REFRIGERATION SCIENCE AND TECHNOLOGY PROCEEDINGS



ICR 2019

THE 25th IIR INTERNATIONAL CONGRESS OF REFRIGERATION

August 24-30 | Montréal, Québec, Canada

25th IIR International Congress of Refrigeration

August 24-30, 2019
Montreal, Canada



INSTITUT INTERNATIONAL DU FROID
INTERNATIONAL INSTITUTE OF REFRIGERATION

ISBN: 978-2-36215-035-7 ISSN: 1025-9031

SCIENCE ET TECHNIQUE DU FROID COMPTES RENDUS

25th IIR International Congress of Refrigeration

www.icr2019.org

August 24-30, 2019
Palais des congrès de Montréal
159 Saint-Antoine St. West
Montréal, Québec,
H2Z 1H2,Canada

Editors

Vasile Minea, Montreal, Canada, minea.vasile@hotmail.com

IS Event Solutions, St-Lambert, Canada, info@iseventsolutions.com

Publisher

International Institute of Refrigeration IIR
Institut International du Froid IIF
177 Boulevard Malesherbes
75017 Paris, France

Sponsors

Diamond





Gold















Silver

















Partners

JARN theNEWS shecco

Exhibitors

ATMOShere (Shecco)
Cemafroid – L'expert du froid
CTi – Calibration Technologies Inc.
Elsevier (International Journal of Refrigeration)
Emerson Commercial; Residential Solutions
Frascold S.p.a
Espace Hydro Québec
IEA Heat Pump Centre
International Institute of Regrigeration (IIR)
International Copper Association (MicroGroove Campaign)
Matelex

STAR Refrigeration Ltd

Copyright and Disclaimer

Copyright and Disclaimer
The information provided in this document is based on the current state of the art and is designed to assist engineers, scientists, companies and other organizations. It is a preliminary source of information that will need to be complemented prior to any detailed application or project. Whilst all possible care has been taken in the production of this document, the IIR, its employees, officers and consultants cannot accept any liability for the accuracy or correctness of the information provided nor for the consequences of its use or misuse. Any opinions expressed herein are entirely those of the authors.
For full or partial reproduction of anything published in this document, proper acknowledgement should be made to the original source and its author(s). No parts of the book may be commercially reproduced, recorded and stored in a retrieval system or transmitted in any form or by any means (mechanical, electrostatic, magnetic, optic photographic, multimedia, Internet-based or otherwise) without permission in writing from the IIR.
Copyright © 2019 IIF/IIR. All rights reserved.

Droit de reproduction et avertissement
Les informations présentées dans ce document sont basées sur l'état de l'art actuel et sont destinées à aider dans leurs travaux les ingénieurs, scientifiques, sociétés et organisations. Elles constituent une source première de renseignements destinée à être complétée avant la réalisation de tout projet ou application. Malgré le soin apporté pour réaliser ce document, l'IIF, son personnel et ses consultants se dégagent de toute responsabilité sur la précision et l'exactitude des informations fournies et les conséquences de leur bonne ou mauvaise utilisation. Les opinions émises n'engagent que la responsabilité de leurs auteurs.
Toute reproduction partielle ou totale du contenu du document ne pourra être faite que sous réserve de citation précise de la source originale.
De plus, toute reproduction partielle ou totale du contenu du document sera soumise à l'autorisation écrite de l'IIF si cette reproduction est faite dans une intention commerciale, quelle que soit la forme de cette reproduction, enregistrement, stockage ou transmission (mécanique, électrostatique, magnétique, optique, photographique, multimédia, Internet ou autres).
Tous droits réservés. © 2019 IIF/IIR.

International Institute of Refrigeration IIR
Institut International du Froid IIF
177 boulevard Malesherbes, 75017 Paris, France
e-mail: iif-iir@iifiir.org

TABLE OF CONTENTS

KEYNOYES

1374 1
Prediction of food thermal properties to enable accurate design of food refrigeration processes
Donald Cleland

1746 14
Thermodynamics of the new refrigerants
Mark McLinden

1832 29
Rational approach to heat pump refrigerant charge reduction
Pega Hrnjak

1833 41
Recent developments in HVAC&R systems utilizing two-phase ejector for expansion work recovery
Stefan Elbel

1834 53
Recent advances in elastocaloric cooling technologies: where they stand and what prospects are
David Catalini, Yunho Hwang

1835 63
Vapor compression heat pumps with refrigerant mixtures
Jiazhen Ling, Yunho Hwang, Reinhard Radermacher

1836 74
Certification of conformity and performance in the cold chain
Gérard Cavalier

1837 86
Magnetocaloric refrigeration and heat pumping: The present, tomorrow, and the future
Andrej Kitanovski, Katja Klinar, Urban Tomc

1839 108
Advances on slurries and phase-change materials
Laurence Fournaison

1843 118
Current status and new developments on high temperature heat pumps
Dereje Ayou, José Miguel Corberán, Alberto Coronas

1846 130
Renewable energy technologies in air conditioning: State-of-the-art and perspectives
Renato Lazzarin

1879 142
Highly efficient heat pump with desiccant coated evaporator and condenser: Principle and application
Ruzhu Wang, Lingji Hua, Tianshu Ge, Yaodong Tu, Xiangyu Sun

1892 154
Evaporative heat transfer characteristics of low GWP refrigerants in plate heat exchangers
Yongchan Kim, Dongchan Lee

1893 158
Cryopreservation of human cardiovascular tissues: clinical application and storage devices
Noboru Motomura

SECTION A

A1 Commission

0117 162
Study on thermodynamic process in pulse tube using molecular dynamics simulation
Yingxia Qi, Yanjin Che, Shuai Pan, Haifeng Yang

0258 170
Optimization of energy charge/discharge scenarios of liquid air energy storage system in cold storage warehouse and economic analysis in case of PV power plant
Cyrine Damak, Denis Leducq, Minh Hong Hoang, Amine Hamzi, Anthony Delahaye

0343 178
Performance study of asymmetric looped travelling-wave thermoacoustic engine driven by low-grade heat
Rui Yang, Yi Wang, Tao Jin, Ke Tang

0429 183
Investigations of a 450 g micro moving-coil linear compressor operating at 200 Hz
Jiaqi Li, Jun Tan, Rui Zha, Tao Zhang, Yongjiang Zhao, Bangjian Zhao, Haizheng Dang

0456 191
A practical calibration procedure for the balanced ambient room type calorimeter in testing the cooling capacity of room air conditioner
Chenzhe Hang, Haiyun Zhang, Dinghua Xu, Guoyuan Ma

0487 199
Problems in design of cooling systems for particle detectors and relevant electronics
Vaclav Vacek, Martin Doubek

0585 207
A molecular dynamics study of cryogenic gas nucleation at high supersaturation
Wan Sun, Zaiyong Ma, Shanshan Bu, Luteng Zhang, Liangming Pan

0779 213
Study on supercooling degree of water-based graphene oxide nanofluids
Jiangqing Wang, Yudong Liu, Xinqiao Jin, Wantao Shi

0930 221
Study on boiling - cooling by using frost layer
Taiyo Sugino, Hidetoshi Hidetoshi

0949 226
Numerical research of driving mechanism for geyser developing in cryogenic propellant feedline
Hongwei Mao, Yanzhong Li, Lei Wang, Jiaojiao Wang

0967 234
Numerical modeling and experimental investigations on a 18 kW Oxford-type moving-coil linear compressor
Jun Tan, Jiaqi Li, Rui Zha, Tao Zhang, Bangjian Zhao, Yongjiang Zhao, Haizheng Dang

0971 243
Investigations on a novel automatic temperature control method and electronics for multi-stage Stirling-type pulse tube cryocoolers
Jun Tan, Tao Zhang, Rui Zha, Jiaqi Li, Yongjiang Zhao, Bangjian Zhao, Haizheng Dang

0975 252
Computational fluid dynamics modeling and experimental verification of a Stirling-type pulse tube cryocooler with a cooling capacity of 700 W at 77 K
Jiaqi Li, Jun Tan, Rui Zha, Tao Zhang, Yongjiang Zhao, Bangjian Zhao, Haizheng Dang

0998 260
Theoretical analyses and experimental verifications of a four-stage Stirling-type pulse tube cryocooler reaching 3 K
Rui Zha, Tao Zhang, Jun Tan, Jiaqi Li, Yongjiang Zhao, Bangjian Zhao, Haizheng Dang

1020 267
Numerical simulations and experimental verifications of a three-stage gas-coupled 4.0 K Stirling-type pulse tube cryocooler
Rui Zha, Tao Zhang, Jun Tan, Jiaqi Li, Yongjiang Zhao, Bangjian Zhao, Haizheng Dang

1023 275
Experimental studies on heat transfer coefficient for boiling of hydrocarbon mixture in shell-side of coil-wound heat exchanger for LNG production
Yaroslav Samokhvalov, Andrey Kolesnikov, Alexander Krotov, Alexey Parkin, Anatoly Zherdev

1027 282
Recent advances in single- and multi-stage Stirling-type pulse tube cryocoolers in SKLIP/SITP/CAS
Haizheng Dang, Jun Tan, Rui Zha, Jiaqi Li, Tao Zhang, Yongjiang Zhao, Bangjian Zhao, Han Tan, Renjun Xue

1063 290
Computational fluid dynamics simulations and experimental investigations on a 1-2 K Joule-Thompson cryocooler precooled by a three-stage Stirling-type pulse tube cryocooler
Tao Zhang, Rui Zha, Jun Tan, Jiaqi Li, Yongjiang Zhao, Bangjian Zhao, Haizheng Dang

1141 298
Non-condensable helium effect on heat and mass transfer characteristics inside a liquid hydrogen tank
Lei Wang, Tian Yan, Jiaojiao Wang, Fushou Xie, Yanzhong Li

1311 306
Investigation on thermal conductivity of nanoencapsulated phase change materials
Lisi Jia, Ying Chen

1434 312
Investigations on the thermodynamic characteristics of a high-efficiency three-stage linear compressor system for a 1-2 K Joule-Thompson cryocooler
Tao Zhang, Rui Zha, Jun Tan, Jiaqi Li, Yongjiang Zhao, Bangjian Zhao, Haizheng Dang

1452 320
A review of battery thermal management in electric vehicles
Lingyu Zheng, Xuelai Zhang

1510 329
Numerical investigation of pulse tube refrigerator with inertance tube-gas reservoir phase modulation
Wenbin Wang, Liang Chen, Menglin Liang, Yanjie Liu, Shuangtao Chen, Yu Hou

1525 338
Simulation and analysis of the influence of wind flow on the evolution of hydrogen vapor cloud
Yuanliang Liu, Gang Lei, Jianjian Wei, Tao Jin

1653 345
Integrated cryogenic quantum refrigeration of electrons
Kazuaki Yazawa, Ali Shakouri

1690 351
CO2 cooling challenges at CERN for the future phase 2 upgrade program
Bart Verlaat, Paolo Petagna, Lukasz Zwalinski, Jerome Daguin, Dina Giakoumi, Viren Bhanot, Michele Battistin, Armin Hafner, Johann Collot, Dominique Bondoux, Hans Postema, Paola Tropea

1699 360
Design and numerical simulation of a cold compressor for large scale superfluid helium cryogenic system
Xinbo Dong, Jihao Wu, He Su, Jinzhen Wang, Cui Lv, Huiming Zou

1732 369
Advanced cryogenic insulation systems
James Fesmire, Adam Swanger

1890 377
Experimental investigation of the cascade type non-flammable mixed refrigerant Joule-Thomson refrigerator for 100K cooling temperature
Cheonkyu Lee, Sangkwon Jeong, Hyo Jae Jeong, Seon-Chang Kim, Dong An Cha

A2 Commission

0372 385
Ways of heat accounting of the ortho-para conversion at simulation of hydrogen liquefier cycles
Sergei Parshin, Ekaterina Navasardyan, Ivan Arkharov, Aleksey Arkharov

0375 393
Helium, hydrogen and methane liquefaction with Reverse-Brayton & Joule-Thomson cycles, boosted by sub-sink cooled compression and hybrid compression or coabsorbent technology ultra-low temperature ref
Mihail-Dan Staicovici

0980 401
Research of mixed refrigerant cycle for liquefaction of natural gasdepending on ambient conditions and its regulation
Alexander Krotov, Andrey Kolesnikov, Yaroslav Samokhvalov, Dmitry Zhidkov, Maxim Vasilev, Roman Kuznetsov, Anatoly Zherdev

0987 407
Numerical investigation on flow boiling characteristics of liquified natural gas in FLNG plate-fin heat exchanger under sloshing conditions
Haitao Hu, Jianrui Li, Haoxian Wang, Guoliang Ding, Chunlin Wu, Hui Chen, Zhanyang Xing

1067 415
Liquefied natural gas cold recovery for heavy-duty vehicles smart management
Alessia Arteconi, Daniele Fiaschi, Luca Cioccolanti, Carlo Maria Bartolini, Fabio Polonara

1405 422
Innovative elements for a liquid air energy storage system
Gregor Trommler, Martin Klupsch, Detlef Eggers, Philipp Bobsin, Christian Wendt, Niklas Bohne

1577 429
Numerical analysis on cavitation of LNG in micro clearance of self-lubricated journal bearing
Yu Wang, Yu Hou, Yu Guo, Xiufang Liu, Tianwei Lai

1596 437
Performance analysis method for intermediated fluid type LNG vaporizers considering fluid properties
Kosuke Higashi, Chieko Kondo, Yukihiro Higashi, Shigeru Koyama

1665 445
Theoretical analysis of supersonic phase change for carbon dioxide in a de Laval nozzle
Julian Restrepo, Andres Bolanos-Acosta, José Simões-Moreira

SECTION B

B1 Commission

0059 452
Surface tension measurement and modeling work for new low GWP working fluids
Chieko Kondou, Jamal El Abbadi, Christophe Coquelet, Céline Houriez, Michel Masella, Yukihiro Higashi

0060 460
Molecular simulation for surface tension of new low GWP working fluids
Céline Houriez, Michel Masella, Chieko Kondou, Yukihiro Higashi, Jamal El Abbadi, Christophe Coquelet

0063 468
Using Al2O3-water nanofluid to investigate the spray cooling heat transfer performance on a heated surface
Tong-Bou Chang, Tsung-Han Lin, Jhong-Wei Huang

0065 474
An experimental study on the evaporation heat transfer and pressure drop of R-1234ze(E) in a shell and plate heat exchanger
Chang Uk Jo, DongChan Lee, Dongwoo Kim, Yongchan Kim

0067 480
Numerical benchmark for air vortex tube flows using a 2^(5-1) resolution V fractional factorial design
Junior Lagrandeur, Sergio Croquer, Sébastien Poncet, Mikhail Sorin

0069 488
A new thermodynamic model for the prediction of air vortex tube performances
Junior Lagrandeur, Sébastien Poncet, Mikhail Sorin

0078 496
Finite-volume modelling of water solidification inside ice trays: A novel enthalpic formulation
Lucas Barboza, Felipe Loyola, Christian Hermes

0116 504
Simulations of saturated vapor pressures of single refrigerants by COSMO-RS
Yingxia Qi, Danping Ma, Hua Zhang, Shuai Pan, Haifeng Yang

0134 515
Performance of R466A, a non-flammable replacement for R410A, in unitary air-conditioning and transport refrigeration
Kenneth Schultz, Steve Kujak

0138 523
Experimental investigation of R290 during flow condensation and adiabtic two phase flow
Simon Fries, Andrea Luke

0144 531
Replacements for R410A with GWPs less than 300
Kenneth Schultz

0148 539
Evaluation of refrigerants leakage ratios based on electronic logging and reporting system
Peter Tomlein, Michal Tomlein, Matúš Tomlein

0162 547
(Micro) Fluidic thermal switches: a review of the principles for caloric technologies
Katja Klinar, Urban Tomc, Andrrej Kitanovski

0164 555
Investigation of the nucleation temperature of different heat exchanger surfaces in an ice store
Ursina Oechsle, Klaus Spindler

0167 563
Investigation of combination of a rotary vane expander and an expansion valve in a refrigeration system
Rahul Thakur, Anarghya Ananda Murthy, Alison Subiantoro

0171 571
A numerical framework for the one-dimensional modelling of refrigerator components
Luka Lorbek, Andrej Kitanovski

0186 579
An experimental analysis of the use of thermal storage materials in natural-draft condensers of household refrigerators
Joel Boeng, Julius Mihr, Carla Rametta, Claudio Melo

0189 587
Optimization potentials for the absorber and the generator of an ammonia-water absorption heat pump
Nico Mirl, Klaus Spindler

0191 595
Scaling parameters between ammonia and water
Klaus Spindler

0203 603
Measurement of pool nucleate boiling heat transfer coefficient of R1234yf at saturation
Yoshinori Takaishi, Kou Kato

0205 609
Effect of pressure pulsation on COP in two-stage-compression vapor-injection cycle
Sachio Sekiya, Atsushi Kubota, Masayuki Nonaka, Hitashi Daisaka

0219 617
Experiments on flow boiling characteristics of R32/lubricant oil mixtures in a multiport tube with circular minichannels
Daisuke Jige, Shogo Kikuchi, Hikaru Eda, Norihiro Inoue

0225 625
R513A condensation inside a small sized microfin tube
Andrea Diani, Luisa Rossetto

0227 633
Review of next generation low GWP refrigerants for chiller products
Stephen Kujak, Kenneth Schultz

0234 641
Compressed liquid density measurement and correlation for CIS-1-chloro-2,3,3,3-tetrafluoropropene (R1224YD(Z))
Laura Fedele, Sergio Bobbo, Mauro Scattolini, Claudio Zilio, Ryo Akasaka

0236 649
Utilization of CO2 and R1234ze(E) as refrigerant: determination of mixture volumetric properties at the vicinity of critical point
Jiangjun Xie, Alain Valtz, Christophe Coquelet, Haitao Hu

0243 657
Fundamental study on continuous pipe transportation of ice slurry
Tatsunori Asaoka, Daiki Hoshina

0251 662
Measurements of solubility and kinematic viscosity data of refrigerants-lubricants oil mixtures
Julien Brocus, Alain Valtz, Pascal Theveneau, Yannick Beucher, Florence De Carlan, Jean-Marie Fourmigue, Christophe Coquelet

0254 670
Transfer processes in the thermosyphon employing graphene oxide and silica nanofluids
Agnieszka Wlazlak, Bartosz Zajaczkowski, Zbigniew Krolicki, Michal Woluntarski, Matthias Buschmann

0263 680
A density-based solver using real gas properties for R744 supersonic flashing simulations
Yu Fang, Yann Bartosiewicz, Sébastien Poncet, Hakim Nesreddine

0264 688
A novel analytical accelerated life model to understand refrigerant chemical stability
Stephen Kujak, Elyse Sorenson

0265 696
Liquid-to-suction heat exchanger assessment using new synthetic refrigerants to replace R-134a
Adrián Mota Babiloni, Joaquín Navarro-Esbrí, Francisco Molés, Carlos Mateu-Royo, Ángel Barragán-Cervera, Marta Amat-Albuixech

0294 704
Experimental investigation on melting process of a phase change material with embedded heat pipes in a vacuum insulated cold thermal energy storage panel
Shen Tian, Qifan Yang, Shuangquan Shao, Shengchun Liu

0299 710
Experimental and numerical investigations on thermal conductivity of Al2O3/ethylene glycol water and TiO2/ethylene glycol water nanofluids
Rajeev Kukreja, Nandyala Mahesh

0310 720
Thermal boundary layer at a periodically magnetized Gd plate with mean flow
Zhe Lei, Kerstin Eckert

0315 725
Experimental study of R1234yf as a low global warming potential alternative for R134a in an oil-free vapour compression refrigeration system
Zhaohua Li, Kun Liang, Hanying Jiang

0317 732
Performance of an oil-free vapour compression refrigeration system using R134a
Zhaohua Li, Kun Liang, Hanying Jiang

0319 739
R1234ze(Z) and R1233zd(E) vaporisation inside a brazed plate heat exchanger (BPHE)
Giovanni Longo, Simone Mancin, Giulia Righetti, Claudio Zilio

0328 747
New generation of low-charge ammonia unit coolers
Stefano Filippini, Umberto Merlo, Lorenzo Noto La Diega, Matteo Carmelo Romano, Ennio Macchi

0353 755
Design and operation of a thermal harshness test facility for electric motors in hermetic environments
Neal Lawrence, Stefan Elbel

0383 763
Experimental study on a air-conditioning system using membrane dehumidification module
Seok Ho Yoon, Dong Ho Kim, Young Kim, Jungchul Kim, Howon Byun

0388 769
Development of vapor pressure model for mixed liquid desiccants near saturated solubility
Chunwen Che, Yonggao Yin

0389 777
Experimental investigation on the instability of a two-phase loop thermosyphon with three evaporators
Hainan Zhang, Shuangquan Shao, Changqing Tian

0390 781
2-D models of magnet and active magnetocaloric regenerator
Lifen Yuan, Suxin Qian, Jianlin Yu, Gang Yan

0404 789
R1224yd(Z) flow boiling inside a mini microfin tube
Giovanni Longo, Giulia Righetti, Claudio Zilio, Simone Mancin

0408 797
R1233zd(E) and R1234ze(Z) condensation inside a 4 mm horizontal smooth tube
Giovanni Longo, Simone Mancin, Giulia Righetti, Claudio Zilio

0442 804
Analysis of the P-T and T-S phase boundary in discriminating suitable low global warming potential and low flammability refrigerants
Moonis Ally, Vishaldeep Sharma, Kashif Nawaz

0445 813
Simultaneous measurements of flow-induced noise and two-phase flow regime in expansion valves
Yingyue Zhang, Stefan Elbel

0464 821
Measurement of Sound Speeds in the Liquid Phase of Hydrochlorofluoroolefins (HCFO)
Takashi Nishiyama, Tomohiro Honda, Lei Gao, Ryo Akasaka

0468 825
Pressure drop and void fraction of vertical and horizontal adiabatic two-phase flow in a plate heat exchanger single channel with uniform gas-liquid distribution
Susanne Buscher

0476 834
A fundamental equation of state for lubricant-refrigerant mixtures with optimization based on transport and interfacial properties
Tobias Göpfert, Christiane Thomas, Ullrich Hesse

0478 842
Measurement of thermophysical properties of low-viscous polyol ester lubricants in carbon dioxide, ethane and ethylene atmospheres
Tobias Göpfert, Christiane Thomas, Ullrich Hesse

0502 850
Heat transfer model of superheated vapor bubbling in liquid in multi-stage refrigeration systems
Lorenzo Carrieri, Gianpiero Colangelo, Giuseppe Starace

0508 859
Simulation investigation of evaporating tower in heat pump air circulation evaporation separation System for High Salinity Wastewater
Liang Chen, Qingqing Li, Sumin Jin

0512 867
Flow patterns of vertical and horizontal adiabatic two-phase flow in a plate heat exchanger single channel with uniform gas-liquid distribution
Susanne Buscher

0514 876
Calibration of a simulation tool for fixed-bed adsorption household refrigerators and determination of optimal design parameters
Mike Jäger, Karsten Düwel, Kristian Hurtig, Roland Kühn

0515 884
Coupling of a two-phase natural circulation cooling system with latent heat storage for aircraft applications
Björn Albertsen, Gerhard Schmitz

0516 892
First results of a directly air-cooled fixed-bed adsorber for a refrigerator driven by waste heat
Kristian Hurtig, Karsten Düwel, Mike Jäger, Roland Kühn

0531 900
The evaluation of working pairs for single absorption cycle based on excess Gibbs free energy
Yibo Fang, Jiongliang Huang, Yuwen Zhou, Kangli Bao, Xiaogang Qiao, Xiaohong Han, Guangming Chen

0532 908
Visual study on the effect of SiO2/water and CuO/water nanofluids on the start-up and heat transfer performance of pulsating heat pipe
Kangli Bao, Yibo Fang, Chenyi Xu, Xiaosheng Ji, Xiaogang Qiao, Xiaohong Han, Guangming Chen

0551 916
Performance of magnetocaloric pin regenerators by direct numerical simulation
Ibai Mugica Guerrero, Sebastian Poncet

0552 924
Alternatives to high GWP refrigerant in refrigeration & air-conditioning applications
Thomas Michineau, Olivier Calmels, Denis Clodic, Stéphanie Barrault

0569 932
A new model for droplets growth during their onset of freezing on flat surfaces under air forced convection
Lorenzo Cremaschi, Ellyn Harges, Burak Adanur

0594 940
Thermal performance of a rotary booster driven free-cooling unit for data center
Lianzheng Xue, Shaocong Li, Guoyuan Ma, Feng Zhou, Fuping Li, Xianghui Yan

0595 950
Heat and mass transfer characteristics of liquid desiccant dehumidification process with microencapsulated phase change material slurry
Yufeng Yan, Xiaofeng Niu, Tao Liu, Guojian Shen, Dandan Wang, Yue Zhang

0607 958
Condensation and evaporation of pure refrigerant flowing in small diameter micro-fin tubes
M. Khairul Bashar, Keisuke Nakamura, Keishi Kariya, Akio Miyara

0612 966
Theoretical analysis of energy efficiency on refrigerants in vapor compression refrigeration cycle under different conditions
Jiongliang Huang, Yibo Fang, Kangli Bao, Xiaogang Qiao, Yingjie Xu, Xiaohong Han, Guangming Chen

0631 974
CFD research of the counter-flow spray concentration process in solar energy - air evaporating separation saline wastewater treatment system
Jing Yu, Sumin Jin

0635 982
Investigations of turbulence effect on heat transfer in packed bed of vegetables
Adam Łapiński, Jerzy Gagan, Kamil Smierciew, Dariusz Butrymowicz

0643 990
Experiments on boiling heat transfer and pressure drop of refrigerant mixtures R245fa/R1234ze(E) inside horizontal microfin tubes
Yufei Liu, Kazuhide Watanabe, Daisuke Jige, Norihiro Inoue

0648 998
Generalized COP estimation of heat pump processes for operation off the design point of equipment
Torben Ommen, Jonas Jensen, Wiebke Meesenburg, Pernille Jørgensen, Henrik Pieper, Wiebke Markussen, Brian Elmegaard

0660 1006
Experiments on condensation heat transfer and pressure drop of refrigerant mixtures R245fa/R1234ze(E) inside horizontal microfin tubes
Kazuhide Watanabe, Yufei Liu, Daisuke Jige, Norihiro Inoue

0673 1014
Controlling vapor quality of R245fa in a microchannel evaporator
Stanislawa Sandler, Bartosz Zajaczkowski, Zbigniew Krolicki

0680 1022
Water (R718) as a low GWP alternative
Hans Madsboll, Alexander Pachai

0682 1030
The experimental investigation of the influence of fullerene C60 additives in compressor oil on the coefficient of performance of refrigeration system
Vitaly Zhelezny, Guangming Chen, Olga Khliyeva, Nikolai Lukianov, Kostyantyn Shestopalov, Serhii Kornievich

0701 1038
Optimization analysis on the performance of a vapor injection air-source heat pump with single screw compressor
Shanwei Liu, Yuanwei Lu, Yuting Wu, Biao Lei, Ruiping Zhi, Chongfang Zhi

0702 1046
Heat transfer and pressure drop characteristics of wet air flow in metal foams with different structures and surface wettability during dehumidifying conditions
Haitao Hu, Zhancheng Lai, Guoliang Ding

0725 1054
Visualization investigation on the expansion state of the primary flow in a transcritical CO2 two-phase ejector
Yafei Li, Jianqiang Deng, Li Ma, Yang He

0726 1062
Increasing the performances of a CO2 refrigeration system using cool thermal energy storage for subcooling: a supermarket application
Benedicte Ballot-Miguet, Gilles Dejardins, Bastien Quaro, Amaury Defruit, David Rousset

0727 1070
Condensation heat transfer and pressure drop of NH3 and NH3/H2O within a plate heat exchanger
Xuan Tao, Elias Dahlgren, Carlos Infante Ferreira

0738 1078
Performance analysis of a thermoelectric assisted indirect evaporative cooling system considering condensation from primary air
Ming Gao, Yuanyuan Zhou, Jianlin Yu, Yanshun Yu

0742 1086
Examining low global warming potential hydrofluoroolefin-hydrofluorocarbon blends as alternatives to R-404A
Stephen Spletzer, Jethro Medina, Joshua Hughes

0746 1094
Flow visualization of ammonia inside a gasketed plate heat exchanger condenser
Maaike Leichsenring, Xuan Tao, Carlos Infante Ferreira, Joost Kirkenier

0751 1102
Performance simulations of heat and mass transfer of a novel compound absorber
WeiXing Yuan, Yu Li, YuXue Guo, Bo Yang

0758 1110
Experimental study of the impact of crystallization parameters on properties of modified and reinforced ice structures intended for sports facilities and the Arctic
Galina Goncharova, Vyacheslav Buznik, Nikolay Razomasov, Georgy Nuzhny

0767 1118
Safety related properties of low-GWP refrigerants
Enis Askar, Volkmar Schröder, Tobias Göpfert, Ullrich Hesse, Erik Winterleitner, Michael Schwarze

0773 1125
A magnetic refrigeration prototype operating with a rare-earth-free magnetic field source
Urban Tomc, Katja Klinar, Simon Nosan, Franc Majdič, Joško Valentinčič, Jure Mencinger, Andrej Ljubenko, Dejan Dren, Andrej Kitanovski

0804 1133
Comparison of R-404a, R-448A and R-452A as drop-in replacements for R-218 in special applications
Martin Doubek, Václav Vacek

0809 1141
Void fraction and flow regime of in-tube condensation in a vapor-compression system
Jiange Xiao, Pega Hrnjak

0812 1150
Heat transfer and pressure drop model of in-tube condensation in a vapor-compression system
Jiange Xiao, Pega Xiao

0818 1159
Flow boiling of binary mixture in finned compact heat exchangers
Ines Ben El Mekki, Marine Andrich, Pascal Tobaly, Brice Tremeac, Florine Giraud, Marie-France Terrier

0821 1167
Effect of lubricating oil on flow boiling heat transfer of low-GWP refrigerants in extruded multi-port tubes
Eiji Hihara, Shizuo Saitoh, Chaobin Dang

0822 1174
Disproportionation reaction of HFO-1123 refrigerant
Makoto Ito, Zhihua Zhang, Chaobin Dang, Eiji Hihara

0824 1182
Experimental study of method for charge composition determining for Joule–Thomson multicomponent mixed-refrigerant refrigerator
Evgeny Bychkov, Anatoly Zherdev, Boris Makarov, Yaroslav Samokhvalov

0831 1190
Refrigerants With Low Environmental Impact For Refrigeration Systems
Ankit Sethi, Samuel Yana Motta

0838 1199
Flow boiling heat transfer and pressure drop of hydrocarbons R600a and R290 in a multiport mini channel tube
Jacqueline Copetti, Mario Macagnan, Jeferson OLiveira, Priscila Silva

0839 1207
Signal analysis and mass measurement based calibration of capacitive sensors for void fraction and flow regimes in horizontal and vertical round tubes using R134a
Hongliang Qian, Pega Hrnjak

0840 1215
Visualization of two phase flow through distributors and effect on performance of evaporators
Yufang Yao, Raghu Kunapuli, Pega Hrnjak

0844 1223
Flow patterns and pressure drop of vertical upward flows in a tube with header-like protrusions with R134a
Hongliang Qian, Pega Hrnjak

0857 1231
Modified flow pattern maps for flow boiling in horizontal micro-finned tubes considering the effect of helix angle
Cheng-Min Yang, Pega Hrnjak

0858 1239
Analysis and quantification of generated bubbles in flow boiling through diabatic visualization
Cheng-Min Yang, Pega Hrnjak

0871 1247
Experiments on boiling/condensation heat transfer and pressure drop of refrigerant HFO1336mzz(E) and the mixture inside a horizontal microfin tube
Norihiro Inoue, Yufei Liu, Kazuhide Watanabe, Daisuke Jige

0875 1255
Experimental study on falling film evaporation heat transfer of ammonia on horizontal tubes
Ikuro Akada, Kenichi Obata, Masashi Kato, Kousaku Nishida, Norihiro Inoue

0898 1263
Steam condensation heat transfer coefficient in large, flattened-tube air-cooled condensers
William Davies, Pega Hrnjak

0906 1271
Capacity and pressure drop in a large, flattened-tube air-cooled condenser for power plants
William Davies, Pega Hrnjak

0907 1279
Heat transfer and flow characteristics of condensing flow in a quadrilobed tube
Tomonori Asano, Hitoshi Asano, Hitoshi Hara

0909 1287
Air-water two-phase flow distribution in a manifold having four indoor-unit connections of a VRF system
Jihwan Jeong, Seongkwan Ham, Siyoung Choi

0952 1295
Flow boiling heat transfer and pressure drop for R134A and RL32H in multi-channel tube
Xiuwei Yin, Wen Wang, Vikas Patnaik, Jin-Shen Zhou, Xiang-Chao Huang

0954 1308
Experimental investigation on the supercooling effect of fluids confined in non-metallic vessels using pure water and silicon carbide
Sebastian Gund, Michael Kauffeld

0990 1316
Study on air conditioner with dense membrane
Hyunjeong Lim, Sangmi Choi, Yeonjoo Cho, Soyeon Kim, Minsung Kim

1011 1322
Measurements of isobaric heat capacity of R1234yf
Noboru Kagawa, Atsushi Matsuguchi, Koichi Watanabe

1014 1329
Investigation into low viscosity refrigeration oil for refrigerators
Yohei Shono, Fumiyuki Nara, Takeshi Okido, Kiyomi Sakamoto

1033 1335
Comparative analysis of ionic liquids as sorptive media for absorption cooling systems
Hifni Ariyadi, Niccolo Giannetti, Seiichi Yamaguchi, Kiyoshi Saito

1034 1343
Overview on experimental techniques for heat flux and heat transfer estimations, during non-dropwise condensation
Marie-Adélaïde Cremieux, Florine Giraud, Jacopo Seiwert, Frédéric Crayssac, Marc Wagner, Christophe Marvillet, Brice Tremeac

1052 1351
Ammonia/ionic liquid absorption in a plate heat exchanger: a modeling study
Meng Wang, Carlos Infante Ferreira

1075 1359
A study on the operating parameter optimization of solid desiccant heat pump based on a real-time algorithm
Lingji Hua, Tianshu Ge, Ruzhu Wang

1083 1368
Performance characteristics of a plate fin heat exchanger
Mohammad Sultan Mahmud, Md. Emamul Kabir

1095 1376
Void fraction characteristics of adiabatic one-component vertically upward two-phase flows in circular and non-circular small diameter tubes
Hitoshi Asano, Hideki Murakawa

1107 1384
Solar driven Organic Rankine Cycle – ab/adsorption cogeneration systems
Carlos Infante Ferreira, Tryfonas Roumpedakis

1108 1392
Characteristics of refrigerant leaks from small HVAC&R systems
Viral Patel, Ahmad Abu-Heiba, William Miller, Van Baxter

1129 1400
Aqua ammonia as secondary refrigerant in ice rink applications
Jörgen Rogstam, Simon Bolteau, Cajus Grönqvist, Juris Pomerancevs

1134 1408
Methodology to estimate vapor quality of refrigerant leaks
William Miller, Viral Patel, Ahmad Abu-Heiba, Van Baxter

1150 1417
Reduced-order model to estimate safe flammable refrigerant charge limits for a one-room air conditioner
K. Dean Edwards, Ahmad Abu-Heiba, Miroslav Stoyanov, Mingkan Zhang, Ahmed Elatar, Viral Patel, Van Baxter, Charles Finney, Omar Abdelaziz

1164 1426
Screening of surface active agents to enhance absorption in ammonia-water systems
Girish Kini, Srinivas Garimella

1174 1435
Boiling heat transfer of new zeotropic mixtures
Arianna Berto, Costantino Guzzardi, Marco Azzolin, Stefano Bortolin, Davide Del Col

1178 1443
A multilayer desiccant dehumidification system
Jubair Shamim, Lili Yu, Soumyadeep Paul, Wei-Lun Hsu, Hirofumi Daiguji

1188 1451
Gas to liquid transfer enhancement during hydrate crystallization: Case study of CO2 hydrate for cold storage and transport
Véronique Osswald, Amokrane Boufares, Pascal Clain, Elise Provost, Didier Dalamzzone, Hong Minh Hoang, Laurence Fournaison, Anthony Delahaye

1197 1459
Heat transfer mechanisms during refrigerant condensation when varying inclination
Marco Azzolin, Stefano Bortolin, Arianna Berto, Pascal Lavieille, Marc Miscevic, Davide Del Col

1209 1467
Experimental analysis of transcritical CO2 booster refrigeration system with heat recovery and ejector expansion
Kundan Kumar, Simarpreet Singh, Parmod Kumar, Prakash Maiya, Armin Hafner, Krzysztof Banasiak, Petter Neksa

1223 1475
Online composition measurements of refrigerant mixtures by optical fibers and infrared spectroscopy
Pascal Tobaly, Marie-France Terrier

1234 1483
Influence of thermophysical properties in nucleate boiling
Niklas Buchholz, Andrea Luke

1252 1491
Flow patterns of some new low GWP refrigerants during evaporation in small tube
Houpei Li, Pega Hrnjak

1255 1499
Heat transfer coefficient, pressure drop, and flow visualization for some new low GWP refrigerants during evaporation in small tube
Houpei Li, Pega Hrnjak

1256 1507
Droplet injection at the diffuser outlet in an ejector-based refrigeration cycle working with R245fa
Mehdi Bencharif, Sébastien Poncet, Said Zid, Hakim Nesreddine

1267 1515
Two-phase flow distribution in dual-compartment microchannel heat exchanger header
Mark Anthony Redo, Jongsoo Jeong, Seiichi Yamaguchi, Kiyoshi Saito, Hyunyoung Kim

1269 1523
Numerical study of heat and mass transfer absorption processes using a horizontal flooded-liquid film in ammonia-water mixtures
Beethoven Narváez-Romo, José R. Simões-Moreira

1276 1531
Mapping of Coefficient of Performance for large-scale ammonia heat pumps for district heating systems
Pernille Jørgensen, Torben Ommen, Wiebke Markussen, Brian Elmegaard

1278 1542
Flow boiling heat transfer of refrigerants HFO-1234yf and HFC-134a in a chevron plate heat exchanger
Chien-Yuh Yang, Kuan-Ting Chen, Hamid Nalbandian

1282 1550
New low global warming halogenated olefin working fluids for use in two-phase cooling
Jason Juhasz, Luke Simoni

1283 1558
Pool boiling heat transfer measurements on a horizontal plate with a low global warming potential refrigerant
Ilya T'Jollyn, Jasper Nonneman, Michel De Paepe

1290 1565
Performance measurements of a two stage CO2 refrigerator and SEPR comparison with low-GWP alternative
Biagio Citarella, Rita Mastrullo, Alfonso Mauro, Massimiliano Sfragara, Marcello Tammaro

1292 1573
Long term viability of R-513A in a stationary refrigeration system
Jethro Medina, Joshua Hughes, Ryan Coombs

1297 1580
Experimental data during flow boiling of refrigerants R448A and R452A
Gianluca Lillo, Rita Mastrullo, Alfonso Mauro, Luca Viscito

1303 1588
Experiments on condensation heat transfer and visualization of flow pattern with R1234ze(E) inside horizontal 4 mm small-diameter microfin tubes
Masataka Hirose, Daisuke Jige, Norihiro Inoue

1316 1596
Use of Diamond/POE nanolubricant in a refrigeration system operating with R410A and R32
David Marcucci, Luiz Freitas, Enio Bandarra Filho

1320 1602
Two-Phase refrigerant distribution of vertical header with insertion structure of branch pipe for multi type air conditioner
Yoji Onaka, Takashi Matsumoto, Hiroyuki Okano

1323 1607
Numerical simulation on buoyancy-induced deterioration of supercritical heat transfer
Jiacheng He, Chaobin Dang, Eiji Hihara

1327 1614
Permeability of PTFE flat-type membrane for absorption chiller
JIACHENG HE, Chaobin Dang, Eiji Hihara

1328 1622
The developing of lower GWP refrigerants
Shun Ohkubo, Felix Flohr, Kenji Goboh, Tatsumi Tsuchiya, Hitomi Arimoto, Yuzo Komatsu

1338 1627
Improvement of CO2 hydrate slurry transportation in flow loop: effect of anti-agglomerant additives on rheological properties
Pascal Clain, Amokrane Boufares, Fatima Benmesbah, Amira Zennoune, Véronique Osswald, Hong Minh Hoang, Didier Dalmazzone, Anthony Delahaye, Laurence Fournaison

1347 1635
The R744 vapour compression test rig designed for visualisation of two-phase flow inside ejectors
Michal Haida, Rafal Fingas, Wojciech Szwajnoch, Jakub Bodys, Michal Palacz, Jacek Smolka, Andrzej Nowak

1363 1644
Condensation and evaporation heat transfer characteristics of pure and binary-mixture HFO refrigerants inside a plate heat exchanger
Keishi Kariya, Akio Miyara

1376 1652
Experiment study on spreading and horizontal motions of Lithium Bromide solution droplets on horizontal tubes
Yueting Yang, Xiaoyun Xie, Yi Jiang

1402 1661
Thermodynamic cycle analysis and experimental investigation on a three-stage vapor injection air source heat pump
Huan Zhao, Peiyu Lei, Yujie Huang, Youlin Zhang, Jun Shen

1412 1668
The preparation of paraffin/EVA/graphene phase change materials and its thermal properties analysis
Changling Wang, Xiaosong Zhang, Zhenghao Liu

1430 1676
Options for low-global-warming-potential and natural refrigerants - Performance for heat pump application and analysis of systemic irreversibilities
Kashif Nawaz, Moonis Ally, Vishaldeep Sharma

1433 1685
A practical heat and mass transfer model between air and ionic liquid solution in an internally cooled dehumidifier with partial wetting
Richard Jayson Varela, Niccolo Giannetti, Hifni Ariyadi, Seiichi Yamaguchi, Kiyoshi Saito, Xin-Ming Wang, Hiroshi Nakayama

1465 1693
A new fundamental equation of State for trans-1-chloro-3,3,3-trifluoro-1-propene [R-1233zd(E)]
Ryo Akasaka, Eric Lemmon

1503 1701
Performance analysis of different ternary NH3-H2O-salt absorption heat pump cycle combined with electrodialysis technique
Mengkai Xu, Shuhong Li, Kai Du

1508 1709
Analysis of the arrangement and effects of air layer in external thermal insulation walls in hot summer and cold winter zone in China
Chengcheng Xu, Shuhong Li, Kaikai Zou, Kai Du

1532 1718
N2O-CO2-mixtures as refrigerants for temperatures below -50 °C
Michael Kauffeld, Timo Maurath

1535 1726
Experimental study of R454B drop-in performance in a R410A liquid-to-water heat pump
Ignacio Ortega, Jaime Sieres, Fernando Cerdeira, Estrella Álvarez, J. Alberto Dopazo

1541 1734
Development of a new optical method to quantify local air-side heat transfer coefficient
Min Che, Stefan Elbel

1543 1742
Application of a new method to quantify local air-side heat transfer coefficient on fundamental geometries
Min Che, Stefan Elbel

1547 1750
An experimental study of evaporative coolers using elliptic tubes
Jian-Cheng Fang, Liang-Han Chien, De-Cian Chen

1563 1758
Experimental assessment of a detachable plate falling film heat and mass exchanger couple using lithium bromide and water as working fluids
Tianle Hu, Yuhao Yi, Xiaoyun Xie, Yi Jiang

1586 1767
Experimental research and numerical simulation of periodic frost melting progress
Zheng Ren, Xingqun Zhang, Xiaojun Dong, Beile Zhang, Xiaozhuan Chen, Yu Hou, Tianwei Lai

1598 1775
Increasing the efficiency of a carbon dioxide refrigeration system using a pressure exchanger
Brian Fricke, Kashif Nawaz, Ahmed Elatar, Vishaldeep Sharma

1608 1782
Thermodynamic properties of binary mixtures of Trifluoroethene (HFO1123) + 2,3,3,3-Tetrafluoroprop-1-ene (HFO1234yf)
Naoya Sakoda, Jiang Shiheng, Masaya Nakazaki, Yasuyuki Takata, Yukihiro Higashi

1633 1788
Sorption materials for the safe use of flammable refrigerants in cooling/heating cycles
Christian Sonner, Sebastian-Johannes Ernst, Gunther Munz, Lena Schnabel, Thore Oltersdorf

1643 1797
A new analytical model for concrete sensible thermal energy storages simulation
Luca Doretti, Francesca Martelletto, Simone Mancin

1654 1805
Optimized 3D periodic structures for advanced Latent Thermal Energy Storages (LTESs) via additive manufacturing
Giulia Righetti, Gianpaolo Savio, Roberto Meneghello, Luca Doretti, Simone Mancin

1686 1813
Performance evaluation on heat pump water heater with drop-in refrigerant R1234yf and condenser size modification
Ce Shi, Pega Hrnjak

1726 1821
Experimental analysis of the hydrofluidization freezing system for small fruits and vegetables
Michał Palacz, Edyta Piechnik, Wojciech Adamczyk, Michal Stebel, Jacek Smolka

1768 1829
Numerical investigation of cooling properties of La0.6Ca0.4MnO3 in an active magnetic regenerator system
Aicha El Boukili, Hamid Ez Zahraouy, Mohammed Hamedoun, Abdelilah Benyoussef, Mohamed Balli, Omar Mounkachi

1849 1837
Energy saving in refrigeration machines based on the use of mini-channel technologies
Kouadio Fabrice

1860 1844
Study of heat exchange process in heat exchangers of refrigerating systems using electric hydraulic aerosols
Mikhail Voronin, Boris Babakin, Georgy Belozerov, Sergey Babakin

1874 1848
Why and which Insulation materials for refrigerators!
Sankarshan Verma, Harjit Singh

1875 1855
Experimental investigation of evaporation of propane (R290) in small pipes
Ehsan Allymehr, Trygve Eikevik, Armin Hafner

B2 Commission

0061 1863
Gas supersonic ejector performance with droplet injection: comparison of CFD and thermodynamic modelling
Sergio Croquer, Sébastien Poncet, Zine Aidoun

0076 1871
Quasi-steady-state simulation of the on-off behaviour of household refrigerators: a self-tuning approach
Guilherme Santos, Adriano Ronzoni, Christian Hermes

0139 1879
Design of a cold thermal energy storage unit for industrial applications using CO2 as refrigerant
Håkon Selvnes, Armin Hafner, Hanne Kauko

0141 1887
Control optimization for cold-room (walk-in) refrigeration units
Pere Moreno, Xavier Albets-Chico, Gabriel Zsembinszki, Alvaro de Gracia, Jose Miguel Maldonado, Luisa F. Cabeza

0142 1895
Experimental comparison of the use of R134a and R1234ze(E) in a semi-hermetic reciprocating compressor
Luca Molinaroli, Andrea Lucchini, Luigi Colombo

0143 1903
A smart early detection system for gas leaks in refrigeration applications
Xavier Albets-Chico, Pere Moreno, Xavier Palomino, Ricard Rovira, Miguel Angel Gonzalez

0160 1912
Numerical and experimental study of the heat transfer for the ammonia condensers
Drughean Liviu, Girip Alina Viorica, Ilie Anica, Dumitrescu Rodica

0170 1920
Thermodynamic and numerical analysis of the ejector performance at off-design operation modes
Guangming Chen, Oleksii Volovyk, Volodymyr Ierin, Kostyantyn Shestopalov

0184 1928
A new correlation to predict the heat transfer rate of natural-draft wire-on-tube condensers
Rodolfo Espindola, Fernando Knabben, Joel Boeng, Claudio Melo

0187 1936
An experimental and numerical investigation of HC-600a flow through electronic expansion valves for small refrigerating appliances
Fernando Knabben, Claudio Melo

0202 1944
Experimental analysis of the use of R290 in a small ice maker
Luca Molinaroli, Guido Romagnoli, Tommaso Vania, Sergio Zanzottera

0213 1952
Investigation of heat exchange of ice slurry flow in a coil
Natalia Mednikova, Georgy Belozerov, Viktor Pytchenko

0229 1957
Energetic and exergetic analyses of ejector cooling cycle with feed pump driven by expander
Guangming Chen, Volodymyr Ierin, Oleksii Volovyk, Kostyantyn Shestopalov

0235 1965
Synthesis and characterization of nano-PCM in water for phase-change secondary refrigerants applications
David Cabailero, Filippo Agresti, Simona Barison, Stefano Rossi, Sergio Bobbo, Laura Fedele

0255 1974
Dynamic model of heat and mass transfer in a closed ventilated and refrigerated display cabinet loaded with products
Sébastien Bussonniere, Valérie Sartre, Jocelyn Bonjour

0273 1982
Energy performance of industrial cold storage facilities
Andy Pearson

0275 1990
Continuous monitoring of energy performance in industrial systems
Andy PEARSON

0290 1999
Heat transfer characteristics of R-134a inside an inclined helical coiled tube-in-shell type condenser
Anand Solanki, Ravi Kumar

0313 2008
Sensor-less position detection of oil-free linear compressor for refrigeration
Hanying Jiang, Kun Liang, Zhaohua Li

0320 2014
Condensation characteristics of R134A and R404A in horizontal micro finned tubes
Rajeev KUKREJA, Sanjeev SINGH

0326 2023
High efficiency air cooled heat exchangers for CO2 applications
Stefano Filippini, Umberto Merlo, Giovanni Mariani, Livio Perrotta

0337 2031
Study on method ensuring safety of built-in refrigerated display cabinet using R290
Koji Yamashita, Yoshihisa Sakamoto, Toshimasa Kato, Shigeki Ishihara, Akira Kobayashi, Hidekazu Kainuma, Makoto Sato, Katsuyuki Osawa, Hiroshi Nagai, Masahiko Nakagawa

0347 2039
Performance of a non-uniform width rotating discharge valve in the revolving vane (RV) compressor
Kim Rui HENG, Kim Tiow OOI, Weng Kong CHAN

0365 2047
Experimental study on frost suppression performance of super-hydrophobic surface
Yaxiu Gu, Xinglong Wang, Tingting Wen, Aiping Zheng, Song Pan

0367 2053
Theoretical analysis and experimental design of a new evaporative condenser
Yaxiu Gu, Yang Zou, Song Pan, Aiping Zheng, Junwei Wang, Guangdong Liu

0373 2061
A novel marine ejector-refrigeration rotary-desiccant air-conditioning system and its working fluid analysis
Chaoyu ZHENG, Chenxu ZHAO, Wu CHEN

0374 2069
Smart control of screw compressors in industrial conditions
Jacques Guilpart

0379 2076
Design parametric study of a lateral configured diabatic straight capillary tube with R-134a
Santhosh K. Dubba, Ravi Kumar

0405 2082
Thermodynamics analysis of CO2 refrigeration cycles working with mechanical subcooling systems
Laura Nebot-Andrés, Rodrigo Llopis, Jesús Catalán-Gil, Daniel Sánchez , Daniel Calleja-Anta , Ramón Cabello

0407 2090
Performance analysis of vapor compression refrigeration systems with oil-free linear compressor vapor injection and regeneration
Xinye Zhang, Davide Ziviani, James Braun, Eckhard Groll

0413 2098
Water vaporization inside a smooth plate-type heat exchanger at subatmospheric pressure: impact of the channel thickness
Florine Giraud, Lisa Fluro, Brice Tréméac

0417 2106
Wet compression with NH3-CO2-H2O
Dionne Gruijthuijsen, Vilborg Gudjonsdottir, Carlos A. Infante Ferreira

0449 2114
Effect of punching holes on the thermofluids characteristics of wavy fin-and-tube heat exchangers
Ali Sadeghianjahromi, Chi-Chuan Wang

0459 2122
A detailed dynamic modeling of the split-type air conditioner
Yang Yang, Chengqin Ren, Lei Yu, Zhao Wang, Yangda Wan

0474 2130
The potential of water as a refrigerant - past, present and future approaches
Florian Hanslik, Juergen Suess, Juergen Koehler

0482 2138
Dynamic simulation of a triple-effect absorption chiller with a reverse-parallel solution flow
Sangmoo Han, Hojin Seo, Sungmin Woo, Siyoung Jeong

0483 2143
A table-top demonstration unit for CO2-sublimation cycles
Yixia Xu, Thomas Tannert, Ullrich Hesse

0486 2151
Experimental analysis on the thermal performance of a R290 air source heat pump water heater
Dehua Cai, Lijuan Niu, Guogeng He

0488 2159
Refrigerant-distribution characteristics of a horizontal header with branch holes of 0.3 mm in diameter
Kazuhiro Endoh

0541 2175
Experimental evaluation of low-GWP replacements of R-404A in a stand-alone commercial cabinet for fresh product
Daniel Calleja-Anta, Laura Nebot-Andrés, Jesús Catalán-Gil, Rodrigo Llopis, Daniel Sánchez, Ramón Cabello

0558 2183
Modeling the heat transfer and the pressure loss in flat fin-and-tube compact heat exchangers
Martim Aguiar, Pedro Gaspar, Pedro Silva

0562 2191
Further development and experimental testing of a resistive sensor for monitoring frost formation in refrigeration systems
Martim Aguiar, Pedro Gaspar, Pedro Silva

0564 2200
Comparisons of electrochemical compression processes for different working fluids
Joseph Baker, Yunho Hwang, Reinhard Radermacher, Chunsheng Wang

0570 2208
Integration of Supermarket's CO2 Refrigeration System and Geothermal Storage
Mazyar Karampour, Carlos Mateu-Royo, Jörgen Rogstam, Samer Sawalha

0571 2216
Design optimization of an air-cooled bifurcated tube heat exchanger
Zhiwei Huang, Jiazhen Ling, Vikrant Aute, Yunho Hwang

0638 2223
A study on novel high efficiency vane compressor
Yusheng Hu, Huijun Wei, Jia Xu, Pengkai Wan, Fayou Luo, Fei Wu, Liping Ren

0644 2231
Experimental investigations of two-phase ejector operating with isobutane
Adam Dudar, Kamil Smierciew, Dariusz Butrymowicz, Jerzy Gagan

0646 2239
Thermodynamic analysis of zeotropy mixtures for ejection refrigeration cycle
Jerzy Gagan, Paweł Jakonczuk, Kamil Smierciew, Dariusz Butrymowicz

0657 2247
Thermodynamic analysis of performance of two-phase injector
Andrzej Pawluczuk, Kamil Smierciew, Dariusz Butrymowicz

0665 2255
Analysis of heat recovery system for air-conditioning application in motor yachts
Mateusz Kedzierski, Kamil Smierciew, Dariusz Butrymowicz, Jerzy Gagan

0670 2263
Virtual-prototype-based development of household refrigerator-freezer appliances
Primoz Poredos, Andrej Ljubenko, Andrej Kitanovski, Alojz Poredos

0686 2272
Absorption heat pump using R1234ze(E) and ionic liquid for PEMFC (Proton-Exchange Membrane Fuel Cells) vehicles
Gabyong Kim, Han Sol Jung, Hyun Jin Kim, YongTae Kang

0717 2280
Design of heat pipe heat sink used for cooling controller of inverter air conditioner
Guanghui Xia, Dawei Zhuang, Guoliang Ding

0719 2288
Research on heat transfer of the closed-loop thermosyphon system with microencapsulated phase change material suspension
Yixuan Li, Shugang Wang, Jihong Wang, Xunjia Deng, Tengfei Zhang, Zhenjun Ma

0728 2296
Electrical demand side flexibility from refrigeration systems with thermal energy storage based on a model predictive control strategy: Influence of model uncertainties
Daniel Pfeiffer, Sebastian Haußer, Stefan Hudjetz, Martin Becker

0781 2304
A new design method of vortex tube based on unsteady processing vortex core and its experimental verification
Bo Zhang, Xiangji Guo

0828 2312
A study of ice-slurry production process based on electric heating of heat transfer surface
Andrey Kolesnikov, Alexander Krotov, Dmitry Pronin, Anna Egorova, Yaroslav Samokhvalov, Anatoly Zherdev

0829 2318
Future refrigerant mix estimates as a result of the European Union regulation on fluorinated gases
Pavel Makhnatch, Adrián Mota-Babiloni, Rahmatollah Khodabandeh

0835 2326
Performance analysis of finned-tube CO2 gas cooler with advanced CFD modelling development and simulation
Yunting Ge, Xinyu Zhang

0836 2335
Numerical simulation of phase separation in the second header of microchannel condenser
Jun Li, Pega Hrnjak

0841 2343
Optimization of a procedure for model calibration using a method based on scattered data interpolation
Sergio Morales, Carles Oliet, Jesús Castro, Joaquim Rigola, Assensi Oliva

0853 2351
Design recommendations for plate heat exchangers in heat pumps using pure and mixed refrigerants
Roberta Mancini, Benjamin Zühlsdorf, Wiebke Brix Markussen, Brian Elmegaard

0854 2359
Optimization of copper-tube coils for energy-efficiency and charge reduction in heat pumps, air conditioners and refrigerators
Nigel Cotton, Hal Stillman, Dennis Nasuta, Yoram Shabtay

0889 2367
Experiments on condensation heat transfer and tube bundles simulation with falling liquid film of R245fa / R134a outside enhanced tubes
Tomonobu Matsuno, Hiroyuki Takahashi, Norihiro Inoue

0892 2375
Analysis of rigid rotor of magnetic refrigeration compressor
Yusheng Hu, Xiaobo Zhang, Fang Zhang, Gao Gong

0894 2383
Multibank microchannel heat exchanger pass optimization using integer permutation based genetic algorithm
Zhenning Li, Jiazhen Ling, Vikrant Aute

0914 2391
Combustion suppression effect of additives for lubricating oil during Diesel explosion at pump-down of air conditioner
Tomohiro Higashi, Chaobin Dang, Eiji Hihara, Yuji Shitara

0946 2399
Data-driven modelling of a R744 refrigeration system with parallel compression configuration
Glenn Andreasen, Jakob Stoustrup, Roozbeh Izadi-Zamanabadi, Ángel Á. Pardiñas, Armin Hafner

0947 2408
Comparing energy consumption and life cycle costs of industrial size refrigeration systems
Thomas Lund, Morten Skovrup, Mads Holst

0963 2416
Characteristics of heat transfer on a microchannel flat tube applied to air-to- refrigerant heat exchangers of air conditioners using R32
Chen Zheng, Tomoki Hirokawa, Ryuhei Kaji, Hirokazu Fujino

0989 2424
Experimental tests using deactivation of coolant fluid circulation to mitigate frost formation on the heat exchanger surface
Pedro Panoias, Pedro Silva, Pedro Gaspar, Luis Pires, José Nunes

0997 2431
A study on flow boiling heat transfer in non-uniformly heated parallel mini-channels by numerical analysis
Kizuku Kurose, Takuya Kawasuso, Kazushi Miyata, Yoshinori Hamamoto, Hideo Mori

1010 2439
Investigation of magnetic field effect on frost formation on substrate
Yu Meng, Bin Liu, Rui Zhang, Aiqiang Chen, Georges El Achkar, Rachid Bennacer

1018 2448
Thermal design of a vaporizer for cold recovery from LNG-regasification using CO2 as heat transfer media
Antonio Atienza-Márquez, Joan Carles Bruno, Atsushi Akisawa, Alberto Coronas

1030 2456
The advantages of natural working fluids
Armin Hafner

1032 2465
Method of on-site determination of refrigerating machine efficiency
Yurii Baidak, Iryna Vereitina

1042 2473
Effects of operating conditions on reciprocating room temperature magnetic refrigeration system
Georges El Achkar, Bin Liu, Qi Wang, Rachid Bennacer

1057 2479
Chiller fault diagnosis with the technology of imbalanced data
Yuqiang Fan, Hua Han, Xiaoyu Cui, Hao Wu, Ling Xu, Hailong Lu, Hui Geng

1081 2487
Case study of the adsorption chiller driven by combined municipal heat and solar energy
Tomasz Halon, Paweł Lukmin, Malgorzata Szyc, Boguslaw Bialko, Bartosz Zajaczkowski

1086 2496
Comparison of compressor control strategies for solar direct drive refrigeration systems
Jonas Jensen, Hendrik Moeller, Ivan Katic, Per Henrik Pedersen, Wiebke Markussen

1088 2504
Demand side management of a commercial refrigeration system with cold thermal energy storage
Gianluca Coccia, Alessia Arteconi, Paola D'Agaro, Fabio Polonara, Giovanni Cortella

1099 2512
Modelling of a diphasic CO2 ejector for cooling circuit
Pierre-Henri Nattes, Brice Tremeac, Marie-France Terrier, Pascal Tobaly

1105 2520
Variable capacity operation of a vapor ejector equipped with an adjustable needle
Michel Poirier, Christopher Reddick, Hristo Sapoundjiev

1123 2528
Design optimization of high performance, reduced charge condensers with novel tube shapes
James Tancabel, Vikrant Aute, Jiazhen Ling, Reinhard Radermacher

1143 2536
Steps toward standardized calculations of LCCP
Paul de Larminat

1145 2544
Design of experiments methodology for the characterization of the performance map of refrigeration and heat pump units
José Corberan, Javier Marchante-Avellaneda, Emilio Navarro-Peris, Belén Llopis

1165 2552
Experimental analysis of the intermediate conditions of a variable speed vapor-injection scroll compressor working with R-410A
Fernando Tello-Oquendo, Bertrand Deschene, Emilio Navarro-Peris, Jose Gonzalvez, Vincent Lemort

1183 2560
Prediction of two-phase flow boiling heat transfer coefficient of refrigerants in minichannel multiport tubes
Jong-Taek Oh, Nguyen Ba Chien, Kwang-Il Choi

1185 2568
Cesium and ammonium slats as low temperature secondary fluids
Monika Ignatowicz, Lorenzo Barcarolo, Åke Melinder, Luca Molinaroli, Björn Palm

1201 2576
Comparison of efficiency increasing methods in CO2 refrigeration systems
Christian Doerffel, Thomas Tannert, Ullrich Hesse

1202 2583
Design and experimental results of a hybrid water/lithium bromide absorption/compression chiller
Martin Helm, Thomas Eckert, Christian Schweigler

1203 2591
Design considerations for dynamically operated large-scale ammonia heat pumps
Wiebke Meesenburg, René Kofler, Torben Ommen, Wiebke Markussen, Brian Elmegaard

1208 2599
Transient thermal management of vapor cycles to simulate aircraft electrical envirnoment control systems
Nicolás Ablanque, Santiago Torras, Carles Oliet, Joaquim Rigola, Carlos Pérez-Segarra

1211 2607
Thermal system oriented heat exchanger models. Focus on moist air liquid cooled units with dehumidification
Santiago Torras, Carles Oliet, Nicolás Ablanque, Joaquim Rigola

1221 2616
Monitoring energy efficiency of refrigerating systems under real operating conditions - methods and recommendations
Stefan Hudjetz, Peter Köhler, Martin Becker

1227 2624
Performance monitoring of closed cooling towers for fouling detection
Björn Nienborg, Subramanian Santhanam, Marc Mathieu, Alexander Schwärzler, Katharina Conzelmann, Lena Schnabel

1231 2633
Energy improvements in a stand-alone transcritical refrigeration system using a low-GWP mixture of CO2/R1270
Daniel Sánchez García-Vacas, Ramón Cabello López, Rodrigo Llopis Domènech, Jesús Catalán Gil, Laura Nebot Andrés, Daniel Calleja Anta, Eduardo Gil Miñana

1241 2641
A theoretical and experimental analysis of n-butane application for household refrigerators
Adriano Ronzoni, André Furlan, Gustavo Montagner, Mario Straub, Didier Siegel

1273 2649
Characterisation of the behaviour of a CO2 water/water heat pump for hot water generation
José García-Cascales, Fernando Illán-Gómez, Francisco Sánchez-Velasco, Víctor Sena-Cuevas, Rafael Molina-Valverde

1287 2657
Active control of external volume flow rates for single effect absorption chillers
Stefan Petersen, Walther Hüls, Christopher Paitazoglou, Jan Albers

1289 2665
Heat rejection coolers for absorption chillers - theory and field test results
Wolfgang Lanser, Rupert Graf, Martin Schröder, Carsten Hausherr

1321 2673
Multi-input multi-output (MIMO) artificial neural network (ANN) models applied to economized scroll compressors
Davide Ziviani, Ammar Bahman, Eckhard Groll

1346 2682
Compressor characteristics of an oil-free, two phase rotary vane motor for water-steam applications
Espen Verpe, Michael Bantle, Steinar Faanes, Nikolai Slettebø, Trygve Magne Eikevik

1361 2690
Development of a dynamic model for ice-on-coil external melt storage systems
Jasper Nonneman, Michiel De Vos, Hugo Monteyne, Wim Beyne, Michel De Paepe

1404 2698
Neuronal network in a refrigerating laboratory
Vincent Moizan, Thomas Suquet, Frantz Latchan, Xining Wu, Nicolas Boudet

1431 2706
Experimental comparison of the heat transfer performance of R134a and R1234ze(E) in a hybrid film evaporator
Giuseppe Censi, Loris Giancotti, Andrea Padovan

1439 2714
Experimental and numerical study of heat transfer in evaporation and condensation with R410A, R32 and R454B in a finned tube heat exchanger
Pierre Pardo, Michèle Mondot, Nicolas Gaillard

1440 2723
Thermal resistance analysis for fin-and-tube phase change thermal energy storage unit
Hao Chen, Xiangfei Liang, Yingwen Wu

1498 2731
Development of macroscopic two-phase flow model based on equivalent porous media approach for plate and fin heat exchanger
Cédric Septet, Jean-Michel Hugo, Georges El Achkar, Olivier Le Metayer

1522 2739
Modeling of spray evaporators for salt solutions
Daniel Boman, Srinivas Garimella

1564 2746
Experimental investigations of the single-phase flow distribution in brazed plate heat exchangers and its impact on the heat exchanger performance
Wenzhe Li, Pega Hrnjak

1565 2754
Theoretical analysis of the end-plate effect on heat transfer in brazed plate heat exchangers
Wenzhe Li, Pega Hrnjak

1597 2762
Influence of commercial refrigeration system design and refrigerant options on life cycle climate performance
Brian Fricke, Michael Petersen, Gustavo Pottker

1669 2770
Adsorption dynamics of MOF coatings for waste heat driven cooling
Thomas Gindre, Thore Oltersdorf, Clemens Dankwerth, Christian Scheffler, Martin Kolouch, Lena Schnabel

1698 2778
Replacement of R-404A refrigerant in supermarkets
Olivier Calmels, Thomas Michineau, Thomas Suquet

1702 2784
Refrigerant handling practices and their evolution over the last decade
Olivier Valet, Gérald Cavalier

1738 2792
Effects of cooling method for condensation heat transfer in plate-fin heat exchanger
sho fukuda, shohei oishi, nobuo takata, takahiko miyazaki, shigeru koyama

1757 2798
Numeral simulation on characteristics of cooling heat transfer and pressure drop of supercritical pressure fluids flowing in a chevron-type plate heat exchanger
Yuki Yamasaki, Naoto Watanabe, Kazushi Miyata, Hideo Mori, Yoshinori Hamamoto, Shuichi Umezawa, Katsuhiko Sugita, Kizuki Kurose

1772 2805
Amorphous Silica Nanosprings: a candidate for improving condensation heat transfer performance
Nickolas Schmiesing, Andrew Sommers, Giancarlo Corti

1870 2813
CO2 ejector modelling using CFD: Current Status
Knut Ringstad, Yosr Allouche, Paride Gullo, Krzysztof Banasiak, Armin Hafner

1872 2823
Optimization of water cooled low charge propane integral display cabinet with dedicated variable speed compressor solution
Kristian Huchtemann, Eric Winandy, Stéphane Bertagnolio

SECTION C

C1 Commission

0169 2831
Loss of mitochondrial function and accumulation of acidic vesicular organelles under low-temperature incubation in HaCaT cells
Yukitoshi Nagahara, Natsumi Uchida, Tomoki Midorikawa, Norio Murase, Takahisa Shinomiya

0498 2837
Ultra-fast vitrification experiment of hamster ovary cells utilizing thin film evaporation
fengmin su, Yiming Fan, he xu, nannan Zhao, Yulong Ji, hongbin ma

0572 2846
Instant cryopreservation of porcine heart valves and aortic segments in low-viscous polydimethylsiloxane - first results
Stanislav Lauk-Dubitskiy, Lyubov Severgina, Igor Korovin, Alexey Shakurov, Alexander Pushkarev, Roman Komarov, Dmitrii Britikov, Ivan Novikov

1555 2853
Study on proline as cryoprotectant in cryopreservation
Ziqiao Sun, Yazhou Li, Wei Rao

1574 2860
Measurement method of actual temperature in whole- and partial- cryotherapy device during exposure: A new approach to optimized treatment protocols
Romain Bouzigon

1859 2868
What everybody should know about whole-body cryotherapy/cryostimulation: An up-dated mini review
Benoit Dugue, Wafa Douzi, Pierre Carette, Olivier Dupuy

1864 2872
What is the future of using whole body cryostimulation (WBC) in medicine?
Elzbieta Miller, Ewa Zielinska

C2 Commission

0049 2879
A simplified heat transfer model of a closed refrigerated display cabinet
Nattawut Chaomuang, Onrawee Laguerre, Denis Flick

0178 2887
Modelling the airflow inside a refrigerated semitrailer loaded with pork carcasses
Mouna Merai, Steven Duret, Jean Moureh, Onrawee Laguerre, Denis Flick

0215 2895
Study of freezing process and short-term storage of meat using electroconvection
Boris Babakin, Mikhail Voronin, Georgy Belozerov

0216 2901
Control of the process of structure formation of "premium" class ice cream using monostabilizers
Antonina Tvorogova, Natalia Kazakova, Tatyana Shobanova, Georgy Belozerov

0250 2908
Development of multi-criteria analysis approach considering food safety, food waste and energy consumption indicators for food plants: application to production process of puff pastry
Steven Duret, Hong Minh Hoang, Evelyne Derens-Bertheau, Erwann Hamon, Valérie Stahl, Laurent Guillier, Jean Christophe Augustin, Anthony Delahaye, Onrawee Laguerre

0303 2916
Freezing and storage of seaweed
Tom Nordtvedt, Erlend Indergård, Pierrick Stevant

0305 2924
Chilling of pelagic fish onboard Norwegian fishing vessels
Tom Nordtvedt, Kristina Widell

0322 2932
Development of prediction model of leaf vegetable product coupled photosynthetic rate and growth curve of leaf area under air-conditioning environment in plant factory
Atsumasa Yoshida, Koji Moriuchi, Yasushi Ueda, Shinichi Kinoshita

0385 2940
Effect of permanent magnetic field and alternating magnetic field on the cherry quality during the freezing process
Junyan Tang, Shuangquan Shao, Huiming Zou, Changqing Tian

0421 2948
Optimizing design and operation of chilling tank for Atlantic salmon
Kristina Widell, Tom Ståle Nordtvedt, Ignat Tolstorebrov, Inge Fossen

0424 2956
Refrigeration to prevent food losses
Kristina Widell, Pranab Raj Dhakal, Maitri Thakur, Armin Hafner

0450 2964
Numerical heat transfer model for industrial chilling installations
Duy Hoang, Simon Lovatt, James Carson, Jamal Olatunji

0451 2972
Experimental study on effects of packing arrangment and plastic liner bag on freezing rates of bulk packed chicken drumsticks
Duy Hoang, Simon Lovatt, James Carson, Jamal Olatunji

0457 2980
Cold-chain monitoring of fresh food distribution converging internet of thing and dynamic prediction technology
Byeong-Sam Kim, Ji-Young Kim, Jong-Hoon KIm, Ki-Hyun Kwon, Seung-IL Oh, He-Ok Lee, Junemo Koo, Samuel M Yimenu

0560 2988
Numerical modelling of thermal processes in Chinese cabbage cold storage chamber using varaible turbulence models
Kamil Smierciew, Mirosława Kołodziejczyk, Jerzy Gagan, Dariusz Butrymowicz

0574 2996
Influence of thermal properties of brown seaweeds (Saccharina latissima) on atmospheric freeze-drying process in fluidized bed
Ignat Tolstorebrov, Trygve Eikevik, Maren Sæther

0575 3004
The use of nanoencapsulated essential oils embedded in the ice has an antimicrobial effect and extends the shelf life of refrigerated fresh sea bream with ice toping
Antonio Lopez-Gomez, Laura Navarro-Segura, Maria Ros-Chumillas

0576 3010
The treatment with vapors of essential oils in the vacuum cooling has a significant effect on surface microbial decontamination of fresh vegetables
Antonio Lopez-Gomez, Maria Ros-Chumillas, Sonia Soto-Jover, Laura Navarro-Segura, Laura Buendia-Moreno, Vera Antolinos-Lopez, Maria Sanchez-Martinez

0650 3018
The impact of storage temperature on postharvest quality and chilling injury of 'Okubao' peaches
Lijun Sun, Qi Zhang, Sheng Liu, Jinhua Zuo, Zhongyang Fan, Yan Li, Junyan Wang, Yufu Zhong, Xiaoming Duan

0813 3026
Food thermal distribution-based control of industrial freezers
Cyril Toublanc, Lionel Boillereaux

0827 3034
Study of convective heat transfer and chilling kinetics of Atlantic salmon in refrigerated sea water: experiments and modelling
Ignat Tolstorebrov, Trygve Eikevik, Kristina Widell, Tom Ståle Nordtvedt

0830 3043
Challenges of effective chilling of Atlantic salmon in refrigerated sea water: field tests
Ignat Tolstorebrov, Kristina Widell, Tom Ståle Nordtvedt, Trygve Eikevik

0847 3051
Crushed ice including nanoencapsulated clove essential oil improves animal welfare in farmed sea bass during stunning and slaughtering
Antonio Lopez-Gomez, Amanda Lopez-Canovas, Maria Ros-Chumillas, Isabel Cabas, Alfonsa Garcia-Ayala

0866 3059
Experimental study of the consequences of controlled atmosphere conservation environment on cherry characteristics
Luis Andrade, José Nunes, Maria Simões, Diogo Morais, Cristina Cannavarro, Christophe Espírito Santo, Pedro Gaspar, Pedro Silva, Mafalda Resende, Catarina Caseiro, Helena Beato, Yuran Belane

0950 3067
Industrial storage of root vegetables - energy and quality aspects
Erlend Indergaard, Mette Thomsen, Belachew Tadesse, Berit Nordskog, Pia Heltoft, Tom Nordtvedt, Kristina Widell

0962 3078
The effect of supercooling-freezing on inhibition of ice recrystallization during storage
Yasuho Ishikawa, Manabu Watanabe, Toru Suzuki

1022 3085
Fractal structure evolution of moisture-containing porous media under the weak potential difference in case of garlic stems
Lin Chai, Bin Liu, Yu Meng, Aiqiang Chen, Georges El Achkar, Rachid Bennacer

1058 3093
Quantifying experimental uncertainty in large-scale pre-cooling operations
Jamal Olatunji, Young-Min Shim, Andrew East

1084 3101
Experimental measurements of the pressure drop loss coefficient for vent configurations of packaging designed for air cooling of horticultural products
Nicolas Tapia, Richard Love, Emilia Nowak, Andrew East

1090 3109
Effects of continuous cooling on physiological and biochemical indexes of the blue mussels
Zejin Wang, Dechao RAO, Ying HUANG, Zhenshan LIN, Jinhua Tong

1096 3118
X-ray CT-based CFD study to investigate the cooling process of packed pear fruit
Willem Gruyters, Zi Wang, Pieter Verboven, Bart Nicolaï

1110 3125
Effect of dynamic storage temperatures on microstructure of frozen carrot imaged by X-ray computed tomography
Vicent Victor, Ndoye Fatou Toutie, Verboven Pieter, Nicolaï Bart, Alvarez Graciela

1168 3133
Cold thermal energy storage with low-temperature plate freezing of fish on offshore vessels
Espen Verpe, Ignat Tolstorebrov, Alexis Sevault

1192 3141
Cryo-differential scanning calorimetry as a tool to monitor polysaccharide transformations
Antonio Molina-García, Eva Gomez-Ordoñez, Pilar Ruperez

1194 3149
Connected Indexes for food product temperature and quality monitoring
Xavier Albets-Chico, Pere Moreno, Israel Muñoz, Josep Comaposada, Sara Bover, Anna Jofre, Ricard Rovira

1206 3157
Airflow design in refrigerated retail display cabinets and its impact on food quality
Ana Marques, Edward Hammond, Shaun Pitchers, David Vagg

1215 3165
Characterization of sorbet microstructure by using X-Ray Microtomography
Veronique Masselot, Veronique Bosc, Hayat Benkhelifa

1272 3172
Influence of 2.45 GHz microwave radiation supplied with or without intermittency on the size of ice crystals during an innovative freezing process
Mathieu Sadot, Olivier Rouaud, Sylvie Chevallier, Sébastien Curet-Ploquin, Alain Le-Bail, Michel Havet

1288 3179
Physics of freezing under electromagnetic conditions: a review
Alain LE-BAIL, P.K. JHA, Epameinondas XANTHAKIS, Michel HAVET

1294 3186
Current status and future trends of monitoring technologies for food products traceability
Diogo Morais, Pedro Gaspar, Pedro Silva, Luís Andrade, José Nunes

1308 3194
Application of time-scale approach on fruit simulator for postharvest cool-chain optimization
Huijian Huang, Mark Tunnicliffe, Young-Min Shim, John Bronlund

1333 3202
Design of a CO2 heat pump drier with dynamic modelling tools
Michael Jokiel, Michael Bantle, Christian Kopp, Ingrid Camilla Claussen, Ignat Tolstorebrov

1399 3210
Suppression of damage on frozen fish by the post-harvest treatment using ice slurry
Kensuke Nishi, Manabu Watanabe, Toru Suzuki

1442 3216
Study of intelligent antibacterial and antioxidant poly(vinyl) alcohol active film on the fresh-keeping effect and quality dynamic monitoring of pseudosciaena crocea
Jing Xie, Zhipeng Tang, Chenwei Chen

1446 3223
Effects of nozzle structures of air Impinging freezer on heat transfer characteristics on the steel strip
Jing Xie, Yuyan Liu, Jinfeng Wang

1463 3232
Modelling freezing of food products at ice crystals scale
Violette Mulot, Christophe Doursat, Hayat Benkhelifa, Fatou-Toutie Ndoye, Didier Pathier, Denis Flick

1478 3240
Forced-air cooling of dairy product in pallets : influence of process parameters on energy and quality
Michel Havet, Edith Patissier, Luc Guihard, Victor Grivier, Fabien Baticle, Benoit Gardes, David Huffschmidt

1639 3248
Effects of on-board bleeding methods and superchilling on quality of cod and saithe
Sæmundur Elíasson, Sigurjon Arason, Bjorn Margeirsson, Arnljotur Bergsson, Olafur Palsson

1674 3256
Influence of different nozzle forms on heat transfer characteristics of quick freezer
Jinfeng WANG, Jing Xie, Dazhang Yang

1765 3264
Diagnosis of the freeze-drying process through the ultrasonic technology
Chin-Chi Cheng, Yen-Hsiang Tseng, Hong-Ping Cheng

SECTION D

D1 Commission

0055 3270
Optimal control of thermal energy storage for a solar energy driven refrigeration plant to cool a fruit storage facility
Leo Lukasse, Edo Wissink

0068 3278
Influence of coil geometrical parameters on the solidification process in an ice on coil cold storage system
Seyed Soheil Mousavi Ajarostaghi, Sebastien Poncet, Mojtaba Aghajani Delavar, Kurosh Sedighi

0124 3286
Reducing energy demand using cooling efficiently (REDUCE)
Jolyon Axelrod, Graeme Maidment

0190 3296
Experiences with selecting natural refrigerant solutions for small capacity industrial food production and temperature controlled storage applications
Robert Lamb

0233 3304
Performance of domestic refrigerators in laboratory and home environments
Judith Evans, Alessandro Biglia, Andrew Gemmell, Helen Foster

0280 3312
The impact of retrofitting doors on performance of a retail display cabinet
Tim Brown, Alan Foster, Judith Evans

0285 3320
Defrosting performance and control strategy with hot gas bypass for medical refrigerator
Lifen Yuan, Suxin Qian, Jianlin Yu, Gang Yan

0307 3327
Modelling and development of high-pressure-lift ejector for low temperature evaporators in R744 refrigeration systems for supermarkets
Krzysztof Banasiak, Ángel Pardiñas, Ekaterini Kriezi, Armin Hafner

0351 3335
Permanent magnet synchronous motors for commercial refrigeration
Bryan Becker, Brian Fricke

0395 3343
Thermophysical roperties of water-based carbon nanotubes nanofluid as cold storage media
Meibo Xing, Ruixiang Wang

0412 3349
Application of demand response in cold room: evaluation of energy performance using different modelling aproaches
Mahdjouba Akerma, Hong Minh Hoang, Alan Le Montagner, Denis Leducq, Nedra Mellouli-Nauwynck, Anthony Delahaye, Ronia Ben Abdallah

0448 3357
A2L refrigerants leak and ignition testing for a walk-in cooler system
Xudong Wang

0466 3363
Real energy efficiency of DX NH3 versus HFC
Stefan Jensen

0537 3371
Applicability of numerical code for simulation of ice-slurry flows in heat exchangers
Shaimaa Hefny, Thomas Tannert, Ullrich Hesse

0548 3379
Operation costs for heat recovery from supermarkets to district heating grids
Christian Heerup

0690 3387
Load peak shifting using phase change materials in retail display cabinets: an experimental investigation
Ronia Ben Abdallah, Denis Leducq, Olivier Pateau, Hong Minh Hoang, Bénédicte Ballot-Miguet, Anthony Delahaye, Laurence Fournaison, Elyamin Dahmana

0771 3395
Combined refrigeration, heating and air conditioning systems in supermarkets: seeking energy efficient solutions
Paola D'agaro, Michele Coppola, Giovanni Cortella

0776 3403
Dynamic modelling of a refrigerated cabinet with integrated phase change material thermal storage
Michael Jokiel, Hanne Kauko, Krzysztof Banasiak, Alexis Sevault

0784 3411
Subcooling with AC and adiabatic gas cooling for energy efficiency improvement: field tests and modelling of CO2 booster systems
Giovanni Cortella, Michele Coppola, Paola D'agaro

0787 3419
Experimental evaluation of a multi-ejector trans-critical CO2 system for supermarkets
Simarpreet Singh, Armin Hafner, Krzysztof Banasiak, Prakash Maiya, Petter Neksa

0860 3428
Flow characteristics of silica hard-shell microcapsule slurries treated with additives
Hiroshi Suzuki, Sohei Usa, Ruri Hidema

0861 3437
Numerical and experimental evaluation of the aerodynamic drag of the air curtain in vertical open refrigerated display cases
Samuel Nascimento, Gustavo Heidinger, Pedro Gaspar, Pedro Silva

0869 3445
Energy savings in supermarket using control theory
Min-Lun Chai, Yen-Tin Shien, Wen-Der Hsieh

0983 3452
Characterization of refrigeration systems in the Portuguese food processing industry
Diogo Morais, Pedro Silva, Pedro Gaspar, Luis Pires, Luis Andrade

1006 3460
Extending the autonomy time of an icelined solar powered vaccine cooler
Jonas Jensen, Christoffer Busk, Claus Cording, Per Henrik Pedersen, Wiebke Markussen

1024 3468
Direct drive solar coolers
Per Pedersen, Ivan Katic, Wiebke Brix Markussen, Jonas Kjær Jensen, Claus Cording, Hendrik Moeller

1044 3476
CO2 commercial refrigeration system in Jordan
Nour Abdin, Armin Hafner, Sergio Girotto, Franziska Menten, Yannick Pruss, Riccardo Savigliano

1047 3484
First field test results of a solar thermal off-grid refrigerator for vaccines
Roland Kühn, Kilian Mähne, Karsten Düwel, Christoph Göller, Julia Römer

1091 3493
Energy efficiency in cold store refrigeration systems
Alessia Arteconi, Anna Lauri, Lino Casalena, Fabio Polonara

1103 3501
Global market and policy trends for CO2 in refrigeration
Klara Zolcer Skacanova, Anti Gkizelis

1154 3509
Monitoring of a CO2 commercial refrigeration system serving a supermarket in Southern Europe
Simone Dugaria, Marco Azzolin, Livio Calabrese, Silvia Minetto, Davide Del Col

1266 3517
NOT-in-kind approach to remote monitoring in CO2 refrigeration systems
Silvia Minetto, Giacomo Tosato, Sergio Girotto, Antonio Rossetti, Sergio Marinetti, Krzysztof Banasiak

1296 3525
Comparing open and closed vertical refrigerated display cabinets at mild and tropical external environments
Gustavo Heidinger, Samuel Nascimento, Pedro Gaspar, Pedro Silva

1571 3534
Snowmelting and solutions for outdoor snow storage
Marianne Heimdal, Trygve Eikevik, Ignat Tolstorebrov

1663 3542
Sizing of thermal energy storage with phase change materials for a battery-free solar powered refrigerator
Adriana Coca-Ortegón, Juan Prieto, Alberto Coronas

1790 3550
Energy mapping of large refrigerated warehouses co-located with renewable energy sources across Europe
Kostadin Fikiin, Paola Mazzucchelli, Alan Foster, Judith Evans, Stepan Akterian, Graciela Alvarez , Denis Leducq, Mihn Hoang , Gabriel Garcia , Liz Varga , Ian Truckell , Tim Brown, Ina Colombo

1794 3558
Dynamic energy model of a refrigerated warehouse operating synergistically with a cryogenic energy storage system
Borislav Stankov, Kostadin Fikiin, Gabriel Garcia, Alicia Kalm, Marionel Estevez, Raquel Garde

1861 3566
Experimental investigation on the integration of cold energy storage into a R744 refrigeration system
Yosr Allouche, Armin Hafner

D2 Commission

0043 3574
Numerical modeling of heat and mass transfer in a refrigerated truck trailer
Sergio Croquer, Alla Eddine Benchikh Lehocine, Sebastien Poncet

0054 3582
An airflow enhancing floor cover to improve temperature uniformity in maritime refrigerated containers
Leo Lukasse, Marcel Staal, Edo Wissink

0131 3590
Strategy for improved temperature control in the supply and processing stages of Surimi cold chain in India
Mani Sankar Dasgupta, Srikanta Routroy, Kristina Widell, Souvik Bhattacharyya, Maitri Thakur

0149 3598
Surimi value chain in India: a strategy for improved resource utilization
Srikanta Routroy, Manisankar Dasgupta, Maitri Thakur, Souvik Bhattacharyya, Kristina N. Widell

0163 3606
Combination of vacuum insulated panels and phase change materials in temperature-controlled containers
Abbes Kacimi, Gilles Labranque

0179 3615
Experimental characterization and modelling of refrigeration of pork carcasses during transport in field conditions
Onrawee Laguerre, Mouna Merai, Steven Duret, Evelyne Derens, Alain Leroux, Denis Flick

0306 3623
Design and application of a novel cold chain pallet using a phase change material
Guanghai Liu, Junzhang Wu, Ruhe Xie, Judith Evans, Alan Foster

0352 3633
Design and performance evaluation of an R744 multi-temperature refrigerated container
Neal Lawrence, Stefan Elbel, Pega Hrnjak

0422 3641
Live transport of Norway lobster with mobile RSW system for an international market
Robert Wolff, Guro Tveit, Kristina Widell, Ulf Erikson, Erlend Indergård, Tom Ståle Nordtvedt

0555 3649
Experimental assessment of the difference between new refrigerated trucks and their corresponding prototypes
Claudia Capo, Frantz Latchan, Thomas Michineau, Jean-Marc Petit , Rémi Revellin , Jocelyn Bonjour , Gérald Cavalier

0713 3657
Towards a comprehensive modelling framework for flammable refrigerant leaks in transport containers
Hugh O'Reilly, Dermott Crombie, Rory Monaghan, Padraig Molloy

0754 3657
Comparison of novel environmental control systems in aircrafts based on a vapor compression cycle
Steffen Golle, Ullrich Hesse

0805 3673
Laboratory determination of hazardous R40 concentration in HFC-134a systems, application to intermodal container refrigeration and pacification technique
Richard Lawton, Christopher Rhodes, Paul Clarke

0814 3681
Influence of temperature sensors on temperature control of marine reefers
Santiago Martinez Ballester, M. Angel Ferrer-Blas

1089 3688
Intelligent fault detection for refrigerated reefer containers
Jorrit Wronski, Ragnar Jónsson

1200 3696
Numerical transient simulation of the insulating performance of a refrigerated truck body
Paolo Artuso, Antonio Rossetti, Silvia Minetto, Sergio Marinetti, Davide Del Col

1205 3704
Innovative layout for electric powered refrigeration for insulated trucks: the integration of photo-voltaic generator
Antonio Rossetti, Silvia Minetto, Sergio Marinetti, Paolo Artuso

1312 3712
Factors affecting energy consumptions and carbon footprint in refrigerated road transport: a brief review of recent advances in technology, materials and methods
Rita Mastrullo, Alfonso Mauro, Girolamo Panozzo

1407 3720
Experimental investigation of a multi-temperature insulation box with phase change materials for cold storage
Xiaofeng Xu, Xuelai Zhang, Sheng Liu

1688 3729
Emission testing of a transport refrigeration unit
Richard Lawton, Tobias Mynott, Nicholas Marshall, Brian Robinson

1689 3737
Ageing in of in-service refrigerated transport vehicles: a statistical analysis
Claudia Capo, Jean Marc Petit, Rémi Revellin, Jocelyn Bonjour, Gérald Cavalier

1691 3745
Refrigeration container fires during intermodal transportation
Richard Lawton, Christopher Rhodes, Paul Clarke

1692 3751
Insulated bodies for refrigerated transport vehicles: past, present and future construction techniques
Claudia Capo, Nicolas Boudet, Gérald Cavalier

1695 3759
Ageing of insulated marine containers
Richard Lawton, Christopher Rhodes, Tobias Mynott

1764 3765
Food losses during refrigerated transport: a socio-economic analysis
Merdji M'hamed, Capo Claudia, Gerald Cavalier, Thomas Michineau

SECTION E

E1 Commission

0071 3773
Evaluation of photovoltaic cooling application to a data center
Adenilson Belizário, José Roberto Simões Moreira

0161 3781
Theoretical and experimental studies on the influence of subcooling of the liquid in air-conditioning system
Nichita Madalina, Negrutiu Catalin, Cublesan Valentin, Razvan Calota, Liviu Drughean

0208 3788
Dynamic modeling and control strategy of a transcritical CO2 cycle for a multi-temperature refrigerated container system for military applications
Riley Barta, Davide Ziviani, Jason Hugenroth, Eckhard Groll

0292 3796
Investigation of two-phase injected compression with economization for high temperature application
Ammar Bahman, Davide Ziviani, Eckhard Groll

0435 3804
Development of a propane double duct room air conditioner
Giulia Righetti, Matteo Campidelli, Oreste Bottaro, Claudio Zilio

0509 3812
First measurement results of cooling and heat-pump operation of an environmental test chamber using co2 as refrigerant
Andreas Wagner, Thomas Tannert, Ullrich Hesse

0511 3820
Optimal operation of HVAC system incorporated with online performance evaluation based on operation data
Wantao Shi, Jiangqing Wang, Xinqiao Jin

0565 3828
New unitary air condition system design for flammable refrigerants and ventilation
Hanlong Wang, Yunho Hwang

0573 3835
Hydrocarbon refrigerant for building air conditioning application in Indonesia: performance and safety analysis
Ardiyansyah Yatim, Muhammad Alhamid, Agus Pamitran, Nandy Putra, Budihardjo Budihardjo

0598 3843
Evaporative coolers of gases and liquids with a lowered level of cooling
Guangming Chen, Alexander Doroshenko, Kostyantyn Shestopalov

0621 3851
Energy and exergy analysis of flat plate solar air heater with micro-heat pipes arrays (MHPA)
Tingting Zhu, Yanhua Diao, Yaohua Zhao

0622 3859
Heat transfer analysis of double U-tube ground heat exchanger of closed loop ground source heat pump system during space cooling application for Indian climatic conditions
Murugesan Krishnan, Satish Kumar, Jivlal Pandit

0642 3867
Numerical modelling of thermal comfort for auditory halls
Aneta Bohojło-Wiśniewska, Mirosława Kołodziejczyk, Dariusz Butrymowicz, Adam Dudar, Michał Łukaszuk, Kamil Smierciew

0658 3875
A study on cost-efficiency relationship analysis of air conditioner in Korea
Daehoon Kim, Jinho You, Younsung Choi, Heejeong Kang, Jeongsik Seo, Wonyoung Park

0662 3883
Marine application of waste heat to drive ejection refrigeration system
Mateusz Kedzierski, Kamil Smierciew, Dariusz Butrymowicz, Jerzy Gagan

0672 3891
Dynamic testing to better reflect real use for the seasonal performance of air conditioners
Carsten Palkowski, Stefan Schwarzenberg, Anne Simo

0679 3900
Improvement of efficiency of a geothermal heat pump installation
Pierre Azar, Chantal Maatouk

0722 3908
A method to calculate the maximum APF for inverter air conditioners
Tao Ren, Jiamin Shen, Guoming Wu, Guoliang Ding, Yongxin Zheng, Yifeng Gao, Ji Song

0730 3916
The application and risk assessment of R290 in split type household air conditioners
Guogeng He, Wei Sun, Weier Tang, Dehua Cai, Sai Zhou

0797 3924
Experimental investigation of CO2 systems for Indian supermarkets with parallel configuration of multiejectors (INDEE)
Krzysztof Banasiak, Simarpreet Singh, Armin Hafner, Prakash Maiya, Petter Neksa, Ángel Pardiñas

0800 3932
Energy and economic approach for the use of thermal energy storage on district cooling: impact of scenario and materials
Hong Minh Hoang, Thomas Dufour, Veronique Osswald, Pascal Clain, Laurence Fournaison, Anthony Delahaye

0845 3940
Direct integration of a latent heat storage in the refrigerant cycle of a multi-split variable refrigerant flow system
Timo Korth, Felix Loistl, Christian Schweigler

0849 3948
Cooling demand: a challenging issue for new buildings in moderate climates
Dorota Chwieduk

0865 3957
Control analysis of VRF type air-conditioner for demand response
Kuniyasu Matsumoto, Kiyoshi Saito, Seiichi Yamaguchi, Keisuke Ohno

0927 3965
Experimental investigation on a novel semi-coupled desiccant heat pump system
Fanli Lu, Tianshu Ge, Yong Li, Yanjun Dai, Ruzhu Wang

0936 3973
Effects of cooling surface micro-machining shapes on frosting curves
Agui Haruka, Ohkubo Hidetoshi, Matsushita Sho

0944 3979
Formation and growth of frost crystals on micro-sized objects llaced in boundary layer
Hidetoshi Ohkubo, Haruka Agui, Shohi Yokoyama, Sho Matsusita

1056 3987
Experimental study on oil charge impact on a scroll compressor energy performance
Ghady Abou Rached, Joelle Rizk, Assaad Zoughaib, Bruno Deboux

1102 3994
Modelling and dynamic simulation of a liquid desiccant system coupled to a heat pump for air conditioning applications
Juan Prieto, Antonio Atienza-Márquez, Alberto Coronas

1112 4002
Simulation and optimization of water-based hybrid VRF systems with bifurcated bare-tube heat exchangers
Ransisi Huang, Zhiwei Huang, Jiazhen Ling, Vikrant Aute

1126 4010
Improving performance of a rechargeable personal cooling system with low GWP refrigerants
Rohit Dhumane, Yiyuan Qiao, Jiazhen Ling, Vikrant Aute, Yunho Hwang, Reinhard Radermacher

1135 4018
Performance characteristics of a residential air conditioning system with subcooling control
Bruno Yuji Kimura de Carvalho, Pega Hrnjak

1149 4026
Experimental research on the heating performance of a flat heat pipe heating system integrated with a phase change material and a thermoelectric unit
Hongli Sun, Borong Lin

1159 4037
Performance evaluation and strategies of subcooling control in residential heat pump systems
Bruno Yuji Kimura de Carvalho, Pega Hrnjak

1195 4045
Experimental investigation and mathematical modelling of the desiccant wheel of a hybrid air conditioning system
Pradeep Sahoo, Manoj Kumar, Manish Mishra

1228 4053
Covering peak loads with phase change materials in a geothermal and desiccant assisted air conditioning system
Finn Richter, Peter Niemann, Gerhard Schmitz

1244 4061
Identification of vapour compression air conditioning system behaviour using Bayesian regularization neural network
Sholahudin Sholahudin, Keisuke OHNO, Seiichi YAMAGUCHI, Kiyoshi SAITO

1247 4069
Development of an ice storage integrated into a mono-split air conditioning system for increase of photovoltaic self-consumption
Carsten Heinrich, Myrea Richter, Tobias Franzky, Felix Stelzer, Mathias Safarik, Ralf Herzog

1354 4077
A novel dehumidification system using zeotropic refrigerants
Xingru Liu, Xiangfei Liang, Mingyue Huang

1459 4084
Comparative analysis of vacuum membrane distillation regenerator and traditional regenerator in liquid desiccant air conditioning system
Junming Zhou, Xiaosong Zhang

1496 4092
A proposed hyper-gravity liquid desiccant dehumidification system and experimental verification
Yangyang Gu, Xiaosong Zhang

1514 4100
Analysis on potential to enhance the energy efficiency of inverter air conditioners
Mengdi CUI, Baolong WANG, Lianrui DING, Wenxing SHI, Xianting LI

1538 4108
Flow characteristic of a two stage high speed centrifugal blower via CFD simulation
Wun-Huei Chih, Kuo-Shu Hung, Yean-Der Kuan, Huang-En Lin, Jeng-Min Huang, Chung-Che Liu

1566 4116
Energy efficiency of a fresh air pre-handling system integrated with pipe-embedded envelopes by utilizing shallow geothermal energy
Weihua Lyu, Xianting Li, Shuai Yan

1587 4124
Investigation on the feasibility of using wood pulp fiber paper as substrate of rotary desiccant wheel for dehumidification
Xuannan Wu, Tianshu Ge, Yanjun Dai, Ruzhu Wang

1619 4131
Numerical study on performance comparison for sub-cooling methods using a sub-cooler in a multi-split variable refrigerant flow (VRF) system
Taemin Lee, Byungchae Min, Gyungmin Choi, Heunghee Bae

1626 4139
Assessing fresh air rate for theatre buildings using particle mass balance principle
Yuchen Shi, Xiaofeng Li

1627 4146
Experimental study for transcritical R744 refrigeration system with ejector installed
Gu Hwang Kang, Sun Ik Na, Min Soo Kim

1706 4153
Comparison of two indirect cooling processes to produce cold water
Yi Jiang, Xiaoyun Xie

1709 4161
A novel indirect evaporative chiller to realize anti-freezing of cooling tower used in data center systems
Xiaoyun Xie, Hua Cai, Yi Jiang

1721 4169
Discrete modeling of fin-tube heat exchangers accounting for cross-fin conduction
Omer Sarfraz, Saad Saleem, Christian Bach, Craig Bradshaw

1761 4177
Study on risk assessment of air conditioner using R290
Atsushi Baba, Kenji Takaichi, Shigeharu Taira, Tsutomu Imoto, Shyunji Itakura, Hironori Mori, Hiroaki Makino, Koji Yamashita, Hiroichi Yamaguchi

1788 4184
The effects of antifreeze in the circulating water on the operation performance of ground heat exchangers
Xiuqin Yang, Xiang Zhou, Xu Zhang

1795 4193
Durability investigation on electrolytic dehumidifier with polymer electrolyte membrane for air-conditioning systems
Ronghui Qi, Dujuan Li, Lizhi Zhang

1808 4199
Numerical simulation for heat transfer performance of a prefabricated ceiling radiant cooling panel with air layer
Dong Xie, Jin zhi Liu, Hanqing Wang

E2 Commission

0128 4207
Numerical performance investigation of a CO2 heat pump and refrigeration system for a Nordic hotel
Silje Marie Smitt, Armin Hafner

0155 4215
Photovoltaic/Thermal (PV/T) to drive a dual source heat pump (ground and PV cooling): performance analysis in a real application
Renato Lazzarin, Marco Noro

0156 4223
Solar thermal and ground source absorption heat pump: energy analysis for a nearly Zero Energy Building
Renato Lazzarin, Marco Noro, Oscar Zanni

0214 4231
Experimental analysis of a gas-fired absorption heat pump with a refrigerant cooled flue gas heat exchanger
Philipp Wagner, Rene Rieberer

0242 4239
High temperature heat pump using HFO and HCFO refrigerants – system design and experimental results
Cordin Arpagaus, Ralph Kuster, Frédéric Bless, Manuel Prinzing, Michael Uhlmann, Elias Büchel, Stefan Frei, Jürg Schiffmann, Stefan Bertsch

0252 4248
Novel high-efficient open sorption system using multilevel cascade reactors for space heating
Yannan Zhang, Ruzhu Wang

0259 4254
High temperature heat pumps – Theoretical study on low GWP HFO and HCFO refrigerants
Cordin Arpagaus, Manuel Prinzing, Ralph Kuster, Frédéric Bless, Michael Uhlmann, Jürg Schiffmann, Stefan Bertsch

0286 4262
Overview on HCFO-R1233zd(E) use for high temperature heat pump application
Nikhilkumar Shah, Donal Cotter, Neil Hewitt

0293 4270
A novel air-source heat pump system with integrated desiccant for electric vehicles
Li Zhang, Katsumi Hashimoto, Hiromi Hasegawa, Michiyuki Saikawa

0308 4278
Experimental investigation of a heat pump assisted drum drying system using propane (R290) as working fluid
Espen Storslett, Trygve Eikevik

0325 4286
Investigation of an air source heat pump water heating system working at wide temperature scale
Jianyong Chen, Ying Chen, Xianglong Luo, Zhi Yang

0400 4294
Implementation of a 25kW NH3-H2O absorption resorption refrigeration unit in the heating, cooling and refrigeration structure of a supermarket
Oliver Ziegler, Ullrich Hesse

0415 4302
Operating characteristics of heat pump type ventilation heat recovery system in the winter
Lei Wang, Guoyuan Ma, Anna Ma, Feng Zhou, Fuping Li

0444 4310
A hardware-based heat pump water heater design model for quasi-steady-state simulation
Bo Shen, Kashif Nawaz, Ahmed Elatar, Van Baxter

0453 4318
Modeling and optimization for the external heat exchanger of CO2 heat pump applied for electric vehicles
Yiyu Chen, Huiming Zou, Junqi Dong, Changqing Tian

0467 4327
Research progress of air source heat pump heating system suitable for cold area applications
Anna Ma, Guoyuan Ma

0473 4333
Thermodynamic performance of triple-loop heat pump ventilation recovery system
Anna Ma, Guoyuan Ma, Lei Wang, Feng Zhou, Mingjian Jiang, Xianghui Yan

0495 4340
Waste heat recovery from urban electrical cable tunnels
Akos Revesz, Gareth Davies, Maidment Graeme, Joanna Kuleszo, Rob Liddiard, Hector Altamirano, Alex Davenport, Boris Yazadzhiyan

0497 4348
Experimental study of residential air-to-air heat pump performances in the field
Cong Toan Tran, Philippe Riviere, Dominique Marchio, Christine Arzano-Daurelle, Assaad Zoughaib

0533 4356
A new self-driven loop heat pipe used in HVAC systems: feasibility analysis
Xiaorui Yang, Penglei Zhang, Xingwang Li, Dalin Zhang

0540 4366
Development of photovoltaic thermodynamic driven chiller, application to air conditioning and cooling storage
Philippe Esparcieux, Olivier Baup, Daniel Mugnier, Christophe Weber, Christophe Marvillet

0543 4374
Ammonia - carbon adsorption heat pump development
Robert Critoph, Steven Metcalf, Angeles Rivero Pacho

0547 4381
Efficiency evaluation of borehole heat exchangers in Nunavik, Québec, Canada
Nicolò Giordano, Luca Riggi, Simone Della Valentina, Alessandro Casasso, Giuseppe Mandrone, Jasmin Raymond

0584 4389
Performance evaluation and validation of a novel heat pump water heater with D-shaped condenser coils
Ce Shi, Pega Hrnjak

0603 4399
Heat and mass transfer characteristics of molded activated carbon/methanol pair for adsorption cooling
Chieko Shibata, Akio Kodama, Hidenori Higashi, Takafumi Seto, Yoshio Otani, Mikio Kumita

0613 4407
Performance optimization of ground water heat pump system for space heating and cooling applications
Murugesan Krishnan, Mahalingesh Satalagaon, Hywel Thomas

0645 4415
Integration of a compact two fluid PCM heat exchanger into the hot superheated section of an air source heat pump cycle for optimized DHW generation
Johann Emhofer, Tilman Barz, Klemens Marx, Felix Hochwallner, Luisa Cabeza, Gabriel Zsembinszki, Andreas Strehlow, Birgo Nitsch, Michael Weiß

0647 4424
Performance of ground source heat pump that uses direct expansion method for supplying hot water
Ryoichi Nishizawa, Tetsuaki Takeda, Shuhei Isiguro, Yuki Marumo

0649 4431
Thermal performance of underground heat exchanger for ground source heat pump that uses direct expansion method
Ryosuke Okazawa, Tetsuaki Takada, Syuhei Ishiguro

0689 4439
Gas dynamic analysis of a rotary compressor with vapor injection
Wei Sun, Guogeng He, Dehua Cai, Sai Zhou, Yu Gao

0712 4447
Pore-scale unsteady CFD simulation of a thermal storage system for optimum design
Peiyu Hu, Shugang Wang, Jihong Wang, Shuang Jiang, Tengfei Zhang, Zhenjun Ma

4455 4463
Modelling and experimental evaluation of a condenser for a heat-pump tumble dryer
Nada Petelin, Pero Gatarić, Andrej Kitanovski, Alojz Poredoš

0734 4463
Industrial heat pumps in the UK - current constraints and future possibilities
Neil Hewitt, Mingjun Huang, Nik Shah

0750 4471
Sorption heat pump for flue gas condensation of biomass-fired boilers
Tina Hermann, Julian Geier-Pippig, Christian Schweigler

0753 4479
Multi-objective optimization of water tank of carbon dioxide heat pump water heater based on improved nondominated sorting genetic algorithm
Yingjie Xu, Enteng Li, Yuangong Huang, Xiaohong Han, Qin Wang, Guangming Chen

0761 4487
Simulation of the ammonia-water absorption heat pump system
WeiXing Yuan, yuxue Guo, yu Li, Bo Yang

0775 4494
Thermodynamic analysis of a novel high-temperature heat pump for low-grade waste heat recovery
Carlos Mateu-Royo, Joaquín Navarro-Esbrí, Francisco Molés, Adrián Mota-Babiloni, Marta Amat-Albuixech

0778 4502
Theoretical and experimental investigation on a very high temperature heat pump with water refrigerant
Di Wu, Bin Hu, RuZhu Wang

0789 4511
Absorption cooling system with optimized heat exchange network for efficient waste heat recovery
Zhenyuan Xu, Ruzhu Wang, Chun Yang

0802 4519
Simulation and optimization analysis of a dual-source R744 two-stage parallel compression hot water heat pump system
Hongxia Zhao, Yiming Wang

0832 4527
Decarbonisation of industrial processes with heat pumps
Veronika Wilk, Michael Lauermann, Franz Helminger

0884 4535
Application of R1224yd(Z) as R245fa alternative for high temperature heat pump
Takenobu Kaida, Masato Fukushima, Koichiro Iizuka

0905 4543
Thermal performance of ground source heat pump using steel pipe pile for house
Tomoya Aoki, Tetsuaki Takeda, Shuhei Ishiguro, Osamu Yoda, Hiroji Okubo

0960 4550
Development of water-lithium bromide absorptions chillers based on asymmetric plate heat exchangers
Lutz RICHTER, Carsten HEINRICH, Christian KEMMERZEHL, Mathias SAFARIK, Mike OTTO, Gregor WEIDNER, Bodo BURANDT, Ralf HERZOG

0970 4559
Comparison of configurations of high-temperature heat pumps for biogas-upgrading
Franz Helminger, Michael Lauermann, Alexander Baumhakel, Gerwin Drexler-Schmid

0973 4567
Turbo-compressor for R-718: Simulation and verification of a two stage steam compression cycle
Michael Bantle, Christian Schlemminger, Marcel Ahrens

0978 4575
Energy conservation effect based on the change of supercooling in water flow rate exchanging heat in condenser of refrigerated cabinet(s) using PCM
Toshiyasu Watanabe, Tatsutoshi Nakamura, Akira Yasukochi, Sangchul Bae, Masafumi Katsuta

0979 4582
Design of a 2-salt thermochemical heat transformer for industrial waste heat upgrading
Marc Clausse, Benoît Michel

0995 4590
New tap water heat pump using propane refrigerant
Per Pedersen, Asbjoern Vonsild, Torben Lauridsen

1013 4599
Heat from underground energy London (Heat FUEL)
Henrique Lagoeiro, Gareth Davies, Daniel Curry, Graeme Maidment, Akos Revesz, John Bielicki, Gareth Faulks

1055 4608
Screening of heat pump performance improvements obtained through gradual heating using a tank system
René Kofler, Brian Elmegaard, Claus Madsen, Lars Olsen, Wiebke Markussen

1059 4616
Semi-theoretical model of ionic liquid wetting characteristics on a gas-liquid finned-tube contactor
Niccolo Giannetti, Richard Varela, Hifni Ariyadi, Seiichi Yamaguchi, Kiyoshi Saito, Xin-Ming Wang, Hiroshi Nakayama

1111 4624
Field measurements of CO2 refrigeration systems with heat recovery in retrofitted ice rinks
Simon Bolteau, Cajus Grönqvist, Jörgen Rogstam

1117 4632
Performance of high temperature heat pump for simultaneous and efficient production of ice water and process heat
Christian Schlemminger, Eirik Svendsen, Sverre Steffanussen Foslie, Michael Bantle, Opeyemi Bamigbetan, Petter Nekså

1125 4640
Performance evaluation of CO2-based mixture refrigerants in ground-source heat pump with ejector
Wei Wu, Michael Leung, Xianting Li

1131 4649
Desing of a system to produce domestic hot water based on a water to water heat pump booster
Estefania Hervas-Blasco, Emilio Navarro-Peris, Jose Corberan

1133 4657
Analysis of the performance of developed EVI air source heat pump with heat demand during seasonal operations
Ming Jun Huang, Yan Jun Dai, Nikhilkumar Shah, Christopher Wilson, Neil Hewitt

1158 4665
A field study on frosting suppression for air source heat pumps by adjusting operation strategies of multi-parallel compressors
Shimin Liang, Shiqiang Zhang, Wei Wang, Yuying Sun, Yiming Cui, Zhaoyang Li, Shiming Deng

1166 4673
Comparison of zeotropic working fluid mixtures in different heat pump cycles
Benjamin Zühlsdorf, Jonas Jensen, Lars Reinholdt, Brian Elmegaard

1169 4681
Waste heat driven ammonia-water absorption chiller for high temperature residential-scale applications
Girish Kini, Michael Tambasco, Sriram Chandrasekharan, Srinivas Garimella

1184 4689
Transcritical industrial heat pump using HFO's for up to 150°C hot air supply
Gisèle Abi Chahla, Yannick Beucher, Assaad ZOUGHAIB, Florence de Carlan, Jacques Pierucci

1186 4697
Trans-critical vapor compression cycle using butane (R600) as refrigerant for industrial waste heat recovery
Manuel Verdnik, René Rieberer, Heinz Moisi

1193 4705
Thermodynamic analysis and selection of refrigerants for high-temperature heat pumps
José Corberan, Abdelrahman Hassan, Jorge Payá

1246 4713
Large-scale mechanical vapor recompression drying process in superheated steam
Hans Madsboll, Kasper Larsen

1251 4721
Control strategy of two stage CO2 heat recovery systems in ice rinks
Sotirios Thanasoulas

1253 4729
High temperature industrial heat pumps utilising natural working fluids
Petter Nekså, Michael Bantle, Christian Schlemminger, Opyemi Bamigbetan

1325 4737
Radiation absorption and heat collection characteristics of graphene/paraffin composite phase change material
Lanxiong Ouyang, Guoying Xu, Junhui Yan, Kai Du

1341 4745
Novel air conditioning system using desiccant coated heat exchanger
Tomohiro Higashi, Chaobin Dang, Eiji Hihara, Li Zhang

1348 4754
Hydrocarbons as natural refrigerants for heat pump water heating applications
Kashif Nawaz, Bo Shen, Ahmed Elatar, Van Baxter, Omar Abdelaziz

1355 4763
Ejector based climate control systems with heat and mass recuperation through the Maisotsenko cycle
Oleksii Drakhnia, Dmytro Buyadgie, Olexiy Buyadgie, Takahiko Miyazaki, Valeriy Maisotsenko

1370 4771
Thermodynamic analysis of an absorption heat transformer based on experimental measurements
José Corrales Ciganda, Falk Cudok, Marvin Schloesser, Manuel Wahl, Dominik Metzner

1375 4779
Compact exhaust air/supply air heat pump with recirculation with energy recovery in renovated multi-storey-buildings
Fabian Ochs, Dietmar Siegele, Georgios Dermentzis, Toni Calabrese

1403 4787
Simulation on the performance of gas-fired boiler with flue gas heat recovery utilizing gas engine driven heat pump
Wei Chen, Sheng Shang, Wenxing Shi, Baolong Wang, Yang Cao, Xianting Li

1436 4794
Performance study of air source heat pump with multiple parallel outdoor machines defrosting alternatively
Niu Jianhui, Xu Shuxue, Ma Guoyuan

1461 4803
Assessment of the influence of the intermediate pressure on the optimal gas cooler pressure in a one-stage CO2 heat pump with gas bypass for hot water generation
Fernando Illán-Gómez, José Ramón García-Cascales, Francisco Javier Sánchez-Velasco, Víctor Francisco Sena-Cuevas

1471 4811
Development of hybrid VRF using R32 refrigerant
Soshi Ikeda, Katsuhiro Ishimura, Jun Nishio, Hiroyuki Okano

1521 4819
A dual-function absorption heat pump cycle for space conditioning and water purification
Daniel Boman, Srinivas Garimella

1537 4827
Alternative energy storage using a domestic hot water solar-assisted heat pump with PV collector/evaporator and HC refrigerant
Cesar Isaza-Roldan, William Quitiaquez, Cesar Nieto-Londoño, Luis Fernando Toapanta, Isaac Simbaña

1550 4840
Experimental study on the wetting characteristics of a liquid-level-lifting type asymmetrical overflow distributor
Yuhao YI, Tianle HU, Yi JIANG, Xiaoyun XIE

1570 4848
Dynamic behavior study of multi-section vertical absorption heat exchanger
Chaoyi Zhu, Xiaoyun Xie, Yi Jiang

1579 4856
A novel heat-driven thermoacoustic refrigeration system for food refrigeration applications
Huizhi Wang, Limin Zhang, Jianying Hu, Guoyao Yu, Zhanghua Wu, Ercang Luo

1594 4861
A novel flue gas total heat recovery system combining direct-contact condensation with liquid desiccant absorption
Xiaoyue Zhang, Junda Wu, Zhen Li

1638 4867
Development of a two-stage balanced absorption-resorption heat pump cycle with multiple internal heat recovery for space heating
Teng Jia, Yanjun Dai

1641 4875
Exergy analysis of vapour injection system with intermediate heat exchanger using R32/R1234ze(E) mixture
Zuo Cheng, Baolong Wang, Wenxing Shi, Xianting Li

1644 4883
Comparing integrating configurations of latent heat storage in heat pump heating systems
Tianhao Xu, Yingrui Hao, Samer Sawalha

1668 4891
A gas-fired heat-driven thermoacoustic heat pump for winter heating
Yanlei Sun, Jianying Hu, Ercang Luo, Limin Zhang, Kaiqi Luo, Zhanghua Wu

1694 4899
Applications of absorption heat exchangers for kinds of waste heat recovery systems
Yi Jiang, Xiaoyun Xie

1715 4907
Effect of surface roughness on heat transfer in a thermal energy storage system employing microencapsulated phase change material slurry
O.F. Alasfoor, S.A. Sherif

1750 4918
Performance improvement of heat pump water heater by modifying water temperature stratification on tank side
Ce Shi, Pega Hrnjak

1791 4926
COP tests of a rotation heat pump
Andreas Längauer, Bernhard Adler, Christian Rakusch, Karl Ponweiser

1815 4934
Experimental study on a water and air source high-temprature heat pump using a low GWP refrigerant
Choyu Watanabe, Shuto Tomita, Motoki Yamada, Toshiyuki Nakamura, Tomoyuki Yamada, Atsuki Hattori, Tadayoshi Aono

1869 4942
Development of ammonia-water hybrid absorption-compression heat pumps
Marcel Ulrich Ahrens, Armin Hafner, Trygve Magne Eikevik

1876 4950
Experimental measurements and techno-economic analysis of a compact DHW heat pump powered by photovoltaic energy
Pedro Vicente-Quiles, Damian Crespi-Llorens, Francisco Aguilar-Valero

1878 4958
Performance testing of a geothermal heat pump system in a Canadian residential building
Mohamed R.H. Abdelsalam, Aqeel Zaidi

TOPIC S: SUSTAINABLE AND HIGH PERFORMANCE BUILDINGS

0217 4965
Performance analysis of the metamaterial based cool roof for single-family houses
Saihong Tang, Kai Zhang, Lufang Chen, Mingquan Ma, Jinxiang Liu, Xiaofeng Niu

0283 4973
Benchmarking of supermarket energy consumption
Alan Foster, Tim Brown, Judith Evans, Graeme Maidment

0885 4981
Evaluation of the heat and energy performance of a data center for a new efficiency index: energy usage effectiveness - EUE
Alexandre Santos, Pedro Dinis Gaspar, Heraldo José Lopes de Souza

0908 4989
Building energy management in energy-hub manner based on economic model predictive control
Jiangyu Wang, Jiangyan Liu, Guannan Li, Yabin Guo, Huanxin Chen, Yue Yuan, Yao Huang

0966 4997
Quantification of energy flexibility from air conditioning in residential buildings
Alice Mugnini, Fabio Polonara, Alessia Arteconi

1046 5006
Proof of concept for a building integrated solid state heat pump
Sietze Van Der Sluis

1330 5014
Rigorous assessment of low GWP refrigerants in heat pumps from an ecologic perspective using Life Cycle Assessment (LCA)
Christian Vering, Moritz Lauster, Dirk Müller

1499 5022
Analysis on the characteristic of heat absorbed by the pipes in pipe-embedded double-skin façade (PDSF)
Shuai Yan, Xianting Li

1518 5030
Autonomy of low energy residential houses in Belgium using photovoltaic panels and energy storage
Hugo Monteyne, Katarina Simic, Marija Lazova, Jelle Laverge, Michel De Paepe

1770 5039
Parametric study by means of 3D CFD to improve the airflow pattern and temperature distribution in data center rooms
Diogo Macedo, Radu Godina, Pedro Gaspar, Pedro Silva, Miguel Covas

1891 5047
Development of thermal energy storage system for peak thermal demand of apartment using *phase change material*
Hyo Jae Jeong, Dongho Park, Sung Yong Park, Dong An Cha, Jong Hyeon Peck, Kyung Min Kim, Won Seok Chang, Mun Sei Oh

Manuscript ID: 1374
DOI: 10.18462/iir.icr.2019.1374

Prediction of food thermal properties to enable accurate design of food refrigeration processes

Don J. CLELAND[(a)]

[(a)] Centre for Postharvest & Refrigeration Research, Massey University
Palmerston North 4442, New Zealand, d.cleland@massey.ac.nz

ABSTRACT

Optimal design and operation of food refrigeration processes requires knowledge of thermal properties including density, specific heat capacity (and hence enthalpy), thermal conductivity and initial freezing point. Measurement of such properties is time-consuming and expensive given the wide range of foods and variations in composition and structure. Simple methods to predict properties from composition data are desirable. Density and heat capacity are volume and mass weighted-averages of the food components respectively. Thermal conductivity is a volume-based property but also depends on structure. Further important considerations are the effects of air voids contained with the food or packaging system, and ice for frozen foods. The recommended method uses a parallel model for components other than ice and air; the Levy model for ice, and an Effective Medium Theory model for air voids. All models are generally applicable and only the method to estimate the bound water used to estimate the ice fraction has any empirical coefficients. Comparisons against experimental data for a range of products and a worked example show the accuracy and utility of the methods.
Keywords: Thermal properties, Prediction models, Effect of ice, Air voids.

1. INTRODUCTION

Most food processing and preservation systems involve heating or cooling steps, particularly if a refrigerated supply chain is employed. Accurate prediction of the rate of heat transfer and temperature change is critical if the design and operation of such heating and cooling processes is to be optimised (Datta, 2016). For refrigeration processes, the optimisation might include:

a. Ensuring that the rate of temperature change is appropriate to maintain product quality (e.g. not too fast if product susceptible to chill injury, cold-shortening or similar effects; not too slow if microbial growth, respiration or other temperature-related reactions will quickly spoil the product at higher temperatures).
b. Correctly sizing of equipment to ensure there is sufficient residence time for the desired temperature change to occur.
c. Selecting air velocity that achieves the desired rate of heat transfer whilst keeping fan power, energy use and operating costs low.
d. Selecting cooling medium temperatures that achieves the desired rate of heat transfer whilst keeping refrigeration system capital and running (energy) costs acceptably low.
e. Other trade-offs between product quality deterioration and the costs and sustainability of the refrigeration system.

Imprecision in heat transfer predictions arise from two main sources:

1. Shortcomings in the prediction method (model). These shortcomings might arise from assumptions and simplifications made in formulating the model so that it may significantly deviate from the real world situation (e.g. some heat transfer mechanisms assumed negligible; simplified geometry, homogeneous rather than heterogeneous composition) or imprecision in how the model is solved (e.g. accuracy of the time and space discretization for numerical methods)
2. Uncertainty in the input data that the model requires (e.g. size and geometry of the product and food types within a product item, variation in process conditions such as cooling medium temperature and velocity (and hence heat transfer coefficients) with time and position, product thermal properties including uncertainty due to composition variations).

For many cooling and freezing application, semi-analytical (semi-empirical) and numerical models are available with accuracy better than ±10% if accurate input data is available. In particular, modern software packages, such as Comsol Multi-Physics^{TM}, allow all heat and mass transfer mechanisms to be included, carter for complex geometries and compositions (e.g. mixtures of food types), handle time and position-variable operating conditions, can incorporate temperature variable properties including latent effects and moving boundaries, and provide automate grid generation and time-stepping solver controls to minimise numerical approximation uncertainty. Modern computing power mean that the computational overhead of using fine grid meshes and including complex multi-scale mechanisms is seldom a constraint. However, such complicated models come at the expensive of much more intensive data requirements so simpler semi-analytical models with simpler data requirement are often just as accurate and can be preferred due to their simplicity to understand and use (Gulati & Datta, 2013).

The impact of thermal property uncertainty on prediction accuracy can be significant Larkin et al., (2004). At high Biot number conditions (internal resistance to heat transfer is controlling) then a ±10% uncertainty in thermal conductivity results in a ±10% uncertainty in cooling or freezing rate for a solid product (directly proportional), although this reduces to about ±3% uncertainty at a Biot number of 1 (balance between internal and external resistance to heat transfer). Similarly, a ±5% uncertainty in heat capacity (or enthalpy) results in a proportional ±5% uncertainty in cooling or freezing rate for all situations.

Therefore further refinement of semi-analytical prediction methods or use of the more advanced features available in numerical heat and mass transfer packages are seldom worthwhile unless input data uncertainty can be addressed i.e. the accuracy of the prediction is often controlled more by the accuracy of input data than that of the prediction method (Datta, 2007; Ho et al., 2013).

For food refrigeration processes, the key thermal properties required are density, specific heat capacity, enthalpy, thermal conductivity and initial freezing point, T_{if}. In addition, to understand the change in properties at temperature below T_{if}, it is usually desirable to know the split between unfrozen water and frozen water (ice) because ice thermal properties are significant different to those for water resulting in a step-change in most properties (Figure 1).

Some might argue that prediction of properties is unnecessary because there are comprehensive sources of property data on-line and in the literature (e.g. Nesvadba et al., 2004; Rahman, 2009; ASHRAE, 2018) or that the properties can be directly measured. In terms of undertaking accurate property measurements across the full temperature range, the challenges include:

i. The high cost of appropriate instrumentation and the long time to perform the measurements to high accuracy.
ii. Measurements just below the T_{if} have high uncertainty because of the rapid change in properties in this temperature range as shown in Figure 1 (Murakami & Okos, 1996).
iii. Measurement for foods including significant air voids is difficult so often measurements are only taken for the “solid” food with air voids eliminated.
iv. Measurements being only practical for single food types and not composite heterogeneous food products (e.g. pizza). Many measurement systems require very small samples and getting a representative sample for a heterogeneous product is difficult, and there are variations in properties with change in food type within a product.
v. Measurements cannot be undertaken without samples and so properties for conceptual designs before the production facility is constructed must rely on laboratory or pilot scale samples which may differ slightly in composition from full-scale samples.

The weaknesses of published data include:

i. Most of the data are for minimally processed food or single food types and not for composite heterogeneous food products or for foods with air voids.
ii. Variation of the properties with temperature is rarely available (constant fully frozen or unfrozen values only) especially at temperature just below T_{if} where changes are rapid.
iii. The variations with variety and time of seasonal (natural products) or with changes in composition (e.g. water content or porosity) are seldom provided and often the exact composition of the product is not stated.
iv. The accuracy of the data can be dubious because the measurement methods were inappropriate or poorly executed (Carson, 2017). Further, some of the published data that purports to be measured is actually predicted from typical composition data.

v. The data is seldom available for a new product or a new formulation of an existing product.

Modern numerical methods allow the different food types in a heterogenous food product to be modelled discretely (e.g. Ho et al., 2013). However, the extra data preparation requirements related to defining the geometry of each food type in a product item and the normal variability in this geometry across a production run mean that the most common approach is to treat the product as homogeneous and use of effective property values for the whole product item.

Therefore there is an on-going need for prediction of effective thermal properties of complete food products from knowledge of the food composition (which is usually known or is simple and low cost to measure). The purpose of this paper is to recommend accurate yet simple to implement methods to predict effective product thermal properties from composition data in the temperatures range most relevant to refrigerated foods, taking into account change in ice fraction below the freezing point, the presence of air voids and, for packaged food items, the effect of packaging.

2. RECOMMENDED PREDICTION METHODS

There are a large number of empirical property prediction methods. In general terms, these are only accurate for the temperatures ranges, food types, and compositions for which they were derived. Whenever possible methods based on physical principles without empirical curve-fitted constants and/or terms are recommended because they are more likely to be generally applicable.

The literature related to prediction of thermal properties is vast (e.g. Carson, 2006; Gulati & Datta, 2013). Therefore, in this paper citations are limited to references giving the recommended methods, providing good overviews of the literature, or providing key examples in an area.

The basis of the prediction method is to consider the food as homogenous and isotropic comprising a mixture of components – water, ice if below T_{if}, proteins, fats/lipids, minerals (ash), carbohydrates, other solids (e.g. fibre), air voids and occasionally packaging internal to the product item. Sometimes there is a distinct and defined structure e.g. fat layers, emulsions, distribution of air voids, and these may lead to some properties being anisotropic (e.g. parallel vs perpendicular to fibres in muscle) but the recommended methods assume homogeneity. The required information is the mass fraction of each of the components (composition) plus the bulk density of the food.

Refrigerated foods are generally high moisture (low moisture foods usually do not need to be refrigerated because their low water activity already provides a preservation effect), thus the characteristics of refrigerated food are dominated by their water content. The standard conceptual model is to consider food a mixture of solutes in the water plus ice (below T_{if}) and other solids. The solutes depress T_{if} below 0°C, and because pure ice freezes out of the water solution, the solutes because more concentrated and freezing point depression increases. Thus freezing occurs over a range of temperatures. Some of the non-water components are considered to mainly affect freezing point depression (e.g. low molecular weight solutes such as minerals/ash), some mainly affect the availability of water to freeze (e.g. water bound to macro-molecules such as protein and carbohydrates), and some have negligible effect on the water phase (e.g. fats/lipids).

2.1. Initial Freezing Temperature (T_{if})

The initial freezing temperature is important to know in order to avoid freezing in a product chilling process, as a parameter in the prediction of rates of freezing, and as a factor affecting the temperature-ice fraction relationship. As pointed out by Larkin et al. (1984), accuracy in the order of ±0.05 to 0.1°C is required so thermal properties and hence cooling rate prediction uncertainty is less than 5%.

Measurement of T_{if} is often practical and low cost, so if available to high accuracy, use of a measured value is recommended. If required, the best prediction methods are based on freezing point depression theory (Raoult's Law) with the food being considered as a mixture of solutes in water (e.g. Miles et al., 1997). That proposed by Boonsupthip & Heldman (2007) is recommended:

$$\frac{1}{T_{if} + 273.15} = \frac{1}{273.15} - \frac{R}{M_w L_w} \ln \frac{(x_{tw} - x_{bw})/M_w}{(w_{tw} - w_{bw})/M_w + \sum_{j \text{ not } w} (x_j / M_j)} \quad \text{Eq. (1)}$$

Note that for the summation term in Eq.(1), it is recommended that proteins, carbohydrates (except simple sugars) and fibre are assumed to have a M_j of 50 kDa and so have little effect, that fats are ignored, and that the focus is on low molecular weight solutes such as minerals, acids, bases and mono- and di-saccharides with a minimum molality of 50 μmol.100 g^{-1}.

2.2. Ice Fraction (x_{ice})

For properties below T_{if} it is necessary to predict the ice fraction, x_{ice}, and hence the remaining fraction of unfrozen water ($x_w = x_{tw} - x_{ice}$) due to the large differences in properties. Miles et al. (1997) and others (e.g. Chen 1985) showed that the following theoretical relationship holds for food systems with low concentrations of solutes:

$$x_{ice} = \left(x_{tw} \quad x_{bw}\right)\ 1 \quad \frac{T_{if}}{T} \qquad \text{Eq. (2)}$$

Eq.(2) required the bound water to be estimated. While for many foods, bound water is primarily associated with protein, the linear relationship proposed by Schwartzberg (1976) is generally used:

$$x_{wb} = \quad _j b_j x_j \qquad \text{Eq. (3)}$$

Various references such as Chen (1985), Pham (1987) and Miles et al (1997) suggest empirical values of b_j for different food groups and components based on fit to measured data. The equation proposed by Pham et al. (1996) is recommended as it is potentially the most generally applicable:

$$\frac{x_{bw}}{x_{tw}} = 0.342\left(1 \quad x_{tw}\right) \quad 4.510\ x_{ash} + 0.167\ x_p \qquad \text{Eq. (4)}$$

Pham (2014) found the following relationship proposed by Tchigeov (Fikiin, 1998) to be slightly more accurate than Eq. (2) in the ranges -45°C < T < T_{if} and -2°C < T_{if} < -0.4°C:

$$x_{ice} = \frac{1.105\ x_{tw}}{1 + \dfrac{0.7318}{\ln(T_{if} \quad T + 1)}} \qquad \text{Eq. (5)}$$

However, Eq.(5) is fully empirical so the more mechanistic approach of Eq.(2) and (4) is preferred.

2.3. Density (ρ)

Density is a volume based property and so effective density is simply a volume-weighted average of the components. Given the density of air is negligible relative to the other components and the weight of air in the food cannot be easily measured, the most common approach is to estimate the density of the "solid" food ignoring the air voids:

$$\frac{1}{_{solid}} = \quad _j \frac{x_j}{_j} = \frac{1}{\quad _j {}_j v_j} \qquad \text{Eq. (6)}$$

Knowing the food bulk density, the volume faction of air (porosity), v_{air}, can be estimated using:

$$_e = \quad _{solid}\left(1 \quad v_{air}\right) = \quad _j {}_j v_j \qquad \text{Eq. (7)}$$

In this paper, porosity refers to the fraction of air voids only. In contrast, in other parts of the food literature (e.g. drying) and in other fields (e.g. soil science), porosity is often defined to be the total of the air and water volume fractions.

2.4. Specific Heat Capacity (c)

Specific heat capacity is simply a mass-weighted average of the component heat capacities plus the apparent heat capacity due to water phase change to ice using the differential form of Eq. (2):

$$c_e = \quad _j c_j x_j \quad \left[L_w + \left(c_w \quad c_{ice}\right)T\right]\frac{dx_{ice}}{dT} = \quad _j c_j x_j \quad \left[L_w + \left(c_w \quad c_{ice}\right)T\right]\left(x_{tw} \quad x_{bw}\right)\frac{T_{if}}{T^2} \qquad \text{Eq. (8)}$$

Of course, above T_{if}, the second (latent heat) term in Eq. (8) is omitted. If the prediction method required the latent heat separately from the specific heat capacities, then the differential term in Eq. (8) is omitted and the latent heat is estimated using:

$$L_e = L_{w@T_{if}} \left(x_{tw} \quad x_{bw} \right) \qquad \text{Eq. (9)}$$

The latent heat of solidification of fats, while smaller than that for water, can be significant for some foods above T_{if}. Fats are usually a mixture of lipids with different melting points so the latent heat is released over a wider temperature range than for water. Also, fat solidification is not influenced by the concentration of solutes in the aqueous phase. Therefore, if significant fat phase change is likely over the temperature range of interest, then adding a further term to Eq. (8) is recommended. The term is the cumulative latent heat of solidification of the fats divided by the temperature range over which the phase change will occur and is only added for phase change temperature range.

2.5. Enthalpy (*h*)

If required, the difference in the enthalpy of the food from the datum temperature can be estimated by analytical or numerical integration of Eq. (8) as follows:

$$h_e = \int_{T_{datum}}^{T} c_e \, dT \qquad \text{Eq. (10)}$$

2.6. Thermal Conductivity (*k*)

Thermal conductivity is the most difficult thermal property to estimate because as well as being volume rather than mass based, it also depends on the structure of the components within the food (i.e. how the components are configured relative to each other). This is particularly important when there is a large difference in component thermal conductivity. There is considerable literature on thermal conductivity prediction models (e.g. Carson, 2006; Rahman, 2009). The sequential multi-stage method proposed by Carson et al. (2016) is recommended. It divides foods into four classes based on the ratio of the maximum and minimum thermal conductivity components:

I. Unfrozen, non-porous foods ($k_w/k_{solids} \approx 3$)
II. Frozen, non-porous foods ($k_{ice}/k_{solids} \approx 12$)
III. Unfrozen, porous foods ($k_{water}/k_{air} \approx 25$)
IV. Frozen, porous foods ($k_{ice}/k_{air} \approx 100$)

If the ratio is low, knowledge of the structure, and hence the choice of thermal conductivity model is less critical. In the approach, Class II foods are considered as being a mixture of a Class I food and ice, Class III foods are considered as being a mixture of a Class I food and air, and Class IV foods are considered as being a mixture of Class II foods and air. This approach is illustrated schematically in Figure 2.

For Class I food components the Parallel model is used, since it is the simplest model yet provides sufficient accuracy and allows for any number of components:

$$k_I = \sum_j k_j v_j \qquad \text{Eq. (11)}$$

For Class II foods the presence of ice is be accounted for using Levy's model (Levy, 1981):

$$k_{II} = k_{ice} \frac{2k_{ice} + k_I \quad 2(k_{ice} \quad k_I)F}{2k_{ice} + k_I + (k_{ice} \quad k_I)F} \qquad \text{Eq. (12)}$$

$$F = \frac{2/G \quad 1+2(1 \quad v_{ice}) \quad \sqrt{[2/G \quad 1+2(1 \quad v_{ice})]^2 \quad 8(1 \quad v_{ice})/G}}{2} \qquad \text{Eq. (13)}$$

$$G = \frac{(k_{ice} \quad k_I)^2}{(k_{ice} + k_I)^2 + k_{ice}k_I/2} \qquad \text{Eq. (14)}$$

The Levy model physically represents the structure where the two components are mixed in a combination of one dispersed in the other which is continuous and vice versa in proportions such that the composite conductivity is the same (i.e. a mixture of the two versions of the well-known Maxwell-Eucken model for a dispersed phase in a continuous phase). This is appropriate because water is generally present throughout a food and when most of this water freezes, the ice is often extra-cellular and/or forms through a combination of crystal growth of dentrites and new nucleation. Hence the ice is often a mixture of being continuous through the food and dispersed within the rest of the food components, which broadly matches the structure assumed in the Levy model.

For Class III and IV foods, the Effective Medium Theory (EMT) model is used to represent the effect of air voids. The respective equations are:

$$k_{III} = \frac{(3v_{air} \quad 1)k_{air} + [3(1 \quad v_{air}) \quad 1]k_I + \sqrt{\{(3v_{air} \quad 1)k_{air} + [3(1 \quad v_{air}) \quad 1]k_I\}^2 + 8k_I k_{air}}}{4} \quad \text{Eq. (15)}$$

$$k_{IV} = \frac{(3v_{air} \quad 1)k_{air} + [3(1 \quad v_{air}) \quad 1]k_{II} + \sqrt{\{(3v_{air} \quad 1)k_{air} + [3(1 \quad v_{air}) \quad 1]k_{II}\}^2 + 8k_{II} k_{air}}}{4} \quad \text{Eq. (16)}$$

The effect of porosity on thermal conductivity is complicated by the widely differing structures that porous foods may have. Air may be dispersed as "bubbles" in a continuous matrix (e.g. ice cream or bread), it may form a continuous phase, as is the case with particulate foods (e.g. bag of peas or grated cheese), in some cases it may exist as a mixture of both dispersed and continuous phases, or both the air and food solids can be continuous but inter-twined (e.g. sponges). In some cases, the air may be in "layers" (e.g. trapped between fillets or steaks within a packaged item) and these layers may be parallel or perpendicular to the direction of heat flow. It can be inferred that when porosity is low (e.g. $v_{air} < 0.3$), then the air is more likely to be dispersed, and when porosity is high (e.g. $v_{air} > 0.7$), then the air is more likely to be continuous.

There are two forms of the Maxwell-Eucken model depending which phase is dispersed and which is continuous. The EMT model represents the structure where all the components are randomly dispersed with each other (co-dispersed). It closely approximates the two versions of the Maxwell-Eucken model at low and high porosity respectively, and the transition at intermediate porosity is plausible for such foods. Hence the EMT model is recommended if a single model is to be used without prior or definitive knowledge of how the air voids are distributed (Carson et al., 2016). If the air void structure is known, then the matching model should be used instead of Eq.(15) and (16).

2.7. Volume Fractions and Component Property Values

Volume fractions can be calculated from mass fractions using:

$$v_j = x_j \frac{e}{j} \quad \text{Eq. (17)}$$

When estimating intermediate thermal conductivity values (e.g. k_I for k_{II} or k_{III} values, or k_{II} for k_{IV} values), then the intermediate volume fractions should only include the components appropriate for that Class as shown in Figure 2, and the volume fractions for these components should sum to 1.

Table 1 gives the properties of the various components in food as a function of temperature (Choi & Okos, 1986) as well as the constant values often used to make predictions where singular values are required rather than full temperature-variable values. It is extremely important to note that this Table corrects typographical mistakes in the original paper by Choi & Okos (1986) that unfortunately have often been repeated in other references. The corrections are to the second coefficient for thermal conductivity for fat and the constants for specific heat capacity for water. For temperatures above 10°C, Phinny et al. (2017) shows that linear version of the equations are just as accurate as the quadratic version, that greater accuracy is achieved by subdividing carbohydrates into simple and complex carbohydrates for all properties, and that for fat specific heat capacity adding terms related to the oleic and linoleic fatty acid content also improves accuracy. For refrigerated foods, the key processes are generally below 10°C so the Table 1 models are recommended.

2.8. Air Voids (Porosity) and Packaging

The above thermal conductivity equations assume that air voids are sufficiently small that no natural convection within them. If natural convection is a possibility then a simple approach is to use a larger value for the air thermal conductivity than the still air values given in Table 1.

The prediction equations include the effect of air voids that are internal to the food items being heated or cooled. However, more generally, the effect of air voids depends on their location. Some air voids are an inherent part of the product (e.g. air in bread or dough; porosity of fruit such as an

apple with spaces between the cells and in the vascular structure), while some air voids are created when food items are combined into a product item (e.g. air within grated cheese on a pizza or air between fish fillets layered in a carton). Such air voids internal to the product item affect the thermal properties (density & thermal conductivity), and should be included in the above methods.
However, some air voids exist as air gaps between the outside of the food itself and the packaging that makes the food into a food product or item. Such air voids generally have greatest effect on the surface heat transfer and should be taken into account when the surface heat transfer coefficients are estimated.
Similar logic applies for packaging. Packaging on the outside of an item to be heated or cooled mainly affects the surface heat transfer coefficient and should not be considered part of the food item for which thermal properties are calculated. The dimensions of the food item should also be adjusted to the outside of the food itself (often the inside of the packaging subtract air gaps thicknesses) when heat transfer predictions are made. Sometimes there is packaging on the inside of the product item (e.g. internal cartons faces in a pallet of cartons) that should be treated as affecting the effective thermal properties of the product items. The above equations can be used by treating the packaging as another food component. Table 1 includes typical property values for some common packaging constituents. The thermal conductivity values are of the same order of magnitude as the non-water components of food so for Class I foods they should be considered another "solid" components (i.e. excluding ice, water or air). The heat capacity of most packaging is low compared to the food (for medium and high moisture foods) so ignoring the thermal mass of the external packaging (i.e. only considering its thermal resistance on the surface heat transfer coefficient) normally has minimum effect on the accuracy of the prediction of heat transfer rate.
Some packaging acts to trap air but has negligible mass (e.g. plastic wrap) and can be ignored except for the air voids it creates. Further, some packaging types have internal air (e.g. corrugated cardboard). In these cases, if the packaging is internal to the product item, the internal air should be added to the air voids for the whole product item and the rest of packaging assumed "solid" without air voids.
Defining the product item geometry is a critical decision in prediction of heat transfer for foods. The recommended approach is to define the product item as the smallest element to which the cooling medium comes into contact with sufficient flowrate to prevent stagnancy. Thus for a pallets with tightly stacked cartons such that air cannot penetrate into or between cartons then the product item is the whole pallet and packaging and air voids should be subdivided into those that are internal or external to the pallet. For a pallet where air penetrates between cartons but not into cartons, then the item might be a column or layer of cartons or a possibly a single carton if there are gaps for air flow across most carton faces. For cartons which air flows through (e.g. through handholds or vent holes), then the product item might best be defined as a single item within the carton (e.g. a single fruit or a layer of fruit) depending on the internal carton geometry.

3. PREDICTION ACCURACY

The prediction accuracy of the proposed methods for density, specific heat capacity and enthalpy are well established and proven (Murakami & Okos, 1989; Rao et al., 2005; Rahman, 2009). The main uncertainty relates to estimating T_{if} and ice fraction and hence properties for frozen foods in the temperature just below T_{if} will be less accurate. These properties are strongly mass-dependent, so their accuracy for porous foods is not significantly worse.
Prediction of thermal conductivity, especially for frozen and porous food, has far greater uncertainty. There is limited reliable measured data for foods that also give details about the mass fractions of components and porosity that allows the testing of prediction methods. There are fewer data for frozen foods (Class II) than unfrozen foods (Class I) and very few data for porous foods likely to be refrigerated (Class III and IV). There is virtually no measured effective values for composite product items that are a mixture of food and packaging including air voids.
Carson et al. (2016) compared Eq.(11) with measured data from Willix et al. (1998) for 13 unfrozen, non-porous (Class I) foods at 20°C. The average absolute deviation between measured data and predictions were less than 6% and were not bettered by any other generally applicable prediction models. For the same 13 foods at -20°C (Class II), the average absolute deviation between measured data and predictions from Eq.(12) were less than 18%. While some other

generally applicable prediction models were slightly more accurate on average, the differences were not significant given uncertainty in estimating ice fraction for all methods, and the greater uncertainty of the measured data at frozen temperatures.

None of the measured data for Class III foods were for foods likely to be refrigerated, but the average absolute deviation between measured data and predictions from Eq.(15) were less than 15% and Eq.(15) was the most accurate generally applicable model by a significant margin.

The only Class IV food for which reliable measured data were available was for ice cream (Cogne et al., 2003). The average absolute deviation between measured data and predictions from Eq.(16) was about 20% (Carson et al., 2016). The deviations were higher at high porosity. Ice cream is quite unique in that the air in it remains as dispersed discrete bubbles even at high porosity. Therefore, the high porosity ice cream data is a case where the EMT model for Class IV foods may be less appropriate than other models such as Maxwell-Eucken (Wang et al., 2010). Given, that EMT model (Eq. (15) worked well for Class III foods and for ice cream at low porosity, its use as the recommended general method is still justified.

4. WORKED EXAMPLE

A carton of deboned beef is to be frozen. The carton has a net weight of 27.2 kg and the inside dimensions after freezing are 165 mm high, 530 mm long and 360 mm wide. The beef T_{if} is -0.8°C and the mass fractions of the beef basic components are: total water 68%, protein 19%, fat 12%, and other solids (ash) 1%. The thermal properties of the beef in the carton at -20°C are required.

The product item is the meat to be frozen inside the carton (the cardboard carton itself is assumed to affect the surface heat transfer coefficients rather than the thermal properties). It is anticipated that there are 2 mm wide air gaps between the beef and the carton on all faces except the bottom of the carton. Hence the product data is:

x_{tw} = 0.68 x_p = 0.19 x_{fat} = 0.12 x_{ash} = 0.01

T_{if} = -0.8°C T = -20°C product mass = 27.2 kg

product volume = (0.165-0.002) ×(0.36-2×0.002)×(0.53-2×0.002) = 0.03052 m^3

Step 1 – Initial Freezing Point: In this case T_{if} is known so Eq.(1) can be used to back-calculate the molality term if fat is ignored as a solute, after Eq.(4) is used to estimate the bound water:

$$x_{bw} = x_{tw}\left[0.342\left(1 \quad x_{tw}\right) \quad 4.510\ x_{ash} + 0.167\ x_p\right] = 0.68 \cdot \left[0.342\left(1 \quad 0.68\right) \quad 4.510 \cdot 0.01 + 0.167 \cdot 0.19\right] = 0.06533$$

$$\frac{1}{T_{if} + 273.15} = \frac{1}{273.15} \quad \frac{\mathrm{R}}{M_w L_w} \ln \frac{(x_{tw} \quad x_{bw})/M_w}{(w_{tw} \quad w_{bw})/M_w + \underset{j\ not\ w}{\quad} (x_j / M_j)}$$

$$\frac{1}{0.8 + 273.15} = \frac{1}{273.15} \quad \frac{8.314}{18.02 \cdot 333.5 \cdot 1} \ln \frac{(0.68 \quad 0.06533)/18.02}{(0.68 \quad 0.06533)/18.02 + \underset{j\ not\ w}{\quad} (x_j / M_j)}$$

$$(x_j / M_j) = 0.0002662 \quad \text{and taking} \quad x_j = 1 \quad 0.68 \quad 0.12 = 0.20 \ \text{gives} \ M_j = 752$$

The net effect is that the 20% of the meat that is not water or fat, on average behaves like solute with a molecular weight of 752. These values might be able to be used to predict T_{if} for similar meat products with different water and fat contents.

Step 2 - Ice Fraction: The ice fraction is estimated from Eq.(2). At -20°C:

$$x_{ice} = \left(x_{tw} \quad x_{bw}\right)\ 1 \quad \frac{T_{if}}{T} = \left(0.68 \quad 0.06533\right)\ 1 \quad \frac{0.8}{20} = 0.5901$$

Thus the mass fraction of unfrozen water at -20°C is: $x_w = x_{tw} - x_{ice}$ = 0.68 – 0.5901 = 0.0899

Step 3 – Densities: Using the Table 1 equations the component densities at -20°C are:

$_{ice} = 919.5\ \mathrm{kg.m^{--}}$ $_{w} = 995.6\ \mathrm{kg.m^{--}}$ $_{p} = 1340.3\ \mathrm{kg.m^{--}}$ $_{fat} = 933.9\ \mathrm{kg.m^{--}}$ $_{ash} = 2429.4\ \mathrm{kg.m^{--}}$

The density of the beef at -20°Cwithout air voids is estimated using Eq.(6):

$$\frac{1}{_{solid}} = \quad \frac{x_j}{_j} = \frac{0.5901}{919.5} + \frac{0.0899}{995.6} + \frac{0.19}{1340.3} + \frac{0.12}{933.9} + \frac{0.01}{2429.4} \qquad _{solid} = 993.6\ \mathrm{kg.m^{-3}}$$

Step 4 – Volume Fractions: The volume fractions (excluding air voids) are estimated using Eq.(17):

$$v_{ice} = x_{ice}\frac{\rho_e}{\rho_{ice}} = 0.5901 \cdot \frac{993.6}{919.5} = 0.6377 \quad \text{Similarly, } v_w = 0.0897, v_p = 0.1409, v_{fat} = 0.1277, v_{ash} = 0.0041$$

Step 5 – Bulk Density and Porosity: The bulk (effective) density can be estimated from the mass and volume of the product and allows the porosity to be estimated from Eq.(7):

$$\rho_e = \frac{\text{mass}}{\text{volume}} = \frac{27.2}{0.03052} = 891.1 \text{kg.m}^{-3} \qquad \rho_e = \rho_{solid}(1 - v_{air}) = 993.6 \cdot (1 - v_{air}) \qquad v_{air} = 0.1031$$

Step 6 – Specific Heat Capacity: Using the Table 1 equations the component specific heat capacities at -20°C are:

$c_{ice} = 1.941 \text{kJ.kg}^{-}.\text{K}^{-}$ $c_w = 4.528 \text{kJ.kg}^{-}.\text{K}^{-}$ $c_p = 1.984 \text{kJ.kg}^{-}.\text{K}^{-}$ $c_{fat} = 1.953 \text{kJ.kg}^{-}.\text{K}^{-}$ $c_{ash} = 1.053 \text{kJ.kg}^{-}.\text{K}^{-}$

The effective heat capacity of the beef at -20°C is estimated using Eq.(8):

$$c_e = \sum_j c_j x_j + [L_w + (c_w - c_{ice})T](x_{tw} - x_{bw})\frac{T_{if}}{T^2}$$

$$= 1.941 \cdot 0.5901 + 4.528 \cdot 0.0899 + 1.984 \cdot 0.19 + 1.953 \cdot 0.12 + 1.053 \cdot 0.01$$

$$[333.5 + (4.528 - 1.941) \cdot (-20)] \cdot (0.68 - 0.06533) \cdot \frac{0.8}{(-20)^2} = 2.174 + 0.346 = 2.520 \text{ kJ.kg}^{-1}.\text{K}^{-1}$$

At -20°C, only 14% (0.346/2.520) of the effective heat capacity is due to the latent heat of some of the residual water freezing.

Step 7 – Thermal Conductivity: At -20°C the beef is a Class IV food (frozen and porous) so calculation of the effective thermal conductivity required a 3 stage calculation (Figure 2). Using the Table 1 equations the component thermal conductivities at -20°C are:

$k_{ice} = 2.385 \text{ W.m}^{-}.\text{K}^{-}$ $k_w = 0.533 \text{ W.m}^{-}.\text{K}^{-}$ $k_p = 0.154 \text{ W.m}^{-}.\text{K}^{-}$

$k_{fat} = 0.186 \text{ W.m}^{-1}.\text{K}^{-1}$ $k_{ash} = 0.300 \text{ W.m}^{-1}.\text{K}^{-1}$ $k_{air} = 0.0225 \text{ W.m}^{-1}.\text{K}^{-1}$

Eq.(11) is used to estimate k_I for the components other than ice or air. The volume fractions including ice are all divided by (1 - v_{ice}) so they sum to 100%:

$$k_I = \sum_j k_j v_j = \frac{0.533 \cdot 0.0897 + 0.154 \cdot 0.1409 + 0.186 \cdot 0.1277 + 0.300 \cdot 0.0041}{1 - 0.6377} = 0.2608 \text{ W.m}^{-1}.\text{K}^{-1}$$

Eq.(12) to (14) are used to add in the effect of ice to estimate the k_{II} value (frozen, non-porous):

$$G = \frac{(k_{ice} - k_I)^2}{(k_{ice} + k_I)^2 + k_{ice}k_I/2} = \frac{(2.385 - 0.2608)^2}{(2.385 + 0.2608)^2 + 2.385 \cdot 0.2608/2} = 0.6172$$

$$F = \frac{2/G - 1 + 2(1 - v_{ice}) - \sqrt{[2/G - 1 + 2(1 - v_{ice})]^2 - 8(1 - v_{ice})/G}}{2}$$

$$= \frac{2/0.6172 - 1 + 2 \cdot (1 - 0.6377) - \sqrt{[2/0.6172 - 1 + 2 \cdot (1 - 0.6377)]^2 - 8 \cdot (1 - 0.6377)/0.6172}}{2} = 0.4707$$

$$k_{II} = k_{ice}\frac{2k_{ice} + k_I - 2(k_{ice} - k_I)F}{2k_{ice} + k_I + (k_{ice} - k_I)F}$$

$$= 2.385 \cdot \frac{2 \cdot 2.385 + 0.2608 - 2 \cdot (2.385 - 0.2608) \cdot 0.4707}{2 \cdot 2.385 + 0.2608 + (2.385 - 0.2608) \cdot 0.4707} = 1.199 \text{ W.m}^{-1}.\text{K}^{-1}$$

Finally, Eq.(16) is used to estimate k_{IV} including the effect of the air voids:

$$k_{IV} = \frac{(3v_{air} - 1)k_{air} + [3(1 - v_{air}) - 1]k_{II} + \sqrt{\{(3v_{air} - 1)k_{air} + [3(1 - v_{air}) - 1]k_{II}\}^2 + 8k_{II}k_{air}}}{4}$$

$$= \frac{(3 \cdot 0.1031 - 1) \cdot 0.0225 + [3 \cdot (1 - 0.1031) - 1] \cdot 1.199}{4}$$

$$+ \frac{\sqrt{\{(3 \cdot 0.1031 - 1) \cdot 0.0225 + [3 \cdot (1 - 0.1031) - 1] \cdot 1.199\}^2 + 8 \cdot 1.199 \cdot 0.0225}}{4} = 1.019 \text{ W.m}^{-1}.\text{K}^{-1}$$

The full set of properties for the meat carton product across the temperature range from -40°C to 20°C is shown in Figure 1. The effective heat capacity is expressed as a volumetric value (i.e. the product of effective density and effective specific heat capacity).

5. CONCLUSIONS

Methods to predict the thermal properties of refrigerated foods from information about their composition only are presented. The methods utilise mechanistic rather than empirical models whenever possible so that they are more likely to be generally applicable. Advice and methods to taken into account air voids (porosity) and packaging are provided including how to define the product item for composite systems such as cartons or pallets of packaged food products. For well-defined product geometries and composition, the predictions should be accurate within ±10% for non-porous food (slightly less accurate for frozen foods) and ±20% for porous foods which is sufficiently accurate for most heating and cooling process analysis purposes.

ACKNOWLEDGEMENTS

The synthesis of the ideas and methods presented in this paper have been developed over a long period of time and many research programmes at Massey University and research collaborators. I would like to acknowledge the contribution of my colleagues to the ideas that are summarised in this paper particularly James Carson, Jianfeng Wang, Andrew Cleland, Mike North, Simon Lovatt, David Tanner, Tuan Pham, Nevin Amos, Jim Willix, TC Chadderton and Richard Love.

NOMENCLATURE

b	bound water coefficient	*air*	air
c	specific heat capacity ($J.kg^{-1}.K^{-1}$)	*ash*	ash
F,G	intermediate variables (Eq. 13 & 14)	*bw*	bound water
h	enthalpy ($J.kg^{-1}$)	*carb*	carbohydrate
k	thermal conductivity ($W.m^{-1}.K^{-1}$)	*e*	effective
L	latent heat of fusion ($J.kg^{-1}$)	*fat*	fat
R	gas constant (8.314 $J.mol^{-1}.K^{-1}$)	*fibre*	fibre
v	volume fraction	*ice*	ice
ρ	density ($kg.m^{-3}$)	*if*	initial freezing point
M	molecular weight ($g.mol^{-1}$; Da)	*j*	jth component
T	temperature (^oC)	*p*	protein
x	mass fraction	*solid*	food without air voids
Subscripts		*t*	total
I,II,III,IV	food class (Section 2.6)	*w*	water (unfrozen)

REFERENCES

ASHRAE 2018. ASHRAE Handbook of Refrigeration. American Society of Heating Refrigeration and Air-conditioning Engineers, Atlanta GA.

Boonsupthip, W., Heldman, D.R., 2007. Prediction of Frozen Food Properties during Freezing Using Product Composition. J. Food Science, 72, E254-E263.

Carson, J.K., 2006. Review of effective thermal conductivity models for foods. Int. J. Refrigeration, 29, 958–967.

Carson, J.K., 2017. Use of simple thermal conductivity models to assess the reliability of measured thermal conductivity data. Int. J. Refrigeration, 74, 458–464.

Carson, J.K., Wang, J., North, M.F., Cleland, D.J., 2016. Effective thermal conductivity prediction of foods using composition and temperature data. J. Food Engineering, 175, 65-73.

Chen, C.C., 1985. Thermodynamic analysis of the freezing and thawing of foods: ice content and Mollier diagram. J. Food Science, 50, 1163-1166.

Choi, Y., Okos, M.R., 1986. Effects of temperature and composition on the thermal properties of foods. In: Le Mageur, M., Jelen, P., Food Engineering and Process Applications, Elsevier Applied Science, London, 93-101.

Cogné, C., Andrieu, J., Laurent, P., Besson, A., Nocquet, J., 2003. Experimental data and modelling of thermal properties of ice creams. J. Food Engineering, 58, 331-341.

Datta, A.K., 2007. Porous media approaches to studying simultaneous heat and mass transfer in food processes. II: Property data and representative results. J. Food Engineering, 80, 96-110.
Datta, A.K., 2016. Towards computer-aided food engineering: Mechanistic frameworks for evolution of product quality and safety during processing. J. Food Engineering, 176, 9-27.
Fikiin, K.A., 1998. Ice content prediction methods during food freezing: a survey of the Eastern European literature. J. Food Engineering, 38, 331-339.
Gulati, T., Datta, A.K., Enabling computer-aided food process engineering: Property estimation equation for transport phenomena-based models. J. Food Engineering, 116, 483-504.
Ho, Q.T., Carmeliet, J., Datta, A.K., Defraeye, T., Delele, M.A., Herremans, E., Opara, L., Ramon, H., Tijskens, E., van der Sman, R., van Liedekerke, P., Verboven, P., Nicolai, B.M., 2013. Multiscale modelling in food engineering. J. Food Engineering, 114, 279-291.
Larkin, J.L., Heldman, D.R., Steffe, J.F., 1984. An analysis of factors influencing precision of thermal property values during freezing. Int. J. Refrigeration, 7, 86-92.
Levy, F.L., 1981. A modified Maxwell–Eucken equation for calculating the thermal conductivity of two-component solutions or mixtures. Int. J. Refrigeration, 4, 223–225.
Miles, C.A., Mayer, Z., Morley, M.J., Houska, M. 1997. Estimating the initial freezing point of foods from composition data. Int. J. Food Science & Technology, 32, 389-400.
Murakami, E.G., Okos, M.R., 1989. Measurement and prediction of thermal properties of foods. In: Singh, R.P., Medina, A.G., Food Properties and Computer Aided Engineering of Food Processing Systems, Kluwer Academic Publishers, New York, 3–48.
Murakami, E.G., Okos, M.R., 1996. Calculation of initial freezing point, effective molecular weight and unfreezeable water of food materials from composition and thermal conductivity data. J. Food process Engineering, 301-320.
Nesvadba, P., Houska. M., Wolf, W., Gekas, V., Jarvis, D., Sadd, P.A., Johns, A.I., 2004. Database of physical properties of agro-food materials. J. Food Engineering, 61, 497–503.
Pham, Q.T., 1987. Calculation of bound water in frozen food. J. Food Science, 52, 210-212.
Pham, Q.T., 1996. Prediction of calorimetric properties and freezing time of foods from composition data. J. Food Engineering, 30, 95–107.
Pham, Q.T., 2014. Food Freezing and Thawing Calculations, Springer, New York.
Phinney, D.M., Frelka, J.C., Heldman, D.R., 2017. Composition-based prediction of temperature-dependent thermophysical food properties: reevaluating component groups and prediction models. J. Food Science, 82, 6-15.
Rao, M.A., Rizvi, S.S.H., Datta, A.K., 2005, Engineering Properties of Foods, 3rd edition. Taylor & Francis, Boca Raton, FL.
Rahman, M.S., 2009. Food Properties Handbook, 2nd Edition, CRC Press, Boca Raton.
Schwartzberg, H., 1976. Effective heat capacities for the freezing and thawing of foods, J. Food Science, 41, 152-156.
Shitzer, A., 2006. Wind-chill-equivalent temperatures: regarding the impact due to the variability of the environmental convective heat transfer coefficient. Int. J. Biometerology, 50, 224-232.
Wang, J.F., Carson, J.K., North, M.F., Cleland, D.J., 2010. Prediction of thermal conductivity for frozen foods with air voids. Proceedings 1st IIR International Cold Chain Conference, Cambridge, UK, Paper #173.
Willix, J., Lovatt, S.J., Amos, N.D., 1998. Additional thermal conductivity values of foods measured by a guarded hot plate. J. Food Engineering, 37, 159–174.

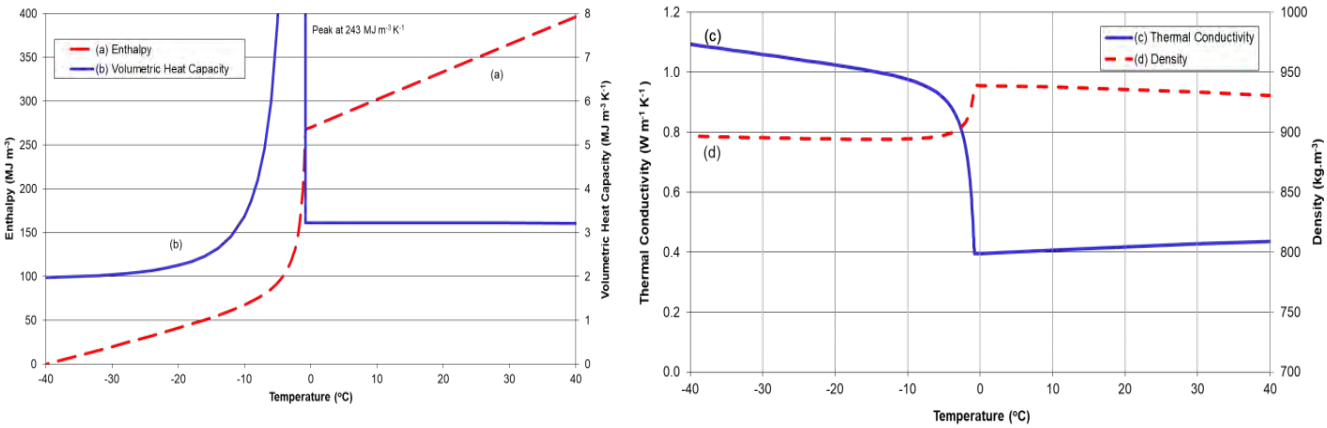

Figure 1: Thermal properties as a function of temperature for a typical high moisture food with air voids (worked example).

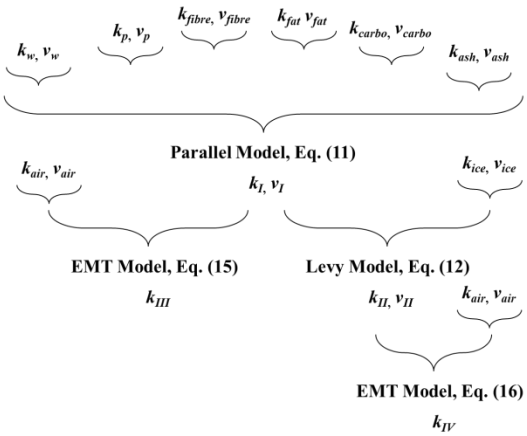

Figure 2: Schematic representation of the sequential approach for predicting the thermal conductivity of foods for the four classes of foods.

Table 1. Thermal properties of major components of foods (adapted from Choi & Okos, 1986)

Property	Component	Temperature Dependent Prediction Equation	Constant
Density ρ_j ($kg.m^{-3}$)	Water	$= 9.9718 \cdot 10^{2} + 3.1439 \cdot 10^{-3} T \quad 3.7574 \cdot 10^{-3} T^{2}$	1000
	Ice	$= 9.1689 \cdot 10^{2} \quad 1.3071 \cdot 10^{-1} T$	920
	Protein	$= 1.3299 \cdot 10^{3} \quad 5.1840 \cdot 10^{-1} T$	1300
	Fat	$= 9.2559 \cdot 10^{2} \quad 4.1757 \cdot 10^{-1} T$	930
	Carbohydrate	$= 1.5991 \cdot 10^{3} \quad 3.1046 \cdot 10^{-1} T$	1500
	Fibre	$= 1.3115 \cdot 10^{3} \quad 3.6589 \cdot 10^{-1} T$	1300
	Ash	$= 2.4238 \cdot 10^{3} \quad 2.8063 \cdot 10^{-1} T$	2400
	Air	$= 1.3180 \quad 4.8312 \cdot 10^{-3} T \quad 1.1237 \cdot 10^{-5} T^{2} \quad 3.428 \cdot 10^{-7} T^{3}$	1.29
Specific Heat Capacity c_j ($kJ.kg^{-1}.K^{-1}$)	Water ($\theta>0^{o}C$)	$c = 4.1289 \quad 9.0864 \cdot 10^{-5} T + 5.4731 \cdot 10^{-6} T^{2}$	4.18
	Water ($\theta<0^{o}C$)	$c = 4.1289 \quad 5.3062 \cdot 10^{-3} T + 9.9516 \cdot 10^{-4} T^{2}$	4.28
	Ice	$c = 2.0623 + 6.0769 \cdot 10^{-3} T$	2.00
	Protein	$c = 2.0082 + 1.2089 \cdot 10^{-3} T \quad 1.3129 \cdot 10^{-6} T^{2}$	2.00
	Fat	$c = 1.9842 + 1.47339 \cdot 10^{-3} T \quad 4.8008 \cdot 10^{-6} T^{2}$	1.95
	Carbohydrate	$c = 1.5488 + 1.9625 \cdot 10^{-3} T \quad 5.9399 \cdot 10^{-6} T^{2}$	1.50
	Fibre	$c = 1.8459 + 1.8306 \cdot 10^{-3} T \quad 4.6509 \cdot 10^{-6} T^{2}$	1.80

	Ash	$c = 1.0926 + 1.8896 \cdot 10^{-3}T - 3.6817 \cdot 10^{-6}T^2$	1.05
	Air (Shitzer, 2006)	$c = 1.0051 + 8.64629 \cdot 10^{-7}T + 4.8700 \cdot 10^{-7}T^2 + 8.0004 \cdot 10^{-9}T^3 + 5.4 \cdot 10^{-11}T^4$	1.005
	Packaging	$c_{carboard} \quad 1.4; c_{plastic} \quad 1.6$	
Thermal Conductivity k_j (W.m^{-1}.K^{-1})	Water	$k = 5.7109 \cdot 10^{-1} + 1.7625 \cdot 10^{-3}T - 6.7036 \cdot 10^{-6}T^2$	0.54
	Ice	$k = 2.2196 - 6.2489 \cdot 10^{-3}T + 1.0154 \cdot 10^{-4}T^2$	2.35
	Protein	$k = 1.7881 \cdot 10^{-1} + 1.1958 \cdot 10^{-3}T - 2.7178 \cdot 10^{-6}T^2$	0.16
	Fat	$k = 1.8071 \cdot 10^{-1} - 2.7604 \cdot 10^{-4}T - 1.7749 \cdot 10^{-7}T^2$	0.19
	Carbohydrate	$k = 2.0141 \cdot 10^{-1} + 1.3874 \cdot 10^{-3}T - 4.3312 \cdot 10^{-6}T^2$	0.20
	Fibre	$k = 1.8331 \cdot 10^{-1} + 1.2497 \cdot 10^{-3}T - 3.1683 \cdot 10^{-6}T^2$	0.18
	Ash	$k = 3.2962 \cdot 10^{-1} + 1.4011 \cdot 10^{-3}T - 2.9069 \cdot 10^{-6}T^2$	0.30
	Air	$k = 2.4125 \cdot 10^{-2} + 7.9976 \cdot 10^{-5}T - 3.4657 \cdot 10^{-8}T^2$	0.024
	Packaging	$k_{carboard} \quad 0.07; k_{plastic} \quad 0.1$	
Latent Heat of Fusion L_j (kJ.kg^{-1})	Water	$L = 333.5 + (c_w - c_{ice})T$	334
	Fat	Depending on lipid profile, add mass-averaged latent heat to heat capacity across the melting/solidification temp. range	

Manuscript ID: 1746
DOI: 10.18462/iir.icr.2019.1746

Thermodynamics of the new refrigerants[1]

Mark O. McLINDEN[(a)]

[(a)]Applied Chemicals and Materials Division, National Institute of Standards and Technology
325 Broadway, Boulder, Colorado 80305 USA, markm@boulder.nist.gov

ABSTRACT

As the refrigeration industry moves towards refrigerants with low global-warming potential, the number of acceptable refrigerants is decreasing due to environmental constraints, but, at the same time, new options are becoming available. These "new" refrigerants include new molecules, such as the HFOs (hydrofluoroolefins) containing a carbon-carbon double bond, as well as some very "old" fluids, such as ammonia and carbon dioxide. The HFC (hydrofluorocarbon) refrigerants, although being phased down, remain in use—especially as blend components. Here, the thermodynamic characteristics that underpin the choice of a refrigerant are reviewed; together the environmental and thermodynamic constraints result in a limited number of suitable fluids. Refrigerants have differing thermodynamic characteristics, and these determine their relative performance in a refrigeration cycle. The design engineer must recognize and balance the tradeoffs presented by different refrigerants and design the system to best accommodate the properties of the chosen fluid.
Keywords: Ammonia, Carbon Dioxide, GWP, Hydrofluoroolefins, Refrigerants, Refrigeration Cycle, Thermodynamic Properties

1. INTRODUCTION

The Kigali Amendment to the Montreal Protocol, which mandates a phase-down of the production of hydrofluorocarbon (HFC) refrigerants, entered into force January 1, 2019. But even before this milestone was reached numerous regional and national regulations concerning the use of HFCs were already in place. For example, the "F-gas" regulations in the European Union (European Environment Agency, 2014) mandate maximum values of GWP (global warming potential) for refrigerants in various applications, as well as specifying training and reporting requirements. In the United States, the Significant New Alternatives Policy (SNAP) of the U.S. Environmental Protection Agency (US EPA, 2018) prohibits or allows specific refrigerants in various applications. The need to identify alternative low-GWP fluids is obvious.

This paper first provides a brief perspective on the environmental impacts of the HFCs and other refrigerants. The main discussion is on the thermodynamic characteristics of refrigerants; the focus is on "new" molecules, such as the hydrofluoroolefins (HFOs), but "old" fluids (*e.g.*, CO_2, ammonia, and hydrocarbons) that might be "new" to particular application areas are also discussed. Results of previous searches for replacement fluids are summarized in Section 3, and the results of such studies are discussed in terms of fundamental thermodynamic properties. Section 4 discusses the thermodynamic underpinning of some of the trade-offs associated with the HFO refrigerants and with flammability, in particular. Means to adapt to the differing characteristics of "new" fluids are discussed in Section 5. Finally, brief conclusions are presented.

2. BACKGROUND—ENVIRONMENTAL PROPERTIES OF REFRIGERANTS

Emissions of HFCs currently account for only a small fraction of anthropogenic climate change—about 1 % of the total radiative forcing due to all greenhouse gases, including CO_2, CH_4, and N_2O (WMO, 2018). The Kigali Amendment and other regulations are driven by estimated large increases in future emissions predicted under "business as usual" scenarios (Velders *et al.*, 2009, 2015). With the HFC phasedown of the Kigali Amendment, Velders (2016) estimates that the surface temperature increase from HFCs will be limited to 0.06 K by the end of the century compared to 0.3 K to 0.5 K with "business as usual," as shown in Fig. 1.

[1] Contribution of the National Institute of Standards and Technology, not subject to copyright in the United States.

The environmental characteristics of selected refrigerants, as compiled by the World Meteorological Organization (WMO, 2018), are listed in Table 1. The GWP parameter was first presented by the Intergovernmental Panel on Climate Change (Houghton *et al.*, 1990) as a simple metric for comparing the impact of different gases on the climate system. The GWP of a gas is relative to that of carbon dioxide; furthermore, it is calculated over some time interval, or "time horizon." A time horizon of 100 years is most commonly used (including in regulations) and is referred to as GWP_{100}. Other time horizons are sometimes used, and Table 1 also lists the GWP_{20}—the value for a 20-year time horizon. For long-lived gases, such as R-12 (a chlorofluorocarbon or CFC), the GWP_{100} and GWP_{20} are similar. For gases with lifetimes on the order of a few decades or less (*e.g.*, the HFCs), however, the GWP_{20} is substantially higher than the GWP_{100} because the climate impact of such gases is concentrated in the initial years following their release into the atmosphere. When calculating over a longer time horizon, the impact in the later years is small, and the GWP_{100} basically "averages out" the impacts. This indicates that the short-term climate impact of the HFCs can be understated by their GWP_{100}. But it also underlies the opportunity for mitigating, by mid-century, the climate impacts of refrigerants by phasing down the HFCs: CO_2 is long-lived in the atmosphere, and so the benefits of any reduction in its emissions are damped by its existing concentration in the atmosphere. A phase-down of HFC emissions, on the other hand, has much more immediate benefits.

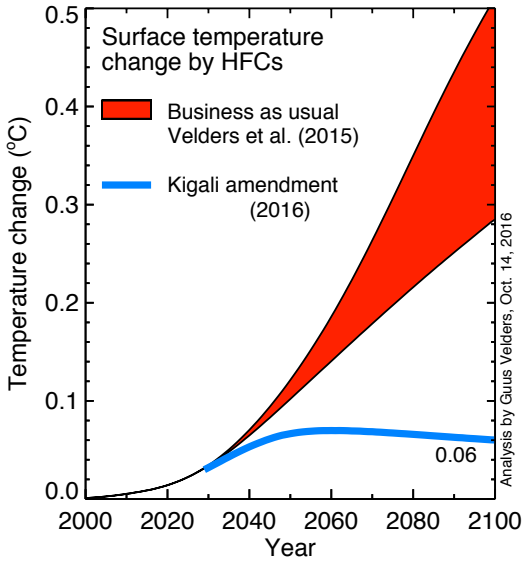

Figure 1. Projected global average surface temperature increase assuming compliance with the Kigali Amendment to the Montreal Protocol compared to "business as usual;" analysis of Velders (2016); figure used with permission.

Table 1. Environmental characteristics of selected refrigerants.†

R-number	Formula	T_{NBP} (°C)	Lifetime (years)	ODP	GWP_{20}	GWP_{100}
CFCs and HCFCs						
R-12	CCl_2F_2	–29.8	102	0.73–0.81	10800	10300
R-22	$CHClF_2$	–40.8	11.9	0.024–0.034	5310	1780
R-123	$CHCl_2CF_3$	27.8	1.3	0.01	290	80
HFCs						
R-32	CH_2F_2	–51.7	5.4	0	2530	705
R-125	CHF_2CF_3	–48.1	30	0	6280	3450
R-134a	CH_2FCF_3	–26.1	14	0	3810	1360
R-152a	CH_3CHF_2	–24.0	1.6	0	545	148
HFOs and HCFOs						
R-1233zd(E)	$CF_3CH=CHCl$	18.3	0.071	<0.0004	13.5	3.7
R-1234yf	$CF_3CF=CH_2$	–29.5	0.029	0	1	<1
R-1234ze(E)	$CF_3CH=CFH$	–19.0	0.045	0	4	<1
Natural fluids						
R-290	$CH_3CH_2CH_3$ (propane)	–42.1	0.041	0	<1	<1
R-717	NH_3 (ammonia)	–33.3	"few days"	0	<1	<1
R-744	CO_2 (carbon dioxide)	–56.6‡	–	0	1.00	1.00

†Environmental data from WMO (2018); T_{NBP} from REFPROP (Lemmon *et al.*, 2018).

‡Triple-point temperature

While the many of the HFCs have high values of GWP, recall that they were developed and implemented to replace ozone-depleting substances (ODSs), primarily the CFCs and HCFCs. Many of the CFCs and HCFCs also have high values of GWP (see Table 1); for example the GWP_{100} of the refrigerant in automotive systems was reduced by a factor of 7.5 (10300 to 1360) when R-12 was replaced with R-134a. Thus, the Montreal Protocol, which was originally targeted at stratospheric ozone protection, has already had a tremendously positive impact on climate, as reported by Velders *et al.* (2007). In that analysis, Velders *et al.* consider a scenario in which the 1987 Montreal Protocol (and subsequent amendments) was not implemented. Without any action, the radiative forcing (*i.e.*, impact on climate) of the ODSs would have been comparable to CO_2 emissions by 2010. Instead, the actual emissions of the ODSs peaked in 1988 at an equivalent equal to 43 % of that of CO_2 emissions. Even today, R-12 remains the fourth-most powerful greenhouse gas because of past emissions, behind CO_2, methane, and N_2O (WMO, 2018). By 2010 the Montreal Protocol had avoided emissions of approximately 10 Gt CO_2[eq] (*i.e.*, emissions equivalent to 10 gigatonnes of CO_2) per year; by comparison, global CO_2 emissions from fossil fuels and industrial processes were 32 Gt per year in 2010 (IPCC 2014). Put another way, the Montreal Protocol has delayed climate change by 7–12 years, according to Velders *et al.* (2007).

Thus, by rapidly phasing out the CFCs and other ODSs in the 1990s, the refrigeration industry has already avoided substantial climate impacts, and with the HFC phasedown called out in the Kigali Amendment to the Montreal Protocol the industry will make further substantial contributions.

3. REPLACEMENT FLUIDS

The objective of a refrigeration system is not to circulate a fluorinated chemical around a cycle with various changes in phase, but rather to move heat from a lower to a higher temperature to accomplish a useful purpose—keeping food from spoiling (*i.e.*, refrigeration), providing a comfortable living environment in a warm climate (*i.e.*, air conditioning), or providing efficient space heating (*i.e.*, heat pumping). Are replacement fluids required at all? Might there be alternative means of providing the desired heat transfer? Indeed, various alternative technologies (termed “not-in-kind replacements”) are possible, and these have been summarized by Goetzler *et al.* (2014). These technologies have been known for many years (even decades), yet vapor-compression refrigeration technology dominates the market because it is efficient, reliable, and cost-effective. While not-in-kind technologies must be continually evaluated, the most prudent path would seem to be finding more-or-less direct replacements for the high-GWP refrigerants so that the existing industrial base for manufacturing, installing, and servicing refrigeration equipment can (with, perhaps, some modifications) be retained.

3.1. Requirements of a Refrigerant

The requirements of a replacement refrigerant have been considered by numerous authors including McLinden and Didion (1987), Calm and Didion (1997), and Kujak and Schultz (2016). Always at the top of the list is the need for chemical stability within the sealed refrigeration system; next are health and safety considerations. Environmental considerations (*e.g.*, ODP and GWP) are obviously important—they are the reason new fluids are currently under consideration. Practical requirements such as cost and materials compatibility also factor in.

A refrigerant must also possess certain thermodynamic characteristics for it to function. Since a refrigerant absorbs and releases heat primarily through evaporation and condensation, a high latent heat of vaporization might seem to be desirable. A boiling point temperature low enough that air will not leak into a system is desirable; but the boiling point should not be so low that the system pressures are “too high.” A high discharge temperature upon compression will lower the efficiency of the cycle, but conversely, “wet compression” must be avoided in most types of compressors.

3.2. Exploration of Thermodynamic Space

But how are these seemingly disparate thermodynamic characteristics related, and how is one to identify a refrigerant satisfying them? McLinden *et al.* (2012) and Domanski *et al.* (2014) approached this problem by defining fluids in terms of a small number of fundamental thermodynamic characteristics. Thus, they considered the full range of possible thermodynamic behaviour, rather

than scanning a finite number of known fluids (which would reveal no new fluids). They termed this approach the "exploration of thermodynamic space."
The fluid thermodynamic properties were modeled by an "extended corresponding states" (ECS) approach (Huber and Ely, 1994). Corresponding states is the observation that the properties of fluids are similar when scaled by their critical point parameters, T_c and p_c, where the critical point is the state where the saturated liquid and saturated vapor approach one another. Key to this method is a "reference fluid" to which the properties of the unknown fluid are scaled. This method is "extended" by additional parameters; the most significant were the heat capacity of the vapor (C_p°) and the acentric factor, ω, which is related to the slope of the vapor pressure curve. The range of the parameters considered is given in Table 2. The critical temperature is not as familiar as the normal boiling point temperature, T_{NBP}, but the two are related, and here both are used. (Other parameters were considered, but they were found to be of minor importance. (Domanski *et al.*, 2014))

Table 2. Fluid parameters varied in the optimization runs and their ranges.

Parameter	Units	Range
reference fluid	–	propane –or– R-32
T_c	K	305 ~ 650
p_c	MPa	2.0 ~ 12.0
ω	–	0.0 ~ 0.6
C_p°(300 K)	J·mol^{-1}·K^{-1}	20.8 ~ 300

3.3. Optimum Thermodynamic Characteristics

Any optimization requires objective function(s), and the coefficient of performance (COP) and volumetric capacity (Q_{vol}) were selected for a cycle operating between an evaporation temperature of 10 ˚C and a condensation temperature of 40 ˚C.
This exploration of thermodynamic space indicated a trade-off between efficiency and volumetric capacity. Refrigerants with a high critical temperature gave high efficiency, but low capacity; fluids with a relatively low T_c resulted in the converse. A critical pressure at the upper limit of the range resulted in both high efficiency and high capacity, while an acentric factor near the lower limit was optimal. The optimum value of the vapor heat capacity varied with the cycle; a relatively low value was best for the simple vapor compression cycle, while a higher value was optimal for a cycle with internal heat exchange between the condenser outlet and compressor inlet. These results are presented in Fig. 2; a clear efficiency-versus-capacity tradeoff is seen for both the simple vapor-compression cycle (Fig. 2(a)) and the cycle with internal heat exchange (Fig. 2(b)). Fig. 2 also shows the "Pareto front" comprising the set of hypothetical fluids having thermodynamic parameters offering the highest COP for a given Q_{vol} and vice-versa; this defines the upper limit of performance that is allowed by thermodynamics. (The inverse of COP and Q_{vol} are plotted to yield a minimization, which is the convention for this type of problem.) For selected "real" refrigerants, the cycle with the LL/SL heat exchanger shows a much smoother variation of COP versus Q_{vol} compared to the simple cycle.

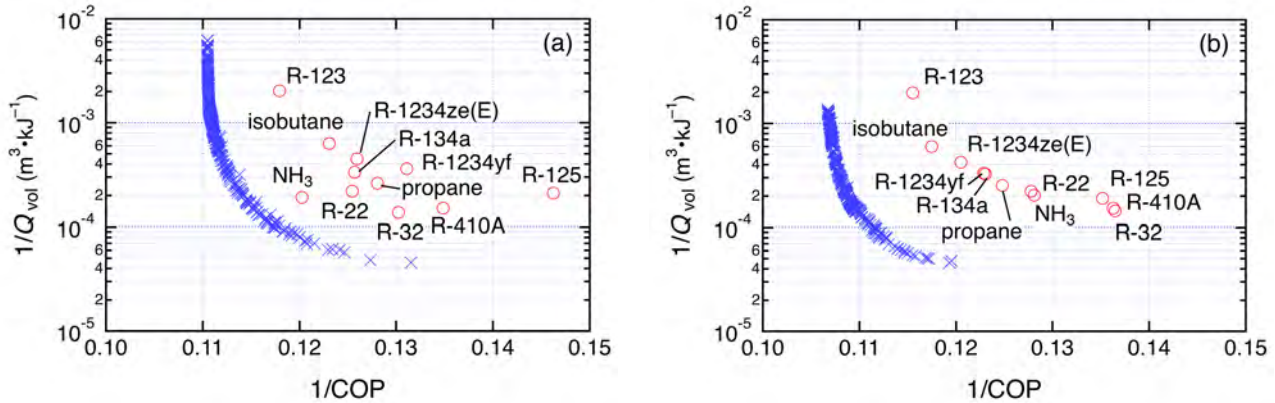

Figure 2. Pareto front (×) and selected current refrigerants (○) for different cycle options: (a) simple vapor compression cycle; (b) cycle with 100 % effective LL/SL heat exchanger; figure from McLinden et al. (2012).

These effects can be understood by examining the vapor-compression cycle on diagrams of temperature versus entropy (T–s) or pressure versus enthalpy (p–h). Figure 3(a) contrasts R-134a (T_c = 374 K) with R-123 (T_c = 457 K) on (T–s) coordinates. Shown is the ideal cycle, *i.e.*, a cycle with compression at constant entropy, expansion at constant enthalpy, zero pressure drop in the condenser and evaporator, and saturated vapor entering the compressor; shown is a cycle with an evaporation temperature of –20 ˚C and a condensation temperature of 30 ˚C. As the cycle moves to a lower temperature relative to the critical temperature the width of the vapor dome increases, providing a larger refrigeration effect per unit mass of refrigerant. The potential refrigeration effect lost in the expansion process (as a percentage of the total heat of vaporization) decreases. Both of these effects increase the efficiency of the cycle.

The effect of critical pressure is shown on (p–h) coordinates in Figure 3(b), which compares R-134a with ammonia. While the normal boiling point temperatures of R-134a and ammonia are similar (T_{NBP} = 247.1 K for R-134a versus T_{NBP} = 239.8 K for ammonia) the critical pressure of ammonia (p_c = 11.4 MPa) is nearly three times that of R-134a (p_c = 4.06 MPa); the result is that, the cycle is pushed "lower" in the vapor dome, which somewhat analogous to the effect of T_c seen in Figure 3(a).

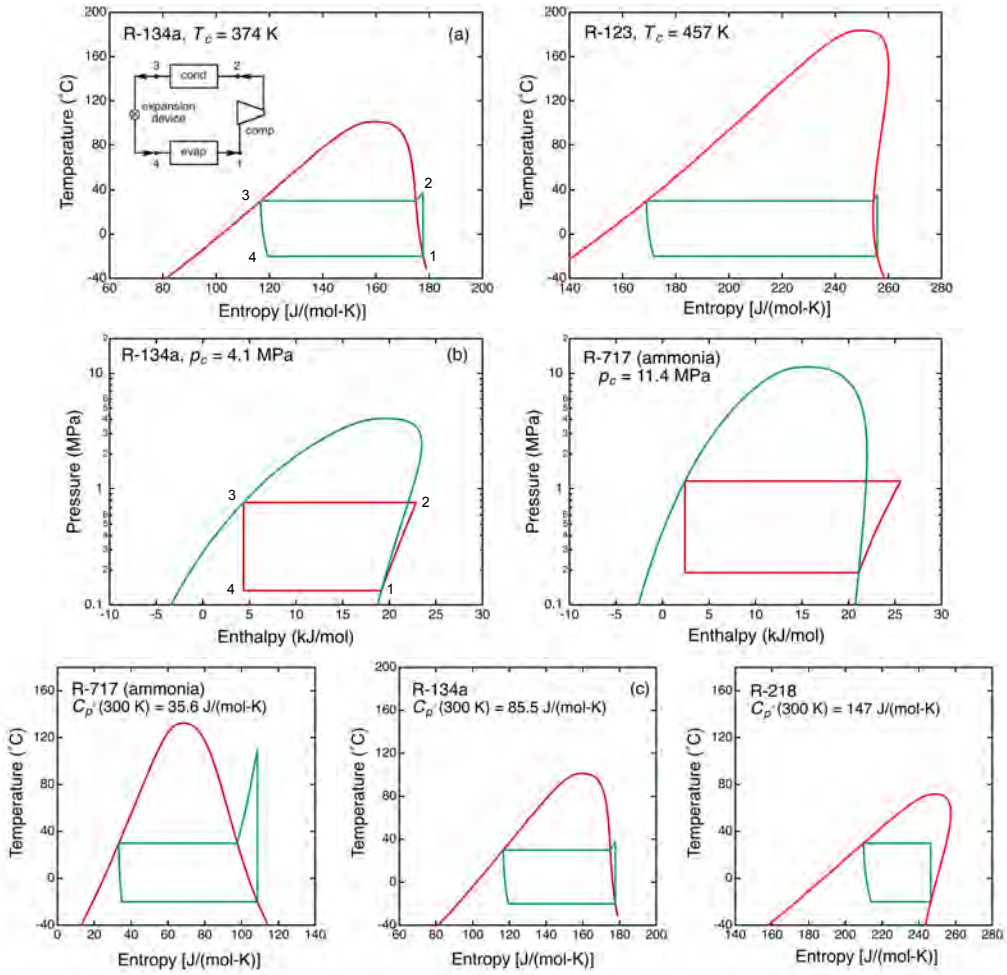

Figure 3. Effect of thermodynamic parameters on the shape of the saturation dome; (a) effect of critical temperature, T_c, on (T–s) coordinates; (b) effect of critical pressure, p_c, on (p–h) coordinates; (c) effect of vapor molar heat capacity, C_p^0, on (T–s) coordinates.

The effect of the vapor heat capacity is shown in Figure 3(c), which compares ammonia, R-134a, and R-218; for these fluids the C_p° (at T = 300 K) varies from 35.6 J·mol^{-1}·K^{-1} to 147 J·mol^{-1}·K^{-1}. With the low C_p° of ammonia the vapor dome is "upright;" this results in a high compressor discharge temperature (which decreases efficiency), but the expansion losses are relatively small (increasing efficiency). As the value of C_p° increases the vapor dome increasingly "leans over." With the high C_p° of R-218 the result is "wet compression" (where an isentropic compression process starting with saturated vapor would result in a two-phase state exiting the compressor); the saturated-liquid (left) side of the saturation dome is also much more tilted, resulting in increased expansion losses. The result of these offsetting effects is that there is an optimal value of C_p° for a given cycle; in this

example the C_p° of R-134a is near optimal for the simple vapor compression cycle. For a cycle with a liquid-line/suction-line heat exchanger, the optimum shifts to a higher value of C_p° as discussed by McLinden (1990) and Domanski (1995). C_p° stems from intramolecular degrees of freedom, with each mode of internal vibration, bending, etc. adding to C_p°. The magnitude of each contribution increases with the mass of the atoms involved, so that, for example, substituting a fluorine for a hydrogen will increase the C_p°. These effects and the relationship between C_p° and the shape of the saturation dome are discussed by Morrison (1994).

The comparisons in the previous three paragraphs were on a molar basis, rather than the mass basis familiar in the refrigeration field. A molar basis is often the natural choice when discussing fluid properties. Ammonia is well known for having a large enthalpy of vaporization (on a mass basis) compared to other refrigerants, as shown in Fig. 4(a). On a molar basis, however, ammonia has only a slightly higher enthalpy of vaporization (Fig. 4(b)). The large enthalpy of vaporization per kilogram of ammonia is largely due to its low molar mass (17.03 g·mol^{-1} for ammonia, 44.10 g·mol^{-1} for propane, and 102.03 g·mol^{-1} for R-134a). The enthalpy of vaporization on a molar basis of a fluid at its boiling point is approximately proportional to the normal boiling point temperature; this was observed by Trouton (1884) and is known as Trouton's rule.

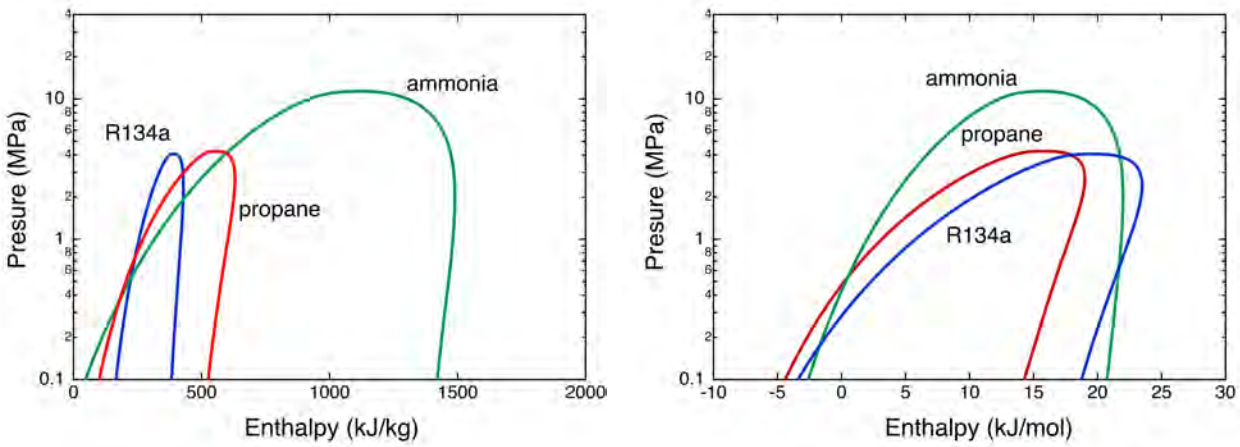

Figure 4. Saturation dome on (*p–h*) coordinates for three refrigerants; (a) mass basis; (b) molar basis.

The above analysis assumed an ideal cycle with zero pressure drop in the condenser and evaporator. With the inclusion of pressure drop and heat-transfer limitations (*i.e.*, consideration of the transport properties of viscosity and thermal conductivity), however, the situation can be quite different. Fig. 5 shows the results of cycle simulations carried out by McLinden *et al.* (2017) for a cycle typical of air conditioning (T_{cond} = 10 ˚C and T_{evap} = 40 ˚C) and which included a simplified and generalized pressure drop model; the COP versus capacity tradeoff has disappeared. Instead, there is a broad optimum in COP corresponding to medium-to-high pressure refrigerants. This was also discussed by Domanski *et al.* (2017).

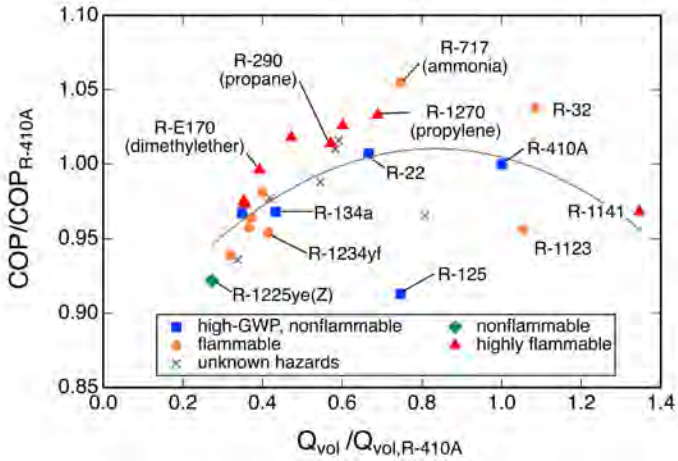

Figure 5. COP and Q_{vol} of selected low-GWP fluids in the basic vapor-compression cycle relative to R-410A including pressure drop and heat-transfer limitations; the curve indicates the general trend; figure adapted from McLinden *et al.* (2017).

3.4. Database Screenings

The purpose of the "exploration of thermodynamic space" was to define the desired thermodynamic characteristics of a refrigerant. Combining those parameters with desired environmental characteristics (*i.e.*, low GWP and zero, or near-zero, ODP) of a refrigerant, Kazakov *et al.* (2012) and McLinden *et al.* (2014, 2017) carried out a series of database screenings to identify fluids having those characteristics. These made use of the PubChem database (Kim *et al.*, 2016), a public-domain listing of more than 60 000 000 chemicals.

Flammability was estimated in the 2012 screening and highly flammable fluids were eliminated. Toxicity was also estimated based on a set of "markers and associated rules." At this point the critical parameters were estimated and those with $300 < T_c < 550$ K were retained; finally, chemical groups known to be generally unstable were screened out, resulting in ~1200 candidate fluids. The analysis of McLinden *et al.* (2014) built upon these 1200 candidate fluids and down-selected to a set of 62 fluids based primarily on $T_c < 400$ K and other thermodynamic characteristics; after considering toxicity and stability in more detail, only about a dozen candidates remained.

Because of the dearth of fluids with characteristics similar to R-410A McLinden *et al.* (2017) carried out a second screening. Here, flammable fluids were not automatically screened out, and the initial screen was $320 < T_c < 420$ K; only 138 fluids were identified. This number was small enough to permit a "manual" examination of toxicity and stability. Cycle calculations were also carried out, and fluids with low COP and/or volumetric capacity were screened out. The final result was a list of 27 fluids; these comprised hydrocarbons, HFCs, HFOs, CO_2, ammonia, and a total of five compounds with oxygen, nitrogen and/or sulfur.

3.5. Other Fluids

The database search of McLinden *et al.* (2017) resulted in a list of 27 fluids with the assertion that it would be "highly unlikely that any better-performing fluids will be found." The list already included several fluids that failed the stated screening criteria, but were added because of commercial interest. These included R-1123; it was identified as unstable (Tanaka *et al.*, 2014), but a blend with R-32 may be stable (Hashimoto et al., 2019). Have any additional fluids been identified in the intervening time? Domanski *et al.* (2017) added R-1132a to the list. This fluid was included in the original screening but was rejected based on an indication of high toxicity (NIOSH, 2007); later data resulted in a "class A" toxicity rating (ASHRAE, 2017).

The iodine-containing CF_3I has generated considerable interest recently as a low-GWP option that might be used to suppress the flammability of blends (McGowan, 2019). An application to classify CF_3I as "A1" (low-toxicity, nonflammable) under ASHRAE Standard 34 has been submitted (ASHRAE, 2018). This fluid was considered by Kazakov *et al.* (2012). The C–I bond is very weak, and is readily photolyzed by UV light; thus, it did not fit within the estimation scheme for GWP developed by Kazakov. CF_3I and other iodine-containing compounds were investigated in the 1990s during the search for CFC replacements (Calm 2012, Nimitz and Lankford 1994) and again in the early 2000s in the program sponsored by the Society of Automotive Engineers to identify

replacements for R-134a in automotive air-conditioning systems (Brown, 2013). Interest waned in the iodine-containing compounds on both occasions because of stability and toxicity concerns. Thus, iodine was not included in the list of eight elements making up the fluids in the database searches of Kazakov *et al.* (2012) and McLinden *et al.* (2014, 2017).

But why are there no other fluids? In organic chemistry, molecules are categorized by the functional group(s) they possess. The HFCs belong to the fluorinated alkane category. The alkanes comprise one or more carbon atoms with hydrogens attached to each carbon as needed to satisfy the requirement that each carbon atom be bonded to four neighbors. In the fluorinated alkanes, some of the hydrogens are simply replaced by fluorine. The alkenes (also known as olefins) are a variation on the alkanes with one or more of the carbon-carbon bonds replaced with a double bond, with each double bond "counting" as two neighbors.

Many other functional groups are well known, and some of these are shown in Figure 6. These are, for the most part, not suitable as refrigerants in moderate-to-high pressure systems because the normal boiling points for even the simplest examples are too high. The simplest alcohol, for example, is methanol with T_{NBP} = 65 ˚C. Acetone is the simplest ketone with T_{NBP} = 56 ˚C. Substitution of hydrogen with other atoms generally increases the boiling point. Functional groups with T_{NBP} low enough to serve as the basis for moderate-to-high-pressure refrigerants include the ethers (C-O-C) and the amines (comprising a central nitrogen with three attached groups). All such compounds were included in the database searches, but apart from dimethyl ether, ammonia, and a very few others, they were rejected because of high GWP_{100}, high T_c, or other factors.

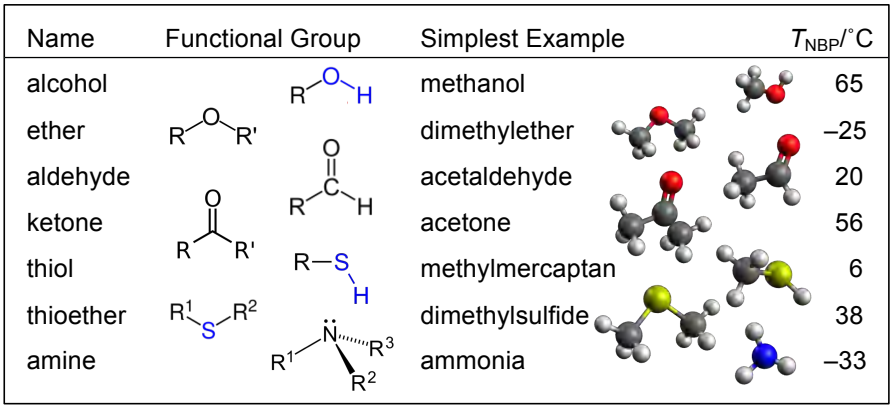

Figure 6. Selected functional groups of organic chemistry containing oxygen, sulfur, or nitrogen, with the simplest example of each also shown; R, R', R^1, R^2, R^3 indicate attached hydrogens or alkyl groups.

4. TRADEOFFS

When Midgley famously introduced R-12 at the 1930 meeting of the American Chemical Society by inhaling a lungful of the refrigerant and using it to extinguish a burning candle (Midgley and Henne, 1930; Downing, 1988), it seemed that the perfect refrigerant had been found. It was nonflammable, of low toxicity, and was simple and cheap to manufacture. It had good thermodynamic properties, and, in fact, its properties were nearly a perfect match to the simple vapor-compression cycle (McLinden, 1990). But, of course, it was later found to deplete stratospheric ozone and have a high GWP. Since the mid-1970s the task of identifying suitable refrigerants has faced an increasing list of constraints. So, while these constraints have restricted the choice of fluids (*e.g.*, CFCs and HCFCs are no longer available), they have also opened up interest in other fluids. The phaseout of the ozone-depleting fluids, for example, sparked a resurgence of interest in the long-known natural fluids (*e.g.*, ammonia, hydrocarbons). Likewise, the lack of an obvious low-GWP, nonflammable, high-pressure replacement for some of the HFCs has opened a discussion on how fluids with at least some degree of flammability might be safely implemented in a wider variety of systems.

4.1. Hydrofluoroolefins

The hydrofluoroolefins (HFOs) are the focus of intense development efforts by the refrigeration industry, and the carbon-carbon double bond that defines the chemical class of "olefin" is at the heart of the trade-offs seen with the HFOs. It is the reactivity of the double bond to the atmospheric

hydroxyl radical that results in the very low atmospheric lifetimes and GWP values of the HFOs. The reactivity of the olefins, both in the atmosphere and in refrigeration equipment, is discussed by Kujak and Sorenson (2018).

The most-common HFC refrigerants (R-134a, R-125, R-32, etc.) are based on one or two carbon atoms, and several have a T_{NBP} in a suitable range, see Figure 7. The two-carbon HFOs, on the other hand, have normal boiling point temperatures that are too low for most refrigeration applications, as shown in Fig. 7(a). R-1132(Z) and R-1132(E) have T_{NBP} in a desirable range, but very little data are available on these two fluids, and even the values of T_{NBP} plotted in the figure are estimated values (McLinden *et al.*, 2014). Thus, most of the development efforts are focused on the three-carbon HFOs, and here there are a number of fluids with –40 ˚C < T_{NBP} < –20 ˚C; see Fig. 7(b). But a three-carbon HFO is a more complicated molecule than a one- or two-carbon HFC, and this results in a higher vapor molar heat capacity and a vapor dome that is "skewed" to the right. This has implications for the optimal cycle as discussed in Section 3.3.

The best-known HFO is R-1234yf, and this fluid is "marginally flammable" with an ASHRAE Standard 34 flammability classification of "2L" (ASHRAE, 2016a). There is often the perception that some degree of flammability is inevitable with the HFOs. Figure 7 indicates flammability and shows that this is not true, but that, compared to the HFCs, additional fluorines are needed with the HFOs to offset the flammability of the carbon-carbon double bond. For example, the four fluorines of R-134a are sufficient to yield a nonflammable fluid, while the four fluorines on R-1234yf are not; the three-

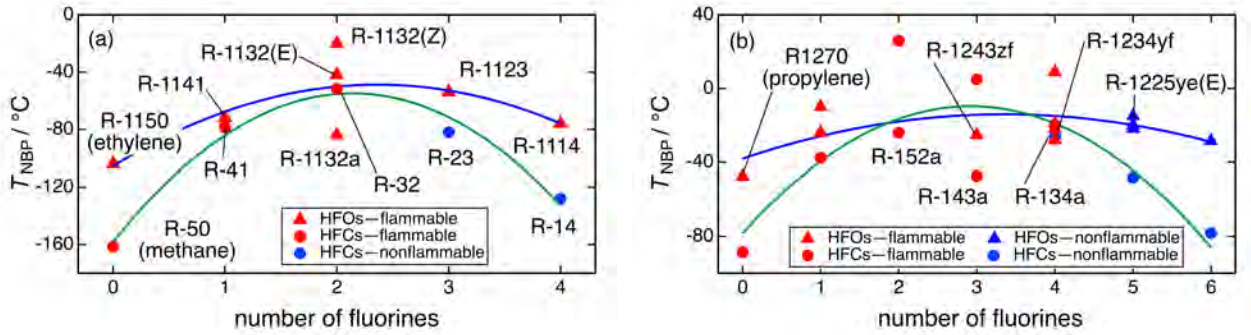

Figure 7. Variation of normal boiling point temperature T_{NBP} with the number of fluorines on the molecule;
(a) one-carbon HFCs and two-carbon HFOs; (b) two-carbon HFCs and three-carbon HFOs.
The curves indicate the general trends in T_{NBP}. Flammability is indicated with a color code.

carbon HFOs require five fluorines for nonflammability (*e.g.*, R-1225ye(E)). For the two-carbon HFOs even the fully fluorinated R-1114 is flammable. The situation with the four-carbon HFOs is better; for example R-1336mzz(Z), with six of the eight hydrogens replaced with fluorine, is nonflammable.

4.2. Flammability versus GWP

Among the HFCs, a trade-off between flammability and GWP is somewhat inevitable. Flammability is determined by both thermodynamic and kinetic considerations. Flammability is the reaction of a material with oxygen, with the release of heat. A reaction is thermodynamically favorable when the change in Gibbs free energy (G) of the products compared to the reactants (*i.e.*, oxygen plus refrigerant as the "fuel") is negative; $G = H - TS$ so that:

$$\Delta G = (H - TS)_{products} - (H - TS)_{reactants} = \Delta H - T\Delta S \quad \begin{matrix} < 0: \\ > 0: \end{matrix} \quad \begin{matrix} \text{reaction } \textit{favorable} \\ \text{reaction } \textit{un}\text{favorable} \end{matrix} \qquad \text{Eq.(1)}$$

Thus, a reaction with a negative ΔH and positive ΔS will be thermodynamically favorable. A negative value of ΔH for the reaction corresponds to the release of heat, and a positive ΔS means an increase in entropy. A larger number of product molecules compared to reactant molecules generally corresponds to an increase in entropy. The enthalpy term usually dominates, so that reactions that release more heat are more favored; in other words, a larger heat of combustion roughly correlates with "more flammable."

But kinetics, or the speed of the reaction, is also important. A block of wood sitting in air is thermodynamically unstable: It "wants" to burn, but the unfavorable kinetics of the reaction at room temperature prevents it from bursting into flame. The wood (or at least a small bit of it) must be

heated sufficiently to volatilize a portion of it, and the resulting gases must then be further energized (*e.g.*, with a spark) for the combustion reaction to begin. Linteris *et al.* (2019) consider kinetics in their method to estimate flammability.

Another way to look at flammability is in terms of the overall chemical stability of the molecule, as expressed by the enthalpy of formation, ΔH_f. This quantity is calculated as the enthalpy change of a hypothetical reaction forming the compound from its elements. As the value of ΔH_f becomes more negative, the more stable the molecule is. Fig. 8 plots the ΔH_f versus the number of fluorine atoms for the ethane-based (two-carbon) HFCs; the ΔH_f becomes steadily more negative from the highly flammable R-170 (ethane, CH_3CH_3) to the nonflammable R-116 (CF_3CF_3). This trend is a result of the great stability of the carbon–fluorine bond; it takes considerable energy to break a C–F bond, and thus R-125 is "more nonflammable" and has a greater ability to suppress the flammability of a blend compared to R-134a.

The C–F bond also absorbs infrared radiation, and this is the root of the radiative forcing seen with the HFCs. As the number of fluorines on the molecule increases the infrared absorption increases, but also the number of hydrogens must decrease, and it is the reaction of hydrogen with atmospheric hydroxyl that degrades HFCs in the atmosphere. This combined effect results in GWP_{100} values increasing from <1 for R-170 (Hodnebrog *et al.*, 2018) to 11100 for R-116 (WMO, 2018). The HFOs also have C–F bonds and have a similar absorption of infrared radiation, but their much, much shorter atmospheric lifetimes result in very low GWP values. Thus, the HFOs can sidestep the flammability versus GWP trade-off—except that the flammability versus fluorine-number relationship discussed in Section 4.1 means that there are a smaller percentage of possible HFOs that are nonflammable.

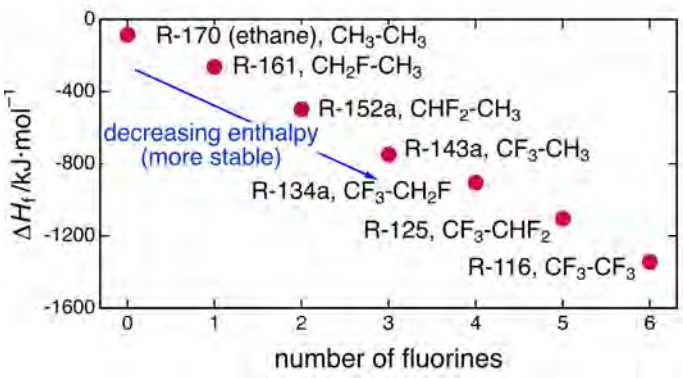

Figure 8. Variation of enthalpy of formation, ΔH_f, with number of fluorines for the two-carbon HFCs.

4.3. Refrigerant Mixtures

Blending different refrigerants to obtain a desired set of attributes has a long history. Indeed, in 1928 when Midgley was told by Kettering that "the refrigeration industry needs a new refrigerant if they every expect to get anywhere" Midgley was "doubtful that we would be able to find a single substance suitable to the task but that there might be some hope of greatly reducing the existing hazards by using mixtures" of nontoxic, but flammable compounds with nonflammable, but toxic compounds (Midgley, 1937). Midgley, of course, went on to develop the (pure-fluid) CFCs, but mixtures are now quite common. By 2016, ASHRAE Standard 34 (ASHRAE, 2016a) listed 112 refrigerant blends. Apart from R-134a in home refrigerators and automotive air-conditioning systems, the HFCs are primarily used as blend components (*e.g.*, R-410A, R-404A, R-507A). For example, R-410A, a blend of R-32 and R-125, takes advantage of the good COP of R-32 (see Fig. 5) while mitigating its flammability and high discharge temperature. Refrigerant blends offer a way to balance tradeoffs, but they come with some tradeoffs of their own. Blends can fractionate, meaning the the composition of the liquid and vapor phases are different; a leak from one phase will result in a changing composition over time. The tradeoff of temperature glide is discussed in Section 5.4.

5. DISCUSSION—ADAPTING TO NEW FLUIDS

While a drop-in replacement refrigerant requiring no changes to equipment design is appealing, the properties of low-GWP fluids will generally be different than the refrigerants they are replacing.

Recognizing and adapting to these differences will be required to maximize the safety, efficiency, and reliability of new systems.

5.1. Cycles

As discussed in Section 4.1, the HFO refrigerants are more complex molecules than the HFCs they may replace and, as such, may benefit from a modified cycle. Domanski (1995) showed theoretically that virtually any refrigerant could be made to operate efficiently with cycle modifications designed to minimize throttling losses. Such losses cannot be recovered completely, however, because economizers, ejectors, and intra-cycle heat exchangers are themselves subject to irreversibilities. The thermodynamic properties of the HFO refrigerants are not greatly different than the HFCs, and simple modifications, such as a liquid-line/suction-line heat exchanger, an ejector, or a two-stage economizer cycle, are worthwhile to consider.

Carbon dioxide has the considerable advantage of an "A1" (lower toxicity, nonflammable) safety classification and a GWP = 1.00. Its relatively low critical temperature of 304.1 K, however, results in a supercritical cycle under many operating conditions. This means that the high-side heat exchanger is no longer a "condenser" but, rather, a "gas cooler." This does not fundamentally change the cycle, but it does require careful design (especially control of the expansion process) to avoid significant energy penalties. The use of CO_2 has been considered by many authors; see for example, the proceedings of the biennial IIR Gustav Lorentzen Conferences on Natural Refrigerants.

5.2. System Technology

The difficulty of finding a nonflammable and low-GWP refrigerant is most acute for medium- and high-pressure systems (*e.g.*, those currently employing R-134a or R-410A) (Domanski *et al.*, 2017). There are more choices among low-pressure refrigerants (*e.g.*, R-1233zd(E) and R-1336mzz(Z)). The lower-pressure refrigerants are generally more complex molecules, and with each additional carbon atom in a molecule, the number of possible permutations and combinations for adding fluorine and/or chlorine increases exponentially. Furthermore, the fraction of those that are nonflammable increases, as discussed in Section 4.2.

But while low-pressure refrigerants are commonly used in large chillers based on centrifugal compressors and flooded evaporators, they carry a significant pressure-drop penalty with the compressor and heat-exchanger technologies commonly used in small unitary systems. To extend turbo-compressor technology to smaller systems, the U.S. Department of Energy has funded a project to "demonstrate a high efficiency centrifugal compressor design … in the 1.5- to 10-ton range" (*i.e.*, 5.3 kW to 35 kW cooling capacity) (U.S. DOE, 2015). Verma (2018) stated that the refrigerant to be used was proprietary, but that it was a "low-GWP, nonflammable, high-efficiency refrigerant" with "lower superheat." These characteristics suggest a more-complex, lower-pressure molecule, as discussed in Section 4.1. Thus, different technologies might expand the range of refrigerant choices.

5.3. System Configuration

Natural refrigerants, such as ammonia and hydrocarbons, have excellent thermodynamic characteristics and were among the highest-efficiency fluids identified in the cycle simulations carried out by McLinden *et al.* (2017) and Domanski *et al.* (2017). Their application to many types of systems, however, is constrained by the limited charge sizes allowed by safety codes (*e.g.*, ASHRAE, 2016b). Such charge limits are considerably relaxed if the refrigeration system sits outside the occupied space, and this would imply a separate heat-transfer loop. This has long been the normal practice with water chillers. More recently, supermarket systems have employed a central machine room with an ammonia-based system and heat-exchange loops to the display cases, with CO_2 serving as the heat-transfer fluid (Pearson and Campbell, 2010). Such a system also avoids the often-high leakage rates of high-GWP refrigerants experienced with long piping runs that feed direct-expansion evaporators in the display cases.

Heat-exchange loops could also be applied to other systems, such as residential air conditioning. A factory-sealed refrigeration system could more easily achieve very-low leakage rates as well as reduced refrigerant charge—minimizing the environmental impact if a high-GWP refrigerant were used or reducing the safety hazards of a flammable or toxic refrigerant. A separate loop would, however, incur an efficiency penalty (Payne *et al.*, 1999).

5.4. Temperature Glide With Refrigerant Mixtures

With a refrigerant mixture, condensation and evaporation at a constant pressure are no longer constant-temperature processes (except for the special case of an azeotropic blend), but rather, take place over a range of temperature—the so-called temperature glide. (The temperature glide is defined as the "difference between the starting and ending temperatures of a phase change process" (ASHRAE, 2016a).) With proper heat exchanger design, such a temperature glide can be exploited to more closely match the temperature profile of the fluid (*e.g.*, air) being heated or cooled, thus increasing the efficiency of the cycle. This idea traces back to Lorenz (1894) and is sometimes called the Lorenz cycle. While many refrigerant blends are in common use today, most of these are azeotropic or "near-azeotropic" blends with temperature glides of, at most, a few kelvins. Blends with larger glides are perceived to not be compatible with common cross-flow refrigerant-to-air heat exchangers and to present servicing difficulties because fractionation of the blend components can occur.

The pressure drop down the length of the condenser and evaporator also results in a temperature glide (even with a pure-fluid refrigerant), because the saturation temperature decreases along with the pressure. This effect would amplify the temperature glide of a blend in the condenser but reduce it in the evaporator. This effect could be used to reduce the heat-transfer irreversibilities in a cross-flow evaporator. Seeton (2018) suggested exploiting this effect to the extreme by combining a high-glide blend with a very-high pressure drop down the length of the evaporator (essentially moving some portion of the expansion process into the evaporator), achieving a more nearly isothermal evaporation process. This idea has not been tested, but is mentioned as an example of an out-of-the-box idea that could circumvent some of the trade-offs being encountered with low-GWP refrigerants. For example, CO_2 offers the possibility to reduce flammability, but blends with a high concentration of CO_2 often have very-high glides. On the other hand, the use of relatively low-pressure refrigerants often entails significant pressure drop penalties that might be mitigated by this approach.

When optimizing systems with different blends and temperature glides the heat-exchanger geometry is a design parameter, but the constraint of a constant total heat-exchanger area is often assumed. This corresponds to an approximately constant-cost constraint. Zühlsdorf *et al.* (2019), on the other hand, argue that the potential for higher efficiency when fully utilizing the temperature glide of blends justifies (and might require) a higher initial cost.

5.5. Flammability

While the tradeoff of GWP versus flammability was linked to thermodynamic factors in Section 4.2, the adaptations necessary to safely implement a flammable refrigerant are in the realm of safety engineering. Thermodynamic properties might, however, be a factor if different system configurations are considered.

6. SUMMARY AND CONCLUSIONS

This paper has considered some of the thermodynamic considerations underlying the selection of alternatives to the high-GWP refrigerants. A fluid must possess certain fundamental thermodynamic properties to be suitable for use as a refrigerant, with the critical temperature and pressure and the heat capacity of the vapor having the largest impact on efficiency. Thermodynamics, in the form of the enthalpy of formation and free energy of reaction, underlie the flammability of a fluid. The different thermodynamic properties of the "new" refrigerants may require modifications to the cycle or system configuration.

Calm (2008) introduced the concept of "refrigerant generations," and he characterizes the current, fourth generation of refrigerants as driven by "attention to global warming." Later, Calm (2012) posited that, in view of limited options, a fifth generation, which would "re-examine previously discarded candidates", may be forthcoming as the full range of tradeoffs are considered. But the results of McLinden *et al.* (2017) indicate (as summarized in Section 3.4) that there are no fundamentally new classes of chemicals available for use in vapor-compression refrigeration systems. While the "re-examination" discussed by Calm (2012) may well occur, the situation may be to return (recycle?) to earlier generations, such as the ammonia, CO_2, and hydrocarbons of the first generation of "whatever works." Let us hope that we are not forced back to a "generation zero" of harvesting ice from frozen lakes.

NOMENCLATURE

CFC	chlorofluorocarbon
COP	coefficient of performance
C_p°	heat capacity in the limit $p \rightarrow 0$
GWP	global warming potential
GWP_{20}	global warming potential for a time horizon of 20 years
GWP_{100}	global warming potential for a time horizon of 100 years
h, H	enthalpy
HCFC	hydrochlorofluorocarbon
HFC	hydrofluorocarbon
HFO	hydrofluoroolefin
ODP	ozone depletion potential
ODS	ozone depleting substance
p	pressure
Q_{vol}	volumetric heating or cooling capacity
s, S	entropy
T	temperature
ΔH_f	heat of formation
Δ	change in a quantity
ω	acentric factor

Subscripts

c	critical point value
NBP	normal boiling point

Superscripts

o	ideal-gas state

REFERENCES

ASHRAE, 2016a. ANSI/ASHRAE Standard 15-2016 Safety Standard for Refrigeration Systems. American Society of Heating, Refrigerating and Air-Conditioning Engineers, Atlanta, GA USA.

ASHRAE, 2016b. ANSI/ASHRAE Standard 34-2016 Designation and Safety Classification of Refrigerants. American Society of Heating, Refrigerating and Air-Conditioning Engineers, Atlanta, GA USA.

ASHRAE, 2017. Addendum f to ANSI/ASHRAE Standard 34-2016: Designation and Safety Classification of Refrigerants. American Society of Heating, Refrigerating and Air-Conditioning Engineers, Atlanta, GA USA.

ASHRAE, 2018. Proposed Addendum t to Standard 34-2016, Designation and Safety Classification of Refrigerants. American Society of Heating, Refrigerating and Air-Conditioning Engineers, Atlanta, GA USA.

Brown, J.S., 2013. Introduction to hydrofluoro-olefin alternatives for high global warming potential hydrofluorocarbon refrigerants. HVAC&R Research 19, 693-704.

Calm, J.M., 2008. The next generation of refrigerants—Historical review, considerations, and outlook. Int. J. Refrig. 31, 1123-1133.

Calm, J.M., 2012. Refrigerant transitions … Again, 2012 ASHRAE/NIST Refrigerants Conference. ASHRAE, Inc., Gaithersburg, MD USA.

Calm, J.M., Didion, D.A., 1997. Trade-offs in refrigerant selection: Past, present and future, ASHRAE/NIST Refrigerants Conference: Refrigerants for the 21st Century, Gaithersburg, MD USA, October 6-7, pp. 6-19.

Domanski, P.A., 1995. Minimizing throttling losses in the refrigeration cycle, 19th International Congress of Refrigeration. IIF/IIR, The Hague, The Netherlands, pp. 766-773.

Domanski, P.A., Brignoli, R., Brown, J.S., Kazakov, A.F., McLinden, M.O., 2017. Low-GWP refrigerants for medium and high-pressure applications. Int. J. Refrig. 84, 198-209.

Domanski, P.A., Brown, J.S., Heo, J., Wojtusiak, J., McLinden, M.O., 2014. A thermodynamic analysis of refrigerants: Performance limits of the vapor compression cycle. Int. J. Refrig. 38, 71-79.

Downing, R.C., 1988. Fluorocarbon refrigerants handbook. Prentice-Hall, Inc., Englewood Cliffs, New Jersey USA.

European Environment Agency, 2014. Regulation (EU) No 517/2014 of the European Parliament and of the Council of 16 April 2014 on fluorinated greenhouse gases and repealing Regulation (EC) No 842/2006.

Goetzler, W., Zogg, R., Young, J., Johnson, C., 2014. Energy Savings Potential and RD&D Opportunities for Non-Vapor-Compression HVAC Technologies, Report to U.S. Department of Energy.

Hashimoto, M., Otsuka, T., Fukushima, M., Okamoto, H., Hayamizu, H., Ueno, K., Akasaka, R., 2019. Development of New Low-GWP Refrigerants: Refrigerant Mixtures Including HFO-1123. Sci. Tech. Built. Environ. 25.

Hodnebrog, Ø., Dalsøren, S.B., Myhre, G., 2018. Lifetimes, direct and indirect radiative forcing, and global warming potentials of ethane (C_2H_6), propane (C_3H_8), and butane (C_4H_{10}). Atmos. Sci. Lett. 19, e804.

Houghton, J.T., Jenkins, G.J., Ephraums, J.J., Eds., 1990. Climate Change: The IPCC Scientific Assessment. Cambridge University Press, Cambridge, England.

Huber, M.L., Ely, J.F., 1994. A predictive extended corresponding states model for pure and mixed refrigerants including an equation of state for R134a. Int. J. Refrig. 17, 18-31.

IPCC, 2014. Climate Change 2014: Synthesis Report. Contribution of Working Groups I, II and III to the Fifth Assessment Report of the Intergovernmental Panel on Climate Change, Pachauri, R.K., Meyer, L.A. (Eds.). IPCC, Geneva Switzerland.

Kazakov, A., McLinden, M.O., Frenkel, M., 2012. Computational design of new refrigerant fluids based on environmental, safety, and thermodynamic characteristics. Ind. Eng. Chem. Res. 51, 12537-12548.

Kim, S., Thiessen, P.A., Bolton, E.E., Chen, J., Fu, G., Gindulyte, A., Han, L., He, S., Shoemaker, B.A., Wang, J., Yu, B., Zhang, J., Bryant, S.H., 2016. PubChem substance and compound databases. Nucleic Acids Res. 44, D1202-D1213.

Kujak, S., Schultz, K., 2016. Insights into the next generation HVAC&R refrigerant future. Sci. Tech. Built Environ. 22, 1226-1237.

Kujak, S., Sorenson, E., 2018. Haloolefins Refrigerants. ASHRAE J. 60, 28-35.

Lemmon, E.W., Bell, I.H., Huber, M.L., McLinden, M.O., 2018. NIST Standard Reference Database 23: Reference Fluid Thermodynamic and Transport Properties—REFPROP, Version 10.0. National Institute of Standards and Technology, Gaithersburg, MD USA.

Linteris, G.T., Bell, I., McLinden, M.O., 2019. An empirical model for refrigerant flammability based on molecular structure and thermodynamics. Int. J. Refrig. (in press).

Lorenz, H., 1894. Beiträge zur Beurteillung von Kühlmaschinen. Zeitschrift des VDI 38, 62-68.

McGowan, M.K., 2019. Progress report on alternative refrigerants. ASHRAE J. 61, 38-41.

McLinden, M.O., 1990. Optimum refrigerants for non-ideal cycles: An analysis employing corresponding states, USNC/IIR–Purdue Refrigeration Conference and ASHRAE-Purdue CFC Conference, W. Lafayette, IN USA, July 17-20, pp. 69-79.

McLinden, M.O., Brown, J.S., Brignoli, R., Kazakov, A.F., Domanski, P.A., 2017. Limited options for low-global-warming-potential refrigerants. Nat. Comm. 8, 14476.

McLinden, M.O., Didion, D.A., 1987. CFCs: Quest for Alternatives. ASHRAE J. 29, 32-42.

McLinden, M.O., Domanski, P.A., Kazakov, A., Heo, J., Brown, J.S., 2012. Possibilities, limits, and tradeoffs for refrigerants in the vapor compression cycle, 2012 ASHRAE/NIST Refrigerants Conference. ASHRAE, Inc., Gaithersburg, MD USA.

McLinden, M.O., Kazakov, A.F., Brown, J.S., Domanski, P.A., 2014. A thermodynamic analysis of refrigerants: Possibilities and tradeoffs for Low-GWP refrigerants. Int. J. Refrig. 38, 80-92.

Midgley, T., 1937. From the periodic table to production. Ind. Eng. Chem. 29, 241-244.

Midgley, T., Henne, A.L., 1930. Organic fluorides as refrigerants. Ind. Engr. Chem. 22, 542-545.

Morrison, G., 1994. The shape of the temperature-entropy saturation boundary. Int. J. Refrig. 17, 494-503.

National Institute for Occupational Safety and Health, 2007. NIOSH Pocket Guide to Chemical Hazards. U.S. Department of Health and Human Services.

Nimitz, J., Lankford, L., 1994. Refrigerants containing fluoroiodocarbons (FICs), 1994 International Refrigeration Conference, W. Lafayette, IN USA, July 19-22, pp. 255-260.

Payne, W.V., Domanski, P.A., Muller, J., 1999. A study of a water-to-water heat pump using hydrocarbon and hydrofluorocarbon zeotropic mixtures, NISTIR 6330. National Institute of Standards and Technology, Gaithersburg, MD USA.

Pearson, A., Campbell, A., 2010. Using CO_2 in supermarkets. ASHRAE J. 52, 24-28.

Seeton, C., 2018. Personal communication, Shrieve Chemical Company, The Woodlands, TX USA.

Tanaka, T., Okamoto, H., Ueno, K., Irisawa, J., Otsuka, T., Nogami, T., Dobashi, R., 2014. Development of a new low-GWP refrigerant composed of HFO-1123 (trifluoroethylene), AIChE Annual Meeting. American Institute of Chemical Engineers, Atlanta, GA USA.

Trouton, F., 1884. IV. On molecular latent heat. The London, Edinburgh, and Dublin Philosophical Magazine and Journal of Science 18, 54-57.

U.S. DOE, 2015. Energy Department Invests Nearly $8 Million to Develop Next-Generation HVAC Systems for Buildings (press release). U.S. Department of Energy, https://www.energy.gov/eere/articles/energy-department-invests-nearly-8-million-develop-next-generation-hvac-systems.

U.S. Environmental Protection Agency, 2018. Significant New Alternatives Policy (SNAP): SNAP Regulations, https://www.epa.gov/snap/snap-regulations#notices.

Velders, G.J.M., 2016. unpublished analysis based on Velders, *et al.* (2015).

Velders, G.J.M., Andersen, S.O., Daniel, J.S., Fahey, D.W., McFarland, M., 2007. The importance of the Montreal Protocol in protecting climate. Proc. Natl. Acad. Sci. USA 104, 4814–4819.

Velders, G.J.M., Fahey, D.W., Daniel, J.S., Andersen, S.O., McFarland, M., 2015. Future atmospheric abundances and climate forcings from scenarios of global and regional hydrofluorocarbon (HFC) emissions. Atmos. Environ. 123, 200-209.

Velders, G.J.M., Fahey, D.W., Daniel, J.S., McFarland, M., Andersen, S.O., 2009. The large contribution of projected HFC emissions to future climate forcing. Proc. Natl. Acad. Sci. USA 106, 10949-10954.

Verma, P., 2018. High Efficiency Low GWP Compressor, U.S. Department of Energy, Building Technologies Office 2018 Peer Review, Arlington, VA USA, https://www.energy.gov/sites/prod/files/2018/06/f52/312106_Verma_043018-1600.pdf

WMO (World Meteorological Organization), 2018. Scientific Assessment of Ozone Depletion: 2018, Global Ozone Research and Monitoring Project–Report No. 58. WMO, Geneva, Switzerland.

Zühlsdorf, B., Jensen, J.K., Elmegaard, B., 2019. Heat pump working fluid selection-economic and thermodynamic comparison of criteria and boundary conditions. Int. J. Refrig. 98, 500-513.

Manuscript ID: 1832
DOI: 10.18462/iir.icr.2019.1832

Rational approach to refrigerant charge reduction

Pega HRNJAK
University of Illinois at Urbana-Champaign, Department of Science and Engineering,
Urbana, IL, 61820, USA
Creative Thermal Solutions,
Urbana, IL, 61802, USA, pega@illinois.edu

ABSTRACT

This paper presents an overview of the reasons for charge reduction in air conditioning and refrigeration systems and discusses strategies for charge reduction: in compressors (oil), vessels, pipes, and heat exchangers. The focus is on heat exchangers, microchannel in particular. In addition to a trivial reduction of internal volume as a strategy for charge reduction, the effect of mass flux on void fraction and needed manipulation of circuiting is presented. A framework and example of comparison between refrigerants based on their potential for low condenser charge is provided.
Keywords: Refrigerant, Safe and efficient operation

1. INTRODUCTION

1.1 Reasons for charge reduction

Reduction of refrigerant charge (inventory) is attractive for any refrigerant for several reasons:

- Low charge may expand the possibilities for some very good refrigerants (high cycle efficiency, high heat transfer/pressure drop performance, etc.) in areas and locations where either these fluids are totally restricted or only allowed in limited quantities due to flammability or toxicity issues. This is particularly true for fluids like ammonia and hydrocarbons which in some applications and locations are already accepted below certain levels (typically 150 kg for NH_3 and 150 or 50 g for HCs).
- System efficiency could be increased in cycling when refrigerant migration in off periods is significant.
- Direct environmental effects (limited importance for ammonia or hydrocarbons) are reduced: ozone depleting issues if any, global warming issues, etc… especially in the case of catastrophic leaks.

Reduction of the first costs for refrigerant and lubricant expenses (again not very important for ammonia or hydrocarbons since they are very inexpensive).

1.2 Possible drawbacks of low charge

Reducing charge beyond some point could result in problems in operation such as:

- If receiver is inadequate, then small leaks will result in insufficient charge thus reducing performance.
- If charge reduction is achieved by reducing the hydraulic diameter of pipes too severely, then pressure drops and flashing may affect efficiency and perhaps capacity.
- Reduced reliability of pumps (if present) due to possible vapor entrainment and cavitation.

STRATEGIES FOR CHARGE REDUCTION:

1.3 In the system

The first and almost trivial option for charge reduction is to add another fluid loop in the refrigeration system and in that way reduce the primary refrigerant charge. These options could be either cascades or secondary refrigerant loops which actually turn a refrigeration system into a chiller with either single or two phase secondary refrigerants. These options were, and are, very popular for their simplicity. Refrigerant in the primary (or only) system is in each component: compressor, vessel(s), liquid, two phase and suction lines, and finally, heat exchangers

Reducing refrigerant charge in compressor by a) reducing the internal volume b) reducing the quantity of lubricant and c) reducing refrigerant solubility (if reasonable). Needless to say, reduction of the volume on the high side yields greater results than on the suction due to density difference. A part of lubricant charge in the compressor is a function of refrigerant charge in the system to allow for oil retention in the system. Minimized internal volume of the system in refrigerant charge reduction process makes request for lubricant charge reduction stronger. Acceptance of that request will result in further refrigerant charge reduction. Reduction of liquid quantities in vessels can be achieved by reducing their volume and liquid levels

Reduction of the refrigerant charge in pipes is typically achieved by reducing internal volume (diameter and possibly even length). Reduction of diameter results in increased pressure drops. Pressure drops in liquid lines do not affect the system performance but can cause non-desirable flashing which affects the operation of flow controllers. Pressure drops in suction lines affect system efficiency and therefore may not be advisable

The most attractive and important strategy is to reduce the charge in heat exchangers. Reduction of refrigerant charge in heat exchangers is always related to a reduction in internal volume. One must be careful to balance the adverse effects regarding either increased pressure drop or reduced heat transferred

1.4 In heat exchangers

Every refrigerant inventory reduction strategy is related to reducing the internal volume. It is a great advantage that reduction of the volume is proportional to the channel diameter squared while heat transfer area is a linear function of the diameter. Nevertheless reduction of the internal volume is just one, relatively trivial, path to reaching the objective

In the cases of spray evaporators, significant charge reductions were achieved compared to shell and tube even for the same volume.

To provide sufficient capacity with in-tube flow heat exchangers, it is necessary to provide a refrigerant flow that is inversely related to the latent heat of vaporization (h_{fg}). Therefore, refrigerants with larger values latent heats will have lower mass flow rates for the same capacity and all else being equal, will have lower pressure drop compared to those that require higher flow rate. These lower pressure drops may then allow for smaller diameter tubes to be utilized.

Heat transfer effects of the charge reduction strategies are related to refrigerant side heat transfer. Higher heat transfer coefficients mean that smaller surfaces are required for a given duty. The effect of refrigerant heat transfer coefficient is greater for heat exchangers where the refrigerant side is a relatively large component of the total heat transfer resistance. As an example, charge is easier to be minimized in heat exchangers such as water cooled condensers or chiller evaporators where water, rather than air, is heated or cooled. This is because a greater heat transfer area is required for a given capacity in the case of a heat exchanger with air due to its lower overall heat transfer.

coefficient. Thus, it will be easier to reduce the charge of refrigerants that have thermophysical properties which provide higher heat transfer coefficients (specific heat, conductivity, latent heat of vaporization, etc.). In addition, those refrigerants that allow flow regimes that are better for heat transfer (annular or intermittent in evaporation or mist in condensation) or geometries that stimulate such flow regimes (i.e. microfins) will provide better opportunities for change reduction. Whether these opportunities will be realized is a function the adequacy of the design.

Every reduction of internal diameter, with everything else being the same, will increase pressure drop. The option to reduce the pressure drop in the same diameter tube with the same fluid is to reduce the length of the tube or decrease flow through the tube. This drives heat exchanger design towards parallel flows of small diameter tubes with the shortest possible circuits. That practically means a single pass design with very small channel diameters. That indicates a parallel heat exchanger design with single pass as an asymptote

Nevertheless, the reality is more complex than this straight forward direction. The main goal should be to optimize system COP for a given mass flow by studying the interplay of heat transfer and pressure drop. A fine discussion of this subject was given by Cavallini, 2011.

When calculating the refrigerant charge in a heat exchanger, engineers typically use void fraction, α (α=Vapor volume/(Vapor+Liquid Volumes)) as a main variable. Fig. 1 presents the relationship between R134a and void fraction in a microchannel tube (Nino et. al. 2002).

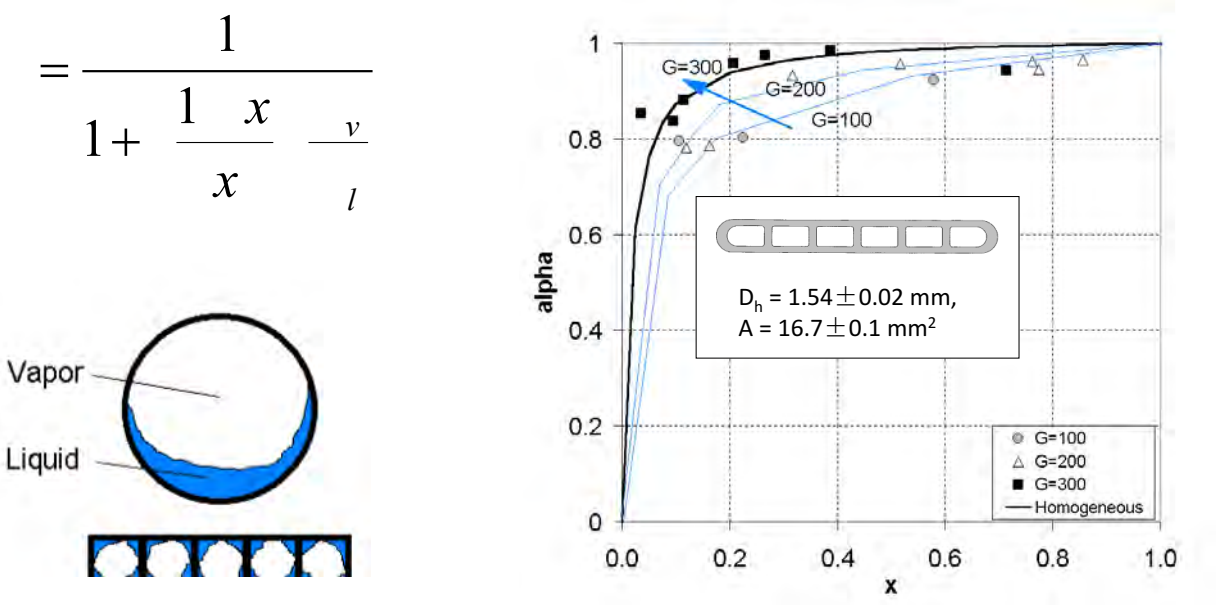

Figure 1: Void fraction: relationship, concept, and some values

Void fraction is a misnomer. There are no voids in any heat exchanger. Better name would be "vapor volume fraction". Even more, we are interested not in vapor but instead in liquid because liquid carries the mass of refrigerant which we are trying to reduce. So, the mass of liquid M_l can be presented as:

$$\boldsymbol{M_l = \int_0^L (1-\alpha)\rho_l A dz} \qquad \text{Eq. (1)}$$

And the total mass is calculated as:

$$\boldsymbol{M = M_l + M_v = \sum(1-\alpha_i)\rho_l A \Delta z_i + \sum(\alpha_i)\rho_v A \Delta x z_i} \qquad \text{Eq. (2)}$$

It is very important to have in mind that the void fraction is a function of mass flux (this fact even some void fraction correlations neglect). This relationship is a very important tool when designing to

reduce refrigerant charge. The trend is the same as discussed above: reduction in diameter increases mass flux and increases void fraction, consequently reducing charge. This trend was obvious from the graph shown in Fig. 1.

There is a practical difficulty when following the strategy described above. When a higher capacity of a heat exchanger is desired, the number of parallel passes increases; consequently headers where channel flows will merge are becoming larger. Flow regimes in headers are less well described and much less predictable, but typically void fractions are lower in header than in tubes.

Probably the best known low charge heat exchangers based on reduction of internal volume are of the microchannel type. They offer extremely low charge (less than 10 g/kW even for air on the other side), unless the headers are designed incorrectly. Hrnjak and Litch (2001) reported charges of 18 g/kW for a 15 kW air cooled microchannel ammonia chiller with refrigerant charge of 6 g/kW in a condenser only. Traeger and Hrnjak (2005) reported an R290 system with 8-10 g of charge in a 1kW serpentine microchannel evaporator. There are some microchannel heat exchanger designs with water as the fluid on the other side (see Palm, 2009).

Other effective low charge heat exchangers are the plate type. They are better known in chiller applications and are typically made of stainless steel which is either brazed with copper or nickel or else are gasketed. Similar variations are becoming more common in plate and shell designs. Plate heat exchangers with air on the other side are predominantly used in automotive a/c systems as evaporators. Typical refrigerant charges in larger heat exchangers (Pearson, 2003) are 1 kg/kW, 0.5 kg/kW, and 0.25 kg/kW for shell and tube, plate, and gravity fed plate heat exchangers, respectively.

Z. Ayub, (1996) reports on low charges (54 g/kW) in large spray evaporators for ammonia (4MW).

2. INFLUENCE OF MASS FLUX ON CHARGE REDUCTION

Even though void fraction has been studied extensively [see Zivi, (1964), Butterworth, (1975), Newell, (1999), Adams et al., (2003) & (2006), etc.]. Mass flux effects were not always considered. Typically, for a given fluid and local quality, increasing the mass or heat flux, will alter flow regimes in a way that increases void fraction thus reducing charge.

Nino et al, (2002) showed the effect of mass flux on the void fraction for R134a in microchannel tubes (Fig. 1), while Adams, Hrnjak, and Newell, (2003) shed some light on void fraction for ammonia (shown in Figs 2 and 3), carbon dioxide, and R245fa in microchannels. Figs 2 and 3 present void fraction as a function of quality for three mass fluxes, along with correlation predictions from the homogenous and Nino et al., (2002) models. It is obvious, despite some scattering of experimental data that higher mass fluxes result in higher void fractions (reduced refrigerant charges). Photos in Figs 4, 5, and 6 [from Niño, Hrnjak, & Newell, (2002)] provide visual evidence of the same trend, in transparent microchannels, for R134a, R410a, and air-water (whose fluid flow resembles ammonia).

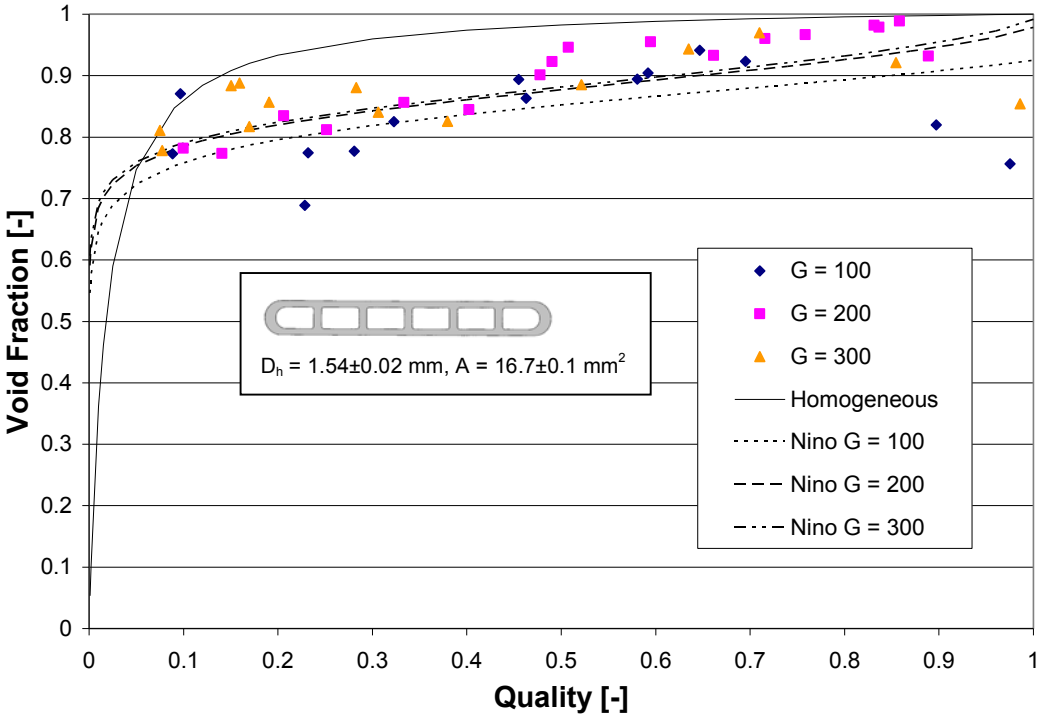

Fig. 2: Void fraction of ammonia in a six port microchannel tube, Adams, Hrnjak and Newell, 2003

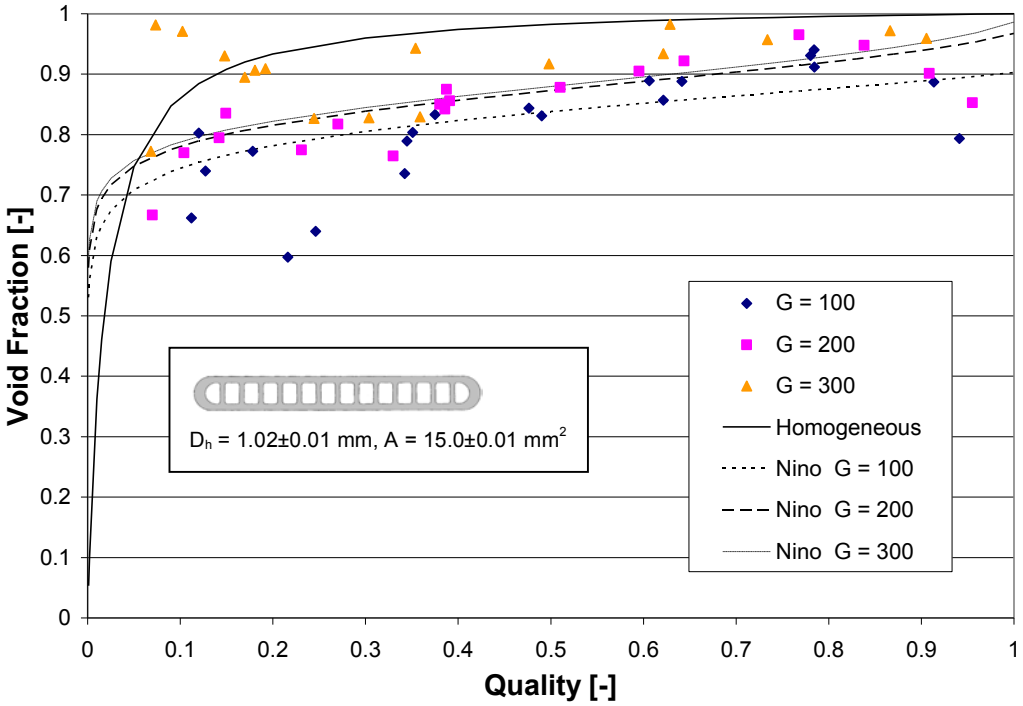

Fig. 3: Void fraction of ammonia in a 14 port microchannel tube, Adams, Hrnjak and Newell, 2003

A comparison between the predictions from a 3-zone approach and a 5-zone approach is shown in Fig. 6. For the 3-zone approach, Churchill correlation and correlation by Friedel (1979) are used. There is obvious underprediction in the CSH region due to the neglect of liquid-vapor interaction, which is the waves mentioned above. Using the 5-zone approach in this section, the underprediction is corrected and the overall accuracy of the model prediction improves. The 5-zone approach also creates a seamless line throughout all 5 regions, which is hardly achieved by the 3 zone approaches. The seemingly continuous curve in Fig. 6 with the 3-zone approach is artificially created by using

Churchill instead of Blasius equation in the Friedel correlation. In this way the effect of surface roughness can be consistence in SH, TP and SC regions. Fig. 7 shows the comparison between the predictions by the 5-zone approach and the experimental data, which is from the condensation of R32, R134a and R1233zd(E) at 30 ^{o}C in 4 and 6 mm tubes under mass fluxes ranged from 100 to 400 kg m^{-2} s^{-1}. The model predictions have a difference smaller than 10% with the experimental data, most of which are in the lower magnitude region. This is probably due to the systematic error when the pressure drop is small. New experiments on mixtures and microchannels are on the way.

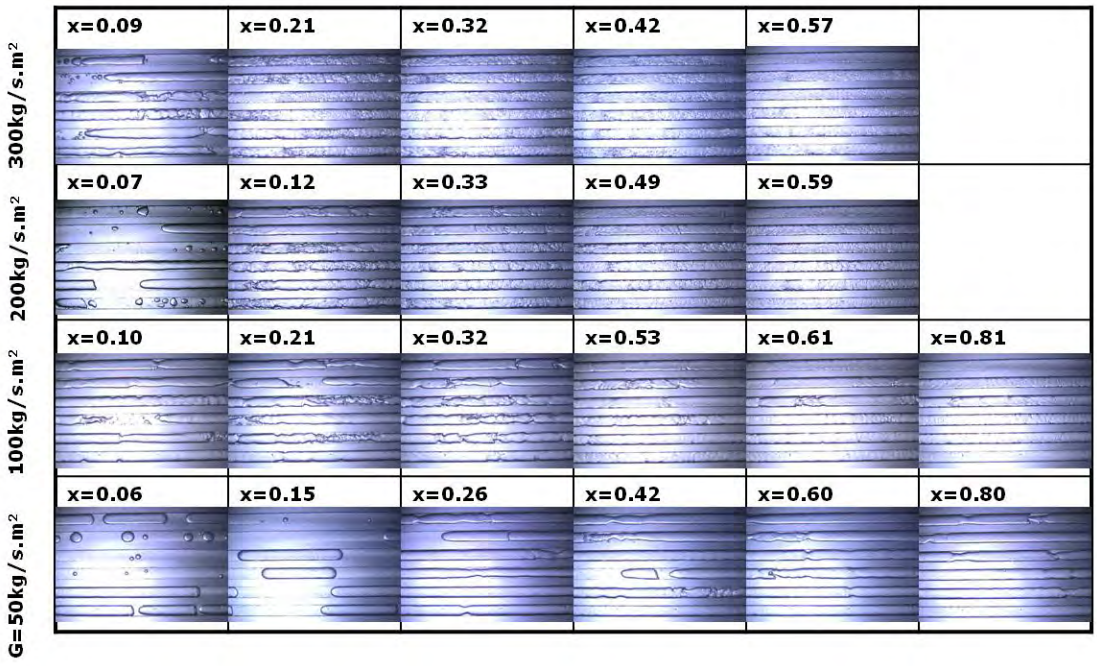

Fig. 4: Void fraction as a function of mass flux and quality (R134a, 9 ports of 1 mm), Nino, Hrnjak, Newell, 2003

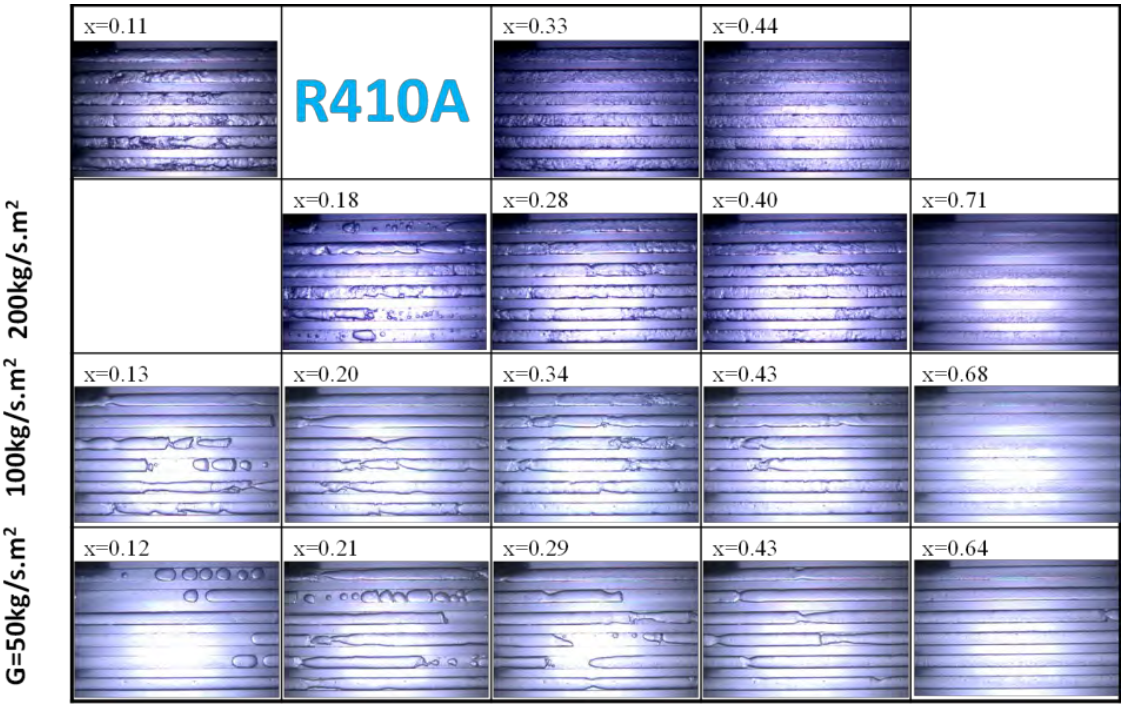

Fig. 5: Void fraction as a function of mass flux and quality (R410A, 9 ports of 1 mm), Nino, Hrnjak, Newell, 2003

Fig. 6: Void fraction as a function of mass flux and quality (Air-Water, 9 ports of 1 mm), Nino, Hrnjak, Newell, 2003

3. POTENTIAL FOR CHARGE REDUCTION IN SOME REFRIGERANTS

As discussed previously, it is clear that low charge is beneficial for every refrigerant in every application.

Comparisons of refrigerants based on their efficiency are common. The basis for efficiency comparison is cycle analysis (typically Rankine or Evans-Perkins). Cycle analysis involves significant simplification that could be even misleading in some cases. It does not include realities of the heat exchanger (heat transfer, pressure drops, power for air or water movers, etc.). That approach is based on thermodynamics and is accepted as a first approximation in the comparative analysis.

It would be interesting to know whether refrigerants can be compared based on their potential for charge reduction. We will try to present here the concept to compare refrigerants based on their potential for charge reduction in heat exchangers and illustrate it with an example. The concept is in principle based on assumption that refrigerant which is less sensitive to reduction of internal volume and has less (high void fraction) and lighter (lower density) liquid has greater potential for charge reduction. The sensitivity to reduction of internal volume is defined by reduction of COP due to pressure drop. Pressure drop is a function mostly of mass flow rate determined by (available) portion of latent heat, specific volume of vapor, and viscosity of liquid.

3.1 Approach for comparison

As said above, the most logical starting point for reducing charge in heat exchangers begins with the reduction of internal volume. A result of reducing the pipe diameter is increased pressure drop. The fair comparison of refrigerants should be based not on equal pressure drop itself but on the effect pressure drop has on efficiency (COP) while maintaining the same capacity.

The heat transfer on both sides (not only on refrigerant that is mostly affected when varying design options for charge reduction) is important and affects the result. That is the reason why maintaining identical air side is important. To maintain identical outside (air-side) conditions for each refrigerant, the heat exchanger type selected is the microchannel serpentine (two circuits) shown in the Fig. 7 and with dimensions given in Table 1. Selection of microchannel type is due to its relevance today and for its anticipated acceptance by more manufacturers. In addition, high heat transfer coefficients and fin enhancement place this type of heat exchanger between conventional round tube plate fin types and water cooled or cooling types, providing a more universal basis for conclusion. A serpentine design was selected to avoid uncertainties in predicting the charge in headers for various refrigerants. The serpentine design does not reduce the generality of the conclusions or even limit the increase in mass flux.

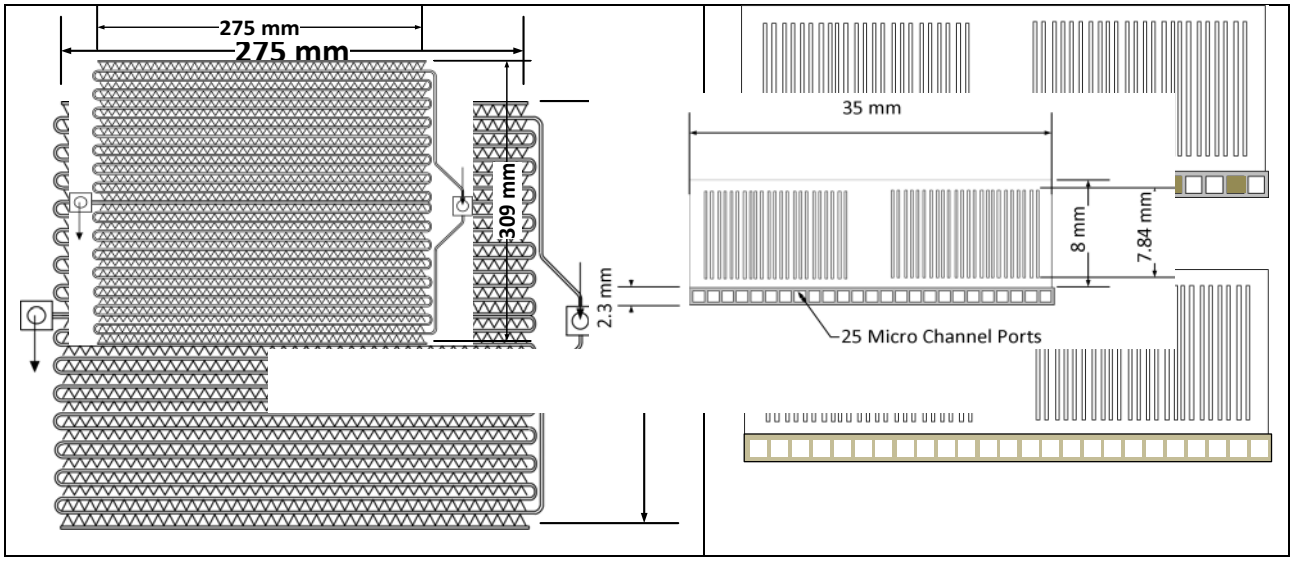

Fig. 7: Baseline serpentine condenser design

Tab. 1: Geometry of the condenser

Fins		Tubes		Overall	
Fin height [mm]	8	Number of tubes (circuits)	2	Width [mm]	275
Fin depth [mm]	35	Tube thickness [mm]	2.3	Height [mm]	200
Fin thickness [mm]	0.15	Tube depth [mm]	35	Depth [mm]	30
Fins per inch [in^{-1}]	15	Number of ports [-]	25	Circuits [-]	2
Fin pitch [mm]	1.41	Hydraulic diameter [mm]	Varies	Runs per circuit [-]	10
Louver height [mm]	7.84	Absolute roughness [mm]	0.001	Air HT area [m^2]	1.612
Louver pitch [mm]	1.72				
Louver angle [^{o}]	27				

For the example presented here, the internal diameter of the channel was the only variable in the model used to adjust refrigerant pressure drop. In the experiments it was easier to vary the number of active channels and the model was adjusted to facilitate validation.

To estimate the condenser charge required for different refrigerants, the internal volumes (diameters) of identical baseline heat exchangers are shrunk to create a pressure drop which causes an equal (here selected 1%) reduction in COP. Certainly, 1% is arbitrary value, but it is equal for each refrigerant. One could question if equal penalty is fair, Wujek, (2012). More about this subject may be found in Hrnjak (2009) and Padilla and Hrnjak (2012).

The adopted model takes into account the effect of the ratio between the refrigerant and air side heat transfer areas when iterating to find the solution.

A fair comparison of minimum refrigerant charges requires maintaining the system capacity while modeling heat exchangers with the same face area, exterior tube dimensions, identical fins, and same operating conditions on the air side (velocity, temperature, humidity). Additionally, the effect of the condenser on the rest of the refrigerant side of the system should be the same. Here it is defined as a 1% difference between COPs of the system with a real condenser and one without pressure drop on the refrigerant side. The condenser channel diameter is modified to generate the same degradation of COP due to refrigerant side pressure drop compared to an ideal condenser (without pressure drop) while maintaining the same evaporator capacity. A similar option would be to vary the number of active channels while maintaining the channel diameter and the outer dimensions of the flat tube. This approach has been tested experimentally in Hoehne and Hrnjak, (2004).

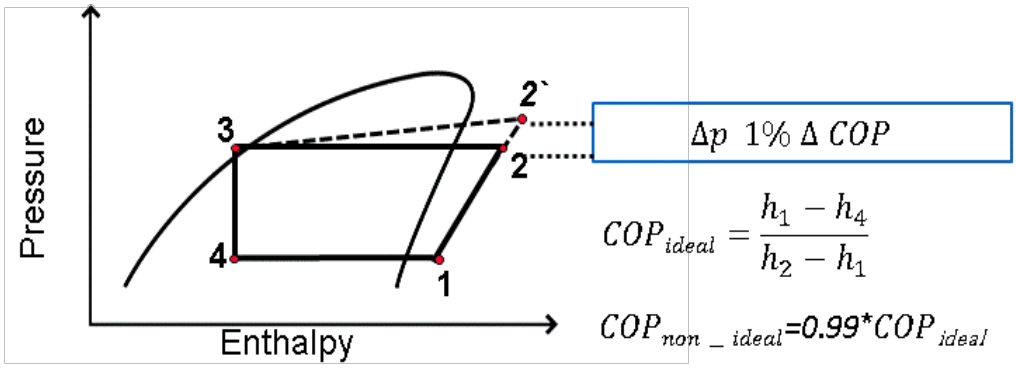

Fig. 8: Illustration of the logic – pressure drop that causes 1% change in COP

Fig. 8 compares the "ideal" baseline cycle, in solid line, to the "real" cycle, with pressure drop, shown with the dashed line. The pressure drop in the "real" condenser is set to cause a 1% reduction in COP compared to "ideal" cycle. Isenthalpic expansion and isentropic compression are assumed in the ideal cycle for all fluids. The Zivi void fraction model was used because it is refrigerant independent but consequently the effect of mass flux was not reflected. These assumptions do not affect the generality of conclusions. Cycle operating conditions in this example are: $T_{evaporation}$=0°C, T_{airin}=20°C, superheat 5 K. Based on the evaporator and condenser models, the necessary charge to achieve 1 kW cooling capacity for various refrigerants is evident from the Fig. 9. Additionally, the "real" hydraulic diameter of the condenser to minimize charge with only 1% degradation in COP can be found, and to make more plastic presentation, the size of the squares represent the relative sizes of the channel. Ammonia requires the lowest charge but not the smallest tube size. Isobutane requires a much larger tube diameter.

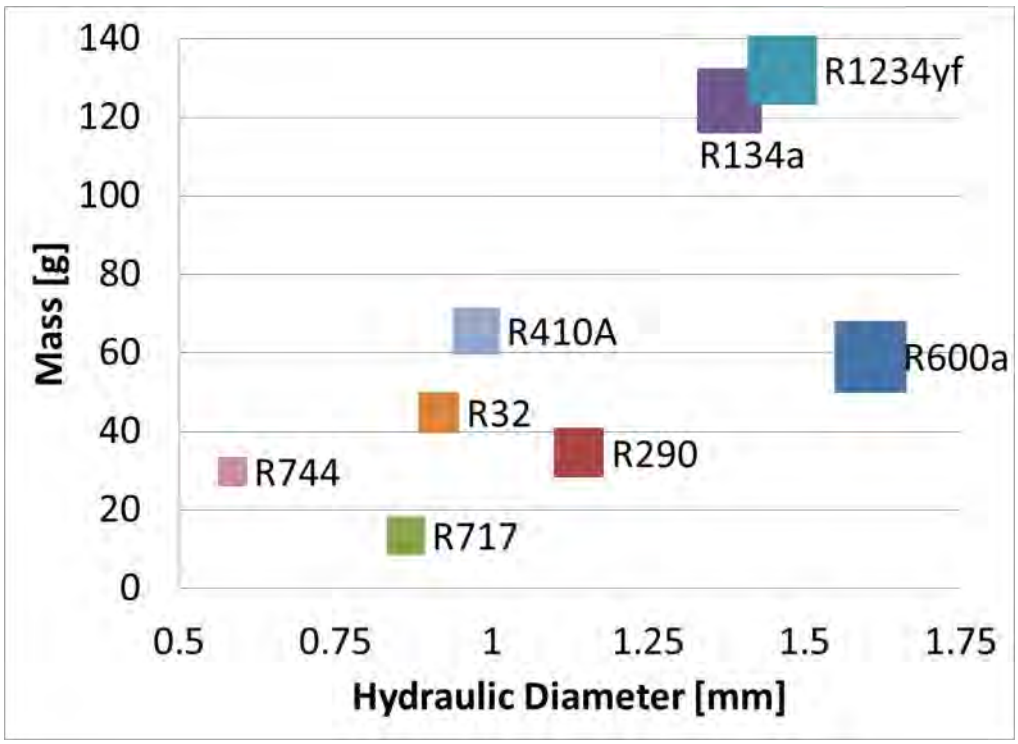

Fig. 9: Refrigerant charge and hydraulic diameter of serpentine condenser for 1kW refrigeration system causing 1% difference from ideal COP due to condenser pressure drop

R717 and R744 show the best potential for low charge systems but for different reasons. R717 is known to have a very high pressure drop for a given mass flux because of very low vapor density (see second to last column in Table 2) which causes higher velocity for a given mass flow rate in comparison to other fluids. However, due to its very high latent heat (h_{fg} = 1167 kJ/kg), the mass flow needed for the same capacity is significantly lower for R717 than for any other fluid. The sensitivity of ammonia to pressure drop is neither exceptionally low nor high in comparison to the other fluids shown in Table 2 (column 5, ΔP). Since vapor density is very low for ammonia, the total mass is the lowest for a given void fraction. Light vapor is helpful in building a low charge system.

Carbon dioxide (R744) has different characteristics than ammonia. R744 has a low sensitivity to pressure drop, which means that high pressure drop will not result in high temperature drop. The sensitivity to pressure drop is given in Table 2, Column 5. The potential for building a low charge R744 system comes from having low pressure drop (due to dense vapor) and very low sensitivity to pressure drop. The small channel sizes, dense vapor, and low sensitivity to pressure drop indicated that microchannel heat exchangers are ideal for R744. Because R744 has a dense vapor, it will have more refrigerant mass at a given void fraction and internal volume

The largest hydraulic diameter is required for R600a (Isobutane) mostly because of the lighter vapor (second to ammonia). The combination of both light vapor and liquid keeps the charge reasonably low even with the largest diameter.

The two refrigerants that require the highest charge are R1234yf and R134a even though their individual thermophysical properties are balanced. High density of liquid combined with high sensitivity to pressure drop requires significantly greater charge than other fluids presented here.

Tab. 2: Refrigerant charges in evaluated condenser serving 1 kW evaporator based on pressure drop that causes 1% COP reduction compared to idealized (∆P=0 cycle)

Fluid	Ref. Mass	Hydr. Diam.	Mass Flow	∆P [1 % COP reduction]	COP Ideal	Cond. Temp.	Rejected Heat	Liquid Density	Sat. Vapor Density	Latent Heat
	[g]	[mm]	[g/s]	[kPa]	[-]	[C]	[kW]	[kg/m^3]	[kg/m^3]	kJ/kg]
R717	13.4	0.86	0.86	7.45	10.0	24.6	1.043	604	7.72	1169.0
R744	29.8	0.59	5.94	35.79	7.0	24.3	1.103	725	234.70	125.9
R290	34.4	1.14	3.15	6.58	9.6	25.2	1.048	492	20.72	335.7
R32	44.9	0.92	3.63	11.46	9.4	24.8	1.054	963	47.12	271.7
R600a	59.1	1.61	3.31	3.17	9.8	25.5	1.067	550	9.285	329.4
R410A	65.6	0.98	5.32	11.65	9.4	25.1	1.067	1063	66.15	187.8
R134a	124.2	1.38	5.96	5.52	9.5	25.6	1.094	1206	32.88	177.7
R1234yf	132	1.46	7.52	5.41	9.3	25.6	1.077	1091	38.42	145.6

4. SUMMARY AND CONCLUSIONS

This paper presented reasons for charge reduction and strategies for the actions:

1. Introduction of another (secondary) fluid
2. In the compressor:
    - Reducing the internal volume
    - Reducing quantity in lubricant
    - Reducing solubility to reduce refrigerant absorption.
3. In vessels by reducing volume and liquid levels.
4. In pipes by reducing internal volume (diameter and possibly even length).
5. In heat exchangers by reducing tube diameter and length

Because it is the most attractive, the last strategy is elaborated in detail. Obviously, to reduce the charge internal volume needs to be reduced, but the most important is to take in consideration effects of heat transfer balance and mass flux on void fraction.

Special attention is given to explore and design a methodology for fair way of comparing refrigerants based on their potential to be used in low charge condensers.

NOMENCLATURE

A = Area [m^2]
α = void fraction [-]
L = total length [m]
m= mass [g]
ρ = density [kg/m^3]
x = quality [-]
z = length

Subscripts
l = liquid
v = vapor
i = counter

REFERENCES

Adams, D., P. Hrnjak, and T. Newell, 2003, Pressure Drop and Void Fraction in Microchannels Using Carbon Dioxide, Ammonia, and R245FA as Refrigerants, ACRC Report TR221

Adams, D. C., J. D. Burr, P. S. Hrnjak, and T. A. Newell, 2006, “Void Fraction of CO2 and Ammonia in Multiport Aluminum Microchannel Tubes,” Proceedings of the 11th International Refrigeration and Air Conditioning Conference at Purdue, West Lafayette, IN

Butterworth, D. 1975. A Comparison of Some Void-Fraction Relationships for Co-Current Gas-Liquid Flow" International Journal of Multiphase Flow, 1: 845-850.

Cavallini, A. 2012. IIR Gustav Lorentzen conference on natural refrigerants, Delft

Hoehne M.R., Hrnjak P.S., 2004, Charge minimization in systems and components using hydrocarbons as a refrigerant, Air Condition and Refrigeration Center, University of Illinois, Technical Report 224

Hrnjak P.S. 2010, Developments in charge reduction and microchannel technology: Mass flux as a way to affect void fraction – charge, 2nd IIR Workshop on Refrigerant Charge Reduction, KTH, Stockholm

Hrnjak P.S. 2009, Refrigerant charge reduction: strategies and experience, 1st IIR Workshop on Refrigerant Charge Reduction, Cemagref Antony, France

Hrnjak, P., 2012, Technologies needed to advance the position of major natural refrigerants: HC, NH3 or CO2, IIR Gustav Lorentzen conference on natural refrigerants, Delft

Litch A.D., Hrnjak P.S., 1999, Condensation of ammonia in microchannel heat exchangers, Air Condition and Refrigeration Center, University of Illinois, Contract Report 22

Hrnjak, P. A. Litch, 2001. Charge Reduction in Ammonia Chiller Using Air-Cooled Condensers with Aluminum Microchannel Tubes, Proceedings of International Institute of Ammonia Refrigeration Conference Long Beach, CA, 235-267

Newell, T.A. et al. 1999. An Investigation of Void Fraction in the Stratified/Annular Flow Regions in Smooth, Horizontal Tubes In Review for International Journal of Multiphase Flow

Niño V., P. Hrnjak, T. Newell, 2002, Characterization of Two-Phase Flow in Microchannels ACRC TR202

Palm, B. 2009. Summarizing a Decade of Experience on Charge Reduction for Small HC, Ammonia and HFC Systems, 1st IIR Workshop on Refrigerant Charge Reduction, Paris

Padilla Y, P. Hrnjak, 2012 Experimentally Validated Microchanel Heat Exchanger Performance And Charge Predictions Used To Compare Charge Reduction Potentials Of Some Refrigerants, 10th IIR Gustav Lorentzen Conference on Natural Refrigerants, Delft, The NetherlandsTraeger K.M., Hrnjak P.S., 2005, Charge minimization of microchannel heat exchangers, Air Condition and Refrigeration Center, University of Illinois, Technical Report 251

Wujek, S. 2012, Personal communication

Zivi S.M., 1964, Estimation of steady-state steam void fraction by means of the principle of minimum entropy production, J. Heat Transfer, 86 Trans. Am. Soc. Mech. Engrs, Series C (1964), 247–252..

Manuscript ID: 1833
DOI: 10.18462/iir.icr.2019.1833

Recent developments in HVAC&R systems utilizing two-phase ejector for expansion work recovery

Stefan ELBEL[a,b]

[a] Air Conditioning and Refrigeration Center
Department of Mechanical Science and Engineering
University of Illinois at Urbana-Champaign
1206 West Green Street, Urbana, IL 61801, USA, elbel@illinois.edu

[b] Creative Thermal Solutions, Inc.
2209 North Willow Road, Urbana, IL 61802, USA, stefan.elbel@creativethermalsolutions.com

ABSTRACT

This paper gives an overview of the technical challenges encountered with two-phase ejector refrigeration systems. Of particular interest are attainable improvement potentials for different working fluids, including CO_2 and as well as lower pressure refrigerants such as R410A or R1234yf. Numerous ways of how to best integrate the ejector have been studied. Besides the standard two-phase ejector cycle it is also possible to utilize the recovered expansion energy to drive evaporator overfeed or to provide cooling at different temperature levels. Ejector design plays an important role in achieving high work recovery efficiencies, but the design of other system components, such as the evaporator or the vapor/liquid separator that many of the cycle architectures require are equally influential and offer large improvement potentials. Finally, the paper will give an overview of various ejector control options which are important, especially when capacity modulation requirements need to be met.

Keywords: Two-phase Ejector, Expansion Work Recovery, COP, Cycle Improvement, Energy Efficiency

1. INTRODUCTION

In vapor-compression refrigeration cycles, throttling devices such as capillary tubes, short tube orifices, and expansion valves are used as robust and cost-effective solutions for expanding the refrigerant from the higher condensing or gas cooling pressure to the lower evaporation pressure. However, the physical process during throttling is irreversible. The isenthalpic pressure reduction inflicts a dual penalty on the system in the form of reduction in cooling capacity as well as increase in required compression work. This results in lower COP of the actual vapor-compression refrigeration cycle compared to an ideal Carnot refrigeration cycle. COP reduction due to the isenthalpic process in the expansion valve can be lessened by many different methods. One of the simplest methods is internal heat exchange that reduces the generation of flash gas during expansion by introducing more subcooling at the inlet of the expansion device. However, methods that involve expansion work recovery are known to be more beneficial in terms of cycle efficiency and cooling capacity. A common feature of methods that involve work recovery is that they attempt to utilize the kinetic energy released during the pressure reduction of the fluid as it passes from the high- to the low-pressure side to save compressor work instead of dissipating it in a throttling process. Meanwhile, an isentropic expansion process is approached rather than isenthalpic throttling. This increases cooling capacity because the specific enthalpy at the evaporator inlet is reduced. Therefore, devices that can approach expansion closer to isentropic process are worth exploring.

An ejector is a device that uses the expansion of a high-pressure (motive) fluid to entrain and compress a low-pressure (suction) fluid by means of momentum transfer between the two streams of fluid. The motive fluid is expanded through a usually converging-diverging (though sometimes converging-only) nozzle to high velocity and low pressure. This high velocity and low pressure is used to entrain the suction fluid through the suction nozzle; the motive and suction fluids are then mixed in the mixing section. The high-speed mixed flow is then decelerated in the diffuser and static pressure is recovered, resulting in a pressure increase provided to the suction stream across the ejector.

2. WORKING FLUIDS USED WITH EJECTOR CYCLES

The amount of COP improvement that can be obtained with the ejector cycle depends on many factors including the properties of the fluid that is being used. Fluids with greater irreversibility or throttling loss (difference between isentropic and isenthalpic expansion) in the expansion device of the DX cycle offer greater opportunity for improvement. Fluids with a higher mass flow rate for a given capacity may also benefit from expansion work recovery, as larger mass flow rate also increases the total irreversibility in the expansion device. Figure 1 compares the specific throttling loss for three different refrigerants (CO_2, R410A, and R134a) as seen in a temperature-specific entropy diagram. Note again that total throttling loss is also proportional to mass flow rate; for the same capacity, the mass flow rate for each fluid is inversely related to the enthalpy difference in the evaporator. Overall, CO_2 has significantly higher throttling loss compared to low-pressure fluids, especially at elevated ambient temperatures where a CO_2 cycle would operate in transcritical mode; this means that CO_2 has much greater opportunity for COP improvement when using a work recovery device such as an ejector.

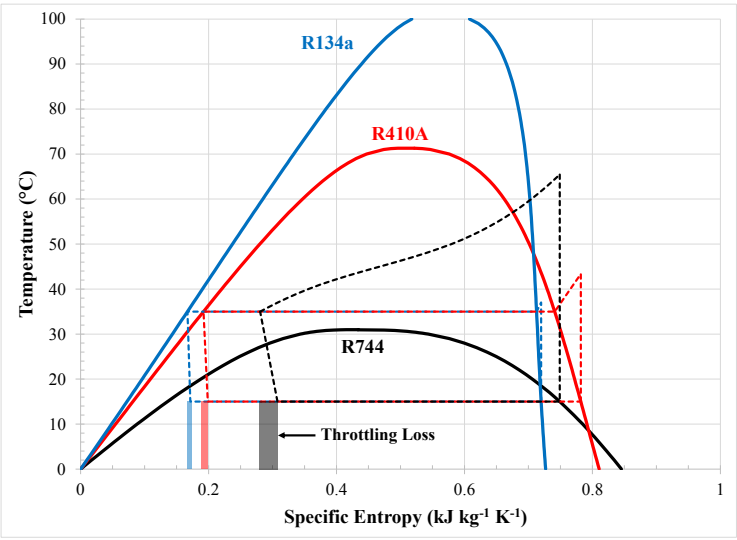

Figure 1: Vapor-compression cycle with isenthalpic expansion shown on temperature-specific entropy diagram for R744 (CO_2), R410A, and R134a

Table 1 presents simulation results for a typical ejector cycle for the three refrigerants mentioned before. It is obvious that CO_2, even when an IHX is used, shows the largest improvement potential for the ejector. While the numbers presented are based on ideal cycle assumptions, measurements on real ejector systems confirm these trends. COP improvement potentials for transcritical CO_2 systems are found in the range of 15 to 30%. For R410A or comparable HFO replacements, realistic COP increases are on the order of 10 to 15%, while for low pressure fluids such as R134a, R1234yf, etc., the attainable COP gain is approximately 5%. The exact numbers depend of course on the application and performance level of the baseline system to which the ejector system is being compared. A large difference between heat sink and heat source temperature further increase the potential for work recovery. Suitable applications include air-conditioning at elevated ambient temperatures, commercial refrigeration systems, low-temperature heat pumps, heat pump water

heater systems, and many more. Additional details regarding work recovery potentials can be found in Elbel and Lawrence (2016).

Table 1. Comparison of ejector improvement potentials for various refrigerants for following thermodynamic cycle conditions and assumptions: Q_{evap} = 2 kW; T_{evap} = 15°C; R134a/R410A: T_{cond} = 35°C, ΔT_{SC} = 0 K; CO_2: P_{gc} = 90 bar, $T_{gc,out}$ = 35°C

Refrigerant	Specific Throttling Loss (kJ kg^{-1})	Mass Flow Rate (g s^{-1})	Total Throttling Loss (kW)	Maximum COP Improvement (%)
CO_2 (no IHX)	7.10	17.0	0.121	**56.5**
CO_2 (ε_{IHX} = 0.6)	5.54	13.8	0.076	**38.8**
R410A	1.95	11.9	0.023	**17.6**
R134a	1.27	12.7	0.016	**12.4**

The use of ejectors for work recovery in vapor-compression systems has been a topic of research for approximately the past 25 years. Early work in the 1990's focused on theoretical performance predictions and component performance tests using low-pressure refrigerants. Approximately ten years ago, a significant amount of research began on the application of two-phase ejectors to transcritical CO_2 cycles. CO_2 has been seen recently as a possible alternative refrigerant that could replace current HFC refrigerants that are being phased out, and as discussed above, the application of ejector technology to CO_2 systems could improve efficiency substantially. As a result, much of the focus of two-phase ejector research in the past ten years has been on transcritical CO_2 cycles. Several numerical studies on transcritical CO_2 ejector cycles were published in 2004, while the first detailed experimental investigation was published in 2008; numerous additional experimental studies appeared since.

3. EJECTOR CYCLE INTEGRATION

3.1. Standard Two-phase Ejector Cycle

The most commonly considered cycle using an ejector for expansion work recovery is shown in Figure 2 for transcritical operation. This cycle is often referred to as the standard ejector cycle. This cycle was first patented by Gay (1931) but was largely neglected for many years until Kornhauser (1990) reported the first detailed theoretical analysis of the cycle. Kornhauser (1990) was the first to analyze the performance of the standard ejector cycle. He used a thermodynamic state point model for the cycle and the zero-dimensional constant-pressure mixing model for the ejector to investigate the ability of the standard ejector cycle to improve COP with several different refrigerants. He observed that the COP of the ejector cycle was strongly dependent on the specified efficiencies of the ejector components and that the maximum COP improvement achieved by the ejector cycle compared to a cycle with an isenthalpic expansion (DX cycle) ranged from 12 to 30 % depending on the refrigerant. A similar study was performed by Domanski (1995) with 38 different refrigerants, predicting up to 80 % COP improvement. Much of the recent work on two-phase ejectors has focused on transcritical CO_2 systems. Elbel and Hrnjak (2004) and Li and Groll (2005) used numerical models to analyze the performance of a transcritical CO_2 ejector cycle; both of these studies showed that, similar to a transcritical CO_2 DX cycle, the COP of a transcritical CO_2 ejector cycle can be maximized by optimizing gas cooler pressure. Further discussion of gas cooler pressure optimization in CO_2 ejector cycles will be provided in the sections on experimental studies and ejectors in real systems below.

It will also be one of the focuses of the experimental investigation reported in this study. Numerous additional studies have also theoretically investigated the transcritical CO_2 ejector cycle, though the conclusions of these studies were similar to those of Elbel and Hrnjak (2004) and Li and Groll (2005).

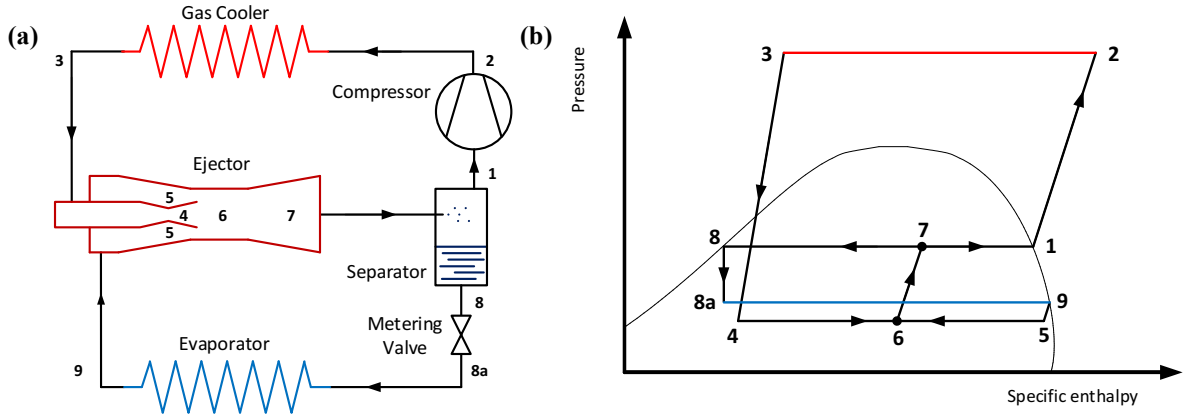

Figure 2: Standard ejector cycle for transcritical operation represented as (a) schematic diagram and (b) pressure-specific enthalpy diagram.

3.2. Ejectors in Liquid Recirculation Cycles

The standard ejector cycle uses the ejector to lift the pressure of the fluid at the evaporator outlet, which results in higher compressor suction pressure. In this sense, the work recovered in the ejector is used to directly supplement the work of the compressor. However, this is not the only way that the work recovered by the ejector can be used to improve cycle performance, as the work recovered in the ejector can be used to pump excess liquid through the evaporator, resulting in an evaporator that is overfed with liquid. This liquid overfeed or liquid recirculation effect increases the mass flux through the evaporator and eliminates evaporator dryout, resulting in improved evaporator performance. Thus, the work recovered in the ejector can also be used to improve evaporator performance, which indirectly unloads the compressor. Figure 3 shows a schematic of the ejector recirculation cycle in which the ejector is used to recirculate liquid through the evaporator. This cycle was patented by Phillips (1938).

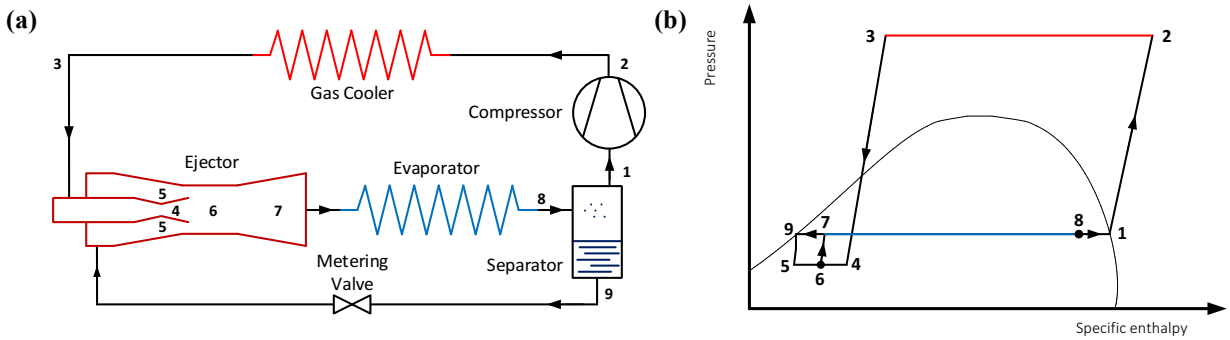

Figure 3: Ejector recirculation cycle shown as (a) schematic and (b) pressure-specific enthalpy diagram

Liquid overfeed was actually the first widely used application of ejectors for work recovery before research began on the standard ejector cycle (Lorentzen, 1983). However, only a limited amount of research can be found on the ejector recirculation cycle in the open literature, possibly because the operation and performance of the cycle are thought to be well understood already. Furthermore, the positive effects of this indirect method of utilizing expansion work to improve the cycle are not directly visible from simple state point models since the improvement mechanism relies on improving evaporator effectiveness by eliminating or reducing dryout. Industrial refrigeration systems utilizing refrigerant pumps for liquid overfeeding target the same improvement mechanism; however, in those cycles electric power has to be spent to operate the pump, while in the ejector recirculation cycle, expansion work is used to achieve overfeed. Note that the standard ejector cycle can also use the ejector to recirculate liquid and improve evaporator performance while simultaneously using the ejector to directly unload the compressor. With the exception of the present study, no research has

focused on modeling of the ejector recirculation cycle or comparing the standard ejector and ejector recirculation cycles.

One factor that affects the amount of COP improvement that can be achieved with a recirculation cycle is the amount of additional liquid being fed into the evaporator. The amount of additional liquid being fed into the evaporator (the amount of recirculation) can be quantified by the circulation number (*n*), defined as the total mass flow rate of liquid supplied to the evaporator divided by the mass flow rate of refrigerant that is vaporized in the evaporator, as defined by (ASHRAE, 2014) and shown in Eq. (1). By performing an energy balance on the refrigerant that is vaporized in the evaporator, an expression for mass flow rate of vaporized refrigerant can be obtained and used to calculate circulation number, as also shown in Eq. (1). ASHRAE (2014) also defines the overfeed ratio (*OR*) as the mass ratio of liquid to vapor at the evaporator outlet, as shown in Eq. (2).

$$n = \frac{\dot{m}_{evap,total}}{\dot{m}_{evap,vaporized}} = \frac{\dot{m}_{evap,total}\left(h_v\left(P_{evap,out}\right) - h_{evap,in}\right)}{\dot{Q}_{evap}} \quad \text{Eq. (1)}$$

$$OR = \frac{\dot{m}_{liquid,evap,out}}{\dot{m}_{vapor,evap,out}} = \frac{1 - x_{evap,out}}{x_{evap,out}} \quad \text{Eq. (2)}$$

When using the ejector recirculation cycle, it must be determined if the total mass flow rate at the evaporator inlet or the mass flow rate of liquid at the evaporator inlet should be used in the numerator of the circulation number definition, as there will often be a significant amount of vapor present at the evaporator inlet in this cycle. For the forced standard ejector cycle, this would not be a problem as the amount of vapor at the evaporator inlet is generally very small and would not have a significant effect on the calculated value of circulation number. In this study, the total evaporator inlet mass flow rate (liquid and vapor) is used in the numerator of the circulation number for all cycles.

The amount of overfeed can also be measured with the recirculation ratio (*R*), defined as the evaporator mass flow rate over the condenser/gas cooler mass flow rate, as shown in Eq. (3). It is easy to see that for the standard ejector cycle, the recirculation ratio is equivalent to the entrainment ratio of the ejector, which is defined as the ejector suction mass flow rate divided by the ejector driving or motive mass flow rate, as shown in Equation (4). It can also be seen that for the ejector recirculation cycle, the recirculation ratio is equal to the ejector entrainment ratio plus one, as also pointed out by Li *et al.* (2014) and shown in Equation (5).

$$R = \frac{\dot{m}_{evap}}{\dot{m}_{cond}} \quad \text{Eq. (3)}$$

$$R_{StandardEjecCycle} = \Phi_m \quad \text{Eq. (4)}$$

$$R_{EjecRecircCycle} = 1 + \Phi_m \quad \text{Eq. (5)}$$

In comparison to the circulation number, the recirculation ratio is relatively easy to understand and use, and its definition is valid for any evaporator outlet state. Furthermore, as shown above, the recirculation ratio can be directly related to the entrainment ratio of the ejector for both of the ejector cycles. However, the recirculation ratio is simply a ratio of mass flow rates and does not provide any direct information about the amount of overfeed in the evaporator like the circulation number does.

3.3. Alternate Two-phase Ejector Cycles

Numerous examples of alternate vapor-compression cycles using an ejector for work recovery can be found in the open literature. One example of an alternate ejector work recovery cycle is shown in Figure 4. The flow at the outlet of the condenser or gas cooler is split; one stream becomes the motive flow of the ejector while the other stream is isenthalpically expanded and sent to an evaporator before becoming the suction flow of the ejector. The two-phase flow at the outlet of the ejector is sent to a second, higher temperature evaporator before entering the suction of the compressor. Because the flow at the outlet of the condenser (subcritical operation) is split, this cycle will be referred to as the COS (condenser outlet split) ejector cycle (Lawrence and Elbel, 2013). The pressure lift provided by the ejector causes a lift in saturation temperature between the two

evaporators, meaning that the COS ejector cycle offers the opportunity to provide cooling capacity at two different temperatures. This may initially seem like an attractive cycle for systems that require two different evaporation temperatures, such as refrigeration systems with medium-temperature (MT) and low-temperature (LT) evaporators. However, it must be noted that the difference in temperature between the evaporators and the ratio of capacities of the evaporators are not independent but are a function of ejector operation. The temperature difference is controlled by the pressure lift of the ejector, while the ratio of capacities is related to the entrainment ratio of the ejector; because ejector pressure lift and entrainment are related, there is a trade-off between greater temperature separation between the evaporators and greater low-temperature evaporator capacity. In addition, depending on the fluid, the achievable temperature difference between the two evaporators, which is the temperature lift achieved by the ejector, may only be about 1 to 2 K, which is too small for what is needed in typical two-temperature applications. Thus, despite the two different evaporation temperatures, the two evaporators in this cycle may be best suited for cooling the same stream of fluid; note that the two evaporators may allow for separation of latent and sensible loads in this case.

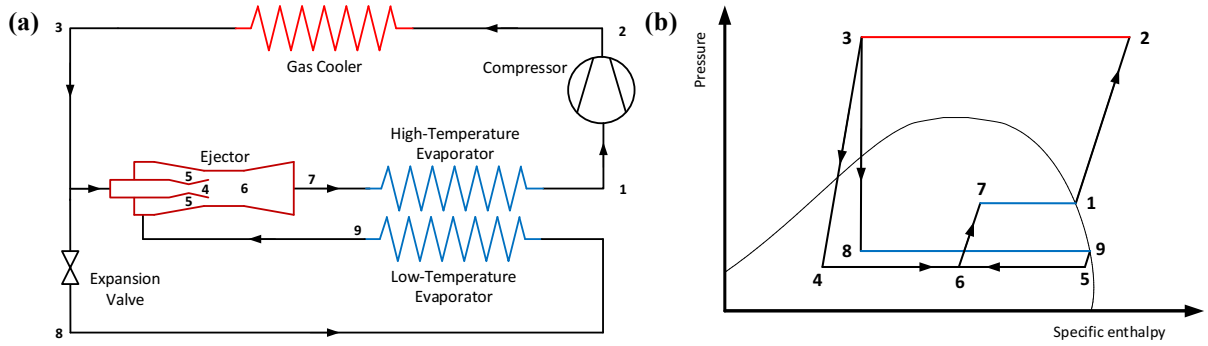

Figure 4: Alternate ejector cycle for transcritical operation represented as (a) schematic diagram and (b) pressure-specific enthalpy diagram

Lawrence and Elbel (2013) noted several advantages that the COS ejector cycle offers in comparison to the standard ejector cycle. The COS ejector cycle does not have a liquid-vapor separator; the large size and potential inefficiency of a separator may not be allowable for some applications. The COS ejector cycle is also better suited for off-design performance. If the ejector in the standard ejector cycle fails to entrain sufficient mass flow, due to poor ejector design or conditions of low work recovery, then the cycle will lose significant capacity and COP; the COS ejector cycle would not lose capacity in either evaporator if the ejector failed to entrain properly because all flow passes through the compressor. The COS ejector cycle could also potentially offer better oil return than the standard ejector cycle because there is no opportunity for oil separation in parallel loops.
There are numerous additional alternate ejector cycle options that have been proposed and analyzed in the open literature. The majority of these alternate cycles have been proposed more recently, mainly since 2012 once the operation and performance of the standard ejector cycle was better understood. Chen *et al.* (2015) provide an overview of many of the different cycle options that use an ejector for work recovery. However, it should be noted that few of the alternate ejector cycles sufficiently address issues such as off-design operation, separator inefficiency, or oil return that likely limit the use of ejector cycles in real applications. Nonetheless, it may be worth considering the COS ejector cycle or other alternate ejector cycles that offer practical advantages for real applications in future experimental studies, especially when working with fluids that offer less improvement from expansion work recovery.

4. INFLUENCE OF EVAPORATOR DESIGN

High ejector cycle efficiency requires optimized ejector designs. However, it is often overlooked that other cycle components, such as heat exchangers, vapor-liquid separator, and oil management require optimization as well. If that is not the case, it is easily possible that the performance improvements obtained with the ejector are not strong enough to offset performance losses caused

by other components in the cycle that are not optimized. For the purpose of illustration, experimental results with two different ejector cycles and two different evaporator designs are presented next.

4.1. Test Conditions

Compared are the performance of the standard ejector cycle and the ejector recirculation cycle. The refrigerant is R410A. The comparison is performed with both Evaporator A and with Evaporator B in order to see the effect that refrigerant-side cross-sectional area can have on the performance of the cycles. Evaporators A and B have exactly the same exterior dimensions on the air side. The only difference is that Evaporator B has approximately 50 % of the cross-sectional area on the refrigerant side. This was achieved by purposefully blocking every other microchannel port during the manufacturing process. More details can be found in Lawrence and Elbel (2016).
Table 2 shows the system conditions that were used in this section. Evaporator air inlet temperature and flow rate were the same for all tests. Condenser air flow rate was the same for all tests, but condenser air inlet temperature was varied for some tests. The condenser outlet state (ejector inlet state) was approximately saturated liquid due to the presence of the receiver at the condenser outlet. The capacity was kept the same for all tests (1.0 kW) by adjusting compressor speed; this value of capacity was chosen to ensure that the compressor could achieve the desired capacity for all cycles and conditions. In order to investigate different amounts of evaporator overfeed, the evaporator flow rate (outlet state) was adjusted for different tests using the metering valve in each of the ejector cycles. The DX cycle was operated with 3 K of superheat at the evaporator outlet. The system was charged with enough refrigerant to ensure a reasonable liquid level in the liquid-vapor separator for all conditions; this ensured that only liquid would flow to the evaporator in the standard ejector cycle.

Table 2. Operating conditions used in R410A experiments

Parameter	Unit	Value
$T_{evap,air,in}$	°C	27
$\dot{V}_{evap,air}$	$m^3\ s^{-1}$	0.100
$T_{cond,air,in}$	°C	35, 39, 42
$\dot{V}_{cond,air}$	$m^3\ s^{-1}$	0.200
$\dot{Q}_{evap}$	kW	1.0
$x_{cond,out}$	-	0.0
R	-	0.67 – 1.64
$\Delta T_{SH,DX}$	K	3

4.2. Comparison of Standard Ejector and Ejector Recirculation Cycles

The results comparing the performance of the two ejector cycles with Evaporator A are shown in Figure 5 with the evaporator outlet state for each point indicated (same capacity for each point). Performance is reported in terms of the COP Ratio; capacity was the same for each test. The amount of recirculation is measured with the Recirculation Ratio, Eq. (3). It can be seen that the ejector recirculation cycle can achieve up to 16 % COP improvement, though COP of this cycle increases only slightly beyond a recirculation ratio of 1.1. The improvement in COP obtained with the ejector recirculation cycle comes solely from improving the performance of the evaporator; the pressure lift of the ejector is only used to overcome pressure drop in the low-pressure circuit and cannot be used to directly lift compressor suction pressure. The performance of the evaporator in the ejector recirculation cycle is improved in comparison to that of the DX cycle because dryout is eliminated and mass flux is increased by the additional liquid being recirculated by the ejector. Theoretically, the ejector recirculation cycle should have the same performance as the DX cycle if the metering valve is closed (recirculation ratio of 1.0) and the evaporator is operated with the same superheat as the DX cycle. This case is shown in the figure where the ejector recirculation cycle has a recirculation ratio of 1.0 and an evaporator outlet superheat of 3.7 K; the COP is within 1 % of the DX cycle COP. Note that this comparison is only shown to demonstrate that the ejector recirculation cycle without any recirculation and the DX cycle are essentially the same; the ejector recirculation cycle would never be operated this way in a real application. If some amount of recirculation is used and the

superheat at the end of the evaporator is eliminated, then the ejector recirculation can achieve significantly higher COP than the DX cycle.

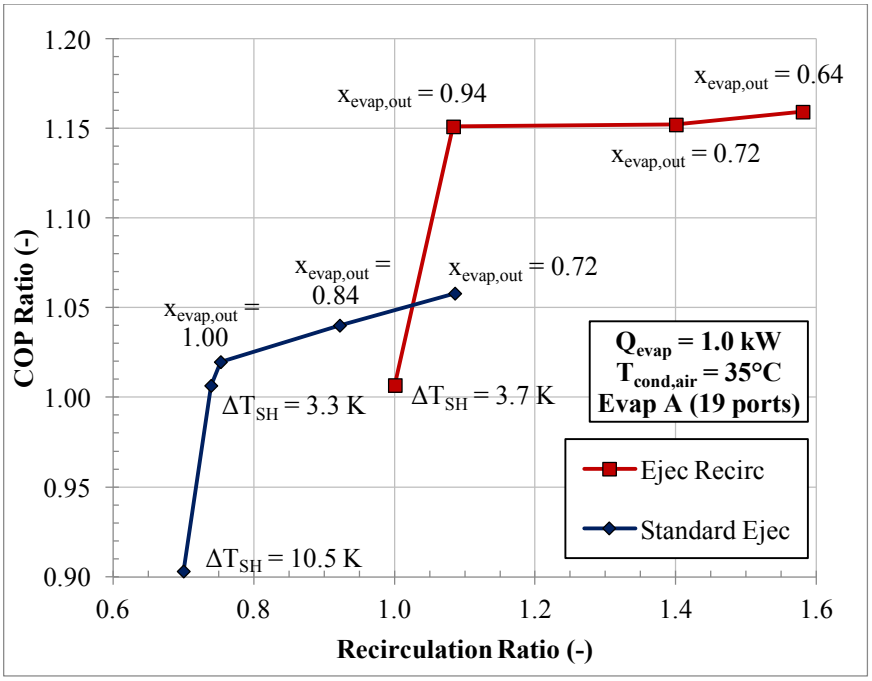

Figure 5: COP improvement obtained with standard ejector and ejector recirculation cycles as a function of recirculation ratio using Evaporator A

Figure 5 also shows that the standard ejector cycle achieves noticeably lower COP despite being the more commonly considered of the two ejector cycles. If the standard ejector cycle is operated with 3 K superheat to match the evaporator outlet state of the DX cycle, it is only able to achieve about 1 % COP improvement over the DX cycle. On the other hand, if the ejector is used to recirculate excess liquid through the evaporator in addition to lifting compressor suction pressure, then the standard ejector cycle is able to achieve up to 6 % COP improvement at an evaporator outlet quality of 0.72. These results for both ejector cycles indicate that with Evaporator A, it is better to use the ejector to eliminate superheat and overfeed the evaporator rather than directly lift compressor suction pressure. Note that difficulty was encountered in obtaining readings at higher evaporator mass flow rates, as the mass flow meter upstream of the evaporator in the standard ejector cycle produced unstable readings at higher flow rates; as a result, data could not be obtained for higher recirculation ratios. It would be expected that the COP of each ejector cycle reaches a maximum and then begins to decrease at higher recirculation ratio as refrigerant pressure drop becomes more significant.

4.3. Effect of Evaporator Design on Ejector Cycle Comparison

The previous results have shown that an evaporator with too large refrigerant-side cross-sectional area and too low refrigerant mass flux can have a negative impact on the performance of the evaporator in the standard ejector cycle, limiting the opportunity to improve COP with this cycle; for the present case, the standard ejector cycle mass flux was less than 50 kg m^{-2} s^{-1} with Evaporator A for a saturated outlet. However, if a different evaporator that was not penalized as severely by reduced mass flux were used, it is possible that greater COP improvements could be achieved. Thus, the comparison of the ejector cycles was repeated with Evaporator B, which had 10 microchannel ports in each tube (same port size) rather than 19. Using Evaporator B results in approximately half the refrigerant-side cross-sectional and heat transfer area but double the evaporator mass flux for a given mass flow rate, which increases the refrigerant-side heat transfer coefficient. The COP Ratio obtained with the two ejector cycles with Evaporator B is shown in Figure 6 along with the previously presented Evaporator A results for comparison. It can be seen that with Evaporator B, the standard ejector cycle achieves up to 9 % COP improvement, meaning that, as intended, the evaporator with lower refrigerant-side cross-sectional area has improved standard

ejector cycle performance. Note again that difficulty was encountered obtaining stable evaporator mass flow rate readings for higher values of recirculation number; a slight further increase in COP would be expected in this case if the evaporator were overfed in the standard ejector cycle. Interestingly, the ejector recirculation cycle achieves up to 13 % COP improvement with Evaporator B, meaning that an evaporator with lower refrigerant-side cross-sectional area hurts ejector recirculation cycle performance.

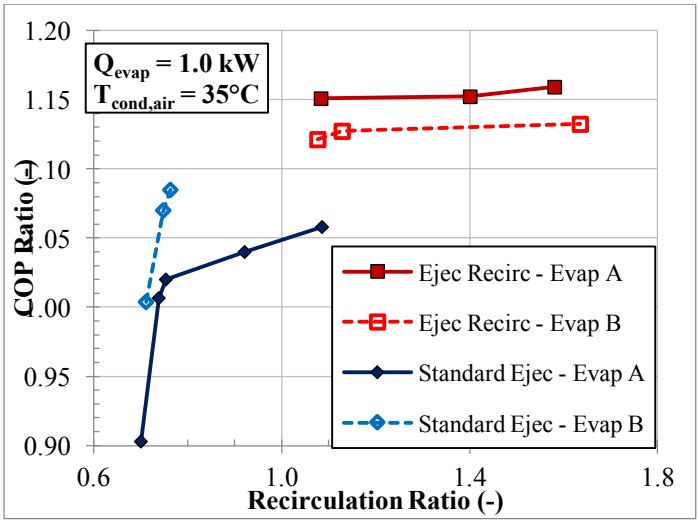

Figure 6: Comparison of performance of ejector cycles with different evaporators

5. EJECTOR CYCLE CONTROL

Another important topic is the control of the ejector and its cycle. For transcritical CO_2 the control of high side pressure represents an important parameter to optimize cycle performance.

A conventional (fixed geometry) ejector cannot actively control high-side pressure on its own, meaning that some additional means of control must be added to the cycle. Figure 7 shows several options for controlling the ejector in order to control high-side pressure. Figure 7(a) shows the adjustable ejector, while Figure 7(b) shows parallel ejectors; both of these options are being pursued and commercial solutions have been introduced to the market. Figure 7(c) shows an expansion valve in series with the ejector (to increase high-side pressure) and an expansion valve in parallel with the ejector (to decrease high-side pressure). The use of an expansion valve to control ejector cycle high-side pressure works well; however, it is associated with throttling losses in the valve. Nevertheless, this could be an attractive option for to implement a low-cost ejector control strategy.

In addition, vortex control offers a new way of providing ejector control. Zhu and Elbel (2016, 2017, 2018) were the first to experimentally investigate the influence of nozzle inlet vortex on the nozzle restrictiveness on initially subcooled flashing flow expanded through convergent-divergent nozzles. This novel two-phase nozzle restrictiveness control mechanism by adjustable nozzle inlet vortex, called vortex control, requires no change to the physical dimensions of the nozzle geometry. A nozzle with inlet vortex was called vortex nozzle (or swirl nozzle). Zhu and Elbel's experiments on vortex nozzle with initially subcooled R134a showed that the strength of the nozzle inlet vortex can change the restrictiveness of the two-phase convergent-divergent nozzle without the need for changing the nozzle geometry. The nozzle becomes more restrictive as the strength of the vortex increases. With vortex control, the mass flow rate can be reduced by 42% under the same inlet and outlet conditions. Vortex control can therefore be seen as a way of modulating the discharge coefficient of the motive nozzle. The control range of inlet pressures and mass flow rates that can be achieved by vortex control appears to be large enough to be suitable for numerous technical applications. This novel mechanism can potentially provide flow control with less sacrifice of nozzle efficiency, which is extremely important for ejector cooling cycle performance.

It is also less vulnerable to clogging since the flow control is achieved without changing the flow area. A variety of different expansion devices, in addition to ejectors, could potentially benefit from this new control mechanism, including actively controlled flow metering devices for superheat control in

subcritical applications or high-side pressure control in transcritical systems. Furthermore, the new vortex control mechanism can possibly lead to alternative self-regulating expansion valve designs. Here, some first results are presented when a vortex-controlled ejector is implemented into a transcritical CO_2 system.

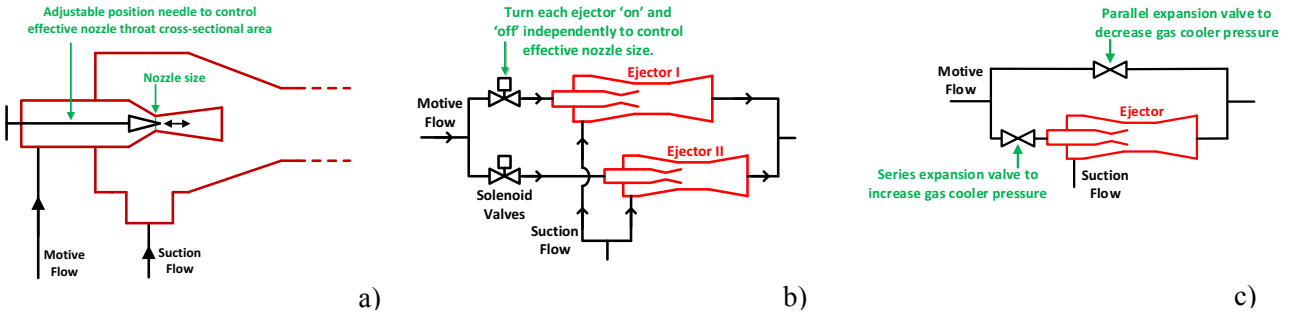

a) b) c)

Figure 7: Diagrams of methods to control high-side pressure in an ejector cycle using (a) adjustable ejector, (b) parallel ejector arrangement, and (c) expansion valve in series or parallel with ejector

Table 3 shows the ejector test conditions for comparison of vortex control and expansion-valve control. The conditions are obtained by operating the system with no vortex control/valve control applied to the ejector when evaporator air-side inlet temperature and air flow rate are 27 ˚C and 275 L/s, respectively, gas cooler air-side inlet temperature and air flow rate are 35 ˚C and 500 L/s, respectively, and compressor speed is 1494 min^{-1}.

Table 3. Ejector test conditions

IHX high-side outlet temperature (˚C)	Suction inlet pressure (kPa)	Suction inlet temperature (°C)	Motive flow rate (g/s)	Suction flow rate (g/s)
31.9	3802	7.4	43.1	22.8

Figure 8 shows the variation of ejector pressure lift and total work recovery efficiency, respectively. The total work recovery efficiency is defined according to Eq. (6) with IHX outlet pressure for expansion valve control and vortex control.

$$\eta_{exp} = \phi_m * \frac{h(P_{diff,out}, s_{s,in}) - h_{s,in}}{h_{exp,in} - h(P_{diff,out}, s_{exp,in})} \quad \text{Eq. (6)}$$

When there is no control, the IHX high-side outlet pressure at the conditions presented in Table 3 is 8736 kPa. After the application of expansion valve control and vortex control, the IHX high-side outlet pressure increases at constant motive flow rate and IHX high-side outlet temperature. When the maximum inlet vortex is applied, an increase of 1161 kPa for the IHX high-side outlet pressure can be achieved, which is believed to be large enough for high-side pressure control for many applications. Again, it should be emphasized that this pressure increase was achieved without changing the physical geometry of the ejector. Instead, the application of the vortex increases the vapor generation rate inside the ejector and reduces the degree of thermal non-equilibrium. The enhanced vapor generation rate, which is believed to mostly take place inside the diverging part of the motive nozzle results in the same effect that a more restrictive nozzle throat diameter would have. Therefore, vortex control has been proven to be an effective nozzle restrictiveness control mechanism that can be used for the control of ejector cooling cycles. For the same level of high side pressure control, the ejector with vortex control provides slightly less pressure lift and total work recovery efficiency than expansion valve control with the current design. For 1349 kPa increase in IHX high-side outlet pressure, total work recovery efficiency of the ejector with expansion valve control drops from 27.2% to 20.5%. As a comparison, for 1161 kPa increase in IHX high-side outlet pressure, the total work recovery efficiency of the ejector with vortex control drops from 27.2% to 18.5%. This is the first attempt to apply vortex control to an ejector operating in an actual system and the ejector design has yet to be optimized for accommodation of the ejector inlet vortex. Nevertheless, these first results are extremely promising.

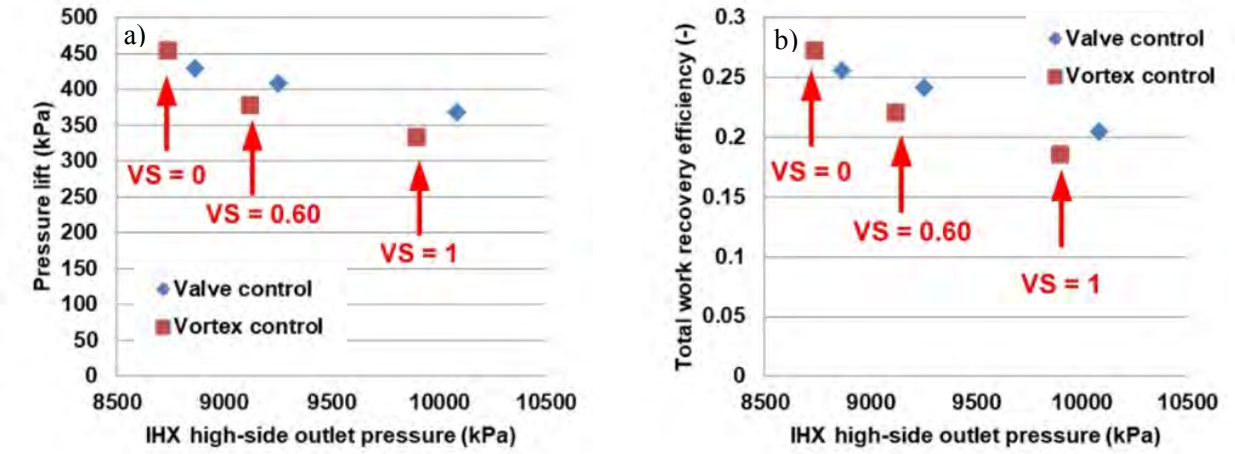

Figure 8: Variation of a) ejector pressure lift and b) total work recovery efficiency with IHX high-side outlet pressure

6. CONCLUSIONS

This paper summarized some of the recent developments in the area of two-phase ejectors used to recover expansion work in HVAC&R applications. While most attractive for fluids and cycles with high throttling losses, such as transcritical CO_2, the use of ejectors still makes sense for various applications using lower pressure refrigerants. Numerous integration options for ejectors exist and the recovered expansion work can be utilized in different ways, for example to raise the compressor suction temperature, to provide cooling at different temperature levels, or to improve evaporator performance through liquid overfeed. It has also been shown that design and optimization is not only important for the ejector itself, but also for other system components, such as the evaporator or the vapor-liquid separator. It needs to be ensured that potential inefficiencies of these other system components don't outweigh the positive performance impact provided by the ejector. It has also been shown that numerous approaches exist to implement ejector and cycle control, including adjustable motive nozzle throat area mechanisms, parallel ejectors, or vortex control. Ejectors in HVAC&R remain an interesting and intriguing topic and the onset of successful commercialization warrants continued research and development.

ACKNOWLEDGEMENTS

The author would like to thank the member companies of the Air Conditioning and Refrigeration Center at the University of Illinois at Urbana-Champaign for their support. Contents of this publication were adopted from the PhD thesis of Dr. Neal Lawrence.

NOMENCLATURE

Variables and Abbreviations		**Greek**	
COP	coefficient of performance (-)	ΔT	temperature difference (K)
COS	condenser outlet split	ε_{IHX}	IHX effectiveness (-)
DX	direct expansion	Φ_m	Mass entrainment ratio (-)
Ejec	ejector		
Evap	evaporator	**Subscripts**	
h	specific enthalpy (kJ kg^{-1})	air	referring to air flow
IHX	internal heat exchanger	cond	condenser
LT	low temperature	diff	diffuser
MT	medium temperature	evap	evaporator
$\dot{m}$	mass flow rate (kg s^{-1})	exp	expansion valve
n	circulation number (-)	gc	gas cooler
OR	overfeed ratio (-)	in	inlet
P	pressure (kPa)	liquid	referring to liquid

Q	capacity (kW)	m	referring to motive flow
R	recirculation ratio (-)	out	outlet
Recirc	recirculation	s	process at constant spec. entropy
Standard	standard ejector cycle	SH	superheat
s	specific entropy (kJ kg^{-1} K^{-1})	total	referring to total mass flow rate
T	temperature (K)	v	referring to saturated vapor
VS	vortex strength (-)	vapor	referring to vapor
x	vapor mass fraction (-)	vaporized	referring to vaporized mass flow

REFERENCES

American Society of Heating, Refrigeration, and Air Conditioning Engineers (ASHRAE), 2014. *Refrigeration Handbook*, Chapter 4 Liquid Recirculation, Atlanta, GA, USA.

Chen, J., Jarall, S., Havtun, H., Palm, B., 2015. A review on versatile ejector applications in refrigeration systems. *Renew. Sustain. Energy Reviews* 49: 67-90.

Domanski, P., 1995. Theoretical evaluation of the vapor-compression cycle with a liquid-line/suction-line heat exchanger, economizer, and ejector. National Institute of Standards and Technology (NIST), Report NISTIR 5606, Gaithersburg, MD, USA.

Elbel, S.W., Hrnjak, P.S., 2004. Effect of internal heat exchanger on performance of transcritical CO_2 systems with ejector. 10th International Refrigeration and Air Conditioning Conference at Purdue, West Lafayette, IN, USA, Paper R166.

Gay, N.H., 1931. Refrigerating system. U.S. Patent 1,836,318.

Li, D., Groll, E.A., 2005. Transcritical CO_2 refrigeration cycle with ejector-expansion device. *Int. J. Refrigeration* 28: 766-773.

Kornhauser, A.A., 1990. The use of an ejector as a refrigerant expander. 1990 USNC IIR-Purdue Refrigeration Conference, West Lafayette, IN, USA.

Li, Y., Tan, L., Zhang, X., Du, K., 2014. Experimental evaluation of an ejector as a liquid re-circulator in falling film water chiller. *Int. J. Refrigeration* 40: 309-316.

Lawrence, N., Elbel, S., 2013. Theoretical and practical comparison of two-phase ejector refrigeration cycles including First and Second Law analysis. *Int. J. Refrigeration* 36: 1220-1232.

Elbel, S., Lawrence, N., 2016. Review of recent developments in advanced ejector technology. *Int. J. Refrigeration* 62: 1-18.

Lawrence, N., Elbel, S., 2016. Experimental investigation on the effect of evaporator design and application of work recovery on the performance of two-phase ejector liquid recirculation cycles with R410A. *Appl. Therm. Engr.* 100: 398-411.

Lorentzen, G., 1983. Throttling, the internal haemorrhage of the refrigeration process. *Proc. Inst. Refrigeration*, 80: 39-47.

Phillips, H.A., 1938. Refrigeration system. U.S. Patent 2,123,021.

Zhu, J., Elbel, S., 2016. A new control mechanism for two-phase ejector in vapor compression cycles for automotive applications using adjustable motive nozzle inlet swirl. SAE Int. J. Passeng. Cars - Mech. Syst. 9(1): 44-51.

Zhu, J. and Elbel, S., 2017. Influence of nozzle divergent part length and throat diameter on vortex control of initially subcooled flashing flow. SAE Int. J. Passeng. Cars - Mech. Syst. 10(1): 121-127.

Zhu, J. and Elbel, S., 2018. Experimental investigation of a novel expansion device control mechanism: vortex control of initially subcooled flashing R134a flow expanded through convergent-divergent nozzles. Int. J. Refrigeration 85: 167-183.

Manuscript ID: 1834
DOI:10.18462/iir.icr.2019.1834

Recent advances in elastocaloric cooling technologies: Where they stand and what prospects are

David CATALINI, Yunho HWANG*

Center for Environmental Energy Engineering, Department of Mechanical Engineering, University of Maryland, College Park, MD, 20742, United States, *yhhwang@umd.edu

ABSTRACT

Elastocaloric cooling is as a solid-state cooling technology undergoing early stage research and development. This study presents a general introduction of core concepts common to all caloric cooling technologies and a review of the recent progress made in the elastocaloric Cooling field with respect to materials, mathematical modelling at the system and material levels, and system integration. Multiple compositions were recently studied. Some by adding alloying elements to traditional systems to tune the transformation temperature and increase fatigue life. Other are multiferroic alloys, which are materials that can respond simultaneously to additional stimuli (electric or magnetic field) besides strain to leverage multiple caloric effects at once. Influence of additional variables like texture, strain rate, martensitic transformation paths and hysteresis in material's performance have also been further studied. Fundamental thermodynamic principles were applied to further understanding elastocaloric effect, and through mathematical description of the heat transfer process coupled with phase transformation new approaches to materials and characterization. System integration with heat recovery and regeneration strategies were also reviewed.
Keywords: Caloric cooling, Elastocaloric cooling.

1. INTRODUCTION

Vapor compression cycle (VCC) has been developed and optimized over the last 100 years to provide cooling in residential and industrial buildings, and vehicles. However, its usage has resulted in unpredicted environmental damages such as depleting the ozone layer and causing the global warming when its working fluid leaks into the atmosphere. Because of this, it is important to replace VCC by developing a superior technological alternative without environmental costs. One way the scientific community is exploring to tackle this problem is to develop heat pumping cycles using caloric materials. The immediate benefit of this approach is the elimination of the harmful refrigerant, because caloric materials can serve as solid-state refrigerants. The grand challenges are to keep developing materials with ever-increasing performance and just as important to integrate these materials into systems efficiently. Caloric materials undergo a reversible change in entropy when an external field is either applied or removed. In materials science and statistical thermodynamics, entropy allows for a quantitative measure of changes in the degree of order in the atomic structure of the material. When the order in the structure of the material increases, the entropy increases. When the order decreases, the entropy decreases. Significant changes in microstructural order can take place by phase transitions, and the key characteristic in caloric materials these transitions can be induced by the external field and they involve a quantitatively significant entropy change. Ultimately, these entropy changes manifest themselves as temperature change of the material when the external field is applied or removed adiabatically and as a heat transfer between the material and the surroundings when the external field is applied/removed isothermally. Based on the nature of the external field to which the caloric materials respond to they are classified as magnetocaloric (the application of a magnetic field induces a change in magnetization), electrocaloric (the application of an electric field induces a change in polarization) and elastocaloric materials (the application of a stress field induces a strain and change in crystallographic symmetry). When materials respond to multiple fields simultaneously, they are referred to as multicaloric.

This paper is organized as following. First, a general perspective of cooling with caloric materials is presented and some of the main concepts of caloric cooling are expanded in order to set the necessary background for the discussions that follow. Second, the main results of the recent elastocaloric cooling bibliography are analyzed and summarized with respect to materials research, system integration examples and modeling.

2. Solid State Cooling

2.1. General perspective of cooling with caloric materials

A few review papers were published in recent years. Liu et al. (2016a) provided general introduction of caloric cooling and performance improvements with ferroelectrics. Mañosa and Planes (2016, 2017) conducted a very thorough study of elastocaloric material systems, thermodynamics, crystallography and examples. Qian et al. (2016) reviewed elastocaloric materials, cycles and system integrations from a mechanical engineering perspective. Vitalij et al. (2016) provided a very insightful review of caloric refrigeration. Similarly, Xie et al. (2017) reviewed caloric cooling with special focus on comparing elastomers with traditional caloric cooling materials.

The amount of entropy available for a caloric effect is highly dependent on the nature and characteristics of the phase transition and it is important to distinguish between first-order and second-order transitions. If the first derivatives of the molar Gibbs free energy are discontinuous at the temperature-pressure boundary between physical states A and B, the transition between them is, by definition, a first-order transition. Melting and boiling are examples of first-order transitions. If the first derivatives are continuous, but the second derivatives are discontinuous, then the transition is a second-order transition. Glass transitions in polymers, order-disorder phenomena in solid solutions, ferromagnetic transitions and some transitions between superconducting and non-superconducting states are examples of second-order transitions (Ragone, 1994). In general, first-order phase transitions exhibit the best caloric performance but take place over a very narrow temperature range and also present hysteresis and while the second-order transitions offer a moderate caloric performance, they can occur over a wider temperature range and with less hysteresis.

Phase transition character can be modified by adjusting the chemical composition of the material and that is where a large amount of the research efforts in materials science are directed towards, to find the optimal compromise for a certain application. The difference between first and second order transitions can be understood by comparing the constant temperature cooling by an evaporating liquid versus the cooling by a simple gas expansion. The first order transition and liquid evaporation utilize the enthalpy of transformation (evaporation) to increase their entropies at a constant temperature, while the second order magnetic phase transition and gas expansion do not (Pecharsky and Gschneidner, 1997).

In order to build a heat pump using a solid caloric material as a refrigerant it is possible to use a heat transfer fluid to transfer heat between the caloric material and the heat sink and reservoir. By alternating steps of applying a field to induce the caloric transformation, heat rejection, removing the field to reverse the caloric transformation and heat absorption a thermodynamic cycle can be designed. Within the scope of this review, it is important for the reader to become familiar with the cascaded regenerator configuration and thermodynamic cycle. It has been successfully applied in magnetocaloric and elastocaloric cooling systems and it offers a very effective way to increase the temperature lift of the heat pump.

2.2. Elastocaloric cooling

In elastocaloric materials a stress field induces a reversible phase transformation and with it a change in entropy in isothermal conditions or a change in temperature in adiabatic conditions. The nature of the phase transformation is dependent of the material system.

2.2.1. Material elastocaloric effect measurement

The first step in the analysis of the fitness of a potential alloy system is to quantify the elastocaloric effect. This can be done through direct or indirect methods. On the one hand, direct methods are designed to measure the adiabatic temperature changes during loading and unloading of the material. The main shortcoming of these methods is that it is difficult to assure the adiabatic boundary condition. This results in an underestimation of the property. On the other hand, indirect methods are based on measuring either the stress-strain curves at different constant temperatures or strain-temperature curves at different constant stresses. The data is post processed to apply the corresponding Maxwell relation, Eq. (1), or the Clausius-Clapeyron equation, Eq. (2), and calculate the isothermal entropy change. One of the shortcomings of this kind of methods is that in order to obtain accurate data a large number of constant temperature or constant stress data sets would be required. In order to overcome this it is possible to use a phenomenological model which can predict the superelastic response as a function of stress and temperature (Tušek et al., 2016). The elastocaloric properties can also be obtained from calorimetry measurements (Gràcia-Condal at al., 2018).

$$\Delta S_{iso} = \frac{1}{\rho}\int_{\sigma_1}^{\sigma_2}\left(\frac{\partial \varepsilon}{\partial T}\right)_{\sigma} d\sigma \qquad \text{Eq. (1)}$$

$$\left(\frac{d\sigma}{dT}\right)_{cr} = \rho \frac{\partial S}{\partial \varepsilon} \quad \text{Eq. (2)}$$

2.2.2. Material figures of merit

Figures of merit are useful parameters defined to guide the development of new and better materials. These figures of merit require the use of quantities like heat capacity, isothermal entropy and adiabatic temperature change, which are measured by the methods previously described. It is difficult to define a single figure of merit to unequivocally rank a set of materials. Some figures of merit are used to measure the magnitude of the effect, like the quotient between the latent heat of the transformation and the heat required to increase the temperature of the material by a certain amount of degrees (Qian et al., 2016). Others are calculated to take into consideration the efficiency of the effect, like the quotient between the volume-normalized latent heat of the phase change to the volume-normalized work required to drive the thermodynamic cycle (Moya et al., 2015). A new simple material-based figure of merit called "temperature-averaged entropy change" has been proposed, Eq. (3).

$$TEC\left(\Delta T_{lift}\right) = \frac{1}{\Delta T_{lift}} \max_{T_{mid}} \left\{ \int_{T_{mid}-\frac{\Delta T_{lift}}{2}}^{T_{mid}+\frac{\Delta T_{lift}}{2}} \Delta S(T)_{\Delta H,T} dT \right\} \quad \text{Eq. (3)}$$

Materials with a large entropy change over a narrow temperature window are the most promising for layered regenerators, while materials with a wider temperature profile can be competitive if fewer layers or even a single layer is desired (Griffith et al., 2018).

2.2.3. Phase transitions and transformation mechanisms

Conventional superelastic alloys such as Ni-Ti and Cu-based alloys exhibit a typical first-order martensitic transformation. Other alloys, like Fe-Pd, exhibit a weak first-order (second-order like) martensitic transformation. Each kind of transformation has its particular characteristics (Xiao et al., 2018) and a series of articles have been published to describe more specific details about the weak first-order martensitic transformation in Fe-Pt system (Fukuda and Kakeshita, 2017; Kakeshita et al., 2016) and in the transformation mechanism in Ni-Ti system (Soto-Parra et al., 2016). This last one is particularly interesting because it shows how through heat treatment it is possible to induce different transformation paths from B2 (Austenite) to B19' (Martensite), including or bypassing an intermediate phase, R. This is of particular importance because when compared to the B2 to B19' direct transformation, the B2 to R transformation occurs with small hysteresis and higher cycling stability. The penalty for this instability is a loss in latent heat, because to retain these properties the material should not be transformed from R to B19', and thus a fraction of the entropy is never used.

2.2.4. Composition

The material properties of the main material systems and their comparison can be found in some articles with a broad reach (Qian et al., 2016; Mañosa and Planes, 2017; Wu et al., 2017). In general, there are two main families of superelastic alloys: non-magnetic and magnetic. Within the non-magnetic family there are Ni-Ti-based and Cu-based. In the last few years the systems that were explored within the Ni-Ti family were the Ni-Ti alloyed with V and Hf, and the Ti-rich Ni-Ti-Cu system alloyed with Co, Fe and V. Addition of V to Ni-Ti enhances the efficiency and functional stability of the elastocaloric effect of Ni-Ti (Kim et al., 2018). Ni-Ti alloys with Hf additions have been studied from the shape memory effect perspective noting the high work output of the alloy, and from the elastocaloric effect perspective it has been compared with multiple other systems with no particularly notable behavior (Wu et al., 2017). The Ti-rich Ni-Ti-Cu system is known for its high functional and structural stability and small hysteresis. The addition of Co or Fe alloying allows for a reduction of the transformation temperature while maintaining high transformation enthalpies (Chluba et al., 2016; Ossmer et al., 2016). A very interesting progression of this concept is the manufacturing of alloy samples with a composition gradient (and thus a tuned transformation temperature gradient) which is very useful for an active regeneration cycle, in which a temperature gradient is developed along the elastocaloric material during operation. If the temperature gradient matches the materials transformation temperature gradient, the transformation stress along the alloy sample is minimized. Alloy samples like the one shown in Fig. 1 have been manufactured in thin films with remarkable results (Bumke et al., 2018).

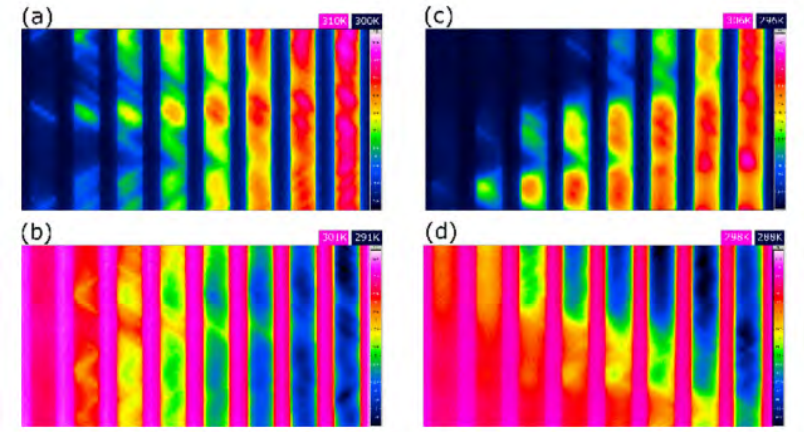

Figure 1: The local evolution of the elastocaloric effect visualized by IR-measurements (a) Forward and (b) reverse transformation without transformation gradient; (c) forward and (d) reverse transformation with a transformation gradient. Test conditions: strain rate of 0.05 s^{-1}, time interval at 100 ms (Source: Bumke et al., 2018)

The studies for the Cu-based alloys were in the Cu-Al-Mn and Cu-Al-Zn systems. One of the main benefits of the Cu-based alloys is that a lower transformation stress is required to induce the elastocaloric effect (Qian et al., 2016). Giant elastocaloric effects have been measured for both systems, Cu-Al-Mn (Xu et al., 2016) and Cu-Al-Zn (Gràcia-Condal et al., 2018), and also superelastic properties at very low temperatures (Niitsu, Kimura, Omori, and Kainuma, 2018).

Within the magnetic family we can find the Ni-based, Fe-based and Mn-based. Their magnetism is an additional system whose order also contributes to the total material's entropy, besides the lattice. In this special group of materials, the structural change due to the martensitic transformation is accompanied by changes in the materials magnetization. Unlike their non-magnetic counterpart, alloys in the magnetic family are brittle, so one of the main objectives in doping the alloys is to improve their ductility (Mañosa and Planes, 2017). The Ni-based alloys are almost as studied as the Ni-Ti based. However, the studies are spread over a larger amount of compositions. The elastocaloric effect in this type of materials is not as big as in the non-magnetic family, most of the studies are oriented to the study of the transitions from the microstructure and texture perspectives, and did not show any record breaking latent heat values. The most recent studies are about Ni-Mn-Sn (Sun et al., 2016) with alloying elements Co (Yang et al., 2016) and Cu (Wójcik et al., 2017; Li et al., 2017); Ni-Mn-In with alloying elements Co (Zhao et al., 2017), B (Yang et al., 2017), Tb (Shen et al., 2017), Ga (Wang et al., 2017) and Cr (Henández-Navarro et al., 2018); Ni-Mn-Ga with alloying element Cu (Zhao et al., 2017) ; Ni-Ga with alloying elements Fe (Álvarez-Alonso et al., 2017) and Co (Shen et al., 2017); and last of all Ni-Al-Co (Khan et al., 2018). The studies within the Fe-based alloys are limited and the compositions are Fe-Pd (Xiao et al., 2016) and Fe-Pt (Fukuda and Kakeshita, 2017). The transition in these alloys is weakly first-order, and as such the entropy change is low, with a low hysteresis. Only one Mn-based system was studied and that was Mn-Cu (Cui et al., 2017).

Outside of these two main categories there are also soft materials. The main representatives are natural rubber and P(VDF-TrFE-CTFE). Caloric effects in PVDF-Polymers is mostly related to stress-induced crystallization (Xie et al., 2017). Recent study explored the elastocaloric effect in carbon nanotubes and graphene (Lisenkov et al., 2016).

2.2.5. Cycles

A description of the feasible thermodynamic cycles that can be applied in an elastocaloric heat pump have been described by Qian et al. (2016) and Schmidt et al. (2016). In order to increase the temperature lift of the system, heat recovery mechanisms are necessary (Qian et al., 2017; Qian et al., 2015). From the different cycles that include heat recovery strategies, the active regeneration cycle has proven to be very successful in magnetocaloric systems and now in elastocaloric systems. A regenerator is a storage type heat exchanger. Cold and hot fluids flow alternatively through the same flow passages and hence the heat transfer is intermittent. When the hot fluid flows over the heat transfer surface the thermal energy from the hot fluid is stored in the regenerator wall, and thus the hot fluid is being cooled. As a cold fluid flows through the same passages later, the regenerator wall gives up thermal energy, which is absorbed by the cold fluid (Shah and Sekulic, 2003). An active (elastocaloric) regenerator, unlike a passive one, is made out of an elastocaloric material and it serves the dual function as heat storage medium and a heat

source (or sink), and it becomes a heat source (or sink) when the forward (or reverse) transformation takes place. The thermodynamic cycle consists of the following steps: first, the elastocaloric material is subjected to the stress field and the phase transformation is induced adiabatically (so the temperature of the regenerator wall increases); second, the heat transfer fluid is pumped through the regenerator to the hot heat exchanger where heat is rejected (and the temperature of the regenerator wall decreases); third, the stress field is released and the reverse phase transformation takes place adiabatically (so the temperature of the regenerator wall further decreases); and fourth, the heat transfer fluid is pumped through the regenerator to the cold heat exchanger where heat is absorbed (and the temperature of the regenerator increases) and the cycle repeats all over again. At the right frequency and flowing the right amount of water in each heat exchange step, a temperature gradient will be developed from one end to the other of the regenerator.

2.2.6. System integration

Several laboratory systems were developed and studied around the world. A system based on tension of the elastocaloric material to induce the transformation and using the active regeneration cycle exhibited a temperature span of 15.3 K on the water side and COP values of up to 7 (Tušek et al., 2016). Further development showed a temperature span of 17.6 K and 19.9 K (Engelbrecht et al., 2017). Some preliminary reports about materials properties of the Ni-Ti plates used for the regenerators (Tušek et al., 2016) and the effects of surface finish (Engelbrecht et al., 2016) were published too as shown in Fig. 2.

A two reciprocating beds single stage system was designed and it's performance was studied over a wide range of conditions through an optimization formulation allowing for an increase of 51% of COP from 1.8 to 2.8 (Qian et al., 2015). The next iteration of this design duplicated the amount of beds and used a hydraulic actuator to apply the stress and induce the transformation. The design characteristics were published (Qian et al., 2016) and the system was later built and tested. A maximum temperature lift of 8 K at zero cooling capacity, and a maximum cooling capacity of 150 W at zero temperature lift was measured. The last two configurations allowed to have work recovery. The design was flexible enough to allow for the application of an active regeneration cycle on the same structure and the maximum temperature lift value measured by the authors was 22.5 K at 5% strain. Some components of the system are shown in Fig. 2.

Another system is based on Ni-Ti thin film and foils. A thorough analysis of design alternatives were presented by Ossmer et al. (2016). The figure shows one of those configurations in which the mechanical loading is realized through deflection of the bridge center in out-of-plane direction. The heat source and sink in this design are copper blocks and the heat transfer between them and the elastocaloric material is through direct contact, there is no heat transfer fluid involved. This configuration allows for work recovery as shown in Fig. 2 (Bruederlin et al., 2017).

2.2.7. Modeling, experimental and analytical methods

Models require material and heat transfer data that need to be measured. On one hand, very specific experimental apparatus was developed in the last few years to measure the data it is necessary to feed the models. On the other hand, models were used to develop analytical tools and new methods to estimate material and heat transfer quantities from open literature data. An example of the experimental apparatus design for elastocaloric cooling measurements and analysis can be seen in literature (Schmidt et al., 2016). A data reduction technique was proposed to predict the adiabatic temperature change of the material by doing multiple tests within moderate strain rates and doing a non-linear least squares fitting method instead of doing test at ultrahigh strain rates and adiabatic conditions. A byproduct of the method is the estimation of the heat transfer coefficient (Qian et al., 2017b). A method to accurately predict work and coefficient of performance was also published (Qian et al., 2018). Different approaches to system modeling have been implemented. A lumped element model approach, in which the heat component due to the martensitic transformation is approximated as a variable source only function of the martensite transformation rate (considered only a function of the strain rate), was implemented and solved as a thermal network and showed satisfactory agreement with the experiment (Bruederlin et al., 2017). In more complex systems, like an active regenerator, in which a temperature gradient is developed across the elastocaloric material, it is necessary to use the phase transformation kinetic equation based on the Müller-Achenbach-Seelecke model (Seelecke and Müller, 2004), which allows to determine the martensite transformation rate as a function of the temperature as well as the stress. A system level study with an extensive parametric analysis of design variables was published by Qian et al. (2017a). Another examples of the application of that material thermodynamic model were also published by Wendler et al. (2017) and Welsch et al. (2018).

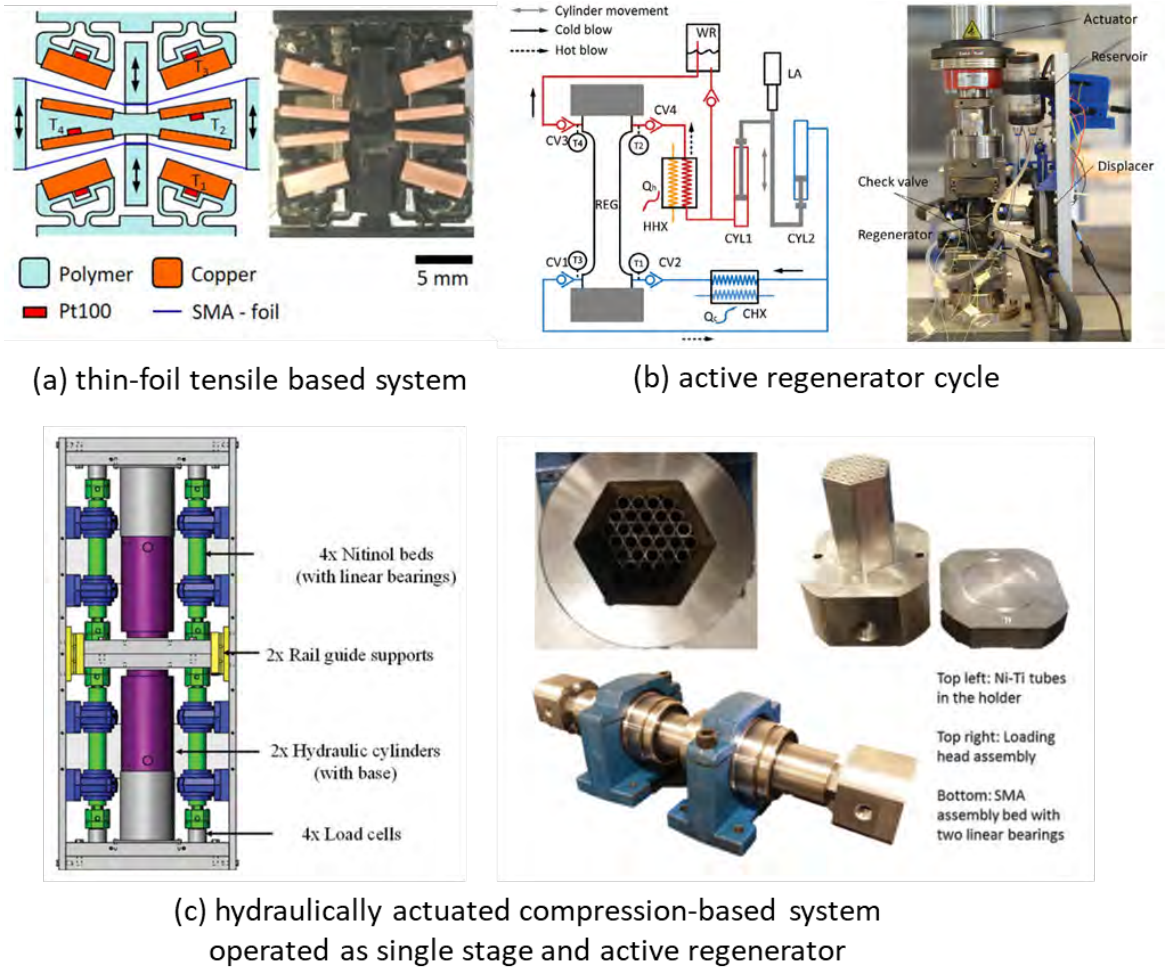

Figure 2: Three different elastocaloric cooling system configurations

General theory about regenerator design applies to this application and specific mathematical models, numerical implementation and comparison with experimental data can be found also in recent work by Trevizoli and Barbosa (2017).

3. CONCLUSIONS

Due to recent environmental concerns, the development of cooling technologies that use only environmentally friendly heat transfer fluids and more efficient than current vapor compression technology becomes an important research topic. Studies on caloric cooling technologies are rather new. However, significant progress was made in elastocaloric cooling field. From the materials point of view, new SMA materials have been developed with longer fatigue life and a tuned composition along its length. This can be important for the fabrication of regenerators in which the transformation temperature is as close as possible to the temperature of the material in operating conditions right before the transformation. This will keep the stress required to a minimum. Analytical tools were developed to estimate material properties with simplified experimental set ups, and experimental rigs were developed to increase the accuracy of the material properties measurements. The temperature lift performance of the systems in operation is setting new records. While researches on elastocaloric cooling are still on early stage of development, many research outcomes have revealed its potential and its worth for future development.

ACKNOWLEDGEMENTS

We gratefully acknowledge the support from the Center for Environmental Energy Engineering (CEEE) at the University of Maryland.

REFERENCES

Álvarez-Alonso, P., Aguilar-Ortiz, C. O., Villa, E., Nespoli, A., Flores-Zúñiga, H. and Chernenko, V. A., 2017. Conventional and inverse elastocaloric effect in Ni-Fe-Ga and Ni-Mn-Sn ribbons. *Scripta Materialia 128©, 36-40.*.

Bruederlin, F., Ossmer, H., Wendler, F., Miyazaki, S., and Kohl, M., 2017. SMA foil-based elastocaloric cooling: from material behavior to device engineering. *J. Phys. D: Appl. Phys 50(42)*.

Bumke, L., Chluba, C., Ossmer, H., Zamponi, C., Kohl, M., and Quandt, E., 2018. Cobalt Gradient Evolution in Sputtered TiNiCuCo Films for Elastocaloric Cooling. *Physica Status Solidi (B) Basic Research 255, 1700299*.

Chluba, C., Ossmer, H., Zamponi, C., Kohl, M., and Quandt, E., 2016. Ultra-Low Fatigue Quaternary TiNi-Based Films for Elastocaloric Cooling. *Shape Memory and Superelasticity 2: 95-103.*

Cui, S., Wan, J., Zuo, X., Chen, N., Zhang, J., and Rong, Y., 2017. Three-dimensional, non-isothermal phase-field modeling of thermally and stress-induced martensitic transformations in shape memory alloys. *International Journal of Solids and Structures 109: 1-11*.

Engelbrecht, K., Tušek, J., Eriksen, D., Lei, T., Lee, C. Y., Tušek, J., and Pryds, N., 2017. A regenerative elastocaloric device: Experimental results. *Journal of Physics D: Applied Physics 50, 424006.*

Engelbrecht, K., Tušek, J., Sanna, S., Eriksen, D., Mishin, O. V., Bahl, C. R. H., and Pryds, N., 2016. Effects of surface finish and mechanical training on Ni-Ti sheets for elastocaloric cooling. *APL Materials 4, 064110*.

Fukuda, T. and Kakeshita, T., 2017. Elastic-like deformation and elastocaloric effect of a partly ordered iron-platinum alloy exhibiting a weak first-order martensitic transformation. *Journal of Physics D: Applied Physics 50, 404003*.

Gràcia-Condal, A., Stern-Taulats, E., Planes, A., Vives, E., and Mañosa, L., 2018. The Giant Elastocaloric Effect in a Cu–Zn–Al Shape-Memory Alloy: a Calorimetric Study. *Physica Status Solidi (B) Basic Research 255, 1700422*.

Griffith, L. D., Mudryk, Y., Slaughter, J., and Pecharsky, V. K., 2018. Material-based figure of merit for caloric materials. *Journal of Applied Physics 123, 034902*.

Henández-Navarro, F., Camarillo-Garcia, J.-P., Aguilar-Ortiz, C.-O., Flores-Zúñiga, H., Ríos, D., González, J.-G., and Álvarez-Alonso, P., 2018. The influence of texture on the reversible elastocaloric effect of a polycrystalline Ni50Mn32In16Cr2 alloy. *Applied Physics Letters 112, 16401*.

Kakeshita, T., Xiao, F., and Fukuda, T., 2016. Large elastic strain and elastocaloric effect caused by lattice softening in an iron-palladium alloy. *Philosophical Transactions of the Royal Society A: Mathematical, Physical and Engineering Sciences*, *374*(2074), 20150312.

Khan, M. T., Wang, Y., Wang, C., Liao, X., Yang, S., Song, X., and Ren, X., 2018. Combination of conventional elastocaloric and magnetocaloric effects in a Co37Ni35Al28ferromagnetic shape memory alloy. *Scripta Materialia 146: 182-186*.

Kim, Y., Jo, M.-G., Park, J.-W., Park, H.-K., and Han, H. N., 2018. Elastocaloric effect in polycrystalline Ni 50 Ti 45.3 V 4.7 shape memory alloy. *Scripta Materialia 144*: 48–51.

Li, Y., Sun, W., Zhao, D., Xu, H., and Liu, J., 2017. An 8 K elastocaloric temperature change induced by 1.3% transformation strain in Ni44Mn45 − xSn11Cuxalloys. *Scripta Materialia 130:278-282.*.

Lisenkov, S., Herchig, R., Patel, S., Vaish, R., Cuozzo, J., and Ponomareva, I., 2016. Elastocaloric Effect in Carbon Nanotubes and Graphene. *Nano Letters 16: 7008-7012*.

Liu, Y., Scott, J. F., and Dkhil, B., 2016. Some strategies for improving caloric responses with ferroelectrics. *APL Materials 4, 064109*.

Mañosa, L., and Planes, A., 2016. Mechanocaloric effects in shape memory alloys. *Philosophical Transactions of the Royal Society A: Mathematical, Physical and Engineering Sciences 374, 20150310*.

Mañosa, L. and Planes, A., 2017. Materials with Giant Mechanocaloric Effects: Cooling by Strength. *Advanced Materials 29, 1603607*.

Moya, X., Defay, E., Heine, V., and Mathur, N. D., 2015. Too cool to work. *Nature Physics*, *11:*202-205.

Niitsu, K., Kimura, Y., Omori, T., and Kainuma, R., 2018. Cryogenic superelasticity with large elastocaloric effect. *NPG Asia Materials 10, e457*.

Ossmer, H., Chluba, C., Kauffmann-Weiss, S., Quandt, E., and Kohl, M., 2016. TiNi-based films for elastocaloric microcooling - Fatigue life and device performance. *APL Materials 4, 064102*.

Ossmer, H., Wendler, F., Gueltig, M., Lambrecht, F., Miyazaki, S., and Kohl, M., 2016. Energy-efficient miniature-scale heat pumping based on shape memory alloys. *Smart Materials and Structures 25, 085037*.

Pecharsky, V. K., Cui, J., and Johnson, D. D., 2016. (Magneto)caloric refrigeration: Is there light at the end of the tunnel? *Philosophical Transactions of the Royal Society A: Mathematical, Physical and Engineering Sciences 374, 20150305*.

Pecharsky, V. K. and Gschneidner, K. A., 1997. Tunable magnetic regenerator alloys with a giant magnetocaloric effect for magnetic refrigeration from ~20 to ~290 K. *Applied Physics Letters*, *70*(24):3299–3301.

Qian, S., Alabdulkarem, A., Ling, J., Hwang, Y., and Radermacher, R., 2015. Study on Performance Improvement of a Compressive Thermoelastic Cooling System Using Single Objective Optimization. In *ASME 2015 9th International Conference on Energy Sustainability collocated with the ASME 2015 Power Conference, the ASME 2015 13th International Conference on Fuel Cell Science, Engineering and Technology, and the ASME 2015 Nuclear Forum,* ES2015-49745.

Qian, S., Geng, Y., Wang, Y., Ling, J., Hwang, Y., Radermacher, R., and Cui, J., 2016. A review of elastocaloric cooling: Materials, cycles and system integrations. *International Journal of Refrigeration 64:1-19*.

Qian, S., Geng, Y., Wang, Y., Muehlbauer, J., Ling, J., Hwang, Y., and Takeuchi, I., 2016. Design of a hydraulically driven compressive elastocaloric cooling system. *Science and Technology for the Built Environment 22(5): 500-506*.

Qian, S., Geng, Y., Wang, Y., Pillsbury, T. E., Hada, Y., Yamaguchi, Y., and Takeuchi, I., 2016. Elastocaloric effect in CuAlZn and CuAlMn shape memory alloys under compression. *Philosophical Transactions of the Royal Society A: Mathematical, Physical and Engineering Sciences 374, 20150309*.

Qian, S., Ling, J., Hwang, Y., Takeuchi, I., and Radermacher, R., 2015. Modeling and Optimization of a Novel Heat Recovery Design for Thermoelastic Cooling Systems. Proceedings of the ASME IMECE, 52614.

Qian, S., Nasuta, D., Rhoads, A., Wang, Y., Geng, Y., Hwang, Y., and Takeuchi, I., 2016. Not-in-kind cooling technologies: A quantitative comparison of refrigerants and system performance. *International Journal of Refrigeration 62:177-192*.

Qian, S., Yu, J., and Yan, G., 2017. A review of regenerative heat exchange methods for various cooling technologies. *Renewable and Sustainable Energy Reviews*, *69:*535–550.

Qian, S., Yuan, L., Hou, H., and Takeuchi, I., 2018. Accurate prediction of work and coefficient of performance of elastocaloric materials with phase transformation kinetics AU. *Science and Technology for the Built Environment*, *24*(6), 673–684.

Qian, S., Yuan, L., Yu, J., and Yan, G., 2017a. Numerical modeling of an active elastocaloric regenerator refrigerator with phase transformation kinetics and the matching principle for materials selection.

Energy 141:744-756.

Qian, S., Yuan, L., Yu, J., and Yan, G., 2017b. The mechanism of Δt variation in coupled heat transfer and phase transformation for elastocaloric materials and its application in materials characterization. *Applied Physics Letters 111, 223901*.

Ragone, D. V., 1994. Thermodynamics of Materials, Volume 1. *Thermodynamics of Materials, Volume 1, by David V. Ragone, ISBN 0-471-30885-4. Wiley-VCH, October 1994*, 336.

Schmidt, M., Kirsch, S. M., Seelecke, S., and Schütze, A., 2016. Elastocaloric cooling: From fundamental thermodynamics to solid state air conditioning. *Science and Technology for the Built Environment 22(5):475-488*.

Schmidt, M., Ullrich, J., Wieczorek, A., Frenzel, J., Eggeler, G., Schütze, A., and Seelecke, S., 2016. Experimental Methods for Investigation of Shape Memory Based Elastocaloric Cooling Processes and Model Validation. *Journal of Visualized Experiments 111, e53626*.

Seelecke, S., and Müller, I., 2004. Shape memory alloy actuators in smart structures: Modeling and simulation. *Applied Mechanics Reviews 57*(1):23–46.

Shah, R. K., and Sekulic, D. P., 2003. *Fundamentals of heat exchanger design*. John Wiley and Sons.

Shen, A., Zhao, D., Sun, W., Liu, J., and Li, C., 2017. Elastocaloric effect in a Co50Ni20Ga30 single crystal. *Scripta Materialia 127:1-5*.

Shen, Q., Zhao, D., Sun, W., Li, Y., and Liu, J., 2017. The effect of Tb on elastocaloric and mechanical properties of Ni-Mn-In-Tb alloys. *Journal of Alloys and Compounds 696:538-542*.

Soto-Parra, D., Vives, E., Mañosa, L., Matutes-Aquino, J. A., Flores-Zúñiga, H., and Planes, A., 2016. Elastocaloric effect in Ti-Ni shape-memory wires associated with the B2↔B19' and B2↔R structural transitions. *Applied Physics Letters 108, 071902*.

Sun, W., Liu, J., Lu, B., Li, Y., and Yan, A., 2016. Large elastocaloric effect at small transformation strain in Ni45Mn44Sn11 metamagnetic shape memory alloys. *Scripta Materialia 114:1-4*.

Trevizoli, P. V., and Barbosa, J. R., 2017. Thermal-hydraulic behavior and influence of carryover losses in oscillating-flow regenerators. *International Journal of Thermal Sciences 113:89-99*.

Tušek, J., Engelbrecht, K., Eriksen, D., Dall'Olio, S., Tušek, J., and Pryds, N., 2016. A regenerative elastocaloric heat pump. *Nature Energy 1, 16134*.

Tušek, J., Engelbrecht, K., Mañosa, L., Vives, E., and Pryds, N., 2016. Understanding the Thermodynamic Properties of the Elastocaloric Effect Through Experimentation and Modelling. *Shape Memory and Superelasticity 2(4):317-329*.

Tušek, J., Engelbrecht, K., and Pryds, N., 2016. Elastocaloric effect of a Ni-Ti plate to be applied in a regenerator-based cooling device. *Science and Technology for the Built Environment 22(5):489-499*.

Wang, J., Yu, Q., Xu, K., Zhang, C., Wu, Y., and Jiang, C., 2017. Large room-temperature elastocaloric effect of Ni57Mn18Ga21In4alloy undergoing a magnetostructural coupling transition. *Scripta Materialia 130:148-157*.

Welsch, F., Ullrich, J., Ossmer, H., Schmidt, M., Kohl, M., Chluba, C., and Seelecke, S., 2018. Numerical simulation and experimental investigation of the elastocaloric cooling effect in sputter-deposited TiNiCuCo thin films. *Continuum Mechanics and Thermodynamics 30(1):53-68*.

Wendler, F., Ossmer, H., Chluba, C., Quandt, E., and Kohl, M., 2017. Mesoscale simulation of elastocaloric cooling in SMA films. *Acta Materialia 136:105-117.*

Wójcik, A., Maziarz, W., Szczerba, M. J., Sikora, M., Żywczak, A., Aguilar-Ortiz, C. O., … Chernenko, V. A., 2017. Transformation behavior and inverse caloric effects in magnetic shape memory Ni44-xCuxCo6Mn39Sn11 ribbons. *Journal of Alloys and Compounds*. *721:172-181.*

Wu, Y., Ertekin, E., and Sehitoglu, H., 2017. Elastocaloric cooling capacity of shape memory alloys – Role of deformation temperatures, mechanical cycling, stress hysteresis and inhomogeneity of transformation. *Acta Materialia 135:158-176*.

Xiao, F., Fukuda, T., Jin, X., Liu, J., and Kakeshita, T., 2018. Elastocaloric Effect Associated with Different Types of Martensitic Transformations: Typical First-Order and Weak First-Order Ones. *Physica Status Solidi (B) Basic Research 255, 1700246*.

Xiao, F., Liang, X., Jin, X., Nie, Z., Kakeshita, T., and Fukuda, T., 2016. Stable elastocaloric effect under tensile stress of iron-palladium alloy and its in situ X-ray observation. *Acta Materialia 118:88-94*.

Xie, Z., Sebald, G., and Guyomar, D., 2017. Comparison of elastocaloric effect of natural rubber with other caloric effects on different-scale cooling application cases. *Applied Thermal Engineering 111:914-920*.

Xu, S., Huang, H. Y., Xie, J., Takekawa, S., Xu, X., Omori, T., and Kainuma, R., 2016. Giant elastocaloric effect covering wide temperature range in columnar-grained Cu71.5Al17.5Mn11 shape memory alloy. *APL Materials 4, 106106*.

Yang, Z., Cong, D. Y., Huang, L., Nie, Z. H., Sun, X. M., Zhang, Q. H., and Wang, Y. D., 2016. Large elastocaloric effect in a Ni-Co-Mn-Sn magnetic shape memory alloy. *Materials and Design 92:932-936*.

Yang, Z., Cong, D. Y., Sun, X. M., Nie, Z. H., and Wang, Y. D., 2017. Enhanced cyclability of elastocaloric effect in boron-microalloyed Ni-Mn-In magnetic shape memory alloys. *Acta Materialia 127:33-42*.

Zhao, D., Castán, T., Planes, A., Li, Z., Sun, W., and Liu, J., 2017. Enhanced caloric effect induced by magnetoelastic coupling in NiMnGaCu Heusler alloys: Experimental study and theoretical analysis. *Physical Review B 96, 224105*.

Zhao, D., Liu, J., Feng, Y., Sun, W., and Yan, A., 2017. Giant elastocaloric effect and its irreversibility in [001]-oriented Ni45Mn36.5In13.5Co5meta-magnetic shape memory alloys. *Applied Physics Letters 110, 021906*.

Manuscript ID: 1835
DOI: 10.18462/iir.icr.2019.1835

Vapor compression heat pumps with refrigerant mixtures

Jiazhen LING, Yunho HWANG, Reinhard RADERMACHER*

4164 Glenn Martin Hall, University of Maryland, College Park, MD 20742

United States

Tel: 1-301-405-5286

raderm@umd.edu

ABSTRACT

Refrigerant mixtures are widely considered as the next-generation environment-friendly refrigerants because they allow to tune refrigerant properties for the best compromise between conflicting goals: lower global warming potential (GWP), zero ozone depletion potential (ODP), low or no flammability and toxicity. Nevertheless, refrigerant mixtures can behave quite differently during evaporation and condensation than pure refrigerants. This paper first discusses key differences between pure and mixed refrigerants, presents a case study on the impact of mixtures on heat exchanger design and quantifies the potential efficiency losses/gains using a large temperature glide mixtures. The paper further details the benefit of mixtures on capacity control.
Keywords: Refrigerant mixtures, Cycle efficiency, Heat pump, Temperature glide

1. INTRODUCTION

Refrigerant mixtures have become commonly used for air-conditioning and refrigeration applications since the phase out of CFCs. Those refrigerant mixtures typically consist of two or more pure refrigerants. Since every constituent has its own properties such as density, normal boiling point and latent heat, the mixing process, which typically generates little interactions among different types of molecules, often leads to a so-called zeotropic mixtures that have never the same vapor phase and liquid phase mass fraction in the vapor-liquid equilibrium state [1]. Such a behavior is unique and distinguishes the zeotropic mixture from pure refrigerants most significantly in the two-phase region.

To provide a further explanation on this uniqueness, we begin with a temperature-mass fraction diagram (Figure 1).

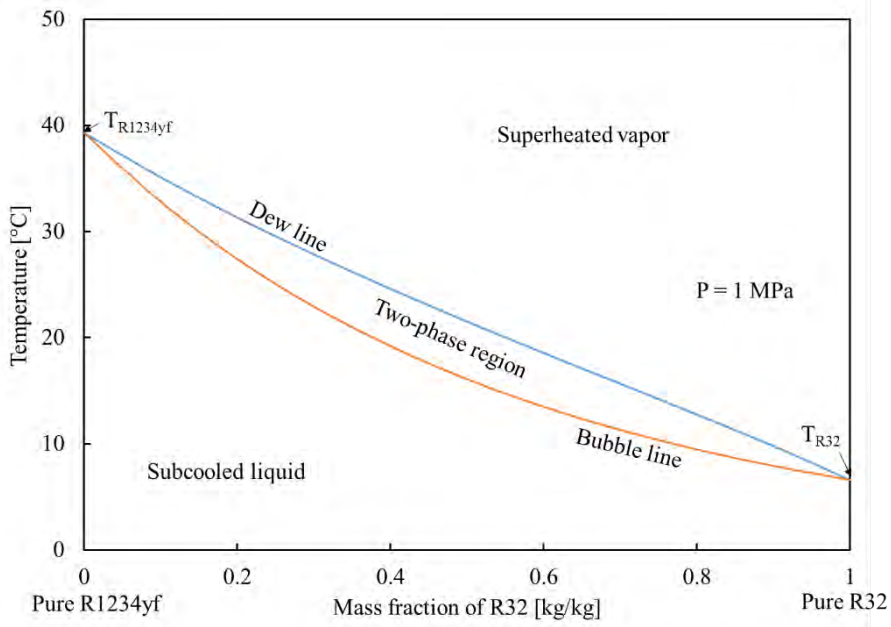

Figure 1: Saturation temperature and temperature glide of R1234yf/R32 mixture

When the liquid and vapor phases of a mixture coexist in equilibrium, the saturation temperature varies with the mass fraction even though the pressure is constant. This behavior contrasts with a pure fluid where T_{sat} remains constant. Figure 1 shows the temperature-mass fraction diagram (T-x diagram) for a mixture of two components, R1234yf and R32, at constant pressure of 1.0 MPa. The X-axis shows the mixture's mass fraction ranging from 0 to 1 with the two endpoints representing pure R1234yf and R32, respectively. The area below the bubble line represents the mixture in the subcooled liquid phase. The area above the dew line represents superheated vapor. The area enclosed by the lens formed by the dew line and bubble line is the two-phase region. The boiling point for a mixture of mass fraction x is located on the bubble line at that mass fraction. The bubble line indicates the saturation temperature at which the first vapor bubble is formed for the specified pressure and mass fraction when the temperature is raised from the subcooled liquid region to the saturation value.

From Figure 1, we notice the boiling points of the pure refrigerants are quite different. R32 has a saturation temperature of 6.6°C at 1 MPa, while R1234yf has a saturation temperature of 39.3°C at 1 MPa. That is to say, at the same temperature, R32 has a higher saturation pressure than R1234yf does, and the molecules of R32 are therefore more readily entering the vapor phase. Consequently, in the saturated vapor phase of the mixture, there is a higher mass fraction of R32. This means the mixture has a different mass fraction in the saturated vapor phase from than in the saturated liquid phase.

The vapor composition of that first bubble generated at onset of boiling is indicated by the intersection of the saturation temperature of the liquid phase with the Dew line. Thus, the horizontal distance between the dew line and the bubble line is a measure for the difference in the vapor and liquid phase compositions. This fact has important implications, it leads to changes in mixture concentration during the operation of the system through selective storage of refrigerant inventory within the system and also to potential changes in refrigerant composition through refrigerant leaks.

The boiling points of the pure components, R1234yf and R32 are found on the respective ordinates. The dew line defines the temperature at which the first liquid droplet is formed when a superheated gas mixture of a given mass fraction is cooled at constant pressure. When we draw a vertical line originating from mass fraction x, which is between 0 and 1, it will intersect both the dew line and the bubble line. The vertical distance between the two points of that intersection is called temperature

glide. For zeotropic mixtures, the temperature glide is non-zero and denotes the temperature difference between the temperature at which evaporation begins with the first vapor bubble and ends with the last droplet evaporated.

It should be noted that, for certain refrigerant mixtures (usually those where the boiling points of the constituents are close), there exists a composition that makes the refrigerant mixture act as a single refrigerant (see Figure 2 for a an example schematic). It is called azeotropic mixture. For example, the commonly used refrigerant R507A, 50%/50% mass fraction of R143a/R125, has virtually no temperature glide at various pressures (see figure 3). Strictly speaking R410A, a mixture of R32/R125 (50/50 in mass fraction) also has a small temperature glide of 0.12 K, but no azeotropic point. However, for all practical considerations, R410A behaves as a pure refrigerant. .

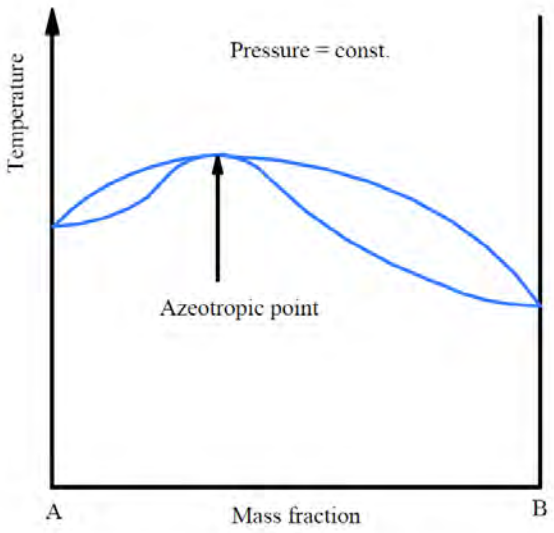

Figure 2: Saturation temperature and temperature glide of an azeotropic mixture[2]

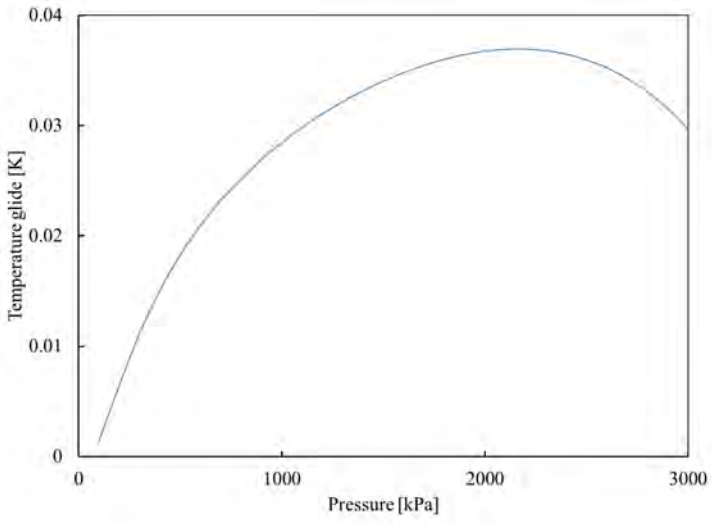

Figure 3: Temperature glide of R507A at various saturation pressure levels

2. Effect of temperature glide on heat exchanger design

The temperature glide significantly affects the design of air-to-refrigerant heat exchangers. For a pure refrigerant, the saturation temperature remains constant if the pressure drop is neglected during evaporation and condensation. Thus, the approach temperature, defined as the temperature

difference between two fluids, is only affected by the change of the air temperature. On the contrary, when the refrigerant is a zeotropic mixture, refrigerant saturation temperature increases significantly according to the temperature glide during evaporation and decreases during condensation. This makes the approach temperature dependent on both fluid temperatures and therefore demands a careful design on the refrigerant flow path vs the airflow path. Generally, the larger the temperature glide of a mixture, the smaller the approach temperature and the more important the appropriate heat exchanger design. Figure 4 shows an example of approach temperature profiles of a heat exchanger when considering two different mixtures, R404A (R125, 0.44; R143a, 0.52 and R134a, 0.04) and R448A (R32, 0.26; R125, 0.26; R134a, 0.21; R1234ze, 0.07 and R1234yf, 0.2).

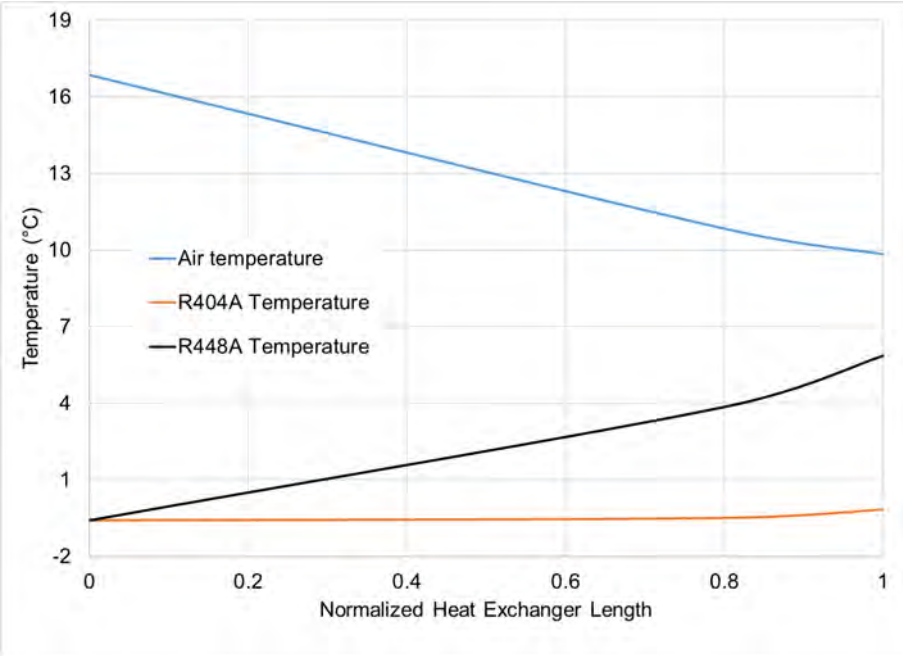

Figure 4: Temperature profiles of a conceptual parallel flow heat exchanger using zeotropic mixtures

Both refrigerants are zeotropic mixtures but with different temperature glides. R404A has merely a temperature glide of 0.47K at 0.82 MPa pressure (10 °C saturation temperature) and hence behaves more like a pure refrigerant. In contrast, R448A has a temperature glide of 5.38K at 0.85 MPa (10 °C saturation temperature). The difference in the temperature glide can be explained by their constituents' normal boiling point (NBP) differentials. As Table 1 indicates, the top two constituents of R404A, in terms of mass fraction, have only 0.85K differential in boiling points. R134a, however, has a significantly higher boiling point, but only 4% in mass fraction. In contrast, the top three constituents of R448 have NBPs ranging from -26C to -51C, each of which has at least 21% in mass fraction. The differential in saturation temperatures leads to different temperature profiles when the two refrigerant mixtures are compared Figure 4 The heat exchanger at issue is a parallel flow evaporator with incoming air temperature of 17°C for both cases. In both cases, refrigerant inlet temperature is -0.6°C and since the heat exchanger has a parallel flow configuration, the inlet of the heat exchanger, denoted by the normalized HX length at 0 , has the maximum approach temperature of 17.6 K. As heat transfer continues along the heat exchanger, R404A always demonstrates a larger approach temperature than R448A. At the exit of the heat exchanger, R404A still has an approach temperature of 12K while R448A has only 5K. It is obvious that the larger temperature glide of R448A causes an overall smaller temperature difference across the heat exchanger. As denoted by Eqn. 1, a smaller temperature differential will result in a reduced heat exchanger capacity.

$$Q_{cap} = UA * \delta T \qquad \text{Eq. (1)}$$

Where Q_{cap} is the heat exchanger capcity; UA represents the UA value; δT is the temperature difference of two fluids.

To better quantify the heat exchanger capacity drop caused by the temperature glide, we design a simple 60-tube and 2-row air-to-refrigerant coil (Figure 5). Air flows from left to right in the picture and the color represents refrigerant temperature in the tubes. Because of the color inversion, warm color represents higher temperature; cool color represents lower temperature. Such a coil is commonly used as evaporator in refrigerating systems and due to its relatively large tube number in a row, we can see a significant impact on capacity drop due to the temperature glide. When both refrigerants, with the same inlet saturation temperature, mass flow and inlet quality, flow in a parallel manner to air (top picture), R404A has a capacity of 1.5 kW which is 26.7% larger than that of R448A (capacities are tabulated in Table 2). Because the air side parameters and coil geometries are identical, the difference in capacity has to be a result of different approach temperatures. To support this conclusion, we plot the approach temperature at each segment of the coil and then compare them for both refrigerants. The approach temperature, in both cases, are only similar to each other at the coil inlet and outlet which is due to the same inlet flow condition and a proper coil sizing, respectively. R404A has a larger approach temperature up to 1K than R448A in the remainder of the coil.

This case study on parallel heat exchanger stresses the importance of mitigating the capacity penalty from high temperature-glide mixture. As an example of such mitigation, we design the R448A coil to be a counter flow configuration. In the bottom picture of Figure 5, we can see the refrigerant now flows from right to left while air still flows from left to right. In Table 2, noticeably, the capacity of the counter flow heat exchanger increases by 27%, from the original 1.1 kW to 1.4 kW. A closer examination on the approach temperature profile (Figure 6) of the counter flow case reveals the reason behind this improvement. For the counter flow case, the inlet approach temperature does not reach as high as the parallel flow case, but in the later HX section, it never drops as quickly as that in the parallel flow case. The overall approach temperature in the counter flow case turns out to be 0.85K higher than that in the parallel one which substantiates the capacity improvement.

Table 1: Normal boiling point of mixture component

R404A (top 3 constituents only)			R448A (top 3 constituents only)		
Constituent	Mass Fraction	Normal Boiling Point	Constituent	Mass Fraction	Normal Boiling Point
R143a	0.52	-47.24 °C	R32	0.26	-51.64 °C
R125	0.44	-48.09 °C	R125	0.26	-48.09 °C
R134a	0.04	-26.07 °C	R134a	0.21	-26.07 °C

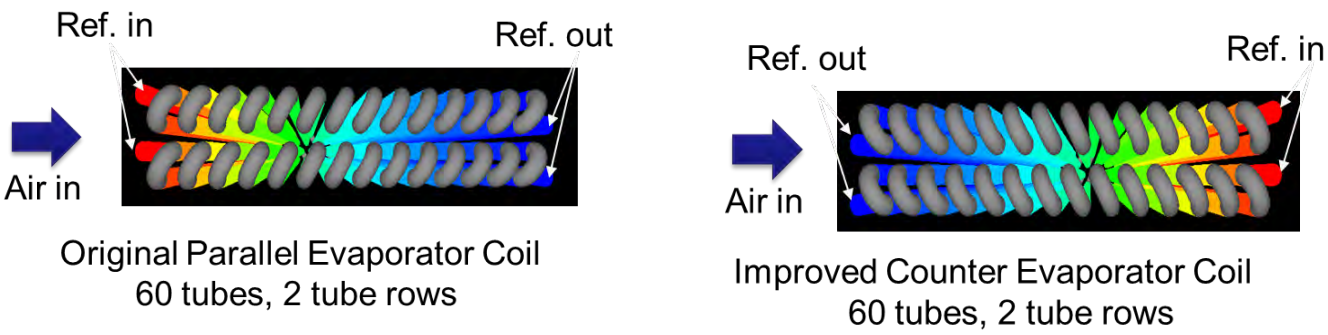

Figure 5: Case study: parallel flow vs counter flow heat exchangers using mixtures

Table 2: Temperature glide and capacity comparison

	R404A	R448A (Parallel Flow)	Improved R448A (Counter Flow)
Temp. Glide	0.1 K	5.8 K	5.8 K
Capacity	1.5 kW	1.1 kW	1.4 kW

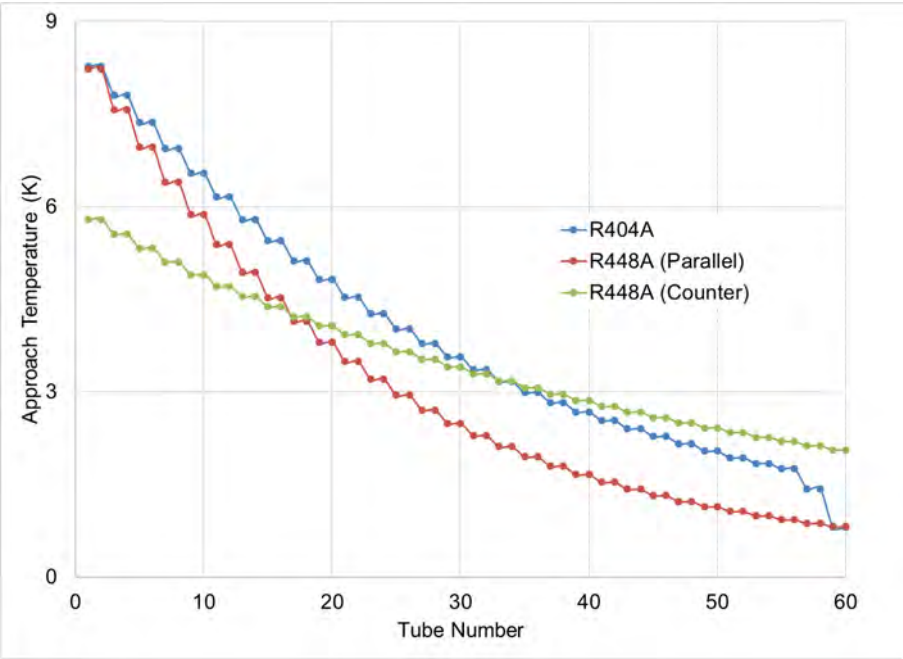

Figure 6: Approach temperature profiles of R404A and R448A heat exchangers

3. TEMPERATURE GLIDE EFFECT IN A VAPOR COMPRESSION CYCLE

We can extend our knowledge on the impact of a mixture's temperature glide by constructing a vapor compression cycle that uses the above-mentioned coils. With the help of the cycle, we not only eliminate the arbitrary assumption of refrigerant inlet conditions, but also start to explore the impact of temperature glide on compressor power consumption and system COP. A better heat exchanger design benefits the cycle efficiency by increasing the evaporating temperature and/or reducing the condensing temperature. This helps reduce the temperature lift across a compressor. A higher evaporating temperature can also increase the refrigerant suction density so that, under a fixed rotation speed, a compressor delivers a higher mass flow rate and therefore capacity. In this case, we further designed a two-row, 28 tubes coil as a condenser and an efficiency-based compressor with 65% isentropic efficiency and 95% volumetric efficiency. The cycle has a prescribed 5.5 K sub-cooling and 5K superheat for all cases. It should be noted that, for the sake of clarity and simplicity, we only study the impact of temperature glide on the system level by varying the design of the evaporator only. In all cases, the condenser and the compressor remain the same. The results of three cases including one R404A baseline, two different R448A cycles, the parallel flow and counter flow version, are tabulated in Table 3. We found the system capacity in all three cases behaved

consistently with their individual coil cases. The parallel design for R448A has the least capacity among the three, 16% less than the baseline. The evaporating temperature of the R448A system is 4K lower than the R404A system which leads to both reduced capacity and COP. On the other hand, the counter flow design has an evaporating temperature much closer to the R404A baseline, which successfully makes up both the capacity and COP losses. We can therefore conclude that, without proper design of the refrigerant mixture path, the temperature glide of a mixture may negatively impact the system capacity and efficiency. However, once a heat exchanger is sufficiently large so that the capacity demand is met, the temperature glide improves the system efficiency due to either an elevated evaporating pressure and/or a reduced condensing pressure. McLinden and Radermacher [3] thoroughly investigated the cycle efficiency improvement when properly exploiting the mixture temperature glide. The paper also includes successful cycle designs using mixtures.

With this conclusion in mind, we embark on exploring some benefits of using mixtures such as more flexible capacity control.

If we recall Figure 1 on the relationship between saturation temperature and mass fraction, the temperature glide of the mixture can vary according to mixture compositions. Consider the conclusion we just drew on temperature glide and capacity, we can infer that a system's capacity can be controlled to some extent, without the aid of mechanical means, through the change of refrigerant composition circulating inside the vapor compression cycle. The ability of capacity control without cycling the compressor is attractive because it reduces air conditioner's performance degradation during frequent on-and-off cycles. There exist multiple cycle configurations to actively alter the composition of various mixtures, most of which use at least one accumulator so that more less-active constituent in the mixture can be stored in the accumulator whereas the more-active one remains circulating in the cycle and dominating its performance.

Table 3: Cycle-level capacity and efficiency comparison on various evaporator designs

	R404A System	R448A System (Parallel flow)	R448A System (Counter flow)
Cooling Capacity (W)	1489	1247	1557
Compressor Power (W)	450	424	453
Evaporating Temperature (°C)	-3.46	-7.94	-4.24
COP	3.31	2.94	3.44

As one example, Etherington and Cannon[4] developed a variable capacity refrigeration cycle using an accumulator with a special molecular sieve that is selectively reactive to a certain refrigerant. As compared to the conventional refrigeration cycle with four basic components (evaporator, condenser, compressor, and expansion device), the one accumulator cycle (OAC) has an additional accumulator as shown in Figure 7. The accumulator is installed across the high and low pressure sides and connected on one side to the condenser outlet before the expansion device and on the other side to the compressor suction after the evaporator outlet. Both sides of the accumulator can be shut off with valves C and D. Etherington and Cannon proposed to use a molecular sieve that only absorbs one refrigerant, in this case R22 in the accumulator when the cycle is charged with R12/R22. The cycle operation is explained as follows. Let's assume that a binary zeotropic mixture of R12 and R22 is charged in the cycle. A normal boiling point of R12 and R22 are –29.8°C and –40.8°C. R22 has a higher saturation pressure and larger latent heat than those of R12. For example, the saturation pressures of R12 and R22 are 423 kPa and 681 kPa, respectively at 10°C saturation temperature. The latent heats of R12 and R22 are 148 kJ/kg-K and 196 kJ/kg-K, respectively at 10°C saturation

temperature. Therefore the mixture circulating in the cycle will have a richer composition of R22 and, latent heat and higher suction pressure which increases the suction density and consequently the refrigerant mass flow rate. Therefore a R22 rich mixture works at higher operating pressures and provides more capacity. When the system capacity is larger than the load, there is a need for reducing capacity. Then valve C is opened and valve D is closed. Thus R22 is absorbed into the molecular sieve selectively. In this case, the R22 mass fraction of the circulating mixture becomes lower than the originally charged mass fraction. The system capacity is reduced due to the increase in R12 content. When the system capacity is smaller than the load, there is a need for restoring system capacity. Then valve C is closed and valve D is opened. An electric heater helps to desorb the R22 that is absorbed in the molecular sieve. In this case, the R22 mass fraction of circulating mixture becomes the same as the originally charged mass fraction. The system capacity is restored.

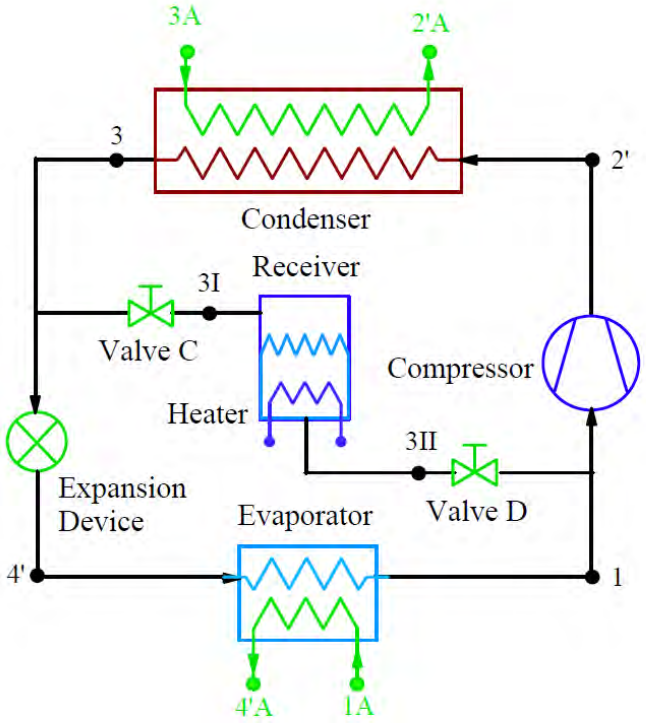

Figure 7: One-receiver design on mixture capacity control

We created a vapor compression cycle model to better quantify the capacity control described above. Since the R32 and R1234yf pair was previously mentioned, we continue to use them as our mixture at issue. It should be noted that the created model does not fully represent the cycle in Figure 6. We don't actually consider the design of the receiver (accumulator) but rather make assumptions about the outcome. We assume the receiver works perfectly and helps control the concentration of the R32 as needed from 30% to 60%. We simulated the cycle under AHRI standard cooling test condition (Table 4). The system simulations show that for the pair of R32/R1234yf, as the mass fraction of R32 decreases by 10%, the cooling capacity is off by up to 4% (Figure 8). The deviation of cooling capacity shows a monotonic decrease as the R32 mass fraction decreases. This is due to both the change in operating pressures and a higher heat of vaporization of R32 than that of R1234yf. We first compare the difference in latent heat. At 300 K, R32 has a heat of vaporization of 267.1 kJ/kg while R1234yf has a heat of vaporization of 143.87 kJ/kg. As the R32 mass fraction is reduced by 10%, the COP reduces in a similar manner as the cooling capacity. It can be found from Figure 7 that the compressor power consumption reduction is almost negligible compared with cooling capacity reduction.

Table 4: ASHRAE Standard 116 (2010) Test Condition [5]

	Indoor conditions		Outdoor conditions	
ASHRAE Test A condition	26.7 °C (dry bulb)	19.4 °C (wet bulb)	35 °C (dry bulb)	N/A (wet bulb)

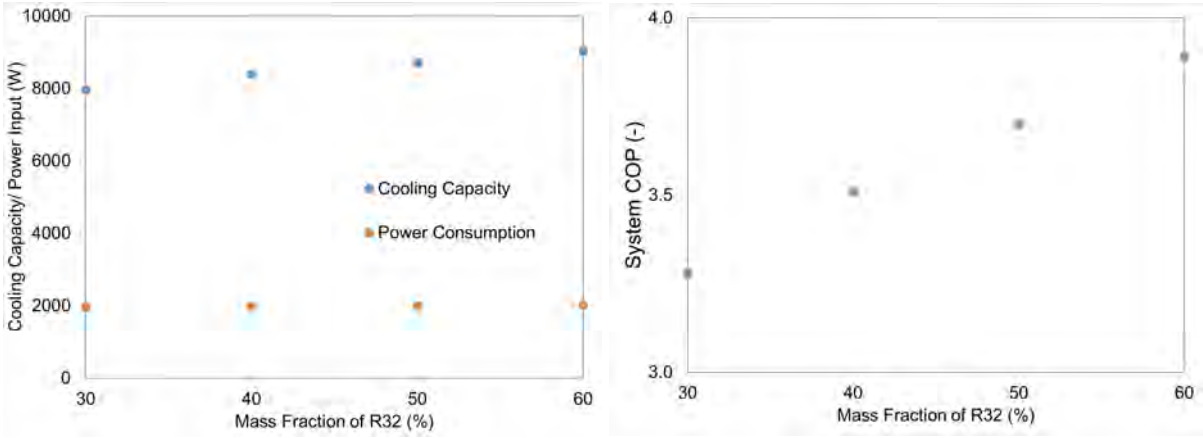

Figure 8: Cooling capacity, power input and system COP at various R32 mass fractions

Regarding the operating pressures, as the mass fraction of R32 decreases, the operating pressures decrease too (Figure 9). For every 10% lesser R32, both condensing and evaporating pressures reduce up to 7%.

This is because R1234yf has a high boiling point of 243.7K which leads to much lower operating pressure. When R32 mass fraction reduces, the operating pressure of the blend turns towards lower pressure. The vapor specific heat of R1234yf at 300K is 1.065 kJ/kg which is lower than that of R32. The discharge temperature is therefore decreased by 0.4 K to 0.5 K as the R32 mass fraction shifts by 10%.

(Figure 10).

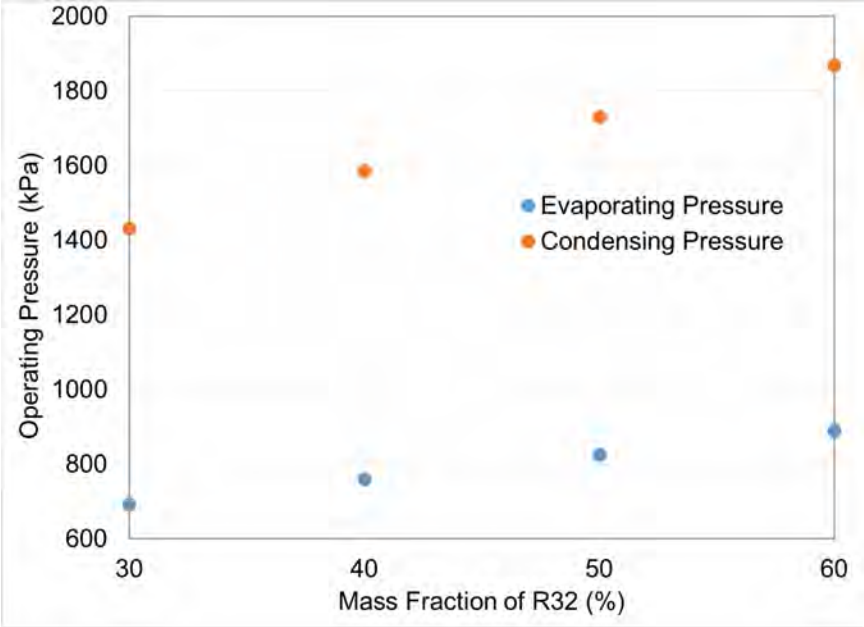

Figure 9: System condensing pressure and evaporating pressure at various R32 mass fractions

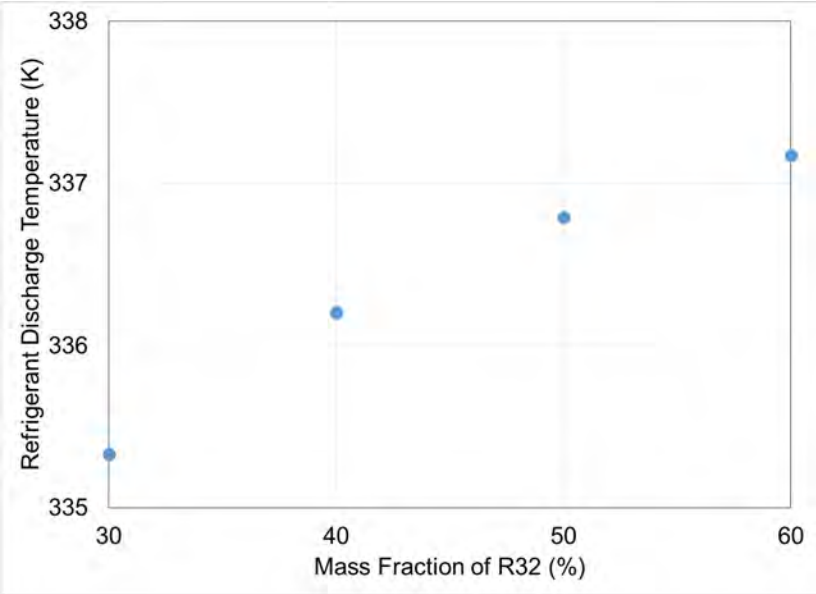

Figure 10: System discharge temperature at various R32 mass fractions

4. CONCLUSIONS

The paper discusses refrigerant mixtures and their applications in heat exchangers and vapor compression cycles. Most mixtures are zeotropic ones and therefore exhibit a temperature glide during evaporation and condensation. The temperature glide may cause capacity losses due to a reduced approach temperature in heat exchangers. Without a proper design, heat exchanger may lose up to 27% of its capacity when using a zeotropic mixture having 5.2 K temperature glide. However, by simply changing the refrigerant path to be counter flow, such capacity loss can be minimized. When the air-to-refrigerant mixture heat exchanger can deliver the required capacity, the

reduced approach temperature resulting from the temperature glide can improve the system efficiency. Refrigerant mixture has the benefit of control system capacity by altering its composition circulating in the cycle. The paper studies a R1234yfa/R32 mixture and reports a 4% cooling capacity reduction for every 10% reduction in R32 concentration.

ACKNOWLEDGEMENT

The authors would like to thank the Center for Environmental Energy Engineering's sponsors for their financial support.

REFERENCES

[1] http://en.wikipedia.org/wiki/Zeotropic_mixture

[2] Radermcher R., Hwang Y., 2005, Vapor Compression Heat Pumps with Refrigerant Mixtures, CRC Press

[3] McLinden M.O., Radermacher R., 1987, Methods for comparing the performance of pure and mixed refrigerants in the vapour compression cycle, International Journal of Refrigeration,

Volume 10, Issue 6, Pages 318-325.

[4] Etherington, T., Cannon P., 1960, Variable capacity refrigeration, US Patent 2951350

[5] ASHRAE Standard 116-2010 - Methods of Testing for Rating Seasonal Efficiency of Unitary Air Conditioners and Heat Pumps (ANSI Approved)

Manuscript ID: 1836
DOI: 10.18462/iir.icr.2019.1836

Cold chain certification

Gérald CAVALIER[(a)]

[(a)] Cemafroid, 5 Avenue des Prés - Fresnes cedex - France
gerald.cavalier@cemafroid.fr

ABSTRACT

Cold chain is indispensable to ensure perishable goods safety in our societies. It has strongly developed for more than 150 years and will develop even more during the next decades. As far as safety is involved its guarantee is searched and it is also the case for cold chain from its early beginning with Charles Tellier in 1876. With the increasing place of cold chain and its energy needs, it is now also necessary to ensure cold chain environmental efficiency.
Certification is a way to guarantee safety and performance. Since the beginning, alongside with cold chain development, certification schemes were developed, through tests in a first time, then with product certification and then companies and staff certification. An overview of the available certification systems allows understanding the potential of certification to guarantee cold chain conformity and performance and to help its development all around the world.
The analysis of cold chain certification development in 2019 in the world from farm to fork and from laboratory to pharmacy underlines the necessity of harmonisation of the standards and their development all around the world to improve the safety of cold chain and its environmental performance and reduce its energy consumption
Keywords: Cold Chain, Certification, Tests, Label, Performance.

1. INTRODUCTION

Cold chain was invented nearly hundred fifty years ago in France by Charles Tellier who, for the first time, transported fresh meat from France to Argentina and back in 1876. The issue for Tellier was already to certify the quality and security of the meat after its transport and his greater challenge to convince people of the tremendous interest of these new technologies for them and for their health: "*Ils prouveront mieux la vérité des faits que tout ce que je pourrais dire* (They will better prove the truth of facts than all the things I may say)."
Nowadays cold chain is indispensable for our society. It is the guarantee of food security for fresh and frozen products and consumers want the guarantee of their food quality that is to say also the guarantee of the cold chain. It is also a demand of all the professionals along the cold chain who endorse the responsibility of the food safety of their products. It is also the case for thermos-sensible pharmaceuticals and health products which requires cold chain. The patient wants to be sure of their quality, including the continuity of cold chain from farm to fork and from laboratory to lavatory.
In the same time cold chain requires energy and its environmental impact is important. The consumer also wants a sustainable cold chain with energetic and environmental labelling ensuring the performance of the equipment and the governments ask for energy savings and sustainability.
To face these two challenges, cold chain should prove its quality and performances on an independent way. Since the first cold chain certification systems at different levels were developed either by manufacturer, by users or by the authorities willing to develop cold chain and guarantee food but also health products, safety and security.
This paper first tries to describe all the development of certification schemes of equipment, people, systems or companies all along with cold chain development, and then it presents the different certification systems and models in regard with cold chain specificities. Finally the author analyses the present situation with the available cold chain certification schemes and the gaps to be filled to guarantee to users, consumers and authorities the quality and the performance of cold chain all over the world for all kind of products.

2. COLD CHAIN CERTIFICATION DEVELOPMENT

Since its early beginning, cold chain had to prove its quality and performances. Tellier faced many objections and when he summarised his work in 1910 he noted that he proved the capacity of the machines to produce cold, the capacity of the insulation to preserve it and finally the quality of the meat after its storage and transport under controlled temperature: the performance of the equipment and the conformity of the result, the two pillars of most of our certification systems nowadays. Obligations of means or obligation of results are too often opposed but Tellier reminds us that they are fully complementary.

2.1. Cold Rooms, Cold Chambers and Ice-coolers, the oldest Cold Chain Equipment

Deriving from the ancient icehouses, cold chambers are certainly the oldest cold chain equipment, introduced before the chain. Recently a standardisation of testing and dimensioning was intended in Europe in the frame of CEN TC44. If this work proposes dimensioning rules it is not bringing yet to certification.
On the pharmaceutical cold chain cold chambers and ice-coolers for vaccines and blood testing methods and certification have been defined by WHO in its SQP (Service Quality Plan) program which covers most of the equipment's for vaccines cold chain from packaging to delivery including traceability devices. The SQP certification scheme is a type certification of the products.

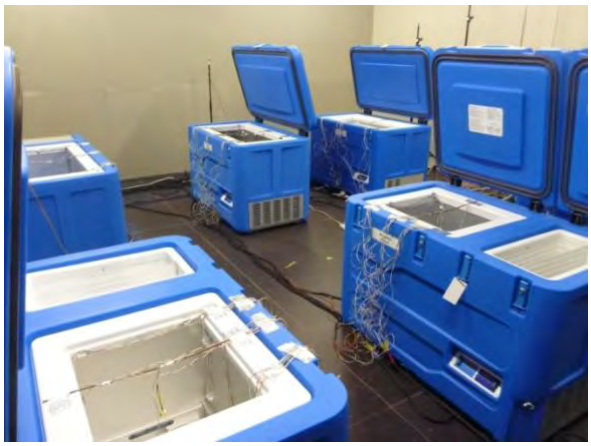

Figure 1: test of an ice cooler for vaccine transportation according to OMS PQS certification protocols.

2.2. Refrigerated Transport Certification: more than a century of history

Just after the first International Congress of refrigeration in Paris in 1908 and the creation of the French Refrigeration Association and the International Institute of Refrigeration the same year, the first cold chain test station is built in Chateaurenard in the south of France in 1910 (see Fig. 2). Its objective was to measure the insulation performance of the refrigerated rail coaches and their capacity to preserve and transport perishable foodstuff under controlled temperature. It was certainly the first attempt to elaborate standard testing methodologies for cold chain equipment on an independent way in a dedicated laboratory, the ancestor of present ATP testing stations and the first cold chain independent laboratory.

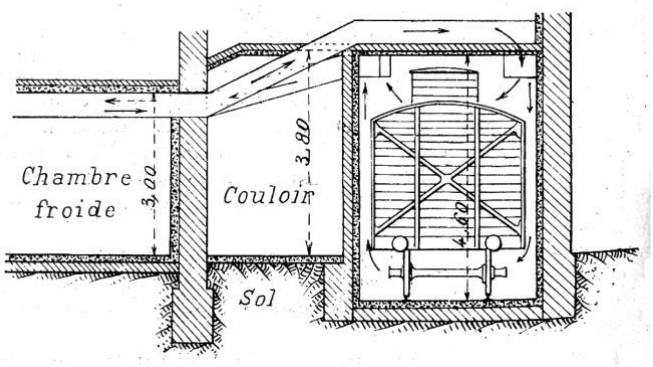

Figure 2: Type test of a refrigerated wagon in Chateaurenard test station (1910).

Refrigerated transport long remained the weak point of cold chain. Without refrigerated transport there is no cold chain continuity and then no cold-chain at all. Invented in 1876, cold chain real met a large scale development in the world during and after First World War with the need to feed the armies on the front and then the development of terrestrial refrigerated transport and refrigerated transport equipment at large scale. After the World War the refrigerated transport fleet has tremendously increased. In France for instance it was multiplied by more than 10 in four years. With cold storages, refrigerated rail coaches and cold chambers, a network has been developed to offer a continuous cold chain. To assess the performances of their equipment the army wanted standards and tests. Henri Bénard, the famous physicist, served during the war as officer in the military cold chain scientific commission and he conceived new methods for the measurements of the thermal diffusivity of the insulated wagons walls published after the war in 1919 and 1921. It was the first standard for measurement of refrigerated transport equipment performances.
In France these equipment were given by the government to create refrigerated logistics companies between 1919 and 1927.
The Second World War marked also an important change in cold chain with the strong development in the 40s and after of the refrigerated road transport. One of the first refrigerated trucks appeared in the late 30s in the United States of America arrived in Europe in the mid-40s. The new equipment allowed a larger and broader development of cold chain introducing also new challenges for manufacturers, users and consumers. Cold chain developed its network on more international bases. Following its 40 years' experience in testing and certification of refrigerated transport equipment, France published in 1952 a regulation requiring minimum performances of insulation and minimum refrigeration capacities for refrigerated trucks. This regulation was including the measurement methodology, the classification of the equipment depending of their type and performances, and individual certification of each refrigerated van, truck or trailer. New tests stations were created to face the increasing demand of tests and certification of equipment. One of these was the ATP test station in Antony (France) for the certification of refrigerated transported equipment (see Fig. 3).

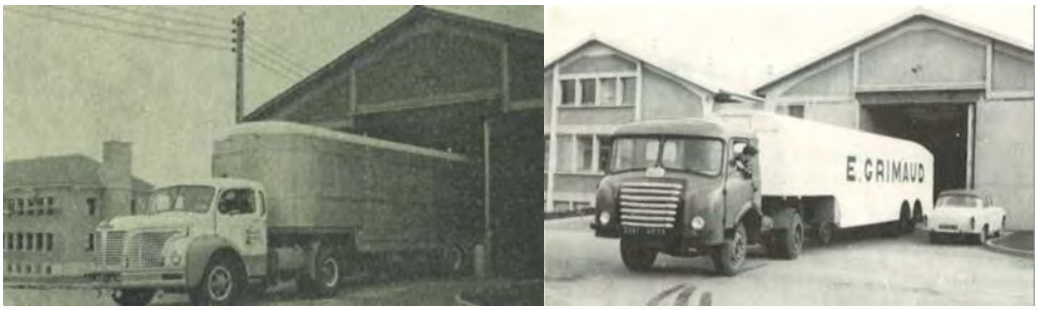

Figure 3: tests of refrigerated trucks in the 50s in Antony ATP test station.

With the increase of international exchanges and the control of customs it appeared preferable to reduce the openings of the refrigerated transport equipment for their control. The development of an international recognition of the performance of the refrigerated transport equipment was necessary. In the frame of Economic Commission for Europe of the United Nations started discussions that ended in 1970 with the signature of the International Agreement concerning the

International Carriage of Perishable Foodstuffs and on the Special Equipment to be used for such Carriage, referred to as “ATP”. It became the first international certification scheme for cold chain. To date, fifty two countries in the world have signed this agreement and some others have copied it in their own regulation and standards. This agreement requires minimum performances for all terrestrial refrigerated transport equipment used for international transport and the certification and regular recertification of each piece of equipment. With the aim of guaranteeing food security all along the transport, these performances and certification system is required both for the insulation of the refrigerated enclosure and for the refrigerating unit.
Since 1970, as a matter of fact, some countries such as Russia, Italy, Spain, Morocco or France have also decided in their national regulation, to apply ATP rules to all refrigerated transport in their country. They want to reinforce their food security taking into account the specificity of their food chain, alimentation habits but also their climatic constraints.
Fig. 4 shows the ATP certification scheme as implemented in France in 2019. The insulation performance of a refrigerated vehicle used in the carriage of perishable foodstuffs is quantified through the overall insulation coefficient, so called K coefficient. As shown if Fig. 4, the French Regulation requires that this coefficient is measured for all the in-service vehicles after twelve years from their owner whereas immediately after the manufacturing only the K coefficient of the prototype, K_p, is measured to certify the whole series, for the first six years of life. After the first six years of life the recertification is made for all the in-service equipment through a pull down test, to be repeated after three years of life. At twelve years of life, the K coefficient allows renewing the ATP certificate for other six years, after which the K coefficient test must be repeated for a renewal of a further six years.

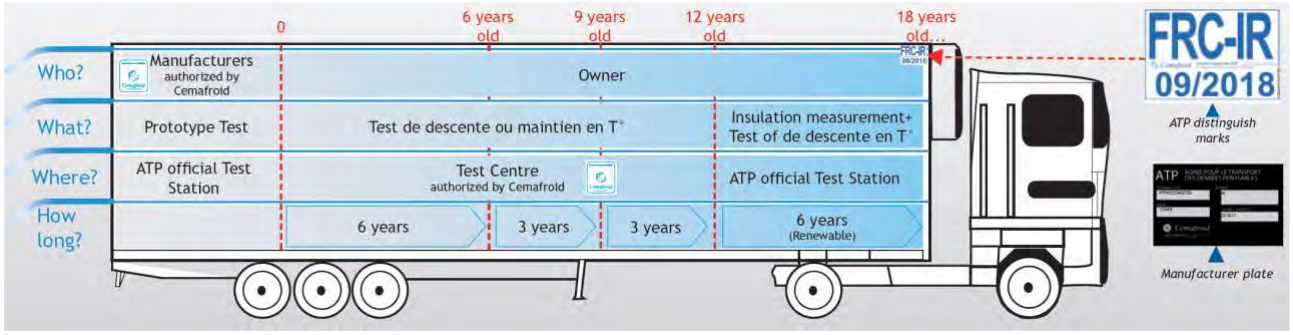

Figure 4: ATP certification scheme as implemented in France in 2019.

2.3. Bulk Milk Coolers

Cold chain is not limited to transport even if refrigerated transport long remained the weak point of cold chain and is still the critical segment in a lot of regions of the world. As stated by Alexandre Monvoisin in 1925 cold chain requires safe products, early refrigeration and continuous refrigeration: the three pillars of the famous Monvoisin tripod. Then, it is not surprising to see the development of testing protocols and certification schemes for other cold chain segments. Among other cold chain segments, milk and dairy products are the most sensitive perishable food products. The industrialisation of their distribution and transformation increased the time between milking and process. In the 70s it became indispensable to cool milk at farm before transport to the dairy. Bulk milk coolers met a fast and important development. French government subsidised them in the 60’s to encourage farmers to improve the quality and security of their milk. It was important to finance with public money only efficient equipment. Then a testing methodology and a voluntary “NF” product label was created based on a certification scheme developed by French agricultural ministry, the manufacturers and the Cemagref technical and research centre. The testing and performance standard then became European and is referenced today as EN 13732.

2.4. Refrigerated Display Cabinets

At the end of the chain, fresh and frozen products are distributed to the consumer most of the time in display cabinets. Nearly 100 million of these display cabinets are in service in the world. At the end of cold chain, with an important turnover of products, a strong lighting of the stuff, an increasing number of customers taking their shopping directly in the refrigerated cabinets, these equipment most of the time open are one of the most critical component of cold chain.
An international testing and performance standard was developed to assess the performances of refrigerated cabinets in different ambient conditions, for different foodstuff temperature and

including their energy consumption. It is referenced ISO 23953. Type certification has been developed on this standard.

2.5. Temperature Recorders and Thermometers

In the same time the demand of traceability of cold chain increased and raised the issue of the performance of the thermometers and temperature recorders in cold chain and particularly in cold chain logistics where the conditions of operation may be difficult. Testing and performance standards were also developed with a type certification of temperature recorders on national approbation lists. A French standard was created by Cemagref in the 80's and became then European standard under the reference EN 12 830. It has been recently revised in 2018 including new classes of performances and enlarging its scope to pharmaceutical cold chain.
Another standard EN 13 485 was developed for testing and performances of thermometers. It was also indispensable to set rules for calibration and verification of thermometers and temperature recorders, it is done with the EN 13 486 standard. These two last standards are currently in revision by CEN. A first standard for testing and performances of temperature indicators and integrators were also developed and published in France under the number NFX-18 100.
These three voluntary European standards should be fulfilled by thermometers and temperature recorders used in deep frozen food cold chain in application of European EU 37/2005 regulation. This equipment should be type certified and individually calibrated and checked.

3. CERTIFICATION SCHEMES

Certification may be mandatory and imposed by international, national or regional regulations. In cold chain it is the case of ATP for refrigerated transport equipment. It may also be voluntary such as "NF Refroidisseurs de lait en vrac" ("NF bulk milk coolers") label for bulk milk coolers for example. It may also be required for public or private funding's such as WHO SQP (Service Quality Plan) label. Voluntary or mandatory, certification has different level from type certification to product certification with control of production, it may be self-certification by the manufacturer such as CE mark with a rather low reliability, delivered by a second or a third independent party with a high level of confidence most of all when the certification body is accredited such as Cemafroid certification body for ATP new equipment certification.

3.1. Equipment Testing and Type Certification

Equipment certification is the most common, even in cold chain. Generally based on testing and performances standards, equipment certification may nevertheless have different level. The first level of certification is "type certification" based on the test of a representative sample of a model. The laboratory assesses the performance of the tested equipment and it may be considered, if the production is of quality, that the other equipment pieces built on the same reference offer the same performances. Generally, a type certificate describes the given performances and the certified product. The type certificate is related to a model or type of equipment, never to each individual piece of equipment.

3.2. Products Certification

The equipment certification may be a little bit more accurate with a quality control of the production through audits of the plants for instance. This offers a better guarantee of the production quality. It may be based on the product certification standard ISO 17 065.
The better guarantee is offered by a product certification based on the same standard and principles but including production controls of each piece of equipment produced and an independent random selection of a piece of equipment for the measurement of its performances by an independent accredited laboratory. The third party production control under accreditation is the must in term of product certification.
The ultimate certification is based on a systematic full test of each piece of equipment, but this approach is extremely expensive and generally economically unviable. It is totally inapplicable to cold chain. It is preferable to set an appropriate intermediary independent certification system.
The cost of these different systems is of course rather different but the level of guarantee offered too.

3.3. People Certification

Even with the best equipment cold chain may be inefficient with unskilled people. It is an increasing issue with the growing complexity of the systems and their faster evolution. Training of staff is indispensable at all level of the companies, but also at the customer level.
The increasing complexity of refrigeration requires trained people either to implement, to maintain or to use the cold chain facilities and systems. Training were developed with cold chain development in all the countries and refrigeration diplomas created from operators level to engineers. The French Refrigeration Association for example developed technicians and engineers diplomas with Conservatoire National des Arts et Metiers in the frame of Institut Français du Froid Industriel (IFFI) which still exist.
More recently it appears that the progress of techniques and regulations required regular control of the knowledge and practices of the operators. In Europe a certification of operators was set in 2007 in the frame of F-gases regulation EU 842/2006 replaced then by EU 517/2014, in order to reinforce the containment of refrigeration systems and reduce refrigerant losses in the atmosphere. Since 2008, hundred thousands of staffs have been certified in Europe for F-gas manipulation. If in some countries this certification is not limited in time, in most of the European countries it is a five or ten years certification. A report of the European commission stated that in 2016 already more than 160 000 people had been certified in more than 40 000 certified companies.

3.4. Cold Chain Certification

The Graal for cold chain certification would be of course the full cold chain certification. With an important number of segments, equipment and operators, it is a great challenge and a complex system. Till now no system exists for the full cold chain certification from farm to fork or from laboratory to lavatory.
Before the certification of the full cold chain it will certainly be necessary to certify all the equipment and operators of the chain which is not already done.
The development of communication facilities and big data will certainly help developing a global certification, even without a certification of each individual element.

3.5. Certification Bodies

The first level of certification, which is not really one, is auto certification by the manufacturer such as for most of the CE mark in Europe. Auto-certification does not give really more than a commercial trade mark for the consumer or the user.
Most of these certifications are delivered by independent third parties, either for type certifications or for products and services certifications. Nevertheless an efficient certification system also requires a public and well documented certification system accessible to everybody with no restrictions.
The most robust certification labels are delivered by accredited bodies. The accreditation bodies should be members of the international network of accreditation bodies the International Accreditation Forum (IAF) at international level and the European co-operation for Accreditation (EA) at European level. Certification bodies should be accredited according to the international standard ISO 17 065.
Nevertheless, some intergovernmental organisations, such as World health organisation (WHO) in the frame of its SQP program, also deliver accreditation for laboratories and certification bodies.

3.6. Accreditation Bodies

At the top of the systems there are the accreditation bodies. Laboratories and certification bodies should be accredited to assess and insure the quality of their service and the independence of their decisions. Each country has its own accreditation body such as Accredia in Italy, UKAS in United Kingdom, ENAC in Spain or COFRAC in France. The accreditation bodies gathered in associations and assess their performances on the base of peer revues. The international laboratories accreditation cooperation (ILAC) coordinates testing accreditation bodies while European Accreditation (EA) coordinates certification accreditation bodies. The members of European Accreditation are shown in Fig. 5.



Figure 5: Members of European accreditation.

4. COLD CHAIN CERTIFICATION TODAY AND FUTURE NEEDS

It is interesting to map the certification systems in operation nowadays for cold chain from farm to fork and laboratory to lavatory.

Table 1 hereunder gives an over view of existing certification schemes for cold chain equipment, companies and staff. It underlines that even if nearly all equipment, companies and staff may be certified in the frame of existing certification schemes, the penetration of certification remains very low. With the development of cold chain, the need of certified equipment, certified commissioners and maintainers and certified staff is major. Nevertheless the number of certified items is still low and the level of the existing certifications sometimes quite basic or poor.

Table 1. Identified certification systems in 2019 for cold chain components

Equipment	name of the certifications	perishable goods concerned	Voluntary or mandatory certification	Nature of certification	standard or regulation	geographical area	total number of certified units in the world	% of units certified
Coldstorage and cold chambers	Certicold HACCP and Certicold Pharma	Perishable Foodstuff, Health products	voluntary	product certification	standard	everywhere		less than 1%
Icecoolers	WHO-PQS	health products	mandatory for some operations	type certification	standard	everywhere	only several models	0%
Refrigerated transport equipment	ATP, Certicold Pharma,	Perishable Foodstuff, Health products	regulation (ATP), Voluntary (Certicold)		regulation	52 countries in the world	nearly 1 million	beetwen 20% and 50%
Insulated and refrigerated packaging	WHO-PQS, Certicold Pharma, Certicold HACCP			type certification	standard	everywhere	many types certified but no individual unit	less than 1%
Display cabinets and vending machines	Energy labelling, Certicold HACCP,	Perishable Foodstuff,		type certification and product certification	standard	everywhere	some ten thouthands units	between 1 and 20 %
Domestic refrigerators	energy labelling	Food	mandatory for some operations	type certification	regulation	everywhere	all type certified but no individual unit	0%

Compagnies	name of the certification	perishable goods concerned	Voluntary or mandatory certification	Nature of certification	standard or regulation	geographical area	total number of certified compagnies	% of units certified
Refrigerants manipulation	F-gaz certification	all	mandatory	Compagnie certification	regulation	EU (28 countries)	40 000	**more than 50%**

Staff	name of the certification	perishable goods concerned	Voluntary or mandatory certification	Nature of certification	standard or regulation	geographical area	total number of certified units	% of units certified
Operators manipulating F-gazes	F-Gaz certification	all	mandatory	Staff certification	regulation	EU (28 countries)	160 000	**more than 50%**

4.1. Bulk Milk Coolers

The voluntary certification system developed in Europe by AFNOR was interrupted a few years ago due to a concentration of the market, an increasing number of models and a now un-adapted certification system even if it was based on a quite well written testing standard EN 13 732.
If the European market of bulk milk coolers is mature and rather limited now, it is booming in developing countries. Equipment of all levels of quality are proposed on the market and a certification would be very useful, first of all for equipment subsidised by international or national public money. It will guarantee a high cold chain performance of the equipment but also a high environmental and energetic efficiency for equipment requiring high energetic consumption. At a broader scale, Certicold HACCP bulk milk coolers offers all over the world an international certification of these key equipment at the really beginning of dairy cold chain.

4.2. Cold Chambers

The oldest cold chain equipment remains till recently out of the standards and certification scope. An European standard referred to as EN 16855-1 was published in 2017 for test and dimensioning of cold chambers no certification scheme has been developed in this frame.
With the development of mobile cold chambers and containers used as cold chambers, professionals have developed recently a referential in the frame of Certicold certification scheme. It is the beginning of cold chambers certification either for foodstuff or for pharmaceuticals cold chain.

4.3. Refrigerated Transport Equipment

Among cold chain equipment, refrigerated transport equipment meet the highest rate of certification. Perhaps, this is due to the fact that it is one of the most critical, due particularly to their movements and constraints. In ATP countries a large number of equipment are certified and in countries such as Russia, Italy, France, Spain or Portugal who decided to apply ATP regulation to all transports, nearly all the refrigerated transport equipment are certified. Figure 6 hereunder shows the implementation of ATP in European and nearby countries, that is to say most of the 52 ATP countries.

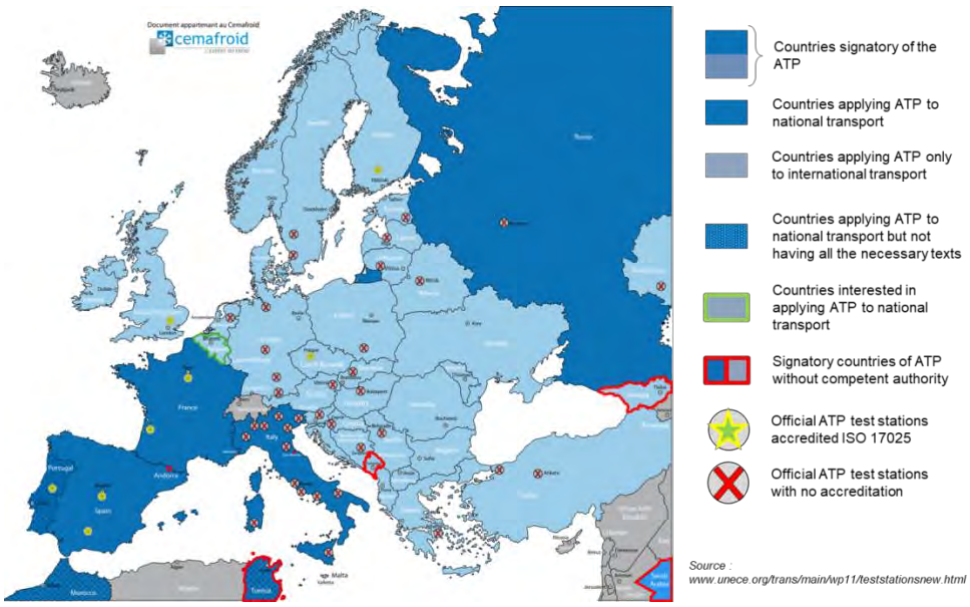

Figure 6: Implementation of ATP in the world in 2019 – Cemafroid©.

With more than 1, 2 million refrigerated transport equipment pieces, Europe account for roughly a third of the world fleet. A large part of this fleet is certified in 2019. It is also the case in other ATP countries. Fig. 7 presents the distribution of the ATP certificates issued in the world in 2017 whereas Fig. 8 presents the ATP refrigerated transport fleets according to UNECE 2012-2018 figures.

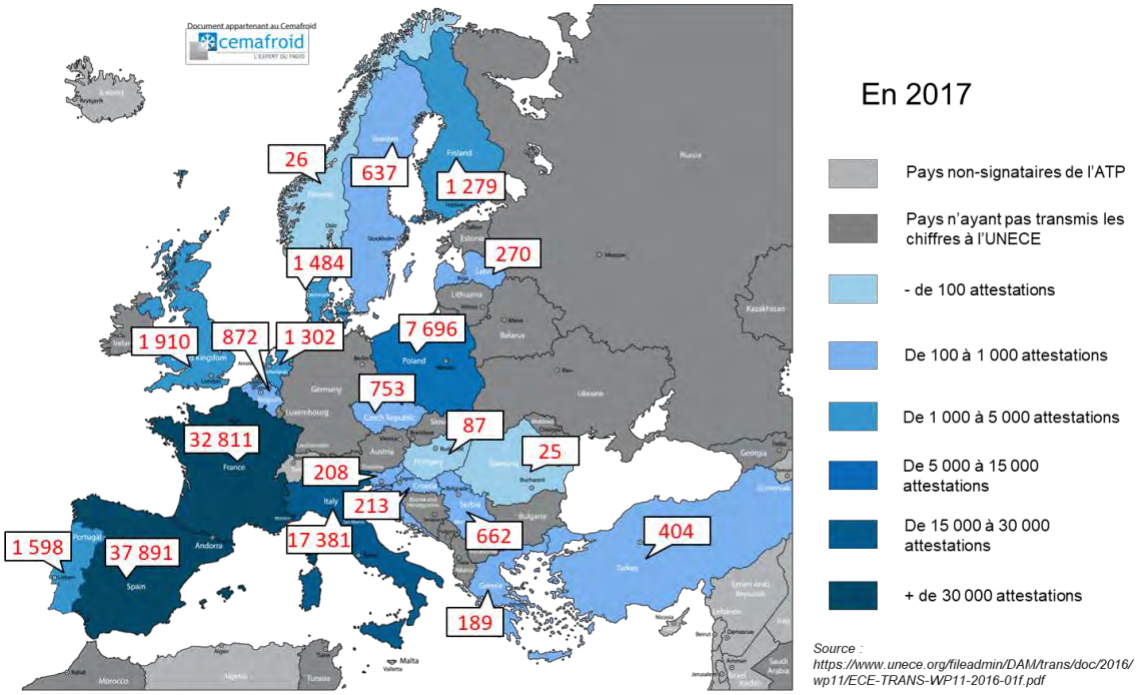

Figure 7: Number of ATP certificates delivered in ATP countries in the world in 2017 – Cemafroid© based on ECE-TRANS-WP11-2016-01.

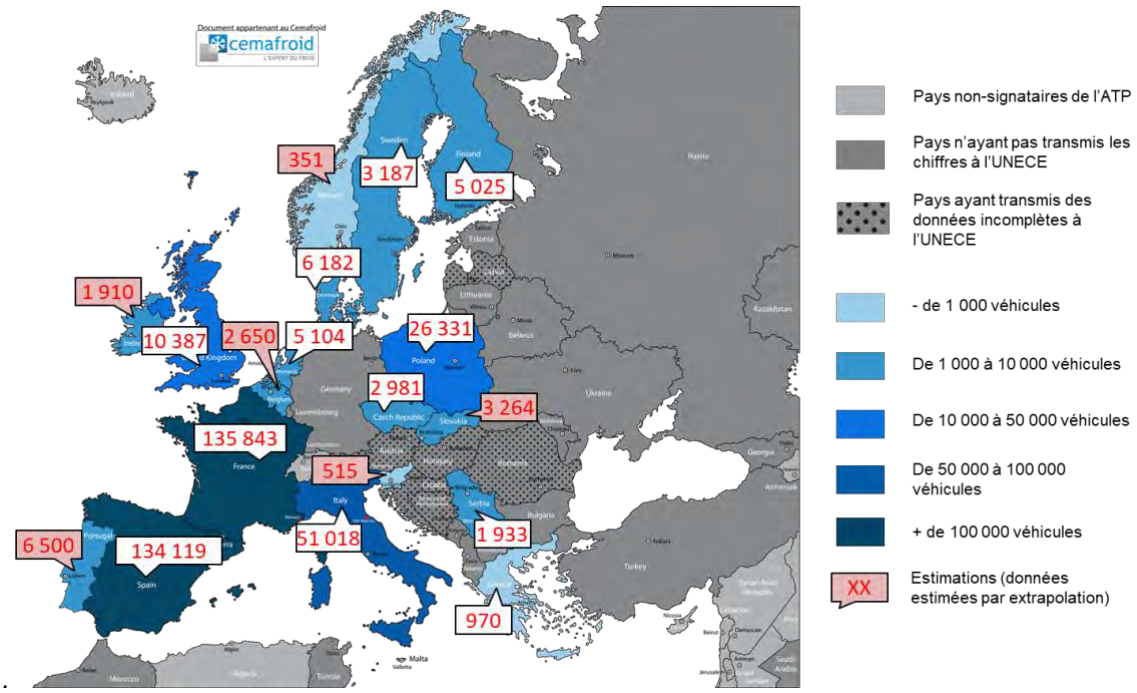

Figure 8: ATP refrigerated transport fleets according to UNECE 2012-2018 figures.

For health products transport, if a lot of manufacturer's labels have been developed, few independent third party public labels are available. Certicold Pharma®, for example, start to develop in many countries with some thousands equipment already certified with a strong link with ATP.

4.4. Refrigerated Packaging

Refrigerated packagings are used for several years for pharmaceutical cold chain. Several testing standards are used such as private American standard ISTA 5b, public French standard NFS 99 700 but most of the time without even type certification.

For the needs of international vaccines distribution, World Health Organisation has developed its PQS certification system including most of vaccines cold chain equipment and particularly insulated and refrigerated transport packaging:

- E001: Cold rooms, freezer rooms, and related equipment
- E002: Refrigerated vehicles
- E003: Refrigerators and freezers
- E004: Cold boxes and vaccine carriers
- E005: Coolant-packs
- E006: Temperature monitoring devices
- E007: Cold chain accessories

The certification of cold boxes and vaccine carriers, coolant-packs and temperature monitoring device according to PQS is mandatory to access the United Nations vaccination programs.

The use of packaging is booming for a few years for distribution of food stuff sold on e-commerce. In Some countries such as China were the traditional cold chain is not so well developed, fresh foodstuff distribution is said to be more important through this canal than throughout the traditional cold chain.

An attempt of foodstuff distribution certification in refrigerated packaging is ongoing in the frame of ISO under the PR NF ISO 23412.

4.5. Display Cabinets

In the world nearly 100 million refrigerated display cabinets contributes to daily distribution of perishables to the consumers all around the world. They are certainly now the critical point for cold-chain at the interface of professional distribution and the consumer. Distributors have for long asked for certification of display cabinet to guarantee their performance and the quality of cold chain in the supermarkets and shops.

With an international standard available it was easier to develop a product certification for display cabinet. The project started in 2006 with Perifem the French technical association of retailers. The

first Certicold HACCP label for display cabinets were issued in 2016 for independent refrigerated display cabinets. It was enlarged in 2018 to remote refrigerated display cabinets. More than 15 000 refrigerated cabinets have been individually certified and marked with Certicold HACCP label. The Certicold HACCP certification system is based on type tests realised in an independent accredited laboratory, construction audits are conducted by the certification body that also randomised each year products on production line to test them in an independent accredited laboratory.

4.6. People Certification

If people certification is well developing all around the world for F-gas manipulation, the certification of people working in cold chain is rather limited. With the tremendous need of training of people in cold chain, we can imagine that people certification will start soon on these items.

4.7. Cold Chain Certification

Cold chain certification remains a dream today. To reach the full cold chain certification it is first necessary to manage all the segments and certify them. Nevertheless some certification schemes apply to cold chain segments.

Night delivery is a solution to improve urban areas logistics. Most of the mega poles do not have more than three days food storage in their urban area. Food distribution is then a sensible item. To improve fresh food distribution reducing its environmental impact, night delivery has strongly developed since a few years in Europe and United States. Nevertheless refrigerated transport is noisy and then may create noise problems at night with neighbours of shops and restaurants. To answer this issue certifications of night deliveries have been developed. It started in the Netherlands with the type certification of silent refrigerated trucks under the Piek Label which then expanded all over Europe. Then this initiative was completed with the certification of the shop to be delivered at night and the transporter able to do so. It began in United Kingdom with Noise abatement society project and then in France with Certibruit initiative for night delivery certification. A similar system has also been developed in New York.

5. CONCLUSIONS

Cold chain certification is an issue from the early beginning of cold chain in 1876 with Charles Tellier. All along the hundred and fifty last years, cold chain experts worked together to set certification schemes. From the first tests of cold chain equipment in the early twenty century in the first dedicated laboratories to now, they have developed a full set of certification schemes from type certification to product independent certification.

Nowadays certification schemes are available for nearly all cold chain equipment either mandatory or voluntary. They have proved their interest and their capability to increase the performance of cold chain. Nevertheless they are not implemented all over the world, such as for refrigerated transport equipment. There is then a large potential for development of cold chain equipment certification from farm to fork and laboratory to lavatory all over the world.

People certification has also strongly been developed over the last decades, but mainly in the management of F-gases. There is an important need in this field and it will be a challenge for cold chain industries in a context of major difficulties to recruit competent and qualified staff in a lot of countries.

Finally the global cold chain certification remains a dream today. Nevertheless the fast development of big data, the internet of things, the capacities of data exchanges offer new possibilities to develop a connected cold chain. These technologies will help to assess the global performance of cold chain for each fresh and frozen product transported from farm to fork and laboratory to lavatory. It will not replace the equipment and people certification but will usefully complete it.

The full cold chain certification is then our challenge for the next twenty years.

REFERENCES

Bénard, H. Détermination du coefficient de transmission de la chaleur à travers les parois d'un wagon fortement isolé., Société Française de Physique résumé des communications faites en 1919, séance du 17 janvier 1919.

Bénard, H. Expériences et mesures techniques relatives aux wagons aménagés en France pour le

transport de la viande congelée aux armées. La Revue générale du froid et des industries frigorifiques, numéro de mars avril, mai 1921, réimpression I broichure 24 pages in-4°.

Cavalier, G., Tassou, S. A., 2011. Sustainable refrigerated road transport. 21st Informatory Note on Refrigerating Technologies, International Institute of Refrigeration.

Cavalier G.,2018.Un plan de contrôle de la conformité des engins de transport sous température dirigée.Revue générale du froid n°1167 – janvier 2018.

Cavalier,G. Devin,E.,2012. Towards a certification of night delivery in urban freight transport., 22nd Internoise congress, New-York August 2012.

Lemaire, E. « La station expérimentale du froid de Châteaurenard », Le Génie civil, 24 septembre 1910.

Tellier, C., 1910.Histoire d'une invention moderne, le frigorifique. 1 vol. (XI-456 p.), Édition Ch. Delagrave Paris, DL 1910, Préface de Jacques Arsène d'Arsonval (1851-1940) membre de l'institut et fondateur de l'AFF.

Manuscript ID: 1837
DOI: 10.18462/iir.icr.2019.1837

Magnetocaloric refrigeration and heat pumping: the present, tomorrow, and the future

Andrej KITANOVSKI[(a)], Katja KLINAR[(a)], Urban TOMC[(b)]

[(a)] University of Ljubljana, Faculty of Mechanical Engineering
Ljubljana, 1000, Slovenia, andrej.kitanovski@fs.uni-lj.si

ABSTRACT

The magnetocaloric refrigeration and heat pumping is considered to be one of the most important alternatives to existing vapour-compression technologies. In the past two decades we have witnessed a substantial increase in basic and applied research efforts to bring this technology to the market. Despite the significant research progress that has been made, there are several critical issues that need to be solved in the near future. These concern efficient heat transfer, the reduction or removal of moving parts, and rare-earth-free and stable, energy-efficient magnets and magnetocaloric materials. This article gives an overview and updated information on global research achievements in magnetic refrigeration and heat pumping. The article addresses the most important and also some overlooked solutions that could pave the way for the future developments of magnetocalorics and their realistic market applications.

Keywords: Refrigeration, Heat pump, Magnetocaloric, Cooling, Energy Efficiency.

1. INTRODUCTION

Magnetocaloric refrigeration in combination with heat pumping is one of the most important and most developed ferroic technologies, representing a serious alternative to vapour compression (Goetzler et al., 2014; Qian et al., 2016; Choi et al., 2018). Since the two key milestones that mark the beginning of intensive research in materials science (Pecharsky and Gschneidner, 1997) and device development (Zimm et al., 2003), a substantial number of new magnetocaloric materials and conceptual devices have been developed. Today, we are witnessing enormous progress in magnetocaloric technology, but at the same time many open and unresolved problems represent a serious challenge to the development of competitive market applications. In this article, we review the past 5 years of developments in magnetocaloric technology. Since several critical issues need to be solved in the near future, a special emphasis is put on solutions that are required for magnetocaloric refrigeration combined with heat pumping to become a competitive technology. These issues address the present problems related to magnetocaloric materials, regenerators and heat transfer, magnetic field sources, as well as the hydraulics. Simultaneously, guidelines for short-term research activities are presented, which could lead to substantial improvements with respect to the costs and energy efficiency of tomorrow's magnetocaloric devices. Some of the newest research activities indicate that future magnetocaloric devices can efficiently operate, even with no moving parts. The following sections provide the reader with a review of the state of the art for **the past 5 years of activities** and **future perspectives** for magnetocalorics.

2. THE MAGNETOCALORIC REFRIGERATOR/HEAT PUMP

A typical magnetocaloric device consists of a magnetocaloric material in the form of the regenerator's matrix, through which the working fluid oscillates. Different hydraulic means can be provided for the fluid's propulsion, which enables heat transfer to external (heat source or heat sink) heat exchangers. A variable magnetic field source is required for the periodic magnetization/demagnetization process. This is usually provided by a static permanent-magnet assembly (which requires the motion of the

regenerator's matrix) or by a magnet assembly that moves over the static regenerator matrix. The most comprehensive description of devices and thermodynamics, their operation with different configurations, including particular parts, can be found in (Kitanovski et al., 2015a). Since the research domain is rapidly developing, with significant new achievements, the following sections present an up-to-date overview of research activities in each particular subdomain of magnetocalorics.

2.1. Magnetocaloric materials

At the beginning of this section it is worth highlighting two important projects, one of which was recently closed. The results of the German Ferroic Cooling programme led to very important findings in tailoring new or improved magnetocaloric materials and processing methods for regenerators. Some of the latest research results of the group of researchers involved in several different projects can be found in a special issue, edited by Fähler, (2018); however, a complete list of references from the programme can be found at the following website (www.ferroiccooling.de). Another important and ongoing project concerns a consortium of research institutes and companies from the USA (www.caloricool.org), as part of the Energy Materials Network (US Dept. of Energy).

In both the above-mentioned activities, an important part of the investigations related to recyclability, processing methods for regenerators, the search for new, rare-earth-free magnetocaloric materials, and an improvement of the properties (reduction of the hysteresis, improvement of the thermal conductivity, elasticity, etc.). These are also issues that were the subject of recent research activities by other groups around the world.

The most recent and most comprehensive review of magnetocaloric materials can be found in Franco et al., (2018). The latest review on manganese-based magnetocaloric materials can be found in the work of Chaudhary et al., (2019). Another interesting publication came from Lyubina, (2017a), who made a review of magnetocaloric materials with an adiabatic temperature change higher than 2 K/Tesla.

In general, the most applicable magnetocaloric materials can be divided into four main groups: Gd and its alloys, La–Fe–Si-based materials, Mn–Fe–P-based materials, and Ni–Mn-based Heusler alloys Waske et al., (2018). However, research is ongoing to find new candidate materials (Pecharsky et al., 2016; Brück et al., 2016). A systematic search for new magnetocaloric compounds can be found in Bocarsly et al., (2017), who screened 134 ferromagnetic materials and an additional 30 compounds for their potential as magnetocalorics. A very comprehensive study, performed by Zarkevich et al., (2018), was based on theoretical and computational methods, and served as a guide for a later experimental investigation. The authors report on assessments of more than 1000 materials, which led to the selection of the 10 best materials to be evaluated experimentally.

Hysteresis represents an important drawback of magnetocaloric materials. In recent years, great efforts have been invested to solve this problem for certain magnetocaloric materials. For instance, Gutfleisch et al., (2016) investigated the mechanisms behind the thermal hysteresis of La–Fe–Si-based, Heusler-based and Fe_2P-based compounds. In their work, they summarized the main causes of hysteresis in different magnetocaloric materials and discussed the possibilities to reduce it. Additional work on mastering the hysteresis problem in Heusler alloys can be found, e.g., in (Gottschall et al., 2017; Cohen, 2018).

2.1.1. Resources & Environmental issues

Gauß et al., (2017) evaluated to what extent the raw materials needed to produce magnetic refrigeration for the mass market are critical in terms of demand and supply. They found that Gd-based materials are critical, with La–Fe–Si-based or Mn–Fe–P-based being substantially less problematic. Moreover, their evaluation of Nd and Nd–Fe–B as the candidate permanent-magnet material for magnetic refrigeration has shown that these kinds of materials will represent a significant

bottleneck at a later innovation stage when magnetic cooling technology would potentially dominate the main markets. Another comprehensive study was performed by Tunsu and Petranikova, (2018). They investigated the recycling process by assessing the use of hydrometallurgy to recover the REEs from commercial magnetocaloric materials containing cerium, iron, lanthanum, manganese and silicon. A very important study was performed by Aprea et al., (2015a) who numerically investigated and compared the TEWI index (Total Equivalent Warming Impact), which relates to direct and indirect contributions to global warming. In the study several different first- (FOMT) and second-order (SOMT) magnetic refrigerants were analysed. The study showed that $GdSi_2Ge_2$ and $LaFe_{11.384}Mn_{0.356}Si_{1.26}H_{1.52}$ have a TEWI index always lower than that of a vapour-compression plant. Furthermore, the TEWI of the AMR cycle working with FOMT materials is always better than that of SOMT materials. In 2018, their study was extended to include other caloric materials Aprea et al., (2018).

2.1.3. Adiabatic temperature change

The remaining problem today regards the magnetocaloric effect in terms of the adiabatic temperature change. Despite the fact that the problem of small adiabatic temperature changes has been seriously addressed by the magnetocaloric community, researchers still tend to relate a large magnetocaloric effect to the entropy change, except for a few publications, such as, for instance, those Lyubina, (2017a). Since the heat transfer is not reversible, nor an ideal process, it always requires a temperature gradient for the heat to flow. A small adiabatic temperature change of, e.g., $\Delta T_{ad} < 2$ K, therefore, cannot lead to a high energy efficiency of the device. Despite the very large efforts made in tailoring and improving, e.g., the Heusler alloys, the present small adiabatic temperature change greatly restricts their application for refrigeration and heat pumping. The solution to this problem is, of course, not in the application of very high magnetic fields. Since the future of magnetocaloric technology strongly depends on the compactness (cost), this also relates to the number of thermodynamic cycles per unit of time (frequency). A magnetocaloric material that does not perform a nearly reversible and high magnetocaloric effect at a high frequency of operation >10 Hz (i.e., dynamic magnetocaloric effect), is greatly restricted for future applications (see e.g. Aliev et al., 2016; Gottschall et al., 2016).

2.1.4. Refrigeration capacity / Figure of merit

In vapour compression, the refrigerant's capacity is related to the enthalpy difference of the refrigerant during the evaporation process. In analogy with conventional refrigeration, as well as from the thermodynamic point of view, the most correct way to characterize the refrigerant's capacity lies in the process of the isothermal entropy change at a certain temperature level. Therefore, regardless of the process in which the magnetocaloric material is used (cascade system, regeneration) this can simply be given by the following expression: $q = T \cdot \Delta s$, where *T(K)* is the temperature at which the capacity is defined and Δs corresponds to the total isothermal entropy change of the magnetocaloric material. However, in order to characterize the applicability of the magnetocaloric material, the definition of the ideal refrigeration capacity is not sufficient, especially because it does not concern the adiabatic temperature change, which is crucial for efficient heat transfer and real applications. A very valuable information can be found in a recent publications of Niknia et al.,(2017) and (Griffith et al., 2018), where different figures of merit are used as indicators for a magnetocaloric material's refrigeration quality.

2.2. Regenerators and their processing

In this section we will present the activities of the past 5 years that relate to the material science and engineering of magnetocaloric regenerators. Concerning the number of publications, this domain represents, after the publications on materials, one of the most active domains in the field of magnetocalorics. In general, magnetocaloric regenerators can be divided into two main groups today: packed beds and ordered structures (Figure 1). Most of the activities relate to the engineering

problems of heat transfer, fluid dynamics, as well as the processing methods for tailored structures with the desired magnetocaloric, thermal or mechanical properties.

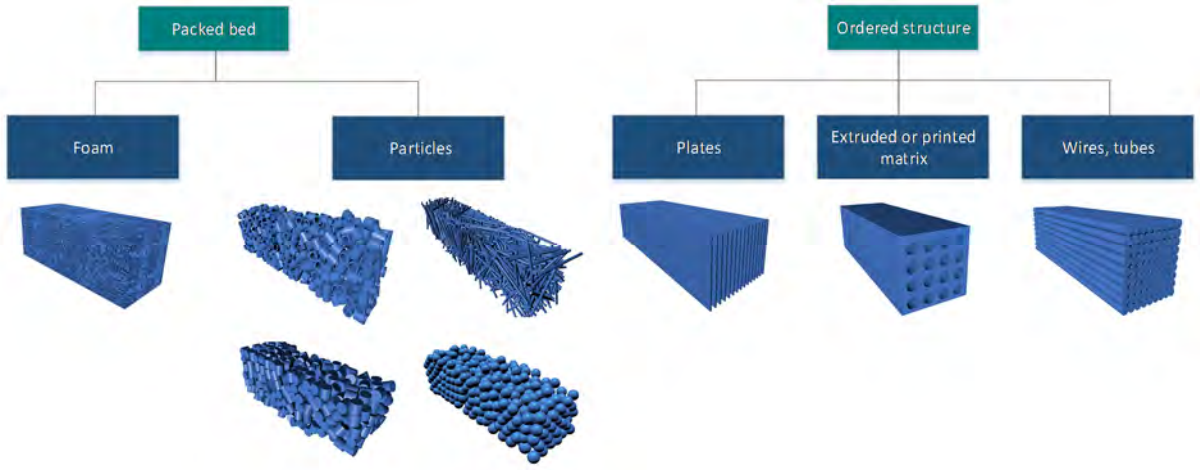

Figure 1: An example of the different types of magnetocaloric regenerators

2.2.1. Numerical modelling and experiments on layered regenerators

Since the magnetocaloric effect is restricted by the temperature interval, the use of multiple layers of magnetocaloric materials with different Curie temperatures enables applications with larger temperature intervals, which are required in real devices. This layering also leads to the increased power density of the device and an improvement in its efficiency (Richard et al., 2004). The largest number of layers was investigated by Zhang et al., (2017), who evaluated by numerical simulations the operating performance of an AMR consisting of 16 layers based on the La–Fe–Mn–Si–H compound. Chiba et al., (2015) performed experiments on a composite material based on different fractions of La–Fe–Co–Si compounds with different Curie temperatures in the temperature range 275–315K, which lead to a rather small adiabatic temperature change over a large temperature span. Additional numerical and experimental studies were performed by the same authors in 2017 (Chiba, 2017). In this particular case, the two parallel-plate regenerators consisted of four La–Fe–Co–Si compounds with different Curie temperatures. Monfared and Palm, (2015) carried out a numerical study by predicting four hypothetical layers of a packed-bed regenerator. Teyber et al., (2016) made a study of the impact of layering on an AMR's performance based on a numerical evaluation and experiments with four regenerator compositions comprised of two-layers of magnetocaloric materials. Whereas the first Gd layer represented the highest Curie temperature, the second layer used Gd and three compositions of $Gd_{1-x}Y_x$. The tests and numerical simulations were performed for the same size and operating conditions for all four regenerators. The best results were obtained for the regenerators with two layers. An optimization method using neural networks for n-layers of any magnetocaloric material was developed by Tomc, (2016), who also experimentally validated the model on three different parallel-plate regenerators layered with La–Fe–Co–Si compounds. An interesting finding from the optimization revealed that there exists an optimal finite number and an optimal length for a particular layer of the magnetocaloric compound. A study which considered up to 8 layers of La–Fe–Mn–Si–H, a hypothetical Gd-like compound and mixed layers of the first- (FOPT) and the second-order materials (SOPT) was performed for by Lei et al., (2016). Whereas the layers of only SOPT materials can lead to higher cooling powers, such regenerators require a substantially larger number of layers. In contrast, the layering with only FOPT (Gd-like) materials is more sensitive to their Curie temperature. The results reveal that the most efficient solutions can be obtained by mixing different SOPT and FOPT materials. Kamran et al., (2016) developed a hybrid numerical model in which they studied the performance of layered AMRs based on Gd-like and La–Fe–Co–Si-type compounds. The verification of the model was performed using existing experimental

data from the literature, as well as from their own experiments. The latter related to two microchannel regenerators, each having two layers of magnetocaloric material. The experimental investigation of $MnFeP_{1-x}$ As_x was performed by Govindappa et al., (2017) for five different matrices: three layers; six layers; and three, eight-layer regenerators. In the study, the thickness of a particular layer was varied. Similar to the case of Tomc (2016), the authors conclude that there is a trade-off between the number of layers and the layer thickness. A too large number of layers will lead to a mismatch in the regenerator's operating temperature range. Another important numerical study on the layering of the regenerator with 10 layers; however, with variable cross-sections (tapering) along the length of the regenerator, was performed by Dall'Olio et al., (2017). The authors revealed that tapering represents a small disadvantage for the performance, except for a small range of negative angles where the system can gain a small improvement in efficiency. An interesting review was published by Balli et al., (2017). There, not only the fundamental properties of recently reported magnetocaloric materials, but also their thermodynamic performance in functional devices were discussed. Teyber et al., (2018a) developed and experimentally validated a semi-analytical model over a broad range of operating conditions and regenerator compositions using two second-order magnetocaloric materials. The results of the study revealed that the model demonstrates good predictive capabilities using experimental data. The authors also state a record (no-load) temperature span of 40 K obtained from a permanent-magnet-based device. Christiaanse et al., (2018) experimentally evaluated the performance of six different regenerators with five different layers of Mn–Fe–Si–P compounds. The authors concluded that a closer "temperature span" spacing improves the performance of the regenerator. When a spacing in excess of 10 K was used, the beds seemed to function independently of each other. One of the latest publications relates to the work of Monfared and Palm, (2018), who numerically investigated and compared the performances of different layered AMRs in order to find out how much the properties of magnetocaloric materials need to be improved before magnetic refrigeration systems outperform vapour-compression ones.

2.2.2. Numerical modelling and experiments with single material regenerators

A large number of studies were dedicated to the numerical performance assessment of active magnetocaloric regenerators (AMRs). For instance, a new procedure to quantify the AMR's performance based on entropy-generation minimization was proposed and investigated by Trevizoli and Barbosa, (2015). The authors performed a comprehensive numerical study of Gd-based packed-bed regenerators operating with a magnetic field change of 1.5 Tesla with a variable frequency between 1 and 4 Hz. A different study was performed by the same authors (Trevizoli and Barbosa, 2017a), where they investigated the thermal-hydraulic behaviour and the influence of the carry-over losses in the AMR. Torregrosa-Jaime et al., (2015) proposed a new finite-difference scheme that optimally combined the explicit and implicit techniques in order to solve the one-dimensional conjugate heat-transfer problem of the AMR. Qian et al., (2017) proposed a new approach for the evaluation of the performance of the active magnetocaloric regenerator (AMR) based on given critical parameters proposed in this study. The critical parameters were derived from the energy equations that were used to describe the transient energy-transfer processes in the AMR for both the magnetocaloric materials and the heat-transfer fluid. An open-source DNS solver for the simulation of AMR cycles was developed by Mugica et al., (2018). The model can be exploited for a variety of regenerator geometries and properties and can be adopted for other caloric technologies. Interesting research was performed by Plait et al., (2018), who developed and experimentally verified a new magnetostatic model based on a reluctance network. The model serves for the calculation of the internal magnetic field and the internal magnetic flux density of the active magnetocaloric material (gadolinium, Gd) inside the air gap of a magnetic circuit. According to the authors, the semi-analytical model leads to a substantial decrease in the computation time and offers (compared to a 3D finite-element model) a similar precision for all the magnetic quantities in the whole magnetocaloric system.

Researchers are finding improvements in designing different geometries of magnetocaloric structures with a high heat-transfer surface or improved thermal properties. A large number of publications report on numerical modelling for a number of different geometries.

A comprehensive 1D numerical work on an AMR's performance evaluation for six different geometries was performed by Lei et al., (2017a). The following Gd-regenerator geometries were considered in the study: packed sphere bed; parallel-plate matrix; circular micro-channel matrix; rectangular micro-channel matrix; and packed screen bed. A comprehensive study was also performed by Trevizoli et al. (2017b), who investigated different spheres, plates and pins.

You et al., (2018) numerically (Ansys Fluent) investigated Gd materials processed into a twin-wedged shape. The results of the study reveal that when long Gd plates are replaced by twin-wedged Gd elements, the maximum refrigeration temperature span and the specific refrigeration capacity can be noticeably improved.

Aprea et al. (2015b) presented a comparison between experimental and 2D multiphysics numerical results for a packed-bed AMR. C. Aprea et al., (2017a) reported on extended multiphysics 2D numerical modelling for two different magnetocaloric regenerators made of gadolinium: a packed bed and parallel plates. The authors indicated under which operating conditions the packed-bed configuration is preferred to parallel plates and vice versa. The same author (Aprea et al., 2017b) made numerical simulations using a two-dimensional model of AMR regenerators for six different magnetocaloric materials. The results of the study were validated with previously performed experimental results from two different situations (zero-load and iso-load). A similar, but substantially more extended, study as a numerical and experimental investigation was reported in Aprea et al. (2018a). An interesting study was made by Aprea et al. (2018b) who made a comparison of the energy performances for different caloric materials (magnetocaloric, elastocaloric, barocaloric and electrocaloric) operating in an active caloric regenerator. The study under the predicted assumptions revealed the superiority of PLZT electrocaloric materials over other types of caloric materials.

The largest number of numerical simulations, models and experimental verifications was made for a single geometry of a particular magnetocaloric material. Below we indicate the work published since the 2015.

Lionte et al., (2015) presented the results of a simulation performed using a 2D numerical model of an AMR based on Gd parallel plates. Meddeb et al., (2015) reported a numerical study performed for different operating conditions of a Gd-based AMR. A one-dimensional model was created by Schroeder and Brehob, (2016) to determine the periodic steady-state cooling power of an AMR. Pavlukhina et al., (2016) made a parametric three-dimensional heat-transfer study in order to investigate the relaxation time of a regenerator consisting of microwires of a Ni_2MnIn Heusler alloy. The diameter of the magnetic wires was varied from 10 to 50 μm, while the length was fixed at 1 mm. The calculations showed that, depending on the fluid-flow velocity, the relaxation time varied from approximately 0.6 to 2 ms. Trevizoli et al., (2016 c,d) made an experimental assessment of a packed-bed active magnetic regenerator (AMR) composed of 0.55-mm Gd spheres subjected to a rectified sinusoidal magnetic flux density in phase with a sinusoidal fluid-flow waveform. The operating AMR frequency was set to 0.25, 0.5 and 1 Hz. Moreover, a mathematical model of the AMR was developed and verified. The model took into account most of the losses that take place in the AMR (including the demagnetizing losses), where the heat interaction with the external environment and the presence of dead (void) volumes between each end of the regenerator and the hot and cold heat exchangers was found to be the main factors that affect the AMR. Another study was performed by Ezan et al., (2017), who applied a decoupled multiphysics numerical approach by using a commercial CFD Ansys-Fluent, with incorporated user-defined functions. The analysis was performed for a parallel-plate Gd AMR and a cooling system under different operating conditions. You et al., (2017) investigated a two-dimensional numerical model with ANSYS Fluent for the unsteady conjugate heat transfer of an AMR with Gd plates. Nakashima et al., (2018a,b) experimentally and numerically investigated the influence of the flow-rate waveform and the mass imbalance on the performance of AMRs based on packed-bed Gd.

2.2.3. Processing of regenerators

One of very important domains of research regards the processing of magnetocaloric materials into different shapes with low viscous losses, improved thermal and magnetocaloric properties, as well as a large heat-transfer surface. Moreover, the manufacturability and the mechanical stability are two very important parameters that relate to the present and future work in magnetocalorics.

Despite the fact that gadolinium is a reference material, also from the point of view of manufacturability, the results of Taskaev et al., (2015) show that severe plastic deformation dramatically changes the thermodynamic properties of Gd. Namely, the large reduction in the specific heat observed in the vicinity of the Curie temperature was suggested to be due to the suppression of the magnetic contribution to Cp. The authors found the appropriate conditions for annealing in order to restore the magnetocaloric properties of the previously cold-rolled gadolinium. Another interesting and comprehensive experimental research work with Gd was carried out by Trevizioli et al., (2017b). The authors first constructed stainless-steel samples with different geometries: parallel-plate, pin array and a packed bed of spheres and after testing designed the appropriate gadolinium regenerators.

Most of the recent work in processing regenerators relates to the use of La-based magnetocaloric materials, especially due to their brittleness. Radulov et al., (2015) reported on cold processing into polymer-bonded $La(Fe,Mn,Si)_{13}H_x$ thin plates. The authors applied two different methods: wire-saw cutting and cold rolling. Furthermore, the corrosive behaviour of the plates in different heat-transfer fluids was investigated. The adiabatic temperature change and the magnetic entropy change of the plates were observed over a 7-month period in order to evaluate their applicability in a real device. Bahl et al., (2017) processed and experimentally validated the magnetocaloric properties and the AMR performance of tailored bonded plates made by hot pressing $La_{0.85}Ce_{0.15}Fe_{11.25}Mn_{0.25}Si_{1.5}H_y$ particles and resin. The plates were prepared with 5 wt% resin, and from the density measurements it was found that the volume ratio of the magnetocaloric material in the plates was 0.53, due to the resin and porosity. The best operating conditions for the plate regenerator were determined, for which a temperature span of 6.4 K was measured along the plates. The experimental validation of the epoxy bonded regenerators of both spherical and irregular $La(Fe,Mn,Si)_{13}H_y$ particles was made by Lei et al., (2018). A five-layer epoxy-bonded AMR using spherical $La(Fe,Mn,Si)_{13}H_y$ particles was tested in a small reciprocating magnetic refrigerator. Radulov et al., (2017a) created and tested a porous body regenerator from metal-bonded $La(Fe,Mn,Si)_{13}H_x$ powder. The authors concluded that the metal coating of the particles significantly increases the corrosion resistance of the regenerator. By bonding the metal-coated particles together, the mechanical stability of the regenerators is increased and no sedimentation, segregation or channel building due to particles movement was observed. The authors pointed out that the disadvantage is that the arbitrarily shaped $La(Fe,Mn,Si)_{13}H_x$ particles can affect the channel structure of the porous body and can result in blind or closed channels, which would limit the utilization of the regenerator. In another study Wenkai et al., (2017) processed La–Fe–Si–H with indium as the binding material by hot pressing. Similar work was performed by Liu et al. (2015), involving the hot-press bonding of Cu with a La-Fe-Si alloy. Another work reports an improvement of the intrinsic brittleness and relatively low thermal conductivity in La–Fe–Si–H alloys. Shao et al., (2017) proposed the fabrication of stable La–Fe–Si–H blocks and plates by adding extra α-Fe as the reinforcing phase to enhance the mechanical integrity. Much better bending strength compared to that in the stoichiometric composition was observed in the samples, which also withstood 105 magnetic field cycles without losing their mechanical integrity. The authors also reported on a reproducible ΔT_{ad} with a thermal conductivity of 6 W/mK. The powder extrusion and sintering of a magnetocaloric La–Ce–Fe–Mn–Si alloy into well-ordered structures of the AMR was carried out by Wieland and Petzoldt (2017). Large efforts were invested in processing magnetocaloric powders with metals, for instance, with Field's alloy binders (Radulov et al., 2017b). Another interesting and very important study relates to the powder-in-tube-processing of lanthanum compounds in a steel jacket-tube, which was reported by Funk et al., (2018). Such solutions substantially improve the mechanical and chemical stability of the magnetocaloric regenerator. Researchers are also focusing on methods to process magnetocaloric regenerators via metallic additive manufacturing Lyubina, (2017b).

Karpenkov et al., (2016) performed research on two methods for assembling Y_2Fe_{17} rapidly quenched ribbons into regenerators as stacked 100-μm-thick plates with 100-μm gaps: the first method consisted of gluing rapidly quenched ribbons using thermos-conductive epoxy, while the second method was focused on the sintering of stacked ribbons at a temperature of 30 K below the melting point of the Y_2Fe_{17} phase.

A particular domain of processing relates to wires made of a magnetocaloric material. An experimental validation of Gd wires was conducted by Kondo et al., (2016). Work on producing magnetocaloric wires was also published by Varga et al., (2015). They showed that it is possible to produce glass-coated microwires based on Heusler alloys (NiMnGa- and NiMnInCo-based microwires). According to the authors, the wires can be characterized by small dimensions (high surface-to-volume ratio) and allow applications in a wide range of materials without any variation in their mechanical properties, and insulating glass coating, which prevents the microwire from chemical and electrical interactions with the surroundings and enhances the mechanical strength of the Heusler-based metallic nucleus. Sheng et al., (2018) reported comprehensive experimental research in which they designed different microwires of $Gd_{20}Ho_{20}Er_{20}Al_{20}TM_{20}$ (TM=Fe, Co and Ni).

2.3. Hydraulics

Besides the regenerators and the related viscous losses, today the hydraulic system is one of largest burdens that restricts AMR-based devices from operating efficiently at high frequencies. Two main types of hydraulic systems are being applied in magnetocalorics (Fig.2). In most systems that apply an AMR, the magnetocaloric material is at rest (rotating or switching the magnetic field) or the AMR is periodically exposed to a magnetic field provided by a static magnetic field source. Since the fluid must oscillate through the regenerator, a bi-directional fluid-pumping system can provide the desired fluid flow. In the case of a static regenerator, this can be done by displacement (hydraulic, pneumatic, electro-magnetic or mechanical), a membrane pump or a peristatic pump. A tandem pump system can also provide the oscillatory flow. Check valves or cam valves (Teyber et al., 2017a; Trevizoli et al., (2016c) are, in such cases, a sufficient means to keep the system running. In the case of a static regenerator, a unidirectional pump system can be applied as well. However, such a system requires a valve system (rotary valve or assembly of, e.g., electromagnetic valves), which enables the continuous operation of the pump while maintaining the oscillation of the fluid flow. In another case, which relates to the movement of the regenerator in a static magnetic field source, the unidirectional pump is supported by a valve system that includes rotary valves (Lozano et al., 2016; Nakashima et al., 2018a) cam valves (Eriksen et al., 2015; Fortkamp et al., 2018) or electromagnetic valves (Cardoso et al., 2016).

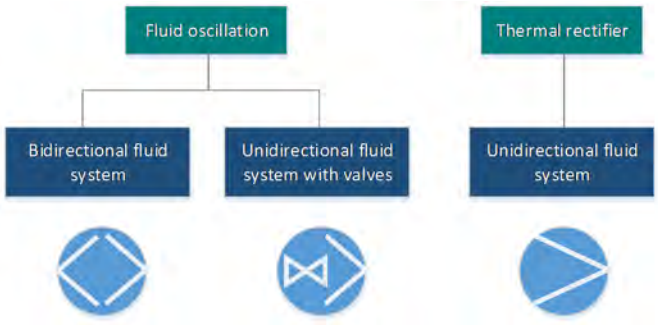

Figure 2: The main principles for the fluid propulsion in magnetocalorics

One of the remaining problems regards the fluid-flow maldistribution in the AMR, which was also a subject of earlier research; however, it can also be found as a topic in recent years (Dall'Olio et al, 2017, Trevizoli et al.,2018). Among the recent publications, it worth mentioning an interesting work by Lionte et al. (2018), who proposed a concept that they call “the by-pass flow” and which enables a continuous flow of fluid. The major problem still remains how to provide an efficient hydraulic system for a higher frequency of operation, e.g., beyond 5 Hz, while maintaining the pressure and the fluid control without dead volumes. Moreover, researchers should tend to find solutions that enable a simplification in the direction of a unidirectional pumping system with simple and low-cost valve systems. This is why the thermal rectification, described in a later section, is also an important subject for future research.

2.4. Magnetic field sources

The magnetic field source represents the heaviest and by far the most expensive part of the magnetocaloric refrigerator or heat-pump system (Kitanovski et al., 2015a), R. Teyber et al., 2017b, R. Teyber et al., 2018b). A full list of the research in the field of magnetic field sources up to 2015 is presented in Kitanovski et al, (2015a,b). Since 2015, most of the work relates to the optimization and design of the permanent-magnet assemblies based on a Halbach array. A comprehensive numerical and experimental study on the design of a nested Halbach assembly was performed by Trevizoli et al., (2015b). You et al. (2016a) presented the results of a numerical simulation of a multi-polar Halbach cylindrical magnet. A numerical study on different design configurations for a rotary permanent-magnet assembly was performed by Lorenz and Kevlishvili, (2017). An interesting study was performed by Fortkamp et al., (2017), who presented the analytical solution for a concentric two-pole Halbach cylinder. Celik and Kural, (2017) performed a numerical simulation on an octagonal Halbach permanent-magnet assembly. Mira et al., (2017) numerically studied the influence of a magnetic sample on the applied magnetic field inside the air gap of a magnetic circuit. For the purpose of the study, different magnetic sources, including an electromagnet, a permanent magnet in a soft ferromagnetic toroidal yoke, as well as 2D and 3D Halbach cylinders, were considered. Additional work with regards to the optimization of the topology of magnetic field sources was performed by Bjørk et al., (2017), Lee et al., (2017) and You et al., (2016a). Besides the research on the design and optimization of magnetic field sources, researchers are also studying problems that relate to rare-earth-based magnetic field sources. This relates to the problem of the supply chain (De Almeida et al., 2017), the reduction of the rare-earth materials and the recycling of magnets (Skokov and Gutfleisch, 2018; Diehl et al., 2018). As an answer to the aforementioned problems, the team from the University of Ljubljana recently (Klinar et al, 2019) introduced an electromagnetic field source with a rather high energy efficiency and the capability of operating at very high frequencies, which is a consequence of a specially designed electronic circuit with a capacitor. The present activities at the University of Ljubljana are the development of a rare-earth-free, hybrid and static electric-permanent magnet assembly. The preliminary results show that such a magnetic field source can, at a high frequency of the operation (e.g. >15 Hz) compete with the energy efficiency of Nd–Fe–B-based rotary magnets. The authors believe that this finding opens up the future guidelines for magnetic field sources in magnetocalorics. In Fig. 3, different types of magnetic field sources are presented, most of which are the subject of theoretical or experimental research activities in the domain of magnetocaloric energy conversion.

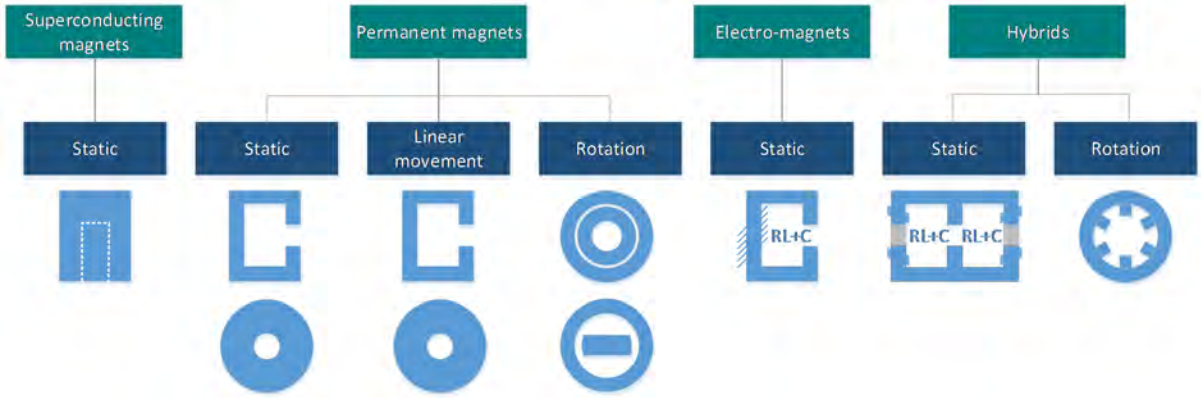

Figure 3: The main types of magnetic field sources in magnetocalorics

Additionally to such types, the newest types, e.g., static hybrid magnets, are added. The notation LR+C relates to the magnetic circuit, which comprises the capacitor.

2.5. Thermal rectification

It is well known today that the concept of active magnetic regeneration cannot lead to a high frequency of operation (e.g., above 5 Hz while maintaining the desired and high energy efficiency) due to the limits of heat transfer and high viscous losses. It is also clear that magnetic refrigeration and heat pumping, as an alternative to most applied refrigeration and heat-pump applications, need to represent not only energy efficient, but substantially more compact devices. This is why the concept of a thermal diode or thermal switch should be applied in magnetocalorics near room temperature. A comprehensive review of the potential applications for thermal diodes and thermal switches can be found in Kitanovski et al., (2015a). In the magnetocaloric community, several researchers are today involved in finding appropriate solutions. Since 2015, researchers have performed work by investigating the implementation of thermal diodes through the application of Peltier modules (De Vries and Van der Meer, 2017; Monfared 2017; Lu et al., 2019) . A theoretical study was performed by Wu et al., (2018), who performed the numerical simulation for a solid-state magnetic refrigerator. Some of the recent studies relate to the application of nanofluid switches (Puga et al., 2017) and the heat-pipe principle (Bartholomé et al., 2017). A solid-solid interface thermal rectification was theoretically studied by Zhang et al., (2016). Lei et al., (2017) performed a numerical and experimental study in order to evaluate the potential mechanisms of magneto-hydrodynamic (MHD) convection to be applied in magnetic refrigeration.

Despite the range of research that is ongoing with different activities, most researchers in the magnetocaloric community still did not touch this very important subject as the future solution. However, a large number of activities in the field of thermal rectification can be found in other domains of research, including other types of caloric technologies. The most recent and the most comprehensive review of thermal rectification can be found in Wehmeyer et al.,(2017). Below in Fig.4 we denote the three main areas in which mechanisms for thermal rectification, which should be the subject of future research activities in magnetocalorics, are presented. The solid-state rectification relates to solid-state principles, which can be electrically, magnetically or thermally actuated. Many of these mechanisms are based on the nano-engineering of future functional materials. The mechanical actuation is mostly the contact switches, which may also efficiently operate on a very small scale. At the moment, the most promising mechanisms are fluidic thermal switches, most of which can also be considered a part of the rapidly developing domain of microfluidics.

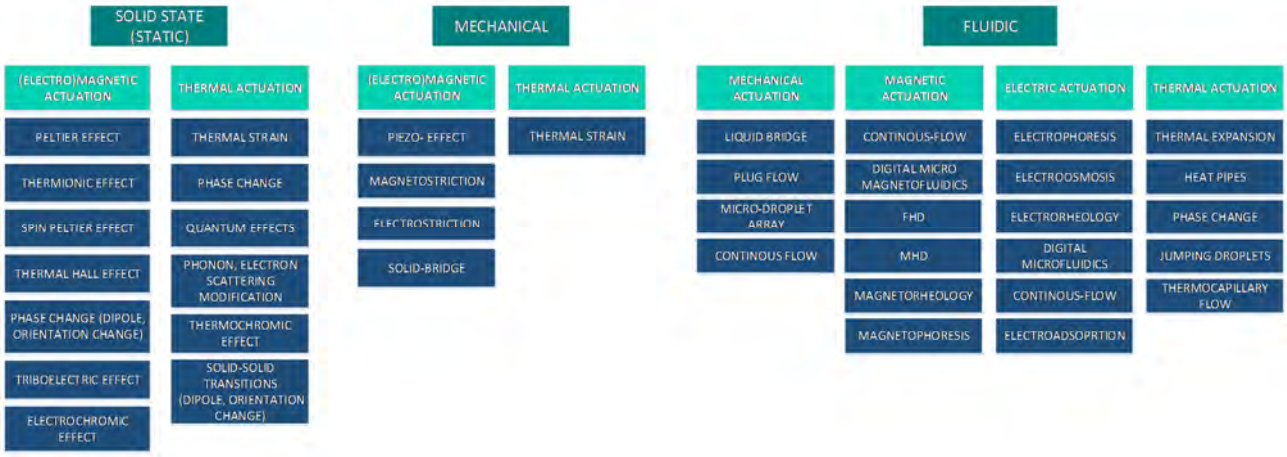

Figure 4: The main types of thermal rectification mechanisms

2.6. Prototypes and devices

By 2015, about 70 conceptual experimental magnetocaloric devices had been developed worldwide (Kitanovski et al, 2015a,b), and since then a number of new prototypes, being presented in this article, were investigated. One of the latest reviews of magnetocaloric devices can be found in the publications of Trevizoli et al., (2016) or Zimm et al., (2018). The lifetime cost analysis and the life-cycle assessment were studied by Bjørk et al., (2016) and Luglietti et al., (2017).

Mahdy et al., (2015) from the Technical College and UOT Baghdad, Iraq, developed a magnetocaloric testing device, consisting of a Halbach permanent-magnet assembly. In Korea, Lee (2015) developed a small AMR refrigeration apparatus with a permanent-magnet array. Velázquez et al., (2016) from the University of Zaragoza, Spain, designed and tested a reciprocating magnetocaloric device, consisting of a Halbach permanent-magnet assembly. In Poland, Kolano et al., (2016) presented the design and performance of a reciprocating experimental magnetocaloric device consisting of a 0.8-T permanent-magnet assembly. In Sweden, Monfared (2018) reported on a comprehensive study by numerical simulations and the experimental validation of the performance of regenerators for a rotary magnetic refrigeration device. The device was, for the first time, presented in an international journal.

Since many of the existing devices are being improved over recent years, it is in some cases difficult to distinguish between publications that report on a new prototype and those that are related to its improvement or experimental work under different conditions. For this reason the following text relates to the work of particular groups. A large number of activities are from the groups at the universities of Salerno and Napoli, Italy. Aprea et al. ,(2015c) reports on experiments and testing of the previously reported geothermal rotary permanent-magnet magnetic refrigerator with a maximum no-load cooling power of 190 W and the highest COP of 2.2, and a cooling power of 100 W at a temperature span of 6 K with a corresponding COP of 0.6. Aprea et al., (2016c) additionally report on a comprehensive investigation of the energy performance of a prototype device. The same group (Aprea et al., 2017c) implemented artificial neural networks in order to maximize the performance of a rotary magnetic refrigerator. A group of institutes from Parma, Bologna and Rimini in Italy (Albertini et al., 2017) report on a preliminary study of a rotary magnetocaloric refrigerator prototype, consisting of four static AMRs and a rotor consisting of two permanent-magnet assemblies. In France, Lionte et al., (2018) report on numerical simulations and tests on a specially designed rotary magnetic refrigeration experimental device. The group from DTU, Denmark, reported (Fortkamp et al., 2018) on the modification of a rotary magnetic refrigeration device in order to perform experiments of different fluid-flow profiles in rotary beds. In another publication Lei et al., (2018) described a reciprocating testing device that was used for the experimental evaluation of AMRs. Johra et al., (2018) report on a numerical evaluation of a magnetic heat pump (part of the Danish project ENOVHEAT: http://www.enovheat.dk/) which can be integrated into a single hydronic loop, including a ground-source heat exchanger and a radiant under-floor heating system. The magnetic heat-pump

system design and its numerical evaluation were presented in Johra et al., (2019). The Brazilian prototype developed and reported by Lozano et al., (2016) from the group of the Federal University of Santa Catarina provided a cooling power of 80.4 W for a temperature span of 7.1 K, with the corresponding COP = 0.54. The performance evaluation of the system was additionally presented by Capovilla et al., (2016). Trevizoli et al., (2017b) reported on experiments with different porous-matrix geometries for active magnetic regenerators, where they obtained a COP of 1.9 for a cooling power of 7 W and a temperature span of 6 K. At the University of Victoria, Canada, Niknia et al., (2016) performed a numerical and experimental analyses (on a previously reported device) in order to study the impact of losses on the performance of the magnetic refrigerator. Another group from the Université de Sherbrooke reported on a numerical sensitivity analysis of magnetic refrigeration, which included a multi-objective optimization by applying a genetic algorithm. In the USA, groups of researchers (Benedict et al, 2017a) from the General Electric Appliances, University of Florida, and University of Louisville reported on the experimental impact of magnet and regenerator design on the refrigeration performance, by using an existing rotary magnetic refrigeration device. In another study, the evaluation of the existing prototype, operating as the heat pump, was evaluated (Benedict et al, 2016). The same group performed a study on the engineering view of the impact of magnetocaloric properties on refrigeration performance and machine design (Benedict et al, 2017b). The group from California State University reported (Bernal et al., 2016) on the testing of a reciprocating device for AMRs, consisting of an N52 magnet with a magnetic field strength of approximately 0.9 Tesla. The same year, another work was presented by the California Baptist University (Abdelmessih et al., 2016), which looks at the design and preliminary experiments for a magnetic cooling apparatus, consisting of a 1-T permanent-magnet assembly with the movement of the magnetocaloric regenerator by applying a high torque servo motor. In China, a group of researchers (Gao et al., 2016) from the Chinese Academy of Sciences, Hebei University of Technology and the University of Technology Beijing published a very interesting study on a hybrid Stirling-magnetocaloric prototype device. The modelling of a room-temperature magnetocaloric cooling system in MATLAB Simulink was presented by the group from the Xi'an Jiaotong University (Qian et al., 2018). A compact experimental apparatus from tests on magnetocaloric wires was presented in a publication of Kondo et al., (2016) from Fujikura Corporation. The authors are aware that many of the research activities are ongoing in Japan with regard to the prototyping of devices and within national projects. In the following years we will certainly witness a number of different publications. The group of researchers (Ezan et al., 2016) from Dokuz Eylul University, Ege University, Yasar University, and Izmir Institute of Technology, Turkey, performed a numerical modelling of a magnetic cooling system by implementing Ansys Fluent software. From the same universities, the researchers (Ekren et al., 2017) developed a magnetic refrigerator experimental device, consisting of a linear motion system and a pair of 0.7-T permanent-magnet assemblies.

3. CONCLUSIONS

Fig. 5 presents a rather speculative view of the future developments of magnetocaloric refrigeration and heat pump technology. The ideal power denoted in the Fig.5 (left) shows the refrigeration capacity as presented in Section 2.1.4. as the enthalpy difference during the isothermal demagnetization process of a range of magnetocaloric materials, multiplied by the frequency of the operation. If the development continues, we will see a dramatic change in magnetocaloric devices, capable of working at high frequencies. This relates to new approaches in engineering, such as the embodiment of magnetocaloric materials with thermal rectifiers. Such solutions do not require an oscillatory fluid flow; therefore, a simplification of the pumping systems can be expected. Moreover, the most recent developments in finding rare-earth-free static hybrid magnetic field sources will not only enable a very high frequency of the operation, but will also lead to a substantial cost reduction and an improvement of the technology's environmental footprint.

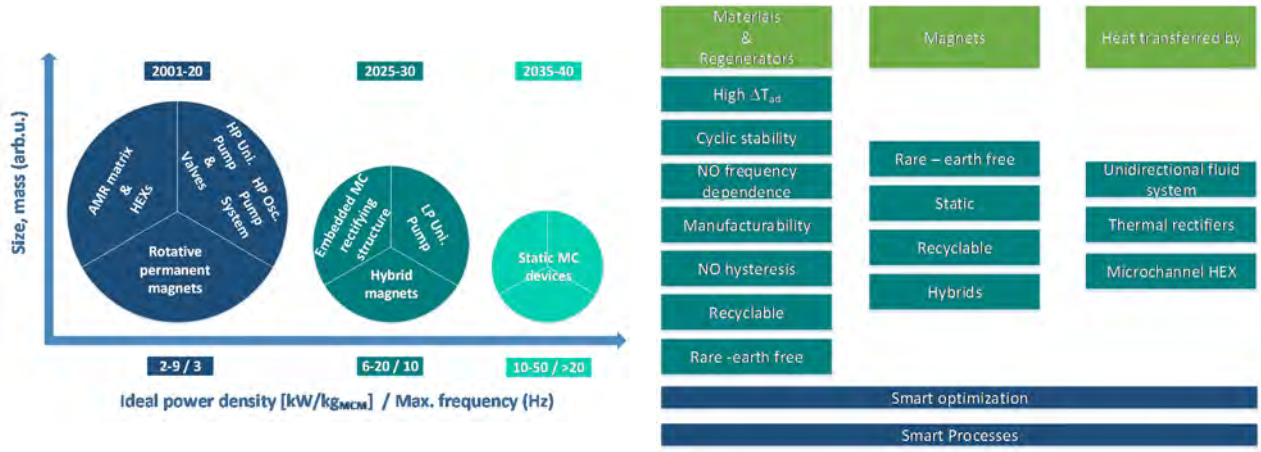

Figure 5: The magnetocalorics: the present, tomorrow, and the future

The long-term future of magnetocaloric devices, especially with the development of the nano-engineering domain, could lead to fully embodied systems with integrated magnetic field sources. For such developments, the required research activities are shown in fig.5 (right). These are, in some cases, completely new approaches, which do not necessarily rely on existing research achievements. K.A.Gschneidner, at the unveiling of the prototype at the Astronautics Technology Center in Madison, Wisconsin, on February 20, 1997, remarked that "*To those that have been and are working in the field: the limitations of magnetic refrigeration are only in the minds of the individual engineers and scientists*".

REFERENCES

Abdelmessih, A.N., Bartholomae, P.W., Casillas, M.L., Goolsby, B.D., Langley, M.M., Livoni, L.A., Logan, T.W., Perhach, N.J., Replogie, J.J., Swann, D.R., Williams, G.M., 2016. Design of a magnetic cooling device using gadolinium alloy and permanent magnets, in: Proceedings of ASME 2016 Heat Transfer Summer Conference. ASME, Washington, USA.

Albertini, F., Bennati, C., Bianchi, M., Branchini, L., Cugini, F., Pascale, A. De, Fabbrici, S., Melino, F., Ottaviano, S., Peretto, A., Rosati, J., Solzi, M., 2017. Preliminary Investigation on a Rotary Magnetocaloric Refrigerator Prototype. Energy Procedia 142, 1288–1293.

Aliev, A.M., Batdalov, A.B., Khanov, L.N., Koledov, V. V., Shavrov, V.G., Tereshina, I.S., Taskaev, S. V., 2016. Magnetocaloric effect in some magnetic materials in alternating magnetic fields up to 22 Hz. J. Alloys Compd. 676, 601–605.

Aprea, C., Cardillo, G., Greco, A., Maiorino, A., Masselli, C., 2016a. A rotary permanent magnet magnetic refrigerator based on AMR cycle. Appl. Therm. Eng. 101, 699–703.

Aprea, C., Cardillo, G., Greco, A., Maiorino, A., Masselli, C., 2015b. A comparison between experimental and 2D numerical results of a packed-bed active magnetic regenerator. Appl. Therm. Eng. 90, 376–383.

Aprea, C., Greco, A., Maiorino, A., 2017c. An application of the artificial neural network to optimise the energy performance of a magnetic refrigerator. Int. J. Refrig. 82, 238–251.

Aprea, C., Greco, A., Maiorino, A., 2015c. GeoThermag: A geothermal magnetic refrigerator. Int. J. Refrig. 59, 75–83.

Aprea, C., Greco, A., Maiorino, A., Masselli, C., 2018a. Energy performances and numerical investigation of solid-state magnetocaloric materials used as refrigerant in an active magnetic regenerator. Therm. Sci. Eng. Prog. 6, 370–379.

Aprea, C., Greco, A., Maiorino, A., Masselli, C., 2018b. Solid-state refrigeration: A comparison of the energy performances of caloric materials operating in an active caloric regenerator. Energy 165, 439–455.

Aprea, C., Greco, A., Maiorino, A., Masselli, C., 2018. The environmental impact of solid-state materials working in an active caloric refrigerator compared to a vapor compression cooler 36, 1155–1162.

Aprea, C., Greco, A., Maiorino, A., Masselli, C., 2017a. A two-dimensional investigation about magnetocaloric regenerator design: parallel plates or packed bed? J. Phys. Conf. Ser. 9.

Aprea, C., Greco, A., Maiorino, A., Masselli, C., 2017b. Analyzing the energetic performances of AMR regenerator working with different magnetocaloric materials: Investigations and viewpoints. Int. J. Heat Technol. 35, S383–S390.

Aprea, C., Greco, A., Maiorino, A., Masselli, C., 2016c. The energy performances of a rotary permanent magnet magnetic refrigerator. Int. J. Refrig. 61, 1–11.

Aprea, C., Greco, A., Maiorino, A., Masselli, C., 2015a. Magnetic refrigeration: An eco-friendly technology for the refrigeration at room temperature. J. Phys. Conf. Ser. 655.

Bahl, C.R.H., Navickaitė, K., Neves Bez, H., Lei, T., Engelbrecht, K., Bjørk, R., Li, K., Li, Z., Shen, J., Dai, W., Jia, J., Wu, Y., Long, Y., Hu, F., Shen, B., 2017. Operational test of bonded magnetocaloric plates. Int. J. Refrig. 76, 245–251.

Balli, M., Jandl, S., Fournier, P., Kedous-Lebouc, A., 2017. Advanced materials for magnetic cooling: Fundamentals and practical aspects. Appl. Phys. Rev. 4.

Bartholomé K., Hess T., Winkler M., Mahlke A., K.J., 2017. New Concept for High-Efficient Cooling Systems Based on Solid-State Caloric Materials as Refrigerant, in: Junior C., Jänsch D., D.O. (Ed.), Energy and Thermal Management, Air Conditioning, Waste Heat Recovery. ETA 2016. Springer, Cham, pp. 178–186.

Benedict, M.A., Sherif, S.A., Beers, D.G., Schroeder, M.G., 2016. Design and performance of a novel magnetocaloric heat pump. Sci. Technol. Built Environ. 22, 520–526.

Benedict, M.A., Sherif, S.A., Schroeder, M., Beers, D.G., 2017a. The impact of magnetocaloric properties on refrigeration performance and machine design. Int. J. Refrig. 74, 574–581.

Benedict, M.A., Sherif, S.A., Schroeder, M., Beers, D.G., 2017b. Experimental impact of magnet and regenerator design on the refrigeration performance of first-order magnetocaloric materials. Int. J. Refrig. 74, 188–197.

Bernal, I., Guido, H., Rautus, S., Piacenza, J., 2016. Toward an Experimental Design Approach for Magnetocaloric Refrigeration Systems, in: Proceedings of the ASME 2016 IDETC/CIE. ASME, North Carolina.

Bjørk, R., Bahl, C.R.H., Insinga, A.R., 2017. Topology optimized permanent magnet systems. J. Magn. Magn. Mater. 437, 78–85.

Bjørk, R., Bahl, C.R.H., Nielsen, K.K., 2016. The lifetime cost of a magnetic refrigerator. Int. J. Refrig. 63, 48–62.

Bocarsly, J.D., Levin, E.E., Garcia, C.A.C., Schwennicke, K., Wilson, S.D., Seshadri, R., 2017. A Simple Computational Proxy for Screening Magnetocaloric Compounds. Chem. Mater. 29, 1613–1622.

Brown, T.D., Bruno, N.M., Chen, J.H., Karaman, I., Ross, J.H., Shamberger, P.J., 2015. A Preisach-Based Nonequilibrium Methodology for Simulating Performance of Hysteretic Magnetic Refrigeration Cycles. Jom 67, 2123–2132.

Brück, E., Yibole, H., Zhang, L., 2016. A universal metric for ferroic energy materials. Philos. Trans. R. Soc. A Math. Phys. Eng. Sci. 374.

Capovilla, M.S., Lozano, J.A., Trevizoli, P. V., Barbosa, J.R., 2016. Performance evaluation of a magnetic refrigeration system. Sci. Technol. Built Environ. 22, 534–543.

Cardoso, P.O., Destro, M.C., Alvares, M.G., Lozano, J.A., De Negri, V.J., Barbosa, J.R., 2016. Modeling of a novel digital hydraulic system for a magnetic refrigerator, in: IIF-IIR (Ed.), Seventh IIF-IIR International Conference on Magnetic Refrigeration at Room Temperature, Thermag VII. Torino, pp. 11–14.

Celik, S., Kural, M.H., 2018. Octagonal Halbach Magnet Array Design for a Magnetic Refrigerator. Heat Transf. Eng. 39, 391–397.

Chaudhary, V., Chen, X., Ramanujan, R. V., 2019. Iron and manganese based magnetocaloric materials for near room temperature thermal management. Prog. Mater. Sci. 100, 64–98.

Chiba, Y., 2017. Experimental and Numerical Study of the Behavior of a Multilayer for Active Magnetic Refrigerator Based on La-Fe-Co-Si 53.

Chiba, Y., Smaili, A., Sari, O., Hu, J., 2015. Composite material based on LaFe(Co,Si) for active magnetic regenerator operating near room temperature, in: 6th International Renewable Energy Congress (IREC). IEEE.

Choi, S., Han, U., Cho, H., Lee, H., 2018. Review: Recent advances in household refrigerator cycle technologies. Appl. Therm. Eng. 132, 560–574.

Christiaanse, T. V., Trevizoli, P. V., Misra, S., Carroll, C., Van Asten, D., Zhang, L., Teyber, R., Govindappa, P., Niknia, I., Rowe, A., 2018. Experimental study of 2-layer regenerators using Mn-Fe-Si-P materials. J. Phys. D. Appl. Phys. 51.

Cohen, L.F., 2018. Contributions to Hysteresis in Magnetocaloric Materials. Phys. Status Solidi Basic Res. 255, 2–9.

Dall'Olio, S., Lei, T., Engelbrecht, K., Bahl, C.R.H., 2017. The effect of tapering on a magnetocaloric regenerator bed. Int. J. Refrig. 84, 300–308.

De Almeida, A.T., Fong, J., Falkner, H., Bertoldi, P., 2017. Policy options to promote energy efficient electric motors and drives in the EU. Renew. Sustain. Energy Rev. 74, 1275–1286. https://doi.org/10.1016/j.rser.2017.01.112

de Vries, W., van der Meer, T.H., 2017. Application of Peltier thermal diodes in a magnetocaloric heat pump. Appl. Therm. Eng. 111, 377–386.

Diehl, O., Schönfeldt, M., Brouwer, E., Dirks, A., Rachut, K., Gassmann, J., Güth, K., Buckow, A., Gauß, R., Stauber, R., Gutfleisch, O., 2018. Towards an Alloy Recycling of Nd–Fe–B Permanent Magnets in a Circular Economy. J. Sustain. Metall. 7, 1–13.

Ekren, O., Yilanci, A., Ezan, M.A., Kara, M., Biyik, E., 2017. Performance Assessment of a Near Room Temperature Magnetic Cooling System. Energy Procedia 107, 188–192.

Eriksen, D., Engelbrecht, K., Bahl, C.R.H., Bjørk, R., Nielsen, K.K., Insinga, A.R., Pryds, N., 2015. Design and experimental tests of a rotary active magnetic regenerator prototype. Int. J. Refrig. 58, 14–21.

Ezan, M.A., Ekren, O., Metin, C., Yilanci, A., Biyik, E., Kara, S.M., 2017. Numerical analysis of a near-room-temperature magnetic cooling system. Int. J. Refrig. 75, 262–275.

Fähler, S., 2018. Caloric Effects in Ferroic Materials: New Concepts for Cooling. Energy Technol. 6, 1394–1396.

Fortkamp, F.P., Eriksen, D., Engelbrecht, K., Bahl, C.R.H., Lozano, J.A., Barbosa, J.R., 2018. Experimental investigation of different fluid flow profiles in a rotary multi-bed active magnetic regenerator device. Int. J. Refrig. 91, 46–54.

Fortkamp, F.P., Lozano, J.A., Barbosa, J.R., 2017. Analytical solution of concentric two-pole Halbach cylinders as a preliminary design tool for magnetic refrigeration systems. J. Magn. Magn. Mater. 444, 87–97.

Franco, V., Blázquez, J.S., Ipus, J.J., Law, J.Y., Moreno-Ramírez, L.M., Conde, A., 2018. Magnetocaloric effect: From materials research to refrigeration devices. Prog. Mater. Sci. 93, 112–232.

Funk, A., Freudenberger, J., Waske, A., Krautz, M., 2018. Getting magnetocaloric materials into good shape: Cold-working of La(Fe, Co, Si)13by powder-in-tube-processing. Mater. Today Energy 9, 223–228.

Gao, X.Q., Shen, J., He, X.N., Tang, C.C., Li, K., Dai, W., Li, Z.X., Jia, J.C., Gong, M.Q., Wu, J.F., 2016. Improvements of a room-temperature magnetic refrigerator combined with Stirling cycle refrigeration effect. Int. J. Refrig. 67, 330–335.

Gauß, R., Homm, G., Gutfleisch, O., 2017. The Resource Basis of Magnetic Refrigeration. J. Ind. Ecol. 21, 1291–1300.

Goetzler, W., Zogg, R., Young, J., Johnson, C., 2014. Alternatives to Vapor Compression HVAC Technology. ASHRAE J. 12–23.

Gottschall, T., Skokov, K. P., Scheibel, F., Acet, M., Zavareh, M.G, Skourski, Y., Wosnitza, J., Farle, M., Gutfleisch, O., 2016, Dynamical Effects of the Martensitic Transition in Magnetocaloric Heusler Alloys from Direct ΔTad Measurements under Different Magnetic-Field-Sweep Rates. Phys. Rev. Applied 5, 024013.

Gottschall, T., Stern-Taulats, E., Mañosa, L., Planes, A., Skokov, K.P., Gutfleisch, O., 2017. Reversibility of minor hysteresis loops in magnetocaloric Heusler alloys. Appl. Phys. Lett. 110.

Govindappa, P., Trevizoli, P. V, Campbell, O., Niknia, I., Christiaanse, T. V, Teyber, R., Misra, S., Schwind, M.A., van Asten, D., Zhang, L., Rowe, A., 2017. Experimental investigation of MnFeP 1–x As x multilayer active magnetic regenerators. J. Phys. D. Appl. Phys. 50, 315001.

Griffith, L.D., Mudryk, Y., Slaughter, J., Pecharsky, V.K., 2018. Material-based figure of merit for caloric materials. J. Appl. Phys. 123.

Gutfleisch, O., Gottschall, T., Fries, M., Benke, D., Radulov, I., Skokov, K.P., Wende, H., Gruner, M., Acet, M., Entel, P., Farle, M., 2016. Mastering hysteresis in magnetocaloric materials. Philos. Trans. R. Soc. A Math. Phys. Eng. Sci. 374.

Jawad Mahdy, A.M., Mohammad, W.S., Mortada, T.K., 2015. Practical Study of Magnetic Refrigeration Performance and Optimization. IOSR J. Mech. Civ. Eng. Ver. II 12, 2320–334.

Johra, H., Filonenko, K., Heiselberg, P., Veje, C., Lei, T., Dall'Olio, S., Engelbrecht, K., Bahl, C., 2018. Integration of a magnetocaloric heat pump in a low-energy residential building. Build. Simul. 11, 753–763.

Johra, H., Filonenko, K., Heiselberg, P., Veje, C., Lei, T., Dall'Olio, S., Engelbrecht, K., Bahl, C., 2019. Integration of a magnetocaloric heat pump in an energy flexible residential building, Renewable Energy 136, 115-126.

Kamran, M.S., Ali, H., Farhan, M., Tang, Y.B., Chen, Y.G., Wang, H.S., 2016. Performance optimisation of room temperature magnetic refrigerator with layered/multi-material microchannel regenerators. Int. J. Refrig. 68, 94–106.

Karpenkov, D.Y., Skokov, K.P., Liu, J., Karpenkov, A.Y., Semenova, E.M., Airiyan, E.L., Pastushenkov, Y.G., Gutfleisch, O., 2016. Adiabatic temperature change of micro- and nanocrystalline Y2Fe17heat-exchangers for magnetic cooling. J. Alloys Compd. 668, 40–45.

Kitanovski, A., Tušek, J., Tomc, U., Plaznik, U., Ožbolt, M., Poredoš, A., 2015a. Magnetocaloric Energy Conversion. Springer, Switzerland.

Kitanovski, A., Plaznik, U., Tomc, U., Poredoš, A., 2015b. Present and future caloric refrigeration and heat-pump technologies. Int. J. Refrig. 57, 288–298.

Klinar, K., Tomc, U., Jelenc, B., Nosan, S., Kitanovski, A., 2019. New frontiers in magnetic refrigeration with high oscillation energy-efficient electromagnets. Appl. Energy 236.

Kolano, R., Kolano-Burian, A., Hreczka, M., Polak, M., Szynowski, J., Tomaka, W., 2016. Magnetocaloric cooling device with reciprocating motion of the magnetic field source. Acta Phys. Pol. A 129, 1205–1209.

Kondo, M., Ueno, K., Takeuchi, K., Nomura, R., Kizaki, T., 2016. Effects of magnetocaloric wire on increase in refrigeration cycle. Seventh II-IIr Int. Conf. Magn. Refrig. Room Temp. Thermag VII 43--46.

Lee, J., Nomura, T., Dede, E.M., 2017. Topology optimization of Halbach magnet arrays using isoparametric projection. J. Magn. Magn. Mater. 432, 140–153.

Lee, J.S., 2015. Experimental results for active magnetic regenerative refrigeration apparatus using twin beds. J. Mech. Sci. Technol. 29, 2237–2241.

Lei, T., Engelbrecht, K., Nielsen, K.K., Neves Bez, H., Bahl, C.R.H., 2016. Study of multi-layer active magnetic regenerators using magnetocaloric materials with first and second order phase transition. J. Phys. D. Appl. Phys. 49.

Lei, T., Engelbrecht, K., Nielsen, K.K., Veje, C.T., 2017a. Study of geometries of active magnetic regenerators for room temperature magnetocaloric refrigeration. Appl. Therm. Eng. 111, 1232–1243.

Lei, T., Navickaitė, K., Engelbrecht, K., Barcza, A., Vieyra, H., Nielsen, K.K., Bahl, C.R.H., 2018. Passive characterization and active testing of epoxy bonded regenerators for room temperature magnetic refrigeration. Appl. Therm. Eng. 128, 10–19.

Lei, Z., Raebiger, D., Eckert, S., Eckert, K., 2017. Liquid Metal Based Magnetic Cooling : Velocity Measurements. Magnetohydrodynamics 53, 403–410.

Lionte, S., Risser, M., Vasile, C., Elouad, L., Muller, C., 2018. Adapting an active magnetic regenerator to a continuous fluid flow application. Int. J. Refrig. 85, 303–313.

Lionte, S., Vasile, C., Siroux, M., 2015. Numerical analysis of a reciprocating active magnetic regenerator. Appl. Therm. Eng. 75, 871–879.

Liu, J.P., Zhang, M.X., Shao, Y.Y., Yan, A.R., 2015. LaFe11.6 Si1.4/Cu Magnetocaloric Composites Prepared by Hot Pressing. Magn. IEEE Trans. 51, 1–2.

Lorenz, L., Kevlishvili, N., 2017. Designing of Halbach cylinder based magnetic assembly for a rotating magnetic refrigerator. Part 1: Designing procedure. Int. J. Refrig. 73, 246–256.

Lozano, J.A., Capovilla, M.S., Trevizoli, P. V., Engelbrecht, K., Bahl, C.R.H., Barbosa, J.R., 2016. Development of a novel rotary magnetic refrigerator. Int. J. Refrig. 68, 187–197.

Lu, B., Wu, J., He, J., Huang, J., 2019. Heat transfer optimization of a fully solid state micro-unit regeneration magnetic refrigerator. Int. J. Refrig. 98, 42–50.

Luglietti, R., Rosa, P., Pastore, A., Terzi, S., Taisch, M., 2017. Life Cycle Assessment Tool Implemented in Household Refrigeration Industry: A Magnetic Cooling Prototype Development. Procedia Manuf. 8, 231–238.

Lyubina, J., 2017a. Magnetocaloric materials for energy efficient cooling. J. Phys. D. Appl. Phys. 50.

Lyubina, J., 2017b. Synthesis of magnetocaloric LaFe 11.6 Si 1.4 alloy by spark plasma sintering 6–10.

Meddeb, Z., Sidhom, R. Ben, Azaeiz, K., Jeday, M.R., 2015. Thermodynamic Study of the Active Magnetic Regenerative Refrigeration in Transitional Regime 1, 49–53.

Mira, A., De Larochelambert, T., Espanet, C., Giurgea, S., Nika, P., Bahl, C.R.H., Bjørk, R., Nielsen, K.K., 2017. Influence of magnetization on the applied magnetic field in various AMR regenerators. J. Appl. Phys. 122.

Monfared, B., 2018. Design and optimization of regenerators of a rotary magnetic refrigeration device using a detailed simulation model. Int. J. Refrig. 88, 260–274.

Monfared, B., 2017. Simulation of solid-state magnetocaloric refrigeration systems with Peltier elements as thermal diodes. Int. J. Refrig. 74, 322–330.

Monfared, B., Palm, B., 2018. Material requirements for magnetic refrigeration applications. Int. J. Refrig. 96, 25–37.

Monfared, B., Palm, B., 2015. Optimization of layered regenerator of a magnetic refrigeration device. Int. J. Refrig. 57, 103–111. https://doi.org/10.1016/j.ijrefrig.2015.04.019

Mugica, I., Poncet, S., Bouchard, J., 2018. An open source DNS solver for the simulation of Active Magnetocaloric Regenerative cycles. Appl. Therm. Eng. 141, 600–616.

Nakashima, A.T.D., Dutra, S.L., Trevizoli, P. V., Barbosa, J.R., 2018a. Influence of the flow rate waveform and mass imbalance on the performance of active magnetic regenerators. Part I: Experimental analysis. Int. J. Refrig. 93, 236–248.

Nakashima, A.T.D., Dutra, S.L., Trevizoli, P. V., Barbosa, J.R., 2018b. Influence of the flow rate waveform and mass imbalance on the performance of active magnetic regenerators. Part II: Numerical simulation. Int. J. Refrig. 93, 159–168.

Niknia, I., Campbell, O., Christiaanse, T. V., Govindappa, P., Teyber, R., Trevizoli, P. V., Rowe, A., 2016. Impacts of configuration losses on active magnetic regenerator device performance. Appl. Therm. Eng. 106, 601–612.

Niknia, I., Trevizoli, P. V., Christiaanse, T. V., Govindappa, P., Teyber, R., Rowe, A.,2017, Material screening metrics and optimal performance of an active magnetic regenerator. J. Appl. Phys. 121, 064902.

Pavlukhina, O., Sokolovskiy, V., Buchelnikov, V., 2016. Modeling of heat transfer processes in Ni2MnIn magnetic wires. Phys. Status Solidi Appl. Mater. Sci. 213, 390–398.

Pecharsky, V.K., Cui, J., Johnson, D.D., 2016. (Magneto) caloric refrigeration : is there light at the end of the Subject Areas : Phil. Trans. R. Soc. Lond. A 374, 20150305.

Pecharsky, V.K., Gschneidner, Jr., K.A., 1997. Giant Magnetocaloric Effect in Gd5(Si2Ge2). Phys. Rev. Lett.

Plait, A., Giurgea, S., de Larochelambert, T., Nika, P., Espanet, C., 2018. Low computational cost semi-analytical magnetostatic model for magnetocaloric refrigeration systems. AIP Adv. 8, 095204.

Puga, J.B., Bordalo, B.D., Silva, D.J., Dias, M.M., Belo, J.H., Araújo, J.P., Oliveira, J.C.R.E., Pereira, A.M., Ventura, J., 2017. Novel thermal switch based on magnetic nanofluids with remote activation. Nano Energy 31, 278–285.

Qian, S., Nasuta, D., Rhoads, A., Wang, Y., Geng, Y., Hwang, Y., Radermacher, R., Takeuchi, I., 2016. Not-in-kind cooling technologies: A quantitative comparison of refrigerants and system performance. Int. J. Refrig. 62, 177–192.

Qian, S., Yuan, L., Yu, J., Yan, G., 2018. Variable load control strategy for room-temperature magnetocaloric cooling applications. Energy 153, 763–775.

Qian, S., Yuan, L., Yu, J., Yan, G., 2017. Critical parameters in design of active magnetocaloric regenerators for magnetic refrigeration applications. Int. J. Refrig. 84, 151–164.

Radulov, I.A., Karpenkov, D.Y., Skokov, K.P., Karpenkov, A.Y., Braun, T., Brabänder, V., Gottschall, T., Pabst, M., Stoll, B., Gutfleisch, O., 2017a. Production and properties of metal-bonded La(Fe,Mn,Si)13Hxcomposite material. Acta Mater. 127, 389–399.

Radulov, I.A., Karpenkov, D.Y., Specht, M., Braun, T., Karpenkov, A.Y., Skokov, K.P., Gutfleisch, O., 2017b. Heat Exchangers from Metal-Bonded La(Fe,Mn,Si)13Hx Powder. IEEE Trans. Magn. 53, 1–7.

Radulov, I.A., Skokov, K.P., Karpenkov, D.Y., Braun, T., Gutfleisch, O., 2015. Polymer-Bonded La(Fe,Mn,Si)13H<italic>x</italic> Plates for Heat Exchangers. IEEE Trans. Magn. 51, 1–4.

Richard, M.A., Rowe, A.M., Chahine, R., 2004. Magnetic refrigeration: Single and multimaterial active magnetic regenerator experiments. J. Appl. Phys. 95, 2146–2150.

Roy, S., Poncet, S., Sorin, M., 2017. Sensitivity analysis and multiobjective optimization of a parallel-plate active magnetic regenerator using a genetic algorithm. Int. J. Refrig. 75, 276–285.

Ryu, K.S., Nahm, S.H., Jung, J.K., Baek, S.W., 2017. Design and fabrication of 2-T rotating halbach magnet for magnetic refrigerator. J. Magn. 22, 65–68.

Schroeder, M.G., Brehob, E., 2016. A flexible numerical model of a multistage active magnetocaloric regenerator. Int. J. Refrig. 65, 250–257.

Shao, Y., Liu, J., Zhang, M., Yan, A., Skokov, K.P., Karpenkov, D.Y., Gutfleisch, O., 2017. High-performance solid-state cooling materials: Balancing magnetocaloric and non-magnetic properties in dual phase La-Fe-Si. Acta Mater. 125, 506–512.

Sheng, W., Wang, J.Q., Wang, G., Huo, J., Wang, X., Li, R.W., 2018. Amorphous microwires of high entropy alloys with large magnetocaloric effect. Intermetallics 96, 79–83.

Skokov, K.P., Gutfleisch, O., 2018. Heavy rare earth free, free rare earth and rare earth free magnets - Vision and reality. Scr. Mater. 1–6.

Taskaev, S., Skokov, K., Khovaylo, V., Buchelnikov, V., Pellenen, A., Karpenkov, D., Ulyanov, M., Bataev, D., Usenko, A., Lyange, M., Gutfleisch, O., 2015. Effect of severe plastic deformation on the specific heat and magnetic properties of cold rolled Gd sheets. J. Appl. Phys. 117, 1–6.

Teyber, R., Trevizoli, P. V., Christiaanse, T. V., Govindappa, P., Niknia, I., Rowe, A., 2018a. Semi-analytic AMR element model. Appl. Therm. Eng. 128, 1022–1029.

Teyber, R., Trevizoli, P. V., Christiaanse, T. V., Govindappa, P., Niknia, I., Rowe, A., 2017b. Permanent magnet design for magnetic heat pumps using total cost minimization. J. Magn. Magn. Mater. 442, 87–96.

Teyber, R., Trevizoli, P. V., Christiaanse, T. V., Govindappa, P., Niknia, I., Rowe, A., 2016. Performance evaluation of two-layer active magnetic regenerators with second-order magnetocaloric materials. Appl. Therm. Eng. 106, 405–414.

Teyber, R., Trevizoli, P. V., Christiaanse, T. V., Govindappa, P., Rowe, A., 2018b. Topology optimization of reduced rare-earth permanent magnet arrays with finite coercivity. J. Appl. Phys. 123.

Teyber, R., Trevizoli, P. V., Niknia, I., Christiaanse, T. V., Govindappa, P., Rowe, A., 2017a. Experimental performance investigation of an active magnetic regenerator subject to different fluid flow waveforms. Int. J. Refrig. 74, 36–44.

Tomc, U., 2016. Improvements to the heat transfer of an active magnetic regenerator : Doctoral Thesis. University of Ljubljana. 147 p.

Torregrosa-Jaime, B., Corberán, J.M., Payá, J., Engelbrecht, K., 2015. An efficient numerical scheme for the simulation of parallel-plate active magnetic regenerators. Int. J. Refrig. 58, 121–130.

Trevizoli, P. V., Barbosa, J.R., 2017a. Thermal-hydraulic behavior and influence of carryover losses in oscillating-flow regenerators. Int. J. Therm. Sci. 113, 89–99.

Trevizoli, P. V., Barbosa, J.R., 2015a. Entropy Generation Minimization analysis of oscillating-flow regenerators. Int. J. Heat Mass Transf. 87, 347–358.

Trevizoli, P. V., Christiaanse, T. V., Govindappa, P., Niknia, I., Teyber, R., Barbosa, J.R., Rowe, A., 2016a. Magnetic heat pumps: An overview of design principles and challenges. Sci. Technol. Built Environ. 22, 507–519.

Trevizoli, P. V., Lozano, J.A., Peixer, G.F., Barbosa, J.R., 2015b. Design of nested Halbach cylinder arrays for magnetic refrigeration applications. J. Magn. Magn. Mater. 395, 109–122.

Trevizoli, P. V., Nakashima, A.T., Peixer, G.F., Barbosa, J.R., 2017b. Performance assessment of different porous matrix geometries for active magnetic regenerators. Appl. Energy 187, 847–861.

Trevizoli, P. V., Nakashima, A.T., Peixer, G.F., Barbosa, J.R., 2016c. Performance evaluation of an active magnetic regenerator for cooling applications - part 1: Experimental analysis and thermodynamic performance. Int. J. Refrig. 72, 192–205.

Trevizoli, P. V., Nakashima, A.T., Barbosa, J.R., 2016d. Performance evaluation of an active magnetic regenerator for cooling applications – part II: Mathematical modeling and thermal losses. Int. J. Refrig. 72, 206–217.

Trevizoli, P. V., Peixer, G.F., Nakashima, A.T., Capovilla, M.S., Lozano, J.A., Barbosa, J.R., 2018. Influence of inlet flow maldistribution and carryover losses on the performance of thermal regenerators. Appl. Therm. Eng. 133, 472–482.

Tunsu, C., Petranikova, M., 2018. Perspectives for the recovery of critical elements from future energy-efficient refrigeration materials. J. Clean. Prod. 197, 232–241.

Varga, R., Ryba, T., Vargova, Z., Michalik, S., Zhukova, V., Zhukov, A., Sanchez Llamazares, J.L., Quintana-Nedelcos, A., 2015. Magnetocaloric effects in magnetic microwires for magnetic refrigeration applications, Magnetic Nano- and Microwires: Design, Synthesis, Properties and Applications. Elsevier Ltd.

Velázquez, D., Estepa, C., Palacios, E., Burriel, R., 2016. A comprehensive study of a versatile magnetic refrigeration demonstrator. Int. J. Refrig. 63, 14–24.

Waske, A., Gruner, M.E., Gottschall, T., Gutfleisch, O., 2018. Magnetocaloric materials for refrigeration near room temperature. MRS Bull. 43, 269–273.

Wehmeyer, G., Yabuki, T., Monachon, C., Wu, J., Dames, C., 2017. Thermal diodes, regulators, and switches: Physical mechanisms and potential applications. Appl. Phys. Rev. 4.

Wenkai, P., Yungui, C., Yongbai, T., Lingtong, Z., Huaqiang, G., 2017. Indium-Bonded LaFe 11.6 Si 1.4 H 1.02 Magnetocaloric Composites by Hot Pressing. Rare Met. Mater. Eng. 46, 2384–2388.

Wieland, S., Petzoldt, F., 2017. Powder-extrusion and sintering of magnetocaloric LaCe(FeMnSi)13 alloy. J. Alloys Compd. 719, 182–188.

Wu, J., Lu, B., Liu, C., He, J., 2018. A novel cascade micro-unit regeneration cycle for solid state magnetic refrigeration. Appl. Therm. Eng. 137, 836–847.

You, Y., Guo, Y., Xiao, S., Yu, S., Ji, H., Luo, X., 2016a. Numerical simulation and performance improvement of a multi-polar concentric Halbach cylindrical magnet for magnetic refrigeration. J. Magn. Magn. Mater. 405, 231–237.

You, Y., Wu, Z., Chen, P., Ji, H., Zeng, X., Xu, X., Dai, F., 2018a. Improving magnetic refrigerator performances by enhancing convection heat transfer with staggered twin-wedged elements. Appl. Therm. Eng. 132, 423–431.

You, Y., Wu, Z., Xiao, S., Li, H., Xu, X., 2017. A comprehensive two-dimensional numerical study on unsteady conjugate heat transfer in magnetic refrigerator with Gd plates. Int. J. Refrig. 79, 217–225.

You, Y., Wu, Z., Yang, Y., Yu, J., Zhang, D., Zhang, Z., 2018b. Refrigeration Performance and Entropy Generation Analysis for Reciprocating Magnetic Refrigerator with Gd Plates. Entropy 20, 427.

You, Y., Yu, S., Tian, Y., Luo, X., Huang, S., 2016b. A numerical study on the unsteady heat transfer in active regenerator with multi-layer refrigerants of rotary magnetic refrigerator near room temperature. Int. J. Refrig. 65, 238–249.

Zarkevich, N.A., Johnson, D.D., Pecharsky, V.K., 2018. High-throughput search for caloric materials: The CaloriCool approach. J. Phys. D. Appl. Phys. 51.

Zhang, M.., A. M. Momen;, Abdelaziz, O., 2016. Preliminary Analysis of a Fully Solid State Magnetocaloric Refrigeration. Int. Compress. Eng. Refrig. Air Cond. High Perform. Build. Conf. 1–10.

Zhang, M., Abdelaziz, O., Momen, A.M., Abu-Heiba, A., 2017. A numerical analysis of a magnetocaloric refrigerator with a 16-layer regenerator. Sci. Rep. 7, 1–12.

Zimm, C., Boeder, A., Mueller, B., Rule, K., Russek, S.L., 2018. The evolution of magnetocaloric heat-pump devices. MRS Bull. 43, 274–279.

Zimm, C.B., Sternberg, A., Jastrab, A.G., Boeder, A.M., Lawton, L.M., Chell, J.J., 2003. Rotating bed magnetic refrigeration apparatus. US6526759B2.

Manuscript ID: 1839
DOI: 10.18462/iir.icr.2019.1839

Practical aspects on slurries for refrigeration and air conditioning

Laurence FOURNAISON

Irstea GPAN, 1 rue Pierre-Gilles de Gennes, CS 10030, 92761 Antony Cedex, France.
laurence.fournaison@irstea.fr

ABSTRACT

Refrigeration industry is facing stronger regulation related to the use of refrigerants. Secondary refrigeration is a technology that can divide up to a factor 10 the amount of refrigerant contained in a system. In order to make the system more efficient the use of diphasic fluids is an interesting solution. Four types of phase change material (pcm) slurries, ice slurries, pcm emulsion, encapsulated phase-change materials, hydrate slurries can be suitable for many refrigerating applications. Currently the industrial use of these diphasic secondary refrigerants is uneven due to their readiness level. This paper presents for each fluid the generation process, their industrial deployment and the issues hampering their development.
Keywords: Slurry, Hydrates, Ice, Emulsion, Encapsulation.

1. INTRODUCTION

Refrigeration industry is directly affected by the phasing down of HFC refrigerants. Indeed, the EU's F-GAS regulation phasing down the use of HFCs has led the profession to propose alternative fluids. In this context, new HFO-type fluids are being marketed and there is an increased use of so-called natural fluids, CO2, NH3 and hydrocarbons. Nevertheless, the latter may be subject to high safety constraints due to their risk of explosion or toxicity. Any innovative technology that minimizes the use of refrigerant is expected to fulfil environment purposes as soon as its efficiency is not altered. Then, secondary refrigeration becomes an interesting alternative as the cooling unit can be confined in the engine room which allows a significant reduction of the refrigerant mass and an environment friendly fluid delivers the cold to the place of use. On the other hand, this solution is more energetic due to the presence of an intermediate heat exchanger and circulation pumps that creates exergetic losses (Guilpart et al. 2006). Despite these disadvantages secondary refrigeration is widely used for air conditioning with chilled water and is gradually developing in the commercial cold sector. More recently, the development of secondary diphasic fluids, such as ice slurries, hydrate slurries or PCM (Phase Change Materiel) slurries suggests a new alternative for industrial cold applications. This paper aims at comparing the different types of diphasic fluids, their generation, their development and the issues encountered with these fluids.

2. SECONDARY REFRIGERATION

Secondary refrigeration is a very well-known technology commonly used for air conditioning applications. It consists in a primary refrigeration system containing the refrigerant and a secondary loop containing the "secondary fluid" (Figure 1). This technology allows to divide by up to a factor 10 the mass of primary refrigerant. This possibility is well adapted to the strong regulation related to the phasing down of the HFC fluids, and provides the ability to use some flammable fluids, as natural fluids or HFO. Furthermore in case of further regulation on fluids, the retrofitting of the system will be easier. The secondary fluid can be of any kind as soon as it has the right properties to deliver the best efficiency. For example, the fluid should have good thermal properties, (consistent with the application temperature, high thermal capacity, high thermal conductivity, low viscosity), nontoxic, nonflammable, environmentally friendly, non-corrosive and should be inexpensive. Then many aqueous mixtures are available, containing salts or alcohols or even ammonia. Among all possible mixtures, there is certainly no ideal solution, but one or more solutions that respond to a compromise between all properties depending on the application. A huge collection of data has been provided by (Melinder, 1997) which is a very good support in the selection of the fluid for the application.

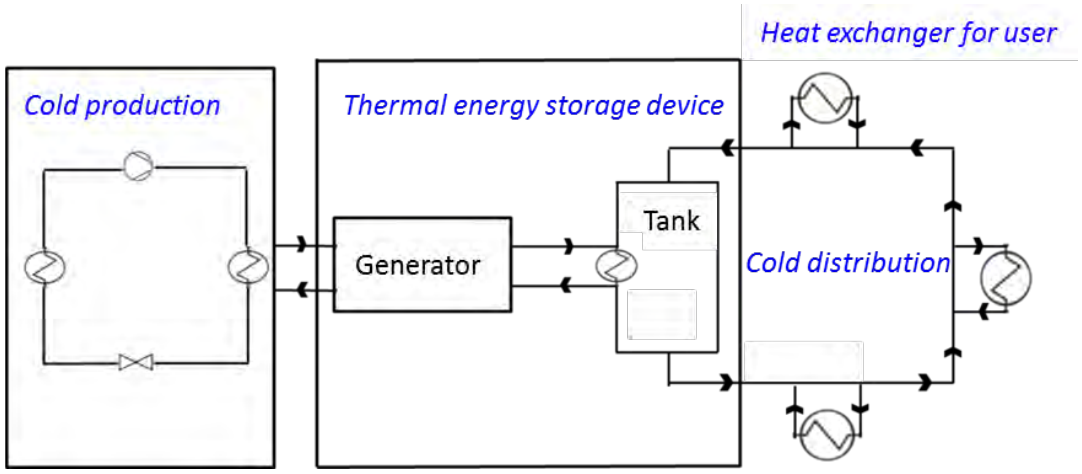

Figure 1: Secondary refrigeration.

Nether the less, the addition of a heat exchanger between the primary fluid and the secondary fluid degrades the energy and produces exergetic losses. Furthermore, in the case of direct expansion, the compression of the refrigerant drives the fluid towards the evaporator. In the case of secondary refrigeration, a pump must be added on the secondary fluid side to reach each terminal unit and therefore consumes energy.

The use of secondary refrigerants with high energetic capacity is a valuable solution to face these exergetic losses. Indeed, they take advantage of the additional latent heat of the PCM in the secondary refrigerant for cold energy distribution to the terminal units. In fact, phase change energy (latent heat) is much higher than that of sensible heat during temperature raise. For example, the heat exchanged by 1 kg of water-glycol mixture with a temperature glide of 5 K is about 5 times less than that contained in the same water-glycol mixture containing 30% of ice.

The liquid-vapor fluids can't be selected as the density difference between the 2 phases is very large and not convenient for secondary systems. So solid-liquid fluids will be here after discussed. There are several types of diphasic solid-liquid fluids, also called slurries that can be used for secondary refrigeration (Youssef et al., 2013). Two-phase secondary refrigerants cover a wide range of phase-change fluids and can be divided into four sub-groups (Figure 2): (a) ice slurries; (b) emulsion; (c) encapsulated phase-change materials; (d) hydrate slurries.

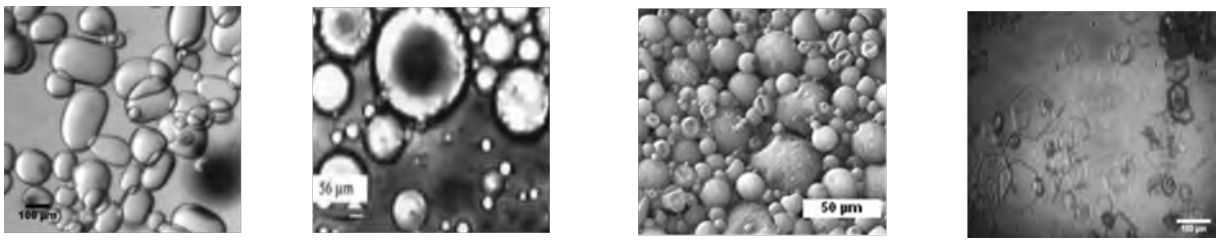

Figure 2: photograph of slurries (a) ice slurry, (b) pcm emulsion, (c) encapsulated pcm, (d) hydrate slurry.

Currently, two-phase secondary refrigerant slurries are not widely used. Apart from ice slurries for applications below 0 °C, only hydrate slurries have been used in industrial applications. In the following section details about each PCM slurry will be given, such as the generation process, their use and the issues encountered with these fluids. The temperatures in the scope of the study range from -40 °C to 10 °C.

3. PCM SLURRIES

In the literature few articles presents a review on different Phase Change Slurry (PCS) systems that can be used at positive temperatures (Delgado et al. 2012),(Zhang,et al. 2010). There are many reviews on each PCS system, as ice slurry (IS), microencapsulated phase change slurry (MS), clathrate hydrate slurry (HS), phase change material emulsions (E) (Figure 3). This paper will firstly give the definition of each type of PCS, then the generation process, their industrial development as well as the major issues of the slurries to face industrial development

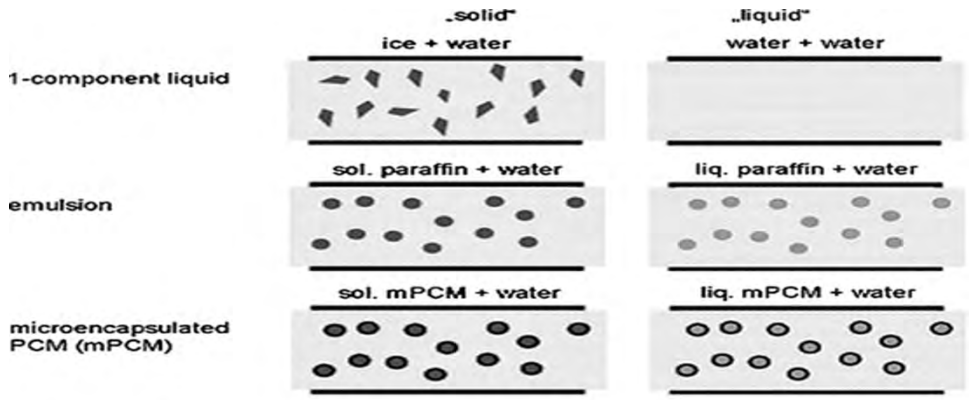

Figure 3: Different kinds of slurries (Harald and Cabeza 2008).

3.1. Type

3.1.1. Emulsion

Emulsions are two-phase liquid-liquid systems, where one liquid (disperse phase) is dispersed in another (continual phase) in the form of droplets. Two types of emulsions are mainly distinguished, depending upon which kind of liquid forms the continuous phase:

- Oil-in-water (O/W) for oil droplets dispersed in water
- Water-in-oil (W/O) for water droplets dispersed in oil

In the case of PCM, the emulsion (PCE) is a mixture of the solution and a phase change material (PCM) (Shao et al., 2015). PCM is directly dispersed in water and generally paraffin wax is used as pcm medium. Paraffin is a well-known PCM, as it has suitable properties for the application, is safe, reliable, inert and non-corrosive. But they have some undesirable properties such as low thermal conductivity and are flammable and not environmentally friendly material. Paraffin wax has also the main advantage to show little volume changes on melting (Sharma et al., 2009) and to release a high amount of latent heat. Paraffin waxes consist in n-alkanes CH3-(CH2) n-CH3. The longer the n-alkane chain the higher the melting point and the latent heat. Then this mixture is more suitable for air conditioning application for a temperature range around 10 to 20 °C than for refrigeration. For example, the kind of paraffin that can be used is tetradecane (Tm=5.9 °C, L=227 kJ.kg-1), or pentadecane CH3-(CH2)13-CH3 (Tm=10 °C, L=206 kJ.kg-1) and hexadecane CH3-(CH2)14-CH3 (Tm=18 °C, L =236 kJ.kg-1). As the cost of pure paraffin is very high, products with polymers blends such as RT6, RT10 and RT18 from Rubitherm Technologies GmbH, which have similar properties as pure paraffin, are preferred. By mixing different paraffin, melting points between those of pure paraffin can be obtained [(Bo et al., 1999), (Choi et al. 1992), (Kousksou et al., 2010)].

3.1.2. Microencapsulated Slurry

Microencapsulated slurries consist in encapsulating or trapping PCM in any way to form particles. When encapsulating, a fin film forms the microcapsules. When stabilized, the PCM is enclosed in a support material with a cross linked structure to form the stabilized PCM. Both are suspended in water to form the slurry.

The PCM contained in the particle is usually Paraffin, as its swelling during phase change is small, and the enthalpy is high enough for the use.

3.1.3. Ice Slurry

Ice slurries consist in small ice particles (around 100 m) dispersed in an aqueous solution. The ice particles are formed while decreasing an aqueous mixture below its freezing point temperature. Then the carrying fluid and the phase-change material are identical (e.g. water-ice system).The lower the temperature, generated is organic or non-organic. The initial additive concentration will define the phase change temperature of the mixture. Ice slurries are very attractive due to their high energetic density related to the latent heat of the ice crystals which is 333 $kJ.kg^{-1}$,but there are more efficient at temperature below 0 °C.

3.1.4. Hydrate Slurry

Gas hydrates are crystalline compounds, similar to ice, are composed of water and guest molecules (gas or liquids). They are generally formed under high pressures and low temperatures. Water molecules (host molecules) form a lattice structure and gas molecules (guest molecules) occupy the interstitial vacancies of the lattice. The gas hydrate has mainly one of the following structures (Sloan, 1998): cubic structure I (SI), cubic structure II (SII) or hexagonal structure H (SH). A gas hydrate is called "simple hydrate" when it contains one type of guest molecules and mixed hydrate when it contains many types of guest molecules.
Semi clathrate hydrates of quaternary salts (Dyadin and Udachin, 1984; Jeffrey and McMullan, 1967),) like TBAB (Tetra-n-butylamonium) can also form with water. In these hydrates, some cages are broken to encage big guest species such as TBAB, and water molecules of the structure are partially replaced by the atoms of guest species.

3.2. Generation

All kinds of PCM slurry presented above are usually used for secondary refrigeration. The basic architecture of the system consists in generating the slurry with a refrigeration unit via a heat exchanger. In the case of emulsion or encapsulate slurry, the pcm “particles freeze, but for hydrate or ice slurries crystals form in the carrying liquid. The fluid is then pumped towards the terminal units. Then at that point, the PCM in the carrier fluid delivers the cooling flux by latent heat in a heat exchanger. The design of the refrigeration loop defines the PCM content necessary to face the cooling demand of the users. Finally, in order to make the system more efficient, a thermal storage tank is frequently associated. The best efficiency is obtained when storing energy in a tank during night time, as the COP is higher and release energy at peak hours during daytime (Kauffeld et al., 2005). Another benefit of the storage is the downsizing of the refrigeration unit, and also it gives the possibility to face heat waves.

3.2.1. Emulsion

Generation of emulsions is a well-known process (Shao et al. 2015). Indeed, water and paraffin are not miscible fluids. Therefore some emulsification process must be performed to obtain an emulsion. Since the emulsification of two unmixable liquids involves a high rise in the surface energy, emulsions are not stable and a third component is needed to stabilize the system. Surfactants are indispensable components used for oil and water based emulsions. Although emulsification process can be carried out by 2 types of process: High-energy method or low-energy method. High energy methods usually involve mechanical energy as high-pressure homogenizers, high-shear stirrers, and ultrasound generators to break large droplets into small ones. Those have the advantage of providing reproducible pcm droplet size emulsions (McClements, 2011). Emulsion can also be obtained by using Phase Inversion Temperature PIT (Schalbart et al., 2010), which changes the curvature of the surfactant. It provides smaller droplets and is cheaper to produce.
The emulsion properties as droplet size distribution or rheological properties are highly depending on the choice of the emulsifier and its concentration and their formation process.

3.2.2. Microencapsulate Slurry

Microencapsulate slurry here includes both pcm that is trapped in a shell as well as the shape stabilized slurries.
Encapsulation is a process of covering the PCM with a suitable coating or shell material. A primary purpose of encapsulation is holding the liquid and/or solid phase of the PCM and keeping it isolated from the surrounding. Microencapsulation techniques have been well developed, mainly by the pharmaceutical industries (Egolf et al., 2003). Microencapsulation can be spherical or rod-shaped particles and are made using a thin and high molecular weight polymeric film.

Stabilized slurries for which the phase-change material is retained inside porous particles of suspensions in a non-water-miscible carrying liquid. For example (Royon et al., 2009) has proposed particles containing a water concentration near close to 90%. Water is introduced, by using a chemical process, inside a three-dimensional network of polymer to form PCM particles.
Some other stabilized slurry can be obtained by mincing stabilized paraffin (Ionescu et al., 2007).

3.2.3 Ice Slurry

An ice slurry generator is necessary to produce ice slurries, the use of a heat exchanger is not sufficient. Generally the aqueous solution is cooled with a chiller, and the water freezes on a cold surface. Scrapers, as rotating blades or brushes to remove the ice layer from the surface. The ice crystals are then driven by the slurry flow and further crystallization occurs in the fluid with the generation of fine crystals in the fluid. The amount of ice produced in the system is determined by the initial additive concentration and the final temperature of the fluid. By lowering the temperature, the ice content increases and the additive concentration in the fluid increases. Scraped surface heat exchangers are the most widely used generators in industry, but some other types as vacuum ice generator and subcooling generator can also be encountered (Figure). The first one is based on the properties of the triple point of water, where the 3 water phases (ice, liquid and gas) are co-existing. The water is contained in a tank under a pressure of 6 mbar at 0 °C. The water vapour is extracted and water freezes in the tank to form the ice slurry at 0 °C. In the case of subcooling generator, water is cooled few degrees below 0 °C, and a mechanical or thermal shock converts water into ice. A new generator has appeared recently, called hydroscraped heat exchanger. There are 2 plate heat exchangers in parallel. The ice slurry is produced while flowing through one of the heat exchangers. A pressure gauge controls the pressure drop between the inlet and the outlet of the fluid. When it becomes too high, the flow is deviated to the other heat exchanger and so on.

3.2.4. Hydrate slurry

Gas hydrate slurries have the advantage of being able to form without mechanical parts. Indeed the aqueous solution containing gas is cooled until it reaches the equilibrium state (temperature and pressure) where hydrate crystals appear in the aqueous solution to become slurry.
In the case of salt hydrates slurries, the generation is similar to that of ice slurries. Then scraped heat-exchanger or plate heat exchangers are used.

3.3. Use

3.3.1. Emulsion

The use of PCM emulsion for secondary refrigeration is based on the following cycle. The “warm” emulsion containing liquid pcm droplets in water flows through a heat exchanger (generally the evaporator of a refrigerating unit) to cool the emulsion. The heat flux must be sufficient to freeze the pcm droplets. Then the emulsion is pumped towards the terminal units. At this location, the emulsion provides cooling energy as the PCM droplets melt in a warmer environment. Then the melted emulsion is cooled again to freeze and starts a new cycle.
Currently, most emulsions are in the development stages and therefore there are no publications related to their application at industrial level. Many test rigs have been developed mainly for air conditioning in a test room or in an office. They prove to give efficient results concerning the efficiency of the process(Inc L.T.D, 2006). It is however widely agreed that they have great potential as cold storage material and heat transfer fluid for heating and cooling systems. Some lab tests have been carried out generally for the air conditioning.

3.3.2. Microencapsulate Slurry

Similarly to emulsions microencapsulate slurry have no industrial nor commercial applications using these fluids. They are often incorporated in gypsum board, plaster, and concrete used in buildings, but not as slurry.

3.3.3. Ice Slurry

The major interest in using ice slurries is the high energy content of the fluid. Indeed, the latent heat of ice is 333 $kJ.kg^{-1}$, so the energy contained in the ice slurry with 30% ice content is about 5 times higher than that contained in a single phase fluid submitted to a temperature glide of 5 K.

Ice slurries are industrially developed all over the world, but the most important application is in Japan, and in Asia where the climatic conditions and the cost of energy promotes thermal storage by latent heat. So in these countries, ice slurry is produced and is immediately stored. The liquid phase of the slurry which temperature is below 0 °C is then pumped towards the terminal units.
In contrary in Europe, ice slurry is pumped towards the terminal units through pipes and heat exchangers. The ice concentration of the slurry at the outlet of the generator should remain below 30 % to ensure flow assurance in the pipes and the velocity must be higher than 1 $m.s^{-1}$ to maintain the homogeneity of the fluid.
Finally, in the fishing industry, ice slurry made from sea water are widely used to cool and preserve fish.

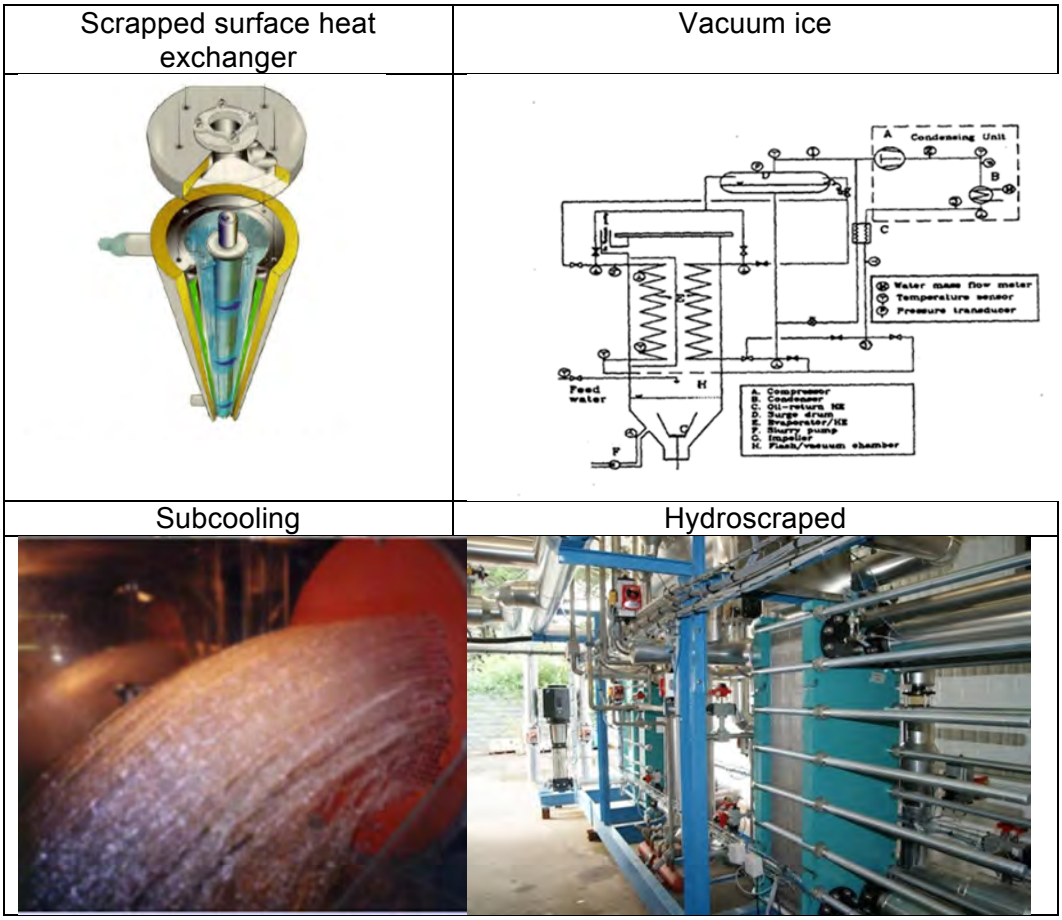

Figure 4: Different types of ice slurry generators.

3.3.4. Hydrate Slurry

Currently, in the case of gas hydrate, only CO_2 gas hydrate slurries are used as secondary refrigerants (Fournaison et al., 2004). The properties of this slurry are very interesting as its dissociation enthalpy is 500 $kJ.kg^{-1}$. As a result, CO_2 hydrate slurries can contain and carry large energy quantities ((Fournaison et al., 2004), (Marinhas et al., 2006). Also CO_2 hydrate phase change temperature can be adapted between 0 and 20 °C depending on the gas pressure. Therefore, it can be used for both refrigeration and air conditioning. However, the use of CO_2 hydrates in cooling systems requires formation pressure higher than 1 MPa. The developing state of this technology is still at a pilot level in laboratories.
Semi clathrate hydrates of quaternary salts, asTetra-n-butylammonium bromide (TBAB) hydrate form at atmospheric pressure (Lin et al., 2014). TBAB hydrate slurries were studied due to their potential suitability for air-conditioning applications (stable between 273 and 285 K). Nevertheless, the generation of TBAB hydrate slurries could have the same drawbacks as ice slurries related to the use of mechanical generators. Moreover, the dissociation enthalpy of TBAB hydrate (~200 $kJ.kg^{-1}$) (Mayoufi et al., 2011) is lower than that of ice (333 $kJ.kg^{-1}$). This kind of hydrate slurry is well

developed and has industrial plants for air conditioning. (Ogoshi and Takao, 2004) have shown 30%power consumption less with this system compared to chilled water system.

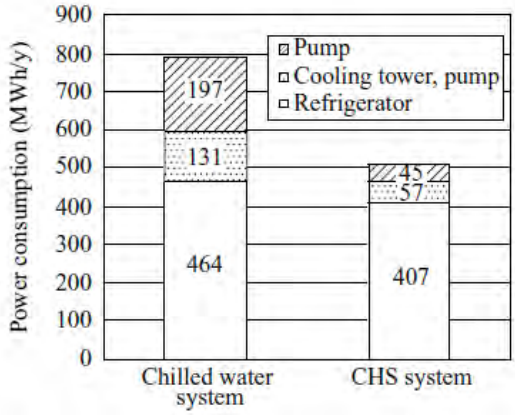

Figure 5: Power consumption for chilled water system and CHS system (Ogoshi and Takao, 2004).

3.4. Issues

For all the slurries the online energy measurement is a technical lock. The issue is different for emulsion and encapsulated slurry than for ice or hydrate slurry. Indeed, for the first two slurries, when the fluid is warm, the pcm particles are liquid and become solid when they freeze. The solid content remains the same whatever the pcm state and it is very difficult to determine the amount frozen PCM in a particle. In the case of hydrate or ice slurries, when the fluid is warm, there is no solid content. In this case, the energy content can be calculated with 2 parameters: initial additive or gas concentration and the fluid temperature. The result is accurate when both the concentration and the temperature are known precisely. Some energy content online sensors based on the measurement of density, calorimetry, spectrometry, pressure drop, sound velocity have been tested but none are both cheap and accurate (Fournaison et al., 2001). The development of slurries is also hampered by other technical issues.

3.4.1. Emulsion

The main barrier affecting the use of emulsion is their stability over time and after freezing and melting cycles. Their stability over time depends on the right choice of surfactants in order to maintain surface energy sufficient. Usually, more than one surfactant is introduced in the water paraffin mixture. The proportion of each additive is important for both the stability over time and the size of the paraffin droplets, which also have an effect on the subcooling degree. The subcooling effect should be avoided because it induces higher energy consumption as the evaporating temperature must be lower than the melting temperature of the paraffin. (Huang et al., 2009) carried out studies on the relationship between the size of the PCM droplets in the emulsion and the subcooling degree. The authors mentioned a clear trend to lower melting temperatures with smaller droplet diameters as is generally expected, up to 2 K lower for the smallest droplets compared to the non-emulsified PCM form. The effect tends to increase as soon as the dimension of the droplet gets below 10 µm. This has also been shown by (Inaba et al., 1994) who measured a subcooling degree of 5.8 K of tetradecane droplet emulsions with a mean diameter of 3.4 µm and of 2.6 K in bulk tetradecane. For the application a compromise must be found between a better heat exchange with smaller droplets, as they will freeze (or melt) more quickly when they are small, but the subcooling degree would be higher.

The second issue with emulsions is related to their stability over time. Indeed, the emulsions can separate into liquid PCM phase and water phase as time passes or when freezing and melting are repeated, but in recent years, emulsions with high stability and durability under extended heating and cooling cycles have been reported (Morimoto et al., 2019).

3.4.2. Microencapsulate Slurry

The suitability of the shell used in encapsulating specific core PCM is a key issue in order to ensure proper thermal performance of the MPCM [13,29,30], especially in preventing PCM leakage when it melts

The development of encapsulated slurry and stabilized slurry are hampered by the reliability of the encapsulation. Indeed, the capsule is subject to high shear when flowing through pumps. This can damage the shell or the matrix and leakage can occur making the fluid unusable.

Similarly to emulsions the smaller the particles, the higher the subcooling degree.

3.4.3. Ice Slurry

Even though this technology is widely spread, its development is hampered by the cost of the ice generators compare to monophasic fluids. The generators have become more reliable and their servicing costs have been reduced. New ice slurry generator designs continue to be developed, so that in the future less expensive and problem-free ice slurry generators should become available.

Ice slurries systems are relevant for refrigeration applications but not for air conditioning, due to the low evaporation temperature. Moreover, as ice slurries are diphasic fluids, the homogeneity of the fluid must be controlled and an adequate management of the ice content is important. This is of main concern also for storage, as the ice density is lower than that of the carrying fluid and the stirring should maintain the fluid homogeneous.

3.4.4. Hydrate Slurry

The CO_2 hydrate slurries form under pressure around 20 bar, and currently industry is reluctant to use these kinds of fluids for secondary refrigeration. Some studies are carried out to decrease the hydrate formation pressure by adding some additives or other salts to form mixed hydrates [ref (Mayoufi et al., 2010)]. The research seems promising, as the pressure can drop up to 75 %, but the dissociation enthalpy is thus also reduced.

Salt hydrates present the same difficulties as ice slurries concerning their generation as scraped surface heat exchangers are generally necessary.

Finally, the thermo physical properties and the pressure drop or heat transfer behaviour of the slurry are of major importance for choosing the most adequate slurry for an application. The pressure drop is increased when the slurry is frozen which is a drawback, but it is balanced by a higher heat transfer.

4. CONCLUSION

Four diphasic secondary refrigerants have interesting thermal properties to render secondary refrigeration more efficient than with monophasic fluids. These are emulsions, encapsulated slurries, ice slurries and hydrate slurries. Their industrial readiness is uneven due to specific issues encountered by each fluid. Currently ice slurries and salt hydrates slurries have industrial applications but their efficiency or technical performances can be improved to expect further spreading of the technology. Emulsion, encapsulated pcm and gas hydrates slurries need further research to expect to have industrial development. The drawback of the emulsions and encapsulated slurry is the aging of the fluid under extended freezing and melting cycles and for gas hydrates slurry is the high pressure of the system.

5. REFERENCES

Bo, H., E. M. Gustafsson,F. Setterwall,1999. Tetradecane and hexadecane binary mixtures as phase change materials (PCMs) for cool storage in district cooling systems. Energy 24(12),1015-1028.

Choi, E. S., Y. I. Cho,H. G. Lorsch,1992. THERMAL-ANALYSIS OF THE MIXTURE OF LABORATORY AND COMMERCIAL GRADES HEXADECANE AND TETRADECANE. International Communications in Heat and Mass Transfer 19(1),1-15.

Delgado, M., A. Lazaro, J. Mazo,B. Zalba, 2012. Review on phase change material emulsions and microencapsulated phase change material slurries: Materials, heat transfer studies and applications. Renewable and Sustainable Energy Reviews 16(1),253-273.

Dyadin, Y. A.,K. A. Udachin,1984. Clathrate formation in water-peralkylonium salts systems. Journal of Inclusion Phenomena and Molecular Recognition in Chemistry 2(1-2),61-72.
Fournaison, L., J. M. Chourot,J. Guilpart,2001. Méthodes de mesure de concentration en glace. 4th workshop on ice slurries IIR-IIF, Osaka, JPN.
Fournaison, L., A. Delahaye, I. Chatti,J. P. Petitet, 2004. CO2 hydrates in refrigeration processes. Industrial & Engineering Chemistry Research 43(20), 6521-6526.
Guilpart, J., E. Stamatiou, A. Delahaye,L. Fournaison,2006. Comparison of the performance of different ice slurry types depending on the application temperature. International Journal of Refrigeration 29(5), 781-788.
Harald, M., Cabeza, L. F., 2008. Heat and cold storage with PCM, Springer.
Huang, L., M. Petermann,C. Doetsch, 2009. Evaluation of paraffin/water emulsion as a phase change slurry for cooling applications. Energy 34(9),1145-1155.
Inaba, H., S. Morita,S. Nozu,1994. Fundamental study of cold heat-storage system of o/w-type emulsion having cold latent-heat-dispersion material, Part 1. Heat Transfer Japan Research 23(3),292–312.
Inc, L. T. D.,2006. A Phase change material slurry system to decrease peak air conditioning loads, in: for C.E. Commision (Ed.) CEC-500-2006-026,. (http://www.energy.ca.gov/pier/portfolio/Content/06/EISG/A%20PCM%20Slurry%20System%20to%20Decrease.htm).
Ionescu, C., P. Haberschill, I. Kiss,A. Lallemand, 2007. Local and global heat transfer coefficients of a stabilised ice slurry in laminar and transitional flows. International Journal of Refrigeration-Revue Internationale Du Froid 30(6), 970-977.
Jeffrey, J. A.,R. K. McMullan,1967. The Clathrate Hydrates. Progress in inorganic chemistry. New York, John Wiley & Sons, Inc. 8, 43-108.
Kauffeld, M., M. Kawaji, P. W. Egolf, A. Melinder,T. W. Davies,2005. Handbook on Ice Slurries - Fundamentals and Engineering. Paris, France, IIF-IIR.
Kousksou, T., A. Jamil, T. El Rhafiki,Y. Zeraouli, 2010. Paraffin wax mixtures as phase change materials. Solar Energy Materials and Solar Cells 94(12), 2158-2165.
Lin, W., D. Dalmazzone, W. Fürst, A. Delahaye, L. Fournaison,P. Clain,2014. Thermodynamic properties of semiclathrate hydrates formed from the TBAB + TBPB + water and CO2 + TBAB + TBPB + water systems. Fluid Phase Equilibria 372(0), 63–68.
Mayoufi, N., D. Dalmazzone, A. Delahaye, P. Clain, L. Fournaison,W. Fürst, 2011. Experimental data on phase behavior of simple tetrabutylphosphonium bromide (TBPB) and mixed CO_2 + TBPB semiclathrate hydrates. Journal of Chemical & Engineering Data 56(6), 2987-2993.
Mayoufi, N., D. Dalmazzone, W. Fürst, A. Delahaye,L. Fournaison, 2010. CO_2 Enclathration in Hydrates of Peralkyl-(Ammonium/Phosphonium) Salts: Stability Conditions and Dissociation Enthalpies. Journal of Chemical & Engineering Data 55(3),1271-1275.
McClements, D. J., 2011. Edible nanoemulsions: fabrication, properties, and functional performance. Soft Matter 7(6), 2297-2316.
Melinder, A. 1997) Thermophysical Properties of Liquid Secondary Refrigerants. Paris, IIR Edition.
Morimoto, T., Y. Kawana, K. Saegusa,H. Kumano, 2019. Supercooling characteristics of phase change material particles within phase change emulsions. International Journal of Refrigeration-Revue Internationale Du Froid 99, 1-7.
Ogoshi, H., S. Takao, 2004. Air-conditioning system using clathrate hydrate slurry. JFE Technical Report 3,1-5.
Royon, L., D. Jacquier,P. Mercier, 2009. Flow investigation of phase change material (PCM) slurry as a heat transfer fluid in a closed loop system. International Journal of Energy Research 33(4), 333-341.
Schalbart, P., M. Kawaji,K. Fumoto, 2010. Formation of tetradecane nanoemulsion by low-energy emulsification methods. International Journal of Refrigeration 33(8),1612-1624.
Shao, J., J. Darkwa,G. Kokogiannakis, 2015. Review of phase change emulsions (PCMEs) and their applications in HVAC systems. Energy and Buildings 94, 200-217.
Sharma, A., V. V. Tyagi, C. R. Chen,D. Buddhi, 2009. Review on thermal energy storage with phase change materials and applications. Renewable and Sustainable Energy Reviews 13(2), 318-345.
Sloan, E. D.,1998. Clathrate hydrates of natural gases. New York, Marcel Dekker Inc.

Youssef, Z., A. Delahaye, L. Huang, F. Trinquet, L. Fournaison, C. Pollerberg,C. Doetsch, 2013. State of the art on phase change material slurries. Energy Conversion and Management 65(0),120-132.
Zhang, P., Z. W. Ma,R. Z. Wang, 2010. An overview of phase change material slurries: MPCS and CHS. Renewable and Sustainable Energy Reviews 14(2), 598-614.

Manuscript ID: 1843
DOI: 10.18462/iir.icr.2019.1843

Current status and new developments on high temperature heat pumps

Dereje S. AYOU[(a)], José Miguel CORBERÁN[(b)], Alberto CORONAS[(a)]

[(a)]CREVER-Group of Applied Thermal Engineering, Universitat Rovira i Virgili, Av. Països Catalans 26, Tarragona, Spain, e-mail: alberto.coronas@urv.cat
[(b)]IUIIE, Universitat Politècnica de València, Camino de Vera s/n, ed. 8E cubo F 5°, 46022 Valencia, Spain

ABSTRACT

This review highlights the current status and new developments on high-temperature heat pumps with heat supply temperatures above 90°C. Besides the vapor compression heat pumps, the focus of this work is on absorption heat pumps, absorption heat transformers and compression-resorption heat pumps. Moreover, recent advancements in compressor technologies and working fluids for high-temperature vapor compression heat pumps are also highlighted. A few manufacturers are available in the high-temperature heat pump market segment that can supply single-stage water/LiBr absorption heat transformer and ammonia/water compression-resorption heat pump technologies. The heating capacity range of the commercial LiBr heat transformers is from 150 to 10,000 kW, while the thermal COP is between 0.45 and 0.50 at the temperature lift of up to 50 K. The commercially available compression-resorption technology delivers heat up to 120°C, while the obtained electrical COPs are about 6.1 (at 22 K lift), 4.3 (at 65 K lift) and 2.4 (at 75 K lift). Many theoretical and experimental studies have been carried out in order to extend the limit of achievable temperature lift and COP of high-temperature heat pumps.
Keywords**:** Heat Pump; High-Temperature, Absorption, Heat Transformer, Resorption, Compression, Industrial Applications.

1. INTRODUCTION

Industries need to reduce their carbon footprints in order to meet future carbon budgets set by international agreements such as the COP 21 (the 2015 Pairs climate conference). Thus, renewable and low carbon energy will replace fossil fuel options. Heat pumps will be one key technology for such sustainable energy transition. Nowadays heat pumps have gained increasing attention not only for residential but also for industrial applications. High-temperature heat pumps (HTHPs) offer an opportunity to upgrade low-to-medium temperature heat sources to high-temperature useful heat for industrial processes. The high-temperature heat (above 100°C) can be used in steam production, district heating or re-integrated into the industrial process thereby increases the efficiency of the system/process. HTHPs find their application in various sectors of industry (e.g., chemical, beverage, and paper). There have been lots of advancements in heat pump technology at lower heat delivery temperature (< 90°C), however, much lower progress has been made at high temperatures.

HTHPs are usually mentioned in connection with industrial applications where the need for heat sources at high temperatures (> 100°C) is frequent. In several research studies, one can find references to high temperature for heat pumps for any application above 60 - 70ºC, which is the usual limit for sanitary hot water production (to inhibit the growth of Legionella bacteria). District heating systems usually operate at higher temperatures, around 80ºC (3rd Generation), but heat pumps working in such sector must produce hot water in the range 80 to 90ºC. Cleaning and some process applications also operate at this level of temperatures, slightly below 100ºC. The heat pumps producing hot water at these temperatures are already available in the market. Only a few heat pump manufacturers supply heat pumps able to produce hot water at 90°C and above (Arpagaus et al., 2018). HTHPs are referred in this paper to those supplying heat at temperatures higher than 90°C.

To date, a limited number of reviews related to HTHP have been published and are briefly reviewed as follows. Arpagaus et al. (2018) and Bamigbetan et al. (2017) reviews were dedicated to vapor compression heat pumps, while Zhang et al. (2016) considered all types of heat pump systems and technologies with emphasis on industrial applications of heat pumps in China. Moreover, Xu and Wang (2017) reviewed the current status and future development of absorption heat pumps for the reuse of waste heat by emphasizing on three main aspects of the technology including absorption cycles, working pairs, and applications.

An excellent overview on the current state of the art and technology of HTHP can be found in a recent paper of Arpagaus et al. (2018), which contains a vast amount of detailed technical and scientific information about HTHPs. They were focused on the market status of HTHPs based on closed-cycle compression heat pump technologies, performance analysis of these cycles and their suitable refrigerants. The authors considered more than 20 HTHPs from 13 manufacturers, which have been identified on the market that are able to provide the heat supply temperature of at least 90°C and maximum of 165°C. The food, paper, metal, and chemical industries are potential application areas of the HTHP technologies with heating capacity in the range of 20 kW and 20 MW, while their electrical COP values vary between 2.4 and 5.8. These heat pumps are typically based on single-stage vapor compression cycle architecture and with their modifications (inclusion of internal heat exchanger, subcooler, economizer and flash tank(for steam generation)). Also, they differ mainly in the type of compressor and refrigerant employed in the system. The main type of compressor used in such systems are twin-screw, piston, screw, and two-stage turbo machine while the refrigerants used are R245fa, R717, R744, R134a or R1234ze(E). Moreover, the refrigerants R1336mzz(Z), R718, R245fa, R1234ze(Z), R600, and R6001 were examined in detail and R1336mzz(Z) enables to achieve exceptionally high heat supply (sink) temperatures of up to 160°C.

Bamigbetan et al. (2017) review work was focused on the use of natural refrigerants (e.g., ammonia, carbon dioxide, water, butane, propane) for HTHPs. Their review has shown the different challenges for the implementation of these HTHPs such as fluid selection, component development to system optimization to mention a few, while, discussing the possible innovative solutions to address these challenges. The HTHPs with natural refrigerants have shown to be a potential environmental friendly solution with the capabilities of energy efficiency increase in industrial processes. The research advances and development in the application of industrial heat pumps in China with the emphasis on three industrial fields (drying of wastewater sludge, crude oil heating in oil field, and process heating in printing and dying) were carried out by Zhang et al. (2016). The review addresses research progresses on refrigerants and different type of systems (i.e., multi-stage, double-effect, compression-absorption, solar assisted and commercial heat pump systems). Chua et al. (2010) have reviewed heat pump systems, focusing on performance enhancement methods (e.g., multi-stage cycles), hybrid heat pump systems, and their applications in selected industries. Whereas, Arpagaus et al. (2016) were focused on the multi-temperature applications of mechanically-driven heat pumps and refrigerators. The present review article is envisioned to complete and address recent advancements on HTHP technologies that have aimed to supply heat at a temperature above 90°C. In this review, absorption heat pumps, compression-resorption heat pumps and vapor compression heat pumps for high-temperature applications are discussed with emphasis on new developments.

2. HIGH-TEMPERATURE HEAT PUMP SYSTEMS AND TECHNOLOGIES

HTHP technologies are classified into three main types; namely, vapor compression heat pump, absorption heat pump and the combination of compression and absorption technologies. In this section and subsequent sections, we focused on these technologies at high-temperature applications.

2.1. Vapor compression based heat pumping

HTHP technology based on mechanical vapor compression process is the most exhaustively studied heat pumping option, and the reader is referred to Arpagaus et al. (2018, 2016). From the thirteen manufacturers mentioned above, only two (Kobe Steel and Viking Heat Engines SA) offer HTHPs

with maximum heat supply temperature above 130°C (Arpagaus et al., 2018). The rest of the manufactures offer HTHPs with maximum heat supply temperatures between 90 and 130°C, and of which five of them only offer at 90°C. The company Kobe Steel offers an HTHP (Kobelco SGH 120) with a nominal capacity of 380 kW producing saturated steam at 120°C, from a water heat source stream from 25 to 65°C with a Coefficient of Perforformance (COP) of 3.2 at 65°C heat source temperature. This unit incorporates an especially designed two-stage screw compressor and uses R245fa as a refrigerant. Furthermore, Kobe Steel also offers a heat pump unit (Kobelco SGH165) producing steam at 165°C by using a vapor recompression process. Viking Heat Engines SA offers a heat pump (HeatBooster HBS4) able to produce hot water at temperature up to 160°C with heating capacity up to 200 kW (Viking Heat Engines, 2018). It employs an especially designed piston compressor (designed together with AVL – an engine designing company) using R245fa or R1336mzz-Z refrigerants.

2.2. Absorption based heat pumping

Absorption heat pumps (Type I Heat Pumps, AHPs) and absorption heat transformers (Type II Heat Pumps, AHTs) can be used to upgrade industrial waste/excess heat to useful temperature levels. Since the heat pumping in AHTs is a temperature increasing process, the AHTs are referred as temperature boosters. Whereas in the case of AHPs the heat pumping process is heat increasing process, hence the AHPs are referred as heat amplifiers. The AHPs require high-temperature driving-heat source (T_{dhs}) in order to upgrade the heat source at low-temperature (T_{hs}) to an intermediate useful temperature level (T_{supply}). AHTs upgrade a portion of the heat from the heat source (T_{hs}) to a higher temperature level (T_{supply}), while rejecting the rest of the heat at low temperature (T_{amb}) to the heat sink (e.g., ambient).

The most commonly employed working pairs, refrigerant/absorbent pairs, in the AHPs and AHTs are ammonia/water and water/LiBr mixtures. The single-effect AHP and AHT are the simplest/basic configurations for AHP and AHT technologies. However, the single-effect AHP and AHT are limited in the temperature lift (defined as $\Delta T_{lift} = T_{supply} - T_{hs}$). The COP of a single-effect AHP is also limited regardless of the driving-heat source temperature level. Hence, there are two ways to improve the performance of AHPs and AHTs: either to increase the efficiency of the heat pump (i.e., higher COP) or enlarge the temperature lift while maintaining the COP or with a small reduction on the COP. The multi-effect and GAX (generator-absorber heat exchange) concepts are used to enhance the energy efficiency, while the double-lift concept is used to increase the temperature lifts of AHPs and AHTs (Alefeld and Radermacher, 1994). Therefore, for instance, the double-effect AHP (DEAHP) is more energy efficient than the single-effect AHP, however, it is more appropriate for conditions where the heat source is at a high-temperature and small temperature lift is needed (Zhang et al. 2016).

2.2.1. Absorption Heat Pump

The cycle configurations of AHPs are the same as those of absorption refrigeration cycles, except that the desired outputs are different – heating in the case of the heat pump cycle while refrigeration effect for refrigeration cycles. The single-effect AHP consists of seven main components an absorber, condenser, evaporator, desorber, solution heat exchanger, solution circulation pump and expansion device. The single-effect ammonia/water AHP is not suitable for industrial heat pumping applications above 90°C with market available standard components, but it is usually used for residential heating and hot water production below 80°C. It is due to the high operating pressures at these heat supply temperatures, e.g., at temperatures higher than 95°C the corresponding pressure is above 53 bar for ammonia composition of 96% (in mass). The single-effect water/LiBr AHP is also limited in application range due to the working pair water/LiBr adverse characteristics such as crystallization, corrosion, and instability at high temperature. Hence, the heat supply temperature levels in single-effect AHP may reach approximately 100°C (Zhang et al., 2016).

The single-effect water/LiBr AHPs developed by LG Electronics (2018) are designed to supply heating up to 55 - 90°C with a heating capacity higher than 300 kW (349 to 30,218 kW). The French manufacturer CNIM provides single-effect water/LiBr AHPs with heat supply temperature 60 to 80°C at a COP of about 1.7 (CNIM, 2019). The heat source temperature is between 25 and 35°C. Hot

water, steam, gas, and hot oil can be used as a driving heat source in the range of 90 to 500°C. Two DEAHPs with a heating capacity of 150 kW has been installed at the experimental test facility of Plataforma Solar de Almería (Spain) (Alarcón-Padilla et al., 2010). This DEAHP is operated to supply hot water at about 65°C to the multi-effect desalination unit using driving steam at 150°C.
A two-stage water/LiBr absorption machine was developed by the company ENTROPIE (now CNIM). The machine can operate in two modes as a chiller and as a heat pump. When it works as double-effect chiller it is driven by heat at 170°C using natural gas boiler (at high-pressure desorber) and can take also heat at low-pressure desorber (e.g., using heat from solar thermal collectors). The machine can also work as a double-lift heat pump delivering heat at 70 - 100°C using driving hot water at 160°C with a COP of 1.3 (Figueredo, 2012).

2.2.2. Absorption Heat Transformer

The single-stage water/LiBr AHT is the most commonly investigated configuration in the literature. The technical challenges (e.g., corrosion at high temperature) associated with this system are similar to the challenges experienced in the design of double-effect water/LiBr chillers, which are dressed effectively in the manufacturing of such technology (Herold et al., 2016). The single-stage water/LiBr AHT can increase about 50% of the waste heat energy by up to 50°C (typically in the range of 30 - 40°C (Parham et al., 2014)). Hence, such systems are ideally suited to applications in which only a relatively small temperature increases are needed.

The single-stage water/LiBr AHTs from LG Electronics (2018) is designed to supply heat up to 120°C, with a heating capacity higher than 300 kW. It utilizes hot water at 70°C as a driving heat source. However, in order to obtain greater temperature lifts (above 50 K), advanced AHT cycles must be used. Using advanced AHTs with an increased number of stages decreases the quantity of energy which may be upgraded (i.e., reduced COP); but it enables higher temperature lifts to be attained. In the literature, two types of two-stage AHT cycles are often considered, which are referred as: double (lift) absorption heat transformer (DAHT) and double-stage absorption heat transformer (DSAHT) (Donnellan et al., 2015). The DAHT uses the concentrated solution coming from the desorber as the absorbent in the absorber-evaporator unit. Hence, the DSAHT has more components and needs more investment in equipment, whereas DAHT is considerably simpler than the DSAHT. Besides, for much higher temperature lifts, the triple-stage water/LiBr AHTs may be used to attain temperature lifts of up to 145 K by upgrading about 20% of the available waste heat.

2.3. Resorption based heat pumping

The resorption concept is according to two basic principles. First, the working pair is a zeotropic mixture with large boiling temperature difference (e.g., ammonia/water). Second, the condensation and evaporation processes (in the reverse Rankine cycle) are replaced by absorption (in a resorber) and desorption (in a desorber) processes, respectively. Since the evaporation of the working pair is not complete, the remaining liquid from the desorber is pumped to the resorber, which forms a solution circuit between the desorber and resorber referred as resorption circuit. There are different possibilities to combine the resorption circuit with mechanical vapour compression and solution circuit of both AHP and AHT. Therefore, the combined/hybrid heat pump types are realized, which are compression-resorption heat pump (CRHP), absorption-resorption heat pump (ARHP) and resorption-absorption heat transformer (RAHT).

The advantages of CRHP, ARHP and RAHT cycles over the individual cycles (i.e., absorption cycle and compression cycle) are, first, the reduction of high vapor pressure relative to the pure refrigerant (in the working pair). Second, the temperature glides of the absorption and desorption processes compared to isothermal condensation and evaporation processes of pure refrigerants. These infer that *(i)* – these heat pumps approach the reversible cycle (e.g., Lorenz cycle) with variable temperatures - which can result in an increased COP due to reduction of entropy generation in the non-isothermal heat addition and rejection processes, *(ii)* – they can achieve higher supply temperatures than the individual cycles at the same operating pressure, and *(iii)* – it has additional degrees of freedom for operational flexibility. Hence, the CRHPs, ARHPs, and RAHTs are appropriate technologies for high-temperature industrial process heat supply and waste/excess heat recovery as these processes often require large sink-source temperature glides.

As the CRHP is a combination of two different types of technologies, i.e., absorption and vapor compression so that the CRHP benefits from both technologies' best features. The CRHP cycle combines the advantages of the compression cycle (higher performance, i.e., higher COP) and absorption heat pump (high-temperature lifts and temperature gliding). The cycle is also known as vapor compression cycle with solution circuit (Groll, 1997); moreover, it is also referred as hybrid absorption-compression cycle in the literature (Jensen, 2016). The single-stage CRHP using an ammonia/water mixture is a promising technology for high-temperature applications using existing standard commercial components (Jensen, 2016).

In addition to single-stage CRHP cycle, there are several possibilities to combine the vapor compression (either with single or multi-stage compression processes) with advanced absorption heat pump technologies in order to improve the performance or extend operating ranges. For instance, two-stage compression with internal heat recovery CRHP (Jensen, 2016; Wersland et al., 2018) and CRHP with absorber-desorber heat exchange (Groll, 1997) have been investigated in the literature. Wersland et al. (2018) studied the performance of ammonia/water CRHP using two types of compressors: a single-stage screw compressor and two-stage piston compressor. The study was carried out at a heat source temperature of 30°C to obtain a heat at 115°C from 95°C. It was obtained a COP of 1.37 and 2.04 for screw compressor and two-stage piston compressor, respectively. Kabelac et al. (2018) investigated the performance of single-stage ammonia/water CRHP with open screw compressor using the experimental test rig built at the Institute for Thermodynamics in Leibniz Universität Hannover (Germany). They obtained a maximum of 2.5 electrical COP at the highest temperature lift of 43 K when the heat source at 59°C, and it delivers a heating output of 40 kW.

3. PERFORMANCE COMPARISON OF DIFFERENT HEAT PUMP CYCLES

For heat pumps operating at two temperature levels, such as VCHP with pure working fluids, their theoretical maximum COP (COP_{ideal}) is described by Carnot COP. The ideal COP of VCHP and CRHP are dependent only on these two temperature levels, which are represented by average entropic temperatures for heat transfer processes occurring at variable temperatures. Then, the ideal COP is defined as $COP_{ideal} = \hat{T}_{supply}/(\hat{T}_{supply} - \hat{T}_{hs})$ where $\hat{T}_{supply}$ and $\hat{T}_{hs}$ are average entropic temperatures for heat supply and heat source, respectively, at variable temperatures. However, the actual COP of the heat pump is lower than the ideal COP due to inherent internal and external irreversibilities. Hence, the second law efficiency of the heat pump ($\eta_{II,HP}$, defined as $\eta_{II,HP} = COP/COP_{ideal}$) can be used to evaluate the performance of the heat pump technology with respect to the theoretical maximum performance. It relates the COP to maximum achievable COP for finite heat reservoirs in terms of a Lorenz cycle and therefore, it gives an indication about the potential improvement possibilities. In Fig. 1 (a), the ideal COP of VCHP and CRHP cycles are shown for a temperature lift from 20 to 100 K at a heat source inlet temperature ($T_{hs,in}$) of 60, 70, 80 and 90°C.

The AHP and AHT are operating at least at three temperature levels. Hence, the ideal COP of AHP and AHT are dependent on the three temperature levels: $\hat{T}_{dhs} > \hat{T}_{supply} > \hat{T}_{hs}$ for AHP (Type I heat pump) and $\hat{T}_{supply} > \hat{T}_{hs} > \hat{T}_{cw}$ for AHT. The ideal COP of AHP and AHT are given in Eq. (1).

$$COP_{ideal,AHP} = \frac{\hat{T}_{dhs} - \hat{T}_{hs}}{\hat{T}_{dhs}} \cdot \frac{\hat{T}_{supply}}{\hat{T}_{supply} - \hat{T}_{hs}} \qquad COP_{ideal,AHT} = \frac{\hat{T}_{hs} - \hat{T}_{cw}}{\hat{T}_{hs}} \cdot \frac{\hat{T}_{supply}}{\hat{T}_{supply} - \hat{T}_{cw}} \qquad \text{Eq. (1)}$$

The ideal COPs of AHT and AHP with the driving-heat source inlet temperatures are presented in Fig. 1 (a) at different values of $T_{hs,in}$. The temperature glides in the driving-heat source, heat supply and, heat source streams were assumed as 20 K. The heat rejection stream (i.e., cooling water) inlet/outlet temperatures of the AHT was set at 30/40°C. Furthermore, the thermodynamic performance of the different types of heat pump cycles was reported at high-temperature heat supply conditions (> 90°C) and heat source temperatures. The selected heat pump cycles are single-stage water/LiBr AHT (SSAHT), double-lift AHT with water/LiBr (DAHT), ammonia/$LiNO_3$ resorption absorption heat transformer (RAHT) and ammonia/water single-stage CRHP cycle. These cycles

are relatively less complex than other advanced absorption cycle configurations (e.g., multi-stage multi-effect cycles, GAX cycles) and some of them are implemented practically. The performance and schematics of these heat pump cycles are presented in Fig. 1 (b – e).

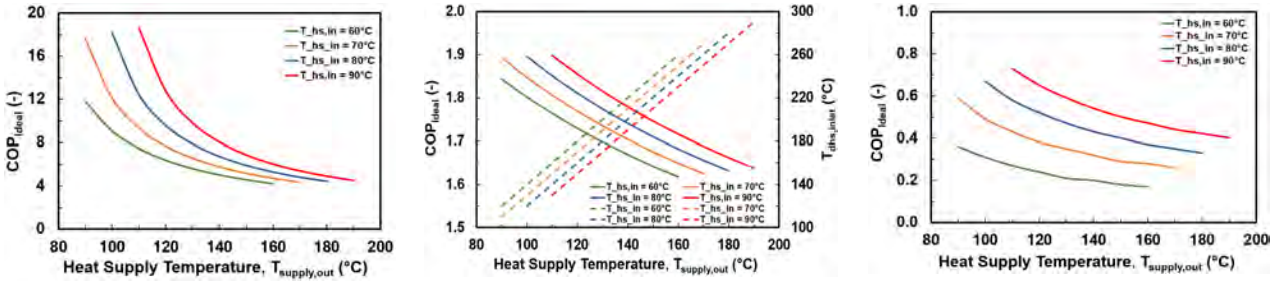

Ideal VCHP/CRHP cycle Ideal AHP cycle Ideal AHT cycle

a) Ideal maximum COP of different types of heat pump cycles with heat transfers at variable temperatures.

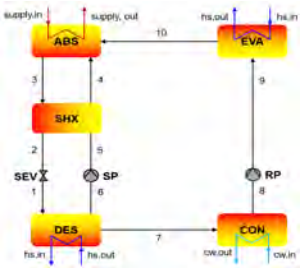

T_{supply} (°C)	130
T_{hs} (°C)	80
T_{cw} (°C)	25
ΔT_{lift} (K)	50
COP[1] (-)	0.480
$\eta_{II,HP}$ (%)	80.3

b) Single-stage water/LiBr AHT (SSAHT)

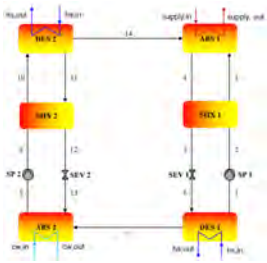

T_{supply} (°C)	120
T_{hs} (°C)	90
T_{cw} (°C)	30
ΔT_{lift} (K)	30
COP[1] (-)	0.401
$\eta_{II,HP}$ (%)	55.6

c) Single-stage ammonia/$LiNO_3$ RAHT

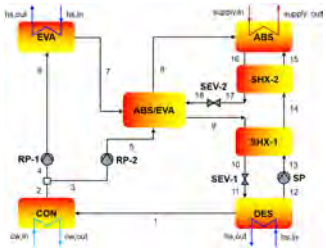

T_{supply} (°C)	160
T_{hs} (°C)	70
T_{cw} (°C)	25
ΔT_{lift} (K)	90
COP[1] (-)	0.313
$\eta_{II,HP}$ (%)	74.4

d) Double AHT with water/LiBr (DAHT)

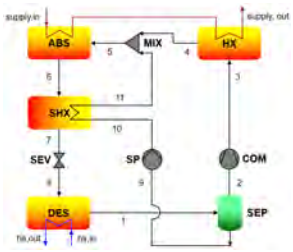

T_{supply} (°C)	100
T_{hs} (°C)	35
T_{cw} (°C)	N/A
ΔT_{lift} (K)	65
COP[2] (-)	4.3
$\eta_{II,HP}$ (%)	51.3

e) Single-stage ammonia/water CRHP

Figure 1. Performance comparison of ideal heat pump cycles, SSAHT, DAHT, RAHT and CRHP.

Note: [1] – thermal COP; [2] – electrical COP; $\eta_{II,HP}$ – second law efficiency of heat pump; N/A – Not applicable.

4. GLOBAL DEPLOYMENT OF INDUSTRIAL HTHP TECHNOLOGIES

The potential of AHT and CRHP technologies to upgrade industrial waste heat (and excess heat) to a useful temperature level (> 90°C) have been implemented in several industrial applications. In Table 1, some of these HTHP industrial deployments are presented. However, limited high-temperature industrial applications are available for AHPs. For instance, the single-effect water/LiBr AHP with a heating capacity of 7.5 MW is installed at the Schweighofer Fibre GmbH (Austria) (IEA, 2014a). It is used to recover waste heat (below 50°C) from the flue gas of the biogas plant and delivered the heat at 95°C. Steam at 165°C from the biomass plant is utilized to drive the AHP. The average COP about 1.6 was achieved for a total operation hour of 37,000 h per annum.

Thermax Ltd (2018) has developed single-stage water/LiBr AHT with heating capacities between 500 and 10,000 kW. They can supply heat at a maximum temperature of 160°C, typically with a temperature lift of 50 K. The COPs are in the range of 0.45 to 0.5. Steam condensate (e.g. from steam turbine), hot water, process condensate between 80 and 150°C are used as a heat source, which either supplied individually or in combination. Thermax single-stage water/LiBr AHT type (shown in Fig. 2(a)) has been used in a poly film manufacturing plant for PV cells. The part of the heat rejected in the cooling process was utilized, by using the single-stage water/LiBr AHT, to generate steam at 4 bar which finds use within the plant. The schematic of the heat recovery process is depicted in Fig. 2(b). Moreover, Thermax single-stage water/LiBr AHTs have been implemented

in food industries in Italy and Germany (Table 1). The AHTs are used to produce hot water at 135°C for drying process of pasta making in the Baronia Pasta Factory (Italy) while hot water produced at 105°C is utilized for vegetable cooling in the pre-cooked meal production process in Renken (Germany). In both cases, hot water at 93°C and 90°C, respectively, from engine jacket water are used as a heat source.

Table 1: Worldwide deployment of absorption heat transformer (AHT) and compression-resorption heat pump (CRHP) technologies for high-temperature (> 90°C) industrial applications.

Company Name (Country)	Manufacturer	Cycle Type	Working Pair	Temperature, T (°C)			Heating Capacity (kW)	COP (-)
				$T_{hs,in/out}$	$T_{cw,in/out}$	$T_{SINK,in/out}$ (ΔT_{lift})		
Asia Silicon Co. Ltd (China)	Thermax Ltd	Single-stage AHT	H_2O/LiBr	108/100	28/38.5	152/157 (49)	~4189	0.47[1]
Baronia Pasta (Italy)	Thermax Ltd	Single-stage AHT	H_2O/LiBr	93/75	N/R	125/135 (60)	~1202	0.46[1]
Renken Germany (Germany)	Thermax Ltd	Single-stage AHT	H2O/LiBr	90/80	N/R	95/105 (15)	~449	0.47[1]
Borregaard ASA (Norway)	Hybrid Energy AS	Single-stage CRHP	NH_3/H_2O	73/46	N/A	70/95 (22)	2000	6.1[2]
Frevar (Norway)	Hybrid Energy AS	Two-stage CRHP	NH_3/H_2O	20/14	N/A	75/95 (75)	800	2.4[2]
Løgumkloster District Heating plant (Denmark)	Hybrid Energy AS	CRHP	NH_3/H_2O	35/17	N/A	35/100 (65)	1300	4.3[2]
Alcohol Industry (Japan)	Johnson Controls HITACHI	Single-stage AHT	H2O/LiBr	N/R	N/R	107/112 (N/R)	2,475	N/R
Not Provided (N/R)	Johnson Controls HITACHI	Single-stage AHT	H_2O/LiBr	90/85	N/R	135/140 (50)	300	0.45[1]
Machinery (N/R)	Johnson Controls HITACHI	Single-stage AHT	H_2O/LiBr	90/85	27/31	133/137 (47)	150	N/R

Note: [1] – Thermal COP; [2] – Electrical COP; cw – Cooling water; hs – Heat source; ΔT_{lift} – Temperature difference between heat sink outlet and heat source inlet (Jensen, 2016); N/A – Not applicable; N/R – Not reported.

Johnson Controls–Hitachi Air Conditioning Solutions offers single-stage water/LiBr AHT with a heating capacity from 150 to 2,475 kW and supply temperature of 70 to 140°C. The AHT uses waste heat, below 100°C, of jacket water of cooled engines, waste heat from industrial processes and distillation units, while rejecting heat at low temperature, e.g. 30°C, to cooling water, underground water or recovery cooling water. A typical example of a single-stage water/LiBr AHT of this manufacturer is used to recover heat of 90°C from hot water of co-generation system to produce steam at 2 bar or deliver hot water at 140°C with heating capacity of 300 kW and COP of 0.45. At the synthetic rubber plant of the Yanshan Petrochemical Corporation (China), an industrial-scale 5 MW single-stage water/LiBr AHT was installed and later expanded to include two other sets of similar AHT with heating capacity of 7 MW (Ma et al., 2003; Zhang et al., 2016). The heat supplied by the AHTs were used to heat hot water for 95 to 110°C, with an average COP of 0.47 and maximum temperature lift of 25 K. The AHTs are used to recover waste heat from steam and organic vapor mixture at 98°C.

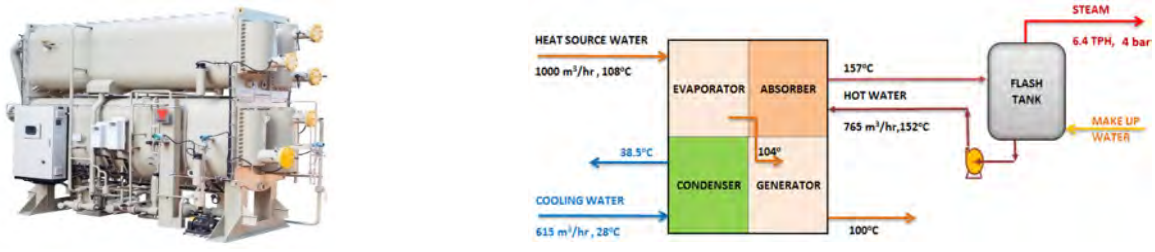

(a) (b)

Figure 2. Single-stage water/LiBr absorption heat transformer installed in poly film manufacturing plant in China (Thermax Global, 2018). Courtesy of Thermax.

The CRHP working with ammonia/water mixture is developed by Hybrid Energy AS (2018). The technology is commercialized by the company for high-temperature industrial heat pumping

applications, with the first commissioning in 2004. It provides heat at temperatures above 110°C by recovering waste/excess heat between 15°C and 65°C using standard refrigeration components (operating below 25 bar). The single-stage CRHP from the Hybrid Energy AS is designed for pre-heating of feed water in Bio-refinery process plant in Borregaard (Norway) and commissioned in 2017. The system has reduced the plant's energy consumption approximately by 60 GWh/year. In 2016, the wastewater and sewage treatment plant of Frevar, in Fredrikstad (Norway), used a two-stage ammonia/water CRHP to recover heat from biogas upgrading plant and treated wastewater. The heat delivered to the central heating system of the plant and, then the hot water (at 95°C) is utilized for industrial processes including preheating of sludge and heating buildings. Løgumkloster district heating plant in Denmark installed the CRHP from Hybrid Energy AS in 2015. The CRHP recovers heat at low temperature (35°C) from concentrated solar power facility and supplies the upgraded heat (from 35 to 100°C) to the district heating network. This heat pump simultaneously provides chilled water at 17°C to processes need cooling in the solar facility.

5. CHALLENGES AND OPPORTUNITIES FOR FUTURE INDUSTRIAL APPLICATIONS

5.1. High-temperature heat pumping challenges

5.1.1. Working fluids

Many pure working fluids have been considered for HTHPs based on vapor compression cycles (Arpagaus et al., 2018). As in other heat pumps (e.g., heat pumps for residential applications), the most important characteristics of the fluids to be considered are the critical temperature and pressure and its volumetric heat capacity at the heat source temperature. Additionally, dry fluids (Retrograde) will need an extra superheat at the evaporator, whereas wet fluids (Anterograde) will tend to produce very high discharge temperatures which could negatively affect the reliability of the compressor. The global warming potential (GWP) and ozone depletion potential (ODP) of the fluids are also important characteristics to be considered for future equipment.

Fig. 3 shows the critical temperature of most employed working fluids with an indication of the kind of fluid they are. The bars, in Fig. 3, connect the NBP (normal boiling point) with the critical temperature of each fluid. One line has been drawn at 150°C just as a reference. As it can be observed in Fig. 3, only a few fluids would be available to work in a subcritical cycle with sink temperatures about 150°C, i.e., R1233zd(E), R365mfc, R1336mzz(Z), pentane, acetone and of course water. Water is maybe an adequate fluid for very high-temperature heat pumping applications, but for the analysed range it still has very low vapor pressure and its compression is very difficult with commercially available compressor technologies. R365mfc is an HFC and has a relatively high GWP (804) and it is an A2 fluid. R1233zd (E) is an HCFO while R1336mzz (Z) is an HFO, both with a very low GWP and with almost null ODP, and they are A1 fluid. Pentane is an HC and so an A3 fluid. High-pressure fluids could work in a transcritical cycle. This would have the advantage of the high glide of the temperature of the fluid along the gas-cooler to match the increase of temperature of the secondary fluid on the sink side. Also, however, sub-critical cycles can exploit this glide by producing a high subcooling.

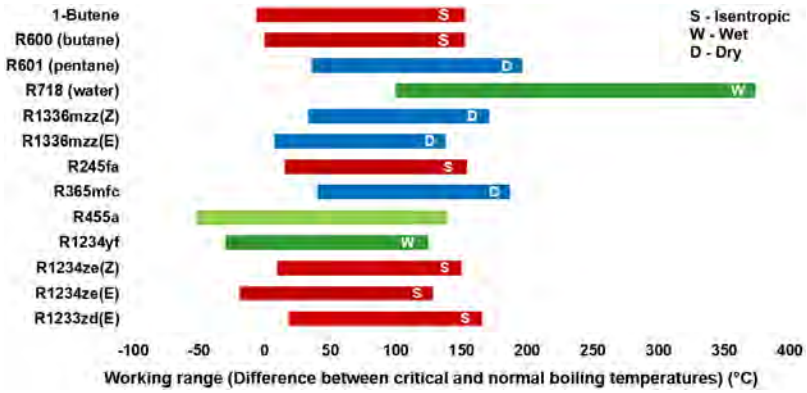

Figure 3. Working range of mostly used working fluids: dry, wet and isentropic working fluids.

One of the main advantages of AHP, AHT, and CRHP technologies is the use of natural working pairs (e.g., ammonia/water, ammonia/$LiNO_3$, water/LiBr. However, these mixtures have their own

drawbacks. The use of ammonia/water mixture in AHP and AHT for high-temperature applications (> 90°C) has an effect of operating at high pressure. The use of water/LiBr limits the temperature lift because of the crystallization potential of LiBr when the temperature drops or LiBr composition increases, while higher heat supply temperatures are restricted due to corrosion and instability of the working pair at high temperature. The solubility of LiBr can be enhanced using additives (e.g., inorganic salts, solvents, ionic liquids). However, it may have an adverse effect on other properties of the mixture such as viscosity, vapor pressure, corrosiveness, etc. Besides its effect on the application ranges, the working pairs can significantly influence the initial capital cost of the unit and dictate required maintenance operations. Therefore, the selection of the working pair is a crucial aspect to be considered for the selection of AHPs and AHTs.

5.1.2. System components

The main challenge of HTHPs based on VCHP and CRHP cycles is the compressor technology. The average and discharge temperatures in this type of HTHP are very high, so all technologies involving potential wearing need to find reliable lubrication warranting a sufficiently long life. Compressors requiring no lubrication would be in principle the most adequate technology. Apart from the lubrication, the electric motor must be also quite special since the high operating temperatures at the evaporator lead to high mass flow rates and high torques. Therefore, the motor required for this application is much larger than the one corresponding to a similar displacement compressor for standard applications. Additionally, the cooling of the motor and the oil is difficult to do with high suction temperatures in hermetic or semi-hermetic compressors. Therefore, the best compressor technology for HTHPs would be turbocompressors. However, the design of these compressors must be specifically done depending on the refrigerant fluid and the operating conditions. Their development is cumbersome and very costly. As each industrial application is different, it is difficult to find cost-effective solutions with this technology except for applications with a large potential market and similar conditions.

Most of the HTHP prototypes that have been tested at high temperatures are working with piston compressors and a few with screw compressors. Électricité de France (EDF) presented an experimental study about an HTHP using a scroll compressor and a new fluid named as ECO3 (IEA, 2014b). This heat pump was able to reach 138°C of condensation temperature with an evaporation temperature of 60°C. The Austrian Institute of Technology (AIT) also reached high temperatures with a 12 kW semihermetic piston compressor working with refrigerant R1336mzz-Z (IEA, 2014b). The condensation temperature is 125°C with a temperature lift of 70 K. Recently, the Norwegian University of Science and Technology (NTNU) and SINTEF investigated an HTHP with semihermetic piston compressor using butene as a refrigerant. The condensation and evaporation temperatures are 115°C and 50°C, respectively, while the compressor discharge temperature is 140°C. Therefore, the maximum attained condensation temperature using volumetric compressors seems to be 125 – 135°C for the moment. The actual efficiency of the compressors at these extreme conditions is relatively low and the reported values of the COP are below 3.0, with about 70 K temperature lift and the highest condensation temperatures. Comparing these COP values with the 50% of ideal (reversible) COP values (i.e., estimated as attainable values) shown in Fig. 1 (a), there is still a significant high margin for improvement. A double-lift water/LiBr AHT was developed and experimentally tested to demonstrate its applicability for steam generation at 8 bar with a lift of about 90 K. This DAHT development was carried out under the research project “Next Generation Heat Pump Technology” supported by NEDO (New Energy and Industrial Technology Development Organization), Ebara Refrigeration Equipment & System Co.Ltd and Waseda University in Japan (Lubis et al., 2017). The authors demonstrated that the technical challenges related to corrosion and crystallization, particularly at high-temperature absorber, was handled well. Thereby, the DAHT system operates steadily and efficiently (at a COP of exceeds 0.3 for a heat source temperature of 84°C). Furthermore, a surfactant additive (2-Ethylhexanol) was used to enhance heat transfer rates. In addition, the European project Indus3Es (2016 – 2020) is developing an AHT for upgrading industrial surplus heat available at low temperature to a useful level below 130°C, depending on the ambient temperature. In this project, two 10 kW lab-scale prototypes and five 50 kW capacity have been tested with the final aim of designing a machine that revalorizes about 200 kW of waste heat from 95 to 135ºC.

5.2. Future opportunities and outlooks

Despite the challenges mentioned above, the opportunities for primary energy savings and reduction of greenhouse gas emissions will continue to build high interest in HTHP applications. Furthermore, there is a necessity to move to low carbon energy solutions and the use of natural refrigerants. It is due to fossil fuel supply depletion, the fuel penalty imposed by governments, and the banning of refrigerants with high GWP and ODP by international agreements. The use of HTHPs as stepping stones towards the replacement of boilers and steam systems, which generates potentially much greater savings where the existing systems have low efficiency. As conventional energy costs are increasing because of imposed legislation by governments, industrial payback period values are easily attainable. Therefore, the need for research and development of HTHP's potential for energy conservation and reduction of CO_2 emissions is enormous.

In the VCHP technology, the main focuses on the R&D fronts are on the working fluids employed in the system and compressor technologies for high-temperature applications. Corberán et al. (2019) studied the performance of an HTHP based on vapor compression cycles for industrial applications, which needs pressurized hot water (> 100°C) and saturated steam or for high-temperature thermal storage applications. They analysed the performance of the HTHP using dry (R1336mzz(Z), R365mfc), wet (water, acetone) and isentropic (R1233zd(E), R245fa, butene) refrigerants. According to their simulation results, the isentropic refrigerants have the highest performance compared to dry and wet refrigerants. From these candidate refrigerants, R1233zd(E) is the most suitable refrigerant regarding safety and performance. However, it reaches a maximum temperature lift of 73 K and acetone seems to be a good candidate for high-temperature lifts. There are two possible R&D directions in order to address the downsides of the conventional working pairs used in the AHP and AHT technologies. They are *(i)* - altering undesirable characteristics of the working pairs and *(ii)* – to identify new working pairs so that to replace the conventional working pairs. Consequently, the temperature lift and the heat supply temperature of the water/LiBr AHT and AHP could be enlarged using additives (e.g., other inorganic salts, solvents, ionic liquids) to increase the solubility of LiBr and reduce corrosion. Another approach is to select other absorbents (e.g., ionic liquids, organic fluids) for natural refrigerants such as ammonia, water, and carbon dioxide.

The CRHPs using wet compression has been considered in the literature due to its promising advantages (Gudjonsdottir et al., 2018). The benefits of wet compression include reduction of consumed power compared to VCHPs and avoid vapor superheating, which is particularly attractive for high-temperature applications. And, the solution pump is not needed. The COP of CRHP with ammonia/water mixture can be increased by above 15% due to the use of wet compression.

As highlighted in the literature, the use of AHTs has several advantages from a thermodynamic viewpoint. However, the economic feasibility of AHTs has not been yet sufficiently reported. Regardless of the amount of heat upgraded by the AHT, unless the AHTs can generate adequate returns on investment so that acceptable short payback periods are obtained, they are unlikely targets for investment. This is mainly due to the system CAPX (capital expenditure). Therefore, more efficient component types should be pursued which can reduce the capital costs of AHTs. Moreover, the price of utilities for example electricity is also extremely influential for economic viability.

The subject of HTHPs has attracted the interest of researchers and companies in the last decade and a considerable number of research projects have been carried out with the aim of developing solutions and assessing the potential performance of these HTHPs. This subject was specifically dealt with in the IEA Annex 35 (IEA, 2014b) dedicated to industrial heat pumps, and it is being currently continued by Annex 48 (IEA, 2016 - 2019). Several recent conferences have included this subject among their topics, and some have organized specific workshops. Among those, it is worth mentioning the Workshop 'Heating and Power from Low-Temperature Heat' in the ICR conference in Yokohama in 2015, the 12th IEA Heat Pump conference, held in Rotterdam in 2017, and the International Workshop on High-Temperature Heat Pumps, held in Copenhagen in September 2017.

6. CONCLUDING REMARKS

High-temperature heat pumps (HTHPs) are regarded as a viable and attractive solution to upgrade low-to-medium temperature industrial waste/excess heat to a useful temperature level for many industrial processes. It can be implemented in a wide range of industries as heat recovery solutions, including beverage, chemical, food, paper, leather, and textile industries. Furthermore, there are ongoing research and development activities to fully utilize the heat recovery potential of HTHPs at a heat supply temperature above 90°C. This paper has reviewed the current status and developments on HTHPs for industrial applications at delivery temperatures above 90°C. Apart from the vapor compression heat pumps (VCHPs), there are different types of heat pump technologies commercially available for high-temperature applications. The technologies are mainly absorption heat transformer (AHT) and compression-resorption heat pump (CRHP). These technologies use natural working fluid mixtures, e.g., ammonia/water and water/LiBr, which have no GWP and ODP.

The market available HTHPs based on absorption technology are mostly the single-stage water/LiBr AHT with heating capacity between 150 and 10,000 kW. The thermal COPs are in the range of 0.45 to 0.5. The heat supply temperature of these heat pumps can reach up to 160°C with a temperature lift of up to 50 K. A few heat pump applications are available for high-temperature heat supply, between 90 and 100°C, using single-effect water/LiBr AH, while there is no ammonia/water single-effect AHP for supply temperature higher than 90°C due to high operating pressure to use standard components. The current technology based on ammonia/water CRHP delivers heat up to 120°C. The obtained electrical COPs of the CRHP technology are about 2.4 (at 75 K lift), 4.3 (at 65 K lift) and 6.1 (at 22 K lift). The theoretical and experimental studies carried out by several researchers in the literature have shown that higher temperature lift (above 85 K) could be obtained using double-lift water/LiBr AHT with a potential of converting more than 30% of industrial waste/excess heat at alow-to-medium temperatures to a useful high-temperature level.

Finally, there is a strong potential for AHT and CRHP technologies for high-temperature lift and heat supply temperature above 160°C, which is the current limit for VCHP technology. Therefore, in order to capitalize these potentials, future research and development activities are mainly directed towards the following areas: *(i)* – on working fluid pairs to alleviate the drawbacks of the conventional working fluid mixtures, *(ii)* – system components size reduction so that the size and capital cost of the heat pump reduced, and *(iii)* – system (cycle) configurations to obtain higher temperature lift than the single-stage AHT, while maintaining the COP or with reasonable lower COP values.

ACKNOWLEDGMENTS

Dereje S. Ayou gratefully acknowledges the Martí-Franquès postdoctoral fellowship (2017PMF-POST2). Authors are grateful for financial support to FEDER/EU and MINECO (DPI2015-71306-R).

REFERENCES

Alarcón-Padilla, D.C., García-Rodríguez, L., Blanco-Gálvez, J., 2010. Design recommendations for a multi-effect distillation plant connected to a double-effect absorption heat pump: A solar desalination case study. Desalination 262, 11–14.

Alefeld, G., Radermacher, R., 1994. Heat conversion systems. CRC Press, Inc.

Arpagaus, C., Bless, F., Schiffmann, J., Bertsch, S.S., 2016. Multi-temperature heat pumps: A literature review. Int. J. Refrig. 69, 437–465.

Arpagaus, C., Bless, F., Uhlmann, M., Schiffmann, J., Bertsch, S.S., 2018. High temperature heat pumps: Market overview, state of the art, research status, refrigerants, and application potentials. Energy 152, 985–1010.

Bamigbetan, O., Eikevik, T.M., Nekså, P., Bantle, M., 2017. Review of vapour compression heat pumps for high temperature heating using natural working fluids. Int. J. Refrig. 80, 197–211.

CNIM, 2018. <https://cnim.com/en/businesses/energy-management-and-efficiency/our-references>

Chua, K.J., Chou, S.K., Yang, W.M., 2010. Advances in heat pump systems: A review. Appl. Energy 87, 3611–3624.

Corberán, J.M., Hassan, A.H., Payá-Herrero, J., 2019. Thermodynamic analysis and selection of refrigerants for high-temperature heat pumps, in: 25th IIR International Congress of Refrigeration. Montreal [to be presented].

Donnellan, P., Cronin, K., Byrne, E., 2015. Recycling waste heat energy using vapour absorption heat transformers: A review. Renew. Sustain. Energy Rev. 42, 1290–1304.

Figueredo, G.R., 2012. Caracterización Experimental y Modelización de una Enfriadora de Absorción de Simple/Doble Efecto de H2O/LiBr con Accionamiento a dos Temperaturas para Climatización de Edificios. PhD thesis (in Spanish), Universitat Rovira i Virgili, Spain.

Groll, E.A., 1997. Modeling of absorption/compression cycles using working pair carbon dioxide/acetone. ASHRAE Trans. 103, 863–872.

Gudjonsdottir, V., Infante Ferreira, C.A., Goethals, A., Kiss, A.A., 2018. Measures to minimize entropy production in compression-resorption heat pumps, in: 13th IIR Gustav Lorentzen Conference on Natural Refrigerants, Valencia (Spain).

Herold, K.E., Radermacher, R., Klein, S.A., 2016. Absorption Chillers and Heat Pumps, 2nd ed. CRC Press, Inc.

Hitachi Johnson Controls, 2018. <https://www.jci-hitachi.com/products/chiller/cogene/1121.html>.

Hybrid Energy AS, 2018. <https://www.hybridenergy.no/reference-plants/>.

IEA, 2016 - 2019. Industrial Heat Pumps, Second Phase Annex 48.

IEA, 2014a. Application of Industrial Heat Pumps, Final Report, Part 1, Report no. HPP-AN35-1.

IEA, 2014b. Applications of industrial heat pumps, IEA heat pump program Annex 35/13.

Indus3Es European Project, 2016 - 2020. <http://www.indus3es.eu/>.

Jensen, J.K., 2016. A numerical study of the ammonia-water hybrid absorption-compression heat pump. Ph.D. Thesis, Technical University of Denmark (DTU), Denmark.

Kabelac, S., Hartmann, K., Kruse, H., Tokan, T., Loth, M., Stegmann, J., Markmann, B., 2018. Experimental results of an absorption-compression heat pump using the working fluid ammonia/water for heat recovery in industrial processes. Int. J. Refrig. 99, 59–68.

LG, 2018. <https://www.lg.com/global/business/air solution/chiller/absorption-heat-pump>.

Lubis, A., Giannetti, N., Yamaguchi, S., Saito, K., Inoue, N., 2017. Experimental performance of a double-lift absorption heat transformer for manufacturing-process steam generation. Energy Convers. Manag. 148, 267–278.

Ma, X., Chen, J., Li, S., Sha, Q., Liang, A., Li, W., Zhang, J., Zheng, G., Feng, Z., 2003. Application of absorption heat transformer to recover waste heat from a synthetic rubber plant. Appl. Therm. Eng. 23, 797–806.

Parham, K., Khamooshi, M., Tematio, D.B.K., Yari, M., Atikol, U., 2014. Absorption heat transformers - A comprehensive review. Renew. Sustain. Energy Rev. 34, 430–452.

Thermax Global, 2018. <https://www.thermaxglobal.com/thermax-absorption-cooling-systems/heat-transformer/>.

Viking Heat Engines, 2018. <http://www.vikingheatengines.com/upl/files/146955>.

Wersland, M.B., Eikevik, T., Tolstorebrov, I., 2018. Investigation of a Hybrid Compression Absorption Heat Pump, 13th IIR Gustav Lorentzen Conference on Natural Refrigerants..

Xu, Z., Wang, R., 2017. Absorption heat pump for waste heat reuse: current states and future development. Front. Energy 11, 414–436.

Zhang, J., Zhang, H.H., He, Y.L., Tao, W.Q., 2016. A comprehensive review on advances and applications of industrial heat pumps based on the practices in China. Appl. Energy 178, 800–825.

Manuscript ID: 1846
DOI: 10.18462/iir.icr.2019.1846

Renewable energy technologies in air conditioning: State of the art and perspectives

Renato LAZZARIN

Department of Management and Engineering – University of Padova
Vicenza, 36100, Italy, renato@gest.unipd.it

ABSTRACT

An increasing demand for space cooling is expected due to the economic growth in developing countries (often with hot climates), to the increasing use of electric appliances in homes and offices that increase internal gains and to the global warming.
Just global warming suggests to provide larger fractions of space cooling using renewable energy technologies.
A first rough classification considers passive (or almost passive) and active technologies. The former include evaporative cooling, radiative cooling, natural ventilation, the use of aquifers or of the ground. The latter mean mainly solar cooling, but also cooling using biomass, considering renewable technologies for air conditioning only when the renewable energy is directly applied to the cooling plant and not for producing electricity for the grid. The technologies are often well experimented and some of them are approaching or even reached the economic parity with the conventional air conditioning systems.
Keywords: Air conditioning; Solar cooling; Evaporative cooling; Radiative cooling; Natural ventilation

1. INTRODUCTION

Space heating and cooling represents a large proportion of global energy demand. Buildings are considered responsible for about 30-45% of the demand with different percentages from country to country (Santamouris and Kolokotsa, 2013). The energy demand for space heating is currently greater than the energy required for space cooling. However extensive applications of insulation and advanced heating technology (from condensing boilers to heat pumps) are reducing the energy demand for heating, at least in the developed world. On the contrary the energy demand for space cooling is forecast to increase dramatically in the next years.
The reasons are many:

- Higher comfort standards will be requested in developing countries as their income is growing. Climate is frequently hot in those countries.
- The use of electric appliances in homes and offices together with other plug loads is rapidly increasing, producing internal heat gains, whose importance is higher when the building is well insulated.
- Modern architecture, that is widespread in every country, is largely using glass, emphasizing the loads due to the incoming solar radiation.
- Heat island effect with the related temperature increase in the urban environment produces a high penetration of air conditioning.
- Global warming can only make this picture worse.

This increasing air conditioning penetration produces important consequences on the energy consumption of buildings with a strong impact on the peak electricity demand. As a consequence utilities shall build up new power plants. The forecast for 2030 in India indicates an extra peak electricity demand of 143 GW (Santamouris, 2016). This additional capacity could require more than 300 new coal fired 500 MW power plants. The combined effects of global warming, income growth and population increase might double the energy use for space cooling in the next 20 years. The IEA forecast indicates a growing of energy demand for space cooling from 87 Mtoe in 2012 to more than 200 in 2050 (IEA, 2012).
Renewable energy technologies can satisfy a relevant fraction of the increasing cooling demand, particularly where solar radiation is abundant, being at the same time one of the main items of the

cooling request. The available technologies are countless. However only few of them have practical applications, finding often utilization only in special climate and ambient conditions.
A first natural technologies classification may be proposed:

- Passive (or almost passive) technologies.
- Active technologies.

2. PASSIVE TECHNOLOGIES

Passive cooling concerns different possible actions that include prevention of heat gains, reduction of heat gains and heat dissipation. The first two measures will not be here considered: they range from solar shielding to green roofs to more efficient lighting and they often involve the architect's ability in a proper building design.
Heat dissipation technology is aimed to exchange the excess heat of a building with a lower temperature sink, like the sky, the ground, the water or the ambient air. The requirements are (Santamouris and Kolokotsa, 2013):

- The existence of an environmental heat sink with a suitable temperature difference with the heat to be dissipated;
- A thermal coupling between the building and the sink.

The heat dissipation processes here considered are:

- Radiative cooling toward the sky.
- Night ventilation cooling.
- Coupling of the room to be cooled with the ground or an aquifer.
- Evaporative cooling.

2.1. Radiative cooling toward the sky

The atmosphere absorbs most of the infrared radiation emitted by the earth. The absorption is mainly due to water vapor, carbon dioxide and ozone. However these gases present a very weak absorption band in the 8-12 μm interval: this interval is called "atmospheric or sky window" through which the earth sees almost directly the chill sky with a downward emission from high altitudes where the temperature can be up to 50 K below the ambient temperature (Zeyghami et al., 2018). The cooling is particularly effective for clear sky and a dry atmosphere, whereas a cloudy sky is practically opaque to infrared radiation and radiative cooling is almost negligible.
Under the most favorable conditions the net thermal exchange between a horizontal black surface exposed to a nocturnal sky and kept at ambient temperature is of the order of 100 Wm^{-2}. Nocturnal cooling is mainly due to radiative cooling. In ancient Iran and India this effect allowed to make ice even for ambient temperature higher than 0 °C. Radiative cooling toward the sky is present also during daytime, but the incident solar radiation prevails.
When the temperature of a surface to be cooled is higher than the air temperature, radiative cooling strongly enhances the thermal dissipation. On the contrary for sub-ambient temperatures thermal gains from convection and conduction set to zero the possible dissipation already for differences of 5-6 °C. Two possible strategies were conceived to remediate:

- A wind cover.
- A selective radiator.

A wind cover reduces the convective heat transfer from the air to the emitting surface. It should be transparent in the infrared. For example a sheet of polyethylene is low cost and presents a 0.85 transmission in the infrared. Experimental surveys demonstrated a net exchange of 40-50 Wm^{-2} for a 5 °C cooling below ambient temperature even with high air humidity (Lazzarin, 1979).
An ideal selective radiator is highly reflective outside the sky window whereas is highly absorptive inside. It is possible to approach this behavior with suitable coatings of the surface to be cooled. This strategy is preferable when a greater sub-ambient temperature is desired, whereas a not selective emitter is better for maximum cooling just below and above the ambient temperature (Lu et al., 2016).
As previously mentioned the radiative cooling effect is operative even during daytime. Some researchers developed selective surfaces able to reflect 97% of the incident sunlight maintaining the desired selective properties inside the sky window. Exposed to direct solar radiation of 850 Wm^{-2} intensity, this special cooler maintained a cooling power of 40 Wm^{-2} at ambient temperature (Raman et al., 2014). However these surfaces are manufactured with non-fabrication techniques which are at present very expensive.
I like to close the presentation of radiative cooling effect proposing two different application schemes (figure 1).

The first sketches an ancient building with an enclosed courtyard, for example a Roman villa (Trombe, 1967), while the other represents a possible hybrid system that combines the nocturnal radiative cooling and a conventional chiller (Zhang and Niu, 2012). The Authors evaluated a possible energy saving between 62% and 77% with respect to the only conventional chiller in two Chinese cities with a dry climate and low nocturnal ambient temperatures.

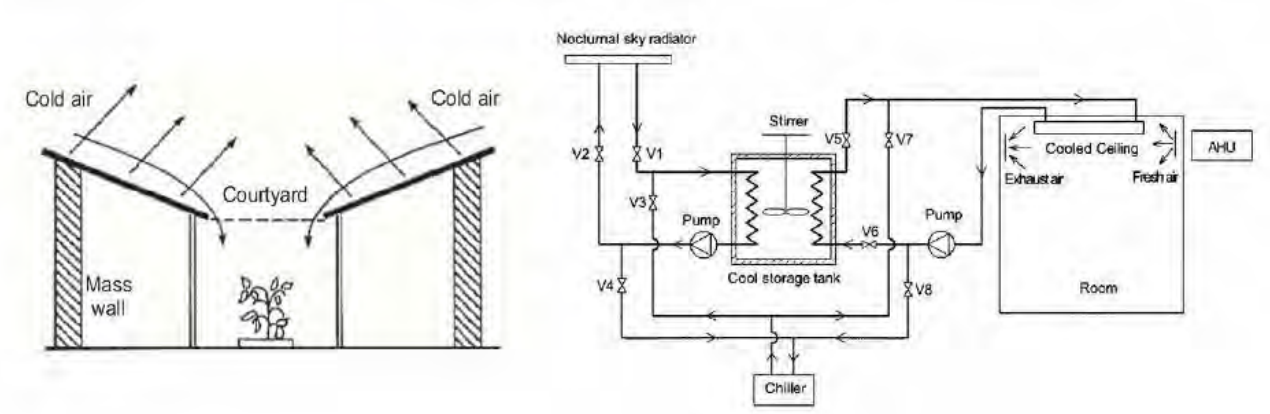

Figure 1 Schematic of an ancient building with a central courtyard and a modern hybrid nocturnal radiator-conventional system

2.2. Night ventilation cooling

During the night period the ambient air usually cools down mainly just for the effect of the radiative cooling. Thus night ventilation allows to dissipate the heat gains absorbed by the building during the daytime. Outdoor nocturnal air is introduced into the building as to cool down the building structure, exhausting the inside warmer air. The building can be equipped with a ventilation system so that the air is forced inside through the Air Handling Unit (AHU) or the ventilation can be driven by a natural force, for example by a stack or wind pressure difference. Night ventilation cooling can be applied in office buildings where the utilization is almost exclusively in the daytime.

The cooling potential is strongly influenced by the thermal excursion between day and night, by the air flow rate and by the thermal capacity of the building. As illustrated in figure 2, a thermal mass realized by concrete slabs, heavy weight mass walls or Phase Change Materials (PCM) incorporated in the building structure smooth the daytime load due to solar radiation and store the cooling effect of nocturnal ventilation.

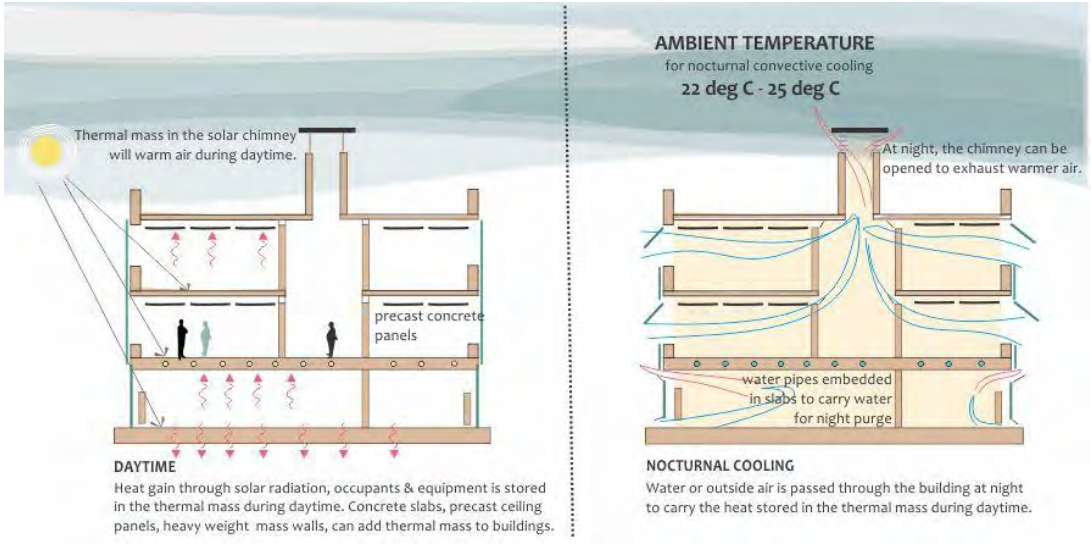

Figure 2 – Operation day/night of a building that exploits nocturnal cooling driven by natural forces (Web ref., Jan. 2019)

2.3. Coupling of the room to be cooled with the ground or an aquifer

Below 2-3 m deep the ground has an almost constant temperature during the year and well lower than the summer air temperature. Aquifers present a similar behavior. The coupling of the building with the ground is usually obtained through buried pipes (figure 3). The cooling effect is influenced by many parameters, besides obviously the geographical location, the depth of the pipes, the length, the pipe radius, the air velocity. A peak cooling capacity is estimated at 45 Wm^{-2} of pipe area with a seasonal energy performance of about 10 $kWhm^{-2}$.

If an aquifer is available heat dissipation can be more effective. Two wells must be drilled: one for withdrawal and the other for reinjection at a proper distance one from another as to avoid a possible detrimental mixing (figure 4). The aquifer temperature is often between 10 and 15 °C: then it can be useful both for cooling but also for a winter preheating. Even if ground and aquifer are mostly used with heat pumps, direct use for cooling and preheating is encountered. For example at Groene Hart Hospital in the Dutch city of Gouda two wells spaced 150 m from each other supply 60 m^3h^{-1} of water at a summer temperature between 8 and 12 °C which is reinjected at about 17 °C. In winter the availability from the previous reinjection well at about 15 °C allows an air preheating with the water reinjected at 7 °C. Of course the system presents an energy cost for lift and circulation pumps: for the just described plant the average seasonal COP is claimed at 13.5.

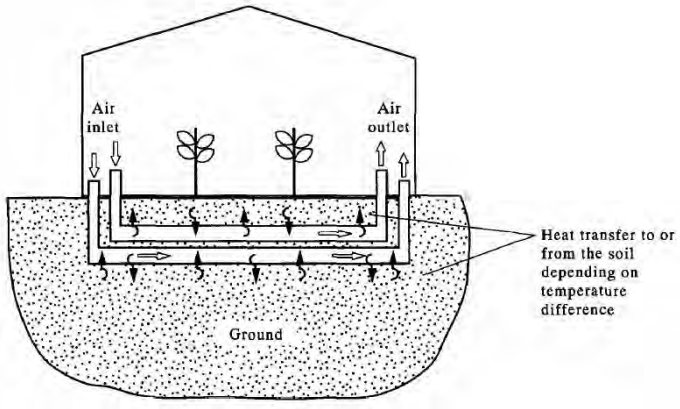

Figure 3 – Use of buried pipes in cooling of a greenhouse (Santamouris et al. 1995)

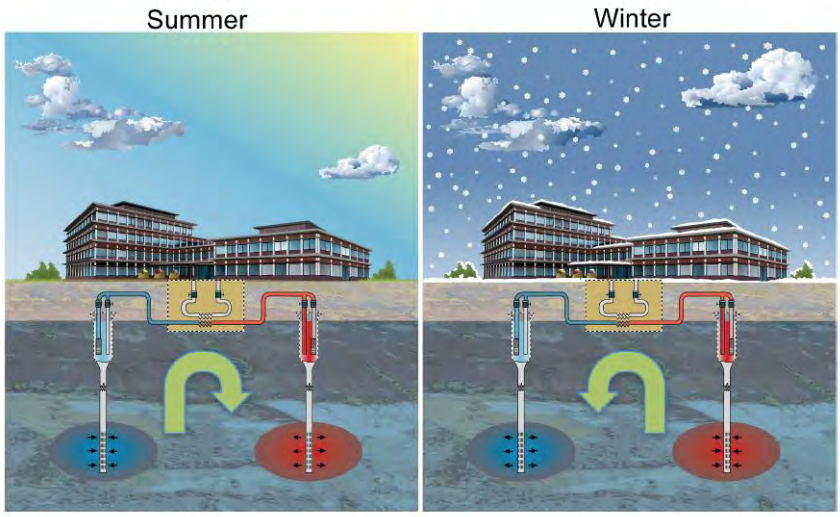

Figure 4 – Two wells (withdrawal-reinjection) for the use of an aquifer both for summer cooling and winter preheating (Barrios, 2015)

2.4. Evaporative cooling

Cooling effect deriving from an adiabatic saturation process of an air flow (evaporative cooling) is well known: injecting fine droplets of water at (quite) constant enthalpy into an air flow causes humidity to increase and temperature to decrease. When the air flow is outside (external) air, you have direct evaporative cooling. Such a technique is useful when outside air enthalpy is lower than inside air and, at the same time, humidity ratio is enough lower than inside air to be able to face eventual internal latent loads. The temperature limit of evaporative cooling is imposed by the wet

bulb temperature of the air to be cooled (figure 5). A particular technology must be cited that allows to approach the dew-point, using direct/indirect evaporative cooling in the so called Maisotsenko cycle (Jiradi and Riffat, 2014). Even if direct evaporative cooling can be considered an effective and cheap cooling technology, some drawbacks must be considered:

- It can be used only in a hot and dry climate where the latent loads are low.
- The supplied air can arrive at too high a moisture content as to require a subsequent dehumidification.
- A water supply is required with a potential high water consumption (Guan et al., 2015).
- The humidifier needs a proper maintenance to avoid the risk of bacterial growth.

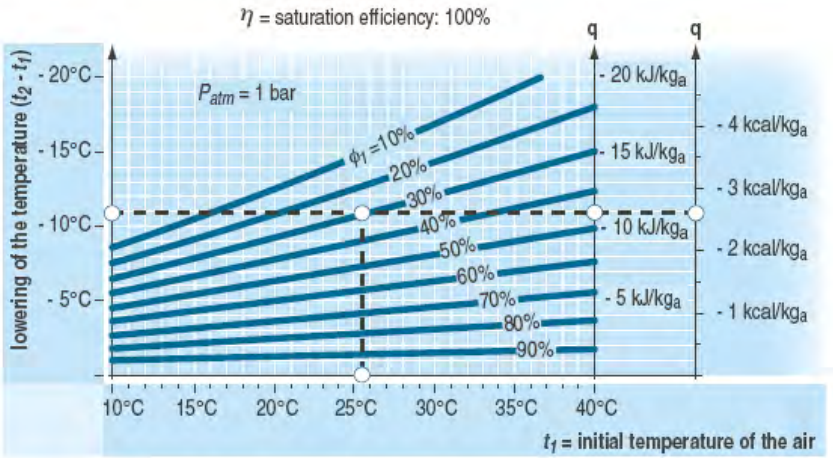

Figure 5. Specific cooling energy (q) and lowering of the temperature (final temperature t_2 – initial temperature t_1) obtainable by adiabatically humidifying air, with a saturation efficiency η = 100%, according to the initial temperature (t_1) and the relative humidity (φ_1)

These drawbacks can be faced with some measures, such as the use of atomizing humidifiers with pressurized and once-through water that minimizes a possible bacterial growth (Lazzarin and Nalini, 2004) or the indirect evaporative cooling where humidified outside air cools the air introduced into the room. The process is more effective when the humidified air is the discharged air as temperature and humidity are generally more favorable.

The most effective process is the so called two stage system where indirect and direct cooling are used (figure 6). A stream G_E of outside air exchanges heat with a stream of humidified exhausted air without changing its moisture content. A subsequent proper humidification can allow to reach the desired input conditions.

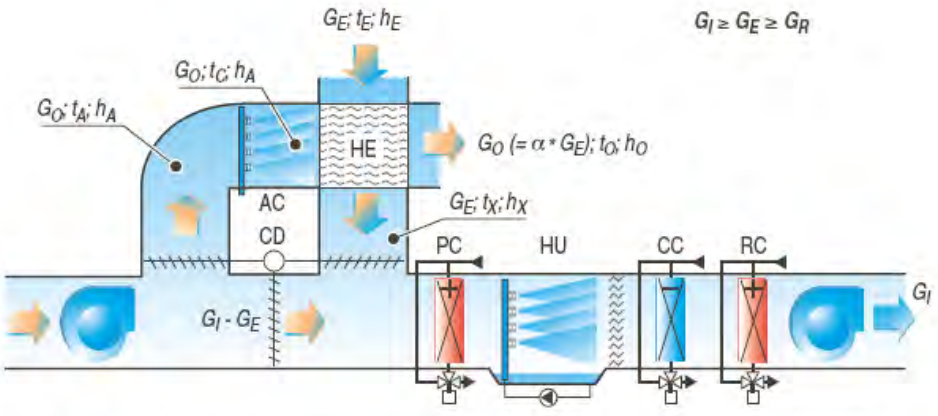

CD	Combined dampers	HE	Heat exchanger
PC	Preheating coil	G_I	Total air flow-rate
HU	Adiabatic humidifier	G_E	Outside air flow-rate
CC	Cooling coil	G_{vent}	Minimum renewal air flow-rate
RC	Post-heating coil	G_O	Exhaust air flow-rate
AC	Adiabatic cooler	α	Ratio between G_O and G_E

Figure 6 – Scheme of a possible indirect/direct evaporative cooling plant

Passive cooling technologies usually offer a marginal contribution to a building air-conditioning, so that many authors propose a hybrid system which couples various passive technologies (Heidarinejad et al., 2010) (Farahani et al., 2010). More frequently the hybrid system is realized with passive and active technologies.
Solar radiation intensity strongly influences the cooling demand. Therefore a lot of research work has been devoted to solar cooling since the 1973 first energy crisis. Solar energy can be exploited obtaining heat with thermal solar collectors or electricity with PV cells. Solar cooling requires a further transformation of heat or electricity into cooling that is neither simple nor cheap (Noro and Lazzarin, 2014). A system is usually required that is particularly complex when the starting point is heat.
Several physical principles can be exploited to produce solar cooling using either PV electricity or thermal solar. Some examples are thermoelectric, thermoacoustic or magnetic refrigeration using electricity and ejector or electrochemical refrigeration for heat driven systems (Kim and Infante Ferreira, 2008). However the just listed technologies are under development and very few products or no equipment at all are commercially available (IIR, 2017).
The main alternatives to produce a cooling effect by solar energy are represented in figure 7 for equipment present on the market. The variety of heat driven systems is apparent.

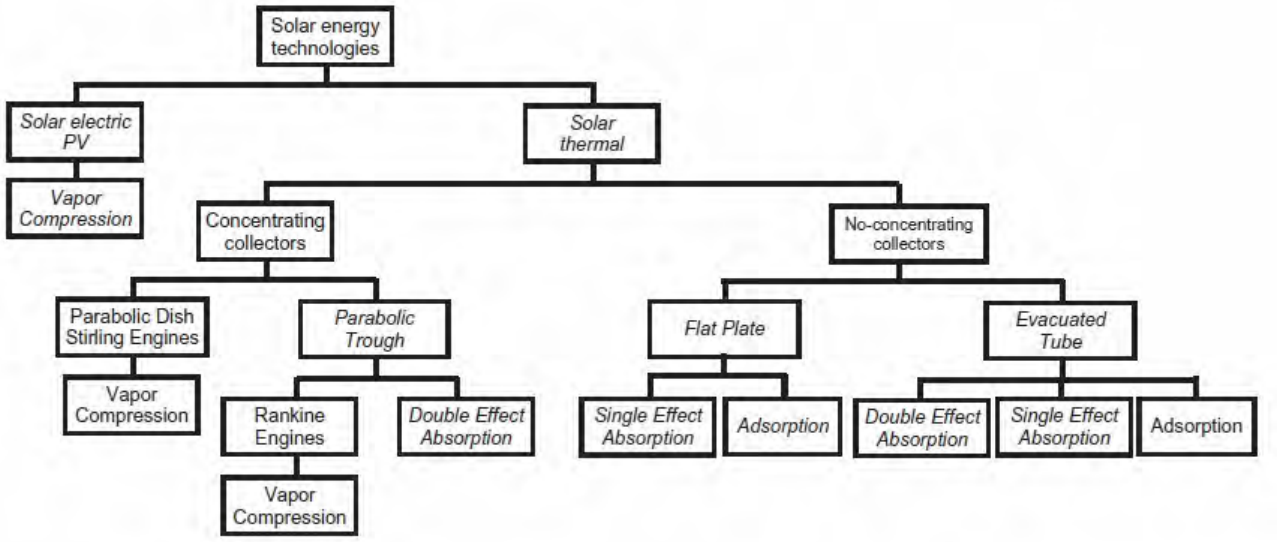

Figure 7 - Alternative routes from solar energy into cooling effect

3.1. Solar thermal cooling

The physical principle, apart the transformation of the collected heat into mechanical work, is the sorption process that uses the physical or chemical attraction between a pair substances: the sorbent and the refrigerant. Sorption can be operated within a liquid and the process is usually an absorption. When sorption is operated in a solid, the term adsorption is used.
The first discriminating factor when the cooling technology is selected is the available temperature. Different solar collectors technologies allow different temperatures at an acceptable efficiency.
In the past the most widespread solar collector was the flat plate collector (FPC). If the plate is selective[1] it can operate till, say, 90 °C. Chinese mass production recently led the Evacuated Tube Collector (ETC) at the top of the sales: the careful reduction of the possible heat losses allows to collect solar heat at temperatures of the order of 160 °C. Off course ETCs can work at 90 °C at a higher efficiency, that exceeds the FPC's at the same temperature. Both FPCs and ETCs are fixed collectors. Some tracking collectors were recently put on the market. The most common technology is the Parabolic Trough Collector (PTC) where a reflector focuses the direct solar radiation parallel to the collector axis onto the receiver placed on the focal line where a receiver heats up a fluid to a temperature that can exceed 200°C, as the small receiver area minimizes thermal losses. The tracking system operates on a single axis that is oriented in the N-S direction or E-W direction.

[1] A selective plate is highly absorbent in the solar spectrum and highly reflective in the infrared

Another less widespread concentrating technology on the market is based on Fresnel reflective optics, where particular reflectors concentrate sunlight at a common focal point similarly to PTCs.

Thermal collector efficiency η is defined as the ratio of useful thermal energy collected Q_u and impinging solar radiation I_β onto the collector in the same time period (A_c is the area of the collector):

$$= \frac{\frac{Q_u}{A_c}\,\mathrm{d}t}{I\ \mathrm{d}t} \qquad \text{Eq. (1)}$$

The solar collector efficiency can be formulated by a second order curve as a function of the so called reduced temperature T_m^* that is the difference between the average temperature of the fluid in the collector and the ambient temperature divided by the solar radiation intensity (t_m is the arithmetic average between inlet and outlet temperature and t_a is the ambient temperature):

$$T_m^* = \frac{t_m \quad t_a}{I} \qquad t_m = t_{in} + \frac{T}{2} \qquad = \ _o \quad a_1 T_m^* \quad a_2 I \ (T_m^*)^2 \qquad \text{Eq. (2)}$$

Figure 8 gives a picture of the three solar collectors typologies and Figure 9 represents typical efficiency curves.

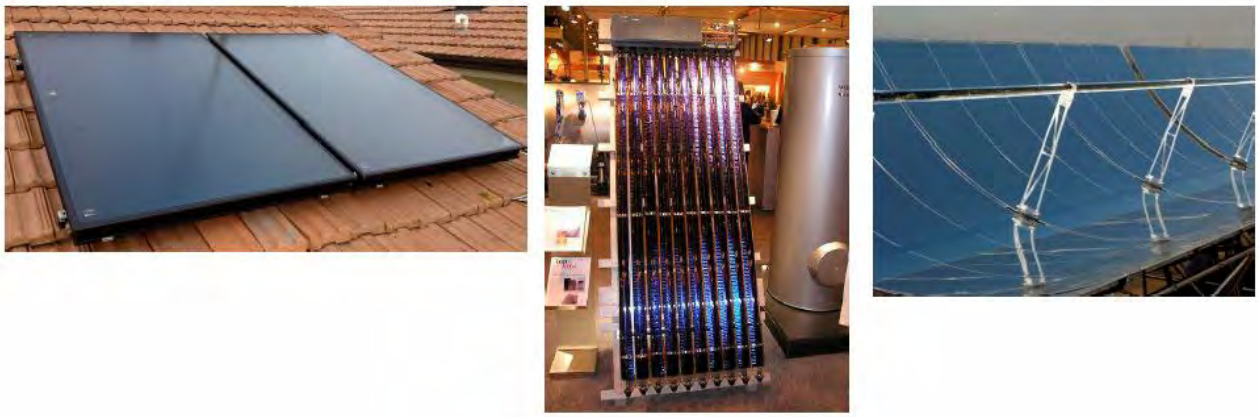

Figure 8 – From left to right: Flat Plate, Evacuated Tube and Parabolic Trough Collectors

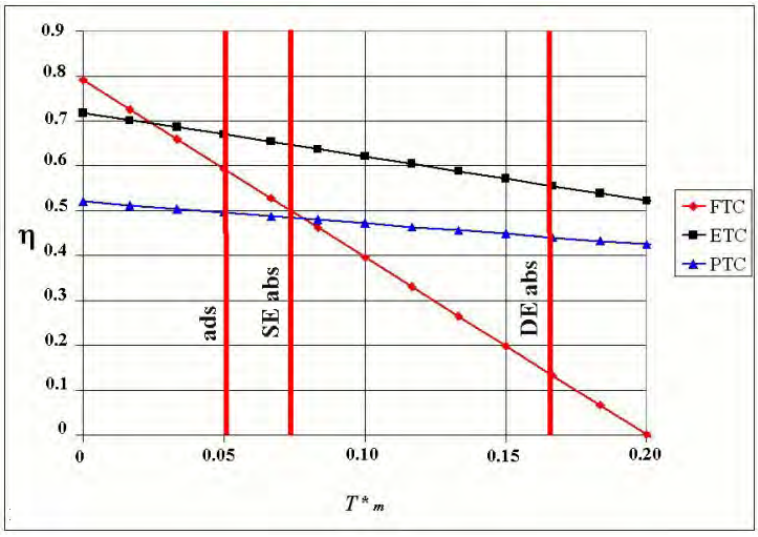

Figure 9 – Typical efficiency curves of the three typologies of considered solar collectors (FPC – Flat Plate (selective) Collector, ETC – Evacuated Tube Collector, PTC – Parabolic Trough Collector)

Table 1 reports possible coefficients of the efficiency curves of high performance solar collectors. The first coefficient η_o, the so called zero loss collector efficiency is well lower for PTCs due to its inability to exploit the most of diffuse radiation. The second coefficient a_1 is strictly connected with thermal losses, that are lower the lower the coefficient.
As previously mentioned, the cooling technology strongly depends on the available temperatures of heat supply. Another important factor in a cooling cycle is the sink temperature. The usual heat sink is the outside air, that can be employed in a dry cooler or in an evaporative cooler or cooling tower. Broadly speaking**,** the main alternatives are the following (Lazzarin, 2014):

- Adsorption chillers, water as refrigerant adsorbed by silica gel or zeolite. Their operative temperature can be as low as 60-70 °C with rather modest COP[2] of the order of 0.4-0.5. The machines are bulky and weighty. They should preferably cooled by a cooling tower.
- Single effect (SE) absorption chillers, water as refrigerant absorbed by an aqueous solution of LiBr or ammonia as refrigerant absorbed by water. The couple H_2O-LiBr requires a temperature of about 80-90 °C arriving at a COP of 0.7-0.8. A cooling tower must be their heat sink to avoid the risk of crystallization. The couple NH_3-H_2O can be air cooled. However the requested temperature is of the order of 140-160 °C and the COP even with the most efficient GAX cycle can be slightly higher than 0.7.
- Double effect (DE) absorption chillers, again water as refrigerant absorbed by an aqueous solution of LiBr. Higher temperatures and pressures in the solution regeneration allow to operate a free lower pressure solution regeneration. Consequently the COP is higher and can exceed 1.2 at a temperature of about 160 °C. A cooling tower must be provided.
- Desiccant cooling system: unlike the previous systems, that operate in a closed cycle, it is an open cycle that treats directly the air to be conditioned. As such it will be separately described.

As far as the closed cycle chillers are concerned, the coupling with solar collectors is illustrated in figure 9, where the vertical lines represent a possible value of the reduced temperature T_m^* in a sunny summer day. Clearly the use of a PTC is inappropriate with an adsorption chiller, whereas the same is true for a FPC with a double effect or NH_3-H_2O chiller.
To complete the picture the proposal of a so called half-effect H_2O-LiBr cycle must be cited (Kim and Infante Ferreira, 2009). The cycle was conceived to allow an air cooling even in extreme hot climate at the price of a COP as low as 0.3-0.4 even with a temperature above 80 °C of the supplied heat. No such a device is actually on the market.

	FPC	ETC	PTC
η_o	0.791	0.718	0.52
a_1 ($Wm^{-2}K^{-1}$)	3.94	0.974	0.52
a_2 ($Wm^{-2}K^{-2}$)	0.012	0.005	0.0031

Table 1 - Parameters of the efficiency curve of three solar collectors (FPC e Flat Plate (selective) Collector, ETC e Evacuated Tubular Collector, PTC e Parabolic Trough Collector).

The scientific literature on solar thermal driven cooling is really abundant, starting from first reports on solar houses in the ’70 (Lazzarin and Noro, 2018). Equipment regarding chillers, solar collectors, auxiliaries as storage systems or controls are all available, Nonetheless the last recording of installations worldwide arrives at only 1,200 plants till 2014, most in Europe (Montagnino, 2017). In that same year, more than 100 million units vapor compression conditioners were sold. The reasons of such a poor performance must be found not only on the high cost of the systems, but also on their complexity. Not only solar collectors and heat driven chillers must be provided, but also suitable storages, better if one hot and one cold, and an intricate circulation system with related pumps, whose parasitic power must be not underestimated. A good design is a difficult task that must keep in mind some fundamental principles, actually ten key principles (Neyer et al., 2018).
To evaluate thermodynamically the various alternatives a possible parameter is the Overall System Efficiency (OSE):

[2] COP of a thermal driven chiller is the ratio between the cooling effect and the supplied heat to regenerate the solution or the adsorbent

Eq. (3)

$$\mathrm{OSE} = \frac{q_0}{I} = \frac{q_0}{q_g}\frac{q_g}{I} = \mathrm{COP}_{\mathrm{th}}$$

that is the ratio between the specific cooling effect per unit area solar collector and the solar radiation intensity onto the collectors. It can be obtained as the product of the COP and the solar collector efficiency. On a summer daily basis it can be of 20% for adsorption chillers, exceeding 40% for SE absorption and even 50% for DE absorption (with ETCs). Air cooled NH_3-H_2O remain below 30%.

3.2. Desiccant cooling

Due to the peculiarity of the system it is separately discussed even if it is thermally driven and the physical principle is always ad/absorption.
The air to be introduced into the room is processed with sorption dehumidification, natural cooling and humidification (Gommed and Grossman, 2007)
To illustrate how it works, one of the possible operative modes can be described: the ventilation mode with all fresh air. An air stream from the outside is dehumidified by a desiccant: the stream is now hot and dry and it is cooled down by the return air from the conditioned space that is first cooled by direct evaporation of water. The return air, now warm and humid, is further heated by solar heat so that it can regenerate the desiccant. The outside air, cooled down in the heat exchanger by the return air, can be directly supplied to the conditioned space as dry air or can be further cooled down by a suitable evaporative cooling. Figure 10 illustrates a possible scheme operating with a solid-desiccant dehumidification wheel, a rotary heat exchanger and evaporative coolers; desiccant regeneration is produced by a heating coil powered by a solar collector. Liquid desiccant schemes are also available.
They do not produce chilled water but directly treat the ventilation air and can be applied only in all air installations. Nevertheless a COP can be defined as the ratio between the cooling effect and the heat requested to regenerate the desiccant. Indicatively a possible value is 0.7-0.8, even if strongly dependent on operating conditions (Henning, 2007). The comparison with the previously described system is not completely appropriate, as desiccant cooling provides a complete AHU particularly suitable for high ventilation rates or high dehumidification requests.

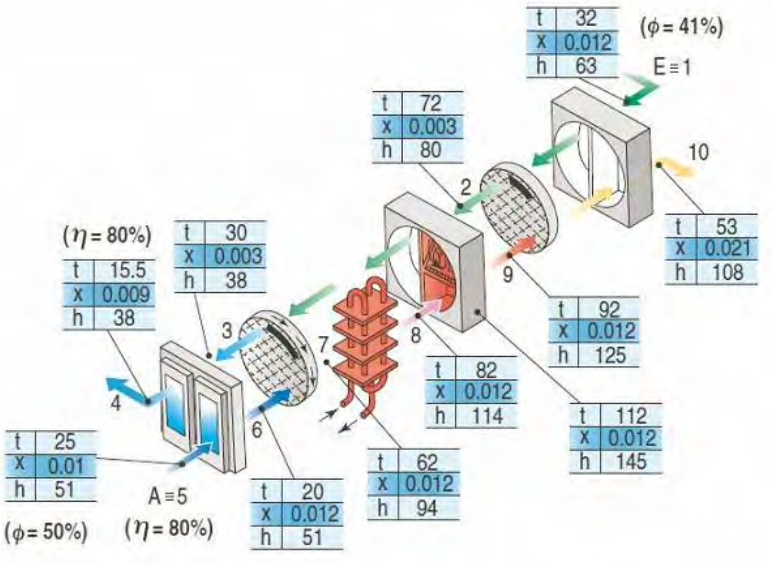

Figure 10 – Solid desiccant solar driven cooling system (Lazzarin and Nalini, 2004): t=temperature, °C; x= specific humidity, kgkg$_a^{-1}$; h=enthalpy, J kg$_a^{-1}$.

3.3. PV driven solar cooling

The most obvious option for PV driven system is the vapor compression, very similar to conventional refrigeration equipment, with the compression eventually driven by a DC motor (Figure 11). The performance of the system is usually given by the COP (Coefficient of Performance), calculated as follows:

$$COP = \frac{q_o}{E} \qquad \text{Eq. (4)}$$

where q_0 is the specific cooling per unit PV area and E is the correspondent supplied energy.
Also for PV driven systems an OSE can be defined:

$$OSE = \frac{q_0}{I} = \frac{q_0}{E}\frac{E}{I} = COP \qquad \text{Eq. (5)}$$

and it can be evaluated as the product of the vapor compression COP and the PV efficiency.

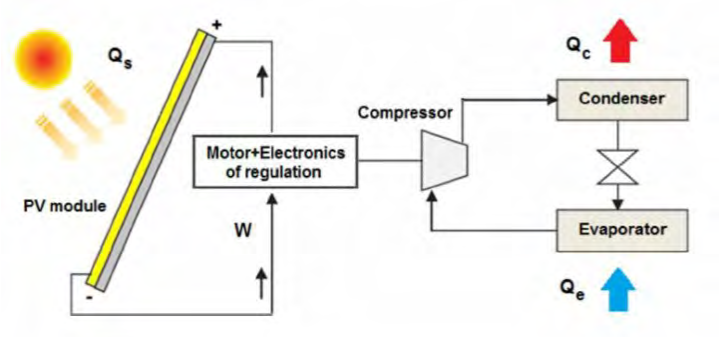

Figure 11 – Scheme of a solar PV driven compression air conditioner (Kim and Ferreira, 2008)

The actual commercial PV modules efficiency ranges between 13 and 17% in standard conditions (solar radiation intensity: 1000 Wm^{-2}, cell temperature: 25°C). As the efficiency is negatively influenced by higher temperatures, it decreases in hot sunny days.
PV module efficiency has been steadily increasing these last years and commercial PV module efficiency is forecast to be about 19% in 2020 and 21% in 2030 (IEA, 2014).
The COP of the vapor compression chiller strongly depends on evaporator and condenser temperatures and on the quality of the equipment. Nowadays an air cooled chiller may present a COP of 3, exceeding 4 when cooled by a cooling tower. Higher quality (and more expensive) chillers are already on the market with COP respectively above 4 and between 5 and 6.
The result of the rising efficiency of both the components produces the summary picture of figure 12, where the OSE comparison between the previously described thermal driven system and the PV driven is carried out in the two climates of Brussels (cold climate) and Trapani (warm climate) in the most sunny summer month, respectively June and August (Lazzarin and Noro, 2018). The more favorable behavior of the PV driven system in Brussels is due to the lower operative temperature of the PV cells and of the cooling medium.

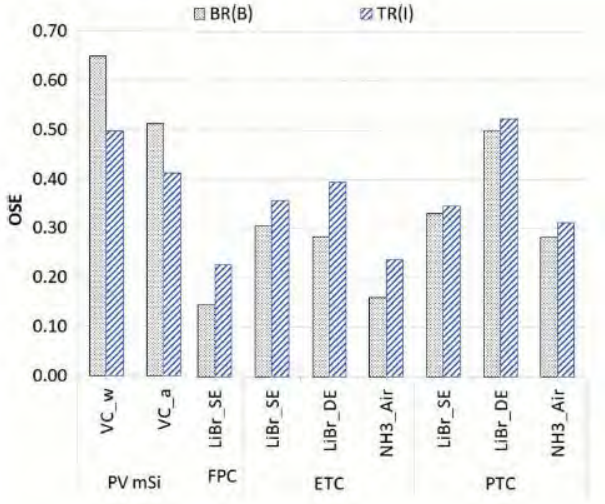

Figure 12 - Overall System Efficiency of different solar cooling solutions; mSi, monocrystalline Silicium cells; VC-w and VC-a, vapor compression chiller, water or air cooled

4. CONCLUSIONS

If the energy efficiency comparison appears unfavorable for the solar thermal cooling, when the costs of investment are considered, no competition seems possible. PV modules cost has been continuously decreasing with a dramatic reduction in the last ten years. The coupling of increased efficiency and decreasing cost, due to mass production, led from a cost of about 5 €Wp^{-1} in 2005 to 3€ in 2010, 1.5€ in 2015 and to less than 0.5 € in 2017 (NREL, 2017). Even adding BOS and installation costs, the final cost is less than 2 € . Moreover the chiller cost is about a half than for absorption equipment and the whole system is by far simpler. For example the storage function is actually assumed by the grid in an easy and cheap way. And now the competition of solar electric cooling in terms of overall cost is rather with conventional air-conditioning.

Game over, then? Not yet completely. In the last years the enormous increase of ETC installations in China (37 million m^2, of which about 85% ETC in 2017) led to an impressive cost reduction at a level three times lower than in the European market for the ETCs and this reduction is going on. However an equivalent market has not arisen for the absorption chillers.

A middle way could derive from a hybrid of PV and solar thermal collector, that is the so called PV cogeneration, shortly PV/T or directly PVT. The starting point is the fact that for an excellent PV module less than 20% of solar energy is turned into electricity. The left 80% must be dissipated. In a PVT the unwanted heat is instead exchanged with a fluid, air or water, so that it can be useful heat. In the past the risk of a damage of the PV cells in stagnation conditions led to avoid glazed solutions so that a low level heat was available. Some experiments were also conducted for using a PVT for night radiative cooling (Eicker and Dalibard, 2011). The development of PV cells that can tolerate high temperature or the utilization of PVT in a dual source heat pump system might allow to build up solar driven plants producing all year building heating and cooling.

The author and his team are designing and realizing a plant for heating and cooling of a nZEB with DHW production, that not only provides all the required energy on a yearly basis, but it makes also available an energy surplus for the grid. A simplified scheme of the system is represented in figure 13. The two possible sources for the heat pump are PVT thermal contribution and the ground. Not represented is the heating or preheating of DHW by PVT. The PVT thermal surplus (mainly in summer) recharges the ground: this permits a PVT cooling that favors the electrical efficiency.

Details of this plant is reported just in this Congress (Lazzarin and Noro, 2019).

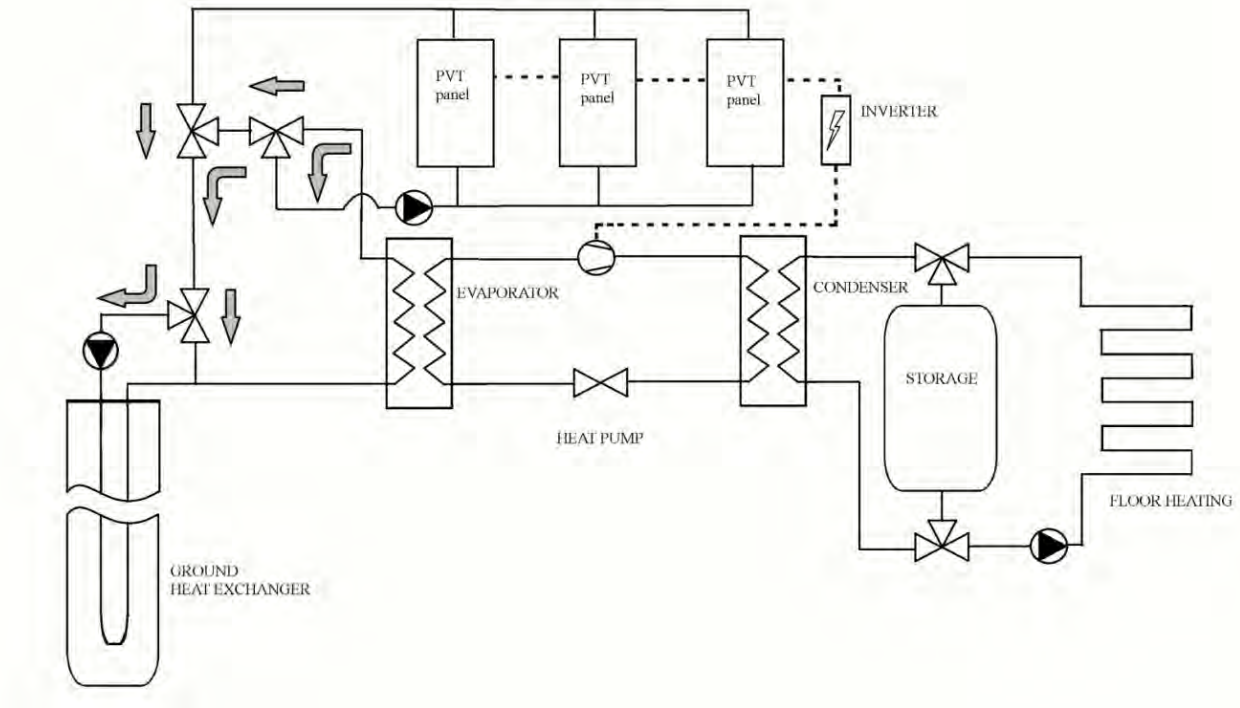

Figure 13 – Dual source heat pump plants PVT modules and ground thermal probes

REFERENCES

Barrios, M., 2015. Evaluation of an aquifer thermal energy storage (ATES) for the city hospital in Karlsruhe (Germany), Master Thesis, KIT and Uppsala Universitet.

Eicker, U., Dalibard, A., 2011. Photovoltaic–thermal collectors for night radiative cooling of buildings, Solar Energy, 85, 1322–1335.

Farahani, M.F., Heidarinejad, G., Delfani, S., 2010. A two-stage system of nocturnal radiative and indirect evaporative cooling for conditions in Tehran, Energy and Buildings, 42, 2131–2138.

Gommed, K., Grossman, G., 2007. Experimental investigation of a liquid desiccant system for solar cooling and dehumidification. Sol. Energy 81, 131–138.

Guan. L., Bennett, M., Bell, J., 2015. Evaluating the potential use of direct evaporative cooling in Australia, Energy and Buildings, 108, 185–194.

Heidarinejad, G., Farahani, M.F., Delfani, S., 2010. Investigation of a hybrid system of nocturnal radiative cooling and direct evaporative cooling, Building and Environment, 45, 1521–1528.

Henning, H.M. 2007. Solar assisted air conditioning of buildings: an overview, Applied Thermal Engn., 27, 1734-1749.

IEA, 2012. IEA Solar_Heating_Cooling_Roadmap_2012_WEB.

IEA, 2014. IEA Solar Photovoltaic Energy Technology Roadmap, 2014 Edition

IIR, 2017. Solar cooling, 34th Informatory Note on Refrigeration Technologies.

Jiradi, M., Riffat, S., 2014. Experimental and numerical investigation of a dew-point cooling system for thermal comfort in buildings, Applied Energy, 132, 524–535.

Kim, D.S., Infante Ferreira, C.A., 2008. Solar refrigeration options-a state-of-the-art review, Int. J. of Refrigeration, 31(1), 3-15.

Kim, D.S., Infante Ferreira, C.A., 2009. Air-cooled LiBr–water absorption chillers for solar air conditioning in extremely hot weathers, Energy Conversion and Management, 50, 1018–1025.

Lazzarin, R., 1979. On natural radiative cooling, La Termotecnica, 23, 345-355.

Lazzarin, R., 2014. Solar cooling: PV or thermal? A thermodynamic and economical analysis, Int. J. of Refrigeration, 39, 38-47.

Lazzarin, R., Nalini, L., 2004. Air humidification: technical, health and energy aspects, Carel, Brugine, pp. 1-600.

Lazzarin, R., Noro, M., 2018. Past, present, future of solar cooling: Technical and economical considerations, Solar Energy, 172, 2–13.

Lazzarin, R., Noro, M., 2019. Photovoltaic/Thermal (PV/T) to drive a dual source heat pump (ground and PV cooling): performance analysis in a real application, submitted to the Int. Cong. of Refrigeration, Montreal.

Lu, X., Xu, P., Wang, H., Yang, T., Hou, J., 2016. Cooling potential and applications prospects of passive radiative cooling in buildings: The current state-of-the-art, Ren. and Sust. Energy Rev., 65 1079–1097.

Montagnino, F.M., 2017. Solar cooling technologies. Design, application and performance of existing projects, Solar Energy, 154, 144–157.

Neyer, D., Ostheimer, M., Mugnier, D., White, S., 2018. 10 key principles for successful solar air conditioning design – A compendium of IEA SHC Task 48 experiences, Solar Energy, 172, 78–89.

Noro, M., Lazzarin, R., 2014. Solar cooling between thermal and photovoltaic: An energy and economic comparative study in the Mediterranean conditions, Energy, 73, 453-464.

NREL, 2017. U.S. Solar Photovoltaic System Cost Benchmark: Q1, Technical Report NREL/TP-6A20-68925.

Raman, AP, Anoma, MA, Zhu, L, Rephaeli, E., Fan, S., 2014. Passive radiative cooling below ambient air temperature under direct sunlight, Nature, 515, 540–4.

Santamouris, M., 2016. Cooling the buildings – past, present and future, Energy and Buildings 128 617–638.

Santamouris, M., Kolokotsa, D.,2013. Passive cooling dissipation techniques for buildings and other structures: The state of the art, Energy and Buildings 57, 74–94.

Santamouris, M., Mihalakakou, G., Balaras, A., Argiriou, A., Asimakopoulos, D., Vallindras, M., 1995. Use of buried pipes for energy conservation in cooling of agricultural greenhouses, Solar Energy 55 2, 111-124.

Trombe, F., 1967. Perspectives sur l'utilisation des rayonnements solaires et terrestres dans certaines regions du monde, Rev. Gen. Therm., 6(70), 1285– 314.

Web ref. Jan. 2019. http://www.nzeb.in/knowledge-centre/passive-design/thermal-mass/

Zeyghami, M., Goswami, D.Y., Stefanakos, E., 2018. A review of clear sky radiative cooling developments and applications in renewable power systems and passive building cooling, Solar Energy Mat. and Solar Cells, 178, 115–128.

Zhang, S., Niu, J., 2012. Cooling performance of nocturnal radiative cooling combined with microencapsulated phase change material (MPCM) slurry storage, Energy and Buildings, 54, 122–130.

Manuscript ID: 1879
DOI: 10.18462/iir.icr.2019.1879

Highly efficient heat pump with desiccant coated evaporator and condenser: principle and application

Ruzhu WANG[(a)], Lingji HUA[(a)], Tianshu GE[(a)], Yaodong TU[(a)], Xiangyu SUN[(a)]

[(a)] Institute of refrigeration and cryogenics, Shanghai Jiao Tong University,
800 Dongchuan road. Minhang District, Shanghai 200240, China, rzwang@sjtu.edu.cn

ABSTRACT

Nowadays, comfortable and efficient heating, ventilation, and air conditioning (HVAC) systems in buildings are highly desirable. Traditional vapor-compression devices exhibit a low coefficient of performance (COP) (typically 2.8–3.6) due to the cooling-based dehumidification. Temperature-and humidity-independent control (THIC) systems have been proposed to overcome the challenges; however, their COP is hindered by the sorption heat effect. Here, we report on a solid desiccant heat pump (SDHP) based on desiccant coated evaporators/condensers (DCEs/DCCs). The desiccants adsorb moisture almost isothermally and can be regenerated by the condensation heat. With the optimized refrigerant and desiccant, our proposed DCCs/DCEs feature a weakly-coupled heat and mass transfer. The system exhibits a COP of 6~7, doubling the efficiency of heat pumps currently used in household, which opens a window for the future development of HVAC systems and also a broad range of THIC applications.
Keywords: Desiccant Coated Heat Exchanger, Solid Desiccant Heat Pump, Weakly-couple Heat and Mass Transfer, Desiccant

1. INTRODUCTION

Improving energy efficiency with adequate humidity control capacity and sufficient fresh air ventilation is a long-standing focus of HVAC systems. A traditional vapor-compression (VC) air conditioner, which adopts the cooling-based dehumidification method to handle sensible and latent loads altogether, operates at a lower evaporation temperature (5–7°C). This results in a lower COP (2.8–3.6, in general). To solve this problem, considerable efforts have been made to develop efficient alternative refrigeration systems such as caloric-based technologies(Bansal, 2016) and innovative system designs such as temperature-and humidity-independent control (THIC)(Tao et al., 2014). Although caloric-based technologies show great potential for energy savings, they are still far from being practically applied. A THIC system usually consists of a thermally driven dehumidification unit and a VC specializing in handling the sensible heat load. It was reported that THIC systems might save 25–50% of electrical consumption(Tao et al., 2014) by adopting a higher evaporation temperature. However, the COP (latent load divided by primary thermal energy input) of current solid-desiccant systems is quite small, typically ranging from 0.5 to 1.0(Lowenstein, 2008) due to high regeneration temperature. Even though solar heat or industrial waste heat can sometimes be used, a large volume and high utility cost limits the large-scale application of solid-desiccant systems in residential buildings.

It is quite natural to consider whether desiccant dehumidification could be used isothermally, while desiccant regeneration can be handled by the waste heat (condensing heat) from the air-conditioning system. The sensible load is handled in the same way as before, by convection, but without overcooling (an evaporation temperature approximately 15–17°C). Therefore, the processed air leaving the evaporator satisfies the requirement for supply air. This is the first time, to our knowledge, that a high-efficiency approach has been devised that inherits advantages of THIC, but also has the merits of compactness, low cost, and realization of the effective utilization of condensation heat..

2. IDEAL THERMODYNAMIC PROCESS OF THE HVAC

As mentioned before, traditional VC system, traditional desiccant cooling system, hybrid desiccant air-conditioning system and solar desiccant cooling system are representative techniques of HVAC,

with their air treatment processes depicted in Fig. 1(a). (taking Shanghai summer condition as an example: two mixed flows of outdoor air (OA: 35°C, 60%RH) and indoor air (RA: 25°C, 50%RH), denoted as MA1 and MA2, are processed in the device and then discharged respectively as supply air (SA) and exhausted air (EA)).

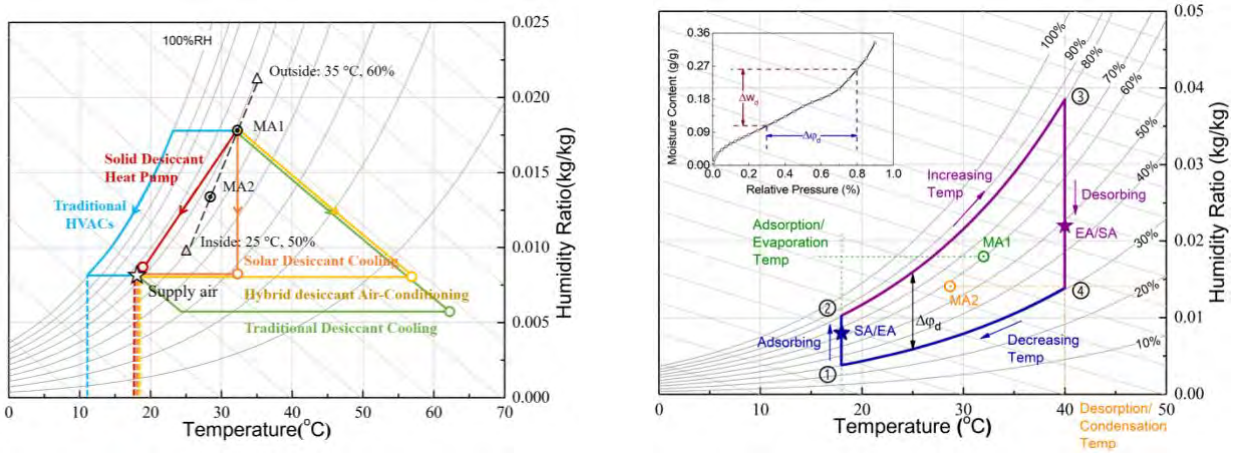

Figure 1: The thermodynamic process of the air and desiccant in SDHP(Hua et al., 2019)

The most compact and widely-adopted system, traditional VC, takes advantage of the cooling dehumidification technique and condenses the excess moisture in MA1 by directly cooling it down to the dew point of the desired SA. Therefore, the outlet air of the evaporator would be with satisfying humidity but low temperature (SA dew point<SA dry-bulb temperature) and need to be reheated before exhausting. Such process of overcooling and reheating is a waste of energy.

The traditional desiccant cooling(Jia et al., 2007) and the hybrid desiccant air-conditioning(Jia et al., 2006), as indicated by their names, manipulate the air humidity via desiccant. The desiccation process in such system, without a cooling source, is normally isenthalpic and features high outlet temperature due to the release of adsorption heat. Auxiliary sensible handling equipment is thus imperative to be adopted.

Air flowing through a solar desiccant cooling device would at first experience a process of latent heat handling in the desiccant coated heat exchangers (DCHEs) without temperature change. That is, the side effect of the sorption heat can be suppressed by the single-phase cooling media. Afterwards, the air should be further cooled via VC or other methods(Saeedand Al-Alili, 2016). The ideal process of the sensible and latent heat handling, otherwise, should be more straightforward, as indicated with the red curve in Fig. 1(a).

The sorption isotherm of a typical desiccant is shown in the sub-graph of Fig. 1(b). The curve is assumed insensitive to temperature variation, indicating the biunivocal correlations between the moisture content of the material and the relative humidity ratio of the air in (thermal and concentration) equilibrium with it. Therefore, the points in psychrometric chart can also present solid desiccant conditions(Li et al., 2010). Fig. 1b then illustrates the ideal adsorption-desorption cycle of the solid material which can realize the above-mentioned process of air handling. The desiccant at point ① is cold and dry, hence it can dehumidify and simultaneously cool down the air flowing through it (MA1). A cold source is imperative to facilitate the process by taking away the sensible and adsorption heat transferred to the desiccant timely (①-②). After a while, the adsorption ability of the adsorbent begins to decay, due to the abundant moisture inside. It is then the time to introduce a hot source to warm the desiccant up (②-③) and trigger the desorption. During the following regeneration process (③-④), the coated desiccant at a relatively high temperature releases heat and water vapor into the MA2, and the heat source keeps heating the desiccant to compensate the sensible and latent heat dissipation. After the material is sufficiently dried up, it should be again cooled by the cold source, retuning to point ①.

In summer/winter, MA1/MA2 is treated by the process ④-①-②/②-③-④, and then discharged as supply air to manipulate the indoor environment. Assuming efficient mass and heat transfer, the processed air is always approaching equilibrium with the desiccant. The averaged supply air temperature and humidity are defined as in Eq. (1). Accordingly, to supply air of stable temperature, processes ①-② and ③-④ are expected to be isothermal. Also, temperature variation processes ②-③ and ④-① should be as quick as possible, so that there is scarcely any mass transfer to the

air during the periods. That is, ②-③ and ④-① are along the iso-relative humidity lines in the psychrometric chart.

$$\begin{cases} summer: \overline{T_{SA}} = \int_{④\to①\to②} T_{SA}(t)dt \Big/ \Delta t_{ad}, \overline{Y_{SA}} = \int_{④\to①\to②} Y_{SA}(t)dt \Big/ \Delta t_{ad} \\ winter: \overline{T_{SA}} = \int_{②\to③\to④} T_{SA}(t)dt \Big/ \Delta t_{de}, \overline{Y_{SA}} = \int_{②\to③\to④} Y_{SA}(t)dt \Big/ \Delta t_{de} \end{cases} \quad \text{Eq. (1)}$$

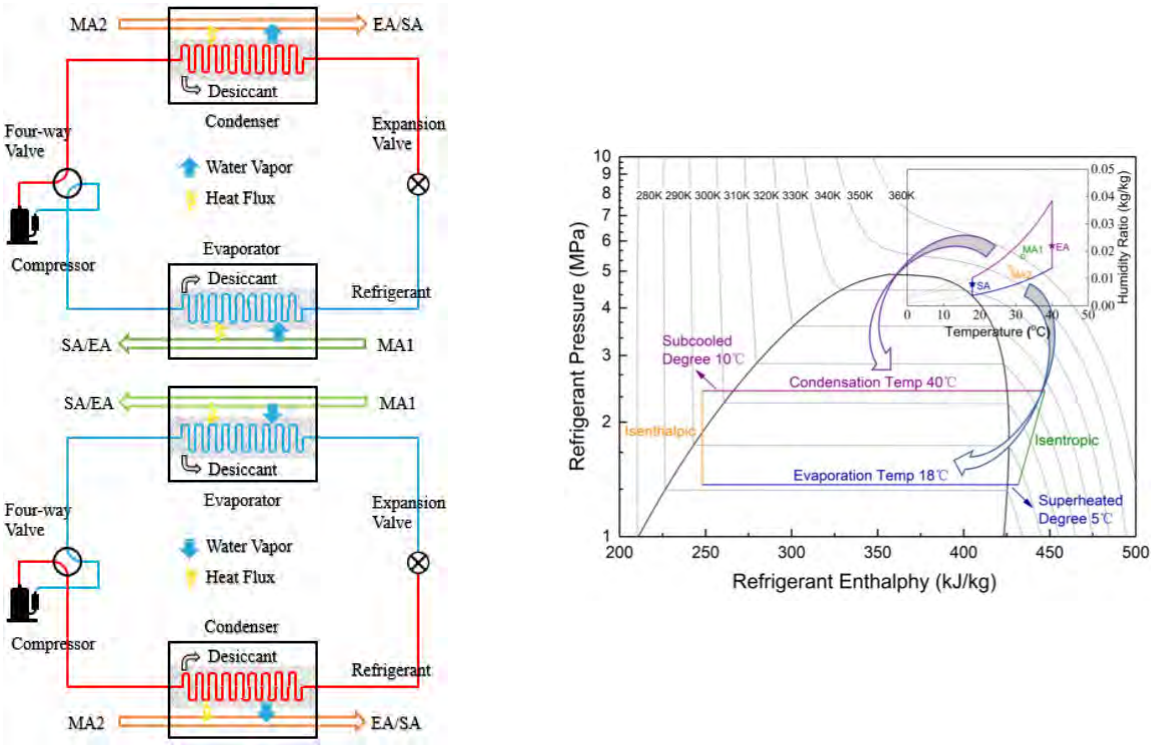

(a) (b)

Figure 2: The schematic of SDHP and its working principle(Hua et al., 2019)

To implement the above cycle, the desiccant is coated onto the surface of a traditional air-to-refrigerant heat exchanger (DCHE). Refrigerant can facilitate the operation of DCHEs by removing the adsorption heat/replenishing the heat used for regeneration in time during cooling/heating phase. The solid desiccant heat pump (SDHP, as shown in Fig. 2) is then proposed to combine a VC system with DCHEs (transforming to DCEs/DCCs).

Same as the conventional VC system, the refrigerant in the SDHP operates as depicted in Fig. 2 (a): after absorbing the heat in the evaporator, the refrigerant vapor is compressed in the compressor, condenses in the condenser and expands through the throttling device, then the cold refrigerant goes to the evaporator again. The evaporator/condenser in this system would adsorb/desorb heat and moisture to/from the air simultaneously if facilitated by the cold/hot fluid. Then, when the evaporator/condenser is saturated/dried up, it is time to switch over the four-way valve, exchanging the position between the evaporator and the condenser. Thus, the SDHP features a process of periodic switchover of the evaporator and condenser. The air duct should also be re-constructed, to persistently guide the cooling air into the condenser. Fig. 2(b) emphasizes that the evaporation/ condensation of refrigerant coincides with the process ④-①-②/②-③-④ of the desiccant.

3. REFRIGERANT AND DESICCANT SCREENING

3.1. New Operational Temperature

As shown in Fig. 3(a), the adsorbed water amount of local desiccant and the water vapor concentration in desiccant pores are correlated by the sorption isotherms. Hysteresis phenomenon

of the desorption isotherms is observed for typical mesoporous desiccant. Isotherms at different temperature seem divergent, however, when the adsorbed water content is depicted against water vapor relatively humidity in pores, the isotherms approximately coincide with each other (Fig. 3(b)). The process ①-②-③-④ shown in Fig. 1(b) can also be depicted in Fig. 3(a). As the time of adsorption/desorption goes by ($t\to\infty$), the water vapor in desiccant pores would reach equilibrium with the external airflow. It is assumed in our study that the condenser has been regenerated completely before it is transformed into the evaporator (set as time origin). That is:

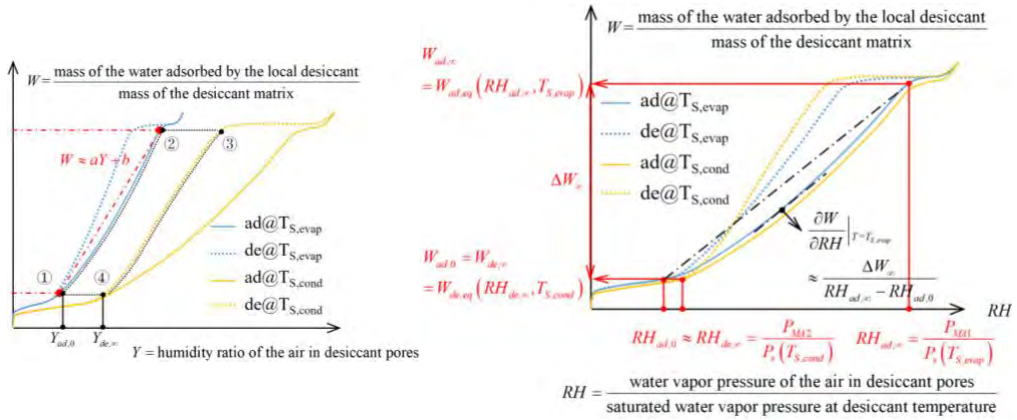

(a) (b)

Figure 3: The isotherms of typical mesoporous desiccants

$$Y_{de,\infty} \triangleq Y_{da}\big|_{t=0-} = Y_{MA2}, P_{de,\infty} \triangleq P_{da}\big|_{t=0-} = P_{MA2},$$
$$\Rightarrow RH_{de,\infty} \triangleq RH_{da}\big|_{t=0-} = \frac{P_{MA2}}{P_s\left(T_{S,cond}\right)}, W_{de,\infty} \triangleq W_d\big|_{t=0-} = W_{eq}\left(RH_{de,\infty}, T_{S,cond}\right) \quad \text{Eq. (2)}$$

$$W_{ad,0} \triangleq W_d\big|_{t=0+} = W_{de,\infty} \Rightarrow RH_{ad,0} \triangleq RH_{da}\big|_{t=0+} = RH_{eq}\left(W_{eq,de}\left(RH_{de,\infty}, T_{S,cond}\right), T_{S,evap}\right) \approx RH_{de,\infty}$$
$$\Rightarrow Y_{ad,0} \triangleq Y_{da}\big|_{t=0+} = 0.622\frac{RH_{ad,0}P_s\left(T_{S,evap}\right)}{P_{atm} - RH_{ad,0}P_s\left(T_{S,evap}\right)} = 0.622\frac{P_{MA2}P_s\left(T_{S,evap}\right)}{P_{atm}P_s\left(T_{S,cond}\right) - P_{MA2}P_s\left(T_{S,evap}\right)} \quad \text{Eq. (3)}$$

$W_{eq,ad}(RH,T)$ and $W_{eq,de}(RH,T)$ are respectively adsorption and desorption isotherms of desiccant, with $RH_{eq,ad}(W,T)$ and $RH_{eq,de}(W,T)$ as their inverse functions at temperature T. Obviously, in summer condition, the desiccant surface temperature and humidity at evaporation phase are restricted by the supply air conditions (T_{SA}, Y_{SA}), as shown in Eq. (4).

$$\begin{cases} T_{S,evap} < T_{SA} \\ Y_{ad,0} < \overline{Y_{SA}} \Rightarrow 0.622\dfrac{P_{MA2}P_s\left(T_{S,evap}\right)}{P_{atm}P_s\left(T_{S,cond}\right) - P_{MA2}P_s\left(T_{S,evap}\right)} < \overline{Y_{SA}} \end{cases} \quad \text{Eq. (4)}$$

$$\begin{cases} T_{evap} = T_{S,evap} - 2^oC = T_{S,evap} - 2^oC = T_{SA} - 6^oC, T_{cond} = T_{S,cond} + 2^oC \\ Y_{ad,0} = \overline{Y_{SA}} - 4\,g/kg \end{cases} \quad \text{Eq. (5)}$$

Based on the above estimation (Eq. (5)), the range of system evaporation and condensation temperature can be obtained (Fig. 4). According to Fig. 4, under typical summer conditions (supply air condition: 16-22ºC, 7.5-9.5g/kg, regeneration air condition: 17-30g/kg), the evaporation and condensation temperature of the SDHP are respectively among the interval 10-20ºC and 40-50ºC. The governing equations illustrating the mass transfer process of the system is derived as in Eq. (6), with the initial and boundary conditions listed in Eq. (7). Eq. (6)–(7) can be simplified to get analytical solution Eq. (8), which reveals that the dehumidification capacity of the SDHP is governed by DCHE configurations, air flow field, switchover period, operational conditions and desiccant properties. In

the respect of desiccant, two parameters $\rho_d \Delta W_\infty$ and $a\rho_d$ in Eq. (8) are proposed as criteria for desiccant screening, with their physical meanings illustrated in Fig. 3(b) and Eq. (9). Based on Eq. (9), variables ΔW_∞ and a are nearly proportional.

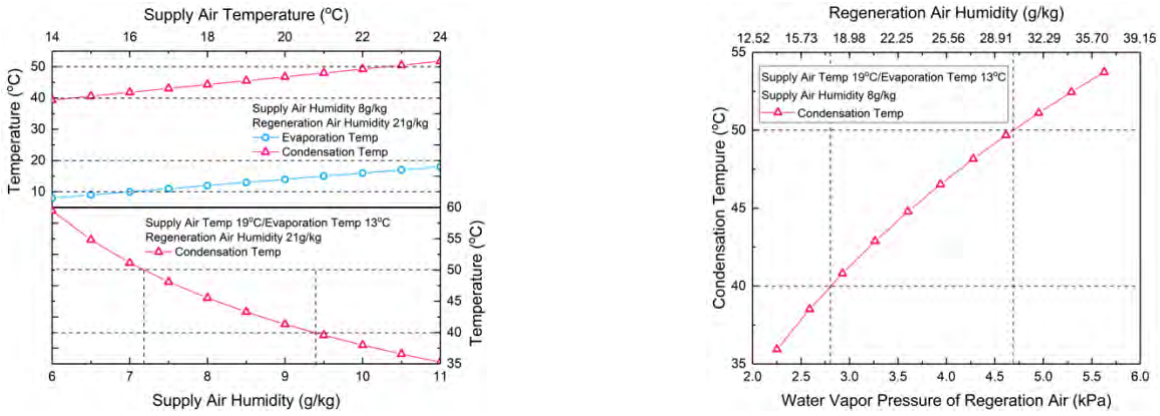

(a) (b)

Figure 4: The estimated operational temperature of the SDHP under typical summer conditions

$$\begin{cases} \dfrac{\partial(\varepsilon_{da}\rho_a Y_{da})}{\partial t}+\dfrac{\partial(\rho_d W_d)}{\partial t}=\dfrac{\partial}{\partial n}\left[D_G\dfrac{\partial(\varepsilon_{da}\rho_a Y_{da})}{\partial n}\right]+\dfrac{\partial}{\partial n}\left[D_S\dfrac{\partial(\rho_d W_d)}{\partial n}\right] \\ \dfrac{\partial(\rho_a Y_a)}{\partial t}+\dfrac{\partial(\rho_a u_a Y_a)}{\partial x}=\dfrac{1}{l_a}K_y\left(Y_{da}\big|_{n=\delta_d}-Y_a\right) \end{cases} \quad \text{Eq. (6)}$$

$$\begin{cases} -D_G\dfrac{\partial(\varepsilon_{da}\rho_a Y_{da})}{\partial n}-D_S\dfrac{\partial(\rho_d W_d)}{\partial n}=K_y\left(Y_{da}\big|_{n=t_d}-Y_a\right) \\ Y_a\big|_{x_1=0}=Y_{a,in} \end{cases} \quad \text{Eq. (7)}$$

$$W_d(t)-W_{ad,0}=\left(1-e^{-\frac{K_y}{at_d\rho_d}t}\right)\Delta W_\infty \Rightarrow Y_{MA1}-\overline{Y_{SA}}=\frac{A_y\rho_d t_d}{A_f\rho_a u_a}\frac{1}{\Delta t_{ad}}\left(1-e^{-\frac{K_y}{at_d\rho_d}\Delta t_{ad}}\right)\Delta W_\infty \quad \text{Eq. (8)}$$

$$\begin{cases} a=\dfrac{\partial W_d}{\partial Y_{da}}\Big|_{T=T_{S,evap}}=\dfrac{\partial W_d}{\partial RH_{da}}\dfrac{\partial RH_{da}}{\partial Y_{da}}\Big|_{T=T_{S,evap}}\approx\dfrac{\Delta W_\infty}{RH_{ad,\infty}-RH_{ad,0}}\dfrac{\partial RH_{da}}{\partial Y_{da}}\Big|_{T=T_{S,evap}} \\ \Delta W_\infty \square\ W_{ad,\infty}-W_{ad,0}=W_{eq,ad}\left(\dfrac{P_{MA1}}{P_s(T_{S,evap})},T_{S,evap}\right)-W_{eq,de}\left(\dfrac{P_{MA2}}{P_s(T_{S,cond})},T_{S,cond}\right) \\ \dfrac{\partial RH_{da}}{\partial Y_{da}}\Big|_{T=T_{S,evap}}\approx \text{const at one specific temperature} \end{cases} \quad \text{Eq. (9)}$$

3.2. Refrigerant Screening

The adopted refrigerant in SDHP should be compatible with the new operational temperature range. Promising candidates are HFC refrigerants and novel refrigerant R-1234yf, with their properties listed in Table 1. and Fig. 5. The optimal ones for SDHP is R410A and R32 due to their high COP and volumetric refrigeration capacities.

Table 1. The important properties of refrigerant candidates

Medium	System*	Low Pressure (MPa)	High Pressure (MPa)	Pressure Ratio	COP	Discharge Temp (°C)	Volumetric Refrigeration Capacities (MJ/m^3)	Viscocity (μPa•s)
R152a	VC	0.3148	1.0368	3.29	5.68	61.6	2.24	9.334
	SDHP	0.4386	1.0368	2.36	8.15	58.2	3.17	9.691

R134a	VC	0.3497	1.1599	3.32	5.43	53.8	2.32	10.9111
	SDHP	0.4884	1.1599	2.37	7.85	52.6	3.34	11.291
R32	VC	0.9514	2.7948	2.94	5.19	80.3	5.8	11.751
	SDHP	1.2808	2.7948	2.18	7.44	71.6	7.89	12.258
R407C	VC	0.5469	1.7536	3.21	4.99	61.1	3.28	11.756
	SDHP	0.7557	1.7536	2.32	7.20	58.1	4.66	12.163
R410A	VC	0.9362	2.7335	2.92	4.95	66.9	5.15	12.479
	SDHP	1.2584	2.7335	2.17	7.11	62.4	7.09	13.046
R417A	VC	0.5471	1.6389	3.00	4.89	52.5	2.73	11.348
	SDHP	0.7415	1.6389	2.21	7.14	51.8	3.94	11.775
R1234yf	VC	0.3729	1.1538	3.09	5.11	46.9	2.14	11.363
	SDHP	0.5103	1.1538	2.26	7.5	47.6	3.08	11.807
R22	VC	0.5841	1.7292	2.96	5.47	67.3	3.66	11.578
	SDHP	0.7893	1.7292	2.19	7.84	62.5	5.03	12.025

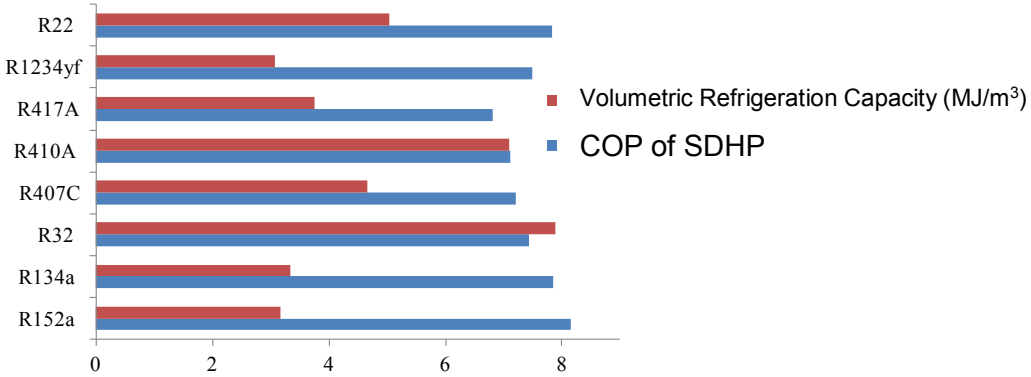

Figure 5: COP and volumetric refrigeration capacities of refrigerant candidates

3.3. Desiccant Screening

To find the optimal desiccant, a comprehensive comparison of water adsorption quantity and regeneration ability between different desiccants is given in the following figure (Fig. 6). Notably, composite desiccant materials have improved water adsorption capacity with the support of impregnated salts. And by proper selection of host matrix and immersed salts, i.e. clay/chlorine salt composite materials, regeneration temperature as low as 40°C can be achieved.

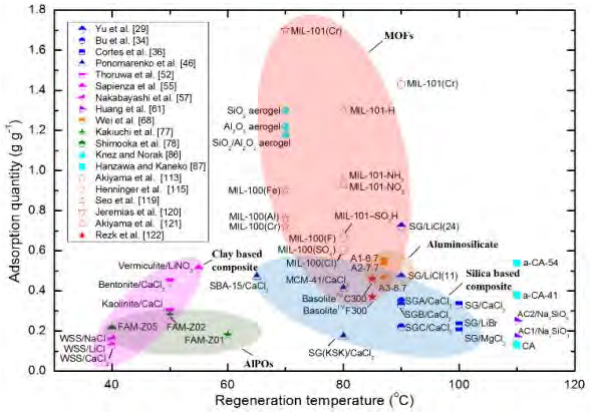

Figure 6: Water adsorption quantity and regeneration ability of recent desiccants(Zheng et al., 2014)

In our study, composites desiccant consisted of different salts (LiCl, LiBr, CaCl2) and host matrix (SGA-microporous silica gel, SGB-mesoporous silica gel, SGC-wide meshed silica gel, SBA-15, MCM-41, AC-active carbon, ACF-active carbon fiber, DE-mesoporous diatomaceous tourmaline) are manufactured and tested in order to match the dehumidification demand of the novel system. The results are illustrated in Fig. 7-8 and Table 2. It is noteworthy that, for composite desiccants, the adsorption amount is not only restricted by its water adsorption capacity, but also pore volumes V_t

(Eq. (10)), which can be derived from the nitrogen isotherms. Otherwise, adsorbed liquid would overflow from the pores and results in lyolysis. That is, the screening criteria for composite desiccant is to maximize $\rho_d \Delta W$ rather than $\rho_d \Delta W_\infty$. According to Table 2., the optimized desiccant is made by impregnating the salt LiCl into mesoporous silica gel SGB.

$$\Delta W = min\left(\Delta W_\infty, \Delta W_{limit}\right), \Delta W_{limit} = \rho_{water} V_t \quad \text{Eq. (10)}$$

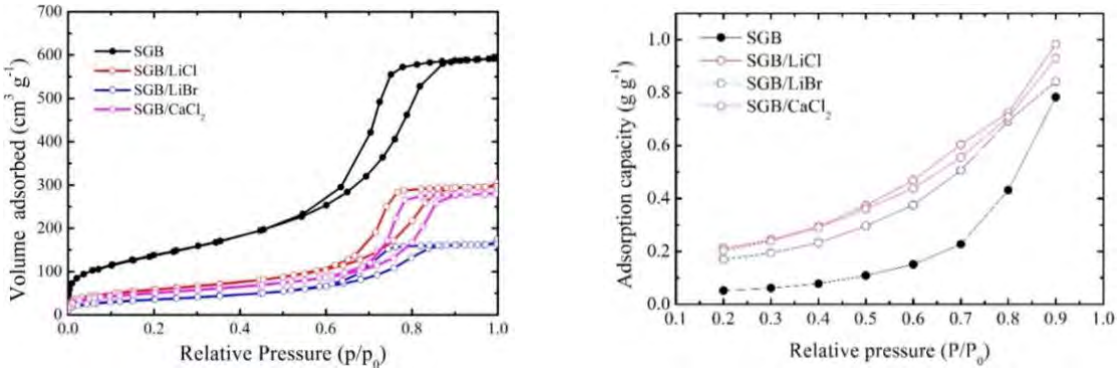

(a) (b)

Figure 7: (a) Nitrogen and (b) water sorption isotherms of composite desiccants (Zheng et al., 2014)

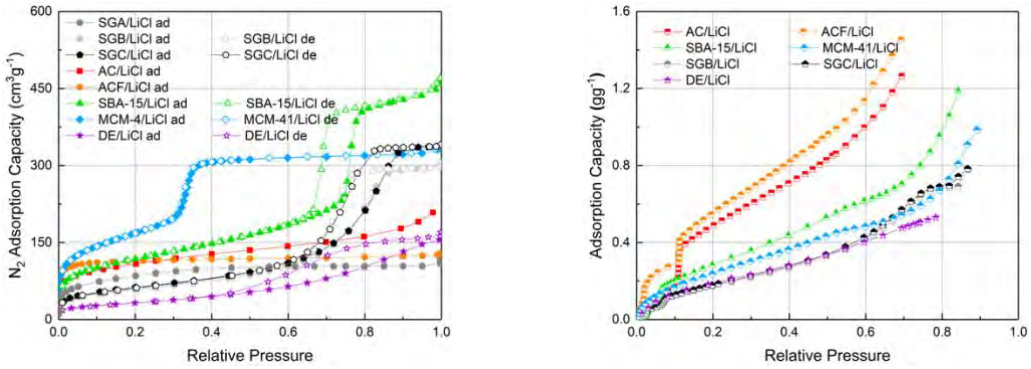

(a) (b)

Figure 8: (a) Nitrogen and (b) water sorption isotherms of composite desiccants with different matrix

Table 2. Important parameters of composite desiccants with different matrix

Desiccant	$\triangle W_\infty$ (g/g)	$\triangle W_{limit}$ (g/g)	$\triangle W$ (g/g)	ρ_d (kg/m^3)	$\rho_d \triangle W$ (kg/m^3)
SGB/LiCl	0.37	0.54	0.37	933	345
SGC/LiCl	0.38	0.69	0.38	900	342
MCM-41/LiCl	0.30	0.40	0.30	267	80
SBA-15/LiCl	0.42	0.81	0.42	233	98
AC/LiCl	0.70	0.11	0.11	1367	150
ACF/LiCl*	0.83	-	0.83	267	221
DE/LiCl	0.35	0.16	0.16	1267	202

4. HEAT AND MASS TRANSFER PROCESS OF THE DCHE

4.1. The Heat and Mass Transfer Coefficient

An experimental apparatus is associated with an open loop flow system that has been fabricated and designed to obtain the heat transfer, mass transfer, coefficient of performance and pressure drop characteristics of DCHE and conventional heat exchanger. The experimental setup is

schematically illustrated in Fig. 9, while the configuration of the DCHEs, along with its manufacture process, is shown in Fig. 9(a).
The obtained results is summarized in Fig. 10. Generally, the desiccant coating slightly subdues the heat transfer capacity of the heat exchangers, on the other hand, the friction is obviously enhanced by the coarse surface. The mass transfer performance of the DCHE is also analysed. The data reveal that the DCHE can handle around 10-60g moisture per second per area, which is a remarkable amount for a household dehumidifier.

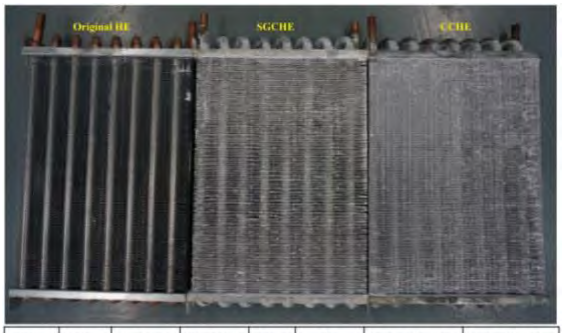

Fin length (mm)	Fin width (mm)	Fin depth (LDCHE) (mm)	Fin depth (SDCHE) (mm)	Fin pitch (mm)	Fin thickness (m)	Outer diameter of the tubes (mm)	Inner diameter of the tubes (mm)
300	300	88	44	2	0.105	10.5	9.87

(a)

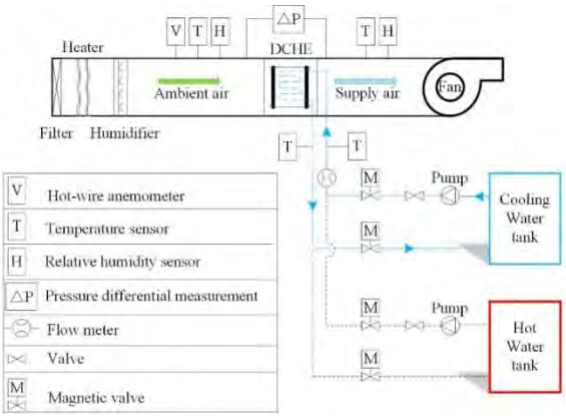

(b)

Figure 9: Schematic diagram of the (a) DCHE (b) experimental set-up(Sun et al., 2017)

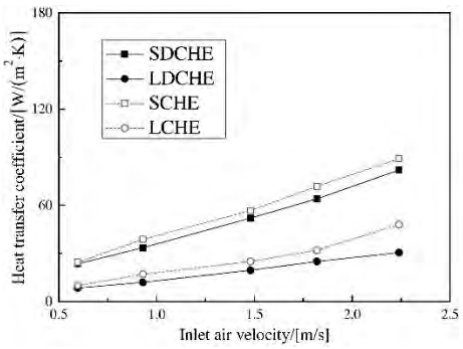

(a)

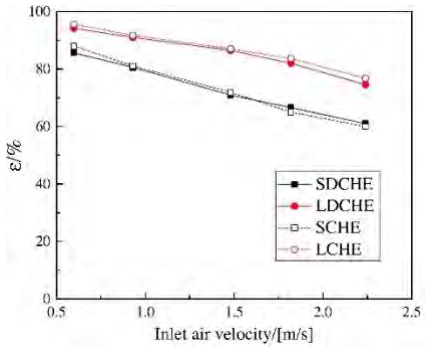

(b)

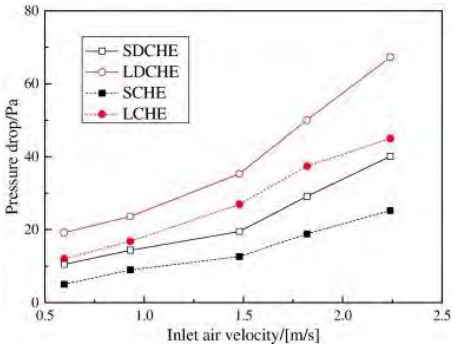

(c)

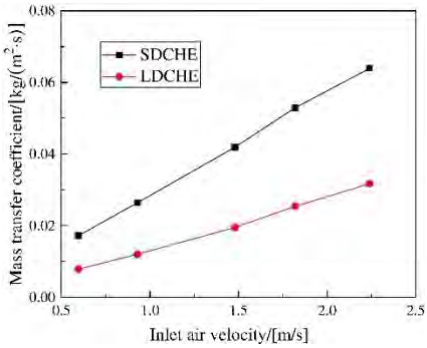

(d)

Figure 10: (a) Heat transfer coefficient (b) Effectiveness of heat exchangers (c) Mass transfer (d) Pressure drop of different type of DCHE(Sun et al., 2017)

4.2. The Weakly-Coupled Heat and Mass Transfer

Based on lumped parameter method, the heat and mass transfer model of the DCHE can be derived as in Eq. (11). Analytical solution of Eq. (11) is then listed in Eq. (12). During the process ②-③ and ④-① shown in Fig. 1(b), energy is consumed to overcome the cold-hot offset of DCHE due to the switchover, while the coefficient K_F in Eq. (12) denotes the rate of this process. A high value of K_F

could facilitate the DCHE by accelerating the temperature variation process and decreasing the energy consumption during the process. Meanwhile, the coefficient K_S dominates the tendency of SA humidity. To implement the ideal process shown in Fig. 1, the value of K_F and K_s should be larger than 0.25 and 0.001 s^{-1} respectively.

$$\begin{cases} \dfrac{\overline{T}_a - T_{HX}}{R_a} = G_a C_{p,a}\left(T_{ai} - T_{ao}\right) \\ \dfrac{\overline{T}_a - T_{HX}}{R_a} - \dfrac{T_{HX} - \overline{T}_r}{R_r} + M_d \dfrac{\partial\left(q_{st} W_d\right)}{\partial t} = C_{p,HX} M_{HX} \dfrac{\partial T_{HX}}{\partial t} \\ G_r C_{p,r}\left(T_{r,i} - T_{r,o}\right) + \dfrac{T_{HX} - \overline{T}_r}{R_r} = C_{p,r} M_r \dfrac{\partial T_r}{\partial t} \\ M_d \dfrac{\partial W_d}{\partial t} = G_a\left(Y_{ai} - Y_{ao}\right) \end{cases} \quad \text{Eq. (11)}$$

$$\begin{cases} T_{ao} = T_{ao,\infty} + \left(T_{ao,0} - T_{ao,\infty}\right) e^{-K_F t} = M + N e^{-K_F t}, K_F \geq 0.25 s^{-1} \\ Y_{ao} = Y_{ai} - \dfrac{M_d \Delta w_\infty K_s}{G_a} e^{-K_s t}, K_S \geq 0.001 s^{-1} \end{cases} \quad \text{Eq. (12)}$$

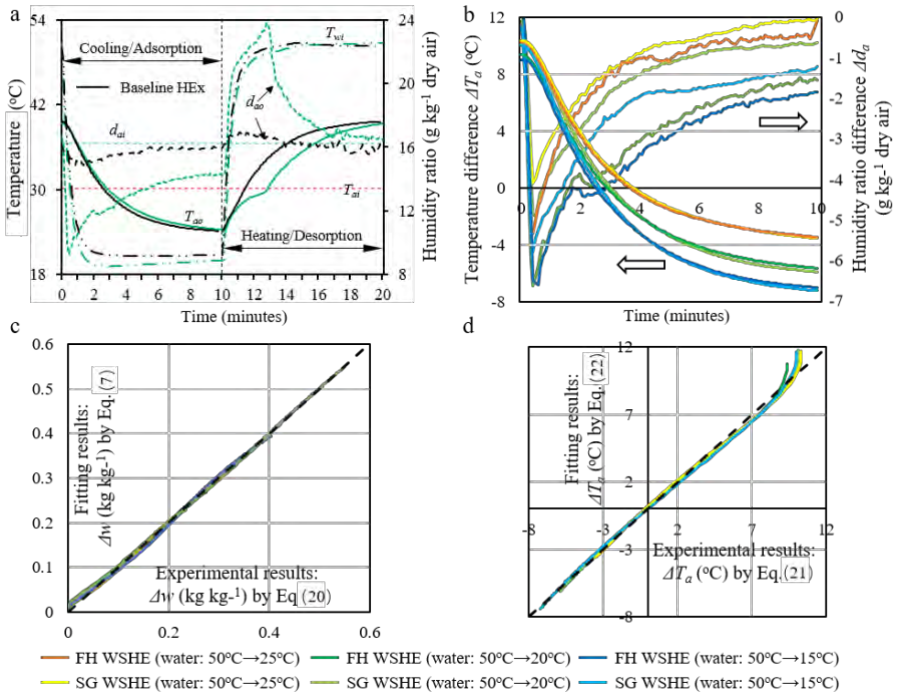

Figure 11: (a) Typical evolutions of outlet air temperature and humidity ratio (b) Transient temperature difference ΔTa and humidity ratio ΔYa (c)/(d) Comparison of the experimental results ΔWd/ΔYa with the theoretical predictions(Tu et al., 2017)

Eq. (12) can be validated by curve-fitting the experimental data. The values of the fitting parameters, M, N, K_F, ΔW_∞ and K_S are listed in Table 3. Comparing the values of K_F and K_s listed in Table 3., it can be seen that with the inlet water temperature T_{ri} decreasing, K_F nearly keeps static while K_s jumps down sharply for both DCHEs. This seems to suggest that the change rates of outlet air temperature T_{ao} and humidity ratio Y_{ao} are independent. The K_F is much smaller than the desired value due to the finite specific heat of single-phase refrigerant. If two-phase media is adopted, the K_F can be improved remarkably (>0.25s^{-1}). In this case, the K_s is two order of magnitude less than K_F. That is, the temperature-variation in DCHE can reach to a stable value quickly, while the humidity-variation can be approximated as a linear function with time. Correspondingly, the averaged SA

temperature and humidity can be altered separately by varying evaporation temperature and switchover period.

Table 3. Test conditions and curve-fitting parameters(Tu et al., 2017)

Test conditions				Temperature difference (ΔT_o) [Eq.(22)]							Water uptake (Δw) [Eq.(7)]				
WSHE & T_{wi}	Th °C	Tc °C	T_{ai} °C	M °C	Stand Error	N °C	Stand Error	K_t $\times 10^3 s^{-1}$	Error R^2	Y	Iw_o kg kg^{-1}	Stand Error	Ks $\times 10^3/s^{-1}$	Stand Error	n
FH WSHE @ 25°C	50.4	25.4	30.9	-3.93	0.06	15.42	0.08	6.01	8.0E-05	1.16	0.2399	1.1E-03	5.15	6.0E-05	0.075
FH WSHE @ 20°C	50.6	20.0	30.5	-6.36	0.07	17.14	0.08	5.60	8.0E-05	1.08	0.6722	3.4E-03	2.32	2.0E-05	0.086
FH WSHE @ 15°C	50.4	17.5	30.2	-7.82	0.08	18.55	0.10	5.65	9.0E-05	1.09	0.7960	6.9E-03	1.95	3.0E-05	0.081
SG WSHE @ 25°C	50.2	25.1	30.9	-4.10	0.07	15.83	0.08	5.77	9.0E-05	1.12	0.1837	6.8E-04	5.73	6.0E-05	0.062
SG WSHE @ 20°C	50.3	20.4	30.6	-6.82	0.08	18.61	0.10	5.45	9.0E-05	1.07	0.2945	1.5E-03	4.08	5.0E-05	0.066
SG WSHE @ 15°C	50.1	17.2	30.1	-8.12	0.081	19.79	0.10	5.60	8.0E-05	1.05	0.4871	4.5E-03	2.75	5.0E-05	0.068

5. HIGHLY EFFICIENT HEAT PUMP

5.1. Simulation Study

The dynamic mathematical models for core components and the SDHP system are built to clarify and to guide the experimental study. Fig. 12 illustrates the calculation algorithm of the system model. Under dynamic operation, the process is repeated every time step with the updated initial conditions from one time step before.

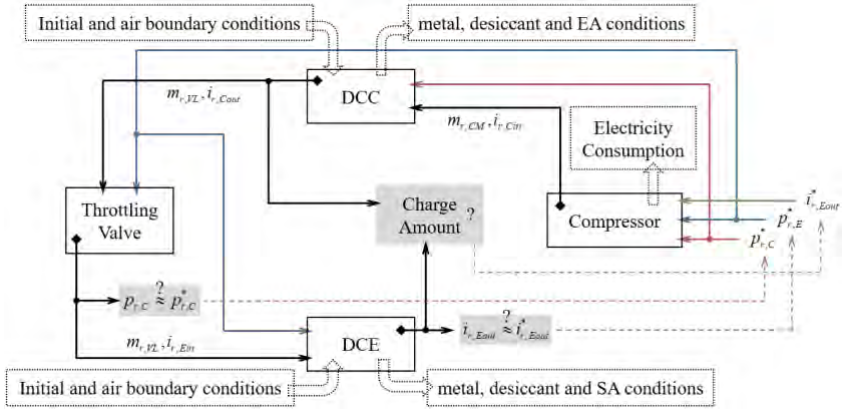

Figure 12: Framework of the system simulation of the SDHP(Hua et al., 2019)

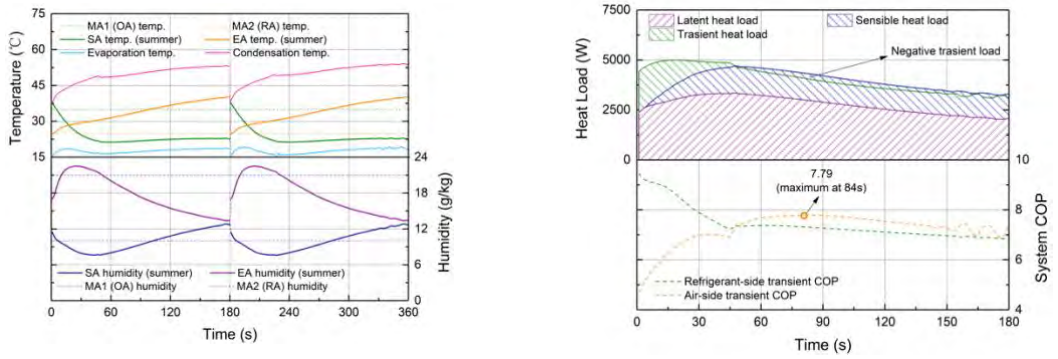

(a) (b)

Figure 13: The characteristics and performance of the different elements of the SDHP (a) outlet air and refrigerant conditions (b) heat load and estimated COP(Hua et al., 2019)

The numerical study shows that, after several minutes of fluctuation and quick self-regulation, the SDHP features periodical performance given arbitrary initial conditions. According to Fig. 13(a), within one cycle, the evaporation temperature fluctuates between 16°C and 19°C, while the condensation temperature gradually increasing from 38°C to 52°C. It also reveals that the humidity

removal/regeneration in DCEs/DCCs happens together with the temperature reduction/recover, and thus validates the possibility of the simultaneous handling of sensible and latent load in such system. The averaged supply air condition is 23ºC, 9g/kg. The enthalpy increase of the refrigerant in SDHP does not equal the enthalpy decrease of the air, due to the existence of the transient heat load. The air-side value is deemed more reasonable. The COP calculated at the air-side, as shown in Fig. 13(b) obtains a maximum of 7.79 at 84s with the averaged value of 7.19.

5.2. Experimental Study

For the first demonstration of this approach, we developed a single packaged SDHP including two parts, a vapor compression loop and air ducts, both of which are located in a cabinet with two air inlets (outdoor air, OA, and return air, RA) and two air outlets (supply air, SA, and exhaust air, EA) (Fig. 14). Two identical DCHEs in a vapor compression loop work as an evaporator or condenser interchangeably with the assistance of a four-way valve. Correspondingly, the processing air (mix of OA and RA) and the exhaust air (mix of OA and RA) can be switched to the evaporator and condenser by using the front duct air switch. The outlet air of the evaporator and condenser can be directed to SA and EA by utilizing the back duct air switch.

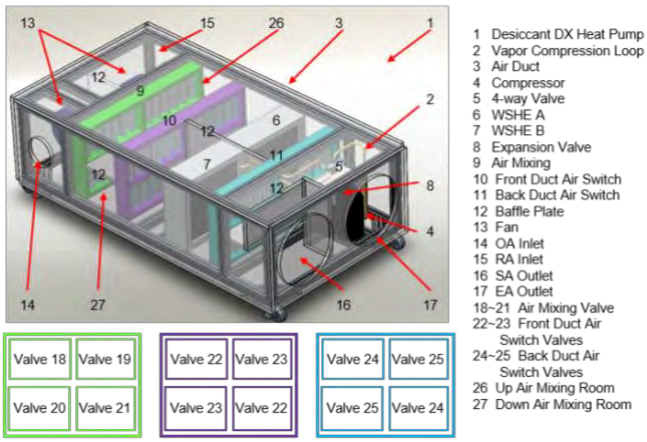

Figure 14: Schematic of the single packaged SDHP system(Y.D. Tu et al., 2017)

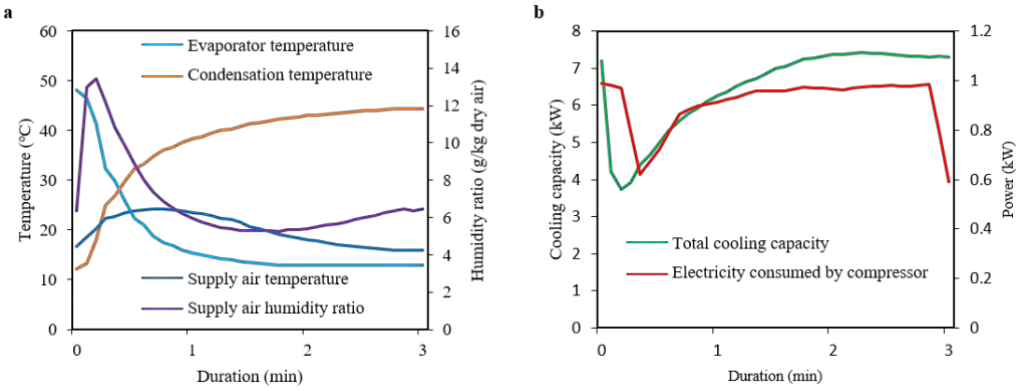

Figure 15: (a)Supply air and (b) energy performance of the SDHP under typical summer condition(Y.D. Tu et al., 2017)

The performance of the demonstration has been tested under a common scenario in Summer for room air conditioning (outdoor 35°C/60% RH and indoor 25°C/50%RH, 70% outdoor fresh air). The experimental results (Fig. 15) show that the condensation temperature approaches 43°C, the evaporation temperature is approximately 13°C, the average supply air dry bulb temperature is approximately 20°C, the humidity ratio is approximately 8.5g/kg dry air (50%RH), and the power consumed by the compressor and fans are roughly 980 and 149 W, respectively. In other words, the total cooling capacity is 7.0 kW with a compressor COP of approximately 7.14 and a system COP of 6.2. These are nearly double the values of current conventional room air conditioners.

6. CONCLUSIONS & PERSPECTIVES

In this study, a novel heat pump system-solid desiccant heat pump, its construction process and evaluation method is comprehensively analyzed. The significant findings are listed as followed:

1. Based on the new operational temperature, the optimal refrigerant is R410A and R32.
2. Based on the mass transfer mechanism, the screening criteria (maximizing $\rho_d \Delta W$) for desiccant is proposed. The composite desiccant LiCl/mesoporous silica gel is regarded as appropriate one.
3. The desiccant-coated heat exchangers feature weakly-coupled heat and mass transfer process.
4. Simulation and experimental study shows that the system COP is around 7.2 under typical Summer conditions, doubling the efficiency of pumps currently used in conventional room air conditioners.

The above research results have shown the great potential for comfortable and high efficient HVAC system by using DCEs/DCCs. Such idea could be used for air-duct HVAC systems effectively, it is especially recommended to the uses in high humidity areas due to its high capability in handling of latent heat, public buses and trains due to high demand on fresh and also clean air, comfortable AC for the old people and young children and the patients in hospitals. it could be also used independently as a dehumidification equipment with significant efficiency improvement in comparison with conventional dehumidification systems (desiccant rotor, liquid desiccant tower, low temperature condensing devices).

ACKNOWLEDGEMENTS

This work was supported by the Key Program of National Natural Science of China (Grant No.51336004) and the Foundation for Innovative Research Groups of the National Natural Science Foundation of China under the contract No. 51521004.

REFERENCES

Bansal, P., 2016. Latest developments in not-in-kind refrigeration technologies. Science and Technology for the Built Environment 22(5), 473-474.

C. X. Jia, Y. J. Dai, J. Y. Wu, and R. Z. Wang, 2006. Analysis on a hybrid desiccant air-conditioning system. Applied Thermal Engineering 26(17), 2393-2400.

Hua, L. J., Ge, T. S., and Wang, R. Z., 2019. Extremely high efficient heat pump with desiccant coated evaporator and condenser. Energy 170, 569-579. doi:https://doi.org/10.1016/j.energy.2018.12.169

Jia, C. X., Dai, Y. J., Wu, J. Y., and Wang, R. Z., 2007. Use of compound desiccant to develop high performance desiccant cooling system. Internation Journal of Refrigerant 30(2), 345-353.

Li, Z., Liu, X. H., Lun, Z., and Jiang, Y., 2010. Analysis on the ideal energy efficiency of dehumidification process from buildings. Energy and Buildings 42(11), 2014-2020.

Lowenstein, A., 2008. Review of Liquid Desiccant Technology for HVAC Applications. HVAC&R Research 14(6), 819-839.

Saeed, A., and Al-Alili, A., 2016. A review on desiccant coated heat exchangers. Science and Technology for the Built Environment. doi:10.1080/23744731.2016.1226076

Sun, X. Y., Dai, Y. J., Ge, T. S., Zhao, Y., and Wang, R. Z., 2017. Comparison of performance characteristics of desiccant coated air-water heat exchanger with conventional air-water heat exchanger – Experimental and analytical investigation. Energy 137, 399-411.

Tao, Z., Liu, X., and Jiang, Y., 2014. Development of temperature and humidity independent control (THIC) air-conditioning systems in China—A review. Renewable and Sustainable Energy Reviews 29(7), 793-803.

Tu, Y. D., Wang, R. Z., Hua, L. J., Ge, T. S., and Cao, B. Y., 2017. Desiccant-coated water-sorbing heat exchanger: Weakly-coupled heat and mass transfer. International Journal of Heat and Mass Transfer 113, 22-31. doi:https://doi.org/10.1016/j.ijheatmasstransfer.2017.05.047

Y.D. Tu, R.Z. Wang, T.S. Ge, and X. Zheng, 2017. Comfortable, high-efficiency heat pump with desiccant-coated, water-sorbing heat exchangers. Scientific Reports 7(2), 40437.

Zheng, X., Ge, T. S., and Wang, R. Z., 2014. Recent progress on desiccant materials for solid desiccant cooling systems. Energy 74(1), 280-294.

Zheng, X., Ge, T. S., Wang, R. Z., and Hu, L. M., 2014. Performance study of com,posite silica gels with different pore sizes and different impregnating hygroscopic salts. Chemical Engineering Science 120(120), 1-9.

Manuscript ID: 1892
DOI: 10.18462/iir.icr.2019.1892

Evaporation heat transfer characteristics of low GWP refrigerants in plate heat exchangers

Yongchan Kim[(a)], DongChan Lee[(b)]

[(a)] Department of Mechanical Engineering, Korea University
Seoul, 02841, Republic of Korea, yongckim@korea.ac.kr
[(b)] Graduate School of Mechanical Engineering, Korea University
Seoul, 02841, Republic of Korea, ldc1120@korea.ac.kr

ABSTRACT

This study investigates evaporation heat transfer characteristics of several refrigerants with low global warming potential (GWP) in different types of plate heat exchangers. Brazed plate heat exchanger and shell and plate heat exchanger, which are widely used in a refrigeration system, are used as test sections. Hydrofluoroolefin (HFO) refrigerants with low GWP such as R1234yf, R1234ze(E), and R1233zd(E) are used as working fluids. The evaporation heat transfer coefficient and pressure drop of the low GWP refrigerants in the plate heat exchangers are measured and analyzed by varying the saturation temperature, mass flux, vapor quality, and heat flux. Based on the performance comparison between the plate heat exchangers, the brazed plate heat exchanger shows higher heat transfer coefficient, whereas the shell and plate heat exchanger exhibits an advantage in the low pressure drop.

Keywords: Low GWP, Alternative refrigerant, Plate heat exchanger, Shell and plate heat exchanger.

1. INTRODUCTION

Conventional refrigerants with high global warming potential (GWP) have been restricted by the regulations (UNFCCC, 1992, EU, 2006) that prohibit greenhouse gas emissions. Numerous studies (Hossain et al., 2013, Vakili-Farahani et al., 2013, Jankovic et al., 2015) have been carried out to propose appropriate alternative refrigerants for given applications. Hydrofluoroolefin (HFO) refrigerants, which have ultra-low GWP (GWP less than 10), have been proposed as powerful candidates for alternative refrigerants. HFOs exhibit short atmospheric lifetime owing to an unstable double bond in the molecule.

The heat transfer coefficient and pressure drop of a refrigerant are important parameters to optimally design heat exchangers in a refrigeration system. Especially, it is required to investigate the heat transfer characteristics of low GWP refrigerants in advanced heat exchangers to cope with the environmental issues. In addition, plate heat exchangers have been widely adopted in refrigeration industries owing to high compactness and efficiency. Accordingly, it is essential to develop empirical correlations of the Nusselt number and two-phase friction factor for optimal design of the plate heat exchangers. Experiments with smooth tubes have been conducted extensively (Diani et al., 2014, Guo et al., 2018, Longo et al., 2019). However, comprehensive experimental studies on the heat transfer characteristics of low GWP refrigerants in the advanced plate heat exchangers are very limited. In this study, the evaporation heat transfer characteristics of low GWP refrigerants including R1234yf, R1234ze(E), and R1233zd(E) were measured in a brazed plate heat exchanger (BPHE) and a shell and plate heat exchanger (SPHE), which are commonly used heat exchangers in refrigeration industries. The heat transfer characteristics of the low GWP refrigerants were analyzed according to operating parameters. Finally, the heat transfer performances of the plate heat exchangers were compared.

2. EXPERIMENTAL SETUP

2.1. Experimental Apparatus

The experimental setup consists of three flow loops: refrigerant, water, and ethylene glycol. The refrigerant loop is composed of a liquid pump, pre-heater, test section, condenser, and receiver. The pump circulates the refrigerant through the test section. The pre-heater controls the inlet vapor quality of the refrigerant entering the test section. After the refrigerant evaporates in the pre-heater and test section, it flows to the condenser which absorbs heat from the refrigerant. Accordingly, the refrigerant fully condenses in the condenser and flows back to the receiver. The related process is described in Fig. 1. The water loop is connected to the test section in order to supply heat. The water and ethylene glycol loop are connected to cooling and heating chillers, separately. The ethylene glycol loop is assembled with the condenser in the refrigerant loop to control the saturation temperature of the test section.

The commercial BPHE and SPHE, which are manufactured by SWEP and FROST, respectively, are used as test sections. The major differences between the plate heat exchangers are the geometry of the plate and the configuration of the channel. The shape of the BPHE is rectangular, while that of the SPHE is circular. As shown in Fig. 2, the refrigerant channel is surrounded by the water channel in the SPHE, whereas the two flow channels are configured side by side in the BPHE. Both plate heat exchangers have chevron angle of 60º.

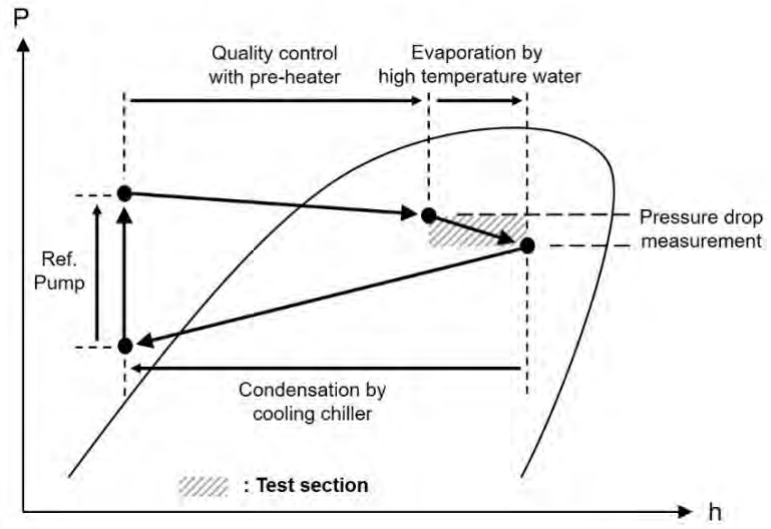

Figure 1 : P-h diagram of the experimental process

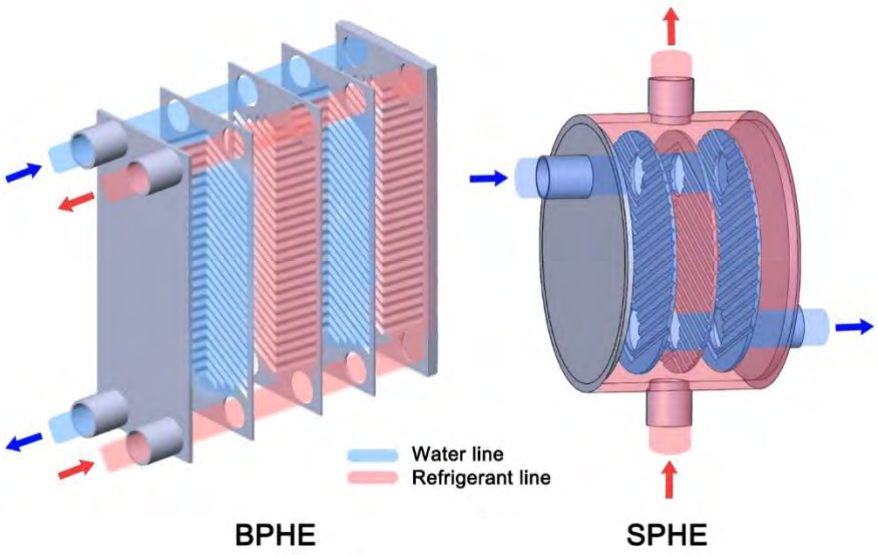

Figure 2 : Geometries and flow channel configurations of BPHE and SPHE

2.2. Test Condition

The evaporation heat transfer characteristics of the low GWP refrigerants in the plate heat exchangers were measured by varying the saturation temperature, mass flux, vapor quality, and heat flux. The saturation temperatures for R1234yf and R1234ze(E) were set to 5–15℃, and that for R1233zd(E) was set to 60–80 ℃. The main applications for the former two refrigerants are refrigeration cycles, whereas R1233zd(E) is mainly used in an organic Rankine cycle (ORC) in which the working temperature of the evaporator is high. In the BPHE, the mass flux, vapor quality, and heat flux were varied in the range of 21–58 kg s^{-1} m^{-2}, 0.1–0.9, and 3–10 kW m^{-2}, respectively. Since the size of the commercial SPHE was generally larger than that of the BPHE, the mass flux and heat flux were downgraded to 20–40 kg s^{-1} m^{-2} and 2.7–6.8 kW m^{-2}, respectively.

3. RESULTS AND DISCUSSION

The frictional pressure drop was influenced by viscosities and densities of the liquid and vapor phases. The large density difference between the liquid and vapor phases of R1234ze(E) resulted in a higher pressure drop owing to the high velocity difference between the phases. Since the viscosity and density differences of R1234ze(E) were 22% and 7%, respectively, higher than those of R1234yf, R1234ze(E) exhibited a higher pressure drop. In addition, the large liquid-vapor density ratio of R1234ze(E) caused high void fraction, resulting in a thin liquid film. Accordingly, the thin liquid film accelerated the evaporation process, which is the key mechanism for convective boiling. Therefore, the evaporation heat transfer coefficients of R1234ze(E) were higher than those of R1234yf even though R1234ze(E) showed 12% lower thermal conductivity than R1234yf.

Fig. 3 compares the heat transfer coefficient and pressure drop of R1234ze(E) in the BPHE and SPHE. The differences in flow characteristics between the plate heat exchangers can be explained by geometric configurations. Since the channel of the SPHE is a circular shape, the liquid phase tends to flow toward the perimeter of the channel, while the vapor phase flows straight to the outlet port. The detouring flow path in the liquid phase could reduce the effect of the corrugation. Therefore, the heat transfer coefficient and frictional pressure drop of the SPHE were lower than that of the BPHE owing to the decreased turbulent flow. Exceptionally, the evaporation heat transfer coefficients of the BPHE at high vapor qualities with the mass flux of 30 kg s^{-1} m^{-2} were lower than those of the SPHE. At the high vapor qualities with the low mass flux condition, the evaporation heat transfer coefficient decreased as the vapor quality increased, which was also reported in the previous studies (Táboas et al., 2012, Lee et al., 2014). This may be due to the partial dry-out at the low mass flux condition. The dry-out quality in the SPHE was higher than that in the BPHE because the liquid phase concentrated at the perimeter of the channel helped to wet the plate surface at the low mass flux condition.

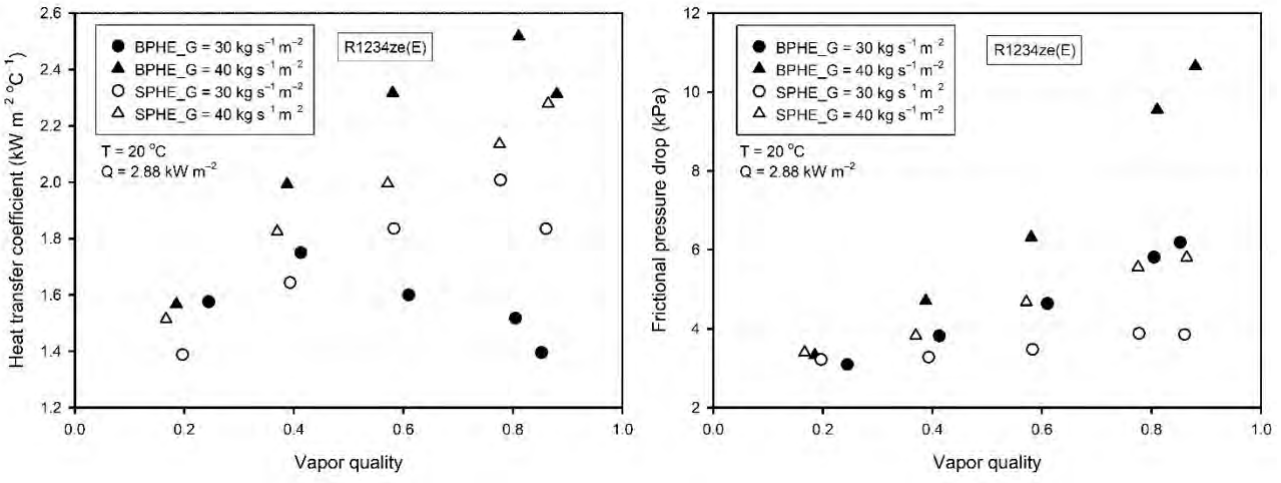

Figure 3 : Comparison of heat transfer performance between BPHE and SPHE.

4. CONCLUSIONS

The experiments were performed to evaluate the evaporation heat transfer characteristics of the alternative refrigerants with low GWP in the plate heat exchangers. The properties such as the thermal conductivity, densities of liquid and vapor, and viscosity influenced the evaporation heat transfer characteristics of each refrigerant. R1234ze(E) showed higher heat transfer coefficient and pressure drop than R1234yf because of its high-density difference between the liquid and vapor phases. The heat transfer characteristics were also compared between the BPHE and SPHE. Based on the performance comparison, it was found that the shape of the flow channel was the major reason for the different trends in the heat transfer performance. Since the circular shape of the flow channel made the liquid phase flow along the perimeter of the channel, the flow in the SPHE was less affected by the plate corrugation. Accordingly, the BPHE had strength in the heat transfer perspective, while the SPHE was preferable in terms of the pressure drop.

REFERENCES

Diani, A., Mancin, S., Rossetto, L., 2014. R1234ze(E) flow boiling inside a 3.4 mm ID microfin tube. Int. J. Refrigeration 47, 105-119.

EU, 2006. DIRECTIVE 2006/40/EC OF THE EUROPEAN PARLIAMENT AND OF THE COUNCIL of 17 May 2006 relating to emissions from air-conditioning systems in motor vehicles and amending Council Directive 70/156/EEC. Official Journal of the European Union.

Guo, Q., Li, M., Gu, H., 2018. Condensation heat transfer characteristics of low-GWP refrigerants in a smooth horizontal mini tube. Int. J. Heat and Mass Transf. 126(B), 26-38.

Hossain, A., Onaka, Y., Afoz, H.M.M., Miyara, A., 2013. Heat transfer during evaporation of R1234ze(E), R32, R410A and a mixture of R1234ze(E) and R32 inside a horizontal smooth tube. Int. J. Refrigeration 36(2), 465-477.

Janković, Z., Atienza, J.S., Suárez, J.A.M., 2015. Thermodynamic and heat transfer analyses for R1234yf and R1234ze(E) as drop-in replacements for R134a in a small power refrigerating system. Appl. Therm. Eng. 80, 42-54.

Lee, E., Kang, H., Kim, Y., 2014. Flow boiling heat transfer and pressure drop of water in a plate heat exchanger with corrugated channels at low mass flux conditions, Int. J. Heat and Mass Transf. 77, 37-45.

Longo, G.A., Mancin, S., Righetti, G., Zilio, C., 2019. Saturated vapour condensation of R134a inside a 4 mm ID horizontal smooth tube: Comparison with the low GWP substitutes R152a, R1234yf and R1234ze(E). Int. J. Heat and Mass Transf. 133, 461-473.

Táboas, F., Vallès, M., Bourouis, M., Coronas, A., 2012. Assessment of boiling heat transfer and pressure drop correlations of ammonia/water mixture in a plate heat exchanger, Int. J. Refrigeration 35, 633-644.

UNFCCC, 1992. Kyoto protocol to the United Nations framework convention on climate change.

Vakili-Farahani, F., Agostini, B., Thome, J.R., 2013. Experimental study on flow boiling heat transfer of multiport tubes with R245fa and R1234ze(E). Int. J. Refrigeration 36(2), 335-352.

Manuscript ID: 1893
DOI: 10.18462/iir.icr.2019.1893

Cryopreservation of human cardiovascular tissues: clinical application and storage devices

Noboru MOTOMURA
Toho University, Sakura Medical Center, Department of Cardiovascular Surgery
285-8741 Sakura-City, Chiba, Japan, noboru@motomura.org.

ABSTRACT

Cryopreservation technology is used in some places of biomedical area. As a cardiac surgeon, I have seen for a long time that cryopreservation technology is used in the most serious condition patients in our field. That is the infectious disease of cardiac valves, especially infection of artificial valve and graft. In this lecture I will show why cryopreservation has an important role in this particular area, and that procedure how the cryopreservation valve is used. Also I will discuss some storage issues to be invented.
Keywords: tissue allograft, cryopreservation, homograft, lazer sealer, cryobag

1. INTRODUCTION

Cryopreservation of human tissues has been performed more than over 30 years. Before an artificial prosthesis came to the world, human allograft tissues were used as surgical prostheses. Since artificial prostheses were available, fresh human allograft tissues disappeared and low temperature preservation tissues appeared. Because of quality problem, low temperature method was replaced to cryopreservation method. In cardiovascular field, almost all prostheses are covered by artificial prostheses. Cryopreserved allografts have been used in infected tissues, like heart valve, aorta, and infected artificial prostheses. These cryopreserved tissues are preserved under the liquid nitrogen level and the tissues are viable practically forever at the cellular level. Clinically the cryopreserved human cardiac aortic valves are used for patients with infected endocarditis or prosthetic heart valve endocarditis. In order to preserve the tissues under minus 180 degree Celsius, the preservation package is made of Teflon base material. These packages need high temperature, over 400 degree Celsius to seal them, and sealer needs special features than conventional heat sealer.

2. CRYOPRESERVATION OF HUMAN TISSUE ALLOGRAFT IN CARDIOVASCULAR AREA

In cardiovascular surgery area, cryopreserved human tissues are used in the tissue infection cases, like cardiac valve endocarditis, cardiac valve prosthetic endocarditis, artificial graft infection, etc. Initially for these valve infection cases, human allograft tissue valves preserved in refrigerator level temperature and not cryopreservation temperature had been used. Because viability of valvular cell (fibroblast) cannot be maintained after 2 weeks preservation in 4 degree Celsius, long-term outcome of such valve replacement was worse than cryopreserved valves (O'Brien et al. 1987). Since then, all of the allograft cardiac valves were preserved in cryopreservation manner.

2.1. Indication

Because artificial valve has spread all over the world and the quality of it is excellent, almost all valve replacement is done with artificial valve, and not cryopreserved allograft valve. Cryopreserved allograft cardiac valve is used mainly for infectious valve disease, because cryopreserved valve is viable and has the feature of anti-infection. Once infection occurred in cardiac valve, artificial valve has to be removed completely and viable cryopreserved cardiac valve is the first choice.

2.2. Mechanism of Anti-Infection Feature

The reason why viable cryopreserved allograft valve is stronger to infection than artificial valve has been unknown for a long time. We found the mechanism of anti-infection property of allograft by animal experiment using rat and methicillin-resistant Staphylococcus aureus (MRSA) microbes

(Saito et al., 2008). In order to fight against microbes, cardiac valve tissue needs to be viable. If not viable, like artificial valve or graft, microbes cannot be eliminated.

2.3. Tissue Allograft Donors

Cardiac valves are extracted from deceased body after taking informed consents. The body was appropriately prepared to keep sterilized in an operating theater. In order to keep sterile, cardiac valves are extracted within 6 hours of heart stop. Under the sterile and cooled condition, the tissues are carried to a processing facility.

2.4. Cryopreservation Method

The allograft tissues are dipped under a medium (RPMI or M119, etc.) with several kinds of antibiotics for 48 hours. This sterilization protocol is depending on the process facilities. Then the tissues are trimmed under a clean bench and placed into the cryopreservation bag with cryopreservation medium. Usually culture medium (RPMI, etc) and 10% dimethyl sulfoxide (DMSO) without antibiotics are used for the cryopreservation for cardiovascular tissues.

2.5. Storage Bag

Because the bag must be tolerable to the liquid nitrogen temperature, many facilities use aluminum or Teflon base bag. The tissues must be strictly kept in sterile, and it is packed in an inner bag which is placed in an outer bag. If aluminum bag is used, we cannot see inside and cannot check the tissue condition. So, we choose Teflon base bags.
As Teflon base bag is expensive, we invented our own bags. This bag will cover several kinds of shapes to adapt many types of tissues and cells (Figure 1). In case of Teflon material, bag sealing method requires higher temperature (over 400 degrees) than other usual bags (100-120 degrees). So, usual laboratory heat sealer will not work. We invented a laser beam bag sealer system. By this new machine we can design sealing line in any shape; straight, circle, angle, zigzag, etc, as you like (Figure 2).

2.6. Program Freezer

Doubly packed tissues are placed into a programmable freezer. The bag was placed in a stainless container to protect the bag. The container is cooled down at a rate of minus 1 degree per minutes until minus 40 degree, then speed is raised to 5 degree per minutes until minus 80 degree. Then the frozen container is moved to main storage tank using liquid nitrogen supply. These containers are stored under the vapor phase of liquid nitrogen, not liquid phase, in order to avoid break down the bags or protect cold injury from handling personnel.

2.7. Surgery

The cryopreserved cardiac allograft valve is shipped to a hospital using a dry shipper. The dry shipper can keep inside minus 150 degree Celsius for 5 to 10 days depending on the absorbed liquid nitrogen volume. The container is placed under the room temperature for 20 minutes in the operating theater. Then outer bag is cut and opened in a sterile manner and the inner bag is moved to sterile warm saline quietly. When inside tissue is completely thawed, the tissue is moved to another pot for rinsing. As DMSO is toxic to thawed tissue, it is gently rinsed with stepwise saline. Finally, the thawed valve is handed to a surgeon.

2.8 Outcome

The outcome of valve infection surgery is bad, because preoperative patient condition is bad and deformity of cardiac valve and surrounding area is serious. If such patients do not receive surgery, as many as half of them could not survive. So, the mortality rate of such surgery is as high as 15 to 35% if cryopreserved allograft valve is not used. The mortality rate of prosthetic valve endocarditis using cryopreserved allograft cardiac valve is roughly 15% which is quite reasonable, thinking of the patients' serious condition.

3. CONCLUSIONS

In some cardiac surgery area, like prosthetic valve infection, cryopreserved human cardiac valve is quite effective. Innovation of storage bag and sealing system can help to extend these precious tissues. Cryopreservation technology is indispensable for such serious patients.

REFERENCES

O'Brien, M.F., Stafford, E.G., Gardner, M.A., 1987. A comparison of aortic valve replacement with viable cryopreserved and fresh allograft valves, with a note on chromosomal studies. Journal of Thorac Cardiovasc Surgery 94,812-823.

Saito, A., Motomura, N., Kakimi, K., 2008. Vascular allografts are resistant to methicillin-resistant Staphylococcus Aureus via Indoleamine 2,3-Dioxygenase in Murine Model. Journal of Thorac Cardiovasc Surgery 136,159-167.

Figure 1. Teflon base cryopreservation storage bag. By using the laser beam sealing system, the sealing line can be designed as you want, like this bag. The sealing line can be drawn in straight, angle, circle, spiral, zigzag, etc.



Figure 2. Laser sealer. Cryopreservation bag which can be stored under liquid nitrogen level is made of Teflon base materials. To seal the Teflon based storage bag, laser beam sealing system is needed. This sealer is designed to seal the Teflon base storage bag easily and securely in a sterile manner by the laser beam system.

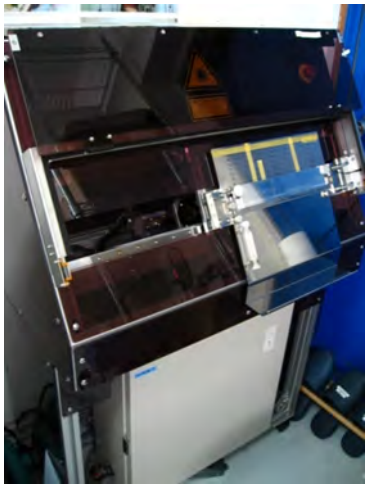

Manuscript ID: 117
DOI:10.18462/iir.icr.2019.0117

Study on thermodynamic process in pulse tube using MD simulation

Yingxia QI [(a)], Shuai PAN[(b)], Yanjin CHE[(b)] , Haifeng YANG[(b)]

[(a)]Department of Energy and Power Engineering, University of Shanghai for Science and Technology
Shanghai, 200093, China, Email: qipeggy@126.com
[(b)] Graduate School of Energy and Power Engineering, University of Shanghai for Science and Technology

ABSTRACT

To explore the mechanism of temperature gradient establishment along the pulse tube, the oscillation flow of helium gas in the pulse tube with no regenerator and heat exchangers was studied using molecular dynamic simulations on NVE ensembles. The EAM/FS and UFF atomic potential was used for Fe and He atoms, respectively. The simulation results show that the temperature, pressure gradients are varied during a whole expansion process. The axial speed is varied from small to maximum quickly and then down to zero gradually by fluctuation. The phase of pressure is leaded to the speed by 72° at the hot end during the expansion process. The phase angle difference between the pressure and the speed waves is not changed with the tube length. The cold temperature after expansion is decreased with the increase of the tube length and the pressure ratio. From the energy efficiency, it should be circumspect to increase the pressure ratio.
Keywords: Micro Pulse Tube, Length, Pressure Ratio, Low Temperature, Temperature Gradient, Molecular Dynamics Simulation.

1. INTRODUCTION

Pulse tube refrigerator has no moving parts, causing high reliability in terms of low vibration, EMI, etc. (Radebaugh R, 2000). Now the pulse tube refrigerator is widely used in aerospace, military, cryogenic electronics, low-temperature medicine, meteorology, gas liquefaction and other fields. Although the structure of pulse tube refrigerator is relatively simple but the formation mechanism of the temperature gradient along the axial tube is very complicated.

Currently, there are several different theories and explanations for the thermodynamic principle of the pulse tube refrigerator. In 1966, (Gifford and Longsworth, 1966) proposed the theory of surface pump heat to explain the mechanism of pulse tube refrigeration, in which it is said that the gas micelle in compression and expansion pump the heat from the cold end to hot end along the wall. However this theory is only applicable to analysis of basic pulse tube. In 1984, Mikulin et al. (1984) proposed a classical analysis method. This method calculates the effective cooling capacity of the complete cycle in the ideal case based on the heat balance equation and the known thermodynamic formula, and finally gets the total refrigerating capacity and efficiency of the modified pulse tube refrigerator. In 1986, Radebaugh et al. (1986) proposed enthalpy flow modulation theory. The relationship between enthalpy flow and pressure / velocity is revealed by the use of energy conservation and mass conservation law. The theory of enthalpy flow phase modulation explains the mechanism of the orifice pulse tube cooler, especially the phase modulation between the small holes and the gas reservoirs. In 1987, Peter et al. (1987) proposed vector analysis method. The sinusoidal vectors can be represented by the rotation vector in the case of small compression ratio. Through vector analysis, the variations and interrelations of the internal parameters can be revealed. However, this method is more idealized, and the calculation results are only qualitatively coincidence with the experimental results. In 1996, Liang et al. (1996) proposed thermodynamic non-symmetry effect to illustrate the refrigeration process in a PTR. By establishing the model, the gas in the pulse tube was divided into the gas in the hot sticky layer near the wall and the gas in the central space. The refrigeration mechanism is the sum of surface heat pump and thermodynamics asymmetric effects and the cooling amount of the pulse tube is the sum produced by the two parts of the gas. In 2004, Luo et al. (2004) proposed the mesoscopic thermodynamic theory to investigate

the thermodynamic cycles in the regenerator. But these theories are short of detailed descriptions for complex gas flow and heat transfer phenomenon in the PTRs. As early as 1969, Rott (1969) established the thermo acoustic theory. The pulse tube refrigerator produces time-average cooling effect depending on the heat interaction between the oscillating fluid and solid medium, but it is limited to the thermal acoustic effect of the acoustic standing wave. The thermo acoustic theory was used to analyze and calculate the pulse tube refrigerator (Xiao Jiahua, 1991). In addition, there are still other analysis methods, such as electrotechnics analogical analysis, network analysis, gas working analysis, etc.(Shaoshuai Liu et al.,2017; Jingyuan Xu et al., 2017; Tian Lei et al.,2016). By numerical simulation method (Y.L. He et al.,2009; Chao Gu et al.,2012; Sachindra Kumar Rout et al.,2017; Qunte Dai et al.,2015), the performance of the PTR and the dynamic characteristics of flow and heat transfer in the pulse tube were obtained, which can explain the experiment results reasonably.

In present work, the formation mechanism of the temperature gradient along pulse tube was investigated using molecular dynamics method. By observing the atomic motions and velocities, the temperature, pressure and speed variations with time in the expansion process were obtained based on statistical thermodynamics.

2. METHODOLOGY

2.1. Physical Mode

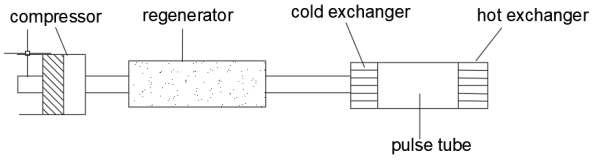

Figure 1: A schematic view of basic type pulse tube refrigerator

Fig. 1 shows a schematic view of a basic type pulse tube refrigerator. The pulse tube is an only a component that separates the gas into a hot end and a cold end. In this paper, the formation process of the temperature gradient in the pulse tube by gas oscillation flow was investigated using molecular dynamics simulations.

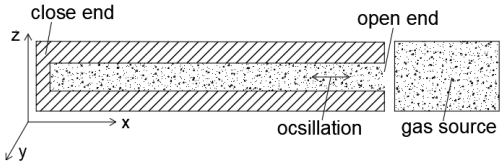

Figure 2: Simulation model of the pulse tube

The simulation model of the pulse tube was shown in Fig. 2. It consists of a half-closed slit channel and a gas source. The gas source has a high pressure or low pressure corresponding to a compression or expansion process initially. In order to study the cooling capacity of gas separately, the heat exchangers at the two ends were eliminated. Also the gas has no heat exchange with the wall of the channel.

2.2. Intermolecular Potential Models

The interactions between Fe and Fe molecules are described by Embedded Atom Method (EAM/FS) (Finnis M W et al.,1984) with the form of Eqn.1. The EAM/FS potential function parameters used in this paper are adopted from the work of Mendelev and Han (2003) in 2007. For the interactions between He-He and He-Fe, the Lennard-Jone potential is used with the expression of Eq. (4). The specific parameter values are shown in table 1.

$$E_i = F_\alpha\left(\sum_{j\neq i}\rho_{\alpha\beta}(r_{ij})\right) + \frac{1}{2}\sum_{j\neq i}\varphi_{\alpha\beta}(r_{ij}) \quad \text{Eq. (1)}$$

$$\rho_i = \sum_{j\neq i}\rho_j(r_{ij}) \quad \text{Eq. (2)}$$

$$\rho_i(r_{ij}) = \sum_{k=1}^{2} A_k (R_k - r_{ij})^3 H(R_k - r_{ij}) \quad \text{Eq. (3)}$$

$$U_{ij} = 4\varepsilon \left[\left(\frac{\sigma}{r_{ij}}\right)^{12} - \left(\frac{\sigma}{r_{ij}}\right)^{6} \right] \quad r_{ij} \le r_c \quad \text{Eq. (4)}$$

$$\varepsilon_{12} = \sqrt{\varepsilon_1 \epsilon_2} \quad \text{Eq. (5)}$$

$$\sigma_{12} = \frac{1}{2} (\sigma_1 + \sigma_2) \quad \text{Eq. (6)}$$

Table 1. L-J potential function parameters

pair	ε (eV)	σ(Å)
He-He	0.000607098	2.103
He-Fe	0.0178726	2.20175

The temperature of a block of atoms was calculated by Eq. (7):

$$T_{cal} = \frac{\sum m_i \, (v_{i,x} - \bar{v}_x)^2 + (v_{i,y} - \bar{v}_y)^2 + (v_{i,z} - \bar{v}_z)^2}{3\mathrm{N}k_B} \quad \text{Eq. (7)}$$

Where m is the atomic mass, v is the velocity of the atom, $\bar{v}$ is the mass-center velocity of the grid, N is the number of the atoms in the grid, K_B is the Boltzmann constant.
The pressure is calculated by the ideal gas equation-of-state.

2.3. Molecular Dynamics Simulation

The system is a channel with L×H×B nm3. L is equal to 286nm, H is 100nm and B is 1.43 nm. This is a unit size.
The system is divided into two equal parts. The left one is used for the high pressure gas, the right one is used for the low pressure gas. The simulation model is shown in Fig. 3. Then the gas pressure difference between them causes an expansion process in the left side.

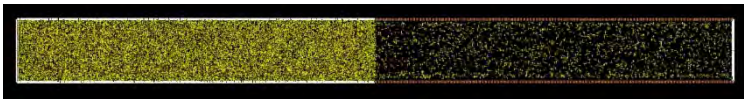

Figure 3: The simulation mode for pulse-tube refrigeration.
Left: high pressure gas, right: low pressure gas

The elastic reflect periodic boundary conditions were imposed on three directions.
The simulations were carried out firstly on NVT ensemble with 1×10^5 steps for getting the wanted system temperature of 300K, and then on NVE ensemble to obtain the acquired data. The Langevin method was selected for the temperature control. The cutoff distance for the Lennard-Jones interactions was 7.15Å. The Velocity-Verlet algorithm with a time step of 0.8 fs was used to solve the equations of motion. The positions and velocities of He atoms were recorded every 50000 steps. The simulations were run on LAMMPS software.

3. RESULTS AND DISCUSSIONS

Along the axial direction (x axis), the system was divided into grids every 200 Å. The origin was located at the hot end of the channel. The temperature, pressure, and velocity were the average values over each grid.

3.1. Time-Variation of Axial Distributions

The model in this section is 6L×3H×1B, i.e. 3400 nm ×300 nm. The expansion length is 3L. The pressure of 0.1 MPa contains 8887 He atoms while 0.6 Mpa contains 53322 He atoms.
The variations of the distributions of the temperature, pressure, atomic number density and the velocity along the axial direction with the time are shown in Figs. 4a to 4c.

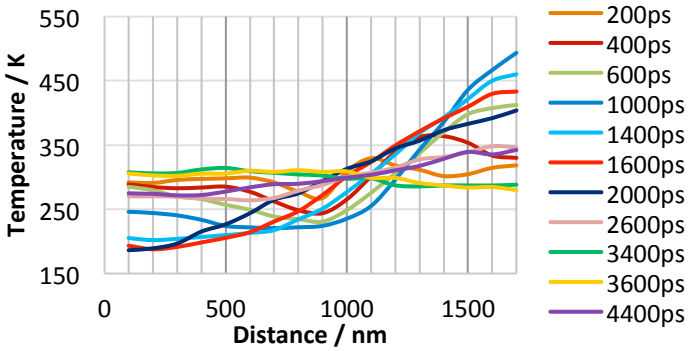

Figure 4a: The time-variation of the axial temperature distribution

From the Fig. 4a, it could be seen that the axial temperature gradient was formed along the axial direction and changed with time. The temperature at the interface of the high and low pressure gas source (800-900 nm) was decreased firstly, and then the cold temperature spread to the left end (100-200 nm) gradually. At 1600 ps, the temperature at the left end reached to the lowest temperature 186 K.

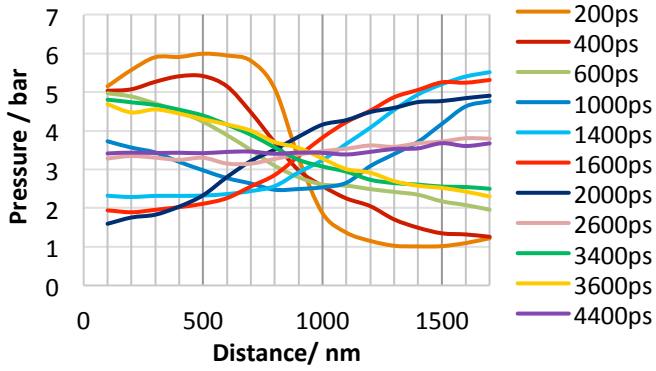

Figure4b: The time-variation of the axial pressure distribution

The time-variation of the pressure distribution along the axial direction is shown in Fig. 4b. The pressure dropped started from the interface of the high and low pressure gas source and then transferred to the left hot end. The lowest pressure at the hot end reached to 1.6 atm. After that it could be seen that the pressure was oscillating around the average value of 3.5 atm. For the ideal isentropic expansion with pressure ratio of 1.6/6, the temperature after expanding is 177 K. Therefore, the simulation result 186K was acceptable.
Figure 4c shows the time-variation of the axial speed distribution along the axial tube. The speed was the axial speed of the mass-center of each grid. It could be seen that the speed presented a normal distribution. At first, the maximum speed was located near to the centre of the system (2000nm), i.e., the interface of the high and low pressure gas source. Then the speed was firstly increased with the peak position transferring to the right and next decreased with moving to the left. After that it could be seen that the speed was oscillating around 0. It was noted that the velocities at the two ends of the system were almost zero throughout the process.

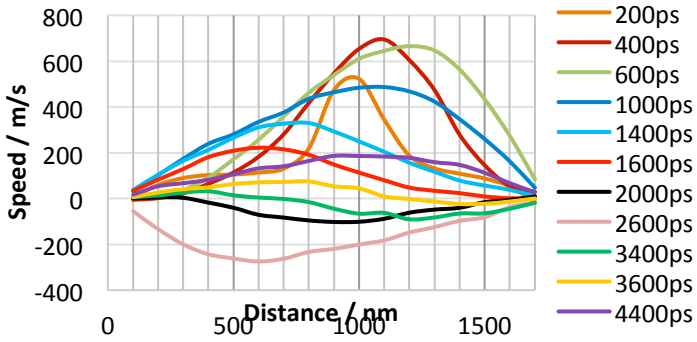

Figure 4c: The time-variation of the axial speed distribution

3.2 Variation of Tube Length

The system length was changed from 6L to 12L (1700 nm to 3400 nm). The expansion length is 6L.

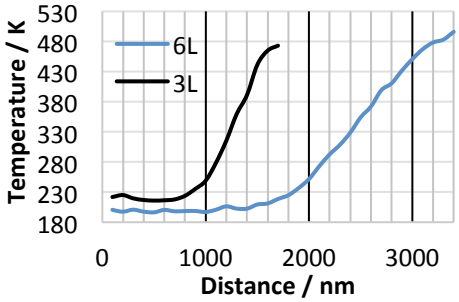

Figure 5: The comparison of transient axial temperature distributions with different length

From Fig. 5, it could be seen that the temperature span is increased with the increase of the tube length and the lowest temperature is decreased with the increase of the tube length. This is interpreted as that the longer length resulted in the smaller axial heat conduction.

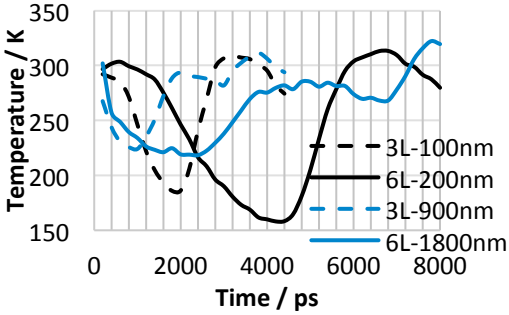

Figure 6: The comparison of temperature time-variations with different length

From Fig. 6, it could be seen that the maintaining time of the cold end (3L-900 nm, 6L-1800 nm) at the lowest temperature is increased with the increase of tube length. However, the lowest temperature at the hot end is decreased with the increase of the tube length. But before 2500 ps, the hot end temperature is increased with the increase of the tube length.

Fig. 7 shows the initial pressure distribution and the transient pressure distribution at which the pressure at the hot end reached the maximum. It could be seen that the pressures in the 6L tube are lower than that in the 3L tube at the same relative positions inside the expansion region (smaller than half of the tube length). The maximum pressure reached after the expansion at the hot end in the 6L tube is a little lower than that in the 3L tube, 0.140 Mpa and 0.169 Mpa, respectively. Therefore, the pressure loss is 0.040 Mpa and 0.069 Mpa for 6L and 3L length, respectively. This indicates at least that the longer length doesn't result in the larger pressure loss in the pulse tube.

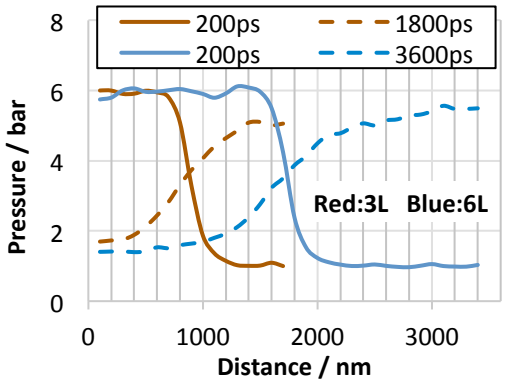

Figure 7: The comparison of pressure distributions with different length.

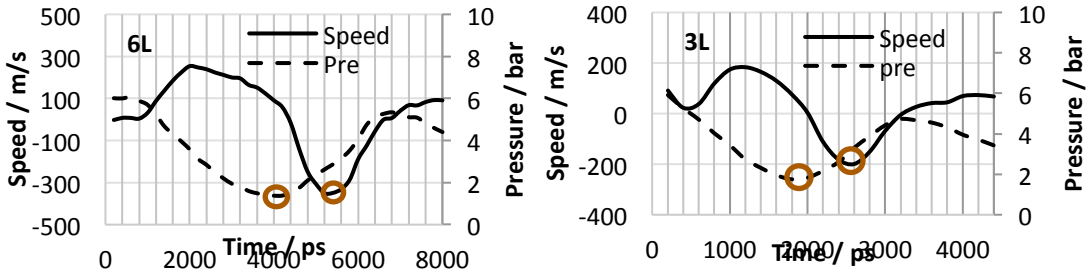

Figure 8: The comparison of phase time differences between pressure and speed waves at the hot end with different length

From Fig. 8, it could be seen that the phase of the pressure wave at the hot end is ahead of the speed wave by about 72°, but the phase difference is almost same for different tube length. Therefore it is concluded that the phase angle difference between the pressure and speed wave is not changed with the length.

3.3 Variation of Pressure Ratio

The model in this section was 6L×3H×1B, i.e. 3400 nm ×300 nm. The expansion length was 3L. Therefore, the hot end is around 100-300nm and the cold end is around the centre (800-900 nm). For comparison, the two models with different pressure ratios were constructed. The initial pressures of high pressure gas sources were 1.2 Mpa and 0.6 Mpa, respectively with the same low pressure of 1.0 Mpa. So the pressure ratios were 12 and 6, respectively.

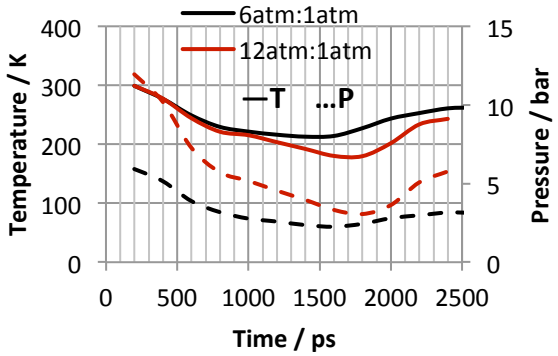

Figure 9: Comparison of temperature and pressure variations at 600 nm with different pressure ratios

In Fig. 9, the temperature and pressure variations at the cold end (600 nm) are presented. It could be seen that the temperature after expanding is decreased with the increase of the pressure ratio. The lowest temperature is 214K and 180K, respectively. The temperature ratio is only 0.841 with

the pressure ratio increased from 6 to 12. However, for the isentropic expansion, it follows Eq. (8):

$$\frac{T_{2a}}{T_{2b}} = \left(\frac{p_{1b}}{p_{1a}}\right)^{\frac{k-1}{k}} \quad \text{Eq. (8)}$$

If $T_{1a} = T_{1b} = 300K$, $p_{1b} = 0.6\ Mpa, p_{1a} = 1.2Mpa$, $p_{2b} = p_{2b} = 1.0Mpa$, Then $T_{2a}/T_{2b} = 0.758$. This means that the effect of the increase of the pressure ratio is weaker in the pulse tube than in the expander.

From Fig. 9, it could also be known that the lowest pressure after expanding for two models is 3.06 and 2.26 Mpa with the initial pressure being 12 and 6 Mpa, respectively. So the actual pressure ratio is 3.92 and 2.65, respectively. Hence the actual pressure ratio is only 0.33 and 0.44 times of the ideal ratio, respectively. From the energy efficiency, larger pressure ratio 12 is not better than lower pressure ratio 6.

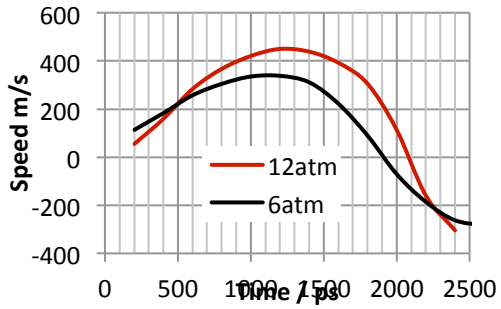

Figure 10 Comparison of axial speed variations at 600 nm with different pressure ratios

From Fig.10, it could be seen that the axial speed at the cold end is increased with the increase of the pressure. The speed is 450 and 338 m/s for 12 and 6 pressure ratios, respectively.

4. CONCLUSIONS

To explore the formation mechanism of temperature gradient along the pulse tube, the expansion process of gas in the pulse tube was investigated by molecular dynamic simulations. The simulation results show that the temperature, pressures, axial speed are varied sinusoidally. Therefore, there is an intrinsic frequency for oscillation flow in a pulse tube. This intrinsic frequency was related with the pressure difference and tube length. The phase of the pressure wave is leaded to that of speed wave at the hot end. As the optimum periodic times were different for hot and cold ends, this is why the phase shifters at hot or cold end could increase the efficiency of the PTR.

REFERENCES

Radebaugh R, 2000. Development of the pulse tube refrigerator as an efficient and reliable cryocooler. Int. J. Proceedings of the Institute of Refrigeration, London, 96：11-31.

W. Gifford, R. Longsworth, 1966. Surface heat pumping, Adv. Cryo Eng. 11: 171–181.

E.A. Mikulin, A.A. Tarasov, M.P. Shkrebyonock, 1984. Low-temperature expansion pulse tubes, Adv. Cryo Eng. 29 :629–637.

R. Radebaugh, S. Herrmann, 1986. Refrigeration efficiency of pulse-tube refrigerator, in: 4th International Cryocoolers, Conference, 119 p.

S. Peter, R. Radebaugh, 1987. Development and experimental test of an analysis model of the orifice pulse tube refrigerator, Adv. Cryo Eng. 33: 851–859.

J. Liang, A. Ravex, P. Rolland, 1996. Study on pulse tube refrigeration Part 1: thermodynamic non-symmetry effect, Cryogenics 36 (2) :87–93.

E. Luo, W. Dai, Z. Wu, et al., 2004. Meso-scope thermodynamic theory for cyclic flow engines,

Cryogenics 1 1–11.

Rott N. ,1969.Damped and thermally driven acoustic oscillations in wide and narrow tubes. ZAMP.

Jiahua X., 1991.Thermal acoustic effect and thermoacoustic theory of retractable cryogenic refrigerator [D]. Beijing: Institute of Physics CAS.

Shaoshuai L., Xi C., Ankuo Z., Zhenhua J., Yinong W., Hua Zhang, 2017. Investigation of the inertance tube of a pulse tube refrigerator operating at high temperatures. Energy 123: 378-385.

Jingyuan X., Guoyao Y., Limin Z., Wei D., Ercang L., 2017. Theoretical analysis of two coupling modes of a 300-Hz three-stage thermoacoustically driven cryocooler system at liquid nitrogen temperature range. Applied Energy 185: 2134–2141.

Tian L., John M. Pfotenhauer, Wenjie Z., 2016.Analysis and comparison of different phase shifters for Stirling pulse tube cryocooler. Cryogenics 80 : 63–73.

Y.L. He, Y.B. Tao, F. Gao, 2009. A new computational model for entire pulse tube refrigerators: model description and numerical validation, Cryogenics 49: 84–93.

Chao G., Yuan Z., Junjie W., Wei J., Qiang Z., 2012. CFD analysis of nonlinear processes in pulse tube refrigerators: Streaming induced by vortices, International Journal of Heat and Mass Transfer, 55:7410-7418.

Sachindra K. R., Arun K. B., Sisir D. and Ranjit K. S., 2017. Numerical analysis of a modified type pulse tube refrigerator. Energy Procedia, 109: 456-462.

Qunte D., Yanyan C., Luwei Y., 2015. CFD investigation on characteristics of oscillating flow and heat transfer in 3D pulse tube. International Journal of Heat and Mass Transfer, 84: 401–408.

Finnis M W, Sinclair J E, 1984. A simple empirical N body potential for transition metals[J]. Philos Mag A, 50(1):545

M. I. Mendelev, S. Han, D. J. Srolovitz, G.J. Ackland, D. Y. Sun, 2003. Development of new interatomic Potentials appropriate for crystalline and liquid iron, Philosophical Magazine, 83(35): 3977-3994

ID: 258
DOI: 10.18462/iir.icr.2019.0258

Optimization of charge/discharge scenarios and economic analysis of a liquid air energy storage system used in combination with a photovoltaic power source and a cold storage warehouse

Cyrine Damak[1], Denis Leducq[1], Minh Hong Hoang[1], Amine Hamzi[1], Anthony Delahaye[1]

[1]IRSTEA (Institut de Recherche en Sciences et Technologie de l'Environnement et de l'Agriculture), ANTONY, 92160, France
cyrine.damak@irstea.fr

ABSTRACT

Intermittency of renewable energy generation and electricity tariff variation make necessary the analysis and optimization of different scenarios of charge/discharge cycle timing and duration of a Liquid Air Energy Storage (LAES) and the economics related to each case.
Solar irradiation and PhotoVoltaic (PV) power plant size, electricity prices, on-site electricity demand throughout the day/month/season and year are key factors here for the scenarios optimization in terms of cost of electrical energy consumed from the grid. These factors are also useful to determine the maximum allowed investment of the LAES and the payback time according to each case scenario.
Self-sufficiency and positive economics of the LAES combined to cold warehouse are reached when PV power plant surface and solar irradiation are high enough. Therefore, there are optimal PV dimensions depending on the round trip efficiency of the LAES, the power capacity discharge/charge ratio of the system and the geographic location of the site. Main results suggest that LAES can only be profitable when electricity from grid is expensive.
Keywords: Cryogenic storage, LAES, Optimization of energy scenarios, economical analysis

1. INTRODUCTION

Recently, cryogenic energy storage and more particularly Liquid Air Energy Storage LAES has drawn the attention of both academic and industry due to environmentally friendly grid-scale technology. LAES is adapted to large scale (grid scale) application, while refrigerant cycle system or ice storage system are limited to small storage size. Besides, the temperature reached in case of LAES is very low (-196°C) which makes the system very different from the refrigerant cyle system or ice storage system in terms of field of application. The idea of cryogenic energy storage was firstly proposed by E.M Smith, at university of New Castle in 1977 (Smith, 1977) using the energy of liquid air as the cryogenic energy. A particular configuration of LAES systems is to use excess cold energy from the electricity recovery process for food factory or refrigerated warehouse. This improves the profitability of the whole process. On one hand, this helps to reduce the electrical consumption of the warehouse refrigeration unit while maintaining adequate temperatures inside the warehouse. On the other hand, direct expansion of liquefied cryogen at high pressures (in this case liquid air) through multi-stage turbines allows electrical energy recovery.
This work investigates the economics related to this system based on the study of an Optimal Control (OC) strategy for charging/discharging/generation of cold energy in the warehouse depending on the electricity tariff and the geographical location. Once the optimal strategy defined, a techno-economic study corresponding to the operating schedule can be conducted to evaluate the economic performance of the system. The OC strategy of this research work is developed for a cost function that aims to minimize the cost of electricity purchased from the grid and maximize the

usage of the LAES. Thereafter, results of scenarios' analysis will lead to investigate economic feasibility of the storage system. The annual savings achieved, or losses generated are calculated to determine the investment threshold allowed for the LAES system as well as the CapEx and the payback period of the reference case.
In the current work, the case study is a refrigerated warehouse supplied by a PV power plant located in Belgium. The objective of the study is, therefore to evaluate energy optimization control and economic benefit from the integration of LAES in this site.

2. ENERGY MANAGEMENT STRATEGIES METHODOLOGY AND SIMULATIONS

This section describes the dynamic energy model of the whole system on-site for the OC strategy. First, the layout model is analyzed and the LAES storage system is described. Second, methodology of the OC strategy and economics is detailed. Finally, results of simulation are given in the final parts.

2.1 Schematic model layout

The proposed system analyzed in this work is composed of 4 sub-models: the power utility grid, PV modules, LAES and the warehouse with the power flow shown in Fig. 1. The refrigeration load of the warehouse is mainly covered by the PV power plant. When energy delivered by the PV plant is in excess, surplus of generated energy is used for air liquefaction unit. When PV plant no longer produces electricity, air is being expanded through the turbine-generator set to meet the refrigeration load. The power grid is then used only in the case where neither the PV nor the storage system are able to supply the warehouse demand. The study is only focused on the excess renewable generation storing approach and not storing it from off-peak electricity grid. No resale to the grid is considered when the PV power plant produces energy excessively, only the profitability of the LAES integration is considered in the current study.
The following control variables to be optimized are represented by the arrows in Fig. 1.
$P_{PV\ TO\ WAREHOUSE\ (t)}$ is the PV power used to directly supply the warehouse; $P_{PV\ TO\ LAES\ (t)}$ is the power for charging the LAES by the excess PV generation, $P_{LAES\ TO\ WAREHOUSE\ (t)}$ is the power generated from the turbine-generator set to supply the warehouse, $P_{GRID\ TO\ WAREHOUSE\ (t)}$ is the grid power used to supply the warehouse.

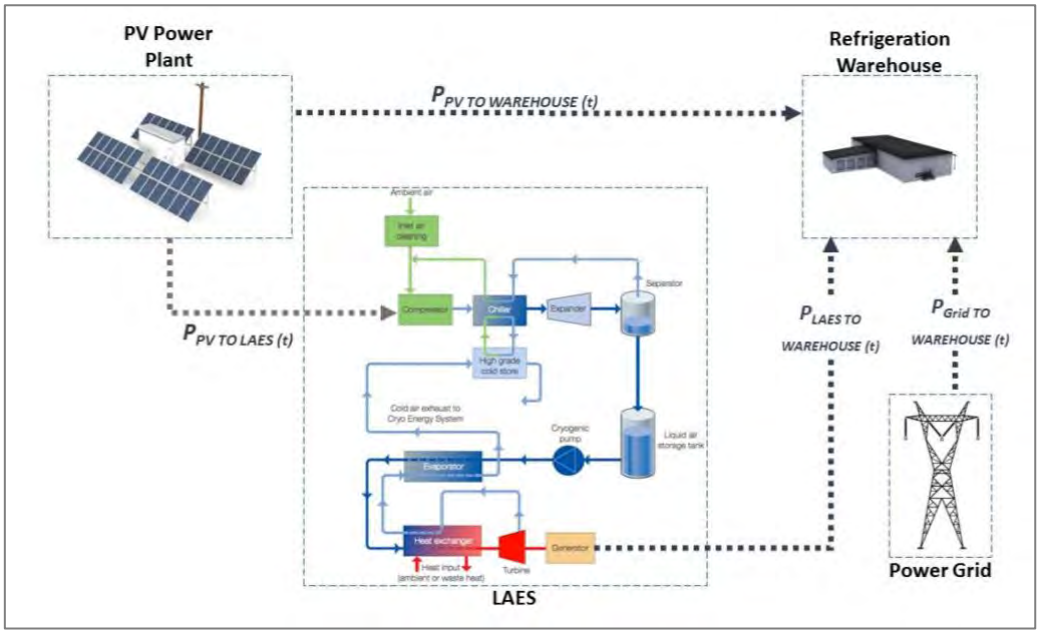

Fig. 1: Schematic layout of the model (Negro et al., 2018)

2.2 Presentation of the storage system

The LAES system comprises three main parts: the charging, storage and discharging processes. During charging phase, excess of renewable electricity is used for air liquefaction. Later at night when PV panels no longer produce electricity, the air is evaporated and expanded in turbines to

generate electricity. Cold energy from the evaporation of liquid air is stored and used for liquefaction needs and also for refrigerated warehouse supply. Besides, hot storage captured from inter-coolers of the liquefaction part is used to "super-heat" air before expansion. More detail about the LAES process can be found in (Negro et al., 2018)

2.3 Methodology of the optimization

The non-linear optimization problem can be solved using the Generalized Reduced Gradient Method as implemented in the standard Microsoft Excel Solver. Simulations are done for a duration 24 hours with a time lapse called "t" from 1 to 24 reflecting 1AM to 12PM.

Assumptions for each sub-model are given in Table 1 and they were made as follow:

Table 1: Set parameters for the simulation

Parameter	Unit	Value
Peak Rated power of PV panels* under a solar irradiation of 1kW/m²	MWp	1
Off-peak tariff**	€/kWh	0,0662
Peak tariff**	€/kWh	0,0842
Round Trip Efficiency***	-	0,25
Exergy efficiency *	-	0,3
Thermal energy load for refrigerated warehouse for winter case***	kWh/day	1500
Thermal energy load for refrigerated warehouse for summer case***	kWh/day	2000
LAES size***	kW/kW	180/60
Minimum power of PV panels*	kW	20
Maximum power of PV panels*	kW	80

(*) author assumption; (**) onsite data; (***) Thermodynamic simulation results (not included in the current work)

2.4 Sub-models

2.4.1 Power PV plant

The sum of the power delivered by the PV plant to charge the LAES and to supply the refrigeration load must be less than the power delivered by the PV panels at any instant *t.*

$$0 \leq P_{PV\ TO\ LAES\ (t)} + P_{PV\ TO\ WAREHOUSE\ (t)} \leq P_{PV,} \qquad \text{Eq. (1)}$$

2.4.2. Power grid

Night off-peak hours are set by the distribution system operator and are on average between 10 pm and 7 am. However, for the rest of the time, a peak hour tariff is applied:

$$p_{(t)} = \begin{cases} p_{0\ (t)} = 0{,}0662\ €/\text{kWh} & \text{if } t \in [22, 24]\ \cup\ [0, 7] \\ p_{1\ (t)} = 0{,}0842\ €/\text{kWh} & \text{if } t \in [7, 22] \end{cases} \qquad \text{Eq. (2)}$$

2.4.3. LAES

The LAES is charged with the excess of renewable energy from the PV panels $P_{PV\ TO\ LAES\ (t)}$. The recovered energy $P_{LAES\ TO\ WAREHOUSE\ (t)}$, consists of the electricity produced by the turbines during the system discharge stage and electricity saved by cooling the warehouse with liquid air from the LAES system. The State Of Energy $SOE_{(t)}$ of the LAES at any given time *t* and the flow of power from *t-1* to *t* is given in Eq. (3):

$$SOE_{(t)} = SOE_{(t-1)} + (RTE \times P_{PV\ TO\ LAES\ (t)} - P_{LAES\ TO\ WAREHOUSE\ (t)}) \times TP \qquad \text{Eq. (3)}$$

2.4.4. Refrigeration warehouse

The conversion of the thermal energy to its equivalent in terms of electrical energy is done by means of COP and it is expressed by Eq. (4) and Eq. (5):

$$COP = COP_{Carnot} \times \eta_{ex} = \left(\frac{T_c}{T_h - T_c}\right) \times \eta_{ex} \qquad \text{Eq. (4)}$$

$$\sum_{t=1}^{N} COP_{(t)} \times P_{WAREHOUSE(t)} \times TP = Q_{f,tot} \quad (kWh) \qquad \text{Eq. (5)}$$

2.4.5. Objective function:
The control strategy needs to identify the most beneficial periods in order to minimize the purchase of electricity in the grid. As described in the equation below the optimal system control strategy will be the one that minimizes the grid electricity purchased.

$$G = \sum_{t=1}^{N} TP \times p_{(t)} \times P_{GRID\ TO\ WAREHOUSE(t)} \qquad \text{Eq. (6)}$$

2.4.6. Variable constraints:
At any instant *t*, the sum of the supplied power to the warehouse must be equal to the instantaneous refrigeration load.

$$P_{PV\ TO\ WAREHOUSE\ (t)} + P_{LAES\ TO\ WAREHOUSE\ (t)} + P_{GRID\ TO\ WAREHOUSE\ (t)} = P_{WAREHOUSE\ (t)} \qquad \text{Eq. (7)}$$

The sum of the power delivered by the PV plant to charge the LAES and to supply the refrigeration load must be less than the power delivered by the PV panels at any instant *t.*

$$P_{PV\ TO\ LAES\ (t)} + P_{PV\ TO\ WAREHOUSE\ (t)} \leq P_{PV\ (t)} \qquad \text{Eq. (8)}$$

2.4.7 Variable limits
The warehouse and the LAES are modelled as variable parameters which can be controlled from an upper to a lower set range for each sampling time period of the simulation horizon. These constraints can be expressed as:

$$20 \leq P_{WAREHOUSE(t)} \leq 80 \quad (kW) \qquad \text{Eq. (9)}$$
$$0 \leq P_{PV\ TO\ LAES(t)} \leq 240 \quad (kW) \qquad \text{Eq. (10)}$$
$$0 \leq P_{LAES\ TO\ WAREHOUSE(t)} \leq 60 \quad (kW) \qquad \text{Eq. (11)}$$
$$0 \leq SOE_{t)} \leq 1704 \quad (kWh) \qquad \text{Eq. (12)}$$

2.4.8. Proposed algorithm
The GRG algorithm solver is formulated as follows:

$$min_x f^T x \text{ Subject to } \begin{cases} A.x \leq b \\ A_{eq}.x = b_{eq} \\ lb \leq x \leq ub \\ c(x) \leq d \\ c_{eq}(x) = d_{eq} \\ x_i \in z \end{cases} \qquad \textit{Eq. (13)}$$

- *Linear equalities*

A_{eq} is a $k \times n$ sparse matrix, b_{eq} is a $k \times 1$ vector.

- *Linear inequalities*
- A_{eq} is a $k \times n$ sparse matrix, b_{eq} is a $k \times 1$ vector
- *Decision variable bounds*

lb and ub are $n \times 1$ vectors indicating the lower and upper bounds respectively.

- *Nonlinear inequalities*

c is a $u \times 1$ vector of functions containing constraints, d is a $u \times 1$ vector.

- *Nonlinear equalities*

c_{eq} is a $v \times 1$ vector of functions containing nonlinear equality constraints, d_{eq} is a $v \times 1$ vector.

2.2 Simulation results and discussion

As a key factor determining the optimum energy scenario, the solar irradiation is herein studied by comparing a typical day of January and another day of July. According to solar irradiation of the location, the optimal schedule in January Fig. 2.a shows the refrigeration load is assured by the grid during the night. The refrigeration load during this time remains at its minimal value so as to

decrease the grid energy cost. At around 10:00 AM, the solar panels take over to supply the warehouse. In the meantime, the decision making of the OC is to maximize the refrigeration load (66 kW at 11:00) to take advantage of free photovoltaic electricity and also to turn on the charging of the LAES. The warehouse is only supplied by the LAES from 18 :00 to 22 :00 (almost 4 hours). A little pic of grid energy consumption appears between 16:00 and 18:00 it corresponds to the time adjustment required for the LAES to meet the load regarding decreasing PV energy production. The discharge time is below the LAES real discharge capacity due to unsufficient duration of charging (low PV panels production). A more optimistic scenario of July is represented by Fig. 2.b where the site is entirely self-sufficient. LAES can supply the refrigerated warehouse during the night-time. The OC switches to LAES for the energy supply when PV panels can no longer produce electricity.

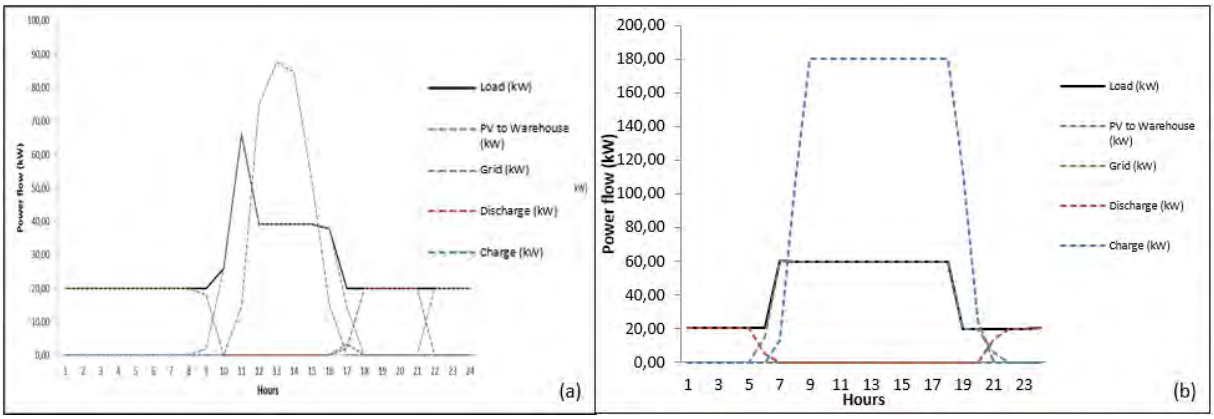

Fig. 2: Optimal energy scenario in a typical winter day (January) (a) and in a typical summer day (July) (b)

Daily energy and cost savings of both cases are summarized in Table 2 and Table 3 for the winter case and the summer case respectively. Energy profiles and values of daily cost savings shows the evidence of the solar irradiation major impact on the energy distribution and cost savings from the LAES integration. Nonetheless, further investigations are needed to evaluate the representativeness of the 16 or 11€/day regarding the project CapEx.

Table 2: Daily cost savings in January

Month	Baseline Energy (kWh)	Optimal Energy (kWh)	Baseline Cost (€)	Optimal Cost (€)	Saved Energy (%)	Saved Cost (%)
January	323,68	241,51	23,66	16,74	25,39	29,25

Table 3: Daily cost savings in July

Month	Baseline Energy (kWh)	Optimal Energy (kWh)	Baseline Cost (€)	Optimal Cost (€)	Saved Energy (%)	Saved Cost (%)
July	184,65	0	11,78	0	100	100

The combination of the LAES to PV panels as renewable energy technology requires optimal meteorological conditions to be profitable. 4 cities representing different climates, both in winter and summer are chosen as subject for this study to investigate LAES profitability under different solar irradiation.

Table 4: Total electricity supplied to the warehouse for the summer case

	Total Electricity Supplied (kWh)	PV Supply (%)	LAES Supply (%)	Grid Supply (%)
Riyadh - KSA	1776,95	54,57	34,11	11,32
Seville - Spain	1493,47	64,26	35,74	0
Helsinki	890,02	64,37	35,63	0
Québec	929,91	48,61	51,39	0
Belgium	966,59	80,90	19,10	0

Table 5: Total Electricity Supplied to the warehouse for the winter case

	Total Eletricity Supplied (kWh)	PV Supply (%)	LAES Supply (%)	Grid Supply (%)
Riyadh	841,00	50,40	49,60	0
Seville	855,57	50,74	41,88	7,38
Helsinki	646,68	37,11	0	62,89
Québec	603,57	37,01	47,06	15,93
Belgium	626,68	48,44	13,11	38,54

The summer simulation for almost every city (Table 4) clearly shows that the warehouse load can be entirely assured without making use of the power grid, except for Saudi Arabia where the 1 MWp PV plant supported by the LAES plant seems unable to meet the high refrigeration load of the warehouse. In this case, a slight increase in the size of the PV plant or a more efficient storage system are needed to outweigh high ambient temperatures reflected in high-energy consumption.
On the other hand, in almost all cases of the winter model (Table 5), PV power plant is only responsible of the reduction of the energy drawn from the grid with differences from one city to another. Despite the low temperature in Helsinki, and therefore the low refrigeration demand, the low solar irradiation makes it hard for the PV power plant to supply both the warehouse and the storage system. The weather conditions allow the system to be self-sufficient by assuring both charging the LAES and supplying the refrigerated warehouse.
As a conclusion, the system represents the highest performance in areas characterized by a moderately warm climate and sunny throughout the year. Ideally, the system should be implemented in a Mediterranean region as southern Europe or North Africa.

3. TECHNO-ECONOMIC ANALYSIS OF THE LAES

This section investigates technical and economic feasibility of the LAES powered by the PV power plant.

3.1 Methodology:

This study is presented in the form of a sensitivity analysis in which the annual savings achieved are evaluated varying 4 parameters: the RTE of the LAES, the PV plant peak power, the ratio of discharge to charge power (D/C) and the geographic location. When parameters are not under study, they are fixed as in the previous paragraph. The economic analysis is based on the annual economic savings calculated as the difference between the yearly energy costs before and after the integration of the energy storage. To achieve this purpose, 3 cases are studied:
Case 1: Only the grid supplies the warehouse; **Case 2:** Warehouse is supplied by both the PV plant and the grid; **Case 3:** The storage system is integrated.

The cost of energy is calculated on the basis of the cost of electricity drawn from the grid and the hourly cost of photovoltaic electricity estimated by Eq. (14).

$$Hourly\ PV\ Cost\ = \frac{1{,}2 \times Peak\ Power\ (Wp)}{Lifespan \times 365 \times 24} \qquad (€/h) \qquad \text{Eq. } \textit{(14)}$$

3. RESULTS AND DISCUSSION

Profiles in Fig. 3a shows that the annual savings allow a maximum value of **9684,04 €**. The lower the DP/CP ratio, the lower this value is reached with low RTE values. The results show that the RTE must be increased by at least 5% to reach the maximum value of the savings achieved.

According to Fig. 3.b, the values of the savings achieved remain constant for most cities from a RTE of 25%. For Brussels, the results show that the system can only be self-sufficient from a RTE of 30% (where the savings stabilize around a value of **9684,04 €**. In accordance with the results of the OC strategy carried out in the previous chapter, Seville represents in this analysis the ideal case for the integration of the storage system considering the interesting value of the realized savings of around **11 383 €**.

As illustrated by Fig. 3.c, the results achieved show that for the various RTEs, the curves are increasing until they reach a maximum of savings corresponding to a certain PV plant size, and then decreasing slightly. This is because the larger the PV plant is, the more energy is stored, and the less electricity is drawn from the grid.

Table 6 shows for each RTE value the optimal PV plant size and the corresponding annual savings. Those savings are used to define an investment threshold not to be exceeded for the storage system. The investment threshold is calculated by multiplying the value of the annual savings achieved by the estimated life of the LAES estimated at 25 years.

Table 6: Optimal Size of PV Power Plant and Threshold Investment function of RTE

RTE (%)	PV Plant Peak Power (kWp)	Annual Savings (€/an)	Investment Threshold (€)
25%	154	3 429,17 €	**85 729,29 €**
30%	155	3 447,26 €	**86 181,61 €**
40%	155	3 484,41 €	**87 110,13 €**
50%	162	3 536,47 €	**88 411,77 €**
100%	395	6 968,56 €	**174 214,08 €**

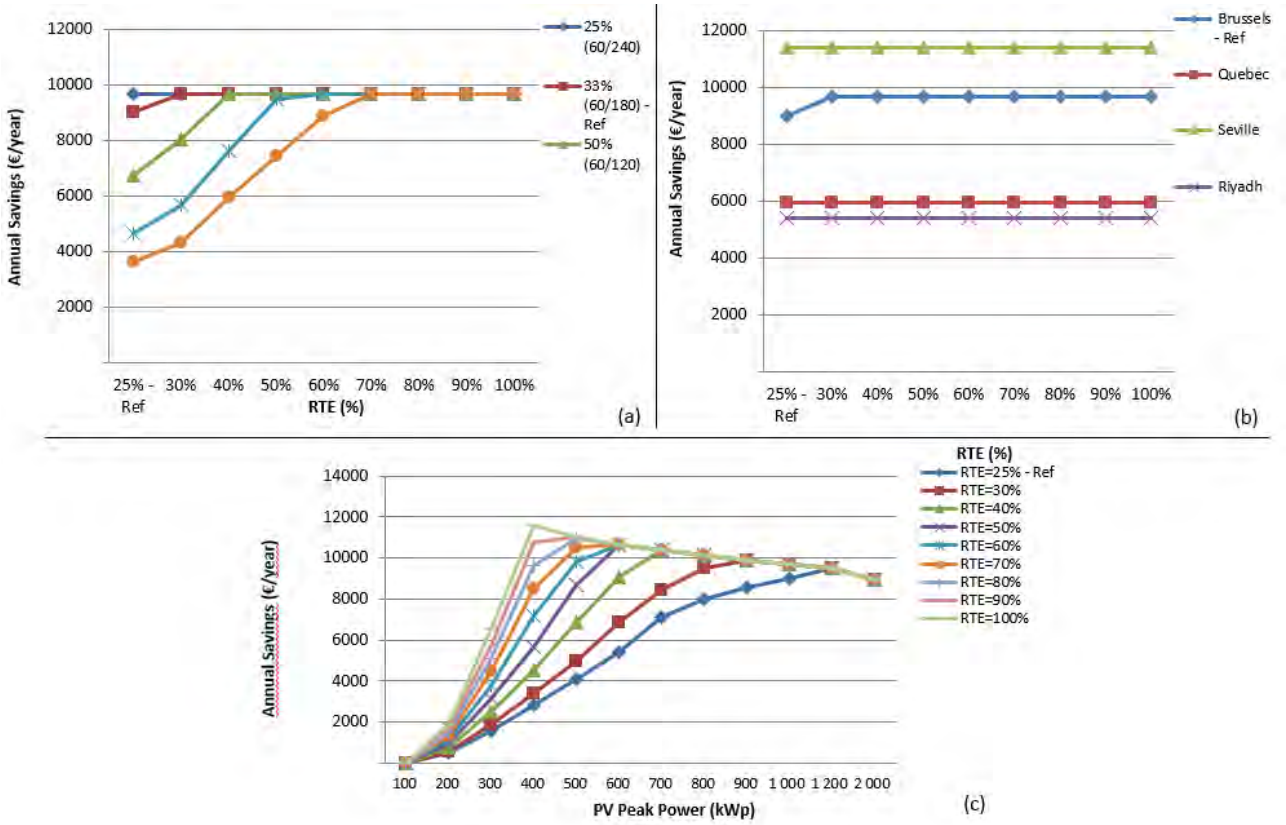

Fig. 3: Sensitivity behavior of the annual savings of the LAES integration regarding 3 parameters : (a) D/C ratio of LAES; (b) geographical location of the system; (c) Peak rated power of PV panels

4. CONCLUDING REMARKS AND PERSPECTIVES

It has been found that the LAES makes the refrigeration warehouse energy self-sufficient in summer while in winter, the storage system is only able to reduce the electricity drawn from the grid. Results of simulations showed that warm climate and sunshine throughout the year make the system more profitable than in regions where it is almost cloudy. This is due to the fact that the LAES is combined in this particular case to a PV power plant, and production of electrical energy is directly linked to solar irradiation. In other cases, if the LAES is connected to a wind farm for instance, results could be completely different from the present case. The techno-economic sensitivity analysis evaluated the annual savings achieved based on several key factors in the sizing of the LAES such as the LAES's RTE, the resale to purchase price ratio of electricity, the charge-to-discharge power ratio and the size of the PV plant. For the reference case, results showed that the system realized an annual savings of 8993,95 €. The capital investment cost computation shows that despite the significant annual savings achieved, LAES remains not very attractive given its high estimated payback period. In agreement with previously published research, this work has shown that, the economic profitability of the LAES system is very low given high CapEx values. The future of this technology could be even brighter if future research focuses on improving the technical performance of the system, so that the technology becomes accessible and mature, therefore more realizations could be made and the corresponding investment costs could decrease. In addition, under current market conditions, the system can have a large economic benefit if installed in a country where electricity prices are high.

REFERENCES

Smith, E.M., 1977. *STORAGE OF ELECTRICAL ENERGY USING SUPERCRITICAL LIQUID AIR.* Proceedings of the Institution of Mechanical Engineers. 191(1): p. 289 298.

Negro D., Evans J., Brown T., Foster A., 2018. Modelling of liquid air energy storage applied to refrigerated cold stores. 10.18462/iir.iccc.2018.0027.

Manuscript ID: 343
DOI: 10.18462/iir.icr.2019.0343

Performance study of asymmetric looped travelling-wave thermos-acoustic engine driven by low-grade heat

Rui YANG[(a)(b)], Yi WANG[(a)] , Yuanliang LIU[(a)], Tao JIN[(a)] , Ke TANG[(a)]

[(a)] Institute of Refrigeration and Cryogenics/Key Laboratory of Refrigeration and Cryogenic Technology of Zhejiang Province, Zhejiang University
Hangzhou 310027, P.R. China, jintao@zju.edu.cn
[(b)] Faculty of Civil and Environmental Engineering, Technion-Israel Institute of Technology
Haifa 3200003, Israel, rui.yang@technion.ac.il

ABSTRACT

Thermoacoustic engine is a promising approach in recovering heat energy with the attracting characteristics of high reliability and environmental friendliness. However, a traditional thermoacoustic engine/refrigerator cannot utilize low-grade thermal energy. This work aims to initiate the thermoacoustic oscillation at very low hot end temperature and to realize the efficient thermoacoustic conversion when driven by low grade heat. Looped thermoacoustic engines with asymmetric configuration are proposed and constructed. The lowest onset temperature is only 29°C (with the temperature difference of 17°C). A thermoacoustic electricity generator driven by the heat source below 200°C is also then developed. A thermal-to-electric efficiency of 5% and an output electric power of 87 W were recently achieved when the hot end temperature is about 180°C, with He-Ar mixture as the working fluid. The results indicate that the asymmetric looped thermoacoustic engine can be utilized as a novel technical method for the recovery of low-grade heat.

Keywords: Thermoacoustic Engine, Travelling-Wave, Thermoacoustic Engine, Thermoacoustic Electric Generator, Thermoacoustic Refrigeration, Low-Grade Thermal Energy.

1. INTRODUCTION

Thermoacoustic heat engine is a type of energy conversion machine, converting thermal energy into mechanical energy or consuming mechanical energy to pump heat, with the outstanding characteristics of high reliability and environmental friendliness (Jin et al., 2015). The former merit comes from the fact that there is no moving part in it, and the latter one is ascribed to the working fluids which are always gases ozone depletion. Under the background of energy and environment crisis, the thermoacoustic heat engine powered by low-grade thermal energy (waste heat, geothermal energy and solar thermal energy, etc.) has become a hot research area, facing but not limited to the applications of electricity generation, refrigeration, water pumping, circulation and pressurization (Timmer et al., 2018; Hou et al., 2018; De Blok, 2012; Zolpakar et al., 2016).

A travelling-wave thermoacoustic engine, which runs by virtue of a reversible thermodynamic cycle, is generally regarded as more efficient than a standing-wave thermoacoustic engine. The conception of travelling-wave thermoacoustic engine was proposed by Ceperley (Ceperley, 1979). He tried to control the phases of velocity and pressure of oscillating gas parcels by the travelling wave, thus to realize a reversible thermodynamic cycle similar to Stirling cycle. However, the low acoustic impedance in the regenerator caused severe viscous loss, leading to poor thermal efficiency. The thermoacoustic Stirling heat engine, which could achieve travelling-wave acoustic field as well as high acoustic impedance in the regenerator by proper combination of the looped structure and the resonator (Backhaus and Swift, 1999), dramatically improved the efficiency of travelling-wave thermoacoustic engines, which is comparable to that of a car engine. However, the required heat sources are generally with relatively high temperature (Backhaus and Swift, 1999), which will severely limit its practical application scope. In 2010, de Blok improved the looped travelling-wave thermoacoustic engine by inserting multiple thermoacoustic cores in the loop, and

the required temperature of heat source has been significantly lowered. The multi-stage travelling-wave thermoacoustic engine was expected to realize a relative Carnot efficiency of 40% when driven by the heat sources below 200°C (De Blok, 2012). However, there still lacks comprehensive understanding on the mechanism of a multi-stage looped travelling-wave thermoacoustic engine (LTTAE). Besides, the existing LTTAE generally depends on its symmetric configuration to ensure the regenerators at the position where the travelling-wave component dominates.
This work focuses on the LTTAE with asymmetric configuration to make good use of the merits of efficient thermoacoustic engine in the travelling-wave acoustic field. Systematic experiments have then been carried out, especially focusing on onset temperature, pressure ratio and heating temperature. Preliminary experiments have also been performed to verify the applicability on the electric generation and refrigeration with low-grade thermal energy.

2. EXPERIMENTAL APPARATUS

Fig. 1a presents the schematics of 1-stage LTTAE (excluding the stages represented by dashed line) and 3-stage LTTAE (including the stages represented by dashed line), while Fig. 1b presents the schematics of 2-stage and 4-stage LTTAEs. The distances between the adjacent regenerators are all 1/4 λ in the 2-stage, 3-stage and 4-stage LTTAEs. To achieve high acoustic impedance, the cross-sectional area of the thermoacoustic core, which includes a hot heat exchanger (HHX), a regenerator (REG) and an ambient heat exchanger (AHX), has been locally enlarged. For the 1-stage and 3-stage LTTAEs, the compliance tube (a locally enlarged tube) has been adopted to adjust the acoustic field. Dimensions of the main parts are listed in Table 1. The total length of the loop is 8.4 m.

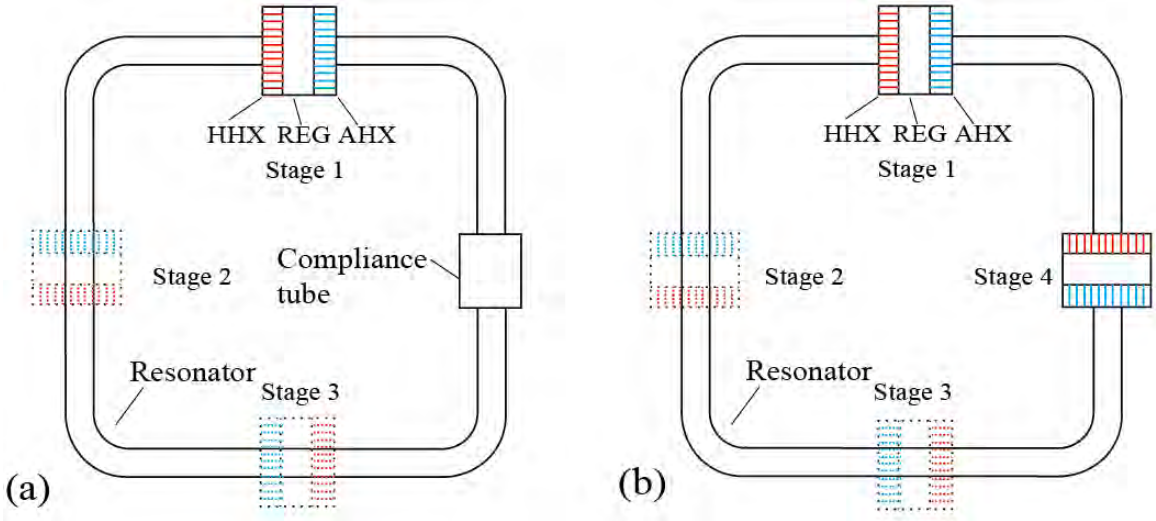

Figure 1: Schematic of the LTTAEs. (a) 1-stage and 3-stage LTTAEs. (b) 2-stage and 4-stage LTTAEs

Table 1. Dimensions of the main parts of LTTAEs

Items	HHX	REG	CHX	Resonator	Compliance tube
Length (mm)	30	30	30	8160	90
Diameter (mm)	99	99	99	26	72

3. RESULTS AND DISCUSSION

The onset temperature, the heating temperature to initiate the thermoacoustic system to oscillate, is a determining factor in the quality of the utilizable thermal energy. One of the key parameters

controlling the onset process is the normalized frequency $\omega\tau$ (Yazaki et al., 1979), where ω is the angular frequency, and τ is defined as $r_h^2/2\alpha$ (r_h is the hydraulic radius of the regenerator, α is the thermal diffusivity). If $\omega\tau>>1$, the gas parcel moves in the channel isentropically and approximately reversibly. If $\omega\tau$ is close to 1, the incomplete heat transfer will happen, leading to thermodynamically irreversible movement. If $\omega\tau<<1$, complete heat transfer happens, making the gas in the channel move reversibly, equilibrating at the local wall temperature. However, a severe viscous loss may also occur. Fig. 2 presents the onset temperature of four LTTAEs under different values of $\omega\tau$ with CO_2 as the working fluid. $\omega\tau$ was changed by adjusting the mean pressure. It can be noted that the onset temperature drops with the elevated $\omega\tau$ at first, then it gradually becomes stable. All the four LTTAEs can start to oscillate with a heating temperature below 60°C when $\omega\tau$ is above 0.1. The lowest onset temperature is only 29°C (the cooling temperature is 12°C, the mean pressure is 1 MPa or 1.5 MPa).This result indicates that the thermoacoustic engine can oscillate under a quite low heating temperature, showing the promising usability of low-grade heat source. Figure 3 shows the pressure ratio (defined as the ratio of maximum over minimum of the pressure amplitude, representing the oscillation intensity) versus heating power under 1 MPa filling pressure. It can be seen that the rise of heating power will lead to the increase in pressure ratio, since the thermoacoustic conversion is enhanced. In the experiments, the highest pressure ratio is 1.27, when the mean pressure is 1 MPa and the heating power is 4200 W at the corresponding heating temperature of 170°C.

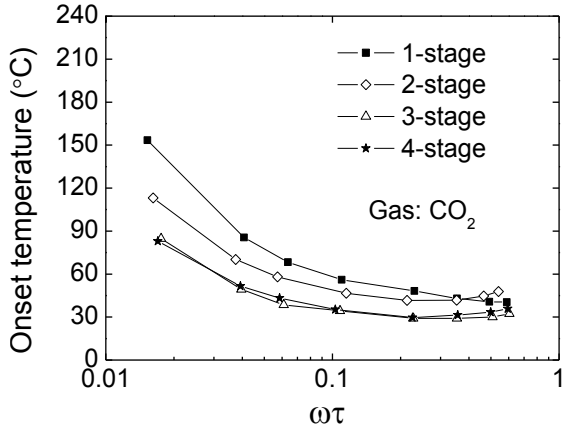

Figure 2: Onset temperature vs. normalized frequency

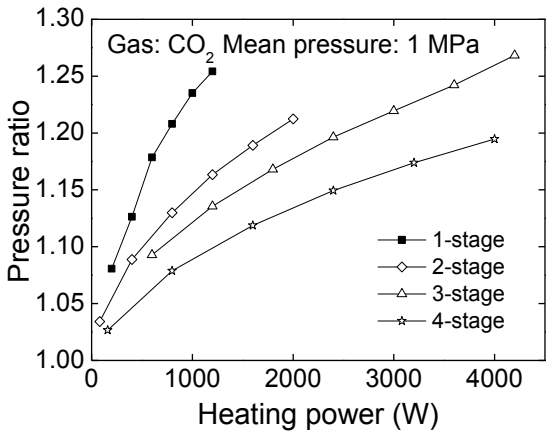

Figure 3: Pressure ratio vs. heating power

To verify the applicability of the LTTAE with low-grade thermal energy, an electric generator driven by 3-stage LTTAE, as shown in Fig. 4, has been studied. A binary mixture of helium and argon was adopted as the working fluid. Fig. 5 shows the output electric power and thermal efficiency (defined as the ratio of output electric power to heating power) with different heating powers when the mean pressure is about 2.5 MPa. When the heating power is 1770 W, the efficiency reaches its maximum value 5%, corresponding to the relative Carnot efficiency of 15% (the corresponding heating temperature is 190°C). It should be noted that the conversion from acoustic power to electricity in the linear alternator is yet far from high efficiency, considering that it is modified from an existing linear compressor by simply reversing its functioning direction. Further optimization is of great necessity and has been scheduled in our near future efforts.

Another promising application is the thermoacoustic refrigerator. Ascribed to its characteristic of no any moving part, it is convenient to switch between the engine and the refrigerator for a thermoacoustic system. Figure 6 shows a thermoacoustic refrigerator modified from the 2-stage LTTAE. When in operation, the thermal energy is converted into the acoustic power within the engine stage, and the amplified acoustic power is delivered through the resonator to the refrigerator stage, which pumps heat from the CHX to the AHX by consuming the acoustic power. In this way, the cooling effect occurs. The onset temperature of the thermoacoustic refrigerator, as shown in Figure 7, is significantly higher than that of the thermoacoustic engine, as shown in Figure 2, because much more acoustic power is required to overcome the resistance in the refrigerator stage. Figure 8 presents the heating temperature, the overall thermal efficiency (i.e.,

the ratio of cooling power over heating power) and the cooling power with different heating power, when the cooling temperature is 0°C. The heating temperature increases steadily with the rise of heating power, as well as the cooling power. The overall thermal efficiency also goes up as heating power is increased, but it seems to approach a plateau when the heating power is higher than 800 W. In the experiments, the highest overall thermal efficiency is 6.7%, with the corresponding cooling power of 94 W and heating temperature of 314 °C. Due to the fact that this system, although running as a refrigerator, was not originally designed for this aim, the overall thermal efficiency is not optimal. Future study on this thermoacoustic refrigerator has also been in our schedule.

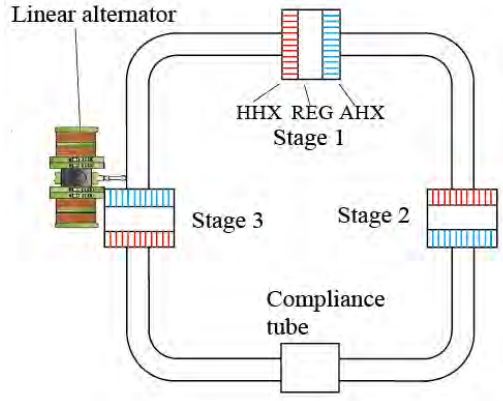

Figure 4: Schematic of the thermoacoustic electric generator

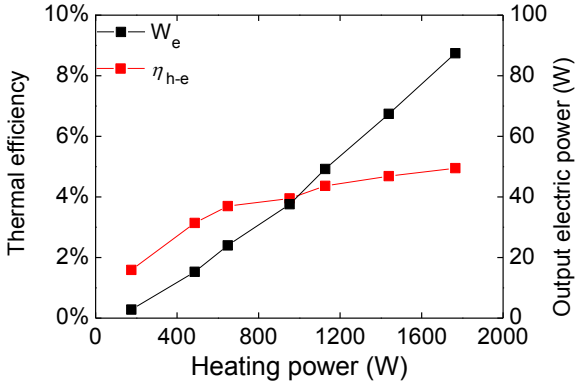

Figure 5: Thermal efficiency and output electric power vs. heating power

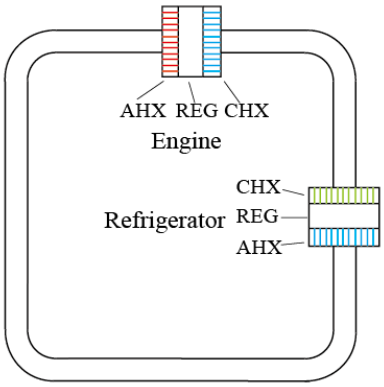

Figure 6: Schematic of thermoacoustic refrigerator

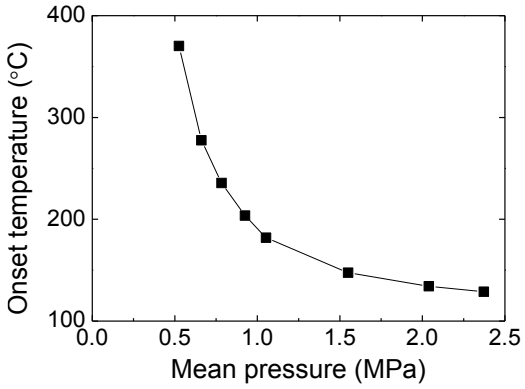

Figure 7: Onset temperature of thermoacoustic refrigerator vs. mean pressure

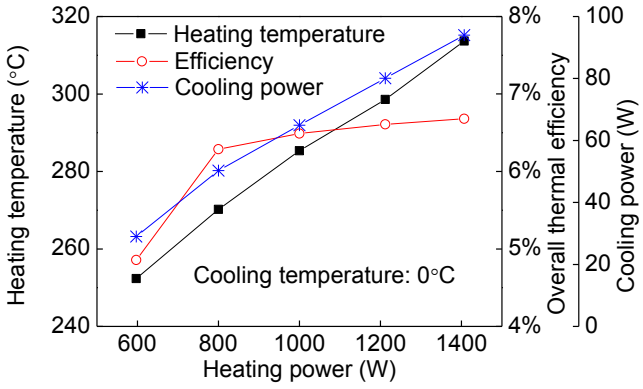

Figure 8: Heating temperature, overall thermal efficiency and cooling power vs. heating power

4. CONCLUSIONS

In summary, the looped travelling-wave thermoacoustic engines (LTTAEs) with 1-4 stages are proposed for low grade heat recovery. Results show that they could realize converting heat energy into acoustic power at a heating temperature even lower than 50°C. The lowest onset temperature is only 29°C, when the cooling temperature is 12°C and the CO_2 of 1 MPa or 1.5 MPa is adopted). A thermoacoustic electricity generator driven by the heat source below 200°C has also been developed, and a thermal-to-electric efficiency of 5% and an output electric power of 87 W are achieved. A preliminary experimental verification of the thermally driven thermoacoustic refrigerator has also been conducted. The highest overall thermal efficiency of 6.7% was achieved, with the corresponding cooling power of 94 W and heating temperature of 314 °C.

ACKNOWLEDGEMENTS

This work is financially supported by the National Natural Science Foundation of China (Grant No.51576170), the National Key Basic Research Program of China (Grant No. 2016YFB0901403).

REFERENCES

Backhaus, S., Swift, G.W., 1999. A thermoacoustic Stirling heat engine. Nature 399(6734), 335-338.

Ceperley, P.H., 1979. A pistonless Stirling engine—the traveling wave heat engine. J. Acoust. Soc. Am. 66(5), 1508-1513.

De Blok, K., 2012. Multi-stage travelling wave thermoacoustics in practice. In: 19th International Congress on Sound and Vibration Vilnius: International Institute of Acoustics and Vibration (IIAV) and Vilnius University, Lithuania, 1-8.

Hou, M., Wu, Z., Yu, G., Hu, J., Luo, E., 2018. A thermoacoustic Stirling electrical generator for cold exergy recovery of liquefied nature gas. Appl. Energy 226, 389-396.

Jin, T., Huang, J., Feng, Y., Yang, R., Tang, K., Radebaugh, R., 2015. Thermoacoustic prime movers and refrigerators: thermally powered engines without moving components. Energy 93(1), 828-853.

Timmer, M.A.G., de Blok K., van der Meer T.H., 2018. Review on the conversion of thermoacoustic power into electricity. J. Acoust. Soc. Am. 2018, 143(2), 841-857.

Yazaki, T., Iwata, A., Maekawa T, Tominaga, A., 1998. Traveling wave thermoacoustic engine in a looped tube. Phys. Rev. Lett. 81(15), 3128-3131.

Zolpakar, N.A., Mohd-Ghazali, N., El-Fawal, M.H., 2016. Performance analysis of the standing wave thermoacoustic refrigerator: A review. Renew. Sust. Energ. Rev. 54, 626-634.

Manuscript ID: 429
DOI: 10.18462/iir.icr.2019.0429

Investigations of a 450 g micro moving-coil linear compressor operating at 200 Hz

Jiaqi LI [(a), (b)], Jun TAN [(a), (c)], Rui ZHA [(a), (b)], Tao ZHANG [(a), (b)], Yongjiang ZHAO[(a), (b)], Bangjian ZHAO[(a), (b)], Haizheng DANG [(a), (c)]

[(a)] State Key Laboratory of Infrared Physics, Shanghai Institute of Technical Physics, Chinese Academy of Sciences, Shanghai, 200083, China, bb22ufo@163.com; haizheng.dang@mail.sitp.ac.cn
[(b)] University of Chinese Academy of Sciences, Beijing, 100049, China
[(c)] Shanghai Boreas Cryogenics Co., Ltd, Shanghai, 200434, China,

ABSTRACT

This paper presents the design and optimization of a micro moving-coil linear compressor for Stirling-type pulse tube cryocoolers. The overall mass of the compressor is less than 450 g. It is designed to operate at a high frequency of around 200 Hz, which is developed with the modified scaling method based on the typical mid-sized compressors in the authors' laboratory. The scaling factors of moving mass and linear motor are studied in detail. A three-dimensional model is built to simulate the magnetic field in the micro linear compressor. The non-uniform magnetic field influences the direction of the specific thrust which decreases the efficiency of the linear compressor. The micro linear compressor is worked out and then coupled with a pulse tube cold finger, which can provide a cooling power of 0.85 W at 77 K.
Keywords: Linear Compressor, Magnetic Field, Miniaturization, Pulse Tube, Simulation.

1. INTRODUCTION

The Stirling-type pulse tube cryocooler (SPTC) is attractive for cooling infrared focal planes, filters and cold optics, because there is no moving part at the cold end which results in long life and high reliability. The SPTC is composed of the linear compressor and the pulse tube cold finger (PTCF). The linear compressor, used to produce the oscillating pressure wave, serves as the energy source of the SPTC and is the only moving part inside the SPTC. The miniaturization of a PTCF is much easier compared to the linear compressor because there is no moving part in it. The miniaturization of linear compressor is the core of the work since it has not only high-speed moving pistons but also delicate and subtle magnetic circuits in it.

Several researchers have worked on the miniaturization of the linear-compressor-driven SPTC. Petach et al. (2007) developed a micro SPTC for space flight payloads with a 415 g moving-coil micro linear compressor. This compressor is scaled down from the flight heritage compressor. Olson et al. (2014) developed a lightweight cryocooler which weights 310 g for tactical and space applications. The micro moving-magnet compressor with less than 200 g used the same long-life technology of Lockheed Martin's large compressors: long-life flexure-bearing clearance-seal technology. Nast et al. (2014) developed a 210 g moving-magnet compressor driven SPTC with cooling capacity of 0.85 W at 150 K with 10 W of input power. The flexure-bearing and the clearance-seal technology were used for the linear compressor.

In the authors' laboratory, a micro SPTC had been developed with an 800 g moving-coil linear compressor operating at 90-170 Hz (Zhao et al., 2018). Then, a 700 g moving-coil linear compressor was developed for a micro SPTC. After that, by using the modeling of the magnetic field of the linear motor and optimized the size, a 500 g micro linear compressor is worked out and tested with a micro PTCF which could produce 1.2 W of cooling power at 77 K.

In this paper, we present the investigation of a 450 g micro linear compressor operating at 200 Hz. The micro linear compressor is developed with the modified scaling method based on the typical mid-sized compressors in the authors' laboratory (Dang, 2012; Dang, 2015; Zhang et al., 2015). The scaling factors of moving mass and linear motor are studied in detail. A three-dimensional model is built to simulate the magnetic field in the compressor. The micro linear compressor is worked out and then tested with a micro pulse tube cold head.

2. MICRO LINEAR COMPRESSOR DESIGN

Fig. 1 shows a schematic of a typical dual-opposed moving-coil linear compressor, which is composed of the permanent magnet, the return irons and the moving coil, the cylinder, the pressure vessel, the linear motor, the flexure springs and the pistons. The flexure-bearing and the clearance-seal technologies are employed.

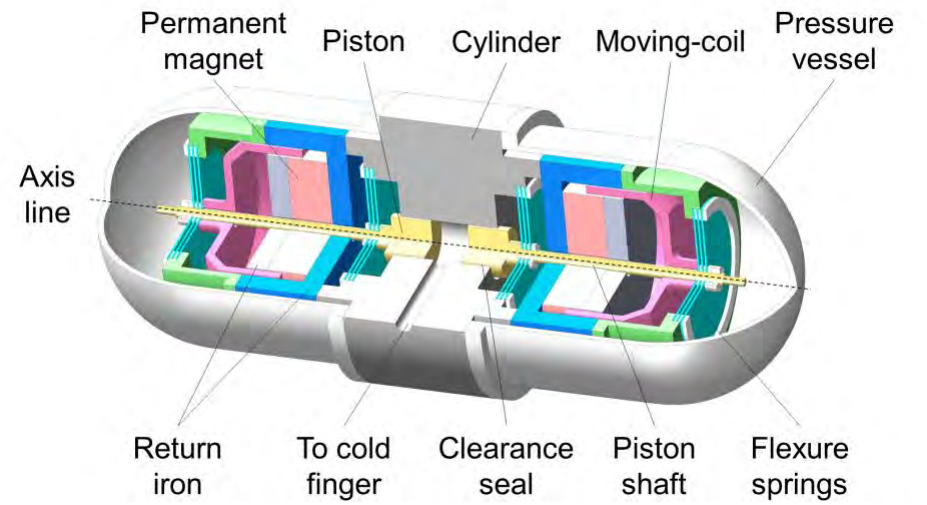

Figure 1: Schematic of a moving-coil dual-opposed linear compressor

2.1. Modified Scaling Method for Micro Linear Compressor

The modified scaling factors were proposed in the same laboratory (Zhang, 2015), which are benefit for making the structure more appropriate and decreasing the difficulty of the manufacture. In the process of scaling, only some key components are scaled while other ones keep unchanged.
Table 1 shows the modified scale factors compared to the original scale factors (Marquardt et al., 1992) for the micro linear compressor.

Table 1. Scaling factors for the micro linear compressor

Parameters	Modified scale factor	Original scale factor
Frequency, f	1/K	1/K
Diameter of piston, D	K	$K^{3/2}$
stroke, S_p	K	K
Thickness of coil, (D_{oc}-D_{ic})	1	K
Width of coil, w_c	Modified calculating	K
Volume of coil, V_c	K^2	K^3
Mechanical spring stiffness, k_m	K	K^2
Forces	K^2	K^3
Diameter of flexure spring, D_s	Modified calculating	K
Thickness of flexure spring, t_s	Standard dimensions	K
Number of flexure spring, N_s	0.5	K
Thickness of clearance gap, t_{gap}	$K^{2/3}$	K
Moving mass, m	K^3	K^4
Gas spring stiffness, k_g	K	K^2

Besides the parameters in Table 1, the no-load characteristics which represent the intrinsic properties of the linear compressor should also be analyzed. In this case, K is 0.51 and the resonant frequency will be 100 Hz considering the limitation of the size and manufacture technology.

2.2. Partial Scaling

Based on the theoretical analysis in section 2.1, the designed linear compressor will work at 100 Hz with an overall weight of 500 g. In this paper, the goal of the frequency is 200 Hz. And thus the parameters of the piston and flexure springs must be changed to fulfill the requirement. Meanwhile, the output power and the efficiency of the micro linear compressor changes slightly. The resonant frequency is given by:

$$f_n = \frac{1}{2\pi}\sqrt{\frac{k_m + k_g}{m}} \quad \text{Eq. (1)}$$

where k_g is the gas spring stiffness, k_m is the mechanical spring stiffness and m is the mass of the piston.
k_m is determined by the flexure springs. There are several important dimensional parameters such as the number of the flexure springs N_s, the thickness t_s, the diameter D_s, the length of the spring arm L_s and the width of the spring arm w_s. The mechanical spring stiffness is equal to the axial stiffness of the flexure spring which can be expressed as follow:

$$k_m = \frac{3N_s E w_s t_s^3}{L_s^3} \propto \frac{N_s E t_s^3}{D_s^3} \quad \text{Eq. (2)}$$

where w_s and L_s are proportional to D_s.
When coupled with the cold finger, the gas and the piston surface can be regarded as a spring. And the gas spring stiffness can be given by:

$$k_g = \frac{a_p \Delta P}{s} cos\varphi \quad \text{Eq. (3)}$$

where a_p is the areas of the piston surface, ΔP is the amplitude of the dynamic pressure.
In this paper, the goal is to obtain a 450 g linear compressor operating at 200 Hz, with further optimization on the theoretical designed 500 g linear compressor given above. So, the f_n should be equal to 200 Hz with the scale factor of 1/K. Thus, both the scale factors of m and N_s should be changed to K.

$$k_m \propto 1/K \quad \text{Eq. (4)}$$
$$k_g \propto 1/K \quad \text{Eq. (5)}$$
$$\mathrm{m} \propto \mathrm{K} \quad \text{Eq. (6)}$$

The resonant frequency can be given by:

$$f_n = \frac{1}{2\pi}\sqrt{\frac{k_m + k_g}{m}} \propto 1/K \quad \text{Eq. (7)}$$

Under this circumstance, the linear compressor will resonate at 200 Hz. The power delivered by the motor can be given by:

$$\langle \dot{W}_{motor} \rangle = \pi s f \left|\vec{F}\right| \quad \text{Eq. (8)}$$

The PV power from the compressor can be defined by:

$$\langle \dot{W}_{PV} \rangle = \frac{\pi}{2} f P_1 V_c \sin\varphi = \frac{\pi^2}{8} f s D_p^2 \Delta P \quad \text{Eq. (9)}$$

The motor efficiency can be expressed by:

$$\eta_e = \frac{\langle \dot{W}_{PV} \rangle}{\langle \dot{W}_{motor} \rangle} = \frac{\frac{\pi^2}{8} f s D_p^2 \Delta P}{\pi s f \left|\vec{F}\right|} = \frac{\pi D_p^2 \Delta P}{8\left|\vec{F}\right|} \quad \text{Eq. (10)}$$

The re-designed micro linear compressor has almost the same motor efficiency as that of the 500 g one. In the analysis, the current of the linear compressor *i* and the piston displacement *x* can be expressed as:

$$x = X_m \cos 2\pi ft \quad \text{Eq. (11)}$$

$$i = -I_m \sin(2\pi ft - \theta) \quad \text{Eq. (12)}$$

where X_m and I_m are the amplitudes of the piston displacement and the current, respectively. θ is the phase angle between the piston velocity and the motor force. The force balance can be expressed as:

$$m\ddot{x} + c\dot{x} + k_m x + F_p = BL_w I \quad \text{Eq. (13)}$$

Substituting Eq. (11) and Eq. (12) into Eq. (13), and I_m can be expressed as:

$$I_m = \frac{X_m}{BL_w}\sqrt{(k_m - 4m\pi^2 f^2)^2 + 4c\pi^2 f^2} \quad \text{Eq. (14)}$$

When the terms BL_w, k_m, m, f, c, R and L are fixed, the amplitudes of the current are in proportion to the piston displacement amplitude. Therefore, the stroke can be controlled directly by changing the current. Eq. (14) can be rewritten as:

$$I_m = \frac{X_m k_m}{BL_w}\sqrt{(1-\tau^2)^2 + 4\tau^2\xi^2} = \frac{X_m k_m}{BL_w}\sqrt{\tau^4 + 2(2\xi^2 - 1)\tau^2 + 1} \quad \text{Eq. (15)}$$

where the frequency ratio $\tau = f/f_n$ and the damping ratio $\xi = \frac{c}{2\sqrt{mk_m}}$ are non-dimensional coefficients. The optimal frequency ratio is founded to be $\tau_{opt} = \sqrt{1-2\xi^2}$.

2.3. Optimization of Magnetic Structure

The efficiency of the linear motor significantly influences the performance of the linear compressor. The linear motor force, maximum input power and motor efficiency will be directly affected by the magnetic field intensity inside the air gap of the linear motor. When the material of the permanent magnet is chosen, the magnetic field intensity and distribution will be determined by the dimensional parameters of the magnetic circuit. In order to obtain a steady sinusoidal force by the moving coil, the magnetic field intensity in the air gap should be uniform. So, a three-dimensional theoretical model for the micro magnetic structure is established as follows.

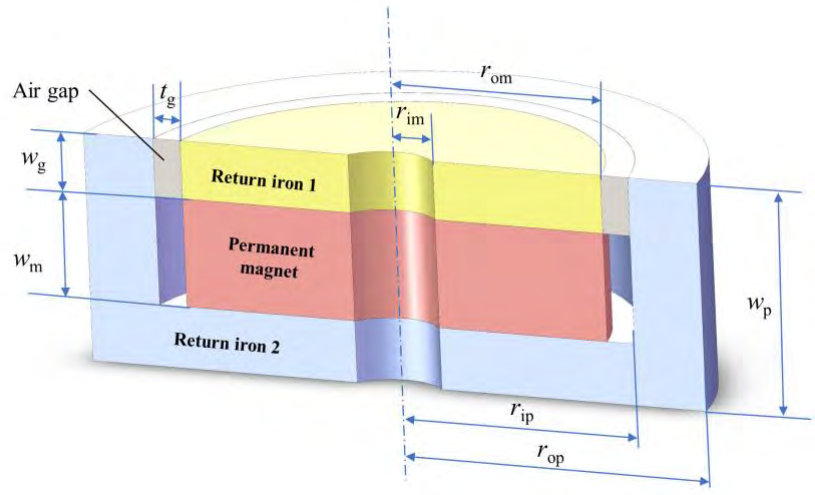

Figure 2: Key parameters of the magnetic structure

Fig. 2 shows some important parameters of the model of linear motor which consists of the air gap, the permanent magnet, the return irons, and the coil. There are several important geometrical

parameters such as the width of air gap w_g, the thickness of air gap t_g, the width of permanent magnet w_m, and the outer radius of permanent magnet r_{om}.
Simulations of the magnet circuit have been put forward with different geometries. The optimal case is chosen under the circumstances that the magnetic field is uniform and the magnetic field intensity is larger than 1 T. Fig. 3 shows the simulation results of the optimal case. The magnetic field inside the air gap is uniform, and the lowest magnetic field intensity is 1.02 T which can fulfill the requirements of the design. In Fig. 3b, magnetic field intensity of most parts of the return irons is in the range from 1.28 T to 1.646 T. Although, there still exists some parts which have only 0.002 T inside. they are far from the moving coil and thus will not affect its movement.

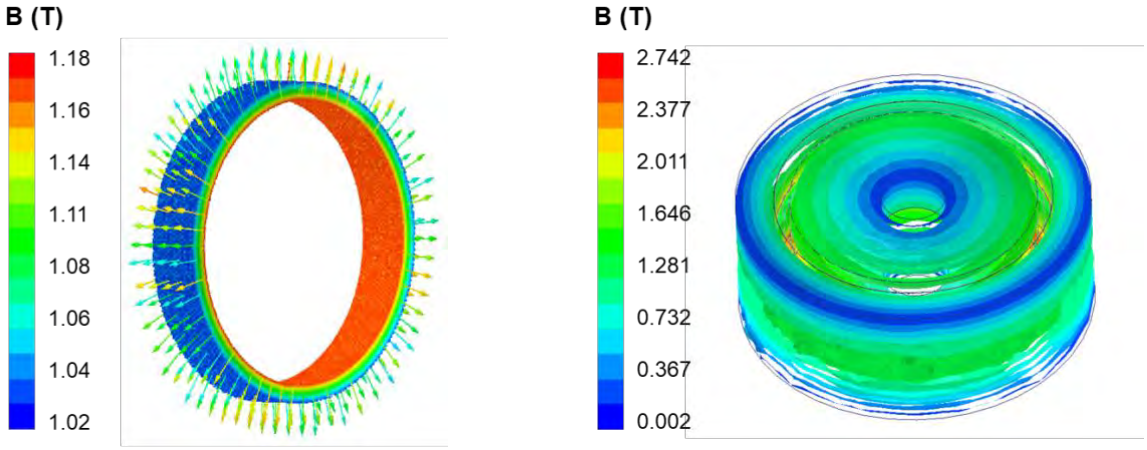

(a) (b)

Figure 3: (a) Magnetic field inside the air gap (b) Magnetic field inside the return irons

2.4. Simulation of Micro Compressor Coupled with Micro PTCF

A micro PTCF is designed to couple with the developed micro linear compressor. The simulated cooling performances with different frequencies are shown in Fig. 4. It can be observed that the cooling capacity increases sharply when the frequency rises from 190 Hz to 198 Hz. Then, it turns to drop when the frequency increases from 200 Hz to 210 Hz. The optimal frequency of the SPTC is around 200 Hz and a cooling capacity of 1.04 W at 77 K can be achieved with 90% of full stroke.

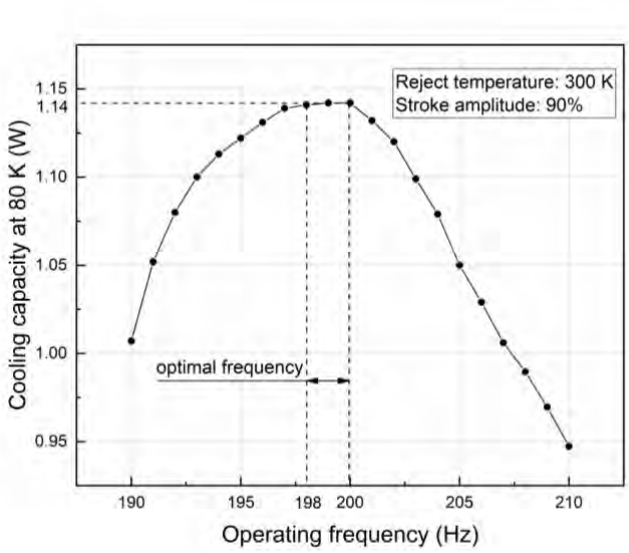

Figure 4: Variations of cooling capacity with operating frequency

3. EXPERIMENTAL RESULTS

3.1. Manufacture of Micro Linear Compressor

Based on the design and optimization, the micro linear compressor is manufactured. Fig. 5 shows the photos of the micro linear compressor and several key components. Fig. 5a shows the micro linear compressor compared to a cola can. The overall mass of the linear compressor is 450 g. Fig. 5b shows the comparison between the original piston and the scaled one. Fig. 5c and 5d show the magnetic structure and the coil of the developed linear motor, respectively.

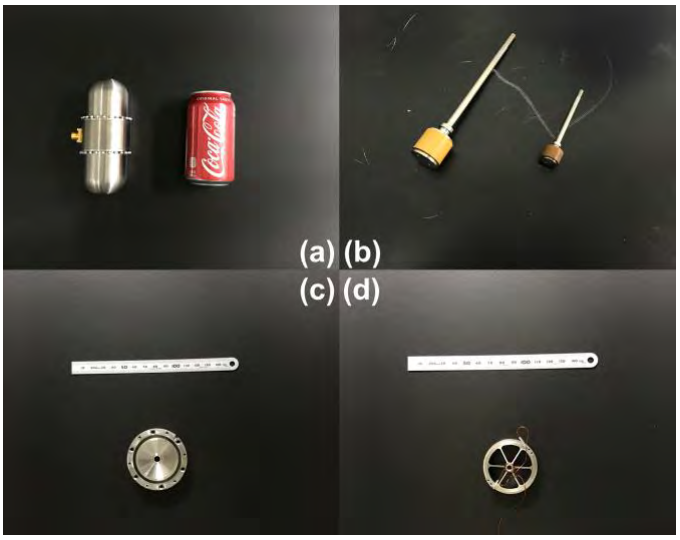

Figure 5: Photos of some important components of the micro linear compressor

Fig. 6 shows the comparison between the simulated and experimental results, in which the changing trends of the magnetic field intensity are similar. The magnetic field intensity decreases from the inside of the air gap to the outside. The measured magnetic field intensity in the air gap varies from 0.9 T to 0.92 T, which is about 0.2 T lower than the simulated ones. There are two reasons for the discrepancy. First, the actual permanent magnet is not full magnetized, and thus the actual magnetic field intensity in the air gap is reduced. Second, there are fixed holes on the return iron 2, which has a negative effect on magnetic field intensity.

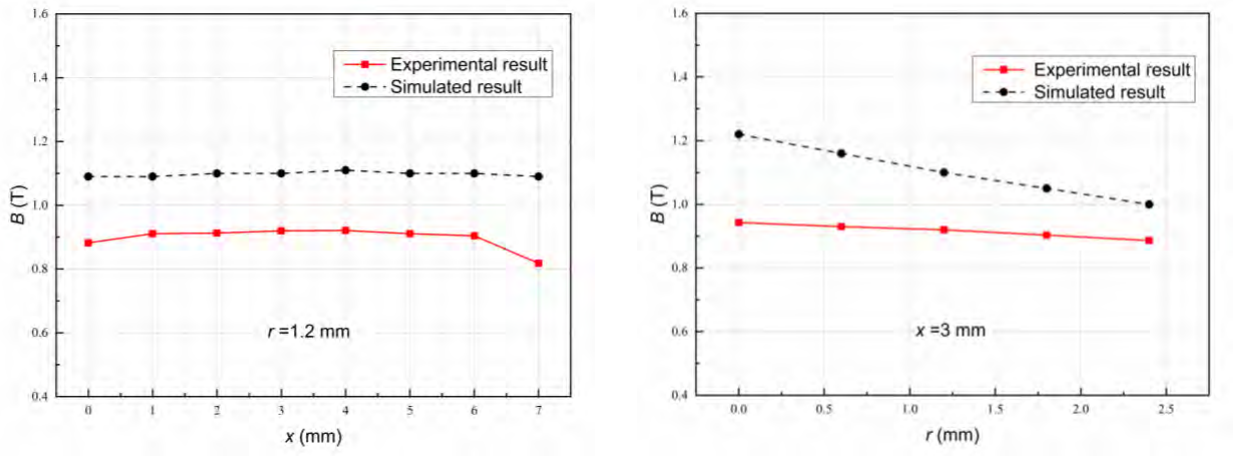

(a) (b)

Figure 6: Simulated and experimental results: (a) the average magnetic field intensities in axial direction at r=1.2 mm. (b) the magnetic field intensities in radial direction at x=3 mm

3.2. Experimental Results of PTCF Coupling with Micro Linear Compressor

An actual micro PTCF is worked out based on the design and optimization. Then the developed micro linear compressor is coupled with the micro PTCF and tested. Fig. 7 shows the experimental

results, in which fig. 7a shows the variations of efficiency of the linear compressor and cooling capacity with different operating frequencies. The optimal operating frequency is 199 Hz which is slightly lower than the simulated one. And it can be observed that the changing trend of the motor efficiency is similar to that of the cooling capacity at 80 K. And both of them rise with the increasing frequency if the frequency is lower than 199 Hz. When the frequency continues increasing, both of them decrease. Fig. 7b shows the performance of the SPTC driven by the micro linear compressor at 199 Hz. A cooling power of 0.85 W at 77 K can be obtained with an input power of 50 W. The result is slightly lower than the simulated one. The reason for this is that the average magnetic field intensity is slightly lower than the simulated one which results in a decrease of the performance of the linear compressor and cooling power. Also, the dimensional parameters of the experiments are slightly different from the simulated ones which also leads to the discrepancy on cooling power.

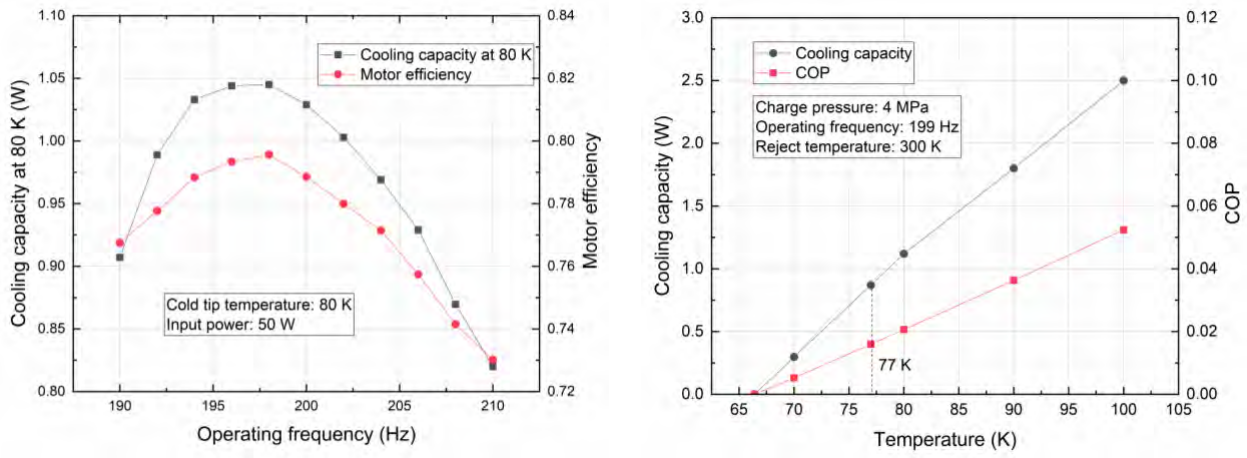

(a) (b)

Figure 7: (a) Variations of compressor efficiency and cooling capacity with different operating frequency (b) Variations of cooling capacity and COP with cold tip temperature

4. CONCLUSIONS

This paper presents theoretical and experimental investigations of a 450 g linear compressor operating at 200 Hz. The micro linear compressor is designed by using the modified scaling method, and then it is optimized by adjusting the moving mass and flexure springs. The linear motor is optimized based on magnetic field simulation. The experimental and simulated results are compared and they have the similar changing trends. The magnetic field intensity of the experiments is only slightly lower than that of the simulation. The reasons for the small discrepancy are that the actual permanent magnet is not full magnetized and that the return iron has a fixed hole in it. The micro linear compressor is worked out and then tested by coupling with a micro pulse tube cold head. The compressor input power is 50 W and the SPTC has a cooling power of 0.85 W at 77 K.

ACKNOWLEDGEMENTS

This work is financially supported by the Aeronautical Science Foundation of China (No. 20162490005) and Shanghai Municipality (Nos. 18511110100, 18511110101, 18511110102).

NOMENCLATURE

a_p	areas of the piston surface (m2)	m	moving mass (kg)
D	diameter of piston (m)	N_s	number of flexure spring
D_s	diameter of flexure spring (m)	ΔP	amplitude of the dynamic pressure (Pa)
D_{oc}	outer diameter of coil (m)	r_{om}	outer radius of permanent magnet (m)

D_{ic}	inner diameter of coil (m)	s	stroke (m)
D_p	diameter of piston (m)	t_s	thickness of flexure spring (m)
D_s	diameter of flexure spring (m)	t_{gap}	thickness of clearance gap (m)
E	Young's modulus	t_g	thickness of air gap (m)
F	force (N)	V_c	volume of coil (m3)
f	frequency (Hz)	w_c	width of coil (m)
f_n	resonant frequency (Hz)	w_g	width of air gap (m)
K	scale factor	w_m,	width of permanent magnet (m)
k_m	mechanical spring stiffness (N/m)	w_s	width of the spring arm (m)
k_g	gas spring stiffness (N/m)	W_{motor}	power delivered by motor (W)
L_p	length of piston (m)	W_{PV}	pV power (W)
L_s	length of the spring arm (m)	η_e	motor efficiency

REFERENCES

Dang, H.Z., 2012. High-capacity 60 K single-stage coaxial pulse tube cryocoolers. Cryogenics 52, 205-211.

Dang, H.Z., 2015. Development of high performance moving-coil linear compressors for space Stirling-type pulse tube cryocoolers. Cryogenics 68, 1-18.

Marquardt, E., Radebaugh, R., Kittel, P., 1992. Design equations and scaling laws for linear compressor with flexure springs. International Cryocooler Conference, Cryocoolers, 783-804.

Nast, T.C., Roth, E., Olson, J.R., et al., 2014. Qualification of Lockheed Martin Micro Pulse Tube Cryocooler to TRL6. International Cryocooler Conference, Cryocoolers, 45-50.

Olson, J.R., Champagne, P., Roth, E., et al., 2014. Microcryocooler for Tactical and Space Applications. Cryogenic Engineering Conference, AIP Conference Proceedings, 357-64.

Petach, M., Waterman, M., Tward, E., et al., 2007. Pulse Tube Microcooler for Space Applications. International Cryocooler Conference, Cryocoolers, 89-93.

Petach, M., Waterman, M., Pruitt, G., et al., 2009. High Frequency Coaxial Pulse Tube Microcooler. International Cryocooler Conference, Cryocoolers, 97-103.

Zhang, L., Dang, H.Z., Tan, J., et al., 2015. Theoretical and experimental investigations on the partial scaling method for the Oxford-type moving-coil linear compressor. Cryogenics 69, 26-35.

Zhao, Y.B., Yu, G.R., Tan, J., et al., 2018. CFD modeling and experimental verification of oscillating flow and heat transfer processes in the micro coaxial Stirling-type pulse tube cryocooler operating at 90–170 Hz. Cryogenics 90, 30-40.

Manuscript ID: 456
DOI: 10.18462/iir.icr.2019.0456

A practical calibration procedure for the balanced ambient room type calorimeter in testing the cooling capacity of room air conditioner

Haiyun ZHANG[(a)], ChenzheHANG[(a)], Dinghua XU[(a)], Guoyuan MA[(b)]

[(a)] National Institute of Metrology
Beijing, 100013, China, zhanghy@nim.ac.cn
[(b)] Beijing University of Technology
Beijing, 100029, China, magy@bjut.edu.cn

ABSTRACT

The balanced ambient room type calorimeter is generally used as the cooling capacity measurement standard equipment in the air conditioner industry. However, the calibration procedure is not investigated. In this study, based on the empty-load situation of calorimeter, the calibration model is proposed in order to restrain the error of heat balance caused by long-term use. Besides, two new parameters, which are background value of indoor-side and outdoor-side, are presented in accordance with the calibration model. Experiments are designed to obtain these two parameters and three heat leakage coefficients of partition wall, as well as the calibration procedure and application method of the parameters are illustrated. The corrected calorimeter measures ten different window type air conditioners in one year. The results show that the absolute value of heat balance is less than 2% in the cooling capacity range of 2000W~4500W and 1% in the range of 4500W~7000W.
Keywords: Calibration, Calorimeter, Heat balance, Cooling capacity.

1. INTRODUCTION

The balanced ambient room type calorimeter (ANSI/ASHRAE 16, 2014; GB/T 7725, 2004; ISO 5151, 2017), as shown in Figure 1, which provides approximate thermal insulators based on the conservation of energy and mass, converts the cooling capacity measurement into the measurements of electrical power, heat exchange of cooling coil, heat leakage of partition walls, heat transfer caused by evaporation and condensation water, et. al. Normally, the calorimeter has four test rooms, two of them are test chamber(shown as 2 and 10 in Figure 1), and the other two are controlled-temperature air spaces(shown as 1 and 12 in Figure 1). In order to decrease the heat leakages of partition wall, the air space can adjust the temperature to the test chamber's. Although calorimeter has more measurement parameters than the indoor air enthalpy test method apparatus (ANSI/ASHRAE 58, 2014), the calorimeter is used as the cooling capacity measurement standard equipment in the room air conditioner industry because of the higher accuracy (Néstor, 2009).

Various type of sensors and instruments are installed in the calorimeter, and the measurement parameters include electrical power, temperature, pressure, flow and mass. Due to the long-term use of calorimeter, the measurement results of the sensors and instruments possibly drift, and this situation can lead to the unpredictable error of cooling capacity measurement. Therefore, periodic check, calibration and correction for the sensors and instruments are essential to the accuracy of calorimeter. For now, the calibration procedure of calorimeter focus on the sensors and instruments which can be calibrated in the field, such as the resistance temperature detectors, the pressure transmitters and the digital power meters. The procedure, which regards the sensors, the data acquisition unit and the software as a integrated system, conducts the field calibration with the external sources. This part of procedure, which is proven by the practical calibration, is well applied in China air conditioner industry.

However, a part of sensors are inappropriate to the field calibration because of the field restrictions. For example, the thermocouples on the partition walls, which are dispersive in position, and surround which the space is narrow and small for the calibration equipments. Anther example, the flow meter of cooling water, which need to disassemble because of the deficiency of calibration

ports in the cooling water pipeline. For these sensors, the field calibration is usually not conducted, or the period of calibration is extended in practice. But this handling way can result in some issues, around which the zero drift of heat balance measurement is most apparent, to the accuracy of calorimeter.

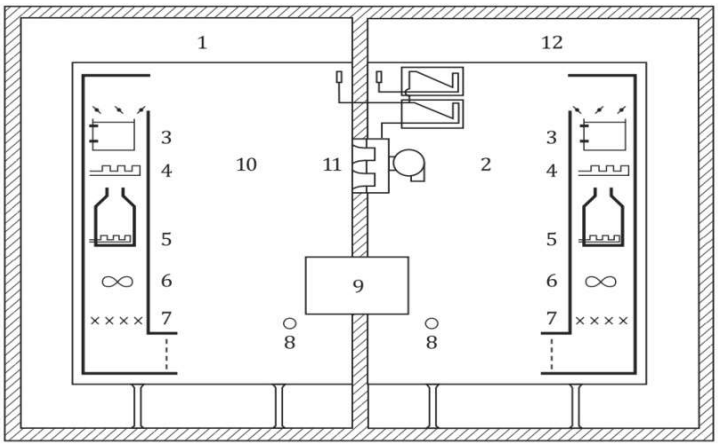

1 indoor-side air space, 2 outdoor-side test chamber, 3 cooling coil, 4 heating coil, 5 humidifier, 6 fan, 7 mixer, 8 air sampling tube, 9 equipment under test, 10 indoor-side test chamber, 11 pressure equalization device, 12 outdoor-side air space.

Figure 1: Room type calorimeter

In this study, the calibration model, which converts the field calibration of thermocouples into the measurement of the coefficients of heat leakage, is proposed based on the empty-load situation of calorimeter. And the practical calibration procedure, which ensure the measurement accuracy of energy flow, improves the issue of heat balance zero drift. Finally, this procedure is applied to a calorimeter, and the heat balance measurement results verify its practicality.

2. THE CALIBRATION MODEL OF CALORIMETER

The objective of calorimeter calibration is to guarantee the accuracy of heat flow measurement. The heat flow, which is related to the sensors unsuitable for filed calibration, is the heat leakage of partition wall. The heat leakage is the product of the temperature measurement results and the heat leakage coefficients. Under the condition that the temperature measurement sensors can not be calibrated, the accuracy of heat flow measurement also can be achieved through the adjustment of heat leakage coefficients.

Therefore, in order to obtain the coefficients of heat leakage, the calibration model of calorimeter is established based on the simplest measurement situation which eliminates unnecessary interference factors caused by the air conditioner under test, water evaporation and condensation.

In accordance with the analysis of heat flow, the simplest measurement of calorimeter is the empty-load situation, under which the pressure equalization device and humidifier are closed. The energy flow chart of the empty-load is shown as figure 2.

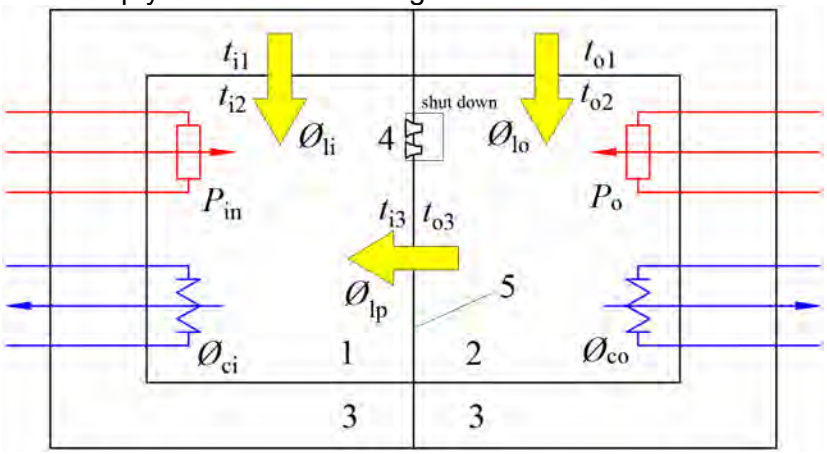

1 indoor-side test chamber, 2 outdoor-side test chamber, 3 controlled-temperature air space, 4 pressure equalization device, 5 the separating partition of test chambers.

Figure 2: The integrated calibration model under empty load

From Figure 2, it can be seen that only three kinds of energy flow are involved, they are the electrical power flowing in the test chambers (red arrows in Figure 2), the heat removed by cooling coils (blue arrows in Figure 2) and the heat leakage of the partition walls (yellow arrows in Figure 2). According to the conservation of energy, the energy that flowing in a test chamber equals to the energy flowing out. As a result, the indoor-side cooling capacity can be expressed as

$$\phi_{\mathrm{tci}} = P_{\mathrm{in}} - \phi_{\mathrm{ci}} + \phi_{\mathrm{li}} + \phi_{\mathrm{lp}} \qquad \text{Eq. (1)}$$

Similarly, outdoor-side heating capacity can be expressed as

$$\phi_{\mathrm{tco}} = \phi_{\mathrm{co}} - P_{\mathrm{o}} - \phi_{\mathrm{lo}} + \phi_{\mathrm{lp}} \qquad \text{Eq. (2)}$$

Bring $\phi_{\mathrm{li}} = L_{\mathrm{i}} \cdot (t_{\mathrm{i1}} - t_{\mathrm{i2}})$, $\phi_{\mathrm{lo}} = L_{\mathrm{o}} \cdot (t_{\mathrm{o1}} - t_{\mathrm{o2}})$ and $\phi_{\mathrm{lp}} = L_{\mathrm{p}} \cdot (t_{\mathrm{o3}} - t_{\mathrm{i3}})$ into Eq.(1) and Eq.(2), we have

$$\phi_{\mathrm{tci}} = P_{\mathrm{in}} - \phi_{\mathrm{ci}} + L_{\mathrm{i}} \cdot (t_{\mathrm{i1}} - t_{\mathrm{i2}}) + L_{\mathrm{p}} \cdot (t_{\mathrm{o3}} - t_{\mathrm{i3}}) \qquad \text{Eq. (3)}$$

$$\phi_{\mathrm{tco}} = \phi_{\mathrm{co}} - P_{\mathrm{o}} - L_{\mathrm{o}} \cdot (t_{\mathrm{o1}} - t_{\mathrm{o2}}) + L_{\mathrm{p}} \cdot (t_{\mathrm{o3}} - t_{\mathrm{i3}}) \qquad \text{Eq. (4)}$$

The Eq.(3) and Eq.(4) are the calibration model of calorimeter.
Moreover, in this model, the room type calorimeter is working under empty-load situation. In other words, there is no air conditioner under tested, which means indoor-side cooling capacity and outdoor-side heating capacity equal to zero. Then, the calibration model can be expressed as

$$P_{\mathrm{in}} - \phi_{\mathrm{ci}} + L_{\mathrm{i}} \cdot (t_{\mathrm{i1}} - t_{\mathrm{i2}}) + L_{\mathrm{p}} \cdot (t_{\mathrm{o3}} - t_{\mathrm{i3}}) = 0 \qquad \text{Eq. (5)}$$

$$\phi_{\mathrm{co}} - P_{\mathrm{o}} - L_{\mathrm{o}} \cdot (t_{\mathrm{o1}} - t_{\mathrm{o2}}) + L_{\mathrm{p}} \cdot (t_{\mathrm{o3}} - t_{\mathrm{i3}}) = 0 \qquad \text{Eq. (6)}$$

In Eq.(5) and Eq.(6), only three coefficients of heat leakage L_{i}, L_{p} and L_{o} are unknown, and the other parameters can be measured through the experiments. Then the coefficients of heat leakage can be obtained.
However, when these coefficients are brought back to Eq.(3) and Eq.(4) with the experiments data, the indoor-side cooling capacity ϕ_{tci} and outdoor-side heating capacity ϕ_{tco} not equal to zero. And ϕ_{tci} and ϕ_{tco} should be treated as the measurement background values of the calorimeter, which denoted by B_{i} and B_{o}.
To sum up, the system parameters include three coefficients of heat leakages and two background values.

3. THE MEASUREMENT METHOD OF SYSTEM PARAMETERS

According to Eq.(5) and Eq.(6), the coefficients of heat leakage and background values can be calculated by designed experiments. The set values of ambient temperature are shown in Table 1.

Table 1. Ambient temperature set values (dry bulb temperature, ℃)

Experiment No.	Indoor-side test chamber	outdoor-side test chamber	Indoor-side air space	outdoor-side air space
1	20	40	20	40
2	20	20	40	40
3	27	35	27	35

From Table 1, under the conditions of experiment 1, the heat mainly flows from the outdoor-side test chamber into the indoor-side test chamber through partition wall because of the obvious temperature difference between the two test chambers. On the contrary, under the conditions of experiment 2, the heats mainly flow from the air spaces into the test chambers through the surrounding walls because of the obvious temperature difference between the two sides of surrounding walls. The experiment 3, which is similar to T1 Standard cooling capacity rating conditions (ISO 5151, 2017), aims to obtain the background values of empty-load situation.
The coefficients of heat leakage can be obtained from the experiment 1 and experiment 2. For the purpose of measurement accuracy, the temperature difference are extended to 20℃ shown in Table 1. In accordance with Eq.(5) and Eq.(6), we have

$$P_{\text{in-c1}} - \phi_{\text{ci-c1}} + L_{\text{i}} \cdot \left(t_{\text{i1-c1}} - t_{\text{i2-c1}}\right) + L_{\text{p}} \cdot \left(t_{\text{o3-c1}} - t_{\text{i3-c1}}\right) = 0 \quad \text{Eq. (7)}$$

$$\phi_{\text{co-c1}} - P_{\text{o-c1}} - L_{\text{o}} \cdot \left(t_{\text{o1-c1}} - t_{\text{o2-c1}}\right) + L_{\text{p}} \cdot \left(t_{\text{o3-c1}} - t_{\text{i3-c1}}\right) = 0 \quad \text{Eq. (8)}$$

$$P_{\text{in-c2}} - \phi_{\text{ci-c2}} + L_{\text{i}} \cdot \left(t_{\text{i1-c2}} - t_{\text{i2-c2}}\right) + L_{\text{p}} \cdot \left(t_{\text{o3-c2}} - t_{\text{i3-c2}}\right) = 0 \quad \text{Eq. (9)}$$

$$\phi_{\text{co-c2}} - P_{\text{o-c2}} - L_{\text{o}} \cdot \left(t_{\text{o1-c2}} - t_{\text{o2-c2}}\right) + L_{\text{p}} \cdot \left(t_{\text{o3-c2}} - t_{\text{i3-c2}}\right) = 0 \quad \text{Eq. (10)}$$

where the subscript -c1 denotes the results of experiment 1, and the subscript -c2 denotes the results of experiment 2.
In experiment 1, the temperature differences of surrounding walls are very small. Similarly, in experiment 2, the temperature difference of partition wall is also very small. Then, Eq. (7) to Eq. (10) can be simplified as

$$P_{\text{in-c1}} - \phi_{\text{ci-c1}} + L_{\text{p}} \cdot \left(t_{\text{o3-c1}} - t_{\text{i3-c1}}\right) = 0 \quad \text{Eq. (11)}$$

$$\phi_{\text{co-c1}} - P_{\text{o-c1}} + L_{\text{p}} \cdot \left(t_{\text{o3-c1}} - t_{\text{i3-c1}}\right) = 0 \quad \text{Eq. (12)}$$

$$P_{\text{in-c2}} - \phi_{\text{ci-c2}} + L_{\text{i}} \cdot \left(t_{\text{i1-c2}} - t_{\text{i2-c2}}\right) = 0 \quad \text{Eq. (13)}$$

$$\phi_{\text{co-c2}} - P_{\text{o-c2}} - L_{\text{o}} \cdot \left(t_{\text{o1-c2}} - t_{\text{o2-c2}}\right) = 0 \quad \text{Eq. (14)}$$

Further, the coefficients of heat leakage are expressed as

$$L_{\text{p}} = \frac{P_{\text{in-c1}} - \phi_{\text{ci-c1}} - P_{\text{o-c1}} + \phi_{\text{co-c1}}}{2 \cdot \left(t_{\text{i3-c1}} - t_{\text{o3-c1}}\right)} \quad \text{Eq. (15)}$$

$$L_{\text{i}} = \frac{P_{\text{in-c2}} - \phi_{\text{ci-c2}}}{\left(t_{\text{i2-c2}} - t_{\text{i1-c2}}\right)} \quad \text{Eq. (16)}$$

$$L_{\text{o}} = \frac{\phi_{\text{co-c2}} - P_{\text{o-c2}}}{\left(t_{\text{o1-c2}} - t_{\text{o2-c2}}\right)} \quad \text{Eq. (17)}$$

The background values B_{i} and B_{o} can be obtained from the measurement method or the calculation method.
When the measurement method is adopted, the background values can be measured through the experiment 3 with the coefficients which are obtained from experiment 1 and experiment 2. The background values can be expressed as

$$B_{\text{i}} = P_{\text{in-c3}} - \phi_{\text{ci-c3}} + L_{\text{i}} \cdot \left(t_{\text{i1-c3}} - t_{\text{i2-c3}}\right) + L_{\text{p}} \cdot \left(t_{\text{o3-c3}} - t_{\text{i3-c3}}\right) \quad \text{Eq. (18)}$$

$$B_{\text{o}} = \phi_{\text{co-c3}} - P_{\text{o-c3}} + L_{\text{p}} \cdot \left(t_{\text{o3-c3}} - t_{\text{i3-c3}}\right) - L_{\text{o}} \cdot \left(t_{\text{o1-c3}} - t_{\text{o2-c3}}\right) \quad \text{Eq. (19)}$$

where the subscript -c3 denotes the results of experiment 3.
When the calculation method is adopted, the background values can be calculated by Eq.(7) and Eq.(8) because experiment 1 is similar to the experiment 3. The background values can be expressed as

$$B_{\text{i}} = P_{\text{in-c1}} - \phi_{\text{ci-c1}} + L_{\text{i}} \cdot \left(t_{\text{i1-c1}} - t_{\text{i2-c1}}\right) + L_{\text{p}} \cdot \left(t_{\text{o3-c1}} - t_{\text{i3-c1}}\right) \quad \text{Eq. (20)}$$

$$B_{\text{o}} = \phi_{\text{co-c1}} - P_{\text{o-c1}} + L_{\text{p}} \cdot \left(t_{\text{o3-c1}} - t_{\text{i3-c1}}\right) - L_{\text{o}} \cdot \left(t_{\text{o1-c1}} - t_{\text{o2-c1}}\right) \quad \text{Eq. (21)}$$

Both of the above methods can be applied to get the background values. The measurement method is closer to the actual measurement situation, and the calculation method can reduce the experimental workloads. In practice, it can be selected according to the requirements.

4. RESULTS AND APPLICATION

4.1. The results of system parameters

In order to ensure the accuracy of measurement data, some preparations should be made before the measurements of the system parameters.

A) The calibration and correction to the electrical power measurement system. The sensors and instruments in electrical power measurement system normally includes the digital power meters and the current transformers, and they all should be calibrated and corrected.

B) The calibration and correction to the resistance temperature detectors which measure the inlet water temperature and the outlet water temperature of the cooling coil. We suggest the fitting correction for the purpose of the accuracy in the full range of temperature measurement.

Then, the pressure equalization device should be closed throughout the measurements of system parameters, and the ambient temperatures of the calorimeter should be set according to Table 1. Besides, the mass flows of the cooling water for the cooling coils in indoor-side test chamber and outdoor-side test chamber are both set at 400 kg/h, and the temperature of the cooling water tank is set at 10 ℃. The measurement results are shown in Tables 2, 3 and 4.

Table 2. Measurement results from experiment 1

No.	P_{in}(W)	Φ_{ci}(W)	P_o(W)	Φ_{co}(W)	t_{i1}(℃)	t_{i2} (℃)	t_{i3} (℃)	t_{o1} (℃)	t_{o2} (℃)	t_{o3} (℃)
1	3549.9	3564.9	12977.2	12765.5	20.25	19.90	20.14	39.96	40.21	39.74
2	3556.4	3570.7	12988.7	12784.6	20.25	19.90	20.14	39.97	40.19	39.73
3	3547.6	3579.6	13018.0	12793.3	20.25	19.90	20.14	39.97	40.16	39.68
4	3748.8	3787.5	13373.1	13120.0	20.28	19.92	20.13	39.97	40.05	39.47
5	3755.1	3797.2	13253.5	13027.5	20.28	19.92	20.13	39.99	40.07	39.50
6	3765.2	3800.9	13163.5	12955.5	20.26	19.93	20.14	40.01	40.08	39.49
7	3792.9	3831.5	12369.8	12067.0	20.30	19.92	20.10	39.99	40.01	39.45
8	3793.7	3824.9	12311.3	12063.8	20.30	19.93	20.09	40.00	40.05	39.47
9	3784.3	3816.6	12280.8	12062.9	20.30	19.92	20.09	40.02	40.06	39.46
Average	3699.3	3730.4	12859.5	12626.7	20.27	19.92	20.12	39.99	40.10	39.55

Table 3. Measurement results from experiment 2

No.	P_{in}(W)	Φ_{ci}(W)	P_o(W)	Φ_{co}(W)	t_{i1}(℃)	t_{i2} (℃)	t_{i3} (℃)	t_{o1} (℃)	t_{o2} (℃)	t_{o3} (℃)
1	3426.8	3760.5	3302.0	3777.9	39.68	20.19	19.90	39.62	20.44	19.95
2	3429.4	3755.1	3336.2	3761.4	39.69	20.19	19.87	39.90	20.42	19.92
3	3408.5	3744.0	3346.4	3746.4	39.69	20.19	19.87	39.61	20.39	19.90
Average	3421.6	3753.2	3328.2	3761.9	39.69	20.19	19.88	39.71	20.42	19.92

Table 4. Measurement results from experiment 3

No.	P_{in}(W)	Φ_{ci}(W)	P_o(W)	Φ_{co}(W)	t_{i1}(℃)	t_{i2} (℃)	t_{i3} (℃)	t_{o1} (℃)	t_{o2} (℃)	t_{o3} (℃)
1	6540.4	6509.0	9996.7	9845.4	27.22	26.93	26.97	35.02	35.07	34.68
2	6533.7	6505.8	10017.8	9852.7	27.23	26.93	26.96	35.04	35.08	34.68
3	6511.8	6488.2	9990.1	9851.9	27.23	26.93	26.96	35.04	35.09	34.68
4	6528.3	6500.4	10001.1	9850.3	27.23	26.93	26.97	35.03	35.08	34.68
Average	6528.6	6500.9	10001.4	9850.1	27.23	26.93	26.97	35.03	35.08	34.68

Table 2 shows 9 groups of measurement results under the conditions of experiment 1. According to Eq.(15), the calculated results is in the range from 5.6 W/℃ to 8.8 W/℃, and the average value 6.8 W/℃ is used as the coefficient of heat leakage L_p.

Table 3 shows 3 groups of measurement results under the conditions of experiment 2. According to Eq.(16) and Eq.(17), the calculated results of L_i and L_o are in the range from 16.7 W/℃ to 17.2 W/℃ and from 20.8 W/℃ to 24.8 W/℃ separately, the average value 17.0 W/℃ and 22.5 W/℃ are used as the coefficients of heat leakage L_i and L_o.

When the calculation method is adopted, three coefficients of heat leakage are brought back to Eq.(20) and Eq.(21), the calculated results of background value B_i is in the range from 95.7 W to

124.9 W, and the average value is 107.0 W. And the calculated results of background value B_o is in the range from -170.8 W to -65.9 W, and the average value is -98.2 W.
When the measurement method is adopted, 4 groups of measurement results under the conditions of experiment 3 are shown in Table 4. In accordance with Eq.(20) and Eq.(21), the measurement results of background value B_i is in the range from 81.2 W to 88.8 W, and the average value is 85.2 W. And the measurement results of background value B_o is in the range from -111.7 W to -84.6 W, and the average value is -97.8 W.

Table 5. Results of system parameters

Method	B_i (W)	B_o (W)	L_i (W/°C)	L_p (W/°C)	L_o (W/°C)
Calculation method	107.0	-98.2	17.0	6.8	22.5
Measurement method	85.2	-97.8			
Average	96.1	-98.0			

The results of system parameters are shown in Table 5. It can be seen that the results of B_o obtained from the two methods are very close. But the difference between the results of B_i obtained from the two methods is 21.8 W. Under the condition that much higher measurement accuracy is required, we suggest that the average values of B_i and B_o should be adopted in the measurement of cooing capacity.

4.2. Application of the system parameters

The using conditions of the system parameters are determined based on the measurement situation of the calorimeter. Three coefficients of heat leakage should be applied to all of the measurement situation. The application of two background values is according to the working situation of the cooling coil in the test chamber.
The measurement of air conditioner using the calorimeter is the comparison of the different measurement situation of the calorimeter. If the calibration model is considered as the basic situation, the measurement results of the indoor-side and outdoor-side are the background values B_i and B_o. Moreover, this basic situation is based on the empty-load measurement under which the cooling coils in the test chambers are all running. Then, an air conditioner is installed in the calorimeter. Under this load situation, the measurement results of indoor-side cooling capacity and outdoor-side heating capacity are denoted by $\Phi_{tci\text{-}t}$ and $\Phi_{tco\text{-}t}$. Due to the difference of measurement results under two situations is caused by the air conditioner under test, therefore the cooling capacity and heating capacity of the air conditioner are $\Phi_{tci\text{-}t} - B_i$ and $\Phi_{tco\text{-}t} - B_o$.
In practice, the cooling coil in the indoor-side test chamber is possibly not working. For the basic situation, if the cooling coil does not remove heat from test chamber, the heating coil is not necessary. Under this basic situation, the energy flows of the indoor-side test chamber only include the heat leakages, which have been considered in the cooling capacity measurement. Therefore, the background value of indoor-side B_i equals to zero, and the cooling capacity of indoor-side is $\Phi_{tci\text{-}t}$.
The application of the system parameters, especially the application of the background values, can improves the issues of heat balance zero drift. To verify the effect of the system parameters, the results in Table 5 is applied to the calorimeter. And 10 window type air conditioners are measured using the calorimeter in one year, the arrangement photos are shown in Figure 3.

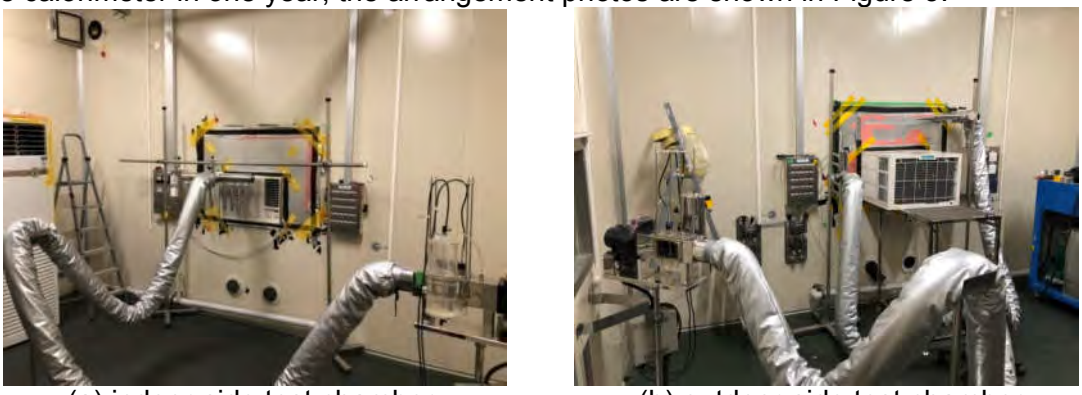

(a) indoor-side test chamber (b) outdoor-side test chamber

Figure 3: Arrangement photos of window type air conditioner in the calorimeter

The heat balance results of the 10 measurements are shown in Figure 4. The results show that the absolute value of heat balance is less than 2% in the cooling capacity range of 2000W~4500W and 1% in the range of 4500W~7000W.

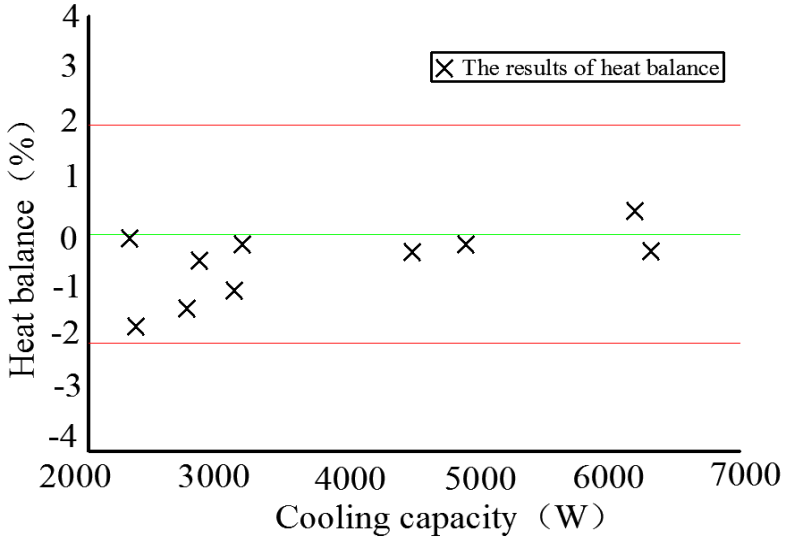

Figure 4: Heat balance results measured by room type calorimeter

5. CONCLUSIONS

In this study, the calibration model of the balanced ambient room type calorimeter is established based on the empty-load situation. In accordance with the model, the system parameters, which include three coefficients of heat leakage and two background values of test chamber, are proposed to improve the issue of heat balance zero drift. And the calibration procedure of system parameters, which is given by the designed experiments, is applied to the calorimeter. Then the using conditions of the parameters are analyzed, and we conclude that the background value of indoor-side test chamber can be obtained through the measurement method or the calculation method under the condition that the cooling coil is working; the background value equals to zero under the condition that the cooling coil is not working. The parameters are applied to the calorimeter which measures 10 different window type air conditioners in one year. The results show that the absolute value of heat balance is less than 2 % in the cooling capacity range of 2000W~4500W and 1% in the range of 4500W~7000W.

ACKNOWLEDGEMENTS

This work is funded by the National Key Research and Development Program of China (No. 2018YFF0212404).

NOMENCLATURE

Φ_{tci}	indoor-side cooling capacity (W)	P_{in}	total electrical power consumed by indoor-side test chamber (W)
Φ_{tco}	outdoor-side heating capacity (W)	Φ_{ci}	cooling capacity of indoor-side cooling coil (W)
Φ_{li}	heat leakage of indoor-side surrounding wall (W)	Φ_{lp}	heat leakage of separating partition wall (W)
Φ_{co}	cooling capacity of outdoor-side cooling coil (W)	P_o	total electrical power consumed by outdoor-side test chamber (W)
Φ_{lo}	heat leakage of outdoor-side surrounding wall (W)	L_i	coefficient of heat leakage through indoor-side surrounding wall
B_i	Background value of indoor-side cooling capacity (W)	L_p	coefficient of heat leakage through partition wall
B_o	Background value of outdoor-side heating	L_o	coefficient of heat leakage through

capacity (W)

t_{i1} external surface average temperature of indoor-side test chamber surrounding wall (℃)

t_{i2} Internal surface average temperature of indoor-side test chamber surrounding wall (℃)

t_{i3} indoor-side average temperature of partition wall (℃)

outdoor-side surrounding wall

t_{o1} external surface average temperature of outdoor-side test chamber surrounding wall (℃)

t_{o2} Internal surface average temperature of outdoor-side test chamber surrounding wall (℃)

t_{o3} outdoor-side average temperature of partition wall (℃)

REFERENCES

ANSI/ASHRAE 16-1983 (RA 2014), 2014. Method of Testing for Rating Room Air Conditioners and Packaged Terminal Air Conditioners. American Society of Heating, Air-Conditioning and Refrigeration Engineers, Inc., Atlanta, 2-10.

ANSI/ASHRAE 58-1986 (RA 2014), 2014.Method of Testing for Rating Room Air-Conditioner and Packaged Terminal Air-Conditioner Heating Capacity. American Society of Heating, Air-Conditioning and Refrigeration Engineers, Inc., Atlanta, 2-10.

GB/T 7725, 2004. Room air conditioners. China National Institute of Standardization, China, 19-62.

ISO 5151, 2017. Non-ducted air conditioners and heat pumps - Testing and rating for performance. International Organization for Standardization, Geneva, Switzerland, 1-33.

Néstor, F.D., 2009. Methodology for uncertainty calculation of net total cooling effect estimation for rating room air conditioners and packaged terminal air conditioners. J. International Journal of refrigeration 32(2009), 1472-1477.

Manuscript ID: 487
DOI: 10.18462/iir.icr.2019.0487

Problems in design of cooling systems for particle detectors and relevant electronics

Vaclav VACEK[(a, b)], Martin DOUBEK[(a)]

[(a)] Czech Technical University in Prague, Department of Physics, Technická 4, 16607 Prague 6, Czech Republic
[(a)] Unicorn College s.r.o., V Kapslovně 2, 13000 Prague 3, Czech Republic
e-mail vaclav.vacek@fs.cvut.cz

ABSTRACT

We present the main design approaches for cooling systems of particle detectors and their electronics. The paper summarizes our 25 years-long participation and experience in design and implementations of cooling systems for major detector projects at CERN. We present some typical use cases that differ in cooling power and employ different refrigerants or refrigerant mixtures.
The first use case deals with a small, lightweight mobile device using air as cooling medium that is aimed for applications requiring cooling power up to thousand watts or lower and temperatures down to -40°C.
The second use case represents evaporative system using fluorocarbon refrigerants (as both a single fluid and mixtures) capable of cooling the electronics down to -30°C. The unusual demand for vapour tubes without thermal insulation resulted in special design measures to keep surfaces of exhaust pipes from evaporator above a dew point.
The results achieved in the above use cases will reflect running condition experience on typical installations, now in service for more than 8 years. Notes about mathematical modelling and simulation will indicate a reduction in development and experimental time needed for verification of the final solutions.
Keywords: cooling systems; detectors and electronics; refrigerants, fluorocarbons; sonar-based analyser/flowmeter.

1. INTRODUCTION

Our research group from the Department of Physics has participated in detector cooling projects at CERN over the last 25 years. Experience collected during that period leads us to the statement that special cooling systems (CS) designed for the particle detector cooling, and also for cooling of high-tech, electronics have many specific features that require a different approach when compared to the traditional refrigeration industry applications, both in design period, and later during the actual implementation of the projects. We have acquired most of our experience through our participation in design and commissioning of the cooling system for the Inner detector (ID) of the ATLAS project. We have participated mainly in design, development and testing of the cooling structures of the pixel part of the Atlas experiment that later resulted in selecting a common evaporative cooling system, also for the second part of the inner detector, i.e. its strip part. The cooling system has been described many times in literature (Attree et al., 2008) and (Hallewell et al., 2007). It is modified compressor-condenser system with cooling power about 70 kW circulating approximately 1.13 kg/s of R 218 refrigerant through 204 loops with different mass flow rates to keep silicon surface of the detectors approximately at - 7°C. Each loop is equipped with pressure regulator (PR), backpressure regulator (BPR) and shut off valves, all pneumatically operated. The complexity of this work allows us to outline some major differences that one has to consider in this special field and we summarize these differences as follows:

- We are cooling down unique and extremely expensive high-tech electronics that will not be possible to replace if some damage or failure of the cooling system occurs. All parts must be continuously cooled and maintained at the required temperature over the lifetime of the experiment (more than 10 years). So generally used COP efficiency of CS is not the highest

priority in the applications but the fact that we have to supply refrigerant to the evaporators all the time and achieve the required temperature according to the specifications of the electronics is more important.

- The most of the experience and standard parts known in the refrigeration industry are excluded due to the working environment (radiation and strong magnetic field).
- The evaporator tubes are often supporting elements for the delicate and very expensive detector electronics. They have to be extremely light, but firm due to the alignment needs.
- Space constrains (available space is unfortunately „shrinking" during the assembly once the engineering specifications are revised) limiting the possibility of insulation and make refrigerant tube layouts very complex with large number of bends and connectors (i.e. potential threats of leaks …).
- Limited accessibility inside of the detectors structure does not allow servicing of the cooling components and it must ensure that parts lifetime exceeds several years (often more than 10 years).
- Thermal interference with other detector sections is to be minimized.
- One has to face floating required specification during the design period and construction process (in pressure, temperature and power dissipation specifications).
- In addition, there is missing information about important thermophysical properties of the relevant radiation-hard fluids and mixtures used in this field, two-phase capillary flow, etc.
- Green refrigerants and heat transfer fluids (with low GWP) are not radiation hard in general. Flammable fluids are immediately excluded since the installations are usually located in underground areas.
- Aspects of dielectric properties are vitally important because of potential leaks due to the many necessary connections within the layouts, including chemical stability of refrigerants to such extend that sometimes environmental issues are getting lower priority.

We can also outline what may help to cope with challenges outlined above:

- Great courage and endless tolerance if design parameters of the cooling are changed by physicists during development or even implementation period.
- Solid information and knowledge about thermophysical properties of relevant fluids (fluoroinert/fluorocarbon family, CO_2 and others).
- Use of the simulation models whenever possible and solid and critical comparison with experimental results.
- Background for the tests require reliable DAQ systems including sensors, and detailed commissioning and verifications of all key components is the must.
- Careful scaling up of the cooling system set-up, one or more small-scale mockup system should be constructed and commissioned prior to the full-scale system realization.
- In general, turnkey industrial solutions are not suitable, and developing of a tailored system is often the only solution.

Over the years, we have prepared and published several works where one can find useful information about several topics pointed out above, just to emphasize and highlight some of them:

- Data about the most fluorocarbons, derived both via semi-empirical approach and simulation (SAFT EOS, MC and MD simulations) some new SOS experimental data (C_4F_{10}, C_3F_8, C_2F_6 and mixtures), HTC data from measurements, Henri constant for fluorocarbons (Hallewel et al., 2010), (Vacek et al., 2000), (Vacek et al., 2013) and (Doubek et al., 2017).
- Two phase capillary flow simulation model are available (including contamination impact) and they can result in less experimental work when for instant one has to trim large number of various capillaries (Vacek at al., 2009), (Vins at al., 2010).
- Many experimental cooling circuits were prepared and used by us ranging in power from 200W to 22 kW (with steps at 500W, 1kW, 6 kW) and used for the commissioning of pixel, SCT part of ID ATLAS and Roman pot type detectors (RP) of TOTEM (Anelli et al., 2008), (Vacek et al., 2011), both as prototypes and final design structures.

We would like to introduce two typical use cases of nonstandard cooling applications that were recently developed in our Prague laboratory by our research team with a great help from our M.Sc. and PhD students.

2. TWO TYPICAL USE CASES

Due to the given scope of the conference paper, we would like to present in more detail two use cases of interesting solutions in the cooling of detectors and their electronics. Both use cases are

dealing with lower energy dissipation (cooling power) but they have great potential for many different applications in electronics cooling even outside the field of particle physics (Vacek and Doubek, 2016). The first use case describes application of Vortex tube in a laboratory cooling system ideally suited for cooling down a single chip or board during development work. The system is currently deployed and works for detectors with dissipation powers up to hundred watts. It is in use for small detectors of RP type within the AFP (Atlas Forward Physics) experiment. The second use case will describe evaporative cooling system with the cooling power around 1.5 kW serving primarily for commissioning of the various types of RP detectors (both silicon and diamond types) in the TOTEM experiment (Vacek et al., 2011). The circuit has a great variability in setting up the running conditions and it is suited to accept various refrigerants and even mixtures. It allows non-insulated lines due to the effective compact heat exchanger placed after the evaporator increasing low refrigerant vapour temperature fast above the dew point.

2.1. Enhancing the Cooling Power of the AIRCOOLER-Split

In addition to our large projects, we have been often approached by physicists and by electronic engineers with requests to develop simple, easy-to-use and maintenance-free system, which could fulfil their “cooling needs”. Both for laboratory purposes during development periods followed by simple “on table” commissioning procedures. In addition, even to develop a device that could be used for low-power dissipation installations (several tens or hundreds of watts) in the LHC (Large Hadron Collider) tunnel, where the cooling device must function in an environment with a strong magnetic field and a high level of radiation. Such problematic surroundings very often preclude the use of ordinary commercially available devices.
We have developed three types of units for production lines called AIRCOOLERS. Details are published in (Vacek and Doubek, 2016) and the most frequently used device is labelled as the AIRCOOLER_Split (ACS). The model in Fig. 1 is now cooling 4 pieces of the RP type of detectors in the LHC tunnel for more than 5 years without any failure, namely because our devices are mobile, very compact and have no moving parts. They do not require a refrigerant or electricity, just compressed air and can function for a long period without maintenance.

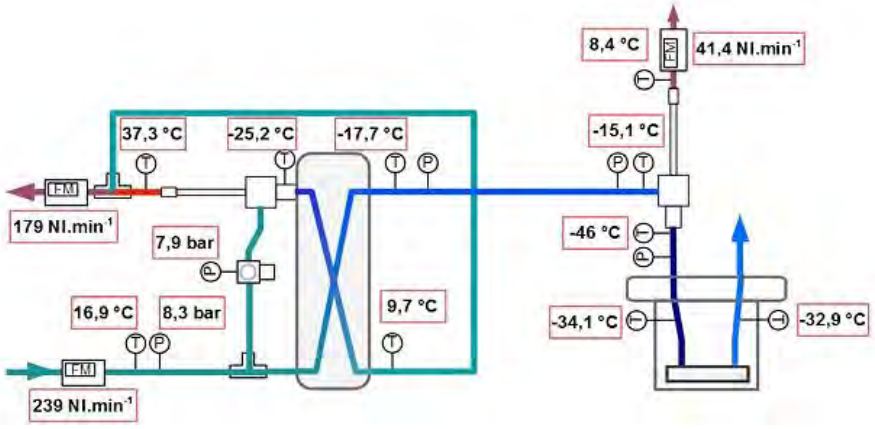

Figure 1: The ACS typical temperatures, pressures and flow for 17°C input air

Our typical arrangement of the AIRCOOLER is two-stage cooling system that is composed of two main parts. The main pre-precooling box reduces the air temperature in the first stage to a moderate temperature (around +2°C), and an additional connected single vortex tube cools the air down to the required level in the second stage. The box includes a plate heat exchanger, a pilot-operated pressure regulator and the first vortex tube for precooling the air passing through the heat exchanger. The second VT is to be placed as close as possible to the heat source that is to be cooled down, i.e. a heat exchanger cooling down the electronics. The integration of the second vortex tube in to the cooled device flange improves process efficiency and lowers airflow temperature down by 5°C. Since the cold air provides desired cooling effect, and even if it passes wiggle path inside the heat exchanger it has its limits due to the simple Newton equation for heat flux is

$$\dot{q} = \alpha \cdot A\,(t_w - t_{air}) \qquad \text{Eq. (1)}$$

where both heat transfer coefficient α and temperature difference between wall and air temperature $\Delta t = (t_w - t_{air})$ has its limits, so the last value that can be changed is the inner contact surface A between flowing air and solid wall. The heat transfer can be enhanced by roughening the inner surface or introducing inner fins inside the heat exchanger, both interventions being problematic. Despite the fins, the inner surface still features a relatively small area for the heat exchange. The air flows through the heat exchanger with limited cooling effect and leaves the exchanger while still having low temperature.

We have prepared heat exchangers filled with metal foams that can be manufactured easily. The empty sections between baffles were filled with copper foam to enlarge the internal surface available for the heat exchange as the second design test sample – see Fig. 2. The foam was cut into pieces slightly higher than the inner cavity height. Then compressed by flat cap on top of the heat exchanger. This ensures a solid thermal contact between all inside heat exchanger surfaces.

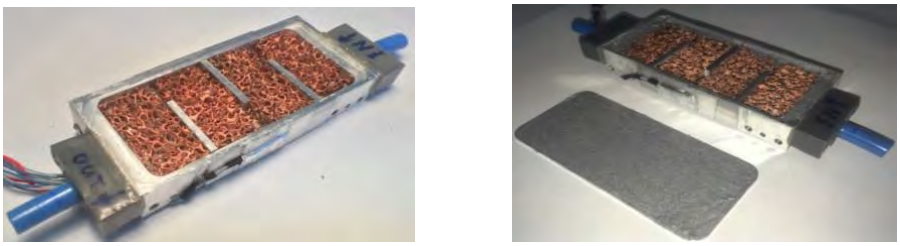

Figure 2: Heat exchanger with copper foam inserted in between the baffles

In order to increase the thermal contact between the copper foam and the heat exchanger surface it was later decided to use aluminium-filled epoxy for the next design test sample. The epoxy with metal filler can provide better thermal conductivity than simple epoxy resin. Moreover, it can further increase the contact area between the foam and the body of the exchanger.

The assembled heat exchanger was placed inside a cylindrical vacuum chamber made of acrylic glass to simulate condition within the Roman Pot detector. A vacuum pump was connected to the chamber to keep the constant pressure of 100 mbar in it.

The AIRCOOLER SPLIT model has one vortex tube outside of box attached directly to the Roman Pot flange supplying the stream of cooling air. The PLC regulation allowed us to maintain both constant output cooling air temperature and a shorter stabilization time of the system.

Each different heat exchanger design under investigation has been tested under the same conditions, i.e. with the same nominal input pressure of 8 bars into the AIRCOOLER and cooling air temperature at the inlet into the heat exchanger at -25°C.

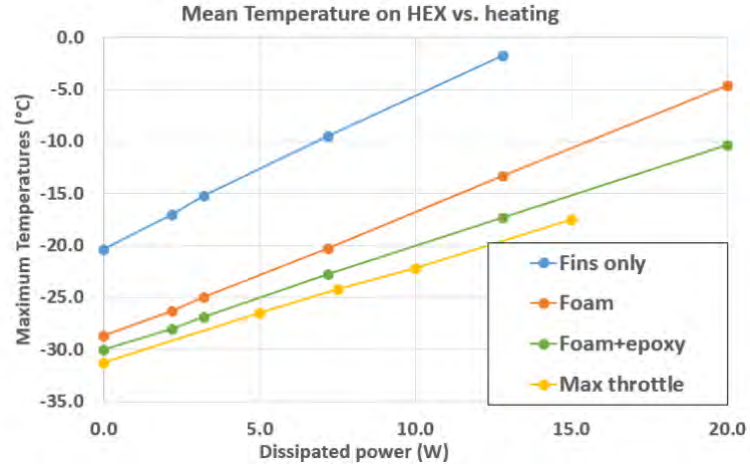

Figure 3: Heat exchanger with copper foam inserted in between the fins

The measurements illustrated in Fig. 3 show that heat exchanger with copper foam filler inside the heat exchanger cavity can significantly increase its cooling performance. Results have also indicated much better temperature distribution along the effective heat exchanger surface for all heat fluxes. Therefore, the heat exchanger, equipped with foam metal filler substituting finned or grooved

surfaces, is capable of handling higher heat fluxes and provides lower surface temperatures. Max throttle mode represents maximal airflow through the device.

2.2. Pilot Versatile Cooling Circuit for the TOTEM Project

The primary circuit purpose was to provide a widely adjustable cooling power for the final TOTEM CS development and commissioning of the RP detectors of the CERN TOTEM experiment (Oriunno et al., 2007). The setup is used to experiment with different elements of the final particle detectors cooling circuits e.g. heat exchangers, capillary tubes, evaporators and basic elements of the relevant cooling circuit control system including monitoring sensors.

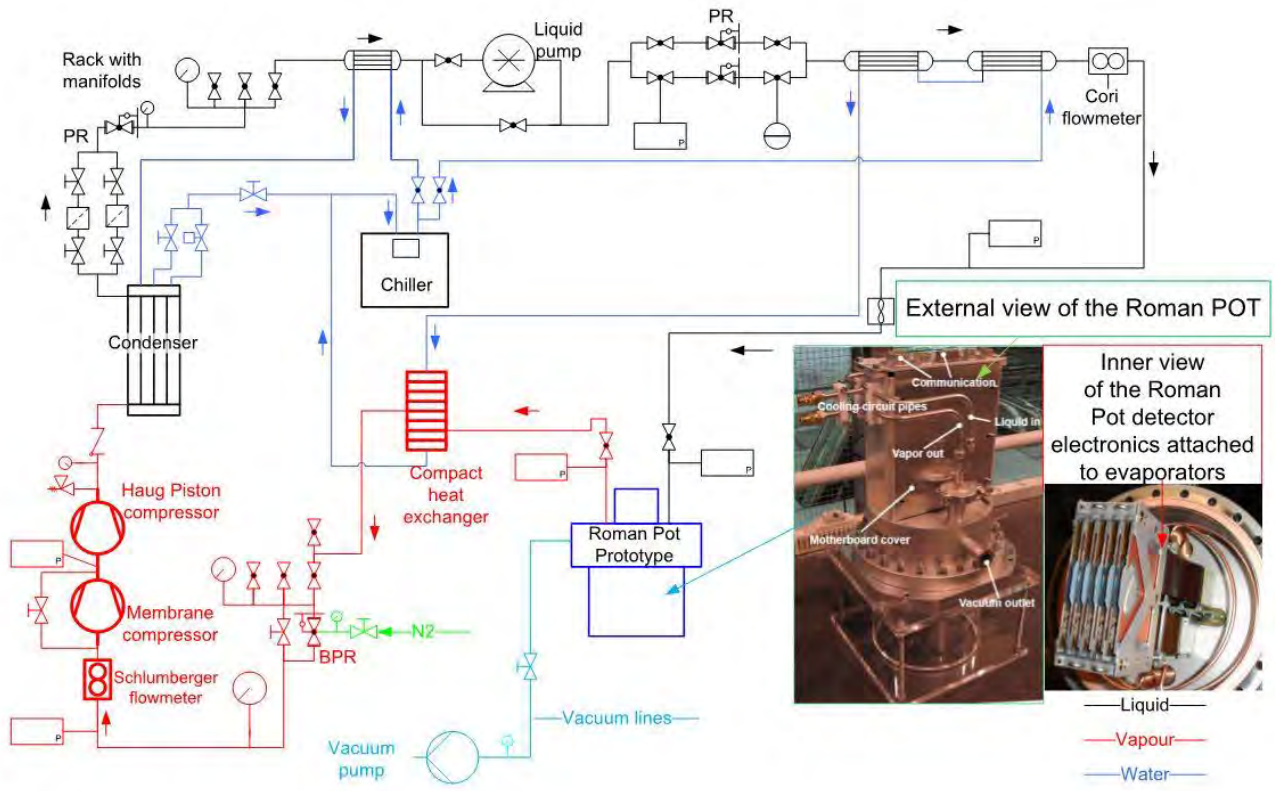

Figure 4: Principal schematics of the versatile cooling circuit

The circuit shown in Fig. 4 comprises two oil-free compressor units (piston and membrane units serving as the booster to cover refrigerant mass flow in the range of 1 to 9 g/s, if required) using the fluorocarbon refrigerant R218 (other fluorocarbons can be used as well: R610 or mixtures of R218 and R116). The use of refrigerants R-404A, R-452A and R-449A was also successfully tested. The heat of condensation is wasted through air-cooling and a supporting water circuit using independent chillers unit. The circuit is capable of reaching up to 1MPa liquid line pressure or up to 1.6MPa with a liquid pump. A DAQ system based on ELMB technology is connected by CANBUS to a PC with installed PVSS II software. A large number of tuning control devices provides a very wide operation parameter field.

There are over 25 sensors of different type on the main manifold measuring running temperatures, pressures and mass-flow on both the liquid and the vapour lines around all circuits. Cooling circuit can handle up to three RP's at once, but each of them can be separated from the main cooling loop using attached operational manifold. This feature provides an option to exchange any RP out of three and still keep small cooling plant running. The total number of sensors including those installed inside the RP's exceeds 70.

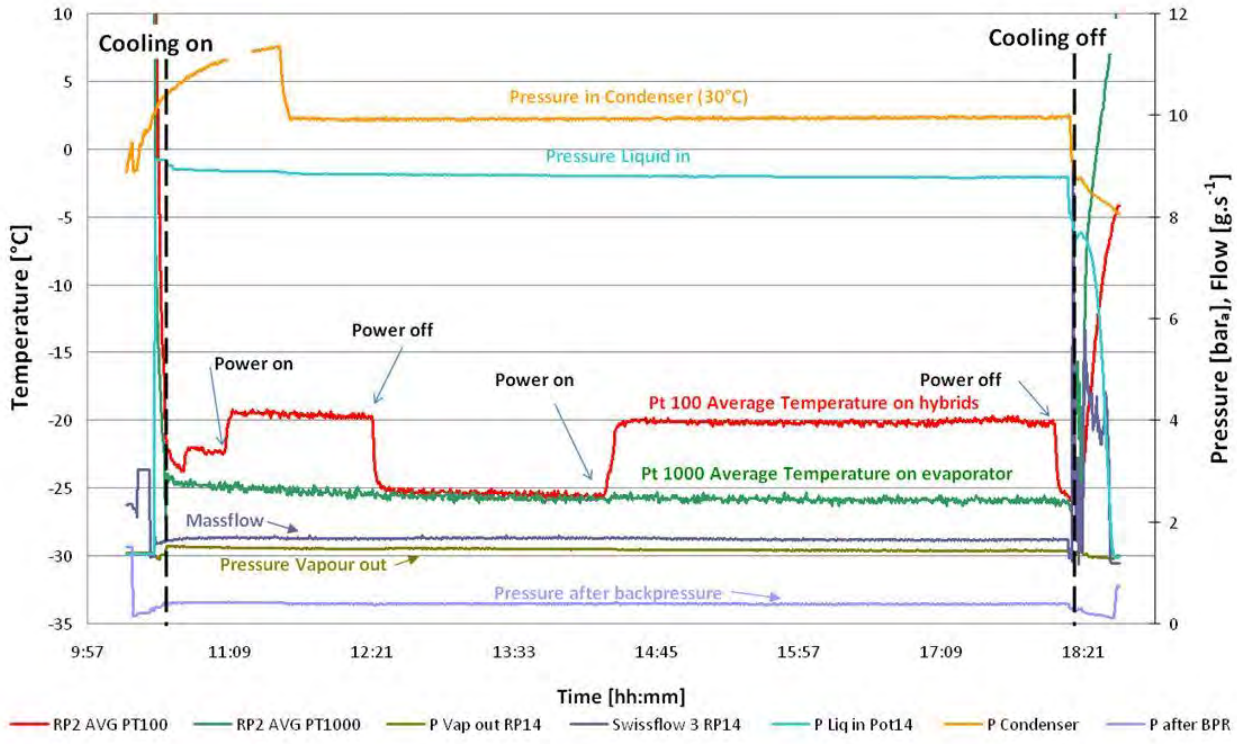

Figure 5: Typical commissioning run lasting more than 8 hours

Data displayed in Fig. 5, covering all day commissioning run, clearly demonstrate a stable performance of the cooling system. It is demonstrated by the stable temperature of the condenser, evaporator and the constant refrigerant flow. One can also note the sections of the run where silicon detectors have collected collision data and at the same time, the electronics were powered on. Please see the red line profile showing temperature of the electronic hybrid chips.
A special attention has been devoted to preventing insulation around the exhaust vapour lines and at the same time to make sure that no condensation takes place on the surface of those lines. Single water compact heat exchanger in Fig. 6 raises the temperature of the returning vapour from all three RP installed unit.

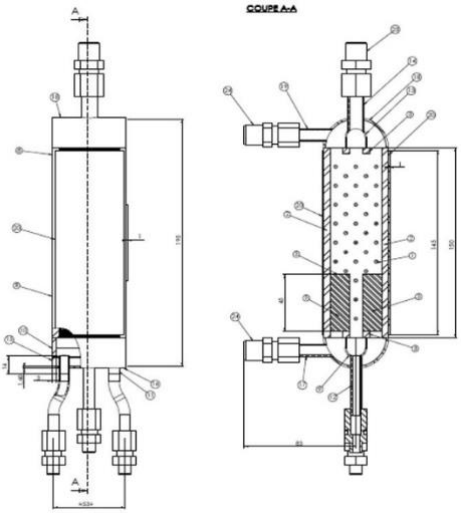

The device can efficiently increase vapour temperature due to the enhanced heat transfer extended surface between liquid (water) on one side and C_3F_8 (vapour) on the other side, see Fig. 7.

The device allows increase of vapour temperature (by 50ºC) over the short distance (150mm) while still keeping pressure drop of vapour section at relatively small values (less than 10kPa). It also turned out that search for minimal required flow of water (6 $cm^3.s^{-1}$ at vapour flow up to 5$g.s^{-1}$ @ -30ºC) passing through the still fully functioning heat exchanger makes it a self-tuning unit which does not need any additional control system.

Figure 6: Compact heat exchanger

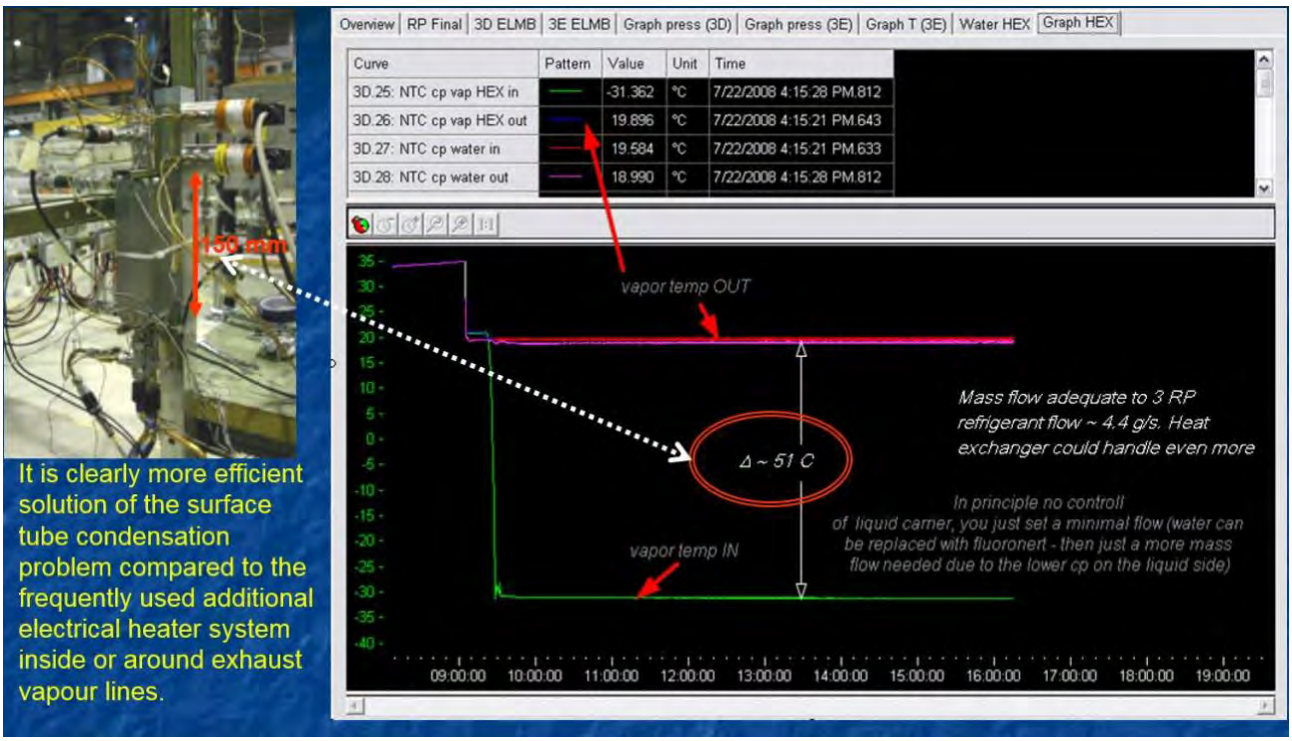

Figure 7: Screen shot showing the overall performance of the compact heat exchanger

Moreover, since both fluids are separated by stainless steel there is no need to tackle problems with compatibility of the refrigerant and sensitive elements of the heaters, seals around wires, and there is no need for an expensive control system. Securing the minimal water flow through the heat exchanger keeps the device perfectly functioning for wide range of conditions.
The circuit has been used for the many trial runs with various refrigerant mixtures and it has shown its outstanding versatility and reliability over more than 12 years.

3. CONCLUSIONS

We have collected number of experiences over the last 25 year while designing, realizing various refrigeration circuits for the particle detector applications and electronics cooling. We have pointed out very frequent problems and obstacles that one will meet in this specific field.
This time we have put our attentions on the smaller cooling devices. We have also summarized the research procedures that have helped us significantly to solve the problems that have arisen, such as the lack of knowledge about the thermo-physical properties of the refrigerants used or their mixtures. This is a very topical topic in looking for coolants for our applications so we are more environmentally friendly. Mathematical modelling of the two-phase capillary flow has significantly helped us to reduce the experimental time when preparing a large number of significantly different capillaries.
An interesting application described in the section on air coolers is definitely an effort to improve the conditions for increasing the heat flux from the internal walls of the heat exchanger into the gaseous media (in our case air). After many attempts to expand the inner surface of the heat exchangers, like traditional fins or for instance experiments with the use of PGS foils, it appears that very efficient method are fillers from foamed metals.
Another interesting circuit is the application originally designed for commissioning measurements on the TOTEM experiment. By a gradual development and improvement of the system, we have ended up with a very flexible system, which was also used for experiments with a wide spectrum of refrigerants, including mixtures. Probably the most exciting part of the circuit is the compact and efficient heat exchanger (the gas/liquid type), which practically does not require complex regulation and completely replaces the traditional and often used solutions. The electrical heater to achieve required thermally neutral solutions of the particle detectors are frequent solution of the problem. The necessary installed electrical power in many cases achieves the magnitude of the cooling power. Both in details presented use cases accompany the basic experimental data.

ACKNOWLEDGEMENTS

Authors would like to express their gratitude to large number of colleagues with whom we had a privilege to cooperate within the last 25 years either at CERN or in Prague. We also appreciate help and support coming through following grants: LM2015058 and LTT17018, kindly provided by the Czech Ministry of Education.

REFERENCES

Anelli, G., Antchev, G., Aspell, P., Avati, V., et al., 2008. The TOTEM Experiment at the CERN Large Hadron Collider. J Instrum., 3 (S08007).

Attree, D., Anderson, B., Anderssen, E. C., et al., 2008. The evaporative cooling system for the ATLAS inner detector. J Instrum., 3 (P07003).

Doubek, M. Haubner, M. Vacek, V. et al., 2017. Measurement of heat transfer coefficient in two phase flows of radiation-resistant zeotropic C2F6/C3F8 blends. Int. J. Heat Mass Transfer.113, 246-256.

Doubek, M., Vacek, V., Hallewell, G., 2016. Speed-of-sound based sensors for environmental monitoring. 15th IEEE Sensors Conference, Orlando, FL, NOV 03, 1400-1402.

Hallewell, G.,Hoffmann, D., Vacek, V., 2007. A versatile evaporative cooling system designed for use in an elementary particle detector. Int. J. Thermophys. 28 (5), 1730-1740

Hallewell, G., Vacek, V., Vins, V., 2010. Properties of saturated fluorocarbons: Experimental data and modeling using perturbed-chain-SAFT. Fluid Phase Equilibr. 292 (1-2), 64-70.

Oriunno, M., Battistin, M., David, E., et al., 2007. Design and prototype studies of the TOTEM Roman pot detectors. Nucl. Instrum. Methods Phys. Res., Sect. A. 581, 499–503.

Vacek, V., Doubek, M., 2016. Air-Driven Cooling Device for Hi-Tech Electronics. Proceedings of the 12th IIR Gustav Lorentzen Natural Working Fluids Conference, Heriot Watt Univ, Edinburgh, AUG 21-24

Vacek, V., Hallewell, G., Ilie, S., Lindsay, S., 2000. Perfluorocarbons and their use in cooling systems for semiconductor particle detectors. Fluid Phase Equilibr. 174 (1-2), 191-201.

Vacek, V., Vins, V., 2009. Two-Phase Flow Analyses During Throttling Processes. Int. J. Thermophys. 30 (4), 1179-1196

Vacek, V., Vitek, M., Doubek, M., 2013, Velocity of sound in Perfluoropropane (C3F8), Perfluoroethane (C2F6) and their mixtures. Fluid Phase Equilibr., 351 (SI), 53-60.

Vacek, V., Vitek, M., Doubek, M., 2011, VERSATILE REFRIGERATION CIRCUIT DEVELOPED FOR THE PARTICLE DETECTOR COMMISSIONING. Proceedings of the 23RD IIR INTERNATIONAL CONGRESS OF REFRIGERATION, Book Series: Congress International du Froid-International Congress of Refrigeration. 23, 3376-3382.

Vins, V., Hruby, J., Vacek, V., 2010. Numerical simulation of gas-contaminated refrigerant two-phase flow through adiabatic capillary tubes. Int. J. Heat Mass Transfer. 53 (23-24), 5430-5439.

Manuscript ID: 585
DOI: 10.18462/iir.icr.2019.0585

A molecular dynamics study of cryogenic gas nucleation at high supersaturation

Wan SUN[(a)], Zaiyong MA[(a)], Shanshan BU[(a)], Luteng ZHANG[(a)]

(a) Key Laboratory of Low-Grade Energy Utilization Technologies & Systems (Chongqing University), Ministry of Education, Chongqing 400044, China, sunwan@cqu.edu.cn

ABSTRACT

Nucleation plays a key role in the cryogenic field, such as supersonic separator, wind tunnel design, and two-phase turbo-expander. However, a lack of accurate knowledge on intermolecular potentials and uncertainties in some key physical properties make it difficult to understand the nucleation mechanism. In this paper, molecular dynamics (MD) simulation is conducted to investigate the micro-scale process of cryogenic gas nucleation at high supersaturation. The Lennard-Jones potential model is used to describe interactions between particles and the Newton equation of motion is solved via Velocity-Verlet method. Based on simulated microscopic quantities, nucleation rate and Wilson point are calculated, and compared with the results from classical nucleation theory. The influences of the supersaturation on the nucleation process also are explored, both of which determine the onset of nucleation and generation rate of cluster.
Keywords: Nucleation, Condensation, MD simulation, Argon.

1. INTRODUCTION

Nucleation is the first step in the formation of a new thermodynamic phase. It has a lot of practical consequences in the physical sciences and engineering fields, such as atmospheric physics, aerospace science, material science, polymer technology and metallurgical technology. In the refrigeration and cryogenic fields, nucleation at high supersaturation also has an important significance as a key process of phase change flow, such as the supersonic gas-liquid separator used for removal of water and heavy hydrocarbons (Bian et al., 2019;Rajaee Shooshtari et al., 2018), the wind tunnel design (Wegener, 1987,1991), and two-phase turbo-expander used in air separation plants (Niu et al., 2019; Sun et al., 2018) or ORC (Nithesh and Chatterjee, 2016). However, a lack of accurate knowledge on intermolecular potentials and uncertainties in some key physical properties for cryogenic fluids make a challenge to understand the microscopic mechanism of nucleation.

Since the classical nucleation theory (*CNT*) was proposed and developed in the early 20th century by Farkas, Becker and Döring, Volumer, Zeldovish and Frenkel (Kalikmanov, 2013), great efforts have been put into well understanding and accurate prediction of nucleation. Due to the capillary phenomenological assumptions, such as macroscopic droplets and thermodynamic equilibrium, were adopted in the derivation of CNT, which greatly limited the calculation accuracy and scope of application, many scholars then reviewed the nucleation theory to seek the correct calculation method of nucleation rate. The typical corrections include such as Coutrney (1961) mass action law correction, Kantrowitz (1951) non-isothermal effect correction and Girshick and Chiu (1990) self-consistency correction.

Whether phenomenological, density functional or semi phenomenological, the nucleation process is solved by simplifying certain assumptions, which are usually caused by insufficient understanding of the detailed information of material molecules. In recent years, with the development of computer technology, molecular simulation provides us with a powerful tool to understand the molecular dynamic evolution process and molecular microstructure changes. Michal et al. (2015) simulated the nucleation process of water vapor in the canonical ensemble using DL_POLY software based on MD method, and described the kinetic process of molecular cluster formation. Bykova and Gorbachev (2017) developed two new mathematical models to describe the formation and growth of water vapor molecular clusters using MC method and based on the classical

nucleation-corrected theory and kinetic nucleation theory, and analyzed the influence of the formation mechanism of dimer on the distribution function of molecular cluster size.
In this study, we use a large system consisting of 4000 vapor molecules, and conducted an MD simulation to directly observe the nucleation of cryogenic gas under high supersaturation. Based on the simulation, the dynamic behavior of cluster formation is revealed, from which the nucleation rate is evaluated and compared with classical nucleation theory. Meanwhile, the influence of supersaturation on the nucleation process also is explored.

2. CLASSICAL NUCLEATION THEORY

Nucleation is the first step in the formation of a stable new phase from a metastable non-equilibrium mother phase, also could be described as the formation of small clusters of new phase due to statistical fluctuation. This fluctuation means that once these clusters with less than critical radius r^* will tend to evaporate, while with larger than r^* will grow further and lead to the formation of a stable new phase. The simplest description of the fluctuation is the liquid droplet model, generally called the capillarity approximation, in which a cluster is treated as a spherical droplet of a well-defined radius with bulk liquid properties and is assumed to be in thermal equilibrium with the surrounding gas. With these assumptions, the classical nucleation theory was developed by Farkas, Becker and Döring, Volumer, Zeldovish and Frenkel (Kalikmanov, 2013). The main result of the *CNT* derived a common equation for the nucleation rate as follows:

$$J = J_0 \exp\left(-\frac{\Delta G^*}{k_B T_g}\right) \quad \text{Eq. (1)}$$

where J_0 is kinetic pre-exponential factor determined by varying corrections of *CNT*, ΔG^* refers to the Gibbs free energy change as the energy barrier that the formation of new phase must overcome. In *CNT*, the computed expression for nucleation rate and critical radius of nuclei are given by:

$$J_{CNT} = \frac{\rho_g^2}{\rho_l}\sqrt{\frac{2\sigma}{\pi m_1^3}}\exp\left(-\frac{16\pi\sigma^3}{3\rho_l^2\left(k_B T_g\right)\left(R_g T_g\right)^2\left(\ln S\right)^2}\right) \quad \text{Eq. (2)}$$

where σ is the bulk surface tension; the supersaturation ratio S is defined as the ratio of local pressure p and saturated pressure p_{sat} at gas local temperature. The critical radius and critical cluster number can be obtained as follows:

$$r^* = \frac{2\sigma}{\rho_l R_g T_g \ln\left(p/p_{sat}\right)} \quad \text{Eq. (3)}$$

$$n^* = \left(\frac{2}{3}\frac{\sigma_\infty s_1}{k_B T \ln\left(p/p_{sat}\right)}\right)^3 \quad \text{Eq. (4)}$$

where

$$s_1 = \left(36\pi\right)^{1/3}\left(v^l\right)^{2/3} \quad \text{Eq. (5)}$$

is the surface area of a monomer. v^l is a molecular volume of the liquid phase.

3. SIMULATION METHOD

The intermolecular potential Lennard-Jones 12-6 (Nicolas et al., 1979) was employed for the molecular dynamic simulation with the LAMMPS numerical computational too. The interaction potential in Lennard-Jones type is defined as:

$$u(r) = 4\varepsilon\left[\left(\frac{\sigma}{r}\right)^{12} - \left(\frac{\sigma}{r}\right)^{6}\right] \quad \text{Eq. (6)}$$

where r is the distance between centers of atoms, ε is the depth of the potential well and σ is the finite distance at which the inter-particle potential is zero. For the argon, the σ, ε and m are 0.34 nm, 1.67×10^{-21} J, and 6.63×10^{-26} kg. Thus, the reduced temperature is 119.8 K. The unit times is:

$$\tau = \sqrt{\frac{m\sigma^2}{\varepsilon}} = 2.15 \text{ ps} \quad \text{Eq. (7)}$$

The cell size is $35\times35\times35$ in the dimensionless unit. The cutoff radius is 5.0, and no tail correction is made for energy calculation. The number of atoms was set to be 4000 as arrangement of FCC type. The periodic boundary condition is used for the approximation of nucleation in macroscopic system. The gas was equilibrated in an NVT ensemble at reduced temperature T^*=1.25 for 10000 steps with the time step 0.005τ. Then the system temperature was set to a supercooled state, including T^*=0.68, 0.7, 0.72 and 0.74, for 90000 steps. The temperature was controlled by the Nose-Hoover style. The developments of pressure and temperature are displayed in Fig. 1.

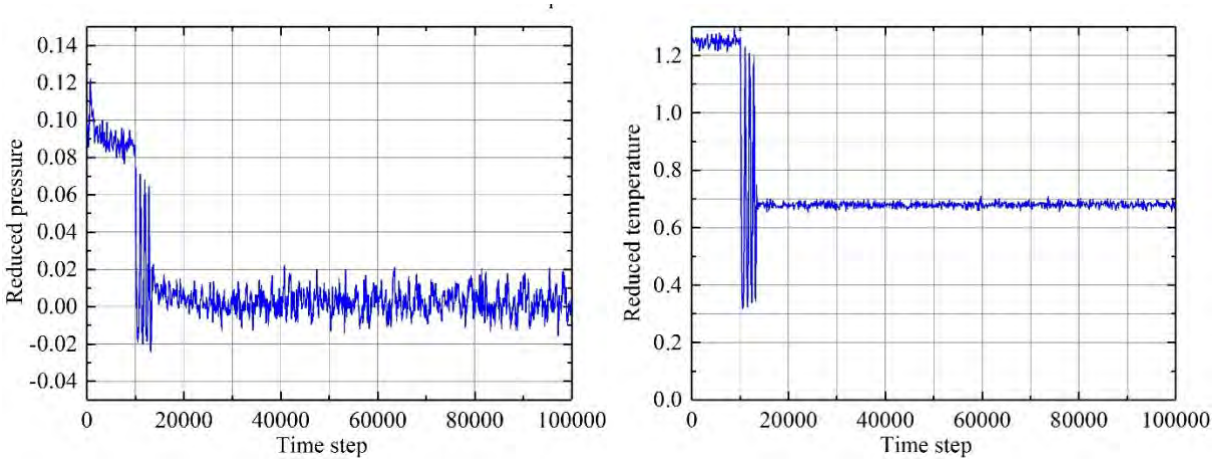

(a) Pressure (b) Temperature

Figure 1: Development of pressure and temperature.

4. RESULTS AND DISCUSSIONS

Molecular configurations for T^*=0.68 are present in Fig. 2. The start configuration for supercooled state at time = 50τ seems almost uniform (Fig. 2a). At time = 150τ (Fig. 2b), the atoms converge to gather and clusters of various sizes are observed at time = 300τ (Fig. 2c). At the end time (Fig. 2d), several largest clusters are formed, the largest of which consists of 1147 atoms.

In order to calculate the nucleation rate, the Stillinger method (Fisher, 1999) is employed to define the cluster size. In this method, we assume two neighbored molecules to be in one cluster when their center-of-mass distance is less than 1.5σ. According to *CNT*, in the nucleation process, only when the droplet radius is larger than the critical cluster size the metastable cluster can continue to grow and form into steady-state liquid phase. The molecules number of the critical cluster, calculated from Eq. (4), is used for the data statistics of MD simulation results. Fig. 3 records the total cluster number at different times for varying supersaturations. In this paper, four types of supersaturation (S = 4.44, 3.35, 2.57 and 2.00), generated by define different temperature (T^* = 0.68, 0.7, 0.72 and 0.74) are investigated. The slope of curve in Fig. 3 refers to the number of generated clusters in unit time in the simulated box. Thus, the nucleation rate could be obtained and listed in Table 1 compared with the nucleation rate predicted by *CNT*. It can be inferred that the nucleation rate predicted by MD simulation is larger than that calculated by CNT. Due to the limitation of molecule number, the difference between CNT and MD becomes larger with the supersaturation decreases. This is because that a lower supersaturation will lead to a larger number of critical

cluster. As a result, a sufficient number of molecules is required for the investigation of nucleation.

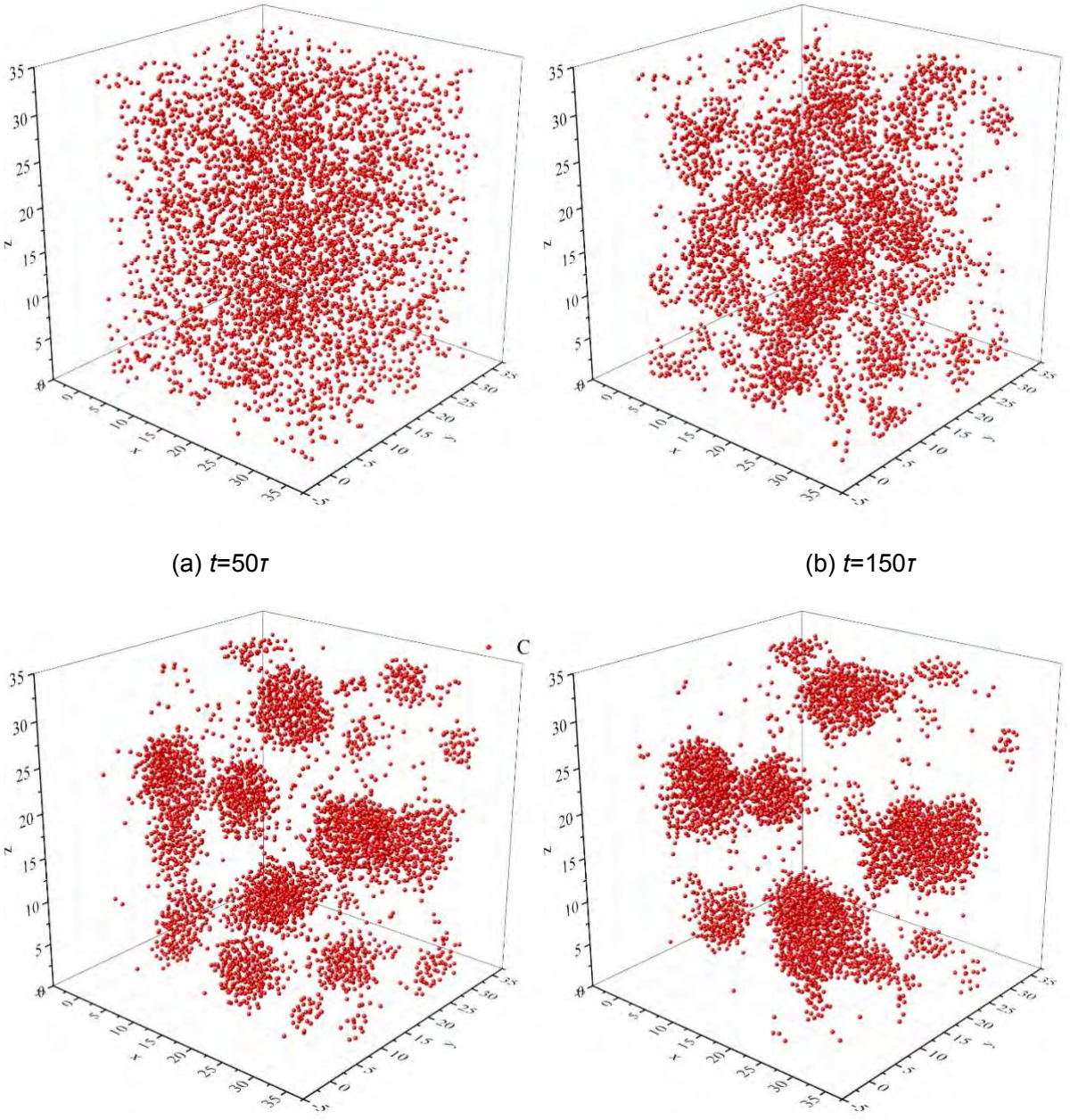

(a) t=50τ (b) t=150τ

(c) t=300τ (d) t=500τ

Figure 2: Sequential snapshots of the MD simulation (T^*=0.68).

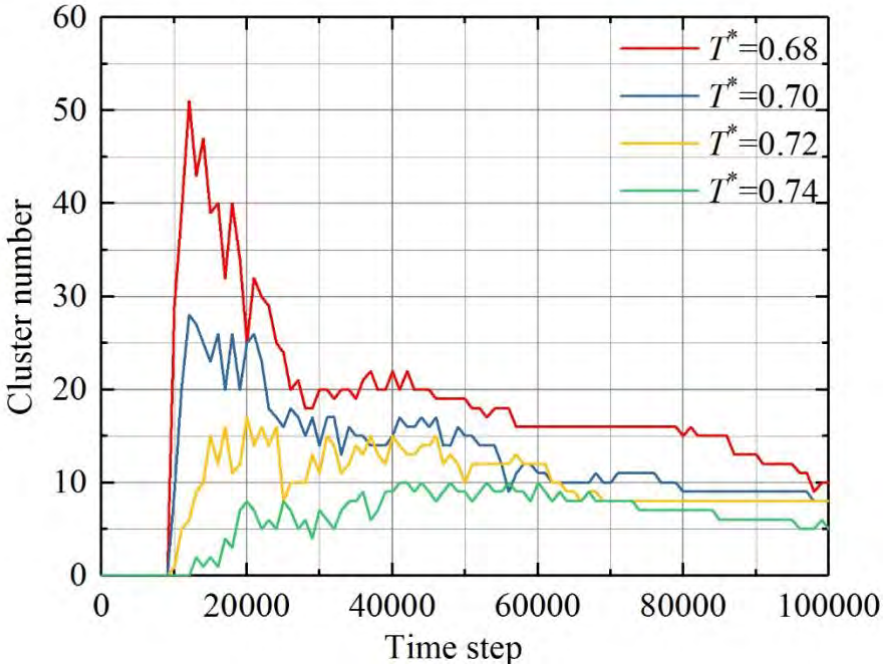

Figure 3: The development of cluster number against the time for varying supersaturations.

Table 1 Comparison of nucleation rate between CNT and MD

T^*	Critical cluster number $(n)^*$	Nucleation rate ($J \cdot m^{-3} \cdot s^{-1}$)	
		CNT	MD
0.68	18	9.77×10^{29}	5.92×10^{32}
0.70	31	5.03×10^{27}	8.28×10^{30}
0.72	60	3.96×10^{23}	3.70×10^{28}
0.74	138	1.10×10^{15}	2.96×10^{27}

5. CONCLUSIONS

This paper investigated the argon nucleation at high supersaturation with the help of molecule dynamic simulation. The results demonstrate that the formation of cluster in nucleation could be successfully predicted with MD simulation. For T^*=0.68 and 0.7, the nucleation rate predicted by MD are three orders of magnitude higher than the values calculated by *CNT*. Whereas, when the supersaturation decreases the predicted nucleation has a great difference compared with *CNT* due to the limitation of simulated atom numbers.

ACKNOWLEDEGMENTS

This project was funded by the National Nature Science Foundation of China (51706025) and the Fundamental Research Funds for the Central Universities (106112017CDJXY140003).

REFERENCES

Bian, J., Cao, X., Yang, W., et al., 2019. Condensation characteristics of natural gas in the supersonic liquefaction process. Energy 168, 99-110.

Bykova, N.Y., Gorbachevb, Y.E., 2017. Mathematical models of water nucleation process for the Direct Simulation Monte Carlo method. Applied Mathematics and Computation 296, 215-232.

Courtney, W.G., 1961. Remarks on homogeneous nucleation. Journal of Physical Chemistry 35, 2249.

Girshick, S.L., Chiu, C.P., 1990. Kinetic nucleation theory - a new expression for the real of homogeneous nucleation from and ideal supersaturated vapor. Journal of Chemical Physics 93(2), 1273-1277.

Fisher, C.A.J., Matsubara, H., 1999. Molecular dynamics investigations of grain boundary phenomena in cubic zirconia. Computational Materials Science 14, 177-184.

Kalikmanov, V.I., 2013. Nucleation theory. New York and London: Springer Netherlands, 2 p.

Kantrowitz, A., 1951. Nucleation in very rapid vapor expansions. Journal of Chemical Physics 19(9): 1097-1100.

Michal, D., Tomáš, N., Jan, H., et al., 2015. Molecular dynamics simulation of vapour-liquid nucleation of water with constant energy. EPJ Web of Conferences 92, 02013.

Nicolas, J.J., Gubbins, K.E., Street, W.B., et al., 1979. Equation of state for the Lennard-Jones fluid. Molecular Physics 37(5), 1429-1454.

Nithesh, K.G., Chatterjee. D., 2016. Numerical prediction of the performance of radial inflow turbine designed for ocean thermal energy conversion system. Applied Energy 167, 1-16.

Niu, L., Chen, X., Sun. W., et al., 2019. Non-equilibrium spontaneous condensation flow in cryogenic turbo-expander based on mean streamline off-design method. Cryogenics 98, 18-28.

Rajaee Shooshtari, S.H., Shahsavand, A., 2018. Optimal operation of refrigeration oriented supersonic separators for natural gas dehydration via heterogeneous condensation. Applied Thermal Engineering 139, 76-86.

Sun, W., Chen, S., Hou, Y., et al., 2018. Numerical studies on the off-design performance of a cryogenic two-phase turbo-expander. Applied Thermal Engineering 140, 34-42.

Wegener, P.P., 1987. Nucleation of nitrogen: experiment and theory. J. Phys. Chem. 91(10), 2479-2481.

Wegener, P.P., 1991. Cryogenic transonic wind tunnels and the condensation of nitrogen. Experiments in Fluids 11(5), 333-338.

Manuscript ID: 779
DOI: 10.18462/iir.icr.2019.0779

Study on supercooling degree of water-based graphene oxide nanofluids

Jiangqing WANG [(a)], Yudong LIU[(b)], Xinqiao JIN[(a)], Xuejun ZHANG[(c)], Wantao SHI[(a)]

[(a)] School of Mechanical Engineering, Shanghai Jiao Tong University, Shanghai, 200240, P. R. China, xqjin@sjtu.edu.cn

[(b)] Key Laboratory of Low-grade Energy Utilization Technologies and Systems, Ministry of Education, Chongqing University, Chongqing, 400044, P. R. China, ydliu2000@163.com

[(c)] Institute of Refrigeration and Cryogenics, Zhejiang University, Hangzhou, 310027, P. R. China

ABSTRACT

Water is usually used as phase-change cold storage material. However, it wastes energy because of its large supercooling degree. Nanofluids can be an alternative cold storage material to solve this problem. Water-based graphene oxide nanofluids with concentration of 20mg/(100ml) and 50mg/(100ml) are prepared by one-step method, and their zeta potential are measured by Laser Size and Zeta Potential Analyzer to analyze the stability of nanoparticles suspension. The correlation models of supercooling degree of deionized water and nanofluids with nucleation rate are established. According to the models, the supercooling degrees of deionized water and two nanofluids are obtained. The results show that the supercooling degree of nanofluid is reduced significantly, and compared to deionized water, the supercooling degrees of 20mg/(100ml) and 50mg/(100ml) nanofluids decrease by 74.8% and 90.3%, respectively. It can be concluded that the graphene oxide nanofluid can be a well alternative cold storage material for energy saving.
Keywords: Cold Storage, Nanofluid, Stability, Supercooling.

1. INTRODUCTION

Cold storage technology can reduce the variation between the peak and valley of electric power demand. Water has been used as a cold storage material for a long time because of its abundance, chemical compatibility and superior energy storage density. However, the high supercooling degree of water is key factor to affect the operating efficiency of the cold storage equipment (Ruddell et al., 2014; Oró et al., 2012; Fan et al., 2011). The application of nanofluids can innovatively reduce supercooling degree of water. Nanofluids is generally prepared by adding a certain proportion of nanomaterials into water, and it is well-dispersed, stabilized, and highly-conductive (Choi, 1995).

Deville et al. (2010) investigated the crystallization process of Al_2O_3/distilled water nanofluids by in situ observations using X-ray radiography and tomography, and concluded that the supercooling degree decreases with the particle size decreasing. Jia et al. (2014) studied the solidification processes of TiO_2 nanofluids and deionized water by differential scanning calorimetry. Their experimental results show that the supercooling degrees of TiO_2 nanofluids without surfactants are approximately 11.5% lower than the supercooling degree of deionized water. Zhao et al. (2015) studied supercooling degree of TiO_2 nanofluids by statistical methods, and found that the average and maximum supercooling degree were lower than deionized water. Zhang et al. (2010) prepared nanofluids by adding α-Al_2O_3, γ-Al_2O_3, and SiO_2 nanomaterials into pure water, and found that their supercooling degrees were significantly reduced compared to pure water. Therefore, the

supercooling degrees of the metal and metal oxide nanofluids were much smaller than the base liquid.
Compared with metals and metal oxides, carbon nanomaterials have higher thermal conductivity and lower density, which promotes heat conduction and stable suspension of nanofluids. In this paper, the supercooling degree of nanofluids is studied, which are prepared by adding graphene oxide nanosheets into deionized water.

2. PREPARATION OF GRAPHENE OXIDE NANOFLUIDS

Graphene oxide nanofluids are prepared by one-step method. Fig. 1 illustrates the schematic diagram of the preparation. The brief preparation process is as follows: 1) Measuring 100 mL of deionized water and 20 mg of graphene oxide nanosheets, and mixing them in a beaker; 2) The ultrasonic horn is immersed in the beaker containing the mixed sample; 3) The ultrasonic oscillator is turned on and shaken for 150 min. And then the preparation of nanofluids with the concentration of 20 mg/100 mL is completed. Similarly, 50 mg/100 mL of graphene oxide nanofluids is prepared.

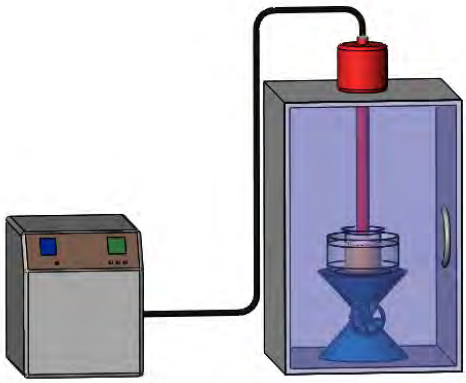

Figure 1: Preparation of graphene oxide nanofluids by ultrasonic oscillator

3. LATENT HEAT OF MELTING OF GRAPHENE OXIDE NANOFLUIDS

This experiment uses a heat flow differential scanning calorimeter to measure the latent heat of melting of nanofluids, as shown in Fig. 2. The measurement results of latent heat of melting are listed in Table 1. The results show that the difference in the latent heat of deionized water and nanofluids is very small. The addition of nanoparticles does not have a great influence on the latent heat of deionized water, because the concentration of nanoparticles is pretty small.



Figure 2: Heat flow differential scanning calorimeter

Table 1. Latent heat of melting of deionized water and nanofluids

Concentration	Latent heat of melting
Deionized water	337.9 kJ/kg
20 mg/100 mL	337.0 kJ/kg
50 mg/100 mL	336.0 kJ/kg

4. SUSPENSION STABILITY OF GRAPHENE OXIDE NANOFLUIDS

The stability of nanofluids is a prerequisite for engineering applications. Since the surface of the graphene oxide nanoparticle contains a large amount of oxygen-containing functional groups such as -OH, C-O-C, -COOH, the oxygen-containing functional group and the water molecule are hydrogen bonded such that the water molecule forms a hydration layer on the surface of the nanoparticle. When the nanoparticles are close to each other, the pressure of the hydration layer increases, causing mutual repulsion between the nanoparticles, which prevents the aggregation of the nanoparticles. In addition, the zeta potential on the surface of the nanoparticle can characterize the electrostatic stabilization between the nanoparticles (Shen, 1991). According to the diffusion electric double layer model, both the diffusion layer and the stern layer, the nanoparticles are surrounded by an ionic atmosphere composed of counter ions. When the nanoparticle moves, a sliding surface is generated somewhere in the diffusion layer, and the potential difference between the sliding surface and the internal solution is the zeta potential. According to the DLVO theory, the total potential between two nanoparticles is the sum of the attraction potential and the repulsion potential. The attraction energy can be determined by Van der Waals force, and the rejection potential can be determined by the zeta potential. When the two nanoparticles are close to each other, the difference between the repulsion potential and the attraction potential reaches a maximum at some point, which is an energy barrier. The larger the zeta potential of the nanofluids, the larger the energy barrier and the more stable the nanofluids. The zeta potentials of two concentrations of nanofluids are measured by Laser Size and Zeta Potential Analyze, as shown in Table 2. The results show that the mean absolute zeta potentials of nanofluids with the concentration of 20 mg/100 mL and 50 mg/100 mL were 30 mV and 42 mV, respectively. According to Hu (2014), two concentrations of nanofluids have great suspension stability.

Table 2. Zeta potential of graphene oxide nanofluids

Concentration	Zeta potential distribution	Mean absolute zeta potential
20 mg/100 mL	0-51 mV	30 mV
50 mg/100 mL	0-75 mV	42 mV

5. SUPERCOOLING DEGREE OF DEIONIZED WATER AND NANOFLUIDS

The cooling curve is the temperature versus time curve in the liquid-solid phase transition process. As shown in Fig. 3, the cooling curve consists of four stages: 1) AB section is the cooling stage of liquid phase; 2) BC section is the formation stage of crystal nuclei. 3) CD section is the growth stage of crystal nuclei; 4) DE section is the cooling stage of the crystal.

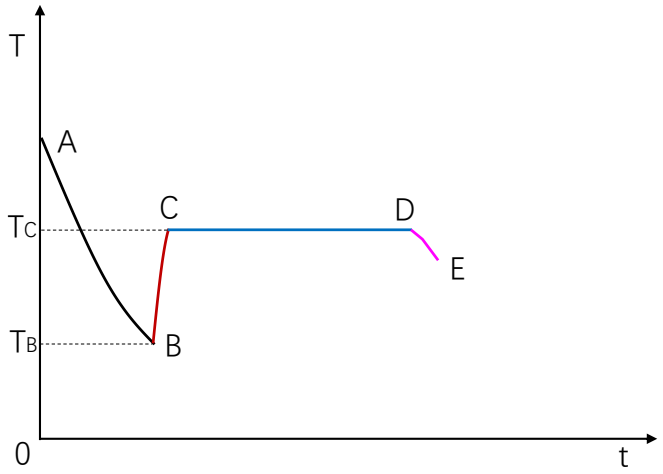

Figure 3: Cooling curve in the liquid-solid phase transition process

The supercooling degree is the difference between the freezing temperature and the lowest temperature of the cooling process, as shown in Fig. 3, it is the difference between T_C and T_B. Fisher et al. (2014) proposed that when the nucleation rate is equal to 1/(cm^3·s), the working fluid is cooled to the lowest temperature (i.e., point B in the cooling curve). Therefore, the supercooling degree can be obtained by determining the correlation between the nucleation rate and the temperature.

5.1. Nucleation Rate of Deionized Water

The nucleation rate refers to the number of critical nuclei that can grow stably in unit volume and unit time. Deionized water nucleates in a homogeneous way. During the nucleation process, it is not affected by the impurity particles or the outer surface of the container and uniformly nucleates and crystallizes. According to classical nucleation theory, the homogeneous nucleation rate of deionized water can be expressed as:

$$J_{dw} = K \cdot N_1 \cdot exp\left(\frac{-\Delta G^*}{K_B T}\right) \quad \text{Eq.（1）}$$

Where K is the kinetic part of the nucleation rate; N_1 is the number of water molecules per unit volume; ΔG^* is the nucleation energy of the crystal; K_B is the Boltzmann constant; T is the thermodynamic temperature.
The kinetic part of the nucleation rate can be expressed as:

$$K = n_s \cdot 4\pi r^2 \cdot Z \cdot \frac{k_B T}{h} \cdot exp\left(-\frac{\Delta g}{k_B T}\right) \quad \text{Eq.（2）}$$

Where n_s is the number of water molecules within jumping distance around the embryo surface/neighboring embryo surface; r is the radius of spherical ice embryo; Z is the Zeldovich factor; h is the Planck constant; Δg is the activation energy.
The nucleation energy can be expressed as:

$$\Delta G^* = \frac{16\pi}{3} \cdot \frac{{v_i}^2 \cdot {\gamma_{iw}}^3}{(k_B T \cdot ln\, S_i)^2} \quad \text{Eq.（3）}$$

Where v_i is the volume of single water molecule in the embryo; γ_{iw} is the interfacial tension of ice-water; S_i is the saturation vapor pressure ratio of water and ice.
Inserting Eq. (2) and (3) into Eq. (1), the homogeneous nucleation rate of deionized water J_{dw} can be expressed as:

$$J_{dw} = K_{pre} \cdot exp\left(\frac{-\Delta g}{k_B T}\right) \cdot exp\left(-\frac{16\pi}{3} \cdot \frac{{v_i}^2 \cdot {\gamma_{iw}}^3}{(k_B T)^3 \cdot (ln\, S_i)^2}\right) \quad \text{Eq.（4）}$$

Where K_{pre} is the pre-exponential factor. K_{pre}, Δg, γ_{iw}, v_i and S_i can be obtained by consulting the literatures (Fletcher, 1964; Ickes et al., 2015; Zobrist et al., 2007; Reinhardt et al., 2013; Smith et al., 1999; Qu and Jiang, 2000; Murphy and Koop, 2005). J_{dw} can be expressed as shown in Eq. (5).

$$J_{dw} = 10^{34} \cdot \exp(-892T/(T-118)^2 + 4.68 \times 10^5 \cdot (20.067 - 0.18T)^3/(T \cdot \eta)) \quad \text{Eq.（5）}$$

Where $\eta = (-210368 - 131.438 \cdot T + 3.32373 \times {}_{10^5}/T + 41729.1 \cdot lnT\ )^2$.

5.2. Nucleation Rate of Nanofluids

The crystal nuclei of the nanofluids form inside the deionized water and on the surface of graphene oxide nanoparticles. Hence, the nucleation rate of nanofluids consists of the homogeneous nucleation rate inside the deionized water and heterogeneous nucleation rate arising from graphene oxide nanoparticles, which leads to:

$$J_{go} = J_{go,hom} + J_{go,heter} \quad \text{Eq.（6）}$$

Where $J_{go,hom}$ is the homogeneous nucleation rate inside deionized water and $J_{go,heter}$ denotes the heterogeneous nucleation rate arising from graphene oxide nanoparticles.
According to Eq. (4), the homogeneous nucleation rates of nanofluids with the concentration of 20 mg/100 mL and 50 mg/100 mL are:

$$J_{go,hom,20} = 9.9991 \times 10^{34} \cdot \exp(-892T/(T-118)^2 + 4.68 \times 10^5 \cdot (20.067 - 0.18T)^3/(T \cdot \eta)) \quad \text{Eq.（7）}$$

$$J_{go,hom,50} = 9.9977 \times 10^{34} \cdot \exp(-892T/(T-118)^2 + 4.68 \times 10^5 \cdot (20.067 - 0.18T)^3/(T \cdot \eta)) \quad \text{Eq.（8）}$$

The heterogeneous nucleation rate of nanofluids is defined as the number of critical nuclei formed on the surface of graphene oxide nanoparticles per unit volume and unit time. The surface of the nanoparticles is simplified to a plane, that is, the crystal nuclei nucleate on the surface of graphene oxide nanoparticles by means of plane nucleation. Therefore, the heterogeneous nucleation rate of the nanofluid can be calculated by two steps: 1) Calculating the number of critical nuclei formed on the surface of the nanoparticle per unit area and unit time; 2) Multiplying the results of first step by the total surface area of the nanoparticles per unit volume to obtain the heterogeneous nucleation rate of the nanofluids.
According to the classical nucleation theory, the number of critical nuclei formed on the surface of the nanoparticles per unit area and unit time can be expressed as:

$$J_{go,sur} = \frac{k_B T}{h} \cdot exp\left(\frac{-\Delta g}{k_B T}\right) \cdot n \cdot exp\left(\frac{-\Delta G^* \cdot f(\theta)}{k_B T}\right) \quad \text{Eq.（9）}$$

Where n is the number density of water molecules at the nanoparticle/water interface, $f(\theta)$ is the compatible function.
The number density of water molecules can be expressed as:

$$n = \left(\frac{\rho_w N_A}{M_w}\right)^{\frac{2}{3}} \quad \text{Eq.（10）}$$

Where ρ_w is the density of water; N_A is the Avogadro constant; M_w is the molar mass of the water molecule.
The compatible function can be expressed as:

$$f(\theta) = \frac{2 - 3\cos\theta + (\cos\theta)^3}{4} \quad \text{Eq.（11）}$$

Where θ is the contact angle between critical nucleus and the surface of nanoparticle.
Liu et al. (2015) pointed out that crystal nucleus can only nucleate on the upper and lower surfaces of graphene oxide nanoparticles. Therefore, the total surface area of nanoparticles per unit volume can be expressed as:

$$S_{go} = 2\varphi_v / H \quad \text{Eq.（12）}$$

Where φ_v is the volume concentration of the nanoparticles; H is the thickness of the nanoparticle. The heterogeneous nucleation rates of nanofluids with the concentration of 20 mg/100 mL and 50 mg/100 mL are expressed as:

$$J_{go,heter,20} = 4.1154 \times 10^{28} \cdot T \cdot exp(-892T/(T-118)^2 + 2.34 \times 10^4 \cdot (20.067 - 0.18T)^3/(T \cdot \eta)) \quad \text{Eq.（13）}$$

$$J_{go,heter,50} = 10.2885 \times 10^{28} \cdot T \cdot exp(-892T/(T-118)^2 + 3.37 \times 10^3 \cdot (20.067 - 0.18T)^3/(T \cdot \eta)) \quad \text{Eq.（14）}$$

5.3. Supercooling Degree and Comparative Analysis

Fisher et al. (2014) proposed that when the nucleation rate of the working fluid is equal to 1/(cm^3·s), it is cooled to the lowest temperature. According to the Eqs. (5) and (6), the supercooling degree of deionized water and the nanofluids with the concentration of 20 mg/100 ml and 50 mg/100 ml can be obtained, as shown in Table 3.

Table 3. Supercooling degree of deionized water and nanofluids

Concentration	Lowest temperature	Experimental supercooling degree	Calculated supercooling degree	Reduction rate
Deionized water	241.65 K	6.8 K	31.50 K	-
20 mg/100 mL	265.22 K	3.6 K	7.93 K	74.8%
50 mg/100 mL	270.11 K	2.1 K	3.04 K	90.3%

Table 3 shows that the experimental and calculated supercooling degree of nanofluids and deionized water are quite different, especially deionized water. I think it is due to the heterogeneous nucleation of the small beaker wall during the experiment. In our experiments, the supercooling degrees of nanofluids and deionized water were measured in the small beaker. For deionized water, its nucleation mode changes from homogeneous nucleation to heterogeneous nucleation. During the experiment, deionized water was first crystallized on the wall of the small beaker, which confirmed the transformation of its nucleation mode. According to the classical nucleation theory, the nucleation barrier of deionized water is significantly reduced. Therefore, the supercooling degree of deionized water has changed from 31.5 K to 6.8 K greatly. Similarly, for nanofluids, the wall of the small beaker increases its heterogeneous nucleation rate of the nanofluid and reduces its supercooling degree.
According to Table 3, the supercooling degrees of deionized water and two concentrations of nanofluids are 31.50 K, 7.93 K and 3.04 K, respectively. Compare with deionized water, the supercooling degrees of nanofluids with the concentration of 20 mg/100 ml and 50 mg/100 ml are reduced by 74.8% and 90.3%, respectively. Because the nucleation energy on the surface of the nanoparticle is $f(\theta)$ times of that inside the deionized water, the nucleation barrier is effectively reduced, resulting in a significant decrease in the supercooling degree of the nanofluid. In addition, compared to 20 mg/100 mL of nanofluids, the supercooling degree of nanofluids with the concentration of 50 mg/100 mL is reduced by 61.7%. Because the crystal nuclei have more heterogeneous nucleation sites as the concentration of nanofluids increases, more critical nuclei can grow stably in the unit volume and the nucleation rate increases, the supercooling degree of nanofluids is reduced. Therefore, graphene oxide nanofluids can replace water and become a new type of phase change cold storage material.

6. CONCLUSIONS

A new type of phase change cold storage material is proposed to reduce the supercooling degree of water. In this paper, graphene oxide nanofluids are prepared, its suspension stability and supercooling degree are analyzed. 20 mg/100 ml and 50 mg/100 ml of graphene oxide nanofluids are prepared by ultrasonic oscillator, and their Zeta potentials are measured by Laser Size and Zeta Potential Analyzer. The results show that the mean absolute zeta potentials of two concentrations of nanofluids are 30 mV and 42 mV, respectively, and the electrostatic stabilization between nanoparticles makes nanofluids have enough stability.

According to classical nucleation theory, analytical formulas between the nucleation rates of deionized water and nanofluids and their supercooling degrees have been established. The supercooling degrees of deionized water and nanofluids with the concentration of 20 mg/100 mL and 50 mg/100 mL were calculated to be 31.50 K, 7.93 K and 3.04 K, respectively. Compared with deionized water, the supercooling degrees of nanofluids with the concentration of 20 mg/100 mL and 50 mg/100 mL decrease 74.8% and 90.3%, respectively. The supercooling degrees of nanofluids are significantly reduced. Therefore, graphene oxide nanofluids can replace water and become a new type of phase change cold storage material.

ACKNOWLEDGEMENTS

The authors gratefully acknowledge the financial support provided by the National Natural Science Foundation of China (Grant No. 51276204).

NOMENCLATURE

h	Planck constant (J×s)	n_s	number of water molecules within the jumping distance (mol×m^{-2})
H	thickness of nanoparticle (m)	N_A	Avogadro constant (mol^{-1})
J_{dw}	nucleation rate of deionized water (cm^{-3} ×s^{-1})	N_1	number of water molecules per unit volume (mol×m^{-3})
J_{go}	nucleation rate of nanofluids (cm^{-3} ×s^{-1})	r	radius of spherical ice embryo (m)
$J_{go,heter}$	heterogeneous nucleation rate of nanofluids (cm^{-3} ×s^{-1})	S_{go}	total surface area of nanoparticles (m^2× cm^{-3})
$J_{go,heter,20}$	heterogeneous nucleation rate of nanofluids with the concentration of 20 mg/100 mL (cm^{-3} ×s^{-1})	S_i	saturation vapor pressure ratio of water and ice
$J_{go,heter,50}$	heterogeneous nucleation rate of nanofluids with the concentration of 50 mg/100 mL (cm^{-3} ×s^{-1})	T	thermodynamic temperature (K)
$J_{go,hom}$	homogeneous nucleation rate of nanofluids (cm^{-3} ×s^{-1})	v_i	volume of single water molecule (m^3)
$J_{go,hom,20}$	homogeneous nucleation rate of nanofluids with the concentration of 20 mg/100 mL (cm^{-3} ×s^{-1})	Z	Zeldovich factor
$J_{go,hom,50}$	homogeneous nucleation rate of nanofluids with the concentration of 50 mg/100 mL (cm^{-3} ×s^{-1})	Greek symbols	
$J_{go,sur}$	nucleation rate of nanofluids on the surface of nanoparticles (m^{-2} ×s^{-1})	Δg	activation energy (J)
K	kinetic part of the nucleation rate (mol^{-1}× s^{-1})	ΔG^*	nucleation energy (J)
K_B	Boltzmann constant (J×K^{-1})	θ	contact angle between crystal nucleus and nanoparticle (°)
K_{pre}	preexponential factor (cm^{-2} ×s^{-1})	γ_{iw}	interface energy between ice and water (J×m^{-2})
M_w	molar mass of water (kg×mol^{-1})	ρ_w	density of water (kg×m^{-3})
n	number of water molecules at the graphene oxide nanoparticle/water interface (mol)	φ_v	volume concentration of nanofluids (m^3×m^{-3})

REFERENCES

Choi, SUS., 1995. Enhancing thermal conductivity of fluids with nanoparticles. ASME International Mechanical Engineering Congress & Exposition, San Francisco, CA, 231(1), 99-105.

Deville, S., Maire, E., Lasalle, A., Bogner, A., Gauthier, C., Leloup, J., et al., 2010. Influence of particle size on ice nucleation and growth during the ice-templating process. Journal of the American Ceramic Society 93(9), 2507–10.

Fan, L., Khodadadi, J.M., 2011. Thermal conductivity enhancement of phase change materials for thermal energy storage: A review ☆. Renewable & Sustainable Energy Reviews 15(1), 24-46.

Fisher, J.C., Hollomon, J.H., Turnbull, D., 2014. Rate of Nucleation of Solid Particles in a Subcooled Liquid. Science 1(1), 41-61.

Fletcher, N.H., 1964. Cloud Microphysics. Science 143(3603), 236-236.

Hu, P.F., 2014. Study on the Supercooling and Nucleation Characteristics of Graphene Oxide Nanofluids under Acoustic Levitation. Chongqing University, Chongqing.

Ickes, L., Welti, A., Hoose, C., Lohmann, U., 2015. Classical nucleation theory of homogeneous freezing of water: thermodynamic and kinetic parameters. Physical Chemistry Chemical Physics Pccp 17(8), 5514-37.

Jia, L., Lan, P., Ying, C., Mo, S., Xing, L., 2014. Improving the supercooling degree of titanium dioxide nanofluids with sodium dodecylsulfate. Applied Energy 124(7), 248-55.

Liu, Y., Li, X., Hu, P., et al., 2015. Study on the supercooling degree and nucleation behavior of water-based graphene oxide nanofluids PCM. International Journal of Refrigeration 50, 80-86.

Murphy, D.M., Koop, T., 2005. Review of the vapour pressures of ice and supercooled water for atmospheric applications. Quarterly Journal of the Royal Meteorological Society 131(608), 1539-65.

Oró, E., Gracia, A.D., Castell, A., Farid, M.M., Cabeza, L.F., 2012. Review on phase change materials (PCMs) for cold thermal energy storage applications. Applied Energy 99(6), 513-33.

Qu, K.Y., Jiang, Y., 2000. Study on the randomness and nucleation rate of the homogeneous freezing. Acta Physica Sinica 49 (11), 2214-9.

Reinhardt, A., Doye, J.P.K., 2013. Homogeneous TIP4P/2005 ice nucleation at low supercooling. Jchemphys 9(9), 8981-95.

Ruddell, B.L., Salamanca, F., Mahalov, A., 2014. Reducing a semiarid city's peak electrical demand using distributed cold thermal energy storage. Applied Energy 134, 35-44.

Shen, Z., Zhao, Z.G., Kang, W.L., 1991. Colloid and surface chemistry. Chemical Industry Press, Beijing.

Smith, R.S., Kay, B.D., 1999. The existence of supercooled liquid water at 150 K. Nature 398 (398), 788-91.

Zhang, X.J., Wu, P., Qiu, L.M., Zhang, X.B., Tian, X.J., 2010. Analysis of the nucleation of nanofluids in the ice formation process. Energy Policy 51(1), 130-4.

Zhao, Q., Zhang, X., Liang, X., Liu, T., Luo, X., 2015. Supercooling and cold energy storage characteristics of nano-media in ball-packed porous structures. Aip Advances 5(4), 1-33.

Zobrist, B., Koop, T., Luo, B.P., Marcolli, C., and Peter, T., 2007. Heterogeneous ice nucleation rate coefficient of water droplets coated by a nonadecanol monolayer. Journal of Physical Chemistry C 111(5), 2149-55.

Manuscript ID: 930
DOI: 10.18462/iir.icr.2019.0930

A study on use of a frost insulation layer for cooling by boiling heat transfer

Taiyo Sugino, Hidetoshi Ohkubo

Graduate School of Engineering, Tamagawa University, Machida-shi, Tokyo, 194-8610, Japan042-739-8904

Sgnta4is@engs.tamagawa.ac.jp

Abstract

The technology of cooling by boiling has been gaining attention in the fields of hardening of metals, nuclear reactors or superconducting coils. The boiling heat transfer involves not only transportation of sensible heat but also the latent heat due to gas-liquid phase transition, and therefore, it produces high heat transfer rates. The purpose of this on-going study is to elucidate the effects on the cooling by boiling heat transfer when a frost-layer coating is formed on the cooling surface. We are currently experimentally investigating the boiling heat transfer characteristics of copper balls in the diameter range of 20 to 30 mm in saturated liquid nitrogen at atmospheric pressure.

The experimental results show that a frost layer coating on the cooling surface has a remarkable effect on the cooling curves of a copper surface.

1. Introduction

In recent times, rapid cooling of low temperature equipment including their piping system has become a necessity. In order to achieve this objective, the heat transfer characteristics in the entire range of boiling, namely from film boiling to nucleate boiling has to be improved. It is well known that a technique to promote cooling rate of boiling from a highly thermally conducting metallic material is to use a thin coating of low conducting material on the metal surface. This phenomenon has been investigated by many researchers including Nishio et al. [1] who coined the terms 'insulation layer paradox' or 'thermal insulation paradox" when referring to effect of this phenomenon. The following findings have been established in relation to this phenomenon.

(1) The nuclear boiling heat transfer coefficient decreases with an increase in the coating thickness.
(2) The film boiling heat transfer coefficient is not affected by the coating thickness.
(3) The degree of superheating at the minimum heat flux point increases with the increase of coating thickness, but it approaches a value specific to the coating material when the coating thickness is increased to certain thickness.

The phenomenon of 'insulation layer paradox' has been investigated with the focus on its utilization in, such as, cooling of steels and super-conductors. Recently, Mazor et al. [2] has succeeded in promoting the cooling rate of a 30mm dia. copper ball dramatically in a pool-boiling experiment by the utilization of a frost coating on the ball. This research is of great interest here in that a coating material of low thermal conductivity has been used to produce a rapid cooling effect, and its application in cooling by boiling using cryogenic liquids has a great potential in the future.

In view of the above background, we investigate here frost layer formation and growth on a sphere, which has not been the focus of the work of Mazor et al. [2], and further, cooling heat transfer characteristics of boiling will be investigated when the sphere surface is coated with a frost layer.

2. Experimental apparatus and Method

2.1 Cooling by boiling heat transfer

Fig. 1 shows a schematic diagram of the apparatus for investigating the cooling by boiling heat transfer. The sphere used in this in study was 25mm in diameter and was made of tough-pitch copper. The sphere was given a mirror-finish and was cleaned in an ethanol container by ultrasonic cleaning method each time before the experiment. The copper sphere's temperature was measured by a K-type thermocouple of 0.1mm wire diameter , and the measurement location was the center of the sphere.

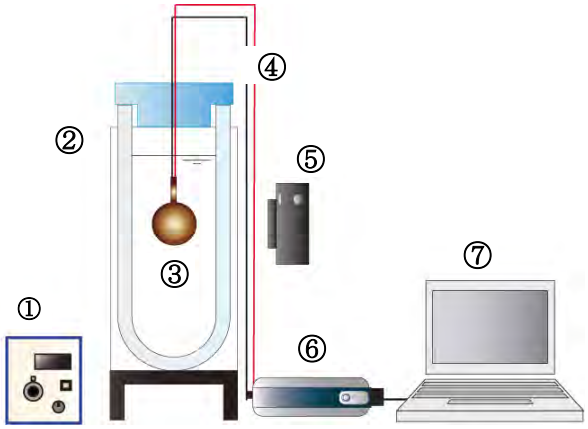

1. Cold light 2. Dewar vessel 3. Copper sphere 4. Thermocouple
5. Camera 6. Data logger 7. Computer

Fig. 1 Schematic diagram of experimental apparatus

The experiment was conducted while the temperature of the sphere changed with time. The temperature history of the spherewas recorded in a data logger, and the heat flux q [W/m^2] from the surface was evaluated by using the lumped-mass approximation.

$$q = \frac{1}{3} r \rho c_p \frac{dT}{d\tau} \quad (1)$$

where, cp is heat capacity of copper [kJ/kg・K], r is radius of the sphere [mm], r is density of copper [kg/m^3], T is cooling surface temperature [K] and t is time [sec].

It is a common practice in boiling heat transfer studies to obtain the heat flux at the cooling surface of a heating block made of copper by the method of lumped-mass approximation, and the error due to this approximation will be limited to only a few percentages if the Biot number (Bi) is less than 0.1. In the case of the present spherical surface system, where saturated pool boiling heat transfer took place subjected to natural convective conditions, Bi was about 0.28 at the most.

2.2 Frost deposition

Frost formation was carried out by the experimental apparatus shown in Fig. 2. The first step was to cool the copper ball to a desired temperature by submerging it in liquid nitrogen in a Dewar vessel. Once the copper ball reached the desired temperature, after maintaining its temperature for 1min, the Dewar vessel was moved to the experimental chamber shown in Fig. 2 while keeping the ball in nitrogen gas in the Dewar. Next, using a heater and humidifier (see Fig. 2), the experimental chamber was maintained at constant temperature and humidity, and after the desired condition was reached, the copper ball was taken out of the Dewar to be fixed in place for making frost on it. Fig. 3 shows typical snapshots of the ball surface, (a) the bare-surfaced copper ball, (b) ball coated with a layer thickness l_f = 0.37mm and (c) ball coated with l_f = 0.49mm. The frost layers formed were very thin as one can still see the color of copper, and they did not break up during the process of cooling by boiling heat transfer.

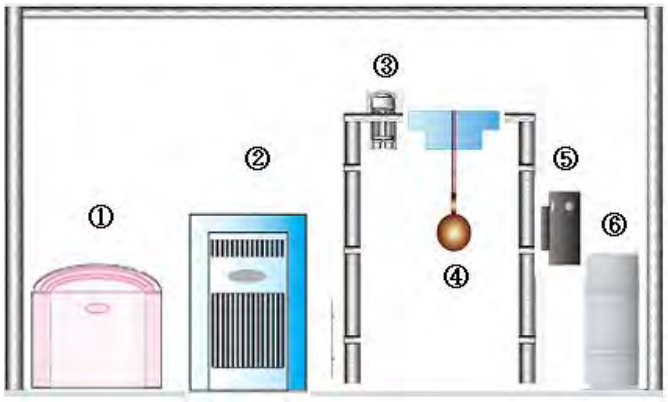

① Heater②Humidifier ③Asman psychrometer ④Copper ⑤Camera⑥Dewar vessel

Fig.2 Schematic diagram of experimental apparatus



(a) d =25mm (b) l_f = 0.37mm (c) l_f = 0.49mm

Fig.3 Typical snapshots of copper ball coated with different frost thicknesses

3. Experimental results and discussion

As the first step in this work, boiling heat transfer characteristics for the copper ball was established. Fig. 4 shows the cooling curves for bare-surface copper balls of diameter d=20 and 25mm. It also shows the cooling curves when the copper ball of d=20mm is coated with frost layers. The experiments each were conducted more than three times, and the typical results of the cooling curves are shown in the figure. The boiling curves were obtained from these cooling curves using Eq.(1), and they are shown in Fig. 5. In this figure, we have also included the boiling curve reported by Mazor et al.[2] for a copper ball of 30mm dia. and the measurements of the degree of superheat at the minimum heat flux point by Nishio-Serizawa [1]. The effect of copper ball diameter on the boiling curve can be seen in the transition region of the boiling curve, but the variation in the temperature at the minimum heat flux point is limited to only a few Kelvins. Thus, it could be confirmed that the use of the method of lumped-mass approximation is adequate to obtain the boiling curve of liquid nitrogen under the saturated boiling condition.

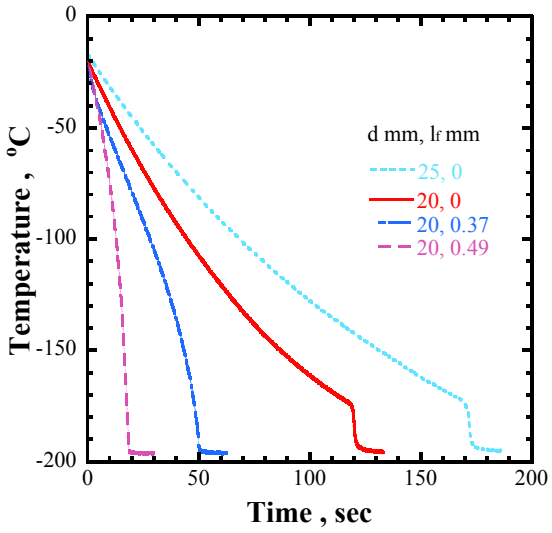

Fig.4 Cooling curves

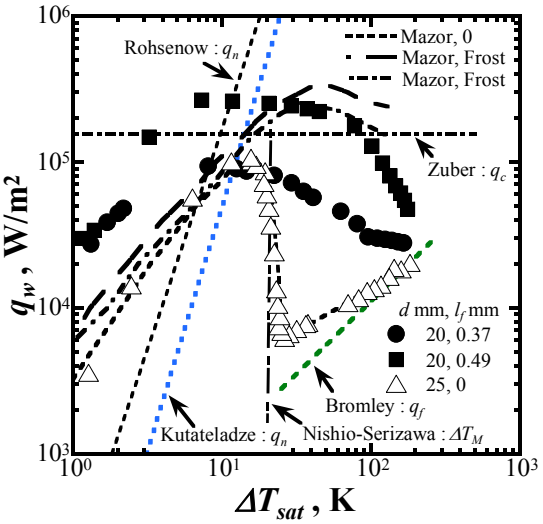

Fig.5 Boiling curves

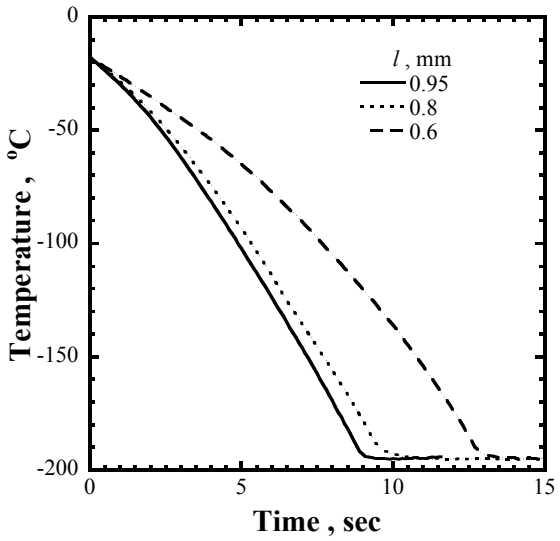

Fig.6 Cooling curves

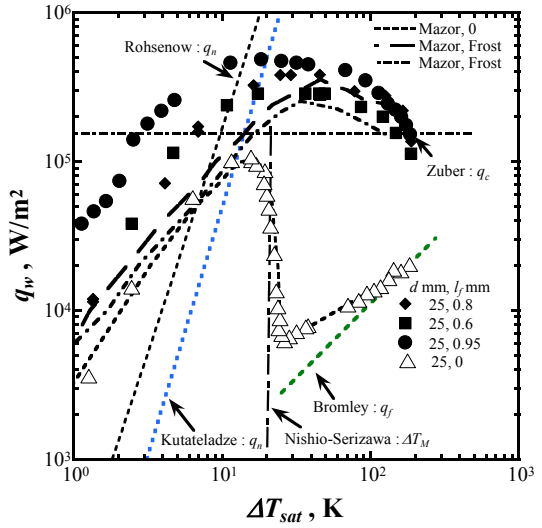

Fig.7 Boiling curves

Next, experiments are conducted using a frost layer as the insulation layer on the copper ball of *d*=25mm. Fig. 6 shows the variation in the cooling curve when the frost layer thickness is varied as a parameter. When a frost layer is used as the thermal insulation layer, a film boiling region could not be observed. Compared to the case of the bare surface (see Fig. 4), the frost coated surface showed a dramatic increase in the cooling rate, which increased with the increase of the frost layer thickness.

Fig. 7 shows the boiling curves obtained from the cooling curves of Fig. 6 in the case of copper ball of *d*=25mm. It shows that the curve for the bare surface has a film boiling region, and that the curves for the frost coated surface exhibit the transition boiling regime from a higher temperature. Mazor et al. [2] used a copper ball of 30mm dia. in their experiments and formed frost coating on the ball in the forced convective flow of a fan under different conditions. In their case, they reported that the minimum heat flux and critical heat flux both showed increases compared to those for a bare surface although thicknesses of the frost coating had not been measured. Further, Li-Peterson [3] has reported that the heat transfer characteristics of a copper plate changed when a wire-mesh was placed on the copper plate.

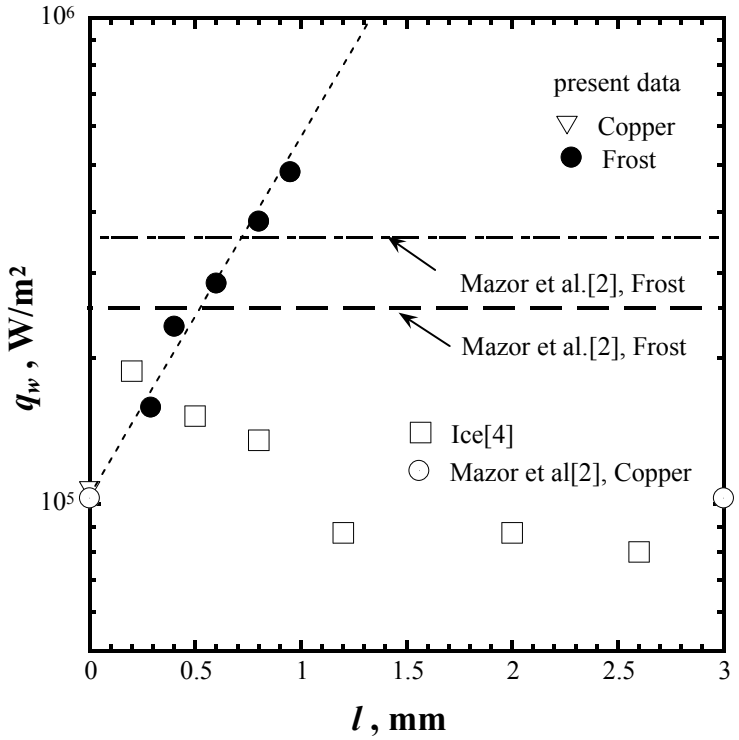

Fig.8 Critical heat flux as a function of coating thickness

Fig. 7 shows that the heat flux in the transition boiling region increases markedly when the ball surface is coated with frost. Further, the heat flux in the nucleate boiling region also shows an increase. Fig. 8 shows the critical heat flux q_{max} as a function of the frost and ice layer [4] thicknesses. The figure shows clearly that the critical heat flux increases with the frost layer thickness; but the ice layer shows a different trend. The cause of these differences can be attributed to thermal conductance and structure of the frost layer. In the case of ice layer, the effect of 'thermal insulation paradox' comes into play reducing the critical heat flux as the ice layer thickness increases.

4. Conclusions

In this work, effect of a surface thermal insulation layer on boiling heat transfer from a copper ball in liquid nitrogen under natural convective conditions was investigated by making frost layers on a copper ball surface. The followings are the findings of this work.

(1) When a frost layer is used as a thermal insulation layer on the cooling surface, the heat flux in the transition boiling region increased markedly.

(2) Similarly, when a frost layer is used as a thermal insulation layer on the cooling surface, both the critical heat flux and heat flux in the nucleate boiling region increased.

It can be anticipated that the findings of this work will be useful for future works on cryogenic applications.

References

[1] Nishio · Serizawa:"Control of Minimum-Heat-Flux-Point temperature by the Thermal Conductance of an Additional Surface-Layer" *The journal of the Japan Society of Mechanical Engineers* (B), 53, 487 (1987), pp. 1061-1064

[2] G.Mazor et al : "Frost formation as a temporary enhancer for quench pool boiling" *Applied Thermal Engineering*, 52(2013), pp.345-352.

[3] Chen Li・G.P.Peterson. : " Parametric Study of Pool Boiling on Horizontal Highly Conductive Microporous Coated Surfaces" *Journal of Heat Transfer*, Vol.129(2007), pp.1465-1475

[4] Agui : "Effects of surface temperature on apparent density and apparent thermal conductivity of frost layer" *Thermophysical Properties* 39(2018), pp229-231

Manuscript ID: 949
DOI: 10.18462/iir.icr.2019.0949

Numerical research of driving mechanism for geyser developing in cryogenic propellant feedline

Hongwei Mao[(a)], Yanzhong Li[(a),(b)], Lei Wang[(a)], Jiaojiao Wang[(a)]

[(a)] Institute of Refrigeration and Cryogenic Engineering, Xi'an Jiaotong University
Xi'an, 710049, China, yzli-epe@mail.xjtu.edu.cn
[(b)] State Key Laboratory of Technologies in Space Cryogenic Propellants
Beijing, 100028, China, yzli-epe@mail.xjtu.edu.cn

ABSTRACT

Geyser would occur in long vertical cryogenic propellant feedline under certain conditions in space launch and propulsion engineering. In order to get a comprehensive knowledge of geyser, a numerical model was established. Geyser phenomenon in a bottom closed liquid oxygen feeding line was studied. Pressure and temperature change were obtained during geyser developing process. The mechanism of geyser is revealed. The results show that the temperature distribution in the tube tends to be low at both end and high in the middle. The geyser process occurs in the LO_2 feed tube could be divided into incubation, eruption and refilling stages. Dramatic pressure fall would occurs in the eruption stage and pressure spike occurs in the refilling stage. The violent depressurization boiling is the main cause of geyser eruption and the condensation induced water hammer caused by vapor condensation in the tube is the main mechanism of pressure spike in the refilling process.
Keywords: Cryogenic Propellant, Liquid Oxygen Feedline, Geyser Phenomenon.

1. INTRODUCTION

Cryogenic liquid propellants, especially liquid hydrogen (LH_2) and liquid oxygen (LO_2) are increasingly used in space launch and propulsion engineering due to their non-toxic, pollution-free and high-specific impulse advantages. Having a low boiling point, cryogenic propellants are quite sensitive to the heat leaks from external thermal environment. Under certain situation, geyser would occur in vertical propellants feed line during the period after missile fueling and prior to launch. The eruption and refilling process of geyser will bring violent pressure fluctuation which is very damaging to propellant feed line. Complex mass and heat transfer mechanism is involved in geyser. Therefore, it is essential to conduct a deep research on geyser phenomenon which is important for the safety launch of rocket.

Geyser is a two phase flow instability phenomenon which have been studied by many researchers in some fields through experiment investigation, theoretical analysis and numerical simulation. Hands (1988) introduced the problem caused by geyser in engineering. Murphy (1965) experimentally investigated the geyser in long vertical tubes with a reservoir at the top and closed at the bottom, and presented a correlation for the prediction of geyser in terms of heating rate, system geometries and fluid properties for cryogenic missile propellant feed designs. But, through experimental study, Kuncoro et al. (1995) pointed out that the correlation to determine geyser occurring or not is not true for some situation. Burkhalter et al. (1968) concentrated on influence of heating rate, fluid temperature and length/diameter ratio on the geyser mechanism. It was shown that the geyser period increased in a linear fashion as reservoir fluid temperature decreased. Morioka et al (1986) simulated the geyser phenomenon in LNG pipes. Aritomi (1992) experimentally investigated the geyser in twin parallel channels in both natural and forced circulations. Casarosa et al. (1983) performed an experimental study of the geyser effect on a two-phase thermosiphon with water as the working fluid. Ozawa et al. (1979) experimentally investigated the effect factors of geyser such as heat flux, flow rate and system pressure. Tae-il et al. (1993) conducted both experimental and numerical studies of effective parameters on the geyser period using a bottom

closed vertical tube. Chiang et al. (1994) investigated the thermos-hydraulic instabilities in the area of geyser under natural circulation. Chen et al. (2015) carried out an experiment investigation of effective parameters on geyser periodicity in a vertical heated system used in a nuclear reactor. Water was used as the experiment fluid.

Although a lot of analysis have been carried out to reveal geyser characteristics, the critical details of geyser are still poorly understood. Thus, in the present paper, CFD approach is adopted to get a comprehensive knowledge of geyser occurs in the liquid oxygen feed tube of rocket. The physical field distribution during geyser process is obtained and analyzed. Pressure and temperature change are presented and discussed, and mechanism of the pressure spike during geyser process is investigated. The present study will provide a more reasonable insight into the geyser behavior in the cryogenic propellant feed line.

2. PHYSICAL AND CFD MODEL

2.1 Physical Model

Fig.1 displays the schematic diagram of a typical LO_2 propellant feed system. It mainly consists of an upper propellant tank and a vertical LO_2 feed tube which is closed at bottom. Foam insulation layer with thickness of 20 mm is sprayed on the pipe and tank surface to reduce heat flux from environment. A 2-D coordinate system is established to describe the geyser phenomenon clearly, and the coordinate origin is set at the center of pipe bottom section. The parameters of system component studied in the present paper are shown in Table 1. In the actual working condition, the size of the tank is huge compared to the pipe under it. The environment heat leak through tank wall will be brought away by liquid convection and evaporation in the liquid gas interface, hence the tank wall could be regarded as adiabatic boundary. The solid zone is not included in the CFD model, and instead a constant heat flux is imposed on the interface between fluid and solid. The heat flux is calculated considering the heat conduct through foam layer and pipe walls with constant temperature boundary which is 300K and 90.19k, respectively. And the heat flux value is 158W/m^2. There is a gas venting device above the upper tank, and it was set as pressure outlet boundary condition. The pressure is constant with a value of 101325Pa. Initial liquid temperature is 90.19K which is the saturated temperature under 101325Pa.

Table 1. Parameters of tube and tank in the CFD model

Component	Inner Diameter(mm)	Height(m)	Wall Thickness(mm)
Pipe1	47	3.5	3
Tank1	1000	1	3
Pipe2	47	5	3
Tank2	2000	2	3

2.2 Phase Change Model

In the present paper, a 2-D model is established by the commercial CFD software FLUENT 16.0 to simulate the geyser phenomenon. The volume of Fluid (VOF) method has been applied for the modeling of multiphase problem. Phase change phenomenon was described by Lee model and implemented by a user-defined function (UDF) which is compiled and embedded into Fluent. In this UDF, the loaded source terms could calculate the direction and magnitude of the phase change in each cell by comparing the temperature of the cell T with the local saturation temperature T_{sat} corresponding to the pressure. The mass transfer during evaporation and condensation can be calculated by Equations, which are embedded as mass sources for vapor and liquid phase in Equation. The corresponding energy transfer term Q is added as an energy source.

$$S_{\mathrm{l}} = -S_{\mathrm{g}} = r_1 \alpha_{\mathrm{l}} \rho_{\mathrm{l}} \frac{(T - T_{\mathrm{sat}})}{T_{\mathrm{sat}}} \qquad \text{Eq. (1)}$$

$$S_{\mathrm{g}} = -S_{\mathrm{l}} = r_2 \alpha_{\mathrm{g}} \rho_{\mathrm{g}} \frac{(T - T_{\mathrm{sat}})}{T_{\mathrm{sat}}} \qquad \text{Eq. (2)}$$

$$Q = Sh_{\mathrm{fg}} \qquad \text{Eq. (3)}$$

Due to the long length of the tube, the static pressure head of liquid column changes significantly with height. The variation of saturation temperature with pressure should be considered. The saturation temperature are derived from NIST at different pressure, and the relation between saturation temperature and pressure is fitted as follows.

$$T_{\mathrm{sat}} = 76.63 + 187.2p - 662.2p^2 + 1485p^3 - 1391p^4 \qquad \text{Eq. (4)}$$

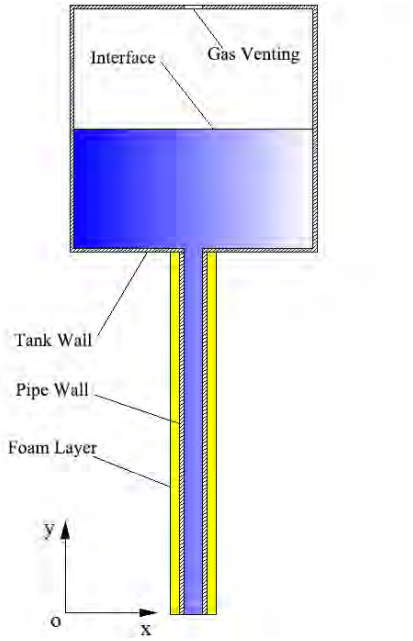

Figure 1: Schematic diagram of LO_2 feeding system

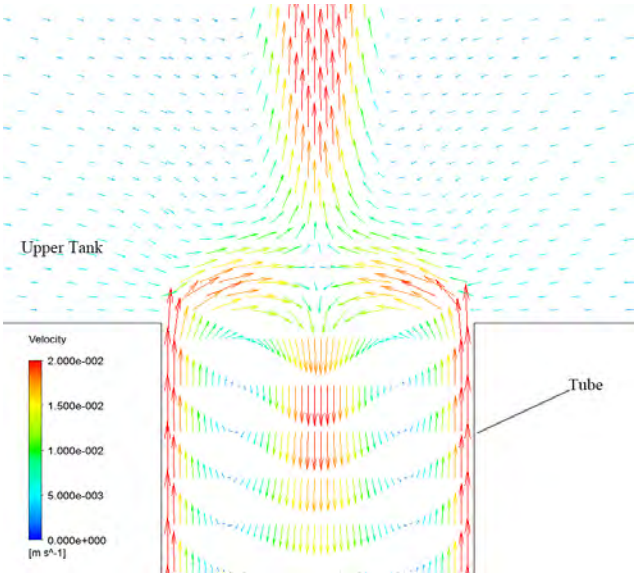

Figure 2: Velocity vector

3. RESULTS AND DISCUSSION

3.1 Natural Convection and Temperature Distribution

Fig.2 displays the development of free convection inside the tube. With heat leak into the pipe, temperature of fluid close to the pipe wall will increase firstly. The fluid within the boundary layer is heated and consequently its density decrease due to the temperature increase. Under the effect of upward buoyancy force, warm fluid moves up along the wall until they arrive the interface between the pipe and upper tank. Afterwards, part of the warm fluid get into the tank, and another part of it moves down along the pipe center after mixing with the cold liquid in the tank.

As pointed out by Murphy (1965), with the development of warm boundary layer, the whole tube section will be occupied. Therefore, the free convection ceases, fluid temperature inside the pipe increase rapidly and eventually leads to the generation of geyser. However, in this paper, the warm boundary layer cannot fill the entire pipe section during the heating process. The free convection will always exist until boiling occurs. Despite the existence of natural convection, the heat from environment cannot be completely brought into the upper tank. Therefore, fluid temperature inside the tube will gradually increases with time.

The heat was brought to the upper part of the tube and the upper tank while the relatively cold fluid flow down to the bottom under the effect of free convection in the pipe. Temperature distribution inside the pipe at 400s is shown in Fig.3. It can be seen that thermal stratification is developed in the lower part of the pipe, and temperature at the pipe bottom is relatively lower due to thermal stratification. The cold liquid was heated when it flows down along the center line. Temperature at the location which near to the interface between the pipe and the upper tank is lowest among the whole part of the pipe. Under the combined effect of free convection and low temperature in the tank, temperature

at the middle region of the pipe is highest, and the temperature distributions trend displayed in Fig.4 a will be maintained until boiling occurs.

Fig.4 gives the temperature changes of pipe center line. It is clear that the overall temperature gradually rises except for the region near the interface between the pipe and the tank. As heat leak continues, a certain location in the upper region of the tube will reach the saturation state first. Before the pipe center temperature reaches the saturation state, there will be some subcooled boiling in the warm boundary layer near the tube wall. With time continuing, the length of tube that temperature is near the saturation state is longer, and the point that boiling could occurs moves down to the bottom of the tube. This temperature distribution field makes more energy accumulated in the lower part of the tube, then, the energy could be violently released when the geyser occurs.

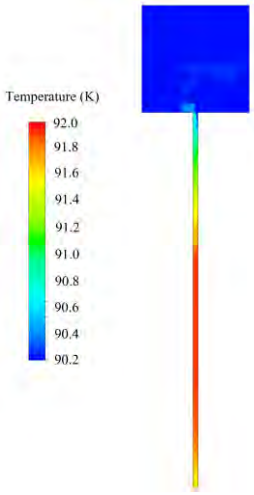

Figure 3: Temperature distribution at 600s

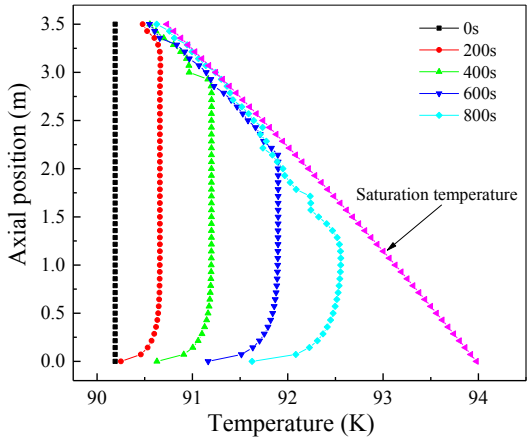

Figure 4: Axial temperature change

3.2 Boiling and Geyser Phenomenon

In order to understand the boiling phenomenon and flow behavior in the geyser process, the phase distribution contours at different times were observed. Phase distribution contours at five representative moments are given in Fig. 5. As shown in Fig. 5, the geyser process occurs in the LO_2 feed tube could be divided into three stages namely incubation, eruption and refilling. As can be seen at 960s in Fig. 5, subcooled boiling occurs in the upper section of the pipe and multiple bubbles disperse in the continuous bulk liquid and travel upward due to buoyancy. With the continuous heat input, the number of bubbles increases while the length of tube that starts to boil becomes longer. The heating period from 0s, and boiling process before eruption could be defined as incubation stage. The presence of bubbles lowers the pressure below and the saturation temperature decreases simultaneously. This in turn provides a self-sustaining violent boiling. The mixture of liquid and vapor erupt into the upper tank in a very short time as shown in Fig. 5 at 1029.8s. At the end of eruption process, void fraction in the pipe reaches the maximum value. Cool LO_2 flow down from the upper tank into the pipe very quickly, as shown at 1031.2s in Fig. 5, causing a considerable water-hammer-effect pressure spike. The LO_2 flowing down process could be defined as refilling of geyser. After refilling process, a new round of energy accumulation process started in the tube until the next geyser occurs. Bubbly flow and churn flow pattern was observed in the geyser process. Taylor bubbles were not able to form during the whole process due to low surface tension and large pipe diameter. Through the phase contours we can see that, the model established in the present paper could simulate the geyser process including eruption and refilling stages.

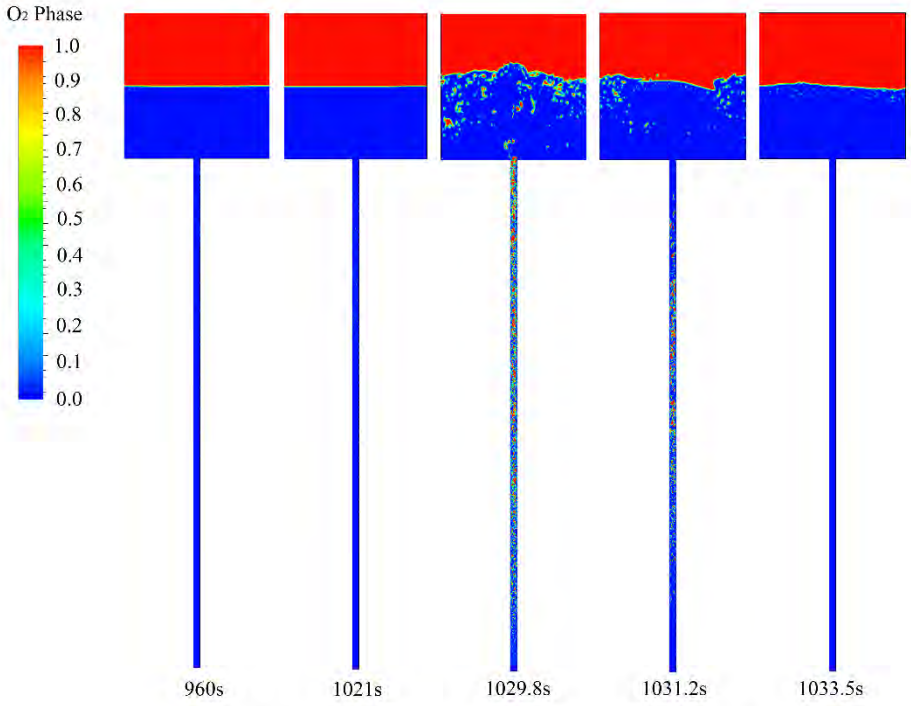

Figure 5: Phase distribution contours at representative moments

3.3 Pressure Change

Fig. 6 gives time variation of pressure at tube bottom and temperature at 0.7m. As seen in Fig. 6, the pressure almost remains constant before 600s. The liquid was heated up in this period of time and the temperature distribution described above was formed. Then, the liquid in the upper section of the pipe starts to boil, and the pressure begin to fluctuate due to bubble formation and movement. In the boiling stage, the temperature in the pipe upper part no longer increases while the temperature in the lower part of the pipe is continuously rising as shown in Fig. 7 and Fig. 8 between 600s and 1020s. The eruption occurred when the number of bubbles and the temperature increase to a certain extent. The pressure and temperature makes a sharp fall coinciding with the explosive eruption. The mechanism of eruption could be revealed by the change in pressure and temperature. The energy accumulated in the liquid becomes very unstable as the heating and boiling going on. Static pressure of the liquid column decreases under the influence of bubbles in the tube. The saturation temperature of liquid with high energy decreases with the decrease of pressure at the same time. Violent depressurization boiling would occur when the local saturation temperature falls below the liquid temperature. This boiling phenomenon is similar to flashing and a great deal of vapor will be produced. The eruption of liquid and vapor is formed while liquid in the pipe is expelled into the upper tank by vapor. During the depressurization boiling process, the energy stored in the liquid was released and taken away by vaporization, hence the liquid temperature decreases. We can see that from Fig. 7 and Fig. 8, temperature decreases coinciding with the local saturation temperature decreases. The eruption is about to cease when the temperature stop decreasing. This means the energy releasing is come to an end, and no more violent boiling exists. The temperature and pressure reach minimum value at the end of eruption, and void fraction in the pipe reaches a high value.

3.4 Pressure Spike Mechanism

After the eruption, a considerable pressure spike is formed by the refilling of cool liquid in the upper tank, as shown in Fig. 6. In order to investigate mechanism of the pressure spike, the process after eruption is studied. When the eruption is about to cease, vapor temperature in the pipe is at saturated level, and higher than the liquid temperature in the upper tank. Condensation caused by contact of subcooled liquid with saturated vapor becomes the main phase change process. The liquid would refill into the tube under the effect of condensation and the gravity. To investigate the dominant factor causing the pressure spike, refilling process considering condensation and gravity effects and only gravity effect is investigated. The condensation mass transfer intensity factor r_2 was set to zero in the

gravity only case to ignore the effect of condensation. And the tube length in this simulation was 5m, the tube diameter was 47mm. The results of the above two situation is depicted in Fig. 9. It is clear that the pressure history is similar to that in the 3.5m-tube-length case when condensation effects is taken into account. However, there is no pressure spike in the gravity only case, and the refilling time is much longer than that of the case when condensation effects is considered. Since there are only two factors which cause refilling of liquid, it implies that vapor condensation is the main factor of the pressure spike. Under the effect of condensation, liquid flow down very quickly and hit the bottom of the pipe or liquid remains in the pipe, and this phenomenon could be called condensation induced water hammer (Wang et al., 2018) and (Daude et al., 2018). This kind of water hammer is usually encountered in water and its vapor transmission system, and a huge pressure spike would be formed. Hence, condensation induced water hammer is the mechanism of the pressure spike in geyser refilling process

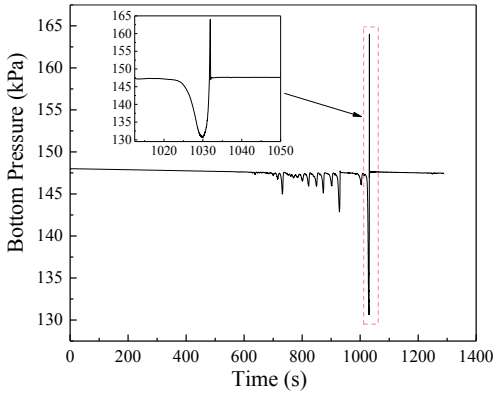

Figure 6: Bottom pressure change

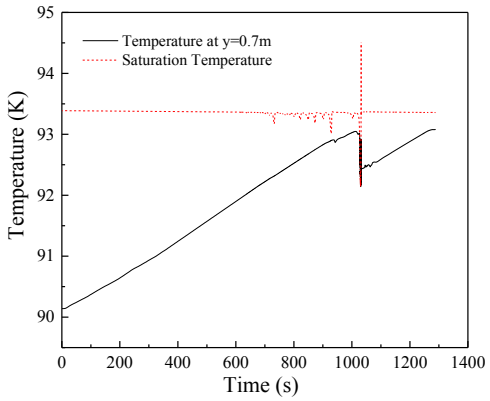

Figure 7: Temperature change at y=0.7m

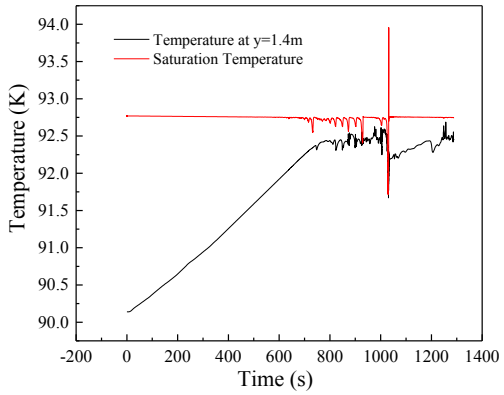

Figure 8: Temperature change at y=1.4m

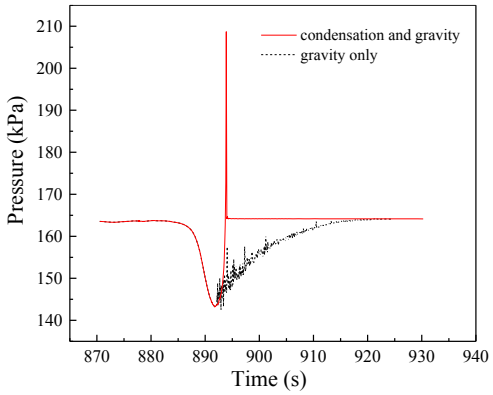

Figure 9: Bottom pressure change under different conditions

4. CONCLUSIONS

In the present paper, geyser phenomenon occurred in bottom closed liquid oxygen feed line is investigated through numerical simulation. The characteristics and mechanism of geyser process is analyzed. Several conclusions are drawn as follow.

(1) Temperature stratification occurs in the feed tube under the effects of natural convention. The temperature distribution in the tube tends to be low at both end and high in the middle. This temperature distribution field makes more energy accumulated in the lower part of the tube, and the energy could be violently released when the geyser eruption occurs.

(2) The geyser process occurs in the LO_2 feed tube could be divided into three stages namely incubation, eruption and refilling. Pressure in the tube falls sharply due to large void fraction in the eruption process. A considerable pressure spike occurs in the refilling stage because of liquid flow down. The model established could simulate the geyser process including eruption and refilling stages.

(3) The violent depressurization boiling is the main cause of geyser eruption. Void fraction in the tube increases rapidly in the depressurization boiling process and liquid column static pressure drops at the same time. The water hammer caused by vapor condensation in the tube is the main mechanism of pressure spike in the refilling process.

ACKNOWLEDGEMENTS

This work was supported by National Natural Science Foundation of China (51876153)

NOMENCLATURE

S_l	Liquid mass source	S_g	Vapor mass source
r_1	vaporizing mass transfer intensity factor (s^{-1})	r_2	condensation mass transfer intensity factor (s^{-1})
α_l	liquid volume fraction	ρ_l	Liquid density (kg/m3)
T	Temperature (K)	T_{sat}	Saturation temperature (K)
α_g	vapor volume fraction	ρ_g	vapor density (kg/m3)
Q	Heat of vaporization or condensation	h_{fg}	Latent heat of phase change
p	Pressure (MPa)		

REFERENCES

Aritomi, M, Jing, H.C., Morib, M, 1992. Geysering in parallel boiling channels. Nuclear Engineering & Design 141(1-2), 111-121.

Burkhalter, J.E., Sforzini, R.H., Tinsley, C.R., 1968. Investigations of geysering in vertical tubes. Journal of Spacecraft and Rockets 5(7), 854-857.

Casarosa, C, Latrofa, E, Shelginski, A., 1983. The geyser effect in a two-phase thermosyphon. Int. J. Heat and Mass Transfer 26(6), 933-941.

Chen, J.B., Yang, S.X., Liao, S.L., Cao, X.W., 2015. Experimental investigation of effective parameters on geyser periodicity in a vertical heated system. Experimental Thermal and Fluid Science 68, 163-176.

Chiang, J-H, Aritomi, M, Inoue, R, Mori, M., 1994. Thermo-hydraulics during start-up in natural circulation boiling water reactors. Nuclear Engineering and Design 146(1), 241-252.

Daude, F., Tijsseling, A.S., Galon, P., 2018. Numerical investigations of water-hammer with column-separation induced by vaporous cavitation using a one-dimensional Finite-Volume approach. Journal of Fluids and Structures, 83, 91-118.

Hands, B.A, 1988. Problems due to superheating of cryogenic liquids. Advance in Cryogenics 28(12), 823-829.

Kuncoro, H, Rao, Y.F., Fukuda, K., 1995. An experimental study on the mechanism of geysering in a closed two-phase thermosyphon. Int. J. Multiphase Flow 21(6), 1243-1252.

Morioka, M, Obama, T, Kouda, Y, Mori, M, Tomura, S, Enya, S, 1986. Simulation of the Geysering Phenomenon in LNG Pipes. Advances in Cryogenic Engineering 31, 1111-1119.

Murphy, D.W., 1965. An Experimental Investigation of Geysering in Vertical Tubes. Advance in Cryogenic Engineering 10, 353-359.

Ozawa, M, Nakanishi, S, Ishigai, s, Mizuta, Y, Tarui, H., 1979. Flow Instabilities in Boiling Channels : Part 2 Geysering. JSME Int. J. 22(170), 1119-1126.

Tae-il, K, Okamoto, K, Madarame, H., 1993. Study on the Effective Parameters for the Geysering Period. Instabilities in Multiphase Flows, 125-136.

Wang, L., Yue, X., Chong, D., Chen, W., Yan J., 2018. Experimental investigation on the phenomenon of steam condensation induced water hammer in a horizontal pipe. Experimental Thermal and

Fluid Science 91, 451-458.

Manuscript ID: 967
DOI: 10.18462/IIR.ICR.2019.0967

Numerical modelling and experimental investigations on an 18 kW Oxford-type moving-coil linear compressor

Jun TAN[(a, c)], Jiaqi LI[(a, b)], Rui ZHA[(a, b)], Tao ZHANG[(a, b)], Bangjian ZHAO[(a, b)], Yongjiang ZHAO[(a, b)], Haizheng DANG[(a, c)]

[(a)] State Key Laboratory of Infrared Physics, Shanghai Institute of Technical Physics, Chinese Academy of Sciences, Shanghai, 200083, China, e-mail address: juntan@mail.sitp.ac.cn; haizheng.dang@mail.sitp.ac.cn
[(b)] University of Chinese Academy of Sciences, Beijing, 100049, China
[(c)] Shanghai Boreas Cryogenics Co., Ltd, Shanghai, 200434, China

ABSTRACT

To achieve a moving-coil linear compressor with the electric input capacity higher than 10 kW is a huge challenge. This paper presents the numerical modelling and experimental investigations on an Oxford-type dual-opposed moving-coil linear compressor with the electric input capacity of 18 kW. A numerical model is established in which systematic analyses about force balance and magnetic circuit are conducted. Optimizations on geometries of the magnet circuit, moving coil and air gap are focused on to enhance the input capacity and also to optimize the motor efficiency. The compressor prototype is developed experimentally, and experimental results are compared with the theoretical analyses. The developed compressor is then coupled with a pulse tube cold finger. At present, experimental results show that the cooler can provide 720 W at 77 K for cooling the high-Tc superconducting facilities with an electric input power of 16.2 kW.
Keywords: Modelling, Experimental Investigation, 18 kW, Moving-Coil, Linear Compressor.

1. INTRODUCTION

The Oxford-type linear compressor, first proposed in the 1970s (Bradshaw et al., 1986; Davey, 1990), has made noticeable progress in the past several decades (Ross, 2007; Dang, 2015). According to the moving component in the linear motor, it can be furtherly classified into the moving-iron, moving-coil and moving-magnet types. The moving-iron type has been firstly studied and developed because of the high cost and lack of high-quality magnets in the early days, but it also introduced extra problems such as low stability and difficult control, simultaneously. After the big breakthrough of permanent magnets, high-energy permanent magnets with considerable cost can be achieved easily. The moving-magnet and moving-coil types had been applied in varieties of scientific and industry fields, such as Stirling cooler, pulse tube cooler and household refrigerator (Bansal et al., 2011; Liang et al, 2017). Especially the moving-coil type, avoiding open circuit axial forces and torques on the moving coil and eliminating the radial forces by structural features, owns high efficiency and reliability, thus has become the prior choice in the applications specially emphasizing the stability and long operation life.

In the cryogenic field, the Oxford-type linear compressor has already become the main driver for the Stirling cooler and Stirling-type pulse tube cryocooler (SPTC) due to the proven high efficiency and reliability for about three decades (Davey, 1990; Marquardt et al., 1993; Bailey et al., 2001; Ross, 2007; Dang, 2015), which are attributed to the sustained studies of the linear compressor and its dynamic and thermodynamic characteristics to a great extent (Bradshaw et al., 2011, 2013; Dang et al., 2016a, 2016b). However, most of these studies mainly focus on the low or medium capacity linear compressor with below 1 kW (always tens of or hundreds of watts) of input power, detailed theoretical and experimental investigations on high capacity compressor (with input power of several kilowatts or tens of kilowatts) have seldom been reported.

For cooling superconducting cables and fault current limiter, hundreds or thousands of watts cooling power at liquid nitrogen temperature are always needed, which necessitates the high capacity

moving-coil linear compressor. In this paper, theoretical and experimental investigations on an 18 kW dual-opposed Oxford-type moving-coil linear compressor will be put forward. Numerical modelling and analyses of the magnet circuit, force balance and the specific design will be described in a detail way. The prototype compressor has been worked out and coupled with a large pulse tube cold finger for cooling the high-Tc superconducting facilities.

2. NUMERICAL MODELLING

Fig. 1 shows the structure of the dual-opposed moving-coil linear compressor to be developed. The dual-opposed configuration is employed which can substantially decrease the fundamental frequency vibration. Each half includes a linear motor, a piston, two sets of flexure springs and several support components. During the operation, the piston, the coil and the flexure springs will oscillate and the clearance acts as the dynamic seal between piston and cylinder, thereby eliminating the source of rubbing wear and providing high reliability which are beneficial for achieving long operation lifetime. The two halves share the same compression chamber and then the PV power will be transported to the cold finger.

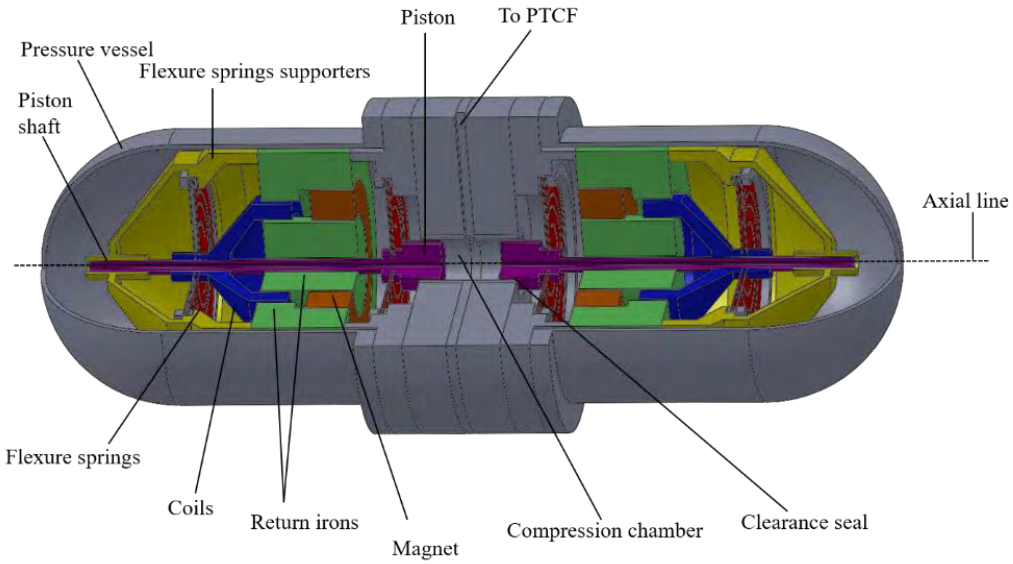

Figure 1: Schematic of a typical moving-coil linear compressor

2.1. Magnetic Circuit Model

According to the working mechanism of the linear motor and the interaction between the compressor and cold finger. The modelling of the linear compressor can be divided into two parts. The first one is the magnetic circuit model which mainly consists of the magnet and return irons. A schematic of the magnetic circuit model for the long-coil type linear compressor is shown in Figure 2. It includes a magnet, a moving coil, two return irons and an air gap. According to the current excitation, the long coil will move up and down periodically and not leave out of the air gap. The centre hole shown in Fig. 2 is used to couple with the piston shaft.

According to the previous study on moving-coil linear compressor in the authors' laboratory [Dang et al., 2016b], the magnetic field intensity should be as high as possible to achieve a high motor efficiency. NdFeB, owning excellent magnetic properties, such as high energy product (BH: 290 kJ/m3) and coercivity (HcB: 880 kA/m), becomes our first choice of magnet material. Then the geometry dimensions will be optimized. The centre hole is far away from the air gap, which draws little effect on the magnetic field intensity distribution in the air gap. Its diameter is determined by the piston shaft. The return iron 1 and the magnet share the same outer diameter which is slightly smaller than the inner diameter of moving coil. Besides, geometry dimensions of the air gap are the key parameters which determine the magnetic field intensity and effective coil volume, thereby affecting the maximum electric input capacity and motor efficiency. Optimizations of them will be discussed in detail in the following.

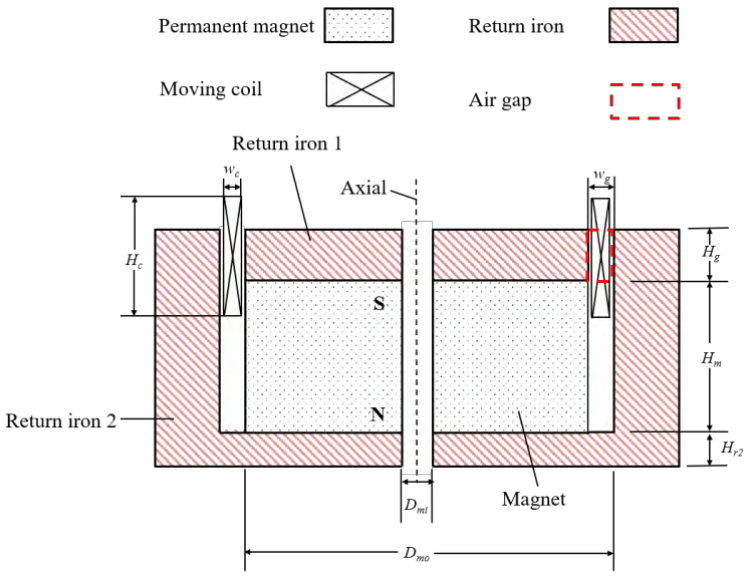

Figure 2: The schematic of magnetic field model

In consideration of the probability of intermittent contact and wear between the moving coil and return irons, the width of the air gap w_g should be a little larger than that of the moving coil w_c. According to the fabrication and assembly experiences on the previous study of linear compressor, the difference is only 15 μm. Theoretically, the width of the air gap w_g should be as small as possible to achieve large magnetic field intensity. But it leads to a short coil length as well. According to the relation between the coil length and motor efficiency shown in Eq. (1), short coil length will lead to the decrease of the motor efficiency. Moreover, it will affect the motor force, thereby reducing the maximum electric input capacity as well. These two aspects are not beneficial for obtaining a large capacity linear compressor with high motor efficiency. In the optimization of air gap geometry, a compromise between the average value of magnetic field intensity and effective coil volume should be made.

$$\eta_{motor} = \frac{B^2 L^2 A_p^{\,2} |Z_a| \cos\theta_a}{|Z_a| \cos\theta_a A_p^2 B^2 L^2 + bB^2 L^2 + R_e A_p^{\,4} \left[\left(|Z_a| \cos\theta_a + b / A_p^{\,2} \right)^2 + \left(|Z_a| \sin\theta_a + \left(k_x - m\omega^2 \right) / A_p^{\,2} \right)^2 \right]} \qquad \text{Eq. (1)}$$

where η_{motor} is motor efficiency, B, A_p, m and L represent magnetic field intensity, piston surface area, moving mass and coil length in the air gap, respectively. Z_a and θ_a are the amplitude and phase angle of the cold finger impedance. R_e, b, k_x and ω represent the coil resistance, damp coefficient, axial stiffness of flexure springs and angular frequency, respectively.

A two-dimensional model of the magnets circuit will be established to explain the above circumstances in a detailed way. The impedance and phase angle of cold finger are regarded as constant. Then the magnetic field distribution in the air gap can be solved by the simulation with Maxwell software. Table 1 gives the simulated results of average magnetic field intensity and motor efficiency with various widths of air gap.

Results show that the average magnetic field intensity decreases monotonously with the width of air gap, while there exists an optimal value for the compressor to achieve the highest motor efficiency. Moreover, with the assumption that the air gap will be full filled with coil wire, the maximum electric input capacity will rise with the growth of air gap width. . According to the simulated results, optimal geometries of the air gap can be determined accordingly. In practice, the diameter of the coil wire cannot be selected arbitrarily and layer number of the coil must be integer, so the air gap cannot be full filled with coil wire. Moreover, in the selection of coil wire dimeter, the rated current which will affect the maximum electric input capacity, should be another important item to be considered.

In addition, a 3D model of the magnet circuit with Maxwell software has also been established to investigate the influences of current excitation on static magnetic field intensity. The simulated results are illustrated in Fig. 3. In the four cases, the current excitation increases from 0 A to 15 A gradually with an interval of 5 A. Results indicate that, large magnitudes of magnetic field intensity appear in

the area of the air gap or near it, and the amplitude of current excitation takes little effect on the static magnetic field distribution in such a magnet circuit configuration, for all cases.

Table 1. Comparisons of compressor performance with different widths of air gap

Width of air gap (mm)	Magnetic field intensity (T)	Motor efficiency	Maximum electric input capacity
6.6	2.22	79.78%	0.976 P
6.8	2.16	79.96%	0.98 P
7.0	2.14	80.02%	P
7.2	2.10	79.98%	1.01 P
7.4	2.06	79.84%	1.019 P
7.6	2.02	79.76%	1.027 P
7.8	2.00	79.68%	1.044 P
8.0	1.97	79.59%	1.056 P

Therefore, in the analyses of moving-coil linear compressor, the magnetic field distribution can be regarded as constant.

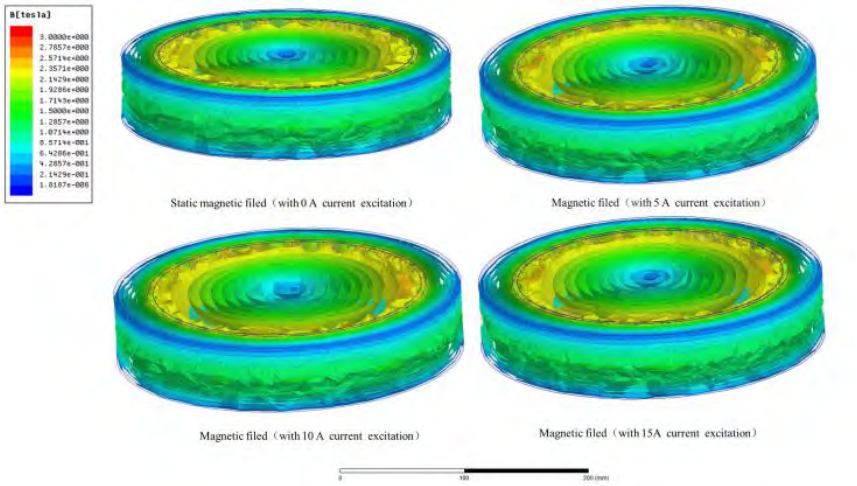

Figure 3: Influences of current excitation on the static magnetic field intensity

2.2. Force Balance Model

The second model of the linear compressor is the force balance. During the operation, the piston, the coil and flexure springs will oscillate according to current excitation. The moving mass includes the piston, moving coil and one third of flexure springs. The force balance model can be summarized as shown in Fig.4 and Eq. (2). Six dynamic forces act on the moving mass, which are the linear motor force, mechanical spring force, gas force on the back side of the piston and that on the front side, viscous dissipation force and inertial force, respectively.

$$\underset{\text{Motor force}}{LBi(t)} = \underset{\text{Inertial force}}{m\frac{d^2x(t)}{dt}} + \underset{\text{Viscous force}}{b\frac{dx(t)}{dt}} + \underset{\text{Mechanical force}}{k_x x(t)} + \underset{\text{Gas force（front）}}{p(t)A_p} - \underset{\text{Gas force（back）}}{p_B(t)A_p} \qquad \text{Eq. (2)}$$

where $p(t)$ and $p_B(t)$ represent the dynamic pressure in the compression space and that on the backside of the piston, respectively. Both phases of the inertial force and mechanical spring force lag the velocity by 90 degrees. During each cycle, these two forces act as springs and no work will be consumed. The work done by the viscous dissipation force will be transformed into heat, while that of the gas force on the front side of the piston will be converted into PV power and then

transmitted to the cold finger. In theory, the value of θ should approximate to 90 degrees to obtain high motor efficiency.

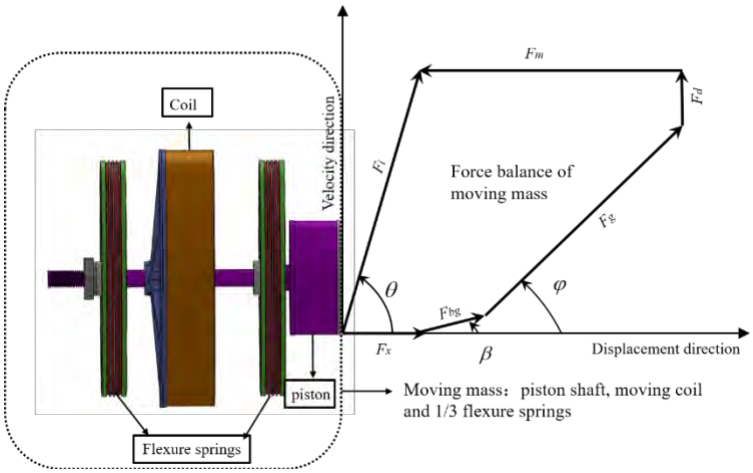

Figure 4: Force balance of the moving mass in linear motor

3. PRIMARY EXPERIMENTAL TESTS AND RESULTS

The permanent magnet and return irons are firstly worked out, installed and integrally magnetized. Experimental tests on the distribution of the magnetic field intensity have ben put forward and a photograph of the test setup is shown in Fig.5. A height measuring instrument, a magnetometer and some supporting structures are used to measure the magnetic field intensity at different positions of the air gap with a relatively high precision.

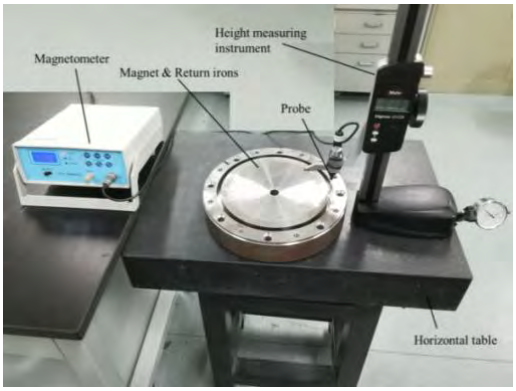

Figure 5: Test setup of the magnetic field intensity

The geometry of the air gap is 7 mm in width and 16 mm in height. Table 2 gives test results of the magnetic field intensity distribution in the air gap with a testing interval of 1 mm in width direction and 2 mm in height direction.

Table 2. Experimental results of magnetic field intensity (mT) distribution

Position in width / Position in height	0 mm	1mm	2mm	3mm	4mm	5mm	6mm	7mm
0 mm	901.6	898.8	902.0	919.0	959.6	1007.6	1078.7	1154.0
2 mm	926.1	931.6	942.3	959.1	986.8	1013.6	1044.8	1069.8
4 mm	938.6	946.9	957.5	971.5	990.9	1007.3	1024.9	1038.9
6 mm	946.7	954.9	964.0	975.4	990.6	1002.9	1016.3	1027.6
8 mm	951.1	958.1	965.7	975.6	989.2	1000.7	1013.8	1025.0
10 mm	951.3	957.6	962.9	970.5	984.2	998.2	1015.5	1030.2
12 mm	965.7	957.4	950.5	949.4	963.9	986.1	1021.5	1054.5
14 mm	1043.5	934.4	893.8	876.1	888.6	920.0	994.9	1120.7
16 mm	677.4	710.4	713.3	715.0	724.9	731.6	742.7	722.7

The zero position in width direction is defined at the inner diameter surface of return iron 2 and that in height direction is defined at the top surface of return iron 1 as shown in Fig.2. Experimental results show that, in the width direction, the magnetic field intensity generally increases from the outside of the air gap to the inside. While in the height direction, largest magnetic field intensity exists at the position of 14 mm. Based on the results, the average value of magnetic field intensity can be calculated and it's equal to 960 mT, which is only about half of the theoretical one as shown in Fig.3. The main reason is that, the magnet with relatively large geometry (the outer diameter of the permanent magnet is 210 mm and that of the return iron 1 reaches 270 mm) is hardly to get full-magnetized with integrated magnetized method.

According to the design and experience of flexure springs applying in our space used linear compressors, three Archimedes spirals are employed in the design and austenitic stainless steel is used in the fabrication. A photograph of the developed flexure springs is shown in Fig.6. The outer diameter of the flexure spring is 200 mm and the inner hole is used to fit the piston shaft with a diameter of 15.5 mm. Both the slot width and thickness are 2 mm. The axial stiffness of the flexure spring is also measured, whose value is 6.2 kN/m for each piece.

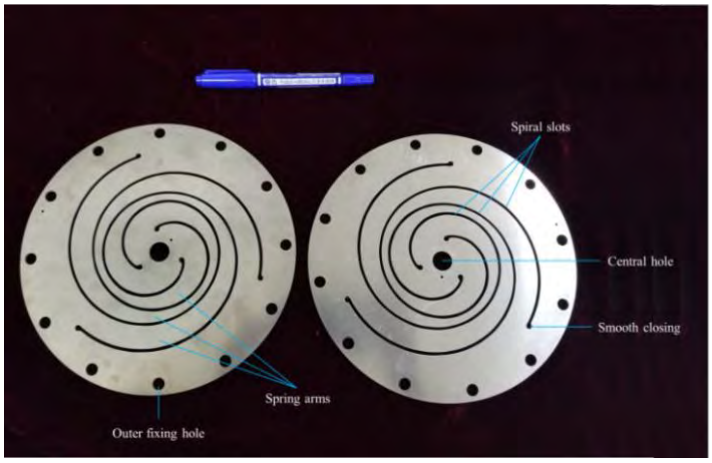

Figure 6: A photograph of the developed flexure springs

The linear compressor is assembled and then tested without coupling a cold finger. Fig. 7 shows the test results of piston oscillation attenuation curve. In the test, the displacement transducer is attached to the piston shaft to monitor the movement of piston. Test results will be displayed in the oscilloscope. Experimental results indicate that, the movement of piston is an attenuated sine wave with a small damp. Results in Fig.7 can be used to evaluate the mechanical damp due to the loss of imperfect elasticity of flexure springs and friction between piston and working gas in the clearance gap.

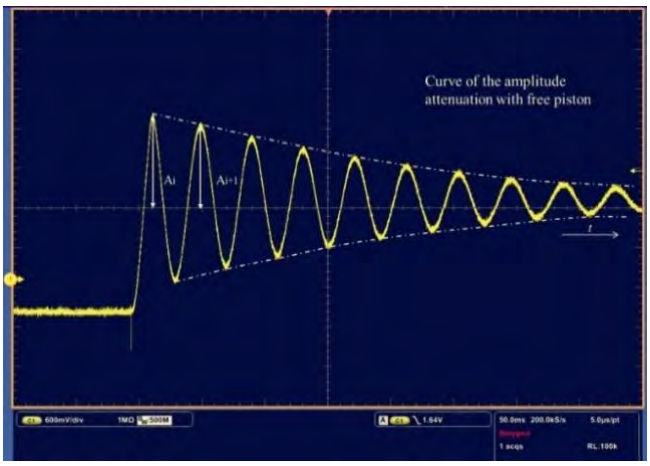

Figure 7: Test setup of the magnetic field intensity

The specific calculated method can be written as:

$$b = 2\ln\frac{A_i}{A_{i+n}}\sqrt{\frac{mk_x}{4\pi^2 n^2 + \left(\ln\frac{A_i}{A_{i+n}}\right)^2}} \qquad \text{Eq. (3)}$$

where A_i represents the amplitude of piston displacement, m is the moving mass and k_x is the axial stiffness of flexure springs, n is the interval number between A_i and A_{i+n}. And the mechanical damp coefficient of the developed compressor is 22.3 N·s/m.

Fig. 8 shows a photograph of the comparison between the developed large capacity linear compressor and our mature medium capacity one (with the maximum input capacity of 300 W). And Fig. 9 shows the details of the half of the linear compressor.The large compressor weights 100 kg with the geometry dimensions of 680 mm in length and 320 mm in outer diameter.

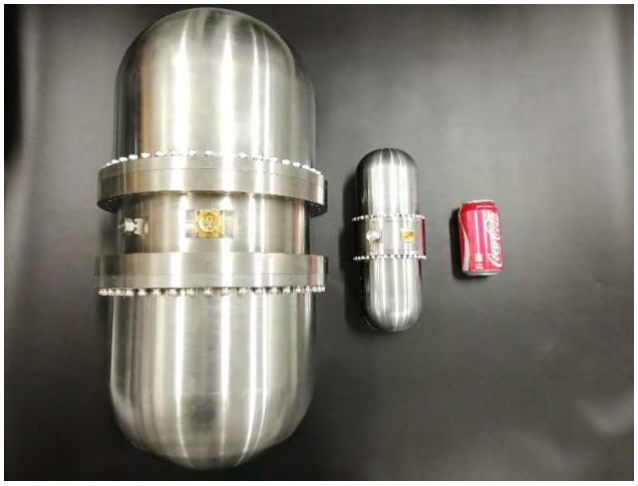

Figure 8: Comparison between the developed compressor and small-scale compressor



Figure 9: A photograph of the details of the developed linear compressor

Moreover, the developed linear compressor has also been coupled with a high capacity pulse tube cold finger and cooling performances are shown in Fig.10. With the increase of cooling capacity, the cooling efficiency of Carnot decrease a little, which mainly caused by the slight attenuation of motor efficiency. At present, with an electric input power of 16.2 kW, a cooling capacity of 720 W at 77 K can be achieved with cooling efficiency higher than 12%. Fig.11 shows the relations between the cooling temperature and motor efficiency. With the decrease of the cooling temperature, the motor efficiency drops slightly, which is the main reason leading to the decrease of cooling efficiency. While, a motor efficiency of 78.5% can be obtained at the cooling tempearture of 77 K. In the near future, some components of the linear compressor will be furtherly optimized, which is expected to have a maximum input capacity of 18.5 kW for the SPTC to acquire a cooling capacity of 800 W at 77 K.

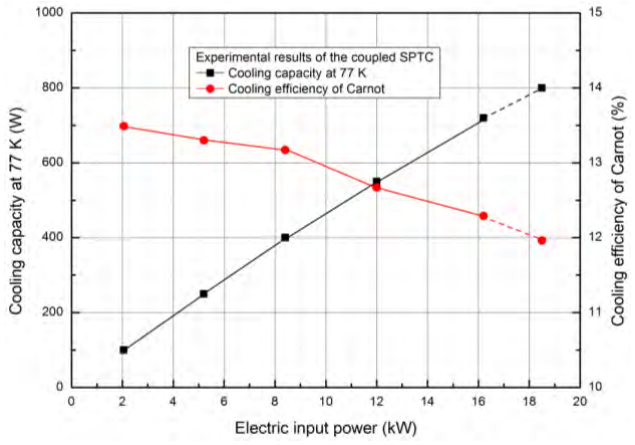

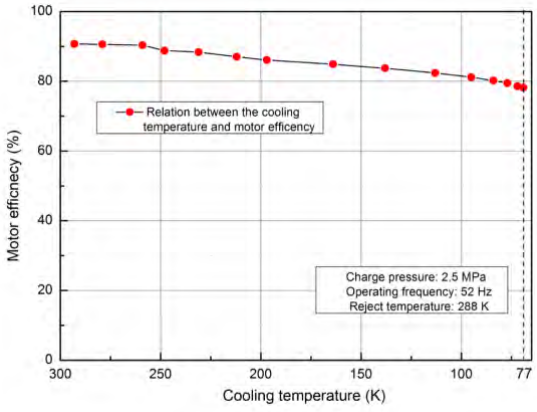

Figure 10: Experimental results of the coupled SPTC

Figure 11: Relations between cooling temperature and motor efficiency

4. CONCLUSIONS

In this paper, the numerical modelling and experimental investigations on an Oxford-type dual-opposed moving-coil linear compressor aiming to obtain the electric input capacity of 18 kW are presented. Numerical models are established in which systematic analyses about force balance and magnetic circuit are conducted. Optimizations on geometries of the magnet circuit, moving coil and air gap are focused on to enhance the input capacity and also to optimize the motor efficiency, simultaneously. The compressor prototype is worked out and then coupled with a pulse tube cold finger. At present, experimental results show that the cooler can provide 720 W at 77 K with an electric input power of 16.2 kW, and a motor efficiency of 78.5% is obtained as well.

ACKNOWLEDGEMENTS

This work was financially supported by The Aeronautical Science Foundation of China (No. 20162490005) and Shanghai Municipality (Nos.18511110100, 18511110101 and 18511110102).

NOMENCLATURE

A_i	piston amplitude (m)	P	electric input power
A_p	piston area (m^2)	$p(t)$	dynamic pressure front of piston (Pa)
B	magnetic field intensity (T)	$p_B(t)$	dynamic pressure back of piston (Pa)
b	damp coefficient (N·s/m)	R_e	coil resistance(Ω)
$i(t)$	current (A)	$x(t)$	piston displacement (m)
k_x	stiffness (N/m)	Z_a	impedance ($Pa·s/m^3$)
L	coil length (m)	η_{motor}	motor efficiency (%)
m	moving mass(kg)	ω	angular frequency(rad/s)
n	interval number	θ_a	phase angle of impedance (degree)

REFERENCES

Bailey, P.B., Dadd, M.W., Hill, N., et al., 2001. High performance flight cryocooler compressor. In: Cryocoolers 11, Kluwer Academic/Plenum Press, New York, pp. 169–74.

Bansal, P., Vineyard E., Abdelaziz, O., 2011. Advances in household appliances-a review. Appl Therm Eng 31, pp.3748-60.

Bradshaw, T.W., Delderfield, J., Werret, S.T., 1986. Performance of the oxford miniature Stirling cycle refrigerator. Adv Cryog Eng 31, pp.801–9.

Bradshaw, C.R., Groll, E.A., Garimella, S.V., 2013. Linear compressors for electronics cooling: Energy recovery and its benefits. Int. J. Refrigeration 36, pp.2007–13.

Davey, G., 1990. Review of the Oxford cryocooler. Adv Cryog Eng 35, pp.1423-30.

Dang, H.Z., 2015. Development of high performance moving-coil linear compressors for space Stirling-type pulse tube cryocoolers. Cryogenics 68, pp.1–18.

Dang, H.Z., Tan, J., Zhang, L., 2016. Theoretical and experimental investigations on the optimal match between compressor and cold finger of the Stirling-type pulse tube cryocooler. Cryogenics 76, pp.33-46.

Dang, H.Z., Zhang, L., Tan, J., 2016. Dynamic and thermodynamic characteristics of the moving-coil linear compressor for the pulse tube cryocooler. Part B: Experimental verifications. Int. J. Refrigeration 69, pp.497–504.

Liang, K., 2017. A review of linear compressors for refrigeration. Int. J. Refrigeration 84, pp.253–73.

Marquardt, E., Radebaugh, R., Kittel, P., 1993. Design equations and scaling laws for linear compressors with flexure springs. In: Cryocoolers 7, pp.783–804.

Ross, Jr. R.G., 2007. Aerospace coolers: a 50-year quest for long life cryogenic cooling in space. In: Timmerhaus KD, Reed RP, editors. Cryogenic engineering: fifty years of progress. Springer,

New York, pp. 225–84.

Manuscript ID: 971
DOI: 10.18462/IIR.ICR.2019.0971

Investigations on a novel automatic temperature control method and electronics for multi-stage Stirling-type pulse tube cryocoolers

Jun TAN[(a, c)], Tao ZHANG[(a, b)], Rui ZHA[(a, b)], Jiaqi LI[(a, b)], Bangjian ZHAO[(a, b)], Yongjiang ZHAO[(a, b)], Haizheng DANG[(a, c)]

[(a)] State Key Laboratory of Infrared Physics, Shanghai Institute of Technical Physics, Chinese Academy of Sciences, Shanghai, 200083, China, e-mail address: juntan@mail.sitp.ac.cn; haizheng.dang@mail.sitp.ac.cn
[(b)] University of Chinese Academy of Sciences, Beijing, 100049, China
[(c)] Shanghai Boreas Cryogenics Co., Ltd, Shanghai, 200434, China

ABSTRACT

The automatic temperature control electronics for the multi-stage Stirling-type pulse tube cryocooler (SPTC) is indispensable in simultaneously maintaining steady cooling temperatures for each stage in practical applications. A novel automatic temperature control method based on expert PID/fuzzy hybrid control method is proposed and its characteristics are elaborated. The design of the control electronics is depicted and the prototype has been tested on a two-stage SPTC providing cooling at 30 K and 85 K, and a three-stage SPTC with cooling temperatures of 90 K, 40 K and 10 K at stages, both developed in the authors' laboratory. Experimental results show that, with the novel control method and developed electronics, high temperature stability of ±0.3 K@85 K and ±0.2 K@30 K can be obtained for the two-stage SPTC and ±0.5 K@90 K, ±0.2 K@40 K, ±0.15 K@10 K are achieved for the three-stage one.
Keywords: Multi-stage, Stirling-type Pulse Tube Cryocooler, Temperature Control, High Stability.

1. INTRODUCTION

With the merits of low vibrations, high reliability, compact structure, high efficiency and long operation life, the Stirling-type pulse tube cryocooler (SPTC) has become one of the most expected cryocooler in a variety of special fields, such as in space and national defense. Recently, there is an increasing interest in providing multiple cooling temperatures in one space-borne cryogenic instruments. For instance, some space equipment has several detectors with different operating temperatures, and some need to simultaneously cool both the detector and optics since the cooled optics contributes to substantially minimize background thermal noise and thus can noticeably enhance the detecting sensitivity. Still some need to simultaneously cool the detector and to remove the parasitic heat loads originating from the support structures and electrical leads (Jensen et al., 2006; Ross, 2006; Jaco et al., 2008; Rabb and Tward, 2010). In order to achieve high signal/noise ratio, the SPTCs are needed to provide steady temperatures to the cooled device, and thus the automatic temperature control becomes a new request to the SPTC.

In recent years, with more and more multi-stage SPTCs been used for practical space missions, the corresponding temperature control electronics has also achieved noticeable developments. For example, in 2009, in cooperation with ITT Industries Space Systems Division, NGST (Colbert et al., 2009) worked out its control electronics of the Pulse Tube Cooler System for Advanced Baseline Imager (ABI) program in the mission of NOAA Geosynchronous Operational Environmental Satellite-R Series (GOES R), in which the electronics could provide a temperature stability of 100 mK peak-to-peak in short-term and ±500 mK in long-term, especially to the second stage.

Generally, there are two methods for the SPTC to achieve automatic temperature control. The first one is to adjust the electric input power. The advantage of this method is power-saving, but the control is relatively complicated owing to that the SPTC is a mechanical-thermodynamic coupled time-hysteresis system. The second one is to apply heat load automatically through thermal balance method. The obvious advantages of this method are simplicity and high precision of temperature control. But it needs the SPTC to provide more cooling powers to achieve the automatic temperature

control, and thus it wastes some cooling powers which reduces the cooling efficiency of the system. Especially in the cases of very low cooling temperatures, extra small cooling powers always need large input power. In the automatic temperature control of our multi-stage SPTC, the above two methods will be combined to achieve high temperature stability and power saving simultaneously.
In recent years, the authors' laboratory has made substantial progress in the development of SPTC, the developed SPTCs include single-stage, two-stage and three-stage, which cover the cooling temperature ranges from 300 K to 4 K, some types of single-stage SPTC have been applied into actual space applications. To meet the demands in space applications, the automatic temperature control system is also developed synchronously. The space-born control electronics for the single-stage SPTC has been reported (Tan, et al., 2015). In this paper, the automatic temperature control electronics for our multi-stage SPTCs (a two-stage SPTC with cooling temperatures of 30 K and 85 K and a three-stage SPTC with cooling temperatures of 10 K, 40 K and 90K) will be presented and the control method based on expert PID/fuzzy hybrid control will be described in detail.

2. COOLERS AND CONTROL ALGORITHM

2.1 Cooler Descriptions

Fig. 1 shows a photograph of a thermally-coupled two-stage coaxial SPTC (Tan and Dang, 2017). It employs one linear compressor, and typically, it can simultaneously achieve 0.6 W at 30 K and 3 W at 85 K with an electric input power of 300 W and a reject temperature of 300 K.

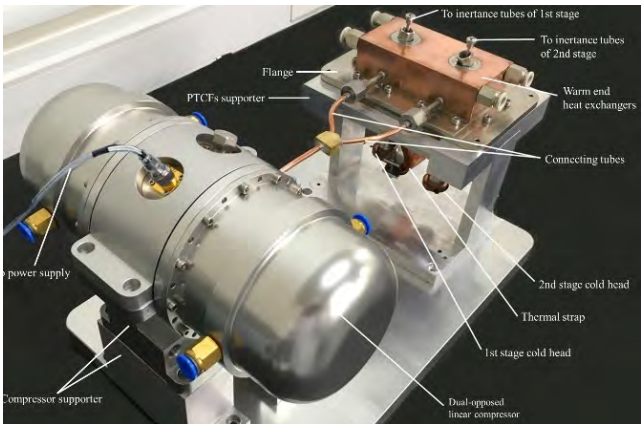

Figure 1: A photograph of the developed two-stage SPTC

Fig. 2 shows a photograph of a three-stage SPTC (Dang et al., 2018). One linear compressor drives for the first two stages and the other one connects to the three stage, with a total input power of 400 W, cooling capacities of 100 mW@10 K, 0.5 W@40 K and 2 W@90 K can be obtained at each stage.

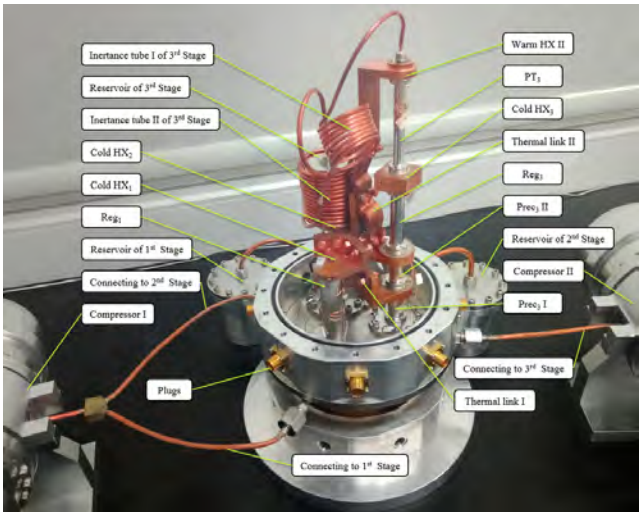

Figure 2: A photograph of the developed three-stage SPTC

2.1 Control algorithm

In the automatic temperature control of the multi-stage SPTC, both the methods of adjusting input power and automatically applying heat load by thermal balance method will be used. The two-stage SPTC is thermally-coupled, and part of the cooling power of the first stage will be used to precool the middle part of the second stage. Therefore, the temperature fluctuation of the first stage will affect the cooling performance and temperature stability of the second stage. Moreover, the two-stage SPTC is driven by only one linear compressor, and adjustment of the input power will influence both the cooling performances of the two stages. In consideration of these points, the temperature of the first stage will be controlled through thermal balance method while that of the second stage by adjusting the input power of the linear compressor.

Fig. 3 shows the closed-loop feedback control block diagram of the two-stage SPTC. Temperature sensors are installed at two cold tips to collect the temperature signals, which will be sent to signal amplifier part and transformed into voltage signals. After that, signals will be furtherly converted into digital signals and sent to controller. According to the designed expert PID/fuzzy hybrid control method, the digital signals will be compared with the set ones and proceeded, then the controller exports the digital control signals. After the digital to analogue(D/A) conversion, two actuators will act on the basis of the digital control signals with the power supply, adjusting the input power of the linear compressor and heat power of the first stage.

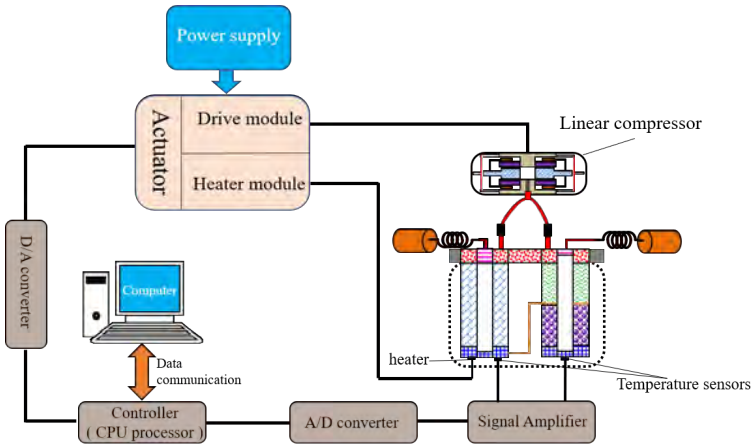

Figure 3: The control block diagram of the two-stage SPTC

Similar to the two-stage SPTC, the three-stage one also employs thermally-coupled staging construction. But the three-stage SPTC owns two linear compressors and three different cooling temperatures. Moreover, phase shifters of the third stage are precooled by the second stage, thus its cooling temperature stability plays a substantial role in the cooling performance and cooling temperature stability of the three stage. Fig. 4 illustrates the control block diagram of the three-stage SPTC.

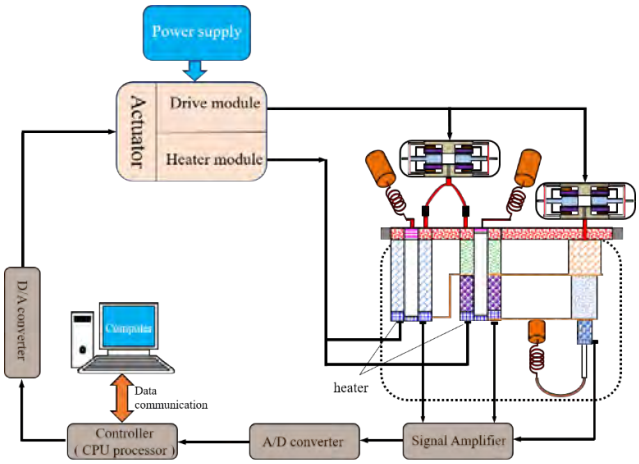

Figure 4: The closed-loop feedback control block diagram of the three-stage SPTC

The basic control loop is similar to that of the two-stage SPTC. The cooling temperature of the third stage reaches 10 K. The ratio of input power to cooling capacity is relatively large, and the third stage is driven by a separated linear compressor. In order to reduce input power and to promote the control precision of the cooling temperature, the temperature of third stage is controlled by adjusting the input power of the linear compressor through closed-loop control. For the first stage, part of its cooling power is used to precool both the middle part of the second stage and first part of the third stage. For the second stage, part of the cooling power is used to precool the second part of the third stage. One compressor and two heaters which can respectively adjust the input power and extra joule heat on the cold tips, are employed to ensure the temperature stability of the first two stages.
The SPTC is a complicated electrical-mechanical-thermodynamic system. Especially for the multi-stage ones, performance of each stage will influence others. It is difficult to establish the accurate mathematical model and to get its transfer function. The expert PID control algorithm is a kind of control algorithms based on the classical PID algorithm. It intelligently uses the knowledge on the control objects and control rules to design the controller. The PID parameters can be designed based on the experts' experience accumulated by many tests on the SPTCs. Moreover, as the transfer function of the SPTC is unknown, fuzzy control is very appropriate for the control. Combined these, a novel control method named expert PID/fuzzy hybrid control is proposed to achieve the automatic temperature control of the multi-stage SPTCs.
For the temperature signals of both stages, the incremental PID will be used in the discretization which can be expressed as Eq. (1) to Eq. (3):

$$u_m(k) = u_m(k-1) + k_n \left\{ k_P \left[e_m(k) - e_m(k-1) \right] + k_S k_I e_m(k) + k_D \left[e_m(k) - 2e_m(k-1) + e_m(k-2) \right] \right\} \quad \text{Eq. (1)}$$

$$\Delta e(k) = e(k) - e(k-1) \quad \text{Eq. (2)}$$

$$\Delta e(k-1) = e(k-1) - e(k-2) \quad \text{Eq. (3)}$$

where k is the sampling sequence number, $u_m(k)$ (m=1, 2 or 3, represents the number of the stage) is the controlled parameter at the moment of k, $e(k)$ and $e(k–1)$ are the errors at the moment of k and $k–1$. k_P is the proportional gain, k_I is the integral gain, k_D is the derivative gain, and k_S is the integral separation coefficient. k_n(n=1,2) is the control coefficient, k_1>1 and 0<k_2<1.
Generally, the operation of the SPTCs will be very steady if the working environmental variation is small. The automatic temperature control system is mainly used to resist large enviromental change and cooler performance deterioration of long time operation. The complete control algorithm of the SPTC is shown in Fig. 5 and the detailed flow chart of the expert PID/fuzzy control algorithm is shown in Fig.6. According to the value and variation of the errors, the detailed expert PID/fuzzy hybrid control algorithm of the multi-stage SPTCs can be summarized as the following four cases.

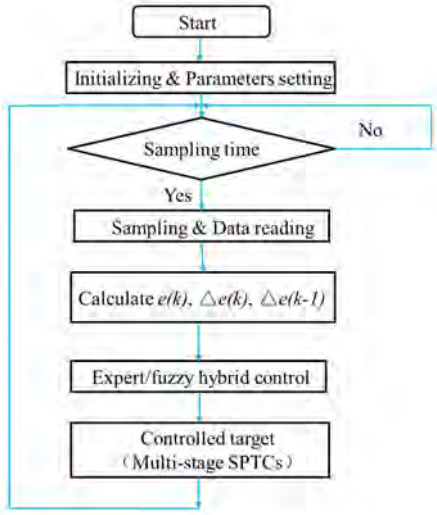

Figure 5: The control algorithm of the whole SPTC

Case 1: $e_m(k)>L_1$. Here L_1 is a relatively large set limit value. In this case, the absolute value of error is very large, which mostly occurs at the start-up process. At this moment, the input power of the compressor should be kept maximum to decrease the absolute value of the error at the maximum rate despite of the variation tendency of the deviation. The control process can be regarded as an open-loop control.

Case 2: $e_3(k)>L_1$, $e_2(k)<L_1$ or $e_1(k)<L_1$. In this case, the difference between the current cooling temperatures of the first stage and the set one becomes small, while those of the second stage and third stage are not. The electric input power of the compressor which supplies the first two stages will be set to a specific value P1 while that of the compressor supplying the third stage separately will be kept to the maximum.

Case 3: $L_2<|e_m(k)|<L_1$. Here, L_2 is another set limit value which is smaller than L_1. Under this circumstance, the differences between two cooling temperatures and the set ones are small. Then, the electric input power of the compressor which supplies the first two stages will be set to a specific value P_1 and that of the compressor supplying the third stage will be set to P_2.

Case 4: $|e_m(k)|<L_2$. If $|e_1(k)|<L_2$, the expert PID control of heat balance will work, and the heat load applied to the first stage will be automatically regulated. If $|e_2(k)|<L_2$, the expert PID control of electric input power of the first compressor will work to adjust the input power of the compressor to make the cooling temperature of the second stage stable. If $|e_3(k)|<L_2$, the expert PID control of electric input power of the second compressor will work. The control algorithms of the expert PID controls mentioned above are the same. The specific is as follow: if $e_m(k)\Delta e_m(k)\geq 0$, general control works to reserve the variation tendency of the error and to reduce the absolute value of error, $k_n = k_2$ and $k_S=0$. If $e_m(k)\Delta e_m(k)<0$ and $\Delta e_m(k)\Delta e_m(k-1)>0$ or $e_m(k)=0$. The absolute value of error changes with a decreasing rate, or the control is in the equilibrium state, and the output of the controller should be kept constant. If $e_m(k)\Delta e_m(k)<0$ and $\Delta e_m(k)\Delta e_m(k-1)<0$. The error is in the extreme state, the absolute value of error is not very large. General control can be applied, $k_n = k_2$ and $k_S=0$. If $|e(k)|<\varepsilon$. Here ε is a relatively small set value. It means the absolute value of error is already very small, and the integral control process should be added to reduce the steady-state error, $k_n = k_2$ and $k_S=1$.

For the two-stage SPTC, the control algorithm is very similar. In Case 4, the expert PID control of heat balance works on the first stage and that of input power takes effect on the second stage.

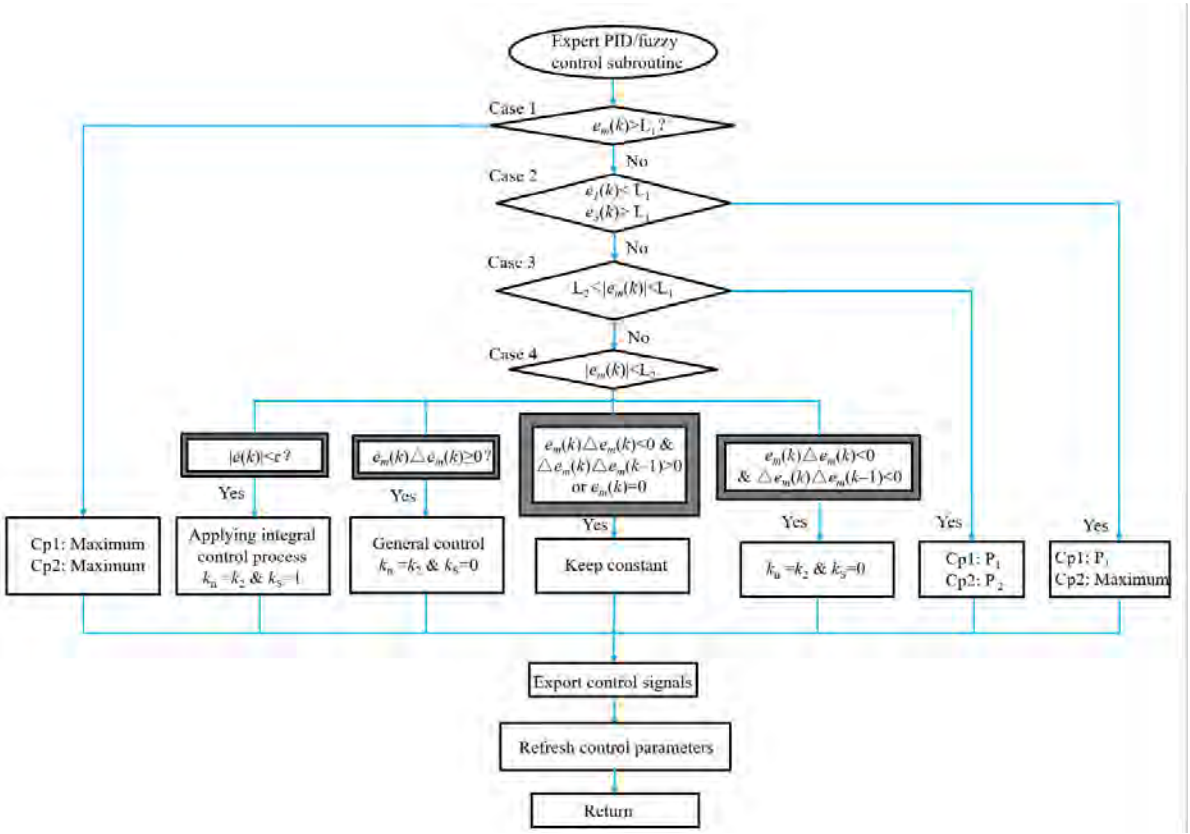

Figure 6: The flow chart of the expert PID/fuzzy control algorithm of the SPTC

3. HARDWARE APPARATUS AND CONTROL SOFTWARE

Table 1 gives a summary of operating parameters of the developed two-stage and three-stage SPTC, and Table 2 shows the key design goals of the control electronics. At present, the temperature stability and energy conversion efficiency are the most concerned. Low mass and wide temperature adaptability are also important terms for the future applications.

Table 1. A summary of operating parameters of two-stage and three stage SPTCs

Parameters	Two-stage SPTC	Three-stage SPTC
Operating frequency	57 Hz	57 Hz (1st, 2nd stages), 32 Hz (3rd stage)
Electric input power	200 W	290 W (1st, 2nd stages), 80 W (3rd stage)
Charge pressure	3 MPa	3.3 MPa (1st, 2nd stages), 1.2 MPa (3rd stage)
Cooling performances	1W @85 K, 0.5 W@30 K	0 W@90 K, 0 W@40K, 100 mW@10 K

The control electronic consists of three parts. The first one is the signal process module, in which the design software of sinusoidal pulse width modulation (SPWM) output and that of the expert PID/fuzzy hybrid control are developed and downloaded from the computer. The second part is the H bridge drive module. The bus voltage is 42 V DC, while the linear compressor employs the AC current to achieve periodical piston compression and expansion. Therefore, with the SWPM signal acting as the control signal, an integrated chip named DRV8412 from Texas Instrument Company is used to efficiently drive the linear compressor under DC power supply. The third part is the temperature collecting module, which mainly includes thermometers, sampling circuit and signal amplifier.

Table 2. Key design goals of the control electronics

Parameters	Design goal
Bus voltage	42 V (DC)
Total power	0-300 W, for one compressor
Frequency of modulated sine wave	10-100 Hz

Efficiency (DC to AC)	>90%
Temperature stability	< ±0.5 K for each stage
Mass	<0.5 kg（not including mounting box）
Geometry dimensions	180 mm*160 mm*100 mm (L * W * H)
Operating temperature adaptability	-40 ºC to 60 ºC

4. EXPERIMENTAL SETUP AND TESTS RESULTS

The control electronic is worked out, and experimental tests of them coupling with SPTCs have been carried out. At first, the automatic cool down process has been tested. Fig.7(a) and (b) shows the automatic cool-down curves of the two-stage and three-stage STPC with the control of the developed electronics devices, respectively. For the two-stage SPTC, a heat load of 1 W is applied on the first stage and 0.5 W is applied on the second stage at the time of start-up. Fig.7(a) shows that it takes about 18 mins for the first stage to achieve the target cooling temperature of 85 K, and 30 mins are needed for the second stage to achieve the cooling temperature of 30 K. Moreover, there are no overshooting in the cool-down processes of both stages, which verifies the control effect of the developed expert PID/fuzzy control method. For the three-stage SPTC, a heat load of 100 mW is added at the time of start-up. Fig.7(b) shows that similar circumstances also occur in the cool-down process of the three stages, there is no temperature overshooting under the control of the developed electronics. It takes about 60 mins for the first two stages to achieve the aimed cooling temperature of 90 K and 40 K. While 80 mins is needed for the third stage to obtain the cooling temperature of 10 K.

Then, long-term temperature stabilities of the SPTCs with the developed control electronics are also tested. Fig.8(a) illustrates the temperature variations of the two-stage SPTC in long-time operation. Once the cooler is in steady state, the temperature fluctuation of the first stage at 85 K is smaller than 0.5 K and that of the second stage at 30 K is below 0.2 K in 2 hours. Fig. 8(b) shows the long-term test results of the three-stage SPTC. Temperature stabilities of ±0.5 K, ±0.2 K and ±0.15 K can be achieved for the three stages operating at the cooling temperatures of 90 K, 40 K and 10 K, respectively. The experimental results of both the two-stage and three-stage SPTCs verify that the proposed novel expert PID/fuzzy control method and the developed control electronics can provide automatic temperature control for the multi-stage SPTCs with high stability.

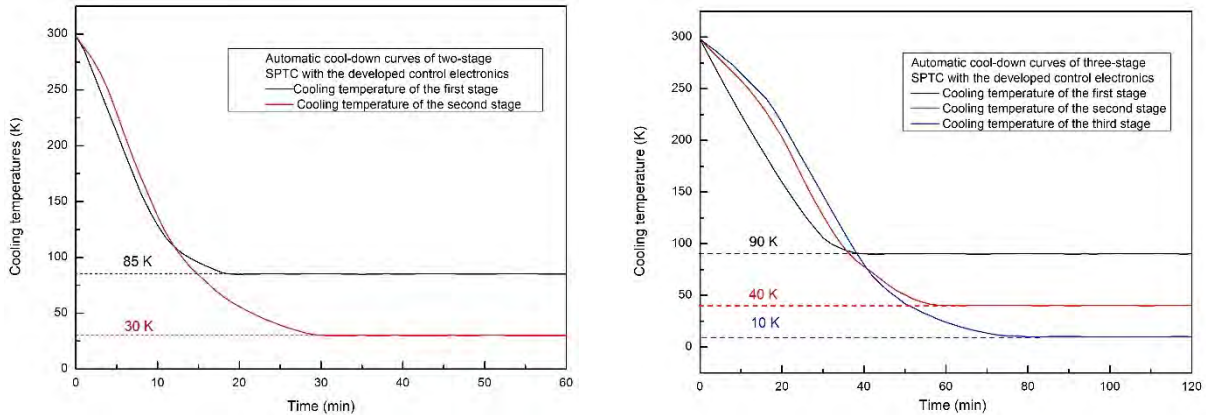

Figure 7: (a) Cool-down curve of two-stage SPTC. (b) Cool-down curve of three-stage SPTC

Then, long-term temperature stabilities of the SPTCs with the developed control electronics are also tested. Fig.8(a) illustrates the temperature variations of the two-stage SPTC in long-time operation. Once the cooler is in steady state, the temperature fluctuation of the first stage at 85 K is smaller than 0.5 K and that of the second stage at 30 K is below 0.2 K in 2 hours. Fig. 8(b) shows the long-term test results of the three-stage SPTC. Temperature stabilities of ±0.5 K, ±0.2 K and ±0.15 K can be achieved for the three stages operating at the cooling temperatures of 90 K, 40 K and 10 K, respectively. The experimental results of both the two-stage and three-stage SPTCs verify that the proposed novel expert PID/fuzzy control method and the developed control electronics can provide automatic temperature control for the multi-stage SPTCs with high stability.

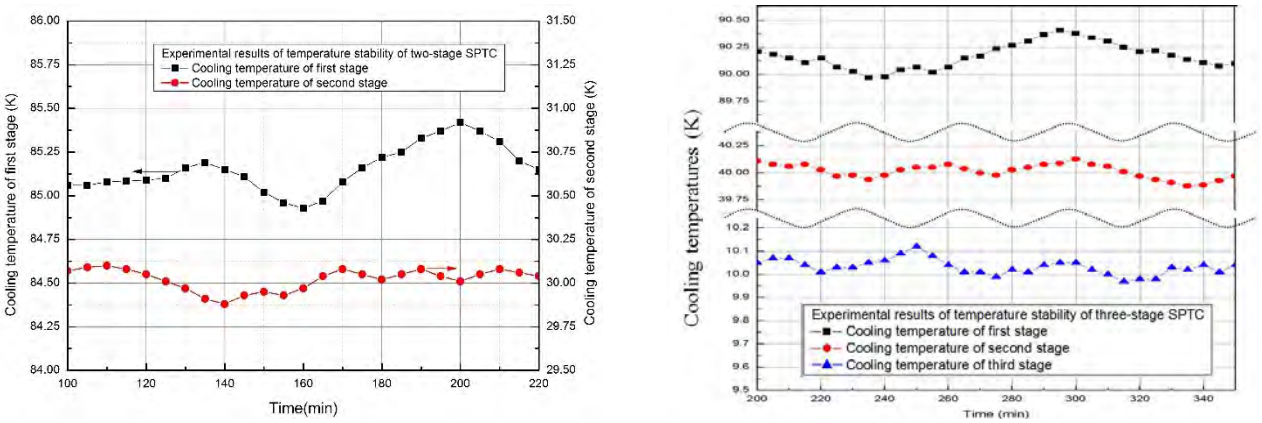

(a) (b)

Figure 8: (a) Experimental tests results of temperature stability of two-stage SPTC, (b) Temperature stability of three-stage SPTC

Moreover, temperature stabilities of the SPTCs with additional external heat disturbence are also tested, especailly for the stage with lowest temperature. Fig.9(a) and (b) show the temperature variations of the two-stage SPTC with additional external heat disturbence of 0.1 W appling at the second stage, and that of the three-stage SPTC with 20 mW appling at the third stage, respectively. During the whole process, the temperature fluctuation of the second stage at 30 K is below 0.2 K, which shown in Fig.9(a). Moreover, Fig. 9(b) shows the stability test results of the three-stage SPTC with additional external heat disturbance of 20 mW. Under this circumstance, a temperature stabilitie of ±0.15 K can be achieved at the cooling temperatures of 10 K for the third stage.

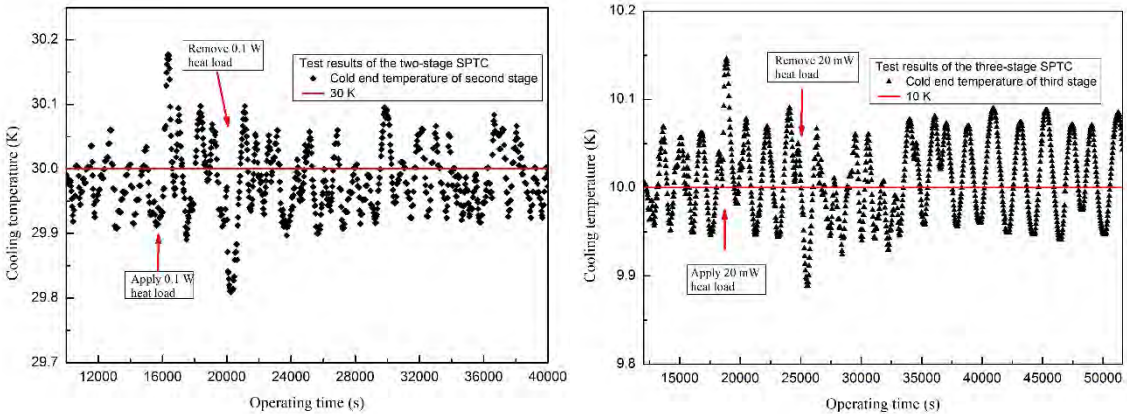

(a) (b)

Figure 9: (a) Experimental tests results of temperature stability of two-stage SPTC with external disturbance, (b) Temperature stability of three-stage SPTC with external disturbance.

5. CONCLUSIONS

In this paper, a novel automatic temperature control method named expert PID/fuzzy hybrid control method is proposed and its control algorithm is detailed elaborated. The design of the control electronics is depicted and the prototype has been tested on a two-stage SPTC providing cooling at 30 K and 85 K, and a three-stage SPTC with cooling temperatures of 90 K, 40 K and 10 K at stages. The experimental results show that, with the novel control method and developed electronics, temperature stabilities of ±0.3 K@85 K and ±0.2 K@30 K can be obtained simultaneously for the two-stage SPTC and ±0.5 K@90 K, ±0.2 K@40 K, ±0.15 K@10 K are achieved for the three-stage one.

ACKNOWLEDGEMENTS

This work was financially supported by The Aeronautical Science Foundation of China (No. 20162490005) and Shanghai Municipality (Nos.18511110100, 18511110101 and 18511110102).

REFERENCES

Colbert R., Pruitt G., Nguyen T., et al., 2009. ABI cooler system protoflight performance. Cryocoolers 15, 49–54.

Dang HZ., Bao DL., Zhang T., et al., 2018. Theoretical and experimental investigations on the three-stage Stirling-type pulse tube cryocooler using cryogenic phase-shifting approach and mixed regenerator matrices. Cryogenics 93, 7-16.

Jaco C., Nguyen T. and Tward E., 2008. High capacity two-stage coaxial pulse tube cooler. Adv Cryog Eng 53, 530–537.

Jensen S.M., Hansen G., Nast T. and Roth E., 2006. Cooling the GIFTS FPA: summary and analysis of engineering test results performed at SDL using the Lockheed Martin two-stage cryocooler. Adv Cryog Eng 51,1513–1520.

Rabb J., Tward E., 2010. Northrop Grumman Aerospace Systems cryocooler overview. Cryogenics 50, 572–581.

Ross Jr RG., 2006. Space coolers: a 50-year quest for long life cryogenic cooling in space. In: Timmerhaus KD and Reed RP, editors. Cryogenic engineering: fifty years of progress, Springer Publishers, New York, 225–284.

Tan J., Dang HZ., Zhao YB., et al., 2015. Investigations on the automatic temperature control electronics of single stage space Stirling-type pulse tube cryocooler. Proceedings of 24th International Congress of Refrigeration, Yokohama, Japan, IIF/IIR, 351.

Tan J. and Dang HZ., 2017. Theoretical and experimental investigations on the cooling capacity distributions at the stages in the thermally-coupled two-stage Stirling-type pulse tube cryocooler without external precooling. Cryogenics 82, 48-61.

Manuscript ID: 975
DOI: 10.18462/iir.icr.2019.0975

Computational fluid dynamics modeling and experimental verification of a Stirling-type pulse tube cryocooler with a cooling capacity of 700 W at 77 K

Jiaqi LI [(a), (b)], Jun TAN [(a), (c)], Rui ZHA [(a), (b)], Tao ZHANG [(a), (b)], Yongjiang ZHAO[(a), (b)], Bangjian ZHAO[(a), (b)], Haizheng DANG [(a), (c)]

[(a)] State Key Laboratory of Infrared Physics, Shanghai Institute of Technical Physics, Chinese Academy of Sciences, Shanghai, 200083, China, bb22ufo@163.com; haizheng.dang@mail.sitp.ac.cn
[(b)] University of Chinese Academy of Sciences, Beijing, 100049, China
[(c)] Shanghai Boreas Cryogenics Co., Ltd, Shanghai, 200434, China

ABSTRACT

This paper presents the computational fluid dynamics (CFD) modeling and optimization of a SPTC with a cooling capacity of 700 W at 77 K for cooling large-scale high-T_c superconducting facilities. This SPTC consists of two cold fingers driven by an 18 kW linear compressor. A two-dimensional CFD model is established to investigate the flow and heat transfer process inside the regenerator. For the aimed high cooling capacity, the flow straighteners become crucial to minimize the turbulence flows in the system. The distribution of temperature in the regenerator is non-uniform due to the flow conditions, which makes the optimization more difficult. The SPTC is worked out based on the theoretical analyses. The cooling capacity of 700 W at 77 K with a relative Carnot efficiency of 11.3% has been achieved experimentally, slightly lower than the simulated 13%.
Keywords: CFD, Heat Transfer, Large Scale, Pulse Tube, Regenerator.

1. INTRODUCTION

In recent years, with the rapid developments of the superconducting technology, the characteristics of no-resistance, high current density and Meissner effect have attracted many fields such as the electric elements, transportation, medical instruments, military defense and scientific experiments. There is an increasing demand for cryogenic systems of the applications mentioned above, especially the high-temperature superconducting electrical technology. Cryocoolers are the key component of cryogenic systems. Compared to conventional cryocoolers such as GM and Stirling cryocoolers, the Stirling-type pulse tube cryocooler (SPTC) without any moving part at the cold head is a better choice due to its long-life and high reliability.

The SPTC is composed of two essential parts: the linear compressor and the pulse tube cold finger (PTCF). There are still some obstacles in the design of a PTCF when the cooling capacity is larger than 500 W. Some special phenomena, such as the non-uniform temperature distribution inside the regenerator and turbulence flows, will occur.

Several proposals were put forward to reduce the influence mentioned above. Imura et al. (2008) developed an in-line SPTC with the cooling capacity of 180 W at 80 K, in which the hard copper meshes were inserted inside the regenerator to reduce the impact of the turbulent flow. Potratz et al. (2008) built a large capacity in-line SPTC with a refrigeration capacity of 1 kW at 77 K by using a 20 kW dual-opposed pressure wave generator. Sophisticated geometry was applied and the streaming had been minimized successfully. Caughley et al. (2015) combined three in-line pulse tube cryocooler with only one diaphragm pressure wave generator, which provided 1250 W of cooling power at 77 K with a Carnot efficiency of 15%. Chart's coaxial SPTC could achieve 650 W of cooling power at 80 K with 15 kW of input power (Spoor, 2014; Spoor, 2016), for which computational fluid dynamics (CFD) were applied to analyze the flow inside the aftercooler and cold head for optimization.

In spite of these studies, rare investigations have been worked on the two coaxial cold fingers coupled with only one linear compressor. In this paper, the CFD modeling and optimization of a SPTC with a cooling capacity of 700 W at 77 K for cooling large-scale high-Tc superconducting

facilities will be presented. A two-dimensional CFD model is established to investigate the flow and heat transfer process inside the regenerator. For the high cooling capacity, the flow straighteners become crucial to minimize the turbulence flows in the system. The distribution of temperature in the regenerator is non-uniform due to the flow, which results in much difficulties in optimization. The SPTC with two cold fingers and one compressor is then worked out based on the theoretical analyses. And the theoretical and experimental results will be compared and discussed.

2. MODEL SETUP

The one-dimensional model is widely used in the design and optimization of the mid-sized SPTC because of the fast speed of the calculation. With the rapid development of the SPTC, the cooling capacity increases gradually which makes the size become larger, and the ratio of the diameter to the length of tubes becomes higher. As a result, the accuracy of the one-dimensional model would decrease. In recent years, to acquire more accurate results and detailed descriptions of the heat and mass transfer process inside the SPTC, two-dimensional (2D) models have been built based on ANSYS Fluent®, and then characteristics of the flow and heat transfer could be presented. However, most studies mainly focus on the mid-sized and micro sized SPTCs, few investigations are conducted on the large capacity which is higher than 300 W using 2D modeling. In this paper, a 2D axis-symmetric CFD model of SPTC with a cooling capacity of 700 W will be established using ANSYS Fluent®, and the characteristics of the SPTC will be studied theoretically and experimentally.

2.1. CFD Model

The typical SPTC has two parts: the linear compressor and the PTCF. The linear compressor is composed of two pistons, two cylinders, two moving-coils, the return irons, the permanent magnet, the flexure springs. The clearance seal technology is applied in the linear compressor. The PTCF consists of the regenerator, the pulse tube, the heat exchangers, the inertance tubes, and the reservoir. The two parts are connected by a tube.

Fig. 1 shows a schematic of the simulation model. Fig. 1 (a) shows a schematic of one compressor coupled with two cold fingers. Since the two cold fingers are the same, to simplify the model of the SPTC, it only includes one cold finger and is set to be axis-symmetric as shown in Fig. 1 (b). The flow straightener is set to be filled with porous materials. The linear compressor in the model is regarded as the pressure inlet.

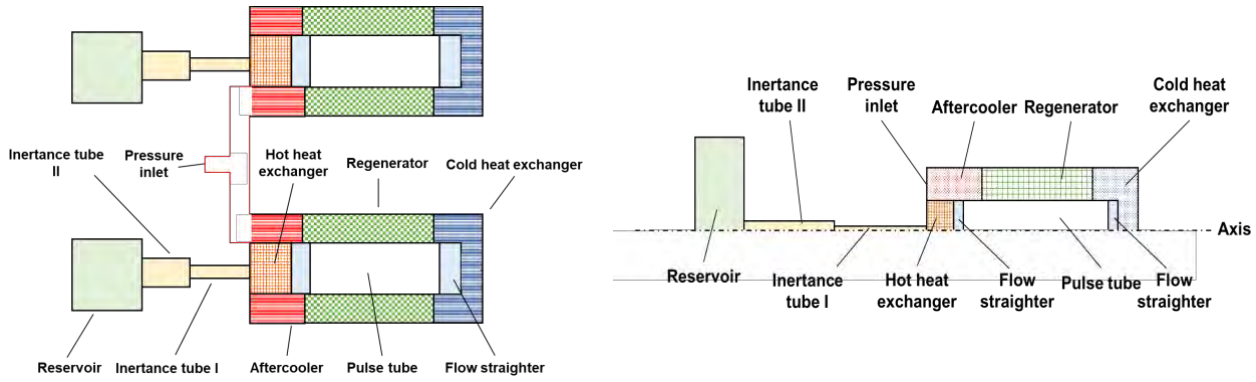

(a) (b)

Figure 1: Schematic of the simulation model

Table 1 shows the boundary conditions of the model. The components which are placed inside the vacuum chamber is set to be adiabatic. The wall temperatures of other components are set to be 300 K.

Table 1. Boundary conditions

Component name	Boundary condition
Aftercooler	300 K (Wall temperature)
Regenerator	Adiabatic
Cold heat exchanger	Adiabatic
Pulse tube	Adiabatic
Hot heat exchanger	300 K (Wall temperature)
Inertance tube 1	300 K (Wall temperature)
Inertance tube 2	300 K (Wall temperature)
Reservoir	300 K (Wall temperature)

The inlet pressure wave can be defined by using the User Defined Function. So, the inlet pressure wave can be given by (Fluent Inc., 2006):

$$p_{in} = p_0 + \Delta p \sin 2\pi f t \quad \text{Eq. (1)}$$

where Δp is the amplitude of the dynamic pressure, f is the operating frequency, and p_0 is the charge pressure of the whole system. The value of f and the p_0 will be given after the optimization. The value of Δp can be calculated based on the results of studies in the same laboratory (Dang, 2012; Dang, 2015).
In the simulation, the governing equations of the model including the mass conservation equation, the momentum conservation equation and the energy conservation equation are given as follows (Fluent Inc., 2006):

$$\frac{\partial \rho_f}{\partial t} + \nabla \cdot \left[\rho_f \vec{u}\right] = 0 \quad \text{Eq. (2)}$$

$$\frac{\partial}{\partial t}\left[\rho_f \vec{u}\right] + \nabla \cdot \left[\vec{u}\vec{u}\right] = -\nabla p + \nabla \cdot \left(\bar{\bar{t}}\right) \quad \text{Eq. (3)}$$

$$\frac{\partial}{\partial t}\left[\rho_f E_f\right] + \nabla \cdot \left[\vec{u}\left(\rho_f E_f + p\right)\right] = \nabla \cdot \left[k_f \nabla T + \left(\bar{\bar{t}} \cdot \vec{u}\right)\right] \quad \text{Eq. (4)}$$

where ρ_f is the density, $\vec{u}$ is the velocity, p is the static pressure, T is the temperature, k_f is the thermal conductivity, $\bar{\bar{t}}$ is the stress tensor and E_f is the total energy of the fluid.
And the mass and the momentum conservation equations of the porous media are (Fluent Inc., 2006):

$$\frac{\partial}{\partial t}\left[\varepsilon \rho_f\right] + \nabla\left[\varepsilon \rho_f \vec{u}\right] = 0 \quad \text{Eq. (5)}$$

$$\frac{\partial}{\partial t}\left[\varepsilon \rho_f \vec{u}\right] + \nabla\left[\varepsilon \rho_f \vec{u}\vec{u}\right] = -\varepsilon \nabla p + \nabla\left(\varepsilon \bar{\bar{t}}\right) + S_i \quad \text{Eq. (6)}$$

where ε is the porosity of the medium, S_i is the source term for the momentum conservation equation, S_i consists of two parts which are the Darcy term and the Forchheimer term (Zhao and Dang, 2016):

$$S_i = -\left[\frac{\mu}{\alpha}\vec{u} + \frac{C_2}{2}\rho_f |\vec{u}| \vec{u}\right] \quad \text{Eq. (7)}$$

where α, C_2 are the permeability and the inertial resistance factor.
The energy conservation equation based on the thermal equilibrium mode is given as follow:

$$\frac{\partial}{\partial t}\left[\varepsilon \rho_f E_f + (1-\varepsilon)\rho_s E_s\right] + \nabla \cdot \left[\vec{u}\left(\rho_f E_f + p\right)\right] = \nabla \cdot \left[k_{eff} \nabla T + \left(\bar{\bar{t}} \cdot \vec{u}\right)\right] \quad \text{Eq. (8)}$$

where k_{eff} is the effective thermal conductivity, ρ_s is the density of the solid and E_s is the total energy of the solid.

2.2. Optimizations of the Dimensional and Operating Parameters

Fig. 2 shows the optimization results. The two key components of the regenerator and pulse tube are optimized with the dimensional parameters of diameter and length. In Fig. 2 (a), it can be observed that there exists an optimal ratio (diameter to length) for the pulse tube to obtain the largest cooling capacities. The cooling power is more than 700 W as expected. Based on that, the radius and the length of the pulse tube are set to be 21 mm and 72 mm, respectively. Fig. 2 (b) shows the optimization results of the regenerator. In this section, the matrix inside the regenerator is the 400-mesh stainless steel (SS) screen. Considering the design goal, the outer radius and the length of the regenerator are set to be 42.5 mm and 52 mm, respectively.

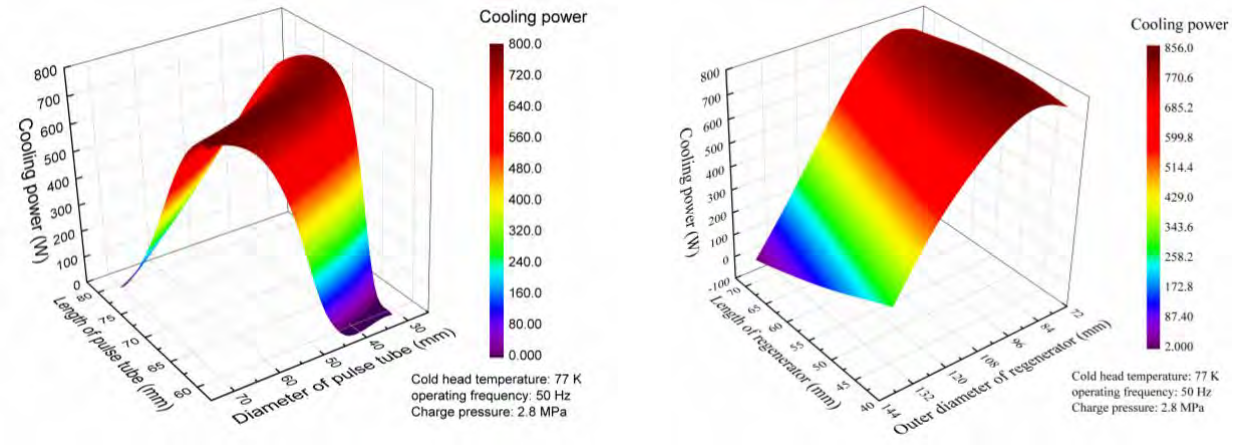

(a) (b)

Figure 2: Optimization results of the dimensions (a) pulse tube (b) regenerator

Fig. 3 shows the variations of cooling power with different operating frequencies and charge pressures. It can be observed that the cooling power is largest when the operating frequency is at around 53 Hz. And the cooling power will increase with the increasing the charge pressure. However, the charge pressure cannot be too high. The additionally added thickness of the regenerator and other components to ensure the mechanical strength for safety will bring more conduction loss which will decrease the cooling power. Considering the design goal, the charge pressure is set to be 2.8 MPa. And the amplitude of the dynamic pressure can be calculated as 0.26 MPa (Dang et al., 2016).

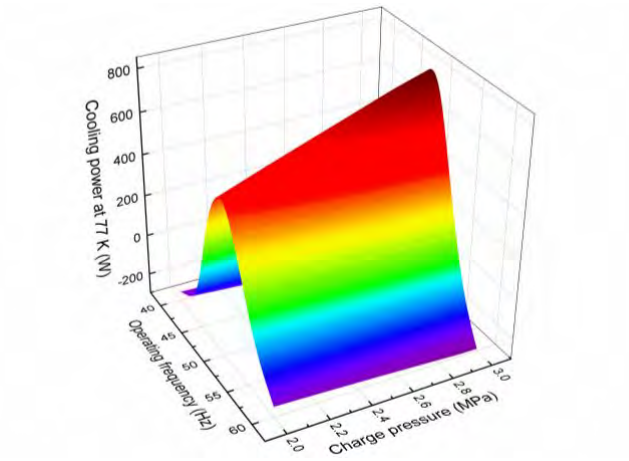

Figure 3: Optimizations of the frequency and charge pressure

3. SIMULATION RESULTS

3.1. Temperature Distribution and Transient Velocity Streamlines

The analysis of the temperature distribution and the transient velocity streamlines helps to investigate the internal process, which is beneficial for the design of the flow straightener structure.

Fig. 4 shows the temperature distribution and the streamlines inside the pulse tube. In Fig. 4 (a), the changes of the temperature are steady. The gas piston can be easily found in the middle of the pulse tube. The largest temperature gradient exists in the area between 14 mm and 43 mm when $\varphi = 0$. And this part moves to the area between 31 mm and 45 mm when $\varphi = 3\pi/2$. Fig. 4 (b) shows the transient velocity streamlines inside the pulse tube during a cycle. Five phases are chosen to show the typical conditions of the flow. The flow in all five phases are uniform and no vortex occurs in the process, which indicates that the flow straightener works well.

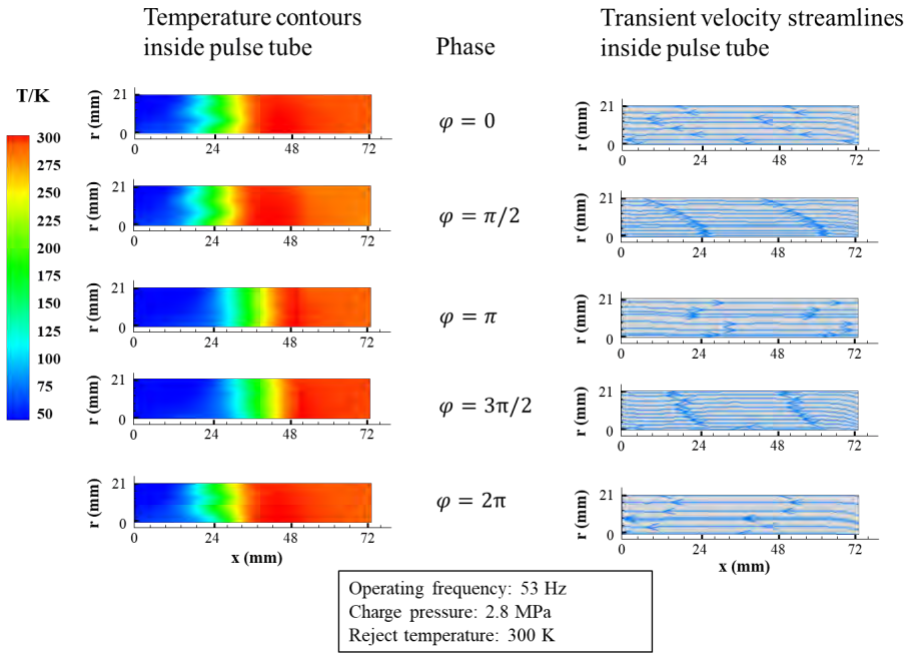

Figure 4: Temperature contours and transient velocity streamlines inside pulse tube

Fig. 5 shows the temperature contours and transient velocity streamlines inside the regenerator. In Fig. 5 (a), the temperature changes slightly during a cycle. But there still exists non-uniform temperature distribution. The phenomenon occurs in the area of 25 mm to 30 mm and that of 40 mm to 45 mm. Although the maximum temperature difference reaches 100 K, the flow inside the regenerator is stable and no vortex occurs.

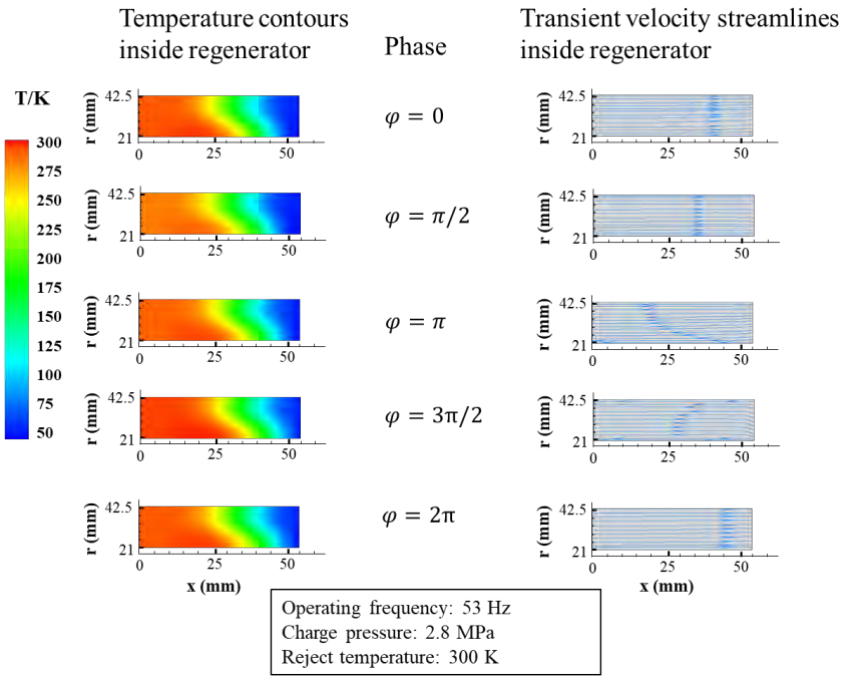

Figure 5: Temperature contours and transient velocity streamlines inside regenerator

3.2. Dynamic Parameters

Fig. 6 shows the dynamic pressure and the mass flow rate inside the pulse tube and regenerator. In Fig. 6 (a), the phase shift of the mass flow rate between inlet and outlet of the pulse tube is 0.035π. The difference of the mass flow rate amplitude between the inlet and outlet of pulse tube is 58 g/s. The phase shift and amplitude variation of the dynamic pressure are small which can be hardly found in the figure. It can be observed that the phase difference between the dynamic pressure and mass flow rate at the inlet of the pulse tube is 0.07π. In Fig. 6 (b), the pressure drop along the regenerator is 0.075 MPa. The phase shift of the dynamic pressure between inlet and outlet is 0.05π. The phase shift of the mass flow rate between inlet and outlet is 0.14π. The difference of the mass flow rate between inlet and outlet of the regenerator is 18.16 g/s, which is much smaller than that of the pulse tube. And the phase difference between the mass flow rate and the pressure wave is 0.105π at the inlet of the regenerator and 0.05π at the outlet, respectively.

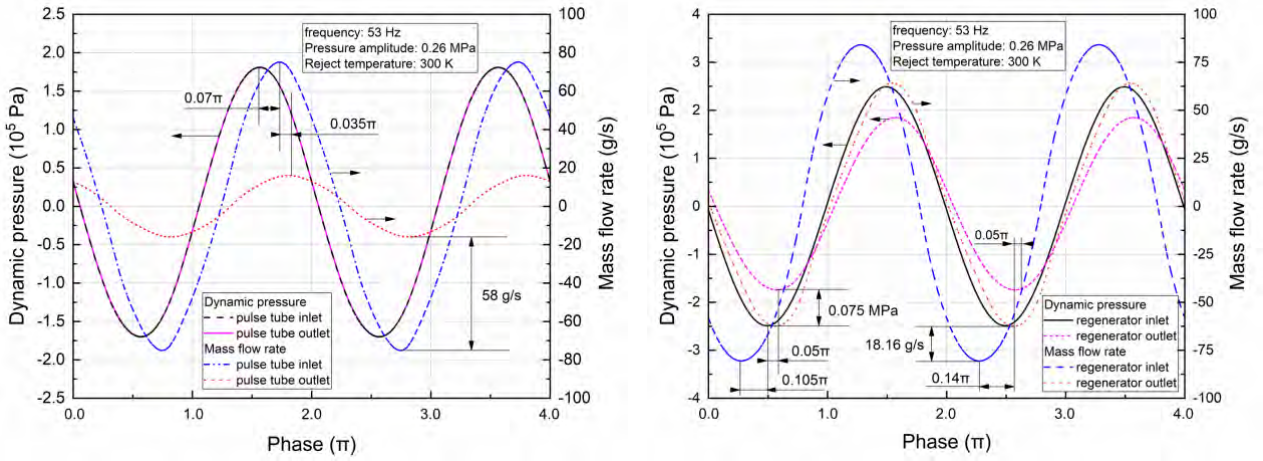

Figure 6: Dynamic pressure and mass flow rate inside (a) pulse tube (b) regenerator

4. EXPERIMENTAL VERIFICATIONS

4.1. Structure Design

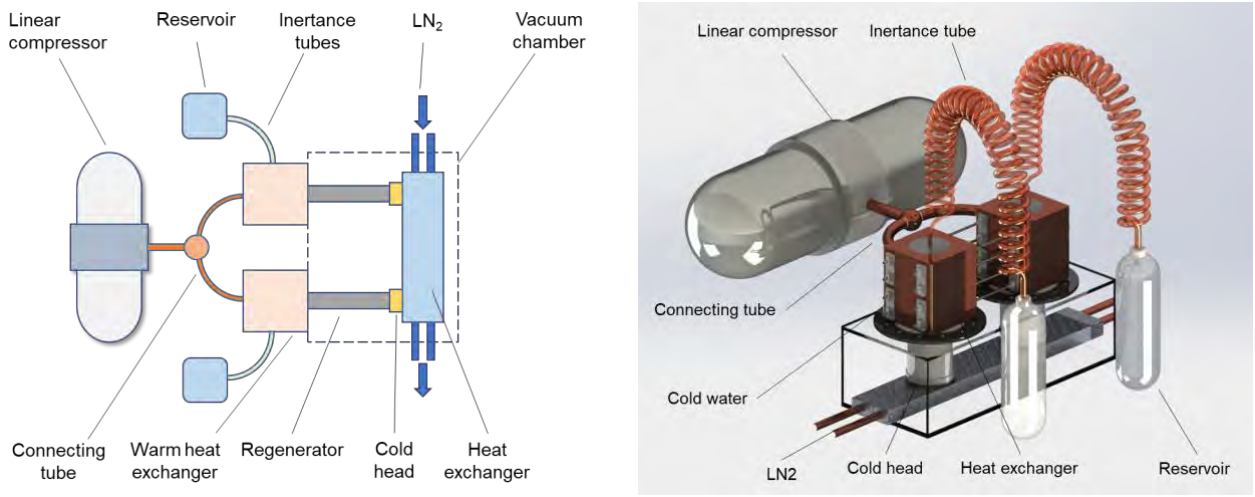

Figure 7: (a) Schematic of the SPTC (b) 3D model of the SPTC

The aimed SPTC which can provide 700 W at 77 K consists of one single compressor and two coaxial PTCFs. Fig. 7 shows a schematic and the three-dimensional (3D) model of the design. The linear compressor and two PTCFs are connected by a Y-shaped copper tube. The two cold fingers

have the same design, and their cold heads are attached to a heat exchanger to transfer the cooling power to cool the liquid nitrogen. The cold fingers are put into a vacuum chamber. The hot heat exchangers are cooled by cycling cold water.

4.2. Experimental Results

Fig. 8 shows the experimental results. The cooling power rises with the increasing cold tip temperature. The cooling power at 77 K reaches 700 W with an input power of 18 kW. The relative Carnot efficiency of the SPTC is 11.3%, which is slightly lower than the theoretical one. The experimental and tested results show the similar changing trends. The reason for limitation of the efficiency between 80 K to 100 K may be that the match between the compressor and cold finger changes when the working status is different.

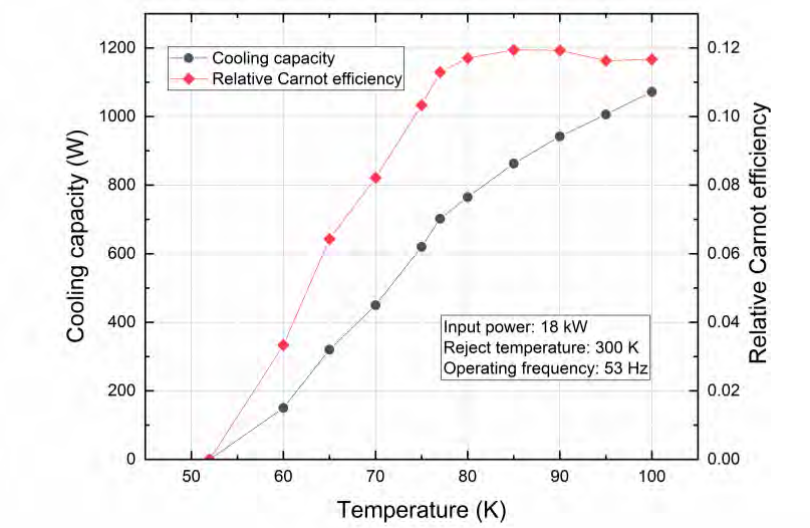

Figure 8: SPTC test results

5. CONCLUSIONS

This paper presents the CFD modeling and experimental verification of a SPTC with a cooling capacity of 700 W at 77 K. This SPTC consists of two coaxial cold fingers coupled with an 18 kW linear compressor. A two-dimensional CFD model is established to investigate the flow and heat transfer process inside the regenerator.

For the high cooling capacity, the flow straighteners become crucial to minimize the turbulence flows in the system. The distribution of temperature in the regenerator is non-uniform due to the flow and the gravity, which makes the optimization more difficult. In the testing, the flow straighteners are designed in detail and the simulation results show that the flow straightener work well. No vortex occurs in the pulse tube and thus the flows inside both regenerator and pulse tube are steady. The gas piston inside the pulse tube is stable and its boundary is clear.

The SPTC is worked out based on the theoretical analyses. A cooling capacity of 700 W at 77 K has been achieved experimentally with a relatively Carnot efficiency of 11.3%, slightly lower than the simulated 13%. The experimental and simulated results show similar changing trends.

ACKNOWLEDGEMENTS

This work is financially supported by the Aeronautical Science Foundation of China (No. 20162490005) and Shanghai Municipality (Nos. 18511110100, 18511110101, 18511110102).

NOMENCLATURE

C_2	inertial resistance factor (m^{-1})	Greek symbols	
E	specific energy ($J\ kg^{-1}$)	α	permeability (m^2)

f	operating frequency (Hz)	ε	porosity
k	thermal conductivity (W m^{-1} K^{-1})	μ	viscosity (Pa s)
k_{eff}	effective thermal conductivity (W m^{-1} K^{-1})	P	density (kg m^{-3})
p	pressure (Pa)	$\bar{\bar{\tau}}$	stress tensor (N m^{-2})
p_0	charging pressure (Pa)		
ΔP	amplitude of the dynamic pressure (Pa)	Subscripts	
S_i	moment source term (N m^{-3})	f	fluid
T	temperature (K)	s	solid matrix
t	Time (s)		
u	velocity (m s^{-1})		

REFERENCES

Caughley, A., Emery, N., Nation, M., et al., 2015. Commercialisation of Pulse Tube cryocoolers to produce 330 W and 1000 W at 77 K for liquefaction. Cryogenic Engineering Conference, IOP, 012060.

Dang, HZ., 2012. High-capacity 60 K single-stage coaxial pulse tube cryocoolers. Cryogenics 52, 205-211.

Dang, HZ., 2015. Development of high performance moving-coil linear compressors for space Stirling-type pulse tube cryocoolers. Cryogenics 68, 1-18.

Dang, HZ., Tan, J., Zhang, L., 2016. Theoretical and experimental investigations on the optimal match between compressor and cold finger of the Stirling-type pulse tube cryocooler. Cryogenics 76, 33-46.

Fluent Inc., 2006. Fluent 6.3 User's Guide. Fluent documentation.

Imura, J., Iwata, N., Yamamoto, H., et al., 2008. Optimization of regenerator in high capacity Stirling type pulse tube cryocooler. Physica C 468, 2178-2180.

Potratz, SA., Abbott, TD., Johnson, MC., et al., 2008. Stirling-type pulse tube cryocooler with 1 kW of refrigeration at 77 K. Cryogenic Engineering Conference, AIP, 42-48.

Spoor, P., 2014. Anomalous temperature and amplitude-dependent performance characteristic of a 1000 W/80 K coldfinger. Adv Cryog Eng, AIP, 1405-1409.

Spoor, P., 2016. Reliable, Practical Kilowatt-class Cryogenics for Superconducting Devices (No. DOE-0000528). Clever Fellows Innovation Consortium, Inc., Troy, NY (United States).

Zhao, YB., Dang, HZ., 2016. CFD simulation of a miniature coaxial Stirling-type pulse tube cryocooler operating at 128 Hz. Cryogenics 73, 53-59.

Manuscript ID: 998
DOI: 10.18462/iir.icr.2019.0998

Theoretical analyses and experimental verifications of a four-stage Stirling-type pulse tube cryocooler reaching 3 K

Rui ZHA[(a),(b)], Tao ZHANG[(a),(b)], Jun TAN[(a),(c)], Jiaqi LI[(a),(b)], Yongjiang ZHAO[(a),(b)], Bangjian ZHAO[(a),(b)], Haizheng DANG[(a),(c)]

[(a)]State Key Laboratory of Infrared Physics, Shanghai Institute of Technical Physics, Chinese Academy of Sciences, Shanghai, 200083, China, cryoray@163.com; haizheng.dang@mail.sitp.ac.cn

[(b)]University of Chinese Academy of Sciences, Beijing, 100049, China

[(c)]Shanghai Boreas Cryogenics Co., Ltd, Shanghai, 200434, China

ABSTRACT

This paper conducts theoretical analyses and experimental verifications of a four-stage Stirling-type pulse tube cryocooler (SPTC) aimed at reaching 3 K for low-T_c superconducting devices and deep space explorations. A computational fluid dynamics (CFD) model is built for the SPTC, in which the irreversible losses in the regenerator are studied and cooling performances simulated. The entropy generations caused by three types of losses including pressure drop, axial heat conduction and ineffective heat transfer are calculated quantificationally and the distributions of them are presented. The four-stage SPTC is then worked out and tested. The experimental results indicate that, by using He-4 and He-3, it reaches no-load temperatures of 4.2 K and 3.5 K, respectively. The SPTC is expected to reach 3 K by matching with a larger capacity compressor.
Keywords: Four-stage Stirling-type Pulse Tube Cryocooler, CFD Model, Regenerator Losses, Theoretical Analyses, Experimental Verifications.

1. INTRODUCTION

The Stirling-type pulse tube cryocooler (SPTC), driven by the linear compressor with flexure springs and clearance seal, has distinct advantages in high reliability, low vibration and long life, and thus plays an important role in many special fields including aerospace, military defense and superconducting, etc. At present, single-stage SPTCs have already been widely used in practical applications at above 25 K, and two-stage ones with cooling powers at both stages, normally varying between 20 K and 180 K, are also becoming mature (Ross Jr, 2006; Dang, 2015; Tan and Dang, 2017). In recent years, three-stage SPTCs were developed to provide cooling at below 20 K (Gao et al., 2017; Dang et al., 2018a; Dang et al., 2018b).

The four-stage SPTC, which is developed based on the three-stage one, is a promising cryocooler candidate for directly reaching 3.0 K or even below used for cooling low-T_c superconducting devices and deep space explorations. It is more robust and reliable than hybrid systems in which a multi-stage SPTC or Stirling cooler is coupled to a Joule-Thomson (J-T) cooler because it eliminates the troublesome components: the J-T valve and the moving displacer.

So far, the feasibility of developing a long-life four-stage SPTC for space applications has been studied. Olson et al. (2006) developed a four-stage SPTC to provide coolings at 6 K and 18 K for Mid-Infrared Instrument (MIRI) in James Webb Space Telescope (JWST). Nast et al. (2007) built a four-stage SPTC for HYPRES cooling requirements which reached a no-load temperature of 3 K.

The previous studies focused on structure design, practical manufacture and performance optimization, whereas the in-deep theoretical analyses of the inner process and operating mechanism are rarely conducted. The four-stage SPTC cold finger (CF) has much more complicated physical structure and operating mechanism than those of single-, two- or three-stage ones. First, the staging configurations of the four-stage CF lead to difficulties in structure design and matching with compressors. Second, the irreversible losses in regenerators at much lower temperatures deteriorate the cooling performance dramatically. Third, the phase characteristics in different regenerators are complex, especially in the fourth stage.

This paper will establish a 2-D axis-symmetric CFD model for the four-stage CF in which the irreversible losses and phase characteristics in the regenerator will be simulated and analyzed in depth. The effects of precooling temperatures and operating parameters on the three types of regenerator losses including pressure drop, axial heat conduction and ineffective heat transfer will be discussed. A four-stage thermally-coupled SPTC will then be developed to verify the above theoretical studies. The simulated and experimental results will be compared and discussed in detail.

2. THEORETICAL ANALYSES

2.1. CFD model

The 2-D axis-symmetric geometry of the fourth stage is shown in Fig. 1. The regenerator has four segmented parts packed with #400 stainless steel (SS) meshes, #500 SS meshes, #600 SS meshes and rare-earth spherical materials, respectively. Table 1 gives the geometric dimensions and boundary conditions of the components.

Table 1. Geometrical dimensions and boundary conditions of the components.

Component	Diameter (mm)	Length (mm)	Boundary condition (K)
Aftercooler	14	5	300 K
Reg I	14	36	Adiabatic
Reg II	12	28	Adiabatic
Reg III	12	28	Adiabatic
Reg IV	12	36	Adiabatic
CHX	-	5	Adiabatic
Pulse tube	8	80	Adiabatic
WHX	8	5	Variable
PHX I	12	5	Variable
PHX II	12	5	Variable
PHX III	12	5	Variable
Inertance tube I	3	320	Variable
Inertance tube II	4	1260	Variable
Gas reservoir	30	55	Variable

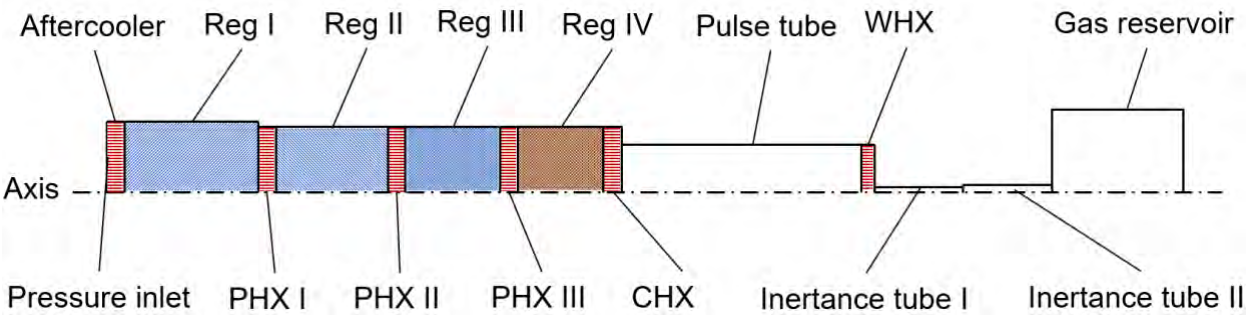

Figure 1: 2-D model for the fourth stage CF.

2.2. Irreversible losses in the regenerator

In the thermal non-equilibrium mode, three types of irreversible losses in the regenerator including axial heat conduction, pressure drop and ineffective heat transfer between fluid and solid are considered, which can be calculated by (Gao and Dang, 2016):

$$\mathrm{d}\langle \dot{S}_{\mathrm{hc}} \rangle = \frac{[(1-\varepsilon)k_{\mathrm{s}} + \varepsilon k_{\mathrm{f}}]A_{\mathrm{r}}}{T^2}\left(\frac{\mathrm{d}T}{\mathrm{d}x}\right)^2 \mathrm{d}x \qquad \text{Eq. (1)}$$

$$\mathrm{d}\langle \dot{S}_{\mathrm{pd}} \rangle = -\frac{\dot{m} Z R}{p} \mathrm{d}p \quad \text{Eq. (2)}$$

$$\mathrm{d}\langle \dot{S}_{\mathrm{ht}} \rangle = h_{\mathrm{fs}} A_{\mathrm{fs}} \frac{(T_{\mathrm{f}} - T_{\mathrm{s}})^2}{T_{\mathrm{f}} T_{\mathrm{s}}} \mathrm{d}x \quad \text{Eq. (3)}$$

where $\mathrm{d}\langle \dot{S}_{\mathrm{hc}} \rangle$ $\mathrm{d}\langle \dot{S}_{\mathrm{pd}} \rangle$ and $\mathrm{d}\langle \dot{S}_{\mathrm{ht}} \rangle$ are the entropy generations caused by axial heat conduction, pressure drop and ineffective heat transfer, respectively. h_{fs} and A_{fs} are the heat transfer coefficient and the effective heat exchange area between fluid and solid, which can be calculated by (Kays and London, 1984; Arp and Radebaugh, 1987):

$$h_{\mathrm{fs}} = \frac{Y \mu C_{\mathrm{p}} \mathrm{Re}}{d_{\mathrm{h}} \mathrm{Pr}^{2/3}} \quad \text{Eq. (4)}$$

$$A_{\mathrm{fs}} = -\frac{4(1-\varepsilon) A_{\mathrm{r}}}{d_{\mathrm{w}}} \quad \text{Eq. (5)}$$

The dimensionless parameter Y are determined empirically for different geometries and Reynolds numbers (Arp and Radebaugh, 1987; Gao and Dang, 2016). For the woven screen meshes,

$$Y = 0.715 \mathrm{Re}^{-0.43} [5.6 + (13.928\varepsilon - 16.363)\varepsilon] \quad \text{Eq. (6)}$$

For the spherical particles,

$$Y = 0.23 \mathrm{Re}^{-0.30} [1.0 + 0.7772(0.38 - \varepsilon)] \quad \text{Eq. (7)}$$

Fig. 2 shows the distributions of three regenerator losses per unit length in each segment of the regenerator. The pressure drop loss accounts for the main part in Reg Ⅰ and Reg Ⅱ (more than 80%) and reduces slightly in Reg Ⅲ. But in Reg Ⅳ, it becomes larger than that in Reg Ⅲ. This is because the porosity of $HoCu_2$ is much smaller than that of SS meshes. The heat transfer loss is a negligible portion of the total losses in Reg Ⅰ and Reg Ⅱ, and it increases sharply near the right end of Reg Ⅲ. In Reg Ⅳ, the heat transfer loss first increases and then decreases, which accounts for 45% of the gross losses. The values near the left end of Reg Ⅳ are smaller than those near the right end of Reg Ⅲ, which means the efficiency of heat transfer between matrix and fluid is effectively enhanced by using $HoCu_2$. The heat conduction loss accounts for a small part in Reg Ⅰ and Reg Ⅱ (around 15%, larger than the heat transfer loss) but turns to be negligible in Reg Ⅲ and Reg Ⅳ (less than 5%).

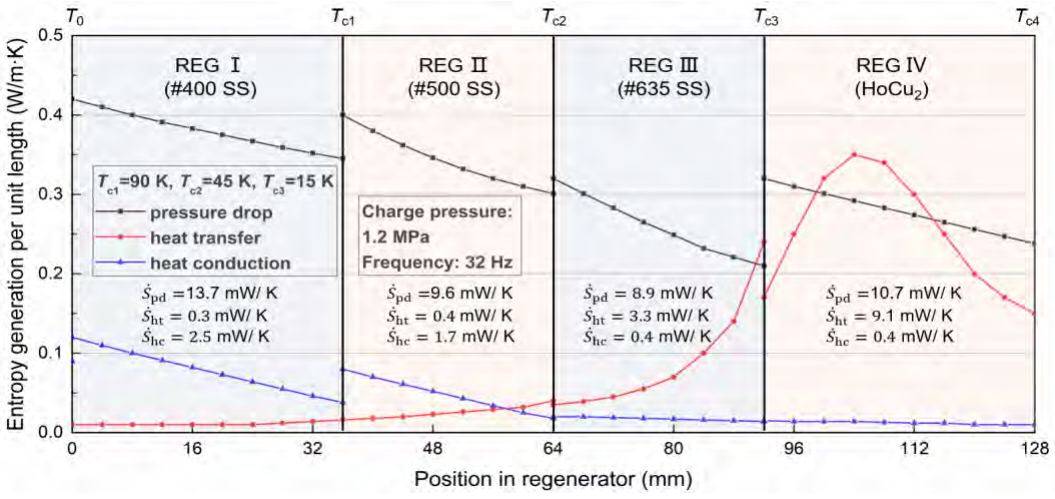

Figure 2: Distributions of regenerator losses with precooling temperatures of 90 K, 45 K and 15 K.

As shown in Fig. 3, the three precooling temperatures change from 90 K, 45 K and 15 K to 120 K, 60 K and 25 K, respectively. The pressure drop loss increases apparently in the whole regenerator. The heat conduction loss increases in Reg Ⅰ and Reg Ⅱ, and basically remains unchanged in Reg Ⅲ and Reg Ⅳ. The heat transfer loss keeps unchanged in Reg Ⅰ and Reg Ⅱ, but decreases in Reg Ⅲ and Reg Ⅳ. These results indicate that, with fixed geometries and matrices of the regenerator, lower precooling temperatures can significantly reduce both the pressure drop loss and the heat conduction loss but may result in the increase of heat transfer loss in Reg Ⅲ and Reg Ⅳ.

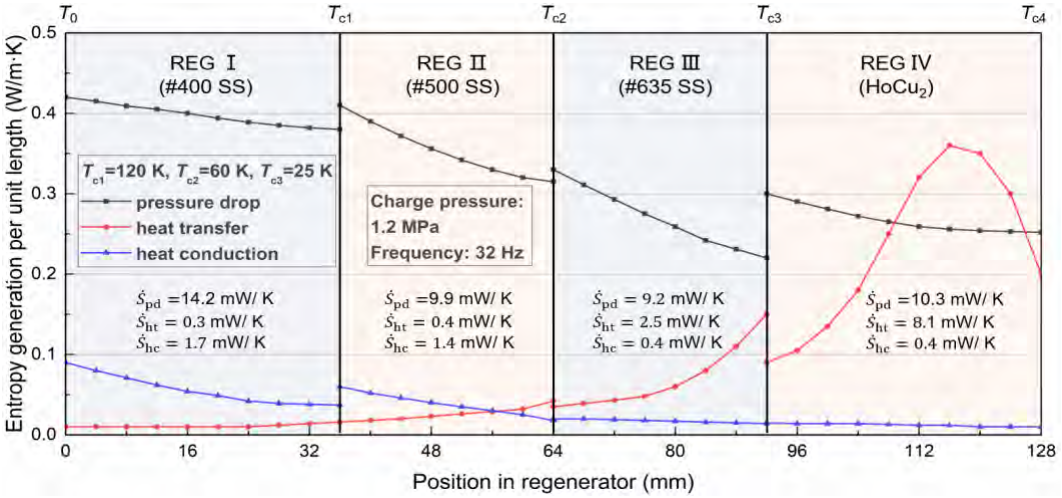

Figure 3: Distributions of regenerator losses with precooling temperatures of 120 K, 60 K and 25 K.

To reduce the heat transfer loss in the regenerator, mixed matrices of Er_3Ni and $HoCu_2$ can be applied in Reg Ⅳ. Er_3Ni is packed near the left end (warm end) while $HoCu_2$ near the right end (cold end), as shown in Fig. 4. In Reg Ⅳ, the pressure drop loss and the heat conduction loss almost keep unchanged, while the heat transfer loss decreases from 9.1 mW×K^{-1} (in Fig. 2) to 7.3 mW×K^{-1} dramatically. These phenomena are probably due to the difference of thermal capacities between Er_3Ni and $HoCu_2$. The thermal capacity of Er_3Ni is larger than that of $HoCu_2$ when the temperature is above 8 K, approximately (Dang et al, 2018a). Thus, Er_3Ni is suitable for matrix at relatively higher temperature which causes smaller heat transfer loss than those of $HoCu_2$.

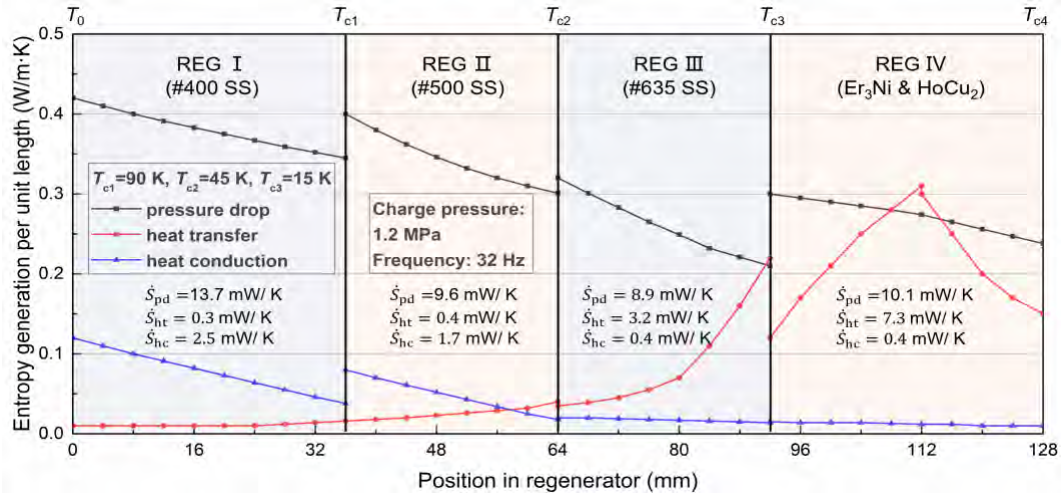

Figure 4: Distributions of three regenerator losses with mixed matrices in Reg Ⅳ.

Fig. 5 shows variations of the entropy generation in Reg Ⅳ and cooling capacity at 5 K with the ratio of L_{4-1} and L_4, where L_4 is the length of Reg Ⅳ and L_{4-1} stands for the length of Er_3Ni. Obviously, the heat transfer loss is reduced by using mixed matrices than by only either Er_3Ni or $HoCu_2$. When the ratio is 0.6, the heat transfer loss gets the smallest value of 7.3 mW×K^{-1} and the

cooling capacity at 5 K becomes the largest. Fig. 6 shows the effects of both operating frequency and charge pressure on the cooling performance. When the operating frequency is around 32 Hz, the cold end achieves the largest cooling capacity at 5 K. In addition, a larger charge pressure will lead to a larger cooling capacity at 5 K. For example, when the operating frequency is 32 Hz and the charge pressures are 1.0 MPa, 1.2 MPa and 1.4 MPa, the cooling capacities are 23 mW, 27 mW and 34 mW, respectively.

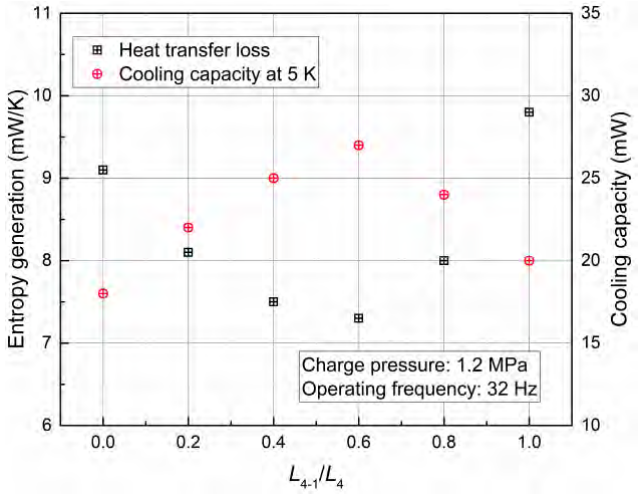

Figure 5: Variations of heat transfer loss in Reg Ⅳ and cooling capacity at 5 K with L_{4-1}/L_4.

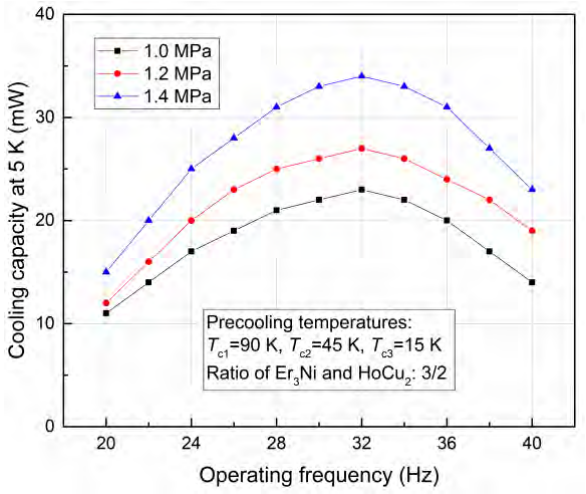

Figure 6: Variations of cooling capacity at 5 K with operating frequency.

3. EXPERIMENTAL RESULTS

To verify the validity of the above results, a four-stage thermally-coupled SPTC is developed and tested. The configuration of the SPTC is shown in Fig. 7 and the experimental setups are presented in Fig. 8. The first two stages are driven by one compressor and the last two stages by the other one. The experimental operating parameters of each stage are shown in Table 2.

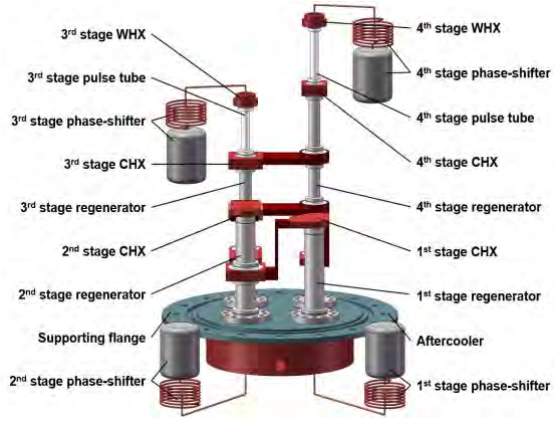

Figure 7: Configuration of the SPTC.

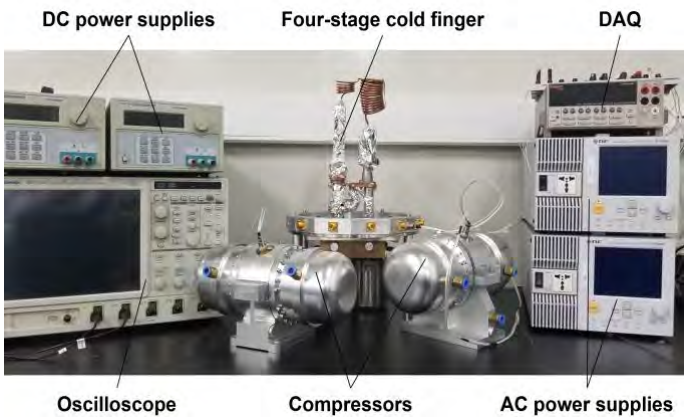

Figure 8: Experimental setups.

Table 2. Experimental operating parameters of each stage.

Conditions	Operating frequency	Charge pressure	Reject temperature	Phase-shifter temperature
1st stage	57 Hz	3.2 MPa	300 K	300 K
2nd stage	57 Hz	3.2 MPa	300 K	300 K
3rd stage	32 Hz	1.2 MPa	300 K	60 K
4th stage	32 Hz	1.2 MPa	300 K	30 K

Fig. 9 shows the cool-down curves of the four stages. The no-load temperatures of the four stages are 82.4 K, 48.0 K, 16.5 K and 4.2 K, respectively, with He-4 as working fluid. The 4th stage also gains a cooling capacity of 12 mW at 5 K, with an electric input power of 450 W. Fig. 10 shows the variations of the 4th stage no-load temperature with operating frequency. The lowest temperature occurs at 32 Hz with He-4 and at 31 Hz with He-3, respectively. The optimal frequency is basically in keeping with the simulated results. While using He-3, the lowest temperature of the 4th stage is 3.5 K. The SPTC has the potential to reach 3 K when a larger capacity compressor is employed to drive the last two stages.

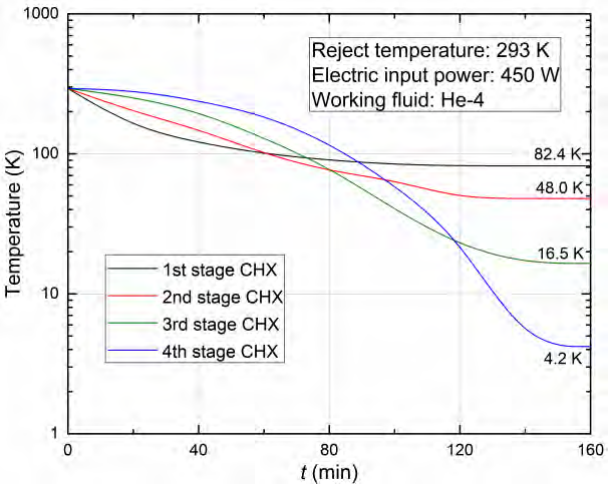

Figure 9: Cool-down curves.

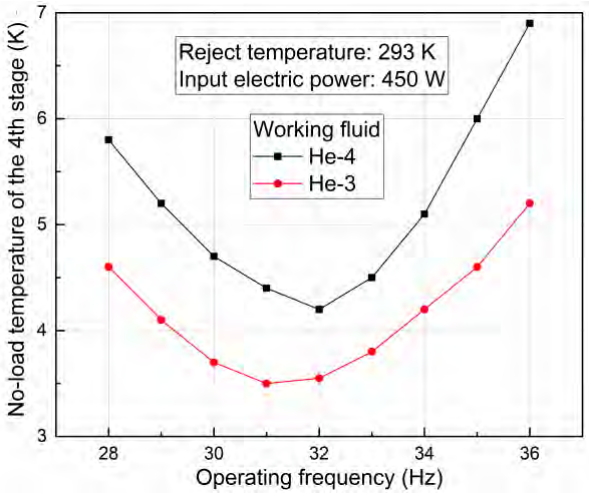

Figure 10: Cooling performance.

4. CONCLUSIONS

This paper conducts theoretical and experimental investigations on a four-stage SPTC aimed to reach 3 K for low-T_c superconducting devices and deep space explorations. A 2-D axis-symmetric CFD model is set up to study the irreversible losses in the regenerator. The pressure drop loss accounts for the main part of gross losses in the first three segments of the regenerator. The heat transfer loss increases rapidly in Reg Ⅳ which accounts for around 45%. Mixed matrices consist of Er_3Ni and $HoCu_2$ are proved to be effective to reduce the heat transfer loss in Reg Ⅳ. The optimal ratio between them is 3:2.

A four-stage SPTC is then worked out based on the above theoretical studies, which experimentally reaches no-load temperatures of 82.4 K, 48.0 K, 16.5 K and 4.2 K with He-4. When using He-3, the no-load temperature of the fourth stage reduces to 3.5 K. The total electric input power is 450 W. The four-stage SPTC is expected to reach 3 K by using a larger capacity compressor to drive the last two stages.

ACKNOWLEDGEMENTS

The work is financially supported by the Aeronautical Science Foundation of China (No. 20162490005) and Shanghai Municipality (Nos. 18511110100, 18511110101, 18511110102).

NOMENCLATURE

A_{fs}	effective heat exchange area between fluid and solid (m^2)	Re	Reynolds number
		Reg	regenerator
A_r	cross-sectional area of regenerator (m^2)	$\dot{S}_{hc}$	entropy generation of heat conduction ($J\times K^{-1}$)
		$\dot{S}_{ht}$	entropy generation of heat transfer ($J\times K^{-1}$)
C_p	heat capacity ($J\times kg^{-1}\times K^{-1}$)	$\dot{S}_{pd}$	entropy generation of pressure drop ($J\times K^{-1}$)
d_h	hydraulic diameter of matrix (m)	t	time (s)
f	frequency (Hz)	T	temperature (K)
h_{fs}	convective heat transfer coefficient	T_f	temperature of fluid (K)

	($W \times m^{-2} \times K^{-1}$)
k_f	thermal conductivity of fluid ($W \times m^{-1} \times K^{-1}$)
k_s	thermal conductivity of solid ($W \times m^{-1} \times K^{-1}$)
L_4	length of Reg Ⅳ (mm)
L_{4-1}	length of Er_3Ni in Reg Ⅳ (mm)
$\dot{m}$	mass flow rate ($kg \times s^{-1}$)
p	dynamic pressure (Pa)
p_a	average pressure (Pa)
Δp	pressure amplitude (Pa)
Pr	Prandtl number
R	gas constant ($J \times kg^{-1} \times K^{-1}$)
T_s	temperature of solid (K)
T_{c1}	temperature of 1st stage cold end (K)
T_{c2}	temperature of 2nd stage cold end (K)
T_{c3}	temperature of 3rd stage cold end (K)
T_{c4}	temperature of 4th stage cold end (K)
T_{ps}	phase-shifter temperature (K)
X	position in different components (mm)
Y	dimensionless parameter of flow
Z	compressibility factor

Greeks

ε	porosity of regenerator matrix
μ	viscosity of fluid ($Pa \times s$)

REFERENCES

Arp, V., Radebaugh, R., 1987. Interactive Program for Microcomputers to Calculate the Optimum Regenerator Geometry for Cryocoolers, AFWAL-TR-87-3040, Flight Dynamics Lab.

Dang, H.Z., 2015. Development of high performance moving-coil linear compressors for space Stirling-type pulse tube cryocoolers. Cryogenics 68, 1–18.

Dang, H.Z., Bao, D.L., Zhang, T., et al., 2018a. Theoretical and experimental investigations on the three-stage Stirling-type pulse tube cryocooler using cryogenic phase-shifting approach and mixed regenerator matrices. Cryogenics 93, 7-16.

Dang, H.Z., Bao, D.L., Gao, Z.Q., et al., 2018b. Theoretical modeling and experimental verifications of the single-compressor-driven three-stage Stirling-type pulse tube cryocooler. Frontiers in Energy, doi: 10.1007/s11708-018-0569-8.

Gao, Z.Q., Dang, H.Z., 2016. Entropy analyses of the three-stage thermally-coupled Stirling-type pulse tube cryocooler. Applied Thermal Engineering 100, 944-960.

Gao, Z.Q., Dang, H.Z., Bao, D.L., et al., 2017. Investigation on a three-stage Stirling-type pulse tube cryocooler for cooling the low-Tc SQUID. IEEE Transactions on Applied Superconductivity 27, doi: 10.1109/TASC.2016.2642584.

Nast, T., Olson, J.R., Roth, E., et al., 2007. Development of Remote Cooling Systems for Low-Temperature, Space-Borne Systems. Cryocoolers 14, 33-40.

Olson, J.R., Moore, M., Champagne, P., et al., 2006. Development of a space-type 4-stage pulse tube cryocooler for very low temperature. Adv. Cryog. Eng. 51, 623–631.

Ross Jr, R.G., 2006. Space coolers: a 50-year quest for long life cryogenic cooling in space. Timmerhaus, K.D., Reed, R.P., Cryogenic engineering: fifty years of progress, New York: Springer Publishers, 225–284.

Tan, J., Dang, H.Z., 2017. Theoretical and experimental investigations on the cooling capacity distributions at the stages in the thermally-coupled two-stage Stirling-type pulse tube cryocooler without external precooling. Cryogenics 82, 48–61.

Manuscript ID: 1020
DOI: 10.18462/iir.icr.2019.1020

Numerical simulations and experimental verifications of a three-stage gas-coupled 4.0 K Stirling-type pulse tube cryocooler

Rui ZHA[(a),(b)], Tao ZHANG[(a),(b)], Jun TAN[(a),(c)], Jiaqi LI[(a),(b)], Yongjiang ZHAO[(a),(b)], Bangjian ZHAO[(a),(b)], Haizheng DANG[(a),(c)]

[(a)]State Key Laboratory of Infrared Physics, Shanghai Institute of Technical Physics, Chinese Academy of Sciences, Shanghai, 200083, China, cryoray@163.com; haizheng.dang@mail.sitp.ac.cn

[(b)]University of Chinese Academy of Sciences, Beijing, 100049, China

[(c)]Shanghai Boreas Cryogenics Co., Ltd, Shanghai, 200434, China

ABSTRACT

This paper conducts theoretical and experimental investigations on a three-stage gas-coupled Stirling-type pulse tube cryocooler (SPTC). A two-dimensional computational fluid dynamics (CFD) model is established in which the interactions between compressor and cold finger (CF) are analyzed and the distributions of PV power simulated as well. The effects of operating frequency and charge pressure on the performances of both compressor and CF are modeled in detail. Based on the above theoretical studies, a three-stage gas-coupled SPTC is then worked out and tested. The experimental results show that it reaches a no-load temperature of 4.5 K. The electric input power and the motor efficiency of the compressor are 320 W and 81.5%, respectively. When using He-3, the no-load temperature reduces further to 4.0 K. Finally, the SPTC prototype shows great potential for 4-10 K space applications due to its compact configuration, high reliability, low vibration and high cooling efficiency.

Keywords: Three-Stage Stirling-type Pulse Tube Cryocooler, Gas-Coupled, CFD Model, PV Power, Theoretical and Experimental Investigations.

1. INTRODUCTION

The Stirling-type pulse tube cryocooler (SPTC), driven by the linear compressor based on clearance seal and flexure springs, achieves high reliability and long operation time at both warm and cold ends, and thus has a strong appeal to many special fields such as aerospace, military defense and superconducting, etc. (Radebaugh, 2000; Ross Jr, 2006; Dang, 2015). In recent years, the development of the SPTCs working in the temperature range of 4–10 K are drawing interest due to their potential applications in deep space exploration and low-T_c superconducting application. (Gao et al., 2016; Gao et al., 2017; Dang et al., 2017; Dang et al., 2018a; Dang et al., 2018b).

In practice, for a SPTC, to achieve the effective cooling capacity at 10 K or below usually needs a three-stage arrangement, for which two typical coupling methods, namely, thermally-coupled and gas-coupled, are often employed. The thermally-coupled arrangement is simple to design the configuration and easy to control the internal flow as well. However, the indispensable thermal straps often introduce considerable irreversible losses and also lead to a complicated system. By contrast, the gas-coupled arrangement eliminates all the external thermal links between stages and thus avoids the potential irreversible losses, which might result in a more compact configuration and a higher cooling efficiency as well. Comparing with the four-stage SPTC developed by the same authors, the three-stage one is mainly for 4-10 K space uses such as long-wave Infrared instruments due to its compactness and high-reliability, while the other one is capable of providing a cooling at below 4 K for single-photon detectors or simultaneous coolings at four temperatures for hybrid optical systems.

In practice, despite the above definite advantages, the application of the gas-coupled multi-stage SPTC is rare, partly due to the great challenge to the considerable complexity of the internal flow in

a gas-coupled multi-stage SPTC system. First, the phase characteristics in the CF become much more complicated due to the branch flows among stages. Second, the distributions of PV power into each stage are hard to control. Third, the matching mechanisms between compressor and CF also becomes more complex, which result in great difficulties in determining the operating parameters such as charge pressure and operating frequency.
This paper aims to establish a CFD model for the three-stage gas-coupled SPTC, in which the interactions between compressor and CF will be analyzed and flow conditions in the CF simulated as well. The distributions of PV power into each stage will be studied quantitatively and the optimal operating parameters determined. A three-stage gas-coupled SPTC prototype and corresponding experimental results will be presented to provide detailed verifications for the theoretical studies.

2. THEORETICAL ANALYSES

2.1. Interactions between the CF and the Compressor

In the compression space, to simplify the analyses, the motion of the piston is assumed to be sinusoidal and then the basic parameters can be written as:

$$x = X\sin\omega t \quad \text{Eq. (1)}$$

$$\dot{U}_{\mathrm{out}} = A_{\mathrm{p}}\omega X\cos\omega t = \omega V_{\mathrm{s}}\cos\omega t \quad \text{Eq. (2)}$$

$$p_{\mathrm{out}} = P_a + \Delta P\cos(\omega t - \theta_{\mathrm{out}}) \quad \text{Eq. (3)}$$

For the linear motor, by neglecting the influence of the back pressure, the force balance is shown as (Dang et al., 2016):

$$LBI = m\frac{\mathrm{d}^2x}{\mathrm{d}t^2} + C_{\mathrm{d}}\frac{\mathrm{d}x}{\mathrm{d}t} + kx + [\Delta P\cos(\omega t - \theta_{\mathrm{out}})]A_{\mathrm{p}} \quad \text{Eq. (4)}$$

where the left part of the equation is the electromagnetic force, and the four terms in the right part stand for inertia force, viscous force, mechanical spring force and gas force, respectively. Substituting Eqs. (1)-(3) into Eq. (4), the motor current becomes:

$$\begin{aligned} I &= \frac{X}{BL}[(k - m\omega^2)\sin\omega t + C_{\mathrm{d}}\omega\cos\omega t] + \frac{\Delta PA_{\mathrm{p}}}{BL}\cos(\omega t - \theta_{\mathrm{out}}) \\ &= \frac{Xk - Xm\omega^2 + \Delta PA_{\mathrm{p}}\sin\theta_{\mathrm{out}}}{BL}\sin\omega t + \frac{XC_{\mathrm{d}}\omega + \Delta PA_{\mathrm{p}}\cos\theta_{\mathrm{out}}}{BL}\cos\omega t \end{aligned} \quad \text{Eq. (5)}$$

To simplify the calculation, assuming *a* and *b* are:

$$a = \frac{Xk - Xm\omega^2 + \Delta PA_{\mathrm{p}}\sin\theta_{\mathrm{out}}}{BL} \quad \text{Eq. (6)}$$

$$b = \frac{XC_{\mathrm{d}}\omega + \Delta PA_{\mathrm{p}}\cos\theta_{\mathrm{out}}}{BL} \quad \text{Eq. (7)}$$

Then the motor current can be expressed as:

$$I = a\sin\omega t + b\cos\omega t \quad \text{Eq. (8)}$$

The motor voltage can be calculated by:

$$U = L_e \frac{dI}{dt} + R_e I + BL \frac{dx}{dt} \quad \text{Eq. (9)}$$

Then, the time-averaged electric power, PV power and Joule loss of the compressor can be expressed as:

$$\dot{W}_e = 2 \times f \int_0^{2\pi/\omega} UI dt = R_e(a^2 + b^2) + \omega BLXb \quad \text{Eq. (10)}$$

$$\dot{W}_{pv} = 2 \times f \int_0^{2\pi/\omega} p\dot{U} dt = \omega V_s \Delta P \cos\theta \quad \text{Eq. (11)}$$

$$\dot{Q}_J = 2 \times f \int_0^{2\pi/\omega} I^2 R_e dt = R_e(a^2 + b^2) \quad \text{Eq. (12)}$$

Because of the dual-opposed configuration of the compressor, the electric power, PV power and Joule loss should be doubled. Then the PV power efficiency and the motor efficiency can be expressed as:

$$\eta_{motor} = \frac{\dot{W}_e - \dot{Q}_J}{\dot{W}_e} = \frac{\omega BLXb}{R_e(a^2 + b^2) + \omega BLXb} \quad \text{Eq. (13)}$$

So far, the interactions between the compressor and the PTCF have been established.

2.2. CFD Modeling

To improve the modeling accuracy, a 2-D CFD model for the three-stage gas-coupled PTCF is established, as shown in Fig. 1. The main geometries of the PTCF are shown in Table 1. The regenerator has three segments, in which the first two ones are packed with #400 stainless steel (SS) meshes and #500 SS meshes, successively, and the last one with mixed spherical particles of Er_3Ni and $HoCu_2$. The compressor is simplified as a moving piston. The initial values of charge pressure, amplitude of the piston displacement and operating frequency will be assigned in advance.

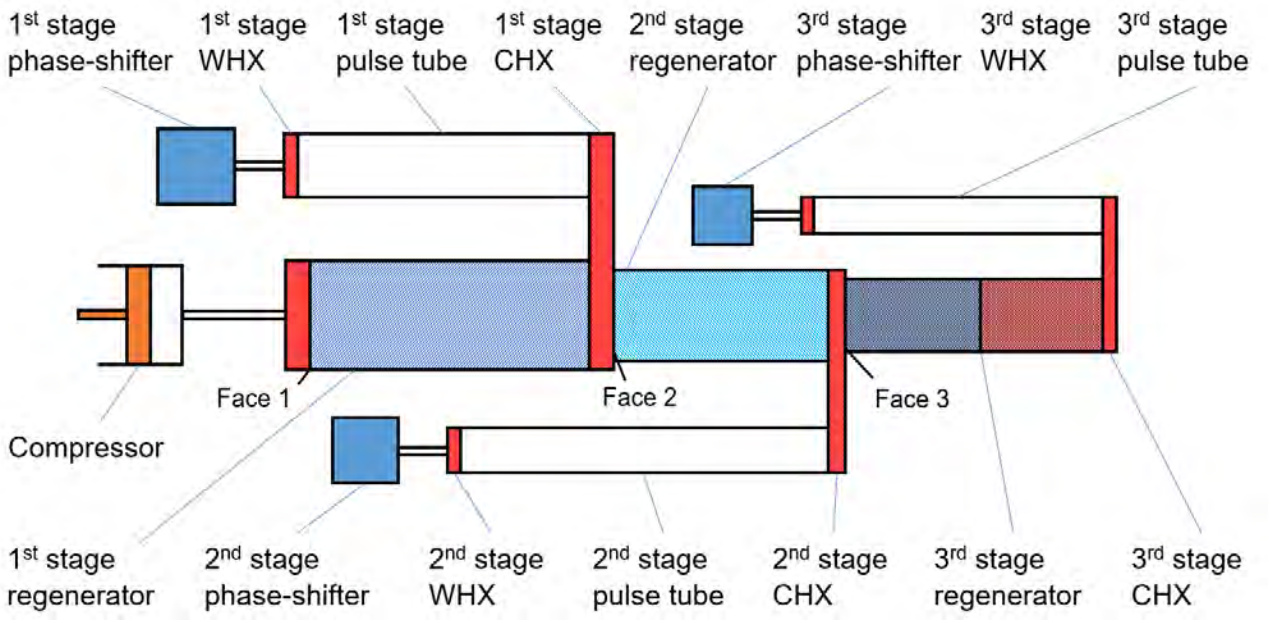

Figure 1: Schematic of the three-stage gas-coupled SPTC.

Table 1. Geometrical dimensions and boundary conditions of the components.

Component	Diameter (mm)	Length (mm)	Boundary condition (K)
Aftercooler	37	6	300 K
1st regenerator	37	69	Adiabatic
1st pulse tube	13	64	Adiabatic
1st inertance tube	2.6	2970	Adiabatic
2nd regenerator	20	47	Adiabatic
2nd pulse tube	10	56	Adiabatic
2nd inertance tube	3.2	3130	45 K
3rd regenerator	14	39	Adiabatic
3rd pulse tube	6	65	Adiabatic
3rd inertance tube	1.7	1320	30 K

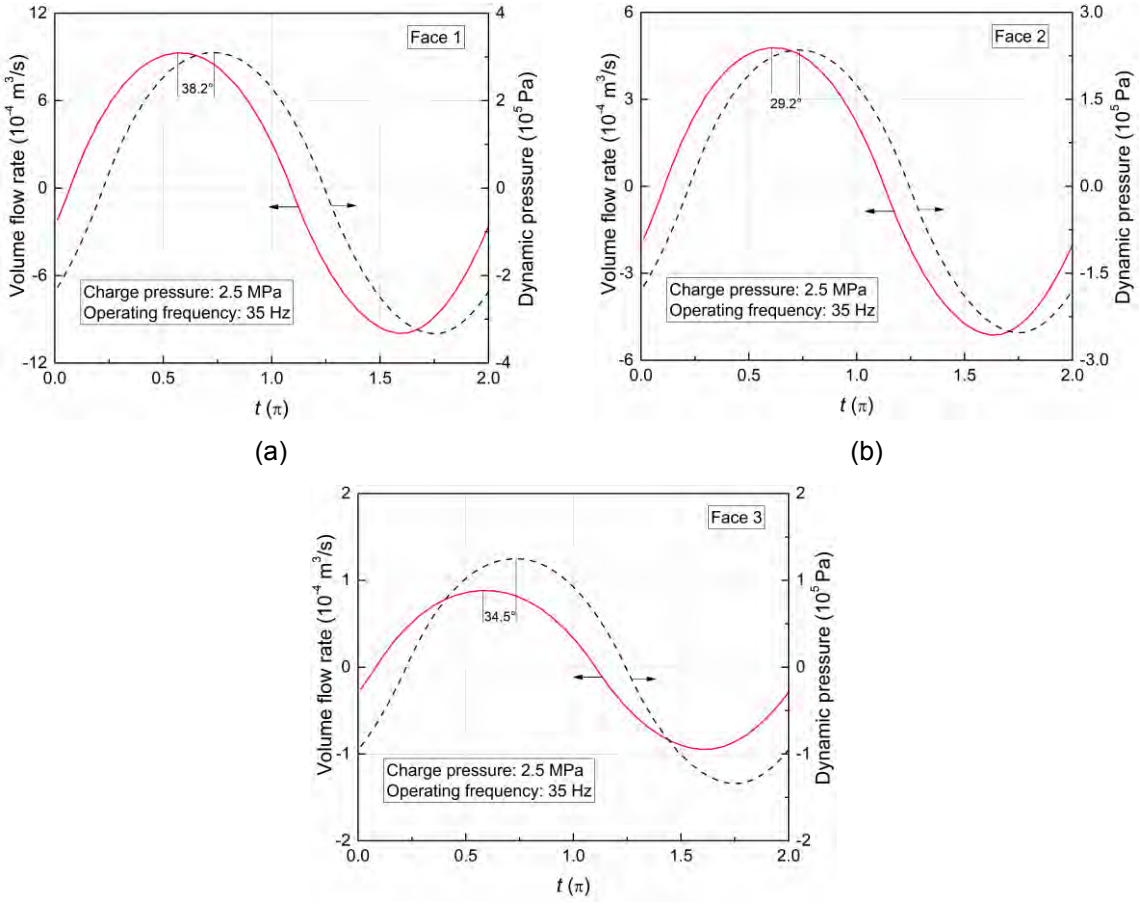

Figure 2: Volume flow rates and dynamic pressures at (a) face 1, (b) face 2 and (c) face 3.

2.3. Discussions on Simulated Results

Figure 2 gives the simulated results of volume flow rates and dynamic pressures at face 1, face 2 and face 3 shown in Fig. 1. When the fluid flows from face 1 to face 3, the volume flow rate first decreases from 9.28×10^{-4} m$^3\times$s^{-1} to 4.85×10^{-4} m$^3\times$s^{-1} and then to 1.74×10^{-4} m$^3\times$s^{-1}, while the dynamic pressure from 3.08×10^5 Pa to 2.35×10^5 Pa and then to 1.34×10^5 Pa. The phase

differences at the three faces are 38.2°, 29.2° and 34.5°, respectively.
The PV power of each stage can be calculated according to Eq. (10). It should be noted that the PV power at face 2 are not the one of the 2nd stage but the one subtracting that of the 3rd stage. Figure 3 presents the variations of PV powers with operating frequency. When the operating frequency increases from 20 Hz to 50 Hz, the gross PV power rises from 180 W to 320 W. The PV powers of the 1st and the 2nd stage also show increasing trends but the one of the 3rd stage first increases and then decreases. Its largest PV power is 58 W at 35 Hz.
Fig. 4 shows variations of electric power and motor efficiency of the compressor with operating frequency and charge pressure. Two following important phenomena can be observed. First, with a certain charge pressure, the gross electric input power increases with the operating frequency but very slowly beyond 40 Hz. In addition, the motor efficiency reaches the maximum value near 40 Hz. Second, a higher charge pressure can lead to a larger electric power and a lower motor efficiency. This is probably due to that a lower charge pressure can efficiently modify the phase conditions, especially in the third stage, and then enhance the compressor performance.

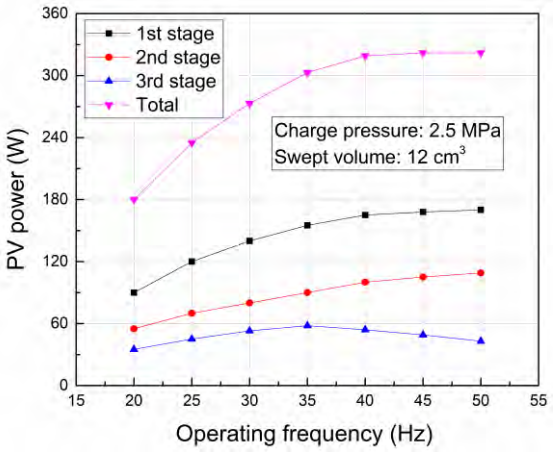

Figure 3: Variations of PV powers with operating frequency.

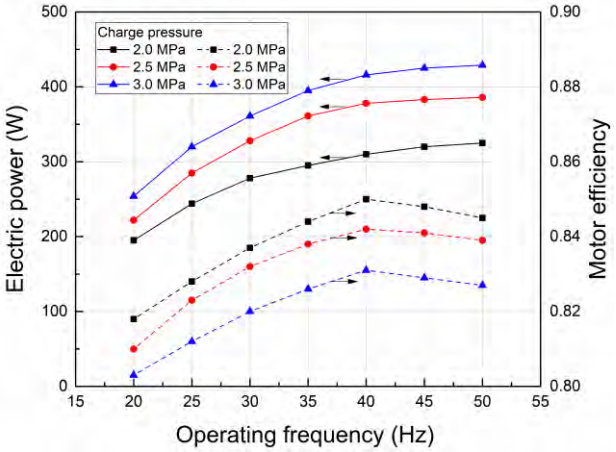

Figure 4: Variations of electric powers and motor efficiencies with operating frequency.

The effects of operating frequency and charge pressure on the cooling performance of each stage are also simulated, as shown in Fig. 5. In the first two stages, the no-load temperatures decrease with the increase of operating frequency. A higher charge pressure also results in the better cooling performance. But in the 3rd stage, the lower charge pressure, the better. The lowest temperature occurs at 35 Hz. It is about 4.3 K with the charge pressure of 2.0 MPa, and 4.25 K with 2.5 MPa.

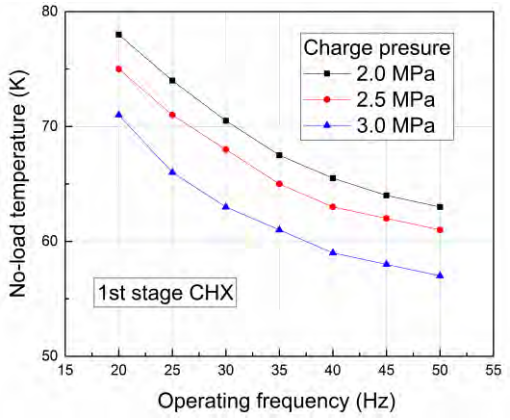

(a)

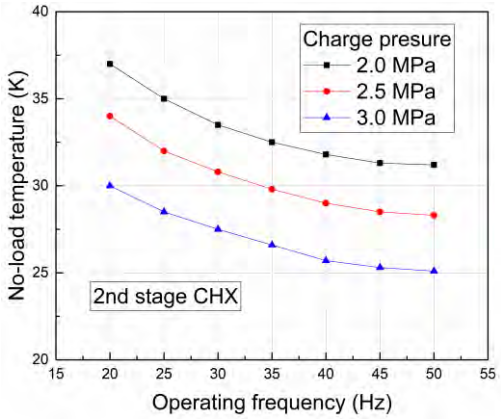

(b)

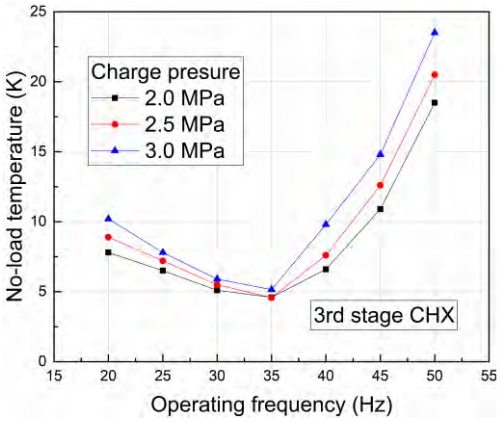

(c)

Figure 5: Variations of no-load temperatures with operating frequency and charge pressure. (a) 1st stage; (b) 2nd stage; (c) 3rd stage.

3. EXPERIMENTAL VERIFICATIONS

Based on the above studies, a three-stage gas-coupled SPTC is then worked out and tested. The configuration of the SPTC is shown in Fig. 6. It is driven by one single linear compressor. Fig. 7 shows the experimental setups.

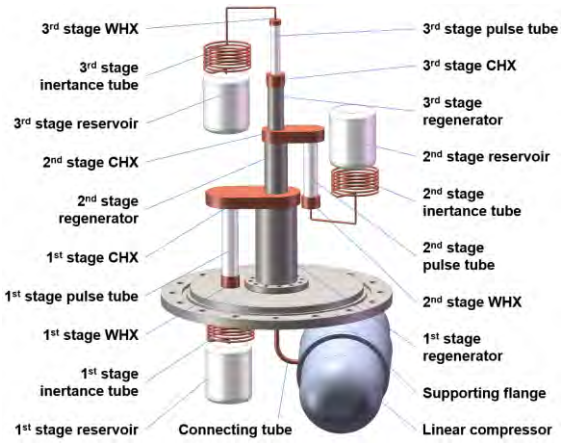

Figure 6: Configuration of the three-stage SPTC.

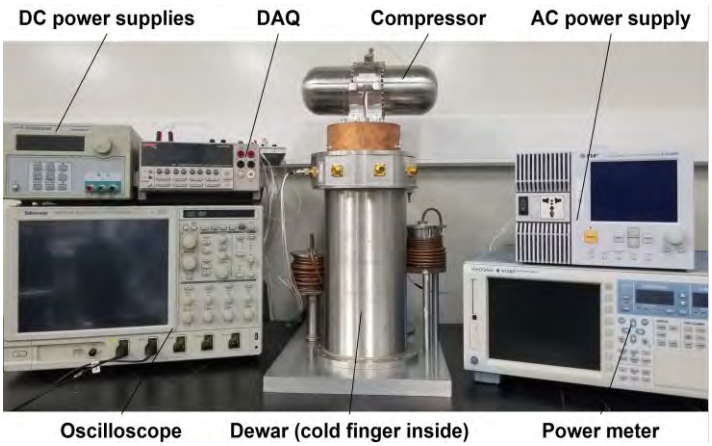

Figure 7: Experimental setups of the three-stage SPTC.

The cool-down curves of the SPTC are shown in Fig. 8. The no-load temperatures of the three stages are 65.5 K, 29.6 K and 4.5 K, respectively. The third stage can also gain a cooling power of 45 mW at 6 K. Accordingly, the charge pressure is 2.5 MPa, the operating frequency is 35 Hz, and the electric input power is 320 W. The third stage has already worked at below the critical temperature of He-4, which might lead to flexible flow and heat transfer characteristics near the cold end and result in irreversible losses. Thus, He-3 is used to improve the cooling performance of the SPTC. According to the results, a lower temperature of 4.0 K is reached under the same working conditions.

The performance of the compressor is tested, as shown in Fig. 9. When the operating frequency increases from 30 Hz to 40 Hz, the electric power increases from 289 W to 336 W. The highest motor efficiency is 81.5% when the operating frequency is around 35 Hz.

With one single compressor and a gas-coupled configuration, the SPTC prototype has significant advantages such as compact configuration, high reliability, low vibration and high cooling efficiency and thus shows great potential for 4-10 K space applications.

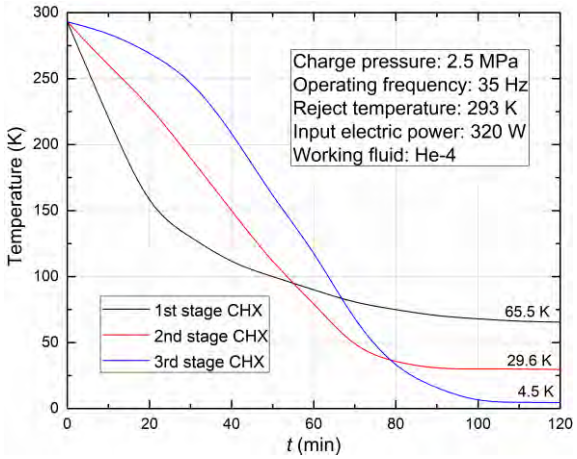

Figure 8: Cool-down curves.

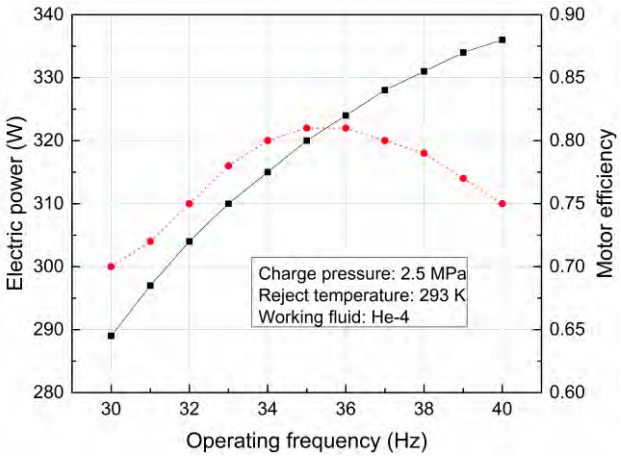

Figure 9: Compressor performance.

4. CONCLUSIONS

This paper establishes a CFD model for the three-stage gas-coupled SPTC. The interactions between the compressor and the CF are established by analyzing the dynamic characteristics in the compression volume. The force balance of the piston is studied, and equations of PV power, electric power and motor efficiency are deducted. The distributions of PV power into each stage are analyzed quantitatively and the cooling performance simulated as well. The optimal operating parameters including charge pressure and operating frequency are determined in this model.

A three-stage gas-coupled SPTC is worked out and tested. No-load temperatures of 65.5 K, 29.6 K and 4.5 K are reached for the three stages, respectively, with an electric input power of 320 W. The cooling power at 6 K is 45 mW. The compressor also achieves a satisfactory motor efficiency of 81.5%. When using He-3, the no-load temperature of the 3rd stage reduces further to 4.0 K.

In view of the obvious advantages such as a single driver, compactness, high reliability and high cooling efficiency, the gas-coupled SPTC has great potential for 4-10 K space applications.

ACKNOWLEDGEMENTS

This work is financially supported by the Aeronautical Science Foundation of China (No. 20162490005) and Shanghai Municipality (Nos. 18511110100, 18511110101, 18511110102).

NOMENCLATURE

A_p	area of piston surface (m^2)
B	magnetic field intensity (T)
C_d	mechanical damp coefficient
d_p	diameter of piston surface (m)
f	operating frequency (Hz)
I	current (A)
k	axial stiffness of flexure springs ($N \times m^{-1}$)
L	length of coil wire (m)
L_e	inductance of coil wire (H)
m	mass of moving part (kg)
p	dynamic pressure (Pa)
P_a	charge pressure (Pa)
ΔP	amplitude of dynamic pressure (Pa)
$\dot{Q}_J$	Joule loss (W)
R_e	resistance of coil wire (Ω)
t	time (s)
T	temperature (K)
T_{ps}	temperature of phase-shifter (K)
$\dot{U}$	volume flow rate ($m^3 \times s^{-1}$)
U	voltage (V)
V_s	swept volume (m^3)
W_e	electric power (W)
W_{PV}	PV power (W)
x	piston displacement (m)
X	piston stroke (m)

Greeks

θ	phase difference between dynamic pressure and volume flow rate
ω	angular frequency
η_{motor}	motor efficiency

REFERENCES

Dang, H.Z., 2015. Development of high performance moving-coil linear compressors for space Stirling-type pulse tube cryocoolers. Cryogenics 68, 1–18.

Dang, H.Z., Tan, J., Zhang, L., 2016. Theoretical and experimental investigations on the optimal match between compressor and cold finger of the Stirling-type pulse tube cryocooler. Cryogenics 76, 33–46.

Dang, H.Z., Tan, J., Zha, R., et al., 2017. Advances in single- and multi-stage Stirling-type pulse tube cryocoolers for space applications in NLIP/SITP/CAS, IOP Conf. Ser.: Mater. Sci. Eng. 278 012008. doi: 10.1088/1757-899X/278/1/012008.

Dang, H.Z., Bao, D.L., Zhang, T., et al., 2018a. Theoretical and experimental investigations on the three-stage Stirling-type pulse tube cryocooler using cryogenic phase-shifting approach and mixed regenerator matrices. Cryogenics 93, 7-16.

Dang, H.Z., Bao, D.L., Gao, Z.Q., et al., 2018b. Theoretical modeling and experimental verifications of the single-compressor-driven three-stage Stirling-type pulse tube cryocooler. Frontiers in Energy, doi: 10.1007/s11708-018-0569-8.

Gao, Z.Q., Dang, H.Z., 2016. Entropy analyses of the three-stage thermally-coupled Stirling-type pulse tube cryocooler. Applied Thermal Engineering 100, 944–960.

Gao, Z.Q., Dang, H.Z., Bao, D.L., et al., 2017. Investigation on a three-stage Stirling-type pulse tube cryocooler for cooling the low-Tc SQUID. IEEE Transactions on Applied Superconductivity 27, doi: 10.1109/TASC.2016.2642584.

Radebaugh, R., 2000. Development of the pulse tube refrigerator as an efficient and reliable cryocooler. In: Proc. of Institute of Refrigeration.

Ross Jr, R.G., 2006. Space coolers: a 50-year quest for long life cryogenic cooling in space. Timmerhaus, K.D., Reed, R.P., Cryogenic engineering: fifty years of progress, New York: Springer Publishers, 225–284.

Manuscript ID: 1023
DOI: 10.18462/iir.icr.2019.1023

Experimental studies on heat transfer coefficient for boiling of hydrocarbon mixture in shell-side of coil-wound heat exchanger for LNG production

Alexander KROTOV[(a)], Ekaterina NAVASARDYAN[(a)], Andrey KOLESNIKOV[(a)], Yaroslav SAMOKHVALOV[(a)], Oleg ZUEV[(a)]

[(a)] Bauman Moscow State Technical University
Moscow, 105005, Russia, s_samokhvalov@mail.ru

ABSTRACT

Coil-wound heat exchangers are widely applied in natural gas liquefiers, but existing heat transfer coefficient correlations are constrained and inaccurate, which leads to overdimension of heat exchangers. Calculation and comparison of correlations for heat transfer coefficient for boiling in shell-side of hydrocarbon mixture are made. Authors developed test installation and test section for measuring heat transfer coefficient for boiling in shell-side of hydrocarbon mixture with various composition, mass flux, temperature and pressure.
Keywords: Azeotropic mixture, Boiling, LNG, Shell.

1. INTRODUCTION

Heat transferring processes between flows with different temperatures occur in heat exchangers. These processes are conformed by common patterns of thermodynamics and heat and mass transfer, but at low working temperatures few factors take place which should be considered in designing compact and effective apparatus.
Spiral wound heat exchangers (SWHE) are widely used for cryogenic applications. The reason for this is high compactness and effectiveness, heat transfer coefficient is 1.5-2 times higher than for tube-and-shell heat exchangers. These advantages precipitate for applying spiral-wound heat exchangers in LNG production.
Base load LNG plants are characterized in that relative footprint of heat exchanging equipment is higher than for other types of plants. It is considered that tendency of LNG plant's capacity growing will be inhibited by manufacturing complexity of the main cryogenic heat exchanger.
SWHE is applied as the main heat exchanger in 90% of existing LNG plants according to Ding et al. (2017). Additional advantages of SWHE in reference to LNG plants designing are robustness, possibility to work with fluids with rapidly changing pressures and temperatures, mechanical durability, no tough requirements for product flow treatment, ease of single unit production. Also, there is technological possibility to place all heat exchangers in a single shell.
Heat exchangers are the main elements of any cryogenic system, especially in natural gas liquefaction plants working on mixed refrigerant technology. According to Narasimhan and Venkatarathnam (2010), the most part of exergy losses, shown on Fig. 1, occur in the main heat exchanger. Entropy-statistical analysis by Arkharov and Semenov (2016), Arkharov et al. (2016a) and Arkharov et al. (2016b) prove meaningful energy "waste" in heat exchanging equipment.
Commonly, technology based on mixed refrigerant cycle is applied for liquefaction of natural gas. Special characteristic of this cycle is presence of multi-flow heat exchanger, at least three flows: first for natural gas, second for mixed refrigerant high pressure flow, third for mixed refrigerant low pressure flow. Natural gas and mixed refrigerant high pressure flows are cooled by return low pressure flow of mixed refrigerant, which is boiling in the shell-side, while natural gas and low pressure mixed refrigerant flows, usually in-tube flows, are cooled and condensed.
Problem of calculation of heat transfer coefficient of in-tube condensation process for hydrocarbon zeotropic mixtures is described by Samokhvalov et al. (2018), it consists inadaptability of pure fluids model to calculate mixed refrigerant and natural gas condensation heat transfer coefficient. The

process comes with fluctuations of component concentrations and different temperatures at the boundary and at the vapour core.
The similar problems are obtained for boiling process of mixed refrigerant, limited number of experiments for boiling of hydrocarbon mixtures in shell-side of SWHE prevent from development of a valid designing method.

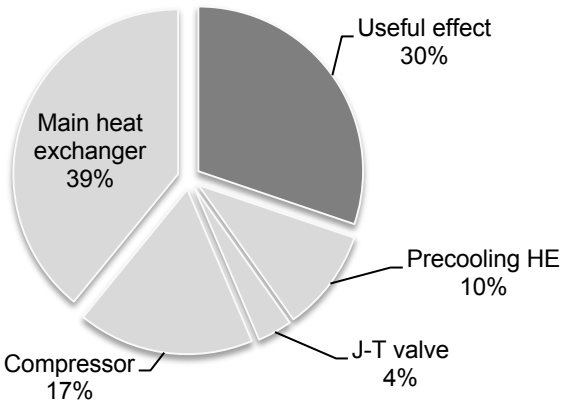

Figure 1: Exergy losses in base load LNG plant.

2. THEORETICAL MODELS

Theoretical models which are based on experimental data for boiling of hydrocarbon mixed refrigerant in the shell-side of SWHE are observed. They include equations based on data acquired by Fredheim et al. (2000), Neeraas et al. (2004) and Hu et al. (2019).
Measurements of heat transfer coefficient by Fredheim et al. (2000) and Neeraas et al. (2004) were carried out on the same test facility. The test section represents model of SWHE with three zones: stabilization zone, isothermal zone and electrically heated zone. The heating elements are placed inside tubes in the heated zone; temperature transmitters are located on the walls of the tubes.
Measurements were made for regimes with Re-number in range from 500-8000 for different hydrocarbon and nitrogen mixtures, detailed parameters are shown in Table 1.
Suggested equation, based on the method from Bays and McAdams (1937), for heat transfer coefficient in dimensionless form for falling film flow in the shell-side of SWHE is presented in Eq.1:

$$Nu_l = a_1 \cdot \left(\frac{d_t}{\delta_c}\right)^c \cdot (Re_l)^b \cdot Pr_l^d \qquad \text{Eq. (1)}$$

where d_t is tube diameter in m; δ_c is reference film thickness in m; Re_l is Reynolds number for liquid; Pr_l is Prandtl number for liquid.
For $Re_l \leq 2000$ constants a_1, b, c, d are taken from Bennett et al. (1986), for $Re_l > 2000$ new constants are given to fit measured data of heat transfer for hydrocarbon mixture in Bays and McAdams (1937) equation. The agreement between measuring and calculation within ±15% with measuring accuracy between ±5 and30%.
Hu et al. (2019) studied flow patterns of boiling film flow and heat transfer coefficient depending on ethane-propane mixture composition; influence of vapour quality on heat transfer and influence of mass flux on heat transfer. The goal of the research was the development of new correlation for calculation of heat transfer coefficient of boiling mixed hydrocarbon refrigerant in shell-side of SWHE. The correlation is based on Ding et al. (2017) equation (Eq. 2) which was developed for pure propane.

$$\alpha = E \cdot \alpha_{con} + S \cdot \alpha_{boil} \qquad \text{Eq. (2)}$$

Hu et al. (2019) fitted coefficients E and S (Eq. 3 and Eq. 4) for convective and nucleate boiling heat transfer coefficients for hydrocarbon mixed refrigerant. These modified parameters reflect composition shift effect and changing of thermophysical properties of the refrigerant during boiling process. In addition, Prandtl number for liquid is introduced to take into account molar composition of the mixture.

$$E = 1 + a_1 \cdot (\varphi^2)^{a_2} \cdot (Re_l)^{a_3} \cdot (Pr_l)^{a_4} \quad \text{Eq. (3)}$$

where φ is two-phase frictional factor.

$$S = b_1 \cdot (We_l)^{b_2} \cdot (Bo_l)^{b_3} \cdot (Pr_l)^{b_4} \quad \text{Eq. (4)}$$

where We_l is Webb number; Bo_l is Boiling number.
Coefficients a_1, a_2, a_3, a_4 and b_1, b_2, b_3, b_4 were found by using nonlinear programming solutions. The correlation agrees with 96% of experimental data within a deviation of ±25%. Parameters of the experiments are shown in Table 1.

Table 1. Operational conditions of the experiments

Method	Composition (Mole %)	Mass flux, $kg \cdot m^{-2} \cdot s^{-1}$	Heat flux, $kW \cdot m^{-2}$	Vapour quality	Pressure, bar	Temperature, °C
Fredheim et al. (2000),	C_1/C_2 (45/55)	49-76	<10	0.1-0.89	3.0-6.0	-125..-96
	C_3/C_2 (90/10)	36-97	<10	0-0.83	2.2-3.9	-30..-12
	C_3/C_2 (85/15)	36-87	<10	0.05-0.94	1.7-4.7	-41..-10
	n-C_4/C_2 (85/15)	45-71	<10	0.07-0.93	1.5-2.5	-25..-2
	n-C_4/C_2 (70/30)	43-84	<10	0.05-0.91	2.0-4.0	-34..-3
	n-$C_4/C_2/C_1$ (80.7/14.3/5.0)	45-69	<10	0.09-0.87	1.7-3.0	-44..-10
	n-$C_4/C_2/C_1$ (65.2/15.4/19.4)	44-70	<10	0.07-0.93	2.5-5.0	-117..-46
	n-$C_4/C_2/C_1/N_2$ (62.6/14.8/18.6/4.0)	46-84	<10	0.08-0.92	2.5-5.2	-122..-63
Neeraas et al. (2004),	C_3/C_2 (90/10)	35-98	<10	-	2.2-3.6	-30..-15
	C_3/C_2 (85/15)	36-89	<10	-	3.6-3.8	-19..-17
	n-C_4/C_4 (70/30)	45-85	<10	-	2.0-4.0	-37..-5
	C_2/C_1 (59/41)	15-96	<10	-	2.0-4.0	-134..-105
Hu et al. (2019)	C_3/C_2 (90/10)	40-80	6-10	0.2-0.9	0.25	-
	C_3/C_2 (70/30)	40-80	6-10	0.2-0.9	0.25	-
	C_3/C_2 (40/60)	40-80	6-10	0.2-0.9	0.25	-

Described methods of calculating heat transfer coefficient of boiling hydrocarbon mixed refrigerant in shell-side of SWHE are based on different equations. First correlation has its origin from equation for falling film flow which includes only convective heat transfer constituent. Whilst the agreement for this correlation is better than for the second one, despite of adding coefficients for composition shift and boiling heat transfer additive.

3. RESULTS AND DISCUSSION

Calculation of the heat transfer coefficient is made for conditions mentioned by Samokhvalov et al. (2018) and Smorodin and Parshin (2018) are shown in Table 2. Thermodynamic properties are calculated by Peng-Robinson equation of state.

Table 2. Parameters of the numerical simulation

Parameter	Value
Composition (mole %)	$n\text{-}C_4/C_3/C_2/C_1/N_2$ (37.3/0.1/24.6/32.8/5.2)
Pressure (bar)	3.0
Mass flux ($kg \cdot m^{-2} \cdot s^{-1}$)	40, 80
Heat flux ($kW \cdot m^{-2}$)	6.0
Vapour quality	0.06-0.96
Temperature (°C)	-147..0
Outer tube diameter (m)	0.012
Winding angle (°)	4
Core diameter (m)	0.12
Shell diameter (m)	0.15
Number of layers	2
Tube surface roughness (μm)	1.5

Heat transfer coefficients are defined for mass fluxes values of 40 $kg \cdot m^{-2} \cdot s^{-1}$ and 80 $kg \cdot m^{-2} \cdot s^{-1}$ (Fig. 2). As a result, correlations of Hu et al. (2019) and Neeraas et al. (2004) have similar results for high Reynolds numbers for vapour quality from 0.05 to 0.75. As for lower mass flows values and greater vapour quality methods have the divergence about 30%.
Authors suggest carrying out additional experiments to investigate heat transfer coefficient of boiling hydrocarbon mixed refrigerant in shell-side of SWHE for mass fluxes from 40 $kg \cdot m^{-2} \cdot s^{-1}$ to 60 $kg \cdot m^{-2} \cdot s^{-1}$ and for vapour fractions greater than 0.7 for different hydrocarbon and nitrogen compositions.

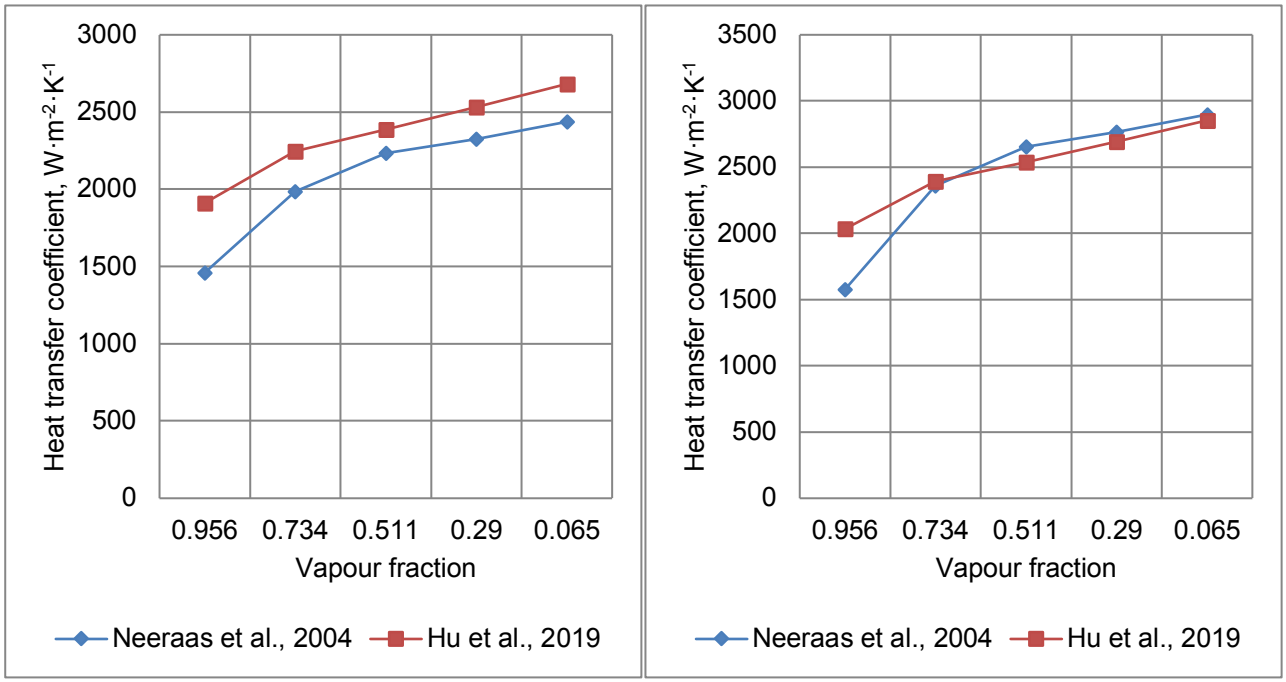

Figure 2: Heat transfer coefficients for different mass fluxes (left – 40 $kg \cdot m^{-2} \cdot s$, right – 80 $kg \cdot m^{-2} \cdot s$).

4. EXPERIMENTAL SETUP

Experimental setup consists of two cycles (Fig. 4): mixed refrigerant cycle and imitation of flow through test section cycle. Setup also includes measuring instruments described in Table 3. Mixed refrigerant cycle provide refrigeration capacity in temperature ranges from -156..-60°C, cooling and condensing test flow before the test section inlet.

The test cycle includes compressor, aftercooler, main spiral-wound heat exchanger and expansion valve. Before the test section electric heater is installed to provide required vapour fraction quality of the flow. Electric heater after the test section is designed to evaporate residual liquid to protect compressor from liquid slugging.

Table 3. Main instruments and their measuring properties

Parameter	Instruments	Measuring range	Accuracy
Temperature	OWEN Pt1000	-196..660°C	0.25%
Mass flow	Emis	10-2000 kg/h	0.15%
Power meter	GW Instek	0.1 W to 12 kW	0.1%
Pressure	Elemer	0 to 40 bar	0.25%
Chromatography	Chromos GC-1000	-	0.2%

Design of the test section of the experimental setup (Fig. 3) is based on the test section developed by Ding et al. (2017). It includes zone for flow stratification and electric heated zone. The heating elements are installed in stainless tubes, temperature transmitters are placed between outer and inner layer as shown on Fig. 3.

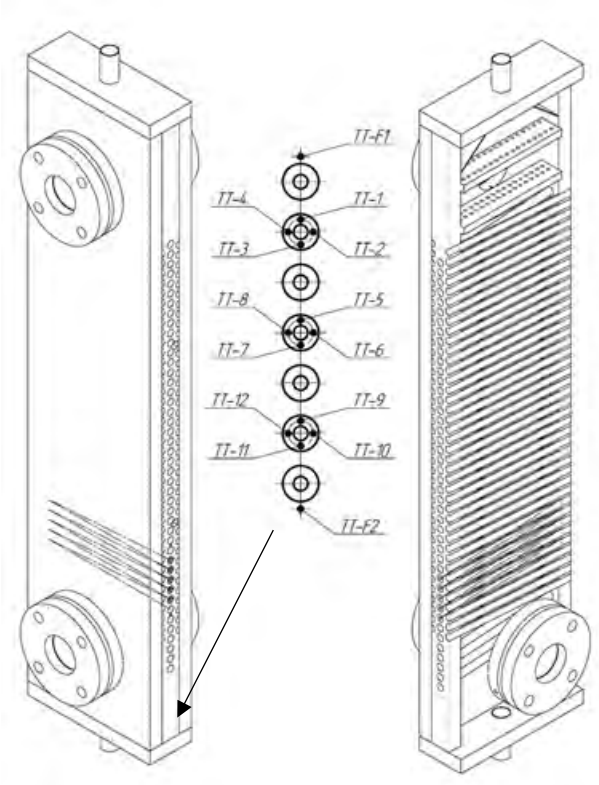

Figure 3: Test section of the experimental setup.

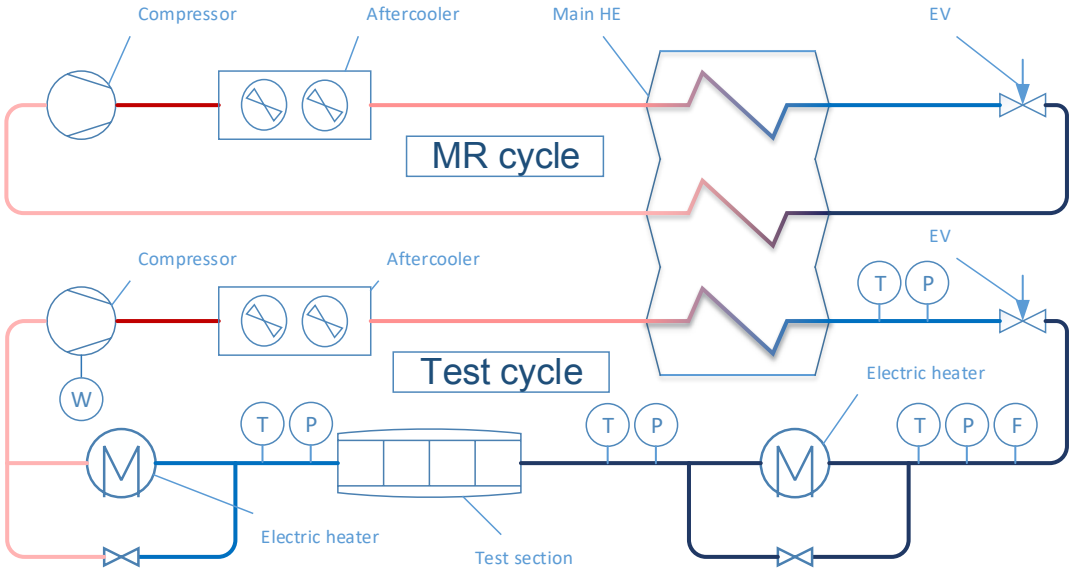

Figure 4: Scheme of the experimental setup.

5. CONCLUSIONS

Designing of the spiral wound heat exchangers for liquefaction of natural gas still causes difficulties, part of the reason is uncertainty in calculation of heat transfer. Authors made literature data analysis of problem of calculation of heat transfer coefficient of boiling mixed hydrocarbon refrigerant in shell-side of SWHE. Calculation and comparison of appropriate correlations are made and found divergences under certain conditions. Test setup with test section is suggested for further research of heat transfer.

REFERENCES

Arkharov, A.M., Semenov, V.Y., 2016. Analysis of Thermodynamic Efficiency of Small-Scale Natural Gas Liquefying Plant Operating on Medium-Pressure Cycle. Chemical and Petroleum Engineering, 51 (9-10), 656-664.

Arkharov, A.M., Semenov, V.Y., Krasnonosova, S.D., 2016. Methodology of Statistical Entropy Analysis of Small-Scale Natural Gas Liquefiers. Chemical and Petroleum Engineering, 51 (9-10), 665-673.

Arkharov, A.M., Semenov, V.Y., Krasnonosova, S.D., Lebedev, S.Y., Kul'byakin, V.P., 2016. Statistical Entropy Analysis and Experimental Study of LNG Plant with Precooling at -70°C. Chemical and Petroleum Engineering 52 (7-8), 468-475.

Bays, G.S., McAdams, W.H., 1937. Heat transfer coefficients in falling film heaters, streamline flow. Indust. Eng. Chem., 29 (11), 1240–1246.

Bennet, D.L., Hertzler, B.L., Kalb, C.E., 1986. Down-flow shellside forced convective boiling. AIChE J. 32 (12), 1963–1970.

Ding, C., Hu, H., Ding, G., Chen, J., Mi, X., Yu, S., Li, J., 2017. Experimental investigation on downward flow boiling heat transfer characteristics of propane in shell side of LNG spiral wound heat exchanger. Int. J. Refrig. 84, 13–25.

Fredheim, A., Jørstad, O., Owren, G., Vist, S., Neeraas, B.O., 2000. Coil, a model for simulation of spiral wound LNG heat exchangers. World Gas Conference, Nice.

Hu, H., Ding, C., Ding, G., Chen, J., Mi, X., Yu, S., 2019. Heat transfer characteristics of two-phase mixed hydrocarbon refrigerants flow boiling in shell side of LNG spiral wound heat exchanger. Int. J. Heat Mass Tran. 131, 611–622.

Narasimhan, N.L., Venkatarathnam G., 2010. A method for estimating the composition of the mixture to be charged to get the desired composition in circulation in a single stage JT refrigerator operating with mixtures. Cryogenics 50(2), 93-101.

Neeraas, B.O., Fredheim, A.O., Aunan, B., 2004. Experimental shell-side heat transfer and pressure drop in gas flow for spiral-wound LNG heat exchanger. Int. J. Heat Mass Tran. 47, (2) 353–361.

Samokhvalov, Y., Kolesnikov, A., Krotov, A., Parkin, A., Navasardyan, E., Arkharov, I., 2018. Heat transfer in the structure of a spiral-wound heat exchanger for liquefied natural gas production: Review of numerical models for the heat-transfer coefficient of condensation for a hydrocarbon mixture in a horizontal tube. Journal of Enhanced Heat Transfer 25 (2), 109-120.

Smorodin, A.I., Parshin, S.A., 2018. Optimization of Refrigerant Composition of Low-Temperature Stage of Dual Mixed Refrigerant Cycle. Chemical and Petroleum Engineering 54 (7-8), 493-498.

Manuscript ID: 1027
DOI: 10.18462/iir.icr.2019.1027

Recent advances in single- and multi-stage Stirling-type pulse tube cryocoolers in SKLIP/SITP/CAS

Haizheng DANG[(a),(c)], Jun TAN[(a),(c)], Rui ZHA[(a),(b)], Jiaqi LI[(a),(b)], Tao ZHANG[(a),(b)], Yongjiang ZHAO[(a),(b)], Bangjian ZHAO[(a),(b)], Han TAN[(a),(b)], Renjun XUE[(a),(b)]

[(a)]State Key Laboratory of Infrared Physics, Shanghai Institute of Technical Physics, Chinese Academy of Sciences, Shanghai, 200083, China, haizheng.dang@mail.sitp.ac.cn
[(b)]University of Chinese Academy of Sciences, Beijing, 100049, China
[(c)]Shanghai Boreas Cryogenics Co., Ltd, Shanghai, 200434, China

ABSTRACT

This paper reviews recent advances in single- and multi-stage Stirling-type pulse tube cryocoolers (SPTCs) developed in the authors' laboratory, in which single-stage coolers operate at 30-200 K, two-stage ones at 15-100 K while three- and four-stage ones cover 2-10 K. Single-stage coolers involving micro, miniature and middle-size ones, with cooling capacities varying from 1.0 W to 50 W, are for cooling infrared and optical devices. Recently high-capacity ones with 800 W at 77 K are developed to cool high-Tc superconducting facilities such as cables and magnets. Two-stage SPTCs are mainly for simultaneously providing cooling at both stages. Three-stage SPTCs are developed to achieve cooling at around 10 K while four-stage ones at below 4 K, both of which can also precool J-T coolers to achieve lower temperatures such as around or below 2 K used for low-Tc superconducting devices or the deep space exploration. The designs of the SPTCs including the compressors are described in which the efforts in enhancing the efficiencies are emphasized.
Keywords: Recent Advances, Single-stage, Multi-stage, Stirling-type Pulse Tube Cryocooler, Review.

1. INTRODUCTION

The pulse tube cryocooler (PTC) is now widely acknowledged as a significant innovation in the regenerative refrigeration technology because it eliminates any moving component at the cold end, which endows it with evident advantages over the conventional regenerative cryocoolers such as GM and Stirling ones in terms of high reliability, long life and low vibration at the cold end (Dang, 2015; Dang et al., 2017). The Stirling-type PTC (SPTC) driven by the linear compressor employing the well-proven flexure springs and clearance technology further realizes the long operation time at the warm end (Dang, 2015; Dang et al, 2016), which makes it an attractive candidate for cooling cryogenic devices used in some special fields such as in space. The past decade has witnessed a rapid development of single- and multi-stage SPTCs in the authors' laboratory and their successful applications in a variety of projects. Recently, new progress has been achieved and this paper will present an overview of these advances.

2. SINGLE-STAGE SPTCS

During the past 10 years, a series of single-stage coaxial, U-type and in-line high efficiency SPTCs covering 20-180 K have been developed in the authors' laboratory for a variety of practical applications, in which several mid-sized ones weighing 4.5-12.0 kg working at 60-110 K are already flown in space (Dang et al., 2017). Continuous advances have been achieved in the mid-sized SPTCs working at below 30 K. At present, using the mixed regenerator consisting of multi-segment matrices to enhance the regenerator performance at the coldest end and also to minimize the overall flowing resistance along the tube, a new no-load temperature of 17.3 K and the cooling power of 0.25 W at 25 K can be achieved with an electric input power of 295 W. However, the much more impressive progresses are about a 650 g micro SPTC operating at high frequencies of over 100 Hz and a 150 kg high-capacity one achieving 800 W at 77 K to be discussed as follows.

2.1 650 g micro coaxial SPTC

Miniaturization of cryocoolers is a worldwide concern because a variety of applications based on optical and electronic technologies only require relatively small cooling powers but do need both light weight and short cool-down time. There exists a wide gap between the requirements and the available cryocoolers. The cooling capacity of a regenerative cryocooler would decrease sharply with reduced size and an effective solution is to increase both charge pressure and cycle frequency. However, the charge pressure has an upper limit in view of safety, while a too high operating frequency often results in the poor heat transfer in the heat exchanger, thereby producing considerable irreversible losses (Zhao et al., 2018).

Based on the developed two-dimensional axis-symmetric CFD model, the oscillating flow and heat transfer process in the micro coaxial SPTC operating at 90-400 Hz had been investigated and a 800 g micro prototype worked out in 2017 (Dang et al., 2017). In 2018, the overall mass was reduced to 700 g and the Engineering Model (EM) of the cooler is achieved (Zhao et al., 2018). And in 2019, the SPTC EM has further decreased to 650 g while keeping the same cooling performance.

Fig. 1 provides a photograph showing the comparisons between the 450 g micro linear compressor and a conventional mid-size one, and Fig. 2 shows the developed 650 g micro SPTC together with a Coke can as the reference object. The micro SPTC has achieved the cooling capacity of 1.0 W at 77 K with an electric input power of 40 W, and the cool-down time from 300 K to the no-load temperature of 50 K is within 5.0 minutes.



Figure 1: Micro and mid-size compressors

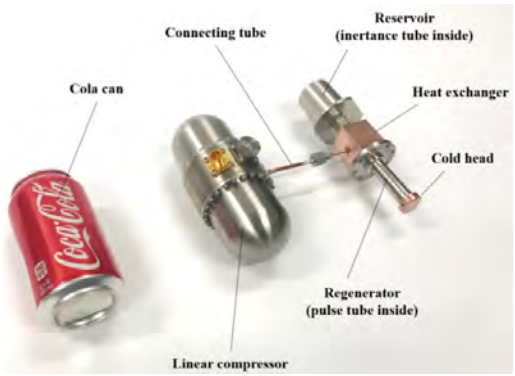

Figure 2: 650 g micro SPTC EM

2.2 High-capacity SPTC with 800 W at 77 K

The continuously increasing demand for electricity has put a strain on the capacity of electric grids around the world. The high temperature superconducting (HTS) cable can provide a feasible solution to the acute problem since it can carry several times more power than the conventional one with the same footprint and operate at a much lower voltage as well. The cryogenic system is indispensible for the HTS cable, in which several requirements are desirable such as low maintenance, high reliability, long operation life, high cooling efficiency, small footprint and acceptable cost. Due to the outstanding merits discussed in the Introduction, the SPTC becomes an attractive candidate for cooling the HTS cable. However, an enormous challenge for the application is the required huge cooling powers. To minimize the number of the cryocoolers in the cryogenic system, the cooling capacity of about 700 W up to several kilo-Watts at 77 K is needed. By contrast, in most cases, the SPTCs usually provide the cooling powers of below 50 W, or even less. In essence, the main challenge comes from the linear compressor serving as the energy origin of the cryocooler system. Generally speaking, most linear compressors have an upper limit of the input power of around 1 kW, but the aimed application would require much more than ten times the conventional upper limit, especially for the moving-coil linear compressors.

In our development program, the moving-coil linear compressor is still adopted for the high capacity SPTC. The main purpose is to avoid open circuit axial forces and torques on the current carrying coil and also to completely eliminate the radial forces in the compressor, which are the key advantages of the moving-coil linear compressor. The design of the compressor is based on the partial scaling method proposed by the same laboratory (Zhang et al., 2015), and the chosen original linear compressor as the basis is the mature mid-size one with an input capacity of 400 W developed mainly for space applications, and the aimed input capacity goal is 16 kW. Fig. 3 shows the photo of the original 400 W linear compressor (middle) and the scaled-up new 16 kW one (up) with a Coke can (below) as the reference object.

The mass of the developed 16 kW compressor is about 100 kg. In order to ease the practical application, the coaxial arrangement is adopted for the pulse tube cold finger and all of the phase-shifters (inertance tubes) are enveloped in the reservoir to achieve a compact system, as used in the mid-size SPTCs (Dang et al., 2017). Fig. 4 shows a photograph of the developed high-capacity SPTC. The overall mass is 150 kg and currently it can provide the cooling power of 800 W at 77 K with the input power of 16 kW. The reject temperature at the cold end is kept at 300 K using the cycling water, and a relative Carnot efficiency of about 14.5% is achieved.



Figure 3: 400 W and 16 kW compressors

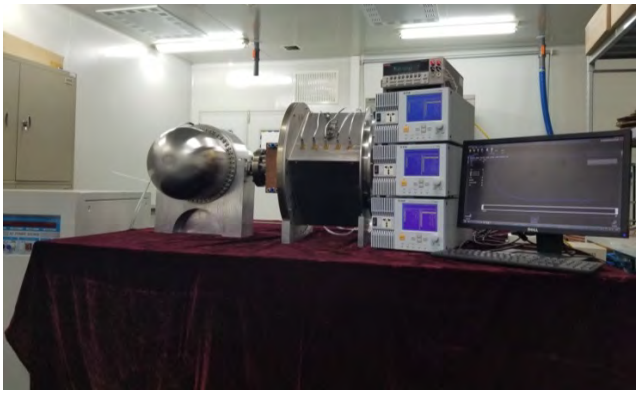

Figure 4: SPTC capable of 800 W at 77 K

3. TWO-STAGE SPTCS

In practice, there is an increasing interest in providing cooling powers at different temperature levels. For example, for many space-borne cryogenic instruments, some have two detectors with differing operating temperatures, and some need to simultaneously cool both detector and optics. In some cases, the use of two separate single-stage SPTCs with two different cooling temperatures is suggested as a viable option. However, a two-stage SPTC driven by a single compressor will have many definite advantages in terms of weight, compactness and system integration. In our development program, the main goal of developing the two-stage SPTCs is to simultaneously achieve the cooling capacities at both stages, in which the second stage normally works in 30-35 K while the first stage usually operates in 80-150 K.

The capacity in distributing the cooling capacities between the stages has been investigated theoretically and experimentally (Tan and Dang, 2017). A theoretical model of the thermally-coupled two-stage SPTC based on the electric circuit analogy with considering real gas effects has been established, and simulations of both the cooling performances and PV power distribution between stages has been conducted. The results indicate that the PV power is inversely proportional to the acoustic impedance of each stage, and the cooling capacity distribution is determined by the cold finger cooling efficiency and the PV power into each stage together. Recently, the two-stage SPTC have made the new progress and the results indicate that it can reach a no-load temperature of 11.6 K and simultaneously achieve 2.0 W at 30 K and 6.0 W at 85 K with an electric input power of 340 W and a reject temperature of 300 K.

4. THREE-STAGE SPTCS

The three-stage SPTCs are developed mainly for the applications at around 10 K, and they can also be used for precooling J-T coolers to achieve liquid helium temperatures. Both thermally-coupled and gas-coupled arrangements of the three-stage SPTC, as shown in Fig. 5 and Fig. 6, have been studied (Gao and Dang, 2016; Dang et al., 2018a; Dang et al., 2018b). And the entropy analysis has been employed as one of the main approaches for their design and optimization (Gao and Dang, 2016).

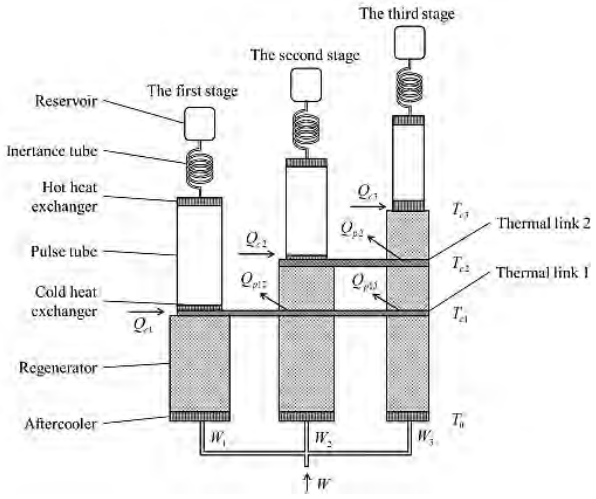

Figure 5: Three-stage thermally-coupled

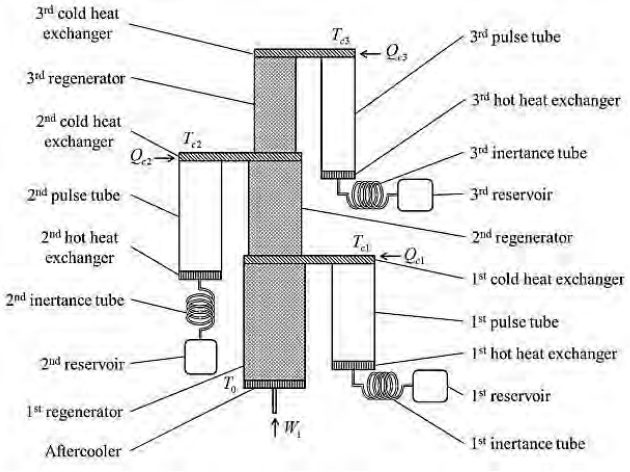

Figure 6: Three-stage gas-coupled

Cryogenic phase-shifting and mixed regenerator matrices are employed to improve the

performance at the third stage (Dang et al., 2018a). Fig. 7 and Fig. 8 show the concepts of cryogenic and ambient phase-shifters, respectively. Simulations of the phase relationship, dynamic pressure and mass flow rate are presented with third-stage phase-shifters at 40 K, 50 K and 293 K, respectively (Dang et al., 2018a). Mixed regenerator matrices of conventional stainless steel meshes and rare-earth materials such as Er_3Ni, $HoCu_2$ and $Er_{0.6}Pr_{0.4}$ are optimized theoretically. Different ratios and combinations are analyzed and compared, and the quantitative analyses by the entropy analysis are made. A three-stage SPTC without external precooling is developed based on the theoretical analyses. In the new experiments, with an overall input power of 370 W, the three-stage SPTC has experimentally reached a no-load temperature of 4.8 K and achieved a cooling capacity of 155 mW at 10 K.

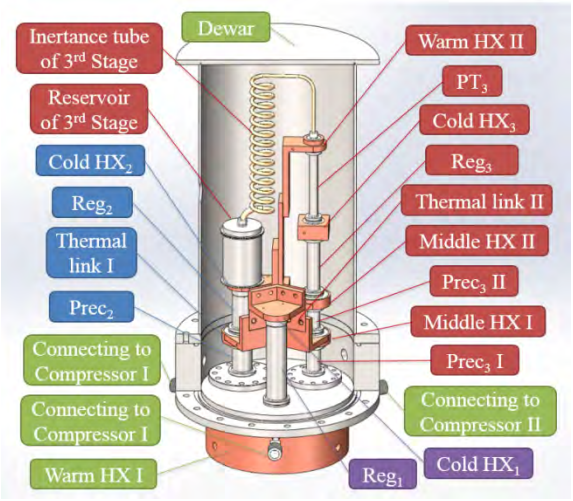

Figure 7: Cryogenic phase-shifter

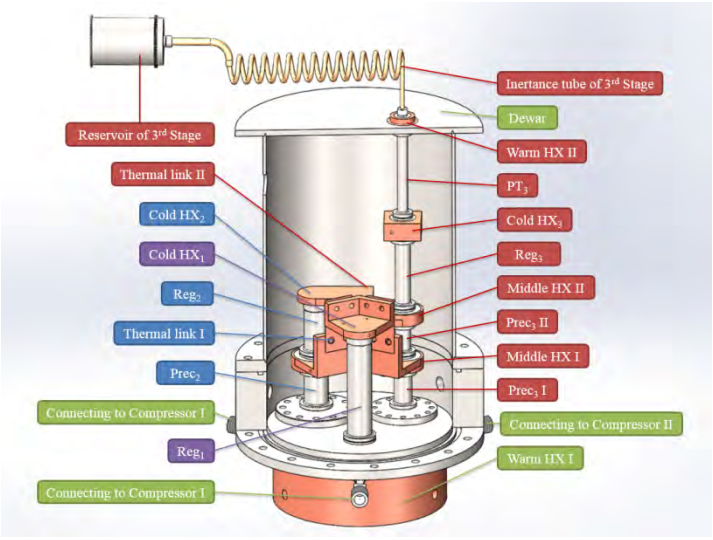

Figure 8: Ambient phase-shifter

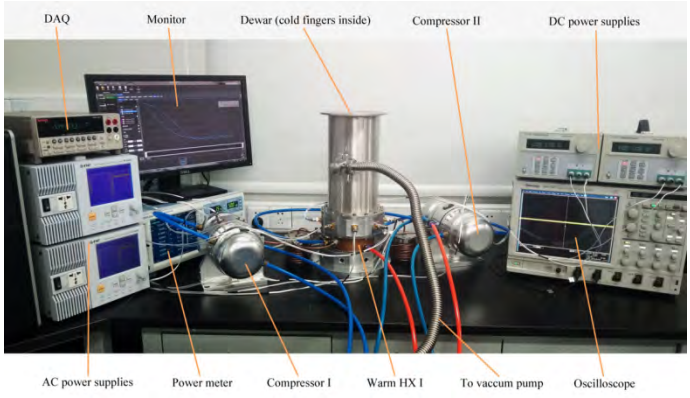

Figure 9: Two-compressor-driven three-stage SPTC

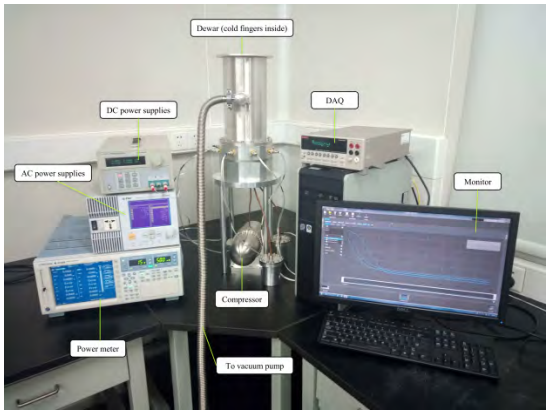

Figure 10: Single-compressor-driven three-stage SPTC

The single-compressor-driven (SCD) three-stage SPTC has also been investigated (Dang et al., 2018b). The main differences between the SCD type and the multi-compressor-driven (MCD) one is that the former is driven by only one linear compressor, which will result in big differences in the distribution of the input acoustic power in each stage and the optimization of the operating parameters. Fig. 9 and Fig. 10 give the set-ups of a two-compressor-driven three-stage SPTC and a SCD counterpart, respectively. In the new experiments, with a total input acoustic power of 370 W,

the SCD three-stage SPTC reaches a no-load temperature of 7.2 K and achieves the cooling capacity of 67 mW at 10 K. The performance of the SCD three-stage SPTC is slightly poorer than that of its MCD counterpart given above, but the advantages of lightweight (20 kg less) and compactness make the former more attractive to practical applications.

Fig. 11 shows a schematic of the three-stage SPTC/J-T hybrid cryocooler. The three-stage SPTC used to precool the J-T cooler employs the completely gas-coupled arrangement and the three cold fingers are driven by only one linear compressor. The first two stages are U-type and the third stage is linear-type. All of the three phase-shifters are placed in the ambient environment. The three cold heads are able to provide adequate cooling capacities for the J-T cooler at three different temperatures, respectively, through the thermal links.

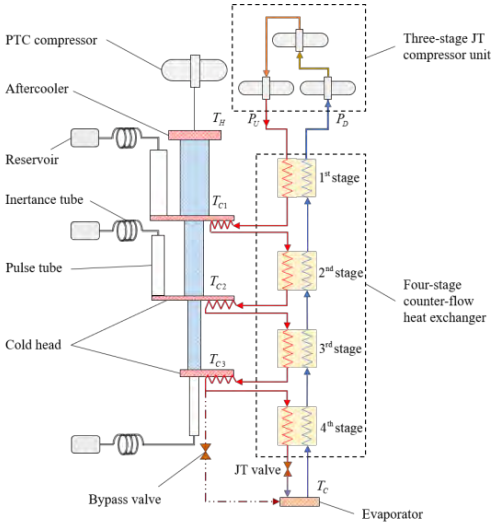

Figure 11: Schematic of three-stage SPTC/J-T hybrid cryocooler

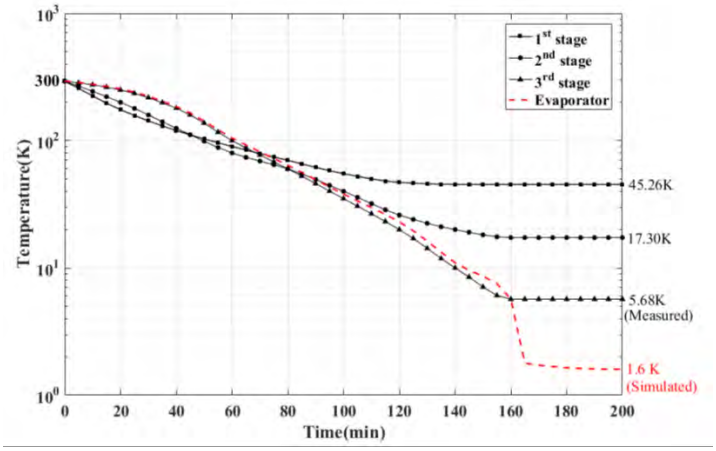

Figure 12: Cool-down curves of three-stage SPTC/J-T hybrid cryocooler

The J-T loop, as shown in Fig. 11, consisting of four-stage counter-flow heat exchangers, a throttling valve and an evaporator, is driven by the three-stage J-T compressor unit formed by three linear J-T compressors and corresponding valves which are used to generate DC flow. To achieve the aimed temperature of 2 K, the first stage compressor of the JT actually acts as a vacuum pump to maintain the required saturation pressure in the evaporator which is much lower than the atmospheric pressure. He-4 or He-3 gas passes through the high-pressure (upstream) channel of the four-stage counter-flow heat exchangers where it is cooled stage-by-stage by the low-pressure (downstream) returning gas and the three cold heads of SPTC. After going through the throttling valve, He-4 or He-3 experiences the drop in both temperature and pressure, with a fraction of liquid working medium producing in the evaporator as the cooling capacity for the device to be cooled.

The cooling performance of the hybrid cryocooler is tested and the cool-down curves are shown in Fig. 12. With a total input power of 390 W, the no-load temperatures of the three stages are 45.26 K, 17.30 K and 5.68 K, respectively, in 200 minutes. A CFD model is established for the hybrid cryocooler in which flow and heat transfer processes are simulated and then the cooling capacities can be optimized by analyzing exergy losses caused by heat transfer. Based on the simulations, if the J-T cryocooler uses He-3 as the working gas, with an input power of 420 W, a no-load temperature of 1.6 K is expected to be obtained by the current test setup (Dang et al., 2019).

5. FOUR-STAGE SPTCS

The four-stage SPTCs are developed to directly reach liquid helium temperatures, which can also be used for precooling a J-T cooler to achieve further lower temperatures, and thus are expected to play an important role in cooling the space low-Tc superconducting devices and in the deep space exploration as well (Dang et al., 2017). A schematic of the four-stage SPTC and the experimental set-up are shown in Fig. 13 and Fig.14, respectively. It has four cold fingers, in which the first two ones are coaxially arranged and driven together by one compressor whereas the last two ones adopt the linear arrangement and are driven by the other compressor. The phase-shifters of the first two stages are put in ambient environment and those of the third and fourth stages in cryogenic one, which are cooled by the second and third stages, respectively.

In the preliminary experiments, it is observed that the fourth stage cold head can achieve a no-load temperature of 4.38 K in about 160 minutes, as shown in Fig. 15 (Dang et al., 2019). We have also built the CFD model for the fourth stage in which the entropy generations caused by the losses can be studied in detail. Based on the model, the cooling performance and the temperature distributions can be simulated. It is shown that if an input power of 510 W is provided and He-3 is used to replace He-4 as the working fluid at the fourth stage, the no-load temperature would further decrease to K. Currently, both of the above two optimization ways are underway (Dang et al., 2019).

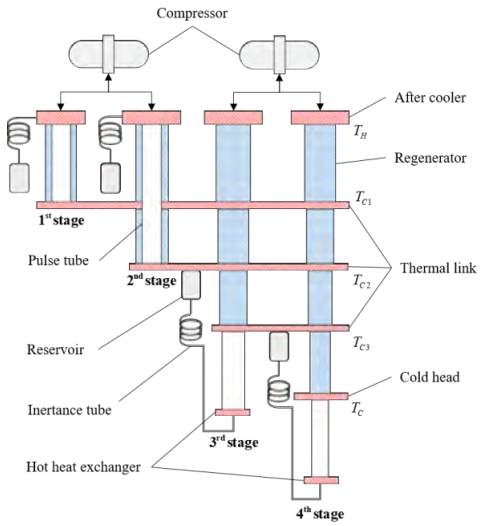

Figure 13: Schematic of four-stage SPTC

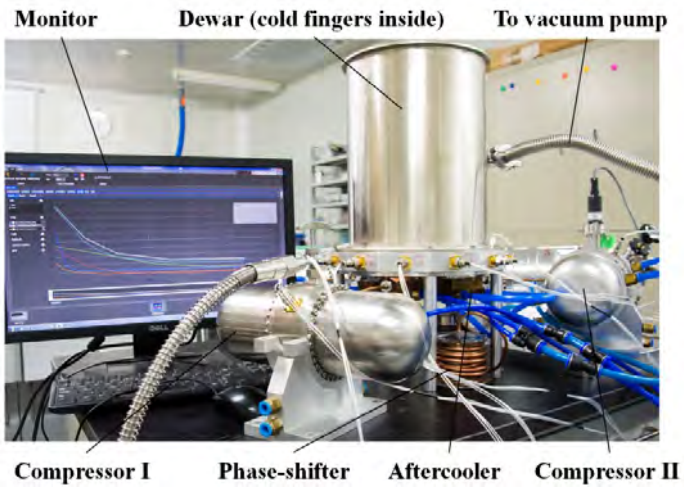

Figure 14: Experimental set-up of four-stage SPTC

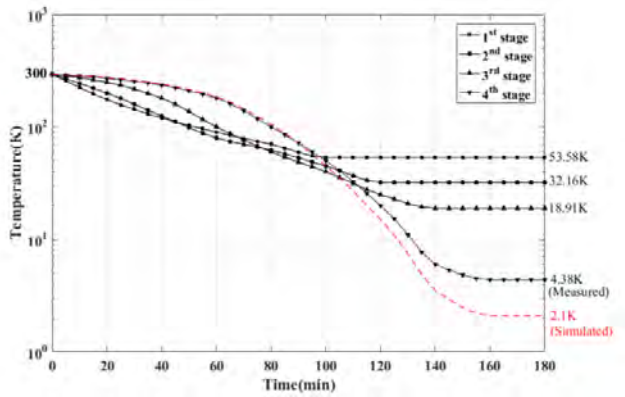

Figure 15: Cool-down curves of each stage of four-stage SPTC

6. CONCLUSIONS

This paper presents a review of recent advances in single- and multi-stage SPTCs in the authors' laboratory. A 650 g micro SPTC and a high-capacity one with 800 W at 77 K are achieved. The two-stage SPTC have made new advances at 30 K and 85 K. The three-stage and four-stage SPTCs have reached 5.68 K and 4.38 K, respectively. Both three-stage SPTC/J-T hybrid cryocooler and four-stage SPTC expected to achieve around 2 K or even below are underway.

ACKNOWLEDGEMENTS

This work is supported by the Aeronautical Science Foundation of China (No. 20162490005) and Shanghai Municipality (Nos. 18511110100, 18511110101, 18511110102).

REFERENCES

Dang, H.Z., 2015. Development of high performance moving-coil linear compressors for space Stirling-type pulse tube cryocoolers. Cryogenics 68, 1-18.

Dang, H.Z., Zhang, L., Tan, J., 2016. Dynamic and thermodynamic characteristics of the moving-coil linear compressor for the pulse tube cryocooler. Part A: Theoretical analyses and modeling. Int. J. Refrigeration 69, 480-496.

Dang, H.Z., and Zhao, Y.B., 2016. CFD modeling and experimental verification of a single-stage inertance tube coaxial Stirling-type pulse tube cryocooler operating at 30-35 K using the mixed stainless steel mesh regenerator matrix. Cryogenics 78, 40-50.

Dang, H.Z., Tan, J., Zha, R., et al., 2017. Advances in single- and multi-stage Stirling-type pulse tube cryocoolers for space applications in NLIP/SITP/CAS, IOP Conf. Ser.: Mater. Sci. Eng. 278 012008. doi: 10.1088/1757-899X/278/1/012008.

Dang, H.Z., Bao, D.L., Zhang, T., et al., 2018a. Theoretical and experimental investigations on the three-stage Stirling-type pulse tube cryocooler using cryogenic phase-shifting approach and mixed regenerator matrices. Cryogenics 93, 7-16.

Dang, H.Z., Bao, D.L., Gao, Z.Q., et al., 2018b. Theoretical modeling and experimental verifications of the single-compressor-driven three-stage Stirling-type pulse tube cryocooler. Frontiers in Energy, doi: 10.1007/s11708-018-0569-8.

Dang, H.Z., Zhang, T., Zha, R., et al., 2019. Development of 2 K space cryocoolers for cooling the superconducting nanowire single photon detector. IEEE Transactions on Applied Superconductivity 29, doi: 10.1109/TASC.2019.2902770.

Gao, Z.Q., and Dang, H.Z., 2016. Entropy analyses of the three-stage thermally-coupled Stirling-type pulse tube cryocooler. Applied Thermal Engineering 100, 944-960.

Tan, J., and Dang, H.Z., 2017. Theoretical and experimental investigations on the cooling capacity distributions at the stages in the thermally-coupled two-stage Stirling-type pulse tube cryocooler without external precooling. Cryogenics 82, 48-61.

Zhang, L., Dang, H.Z., Tan, J., et al., 2015. Theoretical and experimental investigations on the partial scaling method for the Oxford-type moving-coil linear compressor. Cryogenics 69, 26-35.

Zhao, Y.B., Yu, G.R., Tan, J., et al., 2018. CFD modeling and experimental verification of oscillating flow and heat transfer processes in the micro coaxial Stirling-type pulse tube cryocooler operating at 90-170 Hz. Cryogenics 90, 30-40.

Manuscript ID: 1063
DOI: 10.18462/irr.icr.2019.1063

Computational fluid dynamics simulations and experimental investigations on a 1-2 K Joule-Thomson cryocooler precooled by a three-stage Stirling-type pulse tube cryocooler

Tao ZHANG[(a),(b)] , Rui ZHA[(a),(b)], Jun TAN[(a),(c)], Jiaqi LI[(a),(b)], Yongjiang ZHAO[(a),(b)], Bangjian ZHAO[(a),(b)], Haizheng DANG[(a),(c)]

[(a)] State Key Laboratory of Infrared Physics, Shanghai Institute of Technical Physics, Chinese Academy of Sciences, 500 Yutian Road, Shanghai 200083, China, cryotz@163.com; haizheng.dang@mail.sitp.ac.cn

[(b)] University of Chinese Academy of Sciences, No. 19A Yuquan Road, Beijing 100049, China

[(c)] Shanghai Boreas Cryogenics Co., Ltd, 1388 Shuidian Road, Shanghai 200434, China

ABSTRACT

The temperature of 1-2 K is crucial to the low-T_c superconducting and deep space exploration. The Joule-Thomson (JT) cryocooler coupled with a three-stage Stirling-type pulse tube cryocooler (SPTC) is an effective way of achieving the required low temperature and high efficiency. In this paper, a computational fluid dynamics (CFD) model is established for the JT cryocooler, in which the flow and heat transfer processes are simulated and analyzed. The distributions of precooling capacities are optimized by analyzing exergy losses caused by heat transfer. The effects of the three stage precooling temperatures, the precooling capacities and the high pressure before the JT valve on the cooling performance are also studied in depth. The no-load temperatures of 2.2 K and 1.42 K are achieved in the model with He-4 and He-3 as working fluids, respectively. The corresponding experimental verifications are underway.
Keywords: 1-2 K, Cryocooler, SPTC, J-T Cooler, CFD Model, Enthalpy Analysis.

1. INTRODUCTION

The recent years have witnessed the rapid development of the low-T_c superconducting and deep space exploration technologies. For several required detectors such as superconducting nanowire single photon detectors (SNSPDs) and X-ray detectors, the very low temperature of 2 K or even below is critical to their normal operation. Traditionally, a large superfluid helium (He II) cryostat capable of providing a temperature as low as 1.7 K is used to cool the detectors. However, due to the limited volume and evaporation losses, the cryostat's lifetime is very short, such as only several weeks. By contrast, the mechanical hybrid Joule-Thomson (JT) cryocooler is a promising cryocooler candidate for over 5 years operation due to its closed cooling cycle.

For the JT cryocooler aimed to reach 1-2 K, a precooling cryocooler is necessary to provide the cooling power at the temperature which is below the maximum inversion temperature (45.2 K at 0.1 MPa) for He-4. Several researches have been conducted, in which the GM cryocooler and the Stirling cryocooler are employed for precooling (Yoichi et al., 2012; Takeshi et al., 2016). However, the moving components in either GM or Stirling cryocoolers' cold heads inevitably lead to vibration and wear, in which the later dramatically reduces the lifetime and influencing the performance of the detectors. By contrast, the pulse tube cryocooler (PTC) eliminates the moving component at the cold end and thus results in its long life and low vibration. The Stirling-type PTC (SPTC) driven by a linear compressor further achieves the high reliability and long life in the compressor at the warm end, and thus is suitable for a variety of special applications such as in orbit (Dang, 2015). Besides, the multi-stage SPTC is able to precool the JT cold head with two or three stage temperatures from 150 K to less than 10 K. Therefore, the multi-stage SPTC becomes an attractive candidate for precooling the JT cooler, especially for space applications (Dang et al., 2018; Dang, Bao et al., 2018; Dang et al.,

2017).
This paper presents a three-stage SPTC/JT hybrid cryocooler. A computational fluid dynamics (CFD) model is established for the JT cryocooler, in which the flow and heat transfer processes are simulated and analyzed. The boundary conditions are optimized based on the enthalpy analysis. The distributions of precooling capacities are optimized by analyzing exergy losses. The effects of the three stage precooling temperatures, the precooling capacities and the high pressure before the JT valve on the cooling performance are also studied in depth. The experimental investigations are then carried out to verify the simulated results.

2. STRUCTURE DESIGN AND WORKING MECHANISM

Fig. 1 shows the configuration of the three-stage SPTC/JT cryocooler. The three-stage SPTC used to precool the J-T cooler employs the completely gas-coupled arrangement and the three cold fingers are driven by only one linear compressor. The cold fingers are all U-type and all of the three phase-shifters are placed in the ambient environment. The three cold heads are capable of providing adequate cooling capacities for the JT cooler at three different temperatures, respectively, through the thermally coupled Precooling Heat EXchangers (PHEXs).

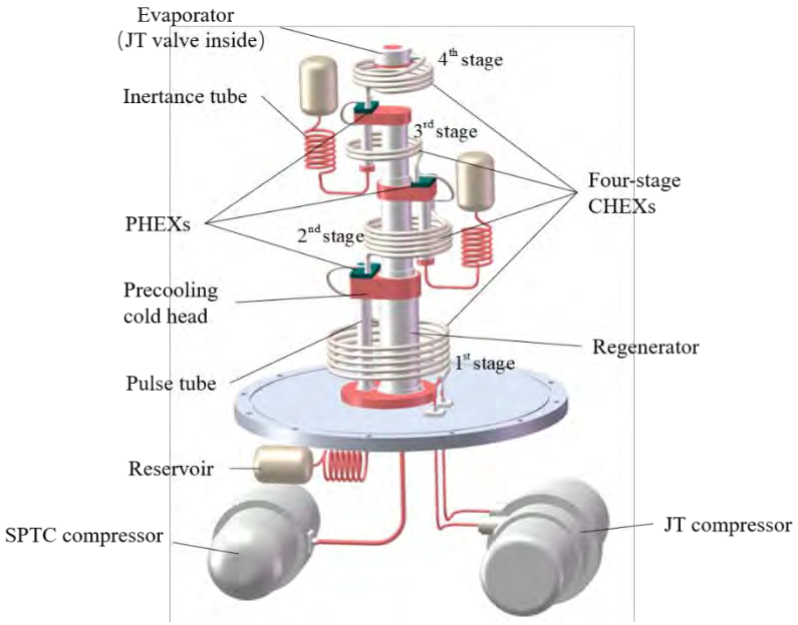

Figure 1: Configuration of the three-stage SPTC/JT cryocooler

The JT cooler, consisting of four-stage Counter-flow Heat Exchangers (CHEXs), three PHEXs, a JT valve and an evaporator, is driven by the JT compressor unit composed of three linear JT compressors and corresponding valves which is used to generate DC flow. In Fig.1, only one JT compressor is demonstrated. Similar to the SPTC, the JT cold head also has no moving component and thus possesses the merits of high reliability, low vibration and long lifetime.
The four CHEXs are all made of stainless steel and adopt tube-in-tube designs, with high-pressure gas flowing in the annular space between the two tubes and the low-pressure gas flowing through the inner tube. The JT valve with a fixed orifice used for a flow impedance for the JT expansion circuit, is integrated inside the evaporator.
Fig. 2 shows a schematic of the operating mechanism in the cryocooler. The effective cooling powers of the three-stage SPTC are 5.8 W at 80 K, 0.72 W at 30 K and 20 mW at 4.2 K, respectively. The working fluid He-4 or He-3 gas passes through the high-pressure (upstream) channel of the four-stage CHEXs where it is cooled stage-by-stage by the low-pressure (downstream) returning gas and the three cold heads of SPTC. After going through the JT valve, the working fluid experiences the isenthalpic expansion with both temperature and pressure decreasing simultaneously. A small amount of liquid coolant is formed in the evaporator, which is used to provide cooling power for the detectors. The vapor pressure of working fluid at the downstream side of the JT valve is determined by the suction pressure maintained at the compressor inlet. When the temperature is below 4 K, the

vapor pressure of He-4 is lower than 100 kPa, such as, about 50 kPa at 3.5 K, 10 kPa at 2.5 K and 5.3 kPa at 2.2 K.

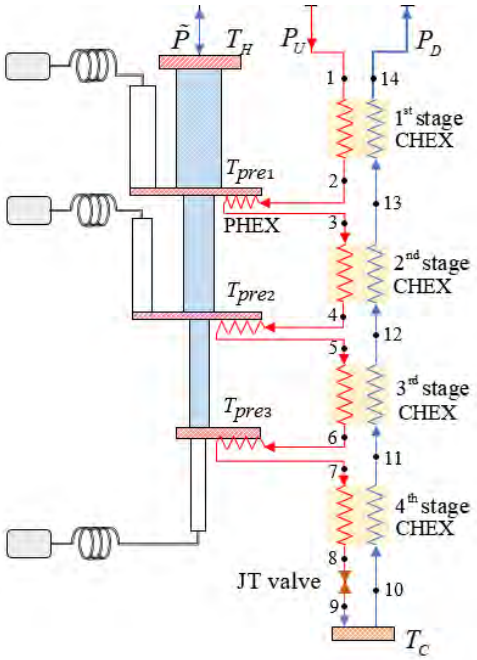

Figure 2: Schematic of working mechanism of the SPTC/JT cryocooler

3. CFD MODEL BUILDING

Generally speaking, a numerical model based on the first law of thermodynamics is convenient and effective to calculate the key parameters in the JT circuit, such as temperature, pressure and enthalpy. However, the flow and heat transfer in the components are much easier to be observed and studied by a CFD model. Therefore, a two-dimensional (2-D) CFD model is established to simulate the flow and heat transfer of the four-stage CHEXs, the three PHEXs and the evaporator, and another numerical model is developed to optimize the parameters of the boundary conditions.

3.1. Model Building

The four CHEXs, three PHEXs and the evaporator are all simplified as 2-D channel flow model. Due to the flow velocity and characteristic lengths of the heat exchangers are very small, the Reynolds number of the fluid does not reach the critical value, and thus the laminar flow model is employed.Fig. 3 shows the axis-symmetric geometry of the first stage CHEX with the length of L. d_{in} and d_{out} are the diameter of the inner tube and outer tube, respectively. The upstream working fluid flow through the outer tube and is cooled from T_1 to T_2 by the downstream one flowing through the inner tube in a counter direction with the temperature from T_{13} to T_{14}.

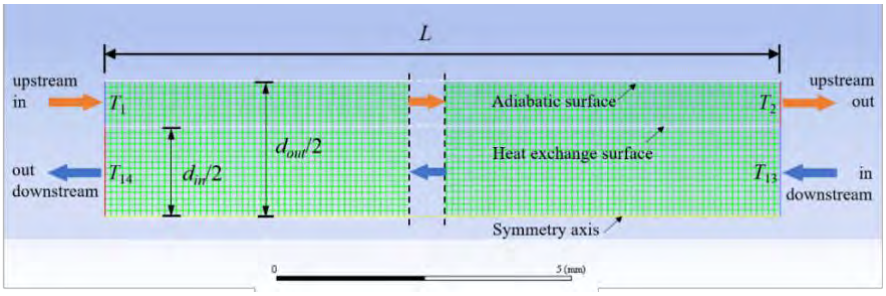

Figure 3: Axis-symmetric geometry of the first stage CHEX

Table 1 gives the geometric dimensions and the boundary condition types of the four CHEXs.

Table 1. Geometrical dimensions and boundary condition types of each stage

Heat exchanger	Length (m)	Diameter (mm)		Boundary condition type	
		Inner tube	Outer tube	Inlet	Outlet
1st	1.3	2	6.5	mass flow rate and temperature	pressure and temperature
2nd	1.0	2	4.2		
3rd	0.7	2	4.2		
4th	1.1	2	4.2		

3.2. Governing Equation

Since helium is in gas or supercritical phase in the CHEXs and PHEXs, the single phase and energy model are employed in the solving model. In the evaporator, part of helium is in liquid phase and heated to the gaseous state, thus the mixture model is used in the model. The conservation equations for the single model and mixture model are given as Eq. (1) and Eq. (2), respectively

$$\frac{\partial(\rho T)}{\partial t} + \nabla \cdot (\rho \boldsymbol{u} T) = \nabla \cdot \left(\frac{\lambda}{c_p} \nabla T\right) + S_T \qquad \text{Eq. (1)}$$

$$\frac{\partial}{\partial t}\left(\sum_{k=1}^{n} \alpha_k \rho_k h_k\right) + \nabla \cdot \left(\sum_{k=1}^{n} \alpha_k \boldsymbol{u}_k (\rho_k h_k + p)\right) = \nabla \cdot \left(\lambda_{eff} \nabla T\right) + S_T \qquad \text{Eq. (2)}$$

In Eq. (2), the subscript index k and n represent the phase number k and the total number of phases, respectively. Other symbols in the two equations are explained in the Nomenclature.

3.3. Boundary Conditions Analysis

The boundary conditions have a crucial effect on the simulated results of the JT cooler performance. With the optimal boundary conditions, the CFD model is the most efficient since it reduces the unnecessary trial-and-error processes. Therefore, a theoretical model based on the enthalpy analysis is developed to calculate and optimize the boundary condition parameters of the model, which is based on the following assumptions:

(1) There are no parasitic heat leaks in the circuit and the heat exchanger is perfectly effective without axial heat conduction;

(2) The compression process is isothermal at the ambient temperature of 300 K;

(3) The heat load is balanced by a maximum generation of cooling capacity;

(4) There is no pressure drop in the isobaric process.

The thermodynamic cycle of the He-4 in the fourth stage CHEX, the JT valve and the evaporator, which is known as the Linde-Hampson cycle, is demonstrated on the *P-h* plane shown in Fig. 3.

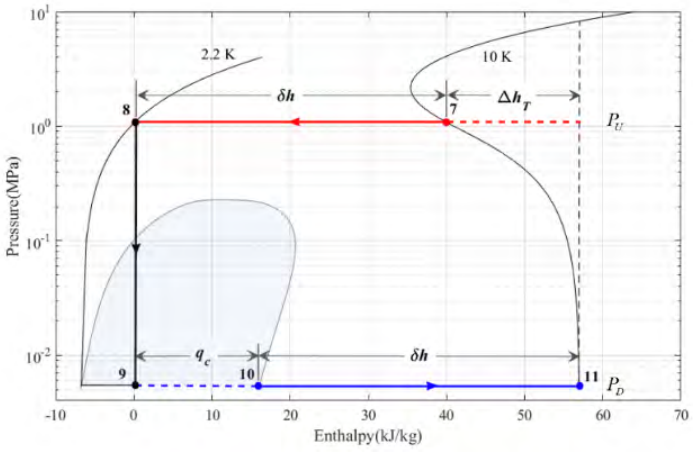

Figure 3: Thermodynamic cycle of He-4 in the last stage of JT circuit

The maximum possible specific cooling capacity q_c is the latent heat of vaporization of the liquid part produced by throttling. Δh_T is the enthalpy change along the constant precooling temperature line from P_D to P_U. Fig.4 shows the pressure dependence of the specific cooling capacity when the third stage precooling temperature T_{pre3} is 10 K. The specific cooling capacity is determined by the smaller one of Δh_T and q_c, which is expressed as,

$$q = min\{\Delta h_T, q_c\} = \begin{cases} \Delta h_T, P_U \le P_{U,opt} \\ q_c, P_U > P_{U,opt} \end{cases} \quad \text{Eq. (3)}$$

where $P_{U,opt}$ is the optimal upstream pressure in MPa at which the specific cooling capacity reaches the maximum.

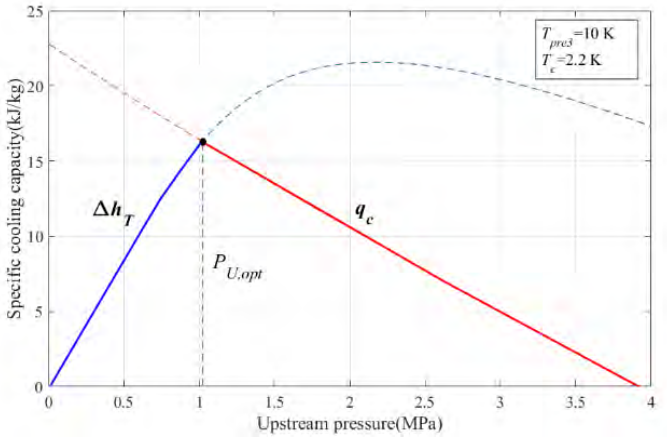

Figure 4: Pressure dependence of specific cooling capacity with the third stage precooling temperature at 10 K

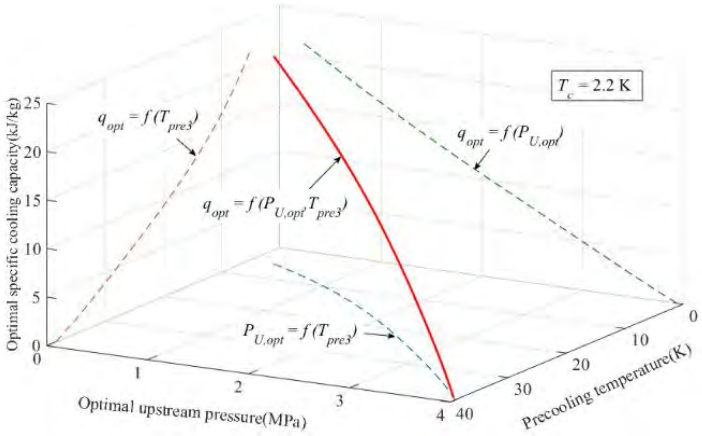

Figure 5: Optimal upstream pressure and precooling temperature dependence of the maximum specific cooling capacity

For each T_{pre3}, there is a $P_{U,opt}$ that maximizes the specific cooling capacity. Fig.5 presents the relationship among the optimal specific cooling capacity, optimal upstream pressure and precooling temperature when the cooling temperature is at 2.2 K. The optimal specific cooling capacity q_{opt} can be expressed by a function of the $P_{U,opt}$ and T_{pre3} as follow:

$$q_{opt} = f(P_{U,opt}, T_{pre3}) = 22.06 - 7.621P_{U,opt} + 0.2075T_{pre3}(T_c = 2.2K) \quad \text{Eq. (4)}$$

Besides, $P_{U,opt}$ is also a function of T_{pre3} which is presented by a quartic polynomial,

$$P_{U,opt} = f(T_{pre3}) = a_0 + a_1 T_{pre3}^1 + a_2 T_{pre3}^2 + a_3 T_{pre3}^3 + a_4 T_{pre3}^4 (T_c = 2.2K) \qquad \text{Eq. (5)}$$

where a_0 to a_4 are the fit coefficients shown in Table 2. It should be noticed that the $P_{U,opt}$ is a monotonically increasing function of T_{pre3}, which means the lower T_{pre3} is, the lower $P_{U,opt}$ to obtain the maximum specific cooling capacity. The optimized function of T_{pre3} and $P_{U,opt}$ is used in the boundary condition settings. The downstream pressure is set to 5.3 kPa, which corresponds to the saturation temperature of 2.2 K for He-4 and 1.42 K for He-3, respectively.

Table 2. Values of the polynomial fit coefficients of Eq. (5).

a_0	a_1	a_2	a_3	a_4
-0.8584	0.2451	-7.239×10^{-3}	1.631×10^{-4}	-1.464×10^{-6}

3.4. Results and Discussions

The simulation mainly focuses on the influence of precooling temperatures on the cooling capacity, the precooling capacity distribution and system exergy of the JT cooler. The simulated results of the optimal cooling capacity changing with the cooling temperature and the third stage precooling temperature are shown in Fig. 6. The cooling capacity of JT cooler Q_c is a product of the specific cooling capacity and the mass flow rate, which has no direct connection with the precooling capacity that is provided by the three-stage SPTC. The optimal cooling capacity $Q_{c,opt}$ is defined as the cooling capacity when the high pressure is $P_{U,opt}$. For a fixed cooling temperature T_c, when T_{pre3} decreases from 40 K to 5 K, $Q_{c,opt}$ first increases and then decreases. For any constant T_c in the range of 2.2 K to 3.0 K, $Q_{c,opt}$ reaches the maximum, that is 70-80 mW, at around T_{pre3}=12 K. Besides, a higher T_c corresponds to a bigger $Q_{c,opt}$, though this influence is very weak compared with the effect of T_{pre3} on $Q_{c,opt}$.

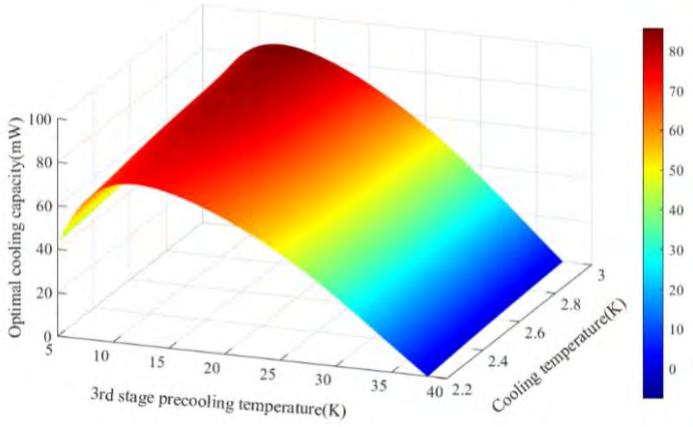

Figure 6: Optimal cooling capacity at different cooling temperature when the third stage precooling temperature varying from 5 K to 40 K

Fig. 7 shows the relationship among precooling capacity distributions, T_{pre1} and T_{pre2} when T_{pre3}=12 K and $\varepsilon = 1$, with the cooling temperature of 2.2 K, mass flow rate of 5.02 mg/s and optimal upstream pressure of 1.29 MPa. The first stage precooling capacity Q_{pre1} is only determined by T_{pre1} and Q_{pre3} only depends on T_{pre2}, while Q_{pre2} is up to both T_{pre1} and T_{pre2}. The value of Q_{pre1} rises with the decline of T_{pre1}, whereas Q_{pre3} increases as the increase of T_{pre2}. Generally, Q_{pre1} is much smaller than Q_{pre3} and the influence extent of T_{pre2} on Q_{pre3} is greater than T_{pre1} on Q_{pre1}. Q_{pre2} rises fast with the drop of T_{pre2} while quite slowly with the increase of T_{pre1}.

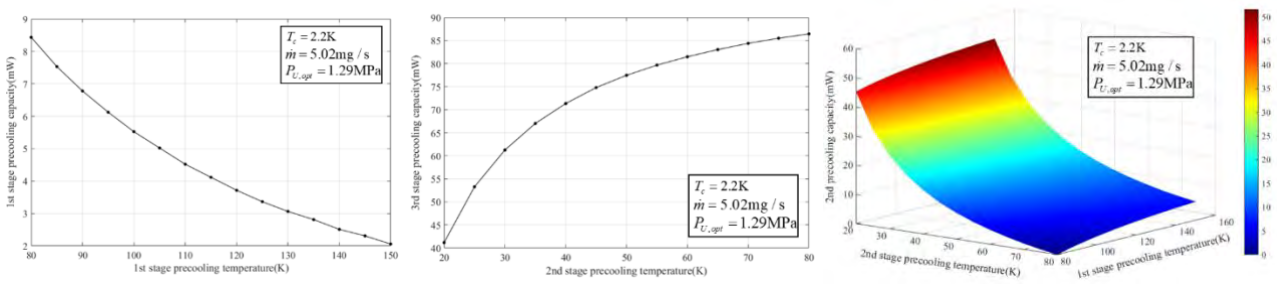

Figure 7: T_{pre1} and T_{pre2} dependence of the precooling capacity distribution with T_{pre3} fixing at 12 K (when $\varepsilon = 1$)

Eq. 6 presents the relationship among the total input exergy of the three PHEXs $\sum_{k=1}^{3} Ex_{pre}$, the total exergy loss caused by the CHEXs and JT valve $|\sum Ex_{loss}|$, and the compressor input exergy Ex_{cpr},

$$\sum_{k=1}^{3} Ex_{pre} = \left|\sum Ex_{loss}\right| - Ex_{cpr} \qquad \text{Eq. (6)}$$

Since the up- and down- stream pressure, as well as the ambient temperature are all constant, Ex_{cpr} is then also a constant value. In this sense, $\sum_{k=1}^{3} Ex_{pre}$ indirectly signifies the general exergy loss of the JT circuit. A smaller $\sum_{k=1}^{3} Ex_{pre}$ means a smaller $|\sum Ex_{loss}|$, which indicates that the total power input to the system is used more efficiently.
Fig. 8 shows the variations of $\sum_{k=1}^{3} Ex_{pre}$ with T_{pre1} and T_{pre2}. Similar to the effects of T_{pre1} and T_{pre2} on Q_{pre3}, T_{pre2} also has a more significant impact on $\sum_{k=1}^{3} Ex_{pre}$ than T_{pre1} dose. For constant T_{pre1}, as T_{pre2} decreases, $\sum_{k=1}^{3} Ex_{pre}$ first slowly increases to a maximum value at about T_{pre2}=25 K, and then gradually decreases.

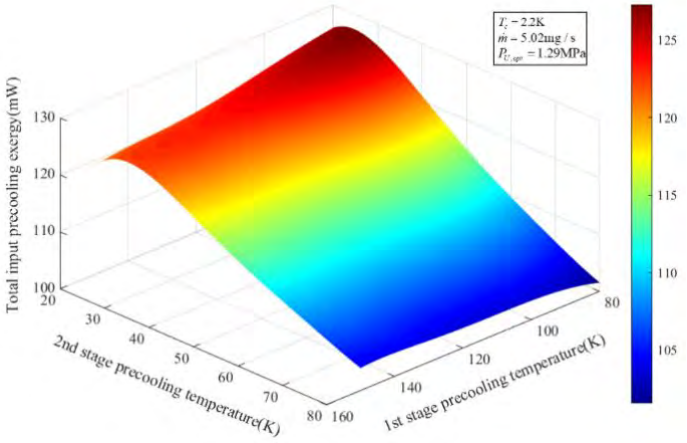

Figure 8: Influence of T_{pre1} and T_{pre2} on the total input exergy of the three PHEXs

In conclusion, considering the above analysis of precooling capacity and exergy, T_{pre2} should be lower than 25 K to reduce the precooling capacity requirement of the third precooling stage and the total exergy loss in the system, while a T_{pre1} higher than 80 K is acceptable due to its negligible effect on both the precooling capacity and total exergy loss.

4. CONCLUSIONS

A JT cooler coupled with a precooling three-stage SPTC is developed to achieve 1-2 K. A two-dimensional CFD model is established to investigate the flow and heat transfer process of the counter-flow heat exchangers, precooling heat exchangers and evaporator, in which a numerical model is used for the boundary conditions to optimize the upstream pressure and specific cooling capacity. The simulated results indicate that for different third stage precooling temperatures, there

exists an associated optimal high pressure that maximizes the specific cooling capacity. The best third stage precooling temperature to obtain the maximum cooling capacity at cooling temperature below 3.0 K is about 12 K. The first and second stage precooling temperatures are analyzed to optimize the precooling capacity distributions and reduce the exergy loss of the JT circuit. The no-load temperatures of 2.2 K and 1.42 K are achieved in the model with He-4 and He-3 as working fluids, respectively. The experimental verifications on the model are underway.

ACKNOWLEDGEMENTS

This work is financially supported by the Aeronautical Science Foundation of China (No. 20162490005) and Shanghai Municipality (Nos. 18511110100, 18511110101, 18511110102).

NOMENCLATURE

c_p	specific heat capacity (kJ×kg^{-1}×K^{-1})	$\boldsymbol{u}$	velocity vector (m×s^{-1})
h	enthalpy (kJ×kg^{-1})	*Greeks*	
P	pressure (Pa)	α	volume fraction
$P_{u,opt}$	optimal upstream pressure	λ	thermal conductivity (W×m^{-1}×K^{-1})
S_T	viscous dissipation term	ρ	density (kg×m^{-3})
t	time (s)	ε	effectiveness of CHEX
T	temperature (K)		

REFERENCES

Dang, HZ., 2015. Development of high performance moving-coil linear compressors for space Stirling-type pulse tube cryocoolers. Cryogenics 68, 1-18.

Dang, HZ., Bao, DL., Zhang, T., et al., 2018. Theoretical and experimental investigations on the three-stage Stirling-type pulse tube cryocooler using cryogenic phase-shifting approach and mixed re-generator matrices. Cryogenics 93, 7-16.

Dang, HZ., Bao, DL., Gao, ZQ., et al., 2018. Theoretical modeling and experimental verifications of the single-compressor-driven three-stage Stirling-type pulse tube cryocooler. Frontiers in Energy.

Dang, HZ., Tan, J., Zha, R., et al., 2017. Advances in single- and multi-stage stirling-type pulse tube cryocoolers for space applications in NLIP/SITP/CAS. Cryogenic Engineering Conference 278, Art. no. 012008.

Takeshi, S., Keishi, T., Osamu, T., 2006. Gifford-McMahon/Joule-Thomson cryocooler with high-flow-conductance counterflow heat exchanger for use in resistance thermometer calibration. Review of Scientific Instruments 77, Art. no. 034902.

Yoichi, S., Keisuke, S., Hiroyuki, S., et al., 2012. Development of mechanical cryocoolers for the cooling system of the Soft X-ray Spectrometer onboard Astro-H. Cryogenics 52, 4-6.

Manuscript ID: 1141
DOI: 10.18462/iir.icr.2019.1141

Non-condensable helium effect on heat and mass transfer characteristics inside a liquid hydrogen tank

Lei WANG, Tian YAN, Jiaojiao WANG, Fushou XIE, Yanzhong LI

Institute of Refrigeration and Cryogenic Engineering, Xi'an Jiaotong University, Xi'an, 710049, China, wanglei-epe@xjtu.edu.cn

ABSTRACT

Existence of non-condensable helium in cryogenic tank ullage may affect the interfacial heat and mass transfer characteristics and also the pressurization performance. In the present paper, helium effect on heat and mass transfer inside a hydrogen tank as well as the associated pressurization performance is studied, and a computational fluid dynamic (CFD) approach is introduced. In the CFD computations, species transfer between helium and propellant vapor is considered, and a modified phase change model accounting for helium effect on heat and mass transfer is also involved. A series of successive pressurization operations are simulated, and the tank pressure evolutions and field distributions are calculated to assist the analysis. The results show that existing of helium in tank ullage could facilitate the mass transfer from liquid to vapor, and a combined effect of more evaporated vapor and non-condensable helium inside ullage could suppress the pressure reduction during vehicle launching process.
Keywords: Tank Pressurization, Launch Vehicle, Liquid Hydrogen, Phase Change.

1. INTRODUCTION

For a typical aerospace vehicle, helium gas is usually used to provide pressurization effect for cryogenic propellant tanks under different stages, including ground pre-pressurization, vehicle ascent period, and on-orbital active pressurization. For a helium injection issue or helium existence issue, complex multi-species heat and mass transfer effect could occur and exert significant influence on the thermodynamic behaviors. In the view of accurate management of propellant system, the helium effect on pressurization as well as other properties should be known clearly in advance.

To reveal helium effect on cryogenic thermodynamic mechanisms, experimental investigations and CFD simulations are usually used to assist the performance analysis under normal gravity and microgravity. For the experiments, Kassemi (2018) presented preliminary results from ZBOT's ground-based research and performed ISS microgravity test that focused on the effects of residual non-condensable gases on both pressurization and pressure reduction trends in a sealed Dewar. Morehead (2016) presented a LOX/LCH_4 prototype planetary lander and hot-fire tests, and a cold helium active pressurization system was incorporated in the fuel systems. CFD approach had been widely used in the fields of tank pressurization and pressure control, and a great deal of CFD models had been constructed aiming at different tanks. For example, Kartuzova and Kassemi (2013, 2017) introduced a CFD model for simulating the fluid dynamics, heat transfer, and phase change during self-pressurization and pressure control via jet mixing of an enclosed tank in microgravity. To reach an accurate prediction, the interfacial heat and mass transfer effect should be emphasized, especially for a helium-existence issue. Through Dalton's partial pressure model and Henry's law, the helium molar fractions in both of gas phase and liquid phase were described by Kim (2012) to examine helium effect on phase change rate. The similar treatment of multi-species phase change had also been utilized by Grayson (2007), Ludwig and Dreyer (2014), and Wang (2017), and CFD models based on Flow-3D and Fluent software had been constructed.

The existing researches of helium pressurization mainly focused on the performance under certain conditions, and the helium effect on heat and mass transfer in different pressurization operations were still lack. Therefore, in the present paper, a CFD model, involving non-condensable helium effect on liquid-vapor phase change, is introduced to reveal the helium effect on mass transfer rate

as well as thermodynamic characteristics under different mission stages. The situations about ground pre-pressurization and depressurization, pressurized discharge during vehicle launching, and ballistic period in 0-g are simulated and analyzed. It is believed that the present paper is beneficial for deep understanding the helium effect on pressurization performance.

2. CFD MODELING

Fig.1 exhibits the schematic diagram of a LH_2 tank. 4-mm-thickness 2219 aluminum alloy plate is used to construct the tank wall. A horizontal-outlet diffuser with outlet area of 0.03 m^2 is adopted to diffuse pressurant gas. To reduce heat load from environment, a composite thermal insulation structure including 20mm foam layer and 20mm multi-layer insulation is used. A preliminary study showed that exterior heat leakage had slight influence on the internal thermodynamic behaviours as well as pressure evolution of cryogenic tank experiencing short time (~minutes), so that adopting approximate heat leakage values seem to be accepted. In this paper, redundant consideration of heat flux boundary conditions of q=300 $W \cdot m^{-2}$ and q=1 $W \cdot m^{-2}$ are used respectively for high-gravity cases and microgravity cases.

Fig. 2 displays tank pressure evolution as well as gravity variation sequence for the present simulations. For the prelaunch helium pressurization operation, room-temperature gas is used to pressurize cryogenic propellant tank from a normal pressure to a specific pressure level and then maintain this level until the engine fire. During vehicle launching, an on-board pressurization system is activated to sustain pre-setting pressure range for the core stages so that the propellant supplement requirements could be met. Comparatively, the cryogenic tank of upper stage may experience a depressurization phenomenon due to no pressurant injection together with heat transfer from warm ullage to its adjacent cold boundaries. For the deep-space exploration mission, the cryogenic tanks of upper stage could experience a zero-gravity ballistic period as well as space varied-gravity operations, so that reorientation of liquid-gas phases may occur and the associated thermodynamic behaviours would be affected. On the whole, pressurization and pressure control play significant role in the cryogenic propellant system, and the properties are closely related to the heat and mass transfer effect inside the cryogenic tanks.

To perform CFD simulations of the present cases, an axisymmetric model is developed and the fluid region together with the metal wall region is considered as simulated objective. VOF method is adopted to solve the multiphase problem. The density of ullage gas is calculated by ideal-gas model. Except Boussinesq approximation is used to consider liquid density, the other thermophysical and thermodynamic properties are supposed as constant values. Due to the non-condensation helium existence in ullage region, the species transport function is involved to consider the species transfer effect. Moreover, near-wall treatment of low-Re k-ε model approach is used to consider the fluid - wall heat transfer.

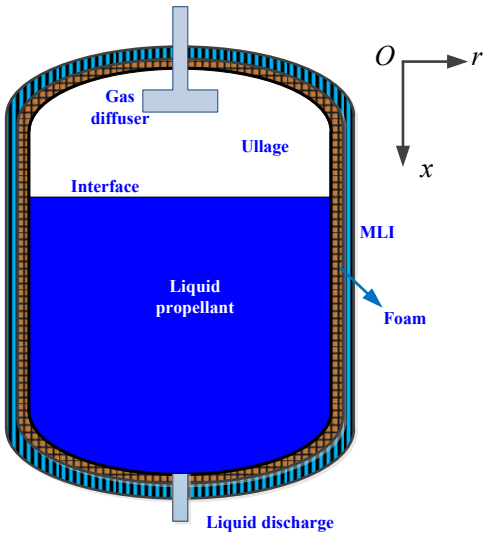

Figure 1: Schematic diagram of LH_2 tank

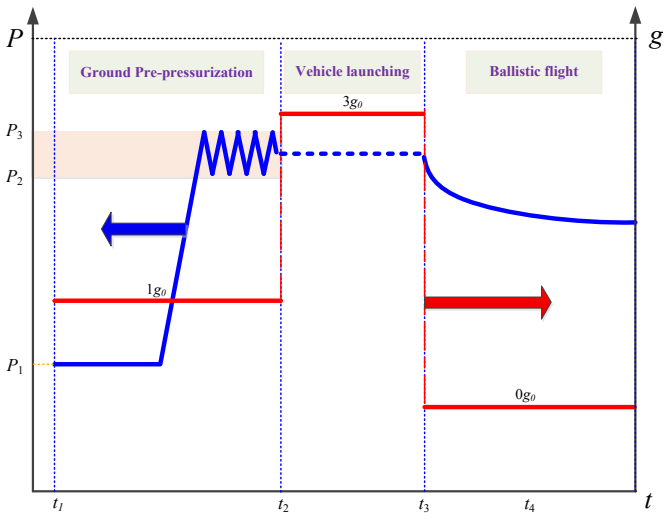

Figure 2: Mission sequence of pressure evolution and acceleration levels

To implement the mass transfer calculation, a modified phase change model based on Schrage's equation is introduced. Similar to Schrage's model, the present model calculates phase change rate through temperature difference between fluid and its saturation state. What's the difference is in Schrage's model the saturation temperature is calculated based on fluid total pressure, while the present model considers saturation temperature through partial pressure of propellant vapor based on Dalton's model. The mathematical mechanisms for the multi-species phase change model are shown below.

For $T > T_{sat}$ (evaporation):

$$\dot{S}_m = \dot{m}_{vl} = -\dot{m}_{lv} = -F\rho_l\alpha_l\frac{|T-T_{sat}|}{T_{sat}} \quad \text{Eq. (1)}$$

For $T<T_{sat}$ (condensation):

$$\dot{S}_m = \dot{m}_{vl} = -\dot{m}_{lv} = F\rho_v\alpha_v\frac{|T-T_{sat}|}{T_{sat}} \quad \text{Eq. (2)}$$

and

$$\dot{S}_E = i_{fg}\dot{S}_m \quad \text{Eq. (3)}$$

$$T_{sat} = T_{sat}(P_v) \quad \text{Eq. (4)}$$

$$P_{total} = P_{He} + P_v \quad \text{Eq. (5)}$$

Here, F denotes the relaxation parameter used for obtaining the rate of mass transfer in a cell of unit volume, and it carries the unit of [s^{-1}]. In the CFD simulations, all of above heat and mass transfer calculations are coded and implemented via customized User Defined Functions (UDF).

3. HE EFFECT ON PRE-PRESSURIZATION BEHAVIORS

Fig. 3 displays the H_2 mass fraction distributions and associated temperature distributions at different times of ground pre-pressurization process. It shows He-H_2 diffusion with each other occurs under the effect of helium gas injection and also the turbulent movement. At the end of this period, an apparent axial concentration distribution and axial temperature distribution are observed. Also, since

the helium diffuses towards liquid surface, He-H_2 mixture instead of a pure H_2 covers the liquid surface, which may affect the mass transfer mechanism in the near-interface region.

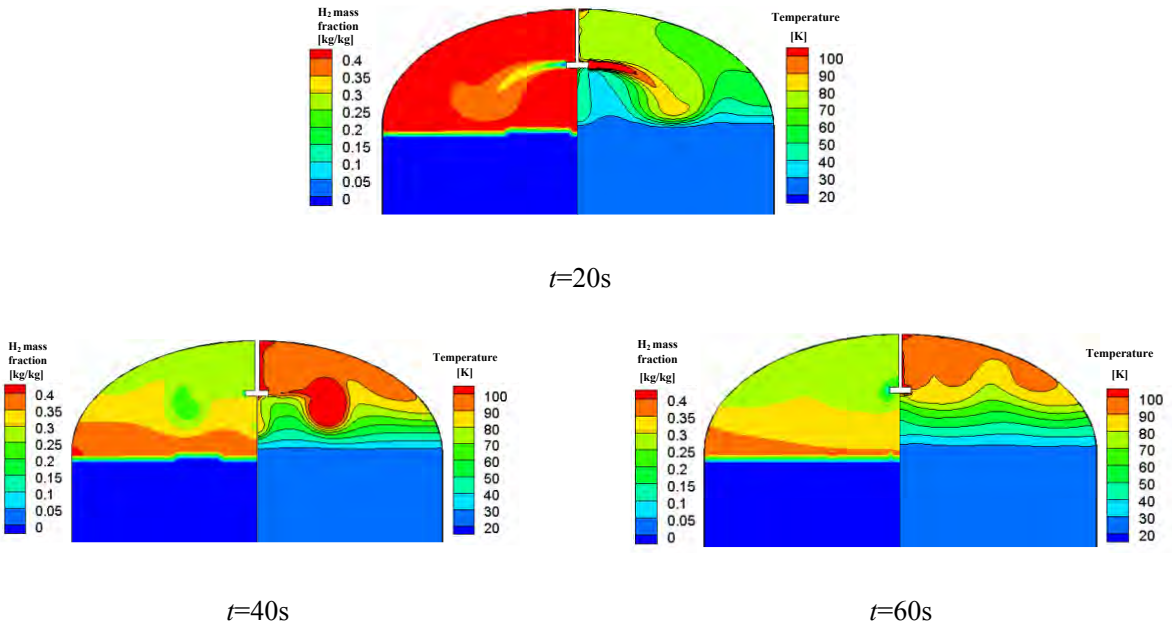

Figure 3: H_2 mass fraction and temperature distributions for pre-pressurization periods

To clearly explain the multi-species effect on pressurization and phase change performance, a pure H_2 case is calculated. Also, the two simulations are extended to involve the depressurization process which could represent the situations of upper stage. Fig. 4 displays the comparisons of pressure and ullage average temperature for pure-H_2 case and H_2-He mixture case. In the two cases, same mole fluxes of gas injection are used. It shows helium existence produces a lower initial temperature at the end of pre-pressurization stage but a more significant temperature decrease in the depressurization process. This is because the heat transfer rate from ullage to its boundaries is mainly determined by the temperature difference. In the pre-pressurization period, helium case obtains less gas injection so that the tank wall has a lower temperature when compared to the pure-H_2 case. Therefore, a larger temperature difference in helium case brings about more heat transfer from ullage to tank wall in the subsequent depressurization period.

Fig. 5 displays the mass transfer amount curves during the pre-pressurization and depressurization periods, and the positive value of ordinate denotes mass transfer from liquid to vapor. It shows helium existence produces a more significant liquid evaporation during pre-pressurization, and this effect even occurs in the subsequent depressurization process although the ullage temperature reduces. Comparatively, pure H_2 case experiences an apparent liquid evaporation in the pre-pressurization period and then a vapor condensation in the depressurization. Moreover, comprehensive analysis of temperature variations as well as mass transfer amount curves indicates that the pressure is mainly determined by ullage temperature variation. For the pure-H_2 case, although mass transfer is transferred from liquid to vapor, which is favour for pressure rise, the tank pressure still decreases under the effect of temperature drop.

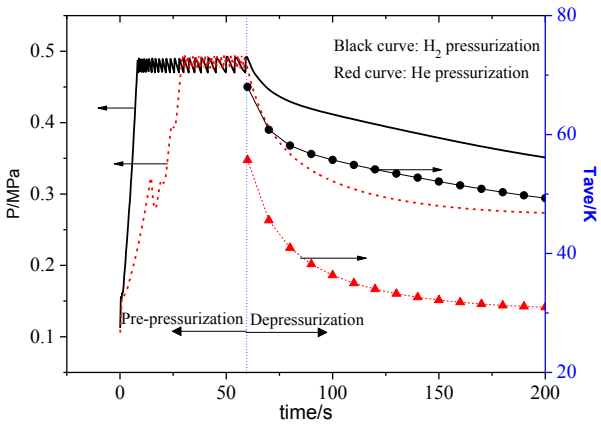

Figure 4: Comparison of pressure and ullage temperature for pure-H_2 and H_2-He mixture cases

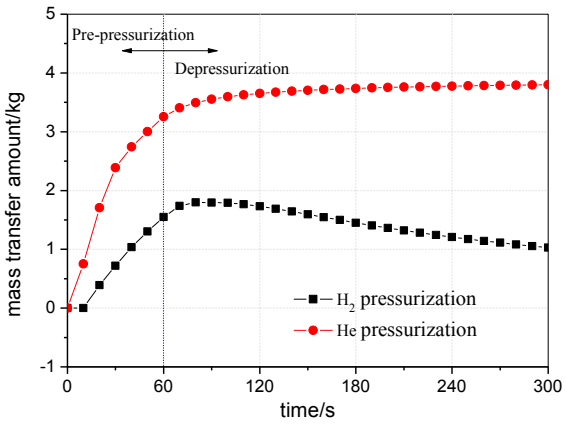

Figure 5: Comparison of mass transfer amounts for pure-H_2 and H_2-He mixture cases

4. HE EFFECT ON PRESSURIZED DISCHARGE PERFORMANCE

Fig. 6 exhibits H_2 mass fraction and associated temperature distributions at different times of pressurized discharge period. It shows with the continuous decline of liquid surface the injected helium impels the high concentration H_2 region flowing downwards. Simultaneously H_2-He diffusion with each other produces a significant concentration axial distribution. Moreover, owing to the pressured gas injection structure, the downward velocity near the wall region is larger than that in the bulk region, and thus a larger fraction of He could be seen in the near wall region, which further results in a distinguishable radial temperature gradient in the lower part of ullage.

Fig. 7 displays the mass transfer amount during the pressurized discharge period. In this case, a constant flux of pressurant gas is adopted, and also the decrease rate of liquid surface is stable. It shows generally the mass transfer mode during this period is liquid evaporation except that vapor condensation occurs in the beginning 5 seconds. This phenomenon could be explained by the specie fraction in the near-surface region together with the ulage pressure. In the beginning, H_2 vapor still occupies a significant fraction. When the temperature of H_2 vapor is larger than its saturation temperature associated with its partial pressure, vapor condensation occurs, as the mechanism in the pre-pressurization stage. With the process proceeding, further penetration of helium specie towards liquid surface region reduces the vapor partial pressure as well as the saturation temperature, so that an increasing tendency of liquid evaporation could be supposed. Moreover, it could be seen that over the whole discharge period, about 2kg mass is transferred from liquid to vapor. Simultaneously, about 70kg helium pressured is injected in this process. Compared to the injected gas, the phase change effect has slight influence on the pressure behaviours even using helium as the pressured gas. Therefore, for a typical short-time discharge event, the phase change effect could be ignored in the pressurization analysis.

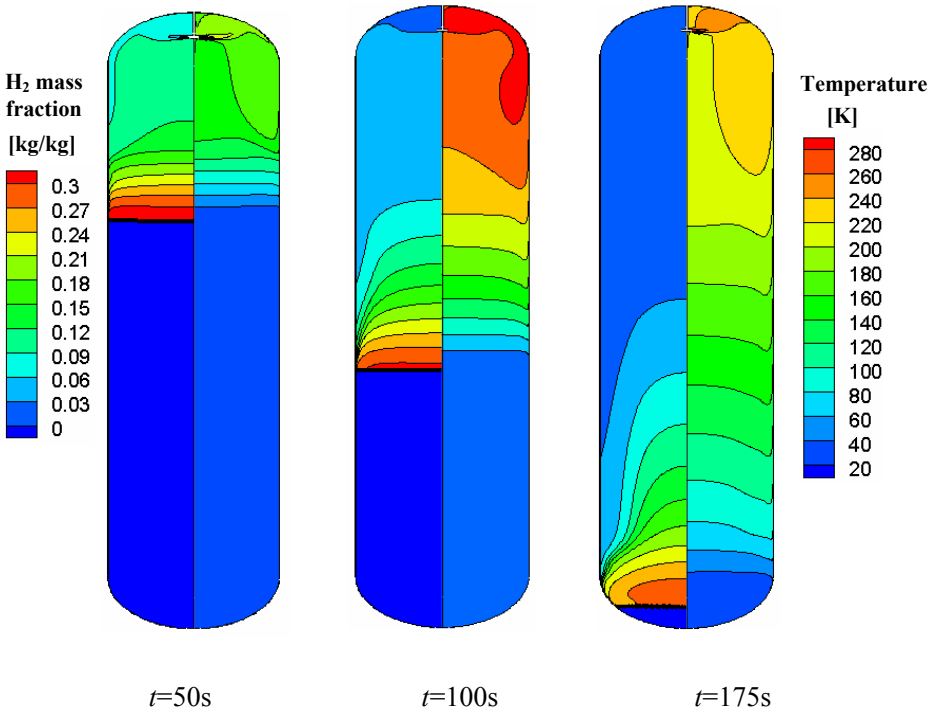

Figure 6: H_2 mass fraction and temperature distributions for pressurized discharge process

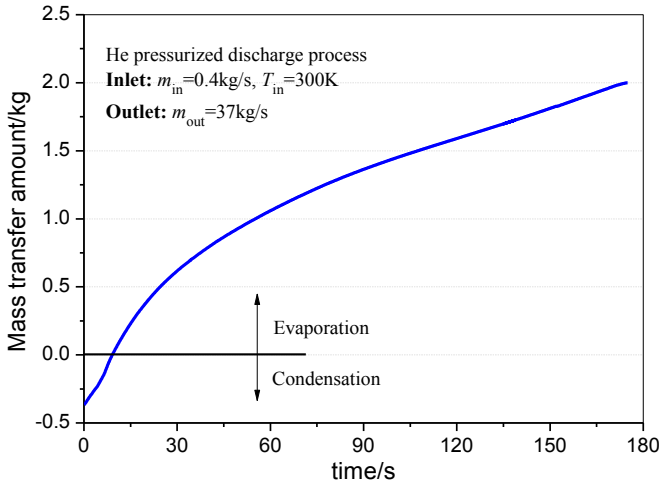

Figure 7: Mass transfer amount for pressurized discharge process

5. HE EFFECT DURING BALLISTIC PERIOD

Fig. 8 exhibits He influence on physical field distribution under 0-g ballistic period, and phase distribution and associated temperature distribution for both of He existence case and pure H_2 case are illustrated. Since no other external force dominates fluid behaviours in 0-g condition, surface tension comes to play the leading role in the field distributions. It could be observed that under 0-g environment, ullage bulk is isolated from the tank wall under surface tension, and an approximate spherical ullage is formed for both of the two cases. It should be noted that the present phase distributions are not the final stable results. The coverage of ullage by liquid phase could bring about weak velocity distribution over the whole fluid region, and under the inertia force effect the formed spherical ullage would experience back and forth movement inside the tank until the final stable position in the tank centre. Comparison of temperature distributions for the two cases indicates that the He existence case has a higher temperature ullage than pure H_2 case. For the pure H_2 case, the coverage of ullage by liquid reinforces the heat and mass transfer between liquid and vapor phase,

and also sufficient phase change could accelerate the process of establishing thermal equilibrium. Comparatively, in the helium existence case, heat transfer in the two-phase system is mainly performed through gas conduction, so that a lower temperature decline rate is produced. Figure.9 displays the pressure evolutions for the two cases during the ullage-coverage periods. It shows He existence in the ullage region produces a larger pressure lower limit, and the stable pressure value could be estimated by the helium amount in the ullage.

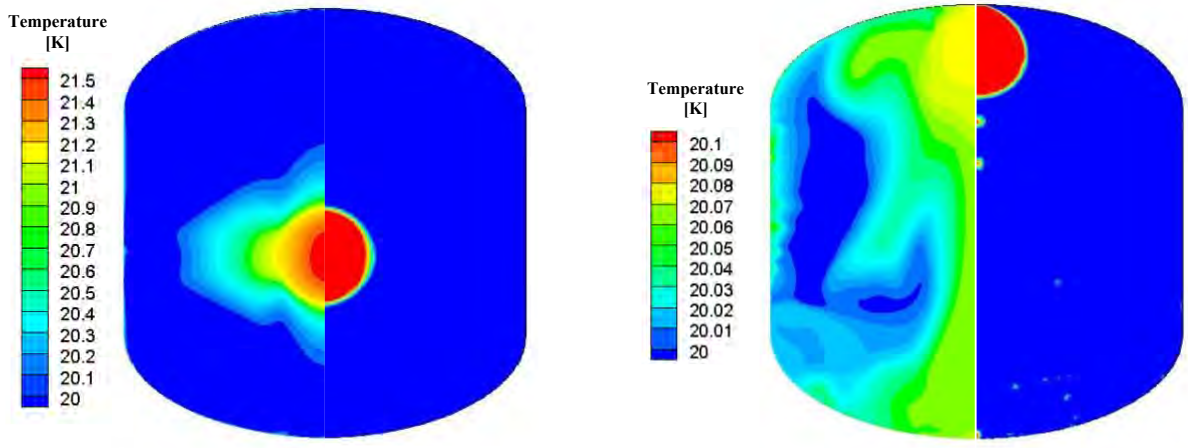

(a) He-H_2 mixture case **(b) pure H_2 case**

Figure 8: He influence on physical field distribution under 0-g condition at *t*=350s (The left side is temperature distribution, and the right side is phase distribution)

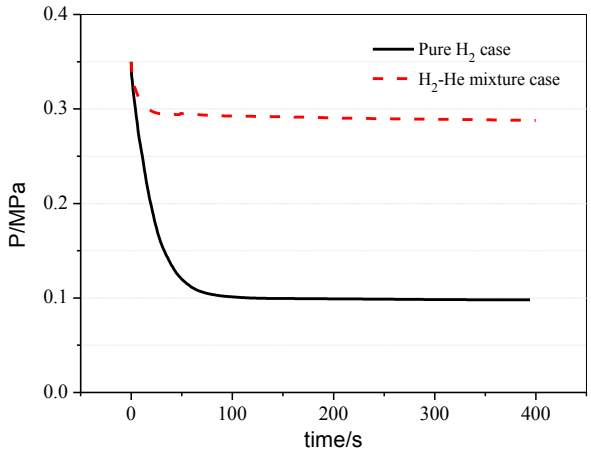

Figure 9: Pressure evolutions for pure-H_2 case and H_2-He mixture case under 0-g condition

6. CONCLUSIONS

Based on the present CFD simulations, He existence influence on the pressure behaviours and interior thermodynamic characteristics for different stages could be drawn as follow.

1) For ground pre-pressurization issue, helium-hydrogen mixing process is driven by pressurant injection inertia force as well as turbulence diffusion. The uniform mixing is not finished within the pressurization time, and an apparent axial concentration distribution could be observed.
2) During pressurized discharge period, helium diffusion towards liquid surface reduces the partial pressure of hydrogen vapor, so that a tendency of liquid evaporation mostly occurs. Compared to the injected pressurant gas mass, the mass transfer amount is weak and has ignorable influence on the pressurization performance.
3) In 0-g ballistic process, helium existence in ullage would provide a higher stable pressure level, and the pressure value could be estimated by the helium amount. Also, the helium existence

slows down the establishment of thermal equilibrium state, and a superheated ullage could be observed after the coverage of ullage by liquid phase.

ACKNOWLEDGEMENTS

This work is supported by National Natural Science Foundation of China (No.51406142).

REFERENCES

Grayson, G., Lopez, A., Chandler, F., Hastings, L., Hedayat, A., Brethour, J., 2007. CFD modeling of helium pressurant effects on cryogenic tank pressure rise rates in normal gravity. 43rd AIAA/ASME/SAE/ASEE Joint Propulsion Conference and Exhibit, Cincinnati, Ohio, AIAA 2007-5524.

Kartuzova, O., Kassemi, M., 2017. CFD prediction of microgravity self-pressurization and pressure control and validation against the tank pressure control experiment. 53rd AIAA/SAE/ASEE Joint Propulsion Conference, Atlanta, GA, AIAA 2017-4660.

Kassemi, M., Hylton, S., Kartuzova, O., 2013. Effect of residual noncondensables on pressurization & pressure control of a zero-boil-off tank in microgravity. 29th ASGSR Conference, Orlando.

Kassemi, M., Hylton, S., Kartuzova, O. 2018. Zero-boil-off tank (ZBOT) experiment-CFD self-pressurization model validation with ground-based & microgravity results, Joint Propulsion Conference, Cincinnati, Ohio, AIAA 2018-4940.

Kim, K.H., Ko, H.J., Kim, K., Jung, Y.S., Oh, S.H., Cho, K.J., 2012. Transient Thermal Analysis of a cryogenic oxidizer tank in the liquid rocket propulsion system during the prelaunch helium gas pressurization. J. Eng. Thermophys-Rus. 21(1),1-15.

Ludwig, C., Dreyer, M.E., 2014. Investigations on thermodynamic phenomena of the active-pressurization process of a cryogenic propellant tank. Cryogenics 63,1-16.

Morehead, R.L., Atwell, M.J., Melcher, J.C., Hurlbert, E.A., 2016. Cold helium pressurization for liquid oxygen/liquid methane propulsion systems: Fully-integrated initial hot fire test results, 52nd AIAA/SAE/ASEE Joint Propulsion Conference, Salt Lake City, UT, AIAA 2016-4682.

Wang, L., Ye, S., Ma, Y., Wang, J., Li, Y., 2017. CFD investigation on helium pressurization behaviors in liquid hydrogen tank, Int. J. Hydrogen Energ. 42, 30792-30803.

Manuscript ID: 1311
DOI: 10.18462/iir.icr.2019.1311

Investigation on thermo-physical properties of aqueous suspension of nanoencapsulated phase change materials

Jiacheng WANG[(a)], Lisi JIA[(a)], Ying CHEN[(a)], Gang Liu[(a)]

[(a)] School of Materials and Energy, Guangdong University of Technology
Guangzhou, 510006, China, e-mail: jialisi@gdut.edu.cn

ABSTRACT

Nanoencapsulated phase change materials (NEPCM) composed of n-octadecane as the core and polymethyl methacrylate as the shell were fabricated by in situ polymerization first and then dispersed into the water to prepare aqueous suspensions by a two-step method. The aqueous suspensions of NEPCMs showed good dispersion stability and had a uniform size distribution. The thermal and rheological properties of the aqueous suspensions of NEPCMs were investigated, emphasizing on the effects of NEPCM concentration and operating temperature. The specific heat capacity and viscosity were measured by a differential scanning calorimeter and a rotational rheometer, respectively. The results showed that as the NEPCM concentration increased, the specific heat capacity of the aqueous suspension decreased slightly in the single-phase region and increased drastically in the two-phase region. The overall specific heat capacity of the aqueous suspension increased with increasing NEPCM concentration. The viscosity of the aqueous suspension of NEPCMs increased with increasing NEPCM concentration and decreased as the temperature increased. It was found that the NEPCM-caused increase in specific heat capacity is more significant than that in viscosity. Thus, the aqueous suspensions of MEPCMs prepared possessed potential for use as a latent functionally thermal fluid for high-efficiency heat dissipation systems.
Keywords: NEPCM Suspension, Dispersion Stability, Specific Heat Capacity, Viscosity.

1. INTRODUCTION

In recent years, micro-electronic components are developing toward micro-miniaturization, high frequency, high power and a high degree of chip integration, the contradiction between high heat flux density and small heat dissipation space becomes considerable evident (Chein and Huang, 2004). The poor thermal performance of the traditional cooling fluids, such as water and oil, can no longer meet the increasingly stringer requirements of the heat dissipation. (Toghraie et al., 2016). Microencapsulated phase change material (MEPCM) is composed of PCM as core and a polymer or inorganic shell to maintain the shape and prevent PCM leakage during the phase change process. The new latent functionally thermal fluid, with MEPCM particles in it, can express greater heat exchange ability owing to the excessive heat storage by MEPCM particles. Therefore, researches on the fluid flow and heat transfer characteristics of the latent functionally thermal fluid have attracted more and more attention (Zhang et al., 2007).

Goel el at. (1994) investigated the flow and heat transfer properties of the water-based MEPCM suspensions for the laminar hydraulically and fully developed flows in a circular tube with a constant wall heat flux. The results showed that the NEPCM suspensions could reduce the rise of the tube wall temperature by up to 50% compared to the single-phase heat transfer fluid in the same dimensionless parameter condition, and the increase in particles size could further reduce the rise of the tube wall temperature by 15%. A study by Chen et al. (2008) indicated that the dimensionless wall temperature of the MEPCM suspensions was lower than that of the pure water in the constant heat flux due to phase change, and also found the heat transfer enhancement ratio of the suspensions containing 15.8% MEPCM could be 1.42 times of that of water and could reduce the pump consumption by up to 67.5% of that of pure water. Kong et al. (2015) utilized the MEPCM suspensions flowing through a coil heat exchanger, and found that it could improve the

heat transfer of the heat exchanger despite the pressure drop of the MEPCM suspensions was higher than that of pure water due to the higher viscosity, and the performance efficiency coefficient value is over 1 for the 4.8% MEPCM suspension.
It has been demonstrated that the MEPCM suspensions could enhance the heat transfer properties in comparison to the pure water in the previous studies. However, the MEPCM particles were found to be easily broken because of the large particles size, resulting in the abrasion and blocking of the tube (Alvarado et al., 2007). Compared to the MEPCM particles, the nanoencapsulated phase change materials (NEPCM) with the particle sizes less than 1μm were much more stable and not easy to be broken. Moreover, the NEPCM particles should be able to further enhance the micro-convection in the base fluid due to the higher ratio of surface area to volume than the MEPCM particles (Lu et al., 2015). To date, few studies on the fluid flow and heat transfer of aqueous suspension of NEPCM particles have been found in the literature. Considering that the heat transfer enhancement of the NEPCM suspension was determined by its improved thermos-physical properties, we focused on the specific heat capacity and viscosity of the aqueous suspension of NEPCM particles in the present study. The thermo-physical properties of the aqueous suspension of NEPCM particles should be closely related to suspension stability. Thus far, few studies have been conducted with the goal of improving the dispersion stability of NEPCM suspensions. In the literature, the commonly used method was to make the density of the base fluid match that of the foreign particles. Therefore, preparation of monodisperse NEPCM particles with uniform size and controlled density was necessary to improve the suspension stability.
In the present study, NEPCM particles consisting of n-octadecane as the core and polymethyl methacrylate as the shell were fabricated using a in situ polymerization approach. Deionized water was chosen as the base fluid. The NEPCM particles were dispersed in the water to prepare stable suspensions. The effects of NEPCM concentration and operating temperature on the thermal and rheological properties of the aqueous suspensions, as well as the specific heat capacity and dynamic viscosity, were investigated to demonstrate the advantages of the NEPCM suspension as heat transfer fluid.

2. EXPERIMENTAL

2.1 Preparation of the NEPCM Suspensions

The nanoencapsulated phase change materials were fabricated using an in situ polymerization approach. Methyl methacrylate, n-octadecane, initiator 2,2-Azodiisobutyronitrile, surfactant Tween-80 and modified zirconium phosphate nanoplatelets were mixed in a three-neck flask as the oil phase, and then the stable emulsion was prepared by slowly adding deionized water with mechanical agitation at 200 rpm and a constant temperature of 313.15 K. The polymerization process was started after the reaction mixture was heated to 343.15 K for 2 h with mechanical agitation at 200 rpm and purged with nitrogen for 30 min. Finally, the resultant NEPCMs were washed with Ethanol and deionized water and dried by vacuum freeze drying for 12h. The aqueous suspension of NEPCM particles was prepared by a two-step method, in which the NEPCM particles were dispersed in the pure water through magnetic stirring first and then ultrasonic vibration. The volume concentrations of the NEPCM suspensions ranged from 1.0% to 6.0%.

2.2 Characterization of the NEPCM Suspensions

The micromorphology of the prepared NEPCM particles was measured using a scanning electron microscope (SEM, S-3400N, Hitachi, Japan). The particle size of the aqueous suspension of NEPCM particles was measured using a particle size analyzer (Delsa NanoC, Beckman Coulter, America). The specific heat capacities of the NEPCM particles and the aqueous suspension of NEPCM particles were analysed using a differential scanning calorimeter (DSC, DSC 3, Mettler Toledo,Switzerland) under nitrogen atmosphere at a heating and cooling rate of 10 K/min. The rotational rheometer (Kinexus ultra+, Malvern, UK) was employed for measurement of the viscosity of the aqueous suspension of NEPCM particles at the operating temperatures of 283.15 K, 293.15 K and 308.15 K.

3. RESULTS AND DISCUSSION

3.1 Micromorphology and Thermal property of the NEPCM Particles

Fig. 1 showed the SEM image of the NEPCM particles. It was observed that the NEPCM particles had a regular spherical shape and a uniform size distribution. The average particle size was around 500 nm. The NEPCM particles with good monodispersity provided convenience for the subsequent preparation of aqueous suspensions of NEPCM particles. The specific heat capacity of the NEPCM particles was measured by DSC analysis and the result was shown in Fig. 2. It could be seen that the specific heat capacity of the NEPCM particles varied with operating temperature. The specific heat capacity of the NEPCM particles in the single-phase regions are about 1.89 $J \cdot g^{-1} \cdot K^{-1}$ (in the solid state) and 2.36 $J \cdot g^{-1} \cdot K^{-1}$ (in the liquid state), respectively. In the two-phase region located in the range of 295.15-315.15K, the specific heat capacity of the NEPCM particles increased due to the phase transition of the core material, and was apparently higher than that in the single-phase region. The maximum specific heat capacity at the temperature of 308.15 K was 26.18 $J \cdot g^{-1} \cdot K^{-1}$. The high specific heat capacity of the NEPCM particles should be able to guarantee the heat transfer performance of the water-based working fluid.

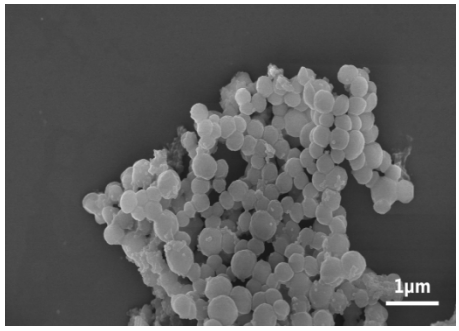

Figure 1: The SEM image of the NEPCM particles

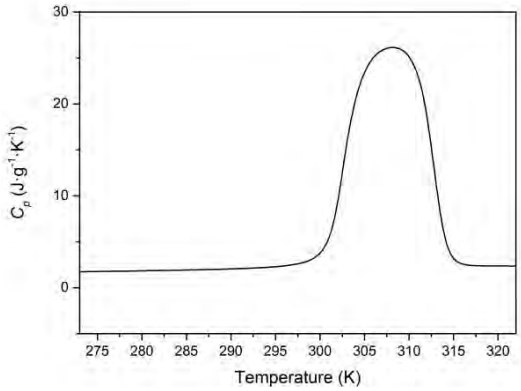

Figure 2: The specific heat capacity curve of the NEPCM particles

3.2 Distribution Stability and Size Distribution of the NEPCM Suspensions

Fig. 3a showed that the sedimentation of the aqueous suspensions of NEPCM particles at different standing times. There were no visible separation or sedimentation observed in these NEPCM suspensions. It was indicated that the aqueous suspensions of NEPCM particles prepared in the study possessed good stability and the NEPCM particles could be well suspend in the base fluid. The particle size distributions of the aqueous suspensions of NEPCM particles at different NEPCM concentrations were shown in Fig. 3b. It was apparent that all the NEPCM suspensions prepared in the study had a narrow size distribution and the average particle size was measured to be around 564.3 nm. It was found that the NEPCM suspensions and the NEPCM particles prepared were approximately equal in particle size, suggesting that the NEPCM particles were uniformly dispersed in the water and almost no aggregation occurred in the NEPCM suspensions. The good dispersion stability achieved in the study could provide an

experimental basis for further investigating the thermo–physical properties of aqueous suspensions of NEPCM particles.

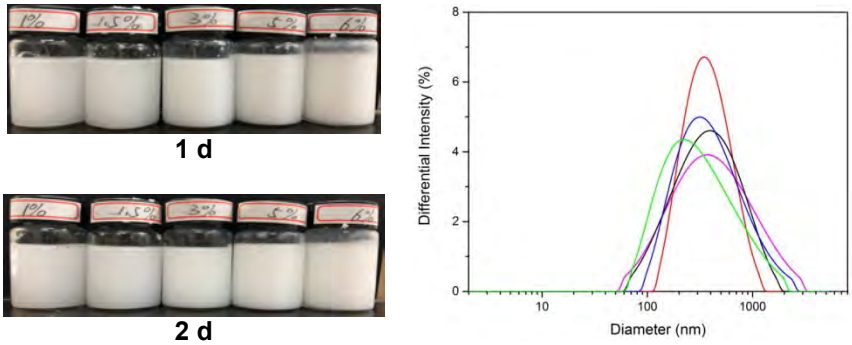

(a) (b)

Figure 3: (a) The sedimentation of the NEPCM suspensions at different standing times and (b) the particle size distributions of the aqueous suspensions of NEPCM particles

3.3 Thermal and Rheological Properties of the NEPCM Suspensions

The specific heat capacity curves of the aqueous suspensions of NEPCM particles measured in the temperature range of 280.13-315.13K were shown in Fig. 4. It could be seen that two typical regions appeared in the specific heat capacity curves of the aqueous suspension. Region 1 was located in the temperature range of 280.13-298.15K and 305.13-315.13K in which no phase transition occurred in the NEPCM particles. Region 2 was located in the temperature range of 298.15-305.13K in which the NEPCM particles endure a phase transition. In the Region 1, the specific heat capacity of the NEPCM suspension decreased as the NEPCM concentration increased due to the lower specific heat capacity of the NEPCM particles compared to the pure water. In the Region 2, the specific heat capacity of the NEPCM suspension increased sharply and was apparent higher than that in the region 1. The maximum value of the specific heat capacity appeared at the temperature of 302.15 K and the NEPCM concentration of 6.0%. Fig. 4 also showed the average specific heat capacity of the NEPCM suspension in the temperature range of 280.13-315.15 K at different NEPCM concentrations. It was obvious that the average specific heat capacity increased with increasing NEPCM concentration. The specific heat capacity reached 13.03 $J \cdot g^{-1} \cdot K^{-1}$ at the NEPCM concentration of 6.0%.

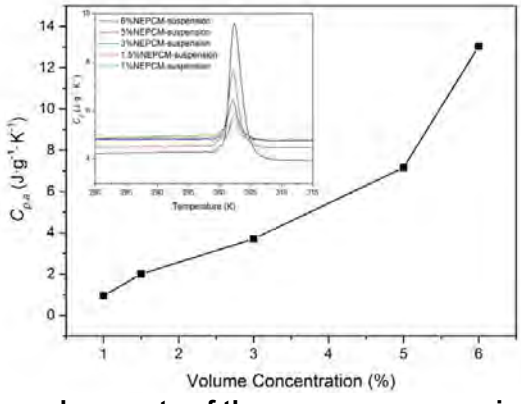

Figure 4: The thermal property of the aqueous suspension of NEPCM particles

The effects of NEPCM concentration and operating temperature on the viscosity of the aqueous suspension of NEPCM particles were presented in the Fig. 5. It could be seen that the viscosity of the NEPCM suspension decreased as the operating temperature increased and increased with increasing NEPCM concentration. Moreover, the effect of NEPCM concentration on the viscosity of the NEPCM suspension was irrelevant to the operating temperature or the state of the NEPCM particles. The NEPCM-caused increase in suspension viscosity was larger in the NEPCM concentration of 1.5-5% than that in the NEPCM concentration of 5-6% and 1-1.5%. It also could be seen that the increase in viscosity of the NEPCM suspension caused by the NEPCM concentration at the lower temperature was larger than that at the higher temperature; and the

increase in viscosity of the NEPCM suspension caused by the operating temperature at the higher NEPCM concentration was larger than that at the lower NEPCM concentration. The maximum increase in viscosity of the NEPCM suspension was about 15.6% at the NEPCM concentration of 6.0% and the temperature of 283.15 K.

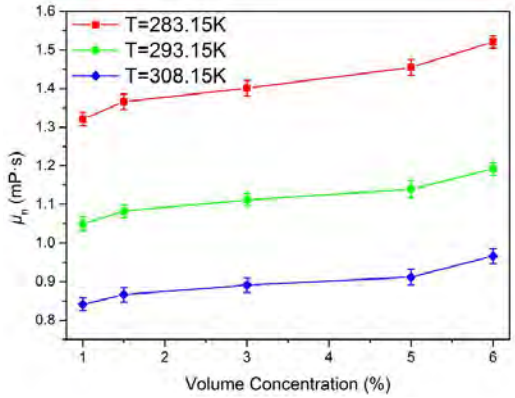

Figure 5: The rheological property of the aqueous suspension of NEPCM particles

4. CONCLUSIONS

In the present paper, the NEPCM particles consisting of n-octadecane as the core and polymethyl methacrylate as the shell were fabricated using a in situ polymerization method. The obtained NEPCM particles had regular shape and uniform sizes. These monodisperse NEPCM particles could steadily dispersed in the base fluid and thus good stability of the aqueous suspension of NEPCM particles was achieved without aggregation. The effects of the NEPCM particles and operating temperature on the specific heat capacity and dynamic viscosity of the NEPCM suspensions were investigated. It was found that the specific heat capacity of the NEPCM suspension increased significantly with increasing NEPCM concentration due to the phase transition of the core material. The viscosity of the NEPCM suspensions also increased due to the NEPCM particles and showed little relationship with the phase state of the NEPCM particles. The NEPCM-caused increase in the specific heat capacity was more significant compared to that in the viscosity. It was suggested that the aqueous suspension of NEPCM particles should have great potential applications in heat transfer.

ACKNOWLEDGEMENTS

The study was supported by the National Natural Science Foundation of China [grant numbers 51606045 and 51876045], and the Guangzhou Science Technology and Innovation Commission [grant number 201704030107].

NOMENCLATURE

C_p	Specific heat capacity ($J \cdot g^{-1} \cdot K^{-1}$)	$C_{p,a}$	Average specific heat capacity ($J \cdot g^{-1} \cdot K^{-1}$)
T	Temperature (K)	μ_n	Dynamic viscosity (mPa·s)

REFERENCES

Chein, R., Huang,G., 2004. Thermoelectric cooler application in electronic cooling. Appl. Therm. Eng 24(14-15), 2207-2217.

Toghraie, D., Chaharsoghi, V., Afrand, M., 2016. Measurement of thermal conductivity of ZnO–TiO2/EG hybrid nanofluid. J. Therm. Anal. Calorim 125(1), 527-535.

Ahammed, N., Asirvatham, L., Wongwises, S., 2016. Effect of volume concentration and temperature on viscosity and surface tension of graphene–water nanofluid for heat transfer applications. J. Therm. Anal. Calorim 123(2), 1399-1409.

Zhou, S., Ni, R., 2008. Measurement of the specific heat capacity of water-based Al2O3 nanofluid. Appl. Phys. Lett 92(9), 93123-5.

Roberts, N. S., Al-Shannaq, R., Kurdi, J., Al-Muhtaseb, S., Farid, M., 2017. Efficacy of using slurry of metal-coated microencapsulated pcm for cooling in a micro-channel heat exchanger. Appl. Therm. Eng 122, 11-18.

Goel, M., Roy, S., Sengupta, S., 1994. Laminar forced convection heat transfer in micro-encapsulated phase change material suspensions. Int. J. Heat Mass Transf 37(4), 593-604.

Chen, B., Wang, X., Zeng, R., Zhang, Y., Wang, X., Niu, J., Li, Y., Di, H., 2008. An experimental study of convective heat transfer with microencapsulated phase change material suspension: laminar flow in a circular tube under constant heat flux. Exp. Therm. Fluid. Sci 32(8), 1638-1646.

Kong, M., Yu, K., Alvarado, J., Terrell, W., 2015. Thermal Performance of Microencapsulated Phase Change Material Slurry in a Coil Heat Exchanger. J. Heat Transf-Trans. ASME 137(7).

Alvarado, J., Marsh, C., Sohn, C., Phetteplace, G., Newell, T., 2007. Thermal performance of microencapsulated phase change material slurry in turbulent flow under constant heat flux. Int. J. Heat Mass Transf 50(9-10), 1938-1952.

Lu, H., Seyf, H., Zhang, Y., Ma, H., 2015. Heat transfer enhancement of backward-facing step flow by using nano-encapsulated phase change material slurry. Numer. Heat Tranf. A-Appl 67(4), 381-400.

Fang, Y., Yu, H., Wan, W., Gao, X., Zhang, Z., 2013. Preparation and thermal performance of polystyrene/n-tetradecane composite nanoencapsulated cold energy storage phase change materials. Energy Conv. Manag 76, 430-436.

Fang, Y., Kuang, S., Gao, X., Zhang, Z., 2009. Preparation of nanoencapsulated phase change material as latent functionally thermal fluid. J. Phys. D-Appl. Phys 42(3), 34-38.

Manuscript ID: 1434
DOI: 10.18462/irr.icr.2019.1434

Investigations on the thermodynamic characteristics of a high-efficiency three-stage linear compressor system for a 1-2 K Joule-Thomson cryocooler

Tao ZHANG[(a),(b)] , Rui ZHA[(a),(b)], Jun TAN[(a),(c)], Jiaqi LI[(a),(b)], Yongjiang ZHAO[(a),(b)], Bangjian ZHAO[(a),(b)], Haizheng DANG[(a),(c)]

[(a)] State Key Laboratory of Infrared Physics, Shanghai Institute of Technical Physics, Chinese Academy of Sciences, 500 Yutian Road, Shanghai 200083, China, cryotz@163.com; haizheng.dang@mail.sitp.ac.cn

[(b)] University of Chinese Academy of Sciences, No. 19A Yuquan Road, Beijing 100049, China

[(c)] Shanghai Boreas Cryogenics Co., Ltd, 1388 Shuidian Road, Shanghai 200434, China

ABSTRACT

The high-efficiency linear compressor is critical to the Joule-Thomson (JT) cryocooler working at 1-2 K. A three-stage linear compressor system is developed. The system components and the inner structure of the compressor are illustrated and described in detail. The electrical, mechanical and thermal energy conversions and the compression losses in the compressor are theoretically analyzed. In particular, the mass flow rates and pressure distributions among the three stages are investigated in depth. An experimental setup is established to test the performance of the three stages separately. The testing results show that, each JT compressor can achieve the aimed suction and discharge pressures. With a total input power of 90.5 W, the developed JT cryocooler is expected to achieve the no-load temperatures of 2.2 K and 1.42 K with He-4 and He-3 as working fluid, respectively. The further experimental investigations and verifications are underway.
Keywords: 1-2 K, Cryocooler, J-T cooler, Linear compressor, Thermodynamics

1. INTRODUCTION

With the rapid development of the deep space exploration and low-T_c superconducting technologies, the associated mechanical cryocooler capable of providing 1-2 K is now desirable. Among all the mechanical cryocoolers, the Joule-Thomson (JT) cooler coupling with a three-stage Stirling-type pulse tube cryocooler (SPTC) is a promising way to reach the required temperatures (Dang et al., 2018; Dang et al., 2018; Dang et al., 2017). For the JT cooler, a direct-steady-continuous (DC) flow with high pressure before the JT valve and low pressure after that is demanded to realize the throttle cooling effect. Therefore, the compressor, as the driver source of the JT cooling loop, is one of the most important components of the entire system.

Generally, a rotary compressor is used to circulate the JT loop, such as in the household refrigerator, and some work has been done to change it to the version that can be employed in the cryogenic JT cooler, such as the GM/JT hybrid cryocoolers. However, it is still knotty if it is used in cryogenic regions. For example, (1) the friction and wear between shaft and cylinder is inevitable; (2) the frozen lubricating oil at low temperature probably clogs the orifice of the JT valve; (3) the volume is large and weight is too heavy. These disadvantages limit its application in many fields, especially for space missions. By contrast, the linear compressor is a reciprocating compressor that utilizes a piston driven by a linear motor to deliver gases at high pressure. The Oxford-type moving-coil dual-opposed linear compressor, with the clearance seal, flexure springs, dual-opposed configuration and flexible design technologies, have the advantages of high reliability, long life time, low vibration and high efficiency (Dang, 2015). Over the past decades, it has been successfully applied in a variety of space missions to drive the Stirling or pulse tube cryocoolers.

This paper presents a high-efficiency three-stage linear compressor system for the JT cooler. Each JT compressor is developed based on the Oxford-type moving-coil dual-opposed linear compressor used for the SPTC. The system components and structure design are described in detail.

Theoretical analyses are made to study the electrical, mechanical and thermal characteristics in the JT compressor. An experimental setup is built to test the system performance. The further investigations on the matching between the three-stage compressor group and the JT loop are underway.

2. SYSTEM COMPONENTS AND STRUCTURE DESIGN

2.1. System Components

Fig. 1 shows the components of the three-stage JT compressor group. It consists of three linear compressors that are connected in tandem. At first, the low-pressure working fluid He-4 or He-3, which is from the first stage of the counter-flow heat exchanger, is taken into the first stage compressor. Then it is compressed stage-by-stage by the compressor group. Finally, the required high pressure is exhausted through the discharge port of the third stage compressor. The Alternating Current (AC) power source is used to drive the compressor group, with W_1, W_2 and W_3 power supply for the first, second and third compressor, respectively.
The system, together with the cold finger of the JT loop, forms the complete closed cycle JT cryocooler. In contrast to the open cycle system, in the closed loop the low pressure p_l and the high pressure p_h, are not independent. Any change in one as a response to varying operating conditions (such as the adjustment of the orifice's size) is accompanied by a corresponding change in the other one. The linkage between the two pressures results from two aspects associated with the conservation of mass and continuity, which are inherently realized by a circulating working fluid operating at steady state in a closed loop. This point will be discussed in detail in the next chapter.

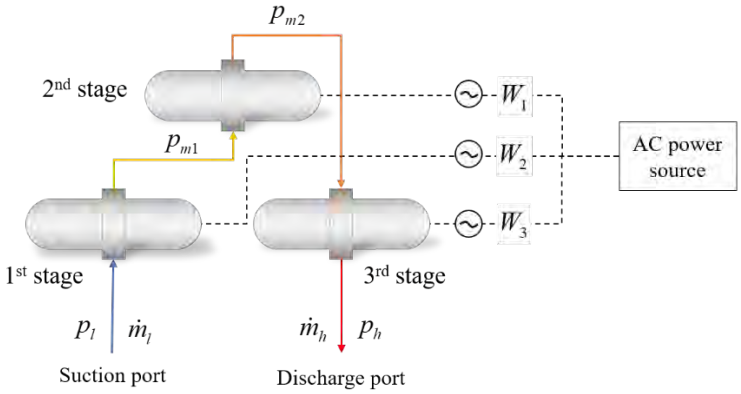

Figure 1: Components of three-stage JT compressor group

2.2. Structure Design

In the three-stage JT compressor group, all of the three compressors have similar structures. Fig.2 shows a schematic of one linear JT compressor, which is similar to the compressor used for the SPTC. It adopts the balanced-opposed arrangement so that the self-induced vibrations from the two halves are cancelled out. Each half comprises a cylinder, a piston with a shaft, two sets of flexure springs, a position transducer, a pressure vessel, and a linear motor composed of a permanent magnet, a moving coil and two return irons. Each piston is driven by the linear motor directly coupled to the piston shaft and reciprocates in its own cylinder. Two sets of flexure springs attached to each piston shaft axially support the piston to achieve the clearance seal, with which the wear between the piston and cylinder is eliminated and the power lost through the clearance becomes negligible compared with the total power delivered by the piston. Each piston is designed to operate resonantly in order to minimize the drive current. Two position transducers are fixed on the piston shafts to closely monitor the respective movements of the pistons (Dang, 2015).

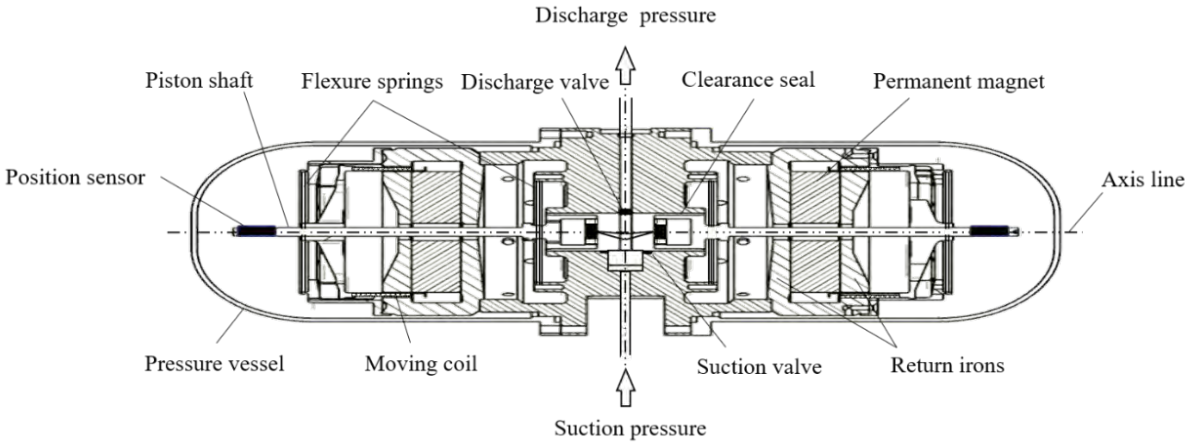

Figure 2: Schematic of dual-opposed linear JT compressor

The suction and discharge valves are mounted in the inlet channel and outlet channel of the cylinder, respectively. They are a kind of relief valves that are used to provide a one-way flow of the working fluid (Sato et al., 2012; Sato et al., 2010). As shown in Fig. 2, the compression process is as follows:
The low-pressure working fluid from the former stage is sucked into the compression space with the action of the pistons through the suction valves, when the pistons move towards the center. The working fluid is compressed, and then exhausted through the discharge valve when the pistons move towards the outside. The exhausted working fluid flows into the next stage JT compressor through the connecting tube. The other compressors work in the same way and supply the high-pressure working fluid to the JT cooling loop. The volume of each pressure vessel is used as a buffer volume for suction pressure of each compressor in order to make a stable flow.

3. THEORETICAL ANALYSES

In a JT compressor, three different forms of energy are included in the energy conversion: the electric energy, mechanical energy and thermal energy. The electric energy is transferred into the mechanical energy through the moving coil acting in the magnetic field, and the mechanical energy is transferred into the thermal energy by pistons acting on the working fluid. The input electric power, movement of the piston and thermodynamic parameters of the working fluid are correlated and the relationship among them are relatively complicated, especially the thermodynamic characteristics in the three different stages of the compressor system. A theoretical model is built to investigate the energy conversion and variations of the thermal parameters in the three-stage system. The compression losses are also analyzed theoretically.

3.1. Linear Motor

To simplify the analyses, the motion of the piston is assumed to be sinusoidal and then it can be written as (Jomde et al., 2018; Jomde et al., 2017; Phadkule et al., 2018)

$$x = \frac{X}{2}\sin\omega t \qquad \text{Eq. (1)}$$

where X is the piston displacement of one stroke and ω is the angular frequency.
For the linear motor, neglecting the influence of the back pressure, the force balance is given as:

$$LBI = M_1\frac{\mathrm{d}^2x}{\mathrm{d}t^2} + C_{\mathrm{d}1}\frac{\mathrm{d}x}{\mathrm{d}t} + K_1x + A_{p1}\Delta P_1 \qquad \text{Eq. (2)}$$

where the left part of the equation is the electromagnetic force, in which L is the coil length, B is

the magnetic field intensity and I is the motor current. The four terms in the right part stand for inertia force, viscous force, mechanical spring force and gas force, respectively. M_1 is the mass of moving coil and piston $C_{\mathrm{d}1}$ is the mechanical damp coefficient of the moving part, K_1 is the axial stiffness of flexure springs, A_{p1} is the cross-sectional area of the piston and ΔP_1 is the pressure difference between the compression chamber and the back side of the piston. t stands for time.
The motor voltage can be calculated by:

$$U = L_{\mathrm{e}}\frac{\mathrm{d}I}{\mathrm{d}t} + R_{\mathrm{e}}I + BL\frac{\mathrm{d}x}{\mathrm{d}t} \qquad \text{Eq. (3)}$$

where L_{e} and R_{e} are coil inductance and coil resistance. R_{e} can be given as:

$$R_{\mathrm{e}} = \frac{16\rho_{\mathrm{c}}\eta V_{\mathrm{c}}}{\pi^2 d_{\mathrm{c}}^4} \qquad \text{Eq. (4)}$$

where ρ_{c} is the resistivity of the coil, η is the filling rate, d_c is the diameter of the coil wire and V_{c} is the available volume in the coil holder.

3.2. Suction and Discharge Valve

Simplified valve motion of the suction and discharge valve, which is used for predicting compressor efficiency, could be achieved from a second-order damping system. The governing equation is:

$$M_2\frac{\mathrm{d}^2 z}{\mathrm{d}t^2} + C_{\mathrm{d}2}\frac{\mathrm{d}z}{\mathrm{d}t} + K_2 z = \Delta P_2 A_{\mathrm{p}2} - f_{\mathrm{s}} - M_2\frac{\mathrm{d}^2 x}{\mathrm{d}t^2} \qquad \text{Eq. (5)}$$

where z is the displacement of valve, $C_{\mathrm{d}2}$ is the damping coefficient of the valve, K_2 is the elastic coefficient, ΔP_2 is the difference between pressures acting on topside and backside of valve, $A_{\mathrm{p}2}$ is the effective area which ΔP_2 is acting on and f_{s} is the stiction and initially installed force.

3.3. Thermal Characteristics

As discussed in the system components section, the linkage between the low-pressures and high-pressure in a closed cycle arises from two aspects associated with the conservation of mass and continuity:
(1) The high-pressure mass flow rate has to match the low-pressure mass flow rate, which is $\dot{m}_l = \dot{m}_h$. This aspect connects the two pressures through the size of the orifice. In case of choked flow conditions, the low-pressure has a minor effect on the mass flow rate, while the high-pressure is the main contributory factor, which is expressed as follow:

$$\dot{m} = \frac{\pi {d_{orf}}^2}{4}\left(\frac{2}{\bar{\kappa}+1}\right)^{\frac{1}{\bar{\kappa}-1}}\sqrt{\frac{2\bar{\kappa}p_h\rho_h}{\bar{\kappa}+1}} \qquad \text{Eq. (6)}$$

where d_{orf} is the JT valve orifice diameter, $\bar{\kappa}$ is the average adiabatic index and ρ_h is the density at p_h before the JT valve.
(2) The total amount of working fluid in the entire loop remains unchanged although the distribution between the two sections, m_l and m_h, may alter. This aspect is associated with the actual pressure values and the volumes before and after the JT valve.
The mass flow rate, which is a constant around the complete JT loop, can be determined from the density and volumetric flow rate at the suction side of the compressor:

$$\dot{m} = \dot{V}\rho(p_l)\eta_V \qquad \text{Eq. (7)}$$

where the volumetric flow rate $\dot{V}$ depends on the swept volume during a single stroke and the frequency of the strokes, and then:

$$V = \frac{1}{4}\pi d^2(2X + \delta)f \quad \text{Eq. (8)}$$

where d is the diameter of the piston, δ is the minimum distance between the two pistons and f is the operation frequency of the compressor.
The volumetric efficiency η_V is the fraction of the swept mass, which is actually transferred and discharged into the high-pressure side. A variety of factors influence the volumetric efficiency of a compressor including its void volume, the content of which is compressed but not discharged, internal leakages induced by the discharge and suction pressure difference, $p_h - p_l$, and at very high flow rates in reciprocating compressors, the inertial impedance of flow into and out of the cylinders. The volumetric efficiency is a moderately decreasing function of the pressure ratio, which is given as:

$$\eta_V = 0.71 + (0.35 - 0.34\kappa)\left[\left(\frac{p_h}{p_l}\right)^{\frac{1}{\kappa}} - 1\right] \quad \text{Eq. (9)}$$

Eq. (9) is applicable to each single stage of the JT compressor. The compression process for all the three compressors is assumed to be isothermal. In this case, the theoretical input power for the entire three-stage JT compressor group reaches the minimum. The pressure distributions among the three stage and the corresponding pressure ratio is determined by Eq. (10):

$$\frac{p_{m1}}{p_l} = \frac{p_{m2}}{p_{m1}} = \frac{p_h}{p_{m2}} = \sqrt[3]{\frac{p_h}{p_l}} \quad \text{Eq. (10)}$$

3.4. Compressor Loss

The compressor losses mainly include three parts: the Joule loss, the valve head loss and the pumping loss.

3.4.1. Joule Loss

The Joule loss of the compressor can be expressed as:

$$\dot{Q}_{\mathrm{J}} = 2\times f\int_0^{2\pi/\omega} I^2\, R_{\mathrm{e}}\mathrm{d}t \quad \text{Eq. (11)}$$

3.4.2. Valve Head Loss

The pressure drop at the valve can be calculated by:

$$\Delta P_v = \rho_{\mathrm{s}}(au + bu^2) \quad \text{Eq. (12)}$$

where ρ_{s} is the estimated stagnation density at the valve port, a and b are constants, and u is the mean flow velocity.

3.4.3. Pumping Loss

The pumping loss though the clearance seal is calculated using the expression for the instantaneous laminar mass flow through an annulus (ignoring acceleration terms):

$$\dot{m}_{\mathrm{seal}}(\phi) = \frac{\pi d\tau^3}{12\mu}\frac{(p_b + p_{dis})}{2RT}\frac{(p_b - p_{dis})}{L_s} \quad \text{Eq. (13)}$$

Where R is the gas constant, L_s is the seal length, μ is the gas viscosity, τ is the radial gap clearance, p_b is the body pressure in the compressor vessel, and p_{dis} is the discharge pressure.

4. PERFORMANCE TESTING

According to a developed numerical model based on the enthalpy analysis, the JT cooler will achieve the optimal cooling capacity at 2.2 K when the high-pressure and the low pressure are 1.29 MPa and 5.32 kPa, respectively. The theoretical mass flow rate is 5.02 mg/s with He-4 as the working fluid. An experimental setup is used to test the compressor performance, as shown in Fig. 3.

The three compressors are tested separately. Two pressure gauges are used to monitor the high and low pressure in the loop. The pressure ratio is controlled by the JT valve and the mass flow rate of He-4 is measured by the mass flow meter (MFM). During the test, the temperature of the JT compressor is kept at 300 K by the cooling water using a constant temperature circulator. The pressure inside the cylinder is measured using the dynamic pressure transducer. The position sensor measures the displacement of the piston through which the volume of a cylinder was calculated. Hence the pressure-volume (P-V) diagrams of the three stages are plotted as shown in Fig. 4. It can be observed that the measured values have a good agreement with the simulated values based on the theoretical analyses.

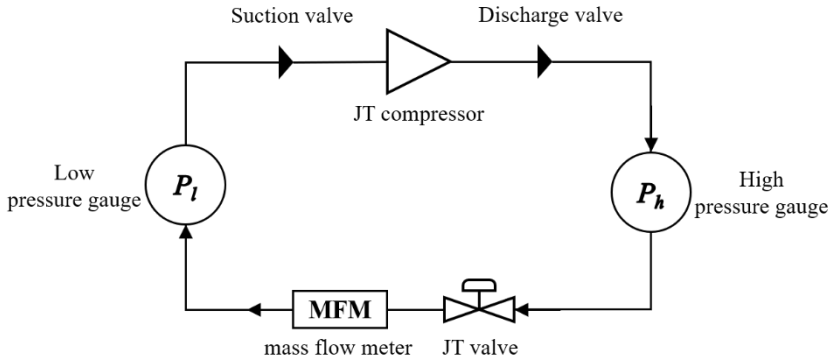

Figure 3: Schematic diagram of JT compressor testing setup

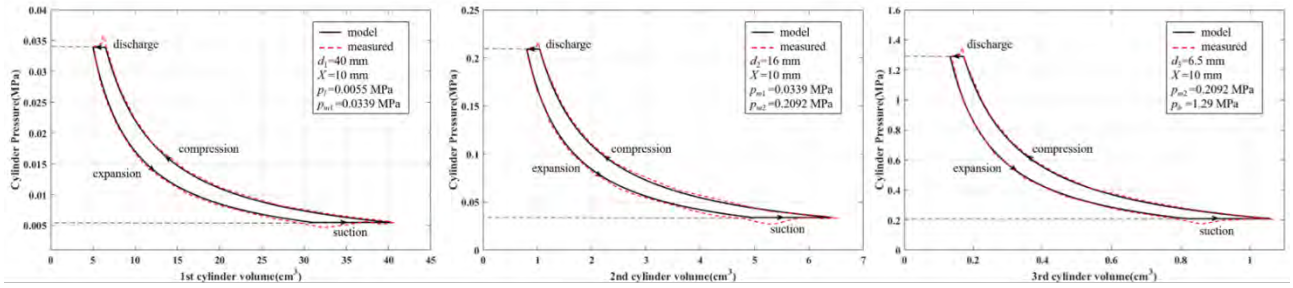

Figure 4: Test results for three JT compressors on P-V diagram

Table 1 gives the design and test parameters of the three JT compressors. The pressure ratio for each stage is about 6.17, and the mass flow rates of the three stages are 4.99, 4.92 and 5.01 mg/s, respectively, which shows a good match for the required value achieving the optimal cooling capacity. The total input power is 90.5 W. The results indicate that, if the three compressors are linked in tandem and coupled with the JT cooling loop, the complete JT cryocooler is expected to operate steadily with the closed cycle. The predicted no-load temperatures are 2.2 K and 1.42 K with He-4 and He-3 as working fluid, respectively.

Table 1. Design and test parameters of three JT compressors

Compressor	Piston diameter (mm)	Piston stroke (mm)	Operation frequency (Hz)	Suction pressure (MPa)	Discharge pressure (MPa)	Mass flow rate (mg/s)
1st	40	10	50	0.0055	0.0339	4.99
2nd	16	10	50	0.0339	0.2092	4.92
3rd	6.5	10	50	0.2092	1.29	5.01

5. CONCLUSIONS

A high-efficiency three-stage linear compressor system used for the 1-2 K JT cryocooler is developed. The system is composed of three JT compressors which linked in tandem. The inner structure is illustrated and described in detail. The electric, mechanical and thermal energy conversions and the compression losses in the compressor are theoretically analyzed. In particular, the mass flow rates and pressure distributions among the three stages are investigated in depth. An experimental setup is established to test the performance of the three stages separately. The testing results show that, each JT compressor can achieve the aimed suction and discharge pressures. The steady mass flow rate matches well with the theoretical required value. With a total input power of 90.5 W, the developed JT cryocooler is expected to achieve the no-load temperatures of 2.2 K and 1.42 K with He-4 and He-3 as working fluid, respectively. The further experimental investigations and verifications are underway.

ACKNOWLEDGEMENTS

This work is financially supported by the Aeronautical Science Foundation of China (No. 20162490005) and Shanghai Municipality (Nos. 18511110100, 18511110101, 18511110102).

REFERENCES

Dang, HZ., 2015. Development of high performance moving-coil linear compressors for space Stirling-type pulse tube cryocoolers. Cryogenics 68, 1-18.

Dang, HZ., Bao, DL., Zhang, T., et al., 2018. Theoretical and experimental investigations on the three-stage Stirling-type pulse tube cryocooler using cryogenic phase-shifting approach and mixed re-generator matrices. Cryogenics 93, 7-16.

Dang, HZ., Bao, DL., Gao, ZQ., et al., 2018. Theoretical modeling and experimental verifications of the single-compressor-driven three-stage Stirling-type pulse tube cryocooler. Frontiers in Energy.

Dang, HZ., Tan, J., Zha, R., et al., 2017. Advances in single- and multi-stage stirling-type pulse tube cryocoolers for space applications in NLIP/SITP/CAS. Cryogenic Engineering Conference 278, Art. no. 012008.

Jomde, A., Anderson, A., Bhojwani, V., et al., 2018. Modelling and measurement of a moving coil oil-free linear compressor performance for refrigeration application using R134a. International Journal of Refrigeration 88, 182-194.

Jomde, A., Anderson, A., Bhojwani, V., et al., 2017. Performance predictions and parametric analysis of valved linear compressor using mathematical model. International Journal of Ambient Energy 39, 456-461.

Phadkule, S., Inamdar, S., Inamdar, A., et al.,2018. Resonance analysis of Opposed piston linear compressor for Refrigerator application. International Journal of Ambient Energy, 1-8.

Sato, Y., Shinozaki. K., Sugita. H., et al., 2012. Development of mechanical cryocoolers for the

cooling system of the Soft X-ray Spectrometer onboard Astro-H. Cryogenics 52, 158-164.

Sato, Y., Sugita, H., Shinozaki, K., et al., 2010. Conceptual design of a cryogenic system for the next-generation infrared space telescope SPICA. Proceedings of SPIE - The International Society for Optical Engineering 77314.

Manuscript ID: 1452
DOI: 10.18462/iir.icr.2019.1452

A review of battery thermal management in electric vehicles

ZHENG Lingyu，ZHANG Xuelai

Institute of Cool Storage Technology, Shanghai Maritime University,
Shanghai 201306, China，zhenglingyu13@stu.shmtu.edu.cn

ABSTRACT

Electric vehicles are widely adopted as the solutions of air pollution and energy crisis. Batteries as electric vehicles' power sources are very important. The most widely used batteries are lithium-ion batteries, Ni-MH batteries, fuel cells and super-capacitors. However, these batteries have different heating problems. The paper studied principle of produced heat of these four type of batteries, reviews the existing batteries' thermal management. Traditional methods as air and liquid and PCM cooling are useful. This paper also introduces other new cooling methods such as heat pipe cooling and multiple cooling methods, as well as the solution to the problem of low temperature start of the batteries in winter. This will facilitate the investigation on advancing the thermal management system to a new generation.

Key words：Battery, Electric Vehicle, PCM, Thermal switch

1. INTRODUCTION

Automobile is one of the main reasons of air pollution and petroleum energy crisis. With the increasing global warming and other environmental problems and the gradual exhaustion of non-renewable energy, countries around the world are competing to develop new energy vehicle technology for high efficiency and low pollution. In recent years, Chinese car ownership has increased year by year. It is expected that by 2020, Chinese car ownership will exceed 200 to million vehicles, and its fuel consumption will account for 57% of the total oil consumption[1]. The severe situation has prompted countries to organize relevant strategies for innovation and development of new energy and intelligent automobiles [2]. New energy vehicles are expected to account for 35% of global car sales by 2040.

Power battery is the main technology of new energy vehicles, which can be divided into biological battery, chemical battery and physical battery [3]. Bio-battery converts bio-energy into electric energy. Physical batteries contain solar cells and supercapacitors that store and release electrical energy through physical changes. According to working properties, chemical batteries are divided into primary batteries (primary batteries), secondary or rechargeable batteries (storage batteries) and fuel cells [4]. Lithium-ion battery is one kind of secondary batteries which is widely used because of its wider operating temperature range, higher safety voltage and lower price. High temperature will lead to the aging of power batteries, which will cause various safety problems. Low temperature will also cause the performance of lithium-ion batteries and fuel cells to decline or even make them unable to start. Therefore, different thermal management systems need to be designed for different power batteries. General cooling methods of power batteries are air cooling, liquid-cooling, phase change cooling, etc. General heating methods are external heating and internal heating.

2. MAIN SECTION

2.1. Lithium ion battery thermal management system

Lithium ion batteries transfer energy through positive and negative electrodes during the charging and discharging process: When the battery is charging up, the lithium-cobalt oxide, positive electrode gives up some of its lithium ions, which move through the electrolyte to the negative, graphite electrode and remain there. The battery takes in and stores energy during this process. When the battery is discharging, the lithium ions move back across the electrolyte to the positive electrode, producing the energy that powers the battery[5].

In the process of charging and discharging, the temperature of the battery will rise because of the inside chemical reaction and resistance. When the temperature rises to a certain limit, the thermal failure of the battery would happen, which will lead to the explosion of the battery, even resulting in huge casualties [6]. Fig. 1 shows a Model S 90D burning due to thermal failure, so the thermal management method of power battery is important.



Fig. 1 a burning Model S 90D

The overall heat generated by the lithium-ion battery during charging and discharging is ohmic heating QJ, reactive heating Qr, side reaction heating Qs and polarization thermal QP.

The calorific value can be expressed by formulas (1) and (2):

$$Q_J = I^2 R_e \tag{1}$$

$$Q_r = nmQI/(MF) \tag{2}$$

The total heating production of lithium ion battery can be calculated by the formula (3) :

$$Q_t = Q_r + Q_J + Q_P + Q_s \tag{3}$$

The Bernardi formula (4) can be used to analysis the thermal characteristics of batteries [7]:

$$q = \frac{I}{V_b}(V - U) + \frac{I}{V_b}(T\frac{\partial U}{\partial T}) \tag{4}$$

In addition, the low temperature will also destroy battery performance, such as increasing the internal resistance of batteries and reducing the discharge capacity of batteries[8].

Therefore, effective thermal management of batteries is particularly important. Liquid cooling, air cooling, phase change material cooling and composite cooling are the main way of thermal management.

2.1.1 Air Cooling System

Air cooling technology uses air as heat transfer medium. It is simple, easy to integrate, no leakage danger, and low maintain cost. Toyota's RAV-4 and Prius have chosen this thermal management system to cool the car battery. air cooling thermal management system is generally divided into parallel and serial [9]. The parallel mode is better than serial [10] and different runner structure design also has a vital impact on the efficiency of system. Zhu Hui found that when the angle between air guide plates and horizontal plane was 4 degrees and the distance between air passages decreased by 2 mm, the air cooling system could maintain the minimum temperature difference between cells at room temperature (25 C)[11]. Xun found that the cooling efficiency could be improved by increasing the size of cooling passage, but it would lead to the unbalanced temperature distribution of battery pack. When the discharge rate of battery is as high as 2C and the Reynolds number of cooling air at the inlet is more than 2000, the volume ratio between cooling passage and battery pack should be more than 0.014 [12]. Park found that the wide flat battery module with small battery gap is more suitable for air cooling vehicle battery thermal management system [13]. Mohammadian used 3D transient thermal analysis method to find that a special type of aluminum pin fin radiator can increase the cooling efficiency of air cooling [14].

With the increasing demand for energy density of lithium-ion batteries air cooling system has been unable to meet the heat dissipation requirements of power batteries. It has become a trend to replace air cooling devices with more effective thermal management systems.

2.1.2 Liquid Cooling System

Liquid cooling system is more effective than air cooling system. Tesla Motors Model S-64P and Audi A3 Sportback e-tron chose this as their thermal management system.

The research of liquid cooling system focuses on the design of microchannel cooling plate, including the structural and fluid characteristics of the system itself. Rao found that changing the flow rate of the inlet liquid could change the maximum temperature and temperature difference of the battery pack [15]. Jia found that the number of pipes had the greatest effect on the average temperature of the cooling plate, followed by the flow rate of coolant, and the height of pipes had the least effect. The number of pipes and the speed of coolant had the same effect on the temperature uniformity [16]. Zhao found that increasing the liquid flow rate of the system can effectively reduce the temperature of the battery and improve the uniformity of the temperature distribution of the battery. Increasing the heat transfer in the vicinity of the battery can also improve the uniformity of the temperature distribution of the battery, but this method has little effect on reducing the temperature of the whole battery module. Increasing the interface area between the battery and the outer wall of the liquid runner can significantly reduce the maximum temperature of the system, but this method destroys the uniformity of the temperature of the whole system [17].

However, the structure of liquid cooling system is complex, which increases the cost of construction and maintenance. At the same time, the liquid cooling system has higher requirements than the air cooling system in mechanical strength and vibration resistance of materials.

2.1.3 Phase Change Material Cooling System

Phase change material (PCM) uses the latent heat of phase change to store energy. Paraffin is a typical PCM used in thermal management system of batteries because of its non-corrosiveness and low price. However, the low thermal conductivity strict the development of it. Therefore, improving the thermal conductivity of paraffin is the prime aim of this technology. The traditional method is

adding something like expanded graphite, nanoparticles and other typical materials to enhance PCM's conductivity. Ling found that 60 wt% RT44HC paraffin/expanded graphite phase change composites can effectively reduce the temperature difference between batteries [18]. Jiang Guiwen found that EG (12%)/PCM (88%) composite PCM could effectively improve the thermal management of lithium batteries. At the same time, he proposed that the radial thermal conductivity of composite materials played a decisive role in the heating rate of batteries, but when the radial thermal conductivity reached a certain value, the heating rate of batteries would not change [19]. However, the thermal conductivity of expanded graphite for paraffin wax is not infinite. Li Zhao found that the thermal conductivity of composites increases gradually with the increase of the mass fraction of expanded graphite to a certain value, and other thermal physical parameters decrease gradually [20]. Lv chooses nano-silica composite PCM for battery thermal management system [21]. In addition to composite materials with high thermal conductivity, heat transfer can also be enhanced by changing the structure of the system. Zhang Yanlai, through experimental testing and numerical analysis, concluded that wrapping PCM into microcapsules with thin films can enhance the heat transfer of natural convection [22].

2.1.4 Heat Pipe Cooling System

Heat pipe is widely used in industry as heat ex-changer.Ye validates that the heat pipe cooling system can effectively control the accumulated heat in the rapid charging process of power batteries [23-24]. Ye designed a flat miniature heat pipe cooling system. The system can keep the temperature between 25 and 40 degrees Celsius and ensure that the temperature difference between batteries is always less than 5 degrees Celsius [25]. Zhao proved that the thermal management system of automobile batteries can rely on ultra-thin heat pipes to quickly dissipate heat [26]. Wang Jian demonstrates by numerical analysis that the average temperature of the battery pack cooled by heat pipe is lower than that cooled by natural convection, and the temperature difference of the battery pack decreases by 2.2 degrees Celsius. With the increase of the length of the condensation section of the heat pipe, the cooling effect of the battery pack will be enhanced. When the length of the condensation section of the heat pipe reaches 50 mm, the cooling requirement of the battery pack can be met [27].

2.1.5 Compound Application of Multiple Thermal Management Systems

A single thermal management method often has many shortcomings, so more and more scholars are trying to pull together different thermal management methods in batteries.

Al-Hallaj designed a composite thermal management system which combines air cooling and phase change materials[28]. Behi designed a heat pipe cooling system assisted by composite phase change materials, which can increase heat dissipation and reduce heat absorption, and avoid thermal damage of battery packs[29]. Krishna designed an effective heat pipe cooling system assisted by nano-reinforced phase change materials [30]. Wang designed a pulsating heat pipe battery thermal management system which combines phase change materials, and found that it is more effective than the pure pulsating heat pipe thermal management system [31].

2.1.6 Low Temperature Heating System

At present, most scholars are only concerned about the heat dissipation of lithium ion batteries, but low temperature will increase the internal resistance of the electrolyte and inhibit the chemical reaction rate, resulting in poor charge-discharge performance of lithium-ion batteries. Therefore,

reasonable heating devices are needed to preheat lithium-ion batteries in winter.

Zhang compared the external heating methods of metal resistance heating film (MRF) and positive temperature coefficient thermistor (PTC), found that the heating effect of MRF was better [32]. Guo designed a battery heating system for all-weather electric vehicles. The system can raise the temperature of the battery from 2.21 (-20.84) to 10.02 (-20.3 C) in 12.4 minutes[33]. However, there is little research in this field, which needs to be developed by scholars in the future.

2.2. Research status of other types of battery thermal management system

2.2.1 NiMH Battery Thermal Management System

With the increase of temperature, the chemical reaction rate will accelerate, which will affect the service life of the battery. The results show that the cycle times of MH-Ni battery decrease by 60% when the working temperature of MH-Ni battery reaches 45 C. Chang Guofeng optimized the structure of thermal management system for MH-Ni batteries in hybrid electric cars. Tests show that the optimized structure can control the local maximum temperature of batteries below 40 C, and the temperature difference between batteries is not more than 5 [34]. Wu Zhongjie has designed a jacketed thermal management system for liquid cooling batteries. The system can control the surface temperature of batteries in the optimum operating range and maintain a uniform temperature distribution [35].

2.2.2 Fuel Cell Thermal Management System

The main heating components of PEMFC are proton exchange membrane fuel cell stack and battery pack. The internal water balance and thermal balance of fuel cells are closely related, so the thermal management of fuel cells is also called water management. When the temperature is low, the internal polarization of the battery is greater, and the ohmic impedance increases [36]. The increase of temperature can promote the electrochemical reaction speed and improve the performance of the battery, but too high temperature can also cause dehydration of the proton exchange membrane and lead to safety problems [37]. The relationship between the theoretical potential and temperature of the fuel cell is formula (5) [38]:

$$E = \frac{\Delta H}{nF} - \frac{T\Delta S}{nF} \tag{5}$$

At present, the working temperature of proton exchange membranes of fuel cells used in the market is 60-80 C, which can not exceed 100 C. Meanwhile, PEMFC contains water, which will freeze below 0 C, then affecting battery start-up. So the cold start problem is what PEMFC needs to solve urgently. Chen Sitong applied phase change materials to the thermal management of PEMFC. It was found that phase change materials could make temperature difference between single batteries smaller, and had obvious advantages in the cold start problem [39]. Shi Haimin invented a fuel cell thermal management system which combines various water circulation systems[40].

2.2.3 Supercapacitor Thermal Management System

Supercapacitor (SC) has the advantages of low internal resistance, but the heat caused by the instantaneous diffusion of ions in electrolyte can not be neglected. The thermal behavior of SC can be simulated by equivalent circuit. Berrueta studied an electrical and thermal model of a Maxwell SC by means of equivalent circuit simulation[41] . Excessive temperature accelerates the aging of SC [42]. Gualous verified that the aging of SC is related to temperature and voltage [43]. The core temperature of SC should be kept below the boiling point of electrolyte. Once the temperature exceeds 81 C, SC will be damaged. So we must also set up cooling system for SC. The current cooling methods are

natural convection cooling method and forced air cooling method.

3. CONCLUSIONS

Future Prospect of Research on Automotive Battery Thermal Management System

3.1 Because of the space limitation of electric vehicles, in the future battery thermal management system design should mainly focus on the smaller size, lighter weight, cheaper cost and more heat dissipation performance. Meanwhile, phase change materials and heat pipe cooling methods are in the laboratory stage, and the ideal state of the laboratory is far from practical application.It is necessary to turn it into reality and deduce and establish the optimization performance models of phase change materials and heat pipes.

2.3.2 The high temperature resistance of MH-Ni batteries is very poor. It is necessary to control the working temperature below 45 C. Therefore, future scholars need to find a more effective way to control the overall battery temperature by improving the internal performance of batteries or enhancing the thermal properties of external thermal management materials.

2.3.3 PEMFC thermal management systems should focus on preventing the battery stack from freezing, and quickly melting the ice through external heating after freezing.

2.3.4 Further study of supercapacitors is making out the aging mechanism and establishing aging models.

NOMENCLATURE

R_e	ohmic internal resistance of battery material	I	Charge and Discharge Current of Batteries
n	cell number	M	electrode quality
Q	electrode chemical reaction and heat generated algebra	M	molar mass
F	Faraday constant (96484.5C/mol)	Q	the heat production rate of the battery
Vb	Battery Volume	U	open circuit voltage
V	working voltage	T	temperature

REFERENCES

[1] MA W X. ,2008, Orientation analysis of vehicle power system development under the influence of energy pressure ,J. Modern Business Trade Industry20(1):274-275.

[2] JIANG L W. , 2017, The development strategy of the intelligent automobile industry will be introduced ,J. Financial Technology Time(10):92-92.

[3] MI L W, Copelel R. , 2017, The tesla revolution: why big oil has lost the energy war，M. China Machine Press.

[4] TANG D L. , 2013, Classification and performance indicators of power batteries for electric

vehicles,J. Auto Maintenance & Repair(4).

[5] ZHAI J Y. , 2008, Pulse charge and discharge management of lithium ion batteries,D. Zhejiang University.

[6] HONG S H, ZHANG X Q, WANG S F,et al. , 2014, Review on application of heat pipe technology in lithium-ion power battery thermal management system,J. Chemical Industry and Engineering Progress 33(11):2923-2927.

[7] LIU A H, GAN X Y, HE P Y,et al. ,2017,Research trends of lithium ion battery thermal model ,J/OL. Journal of Power Supply,1-13.

[8] SUN J L. , 2016, Research on the key technologies of electric vehicle battery management in high latitude and cold region, D. Harbin Institute of Technology.

[9] ZHANG F L., 2013, Research on battery package thermal management of electric vehicles,C // 2013 China Auto Engineering Society annual meeting paper collection. .

[10] TANG Z J, ZHU Q Z., 2013, Research on thermal management technology for power batteries,J. Chinese Journal of Power Sources 37(1):103-106.

[11] ZHU H, ZHANG Y C, ZHU C P,et al. , 2011,Research on thermal management technology for power batteries,J. Chinese Journal of Power Sources(6):8-10.

[12] Xun J, Liu R, Jiao K. , 2013, Numerical and analytical modeling of lithium ion battery thermal behaviors with different cooling designs,J. Journal of Power Sources233:47-61.

[13] Park S, Jung D. , 2013, Battery cell arrangement and heat transfer fluid effects on the parasitic power consumption and the cell temperature distribution in a hybrid electric vehicle,J. Journal of Power Sources227(4):191-198.

[14] Mohammadian S K, Rassoulinejad-Mousavi S M, Zhang Y. , 2015, Thermal management improvement of an air cooling high-power lithium-ion battery by embedding metal foam,J. Journal of Power Sources 296:305-313.

[15] Rao Z, Qian Z, Kuang Y, et al. , 2017,Thermal performance of liquid cooling based thermal management system for cylindrical lithium-ion battery module with variable contact surface,J. Applied Thermal Engineering 123:1514-1522.

[16] Jiaqiang E, Han D, Qiu A, et al. , 2017, Orthogonal experimental design of liquid-cooling structure on the cooling effect of a liquid cooling battery thermal management system,J. Applied Thermal Engineering.

[17] Zhao C, Cao W, Dong T, et al. , 2018, Thermal behavior study of discharging/charging cylindrical lithium-ion battery module cooled by channeled liquid flow,J. International Journal of Heat & Mass Transfer120:751-762.

[18] Ling Z, Wen X, Zhang Z, et al., 2018, Thermal management performance of phase change materials with different thermal conductivities for Li-ion battery packs operated at low temperatures,J. Energy, 144:977-983.

[19] JIANG G W, HUANG J H. , 2017, Preparation and thermal management of expanded graphite/paraffin composite for Li-ion battery,J. Journal of Materials Engineering45(7):41-47.

[20] LI Z, XU S C, CHANG G F, et al. , 2015, Cooling character of PCM embedded in porous

material for battery thermal management,J. Chinese Journal of Power Sources 39(2):257-259.

[21] Lv Y, Situ W, Yang X, et al. , 2018, A novel nanosilica-enhanced phase change material with anti-leakage and anti-volume-changes properties for battery thermal management,J. Energy Conversion & Management:250–259.

[22] ZHANG Y L, WANG S F, et al. , 2012, Enhanced natural convection on the micro capsule phase change material during phase change process,J. Acta Energiae Solaris Sinica33(11):1951-1955.

[23] Ye Y, Shi Y, Saw L H, et al. , 2016,Performance assessment and optimization of a heat pipe thermal management system for fast charging lithium ion battery packs,J. International Journal of Heat & Mass Transfer 92:893-903.

[24] Ye Y, Saw L H, Shi Y, et al. , 2015, Numerical analyses on optimizing a heat pipe thermal management system for lithium-ion batteries during fast charging,J. Applied Thermal Engineering86:281-291.

[25] Ye X, Zhao Y, Quan Z. , 2018,Experimental study on heat dissipation for lithium-ion battery based on micro heat pipe array (MHPA),J. Applied Thermal Engineering 130:74-82.

[26] Zhao R, Gu J, Liu J. , 2015, An experimental study of heat pipe thermal management system with wet cooling method for lithium ion batteries,J. Journal of Power Sources273:1089-1097.

[27] WANG J, GUO H, YE F, et al. , 2016,Numerical simulation of effect of heat pipe cooling device on temperature distribution in lithium-ion battery pack of vehicle,J. Journal of Chemical Industry and Engineering(China) | J Chem Ind Eng 67(z2):340-347.

[28] Al-Hallaj S, Selman J R. , 2004, Thermal modeling of secondary lithium batteries for electric vehicle/hybrid electric vehicle applications ,J. Journal of Power Sources110(2):341-348.

[29] Behi H, Ghanbarpour M, Behi M. , 2017,Investigation of PCM-assisted heat pipe for electronic cooling,J. Applied Thermal Engineering 127.

[30] Krishna J, Kishore P S, Solomon A B. , 2017,Heat pipe with nano enhanced-PCM for electronic cooling application,J. Experimental Thermal & Fluid Science 81:84-92.

[31] Wang Q, Rao Z, Huo Y, et al., 2016, Thermal performance of phase change material/oscillating heat pipe-based battery thermal management system,J. International Journal of Thermal Sciences 102:9-16.

[32] Jianan Zhang, Fengchun Sun, Zhenpo Wang.，2017，Heating Character of a LiMn2O4 Battery Pack at Low Temperature Based on PTC and Metallic Resistance Material,J. Energy Procedia105:2131-2138.

[33] Guo S, Xiong R, Wang K, et al. , 2018, A novel echelon internal heating strategy of cold batteries for all-climate electric vehicles application,J. Applied Energy219:256-263.

[34] CHANG G F, CHEN L T, XU S C, et al., 2009, Structural Optimization Design of Nickel hydrogen Battery Thermal Management System,J. Journal of Tongji University (Natural Science),37(11):1518-1520.

[35] WU Z J, ZHANG G Q. The Liquid Cooling System of the Ni-MH Battery Pack for Hybrid Electric Vehicles,J. Journal of Guangdong University of Technology.

[36] SHEN C H, YU H. , 2015, Research Progress on Key Technologies of the Proton Exchange Membrane Fuel Cell Power System for Vehicle,J. Journal of Wuhan University of Technology37(2):34-39.

[37] ZHANG Y J, LI X H, HUANG H Y, et al. , 2003, Thermal Management of Automotive Fuel Cell Power Systems,J. Automotive Engineering25(6):561-565.

[38] SPIEGEL C, et al. 2008.Designing & building fuel cells,M. Publishing House of Electronics Industry,

[39] CHEN S T, LI W W, WANG X K, et al. , 2016,Thermal management using phase change materials for proton exchange membrane fuel cells,J. Journal of Chemical Industry and Engineering(China) 67(s1):1-6.

[40] SHI H M, HUANG R, YU X L.，2017，Fuel cell thermal management system with regenerative heating function:, CN206353578U[P]..

[41] Berrueta A, Martín I S, Hernández A, et al., 2014, Electro-thermal modelling of a supercapacitor and experimental validation,J. Journal of Power Sources 259(4):154-165.

[42] BEGUIN F, FRACKOWIAK E. , 2014，Supercapacitors: materials, systems, and Applications,M. China Machine Press.

[43] Gualous H, Gallay R, Alcicek G, et al., 2010, Supercapacitor ageing at constant temperature and constant voltage and thermal shock,J. Microelectronics Reliability50(9):1783-1788.

Manuscript ID: 1510
DOI: 10.18462/iir.icr.2019.1510

Numerical investigation of pulse tube refrigerator with inertance tube-gas reservoir phase modulation

Wenbin WANG [(a)], Liang CHEN [(a)], Menglin LIANG [(b)], Yanjie LIU [(b)], Shuangtao CHEN [(a)], Yu HOU [(a),*]

[(a)]Xi'an Jiaotong University
Xi'an, 710049, China, yuhou@mail.xjtu.edu.cn
[(b)]Technical Institute of Physics and Chemistry
Beijing, 100190, China

ABSTRACT

This paper presents a numerical study on a coaxial pulse tube refrigerator(PTR) with inertance tube-gas reservoir as the phase modulation device. A two-dimensional model is developed to describe the oscillating flow in the regenerator, cold-end heat exchanger, pulse tube and warm-end heat exchanger, while a 1D model is employed to describe the phase modulation by the inertance tube. The boundary condition at the warm end of regenerator is the sinusoidal pressure wave of a mean value of 3.0 MPa, an amplitude of 0.07 MPa and a frequency of 34 Hz. Based on the simulation results, the influence of inertance tube-gas reservoir device on the temperature and velocity distribution profile is obtained. The transient variations of velocity near the wall lead that at the other points at the same cross section in the pulse tube. Velocity oscillations with large magnitudes are observed near the center of the cold end heat exchanger due to the presence of the empty volume. Besides, the anisotropy thermal conductivity of porous medium has a significant effect on the performance. The cryocooler can reach a minimum temperature of 86 K when a small value of axial thermal conductivity is applied, which is 15 K lower than that of the case with isotropic thermal conductivity.
Keywords: Pulse Tube Refrigerator, CFD Simulation, Coaxial Type, Inertance Tube.

1. INTRODUCTION

Cryogenic refrigerators have been widely used in the fields of space industry, military application and hypothermal medicine. Compared to other types of cryogenic refrigerators, the pulse tube refrigerator(PTR) without moving parts at its cold head has simple structures, small vibrations, high reliabilities and long lifetimes, which makes it a promising candidate as a space cryocooler, especially in field of infrared detector cooling.

The first generation of pulse tube refrigerator was proposed by Gifford and Longsworth (1964) in the 1960's. Their prototype refrigerator reached a refrigeration temperature of 124 K. Since then, pulse tube refrigerator had been widely studied. The phase shifter, which is one of the research hotspots, is crucial to a pulse tube refrigerator. Up to now, there are several kinds of phase shifter, such as orifice-reservoir, dual-piston, double-inlet valve, and inertance tube. Theoretical analysis and studies show that the inertance tube has the ability to regulate phase difference for a wide range by using the inertance effect of oscillating gas. Meanwhile, the inertance tube provides the function of amplifying the pressure ratio in the pulse tube and avoids producing direct current. Therefore, it is not only applicable for high power pulse tube cryocooler, but also satisfies the requirements of small refrigeration system.

Inertance tube was first applied to the high frequency pulse tube cryocooler by Kanao et al. (1994) and a 114 K of refrigeration temperature was acquired. Researchers tried to explore the mechanism inside inertance tube for many years. Gardner and Swift (1997) carried series of experiments and analyzed the phase shifting mechanism of inertance tube with an electric analogy method. They pointed out that the inertance tube could adjust phase difference in a wide range. Schunk et al. (2005) analyzed the segmented inertance tube combined with fluid network theory and the distributed parameter model followed by validation experiments. They suggested that the

distributed parameter model considered the impedance introduced by tube diameter change of inertance tube and the simulated results was closer to the experimental data than that of the lumped-capacitance model. Radebaugh et al. (2006) developed a transmission line model based on the fluid network theory and the corrected the term of unit length flow resistance. They compared the phase shifting results under both adiabatic and isothermal conditions of inertance tube with experimental data and found that experimental data fell between the predictions of the two cases. They concluded that the inertance tube would be closer to the adiabatic condition with the increase of the ratio of tube diameter to thermal penetration depth. Luo et al. (2004) applied the linear thermoacoustic theory to the analysis of inertance tube and developed a laminar thermoacoustic transmission line model with the simplified turbulent thermoacoustic model, which showed good agreement with the experimental results. Ren et al. (2009) adopted the turbulence correction model to analyze how the temperature affects the phase shifting ability under the conditions with/without a gas reservoir. The concluded that the phase shifting ability increased with the decrease of temperature. Luo et al. used their model to analyze the dimensionless phase shifting map of inertance tubes. Huang et al. (2014) studied the pressure and mass distribution along the axis of the inertance tube-gas reservoir. They found that minimum pressure magnitude exists and it is near the gas reservoir. Mass flow rate is increasing along the tube. Liu et al. (2016) studied the effect of winding mode on inertance tube and concluded that the less the number of winding, the lower temperature the refrigerator coud be reached. Fang et al. (2017) developed a one dimensional analogy model for the inertance tube and coupled it with 2D/3D CFD model of pulse tube refrigerators. The results showed good agreement with experimental data. Liu et al. (2017) studied the temperature of inertance tube on the phase shifting ability and the cooling performance of PTR with a lumped-capacitance model. They found that a shorter inertance tube with a lower temperature could enhance the phase shifting ability but deteriorated cooling performance.

The temperature and velocity distribution inside the PTR is difficult to measure. CFD simulation is a useful tool to predict the flow field inside the pulse tube refrigerator. But the cost is too high for the PTR with a long inertance tube. In present paper, the 1D inertance tube model was employed to reduce the computational cost, and the 2D simulations of PTR are presented. In addition, the effects of axial conduction in the regenerator on the PTR performance are investigated by setting the anisotropic thermal conductivity of the regenerator filler materials.

2. SIMULATION MODEL

2.1. Geometry Model

This study is carried out with a coaxial pulse tube cryocooler as the prototype. The computational domain is presented in Fig. 1. The aftercooler, warm-end heat exchanger(WHX) and cold-end heat exchanger(CHX) are considered as the thermal equilibrium domain while the regenerator is assumed to be a non-thermal equilibrium domain. All of heat exchangers are treated as porous zone. The 2D axisymmetric model was adopted to reduce the number of grid points.

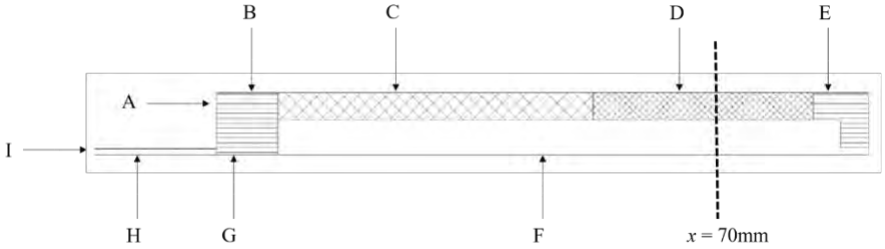

Figure 1: Schematic diagram of pulse tube refrigerator (A - pressure inlet, B - aftercooler, C, D - regenerator, E - cold-end heat exchanger, F - pulse tube, G - hot-end heat exchanger, H - part of inertance tube, I - mass inlet)

Besides, the compressor characteristics are described by the sinusoidal pressure waves, which was implemented by user-defined functions (UDFs):

$$p_{in} = p_0 + \Delta p \sin 2\pi ft \quad \text{Eq. (1)}$$

where p_0 is the inflation pressure and is the Δp pressure amplitude. The values of p_0 and Δp are fixed at 3.0 MPa and 0.07Mpa, respectively. More important, the inertance tube and gas reservoir were cut and replaced by a boundary condition, which is just the purpose the research. Treated as ideal gas, helium was adopted as working fluid, the properties of which were calculated by NIST. As for the material of regenerator and heat exchanger, we adopted 304 stainless steel and copper, respectively. The properties of both helium and stainless steel then were fitted into piecewise polynomial functions of temperature by UDFs.
In the transient simulation, standard *k-ω* model was adopted as the viscous model to make the formulation of a robust y^+–insensitive treatment. Scheme of PISO was selected as pressure-velocity coupling method. Spatial discretization scheme for pressure equation was set to PRESTO!, density, momentum and energy equation second order upwind, turbulent energy and specific dissipation rate equation first order upwind to make sure enough accuracy. Time step Δt in the transient simulation should meet the following condition:

$$\frac{1}{f \cdot \Delta t} \geq 40 \quad \text{Eq. (2)}$$

where *f* is frequency. This simulation selected a time step of 4e-4s.

2.2. Governing Equations

Compared with non-porous zone, the governing equations for porous zones introduce superficial velocity and have different forms with a variable porosity *γ*. They are given as follows:
The continuity and momentum equations are shown as following.

$$\frac{\partial}{\partial t}\left(\gamma\rho_f\right) + \nabla \cdot \left(\gamma\rho_f \vec{v}\right) = 0 \quad \text{Eq. (3)}$$

$$\frac{\partial}{\partial t}\left(\gamma\rho_f \vec{v}\right) + \nabla \cdot \left(\gamma\rho_f \vec{v}\vec{v}\right) = -\gamma\nabla p + \nabla \cdot \left(\gamma\bar{\bar{\tau}}\right) + S \quad \text{Eq. (4)}$$

where *S* and $\bar{\bar{\tau}}$ are the stress tensor and the source term to calculate the effect of porosity. For homogeneous porous media, *S* is given by:

$$S = -\left(\frac{\mu}{\alpha}\vec{v} + \frac{C_2}{2}\rho_f |\vec{v}|\vec{v}\right) \quad \text{Eq. (5)}$$

where *α* is permeability and C_2 is inertial resistance factor.
Energy equation for thermal equilibrium condition:

$$\frac{\partial}{\partial t}\left(\gamma\rho_f E_f + \left(1-\gamma\right)\rho_s E_s\right) + \nabla \cdot \left(\vec{v}\left(\rho_f E_f + p\right)\right) = \nabla \cdot \left(k_{eff}\nabla T + \left(\bar{\bar{\tau}} \cdot \vec{v}\right)\right) \quad \text{Eq. (6)}$$

where k_{eff}, E_f and E_s are effective thermal conductivity of the medium, the total fluid energy and total solid medium energy, respectively. k_{eff} is computed as the volume average of the fluid conductivity and the solid conductivity:

$$k_{eff} = \gamma k_f + \left(1-\gamma\right)k_s \quad \text{Eq. (7)}$$

Energy equations for the non-thermal equilibrium condition for gas and solid phases are

$$\frac{\partial}{\partial t}\left(\gamma\rho_f E_f\right)+\nabla\cdot\left(\vec{v}\left(\rho_f E_f+p\right)\right)=\nabla\cdot\left(\gamma k_f\nabla T_f+\left(\bar{\bar{\tau}}\cdot\vec{v}\right)\right)+h_{fs}A_{fs}\left(T_s-T_f\right) \quad \text{Eq. (8)}$$

$$\frac{\partial}{\partial t}\left(\left(1-\gamma\right)\rho_s E_s\right)=\nabla\cdot\left(\left(1-\gamma\right)k_s\nabla T_s+\left(\bar{\bar{\tau}}\cdot\vec{v}\right)\right)+h_{fs}A_{fs}\left(T_f-T_s\right) \quad \text{Eq. (9)}$$

The distributed parameter model proposed by Schunk et al. (2005) is considered to be the most accurate 1D model to predict the performance of inertance tube. This model is based on the electrical analogy. The basic idea is to make an analogy between pressure amplitude (Δ*p*) and voltage (V) and the mass flow rate (*m*) and current (I). In order to include the velocity effects of the long inertance tube, the inertance tube is divided into several segments. The distributed model is shown in Fig. 2.

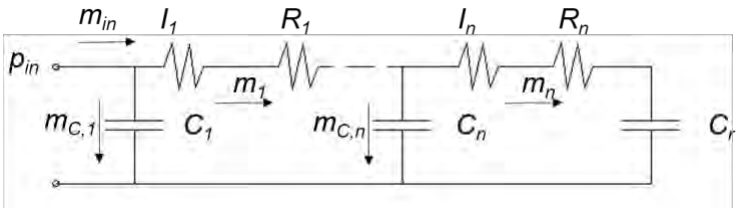

Figure 2: Impedance network of inertance tube and resevior

The compliance(*C*), inertance(*I*) and resistance(*R*) of each segment can be expressed as:

$$C_i=\pi D^2/4\gamma R_g T \quad \text{Eq. (10)}$$

$$I_i=4/\pi D^2 \quad \text{Eq. (11)}$$

$$R_i=64 f_r\dot{m}_i/\pi^3\rho D^5 \quad \text{Eq. (12)}$$

where f_r is the Fanning friction factor, and it is given as:

$$f_r=0.046\,\mathrm{Re}^{0.2} \quad \text{Eq. (13)}$$

The impedance of compliance(*C*), inertance(*I*) and resistance(*R*) is calculated as:

$$Z_{C,i}=1/j\omega C_i \quad \text{Eq. (14)}$$

$$Z_{I,i}=j\omega R_i \quad \text{Eq. (15)}$$

$$Z_{R,i}=R_i \quad \text{Eq. (16)}$$

$$Z_r=\gamma R_g T/j\omega V_r \quad \text{Eq. (17)}$$

$$\dot{m}_i=\dot{m}_{i-1}+\dot{m}_{C,i-1} \quad \text{Eq. (18)}$$

3. RESULTS AND DISCUSSION

3.1. Mass Flow Rate and Pressure Distribution along the Inertance Tube

Fig. 3 shows the mass flow rate and the pressure distribution in the inertance tube. It can be seen the mass flow rate is minimum at the pulse-tube-end while the mass flow rate reaches its maximum at the reservoir-end. The pressure magnitude reaches the minimum at the very end of the pulse tube. The magnitude of pressure fluctuations decreases along axis, which is mainly caused by viscosity of working fluid and frictional resistance. However, the magnitude of mass flow rate increases along the inertance tube. The reason is that the flow impedance is so small at the outlet of inertance tube connected to the gas reservoir that the mass flow rate is large compared to other positions. The pressure magnitude tends to zero at the end connected to the gas reservoir because the large volume of the gas reservoir plays as a buffer to balance the time-varied pressure. As a typical capacitive element, the gas reservoir can lead to a phase difference of 90 degrees while phase difference of other position is dominated by the flow impedance.

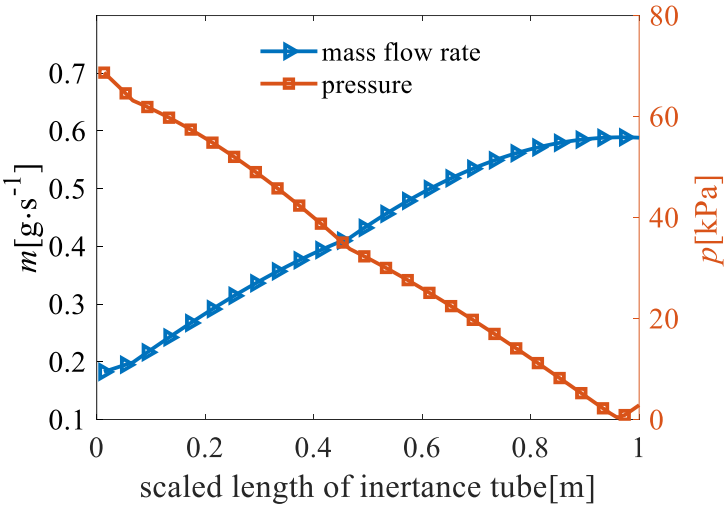

Figure 3: Mass flow and pressure distribution in the pulse tube

3.2. Effects of the Anisotropic Thermal Conductivity of the Porous Medium

The axial conduction in the regenerator is crucial for the PTC performance. For regenerator filled with wired screens, the thermal conductivity can be different between axial and radial directions. In the axial direction, the thermal conduction can be reduced due to a large number of contact between different layers of screens. Therefore, it is interesting to examine the effects of anisotropic thermal conductivity of porous medium on the PTC performance.

In order to illustrate the influence of axial conduction on the PTC performance, the thermal conductivity in the axial direction is set to zero for the anisotropic medium. The predicted cold-end temperatures of PTC with the isotropic medium and the anisotropic medium are 101 K and 86 K, respectively. Because the anisotropic medium can reflect regenerator's performance, we use the results of the condition with anisotropic medium in the following discussion on the temperature and velocity distribution. Fig. 4 shows the variations of pressure and mass flow rate with time at both ends of the pulse tube. Spatial distribution of pressure synchronizes in the entire pulse tube, while mass flow rate does not. It indicates that the pressure leads the mass flow rate at the PT hot-end by 110 degrees and the PT cold-end by 178 degrees, respectively.

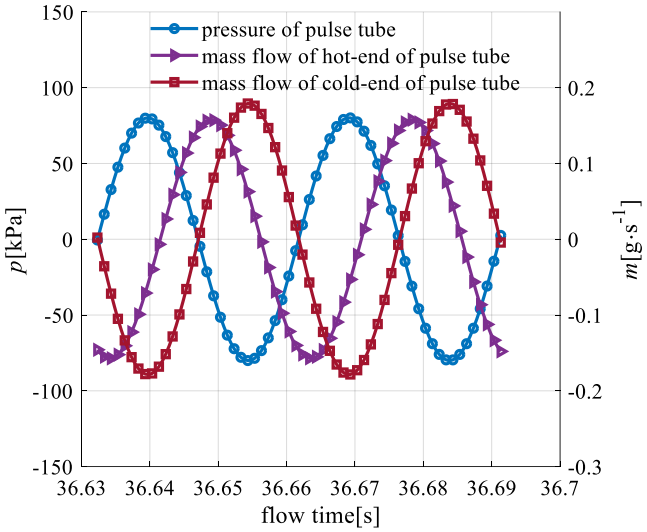

Figure 4: The phase map of pressure and mass flow rate at both ends the pulse tube

3.3. Temperature Distribution in the Pulse Tube

Fig. 5 shows the temperature distribution in the pulse tube over a period. Temperature change is relatively small over a time step. In the regenerator, temperature of working fluid maintains relatively linear and uniform, while in the pulse tube, temperature distribution of working fluid varies along radial direction. The difference of temperature distribution between regenerator and pulse tube is caused by the filler. Because of the large heat capacity of the filler, the temperature sensibility to pressure change in the regenerator comes down and the temperature difference along the radial direction declines. In the pulse tube, the heat capacity and thermal conductivity is dominated by the gas property. So it is more sensible to pressure change, which is why temperature varies along the radial direction with the pressure change. Fig. 6 shows a detailed description of the temperature along the axis in the center of the pulse tube at T/4 and 3T/4 time instances of a period. When the pressure peaks, the working fluid flows slightly from the cold-end to the hot-end and the temperature decreases at the same location. When the pressure reaches the minimum point, the working fluid flows from the hot-end heat exchanger to the cold end, which undergoes a compression process. As a result, the temperature near warm-end heat exchanger goes up a little bit.

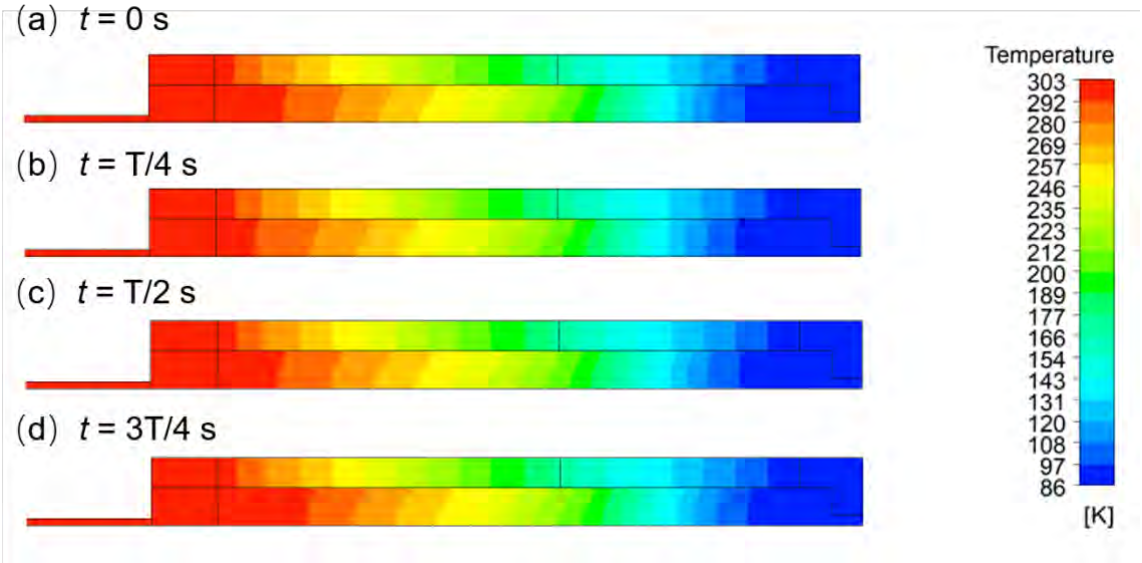

Figure 5: Temperature distribution in the pulse tube over a period

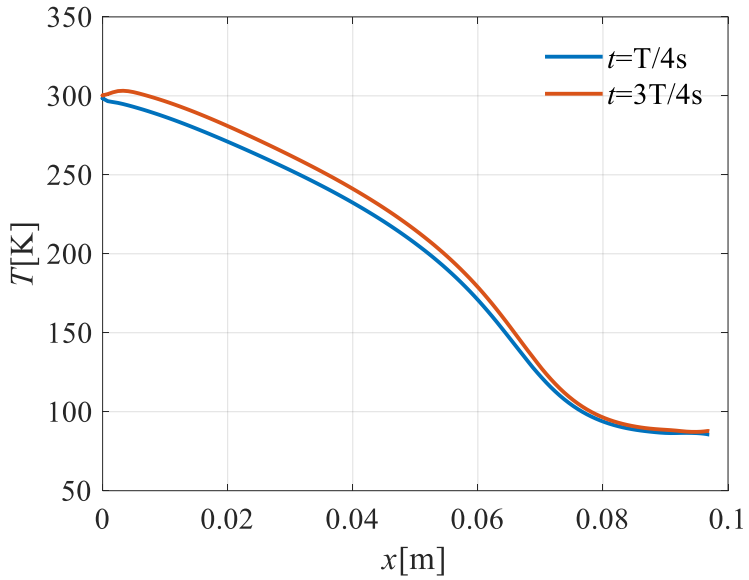

Figure 6: Temperature distribution along the axis of the pule tube at time instances of *t* = T/4 and *t* = 3T/4

3.4. Velocity Distribution in the Pulse Tube

Fig. 7 shows the velocity distribution in the pulse tube over a period. It can be seen there are two notable features about the velocity map. Firstly, the adverse velocity gradient occurs in the near-wall region. At the time instance of T/4, the pressure upstream reaches its maximum, forming a gradient with the downstream pressure. So the fluid at the cold-end is pushed downstream and accelerated. The velocity was relativity low in the region near the wall. On the contrary, at t = 3T/4, gas parcels are squeezed and velocities are increased. Because of the blockage of wall and porous zone, fluid must slow down. Secondly, there is an obvious velocity change at the cold-end of the pulse tube during one period compared to the other regions of the domain.

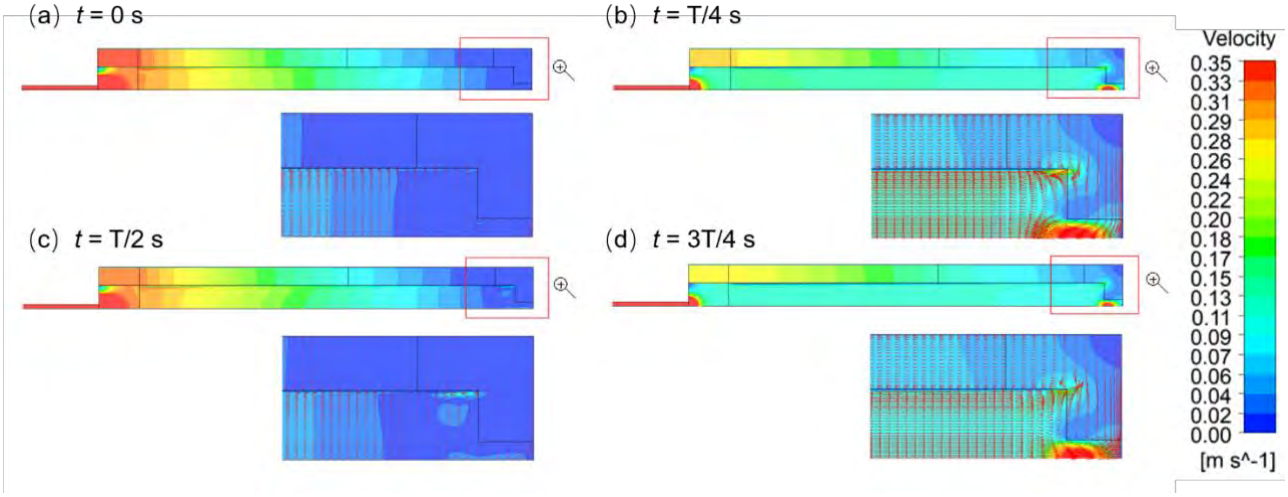

Figure 7: Velocity magnitude distribution of the pulse tube and the vector map at the cold-end pulse tube over a period

Fig. 8 shows the velocity vector map at the location of *x* =70 mm. The phenomenon can be explained using electric analogy. The impedance in the cold-end heat exchanger is higher than that in the pulse tube, so the fluid chooses the least resistance path that is going straight forward to the pulse tube through the corner and the rest of the heat exchanger possessing more resistance has less current. Thereupon, velocity at the corner goes up promptly due to the pressure change. Nevertheless, the response of the rest area of the pulse tube is relatively slow, so the velocity near the wall always leads map change. Accompanied by no-slip wall condition, the velocity diminishes to zero at the wall boundary.

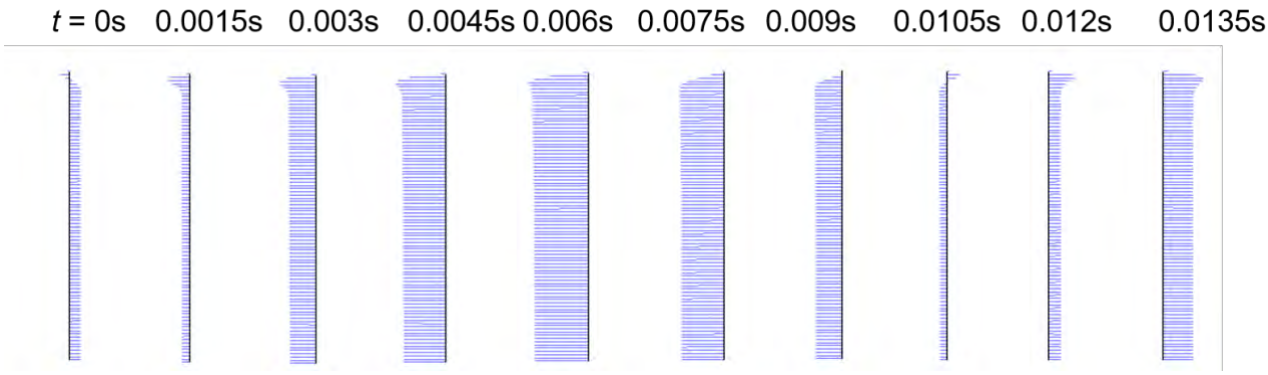

Figure 8: Adverse velocity map at the location of *x* = 70 mm over flow time

Fig. 9 shows the intuitive velocity profile along the axis of the PT central line. It can be seen that the velocity decreases monotonously over the pulse tube at the points of *t* = 0s and *t* = T/2 s. At the points of *t* = T/4 s and *t* = 3T/4 s, the velocity variation is very small over most of the region in the pulse tube, but the velocity increases dramatically first and then decreases near the cold end of the pulse tube. When the flow time reaches to 0 and T/2 s, the pressure change rate in the pulse tube is increased. Consequently, accompanied by the inertance of working fluid, velocity gradient along the axis is formed. As for the flow time of *t* = T/4 s and *t* = 3T/4 s, pressure change rate is almost zero, so the velocity keeps relatively constant. Due to the U turn near the cold end of the pulse tube, the velocity

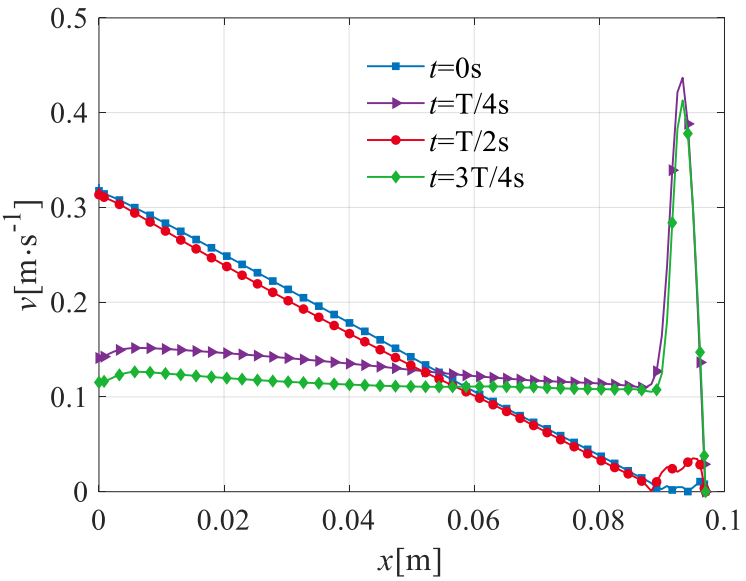

Figure 9: The centreline velocity profile of the pulse tube versus the axis location over a period

4. CONCLUSIONS

In this paper, we perform simulations on a coaxial PTR with inertance tube, and obtain the temperature and velocity fields over the entire refrigerator. The unusual velocity distribution in the lumped area is observed, and the velocity change is out of phase at that same cross-section during a period. Besides, the PTR with anisotropic porous medium has better performance than that with isotropic porous medium due to the lower axial conduction.

ACKNOWLEDGEMENTS

This work was supported by the National key basic research program (613322), by the National Nature Science Foundation of China (51706169), and the Fundamental Research Funds for the Central Universities.

NOMENCLATURE

A	interfacial area density (m^{-1})	C_2	inertial resistance factor (m^{-1})
E	total energy (J)	f	frequency (Hz)
h	heat transfer coefficient ($W \cdot m^{-2} \cdot K^{-1}$)	k	thermal conductivity ($W \cdot m^{-1} \cdot K^{-1}$)
p	pressure (Pa)	Δp	pressure (Pa)
R_g	gas constant ($J \cdot kg \cdot K^{-1}$)	S	stress tensor
t	flow time (s)	Δt	time step (s)
T	temperature (K)		
Greek letter			
α	permeability (m^{-2})	γ	porosity
ρ	density ($kg \cdot m^{-3}$)	μ	molecular viscosity (Pa·s)
ω	angular frequency (Hz)	$\bar{\bar{\tau}}$	source term
Subscript			
0	initial	in	pressure inlet boundary
f	fluid	s	solid
eff	effective thermal conductivity		

REFERENCES

Fang, T., Spoor, P. S., Ghiaasiaan, S. M., 2017. A computational approach for coupled 1d and 2d/3d cfd modelling of pulse tube cryocoolers. IOP Conference Series: Materials Science and Engineering, 278, 012172.

Gardner, D. L., Swift, G. W., 1997. Use of inertance in orifice pulse tube refrigerators. Cryogenics, 37(2), 117-121.

Gifford, W. E., Longsworth, R. C., 1964. Pulse-tube refrigeration. Trans.asme J.eng.ind, 86(3), 264-268.

Huang T., Chen H., Cai J., 2014. Numerical simulation and analysis on oscillating flow in inertance tube. Cryogenics, (3), 22-26.

Kanao, K. I., Watanabe, N., & Kanazawa, Y., 1994. A miniature pulse tube refrigerator for temperatures below 100k. Cryogenics, 34(1), 167-170.

Liu, S., Chen, X., Zhang, A., Jiang, Z., Wu, Y., Zhang, H., 2017. Investigation of the inertance tube of a pulse tube refrigerator operating at high temperatures. Energy, 123, 378-385.

Liu S., Zhang A., Chen X., Kan A., Jiang Y., Zhang H., Wu Y. N., 2016. Effect of coiling ways of inertance tube on performance of pulse tube cryocooler. CIESC Journal, 67(5), 1791-1797.

Luo, E., Radebaugh, R., Lewis, M., 2004. Inertance Tube Models and Their Experimental Verification. Advances in Cryogenic Engeineering: Transaction.

Radebaugh, R., Lewis, M., Luo, E., Pfotenhauer, J. M., Nellis, G. F., & Schunk, L. A., 2006. Inertance Tube Optimization for Pulse Tube Refrigerators. Aip Conference.

Ren, J., Hu J. Y., Luo E. C., Wang X. T. Dai W., 2009. Investigation on phase shifters of pulse tube coolers Part4 : Investigation on phase shifters at low temperature. National Cryogenic Engineering Conference.

Schunk L. O., Nellis G. F., Pfotenhauer J. M.,2005. Experimental investigation and modeling of inertance tubes. Journal of Fluids Engineering, 127(5), 1029-37.

Manuscript ID: 1525
DOI: 10.18462/iir.icr.2019.1525

Simulation and analysis of the influence of wind flow on the evolution of hydrogen vapor cloud

Yuanliang LIU[(a)], Gang LEI[(b)], Jianjian WEI[(a)], Tao JIN[(a*)]

[(a)] Institute of Refrigeration and Cryogenics/Key Laboratory of Refrigeration and Cryogenic Technology of Zhejiang Province, Zhejiang University
Hangzhou, 310027, China, jintao@zju.edu.cn
[(b)] State Key Laboratory of Technologies in Space Cryogenic Propellants
Beijing, 100028, China, leigang_1973@sina.com

ABSTRACT

Potential hazards should be seriously assessed and avoided when handing liquid hydrogen, such as the flammable vapor cloud and the low temperature injury. A three-dimensional CFD model for liquid hydrogen dispersion is developed, with the guidelines proposed by the Working Group of the Architectural Institute of Japan constructing the wind environment. Spills with different vertical wind flow profiles are numerically investigated. The increment in power law exponent of the wind profile hinders the dispersion process, which enlarges the detachment distance on the ground, and reduces the streamwise distance of the flammable vapor cloud. The increased vertical velocity gradient hinders the cloud from rising up. The present work reveals the mechanisms and characteristics of hydrogen cloud evolution in different wind flows.
Keywords: Liquid Hydrogen, Wind Flow, Vapor Cloud, CFD.

1. INTRODUCTION

Hydrogen energy has been widely used for aerospace propulsion (Wang et al., 2016), and shows promising applications in vehicle fuels (Huo et al., 2017; Choi et al., 2013). However, the accidental spills of liquid hydrogen into the environment may cause severe hazards, due to the low temperature of the cryogen, and the flammability and explosion of hydrogen, which poses severe threats to public safety.

The air plays important roles in the dispersion of hydrogen, including mixing with hydrogen to form hydrogen vapor cloud and carrying the vapor cloud to the downwind domain. Many experimental and theoretical researches have been carried out to investigate the wind effects in the past decades. The large-scale liquid hydrogen spill experiments conducted by NASA (Witcofski and Chirivella, 1984; Chirivella and Witcofski, 1986) showed that the initial momentum of liquid spill and the rapid expansion from a liquid to a gas in the cloud created turbulence levels far greater than the atmospheric turbulence, controlling the vapor cloud dispersion in the near field. Sensitivity study for the atmospheric stability was carried out by Middha et al. (2011) with FLACS, and the stable configuration gave the most consistent results with the NASA experimental observations. Jin et al. (2017) numerically analyzed the influences of wind velocity and wind temperature on the cloud dispersion with ANSYS FLUENT. The increased wind speed extends the downwind distance of flammable cloud, and the increased wind temperature retards the hydrogen diffusion. Shao et al. (2018) investigated the cloud dispersion under various weather conditions, including ambient temperature, wind speed and atmospheric pressure. The results show that the hydrogen dispersion is excited with the increased wind speed, while it is impeded with the increased atmospheric pressure.

However, the wind flow in the atmospheric boundary layer where the liquid hydrogen spill occurs is commonly complex, with various vertical velocity profiles and turbulence profiles. In the present work, the guidelines proposed by the Working Group of the Architectural Institute of Japan (AIJ) (Tamura et al., 1999; Tominaga et al., 2008) are adopted to construct the wind environment. Then, liquid hydrogen spills with different vertical wind flow profiles are numerically investigated.

2. MODEL STRATEGIES

2.1. Mathematical Equations

The liquid phase and the gas phase are both assumed to be incompressible, and the single fluid mixture approach is adopted, i.e., the two-phase flow is predicted by solving the transient conservation equations for mixture mass, mixture momentum and mixture enthalpy:

$$\frac{\partial \rho_{\mathrm{m}}}{\partial t}+\nabla \cdot\left(\rho_{\mathrm{m}} \vec{v}_{\mathrm{m}}\right)=0 \quad \text{(Eq. 1)}$$

$$\frac{\partial}{\partial t}\left(\rho_{\mathrm{m}} \overrightarrow{v_{\mathrm{m}}}\right)+\nabla \cdot\left(\rho_{\mathrm{m}} \overrightarrow{v_{\mathrm{m}}} \overrightarrow{v_{\mathrm{m}}}\right)=-\nabla p+\nabla \cdot\left[\mu_{\mathrm{m}}\left(\nabla \overrightarrow{v_{\mathrm{m}}}+\nabla \overrightarrow{v_{\mathrm{m}}}^{\mathrm{T}}\right)\right]+\rho_{\mathrm{m}} g+\nabla \cdot\left(\sum_{i=1}^{2} \alpha_i \rho_i \vec{v}_{\mathrm{dr},i} \vec{v}_{\mathrm{dr},i}\right) \quad \text{(Eq. 2)}$$

$$\frac{\partial}{\partial t} \sum_{i=1}^{n}\left(\alpha_i \rho_i h_i\right)+\nabla \cdot \sum_{i=1}^{n}\left(\alpha_i \vec{v}_i\left(\rho_i h_i+p\right)\right)=\nabla \cdot\left(k_{\mathrm{eff}} \nabla T\right) \quad \text{(Eq. 3)}$$

The local mass fraction of each species in gas phase is calculated by the convection-diffusion equation:

$$\frac{\partial}{\partial t}\left(\rho_{\mathrm{g}} \alpha_{\mathrm{g}} Y_{\mathrm{g},i}\right)+\nabla \cdot\left(\rho_{\mathrm{g}} \alpha_{\mathrm{g}} \vec{v} Y_{\mathrm{g},i}\right)=-\nabla \cdot \alpha_{\mathrm{g}}\left[-(\rho D_{\mathrm{g},i}+\frac{\mu_{\mathrm{t}}}{Sc_{\mathrm{t}}}) \nabla Y_{\mathrm{g},i}\right]+\dot{m}_{\mathrm{lg}}^{i}-\dot{m}_{\mathrm{gl}}^{i} \quad \text{(Eq. 4)}$$

where a modified expression of Lee model is adopted to simulate the liquid-vapor phase change for hydrogen and water (Lee, 1979; Liu et al., 2019):

For evaporation: $\dot{m}_{\mathrm{lg}}^{i}=\gamma_{\mathrm{ev}} Y_{\mathrm{l},i} \cdot \alpha_{\mathrm{l}} \rho_{\mathrm{l}}\left(T_{\mathrm{l}}-T_{\mathrm{sat},i}\right) / T_{\mathrm{sat},i},\ if\ T_{\mathrm{l}}>T_{\mathrm{sat},i}$ (Eq. 5)

For condensation: $\dot{m}_{\mathrm{gl}}^{i}=\gamma_{\mathrm{con}} Y_{\mathrm{g,\,i}} \cdot \alpha_{\mathrm{g}} \rho_{\mathrm{g}}\left(T_{\mathrm{g}}-T_{\mathrm{sat},i}\right) / T_{\mathrm{sat},i},\ if\ T_{\mathrm{g}}<T_{\mathrm{sat},i}$ (Eq. 6)

In addition, the Realizable *k-ε* model (Shih et al., 1995) is adopted here for turbulence closure. The transport equations for *k* and *ε* are:

$$\frac{\partial}{\partial t}(\rho k)+\frac{\partial}{\partial x_j}(\rho k u_j)=\frac{\partial}{\partial x_j}\left[\left(\mu+\frac{\mu_{\mathrm{t}}}{\sigma_{\mathrm{k}}}\right) \cdot \frac{\partial k}{\partial x_j}\right]+G_{\mathrm{k}}+G_{\mathrm{b}}-\rho \varepsilon \quad \text{(Eq. 7)}$$

$$\frac{\partial}{\partial t}(\rho \varepsilon)+\frac{\partial}{\partial x_j}(\rho \varepsilon u_j)=\frac{\partial}{\partial x_j}\left[\left(\mu+\frac{\mu_{\mathrm{t}}}{\sigma_{\varepsilon}}\right) \cdot \frac{\partial \varepsilon}{\partial x_j}\right]+\rho C_1 E \varepsilon-\rho C_2 \frac{\varepsilon^2}{k+\sqrt{\nu \varepsilon}}+C_{1 \varepsilon} \frac{\varepsilon}{k} C_{3 \varepsilon} G_{\mathrm{b}} \quad \text{(Eq. 8)}$$

where $C_1=\max\left[0.43, \frac{\eta}{\eta+5}\right]$, $\eta=\sqrt{2 S_{ij} \cdot S_{ji}} \cdot \frac{k}{\varepsilon}$, $S_{ij}=\frac{1}{2}\left(\frac{\partial u_i}{\partial x_j}+\frac{\partial u_j}{\partial x_i}\right)$, G_{k} is the generation of turbulent kinetic energy due to the mean velocity gradients, and G_{b} is the generation of turbulent kinetic energy due to buoyancy.

The mathematical model has been validated in our previous work (Liu et al., 2019).

2.2. Wind Flow Field

The wind environment adopts the guidelines proposed by AIJ (Tamura et al., 1999; Tominaga et al., 2008), which were based on the cross-comparison between CFD predictions, wind tunnel test results and field measurements. The vertical profile of velocity, turbulent intensity and turbulent length scale of the wind in the atmospheric boundary layer under different terrain subcategories were given in the guidelines. Table 1 lists the wind profiles involved in the present work, where *β* is the power law exponent determined by terrain category, and Z_{G} is the boundary layer height. The power law vertical velocity profile is expressed as $u(z)=u_0\left(z / z_0\right)^{\beta}$, where the reference height z_0 is 10 m. The vertical profiles of turbulent intensity $I(z)$ and turbulent length scale $L(z)$ are expressed as $I(z)=0.1(\mathrm{z}/\mathrm{z_G})^{-\beta-0.05}$ (*z* ≥ 5 m) and $L(z)=100(\mathrm{z}/30)^{0.5}$, respectively. For the height below 5 m, the turbulent intensities for three terrains are 0.18, 0.23 and 0.31, respectively. Then, the turbulent kinetic energy *k*(*z*) and turbulent dissipation rate *ε*(*z*) can be achieved:

$$k(z)=\frac{3}{2}[u(z) I(z)]^2 \quad \text{(Eq. 9)}$$

$$\varepsilon(z)=C_{\mu}^{3/4} k(z)^{1.5} / L(z) \quad \text{(Eq. 10)}$$

Table 1. AIJ recommendations for wind profiles under different terrain categories

Category	I	II	III
Site condition	Open, no significant obstruction	Open, few obstruction, grass land	Suburban, wooded terrain
β	0.10	0.15	0.20
Z_G	250 m	350 m	450 m

2.3. Boundary Conditions

The calculation domain is schematically shown in Fig. 1. The dimensions are 200 m, 60 m and 80 m in streamwise (x), cross-wind (y) and vertical (z) directions, respectively, and the symmetry plane (y=0) is adopted so as to reduce the calculation cost. The source is represented by a horizontal cross section with the size of 0.25 m × 0.5 m, with the center located at (20.25, 0, 0.5). A fence with a height of 0.61 m, a thickness of 0.25 m, and an inner diameter of 9.1 m is also set up.

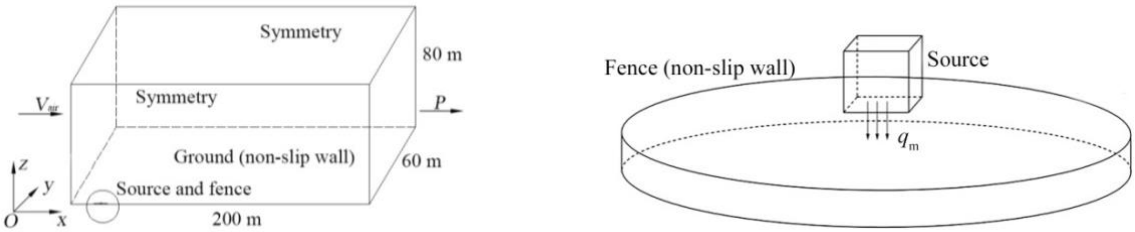

(a) Basic domain and boundary conditions (b) Locally enlarged figure around the source

Figure 1: Illustration of the physical model of liquid hydrogen spills

Mass flow inlet condition is specified at the source exit. The total mass flow rate is 9.52 kg/s, with the liquid mass fraction of 65%. The temperature of hydrogen at the source exit is set to be 20.35 K, and the spill time is 38 s. The ground is modelled as no-slip wall, with initial temperature of 288 K. The outlet of the domain is set as the pressure out boundary with the pressure of 101,325 Pa. In addition, the top and back of computational domain are set as symmetry. The vertical profiles of wind velocity and wind turbulence are given in the inlet domain. The relative humidity and the temperature of the air are 29.3% and 288 K, respectively. Before the spill occurs, a steady calculation is performed to achieve the wind flow field.

3. RESULTS AND DISCUSSION

In the simulations, the reference wind velocity is 2.2 m/s at 10 m height, and the wind flow profiles adopted are listed in Table 1, with the power law exponents of 0.10, 0.15 and 0.20. Fig. 2 and Fig. 3 show the vertical distributions of wind velocity and wind turbulent intensity, respectively.

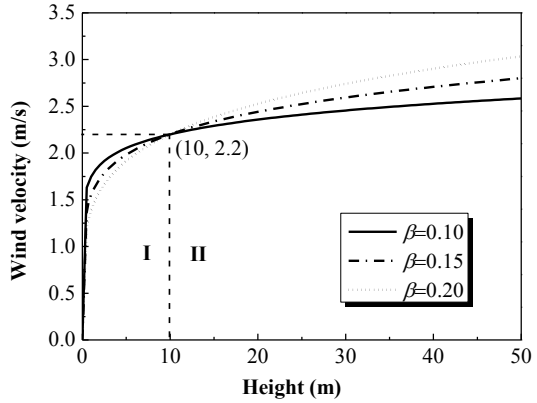

Figure 2: Vertical distribution of wind velocity

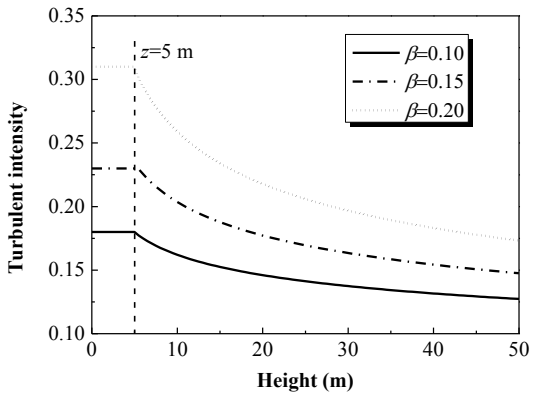

Figure 3: Vertical distribution of turbulent intensity

Fig. 4 illustrates the hydrogen concentration contours on the symmetry plane at *t*=25 s, and Fig. 5 shows the cloud dimensions for the flammability hazard (hydrogen volume fraction above 4%) and the detonation hazard (hydrogen volume fraction above 18.3%). It can be seen that the height and the streamwise distance of the flammable cloud decreases with the increment in power law exponent of the wind flow, while the detachment distance shows opposite trend, indicating less buoyancy of the cloud. In addition, the dimensions for potential detonation hazard increase with power law exponent, which worsens the situation.

The dimensions of the flammable cloud during the whole dispersion process with different power law exponents are listed in Table 2, including the streamwise distance, the height and the detachment distance on the ground. Compared with the variation in cloud height, the variation in streamwise distance is less sensitive to *β*. When increasing *β* from 0.10 to 0.20, the streamwise distance reduces by 9.52%, compared to 28.9% in height reduction.

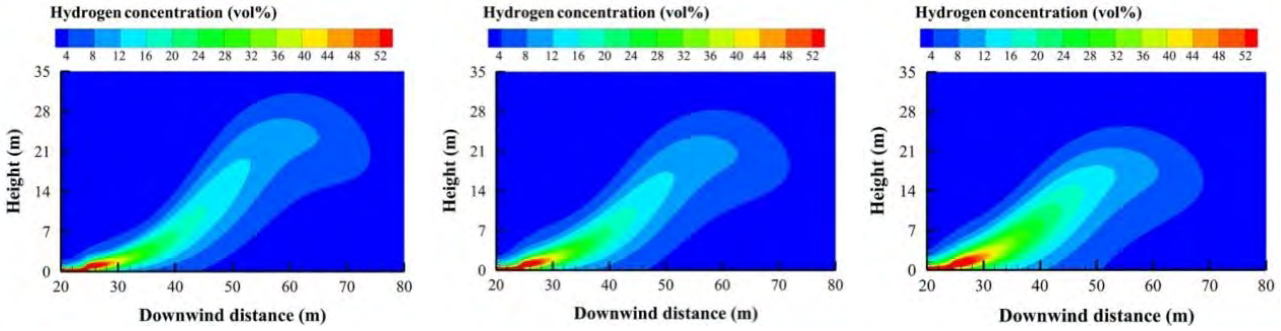

(a) *β*=0.10 (b) *β*=0.15 (c) *β*=0.20

Figure 4: Hydrogen concentration contours on the symmetry plane at *t*=25 s

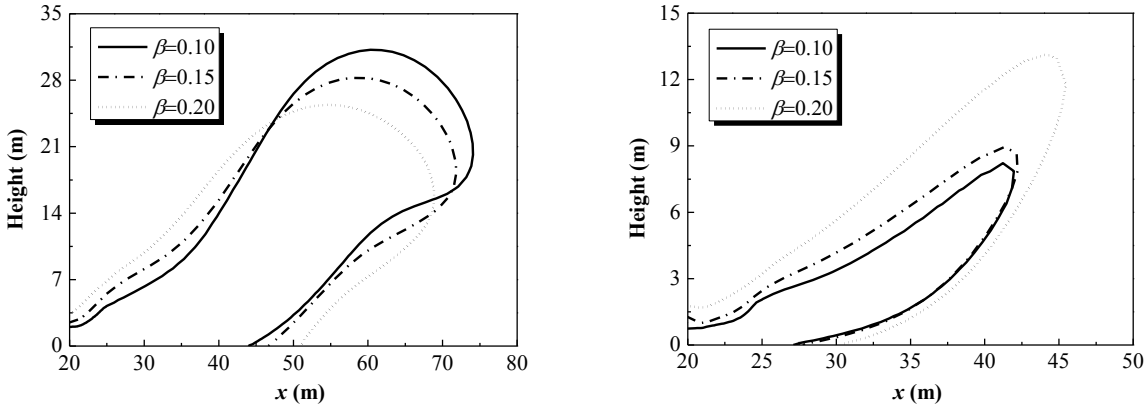

(a) Flammable cloud (b) Detonation cloud

Figure 5: Dimensions of the cloud on the symmetry plane at *t*=25 s

Table 2. Dimensions of the flammable vapor cloud during the whole dispersion process

β	0.10	0.15	0.20
Streamwise distance	84 m	81 m	76 m
Height	45 m	37 m	32 m
Detachment distance	31 m	35 m	42 m

As shown in Fig. 3, the wind turbulence increases with the power law exponent *β*. The increased turbulent intensity will promote the dispersion of hydrogen vapor cloud. However, the results show that the increment in *β* hinders the dispersion process, with the enlarged detachment distance on the ground, and the reduced streamwise distance and height. A possible explanation is that the increased vertical velocity gradient of the wind prevents the cloud from going up. The cloud will then be less lifted and consequently have a reduced contact area with the incoming wind, which hinders the mixing and carrying process.

Four locations downwind the source are selected to investigate the variations of hydrogen concentration with time in the human activity domain. The results are shown in Fig. 6. The heights

of the locations are 0.8 m, and the downwind distances to the source are 3 m, 8 m, 15 m and 25 m, respectively. For the locations near the source (Location 1 and Location 2), the hydrogen concentration is lower in the beginning of the spill process for a larger power law exponent. However, when the cloud has spread for a certain time (approximately 25 s for both locations), the hydrogen concentration begins to increase with power law exponent. Meanwhile, the locations relatively farther from the source (Location 3 and Location 4) are exposed to the vapor cloud with higher hydrogen concentration for most of the time when the spill occurs in the wind flow with a larger power law exponent. The results indicate that the increment in power law exponent will make the near ground domain get exposed to higher hydrogen concentration, especially for the domains away from the source, which puts more threats to the surroundings.

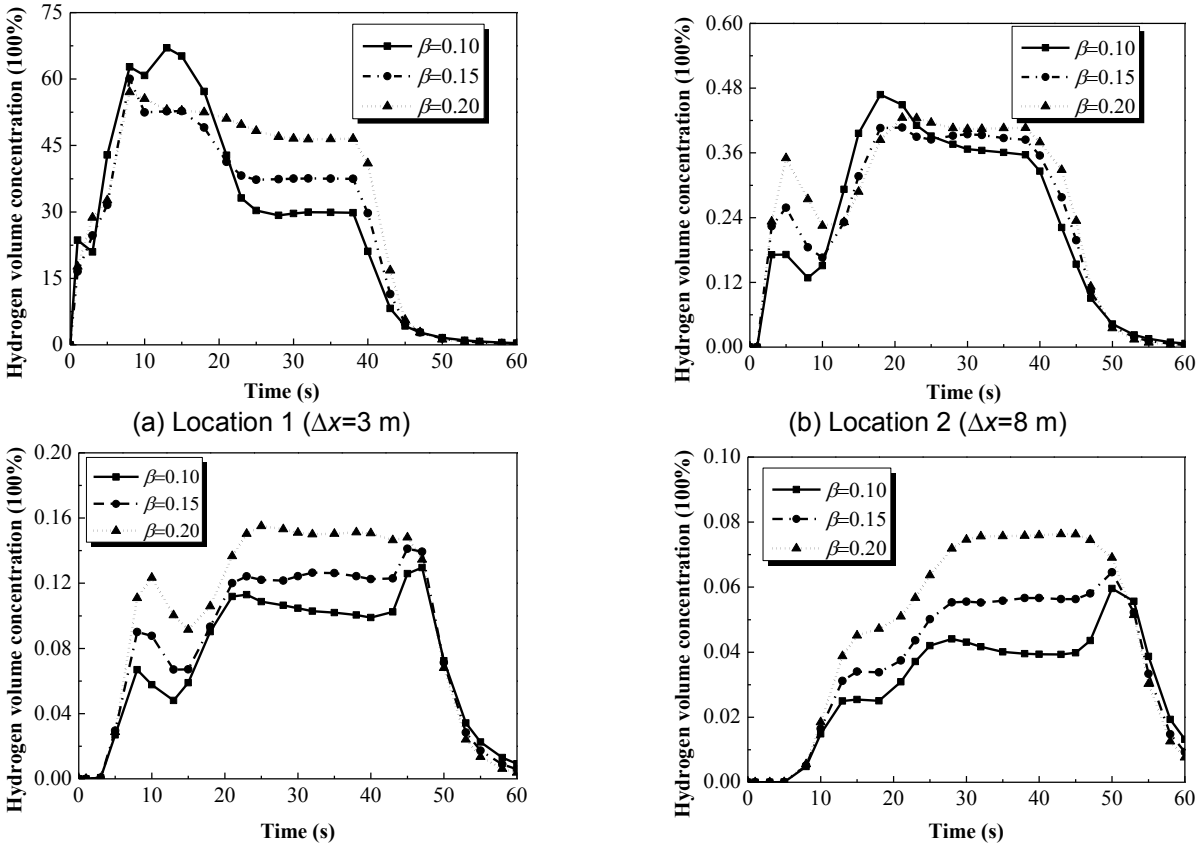

(a) Location 1 (Δ*x*=3 m) (b) Location 2 (Δ*x*=8 m)

(c) Location 3 (Δ*x*=15 m) (d) Location 4 (Δ*x*=25 m)

Figure 6: The concentration versus time histories for the locations 0.8 m above the ground

4. CONCLUSIONS

Liquid hydrogen spills under different wind flows are numerically predicted. The wind flow is represented by the power law vertical profile proposed by AIJ. The effects of vertical wind flow profiles on the evolution of hydrogen vapor cloud are analyzed. The main conclusions that can be drawn from the simulations are as follows.

The increased vertical velocity gradient of the wind prevents the cloud from going up. The cloud dispersion is hindered by the increased power law exponent of the wind profile, with the reduced streamwise distance and height, and the enlarged detachment distance on the ground. The increment in power law exponent makes the near-ground domain get exposed to higher hydrogen concentration, especially for the domain away from the source.

ACKNOWLEDGEMENTS

This study is financially supported by the National Key Basic Research Program of China (No. 613322) and the National Natural Science Foundation of China (No. 51676213).

NOMENCLATURE

u	horizontal velocity (m/s)	Greek symbols	
p	pressure (Pa)	α	volume fraction
t	time (s)	μ	viscosity, kg/(m·s)
v	velocity (m/s)	ε	turbulent energy dissipation rate (m^2/s^3)
$v_{dr,i}$	drift velocity for phase i (m/s)	β	power law exponent
h	enthalpy (J/kg)	ρ	density (kg/m^3)
T	temperature (K)	Subscripts	
$\dot{m}$	rate of mass transfer ($kg/(s \cdot m^3)$)	0	reference value
Y	Mass fraction of species in phase	m	mixture phase
k_{eff}	effective heat conductivity (W/(m·K))	l	liquid phase
g	gravity acceleration (m/s^2)	g	gas phase
n	number of phases	sat	saturation
k	turbulent kinetic energy (m^2/s^2)	i	liquid phase or gas phase
z	height (m)	l,i	species i in liquid phase
I	turbulent intensity	g,i	species i in gas phase
L	turbulent length scale (m)		

REFERENCES

Chirivella, J. E., Witcofski, R. D., 1986. Experimental results from fast 1500 gallon LH_2 spills. Cryogenic Properties, Processes and Applications 251(82): 120-140.

Choi, J., Hur, N., Kang, S., Lee, E. D., Lee, K. B., 2013. A CFD simulation of hydrogen dispersion for the hydrogen leakage from a fuel cell vehicle in an underground parking garage. Int. J. Hydrogen Energy 38(19): 8084-8091.

Huo, S., Park, J. W., He, P., Wang, D., Jiao, K., 2017. Analytical modeling of liquid saturation jump effect for hydrogen alkaline anion exchange membrane fuel cell. Int. J. Heat Mass Transfer 112: 91-902.

Jin, T., Wu, M., Liu, Y., Lei, G., Chen, H., Lan, Y., 2017. CFD modeling and analysis of the influence factors of liquid hydrogen spills in open environment. Int. J. Hydrogen Energy 42(1): 732-739.

Lee, W. H., 1979. A pressure iteration scheme for two-phase flow modeling. Los Alamos National Laboratory: LA-UR-79-975.

Liu, Y., Wei, J., Lei, G., Wang, T., Lan, Y., Chen, H., Jin, T., 2019. Modeling the development of hydrogen vapor cloud considering the presence of air humidity. Int. J. Hydrogen Energy 44(3): 2059-2068.

Middha, P., Ichard, M., Arntzen, B. J., 2011. Validation of CFD modeling of LH_2 spread and evaporation against large-scale spill experiments. Int. J. Hydrogen Energy 36(3): 2620-2627.

Shao, X., Liang, P., Li, Q., Li, Y., 2018. Numerical investigation of flammable cloud on liquid hydrogen spill under various weather conditions. Int. J. Hydrogen Energy 43(10): 5249-5260.

Shih, T. H., Liou, W. W., Shabir, A., Zhu, J., 1995. A new eddy viscosity model for high Reynolds number turbulent flows: model development and validation. Comput. Fluids 24(3): 227-238.

Tamura, Y., Ohkuma, T., Okada, H., Kanda, J., 1999. Wind loading standards and design criteria in Japan. J Wind Eng Ind Aerod 83(1-3): 555-566.

Tominaga, Y., Mochida, A., Yoshie, R., Kataoka, H., Nozu, T., Yoshikawa, M., Shirasawa, T., 2008. AIJ guidelines for practical applications of CFD to pedestrian wind environment around buildings. J Wind Eng Ind Aerod 96(10): 1749-1761.

Wang, L., Zhu, K., Xie, F., Ma, Y., Li, Y., 2016. Prediction of pool boiling heat transfer for hydrogen in microgravity. Int. J. Heat Mass Transfer 94: 465-473.

Witcofski, R. D., Chirivella, J. E., 1984. Experimental and analytical analyses of the mechanisms governing the dispersion of flammable clouds formed by liquid hydrogen spills. Int. J. Hydrogen Energy 9(5): 425-435.

Manuscript ID: 1653
DOI: 10.18462/iir.icr.2019.1653

Integrated cryogenic quantum refrigeration of electrons

Kazuaki YAZAWA[(a)], Ali SHAKOURI [(a)]

[(a)] Birck Nanotechnology Center, Purdue University
West Lafayette, Indiana, 47907, USA, kyazawa@purdue.edu

ABSTRACT

Many quantum computing approaches require deep cryogenic refrigeration to preserve quantum coherence using superconducting or high electron mobility topological materials. State-of-the-art cryo-refrigerators achieve 20 mK with a step at 4 K using a regenerative Gifford-McMahon cycle with a total COP of 10^{-9}. Huge amount of energy is required to cool the lattice while conduction electrons are the ones used for information processing. High performance computing requires very fast operations on qubits. Here we investigate the possibility to develop thermodynamic cycles for transient cryogenic cooling of non-equilibrium electrons inside the quantum computer circuit. Under moderate cryogenic conditions and in picosecond range, compression and expansion of Fermionic electron gas can be achieved without exchanging energy with the lattice. Device geometries are investigated for modulating electrostatic confinement of electrons to mimic Joule-Thomson refrigeration. Preliminary investigation of COP is also reported.
Keywords: Cryogenic Cooling, Joule-Thomson Effect, Non-Equilibrium Electrons, Thermoelectrics.

1. INTRODUCTION

We study the potential to utilize electron gas in a solid as a refrigerant. This concept is based on the same thermodynamic behaviour of non-equilibrium electron (NEs) considered as a working fluid for a solid-state heat engine (Yazawa and Shakouri, 2016). Many quantum computing approaches require deep cryogenic refrigeration to preserve quantum coherence using superconducting (Ladd, 2010) or high electron mobility topological materials (Wan, 2015). State-of-the-art cryo-refrigerators achieve 20 mK with a step at 4 K using a regenerative Gifford-McMahon cycle with a total coefficient of performance (COP) of around 1 per billion (10^{-9}) by multiplying the COPs that are about 10^{-4} to reach 4K (Satoh, 2002) and 10^{-5} to reach 20 mK (Hornibrook, 2015), respectively. Huge amount of energy is required to cool the lattice while conduction electrons are the ones used for information processing. Such sub-Kelvin cooling effort is indispensable since removal of relatively large noise (decoherence) by thermal fluctuation is critical for the very fast operations on qubits in high performance computing. Electron-phonon interactions are one the major contributors limiting the coherence of electronic wavefunction in a solid. Due to the large difference in the number of electrons and the lattice atoms per unit volume, their scattering times can be very different. For instance, phonons take more than 100s femto seconds to respond in gallium arsenide (GaAs) at room temperature. Within that short duration of time, highly excited NEs can move across the solid without interacting phonons (thermalization). Based on this mechanism, we investigate the possibility to develop thermodynamic process or cycle for highly transient cryogenic cooling of electrons, which may be potentially applicable to directly cool electrons in a quantum computer circuit. Phonons scattering times are slower under cryogenic temperatures hence transient cooling in 10s of picosecond range may be possible. The device structure can be similar to high electron mobility transistors (HEMTs) where the confinement of the 2D electron gas can be modulated by electrostatic confinement of electrons mimicking Joule-Thomson effect. Preliminary investigation for COP is also reported.

2. NON-EQUILIBRIUM REFRIGERATION

Before handling non-equilibrium electrons (NEs) as a gas, we consider the general characteristics of electrons in the following section. Joule-Thomson effect is considered for refrigeration process using NEs through expansion of electron gas in a confined volume of semiconductor solid. It is in contrast to what we investigated the compression by using electrical filed plus geometric confinement

for a thermodynamic power generator in our previous study. A preliminary discussion of the device consideration is followed by the performance analysis in later sections.

2.1. Non-Equilibrium Fermi Gas

Electrons in a solid follow Fermi-Dirac energy distribution according to the Pauli Exclusion Principle. Free electrons occupy an energy level over conduction band of a semiconductor are considered as energy carriers freely moving inside a confined solid space (lattice). Behaviour of the free electrons is commonly accepted as a Fermi gas. The non-equilibrium energy distribution of electrons happens within 100s femto seconds (e.g. GaAs) after excitation (Langot, 1996) and before electron-phonon interactions begin to dominate energy transport (Sarma, 1990;Harris, 1998).
In order to develop a refrigeration mechanism, the characteristics of the Fermi gas are reviewed here. Let's assume a carrier density n per unit volume in a semiconductor material. The carrier density is controlled by introducing foreign species to the lattice by a doping process so that excess electrons can be added. Once the device is biased, the Fermi level E_F in eV is determined by the contacts. With bandgap E_g in eV as the intrinsic material property, the carrier (electron) density is a function of electron temperature. Note that this temperature does not necessarily match to the lattice when electrons are in a non-equilibrium state (e.g. excited by an ultrafast external input energy).

$$n = \frac{8\pi\sqrt{2}}{h^3} m^{*\frac{3}{2}} \int_{E_g}^{\infty} \frac{\sqrt{\varepsilon - E_g}}{\exp((\varepsilon - E_F)/k_B T)+1} d\varepsilon \qquad \text{Eq. (1)}$$

where h = 6.63x10^{-34} in Jxs is the Planck constant, k_B = 1.38x10^{-23} in JxK^{-1} is Boltzmann constant, m^* is effective mass of electrons relative to the mass in vacuum m_0. For GaAs, m^* = 0.067 m_0. The relationship comes from Fermi distribution times density of state of electrons.
In order to discuss the heat exchange in a confined region, we use a 2-dimensional (2D) electron gas structure, such as high electron mobility transistors (HEMT), which is commonly used in high-speed switching devices (Miura, 1980).
Non-equilibrium electrons (NEs) can be considered as a free gas only in a very short time. When NEs are created by energy input or temperature step pulse, it takes some time for the energy to be transferred to lattice vibrations, which is represented by phonons, through a process called thermalization. Following figure shows the electron-phonon relaxation time for GaAs as an example. At room temperature or lower, the time to respond significantly increases to approximately 10 picoseconds.

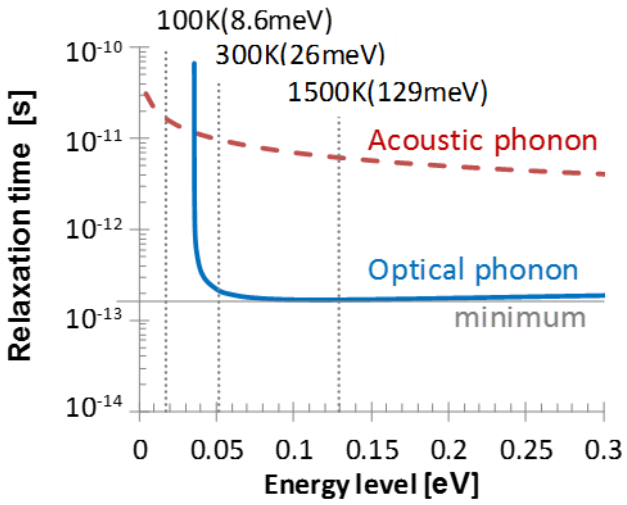

Figure 1: Electron-phonon relaxation time is a strong function of the lattice temperature

2.2. Refrigeration with NE gas

Compression stage for a gas compression cycle can be implemented with NEs. We are handling NEs as single-phase gas for the analysis. Hence the reverse Brayton cycle could be one approach for refrigeration. A challenge for NEs gas cycle is found at heat exchangers especially at the cooling spot. Heat absorption from lattice is low due to the small heat capacity of NEs.

Joule-Thomson effect can be much simpler especially for applications of heat removal from a small region, e.g. Micro Miniature Refrigerators used in optics (Little, 1983). In this study, gas expansion is not a volume increase, but instead, density of particles is reduced using electrostatic potential from a gate, as illustrated in the following Fig. 2.

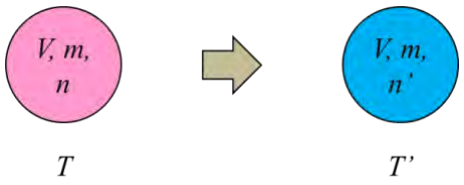

Figure 2: State change by Joule-Thomson effect with NE gas

In the Fig. 2, T represents the particle temperature but not the lattice temperature. Since the particles are in a solid, the volume and mass can be constant and do not change, while particle density n changes. Joule-Thomson coefficient μ_{JT} by definition (Maytal and Pfotenhauer, 2013) is found as the following.

$$\mu_{JT} \equiv \left(\frac{\partial T}{\partial p}\right)_H = \frac{TV}{C_p}\left(\beta - \frac{1}{T}\right) \qquad \text{Eq. (2)}$$

where p is pressure in Pa, T is temperature in K, V is volume in m^3, C_p is effective specific heat at constant pressure in Jxkg^{-1}xK^{-1}. β is the effective volumetric thermal expansion coefficient in K^{-1} as,

$$\beta = -\frac{1}{n}\frac{dn}{dT} \qquad \text{Eq. (3)}$$

One should note that Eq. (2) can be applied to non-degenerate electron gas when Boltzmann statistics is valid. As β is always negative, μ_{JT} is negative. This is not useful for cooling purposes. One can make the Joule-Thomson coefficient positive by transient switching of the Fermi level. The difference in carrier density can be used to create a positive Joule-Thomson coefficient, leading to refrigeration. The change of n by changing in Fermi level E_F in eV is quite sensitive especially at low temperatures. The following figure illustrates the carrier density as function of temperature for different Fermi levels (from 1.3 to 2.0 eV) for the case of GaAs whose bandgap E_g is 1.424 eV. Drastic drop in cryogenic temperature range suggests a large sensitivity of carrier density to temperature and volume. Also, it is understood that electron-electron scattering can be very fast, so electrons can behave as a gas with a single quasi-Fermi level.

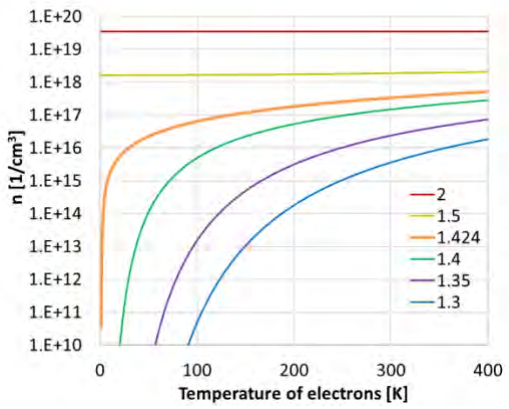

Figure 3: Carrier density as function of temperature for different Fermi levels in eV (different colors) for GaAs (E_g = 1.424 eV)

According to the model Eq. (1), the critical carrier density n to determine $\mu_{JT} = 0$ is calculated and shown in Fig. 4. Fig. 5 shows the change in Fermi level (offset) required to fulfill the critical density as function of temperature. The critical curve with $\mu_{JT} = 0$ is sometimes called as inversion curve.

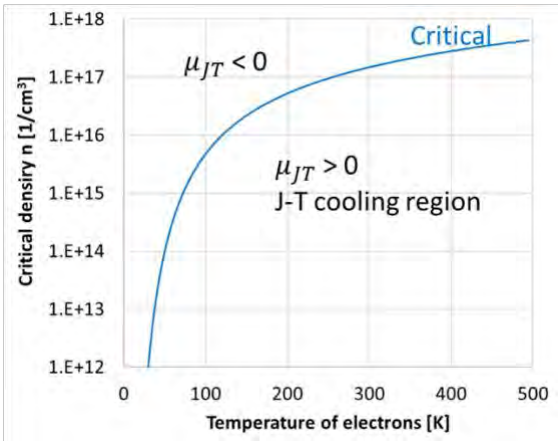

Figure 4: Joule-Thomson critical carrier density as function of temperature.

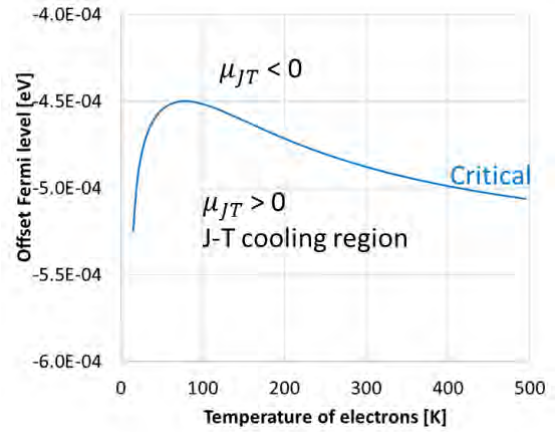

Figure 5: Offset of Fermi level compared to the initial value at 1.42 eV

2.3. Cooling of Hot Spot

Within few picoseconds, high-energy free electrons need to expand. Then, the electron temperature is reduced. In order to benefit from this process to make low noise devices, the region of heat input and expansion process must be small enough to allow non-equilibrium electron transport. The length scale of the cooling spot can be indirectly found by energy relaxation length (Shakouri, 1998) which is 23×10^{-9} m at room temperature in GaAs under 5 kV/cm field and becomes much longer for cryogenic temperatures. Hence, the size of the cooling region should be on the order of submicron to couple of microns. As one potential application, direct cooling of 2D electron gas in the HEMT channel can be considered. This can create a low-noise “classical” electronic device.
For computing via qubits, one should consider devices where there is quantum entanglement (Horodecki, 2009). This is a subject of future study whether if the expansion mechanism clearly matches the dimensions of the qubit information processing region. The dimension depends on specific quantum computing technology, e.g. using spin-orbit coupling, topological insulators, etc.

2.4. Performance

Since NEs are considered as refrigerant, effective heat capacity and the number of energy carriers are the key parameters to investigate. Well-known classical expression of heat capacity in constant volume is $C_v = (2/3)\, k_B T$. This is valid at low electron density when Boltzmann statistics dominates. Due to the Fermi-Dirac statistics for electrons, as described in section 2.1, the specific heat at high concentrations is constrained by Fermi level and determined as,

$$C_V = C_v/n = \frac{\pi^2}{2}\frac{{k_B}^2 T}{E_F} \quad \text{Eq. (4)}$$

where C_V in heat capacity per electron at constant volume in JxK^{-1} (Kittle, 1996). The value of specific heat C_v in Jxm^{-3}xK^{-1} largely differs from ideal gas and can be as small as nearly one hundredth.

At short times, when electrons are in non-equilibrium state, the heat energy absorbed by the available NEs is found as,

$$Q = \int_{n1}^{n2} n\frac{\pi^2}{2}\frac{{k_B}^2 T}{E_F} dn \quad \text{Eq. (5)}$$

where n_1 and n_2 are carrier densities at $T = T_1$ and $T = T_2$, respectively. To make the change from n_1 and n_2, an external energy must be applied at the same time duration, which is

$$W = (n_2 - n_1)e \quad \text{Eq. (6)}$$

Where, e is elemental charge of electron 1.6x10^{-19} in JxeV^{-1}. Calculation result of COP = Q / W is shown in the following figure. The result shows COP in the range of 10^{-3} – 10^{-2}, which is lower compared to off-the-shelf vapor compression cycles at smaller temperature differences near room temperature. Interestingly, however, the COP is larger at larger temperature differences at cryogenic target temperature range. With GaAs, COP of 10^{-3} is significantly higher than that of a state-of-the-art mechanical cryo-refrigeration currently used for quantum computers. The COP seems to be asymptotic to a single value 1.18x10^{-2} as the target temperature approaches sub Kelvin region. This requires additional investigation if this is a fundamental limit. In this model, COP at temperatures below 4 K may require few-electron devices since carrier density is so low. Overall, this initial analysis shows potential for quantum refrigeration of electrons at cryogenic temperatures.

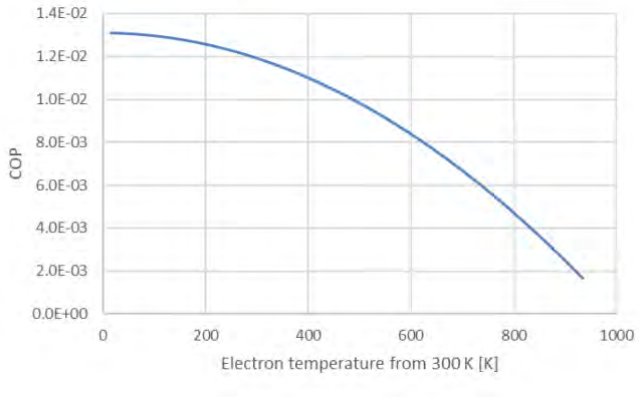

Figure 6: Preliminary COP versus temperature delta from 300 K. This calculation is based on GaAs with E_F = 1.4 eV (Intrinsic career density n = 2.6x10^{16} 1/cm^3)

3. CONCLUSIONS

Nonequilibrium electrons are investigated as a refrigerant via Joule-Thomson effect. Preliminary analysis of key factors and performance limits are presented. We identified a critical carrier density to get positive Joule-Thomson coefficient, where the cooling of electrons can be achieved. Joule-Thomson coefficient is very sensitive and can be controlled via Fermi-level, which could be modified, for example, by very fast changing gate voltage in a 2D electron gas transistor configuration. By directly cooling electrons, a combined functional carrier of information and heat could be considered for the future quantum computing. Heat capacity of electron is very small compared to the lattice, it is a preferable benefit to directly cool free electrons, where significantly smaller power should be required rather than cooling the entire solid. Very preliminary COP analysis suggests several orders of magnitude larger COP if this approach is extended to an integrated qubit device for quantum computing.

NOMENCLATURE

C	Heat capacity ($J \times K^{-1}$)	m	mass (kg)
n	Carrier density (m^{-3})	p	Pressure (Pa)
Q	Heat amount (J)	V	Volume (m^{-3})
W	Electricity (J)	β	Thermal expansion (K^{-1})
μ_{JT}	Joule-Thomson coefficient ($KxPa^{-1}$)		

REFERENCES

Das Sarma, S., Jain, J. K., Jalabert, R., 1990. Many-body theory of energy relaxation in an excited-electron gas via optical-phonon emission, Physical Review B 41(6), 3561-3571.

Harris, J.J., 1998. Growth of fabrication of semiconductor devices for hot-electron research, In: Foxon, C.T., Ed: Balkan N., Hot Electrons in Semiconductors Physics and Devices, Oxford Science Publications, New York, 35-53.

Hornibrook, J. M., Colless, J. I., Conway Lamb, I.D., Pauka, S. J., Lu, H., Gossard, A. C., Watson, J. D., Gardner, G. C., Fallahi, S., Manfra, M. J., Reilly, D. J., 2015. Cryogenic control architecture for large-scale quantum computing, Physical Review Applied 3(2), 024010.

Horodecki, R., Horodecki, P., Horodecki, M. and Horodecki, K., 2009. Quantum entanglement. Reviews of Modern Physics 81(2), 865.

Kittel, C., 1996. Introduction to Solid State Physics Seventh Edition. John Willey & Sons, United States of America, 151 – 155.

Ladd, T.D., Jelezko, F., Laflamme, R., Nakamura, Y., Monroe, C., O'Brien, J.L., 2010. Quantum computers, Nature 464(7285), 45.

Langot, P., Del Fatti, N., Christofilos, D., Tommasi, R., Vallée, F., 1996. Femtosecond investigation of the hot-phonon effect in GaAs at room temperature. Physical Review B 54(20), 14487.

Little, W.A., 1983. Micro miniature refrigerators. U.S. Patent 4,392,362.

Maytal, B.-Z., 2013. Miniature Joule-Thomson Cryocooling Principles and Practice. In: Pfotenhauer, J. M., Springer, New York, 40.

Mimura, T., Hiyamizu, S., Fujii, T., Nanbu, K., 1980. A new field-effect transistor with selectively doped GaAs/n-AlxGa1-xAs heterojunctions. Japanese Journal of Applied Physics 19(5), L225.

Satoh, T., Li, R., Asami, H., Kanazawa, Y., Onishi, A., 2002. Development of a High Efficiency 0.5 W Class 4K GM Cryocooler, Cryocoolers 10, Springer, Boston, MA, 575-580.

Shakouri, A., Lee, E.Y., Smith, D. L., Narayanamurti, V., Bowers, J.E., 1998. Thermoelectric effects in submicron heterostructure barriers, Microscale Thermophysical Engineering 2(1), 37-47.

Yazawa, K., Shakouri, A., 2016. Electrothermal Energy Conversion Using Electron Gas Volumetric Change Inside Semiconductors, Applied Physics Letter 109(4).

Wan, Z., Kazakov,A., Manfra,M.J., Pfeiffer, L.N. West, K.W., Rokhinson, L.P., 2015. Induced superconductivity in high-mobility two-dimensional electron gas in gallium arsenide heterostructures, Nature Communications 6, 7426.

Manuscript ID: 1690
DOI: 10.18462/iir.icr.2019.1690

CO_2 cooling challenges at CERN for the future phase 2 upgrade program

Bart VERLAAT[(a)], Paolo PETAGNA[(a)], Lukasz ZWALINSKI[(a)], Jerome DAGUIN[(a)], Dina GIAKOUMI[(a)], Viren BHANOT[(a)], Michele BATTISTIN[(a)], Armin HAFNER[(b)], Johann COLLOT[(c)], Dominique BONDOUX[(c)], Hans POSTEMA[(a)], Paola TROPEA[(a)], Stefanie BLUST[(b)], Pierre HANF[(a)], Ángel Á. PARDIÑAS[(b)]

[(a)] CERN, Geneva, 1211, Switzerland, bart.verlaat@cern.ch
[(b)] NTNU, Trondheim, 7491, Norway, armin.hafner@ntnu.no
[(c)] LPSC, Université Grenoble Alpes, CNRS/IN2P3, Grenoble, 38026, France, collot@in2p3.fr

ABSTRACT

At CERN, evaporative CO_2 is the baseline cooling solution for the thermal management of the phase-II silicon detectors, which will be installed in 2025 in the ATLAS and CMS experiments. Since 2008 CO_2 cooling is used in 3 detectors with capacities ranging 1 to 15 kW at -30°C. A special pumped cycle was developed to guarantee accurate temperature control under all operational conditions.
The challenges for the upgrade are the large increase of the cooling power (300 - 550 kW), the large number of parallel operating evaporators (~1000x), the low evaporative temperature (-45°C) and the implementation of a primary R744 trans-critical cooling system.
Implementing this R744 primary cooling solution will make the future detector cooling to work fully with natural working fluids (R744 and R718).
This paper describes the design and prototyping phase of the system with surface storage and the new primary R744 system, which bridges the industrial applications of R744 refrigeration to the highly demanding performances of high-energy physics experiments.

Keywords: Refrigeration, Carbon Dioxide, R744, CERN, 2PACL, Transcritical.

1. INTRODUCTION

The CERN Large Hadron Collider (LHC) (Evans et al., 2008) has four detectors. The two largest being CMS (Chatrchyan et al.,2008) and ATLAS (Aad et al., 2008) will undergo a major upgrade in the 3rd long shut down period since the start in 2008. Currently this upgrade is scheduled to take place in 2025. The LHC accelerator will be upgraded to an increased luminosity by a factor of 10. The detectors must be upgraded to cope with this increased luminosity, which requires higher precision, faster electronics and the resistance to higher radiation levels. In both ATLAS and CMS the full inner tracking detector will be replaced and an extra timing detector layer in front of the calorimeters will be installed. Additionally, in CMS a part of the Calorimeter will be upgraded.
All new detectors will use silicon detector technologies, which need effective cooling to remove the relatively large heat produced by the sensors and electronics. To minimize the radiation damage received from the particle flux, the silicon requires to be cold at all times (typically <-10°C for the sensors, leading to -40°C in cooling pipes). The additional design requirement for low mass and hence small cooling pipes have led to the choice of using evaporative CO_2 cooling. CO_2 can work with small cooling pipes due to its high evaporative pressure. It is radiation hard and has the right temperature range for detector operation. The operative temperature range for detector cooling is from 15°C down to -45°C, fitting well in the 2-phase area between the critical point at 31°C and triple point of -56°C.

2. OPERATIONAL CO_2 SYSTEMS AT CERN

Currently at CERN 3 detectors have been equipped with CO_2 cooling and all have run successfully for years. The 1st CO_2 system at CERN was the cooling for the LHCb-Velo detector (Verlaat et al, 2008), which was recently retired since the operation start in 2008. Since then the ATLAS and CMS inner pixel detectors have been upgraded in 2014 and 2016with a similar technology and are operating successfully since then (Daguin et al., 2015).

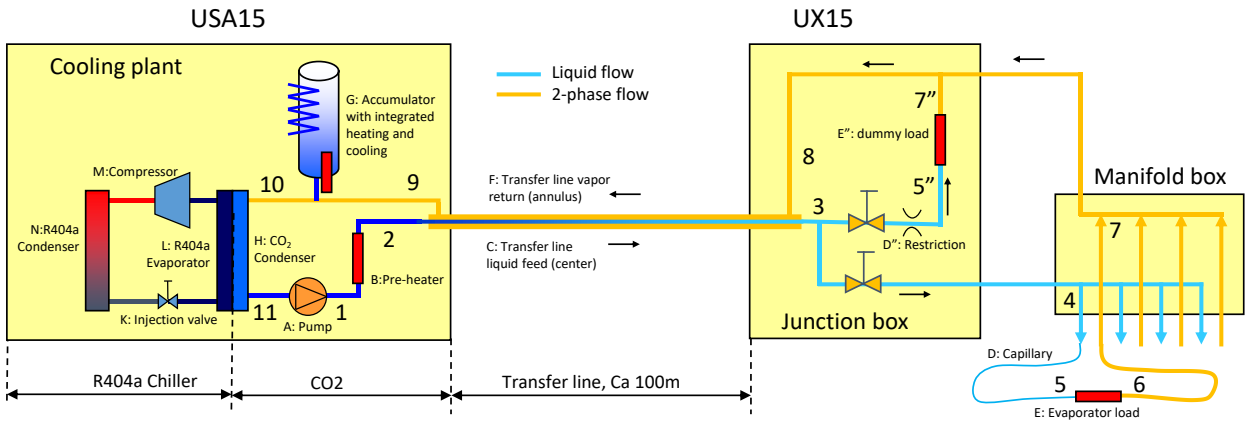

Figure 1: 2PACL concept for detector cooling.

The basic principle of the CO_2 circulation and conditioning through the detectors is the so-called 2-Phase Accumulator Controlled Loop (2PACL) method (Verlaat, 2018). In this cycle, shown in Figure 1 , subcooled liquid CO_2 is pumped through a 100 m long, concentric transfer line towards the cooling loops of the detector, which are situated underground. The subcooled liquid is heated in the concentric transfer line by exchanging heat with the returning 2-phase flow such that the cooling loops are in saturation with a low entrance vapour quality. The cycle is plotted with corresponding numbering of Figure 1 in the PH diagram of Figure 2. Under full load, the vapour quality at the evaporator outlet is about 35%. This low vapour quality range gives the best heat transfer behaviour in the detector cooling loops. The returning flow is in 2-phase state and is condensed and subcooled in a heat exchanger in the plant, which is cooled by an external ch[illed] system.

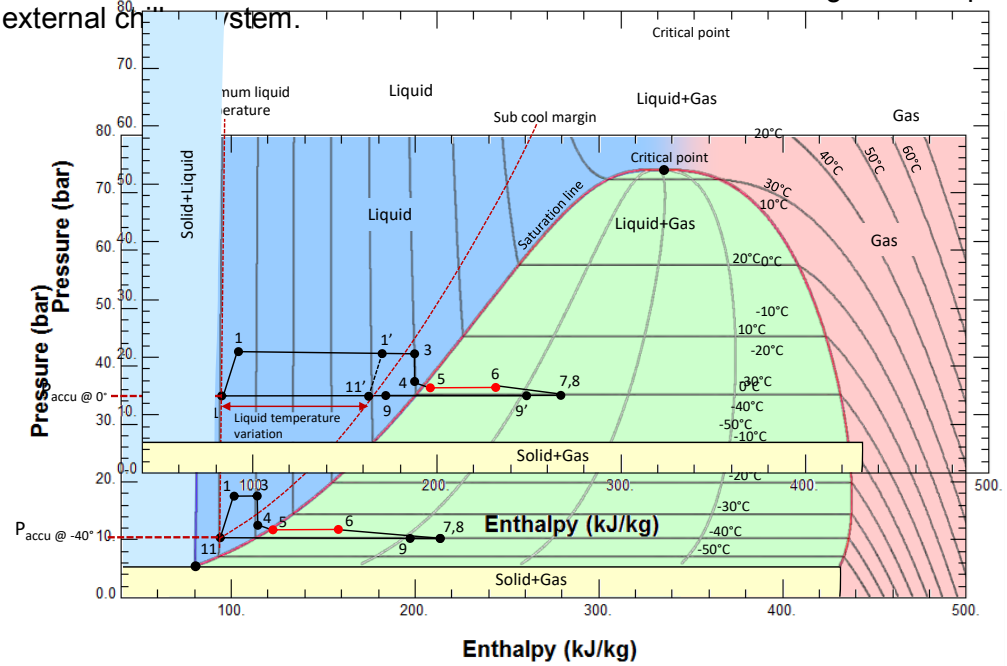

Figure 2: 2PACL operation at two different temperatures in the PH-diagram.

The return line is connected to a 2-phase accumulator, which is pressure controlled by a combination of heating and cooling. This vessel is designed such that always a 2-phase mixture is present and hence the pressure can be controlled by the saturation temperature. The return line pressure drop from the detector loops to the plant is low, so the accumulator has a direct control over the cooling loop pressure and hence temperature with just a slide offset. The 2PACL method proved to be ideal for detector cooling as it can regulate the cooling loop pressure and hence temperature in a very large range from room temperature down to the target temperature for the future detectors as low as -45°C. The room temperature operation is used usually for commissioning when the detectors are exposed to ambient conditions, while during physics operation a cold cooling is needed to guarantee the detector performance. The cooling temperature can be controlled stable within 0.1K independent of the detector headload, which can be switched off or be at full power. During start-up the 2PACL is transferred in a full liquid system to guarantee a slow and controlled cool down of the sensitive detector without thermal shocks of arriving liquid slugs.

3. FUTURE CHALLENGES

The CO_2 cooling needed for the phase 2 upgrade in 2025 has to cool a magnitude more power than the current systems. 300 kW cooling power is needed in ATLAS and 550 kW cooling power in CMS. The needed cooling temperature in the detectors is around -40°C, while current systems operate at -30°C at lowest. This decrease of temperature becomes a challenge as this requires a plant saturation temperature in the order of -45°C. The pumps need several degrees of sub cooling bringing the liquid temperatures below -50°C. This becomes close to the triple point of CO_2, a real hard limit for a CO_2 system. Figure 3 shows a typical temperature profile of a CO_2 cooling circuit from the plant to the evaporator loops in the detector. On the right side, the highest cooling temperature is shown in the detector. From there the temperature decreases towards the cooling plant due to the pressure drop it encounters along the way in the return line. The biggest pressure and hence temperature drops are generally inside the detector cooling loops and the distribution lines called flex lines in this graph. These pressure and hence temperature drops are relatively high as the tubes are smaller than usual due to integration constraints and mass savings. The transfer lines connecting the detector cooling loops to the plant can be larger as there is more space to route them, pressure drop is generally much lower as shown in Figure 3. In the plant the liquid is subcooled by an external primary chiller. A liquid pump is circulating the CO_2. The subcooled liquid from the pump is heated by heat exchange with the return flow in the concentric transfer line. This exchange ensures a proper evaporation in the detector with low vapor quality. In the graph, the blue line (subcooled liquid) approaches the 2-phase return temperature (red line) along the way and follows it to the evaporator in the detector.

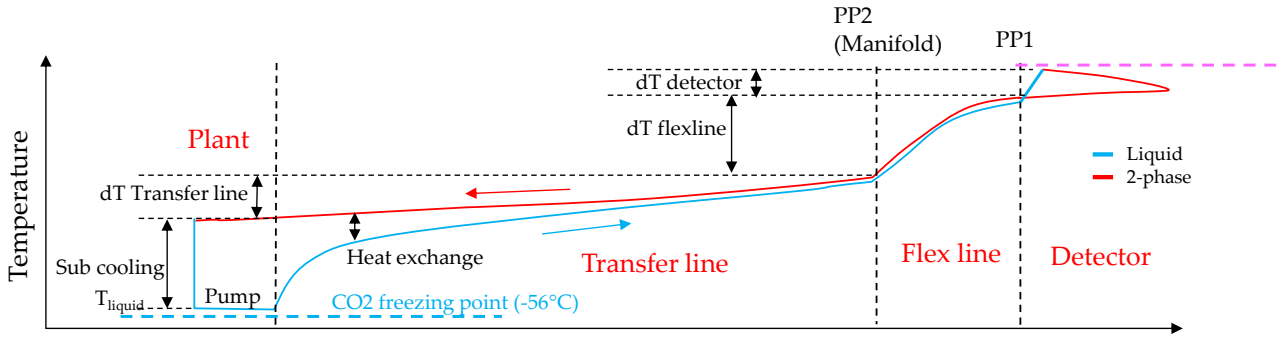

Figure 3: Temperature profile of the cooling system from plant to detector.

A large challenge of cold temperature operation is the stability of the primary cooling. In Fig. 2, a vertical and a diagonal red dotted line are shown. One with an offset to the liquid saturation line, illustrating a minimum sub cooling, and a second one with an offset from the freezing line. State point 11 (11') needs to be in between these two lines for a proper operation. It may vary or remain stable as long as it remains in between. At colder temperatures, the lines come closer together. This means that the primary cooling needs to be more stable and more accurate. At the point where the lines come together, a very stable primary cooling is needed. Stretching the cooling further to lower values would mean that the margins of sub cooling or freezing need to become smaller. This is a large challenge for the future CO_2 cooling systems.

4. CO_2 COOLING PLANTS

The detectors request a total cooling power of several hundred kilowatts. The largest build 2PACL so far is a 15 kW unit for the CMS phase-1 upgrade. The phase-2 upgrade detectors consist of several sub detectors, which might require different temperatures and are in different locations. A segmentation of multiple individual units is foreseen. The current concept for a unit contains a 100 kW cooling plant with a triple remote head membrane pump (Figure 4). This capacity allows the use of known components with a proven heritage of the previous systems. A 100 kW segmentation gives a reasonable amount of plants, which is important for integration and maintenance.

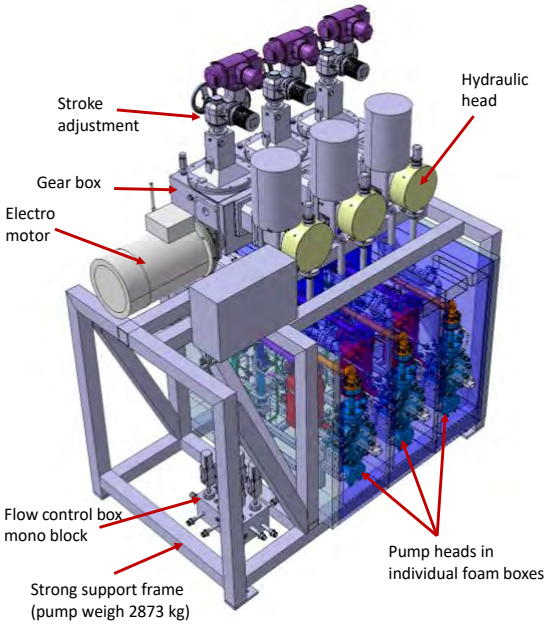

Figure 4: The phase-2 upgrade CO2 cooling plant.

The triple pump head configuration gives the possibility to make smaller plants by removing a pump head. Like this, the plant sharing between the several sub detectors can be optimized. ATLAS is foreseen to be equipped with five double head pump units and one single head pump unit. CMS will have three triple head units and two double head units. Both detectors will have one spare triple head pump that can be swapped with operational units in case of problems or maintenance. Silicon detector cooling must always work, even if the detector power is switched off. If a silicon detector, which has been exposed to a significant radiation, warms up, the damage in the crystal lattice caused by radiation will become worse and can destroy the detection performance. Therefore, the cooling must always stay on, and a serious automatic back-up system guarantees a continuous cold operation, whether there is an electronic heat load or not. **Error! Reference source not found.** shows the layout of the experiment and the different location of system elements. The plants are in the so-called service cavern, which shields them from radiation present in the detector cavern. All other systems like primary cooling and surface storage are on the surface.

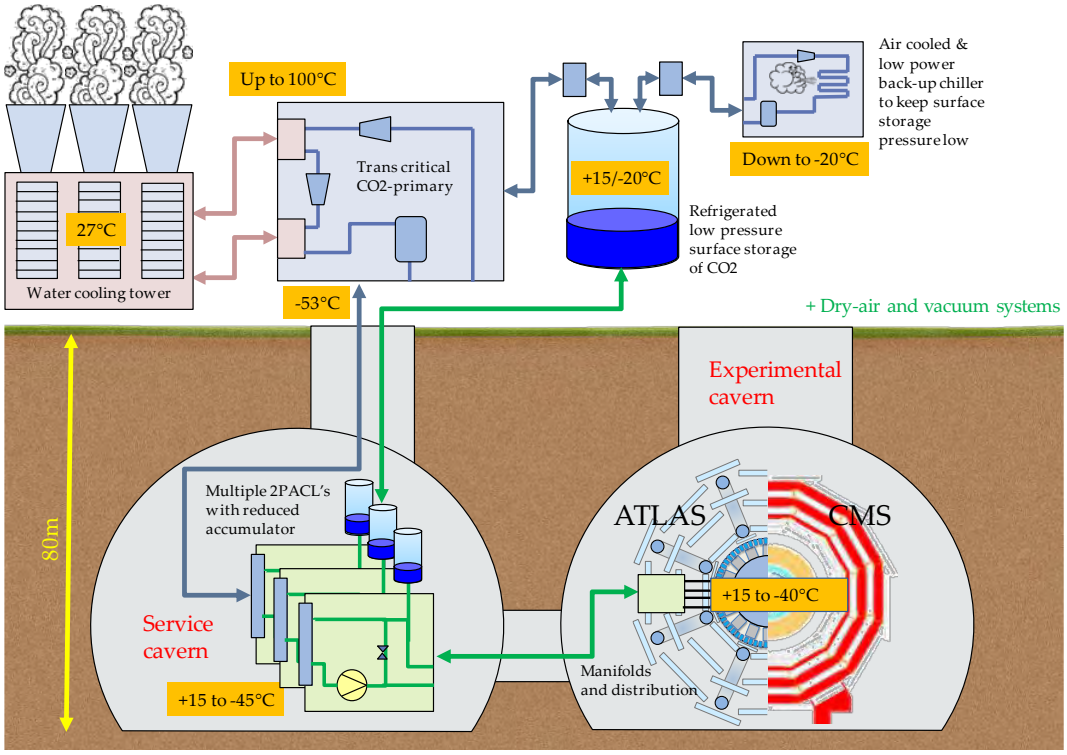

Figure 5: Schematic overview of the experimental area of the ATLAS and CMS detector.

5. SURFACE STORAGE

A 2PACL plant usually has an accumulator volume of about three times the system volume (Verlaat, 2018). With this volume ratio, the accumulator can serve all operational conditions. An accumulator must always have a saturated mixture so the pressure in the system can always be controlled by heating or cooling. The lowest accumulator level usually occurs at start up where the system is liquefied completely under pressure and where the remaining quantity of liquid in the accumulator is minimal due to the increased vapour density and reduced liquid density. The highest levels occur during maintenance when the accumulator is used for storage. The loop volumes for the phase-2 upgrade are significantly larger than the systems we had so far. A traditional 2PACL system will lead to very large high-pressure accumulators, which are expensive to make and have problems fitting in the small space available underground for integration. Typical volumes of a system is in the order of 300-400 litres, which will lead to accumulators of about 1m³ each, which is unacceptable.

During operation, the system parameters are very stable. This means that the power and accumulator set-point temperature are constant. Consequently, there are no large fluid content fluctuations in the accumulator. Therefore, the use of a smaller accumulator as control device is possible under these conditions. A system with an undersized accumulator must have different charges as a function of its operational temperature or heat load. For the future systems, the variable charge is obtained by fluid exchange with a common supply, which is located at the surface, where sufficient integration capacity is present. A schematic overview of the integration situation with respect to surface storage is shown in **Error! Reference source not found.**. The 2PACL system with surface storage integration is shown in Figure 6. A simple 2PACL would have only the valves VL2 and VL3. The surface storage need the extra valves VL1, VL4, VL5 and VL6. The surface storage pressure is kept low such that standard cryogenic storage vessels can be used. The final design pressure is still under investigation based on the availability of equipment. At cold operation of the 2PACL the accumulator set-point is below the surface storage pressure and a fill of CO_2 from the surface is achieved by VL5. In case a fluid return to surface is needed VL6 is opened. This requires a pump discharge pressure, which is higher than the surface storage pressure. The pump must work with typical pressure differences of about 20 bar or more to be able to do so. The pressure drop over the cooling lines towards the detector is, typically, 10-20 bar as the distribution to the many parallel cooling loops require it. The pump is a membrane pump and has a large pressure head capacity for this reason. In case a larger pressure difference than the detector loops is needed, an extra valve VL1 is present to increase the pump discharge.

A key property of the 2PACL method is the pressure stability and hence temperature stability in the detector. A surface storage operation would introduce unwanted instabilities in the system when being active permanently. Under stable circumstances, there is no need for surface storage control. The accumulator is the main pressure control object and surface storage kicks in if accumulator liquid levels reach a certain threshold. Like this, surface storage is only active during dynamic operations such as temperature set point change or power changes. During detector operation when the load is stable we benefit from the pressure and hence temperature stability of a 2PACL system.

The new concept of surface storage will be prototyped in an existing system build to study the cold operation called Baby-DEMO (Zwalinski et al.,2018).

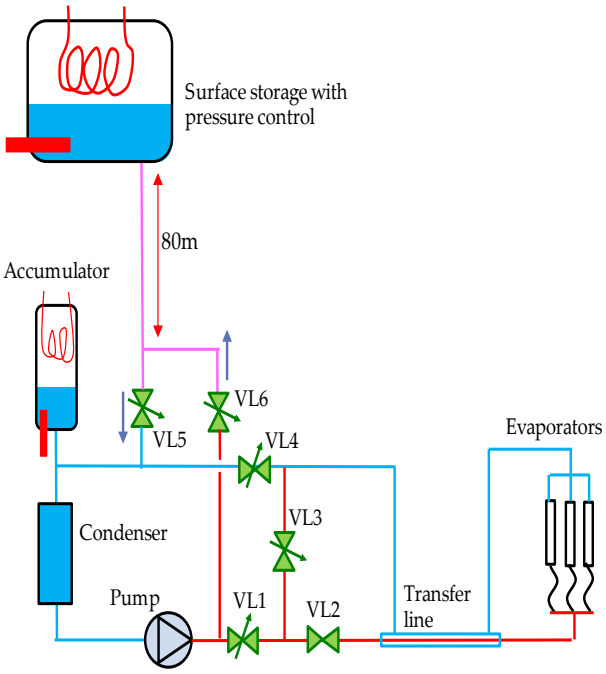

Figure 6: 2PACL system with surface storage.

6. PRIMARY R744 COOLING

As discussed in section 3, a very stable primary cooling source able to cool the CO_2 below -50°C is needed. The primary cooling plant must be placed on the surface, as there is no space in the underground cavern (**Error! Reference source not found.**). The primary cooling must cope with large load variations, and remain stable in evaporation temperature. The primary cooling system uses also CO_2 as working fluid, which is referred to as R744, to distinguish both CO_2 system fluids from each other. R744 is selected as it allows having the evaporators underground and bridging the 80 m height difference between underground and surface within a single system. The use of low-pressure refrigerants will encounter too many losses on the way to the surface; an intermediate brine system would be needed in case. The introduction of R744 in the primary system makes the full detector cooling

to work with natural refrigerants and is in line with the general CERN environmental policy of minimizing all the emissions of Green House Gases (GHG).
The primary R744 cycle is a trans-critical cycle with two compressor stages. Figure 7 shows the concept schematics and **Error! Reference source not found.** shows the operation in the PH-diagram. The system contains of several parallel compressor slices (the green fields), which can be activated as a function of the load. Each compressor slice has a target capacity of 50 kW at -53°C. The last activated slice is doing the fine control of the capacity by the use of a hot gas bypass valve CV12, and is in principle able to operate without any load (full bypass). Like this, the system can operate from no load to full load (300 kW in case of ATLAS and 550 kW in case of CMS) and remain stable within the order of one degree. The final capacity of the system will be tuned with the amount of compressor slices adapted. The example shown in Figure 7 shows two slices and is the prototype, which is currently under design.

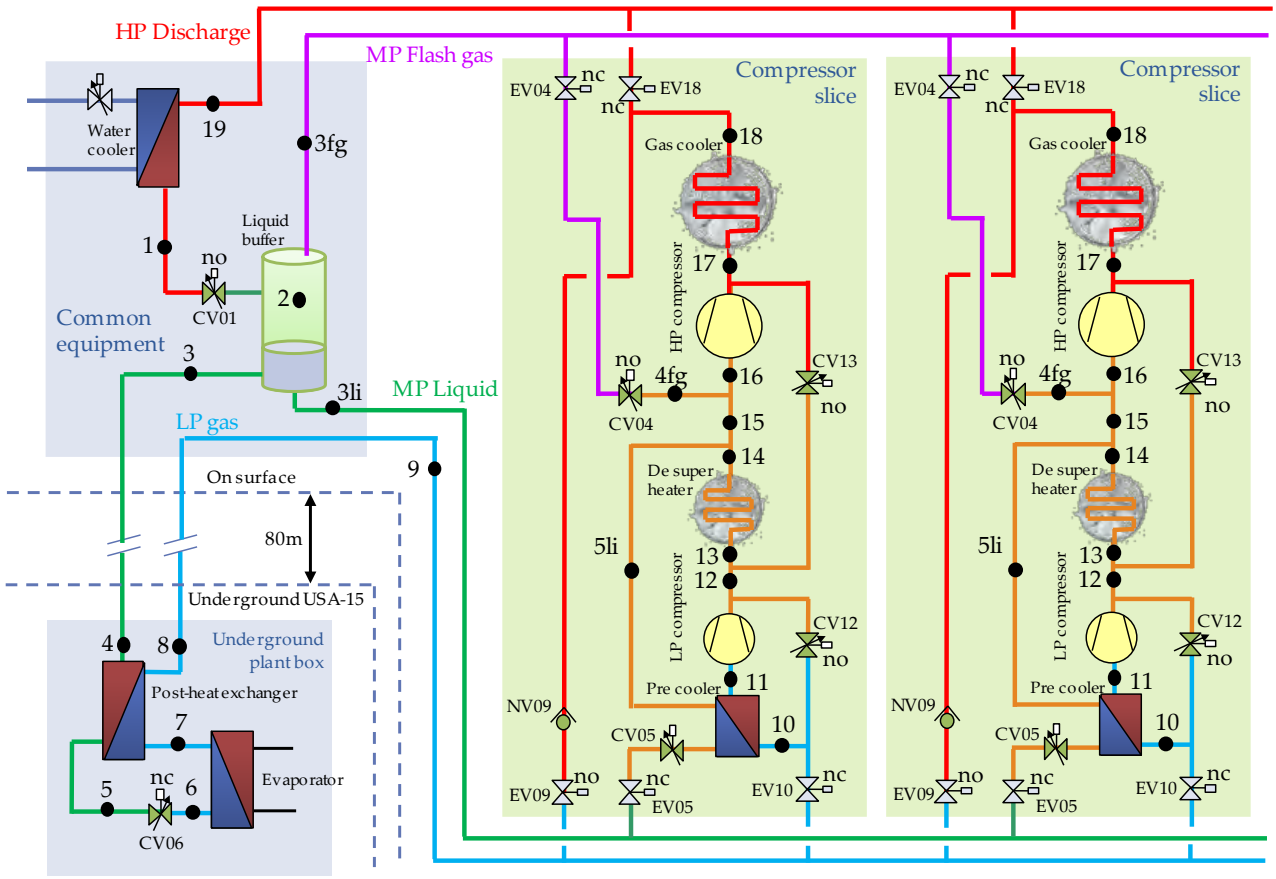

Figure 7: The primary R744 trans-critical cold temperature system.

The evaporators underground have an internal heat exchanger (7-8) to post-heat the evaporator cold gas (7) to ambient temperature conditions with the supplied ambient temperature liquid from the surface. The supply liquid (3) and return gas lines (8) do not need insulation, saving cost and integration space. The warm transport of gas also has the advantage that the losses on the return pressure drop by static height are minimal due to the reduced density of the gas at higher temperatures. A larger return tube solves the impact of the higher speed due to the lower density.

The warm gas is precooled before it enters the LP compressor to minimize the compressor suction superheating (11) and discharge temperature (12). The precooling is achieved by a heat exchange to the liquid inlet of the inter stage cooling (5li). The inter stage pressure is controlled around a saturation temperature of about -15°C and pre cools the warm gas (10) to such similar temperature. An exchange with another circuit was chosen above liquid injection, as liquid injection in a system working close to the triple point pressure risks to make dry-ice. An extra fluid injection is also not favourable for the stability of the suction pressure. The precooling by the heat exchanger in principle allows the plant to work even below the triple point as only gas is present in the suction lines. The risk of liquid and hence ice suction is minimal as the evaporators are 80 m down. To avoid dry-ice formation in the evaporators (6-7), the suction pressure of the compressor slices is controlled to be above the triple point. The losses in pressure of the return line guarantee an offset and safe margin from the triple point in the underground evaporators. Only in case the losses on the way are larger than foreseen, the system above ground can also be operated at a pressure lower than the triple point.

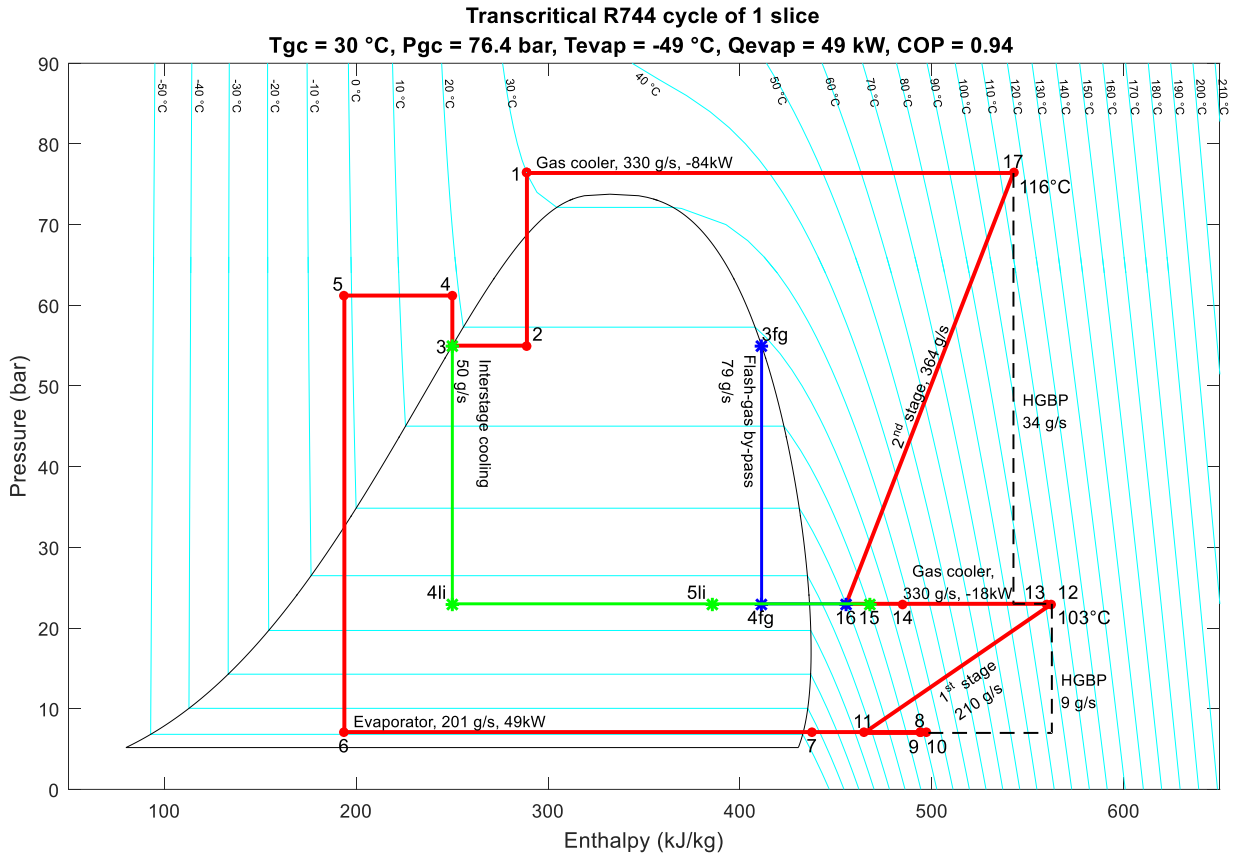

Figure 8: The primary R744 trans-critical system operation in the PH-diagram.

The R744 primary chiller rejects its heat directly to air at both compressor discharges. At the common equipment slice a water cooled heat exchanger is present to guarantee a fixed gas cooler outlet temperature all year long. This combined air/water cooling makes the system not fully dependent on water-cooling. The system is designed such that with a limited functionality loss the system can also run on air cooling only. The usual maintenance period for the water system is in the winter and this has a limited impact on the system performance due to the cold air temperature available for air cooling. A cooling water failure in the summer will reduce the capacity of the system, but is likely to be fine with the build-in margins. In addition, the control of the gas cooler pressure can be introduced to boost the efficiency of gas cooling with the prize of a lower COP, which is very acceptable. All what counts for the detector cooling is the reliability of having a stable cooling.

7. CONCLUSIONS

Since 1999, CO_2 cooling has been developed for detector cooling. Up to now, small detectors have been equipped successfully and the technology is mature enough to be applied in large scale for the phase-2 upgrade in the upcoming mid-twenties. The scaling up being more than a magnitude requires adaptations to the standard operation. Due to the scaling up, a research program is ongoing to reduce the amount of CO_2 underground in the systems. A common CO_2 supply on the surface is being considered. New is also the introduction of the primary cooling to be CO_2 (R744), making the system to be fully working with natural working fluids, paving the road for a green future of CERN.

REFERENCES

Evans, L., Bryant, P., 2008. LHC machine, JINST 3 S08001.

Chatrchyan, S. et al., 2008. The CMS experiment at the CERN LHC, JINST 3 S08004.

Aad, G., Abat, E., Abdallah, J. et al., 2008. The ATLAS experiment at the CERN Large Hadron Collider, JINST 3 S08003.

Verlaat, B., Lysebetten, A. V., Beuzekom, M. V., 2008. CO_2 cooling for the LHCb-VELO Experiment at CERN, In Proceedings of the 8th IFF/IRR Gustav Lorentzen Conference on Natural Working Fluids, Copenhagen, Denmark, CPD 16-T3-08.

Daguin, J., Bortolin, C., Crespo-Lopez, O. et al., 2015. CO_2 cooling for particle detectors: experiences from the CMS and ATLAS detector systems at LHC, and prospects for future upgrades, 24th IIR International Congress of Refrigeration, Yokohama, Japan, ID:0788.

Verlaat, B., Petagna, P., Francescon, A., 2018. Two-phase thermal management of silicon detectors for high energy physics, Encyclopedia of Two-Phase Heat Transfer and Flow III, World Scientific, pp. 335-412.

Zwalinski, L., Bojdol, K. Bortolin, C. et al., 2018. ATLAS Baby-DEMO, Nuclear Instruments and Methods, https://doi.org/10.1016/j.nima.2018.09.093.

Manuscript ID: 1699
DOI: 10.18462/iir.icr.2019.1699

Design and numerical simulation of a cold compressor for large scale superfluid helium cryogenic system

Xinbo DONG[(a,b)], Jihao WU[(a,b)], He SU[(a,b)], Jinzhen WANG[(a,b)] Cui LV[(a)], Huiming Zou[(a)]

[(a)] State Key Laboratory of Technologies in Space Cryogenic Propellants, Technical Institute of Physics and Chemistry, Chinese Academy of Science, Beijing, BJ 10, China, dongxinbo15@mails.ucas.edu.cn

[(b)] University of Chinese Academy of Science, Beijing, BJ 10, China, wujihao@mail.ipc.ac.cn

ABSTRACT

In large scale superfluid helium system, cold compressor is utilized to pump down gaseous helium from saturated liquid helium tank for producing superfluid helium. In this paper, a three-dimensional geometry of the whole stage of the cold compressor is designed and simulation is carried out to verify the performance. Considering the extremely low inlet pressure and temperature of each cold compressors, the real gas effect is considered to design and simulate such flow passages of each stage. To improve the accuracy of the simulation results, helium properties obtained by different equations of state are compared with NIST database. As a result, the ARK state equation maintains the maximum deviation of density and specific heat below 1.8 %. Then it is utilized in CFD simulation and the details on the flow field within the stage is presented.
Keywords: Superfluid Helium, Cold Compressor, Numerical Simulation, EOS.

1. INTRODUCTION

The technical properties of helium II ('superfluid' helium) are presented in view of its applications to the cooling of large particle accelerators, nuclear fusion device and other large-scale scientific facilities. To obtain superfluid helium cooling@2K, it is necessary to maintain an absolute pressure below 3.1 kPa on the heat sink of a 2 K cryogenic system. Bringing the saturated vapor up to atmospheric pressure, thus it requires compression with a pressure ratio exceeding 40. To fulfil the demand of large pressure ratio and producing refrigeration below 2 K, several methods were investigated, such as cold cycle and mixed cycle. Details of the operating principles and advantages of each cycle can be found in the reference (Lebrun and Tavian, 2015). Whatever cycle is used, cold compressor which is short for cryogenic centrifugal compressor must be used to pump flow from a few kPa up to a high pressure. This technology, has been first presented in the Tore Supra tokamak in France (1986) for a helium refrigerator with a capacity of 300 W@1.8K (Gravil et al., 1998). Then, the cryogenic system at CERN-LHC was comprised of a warm compressor (WC) and 4 cold compressors to achieve a capacity of 2.4 kW@1. 8 K. Recently, more and more large scale superfluid helium system, such as CMTF, XFEL, ESS and LCLS-II, is being built. And cold compressors system is chosen as the core component to construct the superfluid helium system (White et al., 2014; Bozhko et al., 2017; Wang et al., 2014; Wang et al., 2017).

It is clear that a better efficiency of the flow passage of the cold compressor will considerably affect the economical parameters of the cryogenic system. Nowadays, a design procedure through a deep understanding of the flow characteristics and the origins and effects of various losses can help designing a normal centrifugal compressor. However, considering the extremely low intake pressure and temperature of the cold compressor, it is almost impossible to observe the flow pattern inside the flow passages on the test rig. With the development of computer technology, numerical simulation technology has become an important and effective tool for studying the internal flow of turbomachinery in cryogenic field. For example, Sam has done 3D turbulent flow analysis of a cryogenic turbo expander for small scale air separation using ANSYS CFX (Sam et al., 2017). ZHANG has obtained the steady operating range of cold compressor, unsteady flow in the case of low mass flow or high pressure ratio by CFD (Zhang et al., 2015). Geng has discussed the influence of the length of the tip clearance between the impeller and shroud by using ANSYS CFX (Geng et al., 2018).

In the development process of the superfluid helium cryogenic system, a series of 3 cold compressors is designed and assembled at TIPC, CAS. In this paper, a three-dimensional geometry of the whole stage of the cold compressor is designed. Simulation, considering the real gas effect, is carried out to verify the performance using the commercial program code ANSYS CFX.

2. MAJOR DIMENSIONAL PARAMETERS OF COLD COMPRESSOR

The large cryogenic refrigeration system for Super-Liquid Helium is being developed in TIPC, CAS, centrifugal compressors are applied to compress pure gaseous helium from 3.3kPa@3. 2K to 45kPa with the mass flow rate of $30g \cdot s^{-1}$. As the pressure ratio up to 14, a series of three stages of cold compressor is adopted. The mechanical structure of the cold compressor is shown in Fig. 1. Based on fundamental estimation and calculation of compressors impeller and diffuser, the pressure ratios of those three-stage compressors are designed as 3.3, 2.5 and 1.8 respectively. Due to space limitations in this paper, only the parameters of the second stage cold compressor will be introduced and analyzed.

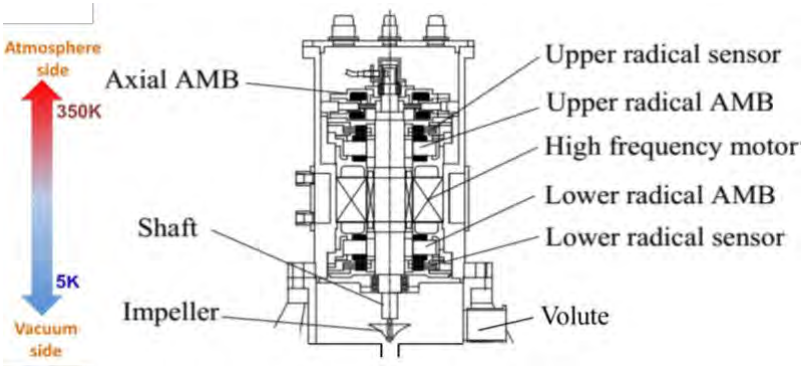

Figure 1: Mechanical structure of the helium cold compressor

The structure diagram of the impeller, diffuser and volute are designed one dimensional by our own programmed code. In order to obtain high efficiency, backward-skewed blades are used. Furthermore, the efficiency of using vane diffuser is higher than that of vaneless diffuser, but as a trade-off, finally a vaneless diffuser is adopted to get a wide operating range. And then based on its data, a three-dimensional model is created which is shown in Fig. 2. The details of its specified parameters are shown in Table 1.

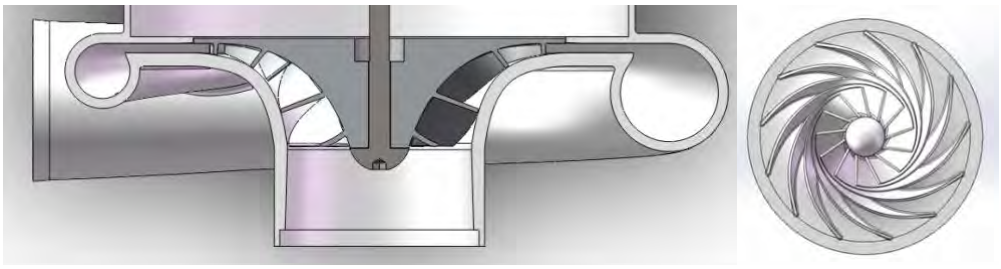

Figure 2: Model of the second stage

Table 1. Detailed geometrical specification of the stage

Item	Parameters	Item	Parameters
Fluid type	Helium	ZR	13
Rotating speed	50000 rpm	R_{1h}	7.3
T_{01}	6.9 K	R_{1t}	18 mm
P_{01}	11.5 kPa	R_2	39 mm
T_{08}	12 K	B_2	3 mm
P_{08}	32 kPa	T_{clr}	0.2 mm
M	30 g/s	R_4	65 mm
Diffuser type	Vaneless	Volute type	Asymmetric circular volute

3. CFD SIMULATION OF COLD COMPRESSOR

3.1 Grid Independence and Boundary Condition

As depicted in Fig. 2, a full-passage steady state model is chosen for the numerical calculation model due to the asymmetric circular volute. The fluid domain of all parts is then exported to ANSYS. While the grid of different group is meshed separately and it is given in Table 2 in details. The mesh generation software Turbo-grid is used to generate a mixed grid for the impeller, which is then imported to CFX to calculate the internal flow inside the impeller. The total mesh number of the full-passage model is approximately 3.7million which has considered sufficiently reliable to ensure mesh independence. The average y+ value is taken as 15 and a k-ε turbulence model is chosen to calculate the flow of cold helium. The integrated 3-D geometry and mesh of various parts are shown in Fig. 3.

In the CFX, the blades, hub and shroud are defined as fixed heat flux walls with the appropriate rotational velocity. The boundary condition at the inlet is set as the total pressure and total temperature with a no pre-whirl state and the boundary at the outlet is set at the mass flow rate accordingly.

Table 2 Mesh specifications for various parts

Domain	Number of elements	Method	Mesh type
Inlet	121580	Sweep	Unstructured hexahedral mesh
Impeller	2651880	ATM optimized	Only structured hexahedral mesh with H/J/C/L type topology
Diffuser	332210	Sweep	Unstructured hexahedral mesh
Volute	652427	Patch conforming method	Unstructured Tetrahedral mesh

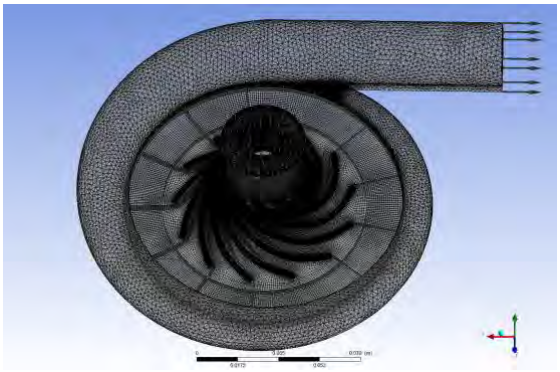

Figure 3: The mesh of the main domain

3.2 Equations of State Used in CFX

In this paper, the commercial code (ANSYS CFX), which has been proved adaptive in the domain of turbomachinery, is used to simulate the flow patterns of the flow passages. Considering the extremely low inlet pressure and temperature of each cold compressor and even some working point inside the impeller may get close to the two phase line. In this situation, merely taken helium as an ideal gas is not enough to get a relative accurate result, so that the effect of real gas should be considered to simulate the flow inside each stage of cold compressor. While Ansys CFX has provided two ways to bring in the real gas effect. One is by building an RGP table and another one is by applicating of several kinds of built-in cubic real gas equations, including the original form of the Redlich-Kwong equation, the Soave-Redlich-Kwong equation (Soave et al,1972) the Peng-Robinson equation(Peng et all, 1976) and the Aungier-Redlich-Kwong equation (Aungier et al, 1995). However, considering the rate of convergence and robustness, the built-in cubic real gas equation is suggested to be employed in the following simulation. In previous work (Zhang et al, 2015 and Geng et al, 2018), none of them has ever mentioned the differences of all these equations for helium property especially in cryogenic and low pressure field. So before using the above equations, the deviation of helium properties between each equation and the actual gas, including density, Cp (specific heat

capacity) and SC (speed of sound), which are all important data for compressor design, is compared in this paper.

3.3 The comparison of different equation

The cubic EOS (equation of state) is an improvement on the ideal gas model in the sense that they try to model the finite volume of the fluid molecules as well as the interactions between them. A general expression for cubic EOS is shown below:

$$p = \frac{RT}{v - b - c} - \frac{a(T)}{v^2 + dv + e} \quad \text{Eq.(1)}$$

The (a(T) ,b,c,d,e) are the coefficients of the EOS .When substituting the general equation $pv = ZRT$ into the above equation results in a cubic equation in terms of Z, the equation is given by:

$$Z^3 + AZ^2 + BZ + C = 0 \quad \text{Eq.(2)}$$

The coefficients (A, B, C) are expressed as:

$$A(T,p) = \frac{-RT - bp + cp + dp}{RT} \quad \text{Eq.(3)}$$

$$B(T,p) = \frac{-RTdp + a(T)p - bdp^2 + cdp^2 + ep^2}{R^2T^2} \quad \text{Eq.(4)}$$

$$C(T,p) = \frac{-RTep^2 - a(T)bp^2 + a(T)cp^2 - bep^3 + cep^3}{R^3T^3} \quad \text{Eq.(5)}$$

After deriving the general basic calculation formula, the coefficients of various states of equations are brought to solve the three most important physical parameters mentioned before. The table 3 shows the comparison of different coefficients of different EOS.

Table 3 Detailed coefficients of each EOS

EOS	a , k	b	c	d	e
RK(Redlich-Kwong)	$a(T) = \frac{0.42747R^2T_c^2}{P_c}\left(\frac{T}{T_c}\right)^{-0.5}$	$b = \frac{0.08664RT_c}{p_c}$	$c = 0$	$d = b$	$e = 0$
SRK(Soave-redlich-Kwong)	$a(T) = \frac{0.42747R^2T_c^2}{P_c}\left[1 + k\left(1 - \sqrt{\frac{T}{T_c}}\right)\right]^2$ $k = 0.48508 + 1.55171\omega - 0.15613\omega^2$	$b = \frac{0.08664RT_c}{p_c}$	$c = 0$	$d = b$	$e = 0$
PR(Peng-Robinson)	$a(T) = \frac{0.45724R^2T_c^2}{P_c}\left[1 + k\left(1 - \sqrt{\frac{T}{T_c}}\right)\right]^2$ $k = 0.37464 + 1.54226\omega - 0.26992\omega^2$	$b = \frac{0.07780RT_c}{p_c}$	$c = 0$	$d = 2b$	$e = -b^2$
ARK(Aungier-Redlich-Kwong)	$a(T) = \frac{0.42747R^2T_c^2}{P_c}\left(\frac{T}{T_c}\right)^{-k}$ $k = 0.4986 + 1.1735\omega - 0.4754\omega^2$	$b = \frac{0.08664RT_c}{p_c}$	$c = \frac{RT_c}{p_c + \frac{0.42747R^2T_c^2}{p_c v_c (v_c + b)}} + b - v_c$	$d = b$	$e = 0$

Then, the density is calculated by:

$$\rho = \frac{1}{v} \quad \text{Eq.(6)}$$

The specific heat capacity can be obtained from the enthalpy, the formulation is given by:

$$Cp = \left(\frac{\partial H}{\partial T}\right)_p \quad \text{Eq.(7)}$$

After incorporating this equation with the EOS, the specific heat capacities can be written as below:

$$Cp = Cp^0(T) + RT\left(\frac{\partial Z}{\partial T}\right)_p + R(Z-1) + T\frac{\log(h)}{\sqrt{d^2-4e}}\frac{d^2a}{dT^2} + \frac{hg}{\sqrt{d^2-4e}}\left(T\frac{da}{dT} - a\right) \quad \text{Eq.(8)}$$

Where the coefficients are given below:

$$Cp^0(T) = n_1 + n_2T + n_3T^2 + n_4T^3 + n_5T^4, \quad h = \frac{\sqrt{d^2-4e} + 2RTZ/p + d}{-\sqrt{d^2-4e} + 2RTZ/p + d}, \quad g = \frac{-4\sqrt{d^2-4e}Rp\left(T\left(\frac{\partial Z}{\partial p}\right)_T + Z\right)}{\left(2RTZ - p\left(\sqrt{d^2-4e} - d\right)\right)^2} \quad \text{Eq.(9)}$$

The speed of sound is calculated by:

$$SC = \sqrt{-\left(\frac{Cp}{Cv}\right)\frac{v^2}{\left(\frac{\partial v}{\partial p}\right)_T}} \quad \text{Eq.(10)}$$

3.4 The Result of Maximum of Different Equation

In order to compare the accuracy of the physical properties of each state equation, the data of helium physical property based on NIST database are introduced to estimate the results. According to the introduction of NIST database, the uncertainties of helium in density are 0.25% at pressures up to 10^9 Pa. The uncertainties in the speed of sound are 0.01% for the vapor phase and for the heat capacities are about 2%. So, we use the physical property value of the NIST database as the reference and then the property calculated by each EOS are summarized by comparing the relative deviation percentage from the NIST reference property.

The detailed results are shown in Fig. 4-6. In single figure, temperature range is from 3K to 25K and pressure range is from 750Pa to 24000Pa. The results show that the error of all cubic equation becomes larger when the state point is close to the two-phase region. Comparing the density results, we can find that all cubic state equations have relative large errors between 3K and 5K, and only the PR equation has the best error at this time. However, when the temperature is between 5k-25K, the error of all equations decreases with the increase of temperature and then the ARK equation has the smallest integrated error. For specific heat capacity and speed of sound, the ARK equation is more superior than other three equations. The maximum error in ARK equation is only occurs when the state point is close the phase transformation point. The value is 1.8% for specific heat capacity and -0.45% for speed of sound.

Based on the above analysis, the property parameters calculated by ARK equation have a good agreement for the real helium gas property. As a result, the ARK equation built-in ANSYS CFX is chosen to simulate the flow pattern inside the impeller and verify the performance of the design.

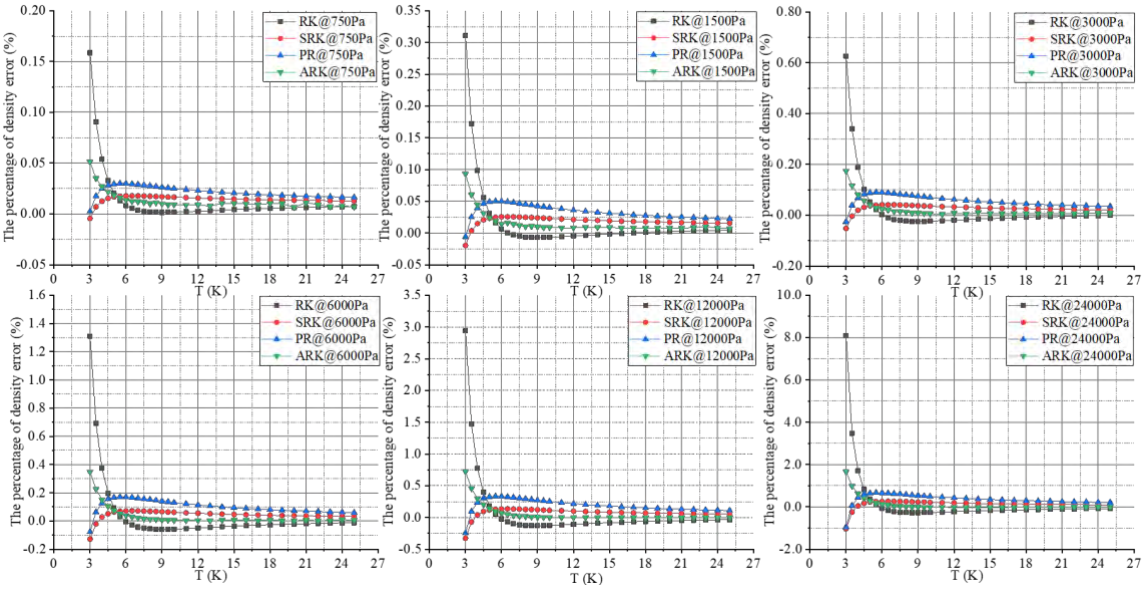

Figure 4: Error of density between RK, SRK, PR and ARK equation from 3K to 25K and 750Pa to 24000Pa

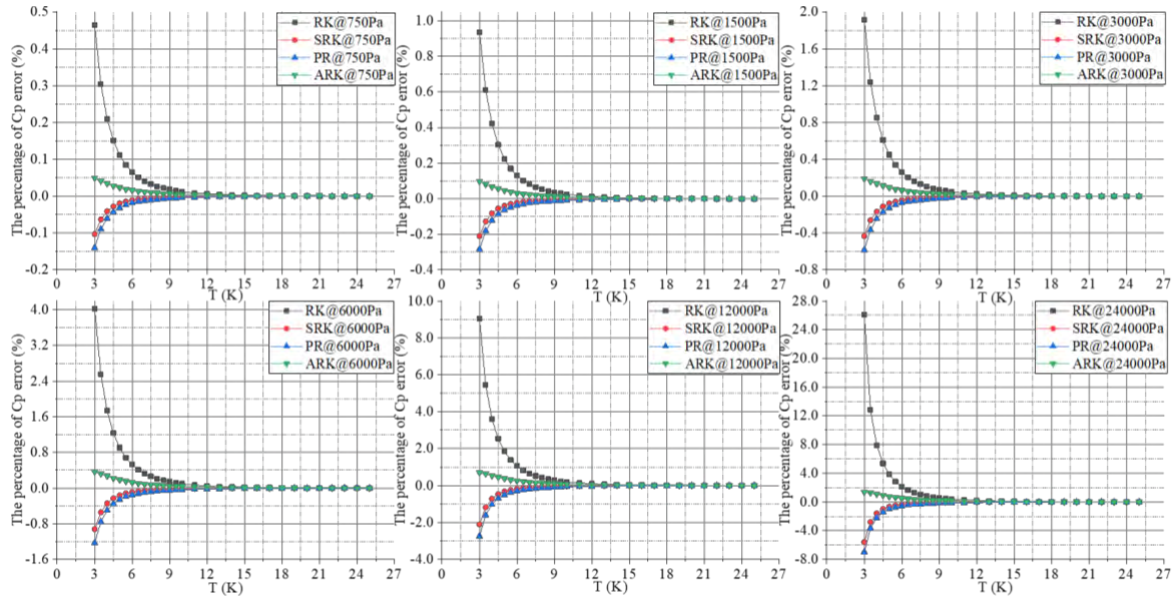

Figure 5: Error of specific heat capacity between RK, SRK, PR and ARK equation from 3K to 25K and 750Pa to 24000Pa

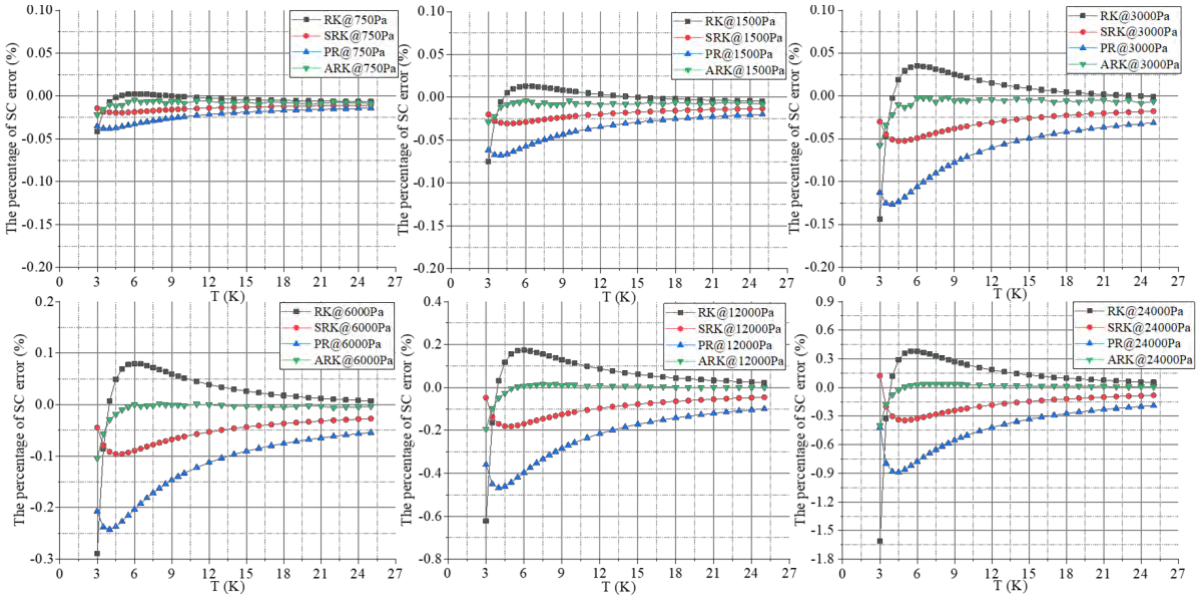

Figure 6: Error of speed of sound between RK, SRK, PR and ARK equation from 3K to 25K and 750Pa to 24000Pa

4. THE PERFORMANCE OF THE DESIGNED COLD COMPRESSOR

In Fig. 7, the simulation results such as the velocity magnitude and the static pressure on the meridional surface of the impeller are shown. As it can be seen from the Fig. 7, the pressure inside the impeller flow path changes smoothly that no large pressure fluctuation occurs alongside the extension of the impeller blade. It can be seen from the figure that the maximum Mach number appears merely near the region of the blade inlet tip in the impeller flow path and the maximum number does not exceed 0.8. The cross sections of streamlines at 10%, 50% and 90% span location of blade height are shown in Fig. 8 respectively. It can also be seen from the streamline diagram of the stage impeller that there is no obvious recirculation zone in the flow field in the impeller flow channel under design conditions. In summary, the overall flow field distribution of the impeller under the design conditions is reasonable.

Unlike piston or screw compressors, each cold compressor has its individual working filed. Leaving the permitted field across the surge line will cause separate flow inside the impeller resulting in a sudden pressure ratio drop or violent vibration of the rotor. So, a full performance map that ranging from near stall conditions to choked conditions which depended on variety rotating speed are shown

in Fig. 9. This figure illustrates that the pressure ratio varies as a function of rotating speed and mass flow. From the figure, we can conclude that the mass flow for stable working region at 50000rpm is from 13.5g/s to 36g/s. And the working point under the design condition has a 50% margin of the surge region at the same pressure ratio. To compare the 1-D design point and the 3-D simulated result, the 1-D design point which mentioned in table 1 is marked in Fig. 9. We can find that the actual 3-D simulation results have a higher-pressure ratio than the 1-D design result at the same mass flow rate. It directly indicate that the compressor we designed has a certain extra margin compared to the demand value, thus totally meet the system requirements.

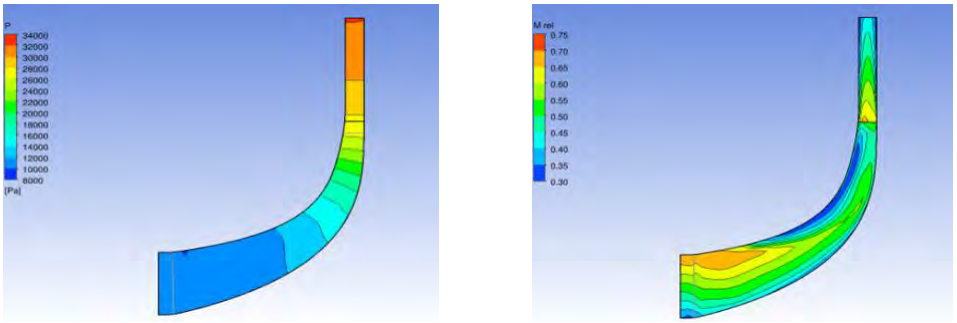

Figure 7: Contours of mean static pressure and Mach number of design point in the meridian plane

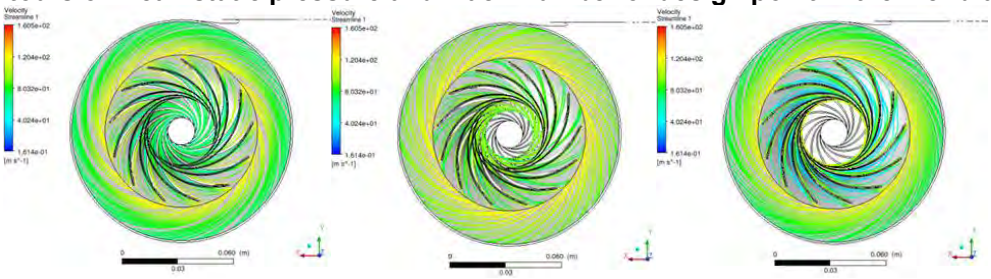

Figure 8: Streamlines of 10%, 50% and 90% blade height cross sections

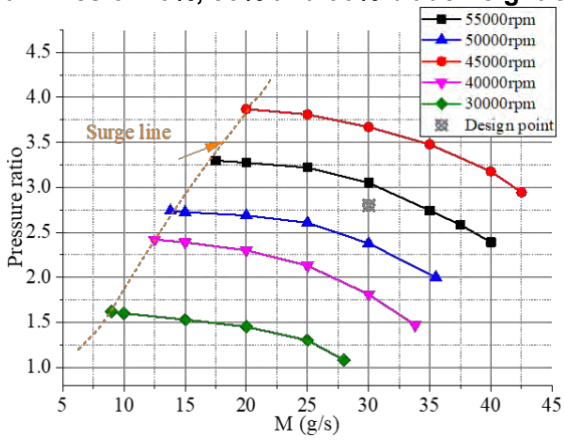

Figure 9: Performance map of the cold compressor

5. CONCLUSIONS

In this study, a single stage of cold compressor is generally designed and a CFD simulation is applicated to verify its performance. To consider the real gas effect and improve the accuracy of the simulation process, different EOS are compared with each other. As a result, the ARK state equation which maintains the minimum error deviation for ρ, Cp and SC is utilized to simulate the details of the flow field within the stage. Finally, the flow characteristics inside the impeller and diffuser together with the performance map are provided to prove that the stage could meet the design requirements.

ACKNOWLEDGEMENTS

This research is financially supported by the funding under the contracts (Major project of the Ministry of Finance: NO: Y5AF021ZD8).

NOMENCLATURE

p	pressure	R_{1h}	Impeller inlet hub radius(mm)
T	temperature	R_{1t}	Impeller inlet tip radius(mm)
R	molar gas constant (8.314472 J×mol^{-1}×K^{-1})	R_2	Impeller exit RMS radius(mm)
V	molar volume (m^3×mol^{-1})	B_2	Impeller exit width(mm)
Z	compressibility factor	T_{clr}	Impeller tip clearance(mm)
ρ	Density (kg×m^{-3})	R_4	Diffuser exit radius(mm)
T_{01}	Total temperature at inlet(K)	Cp	constant-pressure specific heat (J×mol^{-1}×K^{-1})
ω	acentric factor	Cv	constant-volume specific heat (J×mol^{-1}×K^{-1})
P_{01}	Total pressure at inlet(kPa)	Cp_0	Specific heat capacity for ideal gas (J×mol^{-1}×K^{-1})
T_{08}	Total temperature at outlet(K)	SC	Speed of sound(m×s^{-1})
P_{08}	Total pressure at outlet(kPa)	T_C	Critical temperature(5.1935 K)
M	Mass flow rate (g×s^{-1})	V_C	Critical specific volume(5.7524e^{-5} m^3×mol^{-1})
ZR	Number of blades	P_C	Critical pressure
a(t),b,c,d,e	Coefficients of EOS		
$n_{1\text{-}5}$	Coefficients of specific heat capacity for model of ideal gas		

REFERENCES

Lebrun, P., Tavian, L., 2015. Cooling with Superfluid Helium. Proceedings of the CAS-CERN Accelerator School: Superconductivity for Accelerators, CERN Yellow Report CERN-2014-005, 453-476

Gravil, B., Jager, B. ,1998. Experience with a Large Scale He II Refrigeration System at Tore Supra. Advances in Cryogenic Engineering, Boston, Springer, 571-579.

White, M., Martinez, A., Bossert, R., et al. 2014. Cryogenic System for the Cryomodule Test Facility at Fermilab. Advances in Cryogenic Engineering, USA, AIP 1573(1), 179-186.

Bozhko, Y., Escherich, K., Jensch, K., et al. 2017. Commissioning and First Cooldown of XFEL Linac. IOP Conference Series: Materials Science and Engineering, USA, IOP Publishing, 278,012100.

Wang, X.L., Weisend J., Koettig T., et al. 2014. ESS accelerator cryogenic plant. HVAC&R RES 20(3), 296-301

Wang, R., Hansen, B., White, M., et al. 2017. Operational Experience from LCLS-II Cryomodule Testing. IOP Conference Series: Materials Science and Engineering, USA, IOP Publishing, 278(1), 012187.

Sam, A.A., Ghosh, P., 2017. Flow field analysis of high-speed helium turboexpander for cryogenic refrigeration and liquefaction cycles. Cryogenics 82, 1-14.

Zhang, N., Zhang, P., Wu, J.H., 2015. Numerical Study of Unsteady Flow in Centrifugal Cold Compressor. 25th International Cryogenic Engineering Conference and the International Cryogenic Materials Conference in 2014, USA, IOP Publishing, 67, 153-157.

Geng, M.F., Song, Y.T., Cheng, A.Y., et al. 2018. Determination of critical parameters in the EAST subcooled helium system. FUSION ENG DES 131, 84-89.

Aungier, R.H., 1995. A Fast, Accurate real gas equation of state for fluid dynamic analysis applications. J. FLUID ENG. 117(2), 277-281.

Soave, G., 1972. Equilibrium constants from a modified Redlich-Kwong equation of state. CHEM ENG. SCI. 27(6), 1197-1203.

Peng, D.Y., Robinson, D.B., 1976. A new two-constant equation of state. IND. ENG. CHEM. RES 12(11-12), 3069–3078.

Manuscript ID: 1732
DOI: 10.18462/iir.icr.2019.1732

Advanced cryogenic insulation systems

James E. FESMIRE, Adam M. SWANGER

Cryogenics Test Laboratory
NASA Kennedy Space Center
KSC, Florida, 32899, USA,
james.e.fesmire@nasa.gov

ABSTRACT

New materials in recent decades have enabled advances in thermal insulation systems for storage and transfer of cryogens. To preserve the cold and achieve efficient cryogenic systems, a combination of materials, testing, and engineering is required. The total heat leak into any cryogenic assembly is comprised of three main parts: 1) heat leak through the insulation, 2) heat leak through the support structures, and 3) heat leak attributed to piping penetrations and feedthroughs (and their negative effects on the insulation). This "cold triangle" approach provides a basis for evaluating performance benefits of new materials and analyzing the cost effectiveness in overall system design. Provided are thermophysical data for aerogels, aerogel composites, novel multilayered composites, and glass bubbles for standard test conditions of 293 K and 78 K under conditions from high vacuum to ambient pressure. Examples of cryogenic storage tanks show the relative importance of both insulation and structural materials for achieving designs of highest energy efficiency.
Keywords: Insulation, Total Heat Leak, Thermal Analysis, Cryogenic Tanks, Cryogenic Piping, Aerogels, Multilayer Insulation, Energy Efficiency, Integrated System Design.

1. INTRODUCTION

Most systems that are designed to be operated at below-ambient temperatures require thermal insulation for both control and energy-efficiency concerns. For cryogenic systems the need is amplified, and the level of performance must be much higher to properly limit the heat transmission from the ambient environment. Relative to foam-type insulation materials in air, aerogels can reduce the heat flow by about one half (Fesmire and Coffman et al., 2012), and moderately evacuated ("soft vacuum") layered composites can reduce the heat by ten times (Fesmire, 2015). The latest evacuated bulk-fill systems (glass bubbles) can reduce the heat flow by almost 100 times (Scholtens et al., 2008) and highly evacuated multilayer insulation (MLI) systems can reduce the heat transmission by more than 1,000 times compared to foams (Fesmire and Johnson, 2018). With each higher level of thermal performance, the design approach, engineering, and manufacturing execution become progressively more challenging. A fitting combination of materials, testing, and engineering is key to meet the objectives of system control, safety, and performance. Most important, as discussed by Augustynowicz et al. (2000), the thermal performance must justify the cost.

The total heat leakage rate (Q_{total}), or "heat leak," into any cryogenic system is comprised of three main parts in a cold triangle of integration: 1) heat leak through the insulation, 2) heat leak through the support structures, and 3) heat leak attributed to piping penetrations. But real systems have additional heat leak due to practical limitations of fabrication and installation, as well as the negative effects of supports and piping. This additional heat leak for cryogenic systems is accounted for using the insulation quality factor (IQF). The "cold triangle" approach, with the use of the IQF, is readily applied to piping systems, piping connections, cryostats, storage tanks, etc. to determine the best insulation system for a particular case.

2. CALCULATIONS, TESTING, AND MATERIALS

Engineering analysis and thermal testing go hand-in-hand for determining the best insulation system for a given design situation. Conducting analysis and calculations according to standard methods is

essential for fair comparison of different materials and accurate applications of results as detailed by Fesmire (2015). Testing involves the measure of the total heat flow rate through an insulation system under relevant conditions. Relevant conditions typically include a large temperature difference (∆T) and a controlled, steady-state test environment or vacuum level.

2.1 Calculations of Heat Transmission

Calculations for cryogenic insulation systems follow the guidance given in ASTM C1774 *Standard Guide for Thermal Performance Testing of Cryogenic Insulation Systems*. The heat flow rate (Q) in $J \cdot s^{-1}$ or W, also known as "heat leak" is calculated as given in Eq. (1) and the effective thermal conductivity (k_e) in $mW \cdot m^{-1} \cdot K^{-1}$ is further calculated in Eq. (2):

$$Q = \dot{m} h_{fg} = k_e A_e \frac{\Delta T}{\Delta x} \quad \text{Eq. (1)}$$

$$k_e = \frac{Q}{A_e} \frac{\Delta x}{\Delta T} \quad \text{Eq. (2)}$$

Where ṁ is the mass flow rate in $g \cdot s^{-1}$, h_{fg} is the heat of vaporization in $J \cdot g^{-1}$, A_e is the effective area for heat transmission in m^2, ∆T is the temperature difference in K, and ∆x is the thickness in m. For flat plate test apparatuses, the A_e is constant through the thickness of the thermal insulation system. For cylindrical apparatuses or spherical geometries, the A_e is the log-mean area between the inner and outer diameters of the insulation test specimen. The Q is obtained directly by boiloff calorimetry, while other methods are indirect, measuring a combination of electrical power and temperatures.

This real-world heat flow rate includes all modes of heat transmission (radiation, solid conduction, gaseous conduction, and convection). While solid conduction is usually fixed by the system design, the test environment determines the relative amounts of the other components of the total flow of heat. The test environment is defined by the cold vacuum pressure (CVP) (that is, the vacuum level under steady-state operating conditions of the system) and the composition of the residual gas. From the total heat flow rate, the heat flux (q) in $W \cdot m^{-2}$ is calculated; which is the heat flow rate, under steady-state conditions, through an effective area (A_e) in m^2, in a direction perpendicular to the plane of the thermal insulation system as given in Eq. (3):

$$q = \frac{Q}{A_e} \quad \text{Eq. (3)}$$

2.2 Testing of Cryogenic Insulation Systems

Standard laboratory cryostats in both cylindrical (Cryostat-100) and flat-plate (Cryostat-500) geometries are used for testing of various insulation materials and systems (Fesmire et al., 2015). Both are steady-state liquid nitrogen boiloff calorimeters designed for absolute thermal performance measurements. Test conditions include a cold boundary temperature (CBT) of 78 K and a warm boundary temperature (WBT) of 293 K for a temperature difference (∆T) of approximately 215 K. The vacuum level in millitorr (μ), or CVP, is set via a residual flow of nitrogen (or other gas) with continuous pumping and an electronic control-loop to maintain the desired pressure.

Cryostat-100 has a vertical cylindrical cold mass assembly that is 1-m tall by 167-mm diameter, while the Cryostat-500 has a horizontal flat plate cold mass assembly of 204-mm diameter. For high vacuum tests (<0.1μ), each test specimen is heated and evacuated according to standard laboratory procedures. The test methodologies follow ASTM C1774, Annex A1 and Annex A3, respectively.

From the direct experimental test results for heat flux, different heat transmission values can be calculated. The point is to gauge the transmission of heat from a defined "hot surface" to a defined "cold surface" according to Fourier's Theory of Heat. Although there does not exist the convenience of intrinsic thermal properties of materials in the context of these complex systems, calculation of "thermal conductivity" values are useful for several reasons: 1) comparison of different systems tested under similar conditions; 2) comparison of systems with varying thickness; 3) analyzing temperature dependence and different boundary temperatures; and 4) modeling for specific engineered designs.

For this study, two standard definitions from ASTM C1774 are used. The *effective thermal conductivity* (k_e) is defined as the thermal conductivity value through the total thickness of the insulation test specimen (one material, homogeneous non-homogeneous, or a combination of materials) between specified boundary temperatures, and in a specified environment. The *system thermal conductivity* (k_s) is defined as the thermal conductivity value through the total thickness of the insulation test specimen and all ancillary elements such as packaging, supports, seams, joints, getter packages,

enclosures, etc.—in other words, k_s is always determined using the total distance between the hot and cold surfaces. The k_e or k_s, as applicable, and q are calculated for the standard ΔT of 215 K. Each test is for a given CVP environment of nitrogen gas as indicated. Physical characteristics include the as-tested thickness and density.

2.3 Insulation Materials Data

Data in terms of k_e for a variety of insulation materials and systems, tested under representative and similar conditions, are presented as a variation CVP in Fig. 1. Included are two MLI systems, one with

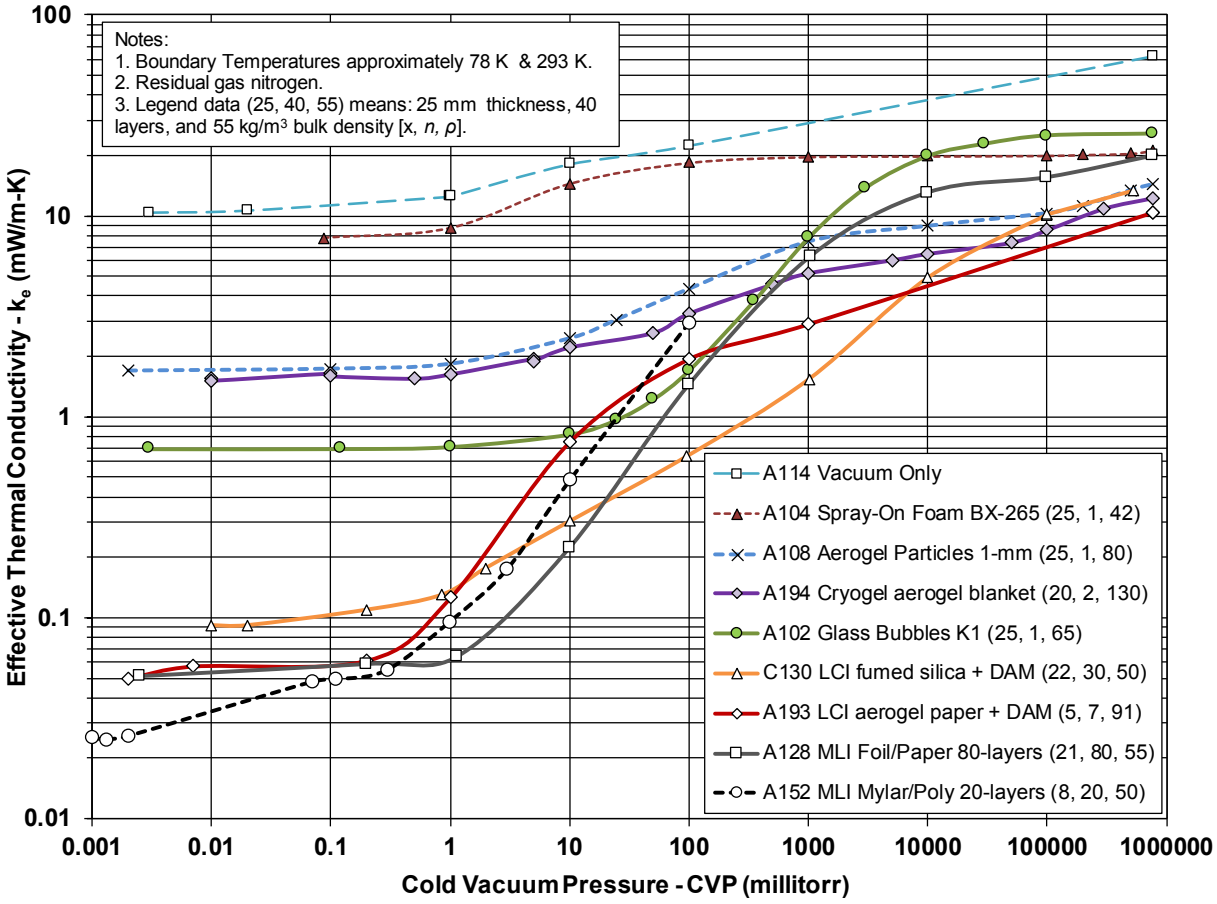

Figure 1: Cryostat test data for thermal insulation systems tested at 293 K / 78 K

Table 1. Select thermal conductivity data for cryogenic thermal insulation systems

Thermal Insulation System	Ref. No.	†Density	CVP	*k_e
		kg·m^{-3}	μ	mW/m-K
Glass Bubbles Type K1	A102	65	<0.1	0.70
			100	1.7
			760,000	26
Aerogel Particles (1-mm diameter)	A108	80	<0.1	1.7
			100	4.3
			760,000	14
LCI with fumed silica & Mylar	C130	50	<0.1	0.09
			100	0.64
			530,000	13.4
MLI 80-layers Foil and Paper	A128	55	<0.1	0.051
			100	1.5
			760,000	20
MLI 20-layers Mylar and Poly Net	A152	50	<0.1	0.026
			100	3.0
			760,000	18 (est.)

†As-tested *For boundary temperatures of 293 K and 78 K

80 layers of aluminum foil and micro-fiberglass paper and another with 20 layers of double-aluminized Mylar (DAM) and polyester netting (Fesmire and Johnson, 2018). Two different Layered Composite Insulation (LCI) systems are given: LCI with a fumed silica and DAM (Fesmire et al., 2008) and LCI with aerogel paper (0.7-mm) and DAM (Fesmire, 2018). Data for aerogel blanket material (Cryogel® by Aspen Aerogels) are presented (Fesmire et al., 2018). Two bulk-fill materials are given: aerogel particles (white 1-mm diameter) by Cabot and glass bubbles (K1) by 3M (Scholtens et al., 2008).
For general comparison, data for "vacuum only" and a polyisocyanurate foam (BX-265) by NCFI and are also given (Fesmire and Coffman et al. 2012). The boundary temperatures are 293 K (WBT) and 78 K (CBT) in all cases. The physical parameters of thickness, number of layers, and bulk density are also provided in the legend. Table 1 lists select data for the CVP points of high vacuum, moderate vacuum, and no vacuum.

2.4 Structural-Thermal Materials Data

Thermophysical data for a range of different structural-thermal materials used in cryogenic systems data are given in Table 2. Included are polyimide aerogel AeroZero®, Ultem®, Foamglas, Divinycell®, and Rohacell®. Also included are G10 composite, Teflon™, balsa wood, and polyiso spray foam for general reference (NIST; Flynn, 2005). These k_e data were produced using a Macroflash (Cup Cryostat), per ASTM C1774 Annex A4, for boundary temperatures of 78 K (CBT) and 293 K (WBT) and under a compressive load of 34 kPa. The structural-thermal figure-of-merit (F_{ST}) in $K \cdot m \cdot s \cdot g^{-1}$ is calculated via Eq. (4):

$$F_{ST} = \frac{\sigma}{\rho k_e} \text{ x } 10^6 \qquad \text{Eq. (4)}$$

Where ρ is the bulk density in $kg \cdot m^{-3}$, k_e is the effective thermal conductivity in $mW \cdot m^{-1} \cdot K^{-1}$ (with the prescribed CBT and WBT), and σ is the compressive strength in MPa (at ambient temperature).

Newer materials developed in the last decade include AeroFoam, AeroPlastic, and AeroFiber composites (Williams and Fesmire, 2016). These structural-thermal composites composed of hybrid combinations of aerogels, polyimides, and other engineering polymers further demonstrate the possibilities for tailoring systems to achieve specific combinations of light weight, low thermal conductivity, and high strength, along with excellent fire properties (Smith et al., 2009).

Table 2. Thermophysical data for structural-thermal materials used in cryogenic systems

Material	†σ	ρ	*k_e	F_{ST}
	MPa	$kg \cdot m^{-3}$	$mW \cdot m^{-1} \cdot K^{-1}$	$K \cdot m \cdot s \cdot g^{-1}$
G-10 (transverse direction)	448	1,939	467	495
Ultem® 2300 Glass Filled PEI	221	1500	212	695
Teflon™ PTFE	24.1	2,120	253	45
Rohacell® WF-300 PMI foam (14 kPa)	17.8	324	42.1	1,305
Balsa Wood (transverse direction)	7.0	166	45.9	919
AeroZero® polyimide aerogel	1.6	150	28.1	380
Foamglas® Cellular Glass Foam	0.8	118	32.3	210
Divinycell® H45 PVC Foam (14 kPa)	0.6	50	23.8	504
Spray Foam Polyiso BX-265 (14 kPa)	0.4	37	22.6	483

†At ambient temperature *Boundary temperatures 293 K / 78 K; compressive load 34 kPa or as noted.

3. ENGINEERED SYSTEMS ANALYSIS

Five examples of cryogenic systems, three tanks and two piping systems, are shown in Fig. 2. In each case, the optimum approach involves a different combination of materials; and for simplicity and comparison, uniform hot and cold surfaces are assumed. The CVP, ranging from high vacuum (<0.1μ), to normal vacuum (~1μ), to moderate vacuum (~10μ), to soft vacuum (~100μ), to no vacuum

(760,000μ), are also uniquely representative of actual working systems in each case. Demko et al. (2008) present a design tool for heat leak analysis of various geometries and insulation data.

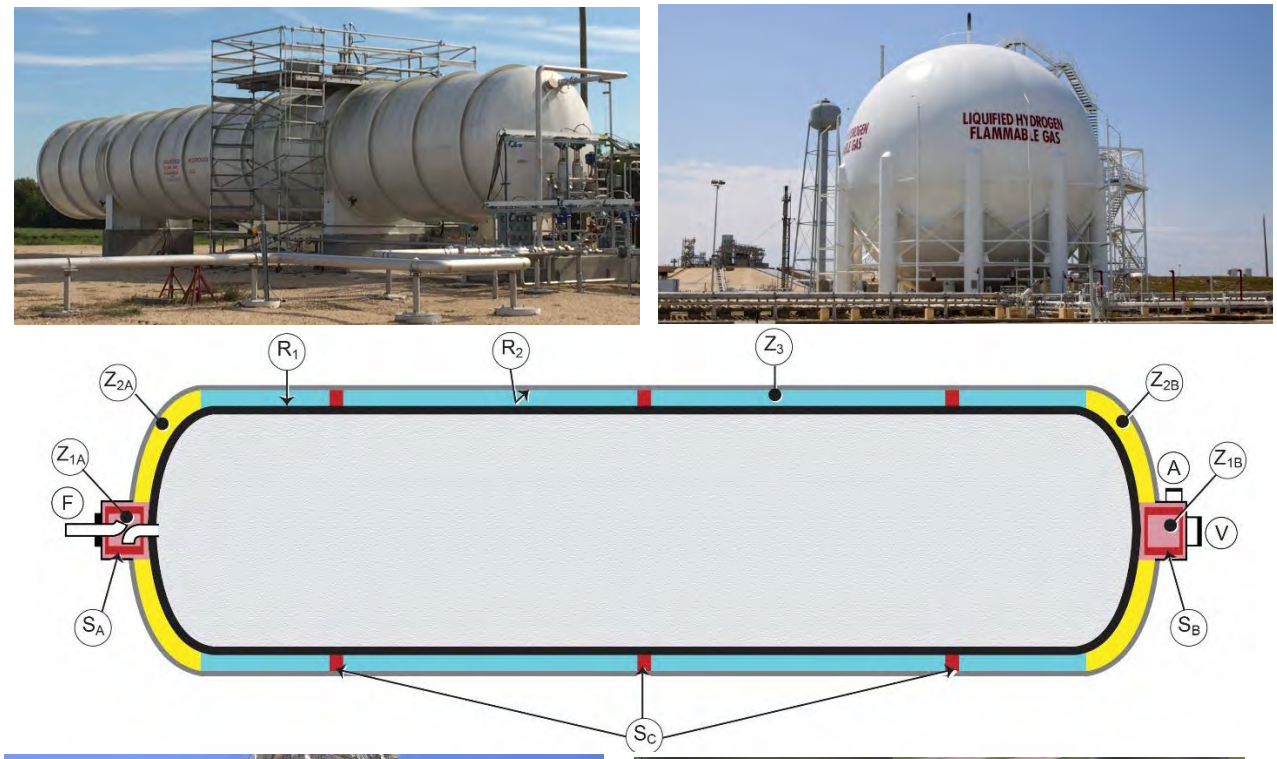



Figure 2: Cryogenic system examples: 1) cylindrical tank (u. left), 2) large spherical tank (u. right), 3) small composite tank (middle), 4) transfer piping (l. left), 5) piping field joint (l. right). **Images: NASA**

3.1 Comparative Analysis of Example Systems

The first example is a 125-m^3 horizontal cylindrical SST tank with a carbon steel outer jacket and a 200-mm annular space. This factory-built, medium-size tank includes an 80-layer MLI system for high vacuum, four G10 pad supports, several piping penetrations, and a 0.6-m diameter manway for internal access and multiple instrumentation feedthroughs. Boiloff testing using LN2 and liquid hydrogen (LH2) is described by Swanger (2018).

The second example is a 3,200 m^3 spherical 304 SST tank (30-mm thickness) with a carbon steel outer jacket (17-mm thickness) and a 1,200-mm annular space. This tank includes 40 vertical SST support rods connecting the inner vessel to the outer jacket, four piping penetrations on the bottom,

and a 0.5-m diameter manway for internal access. The specified boiloff rate is 0.075% per day (LH2) with the original perlite power insulation (Fesmire et al., 2008). In this example the insulation system is glass bubbles which provides an estimated 46% reduction in boiloff, compared to perlite, at moderate vacuum level of 10 millitorr based on field test data by Sass, 2010. An even larger LH2 storage sphere (4,700 m^3), using glass bubbles insulation, is being constructed at the Kennedy Space Center (KSC) for supplying the future space launch programs.

The third tank example is a 100-liter carbon composite tank in a 4:1 cylindrical geometry with a SST outer jacket and an annular space of 23-mm thickness. The LCI system is designed for soft vacuum of 100μ for low cost and to avoid vacuum maintenance. Three polyimide aerogel rings support the inner vessel and a single 12.7-mm diameter piping penetration are also included as depicted for this generalized storage tank concept (Adams et al., 2018).

In addition to the three tanks, two piping systems are also analyzed. Example four is a DN25x80-mm all SST vacuum-jacketed (VJ) pipe segment of 18.3-m length. The ends are thermally guarded with LN2 so that an absolute boiloff test is achieved. The insulation is 20 layers of MLI (aluminized Mylar and paper) with a CVP in the normal vacuum range of approximately 1μ. The cryogenic testing of this pipeline is described by Fesmire, Augustynowicz, and Nagy (2004).

Finally, example five is a DN250x300-mm, double-walled field joint connection (1-m overall length) between two VJ pipe segments. The ends, 425-mm length cones, are treated as the supports, while a straight middle portion is 150-mm length. The insulation system is a complete bulk-fill by aerogel particles (1-mm nominal diameter) of the sealed annular space, which is designed for non-vacuum. The space is optionally backfilled with CO2 for achieving enhanced performance at a cryo-pumped soft vacuum (~100 μ) under cold operating conditions (Johnson et al., 2012).

3.2 The Insulation Quality Factor in System Design

The insulation materials and data given here represent preferred solutions in the relative sense among a vast landscape of different applications. There are many more details and choices to be made for an optimum solution in the final design, but these examples give first order approximations and the interplay among materials, design, installation, manufacturing, and operation.

There is another potentially crucial part of the Q_{total} for a cryogenic system: the additional heat leak due to the insulation quality factor (IQF). The IQF is a first order means of capturing the combined degradation of the insulation's thermal performance due to practical limitations of its installation, and also the negative effects of supports and piping. A high fidelity IQF can only be determined experimentally, but estimates can be obtained via a combination of historical information and analytical methods. As warranted by the design objectives and fidelity required, an individual IQF can be applied to different zones of insulation area, to each support structure, and to each penetration.

In the basic cases presented here, a single IQF is applied for the entire cryogenic assembly as a separate heat leak element of Q_{total} as given in Eq. (5).

$$Q_{total} = Q_i + Q_s + Q_p + Q_{IQF} \quad [\mathrm{W}] \qquad \text{Eq. (5)}$$

Where Q_i is the insulation heat leak, Q_s is the heat leak attributed to the supports, and Q_p is the heat leak due to the piping penetrations, and Q_{IQF} is the heat leak of the insulation quality factor.

Heat leak budgets for the five example systems are summarized in Table 3. Values for the q and k_s are also calculated for each case. In this table, the A_e is the log-mean area between inner and outer shells and the ΔT is equal to 215 K. These cases represent idealized solutions for each situation.

The best thermal insulation system under idealized laboratory conditions is obviously not always the best one to use. In the field joint example, the majority of the heat leak is fixed by solid conduction (75% of Q_{total}) and the annular space is mostly inaccessible for wrapping with MLI. Added to the geometric constraints are the difficulties in field fabrication, for which achieving a long-term high-vacuum in the annular space is not a reasonable expectation. With the option of adding a CO2 backfill to achieve an effect of cryopumping to a soft vacuum, the Q_{total} drops to 30.6 W and the k_s to 8.1 mW/m-K which would be comparable to a high vacuum MLI system in this case.

The Q_{IQF} ranges from zero to 34% of the total. In many real cases, the Q_{IQF} can be as high as or higher than the Q_i. For example, Johnson et al. (2014) show that a small single penetration (12-mm diameter) though an MLI blanket results in an Q_{IQF} that is from one to five times the Q_i. Even in bulk fill systems, the two instances of zero IQF in the two cases given, there can be a problem. Two identical design 3,200-m^3 VJ LH2 storage tanks were built at KSC in 1965, and one ended up with triple the heat leak of the other (3.8 versus 1.1 m^3 per day boiloff losses). Krenn (2012) shows that this problem was eventually determined to be due to a large void within the perlite annular space filling. Therefore, the Q_{IQF} is not just a deviation from the ideal or a degradation of the insulation

material that can be mitigated, but a substantial heat leak potential that must be addressed up front in the design process.

Table 3. Total heat flow rate analysis for different examples of cryogenic systems

Cryogenic System Description	Thermal Insulation System	CVP	Dimensions		Q_i	Q_s	Q_p	Q_{IQF}	Q_{total}	q	k_s
			t	*A_e							
		μ	mm	m^2	%	%	%	%	W		
1) Medium tank, VJ, factory built (125-m^3)	MLI (80 layers) for high vacuum	<0.1	250	229	33.7	17	43.3	6.3	300	1.3	1.5
2) Large tank, VJ, site-built (3,200-m^3)	Bulk-fill glass bubbles, moderate vac	10	1200	1194	74.1	12.9	12.9	0.0	240	0.2	1.1
3) Small composite tank, VJ, conceptual (0.1-m^3)	LCI for soft vacuum	100	23	1.6	68.9	21	10.4	?	14.4	9.0	1.0
4) Piping System, DN25x80-mm, VJ, with 2 bayonet joints, factory built (18.3-m)	MLI (20 layers) for normal vacuum	1	26	3.2	12.0	15	38.3	34.4	20.9	6.5	0.8
5) Piping Field Joint, DN250x300-mm, double-wall, field fabricated (1-m)	Bulk-fill aerogel for non-vacuum	n/a	50	0.88	54.1	27	19	0.0	49.0	55.7	12.9

The elements of heat transmission through an insulation system are highly interdependent, showing that the analysis of the total heat leak is an iterative process. The right design approach depends on the shape, the size, the operational duty cycle, and, of course, the economic objectives.

4. CONCLUSION

A practical methodology for designing cryogenic thermal insulation systems is based on a “cold triangle” approach of insulation, supports, and piping as well as the insulation quality factor (IQF). The total heat leak of the end product is what matters, but to minimize this heat leak in the most cost-effective way, the calculations, testing, and materials data must be covered and the thermal performance understood as a summation of its parts. The approach also provides a basis for evaluating performance benefits of new materials and analyzing the cost effectiveness in overall system design. Provided are thermophysical data for aerogels, aerogel composites, multilayer insulation, novel layered composites, and glass bubbles for standard test conditions of 293 K and 78 K under conditions from high vacuum to ambient pressure. A wide range of reference materials data are also included for direct analytical comparison. Basic data for structural-thermal materials, including ranking of their structural-thermal figure of merit (F_{ST}) are also presented. Examples of different cryogenic storage tanks and piping systems show the relative importance of both insulation and structural materials for achieving designs of highest energy efficiency.

NOMENCLATURE

Q	heat flow rate or heat leak (W)	ρ	bulk density ($kg \cdot m^{-3}$)
k_e	effective thermal cond. ($mW \cdot m^{-1} \cdot K^{-1}$)	σ	compressive strength (MPa)
k_s	system thermal cond. ($mW \cdot m^{-1} \cdot K^{-1}$)	μ	vacuum pressure (millitorr)
$\dot{m}$	mass flow rate ($g \cdot s^{-1}$)	Q_{total}	heat leak, total system (W)
h_{fg}	heat of vaporization ($J \cdot g^{-1}$)	Q_i	heat leak, insulation (W)
A_e	effective area for heat trans (m^2)	Q_s	heat leak, supports (W)
q	heat flux ($W \cdot m^{-2}$)	Q_p	heat leak, piping connections (W)
ΔT	temperature difference (K)	Q_{IQF}	heat leak, IQF (W)
Δx	thickness (m)	F_{ST}	struct-thermal fig-of-merit ($K \cdot m \cdot s \cdot g^{-1}$)

REFERENCES

Fesmire J., Coffman B., Meneghelli B., Heckle K., 2012. Spray-on foam insulations for launch vehicle cryogenic tanks. Cryogenics 52, 251-261.

Fesmire J., 2015. Layered composite thermal insulation system for non-vacuum cryogenic applications. Cryogenics 74, 154-165.

Scholtens B., Fesmire J., Sass J., Augustynowicz S., 2008. Cryogenic thermal performance testing of bulk-fill & aerogel insulation materials. Adv in Cryo. Eng, 53A, AIP, 152-159.

Fesmire J., Johnson W., 2018. Cylindrical cryogenic calorimeter testing of six types of multilayer insulation systems. Cryogenics 89, 58-75.

Augustynowicz, S., Fesmire, J., Wikstrom, J., 2000. Cryogenic Insulation Systems. 20th International Congress of Refrigeration, no. 2000-1147, IIR, Paris.

Fesmire J., 2015. Standardization in cryogenic insulation systems testing and performance data. Physics Procedia 67, 1089-1097.

Fesmire J., Johnson W., Meneghelli B., Coffman B., 2015. Cylindrical boiloff calorimeters for testing of thermal insulations. Adv. in Cryo. Eng., IOP 012056.

Fesmire J., Johnson W., Swanger A., Kelly A., Meneghelli B., 2015. Flat plate boiloff calorimeters for testing of thermal insulation systems. Adv. in Cryo. Eng., IOP 012057.

Fesmire, J., Augustynowicz, S., Scholtens, B., 2008. Robust multilayer insulation for cryogenic systems. Adv. in Cryo. Eng. 53B, American Institute of Physics, 1359-1366.

Fesmire J., 2018. Aerogel-based insulation materials for cryogenic applications. International Cryogenic Engineering Conference, Oxford University, United Kingdom.

Fesmire J., Ancipink J., Swanger A., White S., Yarbrough D., 2017. Thermal cond of aerogel blanket insulation under cryo-vacuum in different gas environments. Adv. Cryo. Eng. IOP 278 012198.

National Institute of Standards (NIST), Applied Chemicals and Materials Division, Properties of solid materials from cryogenic to room temperatures, Boulder Colorado USA.

Flynn T., 2005. Cryogenic Engineering. Marcel Dekker, 467 and 530.

Williams, M., Fesmire, J., 2016. Aerogel hybrid composite materials: designs and testing for multifunctional applications. NASA Tech Briefs Webinar.

Smith, T., Williams, M., Fesmire, J., Sass, J., and Weiser, E., 2009. Fire and engineering properties of polyimide-aerogel hybrid foam composites. Fire and Polymers V, 10, ACS, 148–173.

Demko, J., Fesmire, J., and Augustynowicz, S., 2008. Design tool for cryogenic thermal insulation systems. Advances in Cryogenic Engineering 53A, AIP, 145-151.

Swanger, A., 2018. Large scale cryogenic storage with active refrigeration. Master's Thesis, University of Central Florida.

Fesmire, J., Sass, J., Nagy, Z., Sojourner, S., Morris, D., Augustynowicz, S., 2008. Cost-efficient storage of cryogens. Advances in Cryogenic Engineering 53B, AIP, 1383-1391.

Sass, J., et al., 2008. Thermal performance comparison of glass microsphere and perlite insulation systems for liquid hydrogen storage tanks. Advances in Cryo Eng. 53B, AIP, 1375-1382.

Adams, J, et al., 2018. Integrated Insulation System for Cryogenic Automotive Tanks (iCAT). United States: N. p., Web doi:10.2172/1457536.

Fesmire, J., Augustynowicz, S., Nagy, Z., 2004. Thermal performance testing of cryogenic piping systems. 21st International Congress of Refrigeration, IIR, Paris.

Johnson, W., Fesmire, J., Meneghelli, B., 2012. Cryopumping field joint can testing. Advances in Cryogenic Engineering, AIP Conference Proceedings 1434, 15-27.

Johnson, W., Kelly, A., Fesmire, J., 2014. Thermal degradation of multilayer insulation due to the presence of penetrations. Adv in Cryo Eng, AIP Conference Proceedings 1573, 463-470.

Krenn, A., 2012. Diagnosis of a poorly performing liquid hydrogen bulk storage sphere," Advances in Cryogenic Engineering, AIP Conference Proceedings 1434, 376.

Manuscript ID: 1890
DOI: 10.18462/iir.icr.2019.1890

Experimental investigation of the cascade type non-flammable mixed refrigerant Joule-Thomson refrigerator for 100K cooling temperature

Cheonkyu LEE[(a)], Sangkwon JEONG[(b)], Hyo Jae JEONG[(a)], Seon-Chang KIM[(a)], Dong An CHA[(a)]

[(a)] Thermal & Fluid System R&D Group, Korea Institute of Industrial Technology
Cheonan, 31056, Republic of Korea, cklee@kitech.re.kr, hyojae.jeong@kitech.re.kr, kimsc@kitech.re.kr, cdongan@kitech.re.kr

[(b)] Department of Mechanical Engineering, Korea Advanced Institute of Science and Technology
Daejeon, 34141, Republic of Korea, skjeong@kaist.ac.kr

ABSTRACT

This paper describes the cascade type non-flammable mixed refrigerant (MR) Joule Thomson (JT) refrigerator for the cooling temperature of 100 K. The working fluid for non-flammable MR JT refrigerator is a mixture of Nitrogen, Argon, Tetrafluoromethane (R14, CF_4) and Octafluoropropane (R218, C_3F_8). Experimental work is performed to confirm the design result of the cascade MR JT refrigerator. The lowest temperature is approximately 98.5 K and the maximum cooling capacity records 15 J/g at the 103 K, which is the normalized value with respect to the mass flow rate of the working fluid. The pressure drop at the low pressure side is a critical role to reduce the refrigeration efficiency.

Keywords: Joule-Thomson, non-flammable, mixed refrigerant, COP, high efficiency

1. INTRODUCTION

Nowadays, low temperature cooling technology, namely cryogenic engineering, draws a lot of attention from the industrial area such as High Temperature Superconductor (HTS) application, Liquefied Natural gas (LNG) industries or bio preservation etc. Generally, cryogenic environment stands for the temperature below 123 K or -150 °C (Barron, 1985). Commonly, the Coefficient of Performance (COP) of refrigerator is mainly applied to describe the refrigeration efficiency, as shown in equation (1) (Cengel and Boles, 2006).

$$\mathrm{COP} = \frac{Q_L}{W_{\mathrm{in}}} \qquad \text{Eq (1)}$$

COP, defined as the ratio of the heat absorbed (Q_L) to the required work (W_{in}), has been widely used to express the efficiency of refrigerator. The required work usually means the compression work at room temperature, and the heat, Q_L, is absorbed at low temperature.

One of the main application area for large cryogenic refrigeration technology is HTS power cable cooling (Chakravarthy, 2011). While the complexity of metropolitan city is drastically increasing by concentrating of population, the normal conducting cable cannot transmit the electric demand of urban area (Yang et al, 2013). It is because, the increasing of normal conductor in the urban area is limited due to the high cost and narrow site (Yang et al, 2013).
According to this circumstance, HTS power cables require a safe and reliable cooling scheme. Also, this superconducting system this system should maintain a cooling temperature of 70 K or less (Yang et al, 2013). Previous research mentioned the multi-stage MR J-T refrigerator to achieve the 64 K cooling temperature and high reliability (Lee et al, 2014, Lee et al, 2015). Aforementioned research requires the precooling stage which target temperature is 100 K. Thus, our research group designed

the non-flammable cascade type MR JT refrigerator in the past research (Lee et al, 2017). The design result shows the maximum COP of cascade type non-flammable MR JT refrigerator is 0.216 without any freezing of working fluid itself. Thus, experimental study is conducted to verify the designed cascade type MR JT refrigerator in this research paper.

2. DESIGN RESULT AND EXPERIMENTAL APPARATUS

2.1. Design results from previous research

The main challenge of the non-flammable MR is the freezing of the working fluid itself. Lee et al verified the freezing limitation of non-flammable MR which constitutes Ar, R14 and R218 (Lee et al., 2016). Certain composition of Ar, R14 and R218 mixture showed dramatic freezing temperature depression even below 77 K. According to this result, non-flammable cascade type MR JT refrigerator was designed as 0.216 with the lowest temperature of 97.6 K (Lee et al, 2017). The schematics and thermodynamic state of each points are shown in Figure 1 and Table 1. As mentioned before, this study is conducted to verify the design results of a cascade type non-flammable MR JT refrigerator. This chapter explains the detail of experimental apparatus.
Since the design result has a considerably larger flow rate (20 g/s), the normalized cooling capacities are considered in the experiment, which can be calculated the Eq. (2).

$$\dot{q}_n = \frac{\dot{Q}_L}{\dot{m}_{\text{in}}} \qquad \text{Eq (2)}$$

The required normalized cooling capacity is approximately 17 J/g according to the design result.

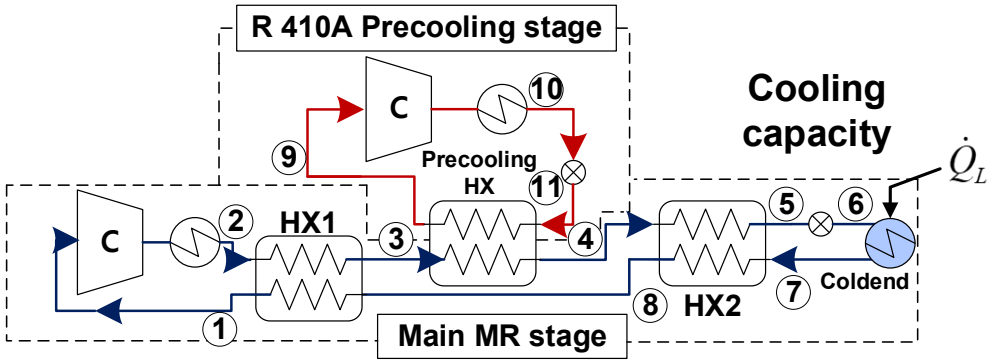

Figure 1. Schematics of cascade type non-flammable MR JT refrigerator

Table 1. Thermodynamic states of each design points

Stream	Temperature	Pressure	Vapor fraction	Refrigerant
	K	kPa	(kg/kg)	
1	297	220	1	
2	300	1400	1	
3	253.9	1400	0.974	
4	247.8	1400	0.921	N_2/Ar/R14/R218
5	108.4	1400	0	0.2/0.3/0.3/0.2
6	97.6	220	0.033	
7	105.2	220	0.267	
8	240	220	1	
9	250.9	287	1	
10	300	1750	0	R410A
11	244.8	287	0.346	

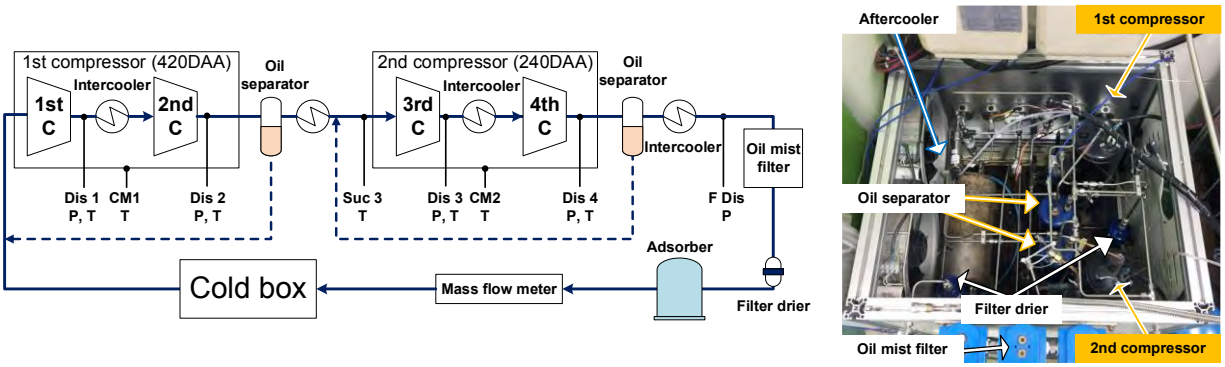

Figure 2. Schematics and photograph of the compressor system

2.2. Experimental apparatus

2.2.1. Compressor system

The compressor system is selected from the previous research (Lee et al, 2014). This compression system is developed by in house fabrication with a series connection by two kinds of commercial 2 stage compressor. To achieve the high purity of working fluid, numerous oil separation mechanism is utilized in this system. Figure 2 shows the schematics of compressor system and photograph of the system.

2.2.2. Cold box

To verify the designed MR JT refrigerator, refrigerator section is utilized as a lab scale. The cold box includes 3 heat exchangers, the evaporator (cold-end), the expansion part (JT valve) and the stirling cryocooler instead of the precooling stage. Figure 3 depicts 3D schematics and the developed cold box system with the JT valve as an expansion part. To control the opening of the orifice, the modified valve stem is installed between the top flange and valve head. The entire cold box covered with multi-layer insulation (MLI), which prevents the radiation heat transfer from the environment to the experimental apparatus.

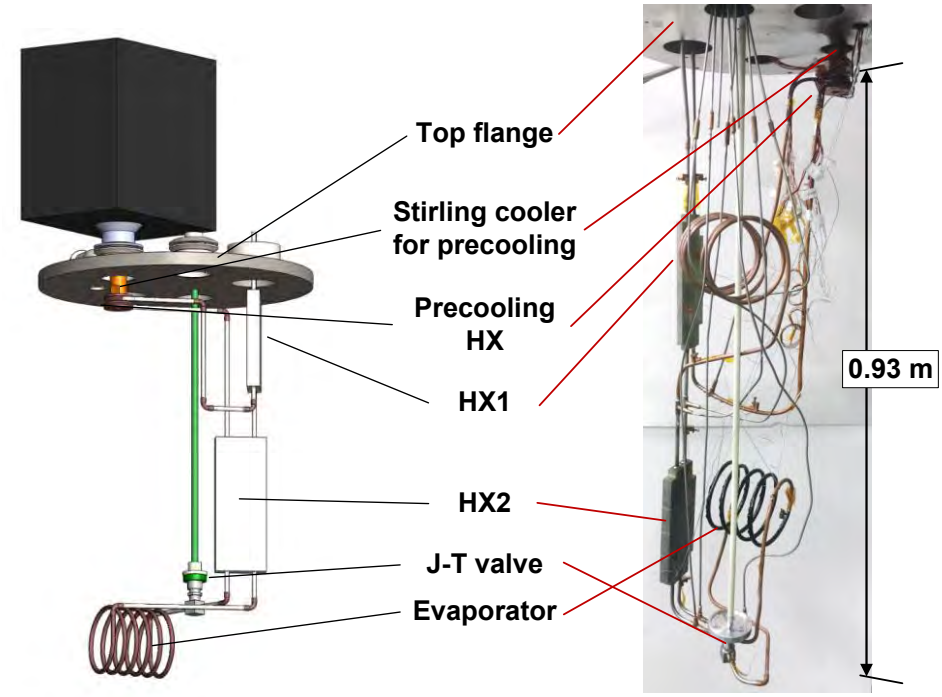

Figure 3. 3D schematics and photograph of cold box part of the MR JT refrigerator

The diffusion bonded printed circuit heat exchangers (PCHEs) are utilized for the heat exchanger 1 (HX1) and heat exchanger 2 (HX2). The single channel has a square type cross section with the 300 μm width. Each plate (layer) has 10 channels in the form of snake shape (Baek et al, 2014). The dimension of the single layer has the height of 210 mm and the width of 77 mm. HX1 has 20-layer (10 layers for hot side and 10 layers for cold side) to utilize the gaseous phase heat transfer, and HX2 has 30-layer (15 layers for hot side and 15 layers for cold side) to cover the two-phase heat transfer. The entire layers are fabricated by using a diffusion bonding process.

A Stirling cooler (Sunpower Inc, Cryotel CUBE) employed precooling stage of cascade type MR JT refrigerator. A machined copper block surrounded with a copper tube is attached to model the precooling heat exchanger. Entire flow path of the cold box mainly applied with 1/4'' stainless steel tube.The exception is only in the evaporator, which is fabricated with a coiled 6.4 mm (1/4 inch) copper tube and the manganin heater is covered with Stycast 2850FT epoxy to examine the cooling capacity.

The whole cold box system is thermally insulated by a vacuum chamber and multi-layer insulation to prevent heat ingress from the environment. The cold box system is maintained at a vacuum condition of approximately 0.13 Pa (10^{-3} torr). 10-layers of MLI (RUAG GmbH, Coolcat 2NW) are applied to cover the entire cold box system.

In the verification experiment, JT expansion part is constructed as a simple metal bellows valve (Swagelok, SS-4-HS). The opening of the JT valve is controlled on the top of the cold box with the extended valve stem made with G-10 tube. The gap between top flange and extended valve stem is sealed with a vacuum fitting (Ultra-Torr, 3/8 inch, Swagelok).

8 temperature sensors and 8 pressure transducers were installed to measure the temperature and pressure of each location, as mentioned in **오류! 참조 원본을 찾을 수 없습니다.** (Main MR stage). Temperature of each points are measured by Silicon diode temperature sensors (Lakeshore Inc, DT-670-SD) and FP 2000 pressure transducers (Honeywell Inc) are selected to get the pressure data. A Coriolis mass flow meter (Bronkhorst, CORI-FLOW M55) is utilized at the discharge of compression system to get the mass flow rate of the MR JT refrigerator. The entire data are collected by a Data acquisition system (National Instruments, SCXI-1000, SCXI-1125, SCXI-1320 and SCXI-1328) and a desktop computer.

2.2.3. Refrigerant charging

Target MR should be carefully blended from the pure components to achieve accurate operating condition of cascade type MR JT refrigerator. The pressure ratio method is performed in the entire system unit. At first, the charging pressure of the compressor is carefully selected according to the desired operating condition (1100 kPa in this research by trial and error). Firstly, the high boiling component (R218) is injected in the compressor system. The pressure ratio of the constituent is set as the molar composition with respect to the charging pressure (P_{R218} = 220kPa). Sequentially, other components (R14, Ar and N2) are carefully charged in the compressor in the same manner. Cold box is simply evacuated with the vacuum pump before connect the compressor system. The partial pressures and the stacked charging pressures are described in Table 2 for each components. This molar composition of the working fluid is confirmed by thermal conductivity detection type gas chromatography (Agilent Technologies, Model 7890B).

Table 2. Charging pressures and partial pressures of each components

Component	Mole fraction [-]	Partial pressure [kPa]	Charging pressure [kPa]	Actual composition by gas chromatography [-]
R218	0.2	220	220	0.202 ±0.01
R14	0.3	330	550	0.296 ±0.01
Ar	0.3	330	880	0.298 ±0.01
N_2	0.2	220	1100	0.204 ±0.01
Total	1	1100	1100	-

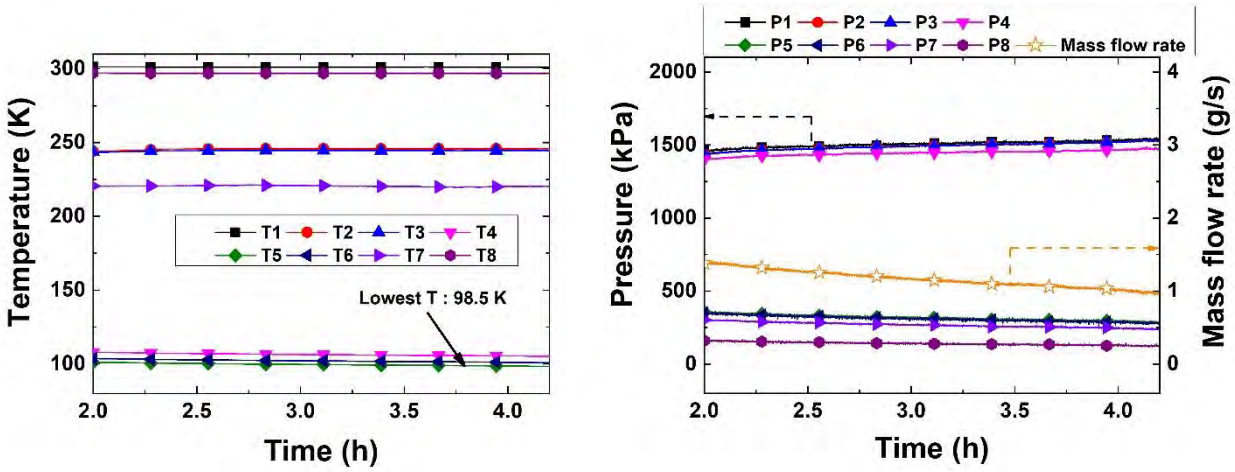

(a) (b)

Figure 4. Steady state experimental results (a) temperature profile and (b) pressure and mass flow rate

3. EXPERIMENTAL RESULTS AND DISCUSSION

3.1. No-load condition

The detailed steady state results are shown in Figure 4 (a) and (b). Figure 4 (a) illustrates the temperature profile of the cold box and Figure 4 (b) represents the pressure and mass flow rate profile of the experimental results. Unfortunately, there is a slight decreasing tendency of the mass flow rate. This is because the concentration of the moisture in the pure refrigerant (R218) is a certain value (higher than 213 K dew point), thus the small amount of moisture is stacked constantly at the lowest condition. At the no-load condition, cascade type MR JT refrigerator reaches the lowest temperature of 98.5 K, which is slightly higher than the design temperature. This higher cold-end temperature is by the considerable frictional pressure drop at the low pressure side. Also, the compressor experiences the compression ratio of 22 at the average mass flow rate of 1.5 g/s due to frictional pressure drop (1550 kPa / 70 kPa).

3.2. Cooling capacity measurement

3.2.1. Experimental result of heating at the evaporator

Figure 5 (a) and (b) present the temperature, pressure and mass flow rate distribution when heat is applied to the evaporator. The temperature after the evaporator (T6) is maintained near 103.4 K in the heat of less than 15 J/g, but it could not maintain the cooling temperature when the heat of

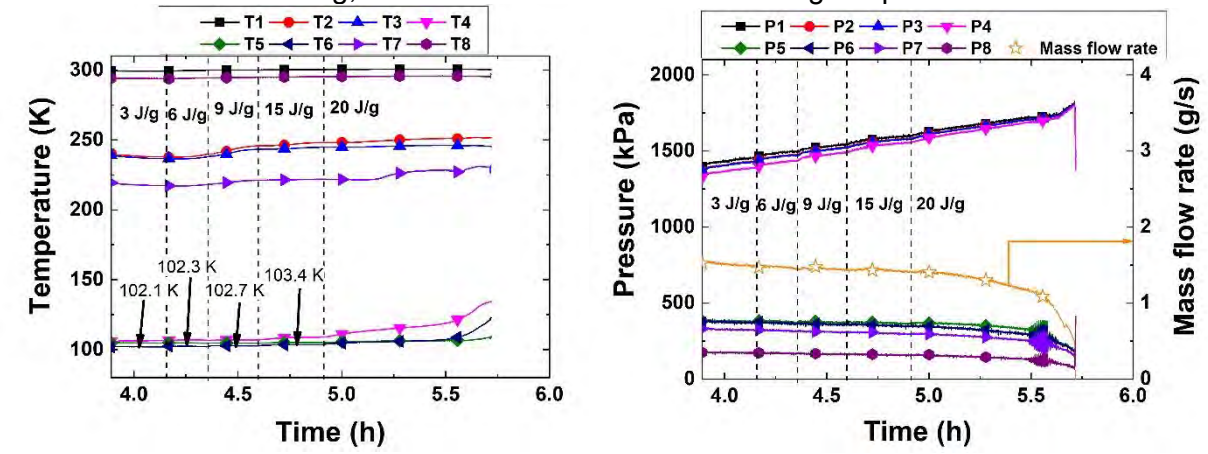

(a) (b)

Figure 5. Experimental result of cooling capacity (a) temperature profile and (b) pressure and mass flow rate

20 J/g is applied at the evaporator. Since the mass flow rate of the working fluid decreases sharply, it can be seen that the operating conditions are completely out. Thus, the cooling capacity of this cascade type MR JT refrigerator is approximately 15J/g.

3.2.2. Discussion of the cooling capacity with pressure drop

Figure 6 illustrates the comparisons of the normalized cooling capacities between experimental results and simulation results according to the temperature. The red line is the design result aforementioned research (Lee et. al., 2017), and the yellow line which is slightly shifted from the design result is the simulation results with the pressure drop in the heat exchanger. The temperature is slightly increased as 103 K when the heat added in the cascade type MR JT refrigerator. Thus, experimental result is well matched with the pressure drop result. Table 3 presents the difference between the experimental results and the simulation results with experimental pressure drop of each stream. Most of discrepancy is due to the pressure drop at the return stream (5,6,7 and 8).

Table 3 Comparisons of the design results and experimental results for 15 J/g heat absorption in the evaporator

Streams	1	2	3	4
Measured temperature [K]	300.2	247.8	244.1	108.4
Calculated temperature [K]	300	253.9	247.8	107.4
T Error = (cal.-exp.)/exp.	-0.6%	2.5%	1.5%	-0.9%
Measured pressure [kPa]	1579	1561	1558	1533
Calculated pressure [kPa]	1400	1400	1400	1400
P Error = (cal.-exp.)/exp.	-11.3%	-10.3%	-10.1%	-8.7%
Streams	5	6	7	8
Measured temperature [K]	103.3	103.4	221.5	294
Calculated temperature [K]	97.5	103.7	240.0	297
T Error = (cal.-exp.)/exp.	-5.6%	0.3%	8.4%	1.0 %
Measured pressure [kPa]	310	300	250	100
Calculated pressure [kPa]	220	220	220	220
P Error = (cal.-exp.)/exp.	-29.0%	-26.7%	-12%	120%

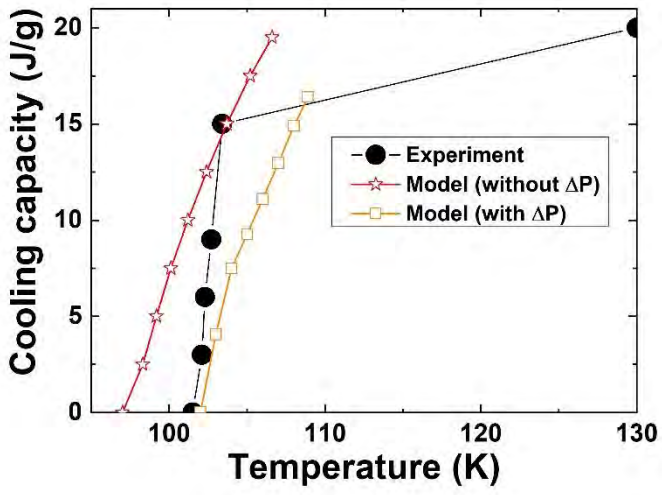

Figure 6. Comparisons of the cooling capacities from the experimental results and simulation results with and without pressure drop

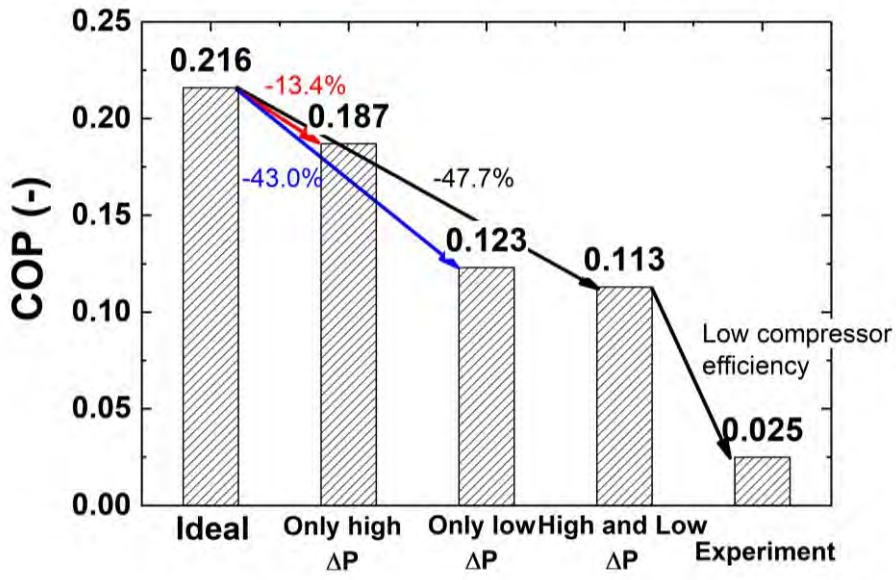

Figure 7. COP comparisons of various simulation conditions and experimental results

3.2.3. COP comparison of simulation and experiment

The electric work consumptions are measured as 359 W and 698 W for 1st compressor and 2nd compressor, respectively by the inverter manufacturer's software (Yaskawa DriveWizard plus, Ver.4.0). The work consumption is significantly higher than the design result. This higher work consumption has two reasons, the one is the pressure drop in the heat exchangers and the other is the compressor efficiency.

To verify the influence of the pressure drop, simulation is conducted with the pressure drop where the value is measured in the experiment. Figure 7 shows the efficiency comparisons of the ideal design result (without pressure drop), the pressure drop result with only high pressure side, the pressure drop result with only low pressure side, the result with both of high pressure side and low pressure side and the experimental result.

If the pressure drop in the heat exchanger apply in the simulation, then the COP of the refrigeration cycle is drastically reduced as 0.113. This simulation also applies the compressor efficiency of 80%, therefore, the total work consumption of the compressors is 198 W. Accordingly, the actual compressor has very poor efficiency approximately 17%.

The simulation result with pressure drop only at the high pressure side is simply calculated with the uniform low pressure of 220 kPa, which is the same as the ideal case. The pressure drop of the high pressure side decreases the COP approximately 17 %. By contrast, the simulation result with pressure drop only at the low pressure side is simply assumed with the uniform high pressure of 1400 kPa. The simulation result of it reduces the COP as 43%. According to this result, it is revealed that the pressure drop at the low pressure side is a critical role to reduce the refrigerator efficiency.

4. CONCLUSIONS AND FUTURE WORKS

Experimental verification of the cascade type MR JT refrigerator is conducted in this paper. The design results are shown as 17 J/g normalized cooling capacity and 97.6 K lowest temperature according to the previous research (Lee et al., 2017). In the experiment, the lowest temperature of the cascade MR JT refrigerator is attained 98.5 K, and the normalized cooling capacity of the cycle is achieved 15 J/g at the temperature of 103 K. After the detail analysis, entire refrigeration cycle efficiency should be discussed in the various factor such as the pressure drop effect of both high

pressure side, low pressure side and compressor efficiency. The main limitations of the experiment are the pressure drop at the low pressure side and the low compression efficiency.

ACKNOWLEDGEMENTS

This work was supported by the project “Pilot Project of Chungbuk Regional Division (Project number: UD19020)”, Funded by the Korea Institute of Industrial Technology (KITECH) in South Korea Agency.

NOMENCLATURE

$\dot{m}$	Mass flow rate (kg/s)	Q	heat (kJ)
W	Work (kJ)		

REFERENCES

Barron, R.F. 1985. Cryogenic systems. Clarendon Press, 32

Baek, S., Lee, C., Jeong, S., 2014. Investigation of two-phase heat transfer coefficients of argon–freon cryogenic mixed refrigerants. Cryogenics, 64(0), 29-39

Cengel, Y.A. and Boles, M.A., 2006. Thermodynamics: an engineering approach. McGraw-Hill, New York, 391-431

Chakravarthy, V.S., Shah, R.K. and Venkatarathnam, G., 2011. A Review of Refrigeration Methods in the Temperature Range 4–300 K. Journal of Thermal Science and Engineering Applications, 3(2), 020801

Lee, C., Yoo, J., Park, C., Jeong, S., 2016, Visualization of the solid–liquid equilibria for non-flammable mixed refrigerants. Cryogenics 75(0), 26-34

Lee, C., Jin, L., Park, C., Jeong, S., 2017. Design of non-flammable mixed refrigerant Joule-Thomson refrigerator for precooling stage of high temperature superconducting power cable, Cryogenics, 81(0), 14-23

Lee, J., Oh, H. and Jeong, S., 2014. Investigation of neon–nitrogen mixed refrigerant Joule–Thomson cryocooler operating below 70 K with precooling at 100 K. Cryogenics, 61(0), 55-62.

Lee, J., Lee, C., Jeong, S., Park, J., Hwang, S.D., Yang, H.S., Jung, S.Y., Lim, J.H., 2015, Investigation on Cryogenic Refrigerator and Cooling Schemes for Long Distance HTS Cable. IEEE Transactions on Applied Superconductivity, 25(3), 5400804

Yang, H. S., Sohn, S. H., Lim, J. H., Yim, S. W., Jeon, H. J., Jung, S. Y., Han, S. C. and Hwang, S. D., 2014. Decompression cooling system operation for HTS power cable in the KEPCO power grid. 2013 Cryogenic Engineering Conference (AIP proceedings) 1573(1), 1678-1684

Manuscript ID: 372
DOI: 10.18462/iir.icr.2019.0372

Ways of heat accounting of the ortho-para conversion at simulation of hydrogen liquefier cycles

Sergei A. PARSHIN[(a)], Ekaterina S. NAVASARDYAN[(a)], Ivan A. ARKHAROV[(a)], Aleksey M. ARKHAROV [(a)]

[(a)] Bauman Moscow State Technical University
Moscow, 105005, Russian Federation, bauman@bmstu.ru

ABSTRACT

The hydrogen ortho-para conversion process simulation is one of the key issues of analytical model development of a hydrogen liquefier. Numerous programs like PRO/II, Aspen HYSYS have no dedicated models for hydrogen conversion process simulation. Thereby, it raises the question of ortho-para conversion hydrogen reactors simulation by artificial ways.
The object of the work is to consider simulation process ways of the hydrogen ortho-para conversion and to find out an optimal one for realization in process simulators. The study is carried out by the computational-analytical method using simulation programs.
Three ways of process simulation are considered. They were compared based on the calculated parameters of each way and analytical outcomes.
The results of the work are as follows: optimal hydrogen ortho-para conversion process simulation way was chosen; the simulated hydrogen liquefier (using the optimal conversion simulation way) was compared with the realized cycle with considered all operating losses.
Keywords: Conversion, Cryogenics, Hydrogen, Liquefaction, Simulation.

1. INTRODUCTION

Hydrogen is considered one of the most promising fuels. The world hydrogen production was about 60 million tons in 2017yr., and the production increase is expected to be 10-15 times due to renewable energy sources by 2050yr. (Klaus et al., 2007). There are many researchers explored the hydrogen use as a fuel and noted its benefits as Eremin et al. (2018), Kavtaradze et al. (2019).
Because of the hydrogen growing demand, the hydrogen production increases of either liquid and gaseous forms, production technological schemes of it are being improved. Moreover, large-capacity hydrogen liquefiers are considered the most promising (Cardella et al., 2017). In that regard, there is a growing need for modeling not only for the entire technological scheme, but also individual equipment, such as ortho-para conversion reactors.
The ortho-para hydrogen conversion effect consists in the spontaneous transition of ortho-modification of hydrogen to para-modification for non-equilibrium concentration of these modifications in hydrogen for given conditions. Hydrogen ortho-para conversion effect leads to additional heat release, the value of which can exceed the latent heat of hydrogen liquefaction (Larsen et al., 1948). Therefore, creation an ortho-para conversion model is one of the main problems of design schemes for hydrogen. Simulation programs like UniSim Design, GIBBS, PRO/II, Aspen Hysys have many different modules (Matveev and Smorodin, 2016), but no one for hydrogen conversion process, raising the question of artificial methods for simulating conversion reactors for hydrogen liquefier cycles.
Nowadays, no article reveals an approach to modeling the ortho-para conversion process, although the modeling of cycles is carried out in the programs mentioned above even in dynamic mode as in Aleksandrov et. al. (2016) and Nagimov et. al. (2016). In some cases, the ortho-para conversion effect is neglected to simplify the calculations.
It has been shown that about 15% of power in hydrogen liquefier cycles is spent on ortho-para hydrogen conversion process (Quack, 2001). Therefore, in the face of increased competition the heat of ortho-para hydrogen conversion should be taken into account for calculation and modeling.

The article objective is to determine the most optimal way to simulate the ortho-para conversion process in hydrogen liquefier cycles in optimization and modelling programs of technological processes.

2. RESEARCH STAGES AND RESULTS EVALUATION

In the framework of the article objective it is considered the real gas state equation choice for hydrogen liquefier cycles modeling. The equation evaluation is based on the handbook (Gamburg, 1989). Three ways of ortho-para conversion process modeling is presented and simulated in the correspond programs. As a result, it is chosen the best fit ways of modeling. Then the hydrogen liquefaction cycle is compared to operated cycles with all losses considered to understand the applicability of chosen way of ortho-para conversion simulation.

2.1. Real gas state equation choice

It highly important to choose the correct gas state equation for considered gas for process simulation. The most popular Peng-Robinson state equation is not match to calculate the hydrogen state parameters (see Figure 1 and Table 1). All state equations possible versions for hydrogen presented in the simulation programs are considered. The following equations were chosen:

- Peng-Robinson state equation (hereinafter PR) presented by Peng and Robinson (1976). The pointed equation is a modification of the van der Waals equation of state. It well describes the fluid density and vapor-liquid equilibrium for hydrocarbon systems.
- Peng-Robinson-Twu state equation (hereinafter PR-Twu) presented by Twu et al. (1995). Cubic state equation modification for Twu and co-authors.
- Peng-Robinson Stryjek-Vera state equation (hereinafter PRSV) presented by Stryjek and Vera. (1986). A modification of the PR equation, extending its range for non-ideal systems.
- The modified Benedict, Webb, and Rubin equation (hereinafter BWRS) for pure components proposed by Han and Starling (1972). The model is used to calculate systems under pressure in both the processing and extraction industries.
- Modified Benedict-Webb-Rubin equation of state (MBWR). Modified 32-term Benedict-Webb-Rubin equation of state for pure components.
- Zudkevitch-Joffee state equation (hereinafter ZJ) presented by Zudkevitch and Joffee (1970). It is a modification of the Redlich-Kwong equation of state. The model is used to calculate vapor-liquid equilibrium for hydrocarbons and systems containing hydrogen.

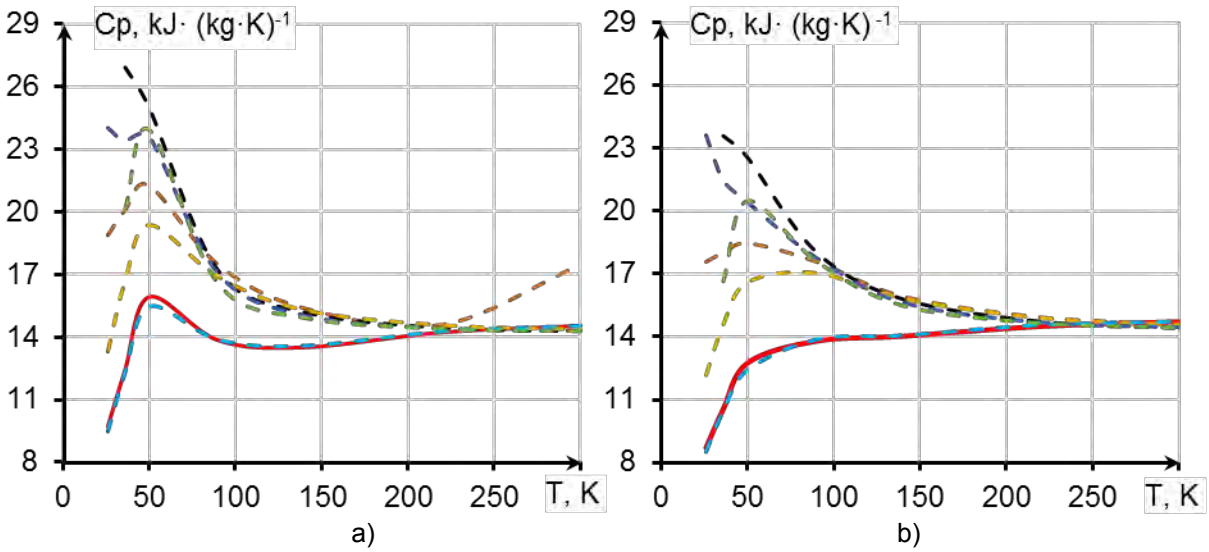

Figure 1: The hydrogen isobar specific heat at two pressures and various temperatures, depending on the equation of state:

reference data (Gamburg, 1989); MBWR; PR-Twu; PR; BWRS; ZJ; PRSV; Cp – hydrogen isobar specific heat in kJ·(kg·K)$^{-1}$; T – temperature in K;
a) gas pressure 10 MPa (100 bar);
b) gas pressure 20 MPa (200 bar).

Since the hydrogen conversion process is discussed in the article for a high pressure cycle, the normal hydrogen heat capacities at pressures of 10 MPa and 20 MPa (Fig. 1) are taken into account to select the equation of state. Additionally, it is considered the boiling point of hydrogen and the latent heat of evaporation (Table 1). Reference data was taken from Gamburg, 1989.

Table 1. The hydrogen boiling point and the heat of evaporation at a pressure p = 101.325 kPa: T_b – hydrogen boiling point in K; q_e – latent heat of hydrogen evaporation in $kJ \cdot kg^{-1}$.

Parameter / property package	Handbook data	PR	PR-Twu	PRSV	BWRS	MBWR	ZJ
T_b, K	20.39	18.69	20.39	21.25	20.28	20.23	20.33
q_e, $kJ \cdot kg^{-1}$	454.2	446.4	455.7	441.4	544.1	445.4	676.3

Based on the data in Fig. 1 and Table 1, it can be seen that the MBWR model is the most correct one for hydrogen properties calculating. For isobaric heat capacity, the maximum error in comparison with reference data is 3%, for boiling temperature and heat of evaporation it is 0.8% and 2% respectively.

2.2. Models of ortho-para conversion heat supply

The ortho-vapor conversion reactors modeling is considered for the three-stage high-pressure hydrogen liquefier cycle (120 MPa) with external nitrogen pre-cooling on the first stage, with part – flow expansion as the second stage, and with JT valve on the third one. The cycle was chosen as an example and is not the main research subject in the article. Results of ways conversion reactors modeling presented in the article can be applied to any hydrogen liquefier cycles.

The scheme is shown in Fig. 2a. The feed flow at point 2 is divided into two: production and circulation flow, the last one removes heat from the production flow increasing the process efficiency (Smith, 1984). It is more close to the real installation schemes. The question was raised that the ortho-para phase of hydrogen backflow is not in equilibrium by Scott, 1959, therefore the characteristics of the flow are unclear. In the article, the conversion of the circulating hydrogen flow was decided to be neglected, since this effect is insignificant (Nandi and Sarangi, 1993).

The cycle comprises a compressor C, an aftercooler CA. Due to hydrogen low inversion temperature of about 204,6 K and to remove the hydrogen heat conversion, a nitrogen pre-cooling bath B is presented, which is modeled as a three-flow heat exchanger. In order to increase the efficiency and to remove the hydrogen conversion heat, an expander E is presented. Also there are 2 HE1/2 heat exchangers, a JT1/2 JT valves and a separator S. The ortho-para conversion reactors R1, R2, R3 are integral parts of the heat exchanger, the nitrogen bath and the separator respectively. The reactors were presented as heaters during simulation. Various schemes of reactors placements into a hydrogen liquefier are presented in (Arkharov et al., 1999). It is implied the use of adiabatic reactors. Since the temperature of hydrogen after HE2 insignificantly differs from the flow temperature at point 5, for the reason there is no need to install an additional heat exchanger at the expander stage.

The implementation of the scheme in Fig. 2a in the simulation programs is not possible in its identical form with the implementation of ortho-para conversion. Therefore, in order to perform calculations in simulation programs, the scheme was partially modified.

Fig. 3 a), b) and c) show various ways for ortho-para conversion reactors realization in simulation programs for hydrogen liquefaction and hydrogen conversion design scheme. The first two ortho-para conversion reactors are designated as heat supply modules to flows R1, R2. The third converter R3 is modeled by supplying heat Q_{R3} to the separator S (Fig. 2 a). Accordingly, schemes a), b) and c) in Fig. 3 are mainly differ in the installation location of the ortho-para reactors R1, R2.

In the first scheme (hereinafter scheme I), shown in Fig. 3 a), the converters R1, R2 are installed on a production flow of hydrogen, as in the designed (real) installations with the peculiarity that the ortho-para conversion heat supply occurs before B, HE2. At the end of the pointed equipment ortho-para conversion takes place in real conditions of designed installations at temperatures in points 3 and 4 respectively. Therefore the conversion specific heat was calculated based on the flow temperature at the outlet of equipment B, HE2 for reactors R1, R2 respectively, according to the Eq. (1) (Arkharov et al., 1999):

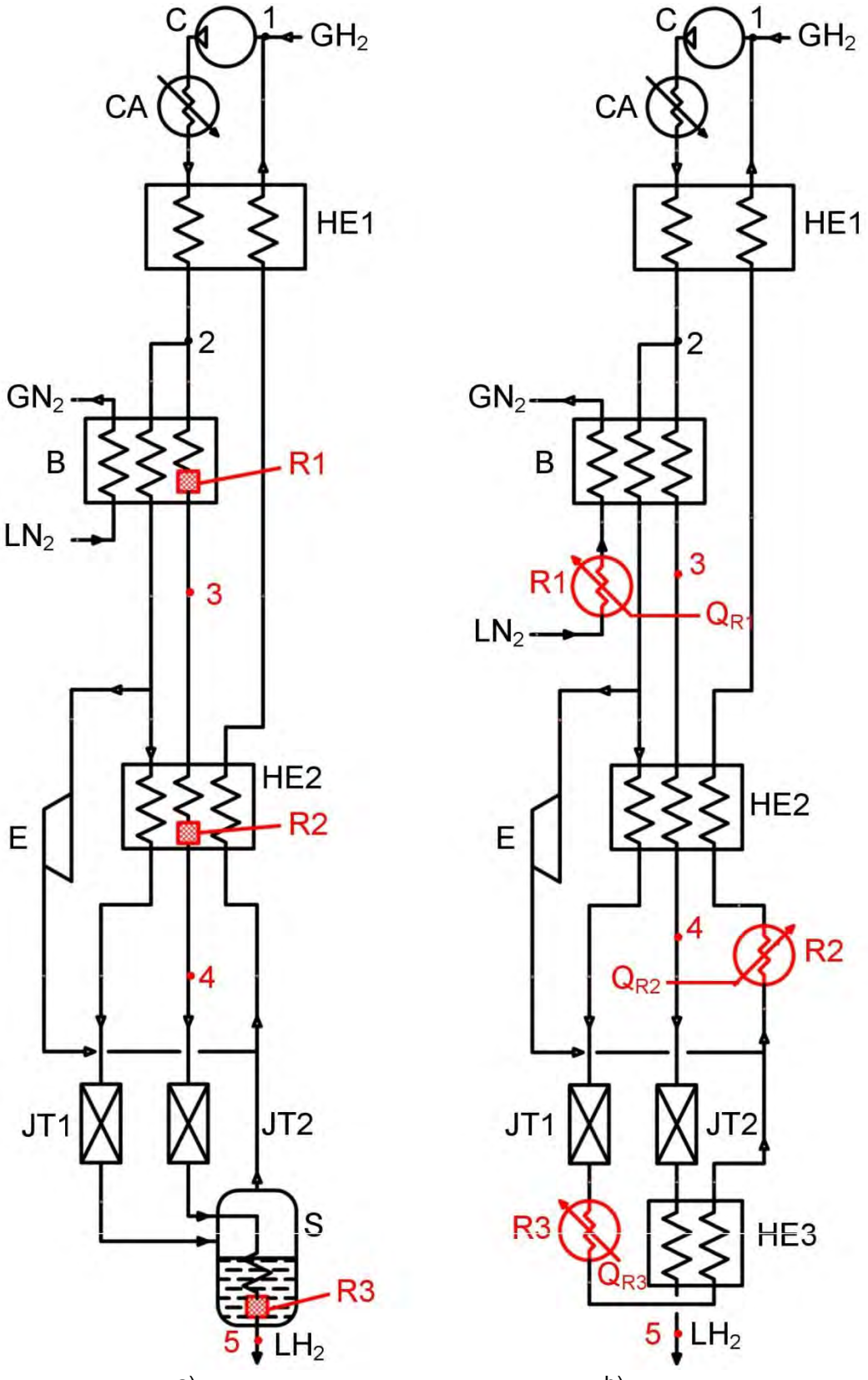

Figure 2: Hydrogen liquefaction cycles:

B – pre-cooling bath; C - compressor; CA – compressor aftercooler; E – expander; GH_2 – gaseous hydrogen; GN_2 – gaseous nitrogen; HE1, HE2, HE2 – heat exchangers; JT1, JT2 – JT valves; LH_2 – liquid hydrogen; LN_2 – liquid nitrogen; Q_{R1}, Q_{R2}, Q_{R3} – ortho-para conversion heat flow in $kJ \cdot h^{-1}$; R1, R2, R3 – ortho-para conversion reactors.

a) preliminary scheme;

b) design scheme.

$$q_{con} = 7{,}05 \cdot (C - C_0) \qquad \text{Eq. (1)}$$

where q_{con} is ortho-para conversion specific heat in $kJ \cdot kg^{-1}$, C_0 is initial (before the considered hortho-para conversion in the reactor) parahydrogen fraction in %, C is parahydrogen fraction in the mixture at reactor temperature (fraction close to equilibrium at the reactor temperature) in %.

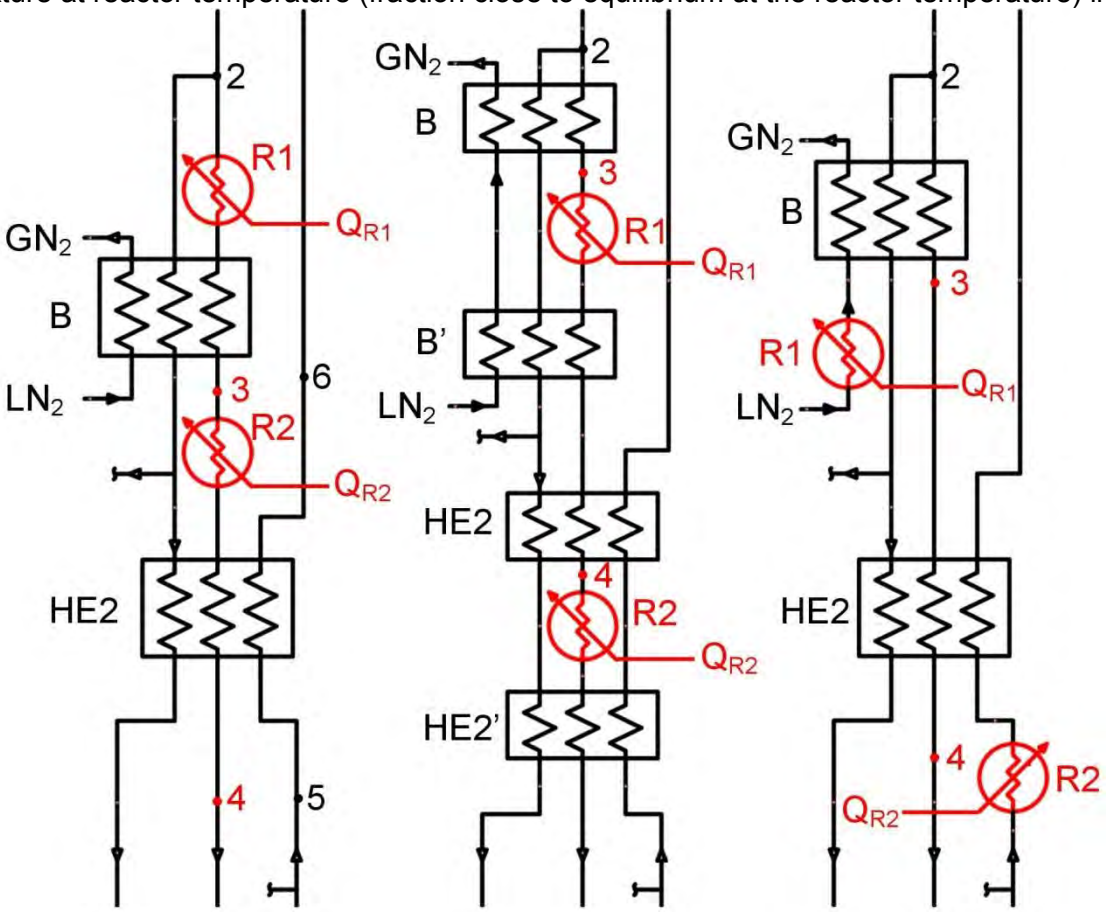

a) b) c)

Figure 3: Various ways to ortho-para conversion reactors modeling in the liquefaction and ortho-para-conversion hydrogen schemes:

HE2, HE2' – heat exchangers; B, B' – pre-cooling baths; GN_2 – gaseous nitrogen; LN_2 – liquid nitrogen; Q_{R1}, Q_{R2} – ortho-para conversion heat flow in $kJ \cdot h^{-1}$; R1, R2 – ortho-para conversion reactors.

a) on the feed flow;

b) on the feed flow with the heat exchangers splitting into two units;

c) on the back flow.

The parahydrogen concentration depends on the temperature and was taken from the data for Malkov et al. (1985) or was calculated by the interpolation method for midvalues. The ortho-para conversion heat was obtained by multiplying the specific heat by the mass flow rate of hydrogen at the specified points.

In the second scheme (hereinafter scheme II), shown in Fig. 3b), it was decided to split the pre-cooling nitrogen bath B and the HE2 heat exchanger from the basic scheme (Fig. 2a) into two corresponding equipment. The equipment B 'and HE2' in Fig. 3b) serve to remove the ortho-para conversion heat from the production flow to backflow. In fact, one nitrogen bath and one heat exchanger are mounted, conversion proceeds inside of the equipment at the presence of catalysts (Berstad et al., 2009). Converters R1, R2 are installed on a production flow of hydrogen, the conversion specific heat was calculated using Eq. (1) with described earlier method, based on the outlet flow temperature of equipment B and HE2 to determine the parahydrogen concentration.

The last scheme (hereinafter scheme III), shown in Fig. 3c), differs from the previous ones in the following. The reactor R1 is installed on the pre-cooling nitrogen flow, R2 is installed on the hydrogen backflow, since the conversion heat is perceived by the backflow on the lower temperature level in comparison with production flow in scheme I. The calculation method and

temperatures selection for determining the parahydrogen concentration is similar to the principle of calculation for the previous schemes.
In order to compare the schemes (ways of orto-para conversion process modeling) in Fig. 3, the following values in Table 2a) were taken as input data (point 1 in Fig. 3). To simplify, the mass flow rate was assumed to be 1 kg·h^{-1}. The compressor characteristic is shown in Table 2 b) for all the specified schemes. The compressor isothermal efficiency was taken for Plastinin (2006).

Table 2. Input data for hydrogen liquefaction schemes:
a) data for the point 1 Fig. 3 a);
b) compressor characteristic.

Parameter	Value
Molar composition	100% H_2
Mass flow G, kg·h^{-1}	1.00
Temperature T, K	300.00
Pressure p, bar(a)	1.00
Vapour mass fraction	1.00

a)

Parameter	Value
Isothermal efficiency	69.00
Suction pressure, bar(a)	1.00
Discharge pressure, bar(a)	120.00
Flow temperature after cooler CA, K	300.00

b)

The nitrogen bath inlet temperature (Fig. 3a, b, c) corresponds to the boiling temperature at a pressure of 1 bar(a). The temperature approach in heat exchangers HE1, HE2 and in the pre-cooling bath B were taken on the basis of recommendations for Arkharov at al. (2009) and equal to 10K, 2K and 3K correspondingly. Hydraulic losses and heat leaks are not considered
The hydrogen mass flow fraction going to the expander E and the flow temperature at point 4 (T_4 in K) are optimization parameters in the cycle. The temperature T4 is set on the basis of the expander mass flow and the temperature approach. The optimization goal is liquefaction coefficient x (unitless). All schemes in Fig. 3 were optimized by the described principle.
Scheme I and scheme III show the same optimization result (Table 3). In the scheme I with placing the ortho-para conversion reactor on the production flow the optimal expander mass fraction is 0.481 with the x coefficient equal to 0.345. For schemes II and III expander flow is equal to 0.648 with a coefficient x equal to 0.122.

Table 3. The parameters of the hydrogen liquefaction schemes

Parameter\scheme	I	II	III
Liquefaction coefficient x	0.345	0.122	0.122
Specific compressor work l_c, MJ·kg^{-1}	22.95	64.30	64.30
Nitrogen mass flow, kg·h^{-1}	5.182	2.849	2.849
Cycle specific work l, MJ·kg^{-1}	100.7	185.7	185.7
Expander mass flow fraction	0.481	0.648	0.648
Temperature in point 4, K	22.67	34.03	34.03
Temperature in point 2, K	199.6	116.2	116.2
Work for nitrogen liquefaction accepted 4,5 MJ·kg^{-1} liquid N_2 (Arkharov et al., 1999)			

Based on Table 3, it can be noted the scheme II and III (Fig. 3 b and c respectively) have the same characteristics. It is explained by the fact that the ortho-para hydrogen conversion heat transfers directly to the cold backflow in scheme III and by means of the HE2 'and B' heat exchangers in scheme II. Hereinafter it is enough to compare scheme I with scheme III.
it can be noted the cycle parameters are differ considerably depending on conversion reactors placement in the simulation cycle (for the liquefaction coefficient the difference is 2.8 times). At first glance, scheme I seems logical strong due to conversion reactors placement, since in the case of a real installation reactors could be mounted also on the production flow and the same equipment could have conversion heat load. In terms of heat transfer the scheme III will be correct, since the conversion heat load transfers at the same temperature level as in the actual installation.

A similar situation is with the scheme II. The ortho-para conversion heat is supplied at the proper temperature level, but by the heat exchangers T2 'and B'. This fact can be confirmed by comparing the cycle parameters in Table 3. In scheme I the heat of conversion Q_{R2} (Fig. 3a) have a slight affect the backflow inlet temperature into the HE2 heat exchanger (Fig. 3a, point 5) and the same one for the production outlet temperature, since the minimum temperature approach in HE2 is at the cold end. It mainly affects the temperature of the backflow from HE2 (Fig. 3a, point 6), increasing it with increasing Q_{R2} and increasing the dimensions of the HE2 heat exchanger by increasing the heat load in it. Consequently the feed flow in the HE1 heat exchanger cools down less than in schemes II and III, which can be seen by comparing the temperatures of point 2 in table 3. Thereby, there is a large heat load on the pre-cooling bath B, which leads to increase in nitrogen consumption in scheme I (Table 3). Thus, the ortho-para conversion heat Q_{R2} affects mainly the consumption of nitrogen in the pre-cooling bath B in scheme I, which is not correct.
Regarding schemes II and III, the first one is most similar to the actual installation in terms of the conversion reactor location and the heat supply point. If a detailed scheme calculation is required, scheme II should be taken into account with R1, R2 converters and B ', HE2' equipment. Additionally, isothermal and continuous conversion (with simultaneous heat conversion removal and production flow cooling, Smorodin and Shuyakov, 2000) could be also simulated by splitting B, B ', HE2, HE2' equipment in scheme II so that the conversion process is close to the isothermal or continuous process of ortho-para conversion. Scheme III allows us to carry out an estimated calculation of the cycle with less time.

2.3. Hydrogen liquefier cycle calculation close to the real cycle

Within the framework of the task, it is proposed to calculate the hydrogen liquefier cycle with ortho-para conversion reactors, taking into account circulation flow, equipment temperature approaches, hydraulic resistances, factor of margin for the liquid nitrogen consumption in the pre-cooling bath, heat leaks in the cycle. The scheme of the cycle is shown in Fig. 2b).
In comparison with the previously presented schemes the new scheme has a HE3 heat exchanger with 1K temperature approach instead of separator S. Due to the hydraulic resistances, the compressor discharge pressure is 13 MPa. The pressure at point 5 is equal to 1,4 bar(a). The conversion heat supplied in the reactor R3 corresponds to the equilibrium concentration of hydrogen ortho-para modification at point 5. The circulation flow is considered.
The accepted values of hydraulic resistances correspond to the recommendations (Arkharov, 2009) are equal to 1% of the equipment inlet pressure for high pressure flows, 2-3% for low pressure flows. For the HE3 the hydraulic loss is 1% of the inlet pressure for both flows. The nitrogen margin in the nitrogen bath B is 15% of the total nitrogen consumption (Arkharov, 1999). Heat losses constitute 3% of the entire cooling capacity of the cycle (Arkharov, 1999).
The results of the calculation of the cycle are presented in Table. 4. It could be seen, such characteristics as the liquefaction coefficient and the cycle specific work correspond to the characteristics for the same cycles (Arkharov et al., 1999).

Table 4. Hydrogen liquefaction scheme close to real cycle

Parameter\scheme	Value
Liquefaction coefficient x	0.252
Specific compressor work l_c, $MJ \cdot kg^{-1}$	32.03
Nitrogen mass flow, $kg \cdot h^{-1}$	4.58
Cycle specific work l, $MJ \cdot kg^{-1}$ liquid H_2	117.1
Cycle specific work l, $MJ \cdot dm^{-3}$ liquid H_2	8.131
Work for nitrogen liquefaction accepted 4,5 $MJ \cdot kg^{-1}$ liquid N_2 (Arkharov et al., 1999)	

3. CONCLUSIONS

As a result of analyzing and calculating methods of ortho-para conversion modeling in simulation programs, it was proposed to use heater model as a reactor to supply the ortho-para conversion heat in hydrogen liquefier cycles to the backflow if an estimated cycle calculation is required. A way of the detailed calculation of the hydrogen ortho-para conversion process was also proposed.

It was shown that an error in the hydrogen ortho-para conversion simulation can lead to a 2.8 times excess of the cycle liquefaction factor relative to the proposed model.
The calculation of the hydrogen liquefier cycle with any losses was also carried out in order to assess the characteristics of the cycle in simulating the ortho-para conversion process by the proposed method.

REFERENCES

Aleksandrov, A. A., Arkharov, I. A., Navasardyan, E. S., & Antonov, E. A. 2016. Modeling of Processes in Microcryogenic Gas Cooler. Chem. Petrol. Eng., 51(9-10), 649-655.

Arkharov, I.A., Aleksandrov, A.A., Navasardyan, E.S., 2009. Theory and calculation of cryogenic system cycles. MGTU lm. N.E. Baumana, Moscow, 159p.

Arkharov, A.M., Arkharov, I.A., Smorodin, A.I., 1999. Cryogenic systems in 2 vol. Vol. 2. Engineering foundation of equipment, plant and systems. Mashinostroenie, Moscow, 720p.

Berstad, D.O., Stang, J.H., Neksa, P., 2009. Comparision criteria for large-scale hydrogen liquefaction processes. Int. J. Hydrogen Energy, 34(3), 1560-1568.

Cardella, U., Decker, L., Klein, H., 2017. Economically viable large-scale hydrogen liquefaction. IOP Conf. Series: Materials Science and Engineering, 171.

Eremin, A. V., Matveeva, N. A., Mikheyeva, E. Y., 2018. Methane and hydrogen ignition with ethanol and butanol admixtures. Journal of Physics: Conf. Series, 946(1), 012063.

Gamburg, D.Yu., 1989. Hydrogen. Properties, production, storage, transportation, application: Ref. Edition. Khimiya, Moscow, 672p.

Han, M.S., Starling, K.E., 1972. Thermo Data Refined for LPG. Part 14: Mixtures. Hydrocarbon Processing, 51 (5),129-132.

Kavtaradze, R., Natriashvili, T., Gladyshev, S., 2019. Hydrogen-Diesel Engine: Problems and Prospects of Improving the Working Process. SAE Technical Paper, No. 2019-01-0541.

Klaus, D. T., Reed, R.P., 2007. Cryogenic engineering. Springer-Verlag Wien, 379p.

Larsen, A.H., Simon, F.E., Swenson, C.A., 1948. The Rate of Evaporation of Liquid Hydrogen Due to the Ortho-Para Hydrogen Conversion. Rev. Sci. Instrum. 19, 266-269.

Matveev, S. A., Smorodin, A. I., 2016. Simulation and Optimization of Amine Purification from Acidic Admixtures at Natural Gas Liquefaction Plants. Chem. Petrol. Eng., 51(11-12), 755-758.

Malkov, M.P., Danilov, I.B., Zeldovich, A.G., Fradkov A.B., 1985. Handbook of Physical and Technical Fundamentals of Cryogenics. Energoatomizdat, Moscow, 432 p.

Nagimov, R. R., Arkharov, I. A., Navasardyan, E. S., 2016. Problems and Development of Methods of Dynamic Simulation of Cryogenic Systems. Chem. Petrol. Eng., 52(7-8), 476-480.

Nandi, T.K., Sarangi, S., 1993. Performance and optimization of hydrogen liquefaction cycles. Int. L. Hydrogen Energy, 18, 131-139.

Peng, D.Y., Robinson, D.B., 1976. A new two-constant equation of state. Ind. Eng. Chem. Fundam., 15(1), 59-64.

Plastinin, P. I., 2006. Reciprocating compressors. Vol. 1. Theory and calculation. Kolos, Moscow, 456 p.

Quack, H., 2001. Conceptual design of a high efficiency large capacity hydrogen liquefier. Adv. Cryog. Eng., 47, 255-263.

Smorodin, A.I., Shuyakov, A.L., 2000. Ortho-para conversion processes in hydrogen liquefier apparatus. Vestnik MGTU, Mashinostroenie, Moscow, 99-111.

Scott, A.J., 1959. Cryogenic Engineering. Van Nostrand, Princetown, 368p.

Smith, E.M., 1984. A possible method of improving energy efficient para-LH_2 production. Int. J. Hydrogen Energy, 9, 913-919.

Stryjek, R., Vera J.H., 1986. PRSV: An improved Peng-Robinson equation of state for pure compounds and mixtures. Can. J. Chem. Eng., 64, 323-333.

Twu, C.H., Coon J.E., Cunningham J.R.,1995. A new generalized alpha function for a cubic equation of state. Part 1. Peng-Robinson equation. Fluid. Phase. Equilib.,105, 49-61.

Zudkevitch, D., Joffee, J., 1970. Correlation and Prediction of Vapor-Liquid Equilibria with the Redlich-Kwong Equation of State. AIChE Journal,16(1), 112-119.

Manuscript ID: 375

DOI: 10.18462/iir.icr.2019.0375

Helium, hydrogen and methane liquefaction with Reverse-Brayton & Joule-Thomson cycles, boosted by sub-sink cooled compression and hybrid compression or coabsorbent technology ultra-low temperature refrigeration

Mihail-Dan STAICOVICI

S.C. VARIA ENERGIA S.R.L., 81 B Mihai Eminescu str., fl. 4, apt. 9,
Bucharest 2, 020 072, Romania, email: mihail_dan_staicovici@yahoo.com,

ABSTRACT

A new gas liquefaction cycle, noted by SCC-HC/CBS-RB&JT, is presented as an improved version of a first cycle introduced in a former author paper. The cycle is a joint of Reverse Brayton (RB), run by helium, and Joule-Thomson (JT), run by the gas to be liquefied. It benefits of new main features, such as: a) the gas precooling at $T_{DI} = -75$°C and $T_{ESS} = 15$°C is boosted by sub-sink cooled compression (SCC), applied to both joint cycles; b) the SCC is performed by Hybrid Compression (HC) or Coabsorbent (CBS) technology, run in the ultra-low temperature refrigeration (ULTR) domain; c) the RB&JT joint is improved, to increase efficiency and feasibility. A simple algorithm for assessment of the specific work consumption and effectiveness of HC and CBS -ULTR technologies, run in different operation conditions by $NH_3 - H_2O$ and NH_3, is given. Next, the SCC-HC/CBS-RB&JT is described and modeled. Depending on ULTR type, the model results of HeL, HL and LNG show $l_{spec,SCC-HC/CBS-RB\&JT}$ is by 10-20 times smaller, up to 7,5 % out of the specific hydrogen heating value and by 2-4 times less, respectively, as compared to l_{spec} of current technologies in kind.

Keywords: hybrid compression technology, coabsorbent technology, thermal-to-work recovery compression, ultra-low temperature refrigeration, helium, hydrogen and methane liquefaction, Reverse-Brayton cycle, Joule-Thomson cycle.

1. INTRODUCTION

The Hybrid Compression (HC) concept and technology have been introduced lately by the author (Staicovici, 2014, 2015a, b, c, 2016a, b, 2017a, b, 2018a, b). HC has the potential to achieve more flexibly and feasibly ultra-low temperature refrigeration (ULTR) and ultra-high temperature heat pump heating (UHTH). Further on, the author enlarged the HC concept, elaborating recently the Partial-Hybrid Compression (PHC) (Staicovici, 2016a) and the Hybrid Compression for Sub-Environmental Cooling Temperature Operation Refrigeration (HC-SECTOR) (Staicovici, 2018b). The PHC and HC-SECTOR have been considered so far in three ULTR-cryogenic studies, of air, natural gas and hydrogen liquefaction, (Staicovici, 2017a, b, 2018a). Out of the three studies, the first two applied a classic technology to the air and natural gas liquefaction. This technology principally consists on one side in gas precooling with either cascades of mechanical vapor compression (MVC) cooling units or with liquid nitrogen, and in the use of the Joule-Thomson expansion cycle (JTEC) and the Linde heat exchanger (LHE), on the other side. The third process, of hydrogen liquefaction (HL), has been modeled differently, taking into account the many recent cycles analyzed, showing improved specific work L_{spec}, $[L_{spec}] = kWhe * (kg\ of\ liquid\ gas)^{-1}$

(Eckroll, 2017). Among them, the Claude cycle is significant. It includes turbo-expanders to precool gas before LHE and yield work (Stamatescu, 1982, Shimko, 2008, Eckroll, 2017)). Also, an effective HL cycle was originally introduced, optimizing a joint between a version of the Reverse-Brayton cycle (RB), named RB expansion cycle (or modified Claude cycle) and the JTEC, (Shimko, 2017). And last but not least, an efficient cycle was proposed by Valenti et al., based also on a RB & JTEC joint (Eckroll, 2017). According to current practice, the interstage-cooling of compression of all technologies mentioned above is done solely with ambient sink source, called ambient cooled compression (ACC) (Staicovici, 2018a), while the precooling processes, used in cryogenic liquefaction to meet JT inversion (JTI), (Hendricks, 1972), are achieved by MVC refrigeration plants, only (except RB / Claude cycle). However, in author recent studies, mentioned above, for the first time the precooling process is considered to be achieved by compression with interstage-cooling at temperatures below ambient sink source temperature, or in short by Sub-sink Cooled Compression (SCC), (Staicovici, 2018a), in order to diminish L_{spec}. Besides PHC and HC-SECTOR, a third ULTR technology will be considered in this work, as well, the Coabsorbent Technology (CBS), introduced by the author at the end of the last decade, (Staicovici, 2014). The cooling of SCC process is modeled in this work considering all mentioned ULTR technologies, i.e. PHC, HC-SECTOR and CBS. Besides SCC, the three ULTR technologies are involved also in all the other cooling processes of a gas liquefaction, such as the precooling below T_{amb} of the y inlet gas mass fraction, as well as in the Thermal-to-Work Recovery Compression (TWRC) processes, (Staicovici, 2014), when it provides the cooling for the Rankine Recovery Cycles (RRC) and for completing the compression interstage cooling (Staicovici, 2018a). The present work continues the author research concerning the gas liquefaction, presenting a new cycle, the SCC-HC/CBS-RB&JT. This cycle improved efficiency as compared to the cycle considered in (Staicovici, 2018a) for HL. For this reason, besides helium liquefaction (HeL), as new study, the paper focuses on former hydrogen and methane liquefaction (LNG) studies too, in order to improve their L_{spec}. The outputs are given for all ULTR technologies mentioned and are compared each other and as well with former results. Finally, conclusions are expressed.

2. RELATIONSHIP OF SCC-HC/CBS-RB&JT WITH EXTERNAL SOURCES WHICH IS CONNECTED TO

The SCC-HC/CBS-RB&JT efficiency depends to an important extend on the heat sources which the HC and CBS are connected to, in order to diminish L_{spec}. For this reason, in this section we give the HC and CBS cooling technologies a look-over with respect to their ULTR specific work consumption and effectiveness in a few different operation conditions, Table 1. Concerning the first, as already known, the HC concept is a two-technology synergy, which lays down the operation of an absorption technology section (ATS) and a mechanical vapor compression technology section (MVCTS), so that MVCTS plays the role of either internal sink and heat or just the internal sink or heat source for ATS, while ATS performs the useful task of cooling or heating, respectively. Referring to the second, CBS is just absorption technology, noted with ATS as well. In Table 1, Eqs. 1 and 5 are the energy balances of ATS and MVCTS, respectively. Also, Eqs. 2, 3 and 4 represent the effectiveness of ATS cooling effect, solution pumping and rectification, respectively, while Eq. 6 is the MVCTS cooling effectiveness. Finally, Eq. (7) expresses the specific work consumed by the power station when supplying the ATS with heat in cogeneration. The specific work consumption of HC or CBS cooling, $COP_c(w)$, is calculated by Eq. (8), or taking into account Eqs. 2-4 and 6, 7, by the final comprehensive Eq. (9). In the lower part of Table 1, we list four different heat supply situations offered by the current practice, together with the resulting $COP_c(w)$ given by Eqs. (10)-(14) as particular cases of Eq. (9).

Table 1. Simple algorithm for assessment of specific work consumption and effectiveness of HC and CBS -ULTR technologies run in different operation conditions by $NH_3 - H_2O$ and NH_3.

$q_A + q_R + q_{rctf} = q_{GR} + q_D + w_p$ Eq. (1); $q_D q_G^{-1} = COP_{c,a}$ Eq. (2); $q_D w_p^{-1} = COP_{c,w}$ Eq. (3)

$q_D q_{rctf}^{-1} = COP_{c,rctf}$ Eq. (4); $q_A + q_R + w_c = q_C$ Eq. (5); $(q_A + q_R) w_c^{-1} = COP_{c,mvc}$ Eq. (6)

$q_{GR} w_{cg}^{-1} = COP_{h,cg}$ Eq. (7); $COP_c(w) = q_D\left(w_p + w_c + w_{cg}\right)^{-1}$ Eq. (8)

$COP_c(w) = \left[COP_{c,w}^{-1} + \left(COP_{c,a}^{-1} + COP_{c,w}^{-1} - COP_{c,rctf}^{-1} + 1\right)COP_{c,mvc}^{-1} + COP_{c,a}^{-1} COP_{h,cg}^{-1}\right]^{-1}$ Eq. (9)

1) *Case of working taking place with external free heat supply, $COP_{cg}^{-1} = 0$, and neglecting the pumping work, i.e. $COP_{c,w}^{-1} \cong 0$.* The $COP_c(w)$ of PHC is assessed by:

$$COP_{c,PHC}(w) \cong COP_{c,mvc}\left(COP_{c,a}^{-1} - COP_{c,rctf}^{-1} + 1\right)^{-1} \quad \text{Eq. (10)}$$

2) *Case of working taking place without any external heat supply, so $COP_{h,cg}^{-1} = 0$, and the pumping work is neglected, i.e. $COP_{c,w}^{-1} \cong 0$.* The $COP_c(w)$ of HC and HC-SECTOR are assessed by:

$$COP_{c,HC}(w) \cong COP_{c,mvc}\left(COP_{c,a}^{-1} - COP_{c,rctf}^{-1} + 1\right)^{-1} \quad \text{Eq. (11)}$$

$$COP_{c,HC-SECTOR}(w) \cong \frac{COP_{c,MVCTS-ESS}}{\frac{COP_{h,MVCTS-ESS}}{COP_{h,MVCTS-G}} COP_{c,ATS}^{-1} + 1} \quad \text{Eq. (12)}$$

3) *Case of working taking place with external free heat supply, $COP_{cg}^{-1} = 0$, and without any compressor use, so that $COP_{c,mvc}^{-1} = 0$.* In this case, of pure absorption, the pumping work is usually very small. However, here it will not be neglected, so $COP_{c,w}^{-1} \neq 0$. Further on the $COP_c(w)$ of Coabsorbent (CBS) cooling technology is assessed by:

$$COP_{c,CBS}(w) = COP_{c,w} \quad \text{Eq. (13)}$$

4) *Case of working supplied by an external heat source resulted for instance from the cogeneration of a power plant.* The $COP_c(w)$ of CBS can be assessed by eqn. (9), where $COP_{c,mvc}^{-1}$=0 and $COP_{c,w}^{-1} \cong 0$, so:

$$COP_{c,cg,CBS}(w) \cong COP_{c,a} COP_{h,cg} \quad \text{Eq. (14)}$$

Table 2. Main ULTR cycles results considered for this work, $T_{DI} = -75$℃; $T_{ESS} = 15$℃.

ULTR cycle	$T_{M,h}$ (℃)	$T_{M,c}$ (℃)	$COP_{c,a}$ (−)	$COP_{c,mvc}$ (−)	$COP_{c,PHC}(w)$ (−)	$COP_{c,HCSECTOR}(w)$ (−)	$COP_{c,CBS}(w)$ (−)
PHC	85,23-127,9	-10 +5	0,4883-0,3241	7,92-21,15	3,152-8,529	-	-
HC $SECTOR$	-51,48 -57,19	-65 -67,5	0,8882-0,9097	-	-	1,852-1,899	-
CBSdt	87	15-18	0,1189-0,1485	0,0	-	-	228,8[1)] 119,9-
CBSqt	58-63	15-18	0,1021-0,0945	0,0	-	-	177,6-171,7
CBSqt[2)]	58	15	0,1021	0,0	-	-	3,063
Cbsqt[3)]	54,5	15	0,1125	0,0	-	-	4,5
Gravel choice	-	-	-	-	7,987	1,872	150

[1)] $\eta_{pump} = 0{,}8$; [2)] Heat supply in cogeneration, $COP_{h,cg} \cong 30$, (Staicovici, 2014) and $COP_{c,mvc}^{-1} = 0$, so Eqn. (14) applies; [3)]Same as [2)] but for $T_{DI} = -70$℃; $T_{ESS} = 15$℃, when $COP_{h,cg} \cong 40$ and $COP_{c,mvc}^{-1} = 0$.

In Table 2 we show results of Eqs. (10)-(14), with $T_{DI} = -75℃, -70℃$, and $T_{ESS} = 15℃$ as main input data. CBSdt and CBSqt are coabsorbent double and quadruple truncated cooling units, respectively, (Staicovici, 2014). Table 2 shows case (4) results, too. HC-SECTOR does not need external heat supply and CBS heat supply is permanent, but $COP_{c,cg,CBS}(w) > COP_{c,HC-SECTOR}(w)$. However, this work considers cases (1) to (3), only, which effectiveness of are shown by the last line in Table 2.

3. SCC-HC/CBS-RB&JT GAS LIQUEFACTION CYCLE

The SCC-HC/CBS-RB&JT gas liquefaction cycle is represented in Fig. 1. It is a joint between the Joule-Thomson (JT) expansion cycle, right side T-s diagram, and the Reverse-Brayton cycle (RB), left side p-v diagram. The RB and JT cycles are run by helium and by the gas to be liquefied, respectively. The RB cycle has a quasi-isothermal compression evolution, 12, $p_2 > p_1$, provided with inter-stage HC-, or CBS-SCC. During the 12 evolution, RB receives compression work L_c. The SCC is done at a temperature $T_{DI} + \delta T$, where T_{DI} is the ULTR temperature produced by HC or CBS, much below ambient temperature T_{amb}, $T_{DI} + \delta T \ll T_{amb}$. HC-, or CBS-SCC is applied to compressed helium until point 2 is reached. This coincides with the turbo-expansion process beginning, covering the quasi-isentropic 23, $p_2 \gg p_3$. In this way, RB is represented in Fig. 1 as a Triangular Reverse-Brayton (TRB) cycle, because point 2 is common to both quasi-isothermal compression and quasi-isentropic expansion evolutions. During the expansion 23 process, TRB delivers work L_{t-e}. At the turbo-expander 23 exit, helium has lowest temperature, $T_3 = T_{32} - \delta T \ll T_2 = T_{DI} + \delta T \cong T_1$. This high helium temperature decrease is caused by the single expansion process with largest work output L_{t-e}, unlike the RB expansion cycle (or modified Claude cycle, Shimko, 2017), where expanders are some and the total work output is small. Next to expansion, helium is sucked by the compressors train on isobar 31 and suffers a heating process till T_1, when receives heat Q_i. Concerning the JT cycle, the fresh y fraction of gas to be liquefied suffers a first precooling process on p_{amb} isobar within the interval $14(T_{amb}, p_{amb}) - 13\ (T_{DI} + \delta T, p_{amb})$, from T_{amb} till $T_{DI} + \delta T$. In point 13 the precooled y fraction joins on same p_{amb} isobar the 1-y superheated fraction of gas resulting from the JT expansion and coming from point $12(T_{11-12}, p_{amb})$, in order to complete the gas mass unit. Subsequently, the gas unit suffers a quasi-isothermal compression evolution $13\ (T_{DI} + \delta T, p_{amb})$ -31 $(T_{DI} + \delta T, p_{31})$, $p_{31} \gg p_{amb}$. In point 31, the compressed gas unit is split in two complementary fractions, $31 - 31 - JT - 32$ and $31 - 31 - RB - 32$ by a 3-way valve. The $31 - 31 - JT - 32$ fraction suffers a second precooling till it reaches an optimum JTI state, $32\ (T_{32}; p_{31})$, in order to minimize L_{spec}. This further precooling process takes place in a gas-gas heat exchanger (see Fig. 1), recovering in countercurrent the cold exergy of fraction 1-y on isobar

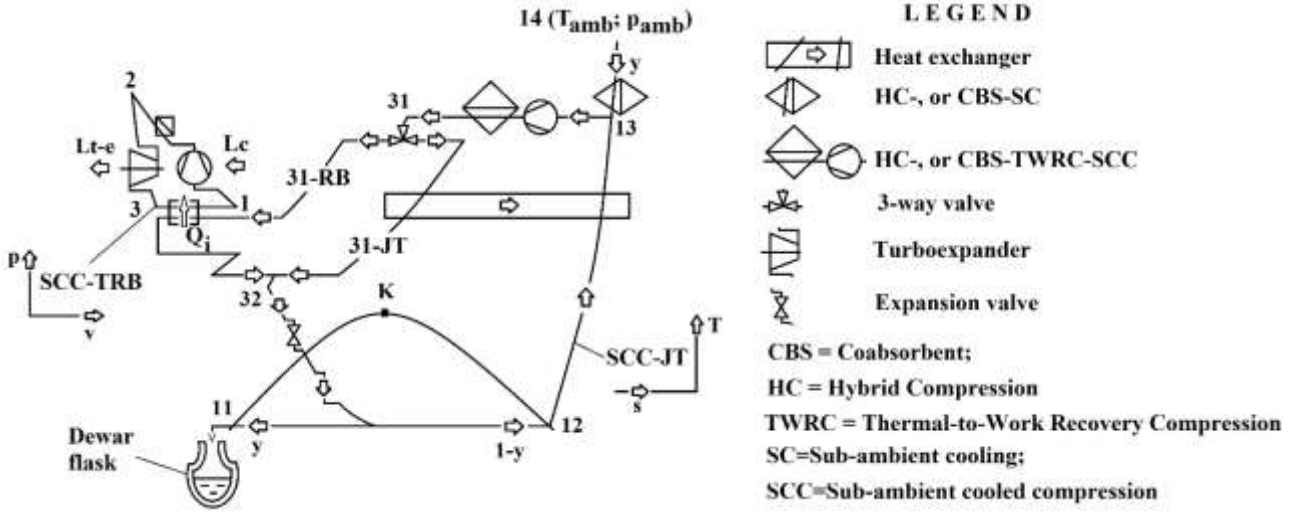

Figure 1. Schematic of the SCC-HC/CBS-RB&JT gas liquefaction cycle.

p_{amb}, between points $12(T_{11-12}, p_{amb})$ and $13\ (T_{DI} + \delta T, p_{amb})$. The second fraction $31 - 31 - RB - 32$ suffers the second precooling as well till the JTI point $32\ (T_{32}; p_{31})$, recovering in countercurrent the cold exergy of TRB helium between points $(T_3; p_3)$ and $(T_1; p_1)$ (see heat Q_i). Further on, the split complementary fractions recombine in point $32\ (T_{32}; p_{31})$. The resulting gas unit to be liquefied is expanded through JTI process expansion valve to obtain the complementary y liquid fraction we look for, state $11(T_{11-12}, p_{amb})$, and the 1-y gas fraction, state $12(T_{11-12}, p_{amb})$, to close cycle.

4. MODEL RESULTS OF SCC-HC/CBS-RB&JT GAS LIQUEFACTION CYCLE

Helium, hydrogen and natural gas liquefaction has been modeled with the help of SCC-HC/CBS-RB&JT cycle, using EES code (Klein, 2017), Fig. 1. All necessary input data are mentioned within the space of figures plotting the results. Next, we start with the HeL.

4.1. Model Results of Helium Liquefaction

The HeL results are plotted in Figs. 2a-c vs. JTI temperature T_{32}. Figs. 2a, c represent data and the specific work and mass, l_{spec} and m_{spec}, respectively, as reverse functions with ULTR parameter. The approach of JTI temperature T_{32} of the critical temperature, $T_{cr,He} = 5{,}195\ K$, improves by cca. two times the functions values, as first important behavior. Second as importance is the ULTR technology parameter. Best results are obtained with CBS and PHC use, followed by HC-SECTOR, as expected. The l_{spec} model results have been compared with results obtained by the already classic quantum HeL technology. To this extent, Quantum Design Co. produces HeL liquefiers with

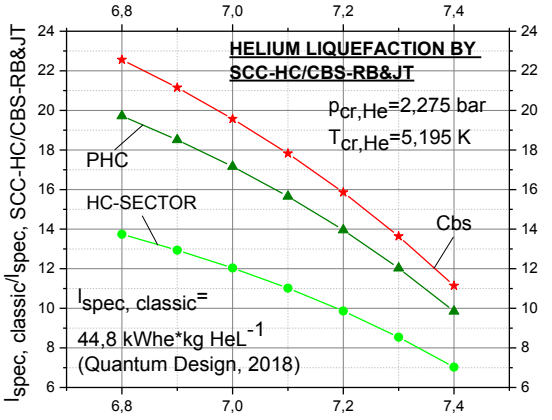

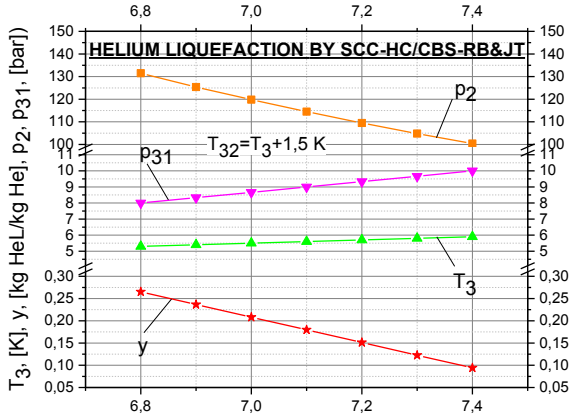

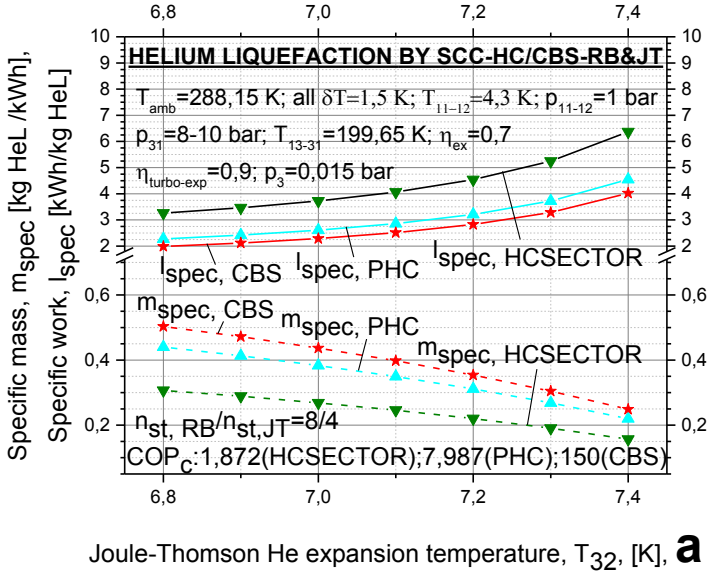

Figures 2a-c. Results of Helium liquefaction, vs. T_{32} JTI temperature.

the following main technical parameters: a) liquefying rate: 30 l/24 h (1,25 l/ h); b) power consumption: 6,5-7,5 kW. From these data, a mean specific work of $l_{spec,classic} \cong 44{,}8\ kWhe * (kg\ HeL)^{-1}$ results. In Fig. 2b we plot the ratio $l_{spec,classic} * \left(l_{spec,SCC-HC/CBS-RB\&JT}\right)^{-1}$ against T_{32}, with ULTR as parameter. Depending on ULTR type, $l_{spec,SCC-HC/CBS-RB\&JT}$ can be roughly by 10-20 times less as compared to $l_{spec,classic}$ of a small-scale HeL production. This benefit is not justified by the larger scale of the cycle at hand, only, but also because SCC-HC/CBS-RB&JT introduces several new efficient technical solutions such as SCC - HC/CBS and an original RB&JT joint to improve effectiveness. The next results, given for HL and LNG, will confirm this statement.

4.2. Model Results of Hydrogen Liquefaction

The new HL results are plotted in Figs. 3a, b. Again, and despite a significant increase of the specific heat, the approach of JTI temperature T_{32} of the hydrogen critical temperature, $T_{cr,H2} = 33{,}15\ K$, improves $l_{spec,SCC-HC/CBS-RB\&JT}$. Indeed, below $T_{32} \cong 36\ K$ all ULTR use show ones of the best l_{spec} model results in HL, today. In this respect, the model with CBS and PHC gives hope to decrease $l_{spec,SCC-HC/CBS-RB\&JT}$ below one tenth of the hydrogen heating value per mass unit, of $33.33\ kWh * kg^{-1}$. To this extent, our model best relative value is here $\frac{2{,}495}{33{,}33} = 0{,}07486 < 0{,}075\ kWhe/kWht$.

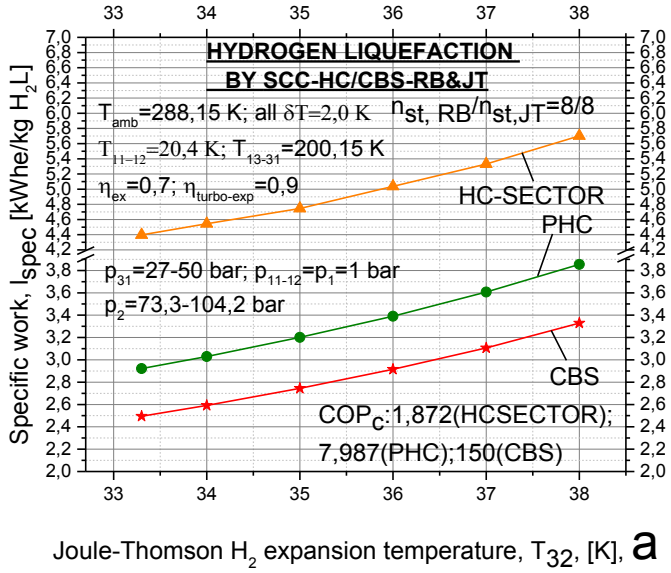

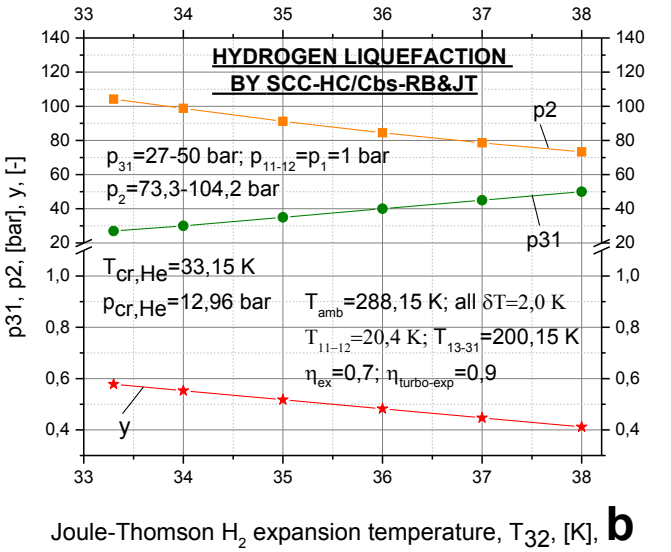

Figures 3a, b. New results of hydrogen liquefaction, vs. JTI temperature, T_{32}.

4.3. Model Results of LNG Liquefaction

The new results of LNG are plotted in Figs. 4a, b. The CH_4 critical point is $T_{cr,CH4} = 190{,}6\ K$, $p_{cr,CH4} = 45{,}99\ bar$. The JT cycle pressure and temperature have been chosen: $p_{31} = 47\ bar$ and $T_{32} = 191{,}5, 185, 180, \dots, 155\ K$, respectively. Our results are compared to the literature data. In (Franco, 2014), after a thorough analysis, the authors conclude that an advanced LNG process consumes today about $l_{spec,classic,LNG} \cong 0{,}805\ kWhe(kg\ LNG)^{-1}$. This actual figure of merit is much higher than the model values given in Fig. 4a. Roughly speaking, from Figs. 4a, b, it results that applying the technology proposed in this paper we can expect to decrease by 2-4 times the actual specific work consumed for LNG, depending on the ULTR used.

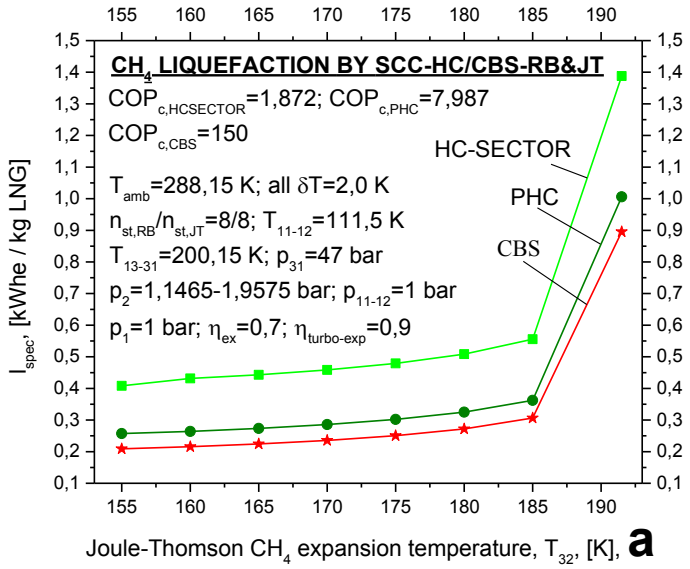

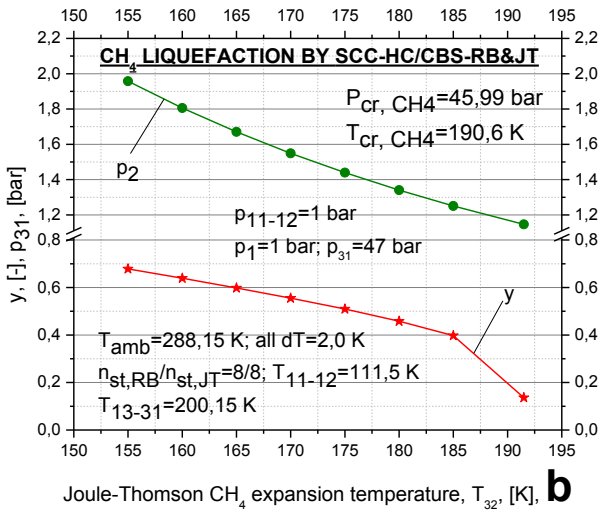

Figures 4a, b. New results of methane liquefaction, vs. JTI temperature, T_{32}.

5. CONCLUSIONS

The paper presents a new gas liquefaction cycle, noted by SCC-HC/CBS-RB&JT. This cycle is an improved version, from constructive and efficiency point of view, of a first cycle introduced in a former paper by the author. The cycle is a joint of the Reverse Brayton (RB) and Joule-Thomson (JT) cycles. It benefits of new main features, such as: a) the gas precooling at $T_{DI} = -75°C$ and $T_{ESS} = 15°C$ is boosted by a sub-sink cooled compression (SCC) technique, applied to both component cycles; b)

the SCC is performed by Hybrid Compression (HC) or Coabsorbent (CBS) technology, run in the ultra-low temperature refrigeration (ULTR) domain; c) the RB&JT joint is improved structurally, to increase efficiency and feasibility. A simple algorithm for assessment of the specific work consumption and effectiveness of HC and CBS -ULTR technologies, run in different operation conditions by $NH_3 - H_2O$ and NH_3, is given. Next, the SCC-HC/CBS-RB&JT is described and modeled. The RB and JT are run by helium and by the gas to be liquefied, respectively. Depending on ULTR type used, the model results of HeL, HL and LNG show $l_{spec,SCC-HC/CBS-RB\&JT}$ is by 10-20 times smaller, up to 7,5 % out of the specific hydrogen heating value and by 2-4 times less, respectively, as compared to l_{spec} of current technologies in kind.

REFERENCES

Eckrol J., 2017, Concepts for Large Scale Hydrogen Liquefaction Plants, NTNU.

Franco A. and Casarosa C., 2014, Thermodynamic and heat transfer analysis of LNG energy recovery for power production. 32nd UIT (Italian Union of Thermo-fluid-dynamics) Heat Transfer Conference. Journal of Physics: Conference Series **547**, IOP Publishing.

Hendricks R.C., Peller I.C, Baron A.K., 1972, Joule-Thomson Inversion Curves and Related Coefficients for Several Simple Fluids, Lewis Research Center, Cleveland Ohio 44135, NASA.

Klein S.A., 2017, Engineering Equations Solver (EES).

Staicovici MD. 2014, Coabsorbent and Thermal Recovery Compression Heat Pumping Technologies. Springer Publishing House, Heidelberg, 501 p.

Staicovici MD. 2015a, Hybrid compression heat pumping cycles based plants. EPO patent file 15075005.7 / EP 15075005.3.

Staicovici MD. 2015b, Hybrid Compression Heat Pumping Cycles Based Plants. Proceedings of the 24th International Congress of Refrigeration: Improving Quality of Life, Preserving the Earth, Yokohama, Japan, IIF/IIR, paper 611.

Staicovici MD. 2015c, Further Research Concerning the Hybrid Compression Cooling and Heating. Termotehnica 1 (AGIR, Bucharest, Romania).

Staicovici MD., 2016a, Advances in Hybrid Compression Technology for Ultra-Low Temperature Achievement. IIR Workshop on Cold Applications in Life Sciences, September 08-09, Dresden.

Staicovici MD., 2016b, Most Feasible Ultra-Low Temperature Refrigeration And Ultra-High Temperature Heating Using Hybrid Compresion Heat Pumping Cycles Based Plants. Silver Medal, EP3051233, EP20150075005/ 20150129, iENA 27-30 October, 2016.

Staicovici MD., 2017a, Research of Partial Hybrid Compression Technology Applied to Ultra-Low Temperature Refrigeration and Air Liquefaction, IIR, Proc. of Cryogenics 2017, 15-19 May, Dresden.

Staicovici MD., 2017b, Research of Partial Hybrid Compression Technology Applied to Ultra-Low Temperature Refrigeration and Natural Gas Liquefaction. Proc. XVII European Conference Milano, 9-10 June.

Staicovici MD., 2018a, Further Research Of Partial Hybrid Compression Technology Applied To Ultra-Low Temperature Refrigeration And Hydrogen Liquefaction. Proceedings of 13th IIR Gustav Lorenzen Conference, Valencia.

Staicovici MD., 2018b, Advances in Hybrid Compression Technology Applied to Ultra-Low Temperature And Industrial Refrigeration. Proceedings of 13th IIR Gustav Lorenzen Conference, Valencia.

Stamatescu C., Peculea M., Vsevolod R., Porneala S., and Barbu H., 1982, Technical Cryogenics (in Romanian). Technical Publishing House, Bucharest.

Shimko M.A., 2008, Innovative Hydrogen Liquefaction Cycle, FY Annual Progress Report, DOE Hydrogen Program.

Manuscript ID: 980
DOI: 10.18462/iir.icr.2019.0980

Research of mixed refrigerant cycle for liquefaction of natural gas depending on ambient conditions and its regulation

Alexander KROTOV [(a)], Andrey KOLESNIKOV [(a)], Yaroslav SAMOKHVALOV[(a)], Dmitry ZHIDKOV[(a)], Maxim VASILEV [(a)]

[(a)] Bauman Moscow State Technical University
Moscow, 105005, Russia, krotov.ax@gmail.com

ABSTRACT

Ambient temperature has sensible influence on parameters of single mixed refrigerant cycle for liquefaction of natural gas: decreasing natural gas inlet temperature and mixed refrigerant temperature in aftercooler in wintertime. System adjusting to ambient conditions can decrease annualized energy consumption. Authors develop simulation model and determine optimal operation parameters depending on ambient temperature. Test installation and procedure to verify model-made data are described. Control operation modes depending on ambient conditions are suggested. Obtained results can be applied at LNG (liquefied natural gas) plants, which are based on single mixed refrigerant cycle with phase separator.
Keywords: LNG, SMR, Ambient Temperature, Optimization, Regulation System.

1. INTRODUCTION

Small-scale LNG plants based on mixed refrigerant are located in different environmental conditions, moreover, some of them work in territories with continental climate, which is notable for cold winters. Influence of ambient conditions for small-scale natural gas liquefaction plants is described by Arkharov and Semenov (2016), Arkharov et al. (2016a) and Arkharov et al. (2016b). Changing working conditions require regulation of working parameters of MR (mixed refrigerant) cycle (refrigerant composition, discharge and suction pressure) to provide optimal operation and decrease exergy losses. Varying the composition of MR is the most common way to adjust to changing ambient conditions according to Xu et al. (2014) and Park et al. (2016). Performing of this regulation method makes a demand for on-line chromatography to control composition of refrigerant, significant reserves for refrigerants to store for charging, flowmeters to measure correction charge. These additions raise a price of plant, it is more sensible for small-scale plants than for medium and large ones.

As an example, Magnitogorsk, Russia is chosen as a location for small-scale LNG plant. There is high demand for liquefied natural gas as a fuel for mining trucks. Besides that, local climate conditions are notable for low ambient temperature at winter and high – for summer, temperature chart is shown on Fig. 1.

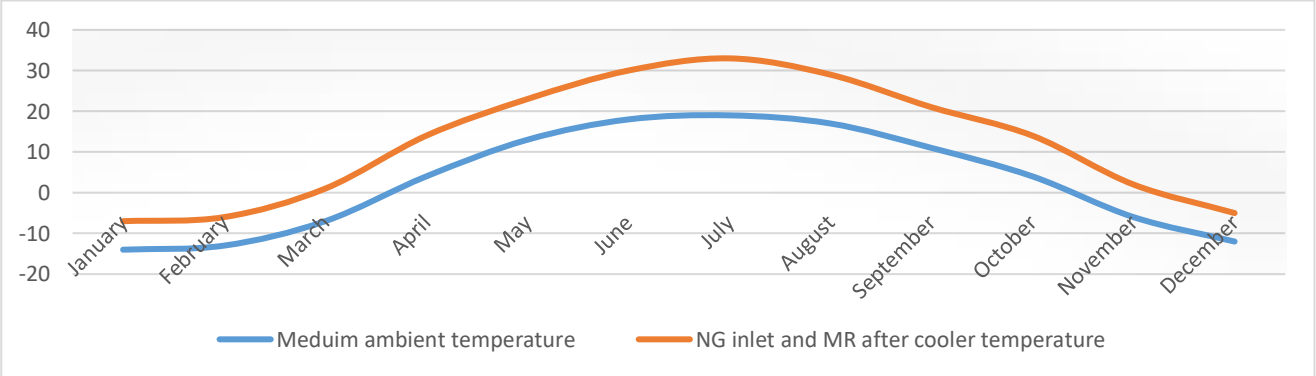

Figure 1: Medium temperature chart for Magnitogorsk, Russia

Authors suggest adjusting method for mixed refrigerant liquefaction cycle to changing ambient conditions. Regulation scheme is presented at Fig. 2. Control loop for mixed refrigerant cycle with phase separator includes separator for low pressure flow S1, separator for high pressure flow S2, refrigerant receiver RR, pump P, flow control valves EV-1, EV-2, expansion valve EV-6, solenoid valve SV-1.
It does not comprise varying of composition with means of external refrigerant storage. Composition of circulating MR changes by variation of two parameters: pressure of refrigerant in receiver RR and liquid refrigerant level in separator S1. The objective of this work is to determine these values by numerical model and validate them by experiment.
Control system works in a certain way: with ambient temperature decreasing, temperature of MR after cooler and inlet NG temperature drop. According to these changings, control system regulates pump P and valves EV-6 and SV-1 to keep appropriate values of pressure and liquid level. Valves EV-1, EV-2 regulate flow distribution to heat exchangers HE-1 and HE-2. Decreasing temperature of MR after condenser leads to increasing of liquid fraction, thuswise, there is lack of high- and mid-boiling components in vapour flow from separator S2. As a result, temperature cross occurs in HE-2 because of insufficient low-pressure flow of MR. To avoid that, HE-2 hot pinch minimum approach is controlled and maintained by flows distribution regulated by valves EV-1 and EV-2.

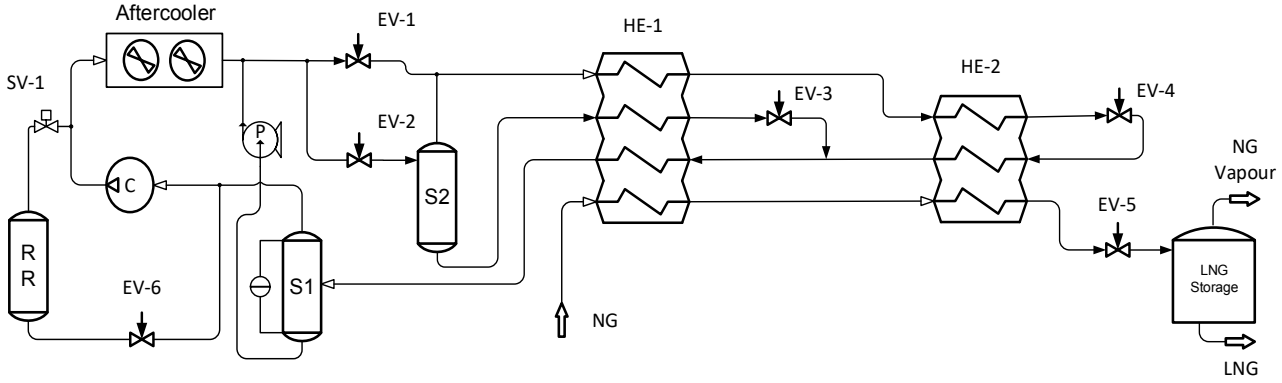

Figure 2: Control system for single MR cycle for natural gas liquefaction cycle with phase separator

2. THEORETICAL MODEL

First step of theoretical approach is modeling and optimization of MR cycle for the worst conditions: temperature of inlet NG (natural gas) and MR after condenser are 45°C. Model is developed in oil and gas processing software «ASPEN HYSYS 8.0». Programs «ASPEN HYSYS 8.0» and «Matlab v.R2016a» are used to solve optimization problems. Parameters of optimization and interaction description are mentioned by Bychkov et al. (2017), Smorodin and Parshin (2018). Optimization constraints are given in Table 1. Model parameters are described in Table 2. By recommendations of Narasimhan and Venkatarathnam (2010) Peng-Robinson equation of state with Li-Kessler enthalpies are applied. Modelling is made with terms of no influence of oil on mixed refrigerant, no heat flux to heat exchangers and expansion valves, parameters are calculated for steady working process, no overheating of suction gas. Mass fractions of components, discharge and suction pressures of mixed refrigerant and intermediate temperature are optimized. Objective function is minimum compressor power duty.
Cycles with composition optimization for other ambient conditions are also optimized with parameters mentioned in tables 1 and 2.

Table 1. Optimization constraints

Parameter	Value
Maximum discharge temperature (K)	403
Minimum approach of upper heat exchanger (K)	7
Minimum approach of lower heat exchanger (K)	3
Refrigerant vapour fraction in suction line	1

Table 2. Parameters of model

Parameter	Value
Compressor efficiency	0.716
Pressure drop of NG flow, %	2.5
Pressure drop of high pressure MR, %	2
Pressure drop of low pressure MR, %	2
After cooler temperature, K	318/303/293/283/273
Natural gas inlet temperature, K	318/303/293/283/273
NG flow rate, kg/h	824
NG inlet pressure, kPa	4000
LNG storage pressure, kPa	600

Second step of theoretical approach is defining amount of refrigerant to bypass to refrigerant receiver RR and amount of liquid low-pressure refrigerant to keep in separator S1. Base cycle for optimization is optimized MR cycle for the worst conditions with temperature of inlet NG and MR after condenser equals to 45°C. Optimization constraints and parameters of model are given in Table 1 and Table 2 respectively. Objective is minimum compressor duty. Variables are suction and discharge pressures, flow fraction to bypass to refrigerant receiver, flow fraction through valve EV-1 and temperature of NG after upper heat exchanger. Amount of liquid low-pressure refrigerant to separate in S1 is calculated automatically.

Fig. 3 shows difference between compressor duties for regulation method and composition optimization method for variety of ambient conditions. Maximum difference of compressor duties stated at temperature 0°C of inlet NG and MR after coolers and does not exceed 4%.

Composition changing of circulating flow for composition regulation method and suggested regulation method are presented at Figures 4 and 5 respectively. Disadvantage of mixed refrigerant composition achieved by suggested method at low ambient temperatures is lack of propane; this may be a problem during starting regimes.

Another outcome for suggested regulation method is tending of single mixed refrigerant cycle with phase separator to work as SMR (single mixed refrigerant) cycle with two three-flow heat exchangers. Flow distribution in mass percentage are shown in Table 3. Flow fraction in refrigerant receiver RR mentioned in table 3 ignore “dead volume” (volume of refrigerant with suction pressure left in receiver after starting regime).

Table 3. Optimization results

Parameter	45	30	20	10	0
Flow fraction in separator S1, mass (%)	0	5,4	12,4	16,2	25,4
Flow fraction in refrigerant receiver RR, mass (%)	0*	3,7*	0,1*	12,1*	5,0*
Flow fraction through EV-1, mass (%)	0	40,3	62,5	65,5	69,3
Flow fraction through EV-2, mass (%)	100	50,6	25,0	7,2	0,3
Intermediate temperature (°C)	-12	-15	-5	-5	-5

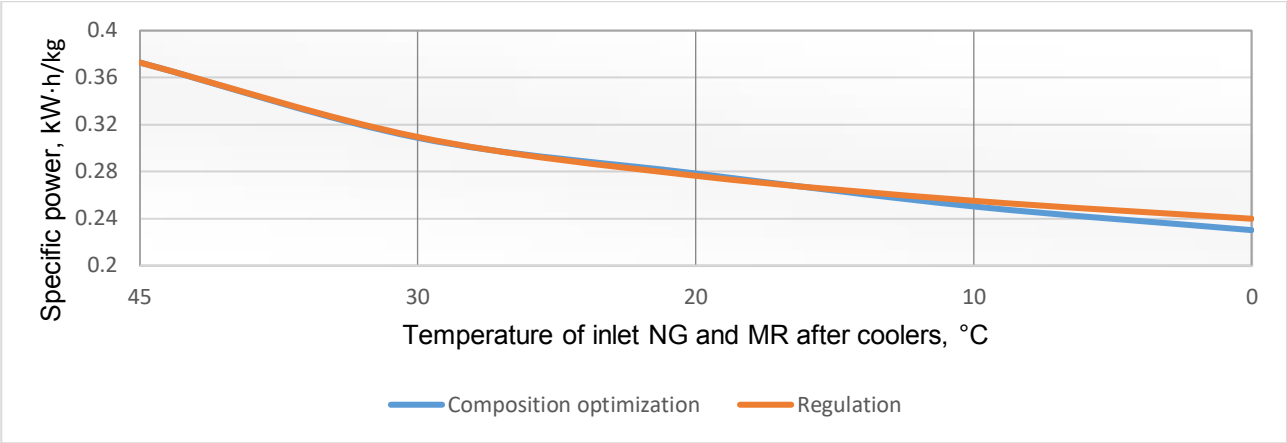

Figure 3: Compressor duty for cycles with different control system

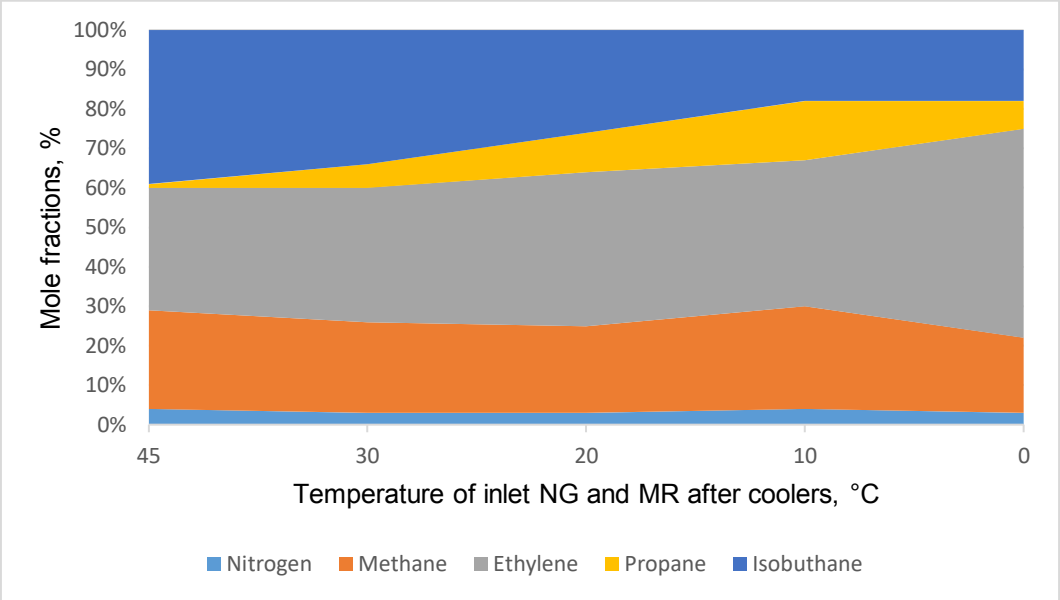

Figure 4: Composition change of circulating flow with composition regulation method

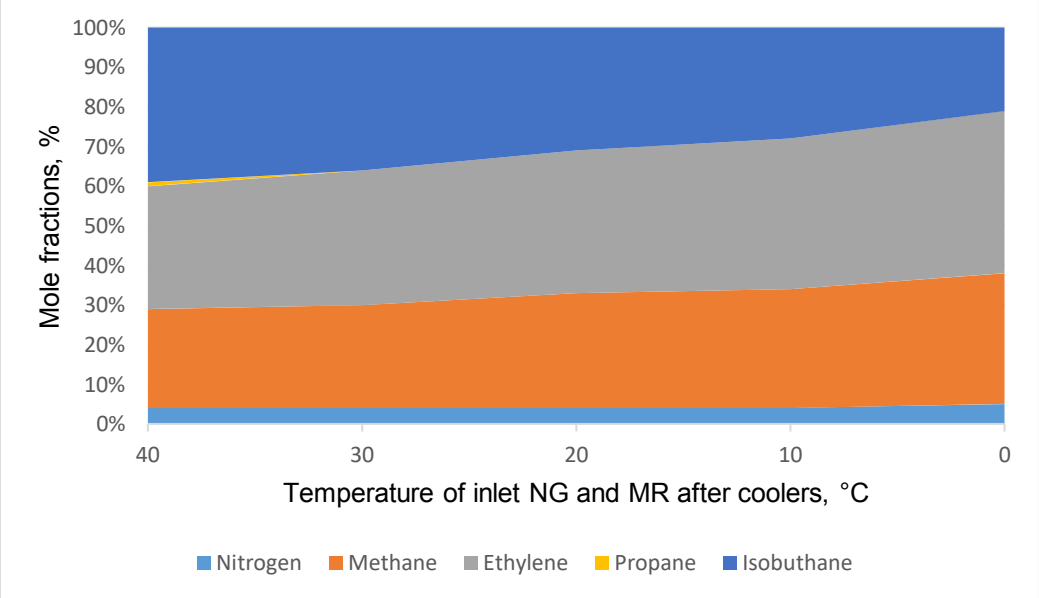

Figure 5: Composition change of circulating flow with suggested regulation method

3. EXPERIMENTAL SETUP

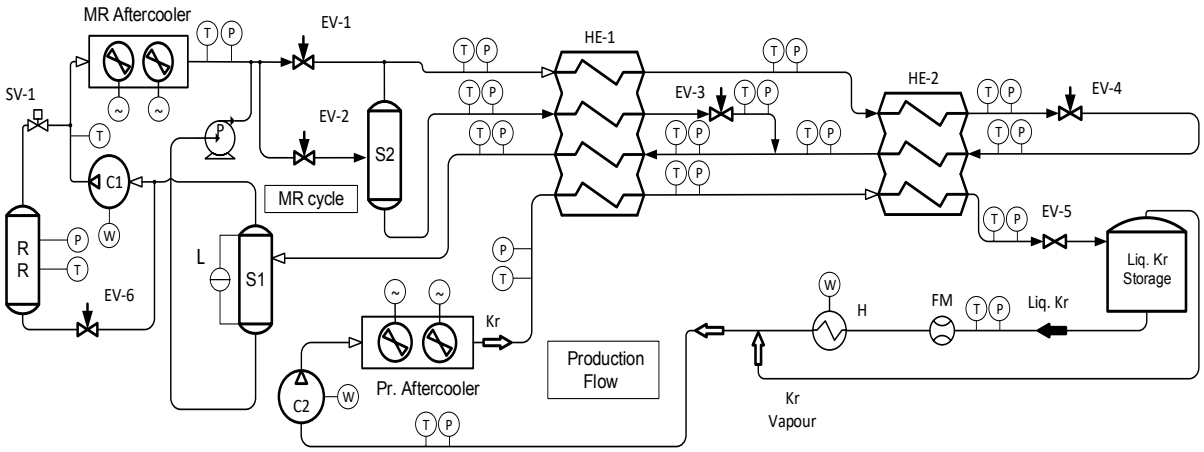

Figure 6: Experimental setup diagram

Experimental setup consists of two cycles (Fig. 6): mixed refrigerant cycle with phase separator and imitation of production flow cycle. Setup also includes measuring instruments described in Table 4. Mixed refrigerant cycle consists of compressor C1, MR aftercooler with variable speed driver fans, separators S1 and S2, pump P, upper spiral-wound heat exchanger HE-1 and lower spiral-wound heat exchanger HE-2, intermediate expansion valve EV-3 and main expansion valve EV-4. Regulation system includes refrigerant receiver RR, expansion valve EV-6, solenoid bypass valve SV-1 and electronic valves EV-1, EV-2. Second loop comprises compressor C2, Pr. aftercooler with variable speed driver fans, expansion valve EV-5, liquid product storage which is a Dewar vessel, electric heater H. Methane is replaced with Krypton for safety reasons, mass flow rate and inlet and storage pressures are changed to be similar with methane temperatures.

Experimental procedure goes in the following way. Mixed refrigerant cycle starts operation at conditions of temperature 45°C of MR out of MR aftercooler. Variable speed fans regulate temperature; experiment goes in winter ambient conditions to reach 0°C temperature after aftercoolers. As process of MR cycle reaches steady working regime (temperature of MR after EV-4 reaches desired value) production flow cycle is turned on. As process stabilizes, all measuring are checked and recorded by SCADA system.

The next step is decreasing flows' temperatures out of aftercoolers to values of 30°C, 20°C, 10°C, and 0°C. Pressure in refrigerant receiver RR and refrigerant level in separator S1 are calculated by method suggested by Bychkov et al. (2019) based on the data obtained from optimization results.

Table 4. Main instruments and their measuring properties

Parameter	Instruments	Measuring range	Accuracy
Temperature	OWEN Pt1000	-196..660°C	0.25%
Mass flow	Emis	10-2000 kg/h	0.15%
Power meter	GW Instek	0.1 W to 12 kW	0.1%
Pressure	Elemer	0 to 40 bar	0.25%
Chromatography	Chromos GC-1000	-	0.2%
Level meter	Sick AG	30…500 mm	<2%

4. CONCLUSIONS AND DIRECTION OF EXPERIMENTAL RESEARCH

Authors suggested regulation method for single mixed refrigerant cycle with phase separator for liquefaction of natural gas with no composition regulation by external sources. Modelling, optimization and comparison of cycles with composition changing regulation method and with suggested regulation method for different ambient conditions are presented. It shows maximum 4%

divergence of specific duties in favor of composition change method for conditions of minus 10°C of ambient temperature. Experimental setup and procedure are described, with following model validation and corrections will be made. Suggested method of regulation on varying ambient conditions allows decreasing capital cost of small scale liquefaction plant with low losses of effectiveness.

REFERENCES

Arkharov, A.M., Semenov, V.Y., 2016. Analysis of Thermodynamic Efficiency of Small-Scale Natural Gas Liquefying Plant Operating on Medium-Pressure Cycle. Chemical and Petroleum Engineering, 51 (9-10), 656-664.

Arkharov, A.M., Semenov, V.Y., Krasnonosova, S.D., 2016. Methodology of Statistical Entropy Analysis of Small-Scale Natural Gas Liquefiers. Chemical and Petroleum Engineering, 51 (9-10), 665-673.

Arkharov, A.M., Semenov, V.Y., Krasnonosova, S.D., Lebedev, S.Y., Kul'byakin, V.P., 2016. Statistical Entropy Analysis and Experimental Study of LNG Plant with Precooling at -70°C. Chemical and Petroleum Engineering, 52 (7-8), 468-475.

Bychkov, E. G., Makarov, B. A., Zherdev, A. A., 2019. Development of a Method of Determining the Component Composition of the Working Fluid of Low-Temperature Throttling Refrigeration Machines Operating with Multicomponent Mixtures of Coolants. Chemical and Petroleum Engineering, Article in Press.

Bychkov, E.G., Samokhvalov, Y.V., Makarov, B.A., Yakovlev, V.I., 2017. Experimental research of low-temperature throttling refrigerator for cryoconservation of medical and biological objects. Journal of Physics: Conference Series, 891(1), article №012109.

Narasimhan, N.L., Venkatarathnam G., 2010. A method for estimating the composition of the mixture to be charged to get the desired composition in circulation in a single stage JT refrigerator operating with mixtures. Cryogenics, 50(2), 93-101.

Park, K., Won, W., Shin, D., 2016. Effects of varying the ambient temperature on the performance of a single mixed refrigerant liquefaction process. Journal of Natural Gas Science and Engineering, 34, 958-968.

Smorodin, A.I., Parshin, S.A., 2018. Optimization of Refrigerant Composition of Low-Temperature Stage of Dual Mixed Refrigerant Cycle. Chemical and Petroleum Engineering, 54 (7-8), 493-498.

Xu, X., Liu, J., Cao, L., Pang, W., 2014. Automatically varying the composition of a mixed refrigerant solution for single mixed refrigerant LNG (liquefied natural gas) process at changing working conditions. Energy, 64, 931-941.

Manuscript ID: 987
DOI: 10.18462/iir.icr.2019.0987

Numerical investigation on flow boiling characteristics of liquefied natural gas in FLNG plate-fin heat exchanger under sloshing conditions

Jianrui LI[(a)], Haitao HU[(a)]*, Weizhe HAN[(a)], Guoliang DING[(a)], Hui CHEN[(b)], Zhigang ZHANG[(b)], Youhu ZHANG[(c)]

[(a)] Institute of Refrigeration and Cryogenics, Shanghai Jiao Tong University
800 Dongchuan Rd, Shanghai, 200240, China, huhaitao2001@sjtu.edu.cn
[(b)] Shanxi Fenxi Heavy Industry Co. Ltd., Taiyuan, Shanxi 030027, China;
[(c)] Hangzhou Zhongtai Cryogenic Technology Co., Ltd., Hangzhou 311402, China

ABSTRACT

Plate-fin heat exchangers (PFHX) are widely used in floating liquefied natural gas (FLNG) facilities, and the PFHX performance may be significantly affected by the FLNG sloshing motions. In the present study, a model for liquified natural gas flow boiling in PFHX under sloshing conditions was established. In the model, the numerical model to simulate the flow and heat transfer was developed, and the sloshing acceleration model was added to reflect the sloshing effect. The proposed model was verified experimetally, and it agrees well with the experimental data. Based on the proposed model, the sloshing motion effects were analyzed. The heaving motion among sloshing conditions has most obvious influence on heat transfer, showing a sloshing impact factor of 38.5%~240.9%; the rotation type of sloshing motion has negligible effect on the heat transfer.
Keywords: Plate-Fin Heat Exchanger, Two-phase Flow, Flow Boiling, Heat Transfer

1. INTRODUCTION

Plate-fin heat exchangers (PFHXs) are widely used in the floating liquefied natural gas (FLNG) facilities due to the advantages of high-efficient, compact structure, low weight and reliability(Jiang et al., 2016.). For PFHXs in FLNG facilities, they operate under sloshing conditions, and the heat transfer characteristics of two-phase fluid in PFHXs would be affected by the additional inertia force (Faheemullah et al., 2016.). For designing PFHXs in FLNG facilities, it is significant to reveal the flow boiling characteristics of liquefied natural gas in FLNG plate-fin heat exchanger under sloshing conditions.

For the fluid flow in PFHXs, the existing research focused on heat transfer characteristics of single-phase fluid (Chen, 2016.; Caoet al., 2016.; Ma et al., 2016.; Aliabadi and Hormozi, 2013.; Yang et al., 2015) and the flow pattern transition of two-phase flow (Wang, 2016.), and there is no literature on flow boiling characteristics of two-phase liquefied natural gas under sloshing conditions. In the existing literatures (Chen, 2016; Cao et al., 2016.; Ma et al., 2016.; Aliabadi and Hormozi, 2013.; Yang et al., 2015.), the effect of structure was analyzed, and flow pattern transition principle under onshore conditions was discussed. However, for flow boiling of two-phase liquefied natural gas in PFHXs under sloshing conditions, the flow pattern will be significantly affected, and the heat transfer characteristics must be different from those obtained for single-phase fluid and for two-phase flow under onshore conditions (Wang and Li, 2016.).

For the effect of of the sloshing conditions, the existing research focused on storage tank equipment (Ushima, 1998.), and single-phase flow in circular tubes(Tan et al., 2009.; Pendyala et al., 2008.; Yan et al., 2011.). But there is no literature on flow boiling of two-phase liquefied natural gas in PFHXs under sloshing conditions.

The objective of this article is to develop a numerical model of flow boiling characteristics of liquified natural gas in PFHXs under sloshing conditions, and to analyze the effect of sloshing conditions on

the heat transfer characteristics in PFHXs.

2. NUMERICAL MODEL

The equations of continuity, momentum and energy conservation are shown in Eqs. (1)~(5). In the equations, the mass source term representing the mass transfer (S_m) is added into the continuity equation to predict the mass transfer rate; the momentum source terms ($\rho\vec{g}$) and (F_σ) presenting gravity and surface tension are added into the momentum equation to describe flow patterns and the effects of different forces; the momentum source term ($\rho(\vec{a}_r + \vec{a}_t)$) represents the additional force of sloshing condition; the energy source term (Q) presenting the latent heat transfer is added into the energy equation; (α_l) and (α_v) in continuity conservation are the volume fraction of gas and liquid, respectively. The additional force of sloshing condition ($\rho(\vec{a}_r + \vec{a}_t)$) is calculated based on the movement of sloshing condition, and the sloshing acceleration ($\vec{a}_r$) and ($\vec{a}_t$) can be derived by second derivativing relative position and angle between fluid and channel, as shown in Eq. (6).

$$\frac{\partial}{\partial t}(\alpha_l \rho_l) + \nabla \cdot (\alpha_l \rho_l \vec{v_l}) = -S_m \quad \text{Eq. (1)}$$

$$\frac{\partial}{\partial t}(\alpha_v \rho_v) + \nabla \cdot (\alpha_v \rho_v \vec{v_v}) = S_m \quad \text{Eq. (2)}$$

$$\alpha_v + \alpha_l = 1 \quad \text{Eq. (3)}$$

$$\frac{\partial(\rho\vec{v})}{\partial t} + \nabla \cdot (\rho\vec{v}\vec{v}) = -\nabla p + \nabla[\mu(\nabla\vec{v} + \nabla\vec{v}^T) - \frac{2}{3}\mu \cdot \nabla\vec{v}I] + \rho\vec{g}' + F_\sigma + \rho(\vec{a}_r + \vec{a}_t) \quad \text{Eq. (4)}$$

$$\frac{\partial(\rho E)}{\partial t} + \nabla \cdot [\vec{v}(\rho E + p)] = \nabla \cdot (k \nabla \theta) + Q \quad \text{Eq. (5)}$$

$$a_t = -A_{\max}(\frac{2\pi}{T})^2 \cos(\frac{2\pi t}{T} + \frac{\pi}{2}) \quad \text{Eq. (6)}$$

The surface tension (F_σ) in momentum conservation is the volumetric force representing the surface tension, and can be calculated in the CSF (Continuous Surface Force) formulation by Eq. (7):

$$F_\sigma = \sigma \frac{\rho \kappa_w \tilde{N} \alpha_w}{\frac{1}{2}(\rho_m + \rho_w)} \quad \text{Eq. (7)}$$

The mass source term (S_m) is expressed as different equations for at vapor-liquid interface or near wall, shown as Eq. (8). At vapor-liquid interface, the mass transfer rate can be calculated based on the difference between local temperature (T_l) and saturation temperature (T_{sat}). At the heating wall, the evaporation mass transfer rate can be derived according to the local heat flux (q).

$$S_m = \begin{cases} coeff \cdot \alpha_l \rho_l \dfrac{(T_l - T_{sat})}{T_{sat}} & (interface) \\ \dfrac{q \cdot A}{h_{fg}} & (nearwall) \end{cases} \quad \text{Eq. (8)}$$

3. SIMULATION DOMAIN AND SOLUTION METHODOLOGY

The simulation domain of a flow channel in PFHXs is shown in Fig. 1. The simulations are based on the commercial software platform ANASYS FLUENT. The Volume of Fluid model combined with a Continuous Surface Force (VOF-CSF model) is applied to represent of the vapor-liquid phase flow with surface tension for simulating the flow patterns. The contact angle boundary condition is set on the tube surface for the VOF-CSF model. All the models developed above are developed by compiling user-defined functions (UDF) in FLUENT. And the standard k-ω model is employed as the

turbulence model for high velocity when vapor quality is large.
Hexahedral structured grids are used for the simulations. The grid independence verfication shows that, as the amount of mesh elements is larger than 102,000, the variations of the heat transfer rate and the average temperature are less than 2%. Therefore, the mesh with 120,000 elements was selected in the persent study.

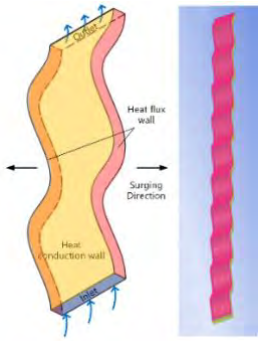

Figure 1: Monthly electricity consumption

4. EXPERIMENTAL VALIDATION

4.1 Experimental Rig and Data Reduction

The schematic diagram of the experimental rig is shown as Fig. 2(a). The main test circuit is composed of a compressor, a plate heat exchanger, an expansion valve, an electric heater and a test sample. The superheated vapor coming out from the compressor is cooled, condensed and subcooled in the front plate heat exchanger and the rear plate heat exchanger. Then the subcooled working fluid goes through the regulating valve to reduce the pressure and temperature, and the two-phase fluid is heated by the front electric heater to get the needed vapor quality; then the working fluid enters into the test section, where the heat transfer coefficient will be tested. Then the working fluid will be heated to superheat state and go back to the compressor.
The test section is shown as Fig. 2(b), and the structure parameters are determined based on the actual heat exchanger used in LNG plants; the fin height is 6.35 mm, and the fin width is 1.4 mm.

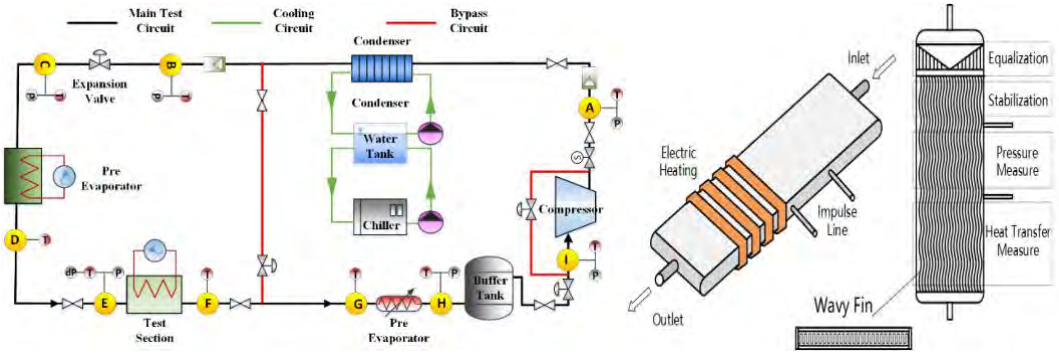

(a) Experimental rig (b) Test section

Figure 2: Experimental rig and test section

The heat transfer coefficient (α) is calculated as Eq. (9):

$$\alpha = \frac{q}{\Delta T} = \frac{q}{(T_{inwall} - \frac{t_{in} + t_{out}}{2})} \quad \text{Eq. (9)}$$

Where, (T_{inwall}) is the inner wall temperature; (t_{in}) and (t_{out}) are the inlet and outlet temperatures, respectively; (q) is the heat flux.

To analyze the sloshing effect, the sloshing impact factor (EF) is defined as the ratio of heat transfer coefficients between the sloshing condition (α_s) and the onshore condition (α_0), as shown in Eq. (10):

$$EF = \frac{\alpha_s}{\alpha_0} \qquad \text{Eq. (10)}$$

4.3 Model Validation

To validate the proposed model, the experiments on the heat transfer characteristics are performed, and the comparison of the heat transfer coefficient between the experimental data and the simulation results under the same operating condition is shown in Fig. 3. The predicted results agree well with the experimental data with an average deviation of 12.6%.

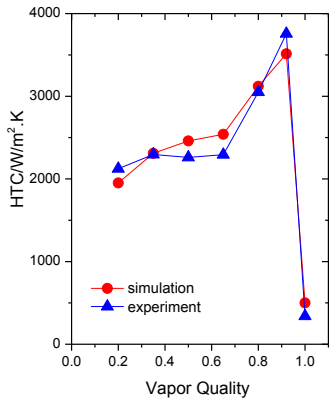

Figure 3: Comparison beween predicted values of proposed model and experimental data (G=40 kg/m²s, *q*=4000W/m²)

5. RESULT DISCUSSIONS

The sloshing conditions include the surging, heaving, yawing and rolling contions. In the present stduy, the heat transfer characteristics under surging, heaving, yawing and rolling contions will be analyzed based on the validated model to reveal the effect of sloshing motions.

5.1 Heat Transfer Characteristics under Surging Condition

Fig. 4a shows the sloshing impact factor (*EF*) values at different vapor qualities under surging conditions. At vapor quality of 0.2, *EF* is within 87.9%~101.3%; as the vapor quality increases, the minimum value of EF increases. At vapor quality of 0.5, *EF* is within 91.4%~106.6%; at vapor quality of 0.8, *EF* is within 96.7%~110.0%. The results show that, as the vapor quality increases, the deterioration effect of surging movement becomes smaller, while the enhancement effect becomes larger.

Fig. 4b shows the sloshing impact factor (*EF*) values under different surging frequency conditions. *EF* is within 89%~104.3% under surging frequency of 0.0833~0.1667. As the frequency increases, *EF* becomes much smaller at 0.1~0.4 surging period. The possible reason is that, at low frequency condition, the liquid will form film on the channel wall due to the inertia force, which resulting in the heat transfer enhancement; as the frequency increases, there is no enough time for the liquid forming film to cover the wall, and the liquid droplets lead to worse heat transfer characteristics compared with the liquid film.

Fig. 4c shows the sloshing impact factor (*EF*) values under different surging amplitude conditions. *EF* varies from 85.9% to 105.5% at surging amplitude of 1~4 m. As the amplitude increases, *EF* increases. The possible reason is that, at larger surging amplitude, the disturbance of fluid is enhanced, and the vapor-liquid slip velocity at non flowing direction is higher; there is less time for liquid formimg droplets, and the phase distribution at the middle of the channel is uniformly distributed, leading to the increment of heat transfer coefficient.

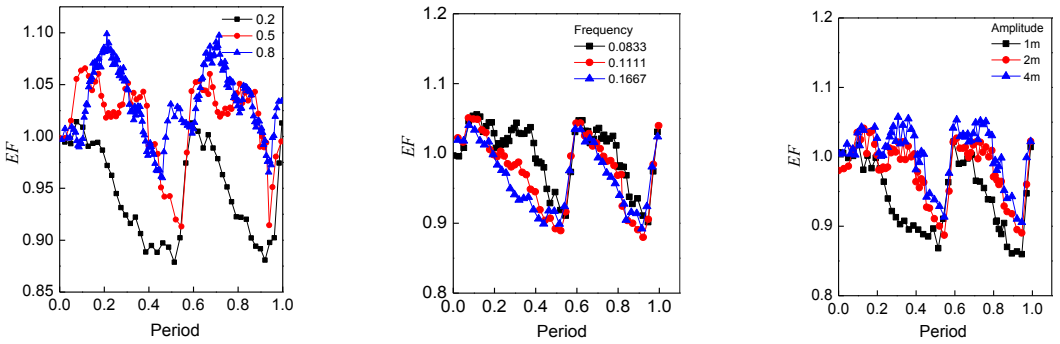

(a) at differentvapor quality (b) at different frequency (c) at different amplitude

Figure 4: *EF* under surging conditions (G = 40 kg·m^{-2} s^{-1}, heat flux = 4000 W·m^{-2})

In order to analyze the effect mechanism of sloshing condition, the comparison of flow patterns between onshore condition and surging condition during an entire surging period (*T*) was performed, as shown in Fig. 5. The operation vapor quality in the figure is 0.5. Under onshore condition, the flow pattern is mist-annular flow, and there is liquid film near the wall and droplet at the middle of the channel. Under surging condition, the liquid phase moves to left side due to the channel movement, and the liquid film thickness of the left side reaches a maximum at the time of 0.25*T*; at 0.25*T*~0.5*T*, the liquid film thickness of the left side decreases, while thie liquid film thichness of the right side increases; as the time goes on, the liquid phase starts to move to the reverse side of the channel, and the liquid film thickness at the right side reaches to a maximum at 0.75*T*; when it comes to the end of a period, the liquid film covers both sides of the wall again.

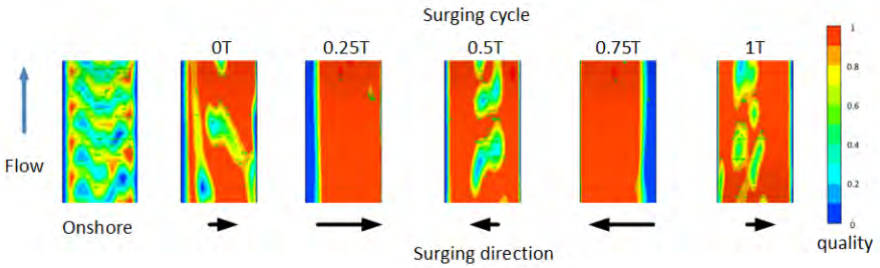

Figure 5: Flow pattern under surging condition (G = 40 kg·m^{-2} s^{-1}, q = 4000 W·m^{-2}, As = 2 m, fs = 0.1667)

5.2 Heat Transfer Characteristics under Heaving Condition

Fig. 6a shows the sloshing impact factor (*EF*) at different vapor quality under heaving conditions. *EF* is within 55.9%~280.0% at vapor quality of 0.2. As the vapor quality increases, the maximum value of *EF* becomes smaller, and the effect of heaving condition on the heat transfer becomes smaller. At vapor quality 0.5, *EF* is within 52.0%~248.1%. At vapor quality of 0.8, *EF* is within 48.8%~228.1%. The maximum value of *EF* appears at the time of 0.25 heaving period. The possible reason for the effect of heaving conditions is that, the heaving direction is parallel to the flow direction, and the relative velocity between fluid and channel wall is sped up at, resulting in a significant heat transfer enhancement at the time of 0.25 heaving period.

Figs. 6b and 6c show the sloshing impact factor (*EF*) under different surging frequency and amplitude conditions. *EF* is within 38.5%~240.9% at surging frequency of 0.0833~0.1667, and it increases with the increasing surging frequency. As the surging amplitude increases from 1 m to 4 m, *EF* increases significantly, and the maximum value of *EF* increases from 138.0% to 344.6%. The results show that, the surging amplitude has a significant effect on the heat transfer characteristics.

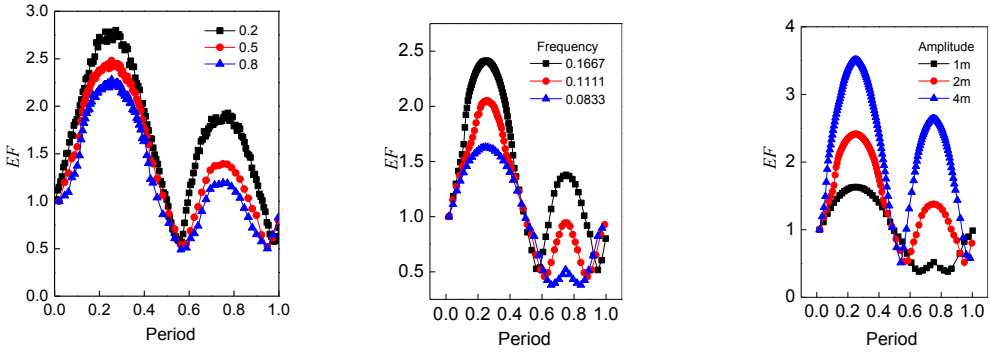

(a) vapor quality (b) frequency (c) amplitude

Figure 6: EF under different heaving conditions (G = 40 kg·m^{-2} s^{-1}, q = 4000 W·m^{-2})

5.3 Heat Transfer Characteristics under Yawing and Rolling Conditions

Fig. 7 shows the sloshing impact factor (*EF*) under yawing and rolling conditions. No obvious influence of yawing and rolling conditions on the heat transfer was found at the whole sloshing period. *EF* is within 99.7%~100.3% under yawing and rolling conditions. The results can be deduced that, the rotation type of sloshing movent has negligible effect on the heat transfer.

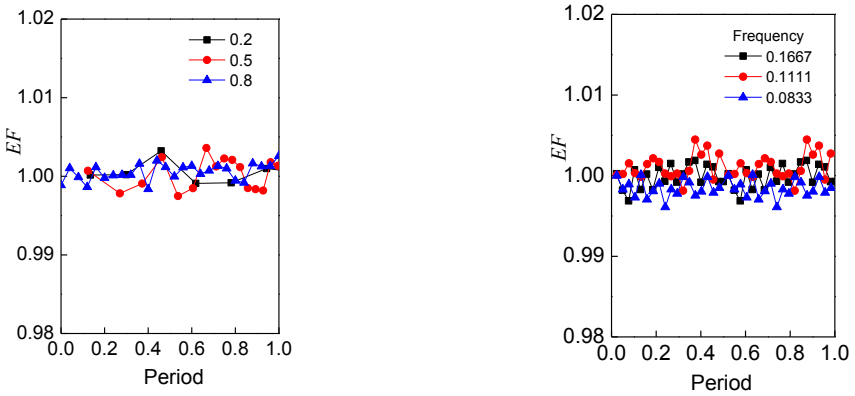

(a) effect of yawing conditions (b) effect of rolling conditions

Figure 7: *EF* under yawing and rolling conditions (G = 40 kg·m^{-2} s^{-1}, q = 4000 W·m^{-2})

6. CONCLUSIONS

1) The numerical model of flow and heat transfer of fluid in channel of PFHXs under sloshing conditions was developed by introducing the mass transfer model, the contact angle model and additional force model into the control equations. The proposed model was validated by experimental data obtained in the present study. The predicted results agree well with the experimental data within an averaged deviation of 12.6%.
2) Based on the validated model, the influence of sloshing conditions (surging, heaving, yawing and rolling contions) on heat transfer characteristics was analyzed.
3) The comparion of flow pattern between the surging contions and onshore conditions was performed. Under onshore conditions, the flow pattern is mist-annular flow, and there is liquid film near the wall and droplet at the middle of the channel. Under surging conditions, the liquid phase moves to one side of the channel due to the channel movement, and the liquid film thickness of the one side reaches a maximum at the time of 0.25 and 0.75 surging period.
4) Among the sloshing conditions, the heaving condition shows the most significant effect on the heat transfer characteristics. The sloshing impact factors (*EF*) under heaving conditions are

within 38.5%~280.0%. The rotation type of sloshing movement has negligible effect on the heat transfer characteristics.

NOMENCLATURE

α_l	volume fraction of gas (-)	T_l	local temperature (K)
α_v	volume fraction of liquid (-)	T_{sat}	saturation temperature (K)
ρ	density (kg.m^{-3})	q	heat flux(W.m^{-2})
$\vec{g}$	gravity (m.s^{-2})	$coeff$	mass transfer coefficient
F_σ	surface tension (N)	h_{fa}	*latent heat*(J.kg^{-1})
Q	energy source term (J)	α	heat transfer coefficient (W.m^{-2}.K)
$\vec{a}_r$	rotation acceleration(m.s^{-2})	T_{inwall}	inner wall temperature (K)
$\vec{a}_t$	transition acceleration (m.s^{-2})	t_{in}	inlet temperatures (K)
S_m	mass transfer source term (kg)	t_{out}	outlet temperatures (K)

REFERENCES

Aliabadi M. K., Hormozi F., 2013. Performance analysis of plate-fin heat exchangers : different fin configurations and coolants. Journal of Thermophysics and Heat Transfer 27(3), 515-525.

Chen T., Wang J., Peng W., 2017. Flow and heat transfer analyses of a plate-fin heat exchanger in an HTGR. Annals of Nuclear Energy108,316-328.

Cao L., Liu J. P., Li R. X. et al., 2016. Experimental study on the mixed refrigerant heat transfer performance in a plate-fin heat exchanger during a single-stage cryogenic period. Applied Thermal Engineering 93,1074-1090.

Faheemullah S., Ji Q., Fan Y.,2016. Evaluating China's natural gas supply security based on ecological network analysis. Journal of Cleaner Production 139,1196-1206.

Jiang Z. A., Wang F. P., Duan Y. Z. et al., 2016. China's gas market under new situations: Trends and countermeasures – Taking Sichuan and Chongqing gas provinces as an example. Natural Gas Industry B, (03):187-194.

Ma H. Q., Hou C. Q., Yang R. X. et al., 2016. The influence of structure parameters on stress of plate-fin structures in LNG heat exchanger. Journal of Natural Gas Science and Engineering 34,85-99.

Ma H. Q., Cai W. H., Yao. Y. et al., 2016. Investigation on stress characteristics of plate-fin structures in the heat-up process of LNG heat exchanger. Journal of Natural Gas Science and Engineering 30,256-267.

Pendyala R., Jayanti S., Balakrishnan A.R., 2008. Convective heat transfer in single-phase flow in avertical tube subjected to axial low frequency oscillations. Heat Mass Transfer 44(7), 857-864.

Tan S.C., Su G.H., Gap P.Z., 2009. Experimental and theoretical study on single-phase natural circulationflow and heat transfer under rolling motion condition. Appl. Therm. Eng. 29, 3160-8.

Ushima S., 1998. Three-dimensional arbitrary Lagrangian-Eulerian numerical prediction method for nonlinear free surface oscillations. International Journal for Numerical Methods in Fluids. 26, 605-623.

Wang Z, Li Y. Z., 2016. Layer pattern thermal design and optimization for multistream plate-fin heat exchangers—A review. Renewable and Sustainable Energy Reviews, 53:500-514.

Yan B.H., Gu H.Y., Yu L., 2011. Numerical research of turbulent heat transfer in rectangular channels inocean environment. Heat mass transfer.

Yang Y. J. ,Li Y. Z., Biao S. et al., 2015. Performance Evaluation of Heat Transfer Enhancement in Plate- fin Heat Exchangers with Offset Strip Fins. physicsprocedia, 67：543-550.

Manuscript ID: 1067
DOI: 10.18462/iir.icr.2019.1067

Liquefied Natural Gas Cold Recovery for Heavy-Duty Vehicles Smart Management

Alessia ARTECONI[(a)], Daniele FIASCHI[(b)], Luca CIOCCOLANTI[(c)], Carlo Maria BARTOLINI[(d)], Fabio POLONARA[(a)]

[(a)] Dipartimento di Ingegneria Industriale e Scienze Matematiche, Università Politecnica delle Marche, via Brecce Bianche 1, 60131 Ancona, Italy, a.arteconi@univpm.it, f.polonara@univpm.it
[(b)] Dipartimento di Ingegneria Industriale, Università degli Studi di Firenze, Via di S. Marta 3, 50139 Firenze, Italy, daniele.fiaschi@unifi.it
[(c)] Università eCampus, C.R.E.A., via Isimbardi 10, 22060 Novedrate (CO), Italy, luca.cioccolanti@uniecampus.it
[(d)] Società per il TRAsferimento TEcnologico e Guida all'Innovation Engineering – S.TRA.TE.G.I.E. srl, via Sandro Totti 3, 60131 Ancona, Italy, c.m.bartolini@strategiesrl.com

ABSTRACT

Liquefied Natural Gas (LNG) is always more and more used as alternative fuel for heavy-duty vehicles because it is more environmentally friendly than traditional fossil fuels. LNG is stored in cryogenic vessels within the truck and must be vaporized before it can be used to supply the engine. Objective of this paper is to evaluate the thermodynamic performance of an innovative system aiming at recovering the cold thermal energy from the LNG vaporization. In general, the cold energy obtained can be used for different applications on-board: vehicle air-conditioning, refrigeration purposes or cooling of engine intake air. With respect to the latter, a thermodynamic analysis of the system proposed is illustrated under different operating conditions and the impact on the overall performance of the LNG fuelled engine of the truck is discussed.
Key Words: LNG, Trucks, Cold Recovery, Engine Intake Air Cooling, Engine Performance, Simulation Analysis.

1. INTRODUCTION

In 2016 the greenhouse gas emissions of the transport sector (including aviation and shipping) accounted for about 27% of the total greenhouse gas emissions in EU-28 countries. Moreover, such emissions (excluding international shipping) were 26% higher than 1990 levels. With reference to the same year, the road transport was responsible for almost 72% of the total greenhouse gas emissions of the sector including international aviation and shipping. According to the European Environment Agency (2018), 44% of these emissions were related to passenger cars and about 19% to heavy-duty vehicles.
In the EU Transport White Paper (2011), a greenhouse gas emission reduction target of 60% compared to 1990 levels has been fixed and, as a consequence, actions need to be implemented. Among the EU policies in the attempt to achieve this goal, the promotion of alternative fuels could have a significant impact especially in the short-medium term. Natural gas (NG) in its liquid form (LNG) is considered the alternative fuel for heavy-duty vehicles that can best substitute conventional fuels, given its availability at competitive prices, high energy density and availability of technology. Indeed, LNG entails: (i) environmental benefit in terms of lower local air pollution and greenhouse gas emissions; (ii) reduced on-board weight and space requirements comparable with diesel fuel; (iii) reduction of dependency on imported oil. LNG has an energy density of 435 $kg \cdot m^{-3}$, more than double the energy density of the compressed natural gas (CNG) at 200 bar (175 $kg \cdot m^{-3}$). This means that an LNG fuelled vehicle can travel up to 2.4 times the distance of the CNG counterpart for a given capacity fuel tank. Alternatively, for a given vehicle range, an LNG fuelled vehicle needs a fuel tank capacity up to 2.4 times smaller than a CNG vehicle. Moreover, an LNG powered vehicle costs less than a CNG powered vehicle for manufacturing. With respect to the environmental impact, Arteconi

et al. (2010) carried out a comparison of the well-to-wheel life cycle greenhouse gas emissions for CNG, LNG and diesel fuel, finding that LNG allows to reduce by 10% the emissions compared to diesel. Moreover, the increasing use of LNG and the development of a proper infrastructure would make possible the deployment of NG resources from various offshore and onshore sites. Furthermore, it can be produced by utilizing low grade coal, recovering coal bed methane or using biogas as methane source to obtain renewable liquefied biogas (LBG).
In general, LNG can be supplied to refuelling stations in two different ways: (i) by purchasing it at the regasification terminal or (ii) by liquefying it on site. Because of the lower LNG terminal purchasing prices the first option is economically advantageous up to terminal distances <2000 km. As a consequence, the distribution phase is of paramount importance for the success of this commodity in the transport sector, but it is still difficult to be fulfilled in many countries, as addressed by Arteconi and Polonara (2013). Thanks also to the EU policy and funded projects (such as the LNG Blue Corridor project), the spread of LNG as vehicle fuel is increased. According to the Natural & bio Gas Vehicle Association (2019), in Italy for example there are 31 L-CNG refuelling stations at present.
LNG is attractive especially for heavy-duty vehicles and big companies of the automotive sector are developing and commercializing their own trucks. Once at the refuelling stations, the LNG is filled into the vehicles and stored on-board in cryogenic tanks, then finally burnt in LNG-adapted engines. In general, because of its low temperature, LNG has a high exergetic content that could be exploited for different purposes. He et al. (2019) summarized all the possible applications of LNG cold recovery, which are mainly power generation, air separation, air conditioning and desalination. Furthermore some researchers focused their attention specifically on the cold energy utilization of LNG on-board. For example, Yan et al. (2016) modified a diesel-fuelled urban bus into an LNG bus and designed the cold energy recovery system. The cold energy of the LNG during its regasification was used for air-conditioning purposes on-board and stored in case of excess. In particular, the authors tested the performance of the LNG bus and compared it with the performance of the vehicle before its modification, finding a significant economic profitability but a reduced engine performance, especially at heavy load conditions. Tan et al. (2010), instead, focused their attention on the heat exchanger to recover the cold energy of the LNG using liquid/solid phase change of water. An experimental investigation was carried out and the authors founded that the internally finned tubes can effectively improve the gas-side heat transfer and the solidification performance of the water outside the tubes. Therefore, this work provided useful insights and reference for the design and optimization of cold energy storage units of LNG refrigerated vehicles.
However, to the best of the authors' knowledge, none of the works reported in literature focused on the on-board cold energy recovery of LNG fuelled trucks to improve the engine performance of the vehicle by cooling the intake air. Indeed the relevant role of the intake air in LNG trucks was already highlighted by Tang et al. (2016). In this work an innovative patent pending (UIBM, 2018) cold energy recovery system from LNG on-board fuel tank of heavy-duty vehicles is presented. After the introduction, Section 2 reports a description of the innovative system under investigation, Section 3 describes the main results and potential of the system. Eventually, Section 4 summarizes the conclusions of the performed analysis.

2. THE COLD ENERGY RECOVERY SYSTEM

2.1 System Description

In a heavy-duty vehicle the fuel consumption mainly depends on the cargo and the engine speed. As a consequence, the cold energy potentially recoverable from the vaporization of the LNG on-board could significantly change during the running of the vehicle. Hence, as already addressed by Yan et al. (2016), the available cold energy of the LNG could differ from the cold energy demand, thus a storage system may be needed to recover the whole energy and maximize the efficiency of the system. In particular, the cold energy of the LNG may be used for several purposes on-board: (i) air conditioning of the cabin; (ii) refrigeration of goods; and (iii) cooling of the engine intake air (by means of a post-cooler) to reduce the fuel consumption and emissions and increase the engine power. With reference to the latter option, some of the authors of this paper patented a novel system to efficiently recover, store and use the cold energy from the LNG fuel vaporization to improve the performance of the heavy-duty engine. Considering a commercial heavy-duty vehicle, at nominal

operating conditions the cold energy from the LNG regasification is higher than the cooling energy requested by the post-cooler. Hence, a storage system allows storing the excess energy to be used for other purposes, decoupling the cooling availability from the cooling demand.
Therefore, the proposed innovative system consists of a cryogenic heat exchanger that allows recovering the cold energy of the LNG fuel supplied to the engine. An Ethylene Glycol Water based solution (EGW) is employed as heat medium to recover the cold energy: a warm tank is used to collect the solution at ambient temperature, while a cold tank stores the surplus cold energy recovered. Such cold energy is partly used in the post cooler (PC) to cool the intake air down to the limit of 0°C, thus avoiding any ice formation due to the water vapour. After heat exchanging with the air, the EGW solution is sent back to the warm tank, where it is mixed with the rest of the returning EGW solution engaged for other cooling purposes. Then, the closed cycle starts again.
Fig. 1 reports a scheme of the LNG smart truck system as patented.

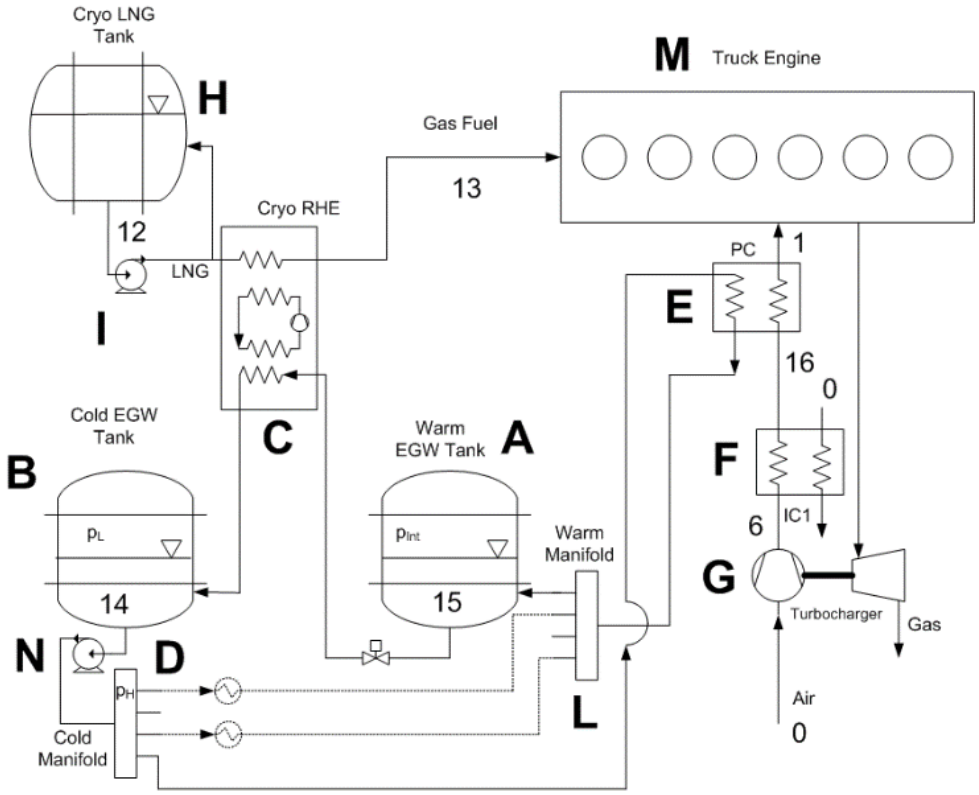

Figure 1: The LNG smart truck system

Therefore, the proposed system allows decoupling the recovery of cold energy and its use on-board. With respect to the size of the warm and cold tanks it depends on several factors: engine truck power and Specific Fuel Consumption (SFC), cooling demands and constraints on board. This aspect is discussed with more detail in Section 3.

2.2 The Simulation Model

The thermodynamic analysis of the cold energy recovery system from LNG on-board fuel tank is performed. The analysis is carried out in steady state conditions and it is aimed at quantifying the cold energy available and at identifying the best potential applications within the heavy-duty vehicle operation. A simulation model is set up for the system under analysis by means of EES (2013). It was assumed that the natural gas stream is composed of 100% methane, stored in the on board tank as saturated LNG at about -126°C (corresponding to a saturation pressure of 0.921 MPa) (Roche, 2009). The EGW solution is composed of 20% content of glycol (mass basis). The Peng-Robinson equation of state is used in the simulation (Peng and Robinson, 1976). The cold tank for the EGW solution is sized in order to store about 10 kWh_{th} and it has a volume of 250 litres.
The Iveco Cursor 8 is considered in this study and its performance chart, on which the engine simulation model is calibrated, is obtained from manufacturer data (Iveco, 2018), as reported in Table

1. In the calculations, the configuration with the minimum SFC value is assumed as the optimized efficiency reference condition. In the latter case the fuel flow rate is equal to 0.0144 kg s^{-1} and the intake air flow rate is 0.2419 kg·s^{-1}. Heat losses and pressure drops are neglected, as first approximation, in the analysis. Once the code is calibrated on the basis of the manufacturer's data (essentially the behaviour of mechanical efficiency, η_m,versus rpm), the performance curves of SFC versus power output with the added post-cooler recovering the cold energy from the LNG gasifier are assessed.

Table 1. Iveco Cursor 8 performance

Power (kW)	rpm	SFC (kg·kWh^{-1})	η_m
110	1000	0.261	0.633
160	1200	0.215	0.768
192	1400	0.209	0.790
220	1600	0.209	0.792
243	1800	0.213	0.777
243	2000	0.2363	0.700

3. RESULTS AND DISCUSSION

3.1. Thermodynamic Analysis

The simulation highlights that the recoverable cold energy rate from the regasification of the LNG in the on-board tank to supply the engine at 15°C is about 10.7 kW. On the other hand, the energy rate necessary to cool down the air intake from 35°C to 0°C in the post-cooler is about 8.8 kW. The thermodynamic properties of the most relevant points in the schematic of Fig. 1 are reported in Table 2.

Table 2. Thermodynamic properties of the main streams in the system schematics in Fig.1.

Stream	Material	Flow rate (kg·s^{-1})	Temperature (°C)	Pressure (MPa)	Vapour fraction
1	Air	0.2419	0	0.182	1
16	Air	0.2419	35	0.182	1
12	LNG	0.0144	-126	0.912	0
13	LNG	0.0144	15	0.912	1
14	EWG	0.0776	-10	0.101	0
15	EWG	0.0776	25	0.101	0

Before entering the post cooler, the compressed intake air is pre-cooled by means of external air at ambient conditions. The inlet air temperature in the post-intercooler (PC) depends on the performance of such intercooler (IC1, see Fig. 1): as much as this temperature is low, as lower the used cold energy is. If the intake air temperature is higher than 42°C, the cold energy recovered by the LNG is no longer sufficient to cool the air down to 0°C, as shown in Fig. 2.

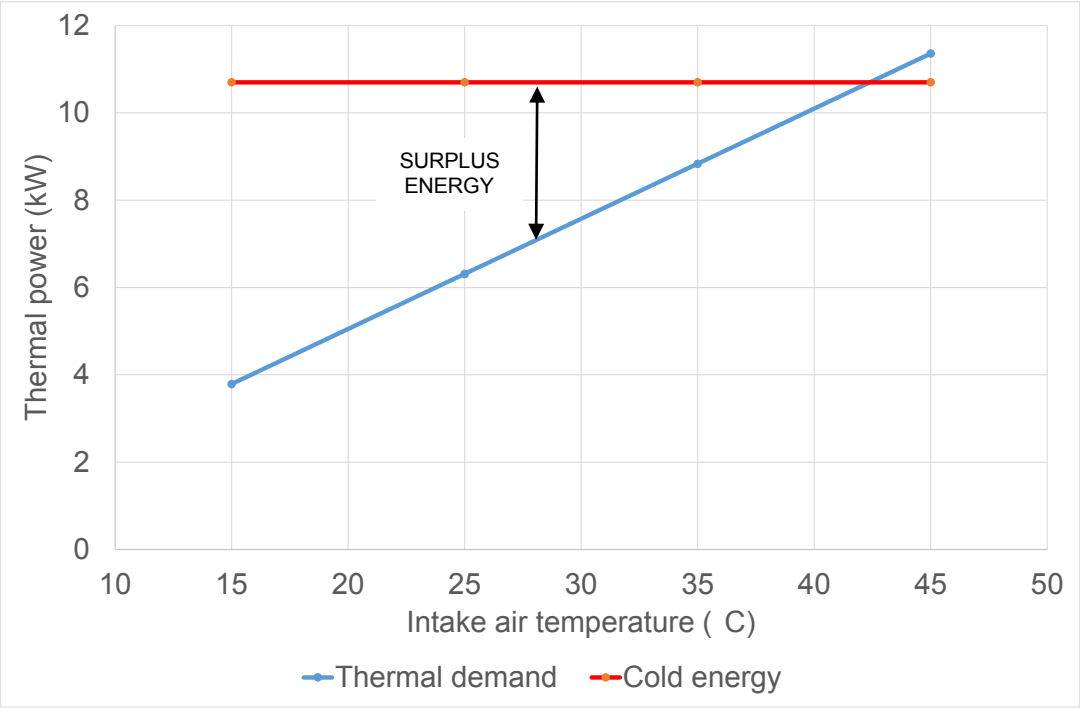

Figure 2: Cold energy used in the post cooler by varying the intake air temperature

Hence, thanks to this innovative cold energy recovery system, the heavy-duty vehicle benefits of:

- an increase of the engine maximum horsepower;
- a reduction of the specific fuel consumption of the engine;
- an improvement of the environmental performance in terms of lower NOx emissions, because of lower combustion temperatures.

This is shown in Figs. 3a and 3b, where the engine SFC and power output respectively with and without post-cooler are represented. A maximum 35 kW power boosting can be achieved thanks to the recovery of the LNG cold energy to cool the intake air.

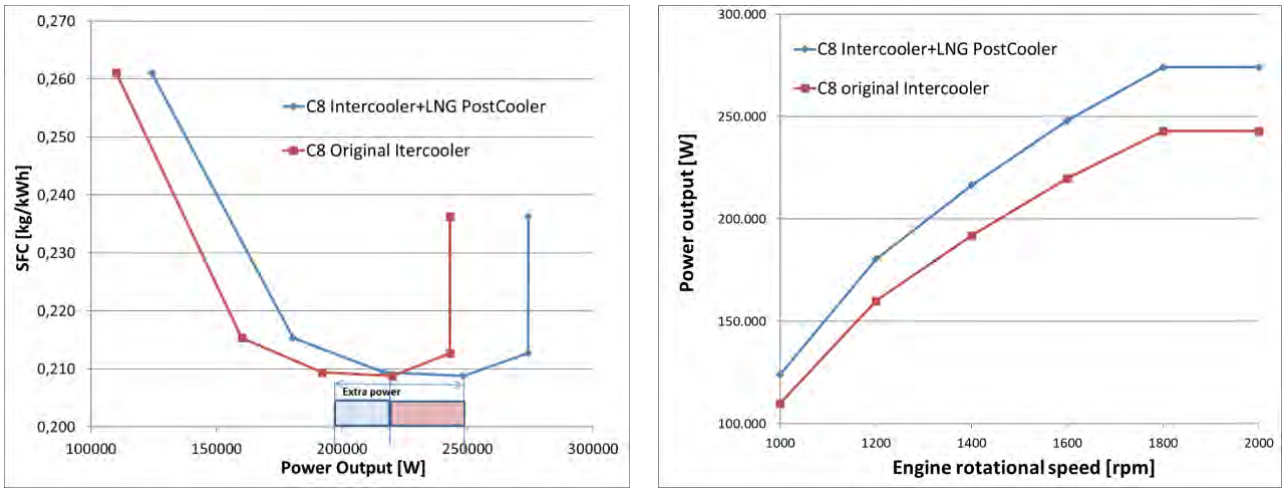

(a) (b)

Figure 3: SFC (a) and Power (b) of the considered engine only with the intercooler (red line) or also with the postcooler (blu line) for an intake air temperature of 0°C

3.2. Cold Energy Recovery Utilization and Future Developments

The excess of the cold energy not used to cool down the intake air temperature (see Fig. 2) can be recovered for other purposes, as for example:

- air conditioning of the heavy-duty vehicle in summer;

- additional cooling for refrigerated trucks;
- load reduction for the intercooler IC1.

All these applications depend on the external environmental conditions and on the dynamic behaviour of the truck during the real road trip. In case the excess cold energy can not be completely used, a back-up procedure should be considered in order to avoid too low temperatures in the cold storage tank.

In particular, the design of the heat exchangers to recover the cold energy must be carefully considered. Especially the Cryo-Recovery Heat Exchanger (Cryo-RHE, C in Fig. 1) needs to be designed taking into account the high temperature difference occurring between the LNG and the EGW heat carrier: the LNG undergoes a very high temperature variation (about 120 °C), whereas the EGW temperature drops of only about 35 °C. For this reason, in order to avoid having too different heat capacities and temperature levels, an intermediate fluid between the evaporating LNG and the EGW could be required.

All these aspects will be object of further future analyses where also the dynamic behaviour of the system will be considered, in order to represent the real transient performance while the LNG level inside the tank decreases and the truck runs in variable traffic and route conditions.

4. CONCLUSIONS

In this paper, an innovative system to recover cold energy from LNG vaporization on-board during fuel supply of heavy-duty trucks is presented. The system allows cold recovery from the LNG regasification to cool the intake air entering the engine. By means of a thermodynamic simulation of the system (i.e. engine and cold energy recovery system), the cold energy available is quantified and the possibility of cooling the intake air down to 0°C is evaluated by varying the inlet air temperature. The positive effect on a specific LNG engine is shown. The system offers a very attractive power boosting potential in the range of 10 – 15%, as well as a reduction in specific fuel consumption. The possible different applications of the excess recovered cold energy is also briefly discussed. Further dynamic analyses are necessary in order to better assess the vehicle performance on the road, under different traffic, load and seasonal conditions.

REFERENCES

Arteconi, A., Brandoni, C., Bartolini, C.M., Polonara, F., 2010. Greenhouse Gas Emissions of Heavy-Duty Vehicles Fuelled by Natural Gas, IANGV 2010 - Roma.

Arteconi, A., Polonara, F., 2013. LNG as vehicle fuel and the problem of supply: The Italian case study, Energy Policy, 62, 503-512.

EU, European Commission, 2011. White Paper 2011, https://ec.europa.eu/transport/themes/strategies/2011_white_paper_en.

EEA, European Environment Agency, 2018, Greenhouse gas emissions from transport, https://www.eea.europa.eu/data-and-maps/indicators/transport-emissions-of-greenhouse-gases/transport-emissions-of-greenhouse-gases-11.

He, T., Chong, Z.R., Zheng, J., Ju, Y., Ling, P., 2019. LNG cold energy utilization: Prospects and challenges, Energy, 170, 557-568.

Iveco, 2018. https://www.iveco.com/switzerland-it/prodotti/pages/stralis_catena_cinematica_cursor8.aspx

Klein, S.A., 2013. EES - Engineering Equation Solver, F-Chart Software, http://www.fchart.com/ees/.

NGVA, Natural & bio Gas Vehicle Association in Europe, 2019, http://www.ngva.eu/stations-map/.

Peng, D.Y., Robinson, D. B., 1976. A New Two-Constant Equation of State, Ind. Eng. Chem.: Fund., 15, 59–64.

Roche, G., 2009. Fueling infrastructure for natural gas trucks. In: Faster Freight–Clean. Air Calif. 2009 Conference, Long Beach - CA.

Tan, H., Li, Y., Tuo, H., Zhou, M., Tian, B., 2010. Experimental study on liquid/solid phase change for cold energy storage of Liquefied Natural Gas (LNG) refrigerated vehicle, Energy, 35, 1927-1935.

Tang, Q., Fu, J., Liu, J., Zhou, F., Yuan, Z., Xu, Z., 2016. Performance improvement of liquefied natural gas (LNG) engine through intake air supply, App. Therm. Eng. 103, 1351–1361.

UIBM, 2018. Impianto di rigassificazione per alimentazione di motori endotermici di veicoli. Patent application n.102017000117283

Yan, F., Xu, B., Liu, N., Zheng, Z., 2016. Study on the Construction of an Urban Liquefied Natural Gas Bus and Its Cold Energy Recovery, Energy Procedia, 104, 515-519.

Manuscript ID: 1405
DOI: 10.18462/iir.icr.2019.1405

Innovative elements for a liquid air energy storage system

Gregor TROMMLER[(a)], Martin KLUPSCH[(a)], Detlef EGGERS[(b)], Philipp BOBSIN[(b)], Christian WENDT[(c)], Niklas BOHNE[(d)]

[(a)] Institut für Luft- und Kältetechnik gemeinnützige Gesellschaft mbH (ILK Dresden),
Dresden, 01309, Germany, gregor.trommler@ilkdresden.de, martin.klupsch@ilkdresden.de
[(b)] RST Rostock System-Technik GmbH
Rostock, 18119, Germany, d.eggers@rst-rostock.de, p.bobsin@rst-rostock.de
[(c)] Ariane Group
Bremen, 28199, Germany, christiandr.wendt@ariane.group
[(d)] Universität Bremen
Bremen, 28199, Germany

ABSTRACT

The ILK Dresden is generally concerned with broadening and increasing the technical and economic efficiency of renewable energy plants as an essential part of the phasing out of nuclear energy and fossil fuels in Germany and Europe. Within the framework of two publicly funded projects, an energy recovery system based on a Cryogenic Rankine Unit and an energy storage system based on Liquid Air Energy Storage (LAES) were developed. Energy recovery is a decisive factor in increasing the efficiency of an energy storage system based on liquid air.
This energy storage is predicated on the principle of liquefied air, in which the existing processes for the liquefaction and regasification have to be adapted to the requirements of the electricity storage to achieve significant efficiency gains and to utilize synergies in the process chain.
The main components of this process are various cold storages, heat storages and flexible electrical energy storage. A cryogenic Rankine plant can also be integrated when the plant specifics are evaluated. The performance and size of the sub-components must be coordinated with the dynamic control processes representing the most important part for increasing efficiency.
Keywords: Energy Storage, Energy Recovery, Efficiency, Liquefier, Cold Storage, Cryogenic Rankine Unit, Liquid Air, Dynamic Control Process.

1. INTRODUCTION

Today, renewable energies already account for a large percentage of the energy mix and their percentage will continue to rise worldwide in the future. Due to the largely decoupled generation and demand of renewable forms of energy, there is a large market for energy storage systems. The aim is not only to buffer peak power but also to realize the base load capacity with renewable energies. The current developments in this application range from hydroelectric power plants to power-to-gas or liquids to batteries and capacitors. All these technologies have their own problems and limitations. We assume that an adapted air liquefaction and regasification process with various loss reduction measures will lead to an electrical energy system that is technically so efficient and cost-effective that it will attract attention compared to alternative storage technologies.
The systems developed within the two publicly funded projects describe a Cryogenic Rankine Unit as energy recovery from the regasification line and a cold storage between the regasification line and the liquefaction line as internal energy storage within a Liquid Air Energy Storage. The developed systems had the primary goal of increasing the efficiency of the Liquid Air Energy Storage. In the following, the main results of the internal cold storage development and the Cryogenic Rankine Unit in a liquid air energy storage system are described with the basic considerations. Furthermore, the

most interesting results of the cold storage simulations carried and their use in the dynamic process simulation of a LAES are presented.

2. MAIN SECTION

2.1. Liquid Air Energy Storage (LAES)

The liquid air energy storage is described by the main components like air compressor with liquefier, liquid air storage and regasification with subsequent conversion into electricity. The loading, storage and discharge process steps are also carried out in this order. The basic process analysis of the described process steps of the LAES was carried out under static consideration. Within the framework of these basic thermodynamic calculations of the LAES, it was shown that only a significant increase in efficiency can be achieved by interconnecting several components within the LAES. These calculations have shown that the use of the cooling energy generated during regasification for pre-cooling in liquefaction results in the significant efficiency gain. The use of this cold is already state of the art (e.g. company “Highview Power”), but the efficiency of its use can be significantly increased.
A more efficient use of this cold is reached by the division of the usable temperature range under consideration of the storage materials usable meaningfully for these temperature ranges and under consideration of the operating modes “loading”, “holding time” and “discharge”. As a result, a meaningful division into three sections (KS 1, KS 2 and KS 3) could be presented. The developed process principle of a liquid air energy storage with three cold storage units is shown in Figure 1.

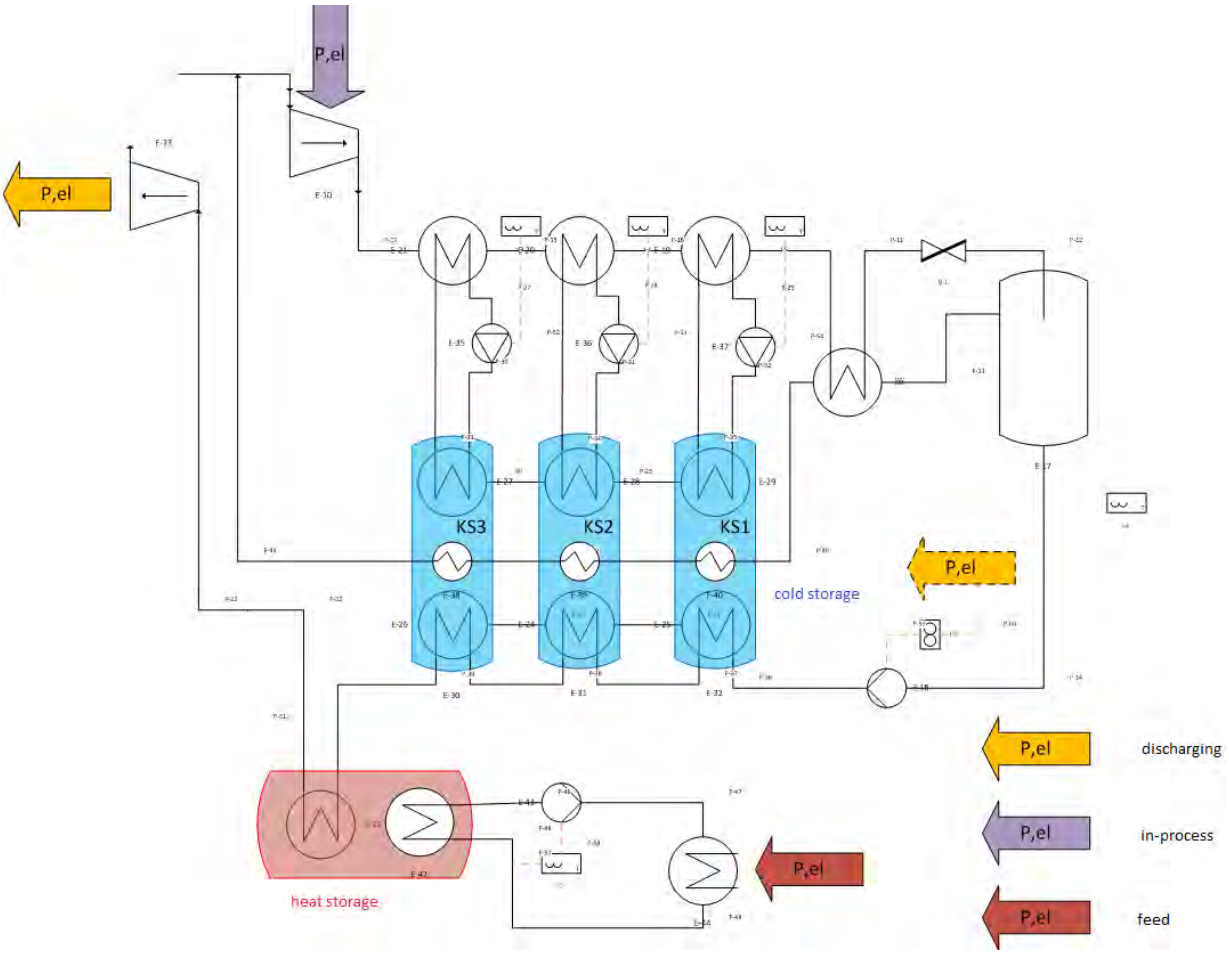

Figure 1: Scheme of the Liquid Air Energy Storage process with three cold storage units

The calculations have shown that the use of three cold storages allows an efficient use of the cold from the regasification process in the liquefaction process of the LAES over the entire temperature

range of the LAES. For a LAES with these three cold storage units and an additional heat storage, an efficiency of more than 55 % is possible.
If for some reason (e.g. location-dependent) the LAES design does not allow direct use of the cold generated by the regasification in the liquefaction, the cold can be used via an additional Rankine process. The Rankine circuit is integrated into the regasification line via a heat exchanger. The process chart is shown in Figure 2.

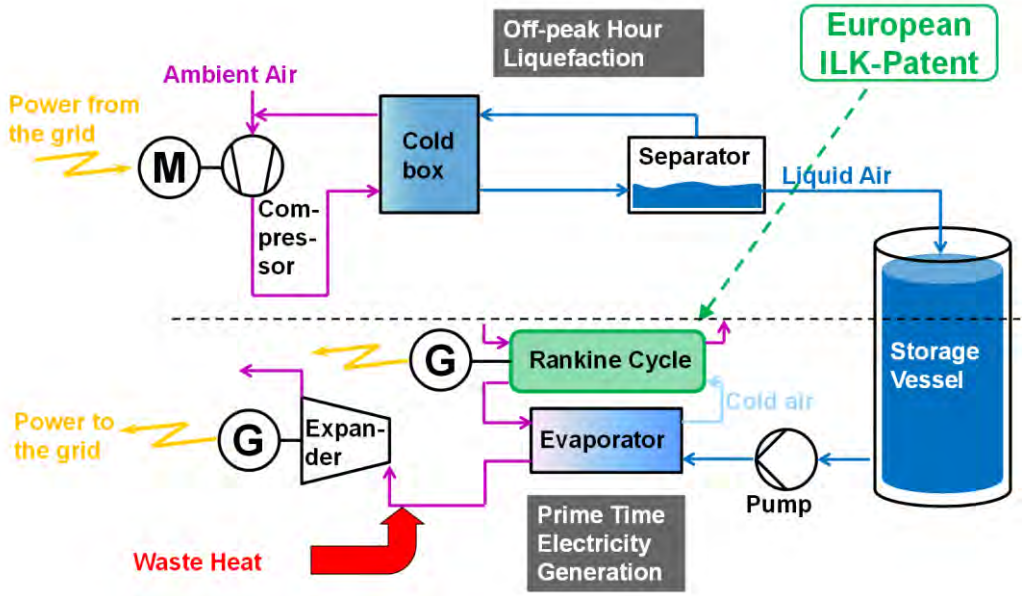

Figure 2: Scheme of the Liquid Air Energy Storage process with the Cryogenic Rankine Unit

For the efficient use of the available temperature level during regasification, the thermodynamic calculations have shown that a three-stage parallel connection of Rankine circuits represents the optimum. An overall LAES efficiency of 50 % can be achieved with this three-stage Rankine process utilization in regasification with additional heat recovery arranged in front of the expansion turbine. The ILK Dresden holds an EU patent (EP000002634383) for this cryogenic Rankine circle development within the regasification at a LAES.

2.2. Cold storage system

The ILK Dresden cooperated within the project content “Cold storage design and performance for use in a LAES” with the company “RST Rostock System-Technik GmbH”, the company “Ariane Group” and the University of Bremen.
In order to determine the optimum cold storage type, a comprehensive candidate evaluation was carried out for cold storage 1 (KS 1) and 2 (KS 2) in the categories technology, costs, risk and marketing. The cold storage type, which gave the maximum value in the sum of the criteria depending on a criteria weighting resulted in the ideal cold storage. These storage types are mixed systems of latent and sensitive storage materials adapted to the respective operating temperatures.
In the further work the focus of the analysis was set on the cold storage 2. It should operate in the temperature range of –140 °C and –60 °C and uses ethanol as a PCM, filled in capsules, and gravel to store the cold energy. This storage was analyzed and compared to a same sized gravel-only cold store. For both cold storage configurations, an operating scenario was simulated with ANSYS Fluent, which consisted of storage, holding time and discharge. During the simulations, temperatures and heat flows were recorded into and out of the system. These data were used to evaluate configuration 1 (ethanol capsules and gravel) and configuration 2 (gravel). Figure 3 shows the temperature fields of the two cold storage configurations 1 (left) and 2 (right), at the end of each simulation.

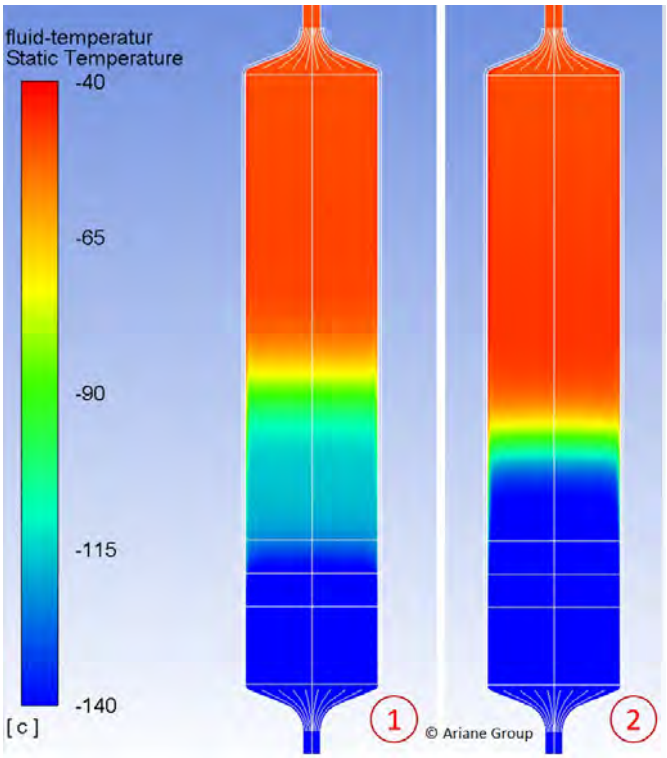

Figure 3: Temperature stratification of the fluid
left: configuration 1 - ethanol capsules and gravel; right: configuration 2: gravel-only.
Simulation in ANSYS Fluent. Steady state condition. End of loading

The analysis presented by Bohne (2018) shows that with 18.2 % of ethanol capsules and 81.8 % gravel, the cold storage unit has an efficiency 2.1 % higher than the gravel-only cold storage unit. In a further 95,2 % of the discharge time, it is able to provide an air temperature below −100 °C compared to the gravel-only cold store, which only meets this requirement for 73,9 % of this time.
In a scaled cold store, functional tests were also carried out on two cold store configurations with regard to unloading. The two configurations differ in the content of the storage medium between 75 % gravel / 25 % ethanol capsules and 100 % gravel. The experimental rig consists of the main components: cold storage, fan, dehumidifier, measurement sensors and liquid nitrogen cooling. The temperatures in the cold store were measured during the tests. Figure 4 shows the experimental rig set up for this task with its assemblies inside the test hall. The dehumidifier was installed in front of the test hall and connected to the test field in the hall via a pipe.
The two function tests start with the cooling of the cold storage, the loading, via liquid nitrogen injection into the air stream. Depending on the uniformity of the liquid nitrogen injection into the air flow of the loading section and above the gravel fill into the cold store, the loading took approximately eight hours.
Immediately after loading, the cold storage is discharged with practically dry air provided by the dehumidifier. For this purpose, the dehumidifier was first operated in bypass mode at the end of the loading process in order to reach the necessary dew point of the air of −30 °C. This procedure took approximately one hour at the time of the test due to the summer outdoor conditions (+30 °C air temperature). The air conditioned in this way had a temperature of +40 °C at the inlet of the cold storage during discharge. The discharge of the cold storage under these conditions took about one hour.
The procedure was carried out in the same way for both cold storage configurations.

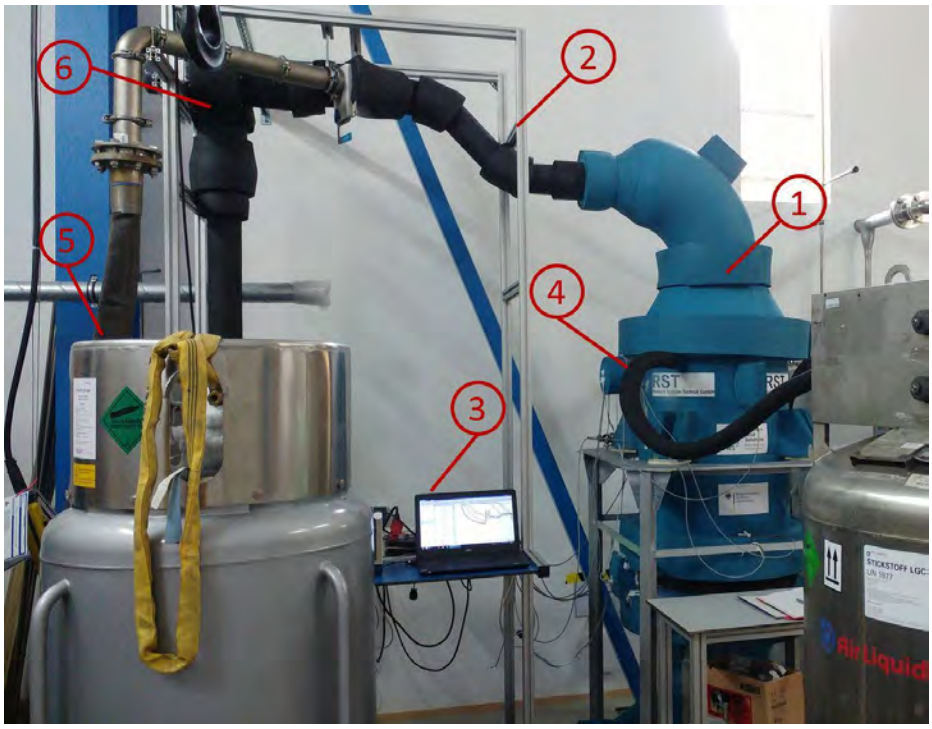

Figure 4: Picture of the test rig: 1 – Cold storage, 2 – pipe system, 3 – measurement station, 4 – first liquid nitrogen supply, 5 – second liquid nitrogen supply, 6 – fan

The measurement data show good accordance for both configurations compared to the simulated assumptions. Small deviations may have been caused by errors in the assumptions or in the test conditions. Further tests under optimized test conditions are still necessary to make a clear statement about the accuracy of the test setup compared to the simulation model.

2.4. Dynamic simulation LAES with cold storage

For the quantitative evaluation of the LAES efficiency, a consideration of the dynamic system behavior was necessary, which links the process simulation with its energy and mass flow balances with the thermal and fluidic simulation model of the developed cold storage model. Depending on the duration and operating parameters of the individual process steps liquefaction and regasification, there are different temperature and storage profiles in the cold store, which influence the efficiency of the next process step liquefaction and regasification. The two main processes of LAES liquefaction and regasification take place at different times. The cold storage stores heat regenerative into the regasification process or out of the liquefaction process by using of secondary circuits. The process diagram used for the simulation is shown in Figure 5.The liquefaction process conforms to the classic LINDE process with pre-cooling.

The air enters the compressor (1), is compressed (2) and cooled back to ambient temperature (3). A part of the gas (4) is then precooled via the “Exhaust gas heat exchanger 1” and the remaining gas flow (5) is precooled in the “Heat exchanger discharge” by the secondary circuit. The combined gas flow (7) is further cooled (8) in “Exhaust gas heat exchanger 2” and then throttled (9) to the low-pressure level. The resulting liquid component is separated and fed into the liquid nitrogen tank (10), while the cold gas component is fed into the “Exhaust gas heat exchangers 1 and 2” as a warm gas to the air sucked in (1).

The liquid air required for regasification is removed from the liquid air tank (14) and pumped by the cryogenic pump to the high-pressure level. The liquid is heated via the “Heat exchanger charging” and, as a supercritical fluid (16), is further adjusted to the ambient temperature level in the “Recooler” and finally expanded in a turbine to perform the work.

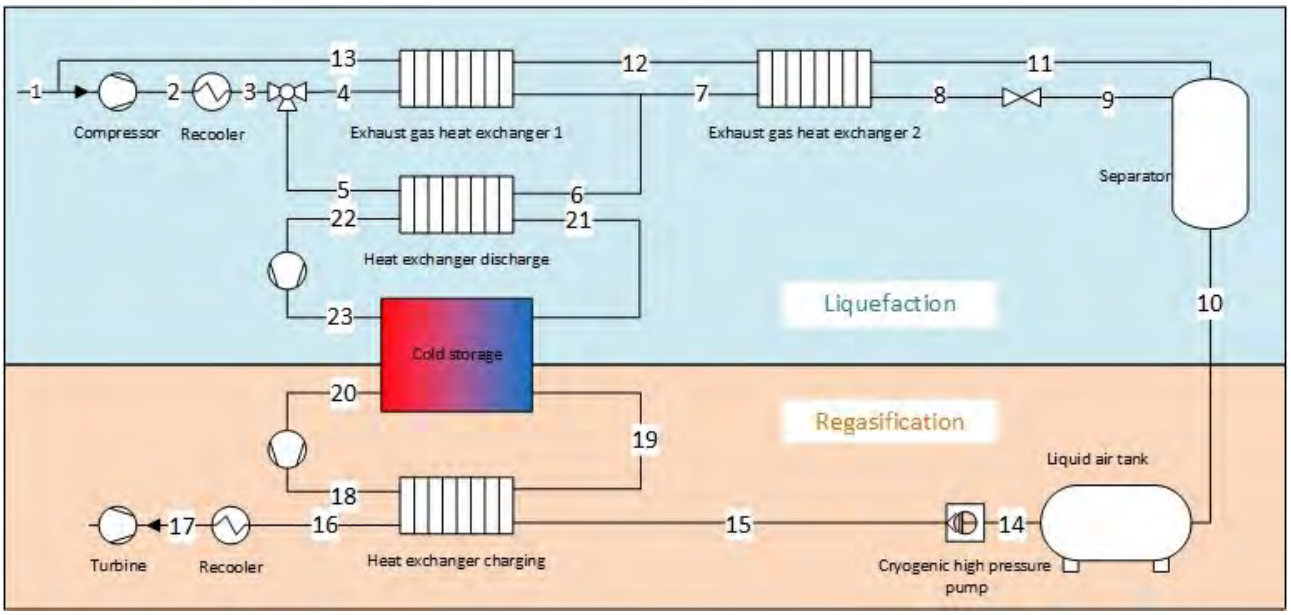

Figure 5: Scheme of the LAES simulation with LINDE liquefaction process and cold storage unit

The software CHEMCAD was used for the representation of the stationary and dynamic simulation of the liquefaction and regasification process. The modelling, discretization of the cold storage in partial sections and transient analysis was carried out with the software ThermXL.
The mode of operation of the sub-processes is designed in such a way that a fixed quantity of air is liquefied during one cycle and is regasified again in the subsequent sub-process. The initial state of the cold storage is the ambient temperature. The simulation begins with the regasification sub-process.
Starting from the warm state of the LAES, seven process steps "liquefaction", "storage" and "regasification" are necessary to put the system into a steady state where a liquefaction work value of 1800 kJ/kg can be achieved. For comparison, the simple LINDE process without the use of external cooling requires under these conditions 9200 kJ/kg liquefaction work. This means that the necessary liquefaction work with use of cold from the regasification process is five times smaller than without this use.
With this dynamic process analysis, a quasi-stationary operating state could be achieved through comparable simulation sequences and operating boundary conditions. On this basis, different liquefaction processes and cold storage models can be compared and optimized.

3. CONCLUSIONS

In order to increase the efficiency of a liquid air energy storage system, an innovative concept - the internal cold storage from regasification for pre-cooling the air in the liquefier - was developed.
For the internal cold storage concept, three cold stores were defined for the entire temperature range available by regasification. Using the example of cold storage 2 the thermodynamic properties were investigated and evaluated. The special feature of this concept is its storage medium, which consists of a latent and a sensitive material in the form of ethanol capsules and gravel. An optimum ratio of the ethanol and gravel content was determined with regard to economic and performance-specific requirements. Both gravel and the ethanol capsules are available separately in piles. The cold store was evaluated by comparing it with a cold store that was identical in design but whose storage medium consisted only of gravel. For both cold storage configurations, an operating scenario was simulated, which consisted of loading, holding time and unloading. The results show that the cold storage concept with the ethanol and gravel can achieve a better efficiency in comparison with the gravel-only cold storage. A further advantage resulting from the results is that the cold storage with gravel and ethanol capsules provides an air flow with a temperature below −100 °C over a longer period than the gravel cold storage. This allows the cold store with ethanol capsules to be used more

efficiently in the LAES plant over a longer period of time. In addition to the simulation, practical functional tests were carried out. The temperature curves within a cold storage are measured during the discharge of two configurations. A repetition of the tests under improved test conditions would make a clear statement possible regarding the accuracy of the test setup in comparison with the simulation model.
To evaluate the dynamic behavior of the cold storage integration into the liquefier process, simulations were performed for the cold run procedure of the LAES up to the steady-state. A proof of the clear reduction of the liquefaction work by integration of the cold from the regasification could be led in such a way. The comparison between different liquefaction processes and different cold-storage systems with changing control parameters can thus follow.
In addition, the ILK Dresden developed a cryogenic Rankine process for the direct use of the cooling energy generated during regasification. The Rankine circuit is integrated into the regasification line via a heat exchanger. For the efficient use of the available temperature level during regasification, the thermodynamic calculations have shown that a three-stage parallel connection of Rankine circuits is the optimum. The ILK Dresden holds an EU patent (EP000002634383) for this cryogenic Rankine circuit development within the regasification of a LAES.

ACKNOWLEDGEMENTS

We would like to thank Thomas Jande, Steffen Richter and Steffen Rackow for their excellent support at the construction of the two test rigs, especially. Furthermore, I would like to thank the Federal Ministry of Education and Research and the Federal Ministry of Economics and Energy for their financial support of these research projects.

NOMENCLATURE

LAES Liquid Air Energy Storage

P,el Electric power

REFERENCES

Bohne, N., 2018. Thermodynamische Analyse eines Kältespeichers für einen Flüssigluft-Energiespeicher. Masterthesis, University of Bremen, Germany

Highview Power: https://www.highviewpower.com/technology/; visited 2019-Jan-10

Manuscript ID: 1577
DOI: 10.18462/iir.icr.2019.1577

Numerical analysis on cavitation of LNG in micro clearance of self-lubricated journal bearing

Yu WANG, Yu HOU, Yu GUO, Xiufang LIU, Tianwei LAI

State Key Laboratory of Multiphase Flow in Power Engineering, Xi'an Jiaotong University
Xi'an, 710049, People's Republic of China, laitianwei@mail.xjtu.edu.cn

ABSTRACT

In the Liquefied Natural Gas (LNG) transportation and storage, pump is required to transport the processed fluid. In order to meet the requirements of hydraulic head, tightness and purity, a high speed full-cryogenic centrifugal pump using LNG as self-lubricant is under development.
To reach the high pump head, the centrifugal LNG pump must be working at high rotational speed. In self-lubricated bearing, sub-ambient pressure will be generated due to the hydrodynamic effect. Hence, cavitation is most likely to occur in micro bearing clearance lubricated with near-saturated LNG.
In order to mitigate cavitation in micro bearing clearance, thermodynamic effect in cavitation-flow is focused on. Numerical analysis of LNG lubricated herringbone bearings is carried out and the bearing characteristics are analysed.
Furthermore, liquid nitrogen(LN_2) test is performed for similarity experiment to verify the simulation and the feasibility of structural optimization.
Keywords: LNG, Pump, Centrifugation, Cavitation, Bearing, Clearance.

1. INTRODUCTION

Cryogenic technology is one of the most effective measures in natural gas transportation and storage. In large scale industrial production of LNG, it is usually stored in vessels with low temperature and atmospheric pressure. The LNG pump plays a vital role in the LNG delivery. Due to its cryogenic characteristics and flammability, higher requirements is imposed on the pump concerning tightness, purity, electrical safety and anti-cavitation. Thus, high speed full-cryogenic centrifugal pump is expected for reliable operation at low temperatures. Because of the high speed operation of the LNG centrifugal pump, silicon carbide and graphite sliding bearings cannot achieve long-term reliable operation owing to abrasion and heat accumulation. Therefore, non-contact hydrodynamic lubrication technology using process fluid as a lubricant becomes an ideal choice. In application of the centrifugal pump, the LNG is in a near-saturated state, and the net positive suction head (NPSH) is relatively low, which might cause the cavitation in micro bearing clearance and breakdown of the transportation system.
Different from boiling, cavitation is the phenomenon that the liquid phase changes to vapor due to the local pressure is lower than the cavitation pressure. In the cavitation process, the growth and equilibrium characteristics of bubbles are closely related to the heat-mass transfer process at the phase interface. In addition, it is also affected by physical properties such as fluid viscosity, surface tension, inertia and thermal diffusivity (Saboni et al., 2016). For cryogens such as LN_2 and LNG, the cavitation is mainly the vaporous type that caused by the depressurization of liquid molecules (Ito et al., 2005). The cavitation of cryogen, that is sensitive to temperature changes, is accompanied by rapid absorption and release of heat. Due to the thermal properties difference, the inception and development of cavitation are phenomenally different between cryogenic process fluids and normal temperature process fluids (Sławomir and Czesław, 2012). On the other hand, cavitation erodes the surface, as well as affecting the flow and pressure field distribution (Tianwei et al., 2014). The noise and vibration caused by the cavitation in the bearing would reduce the operating efficiency of the pump (Kumar and Saini, 2010).
In this article, thermodynamic characteristics in hydrodynamic lubrication is focused on. Numerical analysis of the herringbone grooved journal bearing is carried out. A self-lubricated high speed full-cryogenic centrifugal pump using near saturated liquid was developed. Similarity experiment of the prototype pump was performed in LN_2.

2. CAVITATION THEORY AND MODELING CONSIDERING THERMODYNAMIC EFFECTS

2.1. Effect of Thermodynamic Properties

LNG is a mixture of various chemicals. In this study, for simplification, LNG is assumed to be composed of methane, ethane and propane with molar percentage of 95%, 3% and 2%, respectively. Table 1 lists the relevant physical properties of LNG, LN_2 and water. Sensitivity of the cavitation pressure to temperature of LN_2 and LNG is 16 kPa·K^{-1} (80 K) and 8 kPa·K^{-1} (112 K), respectively. The water is only 0.19 kPa·K^{-1} (298K). For cryogenic fluids and water, the fundamental difference in cavitation is in the thermal properties. Analysis of the dP/dT of LN_2, LNG and water under normal working conditions is shown in the Fig. 1. Compared with water, the saturation pressure to temperature for the cryogens are larger, which indicates that the cryogenic process fluids' cavitation is more temperature sensitive.

Table 1. Comparison of the physical properties of LNG, LN_2 and water

Substance	Liquid phase C_p (J·kg^{-1}·K^{-1})	Liquid phase density (kg·(m^3)$^{-1}$)	Liquid /vapor density ratio	Liquid phase therm. cond. (W·mK^{-1})	Latent heat (kJ·kg^{-1})	Sensitivity of the cavitation pressure (kPa·K^{-1})
LNG (112 K)	3089	452	251	188	496	8.00
LN_2 (80 K)	2055	794	132	139	195	16.00
Water (298 K)	4200	997	43272	687	2257	0.19

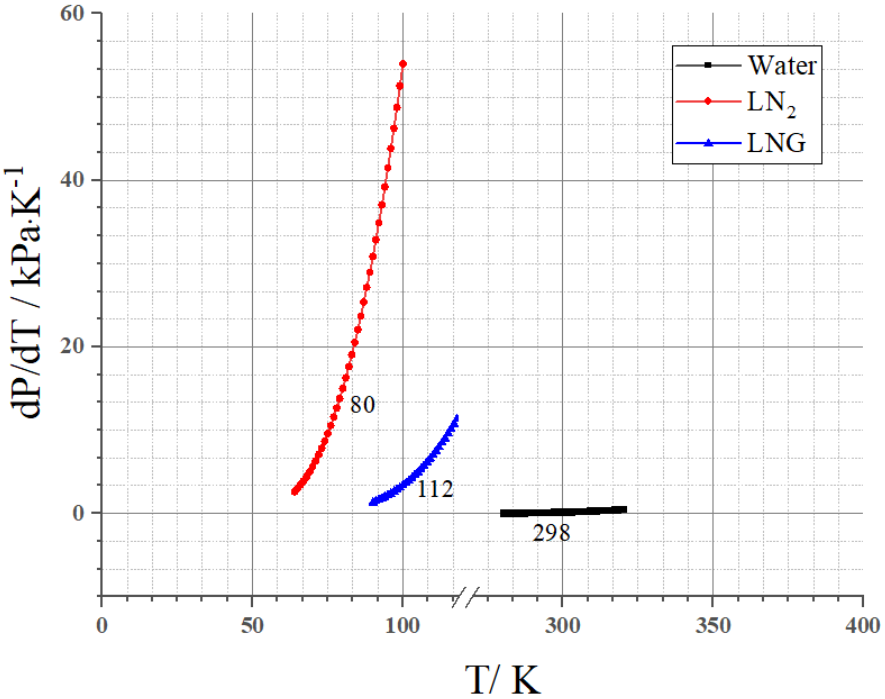

Figure 1: The sensitivity of the cavitation pressure

Based on the theoretical analysis of *B* factor (Stahl and Stepanoff, 1956)., the parameters for measuring the cavitation pressure drop expressed by the height of the liquid column ΔH_v can be obtained by combining the first law of thermodynamics and the equation of state for ideal gas.

$$\Delta H_v = \frac{B(\rho_v L)^2}{\rho_l(\rho_l - \rho_v)C_p T g} \qquad \text{Eq. (1)}$$

where, *B* is the ratio of the total volume of the vapor to the total volume of the liquid in the cavitation zone, C_p is the specific heat capacity of the liquid, L is the latent heat, and g is the acceleration of gravity.
For instance, the bubble volume in the cavitation region is half of the liquid volume when *B*=0.5. With this *B* value, ΔH_v=8.35×10^{-5} m for water (298 K), ΔH_v=0.68 m for LN_2 (80 K), ΔH_v=0.51 m for LNG (112.5 K). Comparing the cavitation pressure drop of the three substances, the thermodynamic effect has a greater influence on the cavitation of cryogenic process fluids. The liquid-vapor density ratio of water is of order 10^5, while the liquid-vapor density ratio for cryogenic fluids is just of order 10^2. Therefore, the cryogenic fluids need more liquid vaporization to form a bubble of the same size as water. In other words, more latent heat is absorbed and the temperature inside the bubble is lower. Moreover, the thermal conductivity of the cryogenic fluids is lower than water, resulting in a more pronounced temperature gradient near the bubbles. As a result, significant temperature drop is caused by the cryogenic cavitation. Further occurrence of cavitation is inhibited due to the thermal sensitivity of the cryogenic fluids.

2.2. Basic Governing Equations and Turbulence Method

In this paper, thermodynamic effect on cryogenic fluid cavitation in micro bearing clearance is considered for numerical simulation using FLUENT. The conservation form of the Reynolds time-averaged N-S equations includes the continuity equation, the momentum equation and the energy equation.

$$\frac{\partial \rho_m}{\partial t} + \nabla \cdot (\rho_m \vec{u}_m) = 0 \qquad \text{Eq. (2)}$$

$$\frac{\partial (\rho_m u_i)}{\partial t} + \frac{\partial (\rho_m u_i u_j)}{\partial x_j} = -\frac{\partial p}{\partial x_j} + \frac{\partial}{\partial x_j}\left[\mu\left(\frac{\partial u_i}{\partial x_j} + \frac{\partial u_j}{\partial x_i} - \frac{2}{3}\frac{\partial u_j}{\partial x_i}\delta_{ij}\right)\right] + \frac{\partial}{\partial x_j}\left(-\rho_m \overline{u_i' u_j'}\right) \qquad \text{Eq. (3)}$$

where, ρ_m is the mixture density, $\vec{u}_m$ is the velocity vector in Cartesian coordinate system, t is the time, p is the pressure, and $u_{i,j}$ is the average speed. $-\rho_m \overline{u_i' u_j'}$ is the time-averaged turbulent pulsation value - Reynolds stress term, and μ is the laminar viscosity coefficient of vapor and liquid mixture which is defined as:

$$\mu = \mu_l \alpha_l + \mu_v (1 - \alpha_l) \qquad \text{Eq. (4)}$$

α_l is the volume fraction of the liquid phase, μ_l is the viscosity coefficient of the liquid phase, and μ_v is the viscosity coefficient of the vapor phase.
Energy equation:

$$\frac{\partial}{\partial t}(\rho_m T) + \frac{\partial}{\partial x_j}\left(\rho_m u_j T\right) = \frac{\partial}{\partial x_j}\left[(k + k_t)\frac{\partial T}{\partial x_i}\right] + S_E \qquad \text{Eq. (5)}$$

where, k is the heat transfer coefficient and k_t is the turbulent heat transfer coefficient, the definition of which depends on the applied turbulence model. S_E is the volumetric heat source term. Take the thermodynamic effect into account, S_E is the product of the vaporization latent heat and mass transfer rate between vapor-liquid phase conversion.
It is especially important to choose a turbulent model reasonably. Because of high curvature of the stream lines in the flow field, the Realizable $k-\varepsilon$ model is selected:

$$\frac{\partial (\rho k)}{\partial t} + \frac{\partial (\rho k u_i)}{\partial x_i} = \frac{\partial}{\partial x_j}\left[\left(\mu + \frac{\mu_t}{\sigma_k}\right)\frac{\partial k}{\partial x_j}\right] + G_k + G_b - \rho\varepsilon - Y_M + S_k \qquad \text{Eq. (6)}$$

$$\frac{\partial (\rho \varepsilon)}{\partial t} + \frac{\partial (\rho \varepsilon u_i)}{\partial x_i} = \frac{\partial}{\partial x_j}\left[\left(\mu + \frac{\mu_t}{\sigma_\varepsilon}\right)\frac{\partial \varepsilon}{\partial x_j}\right] + \rho C_{1\varepsilon} S_\varepsilon - C_{2\varepsilon}\rho\frac{\varepsilon^2}{k + \sqrt{\nu\varepsilon}} + C_{1\varepsilon}\frac{\varepsilon}{k}C_{3\varepsilon}G_b + S_\varepsilon \qquad \text{Eq. (7)}$$

where G_k is the kinetic energy generation term caused by the average velocity gradient, G_b is the kinetic energy generation term due to buoyancy, Y_M represents the fluctuation caused by diffusion. $C_{1\varepsilon}$, $C_{2\varepsilon}$ and $C_{3\varepsilon}$ are empirical constants. σ_k and σ_ε are the Prandtl numbers corresponding to the turbulent kinetic energy ε and the dissipation rate, respectively. S_k and S_ε are user-defined source items.

Based on the Zwart cavitation model and the influence of temperature on mass transfer, an improved cavitation source term considering the thermodynamic effect is obtained (Suguo et al., 2012.):

$$R_e = C_e \frac{\sqrt{k}}{\sigma} \rho_l \rho_v \left[\sqrt{\frac{2P_v - P}{3\rho_l}} - \sqrt{\frac{k}{C_p \rho_l}} \right] (1 - f_v), P \le P_v \qquad \text{Eq. (8)}$$

$$R_c = C_c \frac{\sqrt{k}}{\sigma} \rho_l \rho_l \left[\sqrt{\frac{2P - P_v}{3\rho_l}} - \sqrt{\frac{k}{C_p \rho_l}} \right] f_v, P > P_v \qquad \text{Eq. (9)}$$

where f_v is the vapor phase mass fraction, $\rho_{l,v}$ is the density of the liquid phase and vapor phase, k is the turbulent kinetic energy, σ is the surface tension, C_e and C_c are the empirical coefficients, in the current case, the values are $C_e = 5$, $C_c = 0.001$. P_v is cavitation pressure.

3. NUMERICAL ANALYSIS OF NEAR-SATURATED HYDRO-DYNAMIC BEARING CAVITATION

3.1. Modelling of Fluid Film in Micro Bearing Clearance

According to the principle of hydrodynamic lubrication with near-saturated liquid, a self-lubricated bearing-rotor system is designed in this paper (shown in Fig. 2a). The herringbone bearing's fluid domain (shown in Fig. 2b) is extracted and the hexahedral structured meshing is used.

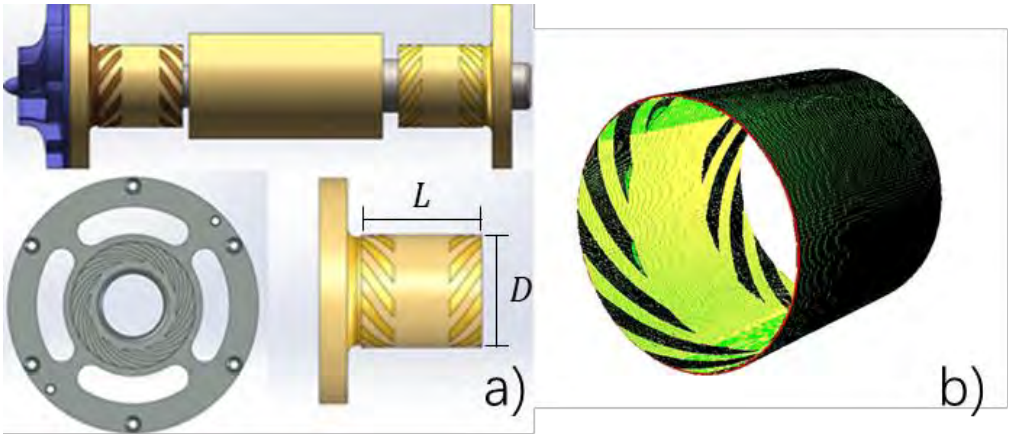

Figure 2: a) Self-lubricating bearing-rotor system, b) Herringbone bearing fluid domain

The self-lubricated journal herringbone bearing analysed in this paper is based on the high speed full-cryogenic centrifugal pump. The main geometrical parameters and operating conditions of the bearing are shown in Table 2

Table 2. Main geometrical parameters and operating conditions of journal bearing

Substance	Bearing diameter (mm)	Bearing length (mm)	Minimum film thickness (μm)	Operation temperature (K)	Subcooled temperature (K)
LNG	25	25	5	112.5	0.5
LN_2				80.5	
Water				298.5	

3.2. Numerical Analysis of Cavitation in Near-Saturated Hydrodynamic Bearing

Cavitation in micro bearing clearance is carried out numerically with LNG, LN_2 and water. The fluid domain is unfolded in accordance with the coordinate system shown in Fig. 3. O_S is the shaft centre, O_B is the bearing centre, β is the attitude angle, and θ is the circumferential direction, *x* is the axial direction.

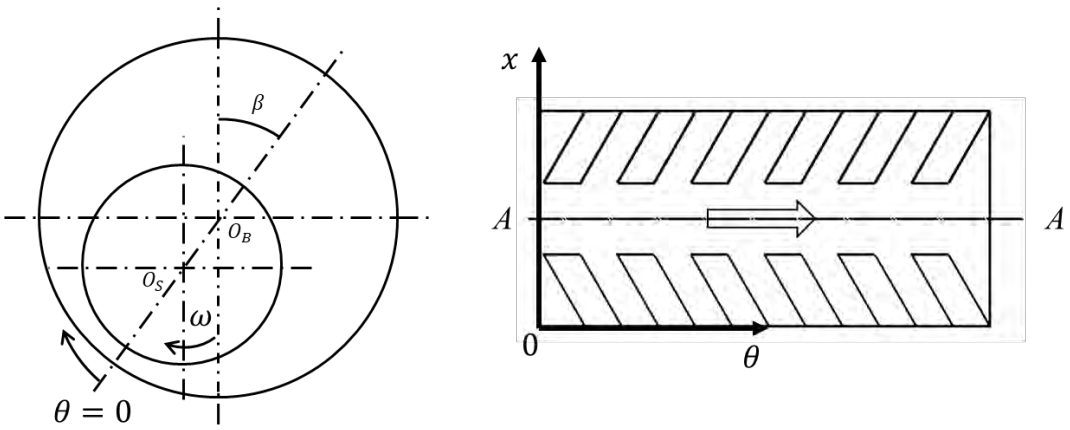

Figure 3: Cylindrical coordinates and Cartesian coordinates

For the three fluids, the volume fractions of vapor phase in the bearing clearance at different rotational speeds are shown in Fig. 4. Cavitation in LN_2 and LNG lubricated bearings have occurred in speed range of 1200-12,000 rpm, and their cavitation distributions are similar. Compared with LN_2, LNG lubricated bearing has a higher volume fraction of vapor phase at the same rotational speed, and cavitation span in circumferential direction is larger. This can be attributed to the thermal properties of LN_2 and LNG have similar trends in the working temperature range. However, cavitation generated by LNG is more intense than that of LN_2 due to the higher sensitivity of the cavitation pressure to temperature. Differently, the water lubricated bearings has no cavitation within the speed range. The distributions of cryogenic process fluids cavitation are all different from the cavitation distribution of water. The reason is that the vapor-liquid density ratio of the cryogenic fluids is relatively small and the cavitation pressure is highly sensitive to temperature. Therefore, the liquid phase transition to the vapor phase is insufficient and the vapor-liquid phase interface is frothier. The vapor phase volume fraction gradient is smaller during the mass transfer process.

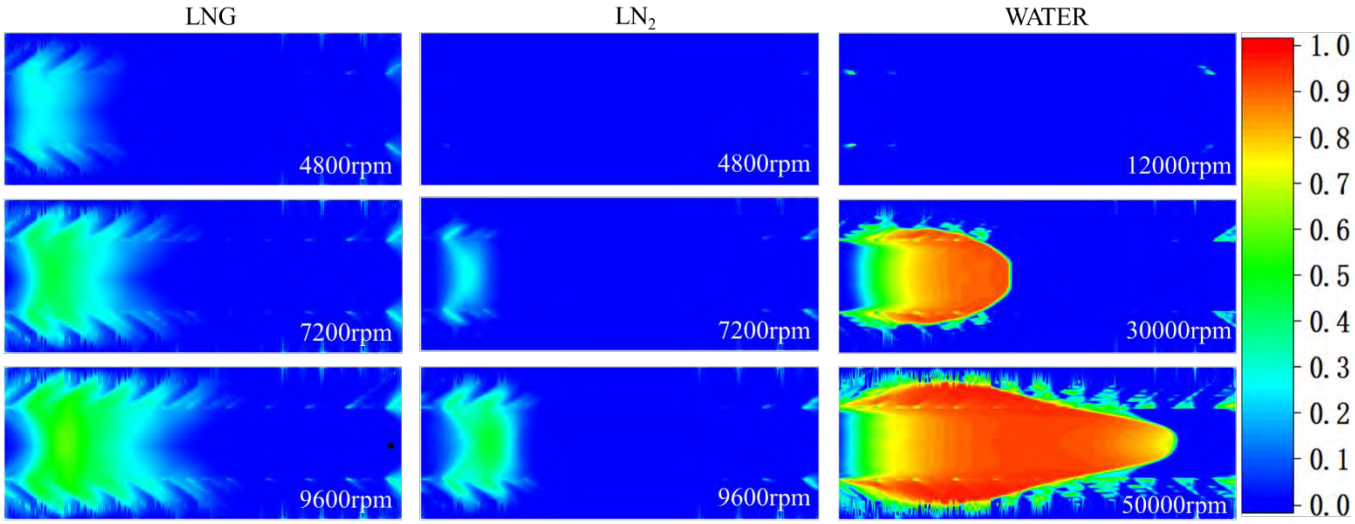

Figure 4: Volume fraction of vapor phase in the journal bearing under different speeds

3.3. The Characteristics of LNG Lubricated Herringbone Bearing

Fig. 5 shows the pressure, temperature and vapor volume fractions of the LNG self-lubricating herringbone bearing at 8400 rpm. Due to the hydrodynamic effect, positive and negative pressure regions are generated in the micro bearing clearance. In the negative pressure region, the pressure is lower than the cavitation pressure and the liquid phase changes to the vapor phase. During this process, heat absorption leads to a decrease in the temperature of the cavitation zone. Comparing the cavitation development of water, the thermodynamic effect of the cryogen can suppress the occurrence of vapor-liquid phase transition and cavitation effectively.

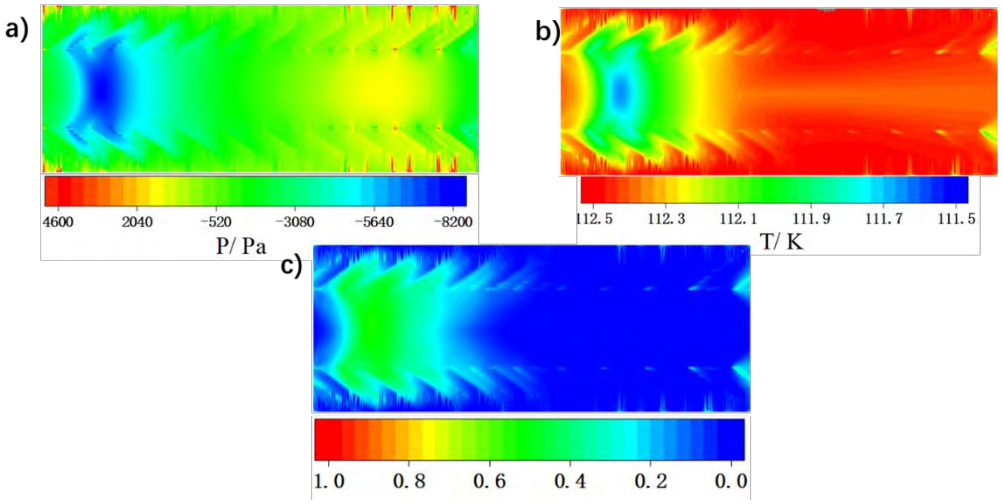

Figure 5: a) Static pressure, b) Temperature, c) Volume fraction of vapor phase in the journal bearing at 8400rpm (LNG)

The pressure, temperature and vapor volume fractions of the intermediate section *A-A* of the LNG self-lubricating herringbone bearing (shown in Fig. 3) at different speeds (4800 rpm, 6000 rpm, 7200 rpm, 8400 rpm, 9600 rpm) is shown in Fig. 6. The positive pressure increases with the increase of rotational speed. The negative pressure region (θ = 0-3.9) gradually increases with the rotational speed. The temperature drop in the region further increases and the cavitation region enlarges (θ = 0-3.0) in circumferential direction. When the rotational speed reaches 9600 rpm, the temperature drop is 1K, the volume fraction of vapor (VOF) is close to 0.56, and the cavitation area is close to 50%.

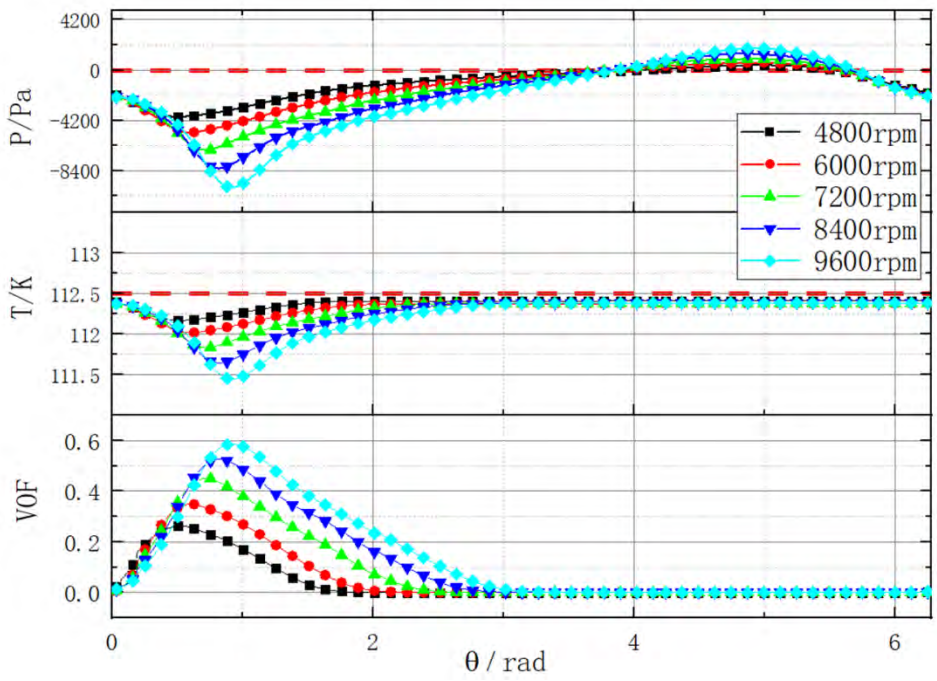

Figure 6: The pressure, temperature and vapor volume fractions of the intermediate section at different speeds

4. EXPERIMENTAL STUDY

The test rig for the high speed full-cryogenic centrifugal pump system is shown in Fig. 7. Using hydrodynamic lubrication with the near saturated liquid (LN_2), centrifugal pump bearings are wear-free and running smoothly at high speeds. The high-speed pump can realize continuous speed regulation in the range 1200-12,000 rpm, which can achieve the adjustment of flow rate and hydraulic head correspondingly. In addition, the high speed full-cryogenic centrifugal pump had small vibrations with amplitude less than 1.5 μm as shown in Fig. 8.



Figure 7: High speed full-cryogenic centrifugal pump system

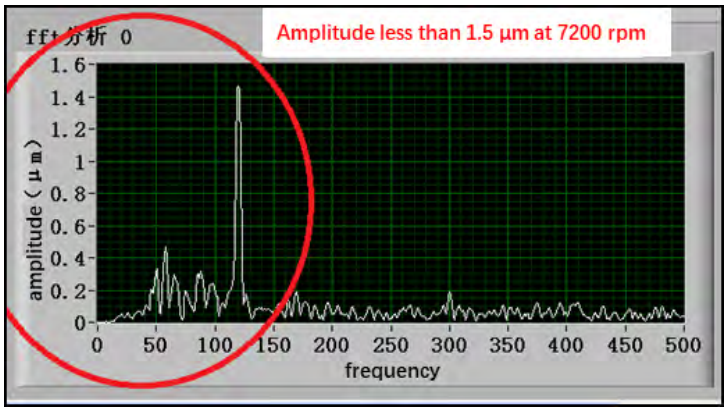

Figure 8: Rotational frequency domain diagram

5. CONCLUSIONS

In this paper, the numerical analysis of cryogen cavitation in the micro bearing clearance is carried out for the high speed full-cryogenic centrifugal pump. A similarity experiment of the high speed full-cryogenic centrifugal pump was carried out, and the following conclusions are obtained:

1.The inception and development of cavitation between cryogenic process fluid and normal temperature process fluid are different. For the cryogenic fluid, its thermodynamic effect is more obvious and the cavitation has been inhibited significantly;

2. For the LNG lubricated journal bearing with cavitation, the maximum pressure drop and temperature drop occur at the position with largest volume fraction of vapor;

3. Feasibility of LNG hydrodynamic lubrication is verified through the experiment using near saturated liquid (LN_2). The test results indicate that the high speed full-cryogenic centrifugal pump can operate smoothly in the cryogenic transport system.

ACKNOWLEDGEMENTS

This project was supported by the National key basic research program (613322) and the National Nature Science Foundation of China (51776148,51776150).

NOMENCLATURE

p	pressure (kPa)	C_p	constant pressure specific heat capacity ($J \cdot kg^{-1}K^{-1}$)
T	temperature (K)	L	latent heat ($KJ \cdot kg^{-1}$)
α	volume fraction	S_E	volumetric heat source term
ΔH_v	cavitation pressure drop(m)	g	acceleration of gravity ($9.8m \cdot (s^2)^{-1}$)
ρ_m	the mixture density ($kg \cdot (m^3)^{-1}$)	$u_{i,j}$	the average speed ($m \cdot s^{-1}$)
μ	viscosity coefficient (Pa·s)	k	heat transfer coefficient ($W \cdot m^{-1}K$ +)
f_v	vapor phase mass fraction	σ	surface tension ($N \cdot m^{-1}$)

REFERENCES

Saboni, A., Alexandrova, S., Karsheva, M., & Gourdon, C., 2016. Mass transfer into a spherical bubble. Chemical Engineering Science 152, 109-115.

Ito, Y., Sawasaki, K., Tani, N., Nagasaki, T., & Nagashima, T., 2005. A blowdown cryogenic cavitation tunnel and cfd treatment for flow visualization around a foil. Journal of Thermal Science 14(4), 346-351.

Sławomir, B., Czesław K., 2012. A numerical analysis of the grooved surface effects on the thermal behavior of a non-contacting face seal. Procedia Engineering 39(7), 315-326.

Tianwei, L., Shanjv, Y., Xingqun, Z., Shuangtao, C., & Yu, H., 2014. Computational fluid dynamic analysis on flow and cavitation characteristics of R134a in centrifugal pump with straight blades. Ciesc Journal 65(z2), 45-51.

Kumar, P., Saini, P., 2010. Study of cavitation in hydro turbines--a review. Renewable & Sustainable Energy Reviews 14(1), 374-383.

Stahl, A., Stepanoff, J., 1956. Thermodynamic aspects of cavitation in centrifugal pumps. ASME Journal of Basic Engineering 78(8), 1691-1693.

Suguo, S., Guoyu, W., & Rui-Yuan, A., 2012. Numerical study of cavitation in cryogenic fluids. Engineering Mechanics 29(5), 61-67.

Manuscript ID: 1596
DOI: 10.18462/iir.icr.2019.1596

Performance analysis method for intermediated fluid type LNG vaporizers considering fluid properties

Kosuke HIGASHI[(a)], Chieko KONDOU[(b)], Yukihiro HIGASHI[(c)], Shigeru KOYAMA[(c)]

[(a)] Kobe Steel L.T.D.
Kobe, 651-2271, Japan, higashi.kosuke@kobelco.com
[(b)]Nagasaki University
Nagasaki, 852-8521, Japan, ckondou@nagasaki-u.ac.jp
[(c)]Kyushu University
Fukuoka, 819-0395, Japan, higashi@i2cner.kyushu-u.ac.jp

ABSTRACT

LNG (Liquefied Natural Gas) vaporizer is widely used all over the world to vaporize LNG by using seawater, etc. as a heating source. Intermediated Fluid type LNG Vaporizer (IFV) is using intermediated fluid between LNG and heating source. Propane has been used as an intermediated fluid conventionally, but new refrigerants except for propane are required because usage environment was diversified recently. In this study, refrigerants substitute for propane applicable to IFV were selected as R32 and R410A. On the basis of some experimental formula, prediction of boiling and condensation heat exchange quantity in tube bundles was also carried out and it enabled to predict actual IFV vaporization quantity with plus or minus 2 percent accuracy. The prediction demonstrated that those selected refrigerants can increase the vaporization rate with IFV from the base line of propane.
Keywords: Condensation, Evaporation, LNG, Tube Bundle.

1. INTRODUCTION

The LNG that was imported from overseas is transported to consumers' locations by vaporizing it using LNG vaporizers. The vaporization of LNG uses heat sources, such as seawater and industrial water. The intermediate fluid type LNG vaporizer (hereinafter referred to as IFV) is a type of vaporizer that uses an intermediate fluid between LNG and the heat source and has a device configuration shown in Fig. 1 (Egashira, 2009). An intermediate fluid is evaporated by being heated by the heating source with the evaporator (E-1), while by being cooled by the cooling source with the condenser (E-2), being condensed, and circulating the inside of the IFV by the thermosiphon phenomenon, it transfers the heat of the heating source to LNG. The IFV is used when cryogenic energy, such as cryogenic power generation or intake air cooling, is used or when the location of use is in a dirty-seawater area. Previously, propane had been used as an intermediate fluid; however, due to recent diversification of operating environments, new refrigerants other than propane are in demand. This study chose, as new refrigerants substitute for propane, R32 and R410A, which have low freezing points. These refrigerants have been widely used for air conditioning; however, their performance when used for a vaporizer has not been grasped. This study examined the feasibility of application of the new refrigerants by developing a calculation model that predicts the vaporization performance of the IFV, verifying it by comparison with operation data of an actual equipment using propane, and predicting the performance when R32 and R410A are used.

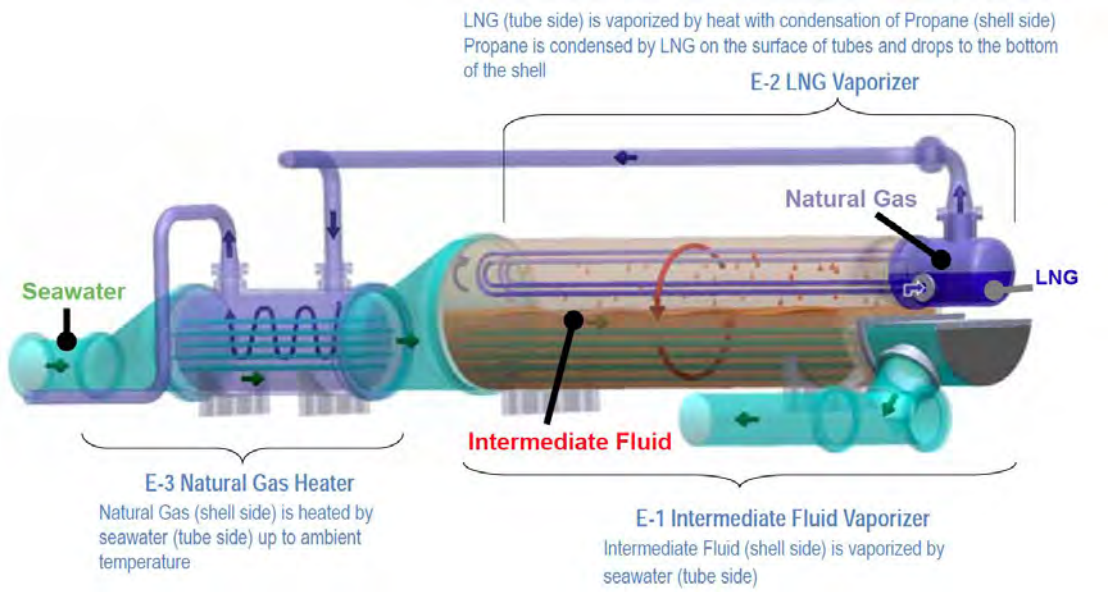

Figure 1: Intermediated Fluid type LNG vaporizer

2. REFRIGERANTS AS NEW INTERMEDIATE FLUIDS

The LNG vaporizer needs to heat LNG from -160°C to ambient temperature. Therefore, the intermediate fluid for the IFV needs to circulate without freezing even in the above temperature range. Also, due to the recent environmental regulations, the ozone depletion potential and the global warming potential need to be taken into consideration as well. As refrigerants that meet these conditions, we chose three types of refrigerants shown in Table 1. Of these refrigerants, R22 has a high ozone depletion potential and hence was removed from the candidates. Although the freezing points of R32 and R410A are higher than that of propane, the possibility of the refrigerants freezing is considered to be low if the circulation of the refrigerants is ensured because the tube wall temperature of the condensing tube is approximately -100 °C. Furthermore, they have relatively low ozone depletion potentials and global warming potentials. Although R410A is a mixed coolant of R32 and R125, since the temperature difference between the boiling point and the dew point is negligibly small, it was handled as an azeotropic coolant in this study. For various physical property values of the refrigerants used in the calculation, we used the physical property calculation software REFPROP 9.1.

3. SIMULATION MODEL

The evaporator and the condenser of the IFV mainly consists of tube bundles; in order to predict the performance, boiling and condensation of the coolant in the tube bundles need to be accurately grasped. This study developed a performance prediction model for each of them.

3.1 Evaporation

Fig. 2 shows rough sketches of the tube bundle of the IFV evaporator. The tubes are arranged in staggered positions in the vertical direction, and bubbles of the generated refrigerant vapor ascend through the tube bundle. The effect of the vapor bubbles reduces the boiling heat transfer rate of the refrigerant in the upper sections of the tube bundle. This study used Eq. (1) by referring to the literature (Ribatski et al., 2008) and calculated the boiling heat transfer coefficient in the tube bundle. The heat transfer coefficient of the heating fluid in the tube was calculated using Eq. (2) by Dittus-Boelter (1930). On the other hand, the heat transfer rate was calculated using the number of transfer units in Eq. (3), considering the stability of the calculation. This calculation was performed by dividing the tube bundle of the evaporator into eight units in the direction of the flow of the heating fluid and following the calculation flow shown in Fig. 3 for each unit. The calculation

temporarily determined the outlet temperature of the heat transfer tube of a unit and calculated the outlet temperature that can balance the heat exchange quantity calculated from the inlet temperature and the outlet temperature of the heat transfer tube with the heat transfer rate calculated with Eq. (3). Assuming that the outlet temperature of one unit is the inlet temperature of the next unit, the calculation was performed repeatedly to obtain the heat exchange quantity of the entire tube bundle.

$$\alpha = f_{\mathrm{wm}} q_{\mathrm{wall}}{}^{0.9-0.3 p_{\mathrm{red}}{}^{0.2}} p_{\mathrm{red}}{}^{0.45} [-\log(p_{\mathrm{red}})]^{-0.8} R_a{}^{0.2} M^{-0.5} \qquad \text{Eq. (1)}$$

$$\mathrm{Nu} = 0.023 Re^{\frac{4}{5}} Pr^{\frac{1}{3}} \qquad \text{Eq. (2)}$$

$$Q = \varepsilon C_{min} (T_{sat} - T_{in}) \qquad \text{Eq. (3)}$$

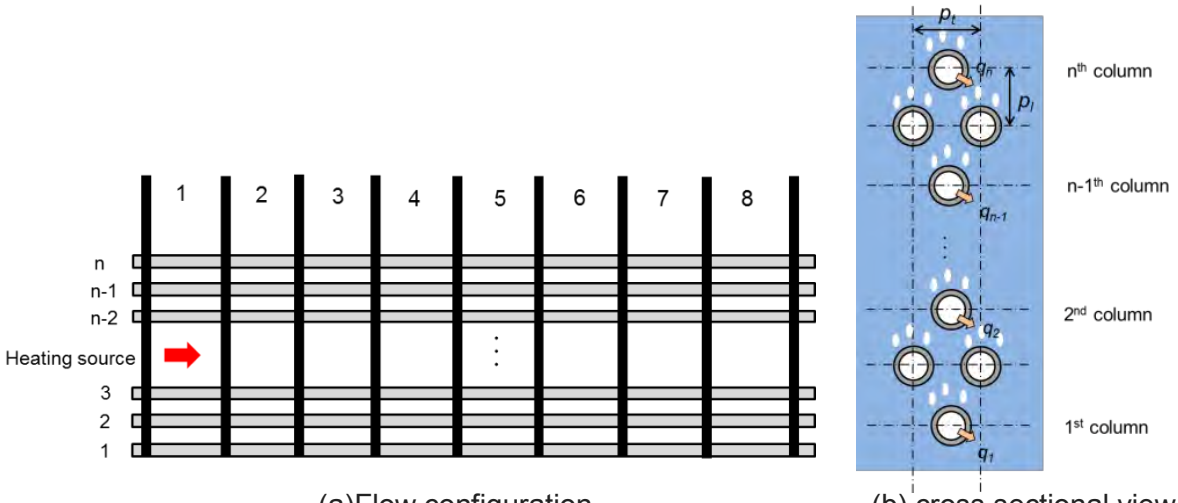

Figure 2: Tube bundle of IFV evaporator

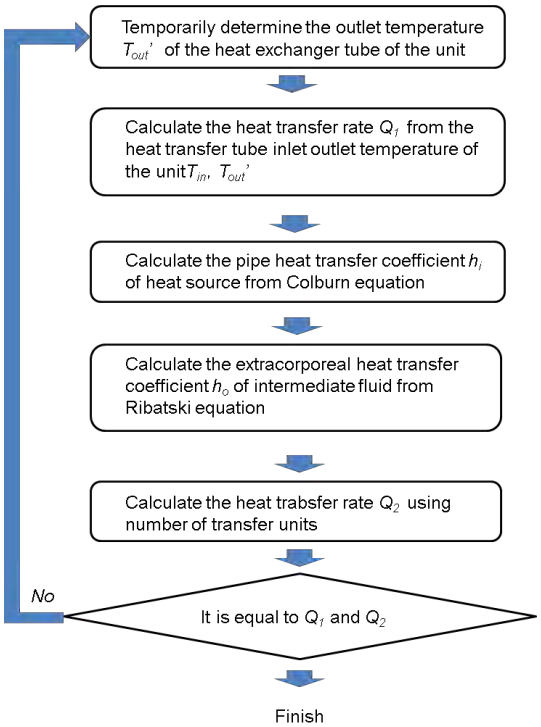

Figure 3: Evaporator calculation flow

3.2 Condensation

Fig. 4 shows rough sketches of the tube bundle of the IFV condenser. In the condenser, U-tubes are arranged in zigzag positions in the height direction, and the generated liquid coolant drips vertically down the tube surfaces. The effect of the liquid film causes inundation in the lower section of the tube bundle, a phenomenon which reduces the condensing heat transfer coefficient of the refrigerants. This study calculated the condensing heat transfer coefficient in the tube bundle that takes the effect of the inundation into account, using Eqs. (4) to (6) with reference to the literature (Honda et al.,1988). In this calculation, Nu_{Dg} represents heat transfer when the condensate flows due to gravity, and Nu_{Df} represents heat transfer when the condensate is uniformly distributed. The heat transfer rate of LNG in the heat transfer tube was calculated using the Dittus-Boelter correlation (1930) because LNG is in a supercritical state and can be simplified as a single-phase fluid. On the other hand, the heat transfer rate was calculated using the number of transfer units as with the evaporator. This calculation was performed by dividing the tube bundle of the condenser into 26 units in the direction of the flow of the heating fluid, including the outward tube and the inward tube and following the calculation flow shown in Fig. 5 for each unit. The calculation temporarily determined the outlet temperature of the heat transfer tube of a unit and the condensing quantity in the inward tube of the U-tube and calculated the outlet temperature that can balance the heat exchange quantity calculated from the inlet temperature and the outlet temperature of the heat transfer tube with the heat exchange quantity calculated with Eq. (3). Assuming that the outlet temperature of one unit is the inlet temperature of the next unit, the calculation was performed repeatedly to obtain the heat transfer rate of the entire tube bundle.

$$Nu_D = \left\{ {Nu_{Dg}}^4 + \left(Nu_{Dg} Nu_{Df} \right)^2 + {Nu_{Df}}^4 \right\}^{1/4} \quad \text{Eq. (4)}$$

$$Nu_{Dg} = {Gr_D}^{1/3} \left\{ \left(1.2/{Re_{fg}}^{0.3} \right)^4 + \left(0.072 {Re_{fg}}^{0.2} \right)^4 \right\}^{1/4} \quad \text{Eq. (5)}$$

$$Nu_{Df} = 0.165 \left(\frac{p_t}{p_l} \right)^{0.7} \left\{ {Re_{vD}}^{-0.4} + 1.83 \left(\frac{q_n}{\rho_v \Delta i_v U_{vn}} \right) \right\}^{\frac{1}{2}} \left(\frac{\rho_v}{\rho_L} \right)^{\frac{1}{2}} \frac{Re_{LD} {Pr_L}^{0.4}}{{Re_{fu}}^{0.2}} \quad \text{Eq. (6)}$$

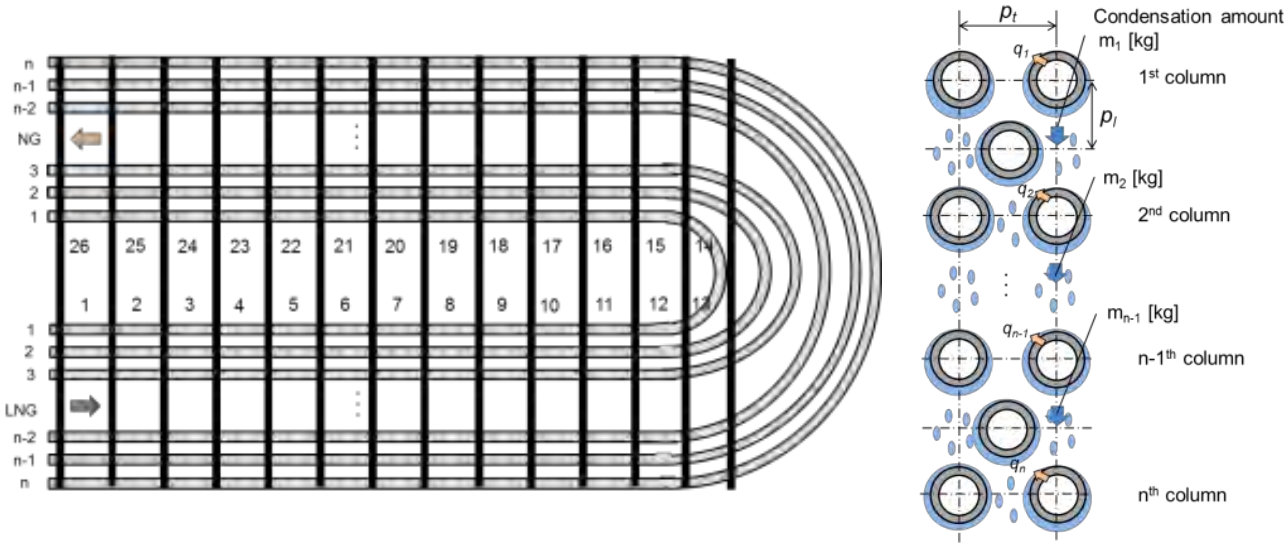

(a) Flow configuration (b) cross sectional view

Figure 4: Tube bundle of IFV condenser

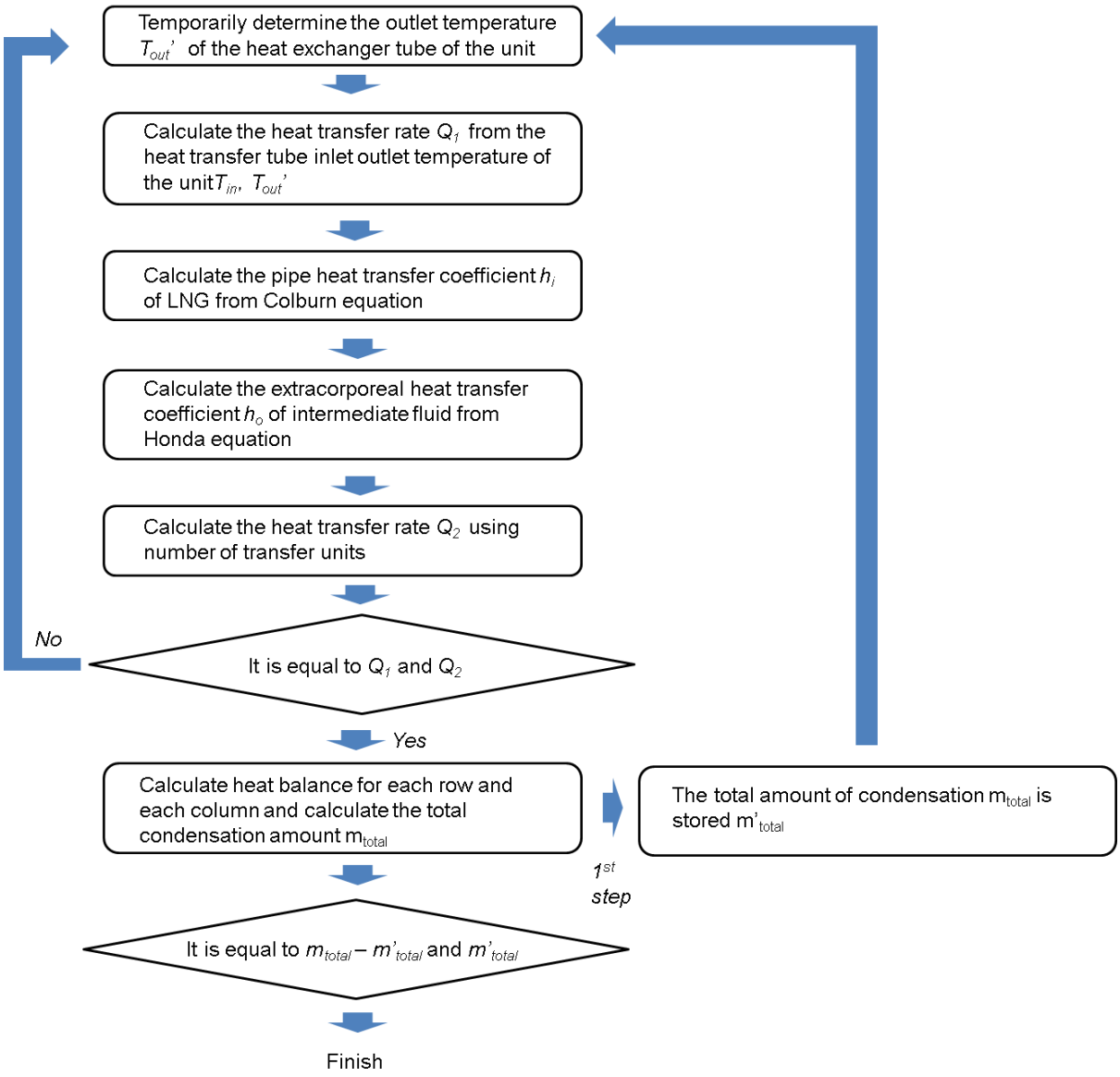

Figure 5: Condenser calculation flow

4. RESULTS AND DISCUSSIONS

Figure 6 shows the heat transfer rate of each unit of the heating fluid in the evaporator. In the lowest tube in the tube bundle, the heat transfer rate is low, and in the second tube from the bottom and upper tubes, the heat transfer rate is improved by promoted convection of the intermediate fluid due to vapor bubbles, which increased the heat transfer rate. Fig. 7 shows the heat transfer rate of each unit of LNG in the condenser. It can be confirmed that the heat transfer rate is greater at the tube influx section where the temperature difference from that of the intermediate fluid is large, and as the temperature difference became smaller, the heat transfer rate gradually decreased. The temperature decreased in order from the upper section to the lower section vertically, which indicates that heat transfer reduction due to inundation is reproduced. The figure shows the result of comparison between the calculation results when the intermediate fluid is propane and the performance of the actual equipment. The performance is successfully predicted with an accuracy of approximately ±1% for the evaporation performance and with an accuracy of approximately ±2% for the condensing performance.

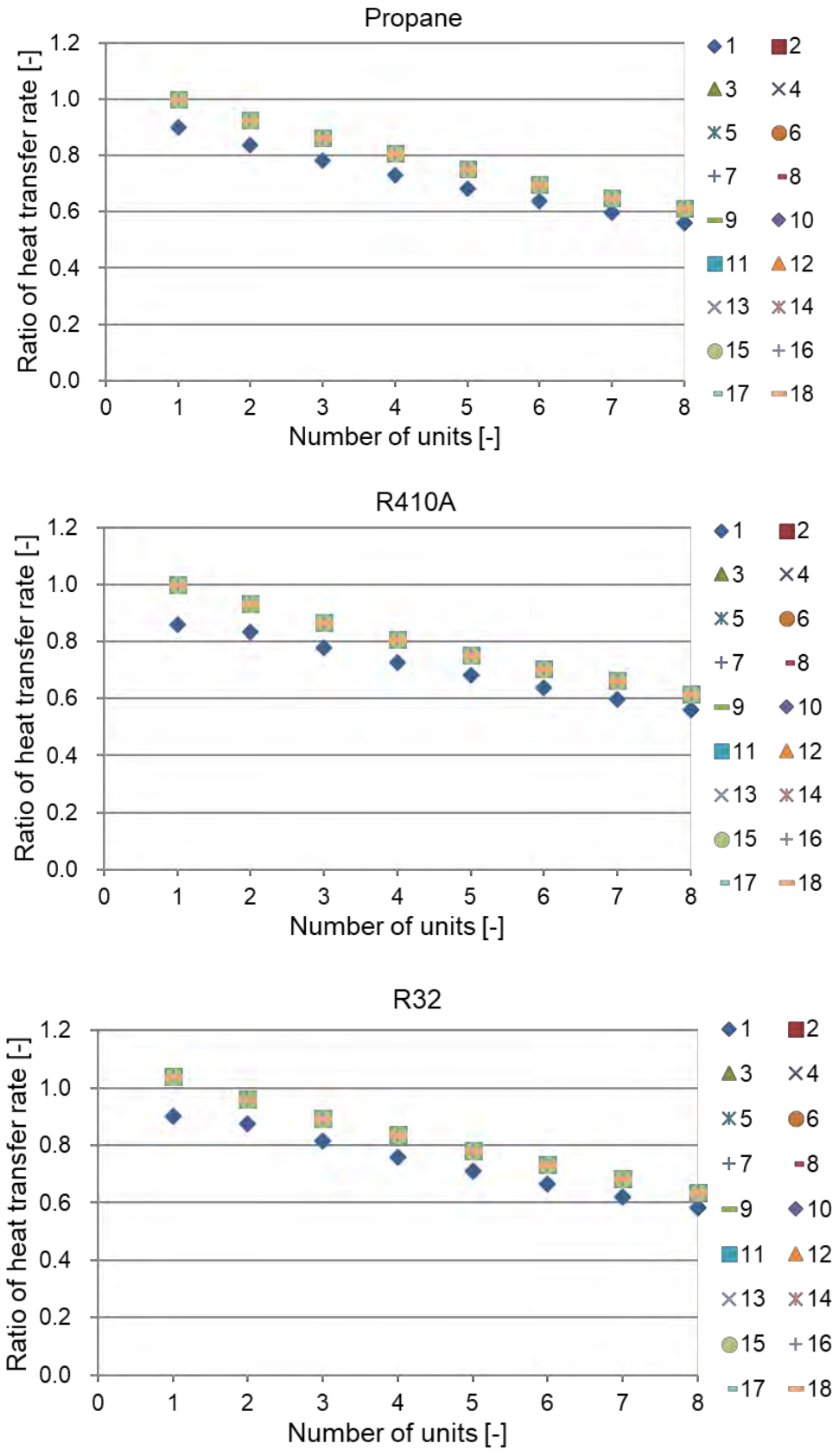

Figure 6: Heat transfer rate in evaporator

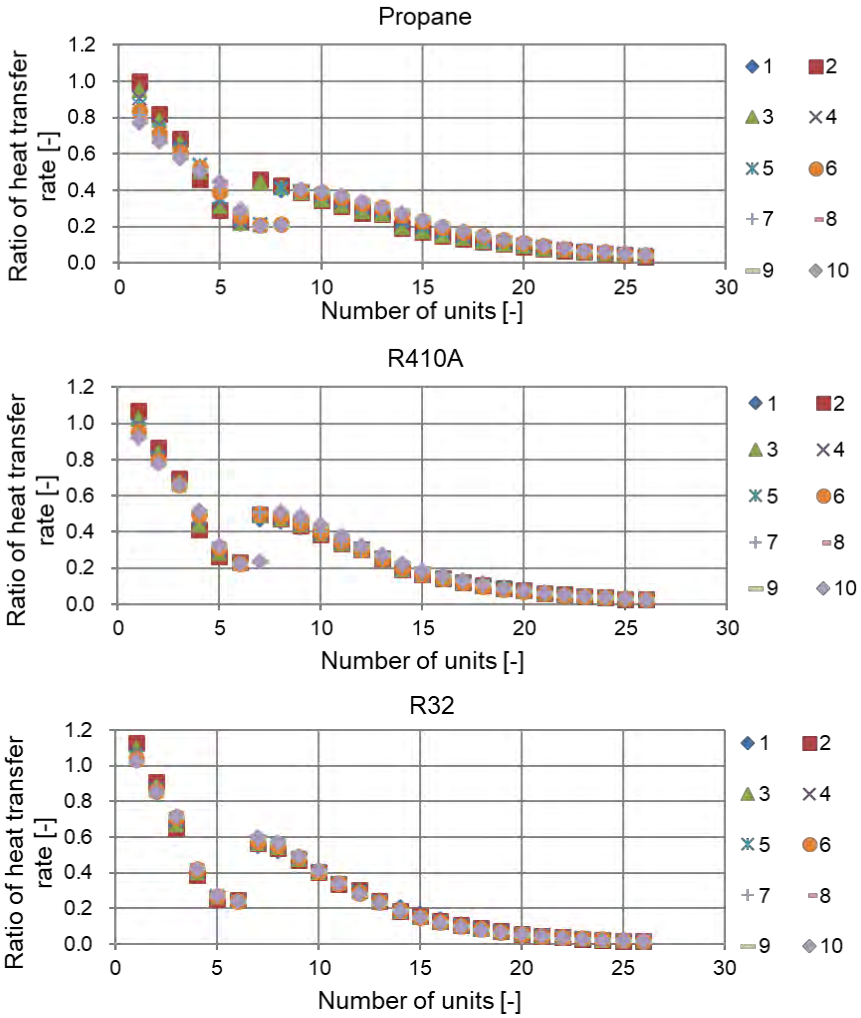

Figure 7: Heat transfer rate in condense

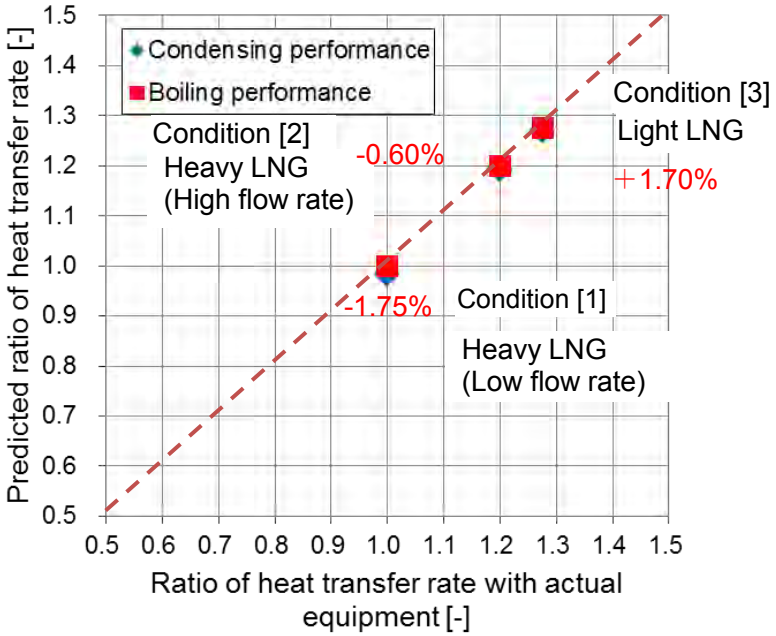

Figure 8: Comparison of heat transfer rate

Using this calculation model, we performed predictive calculation of the heat transfer performance when R32 and R410A are used as an intermediate fluid. The result indicates that the evaporation performance is on the same degree as when propane is used and that the condensing performance improves by approximately 7% with R32 and approximately 4% with R410A. The result also

indicates that the heat transfer tube surface temperature is higher than the freezing point of each refrigerant, suggesting a low possibility of performance deterioration due to freezing on the tube surface. Therefore, in terms of the heat transfer performance of the vaporizer, it was indicated that R32 and R410A can be used in place of propane as an intermediate fluid for the IFV.

5. CONCLUSION

The calculation model predicted with an accuracy of approximately ±1% for the evaporation performance and with an accuracy of approximately ±2% for the condensing performance. The evaporation performance is on the same degree as when propane is used and that the condensing performance improves by approximately 7% with R32 and approximately 4% with R410A.

NOMENCLATURE

C_{min}	:heat capacity on the side of the smaller thermal capacity among the two fluids (W/K)
Gr_D	:Grashof number (-)
M	:molecular weight (kg kmol^{-1})
Nu_D	:Nusselt number (-)
Nu_{Dg}	:Nusselt number (gravity flow) (-)
Nu_{Df}	:Nusselt number (uniform distribution flow) (-)
Pr	:Prandtl number (-)
Pr_L	:liquid Prandtl number (-)
Q	:heat transfer rate (W)
Ra	:arithmetic average roughness (μ m)
Re	:Reynolds number (-)
Re_{fg}	:film Reynolds number (gravity flow) (-)
Re_{fu}	:film Reynolds number (uniform distribution flow) (-)
Re_{vD}	:two-phase Reynolds number (gas) (-)
Re_{LD}	:two-phase Reynolds number (liquid) (-)
T_{in}	:cold fluid inlet temperature (K)
T_{sat}	:saturation temperature (K)
U_{vn}	:tube bundle cross section flow rate (m/s)
f_{wm}	:material constants (-)
p_l	:horizontal pitch (m)
p_t	:vertical pitch (m)
p_{red}	:reduced pressure (-)
ρ_l	:liquid density (kg m^{-3})
ρ_v	:gas density (kg m^{-3})
q_{wall}	:extravascular heat flux
ε	efficiency of a heat exchanger (-)
Δi_v	:latent heat of condensation (J kg^{-1})
α	:boiling heat transfer coefficient (W m^{-2}K^{-1})

REFERENCES

Egashira, S., 2009. Kobe Steel Engineering Reports, 59 (2), 90-93.

Ribatski, G., Saiz Jabardo, J.M., da Silva, E.F., 2008. Experimental Thermal and Fluid Science, 32, 1530-1537.

Dittus, F.W., Boelter, L.M.K., 1930. Heat Transfer in Automobile Radiators of the Tubular Type. Publications in Engineering, University of California, Berkeley, Vol. 2, 443.

Honda, H., Uchima, B., Nozu, S., Nakata, H., Fujii, T, 1988. Transactions of the Japan Society of Mechanical Engineers, Series B, 54 (502), 1453-1460.

Lemmon, E.W., Huber, M. L., McLinden, M. O., Reference fluids thermodynamic and transport properties – REFPROP, NIST standard reference database 23, Version 9.1, Applied Chemicals and Materials Division National Institute of Standards and Technology Boulder, CO 80305 (2013)

Manuscript ID: 1665
DOI: 10.18462/iir.icr.2019.1665

Theoretical analysis of supersonic phase change for carbon dioxide in a de Laval nozzle.

Julián Restrepo, Andrés F Bolaños-Acosta, Jose R Simões-Moreira

SISEA – Alternative Energy Systems Lab., Mechanical Engineering Department
Escola Politécnica, University of São Paulo, Brazil
restrepo@usp.br, afb.acosta@usp.br, jrsimoes@usp.br

ABSTRACT

Carbon dioxide is present in many gases mixtures, such as biogas and natural gas, besides air. This poses an important question on how to extract that gas component at affordable cost and technology.

One of the more promising techniques for carbon dioxide separation is the supersonic separation, which consists in the expansion of the fluid inside a supersonic nozzle and as the temperature falls due to the expansion, clusters (solid or liquid) of carbon dioxide will form leading to a condensation wave within the supersonic nozzle.

Pressure, temperature, and Mach number were calculated using the one-dimensional analysis for real gas. The homogeneous nucleation was calculated using the classical nucleation theory and finally it was estimated the region where the change phase will occur, being located between the Spinodal Line and the homogeneous nucleation (Wilson Line).

Keywords: Carbon Capture, Change Phase, Condensation, Nucleation.

1. INTRODUCTION

Nowadays, natural gas is one of the most important sources of energy in the world (Haghighi et al., 2013). Raw natural gas is not a saleable product because it contains a mix of various hydrocarbon gases with other gases, liquids and solid contaminants (Liu et al., 2014).
For the previous reason dehydration of raw gas is presented as an important goal in operational gas conditioning process (Niknam et al., 2018), helping to avoid the problems that occurs in downstream such as condensation, liquid slugging, and controlling of gas heating value (Speit, Saeid Mokkhatab, William A. Poe, 2006), removing water or heavy hydrocarbons from the gas (Niknam et al., 2017).
Many researches have been focused on the development of new technologies to remove liquids from the gas phase, these dehydration methods are characterized by their huge investment, the complexity of the mechanical structure, the need of large facilities to be implemented and the damage caused by this equipment to the environment (Niknam et al., 2018). Due to these facts, the using of supersonic nozzles for dehydration is a new concept that has been growing in recent years (Niknam et al., 2018).
Some of the advantages of this new technology are: the adding of chemical solvents to the raw natural gas is not required (Haghighi et al., 2013); it does not have rotating parts making it compact; ensure a simple facility with a high availability making it proper to operate in harsh or offshore environments (Liu et al., 2014), it has little loss of thermal energy and hydrodynamic head. However its coefficient of performance is still low, and there seems to be a large gap in the method that evaluates and improves the separation efficiency (Liu et al., 2014).
In a supersonic nozzle, the inlet pressure is exerted to condense the heavy fractions in the gas stream without using any external energy sources(Niknam et al., 2018).
A convergent-divergent nozzle composes the supersonic nozzle, during the supersonic gas expansion; the enthalpy of inlet gas stream is transformed into kinetic energy through an isentropic transition along with a temperature drop, which causes the heavy fractions to be condensed, due to the nucleation.

Therefore, in this paper it is estimated the homogenous nucleation limit for carbon dioxide, this line is also knows as Wilson line and the supersonic expansion inside a de Laval nozzle for a 1-D model with the following assumptions:

- Smooth nozzle profile without boundary layer detachment;
- Steady state flow;
- Inviscid flow;
- No heterogeneous nucleation; and
- Isentropic quasi 1-D flow.

Fig. 1 shows the solution flow chart used in this work, where firstly it was calculated the homogenous nucleation limit along an isothermal line. Next, it was programmed a supersonic solver in Python 3.6 to calculate the supersonic expansion of the carbon dioxide in a de Laval Nozzle, without considering the condensation or solidification effects in the flow.

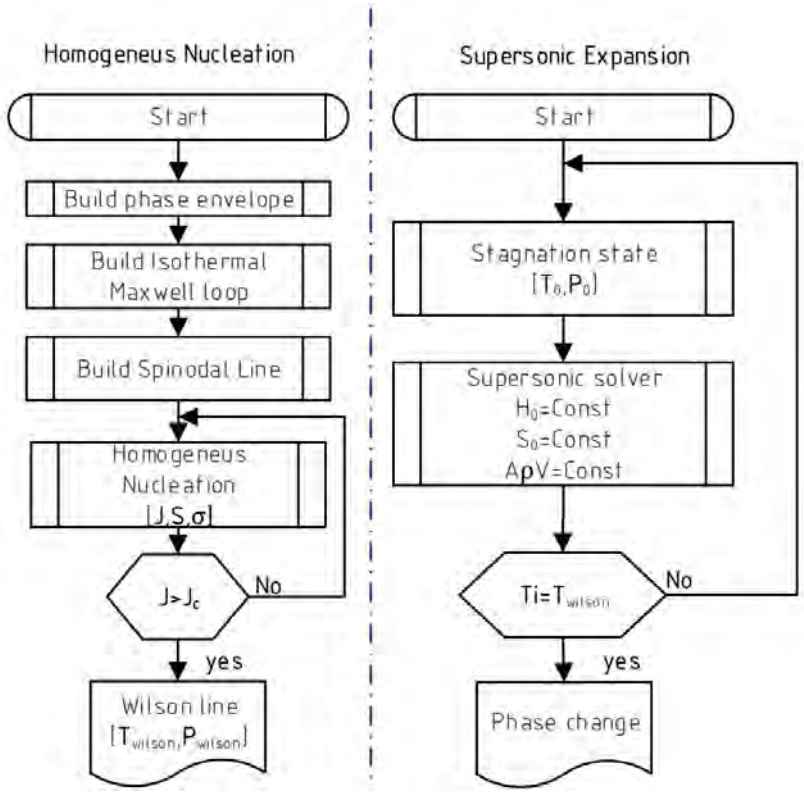

Figure 1: The solution flow chart.

For the nozzle profile was use the divergent-convergent nozzle proposed by Arina´s profile (Arina, 2004) usually used in the literature as a benchmark for different codes. Fig. 2 shows the control volume used in this work. This study is limited to find the conditions required for the phase change starts.

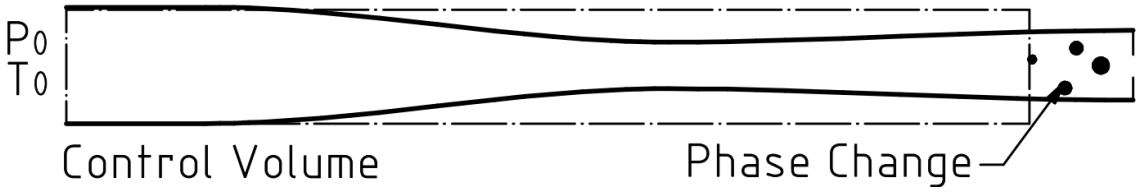

Figure 2: Control volume over an Arina´s converging-diverging supersonic nozzle.

2. MATHEMATICAL MODEL

In next sections, it is presented the mathematical model used in this work related to real gas thermodynamic properties calculations, homogenous nucleation and isentropic supersonic expansion inside a de Laval nozzle.

2.1. Real gas equation of state.

For the estimation of thermodynamic properties and partial derivatives was used CoolProp (Bell et al., 2014), code that handles with several fluids, based on Helmholtz free energy formulation for a multiparameter equation of state. In this work it was used the equation of state proposed by Wagner (Span and Wagner, 1996) which is built in the CoolProp database.

Eq. (1) shows the ideal and residual part of the free Helmholtz energy in a dimensionless form. Eqs. (2) and (3) show the calculation of the ideal and residual part. All these equations are based on the calculation of the non-dimensional temperature and density, Eqs. (4) and (5). The calculation of other thermodynamic properties are possible after the calculation of the dimensionless Helmholtz free energy and their derivatives, such as pressure Eq. (6), specific enthalpy Eq. (7), specific entropy Eq. (8), and, finally, the speed of sound Eq. (9).

$$\alpha = \alpha^0 + \alpha^r \quad \text{Eq. (1)}$$

$$\alpha^0(\rho,T,) = \ln\delta + a_1\ln\tau + a_2 + a_3\tau + a_4\tau^{-1} + a_5\tau^{-2} + a_6\tau^{-3} + a_7\ln[1-\exp(-a_8\tau)] \quad \text{Eq. (2)}$$

$$\alpha^r(\rho,T) = \sum_{k=1}^{6} N_k\delta^{i_k}\tau^{j_k} + \sum_{k=7}^{32} N_k\delta^{i_k}\tau^{j_k}\exp(-\delta^{l_k}) + \sum_{k=33}^{36} N_k\delta^{i_k}\tau^{j_k}\exp(-\phi_k(\delta-1)^2 - \beta_k(\tau-\gamma_k)^2) \quad \text{Eq. (3)}$$

$$\tau = T_c/T \quad \text{Eq. (4)}$$

$$\delta = \rho/\rho_c \quad \text{Eq. (5)}$$

$$p = \rho RT[1+\delta(\frac{\partial\alpha^r}{\partial\delta})_\tau] \quad \text{Eq. (6)}$$

$$\frac{h}{RT} = \tau[(\frac{\partial\alpha^0}{\partial\tau})_\delta + (\frac{\partial\alpha^r}{\partial\tau})_\delta] + \delta(\frac{\partial\alpha^r}{\partial\delta})_\tau + 1 \quad \text{Eq. (7)}$$

$$\frac{s}{R} = \tau[(\frac{\partial\alpha^0}{\partial\tau})_\delta + (\frac{\partial\alpha^r}{\partial\tau})_\delta] - \alpha^0 - \alpha^r \quad \text{Eq. (8)}$$

$$\frac{w^2MW}{RT} = 1 + 2\delta(\frac{\partial\alpha^r}{\partial\delta})_\tau + \delta^2(\frac{\partial^2\alpha^r}{\partial\delta^2})_\tau - \frac{[1+\delta(\frac{\partial\alpha^r}{\partial\delta})_\tau - \delta\tau(\frac{\partial^2\alpha^r}{\partial\delta\,\partial\tau})]^2}{\tau^2[(\frac{\partial^2\alpha^0}{\partial\tau^2})_\delta + (\frac{\partial^2\alpha^r}{\partial\tau^2})_\delta]} \quad \text{Eq. (9)}$$

2.2. Maxwell isothermal reconstruction.

Once the phase envelope for the carbon dioxide was constructed, it is required to build an isothermal line across the two-phase region. Over that line it was calculated the homogenous nucleation limit. Nevertheless, for a multiparameter equation of state based on Helmholtz energy, this isothermal line have several roots compared to with a cubic equation of state. Hence, is required a reconstruction of this line keeping all the important information and fulfilling the Maxwell´s criteria.

It has been used the formulation proposed by Boltachev and Baidakov (2006) and refined by Matthis Thorade (2014). In this formulation it is reconstructed the dimensionless Helmholtz free energy, Eq. (10), and the pressure, Eq. (11), using a polynomial expression. All the adjusting coefficients have to fulfill the conditions established in Eqs. (12), (13), and (14). Eq. (14) is the Maxwell´s rule of equal areas in density terms.

$$\alpha = \alpha_0 - \frac{\alpha_1}{\delta} + \frac{\alpha_2}{\tau}\ln\delta + \frac{\alpha_3}{\tau}\delta + \frac{\alpha_4\delta^2}{\tau} + \frac{\alpha_5}{\tau}\frac{\delta^3}{3} + \frac{\alpha_6}{\tau}\frac{\delta^4}{4} + \frac{\alpha_7}{\tau}\frac{\delta^5}{5} \quad \text{Eq. (10)}$$

$$\frac{p}{\rho_c RT_c} = a_1\tau + a_2\delta + a_3\delta^2 + a_4\delta^3 + a_5\delta^4 + a_6\delta^5 + a_7\delta^6 \quad \text{Eq. (11)}$$

$$\left(\frac{\partial p}{\partial\rho}\right)_T|_{\rho=\rho_l} \;\&\; \left(\frac{\partial p}{\partial\rho}\right)_T|_{\rho=\rho_v} \quad \text{Eq. (12)}$$

$$\left(\frac{\partial^2 p}{\partial\rho^2}\right)_T|_{\rho=\rho_l} \;\&\; \left(\frac{\partial^2 p}{\partial\rho^2}\right)_T|_{\rho=\rho_v} \quad \text{Eq. (13)}$$

$$\int_{\rho_v}^{\rho_v} \frac{p}{\rho^2}d\rho = p_s(\frac{1}{\rho_v} - \frac{1}{\rho_l}) \quad \text{Eq. (14)}$$

After performing the calculations, it was obtained the reconstructed Metastable Maxwell loop as presented in Fig. 3a, where it was also plotted, as an example, the original isothermal line at 295 [K] for carbon dioxide. The analysis showed that it was possible to verify the odd behavior of that isothermal, attaining pressure values higher than the critical one and with several roots within the equilibrium dome, which clearly confirms the data fit behavior of such equation. After reconstructing the isothermal line, it is possible to construct the Spinodal line using the conditions established in Eqs. (12) and (13). The Spinodal curve is presented in Fig. 3b.

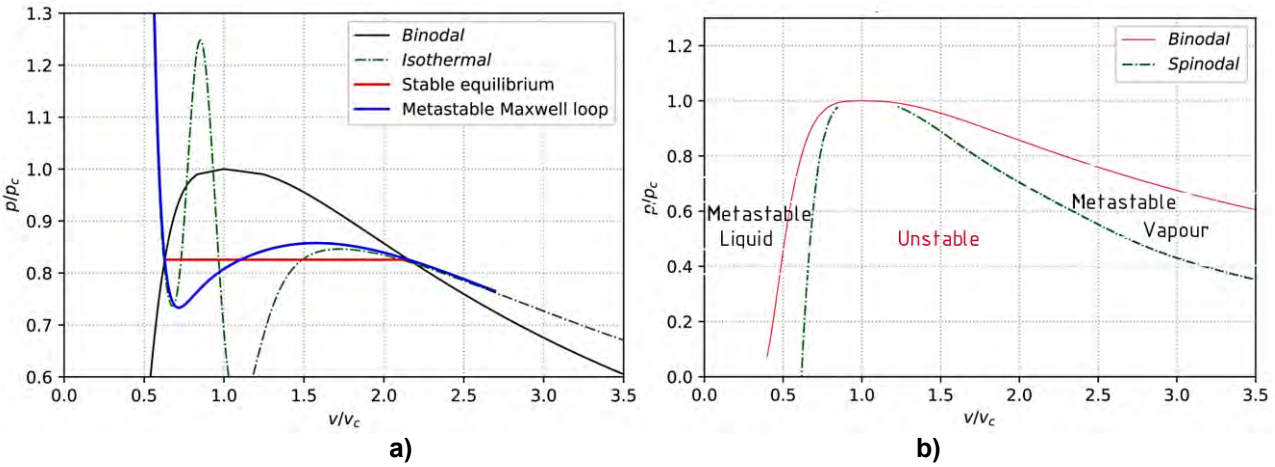

Figure 3: a) Comparison isothermal and Metastable Maxwell Loop for 295 K, b) Spinodal Lines.

2.3. Wilson Line.

Subsequently, the Spinodal and the isothermal lines were calculated, it was estimated the homogeneous nucleation inside the region constrained by the binodal and the Spinodal line. It was used the approach of homogenous nucleation developed by (Pandey, 2014),based on the classical nucleation theory.

In this approach, the nucleation starts when the nucleation rate exceeds a critical value of 10^{20} [$m^{-3}s^{-1}$] (Bier et al., 1990). The nucleation rate was calculated from Eq. (15), considering a non-isothermal factor, Eq. (16). In Eq. (17) it was calculated the critical radius of nucleation as a function of the supersaturation ratio, Eq. (18). That ratio is the relation between the vapor pressure inside the metastable state and the equilibrium pressure for the same isothermal line and it determines the degree of metastability of the expansion.

$$J_{CL} = \frac{\alpha_c \rho_v^2}{C\rho_l}\sqrt{\frac{2\sigma}{\pi m^3}}\exp\left(-\frac{4\pi r^{*2}\sigma}{3kT_v}\right) \quad \text{Eq. (15)}$$

$$C = 1 + 2\frac{\gamma-1}{\gamma+1}\frac{h_v - h_l}{RT_v}\left(\frac{h_v - h_l}{RT_v} - \frac{1}{2}\right) \quad \text{Eq. (16)}$$

$$r^* = \frac{2\sigma}{\rho_l R T_v \ln(S)} \quad \text{Eq. (17)}$$

$$S = \frac{P_v}{P_{eq}} \quad \text{Eq. (18)}$$

With the set of equations (Eqs. 15-18) it was calculated the Wilson Line for carbon dioxide for several isothermal lines inside the two-phase region. The algorithm for the Wilson line starts from the intersection of the bimodal or saturation line with the reconstructed isothermal line in the vapor region. Subsequently, the algorithm starts to go along the isothermal line for several steps looking for the point where the critical homogenous rate is attained, this point is called the Wilson point. After carrying out the procedure for several isothermal lines, the Wilson line is obtained. Those results are shown in Fig. 4 and are compared with experimental data available in literature (Lettieri et al., 2017).

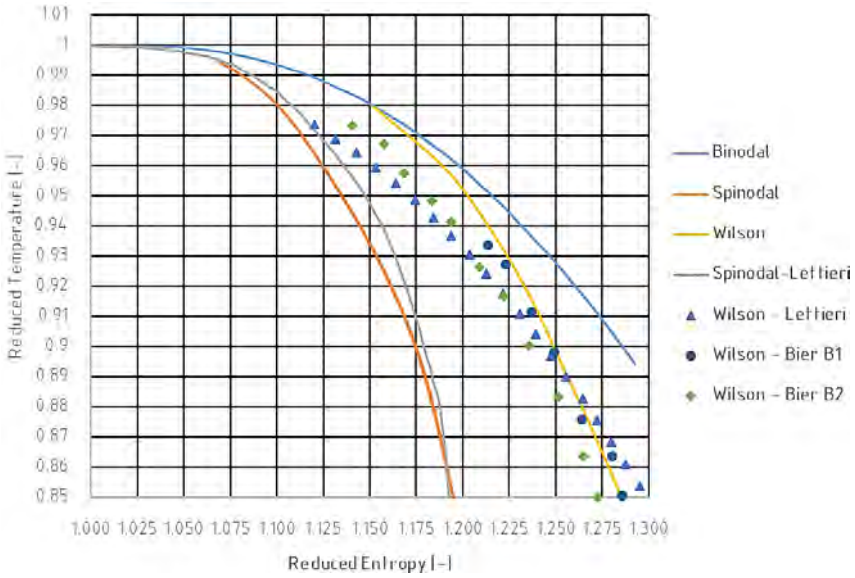

Figure 4: Wilson line validation and Spinodal verification.

2.4. Supersonic Expansion.

In the last sections it is presented the methodology and equations used to find the Spinodal line and the Wilson line for carbon dioxide. In this section, it is presented the model used to simulate the quasi 1-D expansion of carbon dioxide in a supersonic de Laval Nozzle using the Arina´s profile (Arina, 2004). The model does not take into account the effect of condensation in the supersonic flow as it just estimated the conditions and the point where the phase change starts up.

Eq. (19) presents the conservation of the stagnation specific enthalpy that must remain constant along the nozzle, the mass conservation equation is formulated in Eq. (20); Eq. (21) shows the isentropic condition inside the nozzle. Finally, Eq. (22) presents the definition of Mach number.

Was implemented a solver from Scipy in Python 3.6 to calculate the temperature of the flow at each point as a function of the nozzle area and the stagnation entropy, once the temperature is obtained, it is possible to find other thermodynamic properties such as specific enthalpy, density, and the local speed-of-sound, *w*. *V* is the flow velocity.

$$h_0 = h_i + \frac{V_i^2}{2} \quad \text{Eq. (19)}$$

$$A_{inlet}\rho_{inlet}V_{inlet} = A_i\rho_i V_i \quad \text{Eq. (20)}$$

$$s_0 = s_i \quad \text{Eq. (21)}$$

$$M = \frac{V}{w} \quad \text{Eq. (22)}$$

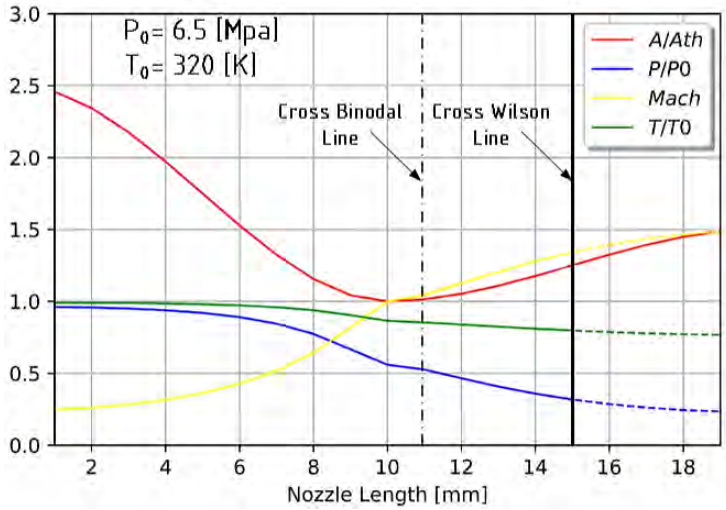

Figure 5: Supersonic expansion in a de Laval nozzle with phase change.

After performing the isentropic solution calculations for the Arina´s profile, it was obtained the temperature, pressure, and Mach number curves within the nozzle, as depicted in Fig. 5. Binodal line and the Wilson line crossing are also shown, and the dashed lines shows the expansion without phase change after the Wilson line. However, in reality, the actual section were nucleation starts off lies between the binodal and the Wilson line, being the latter the metastable limit.

3. CONCLUSIONS

This paper examined the condensation phenomena in an isentropic supersonic expansion of carbon dioxide within an Arina´s nozzle using a real gas approach. It was found that below reduced temperatures of 0.95 a good agreement between experimental data available in literature and the theoretical results.
It was found a good agreement of the Spinodal line after the verification with the work of Lettieri, where the maximum deviation is of 1.1%, showing the good fitting in the reconstruction of the Maxwell isothermal.
The Wilson line obtained could be used to estimate the phase change starts for a no equilibrium process, regardless of the process nature.
The model should be improved to consider the latent heat release as the condensation starts in the supersonic flow, also considering the change in entropy.
The results obtained are good enough for a preliminary design of process and/or equipment; nevertheless, due the complex nature of the non-equilibrium condensation, it is required experimentation and more advanced and realistic models. A further challenge under investigation is to extend the solution procedure to a gaseous mixture containing carbon dioxide.

ACKNOWLEDGEMENTS

The authors would like to thank the sponsorship of Shell and FAPESP through the “Research Centre for Gas Innovation - RCGI” (FAPESP Proc. 2014/50279-4), hosted by the University of Sao Paulo, and the strategic importance of the support given by ANP (Brazil’s National Oil, Natural Gas and Biofuels Agency) through the R&D levy regulation. The last author thanks CNPq for the research scholarship.

NOMENCLATURE

A	area (m^2)	T_c	critical temperature (K)
C	non-isothermal correction factor (-)	T_0	stagnation temperature (K)
J	volumetric nucleation rate ($m^{-3}s^{-1}$)	v	specific volume ($m^3\ kg^{-1}$)
		V	flow velocity ($m\ s^{-1}$)
k_b	Boltzmann constant ($1.38064852\times 10^{-23}$ $m^2\ kg\ s^{-2}\ K^{-1}$)	w	speed-of-sound (ms^{-1})
h	specific Enthalpy ($J\ kg^{-1}$)	α	dimensionless Helmholtz free energy (-)
m	mass of CO_2 (kg)	α^0	ideal dimensionless Helmholtz free energy (-)
M	Mach number (-)	α^r	residual dimensionless Helmholtz free energy (-)
MW	CO_2 molar weight ($44.01\ g\ mol^{-1}$)	α_c	condensation coefficient (-)
P	pressure (Pa)	β	adjusting parameter (-)
P_0	stagnation pressure (Pa)	γ	isentropic expansion ratio (-)
r^*	critical radius (m)	δ	dimensionless density (-)
R	ideal gas constant ($8.314472\ J\ K^{-1}mol^{-1}$)	ρ	density ($kg\ m^{-3}$)
s	specific Enthalpy ($J\ kg^{-1}K^{-1}$)	ρ_c	critical density ($kg\ m^{-3}$)
S	supersaturation ratio (-)	σ	surface tension ($N\ m^{-1}$)
		τ	dimensionless temperature (-)

REFERENCES

Arina, R., 2004. Numerical simulation of near-critical fluids. Appl. Numer. Math. 51, 409–426. https://doi.org/10.1016/j.apnum.2004.06.002

Bell, I.H., Wronski, J., Quoilin, S., Lemort, V., 2014. Pure andPseudo-pure Fluid Thermophysical Property Evaluation and the Open-SourceThermophysical Property Library CoolProp. Ind. Eng. Chem. Res. 53, 2498–2508. https://doi.org/dx.doi.org/10.1021/ie4033999

Bier, K., Ehrler, F., Theis, G., 1990. Spontaneous Condensation in Stationary Nozzle Flow of carbon dioxide in a Wide Range of Density, in: Adiabatic Waves in Liquid-Vapor Systems. Springer Berlin Heidelberg, pp. 129–141.

Boltachev, G.S., Baidakov, V.G., 2006. The thermodynamic properties of nitrogen, argon, oxygen, and their mixtures in the region of the liquid-gas phase transition. Russ. J. Phys. Chem. 80, 501–504. https://doi.org/10.1134/S0036024406040030

Haghighi, M., Abedinzadegan Abdi, M., Hawboldt, K., 2013. Natural Gas Dehydration Using Supersonic Separators with a Novel Design. Offshore Technol. Conf. https://doi.org/10.4043/23974-MS

Lettieri, C., Paxson, D., Spakovszky, Z., Bryanston-Cross, P., 2017. Characterization of Nonequilibrium Condensation of Supercritical carbon dioxide in a de Laval Nozzle. J. Eng. Gas Turbines Power 140, 1–13. https://doi.org/10.1115/1.4038082

Liu, X., Liu, Z., Li, Y., 2014. Investigation on Separation Efficiency in Supersonic Separator with Gas-Droplet Flow Based on DPM Approach. Sep. Sci. Technol. 49, 2603–2612. https://doi.org/10.1080/01496395.2014.938755

Matthis Thorade, 2014. Entropiebasierte Bewertungskriterien für den Wärmeübergang in Kraftwerksprozessen und ihre Relevanz für praktische Anwendungen. Technischen Universität Hamburg-Harburg. https://doi.org/10.15480/882.1207

Niknam, P.H., Mortaheb, H.R., Mokhtarani, B., 2018. Dehydration of low-pressure gas using supersonic separation: Experimental investigation and CFD analysis. J. Nat. Gas Sci. Eng. 52, 202–214. https://doi.org/10.1016/j.jngse.2017.12.007

Niknam, P.H., Mortaheb, H.R., Mokhtarani, B., 2017. Optimization of dehydration process to improve stability and efficiency of supersonic separation. J. Nat. Gas Sci. Eng. 43, 90–95. https://doi.org/10.1016/j.jngse.2017.03.017

Pandey, A., 2014. Numerical Modeling of Non- Equilibrium Condensing Steam Flows. Delft University of Technology.

Span, R., Wagner, W., 1996. A New Equation of State for carbon dioxide Covering the Fluid Region from the Triple-Point Temperature to 1100 K at Pressures up to 800 MPa. J. Phys. Chem. Ref. Data 25, 1509–1596. https://doi.org/10.1063/1.555991

Speit, Saeid Mokkhatab, William A. Poe, J.G., 2006. Handbook of Natural Gas Transmission and processing, Elsevier. Elsevier.

Manuscript ID: 59
DOI: 0.18462/iir.icr.2019.0059

Surface Tension Measurement and Modeling Work for New Low GWP Working Fluids

Chieko KONDOU [(a)], Jamal EL ABBADI[(b)], Céline HOURIEZ[(b)], Michel MASELLA [(c)], Yukihiro HIGASHI[(d)], Christophe COQUELET[(b)]

[(a)] Nagasaki University, School of Engineering,
Nagasaki, 852-8521, Japan, ckondou@nagasaki-u.ac.jp
[(b)] MINES ParisTech, PSL University, CTP - Centre of Thermodynamic of Processes,
Fontainebleau, 77305, France, christophe.coquelet@mines-paristech.fr
[(c)] CEA Saclay, Institut de Biologie et de Technologies de Saclay, Cedex, 91191, France
[(d)] Kyushu University, NEXT-RP in Int. Inst. for Carbon Neutral Energy Research,
Fukuoka, 819-0395, Japan, higashi@i2cner.kyushu-u.ac.jp

ABSTRACT

In this work, the surface tensions of some selected new low GWP (global warming potential) refrigerant mixtures containing HFOs (hydrofluoroolefins) were determined. The surface tension of the HFO-1123/HFC-32 was experimentally determined at temperatures from 265 K to near the critical points and with various compositions. Further, a model associating a cubic equation of state with the linear gradient theory was developed. Good agreement was observed between the experimentally obtained results and those obtained using the developed model.
Keywords: Surface Tension, Measurements, Parachor Method, Linear Gradient Theory.

1. INTRODUCTION

In the Kigali amendment to the Montreal protocol, a phase down schedule for the production and consumption amount of HFCs (Hydro Fluoro Carbons) and HCFCs (Hydro Chloro Fluoro Carbons) was declared for mitigating global warming. According to this schedule, until 2036, developed countries should reduce CO_2 emissions equivalent to 85% from the baseline corresponding to the period 2011–2013. Owing to such circumstances, low GWP (global warming potential) refrigerants are attracting the attention of air conditioning and refrigeration system manufacturers worldwide. The current commercial focus is on HFOs (Hydro Fluoro Olefins) exhibiting a GWP of less than one, with acceptable mild flammability. A binary refrigerant mixture containing HFO1123 and HFC32 is anticipated to be an alternative to HCFC 22 and R410A refrigerants used in stationary air conditioning systems. Although the use of HFO1123 alone causes the risk of disproportionate reactions, this substance has potentially beneficial thermophysical properties as the one of mixture components, coupled with HFC32. However, the physical properties of this refrigerant are not adequately clarified yet. Surface tension is one of the properties having an important role in boiling and condensation heat transfer; however, experimental data in this regard are not yet reported. Surface tension data were precisely measured using a differential capillary-rise-height method in this study. Surface tension was measured using a capillary rise technique; further, a model associating a cubic equation of state with the linear gradient theory was developed for the HFO1123/ HFC32 mixture.

2. MEASUREMENT

Fig. 1 (a) explains the principle of the differential capillary rise method (Heide, 1997). Surface tension was measured in terms of the capillary elevation in a small-diameter tube immersed in a liquid. Two capillaries with inner radii of r_1 = 0.4222 ± 0.0009 mm and r_2 = 0.7526 ± 0.0009 mm were vertically set by a supporting brace in a pressure vessel composed of a glass tube with a 17 mm inner diameter (ID) and 25 mm outer diameter (OD). These capillary radii were precisely measured with mercury

slugs. The pressure vessel filled with a sample refrigerant was placed in a thermostatic bath, and the temperature was kept constant with a fluctuation within ±10 mK. The temperature was measured with a 100 Ω platinum resistance thermometer, calibrated against ITS-90. The uncertainty in temperature measurements was estimated to be within ±5 mK. In the steady state, the capillary rise difference between the two capillary tubes was measured using a digital traveling microscope with a tolerance of 0.01 mm. Fig. 1 (b) shows an example of a charge-coupled device (CCD) image.

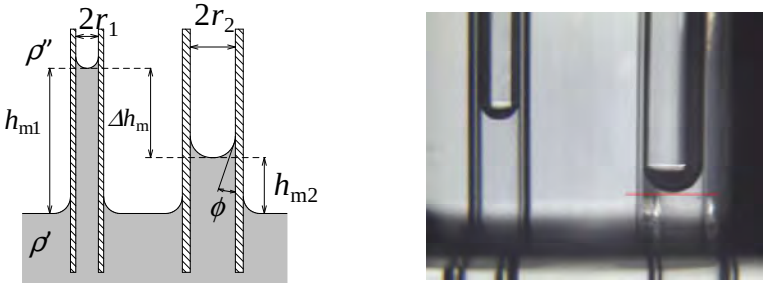

(a) principle (b) CCD image

Figure 1: Differential capillary rise height method

The height difference in the bottom of the meniscus in each capillary tube, Δh_m as shown in Fig. 1 (a), was measured. To obtain the actual differential capillary rise height Δh_c, the measured differential height was corrected using the method proposed by Rayleigh (1916), namely approximating the contact angle ϕ as zero assuming a semi spherical meniscus.

$$\Delta h_c = \Delta h_m + \frac{r_1 - r_2}{3} - 0.1288\left(\frac{r_1^2}{h_{m1}} - \frac{r_2^2}{h_{m2}}\right) + 0.1312\left(\frac{r_1^3}{h_{m1}^2} - \frac{r_2^3}{h_{m2}^2}\right) + \ldots \approx \Delta h_m + \frac{(r_1 - r_2)}{3} \qquad \text{Eq. (1)}$$

The capillary constant a^2 was determined only from the capillary radii and the differential capillary-rise-height. Then, the surface tension σ was determined from the capillary constant and orthobaric liquid and vapour densities ρ_L and ρ_V as follows:

$$\sigma = \frac{a^2\left(\rho_L - \rho_V\right)g_n}{2}, \qquad a^2 = \frac{g\Delta h_c}{g_n\left(1/r_1 - 1/r_2\right)\cos\phi} \approx \frac{g\Delta h_c}{g_n\left(1/r_1 - 1/r_2\right)} \qquad \text{Eq. (2)}$$

where g and g_n correspond to the local gravitational acceleration of 9.79585 m s^{-2} at Nagasaki-city, Japan and normal gravitational acceleration of 9.80665 m s^{-2}, respectively. The orthobaric densities were calculated with REFPROP 9.1. (Lemmon et al., 2013). For HFO1123, the EoS (equation of state) developed by Higashi and Akasaka (2016) was applied.

For the binary mixture HFO1123/HFC32, the following measurement procedure was performed to calculate the orthobaric densities. The total charge amount, m_{total}, and the charge composition, $W_{HFO1123}$, were determined from the mass of each component charged into the pressure vessel.

$$m_{total} = m_{HFO1123} + m_{HFC32}, \qquad W_{HFO1123} = m_{HFO1123}/m_{total} \qquad \text{Eq. (3)}$$

The vapour mass fraction in the vessel, ξ, was determined under a condition such that the total volume was always equal to the internal volume of the pressure vessel.

$$V_{total} = m_{total}\xi/\rho_V\left(W_{HFO1123}, T, \xi\right) + m_{total}\left(1-\xi\right)/\rho_L\left(W_{HFO1123}, T, \xi\right) \qquad \text{Eq. (4)}$$

The compositions in the vapour and liquid phases were calculated at that vapour mass fraction using a default “KW0 model” associated with REFPROP 9.1. Accordingly, the orthobaric vapour and liquid densities were calculated as functions of the charge composition, temperature, and vapour mass fraction.

3. MODELING

3.1. Pure compound

Three main methods can be used for determining the surface tension of a pure compound. The simplest one is a van der Waals type correlation,

$$\sigma = \sigma_0\left(1 - T_r\right)^\gamma \qquad \text{Eq. (5)}$$

The coefficient σ_0 and exponent γ are determined to fit the measurement data. The second one is based on utilising a Parachor (P) for each phase, as seen in Eq. (6). This method also requires the determination of the molar densities $\tilde{\rho}$ of each phase.

$$\sigma = \left(P_L \tilde{\rho}_L - P_V \tilde{\rho}_V\right)^{\theta}, \qquad \tilde{\rho} = \left(\rho / M\right) \times 10^{-3} \quad \text{Eq. (6)}$$

where M represents the molar mass 52.024 g mol^{-1} for HFC32 and 82.025 g mol^{-1} for HFO1123. For a pure component, the value of P for each phase is the same. Eq. (6) also uses an exponent θ and its value is equal or close to 4 (Gasem et al., 1989). The densities of each phase have to be calculated. A fundamental EoS based on Helmholtz energy, developed in REFPROP 9.1, can be used. It is important that the density prediction be very accurate to obtain the best estimation of surface tension.

Further, using an EoS, it is possible to calculate the surface tension directly. This method is based on the gradient theory (GT) and its derivative, the linear gradient theory (LGT), both of which have been extensively described in literature (e.g., Zuo et al., 1997; Miqueu et al., 2003). The gradient theory states that the Helmholtz energy density of an inhomogeneous fluid, in the absence of an external potential, is the sum of two contributions: Helmholtz free energy density of the homogeneous fluid at local composition and a corrective term which is a function of the local density gradient.

$$\sigma = \sqrt{2c} \int_{\tilde{\rho}_V}^{\tilde{\rho}_L} \left(\sqrt{f_0\left(\tilde{\rho}\right) - \sum \tilde{\rho}_i \mu_i + p_{\text{equil}}} \right) d\tilde{\rho} \quad \text{Eq.(7)}$$

Here, c is the influence parameter, $\tilde{\rho}$ is the molar density (mol.m^{-3}), μ_i is the chemical potential of the ith component, f_0 is the Helmholtz free energy density, and p_{equil} is the equilibrium pressure. The equilibrium pressure is calculated using the PR (Peng Robinson) EoS (Peng and Robinson, 1976) with the Mathias Copeman Alpha function Eq. (8).

$$\alpha(T) = \left[1 + n_1\left(1 - T_r\right) + n_2\left(1 - T_r\right)^2 + n_3\left(1 - T_r\right)^3\right]^2 \quad \text{Eq.(8)}$$

Where, T_r is the reduce temperature. The coefficients n_1, n_2, and n_3 in Eq. (8) are optimized using the pure compound vapour pressure data (Mathias and Copeman, 1983). The influence parameter was calculated by using a van der Waals type Equation of State (Bongiorno and Davis, 1975). It was found that $ab^{2/3} \approx 0.61$. The influence parameter is temperature dependent. Several temperature dependency expressions can be used. We considered the one given in Eq.(9) proposed by Miqueu et al. (2003).

$$c = \left(ab^{2/3}\right) \times \left[E\left(\frac{1 - T}{T_{\text{crit}}}\right) + F \right] \quad \text{Eq.(9)}$$

In Eq. (9), a and b represent the cohesive energy parameter and volumetric parameter, respectively (parameters a and b were calculated from the cubic EoS); E and F are adjusted using surface tension data of each of the pure compounds studied.

3.2. Mixture

It is possible to apply the three methods described above for determining the surface tension of mixtures. In the Parachor method, it is necessary to compute the value of the Parachor for each phase by considering a mixing rule.

$$P_{\text{L}} = \sum_{i=1}^{N} x_i P_i \quad \text{and} \quad P_{\text{V}} = \sum_{i=1}^{N} y_i P_i \quad \text{Eq.(10)}$$

Here, x_i and y_i are the representative mole fractions of the i th component in the liquid and vapour phases, respectively.

As for the LGT, mixing rules concerning the determination of parameters a and b of the Cubic Equation of state have to be considered. Concerning the influence parameter, a quadratic mixing rule must be considered.

$$c = \sum_{i=1}^{N} \sum_{j=1}^{N} x_i x_j c_{ij} \quad \text{Eq.(11)}$$

Eq. (11) presents the relation between the influence parameters of the pure compounds. With a Binary Interaction Parameter (BIP) k_{ij} adjusted on experimental data, the parameter c_{ij} in Eq.(11) can be calculated using the influence parameter of each pure component as,

$$c_{ij} = \sqrt{c_i c_j}\left(1 - k_{ij}\right) \qquad \text{Eq.(12)}$$

4. RESULTS AND DISCUSSIONS

4.1. Pure compound

Fig. 2(a) shows the surface tension for pure HFC32 and HFO1123. The symbols and lines correspond to the measured data and calculation results, respectively. The data of HFC32 obtained in the present study agree with the measurement data reported in literature and the correlation proposed by Mulero et al. (2012) implemented using REFPROP within the propagated measurement uncertainty of approximately ±0.2 mNm^{-1}. Thus, the measurement method is validated. The thin solid lines represent the following van der Waals-type correlations.

$$\begin{cases} \sigma_{\mathrm{HFC32}} = 71.47\times10^{-3}\left(1-T/351.26\right)^{1.246} & \text{(Mulero et al., 2012)} \\ \sigma_{\mathrm{HFO1123}} = 61.02\times10^{-3}\left(1-T/331.73\right)^{1.300} & \text{(Kondou and Higashi, 2018)} \end{cases} \qquad \text{Eq. (13)}$$

From the measured surface tension data, the Parachor P was obtained. Fig. 2(b) plots the obtained Parachor that were 92.4 ±1.6 and 120.9 ±1.6 for HFC32 and HFO1123, respectively. The dashed line plotted in Fig. 2(a) shows the calculated surface tension with the obtained Parachor. The calculated value agrees with the measured surface tension within the propagated measurement uncertainty.

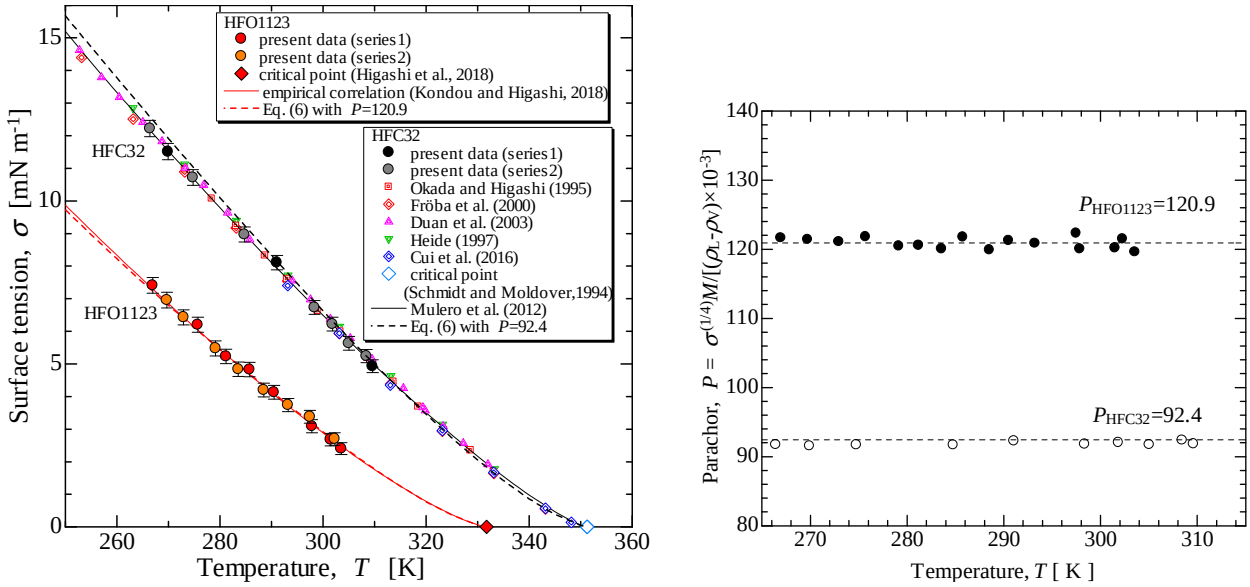

(a) surface tension (b) obtained Parachor

Figure 2: Surface tension for HFC32 and HFO1123 alone and obtained Parachor P (θ = 4)

4.2. Mixture

Fig. 3 shows the phase diagram of the HFO1123/HFC32 to determine the interaction parameter k_{12}. The symbols represent the measured data obtained by Higashi and Akasaka (2016). The parameter k_{12} is determined as 0.034939 to fit these data. The critical parameters and other parameters used in Eq. (8) are listed in Table 1. The adjustable parameters E and F in Eq. (9) were determined from the surface tension data listed in Table 1 for HFC32 and HFO1123.

Table 1: Critical parameters and the parameters used in LGT method

	T_{crit}	P_{crit}	*acentric factor* ω	n_1 in Eq. (8)	n_2 in Eq. (8)	n_3 in Eq. (8)	E in Eq. (9)	F in Eq. (9)
HFC32	351.26	5.782	0.277	0.85552	-1.1255	4.30994	-1.22374	-0.34027
HFO1123	331.73	4.543	0.261	0.77401	-0.8708	4.66050	-1.34234	-0.47698

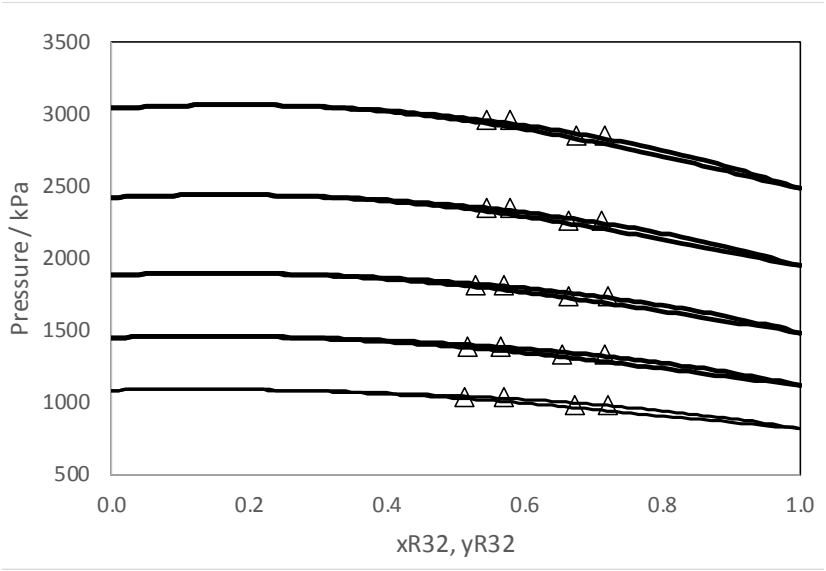

Figure 3: Phase diagram of HFO1123/HFC32 with an interaction parameter k_{12}=0.034939

Figs. 4(a) to 4(d) show the surface tension of the HFO1123/HFC32 at various charge compositions. The circles represent the measured data. The notation $x_{HFO1123}$ denotes the mole fraction variation of the liquid phase in the measurement range, which is slightly lower than the charge mole fraction $X_{HFO1123}$.The diamond symbols represent the critical temperature reported by Higashi and Akasaka (2016). The dashed, thick solid, and dashed-dotted lines respectively represent the calculation results obtained using the Parachor method, LGT, and van der Waals correlation. The purple thin line shows the prediction by Di Nicola et al. (2018) proposed for various HFO/HFC binary mixtures.

For the HFO1123/HFC32, the van der Waals correlation was fitted to the measured data as follows:

$$\sigma_{HFO1123/HFC32} = \begin{cases} 63.52\times10^{-3}\left(1-T/337.48\right)^{1.277} & \text{at } W_{HFO1123}=0.629 \quad X_{HFO1123}=0.518 \\ 64.16\times10^{-3}\left(1-T/339.65\right)^{1.271} & \text{at } W_{HFO1123}=0.519 \quad X_{HFO1123}=0.406 \\ 66.02\times10^{-3}\left(1-T/342.39\right)^{1.264} & \text{at } W_{HFO1123}=0.393 \quad X_{HFO1123}=0.291 \\ 65.99\times10^{-3}\left(1-T/346.85\right)^{1.254} & \text{at } W_{HFO1123}=0.190 \quad X_{HFO1123}=0.130 \end{cases} \quad \text{Eq. (14)}$$

The exponent of van der Waals correlation (γ) is linearly interpolated against the critical surface fraction, and then the coefficient σ_0 is optimized to obtain the best fit with the measurement data. The coefficient varies in a downward convex manner with the charged mole fraction, as shown in Fig. 5. It appears that the coefficient, 65.985, fitted at $X_{HFO1123}$=0.13 is lower than the expected variation indicated by the dashed line.

The values obtained with the parachor method, represented by the dashed line in Fig. 4, agree with the measured surface tension within the uncertainty limit except at a charge mole fraction $X_{HFO1123}$=0.13. At a mole fraction 0.13, the measurement result exhibits a lower value than that predicted using the parachor method. This behavior is also evident in Fig. 6. The blue and red symbols show the surface tension interpolated from the measured data at temperatures of 268 K and 303 K, respectively. The dashed lines show the variation in surface tension predicted by the parachor method at 268 K and 303 K. Similarly, the solid lines represent the prediction by Di Nicola et al. (2018). These two methods exhibit similar behaviors at higher HFO1123 fractions; however, at

mole fractions below 0.3 and 268 K, they deviate. The measured data fall in between the prediction lines of the parachor method and that of Di Nicola et al. (2018).

From the irregularity in the measurement data shown in Figs. 5 and 6, it is inferable that the measured data at a charged mole fraction X_{HFO1123}=0.13 are lower than the true value. Probably, the true value of the van der Waals correlation's coefficient σ_0 at a mole fraction X_{HFO1123} of 0.13 is relatively higher than the center within the propagated measurement uncertainty.

The LGT predictions, plotted with thick solid lines in Fig. 4, show the highest degree of overlap for the measured surface tension with the following correction for parameter CF pertaining to the temperature. CF can be assimilated as a binary interaction parameter.

$$CF = 1-(AT+B) \qquad \text{Eq.(15)}$$

Coefficients A and B are optimized to fit the measurement data and are listed in Table 2. The weakness of the LGT method is the density estimation of the two phases. This parameter is necessary because PR EoS predictions concerning the density of the liquid phase are not very accurate. Selection of the EoS (or parameterization) should be based on density data for both the vapour and liquid phases.

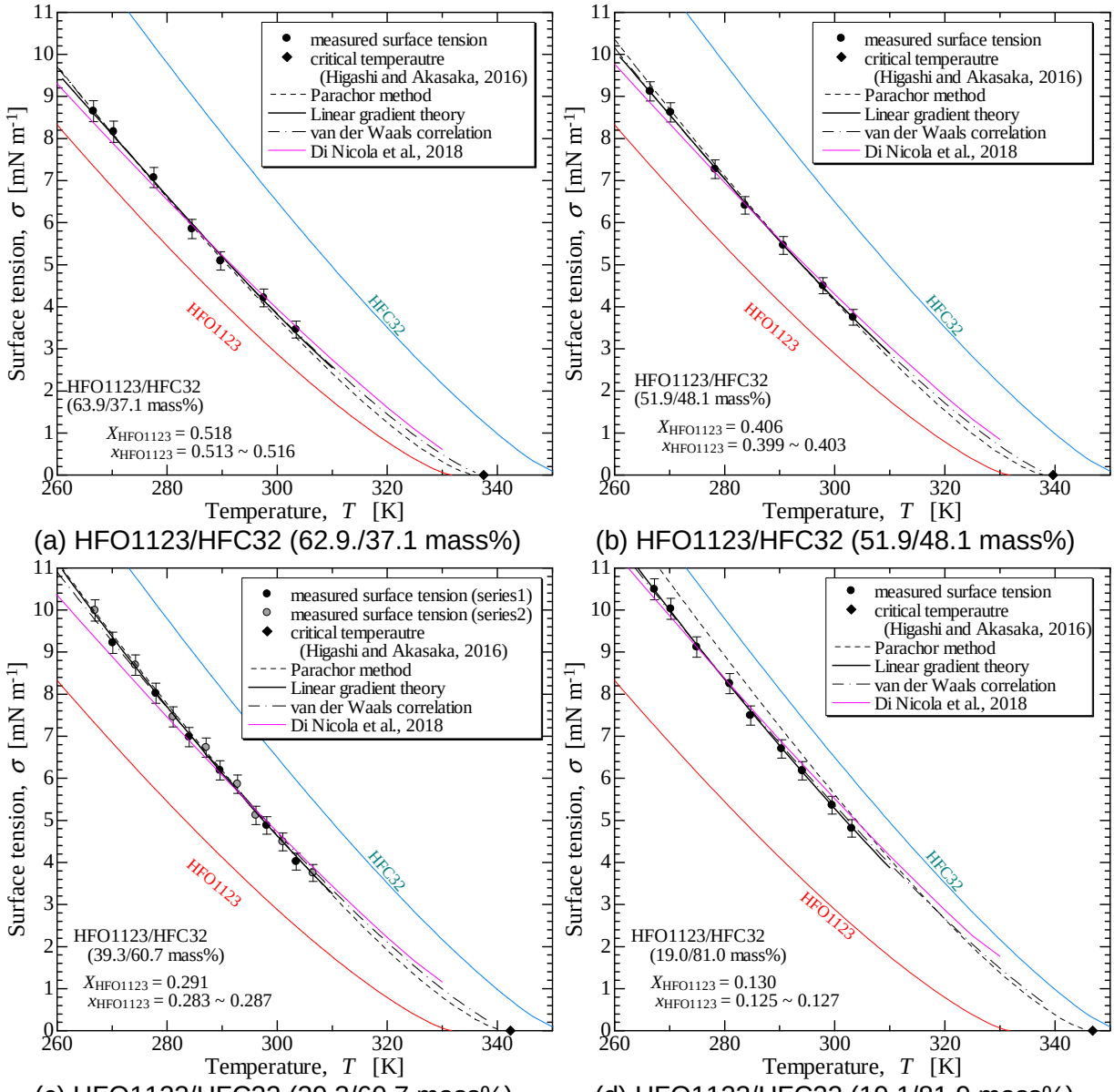

(a) HFO1123/HFC32 (62.9./37.1 mass%)

(b) HFO1123/HFC32 (51.9/48.1 mass%)

(c) HFO1123/HFC32 (39.3/60.7 mass%)

(d) HFO1123/HFC32 (19.1/81.9 mass%)

Figure 4: Measured data and predictions on surface tension for HFO1123/HFC32

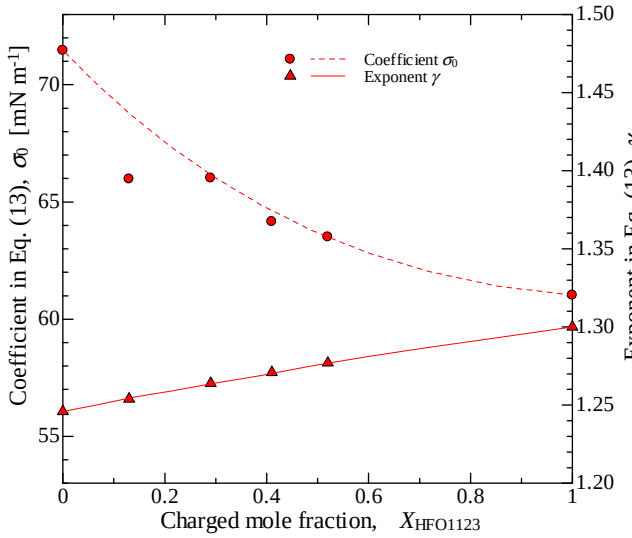

Figure 5: σ_0 variation against a mole fraction

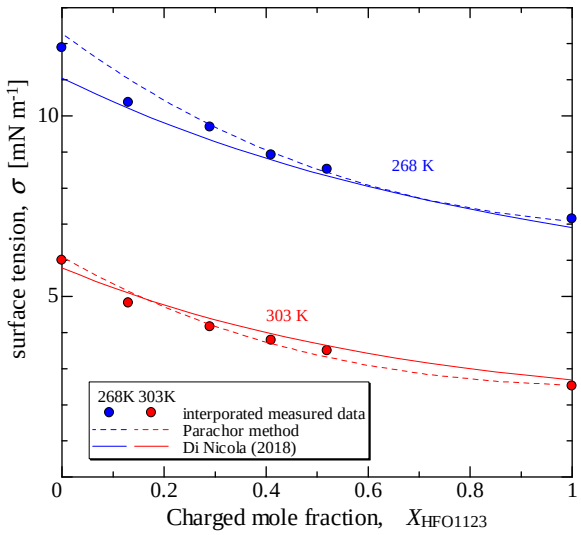

Figure 6: Mole fraction dependence in σ

Table 2: Coefficients A and B in Eq. (14) for adjustable parameter CF

$X_{HFO1123}$	1.0	0.5181	0.4063	0.291102	0.12951	0.0
A	0.0	0.00289	0.00252	0.00249	0.00202	1.0
B	-1.47698	-0.02115	0.08793	0.09090	0.23640	-1.34027

5. CONCLUSIONS

The surface tension data of a binary mixture HFO1123/HFC32 measured by a capillary rise method were delivered. Based on the data, the van der Waals correlation expressing the temperature dependence is fitted at HFO1123 mole fractions of 0.518, 0.406, 0.291, and 0.130. Those are compared with the selected predictions. The Parachor methods and the correlation of Di Nicola et al. (2018) showed good agreement at fractions of 0.518 and 0.406, however slightly deviated at 0.291 and 0.130. The linear gradient theory showed the best agreement. However, the adjustable parameter showed temperature dependency. This is certainly due to the weakness of the cubic EoS concerning density prediction. Experimental density or speed of sound data should be determined in order to select and parametrize the best EoS, and binary interaction parameter for predicting the surface tension in a wide range of temperature and composition. This is very important for the design of evaporators.

ACKNOWLEDGEMENTS

The sample refrigerants are kindly donated by Asahi Glass Co., Ltd., Japan. This work was partially funded by JSPS KAKENHI Grant Number 17K14603 and Asahi Glass Co., Ltd., Japan. The authors are grateful for their support.

NOMENCLATURE

a	:cohesive energy parameter in Eq.(7)
a^2	:capillary constant (m^2)
b	:cohesive energy parameter in Eq.(7)
c	:influence parameter in Eq. (7)
E	:parameter for c in Eq.(9)
F	:parameter for c in Eq.(9)
f_0	:Helmholtz free energy density
g	:local gravitational acceleration (m s^{-2})
g_n	:normal gravitational acceleration (m s^{-2})
k_{ij}	:binary interaction parameter
M	:molar mass (kg/kmol)
m	:mass (kg)
n	:coefficient for saturation pressure used in Eq.(8)
P	:parachor
p	:pressure (Pa)
r_1	:radius of smaller capillary tube (m)
r_2	:radius of larger capillary tube (m)
T	:temperature (K)
T_{crit}	:critical temperature (K)

T_r : reduced temperautre =T/T_{crit} (-)
W :charged composition in mass (kg kg^{-1})
X :charge composition in mole (mol mol^{-1})
x_i :mole fraction in liquid phase of i_{th} component
y_i :mole fraction in vapor phase of i_{th} component
V :volume (m^3)
Δh_c :corrected differential height (m)
Δh_m :measured differential height (m)
ϕ :contact angle (rad)
γ :van der Waals exponent in Eq.(5)
θ :exponent in Eq.(6)
$\tilde{\rho}$:molar density (mole cm^{-3})
ρ :density (kg m^{-3})
σ :surface tension (N m^{-1})
σ_0 :van der Waals coefficient in Eq.(5) (N m^{-1})
ω :acentric factor
ξ : vapour mass fraction in vessel (kg kg^{-1})

REFERENCES

Bongiorno, V., Davis, H.T., 1975. Modified van der Waals theory of fluid interfaces. *Physical Review* A, 12(5), 2213.

Di Nicola, G., Coccia, G., Pierantozzi, M., Tomassetti, S., 2018. Equations for the surface tension of low GWP halogenated alkene refrigerants and their blends. *Int. J. Refrigeration*, 86, 410–421.

Gasem, K.A.M., Dickson, K.B., Dulcamara, P.B., Nagarajan, N., Robinson, R.L., 1989. Equilibrium phase compositions, phase densities, and interfacial tensions for carbon dioxide+ hydrocarbon systems. 5. Carbon dioxide+ n-tetradecane. *J. Chem. Eng. Data* 34(2), 191-195.

Heide, R., 1997. The surface tension of HFC refrigerants and mixtures, *Int. J. Refrigeration*, 20, No. 7, 496-503.

Higashi, Y., Akasaka, R., 2016. Measurements of Thermodynamic Properties for R1123 and R1123 + R32 Mixture. *Int. Refrig. Air Cond. Conf. Purdue*, July 11-14, Paper 1688.

Kondou, C., Higashi, Y., 2018. Surface Tension Measurement for a New Low-GWP Refrigerant HFO-1123 by a Differential Capillary Rise Method. *Trans. Japan Soc. Refrig. Air Cond. Eng.* 35, 403–408.

Lemmon, E.W., Huber, M.L., McLinden, M.O., 2013. Reference fluids thermodynamic and transport properties, Version 9.1, National Institute of Standards and Technology Boulder, CO, USA.

Mathias, P. M., Copeman, T. W., 1983. Extension of The Peng Robinson Equation of State to Complex Mixtures : Evaluation of the Various Forms of the local Composition Concept. *Fluid Phase Equilib.*13, 91-108.

Miqueu, C., Mendiboure, B., Graciaa, a, Lachaise, J., 2003. Modelling of the surface tension of pure components with the gradient theory of fluid interfaces: a simple and accurate expression for the influence parameters. *Fluid Phase Equilib*. 207, 225–246.

Mulero, A., Cachadiña, I., Parra, M.I., 2012. Recommended Correlations for the Surface Tension of Common Fluids. *J. Phys. Chem. Ref. Data* 41, 043105.

Peng, D. Y., Robinson, D. B., 1976. A new two parameters Equation of State. *Ind. Eng. Chem. Fundam.* 15, 59-64.

Rayleigh, L., 1916. On the Theory of the Capillary Tube. *Proc. R. Soc. A Math. Phys. Eng. Sci*. 92, 184–195.

Zuo, Y.X., Stenby, E.H., 1997. Calculation of interfacial tensions with gradient theory. *Fluid Phase Equilib.* 132, 139–158.

Manuscript ID: 60
DOI: 0.18462/iir.icr.2019.0060

Molecular Simulation for Surface Tension of New Low GWP Working Fluids

Céline HOURIEZ[(a)], Michel MASELLA[(b)], Chieko KONDOU[(c)], Yukihiro HIGASHI[(d)], Jamal EL ABBADI[(a)], Christophe COQUELET[(a)]

[(a)] MINES ParisTech, PSL Research University, CTP - Centre of Thermodynamics of Processes, Fontainebleau, 77305, France, celine.houriez@mines-paristech.fr, christophe.coquelet@mines-paristech.fr
[(b)] CEA Saclay, Basic Research Division, Institut Joliot, 91190 Cedex, France, michel.masella@cea.fr
[(c)] Nagasaki University, School of Engineering, Nagasaki, 852-8521, Japan, ckondou@nagasaki-u.ac.jp
[(d)] Kyushu University, NEXT-RP in Int. Inst. for Carbon Neutral Energy Research, Fukuoka, 819-0395, Japan, higashi@i2cner.kyushu-u.ac.jp

ABSTRACT

In this work, the calculated surface tension of selected new low GWP (global warming potential) pure compound refrigerants HFO (hydro-fluoro-olefin) is presented. Molecular simulation methods are used to calculate the surface tension of R-1123 (trifluoroethylene) and of R-1234ze(E) (trans-1,3,3,3-tetrafluoroprop-1-ene), as well as densities at saturation. The results obtained by molecular simulation are compared with recent experimental data.
Keywords: Surface tension; Hydrofluoroolefins; Experimental measurements; Molecular simulation.

1. INTRODUCTION

New-generation refrigerants are proposed for several years, in order to reduce the overall emission of greenhouse gases (Kyoto Protocol, 1997) and to respect the environmental regulations, for instance issued by the European Union (F-gas regulations). In particular, very recently, 150 countries agreed separate timelines for phasing out factory-made hydrofluorocarbon (HFC) gases, which can be 10 000 times more powerful than carbon dioxide as greenhouse gases (Kigali deal, 2016). Due to their low global warming potential (GWP), hydrofluoroolefins (HFOs) arouse interest and have been proposed as replacements for some previous-generation fluids such as HFCs. The detailed knowledge of the physical properties of refrigerants is essential to design and optimize thermodynamic systems involving refrigerants, from the production and separation units to the refrigerant-based systems (such as air-conditioning and refrigeration systems). In the field of refrigeration, there is a strong need for thermophysical and phase equilibrium data of fluids, either to retrofit existing equipment with alternative refrigerants or to replace this equipment. Furthermore, when developing an alternative refrigerant, to obtain detailed experimental data for all the promising candidates can become rapidly expensive and time-consuming. As an important complement to experiment and to larger-scale modeling, molecular simulation studies have emerged in recent years to predict thermophysical properties and phase behavior of pure fluids and mixtures, and to provide a vision of a fluid in terms of molecular interactions. If well calibrated, these techniques can lead to quantitative and predictive results, and they present great advantages, particularly in terms of cost and safety.

The knowledge of surface tension is essential to design refrigerant-based systems, as it plays a very important role in the boiling and condensation heat transfer. In this work, the capacity of molecular dynamics (MD) simulations based on pairwise force fields available in the literature to compute accurate surface tension values, in large temperature ranges, is investigated for two single compound working fluids with low GWP, namely the R-1123 (trifluoroethylene) and the R-1234ze(E) (trans-1,3,3,3-tetrafluoroprop-1-ene). We focus our study first on evaluating the effect of the simulation duration and of the size of the simulated microscopic system on the computed

surface tension. Then, we assess the reliability of these computed surface tension from comparison to recent experiments, in particular those by Higashi and coworkers (Kondou et al 2019, Tanaka et al 2013) and to the results provided by the program REFPROP version 10.0, which is based on the most accurate fluid models currently available (Lemmon et al 2013).

2. MOLECULAR SIMULATION DETAIL

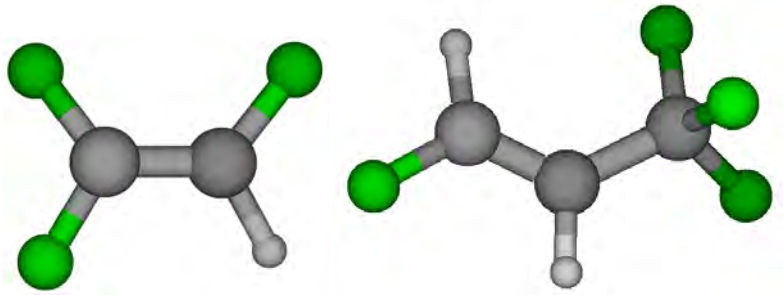

Figure 1: Single compound refrigerants studied in this paper, R-1123 (left) and R-1234ze(E) (right). In grey: carbon atoms; in green: fluorine atoms; in white: hydrogen atoms.

2.1. Force fields

The structure of the compounds studied in this work is shown in Figure 1.The R-1234ze(E) and R-1123 molecules were modeled using force fields developed by Raabe (Raabe et al 2009, Raabe 2012, Raabe 2013, Raabe 2016) for which the total potential energy U is expressed by the standard pairwise functional form:

$$U = \sum_{\text{bonds}} k_r (r - r_0)^2 + \sum_{\text{angles}} k_\theta (\theta - \theta_0)^2 + \sum_{\text{dihedral}} k_\chi [1 + \cos(n\chi - \delta)] + \sum_i \sum_{j>i} \left\{ 4\varepsilon_{ij} \left[\left(\frac{\sigma_{ij}}{r_{ij}} \right)^{12} - \left(\frac{\sigma_{ij}}{r_{ij}} \right)^{6} \right] + \frac{1}{4\pi\varepsilon_0} \frac{q_i q_j}{r_{ij}} \right\} \quad \text{Eq. (1)}$$

These force fields are fully flexible, *i.e.* all the covalent bonds and angles are modeled by the above first two harmonic energy terms of Eq. (1). 1-4 dihedral angles (defined by the four atoms involved in three adjacent covalent bonds) are modelled by the third cosine term. Non-bonded interactions between atoms separated by at least three covalent bonds are described by means of a sum of a Lennard-Jones (LJ) and a Coulombic pairwise terms (the above fourth energy term). Note however that non-bonded interactions between atoms separated by exactly three bonds (1-4 interactions) are scaled by a factor $1/2$ and $1/1.2$, respectively for LJ and electrostatic interactions. Regarding LJ interactions, their parameters for unlike atom pairs $(\varepsilon_{ij}, \sigma_{ij})$ obey Lorentz-Berthelot combining rules

$$\varepsilon_{ij} = \sqrt{\varepsilon_{ii}\varepsilon_{jj}}, \quad \sigma_{ij} = \frac{\sigma_{ii} + \sigma_{jj}}{2} \quad \text{Eq. (2)}$$

Despite these forces fields neglect the dynamic microscopic polarization response, they were shown to provide results in good agreement with experiment for the vapor-liquid equilibrium properties (Raabe 2013, Raabe 2016). However, as far as we know, they have never been tested for the prediction of the surface tension.

2.2. MD and surface tension calculation

MD simulations were performed by means of the POLARIS(MD) code developed at French Alternative Energies and Atomic Energy Commission (CEA) (Coles et al 2015). First, we performed NPT simulations of bulk systems consisting in orthorhombic boxes comprising 686 molecules and

for the sets of temperatures considered to compute surface tension (see below). The box dimensions are (*L*,*L*,2*L*). The systems were modelled using periodic boundary conditions. Coulombic interactions were computed according to the Smooth Particle Mesh Ewald (SPME) summation technique (Darden et al 1997) (to compute the SPME reciprocal energy, we used a grid size of 1 Å, an 8th order Bspline interpolation scheme and no surface term is considered). The cutoff radius of the SPME direct term was set to 12 Å for R-1234ze(E) and to 18 Å for R-1123 (as in the original work of Raabe 2106). These cutoffs were also used for truncating LJ interactions, however we considered standard long range corrections to estimate the energy and virial components corresponding to the truncated LJ interactions. The system temperature and pressure are monitored using the Nosé-Hoover chain thermostat and barostat (Martyna et al 1994) using a coupling constant of 3 ps. We solved the Newtonian equations of motion using the Velocity Verlet algorithm using a time step of 0.1 fs for the harmonic covalent bond and angle energy terms and a time step of 0.5 fs for all the remaining energy terms.

All the bulk orthorhombic boxes were relaxed for 5 ns and they were then placed between two empty regions in the direction of the longest relaxed box dimension $2L_{rel}$, allowing the representation of two liquid-vapor interfaces. These new boxes, whose dimensions are (L_{rel},L_{rel},$6L_{rel}$), were then simulated in the NVT ensemble, using the Generalized Gaussian Moment Thermostat (Liu et al 2000), the coupling constant being 250 fs. NVT simulations were performed according to the same MD scheme detailed above. Once a first equilibration phase of 1 ns is achieved, MD simulations go on until they reach the convergence of the surface tension values for all the temperatures considered.

To calculate the surface tension γ, we employed a thermodynamic route, the Test-Area method developed by Gloor et al (Gloor et al 2005). In this method, the surface tension is expressed as the Helmholtz free energy change associated with infinitesimal perturbations of the reference surface area, in the canonical NVT ensemble:

$$\gamma = \left(\frac{\partial F}{\partial S}\right)_{NVT} = \lim_{\Delta S \to 0} -\frac{kT}{2\Delta S}\left(ln\left\langle \exp\left(-\frac{\Delta U^{+}}{kT}\right)\right\rangle - ln\left\langle \exp\left(-\frac{\Delta U^{-}}{kT}\right)\right\rangle\right) \quad \text{Eq. (3)}$$

Here k is the Boltzmann constant and T is the temperature. $\Delta U^{+} = U(S + \Delta S) - U(S)$ and $\Delta U^{-} = U(S - \Delta S) - U(S)$ are the changes in energy corresponding to an increase/decrease of the surface from S to $S \pm \Delta S$. The brackets $\langle \dots \rangle$ denote temporal averages and the system surface area considered is orthogonal to the longest dimension of the MD orthorhombic boxes. Along a MD trajectory, we estimate $\Delta U^{+}$and ΔU^{-} each 50 fs with the $\Delta S/S$ ratio set to 5 10^{-4}. The computed surface tension γ values are monitored along MD simulations until convergence of the corresponding temporal averages. We denote hereafter γ_{MD} the latter converged surface tension values.

Our MD scheme is based on truncating long range LJ interactions. To estimate the contribution to the surface tension value resulting from this truncation, we assume:

1 - a hyperbolic tangent approximation for the molecular density profile along the simulated box direction orthogonal to the surface area *S*;

2 - the atomic densities to be proportional to the molecular ones, *i.e.* we assume the molecules R-1234ze(E) and R-1123 to adopt a random orientation at the liquid-vapor interface, as in the liquid and vapor phases.

From the above two assumptions we may then estimate the long range correction (LRC) γ_{LRC} to surface tension and corresponding to our MD protocol as follows (see for instance Vega et al 2007 for details)

$$\gamma_{LRC} = 12\pi\varepsilon\sigma^6(\rho^L - \rho^V)^2 \int_0^1 ds \int_{r_c}^{\infty} dr \coth\left(\frac{rs}{d}\right)(3s^3 - s)/r^3 \quad \text{Eq. (4)}$$

Here, ρ^L and ρ^V are the molecular densities in the liquid and the vapor phases, respectively. r_c is the LJ cutoff radius and the parameter $\varepsilon\sigma^6$ obeys

$$\varepsilon\sigma^6 = \frac{1}{2}\sum_{i,j} \varepsilon_{ij}\sigma_{ij}^6 \quad \text{Eq. (5)}$$

Here the sum runs over all atom pairs (*i,j*) that may be defined between two molecules. The surface tension values γ that may be compared to experiment are thus

$$\gamma = \gamma_{MD} + \gamma_{LRC} \quad \text{Eq. (6)}$$

3. RESULTS AND DISCUSSION

We simulated the liquid-vapor systems according to the MD protocol detailed in Section 2.2 for the set of temperatures: 230, 240, 260, 273.15, 283.15, 290, and 300 K, for R-1123. Regarding R-1234ze(E), we considered a larger set of temperatures: 180, 210, 240, 250, 260, 270, 280, 290, 300, 310, and 320 K. Note that the R-1123 and the R-1234ze(E) saturated densities have been previously studied by Raabe, by means of Monte-Carlo simulations in the temperature range 230-330 K for R-1123 and 260-380 K for R-1234ze(E) (Raabe 2016). The results obtained are in very good agreement with experiment for R-1123 and with experiment and/or REFPROP for R-1234ze(E).

3.1 Saturated densities from MD simulations of liquid-vapor systems

From MD simulations we computed the mean molecular density profiles $\rho(z)$ along the axis orthogonal to the liquid-vapor interface (axis denoted hereafter by **z**, whose origin is set to box centers). The density profiles are shown in Figure 2 for the two molecules and for all the simulated temperatures, together with their corresponding fitting hyperbolic tangent functions in the case of R-1234ze(E). The fitting function form is as follows:

$$\rho(z) = \frac{\rho^L + \rho^V}{2} + \frac{\rho^L - \rho^V}{2}\tanh[(z - z_0)/d] \quad \text{Eq. (7)}$$

Here, ρ^L and ρ^V are the fitted mean molecular densities for the liquid and vapor phases, respectively. z_0 is the middle of the liquid-vapor interface (considered as the location of the interface). *d* is the interface thickness, that is the distance domain where the molecular density drops from 95 to 5% of the liquid one. From the R-1123 plots, it appears that all the density profiles can be nicely interpolated by the above tanh function for the whole set of simulated temperatures.

The saturated densities of the inhomogeneous systems obtained during the MD simulations are represented in Figure 3 for R-1123 and R-1234ze(E), and compared to reduced data from experimental surface tension and to REFPROP v10.0 results. For R-1123, molecular simulation results are in very good agreement with experiment, as well as with REFPROP. For R-1234ze(E), molecular simulation results match overall both experimental and/or REFPROP estimates. However, at high temperature (from 300 K), simulation results for the liquid phase are slightly smaller (at most 3.5% of relative error) than the experimental and the REFPROP ones, while saturated vapor densities are overestimated by around 30% at most. Together, all of these results show the saturated densities to be well represented during the molecular simulations of the liquid-vapor systems for both R-1123 and R-1234ze(E), and thus that shows the overall accuracy of the Raabe's force fields and validates our MD protocol.

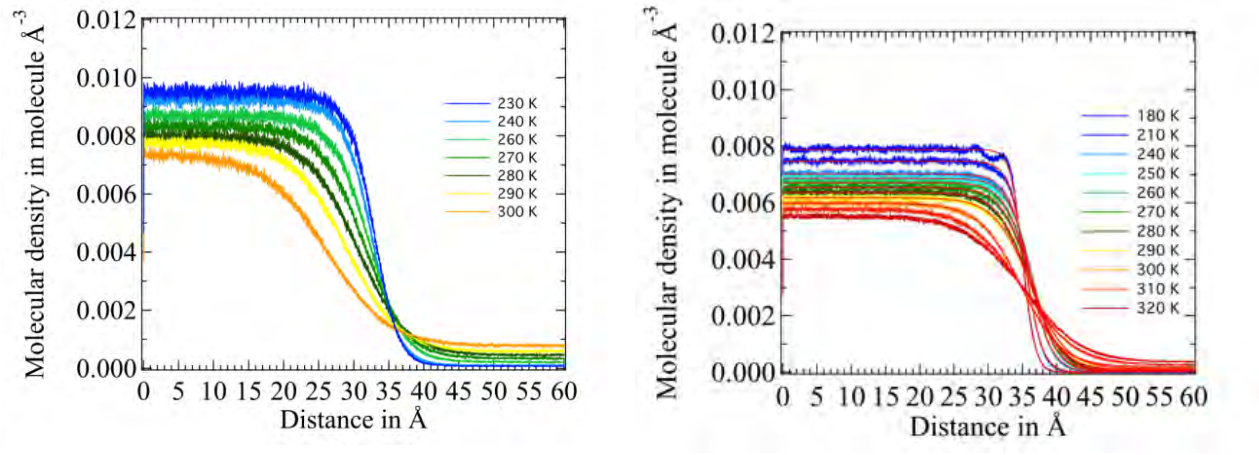

Figure 2: Molecular density profiles in the liquid-vapor systems as a function of the distance along box z axis for R-1123 (left) and R-1234ze(E) (right). For R-1234ze(E), density profiles are shown together with their corresponding fitting hyperbolic tangent functions in red thin lines.

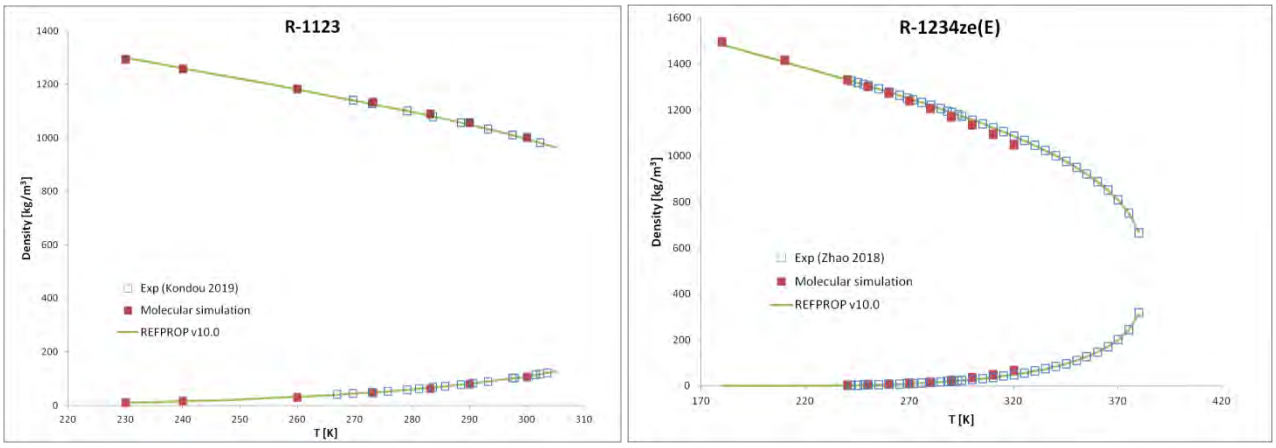

Figure 3: Saturated densities for R-1123 and R-1234ze(E) obtained by MD simulations of liquid-vapor systems, as compared to experiment and to REFPROP calculations.

3.2 Surface tension from MD simulations of liquid-vapor systems

We plotted in Figure 4 the temporal fluctuations of the average of instantaneous surface tension values, allowing the calculation of surface tension γ_{MD} computed according Eq. (3) along the MD simulations of liquid-vapor systems, comprising 686 molecules for the two HFO compounds and the full set of simulated temperatures. In the particular case of R-1234ze(E), we plotted in Figure 5 the temporal fluctuations for systems comprising 1024 and 2000 molecules but for reduced sets of temperatures: from 240 to 320 K and from 240 to 300 K, for 1024 and 2000 molecules, respectively.

Regarding R-1234ze(E), we pushed our MD production runs for 686 molecules systems up to 19 ns. As observed in Figure 4, all the surface tensions are well converged as soon as 7 ns. From the plots in Figure 5, the R-1234ze(E) surface tensions appear to be also well converged for systems comprising 1024 and 2000 molecules around 7 ns and regardless of the temperature. Moreover, the converged surface tensions for these two sizes of systems match those computed for 686 molecules systems within the root mean square deviations of the surface tension computed along our 19 ns MD runs: that is about 0.5 mN/m at low temperatures (from 240 to 270 K) to less than 0.1 mN/M for temperatures above 300 K. These values are considered here as the uncertainties affecting our computed γ_{MD} values, regardless of the compound.

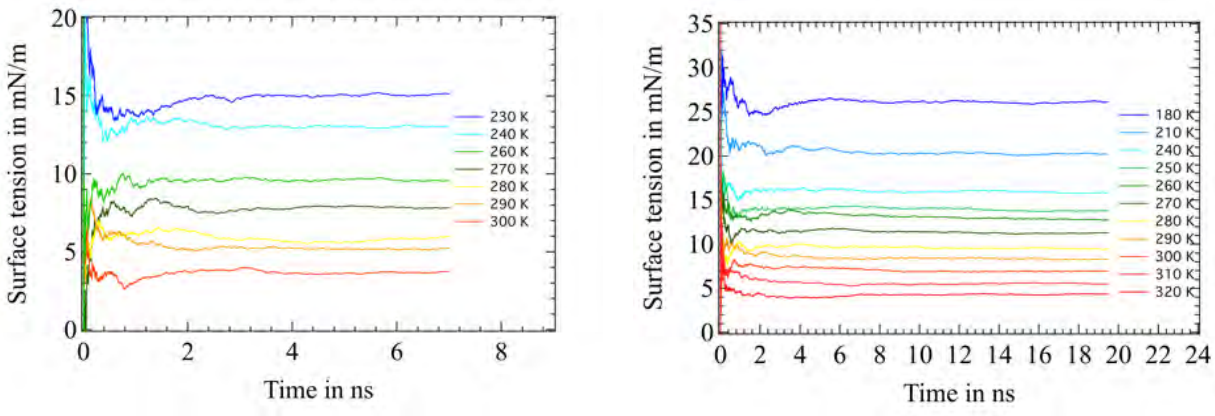

Figure 4: Temporal fluctuations of the average of instantaneous surface tension values, allowing the computation of the surface tension γ_{MD}, for R-1123 (left) and for R-1234ze(E) (right), for systems of 686 molecules.

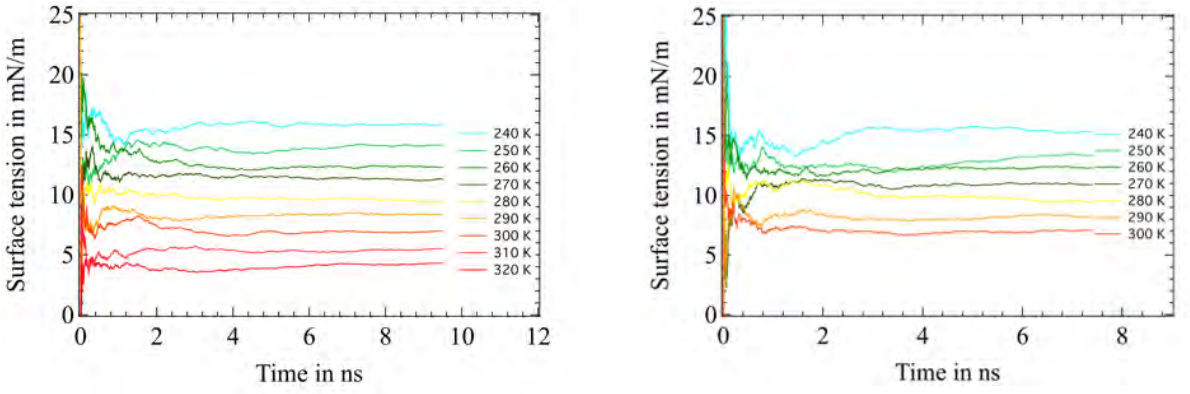

Figure 5: Temporal fluctuations of the average of instantaneous surface tension values, allowing the computation of the surface tension γ_{MD}, for R-1234ze(E) systems comprising 1024 (left) and 2000 (right) molecules.

The surface tensions converge more rapidly for R-1123 compared to R-1234ze(E), regardless of the temperature. They are all well converged as soon as 4 ns. This is why we performed shorter simulations for that compound, 8 ns including the 1 ns equilibration period. The faster surface tension convergence for R-1123 compared to R-1234ze(E) may arise from its less complex molecular structure that favors faster relaxation times, at least to compute surface tensions within the 240-320 K temperature domain.

In all, the above results show our data regarding the surface tensions γ_{MD} to be both well converged at the end of our MD simulations and not sensitive to the size of the liquid-vapor system simulated. From the liquid and vapor mean molecular densities computed from the density plots shown in Figure 2, we estimated the long range correction γ_{LRC} to the surface tension. We checked here also these data to be insensitive to the size of the simulated systems in the case of R-1234ze(E). For temperatures included within 240 and 300 K, the γ_{LRC} values vary at most by 2% among the different system sizes. That represents at most about 0.05 mN/m, a value that we consider as negligible. Hence as γ_{MD} values, the γ_{LRC} estimates are also insensitive to the size of the system simulated and so is the sum $\gamma_{MD} + \gamma_{LRC}$.

3.3 Comparison of surface tensions from MD simulations, experiment and REFPROP data

We plotted in Figure 6 the total MD surface tensions $\gamma_{MD} + \gamma_{LRC}$ as functions of the temperature, together with their experimental and REFPROP counterparts. We may first note that the long range contributions γ_{LRC} are small but not negligible as they amount from about 8 to 15% of the γ_{MD} values for R-1123 and from 15 to 25% for R-1234ze(E). The weaker weight of γ_{LRC} for R-1123 arises from the largest cutoff radius used in the simulations for that compound compared to R-

1234ze(E) (see Section 1.2). Note also that even if the intensity of γ_{LRC} decreases, its weight in the total surface tension estimates is larger and larger as the temperature increases.

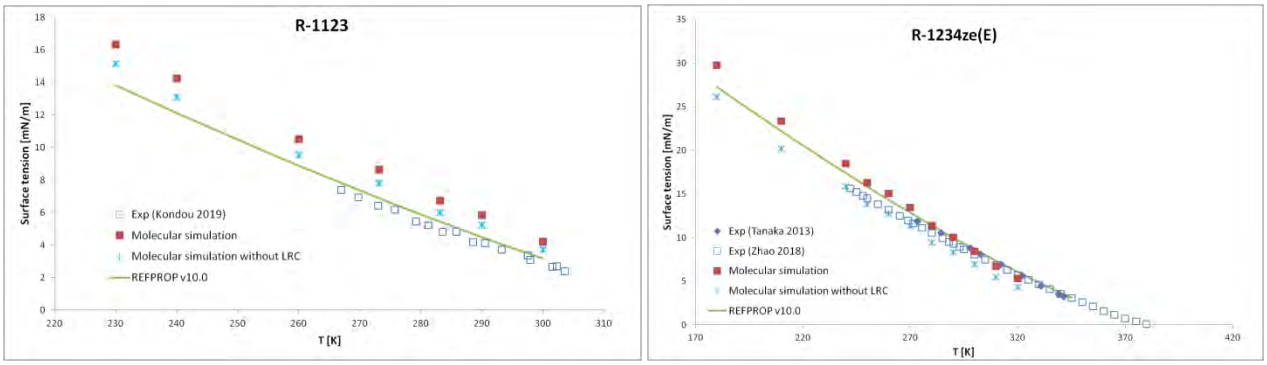

Figure 6: Surface tension for R-1234ze(E) (left) and R-1123 (right) from liquid-vapor system MD simulations, as compared to experiment and to REFPROP estimates.

Regarding R-1234ze(E), we note a remarkable agreement between MD, REFPROP and experimental surface tensions for temperatures larger than 260 K. The surface tensions $\gamma_{MD} + \gamma_{LRC}$ differ more largely from their experimental and REFPROP counterparts for R-1123 than for R-1234ze(E). R-1123 simulation results are systematically larger than REFPROP ones and experiment, by at most 35% between 273 and 300 K (difference of at most 2.2 mN/m).

For temperatures larger than 240 K, the MD surface tensions γ_{MD} and their corrections γ_{LRC} exhibit the same behavior for both R-1234ze(E) and R-1123: they a priori linearly decrease as the temperature increases (the corresponding linear regression coefficient is larger than 0.99 for both compounds). That yields thus a total surface tension $\gamma_{MD} + \gamma_{LRC}$ predicted by MD simulations to be a linear decreasing function of the temperature. However, when accounting for data at lower temperatures, the MD total surface tensions for R-1234ze(E) can be nicely fitted by means of the following power law function of the temperature T (van der Waals-type equation), as experimental data,

$$\gamma(\mathrm{T}) = \gamma_0 \times (1 - \mathrm{T}/\mathrm{T_c})^a \qquad \text{Eq. (8)}$$

Here γ_0, $\mathrm{T_c}$ and *a* are three parameters whose values are 72.38 mN/m, 383 K and 1.41 when all adjusted on simulation results. The obtained value for $\mathrm{T_c}$ match the experimental one (382,51 K as determined in Higashi et al 2010). The latter best numerical value for the power law exponent *a* agrees well with its commonly reported values when analyzing experimental data: about 1.3. However, the prefactor γ_0 is 28% larger than its experimental-based estimates. That may be tied to the inaccuracy of the pairwise force field we used for R-1234ze(E) at low temperature, in particular for the vaporization enthalpy (Raabe 2013).

To conclude, MD simulations by using both force fields for R-1123 and R-1234ze(E) are able to represent accurately the saturated liquid density, as compared to experiment. However, concerning surface tension, molecular simulation results match experiment for R-1234ze(E), while they are larger for R-1123 compared to experimental data. Thus, from our results, accurate predictions regarding saturated liquid densities isn't sufficient for a force field to warrant it to provide reliable predictions for surface tension.

4. CONCLUSIONS

In this work, MD methods used in conjunction with available pairwise force fields are tested to calculate surface tensions in a wide range of temperature for the single HFO compounds R-1123 and of R-1234ze(E), as well as their liquid densities at saturation. The saturated liquid densities are well reproduced for the two compounds as compared to available experimental data, regardless of the temperature. For R-1234ze(E), the computed surface tension values are in very good

agreement with experiment. However, the computed surface tensions regarding R-1123 are systematically overestimated, relative to experiment. Nevertheless, we note that the order of magnitude of the difference in the surface tension values between the two compounds from our MD simulation agrees both with experiment and REFPROP estimates, regardless of the temperature. That shows the ability of the present force fields devoted to HFO to be already accurate enough to provide valuable surface tension data regarding this kind of compounds, data able to complement non exhaustive experimental databases.

REFERENCES

Coles J., Masella, M., 2015. The fast multipole method and point dipole moment polarizable force fields. J. Chem. Phys., 142(2), 024109

Darden T., Toukmaji A., Pedersen L., 1997. Long-range electrostatic effects in biomolecular simulations. J. Chim. Phys. 94(7), 1346-1364

Gloor, G. J., Jackson, G., Blas, F. J., de Migue, l. E., 2005. Test-area simulation method for the direct determination of the interfacial tension of systems with continuous or discontinuous potentials. The Journal of Chemical Physics 123(13), 134703

Kondou, C., E Abbadi, J., Houriez, C., Masella, M., Higashi, Y., Coquelet, C., 2019. Surface Tension Measurement and Modeling Work for New Low GWP Working Fluids. Proceedings of ICR2019, 25e congrès international du froid (IIF), Montréal, Canada

Lemmon, E. W.,Huber, M.L.,McLinden, M. O., 2013. NIST Standard Reference Database 23, NIST Reference Fluid Thermodynamic and Transport Properties, REFPROP, version 10.0

Liu, Y., Tuckerman, M . E., 2000. Generalized Gaussian moment thermostatting: A new continuous dynamical approach to the canonical ensemble. J. Chem. Phys. 112(4), 1685

Martyna G. J., Tobias G. J., Klein M. L., 1994. Constant pressure molecular dynamics algorithms. J. Chem. Phys., 101(5), 4177

Raabe, G., Maginn, E. J., 2009. Molecular Modeling of the Vapor- Liquid Equilibrium Properties of the Alternative Refrigerant 2, 3, 3, 3-Tetrafluoro-1-propene (HFO-1234yf). The Journal of Physical Chemistry Letters 1(1), 93-96

Raabe, G., 2012. Molecular modeling of fluoropropene refrigerants. The Journal of Physical Chemistry B 116(19), 5744-5751

Raabe, G., 2013. Molecular Simulation Studies on the Vapor–Liquid Phase Equilibria of Binary Mixtures of R-1234yf and R-1234ze(E) with R-32 and CO_2. J. Chem. Eng. Data 58(6), 1867-1873

Raabe, G., 2016. Molecular simulation studies in hydrofluoroolefine (HFO) working fluids and their blends. Science and Technology for the Built Environment 22(8), 1077-1089

Tanaka, K., Higashi, Y., 2013. Surface tensions of trans-1,3,3,3-tetrafluoropropene and trans-1,3,3,3-tetrafluoropropene+difluoromethane mixture. Journal of Chemical Engineering of Japan 46(6), 371-375

Vega, C., de Migue, l. E., 2007. Surface tension of the most popular models of water by using the test-area simulation method. The Journal of Chemical Physics 126(15), 154707

Zhao, X., Duan, W., Zeng, X., & Liu, Y., 2018. Measurements of Surface Tension of R1234yf and R1234ze(E). Journal of Chemical & Engineering Data 63(1), 21-26

Manuscript ID: 63
DOI: 10.18462/iir.icr.2019.0063

Using Al2O3-water nanofluid to investigate the spray cooling heat transfer performance on a heated surface

Tong-Bou Chang[(a)], Tsung-Han Lin[(b)], Jhong-Wei Huang[(b)]
Department of Mechanical and Energy Engineering, National Chiayi University, Chiayi, Taiwan
Department of Mechanical Engineering, Southern Taiwan University of Science and Technology, Tainan, Taiwan
Chiayi 600, Taiwan. E-mail: tbchang@mail.ncyu.edu.tw

ABSTRACT

An experimental investigation is performed into the spray cooling heat transfer performance of Al2O3-water nanofluid given four different degrees of subcooling (0°C, 10°C, 20°C and 30°C). The results show that the heat transfer coefficient obtained using a subcooling degree of 20°C is around 8.3%, 8.6% and 15.6% higher than that obtained using subcooling degrees of 10°C, 0°C, and 30°C, respectively. For a heat flux of $q'' = 520\ W/cm^2$, the EDS analysis results show that the surfaces of the samples cooled for 10, 20, 30 and 40 hours, respectively, contain 20.58%, 35.51%, 40.08% and 53.25% Al. The SEM images confirm that the thickness of the deposited layer increases with an increasing spray operating time and leads to a lower heat transfer performance as a result.

Keywords: spray cooling, nanofluid, subcooling, transient heat transfer

1. INTRODUCTION

With the persistent trend toward device miniaturization in many forms of daily life, including 3C products, household appliances, automobile systems, and so on, the development of effective heat dissipation methods has emerged as a major challenge for engineers in recent decades. Choi (1995) showed that the convective heat transfer performance of traditional working fluids such as water, ethylene glycol and oil can be significantly improved through the addition of nanoparticles with a size of around 0~100 nm to form so-called nanofluids. Bang et al. (2005) studied the pool boiling heat transfer performance of Al2O3-water nanofluid on a level heating surface given an average particle size of 47 nm and particle volume fractions of 0.5 vol%, 1 vol%, 2 vol% and 4 vol%, respectively. The results showed that the heat transfer coefficient reduced due to the formation of a low-thermal-conductance nano-adsorption layer on the heated surface. However, the CHF was found to be as much as 32% higher than that for pure water. It was suggested that the enhancement of the CHF was determined by the thickness of the deposited layer, the density of the generated effective nucleation sites, and the physical properties of the surface material. Chakraborty et al. (2010) showed that in the spray cooling of hot steel plates using TiO2-water nanofluid, the heat transfer performance improved with a decreasing surface tension and an increasing nanofluid viscosity.

Chang et al. (2014) investigated the heat transfer performance of jet impingement flow boiling using Al2O3-water nanofluids with nanoparticle additions of 0.0001 vol%, 0.001 vol% and 0.01 vol%, respectively. The results showed that the heat transfer performance of all three nanofluids was poorer than that of pure DI water due to the formation of a nano-adsorption layer with a high thermal resistance on the heated surface. Chang et al. (2012) examined the effect of the particle volume fraction on the spray heat transfer performance of Al2O3-water nanofluid and showed that the spray cooling efficiency improved with a reducing particle concentration due to a lower accumulation of Al nanoparticles on the heated surface. Chang (2015) performed an experimental investigation into the formation of the nano-adsorption layer during spray cooling with Al2O3-water nanofluid. It was shown that for a low nanoparticle addition (0.001 vol%), most of the Al nanoparticles were washed away from the heated surface during the spraying process. However, for higher nanoparticle concentrations, a nano-adsorption layer was formed, which increased the thermal resistance at the heated surface and reduced the benefits of the surface roughness in improving the heat transfer performance.

In the subcooled boiling region, a greater amount of sensible heat can be absorbed by the liquid, and hence the heat transfer coefficient is improved. However, an excessive degree of subcooling suppresses the growth of vapor bubbles, and therefore induces single-phase convection heat transfer with a lower heat transfer efficiency than boiling heat transfer. The present study investigates the spray heat transfer performance of a 0.05 vol% Al2O3-water nanofluid with various degrees of subcooling (0℃, 10℃, 20℃, and 30℃). The results show that the optimal heat transfer performance is obtained using a subcooling degree of 20℃.

2. EXPERIMENTAL EQUIPMENT

As shown in Fig.1a, the experimental system comprised a nanofluid flow loop, a test section containing a heating module and a spray nozzle, a cooling water flow loop, a sub-cooler, a pre-heating system, and a data acquisition system. The details of the experimental setup and data acquisition system are described in the following sub-sections.

2.1 Main flow loop system

In performing the spray cooling tests, nanofluid was drawn from the storage tank by a pump and flowed into a preheat tank to be heated to the specified experimental temperature. The mass flow rate of the nanofluid exiting the preheat tank was adjusted to 0.080 kg/s by means of a bypass valve and the nanofluid was then flowed to the test section. On entering the test section, the nanofluid was sprayed by a liquid-pressurizing nozzle such that it impinged on the heated test plate surface. The evaporated vapor was cooled and condensed in a chiller and then flowed back to the storage tank together with the non-evaporated nanofluid exiting the test section through an outlet valve fitted in the lower surface.

2.2 Test section

The test section comprised a cylindrical stainless steel vessel with a height of 50 cm, an internal diameter of 25 cm, and a thickness of 1 cm. The test section was fitted with two glass ports to permit visualization of the spray cooling process. The observation windows were inter-packed with O-rings to prevent leakage of the working fluids and gases to the environment. Furthermore, to prevent heat loss during the experiments, the outside of the test section was coated with polyurethane. The temperature and pressure within the test section were monitored using a resistance thermometer and an electronic pressure gauge, respectively. In

addition, the upper part of the test section was fitted with a relief valve in order to maintain the chamber at a safe operating pressure.

2.3 Heating module

As shown in Fig.1b, the heating module comprised three resistance-type electrical-heating tubes, a rectangular copper heating block, the copper test piece, and a copper cylinder. The module had an overall diameter and height of 385 mm and 50 mm, respectively. In assembling the heating module, the copper heating block was placed in a rectangular cavity with dimensions of 210 mm x 50 mm x 20 mm (length x width x height). The copper cylinder was then screwed into the heating block and coated first with fiberglass and then with ceramic material to prevent heat loss. The copper test piece was threaded into the top of the copper cylinder and locked in place by a circular Teflon cap.

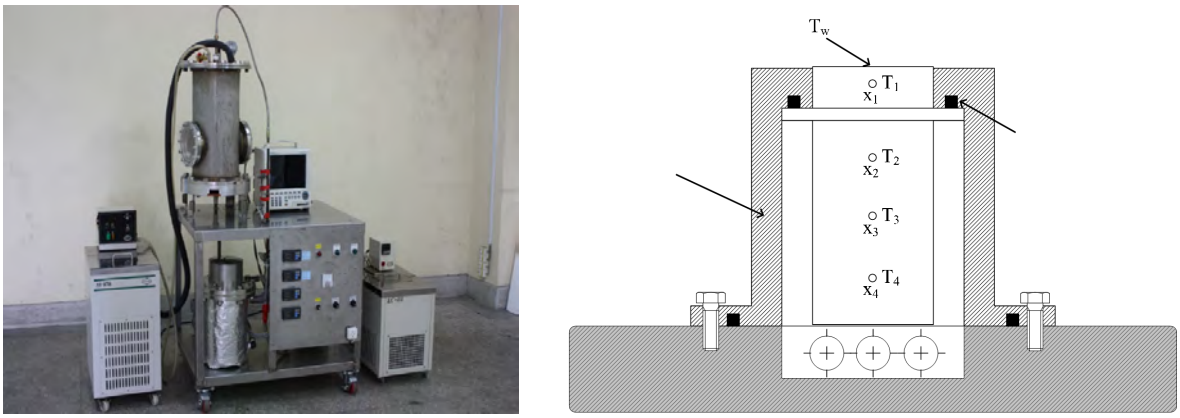

(a) (b)

Fig. 1 The experimental spray cooling system. (a) Photo (b) Schematic illustration of heating module.

2.4 Experimental data reduction

The heat flux (q") at the test plate surface (W/cm^2) was calculated as

$$q'' = \frac{Q}{A}, \qquad \text{Eq.(1)}$$

where

Q: total heating power of three heaters (W),

A: heat transfer area of test plate (cm^2).

The temperature of the test plate surface was derived from the temperature measurements of the thermocouples located at different distances from the heated surface in accordance with a simple one-dimensional thermal conduction assumption, i.e.,

$$T_w = T_2 - \frac{x_2}{x_2 - x_1}\left(T_2 - T_1\right), \qquad \text{Eq. (2)}$$

where

x1: distance of first thermocouple from test plate surface (mm),

x2: distance of second thermocouple from test plate surface (mm),

T1: temperature value recorded by first thermocouple (°C),

T2: temperature value recorded by second thermocouple (°C).

The mean heat transfer coefficient at the test plate surface was then calculated as

$$h = \frac{q''}{T_w - T_{sat}}, \qquad \text{Eq. (3)}$$

where

Tsat: saturation temperature (°C).

3. RESULTS AND DISCUSSIONS

3.1 Effect of subcooling degree on spray cooling heat transfer performance

Fig. 2 shows the variation of the spray cooling heat transfer coefficient with the surface heat flux as a function of the subcooling degree (i.e., 0°C (saturated nanofluid), 10°C, 20°C and 30°C). As expected, the heat transfer coefficient increases with an increasing surface heat flux for all degrees of subcooling. For $q'' \le 200\ W/cm^2$, the heat transfer efficiency is insensitive to the degree of subcooling. However, at higher values of the heat flux, the nanofluid with 20°C subcooling yields the best heat transfer performance, followed by the nanofluids with 10°C, 0°C, and 30°C subcooling, respectively. On average, the heat transfer coefficient obtained using the nanofluid with 20°C subcooling is around 8.3%, 8.6% and 15.6% higher than that obtained using the nanofluids with 10°C, 0°C, and 30°C subcooling, respectively. Furthermore, the heat transfer coefficient obtained using a nanofluid with 30°C subcooling is around 7% lower than that obtained using saturated nanofluid (i.e., 0°C subcooling). In other words, while 20°C subcooling is beneficial in enhancing the spray heat transfer performance, a greater degree of subcooling worsens the heat transfer performance. For a higher degree of subcooling, the sprayed liquid droplets can theoretically absorb more heat before impacting the heated surface (thereby enhancing the heat transfer performance). However, in the present study, the droplets are sprayed with a high speed, and hence experience only a short flying time before impact. Consequently, given a very high degree of subcooling (i.e., 30°C in the present case), insufficient time exists for the droplets to reach the saturation temperature before they impact the surface. As a result, the boiling effect is reduced and hence the heat transfer performance also reduces.

3.2 Effect of spray operating time on spray cooling heat transfer performance

Fig. 3(a), 3(b) and 3(c) show the variation of the heat transfer coefficient with the heat flux of the heated surface as a function of the spray operating time given subcooling degrees of 30°C 20°C and 10°C respectively. It is seen that for all subcooling degrees, the spray operating time has a negligible effect on the heat transfer performance given a low surface heat flux of $q'' \le 200\ W/cm^2$. For $q'' > 200\ W/cm^2$, the heat transfer coefficient decreases with an increasing spray operating time. In other words, the results suggest that $q'' = 200\ W/cm^2$ represents a threshold value above which the effects of spray operating time should be taken into consideration.When performing spray cooling using nanofluids, some of the particles adhere to the heated surface and form an irregular nano-adsorption layer, which increases the thermal resistance of the heated surface and decreases the heat transfer coefficient accordingly. The present results suggest that when spray cooling is performed using a lower surface heat flux, only a few nanoparticles adhere to the heated surface, and of those few particles which do adhere, most are subsequently washed away by the newly-arriving droplets. In other words, despite a longer spray operating time, the thickness of the nano-adsorption layer does not increase, and hence the heat transfer performance remains approximately constant. However, given a higher surface heat flux, a greater number of nanoparticles adhere to the heated surface, and are not fully removed by the subsequently-arriving droplets. Consequently, the thickness of the

nano-adsorption layer increases as the spray cooling process proceeds, and hence the heat transfer performance reduces.

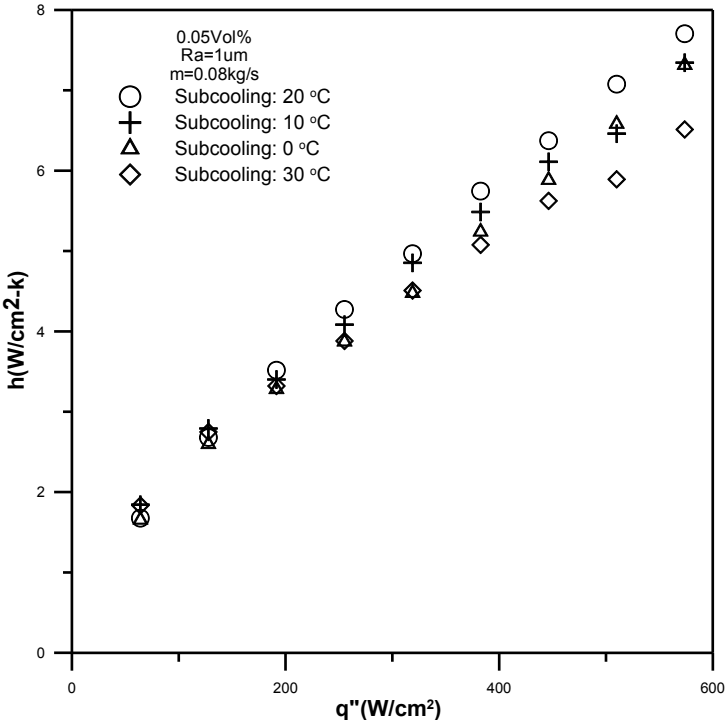

Fig. 2 Effects of subcooling degree on nanofluid spray cooling heat transfer performance.

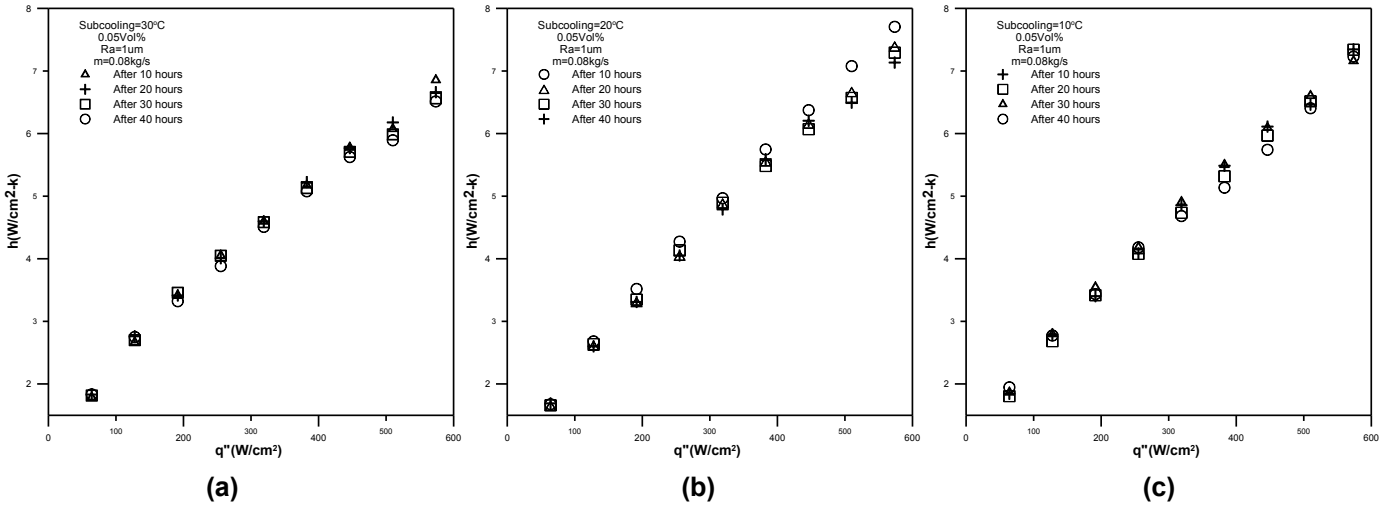

Fig. 3 Effect of spray cooling operating time on nanofluid heat transfer performance given subcooling degree of (a)30°C; (b) 20°C; (c) 10°C.

4. CONCLUSIONS

Previous studies have shown that when performing spray cooling using nanofluids, the nanoparticles form an irregular-shaped nano-adsorption layer on the heated surface, which increases the thermal resistance and reduces the heat transfer efficiency. However, these studies have not examined the effects of the subcooling degree and spray operating time on the formation of this nano-adsorption layer. Accordingly, the present study has performed spray cooling experiments using 0.05 vol% Al2O3-water nanofluid given four different degrees of subcooling (0°C, 10°C, 20°C and 30°C). The experimental results and observations support the following main conclusions.

1. In spray cooling with subcooling degrees of 10°C and 20°C, the liquid drops absorb sensible heat before impacting the heated surface, and hence the heat transfer performance is enhanced. However, given a

higher degree of subcooling, i.e., 30°C, the liquid droplets cannot reach the saturation temperature during their short flight time, and hence the boiling effect at the heated surface is reduced. Consequently, the heat transfer performance is also reduced. Overall, the present results suggest that a subcooling degree of 20°C yields the best heat transfer performance for the current nanofluid and heating conditions.

2. For a heat flux of $q'' \le 200\ W/cm^2$, the spray operating time has a negligible effect on the heat transfer performance. For $q'' > 200\ W/cm^2$, the heat transfer coefficient decreases with an increasing spray operating time. In other words, the results suggest that $q'' = 200\ W/cm^2$ represents a threshold value above which the effects of spray operation time should be taken into consideration.

ACKNOWLEDGEMENT

The authors gratefully acknowledge the financial support provided to this study by the Ministry of Science and Technology (MOST) of Taiwan under grant numbers NSC 101-2221-E-218-016 and MOST 107-2221-E-415-017.

REFERENCES

Bang, I.C., Chang, S.H., 2005. Boiling heat transfer performance and phenomena of Al2O3–water nano-fluids from a plain surface in a pool. Int. J. Heat and Mass Transfer 48, 2407–2419.

Chang, T.B., 2015. Formation of nano-adsorption layer and its effects on nanofluid spray heat transfer performance. Journal of Heat Transfer Trans. ASME, 137(2), 021901.

Chang, T.B., Syu, S.C., and Yang, Y.K., 2012. Effects of particle volume fraction on spray heat transfer performance of Al2O3-water nanofluid. Int. J. of Heat and Mass Transfer 55, 1014-1021.

Chang, T.B., Yang, Y.K., Lin, T.H. 2014. Heat transfer performance of jet impingement flow boiling using Al2O3-water nanofluid. Journal of Mechanical Science and Technology 28, 211-218.

Choi, S.U.S., Eastman, J.A. , 1995. Enhancing thermal conductivity of Fluids with nanoparticles. American Society of Mechanical Engineers ,FED-Vol. 231/MD-Vol. 66, 99-105.

Chakraborty, S., Chakraborty, A., Das, S., Mukherjee, T., Bhattacharjee, D., Ray, R.K., 2010. Application of Water Based-TiO2 Nano-fluid for Cooling of Hot Steel Plate. ISIJ International, 50, 124–127.

Manuscript ID: 65
DOI: 10.18462/iir.icr.2019.0065

An experimental study on the evaporation heat transfer and pressure drop of R-1234ze(E) in a shell and plate heat exchanger

ChangUk Jo [(a)], DongChan Lee [(a)], Dongwoo Kim [(a)], Yongchan Kim [(b)]

(a) Graduate School of Mechanical Engineering, Korea University
Anam-Dong, Sungbuk-Ku, Seoul 02841, Republic of Korea, dnrckd16@gmail.com
(b) Department of Mechanical Engineering, Korea University
Anam-Dong, Sungbuk-Ku, Seoul 02841, Republic of Korea, yongckim@korea.ac.kr

ABSTRACT

A new refrigerant, R-1234ze(E) has emerged to substitute hydrofluorocarbon (HFC) refrigerants, such as R-134a, owing to high global warming potential (GWP). The condensation heat transfer characteristics of R-1234ze(E) have been investigated mainly in plate heat exchangers and horizontal tubes. However, the evaporation heat transfer characteristics of R-1234ze(E) in shell and plate heat exchangers are very limited in the literature. The objective of this study is to investigate the evaporation heat transfer and pressure drop characteristics of R-1234ze(E) in a shell and plate heat exchanger. The evaporation heat transfer characteristics of R-1234ze(E) are measured and analyzed in the shell and plate heat exchanger with the fixed saturation temperature of 15 ºC by varying the mass flux, heat flux, and vapor quality. Moreover, empirical correlations for the evaporation heat transfer coefficient and friction factor of R-1234ze(E) in the shell and plate heat exchanger are developed based on the measured data.
Keywords: Evaporation, Heat Transfer Coefficient, Low GWP, Pressure Drop, R-1234ze(E), Correlation.

1. INTRODUCTION

Based on F-gas regulation, HFC refrigerants with high global warming potential (GWP), such as R-134a and R-410A, are to be prohibited (UN (1998)). As an alternative to R-134a, R-1234ze(E) with low GWP has been studied extensively. In previous studies, R-1234ze (E) mixtures were used to reduce GWP below 150 and to improve the condensation heat transfer coefficient. Koyama et al. (2010) conducted an experiment on the cooling capacity of a mixture of R-1234ze(E) and R-410A. Mota-Babiloni et al. (2016) reviewed the literatures on R-1234ze(E) mixtures. Hossain et al. (2012) measured the condensation heat transfer and pressure drop in a horizontal smooth tube. Liu et al. (2016) also performed experiments and compared experimental results with the correlations for mini channels. Longo et al. (2014) measured the condensation heat transfer and pressure drop in the brazed plate heat exchanger. Moreover, Diani et al. (2016) measured the evaporation heat transfer coefficient and friction factor of R-1234ze(E) in a horizontal microfin tube. Grauso et al. (2013) compared the heat transfer coefficient and frictional pressure drop of R-1234ze(E) measured in a horizontal circular smooth tube with those of R-134a using a flow pattern map. In addition, Kim et al. (2005, 2007) measured the heat transfer coefficient of R-410A in a shell and plate heat exchanger and developed the correlation.

A shell and plate heat exchanger has a shell structure, which is different from conventional heat exchangers. Therefore, the shell and plate heat exchanger is advantageous at more extreme temperatures and pressures. It also has a chevron type plate, similar to the plate used in a plate heat exchanger, which is compact and has excellent heat transfer performance (Park and Kim, 2004).

The objective of this study is to investigate the evaporation heat transfer characteristics of R-1234ze(E) in a shell and plate heat exchanger. The evaporation heat transfer characteristics of R-1234ze(E) are measured and analyzed in the shell and plate heat exchanger with the fixed saturation temperature by varying the mass flux, heat flux, and vapor quality. Furthermore, empirical correlations for the evaporation heat transfer characteristics of R-1234ze(E) in the shell and plate heat exchanger are developed based on the measured data.

2. EXPERIMENTAL METHOD

The heat transfer characteristics of R-1234ze(E) were measured in the shell and plate heat exchanger. Table 1 lists the range of the operating conditions for the experiments. The temperature and pressure of the refrigerant and water were measured with thermocouples and pressure transducers, respectively, at the inlet and outlet of the shell and plate heat exchanger. The saturation temperature of R-1234ze(E) was kept at a constant value of 15 ºC, while varying the mass flux (G), heat flux (Q), and vapor quality (x). The mass flux of the refrigerant was varied from 30–40 kg-m^{-2}s^{-1}. The inlet vapor quality of the refrigerant was varied from 0.1 to 0.75 for each mass flux and heat flux. The heat flux was varied from 0.84–1.05 kW. The exit vapor quality of the refrigerant was calculated from the measured data. After all the processes, the heat transfer coefficient and friction factor were obtained based on the experimental data.

Table 1. Experiment conditions.

Operating variables	Mean vapor quality	Mass flux (kg m^{-2} s^{-1})	Heat flux (kW m^{-2})	Saturation temperature (ºC)
Condition	0.18–0.85	30–40	0.84–1.05	15

3. RESULTS AND DISCUSSION

3.1. Heat transfer coefficient

Fig. 1 shows the heat transfer coefficient of R-1234ze(E) in the shell and plate heat exchanger as a function of the mean vapor quality. The heat transfer coefficient increased with increasing mean vapor quality and peaked at the vapor quality of 0.6. This was because the refrigerant distribution in the shell and plate heat exchanger was improved as the mean vapor quality increased. In addition, the heat transfer coefficient at the heat flux of 1.05 kW was higher than that at 0.84 kW. This was owing to the decrease in the average viscosity of the liquid and vapor as the vapor quality and heat flux increased. The larger the mass flux, the greater the heat transfer coefficient. The reason for the improved heat transfer coefficient was owing to the increase in the turbulence of the refrigerant along with the increase in the mass flux. At the mean vapor quality above 0.7, the heat transfer coefficient decreased rapidly owing to dryout.

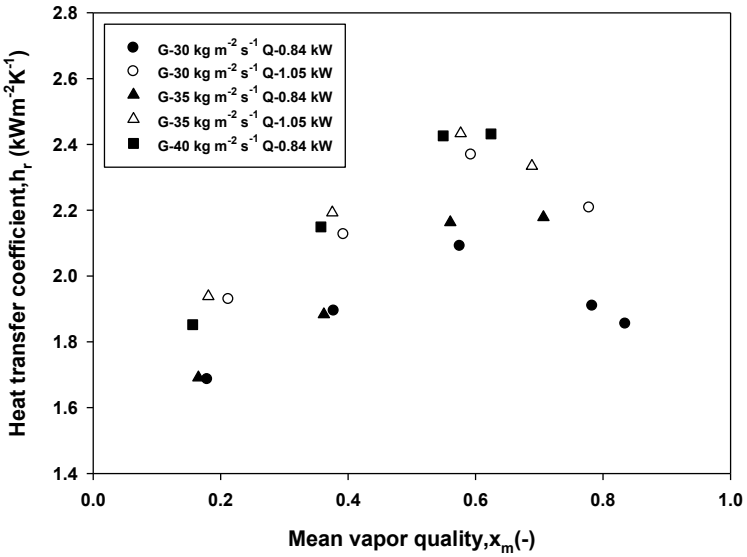

Figure 1: Heat transfer coefficient as a function of vapor quality

3.2. Friction factor

Fig. 2 illustrates the friction factor of R-1234ze(E) in the shell and plate heat exchanger as a function of the mean vapor quality. The friction factor decreased steadily as the mean vapor quality increased. This was owing to the increase in the frictional pressure drop with the increase in the vapor quality by shear stress between liquid film and vapor. The mass flux had a significant effect on the shear

stress caused by the difference in the velocity between liquid film and vapor. Because the heat flux changed thermal properties, such as viscosity, at only low vapor quality less than 0.3, the friction factor increased as the heat flux decreased. At the vapor quality above 0.3, the friction factor was less sensitive to the heat flux as compared to the mass flux. The heat flux and mass flux had less influence on the friction factor with increasing the vapor quality. The friction factor decreased as the mean vapor quality, mass flux, and heat flux increased.

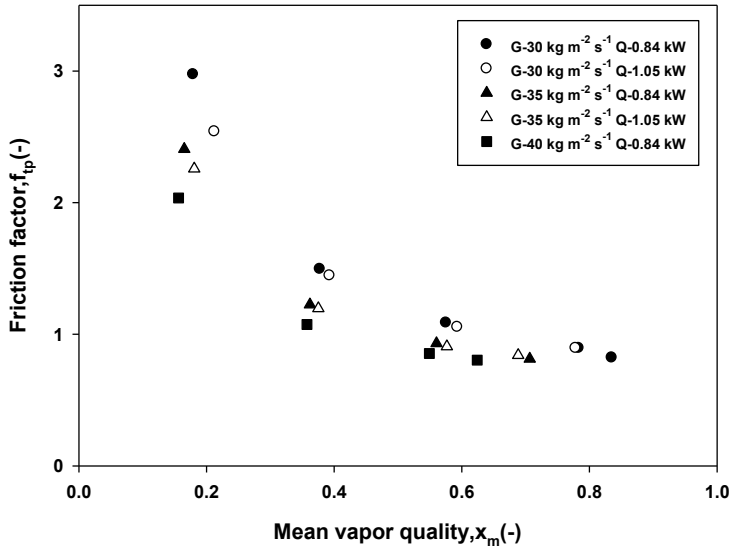

Figure 2: Friction factor as a function of vapor quality

3.3. Correlations

New correlations for the heat transfer coefficient and friction factor of R-1234ze(E) in the shell and plate heat exchanger were developed. As given in Eq. (1), the correlation for the evaporation heat transfer coefficient was developed based on the measured data.

$$h_r = 2926(k/D)\,\mathrm{Re}_{eq}^{\ 0.5836}\,\mathrm{Re}_{fo}^{\ -0.4241}\,Bo_{eq}^{\ 0.5581}\,x^{0.1127} \quad \text{Eq. (1)}$$

where

$$\mathrm{Re}_{eq} = G[(1-x_m)+x_m(\rho_l/\rho_v)^{0.5}]D/\mu_l \quad \text{Eq. (2)}$$

$$\mathrm{Re}_{fo} = G(1-x_m)D/\mu_l \quad \text{Eq. (3)}$$

$$\mathrm{Bo}_{eq} = Q/A/G_{eq}/(i_v - i_l) \quad \text{Eq. (4)}$$

Re_{eq} is the equivalent Reynolds number, Re_{fo} denotes liquid only Reynolds number, and Bo_{eq} indicates the equivalent boiling number.

Fig. 3 shows the comparison of the predicted heat transfer coefficient using Eq. (1) with the measured data. The predictions of the heat transfer coefficient correlation were consistent with the measured data within the deviations of ±15%.

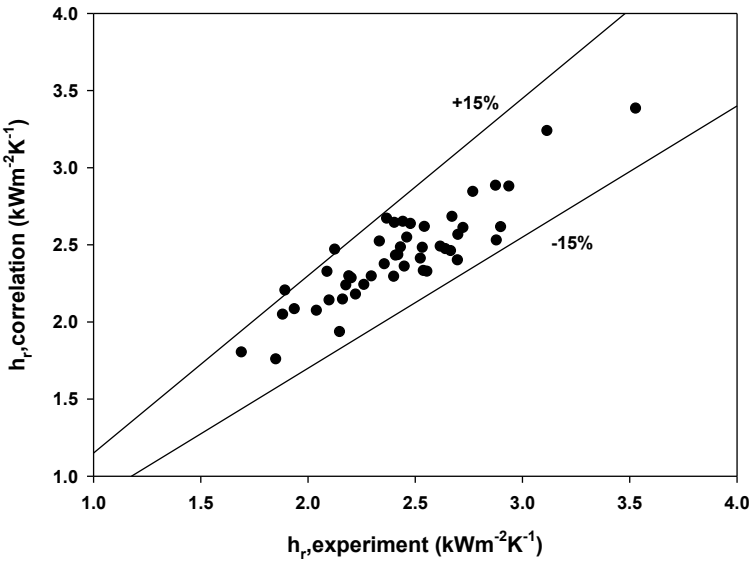

Figure 3: Comparison of correlation of heat transfer coefficient with experimental data.

As given in Eq. (5), the friction factor was developed as a function of the equivalent Reynolds number based on the measured data.

$$f_{tp} = 4861 \mathrm{Re}_{eq}^{-1.102} \quad \text{Eq. (5)}$$

Fig. 4 illustrates the comparison of the predicted friction factor with the measured data. The predicted friction factors were consistent with the measured data within the deviations of ±10%.

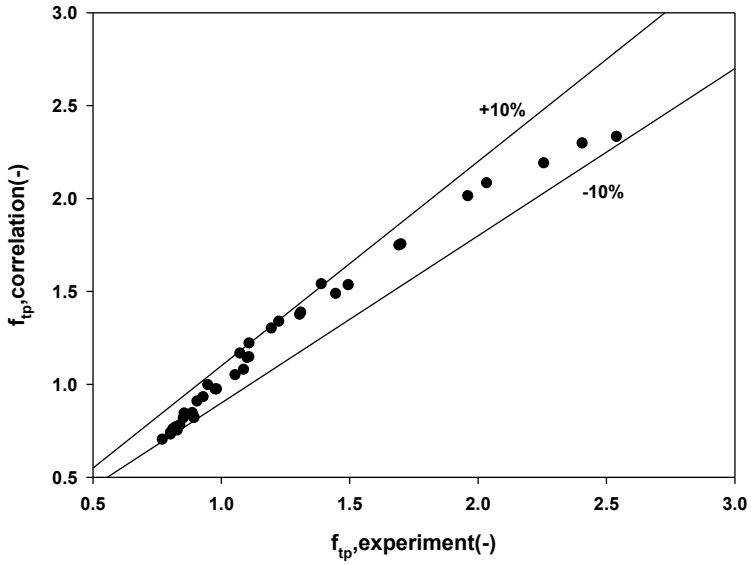

Figure 4: Comparison of correlation of friction factor with experimental data.

4. CONCLUSIONS

In this study, the evaporation heat transfer and pressure drop characteristics of R-1234ze(E) in a shell and plate heat exchanger were investigated as a function of the mass flux, heat flux, and vapor quality. The heat transfer coefficient tended to increase as the vapor quality increased, while the heat transfer coefficient decreased drastically at the vapor quality higher than 0.7 owing to dryout. The friction factor decreased with increasing the vapor quality. In addition, the effect of the mass flux

and heat flux on the friction factor decreased with increasing the vapor quality. The developed correlations for the heat transfer coefficient and friction factor pressure drop showed the consistent results within the deviations of ±15% and ±10%, respectively, as compared with the measured data.

ACKNOWLEDGEMENTS

This research was supported by the Technology Innovation Program (Grant No. 10052926) funded by the Ministry of Trade, Industry & Energy.

NOMENCLATURE

G	mass flux (kg m^{-2} s^{-1})	Q	heat flux (kW)
x	vapor quality(-)	k	thermal conductivity (kW m^{-1} K^{-1})
h	heat transfer coefficient (kW m^{-2} K^{-1})	Re	Reynolds number(-)
D	diameter (m)	f	friction factor(-)
Bo	boiling number(-)	A	heat transfer area (m^{-2})
i	enthalpy (kJ kg^{-1})	ρ	density (kg m^{-3})
μ	viscosity (N m s^{-2})		
Subscripts		r	refrigerant
m	mean	tp	two phase
eq	equivalent	fo	only liquid phase
l	liquid	v	vapor

REFERENCES

Adrián Mota-Babiloni, Joaquín Navarro-Esbrí, Francisco Molés, Ángel Barragán Cervera, Bernardo Peris, Gumersindo Verdú, 2016, A review of refrigerant R1234ze(E) recent investigations, Applied Thermal Engineering, Vol. 95, pp 211–222.

Andrea Diani, Simone Mancin, Alberto Cavallini, Luisa Rossetto, 2016, Experimental investigation of R1234ze(E) flow boiling inside a 2.4 mm ID horizontal microfin tube, International Journal of Refrigeration, Vol. 69, pp 272–284.

Giovanni A. Longo, Claudio Zilio, Giulia Righetti, J. Steven Brown, 2014, Condensation of the low GWP refrigerant HFO1234ze(E) inside a Brazed Plate Heat Exchanger, International Journal of Refrigeration, Vol. 38, pp 250–259.

In-Kwan Kim, Jae-Hong Park, Yong-Ha Kwon, Young-Soo Kim, 2007, Experimental Study on R-410a Evaporation Heat Transfer Characteristics in Oblong Shell and Plate Heat Exchanger, Heat Transfer Engineering, Vol. 28, pp 633–639.

In-Kwan Kim, Young-Soo Kim, Jae-Hong Park, 2005, Experimental Study on R-410A Evaporation Heat Transfer Characteristics in Shell and Plate Heat Exchanger, Journal of the Korean Society of Marine Engineering, Vol. 1, pp 49–59.

Jae-Hong Park, Young-Soo Kim, 2004, Evaporation heat transfer and pressure drop characteristics of r-134a in the oblong shell and plate heat exchanger, KSME International Journal, Vol. 18, Issue 12, pp 2284–2293.

Md. Anowar Hossain, Yoji Onaka, Akio Miyara, 2012, Experimental study on condensation heat transfer and pressure drop in horizontal smooth tube for R1234ze(E), R32 and R410A, International Journal of Refrigeration, Vol. 35, Issue 4, pp 927–938.

Na Liu, Hang Xiao, Junming Li, 2016, Experimental investigation of condensation heat transfer and pressure drop of propane, R1234ze(E) and R22 in minichannels, Applied Thermal Engineering, Vol. 102, pp 63–72.

Shigeru Koyama, Nobuo Takata, Sho Fukuda, 2010, Drop-in Experiments on Heat Pump Cycle Using HFO-1234ze(E) and Its Mixtures with HFC-32, International Refrigeration and Air conditioning Conference, 1155.

S. Grauso, R. Mastrullo, A.W. Mauro, J.R. Thome, G.P. Vanoli, 2013, Flow pattern map heat transfer and pressure drops during evaporation of R1234ze(E) and R134a in a horizontal circular smooth tube: Experiments and assessment of predictive methods, International Journal of Refrigeration, Vol. 36, pp 478–491.

United Nations, 1998, Kyoto Protocol to the United Nations Framework Convention on Climate Change.

Manuscript ID: 67
DOI: 10.18462/iir.icr.2019.0067

Numerical benchmark for air vortex tube flows using a 2^{5-1} resolution V fractional factorial design

Junior LAGRANDEUR[(a)], Sergio CROQUER[(a)], Sébastien PONCET[(a)], Mikhail SORIN[(a)]

[(a)] Mechanical Engineering Department, Université de Sherbrooke
Sherbrooke (Québec) J1K 2R1, Canada,
Junior.Lagrandeur@USherbrooke.ca

ABSTRACT

Computational fluid dynamics models are commonly used to investigate the local fluid flow and heat transfer features inside vortex tubes. For design purpose, extensive calculations are required to optimize the vortex tube and a trade-off must be found between accuracy and computational efforts. A 2^{5-1} resolution IV design is used here with a 2D axisymmetric model of the experiments of Camiré (1995) to evaluate the influence of different modelling parameters on the prediction of the cold mass fraction, the cold outlet temperature and the localization of the stagnation point. This study demonstrates that the k-ω SST turbulence model predicts the cold mass fraction with great accuracy while the standard k-ε model is associated with a significant error. The k-ω SST is used to determine the localization of the stagnation point. This point moves downstream as the cold mass fraction and inlet pressure increase and is affected by the mesh refinement.
Keywords: vortex tube, CFD, factorial design, turbulence, air, physical properties.

1. INTRODUCTION

Georges J. Ranque (1933) invented the vortex tube more than 80 years ago. Even so, the temperature separation mechanism inside the device is still a mystery. Various hypotheses for this effect, often contradicting each other, have been proposed. These have been reviewed by Xue et al. (2010), Devade and Pise (2018) and Lagrandeur et al. (2019a). However, none of these explanations has a broad consensus across the scientific community. The lack of a model to understand and design vortex tubes is believed to be the main factor slowing down the development of this technology (Zhang et al., 2016).

Computational fluid dynamics (CFD) could provide a better understanding of the working mechanism inside vortex tubes. However, the flow through the vortex tube presents many challenges for numerical modelling: compressibility, heat transfer, high levels of turbulence and swirl. Thakare et al. (2015) and Karthikeya Sharma et al. (2017) provided a recent review of CFD simulations of vortex tubes. To the best of the authors' knowledge, the majority of CFD studies are validated using merely one global quantity: the outlet temperature. One exception is the work from Morsbach et al. (2015), who compared the interior velocity profile obtained from filtered Rayleigh scattering with CFD simulation using the k-ω SST and Reynolds stress model (RSM) turbulence models.

With complex flow features like the ones found in vortex tubes, the simulation's hypotheses could have a great impact on its results. Some authors used high precision models like LES (Rafiee and Sadeghiazad, 2016). However, this approach requires very large computation times and is not practical for design purposes. In a recent review, Karthikeya Sharma et al. (2017) indicated that many authors identify the standard k-ε turbulence model as the most suitable to predict T_{0c}. This is surprising since isotropic turbulence models like the standard k-ε model are not well adapted to swirling flows. In this regard, the RSM approach would be a better choice. However, RSM did not perform well for pipe flows (Steenbergen, 1995). Furthermore, it is hard to obtain a converged steady state solution in vortex tubes with differential RSM (Morsbach et al., 2015).

There is a need to determine how well Reynolds average Navier-Stokes (RANS) turbulence models could predict parameters other than the outlets' temperature in vortex tubes. In this work, a 2D axisymmetric model of the experiments of Camiré (1995) is used to benchmark two baseline RANS turbulence models: the standard k-ε and k-ω-SST. Also, two other simulation parameters are investigated: variable physical properties and mesh refinement near the wall. To the best of our

knowledge, it is the first time a low Reynolds approach is used to simulated vortex tube. The impact of using fixed physical properties on outlets' temperatures has been evaluated by Ouadha et al. (2013). They concluded that using variable properties improves slightly the prediction of the cold outlet temperature and modifies the flow profile inside the tube.
In addition to the cold outlet total temperature (T_{0c}), this benchmark will show the effect of these simulation parameters on the cold mass fraction (μ_c) and on the localization of the stagnation point (L_{stag}). Results are compared with the experiments of Camiré (1995) for two values of P_{0in} and μ_c.
To investigate all possible combinations of operational (2) and simulation (3) parameters, 32 simulations are necessary. However, this number is reduced using fractional factorial experiments. As described by Montgomery (2005), fractional factorial experiment allows the investigation of multiple parameters and their low-order interactions with a minimal number of simulations.

2. FRACTIONAL FACTORIAL DESIGN

This work will identify the impact on μ_c, T_{0c}, and L_{stag} of three simulation parameters: turbulence model, variable physical properties and near wall mesh refinement. It is believed that these simulation parameters could have a different effect depending on P_{0in} and μ_c, the two most important operational parameters for vortex tubes (Lagrandeur et al., 2019b).
To make sure potential interactions could be identified, a 2_V^{5-1} fractional factorial design is used. In a resolution V design, there is no main effect or two-factor interaction aliases with each other (Montgomery, 2005). Since low order interactions are most probable, this design will be used to evaluate the impact of the three simulation parameters for two different inlet pressures and two different cold mass fractions with only 16 simulations.

Table 1 details experimental results for the four different conditions studied in this work. These values were chosen because these cold mass fractions correspond approximately to the lower cold outlet temperature (0.4) and maximum cooling power (0.7) in the experiments.

Table 1: Experimental data used to validate the CFD model

Pt	P_{0in} (bar)	Nominal μ_c	Measured μ_c	P_c (bar)	T_{0c} (K)	P_h (bar)	T_{0in} (K)	$\dot{m}_{in}$ (g s^{-1})
1	1.689	0.4	0.409	1.065	285.26	1.120	295.13	5.92
2	1.689	0.7	0.726	1.145	287.68	1.225	295.22	5.63
3	3.080	0.4	0.389	1.170	268.57	1.372	294.22	11.87
4	3.080	0.7	0.696	1.461	276.15	1.731	294.53	11.3

Further in the text when the effect of each factor and their interaction are discussed, this nomenclature will be used:

- *A* is the used turbulence model (standard k-ε or k-ω SST);
- *B* is the inlet pressure (1.7 or 3.08 bar);
- *C* is the nominal cold mass fraction (0.4 or 0.7);
- *D* is the mesh refinement (coarse or fine);
- *E* is for physical properties (fixed or variable);

The generator for this factorial design is *ABCDE*.

3. CFD MODEL

3.1. Geometrical model

The geometry and operational conditions for this study are based on the experiments of Camiré (1995). Table 2 shows the main dimensions of the modelled vortex tube.

Table 2: Main dimensions of the vortex tube.

r_{vt}	L	r_c	L_c	L_n	r_h
12.7 mm	693 mm	8.3 mm	50.8 mm	2.54 mm	6.35 mm

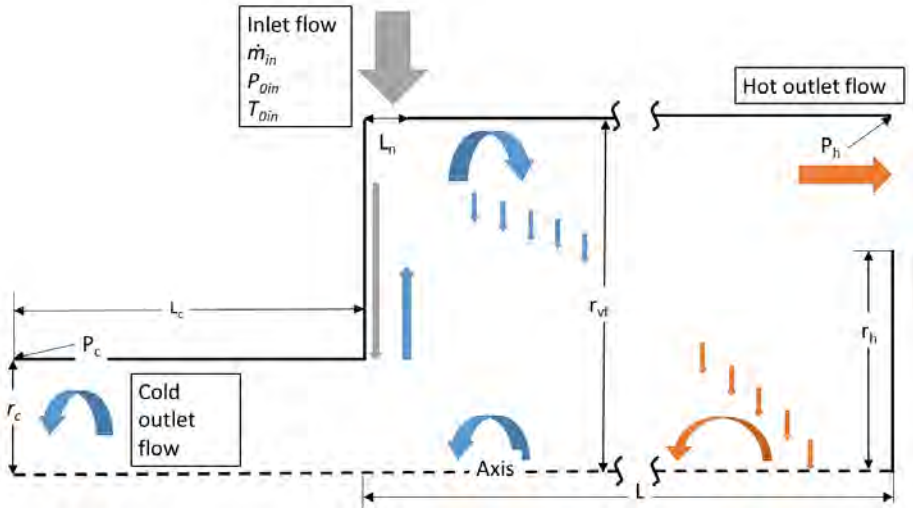

Figure 1: 2D axisymmetric model of the vortex tube of Camiré (1995)

This vortex tube is modelled using a 2D axisymmetric model as shown in Figure 1. 2D simulations have been successfully applied by many authors to model vortex tubes. Some recent examples are the works of Thakare and Parekh (2017), Bazgir and Nabhani (2018) and Dyck and Stratmaan (2018). However, all these studies are limited to the vortex tube itself and neglect the flow in the cold tube. An original feature in this work is the inclusion of part of the cold tube length in the computational domain. The additional length corresponds to the distance between the cold outlet pressure sensor and the cold outlet of the vortex tube in the experimental setup.
Another interesting feature of this model is the inclusion of a detwister near the hot outlet. In the experiments, this is a T-shaped device built from aluminum and inserted inside the tube to stop the rotation before the hot outlet. In the 2D model, this feature is modelled like a rod of 0.8 mm of radius located on the axis. If swirl is small at this point in the tube, this model will be appropriate.

3.2. Governing Equations and Flow Solver

The RANS simulations were carried out using the density based implicit solver of ANSYS Fluent R18.0. All calculations are done assuming steady state flow regimes. Spatial discretization of all flow and turbulence properties is done using the third-order MUSCL scheme with the gradients calculated using the least square cell-based approach.
Fluid density is computed with the ideal gas law. Specific heat (C_p), thermal conductivity (k_t) and dynamic viscosity (μ) were constant or variable depending on the simulated case. When constant flow properties are used, C_p=1.00643 kJ kg^{-1} K^{-1}, k_t=0.0242 kg m^{-1} s^{-1} and μ=1.79x10^{-5} kg m^{-1} s^{-1}. When variable properties are used, μ is computed using the Sutherland's law (White, 2005) and C_p and k_t are evaluated using the polynomial curve fitting equations developed by Ouadha et al. (2013). Two two-equation turbulence models were considered in this work, the standard k-ε and the k-ω SST model. The standard k-ε model is the most popular model in vortex tube studies (Karthikeya Sharma et al., 2017). The k-ω SST model uses a blending function between k-ε far from the walls and k-ω near the walls (Menter, 1994). For both models, a production limiter has been enabled. Thus, the k-ω SST has a built-in wall treatment and no wall function is necessary in this case. For the standard k-ε model, a scalable wall function is used for the coarser mesh and a Menter-Lencher approach for the finer mesh (low-Reynolds number resolution).

3.3. Boundary Conditions

This work uses an original approach to define boundary conditions. First of all, the radial inlet is defined with a fixed velocity instead of using a fixed P_{0in} (Thakare and Parekh, 2017; Bazgir and Nabhani, 2018) or fixed $\dot{m}_{in}$ (Dyck and Stratmaan, 2018). Initial conditions for swirl and density are obtained with the analytic model presented by Lagrandeur et al. (2019b). After the first calculation, both radial and swirl components of the velocity are adjusted iteratively to match the experimental P_{0in} and $\dot{m}_{in}$ values. This approach has the following advantages:

- No backflow occurs at the inlets during the initial stages of the simulation;

- P_{0in} and $\dot{m}_{in}$ are adjusted almost independently by adjusting the associated velocity components without the need to define the inlet flow angle.

At the outlet, pressure is prescribed. However, instead of using a uniform pressure for the whole boundary, a radial pressure equilibrium is used. P_c is defined at the boundary centre in Fluent but it was measured at the wall in the experiments of Camiré (1995). An iterative process is needed to determine the value matching measured and calculated P_c at the wall. It is expected that this boundary condition will be more representative of the swirling flow in the cold tube and will better represent recirculation zones identified by Bin Yusof et al. (2015).
Backflow direction from outlets is defined according to the flow direction of the adjacent cells, including swirl. Backflow temperature is set to the experimental measured outlet temperature. As a consequence, the cold outlet temperature is not representative when significant backflow occurs.
Finally, all walls are considered adiabatic. In the experiments of Camiré (1995), the vortex tube is made of glass, the detwister of aluminum and the cold tube of brass. As found in White (2003), glass is considered smooth, but a roughness height of 2 µm is considered for the detwister and the cold tube surfaces. The only exception is when the Menter-Lencher near-wall treatment is used with the standard k-ε model. In this case, all walls are modelled as smooth walls.

3.4. Meshing

Through the vortex tube, flow variations are expected to be far more important in the radial direction than in the axial direction. Thus, it is advantageous to have cells' boundary perpendicular to the radial direction. As a consequence, the mesh is built using structured rectangular cells elongated in the axial direction, which allows to reduce the total number of cells compared with unstructured triangular meshes.
In this work, two structured grids are built using ICEM v 18.0: one coarsest and one fine achieving a low-Reynolds resolution. The coarsest mesh was built following a grid independence study using condition 4 in Table 1, variable physical properties and the k-ω SST turbulence model. In this study, the number of mesh cells is changed, but the height of the first cell on the vortex tube wall remains unchanged at 0.1 mm. Results of this study are shown in Table 3.

Table 3: Results of the mesh independence study for the coarsest mesh

Number of cells	T_{0c} (K)	μ_c
14 617	281.2	0.624
23 364	281.16	0.621
42 708	281.34	0.625
76 307	281.41	0.626
109 605	281.41	0.626

After slight adjustment, the chosen mesh has 45664 quadrilateral cells. Prediction with this mesh is sufficiently close to the asymptotic value and it is a sufficiently fine to model inlets and outlets. For the case chosen for the mesh validation, y^+<28 everywhere, falling below 1 at some points. A y^+ insensitive wall treatment is required.
The finer mesh achieves a low-Reynolds number resolution at the wall of the vortex tube. This mesh includes 637 551 quadrilateral cells. With a mesh height of 0.0043 mm on the vortex tube wall, y^+<5 everywhere. To get appropriate aspect ratio for all mesh elements, the resulting meshing is finer everywhere in the calculation domain.

4. RESULTS AND DISCUSSION

4.1. General Presentation of Results

Table 4 shows the numerical results for all simulations. It is already visible from these values that the k-ω SST turbulence model is able to accurately predict μ_c in most cases.

Table 4: Numerical results of all simulations in standard order

#	Turb. model	P_{0in} (bar)	μ_c	Mesh	Prop.	T_{0c} CFD (K)	μ_c CFD	L_{stag} (mm)	$\Delta\mu_c$	ΔT_{0c} (K)
1	Standard *k-ε*	1,7	0,4	Fine	var.	282.1	0.09	362	-0.32	-3.3
2	*k-ω* SST	1,7	0,4	Fine	fixed	283.4	0.07	422	-0.34	-2.0
3	Standard *k-ε*	3,08	0,4	Fine	fixed	270.8	0.16	364	-0.23	1.8
4	*k-ω* SST	3,08	0,4	Fine	var.	277.1	0.38	481	-0.01	8.2
5	Standard *k-ε*	1,7	0,7	Fine	fixed	286.5	0.44	461	-0.29	-1.6
6	*k-ω* SST	1,7	0,7	Fine	var.	290.2	0.65	693	-0.08	2.1
7	Standard *k-ε*	3,08	0,7	Fine	var.	277.3	0.49	503	-0.20	0.4
8	*k-ω* SST	3,08	0,7	Fine	fixed	285.4	0.70	693	0.01	8.5
9	Standard *k-ε*	1,7	0,4	Coarse	fixed	285.7	0.14	288	-0.27	0.3
10	*k-ω* SST	1,7	0,4	Coarse	var.	286.0	0.18	382	-0.23	0.6
11	Standard *k-ε*	3,08	0,4	Coarse	var.	274.7	0.28	332	-0.11	5.7
12	*k-ω* SST	3,08	0,4	Coarse	fixed	278.8	0.39	454	-0.00	9.9
13	Standard *k-ε*	1,7	0,7	Coarse	var.	288.8	0.51	398	-0.21	0.8
14	*k-ω* SST	1,7	0,7	Coarse	fixed	292.0	0.71	549	-0.01	3.9
15	Standard *k-ε*	3,08	0,7	Coarse	fixed	283.2	0.57	431	-0.13	6.3
16	*k-ω* SST	3,08	0,7	Coarse	var.	288.4	0.75	693	0.05	11.5

4.2. Influence of the Simulation Parameters on the Cold Mass Fraction

Using a power transform of 1.59 (determined from a Box-Cox's plot), an analysis of variance (ANOVA) of $\Delta\mu_c$ identifies a lot of significant factors. In order, these are: *A, B, C, D, AC, AB, BC, DE, CE* and *E* (see section 2 for the definitions).

As shown in Figure 2, the k-ω SST is always better than the standard k-ε, which always underpredicts μ_c. For all cases, except for P_{0in}=1.7 and μ_c=0.4, the error is almost zero. For this specific case, both standard k-ε and k-ω SST models greatly underpredicts μ_c. This behaviour may be explained by the significant backflow occurring through the cold outlet at this specific condition as shown in Figure 3. For the last two parameters, using a coarser mesh and variable physical properties slightly improve the prediction. For the physical properties, the results are straightforward (see Figure 4). However, the μ_c prediction was expected to be better using the finer mesh. However, the difference is small, so both meshes are appropriated for the μ_c prediction.

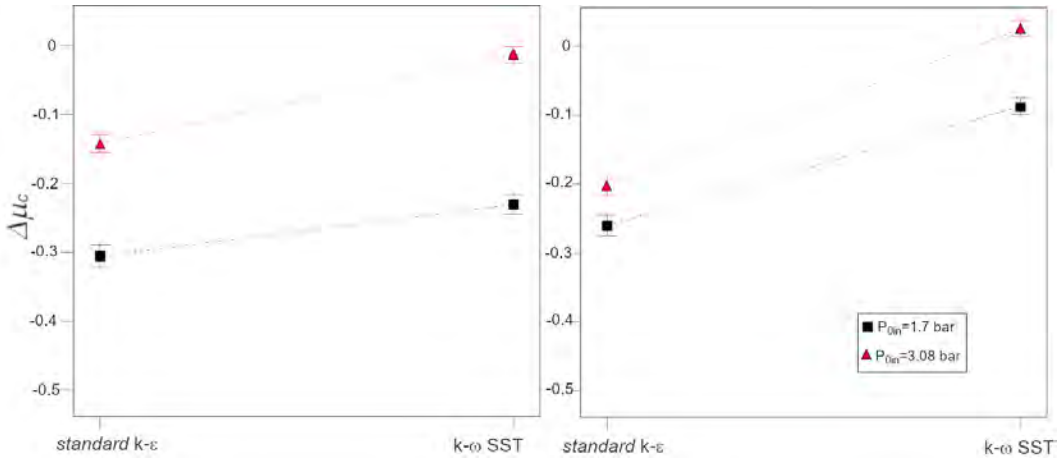

Figure 2: Influence of the turbulence model on $\Delta\mu_c$ for nominal μ_c=0.4 (left) and μ_c=0.7 (right). The black line is for P_{0in}=1.7 bar and the red line is for P_{0in}=3.08 bar. Fine mesh and variable properties are used in this figure.

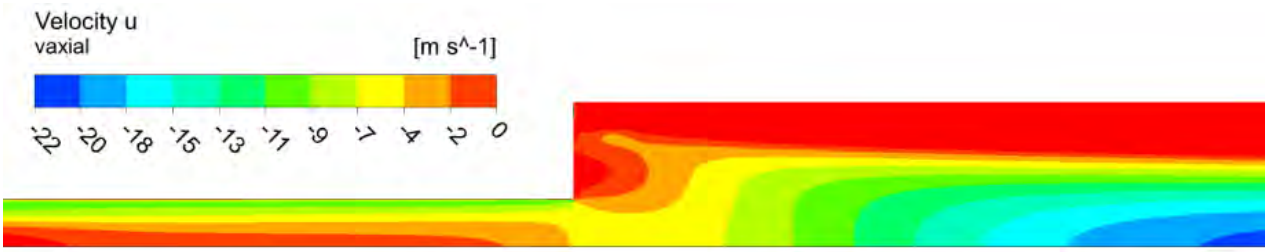

Figure 3: Axial velocity contours using the k-ω SST for fixed physical properties, a fine mesh, P_{0in}=1.7 bar and μ_c=0.4. All areas in red show zones of positive axial velocity.

One possible explanation for the negative impact of the finer mesh is that this effect is aliases with a significant three-factor interaction. In this case, we know that the prediction of this model degrade for a specific combination of *B* and *C*. In consequence, *BC* is an important parameters for the case chosen. Since *A* is the parameter with the most influence on the results and because both *AB* and *AC* are identified as significant parameters, it is probable that *ABC* is significant too. However, *ABC* is aliased with *DE* in this design. A partial fold over, adding eight simulations with the coarse mesh only, could separate these two factors.

4.3. Influence of the Simulation Parameters on the Cold Outlet Temperature

The error on the cold temperature prediction is analyzed with ANOVA without any transformation. Factors influencing significantly the error are *B, A, D* and *AB.* Almost all simulations overpredict T_{0c}. The prediction of T_{0c} is improved by using the finest low-Reynolds number mesh.
The standard k-ε model provides T_{0c} closer to the experimental results at high pressure and for all simulations with the coarsest mesh. However, using the k-ω SST is preferable because μ_c is wrong while using the standard k-ε. Since T_{0c} reduces with μ_c, the standard k-ε cannot be used with confidence. One may correct μ_c by changing the outlets pressure. However, Lagrandeur et al. (2019b) demonstrated that T_{0c} depends mainly on the pressure ratio between inlets and the cold outlet. As a consequence, the improved results may not have a real significance if the wrong value for P_c is used.

4.4. Localization of the Stagnation Point

The ANOVA analysis with a natural logarithm transformation shows that the stagnation point moved with *C, A, D, B, AC* and *BD*. In general, L_{stag} increases with increasing P_{0in} *(B)* and μ_c *(C)*. L_{stag} is higher when the k-ω SST model is used, which could be explained in part because it predicts higher μ_c for the same initial conditions. L_{stag} increases while using the low-Reynolds number mesh.
One surprising fact here comes from the inlet pressure. It was expected that the stagnation point will be strongly influenced by P_{0in}. However, it appears that the effect of pressure is rather small. It is even more visible when the finer mesh is used as shown in Figure 5.

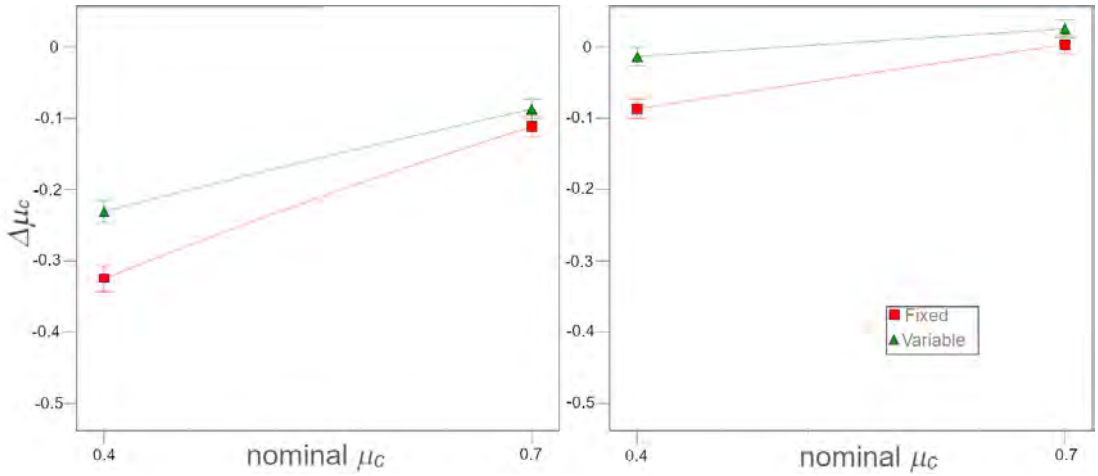

Figure 4: Influence of nominal μ_c on $\Delta\mu_c$ for fixed (red) and variable (green) physical properties using a fine mesh and the k-ω SST model. P_{0in}=1.7 bar (left) and P_{0in}=3.08 bar (right)

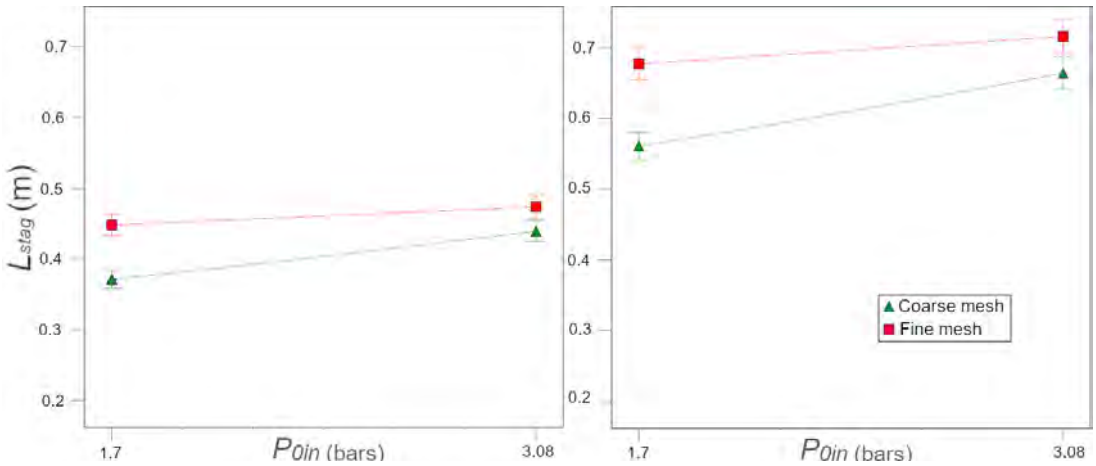

Figure 5: Effect of P_{0in} (in bar) on L_{stag} for coarse mesh (green) and fine mesh (red) using the k-ω SST for μ_c=0.4 (left) and μ_c=0.7 (right).

5. CONCLUSIONS

A benchmark study of two turbulence models against μ_c and T_{0c} with the experimental results of Camiré (1995) has been carried out. Using a 2_V^{5-1} fractional factorial design, this work evaluated the impact of mesh refinement and variable physical properties for two different P_{0in} and two different nominal μ_c.

Results showed that the k-ω SST accurately predicts μ_c for most conditions. One exception is noticed for low P_{0in} and low nominal μ_c where significant backflow occurs from the cold outlet. Except for this case, the k-ω SST underpredicts the temperature separation effect. The standard k-ε model better predicts T_{0c}. Since T_{0c} is proportional to μ_c, the improvement on T_{0c} is related to the error on μ_c.

Using variable physical properties improves the accuracy of μ_c prediction, but has no significant effect on T_{0c}. Mesh refinement improved the prediction of T_{0c}, but it has a slight negative effect on μ_c prediction. This effect may be aliased with a significant three-factor interaction. A partial fold over of this design may solve this problem.

Finally, CFD simulations predicted the localization of the stagnation point inside the tube. The stagnation point moves downstream as μ_c and P_{0in} increase. Additionally, the prediction of L_{stag} is affected by the mesh refinement. In future work, one will needs to determine if L_{stag} changes because of the low-Reynolds resolution near the wall or from the improved mesh resolution near the axis.

ACKNOWLEDGEMENTS

This work is founded by Natural Sciences and Engineering Research Council of Canada (NSERC) and by a Mitacs Acceleration internship grant in partnership with the company Aéroénergie. Aéroénergie is involved in the choice of the research subject and accepts the content of the article prior to publication. They are here all gratefully acknowledged for their support.

NOMENCLATURE

C_p	spec. heat, const. pressure (kJ kg^{-1} K^{-1})	r_h	hot outlet inner radius (mm)
k	turbulent kinetic energy (m^2 s^{-2})	r_{vt}	radius of the vortex tube (mm)
k_t	thermal conductivity (kg m^{-1} s^{-1})	T_{0c}	cold outlet's mean total temperature (K)
L	vortex tube length (mm)	T_{0in}	inlets' total mean temperature (K)
L_c	cold tube length (mm)	y^+	dimensionless wall distance
L_n	nozzles' width (mm)	ΔT_c	error on T_{0c}
L_{stag}	localization of stagnation point (m)	$\Delta\mu_c$	error on μ_c
$\dot{m}_{in}$	total inlet mass flowrate (kg s^{-1})	ε	k dissipation rate (m^2 s^{-3})
P_c	static pressure at the cold outlet (bar)	μ	dynamic viscosity (N s m^{-2})
P_h	static pressure at the hot outlet (bar)	μ_c	cold mass fraction
P_{0in}	total pressure at the inlet (bar)	ω	k specific dissipation rate (s^{-1})
r_c	radius of the cold outlet (mm)		

ANOVA	analysis of variance	RANS	Reynolds average Navier-Stokes
CFD	computational fluid dynamics	RSM	Reynolds stress model

REFERENCES

Bazgir, A., Nabhani, N., 2018. Numerical investigation of the effects of geometrical parameters on vortex separation phenomenon inside Ranque-Hilsch vortex tube using as air separator in helicopter's engine, Aviation 22, 13–23.

Bin Yusof, M.H., Katanoda, H., Morita, H., 2015. Temperature and pressure measurements at cold exit of counter-flow vortex tube with flow visualization of reversed flow, J. Therm. Sci. 24(1), 67–72.

Camiré, J., 1995. Experimental investigation of vortex tube concepts. Master's thesis, University of British Columbia, Vancouver, Canada, 130 p.

Devade, K.D., Pise, A.T., 2018. Issues and prospects of energy separation in vortex tubes. Heat Transfer—Asian Res. 47(3), 461–491.

Dyck, N., Straatman, A., 2018. Energy transfer mechanisms in the Ranque-Hilsch vortex tube, Proceedings of the CSME International Congress, Toronto, Canada, 1–5.

Karthikeya Sharma, T., Amba Prasad Rao, G., Madhu Murthy, K., 2017. Numerical analysis of a vortex tube: a review, Arch. Computat. Methods Eng. 24(2), 251–280.

Lagrandeur, J., Poncet, S., Sorin, M., 2019a. Review of predictive models for the design of counterflow vortex tubes working with perfect gas. Int. J. Therm. Sci. accepted.

Lagrandeur, J., Poncet, S., Sorin, M., Khennich, M., 2019b. Features selection and optimization of counterflow vortex tubes working with air through artificial neural network and thermodynamic modeling. Int. J. Therm. Sci. submitted.

Menter, F.R., 1994. Two-equation eddy-viscosity turbulence models for engineering applications. AIAA J. 32, 1598–1605.

Mongomery, D.C., 2005. Design and analysis of experiments, 6th edition, Wiley, Hoboken, 643 p.

Morsbach, C., Schlüß, D., Franke, M., Doll, U., Burow, E., Beversdor, M., Stockhausen, G., Willert, C. 2015. The flow field inside a Ranque-Hilsch vortex tube, part 2 :Turbulence modelling and numerical simulation. Proceeding of the TSFP-9, Melbourne, Australia, 1–6.

Ouadha, A., Baghdad, M., Addad, Y., 2013. Effects of variable thermophysical properties on flow and energy separation in a vortex tube, Int. J. Refrigeration 36(8), 2426–2437.

Rafiee, S.E., Sadeghiazad, M.B.M., 2016. Three-dimensional computational prediction of vortex separation phenomenon inside the Ranque-Hilsch vortex tube, Aviation 20(1), p. 21- 31.

Ranque, G.J., 1933. Experiments on expansion in a vortex with simultaneous exhaust of hot air and cold air. J. Phys. Rad. 4(7), 112–114.

Steenbergen, W., 1995. Turbulent pipe flow with swirl, PhD thesis, Technische Universiteit Eindhoven, The Netherlands, 188 p.

Thakare, H.R., Parekh, A.D., 2017. Experimental investigation & CFD analysis of Ranque-Hilsch vortex tube, Energy 133, 284-298.

White, F.M., 2003. Fluid mechanics, 5th edition. McGraw Hill, New-York, 866 p.

Xue, Y., Arjomandi, M., Kelso, R., 2010. A critical review of temperature separation in a vortex tube. Exp. Therm. Fluid Sci. 34(8), 1367 – 1374.

Zhang, B., Guo, X., Yang, Z., 2016. Analysis on the fluid flow in vortex tube with vortex periodical oscillation characteristics. Int. J. Heat Mass Transfer 103, 1166 – 1175.

Manuscript ID: 69
DOI: 10.18462/iir.icr.2019.0069

A new thermodynamic model for the prediction of air vortex tube performances

Junior LAGRANDEUR[(a)], Sébastien PONCET[(a)], Mikhail SORIN[(a)]

[(a)] University of Sherbrooke
Sherbrooke (Québec) J1K 2R1, Canada,
Junior.Lagrandeur@USherbrooke.ca

ABSTRACT

A new thermodynamic model is proposed to predict the vortex tube performances. Static temperature drops while high pressure air is accelerated adiabatically through the nozzle. At the inlet, forced vortex, flat axial velocity's profile and constant static temperature are assumed, allowing the calculation of the mean total cold outlet temperature. It has been favourably compared to experimental data from the literature and to a new artificial neural network model.
Results show that most important parameters for design purpose are the inlet to cold outlet pressure ratio to maximize the inlet velocity. The importance of the cold mass fraction is related to its impact on the cold side back pressure and axial velocity. The model shows that the influence of friction and boundary layer flow on the temperature separation is important. Finally, this model is used to identify the optimum cold outlet diameter.
Keywords: Ranque-Hilsch vortex tube, thermodynamic modelling, air, pressure ratio, friction, boundary layer.

1. INTRODUCTION

Since the pioneering work of Ranque (1933), vortex tubes puzzled the scientific community. Many different explanations of the Ranque-Hilsch effect have been proposed as shown in reviews of Xue et al. (2010), Devade and Pise (2018) and Zhang and Guo (2018). However, a proposed working mechanism to well predict the vortex tube performances is still missing. Lagrandeur et al. (2019a) reviewed quantitative models used to predict the performances of counterflow vortex tubes working with perfect gases. However, none of them could predict the vortex tube performances accurately. There is still indeed no commonly accepted model to predict their performances and explain at the same time the energy separation mechanism. The lack of a proper understanding of the Ranque-Hilsch effect is believed to be the major obstacle that limits the broader use of vortex tubes (Zhang et al., 2016).
The review of existing models reveal a lot of similitudes between the different models used to predict the cold outlet temperature (Lagrandeur et al., 2019a). The most important is a simplification of the radial momentum equation for a steady axisymmetric flow with $u_r << u_\theta$, $u_z << u_\theta$, and $\partial/\partial z << \partial/\partial\theta$. Under these assumptions, the radial momentum equation reduces to:

$$\frac{1}{\rho}\frac{\partial P}{\partial r} = \frac{u_\theta^2}{r}. \qquad \text{Eq. (1)}$$

Using Eq. (1), Liew et al. (2012) developed a simple expression to compute the inlet Mach number Ma_{in} based on the pressure difference between the inlets and the cold outlet:

$$\frac{P_{0in}}{P_c} = \left(\frac{r_{vc}}{r_{vt}}\right)^{\gamma Ma_{in}^2}\left(1+\frac{\gamma-1}{2}\mathrm{Ma}_{in}^2\right)^{\gamma/(\gamma-1)}\exp\left(\frac{\gamma}{2}\mathrm{Ma}_{in}^2\right). \qquad \text{Eq. (2)}$$

In this work, a new predictive model is proposed. This model predicts the counterflow vortex tube cold outlet temperature based on a modified version of the two equations given above and on an adequate treatment of the kinetic energy influence on the total temperature. The effects of friction and boundary layer flow will be also investigated. The model performance is benchmarked again experimental data from Camiré (1995) and an artificial neural network developed by Lagrandeur et

al. (2009b). Finally, a parametric analysis enables to identify the optimum working range for a given input pressure.

2. NEW THERMODYNAMIC MODEL TO PREDICT THE COLD OUTLET TEMPERATURE

2.1. Main Hypotheses

This new model analyzes the flow behaviour at the inlet plane of a vortex tube, which includes the cold outlet. In order to solve the Navier-Stokes equations analytically, some assumptions are necessary. In this model, the following hypotheses are used:

- perfect gas;
- axisymmetry;
- forced vortex profile;
- constant Mach number in the vortex chamber;
- $u_\theta >> u_z$;
- $u_\theta >> u_z$;
- variations in the radial direction *r* are more important than variations in the axial direction *z* ($\partial/\partial r >> \partial/\partial z$);
- turbulent quantities are not included in the radial momentum equation;
- compressible flow;
- air is accelerated isentropically in the inlet nozzles;

Most thermodynamic models published to date about vortex tubes used similar hypotheses (Lagrandeur et al. 2009a). An additional hypothesis is necessary to get the axial velocity component in the cold outlet. This velocity is considered invariant in *r* like in fully developed pipe flows.
Finally, the static temperature *T* on the inlet plane is considered as constant. This hypothesis is based on experimental (Gao, 2005) and numerical (Khait et al., 2014) observation of the static temperature profile in vortex tubes.

2.2. Basic Formulation

Under the hypotheses listed in the previous section, the radial momentum equation reduces to Eq. (1). This equation could be solved with $u_\theta = \varpi r$ using the same procedure described by Liew (2013). However, P_c is usually measured at the wall. The cold outlet pressure is moved from the centre to r_c, leading to a modified version of Eq. (2):

$$\frac{P_{0in}}{P_c} = \left(\frac{r_{vc}}{r_{vt}}\right)^{\gamma Ma_{in}^2} \left(1+\frac{\gamma-1}{2}\mathrm{Ma}_{in}^2\right)^{\gamma/(\gamma-1)} \exp\left(\frac{\gamma}{2}\mathrm{Ma}_{in}^2\left(1-\frac{r_c}{r_{vt}}\right)^2\right). \quad \text{Eq. (3)}$$

This equation is used to compute Ma_{in}. Knowing Ma_{in}, the static temperature at the inlet plane is computed using the classical equation for a compressible adiabatic flow (Thompson, 1988):

$$\frac{T_{0in}}{T_{in}} = \frac{T_{0in}}{T_c} = 1+\frac{\gamma-1}{2}\mathrm{Ma}_{in}. \quad \text{Eq. (4)}$$

Integrating Eq. (1) using Ma_{in} as the boundary condition provides the pressure profile:

$$P(r) = P_{in}\left[\exp\left(\gamma \mathrm{Ma}_{in}^2/2\right)\right]^{\left(\frac{r^2}{r_{vt}^2}-1\right)}. \quad \text{Eq. (5)}$$

Density is computed using Eq (5) together with the perfect gas law with constant static temperature. At this point, all flow properties are known on the inlet plane excepted the axial velocity component u_z in the cold outlet. u_z is computed using the cold mass flow rate with this equation:

$$\mu_c \dot{m}_{in} = u_z \int_0^{2\pi}\int_0^{r_c} \rho(r) r \partial r \partial\theta. \quad \text{Eq. (6)}$$

At this point, Eq. (7) is used to derive T_{0c} from the known T_c and the total kinetic energy:

$$\mu_c \dot{m}_{in} C_p T_{0c} = \mu_c \dot{m}_{in} C_p T_c + \mu_c \dot{m}_{in}\frac{u_z^2}{2} + \int_0^{2\pi}\int_0^{r_c}\frac{\varpi^2 r^2}{2} u_z \rho(r) r \partial r \partial\theta. \quad \text{Eq. (7)}$$

2.3. Impact of Friction Losses in Inlets

For vortex tube without vortex chamber, the magnitude of the energy separation depends mainly on the pressure ratio P_{oin}/P_c. That is the reason why one investigates the influence of the pressure losses at the inlets.

To compute the friction losses in inlets, one needs to evaluate the Reynolds number Re_n and the relative roughness ε_n / D_{hn}, with ε_n the nozzle sand-grain surface roughness and D_{hn} the hydraulic diameter of the nozzle. The first step is to determine the flow Mach number at the entrance of the inlet nozzles using the following equation (Thompson, 1988):

$$\frac{\dot{m}_{in}}{A_n \rho_* u_*} = \frac{\mathrm{Ma}_n}{\left(2/(\gamma+1) + \mathrm{Ma}_n^2 (\gamma-1)/(\gamma+1)\right)^{\frac{\gamma+1}{2(\gamma-1)}}}. \quad \text{Eq. (8)}$$

With $u_n = \mathrm{Ma}_n \sqrt{\gamma R_g T_n}$, the nozzle Reynolds number is calculated by:

$$\mathrm{Re}_n = u_n \rho_n D_{hn} / \mu. \quad \text{Eq. (9)}$$

Using data from Camiré (1995), one found here $4.5\times10^7 \le \mathrm{Re}_d \le 1.3\times10^8$.

To compute relative roughness, some assumptions are necessary. Inlet nozzles are circular in the experiment of Camiré (1995). Drilling is the most probable machining operation. From Oberg et al. (2000), drilling produces typical average surface roughness (R_a) equal to 1.6 μm. This value is converted to an approximate value for ε_n using this equation (Adams et al., 2012):

$$\varepsilon_n = 5.863 R_a. \quad \text{Eq. (10)}$$

For the experiment of Camiré (1995), ε_n =0.004. From the Moody chart (White, 2003), the flow is clearly in the fully rough flow regime. Thus, $f \approx 0.028$.

Using classical equation for a Fanno flow (not reproduced here) and with nozzle length of 6.3 mm, a reduced inlet total pressure is computed. From data of Camiré (1995), the reduction in P_{0in} caused by friction remains between 2% and 20%. This is in the same range as the pressure losses measured by Gao (2005).

The difference between the original model and the model including friction losses for μ_c=0.6965 is shown in Table 1. Lagrandeur et al (2019b) present figure showing how friction in the inlet nozzles affects ΔT_{0c} for different μ_c.

Table 1: influence of the proposed improvements on the prediction of the mean total temperature at the cold outlet T_{0c} for P_{0in}=3.08 bar and m_c=0.6965.

Model	T_{0c} (K)	Relative error (%)
Original model	268.6	3.6
Pressure losses in the inlet nozzles	270.5	2.9
Additional 3% for P_c	269.5	3.2
Boundary layer flow from the inlet to the cold outlet	270.5	2.9
Modified model	273.1	1.9
Experimental data (Camiré, 1995)	278.5	-

2.4. Impact of Friction Losses in the Cold Outlet

A numerical study based on the experiment of Camiré (1995) (not reproduced here) shows a pressure drop of 3% between the cold outlet and the pressure sensor location. For μ_c=0.6965, a slight increase of P_c from 1.46 to 1.50 bar creates a difference of 1 K. As a conclusion, the model is sensitive to variations of the cold outlet pressure.

2.5. Impact of the Boundary Layer Flow

The pressure gradient generated by the rotating flow over the wall between the inlets and the cold outlet creates an inward boundary layer flow known as a Bödewadt flow (Schlichting and Gersten, 1999). Because this flow is not involved in the energy transfer process within the tube, its total temperature remains constant (Gutsol, 1997). When this flow reaches the cold outlet, it mixes with the flow coming from the tube and increases the resultant total temperature.

To investigate the influence of this flow, the boundary layer mass flow rate $\dot{m}_{bl}$ is computed from (Gutsol, 1997):

$$\dot{m}_{bl} \approx 25 r_c \rho(r_c) \left[(r_{vt} - r_c) v u_{in,\max} \right]^{1/2}. \quad \text{Eq. (11)}$$

As shown in Table 1, the influence of this parameter is significant at high cold mass fractions. Lagrandeur et al. (2019b) demonstrated it is even more important at low cold mass fractions when the flow in the boundary layer accounts for a greater percentage of the cold outlet flow.

2.6. Comparison Against the Model of Liew et al. (2012) and an Artificial Neural Network

Fig. 1 compares the outputs of the proposed thermodynamic model, of the Liew et al (2012)'s model and of an artificial neural network (ANN) built by Lagrandeur et al. (2019b) against the experimental data of Camiré (1995) for P_{0in}=3.08 bar. This figure confirms that both the artificial neural network and the new thermodynamic model could predict correctly the vortex tube behaviour. Additionally, the new model considering both pressure losses and boundary layer flow improves significantly the predictions of the original model of Liew et al. (2012).

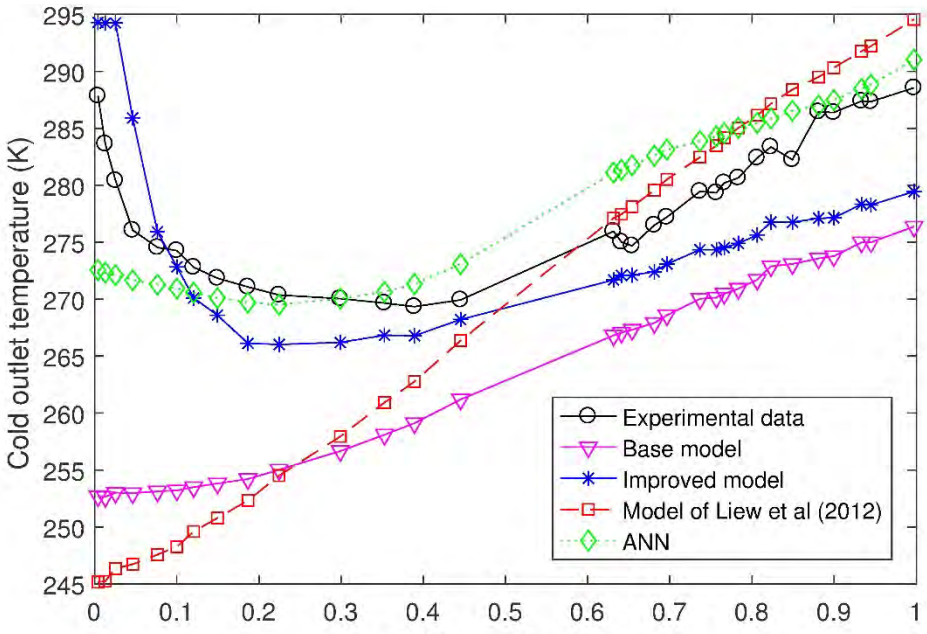

Figure 1: Cold outlet temperature T_{0c} computed by the model of Liew et al (2012), the present thermodynamic model and the ANN model. Comparison with the experimental data from Camiré (1995) for P_{0in}=3.08 bar

Comparison between these methods for other inlet pressures could be found in Lagrandeur et al. (2019b).

3. PARAMETRIC OPTIMIZATION

3.1. Cold outlet radius

Changing cold outlet's radius modify cold outlet's total temperature in two ways. First of all, density and kinetic energy increase with the radius. Increasing the cold outlet diameter allows air with higher total energy to go out by the cold outlet, reducing ΔT_{0c}. This mechanism degrades the performance of the vortex tube and is predicted by Eq. (7).

However, increasing radius of the cold outlet reduces the pressure drop. The cold outlet pressure from experiments of Camiré (1995) for four different values of P_{0in} could be predicted by a single quadratic equation (with a coefficient of determination of 0.998):

$$P_c = 6 \times 10^8 \dot{m}_c^2 + 9.2 \times 10^5 \dot{m}_c + 100566. \quad \text{Eq. (12)}$$

Since P_c varies as the square of the mass flowrate for a given radius, it is expected that P_c will change with the square of the air axial velocity through the cold outlet. Assuming that D_c/D_{vt} ratio does not significantly affect $\dot{m}_{in}$ as demonstrated by Lagrandeur et al. (2019b) using artificial neural networks, the reduced cold outlet pressure is approximated with this relation:

$$P_{c2} - 100566 = \left(P_c - 100566\right)\frac{D_{c1}^2}{D_{c2}^2}, \qquad \text{Eq. (13)}$$

with $_1$ the reference value from the experiment of Camiré (1995) and $_2$ the value for the new D_c. It is important to note that this revised pressure is still applied at the original cold outlet radius when computing Eq. (3). Because of the high angular velocity, pressure at the wall will be higher than this new value.

Fig. 2 shows the results obtained for various D_c/D_{vt} ratios at two different inlet pressures. The best performance at low μ_c occurs for the smallest cold orifice. However, when more air goes out through this orifice with increased μ_c, the reduction in the cold outlet pressure reduces significantly the cold outlet temperature up to 0.5 for the higher inlet pressure and even higher for lower P_{0in}. Lagrandeur et al. (2019b) identify the same optimum ratio using an artificial neural network, but the thermodynamic model provides better insight on the working mechanism of vortex tubes. A literature review provided in the same article agrees with these findings.

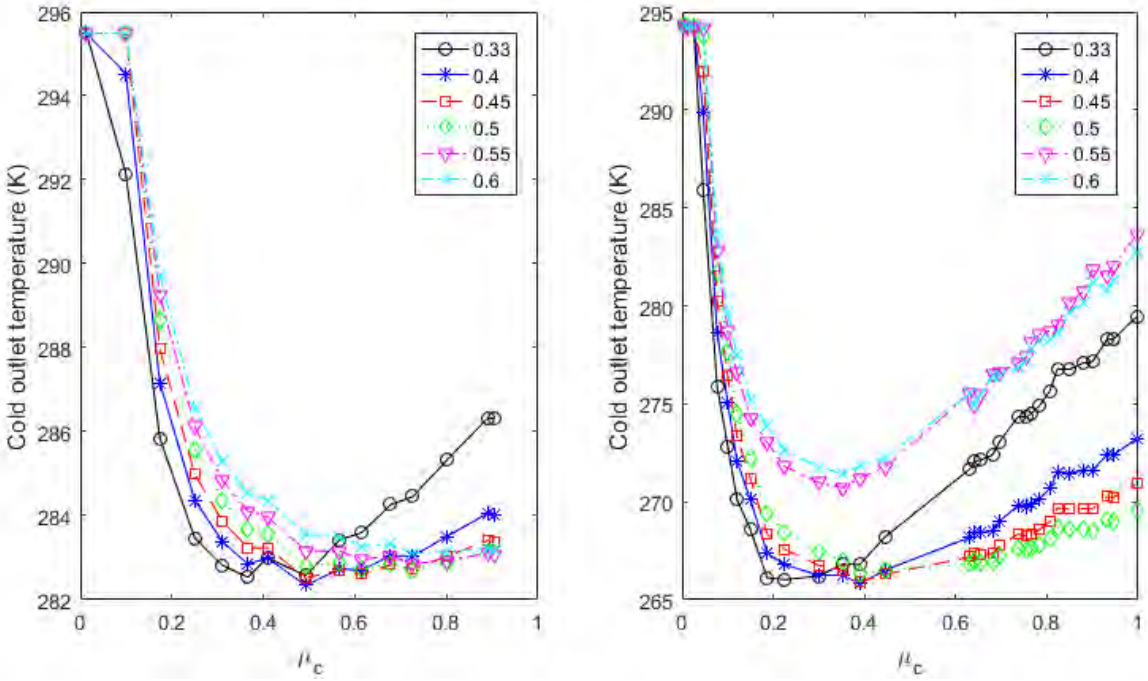

Figure 2: Cold outlet temperature T_{0c} computed by the proposed thermodynamic model including friction and boundary layer flow for various D_c/D_{vt} ratios. Left: P_{0in}=1.7 bar. Right: P_{0in} =3.08 bar.

Finally, this model indicates that the optimal D_c/D_{vt} ratio may change according to other experimental conditions. The advantage of increasing D_c/D_{vt} depends directly on the cold outlet pressure drop downstream of the tube. If back pressure is reduced through a reduced inlet mass flowrate or by removing resistance to air flow downstream of the tube (mass flow meter, piping, valves,…), smaller cold outlets will become more advantageous. It could explain differences in the optimal D_c/D_{vt} ratio identified in the literature by Lagrandeur et al. (2019b).

3.2. Vortex chamber radius

The vortex chamber is a narrow chamber with a radius superior to the hot tube radius. It could improve the performance of vortex tubes in two ways. First of all, this chamber uniformizes the initial vortex to generate an axisymmetric profile at the inlet (Shamsoddini and Abolpour, 2018). Secondly, it prevents sudden expansion at nozzles' outlet when P_{0in}/P_c is high (Fulton, 1965). This second condition makes a vortex chamber necessary to keep $Ma_{in}<1$. Using Eq. (3), this critical pressure ratio is 3.81 if P_c is taken at the middle of the tube.

Fig. 3 shows the effect of the vortex chamber on vortex tubes' performance for a pressure ratio under 3.81. Since this model assumes a constant Mach number in the vortex chamber (Liew et al. 2012), a vortex chamber reduces the maximum Ma_{in} and the temperature drop. Rafiee and Sadeghiazad (2015) reached the same conclusion using a numerical simulation. In consequence, the vortex chamber diameter should be kept to the minimum required to obtain an axisymmetric vortex when P_{0in}/P_c <3.81.

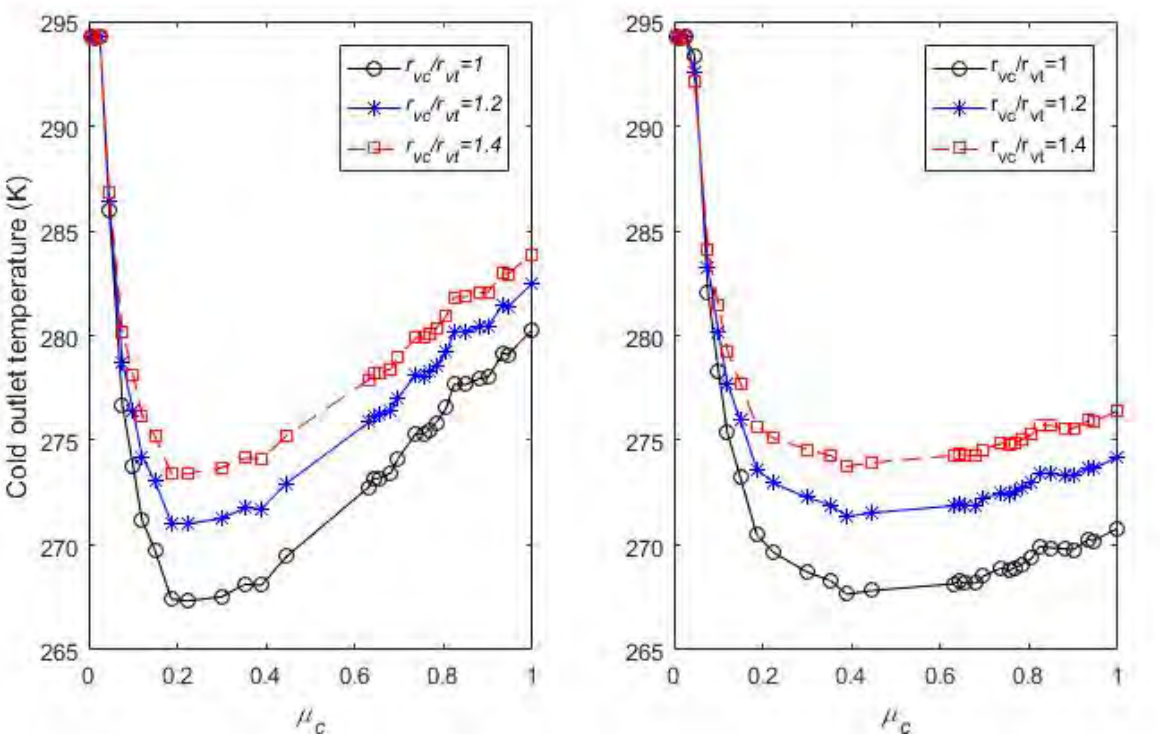

Figure 3: Cold outlet temperature T_{0c} computed by the proposed thermodynamic model including friction and boundary layer flow for various r_{vc}/r_{vt} ratios at P_{0in} =3.08 bar. Left: D_c/D_{vt}=0.33. Right: D_c/D_{vt}=0.5.

4. CONCLUSION

Vortex tubes are puzzling devices. The thermal separation process is still poorly understood, and design tools are lacking. In this work, one proposed a new thermodynamic model to predict vortex tube performances. This model uses the pressure ratio between the inlets and the cold outlet to predict the cold outlet total temperature in a three-step process:

- air is accelerating adiabatically in the inlet nozzles including friction effects (Fanno flow);
- at the inlet, static temperature reaches an equilibrium (isothermal profile) in a well design vortex tube through intense turbulent mixing;
- after going out to the cold outlet, kinetic energy is converted back to thermal energy in an isentropic process to obtain the cold outlet total temperature.

This model compared favourably against experimental data of Camiré (1995) when friction and boundary layer flow are considered in the model. The small remaining discrepancies could be explained by non-optimal conditions inside the tube or by heat exchanges through the vortex tube envelope.

Finally, this model is used to predict the optimal D_c/D_{vt} and r_{vc}/r_{vt} ratios. Increasing D_c/D_{vt} increase T_{0c} by allowing the air to go out faster and reduce it by lowering P_{0in}/P_c through a reduction in the cold outlet pressure. The optimum D_c/D_{vt} identified in this paper (0.5) is in accordance with values reported in the literature and found using an artificial neural network.

On the other hand, the optimal r_{vc}/r_{vt} ratio is 1 for P_{0in}/P_c lower than the critical value of 3.81, meaning that a vortex chamber could reduce the performance of vortex tubes. In consequence, the vortex chamber diameter should be the minimum required to obtain an axisymmetric vortex in the inlet

section. New experimental and numerical work would be helpful to provide the optimal value for the vortex chamber diameter.

ACKNOWLEDGEMENTS

This work is founded by Natural Sciences and Engineering Research Council of Canada (NSERC) and by a Mitacs Acceleration internship grant in partnership with the company Aéroénergie AÉROÉNERGIE. Aéroénergie is involved in the choice of the research subject and accepts the content of the article prior to publication. They are here all gratefully acknowledged for their support.

NOMENCLATURE

C_p	Specific heat at constant pressure (J kg^{-1} K^{-1})	Re_n	nozzles Reynolds number
C_v	Specific heat at constant volume (J kg^{-1} K^{-1})	T_c	cold outlet's static temperature (K)
D_c	cold outlet diameter (m)	T_{in}	inlets' static temperature (K)
D_{vt}	vortex tube's diameter (m)	T_{0c}	cold outlet's mean total temperature (K)
f	friction factor	T_{0in}	inlets' total mean temperature (K)
Ma_{in}	Mach number at inlet (nozzles' outlet)	u_r	radial velocity (m s^{-1})
Ma_n	Mach number at nozzles' inlet	u_z	axial velocity (m s^{-1})
$\dot{m}_{bl}$	mass flowrate in the boundary layer (kg s^{-1})	u_θ	tangential velocity (m s^{-1})
$\dot{m}_c$	mass flowrate through the cold outlet (kg s^{-1})	u_*	velocity magnitude at critical state (Ma_n=1) (m s^{-1})
$\dot{m}_{in}$	total inlet mass flowrate (kg s^{-1})	γ	specific heat ratio (=C_p/C_v)
P_c	static pressure at the cold outlet (Pa)	ΔT_{0c}	total temperature difference between the inlets and cold outlet (K)
P_{in}	static pressure at inlets (Pa)	ε_n	nozzles' sand-grain surface roughness (mm)
P_{0c}	total pressure at the cold outlet (Pa)	μ	dynamic viscosity (N s m^{-2})
P_{0in}	total pressure at the inlets (Pa)	μ_c	cold mass fraction (=$\dot{m}_c/\dot{m}_{in}$)
r_c	radius of the cold outlet (m)	ω	angular velocity (rad s^{-1})
r_{vc}	radius of the vortex chamber (m)	ρ	static density (kg m^3)
r_{vt}	radius of the vortex tube (m)	ρ_*	density at critical state (kg m^3)
R_a	average surface roughness (μm)	ρ_n	static density inside inlet nozzles (kg m^3)
R_g	specific perfect gas constant (J kg^{-1} K^{-1})		

REFERENCES

Adams, T., Grant, C., Watson, H., 2012, A simple algorithm to related measured surface roughness to equivalent sand-grain roughness. Int. J. Mech. Eng. Mecha. 1, 66–71.

Camiré, J., 1995. Experimental investigation of vortex tube concepts. Master's thesis, University of British Columbia, Vancouver, Canada, 130 p.

Devade, K. D., Pise, A. T., 2018. Issues and prospects of energy separation in vortex tubes. Heat Transfer—Asian Res. 47 (3), 461–491.

Fulton, C. D., 1965, Vortex tube, US Patent 3,208,229.

Gao, C., 2005. Experimental study on the Ranque-Hilsch vortex tube. Ph.D. thesis, Technische Universiteit Eindhoven, The Netherlands, 151 p.

Gutsol, A. F., 1997. The Ranque effect. Physics-Uspekhi 40 (6), 639–658.

Khait, A. V., Noskov, A. S., Lovtsov, A. V., Alekhin, V. N., 2014. Semi-empirical turbulence model for numerical simulation of swirled compressible flows observed in Ranque-Hilsch vortex tube. Int. J. Refrigeration 48, 132–141.

Lagrandeur, J., Poncet, S., Sorin, M., 2019a. Review of predictive models for the design of counterflow vortex tubes working with perfect gas. Int. J. Therm. Sci. In press.

Lagrandeur, J., Poncet, S., Sorin, M., Khennich, M., 2019b. Features selection and optimization of counterflow vortex tubes working with air through artificial neural network and thermodynamic modeling. Int. J. Therm. Sci. submitted.

Liew, R., 2013. Droplet behaviour and thermal separation in Ranque-Hilsch vortex tubes. Ph.D. thesis, Technische Universiteit Eindhoven, The Netherlands, 183 p.

Liew, R., Zeegers, J. C. H., Kuerten, J. G. M., Michalek, W. R., 2012. Maxwell's demon in the Ranque-Hilsch vortex tube. Phys. Rev. Lett. 109 (5), 054503.

Oberg, E., Jones, F. D., Horton, H. L., Ryffel, H. H., 2000. Machinery's handbook, 26th Edition. Industrial Press, New-York, 2630 p.

Rafiee, S.E., Sadeghiazad, M. M., 2015, 3D numerical analysis on the effect of rounding off edge radius on thermal separation inside a vortex tube, Int. J. Heat Tech., 33 (1), 83–90.

Ranque, G. J., 1933. Experiments on expansion in a vortex with simultaneous exhaust of hot air and cold air. J. Phys. Rad. 4 (7), 112–114.

Schlichting, H., Gersten, K., 1999. Boundary-layer theory, 8th Edition. Springer, Berlin, 811 p.

Shamsoddini, R., Abolpour, B., 2018, A geometric model for a vortex tube based on numerical analysis to reduce the effect of nozzle number, Int. J. Refrigeration, 94, 49–58.

Thompson, P. A., 1988. Compressible-fluid dynamics, 3rd Edition. RPI, Troy, 665 p.

White, F. M., 2003. Fluid mechanics, 5th Edition. McGraw Hill, New-York, 866 p.

Xue, Y., Arjomandi, M., Kelso, R., 2010. A critical review of temperature separation in a vortex tube. Exp. Therm. Fluid Sci. 34 (8), 1367 – 1374.

Zhang, B., Guo, X., 2018. Prospective applications of Ranque-Hilsch vortex tubes to sustainable energy utilization and energy efficiency improvement with energy and mass separation. Renewable Sustainable Energy Rev. 89, 135–150.

Zhang, B., Guo, X., Yang, Z., 2016. Analysis on the fluid flow in vortex tube with vortex periodical oscillation characteristics. Int. J. Heat Mass Transfer 103, 1166 – 1175.

Manuscript ID: 78
DOI: 10.18462/iir.icr.2019.0078

Numerical simulation of water solidification in square ice trays: A simplified enthalpic formulation

Felipe R. LOYOLA, Lucas Z. BARBOZA, Christian J.L. HERMES

POLO Labs, Department of Mechanical Engineering, Federal University of Santa Catarina
88040900 Florianópolis, SC, Brazil, hermes@polo.ufsc.br

ABSTRACT

Water solidification inside hermetic two-dimensional rectangular cavities is modelled and simulated in the present work aiming at household ice making. A new enthalpic formulation based upon the first-principles of mass, energy and momentum conservation together with the definition of the liquid fraction was developed to track the mushy region interface, where the phase change takes place. The proposed methodology was verified against a classic analytical solution for phase change problems with the numerical predictions following closely the theoretical trends. Comparisons with benchmarks solutions of the open literature are also reported. Finally, household ice making through ice trays is assessed to figure out not only the time required for complete solidification, but also the amount of energy removed in the process. It was observed an increase in the production rate by 35% when a plastic tray is replaced by a thin metal one.

Keywords: Water solidification, Enthalpy method, Two-dimensional model, Finite-volume approach

1. INTRODUCTION

Household consumption of edible ice has been a steadily-increasing market, initiated in ancient civilizations and boosted by the popularization of refrigerators in the first half of the twentieth century. Nowadays, cyclic ice making is a must for any modern refrigerator, among other almost mandatory features such as water dispensing, automatic defrosting and adjustable shelves. For instance, the number of patents filled yearly all over the globe increased from ~100 in 1980 to ~1400 in 2018, revealing a growing interest in the ice making market, whose value is projected to exceed US$ 5.9 billion by 2023 (IMARC, 2018).

An automatic ice maker is a device installed inside a low temperature compartment of a household refrigerator and directly connected to a water source in order to continuously produce ice to be stored in a container placed inside the freezer compartment. In general, automatic ice making relies on filling the tray with water, cooling and freezing water into ice, and harvesting the ice from the tray (Yashar and Park, 2011). A typical ice production rate for a household appliance is only 3 lb per day, although a substantial amount of energy is demanded if compared to the total amount consumed by the refrigerator itself (Meier and Martinez, 1996).

The present work is part of a major project aimed at increasing the ice production rates in household refrigerators with minimal penalty in terms of energy consumption. This paper is particularly focused on modelling the processes of cooling and freezing water into ice, as they respond for half of the total energy consumption of an automatic ice maker, whereas the other half is needed for ice harvesting and storage (Haider et al., 1996).

Water solidification involves complex phenomena that make its mathematical modelling a nontrivial activity. Fig. 1 depicts the evolution of the water temperature over time during the solidification, where the parameter ϕ represents the liquid fraction with ϕ=1 standing for liquid water and ϕ=0 for solid ice, so that $0<\phi<1$ in the two-phase region, i.e. the mushy zone comprised of ice particles in a liquid water suspension (Egolf and Manz, 1994). Starting from a temperature $T_0>T_m$, where T_m is the datum freezing/melting temperature of water (0°C), a certain volume of water can be cooled down to a temperature $T_s \leq T_m$, the onset of solidification. The temperature difference $T_m - T_s$ is called supercooling degree. As the phase change always takes place at T_m, an abrupt temperature change

occurs as the energy removed to freeze water into ice is released to the remaining liquid thus increasing its temperature from T_s to T_m. The solidification process goes on until the volume is fulfilled with ice. Thereafter, the temperature is allowed to decrease below the freezing point (see Fig. 1).

Modelling of the solidification process shall account for all of these phenomena, becoming complex and time-consuming (Alexiades and Solomon, 1993). The present work brings about a simplified mathematical formulation for the water solidification process, which has been developed by means of an enthalpic method based on the first-principles of mass, momentum and energy conservation, heeding the volume expansion during the solidification process as $\rho_{ice}<\rho_{water}$.

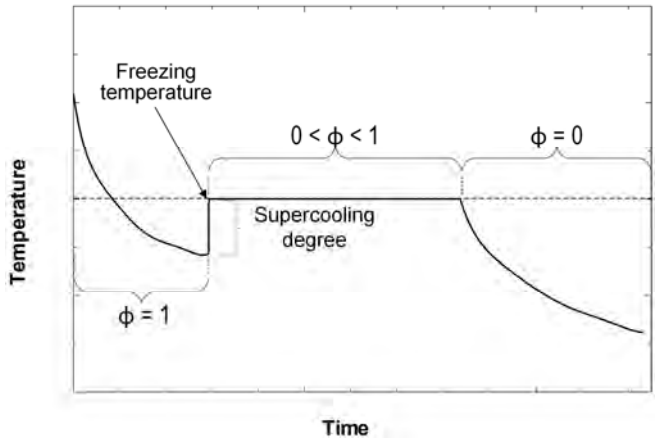

Figure 1: Representation of the water solidification process over time

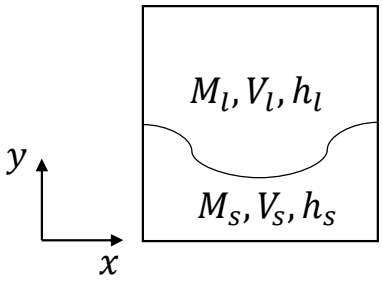

Figure 2: Schematic of a two-phase elementary control-volume

2. MATHEMATICAL MODELLING

The mathematical model was developed for a two-dimensional cartesian domain with dimensions L (horizontal) and H (vertical) that emulate one cavity of an ice tray. The model relies on the first-principles of mass, momentum and energy conservation, whose governing equations are, respectively, as follows:

$$\frac{\partial \rho}{\partial t} + \frac{\partial (\rho u)}{\partial x} + \frac{\partial (\rho v)}{\partial y} = 0 \qquad \text{Eq. (1)}$$

$$\frac{\partial (\rho u)}{\partial t} + \frac{\partial (\rho u u)}{\partial x} + \frac{\partial (\rho v u)}{\partial y} = -\frac{\partial P}{\partial x} + \mu \nabla^2 u \qquad \text{Eq. (2)}$$

$$\frac{\partial (\rho v)}{\partial t} + \frac{\partial (\rho u v)}{\partial x} + \frac{\partial (\rho v v)}{\partial y} = -\frac{\partial P}{\partial y} + \mu \nabla^2 v + g(\rho - \rho_0) \qquad \text{Eq. (3)}$$

$$\frac{\partial (\rho h)}{\partial t} + \frac{\partial (\rho u h)}{\partial x} + \frac{\partial (\rho v h)}{\partial y} = k \nabla^2 T \qquad \text{Eq. (4)}$$

where $\nabla^2() = \partial^2()/\partial x^2 + \partial^2()/\partial y^2$ stands for the Laplace operator, ρ (kg/m³) is the density, k (W/mK) is the thermal conductivity, c_p (J/kgK) is the specific heat, μ (Pa-s) is the viscosity, and h (J/kg) is the specific enthalpy of water or ice, identified by means of the subscripts l or s, respectively. In addition, as mass is conserved for each elementary volume in the domain, it follows that $M = M_l + M_s$. Thus, one can define the liquid fraction, depicted in Fig. 1, as follows:

$$\phi = V_l / V \qquad \text{Eq. (5)}$$

where V and V_l denote the total volume and the part occupied by the liquid phase, respectively, ϕ=1 recalls liquid water and ϕ=0 solid ice, whereas $0<\phi<1$ describes the enthalpy of the two-phase region, where the velocity field was considered null. Therefore, the total enthalpy of fluid in eq. (4) can be written as follows:

$$\rho h = \rho_l h_l \phi + \rho_s h_s (1 - \phi) \qquad \text{Eq. (6)}$$

Hence, the mushy zone can be used to treat the discontinuities of the thermophysical properties (k, c_p) from solid to liquid phases by means of a linear interpolation that depends on the volume fraction of liquid. Moreover, the enthalpy, which varies with the temperature, is computed from

$$h - h_{ref} = c_p(T - T_{ref}) \qquad \text{Eq. (7)}$$

For the liquid phase, the reference values are h_{ref} = 0 J/kg, and T_{ref} = 0°C. Similarly, for the solid phase, h_{ref} = -λ and T_{ref} = 0°C, where λ is the latent heat of solidification of water substance. Substituting eq. (7) into equation (4) with T=0°C for the mushy-zone, the following evolving equation for the liquid fraction can be obtained:

$$\frac{\partial \phi}{\partial t} = \frac{k}{\rho \lambda} \nabla^2 T \qquad \text{Eq. (8)}$$

It is worth noting that eq. (8) comes out with the ice-water interface in the Eulerian domain.

3. NUMERICS

The model was solved by means of the finite-volume method, as described in Patankar (1980), whereas the physical domain was discretized following a uniform Cartesian grid. The resulting linear systems were solved line-by-line through the so-called TDMA (Tridiagonal Matrix Algorithm), while the velocity-pressure coupling was performed by the PRIME method (Maliska and Raithby, 1984). An implicit 2nd-order scheme (Crank-Nicolson) was adopted for the time integration. For instance, for a finite-control volume of size ΔV during a finite time interval Δt, the discretization of eq. (8) yields:

$$\phi \approx \phi^0 + \frac{\Delta t}{\rho \Delta V \lambda} \sum_{faces} \left(\frac{q + q^0}{2} \right) \qquad \text{Eq. (9)}$$

where the symbol q denotes the heat flux across the control surfaces of the finite-control volume (W/m²), whereas the superscript “0” is the heat flux at the previous time-step.

Fig. 3 depicts the typical two-dimensional finite control volume of the discretized domain. While the discretized control volume represents the central node P, the nodes E, W, N, and S stand for the neighbour control volumes at east, west, north, and south, respectively. The indices e, w, n, and s indicate the control surfaces at the east, west, north, and south, respectively, while Δx and Δy represent the control volume dimensions and δx_e, δx_w, δy_n, and δy_s stand for the distances from P to the neighbour nodes.

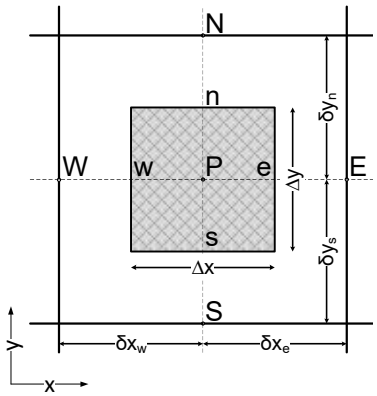

Figure 3: Typical control volume of the discretized domain

The final discretized equation is as follows:

$$A_p \phi_P = A_e \phi_E + A_w \phi_W + A_n \phi_N + A_s \phi_S + B \qquad \text{Eq. (10)}$$

where the source term was linearized, and the power-law interpolation scheme was adopted (Patankar, 1980). A staggered grid for the velocity computation was also applied so that the pressure field is evaluated at the nodes, while the velocities are evaluated at the control surfaces. Fig. 4 depicts the solution algorithm. One can note that the solution is achieved not only by settling the mushy zone location ($0<\phi<1$), but also by correcting the sensible heat in each control volume in the cases when the latent heat removed at a given time is exceeded to comply with the principle of energy conservation. Finally, the simulation ends when the whole domain is fulfilled with ice.

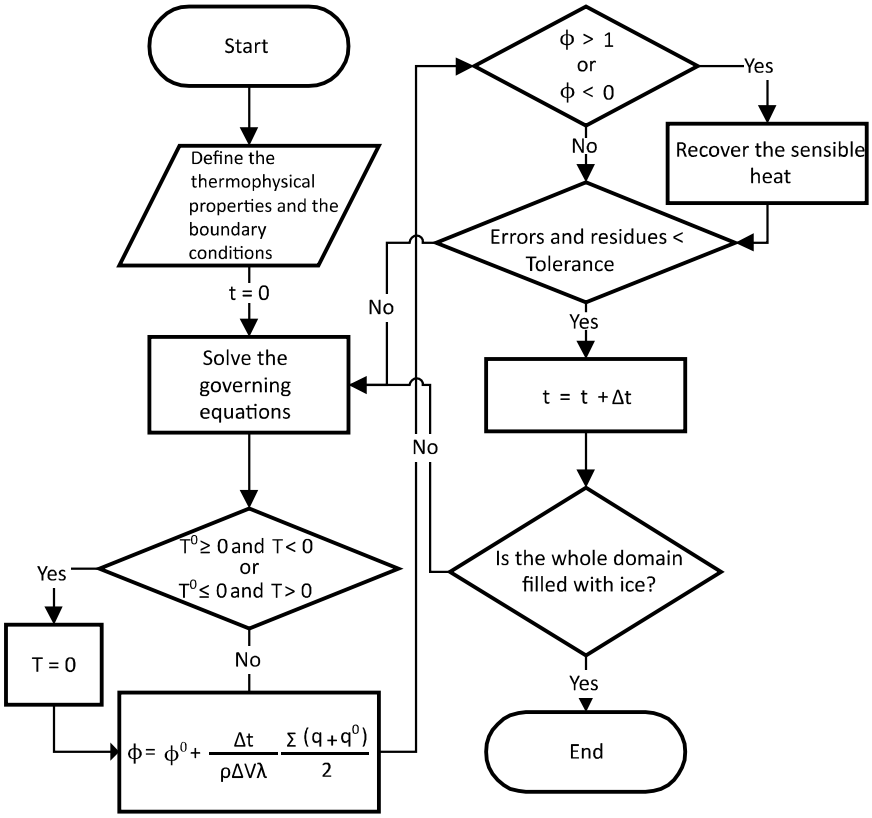

Figure 4: Information flow diagram of the solution algorithm

4. VERIFICATION

The model was coded in *Python* language and verified against analytical solutions for water solidification. In this case, a rectangular cavity of dimensions L and H was considered, with adiabatic side walls and prescribed temperature conditions at the top and bottom walls, as depicted in Fig. 5. Therefore, the heat conduction becomes one-dimensional (from bottom to top), thus representing a typical Stefan problem, whose analytical solution is well-known (Lock, 1990). A uniform Cartesian mesh with 20 x 100 (horizontal x vertical) control-volumes was employed with a time-step of 0.1 seconds.

First, the analysis considered that both phases have the same thermophysical properties of solid at 0°C (see Table 1) and also that there is no fluid displacement, so that the solidification is curtailed to a pure conduction problem. In addition, it was assumed that the water is initially at 0°C (see runs 1 and 2 in Table 2). Later, the initial temperature of the water was changed, so that sensible heat must also be removed until the complete water solidification is achieved (see runs 3 and 4 in Table 2). Finally, simulations with different k and c_p were conducted (see run 5 in Table 2), albeit the density was still considered that of ice.

The results, summarized in Table 2, were compared against the algebraic solutions proposed by Neumann for the Stefan problem, where $Ph=\lambda/c_{p,s}(T_i-T_b)$ denotes the phase-change number (Baehr and Stephan, 2006).

Table 1. Thermophysical properties of water substance

Property	Liquid (@20°C)	Solid (@0°C)	Unity
c_p	4.20	1.96	kJ/kgK
ρ	999.8	917	kg/m³
k	0.72	2.22	W/m²K
λ	335		kJ/kg

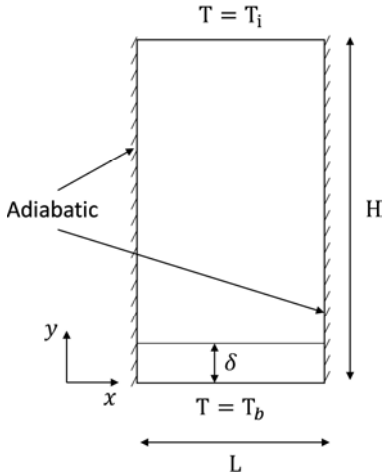

Figure 5: Physical domain and boundary conditions

One can see in Table 2 that the model is able to predict the time evolution of the solidification interface with errors within the 1% thresholds in comparison to the analytical solution. In addition, the amount of energy removed from the physical domain, which corresponds to the sum of the sensible and latent heat, in W/m, was compared with model predictions following closely the experimental trends, with a maximum error of 3% as can be seen in Fig. 6.

Further simulations were carried out by means of the commercial CFD software Star CCM+ (2018) under the same running conditions, but using a mesh with hundreds of thousands of control volumes instead of the 2,000 nodes adopted in the case of the tailormade model. The results are depicted in Table 2, where one can see that the commercial CFD simulations presented errors of the same order of magnitude than those found using the simplified model for the solidification interface, albeit figures below 0.1% were found for the total energy removed from the domain, which is due to the fine mesh adopted in this case.

Table 2. Summary of the verification results

Run	T_b	T_i	Different c_p and k	Ph	Error δ (%) (new model)	Error Q (%) (new model)	Error δ (%) (comm. CFD)	Error Q (%) (comm. CFD)
1	-10	0	No	17.09	0.5	0.39	0.5	0.09
2	-1	0	No	170.9	0.5	0.51	-	-
3	-10	10	No	8.54	0.5	0.31	-	-
4	-1	1	No	85.4	0.5	0.49	-	-
5	-10	10	Yes	8.54	0.9	2.93	0.2	0.01

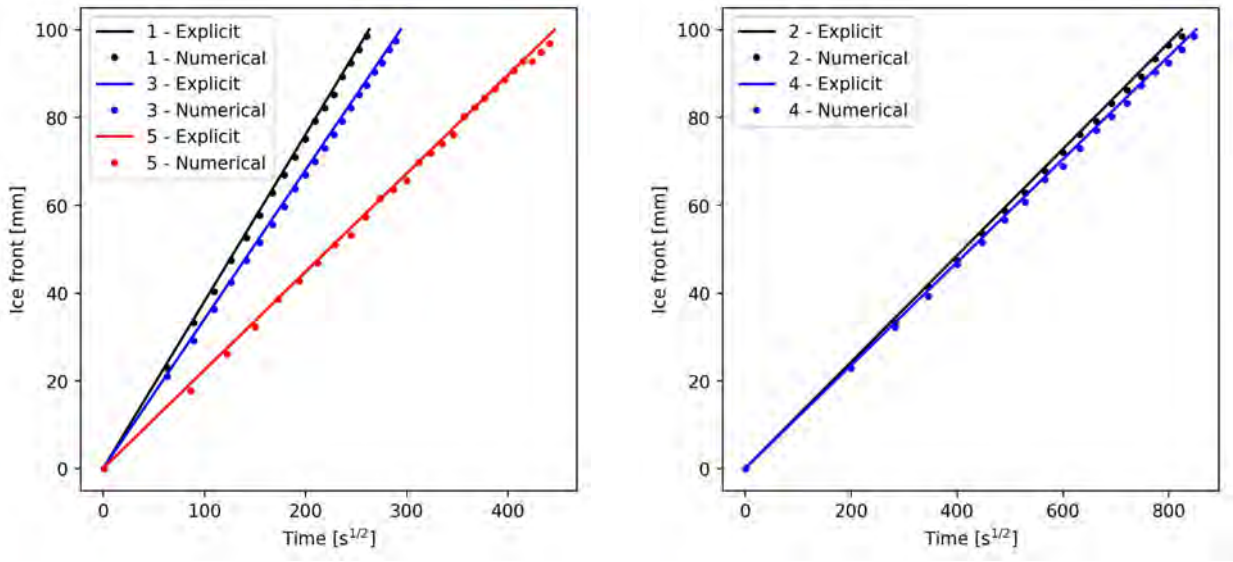

(a) (b)

Figure 6: Phase change interface position over time: (a) runs 1, 3, and 5; (b) runs 2 and 4

A second verification exercise was carried out to evaluate the model suitability to simulate the natural convection in the liquid phase due to the density and temperature variation, and also the volume expansion during the solidification process. The work of Michalek and Kowaleski (2003) was taken as a benchmark, where a square cavity with size of 38 mm filled with water at 278 K was initially exposed to a temperature of 283 K at the left wall and 273 K at the right one, whereas the north and south boundaries were considered adiabatic. The solution (velocity and temperature fields) of the steady-state simulation was used as the initial conditions for the unsteady-state simulations where the temperature of the left border was suddenly decreased from 283 K to 263 K, thus promoting solidification. It is worth to mention that polynomial fittings were used to account not only for the water density variation with the temperature, but also the thermal conductivity, although the heat capacity was considered uniform for both phases. In this case, a Rayleigh number of 2.5×10^7 and a phase-change number of 8 were adopted.

Fig. 7 depicts the temperature fields at three different times: 100, 500, and 1000 s. The 1st column illustrates the results from Michalek and Kowaleski (2003), who used a grid with 145k nodes; the 2nd the results from the tailormade model (40k nodes), and the 3rd the results from the simulation with the commercial CFD software (41k nodes). It can be noticed that the results obtained by the simplified model (present work) agreed well with the benchmark results. Comparing the simulations results with Michałek and Kowaleski (2003) data and the results from the commercial CFD software, the temperature field and ice shape (black band in the temperature scale) agreed quite well.

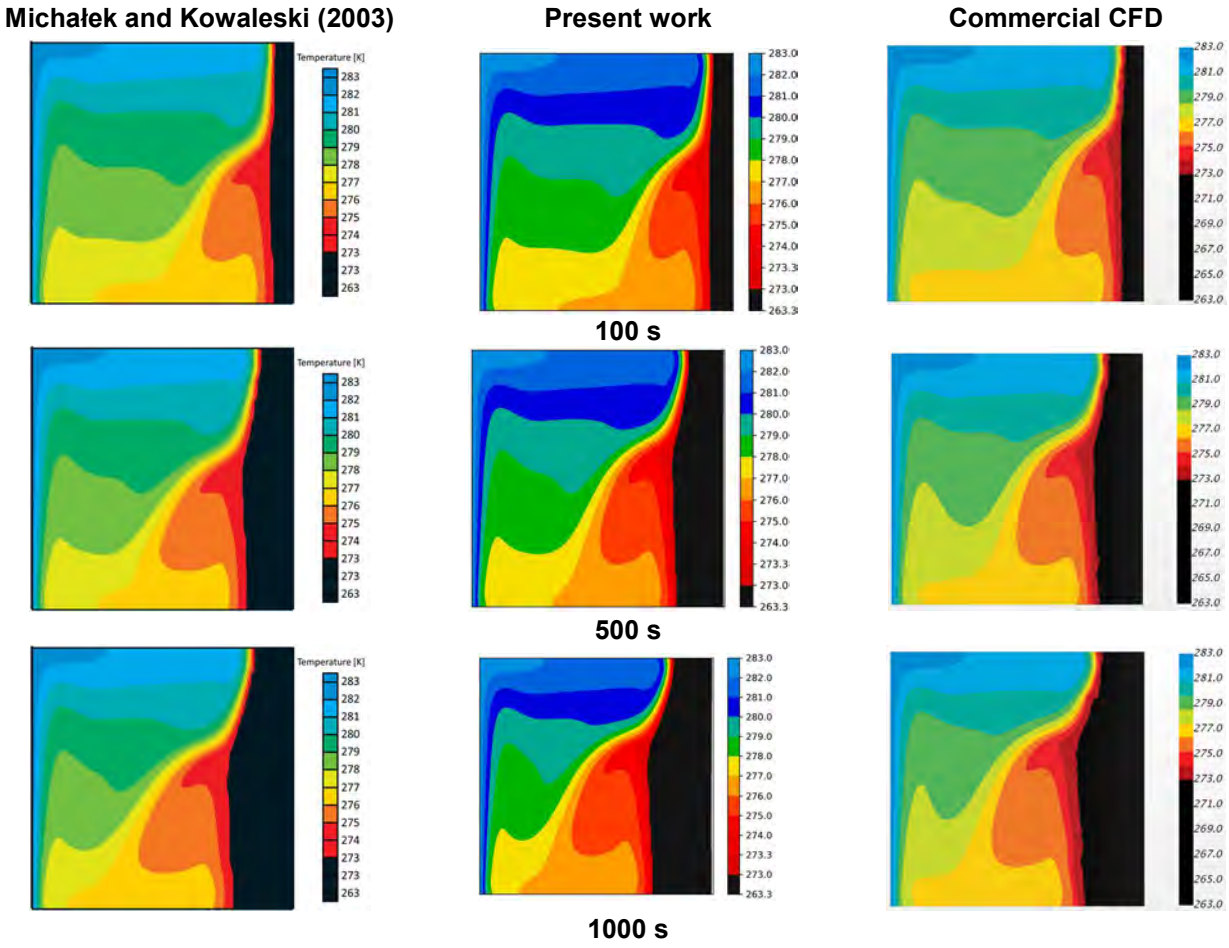

Figure 7: Temperature fields at various time steps obtained by Michalek and Kowaleski (1st column), the present model (2nd column) and commercial CFD package (3rd column)

5. RESULTS

After the verification exercise, the proposed model was employed to simulate the ice production in similar conditions to those found in household refrigerators, where a plastic ice tray is exposed to air at low temperatures inside the freezer compartment. The main aim of these simulations is at estimating the time for total water solidification as well as the overall energy removed from the two-dimensional cavity, in kJ/m. A square Cartesian domain with size of 40 mm was employed, being exposed to a prescribed temperature at the bottom surface, and convection heat transfer at the side and top surfaces, as depicted in Fig. 8. The initial and boundary conditions are as follows:

- $T = T_{initial}$, $x \in [0, L]$, $t = 0$
- $\partial T/\partial x = h(T - T_\infty)$, for $x = 0$ and $x = L$, $y \in [0, L]$, $t > 0$
- $T = T_b$, for $x \in [0, L]$, $y = 0$, $t > 0$
- $\partial T/\partial y = h(T - T_\infty)$, for $x \in [0, L]$, $y = L$, $t > 0$

Table 3 presents the running conditions in terms of the parameters h and T_∞. In addition, the amount of energy removed is calculated until the whole cavity is fulfilled with ice. In all runs, an initial water temperature at 20°C, a mesh with 200 x 200 control volumes, and a time-step of 10^{-2} s were adopted. One can note that the boundary conditions of runs *D* and *E* are more aggressive, where run *A* presents the smoothest condition. Table 3 also emphasizes the difference in solidification time obtained for the cases when the natural convection in the water phase is neglected in comparison to the cases when it is considered as the fluid flow favours the energy dispersion until the water is at the freezing temperature. The difference observed in the total energy removed is due to the temperature distribution of the ice phase at the end of each simulation. Finally, run *E* shows an increase in the production rate by 35% when a plastic tray is replaced by a thin metal one.

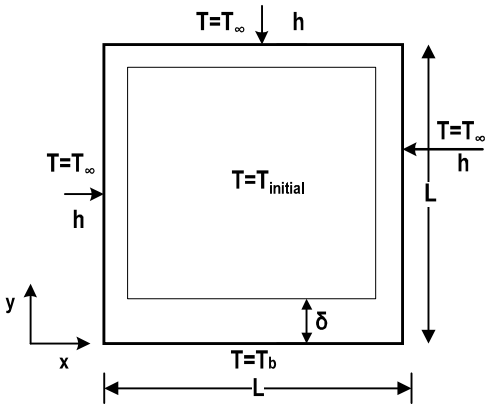

Figure 8: Representation of the physical domain of an ice cube

The computed solidification times are in accordance with experimental evidences obtained in a real ice tray by means of a purpose-built experimental rig constructed at POLO Labs. For an ice cube with 1.4 g of water subjected to different running conditions, such as air flow rates (5 to 25 m³/h) and inlet temperatures (-5 to -25 °C), solidification times ranging from 40 minutes to almost 5 hours were observed, depending not only on the running condition but also on the location of the ice cube in the ice tray (Berno et al., 2019). Such results will be released in a further publication.

Table 3. Boundary conditions and simulation results

Run	T_b (°C)	T_∞ (°C)	h ($W \cdot m^{-2} \cdot K^{-1}$)	Thermal Resistance ($W^{-1} \cdot m^2 \cdot K$)	Conduction Only		Convection	
					Q ($kJ \cdot m^{-1}$)	t (h)	Q ($kJ \cdot m^{-1}$)	t (h)
A	-20	-6	2	0	1175.6	4.99	1097.3	2.08
B	-20	-6	10	0	1156.7	4.40	1036.0	1.83
C	-32	-18	2	0	1199.4	3.13	1168.2	1.54
D	-32	-18	10	0	1178.9	2.55	1098.6	1.29
E	-32	-18	10	0.006	-	-	990.7	1.99

6. FINAL REMARKS

A novel, simplified enthalpic formulation based on the principle of energy conservation was brought about to come out with an evolving equation to track the mushy-zone region over time. The methodology was used together with an Eulerian finite-volume method to solve the heat and fluid flow during water solidification process. The model predictions agreed quite well not only with the classic Neumann solution for Stefan solidification problems but also with a benchmark solution found in the literature. Further simulations aimed at water solidification in ice trays within low temperature compartments of household refrigerator were carried out. The results pointed out that the natural convection inside the cavity reduces the time needed to complete solidification by 50% as the fluid flow intensifies the heat transfer homogenizing the water temperature around 0°C. In addition, in the cases where a plastic tray is used, introducing an extra thermal resistance to the boundary walls, the ice production rate is decreased by 35% if compared with a thin metal tray.

ACKNOWLEDGEMENTS

This work was performed under the auspices of the Brazilian Government funding agencies CAPES, CNPq and EMBRAPII. The authors duly acknowledge the technical and financial support from Whirlpool Corporation, particularly to Messrs. G. Massochin and A. Marcon (Joinville, SC, Brazil), and M. Mezavilla and R. Rodrigues Jr. (Benton Harbor, MI, USA).

REFERENCES

Alexiades, V., Solomon, A.D., 1993. Mathematical Modeling of Melting and Freezing Processes. CRC Press, Boca Raton, 340p.

Baehr, H.D., Stephen, K., 2006. Heat andMass Transfer. Springer, 688p.

Berno, G.M., Loyola, F.R., Hermes, C.J.L., 2019. Experimental evaluation of the solidification time in ice trays, POLO Internal Report, Federal U. of Santa Catarina, Florianópolis, SC, Brazil

Egolf, P.W., Manz H., 1994. Theory and modeling of phase change materials with and without mushy regions. Int. J. Heat Mass Transfer 37(18), 2917-2924.

Haider, I., Feng, H., and Radermacher, R., 1996. Experimental Results of a Household Automatic Icemaker in a Refrigerator/Freezer. ASHRAE Trans.: Symposia, SA-96-7-3, pp. 541-545.

IMARC, 2018. Ice Maker Market: Global Industry Trends, Share, Size, Growth, Opportunity and Forecast 2018-2023, IMARC Group Archive, Report ID 4592317

Kowalewski, T.A., Rebow, M., 1999. Freezing of water in a differentially heated cubic cavity. Int. J. Comput. Fluid Dyn., 11(3-4), 193-210.

Lock, G.S.H., 2005. The Growth and Decay of Ice (Studies in Polar Research). Cambridge University Press, Cambridge, 456p.

Maliska, C.R., Raithby, G.D., 1984. A method for computing three-dimensional flows using non-orthogonal boundary-fitted co-ordinates. Int. J. Numer. Methods Fluids 4(6), 519-537.

Meier, A. and Martinez, M., 1996. Energy Use of Ice Making in Domestic Refrigerators. ASHRAE Transactions, Vol., 102, Pr. 2, pp. 1071-1076.

Michałek, T., Kowalewski, T.A., 2003. Simulations of the water freezing process–numerical benchmarks. Task Quarterly, 7(3), 389-408.

Patankar, S, 1980. Numerical Heat Transfer and Fluid Flow. Hemisphere, New York, 214p.

STAR-CCM+, 2018. STAR-CCM+ user guide version 13.04, Siemens PLM Software.

Yashar, D.A., Park, K.-J., 2011. Energy Consumption of Automatic Ice Makers Installed in Domestic Refrigerators. NIST Technical Note 1697, Gaithersburg, MD, USA

Manuscript ID: 116
DOI:10.18462/iir.icr.2019.0116

Simulations of saturated vapor pressures of single refrigerants by COSMO-RS

Shuai Pan[(b)], Haifeng Yang[(b)], Danping Ma[(b)], Yingxia Qi*[(a)], Hua zhang [(a)]

[(a)] Department of Energy and Power Engineering, University of Shanghai for Science and Technology, Shanghai, 200093, China, Email: qipeggy@126.com

[(b)] Graduate school of Energy and Power Engineering, University of Shanghai for Science and Technology, Shanghai, 200093, China

ABSTRACT

Based on the theory of Conductor like Screening Model for Realistic Solvents (COSMO-RS), the gas-liquid phase equilibrium thermal properties of single refrigerants were simulated. COSMO-RS can predict the thermophysical properties of the fluids only needing the structural information of a single molecule. It is the most effective way of connecting the quantum mechanics and thermodynamics at present. But the relative errors are larger, reaching 10-20% when it is applied for calculations of refrigerants. For this reason, the influences of various parameters on the saturated vapor pressure are studied. The results show that the scale factor of surface area can improve the accuracy of calculation. Under the optimum scale factor of surface area, the simulated values are consistent with the experimental data provided by NIST. The relative error are within ±2%. On this basis, the relation of the size factor with type of refrigerant is analyzed. Finally, the Antoine equations of saturated vapor pressure for various types of refrigerants are fitted.

Keywords: COSMO-RS, refrigerator, vapor-liquid equilibrium data, molecular surface area, scale factor.

1. INTRODUCTION

The research on the thermophysical properties of refrigerant alternatives is one of the hot topics in the international thermodynamics field. However, the theoretical and experimental work on the thermophysical properties of refrigerant alternatives at the micro-scale or molecular level has not been thoroughly explored and studied.

The quantum chemically based Conductor-like Screening Model for Realistic Solvation (COSMO-RS) has developed to a widely accepted and independent novel approach to the simulation of fluid phase equilibria since its first publication in 1995 and developed continuously [1]. Milocco et al [2] predicted the vapor–liquid equilibria (VLE) behavior of some pure refrigerants using DMol3/COSMO-RS calculations with satisfactory quality. COSMO-RS was reasonably accurate for predicting the vapor pressures of aminosilicones [3] and the formaldehyde–water–methanol ternary system [4], and the VLE data of formaldehyde-containing aqueous solutions [5], the LLE data of the ternary systems consisting of {hexane plus benzene plus deep eutectic solvent} [6].

But COSMO-RS has been continuously under the reparameterization in order to improve the prediction accuracy such as for halocarbon thermodynamics [7, 8, 9]. Through making the electrostatic interaction parameter temperature-dependent and the strength of hydrogen-bonding interactions changed with different types of functional groups, the accuracy in VLE predictions is improved from 7.25% and 2.83% to 6.54% and 2.57% in total pressure and vapor phase composition[10]. To predict the vapor liquid equilibrium (VLE) of ethanol and 1,1,1,2,3,3,3-heptafluoropropane (HFC-227ea), Klamt [11, 12] has used two ways of fine tuning towards an improved description of the experimental data. The first way is by adjustment of the fluorine-fluorine vdW interaction parameter τ (F, F) and the second way another is by adjustment polarization charge densities as the unavoidable fluorine–fluorine contacts have an unusually small vdW interaction due to the low polarizability of fluorine. But none of them led to a strong improvement. Reinisch [13] predicted the mutual solubilities of dipropylene glycol dimethyl ether (DPGDME) and water by COSMO-RS by rescaling of the molecular surface areas. Fine tuning of the water and DPGDME

areas led to a good quantitative agreement with experimental data with a maximum deviation of 5.4 mass percent points. To obtain much better agreement with experimental data, Han [14] re-optimized the adjustable parameters of misfit energy constant, hydrogen bond coefficient and effective contact surface area in the popular COSMO-RS to predict the activity coefficients, solubility and vapor-liquid equilibrium (VLE) for the systems containing ionic liquids (ILs).
In this paper, to increase the prediction accuracy of the saturated vapor pressures of single refrigerants by COSMO-RS method, the parameterizations were performed by rescaling of the molecular surface area. Through the fine turning of the scale factor of the COSMO molecular surface area, the mean relative deviation (MRD) is decreased to 2.0 % in the pressure range of 1 to 20 bar. Also, the VLE data for new unknown refrigerants are estimated by re-parameterized COSMO-RS model.

2. COSMO-RS METHODOLOGY

2.1. COSMO-RS equations

COSMO-RS is a "Conductor-like Screening Model for Real Solvents", which is an efficient variant of dielectric continuum solvation methods, and its extension to "Real Solvents", which is a statistical thermodynamics approach based on the results of quantum chemical COSMO calculations [1]. The detailed description of the COSMO-RS theory has been given in Klamt's articles [7–9]. Here, only a short introduction of the basic features are presented for the understanding this article.
COSMO-RS is a two-step procedure. In the first step, quantum chemical calculations are performed for the molecules interested. In these calculations, the continuum solvation model COSMO is applied to simulate a virtual conductor environment for the molecule. In this paper, the quantum chemical calculations for all refrigerate molecules was performed in the ADF module using density functional theory (DFT) with the Beck-Perdew (GGA:BP) exchange-correlation functional, the scalar relativistic ZORA Hamiltoninan, a triple zeta polarized (TZP) small core basis set and an integration accuracy of 6, the Klamt radii, and the Delly surface area for atoms were used [15]. Then the screening charge density σ on the molecular surface was obtained for the molecule.
In the second step, the statistical thermodynamics of the molecular interactions, the screening charge density is used for the quantification of the interaction energy of pair-wise interacting surface segments with regard to the most important molecular interaction modes, i.e. electrostatics and hydrogen bonding. The less specific van der Waals (vdW) interactions or dispersive interactions are taken into account in a more approximate way by element specific dispersion coefficients.
The intermolecular interaction energy is composed of misfit energy, hydrogen bond energy, and van der Waals energy as follows:

$$E_{misfit}(\sigma,\sigma') = \alpha a_{eff} e_{misfit}(\sigma,\sigma') = a_{eff}\frac{\alpha'}{2}(\sigma+\sigma')^2 \quad (1)$$

$$E_{hb}(\sigma,\sigma') = a_{eff} e_{hb}(\sigma,\sigma') = a_{eff} c_{hb} min\{0, min(0,\sigma_{don}+\sigma_{hb}) max(0,\sigma_{acc}-\sigma_{hb})\} \quad (2)$$

$$E_{vdw}(\sigma,\sigma') = a_{eff}(\tau_{vdw}+\tau'_{vdw}) \quad (3)$$

$$E(\sigma,\sigma') = a_{eff} e(\sigma,\sigma') = E_{misfit} + E_{hb} + E_{vdw} \quad (4)$$

where σ and σ' are the screening charge densities of two different segments; a_{eff}, α', c_{hb}, and σ_{hb} are the effective contact surface area, the misfit energy constant, the hydrogen bond coefficient, and the cutoff of hydrogen bond, respectively; σ_{don} and σ_{acc} represent the screening charge densities of hydrogen bond donor and acceptor segments, respectively; and τ_{vdW} is the element-specific adjustable vdW interaction parameter [15].
The ensemble of surface pieces characterizing a liquid system S is described by the distribution function $p_s(\sigma)$, which describes the amount of surface in the ensemble having a screening charge density between σ and $\sigma+d\sigma$, also named "σ-profile". If our liquid system is a pure liquid X, then the σ-profile $p_s(\sigma)$ of the system is identical with the σ-profile $p^{X_i}(\sigma)$ of the pure compound X_i, $p_s(\sigma) = p^{X_i}(\sigma)$. The normalized σ-profile $p^{X_i}(\sigma)$ of the pure compound X_i is calculated by Eq. (5):

$$p_s'(\sigma) = P^{X_i}(\sigma) = \frac{A^{X_i}(\sigma)}{A^{X_i}} = \frac{n_i(\sigma)}{n_i} \quad (5)$$

Where $A^{Xi}(\sigma)$ is the total surface area of all segments with the charge density of σ, A^{Xi} is the total surface area of the compound X_i, $n_i(\sigma)$ is the number of the segments with the charge density of σ, and n_i is the total number of segments of the compound X_i.
The chemical potential of a surface segment with a screening charge density σ in an ensemble having a normalized σ–profile can be described by Eq. (6)

$$\mu_S(\sigma) = -RT \ln\left\{\int d\sigma' p_s'(\sigma') exp\left(\frac{\mu_S(\sigma') - E(\sigma,\sigma')}{RT}\right)\right\} \quad (6)$$

where $\mu_S(\sigma)$ the so-called σ potential, is the chemical potential of an average molecular contact area of size a_{eff} in the ensemble S at temperature T.
The chemical potential of a solute X in the ensemble S is defined by Eq. (7):

$$\mu_S^X = \mu_{res\,S}^X + \mu_{comb\,S}^X = \int p^X(\sigma)\mu_S(\sigma)d\sigma + \mu_{combS}^X \quad (7)$$

Where the combinatorial contribution, which arises from the different shapes and sizes of the molecules, is given by Eq. (8).

$$\mu_{combS}^X = -\lambda RT \ln A_S \quad (8)$$

where A_S is the average molecular surface area as defined in Eq. (9) and λ is a parameter to be adjusted.

$$A_s = \sum_{i\in s} x^i A^{X_i} \quad (9)$$

The chemical potential of the compound X in the ideal gas is given by Eq. (10).

$$\mu_{Gas}^X = E_{Gas}^X - E_{COSMO}^X - E_{vdw}^X + \omega n_{ring}^X + \eta_{gas} \quad (10)$$

Here, E_{Gas}^X and E_{COSMO}^X are the quantum chemical total energies of the molecule X in the gas phase and in the conductor, respectively, and E_{vdw}^X is the vdW energy of the molecule X, which we addressed to the conductor reference state. The adjustable universal parameter η_{gas} connects the reference states in solution and in the gas phase. n_{ring}^X is the number of ring atoms in compound X for ring compounds with and ω an adjustable parameter.

$$\eta_{\mathrm{gas}} = \eta \mathrm{RT} \quad (11)$$

Where η is a adjustable parameter.
The vapor pressure p^X of a pure compound X at arbitrary temperature is estimated via Eq. (12)

$$p^X = exp\left(\frac{\mu_X^X - \mu_{Gas}^X}{RT}\right) \quad (12)$$

where μ_{Gas}^X is the chemical potential of compound X in the gas phase and μ_X^X is the chemical potential of the compound in itself (Eq. 7).
In this study, the values of COSMO-RS parameters are shown in Table 1 and Table 2.

Table 1 General COSMO-RS parameters

rav	0.4	Å	aeff	6.94	Å2
α'	1510	(kcal/mol) Å2/e2	λ	0.13	
fcorr	2.802		ω	-0.212	kcal/mol

chb	8850	(kcal/mol) Å2/e2	η	-9.65	
σhb	0.00854	e/ Å2	chorth	0.816	

Table 2 Element specific parameters

Atom dispersion constants			
element	τvdw kJ/mol/Å2	element	τvdw kJ/mol/Å2
C	-0.0356	O	-0.0333
N	-0.0224	F	-0.026

Theoretically, no input data is needed except for molecular structure in the COSMO-RS theory, it was found that the calculation accuracy would be very poor if none of saturated vapor pressure data P-T is inputted. In the ADF COSMO-RS package, it is optional to input a P-T data. It was certified that the different input points had no effects on the calculation results. In this paper, the standard boiling point data of substance is taken as an input data in the P-T calculations.

2.2. Compound specific fine-tuning

At present, the relative errors of the predictions are larger, reaching 10-20% when it is applied to calculate the properties of refrigerants [11, 12, 13]. This may be because the constant parameters contained in the COSMO-RS equations are fitted using atmospheric liquids rather than high pressure liquids [16], but the refrigerants are turning liquids usually at high pressures. For this reason, the influences of the constant parameters on the calculated saturated vapor pressures are studied. Through a large number of trial-and-error calculations, it was concluded that the change of molecular COSMO surface area can improve greatly the accuracy of the predictions.

The scale factor s of the molecular COSMO surface area As is an input data in the ADF COSMO-RS package. The default value is 1.0. The scaling factor of molecular COSMO surface area for molecule interested were adjusted manually starting from 1 with adding or reducing by trial and error until that the relative error was not decreased any more.

3. SIMULATION RESULTS AND DISCUSSIONS

3.1. Refinement of scale factor of molecular COSMO surface area.

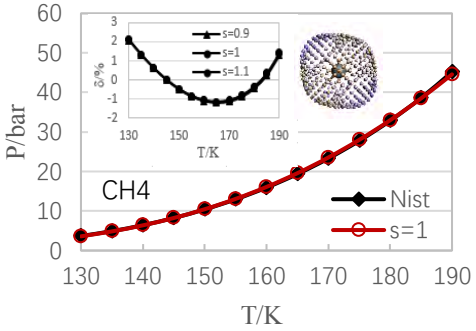

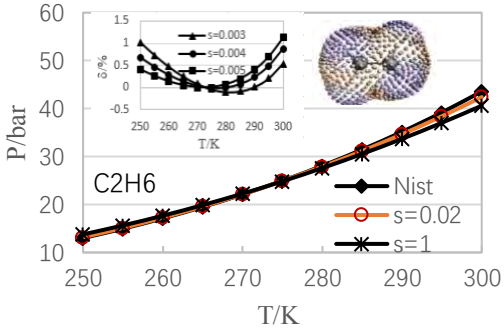

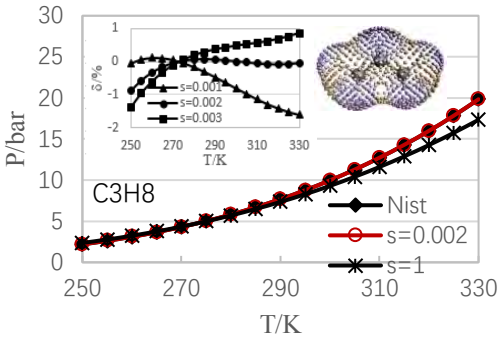
C3H8
Nist
s=0.002
s=1
P/bar
T/K

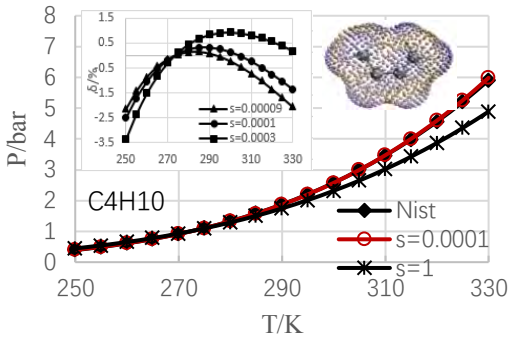
C4H10
Nist
s=0.0001
s=1
P/bar
T/K

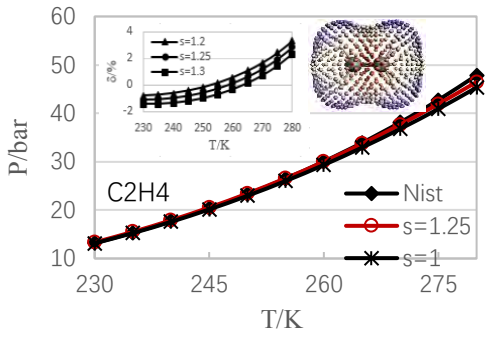
C2H4
Nist
s=1.25
s=1
P/bar
T/K

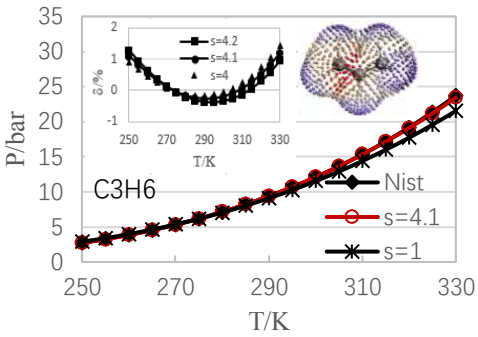
C3H6
Nist
s=4.1
s=1
P/bar
T/K

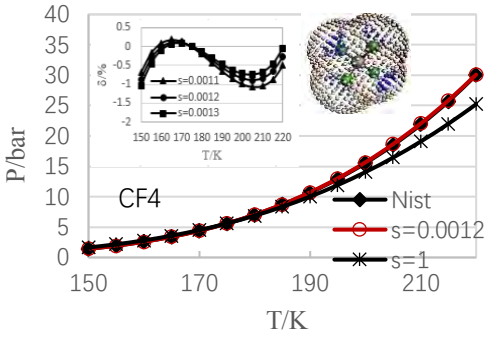
CF4
Nist
s=0.0012
s=1
P/bar
T/K

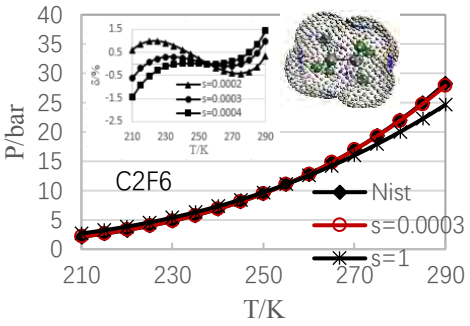
C2F6
Nist
s=0.0003
s=1
P/bar
T/K

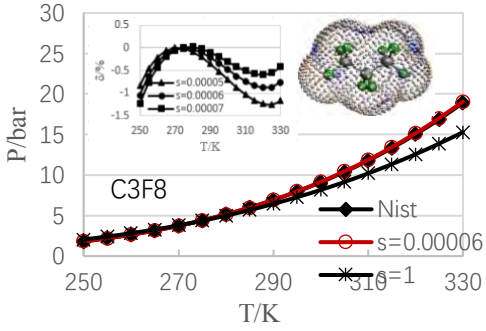
C3F8
Nist
s=0.00006
s=1
P/bar
T/K

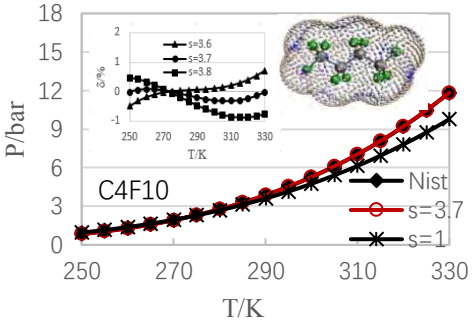
C4F10
Nist
s=3.7
s=1
P/bar
T/K

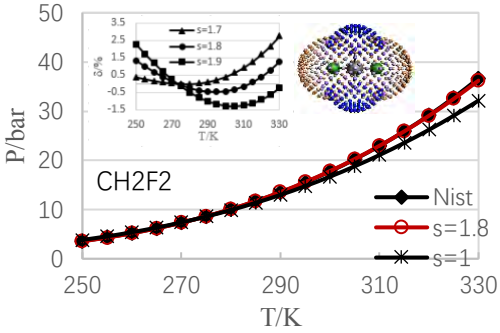
CH2F2
Nist
s=1.8
s=1
P/bar
T/K

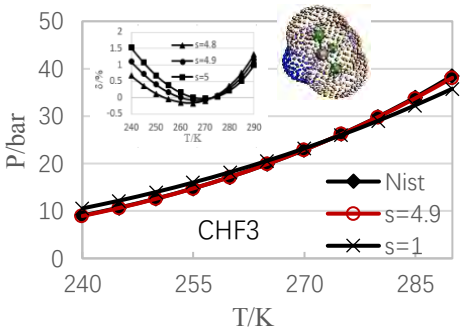
CHF3
Nist
s=4.9
s=1
P/bar
T/K

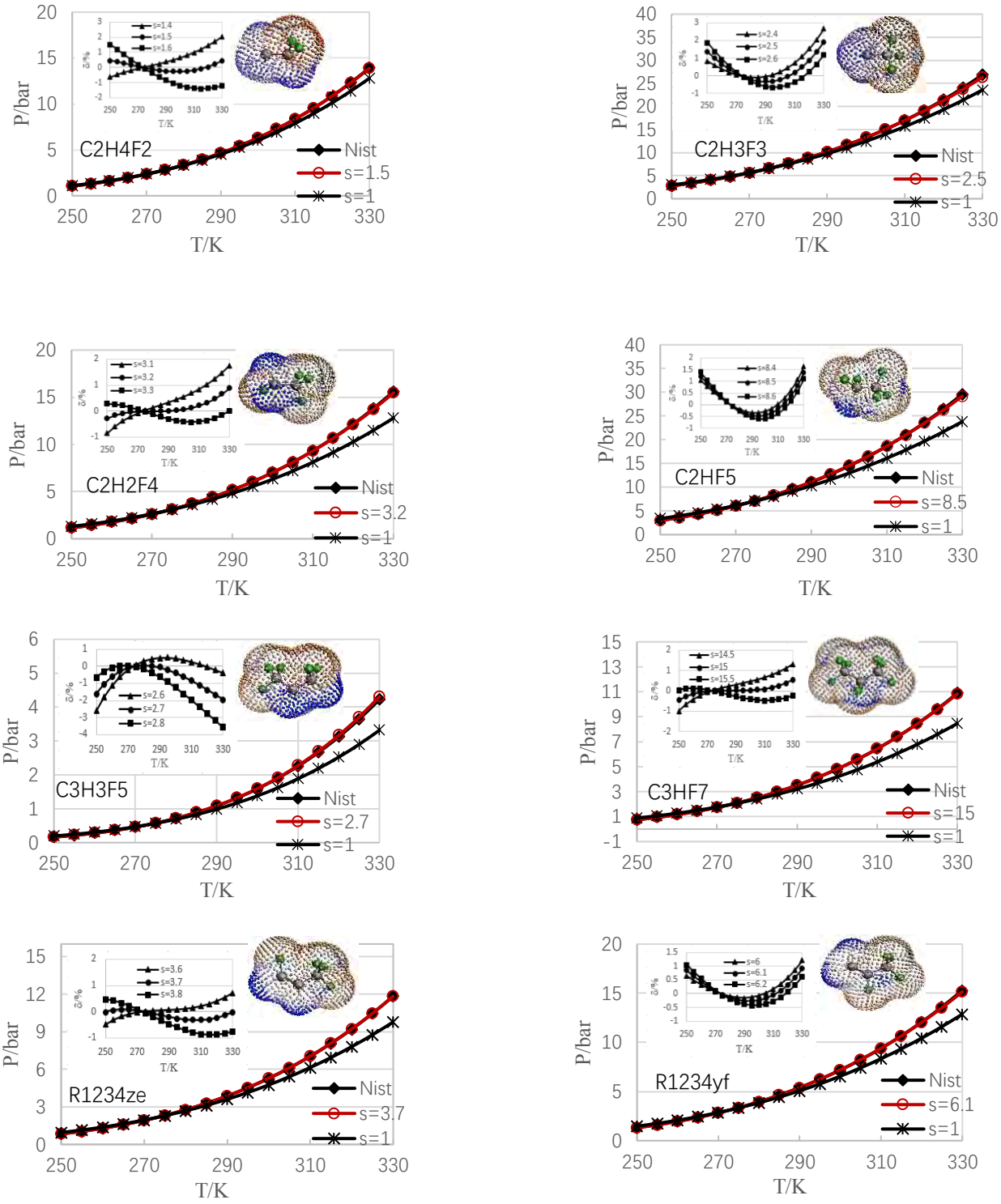

Fig.1 Comparisons of simulated and NIST saturated pressure curves.

In Fig. 1, the simulated saturated pressure curves and NIST dada are presented with the relative deviations between them shown in scaled figures. It was known that the errors were larger in the higher temperature range while smaller in the low temperature. This is because COSMO-RS is valid in the range far from the critical temperature. With the change of the scale factor s of the molecular COSMO surface area, the simulated curves were approaching to the NIST curves and consistent with the NIST curves finally.

In this study, one VLE data at 273.15K was selected as an input data, therefore, the curve would pass through this selected point. It was found when the simulated curve passed through another point on the NIST curve with the change of s, the whole curve would be coincided with the NIST curve. Therefore, if we know the two experimental data, we could predict the whole VLE data by the

method described above.
The optimum scale factors of surface area for different refrigerants are summarized in Table 3. The mean absolute relative error between the simulation results and NIST [16] values in the Table 3 is calculated using the scoring function in Eq. (13):

$$\delta = \frac{100}{\mathrm{n}} \sum_{\mathrm{i}=1}^{\mathrm{n}} \frac{|P_{i,exp} - P_{i,calc}|}{P_{i,exp}} \qquad (13)$$

where PS is the simulated pressure value and PN is the pressure value in NIST. The pressure ranges are from 0.1 to 2.0 Mpa.

Table 3 Optimum scale factors of molecular COSMO surface area for refrigerants.

Type	Name	s	Name	s
Alkanes	CH4(R50)	0.8	C2H6(R170)	0.0045
	C3H8(R290)	0.0008	C4H10(R600)	0.0002
HFs	CF4 (R14)	0.001	C2F6 (R116)	0.00015
	C3F8 (R218)	0.00004	C4F10	0.00002
Alkenes	C2H4(R1150)	1.25	C3H6(R1270)	3.5
HFCs	CH2F2(R32)	1.7	CHF3 (R23)	4.4
	C2H4F2 (R152a)	1.5	C2H3F3 (R143a)	2.2
	C2H2F4 (R134a)	3.3	C2HF5 (R125)	7.9
	C3H3F5 (R245fa)	3.1	C3HF7 (R227ea)	15.5
HFOs	C3H2F4(R1234ze)	3.7	C3H2F4(R1234yf)	5.9

It can be seen from Table 3 that for alkanes and perfluoroalkane, the scale factors are much smaller than 1 and decreased with the increase of the number of C atoms.
For all the alkenes, fluothane (HFC) and fluorene (HFO), the scale factors are greater than 1, and increased with the increase of F atom number.
The scale factors for isomers are different, such as R1234ze and R1234yf.
The s is determined by two factors: the symmetrical characteristic of the molecular structure and the distribution of the surface-screened-charges on the molecular surface. If the molecular structure is more spherically symmetric, s is larger. This is because that for the longer molecule, the contact area between the molecules is limited by the smallest cross section. If the surface-screened-charges on the molecular surface has a stronger polarity, s is larger. Obviously, stronger polarity results in a larger contact area between molecules. In fact, the scale factor s is related with the parameter of the effective contact area aeff. Conclusively, aeff should not be constant for different molecules.
Antoine equation with three parameters is the most commonly used equation of saturated vapor pressure in engineering. It takes the form of:

$$\lg p = a_1 - \frac{a_2}{T + a_3} \qquad (14)$$

The three parameters of Antoine equation for refrigerators studied are fitted according to the simulated data and shown in Table 4.

Table 4 Parameters of Antoine equation fitted according to simulation values and deviations

	a1	a2	a3	Deviations ω
CH4(R50)	6.84	1000.90	270.50	2.13×10-5
C2H6(R170)	7.50	1810.31	273.14	9.84×10-10
C3H8(R290)	7.56	2268.24	273.15	3.41×10-10
C4H10(R600)	7.93	2786.56	273.15	2.01×10-10
CF4 (R14)	7.64	1438.26	273.15	4.83×10-10

C2F6 (R116)	7.79	1960.14	273.15	2.10×10-10
C3F8 (R218)	7.98	2419.72	273.15	2.51×10-10
C4F10	8.10	2814.30	273.15	2.28×10-10
C2H4(R1150)	6.88	1409.72	257.11	4.94×10-5
C3H6(R1270)	6.77	1773.65	242.51	7.70×10-5
CH2F2(R32)	7.62	1886.54	241.04	3.25×10-4
CHF3 (R23)	7.53	1631.28	246.70	1.28×10-4
C2H4F2 (R152a)	7.30	2059.59	238.79	9.51×10-5
C2H3F3 (R143a)	7.04	1794.25	238.63	1.54×10-4
C2H2F4 (R134a)	7.42	2064.65	238.70	1.13×10-4
C2HF5 (R125)	7.26	1831.57	239.20	1.90×10-4
C3H3F5 (R245fa)	7.98	2610.72	239.16	3.38×10-5
C3HF7 (R227ea)	7.23	2103.33	237.35	6.32×10-5
C3H2F4(R1234ze)	7.32	2118.92	239.40	7.95×105
C3H2F4(R1234yf)	6.95	1919.58	236.96	8.34×10-5

3.2. Prediction of saturated vapor pressures.

CH2=CH-CF3(R1243zf), C3F6 and CF3CH=CHCF3 (R1336mzz(Z)) are new kind of refrigerators. But their saturated vapor pressure data are very few. The saturated vapor pressures of them were predicted by COSMO-RS based on the two known experimental data as shown in Fig. 2, 3 and 4. The data are summarized in Table 5. From Fig. 2, it is seen that with the change of s, the curve passes through the other experimental data with the one as the input data in the COSMO-RS calculations. According to the discussions above, when the curve was passing through the two data, the rest part of the curve was coincidence with the experimental data, and the relative errors are ensured within ±0.2%. Similarly, the curves in Fig. 3 and Fig.4 were consistent with the experimental ones. The relative error was ±2.0% for C3H3F3 (R1243zf), while it was within ±5.0% for C3F6, because s of latter couldn't be decreased further more.

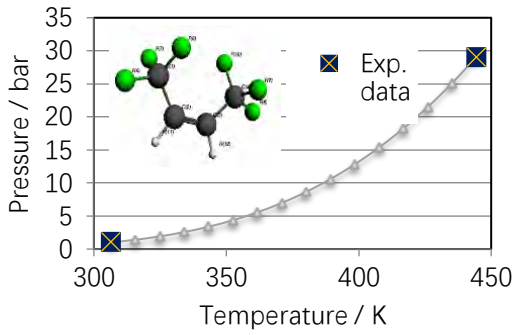

Fig. 2 The Saturated vapor pressures of C4H2F6 (R1336mzz(Z)) predicted by COSMO-RS.

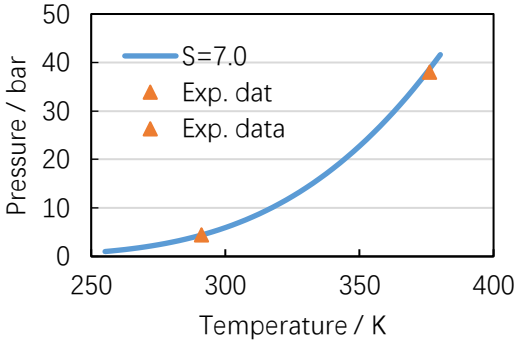

Fig. 3 The Saturated vapor pressures of C3H3F3 (R1243zf) predicted by COSMO-RS.

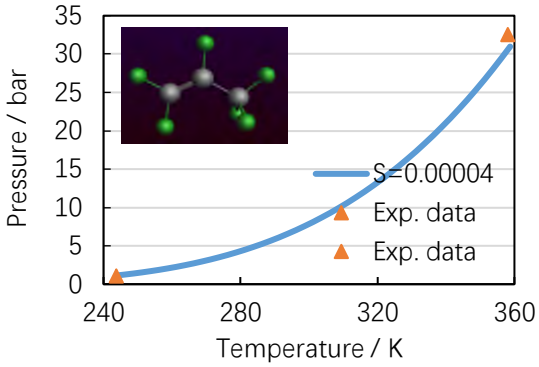

Fig. 4 The saturated vapor pressures of C3F6 predicted by COSMO-RS.

Table 5 Saturated vapor pressures of C4H2F6, C3F6 and C3H3F3 predicted by COSMO-RS.

C4H2F6 CF3CH=CHCF3 (R1336mzz(Z)) S=7.4		C3F6 S=0.00004		C3H3F3 CH2=CH-CF3 (R1243zf) S=7.0	
T / K	Ps / bar	T / K	Ps / bar	T / K	Ps / bar
306.55	1.013	243.75	1.134	255.15	1.013
313.445	1.302	248.75	1.395	260.15	1.281
320.34	1.652	253.75	1.703	265.15	1.603
327.235	2.073	258.75	2.062	270.15	1.985
334.13	2.572	263.75	2.480	275.15	2.435
341.025	3.160	268.75	2.961	280.15	2.961
347.92	3.845	273.75	3.513	285.15	3.570
354.815	4.637	278.75	4.142	290.15	4.272
361.71	5.546	283.75	4.856	291.15	4.424
368.605	6.582	288.75	5.662	295.15	5.073
375.5	7.754	293.75	6.566	300.15	5.983
382.395	9.072	298.75	7.578	305.15	7.009
389.29	10.545	303.75	8.704	310.15	8.160
396.185	12.182	308.75	9.954	315.15	9.445
403.08	13.993	313.75	11.333	320.15	10.871
409.975	15.986	318.75	12.852	325.15	12.447
416.87	18.168	323.75	14.517	330.15	14.180
423.765	20.549	328.75	16.338	335.15	16.077
430.66	23.133	333.75	18.322	340.15	18.146
437.555	25.930	338.75	20.477	345.15	20.394
444.45	28.944	343.75	22.813	350.15	22.827

In conclusion, the prediction accuracy of COSMO-RS is higher for HFCs and HFOs within ± 0.5 while

is lower for HCs and Olefins within ± 1.0% with change of scale factor of molecular surface area.

4. CONCLUSIONS

In this paper, the properties of vapor-liquid equilibria of pure refrigerants are studied by COSMO-RS model, the accuracy of prediction is improved by change of scale factor. Compared to the data provided by NIST, the mean absolute relative errors for alkanes (HCs), alkenes (HOs) and Perfluoroalkanes (FCs), Perfluoroolefines (FOs) are not more than 1.0%, for hydrofluorocarbons (HFCs and HFOs) are smaller than 0.5%. For alkanes and perfluoroalkane, the scale factors are much smaller than 1 and decreased with the increase of the number of C atoms. For all the alkenes, fluothane (HFC) and fluorene (HFO), the scale factors are greater than 1, and increased with the increase of F atom number. The scale factors for isomers are different, such as R1234ze and R1234yf.

As the result, the vapor-liquid equilibrium curves of new single refrigerants was predicted by COSMO-RS method based on the molecular structure and the two experimental vapor-liquid data. The maximum relative errors are ensured within ±2.0 % in the range of 0.1- 2.0 Mpa.

REFERENCES

[1]. Klamt A, Schuurmann G, 1993. COSMO: a new approach to dielectric screening in solvents with explicit expressions for the screening energy and its gradient. Journal of the Chemical Society, 5: 799-805.

[2]. Oliver Milocco, Maurizio Fermeglia, Sabrina Pricl, 2002. Prediction of thermophysical properties of alternative refrigerants by computational chemistry. Fluid Phase Equilibria, 199: 15-21 .

[3]. Robert J. Perry,Sarah E. Genovese, Rachel L. Farnum, Irina Spiry, Thomas M. Perry, Michael J. O'Brien, Hong-bin Xie, De-Li Chen, Robert M. Enick, J. Karl Johnson, Saeed S. Alshahrani, 2014. A Combined Experimental and Computational Study on Selected Physical Properties of Aminosilicones. Industrial and Engineering Chemistry Research. 53(4): 1334-1341.

[4]. Huihong Liu, Zhenmin Bai, Yansheng Liu, Xuqiang Guo, Yu'e Fu, Xinyun Pu, 2016. Interpretation and prediction of the vapor–liquid equilibrium of formaldehyde–water–methanol ternary system by the conductor-like screening model for real solvents. Fluid Phase Equilibria.. 429: 233-241

[5]. Zhenmin Bai, Huihong Liu, Yansheng Liu, Lehuan Wu, 2016. Prediction of the vapor liquid equilibrium of chemical reactive systems containing formaldehyde using the COSMO-RS method [J]. Fluid Phase Equilibria. 415: 125-133.

[6]. Rodriguez NR; Gerlach T; Scheepers D; Kroon MC; Smirnova I, 2017. Experimental determination of the LLE data of systems consisting of {hexane plus benzene plus deep eutectic solvent} and prediction using the Conductor-like Screening Model for Real Solvents. Journal of Chemical Thermodynamics. 104: 128-137.

[7]. Klamt A, Eckert F., 2000. COSMO-RS: a novel and efficient method for the a priori prediction of thermophysical data of liquids. Fluid Phase Equilibria. 172(1):43-72.

[8]. Eckert, F., Klamt, A., 2003, Prediction of halocarbon thermodynamics with COSMO-RS. *Fluid Phase Equilibria* 210 (2003) 117–141.

[9]. Klamt A, Eckert F., 2004. Prediction of halocarbon thermodynamics with COSMO-RS. Fluid Phase Equilibria. 217:53-57.

[10]. Hsieh, C., Sandler, S.I., Lin, S., 2010, Improvements of COSMO-SAC for vapor–liquid and liquid–liquid equilibrium predictions. *Fluid Phase Equilibria* 297 (2010) 90–97.

[11]. Klamt A, Jonas V, Burger T, et al, 1998. Refinement and Parameterization of COSMO-RS. The Journal of Physical Chemistry. 102(26) : 5074-5085 .

[12].Klamt, A., Eckert, F., 2007 Prediction, fine tuning, and temperature extrapolation of a vapor liquid equilibrium using COSMOtherm. *Fluid Phase Equilibria.*. 260:83–189.

[13]. Jens Reinisch, Andreas Klamt, Frank Eckert, Michael Diedenhofen, 2011. Prediction of the temperature dependence of a polyether–water mixture using COSMOtherm. Fluid Phase Equilibria 310 (2011) 7–10.

[14]. Jingli Han; Chengna Dai; Gangqiang Yu; Zhigang Lei, 2018.Parameterization of COSMO-RS model for ionic liquids. Green Energy & Environment.

[15]. ADF COSMO-RS Manual. ADF Program System 2012. Scientific Computing & Modelling NV.

Andreas Klamt, 2016. COSMO-RS for aqueous solvation and interfaces. Fluid Phase Equilibria. 407 : 152-158.

[16]. Lemmon, E. W.; Huber M. L.; McLinden M. O. NIST Standard Reference Database 23: Reference Fluid Thermodynamic and Transport Properties, Ver, 9.1.

Manuscript ID: 134
DOI: 10.18462/iir.icr.2019.0134

Performance of R466A, a non-flammable replacement for R410A, in unitary air-conditioning and transport refrigeration

Kenneth SCHULTZ[(a)]

[(a)] Ingersoll Rand
La Crosse, 54601, USA, kschultz@trane.com

ABSTRACT

Use of R410A is under pressure to be phased down because of its high global warming potential (GWP). The recent Kigali amendment to the Montreal Protocol will necessitate the phase-out of R410A used in air conditioning systems in developed countries by the late 2020s. This will require the industry to begin using R410A replacements by the middle 2020s.
A new refrigerant blend, R466A, has been developed with thermodynamic properties that potentially make it a design compatible replacement for R410A. This new blend offers a 65 % reduction in GWP over R410A and is non-flammable (Class A1). Tests of a blend with very similar composition in an air-cooled chiller and a residential split system heat pump were previously reported. Performance generally met expectations with capacity being slightly lower than R410A and efficiency being slightly lower than R410A in the chiller test and similar to positive in the heat pump test, all consistent with the thermodynamic properties of R466A relative R410A.
This paper presents the results of tests run with R410A (as baseline) and R466A in another residential heat pump and a transport refrigeration unit. Again, performance is generally seen to meet expectations. Capacities ranged from −5 % to +2 % relative to the R410A baselines. Efficiencies ranged from −3 % to +4 % relative to the R410A baselines. These results demonstrate R466A's utility as a lower GWP, design compatible replacement for R410A in a range of HVAC&R equipment. Its classification as non-flammable permits R466A to be used in existing equipment designs, either in new product or as field replacement of reclaimed R410A.
Keywords: Air-Conditioning, Low GWP, R410A, Refrigerated Transport

1. INTRODUCTION

Many low-GWP refrigerant candidates have been evaluated as prospective alternatives to R410A in different types of HVAC&R equipment. These activities began under the Low-GWP Alternative Refrigerants Evaluation Program (AREP) coordinated by the Air Conditioning, Heating and Refrigeration Institute (AHRI, nd). All of the new refrigerants targeted to replace R410A are mildly flammable and are classified as “2L” by ASHRAE Standard 34 (ANSI/ASHRAE, 2016). In AREP I, Schultz and Kujak (2012) and Schultz (2014a,b) tested seven R410A-like replacement candidates. Most of the candidates tested did not perfectly match the capacity of R410A, but were within close proximity (±10 %), and displayed similar, generally positive, efficiencies.
To more closely match R410A characteristics, Hughes and Leck (2015) proposed the blend DR-5A, now designated R454B (68.9 %wt R32 / 31.1 %wt R1234yf), as a replacement for R410A. Kujak and Schultz (2015, 2016) introduced DR-55, now designated R452B (67 %wt R32 / 7 %wt R125 / 26 %wt R1234yf), further optimizing performance, but at the expense of higher GWP matching that of R32. Schultz and Kujak (2016) and Schultz (2016) reported the results of tests on a 14 kW (4 RT) rooftop heat pump and 4 RT residential split heat pump that demonstrate R452B and R454B to be design compatible substitutes for R410A in unitary equipment.
More recently, Schultz and Nayak (2017) reported the results of drop-in tests with R452B and R32 conducted on a 100 RT air-cooled water chiller with R410A as baseline. Chillers typically operate at lower evaporator temperatures and therefore larger temperature lifts than unitary equipment. The chiller’s brazed plate evaporator and microchannel condenser were new components relative to the previous unitary equipment tests with round-tube plate-fin heat exchangers. The cooling capacities with R452B were within 0 to −5 % of R410A while achieving efficiencies 0 to +5 % higher over a

range of ambient temperatures and leaving chilled water temperatures. R32 produced 5 % to 13 % greater capacities than R410A while achieving efficiencies of −2 % to +6 %. Compressor discharge temperatures (CDT) with R452B ran only 3 K to 6 K higher than with R410A. CDTs with R32 ran significantly hotter than R410A by 14 K to 27 K. These results again demonstrate the design compatible nature of R452B to R410A-based equipment.

Schultz and Nayak (2017) also reported the performance of a new refrigerant labelled simply “Exp” at the time. Exp was a precursor to the new blend now designated as R466A. Schultz and Kujak (2019) elucidated the identity of Exp and added performance measurements of a 10.5 kW (3 RT) residential split-system heat pump run with Exp. Exp was observed to be a design compatible replacement for R410A with capacities similar to R452B. COPs with Exp were −4 % to +3 % higher than for R410A as ambient temperature ranged from 18 °C to 52 °C in the chiller tests. In the tests of the residential unit, capacities with Exp were within −5 % to +1 % of R410A while COPs within −2 % to +4 % over the standard rating heating and cooling conditions. This paper reports performance measurements of another residential split-system heat pump and a transport refrigeration unit run with R410A as a baseline and with R466A. (Results from tests in a 14 kW (4 RT) rooftop unit were planned to be reported here as well, however, the tests were not completed in time to be included in the manuscript.)

2. REFRIGERANT CHARACTERISTICS

Characteristics of Exp and R466A are listed in Table 1, along with R410A, R452B, R454B, and R32. Exp and R466A utilize the flame suppressing CF_3I molecule in place of R1234yf to make non-flammable blends. Exp and R466A differ by only 1 % in R32 and CF3I compositions and so are expected to have essentially identical properties and performance characteristics. All of the alternate refrigerants proposed offer a roughly two-thirds reduction in GWP compared to R410A.

Table 1. Compositions, GWPs, and critical properties

Refrig	Composition (% mass)	GWP_{AR4}	GWP_{AR5}	Class	Tcrit (°C)	Pcrit (MPa)
R410A	R32/R125 (50/50)	2088	1924	A1	71.3	4.90
R32	R32 (100)	675	677	A2L	78.1	5.78
R454B	R32/R1234yf (68.9/31.1)	465	467	A2L	80.9	5.58
R452B	R32/R125/R1234yf (67/7/26)	698	675	A2L	79.7	5.50
Exp	R32/R125/CF_3I (50/11.5/38.5)	740	703	–	83.5	5.90
R466A†	R32/R125/CF_3I (49/11.5/39.5)	734	697	A1†	83.8	5.91

† The designation and safety classification of R466A were provisional at the time this manuscript was written. Addendum u to ASHRAE Standard 34-2016 had been released for public review; final approval was not get granted.

Table 2 lists performance characteristics of each refrigerant in a simple single-stage vapor compression cycle operating between an average condensing temperature of 46.1 °C with 8.3 K of subcooling and an average evaporating temperature of 11.4 °C with 8.3 K of compressor suction superheat. These conditions are typical of a unitary piece of equipment running at the AHRI (2012) Standard 210/240 “A Test” rating conditions (26.7 °C dry-bulb / 19.4 °C wet-bulb indoor return air temperature and 35 °C outdoor ambient temperature). A fixed compressor volumetric displacement is assumed and the isentropic efficiency is taken as 0.7. Exp and R466A are seen to have performance characteristics very similar to R452B, indicating that R466A could be a candidate design compatible replacement for R410A as well.

R466A, R454B, and R452B operate at pressures slightly below those for R410A at the same saturation temperature boundary conditions; R32 operates at slightly higher pressures. The CDTs with R466A, R454B, and R452B are expected to be modestly higher than R410A while those with R32 are significantly higher. R466A, R454B, and R452B have small thermodynamic temperature glides of less than 1.5 K that can be easily accommodated in typical HVAC&R equipment and applications that utilize R410A.

Table 2. Simple thermodynamic cycle simulation results

Refrig	∆CAP*	∆COP*	(Pc/Pe)*	mR*	∆CDT (K)	Glide (K)	ρLiq*
R410A	0	0	1	1	0	0.1	1
R32	+0.077	+0.010	1.005	0.722	15.2	0	0.921
R454B	–0.039	+0.016	1.004	0.790	5.4	1.2	0.946
R452B	–0.030	+0.014	1.003	0.813	4.9	1.1	0.952
Exp	–0.022	+0.009	0.993	1.042	6.9	1.4	1.174
R466A	–0.026	+0.009	0.993	1.049	6.9	1.5	1.183

One obvious difference between R466A and the A2L candidates is its heavier liquid density. R32, R454B, and R452B are all somewhat less dense than R410A because of their higher R32 content. R466A contains a significant amount of CF_3I. The high molar mass of the iodine atom (126.9, atomic number 53) in CF_3I results in a high liquid density for CF_3I and of blends containing CF_3I. As a consequence, the optimum refrigerant charge of R466A in a piece of equipment will likely be noticeably larger than of R410A. The lower liquid densities of R32, R454B, and R452B offer the prospect of reduced charges.

3. RESIDNTIAL SPLIT SYSTEM HEAT PUMP

The residential split-system heat pump tested had a nominal rated cooling capacity of 10.5 kW (3 RT) with a nominal COP of 3.5 (12 EER). The test points were taken from AHRI Standard 210/240 (AHRI, 2012). Tests were run at the A and B cooling mode conditions and at the H1, H2, and H3 heating mode conditions; these points are summarized in Table 3 below. Tests were run with R410A (as baseline) and R466A. The capacity was determined from air-side measurements around the indoor coil. The COP was determined by dividing the capacity by the measured electrical power consumption. These measurements do not depend on knowing refrigerant properties.

Table 3. Conditions for residential unit tests.

Test Description	Air Entering Indoor Heat Exchanger		Air Entering Outdoor Heat Exchanger	
	dry-bulb (°C)	wet-bulb (°C)	dry-bulb (°C)	wet-bulb (°C)
cooling mode: A	26.7	19.4	35	n/a
cooling mode: B			27.8	
heating mode: H1	21.1	(<15.6)	8.3	6.1
heating mode: H2			1.7	0.6
heating mode: H3			−8.3	−9.4

Fig. 1 shows the sensitivity of subcooling, capacity (CAP), and efficiency (COP) to variations in R466A refrigerant charge for the A and B rating conditions (cooling mode). Capacity is seen to be insensitive to charge, though it increases slightly as charge increases. Efficiency is maximum at the lower charge (lower subcooling) level and drops quickly at the highest charge and corresponding subcooling. In this case, the liquid level in the condenser displaces area for condensing resulting in elevated condensing pressure and saturation temperature, degrading the efficiency.

The ratios of the capacities and efficiencies (COPs) obtained with R466A relative to R410A are shown in Fig. 2. In the cooling mode tests, the capacity with R466A was within 2 % of that with R410A. The efficiency essentially with R466A match that with R410A, except when overcharged. In the heating mode tests, capacity with R466A was generally within 2 % of that with R410A. A bit of extra charge improved capacity at the two colder ambient temperatures. Efficiency with R466A tended to be within ±2 % of that with R410A. These results are consistent within expectations based on thermodynamic properties along with experimental repeatability and measurement uncertainties. The middle charge of 4.5 kg of R466A appears to be a reasonable compromise to achieve good performance over the full range of operating conditions.

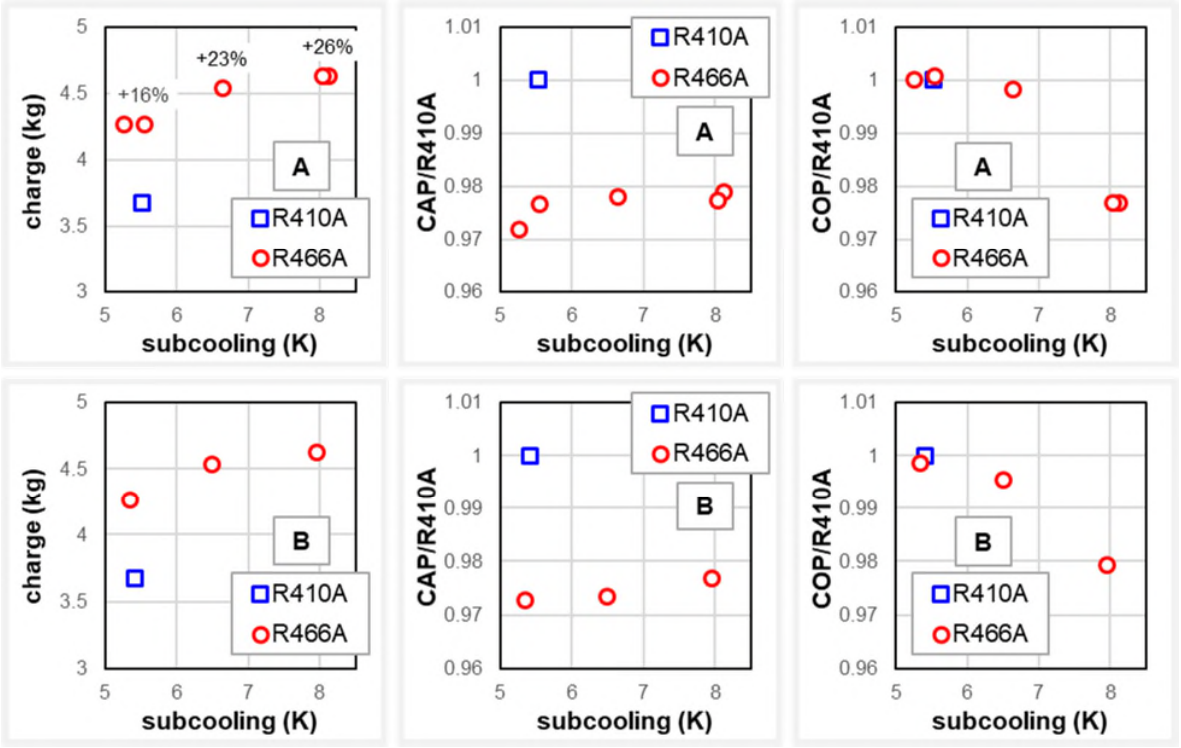

Figure 1. Residential unit capacity (CAP), efficiency (COP), and subcooling as a function of refrigerant charge when operated at the "A" and "B" cooling rating conditions.

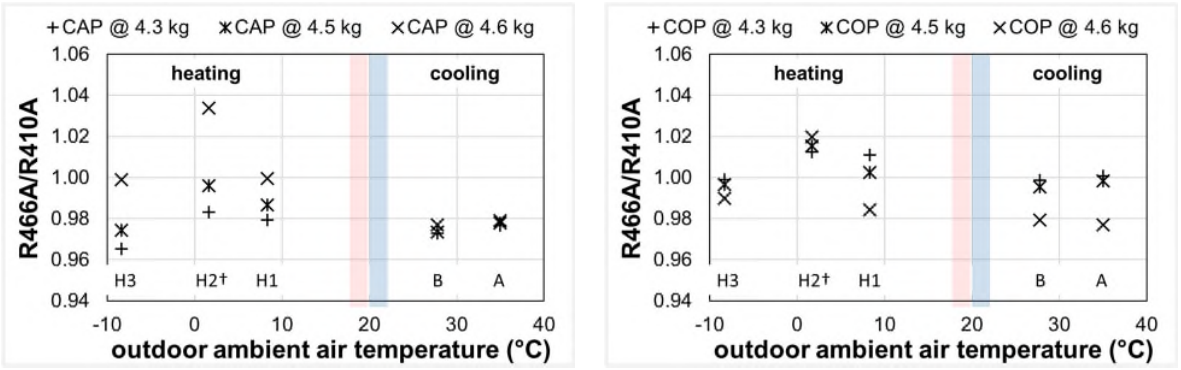

Figure 2. Residential unit capacity and efficiency versus outdoor air temperature. Left) Capacity (CAP). Right) Efficiency (COP). † Note: Frost accumulates during the H2 test. Performance is determined as a time-weighted average over several periodic frost/defrost cycles.

Pressures with R466A entering the condenser (compressor discharge) and leaving the evaporator (compressor suction) were both observed to be slightly lower than with R410A, consistent with expectations based on thermodynamic properties. The corresponding refrigerant saturation temperatures, shown in Fig. 3, were slightly higher in both the condenser and the evaporator with R466A than with R410A.

In condensing mode (whether the outdoor coil in cooling mode or the indoor coil in heating mode), the leaving liquid refrigerant temperature with R466A was closer to the entering air temperature by 1.5 K to 3 K than with R410A. This advantage was partially offset by subcooling with R466A (with middle charge of 4.5 kg) being about 1 K larger than with R410A. In addition, the refrigerant circulation rate with R466A was 3 % to 8 % higher than with R410A, consistent with thermodynamic properties. This resulted in a larger pressure drop through the condenser, forcing the entering (discharge) pressure to be increased in order to push the higher mass flow rate, despite the closer

temperature approach at the outlet. R466A's small thermodynamic temperature glide also adds to the increased pressure drop effect. Modest design changes to the condenser could alleviate the impact of the increased mass flow rate and small temperature glide. On the other hand, R466A's thermodynamic temperature glide, which offsets the pressure drop "glide", appears to have benefited performance in the evaporator. This is consistent with observations made in a rooftop unit run with R452B and R454B (Schultz, 2016), which have thermodynamic temperature glides similar to R466A.

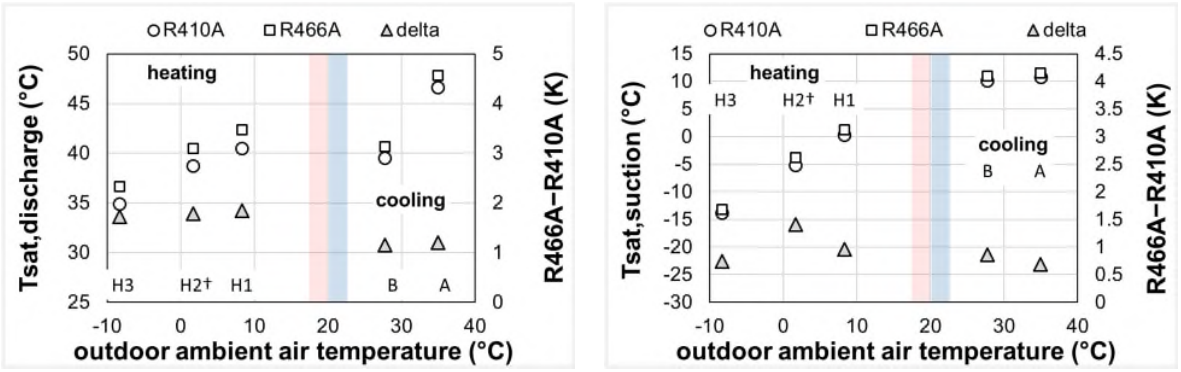

Figure 3. Refrigerant saturation temperatures associated with: Left) Compressor discharge (condenser inlet). Right) Compressor suction (evaporator exit). R446A data points are those with the middle refrigerant charge of 4.5 kg

4. TRANSPORT REFRIGERATION UNIT

Tests of R466A were also run in a transport refrigeration unit designed to use R410A; see Fig. 4. The unit has a nominal capacity of 11 kW at an ambient temperature of 30 °C and a refrigerated box temperature of −20 °C. The compressor is electrically driven. The unit can operate as a heat pump (heating mode), however, performance was measured here only under cooling conditions.



Figure 4. Cut-away view of the transport refrigeration unit tested here

As with the residential unit, measurements of capacity were made from air-side measurements. Efficiency was determined from the air-side capacity and measurement of the electric power consumption, which includes power going to the evaporator and condenser fans as well as the compressor. The tests with R410A were run with the standard unit charge of 8.5 kg. The tests with R466A were run with a unit charge of 9.75 kg (+15 %), based solely on the ratio of liquid densities. No modifications were made to the unit during testing, except to adjust the TXV to produce the desired evaporator leaving superheat with R466A.

The capacities obtained under different operating conditions are shown in Fig. 5, overall efficiencies (COP) are shown in Fig. 6. The labels on the horizontal axis indicate the temperatures of the refrigerated box and the ambient. The first four sets represent a range of typical operating conditions. The last two sets represent extreme conditions, the fifth set having an extremely low box temperature

and the sixth set having an extreme ambient temperature. Both of these conditions result in very large temperature lifts imposed on the system and compressor.

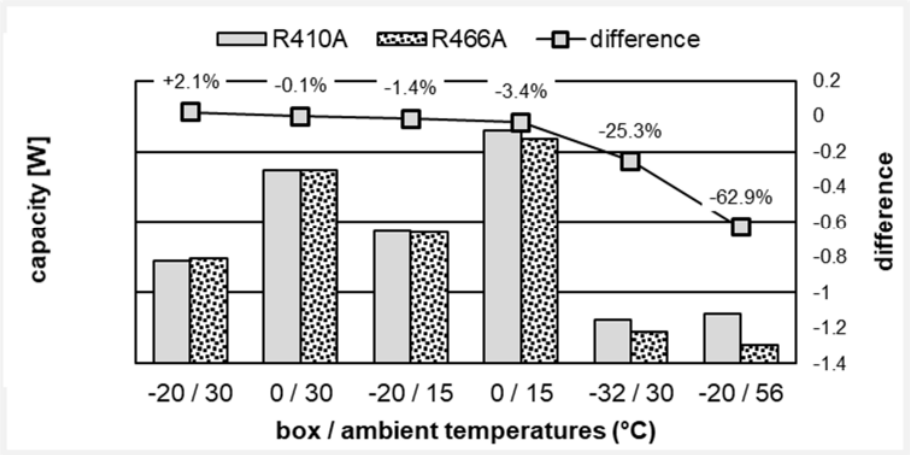

Figure 5. Capacities produced by transport refrigeration unit under various boundary conditions

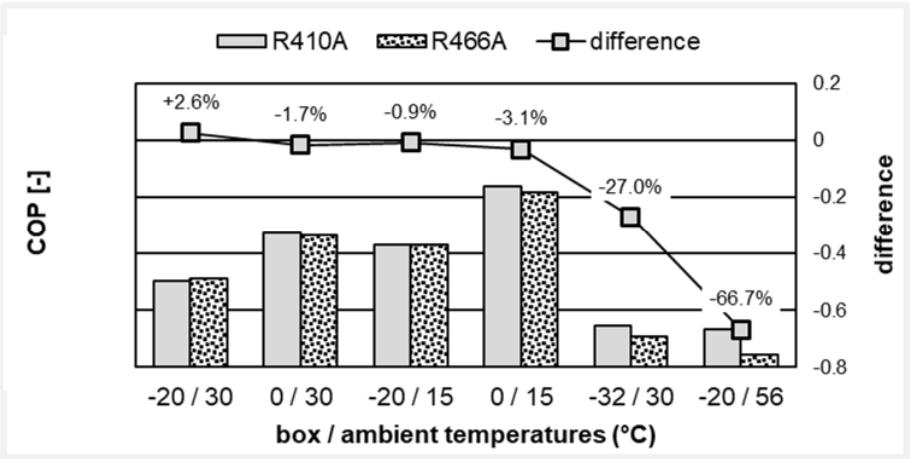

Figure 6. Capacities produced by transport refrigeration unit under various boundary conditions

Under typical operating conditions, R466A was observed to produce capacities that were within −3 % to +2 % of R410A. Efficiencies with R466A were within ±3 % of those with R410A. These results are within expectations based on thermodynamic properties and measurement capabilities. At the two extreme conditions, performance with R466A fell well short of that with R410A. It appears that the TXV was unable to accommodate the higher refrigerant mass flow rate that occurs with R466A under these conditions.

Under the typical operating conditions, the approach of the evaporator entering saturation temperature to the entering air temperature was about 0.5 K larger with R466A than with R10A. However, the approach of the evaporator leaving saturation temperature to the entering air temperature was about 0.5 K smaller with R466A than with R10A. This is likely a beneficial consequence of R466A's small thermodynamic temperature glide offsetting some of the "glide" due to pressure drop, as was seen in the residential unit tests. Evaporator performance appears to be equivalent between the two refrigerants.

The approach of the liquid refrigerant temperature leaving the condenser to the ambient temperature (pinch) was 0.5 K to 1 K better (smaller) with R466A than with R410A. The bubble point temperature at the condenser outlet was similarly lower with R466A than with R410A, indicating similar amounts of subcooling. However, the dew point temperatures at the condenser inlet (compressor discharge) were about 1 K to 1.5 K higher with R466A than with R410A. This is a consequence of the higher

pressure drop across the condenser with R466A due to its higher mass flow rate combined with R466A's thermodynamic temperature glide.
Evaluations indicate that the compressor performance, in terms of an *in situ* isentropic efficiency (which includes the motor efficiency) and the volumetric efficiency were very similar with both R410A and R466A. This is consistent with the general agreement between the observed overall performance measurements with expectations based on thermodynamic properties as modified by the secondary impacts of those properties on heat exchanger performance described above.

5. CONCLUSIONS

Societal demands to protect the earth's environment are resulting in legislative restrictions on the use of high GWP refrigerants, including R410A. A number of candidates to replace R410A have been proposed, such as R452B, R454B, and others, including R32. However, these are all classified as 2L flammable fluids. Implementation of these fluids will require updating of standards and codes, along with safety related equipment designs and service practices.
R466A's A1 non-flammable classification offers the potential for easier and faster replacement of R410A. The results presented here, along with previously published work, indicate that R466A is a suitable replacement for R410A in existing equipment designs from the viewpoint of thermodynamic properties. The two main issues that need to be addressed are accommodating R466A's larger mass circulation rate (mitigating pressure drop effects in heat exchangers, expansion devices, and refrigerant lines) and R466A's higher liquid density which increases the refrigerant charge needed.
Beyond the evaluation of thermodynamic properties and measurements of system performance, a clear understanding of R466A's chemical stability and materials compatibility as well as identification of suitable lubricants is needed to ensure successful deployment.

ACKNOWLEDGEMENTS

Performance measurements of the residential split-system heat pump were provided by the Trane Residential Laboratory in Tyler, TX, directed by Jason LeRoy and executed by Ray Rite and laboratory staff.
Performance measurements of the transport refrigeration unit were provided by Ingersoll Rand's Engineering Technology Center in Prague, Czech Republic, directed by Michal Kolda and executed by Tomáš Kohoutek, Martin Soukup, and laboratory staff.

NOMENCLATURE

CAP	capacity
CDT	compressor discharge temperature
COP	coefficient of performance
GWP	global warming potential
mR*	refrigerant mass circulation rate relative to R410A
Pc	condensing pressure
Pcrit	critical pressure
Pe	evaporating pressure
(Pc/Pe)*	pressure ratio relative to pressure ratio with R410A
RT	Refrigeration Tons (12,000 Btu/hr)
Tcrit	critical temperature
ΔCAP*	difference in capacity relative to R410A
ΔCDT	difference in CDT relative to R410A
ΔCOP*	difference in efficiency (COP) relative to R410A
ρLiq*	ratio of liquid density to R410A

REFERENCES

AHRI, nd, AHRI Low-GWP Alternative Refrigerants Evaluation Program (AREP). http://ahrinet.org/arep.aspx.

AHRI, 2012, ANSI/AHRI Standard 210/240 with Addenda 1 and 2, 2008 Standard for Performance Rating Of Unitary Air-Conditioning & Air-Source Heat Pump Equipment. Arlington, VA: AHRI.

ANSI/ASHRAE Standard 34-2016, Designation and Safety Classification of Refrigerants, ASHRAE, 1791 Tullie Circle, NE, Atlanta GA.

Hughes, J., and T. Leck, 2015, Novel Reduced GWP Refrigerant Compositions for Stationary Air Conditioning. Proceedings of the 24th IIR International Congress of Refrigeration: Yokohama, Japan, August 16-22.

Schultz, K., and S. Kujak, 2012, System Drop-in Test of R-410A Alternative Fluids (ARM-32a, ARM-70a, DR-5, HPR1D, L-41a, L-41b, and R-32) in a 5-RT Air-Cooled Water Chiller (Cooling Mode), Test Report #1 of the AHRI Low GWP AREP. The report is accessible from the AHRI link above.

Schultz, K., 2014a, Performance of R410A and R22 Alternative Lower GWP Refrigerants in a Small (~5 RT) Water Chiller. Presented at the ASHRAE Winter Conference, Jan 19-22, New York City, Conference Paper NY-14-C066.

Schultz, K., 2014b, Performance of R410A and R22 Low GWP Alternative Refrigerants at Elevated Ambient Temperatures, presented at the 15th Int'l Refrigeration and Air Conditioning Conference at Purdue, July 14-17, paper 2381.

Kujak, S., and K. Schultz, 2015, Performance Comparison of Optimized R410A Replacements. Proceedings of the 24th IIR International Congress of Refrigeration: Yokohama, Japan, August 16-22, paper ID 73.

Kujak, S., and K. Schultz, 2016, Optimizing the Flammability and Performance of Next Generation Low GWP R410A Replacements. Presented at the ASHRAE Winter Conference, Jan 24-27, Orlando, Conference Paper OR-16-C015.

Schultz, K., 2016, Behavior of R410A Low GWP Alternative Refrigerants DR-55, DR-5A, and R32 in the Components of a 4-RT RTU, 16th Int'l Refrigeration and Air Conditioning Conference at Purdue, paper 2116.

Schultz, K., and S. Kujak, 2016, Performance of a 4-RT RTU with R410A Low GWP Alternatives, presented at the ASHRAE Annual Conference, 26-29 Jun 2016, St. Louis, Conference Paper ST-16-C065.

Schultz, K., and G. Nayak, 2017, Performance of an Air-Cooled Chiller with R410A Alternatives R452B and R32. Presented at the ASHRAE Annual Conference, Jun 25-28, Long Beach, Conference Paper LB-17-C049.

Schultz, K., and S. Kujak, 2019, Examination of a Novel R410A Replacement, presented at the ASHRAE Annual Conference, Jun 22-26, Kansas City, Conference Paper KC-19-C(TBD).

Manuscript ID: 138
DOI: 10.18462/iir.icr.2019.0138

Experimental Investigation of R290 during Flow Condensation and Adiabatic Two-Phase Flow

Simon Fries[(a)], Andrea LUKE[(a)],

[(a)] University of Kassel, Department of Technical Thermodynamics
Kassel, D-34125, Germany, ttk@uni-kassel.de

ABSTRACT

Tube bundle heat exchangers are widely installed in industrial refrigeration plants. However, there is lack of data and correlations for the design of these apparatus, because the physical phenomena of the heat and momentum transport processes, especially in two phase systems, are not well established. A new test facility is designed by the department of Technical Thermodynamics at the University of Kassel to investigate heat and momentum transfer in horizontal single tubes with hydrocarbons at high pressures in saturation state. The adiabatic two phase flow and condensation are investigated. Therefore the flow patterns, pressure drop and heat transfer are determined for a wide range of saturation pressure, mass flux and vapour quality. Furthermore the influence of the surface structure on the pressure drop is also examined.
Keywords: Condensation, Two-Phase Flow, Pressure Drop

1. INTRODUCTION

Natural gas covers 20% of the worldwide energy demand. Transportation via shipping is an effective way to supply consumers. Therefore the natural gas has to be liquefied by cascade refrigeration plants, which have a high resources demand in construction and require much energy in operation. The tube bundle heat exchangers in those facilities show a significant potential for savings regarding the energy and the resource demands. Therefore the physical phenomena of momentum transport during adiabatic two phase flow as well as the heat transfer during condensation have to be understood in order to prevent oversizing of those heat exchangers.
Friedel (1979) proposed a correlation based on a database of wide variety of fluids, mass fluxes and saturation pressures including many natural refrigerants. The database of Friedel (1979) covers internal tube diameters ranging between 1 mm and 154 mm. In addition further natural refrigerants are investigated by Steiner (1997). However the influence of surface microstructure which has an influence in single phase flow on the pressure drop is not considered in the correlations.
Considering condensation, many refrigerants such as R134a, R125 R32, R410A and R236ea are investigated by Cavallini (2001) in copper tubes with a diameter of 8 mm. Based on these results and the results of Cavallini (1999), Thome (2003) developed a correlation based on flow patterns and the model of Steiner (1997)k for flow boiling. However the single tube in real tube bundle heat exchangers have larger diameter than those investigated by the authors. Hence R290 is investigated by Garimella (2018) for copper tube with diameters till 14.65 mm and mass fluxes up to 450 kg/m²s, which are applied for tube bundle heat exchanger. In real facilities however mild steel is often used as construction material, but limited data is available so far, see Fries (2019).
Recently Shah (2019) published a correlation for condensation heat transfer where many refrigerants in a large variety of parameters are considered. However, the data basis for natural refrigerants in large tube diameters is limited to Fries (2019) and Garimella (2018).

2. EXPERIMENTAL SETUP AND PROCEDURE

The experimental test facility is shown in Fig. 1. The test substance is conveyed by a multiphase pump, into a phase separator, where the gas and the liquid phase are separated due to the buoyancy force. Three fluid loops are connected to the phase separator, whereas two lead to the

measurement section and the last is installed in order to supply the multiphase pump with enough liquid in order to prevent superheating of the pump, which occurs as a result of the compressibility of the gaseous phase. The temperature of that loop is adjusted by Heat exchange HE 3 and HE 1, where HE 3 can be bypassed.

The mass flow of the liquid and gas phase loop connected to the measurement section is regulated by control valves and Coriolis mass flow meter. Due to the large variety of mass flow rates two Coriolis mass flow meters and several control valves are installed. Since the liquid phase is in a saturated state inside the phase separator, it has to be subcooled by heat exchanger HE 4 in order to prevent evaporation because of pressure losses.

The oil separator removes possible contaminations inside the test substance of the sealing oil of the multiphase pump. Both phases pass a static mixer and are conveyed into the measurement section in case of two phase measurements. If single phase transport phenomena are investigated the temperature of the test substance is adjusted by heat exchanger HE 5. After passing the measurement section, the fluid can be post conditioned by heat exchanger HE 2

Two different test sections are used in order to determine the adiabatic two phase flow. The first test section is an insulated drawn copper tube with an internal diameter of 15 mm and a length of 3150 mm, which is used to determine pressure losses during adiabatic two phase flow. The second test section is designed as a shell tube heat exchanger as shown in Fig. 2 with an internal mild steel tube with an internal diameter of 14.65 mm and a brass shell tube. For both test tubes the differential pressure is measured across the whole test section, see Fig. 1. For the second test section the temperature profile is measured in high resolution. Therefore twenty RTD's 100 are inserted inside the annulus. Furthermore the wall temperature of the inner tube is measured at different circumferential and axial positions, as shown in Fig. 2 and table 1.

Additionally the surface roughness of the internal side of both test sections is investigated. The method of focus variation, described by Addy et al. (2016) is applied. The resulting topographies and a representation of a profile are shown in Fig. 3 for copper on the left side and steel on the right side. The mild steel tube has an arithmetic mean surface roughness of 1.80µm, which is approximately six times higher than the roughness of the copper tube with 0.27 µm.

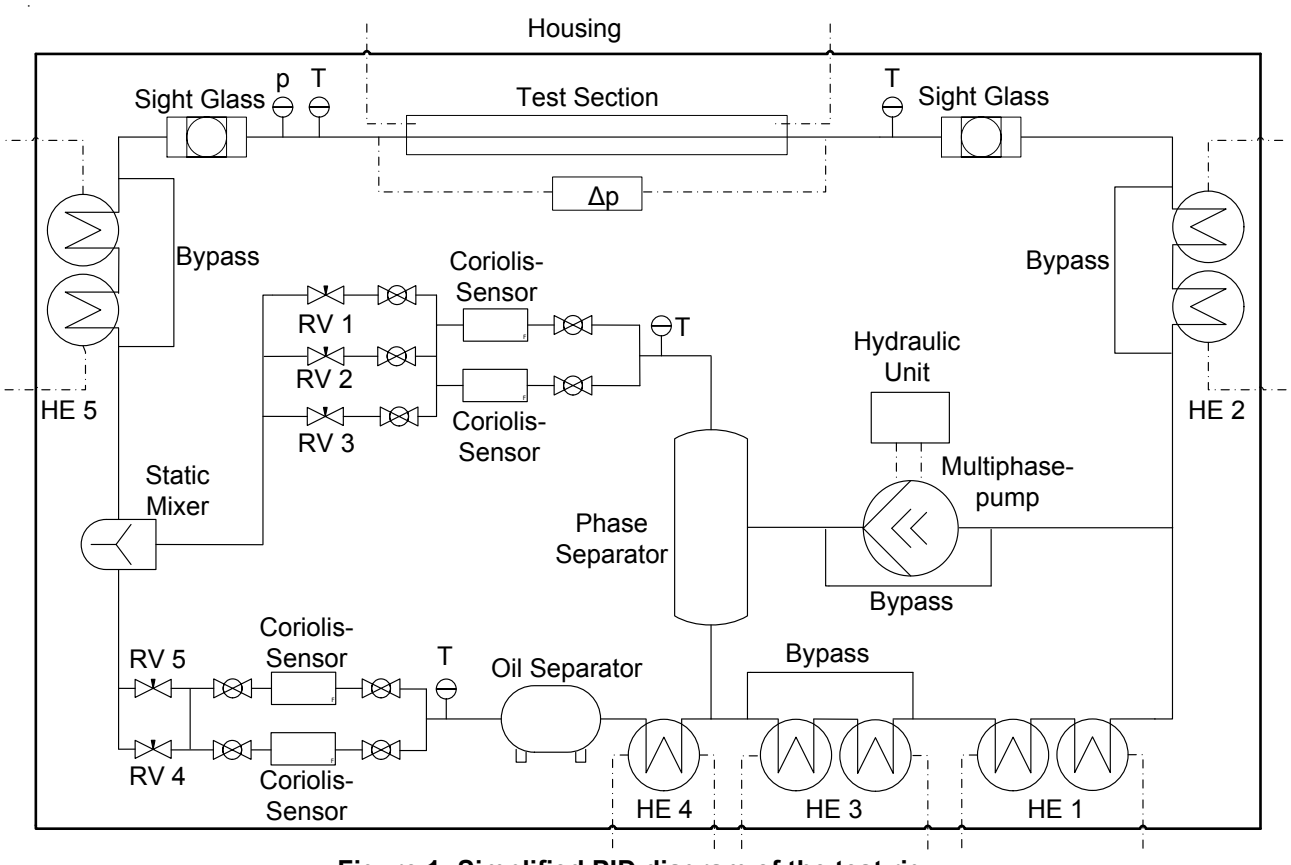

Figure 1: Simplified PID diagram of the test rig

Table 1: Installation positions of the RTD and TC Sensors in Test section

Annulus			Wall		
Measurement Section	axial position	circumferential position	Measurement Section	axial position (from left side)	circumferential position
1 - 19 (odd)	First: 698.5 mm Dist.: 190 mm	0°	1	1070 mm	0 - 360 ° 90° steps
			2	1470 mm	0 - 360 ° 45° steps
2 - 20 (even)	First: 793.5 mm Dist.: 190 mm	180°	3	1870 mm	0 - 360 ° 45° steps
			4	2270 mm	0 - 360 ° 90° steps

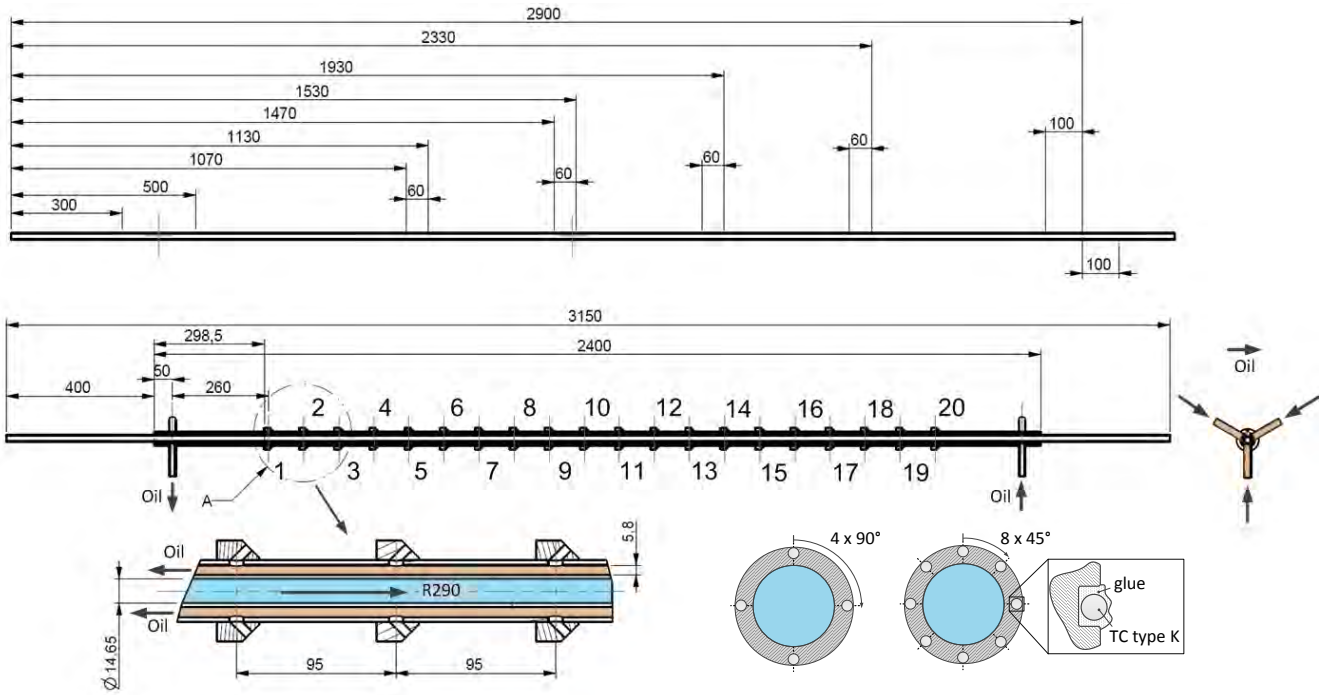

Figure 2: Construction plan of Test Section 2

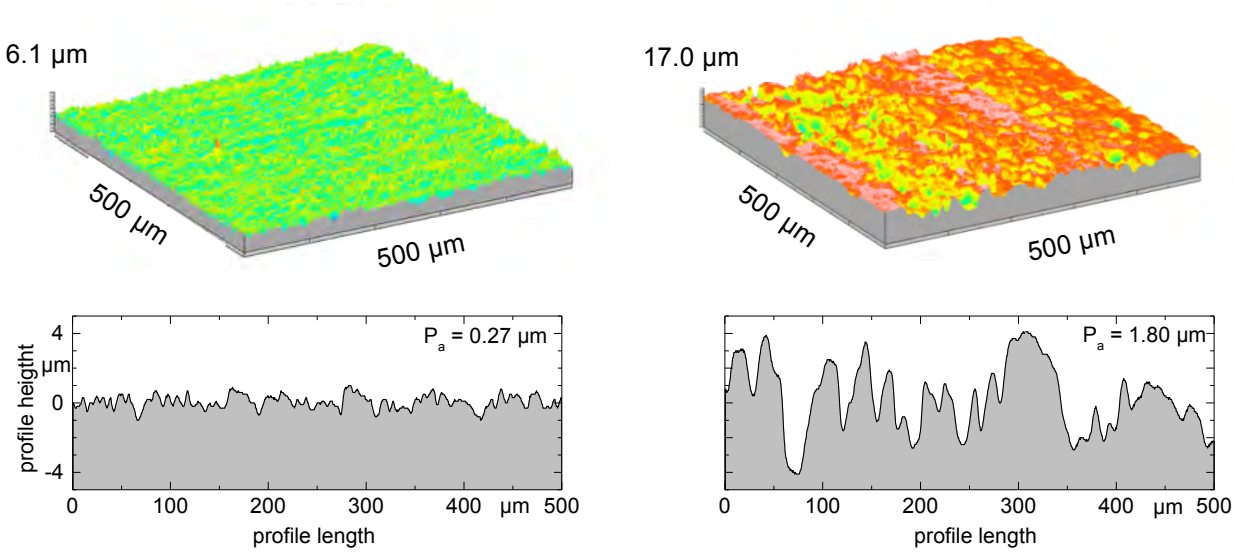

Figure 3: Topographies and profile cuts of the copper tube (left) and mild steel tube (right)

3. DATA REDUCTION

The original evaluation developed by Fries (2019) is slightly alternated. The inlet vapour quality

$$\dot{x}_{in} = \frac{h_s - h_{el}}{h_{ev}} \qquad \text{Eq. (1)}$$

is now determined by Eq. (1) with an energy equation, contrary to the original mass equation. Thereby the subcooling in the liquid loop as well as the superheating due to the pressure loss in the gas loop are taken into account. Therefore the specific enthalpy

$$h_s = \frac{\dot{m}_v h_v + \dot{m}_l h_l}{\dot{m}_v + \dot{m}_l} \qquad \text{Eq. (2)}$$

in the static mixer is determined by Eq. (2) with the gas mass flow rate $\dot{m}_v$ and the liquid mass flow rate $\dot{m}_l$, measured by the respective Coriolis Sensor. The enthalpies h_l and h_v are determined by Eq. (3)

$$h = f(\rho;T) \qquad \text{Eq. (3)}$$

with the equation of state for R290 by Lemmon et al. (2009) with the density and the temperature information.
The heat transfer coefficient is now calculated with Eq. (4) by the radial heat transfer equation

$$\alpha_{i,m} = \frac{1}{r_i \left(\frac{2\pi (T_{Ts,i} - T_{w,av})}{\frac{\partial \dot{Q}}{\partial z}} - \sum_j \frac{1}{\lambda_j} \ln\left(\frac{r_{j+1}}{r_j}\right) \right)} \qquad \text{Eq. (4)}$$

with Eq. (5)

$$T_{w,av} = \frac{1}{k} \sum_k T_{w,k} \qquad \text{Eq. (5)}$$

as mean temperature of the temperature data for all thermocouples on the same axial position. The method to determine the differential $\delta\dot{Q}/\delta z$ is described by Fries (2019).

4. DISCUSSION OF THE EXPERIMENTAL RESULTS

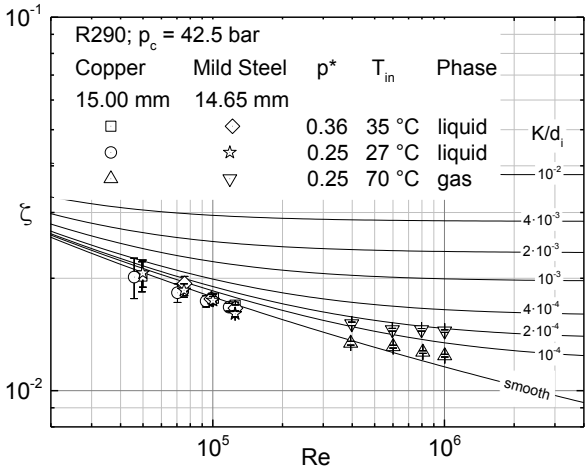

Figure 4: Single Phase Pressure Drop for copper and mild steel tube

At first the pressure drop for adiabatic single phase flow is validated, shown in Fig. 4 for the copper and the mild steel tube in a dimensionless plot. The experimental results of the liquid phase for both test tubes show similar values for the friction factor and are in good agreement with the correlation of Konakov (1946) for smooth tubes.
However for the gas phase only the investigations for the copper tube are in agreement with Konakov (1946), whereas the friction factors in the steel tubes are higher up to 30%. This can be explained by the higher roughness of the steel tube where turbulences occur earlier. This effect cannot be seen for flows with low Reynolds-Numbers since the laminar boundary layer is too thick, so that no turbulence are induced by the higher roughness as explained by Schlichting (2017).
After the validation of the single phase pressure drop, the two-phase pressure drop is investigated for different mass fluxes and different reduced pressures for both test tubes. Generic results for a reduced pressure of 0.5 for the investigations are shown in Fig. 5 for the copper and for the mild steel tube. For both test tubes, the pressure drop is plotted as a function of the vapour quality for different mass fluxes. The pressure drop increases for increasing mass fluxes and vapour qualities. When higher vapour qualities are achieved, the gradient of the pressure drop decreases. Although the pressure drop inside the mild steel tube is significantly higher for single phase gas flow, an increase in the pressure drop is not observed even for higher vapour qualities.
This phenomenon can be explained with the respective flow pattern. For low vapour qualities and low mass fluxes, stratified or stratified wavy flow will occur, where the flow velocities of the gas phase and the liquid phase are similar, yielding low Reynolds-numbers for each phase. Hereby the laminar sub-layer is thicker than the surface roughness profile and hinders the generation of further turbulences. For increasing vapour qualities and mass fluxes, the gas velocity increases but the flow pattern changes. In annular flow, for instance where the gas velocities and therefore the Reynolds-number of the gaseous phase is very high, the gas is not in contact with the wall, but with the liquid phase. Since the liquid phase has a very low velocity, yielding a low Reynolds-number, and is in contact with the wall, the laminar sub-layer will not be affected by the roughness profile.

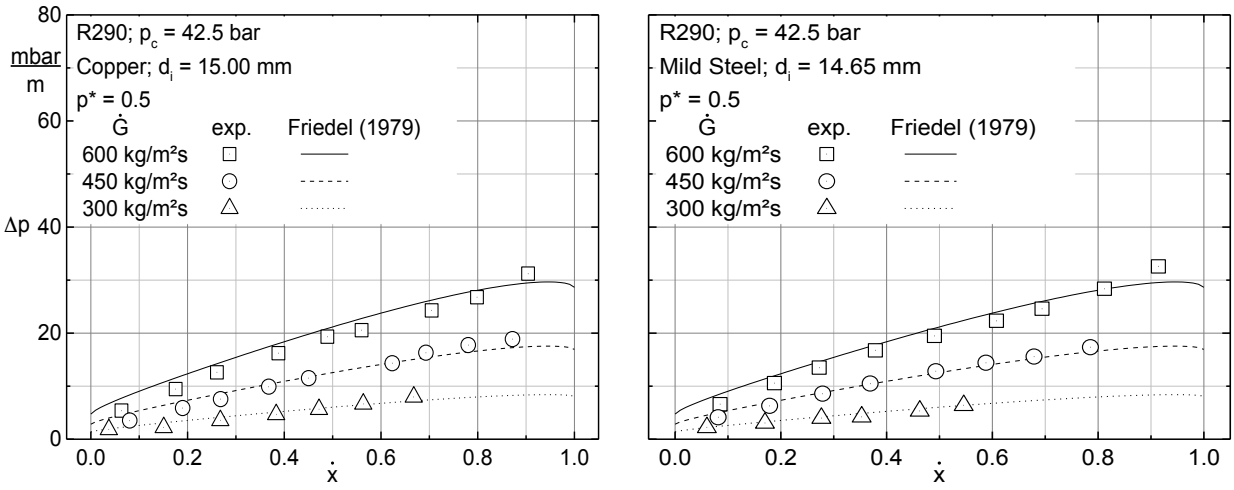

Figure 5: Adiabatic two phase pressure drop inside copper (left) and mild steel (right) tube

In Fig. 6 the pressure drop is illustrated for a reduce pressure of 0.25 and 0.5 for the mild steel tube. As expected the pressure drop is higher for the lower reduced pressure since the phase interaction is more intense, due to the larger difference between the thermophysical properties of the saturated liquid and vapour.

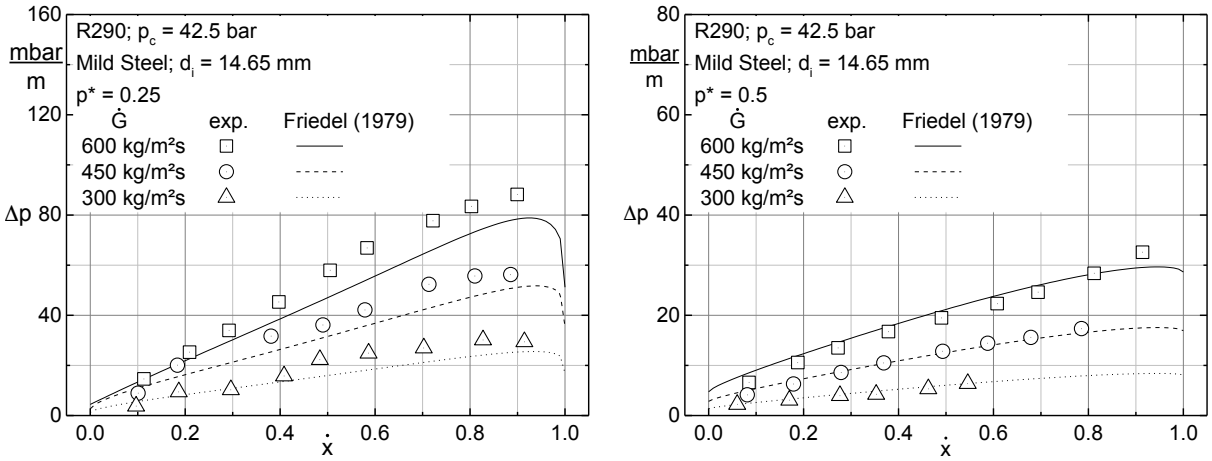

Figure 6: Adiabatic pressure drop of mild steel tube for p* = 0.25 (left) and p* = 0.5 (right)

Before the heat transfer of condensation is investigated, the functionality of the test section is validated with single phase measurements. The heat transfer of liquid and gaseous R290 is measured, over a wide range of Reynolds-numbers. The results are shown in Fig. 7 with a dimensionless plot of the Nusselt-number as a function of the Reynolds-number. The experimental results are in good agreement with the correlation of Gnielinski (2013) and the deviation is within the uncertainty of the correlation, which proves the validity of the test section.

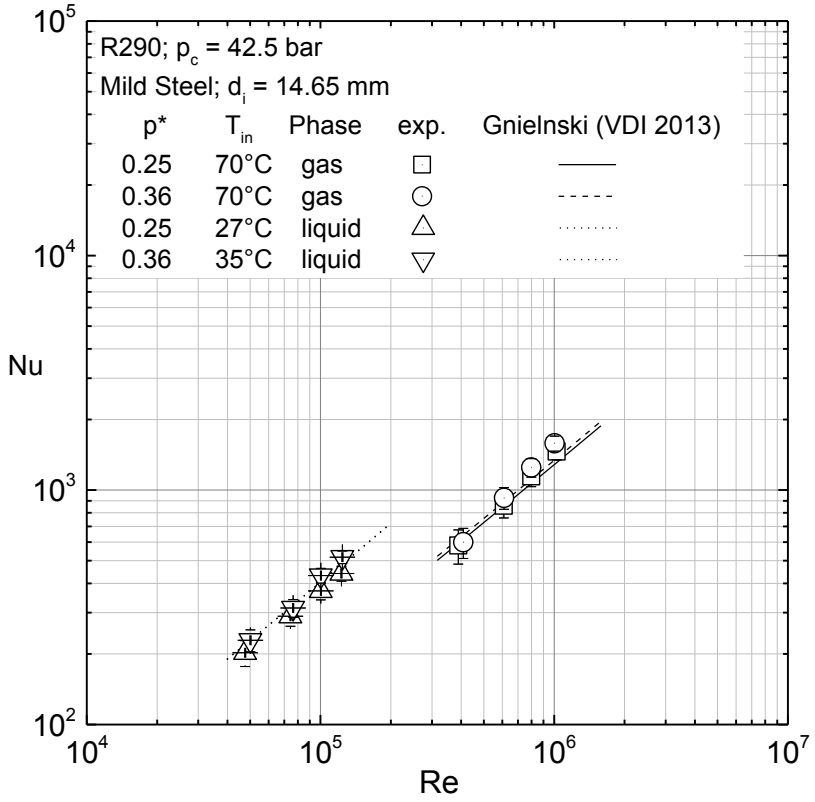

Figure 7: Experimental Results of Singe Phase heat transfer.

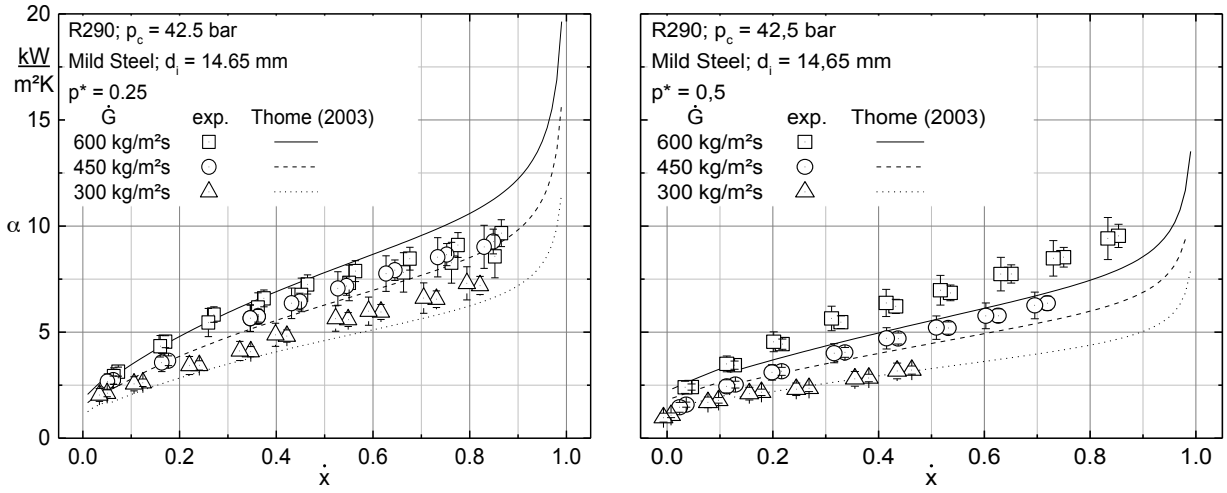

Figure 8: Heat transfer coefficients for p* = 0.25 (left) and p* = 0.5 (right) for condensation

In Fig. 8, the heat transfer coefficient α is shown as a function of the vapour quality for different mass fluxes and two reduced pressures for condensation inside the mild steel tube. The results are compared to the correlation of Thome (2003). The experimental data are underpredicted by the correlation of Thome (2003), however the trend is in good agreement. The experimental values are within the uncertainty range of the correlation. For a reduced pressure of p* = 0.25 and a mass flux of 600 kg/m²s the curvature of the trend is much flatter than predicted by Thome (2003). A possible explanation is, that Thome (2003) calculates mist flow in his flow pattern map and applies that in his calculation for the heat transfer, but annular flow is observed in this experiment, hence the experimental heat transfer is smaller.

Furthermore the heat transfer coefficient decreases with increasing pressure. This can be explained with the lower interfacial interaction, since the difference for thermophysical properties decreases for increasing pressure. Subsequently the vapour density increases and the liquid density decreases, so that the distribution of liquid and vapour changes for increasing pressures. The liquid phase will take more space at higher pressures thus acting as a larger thermal resistance.

5. CONCLUSIONS

The surface roughness of a drawn mild steel tube is six times higher than the roughness of a drawn copper tube. Due to this higher roughness more turbulences are induced in single phase flow at high Reynolds-numbers when the laminar boundary layer is affected by the surface roughness profile. Hence the pressure drop of single phase flow is up to 30% higher in the mild steel tube as compared to the copper tube.

This effect vanishes, when the pressure drop is investigated for gas-liquid flows, even at high vapour qualities. The reason for this is found in the physical phenomena of the different flow patterns. For increasing saturation pressures the pressure drop decreases due to the smaller interfacial interaction. Consequently, the pressure drop can be well predicted with the correlation of Friedel (1979).

The heat transfer during condensation also decreases for increasing saturation pressures for the same reason. The experimental results are in good agreement with the correlation of Thome (2003), considering their trend. The absolute results of the experimental heat transfer coefficients are 15% higher than predicted by Thome (2003), except for p* = 0.25 and a mass flux of 600 kg/m²s, where the difference is significantly higher.

NOMENCLATURE

Symbols

d	diameter (mm)	$\dot{G}$	mass flux ($kg \cdot m^{-2} \cdot s^{-1}$)
h	enthalpy (kJ)	$\dot{m}$	mass flow rate ($kg \cdot s^{-1}$)
K	sand roughness (mm)	p	pressure (bar)
p*	reduced pressure (-)	P_a	arithmetic mean roughness (µm)
$\dot{Q}$	heat flow (W)	r	radius (mm)
T	temperature (°C)	$\dot{x}$	vapour quality (-)
z	position in the tube (m)	α	heat transfer coefficient ($W \cdot m^{-2} \cdot K^{-1}$)
δ	differential (-)	Δ	difference (-)
ζ	friction factor (-)	λ	thermal conductivity ($W \cdot m^{-1} \cdot K^{-1}$)
ρ	density ($kg \cdot m^{-3}$)		

Subscripts

av	average	ev	evaporation
el	evaporation line	i	inner
in	inlet	j	thermal layer
k	counting parameter	Ts	Test substance
v	vapour	w	wall

REFERENCES

Addy, J., Olbricht, M., Müller, B., Luke, A., 2016. Pool Boiling heat transfer on structured surfaces. Proceedings of the 7th European Thermal Sciences Conference, Krakow, Poland, Curran Associates, 519-527.

Cavallini, A., Censi, G., Del Col, D., Doretti, A., Longo, G.A., Rossetto, A., 1999. Condensation heat transfer with refrigerants. Proceedings of the Two-Phase Flow Modeling and Experimental Conference, Pisa, Italy, Editions ETS, 71-88.

Cavallini, A., Censi, G., Del Col, D., Doretti, A., Longo, G.A., Rossetto, A., 2001. Experimental Investigation on condensation heat transfer and pressure drop of new HFC refrigerants (R134a, R125, R32, R410A, R236ea). Int. J. Refrigeration, 24 (1), 73-87.

Fries, S., Skusa, S., Luke, A., 2019. Heat transfer and pressure drop of condensation of hydrocarbons in tubes. J. Heat and Mass Transfer 55 (1), 33-40.

Friedel, L., 1979. Improved friction pressure drop correlations for horizontal and vertical two phase pipe flow. 3R International 18 (7), 485-491.

Garimella, S., Macdonald, M., 2016. Hydrocarbon condensation in horizontal tubes Part I - Measurements. Int. J. Heat and Mass Transfer, 93 (1), 75-85.

Konakov, P. K., 1946. A new equation for the friction coefficient for smooth tubes. Report of the academic society for science of the UDSSR, 51 (7), 503-506.

Lemmon, E.W., McLinden, M.O., Wagner, W., 2009. Thermodynamic Properties of Propane III A Reference Equation of State for Temperatures from the Melting Line to 650 K and Pressures up to 1000 MPa. J. Chem. Eng. Data, 54 (12), 3141-3180.

Shah, M.M., 2019. Improved correlation for heat transfer during condensation in conventional and mini/micro channels. Int. J. Refrigeration, 98 (1), 222-237.

Schlichting H., 2017. Boundary Layer Theory, Springer-Verlag, Berlin, 519-556.

Steiner, D., 1997. Hbb Strömungssieden gesättigter Flüssigkeiten. In: VDI-GVC, VDI-Wärmeatlas, Springer-Verlag, Berlin, 671-676.

Thome, J.R., Cavallini, A., El Hajal, J., 2003. Condensation in horizontal tubes part 2: new heat transfer model based on flow regimes. Int. J. Heat and Mass Transfer, 46 (18), 3349-3363.

Manuscript ID: 144
DOI: 10.18462/iir.icr.2019.0144

Replacements for R410A with GWPs less than 300

Kenneth SCHULTZ[(a)]

[(a)] Ingersoll Rand
La Crosse, 54601, USA, kschultz@trane.com

ABSTRACT

The recent Kigali amendment to the Montreal Protocol will necessitate the phase-out of R410A used in air conditioning systems in developed countries by the late 2020s. This will require the industry to begin using R410A replacements by the middle 2020s. Analyses indicate that the weighted average GWP will need to be 300 or less to reach the overall Kigali targets. The large volume of R410A used in HVAC applications makes this difficult to achieve if the GWPs of its replacements are allowed to be 675 to 750, based on R32 as a benchmark. Three recently introduced molecules offer opportunities to formulate blends with GWPs well less than 675, even achieving GWPs <300. This paper investigates the thermodynamic properties of blends using these new molecules and identifies several specific blend compositions that could serve as lower GWP replacements for R410A. Compromises between important factors are considered, including capacity (match to R410A), efficiency, temperature glide, compressor discharge temperatures, and operating pressures. Beyond their thermodynamic properties, these new molecules present challenges in chemical stability and materials compatibility that are beyond the scope of this paper.
Keywords: R410A, Low GWP, Thermodynamic Property, Glide

1. INTRODUCTION

Release of refrigerants into the atmosphere impacts the environment through their direct Global Warming Potential (GWP). Societal demands to limit climate change are driving regulatory policies and voluntary actions to lower this impact. The Kigali Amendment to the Montreal Protocol (UNEP, nd) is now the key agreement providing a timetable for the phase-down of the use of hydrofluorocarbons (HFCs) with high direct GWPs, just as the original Montreal Protocol is leading to the phase-out of ozone depleting substances (ODSs) such as chlorofluorocarbons (CFCs) and hydrochlorofluorocarbons (HCFCs). This has spurred renewed consideration of "natural" refrigerants such as ammonia (R717), carbon dioxide (R744), and hydrocarbons (R290, R1270, R600, R600a, etc.) as well as the development of alternative lower GWP F-gas chemistries.

R1234yf and R1234ze(E), with GWPs < 1[1], were the first new hydrofluoroolefins (HFOs) to be developed. R1234yf has become the preferred replacement for R134a (GWP = 1300) in automotive air-conditioning. R1234ze(E) is being commercialized as an alternative to R134a in chillers. These fluids are also being employed in a number of new blends designed for a wide range of applications. However, the "low" pressure nature of these fluids limits the amount that can be used in blends intended as replacements for the "high" pressure fluid R410A (GWP = 1924), used extensively in residential, unitary, and VRF equipment, as well as in small chillers.

The timetable called for by the Kigali Agreement is shown in Fig. 1. Calculations based on a weighted average of all refrigerant use today suggest that the average in the future will need to be less than 300 to meet the Kigali phase-down targets. That significant portions of the refrigerants portfolio (e.g., R134a applications and low pressure chillers) have potential to transition to GWPs well below 300 (typically <10) suggests that alternatives for R404A (GWP = 3943) and R410A might be allowed to have somewhat higher GWPs, say <400. The long-term bulk average GWP needed to achieve the Kigali targets depends on the rate of transition away from the high GWP refrigerants and the rate of growth in the overall use of refrigerants, especially by the developing countries.

[1] The GWPs used in this paper are consistent with the 100-year time horizon values listed in the Fifth Assessment Report of the IPCC (Myhre et al, 2013).

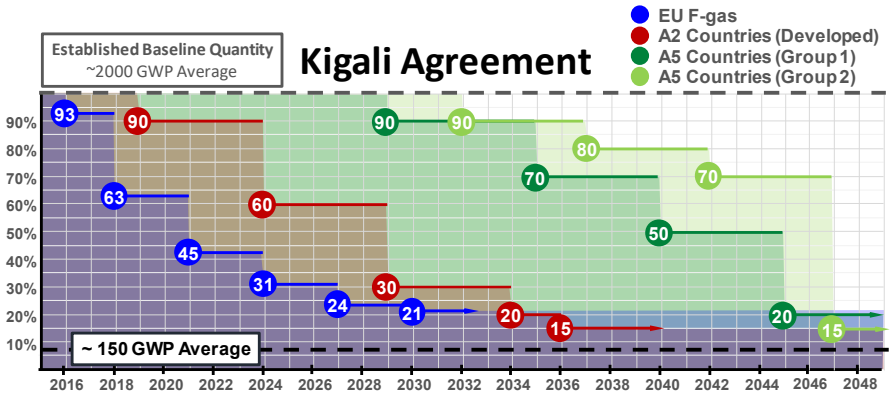

Figure 1. Schematic diagram of the GWP phase-down called for by the Kigali Amendment

Beginning in 2012 under AHRI's (nd) Alternative Refrigerants Evaluation Program (AREP), a number of lower GWP alternatives to R410A have been proposed and evaluated. These fluids all have GWPs between 460 and 715, including R32 (GWP = 677). Although these fluids might be suitable as interim replacements for R410A, they are likely not viable for long-term use.

Chloroiodomethane (CF_3I or R13I1) has a GWP < 1 and was considered as a replacement for Halons in fire suppression agents and as a constituent in low ODP/GWP refrigerant blends in the 1990s (Nimitz and Lankford, 1994). Development stalled until Honeywell submitted an application in 2018 to ASHRAE Standard 34 (abbrev. "Std-34") to revise CF_3I's toxicity levels, followed by a subsequent application for an R410A-like blend containing CF_3I, labelled R466A. Although R466A has the benefit of being non-flammable, its GWP is 697. Although this GWP might be satisfactory for retrofitting R410A in installed equipment; it is again likely too high for long-term use in new equipment. Still, CF_3I can be used in other blends to offer lower GWP alternatives to R410A.

Two "new" HFO molecules have also recently been proposed for use in formulating lower GWP blends to replace R410A. Asahi Glass Corp in 2015 proposed using trifluoroethene (R1123) as a constituent in blends suitable for replacing R410A and R32. (Applications to Std-34 for R1123 and several blends containing R1123 remain tabled as of the date this manuscript was submitted.) Mexichem's 2016 application to Std-34 for 1,1-difluoroethene (R1132a) was approved in 2017. Daikin submitted an application to Std-34 for an R404A-like blend containing R1132a in 2018. It can be imagined that R410A-like blends could be formulated with R1132a as a constituent. Blends containing CF3I, R1123, and R1132a that are potential lower GWP alternatives to R410A are described further in this paper with a focus on thermodynamic properties. Other issues are discussed in Section 6. Select properties of the refrigerants discussed here are summarized in Table 1 at the bottom of the paper.

2. EARLIER PROPOSED R410A REPLACEMENTS

Some of the refrigerants proposed as possible replacements to R410A during AREP are shown in Fig. 2 and Fig. 3. The horizontal axis is the capacity produced in a simple single-stage thermodynamic air conditioning cycle relative to that of R410A assuming a compressor of fixed displacement with an isentropic efficiency of 0.7 and equal average saturation temperatures of 46 °C condensing (with 8 K subcooling) and 11 °C evaporating (with 8 K superheat). Note that using the average of the bubble/flash and dew points can lead to optimistic predictions for blends with large temperature glides of >5 K. Practical performance levels achievable with blends having large glide might be lower than projected here. GWPs range from 460 to 715.

The refrigerant with the 407 GWP has a glide of ~9 K, unacceptably large for typical HVAC applications. R32 by itself is a prospective replacement for R410A, however, its GWP is likely too high for long-term use. The blends contain primarily R32 with R1234yf and/or R1234ze(E); some with small amounts of CO_2, R125, or butane added. Being "low" pressure (R134a-like) fluids, blending R1234yf and R1234ze(E) with R32 results in reduced capacity, so GWP can be lowered only so far while

remaining within, say, 15 % of R410A capacity. Although R125 (GWP = 3170) helps maintain capacity and lowers glide, it adversely impacts the GWP of the blend. CO_2 helps increase capacity, however, its dramatically lower boiling point compared with R32 results in large temperature glides.

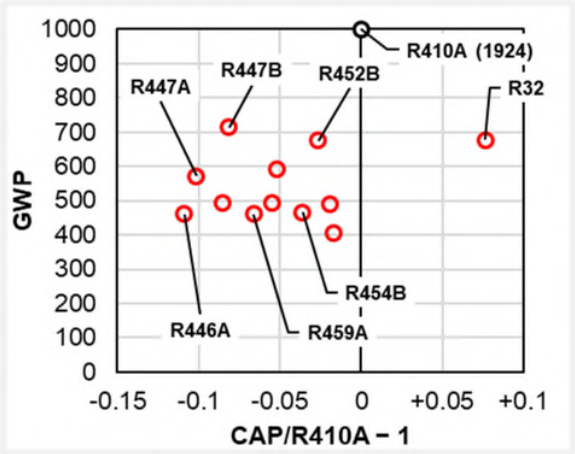

Figure 2. GWP vs capacity relative to R410A of replacements proposed under AREP

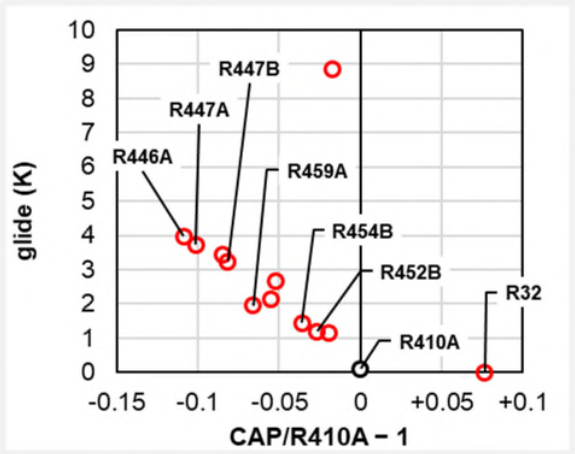

Figure 3. Temperature glide vs capacity of R410A replacements proposed under AREP

Performance characteristics of ternary and concomitant binary blends can be conveniently displayed in "triangle charts" where the axes are the mass fraction of each constituent in the blend. Fig. 4 displays contour lines of the capacity of "R452" series blends (R32 + R125 + R1234yf) relative to that of R410A and of R22. The "R410" (R32 + R125) series runs along the right axis, with R410A at the midpoint. The "R454" (R32 + R1234yf) series runs along the horizontal axis. Properties descriptions for the R454 and R452 series blends are now available in REFPROP v9.1 (Lemmon et al., 2013) and later, including the requisite binary interaction parameters (BIPs). The red line divides the non-flammable (north) and flammable (south) regions.[2] Previous assessments have identified R452B and R454B as "design compatible" replacements for R410A (Schultz and Kujak, 2016).

The R454 series offer the lowest possible GWPs in Fig. 4 (no high GWP R125). A blend of 59 %wt R32 and 41 %wt R1234yf has a GWP of 400 while providing 90 % of R410A capacity, and so could be of interest. To reach a GWP of 300 requires decreasing the R32 content to 43.5 %wt (DR-4), but entails a shortfall of 17 % in capacity. Meeting the long-term GWP target with fluids such as DR-4 could necessitate significant redesign of equipment and product lines, as was required with the switch from R22 to R410A as the industry transitioned away from ODSs.

Fig. 5 shows that R452B and R454B have small thermodynamic temperature glides (<1.5 K). Schultz and Kujak (2016) showed that these small temperature glides had little impact on overall performance in unitary type equipment, with benefits occurring in the evaporator offsetting the small increase in condensing pressure. Note that glide increases modestly as R32 content decreases and R1234yf increases, approaching 7 K at an R32 content of 20-25 %wt. DR-4's glide is 3.5 K, modestly higher than R454B but within the realm of practical experience. Schultz and Kujak (2016) also discuss other quantities, such as thermodynamic COP (increases slightly as increase R32 content, more strongly as increase R1234yf content), mass circulation rate and pressure drop in heat exchangers (decreases as R32 content increases because of wider *Ph* and *Ts* domes), compressor discharge temperatures (CDT, modest increase for R452B and R454A relative to large increase for R32), operating pressures (R4542B and R454B < R410A, R32 > R410A), and liquid density (refrigerant charge for R452B and R454B decreases because of higher R32 content over R410A). Behavior of R454 series blends are further elucidated below.

[2] The flammability line is based on the "local" composition. The fractionation rules in Std-34 need to be addressed to determine if any particular nominal blend would be classified as flammable or not.

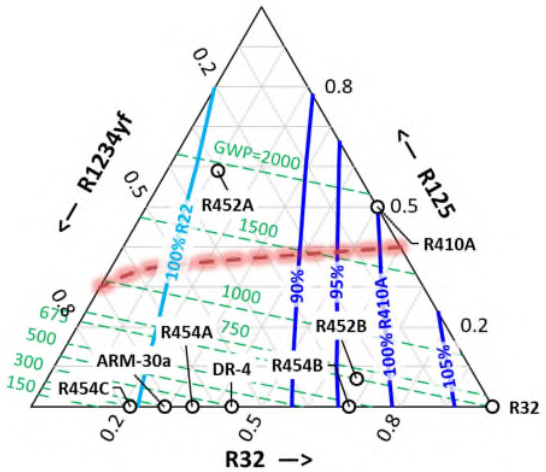

Figure 4. Contour lines of capacity for the R452/R454/R410 series of blends.

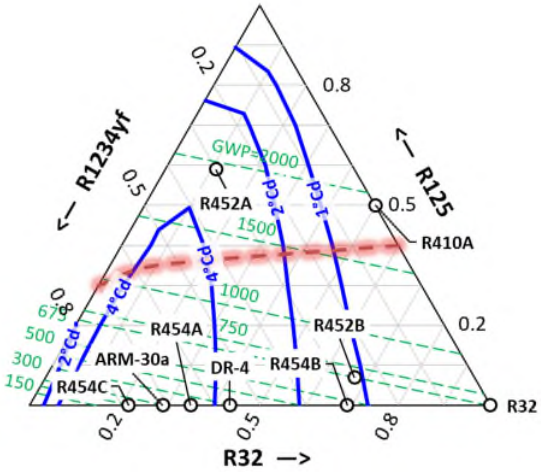

Figure 5. Contour lines of temperature glide for the R452/R454/R410 series of blends.

3. BLENDS COMPRISING TRIFLUOROIODOMETHANE (CF_3I)

Reintroduction of CF_3I (labelled R13I1) back into the refrigerants portfolio offers the potential to create additional lower GWP blends to replace R410A. CF_3I has thermodynamic properties similar to R1234yf while being a flame suppressant. One can therefore imagine replacing R1234yf in the R452 and R454 series blends with CF_3I. Ternary blends of R32 + R125 + CF_3I have received the designation "R466" with the submission of R466A to Std-34.

REFPROP (Lemmon et al., 2013) contains a description of CF_3I properties. REFPROP also has internal algorithms for estimating the BIPs of the R32 + CF_3I and R125 + CF_3I pairs. The estimated BIPs were found to be in reasonable agreement with binary VLE data available in Singh et al. (2013a,b). The data cover a limited range of concentrations at one pressure. Predictions of properties and cycle performance might be subject to lesser or greater uncertainty in various regions of concentrations. Still, this exercise can provide insight into the potential for blends containing R32, R125, and/or CF_3I to replace R410A. Refinement of final blend compositions might be needed once more accurate BIPs are determined.

Contours of capacity relative to R410A and R22 for the R32 + R125 + CF_3I ternary blends (and the associated binaries) are shown in Fig. 6. It is seen that a lower content of R32 is needed to achieve a certain capacity when replacing R1234yf with CF_3I. Again, the red line estimates the divide between the non-flammable (left) and flammable (right) regions. The replacement of flammable R1234yf with flame suppressant CF_3I makes for a larger non-flammable region. R466A is seen to provide a close match to the capacity of R410A while being classified as non-flammable as well as lower toxicity (Std-34 Class A1). Tests of an air-cooled chiller and a residential split system air-conditioner conducted with the blend labelled "A1" by Schultz and Kujak (2018) demonstrated R466A to also be design compatible with R410A.

Comparing Fig. 7 to Fig. 5 indicates temperature glide is smaller as CF_3I is initially added to R32/R125 blends than when adding R1234yf. This allows the glide of R466A to be only slightly larger than for R452B and R454B. However, glide increases dramatically as the CF_3I concentration exceeds 60-70 %wt, making an R466 ternary blend or an R32 + CF_3I binary blend (the "B" series) unsuitable as low GWP replacements for R22 or R404A.

The lowest GWP attainable while matching R410A capacity is about 400 at blend "B1". Fractionation considerations in Std-34 make B1 likely to be classified as flammable. The blend labelled "A3" matches the GWP of R454B. The use of A3 as an alternative to R454B would have the benefit of being potentially non-flammable, but at the expense of about two percentage points in capacity and ~1.5 K increase in glide. Similarly to DR-4 in the R454 series, reaching a GWP of 300 requires decreasing the R32 content to 44 %wt – blend "B2". In contrast to DR-4's 17 % shortfall, the capacity provided by B2 is only 7.5 % lower than R410A. B2's temperature glide is 3.5 K, essentially the same as DR-4's glide. The blends A3 and B2 have thermodynamic COPs that are ~1 % higher than R410A, modestly higher CDTs (~+10 K), and slightly higher mass circulation rates (~+6 %).

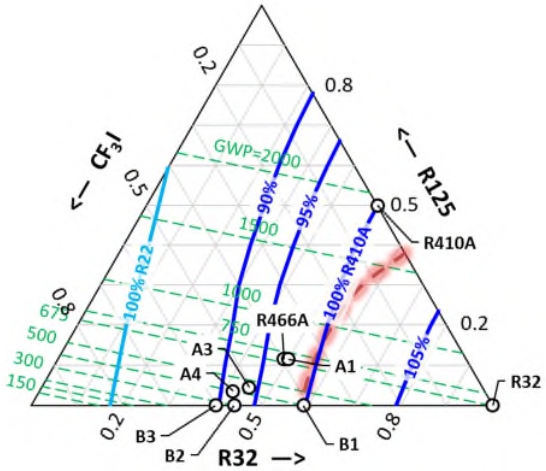

Figure 6. Contour lines of capacity for the R466/[R32+CF_3I]/R410 series of blends.

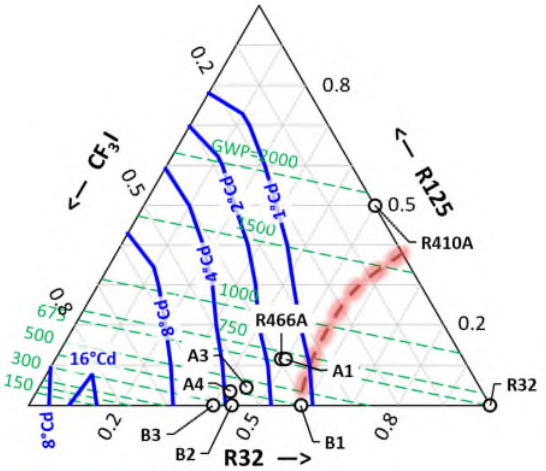

Figure 7. Contour lines of temperature glide for the R466/[R32+CF_3I]/R410 series of blends.

4. BLENDS COMPRISING TRIFLUOROETHENE (R1123)

The operating pressures of R1123 are similar to those of R32 (Table 1), in fact forming a mild azeotrope with R32 and exhibiting near-azeotropic behaviour (small temperature glide) over the full range of concentrations. With a GWP < 1, R1123 blended with R32 lowers the effective GWP in direct proportion to the concentration in mass fraction. R1123 is susceptible to disproportionation, a reaction in which the molecule spontaneously rearranges into other materials with the release of heat. Studies indicate this reaction happens at high temperatures and pressures beyond those experienced in HVAC&R equipment and can be mitigated by mixing (diluting) R1123 with other molecules, such as R32 and R1234yf (Otsuka et al., 2018). The risk of disproportionation appears to be minimized if the mole fraction of R1123 in a blend is maintained below 40 % to 50 %. However, further review will be needed for equipment manufacturers to fully assess the risks associated with disproportionation during the design process.

The work presented here is based on a description of R1123 properties derived using the method of Brown (2008). BIPs for R1123 + R32 were estimated from a few VLE data points presented by Fukushima and Hashimoto (2014). REFPROP's internal algorithm was used to estimate the BIPs for R1123 + R1234yf. Development of more accurate properties descriptions for R1123 and its relevant blending components is underway (e.g., Higashi, 2018).

One way to employ R1123 in refrigerant blends is to consider using the binary pair R1123 + R32 as a lower GWP replacement for pure R32 in the blends considered above, especially the R452/R454 series (R32 + R125 + R1234yf). A set of charts similar to Fig. 4 and Fig. 5 can be constructed with R32 replaced by a blend of R1123 + R32 of a specified ratio. Although these four component blends can have interesting properties, driving toward the lowest possible GWPs suggests minimizing the R125 content and focusing on the R32 + R1123 + R1234yf ternary blends.

Contours of capacity relative to R22, R410A, and R32 are shown for the R32 + R1123 + R1234yf blends in Fig. 8. The lines labelled "50%v" and "40%v" intersect blends in which the mole fraction of R1123 is the stated value. The lines labelled "50/50" and "40/60" indicate fixed relative ratios of R1123 to R32. The blends "C1" and "C2" are binaries of R1123 + R32 submitted to Std-34 in 2015.

The blend "D1" matches the capacity of R410A with a GWP of 300. The R1123 content in D1 is only 25 %mol (%v), well below the threshold for disproportionation. Fig. 9 indicates that D1 has a temperature glide of 2.5 K. D1's thermodynamic COP is ~1 % below R410A, CDT is only ~4 K above R410A, and mass circulation rate is ~5 % lower. Being more aggressive, the blend "D2" matches the capacity of R410A while achieving a GWP of 200. However, the concentration of R1123 falls near the boundary where the risk of disproportionation increases. In addition, the thermodynamic COP falls ~2.5 % below R410A, a consequence of the higher R1123 content. D2's glide is 3 K, still quite reasonable.

The azeotropic nature of the R1123+R32 pair produces a locus of blends with capacities equal to or greater than R32, something not possible with the blends considered above. Blend "D3" offers a

match of R32 capacity while meeting the long-term 300 GWP target. However, D3's thermodynamic COP is ~3.5 % below R32. (R32 offers an ~1 % benefit over R410A). Glide is a mild 1.5 K. Note that the modest temperature glides predicted at high R1234yf concentrations (maximum of <7.5 K) offers potential for formulating lower GWP blends to replace R22 and R404A.

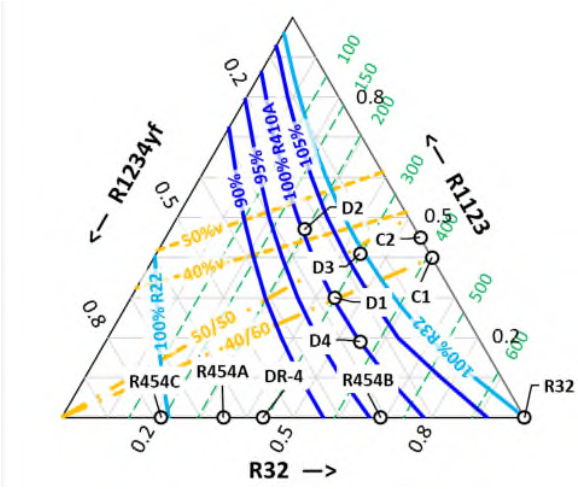

Figure 8. Contour lines of capacity for the R32 + R1123 + R1234yf series of blends.

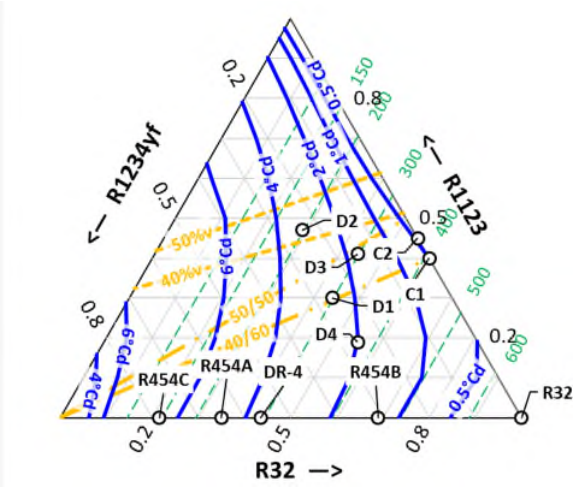

Figure 9. Contour lines of temperature glide for the R32 + R1123 + R1234yf series of blends.

5. BLENDS COMPRISING 1,1-DIFLUOROETHENE (R1132a)

R1132a (aka vinylidene fluoride) has a much lower boiling point and critical temperature (Table 1) than R32. One of its projected uses is in blends to displace R23 and R508A/B in very low temperature applications (evaporator saturation temperatures of <−60 °C). Although an estimate of R1132a's thermodynamic properties can be constructed using the method of Brown (2008), certain features of the resulting description appear unrealistic and call into question its accuracy. In addition, no public information suitable for estimating BIPs with R32 and R1234yf (or other molecules) was available at the time of writing. Detailed simulation of cycle performance will need to wait until more accurate thermodynamic properties are available for R1132a and candidate blending agents. This work is underway (Low, 2018).

Several blends proposed under the AREP (AHRI, nd) and a couple of named refrigerants (R455A and R463A) employ small amounts of CO_2 to enhance capacity and offset some R32 to lower the blend's GWP. As potential alternatives to R404A, the composition of R455A is very similar to R454C with the addition of 3 %wt CO_2 while reducing the R1234yf content, maintaining GWP at 150. It is conceivable that R1132a's lower pressures relative to CO_2 could enable blends to be formulated that displace more R32, lowering GWP, while matching a target capacity. As noted above, a first blend utilizing R1132a has been submitted to Std-34 targeting R404A-like capacity. Further evaluations might reveal compositions suitable for replacement of R410A.

6. OTHER ISSUES

The discussion above is based exclusively on the thermodynamic properties of the various refrigerants and their blends. However, other aspects of a refrigerant or blend are also necessary for eventual successful commercial use in HVAC&R equipment. One of these is the chemical stability of the molecule and the associated materials compatibility concerns. This hurdle was encountered during the first look at CF_3I in the 1990s and is now again an active area of development. As noted above, R1123 is susceptible to disproportionation. Studies to date suggest this risk can be minimized by limiting the concentration of R1123 in a blend. Although this limit looks to be high enough to allow formulation of potentially useful blends, manufacturers will need to conduct proper risk assessments. In addition, classification of R1123 by Std-34 is currently tabled until toxicity studies are concluded. R1132a's toxicity has been classified as A and is expected to be a more stable molecule. However,

R1132a's flammability has been classified as 2 and its higher operating pressures and consequentially higher temperature glides as R1132a content increases could limit the concentration of R1132a in practical blends to replace R410A.

7. CONCLUSIONS

Societal demands to protect the earth's environment are resulting in legislative restrictions on the use of high GWP refrigerants, including R410A. The long-range sustainable limit on GWP may be as low as 300, eliminating R32 and the blends currently being evaluated as long-term refrigerants. The thermodynamic properties of blends utilizing three recently introduced low GWP molecules, CF_3I, R1123, and R1132a, were described here. Blends utilizing these molecules were shown to have properties suitable to replace or displace R410A (and R32). However, achieving a GWP of 300 may require selection of refrigerants with capacities less than R410A, but at least be within 10 % to 15 % of R410A. A number of significant hurdles, such as chemical stability or toxicity classification, must also be overcome for these blends to become practical alternatives to R410A and R32.

ACKNOWLEDGEMENTS

The author wishes to acknowledge the many discussions with and helpful direction from Steve Kujak, Director of Refrigerant Technology for Ingersoll Rand, that shaped the content of this paper.

NOMENCLATURE

BIPs	binary interaction parameters	COP	Coefficient of Performance
CAP	Capacity	GWP	Global Warming Potential
CDT	Compressor Discharge Temperature		

REFERENCES

AHRI, nd, AHRI Low-GWP Alternative Refrigerants Evaluation Program (AREP). http://ahrinet.org/arep.aspx.

ANSI/ASHRAE Standard 34-2016, Designation and Safety Classification of Refrigerants, ASHRAE, 1791 Tullie Circle, NE, Atlanta GA.

Brown, J.S., 2008, Methodology for Estimating Thermodynamic Parameters and Performance of Alternative Refrigerants, ASHRAE Transactions, vol. 114, pt. 1, New York City, paper NY-08-029.

Fukushima, M., and M. Hashimoto, 2014, Development of Low-GWP Refrigerants, JRAIA International Symposium, Kobe, Japan, Nov 20-21.

Higashi, Y., 2018, Evaluation of thermophysical properties, heat transfer characteristics and cycle performance for HFO-1123 mixtures, JRAIA International Symposium, Kobe, Japan, Dec 6-7.

Lemmon, E.W., M.L. Huber, and M.O. McLinden, 2013, NIST Standard Reference Database 23: Reference Fluid Thermodynamic and Transport Properties-REFPROP, Version 9.1, National Institute of Standards and Technology, Standard Reference Data Program, Gaithersburg. See: http://www.nist.gov/srd/nist23.cfm.

Low, B., 2018, Evaluation of Potential Use of R-1132a as a Refrigerant Blend Component, 1st Int'l Conference on the Application of HFO Refrigerants, Birmingham, UK, Sep 2-5, paper ID 1183.

Myhre, G., D. Shindell, F.-M. Bréon, W. Collins, J. Fuglestvedt, J. Huang, D. Koch, J.-F. Lamarque, D. Lee, B. Mendoza, T. Nakajima, A. Robock, G. Stephens, T. Takemura, and H. Zhang, 2013: Anthropogenic and Natural Radiative Forcing. In: Climate Change 2013: The Physical Science Basis. Contribution of Working Group I to the Fifth Assessment Report of the Intergovernmental Panel on Climate Change [Stocker, T.F., D. Qin, G.-K. Plattner, M. Tignor, S.K. Allen, J.

Boschung, A. Nauels, Y. Xia, V. Bex and P.M. Midgley (eds.)]. Cambridge University Press, Cambridge, United Kingdom and New York, NY, USA.

Nimitz, J. and L. Lankford, 1994, Refrigerants Containing Fluoroiodocarbons (FICs), Int'l Refrigeration and Air Conditioning Conference, Paper 256, Purdue University, http://docs.lib.purdue.edu/iracc/256.

Otsuka, T, K. Ueno H. Okamoto, M. Ippommatsu, and R. Dobashi, 2018, Analysis of disproportionation process of trifluoroethylene mixtures, Journal of Loss Prevention in the Process Industries, https://doi.org/10.1016/j.jlp.2018.03.014.

Schultz K. and S Kujak, 2016, Performance of 4-RT RTU with R410A Low GWP Alternatives, presented at the ASHRAE Annual Conference, 26-29 Jun 2016, St. Louis, Conference Paper ST-16-C065.

Schultz K. and S Kujak, 2018, Examination of a Novel R410A Replacement, presented at the ASHRAE Annual Conference, 22-26 Jun 2018, Kansas City, Conference Paper KC-18-C???.

UNEP, nd, Ozone Secretariat, https://ozone.unep.org/ (accessed 16-Jan-2019).

Singh, R., H. Pham, and D. Wilson, 2013a, Azeotrope-like compositions of difluoromethane and trifluoroiodomethane, US patent 8,492,327 B2, Jul 23, 2013.

Singh, R., H. Pham, and R. Richard, 2013b, Azeotrope-like compositions of pentafluoroethane and trifluoroiodomethane, US patent 8,598,107 B2, Dec 3, 2013.

Table 1. Summary of Select Refrigerant Properties

name	GWP	molar mass	Tcrit	Pcrit	T_{bbl} @ 1 atm	T_{dew} @ 1 atm	P_{bbl} @ 25°C	P_{dew} @ 25°C	h_{fg} @ Pdew
			(°C)	(MPa)	(°C)	(°C)	(MPa)	(MPa)	kJ/kg
	single molecules								
CO2	1	44.0	31.0	7.38	–	–	6.43	6.43	120
R1132a	<1	64.0	29.7	4.46	-82.8	-82.8	4.00	4.00	77
R1123	<1	82.0	59.2	4.60	-56.0	-56.0	2.03	2.03	153
R32	677	52.0	78.1	5.78	-51.7	-51.7	1.69	1.69	271
R125	3170	120.0	66.0	3.62	-48.1	-48.1	1.38	1.38	110
R1234yf	<1	114.0	94.7	3.38	-29.5	-29.5	0.68	0.68	145
CF3I	<1	195.9	123.3	3.95	-21.9	-21.9	0.49	0.49	91
	multi-component blends								
R410A	1924	72.6	71.3	4.90	-51.4	-51.4	1.66	1.65	187
R452B	676	63.5	79.7	5.50	-50.7	-50.7	1.59	1.54	222
R454B	467	62.6	80.9	5.58	-50.5	-50.5	1.57	1.52	226
DR-4	295	75.1	84.3	5.17	-49.3	-49.3	1.42	1.25	195
R466A	696	80.7	83.8	5.91	-51.7	-51.7	1.61	1.55	172
A3	448	86.2	87.5	6.10	-51.5	-51.5	1.58	1.46	164
B2	298	88.4	89.5	6.22	-51.5	-51.5	1.56	1.41	162
D1	298	69.5	75.9	5.47	-53.4	-53.4	1.74	1.61	201
D2	197	74.6	72.6	5.26	-54.2	-54.2	1.80	1.63	187
D3	298	67.7	73.2	5.58	-54.7	-54.7	1.86	1.76	200

Manuscript ID: 148
DOI: 10.18462/iir.icr.2019.0148

Evaluation of Refrigerants Leakage Ratios based on Electronic Logging and Reporting System

Peter Tomlein[(a)], Michal TOMLEIN[(a)], Matúš TOMLEIN[(b)]

[(a,b,c)] Slovak Association for Cooling and AC Technology
Šamorín, 931 01, Slovak Republic, szchkt@szchkt.org

ABSTRACT

Success of international F gas agreements depends on effective measures taken responsibly. This paper describes monitoring of leakages based on data recorded using electronic logbooks according to EN 378 and Regulation (EC) No 1516/2007. Advantages of electronic data logging and reporting are shown on the possibilities of automatic analysis, fault detection and comparison, fast access to the full history of leak checks and various forms of output.
Using the implemented system, service engineers can get a quick survey of their customers, cooling circuits, details of all maintenance work and repairs, refrigerants in store, refrigerants added, recovered, reclaimed, and disposed of. This is possible directly at customer sites using tablet and smartphone applications, which also enable the service engineers to create electronic logs of inspections in the field. Experience from reporting of HFC refrigerant emissions shows that the data required by the IPCC methodology divided into several categories of use is difficult to obtain from companies in practice. The concept underlying this work is to take advantage of electronic data logging and reporting, the possibilities of automatic analysis, fast access to the full history and various forms of output.
Electronic data records from refrigerant handling on stock enable summarizing, reporting and analyzing important data in a chosen period. The Slovak data reporting system was launched into operation in the year 2009. We started dividing the data based on field of application in 2012. Weighted mean leakage for all applications, specifically for commercial refrigeration, air conditioning, transport refrigeration, heat pumps, industrial refrigeration, and domestic refrigeration, is calculated automatically. The historical development of the weighted mean leakage is analyzed according to the aforementioned fields of application. Data from the reporting system of monitored cooling circuits are compared with total leakages on national and international level.
This paper is based on the activities of the Slovak Association for Cooling and Air-Conditioning Technology started in the year 2003 supported by the Ministry of Environment. The electronically led documentation was developed from the previous paper form. The evaluated data were collected from service organizations.
Keywords: Accuracy, Computer, Leak, Logging, Refrigerant, Reporting, Statistic.

1. INTRODUCTION

Leakage reporting by category of usage (commercial, industry refrigeration, air conditioning, …) is implemented using a program for logging data about the usage of refrigerants called Leaklog. The function was added to Leaklog in response to the need to compare amounts of leakages according to the aims of the Kyoto Protocol and the methodology of IPCC from 2006 and also the EU Regulation about F gases.
The reporting function includes leakage monitoring by refrigerants and category of usage. An overall scheme of refrigeration reporting is shown in Fig. 1, where data about leakages on equipment from customers is input using Leaklog to the information system of SZ CHKT (Slovak Association for Cooling and AC Technology) and is, subsequently, automatically processed.
Reported data consists of only aggregate values of leakages and amounts of refrigerants in equipment by category of usage. Leaklog does not report any sensitive information about customers. A similar system is operated in Germany by the VDKF organization (Zaremski, 2016), which has published their results and so mutual comparison is possible. Leakage evaluation by VDKF was done in 2011 and 2016 from 260 enterprises and 111 thousand equipment from approximately 15 thousand customers with the total charge of 1790 thousand tons of refrigerants and an average

charge of 16.7 kg of refrigerant per equipment. Web information systems for data collection are operated also in Hungary, Estonia, but their results are not published. Similar web-based information systems are already in development in many other countries.

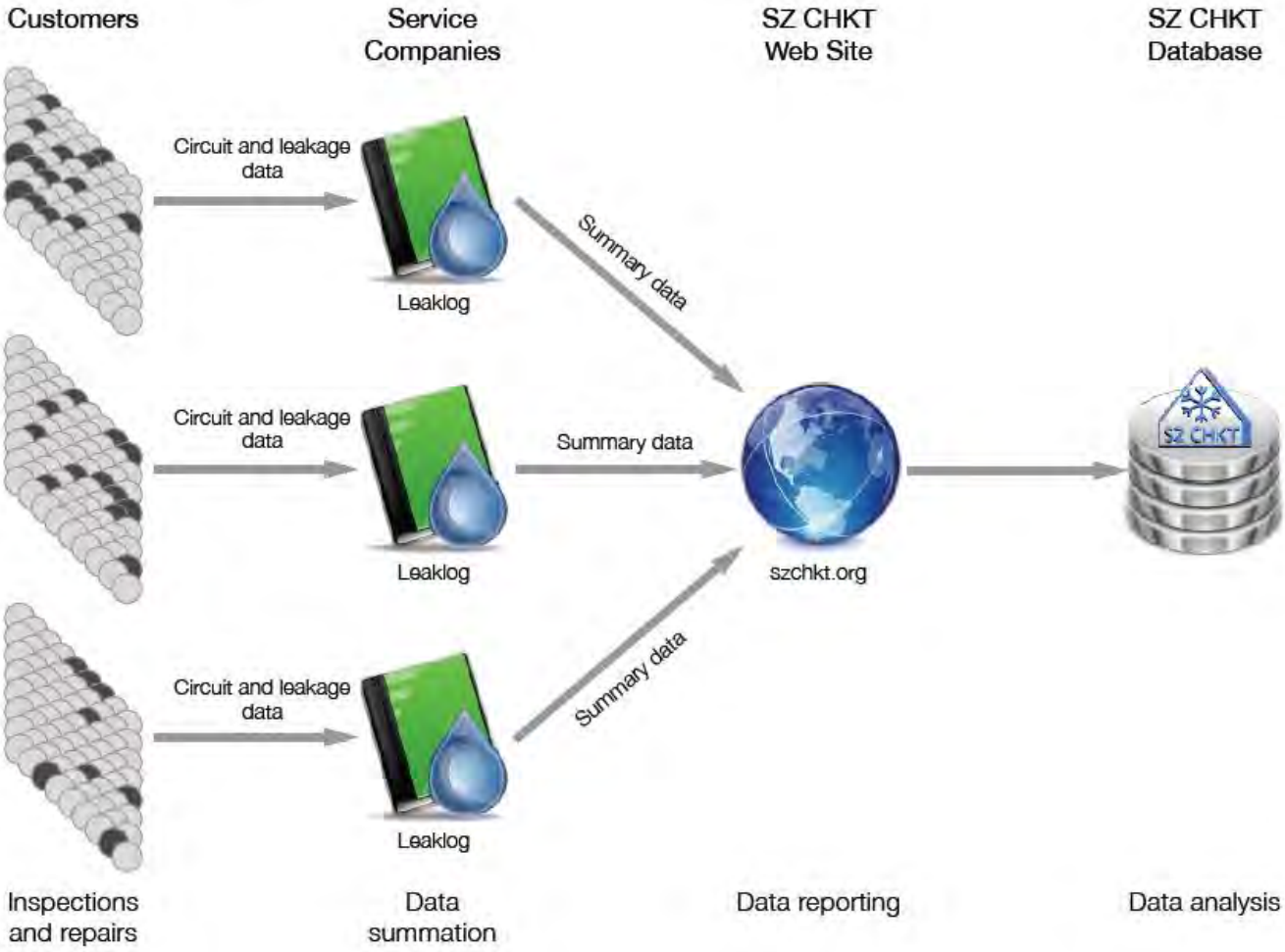

Figure 1: Data flow from customers using Leaklog to the information system of SZ CHKT at www.szchkt.org, where the data is automatically processed

As input to the information system at szchkt.org, two approaches for reporting data are supported:

1. yearly reporting by organizations using Leaklog, and
2. yearly reporting by organizations without Leaklog.

The first approach enables aggregation of precise data from companies, which are logging data about refrigerant movement directly in Leaklog. Using such data, it is possible to calculate average weighted percentage of refrigerant leakage per refrigerant charges in equipment and added amounts of refrigerants. The data is possible to summarize by refrigerant and category of usage (e.g., commercial, industrial cooling, AC and heat pumps).
The second approach enables aggregation of less precise data from all certified companies that may not be using Leaklog. Such summarized data shows trends in purchase development and consumption of refrigerants added to circuits as new charge or due to leakage.
The first approach is more precise as it enables calculation of average weighted percentage of refrigerant leakage by refrigerant and category of usage.

2. LEAKAGES BY CATEGORY OF USAGE

Reporting of leakages by category of usage (commercial, industrial cooling, AC, heat pumps, …) is implemented using the Leaklog software. Summarized amounts of refrigerants by year and category of usage are shown in Fig. 2. Fig. 2 shows added amounts, amounts of refrigerants in equipment, percentage of leakage by individual years for all refrigerants and for selected categories of usage.



Figure 2: Added amount, refrigerant charge in equipment, and leakage percentage by year and usage for all refrigerants

2.1. Survey conditions

In Table 1, SZ CHKT has evaluated leakages from a total of nearly 8 thousand cooling circuits with different categories of usage with a total charge of nearly 200 tons with average leakage of all refrigerants at 4.2 % in the year 2017.
More than 55 refrigeration companies have taken part in the survey from the over 250 companies using the Leaklog software in Slovakia. In total, they reported 181 tons of refrigerants in equipment, which is approximately 20 % of the total charge of refrigerant in equipment in the Slovak Republic. The average charge was at 22.6 kg of refrigerant per circuit.

Table 1. Ratio of refrigerant amount in different categories of usage to total charge

Refrigerant	Category of usage – ratio of refrigerant amount on total refrigerants charges									
	All refrigerants		Commercial cooling		Air Conditioning		Heat pumps		Industr. cooling	
	kg	%	kg	%	kg	%	kg	%	kg	%
All	181252	100	34793	19.2	43313	23.9	4030	2.2	98654	54.4
R134a	29217	100	9619	32.9	4018	13.8	960	3.3	10190	34.9
R404A	26029	100	8213	31.6		0.0		0.0	13794	53.0
R407C	86953	100	10198	11.7	12805	14.7	360	0.4	63292	72.8
R410A	38957	100	5492	14.1	24842	63.8	2348	6.0	6228	16.0

2.1.1. Ratios of refrigerant amount to total refrigerant charges

The ratios of refrigerant amount to total refrigerant charges (181 252 kg) were as follows: R404A (14.3%), R407C (47.9%), R134a (16.12 %), R410A (21.4 %), others (0.28 %).
The ratios of single categories were the following: Commercial (19.2 %), Stationary AC (23.9 %), Industrial (54.4 %), Heat pumps (2.2 %).

From these ratios, we conclude that the most relevant results can be expected in Industrial cooling and Stationary AC, and for refrigerants R134a, R407C and R404A.

2.2. Total charges and leakages

The highest leakages according to Table 2 are found in commercial equipment (7.1 %), then industrial cooling (3.6 %), and AC (2.5 %). Heat pumps were exempted from the evaluation due to comparatively small amounts of refrigerants in included equipment.
Refrigerant R134a, which works with the lowest working pressures, has the lowest leakages in all categories. Similarly, refrigerant R407C shows lower leaks.
Higher leaks were found with refrigerants R404A and surprisingly also R410A. While R410A works with the highest pressures, in most categories as in AC, the expected leaks are lower, as indicated by the lowest average weighted leakage of 2.5 % in Table 2.

Table 2. Refrigerant amounts in equipment by category of usage with average weighted leakages until 1/1/2018

Refrigerant	Category of usage – average weighted leakage									
	All refrigerants		Commercial cooling		Air Conditioning		Heat pumps		Industrial cooling	
	kg	%	kg	%	kg	%	kg	%	kg	%
All	181252	4.2	34793	7.1	43313	2.5	4030	7.7	98654	3.6
R134a	29217	3	9619	3.5	4018	0.4	960	3.1	10190	3.5
R404A	26029	11.5	8213	11.5					13794	11.5
R407C	86953	2.5	10198	8.6	12805	3.1			63292	1.2
R410A	38957	4.3	5492	5.7	24842	3.3	2348	4.7	6228	7

2.3. Comparison of SZCHKT and VDKF results

The introduced results are compared with the results of VDKF (Zaremski, 2016). SZ CHKT has results from a lower number of circuits and lower amounts of refrigerant included in the assessment in relation to VDKF. The weighted average leakages published by VDKF are nearly 50 % lower in total, as well as in the assessed categories of usage of refrigerants. Absolute differences in Table 3 are up to 5 %.
Table 4 shows that by comparing the intensity of leakage by refrigerant, the differences between VDKF and SZ CHKT are higher – up to 5 %. This can partially be explained by the substantially lower amounts of refrigerant in equipment entering into the evaluation.
The highest and most surprising difference is with refrigerant R410A, which is mostly, but not only, charged into AC systems, where leakages are mostly low.
SZ CHKT data has shown 39 % higher total leakages than VDKF in Table 3. These higher differences are probably due to different numbers of reported data and should be lowered in the near future.

Table 3. Comparison of leakage amounts by kind of refrigerant between VDKF and SZ CHKT in the year 2015. Average leakages are compared for all refrigerants by category of usage

Refrigerant	Category of usage– Average weighted leakage in the year 2015									
	All refrigerants		Commercial cooling		AC		Heat pump		Industrial cooling	
	kg	%	kg	%	kg	%	kg	%	kg	%
All SZCHKT	198545	4.7	44012	8,3	47123	2.7	4030	4.4	99306	4.2
All VDKF	1740000	2.9	786000	3.14	149000	1.42	81000	0.79	403000	1.88

Table 4. Leakages by refrigerant in the year 2015. SZ CHKT data shows higher leakages at about 45 up to 84 % than VDKF.

Categories of usage	R134a			R404A			R407C			R410A		
	SZ CHKT	VDKF	Δ%	SZ CHKT	VDKF	Δ%	SZ CHKT	VDKF	Δ%	SZ CHKT	VDKF	Δ%
All categories	5.3 %	2.9 %	45	8.6 %	3.64%	58	4.2 %	1.89%	55	4 %	0.67%	84

2.4. Summary from leakage assessment by refrigerant

Fig. 2 shows by category of usage that leakages of refrigerants R134a, R407C, R410A and R404A are in the range from 2.2 up to 9.5 % including accidents. By refrigerant, the amount of leakage is the lowest for refrigerant R134a, then R407C, and the highest leakages are with refrigerants R410A and R404A.

The assessment shows that using most important refrigerants R134a, R404A, R407C, R410A, the average leakage during the assessed period in monitored categories of usage is under 10 %. The other refrigerants, such as R417A, R422A, R424A, and R507, were found to have higher leakage rates. They were excluded from the assessment due to the lower amounts of these refrigerants used in equipment. The resulting percentage of leakage was seen as not statistically significant enough.

Figs. 4–7 show the development of leakage by refrigerant. Figs. 8–11 show the development of leakage by category of usage in the years 2009–2017.

2.4.1. Price development

Price development of refrigerants in the Slovak Republic copies the price development in the EU. A rapid increase has started only at the beginning of the year 2017. The trend indicates that refrigerants with a GWP of over 2500 are becoming more expensive, and there will be a shortage on the market after the year 2020. The influence of increasing refrigerant prices has not become evident on leakage development (Figs. 3–11), due to the start only during the year 2017.

2.4.2. Leakage trends by refrigerant reported through Leaklog

Leakage trend of all refrigerants in percentage is decreasing as expected, which is reached with high probability due to precautions coming out from EU regulations.

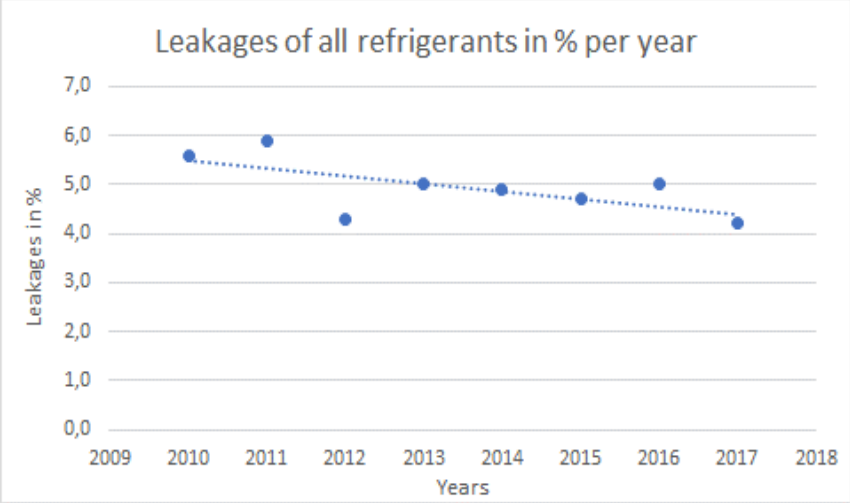

Figure 3: The decreasing leakage trend of all refrigerants in percentage

Leakage rates in Figs. 4–7 have an expected decreasing trend, except for refrigerant R404A. It is not easy to explain this development, but it is known that commercial cooling, where R404A is mostly implemented, has the highest leakages. This could be an effort of customers to have a reserve in store due to the expected lack of R404A and the increasing price.

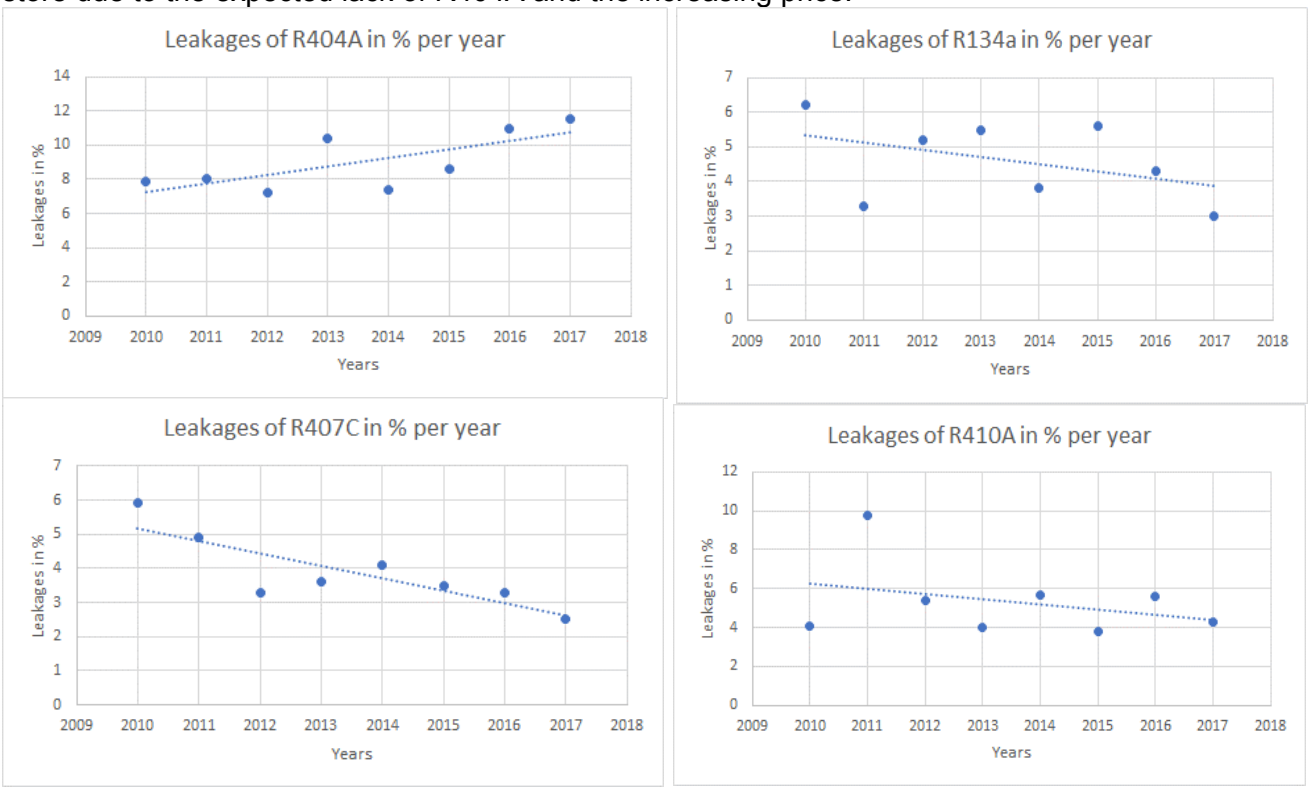

Figs. 4-7: Leakage rates by refrigerant

2.4.3. Leakage trends by category of usage reported through Leaklog

Leakage rates by category of usage, shown in Figs. 8–11, have an expected decreasing trend, except for commercial cooling in Fig. 8, where mostly refrigerant R404A is used, probably due to reserves in customers store.

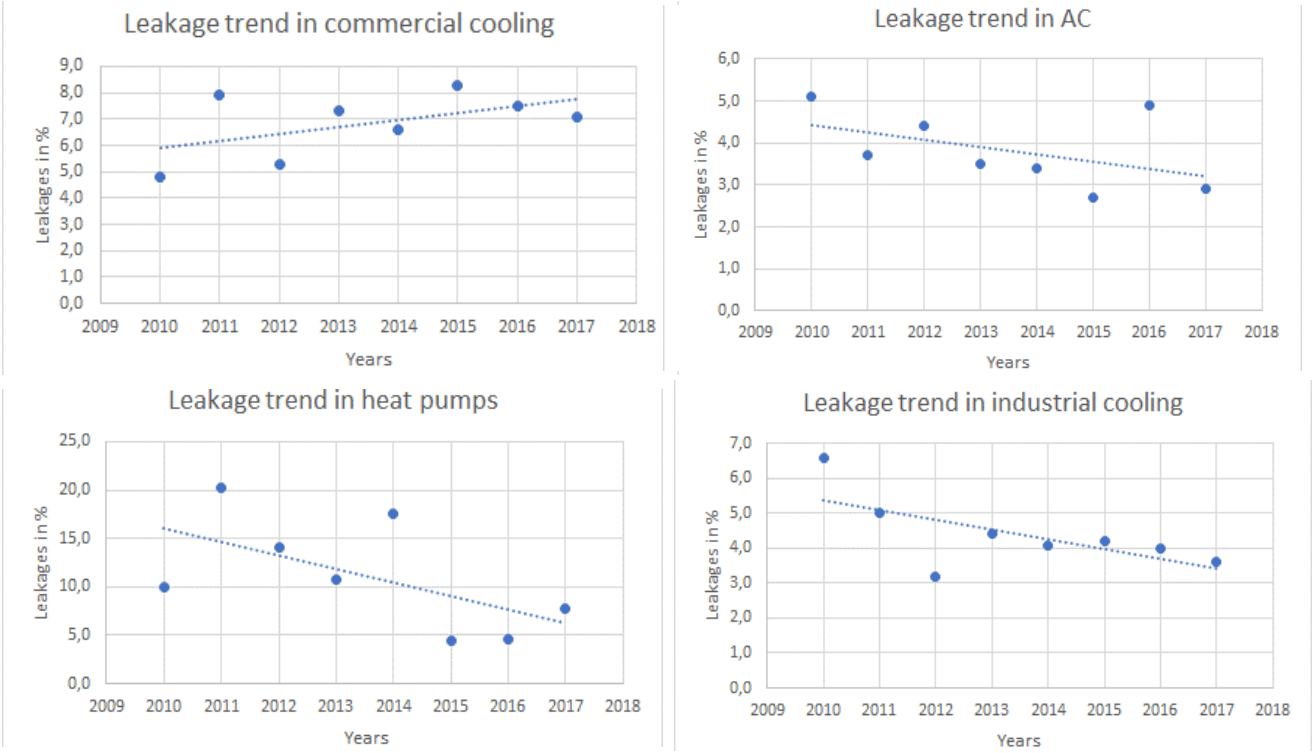

Figs. 8–11: Leakage rates by category of usage

2.4.4. Purchase trends of refrigerants reported by all certified companies

Fig. 12 shows total reported data both with and without Leaklog for refrigerants purchased and added to circuits as new charges and due to leakages. Refrigerants R410A and R407C show a stable trend and R404A has started decreasing trend in 2015.
This is not the case for the purchased amount of R134a, which fluctuates due to mainly changes in commercial cooling and car industry.

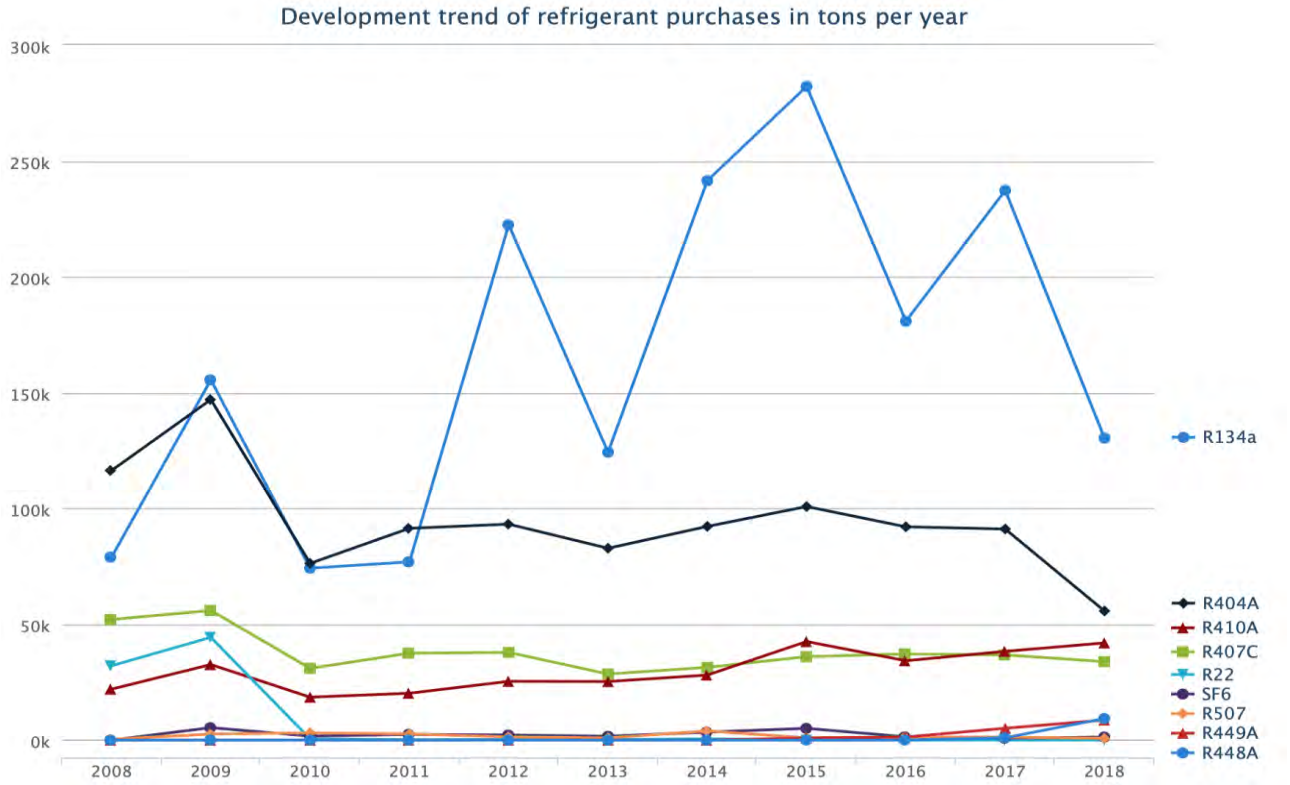

Figure 12: Development trend of refrigerant purchases in tons per year. The trend is mostly stable except for the fluctuating purchases of R134a influenced by the car industry. R404A has started decreasing trend in 2015

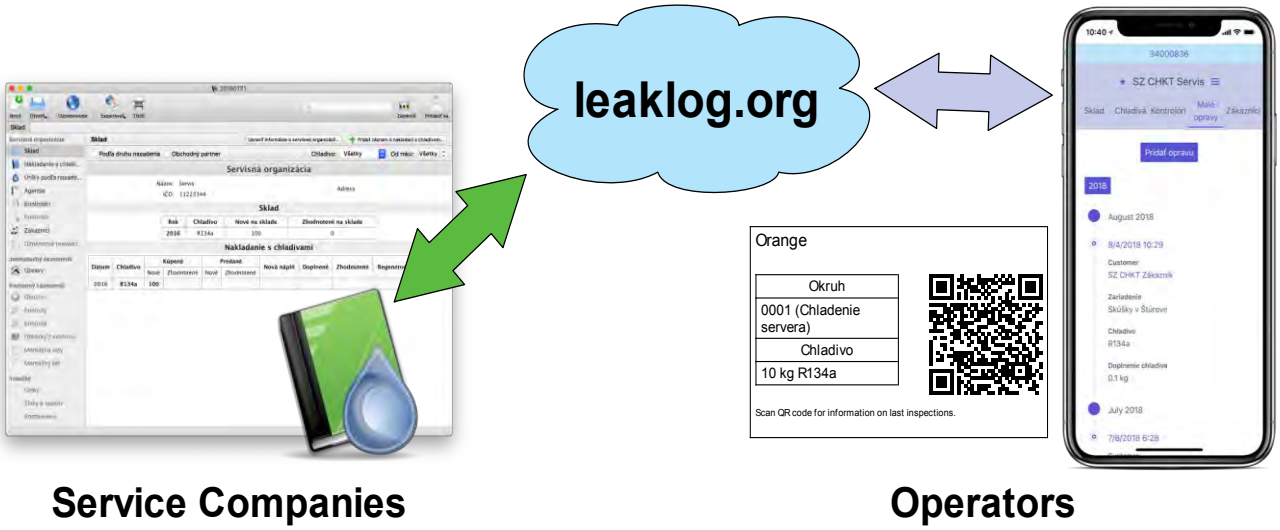

Figure 13: SZ CHKT introduced a new service named Leaklog.org that enables service companies and operators to share information about inspections of cooling equipment. Labels with QR codes placed on equipment link to logbooks with up-to-date information

2.5. Extension of Leaklog for equipment owners and operators

In response to upcoming regulations, SZ CHKT launched an extension of the Leaklog software built for equipment owners and operators intended to enable collaboration and data sharing with service companies. This new web-based solution integrates with existing Leaklog databases managed by service companies and provides an electronic logbook of circuits and inspections for owners and operators.
As shown in Fig. 13, the system offers fast access to circuit data for authorized persons via QR code labels attached to the equipment. The solution aims to replace the existing paper-based workflow and encourage companies to maintain detailed and high-quality data.

3. CONCLUSIONS

Decreasing trend of leakages was confirmed according to data reported through the program Leaklog, which, in the evaluated years, was not influenced by the increasing price of refrigerants or by the lack of refrigerants. Similarly, a decreasing trend was confirmed in the analysis of purchased refrigerants and amounts of refrigerants added to circuits in place of leaked refrigerants.
Comparison of the leakage size according to IPCC methodology from the year 2006 and also EU regulations on F gases has shown, that implemented precautions enabled a decrease in refrigerant consumption and also a decrease of refrigerants consumption added in place of leaked refrigerants. Leaklog enables logging and aggregation of not only summarized amounts of leakages, but also refrigerant usage per cooling circuits and by category of usage. Latest extensions of Leaklog enable service companies to easily share information from inspections with operators and/or owners of cooling circuits.

ACKNOWLEDGEMENTS

This paper is based on the activities of the Slovak Association for Cooling and Air-Conditioning Technology started in the year 2003 supported by the Ministry of Environment. The electronic documentation has been developed from the previous paper-based form. Electronic documentation is running since the year 2009.

NOMENCLATURE

AC	Air Conditioning	*HP*	Heat pumps
CC	Commercial cooling	*IC*	Industrial cooling
SZ CHKT	Slovak Association for RAC	*VDKF*	German Association for RAC

REFERENCES

Barrault, S., 2013. Refrigerant emissions and inventories platform. Proceedings of the IIR Conference on Compressors. Papiernicka, Slovak Republic, 71-71.

Tomlein, P., 2011. Inventory of F gases based on company certification. Proceedings of the IIR Congress, Prague.

Tomlein, P., 2013. Inventory of refrigerants. Proceedings of the IIR Conference on Compressors, Papiernicka, Slovak Republic, 68-68.

Zaremski, W., 2016. Aktualisierter statusbericht über leckgeraten. VDKF-Branchensoftware LEC. VDKF – Branchenbuch.

Regulation of EP and C (EC) č. 842/2006 (Ú. v. EÚ L 161, 14.6.2006) version 517/2014/EÚ

Act of Slovak National Parliament from 19. June 2009, No. 286/2009 Z.z, 348/2015 Z.z. and amendments No. 314/2009 Z.z., 382/2016 Z.z.

Manuscript ID: 162
DOI: 10.18462/iir.icr.2019.0162

(Micro) Fluidic thermal switches: a review of the principles for caloric technologies

Katja KLINAR[(a)], Urban TOMC[(a)], Andrej KITANOVSKI[(a)]

[(a)] University of Ljubljana, Faculty of Mechanical Engineering
Ljubljana, 1000, Slovenia, andrej.kitanovski@fs.uni-lj.si

ABSTRACT

Caloric refrigeration and heat pumping play important roles in a potential future substitute for vapour-compression technology. Although caloric refrigeration is foreseen as one of the most promising alternatives, the current low power density of caloric devices represents a serious hurdle to overcome prior to market applications. In order to improve the power density, the number of thermodynamic cycles per unit of time, denoted as the frequency, has to be increased. Thermal switch mechanisms, which act as a control element for the heat flux, represent a promising solution. They can enable the operation of caloric devices at up to an order higher frequencies compared to existing devices and their principles. This review covers the principles of microfluidic mechanisms that have already been or can be applied as active thermal switches in caloric technologies. The article can serve as a guideline for the future development of compact caloric devices.
Keywords: Refrigeration, Thermal switch, Magnetic refrigeration, Electrocaloric cooling, Elastocaloric cooling, Heat pump, Heat transfer.

1. INTRODUCTION

Caloric refrigeration and heat pumping are considered as important alternatives to existing vapour-compression technologies at room temperature (Brown and Domanski, 2014, Goetzler et al., 2014). Caloric technologies are divided into four groups, based on the driving mechanisms inducing the caloric effect: magnetocalorics (magnetic field), electrocalorics (electric field), elastocalorics (force) and barocalorics (pressure). Materials exhibiting more than one caloric property are called multicaloric.

Due to the many unsolved questions, especially regarding efficient heat transfer and fluid dynamics, the current power density of caloric devices is still lower than that of vapour-compression systems. In order to increase it, the frequency of operation for caloric devices (the number of thermodynamic cycles per unit of time) has to be higher. A promising solution is mechanisms that act as a control element for the heat flux: thermal switches (TSs), thermal diodes, thermal regulators and thermal transistors. The extensive research efforts to find an appropriate thermal control elements in calorics have been underway since 2009 (Epstein and Malloy, 2009, Kitanovski and Egolf, 2010), but the first idea of implementing thermal control element was introduced for the first time by Basiulis et al. in 1988.

This paper presents a selection of the possible principles for fluidic thermal switches that have already been presented in calorics as well as in other different applications, e.g., electronic cooling, microelectromechanical systems (MEMS) or microfluidics. A selection of the best candidates and the proposed future development directions are based on meeting the requirements and the applicability with respect to a caloric device and the required technology readiness level.

2. THE APPLICATION OF THERMAL CONTROL ELEMENTS TO CALORICS

A change in the external applied magnetic, electric, stress or pressure field induces a temperature change in a caloric material. When an external field is applied to a caloric material under adiabatic conditions, its temperature increases with an adiabatic temperature change dT_{ad} and, conversely, when the external field is removed, its temperature decreases by dT_{ad}. After each process of the adiabatic temperature change, heat is transferred either between the caloric material and the heat sink or between the caloric material and the heat source. The majority of caloric devices operate continuously by repeating this thermodynamic cycle by applying an active caloric regenerator. The

active caloric regenerator is a porous structure of caloric material, through which the working fluid flows in an oscillatory, counter flow manner. Even though the active caloric regenerative process is one of the best currently applied solutions, this approach is limited by the operating frequency. The alternatives to active heat regeneration process in calorics, which enable higher operating frequencies, are thermal control elements, especially TSs.
The operation of TS in caloric devices is only efficient if the periodic change in the temperature of the caloric material is coupled with heat transfer to the heat sink or from the heat source. When the temperature of the caloric material rises above the temperature of the heat sink, the heat has to be guided to the heat sink, while the heat-flow rate from the caloric material to the heat source should be as small as possible. In contrast, when the material in the next process is cooled below the temperature of the heat source, the heat flux has to be enabled only from the heat source to the material. For this reason, usually two TSs are needed in caloric technologies, "A" and "B" (Kitanovski et al., 2015a). TS "A" links the caloric material with the heat sink and "B" links the caloric material with the heat source, as presented in Fig. 1. TS could be replaced by a thermal diode, a thermal regulator or a thermal transistor in a similar way.

In analogy to electrical diode, thermal diode rectifies the heat current: the magnitude of the heat flow changes when the polarity of temperature difference between the terminals is switched. The closer look to the transfer function ($\dot{Q}$ vs. ΔT) of thermal diode reveals nonlinearity and asymmetry. The electric analogy to thermal regulator is variable resistor. Its transfer function is also nonlinear, but steeper than that of the thermal diode. Thermal diodes and thermal regulators are materials; whose thermal conductivity is temperature dependent. In contrast to the operation of a thermal diode or thermal regulator, an external force or field drives the TS between the "on" and "off" states. The "on" and "off" state denote the state of lower and higher thermal resistance. Due to the static position of the heat sink, the heat source and the caloric material, a TS in calorics consists of another (solid or fluidic) element, which is usually moved between the caloric material and the heat sink or the heat source. The application of a TS in calorics is presented in Fig 1, a) for a heated and b) for a cooled caloric material. The yellow colour denotes the "on" state of the switch and white (blank), the "off" state, because the switch is could be moved away during the "off" state. The black arrows define the heat-transfer direction, while the number of arrows represents the magnitude of the heat flux.
When the switch is "on", the heat-flux between the opposing surfaces should be a maximum, and when the switch is "off", there should be a minimum heat-flux between the opposing surfaces. TS "A" makes or breaks the thermal contact between the caloric material and the heat sink, and TS "B", between the heat source and the caloric material. They operate in opposite phase: when "A" is "on", "B" is "off".



Figure 1: Heat transfer between a) heated and b) cooled caloric material and heat source/sink with implemented TSs

The typical characterization factor for a TS's operation is the switching ratio, which is the ratio of the thermal resistance r in KW^{-1} between the "on" r_{on} and the "off" r_{off} state, as defined in Eq. (1):

$$R = r_{off} \cdot r_{on}^{-1} \qquad \text{Eq. (1)}$$

A higher ratio of thermal resistances means a better TS, as the difference between the heat-flux for the "on" and "off" states is larger.

3. REVIEW OF THE PRINCIPLES OF A THERMAL SWITCH

Different potential mechanisms of thermal control elements for magnetocaloric technologies were already presented in (Kitanovski et al., 2015b). The principles in this paper were divided into groups

based on the external actuation mechanisms that directly influence the fluid movement: mechanical, electrical and magnetic actuation. The operation of each mechanism is described and schematically presented in figures.

3.1. Mechanical actuation

3.1.1. Micro-droplet array

Fluids can be applied to lower the contact resistance between the solid-solid interface in mechanically actuated TSs. This usually involves a micro-droplet array on an interface, which enables reversible hydrophobic/hydrophilic fluid transitions. The surface covered with droplets is mechanically moved to make or break contact with two opposing surfaces. The concept for calorics is presented in Fig. 2 a) for a heated and b) for a cooled caloric material. The droplets undergo a reversible morphological transition into an almost or a continuous liquid film when they are mechanically compressed by an opposing substrate.

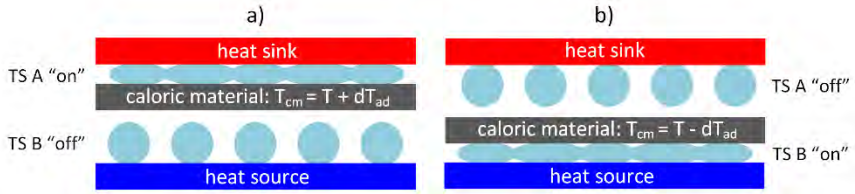

Figure 2: Heat transfer between a) heated and b) cooled caloric material and heat source/sink with the implemented TS of a micro-droplet array. The figure was reconstructed from Jia et al. (2012), Cho et al. (2007) and Cha and Ju (2009)

The thermal resistance between two solids therefore changes from the thermal resistance of the surrounding gas during the "off" state, to the thermal resistance of the fluid during the "on" state. A high thermal resistance ratio R can be achieved, for example, using a combination of liquid-metal droplets and the low thermal conductivity of the surrounding gas. The surface was prepared in different ways, e.g. Jia et al. (2012) and Cho et al. (2007) lithographically patterned hydrophilic islands on silicon substrates for glycerol or mercury droplets, while Cha and Ju (2009) proposed separated hydrophilic micro-channels for water.

3.1.2. Liquid/gas bridge and droplet/plug displacement

Using pumps or pistons we can create a liquid (Jeong et al., 2012) or gas bridge by controlling the volume flow through the entering channel between the caloric material and the heat source/sink. The generated liquid or gas bridge increases the heat-flux due to the lower thermal resistance of the working fluid, which is denoted as the "on" state, as presented in Fig. 3 I. The liquid bridge is broken during the "off" state, while the thermal resistance is higher. A piston or a pump can be applied to displace a drop of different fluid between two different positions, as presented in Fig. 3 II. Yang et al. (2018) implemented the hydraulic actuation of a liquid-metal galinstan droplet into a channel filled with aqueous NaOH. The droplet was alternatively moved between the "on" and "off" positions. When in the "on" position, the heat flux was established between the caloric material and the heat source/sink. They also tested the gravitational actuation by tilting the channel at small angles. Fig. 3 II, a) denotes the operation when the caloric material is heated and 3 II b) when it is cooled.

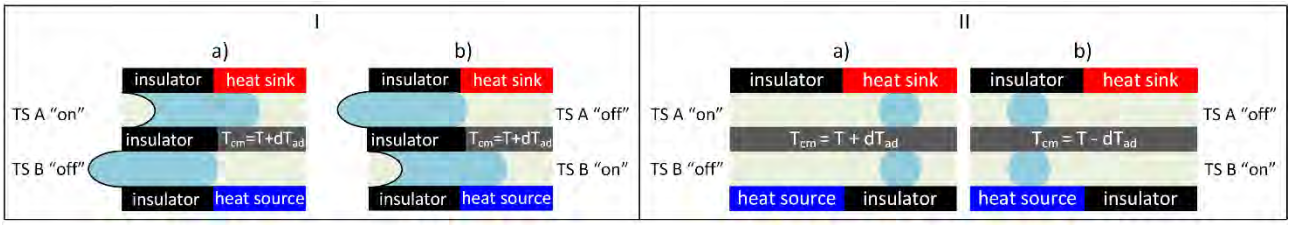

Figure 3: Heat transfer between a) heated and b) cooled caloric material and heat source/sink with an implemented TS using the liquid-bridge principle (I) and the droplet/plug displacement principle (II). The figure I was reconstructed from Jeong et al. (2012) and the figure II from Yang et al. (2018)

3.1.3. Continuous plug flow

Another type of micro-pump application is to provide a continuous plug flow of two different phases – a combination of fluids with high and low thermal conductivity. Hirasawa et al. (2016) implemented such a thermal switch in electrocalorics, where they alternatively pumped water and an air flow through multiple heat sinks and another under the caloric material elements connected to multiple heat sources, as presented in Fig. 4. The water and the air flow were coupled with a temperature change of the caloric material. Water was flowing through the channel when the switch was “on”, and during the “off” mode, the air flow lowered the heat-flux between the caloric material and the heat source/sink. The flows in the channel above and in the channel under the caloric material were of opposite phase. Therefore, in the upper channel the water was hot, while it was cold in the lower channel.

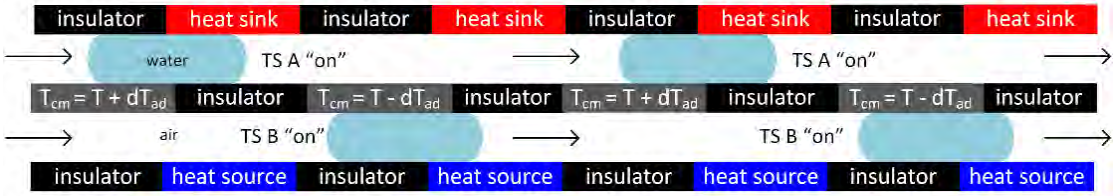

Figure 4: Operation of a TS of air and water plug flow for multiple caloric material elements, heat sources and heat sinks. The figure was reconstructed from Hirasawa et al. (2016)

3.2. Magnetic actuation

3.2.1. Ferrofluidic plugs

Fluid displacement in the micro-channel can be induced by the actuation of ferrofluids in micro-channels by external magnets. As presented by Hartshorne et al. (2004) ferrofluidic plugs can be used as an alternative to pumps or pistons. Another option is to move the ferrofluidic plug, which has a higher thermal conductivity than the surrounding liquid, between two positions and so establish a liquid bridge, similar to the hydraulic displacing presented by Yang et al. (2018) in Fig. 3 II. An example of a ferrofluidic plug actuated by external magnets was presented by Yamahata and Gijs (2004) in Fig. 5 I and Jeon et al. (2017). Similarly Puga et al. (2017) implemented a magnetic nanofluid to a thermal switch, where in the presence of a magnetic field, the nanofluid moved towards the heat sink (“on” state) and remained still when in the “off” state. In this way, the heat is transferred from the caloric material to the heat sink or from the heat source.

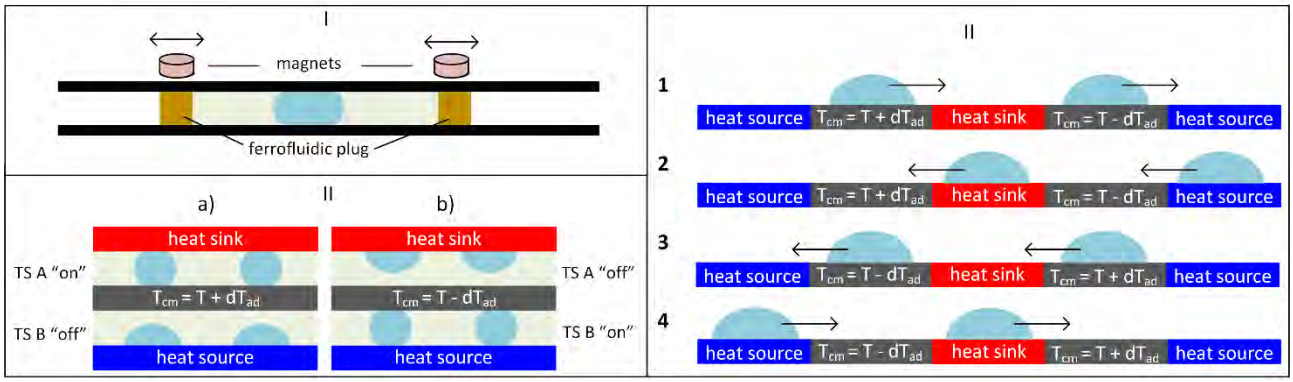

Figure 5: Use of a ferrofluidic plug for fluid displacement by external magnets (I). Vertical magneto-wetting actuation (II) for a) heated caloric material and b) cooled caloric material. Part III presents the operating sequence for the horizontal magneto-wetting actuation (III). The figure was reconstructed from Yamahata and Gijs (2004), Jeon et al. (2017), Puga et al. (2017), Nguyen et al. (2010) and Afkhami et al. (2010)

3.2.2. Magneto-wetting

Another type of magnetic actuation is magneto-wetting, where the surface tension of the fluid is manipulated by an external magnetic field. In this way, the shape of the liquid droplet is modulated to make or break the physical and thermal contact with the heat-transfer surfaces. There are two

main directions of droplet moving, i.e., vertically and horizontally, as presented in Fig. 5 II and III. Nguyen et al. (2010) and Afkhami et al. (2010) analysed the shape, motion and contact angles of ferrofluid droplets driven by a permanent magnet on a planar homogeneous surface. The ferrofluid was a water-based colloidal suspension of magnetic nanoparticles. Fig. 5 II presents a sequence of horizontal movements of the droplets between the caloric material and the heat source/sink. In magneto-wetting the heat is transferred from the caloric material to the heat sink or from the heat source by droplets, which make or break the thermal contact between the opposing surfaces and carry the heat.

3.3. Electrical actuation

The electrical manipulation of fluids in microsystems can be divided into two groups: the continuous-flow microfluidics and digital microfluidics. The continuous-flow microfluidics represents electrohydrodynamics and electrokinetics (e.g. electroosmosis, electrophoresis), where fluid continuously flows through a channel, while the digital microfluidics represents manipulation of the liquid subdivided into droplets (e.g. electro-wetting).

Hehlen et al. (2013) implemented electrohydrodynamic flows in dielectric fluids as thermal switch in electrocaloric refrigerator. They established convective heat transfer by applying electric field across the 500 μm thick gap of commercial hydrofluoroethers. The best achieved switching ratio between conductive and convective heat transfer was 4.7 at 390 V of bias voltage. The operation of the device is presented in Figure 6.

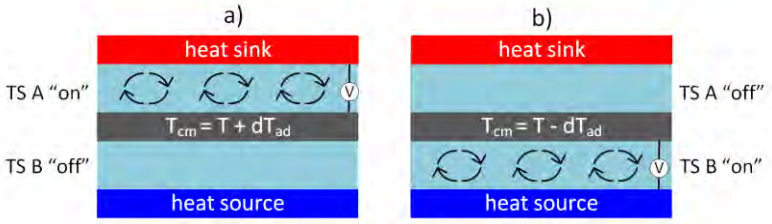

Figure 6: The convective heat transfer is occurred due to applied electric field. The figure was reconstructed from Hehlen et al. (2013)

Epstein and Malloy (2009) and Melo et al. (2016) presented thermal switch using nematic liquid crystals. The thermal conductivity of liquid crystal depends on orientation of molecular director. The application of electric field orientates the molecular director and changes thermal conductivity as presented in Figure 7.

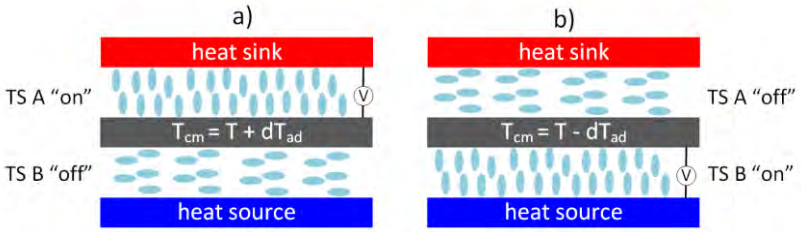

Figure 7: Thermal switch of nematic liquid crystal. The figure was reconstructed from Epstein and Malloy (2009) and Melo et al. (2016)

Electro-wetting is a process similar to magneto-wetting, only that the surface tension of the fluid is manipulated by an external electric field. Therefore, the principle is the same as presented in Fig. 5 I and II. Electro-wetting can be divided into electro-wetting on a dielectric (EWOD), electro-wetting on insulator-coated electrodes (EICE) and electro-wetting on line electrodes (ELE). If the process activates the movement of a droplet, we denote that as electro-capillary flow. In this paper we focused on EWOD only, since there are more applications. Cha et al. (2016) and Gong et al. (2008) demonstrated the actuation of liquid droplets between the beading and spreading states by using a pair of co-planar electrodes, where the ground and bias electrodes were constructed on the same plate. Another option for moving droplets is horizontally within the micro-channel with electrodes positioned on two opposing surfaces of the micro-channel. Kim and Wu, (2005) drove a liquid-metal

droplet in a micro-channel filled with a dielectric fluid. Similar to magneto-wetting, the heat carriers in this TS are manipulated droplets.

4. CONCLUSIONS

A selection of the best candidates and future development directions for caloric TSs at room temperature are based on matching the operating requirements and the applicability of the switch to the caloric device and the technology readiness level. The technology readiness level of the described mechanisms is high, due to increased basic and applied research and rapid prototyping in controlling the heat-flux in electronics, MEMS and microfluidics (Paredes et al., 2015, Morbioli et al., 2018). Most of the presented prototypes in this article were only proof-of-concept devices, so further modifications would improve the switching ratios and the switching time. In addition, they were not built for caloric technologies; therefore, they were not planned or tested at high operating frequencies and tested under operating conditions of caloric device.

In order to characterize the applicability of the presented TSs, we compared the parameters presented in Table 1. The most important parameters are the ratio of the thermal resistance and the switching time. The appropriate TS would have a high thermal resistance ratio and fast operation~ of order of milliseconds.

Table 1. Operating parameters for most applicable thermal switches in caloric technologies

Name	R [/]	Description	Switching time [ms]
Cho et al. (2007)	129 ± 43	**Mechanical actuation (micro droplet array):** mercury droplets on a silicon substrate surrounded by xenon, gap 100 μm wide	<100
Jia et al. (2012)	100	**Mechanical actuation (micro droplet array):** glycerol droplets surrounded by air on a silicon substrate	333
Yang et al. (2018)	70	**Mechanical actuation (plug displacement):** dry 0.9-mm-wide channel with galinstan droplet,	/
Jeong et al. (2012)	1.38	**Mechanical actuation (liquid bridge):** 33.3 μl of water liquid bridge pumped to a 6.25-mm high gap to establish heat transfer between two surfaces	/
Hirasawa et al. (2016)	/	**Mechanical actuation (continuous plug flow):** numerical simulation of water and air plug flow in a channel of thickness 100 μm	100
Puga et al. (2017)	2.6	**Magnetic actuation (magnetic nanofluid):** nanofluid actuated by external magnet in a 1-cm-high gap	33.3
Cha et al. (2016)	2.4 2.7	**Electrical actuation (electrowetting):** vertical EWOD with coplanar electrodes and water vertical EWOD with coplanar electrodes and mercury	<100 100
Hehlen et al. (2013)	4.7 ± 1.1	**Electrical actuation (electrohydrodynamics)** 500 μm gap of hydrofluoroethres, 390 V bias voltage	4000

We present here directions for the future implementation of a TS in caloric technologies. Thermal switch, which enables energy efficient operation of caloric device, should meet the following requirements:

- no or minimal moving parts,
- no or minimal heat generation due to the actuation,
- minimal thermal capacity,
- high switching frequency – above 40 Hz,
- ratio of thermal resistances above 20 (single switch) and above 100 (cascade switches),

- heat flux transmission above 1 W/cm^2
- life expectancy of more than 10^6 cycles.

Thermal control elements are seen as promising solutions for increasing the operating frequency and the energy efficiency of caloric devices. Especially because of the rapid improvement in micro-processing and the fabrication of micro-scale devices, various mechanisms and a variety of different processing methods thermal control elements are available at low cost. However, further basic and applied research has to be performed in order to successfully implement thermal control elements in caloric device that would outperform a conventional caloric device operating with the active-magnetic-regeneration principle.

ACKNOWLEDGEMENTS

The authors acknowledge the financial support of the Slovenian Research Agency for the following projects: Advanced electrocaloric energy conversion, L7-7580 and research core funding No. P2-0223.

NOMENCLATURE

R	ratio of thermal resistances between the "on" and "off" state	r	thermal resistance [K/W]
dT_{ad}	adiabatic temperature change [K]	T	Temperature [K]
T_{mc}	temperature of caloric material [K]		

REFERENCES

Afkhami S, Tyler A.J., Renardy Y., Renardy M., Pierre G. T. St., Woodward R.C., R.J.S., 2010. Deformation of a hydrophobic ferrofluid droplet suspended in a viscous medium under uniform magnetic fields. J. Fluid Mech. 663, 358–384.

Basiulis, A., Beach, R., Berry, R., Verdes, R., 1988. Solid-state electrocalric cooling system and method. US4757688. https://doi.org/US005485919A

Cha, G., Ju, Y.S., 2009. Reversible thermal interfaces based on microscale dielectric liquid layers. Appl. Phys. Lett. 94, 8–11. https://doi.org/10.1063/1.3142866

Cha, G., Kim, C.J., Ju, Y.S., 2016. Thermal conductance switching based on the actuation of liquid droplets through the electrowetting on dielectric (EWOD) phenomenon. Appl. Therm. Eng. 98, 189–195.

Cho, J., Wiser, T., Richards, C., Bahr, D., Richards, R., 2007. Fabrication and characterization of a thermal switch. Sensors Actuators, A Phys. 133, 55–63.

Epstein, R.I., Malloy, K.J., 2009. Electrocaloric devices based on thin-film heat switches. J. Appl. Phys. 106, 1–8.

Goetzler, W., Zogg, R., Young, J., Johnson, C., 2014. Alternatives to Vapor Compression HVAC Technology. ASHRAE J. 12–23.

Gong, J., Cha, G., Ju, Y.S., Kim, C.J., 2008. Thermal switches based on coplanar EWOD for satellite thermal control, in: Proceedings of the IEEE International Conference on Micro Electro Mechanical Systems (MEMS). MEMS, Tucson, USA, pp. 848–851.

Hartshorne, H., Backhouse, C.J., Lee, W.E., 2004. Ferrofluid-based microchip pump and valve. Sensors Actuators, B Chem. 99, 592–600.

Hehlen, M.P., Mueller, A.H., Weisse-Bernstein, N.R., Epstein, R.I., 2013. Electrocaloric refrigerator using electrohydrodynamic flows in dielectric fluids. Laser Refrig. Solids VI 8638, 86380D. https://doi.org/10.1117/12.2004009

Hirasawa, S., Kawanami, T., Shirai, K., 2016. Thermal Performance of Electrocaloric Refrigeration using Thermal Switches of Fluid Motion and Changing Contact Conductance. Am. J. Phys. Appl. 4, 134–139.

Jeon, J., Lee, J.B., Chung, S.K., Kim, D., 2017. On-demand magnetic manipulation of liquid metal in microfluidic channels for electrical switching applications. Lab Chip 17, 128–133.

Jeong, S.H., Nakayama, W., Lee, S.K., 2012. Experimental investigation of a heat switch based on the precise regulation of a liquid bridge. Appl. Therm. Eng. 39, 151–156.

Jia, Y., Cha, G., Ju, Y.S., 2012. Switchable Thermal Interfaces Based on Discrete Liquid Droplets. Micromachines 3, 10–20.

Kim, C., Wu, M.C., 2005. Electrowetting-based driving of liquid metal droplet for reliable RF switching, Air force research laboratory, Aberdeen.

Kitanovski, A., Egolf, P.W., 2010. Innovative ideas for future research on magnetocaloric technologies. Int. J. Refrig. 33, 449–464.

Kitanovski, A., Plaznik, U., Tomc, U., Poredoš, A., 2015a. Present and future caloric refrigeration and heat-pump technologies. Int. J. Refrig. 57, 288–298. https://doi.org/10.1016/j.ijrefrig.2015.06.008

Kitanovski, A., Tušek, J., Tomc, U., Plaznik, U., Ožbolt, M., Poredoš, A., 2015b. Magnetocaloric Energy Conversion. Springer, Switzerland.

Melo, D., Fernandes, I., Moraes, F., Fumeron, S., Pereira, E., 2016. Thermal diode made by nematic liquid crystal. Phys. Lett. Sect. A Gen. At. Solid State Phys. 380, 3121–3127.

Morbioli, G.G., Speller, N.C., Cato, M.E., Cantrell, T.P., Stockton, A.M., 2018. Rapid and Low-Cost Development of Microfluidic Devices Using Wax Printing and Microwave Treatment. Sensors Actuators B Chem.

Nguyen, N.T., Zhu, G., Chua, Y.C., Phan, V.N., Tan, S.H., 2010. Magnetowetting and sliding motion of a sessile ferrofluid droplet in the presence of a permanent magnet. Langmuir 26, 12553–12559.

Paredes, J., Fink, K.D., Novak, R., Liepmann, D., 2015. Self-anchoring nickel microelectrodes for rapid fabrication of functional thermoplastic microfluidic prototypes. Sensors Actuators, B Chem. 216, 263–270.

Puga, J.B., Bordalo, B.D., Silva, D.J., Dias, M.M., Belo, J.H., Araújo, J.P., Oliveira, J.C.R.E., Pereira, A.M., Ventura, J., 2017. Novel thermal switch based on magnetic nanofluids with remote activation. Nano Energy 31, 278–285.

Steven Brown, J., Domanski, P.A., 2014. Review of alternative cooling technologies. Appl. Therm. Eng. 64, 252–262.

Yamahata, C., Gijs, M.A.M., 2004. Plastic micropumps using ferrofluid and magnetic membrane actuation, in: 17th IEEE International Conference on Micro Electro Mechanical Systems. Maastricht MEMS 2004 Technical Digest. IEEE, Maastricht, Netherlands.

Yang, T., Kwon, B., Weisensee, P.B., Kang, J.G., Li, X., Braun, P., Miljkovic, N., King, W.P., 2018. Millimeter-scale liquid metal droplet thermal switch. Appl. Phys. Lett. 112.

Manuscript ID: 164
DOI: 10.18462/iir.icr.2019.0164

Investigation of the nucleation temperature of different heat exchanger surfaces in an ice store

Ursina OECHSLE, Klaus SPINDLER

Institute for Building Energetics, Thermotechnology and Energy Storage (IGTE), University of Stuttgart, Pfaffenwaldring 6, Stuttgart, 70569, Germany, ursina.oechsle@igte.uni-stuttgart.de

ABSTRACT

During loading ice stores, an ice layer forms on the heat exchanger surface once the surface reaches nucleation temperature. The growing ice layer increases the heat conduction resistance; the loading performance decreases.
In this work, the loading performance shall be optimized by changing the surface structure of the heat exchanger to lower the nucleation temperature. The ice store is loaded with an ice-free heat exchanger while ice grows apart from the heat exchanger.
The nucleation temperatures of heat exchangers of different materials with different surface roughness's and hydrophobic plasma coatings are examined in a model ice store. Furthermore, the nucleation temperatures of the heat exchanger surfaces are calculated using the classical nucleation theory and are compared to the experiments.
It is shown that the smoothest heat exchanger surface with a hydrophobic plasma coating lowers the nucleation temperature best. The loading performance is optimized.
Keywords: Coating (Materials), Cooling Load, Icing, Nucleation, Supercooling, Surface Temperature

1. INTRODUCTION

Renewable energies should be used for energy supply to minimize the climate change. The fluctuating supply of renewable energy sources requires energy storage to uncouple the energy demand from the energy supply. One possibility of energy storage is to use ice stores in combination with a cooling device for the air conditioning of buildings. They are used as thermal storages to increase the availability of the cooling supply. At the Institute of Thermodynamics and Thermal Engineering (ITW), an ammonia-water chiller was developed for solar cooling in combination with an ice store. By using ammonia as refrigerant, cold water temperatures of less than 0 °C are reachable and ice growth is possible. The ice store uncouples the cooling supply from the solar radiation and allows a more regular operation of the absorption chiller (Koller et al. 2007; Koller et al. 2012; Zetzsche et al. 2010). Ice stores are characterised by a high storage capacity because of the high enthalpy of fusion of ice of 333 kJ/kg, and small thermal losses. During loading ice stores, an ice layer forms on the heat exchanger surface when the surface temperature comes below the nucleation temperature. The growing ice layer increases the heat conduction resistance; the loading performance of the ice store decreases.
The idea in this work is to control the nucleation mechanism by modifying the heat exchanger's surface. Ideally, the water in the ice store can be supercooled while the ice growth is initiated at nucleation spots apart of the heat exchanger surface. This leads to a better loading performance of the ice store. The storage capacity increases because the ice store can be frozen with smaller heat exchangers.
In this paper, the influence of the surface structure and material on the nucleation temperature is examined. The nucleation temperature of the heat exchanger surface is calculated using the classical nucleation theory. The fundamentals of the model for the nucleation temperature calculation and theoretical results are discussed. Furthermore, the nucleation temperature is examined experimentally by measuring the maximum supercooling of the storage water during a loading procedure of a model ice store. First preliminary results of the experiments will be presented.

2. MODELLING OF THE NUCLEATION TEMPERATURE

Nucleation can occur homogeneously or heterogeneously. In the ice store, heterogeneous nucleation exists on the heat exchanger surface, as the heat exchanger surface is the coldest part in the ice store; see Fig. 1.

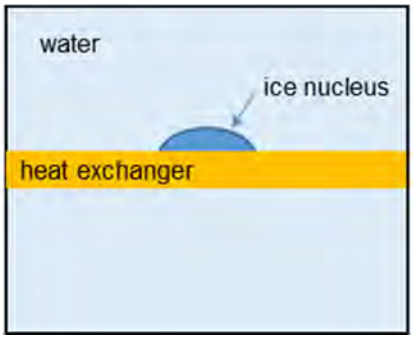

Figure 1: Ice nucleus on the heat exchanger tube in an ice store

The nucleation temperature is calculated in EES (Engineering Equation Solver) using the classical nucleation theory. This theory traces back to the work of Volmer and Weber (1926), Farkas (1927), Becker and Döring (1935) and Volmer (1939). The theory was developed for condensation, e.g. the phase change from vapour to liquid. Turnbull and Fisher (1949) transferred it to the phase change from liquid to solid, as it is for ice nucleation in supercooled water. Fundamental assumptions of the theory are a spherical nucleus; density and surface tension can be described with macroscopic values. Further standard works used for the following remarks are from Fletcher (1958), Dufour and Defay (1963), Defay and Prigogine (1966), Fletcher (1970), Hobbs (1974), Debendedetti (1996), Pruppacher and Klett (1997), Kashchiev (2000) and Vehkamäki (2011).
For the growth of an ice nucleus in supercooled water, molar reorientations at constant pressure and temperature occur. Water-to-water bonds are broken and water-to-ice bonds are created. A water molecule has to break away from its equilibrium position in water and find its equilibrium position in the ice structure. For the diffusion of the water molecule across the water-ice-boundary layer an activation energy must be overcome. The nucleation rate specifies the rate that a built nucleus grows by molecule flow and initiates phase change. The nucleation rate defines how many critical nuclei are built within a second in a defined volume. The heterogeneous nucleation rate J^{het} in supercooled water is defined by Eq. (1).

$$J^{het} = \frac{N_C \cdot k_B \cdot T_{H_2O}}{h} \cdot \frac{v_{ice}}{v_{H_2O}} \cdot \sqrt{\frac{4 \cdot \sigma_{H_2O,ice}}{k_B \cdot T_{H_2O}}} \cdot e^{-\frac{\Delta F_G^{het}}{k_B \cdot T_{H_2O}}} \cdot e^{-\frac{\Delta F_a}{k_B \cdot T_{H_2O}}} \qquad \text{Eq. (1)}$$

During loading an ice store with the water volume $V_{H_2O,St}$, the time when the water has $T_o = 0\,°C$ is t_o. The time when the nucleation temperature T_N is reached is t_N. Then ice growth starts. Assuming that water freezes when one critical nucleus is built, Eq. (2) is valid.

$$\int_{t_o}^{t_N} V_{H_2O,St} \cdot J^{hom} \cdot dt = 1 \qquad \text{Eq. (2)}$$

With a constant cooling rate $C = -dT/dt$, the nucleation temperature T_N can be calculated by Eq. (3).

$$-\frac{V_{H_2O,St}}{C} \int_{T_o}^{T_N} J^{hom} \cdot dT_{H_2O} = 1 \qquad \text{Eq. (3)}$$

For the specific volume of water v_{H_2O}, the specific enthalpy of fusion of ice Δh_f, the interfacial tension between water and ice $\sigma_{H_2O,ice}$, the free activation energy for the diffusion of a water molecule

through the ice-water-boundary-layer ΔF_a, correlations from the literature listed above are used. The free energy of formation of a critical nucleus for heterogeneous nucleation $\Delta {F_G}^{het}$ is calculated by Eq. (4):

$$\Delta F_G^{het} = \frac{1}{3} \cdot \left(\sigma_{H_20,ice} \cdot A_{H_20,ice} + \sigma_{ice,\mathrm{HE}} \cdot A_{ice,\mathrm{HE}} - \sigma_{H_20,\mathrm{HE}} \cdot A_{H_20,\mathrm{HE}}\right) \quad \text{Eq. (4)}$$

The contact area between water and heat exchanger equals, after the ice nucleus growth, the contact area between ice and heat exchanger, see Eq. (5).

$$A_{H_20,\mathrm{HE}} = A_{ice,\mathrm{HE}} \quad \text{Eq. (5)}$$

The equation of Young describes the equilibrium of forces on a drop in a thermodynamic equilibrium. According to Young, a correlation exists between the contact angle θ and the interfacial tensions; see Eq. (6).

$$\cos\theta = \frac{\sigma_{H_2O,HE} - \sigma_{ice,\mathrm{HE}}}{\sigma_{H_2O,ice}} \quad \text{Eq. (6)}$$

Resulting Eq. (7) for the free energy of formation ΔF_G^{het}:

$$\Delta F_G^{het} = \frac{1}{3} \cdot \sigma_{H_20,ice} \left(A_{H_20,ice} - A_{Eis,HE} \cdot \cos\theta\right) \quad \text{Eq. (7)}$$

The contact areas between water and ice and the heat exchanger depend on the structure of the heat exchanger surface. The surface of a rough heat exchanger can be convex or concave; the ice nucleus can grow on a peak or in a notch, see Fig. 2. Besides, in Fig. 2, the geometrical coherences of an ice nucleus growing on a rough heat exchanger surface are visible.

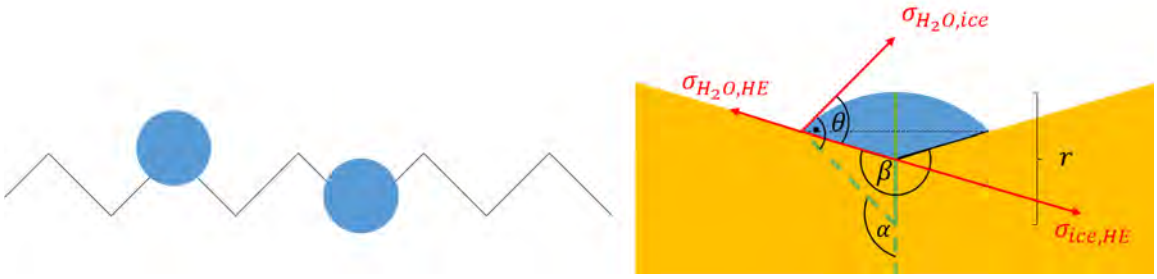

Figure 2: Critical ice nucleus in water on a rough heat exchanger surface for heterogeneous nucleation

The surface area of the ice lens A_{ice,H_2O} (i.e. the contact area between water and ice) and the contact area between ice nucleus and heat exchanger surface $A_{ice,HE}$ are calculated by Eq. (8) and (9). The radius of the ice nucleus r, the contact angle θ, the curvature radius of the heat exchanger surface β and the position angle of the ice nucleus α are used.

$$A_{ice,H_2O}^{het} = 2\pi r^2 \cdot (1 - \cos\alpha) \quad \text{Eq. (8)}$$

$$A_{ice,HE}^{het} = \pi \cdot r^2 \cdot \frac{\sin^2\alpha}{\sin\frac{\beta}{2}} \quad \text{Eq. (9)}$$

It results Eq. (10) for the free energy of formation of a critical nucleus for heterogeneous nucleation ΔF_G^{het}.

$$\Delta F_G^{het} = \frac{1}{3} \cdot \sigma_{H_20,ice} \cdot \pi \cdot {r_G}^2 \cdot \left(2 - 3\sin\left(\frac{\beta}{2} - \theta\right) + \sin^3\left(\frac{\beta}{2} - \theta\right) - \cos^3\left(\frac{\beta}{2} - \theta\right) \cdot \cot\frac{\beta}{2}\right) \quad \text{Eq. (10)}$$

Comparing the free energy of formation of a critical nucleus for heterogeneous nucleation in Eq. (10) to homogeneous nucleation ($\Delta F_G^{hom} = \frac{4}{3} \cdot \sigma_{H_2O,ice} \cdot \pi \cdot {r_G}^2$), it turns out in Eq. (11) that the free energy of formation for heterogeneous nucleation is the free energy of formation for homogeneous nucleation multiplied by the geometry factor $f(\beta, \theta)$ (Li et al. 2017).

$$\begin{aligned} \Delta F_G^{het} &= f(\beta, \theta) \cdot \Delta F_G^{hom} \\ &= \frac{1}{4}\left(2 - 3\sin\left(\frac{\beta}{2} - \theta\right) + \sin^3\left(\frac{\beta}{2} - \theta\right) - \cos^3\left(\frac{\beta}{2} - \theta\right) \cdot \cot\frac{\beta}{2}\right) \cdot \Delta F_G^{hom} \end{aligned} \quad \text{Eq. (11)}$$

The boundary conditions for the formation of a stable nucleus in a notch of the heat exchanger surface are listed in Eq. (12)

$$0 < \beta \leq 180° \qquad 90° - \frac{\beta}{2} < \theta < 90° + \frac{\beta}{2} \qquad \beta > \alpha > 0° \quad \text{Eq. (12)}$$

The boundary conditions for a stable ice nucleus on a peak of the heat exchanger surface are defined in Eq. (13).

$$180° < \beta < 360° \qquad \frac{\beta}{2} - 90° < \theta < 270° - \frac{\beta}{2} \qquad 180° > \alpha > \beta - 180° \quad \text{Eq. (13)}$$

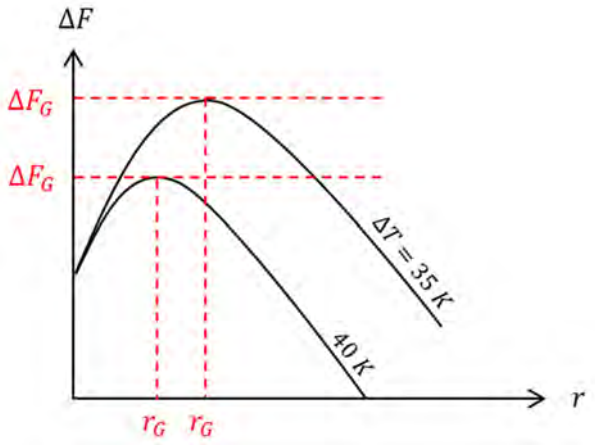

Figure 3: Free energy of formation of a nucleus ΔF depending on the radius of the nucleus r for different supercoolings ΔT

The free energy of formation of an ice nucleus ΔF consists of the required energy to build the new surface of the growing ice nucleus and the gained volume work by releasing the enthalpy of fusion of ice. The free energy of formation of a nucleus versus the nucleus radius for different supercooling is drawn in Fig. 3. For the formation of a critical nucleus, the free energy of formation has its maximum and the critical radius r_G is:

$$r_G = \frac{2 \cdot \sigma_{H_2O,ice} \cdot v_{ice}}{\Delta h_f \cdot \frac{T_o - T_{H_2O}}{T_o}} \quad \text{Eq. (14)}$$

The nucleation temperature of the heat exchanger surface during the cooling process of the ice store can be calculated considering all these information's in Eq. (3). The values of the model ice store for experimental investigations are used for the theoretical calculation.

3. THEORETICAL RESULTS FOR THE NUCLEATION TEMPERATURE

Fig. 4 shows the geometry factor $f(\beta,\theta)$ and the nucleation temperature T_N versus the contact angle θ for different angles of curvature of the heat exchanger surface β, calculated with the above presented model in EES. Exemplary geometrical cases for the formation of stable ice nuclei on heat exchanger surfaces with varied curvature angles β and varied contact angles θ are presented in Table 1.

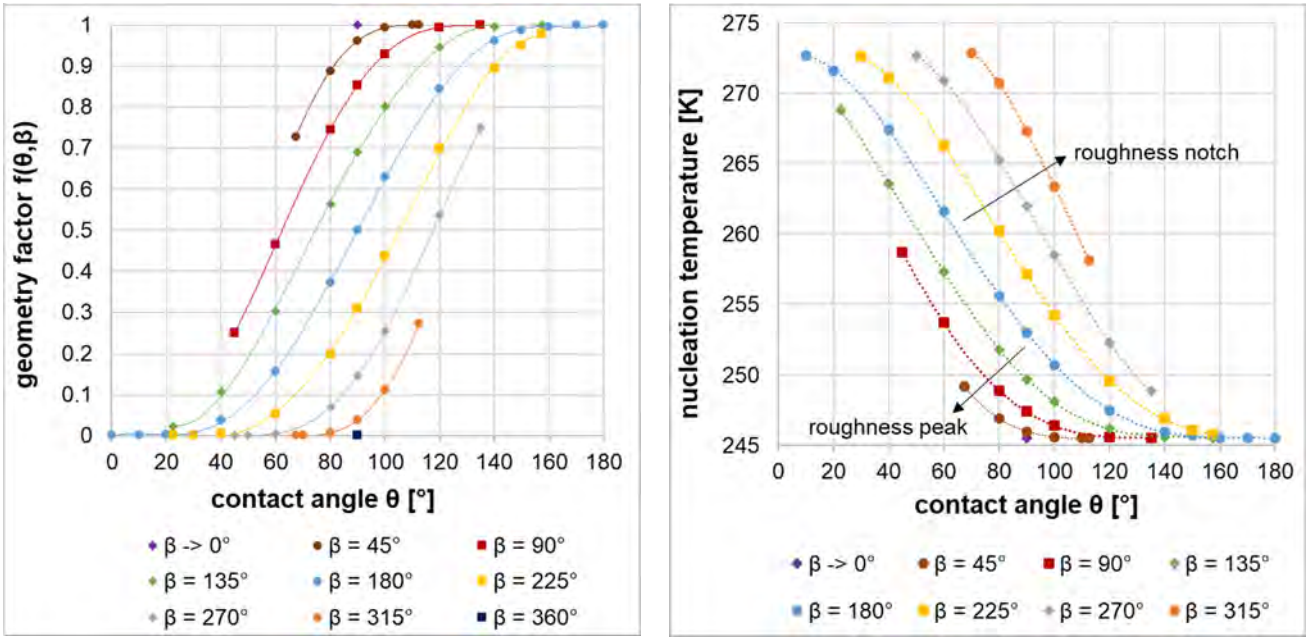

Figure 4: Geometry factor and nucleation temperature over the contact angle θ for different angles of curvature of the heat exchanger surface β

Table 1: Exemplary cases for the formation of stable ice nuclei on heat exchanger surfaces with varied curvature angles β and varied contact angles θ

	$\theta = 0°$	$\theta = 45°$	$\theta = 90°$	$\theta = 135°$	$\theta = 180°$
$\beta \to 0°$	X	X		X	X
$\beta = 90°$	X	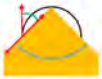			X
$\beta = 180°$	$r_g \to \infty$ 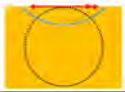	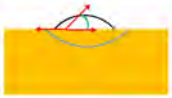	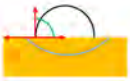	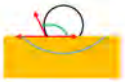	
$\beta = 270°$	X			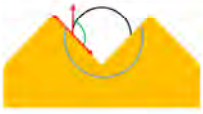	X
$\beta \to 360°$	X	X	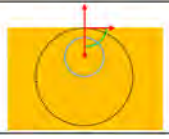	X	X

The nucleation temperature is lowest when homogeneous nucleation can occur. Therefore, the geometry factor must be one. This is the case for decreasing β and growing θ. Then, the contact area between ice and heat exchanger is small and nearly a full ice sphere has to be built. The minimum reachable nucleation temperature is 246 K for a heat exchanger surface with the most pointed peak. However, such a heat exchanger surface also forms a narrow notch where nucleation is initiated already at a low supercooling. Therefore, it is best for the lowering of the nucleation temperature to use the smoothest heat exchanger surface ($\beta = 0°$) with the largest possible contact angle ($\theta \rightarrow 180°$).

4. EXPERIMENTAL RESULTS FOR THE NUCLEATION TEMPERATURE

The experimental setup was presented by Oechsle and Spindler (2016). In a model ice store filled with ultrapure water, demineralized water or tap water different heat exchanger tubes are examined. They differ in their materials (copper, aluminium, stainless steel), their surface roughness's R_a and R_z (electropolished, sandblasted) and their surface plasma coatings. Ethanol flows through the heat exchangers. At the beginning of a loading procedure of the model ice store the ethanol and the water have a temperature of 7 °C. Then, the temperature of the ethanol is set to -2 °C for 6 hours. Afterwards the temperature is reduced in steps of 0.1 K every 30 minutes until ice growth starts at the heat exchanger surface. The minimum water temperature in the model ice store is measured. This leads to the maximum supercooling of the water $\Delta T = T_0 - T_N$ and approximately to the nucleation temperature T_N. For each heat exchanger with each water quality, 10 experiments are done and the mean nucleation temperature is defined. The characteristics of the different heat exchangers are listed in Table 2. First preliminary experimental results for the maximum supercooling reached with the different heat exchangers are listed in Table 3.

Table 2: Characteristics of the different heat exchanger surfaces

Heat exchanger surfaces	Copper (Cu)		Aluminium		Stainless steel	
	R_a [µm]	R_Z [µm]	R_a [µm]	R_Z [µm]	R_a [µm]	R_Z [µm]
Electropolished	0.280	1.786	0.238	1.615	1.07	6.56
Fine sandblasted	0.3	0.705	-	-	-	-
Middle sandblasted	0.985	1.945	-	-	-	-
Electropolished and plasma coated ($\theta = 86.3°$)	0.102	0.636	-	-	-	-

Table 3: Mean maximum reached supercooling with the different heat exchangers during a loading procedure of the model ice store

Heat exchanger surface	Ultrapure water	Demineralized water	Tap water
Cu electropolished	0.9 ± 1.0 °C	0.3 ± 0.5 °C	1.3 ± 0.2 °C
Cu fine sandblasted	0.9 ± 0.4 °C	-	-
Cu electropolished and plasma coated	1.3 ± 0.4 °C	1.0 ± 0.4 °C	2.2 ± 0.3 °C

It turns out, that the smooth electropolished copper surface with plasma coating reaches the highest supercooling. That means it lowers the nucleation temperature best. The lightly alkaline tap water ($pH \sim 8.2$) allows a higher supercooling than the lightly acidic ultrapure water ($pH \sim 6.5$). The neutral demineralized water ($pH \sim 7.4$) leads to the lowest supercooling. The ultrapure water has an electrical conductivity of $0.24 - 0.4\ \mu S \cdot cm^{-1}$, demineralized water of $10.8 - 13.3\ \mu S \cdot cm^{-1}$ and tap water of $281 - 331\ \mu S \cdot cm^{-1}$.
Detailed water analyses regarding the electrical conductivity, the pH number and the chemical and biological composition will follow. Furthermore, the contact angle of each heat exchanger surface has to be defined in the following research.

5. CONCLUSION AND OUTLOOK

The comparison between experimental und theoretical results for the nucleation temperature shows a good qualitative agreement. The smoothest heat exchanger surface with a hydrophobic plasma coating lowers the nucleation temperature best. The loading performance is optimized.
Regarding the quantitative values, a detailed comparison has to be done. From the roughness profiles of the different heat exchanger surfaces, the angle of curvature of the heat exchanger surface β has to be calculated. The different materials or plasma coatings define the contact angle θ, that has to be determined. Then, the nucleation temperature of each heat exchanger surface can be calculated and compared to the nucleation temperatures reached experimentally.
Further experiments will be conducted with the parameter variation of the heat exchanger surface listed in Table 2.

NOMENCLATURE

$A_{ice,HE}$	Contact area between ice nucleus and heat exchanger (m²)	T_N	Nucleation temperature (K)
$A_{H_20,ice}$	Contact area between ice nucleus and water (m²)	v_{ice}	Specific volume of ice (m³×kg^{-1})
$A_{H_20,HE}$	Contact area between water and heat exchanger (m²)	v_{H_2O}	Specific volume of water (m³×kg^{-1})
C	Cooling rate (5,6×10^{-5} K×s^{-1})	$V_{H_2O,St}$	Water volume in the ice store (m³)
$f(\beta,\theta)$	Geometry factor	ΔF	Free energy of formation of a nucleus (J)
h	Plank constant (6.626×10^{-34} J×s)	ΔF_a	Free activation energy for the diffusion of a water molecule through the water-ice-boundary layer (J)
J^{het}	Heterogeneous nucleation rate (m^{-3}×s^{-1})	ΔF_G	Free energy of formation of a critical nucleus (J)
k_B	Boltzmann constant (1.381×10^{-23} J×K^{-1})	ΔF_G^{het}	Free energy of formation for a critical nucleus for heterogeneous nucleation (J)
N_C	Number of water molecules in contact with ice surface (5.3×10^{18} m^{-2})	ΔF_G^{hom}	Free energy of formation for a critical nucleus for homogeneous nucleation (J)
r	Radius of ice nucleus (m)	Δh_f	Specific enthalpy of fusion of ice (J×kg^{-1})
r_G	Critical radius of ice nucleus (m)	ΔT	Supercooling (K) $= T_0 - T_N$
t	Time (s)	α	Position angle of the ice nucleus (°)
t_0	Time when the water has $T_o = 0\ °C$ (s)	β	Angle of curvature of the heat exchanger surface (°)
t_N	Time when the water has T_N (s)	θ	Contact angle (°)
T	Temperature (K)	$\sigma_{H_20,ice}$	Interfacial tension between water and ice nucleus (J×m^{-2})
T_o	Melting temperature of water (273.15 K)	$\sigma_{ice,HE}$	Interfacial tension between ice nucleus and heat exchanger (J×m^{-2})
T_{H_2O}	Water temperature (K)	$\sigma_{H_20,HE}$	Interfacial tension between water and heat exchanger (J×m^{-2})

REFERENCES

Becker, R.; Döring, W., 1935. Kinetische Behandlung der Keimbildung in übersättigten Dämpfen. Annalen der Physik. 5 (24), 719–752.

Debendedetti, P. G., 1996. Metastable Liquids. Concepts and Principles. New Jersey Princeton University Press (Physical Chemistry: Science and Engineering), 411 p.

Defay, R.; Prigogine, I., 1966. Surface Tension and Adsorption Longmans, Green & Co LTD, 432 p.

Dufour, L.; Defay, R., 1963. Thermodynamics of Clouds. International Geophysics Series, vol. 6, 255 p.

Farkas, L., 1927. Keimbildungsgeschwindigkeit in übersättigten Dämpfen. Zeitschrift für physikalische Chemie (125), 236–242.

Fletcher, N. H., 1958. Size Effect in Heterogeneous Nucleation. The Journal of Chemical Physics 29 (3), 572–576.

Fletcher, N. H., 1970. The Chemical Physics of Ice. Cambridge University Press (Cambridge monographs on physics), 271 p.

Hobbs, P. V., 1974. Ice Physics. Oxford Clarendon Press, 837 p.

Kashchiev, D., 2000. Nucleation. Basic Theory with Applications. Oxford Butterworth Heinemann, 529 p.

Koller, T. et al., 2007. Design and Operation of a Small Scale Ice Storage. 2nd International Conference Solar Air-Conditioning. Tarragona. Ostbayerisches Technologie-Transfer-Institut e. V. (OTTI).

Koller, T. et al., 2012. Experimental and theoretical investigations of solidification and melting of ice for the design and operation of an ice store. Int. J. Ref. 35 (5), 1253–1265.

Li, Y. et al., 2017. Ultra-high open-circuit voltage of perovskite solar cells induced by nucleation thermodynamics on rough substrates. Scientific Reports (7), 1–10.

Oechsle, U.; Spindler, K., 2016. Investigation of micro- and nanostructured coatings for heat exchanger surfaces in an ice store. J. Phys.: Conf. Ser. 745 (032135), 1–8.

Pruppacher, H.; Klett, J., 1997. Microphysics of Clouds and Precipitation. 2nd ed. Dordrecht Kluwer Academic Publishers, 948 p.

Turnbull, D.; Fisher, J. C., 1949. Rate of Nucleation in Condensed Systems. The Journal of Chemical Physics 17 (1), 71–73.

Vehkamäki, H., 2011. Classical Nucleation Theory in Multicomponent Systems. Berlin, London Springer, 189 p.

Volmer, M., 1939. Kinetik der Phasenbildung. Die chemische Reaktion, IV, 218 p.

Volmer, M.; Weber, A., 1926. Keimbildung in übersättigten Gebilden. Zeitschrift für physikalische Chemie (119), 277–301.

Zetzsche, M. et al., 2010. Entwicklung einer Ammoniak/Wasser Kälteanlage zur solaren Kühlung - abschließende Bewertung. Jahrestagung des Deutschen Kälte- und Klimatechnischen Vereins AA.II.1.17. Magdeburg, Germany.

Manuscript ID: 167
DOI: 10.18462/iir.icr.2019.0167

Investigation of Combination of a Rotary Vane Expander and an Expansion Valve in a Refrigeration System

Rahul THAKUR[(a)], Anarghya MURTHY[(a)], Alison SUBIANTORO[(a)]

[(a)] Department of Mechanical Engineering,
The University of Auckland, Auckland, New Zealand.
a.subiantoro@auckland.ac.nz

ABSTRACT

Throttling loss is a major source of inefficiencies in a typical refrigeration system. Expanders have been proposed and studied to recover the expansion work previously. In this study, a four-vane rotary expander is developed and will be tested in an R22 refrigeration system. The expander will be installed in combination with an expansion valve to allow for refrigerant flow adjustments. Preliminary experiments were carried out using compressed air as the working fluid to study the expander. The experiments show that the maximum isentropic efficiency was 19% at 561 rpm, the maximum volumetric efficiency was 30% at 1264 rpm and the maximum mechanical efficiency was 7% at 561 rpm. A simulation model was also developed to observe the COP improvements in the modified R22 refrigeration system. The simulation results show that the COP improvements were 2.5-6% and 3.5-8.5% on the heating and cooling sides, in comparison with the benchmark system without an expander.

Keywords: Refrigeration, R22, Expander, Energy, Rotary Vane, Efficiency.

1. INTRODUCTION

Since the mid-20th century, the level of increase in the concentration of greenhouse gasses has been unprecedented (Nakicenovic, 2007). Power generation is one of the major contributors to greenhouse gas emissions (Core Writing Team et al., 2014). In developed countries, building energy use has surpassed the other major sectors such as industrial and transportation (Hossain et al., 2015).

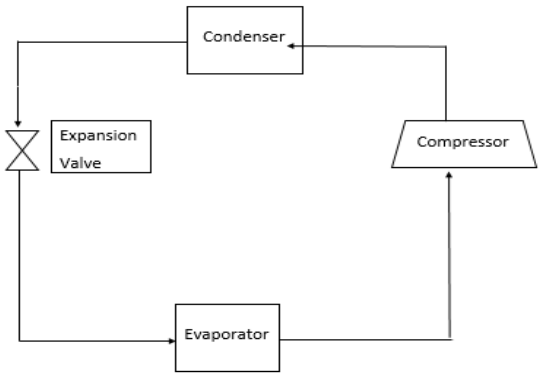

Figure 1 (a): Conventional vapour compression system

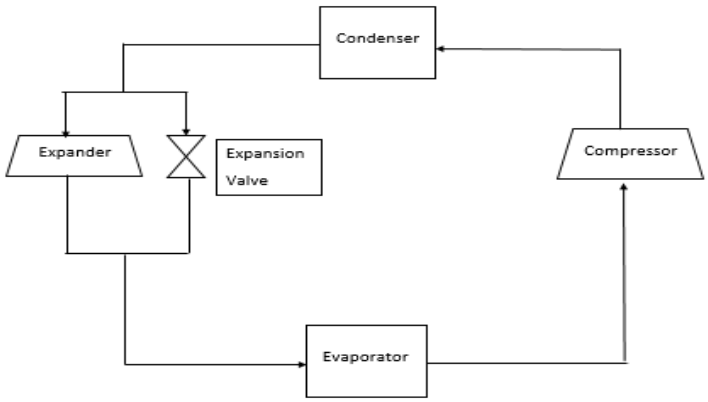

Figure 1 (b): Modified vapour compression system

There has been a steady increase in the energy consumption for both the residential and commercial buildings. The primary consumer of energy in buildings is the Heating and Air Conditioning systems. For example, in the United States, it accounts for 50% of the building energy consumption (DoE, 2012). Therefore, improving the energy efficiency of these systems is imperative. Most refrigerators, heat pumps and air conditioners operate based on the Vapour Compression (VC) cycle principle. The schematic of a conventional VC system is shown in Fig. 1(a). One of the major causes of energy loss in a VC system is the throttling loss that occurs in a conventional expansion valve (Subiantoro

and Ooi, 2015). The throttling process by the conventional expansion device is a sudden expansion process of the refrigerant flowing through the VC system. An expander can be used to overcome the throttling loss by recovering the expansion work to produce useful energy. In addition, an expander expands the fluid more isentropically than a throttling device. Therefore, expanders improve the energy efficiency of a VC system in two ways, by producing power and by providing extra cooling capacity through isentropic expansion. To recover the expansion process, many types of expanders have been studied, such as rotary vane (Fukuta and Yanagisawa, 2003), screw (Stosic et al. 2002), reciprocating (Nickl et al. 2002), scroll (Kohsokabe et al. 2006) and revolving vane (Subiantoro and Ooi, 2009). One of the major practical challenges of this concept at the moment is the loss of the simple flow adjustment possibility that is usually available with an expansion valve (Cao et al., 2016). In this study, a modified VC system shown in Fig. 1(b) is studied, in which an expander is installed in parallel to an expansion valve to still allow a degree of flow adjustment when there is a change in the cooling load. Of course, this will come at the cost of the loss of some expansion energy in the valve. The refrigerant used in the study is R22.

2. TEST SETUPS

2.1. Expander Prototype

A rotary vane type expander was used in this experiment because of its simple structure and its unique port control system which makes it requires no valves in its operation. The inside of the expander is shown in Fig. 2. In this expander, two long and intersecting vanes are used instead of four separate vanes. Having only two vanes meant that there are only two contact points between the vane and the stator wall, instead of four. Therefore, at one end of each vane, there will be a gap between the stator wall and the vane tip. This may reduce friction losses but is expected to amplify the internal leakage.

The key operating characteristics for an expander are its volumetric efficiency, mechanical efficiency and isentropic efficiency. Volumetric efficiency represents the internal leakage of fluid between the suction and the discharge ports. Due to leakage, some of the fluid escapes the expander without expanding and doing any work. The main geometric parameters, together with the inlet/outlet port arrangement of the expander prototype, are shown in the Table 1.

Table 1. Main dimension and parameters

Item	Value
Radius of the rotor	27.7 mm
Radius of the stator	40.7 mm
Length of the cylinder	38.6 mm
Number of vanes	4
Angle range of inlet port	0° – 90°
Angle range of outlet port	225° – 360°



Figure 2: Rotary vane expander prototype

The volumetric efficiency, η_v, is defined as shown in Eq. (1).

$$\eta_v = \frac{\dot{m}_{ideal}}{\dot{m}_{real}} \quad \text{Eq. (1)}$$

The ideal inlet mass flow rate, $\dot{m}_{ideal}$ is calculated by Eq. (2).

$$\dot{m}_{ideal} = \rho \times V_1 \times f \times n_e \quad \text{Eq. (2)}$$

Mechanical efficiency quantifies the frictional losses in the expander that reduce its power output. The mechanical efficiency, η_m, is defined as shown in Eq. (3).

$$\eta_m = \frac{\dot{W}_{real}}{\dot{W}_{ideal}} \quad \text{Eq. (3)}$$

The ideal power, $\dot{W}_{ideal}$ is calculated with Eq. (4) where pressure *P* is calculated with Eq. (5).

$$\dot{W}_{ideal} = \left(\left[\int_{V_1}^{V_2} P dv\right] + P_1V_1 + P_2V_2\right) \times f \times n_e \quad \text{Eq. (4)}$$

$$\frac{P_1}{P_2} = \left(\frac{V_1}{V}\right)^{1.4} \quad \text{Eq. (5)}$$

Lastly, the isentropic efficiency, η_{is}, is defined as shown in Eq. (6).

$$\eta_{is} = \frac{\Delta h_{real}}{\Delta h_{isen}} \quad \text{Eq. (6)}$$

The change in enthalpy is calculated using Eq. (7).

$$\Delta h = C_p \times (T_{in} - T_{out}) \quad \text{Eq. (7)}$$

2.2. Experimental Methodology

The expander was preliminary tested using compressed air for simplicity. The exit of the expander was exposed to the surroundings making it an open system. A schematic diagram of the experimental set up is shown in the Fig. 3. It was tested at various speed with pressures of 4 bar and 5 bar. A dynamometer was used to measure the torque produced by the expander and to control its rotational speed. The rotational speed of the expander was measured using an optical sensor. Thermocouples (type K) were used to find the temperatures of the fluid at the inlet and the outlet of the expander which were then used to find the specific enthalpy (h) and the density (ρ) at both the inlet and the outlet. A flow meter was used to find the flow rate of the fluid into the expander. The degree of accuracy of the measuring instruments of thermocouple and flow meter are $\pm$ 0.5˚C and $\pm$ 1.5%, respectively.

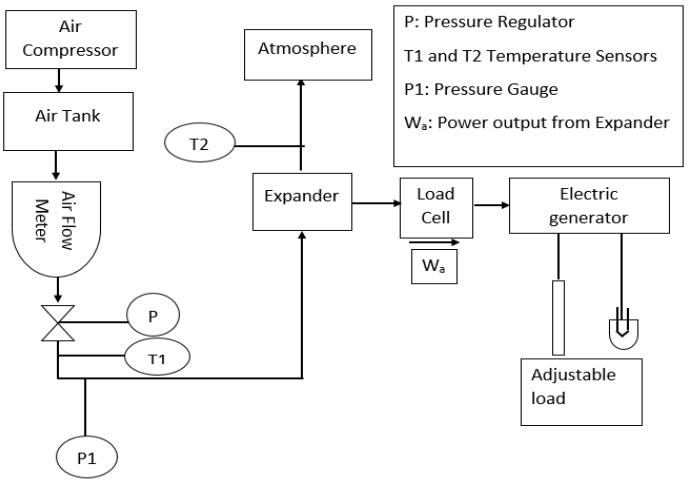

Figure 3. Schematic diagram of the experimental set up

2.3. Simulation of the Refrigeration System

A simulation model was built based on an existing R22 water-cooled heat pump system in our lab. The system had no expander and used only a thermostatic expansion val Mookambika Devi Kripave for expansion. The performance of this system was used for benchmarking in this study. Temperature sensors, flow meters and pressure transducers are installed at various strategic locations in the system. Based on these data, the entropies and enthalpies of the refrigerant at various locations were obtained using the CoolProp database (Bell et al., 2014). The benchmark experimental data of the system is shown in Fig. 4. The compressor isentropic efficiency and maximum volume ratio was found to be 65% and 8.3. The refrigeration cycle was assumed to follow the ideal vapour refrigeration conditions. The condensing temperature was 22°C and evaporating temperature was -30°C**.** The expansion process in an expander was assumed isentropic, and hence the outlet and inlet entropies were the same. With the expander outlet entropy and density known, the other characteristics were calculated using CoolProp database. Subsequently, an isentropic efficiency term (see Eq. 8) was added to account for the expander losses.

$$h_{out} = h_{in-}\eta_s * (h_{in} - h_{out_{isentropic}}) \quad \text{Eq. (8)}$$

The benchmark coefficient of performance (COP) on the cooling and heating sides were 1.804 and 2.769 respectively. The COPs were calculated using Eqs. (9) and (10).

$$\text{COP}_{\text{Benchmark, cooling}} = \frac{\dot{Q}_{Evaporator}}{\dot{W}_{Compressor}} \quad \text{Eq. (9)}$$

$$\text{COP}_{\text{Benchmark, heating}} = \frac{\dot{Q}_{Condenser}}{\dot{W}_{Compressor}} \quad \text{Eq. (10)}$$

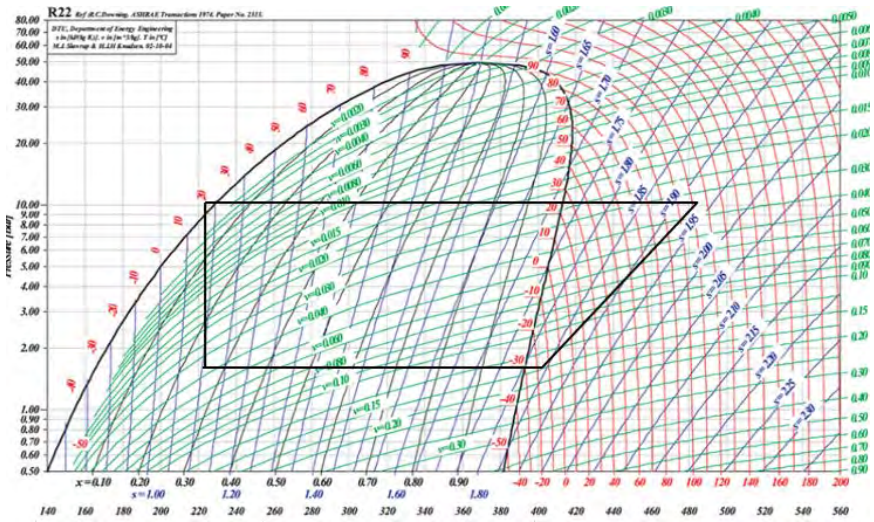

Figure 4: Pressure-enthalpy diagram of the benchmark system (chart from Dowing, 1974)

The mixed fluid property at the junction of the expander and expansion valve outlets was calculated using Eq. (11), where $\dot{m}_{valve}, \dot{m}_{expnader}$ and $\dot{m}_{mixed}$ are the mass flow rate at each location and P can be pressure, enthalpy, etc.

$$P_{mixed} * \dot{m}_{mixed} = P_{valve} * \dot{m}_{valve} + P_{expander} * \dot{m}_{expander} \quad \text{Eq. (11)}$$

With an expander, work is recovered during the expansion process, thus the COPs of a VC system with an expander are defined by Eqs. (12) and (13). It is noted that the cooling capacity at the evaporator may change due to the different expansion process of the refrigerant in an expander.

$$\text{COP}_{\text{expander, heating}} = \frac{\dot{Q}_{Condenser}}{\dot{W}_{Compressor} - \dot{W}_{expander}} \quad \text{Eq. (12)}$$

$$\text{COP}_{\text{expander, cooling}} = \frac{\dot{Q}_{Evaporator,exp}}{\dot{W}_{Compressor} - \dot{W}_{expander}} \quad \text{Eq. (13)}$$

3. RESULTS

3.1. Experimental Results of the Expander

Fig. 5 shows the measured volumetric efficiency of the expander with varying rotational speed at two different inlet pressures. The highest efficiency achieved at an inlet pressure of 4 bar was 30% at 1264 rpm. At 5 bar of inlet pressure, the highest volumetric efficiency was 28% at 1660 rpm. From the trend, it is evident that as the speed rises the volumetric efficiency also rises. This is thought not to be caused by a reduced leakage, like in typical rotary vane machines where the increased speed increases centrifugal force, which reduces the vane tip gap. Rather, it is because of the linear increase of ideal mass flow rate due to the increased speed. This is obvious when volumetric efficiency is expressed as shown in Eq. (14). It is equivalent to Eq. (1), but it demonstrates that high speeds the effect of leakage is minimal.

$$\eta_v = \frac{\dot{m}_{ideal}}{\dot{m}_{ideal} + \dot{m}_{leakage}} \quad \text{Eq. (14)}$$

From the test results, it can also be demonstrated that for the same operating speed, the volumetric efficiency of the 5 bar case was lower than that of the 4 bar case. It is due to the higher-pressure difference between the inlet and the outlet of the expander, which causes more flow to be driven through the gaps.

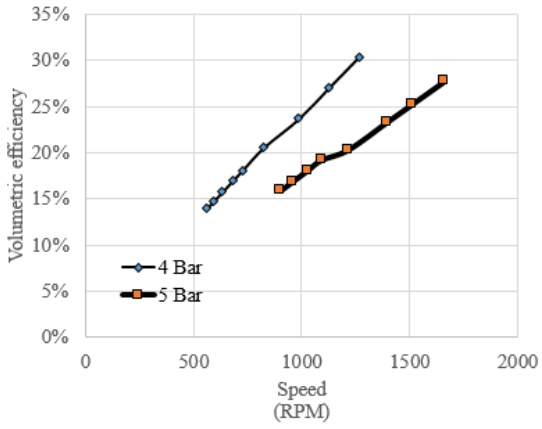

Figure 5: Volumetric efficiency against speed

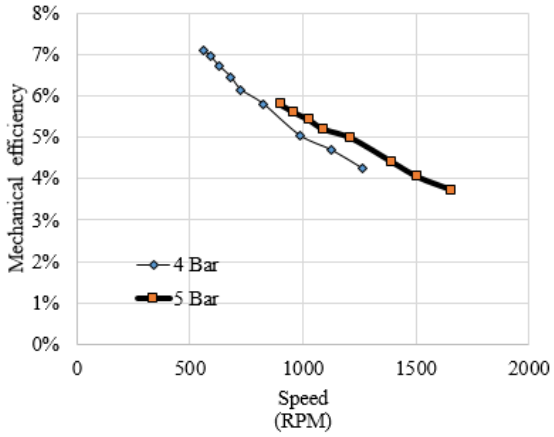

Figure 6: Mechanical efficiency against speed

Fig. 6 shows the test results of the mechanical efficiency against varying speed at two constant pressures. The highest efficiency achieved at a pressure of 4 bar was 7% at 560 rpm. At 5 bar of inlet pressure, the highest mechanical efficiency was 6% at 900 rpm. Both trends are displaying the same behaviour where the mechanical efficiency decreases with increasing speed. Since mechanical efficiency is strongly affected by friction, the decreasing trend demonstrates that friction increases with speed. Increasing rotation speed increases the centrifugal force which increases the contact force between the vane and the wall. High contact force results in more friction and therefore, more losses. The power required to overcome friction rapidly increases because it has a cubic

relation with the rotation speed. This issue was amplified because no suitable form of lubrication system was implemented. Hence, such a trend was observed.
Fig. 7 shows the test results of the isentropic efficiency against varying speed at two constant pressures. The highest efficiency achieved at a pressure of 4 bar was 19% at 560 rpm. At 5 bar of inlet pressure, the highest isentropic efficiency was 10% at 900 rpm. Overall, a decreasing trend was observed from the results. The isentropic efficiency was affected by multiple phenomena. It was affected by the heat transfer between the fluid and the expander, internal leakage in the expander and sudden compression at the exit. The temperature difference between the fluid and the expander wall drives the heat transfer process. The friction between the stator wall and the tip of the vane causes the expander wall to heat up. Therefore, the expander wall tends to have a higher temperature than the fluid. Hence, the temperature of the fluid increases in the heat transfer process. This has a rippling effect on the pressure. So, as the temperature increases, it causes the pressure to rise as well. Therefore, in the expansion process, the pressure drop is lower than that of an ideal case. The internal leakage in the expander causes the mass of fluid inside the expansion chamber to drop. Therefore, at a given volume the pressure inside the expansion volume will be lower for an expander with leakage when compared with an ideal system. This increases the rate of pressure drop throughout the expansion process. This will contribute towards reducing the isentropic efficiency because the rate of pressure drop will be higher than that of an isentropic expansion.
The expander was tested under an open system arrangement. Therefore, the exit pressure of the fluid equalised with the atmospheric pressure. During that process, it causes the fluid to undergo a sudden compression process which deviates the expansion from that of an isentropic expansion. It contributes towards a reduction in the isentropic efficiency. It is a sudden compression process because the expander over expands the fluid due to its high-pressure ratio of 19.1 which was found using Eq. (15).

$$\frac{P_1}{P_2} = \left(\frac{V_2}{V_1}\right)^{1.4} \qquad \text{Eq. (15)}$$

From the three phenomena discussed, the heat transfer between the fluid and the expander wall is responsible for such a trend because it is affected by friction which is dependent on the speed. The leakage phenomenon causes the isentropic efficiency of the higher-pressure case to be lower because leakage increases with increasing pressure as discussed previously. The sudden compression is significant at low pressures such as the ones used in this experiment.

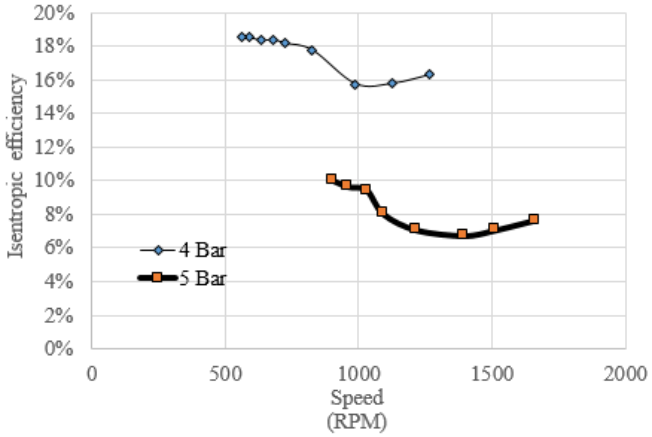

Figure 7: Plot of isentropic efficiency against speed

3.2. Simulation results of the expander with parallel to the throttle valve

The current working vapour compression refrigeration system will be maintained, and the expander will be added in parallel with the throttle valve as shown in Fig. 1(b). The present throttle valve in the R-22 refrigeration system in the laboratory worked with inlet and outlet pressures of 10 bar and 1.5 bar, respectively. Keeping this same inlet condition of 10 bar, it was found that the outlet pressure of the expander was around 4.38 bar. In the present study, the evaporating and condensing

temperatures are chosen from -35˚C to 0˚C and 20˚C to 45˚C, respectively. The expander inlet pressure and outlet pressure are 10 bar and 1 bar, respectively. Fig. 8(a) and (b) shows the COP improvements for the proposed new arrangement. From the graph, it can be observed that COP improvements were between 2.5-6% and 3.5-8.5% in heating and cooling sides respectively. Thus, expander is a promising substitute to improve the performance of the system. The better COP can be obtained at higher condensing and evaporating temperatures.

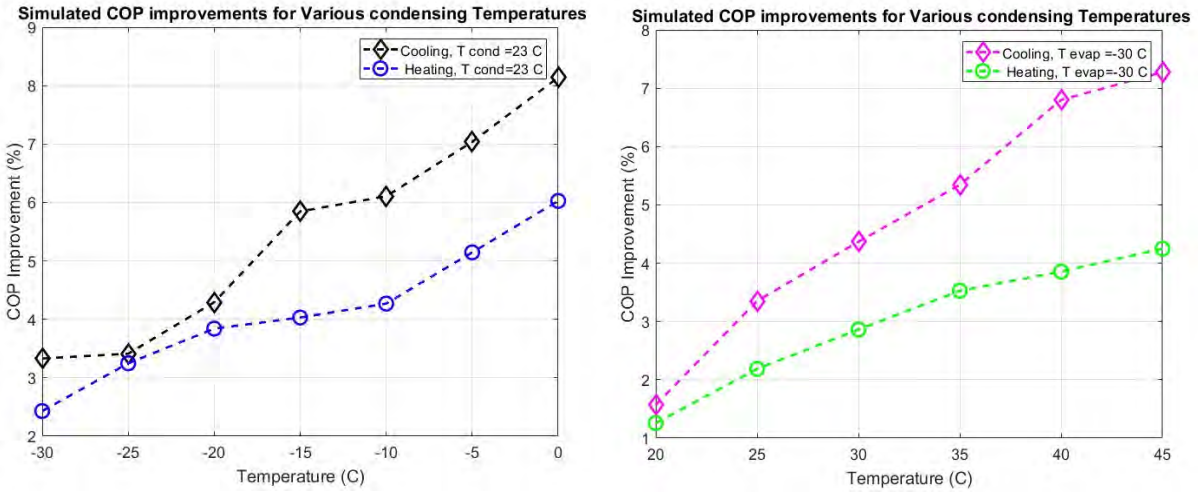

(a) (b)

Figure 8: COP improvements at various condensing and evaporating temperatures

4. CONCLUSIONS

In this paper, a study has been done to test the performance parameter of a four-vane rotary expander. Experiments were carried out with air as the working fluid, and the prototype was found to function steadily. Under the test condition (inlet pressure P= 400 KPa and P=500 KPa, ambient temperature 18˚C) the rotational speed of expander was varied from 561 rpm to 1640 rpm, and its influence on the performance was studied. The results showed that mechanical efficiency and isentropic efficiency varied with rotational speed. The maximum value of the mechanical efficiency and isentropic efficiency were 7% and 19%, respectively, when the rotational speed was about 564 rpm. The maximum volumetric efficiency was around 30% when the rotational speed was about 1264 rpm. A numerical simulation model was then developed to study the performance of this expander in an R22 refrigeration system. To allow for flow adjustment during operation, the expander was installed in parallel to a throttle valve. The study found that the coefficient of performance of the modified system would increase by 2.5-6% and 3.5-8.5% on the heating and cooling sides, respectively. Higher evaporating or condensing temperatures may increase the performance of the system. This preliminary study has shown that the expander prototype can operate smoothly. In the future, the expander will be installed into the heat pump system according to the proposed arrangement and experimental investigation will be carried out.

ACKNOWLEDGEMENTS

The contributions of Martin Ryder, Alan Eaton, Munawwar Abdul Rani, Julie Renault and Quentin Declerck to the project are acknowledged.

NOMENCLATURE

P	pressure (Pa)	η_m	mechanical efficiency (%)
T	temperature (K)	$\dot{m}$	mass flow rate (kg×s^{-1})

V_1	min volume of the expansion chamber (m^3)	η_v	volumetric efficiency (%)
		η_{is}	isentropic efficiency (%)
V_2	max volume of the expansion chamber (m^3)	ρ	density ($kg \times m^{-3}$)
		f	frequency (Hz)
P_1	pressure at the inlet (Pa)	$\dot{W}$	power (W)
Δh	change in specific enthalpy ($J \times kg^{-1}$)	P_2	pressure after expansion (Pa)
		C_p	specific heat capacity ($J \times kg^{-1} \times K^{-1}$)
ω	rotational speed ($rad \times s^{-1}$)		
m	mass (kg)	P_f	power loss due to friction (W)
μ	friction coefficient	r	radius (m)
V	volume (m^3)	n_e	number of vanes

REFERENCES

Bell, H. I., Wronski, J., Quoilin, S. V., 2014. Pure and pseudo-pure fluid thermophysical property evaluation and the open-source thermophysical property library CoolProp. Industrial and Engineering Chemistry Reserach 53, 2498-2508.

Cao, X., Li, Z.Y., Shao, L.L., Zhang, C.L., 2016. Refrigerant flow through electronic expansion valve: Experiment and neural network modeling. Applied Thermal Engineering 92(5), 210–218.

Core Writing Team., Pachauri, K.R., Meyer, A.L., 2014. Climate Change 2014: Synthesis Report. IPCC, Geneva, 151 p.

Dowing, R.C., 1974. ASHRAE Transactions, Paper No. 2313.

DoE, U.S., 2012. Buildings Energy Data Book. Energy Efficiency and Renewable Energy Department, Washington DC, 286 p.

Fukuta, M., Yanagisawa, T., Radermacher, R., 2003. Performance prediction of vane type expander CO_2 cycle. Proceedings of the 21st IIR International Congress of Refrigeration, Washington, D.C, ICR0251.

Hossain, M.S., Li, B., Chakraborty, S., Hossain, M.R., Rahman, M.T., 2015. A Comparative Analysis on China's Energy Issues and CO2 Emissions in Global Perspectives. Sustainable Energy 3(1), 1-8.

Kohsokabe, H., Funakoshi, S., Tojo, K., Nakayama, S., Kohno, K., Kurashige, K., 2006. Basic operating characteristics of CO2 refrigeration cycles with expander-compressor unit. Proceedings of the 11th International Refrigeration and Air Conditioning Conference, Purdue University, West Lafayette, IN, R159.

Nakicenovic, N., 2007. World Energy Outlook 2007. China and India Insights. OECD Publishing, Paris, 672 p.

Nickl, J., Will, G., Kraus, W.E., Quack, H., 2002. Design considerations for a second generation CO2-expander. Proceedings of the 5th IIR-Gustav Lorentzen Conference on Natural Working Fluids, GuangZhou, China, 189-195.

Stosic, N., Smith, I.K., Kovacevic, A., 2002. Twin screw combined compressors and expanders for CO2 refrigeration systems. Proceedings of the 16th International Compressor Engineering Conference, Purdue University, West Lafayette, IN, C21-2.

Subiantoro, A., Ooi, K.T., 2009. Introduction of the revolving vane expander. HVAC&R Research 15, 801-816.

Subiantoro, A., Ooi, K.T., 2015. Expansion Power Recovery in Refrigeration. Handbook of Research on Advances and Applications in Refrigeration Systems and Technologies, Harrisburg, 720-751 p.

Manuscript ID: 171
DOI: 10.18462/iir.icr.2019.0171

A numerical framework for the one-dimensional modelling of refrigerator components

Luka LORBEK[(a)], Andrej KITANOVSKI[(a)]

[(a)] University of Ljubljana, Faculty of Mechanical Engineering
Ljubljana, 1000, Slovenia, luka.lorbek@fs.uni-lj.si

ABSTRACT

This paper presents the development of a numerical framework intended for the modelling of refrigerant flow in components where a one-dimensional pipe flow can be presumed. The goal is to maintain a single modelling paradigm for multiple components. In a vapour-compression system these are the capillary tube, the condenser and the evaporator. The governing equations are discretized according to the finite-volume method and solved with a modified SIMPLE algorithm capable of modelling compressible, phase-changing flow. Test cases were set up and the results show that it is possible to model all three components within a single numerical framework, thus eliminating the need for separate models.
Keywords: Numerical framework, Numerical modelling, Capillary tubes, Evaporator, Condenser, SIMPLE algorithm

1. INTRODUCTION

The development of vapour-compression refrigeration systems is no longer exclusively based on experience and experimental work; it increasingly relies on mathematical models as well. The first models, which date back to the 1970s, such as works by Stoecker (1971), Davis (1976) and Dhar (1978), set the foundations for future models. Over the years, these models have improved in many aspects, such as their complexity, capabilities and computational speeds. One attribute, however, has remained unchanged. While for specific components, such as the compressor shell (Posch, 2016) or ejectors (Mazzelli, 2018), multi-dimensional models do exist; on a system level they are still limited to 0D or 1D models. The major difference between multi-dimensional and 1D models is that in the former all the physical phenomena, such as the shear stresses, that lead to pressure losses are modelled, while in the latter they are usually replaced with empirical or semi-empirical factors that imitate their influence. An example of this is the friction factor, which in the governing momentum equation acts as a sink for momentum, thus imitating the pressure loss.

There are several reasons why this limitation has not been overcome. The nature of the process is extremely complex. It includes turbulent flow, multiphase flow, phase changes, flash evaporation, choking flow, discontinuities and heat transfer. All of these processes are difficult to describe mathematically, and the modelling of some phenomena, such as turbulence and phase change, anyway relies on empirical correlations. Besides their inherent complexity, these processes happen on three different time scales and at least as many length scales. This means that modelling such phenomena would, in most places, require less than millimetre-sized grids in systems with several meters of pipes and time steps of milliseconds in processes that can take up to several hours to reach steady-state conditions. Such a daunting task, however, might not even produce much better results than those of 0D or 1D models, since they can be calibrated to achieve sufficient accuracy for a wide enough spectrum of possible operating conditions. For the reasons explained above, the physics of mathematical models are constrained to one dimension for now. This, however, presents an opportunity, which to the best of the authors' knowledge has not yet been investigated.

Small-scale vapour-compression systems utilize capillary tubes instead of throttling valves as the expansion elements. As the name suggests, a capillary tube is nothing more than a copper tube with a very small diameter and a length of between 1 and 2 meters. Depending on the type of heat exchanger, an evaporator and a condenser can likewise be nothing more than tubes of larger diameter and length, around which there are usually different types of extended surfaces that

increase the heat transfer. From the refrigerants' perspective, excluding of course the compressor, the vapour-compression process in such cases can be considered pipe flow through different diameters. In reality, the flow in evaporators and condensers is different to that in a capillary tube and this may warrant a separate formulation, but while the physics is constrained to one dimension, the mathematical formulation of the refrigerant flow can be the same. The differences between components are in the empirical correlations for the friction factor and the heat-transfer coefficient. There are also slight differences in how the heat transfer is modelled from the refrigerant to the surroundings.

The incentive behind formulating the capillary tube, evaporator and condenser in the same manner is that a single code can model three out of four major components in a vapour-compression system, leaving only the compressor to be modelled separately. Thus, the goal of this research was to create a numerical framework capable of modelling the refrigerator components in which the flow can be considered as pipe flow. The basis for the framework is the iterative SIMPLE algorithm, originally developed by Patankar (1980) for incompressible flows. We upgraded it to enable the modelling of phase change and compressible flow. Because of the multitude of possible inlet/outlet conditions, the numerical model within the framework was designed in such a way that it can accept any inlet/outlet state, be it two phase, liquid or gaseous.

2. GOVERNING EQUATIONS

The first step in developing a fluid-flow model is to decide which phenomena we would like to include in the calculation. We have already explained that we will model only 1D effects. At this point we will also constrain ourselves to steady-state solutions. This means that all the time derivatives are equal to zero. The multiphase flow is considered to be homogenous, meaning that the pressure, velocity and temperature are equal among the gaseous and liquid phases. The effects of gravity, viscous dissipation and the work of pressure forces are not considered.

In the fluid flow the consideration of some phenomena, such as the conservation of mass, is necessary by default. In a differential form (assuming a constant pipe cross-section) this equation is written as:

$$\frac{d(\rho u)}{dx} = 0 \qquad \text{Eq. (1)}$$

In general, an adiabatic capillary tube does not require the modelling of heat transfer and as such the energy equation. Similarly, the heat exchangers (condenser, evaporator), where the pressure drop is often neglected, do not require inclusion of the momentum equation. However, if a single framework is to model all of these components, the momentum equation and the energy equation, describing the conservation of their respective properties, must both be considered.

$$\frac{d(\rho u u)}{dx} = -\frac{dp}{dx} - f_D \frac{\rho u^2}{2D} \qquad \text{Eq. (2)}$$

$$\frac{d(\rho u h_0)}{dx} = \frac{d}{dx}\left(k \frac{dT}{dx}\right) + \frac{4\Delta x}{D} h(T_W - T) \qquad \text{Eq. (3)}$$

A dimensionless factor and a proportionality constant are introduced with Eq. (2) and Eq. (3). The former is the Darcy friction factor *f* and the latter is the heat-transfer coefficient *h*. Darcy's friction factor, a function of the Reynolds number and the relative wall roughness, is determined with the correlation by Churchill (1977). The heat-transfer coefficient is determined from the Nusselt number. For the refrigerant flow, the Nusselt number is determined with the correlation by Gnielinski (1975). The term containing the heat-transfer coefficient represents the heat flow from the refrigerant to the tube wall or vice versa. Axial heat conduction along the fluid is also considered.

Compressible flows also require that the equation of state be considered, so that pressure, temperature and density are coupled. If the flow is in a purely gaseous state and can be considered ideal, the ideal gas law is usually prescribed. However, the flow in capillary tubes, evaporators and condensers will be a mixture of liquid, two phase and gaseous phase. The problem is that the ideal gas law does not apply to liquid or two-phase mixtures. If we wish to retain a single framework, a

solution that is valid for all the phases is required. This is solved by replacing the equation of state with a thermodynamic library, such as REFPROP or CoolProp. These libraries are able to return the density and any other thermodynamic variable of state based on a combination of inputs. Since the vapour-compression process involves several phase changes, it is intuitive to work with pressure and enthalpy. We can thus write:

$$\rho = f(p, h) \qquad \text{Eq. (4)}$$

where *f* is a function call to a thermodynamic library that outputs the density based on the pressure and the enthalpy. Because CoolProp enables so-called low-level function calls, which are considerably faster than high-level calls (standard REFPROP/CoolProp calls), it was chosen as our thermodynamic library.

The equations described above describe the fluid flow of the refrigerant. However, heat transfer from the refrigerant to the surroundings must also be modelled. If the temperature of the surroundings is regarded as constant, which is acceptable since it is a steady-state simulation, one equation for the tube wall is required. It is obtained by a simple energy balance. Eq. (5) shows the equation for the tube wall. It consists of four terms, two describing the heat conduction along the wall and two describing convective heat transfer from the refrigerant and surroundings.

$$U_{o,I} A_{o,I} \left(T^*_{o,I} - T_{W,I}\right) + h_{i,I} A_{i,I} \left(T^*_I - T_{W,I}\right) + k \frac{d^2 T_W}{dx^2} = 0 \qquad \text{Eq. (5)}$$

3. NUMERICAL SOLUTION

3.1. Numerical model

3.1.1. Discretization

The computational domain can be separated into two zones. One for the refrigerant flow and one for the tube wall. Fig. 1 shows a scheme of the discretized computational domain.

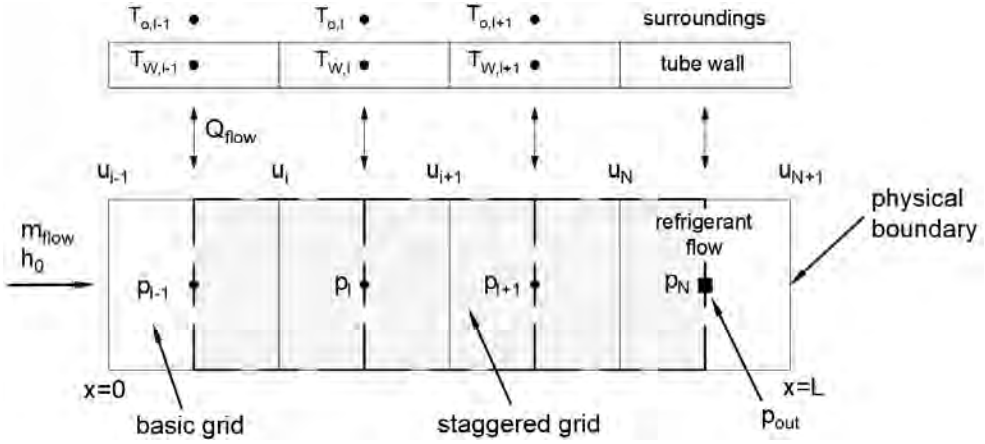

Figure 1: Scheme of the discretized computational domain

The refrigerant zone is divided into control volumes. They can be spaced uniformly or non-uniformly. The non-uniform case is required for the capillary tubes, where the gradients at the outlet are very large and a fine mesh is required there. In this case a growth factor, usually between 1.0 and 1.2, defines the control volume growth from one volume to the next. A factor of 1.2 means that the next control volume will be 1.2 times longer than the one before it.

To prevent the decoupling of pressure and velocity in the liquid zones the momentum equation is solved on a staggered grid, so that the velocities are stored in control-volume faces rather than in control-volume nodes. The finite-volume method was used to discretize the differential form of the governing equations to an algebraic form. A first-order upwind discretization scheme was used and nonlinear terms, such as the first and third term in the momentum equation, were linearized.

3.1.2. Boundary conditions and boundary values

The boundary conditions are separated into two groups. One group for the refrigerant domain and one for the tube wall. They are listed in Table 1 and presented on Fig. 1.

Table 1: Boundary conditions

-	Inlet	Outlet/right border
Refrigerant flow	$\dot{m}_{(x=0)}$ = const., $h_{0(x=0)}$ = const.	$p_{(N)}$ = const.
Tube wall	$T_{(x=0)} = 1.5T_{(1)} - 0.5\,T_{(2)}$	$T_{(x=L)} = 1.5T_{(N)} - 0.5T_{(N-1)}$

Because the conditions at the inlet and the outlet will vary from component to component it is essential that the boundary conditions satisfy all the possibilities. In incompressible flows the rules regarding the proper boundary conditions are not as strict as in compressible flows. This means that the boundary conditions will be selected so that they satisfy the case of a compressible flow. In compressible flows it is highly recommended that the pressure is fixed at the outlet and either the mass flow or the total pressure is prescribed at the inlet, accompanied by the total enthalpy condition. The reason for this is that an absolute pressure must be known at one point to serve as a reference for determining the density. A prescribed mass flow is an upgrade of the velocity inlet condition, where density is also taken into account as it can vary with pressure and enthalpy. The total enthalpy must be prescribed instead of the regular enthalpy if the transformation of internal to kinetic energy or vice versa is to be included. In the case of constant temperature gradients, the temperature at the border is linearly extrapolated from the interior nodes.

The boundary values of the variables that are not prescribed as boundary conditions are extrapolated from the interior or determined indirectly from known variables at the boundary control volume face. For example, if the pressure and the enthalpy are known at the boundary face, the density is computed from the thermodynamic library. As such, they need to be updated in every iteration as the fields inside the domain converge to a solution.

3.2. Modified SIMPLE algorithm

A block diagram of a modified SIMPLE algorithm is presented in Fig. 2. In the initialization, first approximations are made by assuming a pressure and a total enthalpy distribution along the length of the domain. The algorithm then enters a loop and first solves the equations governing refrigerant flow, updates all the thermodynamic variables and empirical factors and then finally solves Eq. (5). The convergence criteria are evaluated, and if they are not satisfied the computation returns to the start of the loop.

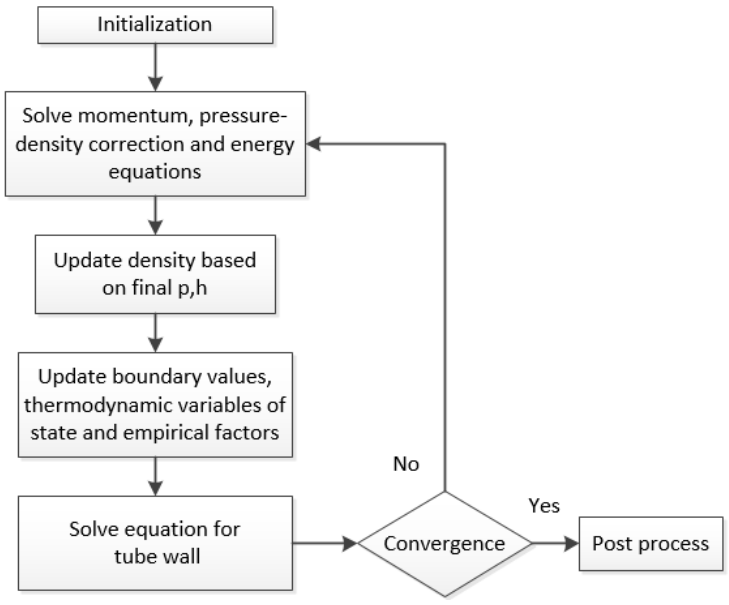

Figure 2: Block diagram of the modified SIMPLE algorithm

4. RESULTS

4.1. Results and case studies

4.1.1. Adiabatic capillary tube

Table 2 shows the test conditions for which we modelled the capillary tube. The case was designed so that the liquid refrigerant enters the capillary tube and upon reaching the saturation pressure it starts evaporating.

Table 2: Adiabatic capillary-tube test conditions

Inlet mass flow [kg/h]	3.25
Inlet total enthalpy [J/kg]	250
Outlet pressure [bar]	1.0
Length [m]	2
Inner diameter [mm]	1.1
Tube roughness [mm]	0.002
Refrigerant	R600a

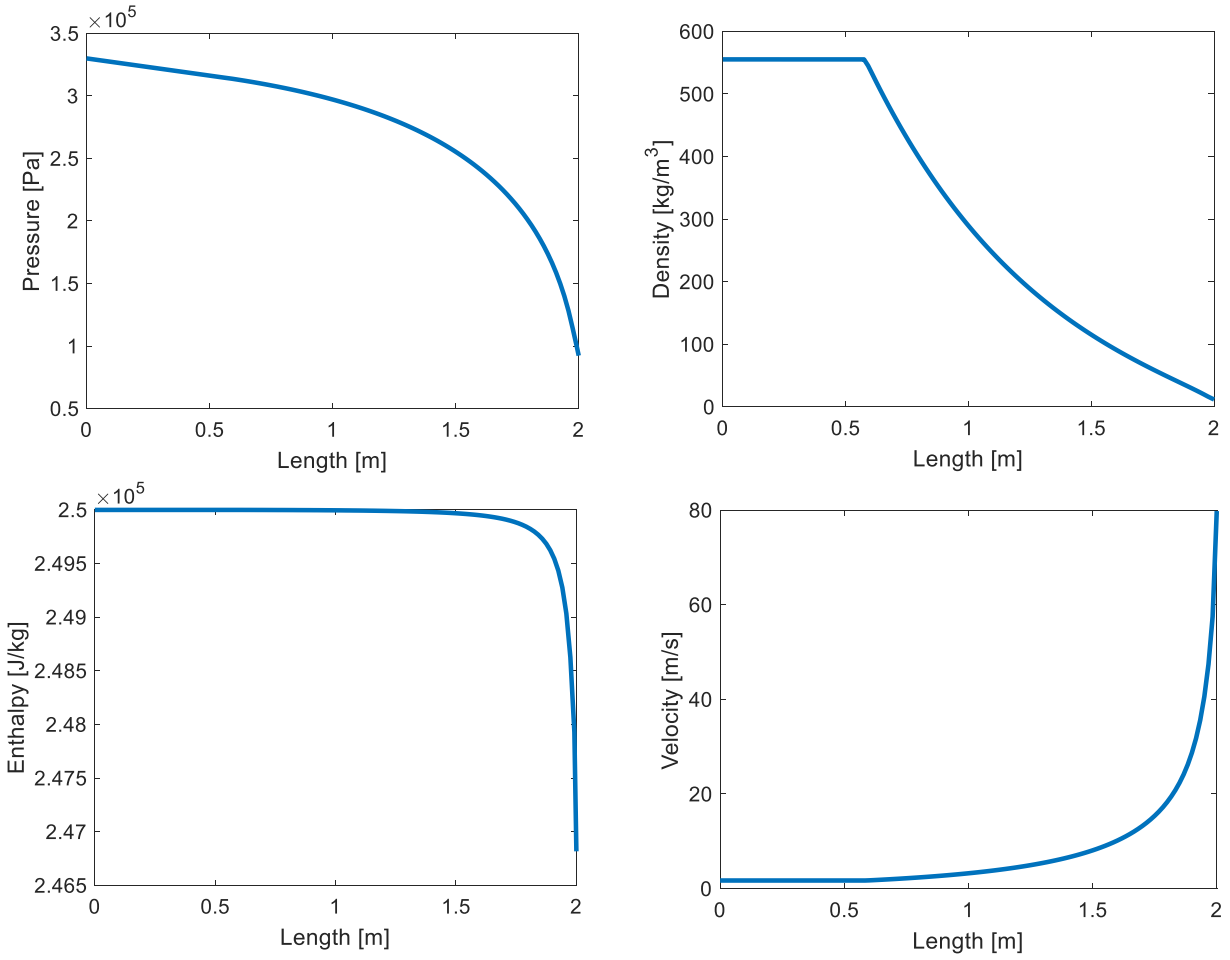

Figure 3: Clockwise: pressure distribution, density distribution, enthalpy distribution and velocity distribution in an adiabatic capillary tube

As long as the refrigerant is in the liquid state the pressure drop is linear. When the refrigerant starts evaporating, the density decreases and since the mass flow must remain constant the velocity increases. In Eq. (2) the velocity in the term describing the pressure losses is to the power of two. This means that the gradient of the pressure in the multiphase zone will increase with the increasing velocity. In an adiabatic system the total energy remains constant. This means that an increase in velocity will lead to a decrease in enthalpy.

4.1.2. Evaporator

Table 3 shows the test conditions for the evaporator. The partially evaporated fluid enters the evaporator and exits as superheated vapour.

Table 3: Evaporator test conditions

Inlet mass flow [kg/h]	3.0
Inlet total enthalpy [J/kg]	300
Outlet pressure [bar]	1.0
Length [m]	14
Inner diameter [mm]	7.0
Tube roughness [mm]	0.002
Outer U×A [W/K]	16.0
Refrigerant	R600a

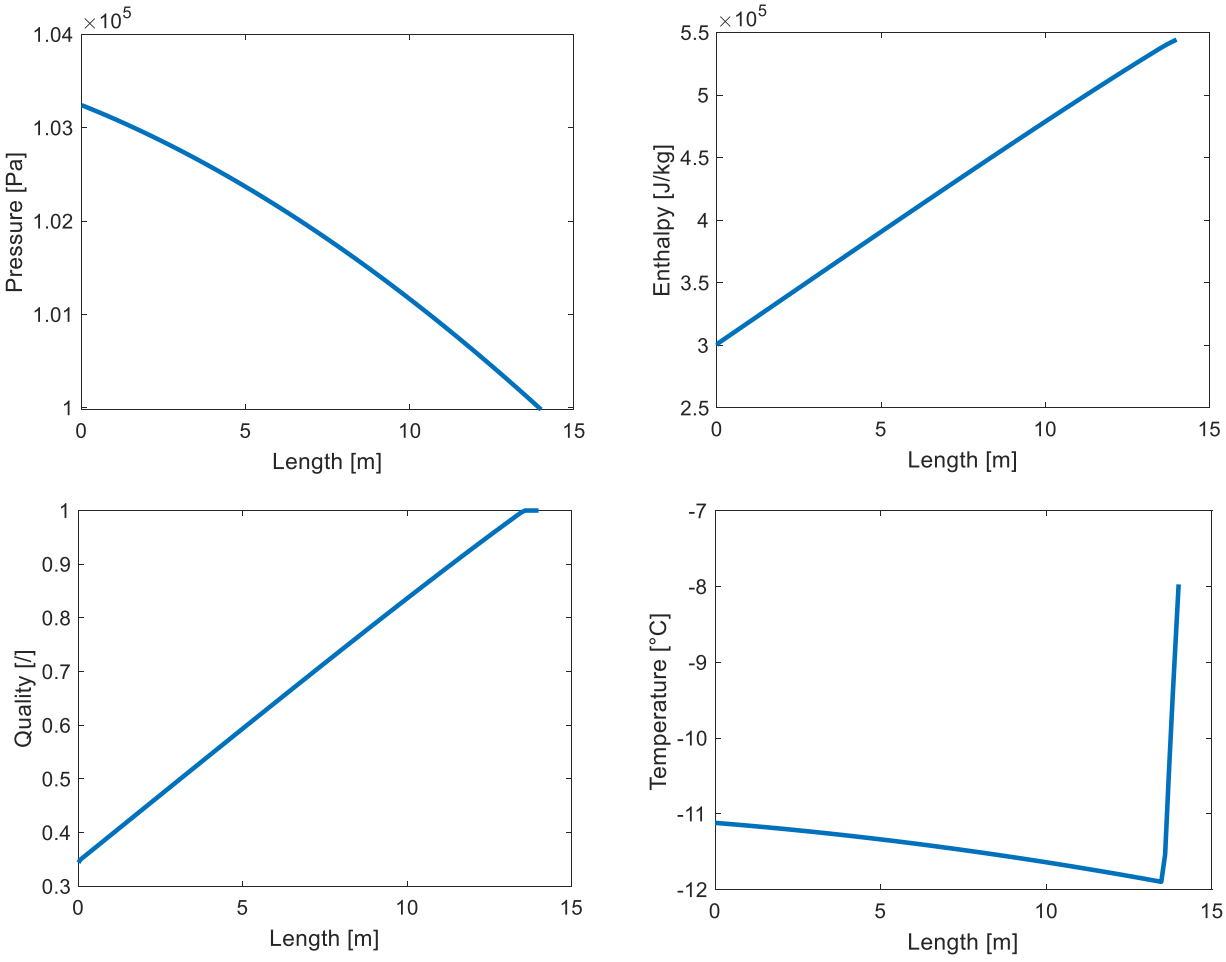

Figure 4: Clockwise: pressure distribution, enthalpy distribution, quality distribution, temperature distribution

Compared to the capillary tube the pressure drop in the evaporator is very small. However, this small change in pressure has a slightly larger impact on temperature, as the temperature drops by 1 K during the evaporation. When the refrigerant evaporates completely it superheats very quickly. As we can see in Fig. 4, it takes around 13.5 meters to evaporate the refrigerant and only 0.5 m to superheat it.

4.1.3. Condenser

Table 4 shows the conditions for the condenser simulation. Superheated vapour enters the condenser and leaves as a subcooled liquid.

Table 4: Condenser test conditions

Inlet mass flow [kg/h]	3.0
Inlet total enthalpy [J/kg]	615
Outlet pressure [bar]	5.0
Length [m]	16
Inner diameter [mm]	7.0
Tube roughness [mm]	0.002
Outer U×A [W/K]	27.0
Refrigerant	R600a

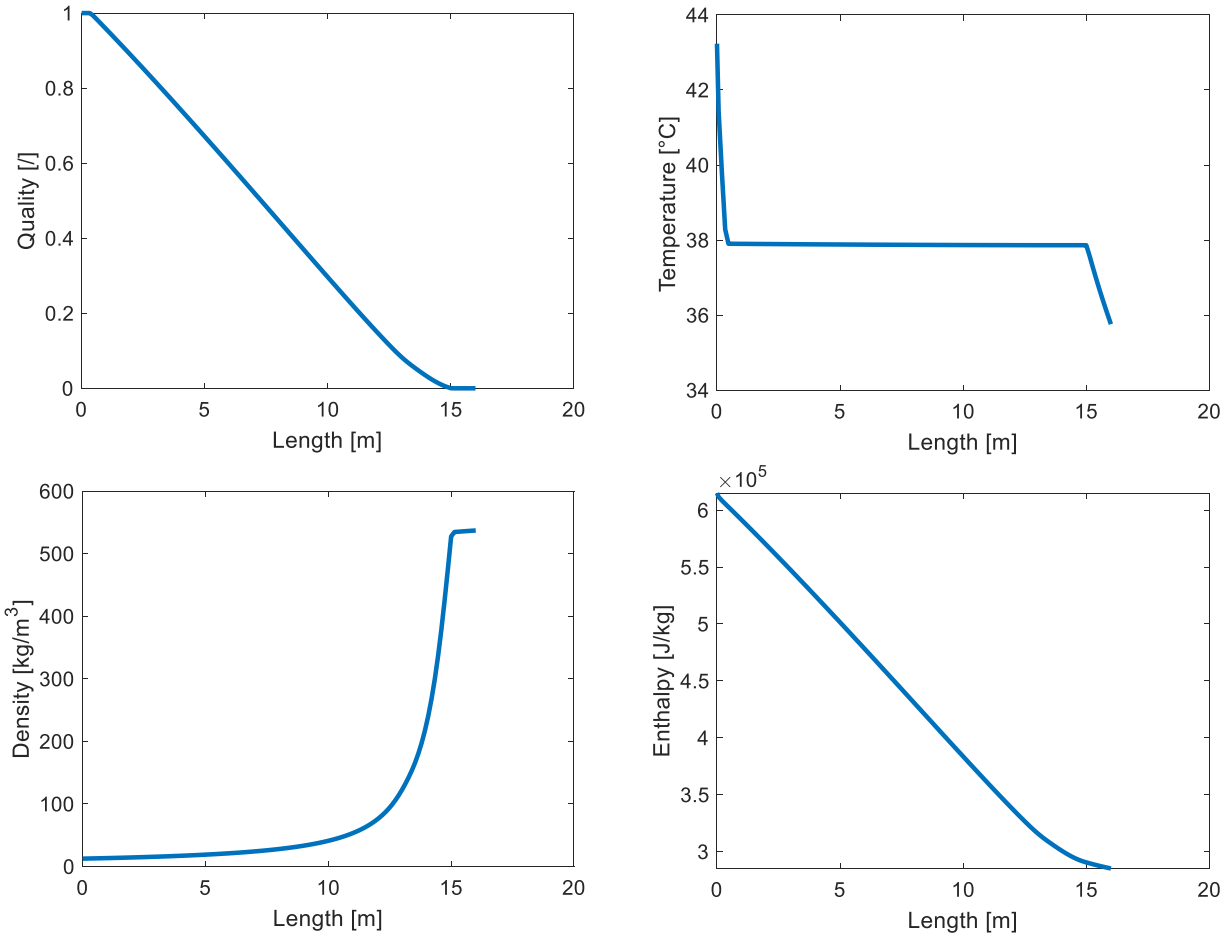

Figure 5: Clockwise: quality distribution, temperature distribution, density distribution, enthalpy distribution

The pressure drop in a condenser is similar in magnitude to that of an evaporator. When superheated vapour enters the condenser it is quickly cooled to the point of saturation. The enthalpy and quality then decrease steadily, while the density increases. When the refrigerant condenses into a liquid completely it subcools and the density is practically constant.

5. CONCLUSIONS

The purpose of this study was to create a numerical framework capable of modelling all the major refrigerator components with pipe flow. The results show that it is possible to create such a framework. Maintaining only one modelling paradigm offers the advantage of better control over the code. Another advantage is that the model must be very flexible by default, if such different components are to be modelled. This means that it is very easy to add different functionalities to the numerical model, such as extra terms describing the different phenomena. In the future, the capability of modelling non-adiabatic or so-called capillary-tube, heat-exchanger components will be added. The model must also be experimentally validated and, if necessary, parameters such as the empirical factor or the heat transfer coefficient need to be calibrated.

ACKNOWLEDGEMENTS

This work was financially supported by the Slovenian Research Agency as part of the Young Researcher PhD program.

NOMENCLATURE

D	diameter (m)	h_0	specific total enthalpy (J×kg^{-1})
h	specific enthalpy (J×kg^{-1})	A	area (m^2)
k	thermal conductivity (W×m^{-1}K^{-1})	x	length (m)
$\dot{m}$	mass flow rate (kg×s^{-1})		
p	pressure (kPa)	U	overall thermal heat-transfer coefficient (W×m^{-2}K^{-1})
T	temperature (K)	c_P	specific heat (J×kg^{-1}K^{-1})
X	vapour quality (/)	f_D	Darcy's friction factor (/)
ρ	density (kg×m^{-3})	u	velocity (m×s^{-1})
$*$	value from previous iteration		
o	outer	i	inner, control volume face
w	wall	l	control volume node

REFERENCES

Churchill, S., 1977. Friction-factor equation spans all fluid-flow regimes. Chemical Engineering 84, 91-91.

Davis, G., Scott, T., 1976. Component modelling requirements for refrigeration system simulation. Proceedings of the Purdue Compressor Technology Conference, West Lafayette, Indiana.

Dhar, M., 1978. Transient analysis of refrigeration system. West Lafayette, Indiana. *Doctoral thesis*.

Gnielinski, V., 1975. Neue Gleichungen für den Wärme- und den Stoffübergang in turbulent durchströmten Rohren und Kanälen. Forsch. Ing.-Wes. 41 (1), 8–16.

Patankar, S., 1980. Numerical heat transfer and fluid flow. McGraw-Hill, USA.

Stoecker, W., 1971. Generalized program for steady state system simulation. ASHRAE Transactions 77, 140-148.

Posch, S., Hopfgartner, J., Heimel, M., Berger, E., Almbauer, R., Stangl, S., 2016. Thermal analysis of a hermetic reciprocating compressor using numerical methods. Proceedings of the International Compressor Engineering Conference, West Lafayette, Indiana.

Mazzelli, F., Giacomelli, F., Milazzo, A., 2018. Numerical modeling of a supersonic steam ejector for a heat powered refrigeration systems. Proceedings of the 13th Gustav Lorentzen Conference, Valencia, Spain.

Manuscript ID: 186
DOI: 10.18462/iir.icr.2019.0186

An experimental analysis of thermal storage materials applied to natural-draft condensers

Joel BOENG, Cláudio MELO

POLO Labs, Department of Mechanical Engineering, Federal University of Santa Catarina
Florianópolis, 88040-970, Brazil, melo@polo.ufsc.br

ABSTRACT

The aim of this work is to study the effect of applying thermal storage materials (TSMs) into natural-draft condensers of household refrigerators. To this end, three types of TSMs were integrated into the wire-and-tube condenser of an appliance. Energy consumption tests were carried out under different system operating conditions with each TSM in order to compare the results with those of an off-the-shelf refrigerator. It was found that the energy consumption benefits are strongly dependent on the contact resistance between the condenser and the material, on the compressor on and off times and on the material thermal capacity, regardless of the ambient temperature. Energy savings of up to 7.4% were achieved with the integration of 700g of a copolymer compound into the condenser of an A++ European appliance.
Keywords: Thermal Storage Material, Refrigerator, Natural-draft Condenser, Energy Consumption.

1. INTRODUCTION

A phase change material (PCM) is a substance with high latent heat of fusion, which is capable of storing and releasing large amounts of energy while changing phase (Bruno *et al.*, 2015). Recently, such materials have been widely used in several applications, such as construction, to increase the thermal inertia of buildings and consequently reduce the costs associated with air conditioning (Cabeza et al., 2011); in preserving food and pharmaceuticals, reducing temperature stratification or prolonging storage time (Phimolsiripol et al., 2008); and as energy regenerators in various applications of thermal systems. Thermal storage materials (TSMs), on the other hand, have a high heat storage capacity without phase changing. Such materials are generally cheaper and might be used for similar applications and purposes. Recent studies showed that the incorporation of PCMs or TSMs into refrigerators can lead to significant performance gains.

Over the past decade, PCM usage into heat exchangers or refrigerated compartments of household refrigerators has grown significantly. According Joybari et al. (2015), most of the studies available in the open literature explore the PCM application in the evaporator or refrigerated compartments. In general, the integration of PCMs into refrigerated compartments or directly into the evaporator causes both a reduction in energy consumption and in the fluctuation of the average temperature of the refrigerated compartment. Moreover, it causes a substantial increase in the time that the refrigerator maintains the temperature at an acceptable level with the compressor off, which brings benefits to the pharmaceutical and food preservation areas or in cases of power outage, for example. Regarding the application of such materials to condensers, most authors reported a significant reduction in the condensing temperature and, consequently, energy consumption.

Cheng et al. (2013) modelled a household refrigerator with integrated PCMs into a natural-draft condenser. The authors state that, under regular conditions without PCM, the condensers operate actively only during the compressor on period. However, the presence of heat storage materials can extend the heat dissipation of the condensers also for the compressor off period. That is, during the compressor on period, a portion of the heat is stored in the material while the other portion is dissipated to the environment. When the compressor shuts off, the heat stored in the material is dissipated. Thus, there is continuous condenser heat dissipation, whether the compressor is on or not. When the heat dissipation occurs during the compressor off period, the heat transfer efficiency is higher, which results in a lower condensing temperature, reducing energy consumption. The

authors further claim that at the beginning of the compressor on period, the PCM temperature is low and the heat storage potential is high, causing a momentary increase of the COP of the system.
Similarly, Sonnenrein et al. (2015a) evaluated the influence of different materials (water, paraffin and a polymer compound) added to a wire-on-tube condenser over the condensing temperature and energy consumption of a household refrigerator. The authors reported a significant decrease in condensing temperature and reductions of up to 10% in energy consumption. Furthermore, Sonnenrein et al. (2015b) also evaluated the performance of a commercial refrigerator equipped with 150g of a copolymer-bound PCM in the evaporator and 500g in the condenser. The authors reported a reduction of up to 8°C in the condensing temperature and up to 7% in energy consumption.
Recently, Rametta (2018) performed experiments with PCMs integrated into a natural-draft wire-on-tube condenser used in a 422-liter frost-free bottom-mount domestic refrigerator. The author investigated the performance of PCMs under different operating conditions. To do so, an external control was developed to vary the compressor on and off periods. At the optimum operating condition, the reduction in energy consumption reached 5.4% with the use of 1.02 kg of water bags between the condenser wires. In this context, the author stated that PCMs should be selected considering the thermal characteristics of the material and the compressor on and off periods.
To the best of the author's knowledge, there are no studies in the open literature that systematically investigated the effects of the TSMs integration on the performance of domestic refrigerators, considering different compressor on and off periods and thermal load. In this context, the present work aims to investigate the effect of thermal storage materials applied to natural-draft condensers. To this end, three materials were selected, with different thermal properties and attaching method to the condenser, and tests were performed under several operating conditions.

2. EXPERIMENTAL WORK

Tests were conducted with a 144-liter all-refrigerator built-in domestic refrigerator with European A++ energy rating. The refrigerator uses a skin-type evaporator, a reciprocating compressor, which operates with 19g of R600a, and a natural-draft wire-on-tube condenser, which is 505mm high and 522mm wide, with 11 tube passes and 144 wires.
The refrigerator was instrumented with temperature, pressure and power transducers. The discharge and suction pressures were measured with absolute pressure transducers with maximum uncertainty of ±0.01bar. The compartment temperatures were measured with T-type thermocouples, with maximum uncertainty of ±0.2°C, which were brazed in small copper cylinders as recommended by IEC62552 (2013). The compressor power was measured with a power integrator. Energy consumption was calculated with maximum uncertainty of ±5.0kWh/year.
Three types of TSMs were integrated into the condenser, namely: (i) commercial PCM OM37P, (ii) water and (iii) polymeric compound (also called bitumen). The physical characteristics of the materials are detailed in Tab. 1. Small bags of water and organic commercial PCM RT44HC were inserted among the condenser wires. In contrast, the bitumen was adhered to the wires and tubes of the condenser due to its softness and adhesive characteristics. The condenser, PCM and TSMs temperatures were measured with T-type thermocouples installed on the respective surfaces.

Table 1. Thermal storage materials characteristics

	OM37P	Water	Bitumen
Mass [kg]	0.50	0.51	0.73
Phase change temperature [°C]	37	0	-
Latent heat of fusion [kJ kg^{-1}]	218	333	-
Specific heat [kJ $kg^{-1}K^{-1}$]	2.0	4.2	1.8
Bag type [-]	aluminum film	aluminum film	-

The performance of the TSMs was evaluated through energy consumption tests based on the requirements of IEC 62552 (2013) standard for built-in refrigerators. All the tests were carried out in a climatic chamber, with controlled ambient temperature and relative humidity. The tests were conducted with different compressor on periods (10, 20 and 30min) and different average

compartment temperatures (0, 4 and 8ºC), covering a significant range of compressor run time ratios. The full combination of these variables resulted in 9 tests per material. Considering the baseline tests (without TSM) and the three different types of materials, the full matrix add up to 36 experimental tests, performed at an ambient temperature of 32°C. Additional tests were performed at 16°C ambient temperature, considering only baseline condition and bitumen.
The original control strategy of the refrigerator has been replaced by an external control with direct actuation in the compressor. The new control operates based on average compartment temperature readings. The desired compressor on time and average compartment temperature are obtained in an iterative process by selecting the on and off compartment temperatures.

3. RESULTS

Figure 1(a) shows the energy consumption results for all configurations tested. As expected, lower compartment temperatures lead to higher thermal loads and, consequently, higher energy consumption. Fig.1(a) also shows that, regardless of the material used, the energy consumption decreases with the reduction of the compressor on time. Figure 1(b) shows the variation in energy consumption caused by the integration of the materials in the condenser, when comparing to the baseline case, including different compartment average temperatures and compressor on periods. The use of bitumen in the condenser resulted in an average 4.8% energy saving. In its turn, the water bags caused an average energy consumption reduction of the order of 2.0%. When the commercial PCM OM37P was used, the average reduction was only 0.6%. Note that generally the energy savings are higher for higher compartment average temperatures, i.e., for lower compressor run time ratios. In addition, reduced compressor on times (10min) also present higher energy savings. The maximum energy consumption reduction (7.4%) was achieved with the highest compartment average temperature (8°C) and the lowest compressor on time (10 minutes).

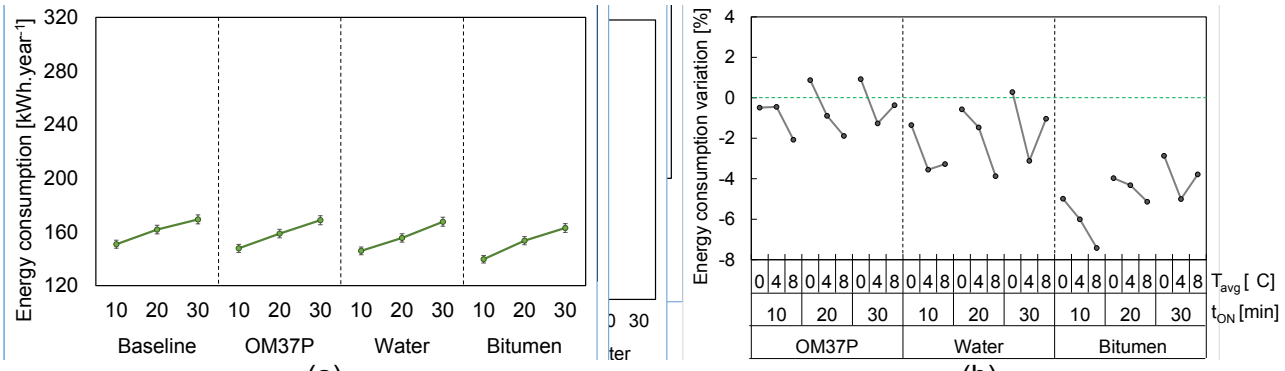

Figure 1: Energy consumption results for all materials and configurations tested

The energy savings caused by the integration of the materials can be explained by the behavior of the system during a complete compressor cycle. Fig. 2(a) shows typical condensing temperatures, for a normalized cycle, of a system with and without PCM. Additionally, Fig. 2(b) shows the difference between both temperatures plotted in Fig. 2(a) ($T_{cond,PCM}$ - T_{cond}). During the beginning of the compressor on period, the heat transfer between the condenser and the PCM is higher due to the high temperature difference, which results in a temporary reduction of the condensing temperature. Therefore, it is noted that the temperature difference shown in Fig. 2(b) is negative (region a), which represents benefits to the system. However, after a certain time, the PCM temperature rises and the condensing temperature curves intersect at the point where the condensing temperature with PCM exceeds the baseline configuration. From this point forward, called cross-point, the heat transfer between the condenser and the PCM is lower, which negatively affects the condensing temperature of the system with PCM (region b). Such behavior clearly indicates that there is a maximum compressor on time that maximizes the system performance with PCM. When the compressor shuts off, the condenser temperature reduction during this period is much slower with the presence of the PCM (region c) due to the thermal inertia of the material. If the compressor is switched on early, the condenser temperature at the beginning of the next cycle will still be high, with negative effects on

system performance. It means that there is also a minimum compressor off period that maximizes the system performance with PCM.

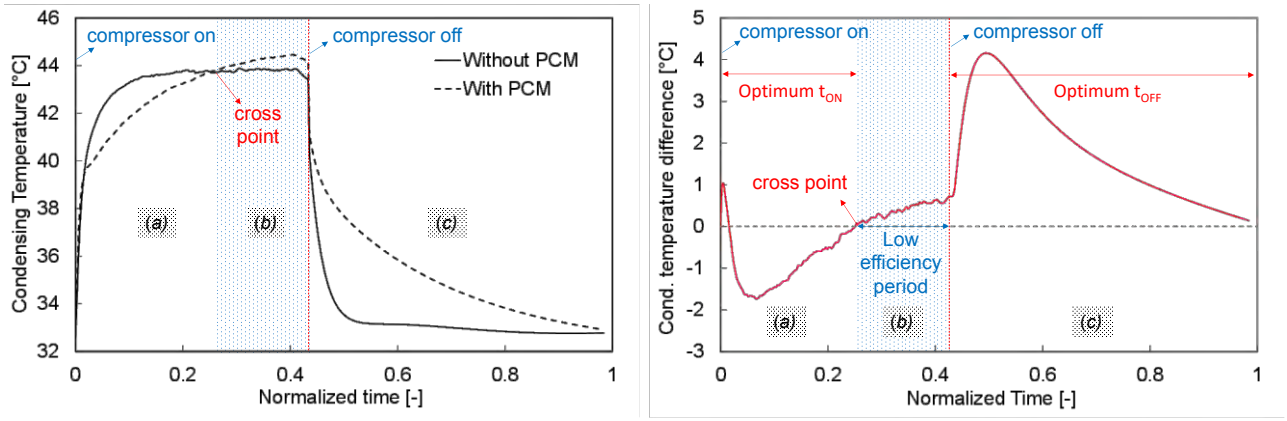

(a) (b)

Figure 2: (a) Condensing temperatures and (b) condensing temperatures difference during an on-off cycle of a system with and without PCM

Fig. 3(a) shows the condensing temperatures during a complete cycle for all materials tested, with 4°C compartment average temperature and 30min compressor on time. In addition, Fig. 3(b) shows the difference of the condensing temperatures with and without TSMs, for the same test conditions. It is noted that the condensing temperature at the beginning of the compressor on time is reduced by the presence of the TSM, reaching the cross-point, and later reducing slowly the temperature during the compressor off time, due to the thermal inertia of the material. These results showed that the beneficial effects of the TSM are proportional to the difference between the condensing temperature curves with and without TSM at the beginning of the compressor on period (see Fig. 3b). The lower the condensing temperature at the beginning of the cycle, the better the system energy performance.

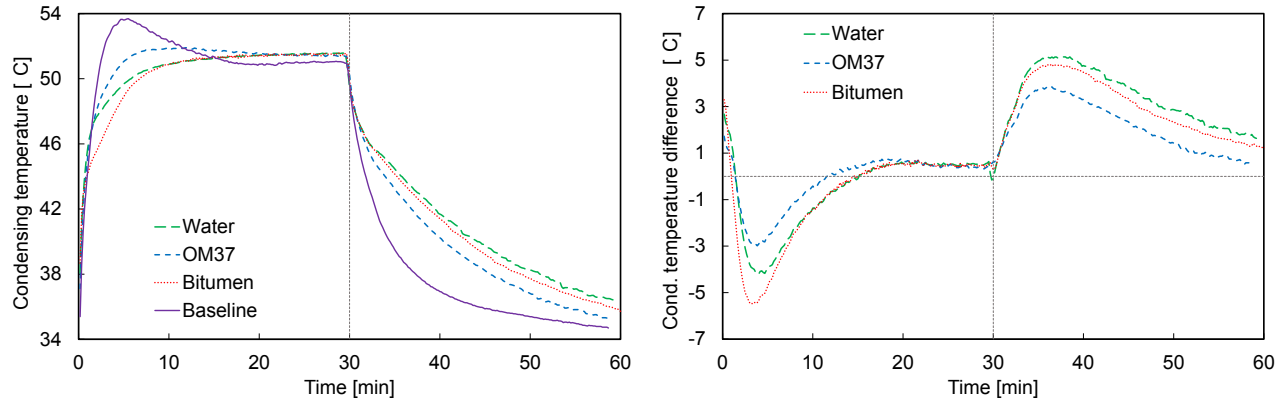

(a) (b)

Figure 3: (a) Condensing temperatures and (b) condensing temperatures difference during an on-off cycle of the test with 4°C compartment average temperature and 30min compressor on period

Fig. 4 shows the condensing temperatures difference of the system with and without bitumen, for the compartment average temperature of 0°C, 4°C and 8°C and compressor on periods of 10min, 20min and 30min (Figures 4a, 4b and 4c, respectively). In these cases, the average compressor run time ratio were 64% (0°C), 46% (4°C) and 35% (8°C), respectively. For higher run time ratios (black lines), the compressor off period is not long enough to provide appropriated condenser temperature reduction at the end of this period, adversely affecting the condensing temperature at the beginning of the next cycle. Note that the attenuation at the condensing temperature at the beginning of the cycle is lower for this condition. As the compressor operating fraction is reduced (blue and red lines), the compressor off period becomes long enough to allow a higher heat rejection of the TSM and

hence the condenser. In this case, the condensing temperature at the beginning of the next cycle is lower due to the higher heat transfer rate. Therefore, it can be concluded that the lower the compressor run time ratio, the greater the system performance with TSM. In fact, the results show higher energy savings for higher compartment average temperatures. All other materials presented similar behavior to bitumen.

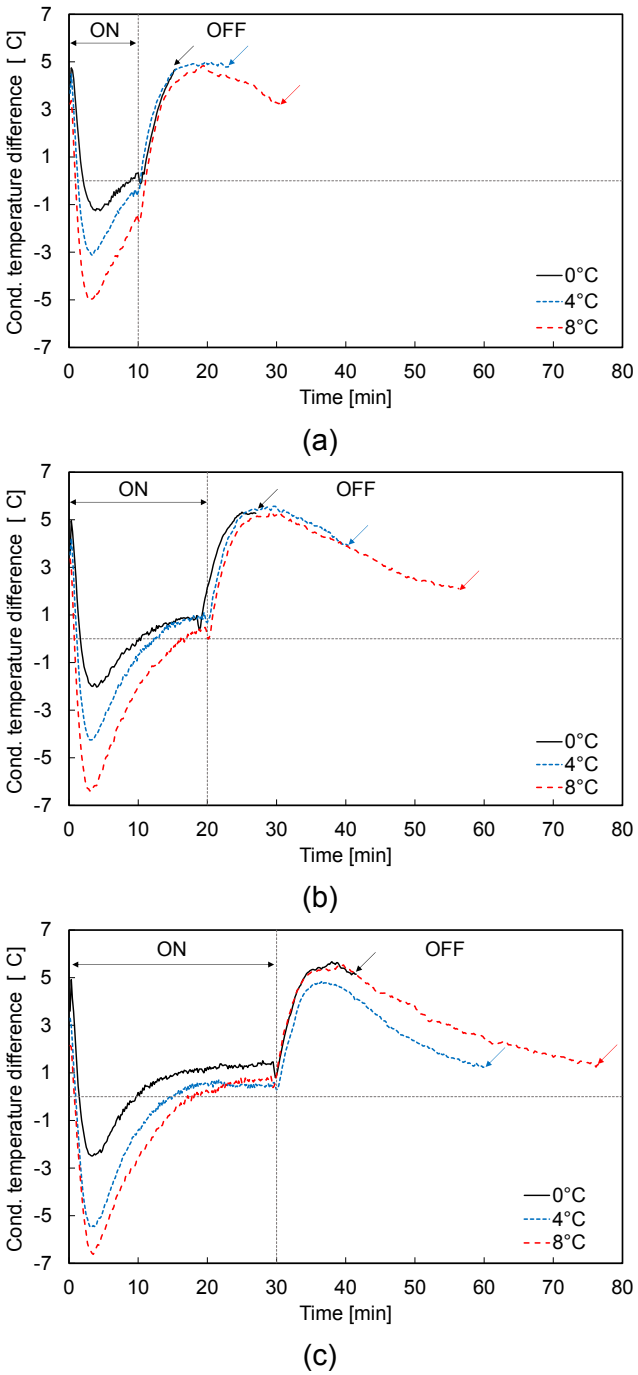

Figure 4: Condensing temperatures difference with and without bitumen during an on-off cycle of the tests with (a) 10min, (b) 20min and (c) 30min compressor on period

When the compressor on time is short (Fig. 4a), the condensing temperature with TSM remains always lower than the condensing temperature of the baseline condition, that is, the temperature difference is always negative during the whole compressor on period, meaning that the cross-point is not reached. On the other hand, as the compressor keeps on for longer periods (figures 4b and 4c), the cross-point is reached, provoking an inefficient operating condition, since the material starts

to act as a thermal resistance in the condenser. In short, the lower the compressor on time, the higher the energy savings.
Moreover, the results indicate that systems which operate with high compressor run time ratio (i.e. low compartment temperature or low compressor capacity) reach the cross-point earlier, due to the reduced compressor off time that harms the condenser temperature reduction during the off period. In contrast, systems that operate with short compressor on time avoid or shorten the cross-point reaching. In other words, the lower the run time ratio and the shorter the compressor on period, the higher the energy savings of TSM equipped systems. Therefore, it can be concluded that there is a maximum compressor on time and a minimum compressor off time that optimizes the performance of the system with TSM. Such periods are dependent on the characteristics of the system and the material, since they depend on the heat rejection rate of the condenser during the compressor on and off cycles, which in turn is a function of the size of the condenser as well as the thermal capacity and attaching method of the TSM with the condenser.
The heat transfer process in natural-draft condensers is dominated by convection, which represents 65% of the total heat exchanged, being the rest rejected to the environment through radiation (Bansal and Chin, 2003). When the TSM is integrated into the condenser, a portion of the heat exchanged occurs through conduction between the material and the tubes and wires. If the contact resistance between the condenser and the material is low, the conduction process becomes dominant, since the conduction thermal resistance is lower when compared to the convection and radiation processes. This phenomenon is most pronounced at the beginning of the cycle, when the TSM is at a lower temperature. As the TSM absorbs heat from the condenser, its temperature increases and the heat transfer by conduction becomes no longer significant (this effect might be delayed for materials with higher thermal capacities). At this moment, depending on the attaching method between the material and the condenser, the presence of TSM may hinder the convection heat transfer, since it can act as a thermal insulation and even change the flow pattern of natural convection, reducing turbulence effects. Therefore, the lower the contact resistance and the greater the thermal capacity, the better the system performance.
In this context, considering the characteristics of each material used in the present work, the thermal capacity of the commercial PCM OM37P was estimated at 12.8 kJK^{-1}, bitumen at 13.9 kJK^{-1} and water at 22.1 kJK^{-1}. Among the materials that presented benefits to the system, bitumen was the most significant (-4.8%), followed by water (-2.0%) and commercial PCM OM37P (-0.6%). Note that there is no direct correlation between the thermal capacity and energy savings, indicating that the material selection should not only consider the thermal capacity. As a matter of clarification, Fig. 5 shows the attachment between the condenser and the (a) bitumen and (b) water bags. Bitumen is a flexible adhesive material that adheres very well to the tubes and wires, minimizing the contact resistance. On the other hand, water bags and commercial PCM were manually placed between the condenser wires, resulting in a significantly higher contact resistance. That is why the bitumen presented a better performance even with a lower thermal capacity.

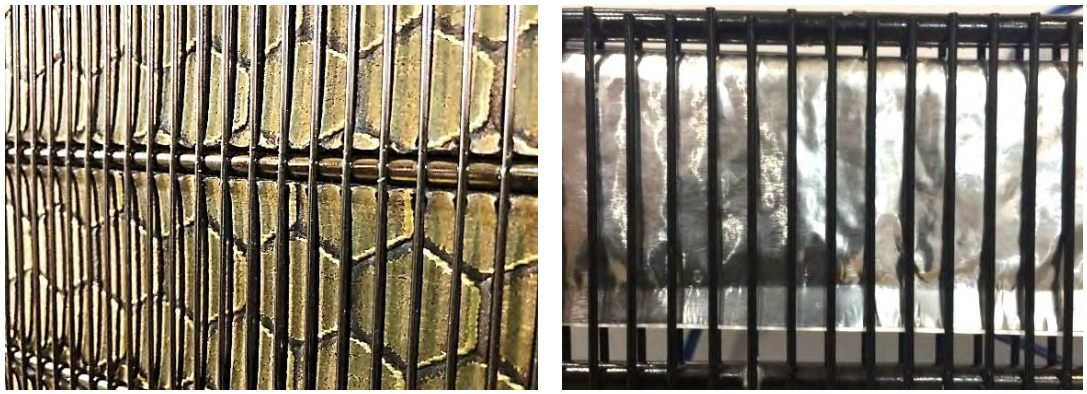

(a) (b)

Figure 5: Condenser attachment with (a) bitumen and (b) water bags

Fig. 6 shows thermographs of the condenser with bitumen obtained with an infrared camera at three instants of a typical cycle: (i) immediately before the compressor turns on, (ii) in the middle of the compressor on time and (iii) just before the compressor shuts off. These images were obtained in

tests with 4°C compartment average temperature and 10min, 20min and 30min compressor on periods. The images show that, for longer periods of compressor on (20 and 30min), the condenser temperature in the middle of the cycle is already high and it is close to the temperature at the end of the cycle. As already mentioned, the heat transfer between the condenser and the TSM decreases until it reaches the cross-point, where it has a negative effect on the condensing temperature, i.e., the heat transfer process at the end of the compressor on period becomes efficient. In other words, shorter is the compressor on period, higher is the benefits. The images also show that, for short compressor on time (10min), the condensing temperature at the compressor start-up is adversely affected. Despite such drawback, the benefits on not reaching the cross-point due to the low off period is higher.

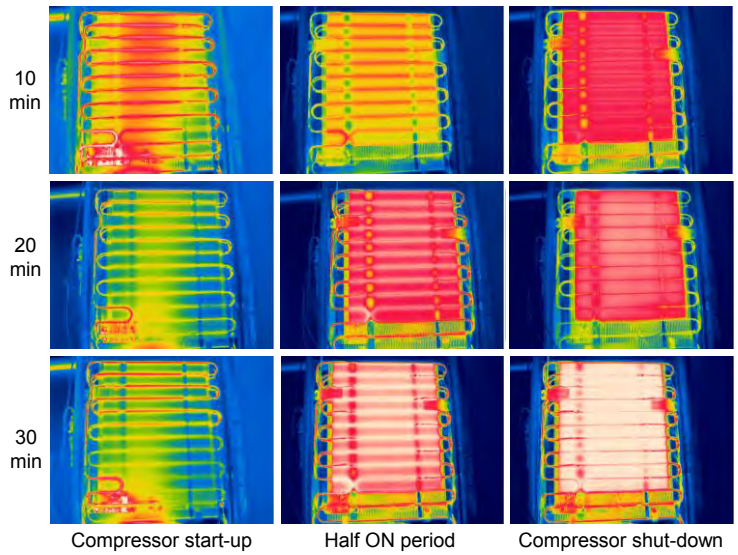

Figure 6: Condenser temperatures with bitumen integrated in the tests with 4°C compartment average temperature and 10, 20 and 30min compressor on time

Finally, the energy consumption tests were also performed at a 16°C ambient temperature. Thus, eighteen additional tests were conducted without TSM and with bitumen into the condenser. It was noted that the energy consumption reduction at 16°C is of the same order of magnitude of the reduction observed at 32°C, which indicates that the performance improvement by the integration of the material into the condenser is not dependent on the ambient temperature.

4. CONCLUSIONS

The present study investigated the effect of the use of thermal storage materials on natural-draft condensers in a A++ European household refrigerator. To this end, three types of TSMs were integrated into the condenser: (i) commercial PCM OM37P, (ii) water and (iii) a polymeric compound. The performance of the TSMs was evaluated through energy consumption tests with different compressor on periods (10, 20 and 30min) and different compartment average temperatures (0, 4 and 8ºC), comprising a significant range of compressor run time ratios.

Considering all operating conditions tested at 32°C ambient temperature, the use of 700g of bitumen into the condenser resulted in an average energy saving of 4.8%. When water capsules and the commercial PCM OM37P were used, the average reduction was of the order of 2.0% and 0.6%, respectively. Energy consumption tests at 16°C ambient temperature were also performed with bitumen integrated into the condenser and the results indicated that the energy savings due to the integration of TSM is not related to the ambient temperature.

It was noted that the energy savings are higher for lower compressor run time ratio and lower compressor on times. Indeed, in the present work, the maximum energy consumption reduction (7.4%) was achieved with the highest compartment average temperature (8°C) and the lowest compressor on time (10min). When the compressor on time is too long, at a given cross-point the

condensing temperature with TSM exceeds the condensing temperature without TSM, then the material acts as a thermal resistance and the condenser starts to operate at an inefficient condition. The results also showed that the contact resistance between the material and the condenser play a role as important as the thermal capacity of the material. That is, the material must be selected and attached seeking to minimize the contact resistance. Finally, it was concluded that there is a maximum compressor on time and a minimum compressor off time that optimizes the system performance. Such periods are dependent on the condenser size, TSM attaching method and material thermal capacity.

ACKNOWLEDGEMENTS

This study was made possible through the financial investment from the EMBRAPII Program (POLO/UFSC EMBRAPII Unit - Emerging Technologies in Cooling and Thermophysics). The authors thank Embraco S.A. for financial and technical support.

REFERENCES

Bansal, P.K., Chin, T., 2003. Heat Transfer Characteristics of Wire-and-Tube and Hot-Wall Condensers. HVAC&R Research 9(3), 277-290.

Bruno, F., Belusko, M., Liu, M., Tay, N.H.S., 2015. Advances in Thermal Energy Storage Systems. In: Using solid-liquid phase change materials (PCMs) in thermal energy storage systems, Woodhead Publishing, Cambridge, 201–246.

Cabeza, L.F., Castell, A., Barreneche, C., de Gracia, A., Fernandez, A.I., 2011. Materials used as PCM in thermal energy storage in buildings: a review. Renewable and Sustainable Energy Rev 15(3), 1675-1695.

Cheng, W.-L., Yuan, X.-D., 2013. Numerical analysis of a novel household refrigerator with shape-stabilized PCM (phase change material) heat storage condensers. Energy. 59(15), 265 – 276.

Hermes, C.J.L., Melo, C., Knabben, F.T., Gonçalves, J.M., 2009. Prediction of the energy consumption of household refrigerators and freezers via steady-state simulation. Int. J. Refrig. 86(7-8), 1311-1319.

Joybari, M.M., Haghighat, F., Moffat, J., Sra, P., 2015. Heat and cold storage using phase change materials in domestic refrigeration systems: The state-of-the-art review. Energy Build. 106(1), 111–124.

Phimolsiripol, Y., Siripatrawan, U., Tulyathan, V., Cleland, D.J., 2008. Effects of freezing and temperature fluctuations during frozen storage on frozen dough and bread quality. J. Food Eng. 84(1), 48 – 56.

Rametta, C.S., 2018. Experimental evaluation of the use of thermal storage materials in household refrigerators. Master's dissertation, Federal University of Santa Catarina, Florianópolis, Brazil.

Sonnenrein, G., Elsner, A., Baumhögger, E., Morbach, A., Fieback, K., Vrabec, J., 2015a. Reducing the power consumption of household refrigerators through the integration of latent heat storage elements in wire-and-tube condensers. Int. J. Refrig. 51, 154-160.

Sonnenrein, G., Baumhögger, E., Elsner, A., Fieback, K., Morbach, A., Paul, A., Vrabec, J., 2015b. Copolymer-bound phase change materials for household refrigerating appliances: experimental investigation of power consumption, temperature distribution and demand side management potential. Int. J. Refrig. 60, 166-173.

Standard IEC 62552, 2013. Household refrigerating appliances - Characteristics and teste methods - Part 1: General requirements, Geneva.

Manuscript ID: 189
DOI: 10.18462/iir.icr.2019.0189

Optimization potentials for the absorber and the generator of an ammonia-water absorption heat pump

Nico MIRL, Klaus SPINDLER

Institute for Building Energetics, Thermotechnology and Energy Storage (IGTE), University of Stuttgart, Pfaffenwaldring 6, Stuttgart, 70569, Germany, Nico.Mirl@igte.uni-stuttgart.de

ABSTRACT

Experimental investigations to identify optimization potentials of an ammonia-water absorption heat pump are performed. In this heat pump, both the absorber and the generator are designed as plate heat exchangers. At the inlet of the absorber, the weak solution is sprayed through a nozzle into the refrigerant vapor, thus creating a high surface for the mass transfer. The advantages of this system are a compact design and a low refrigerant filling quantity.
The aim of these investigations is to identify and classify optimization potentials in heat and mass transfer in the absorber and generator. The potentials in heat transfer are determined using calculated temperature profiles. For an analysis of the mass transfer, the ammonia mass fractions of the strong and the weak solution are calculated with measured densities. By comparison with the theoretically possible ammonia mass fractions, a classification in the areas of heat or mass transfer is carried out for further optimization.
Keywords: Absorber, Absorption System, Ammonia-Water, Generator, Heat Transfer, Mass Transfer, Optimization, Plate Exchanger

1. INTRODUCTION

In German district heating systems, operating temperatures up to 140 °C are available (Paar et al. 2013) while in customer heating systems, temperatures up to 70 °C are required. An improved cooling of the district heating water leads to a reduction of the return temperature. One promising opportunity to achieve an improved cooling is to use the high temperature of the district heating flow to power an absorption heat pump with the working pair ammonia-water and to use the return as heat source for the evaporator (Mirl et al. 2018b). Due to safety regulations for the place of installation, the filling quantity of the absorption heat pump should be less than 10 kg ammonia.
The size and filling quantity of the absorption heat pump is highly affected by the generator. In ammonia-water absorption systems, a vessel-type generator is typically in use (Said et al. 2016; Staedter and Garimella 2018; Aprile et al. 2016). By using a plate heat exchanger as generator, Müller and Spindler (2013) reduced the ammonia filling quantity from 15 kg to 4 kg. However, the coefficient of performance of the absorption system decreased from 0.65 to 0.6. In order to improve the efficiency of the absorption system, the potentials in heat and mass transfer of the plate-type generator have to be investigated.
The absorber mainly influences the efficiency of the whole absorption process (Mittermaier and Ziegler 2015). Many different types of absorbers are studied in literature, such as falling film absorbers (Castro et al. 2009; Triché et al. 2017), bubble absorbers (Cerezo et al. 2010) and spray absorbers (Said et al. 2016; Müller and Spindler 2013; Venegas et al. 2005). The latter absorber type seems to be very compact, due to a high surface for mass transfer within the spray. Müller and Spindler (2013) built a spray absorber where the weak solution is direct sprayed into a plate heat exchanger; the high surface for mass transfer of the spray is combined with the high surface for heat transfer of a plate heat exchanger, working as a falling film absorber.
In the present work, an ammonia-water absorption heat pump with 30 kW heating power has been investigated experimentally. The focus has been on the analysis of the current state of the generator and the spray absorber of the ammonia-water absorption heat pump as well as on the identification and classification of the main optimization potentials. For both, absorber and generator, commercial plate heat exchangers are used, due to their compactness and low costs (Müller and Spindler 2013).

2. EXPERIMENTAL SETUP

The schematic design of the absorption heat pump is shown in Figure 1. The refrigerant vapor (1) is liquefied in the condenser where a part of the useful heat $\dot{Q}_{\mathrm{cond}}$ is extracted from the process. The refrigerant storage tank (2) is used for the intermediate storage of liquid refrigerant. This increases the operating range of the absorption heat pump and compensates temperature fluctuations of the external circuits. The refrigerant heat exchanger increases the efficiency of the process: the liquid refrigerant is subcooled after the condenser (3→4) and the refrigerant vapor (6→7) is superheated. Via the refrigerant expansion valve, the pressure of the liquid refrigerant is reduced to the low pressure of the heat pump (4→5). At the low pressure, the refrigerant can be evaporated at a low temperature level (5→6). At the inlet of the absorber, the refrigerant vapor (7) is mixed with the weak solution (8) in the absorber, resulting in the absorption of the refrigerant. In this process, the absorption heat $\dot{Q}_{\mathrm{abs}}$ is released; therefore, this heat must be transferred to the heating system at a medium temperature level. At the end of the absorption process, the strong solution has an increased ammonia mass fraction ξ_{ss} and is in liquid state (9). The liquid strong solution (9) is led into a pump storage tank. The level of the strong solution in this tank (10) is controlled at a constant value. Via a solution pump, the strong solution is adjusted to the high pressure (11). In order to increase efficiency, a solution heat exchanger is used for internal heat recovery between strong solution (11→12) and weak solution (19→20). Then, the preheated strong solution flows through the dephlegmator (13→14), where internal heat recovery from the refrigerant vapor to the strong solution takes place. Due to the preheating of the strong solution, a two-phase mixture of liquid strong solution and refrigerant gas enters the generator storage tank (14). A connecting pipe (16) between the storage tank and the dephlegmator transports refrigerant vapor to the dephlegmator (17). The liquid strong solution flows to the generator where heat $\dot{Q}_{\mathrm{gen}}$ at a high temperature level is used to evaporate the strong solution (15) partially. In the generator separator, the two-phase flow is separated into refrigerant vapor (18) and weak solution (19). The latter is fed back to the absorber (19→20→8) and reused for the absorption process.

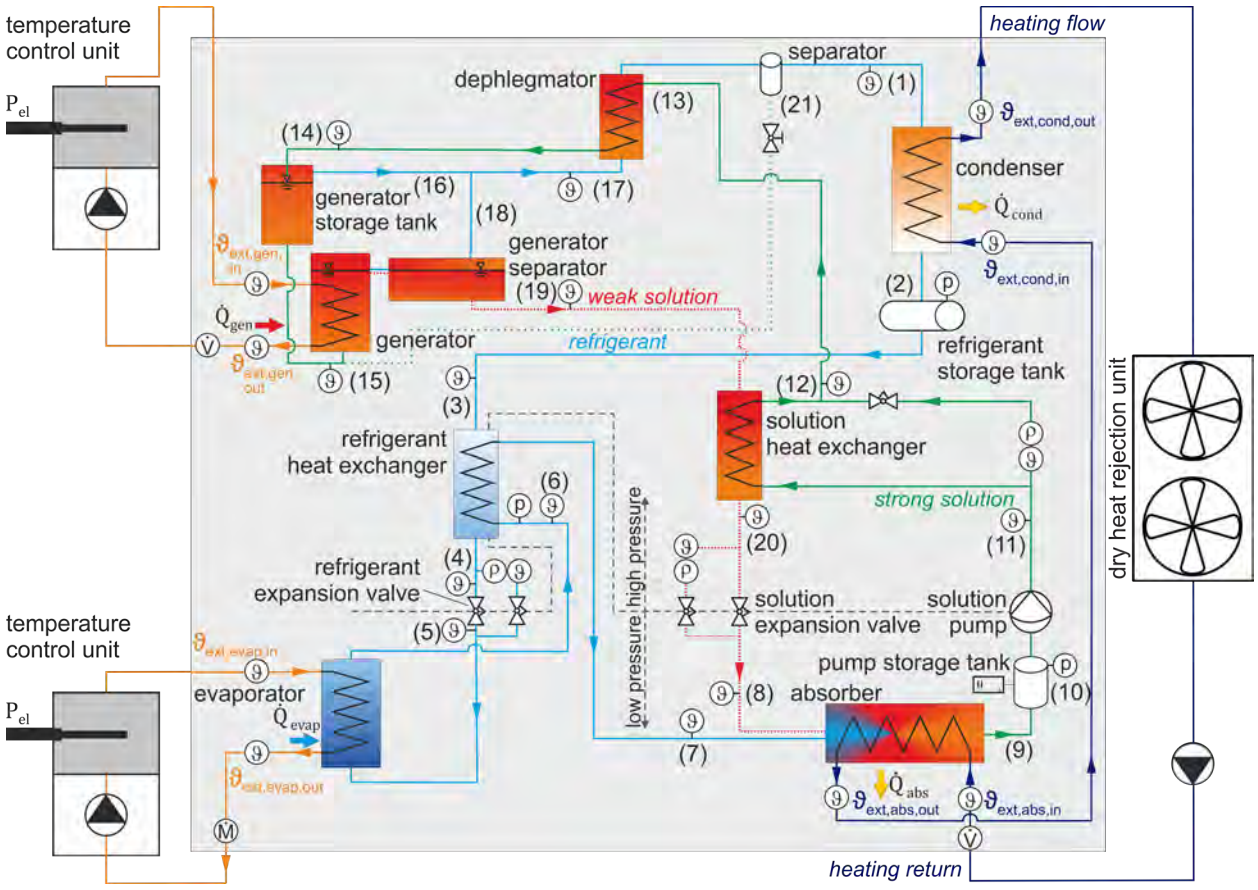

Figure 1: schematic design of the ammonia-water absorption heat pump with measuring locations

Table 1. Uncertainty and quantity of the used measurement

Sensors type	Quantity	Uncertainty
internal fluid temperature (PT100 1/3B)	14	$\pm 1/3 \cdot \left(0.3\ °C + (0.005)\ °C^{-1} \cdot \vartheta\right)$
external fluid temperature (PT100 1/10B)	8	$\pm\ 1/10 \cdot \left(0.3\ °C + (0.005)\ °C^{-1} \cdot \vartheta\right)$
low pressure (0…10 bar)	2	$\pm\ 0.008$ bar
high pressure (0…25 bar)	1	$\pm\ 0.25$ bar
density internal Coriolis flow meter	3	$\pm\ 0.5\ \mathrm{kg\ m^{-3}}$
fluid temperature internal Coriolis flow meter	3	$\pm 0.5\ °C + 0.005\ °C^{-1} \cdot \vartheta$

The refrigerant vapor extracted from the generator is no pure ammonia due to its thermodynamic equilibrium with the solvent water. In order to increase the refrigerant's purity, the vapor is partially condensed in a dephlegmator. In this process, water accumulates predominantly in the liquid phase. This fluid is separated in the separator after the dephlegmator (21) and is fed back to the generator (15). The refrigerant vapor is led to the condenser (1).

The locations of the measuring sensors are also shown in Figure 1. For temperature measurement, PT100 sensors with an accuracy class of 1/10B are installed in the external circuits. Thus, a high accuracy for determining the heat flow of the absorption heat pump is achieved. For safety reasons, pipe-mounted PT100 sensors of an accuracy class of 1/3B are used to measure the temperatures in the refrigerant and solution circuits. By using measured density, pressure and temperature, the ammonia mass fraction of the refrigerant and the solutions can be determined by the equation of state of (Tillner-Roth and Friend 1998). The density of the weak solution and the refrigerant is measured in parallel to the expansion valves with one Coriolis mass flow meter each. For the density measurement of the strong solution, a Coriolis mass flow meter is installed in parallel to the solution heat exchanger. The mass flow through the Coriolis is approx. 2 kg/h. Due to the low mass flow, the heat transfer in the solution heat exchanger is almost unaffected. The advantage of this setup is that the pressure loss of the Coriolis mass flow meter has no influence on the process. However, the mass flow of the solutions cannot be measured.

For the calculation of the total uncertainty, the uncertainties of each measurement system, given in Table 1, were used. The method given in Eq. (1) is used to calculate the uncertainty σ of the measured values, e.g. p, T and ρ, to the state variables, e.g. ξ. In this work, the partial derivatives used in Eq. (1) are calculated as central difference. An example for the central difference of the ammonia mass fraction ξ with respect to the temperature T is given in Eq. (2), assuming that the uncertainty σ_T is used as temperature difference $\Delta T = \sigma_T$.

$$\sigma_\xi = \pm \sqrt{\left(\frac{\partial \xi}{\partial T}\sigma_T\right)^2 + \left(\frac{\partial \xi}{\partial p}\sigma_p\right)^2 + \left(\frac{\partial \xi}{\partial \rho}\sigma_\rho\right)^2} \qquad \text{Eq. (1)}$$

$$\frac{\partial \xi}{\partial T} = \frac{\xi(p, T + \Delta T, \rho) - \xi(p, T - \Delta T, \rho)}{2\Delta T} \qquad \text{Eq. (2)}$$

In order to optimize an absorption heat pump, it is of interest to maximize the absorption and desorption efficiency. The absorption efficiency is defined in Eq. (3) as the ratio of the achieved change of the ammonia mass fraction in the absorber ($\xi_{\mathrm{ss}}^{\rho,\vartheta,p} - \xi_{\mathrm{ws}}^{\rho,\vartheta,p}$) with respect to the change of the ammonia mass fraction in an ideal absorber ($\xi_{\mathrm{ss}}^{x=0,\vartheta_{\mathrm{id}},p} - \xi_{\mathrm{ws}}^{\rho,\vartheta,p}$). Similarly, the desorption efficiency is defined in Eq. (4) as the ratio of the achieved change of the ammonia mass fraction in the generator ($\xi_{\mathrm{ss}}^{\rho,\vartheta,p} - \xi_{\mathrm{ws}}^{\rho,\vartheta,p}$) with respect to the change of the ammonia mass fraction in an ideal generator ($\xi_{\mathrm{ss}}^{\rho,\vartheta,p} - \xi_{\mathrm{ws}}^{x=0,\vartheta_{\mathrm{id}},p}$).

$$\eta_{\xi,\mathrm{abs}} = \frac{\xi_{\mathrm{ss}}^{\rho,\vartheta,p} - \xi_{\mathrm{ws}}^{\rho,\vartheta,p}}{\xi_{\mathrm{ss}}^{x=0,\vartheta_{\mathrm{id}},p} - \xi_{\mathrm{ws}}^{\rho,\vartheta,p}} \qquad \text{Eq. (3)}$$

$$\eta_{\xi,\mathrm{gen}} = \frac{\xi_{\mathrm{ss}}^{\rho,\vartheta,p} - \xi_{\mathrm{ws}}^{\rho,\vartheta,p}}{\xi_{\mathrm{ss}}^{\rho,\vartheta,p} - \xi_{\mathrm{ws}}^{x=0,\vartheta_{\mathrm{id}},p}} \qquad \text{Eq. (4)}$$

In Eq. (3) and Eq. (4), the ideal states $\xi_{\mathrm{ss}}^{x=0,\vartheta_{\mathrm{id}},p}$ and $\xi_{\mathrm{ws}}^{x=0,\vartheta_{\mathrm{id}},p}$ are obtained from the ammonia-water equation of state for saturated liquid ($x = 0$) at the outlet of each plate heat exchanger. The assumption for the solution temperature ϑ_{id} is that an ideal heat exchange takes place, where the temperature difference at the pinch point is zero. However, these efficiencies neither locate the potentials in absorption or desorption nor do they show whether the measured ammonia mass fractions of the solutions are close to thermodynamic equilibrium or not. For this reason, the ammonia mass fractions of each solution are considered directly and the efficiencies are listed for comparability with other works.

3. RESULTS AND CONCLUSIONS

The experimental tests were performed with four operating points of the absorption heat pump, which are shown in Table 2. The operating points have been selected within the project, described in detail in (Mirl et al. 2018a; Mirl et al. 2018b). However, findings on the absorber and on the generator can also be transferred to other operating points. The external inlet temperatures of the evaporator $\vartheta_{\mathrm{ext,evap,in}}$ and the generator $\vartheta_{\mathrm{ext,gen,in}}$ are set and controlled direct by the external temperature control units. The heat capacity rate of these circuits was set to $\dot{W}_{\mathrm{evap}} = \dot{W}_{\mathrm{gen}} = 0.8\ \mathrm{kW/K}$ and kept constant. The external inlet temperature at the absorber $\vartheta_{\mathrm{ext,abs,in}}$ is also controlled direct by the dry heat rejection unit. The external outlet temperature at the condenser $\vartheta_{\mathrm{ext,cond,out}}$, however, is set by reducing the external mass flow rate $\dot{M}_{\mathrm{ext,cond}}$. Due to a series connection, the mass flow rate in the absorber $\dot{M}_{\mathrm{ext,abs}} = \dot{M}_{\mathrm{ext,cond}}$ was also varied. As shown by Triché et al. (2017), a decreasing external mass flow rate reduces the absorption.

The measured values are recorded every 5 seconds over a period of 30 minutes under stable operating conditions. From this, time averages are formed. Those time-averaged values are used for further process evaluation. In order to find the optimal low-pressure level of the heat pump, the low-pressure was varied for each operating point and only those measurements with the highest coefficient of performance are used.

In order to identify the potentials of the absorber and the generator, the ammonia mass fractions of the strong and the weak solution are analyzed for each operating point. The results are presented in Figure 2. The operating points are shown on the x-axis and the ammonia mass fraction is shown on the y-axis. For each operating point, six ammonia mass fractions are calculated: three for the strong solution (ss) and three for the weak solution (ws). The ammonia mass fraction calculated from the measured density ρ of each solution is in the middle of each bar, i.e. $\xi_{\mathrm{ss}}^{\rho,\vartheta,p}$, $\xi_{\mathrm{ws}}^{\rho,\vartheta,p}$. The ammonia mass fractions $\xi_{\mathrm{ss}}^{x=0,\vartheta,p}$ and $\xi_{\mathrm{ws}}^{x=0,\vartheta,p}$ are calculated values by using the measured temperature ϑ and pressure p and assuming that the solution at the outlet of the heat exchanger is a saturated liquid at thermodynamic equilibrium $x = 0$. The highest value for the ammonia mass fraction $\xi_{\mathrm{ss}}^{x=0,\vartheta_{\mathrm{id}},p}$ is the ammonia mass fraction of the strong solution for ideal heat and mass transfer within the absorber. This value is calculated as saturated liquid with given pressure p_{low} and an outlet temperature of the strong solution $\vartheta_{\mathrm{ss,abs,out}}$, which is equal to the inlet temperature of the external circuit $\vartheta_{\mathrm{ext,abs,in}}$. Hence, this value corresponds to the ammonia mass fraction of the strong solution, which can be achieved in an ideal absorber. The lowest ammonia mass fraction $\xi_{\mathrm{ws}}^{x=0,\vartheta_{\mathrm{id}},p}$ of each bar is calculated as saturated liquid at high pressure for an ideal generator.

Regarding the optimization of the absorber and the generator, the differences between the ammonia mass fractions can be interpreted as potentials in absorption or desorption. The differences in the ammonia mass fractions obtained from measured densities $\xi^{\rho,\vartheta,p}$ and those obtained by using the

Table 2. Operating points of the absorption heat pump

Operating Point	$\vartheta_{\mathrm{ext,gen,in}}$	$\vartheta_{\mathrm{ext,evap,in}}$	$\vartheta_{\mathrm{ext,cond,out}}$	$\vartheta_{\mathrm{ext,abs,in}}$	$\dot{M}_{\mathrm{ext,abs}}$
1	110 °C	42 °C	52 °C	40 °C	0.45 kg/s
2	110 °C	30 °C	43 °C	28 °C	0.41 kg/s
3	100 °C	42 °C	52 °C	40 °C	0.31 kg/s
4	100 °C	30 °C	43 °C	28 °C	0.33 kg/s

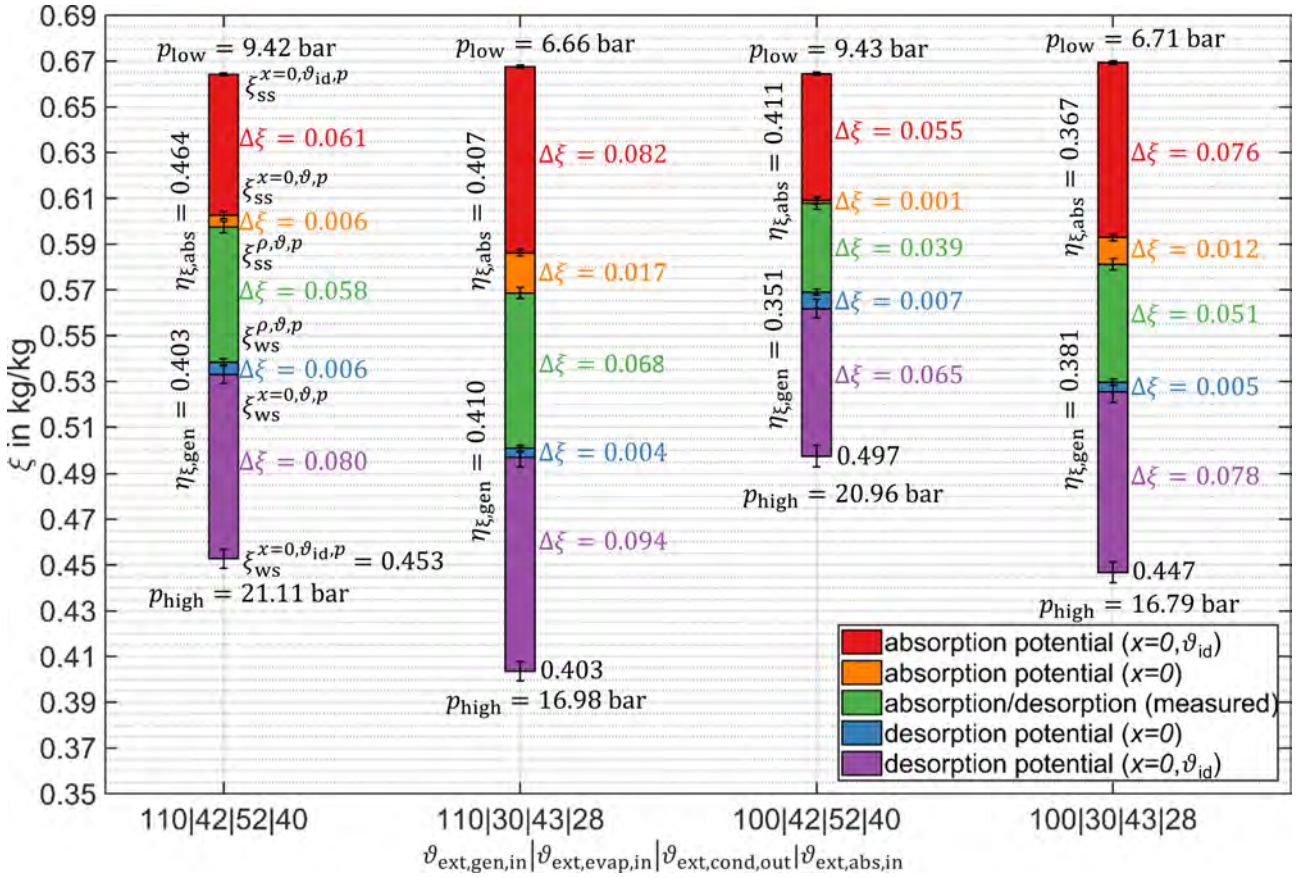

Figure 2: analysis of the ammonia mass fractions of the strong and weak solution

saturated liquid condition $\xi^{x=0,\vartheta,p}$ indicate the potentials in mass transfer within the generator unit and the absorber. For the generator unit, this potential is $0.004 < \Delta\xi < 0.007$ and is therefore within the measurement uncertainty at almost every operating point. In this regard, the generator unit works well. For the absorber, however, the difference of the ammonia mass fraction is in the range of $0.001 < \Delta\xi < 0.017$ and is only in the third operating point within the measurement uncertainty. Hence, there is a potential in mass transfer that could increase the current absorber efficiency for example at operating point 2 from $\eta_{\xi,\mathrm{abs}} = 0.407$ by $\Delta\eta_{\xi,\mathrm{abs}} = 0.102$.

For both, absorber and generator, the differences between $\xi^{x=0,\vartheta_{\mathrm{id}},p}$ and $\xi^{x=0,\vartheta,p}$ are larger in every operating point than the achieved absorption and desorption, respectively. Since $\xi^{x=0,\vartheta_{\mathrm{id}},p}$ is dominantly influenced by the temperature, the coupled heat and mass transfer within the heat exchangers has the highest optimization potential.

For this reason, the heat transfer within the heat exchangers is analyzed more detailed for operating point 2. Therefore, the heat exchangers are divided into $n = 200$ cells with the same heat transfer area A and overall heat transfer coefficient k. The heat transfer equation Eq. (5) is solved for each cell. With Eq. (6) and Eq. (7), the total transferred heat $\dot{Q}$ as well as the mean temperature difference of heat transfer are calculated. With the measured temperatures and the measured total transferred heat $\dot{Q}$ as boundary conditions, the system of equations can be solved iteratively. Hence, the temperature profiles within the heat exchangers can be calculated.

$$\dot{Q}_i = \frac{k \cdot A}{n} \cdot \Theta_{\mathrm{m},i} = \dot{M} \cdot c_p \cdot \Delta\vartheta_i = \dot{M} \cdot \Delta h_i \qquad \text{Eq. (5)}$$

$$\Theta_{\mathrm{m}} = \frac{1}{n}\sum_{i=1}^{n} \Theta_{\mathrm{m},i} = \frac{1}{n}\sum_{i=1}^{n} \frac{\left(\vartheta_{1,\mathrm{in}} - \vartheta_{2,\mathrm{out}}\right)_i + \left(\vartheta_{1,\mathrm{out}} - \vartheta_{2,\mathrm{in}}\right)_i}{2} \qquad \text{Eq. (6)}$$

$$\dot{Q} = \sum_{i=1}^{n} \dot{Q}_i = k \cdot A \cdot \Theta_{\mathrm{m}} \qquad \text{Eq. (7)}$$

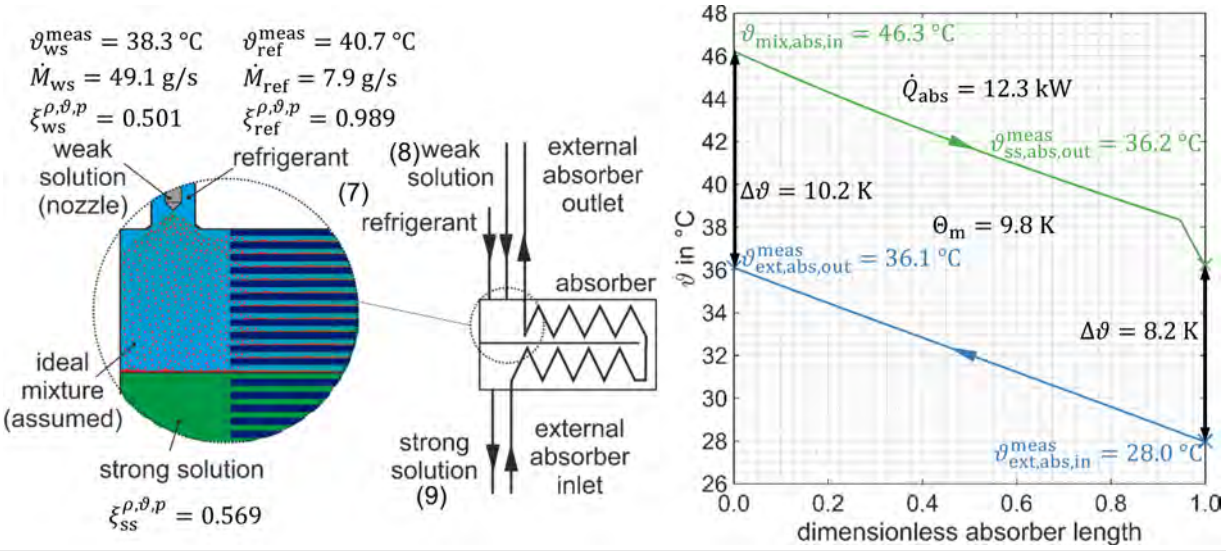

Figure 3: analysis of the temperature profile of the absorber at operating point 2 (110|30|43|28)

The resulting temperature profiles as well as the schematic design of the absorber are shown in Figure 3. For the calculation of the temperature profiles, the two fluids are assumed to be optimally mixed by spraying the weak solution into the refrigerant vapor at the inlet of the absorber. Hence, the inlet temperature of the mixture $\vartheta_{\mathrm{mix,abs,in}}$ can be calculated by the energy balance and thermodynamic equilibrium of the two-phase mixture. The calculated temperature profiles within the absorber are shown in Figure 3 on the right. The dimensionless absorber length is plotted on the x-axis and the temperature is plotted on the y-axis. The measured fluid temperatures are highlighted by the superscript “meas”. The temperature of the ammonia water mixture decreases continuously during heat transfer due to the thermodynamic equilibrium within the two-phase region. The higher temperature decrease of the strong solution in the area of the dimensionless absorber length of > 0.95 is caused by the subcooling of the solution. However, by controlling the pump storage tank to a constant liquid level, vapor from the absorber must also enter the pump storage tank. This indicates that either the distribution of the strong solution on the plate channels is uneven or the liquid phase near the wall is actually subcooled. Hence, there is not enough surface available for mass transfer. Regarding heat transfer, the mean temperature difference of the heat transfer is high at $\Theta_{\mathrm{m}} = 9.8\ \mathrm{K}$. Therefore, the absorber has to be optimized regarding a higher total heat transfer and a better distribution of the flow to the plate channels. A higher heat transfer can be achieved by increasing the absorber length.

Analogous to Figure 3, the temperature profile of the generator at operating point 2 are presented in Figure 4. The strong solution enters the generator at saturated state. Analogous to the absorber, the temperature of the solution changes along the generator length, due to the thermodynamic

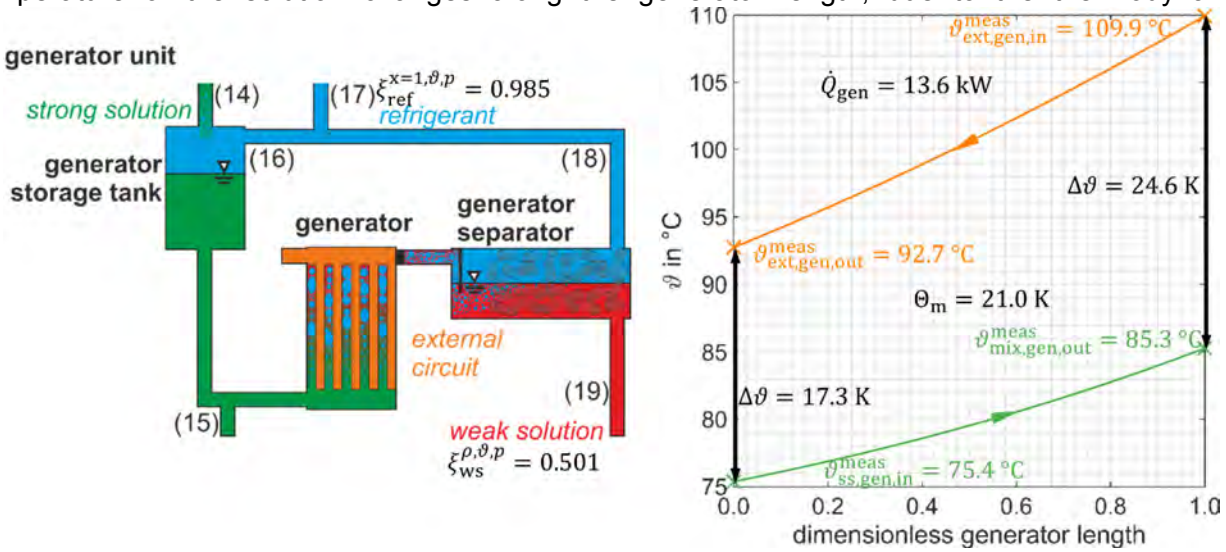

Figure 4: analysis of the temperature profile of the generator at operating point 2 (110|30|43|28)

equilibrium. However, the temperature difference in the external circuit is lower. Hence, the pinch point of the heat transfer is present at the inlet of the weak solution and is $\Delta\vartheta = 17.3\ \mathrm{K}$. This shows that the maximum potential of desorption will be even higher if the external mass flow is increased. However, one aim of Mirl et al. (2018b) is to maximize the temperature difference of the external fluid. Therefore, the mass flow has to be low. Hence, in order to decrease the high mean temperature difference in the generator of $\Theta_\mathrm{m} = 21.0\ \mathrm{K}$ and thereby to increase desorption process, the overall heat transfer coefficient or the heat transfer area have to be increased. Since the plate heat exchanger already consists of 60 plates, it is not appropriate to increase the heat transfer area by adding additional plates. Instead, a direct flow through the plate heat exchanger in conjunction with a multi-pass plate heat exchanger should be investigated to increase the overall heat transfer coefficient.

4. SUMMARY

Experimental investigations to identify and classify optimization potentials in heat and mass transfer of the absorber and generator were performed. For this purpose, the ammonia mass fractions of the strong and weak solution were analyzed at four operating points. This analysis revealed that the absorber efficiency is $0.367 \leq \eta_{\xi,\mathrm{abs}} \leq 0.464$ and the generator efficiency is $0.351 \leq \eta_{\xi,\mathrm{gen}} \leq 0.410$. Hence, the unused potentials in absorption and desorption process at the current state are higher than the achieved degassing range. It was also shown, that the potential in mass transfer at the outlet of the generator unit is $\Delta\xi \leq 0.007$ and therefore almost in thermodynamic equilibrium at all operating points. There is currently no need for enhancing the mass transfer at the generator unit.
A more detailed evaluation of the data showed, that the highest potential for the optimization of the absorber and generator is within the combined heat and mass transfer at the inside of the plate heat exchangers. The potentials were determined by using calculated temperature profiles. The mean temperature of heat transfer at the absorber is $\Theta_\mathrm{m} = 9.8\ \mathrm{K}$ and for the generator $\Theta_\mathrm{m} = 21.0\ \mathrm{K}$. From these analyses, it is pointed out, that the absorber has to be optimized with regard to a uniform distribution of the weak solution and refrigerant vapor to the plate channels as well as to a higher overall heat transfer. At the generator, the heat transfer must also be improved. The use of a direct flow multi-pass plate heat exchanger was suggested as an optimization proposal for the generator.

ACKNOWLEDGEMENTS

The work is based on a project (funding code “19696 N/2”) which is supported within the scope of the "program for promoting joint industrial research (IGF)" by the German Federal Ministry of Economic Affairs and Energy (Bundesministerium für Wirtschaft und Energie, BMWi) on the basis of a decision by the German Bundestag via the Federation of Industrial Research Associations (Arbeitsgemeinschaft industrieller Forschungsvereinigungen, AiF). The authors would like to thank them sincerely for their support.

NOMENCLATURE

A	heat transfer area (m²)	c_p	specific heat capacity (kJ/(kg·K))
h	specific enthalpy (kJ/kg)	k	overall heat transfer coefficient
$\dot{M}$	mass flow rate (kg/s)	n	number of cells
p	pressure (bar)	$\dot{Q}$	heat flow (kW)
T	temperature (K)	$\dot{W}$	heat capacity rate (kW/K)
w	velocity (mm/s)	x	vapor quality
Δ	difference	$\eta_{\xi,\mathrm{abs}}$	absorption efficiency (-)
$\eta_{\xi,\mathrm{gen}}$	desorption efficiency (-)	ϑ	temperature (°C)
Θ_m	mean temperature in heat transfer (K)	ρ	density (kg/m³)
σ	uncertainty in measurement of the variable	ξ	ammonia mass fraction (-)

Subscripts

1	heat-emitting flow	2	heat-absorbing flow
abs	absorber	cond	condenser
evap	evaporator	ext	external circuit
gen	generator	high	high level
i	count index	id	ideal heat exchanger
in	inlet	low	low level
mix	mixture	out	outlet
ref	refrigerant	ss	strong solution
ws	weak solution		

Superscripts

meas	measured value	ρ, ϑ, p	calculated with use of ρ, ϑ, p
$x = 0, \vartheta, p$	calculated with use of $x = 0, \vartheta, p$	$x = 1, \vartheta, p$	calculated with use of $x = 1, \vartheta, p$
$x = 0, \vartheta_{\mathrm{id}}, p$	calculated with use of $x = 0, \vartheta_{id}, p$		

REFERENCES

Aprile, M., Scoccia, R., Toppi, T., Guerra, M., Motta, M. 2016 Modelling and experimental analysis of a GAX NH3–H2O gas-driven absorption heat pump. *Int. J. Refrig.* 66, pp. 145–155.

Castro, J., Oliet, C., Rodríguez, I., Oliva, A. 2009 Comparison of the performance of falling film and bubble absorbers for air-cooled absorption systems. *Int. J. Therm. Sci.* 48 (7), pp. 1355–1366.

Cerezo, J., Best, R., Bourouis, M., Coronas, A. 2010 Comparison of numerical and experimental performance criteria of an ammonia–water bubble absorber using plate heat exchangers. *Int. J. Heat Mass Transf.* 53 (17-18), pp. 3379–3386.

Mirl, N., Schmid, F., Spindler, K. 2018a Experimentelle Untersuchung zur Einbindung einer Ammoniak-Wasser Absorptionswärmepumpe in Fernwärmenetze: Jahrestagung des Deutschen Kälte- und Klimatechnischen Vereins. Aachen, Germany, AA II.1.11.

Mirl, N., Schmid, F., Spindler, K. 2018b Reduction of the return temperature in district heating systems with an ammonia-water absorption heat pump. *Case Studies in Thermal Engineering* (12), pp. 817–822.

Mittermaier, M., Ziegler, F. 2015 Theoretical evaluation of absorption and desorption processes under typical conditions for chillers and heat transformers. *Int. J. Refrig.* 59, pp. 91–101.

Müller, M., Spindler, K. 2013 Effizienzsteigerung einer Ammoniak/Wasser-Absorptions-kältemaschine: Jahrestagung des Deutschen Kälte- und Klimatechnischen Vereins. Hannover, Germany, AA II.1.08.

Paar, A., Herbert, F., Pehnt, M., Ochse, S., Richter, S., Maier, S. et al. 2013 Transformations-strategien von fossiler zentraler Fernwärmeversorgung zu Netzen mit höheren Anteilen erneuerbarer Energien. Heidelberg, Germany.

Said, S.A.M., Spindler, K., El-Shaarawi, M. A., Siddiqui, M. U., Schmid, F., Bierling, B., Khan, M.M.A. 2016 Design, construction and operation of a solar powered ammonia–water absorption refrigeration system in Saudi Arabia. *Int. J. Refrig.* 62, pp. 222–231.

Staedter, M. A., Garimella, S. 2018 Thermodynamic considerations for optimal thermal compressor design. *Int J Ref* 91, pp. 28–38.

Tillner-Roth, R., Friend, D. G. 1998 A Helmholtz Free Energy Formulation of the Thermodynamic Properties of the Mixture {Water + Ammonia}. *J. Phys. Chem. Ref. Data* 27 (1), pp. 63–96.

Triché, D., Bonnot, S., Perier-Muzet, M., Boudéhenn, F., Demasles, H., Caney, N. 2017 Experimental and numerical study of a falling film absorber in an ammonia-water absorption chiller. *Int. J. Heat Mass Transf.* 111, pp. 374–385.

Venegas, M., Rodríguez, P., Lecuona, A., Izquierdo, M. 2005 Spray absorbers in absorption systems using lithium nitrate–ammonia solution. *Int. J. Refrig.* 28 (4), pp. 554–564.

Manuscript ID: 191
DOI: 10.18462/iir.icr.2019.0191

Scaling parameters between ammonia and water

Klaus SPINDLER

Institute for Building Energetics, Thermotechnology and Energy Storage (IGTE),
University of Stuttgart
Pfaffenwaldring 6, Stuttgart, D-70550, Germany, klaus.spindler@igte.uni-stuttgart.de

ABSTRACT

The thermodynamic critical values p_{cr} and T_{cr} are used to obtain corresponding states for the thermophysical properties. The normalized pressure p/p_{cr} has found to be the better scaling parameter. The thermophysical properties of ammonia are presented as function of normalized pressure. The density ratio ρ'/ρ'' and the density difference $\rho'-\rho''$ play an important role in thermosiphons and in two-phase flow heat transfer. Surface tension, viscosity and thermal conductivity influence the process of boiling and condensation. For depressurisation by opening a safety valve, the first derivatives of the enthalpy of vaporization and the density of the saturated liquid with respect to the pressure are relevant. The scaling factors between ammonia and water are given for the thermophysical properties and derivatives in a wide pressure range up to the critical point. The influence of the pressure depending thermophysical properties on boiling and condensation heat transfer of ammonia will be presented.
Keywords: Ammonia, Corresponding State, Thermodynamic Property, Scaling Law, Water, Boiling, Condensation

1. INTRODUCTION

Historically, ammonia has proven to be an excellent natural refrigerant with very good thermodynamic and transport properties. Ammonia has been used as a refrigerant in large industrial refrigeration applications for many years. Ammonia heat pumps for heating and cooling of large non-residential buildings achieve high energy efficiency due to the favorable thermophysical properties. There is a great interest in using ammonia in smaller systems. Water as a refrigerant is one of the oldest natural refrigerants for refrigeration processes down to the freezing point. Water has excellent thermodynamic and chemical properties. A few water vapor compression applications are known (Wobst et al. 2004, Kilicarslan & Müller 2005). Due to worldwide efforts to reduce global warming the use of natural refrigerants must be increased. The thermodynamic and heat transfer behavior of water and ammonia will be analysed using the principle of corresponding state. Based on the normalized values, the scaling parameters between water and ammonia are necessary.

2. THERMODYNAMIC SIMILARITY

The similarity of thermodynamic conditions can be obtained by choosing the thermodynamic variables of state for the fluids. This can be achieved by using the principle of the corresponding states. In general, the similarity can be obtained exactly by fixing one thermodynamic variable of state. A universal, generally valid equation of state is able to describe the thermodynamic behavior of two fluids in a dimensionless form. If the thermodynamic variables are normalized to characteristic thermodynamic states, the theorem of corresponding states can be used. If the thermodynamic critical values of pressure p_{cr}, specific volume v_{cr} and temperature T_{cr} are selected for normalisation, the van der Waals equation will contain only universal constants:

$$\left(\frac{p}{p_{cr}}+\frac{3}{\frac{v}{v_{cr}}}\right)\left(3\frac{v}{v_{cr}}-1\right)=8\frac{T}{T_{cr}} \qquad \text{Eq. (1)}$$

Eq. (1) is called the classical correspondence principle. By using the van der Waals equation, the thermodynamic parameters of state for real fluids cannot be calculated with high accuracy. However, this equation shows that the critical values p_{cr}, T_{cr} and v_{cr} are very useful to obtain corresponding states for the thermal and caloric properties of fluid 1 and fluid 2. Considering a one component system, vapor and liquid can only coexist in the thermodynamic equilibrium along the saturation line. Here, all thermodynamic parameters of state can be expressed by only one parameter of state. If the critical values are used for scaling from fluid 1 to fluid 2, one out of the following conditions will need to be fulfilled:

$$\left(\frac{p}{p_{cr}}\right)_{fluid\ 1} = \left(\frac{p}{p_{cr}}\right)_{fluid\ 2} \qquad \left(\frac{T}{T_{cr}}\right)_{fluid\ 1} = \left(\frac{T}{T_{cr}}\right)_{fluid\ 2} \qquad \left(\frac{\rho}{\rho_{cr}}\right)_{fluid\ 1} = \left(\frac{\rho}{\rho_{cr}}\right)_{fluid\ 2} \qquad \text{Eq. (2)}$$

The normalized pressure has been found to be the best scaling parameter (Mayinger, 1982).
The van der Waals equation in dimensionless (normalized) form shows that the behavior of the normalized specific volume or of the normalized density, as function of the normalized pressure and the normalized temperature, is the same for all substances. In the two-phase region ($T/T_{cr}<1$, $p/p_{cr}<1$) there exist three real solutions of the van der Waals equation. In this region ρ'/ρ_{cr} or ρ''/ρ_{cr} can be calculated by the same function for the model and original fluid. The density ratio ρ'/ρ'' is also a function of the normalized pressure because of

$$\frac{\rho'/\rho_{cr}}{\rho''/\rho_{cr}} = \frac{\rho'}{\rho''} = f\left(\frac{p}{p_{cr}}\right) \qquad \text{Eq. (3)}$$

The relation between the caloric parameters of state (h, c_p, Δh_v, etc.) and the thermodynamic parameters of state (T, p, v) can be deduced from generally valid thermodynamic expressions.
The caloric parameters of state will depend on the normalized pressure in a similar way if the corresponding principle is strictly fulfilled.
Grigull et al. (1968) showed that this thermodynamic corresponding principle can also be applied for transport properties (e.g. thermal conductivity, viscosity). Transport properties can also be given as a function of thermodynamic parameters of state.
The density ratio of saturated liquid and saturated vapor plays an important role in many fluid dynamic and heat transfer processes in gas-liquid two-phase flows. Surface tension, viscosity and thermal conductivity influence bubble growing, evaporation during rapid pressure reduction (flashing) and entrainment. For the simulation of transient processes, e.g. rapid depressurisation by suddenly opening a safety valve, the first derivative of the enthalpy of vaporization or the density of the saturated liquid by the pressure is needed (Mayinger 1982).

3. THERMOPHYSICAL PROPERTIES OF AMMONIA AND WATER

Cooper (1982) showed that the thermophysical properties of water can be expressed as a function of normalized pressure and normalized temperature with a maximum error of a few percent:

$$property = a \cdot \left(\frac{p}{p_{cr}}\right)^b \cdot \left(\frac{T}{T_{cr}}\right)^c \cdot \left(1 - \frac{T}{T_{cr}}\right)^d \qquad \text{Eq. (4)}$$

The coefficients a, b, c, d for the properties ρ', ρ'', $(\rho'-\rho'')$, Δh_v, η', λ', c_p', σ of water are given by Cooper (1982). Ribatski & Jabardo (2000) presented the thermophysical properties ρ', ρ'', c_p', c_p'', η', η'', λ', λ'', h', h'', Δh_v and σ of HFC refrigerants (e.g. R134a, R125, R152a, etc.) as function of normalized pressure and normalized temperature.
In this work, Eq. (4) is applied to the thermophysical properties of ammonia (NH_3). The coefficients a, b, c and d have been obtained by linear regression analysis. The coefficients are given in Table 1 for the individual properties along with the minimum and maximum deviation from the values calculated by REFPROP V9.1 (Lemmon et al. 2013).

The density of saturated liquid and saturated vapor of ammonia (NH_3) is presented in Fig. 1 and Fig. 2, respectively, versus the normalized pressure. The deviation is within ±3 % for the saturated liquid density and within ±6 % for the saturated vapor density of ammonia. Eq. (4) using the normalized pressure and temperature works also well for the transport properties. The thermal conductivity of the saturated liquid is shown in Fig. 3. Near the critical point, the deviation increases due to the anomaly of the thermal conductivity caused by molecule clustering. The dynamic viscosity of saturated liquid is presented in Fig. 4. The deviation is smaller than that for the thermal conductivity. Eq. (4) does not fulfill the boundary values for these properties at p/p_{cr} = 0 and 1. The deviation near the critical point is increased.

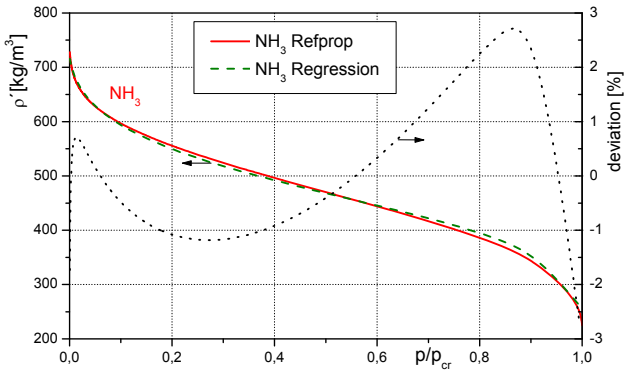

Figure 1: Density of saturated liquid Regression and deviation

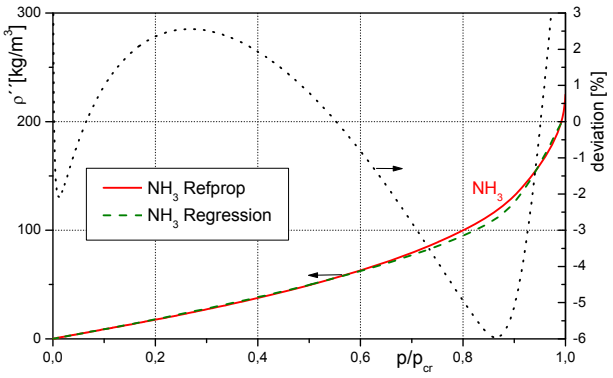

Figure 2: Density of saturated vapor Regression and deviation

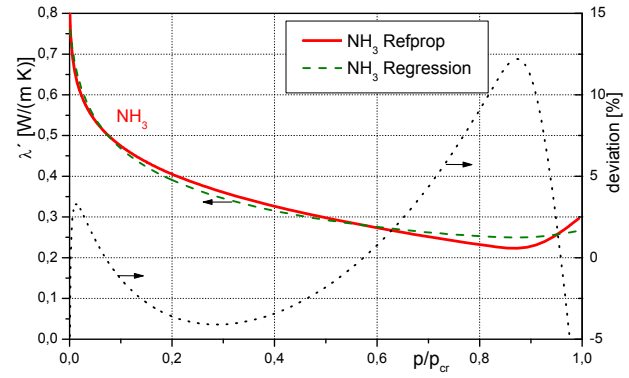

Figure 3: Thermal conductivity of saturated liquid Regression and deviation

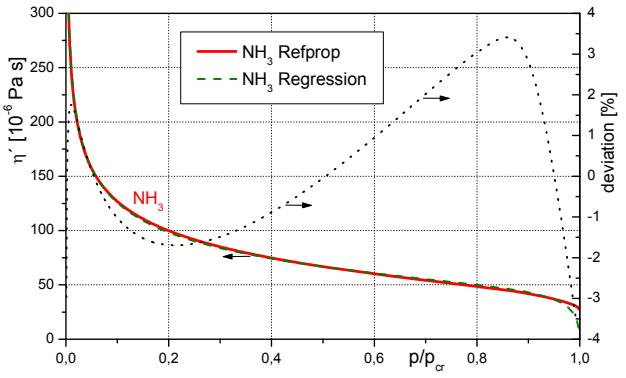

Figure 4: Dynamic viscosity of saturated liquid Regression and deviation

Table 1. Parameters a, b, c, d of Eq. (4) for the different properties of NH_3

property	unit	a	b	c	d	deviation
ρ'	kg/m^3	571.255	0.09784	-1.4206	0.11225	-2.6 to 3.1 %
ρ''	kg/m^3	68.275	0.78741	1.49929	-0.15662	-6.8 to 6.3 %
ρ'/ρ''	-	8.367	-0.68958	-2.92335	0.26887	-8.4 to 10.6 %
$\rho' - \rho''$	kg/m^3	1031.4	-0.02983	0.43793	0.36622	-0.9 to 0.6 %
Δh_v	kJ/kg	1918.85	0.03579	-0.35766	0.39305	-1.4 to 1.4 %
σ	N/m	0.1025	0.02788	-0.22006	1.21042	-0.06 to 0.07 %
λ'	W/(m K)	0.19986	0.36736	-5.58239	-0.04083	-10.2 to 14.8 %
η'	Pa s	$7.0231 \cdot 10^{-5}$	-0.14835	-1.36342	0.11919	-3.5 to 3.7 %
a'	m^2/s	$7.1732 \cdot 10^{-7}$	-0.32663	3.93199	0.77056	-9.1 to 9.3 %
Pr´	-	0.1714	0.08047	-3.87161	-0.76361	-9.4 to 10.8 %

4. SCALING PARAMETERS BETWEEN AMMONIA AND WATER

The comparison of the thermophysical properties of ammonia (NH_3) and water (H_2O) is shown in Fig. 5 to Fig. 16. The properties of ammonia have been calculated with REFPROP V9.1 (Lemmon et al. 2013). The IAPWS-IF97 V1.5 (Wagner et al. 2000) has been used to calculate the properties of water. In most cases, linear scaling factors have been found with except for the dynamic viscosity, the thermal conductivity and the Prandtl number of the saturated liquid. With the scaling factors given in Fig. 1 to Fig. 17 and summarised in Table 2, the values of water have been calculated based on the values of ammonia. These scaled values are presented as dashed lines in the diagrams. These lines are very close to the lines calculated direct for water. Typical maximum deviations between the scaled values and the real values for water are also provided in the diagrams.

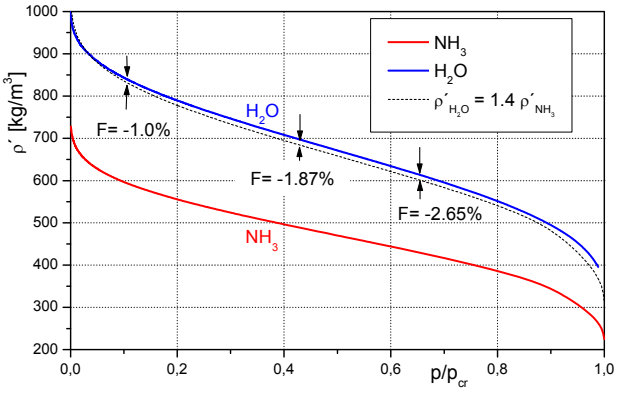

Figure 5: Density of saturated liquid of NH_3 and H_2O, upscaled values and typical deviation

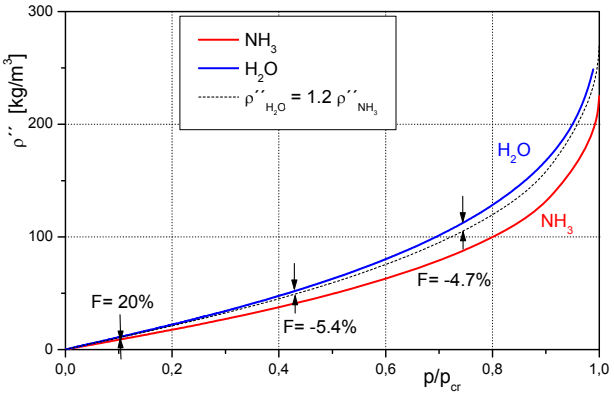

Figure 6: Density of saturated vapor of NH_3 and H_2O, upscaled values and typical deviation

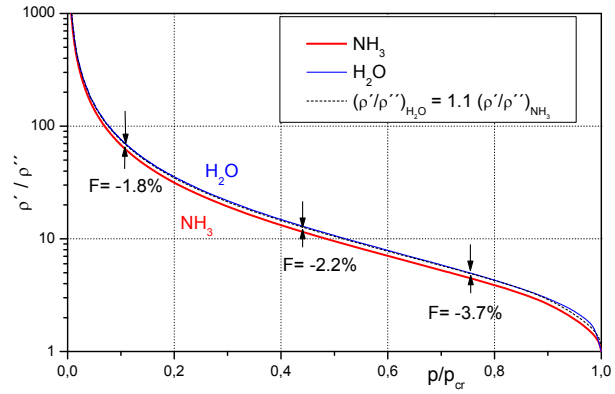

Figure 7: Density ratio of NH_3 and H_2O, upscaled values and typical deviation

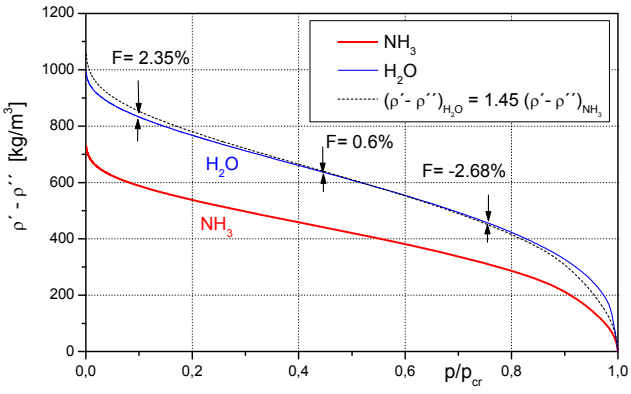

Figure 8: Density difference of NH_3 and H_2O, upscaled values and typical deviation

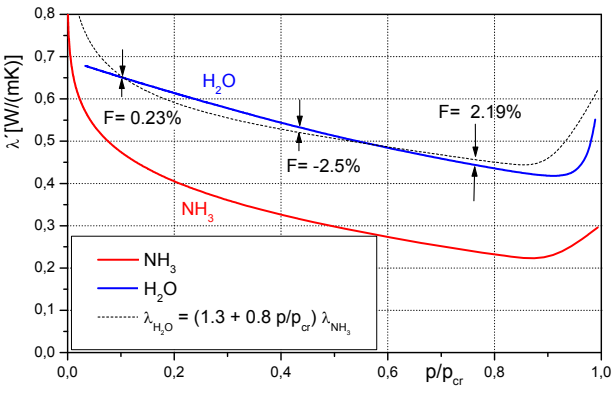

Figure 9: Thermal conductivity of saturated liquid of NH_3 and H_2O, upscaled values and typical deviation

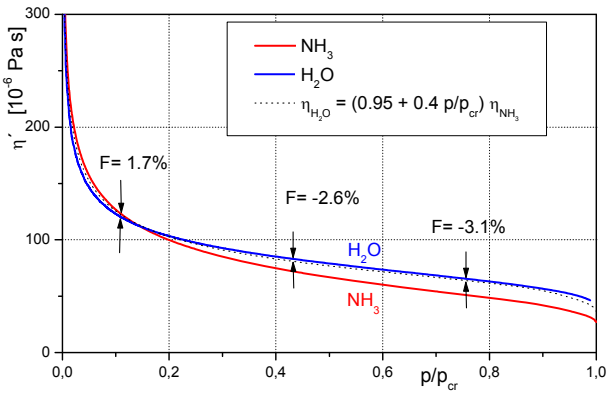

Figure 10: Dynamic viscosity of saturated liquid of NH_3 and H_2O, upscaled values and typical deviation

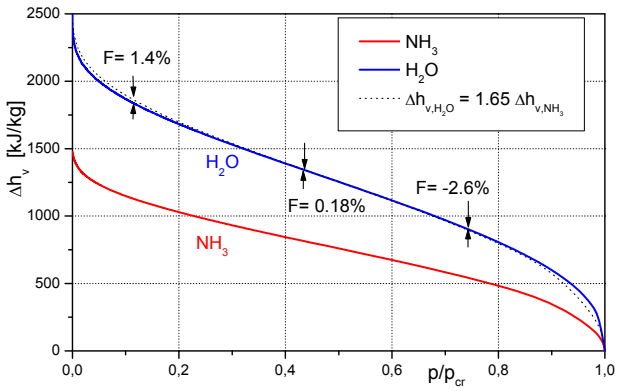

Figure 11: Enthalpy of vaporization of NH_3 and H_2O, upscaled values and typical deviation

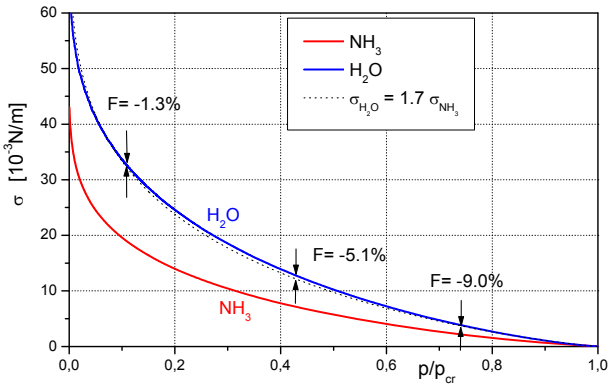

Figure 12: Surface tension

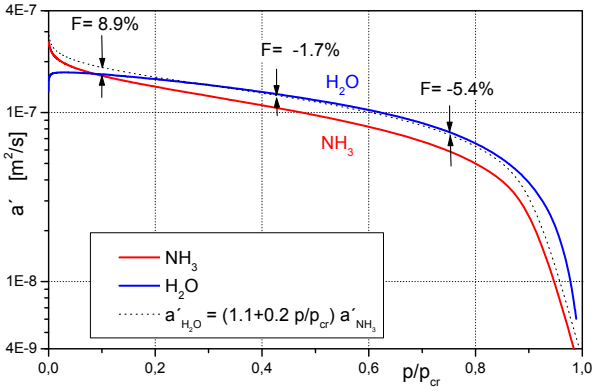

Figure 13: Thermal diffusivity of saturated liquid of NH_3 and H_2O, upscaled values and typical deviation

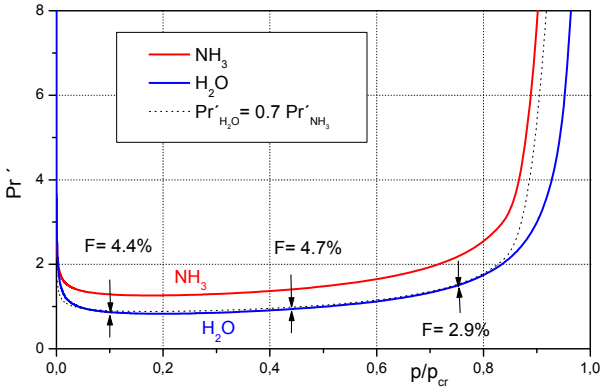

Figure 14: Prandtl number of saturated liquid

Table 2. Scaling factors for NH_3 up to water and R134a up to water in comparison

	NH_3 (this work)	R134a (Spindler, 2001)
saturation pressure	$p_{H2O} = 1.95\ p_{NH3}$	$p_{H2O} = 5.46\ p_{R134a}$
saturation temperature	$T_{H2O} = 1.6\ T_{NH3}$	$T_{H2O} = 1.73\ T_{R134a}$
enthalpy of vaporization	$\Delta h_{v,H2O} = 1.65\ \Delta h_{v,NH3}$	$\Delta h_{v,H2O} = 10\ \Delta h_{v,R134a}$
density of saturated liquid	$\rho'_{H2O} = 1.4\ \rho'_{NH3}$	$\rho'_{H2O} = 0.666\ \rho'_{R134a}$
density of saturated vapor	$\rho''_{H2O} = 1.2\ \rho''_{NH3}$	$\rho''_{H2O} = 0.573\ \rho''_{R134a}$
density ratio	$(\rho'/\rho'')_{H2O} = 1.1\ (\rho'/\rho'')_{NH3}$	$(\rho'/\rho'')_{H2O} = 1.15\ (\rho'/\rho'')_{R134a}$
density difference	$(\rho' - \rho'')_{H2O} = 1.45\ (\rho' - \rho'')_{NH3}$	$(\rho' - \rho'')_{H2O} = 0.666\ (\rho' - \rho'')_{R134a}$
dynamic viscosity	$\eta'_{H2O} = (0.95+0.4\ p/p_{cr})\ \eta'_{NH3}$	$\eta'_{H2O} = (0.45+0.55\ p/p_{cr})\ \eta'_{R134a}$
surface tension	$\sigma_{H2O} = 1.7\ \sigma_{NH3}$	$\sigma_{H2O} = 3.51\ \sigma_{R134a}$
thermal diffusivity of saturated liquid	$a'_{H2O} = (1.1 + 0.2\ p/p_{cr})\ a'_{NH3}$	$a'_{H2O} = 3.2\ a'_{R134a}$
Prandtl number of saturated liquid	$Pr'_{H2O} = 0.7\ Pr'_{NH3}$	$Pr'_{H2O} = (0.25-0.22p/p_{cr}+0.68(p/p_{cr})^2)Pr'_{R134a}$
thermal conductivity of saturated liquid	$\lambda'_{H2O} = (1.3+0.8\ p/p_{cr})\ \lambda'_{NH3}$	$\lambda'_{H2O} = (7.44+1.1\ p/p_{cr})\ \lambda'_{R134a}$
derivative of enthalpy of vaporization by pressure	$(d(\Delta h_v)/dp)_{H2O} = 0.85\ (d(\Delta h_v)/dp)_{NH3}$	$(d(\Delta h_v)/dp)_{H2O} = 1.8\ (d(\Delta h_v)/dp)_{R134a}$
derivative of saturated liquid density by pressure	$(d\rho'/dp)_{H2O} = 0.75\ (d\rho'/dp)_{NH3}$	$(d\rho'/dp)_{H2O} = 0.126\ (d\rho'/dp)_{R134a}$

Table 2 summarises all scaling factors found for scaling from ammonia up to water. For comparison, the scaling factors for R134a, determined by Spindler (2001), are also provided in Table 2. It can be seen that the scaling factors for ammonia are very different to those for R134a.
The lines of the calculated derivatives $d\rho'/dp$ (Fig. 15) and $d\Delta h_v/dp$ (Fig. 16) of ammonia and of the scaled-up values for water show some residual ripples at low normalized pressure because the derivatives are more sensitive to small errors in the thermophysical values.

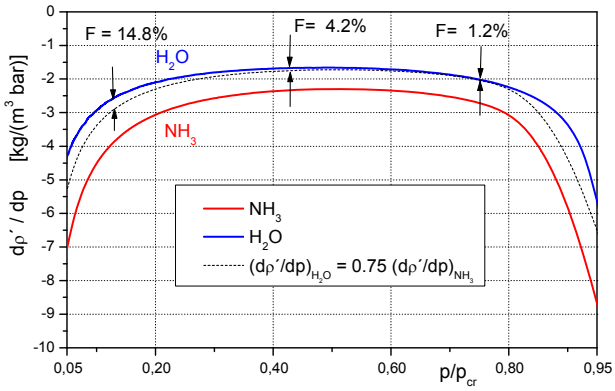

Figure 15: Derivative of saturated liquid density of NH_3 and H_2O, upscaled values and typical deviation

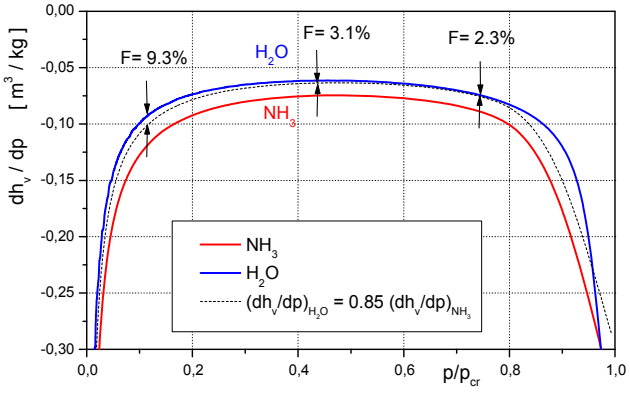

Figure 16: Derivative of enthalpy of vaporization

5. HEAT TRANSFER IN BOILING AND CONDENSATION

Cooper (1982, 1984) showed that boiling heat transfer coefficients can be reduced to a product of powers of the transport properties. These properties can be written in terms of normalized pressure and normalized temperature, see Eq. (4). For water boiling on horizontal cylinders, Cooper found the following equation depending on normalized pressure:

$$\alpha = C_3 \cdot q^{0.69} \left(\frac{p}{p_{cr}}\right)^{0.056} \cdot \left(-log_{10}\frac{p}{p_{cr}}\right)^{-0.7}$$ with C_3 = 7.4 for water. Eq. (5)

Mostinski (1963) applied the principle of corresponding states to nucleate pool boiling. He correlated the data as function of normalized pressure and critical pressure:

$$\alpha = 0.10605 \cdot q^{0.7} {p_{cr}}^{0.69} \cdot F(p/p_{cr})$$ Eq. (6)

with $F(p/p_{cr}) = 1.8(p/p_{cr})^{0.17} + 4(p/p_{cr})^{1.2} + 10(p/p_{cr})^{10}$

The heat flux in Eq. (5) and Eq. (6) must be given in W/m^2 to obtain the heat transfer coefficient in W/(m^2 K). The heat transfer coefficients for H_2O and NH_3 are calculated by using Eq. (6) with the critical pressure 113.33 bar for NH_3 and 220.64 bar for H_2O. The heat transfer coefficients are plotted in Fig. 17 for the heat fluxes 5000, 20000 and 50000 W/m^2. For comparison, the results for H_2O obtained by the Cooper equation (Eq. 5) are also shown. The equation by Mostinski (Eq. (6)) and by Cooper (Eq. (7)) yields about the same heat transfer coefficient for $p/p_{cr} < 0.5$. At $p/p_{cr} > 0.6$, the values calculated by the Cooper equation are higher than the values by the Mostinski equation. In total, the boiling heat transfer coefficient for water is about 1.58 times higher than for ammonia at the same normalized pressure.
The heat transfer coefficient for laminar film condensation is calculated based on the classical film theory by Nusselt:

$$\alpha = 0.943 \frac{g^{1/4}}{(\vartheta_S - \vartheta_W)^{1/4} H^{1/4}} \frac{\rho'^{1/2} \lambda'^{3/4} \Delta h_v^{1/4}}{\eta'^{1/4}}$$ with $H = \pi d_o/2$ Eq. (7)

The condensation heat transfer coefficient for a horizontal tube (outer diameter d_o = 20 mm) and wall subcooling ϑ_S-ϑ_W = 2 K is presented in Fig. 18. The thermophysical properties in Eq. (7) depend on normalized pressure and temperature. The condensation heat transfer coefficient decreases with increasing normalized pressure, whereas the boiling heat transfer coefficient increases with normalized pressure (see Fig. 17). At the same normalized pressure, the condensation heat transfer coefficient for water is about 1.8 times higher at p/p_{cr} = 0.2 and about 2 times higher at p/p_{cr} = 0.8 compared to ammonia.
The influence of the heater material, the surface roughness and the wetting behavior must be considered in addition (see Abbas et al. 2017; Spindler 2010, Spindler 2015).

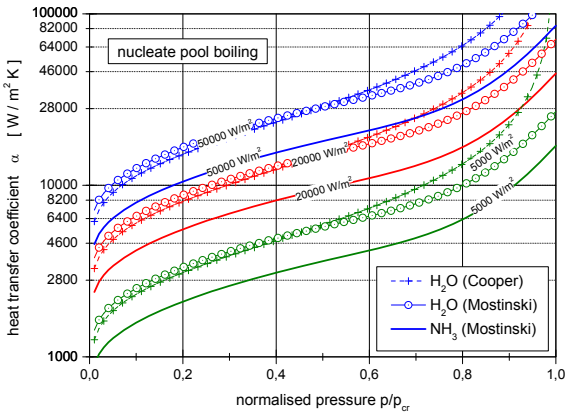

Figure 17: Boiling heat transfer coefficient

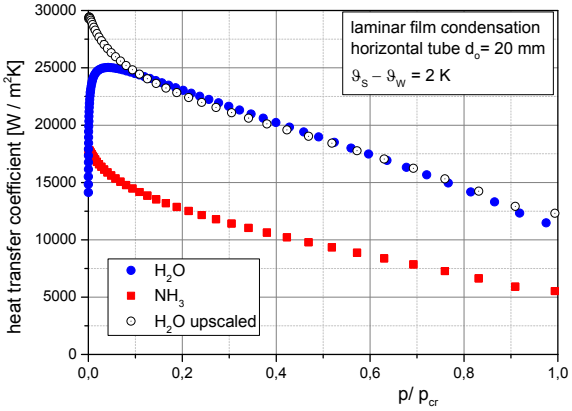

Figure 18: Condensation heat transfer coefficient

6. CONCLUSIONS

The thermophysical properties of ammonia can be correlated with one generally valid correlation only depending on normalized pressure and normalized temperature. The deviation is mostly within ±10%. Linear scaling factors for the thermophysical properties (p, T, Δh_v, ρ', ρ'', (ρ'-ρ''), σ, Pr´) and the derivatives (Δh_v/dp, dρ'/dp) between ammonia and water have been found. For the transport properties (η', λ', a´), the scaling factors depend linearly on the normalized pressure. The deviation between the upscaled values of ammonia to that of water is typically within ±5%. The boiling heat transfer coefficient increases with increasing normalized pressure. The condensation heat transfer coefficient increases with decreasing normalized pressure. Higher evaporation temperature and lower condensation temperature of refrigeration and heat pump cycles yield higher cycle efficiencies. The heat transfer behavior supports this.

NOMENCLATURE

a	thermal diffusivity (m^2/s)	α	heat transfer coefficient ($W/(m^2 K)$)
g	gravitational acceleration (9.81 m/s^2)	η	dynamic viscosity (Pa·s)
d_o	outer diameter of tube (m)	λ	thermal conductivity (W/(m K))
H	heigth (m)	ρ	density (kg/m^3)
p	pressure (bar)	σ	surface tension (N/m)
Pr	Prandtl number	ϑ	Celsius temperature (°C)
v	specific volume (m^3/kg)	Δh_v	enthalpy of vaporization (kJ/kg)
T	absolute temperature (K)	´	saturated liquid
cr	critical value	´´	saturated vapor

REFERENCES

Abbas, A., Ayub, Z.A., Khan, T.S., Ayub, A.H., Chattha, J.A. 2017. A review of correlations for outside boiling of ammonia on single tube and bundles. Heat Transfer Engineering, vol. 39, no. 16, pp. 1425-1436.

Cooper, M.G. 1982. Correlation for nucleate boiling – Formulation using reduced properties. PhysicoChemical Hydrodynamics vol. 3, no. 2, pp. 89-111.

Cooper, M.G. 1984. Heat Flow rates in saturated nucleate pool boiling – A wide-ranging examination using reduced properties. Advances in Heat Transfer 16, pp. 157-239.

Grigull, U., Bach, J., Reimann M. 1968. Die Eigenschaften von Wasser und Wasserdampf nach der “1968 IFC-Formulation”. Wärme- und Stoffübertragung 1, S. 202-213.

Kilicarslan, A., Müller, N. 2005. A comparative study of water as a refrigerant with some current refrigerants. Int. J. Energy Research, 29, pp. 947-959.

Lemmon, E.W., Huber, M.L., Mc Linden, M.O. 2013: REFPROP Vers. 9.1. NIST Standard Reference Database 23, National Institute of Standards and Technology, Gaithersburg, Maryland, United States.

Mayinger, F. 1982. Strömung und Wärmeübergang in Gas-Flüssigkeits-Gemischen. Springer Verlag, Wien, New York.

Mostinski, I.L. 1963. Application of the rule of corresponding states for calculation of heat transfer and critical heat flux (russ.), Teploenergetika 4, pp. 66-71.

Ribatski, G., Jabardo, J.M.S. 2000. Nucleate boiling of Halocarbon Refrigerants: Heat Transfer Correlations. HVAC&R Research vol. 6, no.4, pp. 349-367.

Spindler, K. 2001. The use of refrigerant R134a as model fluid for water. IIR/IIF Commission B1, Thermophysical Properties and Transfer Processes, Paderborn, Germany. A3.9-A3.16

Spindler, K. 2010. Overview and discussion on pool boiling heat transfer data and correlation of ammonia. Int. J. Refrigeration 33, pp. 1292-1306.

Spindler, K. 2015. Enhancement of condensation heat transfer of ammonia on the outside of tubes. 6th IIR Conference Ammonia and CO_2 Refrigeration Technologies, Ohrid, Macedonia.

Stene, J. 2008. Design and application of ammonia heat pump systems for heating and cooling of non-residential buildings. 8th IIR Gustav Lorentzen Conference on Natural Working Fluids, Copenhagen, Denmark.

Wagner, W., Span, R., Bonsen, C. 2000. Wasser und Wasserdampf. Interaktive Software zur Berechnung der thermodynamischen Zustandsgrössen auf der Basis des Industriestandards IAPWS-IF 97, Springer Verlag, Berlin, Heidelberg, Germany.

Wobst, E., Kalitzin, N., Apley, R. 2004. Turbo Water Chiller with Water as Refrigerant. Int. Compressor Engineering Conference, Purdue, United States, July 12-15, paper C 129.

Manuscript ID: 203
DOI: 10.18462/iir.icr.2019.0203

Measurement of Pool Nucleate Boiling Heat Transfer Coefficient of R1234yf at Saturation

Yoshinori TAKAISHI[(a)], Kou KATO[(b)]

[(a)]Kanagawa Institute of Technology
Atsugi, 243-0292, Japan, ytaka@me.kanagawa-it.ac.jp
[(b)]Graduate School, Kanagawa Institute of Technology
Atsugi, 243-0292, Japan

ABSTRACT

This paper describes measurements of the pool nucleate boiling heat transfer coefficient of R1234yf, which has been used as a low GWP alternative for R134a. The measurements were conducted by use of a horizontal platinum heating wire under the pool, saturated conditions. The boiling curves were obtained for heat fluxes up to 220 kW/m^2 and temperatures between 273 K and 294 K whose corresponding saturation pressures lie between 318 kPa and 613 kPa. The boiling data reveal that the heat transfer coefficient increases in proportion to the heat flux to the power of 0.712, and it is also proportional to the saturated pressure to the power of 0.476. The comparison with the similarly measured heat transfer coefficients of R134a indicates that the heat transfer coefficients of R1234yf are slightly less than those of R134a, but their deviations from R134a do not exceed -5%.
Keywords: Measurement, Boiling Heat Transfer Coefficient, HFO, R1234yf, R134a.

1. INTRODUCTION

R1234yf (2,3,3,3-tetrafluoro-1-propene) is a pure unsaturated organic compound called hydrofluoro-olefins (HFOs). It has a low GWP of about 4 and a low toxicity although it has a mild flammability. It is an eminently suitable replacement for R134a in automotive air-conditioning and other refrigerating systems in terms of the thermophysical properties including saturated vapour pressure similar to those of R134a.

Since R1234yf was first proposed and designated as a refrigerant about a decade ago, its boiling heat transfer coefficient, which is needed for evaporator design and others, has extensively been investigated and reported in the literature. Among them are as follows: Park and Jung (2010) reported the nucleate boiling heat transfer coefficient of R1234yf on plain and low fin surfaces. They found that the nucleate boiling heat transfer coefficients are very similar to those of R134a for the two surfaces tested. Saitoh *et al*. (2011) measured the boiling heat transfer coefficient of R1234yf flowing inside a smooth small diameter horizontal tube, and they later investigated the effect of lubricating oil on it (Saitoh *et al*., 2013). Longo (2012) measured the boiling heat transfer coefficient and the pressure drop of R1234yf inside a brazed plate heat exchanger and then concluded that R1234yf exhibits 6% to10% lower heat transfer coefficient than that of R134a. Mortada *et al*. (2012) also measured the local boiling heat transfer coefficient and the pressure drop in mini-channels, and reported that R1234yf presents a local heat transfer coefficient higher than R134a.

This study focuses attention on the pool nucleate boiling for R1234yf at saturation. The measurements are carried out by use of a horizontal platinum heating wire, which seems to be one of the simplest boiling heat transfer systems. The experimental pool nucleate boiling heat transfer coefficients obtained at temperatures 273 K to 294 K are reported. Then the present heat transfer coefficients of R1234yf are compared to those of R134a.

2. EXPERIMENTAL

Fig. 1 shows a schematic diagram of the experimental setup, whose details are given elsewhere (Sato *et al*., 1998). Boiling data were obtained by heating a test liquid at saturation with a horizontal platinum wire, whose diameter and length were 0.1 mm and 20 mm, respectively. The pressure cell filled with the test liquid was immersed in a thermostatic bath. The bath-temperature was controlled

at desired temperatures within a fluctuation of ±0.1 K. A computer regulated the electrical power applied to the platinum wire. Then the electrical current through the platinum wire, *I*, as well as the electrical voltage between the electrodes, *E*, were measured and stored in the computer automatically. The bulk temperature of test liquid at saturation, T_s, was measured with a platinum resistance thermometer. The surface temperature of platinum wire, T_w, was obtained from the correlation equation which related T_w with the electrical resistance of the platinum wire, *R*. Then *R* can be determined from *E / I*. The calibration was carried out prior to the experiment.
Thus the heat transfer coefficient, *h*, is determined from the following equation:

$$h = \frac{q}{\Delta T} \qquad \text{Eq. (1)}$$

where ΔT denotes the wall superheat defined as $\Delta T = T_w - T_s$, and *q* the heat flux from the surface of platinum wire to the test fluid around it. The heat flux, *q*, is determined from *EI / S,* where *S* is the surface area of the platinum wire.

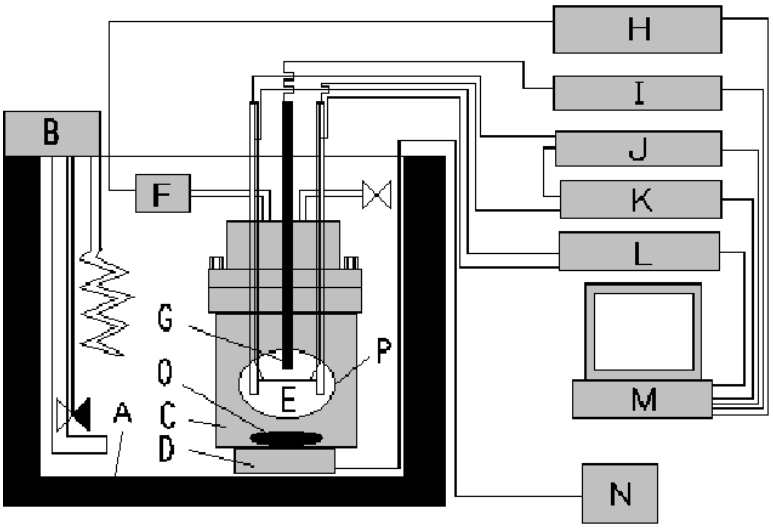

A: thermostatic bath, B: temperature controller, C: pressure cell, D: magnetic stirrer, E: platinum wire, F: pressure sensor, G: platinum resistance thermometer, H: voltmeter for pressure sensor, I: platinum resistance thermometer display, J: ammeter, K: power supply-1, L: voltmeter for platinum wire, M: computer, N: power supply-2, O: magnet rotator, P: sight glass

Figure 1: Experimental setup

3. EXPERIMENTAL RESULTS AND DISCUSSION

3.1. Boiling Data

The measurements were carried out at temperatures between 273.27 K and 294.29 K, whose corresponding saturation pressures were between 318 kPa and 613 kPa. Fig. 2 shows the boiling data of R1234yf for four different saturation temperatures and pressures. The maximum heat flux supplied in the experiment was about 220 kW/m^2.
The boiling data at each saturation temperature was measured under the conditions of both increasing heat fluxes from 0 to 220 kW/m^2 and decreasing heat fluxes from 220 to 0 kW/m^2. The up and down steps in electrical current during the heating cycle were programmed to be ±0.1 A between 0 A and 2.3 A.
Each boiling curve shown in Fig. 2 begins with the natural convection heat transfer at lower heat fluxes. The onsets of nucleate boiling (ONB) during the process of increasing heat flux are depicted by the black-painted markers in Fig. 2

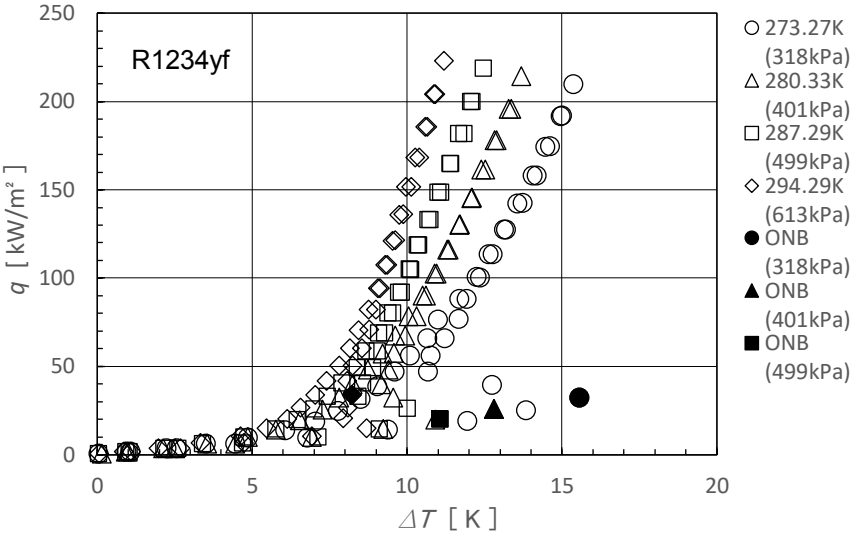

Figure 2: Boiling data for four different saturation temperatures and pressures

The bubble formation at the onset of nucleate boiling means the transition from natural convection heat transfer to nucleate boiling heat transfer. The wall superheat, ΔT, at the onset of nucleate boiling decreased from 15.6 K to 8.2 K as the saturation pressure increases from 318 kPa to 613 kPa. The heat fluxes at the onset of nucleate boiling, however, remained stable around 20 to 30 kW/m^2. The boiling curves had some discrepancy between the processes of increasing and decreasing heat fluxes. The discrepancy tends to become smaller with increasing saturation temperature and pressure. This discrepancy can be called a hysteresis in boiling curves.

In the region of natural convection heat transfer, the relationship between the heat flux, q, and the wall superheat, ΔT, was found to be $q \propto \Delta T^{1.04\sim1.11}$ at temperatures between 273.27 K and 294.29 K. This relationship seems to be similar to $q \propto \Delta T^{1.25}$ which is a typical power law in natural convection heat transfer with a laminar flow.

In the region of nucleate boiling heat transfer, on the other hand, the relationship between q and ΔT was found to be $q \propto \Delta T^{3.06\sim4.15}$ for temperatures 273.27 K to 294.29 K. The similar relationship, $q \propto \Delta T^{3}$, is found in Rohsenow's equation that has widely been used to calculate nucleate boiling heat transfer (Incropera *et al*. 2007).

3.2. Heat Transfer Coefficient with Heat Flux

The nucleate boiling was found to be much more stable in the process of decreasing heat flux than that of increasing heat flux. Thus the nucleate heat transfer coefficient was determined from the boiling data obtained in the process of decreasing heat fluxes from 220 kW/m^2 to 80 kW/m^2, where the nucleate boiling was obviously observed through the sight-glasses of the pressure cell and the thermostatic bath with the naked eyes.

Fig. 3 shows the experimental results of pool nucleate boiling heat transfer coefficients with heat flux for four different saturation temperatures of 273.27 K, 280.33 K, 287.29 K, and 294.29 K. In Fig. 3, the pressure values shown in parentheses are the corresponding saturation pressures.

The overall experimental uncertainty in h was estimated to be less than ±5%. The uncertainty in ΔT resulting from the error in T_w gave the greatest contribution to the overall uncertainty in h.

It was found from the experiment that the pool nucleate boiling heat transfer coefficient is proportional to the heat flux to the power of 0.712. The power of 0.712 for R1234yf is relatively close to the power of 0.745 for refrigerants, which is used in the simplified correlation equation proposed by Stephan and Abdelsalam for nucleate boiling (JSME Data Book 2005). It was also found that the pool nucleate boiling heat transfer coefficient increases in proportion to the saturation pressure to the power of 0.476.

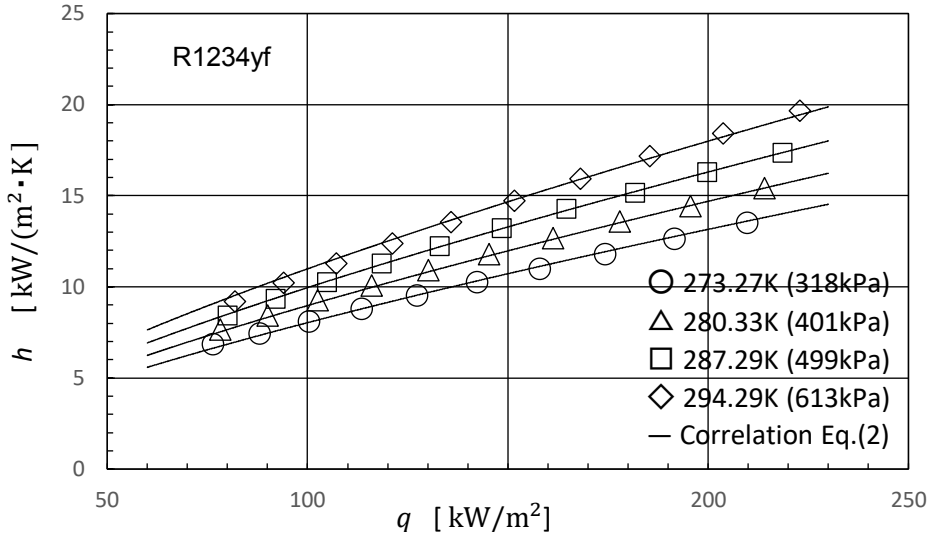

Figure 3: Pool nucleate boiling heat transfer coefficients with heat flux for four different saturation temperatures and pressures

3.3. Correlation Equation

A correlation equation was formulated to represent the experimental pool nucleate boiling heat transfer coefficient, *h*, as a function of heat flux, *q*, and saturation pressure, *P*. The correlation equation is as follows:

$$h = 0.01951 q^{0.712} P^{0.476} \qquad \text{Eq. (2)}$$

where the units used are *h* in kW/(m²·K), *q* in kW/m², and *P* in kPa, respectively.
Fig. 4 shows the deviation plot of experimental pool nucleate boiling heat transfer coefficients from the correlation, Eq. (2). It represents all the experimental data with the deviation less than ±4% and with the absolute average deviation of ±1%. The present correlation, Eq. (2), is valid only in the range of the heat fluxes 80 to 220 kW/m² and the pressures 318 to 613 kPa. In Fiq. 3, the correlation equation is drawn by curved lines.

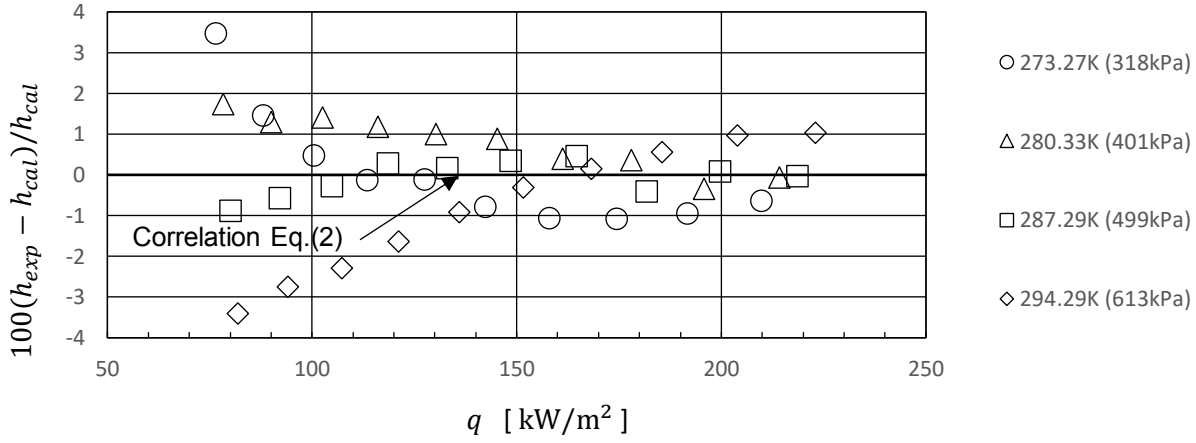

Figure 4: Deviation plot of experimental pool nucleate boiling heat transfer coefficients from Eq. (2)

3.4. Comparison with R134a

Fig. 5 shows the comparison of experimental pool nucleate boiling heat transfer coefficients for R1234yf with those for R134a. The experimental data of R134a were obtained by using the same apparatus and the same method as those described above. The pool nucleate boiling heat coefficient of R1234yf was found to be slightly less than those of R134a. The deviation from R134a, however, is not greater than -5%.

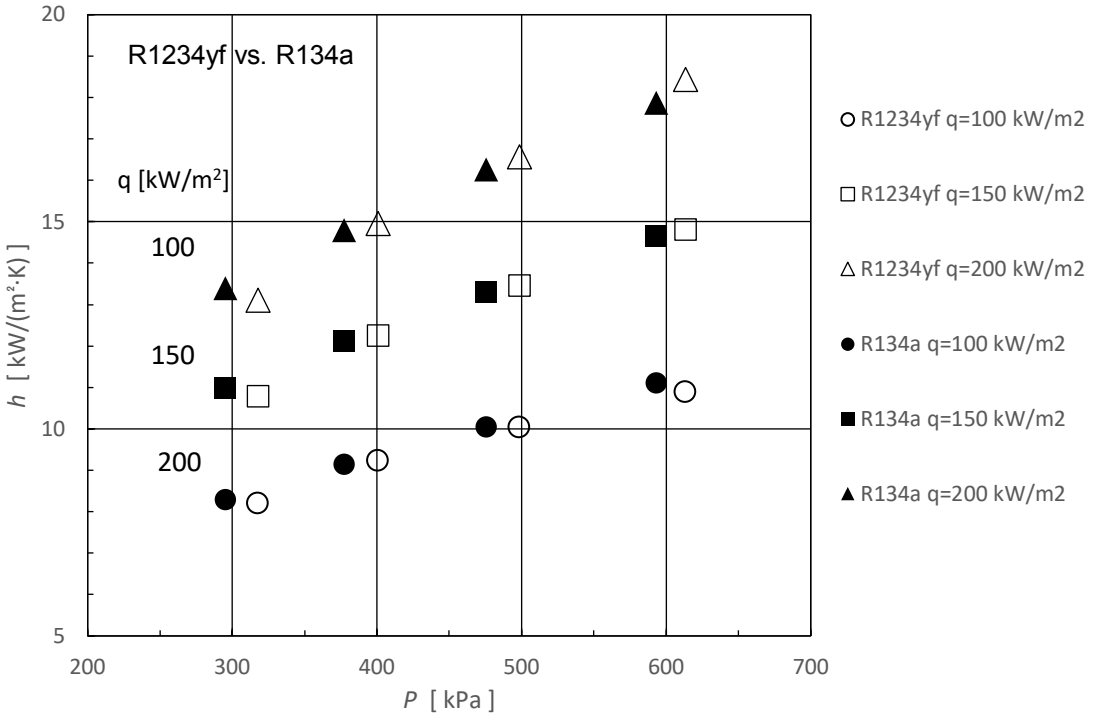

Figure 5: Comparison of pool boiling heat transfer coefficients of R1234yf with those of R134a

4. CONCLUSIONS

The pool nucleate boiling heat transfer coefficient of R1234yf was evaluated experimentally by means of a horizontal platinum wire heating method for the ranges of heat fluxes up to 220 kW/m^2, temperatures between 273 K and 294 K, and pressures from 318 kPa to 613 kPa. The pool nucleate boiling heat transfer coefficients of R1234yf are slightly less than those of R134a, but the deviations of the heat transfer coefficients of R1234yf from those of R134a do not exceed -5% in the range of heat fluxes and pressures the present study has dealt with.

ACKNOWLEDGEMENTS

The authors are grateful to Mr. M. Fukushima of AGC Inc., Japan for his advice about obtaining R1234yf sample bottle.

NOMENCLATURE

h	heat transfer coefficient (kW·m^{-2}·K^{-1})	P	pressure (kPa)
q	heat flux (kW·m^{-2})	T	temperature (K)
ΔT	wall superheat (K)		

REFERENCES

Incropera, F.P, DeWitt, D.P., Bergman, T.L., Lavine, A.S., 2007. Fundamentals of heat and mass transfer 6th edition, John Wiley & Sons, Hoboken, 627-629.

JSME, 2005. JSME Data Book: Heat Transfer 4th Edition, JSME, Tokyo, 128-129.

Longo, G.A., 2012. Vaporisation of the low GWP refrigerant HFO1234yf inside a brazed plate heat exchanger. Int. J. Refrigeration 35, 952-961.

Mortada, S., Zoughaib, A., Arzano-Daurelle, C., Clodic, D., 2012. Boiling heat transfer and pressure drop of R-134a and R-1234yf in minichannels for low mass fluxes. Int. J. Refrigeration 35, 962-973.

Park, K., Jung, D., 2010. Nucleate boiling heat transfer coefficients of R1234yf on plain and low fin surfaces. Int. J. Refrigeration 33, 553-557.

Saitoh, S., Dang, C., Nakamura, Y., Hihara, E., 2011. Boiling heat transfer of HFO-1234yf flowing in a smooth small-diameter horizontal tube. Int. J. Refrigeration 34, 1846-1853.

Saitoh, S., Dang, C., Hihara, E., 2013. Effect of lubricant oil on flow boiling heat transfer of refrigerant R 1234yf in horizontal small-diameter tubes. Trans. of the JSRAE 30(4), 451-462.

Sato, T., Takaishi, Y., Oguchi, K., 1998. Concentration dependence of pool nucleate boiling heat transfer coefficients for R134a and polyol-ester oil systems. Trans. of the JSRAE 15(4), 415-423.

Manuscript ID: 205
DOI: 10.18462/iir.icr.2019.0205

Effect of Pressure Pulsation on COP in Two-Stage-Compression Vapor-Injection Cycle

Sachio SEKIYA[(a)], Atsushi KUBOTA[(a)], Masayuki NONAKA[(b)], Hisashi DAISAKA[(b)]

[(a)] Hitachi, Ltd. Research & Development Group
832-2, Horiguchi, Hitachinaka, Ibaraki, 312-0034, Japan, sachio.sekiya.qo@hitachi.com
[(b)] Hitachi-Johnson Controls Air Conditioning, Inc.
1-16-1, Kaigan, Minato-ku, Tokyo, 105-0022, Japan, masayuki.nonaka@jci-hitachi.com

ABSTRACT

This paper describes experimental results of COP characteristics of two-stage-compression vapor-injection cycle against the injection pipe length. Theoretically, the mass flow rate of vapor injection is determined by the pressure difference between a separator and a compressor's injection port. However, the pressure pulsation of the compressor oscillates the pressure difference and changes the COP of this cycle. In this study, in order to reveal this effect on COP experimentally, COP characteristics were investigated by changing the injection pipe length. The results show that the COP varies cyclically depending on the injection pipe length and this is caused by resonance of pressure wave in the injection pipe.
Keywords: Refrigeration, COP, Resonance, Injection, flash tank

1. INTRODUCTION

As global warming is becoming a serious issue, it is necessary to reduce the energy consumption of air-conditioning systems. Many improvements have been proposed regarding not only component efficiency but also refrigeration-cycle efficiency. A vapor-injection cycle is theoretically known as a highly efficient refrigeration cycle. Nakamura (2010) showed that the pressure change in a compression cylinder decreases the injection mass flow rate (IMF) from a flash tank to a single stage compressor, and decreases COP of the cycle. To address this issue, a vapor-injection cycle with a two-stage rotary compressor was proposed (Nonaka, 2004; Kubota, 2005). This compressor is composed of 1st- and 2nd-stage cylinders connected in series. A vapor refrigerant is injected between the two cylinders so that IMF is not affected by pressure change in the compression cylinders.

However, still there is a possibilities that the IMF would be affected by pressure pulsation generated by intermittent suction and discharge action of the 1st- and 2nd-stage cylinders (Kubota, 2014). If there is no pressure pulsation, the IMF is determined by: 1) the vapor quality in the flash tank and 2) pressure drop from the flash tank to the compressor. The small pressure drop can increase the vapor quality and IMF. Therefore, a shorter injection pipe should be better for obtaining a higher COP. On the other hand, pressure pulsation wave may travel in the injection pipe and effect to the IMF and the cycle COP. This phenomenon makes it difficult to design the injection pipe length.

In this paper, a correlation between the injection pipe length and the cycle COP was discussed using experimental results in order to reveal the effect of pressure pulsation on COP. This paper shows how the COP varies depending on the injection pipe length.

2. TWO-STAGE-COMPRESSION VAPOR-INJECTION CYCLE

Fig. 1 shows pressure-enthalpy diagrams. In the basic cycle shown in Fig. 1(a), a liquid refrigerant from the condenser outlet expands to evaporating pressure, through the evaporator, and flows to the suction of the compressor. The refrigerant is compressed from evaporating pressure to condensing pressure. In the two-stage-compression vapor-injection cycle shown in Fig. 1(b), a liquid refrigerant from the condenser outlet expands to intermediate pressure, and then separates

into liquid and vapor phases in the flash tank. The liquid refrigerant expands further then flows through the evaporator, and enters the suction of the 1st-stage cylinder. The refrigerant is compressed from the evaporating pressure to the intermediate pressure in the 1st-stage cylinder. The vapor refrigerant in the flash tank is injected between the two cylinders then joins the refrigerant discharged from the 1st-stage cylinder. Both are then compressed until arriving at the condensing pressure in the 2nd-stage cylinder.

In this cycle, the mass flow rate through the evaporator is smaller than that of the basic cycle. Thus, the compression power of the 1st-stage cylinder decreases. Moreover, the suction pressure increases because of the smaller pressure drop through the evaporator to the compressor suction. Although the injection reduces the mass flow rate through the evaporator, the enthalpy difference across the evaporator is greater than that of the basic cycle. Therefore, the cooling capacity is almost the same, and the COP improves in cooling mode. In heating mode, the injection increases the mass flow rate through the condenser, but the enthalpy difference across the condenser decreases, so the heating capacity does not change. Therefore, the COP improves since the compression power decreases. This effect of injection varies due to the intermediate pressure because both the vapor quality in the flash tank and the compression power of the two cylinders change. There is an appropriate intermediate pressure for obtaining a higher COP in this cycle.

In fact, the pressure between the two cylinders (Pm) is determined by the displacement ratio of the 1st- and 2nd-stage cylinders, and the pressure of the flash tank (Pt) is higher than Pm by the pressure drop through the injection pipe. If the Pt increases, the amount of vapor decreases because of the lower vapor quality, and the effect of injection decreases. Therefore, smaller pressure drop through the injection pipe is important to obtain larger vapor refrigerant in the flash tank. A shorter injection pipe should be better to obtain a higher COP.

However, considering the pressure pulsation of the compressor, pressure pulsation wave may travel in the injection pipe and effect to the IMF and the cycle COP. In that case, appropriate injection pipe length changes. Therefore, we assumed that an inertial supercharging effect should be considered which may occur at the suction of 2nd cylinder and the injection pipe. This effect occurs at the suction of a rotary compressor (Ito, 1970) and is useful for obtaining larger cooling and heating capacity because it increases the mass flow rate of the compressor. This effect occurs when the vapor refrigerant in a suction pipe is in a resonant state. A resonance wave is formed from the pressure waves generated by the pressure pulsation in the compressor. Resonance occurs when the compressor frequency is the same as the natural frequency of the suction pipe. The natural frequency of the pipe can be calculated as:

$$f_n = (2n-1)/4 \times \left(a_{ref}/L_p\right) \quad \text{(n=1,2,3…)} \qquad \text{Eq. (1)}$$

where f_n is the natural frequency of the pipe in s^{-1}, and a_{ref} is the sound speed of vapor refrigerant in $m.s^{-1}$, and L_p is the pipe length in m.

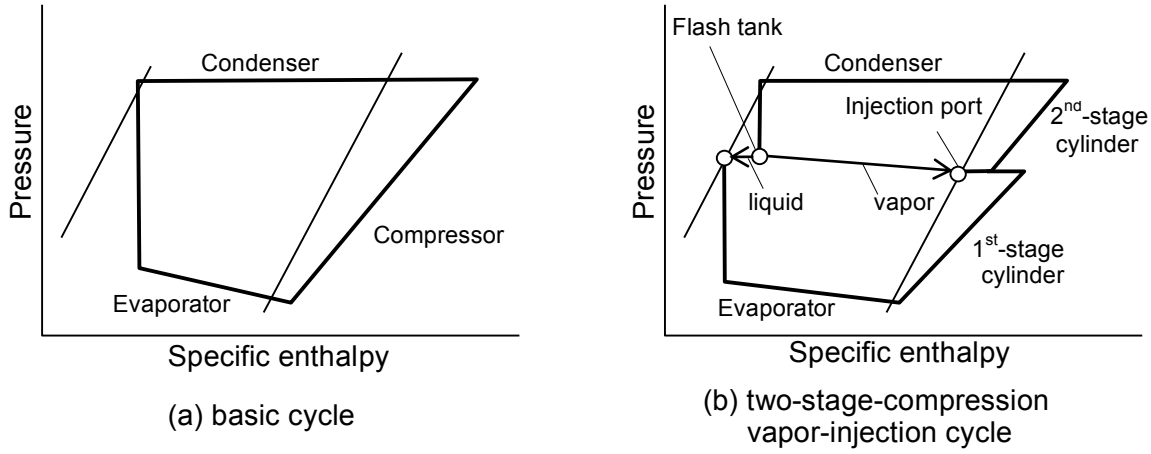

Figure 1: Pressure-enthalpy diagrams

Although the cooling and heating capacity increases with the inertial supercharging effect, the COP does not improve in the basic cycle because of the increased compression power. However, if the inertial supercharging occurs at the 2nd-stage cylinder in the two-stage-compression vapor-injection cycle, the COP might improve because of the increased IMF. There is a pressure pulsation generated by intermittent suction and discharge action of the 1st- and 2nd-stage cylinders in a two-stage compressor.
Therefore, we assumed that this pressure pulsation could cause the inertial supercharging in the 2nd-stage cylinder. We investigated the COP characteristics by focusing on the resonance in the injection pipe. Since f_n is a function of pipe length, we conducted tests at various injection pipe lengths.

3. TESTING SYSTEM

Fig. 2 shows a schematic diagram of the testing system. The system is based on a commercialised residential air conditioner with a rated cooling capacity of 2.8 kW that can be used in both cooling and heating modes. The compressor was replaced with a two-stage rotary compressor, and the flash tank was placed on the liquid line. Expansion valves 1 and 2 were placed on both sides of the flash tank. The injection pipe connected the flash tank to the connecting pipe at the compressor. Two ball valves were placed on the injection pipe. The valves' inner diameters were the same size as the injection pipe, 4.95 mm, so as not to affect the internal pressure waves. The entire injection pipe length (L1) could be changed by replacing the pipe between these two valves. Four pressure sensors were placed on the injection pipe; measurement points P1, P2, P3, and P4 in the Fig 2. A sampling rate for these sensors were 50 kHz. Fig. 3 shows the structure of the two-stage rotary compressor installed in this system. Two cylinders placed in the shell rotated at the same frequency on a common axis. An operation phase difference between two cylinders was 180 degrees. The 1st-stage cylinder was connected to the 2nd-stage cylinder through the 1st-stage discharge chamber and the connecting pipe. Thus, the two cylinders worked as a two-stage compressor. The vapor refrigerant from the flash tank was injected into the connecting pipe through the injection port on it.
The test was conducted in a climatic chamber and the air-enthalpy method was applied to measure the cooling and heating capacity, and the power consumption was also measured to calculate the COP. This facility followed JIS standard (JIS C 9612:2005). The uncertainties for pressure, temperature, air flow rate and power consumption are about ±10kPa, ±0.15℃, ±0.25% and ±0.3%, respectively. The resulting uncertainties for COP is about ±2.1%. The openings of expansion valves 1 and 2 were manually controlled to find the best condition for a higher COP, while keeping the degree of suction superheat at 3 K.

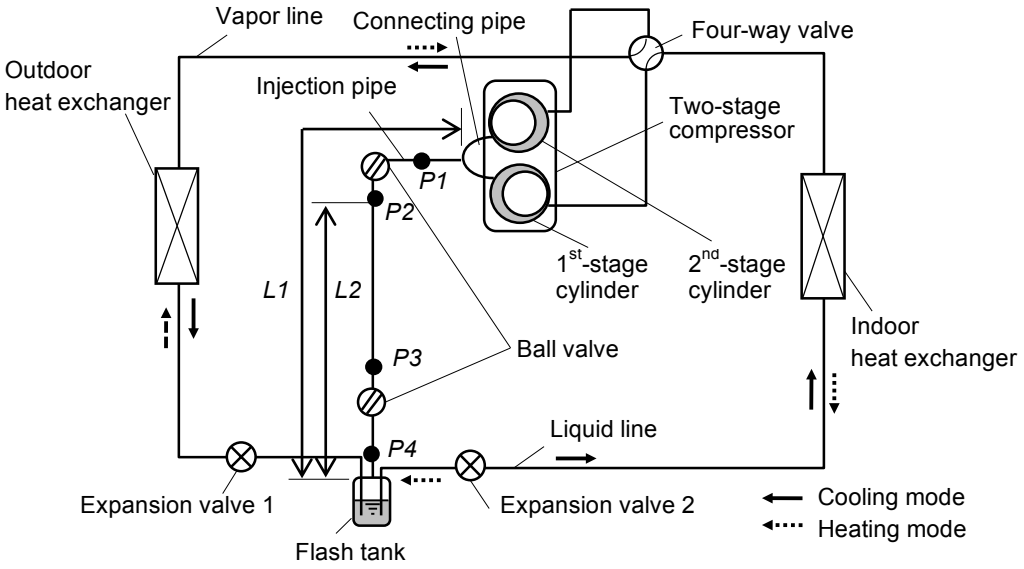

Figure 2: Schematic drawing of test system

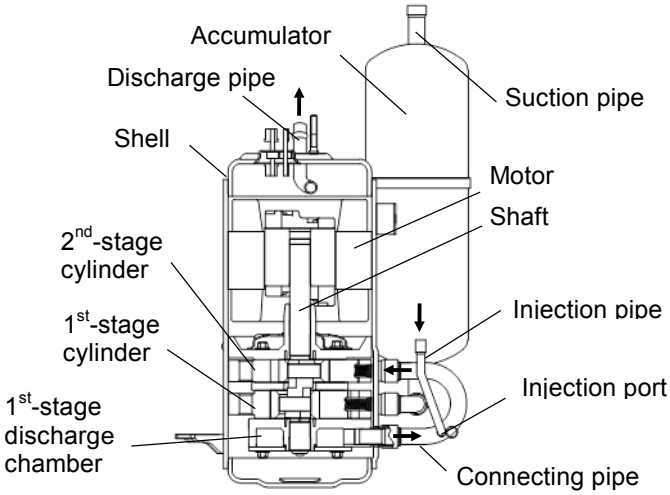

Figure 3: Structure of two-stage rotary compressor

4. RESULTS AND DISCUSSIONS

4.1. Pressure pulsation in injection pipe

We first investigated whether there were pressure waves in the injection pipe, and also whether the waves were originated from the compressor. The test was conducted in cooling mode with a compressor frequency of 31.7 s^{-1}, and L1 was 3140 mm. The pressure at each measurement point was measured. Fig. 4(a) shows the measured pressures against elapsed time. The notation dP on the vertical axis is a deviation from the time average of pressure. To investigate that each pressure wave was originated from the compressor, each elapsed time was modified, as shown in Fig. 4(b). The modified elapsed time was calculated by shifting the time using the traveling time of the vapor refrigerant's pressure waves from the compressor to each measurement point. The distance from the compressor to each measurement point (P1, P2, P3 and P4) was 90, 970, 2700, and 3050 mm, respectively, and the traveling time for each measurement point was 0.6, 6.1, 16.9, and 19.1 ms, respectively.

The results show there were pressure wave in the injection pipe. Although there were differences in shape between each wave in Fig. 4(b), all pressure waves overlapped and the oscillation period of each wave was the same as the compressor rotation period of 31.6 ms. Therefore, it was confirmed that there were pressure waves originated from the compressor in the injection pipe. In this test, the oscillating amplitude at P1 near the compressor was about 100 kPa, that at P2 was smaller, and that at P4 near the flash tank was the smallest at about 25 kPa.

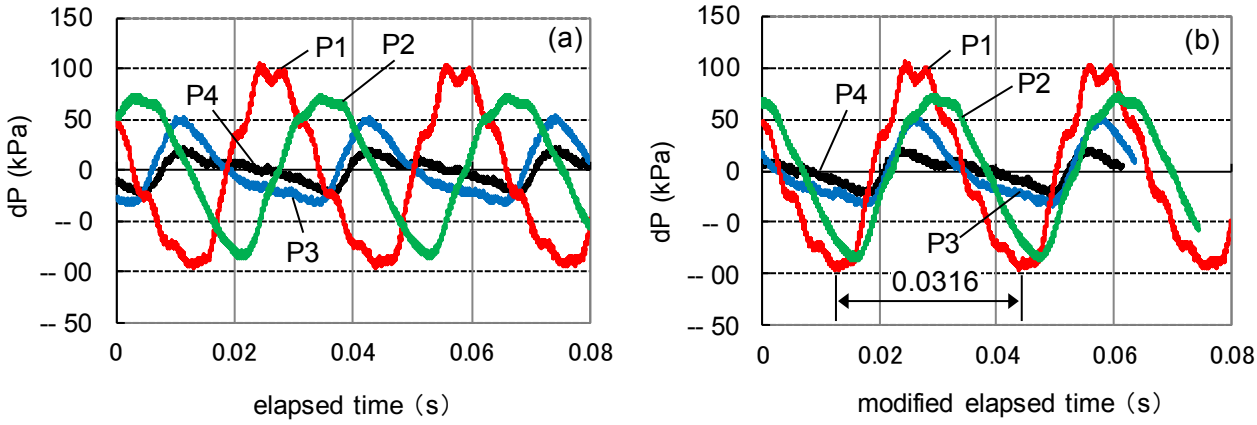

Figure 4: Pressure deviation at each measurement point with L1 of 3140 mm

4.2. COP characteristics against injection pipe length

The COP characteristics against injection pipe length were evaluated to understand the effect of pressure pulsation. The test was conducted by changing the injection pipe length in cooling mode. The experimental conditions are listed in Table 1. The compressor frequency was fixed during each test, and two conditions were used.

Table 1. Experimental conditions in cooling mode

Mode	Cooling
Outdoor temperature (DB/WB) [deg. C]	35/24
Indoor temperature (DB/WB) [deg. C]	27/19
Compressor frequency [s^{-1}]	30.0, 31.7
Injection pipe length [mm]	330 - 7640

Fig. 5 shows the experimental results. The notation %COP on the vertical axis is the COP ratio based on the data for the injection pipe length of 330 mm, which is the shortest injection pipe length in this test. The notation *WLR* on the horizontal axis is non-dimensional parameter which is equivalent to pipe length. The *WLR* is defined as injection pipe length divided by the wavelength of a pressure wave generated by the compressor.

$$WLR = L_{ip} / \left(a_{ref} / f_{comp} \right) \qquad \text{Eq. (2)}$$

where L_{ip} is the injection pipe length in m, and f_{comp} is the compressor frequency in s^{-1}.
The experimental results indicate that: 1) the %COP cyclically oscillated with the change in *WLR*; 2) the %COP had peaks when *WLRs* was 1/4, 3/4, and 5/4; and 3) the interval of each peak was the same as a *WLR* of 1/2. These results agree with Eq. (1). Therefore, the %COP was considered affected by the resonance in the injection pipe generated by the pressure pulsation of the compressor. The %COP difference between peak and bottom reached a maximum of 3%.
Fig. 5 also shows that the peak of %COP gradually decreased by increasing the *WLR*. This is because a larger pressure drop in the injection pipe decreases the COP. This effect is less than 1 % in this test and is smaller than that of the pressure pulsation. As a result, the COP was highest when the *WLR* was 1/4.
WLR can be nearly zero if there is no experimental components such as pressure sensors and valves. The %COP of this condition is assumed to be 99%. Therefore, these results mean that %COP improves by 3% by extending the WLR from nearly zero to 1/4.

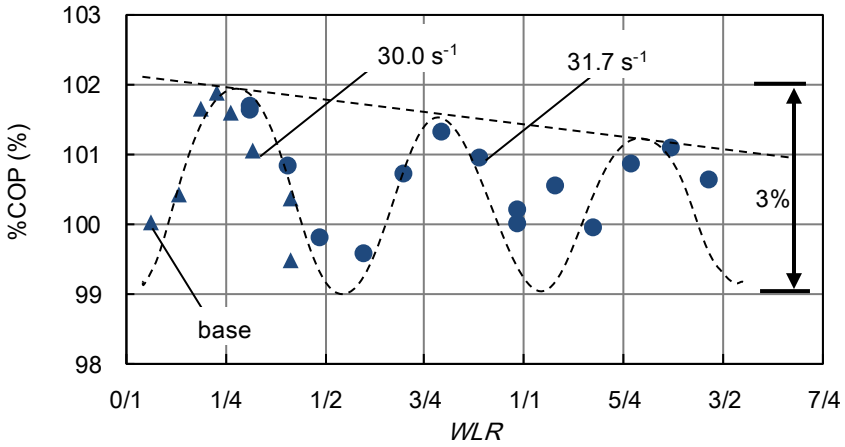

Figure 5: %COP characteristics against *WLR* in cooling mode

4.3. COP characteristics at higher compressor frequency

The %COP is assumed to be oscillate against *WLR* in Fig. 5. However, the data of the different compressor frequency condition do not exactly match. To investigate whether the COP oscillates against *WLR* even at a higher compressor frequency, the compressor frequency was increased to 45.0 s^{-1}. This test was conducted in heating mode. Table 2 lists the test conditions for heating mode.

Fig. 6 shows the experimental results. The *WLR* was calculated using the compressor frequency of this test. The %COP is based on the COP for the injection pipe length of 1670 mm, which is the shortest injection pipe length in this test. As shown in Fig. 6, the %COP represented cyclic oscillation against the *WLR*. The peak value was obtained at *WLRs* of 1/4, 3/4, 5/4, and 7/4. The interval of each peak was a *WLR* of 1/2. These results were the same as those in cooling mode. Therefore, the COP is clearly affected by the pressure pulsation of the compressor and oscillates against *WLR*.

However, compared with the cooling mode, there was no gradual decrease in the peak of the %COP with increasing *WLR*. Moreover, the %COP difference between peak and bottom was about 0.9% in heating mode and was smaller than that in cooling mode, which was about 3%. These results were due to the difference in the magnitude of the pressure drop through the suction pipe. This magnitude was smaller in heating mode than that in cooling mode. Thus, the effect of decreasing the pressure drop lessened. Therefore, the peak of the %COP did not decrease significantly with *WLR* in heating mode compared to that in cooling mode. As a result, the best condition to obtain the highest %COP was a *WLR* of 1/4.

Table 2. Experimental conditions in heating mode

Mode	Heating
Outdoor temperature (DB/WB) [deg. C]	7/6
Indoor temperature (DB/WB) [deg. C]	20/-
Compressor frequency [s^{-1}]	45.0
Injection pipe length [mm]	1670 - 6640

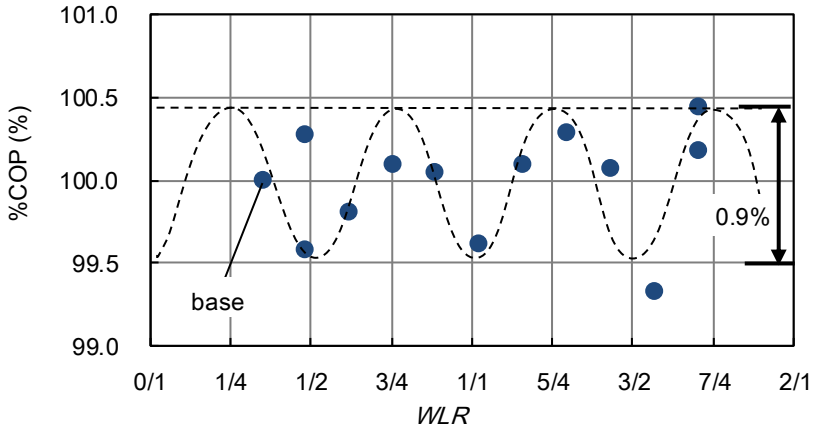

Figure 6: COP characteristics against *WLR* at higher compressor frequency

4.4. Resonance in injection pipe

From the above results, the variation in COP due to injection pipe length was confirmed. Moreover, the COP characteristics can be determined from the *WLR*. Therefore, resonance was considered generated by pressure waves. To confirm whether resonance occurred in the injection pipe, the amplitude characteristics of pressure oscillation was measured by changing the injection pipe length.

Fig. 7 shows the measured pressure at each measurement point against the modified elapsed time. This test was conducted with an L1 of 5140 mm in cooling mode. The vertical axis is a deviation

from the time average of pressure, the same as in Fig. 4. The amplitude of P1, placed near the compressor (pressure-wave source) was the same as that in Fig. 4 and the same as P3 and P4, which were placed near the flash tank. However, the amplitude of P2 placed in the middle of the injection pipe was significantly larger than that in Fig. 4 and larger than that of P1. These results indicated that the amplitude of the P2 varied due to resonance. We then measured whether the amplitude of P2 varied against pipe length.

Fig. 8 shows the results. The vertical axis is the peak-to-bottom amplitude of P2. The notation WLR_2 on the horizontal axis is the *WLR* calculated using L2 as a injection pipe length in Eq. (2). The L2 is the pipe length between the flash tank and P2. The amplitude of P2 had a cyclic oscillation against *WLR*, similar to the COP. It seemed that amplitude of P2 had peaks at *WLRs* of 1/4, 3/4, and 5/4, and the interval of each peak was the same as a *WLR* of 1/2. These results indicate that resonance occurs in the injection pipe due to the reflected pressure wave from the flash tank. Therefore, we concluded that the COP characteristics against *WLR* are caused by change of resonance condition in the injection pipe.

When resonance occurs, an amplitude of the pressure pulsation in the connecting pipe increases. When the pressure in the connecting pipe is high, the 1st-stage cylinder is in a discharge phase and the 2nd-stage cylinder is in a suction phase because the operation phases of the two cylinders are shifted by 180 degrees. Therefore, the mass flow rate of the 2nd-stage cylinder increases because a density of the vapor refrigerant is larger at the high pressure condition. Since the mass flow rate from the 1st-stage cylinder does not increase, IMF increases under this condition. The COP should improve because of the increased IMF.

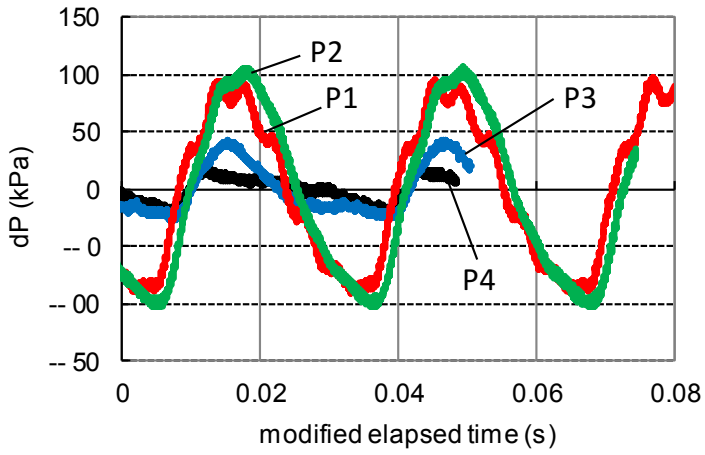

Figure 7: Pressures deviation at each measurement point with L1 of 5140 mm

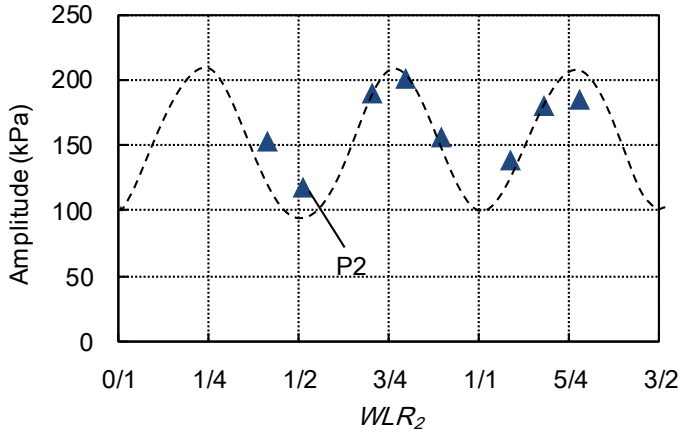

Figure 8: Peak-to-bottom amplitude of P2 against WLR_2

5. CONCLUSIONS

In order to reveal the effect of pressure pulsation on COP, we experimentally investigated the COP characteristics against injection pipe length. We obtained the following conclusions.

1) The COP cyclically oscillates as a function of *WLR,* and this is caused by change of resonance condition in the injection pipe.
2) The effect of pressure pulsation on COP is larger than that of pressure drop in the injection pipe.
3) When WLR is 1/4, the COP reaches the highest value.
4) By extending the WLR from nearly zero to 1/4, the COP improved by 3% in cooling mode and 0.9% in heating mode.

REFERENCES

Ito, S., 1970, “Volume type compressor”, Sangyo Tosho Co., Tokyo, 81-90.

Kubota, A., et al., 2005, Performance of R410A two-stage rotary compressor, Proceedings of the 2005 JSRAE Annual Conference, C313 .

Kubota, A., 2014, Predicting Supercharging Effect in Suction Line in Inverter Rotary Compressor, *Trans. Jpn. Soc. Mech. Eng.*, 80(818).

Nakamura, H., 2010. Study on Refrigeration, Performance Improvement of R410A Room Air Conditioner by Vapor Injection Refrigeration Cycle Using Scroll Compressor, *Trans. JSRAE*, **27**(3), 221-232.

Nonaka, M., 2004, Performance Improvement of Room Air Conditioner with New Injection System, Proceedings of International Symposium on New Refrigerants and Environmental Technology 2004, 97-101.

Manuscript ID: 219
DOI: 10.18462/iir.icr.2019.0219

Experiments on flow boiling characteristics of R32/lubricant oil mixtures in a multiport tube with circular minichannels

Daisuke JIGE [(a)], Shogo KIKUCHI[(b)], Hikaru EDA[(c)], Norihiro INOUE[(d)]

[(a)] Tokyo University of Marine Science and Technology, Tokyo, 135-8533, Japan, djige00@kaiyodai.ac.jp
[(b)] Tokyo University of Marine Science and Technology, Tokyo, 135-8533, Japan, m184002@edu.kaiyodai.ac.jp
[(c)] Tokyo University of Marine Science and Technology, Tokyo, 135-8533, Japan, m164005@edu.kaiyodai.ac.jp
[(d)] Tokyo University of Marine Science and Technology, Tokyo, 135-8533, Japan, inoue@kaiyodai.ac.jp

ABSTRACT

This study experimentally investigated the flow boiling heat transfer and pressure drop of R32/lubricant oil mixtures in a horizontal multiport tube with circular minichannels at a saturation temperature of 15 °C. The effects of mass velocity, heat flux, vapor quality, and oil concentration on the flow boiling heat transfer and pressure drop were clarified. The local heat transfer coefficient of R32/oil mixtures decreased with increasing oil concentration, as compared with that of pure R32, except under conditions of higher heat flux and lower quality. However, considering the increase in the bubble-point temperature with oil mixing, the degradation of heat transfer coefficient with oil mixing was small under conditions of higher mass velocity and quality. The frictional pressure drop of the R32/oil mixture was higher than that of pure R32 and increased with increasing oil concentration. The frictional pressure increased with increasing heat flux in the lower quality region.
Keywords: Boiling heat transfer, Pressure drop, Multiport tube, Minichannel, R32, Lubricant oil

1. INTRODUCTION

In recent years, heat exchangers for air conditioning systems have been required to fulfill the criteria of miniaturization and high performance. Thus, multiport flat tubes consisting of multiple minichannels with a hydraulic diameter of 1 mm or less have gained attention. Moreover, the transition to alternative refrigerants with lower environmental loads is proceeding as a result of regulations on refrigerants for air conditioners, such as the Freon emission control method, and the development of equipment that uses R32, which has a relatively low global warming potential (GWP). Several studies on flow boiling heat transfer in multiport tubes have been reported. Tanaka et al. (2014) visualized two-phase flow patterns and measured boiling heat transfer coefficient using R1234yf in a vertical multiport tube. For a horizontal multiport tube, Kudo et al. (2016) reported experimental results of boiling and condensation heat transfer coefficients using R134a, and investigated the effect of channel shape on heat transfer characteristics. Eda et al. (2018) investigated the boiling heat transfer coefficient of R32 in a horizontal multiport tube with circular minichannels, and confirmed that heat transfer characteristics were similar to those of a macroscale tube under high mass velocity or high heat flux conditions. However, the heat transfer differed under low mass velocity and low heat flux conditions.

In actual machines, lubricant oil mixed with high-temperature and high-pressure refrigerants is discharged from compressors. Previous studies have shown that lubricant oil affects the flow boiling heat transfer and pressure drop characteristics. Filho et al. (2009) reviewed previous studies and found a lack of agreement on the boiling heat transfer characteristics with lubricant oil. However, the pressure drop characteristics exhibited the same trends in all studies they reviewed. It is necessary to accurately clarify the influence of oil on flow pattern, heat transfer, and pressure drop characteristics. However, the influence of the oil varies based on the refrigerant/oil combination and

the channel shape. Numerous studies have evaluated the influence of lubricant oil on flow boiling heat transfer and pressure drop in macroscale tubes. For a multiport tube, Saitoh et al. (2013) visualized the flow pattern inside vertical multiport channels using a R1234yf/POE oil mixture, and reported that many bubbles blocked the flow path. However, further studies are needed to clarify the flow boiling heat transfer of refrigerant/oil mixtures inside a multiport tube.
This study experimentally investigated the flow boiling heat transfer coefficient and pressure drop of R32/PVE oil mixtures in a horizontal multiport tube with circular minichannels, and clarified the influences of oil concentration, mass velocity, heat flux, and vapor quality on these two parameters.

2. EXPERIMENTAL SETUP AND CONDITIONS

2.1. Experimental setup

Fig. 1 shows the experimental setup used in this study. The subcooled liquid refrigerant was discharged from the gear pump, and flowed to water and electric preheaters. The vapor quality of the test refrigerant was adjusted by the heat transfer rate in the electric preheater. The refrigerant then flowed into a test section, in which the heat transfer and pressure drop were measured. The refrigerant temperature and pressure were measured using K-type thermocouples and pressure transducers at the inlets of the electric preheater and the test section. The flow rate and pressure of the refrigerant were adjusted using needle valves and water temperature flowing through a condenser. The oil was charged from the filling/separating loop connected to the test section outlet. A few samples of liquid refrigerant and oil were taken, and the oil concentration was obtained using the measured mass ratio of the refrigerant/oil mixture and the oil.
Fig. 2 shows the test section for measuring heat transfer and pressure drop. The test multiport tube was heated by sheet heaters attached to the upper and lower surfaces of the tube. The wall temperatures at the upper and lower surfaces were measured using K-type thermocouples attached to the outer tube surface at 25 mm intervals. The refrigerant pressure distribution was obtained using pressure measurements at the inlet and outlet of the test tube using absolute and differential pressure transducers. The effective heating length was 300 mm and pressure measuring length was 445 mm. The cross-sectional view of the test multiport tube is shown in Fig. 3. The test tube consisted of 12 circular minichannels with an inner diameter of 0.81 mm, a cross-sectional area of 6.18 mm^2 and an inner perimeter of 30.5 mm.

2.2. Experimental conditions

The experiments were carried out using R32/PVE oil mixtures inside a horizontal multiport tube in a mass velocity range of 50–400 $kgm^{-2}s^{-1}$ and a heat flux range of 5–40 kWm^{-2} at a saturation temperature of 15 °C. The measured heat transfer and pressure drop of the R32/oil mixture were

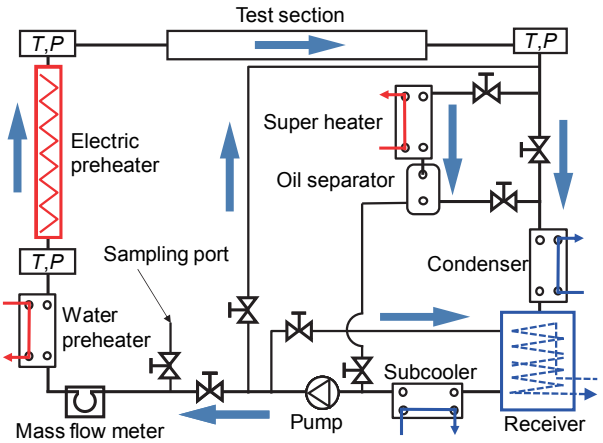

Figure 1: Experimental setup

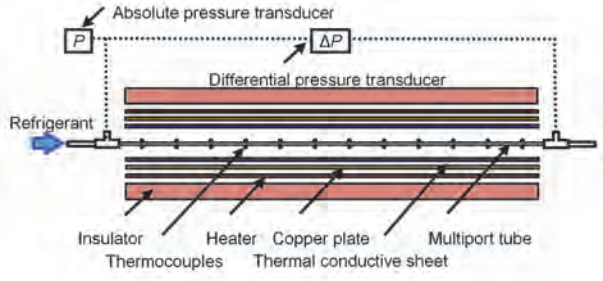

Figure 2: Test section



Figure 3: Cross-sectional view of the test tube

compared with those of pure R32. The thermal properties of R32 were calculated using REFPROP ver.10 (Lemmon et al., 2018).

3. DATA REDUCTION

3.1. Data reduction method

The boiling heat transfer coefficient α_s is obtained using the inner wall temperature T_w and the saturation temperature of the pure refrigerant T_s.

$$\alpha_s = \frac{q}{T_w - T_s} \quad \text{Eq. (1)}$$

where q is the heat flux defined by the actual inner heat transfer area, T_s is the saturation temperature of the pure refrigerant at the measured test pressure. The temperature of the R32/oil mixture changes with increasing oil concentration ratio, and T_s does not remain equal to T_{bub}. The heat transfer coefficient defined using bubble-point temperature is calculated by

$$\alpha_{bub} = \frac{q}{T_w - T_{bub}} \quad \text{Eq. (2)}$$

In this study, preliminary experiments were carried out to obtain the bubble-point temperature of refrigerant/oil mixtures. The temperature of the test R32/PVE oil mixture is correlated using the empirical equation (Eq.(3)) to calculate the bubble-point temperature of R22/oil mixtures that was proposed by Takaishi-Oguchi (1987). The experimental equations, which were modified based on measured temperatures of the test R32/PVE oil mixture, are given in Eqs.(4)–(5).

$$T_{bub} = \frac{A}{\ln(P_s) - B} \quad \text{Eq. (3)}$$

$$A = 66.59 - 1.95C_{o,x} + 23.03{C_{o,x}}^3 + 6.01{C_{o,x}}^5 - 1.4{C_{o,x}}^7 \quad \text{Eq. (4)}$$

$$B = -0.0164 - 0.082C_{o,x} + 0.0926{C_{o,x}}^3 - 0.0396{C_{o,x}}^5 + 0.00428{C_{o,x}}^7 \quad \text{Eq. (5)}$$

where P_s is the saturation pressure in MPa.
The oil concentration in the liquid-phase $C_{o,x}$ is calculated by

$$C_{o,x} = \frac{C_o}{1 - (1 - C_o)x} \quad \text{Eq. (6)}$$

As the oil concentration increases, the liquid density of the test R32/oil mixture decreases, while its surface tension, liquid viscosity, kinematic viscosity, and thermal conductivity increase.

The frictional pressure drop was measured between the inlet and outlet of the test tube for boiling flow. Frictional pressure drop ΔP_F is calculated by the following equation:

$$\Delta P_F = \Delta P_{mes} - \Delta P_a - \Delta P_e \quad \text{Eq. (7)}$$

where ΔP_{mes} is the measured pressure drop, ΔP_a is the acceleration pressure drop calculated by the homogeneous flow model, and ΔP_e is the pressure loss due to the abrupt contraction and expansion at the inlet and outlet of the test tube, as estimated by the equations of Collier and Thome (1994). In this study, $\Delta P_a/\Delta P_{mes}$ and $\Delta P_e/\Delta P_{mes}$ are 12% and 14% or less, respectively.

4. RESULTS AND DISCUSSION

4.1. Boiling heat transfer coefficient

Fig. 4 shows the heat transfer coefficient α_s of pure R32 at mass velocities of 50–400 $kgm^{-2}s^{-1}$ reported by Eda et al. (2018). The data plots in the figure are representative values obtained by measurement heat transfer coefficients for each mass flux and heat flux condition in the vapor quality range of 0.05–0.95 at 0.05 intervals. At lower heat flux, the heat transfer coefficients of pure R32 at mass velocities of 200 and 400 $kgm^{-2}s^{-1}$ increase with vapor quality because of enhanced forced convection. The heat transfer coefficient except for the lowest mass velocity increases with increasing heat flux owing to enhanced nucleate boiling; however, the heat transfer coefficient decreases as heat flux increases, to G = 50 $kgm^{-2}s^{-1}$, because the liquid film around the elongated vapor plugs dried when the flow pattern was plug flow.

Fig. 5 shows the heat transfer coefficient α_s of R32/oil mixture at C_o = 3.7 wt%. The experiments were carried out by changing inlet vapor quality to obtain data in a wide vapor quality range. With the exception of limited condition for low vapor quality and high heat flux, the heat transfer coefficients of the R32/oil mixture are lower than those of pure R32 at each mass velocity and heat flux condition. The heat transfer coefficient of R32/oil mixture decreases drastically compared with pure R32 at lower mass velocities and in higher vapor quality regions. On the other hand, for R32/oil mixture, the increment ratio of the heat transfer coefficient due to increasing heat flux is significant compared with that of pure R32; the heat transfer coefficient of R32/oil mixture is higher than that of pure R32 when the heat flux is 20 kWm^{-2} or more. Regardless of mass velocity, the heat transfer coefficient of R32/oil mixture deteriorates in the high quality region because the oil concentration in the liquid-phase rapidly increases with vapor quality, and strongly affects the heat transfer characteristics.

Fig. 6 shows the effect of oil concentration on heat transfer coefficient for a heat flux of 5 kWm^{-2} and mass velocities of 50, 100, 200, and 400 $kgm^{-2}s^{-1}$. The heat transfer coefficient decreases with increasing oil concentration for any mass velocity condition, especially decreasing drastically at lower mass velocities. Therefore, the heat transfer degradation decreases with increasing mass velocity, and similar trends have been observed by previously reported studies, as reviewed by Filho et al. (2009). The heat transfer coefficient decreases in the higher vapor quality region. The heat transfer coefficient at G = 50 $kgm^{-2}s^{-1}$ dramatically decreases as oil concentrations increase at C_o = 2.2 and 3.7 wt%. At G = 100 $kgm^{-2}s^{-1}$, the heat transfer coefficient dramatically decreases at C_o = 3.7 wt%. At the highest mass velocity, the heat transfer coefficient gradually decreases with increasing oil concentration in the higher vapor-quality region, while there is no effect of oil concentration in the lower vapor-quality region.

Fig. 7 shows the comparison between the heat transfer coefficients α_s and α_{bub} that are calculated using saturation temperature or bubble-point temperature at each of the mass velocity and heat flux conditions. At the mass velocity of 100 kgm^2s^{-1} or below, there is no difference between the heat transfer coefficients α_s and α_{bub}. At higher mass velocities and low heat fluxes, the heat transfer coefficients defined using the bubble-point temperature are higher compared to those defined using the saturation temperature; in other words, increase in bubble-point temperatures affect the heat transfer coefficients. However, despite higher mass velocities, the influence of increasing bubble-point temperatures can negligible when the heat flux is sufficiently large.

Fig. 8 shows the effect of heat flux and oil concentration on heat transfer at x = 0.2. The heat transfer coefficient decreases with increasing oil concentration. The effect of oil concentration on the heat transfer coefficient is significant at heat fluxes of 10 and 20 kWm^{-2}. Compared to pure R32, the heat transfer coefficient deteriorates at oil concentrations of 0.4 and 0.8 wt%; however, it increases as oil concentration increases.

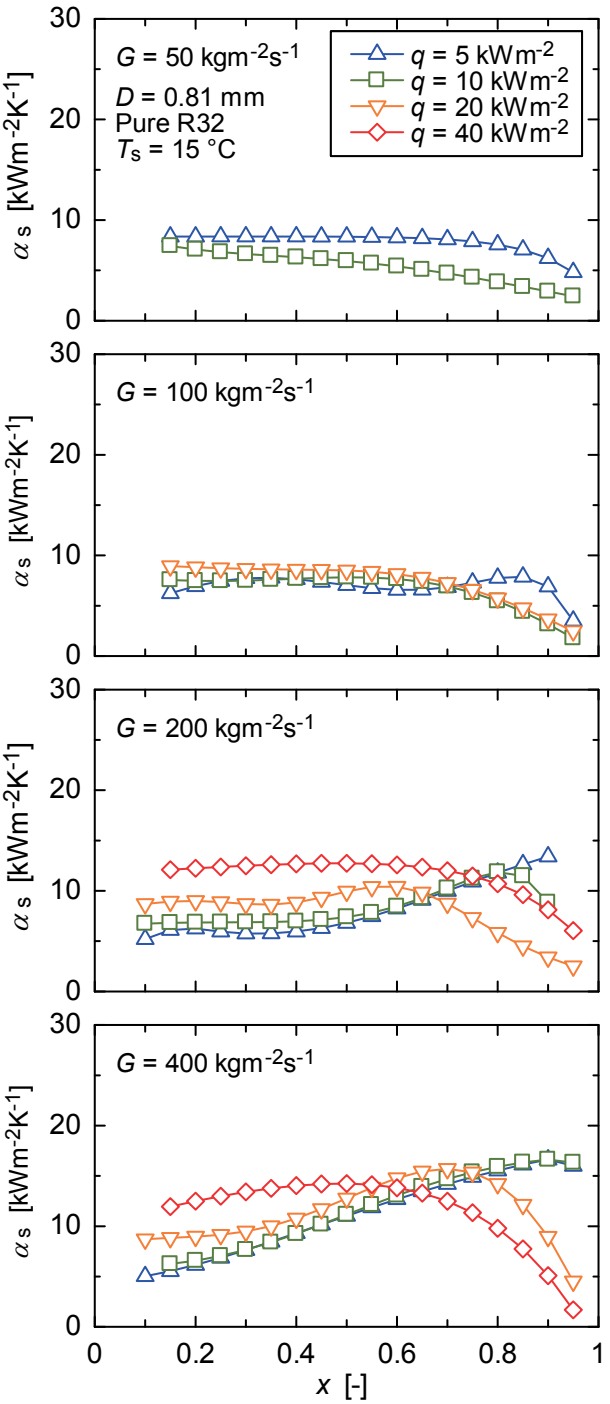

Figure 4: Heat transfer coefficients of pure R32. Data from Eda et al. (2018).

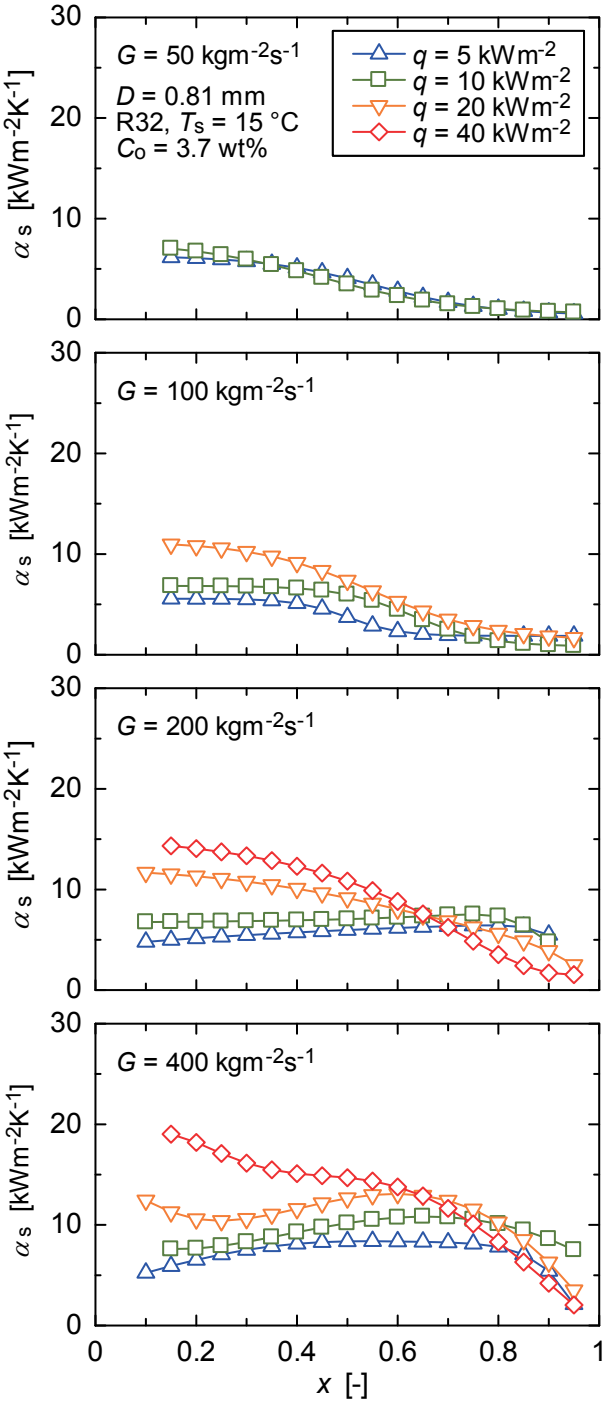

Figure 5: Heat transfer coefficients of R32/oil mixture at C_o=3.7 wt%

4.2. Frictional pressure drop

Fig. 9 shows the effect of oil concentration on frictional pressured drop at a mass velocity of 400 kgm^{-2}s^{-1} and heat flux of 5 kWm^{-2}. The frictional pressure drop of the R32/oil mixture is higher than that of pure R32, and it increases with increasing oil concentrations. In particular, the frictional pressure drop remarkably increases in the higher vapor quality region because oil concentration in the liquid-phase increases greatly as vapor quality increases.

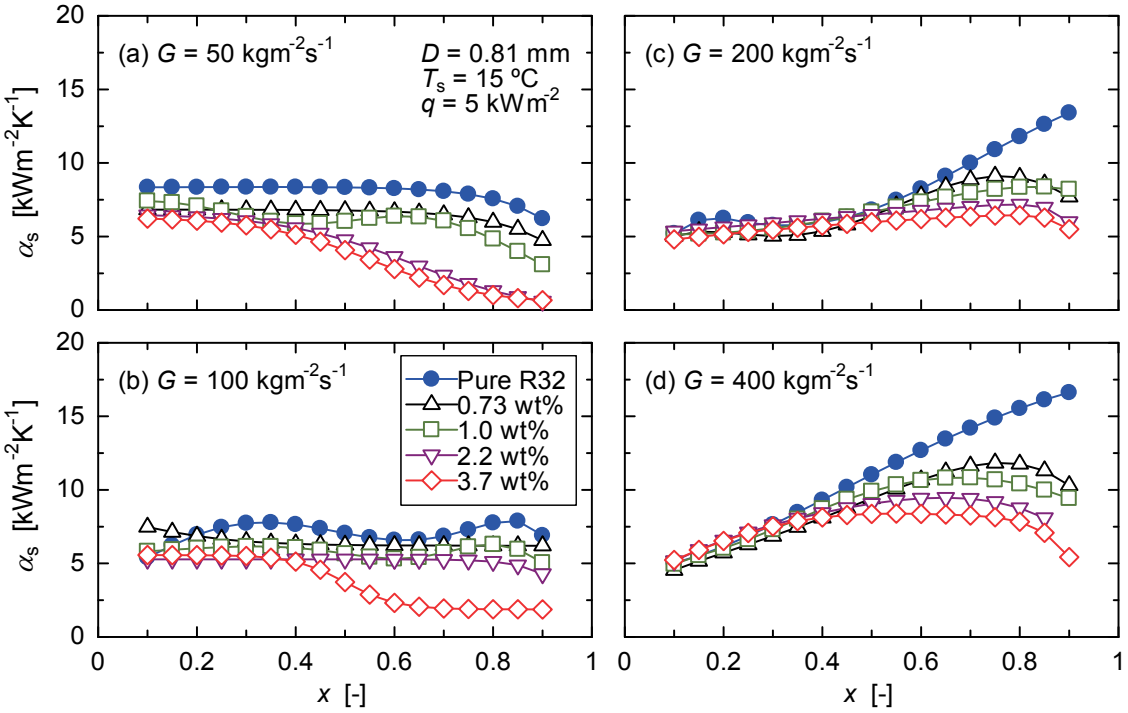

Figure 6: Effect of oil concentration on heat transfer coefficients at mass velocities of (a) 50, (b) 100, (c) 200, and (d) 400 kgm^{-2}s^{-1}

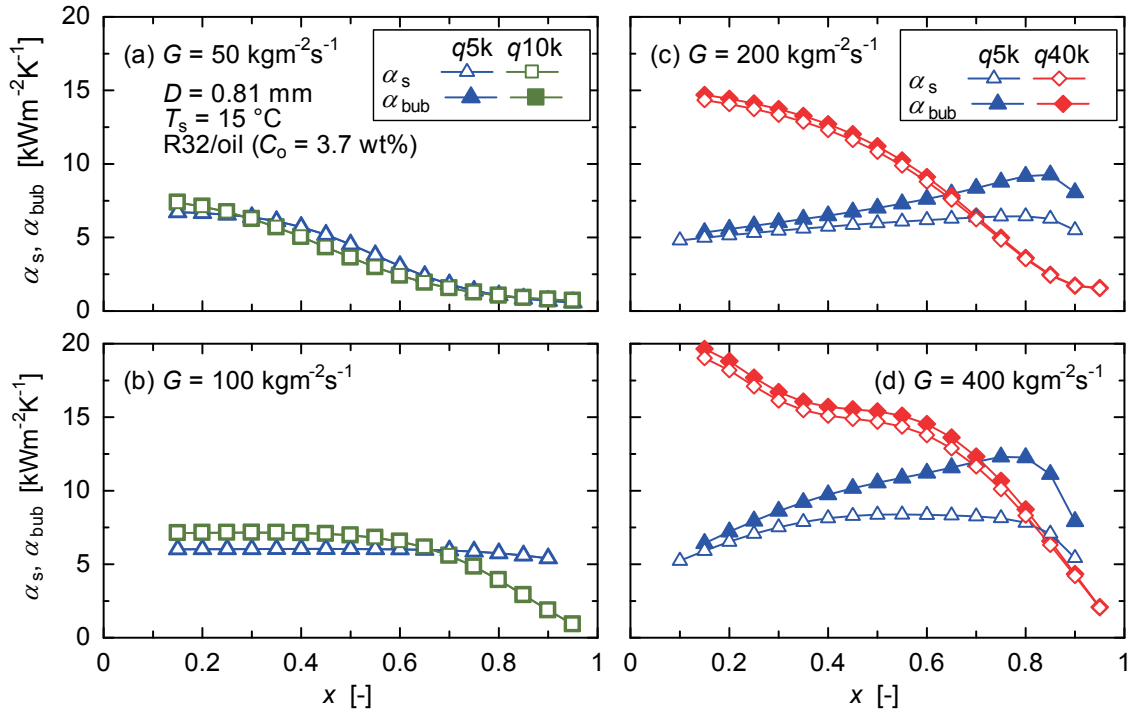

Figure 7: Comparison between heat transfer coefficients α_s and α_{bub} at different mass velocities and heat fluxes

Fig. 10 shows the frictional pressure drops of pure R32 and R32/oil mixture (C_o = 3.7 wt%) for boiling flow. The frictional pressure drops of both substances increase with increasing vapor quality and mass velocity. Comparing the results between pure R32 and R32/oil mixture, the frictional pressure drops of the mixture were 1.3–1.8 times higher than those of pure R32. It is commonly known that the frictional pressure drops of the oil mixture are higher than those of the pure refrigerant; thus, similar trends are observed in this study. Furthermore, the effect of heat flux on the frictional pressure drop characteristics is considered. The effect of heat flux on frictional pressure drop was not evident

for pure R32 (Eda et al., 2018). On the other hand, the frictional pressure drops of the mixture increased with increasing heat flux and oil concentration, for mass velocity range of 200–400 kgm^{-2}s^{-1} and quality range of 0.5 or less. It is assumed that foaming caused by the addition of oil into the refrigerant increased with increasing mass velocity and heat flux, and the bubbles formed due to foaming changed the flow pattern.

5. CONCLUSIONS

This study investigated the flow boiling heat transfer coefficient and pressure drop of R32/PVE oil mixtures by varying mass velocity, heat flux, and oil concentration in a horizontal multiport tube. The local heat transfer coefficient of the R32/oil mixtures decreased with increasing oil concentrations compared with those of pure R32, except for higher heat flux and lower quality region. On the other hand, considering the increase of bubble-point temperature with oil mixing, the degradation of the heat transfer coefficient with oil mixing was small at higher mass velocities and quality regions. The frictional pressure drop of the R32/oil mixture was higher compared with that of pure R32 and increased with increasing oil concentration ratio. The frictional pressure increased with increasing heat flux in the lower quality region.

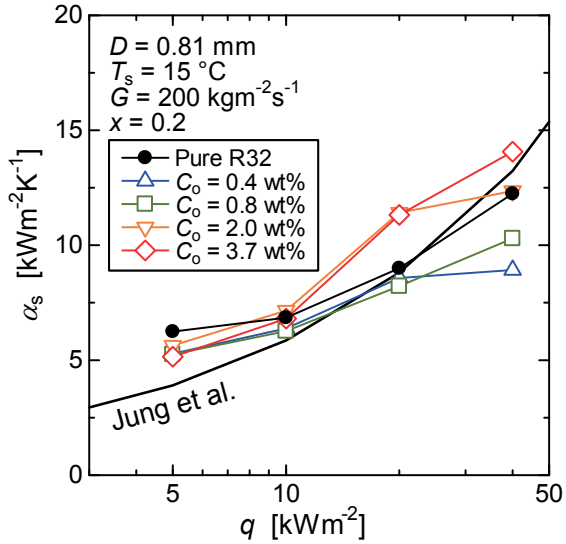

Figure 8: Effects of heat flux and oil concentration on heat transfer

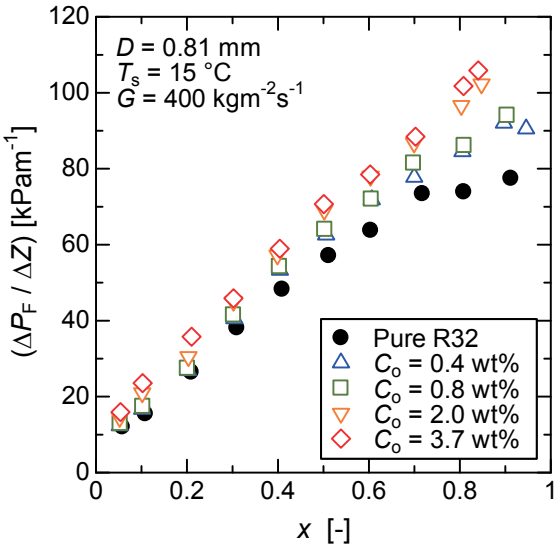

Figure 9: Effect of oil concentration on frictional pressure drop

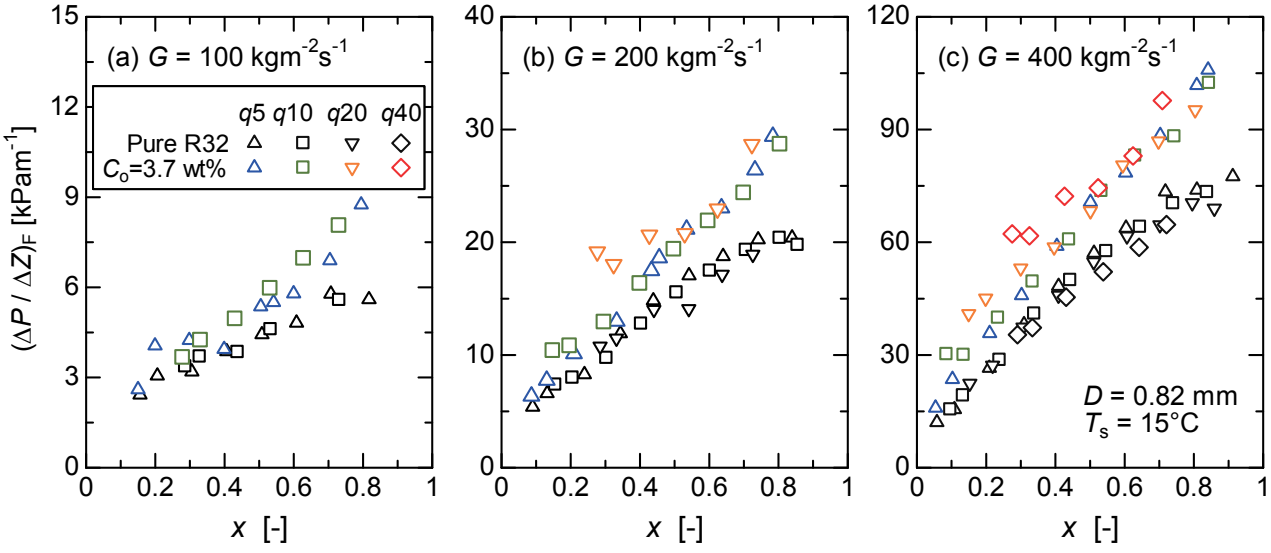

Figure 10: Frictional pressure drops of pure R32 and R32/oil mixture (C_o=3.7 wt%)

ACKNOWLEDGEMENTS

This study was supported by JSPS KAKENHI Grant Number JP15K18292. We would like to express our gratitude to UACJ Corporation, who provided the test multiport tube.

NOMENCLATURE

C_o	oil concentration (wt%)
$C_{o,x}$	oil concentration in liquid phase (wt%)
D	tube diameter (m)
G	mass velocity ($kgm^{-2}s^{-1}$)
P	pressure (Pa)
ΔP	pressure drop (Pa)
q	heat flux (Wm^{-2})
T	temperature (°C)
x	vapor quality (-)

Greek symbol

α	heat transfer coefficient ($Wm^{-2}K^{-1}$)

Subscripts

a	acceleration
bub	bubble-point
e	abrupt contraction and expansion
F	frictional
mes	measurement
s	saturation
w	tube wall

REFERENCES

Collier, J. G. and Thome, J. R., 1994. Convection boiling and condensation, third ed., Oxford university press.

Eda, H., Jige, D. and Inoue, N., 2018. Experimental Study of Boiling Heat Transfer and Pressure Drop of R32 inside Horizontal Multiport Tube with Circular Minichannels, Journal of the Japan Institution of Marine Engineering 53(3), 174–179.

Filho, E. P. B., Cheng, L. and Thome, J. R., 2009. Flow Boiling Characteristics and Flow Pattern Visualization of Refrigerant/Lubricant Oil Mixtures, Int. J. Refrigeration 32(2), 185–202.

Kudo, Y., Nakaiso, K., Kariya, K. and Miyara, A., 2016. Experimental Study on Boiling and Condensation Heat Transfer in a Horizontal Mini Channel, Proc. the 16th International Refrigeration and Air Conditioning Conference at Purdue, USA, 1809.

Lemmon, E. W., Bell, I. H., Huber, M. L. and McLinden, M. O., 2018. Reference fluid thermodynamic and transport properties-REFPROP, Version 10.0, NIST Standard Reference Database 23.

Saitoh, S., Dang, C. and Hihara, E., 2013. Effect of Lubricant Oil on Flow Boiling Heat Transfer of Refrigerant R1234yf in Horizontal Small-Diameter Tubes, Trans. of the JSRAE 30(4), 451–462. (in Japanese)

Takaishi, Y., Oguchi, K., 1987. Measurements of vapor pressure of R-22/oil solutions. In: Proceedings of the 18th International Congress of Refrigeration, Vienna, 217–222.

Tanaka, C., Dang, C. and Hihara, E., 2014. Characteristics of Flow Boiling Heat Transfer in Rectangular Minichannels, Proc. The 15th International Heat Transfer Conference, Japan, IHTC15-9589.

Manuscript ID: 225
DOI: 10.18462/iir.icr.2019.0225

R513A condensation inside a small sized microfin tube

Andrea DIANI[(a)], Luisa ROSSETTO[(b)]

[(a)] University of Padova, Department of Industrial Engineering
Padova, 35131, Italy, andrea.diani@unipd.it
[(b)] University of Padova, Department of Industrial Engineering
Padova, 35131, Italy, luisa.rossetto@unipd.it

ABSTRACT

R513A is a new azeotropic mixture made of R1234yf/R134a (56%/44%). Unlike pure R1234yf, R513A is non-flammable, and it can be used as replacement of R134a for medium and high temperature refrigeration systems. The paper shows some preliminary experimental results during R513A condensation inside a 4.0 mm OD horizontal microfin tube. The microfin tube has an inner diameter at the fin tip of 3.4 mm, it has 40 fins along the inner circumference, and each fin is 0.12 mm high with an apex angle of 43°. Tests are carried out for mass fluxes from 100 to 800 kg m^{-2} s^{-1}, at saturation temperatures of 30 °C and 40 °C. The experimental results are given in terms of heat transfer coefficient and frictional pressure drop. The results show the interesting thermal characteristics of R513A, which can be used in a near future as replacement of the traditional R134a.
Keywords: Azeotropic mixture, Condensation, Heat transfer coefficient, Pressure drop, R513A.

1. INTRODUCTION

R134a is among the most used fluids for refrigeration, air conditioning and heat pump systems. It was proposed as replacement of R22 in the late '90s, thanks to its zero Ozone Depletion Potential (ODP). As time went by, R134a was found to have a strong negative effect on the global warming, since it has a Global Warming Potential (GWP) equal to 1430. Therefore, new fluids or mixtures are needed to replace R134a. These new fluids must have characteristics like those of R134a, and they should be not flammable, in such a way that no new safety arrangements are requested to existing equipment.
HFOs are low GWP refrigerants, but they fall into the A2L flammability class, and so they are considered as mildly flammable. On the contrary, proper mixtures between HFOs and HFCs belong to the A1 flammability class, and so they are not flammable and may be implemented in existing equipment without any safety arrangement. R513A, which is a mixture of R1234yf and R134a (56% and 44% in mass), is a non-flammable azeotropic mixture, with a GWP of 631.
At the current state of the art, studies on R513A are more focused on the evaluation of the performance of vapor compression systems rather than on the evaluation of the heat transfer and fluid flow performances. Mota-Babiloni et al. (2017) compared the performance of R513A and R134a in a vapor compression system. The conclusion of the experimental comparison was that R513A can substitute R134a with only a thermostatic expansion valve adjustment, achieving better performance and a higher cooling capacity.
Yang et al. (2019) performed a comparative experimental study between R134a and R513A in a domestic refrigerator. Considering the pull down, 24-h energy consumption and freezing tests, they concluded that the refrigerant mixture R513A can be a direct drop-in substitute of R134a in the considered refrigeration equipment without any redesign of the entire system. Other studies concerning the comparison among the two refrigerants operating in vapor compression systems can be found in Devecioglu et al. (2018), Mota-Babiloni et al. (2019) and Makhnatch et al. (2019). To authors' knowledge, the two-phase heat transfer behaviour of R513A is almost unexplored.
Microfin tubes were discovered in the '70s, and they have been largely implemented in refrigeration, air conditioning and heat pumps applications. Nowadays, small sized microfin tubes start to appear in the market. Tubes with outer diameters of 5 mm are now commercially available, whereas smaller diameters are still at a research stage. Experimental studies regarding HFCs and HFOs flow boiling inside small sized microfin tubes can be found in the works carried out by Jige et al. (2018), Mancin et al. (2015) and Diani et al. (2018a), whereas condensation heat transfer was studied by Rahman et al. (2017) and Diani et al. (2018b, 2018c).

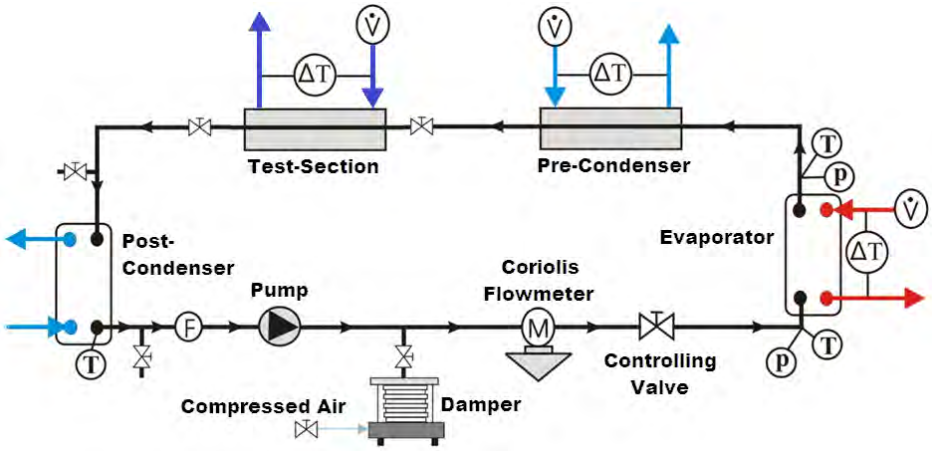

Figure 1: Schematic of the experimental facility

No data during R513A condensation inside small sized microfin tubes can be found in the open literature. This paper starts the experimental project aimed at evaluating the heat transfer coefficient and pressure drop during R513A two-phase heat transfer inside small sized microfin tubes, in order to verify the suitability of the azeotropic mixture R513A as possible substitute of the common R134a from a thermal and hydraulic point of view.

2. EXPERIMENTAL SET UP AND TEST SECTION

The experimental facility is located in the Heat Transfer in Micro-Geometries Laboratory of the Department of Industrial Engineering at University of Padova. A schematic of the experimental set up is reported in Fig. 1. The facility was designed for pressure drop and heat transfer measurements during either flow boiling or condensation. It has a maximum working pressure of 3 MPa and a maximum allowable mass flow rate of 72 kg s^{-1}.
The refrigerant is pumped through the circuit by means of a magnetically coupled gear pump, it is vaporized and superheated in a brazed plate heat exchanger fed with hot water. Superheated vapor then partially condenses in a pre-condenser fed with cold water, which is supplied by a water-cooled chiller, to achieve the desired vapor quality at the inlet of the test section. The pre-condenser is a tube-in-tube heat exchanger where the refrigerant flows in the inner tube, whereas the cold water flows in the annulus. The refrigerant enters the test section at a known mass velocity and vapor quality, where it condenses. The fluid leaves the test section and reaches a post-condenser, which is a brazed plate heat exchanger, where the refrigerant is fully condensed and subcooled. The cold water in the post-condenser is supplied by an air-cooled chiller. The subcooled liquid passes through a drier filter and then it is sent back to the evaporator by the pump. A damper connected to the compressed air line operates as pressure regulator to control the saturation conditions in the refrigerant loop. Further details of the experimental facility can be found in Diani et al. (2018c).

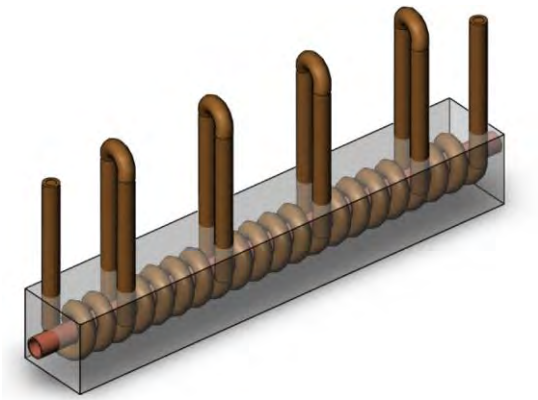

Figure 2: Schematic of the test section

A schematic of the test section is shown in Fig. 2. It consists of a smooth copper tube which is wrapped around the microfin tube. The smooth tube has an inner diameter of 1.9 mm. Cold water, which is supplied by a thermostatic bath, flows in the smooth tube: the cold water is needed to remove heat from the refrigerant condensing inside the microfin tube. The curve between two vertical segments of the smooth tube permits to locate thermocouples for the measurements of the water temperature: thermocouples are attached on the external wall on the top of these curves. In these regions, between two vertical segments, it is possible to attach thermocouples on the external wall of the microfin tube. The microfin tube with the wrapped smooth tube is inserted in an aluminium housing, filled with a melted alloy of tin/lead (40/60), whose melting temperature is around 220 °C, in order to guarantee, after solidification, a thermal contact between the microfin tube and the coils of the smooth tube. The whole test section is effectively thermally insulated from the surrounding environment with AF/Armaflex. The microfin tube under investigation has an inner diameter at the fin tip of 3.4 mm, an outer diameter of 4.0 mm, it has 40 fins along the inner circumference, and each fin is 0.12 mm high with an apex angle of 43°. The helix angle is 18°. The length of the test section is 0.1 m, whereas the length between the pressure ports is 0.33 m.

3. DATA ANALYSIS

The subcooled liquid is pumped to the evaporator where it is vaporized and superheated; the refrigerant temperatures and pressures are measured at both inlet and outlet of the heat exchanger. The vapor quality at the inlet of test section depends on the refrigerant conditions at the exit of the evaporator and on the heat flow rate exchanged in the tube-in-tube heat exchanger, which can be obtained from an energy balance on the cooling water side as given by:

$$q_{PC} = \dot{m}_{w,PC} \cdot c_{p,w} \cdot \left(t_{w,PC,out} - t_{w,PC,in}\right) = \dot{m}_{ref} \cdot \left(h_{vs} - h_{TS,in}\right) \quad \text{Eq. (1)}$$

where $\dot{m}_{w,PC}$ is the water mass flow rate flowing in the pre-condenser, $c_{p,w}$ is the water specific heat at constant pressure, and $t_{w,PC,out}$ and $t_{w,PC,in}$ are the water temperatures at the outlet and inlet of the pre-condenser, respectively. On the right side of Eq. 1, $\dot{m}_{ref}$ is the refrigerant mass flow rate measured by the Coriolis effect flowmeter, and h_{vs} and $h_{TS,in}$ are the refrigerant specific enthalpies at the outlet of the evaporator, which is the inlet of the pre-condenser, and at the outlet of the pre-condenser, which is the inlet of the test section. The vapor quality at the inlet of the test section (x_{in}) can be calculated from the specific enthalpy at the inlet of the test section, derived from Eq. (1), as:

$$x_{in} = \frac{h_{TS,in} - h_L}{h_V - h_L} \quad \text{Eq. (2)}$$

where h_L and h_V are the specific enthalpies of the saturated liquid and vapor, respectively, evaluated at the saturation pressure of the refrigerant measured at the inlet of the test section, calculated with Refprop 10 (Lemmon et al., 2018).
The heat flow rate exchanged in the test section can be calculated as:

$$q_{TS} = \dot{m}_{w,TS} \cdot c_{p,w} \cdot \left(t_{w,TS,out} - t_{w,TS,in}\right) \quad \text{Eq. (3)}$$

where $\dot{m}_{w,TS}$ is water mass flow rate circulated inside the smooth tube wrapped around the microfin tube, and $t_{w,TS,out}$ and $t_{w,TS,in}$ are the water temperatures measured at the outlet and inlet of the test section, respectively. The outlet vapor quality can now be calculated from a energy balance at the test section. From the error propagation analysis, following the procedure suggested by Kline and McClintock (1953), the mean uncertainty on the mean vapor quality (arithmetic average between inlet and outlet vapor qualities) is 0.03. The heat transfer performance of the microfin tube is given in terms of heat transfer coefficient, defined as:

$$HTC = \frac{q_{TS}}{A_D \cdot (\bar{t}_{sat} - \bar{t}_{wall})} \quad \text{Eq. (4)}$$

where $\bar{t}_{sat}$ is the mean saturation temperature, and $\bar{t}_{wall}$ is the wall temperature. A_D is the inner area of a smooth tube with diameter the fin tip diameter. Following the procedure suggested by Kline and McClintock (1953), the mean uncertainty on the heat transfer coefficient is 4.5%.
The hydraulic performance is evaluated in terms of frictional pressure gradient, as:

$$\left(\frac{\mathrm{d}p}{\mathrm{d}z}\right)_f = \left(\frac{\mathrm{d}p}{\mathrm{d}z}\right)_{tot} - \left(\frac{\mathrm{d}p}{\mathrm{d}z}\right)_a \qquad \text{Eq. (5)}$$

The model of Rouhani and Axelsson (1970) was considered to calculate the void fraction, needed to calculate the momentum pressure drop. The gravitational contribution was not considered since the microfin tube is horizontally located.

4. EXPERIMENTAL RESULTS

This section presents the experimental results during condensation of R513A inside the small sized microfin tube under investigation. Experimental tests were carried out for mass velocities, calculated on the cross sectional area of an equivalent smooth tube having an inner diameter equal to the diameter at the tip of the considered microfin tube, from 100 to 800 kg m^{-2} s^{-2}, at saturation temperatures at the inlet of the test section of 30 °C and 40 °C. Every single experimental point is the average value of 100 readings recorded at a frequency of 1 Hz. In these operating conditions, the vapor quality difference between inlet and outlet of test section varies from 0.04 to 0.3, depending on the mass velocity: the higher the mass velocity, the lower the vapor quality difference.
Fig. 3 shows the experimental heat transfer coefficients plotted against the mean vapor qualities for a saturation temperature at the inlet of the test section of 30 °C, for mass velocities *G* from 100 to 800 kg m^{-2} s^{-1}. The heat transfer coefficient at *G* = 100 kg m^{-2} s^{-1} remains almost constant up to a mean vapor quality of 0.5 at a value between 2000 and 2500 W m^{-2} K^{-1}, and then it increases with vapor quality reaching a value of approximately 6500 W m^{-2} K^{-1}. This can be explained considering the different flow patterns: at the lowest mass velocity for low vapor qualities, the flow seems to be stratified, and, as a result, the heat transfer coefficient is weakly affected by vapor quality, i.e. by vapor velocity. On the contrary, as vapor quality increases, the flow seems to be annular, and, in fact, the heat transfer coefficient is highly affected by vapor quality: there is a change of the slope of the trend of heat transfer coefficient at a mean vapor quality between 0.5 and 0.6. This is somehow confirmed by the flow pattern map shown in Fig. 4. Fig. 4 shows the experimental data plotted in the flow pattern map developed by Doretti et al. (2005). The blue dotted line represents the transition between the ΔT-dependent and ΔT-independent regimes. The ΔT-dependent regime (below the dotted line) is linked to gravity controlled flow patterns, such as wavy and smooth stratified flow regime. The ΔT-independent regime (above the dotted line) is linked to shear stress forces, i.e. to annular flow. The flow pattern map confirms that the flow is in stratified regime at low vapor qualities, whereas a transition from stratified to annular flow pattern occurs as the vapor quality increases. Data at *G* = 150 kg m^{-2} s^{-1} for mean vapor qualities lower than 0.4 and the point at *G* = 200 kg m^{-2} s^{-1} at a mean vapor quality of 0.15 seem to be in the stratified regime, and, as a result, their correspondent heat transfer coefficients are between 2000 and 2500 W m^{-2} K^{-1}. All the other experimental data fall in the annular flow regime, and, as a result, their heat transfer coefficient increases as both vapor quality and mass velocity increase.

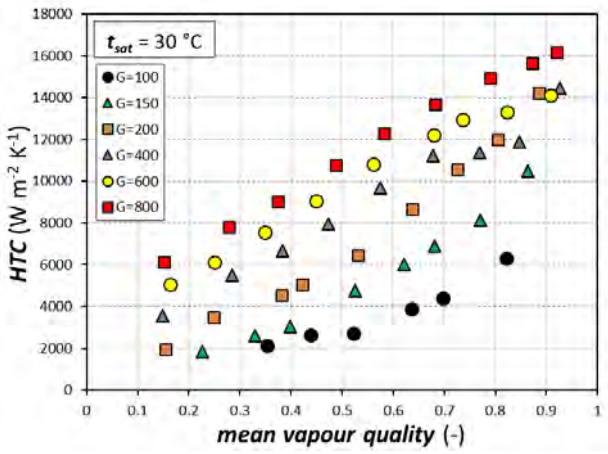

Figure 3: Heat transfer coefficient versus mean vapor quality at t_{sat} = 30 °C. *G* expressed in (kg m^{-2} s^{-1})

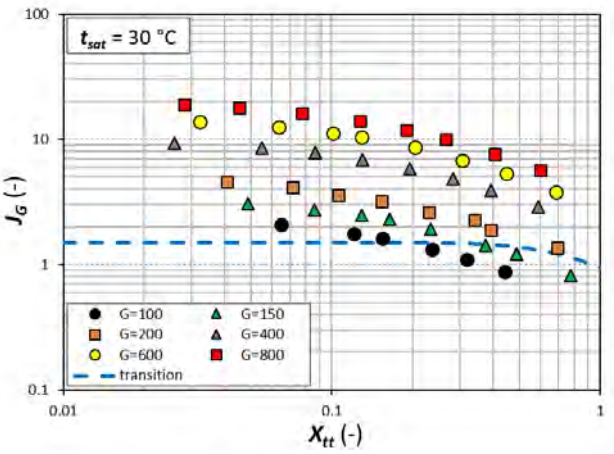

Figure 4: Experimental data at t_{sat} = 30 °C plotted in the flow pattern map developed by Doretti et al. (2005). *G* expressed in (kg m^{-2} s^{-1})

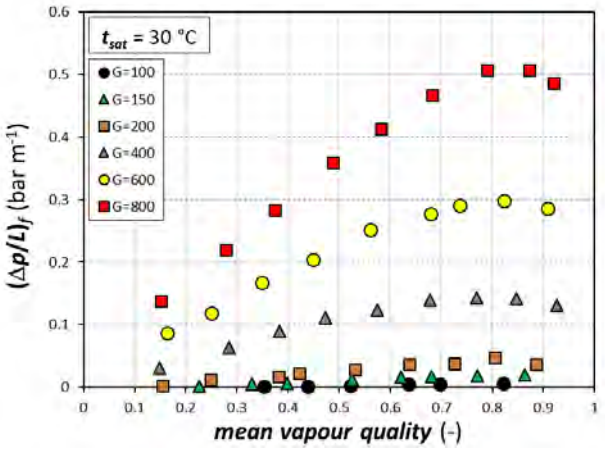

Figure 5: Frictional pressure gradient versus mean vapor quality at t_{sat} = 30 °C. *G* expressed in (kg m^{-2} s^{-1})

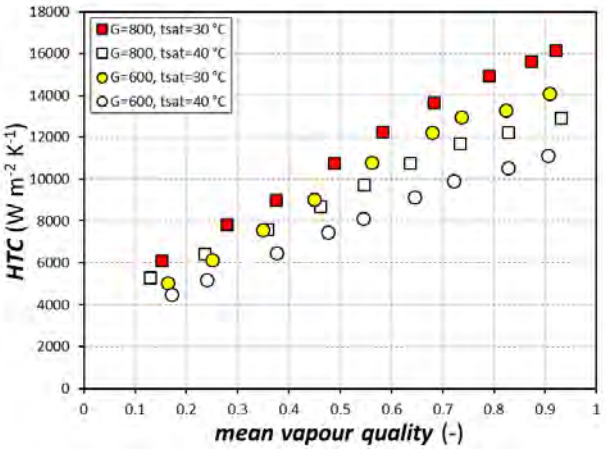

Figure 6: Effect of saturation temperature on the heat transfer coefficient. *G* expressed in (kg m^{-2} s^{-1})

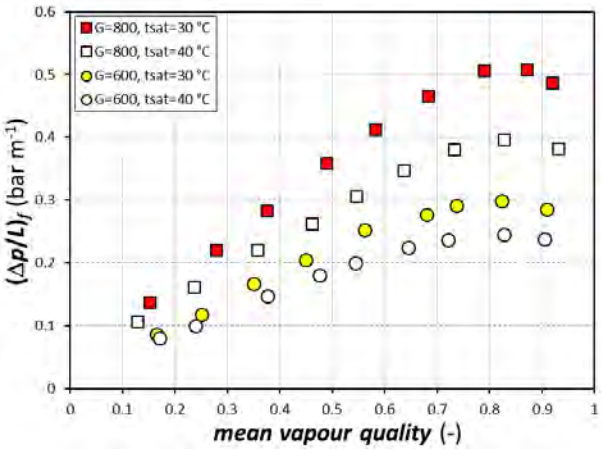

Figure 7: Effect of saturation temperature on the frictional pressure gradient. *G* expressed in (kg m^{-2} s^{-1})

The experimental frictional pressure gradients at t_{sat} = 30 °C are reported in Fig. 5. At constant mass velocity, the frictional pressure gradient increases with vapor quality up to a maximum value, after which it slightly decreases. At constant mean vapor quality, the frictional pressure gradient increases as mass velocity increases.

The effects of the saturation temperature on the heat transfer coefficient and on the frictional pressure drop are reported in Figs. 6 and 7, respectively. Fig. 6 shows the heat transfer coefficient plotted versus the mean vapor quality for G = 600 and 800 kg m^{-2} s^{-1} at two different saturation temperatures at the inlet of the section of 30 °C and 40 °C. A higher saturation temperature implies a higher vapor density, and thus, at constant mass velocity, a lower vapor velocity. This is reflected on the experimental results depicted in Fig. 6: the higher the saturation temperature, the lower the heat transfer coefficient, especially in the high vapor quality region, mainly due to the lower vapor velocity with consequent lower convective effects. The lower vapor velocity at t_{sat} = 40 °C is also reflected on the frictional pressure gradient, as highlighted in Fig. 7: the higher the saturation temperature, the lower the frictional pressure gradient, especially in the high vapor quality region.

5. EMPIRICAL MODELING

This section presents some comparisons between the experimental values of heat transfer coefficient and frictional pressure gradient against the values predicted by empirical correlations

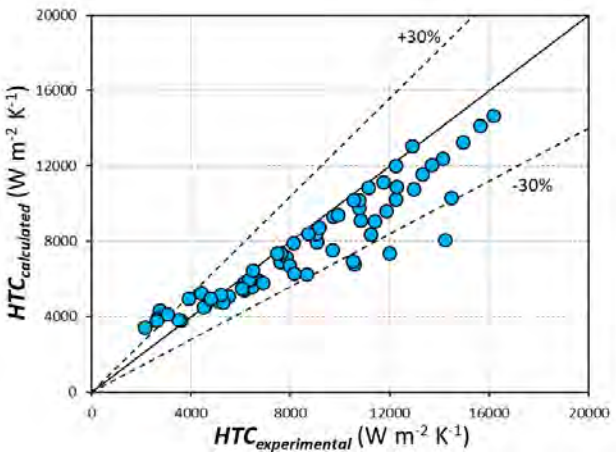

Figure 8: Calculated versus experimental heat transfer coefficients. Model by Cavallini et al. (2009)

available in the literature. The model of Cavalini et al. (2009) was developed to estimate the heat transfer coefficient during condensation of halogenated and natural refrigerants, pure fluids or nearly azeotropic mixtures flowing inside microfin tubes. The model takes into account the refrigerant properties, as well as two-phase flow patterns in microfin tubes and geometrical characteristics of the tubes. It was validated with data including microfin tubes with inner diameter ranging from 5.9 mm and 14.2 mm, fin height from 0.15 mm to 0.38 mm, apex angle from 15° to 90°, helix angle from 7° to 30°, and fin number from 21 to 82, at saturation temperature from -15 °C to 70 °C, and mass velocity between 80 and 890 kg m^{-2} s^{-1}. Even if the smallest considered diameter for the development of the correlation was 5.9 mm, the model is here applied to present data, which were obtained with an inner diameter at the fin tip of 3.4 mm. The model fairly estimates the experimental values, as shown in Fig. 8, with a relative, absolute and standard deviation of -5.1%, 14.9% and 19.9%, respectively.

Diani et al. (2014) proposed a correlation for the estimation of frictional pressure drop during two-phase flow of refrigerants inside small sized microfin tubes. The correlation was developed from experimental data during R1234ze(E) flow boiling inside a microfin tube with an inner diameter at the fin tip of 3.4 mm. The correlation was later validated with other experimental data obtained during flow boiling and condensation of pure refrigerants, at saturation temperatures of 30 °C and 40 °C. The correlation is here applied to the azeotropic mixture R513A. Fig. 9 reports a comparison between the calculated frictional pressure gradient and the experimental counterpart. The model well estimates the experimental values, with a relative, absolute and standard deviation of 2.2%, 8.5% and 12.5%, respectively. Therefore, the model can be considered validated also for azeotropic mixtures.

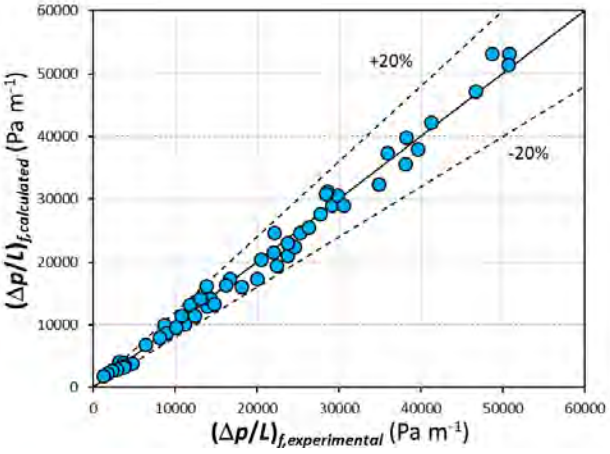

Figure 9: Calculated versus experimental frictional pressure gradients. Model by Diani et al. (2014)

6. CONCLUSIONS

This paper proposed some experimental results during R513A condensation inside a small sized microfin tube with an inner diameter at the fin tip of 3.4 mm. R513A is an azeotropic mixture made of R1234yf and R134a (56% and 44% in mass), which is a possible direct substitute of R134a with a lower GWP. Condensation tests were carried out for mass velocities from 100 to 800 kg m^{-2} s^{-1}, with saturation temperatures at the inlet of the test section of 30 °C and 40 °C.
Some data at the lowest mass velocities and low vapor qualities fall in the ΔT-dependent flow regime, i.e. they are in stratified flow, and so their heat transfer coefficient is weakly affected by vapor quality and mass velocity. All the other experimental data fall in the ΔT-independent flow regime, i.e. they are in annular flow conditions. For these data, the higher the vapor quality, the higher the heat transfer coefficient, and the higher the mass velocity, the higher the heat transfer coefficient.
The comparison between data at t_{sat} = 30 °C and 40 °C revealed the effect of the saturation temperature: the higher the saturation temperature, the lower the heat transfer coefficient and the lower the frictional pressure drop, due to a lower vapor velocity.
The experimental data of heat transfer coefficient and frictional pressure gradient were compared against the values predicted by two empirical correlations available from the literature. The model of Cavallini et al. (2009) is able to estimate the experimental heat transfer coefficients with a relative, absolute and standard deviation of -5.1%, 14.9% and 19.9%, respectively. The correlation of Diani et al. (2014) is able to estimate the frictional pressure gradients with a relative, absolute and standard deviation of 2.2%, 8.5% and 12.5%, respectively.

ACKNOWLEDGEMENTS

The support of the MIUR through the PRIN Project 2017F7KZWS_005 and of the Università di Padova (Project CPDA107382 and Project BIRD172935/17) on this research is gratefully acknowledged. The MS student Luca Vettorato is also gratefully acknowledged.

NOMENCLATURE

A_D	equivalent inner surface area (m^2)	c	specific heat ($J \times kg^{-1} \times K^{-1}$)
G	mass velocity ($kg \times m^{-2} \times s^{-1}$)	h	specific enthalpy ($J \times kg^{-1}$)
HTC	heat transfer coefficient ($W \times m^{-2} \times K^{-1}$)	L	distance between pressure ports (m)
$\dot{m}$	mass flow rate ($kg \times s^{-1}$)	Δp	pressure drop (Pa)
q	heat flow rate (W)	t	temperature (°C)
ΔT	temperature difference (K)	x	vapor quality (-)

Subscripts

a	momentum term	*f*	frictional
in	at the inlet	*L*	saturated liquid
out	at the outlet	*p*	at constant pressure
PC	at the pre-condenser	*ref*	refrigerant
sat	saturation	*tot*	total
TS	at the test section	*V*	saturated vapor
vs	superheated vapor	*w*	water
wall	at the wall		

REFERENCES

Cavallini, A., Del Col, D., Mancin, S., Rossetto, L., 2009. Condensation of pure and near-azeotropic refrigerants in microfin tubes: A new computational procedure. Int. J. Refrigeration 32(1), 162-174.

Devecioglu, A.G., Oruc, V., 2018. Improvement of the energy performance of a refrigeration system adapting a plate-type heat exchanger and low-GWP refrigerants as alternative to R134a. Energy 155, 105-116.

Diani, A., Mancin, S., Rossetto, L., 2014. R1234ze(E) flow boiling inside a 3.4 mm ID microfin tube. Int. J. Refrigeration 47, 105-119.

Diani, A., Rossetto, L., 2018a. Experimental analysis of refrigerants flow boiling inside small sized microfin tubes. Heat Mass Transf. 54(8), 2315-2329.

Diani, A., Campanale, M., Cavallini, A., Rossetto, L., 2018b. Low GWP refrigerants condensation inside a 2.4 mm ID microfin tube. Int. J. Refrigeration 86, 312-321.

Diani, A., Campanale, M., Rossetto, L., 2018c. Experimental study on heat transfer condensation of R1234ze(E) and R134a inside a 4.0 mm OD horizontal microfin tube. Int. J. Heat Mass Transf. 126, 1316-1325.

Doretti, L., Fantini, F., Zilio, C., 2005. Flow patterns during condensation or three refrigerants: microfin tube vs. smooth tube. Proceedings of the IIR International Conference on Thermophysical properties and Transfer Processes of Refrigerants, Vicenza, Italy.

Jige, D., Sagawa, K., Iizuka, S., Inoue, N., 2018. Boiling heat transfer and flow characteristic of R32 inside a horizontal small-diameter microfin tube. Int. J. Refrigeration 95, 73-82.

Kline, S.J., McClintock, F.A., 1953. Describing the uncertainties in single sample experiments. Mech. Eng. 75, 3-8.

Lemmon, E.W., Huber, M.L., McLinden, M.O., 2018. NIST Standard Reference Database 23, NIST Reference Fluid Thermodynamic and Transport Properties, REFPROP, version 10.0. Gaithersburg, MD: Standard Reference Data Program, National Institute of Standards and Technology.

Makhnatch, P., Mota-Babiloni, A., Lopez-Belchi, A., Khodabandeh, R., 2019. R450A and R513A as lower GWP mixtures for high temperature countries: Experimental comparison with R134a. Energy 166, 223-235.

Mancin, S., Diani, A., Rossetto, L., 2015. Experimental measurements of R134a flow boiling inside a 3.4 mm microfin tube. Heat Transf. Eng. 36(14-15), 1218-1229.

Mota-Babiloni, A., Makhnatch, P., Khodabandeh, R., Navarro-Esbri, J., 2017. Experimental assessment of R134a and its lower GWP alternative R513A. Int. J. Refrigeration 74, 682-688.

Mota-Babiloni, A., Navarro-Esbrì, J., Pascual-Miralles, V., Barragan-Cervera, A., Maiorino, A., 2019. Experimental influence of an internal heat exchanger (IHX) using R513A and R134a in a vapor compression system. Appl. Therm. Eng. 147, 482-491.

Rahman, M.M., Kudo, Y., Bashar, M.K., Kariya, K., Miyara, A., 2017. Experimental study on condensation heat transfer and pressure drop inside a 2.13 mm ID smooth and microfin horizontal tube. Proceedings of First Asian Conference on Thermal Sciences – ACTS2017, Jeju Island, South Korea.

Rouhani, S.Z., Axelsson, E., 1970. Calculation of void fraction in the subcooled and quality boiling regions. Int. J. Heat Mass Transf. 13(2), 383-393.

Yang, M., Zhang, H., Meng. Z., Qin, Y., 2019. Experimental study on R1234yf/R134a (R513A) as R134a replacement in a domestic refrigerator. Appl. Therm. Eng. 146, 540-547.

Manuscript ID: 227
DOI: 10.18462/iir.icr.2019.0227

Review of next generation low gwp refrigerants for chiller products

Steve KUJAK[(a)], Ken SCHULTZ[(a)]
[(a)] Ingersoll Rand, 3600 Pammel Creek Road, La Crosse, 54601, USA
skujak@irco.com, kschultz@irco.com

ABSTRACT

The recent Kigali amendment to the Montreal Protocol has initiated regulatory and voluntary actions to limit the direct global warming potential (GWP) of refrigerants used in many applications, including chillers. This paper provides an update on the latest low GWP refrigerant technology for chiller applications. Low GWP refrigerant technology continues to evolve and innovation continues with the development of new refrigerants to replace R123, R245fa, R134a and R410A for chillers, many of which are ultra-low GWP (GWP <10). OEM's continue to expand the introductions of R1233zd(E), R514A, R513A, and R1234ze(E) for large chiller products to replace R123 and R134a. R1224yd(Z) has recently been introduced to replace R245fa. Several flammable R410A replacements, for example R32 and R452B have been previously reviewed, but a new nonflammable refrigerant, R466A, will be compared to the above alternatives for use in R410A chillers
Keywords: R1233zd(E), R514A, R1224yd(Z), R513A, R516A, R1234ze(E), R32, R452B, R466A, R454B Chillers, Centrifugal

1. INTRODUCTION

Introduction of lower GWP refrigerants (<750 GWP) and refrigerants with ultra-low GWPs (<10 GWP) are being introduced into the chiller market place in ever increasing numbers by many OEMs. Many ultra-low GWP refrigerants were introduced starting in 2015 for large capacity centrifugal chillers (~≥1000 kW) and lower GWP refrigerants for screw and scroll compressor based chillers. The reasons for rapid adoption of low GWP refrigerants without significant regulatory pressure is the result of acceptable alternatives being identified that are non-flammable (ASHRAE Class 1) and the financial and climate benefits of rapid adoption outweigh the benefits of waiting for uncertain phase down regulation. Essentially, the industry has recognized that large capacity chillers dependent on high-GWP HFC refrigerants will shortly become obsolete as the result of country actions as the result of meeting their Montreal Protocol commitments in the near future. Building owners worldwide would reduce their investment uncertainty by choosing large capacity chillers utilizing next generation refrigerants or choosing products that are easily retrofitted to the next generation refrigerants (retrofit ready).
Ultra-low GWP refrigerants options that are nonflammable are not available for use in R134a and R410A positive displacement chillers (screw and scroll compressors). Trade-offs need to be made on GWP, flammability and capacity to obtain lower GWP alternatives. The authors have evaluated alternatives for both R134a and R410A chillers. A new nonflammable refrigerant to replace R410A, R466A, was evaluated and results will be discussed in this paper.

2. OVERVIEW OF ALTERNATIVES

2.1 Overview of R-123 and R-245fa Alternatives

There are three new ultra low GWP Olefin alternative refrigerants that have been developed that could be considered replacements for R123 or R245fa (Table 1). One of these new olefin based refrigerants is R514A, an azeotropic blend of R1336mzz(Z) and R1130(E). R514A's composition is 74.7% R1336mzz(Z) and 25.3% R1130(E) by mass. R1233zd(E) and R1224yd(Z) are the other two olefin based refrigerants of interest. All these new lower pressure refrigerants have been listed by ASHRAE Standard 34 as Class 1 non-flammable (ASHRAE 34, 2016). Non-flammability (Class 1)

allows these new refrigerants to be compatible with existing application standards and building codes, and therefore allows their immediate use. Commercial chiller products are now available that utilize R514A, R1233zd(E) and R1224yd(Z).

As shown in Table 1, Fig. 1, and Fig. 2, R514A possesses similar thermodynamic and physical properties to directly replace R123. R1224yd(Z) possesses similar thermodynamic and physical properties to directly replace R245fa. Only R1233zd(E) is different enough to not be considered a direct replacement for either R123 or R245fa. R1233zd(E) has pressures which are 30% to 45% higher than R123 for a given temperature. R1233zd(E) produces 39% more capacity than R123 for a given compressor volumetric displacement. The conditions simulated in the figures and table are for a chiller operating at 4.4°C evaporator saturation temperature and 37.8°C condenser saturation temperature with no suction superheat or condenser subcooling at an 80% isentropic compressor efficiency. Refrigerant properties were computed using REFPROP v9.1 (Lemmon et al., 2013). The fluid properties files for R514A and R1224yd(Z) were provided by the refrigerant suppliers.

Table 1. Summary of Relative Performance Characteristics

Performance Characteristic	R123	R514A	R1233zd(E)	R1224yd(Z)	R245fa
Refrigerant Composition	R123	R1336mzz(Z)/R1130(E)	R1233zd(E)	R1224yd(Z)	R245fa
Composition Weight Percent	100%	74.7%/25.3%	100%	100%	100%
GWP (IPCC, 2013)	79	<2*	1	1*	858
ASHRAE Standard 34 Safety Classification	B1	B1	A1	A1	B1
ODP	0.01	~0.00006	0.00035	0.00012	0
COP	1.00	1.0	0.99	0.99	0.98
Capacity	1.00	0.95	1.39	1.59	1.57
Temp Glide (K)	0	<0.1	0	0	0
Critical Temp (°C)	184	197	167	156	154
Mass Flow Rate	1.0	0.90	1.11	0.95	1.09

*Refrigerant supplier reported value or a calculated value.

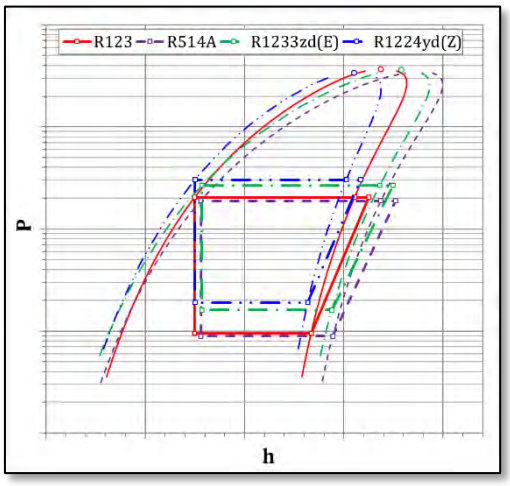

Figure 1. Pressure Enthalpy Comparison for R123, R514A, R1233zd(E) and R1224yd(Z)

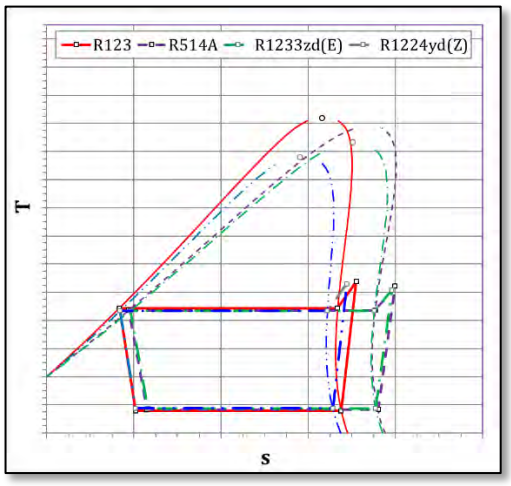

Figure 2. Temperature Entropy Comparison for R123, R514A, R1233zd(E) and R1224yd(Z)

Refrigerant-side heat transfer coefficients (HTCs) have been measured for both the evaporator and condenser with R123, R245fa, R514A, R1233zd(E) and R1224yd(Z) in a single tube heat transfer test rig as shown in Figs. 3, 4, 5, 6, 7 and 8 respectively. R245fa and R123 had roughly the same evaporator performance, but R1233zd(E) and R1224yf(Z) showed 60% better performance than R123 and R245fa. This finding was a pleasant surprise because most next generation R134a refrigerants evaluated by showed equal or reduced performance (Schultz, 2013).

The condenser performance difference between the four refrigerants was less dramatic. R1233zd(E)'s and R1224yd(Z)'s better evaporator (primarily) and condenser (secondarily) performance allows for these to overcome their reduced thermodynamic efficiencies relative to R123 by providing better heat exchanger total approach temperatures as compared to R123. R514A's performance allows similar heat exchanger approach temperatures and overall system efficiencies compared to R123.

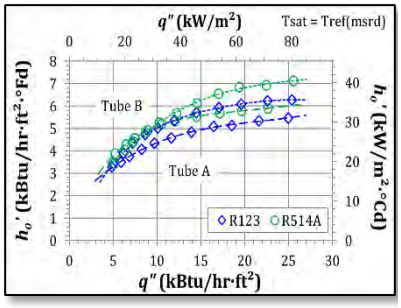

Figure 3. Evaporator heat transfer for R514A

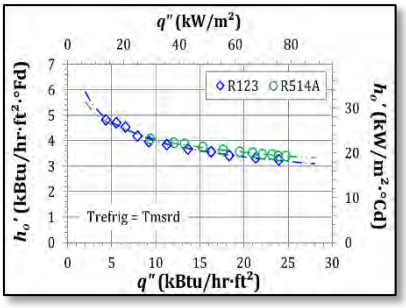

Figure 4. Condenser heat transfer for R514A

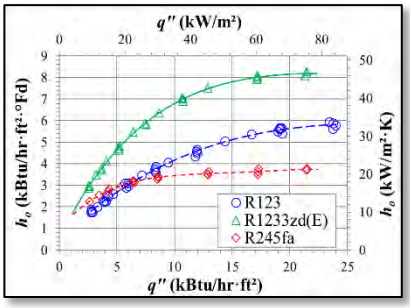

Figure 5. Evaporator heat transfer for R1233zd(E)

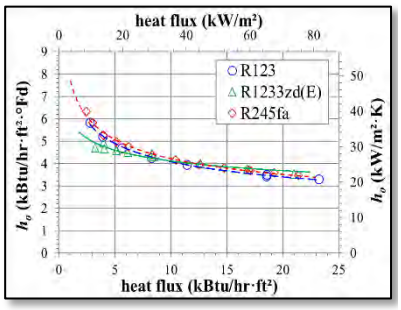

Figure 6. Condenser heat transfer for R1233zd(E)

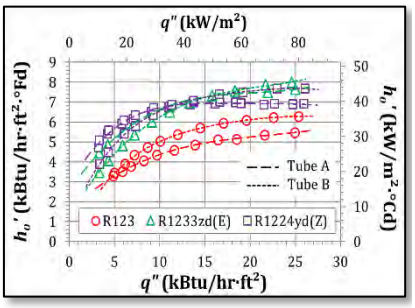

Figure 7. Evaporator heat transfer for R1224yd(Z)

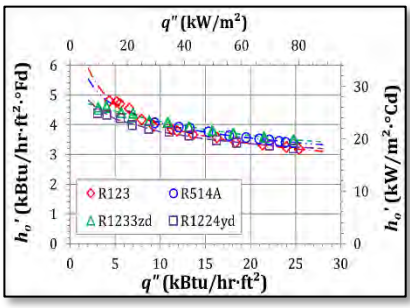

Figure 8. Condenser heat transfer for R1224yd(Z)

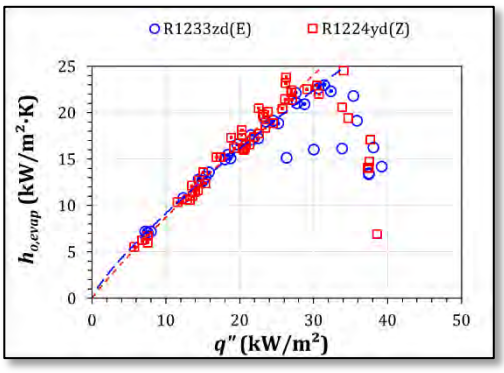

Figure 9. Evaporator HTCs for R1233zd(E) and R1224yd(Z) from tests in a large chiller.

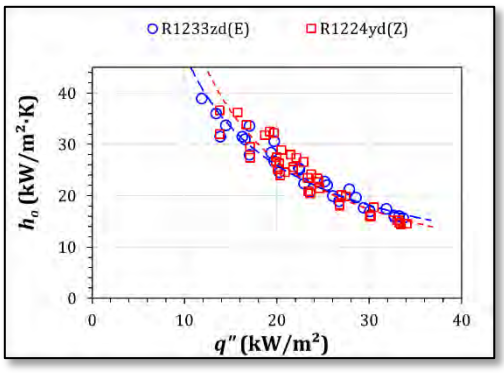

Figure 10. Condenser HTCs for R1233zd(E) and R1224yd(Z) from tests in a large chiller.

In the end, performance in chiller tube bundles is the primary metric that should be used for heat transfer performance comparison. Disappointing heat transfer performance was seen with many R134a alternatives as noted above. These poor results in tube bundles could not be correlated to single tube performance results. Higher performance has been observed in chiller flooded evaporators for both R514A and R1233zd(E) (Schultz and Gallant, 2017). Internal laboratory tests of a large (~5,000 kW) chiller confirmed that the similar high heat transfer performance of R1224yd(Z) and R1233zd(E) observed in the single tube tests translated to large tube bundles, see Figs. 9 and 10. Commercial sales of new production R514A chillers were first reported in 2016 with the simultaneous announcement of the ability to retrofit existing R123 chillers to R514A. Commercial sales of R1233zd(E) chillers were first reported in 2014 with at least six manufacturers now reporting commercially available chillers. Commercial sales of R1224yd(Z) were first reported in 2018.

2.2 Overview of R134a Alternatives

Initial evaluations of prospective alternatives to R134a occurred under the Low-GWP Alternative Refrigerants Evaluation Program (AREP) (AHRI, nd). Schultz (2014) reported the results from tests of several R134a-like refrigerants in a developmental water-cooled screw chiller with a nominal capacity of 810 kW, including R1234ze(E), N-13a, N-13b (now R450A), R513A, and ARM-42a (a predecessor to R516A). As shown in Figs. 11 and 12, R513A and ARM-42a produced predicted capacities and measured capacities very close to R134a. Measured efficiencies were slightly lower than predicted, mainly due to the impacts of somewhat lower heat transfer performance of R513A and ARM-42a in the evaporator and condenser relative to R134a. R1234ze(E) produced capacities 25% less than R134a as predicted. The slight gain in efficiency observed was due to the heat exchangers effectively having larger area per unit capacity, even though the evaporator refrigerant-side heat transfer coefficient with R1234ze(E) was 35% to 40% lower than with R134a. Poor evaporator heat transfer performance with R1234ze(E) has also been noted during other product development testing.

The composition, GWP, safety classification, relative capacity, COP, temperature glide and critical temperature of the refrigerants considered here are listed in Table 2. The performance characteristics of each refrigerant were determined using a simple thermodynamic model. The thermodynamic properties of R134a and R1234ze(E) are based on REFPROP descriptions and the R513A, R516A and R450A properties are also based on REFPROP descriptions with the associated binary interaction parameters provided by the refrigerant suppliers.

Table 2. Summary of Attributes for Evaluated Refrigerants

	R134a	R513A	R516A	R1234ze(E)	R450A
Refrigerant Composition	R134a	R1234yf/ R134a	R1234yf/R152a/R134a	R1234ze(E)	R134a/ R1234ze(E)
Composition, Weight Percent	100%	56%/44%	8.5%/14%/77.5%	100%	42%/58%
GWP_{AR5}	1300	572	130	<1	546
ASHRAE Safety Classification	A1	A1	A2L	A2L	A1
COP	1.00	0.97	0.98	1.00	1.00
Capacity	1.00	1.01	0.96	0.743	0.87
Temperature Glide (K)	0	<0.1	<0.1	0	0.6
Critical Temp (°C)	101	98	99	109	106

The capacities of N-13a and N-13b (now R450A) were lower than predicted. This is likely a consequence of degraded heat transfer coefficients in the evaporator due to the zeotropic nature of these refrigerants. Even though their temperature glides are only 0.6 K, there is additional mass transfer resistance as the compositions fractionate during phase change. This appears to be more significant for the ternary N-13a (R134a, R1234yf, and R1234ze(E)) blend than for the binary N-13b (R134a and R1234ze(E)) blend.

Performance of this chiller was observed to be relatively insensitive to refrigerant charge with the same charge selected for all refrigerants. These tests also demonstrated that the chiller capacity and efficiency were nearly invariant to refrigerant as the cooling water inlet temperature ranged from 18°C to 46°C when referenced to the performance at the nominal design condition of 29.4°C. In addition, the in situ compressor volumetric and isentropic efficiencies were nearly unchanged when applied with the various refrigerants.

Tests with R513A and R516A were also run on air-cooled chiller with similar results. With R513A, capacity matched that with R134a while efficiency was reduced by about 5%. Additional details about these two tests are contained in a report by Schultz and Perez-Blanco (2018). Full capacity with R516A fell only about 2% below the capacity attained with R134a, which is consistent with the prediction based on thermodynamic properties. However, the efficiency (EER or COP) with R516A at full capacity was about 3.5% lower than with R134a, about 1.5% lower than predicted by thermodynamic properties alone.

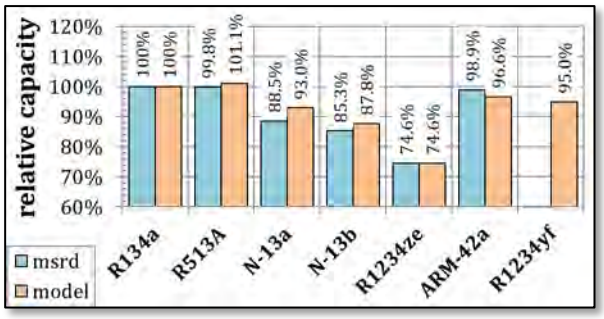

Figure 11. Capacities measured and predicted for the water-cooled chiller relative to R134a.

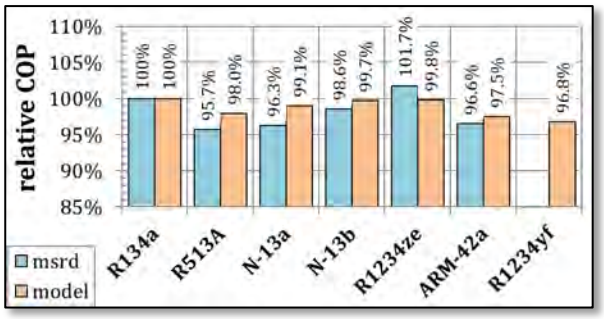

Figure 12. COP measured and predicted for the water-cooled chiller relative to R134a.

2.3 Overview of R410A Alternatives

The composition, GWP, safety classification, relative capacity, COP, temperature glide and critical temperature of the refrigerants considered here are listed in Table 3. The performance characteristics of each refrigerant were determined using a simple thermodynamic model. The thermodynamic properties of R410A and R32 are based on REFPROP descriptions and the R466A, R452B and R454B properties are also based on REFPROP descriptions with the associated binary interaction parameters provided by the refrigerant suppliers.

Three refrigerants, R466A, R452B and R32, offer approximately a two thirds reduction in GWP while R454B offers approximately a three quarters reduction in GWP compared to R410A. R452B, R454B and R32 are well known 2L flammable refrigerants while the R466A is a newly introduced refrigerant blend that is nonflammable. R466A being nonflammable offers the ability of this new refrigerant to be compatible with existing application standards and building codes, and therefore allows its immediate use without having to consider the safety liabilities and costs of using a flammable refrigerant. The authors have done evaluations of these four alternatives in a number of different air conditioning applications; results are described below.

Three of the alternatives, R466A, R452B and R32, were tested in an air-cooled water chiller with a nominal design cooling capacity of 352 kW (100 RT) designed for R410A refrigerant. Additional details about the test conditions are contained in Schultz and Nayak (2017) and Schultz and Kujak (2018). Fig. 13 summarizes the cooling capacity and efficiency (COP) as a function of ambient temperature.

Table 3. Summary of Attributes for Evaluated Refrigerants

	R410A	R466A	R452B	R454B	R32
Refrigerant Composition	R32/R125	R32/R125/R13I1	R32/R125/R1234yf	R32/R1234yf	R32
Composition, Weight Percent	50%/50%	49%/11.5%/39.5%	67%/7%/26%	68.9%/31.1%	100%
GWP_{AR5}	1924	697	675	467	677
ASHRAE Safety Classification	A1	A1	A2L	A2L	A2L
COP	1.00	1.01	1.01	1.01	1.01
Capacity	1.00	0.97	0.98	0.97	1.09
Temperature Glide (K)	0	1.5	1.3	1.4	0
Critical Temperature (°C)	71	84	79	81	78

A 3% drop in the capacity was seen with both R452B and R466A compared to R410A at 6.7°C/35°C operating conditions which is in line with the thermodynamic properties for each refrigerant. R32 yielded an 8.6% increase in capacity as compared to the baseline. The relative capacity varied from about −5% to +1% for R452B and R466A as the ambient temperature increased from 18°C to 52°C. For R32, the relative capacity varied from +5% to +13%. All three alternate refrigerants showed a

modest improvement in capacity over R410A at higher ambient temperatures.R452B refrigerant consistently showed better COP values compared to R410A at all ambient conditions at any given leaving chilled water temperature conditions. The relative COP increased as the ambient temperature increased (0 to +7%). The relative COP varied from −2% to +7 % for R32 and −2% to +4% for R466A. Again, all three alternate refrigerants showed a modest improvement in efficiency over R410A at higher ambient temperatures.

Fig. 14 summarizes the variation of refrigerant temperature at the compressor discharge (CDT) as a function of the ambient temperature relative for all three alternative refrigerants as well as a summary of the absolute difference in CDT to an R410A baseline. The compressor discharge temperatures of R452B were about 3 K to 6 K higher than R410A. With R466A, the CDTs were slightly higher, running about 6 K to 11 K higher than R410A. R32, with its inherent thermodynamic properties, had the highest CDTs, running 13 K to 27 K higher than R410A. The chiller reached its maximum CDT limit while running with 6.7°C and 13.3°C leaving chilled water temperatures as ambient temperatures of ~46°C and ~49°C, respectively. Also, the chiller reached its maximum pressure limit when running with 20°C leaving chilled water temperatures at an ambient temperature of ~49°C. This shows that while R452B and R466A could directly be used in R410A equipment without any major design changes, the system with R32 would require major changes to either accommodate or lower the elevated CDTs, and also would need changes in the heat exchanger design to accommodate the higher operating pressures at high ambient conditions.

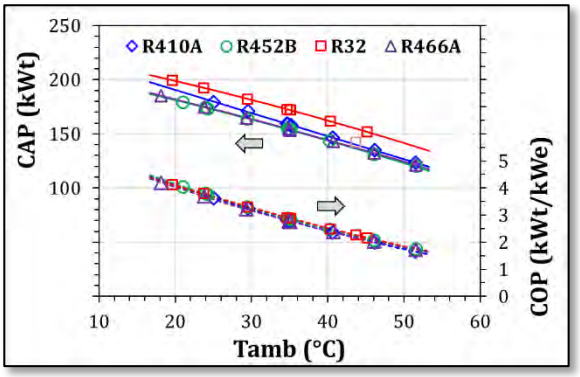

Figure 13. Summary of COP and Capacity (CAP) for Refrigerants Relative to R410A

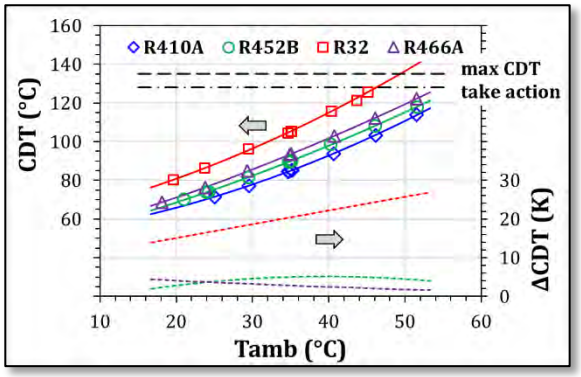

Figure 14. Summary of Compressor Discharge Temperature Relative to R410A

R454B and R452B (described in the referenced paper as DR5A and DR55 respectively) along with R32 were tested in a packaged 14 kW capacity rooftop unit (Schultz and Kujak, 2016). Figs. 15 and 16 summarize the capacity (CAP) and efficiency (COP) variations as a function of ambient temperature relative to R410A. A summary of compressor discharge temperatures (CDT) measured in the testing is shown in Fig. 17 for all three alternatives.

The alternatives produced higher efficiencies than R410A by 3% to 7% (Fig. 15), the advantage increasing slightly for R452B and R454B as ambient temperature increased while the efficiency decreased more quickly for R32 than R410A as the power draw increased as ambient temperature increased. Capacity followed a similar relationship, but to a lesser degree, only increasing 1% to 3% with increasing ambient temperatures (Fig. 16).

For R410A, R4542B and R454B, compressor discharge temperatures increased roughly 0.77 K to 0.83 K for each 1 K increase in ambient temperature. The CDTs with R452B and R454B were 4 K to 7 K higher than R410A, the difference increasing slightly with increasing ambient temperature. With R32, CDTs were elevated over R410A by 11 K at lower ambient temperatures and increased to nearly 25 K over R410A at high ambient temperatures. When running with R32, the maximum CDT operating limit of 120°C was reached near the 49°C ambient temperature. Changes to the unit design to mitigate or accommodate high CDRs would be need to allow the use of R32 at high ambient conditions.

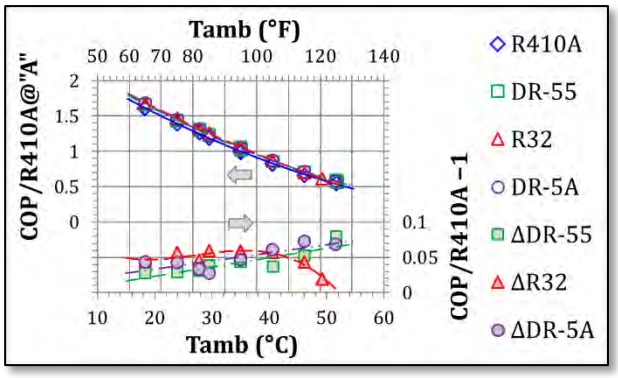

Figure 15. Summary of Coefficient of Performance (COP) Relative to R410A

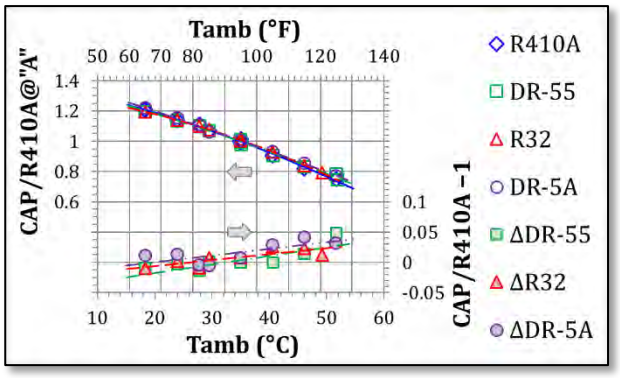

Figure 16. Summary of Capacity (CAP) for Refrigerants Relative to R410A

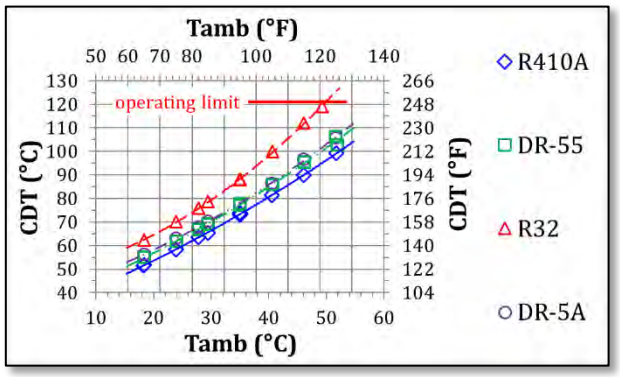

Figure 17. Summary of Compressor Discharge Temperature (CDT) Relative to R410A

3. CONCLUSIONS

Low or ultra-low (<10) GWP, non-flammable and highly efficient refrigerants will be available and have started to emerge as replacements for R123 and R245fa for large capacity centrifugal chillers. These next generation refrigerants include R514A as an alternative for R123 and R1224yd(Z) for R245fa. R1233zd(E) requires a new design platform to be employed. Several OEMs have introduced R1233zd(E) chillers to supplant their R134a products.

R513A has been introduced for both centrifugal and screw compressor chillers, but it has GWP of about ~600 which may not be acceptable long term. R1234ze(E) has also been introduced by many OEMs as an R134a replacement in both centrifugal and screw compressor chiller applications, but R1234ze(E) is flammable and is restricted from wide scale global adoption until standards and codes are updated in the near future. Another R134a like refrigerant, R516A, has GWP of less than 150 and would meet the long term direct GWP sustainability needs, but R516A is also a 2L flammable refrigerant like R1234ze(E), and requires adoption of updated standards and codes. No OEMs have made product announcements using R516A.

A new nonflammable R410A replacement, R466A, has been introduced with equivalent GWP to previously known 2L flammable alternatives R452B, R454B and R32. R466A's performance has been found to be essentially equivalent to R410A in nearly every aspect and should allow for the industry to transition to lower GWP without the need for expensive and complicated safety measures. Products using R454B and R32 have been announced, but few chiller products have been offered for sale.

NOMENCLATURE

CAP	capacity (kilowatts×hour^{-1})
COP	efficiency or coefficient of performance
CDT	compressor discharge temperature (°C)
OEM	original equipment manufacturer

REFERENCES

AHRI, nd, AHRI Low-GWP Alternative Refrigerants Evaluation Program (AREP). http://ahrinet.org/arep.aspx

ANSI/ASHRAE Standard 34-2016, Designation and Safety Classification of Refrigerants, ASHRAE, Inc. Atlanta, GA 30329]

Lemmon, E.W., Huber, M.L., McLinden, M.O. 2013. NIST Standard Reference Database 23: Reference Fluid Thermodynamic and Transport Properties-REFPROP, Version 9.1, NIST, Standard Reference Data Program, Gaithersburg.

Schultz, K., 2014, Performance of R134a Alternative Lower GWP Refrigerants in a Water-Cooled Chiller, presented at the ASHRAE Winter Conference, New York, Conference Paper (NY-14-C065).

Schultz, K. and Gallant, E., 2017, Assessment of Next Generation Refrigerant R514A as Replacement for R123 in Centrifugal Chillers, ASHRAE Winter Conference, Las Vegas, Nevada USA (LV-17-C084).

Schultz, K. and Kujak, S., 2016, Performance of 4-RT RTU with R410A Low GWP Alternatives, presented at the ASHRAE Summer Meeting, St Louis (ST-16-C065).

Schultz K. and Kujak, S., 2018, Examination of a Novel R410A Replacement, presented at the ASHRAE Annual Conference, 22-26 Jun 2018, Kansas City, Conference Paper KC-18-C???.

Schultz, K. and Nayak, G., 2017, Performance of an Air-Cooled Chiller with R410A Alternatives R452B and R32, presented at the ASHRAE Summer Meeting, Long Beach (LB-17-C049).

Schultz, K. and Perez-Blanco, M., 2018, Performance of Low GWP Refrigerant R-516A in an Air-Cooled Chiller, presented at the ASHRAE Winter Meeting, Chicago (CH-18-C063).

Manuscript ID: 234
DOI: 10.18462/iir.icr.2019.0234

Compressed liquid density measurements and correlation for cis-1-chloro-2,3,3,3 tetrafluoropropene (R1224yd(Z))

Laura FEDELE[(a)], Sergio BOBBO[(a)], Mauro SCATTOLINI[(a)], Claudio ZILIO[(b)], Ryo AKASAKA[(c,d)]

[(a)] Istituto per le Tecnologie della Costruzione, Consiglio Nazionale delle Ricerche, Padova, I-35127, Italy, laura.fedele@itc.cnr.it
[(b)] Dipartimento di Tecnica e Gestione dei Sistemi Industriali, Univeristà degli Studi di Padova, Vicenza, I-36100, Italy, claudio.zilio@unipd.it
[(c)] Research Center for Next Generation Refrigerant Properties (NEXT-RP), International Institute for Carbon-Neutral Energy Research (WPI-I2CNER), Kyushu University, 744 Motooka, Nishi-ku, Fukuoka, 819-0395, Japan, ryo-a@ip.kyusan-u.ac.jp
[(d)] Department of Mechanical Engineering, Kyushu Sangyo University, 2-3-1 Matsukadai, Higashi-ku, Fukuoka, 813-8503, Japan

ABSTRACT

The necessity to substitute high-GWP refrigerants gave a large motivation in the study of new halogenated olefins, characterized by GWP values similar to that of natural refrigerants. Within this group, cis-1-chloro-2,3,3,3-tetrafluoropropene (R1224yd(Z)) is one of the most interesting working fluids for applications in centrifugal chillers or Organic Rankine Cycles (ORC), due to its relatively high NBP (287.15 K).
In this paper, 90 experimental compressed liquid density data for R1224yd(Z) will be presented in a wide range of pressures and temperatures. Moreover, 10 saturated liquid density values have been obtained extrapolating the compressed liquid isotherms to the saturated pressure. Liquid densities obtained in this work are compared with calculated values from the equation of state (Akasaka et al., 2017). Totally, the equation well represents the densities, but some data points show larger deviations than the experimental uncertainties. We plan to update the equation based on these densities and other recent measurements.
Keywords: Density; low GWP refrigerant, R1224yd(Z).

1. INTRODUCTION

The more and more evident global warming induced by the emission of greenhouse gases, requires effective measures to face the problem. As well known, HFCs are amongst the controlled gases due to their high GWP. It is therefore necessary to gradually substitute them, with special reference to HVAC&R sector. About this, it is worth citing the European Union's (EU) 2014 F-Gas regulation, which establishes quite short deadlines for the substitution of the present HFCs refrigerants in the most common applications. However, as demonstrated by McLinden et al. (2015), only few tens of chemical compounds characterized by low GWP can be considered as refrigerants. Amongst these, apart from natural fluids such as hydrocarbons, carbon dioxide and ammonia, hydro-fluoro-olefins (HFOs) are the most promising synthetic low GWP group of chemicals. At the same time, at present, as shown in Bobbo et al. (2018), only few or none sets of thermodynamic properties data, necessary to develop reference equations of state, are available for most of the HFOs. Thus, for these fluids, there is the need to produce new sets of experimental data for the most important properties, in particular critical parameters, vapor pressure and PVT properties. Amongst others, very few data are available for R1224yd(Z), a compound that, similarly to R1233zd(E) and R1234ze(Z), is a potential substitute for R245fa for applications in centrifugal chillers or Organic Rankine Cycles (ORC), due to its relatively high NBP (287.15 K). Moreover, R1224yd(Z) is characterized by a very low GWP (<1), and even if its molecule contains one

chlorine atom, the ODP (0.00012) is negligible. It has also a very low toxicity (LC_{50} >200.000 ppm, AEL=500ppm) and it is nonflammable. Thus, from the point of view of environmental compatibility and human safety, it is a very friendly compound. With these premises, this paper presents 90 new experimental compressed liquid density data and 10 extrapolated saturated liquid density values, which will help to improve the fundamental EoS already proposed by Akasaka et al. (2017).

2. EXPERIMENTAL SECTION

2.1. Materials

The sample of R1224yd(Z) (cis-1-chloro-2,3,3,3-Tetrafluoropropene, CF3-CF=CHCl, CAS number 111512-60-8) used for the measurements was supplied by AGC Inc. The declared purity of the material was around 98.4% in mass fraction. Before experimentation, the sample was subjected to several cycles of freezing, evacuation, melting, and ultrasonic agitation to eliminate non-condensable gases. Table 1 reports some basic characteristics of R1224yd(Z).

Table 1. basic characteristics of R1224yd(Z), according to Refprop 10.0

MM (kg/kmol)	NBP (K)	T_{crit} (K)	P_{crit} (MPa)	ρ_{crit} (kg/m^3)	ω (-)
148.487	287.767	428.69	3.337	527.128	0.322

2.2. Experimental apparatus and procedure

The measurements were performed using a stainless steel vibrating tube densimeter (Anton Paar DMA 512). After having obtained a calibration equation correlating the period of oscillation of the vibrating tube with temperature and pressure, the sample density, at given temperature and pressure, was obtained, through the calibration equation, by measuring the period of oscillation. Experimental apparatus, procedure, and calibration have been described in previous papers (Bobbo et al. (2002), Bobbo et al. (2004)) and will be only briefly described here. The densimeter was charged with the sample by means of a circuit of stainless steel tubes connecting the cell and the refrigerant canister. The fluid was pressurized with a syringe pump (Isco Pump 260D). Pressure was measured with a piezoresistive pressure gauge (Druck DPI 145) with an expanded uncertainty of 10 kPa and 0.95 level of confidence, while temperature, controlled with a stability of about ± 0.003 K, was measured by means of a Pt 100 Ω resistance thermometer, with an expanded uncertainty of 0.05 K and 0.95 level of confidence. The densimeter was calibrated by measuring the oscillation period of the U-tube both under vacuum and filled with a fluid of known density, in this case water. For the measurements, after purging and evacuating the system, R1224yd(Z) was charged into the vibrating tube and the associated measurement circuit. At a given temperature, pressure was set at a fixed level by acting on the syringe pump. After stabilization of temperature and pressure, the period of oscillation was acquired. Then, pressure was changed by acting on the syringe pump and a new measurement was taken repeating the same procedure. The expanded uncertainty for the density measurements is estimated to be approximately 0.8 kg·m^{-3}, with 0.95 level of confidence.

3. RESULTS AND DISCUSSION

3.2. Compressed liquid density data

Table 2 and Fig. 1 present the 90 compressed liquid density measurements obtained for R1224yd(Z) along 9 isotherms, evenly spaced from (283 to 363) K, and pressures from close to saturation to 35 MPa.

Table 2. Compressed liquid density experimental data for R1224yd(Z), with the percentage deviations from the values (ρ_{calc}) calculated using the equation of Akasaka et al. (2017), as implemented in Refprop 10.0 [$\Delta\% = (\rho_{calc} - \rho_{exp})/\rho_{calc} \cdot 100$]

T (K)	P (MPa)	ρ (kg/m^3)	Δ% (-)
283.14	34.9997	1480.7	-
283.14	30.0004	1471.6	-
283.15	24.9998	1461.8	-
283.14	20.0003	1451.5	0.11
283.15	15.0005	1440.3	0.10
283.15	9.9999	1428.2	0.09
283.14	4.9995	1415.0	0.08
283.15	2.4999	1407.9	0.07
283.15	0.9998	1403.5	0.07
283.15	0.5001	1402.0	0.07
283.15	0.2500	1401.2	0.06
293.15	35.0005	1461.4	-
293.15	29.9997	1451.5	0.12
293.14	25.0002	1441.0	0.11
293.15	19.9997	1429.8	0.10
293.15	15.0001	1417.6	0.10
293.16	9.9999	1404.4	0.08
293.15	5.0001	1389.8	0.08
293.15	2.4998	1381.9	0.07
293.15	1.0000	1376.9	0.07
293.15	0.5000	1375.2	0.07
293.15	0.2501	1374.3	0.07
303.13	35.0002	1442.2	0.08
303.15	29.9994	1431.7	0.07
303.14	25.0003	1420.4	0.07
303.15	20.0003	1408.2	0.06
303.14	15.0003	1395.0	0.07
303.15	10.0001	1380.4	0.06
303.15	4.9997	1364.3	0.05
303.15	2.4999	1355.3	0.06
303.15	1.0001	1349.7	0.05
303.15	0.5002	1347.7	0.05
303.14	0.2501	1346.8	0.06
313.15	35.0000	1422.5	0.07
313.15	30.0001	1411.2	0.07
313.15	25.0001	1399.1	0.07
313.15	20.0001	1385.9	0.06
313.15	15.0001	1371.6	0.06
313.15	10.0000	1355.6	0.07
313.15	5.0000	1337.5	0.06
313.15	2.5002	1327.5	0.06
313.14	1.0000	1321.1	0.06
313.15	0.5000	1318.8	0.06
313.15	0.3500	1318.2	0.06
333.15	35.0000	1383.4	0.01
333.15	30.0001	1370.5	0.01
333.15	24.9999	1356.5	0.01
333.15	20.0001	1341.2	0.01
333.15	15.0000	1324.1	0.02
333.15	9.9999	1304.7	0.03
333.15	5.0000	1282.0	0.03
333.15	2.4999	1268.9	0.02
333.14	1.0002	1260.3	0.02
333.15	0.5999	1258.0	0.02
343.15	35.0002	1363.7	-0.03
343.15	30.0000	1350.0	-0.02
343.15	25.0000	1334.9	-0.01
343.15	20.0000	1318.3	-0.01
343.15	15.0004	1299.6	0.00
343.15	10.0002	1278.1	0.02
343.15	5.0001	1252.4	0.03
343.15	2.4999	1237.3	0.02
343.15	1.0000	1227.2	0.01
343.15	0.7500	1225.1	0.03
353.15	34.9999	1343.6	-0.03
353.15	29.9999	1329.0	-0.03
353.15	24.9999	1312.8	-0.02
353.16	19.9999	1294.8	-0.01
353.15	14.9999	1274.3	0.02
353.15	10.0001	1250.3	0.03
353.15	5.0000	1221.1	0.04
353.15	2.4999	1203.4	0.03
353.15	0.9999	1191.3	0.01
353.15	0.9000	1190.5	0.01
363.15	35.0000	1323.8	-0.06
363.15	29.9994	1308.0	-0.05
363.15	24.9998	1290.6	-0.03
363.16	19.9999	1271.1	-0.02
363.15	14.9998	1248.6	0.01
363.15	9.9998	1221.9	0.03
363.15	5.0003	1188.3	0.05
363.16	2.4999	1167.2	0.03
363.15	1.2001	1154.2	0.03

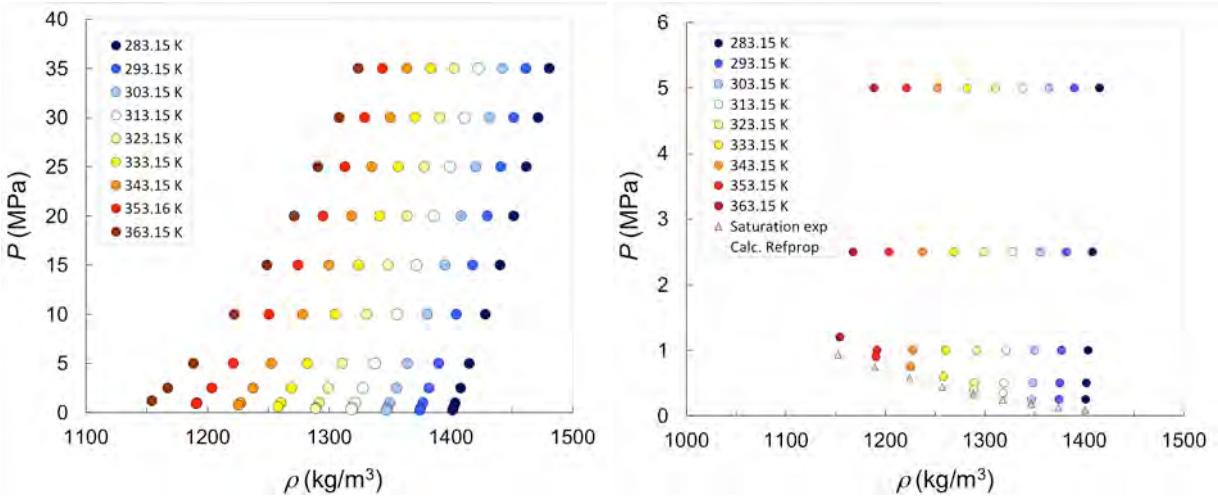

(a) (b)

Figure 1: (a) experimental data distribution in the (ρ−P) plane. (b) distribution of the experimental data at pressures close to saturation. Extrapolated saturated density data are also reported.

3.3. Saturated liquid density extrapolation and correlation

To obtain the saturated liquid density at a given temperature, the isothermal compressed liquid density data below 5 MPa were fitted to a polynomial representing the relation between density and pressure at that temperature. Then, the saturated liquid density was calculated with the polynomial at the given temperature and the corresponding vapor pressure calculated with Refprop 10.0. The extrapolated saturated liquid density (ρ_{sat}) values are reported in Table 2, where they are compared with the saturated liquid densities calculated with Refprop 10.0 ($\rho_{sat\ REFP}$). With these values, a saturated liquid density correlation was developed:

$$\rho_{sat}(\tau) = \rho_{crit}\,(1 + B_1\,\tau^{1/3} + B_2\,\tau^{2/3} + B_3\,\tau + B_4\,\tau^{4/3}) \qquad \text{Eq. (1)}$$

Eq. (1) represents very well the extrapolated saturation density, with AAD%=0.01% and MAD%=0.03%, as shown in Fig. 3(a). The constants B_i of Eq. (1) are reported in Table 3.

Table 2. extrapolated saturation density data and comparison with data calculated with Refprop 10.0 [$\Delta = (\rho_{sat} - \rho_{sat\ REFP})/\rho_{sat\ REFP} \cdot 100$]

T (K)	ρ_{sat} (MPa)	$\rho_{sat\ REFP}$ (kg/m^3)	Δ%
283.15	1400.7	1401.6	-0.06
293.15	1373.9	1374.8	-0.07
303.15	1346.5	1347.2	-0.06
313.15	1317.7	1318.4	-0.05
323.15	1288.5	1288.5	0.00
333.15	1257.1	1257.2	-0.01
343.15	1224.1	1224.2	-0.01
353.15	1189.2	1189.1	0.01
363.15	1152.4	1151.6	0.07

Table 3. Costants B_i for Eq. (1)

B_1	B_2	B_3	B_4
1.950981082	0.044520184	0.98776572	-0.25753216

3.3. Comparison with available fundamental Equation of State

3.3.1. Compressed liquid density data

Liquid densities measured in this work are compared with the fundamental equation of state presented by Akasaka et al. (2017). This equation is currently the only available property formulation for R1224yd(Z). It is worth to note that this equation has been implemented in the database Refprop 10.0: thus, when the database is cited in this paper, it is intended, if not otherwise specified, that the calculations are performed with the equation of Akasaka et al.

Fig. 2 shows relative deviations of the present data from calculated values with the equation. Deviations of Fukushima (2016) experimental data (only compressed liquid), to which the equation was fitted, are also plotted in the figure. In the liquid region, most of the present data are located at lower temperatures and higher pressures than those of Fukushima (2016), and thus comparisons of the present data are done in extrapolated areas of the equation. Because the equation was designed to exhibit proper behavior over wide ranges of temperature and pressure, deviations in the present data agree reasonably with the equation: the maximum absolute and average absolute deviations are 0.12% and 0.046%. However, AAD% become gradually larger as temperature decreases, while it is almost constant as a function of pressure, except at the lowest pressures, where some fluctuation is observed. In any case, the data with maximum deviations, observed at the lowest temperatures (<300 K) and the highest pressures (>25 MPa) exceed the experimental uncertainties. The equation will be updated by fitting it to the present data and other recent measurements, including vapor pressures and liquid-phase sound speeds. The new equation of state will represent all the present data within the experimental uncertainties.

Just to show the potentiality of molecular simulation in prediciting the thermodynamic properties of refrigerants, some preliminary data calculated by Raabe (2017) were compared with the equations of state. 10 compressed liquid density data were calculated by Raabe in the temperature range between 340 K and 420 K, while only two quite high pressures (20 MPa and 30 MPa) were considered. The deviations are relatively large (AAD%=0.34%, MAD%=0.60%), but the results are clearly promising and can be improved in the near future.

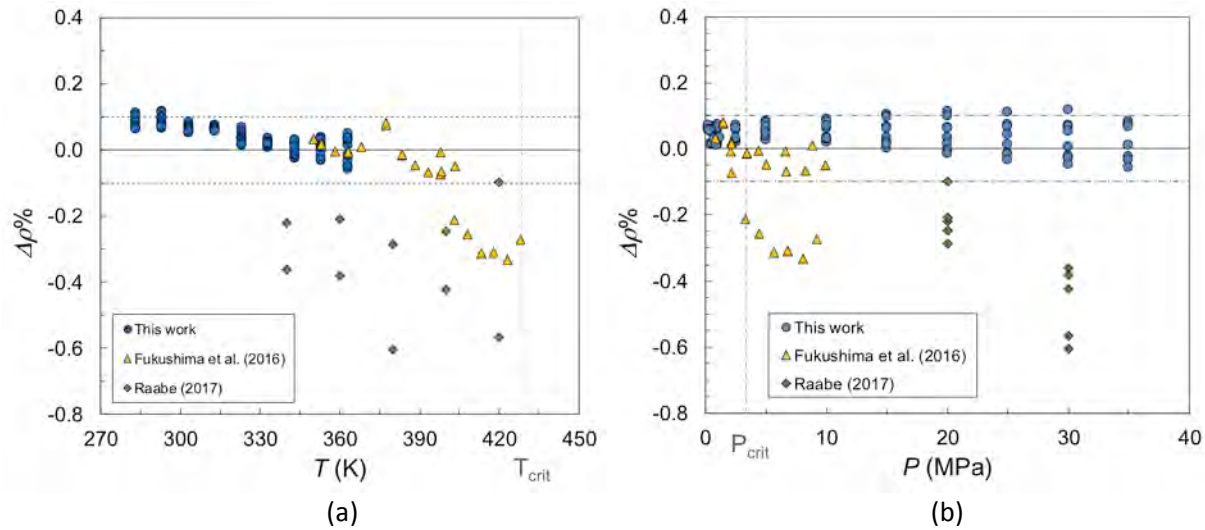

Figure 2: Deviations from Refprop 10.0 of experimental compressed liquid density data measured in this work and those measured by Fukushima et al. (2016) and Raabe et al. (2017). (a) deviations as a function of temperature; (b) deviations as a function of pressure

3.3.2 Saturated liquid density data

The deviations of extrapolated saturated liquid density data, reported in Table 2, from the saturated density calculated with Refprop 10.0, are represented in Fig. 3(b). The data obtained in this work show deviations always within ±0.1%, with AAD%=0.04%, and increase almost monotonously from negative deviations at low temperature to positive deviations at high temperatures. The data of Fukushima (2016) show higher average deviations (AAD%=1.5%) and relatively high maximum deviation (0.35%), with quite scattered behavior in the range of measurements temperature.

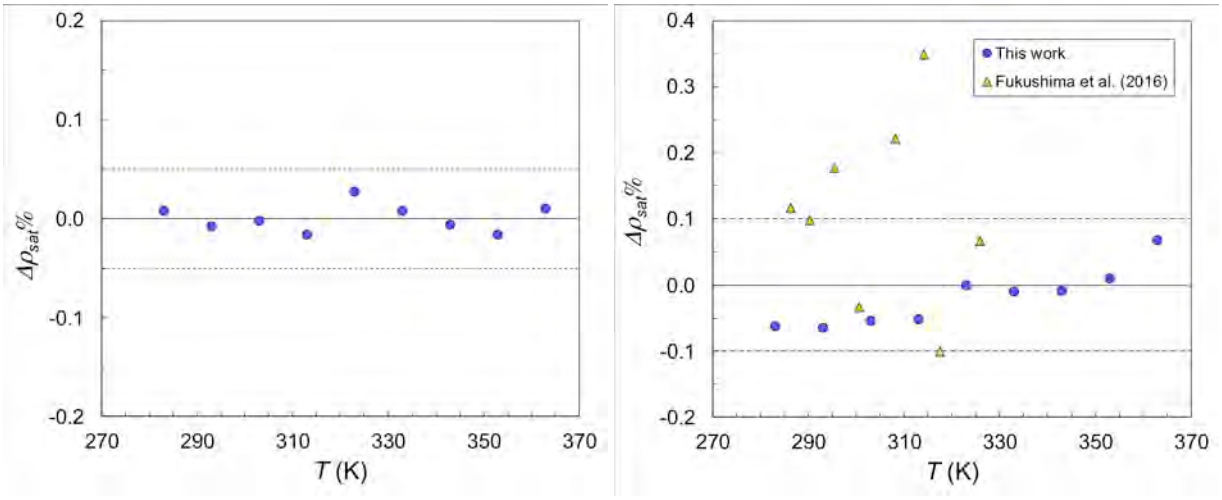

(a) (b)

Figure 3: (a) deviations of this work saturated liquid density values from Eq. (1); (b) deviations of this work saturated liquid density values and those found in the literature from values calculated with Refrpop 10.0

3.5. Comparisons with other hydrofluoroolefins (HFOs)

As anticipated in the introduction, R1224yd(Z) can be considered, like R1234ze(Z) and R1233zd(E), as a low GWP substitute for R245fa due to their similar NBP. In view of the necessity to select one of these fluids for their applications and just to give an idea of their relative volumetric properties in the liquid phase, Figure 4 show the density behavior of these fluids at two isotherms (300 and 360) K. It is evident that R1224yd(Z) is the fluid with the highest density at both temperatures, and this could give some advantage in terms of reduced dimensions for the components of the machines where it could operate as working fluid.

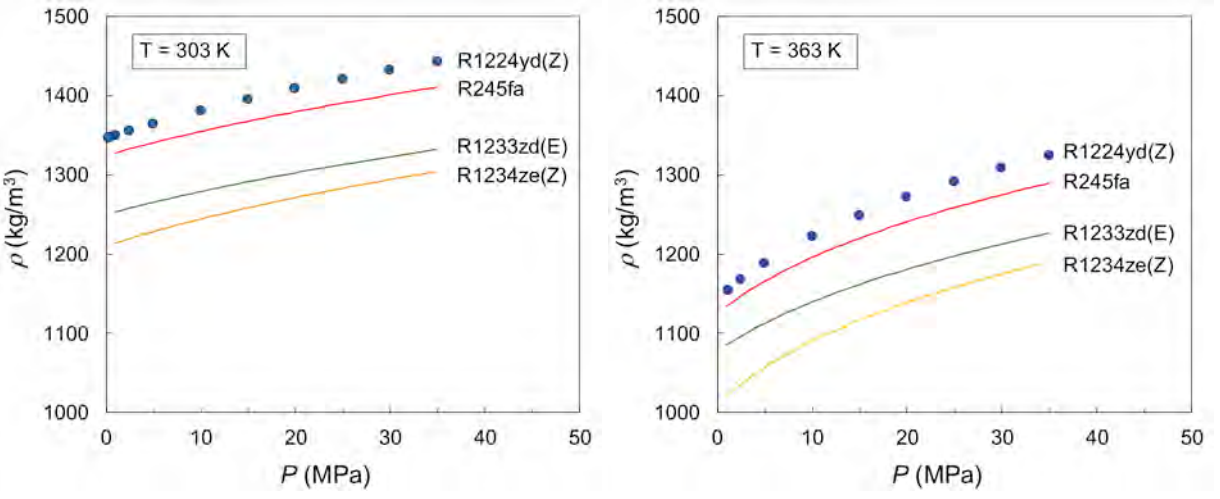

Figure 4: Comparison between the experimental R1224yd(Z) compressed liquid densities at two temperatures (303 and 363) K with those calculated at the same temperatures for three alternative refrigerants (R245fa, R1233zd(E) and R1234ze(Z)

4. CONCLUSIONS

The paper reports 90 compressed liquid density data for the refrigerant R1224yd(Z), measured through a vibrating tube densimeter at isothermal conditions in the range of temperatures between 283 K and 363 K, with pressures from saturation to 35 MPa. A comparison with the fundamental equation of state developed by Akasaka et al. (2017) and implemented in the Refprop 10.0 data base, showed a good agreement (AAD%=0.046%, MAD%=0.12%) between the experimental and the calculated data, especially considering that most of the data are in the extrapolation areas of the equation. The data will be used to further improve the equation of state. Moreover, 10 saturated liquid density data were extrapolated showing a good agreement with the saturation density calculated with the fundamental equation of state. Finally, a correlation was developed to allow the calculation of saturated liquid density as a function of temperature.

ACKNOWLEDGEMENTS

The authors thank AGC Inc. for donating the R1224yd(Z) sample, dr. Raabe (Technische Universität Braunschweig) and dr. Fukushima (Asahi Glass Corporation) for the private communication of density data.
The authors thank Mr. Francesco de Pinto for his help during the measurements.

NOMENCLATURE

AAD%	Percentage Absolute Average Deviation (%)	NBP	Normal Boiling Point (K)
GWP	Greenhouse Warming Potential (-)	P	pressure (MPa)
MM	molar mass (kg kmol^{-1})	T	temperature (K)
MAD%	Percentage Maximum Absolute Deviation (%)		
	Greek Symbols		
ρ	density (kg/m^3)	τ	1-T/T_{crit} (-)
ω	acentric factor (-)		
	Subscripts		
crit	critical	*r*	reduced
sat	saturation	*REFP*	Refprop 10.0

REFERENCES

Akasaka, R., Fukushima, M., Lemmon, E.W., 2017. A Helmholtz Energy Equation of State for cis-1-chloro-2,3,3,3-Tetrafluoropropene (R-1224yd(Z)). 21st European Conference on Thermophysical Properties (ECTP), Graz, Austria, September 3-8, 2017.

Bobbo, S., Di Nicola, G., Zilio, C., Brown, J.S., Fedele, L., 2018. Low GWP halocarbon refrigerants: a review of thermophysical properties, Int. J. Refrig., 90, 181-201.

Bobbo, S., Fedele, L., Scattolini, M., Camporese, R., 2002. Compressed liquid densities, saturated liquid densities, and vapor pressures of hexafluoro-1,3-butadiene (C4F6). J. Chem. Eng. Data, 47, 179−182.

Bobbo, S., Scattolini, M., Fedele, L., Camporese, R., 2004. Compressed liquid densities and saturated liquid densities of HFC-365mfc. Fluid Phase Equilibr., 222−223, 291−296.

Lemmon, E. W., Bell, I.H., Huber, M. L., McLinden, M. O., 2018. NIST Standard Reference Database 23, Reference Fluid Thermodynamic and Transport Properties (REFPROP), version 10.0, National Institute of Standards and Technology: Gaithersburg, MD

Fukushima, M., 2016. Private communication.

McLinden, M.O., A.F. Kazakov, J.S. Brown, Domanski, P., 2014. A thermodynamic analysis of refrigerants: Possibilities and tradeoffs for Low-GWP refrigerants. Int. J. Refrig., 38, 80–92

Raabe, G., 2017. Private communication (preliminary simulation data).

Regulation (EU) No. 517/2014 of the European Parliament and of the Council of 16 April 2014 on fluorinated greenhouse gases and repealing Regulation (EC) No 842/2006 Text with EEA relevance. Off. J. Eur. Union: Legis. 2014, 150, 195−230.

Manuscript ID: 236
DOI: 10.18462/iir.icr.2019.0236

Utilization of CO_2 and R1234ze(E) as refigerant: Determination of mixture volumetric properties at the vicinity of critical point

Jiangjun XIE[(a)], Alain VALTZ[(b)], Christophe COQUELET[(b)], Haitao HU[(a)]

[(a)] Institute of Refrigeration and cryogenics, Shanghai Jiao Tong Univ., 800 Dongchuan Rd, 200240
[(b)] Mines ParisTech, PSL University, CTP- Centre of Thermodynamics of Processes, 35 rue Saint Honoré 77305 Fontainebleau Cedex France
christophe.coquelet@mines-paristech.fr.

ABSTRACT

In recent years, binary and multi-mixture refrigerant have been developed to increase the cycle efficiency and reduce environmental effects. The most promising mixture are composed of R1234yf or R1234ze(E) with HFC or natural refrigerants. However, the experimental data of new mixture is still in short. In this work, we present the results obtained for the temperature-density diagram of CO_2 and R1234ze(E) at the vicinity of the mixture critical point for 4 different compositions. Measurements were done by an equipment whom technique is based on synthetic visual method with observation of disappearance of liquid-vapor interface. Cubic equation of state and Refprop model were used to correlate the data. With cubic EoS, the critical point is determined by considering Heidemann et Michelsen method. The results obtained show a good agreement between experiments and proposed modelling.
Keywords: Working fluid, fluid thermodynamics, experimental work, modeling

1. INTRODUCTION

It was admitted that hydrofluorocarbons (HFC's) are banned for utilisation in refrigeration and climatisation. This is the consequence of an environmental politic started in 1985 with Protocol Montreal: Regulations concerning ozone-depleting substances have prohibited the use and the production of chlorofluorocarbons (CFC's) and of hydrochlorofluorocarbons (HCFC's) worldwide. Consequently, hydrofluorocarbons (HFC's) were proposed as alternative refrigerants but they have non negligible global warning potentials (GWP's). Consequently, after the Kyoto protocol in 1997, regulations concerning GWP have progressively prohibited the utilisation of these latter chemicals. The F-gas regulations (2009) were created in order to plan the utilisation and replacement of these refrigerants. In 2016, at Kigali amendment (2016), the utilisation of HFC was definitively banned. The 2009 F-gas regulation fixes the limits of GWP for each year. In 2018, the objective is to use fluids (pure compounds or mixtures) with GWP < 1300. close to the GWP of R134A (GWP = 1300, Bolaji, 2010). In 2020, the objective will be to use fluids with GWP < 1000. In order to reach the objectives in terms of GWP, two solutions exist: the first one consists in developing new fluids with low GWP values, such as hydrofluoroolefines (HFO's). The second one consists in developing new blends of refrigerants (less than 3 components).

The development of refrigerators, heat pumps or organic Rankine cycle machines requires the knowledge of the thermodynamic properties and the phase diagram of working fluids. For example, to design heat exchangers with and without phase changing, it is important to know the state of the fluid and to evaluate the level of the temperature or pressure glide. In this case, it is important to know if the fluid behaves like a pure component (azeotropic behaviour) or not. So, knowledge of phase diagram is essential. Coquelet and Richon (2009) and Privat and Jaubert (2013) have revisited the Scott and van Konynenburg (1980) classification and applied it to refrigerant-containing systems.

Phase diagram are predicted in general by equation of state. The most famous EoS's are of cubic type, such as equation 1, and all the thermodynamic properties like residual enthalpy can be calculated from such an EoS.

$$P = \frac{RT}{v-b} - \frac{a(T)}{v+ubv-wb^2} \qquad \text{Eq. (1)}$$

where u and w are EoS parameters (for the Peng-Robinson EoS, u = 2 and w = -1), a is the attractive term [Pa.m^3.mol^{-1}] and b is the molar co-volume [m^3.mol^{-1}]. They are very easy to use, do not require a lot of experimental data and can be used to opredcit other thermodynamic properties mlike density or heat capacity. Denisty prediction s are very importnatr in the context of heat transfer (estimation of Reynolds and Prandlt numbers for the estimation of heat transfer coefficient) and for the design of compressor and evaluation of pressur drop.

For the calculation of phase equilibrium, the thermodynamic approach is based on the isofugacity criterion. There are two main ways to solve equality of fugacities. The dissymmetric or "γ-Φ" approach consists in using two different models for describing the vapor phase and the liquid phase: for instance, a cubic EoS like equation 1 for the vapor phase and an activity coefficient model for the liquid phase. Unfortunately, this method is limited to the low or moderate pressures and can not calculate the critical point of a mixture. The second one consists in using a symmetric (or "Φ-Φ") approach. The model is identical for the liquid and vapour phases. Mixing rules are necessary to calculate the parameters *a* and *b* of the EoS for the mixtures. Two types of mixing rules are frequently used:

- The van der Waals mixing rules (known as quadratic mixing rules).
- g^E type mixing rules combining an EoS with an activity coefficient model. The first mixing rule belonging to this approach was developed by Huron and Vidal (1979) with an infinite pressure reference. Other authors used zero pressure reference for low pressure VLE. The thermodynamic models have to represent as accurate enough the phase diagram et so the mixture critical point.

In order to obtain the parameters of a cubic EoS, experimental data are needed, mainly VLE data. Concerning estimation of critical point or densities at the vicinity of critical point, it is recoemmended to use adapated equipment based on synthetic method. In this communication, we proposed to investigate the phase diagram of the binary system CO_2 + R1234ze(E). We will present results reviously published and new results concerning the volumetric properties at the vicinity of the critical point of several mixtures studied.

2. PHASE DIAGRAM OF THE CO_2+R1234ze(E)BINARY SYTEM

This system was previously investigated by Wang et al. (2018). The method of measurement is based on analytical method where the composition of each phase is obtained by analysis after sampling (direct sampling method). An in-house developed apparatus is used in this work to perform the VLE data measurement. Two electromagnetic capillary samplers Rapid On-Line Sampler-Injector (ROLSI®, patent FR 2.853.414) offer precise micro-sampling of mixture equilibrium phases and are connected to a gas chromatograph to analyze phase composition. The method is fully descrbed in the paper of Wang et al.. The Peng Robinson EoS(1976) is used to correlate the data. In order to have the best description of the phase diagram (Coquelet et al., 2009), we have considered the Wong Sandler mixing rule (1992) coupled with the NRTL (Renon and Prausnitz, 1968) activity coefficient model (Eqs 1 to 4). Figure 2 presents the complete phase diagram.

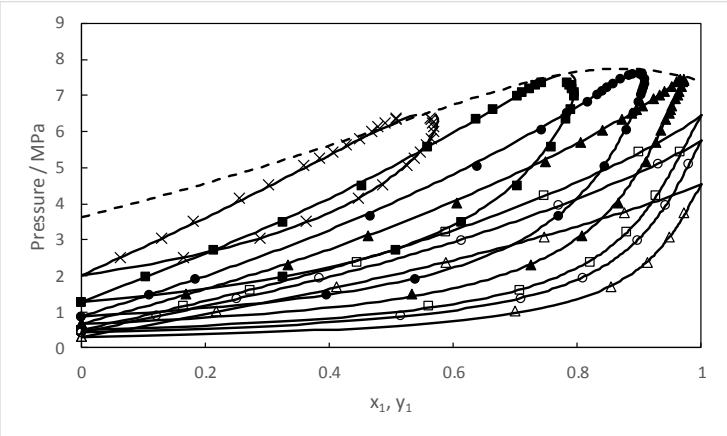

Figure 1: Pressure as a function of CO_2 mole fraction in the CO_2 (1) + R-1234ze(E) (2) mixture at different temperatures and critical line. Solid lines: calculated with PR EoS, Wong-Sandler mixing rules and NRTL activity coefficient. Dashed line: calculated mixture critical line (Wang et al.)

Binary interaction parmeters of the model are adjusted directly to VLE data. Using the power laws with asymptotic behavior at critical point (Ungerer et al., 2005), at a given temperature, the mixture critical composition and pressures can be calculated (Eqs. 2-3) using the experimental data highly close to the critical point.

$$\frac{y+x}{2} - x_c = \lambda_1 (P_c - P) \quad \text{Eq. (2)}$$

$$y - x = \lambda_2 (P_c - P) + \mu (P_c - P)^{\beta} \quad \text{Eq. (3)}$$

x and *y* are molar fraction in the liquid and vapor phases at equilibrium for a given temperature T and at pressure *P*. β =0.325 is a characteristic universal exponent (Sengers et al. 2000). λ_1, λ_2 and μ are adjustable coefficients regressed from experimental VLE data near the critical point. Fig. 2 presents the critical temperature and critical pressure as a function of critical point composition. Heidmann and Khalil algorithm (1980) is employed to compute the critical line with our model. Helmholtz energy is used asthermodynamic potential and it is considered that the critical point corresponds to the limit of stability. In 1998, Stockfleth and Dohrn improved this method by generalizing the previous algorithm. We have chosen their algorithm to compute the critical line using our model. The binary parameters are thus obtained by fitting VLE experimental data in the CO_2 supercritical domain. Mixture critical line is plotted in Fig. 1. The proposed model is in good agreement with experimental data and can predict the phase diagram of the system.
The model developed using VLE data will be used to correlate the new experimental data obtained concerning the volumetric properties of the CO_2+R134ze(E) binary system at the vicinity of the mixtrure critical points.

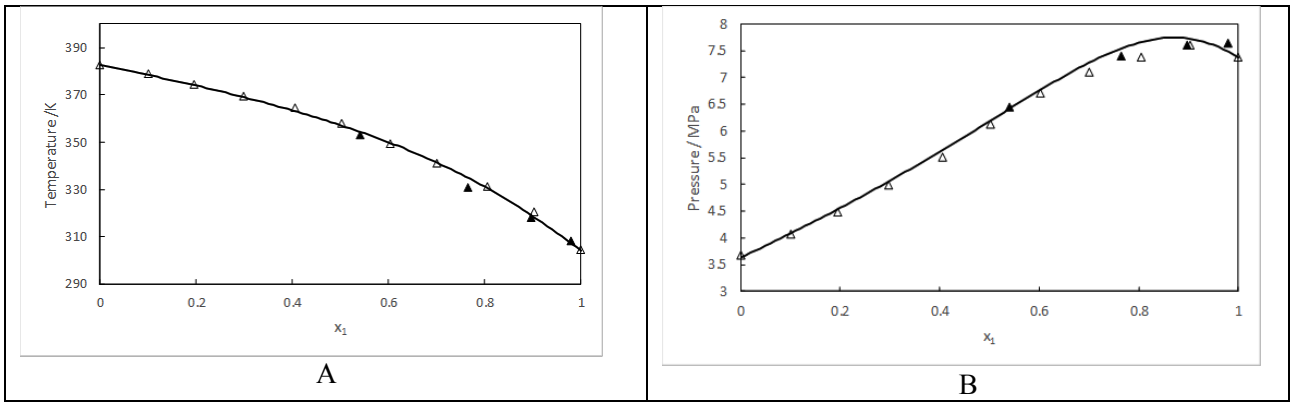

Figure 2: Critical temperature (A) and pressure (B) of the binary system CO_2 (1) + R-1234ze(E) (2). Solid line: calculated using our model. Δ: experimental data from Juntaratchat et al. (2014), ▲: predicted using power laws with asymptotic behavior at critical point.

3. MEASUREMENT OF CRITICAL PROPERTIES AND DENSITIES

The accuracy of the experimental data depends strongly on the method used. Open circuit methods include several different techniques. The method currently apply for the determination of critical properties are generalyy based on synthetic method. The global composition of the mixture is known a priori, so that no sampling and analysis are necessary. The composition of each phase is determined by solving mass balance equations (indirect methods) or the system is brought to its bubble or dew point. Concerning critical point measurements, the technique consists in observing the critical opalescence by controlling the temperature and the flow of the mixture circulating through the equilibrium cell. Fig 3 describes the critical point apparatus. This method was used by Soo et al. (2010) and Juntaratchat et al.(2014) for the determination of critical temperature and pressure.

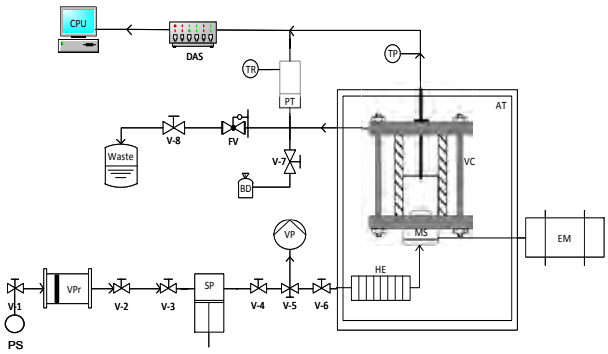

Figure 3: Schematic diagram of the critical point measurement apparatus. PS: pressurized source; VPr: volumetric press; SP: syringe pump; VP: vacuum pump; HE: heat exchanger; EM: electric motor; MS: magnetic stirrer; VC: view cell; AT: air thermostat bath (oven); TP: platinum resistance temperature probe; PT: pressure transducer; TR: temperature regulator; BD: bursting disc; FV: flow regulation valve; DAS: data acquisition system; CPU: central processor unit; V: valve

Volumetric properties data at the vicinity of the critical point are obtained using a "synthetic-visual method". The principle is to add certain amounts of mixture into an equilibrium cell and to measure the temperature and pressure by observing the disappearance of vapor-liquid interface. The Fig. 4 reminds the $T-\rho$ diagrams for a pure component and a mixture. It is important to note that the locations of critical point are different. Similar graph can be plotted by considering $P-\rho$ diagram.

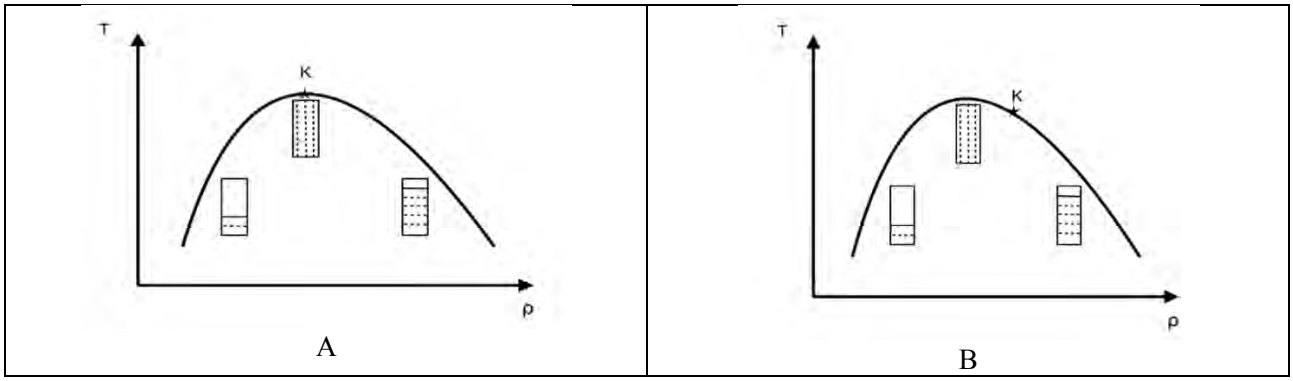

Figure 4: T-ρ diagram for a pure component (A) and a mixture (B)

On the Fig. 4, the curve at left represents the vapor density and the curve at right represents the liquid density. These two curves converge at the critical point, which is noted as 'K'. The corresponding temperature for vapor densities are determined at the moment when the last drop of fluid disappears if the cell is heated and at the moment when the first drop of fluid appears if the cell is cooled down. The corresponding temperatures for liquid densities are determined at the moment when the last bubble disappears if the cell is heated and at the moment when the first bubble appears if the cell is cooled down. For the points at the vicinity of the critical point, the

corresponding temperatures are measured at vapor-liquid equilibrium when the opalescence is observed.

Fig. 5 presents the schematic diagram of the synthetic visual VLE measurement apparatus used for the density measurement at he nvicinity pof the critical point. The apparatus is composed by three main parts: the equilibrium cell, the volumetric pump and the data acquisition unit. The EC is comprised of a sapphire tube which contains the equilibrium mixture, sealed by two titanium flanges respectively at the top and bottom. The top titanium is connected with a platinum probe PP2 and a pressure transducer PT2. The platinum probe aims to measure the temperature at the top of the cell and the pressure transducer is used to measure the pressure in the cell. At the bottom titanium, a magnetic stirrer is installed to accelerate the phase transition and a platinum probe PP3 to measure the mixture temperature at bottom. Three valves are connected with the cell. The mixture is added into the cell when the valve 4 is open and the addition is stopped when the valve 4 is closed. The valve 8 aims to control the usage of the pressure transducer PT2, the real-time pressure data of cell is read when the valve 8 is open. The valve 5 is connected with two values, the valve 6 aims to remove the mixture in the cell and the valve 7 is connected to the vacuum pump. The platinum probe in the middle of the cell PP4 aims to measure the center temperature of the cell. The volume of the cell is 12.8315 ml.

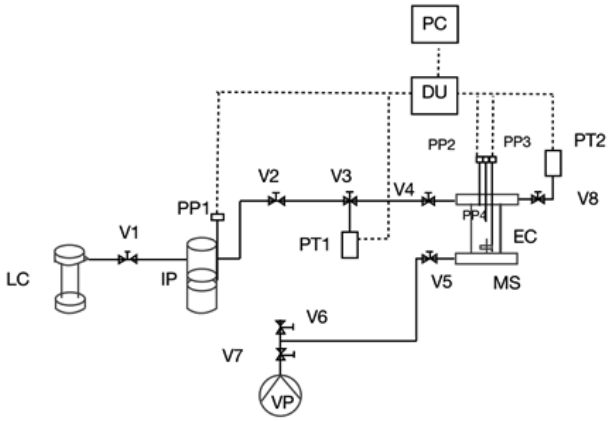

Figure 5: Schematic diagram of synthetic visual VLE measurement apparatus, LC: loading cell; EC: equilibrium cell; V: valve; IP: ISCO pump; PP: platinum probe; PT: pressure transducer; PC: personal computer; VP: vacuum pump; DU: data acquisition/switch unit; MS: magnetic stirrer; Full line: tube; Dotted line: electric wire

The volumetric pump consists of two parts: a syringe pump (ISCO Model 100DM) and a pump controller (ISCO SERIES D). Refrigerant flows into the syringe pump with controlled flowrate and the controller enables to regulate the pressure in the pump. In this work, the pressure of the refrigerant in the ISCO ump is kept at 90 bars. The ISCO pump is connected with a pressure transducer (DRUCK 0-150 bars) PT1 and a platinum probe PP1 to collect the temperature and pressure data in the pump which enables to calculate the density of the refrigerants. The valve 1 is used to control the mixture addition and the valve 3 is used to control the usage of PT1. All the platinum probes and pressure transducers are connected to a LXI data acquisition/switch unit (Agilent 34972A) which is linked to a personal computer using the interface of Agilent BenchLink Data Logger 3. During the experiment, temperatures and pressures collected by the sensors are read and saved in the system.

The volumetric properties experimental data of four CO_2 and R1234ze(E) mixtures using synthetic visual method are presented Table 1. For the mixture 79.6% CO_2 and 20.4% R1234ze(E), there is no data for the pressure due to the limit of operating of the apparatus. An estimation was made for the uncertainties of densities and the order of magnitudes is calculated, where $u(\rho) \cong 10\, mol \cdot m^{-3}$ with u(p)=0.07 MPa and u(T)=0.01 K.

4. PRESENTATION OF THE RESULTS

Our results are presented in Figs. 6 and 7. We can observed that if the mole fraction of CO_2 in the mixture is increasing, the critical point temperature decreases and the temperature difference

between maximum point and critical point increases. We have compared our data with the prediction from our model based on Peng Robinson EoS. In order to do that, we have calculated densities at the bubble and dew pressures. Figs. 6 and 7 reval that the experimental and calculated densities are in good agreement but predicted densities do not respect assympotic behaviour. Corrections like the ones applied in crossover EoS (Dicko and Coquelet, 2010, Janecek et al. 2000) have to be considered to improvge the denisy predictions.

Table 1. Compositon of the systems studied

Expected composition in mole fractions		Real composition in mole fractions	
CO_2	R1234ze(E)	CO_2	R1234ze(E)
0.2	0.8	0.224	0.776
0.4	0.6	0.408	0.592
0.6	0.4	0.6	0.4
0.8	0.2	0.796	0.204

Our results were also compared with the prediction from REFPROP 10 (Lemmon et al., 2013). Binary interaction parameters for the binary system CO_2+R1234ze(E) are implemented. These parameters were adjusted on molecular simulation data from Raabe (2013). Wang et al. have shown that the the prediction of VLE data using REFPROP model are in very good agreement with our experimental data for temperature tower than the critical temperature of CO_2. For temperature higher tghan the critical temperature of CO_2, the data predicted by molecular simulation are not in good agreement with the experimental data (Wang et al.).
Consequently, by analysis the Figs. 6 and 7, we can conclude that fundamental EoS (REFPROP 10) can not be used to predicted density at the vicinity of the mixture critical point and density data are strongly required. Moreover, VLE data for temperature higher than the critical temperature of CO_2 have to be used to fit the binary interaction parameters of the Helmoltz type EoS.

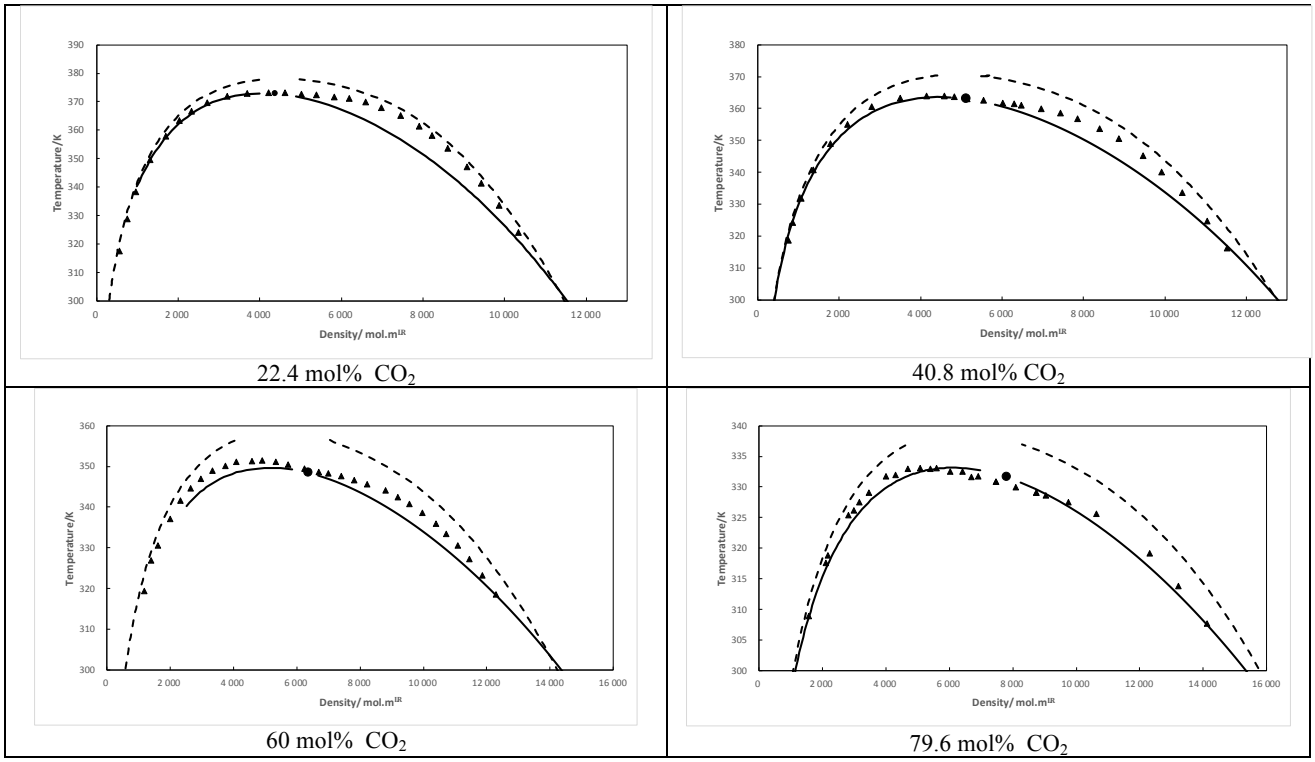

Figure 6: T-ρ diagram for four CO_2 and R1234ze(E) mixture. ▲: our experimental data, solid line: our model, : •: calculated critical point, dashed line: REFPROP v 10, yellow symbol: critical point from Wang et al. (1996)

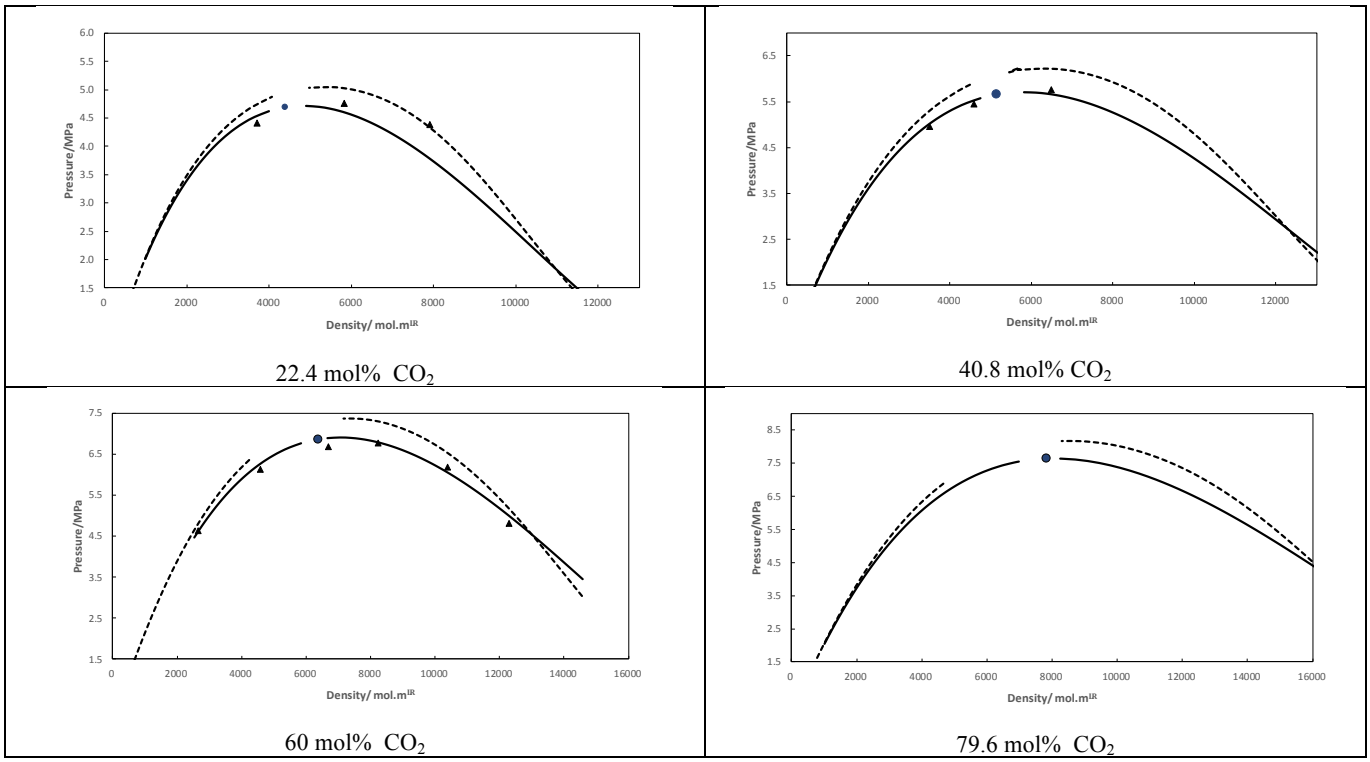

Figure 7: T-ρ diagram for four CO_2 and R1234ze(E) mixture. ▲: our experimental data, solid line: our model, : •: calculated critical point, dashed line: REFPROP v 10, yellow symbol: critical point from Wang et al. (1996)

5. CONCLUSIONS

The accurate knowledge of thermodynamic properties of a refrigerant is necessary to evaluate the performance of a refrigeration or heat pump cycle, due to their direct relation to the energy balance equations (Coquelet and Richon, 2009). Therefore, in order to help evaluating the relevance of this mixture for applications, the vapor liquid equilibrium properties of the binary mixture CO_2 + R1234ze(E) was experimentally investigated, i.e. VLE data (Wang et al. 2018) and new density data at the vicinity of the mixture critical point. These data are very important for the design of transcritical system. Our study reveals without VLE and density data, fundamental EoS like the one program in REFPROP are not accurate enough for the prediction of phase diagram when temperature is higher than the critical temperature of CO_2.

NOMENCLATURE

v	molar volume ($m^3.mol^{-1}$)	P	pressure (Pa)
f	fugacity (Pa)	T	temperature (K)
u,w	equation of state parameter	x,y	liquid and vapour Mole fraction
μ	assymptotic law parameter	λ	assymptotic law parameter
E	excess property	i,j	molecular species
C	critical property		

REFERENCES

Bolaji, B. O. 2010. Experimental study of R152a and R32 to replace R134a in a domestic refrigerator. Energy 35(9), 3793-3798.

Coquelet, C., Chareton, A., Valtz, A. et al. 2003. Vapor-Liquid Equilibrium Data for the Azeotropic Difluoromethane+ Propane System at Temperatures from 294.83 to 343.26 K and Pressures up to 5.4 MPa. J. Chem. Eng. Data 2, 317-323.

Coquelet, C., Richon, D. 2009. Experimental Determination of Phase Diagram and Modeling. Application to Refrigerant Mixtures. Int. J. Refrigeration 32, 1604-1614.

Dicko, M., Coquelet, C. 2011. Application of a new crossover treatment to a generalized cubic equation of state. Fluid Phase Equilib. 302, 241-248.

Heidemann, R. A., Khalil, A. M. 1980. The calculation of critical points," AIChE journal 26,769-779.

Huron, M. J., Vidal, J. 1979. New mixing rules in simple equations of state for representing vapour-liquid equilibria of strongly non ideal mixtures. Fluid Phase Equilib. 3, 255-271.

Janeček, J., Paricaud, P., Dicko, M. et al. 2015. A generalized Kiselev crossover approach applied to Soave-Redlich-Kwong equation of state. Fluid Phase Equilib. 401,16-26.

Juntarachat, N., Valtz, A., Coquelet, C. et al. 2014. Experimental measurements and correlation of vapor-liquid equilibrium and critical data for the CO_2 + R1234yf and CO_2 + R1234ze(E) binary mixtures, Int. J. Refrigeration 47, 141-152.

Lemmon, E. W., Huber, M. L. McLinden, M.O. 2018, NIST Standard Reference Database 23: Reference Fluid Thermodynamic and Transport Properties-REFPROP, Version 10.0, National Institute of Standards and Technology.

NEP, 2017.The Kigali Amendment to the Montreal Protocol: HFC Phase – down . Retrieved online at: http://www.unep.fr/ozonaction/information/mmcfiles/7809-e-Factshe et_Kigali_Amendment_to_MP.pdf

Peng, D.Y., Robinson, D.B.1976. A new two parameters Equation of State. Ind. Eng. Chem. Fund.15, 59-64.

Privat, R., Jaubert, J.N. 2013. Classification of global fluid–phase equilibrium behaviors in binary systems. Chem. Eng. Res. Des. 91, 1807–1839.

Raabe ,G. 2013. Molecular simulation studies on the vapor--liquid phase equilibria of binary mixtures of R-1234yf and R-1234ze (E) with R-32 and CO_2. J. Chem. Eng. Data 58, 1867-1873.

Regulation (EC) No 1005/2009 of the European Parliament and of the Council of 16 September 2009 on substances that deplete the ozone layer (recast).

Renon, H., Prausnitz, J.M. 1968. Local compositions in thermodynamic excess functions for liquid mixtures. AIChE journal*,* 14, 135-144.

Scott, R. L., van Konynenburg, P. H. 1980. Critical lines and Phase Equilibria in Binary van der Waals mixtures, Philos. Trans. R. Soc. 298, 495-594.

Sengers, J. V., Kayser, R., Peters, C., White H. 2000. Equations of state for fluids and fluid mixtures, vol. 5, Elsevier.

Soo, C.B., Theveneau, P., Coquelet, C., Richon, D. 2010. Determination of critical properties of pure and multi component mixtures using a « dynamic-synthetic » apparatus, J. Supercritical Fluids 55, 545-553.

Stockfleth, R., Dohrn, R. 1998. An algorithm for calculating critical points in multicomponent mixtures which can easily be implemented in existing programs to calculate phase equilibria. Fluid phase equilib. 145, 43-52.

Ungerer, P., Tavitian, B., Boutin, A. 2005. Applications of molecular simulation in the oil and gas industry: Monte Carlo methods, Editions Technip.

Wang, S., Fauve, R., Coquelet, C. et al. 2019. Vapor-liquid equilibrium and molecular simulation data for carbon dioxide (CO2) + trans-1,3,3,3-tetrafluoroprop-1-ene (R-1234ze(E)) mixture at temperatures from 283.32 to 353.02 K and pressures up to 7.6 MPa, Int. J. Refrigeration 98, 362-371.

Wong, D.S.H., Sandler, S.I. 1992. A theoretically correct mixing rule for cubic equations of state. AIChE Journal 38, 671-680.

Manuscript ID: 243
DOI: 10.18462/iir.icr.2019.0243

Fundamental study on continuous pipe transportation of ice slurry

Tatsunori ASAOKA [(a)], Daiki HOSHINA [(a)]

[(a)] Shinshu University
Nagano City 380-8553, Japan, asaoka@shinshu-u.ac.jp

ABSTRACT

Ice fixation on the pipe surface causes the blockage accident of ice slurry flow. In this study, we observed behavior of ice slurry flowing in transparent tube and investigated the ice fixation, which caused by adhesion and accumulation of ice particles. We focused the fixation at a contraction part, because the fixation seems to occur around valves or joint parts of the pipe. From the results of the experiment, we suppose the adhesion (initial ice fixation) and the accumulation (growth of the fixed ice) results from the different reasons. As the special feature of ice, the flow condition in front of the contraction part affects the ice fixation. Because of large adhesion force of ice, the block ice flowing from upper stream stacks at the contraction part and leads the ice accumulation.
Keywords: Ice Slurry, Heat Transfer, Fixation, Pipe Transportation.

1. INTRODUCTION

Ice slurry is liquid-solid two-phase mixture, which includes many fine ice particles in water or aqueous solutions. Ice slurry is good as secondary refrigerant and thermal storage material because of its good fluidity, heat transfer capability and heat density. We can transport high density cooling heat by pipe transportation of ice slurry. However, if we use ice slurry under inappropriate conditions, it causes the blockage of the pipe, which must be avoided in practical use. In general two-phase flow, it was known that the blockage occurs with high solid fraction and low flow velocity (Doron and Barnea, 1996). Additionally, ice slurry will have a special feature. For example, in ice slurry, fixation of the ice particles on the pipe surface occurs because of its strong adhesion force of ice, resulting in the blockage. Under the inappropriate condition, ice particles included in the ice slurry adheres and fixes on the pipe surface. Then size of the fixed ice increases owing to accumulation of the other ice particles. The mechanism of the ice fixation should be comprehended to avoid the blockage.

In this study, we observed the behavior of ice slurry flowing in transparent tube and investigated the fixation of ice particles. We focused the fixation at a contraction part in the flow channel, because we found that the fixation seems to occur around valves or joint parts of the pipe, in our previous work (Asaoka et al., 2016).

2. EXPERIMENT APPARATUS

Fig. 1 shows the experiment apparatus. Ice slurry was prepared in the ice slurry tank beforehand. The ice slurry was produced from 5 mass% ethanol solution, and the initial IPF (Ice Packing Factor) is about 20mass%. During the experiment, the ice slurry was circulated via Coriolis flow meter, entrance section and test section by using gear pump. Test section is the transparent acrylic pipe, of which inner diameter is 30mm and length is 200mm, having contraction part, of which diameter is 4mm, length is 15mm, as shown in Fig. 2a. When we investigate the effect of the inflow condition, we use the test section having double contraction parts. As shown in Fig. 2b, two acrylic pipes are combined. The diameter of the upper contraction part is 4mm, and the lower is 12mm. Entrance section, which diameter is the same with the test section; 30mm and the length is 1000mm is established below the test section. We observed the ice slurry flows through the pipes from bottom to up.

Fig. 3 is the photograph of the test section taken in the typical experiment. Under the condition of Fig. 3, the fixation of ice particles do not occur. However, under a specific conditions, the fixation of ice particles occurs around the contraction part.
The flow velocity of the ice slurry was represented as Reynold s Number, Re. For the calculation, inner diameter of the test section (30mm) is used as the characteristics length and kinematic viscosity of the carrier liquid (5 mass% ethanol solution) is used. We can estimate IPF of the ice slurry from the apparent density of the ice slurry, which can be measured by Coriolis flow meter (Kumano, 2010).
The observation was carried out at 3 min interval. The IPF and flow velocity were varied in the experiments. We confirmed the repeatability by performing every experiment 3 times under the same condition.

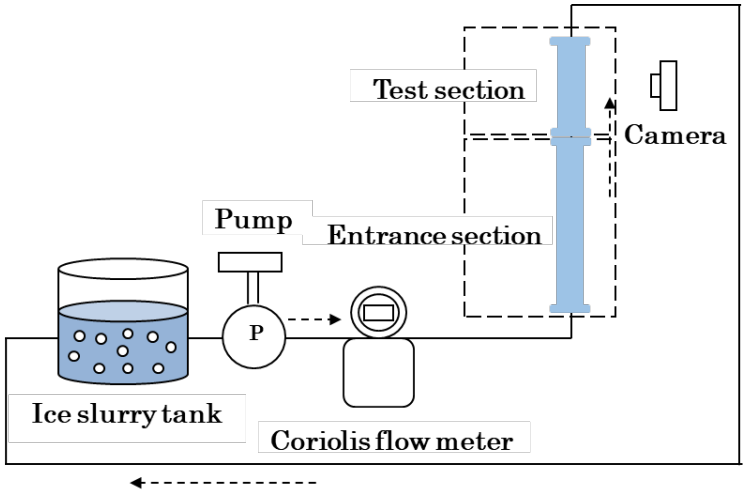

Figure 1: Experiment apparatus



(a) Single contraction **(b) Double contraction**

Figure 2: Photograph of the test section; inner diameter is 30mm



Figure 3: Appearance of ice slurry flow at test section; Re 1000, IPF 20mass%

3. RESULTS AND DISCUSSION

3.1. Fixation Characteristics at the Contraction Part

Fig. 3 shows the pictures of the test section taken during the experiments. White dashed lines in the figures represent the fixed ice. We increased Re from 300 to 1 500 at the 3 min interval. IPF of the slurry was initially 7 mass% and decreased with time.

When Re is 300, as shown in Fig. 4a, ice particles adhered to the wall surface at the contraction part. Then flowing ice particles were trapped and accumulated there, and the size of the block ice, which consist of fixed ice particles, increased. Until Re increased to 1 000, the accumulation of ice particles continued, and the size of the block ice became larger, as shown in Figs. 4b and 4c. The rate of the accumulation decreased as Re increased. Just after Re was increased to 1 500, the block ice was separated from the wall surface and flowed out, as shown in Fig. 4d.

We suppose that the adhesion results from the still ice particles trapped in the dead water region. The separation is occurred by the shear stress between the block ice and flowing slurry. As flow velocity increases, both the size of the dead water region and the shear stress increases. The effect of the shear stress becomes larger around Re is 1 500.

The fixation characteristics are summarized in table 1. We confirmed that if we start the experiment form Re above 1 000, the adhesion do not occur. When Re is 1 000, accumulation occurs but adhesion do not occur. This means that the mechanism of adhesion and accumulation should be different.

We performed each experiment 3 times under the same condition, and confirmed that the results have repeatability. IPF of slurry have little influence on the fixation characteristics.

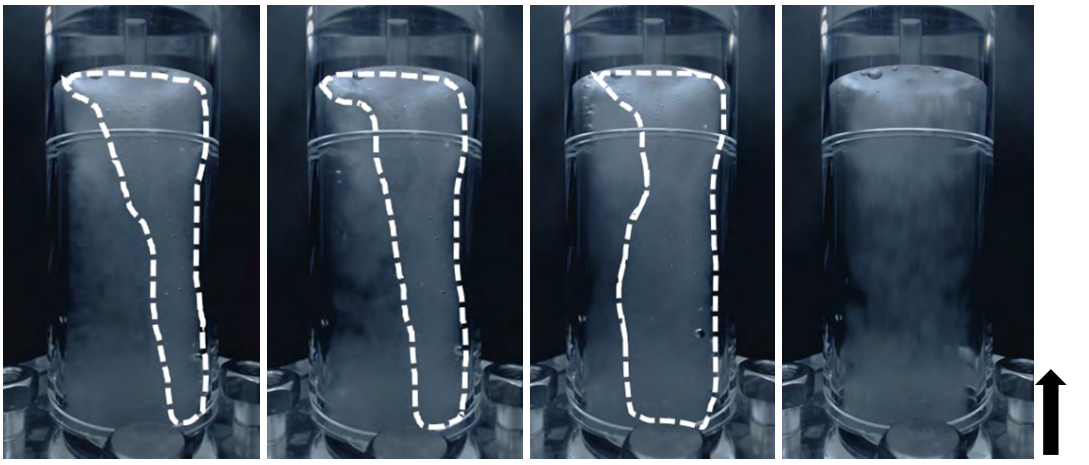

(a) Re = 300 (IPF of slurry, 6.3mass%) **(b) Re = 500 (5.4mass%)** **(c) Re = 1000 (4.9mass%)** **(d) Re = 1500 (4.8mass%)**

Figure 4: Fixation characteristics of ice particles at the contraction part

Table 1. Relationship between the fixation characteristics and Reynolds number

Reynolds number, Re	Adhesion	Accumulation	Separation
300	Yes	Yes	No
500	Yes	Yes	No
1 000	No	Yes	No
1 500	No	No	Yes

3.2. Effect of Inflow Condition

Figure 5 shows the ice fixation at the lower contraction part. We used the test section having double contraction part in this experiment. Re was 1 000, and initial IPF was 21 mass%. As can be seen in the Fig. 5a, ice adhesion occurred at the outlet of the lower contraction part. The size of the block ice, which consist of fixed ice particles, increased by the accumulation like Fig. 5b. Just after Fig. 5b, the block ice separated from the wall accidentally as shown in Fig. 5c. The separated block ice was carried along the slurry flow to the upper contraction part. Then, the block ice stuck at the contraction part and led the ice accumulation.

This should be a special feature for ice, because of its strong adhesion force. The ice particles trapped at lower contraction part agglomerate and formed large block ice. The block ice becomes hard with time. Because the adhesion force of ice is strong, the block ice cannot be broken when it impacts the wall of contraction part, and leads the ice accumulation.

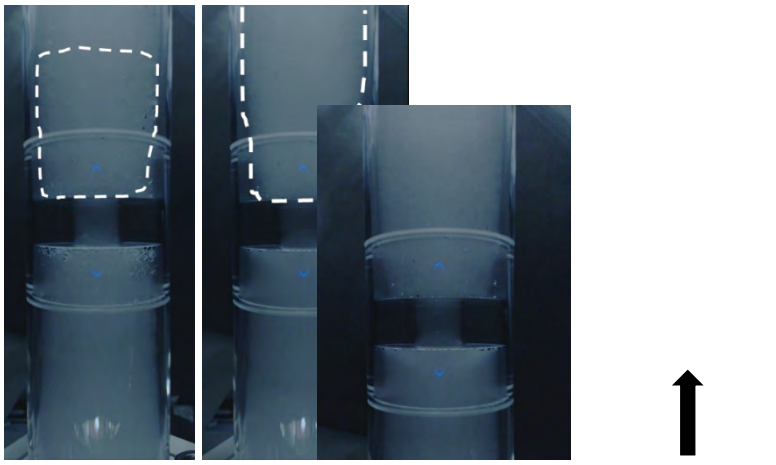

(a) 1min (IPF of slurry, 21mass%) **(b) 12min (16mass%)** **(c) Just after (b)**

Figure 5: Fixation characteristics of ice particles at the lower side of the double contraction part

4. CONCLUSIONS

We observed the behavior of ice slurry flowing in transparent tube and investigated the fixation of ice particles. We focused the fixation at a contraction part, because the fixation seems to occur around valves or joint parts of the pipe. When flow velocity is low, ice particles adhere to the wall surface at the contraction part. Then flowing ice particles are trapped and accumulates there, and the size of the block ice, which consist of fixed ice particles, increases. The rate of the accumulation decreases as flow velocity increases. When flow velocity is large, the block ice is separates from the wall surface due to the share stress between the block ice and flowing slurry. From the result of the experiment, we suppose the adhesion and the accumulation results from the different reasons, because accumulation occurs but adhesion do not occur when Re is 1 000. As the special feature of ice, the flow condition in front of the contraction part affects the ice fixation. When the pipe has the double contraction part, ice adhesion occurs at the outlet of the lower contraction part. If flow velocity is large, the block ice separated from the wall. Then the block ice

stacks at the upper contraction part because of large adhesion force of ice, and it leads the ice accumulation.

ACKNOWLEDGEMENTS

This work was supported by JSPS KAKENHI Grant-in-Aid for Young Scientists (B); Grant Number 15K17986, and Steel Foundation for Environmental Protection Technology.

REFERENCES

Asaoka, T., Tajima, A., Kumano, H., 2016. Experimental investigation on inhomogeneity of ice packing factor in ice slurry flow, International Journal of Refrigeration, 70, 33-41.

Doron, P. and Barnea, D., 1996. Flow pattern maps for solid-liquid flow in pipes, International Journal of Multiphase Flow, 2, 273-283.

Kumano, H., Hirata, T., Shirakawa, M., Shouji, R., Hagiwara, Y., 2010. Flow characteristics of ice slurry in narrow tubes, International Journal of Refrigeration, 33, 1513-1522.

Manuscript ID: 251
DOI: 10.18462/iir.icr.2019.0251

Measurements of solubility and kinematic viscosity data of refrigerants-lubricants oil mixtures

Julien BROCUS[(a),(b)], Alain VALTZ[(a)], Pascal THEVENEAU[(a)], Yannick BEUCHER[(b)], Florence DE CARLAN[(b)], Jean-Marie FOURMIGUE[(b)], Christophe COQUELET[(a)]

[(a)] MINES ParisTech, PSL University, CTP – Centre of Thermodynamics of Processes
Fontainebleau, 77305, France.
[(b)] EDF LAB LES RENARDIERES – Centre R&D
MORET LOING ET ORVANNE, 77250, France.

ABSTRACT

Thermophysical properties of refrigerant-lubricant oil mixtures are of fundamental importance in heat pump systems. In particular, the knowledge of phase diagram of these mixtures as well as kinematic viscosity is very important for the design of the heat pump. Such information can be gathered in data sheets called Daniel plots.
In this work, solubility at saturation of two hydrofluoroolefins (HFO) type refrigerants has been measured in a polyolester type lubricant oil, along with density and viscosity measurements of the liquid phase around room temperature.
P-T-x measurements were carried out by an isothermal isochoric synthetic method at two temperatures, 333 K and 383 K. Two models are also proposed: a cubic equation of state to correlate solubility data and an Eyring type model for the modeling of the kinematic viscosity.
HFOs studied include trans-1-chloro-3,3,3-trifluoroprop-1-ene (R1233zd(E)) and cis-1,1,1,4,4,4-hexafluoro-2-butene (R1336mzz(Z)).

Keywords: Lubricant, Refrigerant, Solubility, Measurement, Viscosity.

1. INTRODUCTION

In a refrigeration or heat pump system, the working fluid comes into contact with the lubricating oil used in the compressor. In most cases, the refrigerant dissolves into the oil phase, forming a mixture. The viscosity of the liquid phase will decrease as a function of the refrigerant concentration. The ensuing lack of lubrication is the main reason for a premature wear and a potential breakdown of the compressor mechanical parts.
This refrigerant-lubricating oil mixture is also an issue for the rest of the system. Even with an efficient oil separator installed, part of the lubricant oil migrates from the compressor to other parts of the system such as the evaporator, condenser, expansion device and piping. If the oil is miscible with the refrigerant over the various temperatures and pressures in the refrigeration cycle, it will naturally flow back to the compressor. However, phase separation, in the form of liquid-liquid-vapor and liquid-liquid equilibria, through the cycle can result in serious problems such as accumulation of oil on the inside of the heat exchanger tubes, reducing heat transfer and overall performance. In addition, the separation into two liquid phases (refrigerant rich and oil rich) prevents the oil flow back, progressively draining the compressor and resulting in a lack of lubrication, reducing its life span.
Hence, to avoid potential issues, the phase and transport properties of the mixture must be understood. Miscibility, solubility and viscosity of the mixture are the main factors to determine the suitability of a refrigerant-lubricating oil couple for a specific application and in particular for predicting reliable oil return.
In spite of their importance, experimental and theoretical studies involving lubricant oils are still scarce and further studies are always necessary. Especially since the restriction on the use of

hydrofluorocarbons (HFCs) as working fluids in heat pumps, refrigeration and air conditioning systems are leading to hydrofluoroolefins (HFOs) as alternatives. In parallel, as new applications for industrial heat pump are being developed, new temperature and pressure ranges are exploited, increasing the need for tools to predict the behaviour of these mixtures.
Data sheets in the form of Daniel Plots contain information about the influence of refrigerants on the viscosity of lubricating oil as shown in Fig. 1. An operating point can be placed at operating conditions (pressure, temperature). The diagram shows how much refrigerant is dissolved in the lubricating oil at saturation. Since the saturation at the equilibrium state is time-related, the concentration at saturation indicates a maximum of concentration at any operating conditions. Hence, the kinematic viscosity read will always be lower than the real viscosity in the system, which adds a safety when designing a cycle.

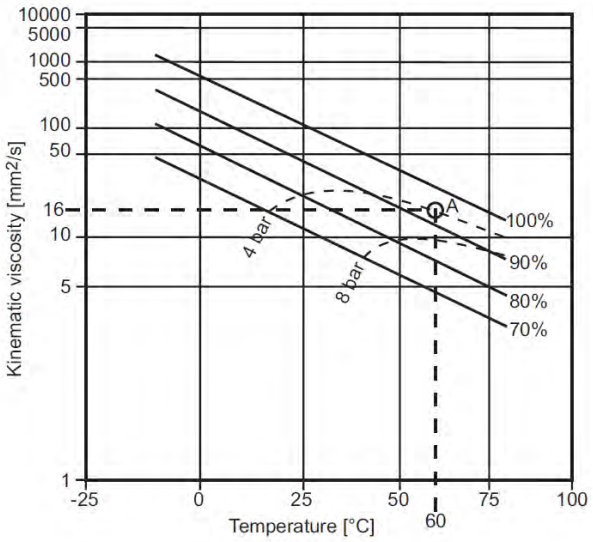

Figure 1: Daniel plot of a RENISO Triton SE55-R134a Mixture (Bock, 2007).

Modeling is necessary to avoid an extensive experimental study which can be costly in resources and in time. Thermodynamic tools such as cubic equations of states can be used to predict the behaviour and thermophysical properties of such mixtures. Nonetheless, experimental work is always necessary to fit model parameters and for the validation of said models.
At this end, an original experimental apparatus has been developed to be able to measure HFO solubility in lubricating oil as well as dynamic viscosity and density of the liquid phase up to 443 K and 10 MPa. The experiments are based on a dynamic synthetic isothermal method. They will provide sufficient measurements to fit models and to be able to reproduce Daniel plots for any refrigerant-lubricant mixture.

2. EXPERIMENTAL MEASUREMENTS

2.1. Experimental method

The synthetic isothermal methods are performed by measuring the pressure of a synthesized multiphase mixture at isothermal conditions. An equilibrium cell is charged with an exactly known amount of the first component before setting the system to the desired temperature. Subsequently, a precisely known amount of the second component is added to the cell, which leads to an increase in the pressure of the system. As the second component dissolves into the liquid phase, the pressure inside the equilibrium cell decreases, eventually reaching an equilibrium value. For this reason, this method is often referred to as pressure-decay method. After equilibration of the system, the pressure and temperature are registered and the composition of the vapour phase is calculated using the material balance from the known total composition, the composition of the vapour phase and the phase densities and volumes. More experimental points along the boiling-point line can be measured by repeating the addition of the second component into the cell.

2.2. Apparatus description

The apparatus used in this work, see Fig. 2, is based on a static-synthetic method as described by Descamps et al. (2005). The equilibrium cell is immersed in a thermo-regulated liquid bath (Lauda Proline RP 3530) which temperature is controlled within 0.01 K.
The equilibrium cell (96.85 cm^3 volume) composed of a sapphire tube pressed between two Hastelloy pieces, is identical to the cell used by Valtz et al. (2002) and Subramoney et al. (2010). The bottom flange holds a magnetic stirring assembly. In order to perform accurate measurement and to check for thermal gradients, two platinum resistance thermometers (Pt100 Ω) are inserted inside wells drilled in both flanges of the equilibrium cell and connected to a data acquisition unit (34972A LXI Data Acquisition Unit). These two Pt100 probes are periodically calibrated against a 25 Ω reference thermometer (Tinsley Precision Instrument) certified by the Laboratoire National d'Essais (Paris, France). The resulting uncertainties on temperature measurements are within ±0.03 K. Pressures are measured by means of two pressure transducers (Druck PTX611, range 0-0.1 MPa and 0-5 MPa) connected as well to the acquisition unit. These transducers are calibrated with a modular pressure controller (PACE 5000). The resulting uncertainties in pressure measurements are within ±0.0003 MPa. Refrigerant and lubricant oil are charged into the cell with two variable volume cylinders connected to an opto-electronic displacement transducer and a pressurizing circuit (nitrogen). Each variable volume cylinder has its own pressure transducer and a platinum resistance thermometer.
A U-tube density measurement apparatus is used for the measurements of liquid phase density. The sample is introduced into a U-shaped borosilicate glass tube that is being excited to vibrate at its characteristic frequency electronically. The characteristic frequency changes depending on the density of the sample. Through precise determination of the characteristic frequency and mathematical conversion, the density of the sample can be measured. This apparatus is thermo-regulated through Peltier elements and the temperature is measured with two integrated Pt100 platinum thermometers. A dynamic viscosity measurement apparatus (Anton Paar Lovis 2000 ME) has been used to measure dynamic viscosity of R1336mzz(Z) – Reniso Triton SE 220 mixtures. This apparatus is based on the Rolling Ball Principle. A ball rolls through a closed, liquid-filled capillary, which is inclined at a defined angle. Three inductive sensors determine the ball's rolling time (the greater the viscosity the longer the rolling time).
Materials. R1233zd(E) was supplied by Climalife with a purity higher or equal to 99.5% in mass. R1336mzz(Z) was supplied by Chemours with a purity higher or equal to 99.5% in mass. The Reniso Triton SE 220 (Polyolester lubricant VG 220) lubricant oil was supplied by Fuchs.

2.3. Procedure

The experimental procedure for the static-synthetic method, as already described in Descamps et al (2005), consists in the introduction of known amount of degassed lubricant oil and refrigerant in the thermostated system. First, the cell, loading and circuit lines are evacuated down to 0.1 Pa. The system is then thermostated at the desired temperature. The degassed lubricant oil is introduced into the equilibrium cell through the loading lines. The displacement of the piston (contained in the variable volume cylinder) and the pressure and temperature of the variable volume cell are recorded. After measurement of the vapour pressure, refrigerant is introduced from another variable volume cell, the pressure and temperature of which are recorded before and after each loading. The system is agitated until the pressure becomes stable, indicating that an equilibrium is reached. The on-line data acquisition unit is connected to a computer to allow real time readings and storage of both pressure and temperature data. More refrigerant is then introduced into the cell through successive loadings.

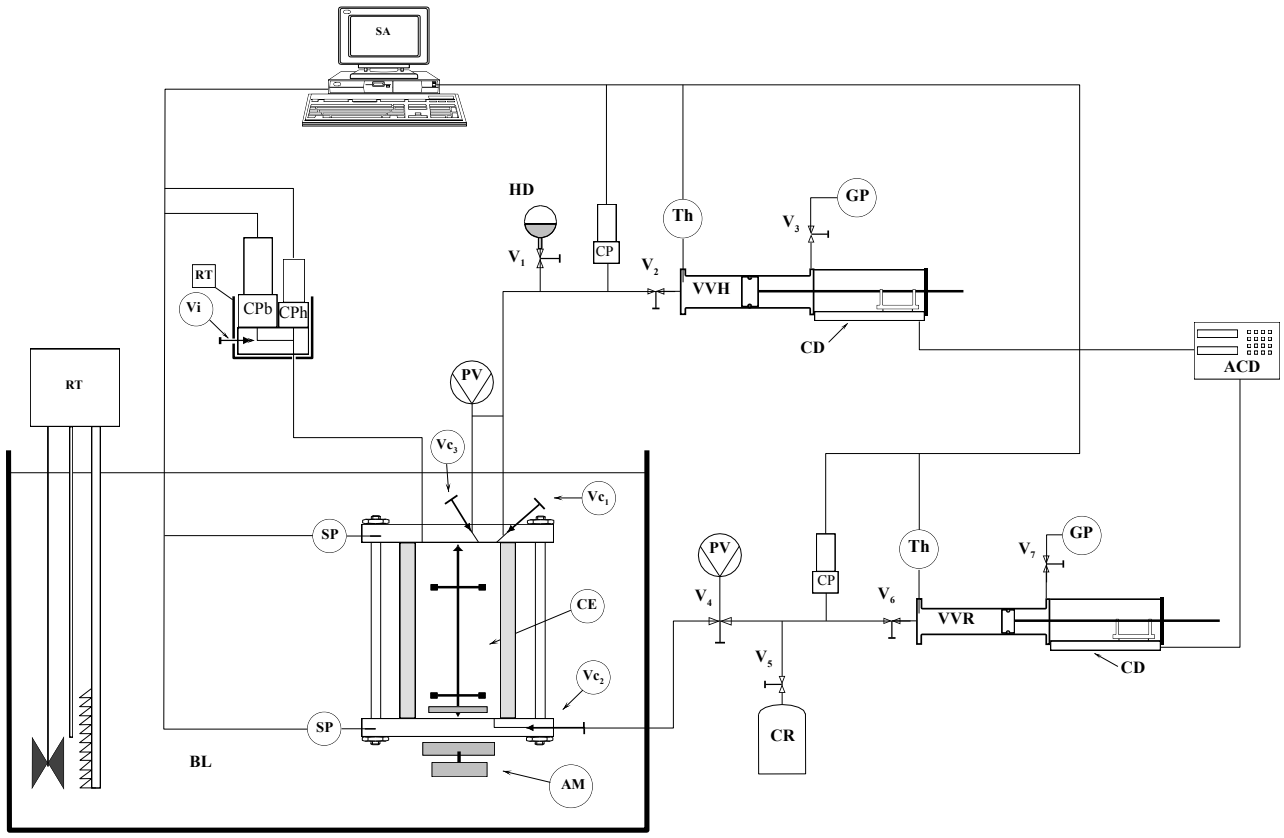

Figure 2: Schematic Apparatus description. RT: Temperature Control; CPb, CPh : Pressure Transducers (Low and High pressure); Vi :Valves; Vci : Loading valves; PV : Vacuum pump; BL : Liquid Bath; SP : Platinum probes; CE : Equilibrium cell; AM : Magnetic stirrer; CR : Refrigerant cylinder; Th : Thermocouple; GP : Pressurizing gas; CD : Displacement transducer: VVR : Variable Volume cell for Refrigerant; VVH : Variable Volume cell for Oil; HD : Degassed Oil; ACD : Displacement acquisition unit; SA : Acquisition unit system.

3. CALCULATIONS

3.1. VLE Data Modeling

The experimental VLE data are correlated using a SRK-type cubic equation of state, shown in equation (1):

$$P = \frac{RT}{v-b} - \frac{a(T)}{v(v+b)} \qquad \text{Eq. (1)}$$

The attractive term a and the co-volume b, are respectively given by equations (2) and (3), while mixture parameters are obtained from equation (4) and (5), as described by Yokozeki (2007) :

$$a = \sum_{i,j=1}^{C} \sqrt{a_i a_j} f_{ij}(T)\left(1 - k_{ij}\right) x_i x_j \qquad \text{Eq. (2)}$$

$$b = \frac{1}{2}\sum_{i,j=1}^{C}\left(b_i + b_j\right)\left(1 - m_{ij}\right)\left(1 - k_{ij}\right)x_i x_j \qquad \text{Eq. (3)}$$

$$f_{ij}(T) = \tau 0_{ij} + \frac{\tau 1_{ij}}{T} + \tau 2_{ij} T, \ o\grave{u}\ f_{ij} = f_{ji}\ et\ f_{ii} = 1 \qquad \text{Eq. (4)}$$

$$k_{ij} = \frac{l_{ij} l_{ji}(x_i + x_j)}{l_{ji} x_i + l_{ij} x_j}, \ o\grave{u}\ k_{ij} = k_{ji}\ et\ k_{ii} = 0 \qquad \text{Eq. (5)}$$

Where $m_{ij} = m_{ji}$ and $m_{ii} = 0$. In this model, there are up to six interaction parameters for each binary pair: l_{ij}, l_{ji}, m_{ij}, $t_{0,ij}$, $T_{1,ij}$, $T_{2,ij}$. The pure component parameters are calculated with equations (6) and

(7). Only a slight change has been made from the original paper of Yokozeki (2001), on the α function. As shown on equations (8) and (9), the first parameter β_0 should not be fitted, but taken as a constant equal to 1 in order to fit the requirements of an α function. In this case, for Tr equal to unity, the alpha function should exactly be equal to one.

$$a_i = 0.427480 \frac{(RT_{c,i})^2}{P_{c,i}} \alpha_i(T) \quad \text{Eq. (6)}$$

$$b_i = 0.08664 \frac{RT_{c,i}}{P_{c,i}} \quad \text{Eq. (7)}$$

$$\alpha(T) = \sum_{k=0}^{\leq 3} \beta_k (1/T_r - T_r)^k, \quad for\ T_r \equiv T/T_c \leq 1 \quad \text{Eq. (8)}$$

$$\alpha(T) = \beta_0 + \beta_1 [exp\{2(1 - T_r)\} - 1], \quad for\ T_r \geq 1 \quad \text{Eq. (9)}$$

3.2. Viscosity Modeling

Since the work of Eyring and his co-workers (Glasstone et al, 1941), based on absolute rate theory, the Eyring's model for predicting kinematic viscosity has been successfully used (Wei and Rowley, 1985; Ji and Lempe, 2006; Lee and Lee, 2001). This model is based on the activation Gibbs energy of flow required to remove molecules from their most favourable state to the activated state. The equation (10) shows the expression of the kinematic viscosity:

$$\eta v = \mathrm{N_A} h_0 exp\left(\frac{\Delta G^{\#}}{RT}\right) \quad \text{Eq. (10)}$$

The activation Gibbs energy of flow can be separated into a pseudo ideal solution part and an excess part as shown in equation (11):

$$\Delta G^{\#} = \Delta G^{\#ID} + \Delta G^{\#E} \quad \text{Eq. (11)}$$

Combining equation (10) and (11), the kinematic viscosity can be expressed as:

$$\eta v = (\eta v)_{\mathrm{ID}} exp\left(\frac{\Delta G^{\#\mathrm{E}}}{RT}\right) \quad \text{Eq. (12)}$$

The viscosity of an ideal mixture can be expressed as a function of the viscosity of the pure components:

$$\ln(\eta v)_{ID} = \sum x_i \ln(\eta_i v_i) \quad \text{Eq. (13)}$$

Wei and Rowley (1985) proposed a simple way to relate the excess activation Gibbs energy of flow to the excess Gibbs free energy, using a proportional factor:

$$\Delta G^{\#E} = -\sigma G^E \quad \text{Eq. (14)}$$

The excess Gibbs free energy of a mixture can be calculated from the fugacity coefficients of the constituent components in mixture and those of pure substances:

$$G^E = RT \sum_{i=1}^{C} x_i \left(\ln \hat{\phi}_i - \ln \phi_i^0\right) \quad \text{Eq. (15)}$$

The fugacity coefficients of the constituent components in mixture and those of a pure substance can be calculated with the cubic equation of state used for the VLE calculations.
It has been reported that the estimated viscosities of mixture had large discrepancies from the real values if σ is treated as a parameter. In order to improve the accuracy of estimation, the parameter σ can be considered as a function of composition.

$$\sigma = 0.876 - 10.1\ln(x) \qquad \text{Eq. (16)}$$

3.3. Results and discussion

The results of the solubility measurements are presented in Fig. 3 with the results of the prediction from the cubic equation of state. The parameters associated with the cubic equation of state are presented in Table 1. The model shows good performance, especially with the R1336mzz(Z), considering that only the first three parameters, m_{12}, l_{12}, l_{21}, have been fitted on experimental data.

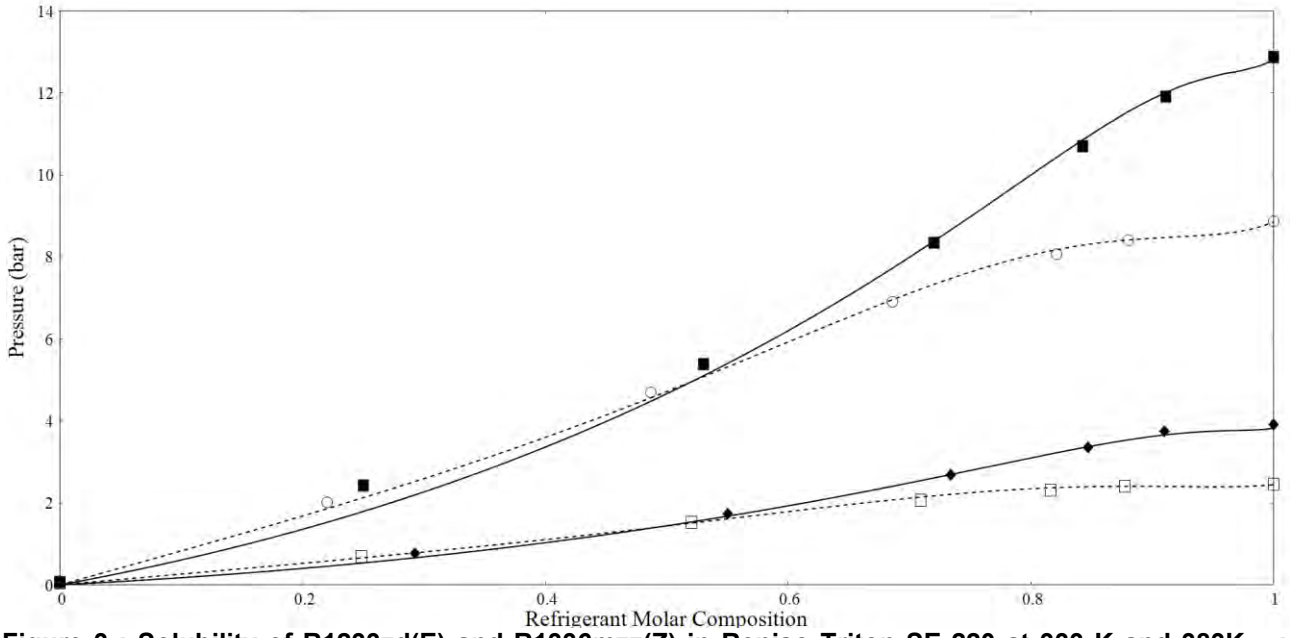

Figure 3 : Solubility of R1233zd(E) and R1336mzz(Z) in Reniso Triton SE 220 at 333 K and 383K. ■: R1233zd(E)-Reniso Triton SE 220 at 383 K; ♦: R1233zd(E)-Reniso Triton SE 220 at 333 K; ○: R1336mzz(Z)-Reniso Triton SE 220 at 383K; □: R1336mzz(Z)-Reniso Triton SE 220 at 333 K.

Table 1 : Cubic equation of state parameters and associated AAD(%).

System	m_{12}	l_{12}	l_{21}	$\tau_{0,12}$	$\tau_{1,12}$	$\tau_{2,12}$	AAD(%)
R1233zd(E)-Reniso Triton SE 220	0.028	0.1	0.01	1	0	0	<5.73
R1336mzz(Z)-Reniso Triton SE 220v	-0.04	0.1	0.05	1	0	0	<2.24

The results of the kinematic viscosity prediction are presented in Fig. 4. Even though the correct trend is obtained, the results are still far from the experimental data. A decisive improvement can be done in the definition of the proportional factor function.

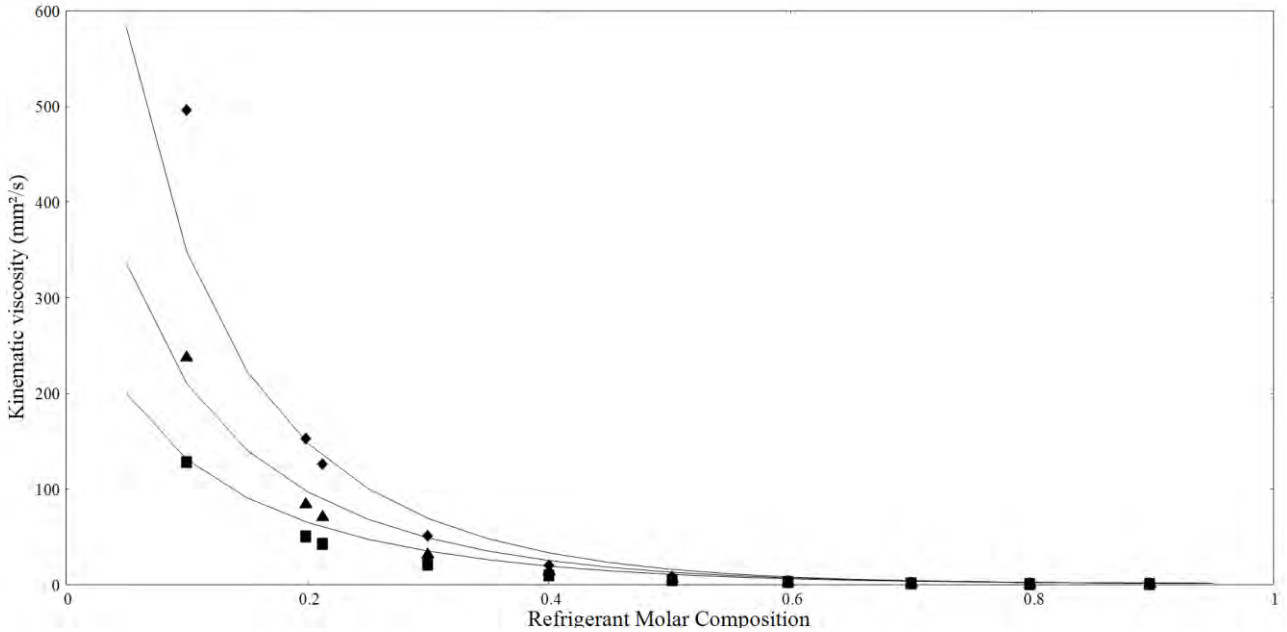

Figure 4 : Kinematic viscosity of a R1336mzz(Z)-Reniso Triton SE 220 mixture at different temperatures (283K, 293K and 303K). ♦:283 K; ▲: 293 K; ■: 303 K; − Eyring model.

4. CONCLUSIONS

In this work solubility measurements of R1233zd(E) – Reniso Triton SE 220 and R1336mzz(Z) – Reniso Triton SE 220 mixtures have been made at 333 K and 383 K. These data have been successfully correlated with a cubic equation of state with AAD below 6%. Density and dynamic viscosity measurements have also been made at 283 K, 293 K and 303 K. An Eyring-type model has been used to predict the corresponding kinematic viscosity. The results are encouraging but additional work needs to be done, especially in the definition of the σ function.
An original experimental apparatus allowing the measurement of VLE data along liquid phase density and dynamic viscosity data is being developed. The new apparatus will provide experimental data sufficient to the fitting of the models used in this work and necessary to predict Daniel plots.

ACKNOWLEDGEMENTS

The authors are grateful for EDF-R&D and the ANRT for the founding of the PhD thesis associated with this work. We would like to thanks Chemours for the sample of R1336mzz(Z). Also we would like to thanks Fuchs for the sample of the Reniso Triton SE 220 oil.

NOMENCLATURE

α	Temperature dependent term	β	Parameter of the alpha function
η	Dynamic viscosity (Pa.s)	σ	Proportional factor
T_{ij}	Binary interaction parameter	φ	Fugacity coefficient
a	Energy parameter of the equation of state ($J.m^3.mol^{-2}$)	b	Molar co volume parameter of the equation of state ($m^3.mol^{-1}$)
f_{ij}	Binary interaction parameter	G	Gibbs Energy ($J.mol^{-1}$)
h_0	Planck's number ($6.62617.10^{-34}$ J.s)	k_{ij}	Binary interaction parameter
l_{ij}	Binary interaction parameter	m_{ij}	Binary interaction parameter
N_A	Avogadro's Number ($6.02204.10^{23}$ mol^{-1})	P	Pressure (Pa)
R	Molar gas constant (8.314472 $J.mol^{-1}.K^{-1}$)	T	Temperature (K)
v	Molar volume ($m^3.mol^{-1}$)	x	Molar fraction

$^{\#}$	Flow property	^{0}	Pure substance
^{E}	Excess property	^{ID}	Ideal substance
$_{C}$	Critical property	$_{i,j}$	Molecular species
$_{ID}$	Ideal substance	$_{r}$	Reduced property

REFERENCES

Bock, W., 2007. Refrigeration Oils. In : Mang, T., Dresel, W., Lubricants and Lubrication, Wiley-VCH, Weinheim, 353-366.

Descamps, C., Coquelet, C., Bouallou, C., Richon, D., 2005. Solubility of hydrogen in methanol at temperatures from 248.41 to 308.20 K. Termochimica Acta, 430, 1-7.

Glasstone, S., Laidler, K.J., Eyring, H., 1941. The Theory of Rate Process. McGraw-Hill, New York.

Ji, W., Lempe, D.A., 2006. Calculation of Viscosities of Liquid Mixtures Using Eyring's Theory in Combination with Cubic Equations of State. Chinese J. Chem. Eng., 14(6), 770-779.

Lee, L., Lee, Y., 2001. The application of the equations of state incorporated with mixing rules for viscosity estimations of binary mixtures. Fluid Phase Equilibria, 181, 47-58.

Subramoney, S.C., Nelson, W.M., Valtz, A., Coquelet, C., Richon, D., Naidoo, P., Ramjugernath, D., 2010. Pure Component and Binary Vapour-Liquid Equilibrium + Modeling for Hexafluoropropylene and Hexafluoropropylene Oxide with Toluene and Hexafuoroethane. J. Chem. Eng. Data, 55, 411-418.

Valtz, A., Coquelet, C., Baba-Ahmed, A., Richon, D., 2002. Vapor-liquid equilibrium data for the propane + 1,1,1,2,3,3,3-heptafluoropropane (R227ea) system at temperatures from 293.16 to 353.18 K and pressures up to 3.4 MPa. Fluid Phase Equilibria, 202, 29-47.

Wei, I.C., Rowley, R.L., 1985. A local composition model for multicomponent liquid mixture shear viscosity. Chem. Eng. Science, 40(3), 401-408.

Yokozeki, A., 2001. Solubility of Refrigerants in Various Lubricants. Int. J. Of Thermophysics, 22(4), 1057-1071.

Yokozeki, A., 2007. Solubility correlation and phase behaviors of carbon dioxide and lubricant oil mixtures. App. Energy, 84, 159-75.

Manuscript ID: 254
DOI: 10.18462/iir.icr.2019.0254

Transfer processes in the thermosyphon employing graphene oxide and silica nanofluids

Agnieszka KUJAWSKA[(a)], Bartosz ZAJACZKOWSKI[(a)], Zbigniew KROLICKI[(a)], Michal WOLUNTARSKI[(b)], Matthias BUSCHMANN[(c)]

[(a)] Wroclaw University of Science and Technology,
Wroclaw, 50370, Poland, agnieszka.kujawska@pwr.edu.pl
[(b)] Institute of Electronics Materials Technology, Warsaw, Poland
Warsaw, 01919, Poland
[(c)] Institut für Luft- und Kältetechnik,
Dresden, 01309, Germany

ABSTRACT

Thermosyphons, as passive heat transfer devices, often assist heat pumps and refrigeration systems. Employing nanoadditives enhance their heat transfer capabilities and in consequence improve performance of thermal systems.
Here, we analyse thermal resistances and time-dependent boiling characteristics of devices filled with water-based silica and graphene oxide nanofluids, known to enhance heat transfer capabilities of water/glycol solutions. The experimental campaign in this work encompassed source temperatures 40-85°C.
Nanofluids reduced thermal resistance of the device at low heat loads. The impact of nanoadditives was restricted to the evaporator section and correlated with the formation of porous layer on the heater's surface.
Additionally, nanofluid affected a pseudo-steady state geyser boiling. The frequency and intensity of geyser events depended on the type of nanofluid, surfactants, and temperatures of heat sources.
Keywords: Boiling, Nanofluid, Porous Surface, Thermosyphon.

1. INTRODUCTION

Thermosyphons, heat pipes, and other similar devices are among the most efficient heat transfer devices known today (Faghri, 2014). Being self-sufficient and having size that easily adapts to the requirements of application, from house heating, electronics cooling, to space applications (Reay and Kew, 2015). A two-phase closed thermosyphon is a sealed tube filled with properly selected working fluid.
Nanofluids, understood as suspensions of particles smaller than 100 nm, improve heat transfer coefficients in thermal systems. As a consequence of the tininess of the nanoparticles and their large specific surface area, a small volume fraction of particles influences transport processes and causes thermal improvement. Even though viscosity increases when fluids are doped with nanoparticles, the negative effect is usually smaller than the possible enhancement of thermal conductivity. For this reason, nanofluids are especially suitable to be used in passive thermal devices such as thermosyphons and heat pipes (Buschmann, 2014).
High efficiency of thermosyphons is achieved due to consecutively occurring phase transitions and thereby the use of latent heat instead of sensible conduction or convection. Working fluid boils due to heat supplied to the evaporator from the external source. Vapour flows through the adiabatic section to the above-located condenser section where heat is released to the cooling medium. Condensed liquid returns to the evaporator section due to gravity.
Despite apparent simplicity, under certain conditions, the stable operation of thermosyphon can be disturbed. In certain range of geometric (diameter and length) and operating (heat flux, filling ratio, etc.) parameter, there is increased probability of geysering, see Casarosa et al. (1982), Lin et al. (1995), and Khazaee et. al (2010). There are four distinct stages of the phenomenon. (1) the liquid in the evaporator section is heated by the external source. (2) Once superheated, a bubble

emerges and grows rapidly to the size of the pipe diameter. (3) The bubble expands in vertical direction, violently pushing the liquid trapped above it upward, in the direction of condenser. (4) condensed liquid returns to the evaporator section and the cycle repeats itself. Very often the phenomenon remains unrecognised, because its detection requires high resolution sensors and continuous pressure measurements. The effect of geysering on the averaged heat transfer performance of thermosyphon seems negligible. However, it causes high mechanical load that leads to shock damage of the device (Smith et al., 2018).
In this work we summarize the experimental study on geyser boiling in the thermosyphon filled with two distinct nanofluids: graphene oxide (GO) and silica dioxide (SiO_2), as well as SDS solution. Boiling curves and thermal resistances of both fluids are compared and discussed. Additionally, we analyse pressure measurements and detect geyser boiling occurrences to determine their intensity. These three factors are then combined in order to determine optimal operating conditions for heat and mass transfer processes in thermosyphon.

2. EXPERIMENTAL STUDY

2.1. Experimental Setup

The analysed closed-loop two-phase thermosyphon was build and installed at ILK-Dresden, Germany. The schematics and details are presented in Fig. 1. The centrepiece is the 1,800 mm copper (CW024A) pipe with an inner diameter of 20 mm and wall thickness of 1 mm. The evaporator and condenser sections are each 400 mm long. Heating and cooling mediums are supplied by copper coils wrapped around each section. The thermosyphon, including all coupling links and all connecting tubes to and from the thermostats, are insulated with a 20 mm Armaflex® insulation shell. The complete test rig is mounted in a vertical orientation on a rack made of aluminium profiles.

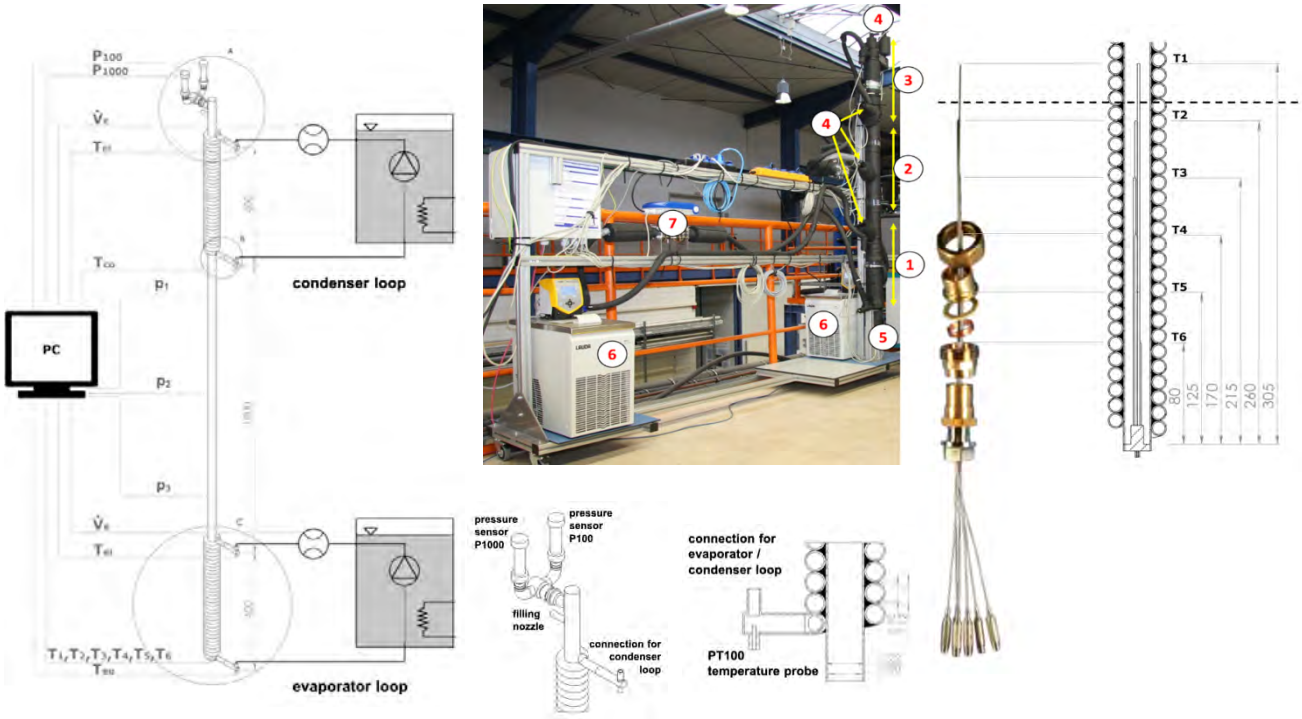

Figure 1: Details of the experimental setup. (1) evaporator, (2) adiabatic section, (3) condenser, (4) pressure transmitters, (5) temperature sensors, (6) thermostatic baths, (7) flow meter. On the right: custom-made temperature probe soldered at the bottom of the evaporator section

Inlet and outlet temperatures of heating and cooling medium are measured with Pt100 sensors. Temperature in the evaporator section is measured with a custom-made probe consisting of six

equidistantly positioned Pt100 sensors. All Pt100s have the working range - 20°C – 150°C with maximum uncertainty ± 0.32 K (calibrated at two-point calibration accuracy ±0.05 K).

Two thermostatic baths (Lauda Eco RE 1050 GW) with a temperature constancy ± 0.02 K supply heating and cooling medium (water). Volume fluxes in the evaporator and condenser are measured using two magneto-inductive flowmeters with a working range up to 0.012 m^3/h and accuracy ± 0.00076 m^3/h at the maximum flux.
Pressure at the top of the device is measured with two piezo-resistive pressure sensors with ranges 0 – 10^4 Pa (TRAFAG 8842) and 0 – 10^5 Pa (TRAFAG 8843) and accuracies ±2.5 Pa and ±250 Pa, respectively. Three additional pressure transmitters (TRAFAG 8842) are installed along the adiabatic section (at heights 500 mm (p3), 900 mm (p2), and 1,300 mm (p1), see Figure 1), each with a measurement range 0 – 400 mbar and accuracy ±50 Pa. Measurement frequency of all pressure signals is 1 kHz.
Data acquisition is carried out using a message device and the ProfiSignal software (Delphin Technology AG, Germany). The message device consists of several components, among them a high-resolution analogue digital converter, which transforms the measurement signals. It is connected with the measurement computer where the data can be monitored online.

2.2. Working Fluids and Measurements

After evacuation, the thermosyphon is filled with 85 ml of working fluid via the filling nozzle in the uppermost part of the device. With these 85 ml, the filling ratio is ~0.68.

2.2.1. Nanofluids

Two GO nanofluids (with and without SDS) has been tested. Both used fluids with graphene oxide (GO) flakes have been supplied by ITME, Warsaw, Poland. The material has been prepared by means of a modified Hummers method (Sadeghinezhad et al., 2015).



Figure 2: The samples of studied nanofluids (before and after experiments). (left) graphene oxide (GO), (right) silica oxide (SiO_2)

Table 1. Properties of analysed nanofluids (all use water as the base fluid)

Working fluid	Nanoparticles concentration	Mean size	Stabilizer concentration
	g/L	nm	g/L
Water	-	-	-
SDS + Water	-	-	0.01
GO	0.1	901	-
GO + SDS	0.1	769	0.01
SiO_2 + KOH	2 % vol	77	(up to pH 10.5)

In presented series of experiments, we compare the behaviour of above-described graphene oxide nanofluids to water-based silica nanofluid. The raw silica material (SIPERNAT® 22 S, Evonik Industries AG, Germany) is dispersed unfractionated with higher concentration and diluted to 2 vol. %. Stabilisation is done with KOH so that a pH-value of 10.5 is achieved. DLS measurement (Zetasizer Nano ZS, Malvern Instruments GmbH, Germany) indicated a mean agglomerate size of 77 nm.

2.2.2. Measurement and cleaning procedure

Each working fluid is measured following a standardised procedure. In both the evaporator heat exchanger coil and the condenser heat exchanger coil, the volume flux is kept constant at 0.012 m^3/h. For each working fluid, two measuring series with condenser inlet temperatures of nominal 15°C and 25°C are conducted. For both series, the inlet temperature at the evaporator coil is varied between 30°C and 85°C with an increment of 5 K. Each measurement starts by adjusting inlet temperatures and volume fluxes of the evaporator and condenser loop. Testing time was one hour for each combination of inlet temperatures.
After each experiment, the device is opened and inspected with an endoscopic SOMIKON®HD camera with a resolution of 2048 x 1536 pixels. After inspection, the interior of the thermosyphon is intensively mechanically cleaned with brushes or emery paper and rinsed with acetone several times. The inner wall is finally cleaned with a lint-free cleaning rag.

3. RESULTS AND DISCUSSION

3.1. Boiling Curves

Boiling curves for all above-listed working fluids were analysed in the series of experiments. The curves presented in Fig. 3 show the amount of heat transferred at a certain evaporator overheating, which is calculated as the difference between the temperature measured at the evaporator wall and the saturated temperature corresponding to the governing pressure.

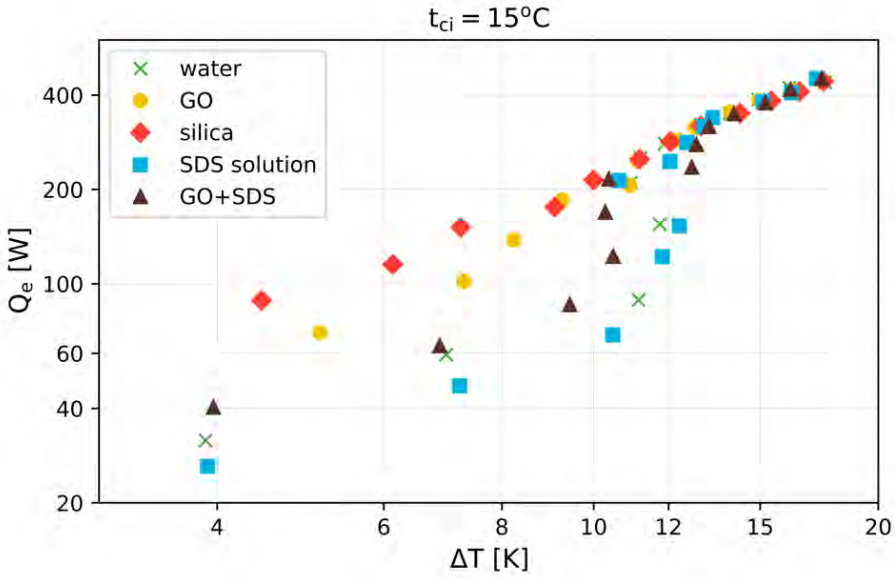

Figure 3: Boiling curves for all tested fluids

The data shows that the introduction of additives reduces superheat corresponding to the particular heat flux. Experiments confirm that the SDS solution is able to transfers slightly less heat than pure deionized water (see Fig. 3). Nanofluids allow to transfer more heat (the amount varies depending on the working fluid), while stabilizer reduces the performance of the device, regardless of the presence of nanoparticles.
Evaporating liquids often require large superheats. In result the nucleation is often delayed. The result is characteristic curve that is visible in Fig.3. This is not the case for nanofluids, for which the nucleation seems to start instantaneously and at much smaller superheats. For example, at 95 W silica nanofluid boils at the superheat that is about half of the superheat registered for pure water.

However, there is no indication that that the enhancement is caused by thermal properties of the nanofluid itself. From other studies of the boiling surfaces (e.g., Wlazlak et al., 2016; Grab et al. 2014; Murshed et al., 2011), we already know that nanofluids tend to accumulate on the surface on the evaporator wall which explains its enhanced heat transfer capabilities (highly conductive rough or porous structure promotes nucleation). GO nanofluid shows similar behavior (Wlazlak et al., 2016), still the enhancement is not as profound as in silica (probably due to distinct shape and chemistry of graphene nanoparticles). This agglomeration, also called baking, significantly influences thermal resistance, which is discussed in the next section.

3.2. Thermal Resistance

Time averaged thermal resistance is defined as the temperature difference between averaged temperatures of heating T_e and cooling T_c medium divided by the capacity of condenser Q_c: $R = (\bar{t}_e - \bar{t}_c)/Q_c$.

At cooling temperature $t_{ci} = 15℃$, water tends to exhibit the highest thermal resistance. Fig. 4 shows normalized thermal resistances calculated for all investigated working fluids at the cooling temperature $t_{ci} = 15℃$. The presence of additives generally lowers the thermal resistance of the device, but the effect is noticeable only for $t_{ei} < 50℃$. For evaporator inlet temperatures $t_{ei} > 50℃$, all fluids express similar values of thermal resistance, regardless of any nano or chemical additives.

Quantitatively, for $t_{ci} = 15℃$ and $t_{ei} = 30℃$ water shows the highest thermal resistance of 0.17 K/W ($\delta R = \pm 2.7 \times 10^{-2}$ K/W). The silica nanofluid creates the lowest thermal resistance with a nearly constant value of 0.088 K/W ($\delta R = \pm 7.2 \times 10^{-3}$ K/W) at $t_{ei} < 50℃$. For $t_{ei} > 50℃$ all fluids determine similar thermal resistance of about 0.076 K/W ($\delta R = \pm 2.1 \times 10^{-3}$ K/W).

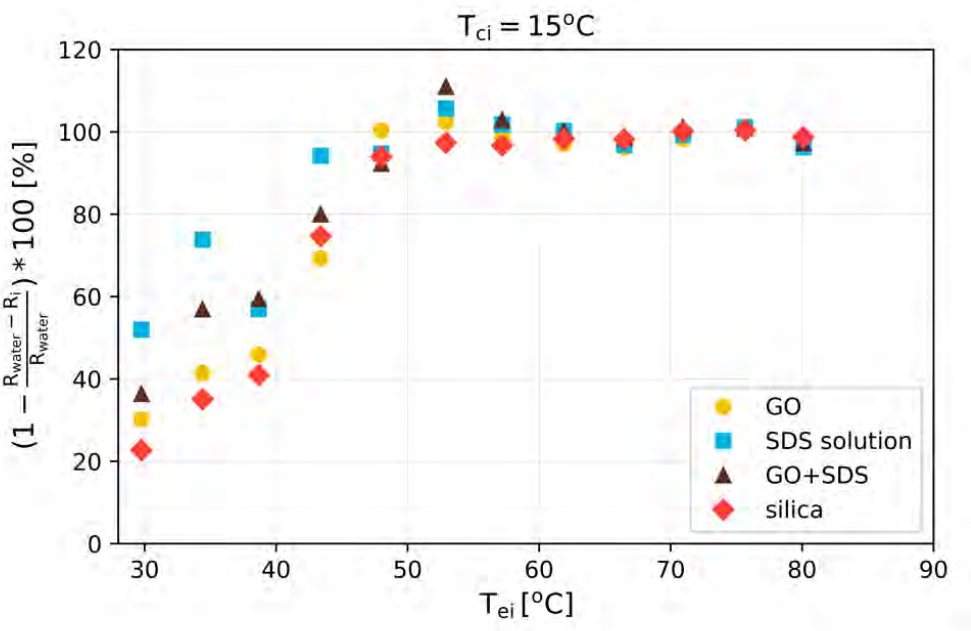

Figure 4: Comparison of thermal resistances of thermosyphon, normalized against thermal resistance of a device filled with water

3.3. Geysering

Experimentally obtained pressure signals show that typical geyser events are characterised by a distinct pattern that consists of a sharp rise followed by a longer lasting decline (see examples in Fig. 5). While the pressure spike occurs within a few milliseconds, following gradual descent needs more time and is partly overlaid by pressure fluctuations. The frequency and amplitude are influenced by the operating conditions. As expected, the geysering is more violent (meaning higher frequency but generally lower amplitude) at higher temperatures and heat fluxes. This result agrees with Casarosa et al. (1982), Lin et al. (1995), and Khazaee et al. (2010).

Among the studied fluids, the geysering pattern is the most noticeable for water and GO nanofluid (see Fig. 6). In the other cases, the distinction between real geysers and the noise is complicated

because the amplitude is often not enough to clearly stand out from the noise. Still, pressure spikes that mark the start of a geyser cycle are usually well above the mean of the pressure distribution.

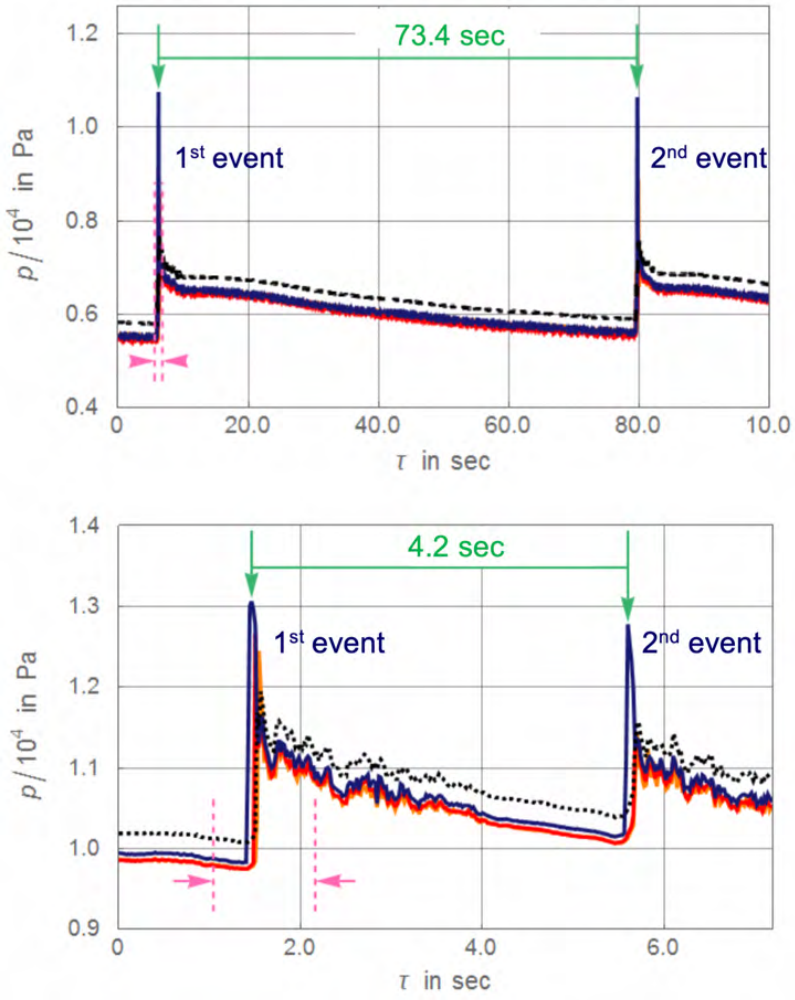

Figure 5: Geyser boiling occurrences showing different frequencies and amplitude. Events registered for distilled water at two heating temperatures: 55°C and 70°C ($t_{ci} = 25$°C)

Pure water produces regular and easily detectable geysering (Fig. 5 and Fig. 6 – top-left). The geyser cycle starts with the characteristic pressure spike that is followed by a region of decaying pressure fluctuations. Occasionally a secondary weaker spike appears. Pressure fluctuations are an echo of this spike, which fade over time.

In order to determine which pressure spikes are the real geyser events, we use time averaged mean pressure to normalise the time dependent pressure distribution. Pressure threshold is set independently for each test. Every peak exceeding this threshold is recognised as the onset of a geyser cycle. Waiting time is defined to avoid misinterpreting pressure fluctuations occurring immediately after geysers. For each case, the threshold and the waiting time are determined individually.

All the other analysed working fluids show different pressure patterns. The feature that is common is that once geysers appear, it takes certain amount of time for the pressure to stabilize, as seen for pure water and GO in Fig. 6.

After operation in the thermosyphon, the nanofluids lost its colouring due to nanoparticles (see comparison in Fig. 2) because the majority of nanoparticles have remained on the walls inside the device. This is a result of violent nature of the boiling phenomena and fact that nanoparticles are not transported by vapor. It may be also a result of geysering that facilitate deposition of nanoparticles on the evaporating surface.

Characteristic features of the pressure distribution of the silica nanofluid are the reduced number of geyser events, the longer lasting period of pressure fluctuations, lower maxima for the initialising pressure peaks, and lower pressure minima of the final pressure drops (see Fig. 6, top-right).

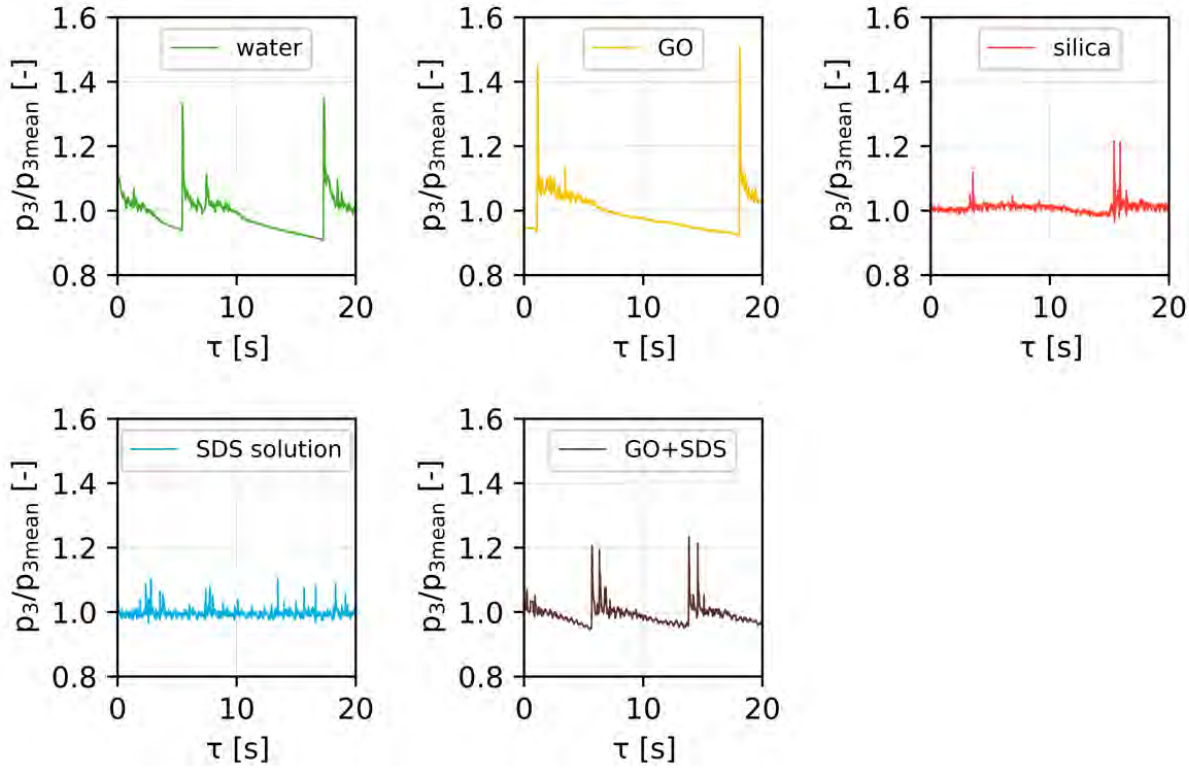

Figure 6: Instantaneous pressure (measured at p_3, see Fig.1) for water, graphene oxide, SiO_2, and also SDS and SDS with graphene oxide. The inlet temperature of cooling water is always 15 °C and the inlet temperature of heating medium is always 85°C

Except a few peaks, the pressure pattern of silica is similar to the one of nucleate boiling-type behaviour. It suggests that under these conditions, there is a continuous process of relatively small bubbles detachment and almost no liquid is pushed upwards towards the condenser. Because silica deposits on the evaporator wall, such behaviour may be caused by changed roughness and wettability of the boiling surface, and in consequence increased nucleation site density.
The SDS solution, which is an ionic surfactant, prevents the geyser boiling entirely (see Fig. 6, bottom-left). Because of reduced surface tension, bubbles cannot reach sizes big enough to eject the fluid gathered above (Wang et al., 2016). Activation of nucleation sites requires less energy, which translates into higher bubble departure frequency and smaller bubble diameters. It is not only the geysers which are prevented by SDS, it is the entire pressure fluctuation which is damped. Some damping behaviour can be observed for GO+SDS nanofluid. Comparison of amplitudes for GO nanofluid (Fig. 6, top-centre) and GO+SDS nanofluid (Fig. 6, bottom-right) shows decreased and more regular pressure fluctuations. In this case however, the geyser boiling is not prevented entirely. As we shown in the earlier paper (Wlazlak et al., 2016), the surfactant seems to attach to the graphene nanoparticles, which reduced the amount of the stabiliser in working fluid. This is the most likely reason for the behaviour of GO+SDS nanofluid.

4. CONCLUSIONS

In the presented paper we have compared three aspects of thermal processes occurring in a two-phase closed-loop thermosyphon for two distinct types of nanofluids: graphene oxide (GO) and silica (SiO_2). In particular, we focused on similarities of boiling curves, thermal resistance, and geysering process. We found that:

- Nanoparticles in the fluid reduce superheat corresponding to particular heat flux and the same heat flux can be transferred by using lower temperature of heating medium. The experiments show that chemical stabilizer (SDS) increased required superheat and, as a consequence, decreased the thermal performance of the device. Altering the working fluid from distilled water to another investigated fluid/suspension shifts the working point of the

thermosyphon, which includes a change of the amount of heat transferred and the temperature levels.

- For $t_{ei} < 50℃$ the presence of additives lowers the thermal resistance of the thermosyphon. For $t_{ei} > 50℃$, working fluid has no effect on thermal resistance, regardless of any nano or chemical additives.
- GO with SDS and silica nanofluids lower the frequency of geysering, in some cases to complete suppression., This effect is more prominent in SiO_2 than in GO.
- The data clearly show that geysering is sensitive not only to the particles in the fluid, but also to the added chemical stabiliser.

ACKNOWLEDGEMENTS

This work is a contribution to the Grant MF140079 and the COST Action (European Cooperation in Science and Technology) CA15119: Overcoming Barriers to Nanofluids Market Uptake (NanoUptake). A.K. acknowledges the Nanouptake COST Action support by STSM grants no. 35922, 37694, 39240.

NOMENCLATURE

p	pressure (kPa)	*R*	thermal resistance K×W^{-1})
Q	cooling capacity, kW	*t*	temperature (°C)

REFERENCES

Buschmann M.H., 2015. Nanofluids in thermosyphons and heat pipes: Overview of recent experiments and modelling approaches, Int. J. Therm. Sci. 72, 1–17.

Casarosa C., Latrofa E., Shelginski A., 1982. The geyser effect in a two-phase thermosyphon, Int. J. Heat Fluid Flow. 26, 933–941.

Faghri A., 2014. Heat Pipes: Review, Opportunities and Challenges, Front. Heat Pipes, 5.

Grab T., Gross U., Franzke U., Buschmann M.H., 2014. Operation performance of thermosyphons employing titania and gold nanofluids, Int. J. Therm. Sci., 86, 352–364.

Khazaee I., Hosseini R., Noie S.H., 2010. Experimental investigation of effective parameters and correlation of geyser boiling in a two-phase closed thermosyphon, Appl. Th. Eng. 30, 406–412.

Lin T.F., Lin W.T., Tsay Y.L., Wu J.C., Shyu R.J., 1995. Experimental investigation of geyser boiling in an annular two-phase closed thermosyphon, Int. J. Heat Mass Transf. 38, 295–307.

Murshed, S.M.S. Nieto De Castro C., V Loureno M.J., Lopes M.L.M., V Santos F.J., 2011. A review of boiling and convective heat transfer with nanofluids, Renew. Sustain. Energy Rev., 15, 2342–2354.

Reay D.A., Kew P.A., 2015. Heat Pipes. Theory, Design and Applications, Fifth ed., 378 p.

Sadeghinezhad E, Mehrali M, Saidur R, Mehrali M, Tahan Lat- ibari S, Akhiani AR, Metselaar HSC., 2015. Experimental investigation of stability and thermophysical properties of carbon nanotubes suspension in the presence of different surfactants. J Therm Anal Calorim. (120), 1193–1201.

Smith, K., Robinson, A. J., & Kempers, R., 2018. Confinement and vapour production rate influences in closed two-phase reflux thermosyphons Part A: Flow regimes. International Journal of Heat and Mass Transfer, *120*, 1241–1254.

Wlazlak A., Zajaczkowski B., Woluntarski M., Buschmann M.H., 2016. Influence of graphene oxide nanofluids and surfactant on thermal behaviour of the thermosyphon, J. Therm. Anal. Calorim. (2018). doi:10.1007/s10973-018-7632-x

Wang J., Li F.C., Bin Li X., 2016. On the mechanism of boiling heat transfer enhancement by surfactant addition, Int. J. Heat Mass Transf, 101, 800–806.

Manuscript ID: 263
DOI: 10.18462/iir.icr.2019.0263

A density-based solver using real gas properties for R744 supersonic flashing simulations

Yu FANG [a, b], Sébastien PONCET [a], Yann BARTOSIEWICZ [b], Hakim NESREDDINE [c]

[a] Université de Sherbrooke
Sherbrooke, J1K2R1, Canada,
yu.fang@usherbroke.ca, sebastien.poncet@usherbrooke.ca
[b] Université catholique de Louvain
Louvain-la-Neuve, 1348, Belgium, yann.bartosiewicz@uclouvain.be
[c] Laboratoire des technologies de l'énergie
Shawinigan, G9N6T6, Canada, nesreddine.hakim@ireq.ca

ABSTRACT

A density-based solver based on the OpenFoam library is coupled with a tabulated equation of state which allows to accurately compute the properties of CO_2 at a reduced computational cost. The homogeneous equilibrium model (HEM) is considered to predict the phase-change phenomenon. The Navier-Stokes characteristic boundary condition is used as the outlet boundary condition to guarantee the accuracy and stability of the simulation. As a result, this solver is suitable to simulate supersonic flashing CO_2 flows in converging-diverging nozzles and supersonic ejectors. Firstly, the flows in the converging-diverging nozzle are simulated under supercritical condition. A good agreement in terms of pressure distribution is obtained. Then, a two-phase CO_2 ejector is investigated numerically. Once again, a good agreement is obtained against experimental wall pressure measurements.
Keywords: R744 two-phase flow, Compressible solver, Real gas properties, Ejector, Flashing nozzle

1. INTRODUCTION

In the context of refrigeration, using CO_2 as the working fluid has several advantages: low cost, non-toxic, relatively low Global Warming Potential (GWP) and zero Ozone Depletion Potential (ODP). It is considered to be a promising alternative to synthetic refrigerants in future energy conversion systems and in the refrigeration industry. It has been proven that replacing the expansion valve by a two-phase CO_2 ejector results in improvements of the cooling capacity and the Coefficient of Performance (COP) of the whole system (Elbel and Hrnjak 2006); (Elbel and Hrnjak 2008) and (Li and Groll 2004). A standard system using a CO_2 two-phase ejector for expansion work recovery is shown in Fig. 1. The motive flow coming from the gas cooler is the supercritical CO_2 fluid. It is expanded through the primary converging-diverging nozzle (from point 3 to point 4). As a result, the motive fluid gains kinetic energy, while decreasing significantly its pressure. The flow state penetrates the liquid saturation curve (blue curve) and finally becomes liquid-vapor phase (point 4). This rapid phase transition is usually named 'flashing'. It occurs often near the throat of the converging-diverging nozzle. Due to the phase transition, the speed of sound decreases rapidly, thus the flow can become supersonic immediately. Hence, at the exit of the motive nozzle, a low-pressure supersonic two-phase jet can be obtained, and it entrains the secondary vapor flow from the evaporator (from point 9 to point 5). These two flows exchange momentum and heat by turbulent mixing. The shock waves may occur during the mixing process. Finally, the mixing flow compresses in the diffuser before entering the liquid-vapor separator (from point 6 to point 7).

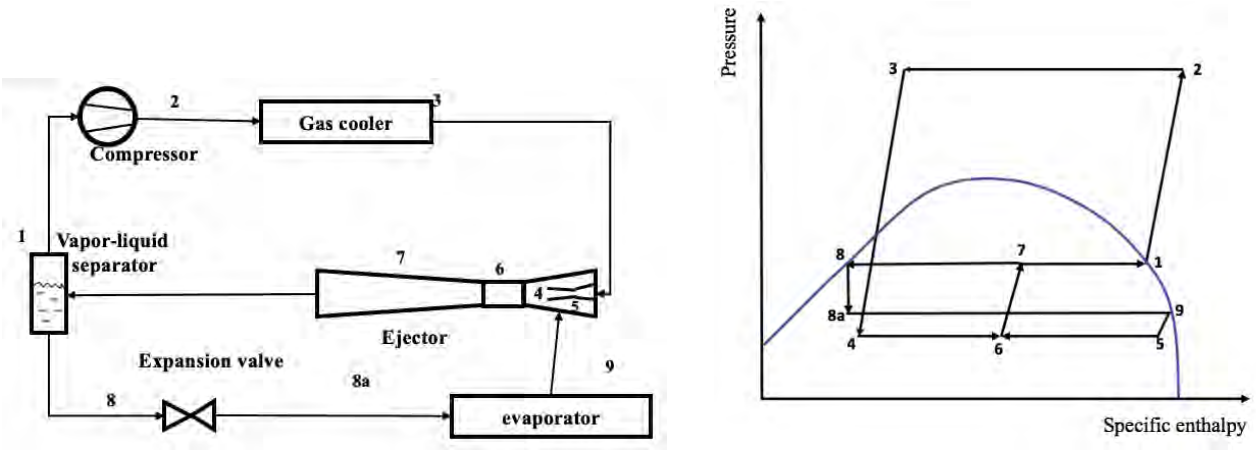

Fig. 1: Schematic of a transcritical CO_2 refrigeration cycle using a two-phase ejector for expansion work recovery and the corresponding p − h diagram.

The converging-diverging nozzle is a major part of the ejector, in which the expansion of the motive flow determines the suction capacity of the secondary flow. The converging-diverging nozzle has been extensively investigated experimentally and numerically. Nakagawa et al. (2009) and Berana et al. (2009) provided a very useful experimental database in terms of pressure and temperature distributions for benchmarking purpose. Several converging-diverging nozzles with different diverging angles were investigated under supercritical and subcritical conditions (Nakagawa et al. 2009) and (Berana et al., 2009). From a numerical point of view, most of CFD simulations of converging-diverging nozzles were performed with pressure-based solvers. Yazdani et al. (2014) considered the cavitation and boiling phase-change models in the pressure-based solver of ANSYS Fluent (ANSYS 2010) to simulate the Nakagawa et al.'s (2009) nozzles. The pressure distributions in the converging and diverging parts agreed well against the experimental measurements except that some numerical oscillations were obtained at the outlet. Ameli et al. (2017) simulated Berana et al.'s (2009) nozzles using Ansys CFX (ANSYS CFX 2015). Abnormal shock waves were predicted near the outlet, which may be attributed to an inappropriate outlet boundary condition. The small angle nozzles in Nakagawa et al.'s (2009) experiments were investigated by Giacomelli et al. (2018). A tabulated property calculation approach based on Refprop (Lemmon et al. 2010) was coupled with the pressure-based solver of ANSYS Fluent. However, different flow fields were obtained by changing the formulation of the sound speed: the subsonic nozzle with a normal shock at the outlet was predicted by the default speed of sound in ANSYS Fluent, while Yazdani et al.'s (2014) formulation predicted a supersonic flow in the whole nozzle with some numerical oscillations observed at the outlet.

The two-phase CO_2 ejector is increasingly investigated by CFD simulations. The pressure-based solver in Ansys Fluent with embedded Refprop database was used to predict two-phase CO_2 flows in ejectors (Smolka et al., 2013); (Palacz et al., 2015); (Haida et al. 2018). The mass flowrate or entrainment ratio were used to assess the numerical model. However, it should be noted that different flow fields could result in the same mass flowrate at inlets and outlet. Hence, the local variables should be investigated, such as the pressure, velocity, vapor quality … The heat and mass transfer mechanisms within a two-phase CO_2 ejector are extremely complex to capture and understand, including transient phase change (flashing), turbulent mixing, condensation and shock waves, shock-boundary layer interactions … In terms of numerical method, each mechanism mentioned above can affect significantly the predictions of the model. The inaccurate prediction of one mechanism can lead to poor predictions, whereas the inaccurate predictions of two different mechanisms can compensate each other and lead to satisfactory results in terms of global parameters. Most of the open literature on two-phase CO_2 ejectors for refrigeration applications has been published based on pressure-based solvers, whereas it is now well known in the fluid mechanics community that density-based flow solvers are required and more suitable for compressible flows. They have been indeed extensively used for water transient simulations, combustion applications, and single-phase ejectors. On the contrary, no CFD simulations based on a density-based solver have been performed for transcritical CO_2 ejectors, which is mainly due to numerical stability issues of commercial solvers and their incapacity to couple a density-based solver with external real gas properties such as the Refprop or any other external subroutines. Hence, in

the present work, the authors develop a new density-based flow solver based on rhoCentralFoam proposed in the OpenFOAM library (Greenshields et al. 2010). The present solver is based on a conservative formulation, which guarantees to correctly capture the acoustic waves within the computational domain. The thermodynamic properties are computed by an accurate and efficient look-up table equation of state (EoS) (Fang et al. 2018) based on Span-Wagner EoS (Span and Wagner 1994) and covering the supercritical, vapor, liquid and vapor-liquid states of CO2. Moreover, the Navier-Stokes characteristic boundary condition (NSCBC) is implemented for the outlet boundary, which insures the correct ingoing and outgoing of acoustic waves at the boundary and so enhances the stability of the simulation. It should be noted that the NSCBC is also coupled with EoS to compute the ingoing and outgoing waves.

2. NUMERICAL MODELLING

The Navier-Stokes equations are solved by the proposed density-based solver. They consist of the conservation of mass (Eq. (1)), momentum (Eq. (2)) and total energy (Eq. (3)), written as:

$$\frac{\partial \rho}{\partial t} + \nabla \cdot (\rho \boldsymbol{U}) = 0 \qquad \text{Eq. (1)}$$

$$\frac{\partial \rho \boldsymbol{U}}{\partial t} + \nabla \cdot (\rho \boldsymbol{U}\boldsymbol{U} + p\boldsymbol{I}) + \nabla \cdot \boldsymbol{T} = 0 \qquad \text{Eq. (2)}$$

$$\frac{\partial \rho E}{\partial t} + \nabla \cdot (\rho E + p)\boldsymbol{U} + \nabla \cdot (\boldsymbol{T} \cdot \boldsymbol{U}) + \nabla \cdot \boldsymbol{j} = 0 \qquad \text{Eq. (3)}$$

The whole system is written under its conservation form in which the conservative variables are the density ρ, the momentum ρ**U** and the total energy ρE. The conservative formulation can allow to accurately capture acoustic waves in compressible flows. The HEM assumptions are considered here, in which the two phases are under thermodynamic and mechanical equilibrium. Hence, all variables in the equations can be written for the two-phase mixture. **T** is the stress tensor written as:

$$\boldsymbol{T} = -2\mu * dev(\boldsymbol{D}) \qquad \text{Eq. (4)}$$

where μ is the dynamic viscosity and **D** denotes the deformation gradient tensor, $\boldsymbol{D} = 0.5(\nabla \mathbf{U} + \nabla \mathbf{U}^T)$. Its deviatoric component is ***dev(D) = D - trace(D)I***, where **I** is the unit tensor. The heat diffusion is presented by Fourier's Law:

$$\boldsymbol{j} = -k \nabla \boldsymbol{T} \qquad \text{Eq. (5)}$$

where k is the thermal conductivity. In practice, the temperature T is converted to the specific internal energy to respect its conservative formulation. To close the system of equations, a tabulated EoS based on Span-Wagner EoS is used to compute the pressure p by the density ρ and specific internal energy e. This tabulated approach was developed by Fang et al. (2018), covering the temperature from 216.59 K (the triple point temperature) to 1000 K and pressures up to 50 MPa. The liquid, vapor and liquid-vapor equilibrium states are included, and the accuracy and computational cost were carefully assessed (Fang et al. 2018). Moreover, the transport properties such as the dynamic viscosity are also implemented according to Vesovic et al. (1989).

From a numerical point of view, the present density-based solver is a Riemann-solver-free segregate solver. The equations are solved sequentially based on the volume finite method using semi-discrete, non-staggered central schemes for collocated variables (Greenshields et al. 2010). The first-order Euler implicit scheme is employed for the temporal discretization. The Kurganov and Tadmor schemes (Kurganov and Tadmor 2001) are considered for the spatial discretization. In order to impose the boundary condition appropriately, the Navier-Stokes characteristic boundary condition is considered for the outlet boundary (Poinsot and Lele 1992) and (Fosso et al. 2012). The ingoing and outgoing characteristic waves are computed and handled at the boundary to insure both accuracy and numerical stability.

The solving procedure can be summarized as follows:

- Compute thermodynamic and transport properties based on the density and specific internal energy.

- Construct interface fluxes by interpolating the conservative variables, $\mathbf{U}^n$, at the previous time step.
- Solve the density equation to obtain ρ^{n+1}.
- Solve the inviscid momentum equation to obtain $(\rho\mathbf{U})^{n+1}$.
- Solve the diffusion equation for the velocity to update $\mathbf{U}^{n+1}$.
- Solve the inviscid energy equation to obtain $(\rho E)^{n+1}$.
- Solve the diffusion equation for the internal energy to update e.
- Compute the conservative variables at boundaries.

3. NUMERICAL RESULTS

3.1. Two-phase converging-diverging nozzle

The converging-diverging nozzle is an important part in a two-phase CO_2 ejector, converting pressure energy to kinetic energy and allowing to entrain the secondary flow. Moreover, the interesting 'flashing' phenomenon occurs near the throat of the converging-diverging nozzle. Here, a 2D rectangular converging-diverging nozzle of Berana et al. (2009) is investigated with similar operating conditions as in two-phase CO_2 ejector applications. The 2D computational domain is meshed with 115140 elements. The Independence of mesh is verified. The simulation is performed without a turbulence model. The inlet conditions are p = 9 MPa and T = 313.15 K, while at the outlet, the pressure is 3.89 MPa. The detailed geometrical parameters are summarized in Tab. 1.

Table 1. Geometrical parameters of the nozzle

d_{in} [mm]	L_c [mm]	H_t [mm]	L_d [mm]	θ [°]
10	15	0.4	20	0.48

d_{in} and H_t denote the height of the inlet and the throat. L_c and L_d represents the length of the converging part and diverging part. θ is the diverging angle. The length of the diverging part of the nozzle was reduced to 8.38 mm in the experiment of Berana et al. (2009). Because no shock waves are in the converging-diverging nozzle this length according to the single-phase isentropic calculation under p = 9.5 MPa. The temperature was measured by thermocouple channels through drilled holes along the nozzle walls. The pressure profile in the converging part is determined by the isentropic calculation. Then, in the diverging part, the saturation pressures are computed by the measured temperatures.

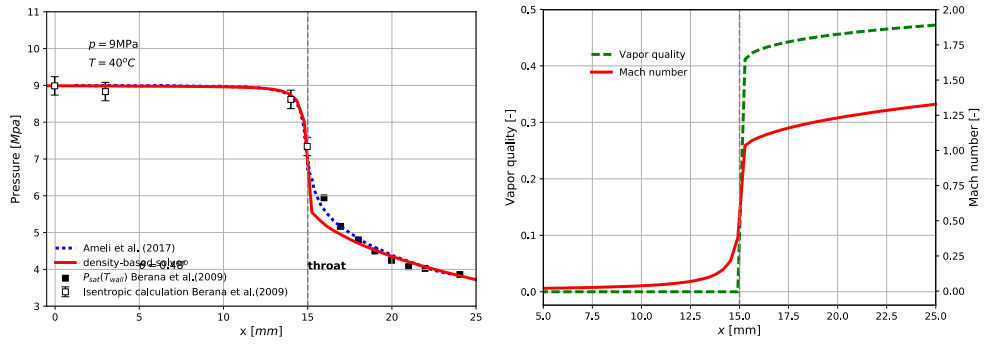

(a) **(b)**

Fig. 2: (a) Pressure profile along the center line of the nozzle compared with the experimental results by Berana et al. (2009). (b) Vapor quality and Mach number distribution along the center line

Fig. 2(a) shows the pressure profile (solid line) compared to the experimental results (markers), while Fig. 2(b) illustrates the vapor quality and the Mach number distributions along the nozzle. Moreover, the pressure profile from Ameli et al. (2017) (blue dashed line) is also presented in the same figure. Slight discrepancies can be observed right after the throat. It is not guaranteed that the differences arise from the two-phase modelling, though the non-equilibrium model was considered by Ameli et al. (2017), because the saturated pressure from the experiment is essentially computed according to HEM assumptions. Another explanation could be the choice turbulence model. The flow is fully

turbulent within the nozzle and the resolution the boundary layer could change the velocity distribution in the cross section and then it could affect the pressure distribution. Hence, more sophisticated turbulence modelling should be applied.
Besides, it can be observed in Fig. 2(b) that the flashing occurs at the throat and the vapor quality is equal to 0.48 at the outlet. In the meantime, the flow reaches sonic conditions at the throat. Afterwards, the flow continues to accelerate in the diverging part and the Mach number is equal to 1.3 at the outlet.

3.2. Two-phase ejector

The simulation of a two-phase CO_2 ejector is performed in this section. Firstly, the 2D ejector is meshed with 278,640 unstructured elements. The maximum Courant number is set to 0.1. The maximum value of the wall coordinate y^+ is around 90. The realizable $k-\varepsilon$ model is considered with a log-wal-function. The main geometrical parameters of the ejector are presented in Table 2 and correspond to an existing experimental set-up available at Laboratoire des Technologies de l'Énergie (LTE, Hydro-Québec, Shawinigan).

Table 2: Geometric parameters of the ejector. Lengths are in millimetres

d_{in}	d_t	d_{prim}	L_c	L_d	d_{mix}	d_{out}	L_d
6	3	3.11	5.598	6.64	4	10	69.2

d_{in}, d_t, d_{prim} denote the diameter of the primary inlet, throat, and outlet, while d_{mix} and d_{out} denote the diameter of the mixing chamber, and the diffuser outlet. l_c, l_d, l_{mix}, and l_{diff} represent the lengths of the primary converging part, the primary diverging part, the mixing chamber and the diffuser, respectively.
At the primary inlet, the CO_2 fluid is in the supercritical state with p = 7.6 MPa and T = 311.9 K. At the secondary inlet, CO_2 is in the vapor state with p = 4.6 MPa and T = 284.1 K. The pressure at the outlet of the ejector is 5.6 MPa which was measured by the pressure probe. Seven pressure probes are displayed along the ejector wall. The probes at the primary inlet, secondary inlet and the outlet provide the boundary conditions for the present simulation. The locations of other probes are shown in Fig. 3 with grey dashed line. Fig.3 compares the pressure distributions obtained experimentally and numerically together with the relative errors for the six streamwise locations.

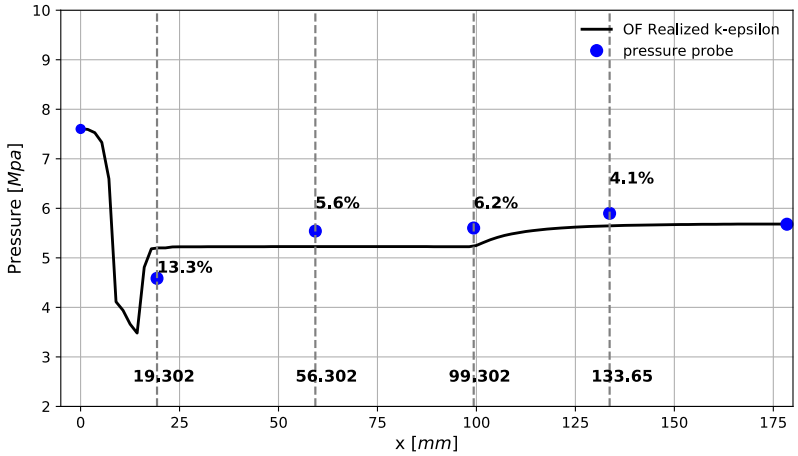

Fig. 3: Pressure distribution along the center line of the ejector (black line). The blue circles illustrate the measurements from pressure probes. The operating condition is p = 7.6 MPa and T = 311.9 K at the primary inlet, p = 4.6 MPa and T = 284.1 K at the secondary inlet and p = 5.6 MPa at the outlet

A good agreement is obtained in the mixing chamber and the diffuser. The maximum relative error (13.3%) is obtained at the beginning of the mixing chamber, where the primary and secondary flows encounter and start to mix. Therefore, the turbulent mixing has a considerable effect here. In order to improve the prediction of turbulence, other turbulence model will be tested including a resolved k-w SST model as well as high fidelity LES approach.
Fig. 4 shows the density gradient map zooming at the primary nozzle and the starting of the mixing chamber. It can be seen that strong density gradients are found at the primary nozzle throat and the

primary nozzle outlet, which correspond to the flashing and the shock waves respectively. It can be seen that the shock wave at the outlet is thick which is the type condensation shock. Moreover, the reflection of the acoustic waves in the primary nozzle and in the mixing layer around the jet are clearly visible according to the density gradient map.



Fig. 4: Density gradient map zooming at the primary nozzle and the starting of the mixing chamber. The operating condition is p = 7.6 MPa and T = 311.9 K at the primary inlet, p = 4.6 MPa and T = 284.1 K at the secondary inlet and p = 5.6 MPa at the outlet

Here, the operating condition may be not appropriate because neither the primary nozzle nor the secondary nozzle is not fully supersonic. This preliminary simulation shows the capacity of the present solver to handle the CO_2 two-phase flow simulations. Other simulations are performing with more appropriate operating conditions.

4. CONCLUSIONS

A density-based solver has been specifically developed for two-phase CO_2 flows. The HEM is coupled with the original solver based on the OpenFoam library to predict the flashing phenomenon. The Navier-Stokes characteristic boundary condition is implemented in order to provide an accurate and stable boundary condition. In addition, all thermodynamic and transport properties of CO_2 are computed by an in-house tabulated approach relying on Span-Wagner EoS. It can be considered as a promising tool to investigate two-phase compressible CO_2 flows in ejectors for refrigeration applications. To demonstrate that, a converging-diverging nozzle and a two-phase ejector have been simulated. Fairly good agreements in terms of pressure have been obtained against existing experimental results. However, more attention should be paid to the turbulence prediction. Hence, RANS simulations with wall-resolved BC and LES should be considered for future investigations.

ACKNOWLEDGEMENTS

Yu Fang and Sébastien Poncet acknowledge the support of the NSERC chair on industrial energy efficiency established in 2014 at Université de Sherbrooke funded by Hydro-Québec, Natural Resources Canada and Rio Tinto Alcan.

NOMENCLATURE

Acronyms		***Symbols***	
CFD	Computational Fluid Dynamics	c	Speed of sound [m. s^{-1}]
COP	Coefficient of Performance	$\boldsymbol{D}$	Deformation gradient tensor [s^{-1}]
EoS	Equation of State	d	Diameter [mm]
GWP	Global Warming Potential	*dev*	Deviatoric
HEM	Homogeneous Equilibrium Model	E	Specific total energy [$J.m^3.kg^{-1}$]
ODP	Ozone Depletion Potential	e	Specific internal energy [$J.m^3.kg^{-1}$]
LES	Large Eddy Simulation	h	Height [mm]
NSCBC	Navier-Stokes Characteristic Boundary Condition	$\boldsymbol{I}$	Unit tensor [-]

RANS	Reynolds Average Navier-Stokes
Greek letter	
μ	Dynamic viscosity [Pa.s]
θ	Diverging angle [º]
ρ	Density [kg.m^{-3}]
Subscripts	
c	Converging part
d	Diverging part
diff	Diffuser
in	Inlet
out	Outlet
prim	Primary nozzle
t	Throat
j	Heat flux [J.m^{-2}.s^{-1}]
k	Thermal conductivity [W.m^{-1}.K^{-1}]
p	Pressure [MPa]
T	Stress tensor [Pa]
T	Temperature [K]
trace	Trace of the matrix
U	Velocity [m.s^{-1}]
y^+	Dimensionless wall distance [-]
Superscripts	
n	Numbering of the time step
T	Transpose of the matrix

REFERENCES

Ameli, A., Afzalifar, A., and Turunen-Saaresti, T., 2017. Non-equilibrium condensation of supercritical carbon dioxide in a converging-diverging nozzle. Proceedings of International Seminar on Non-Ideal Compressible-Fluid Dynamics for Propulsion & Power, Verena, Italy.

ANSYS, 2010. Fluent user's guide. Technical report, ANSYS.Inc.

ANSYS CFX, 2015. Ansys CFX user guide, release 17.0. Technical report, ANSYS Inc.

Berana, M. S., Nakagawa, M., and Harada, A., 2009. Shock waves in supersonic two-phase flow of CO_2 converging- diverging nozzles. HVAC&R Research, 15:1080–1098.

Elbel, S. and Hrnjak, P., 2006. Experimental validation and design study of a transcritical CO_2 prototype ejector system. Proceedings of 7th IIR-Gustav Lorentzen Conference on Natural Working Fluids, Trondheim, Norway.

Elbel, S. and Hrnjak, P., 2008. Experimental validation of a prototype ejector designed to reduce throttling losses encountered in transcritical R744 system operation. Int. J. Refrigeration, 31:411–422.

Fang, Y., De Lorenzo, M., Lafon, P., Poncet, S., and Bartosiewicz, Y., 2018. An accurate and efficient look-up table equation of state for two-phase compressible flow simulations of carbon dioxide. Ind. Eng. Chem. Res., 57:7676—7691.

Fosso, A. P., Deniau, H., Lamarque, N., and Poinsot, T., 2012. Comparison of outflow boundary conditions for subsonic aeroacoustic simulations. Int. J. Numer. Methods Fluids, 68:1207–1233.

Giacomelli, F., Mazzelli, F., and Milazzo, A., 2018. A novel CFD approach for the computation of R744 flashing nozzles in compressible and metastable conditions. Energy, 162:1092–1105.

Greenshields, C. J., Weller, H. G., Gasparini, L., and Reese, J. M., 2010. Implementation of semi-discrete, non- staggered central schemes in a colocated, polyhedral, finite volume framework, for high-speed viscous flows. Int. J. Numer. Methods Fluids, 63:1–21.

Haida, M., Smolka, J., Hafner, A., Palacz, M., Banasiak, K., and Nowak, A. J., 2018. Modified homogeneous relaxation model for the R744 trans-critical flow in a two-phase ejector. Int. J. Refrigeration, 85:314–333.

Kurganov, A. and Tadmor, E., 2001. New high-resolution central schemes for nonlinear conservation laws and convection-diffusion equations. J. Comput. Phys, 160:241–282.

Lemmon, E. W., Huber, M. L., and McLinden, M., 2010. NIST standard reference database 23: reference fluid thermodynamic and transport properties. In REFPROP, Gaithersburg. National Institute of Standards and Technology; Standard Reference Data Program.

Li, D. and Groll, E. D., 2004. Transcritical CO_2 refrigeration cycle with ejector-expansion device. Proceedings of 10th International Refrigeration and Air Conditioning Conference at Purdue, West Lafayette, USA.

Nakagawa, M., Berana, M. S., and Kishine, A., 2009. Supersonic two-phase flow of CO_2 through converging-diverging nozzles for the ejector refrigeration cycles. Int. J. Refrigeration, 32:1195–1202.

Palacz, M., Smolka, J., Fic, A., Bulinski, Z., Nowak, A. J., Banasiak, K., and Hafner, A., 2015. Application range of the hem approach for CO_2 expansion inside two-phase ejectors for supermarket refrigeration systems. Int. J. Refrigeration, 59:251–258.

Poinsot, T. and Lele, S. K., 1992. Boundary condition for direct simulations of compressible viscous flows. J. Comput. Phys., 101:104–129.

Smolka, J., Bulinski, Z., Fic, A., Nowak, A., and Banasiak, K., 2013. A computational model of transcritical R744 ejector based on a homogeneous real fluid approach. Appl. Math. Model., 37:1208–1224.

Span, R. and Wagner, W., 1994. A new equation of state for carbon dioxide covering the fluid region from the triple-point temperature to 1100 K at pressures up to 800 MPa. J. Phys. Chem. Ref. Data, 25(6):1509–1596.

Vesovic, V., Wakeham, W. A., Olchowy, G. A., Sengers, J. V., Watson, J. T. R., and Millat, J., 1989. The transport properties of carbon dioxide. J. Phys. Chem. Ref. Data, 19:763–808.

Yazdani, M., Abbas, A., and Radcliff, T., 2014. Numerical modeling and validation of supersonic two-phase flow of CO_2 in converging-diverging nozzles. J. Fluids Eng., 136(014503).

Manuscript ID: 264
DOI: 10.18462/iir.icr.2019.0264

A novel analytical accelerated life model to understand refrigerant chemical stability

Steve KUJAK[(a)], Elyse SORENSON[(a)]
[(a)] Ingersoll Rand, 3600 Pammel Creek Road, La Crosse, 54601, USA
skujak@irco.com, elyse.sorenson@irco.com

ABSTRACT

A new group of refrigerants known as haloolefins which consist of hydrofluoroolefins (HFOs), hydrochlorofluoroolefins (HCFOs) and hydrochloroolefins (HCOs). These new low-GWP refrigerants may have the potential for decreased chemical stability as compared to the highly chemically stable hydrofluorocarbons (HFCs). Previous generations of chlorofluorocarbons (CFCs) and hydrochlorofluorocarbons (HCFCs) had good product reliability even though there were chemical stability concerns.
This paper summarizes the current highly accelerated life test (HALT) methodologies to qualify a new refrigerant for use. The authors will propose a methodology for extrapolating small scale highly accelerated laboratory results to real life HVACR operational conditions using a simple thermodynamic model and climate zone data. The chemical stability of HCFO-1233zd(E) will be compared to demonstrate the effectiveness of the proposed methodology to validate it's chemical stability for use in chillers. In addition, the chemical stability of HCFC-123 will be used to validate as a baseline of comparison to validate the chemical stability acceptability of R1233zd(E).
Keywords: R1233zd(E), Chemical Stability, Reliability, Chillers, Centrifugal

1. INTRODUCTION

HVACR equipment life expectancies are typically 15 to 25 years depending on the application, with instances of operation in excess of 50 years. Chemical stability of the refrigerant containing systems need to be designed to be stable enough without being replaced during its expected life. The ability to assess the chemical stability of refrigerants in the laboratory has been a dilemma in industry for decades. Investigators are challenged to correlate tens of thousands of system operation hours to data from laboratory scale tests performed over durations of days, weeks or months. Highly accelerated laboratory testing is required because of the impracticality and cost of running equipment for years to validate the chemical stability of the refrigerant. It is common practice in the industry to assess chemical stability of refrigerants using sealed glass tubes per ASHRAE Standard 97 procedures with various system materials at highly accelerated temperatures instead of running equipment (ASHRAE 97, 2007). Typical accelerated conditions for sealed glass tubes experiments can vary with temperatures ranging from 130°C to 200°C for durations of 1 to 4 weeks, with a more common test point established at 175°C for 2 weeks. These HALT temperatures often exceed the inherent thermal capabilities of many organic materials and results from these evaluations may not be relevant to the performance in HVACR equipment.
The proposed numerical methodology was first demonstrated by the authors for R22 unitary product applications (Kujak and Sorenson, 2019). The authors presented the methodology with unitary products since air cooled unitary products typically are the most widely used and typically run at the most harsh ambient and operating conditions. In addition, R22 chemical stability data was available in literature to allow the demonstration of the methodology. In this case study, water cooled chillers operate at lower temperatures in the condenser because of the use of cooling towers for heat rejection. In addition, these systems have typically higher efficiency which drives the operational temperatures lower as well as the refrigerant properties lead to lower compressor discharge superheats. All of these differences combined will lead to the refrigerant being exposed to overall lower temperatures over the life of the equipment and thus will lead to much lower chemical instability.

Ultra-low (<10 GWP) refrigerants options that are nonflammable are available for use as alternatives for R123 and R134a centrifugal compressor driven chillers (Kujak, S. et al., 2018). These alternatives include R514A, R1233zd(E) and R1224yd(Z). The authors have evaluated the chemical stability of R1233zd(E) in HALT testing and R1233zd(E) will be used to demonstrate the effectiveness of the proposed methodology to validate it's chemical stability for use in chillers. In addition, the chemical stability of HCFC-123 will be used to validate as a baseline of comparison to validate the chemical stability acceptability of R1233zd(E).

2. OVERVIEW OF PROPOSED METHODOLOGY

2.1 R1233zd(E) and R123 Chemical Reaction Kinetics

The concept of using reaction kinetics to study the chemical stability of HVACR refrigerants is not novel, and was applied in the past with the use of CFC and HCFC refrigerants. With the introduction of HFCs such as R32, R125, R143a, R134a, the use of rate kinetics has been infrequent or unnecessary, as these refrigerants are largely chemically stable at highly accelerated temperature conditions. Many historic papers studied the reactivity and degradation of these past refrigerants in the presence of lubricant and various metals to determine their suitability for use. These CFC and HCFC fluids, like R11, R12, R502, R123 and R22 while more reactive, were successfully applied in the industry for more than 30 to 50 years. In these early fundamental studies, the chemical stability of the refrigerant and lubricant combinations were evaluated using the sealed tube test approach, a method that is widely applied today to understanding HVACR system chemistry. In these sealed glass tube evaluations, the materials to be tested – typically refrigerants, lubricants, and metals – are sealed in a glass tube, and aged in a heated oven for a specified amount of time to accelerate the aging process. After exposure, the contents in the tube would be analyzed to detect breakdown products for determination of rates of reactivity or decomposition mechanisms. The glass tube approach was employed due to the relative chemical inertness of glass, but more importantly, glass allows the ability to monitor the condition of the materials before, during and after testing. Other approaches to accelerated testing have been applied over the decades, including use of stainless steel pressure vessels (Doerr et al., 1993) and DSC techniques (Kauffman, 1993), however the sealed glass tube approach largely remains the preferred approach in the industry.

As introduced earlier, one must first fully understand the chemical reactions at hand to ensure the refrigerant system being studied and measured is appropriate to model the reaction kinetics. In the case of R123, gas chromatography analysis was utilized to identify and further study its reduction reaction to form R133a via the exchange of one of its chlorine atoms for a hydrogen atom from the lubricant (Eq. 1). Studies of R1233zd(E) indicate the reduction reaction is not the primary reaction which would form R1243zf (Eq 2). The primary reaction seen is a stereoisomer rearrangement reaction where the E (trans) isomer of R1233zd rearranges to form the Z (cis) R1233zd isomer where the chlorine atom shifts from one spatial orientation to another (Eq. 3). Fig. 1 and 2 show the physical change in the atoms in this stereoisomer rearrangement reaction for R1233zd(E). In this study, direct correlation of R1233zd(E) degradation could be inferred by the measurement of R1233zd(Z) produced, due to the stoichiometric relationship of the reactants and products in the isomerization reaction.

$$\text{R123} \rightarrow \text{R133a} + \text{Chloride, dissociation} \qquad \text{Eq. (1)}$$

$$\text{R1233zd(E)} \rightarrow \text{R1243zf} + \text{Chloride, dissociation} \qquad \text{Eq. (2)}$$

$$\text{R1233zd(E)} \rightarrow \text{R1233zd(Z)}, \text{isomerization} \qquad \text{Eq. (3)}$$

Once the reaction kinetics are understood, then the impact on system performance and potential remediation actions need to be understood over the life the equipment. The numerical model presented in this paper presents a methodology to estimate the amount of refrigerant breakdown over the life of equipment operation given various climate zone stresses.

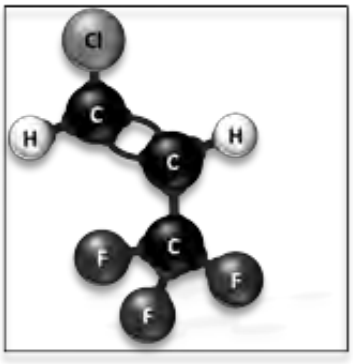

Figure 1: Molecular Diagram of R1233zd(E) Boiling Point = 19°C

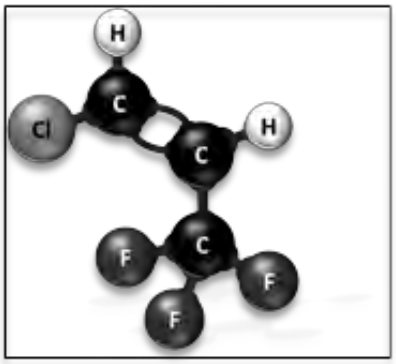

Figure 2: Molecular Diagram of R1233zd(Z) Boiling Point = 39°C

2.2 Arrhenius Theory and R1233zd(E) Reaction Rates

The chemical reaction rate, the rate at which these chemical processes proceed, is dependent on numerous factors. Factors that affect the reaction rate include the nature of the reactant, its physical state (solid/liquid/gas), concentration of various reactants or products, temperature, pressure, and the presence of catalysts which may accelerate or alter the reaction mechanism. The rate at which these reactions occur can be described as the change in concentration of the reactant [A] with respect to time (t). For first order reactions, this rate can be described by the first order rate law in Eq. 4.

$$[A]_t = [A]_0 e^{-kt} \text{ which can be rearranged as: } \ln\frac{[A]_t}{[A]_0} = -kt \qquad \text{Eq. (4)}$$

Rate constants are determined experimentally, and require either; the ability to measure the concentration of the reactant or, knowledge of the chemical reaction and stoichiometry to relate the measured concentration of the products to the depletion of the reactant. If these considerations are not taken into account, the rate study will be ineffective and could lead to confounding results or incorrect conclusions. A typical approach used in evaluating refrigerant stability is to monitor the concentration of a key degradation product (or products) that results from the reactivity of the refrigerant at an elevated temperature for a prescribed period of time.

The knowledge and fundamental understanding of a chemical's reactivity can be further expanded upon through the relationship described by Arrhenius theory (Brown, et al., 2003). Arrhenius argued that for reactants to transform into products, they must first acquire a minimum amount of energy, through heat or other means, called activation energy (E_a). The concept of activation energy is fundamental when describing the sensitivity of reaction rates to temperatures. As the rate constant (k) is utilized to describe the reaction rate at a specific temperature, the Arrhenius theory allows an understanding of the rate constant with respect to temperature (Eq. 5). Rate constants can be measured over a range of temperatures to develop an Arrhenius expression to describe the fluid's reactivity based on the activation energy, E_a, in kilojoules per mole and the pre-exponential factor A, in 1/seconds.

$$k = Ae^{-E_a/RT} \qquad \text{Eq. (5)}$$

Arrhenius theory is fundamental when utilizing accelerated life tests. A typical approach to accelerated testing involves use of elevated temperatures to drive measureable reactions at reasonable time durations. This approach to testing is based on a generalization supported by the Arrhenius theory, in that for many common chemical reactions near room temperature, the reaction rate doubles for every 10°C increase in temperature. This relationship of reaction rate as a function of temperature can then allow a researcher to gain important information on chemical reactivity on a

scale of days as opposed to years. For instance, if the chemical system being studied is a system operating at 100°C for 1 year (365 days), by using the generalization from Arrhenius, an accelerated test could be run at 150°C for 11.4 days to achieve similar chemical reactivity, if reaction mechanisms are not altered by the elevated temperature. Increasing the test temperature by 50ºC results in an increased reaction rate per Arrhenius theory by 32 times (2^5), which is equivalent to doubling of the reaction rate for every 10°C rise in temperature (365 days/32 equals 11.4 days). When the appropriate system is chosen and further studied, valuable information can be gained on the reaction kinetics using the Arrhenius relationship. Knowing the chemical reaction kinetics and degradation species allows one to be able to understand the variables which may promote or inhibit reactions. With this knowledge, strategies can be further developed and implemented to achieve successful applications of HVACR fluids

The authors conducted a number of HALT sealed glass tube studies with various catalyst, at various temperatures and durations. R1233zd(E) was exposed at a 50% refrigerant/50% lubricant mixtures with various iron catalysts and with a combination of copper/steel/aluminium catalyst to understand the amount of isomerization. Temperatures were varied from 110°C to 155°C, which are much higher than highest temperatures seen by chillers in their operational life by approximately 50°C to 100°C. Arrhenius theory indicates that chemical reactions typically double for every 10°C increase in temperature and these HALT temperatures were used to increase the reaction rates by 64 times to 1024 times to understand impact of R1233zd(E) isomerization. The Arrhenius reaction rates are summarized for both R1233zd(E) and R123 in Fig. 3. The R123 reaction rates are from internal studies done in the 1990's by Kujak and are included as a basis of comparison since R123 chillers have a long history of acceptable equipment reliability in water cooled chiller applications.

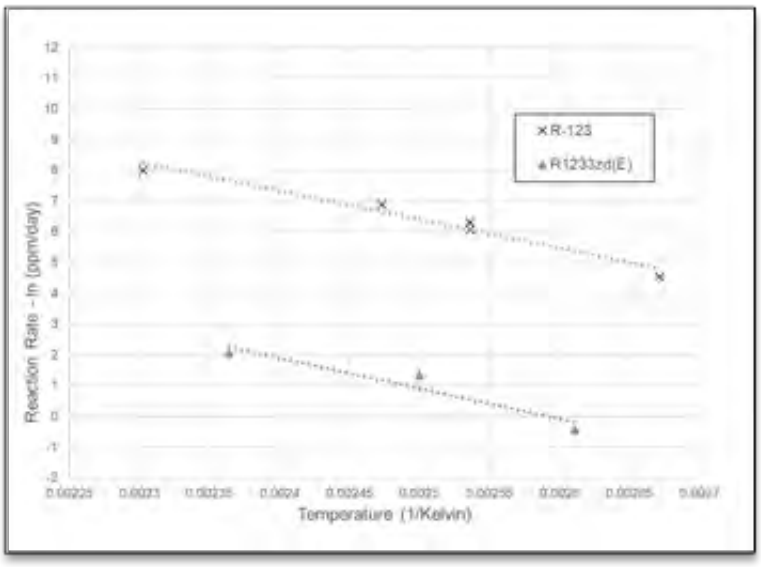

Figure 3: Arrhenius Plot of HALT Test Results for R123 and R1233zd(E) in 50% Refrigerant/50% Lubricant by weight with metal catalysts

3. NUMERICAL MODEL FOR ESTIMATING R123 and R1233zd(E) CHEMICAL STABILITY IMPACTS OVER THE LIFE OF WATER COOLED CHILLERS

Today, published climate zone data is available through resources like ASHRAE Standard 169. It is a simple operation to then use this data in combination with a simple thermodynamic refrigerant model and set the condition of the system to obtain equipment operational characteristics. The climatic data (dry bulb temperature vs hours spent) was obtained for eighteen climate zones that represent most of the globe's climates (ASHRAE 169-2016). Climate data was collected for 2.8°C dry bulb temperature discretized bins from -33°C to 45°C for all climate zones. Climate zones include weather regions from very cold (7), moist zones (6A-0A), dry zones (6B-0B) and marine zones (5C-3C). Fig. 4 provides a summary of all the climate hourly data by the discreet 2.8°C dry bulb

temperature ranges. In addition, ASHRAE 169 contains wet bulb temperatures for each of the climate zones as well. For this study, the wet bulb temperatures are specifically important since the wet bulb will set the water cooled chillers condenser temperatures as the result of the cooling tower effectiveness. The authors determined that climate zone 0A impacts the breakdown of R22 the most because of the long operational hours at elevated temperatures. In this study, the authors will use only climate zone 0A data for this example since it is likely that it is also the worst case climate zone for water cooled chiller operation. Fig. 5 provides a summary of the climate zone 0A hourly data for discreet 2.8°C for both dry and wet bulb temperature ranges. The difference in dry and wet bulb temperatures and hours spent at each condition is stark.

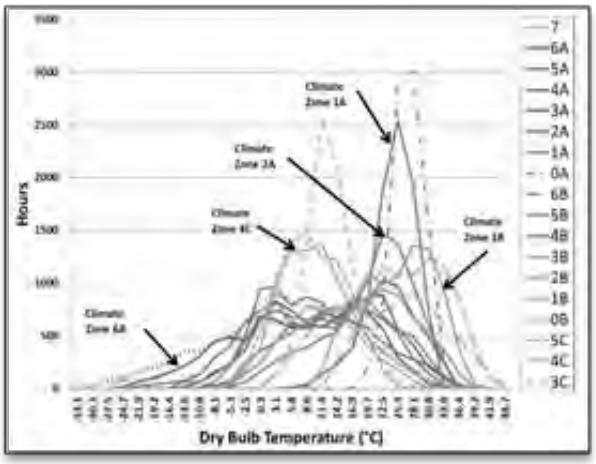

Figure 4: Number of hours spent at various ambient temperatures (dry bulb) by climate zone

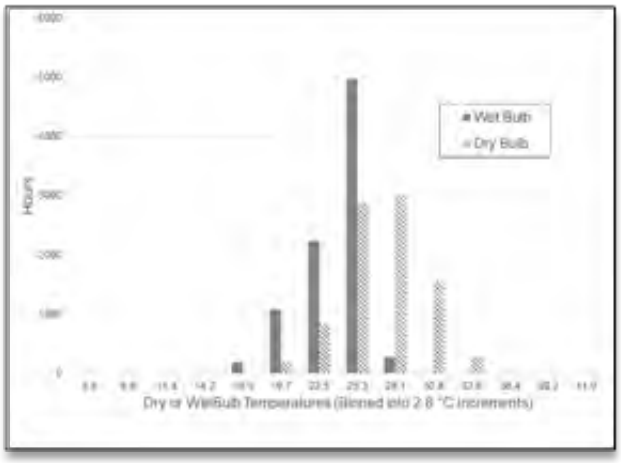

Figure 5: Summary of hours spent at dry and wet bulb temperature for climate zone 0A

Air conditioning is only needed at elevated ambients, starting at temperatures 18.3°C to 23.9°C, depending on the climate zones humidity conditions. It is then easy to understand the amount of time and temperature the equipment will see over its lifetime. Long equipment operation in relatively low ambients climate zones is not of particular interest from a refrigerant chemical stability standpoint since the equipment's operating temperatures and operational hours are low. Climate zones that require long hours of operation at moderate to high ambients can set the worst case from a refrigerant stability stand point because it will drive up the condenser and compressor discharge temperatures. A simple thermodynamic model was run at all the 2.8°C with wet bulb temperature discretized bins to obtain the refrigerant temperatures for the condenser and compressor discharge temperatures. An approach temperature of 3.9°C was used for tower and the wet bulb temperatures to set the entering cooling water temperature to the condenser. The chiller evaporator conditions were set at a constant 5.5°C leaving evaporator temperature and the compressor efficiency was fixed at 80 percent. The condenser leaving water temperature was also fixed at 5.5°C increase over the entering condenser water temperature. Obviously this is worst case scenario since at lower capacity conditions, the chiller would see lower condenser leaving water temperatures, but this assumption was done for the simplifying the analysis. The heat exchangers saturated refrigerant approach temperatures were set at 0.9°C. Superheat and subcooling were set to zero to simplify the analysis and are typical for large capacity economized cycle centrifugal chiller operation.

Next, the amount of time the refrigerant experiences over the life the chiller needed to be determined since refrigerant stability is a function of time spent at a given temperature. A chiller component analysis was conducted and the following times the refrigerant spends in each component were determined per hour of chiller run time. Specific data on the chiller component size and storage are not contained in this paper since this data is proprietary to the manufacturer. A refrigerant molecule spends 0.608 hours, 0.012 hours, 0.380 hours in the evaporator, compressor plus compressor discharge and condenser temperatures per hour of operation. Now an alternate method would be to take a conservative approach and use the maximum temperature obtained by the thermodynamic modeling and apply it to all the refrigerant for all the hours of operation. This worst case scenario analysis was also conducted a basis of comparison as well for this study with using the maximum leaving condenser water temperature (LCWT).

From the analysis of these many contributing factors – reaction kinetics, system component analysis, and operation characteristics specific to the various climate zones – trends in refrigerant degradation can be modeled and applied to estimate potential system impacts. More simply as expressed in Eq. 6, the total refrigerant breakdown is the summation of the breakdown in each component driven by the temperature and time spent in each component. Fig. 7 is a summary of applying the model to see differences in breakdown for both refrigerants when you apply the reaction rates for R123 and R1233zd(E) against operational conditions for climate zone 0A. In addition, an analysis was conducted based on a simplified assumption that all the refrigerant see the highest temperature, LCWT, for all the climate cooling hours.

$$Total\ Refrigerant\ Breakdown = \sum_{Breakdown} Condenser + Evaporator + Compressor + CDT \qquad \text{Eq. (6)}$$

Summarized in Fig. 6, it is evident that the breakdown of R1233zd(E) is about forty times less than R123. R123 has been used successfully in water cooled centrifugal compressor chiller applications over the past 30 years which would indicate that R1233zd(E) will be equally successful in these applications. Further evaluation of the component contributions in this climate zone do not attribute all the modeled degradation to be due to compressor discharge temperature even though it is the highest temperature condition. Given the modeled reaction rates and the residence time in the condenser, >90% of the total refrigerant decomposition is predicted to arise from this component. Even when you apply the highest leaving condenser water temperature to all components at a worst case scenario, you still only see a 4 time increase in breakdown of each refrigerant. The worst case scenario impacts the contributions by the condenser by about two times, the evaporator by forty times and CDT by thirty percent respectively. The increased chemical instability at worse case conditions makes sense since the time the refrigerant spends at increasing temperatures drives the overall reactivity.

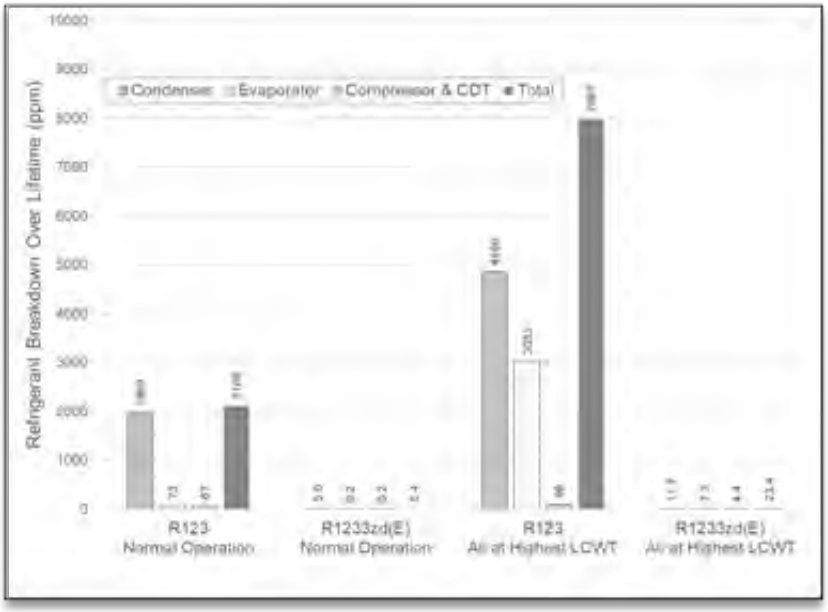

Figure 6: Summary of R123 and R1233zd(E) Breakdown for Climate Zone 0A by Component at Nominal Operation and Worst Case with all Component Temperatures Fixed a Maximum LCWT.

The furthered application and validation of this tool can have additional benefits to the analysis of system reactivity, as it can enable better understanding of the relationship (and limitation) of accelerated sealed glass testing. As discussed in prior sections, the industry commonly uses a sealed glass tube accelerated test point of 175°C for 2 weeks. This time and temperature was arbitrarily chosen to accelerate system reactions to a reasonable time span. It is not an appropriate approach for evaluating suitability of new refrigerants for use in equipment. When the theory of

Arrhenius is used to relate this test temperature to system operations at the most aggressive climate zone (zone 0A), the accelerating factor used is very large, and likely drives reactivity atypical to the dynamic refrigerant system. Assessment of the system modeled using the 0A climate data indicates an average system temperature of 20°C. In using an accelerated test at 150°C (20°C + 150°C ≅ 170°C) above this average temperature, it can be shown using the Arrhenius theory, that the reactivity is being driven at a rate ~32,000x (2^{15}) greater than the reaction rates that would be observed at the average system temperature. This acceleration is equivalent to 1227 years of equipment operation (14 days times 32,000 divided by 365 days per year), which is an unreasonable acceleration factor. The authors have been using a screening test temperatures of 127°C for 7 days as a reasonable acceleration factor for HALT sealed glass testing for water cooled chiller applications using low pressure refrigerants. This temperature is sufficiently high and long enough to get a reasonable amount of acceleration without driving atypical results. In using this time and temperature methodology, the acceleration factor now is reduced to at a rate ~2050 x (2^{11}) greater than the reaction rates that would be observed at the average system temperature. This acceleration is equivalent to ~40 years of equipment operation (7 days times 2050 divided by 365 days per year), which is a more reasonable acceleration factor.

Alternatively, if you choose another system temperature more representative of the maximum compressor discharge temperature modeled with the 0A climate data, we see average system temperatures closer to 33°C. In relating this operational temperature to the standard testing temperature of 127°C, we now see an acceleration of the reactivity by 512 times (2^9), which would relate back to 10 years of the fluid seeing this temperature constantly (7 days times 512 divided by 365 days per year). Alternatively as conducted in this analysis the maximum temperature seen in a component can be used for the estimate of acceleration factor. Compressor discharge temperatures are the highest temperatures seen in all vapour compression cycle. In this analysis, the highest CDT seen is approximately~40°C and we now see an acceleration of the reactivity by 256 times (2^8), which would relate back to 7 years of the fluid seeing this temperature constantly (7 days times 256 divided by 365 days per year). With these examples in mind, it becomes evident and crucial that the researcher understands the implications of accelerated testing in choosing appropriate test conditions to develop accelerated test models.

3. CONCLUSIONS

The approach to refrigerant chemical stability assessments has largely remained the same for the past sixty years since it was established in the industry through research on CFC-12 and HCFC-22. A new numerical approach is proposed using simple thermodynamic models, equipment design characteristics and climate zone data in combination with laboratory determined chemical reaction rates for a specific refrigerant system for determining the appropriate accelerated temperature and time for relation to equipment operation and life.

Ultra-low (<10) GWP, non-flammable refrigerant R1233zd(E) has emerged as replacements for R123, R245fa and R134a in large water cooled centrifugal chillers. This new numerical chemical stability model was applied to R1233zd(E) with using R123 chemical stability as a baseline of comparison. R123 has shown good chemical stability and thus acceptable chiller reliability over the 30 years of it use and the model confirms that R123 would be shown to have limited chemical instability issues over 25 years of operation. R1233zd(E) was demonstrated to have approximately forty times better chemical stability than R123 over 25 years of chiller operation and R1233zd(E) will provide acceptable chiller reliability.

As it is understood that the HVAC system is dynamic, with systems seeing a variety of times and temperatures depending on poor operation from a number of issues, the authors propose using HALT testing temperature of 127°C for 7 days as a temperature and time which could simulate anywhere from 7 to 40 years of water cooled chiller operation depending on various assumption without being too highly accelerated. The 127°C temperature has been used by the authors for the past 30 years when evaluating chemical stability of materials for use in water cooled centrifugal chillers and has been demonstrated to be a reasonable screening temperature and time. Running at higher temperatures could drive unrealistic chemical reactions or reaction rates at nominal operational conditions. With these examples in mind, it becomes evident and crucial that the

researcher understands the implications of accelerated testing in choosing appropriate test conditions to develop accelerated test models.

NOMENCLATURE

CDT	compressor discharge temperature (°C)
HALT	highly accelerated life test
HVACR	heating ventilation air conditioning and refrigeration
LCWT	leaving condenser water temperature
OEM	original equipment manufacturer
PPM	parts per million, by weight

REFERENCES

ASHRAE Standard 97-2007, Sealed Glass Tube Method to Test the Chemical Stability of Materials for Use Within Refrigerant Systems, ASHRAE, Inc., Atlanta, GA 30329.

ASHRAE Standard 169-2016, Weather Data for Building Design Standard, ASHRAE, Inc., Atlanta, GA 30329

Brown, T., et al. 2003. Chemistry The Central Science, 9th Edition, Pearson Education Inc., New Jersey

Doerr, R.G., Lambert, D., Schafer, R., Steinke, D. 1993. Stability Studies of E245 Fluoroether, CF3-CH2-O-CHF2, conference proceedings by ASHRAE.

Kauffman, R., 1993, Accelerated Screening Methods for Determining Chemical and Thermal Stability of Refrigerant-Lubricant Mixtures Part I: Method Assessment. ARTI MCLR Project Number 655-51500

Kujak, S., Schultz, K., and Sorenson, E., 2018, Experiences with Next Generation Low GWP Refrigerants in Centrifugal Chillers, Paper ID 1110,1st International Conference on the Application of HFO Refrigerants, Birmingham, UK.

Kujak, S., and Sorenson, E., 2019, Accelerated Life Methodology for Determining Acceptable Chemical Reactivity in HVACR Systems, presented at the ASHRAE Winter Meeting, Atlanta, Georgia (AT-2019-C064)

Manuscript ID: 265
DOI: 10.18462/iir.icr.2019.0265

Liquid-to-suction heat exchanger assessment using new synthetic refrigerants to replace R-134a

Adrián MOTA-BABILONI, Joaquín NAVARRO-ESBRÍ, Carlos MATEU-ROYO, Francisco MOLÉS, Ángel BARRAGÁN-CERVERA, Marta AMAT-ALBUIXECH

ISTENER Research Group, Department of Mechanical Engineering and Construction, Universitat Jaume I (UJI)
Castelló de la Plana, E-12071, Spain, mota@uji.es

ABSTRACT

The liquid-to-suction heat exchanger (LSHX) is a component added to vapor compression systems that can increase the cooling capacity (CC) and coefficient of performance (COP), depending on the working fluid and operating conditions. This paper evaluates its influence of when hydrofluorolefins (HFOs) and their mixtures are used in typical R-134a operating conditions. Attending to criteria and correlations, the LSHX improves COP for all fluids except for R-152a, presenting the alternatives better results than R-134a. From a theoretical point of view, the LSHX improves less the COP, but the ranking of refrigerants is the same. Then, when tested in an experimental setup with plate LSHX, COP increases are observed but lower those predicted, and the HFO/HFC mixture R-513A is more benefited than the greenhouse gas R-134a. According to these results, the utilization of the LSHX is advisable with new HFO/HFC mixtures in existing or new design refrigeration installations.
Keywords: Vapor compression cycle, Internal Heat Exchanger (IHX), R134a, HFC/HFO mixtures, drop-in replacement

1. INTRODUCTION

Fluorinated gases (F-gases) account for 2% of the European Union's greenhouse gas (GHG) emissions, quantified in CO_2-equivalent (CO_2-eq.) emissions. Three groups are listed as F-gases: hydrofluorocarbons (HFCs), perfluorocarbons and sulphur hexafluoride, being the first ones the more important pollutants. Regulation (EU) No 517/2014 (European Commission, 2014) started to control GHGs on 1 January 2015 in different directions: limiting the total amount that can be put in market, restricting their use in those relevant applications (new types) which more environmentally friendly alternatives are available, and improving their management to reduce the accidental leakages. Consequently, according to the European Environment Agency (EEA), the overall warming effect caused by F-gases in the EU-28 decreased by 2% (CO_2-eq.) compared with 2014 levels (https://www.eea.europa.eu/highlights/eu-goal-on-phase-down), and the global GHG emissions by 22%, compared with 1990 levels (European Environment Agency (EEA), 2018).
F-gas Regulation, for the time being, can be considered as a success regarding climate protection, especially considering that agreed upon in the Kigali Amendment to the Montreal Protocol (Höglund-Isaksson et al., 2017). Kigali Amendment is entered into force on 1st January 2019 after overcoming the minimum number of ratifying countries required. Therefore, it is worth to mention that, in 2017, the EU was 12% below the first HFCs put in the market limit (90% of 2011-2013 levels).
All these numbers reflect that lower global warming potential (GWP) refrigerants are entering into the European refrigeration and air conditioning market, a presence that is becoming more relevant in the coming years as the limit increases. HFCs replacement with environmentally friendly gases must also lead to a better (or at least comparable) system energy efficiency. The fourth generation of refrigerants transition is arising the interest in the improvement of vapor compression system technology and architecture.
R-134a (1 1 1 2-tetrafluoroethane) is a non-flammable HFC with $GWP_{100\text{-}yr}$ (100 years' time period) of 1300 used in medium temperature commercial refrigeration, domestic refrigeration, chillers and mobile air conditioning, among others. In the past, despite the clear energetic benefit caused by the addition of a liquid-to-suction heat exchanger (LSHX), it has not been added for simplicity in some

larger systems (Mota-Babiloni et al., 2015b), or its present as a capillary tube-suction line heat exchanger in other smaller ones (Belman-Flores et al., 2015).
This work aims to investigate, from different perspectives, the benefit that could cause the LSHX in R-134a lower GWP synthetic alternatives. First, the alternatives are presented, and their main characteristics introduced. Then, the LSHX component function and possible consequences are exposed. In the following, different correlations and approaches are used to evaluate the convenience of the LSHX in those fluids. Next, computational simulation is performed to continue the previous assessment. Finally, experimental data is used to validate the previously obtained results, and that will lead to draw the main conclusions of the work.

2. R-134a LOWER GWP ALTERNATIVES

To replace R-134a, the lower GWP synthetic alternatives for R-134a has been selected from the work of (Mota-Babiloni et al., 2017). Hence, the pure refrigerants R-152a, R-1234yf, R-1234ze and the blends R-450A and R-513A have been included. Moreover, the recently registered mixture R-516A (R-1234yf/134a/152a, 77.5/8.5/14.0 by mass percentage) is also considered for the previous analysis. R-444A and R-445A have not been so widely studied as the other mixtures and have been excluded from this work. For these fluids, Fig. 1 contains the temperature-pressure chart and Table 1 the main characteristics. All the thermodynamic properties, included the one presented in this section, are calculated using REFPROP v10 (Lemmon et al., 2018).

Figure 1: Temperature-pressure chart for R-134a and its alternatives

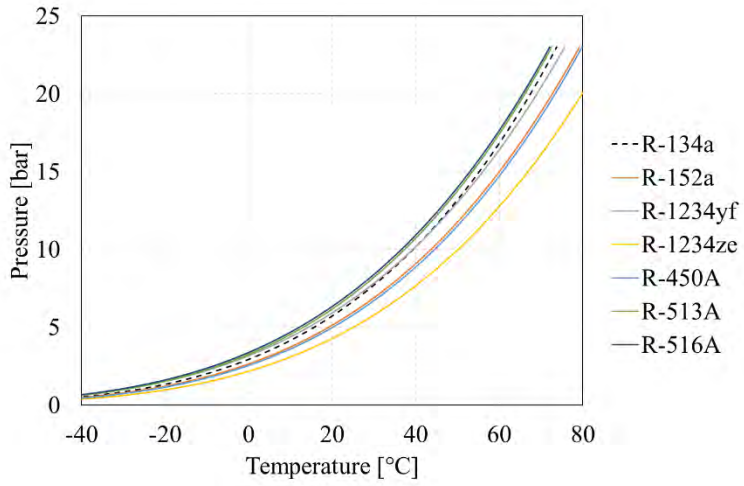

Table 1. Main characteristics for R-134a and its alternatives

	R-134a	R-152a	R-1234yf	R-1234ze	R-450A	R-513A	R-516A
ASHRAE Safety class.	A1	A2	A2L	A2L	A1	A1	A2L
Molar mass [g mol^{-1}]	102.03	66.05	114.04	114.04	108.67	108.43	112.66
P_{crit} [MPa]	4.06	4.52	3.38	3.63	3.82	3.65	3.51
T_{crit} [°C]	101.06	113.26	94.70	109.36	104.47	94.91	92.45
$GWP_{100\text{-}yr}$	1300	124	4	6	604	631	142
$\Delta h_{vap}/(c_{p,L}T_{crit})$	0.42	0.49	0.37	0.38	0.40	0.39	0.37

According to ASHRAE safety classification (ASHRAE, 2016), all selected alternative fluids are low toxic, and R-450A and R-513A are the only fluids that keep the non-flame propagation classification as R-134a, but also are the ones that present higher GWP values, and hence not applicable in European domestic refrigerators, mobile air conditioners or multipack commercial refrigeration systems. The rest of fluids, with GWP below 150, are at least low flammable, being the pure working fluids and R-516A classified as 2L.

The molar mass of alternative fluids is comparable to that of R-134a except for R-152a. Except for R-152a, all the alternative fluids present lower critical pressure than R-134a, being the higher deviation presented by R-1234ze. This information is completed with the temperature-pressure chart, where it can be seen that the refrigerant that shows different behavior to R-134a is R-1234ze. On the contrary, the most similar refrigerants to R-134a are the blends, that in fact include R-134a in their composition.

3. LIQUID-TO-SUCTION HEAT EXCHANGER (LSHX)

The liquid-to-suction heat exchanger (also known as Internal Heat Exchanger, IHX) is an element used to transfer heat between the subcooled liquid at the outlet of the condenser and the superheated gas at the outlet of the evaporator (Fig. 2). As a consequence, the specific enthalpy at the inlet of the expansion device (and at the inlet of the evaporator) is reduced, increasing the refrigerating effect (evaporator enthalpy increase). However, the compressor suctions the refrigerant at a higher temperature and lower pressure. Considering the same compressor operation (frequency, geometric volume and revolutions), it results in a lower mass flow rate given the lower suction density and higher specific compression work due to the higher compression ratio.

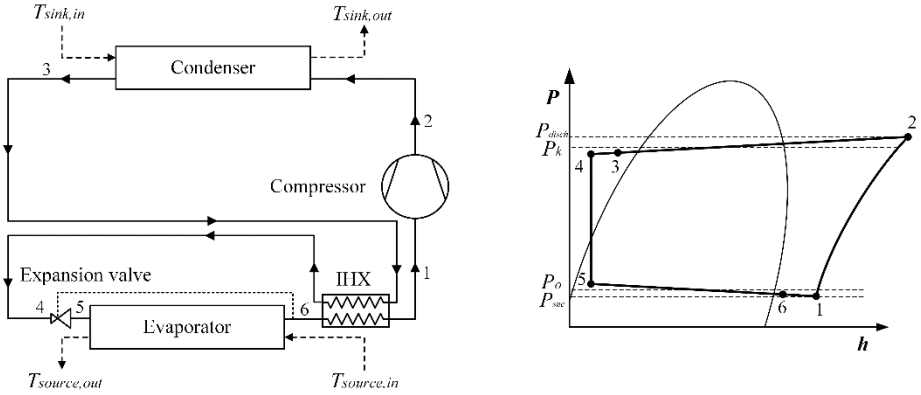

Figure 2: LSHX vapor compression cycle schematic representation and Ph diagram

The energy performance of a vapor compression system is quantified by the coefficient of performance (COP). In cold applications, the COP is defined as shown in Eq. (1). If the electromechanical efficiency is not considered, the COP can be calculated following Eq. (2). Therefore, when the LSHX is used, both parameters that affect the COP are increased and the relative difference compared to a cycle without it will depend on the magnitude of the variation of both enthalpy differences.

$$COP = \dot{Q}_{evap} \Big/ \dot{P}_{comp} \qquad \text{Eq. (1)}$$

$$COP = \Delta h_{evap} \Big/ \Delta h_{comp} \qquad \text{Eq. (2)}$$

It is worth to mention that besides the possible energetic benefits, the LSHX can help to prevent flash gas at the inlet of the expansion valve or compressor flooding. Besides, the LSHX effectiveness and hence the gas LSHX superheating must be controlled to avoid excessive compressor discharge gas temperatures that can worsen the lubricating properties of the oil.

4. CRITERIA AND CORRELATIONS FOR LSHX

Many works have been published to define the energetic benefit provided by the LSHX without computational simulations of the cycle or experimental measurements.
The first approach, provided by Domanski et al. (1994), predicted that the benefit of the LSHX depends on heat capacity, latent heat, and coefficient of thermal expansion (Eq. 3), and concluded that this element would have more considerable influence on those fluids with lower energy performance in the basic cycle.

$$\frac{1}{h_{f,g-e}/\bar{c}_{p,v}-(T_{cond}-T_{evap})\bar{c}_{p,L}/\bar{c}_{p,v}} > \frac{v'_{suction}-v_{suction}}{v'_{suction}(T'_{suction}-T_{suction})} = B_v \quad \text{Eq. (3)}$$

Aprea et al. (1999) simplified the expression to determine the energetic advantage of introducing LSHX, Eq. (4). Eq. (3) and (4) has been applied to the selected refrigerants and show benefit for all of them.

$$c_{p,suction}T_{suction} > \left(h_{suction} - h_{liquid}\right) \quad \text{Eq. (4)}$$

Klein et al. (2000) followed the Domanski et al. (1994) statements to study the cooling capacity enhancement (Eq. 5) and extend the conclusions to the COP. They highlighted that LSHX benefits at low values of D (calculated as $\Delta h_{vap}/(c_{p,L}T_{crit})$) and at high-temperature lifts (L). The first parameter has been presented in Table 1 for the selected refrigerants, and is seen as the most promising refrigerants are the R-1234yf, R-1234ze and R-516A.

$$RCI/_{\varepsilon} = -3.0468 + 19.3484D - 19.091D^2 + 1.2094L + 0.02101L^2 - 5.9980DL - 0.02797DL^2 + 5.52865D^2L \quad \text{Eq. (5)}$$

Klein et al. (2000) also provided correlations to study the cooling capacity or COP deterioration caused by LSHX additional pressure losses. Eq. (6) can correct Eq. (5) results, being only dependent on the temperature lift and the pressure drop proportional to the evaporating pressure.

$$\frac{COP}{COP_{no\ pressure\ losses}} = 1 - (2.37 - 0.0471L + 3.01 \cdot 10^{-4}L^2)\left(\frac{\Delta P_{LSHX}}{P_{evap}}\right) \quad \text{Eq. (6)}$$

Ziegler (2010) developed a dimensionless pseudo-Stefan-number to establish the condition of positive COP variation. Considering also negligible pressure losses at the LSHX, Eq. (7) is obtained. Through this criterion, all refrigerants depict energetic benefit from the LSHX.

$$\frac{c_{p,v}T_{suction}}{\Delta h} = 1 - \frac{c_{p,L}L}{\Delta h} \quad \text{Eq. (7)}$$

Finally, Hermes (2013) developed expressions at constant working pressures or cooling capacity. In the first case, the criterion used is shown in Eq. (8) to (11).

$$\frac{COP_{LSHX}}{COP_{without\ LSHX}} \approx \frac{1+\varepsilon_{LSHX}C_r\frac{\varphi}{1-\varphi}}{1+\varepsilon_{LSHX}\theta} \quad \text{Eq. (8)}$$

$$\varphi = c_{p,L}\left(T_{cond} - T_{evap}\right)/h_{LV} \quad \text{Eq. (9)}$$

$$\theta = \beta\left(T_{cond} - T_{evap}\right) \quad \text{Eq. (10)}$$

$$\beta = \left(\frac{1}{v}\right)\left(\frac{\partial v}{\partial T}\right)_p \quad \text{Eq. (11)}$$

The results obtained with Hermes and Klein et al.'s criteria are presented in Fig. 3. Note that the cooling capacity improvement formula can be used for COP if no variation of power consumption is assumed. It can be seen as the benefit predicted by Hermes is higher than that of Klein et al.'s for all refrigerants except for R-1234ze. As expected, the COP improvement increases with the temperature lift for both criteria and follows that suggested by the $\Delta h_{vap}/(c_{p,L}T_{crit})$ ratio. The only refrigerant which deteriorates COP with LSHX is R-152a (contrary to that predicted by Domanski et al. and Aprea et al. criteria), and the refrigerant with the lower increase is R-134a followed by R-450A. Hence, it can be seen as the presence of R-1234yf in the mixture helps to increase the COP with LSHX, in comparison with R-1234ze as a former component.

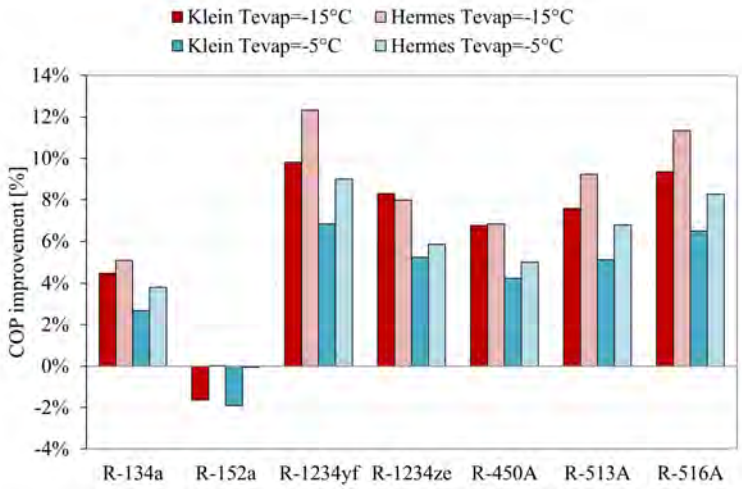

Figure 3: COP improvement using Klein et al.'s and Hermes criteria

A more in-depth analysis of the development, results, assumptions and other characteristics of the mentioned correlations or the parameters used in them can be found in each reference or in papers that use some of them as (Mota-Babiloni et al., 2019; Navarro-Esbrí et al., 2013).

5. THEORETICAL EFFECTS OF LSHX

Mastrullo et al. (2007) carried out a thermodynamic analysis to confirm the benefit of the LSHX in different refrigerants and operating conditions. They agree with (Klein et al., 2000) concluding that the SLHX has the same effect on the COP and the volumetric refrigerating capacity. This work also includes a computational simulation of the COP for the selected refrigerants. The results at a condensing temperature of 32.5 °C and evaporating temperature of -15 and -5°C, volumetric and isentropic efficiency of 0.8, superheating and subcooling degree of 10 and 2 K, and LSHX effectiveness of 0.8 are presented in Fig. 4.

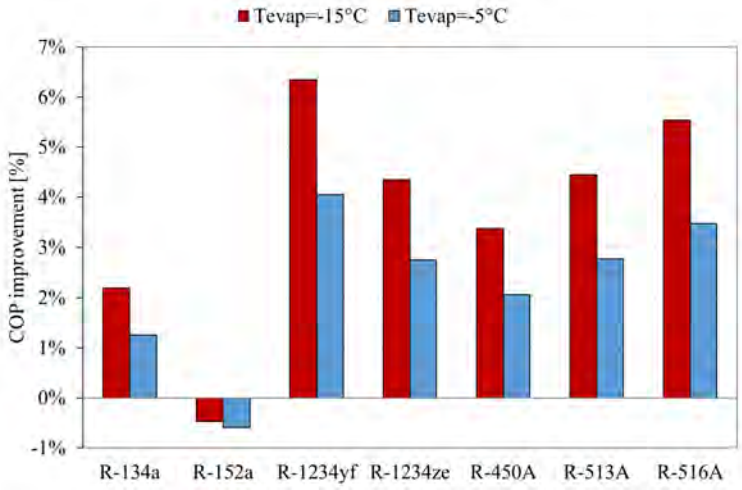

Figure 4: Theoretical COP improvement

Criteria overpredict (almost the double) the benefit of the LSHX, but they agree with the ranking of LSHX benefit and also with the COP deterioration shown by R-152a.

6. EXPERIMENTAL VALIDATION WITH R-513A

Finally, a set of experimental tests are carried out to validate the positive theoretical values obtained with R-134a and its lower GWP alternative, R-513A. The test methodology, experimental setup and analysis of results can be found in (Mota-Babiloni et al., 2019). Additional experimental results with LSHX using R-1234yf, R-1234ze and R-450A can be found in (Devecioğlu and Oruç, 2018; Mota-

Babiloni et al., 2015a; Navarro-Esbrí et al., 2013). The COP experimental results for similar conditions than theoretical analysis are shown in Fig. 5.

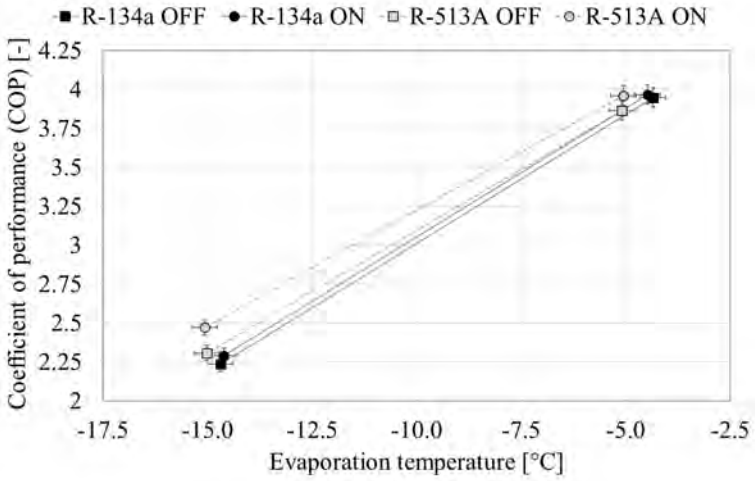

Figure 5: COP results with (ON) and without (OFF) LSHX

Fig. 5 experimentally confirms the great benefit provided by the LSHX to R-134a and R-513A refrigerants, as expected by the correlations, criteria, and theoretical simulation. The COP benefit is more visible at the lower evaporating temperature, in which the heat exchanged in the LSHX is higher (higher temperature difference between gas and liquid lines). R-513A is more benefited by the LSHX, as suggested by the $\Delta h_{vap}/(c_{p,L}T_{crit})$ term.

7. CONCLUSIONS

Refrigeration and air conditioning industry is living today a period of transition from HFCs to more environmentally friendly (lower GWP) refrigerants. The addition of the LSHX offers the possibility to increase the energy performance of vapor compression systems. This work studies the energy performance benefit of including this element in several synthetic refrigerants developed to replace R-134a. The selected alternatives are R-152a, R-1234yf, R-1234ze, R-450A, R-513A and R-516A, which presents similar thermodynamic properties to R-134a and different GWP and flammability characteristics.

The $\Delta h_{vap}/(c_{p,L}T_{crit})$ term can help to quickly determine which alternative refrigerant is going to be more benefited from the introduction of the SLHX. Domanski et al. and Aprea et al. criteria do not predict that R-152a can have worse COP with this element, as the quantitative criteria of Klein et al. and Hermes does. In the same way, Klein et al. and Hermes criteria and theoretical simulation follow the ranking of the $\Delta h_{vap}/(c_{p,L}T_{crit})$ but they have significant differences in the improvement. Experimental results of R-513A and R-134a agrees with the COP benefit, but it is lower than predicted by the criteria.

All the alternative synthetic refrigerants show better COP improvement with LSHX than R-134a, and hence it is recommended to introduce (or maintain) this element in a retrofit replacement. Further experimental studies are required to confirm the negative variation of R-134a, and confirm the positive values of R-516A, a promising low-flammability low GWP mixture.

ACKNOWLEDGEMENTS

Adrián Mota-Babiloni, Carlos Mateu-Royo, and Marta Amat-Albuixech acknowledge the financial support of the Spanish Government, Universitat Jaume I, and Generalitat Valenciana under the grants FJCI-2016-28324, PREDOC/2017/41, and FEDEGENT/2018/002, respectively.

NOMENCLATURE

COP	coefficient of performance (-)	*cond*	condenser
$c_{p,L}$	liquid phase isobaric specific heat (kJ kg-1 K-1)	$c_{p,v}$	vapor phase isobaric specific heat (kJ kg-1 K-1)
crit	critical point	*evap*	evaporating, evaporation
GHG	greenhouse gas emissions	$GWP_{100\text{-}yr}$	global warming potential on a 100-year basis
h	specific enthalpy (kJ kg-1)	HFC	hydrofluorocarbon
HFO	hydrofluoroolefin	L	temperature lift (-)
LSHX	liquid-to-suction heat exchanger	P	pressure (MPa)
$\dot{P}_{comp}$	power consumption (kW)	$\dot{Q}$	heat transfer (kW)
T	temperature (K)	v	specific volume (m3 kg-1)
Δh_{vap}	latent heat of vaporization (kJ kg-1)	Δh_{comp}	specific compressor work (kJ kg-1)
ΔP	Pressure drop (kPa)	ε	Heat exchanger effectiveness (-)
$\beta, \theta, \varphi, D$	Parameters used in LSHX criteria	′	LSHX activated

REFERENCES

Aprea, C., Ascani, M., de Rossi, F., 1999. A criterion for predicting the possible advantage of adopting a suction/liquid heat exchanger in refrigerating system. Appl. Therm. Eng. 19, 329–336. https://doi.org/10.1016/S1359-4311(98)00070-2

ASHRAE, 2016. ANSI/ASHRAE Standard 34–2016 Designation and Safety Classification of Refrigerants.

Belman-Flores, J.M.M., Barroso-Maldonado, J.M.M., Rodríguez-Muñoz, A.P.P., Camacho-Vázquez, G., 2015. Enhancements in domestic refrigeration, approaching a sustainable refrigerator - A review. Renew. Sustain. Energy Rev. 51, 955–968. https://doi.org/10.1016/j.rser.2015.07.003

Devecioğlu, A.G., Oruç, V., 2018. Improvement on the energy performance of a refrigeration system adapting a plate-type heat exchanger and low-GWP refrigerants as alternatives to R134a. Energy 155, 105–116. https://doi.org/10.1016/J.ENERGY.2018.05.032

Domanski, P.A., Didion, D.A., Doyle, J.P., 1994. Evaluation of suction-line/liquid-line heat exchange in the refrigeration cycle. Int. J. Refrig. 17, 487–493. https://doi.org/10.1016/0140-7007(94)90010-8

European Commission, 2014. Regulation (EU) No 517/2014 of the European Parliament and of the Council of 16 April 2014 on fluorinated greenhouse gases and repealing Regulation (EC) No 842/2006. Off. J. Eur. Union. https://doi.org/https://doi.org/10.4271/1999-01-0874

European Environment Agency (EEA), 2018. Annual European Union greenhouse gas inventory 1990–2016 and inventory report 2018, EEA Report/2018. Brussels, Belgium.

Hermes, C.J.L., 2013. Alternative evaluation of liquid-to-suction heat exchange in the refrigeration cycle. Int. J. Refrig. 36, 2119–2127. https://doi.org/10.1016/J.IJREFRIG.2013.06.007

Höglund-Isaksson, L., Purohit, P., Amann, M., Bertok, I., Rafaj, P., Schöpp, W., Borken-Kleefeld, J., 2017. Cost estimates of the Kigali Amendment to phase-down hydrofluorocarbons. Environ. Sci. Policy. https://doi.org/10.1016/j.envsci.2017.05.006

Klein, S.A., Reindl, D.T., Brownell, K., 2000. Refrigeration system performance using liquid-suction heat exchangers. Int. J. Refrig. 23, 588–596. https://doi.org/10.1016/S0140-7007(00)00008-6

Lemmon, E.W., Bell, I.H., Huber, M.L., McLinden, M.O., 2018. NIST Standard Reference Database 23: Reference Fluid Thermodynamic and Transport Properties-REFPROP, Version 10.0, National Institute of Standards and Technology, Standard Reference Data Program. https://doi.org/http://dx.doi.org/10.18434/T4JS3C

Mastrullo, R., Mauro, A.W., Tino, S., Vanoli, G.P., 2007. A chart for predicting the possible advantage of adopting a suction/liquid heat exchanger in refrigerating system. Appl. Therm. Eng. 27, 2443–

2448. https://doi.org/10.1016/j.applthermaleng.2007.03.001

Mota-Babiloni, A., Makhnatch, P., Khodabandeh, R., 2017. Recent investigations in HFCs substitution with lower GWP synthetic alternatives: Focus on energetic performance and environmental impact. Int. J. Refrig. 82, 288–301. https://doi.org/10.1016/j.ijrefrig.2017.06.026

Mota-Babiloni, A., Navarro-Esbrí, J., Barragán-Cervera, A., Molés, F., Peris, B., 2015a. Drop-in analysis of an internal heat exchanger in a vapour compression system using R1234ze(E) and R450A as alternatives for R134a. Energy 90. https://doi.org/10.1016/j.energy.2015.06.133

Mota-Babiloni, A., Navarro-Esbrí, J., Barragán-Cervera, Á., Molés, F., Peris, B., Verdú, G., 2015b. Commercial refrigeration - An overview of current status. Int. J. Refrig. 57. https://doi.org/10.1016/j.ijrefrig.2015.04.013

Mota-Babiloni, A., Navarro-Esbrí, J., Pascual-Miralles, V., Barragán-Cervera, Á., Maiorino, A., 2019. Experimental influence of an internal heat exchanger (IHX) using R513A and R134a in a vapor compression system. Appl. Therm. Eng. 147, 482–491. https://doi.org/10.1016/j.applthermaleng.2018.10.092

Navarro-Esbrí, J., Molés, F., Barragán-Cervera, Á., 2013. Experimental analysis of the internal heat exchanger influence on a vapour compression system performance working with R1234yf as a drop-in replacement for R134a. Appl. Therm. Eng. 59, 153–161. https://doi.org/10.1016/j.applthermaleng.2013.05.028

Ziegler, F., 2010. The multiple meanings of the Stefan-number (and relatives) in refrigeration. Int. J. Refrig. 33, 1343–1349. https://doi.org/10.1016/j.ijrefrig.2010.06.015

Manuscript ID: 294
DOI: 10.18462/iir.icr.2019.0294

Experimental investigation on melting process of a phase change material with embedded heat pipes in a vacuum insulated cold thermal energy storage panel

Shen TIAN[(a)], Qifan YANG[(a)], Shuangquan SHAO[(b)] Shengchun LIU[(a)]

[(a)] Tianjin Key Laboratory of Refrigeration Technology, Tianjin University of Commerce
Tianjin, 300134, China, tianshen@tjcu.edu.cn
[(b)] CAS Key Laboratory of Cryogenics, Technical Institute of Physics and Chemistry
Beijing, 100190, China, shaoshq@mail.ipc.ac.cn

ABSTRACT

By recent interest in overcoming the heat transfer limitations of phase change materials (PCMs), thermal energy storage process that enhanced by embedded heat pipes has received much attention. Due to coupling with heat pipes, the phase change process of PCMs can be indicated or controlled by the operating conditions of heat pipes. In the present paper, a vacuum insulated cold thermal energy storage panel that embedded with heat pipes and PCMs are investigated experimentally. The evaporator section of heat pipes is exposed in air. By applying different air speed and air temperature, melting process of PCM and air temperature difference through the evaporator section of heat pipes are analysed, so as to help to indicate the amount of cold thermal energy in the panel in real time. The study also provides a framework for designing of portable cold thermal energy storage device with controllable energy supply.
Keywords: phase change material, heat pipe, melting behaviour, cold thermal energy storage.

1. INTRODUCTION

Refrigeration is one of the intensive energy consuming technologies. Cold thermal energy storage (CTES) is an energy saving technology that can be effectively combined with different types of renewable energy and can mitigate the problem of instability or mismatch of cold energy supply (Li et al., 2012). This fact make it has always been attracted interest in refrigeration applications such as process cooling, cold chain (Oró et al., 2014) and air conditioning (Qureshi et al., 2011). Generally, there are three thermal energy storage methods: sensible storage, latent storage and thermal-chemical storage (Veerakumar and Sreekumar, 2016). In CTES, latent storage is widely used for its high thermal energy storage density and easily available for applications.

Many researches have studied latent CTES by using PCMs in refrigeration, of which a significant number are aimed at climate-control of refrigerated area. Azzouz et al. (2009) present the experimental results of using a PCM on a household refrigerator, which shows a great improvement of COP. Ahmed et al. (2010) reconstruct the insulation of a refrigerated truck trailer by inclusion of PCMs. A notable reduction in total heat transfer and a more stable indoor temperature is achieved. Nagano et al. (2006) propose a floor supply air conditioning system with PCM packed bed. Experimental results show an increased indoor temperature stabilization. The abovementioned review indicates that CTES has great potential on stable control and energy consumption reduction of refrigeration systems. However, there are also some inevitable problems in applications of CTES: (1) Poor thermal conductivity of PCMs which seriously affects the heat transfer efficiency; (2) For the effect of problem (1), the transient response of CTES is slow that can lead to mismatch of CTES and the coupled/original refrigeration systems.

In consideration of poor thermal conductivity, many researches on heat transfer enhancement by extended heat transfer surfaces have been carried out. Metal fins (Sciacovelli et al., 2015; Rathod and Banerjee, 2015), heat pipes (Nithyanandam and Pitchumani, 2011; Sharifi et al., 2012) and coupled both (Allen et al., 2015) are utilized in the researches. Overall, the embedded extended surfaces methods achieve much higher melting rates with respect to a non-enhanced system.

For the mismatch problem, heat transfer between the CTES and the refrigerated area is mainly by natural convection and radiation with a low air-side heat transfer coefficient (Laguerre et al., 2018). Embedding heat pipes and fins in the CTES is an efficient and cheap solution, which results in an

enhancement/controllable of the global heat transfer at the CETS to realize a quick response to cold thermal energy demand. Meanwhile, melting process that coupling with heat pipes can help indicate the capacity of latent cold thermal energy due to the exported heat transfer process by heat pipes. From abovementioned reasons, in this study, experiments on melting behaviour of a phase change material with embedded heat pipes in a cold thermal energy storage panel is investigated. The outside surface of the panel is vacuum insulated to investigate melting process driven only by heat pipes. The evaporator section of heat pipes is exposed in air. By applying different air speed and input air temperature on the evaporator section, melting process of the PCM and cold thermal energy supply performance of the panel are analysed. The objective is to provide detailed information (temperature distribution, melting process histories and photographic observations) during melting for cold thermal energy supply of cold storage panels embedded with heat pipes.

2. EXPERIMENTAL SET UP AND PROCEDURES

A layout of the experimental apparatus is shown in Fig. 1.

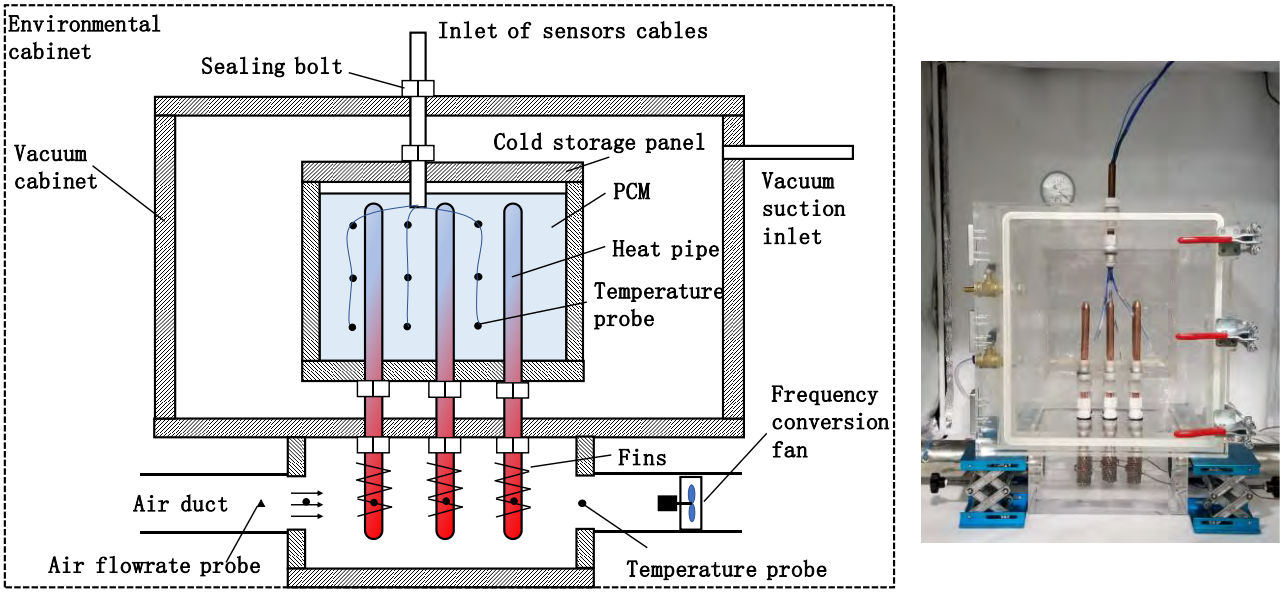

Figure 1: Schematic of experimental apparatus

The PCM (distilled water) is contained in a rectangular panel (160 mm inner height, 180 mm inner length, 80 mm inner width, 20 mm wall thickness) and is subject to heat transfer from six copper-methanol heat pipes (12.7 mm outer diameter). The panel is placed in a vacuum cabinet and well-sealed by sealing bolts to reduce the effect on melting process from surface heat transfer of the panel. The evaporation sections of heat pipes are equipped with fins and heated by airflow through the air duct under the vacuum cabinet. A frequency conversion fan is installed at the end of air duct to regulate air flowrate. To investigate the effect of heat transfer through heat pipes, the temperature of PCM, air inlet, air outlet and evaporation section of heat pipes as well as air speed through air duct are monitored and measured. Meanwhile, photographic observations on PCM by using a camera are also applied during melting process.

The melting experiments of PCM are carried out as followed procedures: (1) Open the door of vacuum cabinet and set up the temperature of environmental cabinet as – 30 °C. It takes 12 hours until the distilled water frozen into ice and the temperature that measured by sensors in the panel are all below – 2 °C. (2) Close the door of vacuum cabinet and turn on vacuum pump. (3) Before turning on the frequency conversion fan, set up temperature of environmental cabinet as required and maintain all the measured parameters are stable. (4) Turn on the regulated power supply of frequency conversion fan as required voltage. (5) Measuring data and taking photos. The specific experimental conditions are listed in Table 1.

Table 1. Specific experimental conditions

No.	Inlet temperature (°C)	Average air velocity ($m \times s^{-1}$)	Initial average temperature in panel (°C)	Final average temperature in panel (°C)	Mass of distilled water (kg)

1	30	3.0	-2.9	10.0	0.98
2		3.5	-3.4	8.3	0.98
3		4.0	-4.2	12.1	0.98
4	50	3.0	-9.5	17.9	0.98
5		3.5	-16.3	18.7	0.98
6		4.0	-3.2	16.4	1.25

3. RESULTS AND DISCUSSIONS

3.1. Photographic observations

The influence of melting process that driven by heat pipes is investigated photographically in this section. Each photograph is taken from the front side view as indicated in Fig. 1. It should be noted that the black-and-white photographs are conversely processed so as to the liquid-solid interface is easily discernible. Therefore, liquid in most of photos appears white and solid appears black.
Photographs during melting for the (a) T_{inlet} = 50 ºC, $\bar{u}$ = 3.0 m×s^{-1} at t = 0 min, t = 60 min, t = 120 min and t = 180 min are shown in Fig. 2 (a). At first, melting liquid near heat pipes is blocked by the front surface of solid that can not be seen. Then by the effect of sequential locations of heat pipes, a larger degree of heat transfer on the left side that close to air inlet results in a larger mass of melting liquid (see Fig. 2 (a) with t = 60 min). After that, for the reason of volume shrinkage of melting liquid, there is a little mass of solid stayed on the top of the panel, which is prevented from falling by inner surface of the panel. At last, all solid became melting liquid.

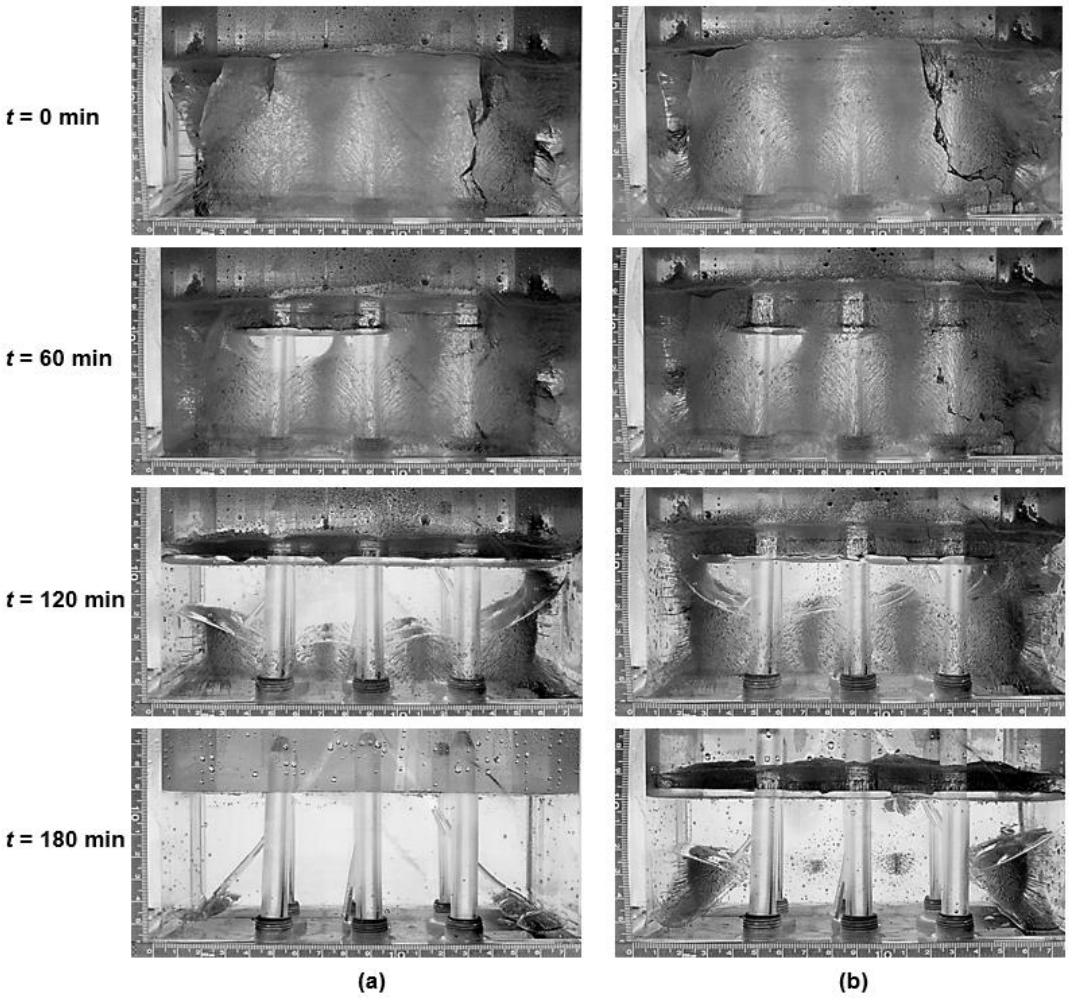

Figure 2: Photographs during melting with heat pipes for the (a) T_{inet} = 50 ºC, $\bar{u}$ = 3.0 m×s^{-1}; (b) T_{inlet} = 30 ºC, $\bar{u}$ = 4.0 m×s^{-1}

Photographs during melting for the (b) T_{inlet} = 30 ºC, $\bar{u}$ = 4.0 m×s^{-1} at t = 0 min, t = 60 min, t = 120 min and t = 180 min show a similar melt pattern. For the symmetry layout of heat pipes, the solid

face appears symmetry forward and backward. It can also be seen that with lower air inlet temperature in 20 °C, melting process almost delay over 1 hour.

3.2. Cold thermal energy supply performance of the panel

Inlet and outlet air temperatures and airflows are measured during melting in different conditions as shown in Table 1. Fig. 3 shows variations of outlet air temperature. There are two main subdivisions: (1) a quick response and sharp rise of outlet air temperature in the first few minutes; (2) relatively stable temperature rises until the melting finish. This fact reveals a noticeable variation of heat transfer degree. This is caused by heat transfer condition variation of PCM, which is in a higher degree of heat transfer for the not enlarged melting liquid area in the first period of time.

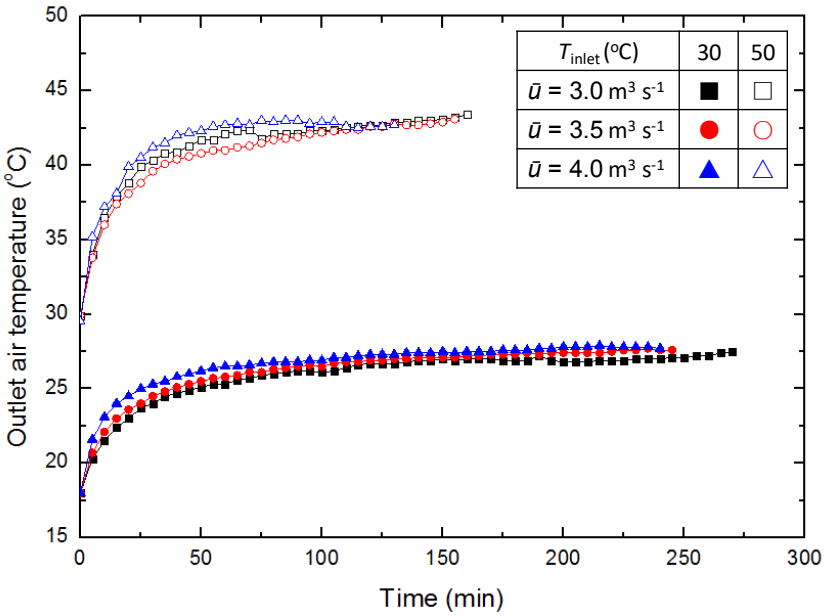

Figure 3: Outlet air temperatures at different inlet air temperatures and airflows

For the reason that the outside surface of the panel is vacuum insulated, heat that received from outside surface is ignored. Therefore, the transient cold thermal energy supply capacity of this panel is equal to the quantity of energy transferred to air divided by time interval, which can be calculated as follows (Stritih and Butala, 2010):

$$Q(t) = \sum_{i=1}^{n} \dot{m} C_p (T_{\text{inlet}} - T_{\text{outlet}}) \qquad \text{Eq. (1)}$$

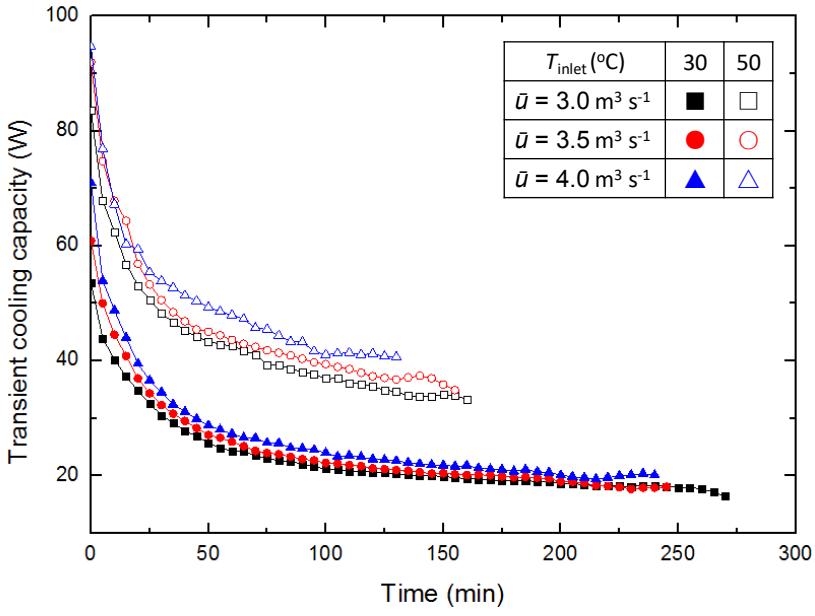

Figure 4: Transient cooling capacity of the panel during melting

Fig. 4 shows the transient cooling capacity of the panel in different experimental conditions. It is a nonlinear cold thermal energy supply that overall affected by inlet air temperature and inlet airflow rates, which decrease with the reduction of the two effectors. The average cooling capacity is at a certain range between 20 W ~ 50 W in the experiments.

4. CONCLUSIONS

This study aims to investigate the melting behaviour of a PCM that only driven by heat transfer from embedded heat pipes. Due to vacuum insulation of outside surface of the panel, melting behaviour of water is revealed and connected by the evaporation section of heat pipes. Different inlet air speeds and air temperatures are provided to the evaporation section and their corresponding effect on melting process is measured. The measurement data of outlet air temperature shows a noticeable variation of heat transfer degree at the not enlarged melting liquid area in the first period of time. The exerted airflow on the evaporation section of heat pipes results on a nonlinear cold thermal energy supply capacity from 20 W ~ 50 W along with variation of air speed and air temperature. The experiments conducted and analysed do not correspond to optimized conditions. Further investigations of liquid fraction histories, different kinds of PCMs and incorporation in CTES systems are necessary to applications in different scenarios. The observed phenomena and measured values can be used to guide model development for purposes of simulating the melting processes coupled with heat pipes and design of portable cold thermal energy storage devices.

ACKNOWLEDGEMENTS

This work is supported by the CAS Key Laboratory of Cryogenics, TIPC (Open Fund No. CRYO201809), Natural Science Foundation of Tianjin (No. 18JCQNJC77500).

NOMENCLATURE

C_p	specific heat capacity ($kJ \times kg^{-1} \times {}^oC^{-1}$)	m	mass (kg)
Q	cooling capacity (W)	T	temperature (^oC)
$\bar{u}$	average air velocity ($m \times s^{-1}$)		

REFERENCES

Ahmed, M., Meade, O., Medina, M. A., 2010. Reducing heat transfer across the insulated walls of refrigerated truck trailers by the application of phase change materials. Energy Conversion and Management 51 (3), 383-392.

Allen, M. J., Sharifi, N., Faghri, A., Bergman, T. L., 2015. Effect of inclination angle during melting and solidification of a phase change material using a combined heat pipe-metal foam or foil configuration. International Journal of Heat and Mass Transfer 80, 767-780.

Azzouz, K., Leducq, D., Gobin, D., 2009. Enhancing the performance of household refrigerators with latent heat storage: An experimental investigation. International Journal of Refrigeration 32 (7), 1634-1644.

Laguerre, O., Chaomuang, N., Derens, E., Flick, D., 2018. How to predict product temperature changes during transport in an insulated box equipped with an ice pack: experimental versus 1-D and 3-D modelling approaches. International Journal of Refrigeration, in press.

Li, G., Hwang, Y., Radermacher, R., 2012. Review of cold storage materials for air conditioning application. International Journal of Refrigeration 35, 2053–2077.

Nagano, K., Takeda, S., Mochida, T., Shimakura, K., Nakamura, T., 2006. Study of a floor supply air conditioning system using granular phase change material to augment building mass thermal storage—Heat response in small scale experiments. Energy and Buildings 38 (5), 436-446.

Nithyanandam, K., Pitchumani, R., 2011. Analysis and optimization of a latent thermal energy storage system with embedded heat pipes. International Journal of Heat and Mass Transfer 54 (21-22), 4596-4610.

Oró, E., Miró, L., Farid, M. M., Martin, V., Cabeza, L. F., 2014. Energy management and CO2 mitigation using phase change materials (PCM) for thermal energy storage (TES) in cold storage and transport. International Journal of Refrigeration 42, 26-35.

Qureshi, W. A., Nair, N. C., Farid, M. M., 2011. Impact of energy storage in buildings on electricity demand side management. Energy Conversion and Management 52 (5), 2110-2120.

Rathod, M. K., Banerjee, J., 2015. Thermal performance enhancement of shell and tube Latent Heat Storage Unit using longitudinal fins. Applied Thermal Engineering 75, 1084-1092.

Sciacovelli, A., Gagliardi, F., Verda, V., 2015. Maximization of performance of a PCM latent heat storage system with innovative fins. Applied Energy 137, 707-715.

Sharifi, N., Wang, S. M., Bergman, T. L., Faghri, A., 2012. Heat pipe-assisted melting of a phase change material. International Journal of Heat and Mass Transfer 55 (13-14), 3458-3469.

Stritih, U., Butala, V., 2010. Experimental investigation of energy saving in buildings with PCM cold storage. International Journal of Refrigeration 33, 1676-1683.

Veerakumar, C., Sreekumar, A., 2016. Phase change material based cold thermal energy storage: Materials, techniques and applications – A review. International Journal of Refrigeration 67, 271-289.

Manuscript ID:299

DOI: 10.18462/iir.icr.2019.0299

Experimental and Numerical Investigations on Thermal Conductivity of Al_2O_3/Ethylene Glycol Water and Tio_2/Ethylene Glycol Water Nanofluids

Rajeev KUKREJA[a], Mahesh NANDYALA[b]

[a,b] Dr. B. R. Ambedkar National Institute of Technology
Jalandhar-144011, Punjab, India. kukrejar@nitj.ac.in, maheshn1481@gmail.com

ABSTRACT

The use of high power density microelectronic devices has led to increased heat flux in electronic chips. Mostly fluids are employed as heat exchanging media in such devices. In the present study, investigations on temperature dependent thermal conductivity of ethylene glycol-water mixture based nanofluids have been carried out. Ethylene glycol and water mixture in the ratio of 30:70 by volume has been used as a base fluid with nanoparticles of Al_2O_3 and TiO_2 with varying concentration varying from 0.25% to 1% by volume. The thermal conductivity of the nanofluids is measured by transient hot wire method in the temperature range of 20°C to 50°C. The experimental results have been compared with the theoretical models to indicate the ability of the models to predict the thermal conductivity and discrepancies were indicated. The maximum increment of 16.07% in the thermal conductivity was observed for 1% Al_2O_3 Nano fluid at 50°C, while the minimum of 0.61%, at 20°C was observed for 0.25% TiO_2.

Key words**:** Ethylene glycol, EGW, Nanoparticles, Nano fluid, Thermal conductivity, Transient hot-wire method.

1. INTRODUCTION

The modern technology has resulted in high power density and ultraspeed microelectronic devices, increasing the heat generated per unit surface area of the electronic chips. Heat transfer rates in variety of applications such as industrial cooling, nuclear reactors, transportation and MEMS have increased drastically in the recent times. Most of the times fluids are employed as heat exchanging media in several equipment, automobiles and heat exchangers. Thermal conductivity of these fluids affects the heat transfer rate and efficiency. Inherent lower thermal conductivity of conventional heat transfer fluids such as water, ethylene glycol and engine oil, is limiting heat transfer efficiency. Thus there is a demand for new heat exchanging fluids with greater thermal conductivity and improved heat transport characteristics. In response to the needs for more efficacious heat transfer systems, researchers and engineers have adopted various heat transfer augmentation methods since the mid-1950s. Thermal conductivity of solids is much higher than liquids. Maxwell (1881) proposed that solid metallic particles of millimeter size, can be dispersed into industrial heat transfer fluids to device new fluids. However coarse particles due to their larger grain size are more susceptible to settling, offer resistance to the flow and cause abrasion on ducts surface. The advancements in nanotechnology open the doors to process and produce powders with average particle sizes of nanometer order. This has helped in applying the Maxwell proposal to enhance the properties of heat exchange media. Due to the very small sizes of the suspended particles nanoparticle fluid mixture could be suitable as heat transfer fluid in many existing heat transfer equipment. Choi et al. (1995) coined the word nanofluids for homogeneous dilute suspension of nanophase particles in

liquids. Nanofluids are the next generation heat transfer fluids and offer enhanced heat transfer performance compared to conventional fluids. This has led to exhaustive research in the area of nanofluids, to understand the mechanisms and parameters affecting the enhancement.

Many researchers have conducted experimental investigations on thermal conductivity of various nanofluids. Masuda et al.(1993) measured the thermal conductivity of Al_2O_3 (13 nm), SiO_2 (12 nm), and TiO_2 (27 nm) water nanofluids. Linear increment of thermal conductivity was observed with volumetric concentration of nanoparticles. An enhancement of 32.4% was observed in the thermal conductivity for 4.3 volume% Al_2O_3/water nanofluid at 31.85° C. Choi et al.(1995) coined the term nanofluids. He theoretically investigated the feasibility and potential of the nanofluids concept. Hamilton et al.(1962) model was employed to explain the effect of shape and concentration of nanoparticles on the enhancement of thermal conductivity of Cu/water nanofluids. Lee et al.(1989) measured the thermal conductivity of EG and water nanofluids at room temperature, with Al_2O_3 and CuO nanoparticles. The study revealed the linear relationship between thermal conductivity and concentration. Hamilton-Crosser model was in agreement with measured thermal conductivity with spherical particle assumption. The author found more than 20% of augmentation in thermal conductivity for 4% volume concentration. Wang et al.(1999) investigated the thermal conductivity performance of nanofluids with Al_2O_3 (28 nm) and CuO (23 nm) nanoparticles by employing steady state parallel plate technique. For 8% volume Al_2O_3/water nanofluid, thermal conductivity enhancement of 40% was achieved. Murshed et al.(2005) studied the effect of shape on thermal conductivity of TiO_2/deionized water nanofluid with rod and spherical shaped particles at room temperature. A nonlinear relationship was observed between thermal conductivity ratio and particle volume fraction, especially at low volume fractions. An increment of 33% and 30% at 5% volume was observed for rod and spherical shaped particles respectively Chopkar et al.(2008) dispersed Al_2Cu (30nm) and Ag_2Al (20nm) nanoparticles into water and ethylene glycol with 1% volume oleic acid as the surfactant. According to the authors, the thermal conductivity of nanoparticles have significant effect on effective thermal conductivity. Effect of particle material is much more pronounced when carbon nanotubes were used for the preparation of nanofluids. Choi et al. (2001) studied the thermal conductivity of MWCNT/synthetic poly (α-olefin) oil based nanofluids at room temperature. 160% enhancement (a thermal conductivity ratio of 2.6) was observed for 1% volume MWCNT/oil nanofluid. The authors noted that such an anomalous enhancement might be due to the liquid nanolayers forming around the nanotubes. Eastman et al. (2001) prepared Cu (10 nm)/EG nanofluids by using a one-step production method. Thioglycolic acid less than 1% volume was added to some of the samples for stabilizing purposes and those samples showed much better enhancement when compared to samples without thioglycolic acid. A 40% increase in thermal conductivity was observed at a particle volume fraction of 0.3% (with thioglycolic acid). Mintsa et al. (2009) studied the effect of nanoparticle size on the thermal conductivity of Al_2O_3 (36 and 47 nm)/water nanofluids, with 0% < ϕ <18% and temperature between 20° C and 50°C. It was observed that the thermal conductivity enhancements were nearly the same for the two different particle sizes of Al_2O_3 nanoparticles at room temperature. However, at higher temperatures Al_2O_3/water nanofluid with smaller particles showed higher enhancement. Xie et al.(2002) investigated the shape effect on thermal conductivity with spherical (26 nm) particles and cylindrical (600 nm) particles. It was found that 4.2% volume water-based nanofluid with spherical particles had a thermal conductivity enhancement of 15.8%, whereas 4% volume nanofluid with cylindrical particles had a thermal conductivity enhancement of 22.9%. Das et al.(2003) studied the temperature dependency of the thermal conductivity of Al_2O_3 (38.4 nm)/water and CuO (28.6 nm)/water nanofluids in the range of 21°C to 51°C. It was found that thermal conductivity enhancement increased from 2% at 21°C to 10.8% at 51°C for 1% volume Al_2O_3/water nanofluid. Temperature dependence of 4% volume Al_2O_3 nanofluid was much more significant. From 20°C to 50°C, enhancement increased from 9.4 to 24.3%. A linear relationship between thermal conductivity ratio and temperature was observed for all the concentrations.

Despite the extensive research in this field, there are differences in experimental investigations and the estimated values of thermal conductivity. Most of the literature is concentrated on single base fluid and higher concentrated EGW mixtures. No data was available in the literature for 30:70 EGW

nanofluids. This motivates the present study to measure the thermal conductivity of 30:70 EGW nanofluids.

2. NANOFLUID PREPARATION

In the present study the nanofluids were prepared by two step method. This method had extensively used in the literature by various authors Duangthongsuk et. al.(2009), Sundar et al.(2010), Peyghambarzadeh et al.(2011), Abbasian et al.(2012), Chougule et al.(2014) etc and found it commercially viable. The Al_2O_3 (40-60nm) and TiO_2 (40-50 nm) nanoparticles were procured . The predetermined weight of nanoparticles corresponding to 0.25% to 1.00% volume concentration were dispersed into the 30:70 EGW basefluid. In this study Cetyle Trimethyl Ammonium Bromide (CTAB) used as a surfactant for stabilized and uniform dispersion of the nanoparticles. Initially the particles were dispersed by using magnetic stirring for 3 hrs. and followed by ultrasonication for 2 hrs.

3. TRANSIENT HOT WIRE METHOD PRINCIPLE

In the present study, KD2 Pro thermal property analyzer was used to determine the thermal conductivity of the nanofluids. It works on a modified transient hot-wire method [20]. Transient hot-wire method is very fast relative to steady-state techniques. In hot-wire method, a wire serving as heater and thermometer was suspended symmetrically in a liquid in a vertical cylindrical container. The modified method uses a platinum wire coated with a thin electrical insulation layer to measure the thermal conductivity of electrically conducting liquids. This method employs the assumption of infinite line source of heat in an infinite medium. The method is called transient because the power is applied abruptly and briefly. The solution to the Fourier's law equation for this case results in the linear relationship between ΔT and $\ln t$. So by applying the known power (q) and obtaining the slope of ΔT versus $\ln t$ between times t_1 and t_2 one can calculate thermal conductivity from eq. (1) given as

$$k = \frac{q}{4\pi(T_2 - T_2)} ln \frac{t_2}{t_1} \qquad \text{Eq.(1)}$$

where T_2-T_1 (ΔT) is the temperature rise of the wire between times t_1 and t_2.

4. EXPERIMENTAL SETUP & PROCEDURE

Fig. 1 shows the schematic representation of the experimental setup. The setup is having KD2 Pro thermal property analyzer to measure the thermal conductivity and a temperature controlled water bath to maintain the constant temperature of the nanofluid to carry out the thermal conductivity measurements at various temperatures. The procedure followed was, nanofluid sample of 30 ml had taken in the small test tube and it is kept in the water bath. The required temperature in the water bath was set by using the controllers on the water bath. Once the nanofluid reaches the set temperature then the KD2 Pro KS-1 sensor was inserted into the fluid and measurements were taken for the thermal conductivity. The same procedure is repeated for different volume concentrations from 0.25% to 1%, over the temperature range of 20°C to 50°C.

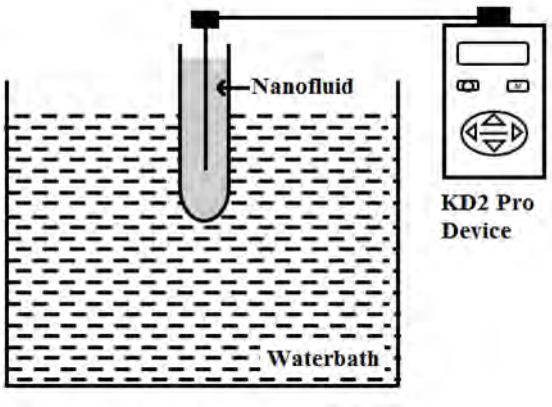

Figure 1: Schematics of experimental setup

5. RESULTS AND DISCUSSIONS

5.1 Stability of the nanofluids

Once the nanofluids were prepared all the samples were kept stable to assess the sedimentation stability of the nanoparticles in the basefluid. It was observed that Al_2O_3 nanofluids were found to be stable for more than 2 days and TiO_2 nanofluids were stable for 6 hrs. After which, visible sedimentation was observed.

5.2 Calibration of the Setup

The KD2 Pro device is calibrated by comparing the measured thermal conductivity of the three different fluids such as glycerin, water and the basefluid (30:70 EGW) considered in the present study. The thermal conductivities of glycerin and water were measured at 20°C and 25°C and compared with the values presented in ASHRAE (2017) handbook. The measurements for ethylene glycol water (EGW) mixture were carried out in the temperature range of 20°C to 50°C and compared with the values available in the ASHRAE (2017) handbook and good accuracy was observed between the measured values and the values from the data book. The error in the measurements was limited to ±5%. This confirms the feasibility of the device to measure the thermal conductivity of nanofluids.

5.3 Comparison of measured thermal conductivity with theoretical models

In the last century, thermal conductivity studies for the composite materials have seen great growth. Many researchers worked on estimating the thermal conductivities for the two phase mixtures. Various models were developed by the researchers to estimate the effective thermal conductivity of the composite materials and multiphase systems by considering the parameters such as thermal conductivity of the liquid phase and solid phase and volume concentrations of the solid phase. The earliest correlation that was known was Maxwell equation. Maxwell (1881) considered the solid-liquid mixtures consisting of spherical particles of the millimeter sized particles in developing the relation but the size effect was not considered in the correlation developed. The Maxwell correlation as given below was extensively used to estimate the thermal conductivity of the nanofluids.

$$\frac{k_{eff}}{k_p} = \frac{k_p + 2k_{bf} - 2\phi\left(k_{bf} - k_p\right)}{k_p + 2k_{bf} + \phi\left(k_{bf} - k_p\right)} \qquad \text{Eq.(2)}$$

Hamilton et.al. (1962) conducted the experimental studies to determine the effective thermal conductivity of the heterogeneous two-component systems and theoretically developed a correlation to find the effective thermal conductivity.

$$\frac{k_{eff}}{k_p} = \frac{k_p + (n-1)k_{bf} - (n-1)\phi(k_{bf} - k_p)}{k_p + (n-1)k_{bf} + \phi(k_{bf} - k_p)} \qquad \text{Eq.(3)}$$

Where n is shape factor given by $n = 3/\lambda$ and λ is the particles sphericity defined as the surface area of the spherical particle (with the same volume of actual particle) to surface area of the actual particle. For spherical particles Maxwell relation Eq. (2) and Hamilton-Crosser relation Eq. (3) are same.

Yu and Choi [22] presented a model for the determination of the effective thermal conductivity of nanofluids by modifying the Maxwell model Eq. (1). In the modification, the effect of the liquid nanolayers formed around nanoparticles was taken into account. The nanoparticle and the layer around it were considered as a single particle and the thermal conductivity of this particle was determined by using effective medium theory.

$$\frac{k_{eff}}{k_p} = \frac{k_p + 2k_{bf} - 2\phi(k_{bf} - k_p)(1-\beta)^3}{k_p + 2k_{bf} + \phi(k_{bf} - k_p)(1-\beta)^3} \qquad \text{Eq.(4)}$$

The measured thermal conductivity data have been compared with the most used correlations available in literature Eq. (1), Eq. (2) and Eq. (3). Comparison was made between the measured thermal conductivity nanofluids and values estimated from the three theoretical models. Present experimental studies evident that the thermal conductivity increases almost linearly with volume concentration. The current study also reveals that the thermal conductivity of nanofluids if a function of the conductivities of both the particles and base fluids. Fig. 2(a) and Fig. 2(b) show the comparison

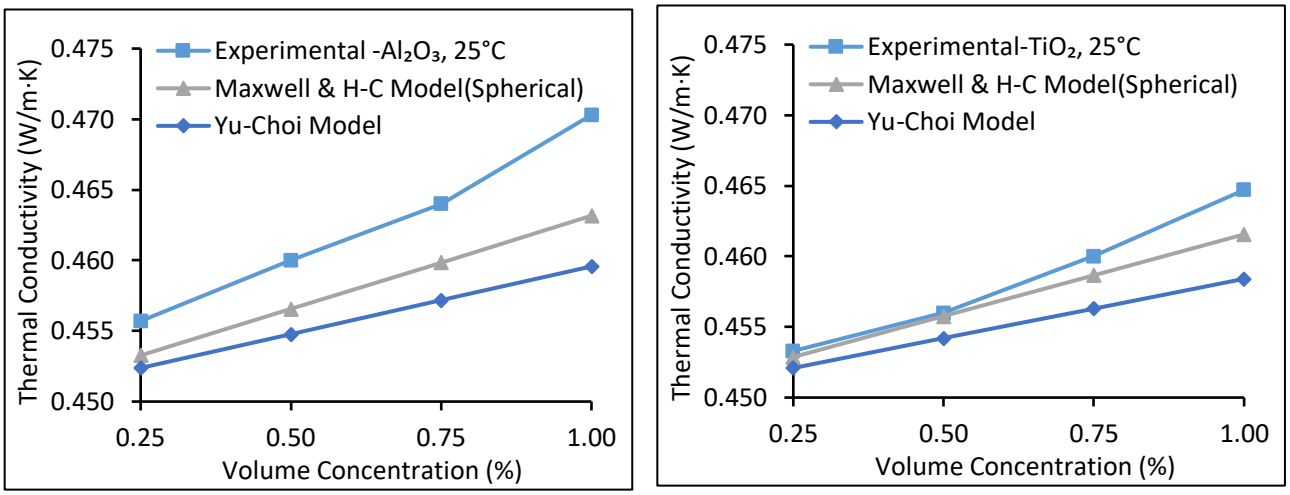

Figure 2: Concentration based comparison of measured Thermal conductivity with theroritical models for (a) Al_2O_3 (b) TiO_2

between measured thermal conductivity values and the corresponding values estimated from the correlations for Al_2O_3 and TiO_2 nanofluids respectively. From the graphs it can be observed that there is no good agreement between the measured and estimated thermal conductivity, which indicates the disability of the models and their inefficiency in estimating the thermal conductivity. The measured thermal conductivity values of significantly higher than the predicted values. This is possible because the effect of the microconvection, Brownian motion and effect of interfacial layers at particle-fluid surfaces. These parameters are significant in enhancing the thermal conductivity of

nanofluids and these combined effects were not accounted in the correlations, which making them inefficient.

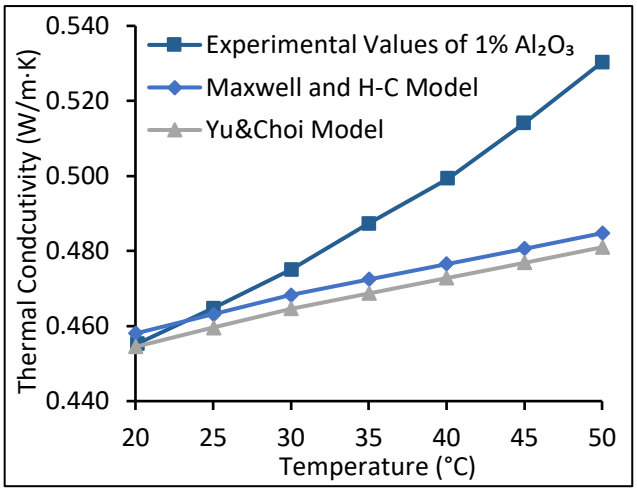

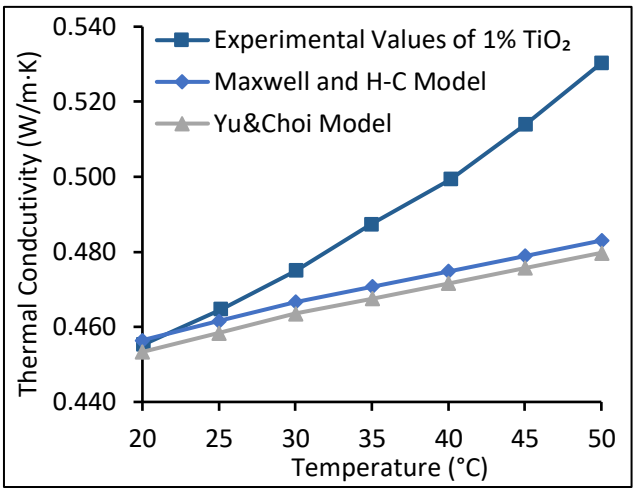

Figure 3: Temperature based comparison of measured Thermal conductivity with theoretical Models for (a) Al_2O_3 (b) TiO_2

Initial measurements were made at the room temperature and the experiments were extended till 50°C. The measured thermal conductivities of nanofluids were compared (Fig.3) with the correlations available. At the room temperature conditions the measured values are in good agreement with the predicted values. As the temperature increases the deviation is observed in measured and predicted values, measured values being larger than the latter. This gives an insight that the temperature plays a dominant role in enhancing the thermal conductivity. There will be a threshold temperature till which the models can predict the values accurately and beyond this they were inefficient. The stochastic motion of the nanoparticles can be seen as the mechanism of enhancement. This random movement is Brownian motion which is highly dependent on the temperature of the fluid. At higher temperatures the Brownian motion quite large leading to the greater increment in the conductivity. The effect of Brownian motion is not consider in the correlations which makes them unable to predict the thermal conductivity accurately at higher temperatures. The comparison for 1% Al_2O_3 and 1% TiO_2 nanofluid was shown in the Fig 3. It can be observed that the same trend is followed for both the nanofluids. From the graph it is concluded that, the correlations are underpredicting the thermal conductivities at the higher temperatures.

5.4 Effect of Concentration and Temperature on Thermal Conductivity

The Fig. 4 shows thermal conductivity data of the different nanofluids as a function of the percentage volume concentration of nanoparticles in the temperature range of 20°C to 50°C. The increment in the thermal conductivity of the nanofluids as the increase in the concentration can be observed from graph. The quantitative increment in the thermal conductivity is marginal for lower concentrations but significant increment can be found at higher concentrations. The investigations revealed that the increase in the concentration, increases the thermal conductivity of the nanofluid. The variation is linear in nature. As the concentration increases no of particles will be more and their collisions strengthen the microconvection and increment in the thermal conductivity. The enhancement is also dependent on the surface area of particles, the increased no. of particles results in higher surface area. The more the number of particles the effective solid phase conductivity is more. The interface layer of liquid medium also behaves as the solid with increased conductivity than the liquid phase. This is the mechanism to augment the conductivity as the concentration increased. This can't be taken as granted, as the higher concentration beyond a certain limit, nanoparticles will agglomerate, leading to negative effect. The lowest increment of 0.83% and 0.61% at ϕ=0.25% while the highest

increment of 16.07% and 12.59% was observed at ϕ=1% concentration, for Al_2O_3 and TiO_2 nanofluids respectively.

The variation of the thermal conductivity with respect to the temperature can also be visualized from the Fig. 4. This variation of the thermal conductivity with temperature is linear and it deviates from the linearity as the temperature increases. The deviation from the linearity can be attributed to the increased Brownian motion, microconvection and collision of particles at higher temperatures and the basefluid thermal conductivity is also a function of the temperature. The effect of the temperature is more prominent as it goes higher and higher. The increment in thermal conductivity at the lower temperature is low, but as the temperature increases the increment in thermal conductivity is more. This can related to the effect of Brownian motion as discussed in the section 5.3. In case of TiO_2 based nanofluids, results indicate the same behavior as the Al_2O_3 nanofluid. The highest increment of 16.07% in the thermal conductivity is observed for the volume concentration of ϕ=1% Al_2O_3 nanofluid at the temperature of 50°C. The lowest thermal conductivity increment is observed for ϕ=0.25% of TiO_2 nanofluid with an increment of 0.61% at 20°C.

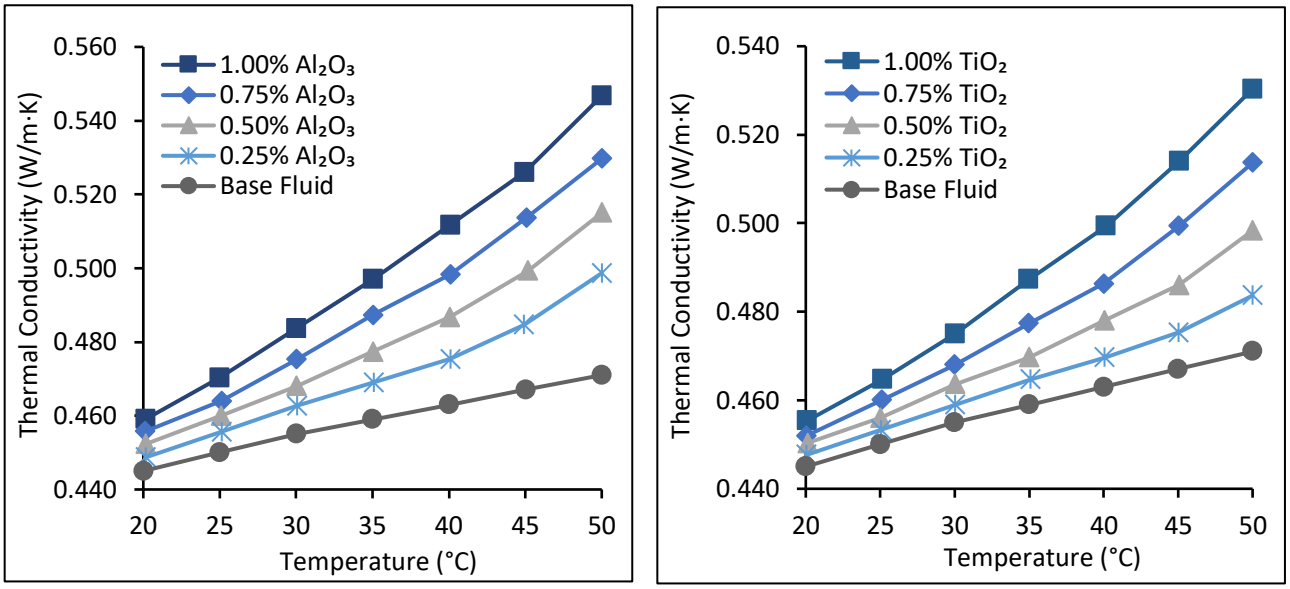

Figure 4: Variation of measured Thermal conductivity with concentration and temperature (a) Al_2O_3 (b) TiO_2

5.5 Effect of Nanoparticle Material on the Thermal Conductivity

For the same concentration the quantitative increment of thermal conductivity for the TiO_2 nanofluids is less than the increment of Al_2O_3 nanofluids. The comparison is shown in Fig. 5. It shows the thermal conductivity values of the 1% concentrated Al_2O_3 and TiO_2 nanofluids. The higher increment in case of Al_2O_3 nanofluids is due to higher thermal conductivity of the Al_2O_3 nanoparticles compared to the TiO_2 Particles, which directly indicates that nanoparticles conductivity will be an important parameter affecting the effective thermal conductivity.

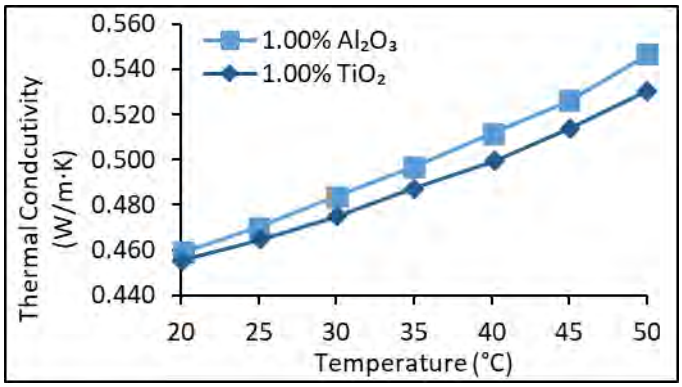

Figure 5: Effect of Nanoparticle Conductivity on effective Thermal Conductivity of Nanofluid

6. CONCLUSIONS

From this experimental study it was found that there is huge potential in nanofluids as advanced heat transfer fluids as the dilute concentrations of nanoparticles resulted significant enhancement in the thermal conductivity. The thermal conductivity of these nanofluids is found to be highly dependent on the temperature, volume concentration and the nanoparticles material. From experimental measurements it is concluded that as the temperature increases the thermal conductivity increases for all the concentration of the nanoparticles. The volume concentration also increases the effective thermal conductivity of the nanofluids. Nanoparticles with higher thermal conductivity will lead to higher effective thermal conductivity of the nanofluids. The highest increment of 16.07% in the thermal conductivity is observed for the volume concentration of 1% Al_2O_3 nanofluid at the temperature of 50°C. The lowest thermal conductivity increment is observed for 0.25% of TiO_2 nanofluid with an increment of 0.61% at 20°C.

NOMENCLATURE

Symbols

k	Thermal Conductivity (W/m·K)
ϕ	Volumetric Concentration
n	Shape Factor
λ	Sphericity
β	Nanolayer Thickness Ratio
t	Time (s)
T	Temperature (°C)
q	Electric Power (W)

Subscripts

eff	Nanofluid
bf	Basefluid
p	Particle

REFERENCES

Choi, S. U. S., Eastman, J. A. 1995. Enhancing Thermal Conductivity of Fluids With Nanoparticles. ASME, *Fluids Engineering Division* 231, 99-105.

Hamilton, R. L., & Crosser, O. K. 1962. Thermal Conductivity of Heterogeneous Two-Component Systems. Industrial & Engineering Chemistry Fundamentals 1(3), 187-191.

Lee, S., Choi, S. U.-S., Li, S., & Eastman, J. A. 1999. Measuring Thermal Conductivity of Fluids Containing Oxide Nanoparticles. Journal of Heat Transfer 121(2), 280-289.

Masuda, H., Ebata, A., Teramae, K., & Hishinuma, N. 1993. Alteration of Thermal Conductivity and Viscosity of Liquid by Dispersing Ultra-Fine Particles. Dispersion of Al_2O_3, SiO_2 and TiO_2 Ultra-Fine Particles. Netsu Bussei 7(4), 227-233.

Maxwell, J. C., 1881. A Treatise on Electricity and Magnetism, 2nd Ed, Clarendon Press.

Murshed, S. M. S., Leong, K. C., & Yang, C. 2005. Enhanced thermal conductivity of TiO2—water based nanofluids. International Journal of Thermal Sciences 44(4), 367–373.

Wang, X., Xu, X., & S. Choi, S. U. 1999. Thermal Conductivity of Nanoparticle - Fluid Mixture. Journal of Thermophysics and Heat Transfer 13(4), 474-480.

Chopkar, M., Sudarshan, S., Das, P. K., & Manna, I. 2008. Effect of Particle Size on Thermal Conductivity of Nanofluid. Metallurgical and Materials Transactions A 39(7), 1535-1542.

Choi, S. U. S., Zhang, Z. G., Yu, W., Lockwood, F. E., & Grulke, E. A. 2001. Anomalous thermal conductivity enhancement in nanotube suspensions. Applied Physics Letters 79(14), 2252-2254.
Eastman, J. A., Choi, S. U. S., Li, S., Yu, W., & Thompson, L. J. 2001. Anomalously increased effective thermal conductivities of ethylene glycol-based nanofluids containing copper nanoparticles. Applied Physics Letters 78(6), 718-720.

Mintsa, H. A., Roy, G., Nguyen, C. T., & Doucet, D. 2009. New temperature dependent thermal conductivity data for water-based nanofluids. International Journal of Thermal Sciences 48(2), 363-371.
Xie, H., Wang, J., Xi, T., & Liu, Y. 2002. Thermal Conductivity of Suspensions Containing Nanosized SiC Particles International Journal of Thermophysics 23(2), 571-580.

Das, S. K., Putra, N., Thiesen, P., & Roetzel, W. 2003. Temperature Dependence of Thermal Conductivity Enhancement for Nanofluids. Journal of Heat Transfer 125(4), 567-574.

Duangthongsuk, W., & Wongwises, S. 2009. Heat transfer enhancement and pressure drop characteristics of TiO2–water nanofluid in a double-tube counter flow heat exchanger. International Journal of Heat and Mass Transfer 52(7-8), 2059-2067.

Sundar, L. S., & Sharma, K. V. 2010. Heat transfer enhancements of low volume concentration Al2O3 nanofluid and with longitudinal strip inserts in a circular tube. International Journal of Heat and Mass Transfer 53(19-20), 4280-4286.

Peyghambarzadeh, S. M., Hashemabadi, S. H., Hoseini, S. M., & Seifi Jamnani, M. 2011. Experimental study of heat transfer enhancement using water/ethylene glycol based nanofluids as a new coolant for car radiators. International Communications in Heat and Mass Transfer 38(9), 1283-1290.

Abbasian Arani, A. A., & Amani, J. 2012. Experimental study on the effect of TiO_2–water nanofluid on heat transfer and pressure drop. Experimental Thermal and Fluid Science 42, 107-115.

Chougule, S. S., & Sahu, S. K. 2014. Thermal Performance of Automobile Radiator Using Carbon Nanotube-Water Nanofluid—Experimental Study. Journal of Thermal Science and Engineering Applications 6(4), 1-6.

Chandra Sekhara Reddy, M., & Vasudeva Rao, V. 2014. Experimental investigation of heat transfer coefficient and friction factor of ethylene glycol water based TiO_2 nanofluid in double pipe heat exchanger with and without helical coil inserts. International Communications in Heat and Mass Transfer 50, 68-76.

Nagasaka, Y., & Nagashima, A. 1981. Absolute measurement of the thermal conductivity of electrically conducting liquids by the transient hot-wire method. Journal of Physics E: Scientific Instruments 14(12), 1435-1440.

ASHRAE Handbook -Fundamentals (SI Edition)-2017.

Yu, W., & Choi, S. U. S. 2003. The Role of Interfacial Layers in the Enhanced Thermal Conductivity of Nanofluids: A Renovated Maxwell Model. Journal of Nanoparticle Research, 5(1-2), 167-171.

Manuscript ID: 310
DOI: 10.18462/iir.icr.2019.0310

Convective heat transfer measurements at the thermal boundary layer of gadolinium

Zhe LEI [a,b], Barbara FRITZSCHE [b], Kerstin ECKERT [a,b]

[a] Transport Processes at Interfaces, Helmholtz-Zentrum Dresden-Rossendorf (HZDR)
Dresden, 01328, Germany
[b] Transport Processes at Interfaces, TU Dresden
Dresden, 01069, Germany
Z.Lei@hzdr.de; K.Eckert@hzdr.de

ABSTRACT

This work reports Mach-Zehnder interferometer measurements on the transient dynamics of heat transfer from a demagnetized gadolinium (Gd) plates into a heat transfer fluid (0.2 M NaOH). The magnetic field is provided by a magnetic assembly with a mean magnetic flux density at Gd plate of 232 mT. First, a heat conduction case is tested by resolving the propagation of the thermal boundary layer emanated from the Gd plates after demagnetization. This result is then compared with the case coupled to a bulk flow with a flow rate of 20 and 30 L/ h, respectively. The temperature adjacent to the Gd plate is extracted for all cases. The more rapid T evolution in the presence of an advective heat transfer process could be verified which clearly demonstrates the capabilities of the measurement setup to resolve the thermal boundary layer down to millimeter range.
Keywords: Interferometer, Heat transfer, Magnetic Cooling, Gadolinium.

1. INTRODUCTION

Magnetic cooling (MC) is an alternative room temperature refrigeration technology which offers certain advantages Gschneidner (2008), Tishin (2014), Engelbrecht(2007) and Yu(2010) compared to conventional cooling based on gas compression. It has the potential of high efficiency, compact design and silent operation, and promises the use of non-toxic solid cooling material and an environmentally friendly heat transfer fluid. This is design-wise potentially compact and more silent operation compared with conventional system as the compressor is replaced with the magnet and vapor-liquid phase change of refrigerant is unnecessary. Principally, this is realized by the magnetocaloric effect (MCE), employing a magnetocaloric material (MCM) functioning simultaneously as a regenerator bed as well as a heat exchanger. With the oscillating direction of heat transfer fluid between the hot and cold end, currently, the active magnetic regenerator (AMR) principle is widely adopted in prototype design and manufacturing. The core of the AMR is a porous structure made up of MCM, frequently realized as a packed sphere bed or as an ensemble of flat parallel plates or lamellar structure, and the heat transfer fluid. Using the AMR, a larger temperature span than just the adiabatic temperature change ΔT_{ad} can be obtained.
There is consensus on the two main bottlenecks which needs to be overcome to further advance the magnetic cooling technology. The first one is that cheaper magnetocaloric material with a bigger caloric effect has to be synthesized, which also possess better mechanical as well as thermodynamic parameters. The second focus is on enhancing the heat transfer that becomes non-ideal in AMR based prototypes despite a higher temperature span bigger than the adiabatic temperature change of the material is provided. The coupling of the regenerator principle and maximizing energy density by bigger portion of magnetocaloric material limits the flow rate of the oscillatory flow. This is due to the pumping loss as a consequence of the bigger flow rate that drops the efficiency of the heat transfer. Due to this reason, the current cycling frequency is humbled to below 1 Hz range. Thus, an attractive method of utilizing the already existing magnetic field together with the injection of a small current in the cold blow process to generate a magnetohydrodynamic (MHD) flow was proven to be a potentially interesting method to enhance the heat exchange without compromising pumping loss by accelerating mean flow rate and decrease cycling frequency. To further advance this idea, a new challenge arises on resolving

temperature field inside the regenerator. Thus it make sense to study the heat transfer in the simplest case, namely from a periodically magnetized and demagnetized plane gadolinium plate into a bulk heat transfer fluid which is in the form of an internal duct flow. With the development of a model cell of high optical quality, the specific boundary of the duct could be replaced by either magnetocaloric material or non-caloric ones for comparison. By means of a Mach-Zehnder interferometer, this paper presents preliminary results of a contactless space- and time- resolved temperature measurement of the thermal boundary layer at the fluid side of a Gd plate with bulk flow Re below 800.

2. SETUP AND DATA PROCESSING ALGORITHM

2.1. Experimental setup

Gadolinium (Gd 99 % pure, Goodfellow Cambridge Ltd.) is employed as a magnetocaloric material. It was machined to a flat plate with smooth surface an area of 50 × 10 mm^2 and a thickness of 2 mm as rolled by the supplier without further polishing. The gadolinium plate is embedded in a building plate made of plexiglass. The building plate on the side facing the heat transfer fluid is flat. The internal flow cell consists of a main part with two accesses for inserting two building plates. This ensures a switchable boundary condition since the material integrated with the plate could vary between plexiglass and a 2 mm thick Gd plate. A measurement region with 10 × 10 mm2 cross section and full length of 110 mm is formed. In the test configuration used in this work the Gd plate serves as bottom boundary, integrated into the center of building plate in streamwise direction while the remaining 3 boundaries are plexiglass. 0.2 M NaOH aqueous solution is used as heat transfer fluid because of its good anti-corrosion property while preserving the properties of water, i.e. optical transparency and thermal diffusivity. Flow is pumped by a magnetic-vane pump at a range of 0 - 100 L/ h. The corresponding Reynolds number, Re, is between 0 and 3000, see Fig. 1, covering the range of most AMRs, i.e. *Re* within 100.

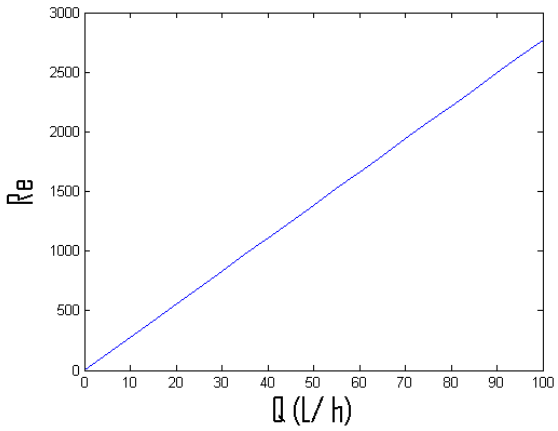

Figure 1: Resulting Reynold number as function of flow rate.

Magnetic field is provided by a self-designed magnetic assembly. The housing part is constituted of a 3D printed non-magnetic ABS frame with two block NdFeB permanent magnet (magnetization N35, size 50 × 50 × 12.5 mm3) with parallel magnetization direction facing each other. The stray field at the outer side is concentrated by soft magnet blocks (Fe 99.8 % pure, Goodfellow Cambridge Ltd.).
The stray field at region of interest is simulated with COMSOL AC/ DC module and the resulting stray field inside the fluid when the magnet is at the fully magnetization position is shown in Fig. 2. The magnet assembly is integrated into an electric mounting stage. A programed linear motion is integrated with the magnetic assembly giving a highest motion speed at 30 mm/s. This module provides a magnetization and demagnetization of the Gadolinium plate, i.e. triggers the magnetocaloric effect.

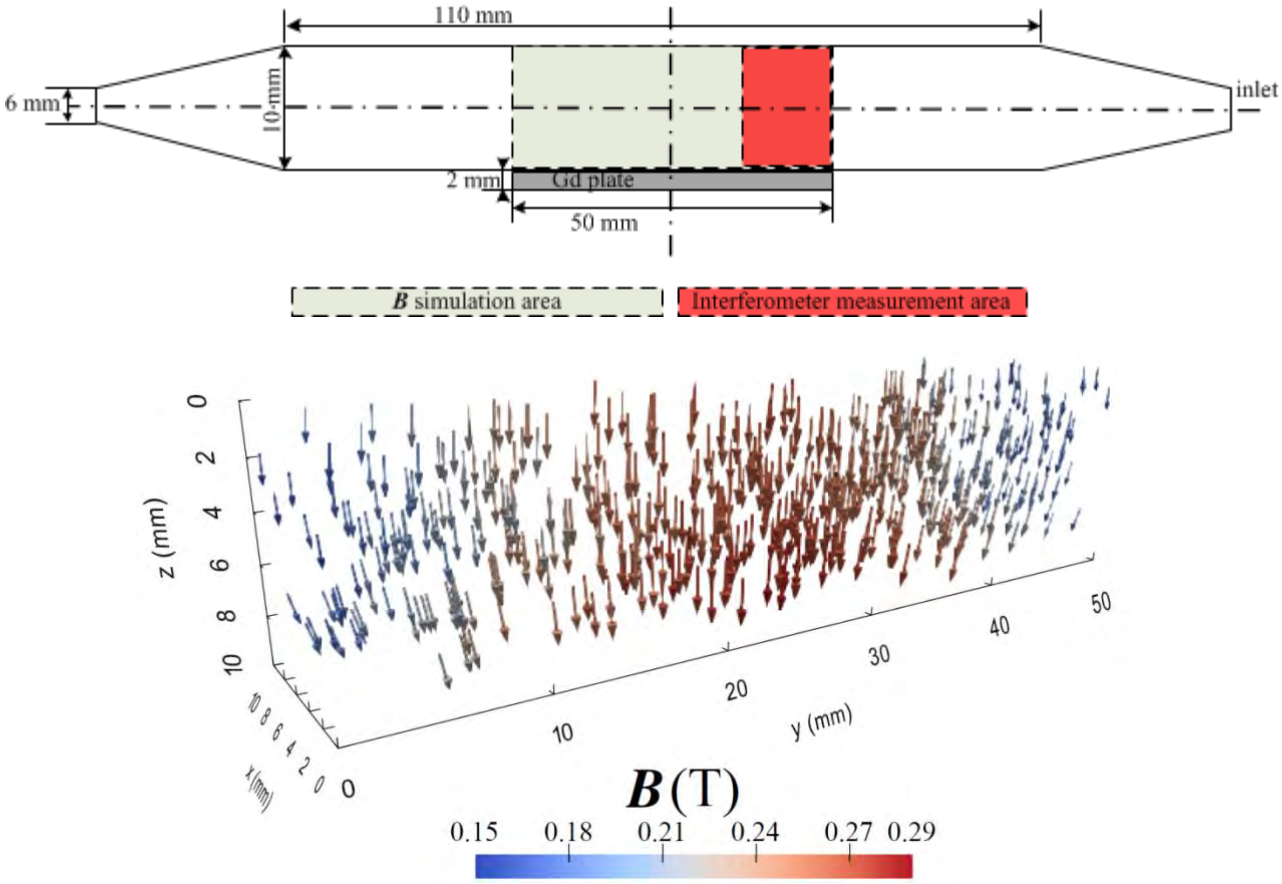

Figure 2: (upper) Experiment sketch and (lower)Stray field of magnet assembly at region spatially occupied by heat transfer fluid at fully magnetization position. Mean flux density at Gadolinium plate with thickness 2 mm is 232 mT.

The Mach-Zehnder interferometer maps the phase difference Δtf(x,y,z) between the cell under study and reference beam, which is related to the difference in the refractive index Δn. The algorithm for computing the Δn from the interferogram recorded is documented in Lei (2015,2016,2017) The temperature change of heat transfer fluid is computed by the correlation with refractive index change correlated by ∂T=∂n. Since $\partial T=\partial n$ is constant, a simplified calculation is obtained.

$$\Delta T = \int_{T_0}^{T} dT(\vec{r'}, t) = \int_{n_0}^{n} \partial T/\partial n \cdot d(n_m(\vec{r}, t)) = \partial T/\partial n \cdot \Delta n_m \qquad \text{Eq. (1)}$$

2.2. Heat transfer at the demagnetization stage

The heat transfer in the demagnetization phase is spatially and temporally resolved using the interferometer. The resolution for all spatial and temporal sampling is 10 m and 0.1 s, respectively. The measurement result is shown in Fig. 3 between 0 s and 4 s where the 0 time indicates the trigger time of demagnetization, i.e. the moving of magnet assembly.

The figure underlines that even small changes in the temperature field can be resolved well by means of the MZI. However, compared to Lei (2015,2016), a foreseen less ideal result appears. A fluid with a high thermal diffusivity serves as a good heat transfer fluid. However, its thermal boundary is more difficult to be resolved by the interferometer. One reason is the fact that the ∂T/∂n for the dilute base is 1=10200K^{-1} which is considerably smaller that for organic solvents like n-decane Lei (ICR2015) where it amounts to 1=2230K^{-1}. From a measurement prospective, the

same given magnetocaloric effect, acting as thermal boundary, results in a less ideal measurement signal in terms of a refractive index change for aqueous solutions compared to organic ones.
By extracting the temperature at the fluid side, the evolution of T at the position adjacent to the Gd plate which locates at the margin of the bottom coordinates is shown in Fig. 4. In fact, due to continuity reason, the fluid directly at the Gd plate could in fact denote the surface temperature distribution of the Gd plate. However, a small misalignment between the collimated beam and the Gd plate is hard to avoid which finally leads to a minor blockage of a sub-millimeter range at thermal boundary. At the vicinity of the Gd plate at the fluid side, temperature decreases gradually due to the heat transfer between fluid and the plate. Then due to the reduced temperature difference between the Gd plate and fluid, a reduced heat exchange rate occurs. The stratification of temperature boundary layer then leads to the peak temperature, see Fig. 4. Compared with pure conduction, a more rapid increase is found in the temperature drop at the fluid side. This is followed by a rapid temperature drop after reaching to a higher value in ΔT. The trend is more pronounced with an increasing bulk flow rate.

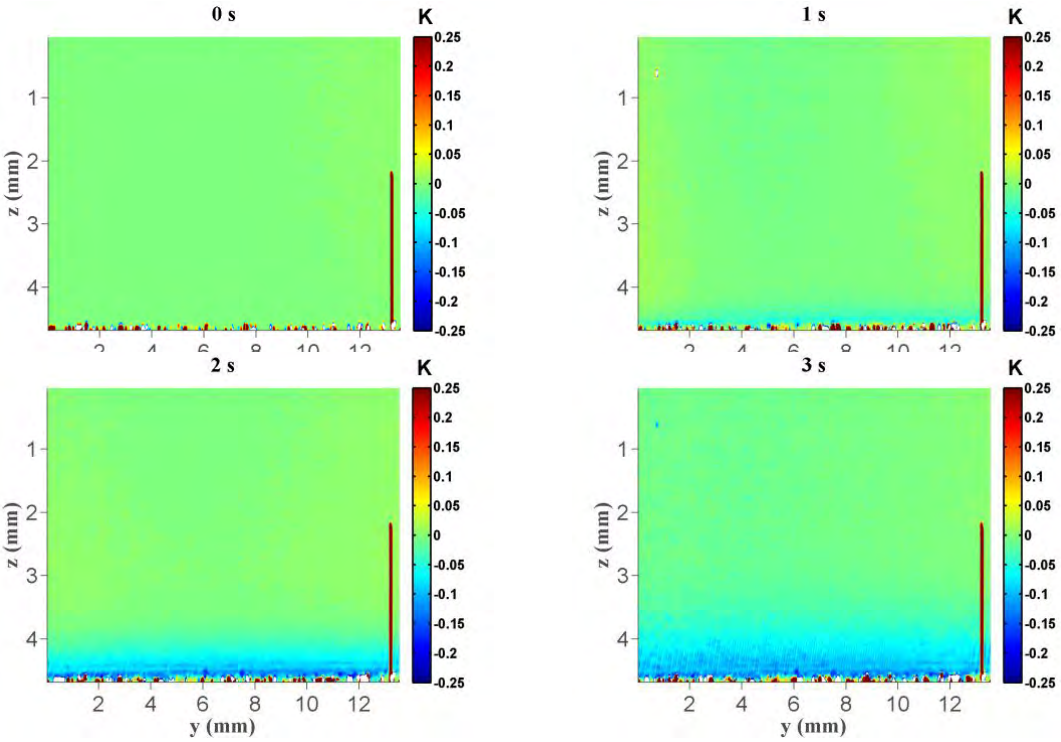

Figure 3: 2D temperature field in a 0.2 M NaOH solution corresponding to the thermal boundary layer of a gadolinium plate. The latter is located at the bottom margin outside the figure. The time 0 s is defined as the time at which the mounting stage with the integrated magnet starts to move and to demagnetize the Gd plate.

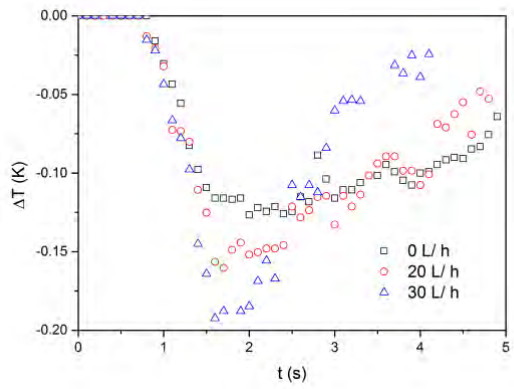

Figure 4: The temperature evolution at the fluid side adjacent to the Gd plate.

3. SUMMARY AND OUTLOOK

This work reports heat transfer measurements of the thermal boundary at a demagnetized Gd plate coupled to bulk flow using a laser based Mach-Zehnder interferometer. First, the heat transfer into a static heat transfer fluid is measured and the resulting temperature evolution in the region demonstrates a heat conduction process as expected. Then, the advective heat transfer is shown with mean flow rate of 56 mm/ s and 83 mm/ s corresponding to a Re number 554 and 832, respectively, is analysed. The temperature adjacent to the Gd plate shows a more rapid warming effect. This is due to the increased local heat transfer forcing a more rapid heat exchange between the heat transfer fluid and the Gd plate. These results demonstrate that it is worth to spend more effort in resolving the temperature field of thermal boundary at both magnetization and demagnetization of Gd. A special focus should be on evaluating the influence of thermal dissipation especially at high flow rate with higher pressure drop when the measurement region is filled with a stack of plates of magnetocaloric material. The prospective work could be carried on with a direct comparison between interferometer result with simulation.

ACKNOWLEDGEMENTS

We acknowledge stimulating discussions about AMR prototypes with Dres. K. Engelbrecht and C.Bahl and Prof. A. Kitanovski. We thank Dr. K. Schwarzenberger for her help with the present work.

REFERENCES

Engelbrecht K., Nellis G., Klein S., Zimm C., 2007. Recent developments in room temperature active magnetic regenerative refrigeration. HVAC&R Research 13(4), 525-42.

Gschneidner, Jr, K. A., Pecharsky, V. K., 2008. Thirty years of near room temperature magnetic cooling: Where we are today and future prospects. Int. J. Refrigeration 31(6), 945-961.

Lei, Z., Eckert, K., 2015 Interferometric measurement of the heat transfer enhancement driven by a magnetohydrodynamic flow at a magnetized gadolinium plate. International Conference of Refrigeration, Yokohama, Japan.

Lei, Z., Haberstroh, C., Odenbach, S. and Eckert, K., 2016. Heat transfer enhancement in magnetic cooling by means of magnetohydrodynamic convection. Int. J. Refrigeration 62, 166-176.

Lei, Z., Yang, X., Haberstroh, C., Pulko, B., Odenbach, S. and Eckert, K., 2015. Space-and timeresolved interferometric measurements of the thermal boundary layer at a periodically magnetized gadolinium plate. Int. J. Refrigeration 56, 246-255.

Lei, Z., Fritzsche, B. and Eckert, K., 2017. Evaporation-Assisted Magnetic Separation of Rare-Earth Ions in Aqueous Solutions. J. Phys. Chem. C 121(44), 24576-24587.

Tishin, A.M., Spichkin, Y.I., 2014. Recent progress in magnetocaloric effect: Mechanisms and potential applications. Int. J. Refrigeration 37, 223229. The sources should be presented as follows:

Yu B., Liu M., Egolf PW., Kitanovski A., 2010. A review of magnetic refrigerator and heat pump prototypes built before the year 2010. Int. J. Refrigeration 33, 1029-1060.

Manuscript ID: 315
DOI: 10.18462/iir.icr.2019.0315

Experimental study of R1234yf as a low global warming potential alternative for R134a in an oil-free vapour compression refrigeration system

Zhaohua LI[(a)], Kun LIANG[(a)], Hanying JIANG[(a)]

[(a)] University of Sussex
Brighton, BN1 9QT, UK, Kun.Liang@sussex.ac.uk

ABSTRACT

As an alternative to the high global warming potential (GWP) hydrofluorocarbons (HFCs), R1234yf synthetic refrigerant from the family of the hydrofluoroolefins (HFOs), has emerged recently as a replacement fluid for R134a, particularly for motor air conditioners. This paper presents an experimental study using R1234yf as a drop-in replacement for R134a in an oil-free refrigeration system. The oil-free refrigeration system was instrumented using both R1234yf and R134a. The experiments were carried out for strokes from 9 mm to 13 mm, pressure ratio from 2.0 to 4.0 and condenser outlet temperatures from 40 °C to 50 °C. The experimental results show that the coefficient of performance (COP) of R1234yf is 12% lower than R134a with condenser temperature of 50 °C and evaporator temperature of 5 °C. Volumetric efficiency of R134a is 5% higher than R1234yf for given conditions. Results of mass flow rate, resonant frequency, and cooling capacity are also reported.
Keywords: R1234yf, R134a, Oil-free vapour compression refrigeration, Cooling capacity, Coefficient of performance.

1. INTRODUCTION

The EU F-Gas Regulation was initiated in 2014 to phase out the refrigerants with global warming potential (GWP) of 150 or more. Traditional hydrofluorocarbons (HFCs) are being replaced by low global warming potential (GWP) refrigerants. R134a is one of the most common commercially used high GWP refrigerants, especially for domestic refrigerator and automobile air conditioner. As the similar saturation pressure, R1234yf is considered as the best replacement for R-134a as a refrigerant in automobile air conditioners. R1234yf is a synthetic refrigerant from the family of the hydrofluoroolefins (HFOs), emerging recently as a replacement for R134a. R1234yf has GWP of 4 while R134a has GWP of 1430 (Vaghela, 2017). The latent heat of R1234yf (148.9 kJ/kg) is about 14% lower than R134a (173.1 kJ/kg) at a temperature of 30 °C. R1234yf is a mildly flammable refrigerant which is qualified to A2L classification in ASHRAE safety group. Oliveira (2015) mentioned that due to low burning velocity, R1234yf can be used safely in air conditioners.
A number of studies have been conducted by researchers to investigate the possibility of substituting R134a in vapour compression refrigeration (VCR) systems. Jankovic et al. (2015) conducted experiments with a small power refrigerating system to compare the performance of R1234yf, R1234ze, and R134a. The result shows that the cooling capacity and COP of R1234yf is 9% and 10% lower respectively compared to R134a. Lu et al. (2013) concluded that the pressure drop for R134a is 5-15% higher than R1234yf due to its higher superficial vapour velocity. Wang (2014) reviewed the system performance of R1234yf refrigerant in air-conditioning and heat pump system indicating that the deterioration of R1234yf is around 0-27% depending on operating conditions. Significant difference between R1234yf and R134a system can occur in condenser.
Despite a lot of comparative studies on R1234yf and R134a, most of the measurements mentioned above involved lubricant oil for compressors. The oil solubility of the refrigerants inevitably affect the heat transfer in evaporator and condenser thus the overall performance. Also, at a low evaporator temperature, lubricant oil can block the tube, especially for the small diameter heat exchanger. The oil-free VCR system can provide significant advantages in selection of refrigerants, minimization of the device, and efficiency improvement. This study compares the performance of

R1234yf with R134a in a novel oil-free VCR system over a wide range of operating conditions. The elimination of oil lubricant enables comparable test conditions for better evaluating the performance of R1234yf and R134a for automobile air conditioning.

2. EXPERIMENTAL APPARATUS

Fig. 1 shows the schematic of an oil-free VCR system and the experimental apparatus. The VCR system consists of two balanced oil-free linear compressors, an off-the-shelf water-cooled coaxial condenser and an evaporator with an electric heater. The details of the linear compressor can be found in Liang et al., (2014). Two identical linear compressors operate in opposite direction to reduce vibration. The specifications of components for the oil-free VCR system are listed in Table 1. The hot compressed refrigerant vapour is released from compressor to condenser. A needle valve is added to adjust the pressure ratio between the condenser and evaporator. The liquid refrigerant flows to the evaporator absorbing the heat from the electric heater then goes back to the compressor. A bleed flow loop using PWM (pulse-width-modulation) controlled solenoid valve allows control of the body pressure in the linear compressor so that the piston offset can be controlled at zero. A PID controller generates a sinusoidal excitation voltage from NI data acquisition card to control the piston displacement. A variac heater controller was used to adjust the heat into the evaporator. A power meter connecting to variac heater controller was used to record the electric heater power. A low-speed data acquisition (LDAQ) was used to record the measured parameters including pressures (discharge, suction, body, evaporator inlet), temperatures (discharge, condenser, evaporator inlet/outlet, suction, body), and mass flow rates (main flow and bleed flow). Pressures, voltage, currents, and displacements were collected by a high-speed data acquisition (HDAQ). The data record speed for LDAQ and HDAQ is 2000 samples and 5000 samples per second respectively. Eight-two steady state were carried out for two refrigerants at different compressor strokes, pressure ratios, frequencies, and condenser temperatures as shown in Table 2. The charge is same for both refrigerants. Before measurements, the compressor was heated by resistors to over 35 °C so that no refrigerant condenses in the compressor. The operating frequency was manually adjusted in LabVIEW for each test condition to ensure resonance.

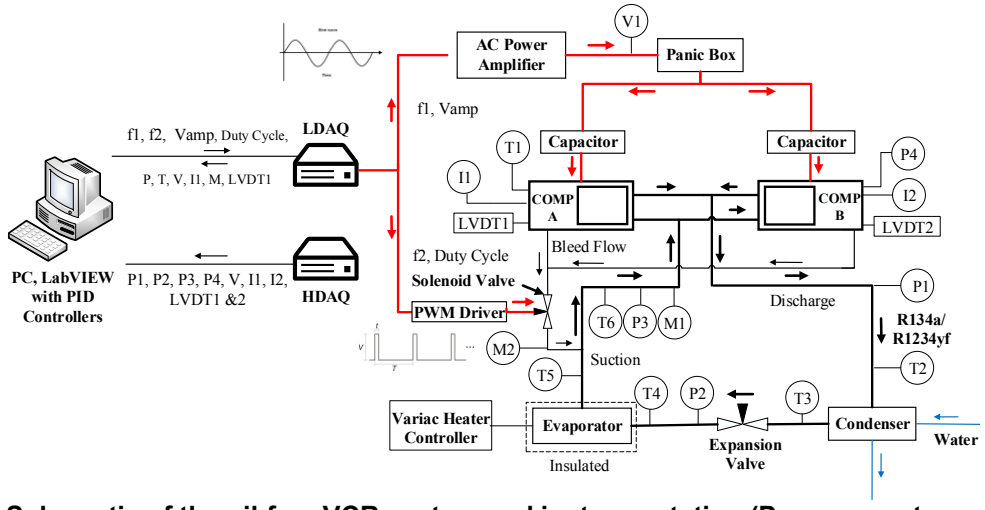

Figure. 1 Schematic of the oil-free VCR system and instrumentation (P: pressure transducer, T: thermocouple, M: mass flow meter, V: voltage sensor, I: current transducer, LVDT: displacement transducer)

Table 1. List of components for the oil-free VCR system

Components	Specifications
Compressor	Two identical oil-free linear compressors working in opposite, piston diameter of 19 mm, maximum compressor stroke of 14 mm, rated power of 100 W for each
Condenser	Coaxial water-cooled, copper, off-the-shelf, coolant connection diameter of 12.7 mm, refrigerant connection diameter of 16 mm
Expansion valve	Needle valve, stainless steel medium flow high pressure
Evaporator	Copper, electric heater (resistance of 50 Ω), length of 128 cm , inner diameter of 7.9 mm, outer diameter of 12.7 mm
Refrigerant	R134a, R1234yf

Table 2. Test conditions for two refrigerants in the oil-free VCR system

Refrigerant	R1234yf, R134a
Charge (g)	250
Pressure ratio	2.0, 2.5, 3.0, 3.5, 4.0
Compressor stroke (mm)	9, 10, 11, 12, 13
Condenser temperature (°C)	40, 45, 50
Operating frequency (Hz)	32-38
Suction temperature (°C)	20-30
Compressor body temperature (°C)	>35
Ambient temperature (°C)	22

3. RESULTS and DISCUSSIONS

3.1. *P-V* Diagram

Fig. 2 shows *P-V* loops for the oil-free VCR system using R1234yf and R134a with a compressor stroke of 12 mm, at a fixed evaporator temperature of 1 °C and a fixed condenser temperature of 40 °C. R1234yf and R134a have similar *P-V* loop thus similar shaft work and power input. Therefore, same capacity compressor can be used to drive the system using R1234yf. Both discharge and suction pressure of R1234yf is higher than R134a due to the higher superheat.

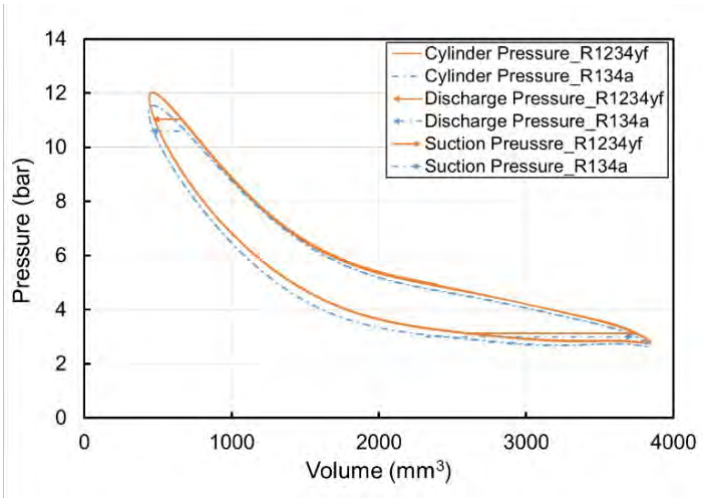

Figure. 2 *P-V* loops for the oil-free VCR system using R1234yf and R134a with a compressor stroke of 12 mm, at a fixed evaporator temperature of 1 °C and a fixed condenser temperature of 40 °C

3.2. Resonant Frequency

To operate the linear compressor at resonance can reduce required input current for the oil-free VCR system thus reduce the copper loss. The resonant frequency can be calculated by mechanical spring rate and non-linear gas spring rate. The very non-linear gas spring curve can be calculated by averaging the in-cylinder pressure P during compression and expansion. The effective nonlinear

spring stiffness of the gas k_g in compression chamber can be expressed as

$$k_g = \left(\int_1^2 PdV - \frac{\oint PdV}{2}\right)\frac{2}{S^2} \quad \text{Eq. (1)}$$

where 1 is the start of compression process, 2 is the end of discharge process, *P* is the in-cylinder pressure, *V* is the cylinder volume, *S* is the compressor stroke.
The resonant frequency f can be calculated as

$$f = \frac{1}{2\pi}\sqrt{\frac{k_g + k_m}{m}} \quad \text{Eq. (2)}$$

where m is the mass of piston (0.66 kg) and k_m is the mechanical spring rate (17 kN/m).

Fig. 3 shows the resonant frequency of the oil-free VCR system using R1234yf and R134a with pressure ratios from 2.0 to 3.0 at a fixed condenser temperature of 40 °C. For both refrigerants, a higher pressure ratio leads to a higher resonant frequency due to higher induced gas spring stiffness. For a fixed pressure ratio, higher compressor stroke causes lower gas spring thus lower resonant frequency. Generally, R1234yf has higher resonant frequency than R134a. This is due to higher suction and discharge pressures for R1234yf (shown in Fig. 2) that lead to higher gas spring stiffness.

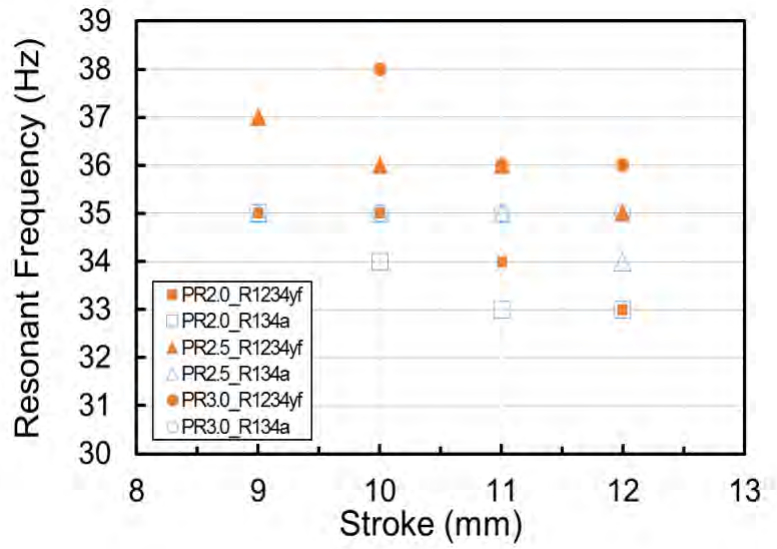

Figure. 3 Resonant frequency against compressor stroke of the oil-free VCR system using R1234yf and R134a with various pressure ratios at a condenser temperature of 40 °C

3.3. Mass Flow Rate

Fig. 4 shows the mass flow rate of R1234yf and R134a varying with the compressor stroke for pressure ratios of 2.0 to 3.5 at a fixed condenser temperature of 40 °C. It can be seen that for a fixed compressor stroke, the mass flow rate decreases as the pressure ratio increases. For a fixed pressure ratio, the mass flow rate of R1234yf and R134a both increase as the compressor stroke increase thus cooling capacity. Overall, the mass flow rate of R1234yf is average 5% higher than R134a. At pressure ratio of 2.5 of compressor stroke of 12 mm, the mass flow rate of R1234yf is 0.36 g/s (16%) higher than R134a. This is due to the higher vapour density of R1234yf in the system. The higher operating frequency of R1234yf also contributes to the high mass flow rate of R1234yf. To produce same amount of mass flow rate for the given pressure ratio, compressor using R1234yf requires lower compressor stroke or displacement (for conventional compressors).

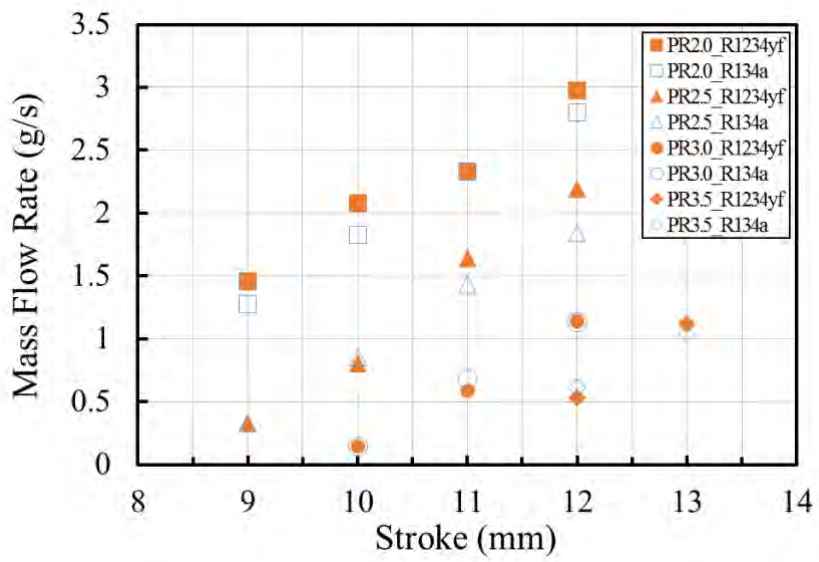

Figure. 4 Mass flow rate against compressor stroke using R1234yf and R134a for pressure ratios of 2.0 to 3.5 at a fixed condenser temperature of 40 °C

3.4. Volumetric Efficiency

The volumetric efficiency was calculated according to the following equation:

$$\eta_V = \frac{\dot{m} R_g T_{suc}}{S A f P_{suc}} \qquad \text{Eq. (3)}$$

where A is the area of piston, f is the operating frequency, T_{suc} is the temperature at the compressor inlet, P_{suc} is the pressure at the compressor inlet, R_g is the specific gas constant and $\dot{m}$ is the mass flow rate.

Fig. 5 shows the volumetric efficiency against the compressor stroke for R1234yf and R134a at a condenser temperature of 40 °C. It can be seen that the volumetric efficiency for both refrigerants increases linearly with the compressor stroke due to decreasing dead volume and increasing of mass flow rate. The volumetric efficiency for both refrigerants decrease with the pressure ratio due to the reduction of mass flow rate. It also can be found that the volumetric efficiency for R1234yf is average 13% lower than R134a.

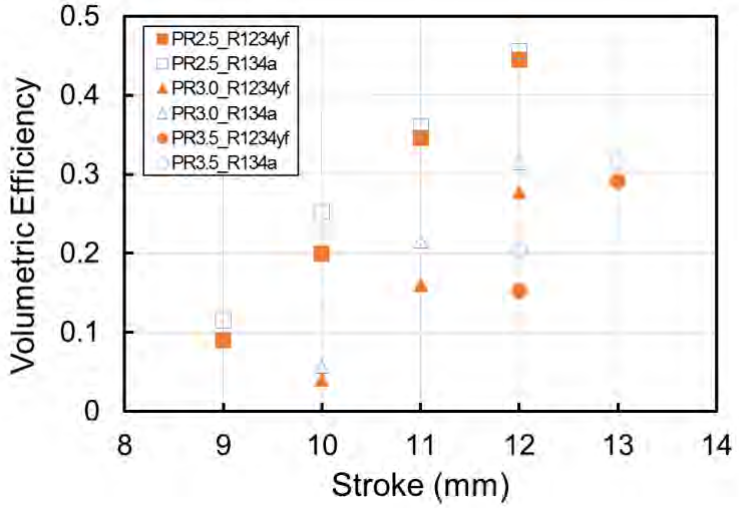

Figure. 5 Volumetric efficiency against evaporator temperature for R1234yf and R134a at a condenser temperature of 40 °C.

3.5. COP and Cooling Capacity

Fig. 6 shows the cooling capacity and COP against condenser temperature for R1234yf and R134a with an evaporator temperature of 5 °C. Both cooling capacity and COP decrease linearly with increasing condenser temperature due to the reduction of the enthalpy difference between evaporator inlet and outlet for R1234yf and R134a. The COP of R1234yf is 10-25% lower than R134a, while the cooling capacity of R1234yf is 10-30% lower than R134a. This is due to smaller enthalpy different between evaporator inlet and evaporator outletIt of R1234yf. It is worth mentioning that with increasing condenser temperature, the difference of COP between R1234yf and R134a decreases as R1234yf is less sensitive to condenser temperature. Though mass flow rate of R1234yf is average 5% higher than R134a, to produce similar cooling capacity to R134a, R1234yf needs to provide a much larger mass flow rate so that large displacement is needed.

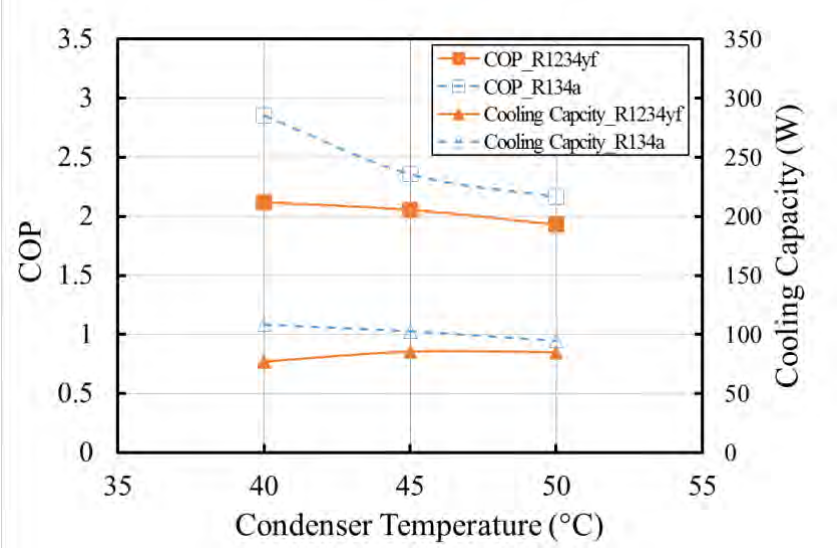

Figure. 6 Cooling capacity and COP against condenser temperature for R1234yf and R134a with evaporator inlet temperature of 5 °C

3.6 Experimental Uncertainty

Pressures, temperature, stroke, current, voltage, and mass flow rate were measured during the experiments. Typically, a set of readings was taken every 15 minutes to allow time for thermal equilibrium to be attained. The measurements of pressure, stroke, and temperature have absolute uncertainties of 0.015 bar, 0.025 mm, and 0.5 °C. The current transducer, voltage transducers, and mass flow rate have accuracies of 0.5%, 0.5%, and 1%, respectively. The combined uncertainties of the calculated values were calculated using a 95% confidence interval. The cooling capacity, COP, and volumetric efficiency have relative uncertainty of 1%, 1.3%, and 0.3%, respectively.

4. CONCLUSIONS

This paper presents an experimental analysis using R1234yf as a drop-in replacement for R134a in an oil-free VCR system for a wide range of operating conditions. Generally, R1234yf provides a lower system performance if it replaces R134a. R1234yf can be used as an alternative to R134a in the device already in operation and new devices. Large displacement compressor for R1234yf will be needed to produce a similar cooling capacity to R134a. Key findings from the experiments are listed below:

(1) For given pressure ratio and compressor stroke, the resonant frequency of R1234yf is higher than R134a due to higher superheat.

(2) At fixed pressure ratio, the mass flow rate of R1234yf is slightly higher than R134a due to the higher vapour density and resonant frequency. Overall, the mass flow rate of R1234yf is average 5% higher than R134a.

(3) With the increase in stroke, the volumetric efficiency for both refrigerants increases and higher pressure tends to have a lower volumetric efficiency due to the reduction of actual piston displacement.

(4) At the condenser temperature of 50 °C and evaporator temperature of 5 °C, the COP of R1234yf is 10% lower than R134a. The COP increases linearly with decreasing condenser temperature. However, the CoP of R1234yf is less sensitive to condenser temperature.

ACKNOWLEDGEMENTS

The Research Development Fund from the University of Sussex (UA016-05) for supporting the instrumentation of the VCR system is acknowledged. The authors are also grateful to Prof Richard Stone, Dr Mike Dadd and Paul Bailey at the University of Oxford for the prototype oil-free linear compressor. The authors are grateful to Andy White and Barry Johnson at the University of Sussex for the lab support.

NOMENCLATURE

A	piston area (mm^2)
COP	coefficient of performance
DAQ	data acquisition
f	frequency (Hz)
GWP	global warming potential
HFC	hydrofluorocarbon
HFO	hydrofluoroolefin
I	current (A)
LVDT	linear variable differential transformer
M	mass flow rate (g/s)
$\dot{m}$	mass flow rate (g/s)
ODP	ozone depletion potential
P	pressure (bar)
PID	proportional-integral-derivative
PR	pressure ratio
PWM	pulse-width-modulation
R	specific gas constant (J/kg/K)
S	stroke (mm)
T	temperature (°C)
V	volume (mm^3) or voltage (V)
VCR	vapour compression refrigeration

Greek symbol

η	efficiency

Subscripts

1	evaporator inlet
2	suction
c	cooling
cond	condenser
g	gas
suc	suction
V	volumetric

REFERENCES

Jankovic, Z. J., Atienza, J. S., and Suarez, J. A. M., 2015. Thermodynamic and heat transfer analyses for R1234yf an R1234ze as drop-in replacements for R134a in a small power refrigerating system. Applied Thermal Engineering, 80, 42-54.

Liang, K., Stone, R., Hancock, W., Dadd, M., and Bailey, P., 2014. Comparison between a crank-drive reciprocating compressor and a novel oil-free linear compressor. International Journal of Refrigeration, 45, 25-34.

Lu, M.-C., Tong, J.-R., & Wang, C.-C., 2013. Investigation of the two-phase convective boiling of HFO-1234yf in a 3.9 mm diameter tube. International Journal of Heat and Mass Transfer, 65, 545-551.

Oliveira, M., Diniz, M., & Deschamps, C., 2015. Thermal modelling and analysis of an oil-free linear compressor. Paper presented at the IOP Conference Series: Materials Science and Engineering.

Vaghela, J. K., 2017. Comparative evaluation of an automobile air-conditioning system using R134a and its alternative refrigerants. Energy Procedia, 109, 153-160.

Wang , C., 2014. System performance of R1234yf refrigerant in air-conditioning and heat pump system. Applied Thermal Engineering, 73, 1412-1420.

Manuscript ID: 317
DOI: 10.18462/iir.icr.2019.0317

Performance of an oil-free vapour compression refrigeration system using R134a

Zhaohua LI[(a)], Kun LIANG[(a)], Hanying JIANG[(a)]

[(a)] University of Sussex
Brighton, BN1 9QT, UK, information@sussex.ac.uk

ABSTRACT

By using a novel linear compressor, lubricant can be eliminated from a vapour compression refrigeration (VCR) system, which offers significant advantages in selection of refrigerants, miniaturization of refrigerator, and heat transfer improvement. In this study, performance of an oil-free VCR system was studied. The system has been constructed using a novel oil-free linear compressor, off-the-shelf condenser unit and an evaporator with electric heater. The oil-free VCR system was instrumented using R134a as refrigerant. The linear compressor was tested with strokes from 9 mm to 13 mm and pressure ratios from 2.0 to 4.0. The refrigerant charge is 300 g, and condenser outlet temperature was controlled from 40 °C to 55 °C. The experimental results show that the oil-free VCR system can achieve a cooling capacity of 311 W and a coefficient of performance (CoP) of 3.65 with a condenser temperature at 40°C, a pressure ratio of 2.5, and a stroke of 12 mm.
Keywords: Oil-free Linear Compressor, R134a, Coefficient of Performance, Cooling Capacity, Vapour compression system

1. INTRODUCTION

Unlike conventional compressors for vapour compression refrigeration (VCR) system, linear compressors can drive the piston without crank mechanism. A free piston is directly driven by linear motor which can provide significant advantages in selection of refrigerants, miniaturization of refrigerator, high efficiency and no need for start and stop. Liang et al. (2014) conducted experiments to compare the performance between oil-free linear compressor and crank-driven compressor. The results indicate that the adiabatic efficiency of linear compressor is more than 20% higher than crank-driven compressor. Bradshaw et al. (2013) developed a compressor model to explore the energy recovery characteristics of a linear compressor and a traditional reciprocating compressor. The results indicated that the linear compressor could operate more efficiently over a wider range of dead (clearance) volumes than the crank-drive compressor. Liang (2017) reviewed the performance of linear compressor indicating that linear compressor has significant advantages over conventional crank-driven compressors. Oil-free operation allows the use of micro-channel heat exchangers for miniature refrigeration system for electronic cooling. Liang et al. (2014) tested an oil-free VCR system with a fixed condenser temperature of 50 °C. The results show that the CoPs are around 3.0 for a pressure ratio of 2.5. Lee et al. (2004) tested a linear compressor for domestic refrigerator. The results show that the system can achieve a coefficient of performance (CoP) of 3.66 at an evaporator temperature of 7.2 °C and a condenser temperature of 54.4 °C.

This study presents an experimental work to evaluate the system performance of an oil-free VCR system using a novel linear compressor. R134a was used as working fluid in this study. Results of specific mass flow rate, motor efficiency, cooling capacity and CoP were reported.

2. INSTRUMENTATION

2.1. Experimental Apparatus

Fig. 1 shows the schematic of an oil-free VCR system and instrumentation using R134a. The test rig consists of two linear compressors, an off-the-shelf water-cooled coaxial condenser and an

evaporator with an electric heater. Two linear compressors were mounted in opposite direction to reduce vibration during the measurement. The details of the linear compressor can be found in Liang et al. (2014). Before measurements, the compressors were heated by resistors to over 35 °C so that no refrigerant condenses in the compressor body. During the measurement, compressed hot refrigerant vapour is released from compressor to condenser. After that, the cooled refrigerant liquid flows to the evaporator via an expansion valve. The pressure ratio depends on the valve lift of the expansion valve. Then, the hot refrigerant vapour flows back to the compressor. A bleed flow loop and a solenoid valve were added to achieve zero piston offset. Compressor stroke and piston offset were controlled by two proportional-integral-derivative (PID) controllers in LabVIEW, respectively. According to measured compressor stroke from linear variable differential transformer (LVDT) displacement transducer, a PID controller generates a sinusoidal excitation voltage from NI data acquisition card to control the piston displacement. The duty cycle of solenoid valve depends on the pulse-width-modulation (PWM) signal which is generated by another PID controller according to the measured piston displacement. A variac heater controller was used to adjust the heat into the evaporator. A power meter connecting to variac heater controller was used to record the electric heater power. A low-speed data acquisition (LDAQ) was used to record the measured parameters including pressures (discharge, suction, body, evaporator inlet), temperatures (discharge, condenser, evaporator inlet/outlet, suction, body), and mass flow rates (main flow and bleed flow). Pressures, voltage, currents, and displacements were collected by a high-speed data acquisition (HDAQ). Forty steady-state tests were conducted for linear compressors. Table 1 shows the test conditions for the oil-free VCR system. The operating frequency of the linear compressor was manually adjusted according to calculated resonant frequency in LabVIEW for each test condition.

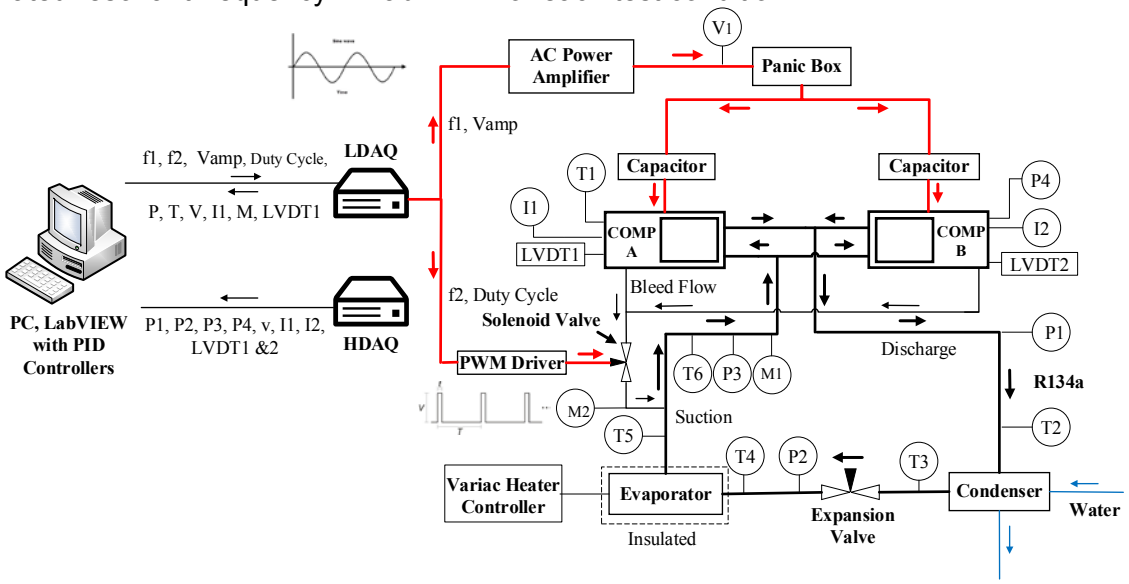

Figure. 1: Schematic of the oil-free VCR system and instrumentation (P: pressure transducer, T: thermocouple, M: mass flow meter, V: voltage sensor, I: current transducer, LVDT: displacement transducer)

Table 1. Test conditions for linear compressor

Refrigerant	R134a
Refrigerant charge (g)	300
Pressure ratio	2.0, 2.5, 3.0, 3.5, 4.0
Compressor stroke (mm)	9, 10, 11, 12, 13
Condenser temperature (°C)	40, 45, 50, 55
Operating frequency (Hz)	32-39

2.2. Polytropic Index and Thermodynamic Efficiency

Due to unavoidable heat transfer through cylinder wall and gas leakage, the compression process and expansion process cannot be considered as adiabatic or isentropic. A correlated polytropic process is realistic. According to ideal gas law, the relationship of in-cylinder pressure, cylinder volume and polytropic index can be expressed as

$$\ln P = -n\ln V + \mathrm{C} \qquad \text{Eq. (1)}$$

where *P* is the in-cylinder pressure, *V* is the cylinder volume, *n* is the polytropic index and C is a constant.

Fig. 2 shows a *P-V* loop in log-scale of R134a with a refrigerant charge of 300 g, a compressor stroke of 12 mm, a pressure of 2.0, and a fixed condenser temperature of 40 °C from measurements. The logged in-cylinder pressure and logged cylinder volume vary linearly during compression and expansion process. Thus, the slope can be considered as the polytropic indexes for two processes. Table 2 lists the polytropic indexes of R134a for pressure ratios of 2.0-4.0. The variation of the polytropic indexes for various pressure ratios is within 12%.

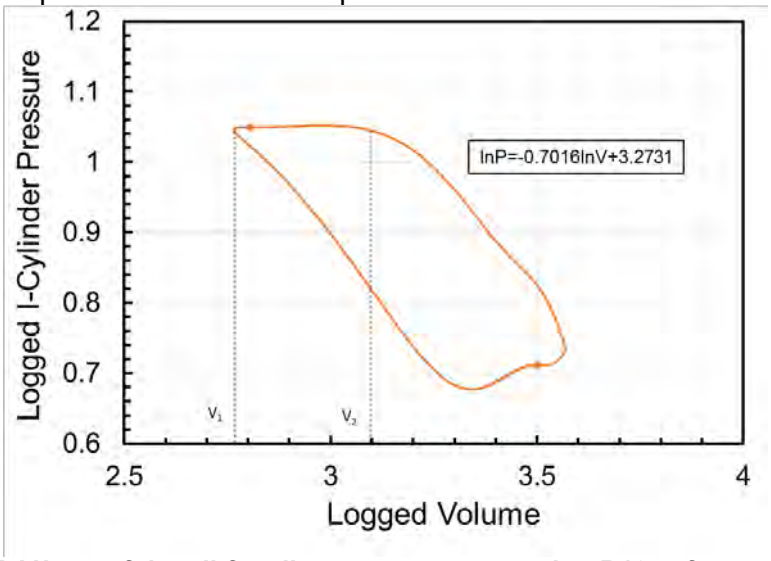

Figure. 2: Logged *P-V* loop of the oil-free linear compressor using R134a for a refrigerant charge of 300 g, a compressor stroke of 12 mm, a pressure of 2.0, and a fixed condenser temperature of 40 °C

Table 2 Polytropic indexes of R134a in linear compressor

Pressure Ratio	2.0	2.5	3.0	3.5	4.0
R134a	0.70	0.72	0.76	0.79	0.73

The thermodynamic power (P_{th}) was calculated according to the following equation

$$P_{\mathrm{th}} = \frac{n}{n-1}\dot{m}\mathrm{R_g}T_{\mathrm{suc}}\left[\left(\frac{P_{\mathrm{dis}}}{P_{\mathrm{suc}}}\right)^{\frac{n-1}{n}} - 1\right] \qquad \text{Eq. (2)}$$

where $\mathrm{R_g}$ is the specific gas constant, $\dot{m}$ is the mass flow rate, T_{suc} is the suction temperature, P_{dis} is the discharge pressure and P_{suc} is the suction pressure.

The thermodynamic efficiency (η_{th}) for the linear compressor can be defined as

$$\eta_{\mathrm{th}} = \frac{P_{\mathrm{th}}}{P_{\mathrm{in}}} \qquad \text{Eq. (3)}$$

where P_{in} is the power input.

3. RESULTS and DISCUSSIONS

3.1. Motor Efficiency, Root Mean Square Value of Current, and Power Input

Fig. 3 shows the motor efficiency and root mean square (RMS) value of current against operating frequency using R134a for a pressure ratio of 3.0, a compressor stroke of 12 mm, and a condenser temperature of 50 °C. At the operating frequency of 37 Hz, the linear compressor is operated at resonant frequency achieving the minimum current for this test condition. Thus, the copper loss can be minimised to improve the motor efficiency of the linear compressor. Fig. 4 shows the motor efficiency and power input against compressor stroke with various pressure ratio at a fixed

condenser temperature of 40 °C. The motor efficiency decreases as compressor stroke increase as induced current becomes larger resulting in a higher copper loss. For a fixed compressor stroke, the motor efficiency increase with pressure ratio due to the reduction of the mass flow rate and shaft force. The maximum motor efficiency is 92.6% at a fixed compressor stroke of 12 mm and a fixed pressure ratio of 3.5 while the minimum is 85.8% at a fixed compressor stroke of 11 mm and a fixed pressure ratio of 2.5. For a fixed pressure ratio, the power input of the oil-free VCR system increases with stroke. For a fixed condenser temperature, the power input decreases with the increase of pressure ratio due to the decrease of shaft force. At a fixed compressor stroke of 12 mm and a fixed pressure ratio of 2.5, the linear compressor requires a power input of 85 W.

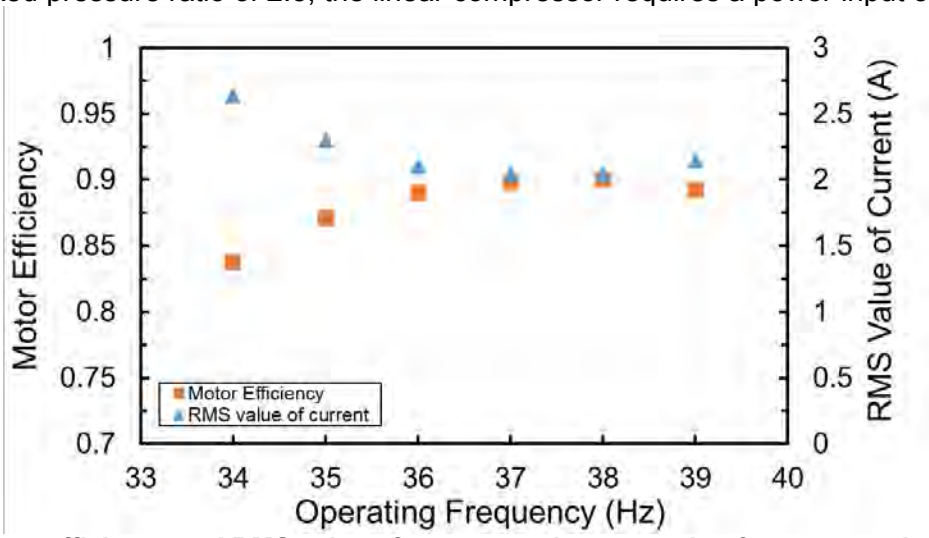

Figure. 3: Motor efficiency and RMS value of current against operating frequency using R134a for a refrigerant charge of 300 g, a pressure ratio of 3.0, a compressor stroke of 12 mm, and a condenser temperature of 50 °C

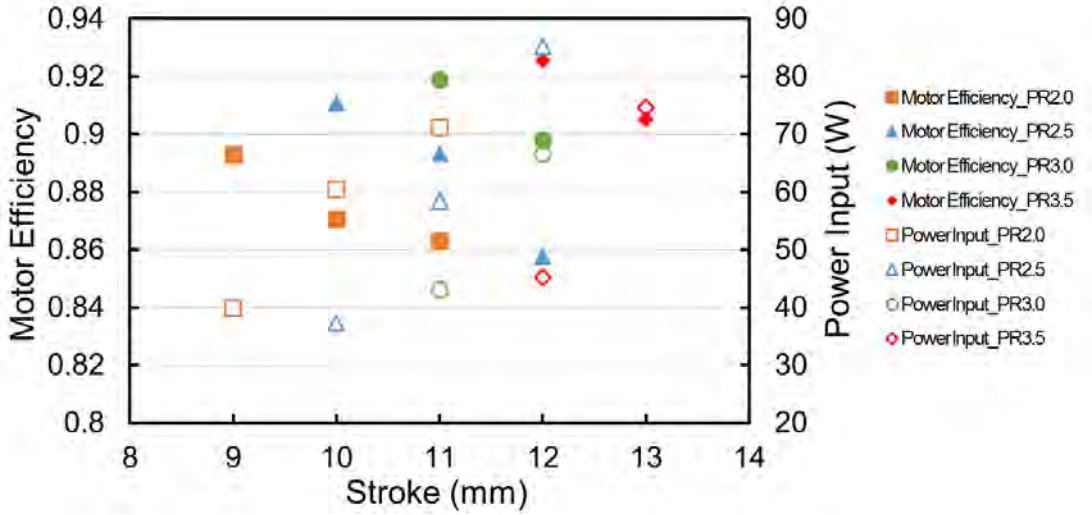

Figure. 4: Motor efficiency and power input against compressor stroke with various pressure ratio at a fixed condenser temperature of 40 °C

3.2. Specific Mass Flow Rate

Fig. 5 shows the specific mass flow rate against pressure ratio using R134a for condenser temperature from 40 °C to 55 °C. It can be seen that for a fixed condenser temperature, specific mass flow rate decreases with the increase of the pressure ratio. This is due to the reduction of the actual piston stroke. For a fixed pressure ratio, the specific mass flow rate decreases with the increase of condenser temperature due to the decrease of the vapour density. At a fixed condenser temperature of 40 °C and a fixed pressure ratio of 2.0, the oil-free VCR system can achieve a specific mass flow rate of 0.034 g/s/W.

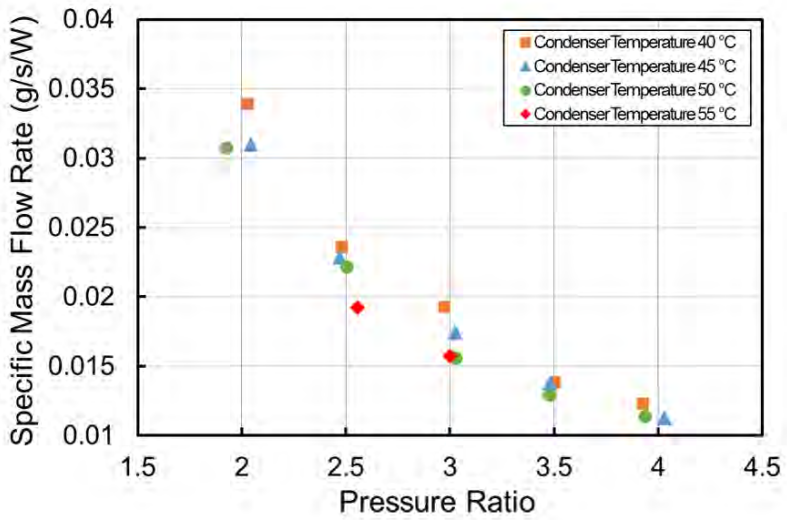

Figure. 5: shows the specific mass flow rate against pressure ratio using R134a for pressure ratios from 40 °C to 55 °C

3.3. Thermodynamic Efficiency

Fig. 6 shows the thermodynamic efficiency against compressor stroke for pressure ratios of 2.0, 2.5, 3.0, and 3.5 at fixed condenser temperatures of 40 °C and 50 °C. The thermodynamic efficiency increases with compressor stroke due to the increase of mass flow rate. For a fixed compressor stroke, the thermodynamic efficiency decrease with the increase of pressure ratio. It is worth mentioning that higher condenser temperature has a negative influence on thermodynamic efficiency. This is due to the higher discharge pressure resulting in higher shaft force thus power input. At a fixed compressor stroke of 10 mm and a fixed pressure ratio of 2.0, the thermodynamic efficiency of the linear compressor at 40 °C (50%) is 5% higher than 50 °C. At a fixed pressure ratio of 3.5, the difference of thermodynamic efficiency between two condenser temperatures is reduced. This is due to the low mass flow rate for both condenser temperatures.

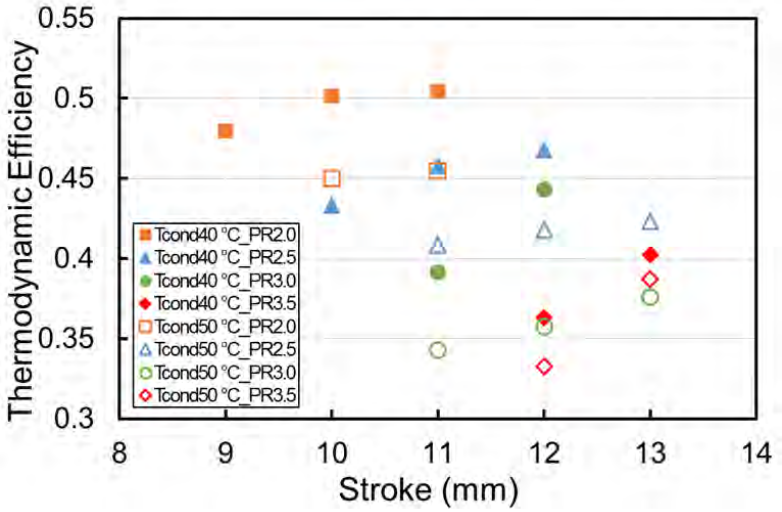

Figure. 6: Thermodynamic efficiency against stroke for pressure ratios of 2.0, 2.5, 3.0, and 3.5 at fixed condenser temperatures of 40 °C and 50 °C

3.4. Cooling Capacity and Coefficient of Performance

Fig. 7 shows the CoP and cooling capacity against condenser temperature of the oil-free VCR system using R134a for pressure ratios of 2.5, 3.0, and 4.0 with a compressor stroke of 12 mm. Both cooling capacity and CoP decrease with the increase of condenser temperature. For a fixed pressure ratio of 2.5, the CoP at a condenser temperature of 40 °C is 30% higher than the CoP at a condenser temperature of 55 °C. For a fixed condenser temperature, the CoP and cooling

capacity decrease as the pressure ratio increases. At a condenser temperature of 40 °C and a pressure ratio of 2.5, the CoP is 3.65 and the cooling capacity is 311 W.

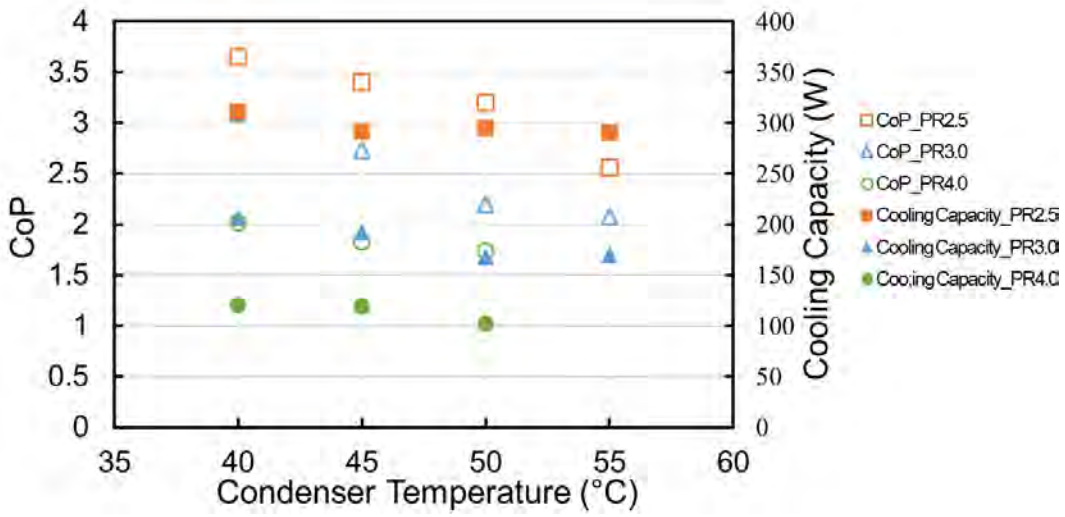

Figure 7: CoP and cooling capacity against condenser temperature of the oil-free VCR system using R134a for pressure ratios of 2.5, 3.0, and 4.0 with a compressor stroke of 12 mm

4. CONCLUSIONS

In this study, the performance of an oil-free VCR system using novel linear compressors was studied. Key findings are listed below:

(1) The motor efficiency decreases with the increase of compressor stroke. For a fixed stroke, the motor efficiency increase with pressure ratio. The maximum motor efficiency is 92.6% at a fixed stroke of 12 mm and a fixed pressure ratio of 3.5.

(2) For a fixed condenser temperature, specific mass flow rate decreases with the increase of the pressure ratio. At a fixed condenser temperature of 40 °C and a fixed pressure ratio of 2.0, the oil-free VCR system can achieve a specific mass flow rate of 0.034 g/s/W.

(3) The thermodynamic efficiency of linear compressor increases with stroke due to the increase of mass flow rate. At a fixed compressor stroke of 10 mm and a fixed pressure ratio of 2.0, the oil-free VCR system can achieve a thermodynamic efficiency of 50%.

(4) Both cooling capacity and CoP for the oil-free VCR system decrease with the increase of condenser temperature. When linear compressor using R134a operates at a stroke of 12 mm, a pressure ratio of 2.0 with a fixed condenser temperature of 40 °C, the system achieves the highest CoP of 3.65.

ACKNOWLEDGEMENTS

The Research Development Fund from the University of Sussex (UA016-05) for supporting the instrumentation of the VCR system is acknowledged. The authors are grateful to Andy White and Barry Johnson at the University of Sussex for the lab support.

NOMENCLATURE

C	constant	*M*	mass flow rate (g/s)
CoP	coefficient of performance	$\dot{m}$	mass flow rate (g/s)
DAQ	data acquisition	n	polytropic index
GWP	global warming potential	*P*	pressure (bar) or power (W)
I	current (A)	PID	proportional-integral-derivative
LVDT	linear variable differential transformer	PR	pressure ratio

PWM	pulse-width-modulation
R	resistance (Ω)
RMS	root mean square
T	temperature (°C)
V	voltage (V)
VCR	vapour compression refrigeration

Greek symbol

η	efficiency

Subscripts

dis	discharge
g	gas
in	input
suc	suction
th	thermodynamic

REFERENCES

Bradshaw, C. R., Groll, E. A., & Garimella, S. V., 2013. Linear compressors for electronics cooling: Energy recovery and its benefits. International Journal of Refrigeration, 36(7).

Lee, H., Jeong, S. S., Lee, C. W., & Lee, H. K., 2004. Linear compressor for air-conditioner. Proceedings of the International Compressor Engineering Conference, C047.

Liang, K., 2017. A review of linear compressors for refrigeration. International Journal of Refrigeration. International Journal of Refrigeration, 84, 253-273.

Liang, K., Stone, R., Dadd, M., & Bailey, P., 2014. A novel linear electromagnetic-drive oil-free refrigeration compressor using R134a. International Journal of Refrigeration, 40, 450-459.

Liang, K., Stone, R., Hancock, W., Dadd, M., & Bailey, P., 2014. Comparison between a crank-drive reciprocating compressor and a novel oil-free linear compressor. International Journal of Refrigeration, 45, 25-34.

Manuscript ID: 319
DOI: 10.18462/iir.icr.2019.0319

R1234ze(Z) and R1233zd(E) vaporisation inside a Brazed Plate Heat Exchanger (BPHE)

Giovanni A. LONGO, Simone MANCIN, Giulia RIGHETTI, Claudio ZILIO

Department of Management and Engineering,
University of Padova, Vicenza, I-36100, Italy,
tony@gest.unipd.it

ABSTRACT

This paper presents the boiling heat transfer coefficients of R1234ze(Z) and R1233zd(E) inside a commercial Brazed Plate Heat Exchanger (BPHE): the effects of heat flux / mass flux, saturation temperature / pressure, outlet conditions and fluid properties are investigated. The boiling heat transfer coefficients are controlled mainly by heat flux / mass flux and evaporator outlet conditions. R1234ze(Z) exhibits boiling heat transfer coefficients higher than those of R1233zd(E). There is a reasonable agreement between the saturated boiling heat transfer coefficients and the calculated values by a model recently proposed by the present authors.
Keywords: GWP; R1234ze(Z); R1233zd(E); boiling; BPHE

1. INTRODUCTION

The Kigali amendment (UNEP, MOP 28 in Kigali, Rwanda, 10-14 October 2016), to the Montreal Protocol established the phase down of traditional HFC refrigerants because their high Global Warming Potential (GWP). The traditional low-pressure HFC refrigerants used in High-Temperature Heat Pumps (HTHP) and Organic Rankine Cycles (ORC) present in general high value of GWP ranging from 1020 of R245fa, to 1370 of R236ea to 9810 of R236fa. A new generation of low-pressure refrigerants with very low-GWP was recently put on the market: the more interesting ones are R1234ze(Z) and R1233zd(E). R1234ze(Z) is a HydroFluoroOlefin (HFO) refrigerant with ODP = 0, GWP ≤ 3, mild flammability (ASHRAE classification A2L), normal boiling point 9.8°C and critical temperature 150.12 °C. R1233zd(E) is a HydroChloroFluoroOlefin (HCFO) refrigerant with ODP ~ 0, GWP ≤ 3, no flammability (ASHRAE classification A1), normal boiling point 19.0 °C and critical temperature 165.5 °C.
This paper presents new and original boiling heat transfer coefficients on R1234ze(Z) and R1233zd(E) inside a commercial Brazed Plate Heat Exchanger (BPHE): the effects of heat flux / mass flux, saturation temperature / pressure, outlet conditions and fluid properties are investigated.

2. EXPERIMENTAL MEASUREMENT AND DATA REDUCTION

The experimental measurements were performed in a test rig already used for proving several HFC, HC, and HFO refrigerants: Longo and Gasparella (2007) gives a detailed description of the experimental rig, the measuring procedures and the data reduction. Fig. 1 presents a schematic view of the experimental rig and Table 1 gives the characteristics of the measuring devices, while Fig. 2 and Table 2 show the geometrical characteristics of the BPHE tested.
The experimental measurements are reported in term of boiling heat transfer coefficient h_r.

Table 1. Specification of the different measuring devices

Devices	Uncertainty (k=2)	Range
T-type thermocouples	0.1 K	-20/80°C
T-type thermopiles	0.05 K	-20/80°C
Abs. pressure transducers	0.075% f.s.	0/1.0 MPa
Diff. pressure transducers	0.075% f.s.	0/0.3 MPa
Coriolis effect flow meters	0.1%	0/300 kg h^{-1}
Magnetic flow meters	0.15% f.s.	100/1200 l h^{-1}
Thermo camera	± 0.1 °C	5 – 150 °C

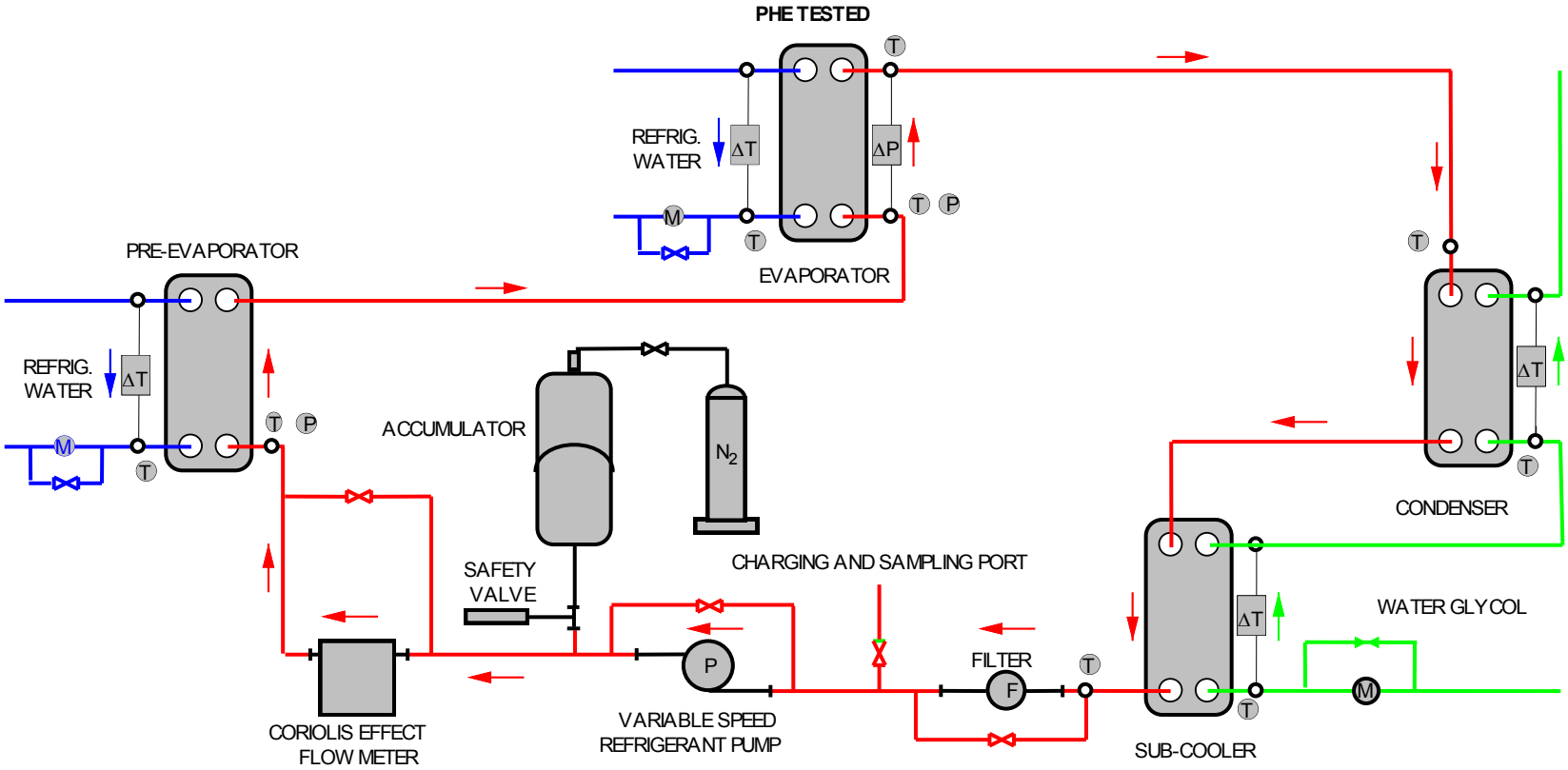

Figure 1: Schematic view of the experimental test rig

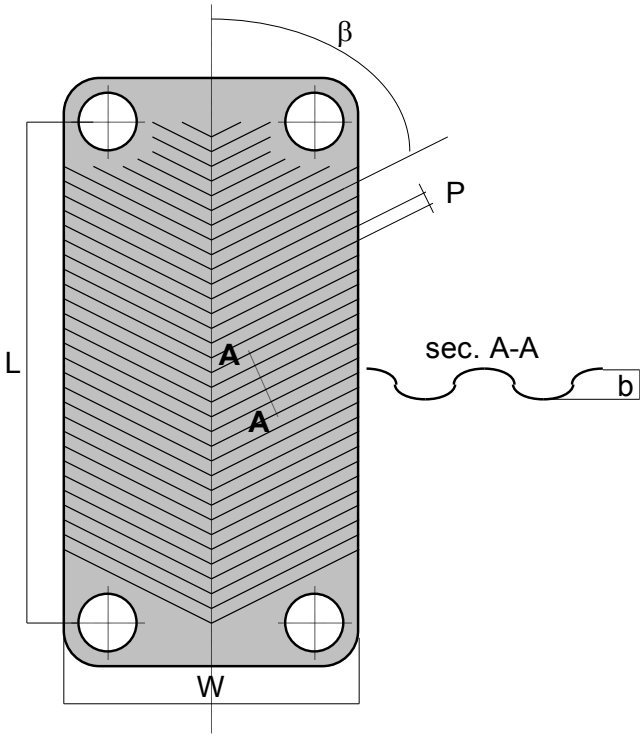

Figure 2: Schematic drawing of the plate

Table 2. Characteristics of the BPHE

Parameter	Measure
Fluid flow plate length *L* (mm)	278.0
Plate width *W*(mm)	72.0
Area of the plate *A*(m^2)	0.020
Corrugation type	Chevron
Angle of the corrugation β(°)	65
Corrugation depth *b*(mm)	2.0
Corrugation pitch *P*(mm)	8.0
Plate roughness R_a(μm)	0.4
Plate roughness R_p(μm)	1.0
Total number of plates	10
Number of effective plates	8
Channels on refrigerant side	4
Channels on water side	5

The boiling heat transfer coefficient h_r is derived from the overall heat transfer coefficient U by determining the water side heat transfer coefficient h_w using a modified Wilson plot technique according with Munley and Manglick (1999). In the saturated boiling tests the overall heat transfer coefficient U is computed with reference to the logarithmic mean temperature difference ΔT_{ln} based on the average saturation temperature T_{sat}. In the boiling and super-heating tests the overall heat transfer coefficient U is computed as the average value between the overall heat transfer coefficient of the boiling portion U_{boil} and that of the super-heating portion U_{sup} weighted on the base of the respective heat transfer area as suggested by Dutto et al. (1991) and Fernando et al. (2004). In this way, it is possible to directly compare the heat transfer performance of an evaporator working only in two-phase heat transfer with that of an evaporator working both in two-phase and super-heating heat transfer.
The refrigerant properties are evaluated by the NIST Standard Reference Database REFPROP 10.0 (Lemmon et al. 2017).

3. ANALYSIS OF THE EXPERIMENTAL RESULTS

The experimental results include 102 R1234ze(Z) data points and 93 R1233zd(E) data points at the saturation temperatures of 30, 35 and 40 °C. Table 3 summarises the operating conditions in the experimental tests. The uncertainty analysis carried out according to Kline and McClintock (1953) evidences a maximum expanded uncertainty (k = 2) within ±12% for the boiling heat transfer coefficients of both the refrigerants tested.

Table 3. Operating conditions during experimental tests

Fluid	Runs	T_{sat} (°C)	X_{in}	X_{out}	ΔT_{sup} (°C)	G_r(kgm^{-2}s^{-1})	q (kW m^{-2})
R1234ze(Z)	102	29.9–40.2	0.19–0.26	0.79–1.00	4.7–10.3	12.6–62.3	2.7–21.6
R1233zd(E)	93	29.9–40.2	0.19–0.25	0.80–1.00	4.7–10.6	10.8–50.0	2.3–15.5

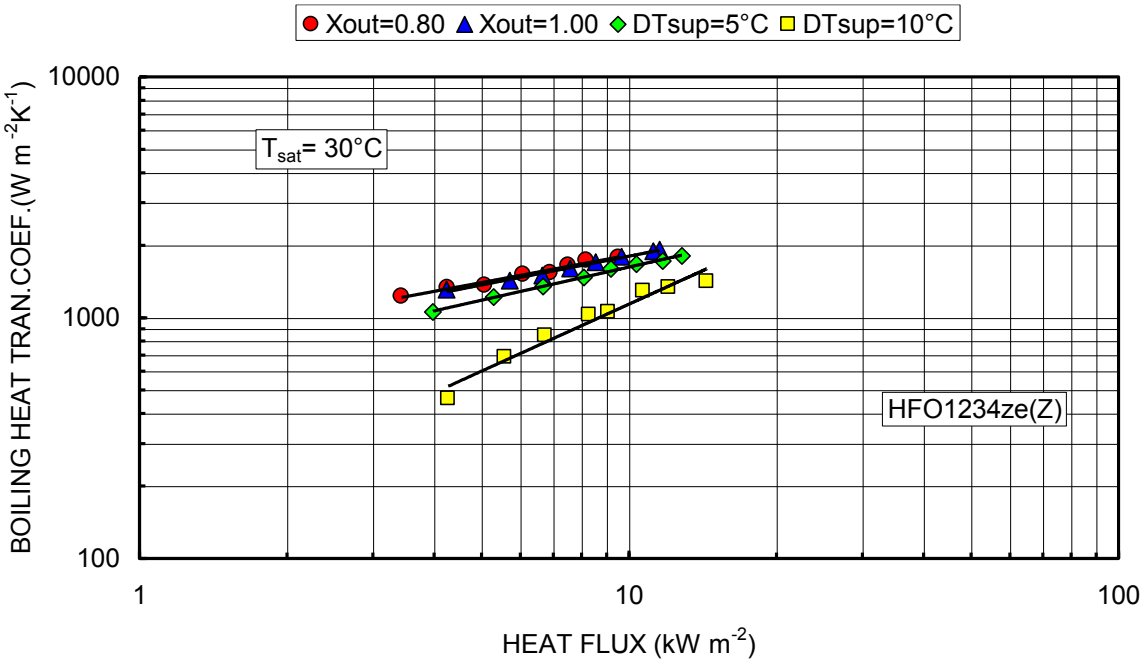

Figure 3a: R1234ze(Z) boiling heat transfer coefficient vs. heat flux at 30 °C

Fig. 3a and 3b, 4a and 4b show the boiling heat transfer coefficients h_r vs. heat flux q and outlet conditions (0.8 and 1.0 vapour quality and 5 and 10 °C vapour super-heating) for R1234ze(Z) and R1233zd(E) at 30 and 40°C of saturation temperature, respectively. It should be noted that in each tested outlet condition the vapour quality change is almost constant, therefore in each experimental run there is a direct relationship between heat flux q and mass flux G and it is difficult to separate the two contributions. The saturated boiling heat transfer coefficient of R1234ze(Z) resulted 17-22% higher than those of R1233zd(E) under the same operating conditions. The saturation temperature / pressure has weak effects on heat transfer coefficients that are controlled mainly by the heat flux / mass flux and by the thermodynamic state of the vapour (saturated or super-heated) at the outlet of the evaporator.

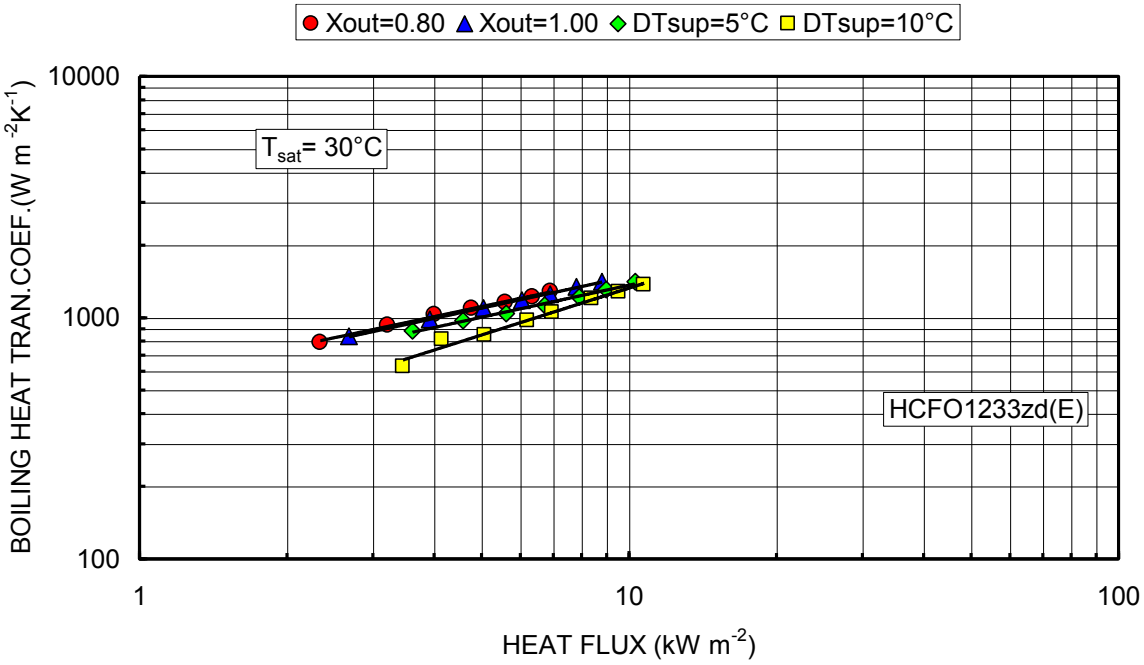

Figure 3b: R1233zd(E) boiling heat transfer coefficient vs. heat flux at 30 °C

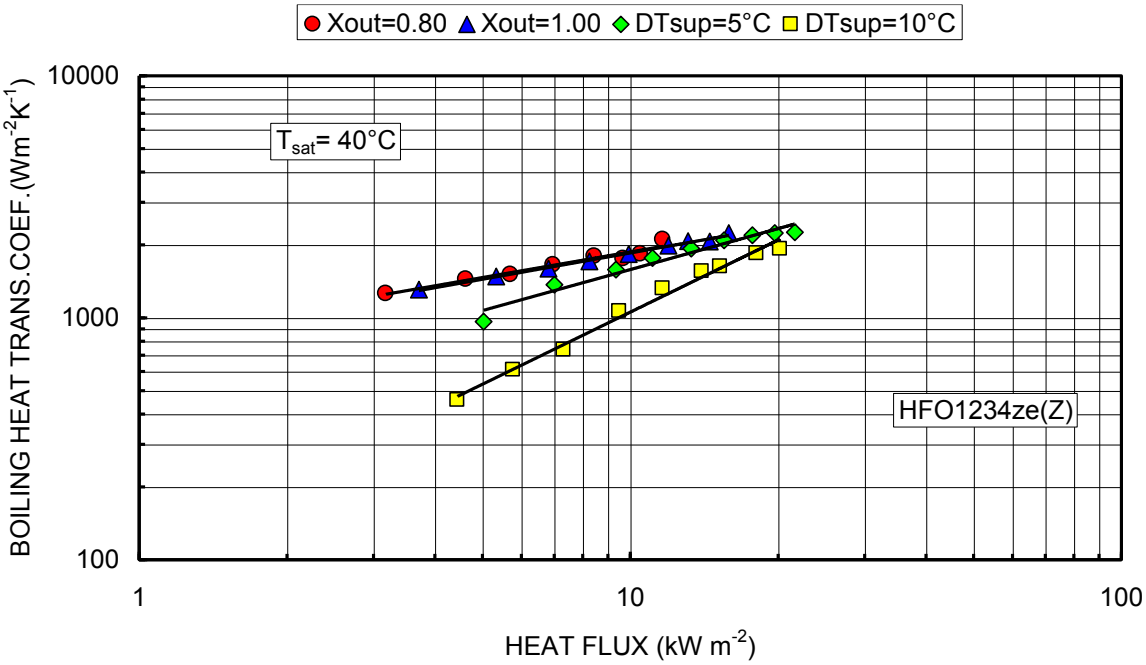

Figure 4a: R1234ze(Z) boiling heat transfer coefficient vs. heat flux at 40 °C

The saturated boiling tests with an outlet vapour quality around 0.8 and 1.00 showed heat transfer coefficients with rather limited difference, within 1 – 2 % for both the refrigerants tested. Differently, a progressive degradation of the heat transfer coefficients can be observed when increasing the outlet vapour super-heating, particularly for refrigerant R1234ze(Z). A penalisation of 11-16 % and of 4 – 9% is observed at 5 °C of outlet super-heating for R1234ze(Z) and R1233zd(E), respectively, while the penalisation increases up to 38 – 44% and 12 – 19% at 10°C of super-heating, for R1234ze(Z) and R1233zd(E), respectively. This penalisation is due to the degradation of the local heat transfer in the evaporator downstream the dry-out point / line. A specific IR thermography analysis was carried out for studying the effects of dry-out and vapour super-heating on the heat transfer coefficient in the evaporator.

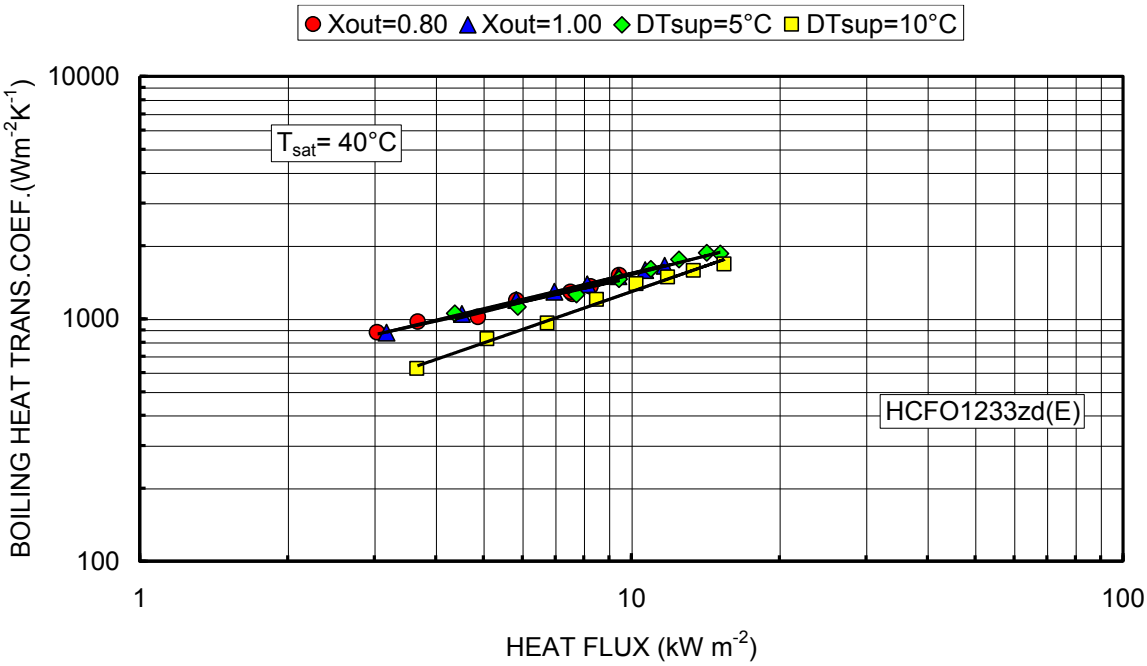

Figure 4b: R1233zd(E) boiling heat transfer coefficient vs. heat flux at 40 °C

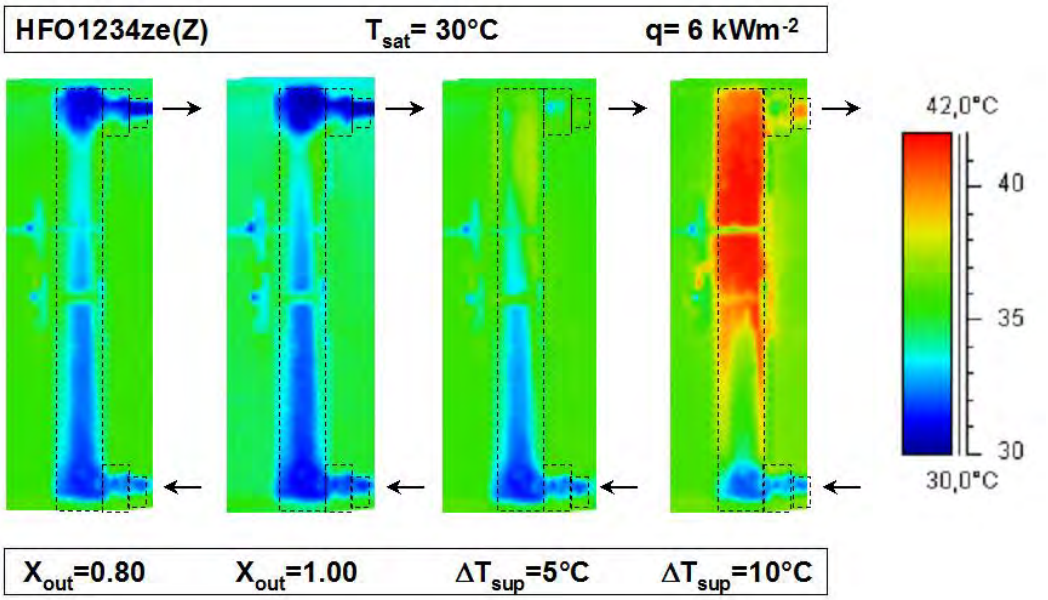

Figure 5a: IR thermography during R1234ze(Z) boiling tests at 30 °C with 6 kWm^{-2} of heat flux.

The flank of the BPHE evaporator was filmed by an IR thermo-camera (temperature uncertainty (k= 2) = ±0.1 °C in the temperature range 5 – 150 °C) to identify the dry-out point / line and to quantify the boiling portion (two-phase heat transfer) and the vapour super-heating portion (gas single-phase heat transfer) of the heat transfer surface area. Fig. 5a and 5b show the IR thermography of the BPHE in the vaporisation tests at 30°C at different vapour outlet conditions (0.8 and 1.0 vapour quality and 5 and 10 °C vapour super-heating) with a heat flux of 6 kWm^{-2} for R1234ze(Z) and R1233zd(E), respectively (the dotted line indicates the BPHE profile). In the saturated boiling tests (0.8 and 1.0 outlet vapour quality) the heat transfer area appears in blue colour which involves two-phase heat transfer at a saturation temperature around 30 °C. In the boiling tests with 5 °C of outlet vapour super-heating around 30-40% and 20-30% of the heat transfer area, for R1234ze(Z) and R1233zd(E) respectively, assumes a yellow-green colour which corresponds to vapour single-phase heat transfer around 35 °C.

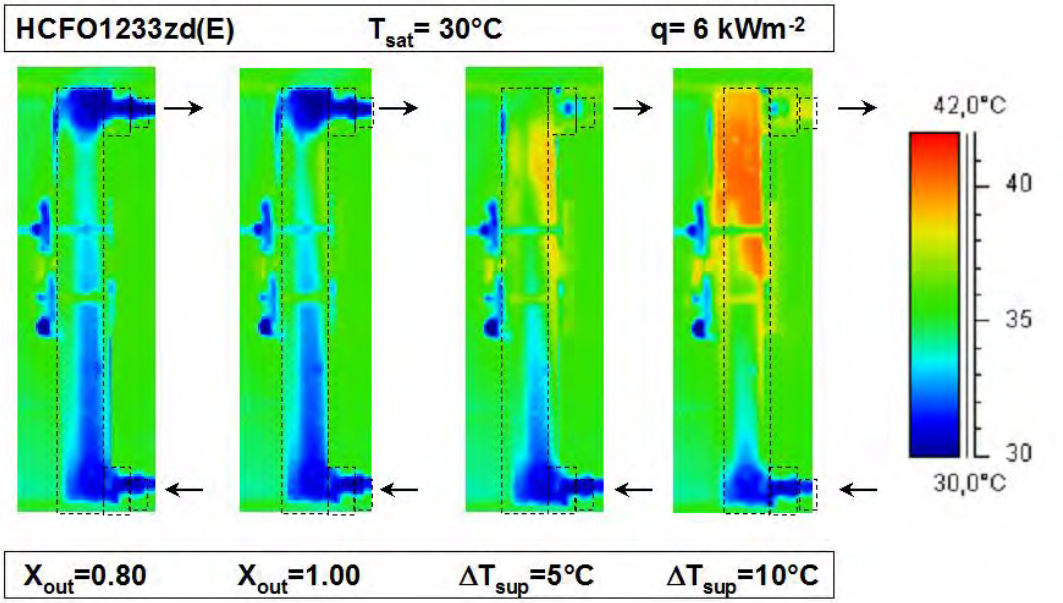

Fig. 5b: IR thermography during R1233zd(Z) boiling tests at 30 °C with 6 kWm^{-2} of heat flux.

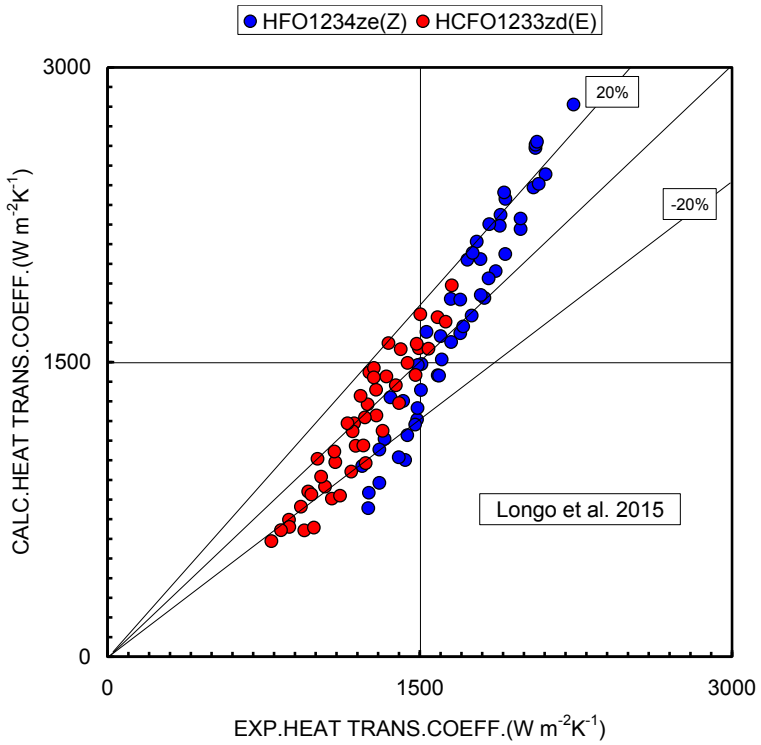

Fig. 6: Experimental vs. calculated saturated boiling heat transfer coefficients .

Increasing the outlet vapour super-heating up to 10 °C, around 50-60% and 40-50% of the heat transfer area, for R1234ze(Z) and R1233zd(E) respectively, presents a red colour which indicates a vapour single-phase heat transfer around 40°C. The increase of the outlet vapour super-heating from 5 to 10 °C produces a consistent degradation of the average boiling heat transfer coefficient of the whole evaporator, particularly for R1234ze(Z), while the penalisation is less evident for R1233zd(E). The IR thermography analysis confirms the results of the heat transfer coefficient measurements quantifying the portion of the heat transfer area affected by vapour super-heating downstream the dryout line.

The saturated boiling heat transfer coefficient were compared with the recent model developed by the present authors for vaporisation inside BPHE (Longo et al., 2015). Fig. 6 shows the comparison between the experimental saturated boiling heat transfer coefficients and the calculated values by the new model: the absolute mean percentage deviation between calculated and experimental data is 14.6 % and 12.1% for R1234ze(Z) and R1233zd(E), respectively. All the experimental data points fall into the convective boiling heat transfer regime.

4. CONCLUSIONS

This paper presents the boiling heat transfer coefficients of R1234ze(Z) and R1233zd(E) inside a commercial Brazed Plate Heat Exchanger (BPHE): the effects of heat flux / mass flux, saturation temperature / pressure, outlet conditions and fluid properties are investigated. R1234ze(Z) and R1233zd(E) are two innovative low-GWP refrigerants particularly interesting as substitutes for traditional working fluids in HTHP and ORC applications.

The boiling heat transfer coefficients are controlled by heat flux / mass flux and evaporator outlet conditions and, in general, they belong to the convective boiling heat transfer regime both for R1234ze(Z) and R1233zd(E). The vapour-superheating at the outlet of the evaporator produces a degradation of the average boiling heat transfer coefficient in the whole evaporator, particularly for R1234ze(Z). There is a reasonable agreement between saturated boiling heat transfer coefficients and the calculated values by a model recently proposed by the present authors. R1234ze(Z) exhibits boiling heat transfer coefficients higher than those of R1233zd(E) under the same operating conditions.

ACKNOWLEDGEMENTS

This research project was partially funded by:
CariVerona Foundation, Verona, Italy, Ricerca Scientifica e Tecnologica 2016-2019:
"*Sostenibilità e autenticazione nutrizionale di filiere lattiero-casearie a tutela del consumatore* ".

NOMENCLATURE

A	area of the plate (m^2)
b	depth of the corrugation (m)
BPHE	brazed plate heat exchanger
G	mass flux (kg $m^{-2}s^{-1}$)
GWP	global warming potential
h	HTC (W $m^{-2}K^{-1}$)
HC	hydrocarbon
HCFO	hydrochlorofluoroolefin
HFC	hydrofluorocarbon
HFO	hydrofluoroolefin
HTHP	high temperature heat pump
k	coverage factor
L	fluid flow plate length (m)
ODP	ozone depletion potential
ORC	organic Rankine cycle
P	corrugation pitch (m)
q	heat flux (W m^{-2})
R_a	roughness (ISO4271/1) (μm)
R_p	roughness (DIN 4762/1) (μm)
T	temperature (K)
U	overall HTC (W $m^{-2}K^{-1}$)
W	width of the plate (m)
X	vapour quality

Greek symbols

β	angle of the corrugation (°)

Subscripts

boil	boiling
in	inlet
out	outlet
r	refrigerant
sat	saturation
sup	super-heat
w	water

REFERENCES

Dutto, T., Blaise, J.C., Benedic, T., 1991. Performances of brazed plate heat exchanger set in heat pump. Proc. of 18th Int. Congr. Refrigeration, Montreal, Canada, 1284-1288.

Fernando, P., Palm, B., Lundqvist, P., Granryd, E., 2004. Propane heat pump with low refrigerant charge: design and laboratory tests, Int. J. Refrigeration 27 761-773.

Kline, S.J., McClintock, F.A., 1954. Describing uncertainties in single-sample experiments. Mech. Eng. 75 3-8.

Lemmon, E.W., Bell, I.H., Huber, M.L., McLinden, M.O., 2017. NIST Reference Fluid Thermodynamic and Transport Properties Database - REFPROP, Version 10.0, National Institute of Standards and Technology, Standard Reference Data Program, Gaithersburg.

Longo, G.A., Gasparella, A., 2007. Heat transfer and pressure drop during HFC refrigerant vaporisation inside a brazed plate heat exchanger . Int. J. Heat Mass Transfer 50 5194-5203.

Longo, G.A., Mancin, S., Righetti, G., Zilio, C., 2015. A new model for refrigerant boiling inside brazed plate heat exchangers (BPHEs). Int. J. Heat Mass Transfer 91 144-149.

Muley, A., Manglik, R.M., 1999. Experimental study of turbulent flow heat transfer and pressure drop in a plate heat exchanger with chevron plates, J. Heat Transfer 121 110-121.

UNEP, 38th Meeting of the Open-ended Working Group (OEWG 38) of the Parties to the Montreal Protocol on Substances that Deplete the Ozone Layer and 28th Meeting of the Parties to the Montreal Protocol (MOP 28), Kigali, 8, 10-14 October 2016.

Manuscript ID: 328
DOI: 10.18462/iir.icr.2019.0328

New generation of low-charge ammonia unit coolers

Stefano FILIPPINI[(a)], Umberto MERLO[(a)], Lorenzo NOTO LA DIEGA[(a)], Matteo Carmelo ROMANO[(b)], Ennio MACCHI[(b)].

[(a)] LU-VE GROUP, Uboldo, 21040, Italy, stefano.filippini@luvegroup.com
[(b)] Politecnico di Milano University, Milano, 20133, Italy, ennio.macchi@polimi.it

ABSTRACT

Industrial refrigeration uses ammonia unit coolers for the principle processes of conservation and freezing of foodstuffs. This paper describes the recent evolution of a unit cooler for NH3 application, aiming to lower the refrigerant charge. The main topics are the use of small tube diameter (1/2”), a new concept of refrigerant distribution, a new methodology of performance calculation, aiming to operate with reduced fluid charge. In fact, the revised construction allows operation with a very limited recirculation ratio number, from the typical 3-4 down to values of 1.8 with major containment of the ammonia charge in the unit cooler and consequently within the entire plant. The article describes the basis of the configuration, the experimental activities carried out to optimize performance and the final product arrangement.

Keywords: ammonia (refrigerant), dry expansion evaporator, evaporator, flooded evaporator, heat exchanger, NH3 (refrigerant), refrigerant charge

1. INTRODUCTION

Since the beginning of refrigeration, ammonia has been judged as one of the best working fluids for medium-large scale refrigeration plants, mostly due to its favourable thermodynamic properties (critical pressure and temperature, molecular complexity and mass): typically, a flooded ammonia system is significantly more efficient than its traditional refrigerant counterpart. Moreover, ammonia has other advantageous characteristics, including low specific cost and good heat transfer properties.
More recently, well known environmental issues have given a strong boost to the adoption of “natural” refrigerants, including ammonia, since they are the most environmentally friendly refrigerants, exhibiting both GWP (Global Warming Potential) and ODP (Ozone Depletion Potential) equal to zero.
However, all ammonia systems have to be designed with safety in mind, since the fluid is a toxic refrigerant, and it is also flammable in certain concentrations. That is why it must be handled with care: in particular, it is of primary importance to reduce the ammonia charge.

2. THE NEW RANGE OF LU-VE INDUSTRIAL AMMONIA UNIT COOLERS

2.1. Design philosophy

The concept, introduced to the refrigeration industry by LU-VE is to adopt compact heat exchanger geometries, achieved by:

- tube diameters lower than conventional solutions (½" vs. ⅝")
- louvered, high efficiency fins

This enables the mass, volume and weight of the heat exchanger to be minimized and increases economic competitiveness. In the particular case of flooded ammonia unit coolers, this concept brought about a dramatic reduction of the internal volume of the coil, and consequently of the

ammonia charge. Moreover, given the high heat transfer coefficients achievable by adopting proper mass velocity and heat flux in the tubes, a large spacing (55 mm) in both row and tube is adopted. This not only gives an optimized heat balance between internal and external surfaces of the exchanger, but also offers a proper large surface for frost deposition. Another relevant feature of LU-VE ammonia unit coolers is the co-current flow arrangement, which enables the most favourable air-ammonia temperature differences across the heat exchanger and facilitates oil discharge thanks to top feeding.

2.2. The new development: low recirculation rates

Conventional evaporators are designed for a recirculation ratio (defined as the ratio between the actual inlet flow rate and the flow rate of generated vapour) of around 4-5. The reason for adopting such high values is based on the need to ensure a correct, nearly uniform, flow distribution among the various circuits and to obtain high internal heat transfer coefficients by means of relatively high mass velocities. However, there are substantial advantages in lowering the ammonia recirculation ratio in the unit cooler:

- lower ammonia mass in the evaporator
- lower flow rates (energy saving in circulation pump, smaller inlet piping and collector diameters, etc.)

The research described in this paper aims to investigate whether it is possible to preserve high unit cooler performance also at low recirculation rates, by the correct selection of circuits and orifices. The research activity was performed in two steps: (i) experimental activity on two unit coolers, with the same coil but with different circuit arrangement - one representative of current production, the other designed for low recirculation rates - and (ii) development of a computational tool, able to predict the complex fluid-dynamic and thermodynamic phenomena occurring in a real ammonia unit cooer.

3. EXPERIMENTAL CAMPAIGN

3.1. Test set up

The tests were performed at the Danish Technical Institute (DTI). The test set up is represented in Fig. 1: it is possible to vary the operating conditions (air temperature, evaporating temperature, ammonia flow rate) to investigate the evaporator capacity variation with these variables. In particular, as discussed below, the ammonia flow rate was varied (and therefore the recirculation rate) for fixed air and evaporating temperature.

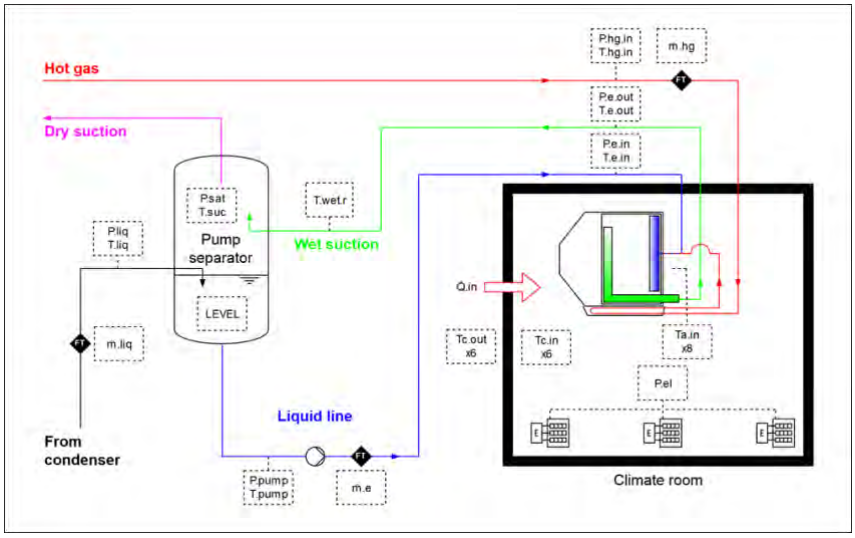

Figure 1: Diagram of DTI ammonia test plant.

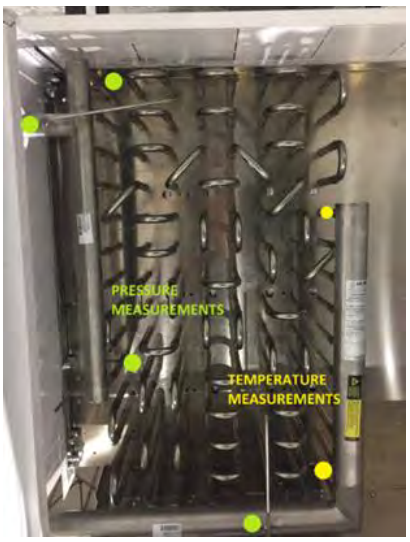

Figure 2: Additional probes.

Three sets of measurements are used to (i) identify the thermodynamic cycle, (ii) verify the temperature uniformity of the air at evaporator inlet, (iii) calculate the evaporator capacity.

The capacity can be computed by two methods: (i) the product of the vapour mass flow rate by the enthalpy difference between saturated vapour and liquid and (ii) the energy balance of the climatic room, given by sum of the electrical power of contrast heaters and thermal power entering the climatic room through the insulated walls. The test is done in steady-state conditions and all quantities are integrated vs time for the test duration (about 30 min). The measure of the liquid flow rate is used to calculate the recirculation rate. Some additional measurements were performed, as depicted in Fig. 2: three differential pressure measurements, located on the upper, medium and top circuit and two temperature measurements, located at the exit of the bottom and top circuit.
Through measurements and calculation pressure test connections permit the evaluation of the pressure drops in the nozzles and along the circuits of the top circuit and the bottom circuit. From these it is possible to assess the mass flowrate distribution through the circuits.
The temperature measurements permit the evaluation of whether superheating occurs at the outlet of the top and bottom circuit.

3.2. Results in term of capacity vs flow rate

The tests were performed on two unit coolers (current production and low recirculation one, see Table 1), at two different operating conditions:

- "High Temperature": Evaporating Temperature= -8°C, Air Temperature = 0°C
- "Low Temperature": Evaporating Temperature= -30°C, Air Temperature = - 22°C

Table 1. Main features of the tested evaporators – C = current design, N = new design.

Tube arrangement	In line		Evaporation temperature	-8/-30	*°C*
Number of tubes	14		ETD ($T_{air,in}$ - T_e)	8	*°C*
Number of rows	8		Design circ. rate (n)	4(C)/2(N)	*[-]*
Tube length	1600	*mm*	Air flow	*15514*	*m³/h*
Pipe outer diameter	13.45	*mm*	Air face velocity	3.285	*m/s*
Pipe inner diameter	12.45	*mm*	Air inlet temp.	0/-22	*°C*
Tube spacing	55x55	*mm*	Number of circuits	11(C)/7(N)	*[-]*
Fin spacing	7.5	*mm*	Tube coil volume	22.98	*dm³*
Fin thickness	0.3	*mm*	Liquid header vol.	0.38	*dm³*
Pipe material	AISI 304		Suction header vol.	0.54	*dm³*
Fins	Aluminium		total volume	23.90	*dm³*

Results are represented in Fig.3, respectively at high and low temperature, as a function of the inlet flow rate.

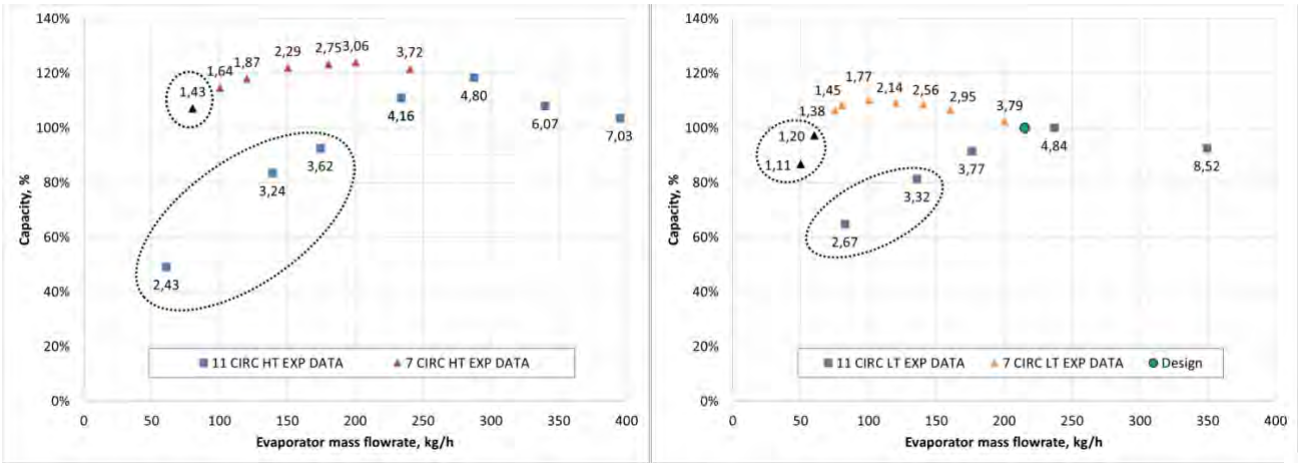

Figure 3: Capacity (referred to the design value at low temp.) vs ammonia flow rate for the two tested evaporators: (left) high temp. (-8°C) and (right) low temp. (-30°C). Numbers refer to the recirculation rate. For points inside the dotted circle superheating at the outlet of the upper circuit was found.

As expected, in all cases there is a value of flow rate which maximizes the capacity. At lower flow rates the capacity decreases, both because the heat transfer coefficient decreases with mass velocity and because the flow distribution experiences increased variations between top and bottom circuits. At higher flow rates the increase of pressure drops caused by large velocities inside the tubes more than counterbalance the increase of heat transfer coefficient. The design flow rate results from the best compromise between these two effects. The measured performance is well predicted for the current production evaporator: actually, the measured capacity reaches its maximum at flow rates slightly larger than the design one, at values of recirculation rate of about 4.8. The new model reaches similar or even higher capacities at flow rates much lower than in the previous case. The capacity remains high in a wide range of recirculation rates, say between 1.5 and 3, thus offering a good performance in a real plant operation, where the capacity can vary for a variety of situations.

The capacity decrease at very low rates is well detected by the temperature measurement at the exit of the top circuit (Fig. 4), which shows the occurrence of superheat in the top circuit: the temperature increases above the evaporation temperature when the pressure drop across the heat exchanger becomes close to the hydrostatic pressure of liquid column in the inlet collector. Fig. 4 depicts also the total (orifice + circuit) pressure drop across the evaporator, at high and low evaporating temperature respectively. At equal flow rate, pressure losses are larger for the low temperature case, due to lower densities of the ammonia vapour.

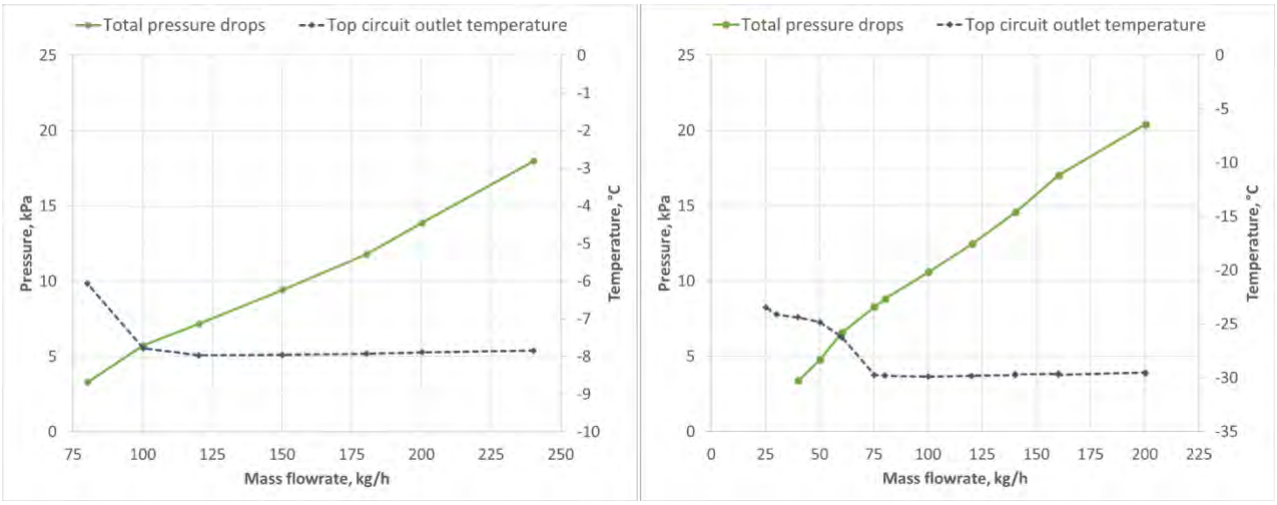

Figure 4: Total pressure drop (solid line) and temperature (dot line) at the end of the top circuit as a function of the inlet mass flow rate. Data refer to the "new evaporator" tested at: (left) high temperature (evaporation temp. = -8°C) and (right) low temperature (evaporation temp. = -30°C)

3.3. Defrost test

Defrost test were carried out to verify that the amount of hot gas flowing inside the heat exchanger was sufficient to perform a satisfactory defrosting also with the new arrangement, with fewer, longer circuits. Fig. 5 describes the flow pattern during defrosting: hot gas enters the tray and then flows inside the exchanger pipes. During the defrost tests the temperature measurements at the outlet of top and bottom circuits of the evaporator were used to detect real end of defrost.

Fig. 6 describes stages of the defrost test procedure. At the beginning a pump down stage is performed for 15 minutes; the liquid line and the fan are shut off while the compressor is running. Then a soft stage of 5 minutes starts, where defrost is initially performed by a small amount of hot gas. Looking at Fig. 6, it is possible to understand that during this stage the heat introduced is used to bring the evaporator near to the temperature of ice melting. The core part is the 23 minutes hard stage which lasts longer than needed. Indeed from Fig. 6 it is possible to assess that ice melting ends after 5 minutes of hard stage, which means a total time of 10 minutes of defrost. Finally, there is a 5-minute dripping stage; the liquid line is open while the fan is still shut off. The measured defrost

efficiency, defined as the ratio between the ideal/real heat required to complete defrost, was as high as 91%.

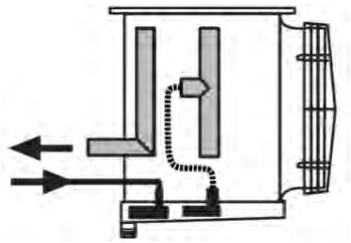

Figure 5: Flow arrangement during defrost

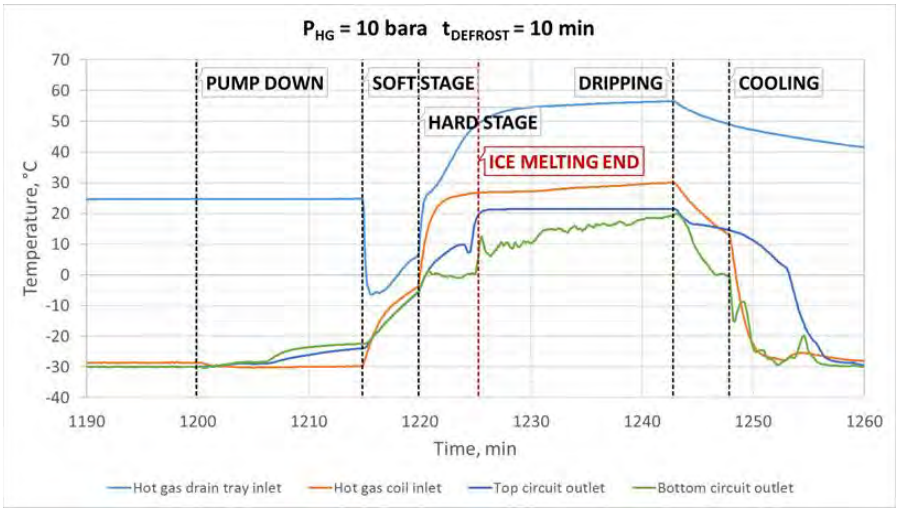

Figure 6: Various stages of the defrost procedure

4. CALCULATION MODEL

The fluid-dynamic and thermodynamic phenomena occurring in a real ammonia flooded evaporator are complex, given that each circuit experiences different heat fluxes, flow rates, vapour qualities at the exit, etc. In the attempt to develop a computer code capable of simulating the performance of such a complex component, the following approach is followed.

1. In order to account for differences among the various circuits, the heat exchanger is divided into five groups of parallel circuits, each group being characterized by a different hydrostatic head.
2. Each circuit is then discretized into 10 sections, following the evolution of fluid quality, pressure, heat transfer coefficient, etc.
3. The distribution of mass flow rate through each group of circuits is calculated by equating the overall pressure change (hydrostatic head + nozzle + heat exchanger tube) between inlet and outlet.
4. Given the mass flow rate for each circuit, the evolution of the heat transfer coefficient along the tube is calculated.
5. When the convergence is reached, it is possible to calculate the energy and mass balance of the whole evaporator.

The problem is solved through two main iteration loops: (i) an external loop, changing the overall pressure drop across the evaporator until the total ammonia mass flow rate is found and (ii) an internal loop, changing the mass flow rate through each circuit until the calculated pressure drop match the value set in the external loop of the previous point.
Empirical correlations are used to calculate heat transfer coefficient and pressure drops along the heat exchanger.

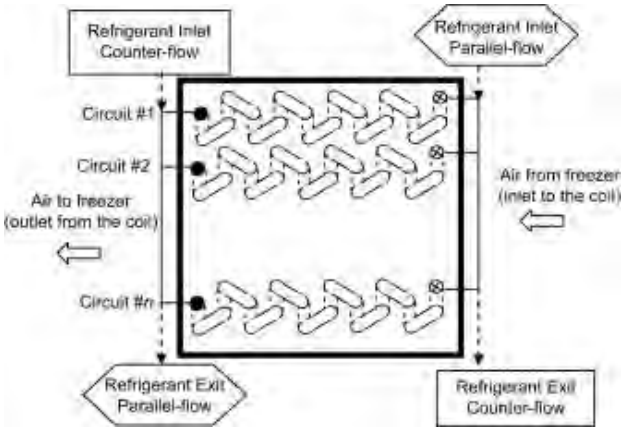

Figure 7: Schematic of the flooded evaporator

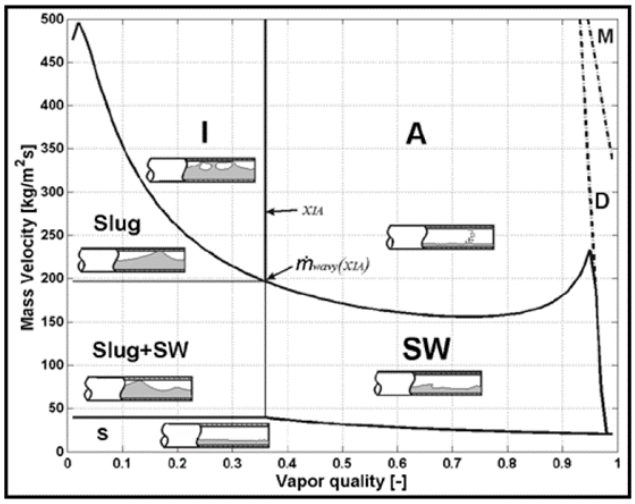

Figure 8: Flow pattern map by model of L. Wojtan et al. assumed as basis for the present calibration.

Relation between heat transfer coefficient, mass velocity, vapour quality and heat flux are derived by L. Wojtan et al. (2005), using the flow regime map by L. Wojtan et al. (2005) (Fig. 8), with an additional coefficient calibrated to fit the experimental data.

Relation between two-phase fluid mass flow rate and pressure drop across the nozzle is derived from CFD calculations, validated by the test with reasonable accuracy. Pressure drops along the heat exchanger tube are calculated with the Lockhart-Martinelli correlation (Fig. 9).

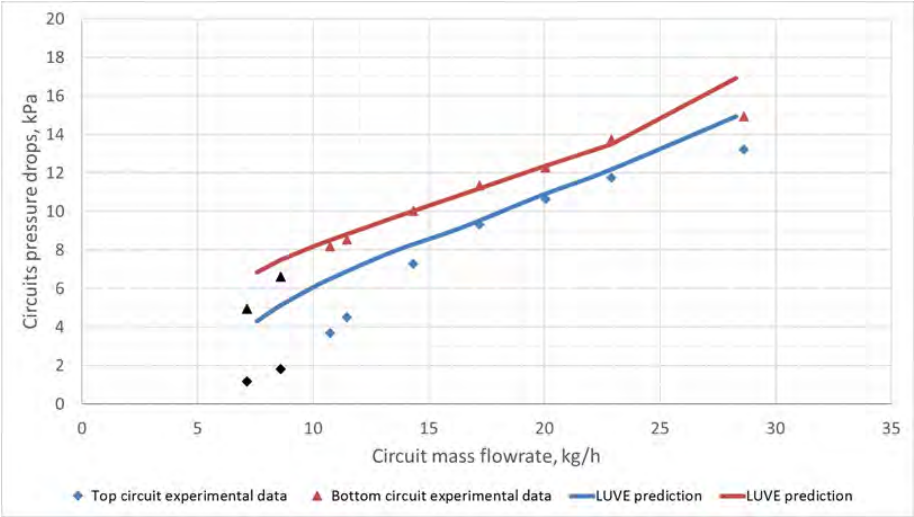

Figure 9: Comparison between experimental data and adopted correlation for predicting pressure drop across the circuit vs average mass flow rate for circuit.

A comparison between the predicted and the measured cooling capacity is given in Fig. 10 for the 7 circuits heat exchanger operated at high and low temperature.

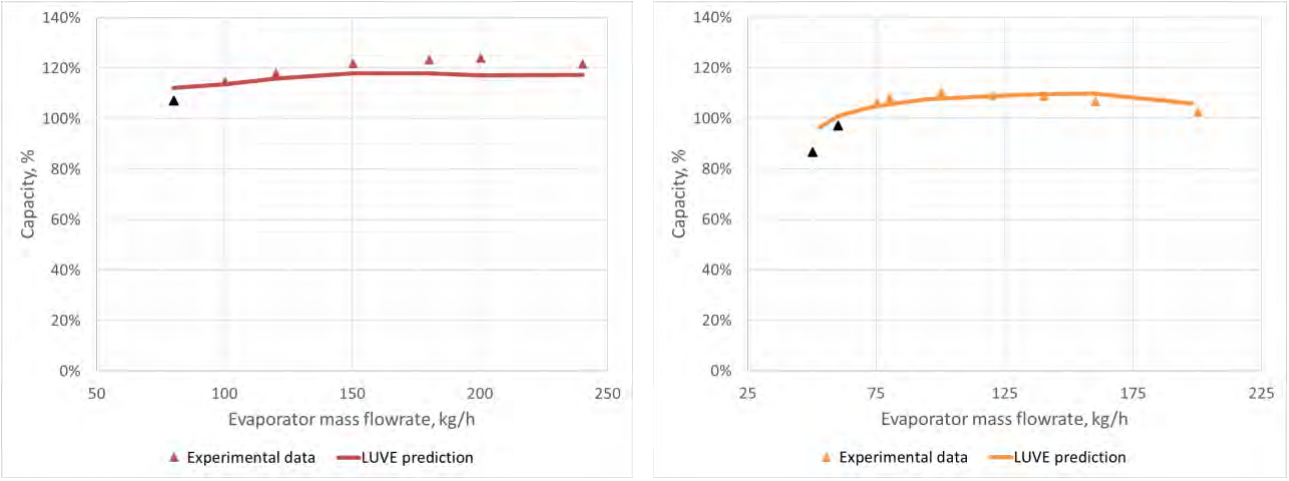

Figure 10: Comparison between experimental and calculated cooling capacity, (left) high temperature and (right) and low temperature cases.

Since the simulation code yields complete information about the velocity field and the vapour quality inside the evaporator, it is possible to calculate the distribution of outlet quality, flowrate and capacity for each circuit (Fig. 11) as well as the void fraction distribution in the heat exchanger, thus calculating with fair accuracy the ammonia charge in the evaporator. As is well known, the charge increases with the recirculation rate.

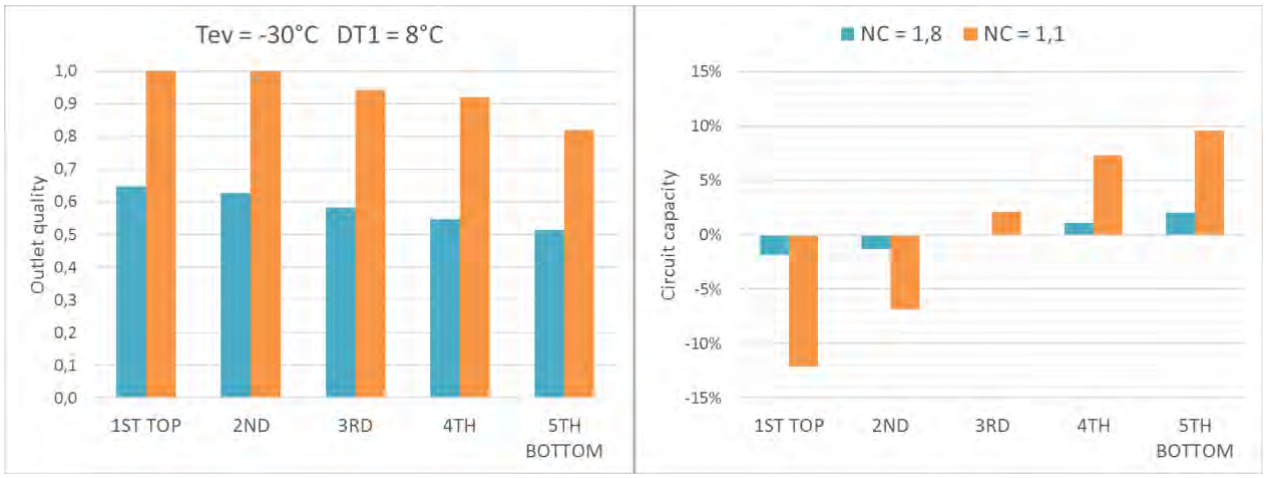

Figure 11 Influence of low and optimum recirculation ratio on outlet quality and capacity: at low recirculation ratio there is uneven flowrate distribution which causes superheat in the top circuits with the consequent capacity loss.

The next table shows an example of these results, giving a comparison of ammonia charges of new and current production evaporator.

Table 2. Ammonia charge in LU-VE flooded unit cooer.

	New unit cooler (7 circuits)	**Current unit cooer (11 circuits)**
	NC = 2	*NC = 4.8*
High temperature	2.3	3.0
Low temperature	1.7	2.1

If the ammonia charge/capacity ratio found in the present paper is compared with conventional flooded evaporators, as the ones described by J. Kristofersson et al. (2017) in a recent paper, we find the results described in table 3.

Table 3. Comparison between a conventional unit cooler and a LU-VE low-charge unit cooler in term of charge/capacity ratio.

	Conventional unit cooler (Tube Ø ⅝" NC=4)	LU-VE present production (Tube Ø ½" NC=4)	LU-VE new model (Tube Ø ½" NC=1.8)
Ratio between liquid holdup and capacity [kg/kW]	0.23	0.10	0.077

We find that LU-VE current production, mainly due to the adoption of a smaller tube diameter, exhibits a reduction of over 50% of ammonia charge for equal capacity versus a conventional unit cooler. The adoption of lower recirculation rates reduces this value for a further 20%.

5. CONCLUSIONS

The future of industrial refrigeration using NH3 as refrigerant has to put the reduction of fluid charge as a main priority. A fundamental contribution is coming from the use of low charge unit cooler design. Efficient heat transfer geometry, with small tube diameter (1/2”), combined with low recirculation rate (1.8) is the solution described in the present paper. An intensive redesign activity coupled with experimental results allowed the reduction of the ratio between liquid holdup and capacity [kg/kW] by 67% compared to conventional unit coolers.
Adopting low recirculation rates is beneficial not only in terms of reduced charge, but also in reducing cost and energy consumption of pump and piping.
The R&D activity continues, aiming to further investigate the possibility of reducing the ammonia charge in the heat exchangers.

REFERENCES

Wojtan L., Ursenbacher T., Thome J.R., 2005. Investigation of flow boiling in horizontal tubes: Part II—Development of a new heat transfer model for stratified-wavy, dryout and mist flow regimes. International Journal of Heat and Mass Transfer, 48 2955–2985.

Wojtan L., Ursenbacher T., Thome J.R, 2005. Investigation of flow boiling in horizontal tubes: Part I—A new diabatic two-phase flow pattern map. International Journal of Heat and Mass Transfer, 48 (2005) 2955–2969.

Kristófersson J., Vestergaard N., Skovrup M., Reinholdt L., 2017. Ammonia charge reduction potential in recirculating systems – calculations. doi: 10.18462/iir.nh3-co2.2017.0005.

Manuscript ID: 353
DOI: 10.18462/iir.icr.2019.0353

Design and operation of a thermal harshness test facility for electric motors in hermetic environments

Neal LAWRENCE [(a)], Stefan ELBEL [(a, b)]

[(a)] Creative Thermal Solutions, Inc.
2209 N. Willow Rd., Urbana, IL 61802, USA
neal.lawrence@creativethermalsolutions.com
[(b)] Air-Conditioning and Refrigeration Center
Department of Mechanical Science and Engineering
University of Illinois at Urbana-Champaign
1206 W. Green St. Urbana, IL 61801, USA

ABSTRACT

This paper discusses the design of a test rig used to simulate thermal cycling of drive motor components immersed in transmission fluid used in hybrid electric vehicles. Unique challenges are encountered in this thermal test due the extreme change in viscosity of the fluid between high and low temperature (150˚C and -20˚C, respectively) as well as the need to simulate powering of the components while undergoing cycling. Addressing the unique challenges requires specific attention to refrigeration system design and control, heat exchanger selection and configuration, fluid pump selection and control, and electrical powering of the motor components. The paper provides details of the test rig and discusses the challenges encountered and specific solutions implemented, with the objective of providing a useful insight for the design of other test rigs for temperature cycling with high-viscosity fluids, especially for the testing of hybrid electric vehicle components.
Keywords: Thermal cycling; harshness testing; system design; heat exchanger configuration; pump selection; electric vehicle components

1. INTRODUCTION

Interest in hybrid electric vehicles has expanded in recent years. With the greater demand of hybrid electric vehicles comes the development of specialized components for the vehicles, such as the components of the electric motors to power the vehicle. Motor components in this application may be subject to more extreme thermal conditions than motors in more conventional industrial applications. For example, a vehicle motor that is exposed to low ambient temperatures during winter while the vehicle is not in operation before being rapidly brought to full power when the vehicle is first used would see a very rapid rise in rate of heat dissipation and thus temperature; repeated thermal cycling of this type over many years can wear down some of the materials used in the electrical components. Thus, it is desirable to perform accelerated thermal harshness testing on such components in order to understand the possible effects of these repeated, rapid temperature swings. Previous studies have reported on the design of thermal cycling facilities for accelerated thermal harshness testing of refrigeration and air-conditioning components (e.g. Wilson and Bowers, 2014; Lawrence *et al.*, 2018). However, these studies focus mainly on thermal cycling of common components in refrigeration systems familiar to refrigeration and air-conditioning engineers and generally under less extreme operating thermal swings. The present study focuses on harshness testing in a different application with a very different working fluid (oil-like fluid in this case) and a different type of component undergoing test.
This paper discusses the design of a thermal cycling facility for testing of components used to power hybrid electric vehicles between high temperature (in the range of 100 to 200°C depending on requirements of test) and low temperature (-20 to 0°C depending on requirements of test) while

immersed in transmission fluid (oil). The unique design challenges presented by the requirements of this test are discussed, and the implemented solutions to address these challenges are described. A brief description of the facility and sample data from the testing are presented. The intent of this paper is to present ideas for design aspects of thermal cycling facilities for electric vehicle components in the expectation that more testing of this type would be needed as the demand for electric vehicles increases.

2. FACILITY DESIGN

2.1 Overall System Concept

Fig. 1 shows a basic schematic of the system. The test pieces were held in separate containers that were filled with the oil, with oil circulated through the each container throughout testing. Cooling was provided by a refrigeration circuit integrated into the test rig; the refrigerant was used to cool the oil, which was then used to cool the test pieces to the desired temperature. Heating was accomplished by extending the three phase leads of the test pieces outside the oil holding containers and providing the proper power to the leads; movement of oil was also required during the heating phase in order to prevent the oil directly in contact with the test piece from overheating. In the specific facility implemented as part of this study, multiple pieces were tested simultaneously, and the system was configured such that half of the test pieces were undergoing cooling while the other half was undergoing heating, with valves allowing each test piece to switch between heating mode and cooling mode; this allows for lower capacity (smaller) equipment for the refrigeration system and lower power (smaller) equipment for heating.

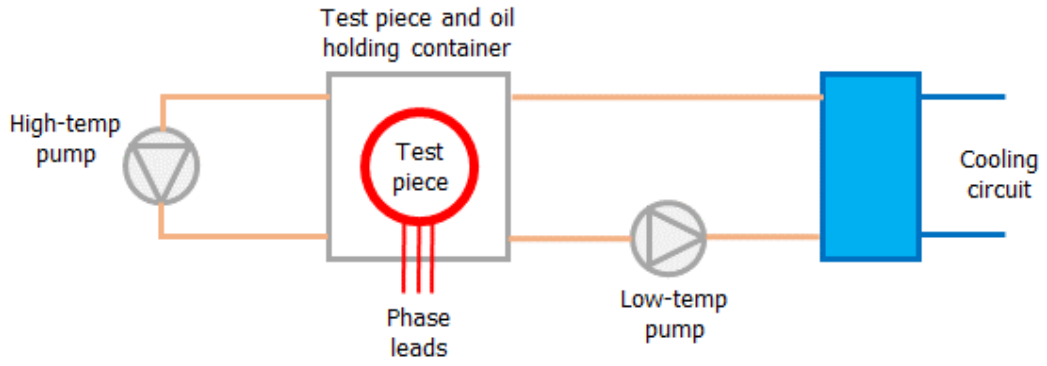

Fig. 1: Schematic of facility for accelerated thermal harshness (cycling) of hybrid vehicle electric motor components immersed in transmission fluid (oil)

Some tuning of the controls was necessary in order to achieve stable operation. For example, the cooling capacity of the refrigeration system had to be adjusted to match the rate at which heat could be removed from the electric test pieces. It is desirable to have as high of cooling capacity as allowed by the tests in order to accelerate testing and make the temperature swings as harsh as possible. However, the cooling capacity is limited by the rate at which the oil can remove heat from the test pieces; if the capacity of the refrigeration system is too high, the oil will be cooled too quickly and become too viscous to pump, resulting in reduced or no oil flow, before the test pieces reach their desired low temperature point. Additionally, the moderate change in density between high and low temperatures as well as the shifting of oil between containers between heating and cooling cycles causes changes in oil level in the holding containers, meaning that proper monitoring of oil level in each container must be implemented to ensure that each test piece is covered with the proper amount of oil throughout testing.

2.2 Design Challenges

The most significant challenge to meeting the testing requirements is pumping of the transmission fluid (oil) over the large range of temperatures. The variation in hydraulic properties with temperature of an oil are in general significantly larger than for water. Fig. 2 shows the variation of the dynamic

viscosity and density of common engine oil over the range of temperatures from 0 to 100°C (data obtained from Incropera *et al.*, 2007). It can be seen that while the density of the oil varies by around 6 % over the temperature range, the dynamic viscosity varies by over two orders of magnitude. For comparison, water at 20°C has a dynamic viscosity of about 1.0 mPa s and varies by a factor of about 6 between 0 and 100°C, which is significant but not nearly as significant as for oil. Detailed data on the properties of the oil used in these tests was not available. However, properties at several points were available; the oil used in the tests had a specific gravity of about 0.84 at 20°C, dynamic viscosities of about 30 mPa s and 12100 mPa s at a temperatures of 40°C and -40°C, respectively, and a pour point of about -50°C.

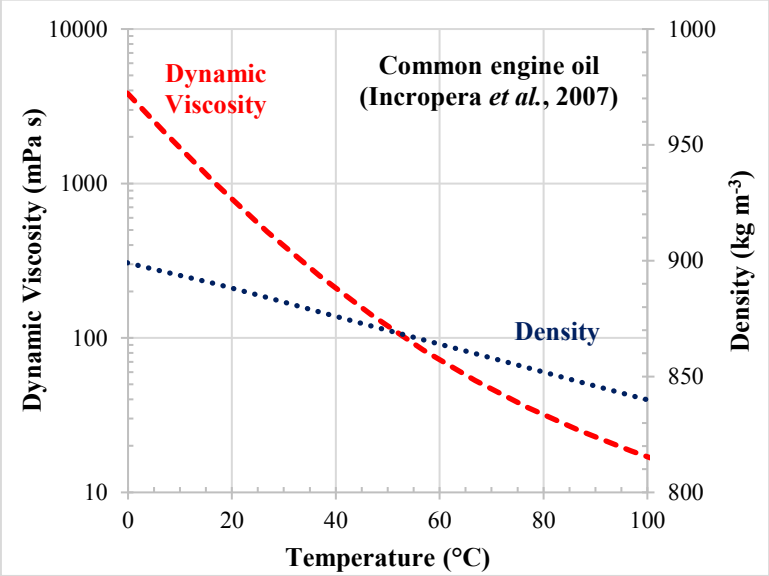

Fig. 2: Variation of dynamic viscosity and density with temperature of common engine oil (data from Incropera *et al.*, 2007)

Heating of the electrical components also presents a challenge in this test. In the actual application, the oil would essentially act as a coolant for the electric drive components, meaning that the components would be at higher temperature than the oil during operation. This means that the heat to raise the temperature of the electrical components should come from the electrical components themselves. As the components are not actually being used as a drive system, all power going into the components during the test can only be dissipated as heat as opposed to being used to propel a vehicle. However, the electrical drive components themselves are essentially long pieces of copper with very low electrical resistance, meaning that very low-voltage, high-current power, which is not commonly available in industrial applications, must be provided to them.

2.3 Fluid Pump Selection and Considerations

Selection of suitable pumps for moving the oil throughout heating and cooling cycles is essential for proper long-term testing. Different types of pumps have advantages and disadvantages that make them each suitable for use with different fluids and systems. However, given the extreme change in fluid properties in this system (specifically viscosity) between high and low temperatures, it was found that different types of pumps were needed to move the oil at different temperatures.

High viscosity fluids are probably best moved with a positive displacement pump, such as diaphragm, screw, piston (pneumatic diaphragm), or gear pumps, as shown in Fig. 3. Diaphragm pumps were chosen because of their ability to meet greater pressure head requirements than some other positive displacement pump options. One difference between diaphragm pumps and other common pumps is that diaphragm pumps are powered by compressed air rather than a motor, meaning that a reliable, continuous, and dry compressed air source must also be installed. With a regulated air pressure used to power the pump, the flow rate of the pump then depends on the required pressure head of the pump, which of course varies significantly as viscosity (temperature) changes; it was estimated that the flow rate of oil at the start of cooling was around 0.8 L s^{-1} but had

dropped to less than 0.2 L s^{-1} by the end of the cooling cycle (lowest temperature); these flow rates corresponded to estimated pressure heads of over 3 bar at the start of cooling cycle and over 5 bar at the end of cooling cycle based on the manufacturer provided pump curve. It was found that nitrile rubber diaphragms were the best material to use in the diaphragm pumps. While PTFE is generally regarded as one of the most compatible plastics for a very wide range of applications, it was found that diaphragm pumps with PTFE diaphragms did not work well at low temperature; it was suspected that the PTFE diaphragms became too stiff while attempting to pump the very viscous, low-temperature oil, and the air pressure was not enough to move the diaphragm, resulting in a loss of oil flow while cooling the test pieces.



Fig. 3: Examples of different types of positive displacement pumps: (a) diaphragm pump, (b) gear pump, and (c) pneumatic diaphragm pump

On the other hand, the rubber diaphragms used in the diaphragm pumps are generally not rated for use with high-temperature fluids, such as the oil reaching around 100°C during heating in these tests. For this reason, a separate selection of pump was made to circulate oil during heating mode. Pumps designed to move high-temperature oil often come in the form of gear pumps, as selected in this facility. In order to ensure that a pump is suitable for use with high temperature fluid, the pump head (gears and housing) should be able to operate at the elevated temperature of interest with suffering accelerated wear; steel gears and housing, as used in the selected pump, are suitable for high temperature and would not be expected to suffer significantly accelerated wear at oil temperatures up to 100°C (selected pump was rated up to 190°C). Additionally, the pump head should be sufficiently separated from the motor such that the high heat from the high temperature oil does not influence motor temperature, such as for the pump shown in Fig. 3(b).
In theory, a gear pump could also have been used to pump the oil at low temperature. The gear pump selected for this system was sized to maintain around 50 K of temperature difference between oil and test piece, with an estimated flow rate of around 0.25 L s^{-1}. A feature of a gear pump that is useful in many applications is that the flow rate of a gear pump varies primarily with pump speed but is not a strong function of pressure head, as long as it operates below its maximum pressure head (275 kPa differential in this case); this means that oil flow rate is expected to remain relatively constant during the heating period even while the oil temperature varies by upwards of 100 K or more. However, if this same pump were used to pump the oil during cooling mode, the much increased viscosity would result in excessive pressure drop and overloading of the pump motor; as noted above, it is estimated that at least 5 bar of pressure head is needed to pump the oil at the end of the cooling cycle. Alternatively, a much larger gear could be used, with the speed controlled as a function of oil temperature; however, tuning the controls for such a solution would not necessarily be any less complex than using separate pumps for different oil temperatures.

2.4 Thermal and Hydraulic Considerations for Heat Exchanger Selection

A common choice for a liquid to two-phase refrigerant heat exchanger, such as the evaporator in this system, is a brazed-plate heat exchanger. The high viscosity of the oil at low temperature necessitates a very large flow area for the oil in order to reduce pressure drop, meaning a very large number of plates. While it is difficult to accurately predict pressure drop through a brazed plate heat exchanger, even for single-phase fluids, it is clear that an undersized evaporator could severely limit the oil flow rate and thus capacity of the system. In order to see the effect of viscosity on pressure drop, the Reynolds number must be determined. For turbulent flow in a smooth tube (as would be

the case for the oil at high temperature), the pressure drop is proportional to the friction factor, which is commonly approximated as being proportional to the Reynolds number to the -0.25 power, as shown in Eq. (1) (Munson *et al.*, 2006). On the other hand, for laminar flow as may be the case for oil at low temperature, the friction factor is inversely proportional to the Reynolds number, as shown in Eq. (2). The dynamic viscosity of the oil increases exponentially to 12100 mPa s as temperature decreases down to -40°C; while the tests do not run down to -40°C, it can be assumed that the dynamic viscosity is still at least 1000 mPa s at the end of the cooling cycle. Thus, for the lowest oil temperature (approximately -20°C), the Reynolds number for a 25 mm ID tube was estimated to be on the order of 300, which is clearly in the laminar regime. This demonstrates that the very high viscosity will have an even more pronounced effect at the lowest temperatures experienced in this system. While this analysis was performed for a round-tube, the same trends would still be expected to apply for a brazed plate heat exchanger, which again highlights the need to use caution and not allow the evaporator to limit the oil flow rate and thus cooling capacity of the system.

$$\text{Turbulent Flow: } \Delta P \sim f \sim Re^{-0.25} \sim \mu^{0.25} \quad \text{Eq. 1}$$

$$\text{Laminar Flow: } \Delta P \sim f \sim Re^{-1} \sim \mu \quad \text{Eq. 2}$$

On the other hand, using a very large heat exchanger to accommodate the high viscosity of the oil will make the evaporator significantly oversized for the capacity of the refrigeration system, meaning that depending on heat exchanger orientation, refrigerant-side thermal performance may be negatively impacted due to very low refrigerant velocity or maldistribution of refrigerant liquid. More specifically, the evaporator in this system had a heat transfer area of about 6.8 m^2, allowing for well over 50 kW of heat transfer (assuming an effective temperature difference of 20 K and an overall heat transfer coefficient of 500 W m^{-2} K^{-1} or more), while the refrigeration system had an average capacity of approximately 10 kW. This indicates that careful attention must be given to the two-phase refrigerant-side of the evaporator.

Clearly, it is desirable to have a counterflow configuration between oil and refrigerant for more effective heat transfer; however, the orientation (whether refrigerant flows upward or downward) must still be determined. As the oil is liquid throughout the system, uniform distribution among the parallel plates is not a concern, and the oil can easily flow upward or downward through the heat exchanger as long as pressure drop is not too high. In terms of the refrigerant compressor oil drainage and return, it is desirable to have the refrigerant fed into the top of the heat exchanger and flow downwards; with this orientation, the oil will drain out of the evaporator by gravity. However, this orientation would require the two-phase refrigerant to be uniformly distributed amongst the parallel plates; for a properly sized heat exchanger, it is possible that fairly uniform distribution could be achieved, but for an oversized heat exchanger, it is very unlikely that refrigerant distribution will be uniform.

Through the course of experiments, it was found that the front half of the evaporator (plates closer to the inlet and outlet ports) was cold, while the rear half of the evaporator was at ambient temperature; this indicates that the majority of liquid refrigerant was distributed amongst the plates in the front of the evaporator, while the rear plates received mainly vapor and thus could not provide any significant cooling capacity, as shown in Fig. 4. For a refrigerant-to-glycol or refrigerant-to-air heat exchanger, this would result in reduced cooling capacity of the heat exchanger but not a complete loss of capacity. However, because the oil in this system becomes exponentially more viscous as the temperature drops, the oil that exchanged heat with the liquid refrigerant was cooled to very low temperature and high viscosity, while the oil that was in contact with vapor refrigerant received almost no cooling. This resulted in the oil in the front of the heat exchanger not flowing at all while the oil the rear of the heat exchanger flowed freely but was not cooled, resulting in little or no net capacity of the heat exchanger. This is a snowball effect similar to frosting of an evaporator; when oil in contact with the liquid refrigerant stops moving and evaporator capacity is lost, the compressor will pull the refrigerant to lower temperature, further cooling the already stagnant oi.

On the other hand, bottom-feed orientation will allow liquid to sit in the inlet header at the bottom of the plate, and with sufficient charge in the system to fill most or all of the inlet header with liquid, all plates should receive a sufficient and mostly uniform amount of liquid, as shown in Fig. 4. In this case, an oil return line between the evaporator inlet and the accumulator is necessary; this will result

in a slight capacity loss for the system, but this can be easily countered with a few percent higher compressor speed. It was found through the course of experiments that the bottom-feed orientation did provide the desired performance.

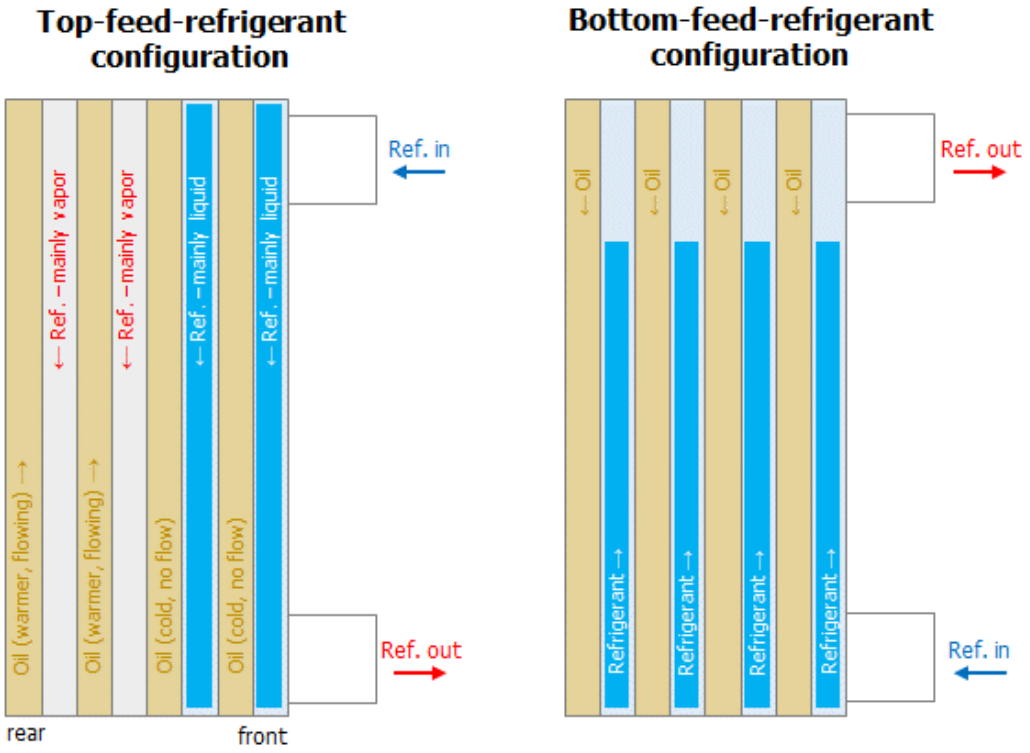

Fig. 4: Side view of brazed-plate evaporator diagraming refrigerant distribution and oil flow for top- and bottom-feeding of refrigerant

An alternative option, not employed in this study, would be to use a 'dual circuit' brazed-plate heat exchanger with a total of three independent circuits. The evaporator could then be configured in such a way that the oil is given two circuits and the refrigerant a single circuit to flow through; this would then yield double the flow area for oil compared to refrigerant and better match extreme difference in viscosity between the two fluids. Additional heat exchanger types, such as a concentric tube heat exchanger with significantly larger annular area for the oil than inner tube area for the refrigerant, are also options; however, it is difficult to find other heat exchanger designs that offer the compactness of a brazed plate heat exchanger.

2.5 Solution for Powering of Electrical Test Pieces

As noted above, it is desirable to have the electrical test pieces act as the heating elements during the heating cycle; as the pieces, when not being used as an actual motor, are essentially long pieces of copper with low electrical resistance compared to actual electric heating elements, low voltage power must be provided to them at very high current in order to achieve the desired heating power. DC power supplies are generally set up to be able to provide low-voltage, high-current power. However, it was desirable to use a form of three phase power so that each phase of the test piece received the same current; a configuration of constant DC power in which all three phases of the test piece receive the same current could not be identified. A VFD, adjusted to output very low voltage, would be capable of providing the necessary power; however, the output terminals of the VFD would need to be sized for the proper current, meaning the VFD would need to be sized for approximately 15 times larger power than it would actually provide in this case. Rather than using a very large, oversized VFD, a properly sized VFD connected to an industrial transformer with a 20:1 ratio was used to decrease the voltage and increase the current; this allowed for a lower-cost solution for providing the same power as a very large VFD.

3. EXPERIMENTAL DATA

An experimental facility based on the above discussion of design concepts was constructed for simultaneous testing for 4 electrical test pieces. The experimental results for several cycles are shown in Fig. 5, with test piece temperature cycling between approximately -10°C and 120°C on 40 minute cycles (completion of both heating and cooling modes).

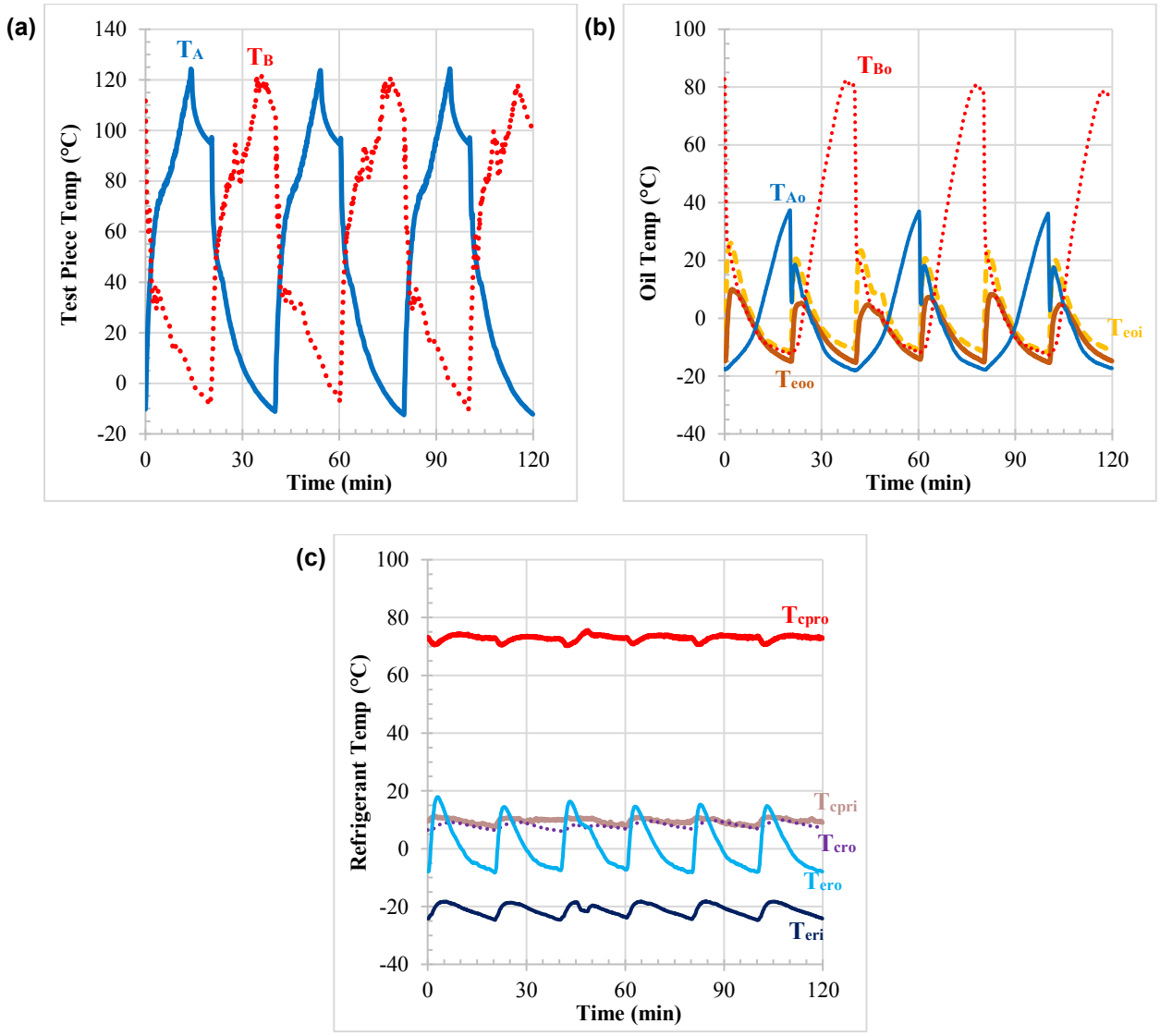

Fig. 5: Experimental results for thermal cycling of test pieces between high and low temperatures of approximately -10°C and 120°C for 40 minute cycles: (a) test piece temperatures, (b) oil temperatures, and (c) refrigerant temperatures

Test piece temperatures were measured with Type-K thermocouples attached to the surface of the test piece, while refrigerant and oil temperatures were measured with Type-K thermocouples mounted on the surface of oil and refrigerant lines. Fig. 5(a) shows the temperature trends of the test pieces. It can be seen that the test pieces have different temperature profiles during heating mode, with test piece A having noticeably higher heating ramp rate than B and consequently a period of time in the second half of the heating cycle where the test piece is powered off. Fig. 5(b) shows the oil temperatures associated with test pieces A and B as well as the oil temperature into and out of the evaporator. Fig. 5(c) shows refrigerant temperatures, with compressor and condenser operation remaining fairly stable while evaporator pressure and superheat vary significantly between the beginning and end of a cooling cycle.

4. SUMMARY

This paper has presented a discussion of the design of a facility for accelerated thermal harshness testing (cycling) of hybrid electric vehicle motor components while immersed in transmission fluid (oil). It has been seen that due to the extreme swings in viscosity of the oil over the range of temperatures required for the test, careful attention must be given to pump selection (including the selection of different pumps for different temperature/viscosity ranges) and heat exchanger selection and configuration. A unique solution for heating of the test pieces was also developed, implemented, and shown to be effective. The experimental results demonstrated that when implemented in a test rig, the design solutions presented in this paper are effective at meeting the requirements of the accelerated thermal cycle testing.

NOMENCLATURE

Symbols and Abbreviations

f	friction factor (-)	VFD	variable frequency drive
PTFE	polytetrafluoroethylene	ΔP	pressure drop (kPa)
Re	Reynolds number (-)	μ	dynamic viscosity (mPa s)
T	temperature (°C)		

Subscripts

A, B	test piece set A and B	i	inlet of component
c	condenser	o	outlet of component, oil
cp	compressor	r	refrigerant
e	evaporator		

REFERENCES

Incropera, F.P., DeWitt, D.P., Bergman, T.L., Lavine, A.S., 2007. Fundamentals of Heat and Mass Transfer, 6th Ed. John Wiley & Sons, Hoboken, NJ, USA, 997 p.

Lawrence, N., Raj, S., Elbel, S., 2018. Assessment of leakage rate and durability of field-made mechanical joints for systems using low-GWP flammable refrigerants (ASHRAE RP-1808). 1st IIR International Conference on the Application of HFO Refrigerants, Birmingham, UK, Paper 115.

Munson, B.R., Young, D.F., Okiishi, T.H., 2006. Fundamentals of Fluid Mechanics, 5th Ed. John Wiley & Sons, Hoboken, NJ, USA, 769 p.

Wilson, M., Bowers, C.D., 2014. Design of accelerated fatigue tests for flame free refrigeration fittings. 15th International Refrigeration and Air Conditioning Conference at Purdue, West Lafayette, IN, USA, Paper 2564.

Manuscript ID: 383
DOI: 10.18462/iir.icr.2019.0383

Experimental Study on the Air-conditioning System using Membrane Dehumidification Module

Seok Ho Yoon, Dong Ho Kim, Young Kim, Jungchul Kim, Howon Byun

Department of Thermal Systems, Korea Institute of Machinery and Materials
Daejeon, 34103, Korea, shyoon@kimm.re.kr

ABSTRACT

Vapor compression systems have technical limitations to reduce power consumption and environmental effects due to chemical refrigerants. Therefore, we are paying attention to a membrane air-conditioning system using water as a refrigerant. Since there is no chemical refrigerator and compressor, power consumption of the membrane air-conditioning system can be greatly reduced and there is no environmental impact such as global warming.
A dehumidifying nanocomposite membrane has been developed. Since this dense membrane has hydrophilic nanochannel, water vapor can be permeated. Therefore, if a difference in water vapor partial pressure occurs using a vacuum pump, this membrane can remove moisture from the supply air.
We built a permeability testing device of the developed membrane. The test cell was placed in a thermo-hygrostat bath. The flow rate, temperature and relative humidity at the inlet and outlet of the test cell were measured and recorded. The water vapor permeability through the membrane was measured to 50 $g/m^2h/kPa$.
The membrane dehumidification module was designed based on this experimental result and assembled with an IEC (indirect evaporative cooler) module for integrating the air-conditioning system. The cooling capacity measured up to 1.2 kW. The feasibility of the membrane air conditioning system has been demonstrated.
Keywords: Non-vapor compression cycle, membrane, dehumidification, indirect evaporative cooler.

1. INTRODUCTION

The amount of energy used for heating and cooling in a residential building is about one third of the total energy consumed. Global energy consumption for summer cooling is soaring that it is burdening the power generation each year. Therefore, it is a big issue to reduce the power consumption of the vapor compression cycle, which is currently responsible for most of the cooling. However, demand for heating and cooling has also exploded recently. Due to the development of construction technology, desert and rainforest areas have been expanded to include the residential environment. The demand for air conditioning equipment of the developing countries in the low-latitude regions with high temperature and humidity throughout the year has increased explosively with the recent economic improvement. It is also expected that this trend will become more severe as global warming causes global climate change. Therefore, the increase in efficiency of existing equipment alone cannot catch up with the increase in energy consumption in the near future. It is absolutely necessary to develop innovative non-vapor compression cycle technology in addition to R&D for the efficiency improvement of existing vapor compression cycle and the development of low GWP alternative refrigerant.
The US Department of Energy (DOE) has produced a report in 2014 that evaluates performance and possibility to enter the market by proposing the ten most promising technologies for non-vapor-compression HVAC Technologies and using a variety of analyzes. Among those, the membrane heat pump can be consisted as a simple system and it is considered that the membrane pump is most likely to be implemented in a short period of time for us.
Membrane heat pump consists of the membrane heat and mass exchanger and vacuum pumps for dehumidification and cooling units. The working fluid is water and this system can achieve cooling and dehumidification without compressor.

2. EXPERIMENTAL SETUP

2.1. Preparation of membrane module

In order to fabricate the dehumidification unit of the membrane heat pump, a membrane having only selectivity for moisture, that is, water passing through without passing air, is essential. More than 30% of the air-conditioning energy is needed for dehumidification. In countries with high humidity in the summer, the load for dehumidification is high. Therefore, if the dehumidification is possible with low energy, the power consumption of the air conditioner can be greatly reduced. Due to recent advances in nanotechnology, it is possible to develop various types of membranes with water channels that are both dense and have higher moisture permeability. In this paper, to make such a membrane, a nanofiber structure having a length similar to or longer than thickness of the membrane is formed in the polymer membrane to form a moisture-permeable channel through front and back of the membrane. However, due to the increase in the viscosity of the coating liquid, there is a limit to the increase of the nanofiber content. There was a limit to improving the moisture permeability with only nanofiber. In order to overcome this limitation, a new organic/inorganic composite membrane was developed. A filler(sNF) having a hydrophilic 1D inorganic substance arranged on the surface of the nanofiber structure was attached.
The plate-type membrane module was constructed as shown in Fig. 1. The membrane was bonded to a non-woven fabric support and attached to a plastic frame with a vacuum suction port along with a spacer to secure the air flow. This membrane module is constructed by stacking several membrane plates and The dehumidification is achieved by the passage of humid air through the gap between the membrane plates. The removed moisture passes through the vacuum line to the outside.

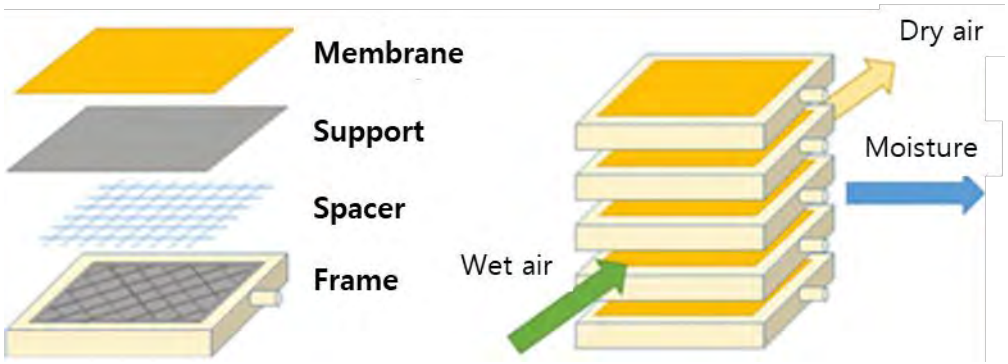

Figure 1: Membrane module configuration

2.2. System design of membrane heat pump

Fig. 2 shows the membrane heat pump system schematic diagram. The membrane heat pump system consists of a dehumidification unit consisting of the membrane module described in Section 2.1 and a cooling unit consisting of Indirect evaporative cooling (IEC) unit. In the dehumidifying unit, two types of vacuum pumps (dry scroll type and diaphragm types) are connected in parallel. The IEC consists of a water loop with a spray nozzle and a water circulation pump. The experiment was conducted in an environment chamber where the temperature and humidity were controlled. And a high-precision temperature and humidity sensor was installed at three places (inlet and outlet of the system and the middle point of dehumidification and cooling unit) shown in Fig. 2.

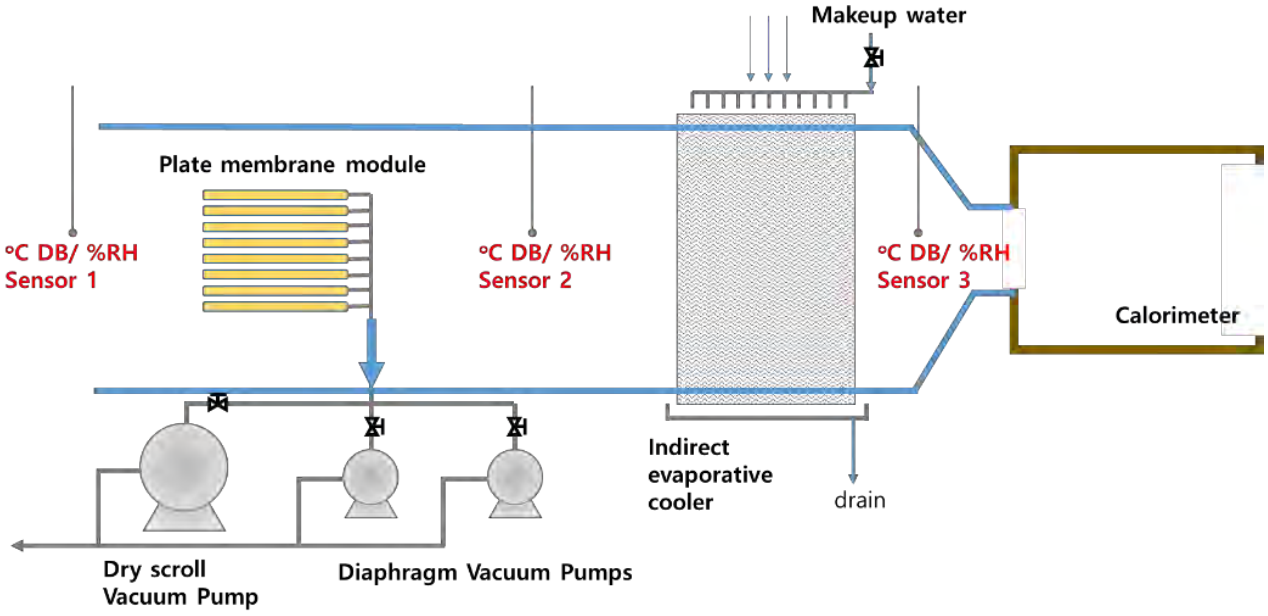

Figure 2: Schematic diagram of experimental setup

3. EXPEIMENTAL RESULTS

3.1. Preliminary performance test of dehumidification module

Preliminary experiments were conducted to investigate the basic performance of the dehumidification module. The air flow rate was fixed at 200 CMH to test the dehumidification performance and the temperature and humidity condition was controlled at 27°C DB / 19°C WB in the environment chamber. Vacuum capacity was adjusted by turning on and off several vacuum pumps. Fig. 3 shows the results of increasing the degree of vacuum up to 215 torr. As shown in Fig. 3, the absolute humidity of the dehumidification unit outlet decreases and the dehumidification capacity increases to 200 W by operating the vacuum pump.

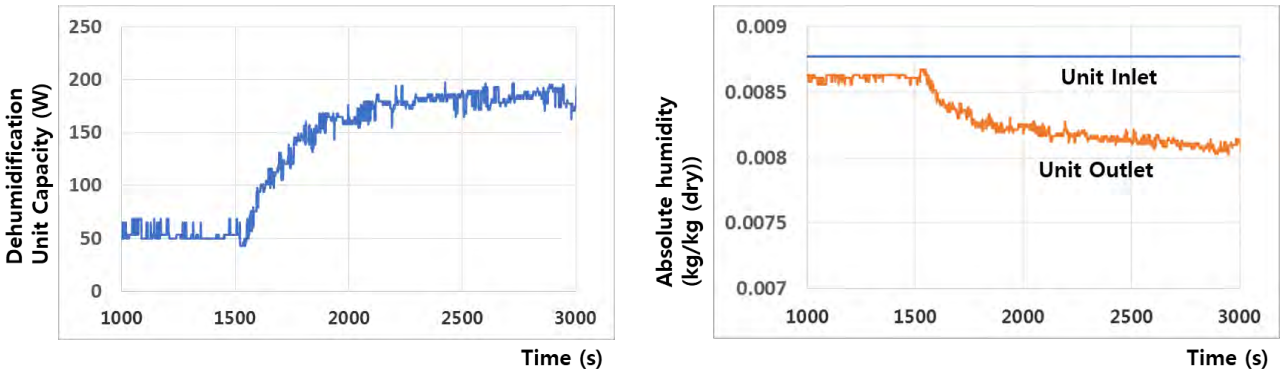

Figure 3: Capacity and absolute humidity of the dehumidification unit

3.2. Preliminary performance test of cooling module

Preliminary experiments were conducted to investigate the basic performance of the cooling module. The air flow rate was fixed at 200 CMH to test the dehumidification performance and the temperature and humidity condition was controlled at 27°C DB / 19°C WB in the environment chamber. During the single operation of the cooling module, it was confirmed that there was no significant change in the absolute humidity of the inlet and outlet of the cooling unit. Although the RH at the outlet of the

cooling unit increased with the beginning of cooling, the temperature at the cooling unit outlet decreased to about 20°C close to the indoor wet bulb temperature (19°C).

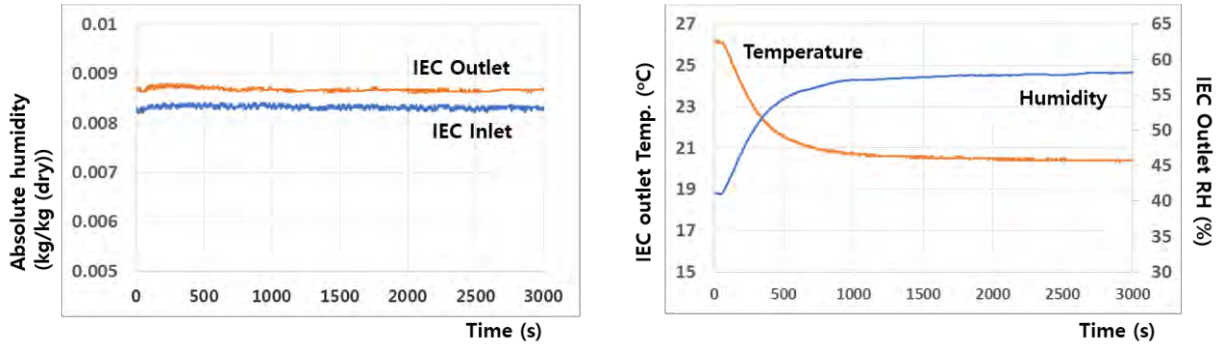

Figure 4: Absolute humidity and temperature of the cooling unit

Fig. 5 shows the enthalpy and cooling capacity measured under the same conditions. The cooling capacity was measured to about 350 W.

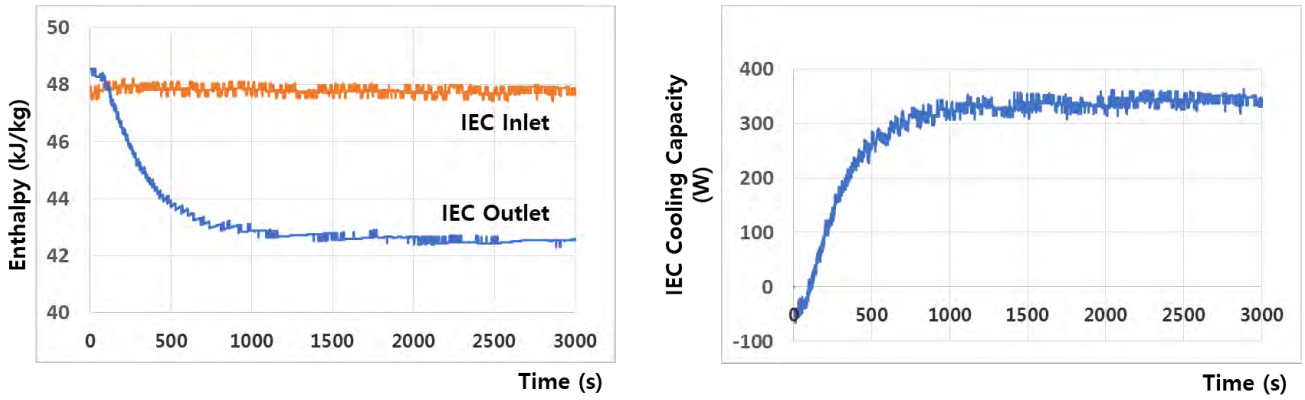

Figure 5: Enthalpy and Capacity of the cooling unit

3.3. Integrated performance test

Combining the dehumidification unit and the cooling unit to build an integrated system and measure the overall system performance. The temperature and humidity condition was controlled at 27°C DB / 19°C WB. The capacity was measured while increasing the airflow so that the optimum capacity was obtained. As the air volume increases, the capacity tends to gradually increase and saturate. The measured results are shown in Fig. 6. The total capacity was measured up to 1070 W when the diaphragm vacuum pump was operated and the performance was measured up to 1200 W with the dehumidification performance increasing when the dry scroll vacuum pump was operated additionally.

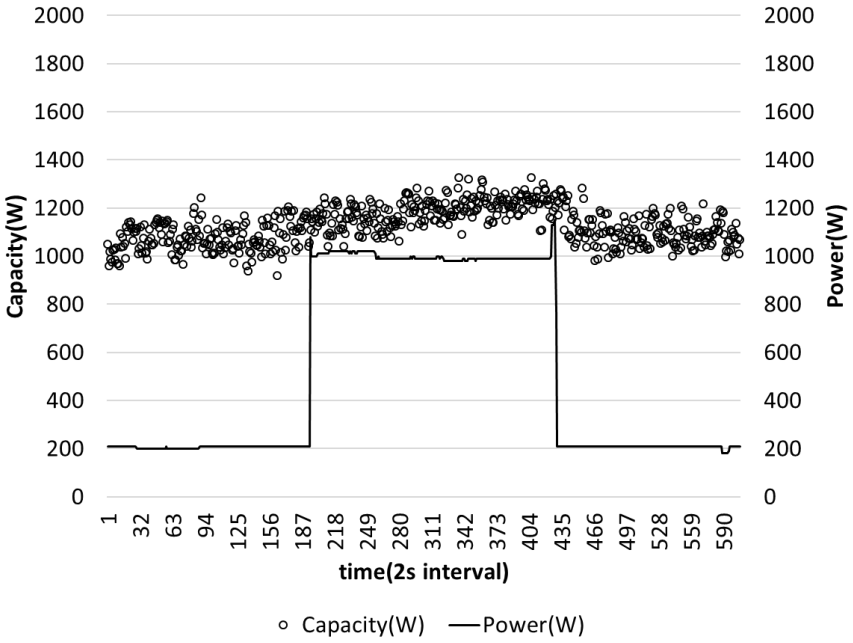

Figure 6: Capacity and power consumption of integrated system

Fig. 7 shows the result of measuring the cooling capacity by varying indoor humidity. The maximum capacity was measured by changing the room temperature / humidity to 27ºC DB / 19ºC WB and 27ºC DB / 21ºC WB. In high humidity conditions, the performance is reduced to 1100W, which is a major cause of degradation of IEC module evaporation performance.

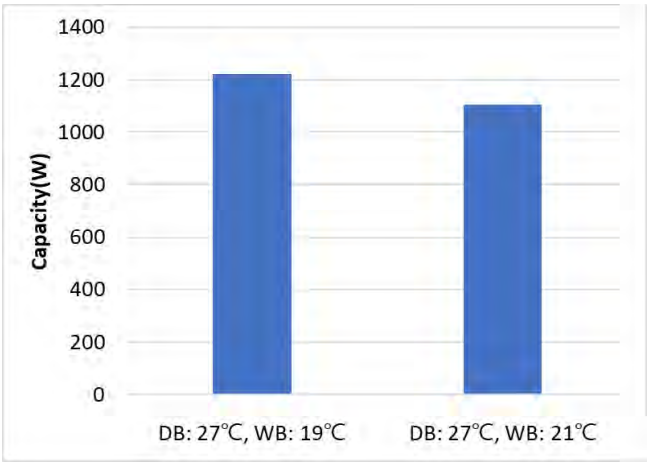

Figure 7: Capacity difference according to humidity condition

4. CONCLUSIONS

In this study, a new concept membrane heat pump without a compressor was developed and its performance was measured. A moisture-permeable membrane was developed to create a dehumidification module, and a cooling module to which IEC was applied was combined to consist an air-conditioner.

In the membrane dehumidification module, the dehumidification performance was measured by operating a vacuum pump. In the cooling module, the cooling capacity due to water injection and evaporation was measured.

Combined dehumidification and cooling unit to create an integrated system. The integrated system showed cooling performance up to 1200 W.

As a result, the feasibility of the membrane heat pump using water as the working fluid was investigated.

ACKNOWLEDGEMENTS

This work was supported by Korea Institute of Energy Technology Evaluation and Planning (Grant Nos. 20168510011420).

REFERENCES

EIA. 2010. Annual Energy Outlook 2010. Energy Information Administration.

DOE Report, 2014, Energy Savings Potential and RD&D Opportunities for Non-Vapor-Compression HVAC Technologies, Building Technologies Office

Woods, J., 2014, Membrane processes for heating, ventilation, and air conditioning, Renew. Sustain. Energy Rev., 33, 290–304.

Bui, T.D.,Chen, F., Nida, A., Chua, K.J., Ng, K.C., 2015, Experimental and modeling analysis of membrane-based air dehumidification, Sep. Purif. Technol., 144, 114–122.

Zaw, K., Safizadeh, M.R., Luther, J., Ng, K.C., 2013, Analysis of a membrane based air-dehumidification unit for air conditioning in tropical climates, Appl. Therm. Eng., 59 (1–2), 370–379.

Manuscript ID: 388
DOI: 10.18462/iir.icr.2019.0388

Development of vapor pressure model for mixed liquid desiccants near saturated solubility

Chunwen CHE[(a)], Yonggao YIN[(a)]

[(a)] School of Energy and Environment, Southeast University
Nanjing, 210096, China, e-mail: y.yin@seu.edu.cn

ABSTRACT

A statistical thermodynamic model is proposed to predict the vapor pressure of mixed liquid desiccant solutions near saturated solubility by re-quantifying the weight of interactions between all species in solution. The model considers that charge interaction between ions and non-charge interaction between all species are still dominant, and charge-dipole interaction between ions and solvent molecules increases with the increase of solute concentration. Rigorous expressions are given to calculate the interactions: ion-ion charge interaction is described by modifying the Fowler-Guggenheim theory, charge-dipole interaction is expressed by combining the McMillan-Mayer osmotic coefficient theory with the Debye-Hückel theory, and non-charge interaction is calculated based on the extended UNIQUAC equation. The prediction accuracy comparison with two typical models shows that the new model has better accuracy for mixed liquid desiccants near saturated solubility.
Keywords: Liquid desiccant near saturated solubility, Vapor pressure, Prediction, Statistical thermodynamic model.

1. INTRODUCTION

As a system to improve humidity control and enhance utilization of low-grade thermal energy, liquid desiccant cooling systems have received increasingly attention in recent decades (Zhao et al., 2016). Generally, the liquid desiccants adopted in this system are electrolyte aqueous solutions near saturated solubility such as lithium chloride (LiCl), lithium bromide (LiBr), calcium chloride ($CaCl_2$), and their binary-solute aqueous solutions. The vapor pressure difference between liquid desiccants and air, as the driving force for mass transfer, plays a vital role in the design and performance evaluation of liquid desiccant cooling systems.

Many thermodynamic models have been introduced to calculate the vapor pressure of liquid desiccant due to its advantages of lower cost and no complicated experimental work. The Debye-Hückel theory (1923) first made it possible to calculate thermal properties of infinite dilution electrolyte solution. Fowler and Guggenheim (1956) proposed a modified equation and extended the Debye-Hückel theory to mixed electrolyte solutions. However, only electrostatic interactions are considered in the Debye-Hückel theory and the modified equation by Fowler and Guggenheim. By taking into short-range (SR) nonelectrolyte interaction, some models such as the Pitzer model (Pitzer, 1973) and the e-NRTL model (Chen et al., 1982) do well work in mixed electrolyte systems in which electrolytes up to a concentration of several moles of solute per kilogram of solvent. Unfortunately, these typical models do not take in account the charge-dipole interactions between ions and solvent molecules, which leads to a poor accuracy for liquid desiccant solutions near saturated solubility in most case. Taking into account charge-dipole middle-range (MR) interaction, Li et al. (1994) presented a g^E model (also known as the LIQUAC model) for electrolyte solutions. The contributions of MR interaction are dominant in the LIQUAC model. However, in practice, charge interaction between ions and non-charge interaction should account a large proportion in all interactions, even in some cases, is greater than that of the charge-dipole interaction.

By considering that ion-ion charge interaction and non-charge interaction between all species are dominant and charge-dipole interaction increases with the increase of solute concentration, a statistical thermodynamic model is proposed to predict the vapor pressure of mixed liquid desiccant solutions near saturated solubility. In the model, the liquid desiccant is treated as a

nonelectrolyte solution with electrostatic interaction and rigorous expressions for the interactions between all species are given. Prediction accuracy of the new model is tested and is compared with two typical models including the LIQUAC model and the e-NRTL model.

2. A STATISTICAL THERMODYNAMIC MODEL

The water activity coefficient can be expressed as the sum of three contributions:

$$\ln \gamma_w = \ln \gamma_w^{LR} + \ln \gamma_w^{MR} + \ln \gamma_w^{SR} \quad \text{Eq. (1)}$$

where γ_w is activity coefficient of water, $\ln f_w^{LR}$ represents the contribution of LR charge interaction between ions, $\ln f_w^{MR}$ expresses the contribution of MR charge-dipole interaction, and $\ln f_w^{SR}$ represents the contribution of SR non-charge interaction.

2.1. Determination of $\ln f_w^{LR}$

$\ln f_w^{LR}$ is calculated as a sum of an excess Gibbs energy term and an empirical linear term of ion strength:

$$\ln f_w^{LR} = \frac{\partial\left[G_{LR}^E/(RT)\right]}{\partial n_w} + B_{LR} I_m \quad \text{Eq. (2)}$$

with

$$I_m = \frac{1}{2}\sum_i m_i z_i^2 \quad \text{Eq. (3)}$$

In Eq. (2) and Eq. (3), G_{LR}^E is excess Gibbs energy, n_w represents the mole number of water, R is gas constant, T is temperature (K), I_m is ionic strength (mol/kg), m_i (mol/kg) is the molality of ion i, z_i is the charge number of ion i, weight coefficient B_{LR} is obtained by fitting experimental data.
Considering that the closest approach distances of ions are different, the Fowler-Guggenheim theory (Fowler and Guggenheim, 1956) is modified to express the excess Gibbs energy based on the statistical thermodynamic theory:

$$G_{LR}^E = -\int_0^1 \sum_i N_i \frac{z_i e\xi}{D} \frac{\kappa\xi}{1+\kappa\xi a_i} d(z_i e\xi) \quad \text{Eq. (4)}$$

where κ is defined as

$$\kappa = \left(\frac{8\pi e^2 d_w N_A}{10^6 DkT} I_m\right)^{0.5} \quad \text{Eq. (5)}$$

and D is calculated through the following empirical temperature dependent function (Mohs and Gmehling, 2013)

$$D(T) = 289.82 - 1.148T + 0.0017843T^2 - 1.053\times10^{-6}T^3 \quad \text{Eq. (6)}$$

In these equation, N_i is the number of ion i, ξ is charging coefficient ($0 \le \xi \le 1$), e is electron charge (4.802×10^{-10} esu), D is dielectric constant of pure water, a_i is the distance of closest approach of ion i, d_w is the density of pure water (kg/m^3), N_A is the Avogadro constant, k is the Boltzmann constant.
By simplifying Eq. (4) and giving it into Eq. (2), $\ln f_w^{LR}$ can be calculated as

$$\ln f_w^{LR} = \sum_i \frac{m_i z_i^2 A_{LR} M_w}{I_m b_i^3}\left[(1+b_i I_m^{0.5}) - 2\ln(1+b_i I_m^{0.5}) - \frac{1}{1+b_i I_m^{0.5}}\right] + B_{LR} I_m \quad \text{Eq. (7)}$$

where

$$A_{LR} = \left(\frac{2\pi N_A d_w}{1000}\right)^{0.5}\left(\frac{e^2}{DkT}\right)^{1.5} \quad \text{Eq. (8)}$$

$$b_i = \frac{\kappa a_i}{I_m^{0.5}} \quad \text{Eq. (9)}$$

In Eq. (7), M_w is the molecular weight of water (kg/mol).
Based on the experimental data in literatures, closest approach distances a_i of all ions i are fitted and are given in Table 1. Weight coefficient B_{LR} is calculated, which is equal to -0.001553.

Table 1. Adjustable parameters in LR, MR and SR interaction terms

i	j	a_j /(10^{-10}m)	$b_{j,i}$ /(kg/mol)	$c_{j,i}$ /(kg/mol)$^{1.5}$	$d_{j,i}$ /(kg/mol)^2	$a^0_{i,j}$ /K	$a^0_{j,i}$ /K	$\delta_{ij,w}$ /K
H_2O	Li^-	73.0845	45088.85	347217.69	-60262.03	-754.9211	2192.2936	-
	Ca^{2+}	8.1783	90179.60	694439.14	-120525.17	-2434.664	-405.7248	-
	Cl^-	45.6901	-45080.43	-347222.63	60263.19	-6417.894	-386.2516	-
	Br^-	2.2437	-45082.54	-347224.81	60263.71	-3045.479	4829.8478	-
Li^+	Cl^-	-	-	-	-	-5348.837	554.5505	17087.82
	Br^-	-	-	-	-	1052.2692	1063.7344	33391.56
Ca^{2+}	Cl^-	-	-	-	-	-5041.758	-4132.356	32173.80
	Br^-	-	-	-	-	506.8548	-2376.33	45184.66
Li^+	Ca^{2+}	-	-	-	-	0	0.3673	-8129.07
Cl^-	Br^-	-	-	-	-	0.002708	-6760.786	107615.9

2.2. Determination of $\ln f_w^{MR}$

The calculation of $\ln f_w^{MR}$ is based on five fundamental assumptions: 1) only charge-dipole interactions between ions and solvent molecules are considered as MR interactions, 2) only the solvent molecules near ions have charge-dipole interaction, while the solvent molecules far away from ions only act as carrier with dielectric constant D to dissolve electrolytes, 3) the McMillan-Mayer osmotic coefficient theory is applicable to the part of solvent molecules with charge-dipole interaction, 4) the ionization of solvent molecules is ignored in the calculation of ionic strength and 5) system temperature is constant.
For the assumption 2), parameter h is assigned to denote the proportion of solvent molecules with charge-dipole interaction in all solvent molecules. According to our previous work, it is more reasonable to express h as

$$h = \frac{h_1 \ln(\sum_i m_i + m_{ref})}{m_w} \quad \text{Eq. (10)}$$

where h_1 is weight factor obtained by correlating experimental data and is 0.040364, subscript i covers all ions, m_w (mol/kg) is the molality of water, m_{ref} indicates reference molality set to 1 mol/kg.
By combining the McMillan-Mayer osmotic coefficient theory (Pitzer, 1977)

$$\phi - 1 = -\frac{1}{6\rho kT}\sum_i\sum_j \rho_i\rho_j \int_0^\infty \frac{d<u_{ij}(r)>}{dr} g_{ij}(r) 4\pi r^3 dr \quad \text{Eq. (11)}$$

with the Debye-Hückel theory (Debye and Hückel, 1923)

$$g_{ij}(r) = g_{ji}(r) = \exp\left(\frac{z_i z_j e^2 \exp[\kappa(a-r)]}{DkT(1+\kappa a)r}\right) \quad \text{Eq. (12)}$$

and using Taylor formula and taking first three terms for Eq. (12), and giving mean potential of charge-dipole interaction between water molecules and ions

$$<u_{w,ion}(r)> = -\frac{\mu_w^2 z_i^2 e^2}{3DkTr^4} \quad \text{Eq. (13)}$$

one obtains based on the statistical thermodynamic theory:

$$\phi\text{-}1=-\frac{hm_w\sum_i m_i z_i^2\frac{8\pi\mu_w{}^2e^2N_A\rho_w}{9\rho D(kT)^2}}{\sum_i m_i+hm_w}\left[\begin{array}{l}(\frac{A_{id}{}^2}{6a_d{}^3}+\frac{A_{id}{}^2}{6a_i{}^3}-\frac{A_{id}}{2a_d{}^2}-\frac{A_{id}}{2a_i{}^2}+\frac{1}{a_d}+\frac{1}{a_i})\\+(\frac{A_{id}}{a_d}+\frac{A_{id}}{a_i}-\frac{A_{id}{}^2}{2a_d{}^2}-\frac{A_{id}{}^2}{2a_i{}^2})(\frac{8\pi e^2d_wN_A}{1000DkT})^{0.5}I_m{}^{0.5}\\+(\frac{A_{id}{}^2}{a_d}+\frac{A_{id}{}^2}{a_i})(\frac{8\pi e^2d_wN_A}{1000DkT})I_m\end{array}\right] \quad \text{Eq. (14)}$$

where

$$A_{id}=\frac{z_iz_de^2\exp(\kappa a)}{DkT(1+\kappa a)} \quad \text{Eq. (15)}$$

In these equations, ϕ is osmotic coefficient, u_w is dipole moment of water, ρ is species number density, $<u_{ij}(r)>$ is potential of mean force between species i and j, g_{ij} is radial distribution function, subscript w represents all water molecules, subscript d represents water molecules with charge-dipole interaction, a_i is the closest approach distance of ion i, a_d is the equivalent closest approach distance of water molecules with charge-dipole interaction, z_d represents the equivalent charge of water molecular with charge-dipole interaction.
Therefore, it is reasonable to assume that $\ln f_w^{MR}$ can be described by the following simple formula

$$\ln f_w^{MR}=-\frac{hm_w\ln[(1-h)x_w]}{\sum_i m_i+hm_w}\sum_i m_i(b_{ion,w}+c_{ion,w}I_m{}^{0.5}+d_{ion,w}I_m) \quad \text{Eq. (16)}$$

where subscript i covers all the ions of solute, x_w is the mole fraction of water in liquid phase, $b_{ion,w}$, $c_{ion,w}$ and $d_{ion,w}$ are adjustable parameters which can be determined as given in Table 1 by correlating experimental data in literatures.

2.3. Determination of $\ln f_w^{SR}$

The expression of the contribution term of non-charge interaction ($\ln f_w^{SR}$) is based on the extended UNIQUAC equation (Sander et al., 1986).

$$\ln f_w^{SR}=1-V_w+\ln V_w-5q_w\left[1-\frac{V_w}{F_w}+\ln(\frac{V_w}{F_w})\right]+q_w\left[1-\ln\left(\frac{\sum_i q_ix_i\psi_{iw}}{\sum_i q_ix_i}\right)-\sum_i\left(\frac{q_ix_i\psi_{wi}}{\sum_k q_kx_k\psi_{ki}}\right)\right] \quad \text{Eq. (17)}$$

with

$$V_w=\frac{r_w}{\sum_i r_ix_i} \quad \text{Eq. (18)}$$

$$F_w=\frac{q_w}{\sum_i q_ix_i} \quad \text{Eq. (19)}$$

$$\psi_{ki}=\exp(\frac{-a_{ki}}{T}) \quad \text{Eq. (20)}$$

$$a_{i,w}=a_{i,w}^0+\theta_i\sum_{j\neq i}\delta_{ij,w}\theta_j \quad \text{Eq. (21)}$$

$$a_{w,i}=a_{w,i}^0+\theta_i\sum_{j\neq i}\delta_{ij,w}\theta_j \quad \text{Eq. (22)}$$

$$\theta_i=\frac{x_iq_i}{\sum_k q_kx_k} \quad \text{Eq. (23)}$$

In these equations, w denotes water, i and k cover all species, x_i is the mole fraction of species i, q_i is the van der Waals surface area parameter of species i, r_i is the van der Waals volume parameter of species i, a_{ki} is the interaction parameter between species k and i, $a^0_{i,w}$ and $a^0_{w,i}$ are reference interaction parameters, $\delta_{ij,w}$ is adjustable parameter and $\delta_{ij,w}=\delta_{ji,w}$. The interaction parameters between ions are assumed to be independent of concentration and $a_{ij} \neq a_{ji}$. The adjustable parameters $a^0_{i,j}$ and $\delta_{ij,w}$ are fitted and are given in Table 1. The van der Waals volume and surface area parameters are from the recommended values by Sander et al. (1986) as listed in Table 2.

Table 2. The van der Waals volume r and surface area q of different species

Species	Li^+	Ca^{2+}	Cl^-	Br^-	H_2O
r	1	1	0.9861	1.2331	0.92
q	1	1	0.9917	1.151	1.4

3. RESULTS AND DISCUSSION

Based on experimental data in literatures, the prediction capability of the new model is evaluated and is compared with that of two typical models (the LIQUAC model and the e-NRTL model) by graph form as elaborated in Figure 1 andFigure 2 qualitatively. Furthermore, absolute average relative deviation in vapor pressure ($AARD-P\%$) is introduced to test the prediction accuracy of model quantitatively as given by

$$AARD-P\% = \frac{1}{N_{data}} \sum_{i=1}^{N_{data}} \left| \frac{P_{espe} - P_{calc}}{P_{espe}} \right| \times 100\% \qquad \text{Eq. (24)}$$

where N_{data} is the number of data points. The $AARD-P\%$ of our model and the two well-known models for mixed liquid desiccant solutions near saturated solubility are compared as shown in Table 3 and Table 4. Figure 1 shows the experimental and calculated vapor pressure of LiCl-$CaCl_2$ aqueous solution at different temperatures and different mass ratios of solutes with a total mass concentration of 40%. From Figure 1, the curves of the new model are close to experimental symbols and closer than that of the other two models in most mass ratios of solutes. The accuracy of the new model increases with the increase of temperature. In addition, it can be clearly seen from Table 3 that the $AARD-P\%$ of our model are much smaller than that of the other two models in most case. It is obvious that the new model has a better capability on the prediction of near saturated LiCl-$CaCl_2$ aqueous solution, which can be explained by taking into account the weight of all interactions reasonably in the new model.

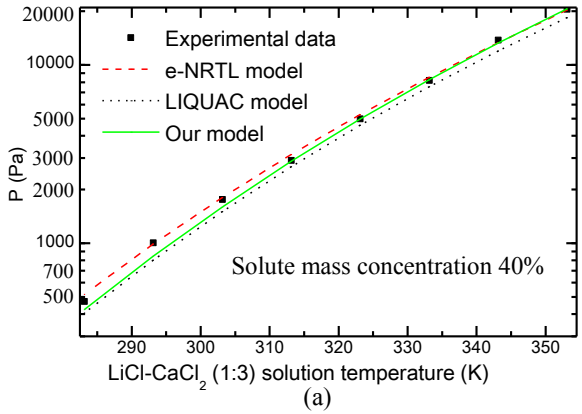

(a)

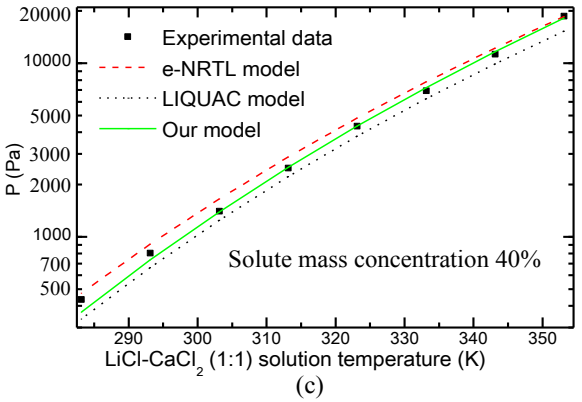

(c)

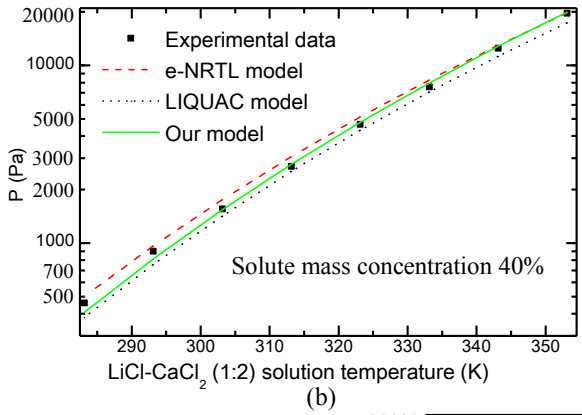

(b)

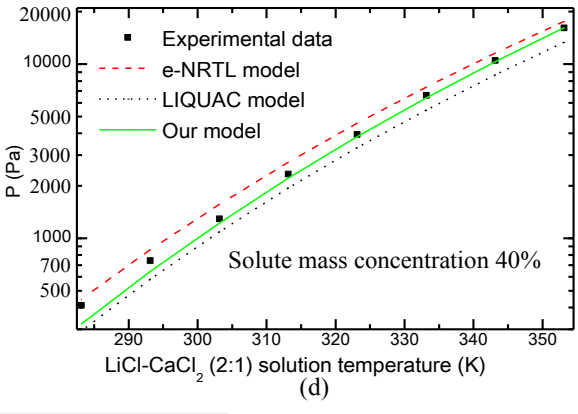

(d)

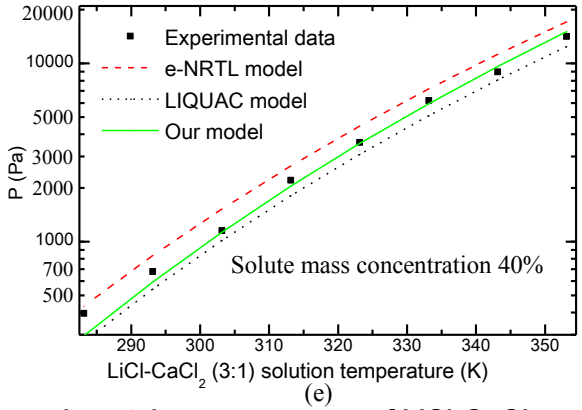

(e)

Figure 1. Calculated and experimental vapor pressure of LiCl-$CaCl_2$ aqueous solution at different temperatures and concentrations

Table 3. Comparison of *AARD-P*% between our model and the other two models for LiCl-$CaCl_2$ aqueous solution

Mass concentration		Temperature range (K)	Number of data points	Experimental data	e-NRTL model (%)	LIQIAC model (%)	Our model (%)
LiCl	$CaCl_2$						
0.1	0.3	283.15-353.15	8	Shen et al. (2016)	4.58	11.68	5.06
0.1333	0.2667		8		8.35	10.25	4.66
0.2	0.2		8		11.24	14.17	4.58
0.2667	0.1333		8		13.80	18.78	6.56
0.3	0.1		8		21.72	16.75	8.01
Mean *AARD-P*%					11.94	14.33	5.77

Figure 2 and Table 4 elaborate the comparison between three models in predicting the vapor pressure of near saturated LiBr-$CaCl_2$ aqueous solution. From Figure 2, it can be found that the accuracy of new model increases with the increase of temperature. In addition, as can be seen from Figure 2 and Table 4, our model is more accurate than the other two models for LiBr-$CaCl_2$ aqueous solution near saturated solubility in most mass ratios of solutes.

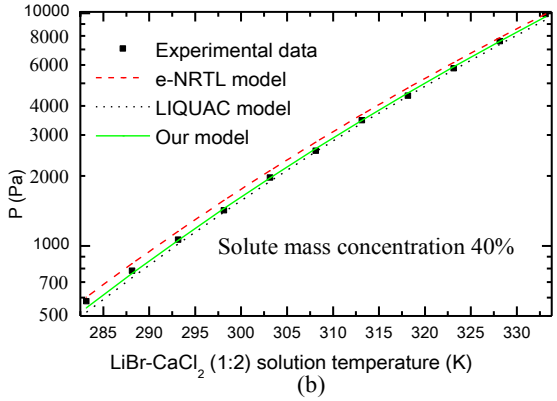

(b)

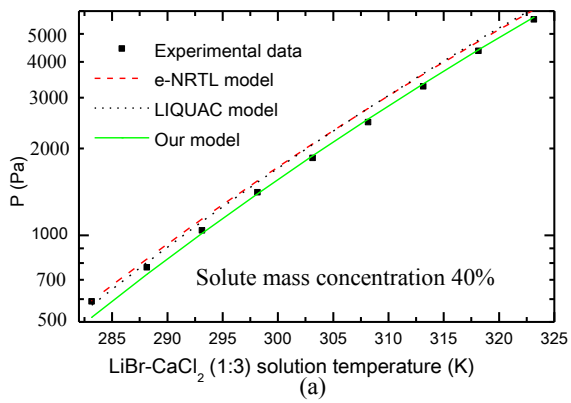

(a)

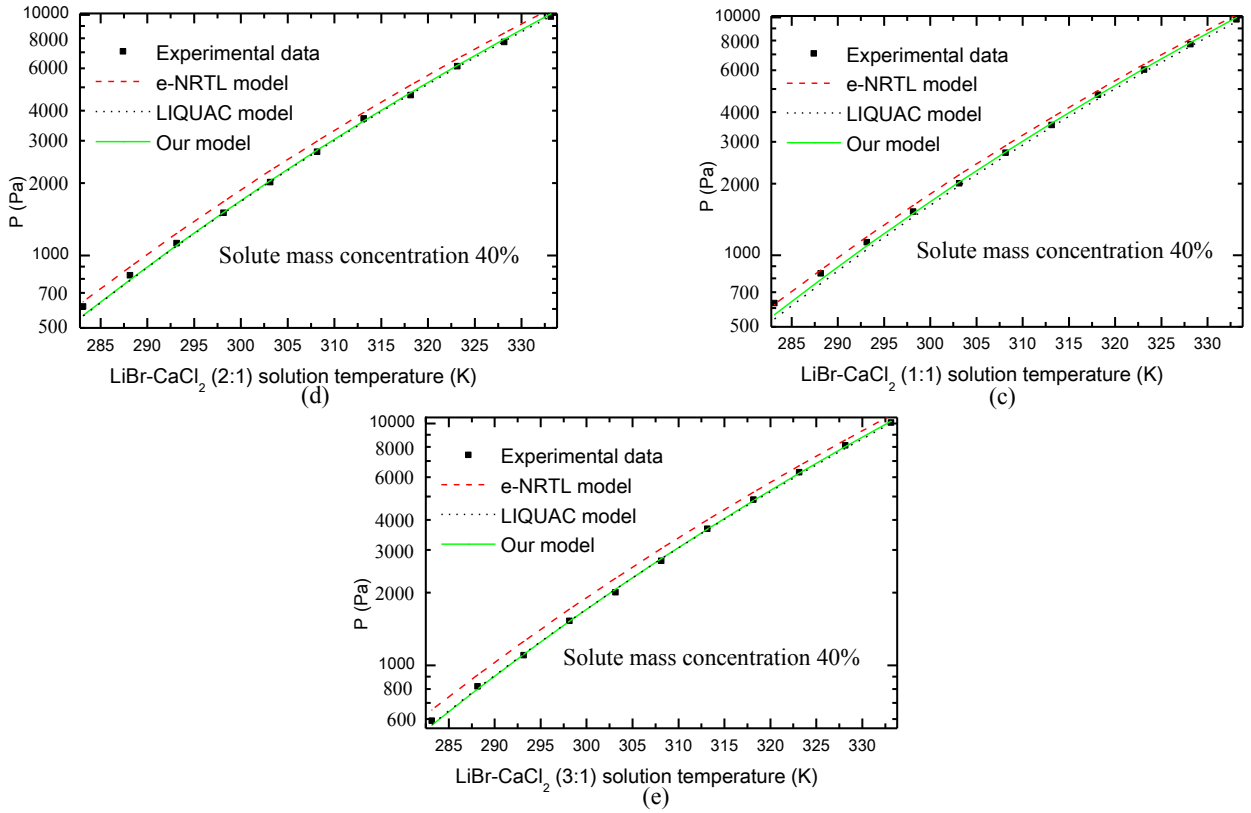

Figure 2. Calculated and experimental vapor pressure of LiBr-$CaCl_2$ aqueous solution at different temperatures and concentrations

Table 4. Comparison of *AARD-P*% between our model and the other two models for LiBr-$CaCl_2$ aqueous solution

Mass concentration		Temperature range (K)	Number of data points	Experimental data	e-NRTL model (%)	LIQIAC model (%)	Our model (%)
LiBr	$CaCl_2$						
0.1	0.3	283.15-333.15	9	Guo (2018)	8.57	3.42	3.31
0.1333	0.2667		11		6.47	3.63	1.89
0.2	0.2		11		5.43	4.71	2.77
0.2667	0.1333		11		8.97	2.16	2.66
0.3	0.1		11		10.06	1.76	1.54
Mean *AARD-P*%					7.88	3.13	2.40

4. CONCLUSION

A new model is proposed in this study to re-quantify the weight of interactions between species in liquid desiccant based on the statistical thermodynamic theory. The new model aims at predicting the vapor pressure of mixed liquid desiccants near saturated solubility. In the model, rigorous expressions are given to calculate the interactions. The prediction accuracy of our model is tested and is compared with the e-NRTL model and the LIQUAC model based on experimental data in literatures. The results show that the new model has a better prediction capability. The superiority of our model increases with the increase of solute concentration or temperature. Furthermore, the paper points out a good model should fully consider the weight of various interactions in liquid desiccants.

ACKNOWLEDGEMENTS

This research was supported by the National Key Research and Development Plan Project of China [grant number 2018YFC0705306] and the National Natural Science Foundation of China [grant number 51776036].

NOMENCLATURE

A_{LR} , b_i	Debye-Hückel parameters	k	Boltzmann constant
$a_{i,w}$, $a_{w,i}$	UNIQUAC interaction parameters	N_A	Avogadro constant
$a^0_{i,w}$, $a^0_{w,i}$	reference interaction parameters	q_i , q_w	van der Waals surface area parameters
B_{LR}	weight coefficient in long-range interaction term	r_i , r_w	van der Waals volume parameters
$b_{ion,w}$, $c_{ion,w}$, $d_{ion,w}$	middle-range interaction parameters between ions and water molecules	m_i , m_d , m_{ref} , m_w	molality (in mol/kg)
D, $D(T)$	dielectric constant of pure water	e	electron charge
d_w	density of pure water (kg/m^3)	ρ , ρ_i , ρ_j	species number densities
$\delta_{ij,w}$	adjustable parameter in short-range interaction term	LR, MR, SR	long-range, middle-range, short-range

REFERENCES

Chen, C., Britt, H.I., Boston, J.F., Evans, L.B., 1982. Local composition model for excess Gibbs energy of electrolyte systems. Part 1: Single solvent, single completely dissociated electrolyte systems. AIChE Journal 28, 588-596.

Debye, P., Hückel, E., 1923. The theory of electrolytes 1. The lowering of the freezing point and related occurrences. Physikalishe zhitschrift 24, 185-206.

Fowler, R., Guggenheim, P.A., 1956. Statistical thermodynamics. Cambridge University Press.

Guo, X., 2018. Research on the performance of mixed solutions to substitute single desiccant in liquid desiccant system, School of Energy and Environment. Southeast University, Nanjing, China.

Li, J., Polka, H.M., Gmehling, J., 1994. A g^E model for single and mixed solvent electrolyte systems: 1. Model and results for strong electrolytes. Fluid Phase Equilibria 94, 89-114.

Mohs, A., Gmehling, J., 2013. A revised LIQUAC and LIFAC model (LIQUAC*/LIFAC*) for the prediction of properties of electrolyte containing solutions. Fluid Phase Equilibria 337, 311-322.

Pitzer, K.S., 1973. Thermodynamics of electrolytes. 1. Theoretical basis and general equations. The Journal of Physical Chemistry 77, 268-277.

Pitzer, K.S., 1977. Electrolyte theory-improvements since Debye and Hueckel. Accounts of Chemical Research 10, 371-377.

Sander, B., Fredenslund, A., Rasmussen, P., 1986. Calculation of vapour-liquid equilibria in mixed solvent/salt systems using an extended UNIQUAC equation. Chemical Engineering Science 41, 1171-1183.

Shen, Z., Yin, Y., Zhang, X., 2016. Measurement and analysis of physical properties of mixed liquid desiccants based on calcium chloride solution. CIESC Journal 67, 3004-3009.

Zhao, X., Li, X., Zhang, X., 2016. Selection of optimal mixed liquid desiccants and performance analysis of the liquid desiccant cooling system. Applied Thermal Engineering 94, 622-634.

Manuscript ID: 389
DOI: 10.18462/iir.icr.2019.0389

Experimental investigation on the instability of a two-phase loop thermosyphon with three evaporators

Hainan ZHANG, Shuangquan SHAO, Junyan TANG, Changqing TIAN

Technical Institute of Physics and Chemistry, CAS
Beijing, 100190, China, zhanghn@mail.ipc.ac.cn

ABSTRACT

Two-phase loop thermosyphon with multiple evaporators is ideal device to achieve multi-source heat transfer and has great application potential. As there are parallel branches in the loop, unstable phenomena often exist. In this paper, the instability of a two-phase loop thermosyphon with three evaporators is investigated experimentally. The results show that the oscillation frequency increases while the amplitude almost remains constant with the increase of heating power; The oscillation frequency decreases slightly while the amplitude increases with the increase filling ratio; In the oscillation, when the temperature of an evaporator reaches the peak value, the temperatures of the adjacent evaporators reach the trough value.
Keywords: Heat Transfer, R134a, Thermosiphon, Two-Phase Flow.

1. INTRODUCTION

The need of multi-source heat transfer is growing with the development of modern industries, e.g., avionics (Xun et al., 2017), super computers (Shoukourian et al., 2017) and data centers (Ling et al., 2016). Loop thermosyphon is a type of heat transfer device with high efficiency compared with traditional air cooling and liquid cooling methods (Oliveira et al., 2016). If there are multiple evaporators and a single condenser in a single loop, it can achieve heat transfer from multiple heat sources to a single cold source with no external power input therefore shows great potential in multi-source heat transfer.

Current studies on loop thermosyphon with multiple evaporators are very limited and there is still a long way to obtain a deep understanding of its flow and heat transfer characteristics. One of the key characteristics is its instability. As there are parallel flow channels in the loop and there is no external driving force, the flow directionality is not very clear therefore its instability is more obvious than common loop thermosyphons. Also, interaction between evaporators also has effect on its instability. Only several references include the results of the instability of loop thermosyphon with multiple evaporators. Tong et al. (2017) studied a loop thermosyphon with two evaporators experimentally, and oscillations of temperature and mass flow rate were observed. Zhang et al. (2018) found unique oscillation phenomena in loop thermosyphon with two evaporators, the feature of which is that when the temperature of a certain evaporator reaches the peak value, the temperature of the other reaches the trough value. Instability of loop thermoysyphon with multiple evaporators is an interesting problem requiring further research.

2. EXPERIMENTAL SETUP

The experimental setup is shown in Fig. 1. The loop thermosyphon consists of three evaporators and one condenser. The condenser is placed a certain height above the evaporators to ensure the gravity head. The internal flow channel of each evaporator is 10 mm $\times$ 10mm $\times$ 60 mm. The condenser is a double pipe heat exchanger. The inside diameter of the inner tube and outer tube is 10 mm and 26 mm, respectively. T type thermocouples are attached on the outside wall along the loop and the data is recorded by a data acquisition instrument. The locations of the thermocouples are presented in Fig. 1. R134a is used as the working fluid and its filling ratio is defined as the ratio

of filling volume to the total internal volume. The inlet temperature of the condenser cooling water is fixed at 20 ℃.

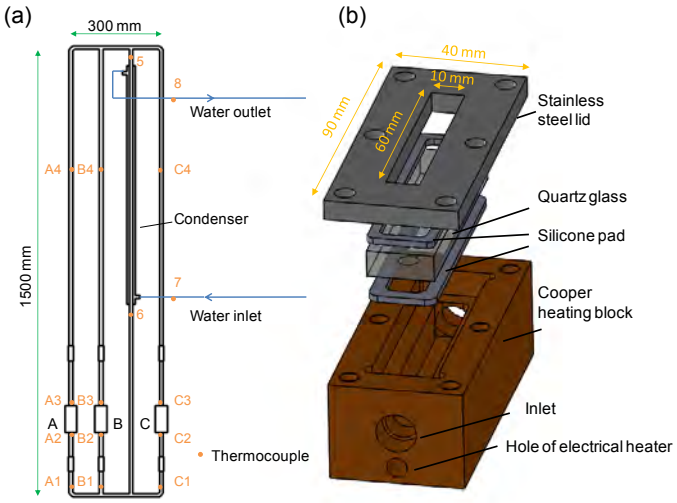

Figure 1: Schematic diagram of experimental setup: (a) Loop; (b) evaporator

3. RESULTS AND ANALYSYS

The temperature oscillations under different heating power are shown in Fig. 2. Only Evaporator B has heating power and the filling ratio is 0.91. The temperatures are measured by Thermocouple B3. The oscillation period and frequency are calculated as the average values during 100 s. It can be seen that the oscillation period decreases with the increase of heating power. The period decreases from 7.41 s to 5.41 s and the frequency increases from 0.135 Hz to 0.185 Hz, when the heating power increases from 36 W to 72 W. While, it can be seen that the effect of heating power on the oscillation amplitude is not very obvious.

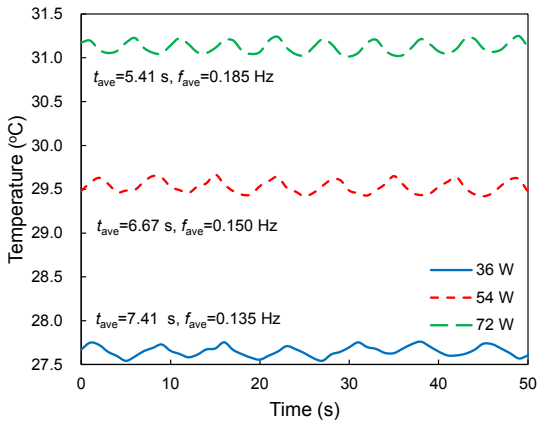

Figure 2: Temperature oscillation under different heating power of Evaporator B when the filling ratio is 0.91

The temperature oscillations under different filling ratios when the heating power of Evaporator B is 90 W are shown in Fig. 3. The temperatures are measured by Thermocouple B3. It can be seen that with the increase of filling ratio, the oscillation frequency decreases slightly. However, the oscillation amplitude increases. Also, oscillation phenomenon is not found when the filling ratio is lower than 0.79. Therefore, oscillation is more significant under higher filling ratios.

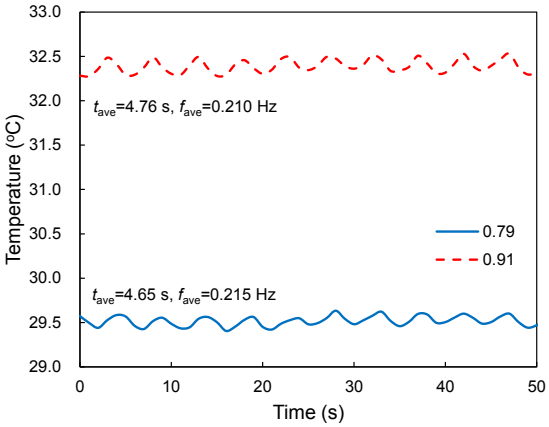

Figure 3: Temperature oscillation under different filling ratios when the heating power of Evaporator B is 90 W

The temperature oscillation when the heating power for each evaporator is 72 W and the filling ratio is 0.79 is shown in Fig. 4. A distinctive feature of this temperature oscillation is that when the temperature of one evaporator reaches the peak value, the temperature of the adjacent evaporator reaches the trough value. The reason is that there is competition between the evaporators as the flow pipe diameter is limited. When the flow boiling of a certain evaporator is relatively strong, the outlet flow of its adjacent evaporator will be restricted. This phenomenon has been found in loop thermosyphon with two evaporators, and it can be seen that it is a common phenomenon in loop thermosyphon with multiple evaporators.

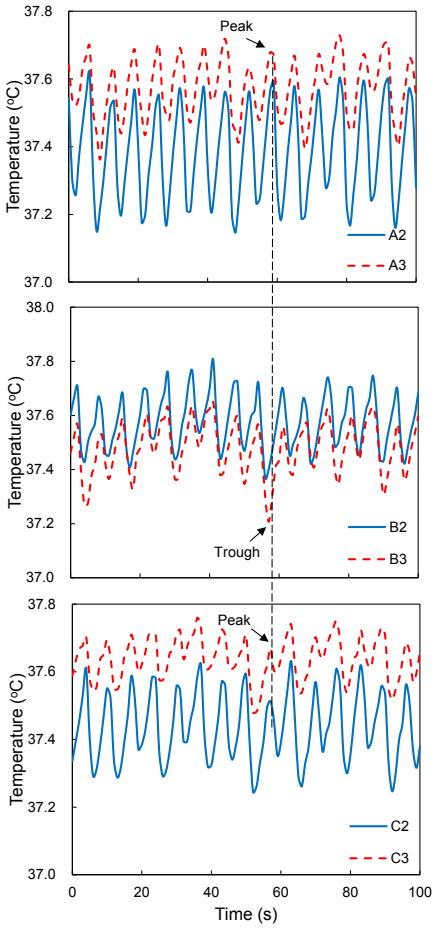

Figure 4: Temperature oscillation when the heating power for each evaporator is 72 W and the filling ratio is 0.79

4. CONCLUSIONS

Loop thermosyphon with multiple evaporators will surely play an important role in the future of multi-source heat transfer. The instability of a loop thermosyphon with three evaporators are invested experimentally in this paper. The main results are summarized as follows:

1) With the increase of heating power, the oscillation frequency increases while the amplitude almost remains constant.
2) With the increase filling ratio, the oscillation frequency decreases slightly while the amplitude increases.
3) For every two adjacent evaporators, the phases of oscillation are almost opposite due to the competition between the evaporators.

ACKNOWLEDGEMENTS

The authors gratefully acknowledge the financial supports from Key Laboratory of Cryogenics, TIPC, CAS (CRYOQN201708) and Talent Cultivation Project of Technical Institute of Physics and Chemistry, CAS (2017-ZHN).

NOMENCLATURE

f	frequency (Hz)	t	time (second)
ave	average	A	Evaporator A
B	Evaporator B	C	Evaporator C

REFERENCES

Ling, L., Zhang, Q., Yu, Y., Liao, S., 2016. Experimental investigation on the thermal performance of water cooled multi-split heat pipe system (MSHPS) for space cooling in modular data centers. Appl. Therm. Eng. 107, 591-601.

Oliveira, J.L.G., Tecchio, C., Paiva, K.V., Mantelli, M.B.H., Gandolfi, R., Ribeiro, L.G.S., In-flight testing of loop thermosyphons for aircraft cooling. Appl. Therm. Eng. 98, 144-156.

Shoukourian, H., Wilde, T., Huber, H., Bode, A., 2017. Analysis of the efficiency characteristics of the first High-Temperature Direct Liquid Cooled Petascale supercomputer and its cooling infrastructure. J. Parallel Distr. Com.107, 87-100.

Tong Z., Liu, X.H., Jiang, Y., 2017. Experimental study of the self-regulating performance of an R744 two-phase thermosyphon loop. Appl. Energy 186, 1-12.

Xun, Q., Xun, B., Li, Z., Wang, P., Cai Z., 2017. Application of SiC power electronic devices in secondary power source for aircraft. Renew. Sustain. Energy Rev. 70, 1336-1342.

Zhang, H., Shao, S., Gao, Y., Xu, H., Tian, C., 2018. The transient response, oscillation and internal flow of a loop thermosyphon with dual evaporators. Int. J. Refrig. 88, 451-457.

Manuscript ID: 390
DOI: 10.18462/iir.icr.2019.0390

2-D Models of Magnet and Active Magnetocaloric Regenerator

Lifen Yuan, Suxin Qian*, Jianlin Yu, Gang Yan

Department of Refrigeration and Cryogenic Engineering, School of Energy and Power Engineering, Xi'an Jiaotong University, Xi'an, Shaanxi, 710049, China, qiansuxin@xjtu.edu.cn

ABSTRACT

A transient two-dimensional model for the parallel plate matrix regenerator is developed to investigate the heat transfer characteristics of oscillating flow. Moreover, the simulated impact of operating frequency on the heat transfer coefficient are presented. To quantitatively describe the influence of operating frequency, this paper compares the heat transfer coefficient calculated by simulations, correlations with the oscillating Reynolds number and correlations with the conventional Reynolds number. In the end, modifications of the empirical correlation are introduced to account for such frequency dependency.

Keywords: Active Magnetocaloric Regenerator, Heat Transfer, Oscillating Flow.

1. INTRODUCTION

Room temperature magnetic refrigeration has developed rapidly in recent years and many prototypes have emerged based on various driving and heat exchange designs (Ram et al. 2018). Jacobs et al. in 2014 demonstrated a rotary system using six layers of LaFeSiH particles, producing 3,042W cooling power under zero temperature span condition and 2,502W cooling power over a span of 11K with a coefficient of performance (COP) around 2 (Jacobs et al. 2014). Prototypes from TU Denmark used two layers of Gd and Gd-Y materials as refrigerant, which performed a COP of 3.6 over a temperature span of 15.5K, corresponding to a maximum second-law efficiency of 18% (Eriksen et al. 2015; Fortkamp et al. 2018). To improve the performance, researchers have focused on various techniques, such as developing novel magnetocaloric materials, increasing the maximum applied magnetic field of the permanent magnet (Trevizoli et al. 2015), optimizing the regenerator geometry with related operating parameters (Hirano et al. 2011). The last approach has attracted substantial attention since it is practical and the first two approaches have encountered bottlenecks (Moos et al. 2014).

The modern magnetocaloric cooling technology is based on the so-called active magnetocaloric regenerator (AMR), in which the magnetocaloric materials work as a regenerator and enables an increase in the temperature span as well as working as a coolant and generating/absorbing heat between the particular phases of the thermodynamic cycle. A typical AMR cycle is generally based on the following four operational steps:

1) Magnetization: Each part of the magnetocaloric material along the AMR is heated up due to the magnetocaloric effect when the magnetic field increases.
2) Fluid flow from the cold side to the hot side (hot blow): The fluid moves through the heated magnetocaloric material to reject heat from the solid.
3) Demagnetization: Each part of the magnetocaloric material along the AMR is cooled down due to the magnetocaloric effect when the magnetic field reduces from given strength to zero.
4) Fluid flow from the hot side to the cold side (cold blow): The fluid moves through the cooled magnetocaloric material to absorb cooling from the solid.

The period of magnetization/demagnetization is t_{mag} and the period of hot/cold blow is t_f, therefore, the period of each AMR cycle and the operating frequency are defined as Eq. (1) and Eq. (2).

$$t_{cyc}=2(t_{mag}+t_f) \quad \text{Eq. (1)}$$

$$fr=1/t_{cyc} \quad \text{Eq. (2)}$$

From a thermodynamic viewpoint, the insufficient heat transfer between the heat transfer fluid and the solid refrigerant is one of the most obvious causes of cooling performance degradation, which is directly or indirectly related to the regenerator geometry. The most common geometrical forms are the packed sphere bed and the parallel plate matrix due to the advantages of easy construction and good heat transfer performance. The former has a higher heat transfer coefficient, while it also leads to an increase in the pressure drop and the viscous dissipation (Tušek et al. 2013), and contrary conclusion can be obtained for the latter (Nielsen et al. 2013). As a matter of fact, the fluid flows in the opposite direction during the processes of hot blow and cold blow, which is called oscillating flow. Due to the reduced blow time, the heat transfer characteristics of oscillating flow are different from the steady state flow, especially at high operating frequencies. However, current simulation models are developed using heat transfer correlations that are based on steady state conditions, and consequently the oscillating flow effect are neglected in order to simplify the calculation (Lei et al. 2015). Moreover, the future of magnetocaloric cooling requires larger power density and thus high operating frequency, which makes it necessary to investigate heat transfer characteristics of oscillating flow.

This paper develops a transient two-dimensional model for the parallel plate matrix regenerator to address the aforementioned problem. The model is designed in the case of the parallel plate matrix regenerator with Gd for a 1.5 T max magnetic field intensity and water as the heat transfer fluid. The specific heat, magnetic entropy and other physical properties of Gd are based on experimental data in the literature. Heat transfer performance for varied operating frequency is investigated. Furthermore, modifications of the empirical correlations to account for such frequency dependency is introduced.

2. REGENERATOR GEOMETRIES

The parallel plate matrix can be built by stacking thin plates with a specified spacing from each other. Here we use a pair of half thin plates and a single channel between them as the geometric model rather than the whole regenerator, since the paper focuses on the study of the heat transfer between the solid and fluid instead of the cooling capacity, temperature span or COP. Half the thickness of two thin plates is simulated because of the symmetry. The schematic diagram of the parallel plate matrix is shown in Fig. 1, where the gray area represents the solid magnetocaloric material and the remaining blue space is the channel of fluid. The length of the plate is 60mm. Each thin plate is 0.5mm thick. The thickness of a single channel between two plates is 0.5mm.

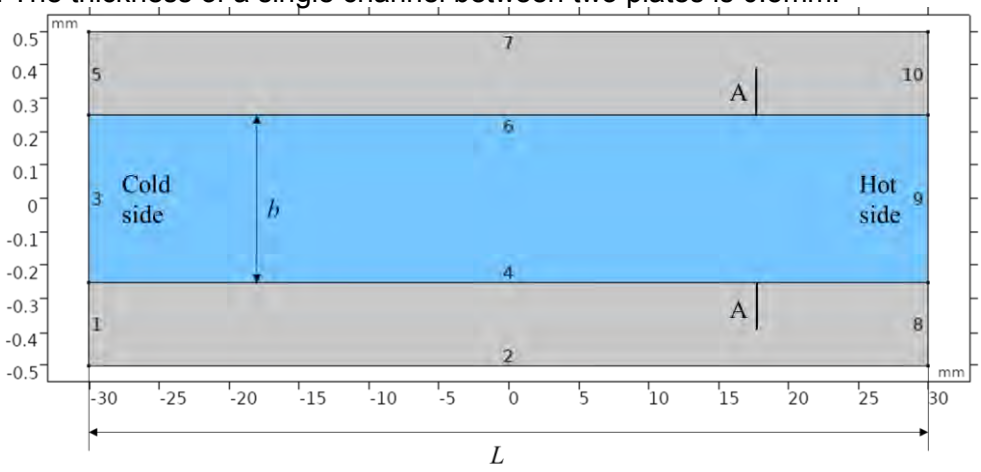

Figure 1: Schematic diagram of the parallel plate matrix

3. NUMERICAL MODEL

3.1. Governing Equations

A two-dimensional model of parallel plate matrix with a single channel is built in COMSOL Multiphysics. Laminar flow and incompressible fluid are assumed. The energy equation is solved to calculate the temperature field in the heat transfer module; the continuity equation and the Navier-

Stokes equations are solved to calculate the velocity and pressure fields in the laminar flow module. The two modules are coupled by non-isothermal flow module. Eq. (3) defines the energy equation of the solid and Eq. (4) defines the mass, energy, momentum equations of fluid, respectively.

$$\rho_s c_s \frac{\partial T_s}{\partial t} = k_s\left(\frac{\partial^2 T_s}{\partial x^2} + \frac{\partial^2 T_s}{\partial y^2}\right) + Q \qquad \text{Eq. (3)}$$

$$\begin{cases} \dfrac{\partial u}{\partial x} + \dfrac{\partial v}{\partial y} = 0 \\ \rho_f c_f\left(\dfrac{\partial T_f}{\partial t} + u\dfrac{\partial T_f}{\partial x} + v\dfrac{\partial T_f}{\partial y}\right) = k_f\left(\dfrac{\partial^2 T_f}{\partial x^2} + \dfrac{\partial^2 T_f}{\partial y^2}\right) \\ \rho_f\left(\dfrac{\partial u}{\partial t} + u\dfrac{\partial u}{\partial x} + v\dfrac{\partial u}{\partial y}\right) = -\dfrac{\partial p}{\partial x} + \mu\left(\dfrac{\partial^2 u}{\partial x^2} + \dfrac{\partial^2 u}{\partial y^2}\right) \\ \rho_f\left(\dfrac{\partial v}{\partial t} + u\dfrac{\partial v}{\partial x} + v\dfrac{\partial v}{\partial y}\right) = -\dfrac{\partial p}{\partial y} + \mu\left(\dfrac{\partial^2 v}{\partial x^2} + \dfrac{\partial^2 v}{\partial y^2}\right) \end{cases} \qquad \text{Eq. (4)}$$

where *ρ, c, T, t, k, μ, u, v* are the density, specific heat, temperature, time, thermal conductivity, dynamic viscosity, fluid velocity in x-direction and y-direction, respectively. The subscript s is for solid and f is for fluid. *Q* as the heat source term in Eq.3 applies the magnetocaloric effect into the model.

3.2. Boundary Conditions

The boundary conditions at the edges of the domain are listed in Table 1. The numbers in Table 1 are corresponding to Fig. 1. Edges 4, 6 are walls. During the processes of adiabatic magnetization and demagnetization, the thermal insulation boundary condition is applied to all the boundaries. In the hot blow process, the temperature T_c is imposed to the cold side of the fluid. In the cold blow process, T_h is set as an isothermal boundary condition on the hot side of the fluid. Edges 2 and 7 are symmetric boundaries.

Table 1 Boundary conditions for fluid and solid domain

Process	1/5/8/10	2/7	3	9
Magnetization/ Demagnetization	$\frac{\partial T_s}{\partial x} + \frac{\partial T_s}{\partial y} = 0$			
Hot blow	$\frac{\partial T_s}{\partial x} + \frac{\partial T_s}{\partial y} = 0$	$\frac{\partial T_s}{\partial x} + \frac{\partial T_s}{\partial y} = 0$	$T_f = T_c$	$\frac{\partial T_s}{\partial x} + \frac{\partial T_s}{\partial y} = 0$
Cold blow	$\frac{\partial T_s}{\partial x} + \frac{\partial T_s}{\partial y} = 0$	$\frac{\partial T_s}{\partial x} + \frac{\partial T_s}{\partial y} = 0$	$\frac{\partial T_s}{\partial x} + \frac{\partial T_s}{\partial y} = 0$	$T_f = T_h$

The velocity vector has been considered positive if fluid flows from the cold side to the hot side, and is set to be negative otherwise. To opportunely model the fluid flow, both the left and right sides of the fluid are set as open boundary, since fluid can enter or leave the domain on either boundaries. The normal stress, namely pressure imposed on the open boundaries is set as a cyclical input signal to simulate the conveying fluid process with circulating pump according to real magnetocaloric cooling systems. Take 1Hz operating frequency as an example, Fig. 2 shows the input pressure profiles varying with time at edges 3 and 9.

3.3. Grid Independence Study

Taking account of the geometric characteristic of the parallel plate matrix, the geometric model containing two half thin plates and a single channel is meshed with 30,000 rectangular cells. The mesh is densified in the cold/hot side and the wall between solid and fluid, in view of the entrance effect and the boundary layer effect, respectively. Grid independence studies are performed with 3,000, 12,000, and 30,000 cells. In addition, the number of cells blow 3,000 leads to divergent results. However, these yields hardly any differences in terms of temperature, pressure or velocity fields.

Take temperature fields as an example, Fig. 3 shows the temperature profiles of magnetocaloric material in the x-direction after the hot blow and cold blow processes. Therefore, in the coming sessions, the grid with 30,000 rectangular cells is applied.

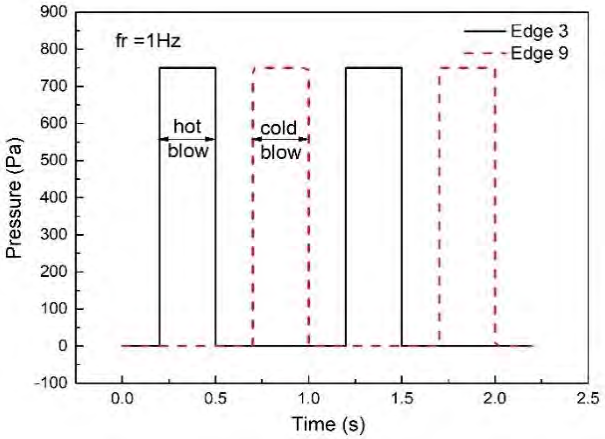

Figure 2: Pressure profiles varying with time at 1Hz at edges 3 and 9

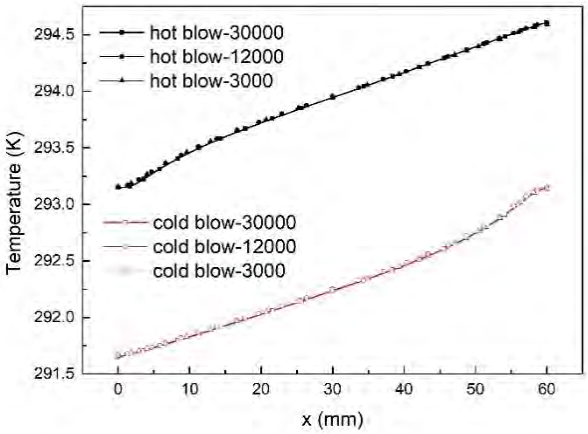

Figure 3: Temperature profiles in the x-direction after the hot blow and cold blow processes

4. NUMERICAL SIMULATIONS AND RESULTS

4.1. Heat Transfer Characteristics of the Parallel Plate Matrix

Convective heat transfer coefficient is the most important indicator, and thus it is used to evaluate the heat transfer performance between the solid and the fluid. The convective heat transfer coefficient is defined as the ratio of heat flux at the wall and the temperature difference between the solid and fluid. Eq. (5) shows the calculation method of the fluid average temperature across the y-direction section, taking the cross section A-A in Fig. 1 for example. The average heat flux, average temperature difference and convective heat transfer coefficient along the wall are defined as Eq. (6), Eq. (7) and Eq. (8), respectively (Yang and Tao 2006).

$$T_{\mathrm{b}} = \frac{\int_0^{b/2} T_{\mathrm{f}}(x,y)u(x,y)\mathrm{d}y}{\int_0^{b/2} u(x,y)\mathrm{d}y} \quad \text{Eq. (5)}$$

$$q''_{\mathrm{w}} = \int_0^{L} k_{\mathrm{s}} \frac{\partial T_{\mathrm{s}}}{\partial y}\mathrm{d}x / L = \int_0^{L} k_{\mathrm{f}} \frac{\partial T_{\mathrm{f}}}{\partial y}\mathrm{d}x / L \quad \text{Eq. (6)}$$

$$\Delta T = \int_0^{L} (T_{\mathrm{w}} - T_{\mathrm{b}})\mathrm{d}x / L \quad \text{Eq. (7)}$$

$$h = q''_{\mathrm{w}} / \Delta T \quad \text{Eq. (8)}$$

where T_{w} is the temperature at the wall. Fig. 4 shows that the operating frequency is a significant contributing factor to the convective heat transfer coefficient. By changing the operating frequency, both the fluid flow and the magnetization durations are changed, while the ratio between those two periods are remained constant, i.e. t_{mag}: t_{f} =2:3. Here, during the hot and cold blow processes, the pressure difference at the inlet and outlet is 750 Pa. The convective heat transfer coefficient presented in this paper is the average value of that from hot blow and that from cold blow.

According to the simulation results in Fig. 4, the convective heat transfer coefficient increases by more than 60% when the operating frequency increases from 1 Hz to 10 Hz. This is an important observation and a key message for the magnetocaloric cooling society, since it has been assumed that the convective heat transfer coefficient does not vary with how fast the system is cycled (Lei et al. 2015; Kamran et al. 2016). Instead, in the previous numerical studies of the AMR, the convective

heat transfer coefficient is determined based on the empirical correlations that are dependent on Reynolds number and properties of heat transfer fluid (Nickolay and Martin 2002). Furthermore, the variation of the convective heat transfer coefficient can be more than 50%, which is a significant factor that should not be omitted. In Fig. 4, the correlation-Ren curve is calculated as following. The Reynolds number, the Nusselt number, the Graetz number and convective heat transfer coefficient are defined as:

$$\mathrm{Ren} = ud_{\mathrm{h}} / \nu \qquad \text{Eq. (9)}$$

$$Gz = d_{\mathrm{h}} \mathrm{Ren}\,\mathrm{Pr}/ L \qquad \text{Eq. (10)}$$

$$Nu = (7.541^{3.592} + (1.841Gz^{1/3})^{3.592})^{1/3.592} \qquad \text{Eq. (11)}$$

$$h = Nuk_{\mathrm{f}} / d_{\mathrm{h}} \qquad \text{Eq. (12)}$$

where d_{h} is the hydraulic diameter; v is the kinematic viscosity , Pr is the Prandtl number of the fluid. The correlation-Ren curve decreases slightly with operating frequency because it takes some time for the velocity to reach its maximum instead of mutation, which is called delayed effect. The delayed effect is significant at high operating frequency, which leads to the reduced average velocity in the hot blow or cold blow process.

Under the limit of 0 Hz, the convective heat transfer coefficient calculated with the empirical correlations often shows excellent agreement with simulation results. Fig. 5 shows the *h*-Ren curves in the steady-state flow condition, in which the geometric model of fluid channel and the boundary conditions are the same as the parallel plate matrix model mentioned above. The deviation of *h* calculated with the simulation and correlations is less than 3%. However, as shown in Fig. 4, large error can be introduced to simulate the heat transfer performance of oscillating flow with the empirical correlations. Furthermore, the results in Fig. 5 can be viewed as an indirect experimental validation since the original correlation is developed by experimental data within 10% error. Not to mention that CFD for single-phase laminar flow is a very mature tool with high accuracy. Therefore, even without any direct support from experiments, the simulation results in the next sections are accurate. The observation from Fig. 4 and Fig. 5 indicate that the contribution of oscillating flow plays an important role in determining heat transfer characteristics of AMR. How to predict it is discussed next.

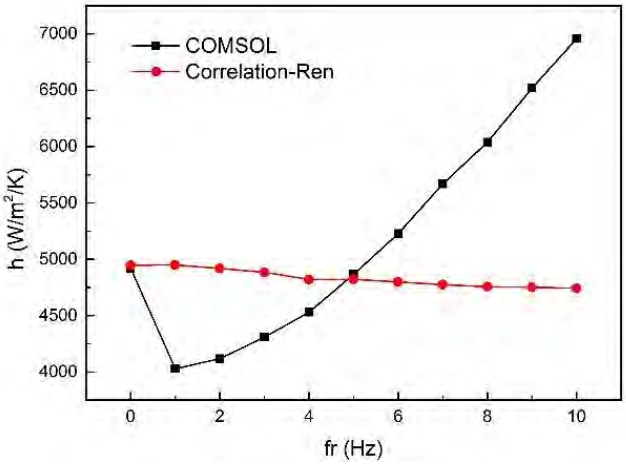

Figure 4: Convective heat transfer coefficient versus different operating frequency (Ren @ 0Hz = 228)

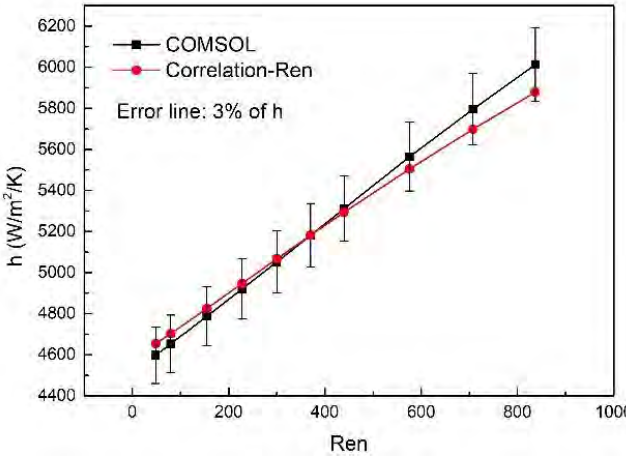

Figure 5: *h*-Ren curves in the steady-state flow (error-bars represent 3% deviation, 0 Hz)

4.2. Modifications to Current Convective Heat Transfer Coefficient Correlations

From engineering application perspective, it is essential to accurately evaluate the convective heat transfer coefficient at different operating frequencies, where the conventional empirical correlations are limited by significant uncertainties as illustrated by Fig. 4. The operating frequency is the most important parameter in an oscillating flow, which is similar to the oscillating flow mixer (OFM) for chemical equipment. In chemical engineering society, it has been well-accepted that the

performance of heat and mass transfer in a vessel can be improved by the oscillating flow (Shipman et al. 2004; Liu and Zhang 2007; Knowles et al. 2007). Therefore, the concept of the oscillating Reynolds number Reo is applied for AMR application, which is defined as Eq. (13). The Nusselt number is able to correlate the oscillating Reynolds number under the condition that Reo is much larger than Ren (Shipman et al. 2004; Liu and Zhang 2007; Knowles et al. 2007).

$$\mathrm{Reo} = \frac{2\pi f r x_0 d_h}{\nu} \qquad \text{Eq. (13)}$$

where *fr* and x_0 are the oscillating frequency and amplitude, respectively. Therefore, ideally the oscillating Reynolds number Reo can be used to replace Reynolds number Ren presented in any conventional correlations to calculate the convective heat transfer coefficient. The oscillating frequency and amplitude correspond to the operating frequency and the length of regenerator in the model, respectively. Fig. 6, Fig. 7, Fig. 8 compare the convective heat transfer coefficient calculated by simulation, correlations with Ren and correlations with Reo under 1 Hz, 5 Hz, and 10 Hz, respectively. Fig. 6 and Fig. 7 shows that the correlations with Reo cannot evaluate *h* accurately under the low operating frequency conditions. However, as was shown in Fig. 8, the correlations with Reo can obtain the equivalent *h* to the simulated results at 10 Hz operating frequency, where Reo is much larger than Ren.

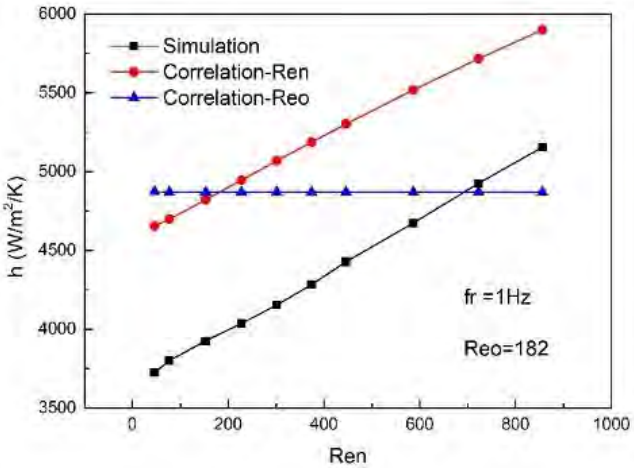

Figure 6: *h*-Ren curves at 1Hz operating frequency

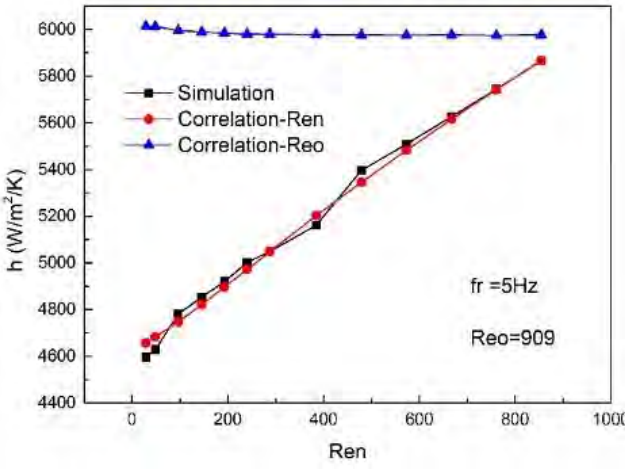

Figure 7: *h*-Ren curves at 5Hz operating frequency

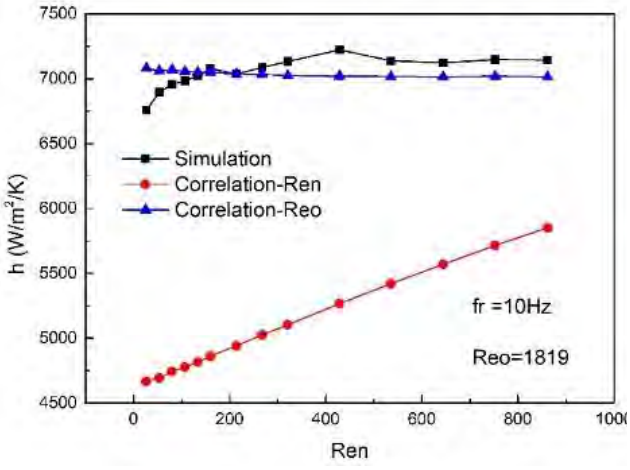

Figure 8: *h*-Ren curves at 10Hz operating frequency

From the above observations, it is clear that neither Ren nor Reo can be applied universally for any frequency or flow rate with acceptable uncertainties. To calculate *h* with correlations accurately at any operating frequency, both Reynolds number should be included as presented in Eq. (14), where the coefficient *m* and *n* reflect the contributions of these two Reynolds numbers to the convective heat transfer coefficient. Based on the results carried out for the parallel plate type AMR, the values

of coefficient *m* and *n* are listed for different operating frequency in Table 2. The two thresholds listed in Table 2 are 5 Hz and 10 Hz based on boundary conditions in this study. The values of these two threshold frequencies may vary, however, they represent the universal feature of AMR and magnetic cooling system with oscillating flow.

1) The first threshold defines "low frequency range" where the heat transfer performance degrades compared with steady state performance. Both Ren and Reo are required and Reo term has a negative coefficient. Unfortunately, due to insufficient time to complete the heat transfer, the current best performing magnetocaloric cooling systems are operated in this range (Jacobs et al. 2014; Eriksen et al. 2015; Fortkamp et al. 2018). This means that if a correlation developed by steady state experiment such as (Nickolay and Martin 2002) is applied for numerical simulation, the simulation results will over-predict the heat transfer and system performance. In other words, ways to improve the heat transfer performance in this range is crucial for AMR and magnetic cooling.
2) Between the first and second thresholds, this domain is the "medium frequency range" where the heat transfer performance is better than that of steady state. Both the Ren and Reo contributes positively to heat transfer and thus both of them should be taken into account for accurate prediction of *h*.
3) It can be considered as "high frequency" when the frequency is beyond the second threshold. The heat transfer coefficient *h* is considerably larger compared with that of steady state. Only Reo is required to predict the *h*. The effect of flow rate becomes negligible to the heat transfer coefficient. For system application, it means smaller flow rate could achieve the same heat transfer performance and therefore provides potential for efficiency improvement as well.

$$h = mf(\mathrm{Ren}) + nf(\mathrm{Reo}) \qquad \text{Eq. (14)}$$

Table 2. The coefficient *m* and *n* corresponding the operating frequency

fr	0	0 < fr ≤ Threshold 1	Threshold 1 < fr ≤ Threshold 2	fr > Threshold 2
m	1	1	0 ≤ m < 1	0
n	0	n ≤ 0	0 < n ≤ 1	1

5. CONCLUSIONS

In this paper, a transient two-dimensional model is built to investigate the heat transfer characteristics of the parallel plate matrix regenerator. From the simulations the following conclusions can be drawn:

1) Different from steady-state flow, the convective heat transfer coefficient in the parallel plate matrix depends on the operating frequency in addition to the fluid velocity because of the oscillating flow of fluid. Comparing with the steady state 0 Hz case, the heat transfer coefficient varies from -18% to 41%.
2) The frequency dependency of heat transfer coefficient can be predicted by a modified correlation based on the oscillating Reynolds number Reo in addition to the conventional Reynolds number Ren. In low and medium region, both Ren and Reo are required. However, in high frequency region, the heat transfer coefficient can be accurately predicted based on only Reo.

ACKNOWLEDGEMENTS

This study is financially sponsored by National Science Foundation of China under grant 51606140.

NOMENCLATURE

AMR	active magnetocaloric regenerator	T_b	average temperature of fluid (K)
b	thickness of flow channel (mm)	T_w	temperature of wall (K)
c	specific heat ($J \cdot kg^{-1} \cdot K^{-1}$)	ΔT	temperature difference (K)
d_h	hydraulic diameter (mm)	t_{mag}	magnetization/demagnetization time (s)
fr	operating frequency (Hz)	t_f	hot/cold blow time (s)
h	heat transfer coefficient ($W \cdot m^{-2} \cdot K^{-1}$)	t_{cyc}	an AMR cycle time (s)
k	thermal conductivity ($W \cdot m^{-1} \cdot K^{-1}$)	*u*	velocity in x-direction ($m \cdot s^{-1}$)

L	length of AMR (mm)	v	velocity in y-direction ($m \cdot s^{-1}$)
m	coefficient (-)	x_0	amplitude (m)
n	coefficient (-)	Greek letters	
Nu	Nusselt number (-)	ν	kinematic viscosity ($m^2 \cdot s^{-1}$)
Pr	Prandtl number (-)	μ	dynamic viscosity (Pa·s]
Q	heat source (W)	ρ	density($kg \cdot m^{-3}$)
q_w''	heat flux of wall ($W \cdot m^{-2}$)	Subscripts	
Ren	conventional Reynolds number (-)	s	solid
Reo	oscillating Reynolds number (-)	f	fluid

REFERENCES

Eriksen, D., Engelbrecht, K., Bahl, C. R. H., Bjørk, R., Nielsen, K. K., Insinga, A. R., and Pryds, N. 2015. Design and experimental tests of a rotary active magnetic regenerator prototype. International Journal of Refrigeration 58:14-21.

Fortkamp, F. P., Eriksen, D., Engelbrecht, K., Bahl, C. R. H., Lozano, J. A., and Jr, J. R. B. 2018. Experimental investigation of different fluid flow profiles in a rotary multi-bed active magnetic regenerator device. International Journal of Refrigeration:S1884651593.

Hirano, S., Kawanami, T., Ikegawa, M., Fumoto, K., and Hirasawa, S. 2011. Analytical Investigation on Regenerative Magnetic Refrigeration with Particle Packed Bed. Transactions of the Japan Society of Refrigerating & Air Conditioning Engineers 27 1:39-47.

Jacobs, S., Auringer, J., Boeder, A., Chell, J., Komorowski, L., Leonard, J., Russek, S., and Zimm, C. 2014. The performance of a large-scale rotary magnetic refrigerator. International Journal of Refrigeration 37 1:84-91.

Kamran, M. S., Ali, H., Farhan, M., Yong, B. T., Yun, G. C., and Hua, S. W. 2016. Performance optimisation of room temperature magnetic refrigerator with layered/multi-material microchannel regenerators. International Journal of Refrigeration 68:94-106.

Knowles, P., Kiger, K., and Scotti, A. 2007. Particle-turbulence interaction and sediment suspension from ripple beds in oscillatory flow. Paper read at Meeting of the Divison of Fluid Dynamics.

Lei, T., Engelbrecht, K., Nielsen, K. K., and Veje, C. T. 2015. Study of geometries of active magnetic regenerators for room temperature magnetocaloric refrigeration. Appl. Therm. Eng. 111:1232-1243.

Liu, H., and Zhang, C. Z. 2007. Numerical Simulation of Flow Field with Turbulence Model in an Oscillatory Flow Mixer. Petro-Chemical Equipment.

Moos, L. V., Nielsen, K. K., Engelbrecht, K., and Bahl, C. R. H. 2014. Experimental investigation of the effect of thermal hysteresis in first order material MnFe(P,As) applied in an AMR device. International Journal of Refrigeration 37 1:303-306.

Nickolay, M., and Martin, H. 2002. Improved approximation for the Nusselt number for hydrodynamically developed laminar flow between parallel plates. International Journal of Heat & Mass Transfer 45 15:3263-3266.

Nielsen, K. K., Engelbrecht, K., and Bahl, C. R. H. 2013. The influence of flow maldistribution on the performance of inhomogeneous parallel plate heat exchangers. International Journal of Heat & Mass Transfer 60 1:432-439.

Ram, N. R., Prakash, M., Naresh, U., Kumar, N. S., Sarmash, T. S., Subbarao, T., Kumar, R. J., Kumar, G. R., and Naidu, K. C. B. 2018. Review on Magnetocaloric Effect and Materials. Journal of Superconductivity & Novel Magnetism 7:1-9.

Shipman, T., Prasad, A., Davidson, S., and Cohee, D. 2004. Evaluation of Mixing Efficiency of a Novel Oscillatory Flow Mixer. American Physical Society.

Trevizoli, P. V., Lozano, J. A., Peixer, G. F., and Jr, J. R. B. 2015. Design of nested Halbach cylinder arrays for magnetic refrigeration applications. Journal of Magnetism & Magnetic Materials 395:109-122.

Tušek, J., Kitanovski, A., and Poredoš, A. 2013. Geometrical optimization of packed-bed and parallel-plate active magnetic regenerators. International Journal of Refrigeration 36 5:1456-1464.

Yang, S., and Tao, W. 2006. Heat Transfer (Forth Edition): Higher Education Press.

Manuscript ID: 404
DOI: 10.18462/iir.icr.2019.0404

R1224yd(Z) Flow Boiling inside a Mini Microfin Tube

G.A. Longo, S. Mancin, G. Righetti, C. Zilio

Dept. of Management and Engineering, University of Padova, Str.lla S. Nicola, 3, VICENZA, 36100-Italy

tony@gest.unipd.it, simone.mancin@unipd.it, righetti@gest.unipd.it, claudio.zilio@unipd.it

1. ABSTRACT

This paper presents the R1224yd(Z) flow boiling heat transfer and pressure drop measurements inside a mini microfin tube with internal diameter at the fin tip of 4.2 mm. The microfin tube was brazed inside a copper plate and electrically heated from the bottom. Sixteen T-type thermocouples are located in the copper plate to monitor the wall temperature. The experimental measurements were carried out at constant mean saturation temperature of 30°C, by varying the refrigerant mass velocity between 100 kg m^{-2} s^{-1} and 200 kg m^{-2} s^{-1}, the vapor quality from 0.3 to 0.95, at three different heat fluxes: 15, 30, 60 kW m^{-2}. The experimental results are presented in terms of two-phase heat transfer coefficient, onset dryout vapor quality, and frictional pressure drop. This new HFO fluid shows promising heat transfer capabilities, which makes it a possible viable substitute of the high-GWP, low-pressure refrigerants.

Keywords: R1224yd(Z), Low-GWP; Flow boiling; Microfin tube, Heat transfer, Pressure drop

2. INTRODUCTION

The R1224yd(Z) is a relatively new HFOs' molecule with GWP<1 and nearly-zero ODP. It has a normal boiling temperature around 14°C, which makes it suitable as blowing agent as well as refrigerant for electronics cooling application and for high temperature heat pumps and chillers.

Since late seventies, microfin tubes have received a lot of attention because they can assure higher heat transfer coefficients compared to smooth tubes, with a relatively small increase of pressure drop. In addition, by means of the fins along the circumference of the tube, microfin tubes facilitate the transition to annular regime, with consequent higher heat transfer coefficients than those during stratified regimes. Furthermore, the vapor quality at the onset of the dryout phenomenon is delayed. Over the last decades, traditional microfin tubes were largely studied, during both flow boiling and condensation. Experimental results regarding heat transfer coefficient, pressure drop, and vapor quality at the onset of the dryout are now available, as well as flow pattern maps and empirical equations for the estimation of those parameters, which can be used to design evaporators and condensers commonly used in traditional air conditioning and refrigeration systems. More recently, microfin tubes with internal diameter smaller than 5 mm are becoming more and more popular because they can be used in the next generation of air conditioning and refrigeration systems, leading to more compact and more efficient heat exchangers. Furthermore, the use of these mini microfin tubes may imply a relevant reduction of the refrigerant charge of the system, thus facing with the new stricter environmental regulations. For these reasons, large manufacturers are exploring the possible use of mini microfin tubes and there is a strong interest in understanding the heat transfer and pressure drop behaviors of these enhanced tubes.

The literature about small diameter microfin tubes (i.e. inner diameter lower than 6 mm or so) is still poor if compared with larger tubes. Among the most recent works, Righetti et al. (2018) experimentally studied the flow boiling heat transfer and pressure drop of R1233zd(E) in a small diameter microfin tube. The authors investigated the effects of the mass flux and of the heat flux on the heat transfer coefficient. Moreover, they evaluated the effects of the thermophysical properties evaluation on the current available models for heat transfer coefficient and pressure drop estimations. Kondou et al. (2013) investigated R32, R1234ze(E), and two R32/R1234ze(E) mixtures, (20:80) and (50:50) by wt.%, flow boiling inside a water heated microfin tube (inner diameter at the fin tip of 4.94 mm) at a saturation temperature of 10°C, heat fluxes of 10 and 15 kW m^{-2}, and mass velocities from 150 to 400 kg m^{-2} s^{-1}. Kondou et al. (2014a) also investigated R1234ze(Z) during flow boiling inside the same microfin tube at different saturation temperatures from 0 to 30°C and at a fixed heat flux equal to 10 kW m^{-2}. The Authors reported the experimental results relative to three

different refrigerant mass velocities, 150, 200, and 300 kg m^{-2} s^{-1}; the results showed that the heat transfer coefficients of R1234ze(Z) were slightly higher than those of R1234ze(E) and R134a at vapor quality values from 0.4 to the thermal crisis while they were slightly lower for vapor qualities lower than 0.4. Furthermore, Kondou et al. (2014b) investigated the boiling performance of high temperature glide refrigerant mixtures containing R1234ze(E) in blend with R744 and R32 (R744/R32/R1234ze(E), (4:43:53) and (9:29:62) by wt.%, inside the same water heated microfin tube, at 10°C of saturation temperature, 10 kW m^{-2} of heat flux and mass velocity ranging from 150 to 600 kg m^{-2} s^{-1}. The Authors compared the boiling results obtained for the ternary mixture with those of the pure fluids and with those obtained for other two binary mixtures of R32/R1234ze(E), (30:70) and (40:60) by wt.%. The heat transfer coefficients of the binary and ternary blends were drastically lower than those measured for the pure refrigerants because of the large mass transfer resistance, which seemed to suppress both the nucleate and forced convective contributions. Diani et al. (2014) compared R1234ze(E) against R134a in a 3.4 mm ID at the fin tip, electrically heated microfin tube at 30°C of saturation temperature by varying the mass velocity from 190 to 940 kg m^{-2} s^{-1} and the heat flux from 10 to 50 kW m^{-2}. The results showed that the flow boiling heat transfer coefficients measured for R1234ze(E) were lower, at least similar, to those for R134a, while the two refrigerants showed similar critical values of vapor quality and heat flux. The same Authors (Diani et al., 2015a) measured the flow boiling performance of R1234yf inside the same mini microfin tube at 30°C of saturation temperature. The Authors investigated the effects of the mass velocity, vapor quality, and heat flux and then compared the experimental data with that measured for R134a (Mancin et al., 2015). Diani et al. (2015b) and Diani and Rossetto (2015) studied R1234ze(E) and R1234yf and R134a, respectively, flow boiling inside a 2.4 mm microfin tube at 30°C of saturation temperature, mass velocity from 375 to 940 kg m^{-2} s^{-1}, and heat flux from 10 to 50 kW m^{-2}. For the R1234ze(E), the Authors found that at low heat flux, the heat transfer coefficient was highly affected by vapor quality, meaning that two phase forced convection was the mechanism which mainly controlled the flow boiling phenomenon. A different situation was found at high heat fluxes, where the heat transfer coefficient was not affected by mass velocity and weakly affected by vapor quality, meaning that the flow boiling process was mainly controlled by nucleate boiling.

Despite the recent work dealing mainly with HFOs listed above, the database for boiling of refrigerants inside relatively small diameter microfin tubes is still limited; furthermore, no data relative to R1224yd(Z) boiling inside microfin tubes can be retrieved in the open literature. This paper presents the R1224yd(Z) flow boiling heat transfer and pressure drop measurements inside a mini microfin tube with internal diameter at the fin tip of 4.2 mm. The experimental measurements were carried out at constant mean saturation temperature of 30°C, by varying the refrigerant mass velocity between 100 kg m^{-2} s^{-1} and 200 kg m^{-2} s^{-1}, the vapor quality from 0.3 to 0.95, at three different heat fluxes: 15, 30, and 60 kW m^{-2}. The experimental results are presented in terms of two-phase heat transfer coefficient, onset dryout vapor quality, and frictional pressure drop.

3. EXPERIMENTAL SETUP AND TEST SECTION

As shown in Fig. 1, the experimental test facility consists of three loops: refrigerant, cooling water, and hot water loops. The rig was designed for heat transfer and pressure drop measurements and flow visualization during either vaporization or condensation of pure refrigerants and refrigerants mixtures inside structured micro- and nano-geometries. The refrigerant is pumped through the circuit by means of a magnetically coupled gear pump, then it is vaporized in a Brazed Plate Heat Exchanger (BPHE) fed with hot water to achieve the desired value of vapor quality. The hot water is supplied by a thermostatic bath; both water flow rate and water temperature can be independently set. The heat flow rate exchanged at the BPHE evaporator is accurately measured by means of a magnetic flow meter and a calibrated T-type thermopile; furthermore, preliminary tests were run to verify the heat balance between refrigerant and water sides, the results showed a misbalance always less than 2%. The refrigerant enters the microfin test tube at a known mass velocity and vapor quality and then it is vaporized by means of a calibrated Ni-Cr wire resistance.

The electrical power supplied to the sample is indirectly measured by means of a calibrated reference resistance (shunt) and by the measurement of the effective electrical difference potential of the resistance wire inserted in the copper heater. The current can be calculated from the Ohm's law.

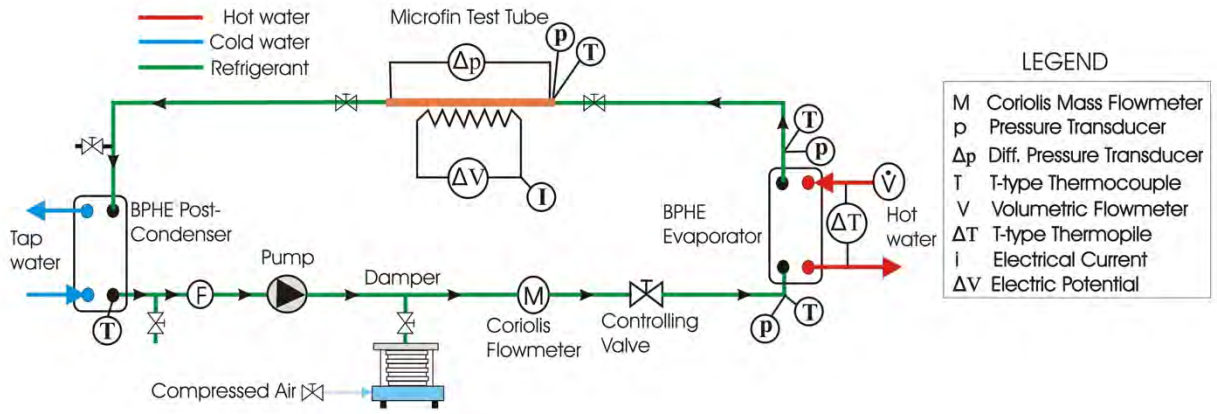

Figure 1: Schematic of the experimental setup

The fluid leaves the test section and enters in a post-condenser, a brazed plate heat exchanger fed with tap water, where it is fully condensed and subcooled. A damper connected to the compressed air line operates as pressure regulator to control the saturation conditions in the refrigerant loop. As shown in Fig. 1, the refrigerant pressure and temperature are measured at several locations throughout the circuit to know the refrigerant properties at the inlet and outlet of each heat exchanger. The refrigerant mass flow rate can be independently controlled by the gear pump and it is measured by means of a Coriolis effect flowmeter. No oil circulates in the refrigerant loop. Table 1 lists the values of uncertainty (k=2) of the instruments used in the experimental facility.

Table1. Instruments uncertainty

Transducer	Uncertainty (k=2)
T-type thermocouples	± 0.1 K
T-type thermopiles	± 0.05 K
Electric power	± 0.26% of the reading
Coriolis mass flowmeter (refrigerant loop)	± 0.10% of the reading
Magnetic volumetric flowmeter (hot water loop)	± 0.2% of FS= 0.33 10-3 m3 s-1
Differential pressure transducer (test section)	± 0.075% of 0.3 MPa
Absolute pressure transducers	± 0.065% of FS= 4 MPa

Table 2. Microfin tube geometry

Characteristic	Value
Outer Diameter	5 mm
Fin Tip Diameter, D	4.2 mm
Apex angle, γ	42°
Helix angle, β	18°
Number of fin, n	40
Fin height, h	0.15 mm
Tube thickness	0.23 mm

The mini microfin tube was brazed inside a guide milled on the top surface of a copper plate, which is 200 mm long, 10 mm wide, and 20 mm high. 16 holes were drilled just 1 mm below the microfin tube, in order to locate as many T-type thermocouples to monitor the wall temperature distribution. Another guide was milled on the bottom side of the copper plate, to host a Nickel-Chrome wire resistance connected to a DC current generator, which supplies the heat flow rate needed to vaporize the refrigerant flowing inside the tube. In order to avoid the abrupt pressure drops due to flow contraction and expansion, a suitable smooth connection to the refrigerant circuit having the same fin tip diameter (D=4.3 mm) was designed and realized to join the test tube with inlet and outlet pipes. Pressure ports are located about 25 mm downstream and upstream of the copper plate, thus the length for pressure drop measurements is 250 mm.
The test section is located inside an aluminum housing filled with 15 mm thick ceramic fiber blanket, to minimize the heat losses due to conduction to the ambient. Table 2 summarizes the main

geometrical characteristics of the tested tube. Given the reported dimensions, the area enhancement with reference to the smooth tube having the same fin tip diameter is equal to 1.62.

4. DATA REDUCTION

As described in the previous section, the subcooled liquid pumped by the magnetically coupled gear pump is vaporized into a BPHE fed with hot water. Thus, the vapor quality at the inlet of the test section can be calculated from a thermal balance at the evaporator, as:

$$q_{evap} = \dot{m}_w \cdot c_{p,w} \cdot \left(t_{w,in} - t_{w,out}\right) = \dot{m}_r \cdot \left(J_{in,TS} - J_{L,sub}\right) \quad \text{Eq. (1)}$$

where $\dot{m}_w$ is the water mass flow rate, $c_{p,w}$ is the specific heat capacity of the water, $t_{w,in}$ and $t_{w,out}$ are the inlet and outlet water temperatures. The right-hand side term of Eq. (1) reports the refrigerant side heat flow rate where $\dot{m}_r$ is the refrigerant mass flow rate while $J_{in,TS}$ and $J_{L,sub}$ are the unknown specific enthalpy at the inlet of the test section and the specific enthalpy of the subcooled liquid entering the BPHE, respectively. Once calculated $J_{in,TS}$, the vapor quality at the inlet of the test section can be estimated by:

$$x_{in,TS} = \frac{J_{in,TS} - J_L}{J_V - J_L} \quad \text{Eq. (2)}$$

where J_L and J_V are the specific enthalpies of the saturated liquid and vapor, respectively, evaluated at the saturation pressure of the refrigerant measured at the inlet of the test section. As already described, the electrical power supplied to the sample is indirectly measured by means of a calibrated reference resistance (shunt) and by the measurement of the effective electrical difference potential of the resistance wire inserted in the copper heater. Preliminary heat transfer measurements permitted to estimate the heat loss (q_{loss}) due to conduction through the test section as a function of the mean wall temperature. The tests were run under vacuum conditions on the refrigerant channel by supplying the power needed to maintain the mean wall temperature at a set value. The measurements were carried out by varying the mean wall temperature from 28°C to 63°C. The results show that the heat loss increases linearly as the mean wall temperature increases (R>0.99). In the tested range of wall temperature, the heat loss by conduction through the test section can be estimated by:

$$|q_{loss}| = 0.2006 \cdot \bar{t}_{wall}\ [°C] - 4.6698 \quad [W] \quad \text{Eq. (3)}$$

thus, the actual heat flow rate q_{TS} supplied to the sample is given by:

$$q_{TS} = P_{EL} - |q_{loss}| = \Delta V \cdot I - |q_{loss}| \quad \text{Eq. (4)}$$

It is worth underlying that the qloss varied from 1.5% to 4.6% of the electrical power supplied. The mean vapor quality, x_{mean} is the average value between the inlet and outlet ones. The two-phase heat transfer coefficient *HTC*, referred to the nominal area *A*, can be defined as:

$$HTC = \frac{q_{TS}}{A \cdot (\bar{t}_{wall} - \bar{t}_{sat})} = \frac{q_{TS}}{\pi \cdot D \cdot L \cdot (\bar{t}_{wall} - \bar{t}_{sat})} \quad \text{Eq. (5)}$$

where $\bar{t}_{wall}$ and $\bar{t}_{sat}$ are defined by the followings:

$$\bar{t}_{wall} = \frac{1}{16}\sum_{i=1}^{16} t_{wall,i} \text{ and } \bar{t}_{sat} = \frac{t_{sat,in}(p_{sat,in}) + t_{sat,out}(p_{sat,out})}{2} \quad \text{Eq. (6)}$$

The hydraulic performance of the microfin tube is given in terms of frictional pressure drop, which was calculated from the measured total pressure drop by subtracting the momentum and gravitational pressure gradients, as:

$$\Delta p_f = \Delta p_t - \Delta p_c - \Delta p_a \quad \text{Eq. (7)}$$

The momentum pressure drops were estimated by the separated model for two-phase flow using

the void fraction calculated with Rouhani and Axelsson (1970) model. Thermodynamic and transport properties are estimated from RefProp v.10 (Lemmon et al., 2018). A detailed error analysis was performed in accordance with Kline and McClintock (1953) using the values of the uncertainty of the instruments listed in Table 1; it was estimated that the uncertainty (k=2) on the two-phase heat transfer coefficient showed a mean value of around ±8%, while the uncertainty on the vapor quality was ±0.03. The pressure drops showed a mean uncertainty of around 8%.

5. EXPERIMENTAL RESULTS

This section presents the experimental results collected during vaporization of the R1224yd(Z) inside the mini microfin tube. The data were collected at constant, mean saturation temperature of 30°C. Table 3 lists the main thermo-physical properties of the R1224yd(Z) at this reference saturation temperature. This refrigerant can be classified as a low-pressure fluid; its critical pressure is 33.4 bar and thus, at these operating conditions, it has a very low reduced pressure, around 0.053. In addition, it has a high saturation temperature drop gradient, around 16.7 K bar^{-1}, a relevant difference between the liquid and vapor densities (ρ_L/ρ_V=121), and a great surface tension, (12.9 mN m^{-1}). It is well known that actual flow boiling heat transfer inside a tube is the result of the combination of the two main heat transfer mechanisms: nucleate boiling and forced convective boiling. Different scenarios can occur as a function of the actual operating test conditions (i.e., mass velocity, vapor quality, and heat flux), thermo-physical properties, and reduced pressure.

Table3. Thermo-physical properties of the R1224yd(Z) at t_{sat}= 30°C. (Lemmon et al., 2018)

p_{sat}	ρ_L	ρ_V	r	λ_L	λ_V	μ_L	μ_V	σ
[bar]	[kg m^{-3}]		[kJ kg^{-1}]	[W m^{-1} K^{-1}]		[μPa s]		[mN m^{-1}]
1.547	1250.6	8.5	188.5	0.073	0.019	470	11.1	13.9

In particular, mass velocity, vapor density, and vapor quality mainly affect the forced convective contribution while heat flux and reduced pressure mainly affect the nucleate boiling. Considering the thermo-physical properties reported in Table 3, this fluid exhibits very low vapor density and high surface tension, which might promote the forced convective boiling rather than the nucleate boiling which is also limited by the very low reduced pressure. These considerations are confirmed by the experimental results plotted in Fig. 2 and Fig. 3 where the effects of the mass velocity and of the heat flux are reported. In particular, Fig. 3 shows the effect of mass velocity on the heat transfer coefficient as a function of mean vapor quality at an imposed heat flux of HF=15 kW m^{-2}. At these operating test conditions, the vapor quality change between inlet and outlet of the test section varies from 0.09 to 0.17. It clearly appears that at all the investigated mass velocities, the heat transfer coefficient increases almost linearly with the vapor quality, meaning that the two-phase forced convection is mainly affecting in the phase-change process. At constant vapor quality, when passing from 100 kg m^{-2} s^{-1} to 150 kg m^{-2} s^{-1}, also the heat transfer coefficient increases. However, the heat transfer coefficients measured at 200 kg m^{-2} s^{-1} are almost similar to those collected at 150 kg m^{-2} s^{-1}. This behavior might be due to the saturation temperature drop related to the high two-phase pressure drops, which increases with both mass velocity and vapor quality. The vapor quality at the onset of the dryout phenomenon occurs earlier at low mass velocity; in fact, it was observed at x_{mean}=0.6, x_{mean}=0.8, and x_{mean}=0.85 at G=100 kg m^{-2} s^{-1}, G=150 kg m^{-2} s^{-1}, and G=200 kg m^{-2} s^{-1}, respectively.

Fig. 3 shows the effect of heat flux on heat transfer coefficient at a mass velocity equal to 200 kg m^{-2} s^{-1}. Considering the results depicted in Fig. 3, it can be stated that at heat flux lower than 30 kW m^{-2}, there is not any noticeable effect of this parameter on the boiling heat transfer, the heat transfer coefficients are almost the same, and they strongly increase with vapor quality. For example, passing from x_{mean}=0.3 to x_{mean}=0.6, the heat transfer coefficient increases from around 7500 W m^{-2} K^{-1} to more that 10500 W m^{-2} K^{-1} When increasing the heat flux to 60 kW m^{-2}, the heat transfer coefficient shows a different behavior: at low vapor quality, the heat transfer coefficients were remarkably higher than those measured at low vapor quality and then they only slightly increased with vapor quality, meaning that the nucleate boiling is affecting the phase change process.

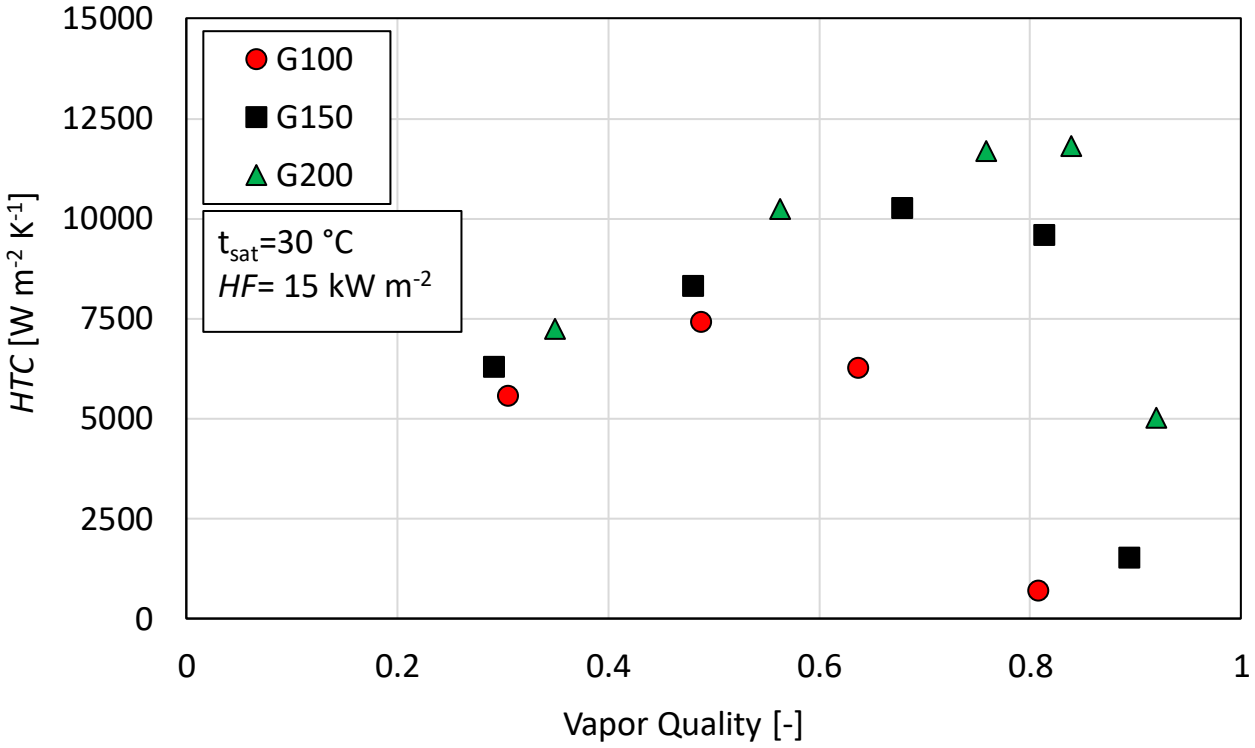

Figure 2: Effect of mass velocity on heat transfer coefficient at *HF*=15 kW m^{-2}.
***G* expressed in [**kg m^{-2} s^{-1}**]**

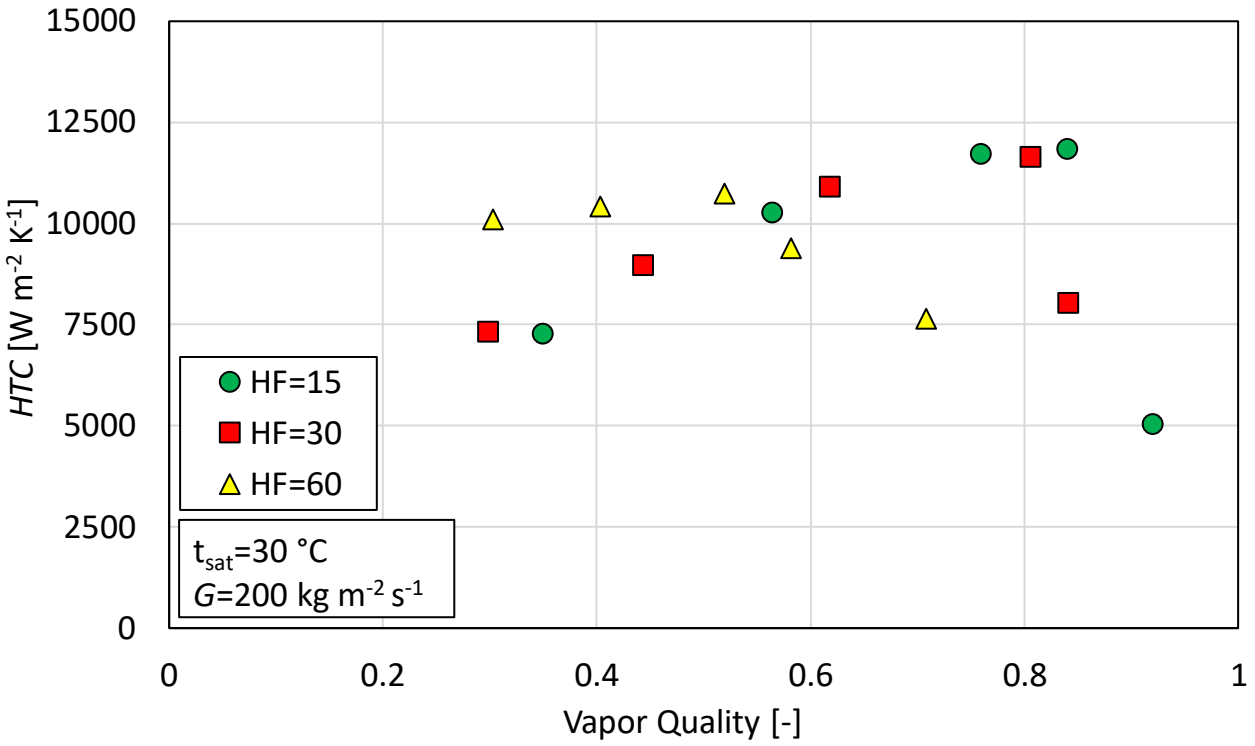

Figure 3: Effect of heat flux on heat transfer coefficient at *G*=200 kg m^{-2} s^{-1}.
***HF* expressed in [**kW m^{-2}**].**

The vapor quality at the onset of the dryout phenomenon occurs earlier as the heat flux increases; in fact, it was observed at x_{mean}=0.85, x_{mean}=0.8, and x_{mean}=0.55 at *HF*=15 kW m^{-2}, *HF*=30 kW m^{-2}, and *HF*=60 kW m^{-2}, respectively.
The experimental frictional pressure gradients are plotted in Fig. 4 as a function of the mean vapor quality, for the sake of clarity, only data relative to an imposed heat flux of 15 kW m^{-2} are reported. The results show that the frictional pressure gradient increases with both the mass velocity and vapor quality.

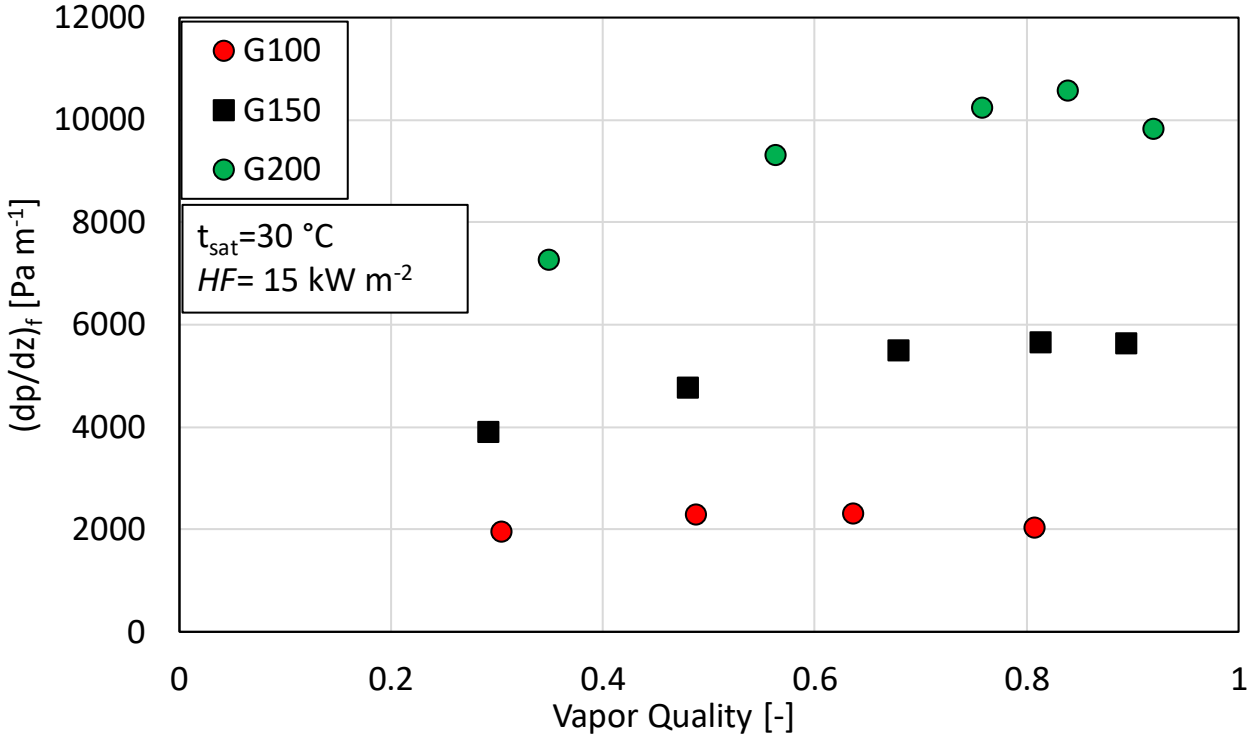

Figure 4: Two-phase frictional pressure drop plotted against the vapor quality as a function of the refrigerant mass velocity, *G* expressed in [kg m^{-2} s^{-1}].

6. CONCLUSIONS

The paper presents experimental heat transfer coefficients and pressure drops measured during R1224yd(Z) flow boiling inside a mini microfin tube with an inner diameter at the fin tip of 4.2 mm. Tests were run at a constant mean saturation temperature of 30°C, by varying the vapor quality from 0.3 to 0.95, the mass velocity from 100 to 200 kg m^{-2} s^{-1}, and the heat flux from 15 to 60 kW m^{-2}. The results confirm that the heat transfer process is controlled by the two main mechanisms that govern the flow boiling phenomenon, i.e. nucleate boiling and two-phase forced convection, and that the prevailing one depends upon the actual operating test conditions. In general, it can be stated that for this low pressure refrigerant, the two-phase forced convection seems to be prevailing over the nucleate boiling. The two-phase frictional pressure drops were also measured. They increase with both mass velocity and vapor quality. Finally, the results highlight the promising heat transfer capabilities of mini microfin tubes during flow boiling; nevertheless, additional heat transfer measurements with different tube diameters, different helical geometries, and different type of refrigerants are surely needed.

7. NOMENCLATURE

A	area (m^2)	*t*	temperature (°C)
$c_{p,w}$	water specific heat capacity (J kg^{-1} K^{-1})	*v*	specific volume (m^3 kg^{-1})
D	fin tip diameter (m)	*x*	vapor quality (-)
G	mass velocity (kg m^{-2} s^{-1})	*Greek symbols*	
h	fin height (m)	Δ	variation

HTC	heat transfer coefficient (W m^{-2} K^{-1})	β	helix angle (°)
HF	heat flux (W m^{-2})	γ	apex angle (°)
J	specific enthalpy (J kg^{-1})	λ	thermal conductivity (W m^{-1} K^{-1})
k	coverage factor (-)	μ	dynamic viscosity (Pa s)
I	electrical current (A)	σ	surface tension (N m^{-1})
L	heated length (m)	*Subscripts*	
$\dot{m}$	mass flow rate (kg s^{-1})	*in*	inlet
n	fin number (-)	*f*	frictional
p	pressure (Pa)	*L*	liquid
P_{EL}	electrical power (W)	*out*	outlet
q	heat flow rate (W)	*r*	refrigerant
r	latent heat of vaporization (J kg^{-1})	*TS*	test section
s	thickness (m)	*w*	water

8. ACKNOWLEDGEMENTS

This research project was partially funded by: CariVerona Foundation, Verona, Italy, Ricerca Scientifica e Tecnologica 2016-2019: “Sostenibilità e autenticazione nutrizionale di filiere lattiero-casearie a tutela del consumatore”. AGC Inc. Chemicals Company (Japan), Wieland-Werke AG, and Generalmeccanica Snc are gratefully acknowledged.

9. REFERENCES

Diani, A., Mancin, S., Rossetto, L., 2014. R1234ze(E) flow boiling inside a 3.4 mm ID microfin tube, Int. J. Refrigeration, 47, 105-119.

Diani, A., Mancin, S., Rossetto, L., 2015a. Flow boiling heat transfer of R1234yf inside a 3.4 mm ID microfin tube, Experimental Thermal and Fluid Science, 66, 127–136.

Diani, A., Mancin, S., Cavallini, A., Rossetto, L., 2015b. R1234ze(E) Flow Boiling Heat Transfer and Pressure Drop Inside a 2.4 mm Microfin Tube, Proc. of ICR 2015, August 16 - 22 - Yokohama, Japan, Paper 549.

Diani, A., Rossetto, L., 2015. Vaporization inside a mini microfin tube: experimental results and modeling, Journal of Physics: Conference Series, 655, 012032.

Kline, S.J., McClintock, F.A., 1953. Describing uncertainties in single-sample experiments. Mech. Eng., 75, 3–8.

Kondou, C., Baba, D., Mishima, F., Koyama, S., 2013, Flow boiling of non-azeotropic mixture R32/R1234ze(E) in horizontal microfin tubes, Int. J. Refrig., 36, 2366-2378.

Kondou, C., Mishima, F., Liu, J.F., Koyama, S., 2014a. Condensation and Evaporation of R134a, R1234ze(E) and R1234ze(Z) Flow in Horizontal Microfin Tubes at Higher Temperature, Proc. of International Refrigeration and Air Conditioning Conference at Purdue, West Lafayette, IN, USA, Paper 1446.

Kondou, C., Mishima, F., Liu, J.F., Koyama, S., 2014b. Condensation and Evaporation of R744/R32/R1234ze(E) Flow in Horizontal Microfin Tubes, Proc. of International Refrigeration and Air Conditioning Conference at Purdue, West Lafayette, IN, USA, Paper 1448.

Lemmon, E.W., Bell, I.H., Huber, M.L., McLinden, M.O. NIST Standard Reference Database 23: Reference Fluid Thermodynamic and Transport Properties-REFPROP, Version 10.0, National Institute of Standards and Technology, Standard Reference Data Program, Gaithersburg, 2018.

Mancin, S., Diani, A., Rossetto, L. 2015. Experimental Measurements of R134a Flow Boiling Inside a 3.4-mm ID Microfin Tube, Heat Transfer Engineering, 36(14-15), 1218-1229.

Righetti, G., Longo, G.A., Zilio, C., Akasaka, R., Mancin, S., 2018, R1233zd(E) flow boiling inside a 4.3 mm ID microfin tube, International Journal of Refrigeration, 91, pp. 69-79.

Manuscript ID: 408
DOI: 10.18462/iir.icr.2019.0408

R1233zd(E) and R1234ze(Z) condensation inside a 4 mm horizontal smooth tube

Giovanni A. LONGO, Simone MANCIN, Giulia RIGHETTI, Claudio ZILIO

Department of Management and Engineering, University of Padova,
Vicenza, I-36100, Italy
tony@gest.unipd.it, simone.mancin@unipd.it, giulia.righetti@unipd.it, claudio.zilio@unipd.it

ABSTRACT

R1233zd(E) and R1234ze(Z) have been proposed as low Global Warming Potential (GWP) refrigerants for high temperature heat pumps. But their application is still not widespread and their heat transfer performance are still poorly investigated. This paper investigates the effects of refrigerant mass flux and mean vapor quality on experimental heat transfer coefficients and frictional pressure drops measured during R1233zd(E) saturated vapor condensation inside a 4 mm ID horizontal smooth copper tube. New experimental tests were carried out at 40 °C of saturation temperature, with refrigerant mass flux in the range 75–200 kg m $^{-2}$ s $^{-1}$ at decreasing vapor quality. The data are compared against some well-known literature correlations and against other experimental data collected by using R1234ze(Z) as two-phase fluid under the same testing conditions.

1. INTRODUCTION

R1233zd(E) and R1234ze(Z) are environmentally friendly molecules proposed to substitute R245fa and other low-pressure high-GWP fluids in many applications (see for instance McLinden et al*., 2014).* R1233zd(E) has GWP=1, close to zero ODP and a normal boiling temperature around 19°C, which makes it suitable as blowing agent as well as refrigerant for electronics cooling application and for high temperature heat pumps and chillers (Righetti et al, 2018). It seems to be advantageous also if applied to Organic Rankine Cycles (ORCs) working with low temperature (t<150 °C) heat sources (Li et al, 2017). For instance, four R1233zd(E) chillers, 26 MW refrigeration each, have been installed to replace the existing R22 ones in order to maintain the Channel Tunnel temperature below 30°C.

R1234ze(Z) is a HFO molecule with zero ODP, an atmospheric lifetime of 10 days (Akasaka et al., 2014) and a GWP lower than 1 (Hodnebrog et al., 2013). Furthermore, it is not toxic and classified as mild-flammable (A2L). In 2009, Brown et al. (2009) were the first Authors to propose R1234ze(Z), as an environmentally friendly substitute of R114 in high temperature heat pumps, thanks to its favorable thermophysical and transfer properties, a critical temperature of 150 °C, a normal boiling point around 9.7 °C, and a relatively high latent heat and thermal conductivity, among others (Lemmon et al., 2017). During years, it has been also proposed as suitable refrigerant for high-temperature applications (Hu et al., 2017) and environmentally friendly drop-in replacement (Giuffrida and Pezzuto, 2017). Longo et al. (2014) measured heat transfer coefficient and pressure drop of R1234ze(Z) during saturated vapor condensation inside a commercial Brazed Plate Heat Exchanger (BPHE).

This paper presents some new experimental tests carried out at 40 °C of saturation temperature, with refrigerant mass flux in the range 75–200 kg m $^{-2}$ s $^{-1}$ at decreasing vapor quality during R1233zd(E) condensation inside a 4 mm smooth tube. Average heat transfer coefficients and frictional pressure drop are analyzed. Following, R1233zd(E) is compared against R1234ze(Z) under the same working conditions.

2. EXPERIMENTAL MEASUREMENTS AND DATA REDUCTION

The experimental facility, shown in Fig. 1, consists of a refrigerant circuit, a water-glycol loop and a refrigerated / cooling water loop. In the first loop the refrigerant is pumped from the sub-cooler into the pre-evaporator, a brazed plate heat exchanger, where it is partially evaporated to achieve the set quality at the inlet of the tubular test section. The refrigerant goes through the test section where it is evaporated and then it comes back to a condenser and a sub-cooler, both brazed plate heat exchangers. A variable speed volumetric pump varies the refrigerant flow rate, whereas a bladder accumulator connected to a nitrogen bottle and a pressure regulator controls the operating pressure in the refrigerant loop. The second loop is able to supply a water-glycol flow at a constant temperature in the range of -10 to 30 °C with a stability within ±0.1 K used to feed the sub-cooler and the condenser, whereas the third loop supplies a refrigerated water flow at a constant temperature in the range of 3 °C to 30 °C with a stability within ±0.1 K used to feed the test section and the pre-evaporator.

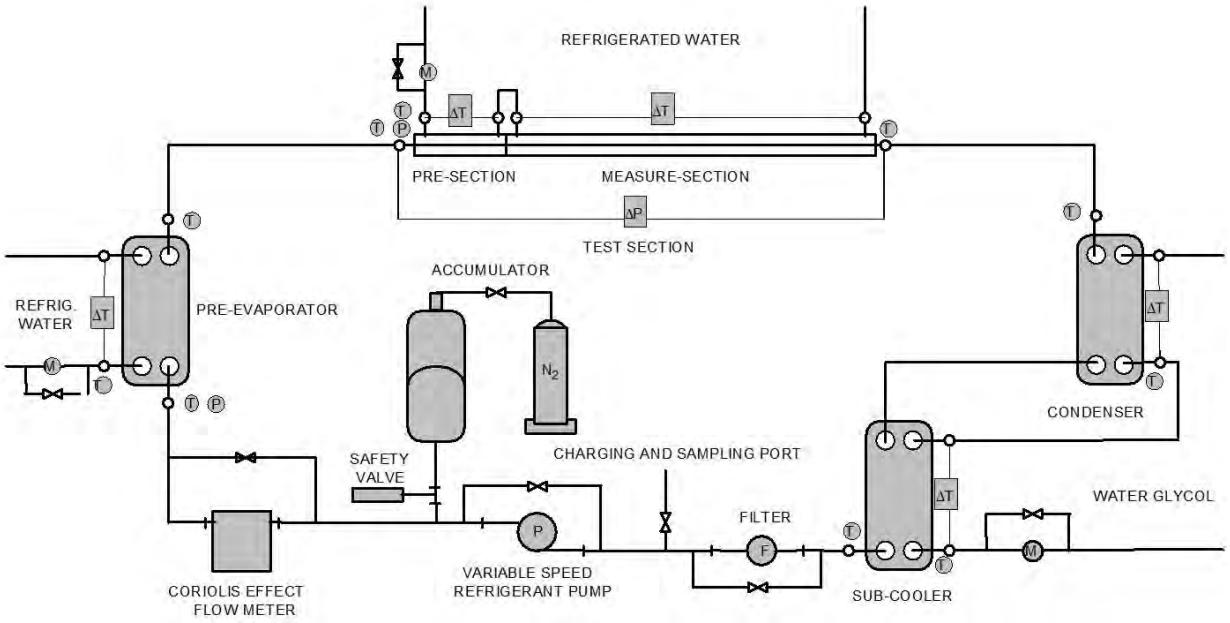

Figure 1: Schematic view of the experimental test rig

The test-section (Fig.2) is a double tube condenser in which the refrigerant vapor condenses in the inner tube while the cooling water flows in the annulus. The test-section is subdivided into two different parts: a pre-section, 200 mm long, in which the refrigerant flow achieves a fully developed flow regime and the measurement section, 800 mm long, in which the heat transfer coefficient is measured. This arrangement is obtained using a single inner smooth tube, 4 mm ID, 1300 mm long and two separated cooling water jackets fed in series. The inner tube is instrumented with four copper-constantan thermocouples embedded in its wall to measure surface temperature. The thermocouples are inserted into two equidistant axial grooves, at the top and the bottom of the cross section, 100 mm from the inlet and outlet of the cooling water. Each groove is sealed with a copper wire fixed by epoxy.

The main features of the different measuring devices are reported in Table 1.

The experimental results are reported in terms of condensation average heat transfer coefficients HTC_r and frictional pressure drop Δp_f. The condensation average heat transfer coefficient HTC_r is equal to the ratio between the heat flow rate Q, the heat transfer area A and the mean temperature difference ΔT:

$$HTC_r = Q / (A\,\Delta T) \qquad \text{Eq. (1)}$$

The heat flow rate Q is derived from a thermal balance on the water-side of the measurement section, the heat transfer area, named A, of the measurement section is equal to the area of the inner surface of the test tube, and the mean temperature difference ΔT is equal to the difference between the arithmetical mean value of the reading of the four thermocouples embedded in the tube wall and the average saturation temperature, derived from the average pressure on refrigerant side.

The frictional pressure drop on the refrigerant side Δp_f is computed by subtracting the inlet / outlet local pressure drop Δp_c, and adding the momentum pressure recovery Δp_a from the total pressure drop measured Δp_t:

$$\Delta p_f = \Delta p_t - \Delta p_c + \Delta p_a \qquad \text{Eq. (2)}$$

Being the test section horizontal, no gravity pressure drops Δp_g occur. For a more detailed data reduction, please refer to Longo et al. (2017).

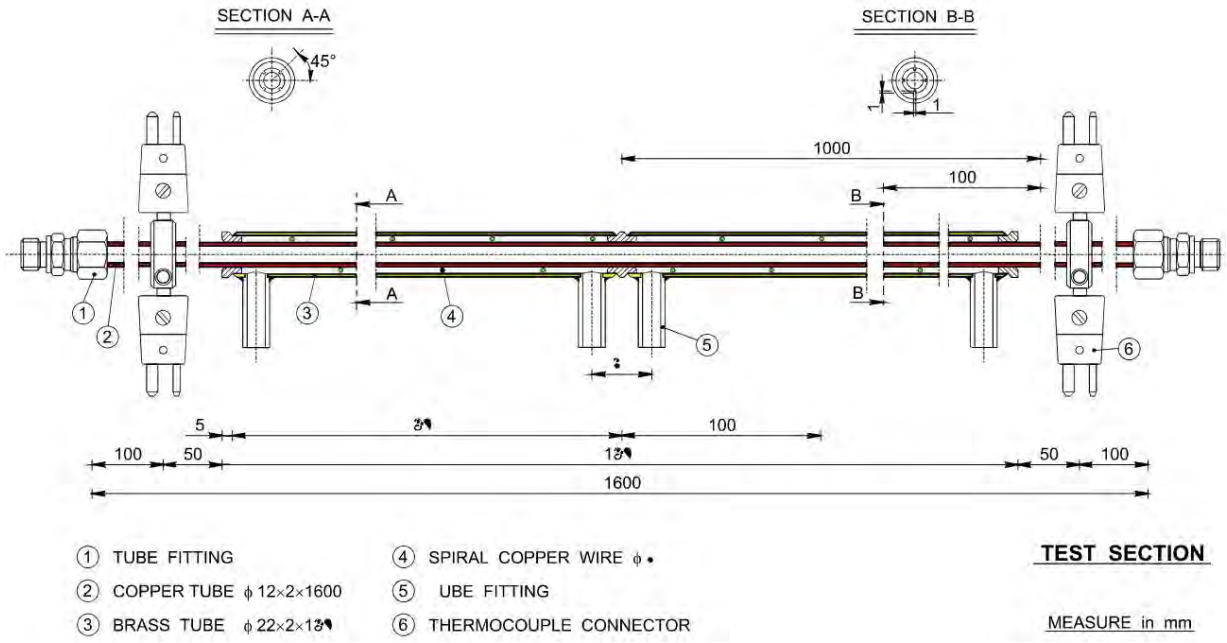

Figure 2: Schematic view of the test section

Table 1. Specification of the different measuring devices

Devices	Uncertainty (k=2)	Range
T-type thermocouples	0.1 K	-20/80 °C
T-type thermopiles	0.05 K	-20/80 °C
Abs. pressure transducers	0.075 % f.s.	0/3.0 MPa
Diff. pressure transducers	0.075 % f.s.	0/0.3 MPa
Coriolis effect flow meters	0.1 %	0/300 kg h^{-1}
Magnetic flow meters	0.15 % f.s.	100/1200 l h^{-1}
Data logger	± 2.7 µV	0/100 mV

3. ANALYSYS OF THE EXPERIMENTAL RESULTS

24 R1233zd(E) experimental condensation tests with refrigerant and water counter-flow was carried out at a saturation temperature of 40 °C, at decreasing vapor quality up to a subcooled liquid condition. They were then compared against 24 experimental tests collected under the same working conditions during R1234ze(Z) condensation in the same test rig. A detailed error analysis performed in accordance with Kline and McClintock (1953) indicates an overall uncertainty within ±14 % and ±18 % for the R1234ze(Z) and R1233zd(E) heat transfer coefficient measurements, respectively and within ±24 % and ±21 % for the total pressure drop, respectively.

Fig. 3 and Fig. 4 show the R1233zd(E) and R1234ze(Z) condensation heat transfer coefficient *HTC* against mean vapor quality at 40 °C saturation temperature and four different refrigerant mass fluxes, namely G=75, 100, 150, and 200 kg m^{-2} s^{-1}. In all the reported measurements, the vapor quality change along the test section was always lower than 0.3.

During condensation inside smooth tubes, the two main dominant heat transfer regimes are gravity controlled and forced convection condensation. In the first regime the condensate drainage, and therefore the heat transfer coefficient, is mainly affected by gravity. It occurs at low vapor quality and low mass fluxes. Whereas, in the second regime the vapor shear controls the two-phase heat transfer mechanism. By analyzing Fig. 3 and Fig. 4, one can notice that heat transfer coefficients increase with the vapor quality, and the slope becomes higher at higher refrigerant mass fluxes, indicating a dominant effect of the forced convection condensation mechanism.
Fig. 5 and Fig. 6 show the R1233zd(E) and R1234ze(Z) condensation frictional pressure drop, evaluated accordingly Eq. (2), against refrigerant mass flux at 40°C of saturation temperature and five different refrigerant mass fluxes, namely G=75, 100, 150, and 200 kg m^{-2} s^{-1}. Frictional pressure drops lower than 2000 Pa were not taken into account, since such data should be affected by a too large uncertainty. As expected, frictional pressure drop increases with the mass flux and the vapor quality.

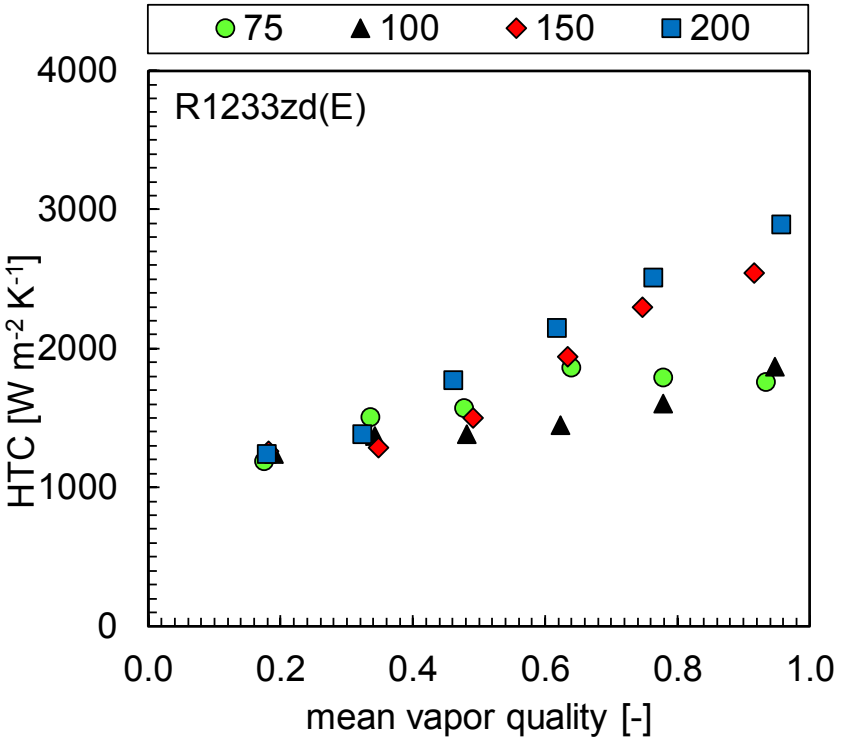

Figure 3: R1233zd(E) condensation heat transfer coefficient vs. vapor quality at 40 °C saturation temperature and mass flux equal to 75, 100, 150, and 200 kg m^{-2} s^{-1}

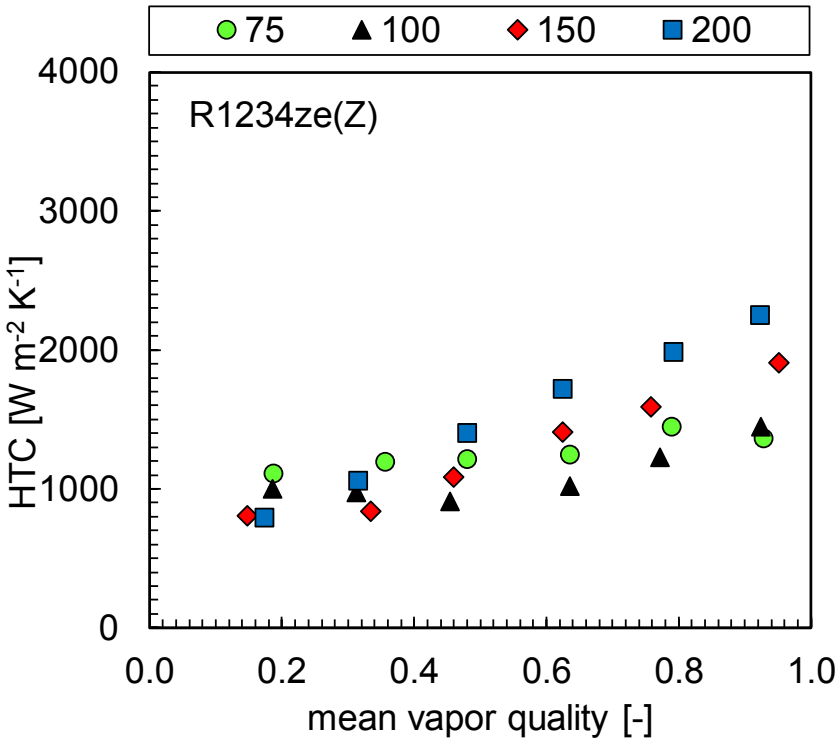

Figure 4: R1234ze(Z) condensation heat transfer coefficient vs. vapor quality at 40 °C saturation temperature and mass flux equal to 75, 100, 150, and 200 kg m^{-2} s^{-1}

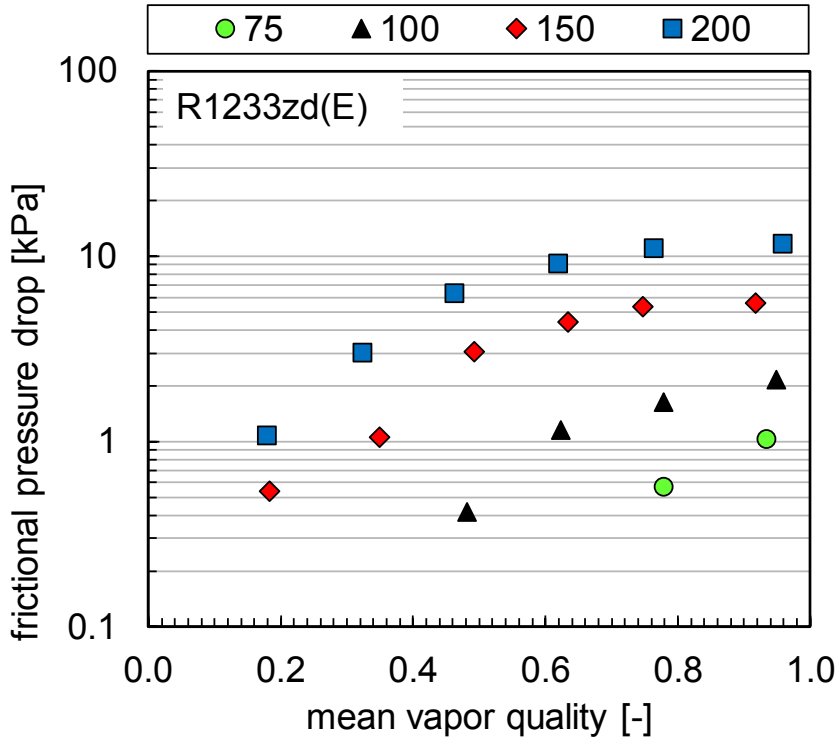

Figure 5: R1233zd(E) condensation frictional pressure drop vs. vapour quality at 40 °C saturation temperature and mass flux equal to 75, 100, 150, and 200 kg m^{-2} s^{-1}

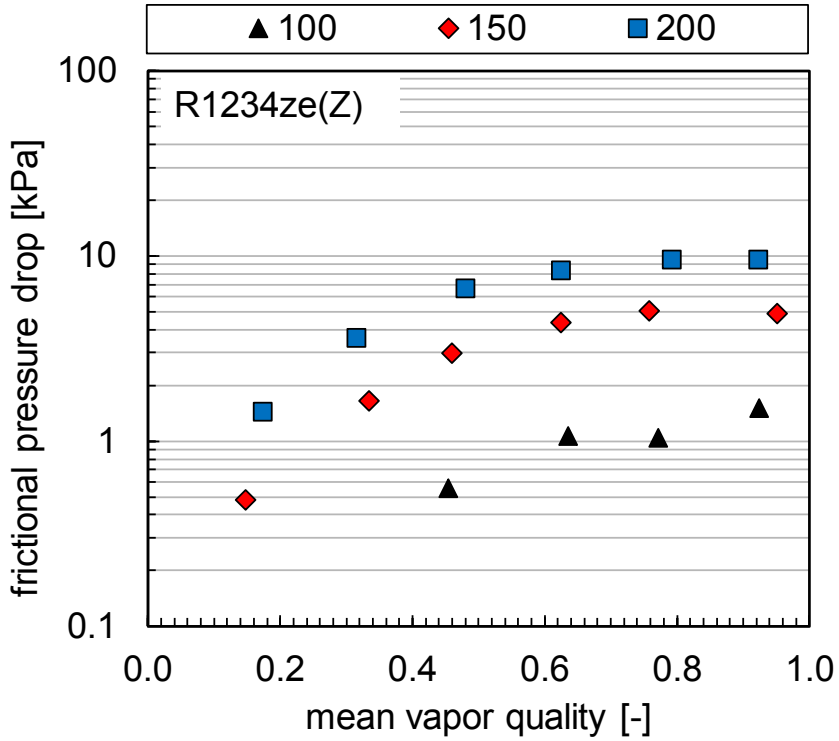

Figure 6: R1234ze(Z) condensation frictional pressure drop vs. vapour quality at 40 °C saturation temperature and mass flux equal to 100, 150, and 200 kg m^{-2} s^{-1}

The present experimental heat transfer coefficients were compared against some well-established heat transfer correlations for condensation inside smooth tubes. The Akers et al. (1959) model satisfactorily predicted the forced convection condensation data in terms of mean relative percentage deviation (MRPD= -7.2 % for R1233zd(E) and MRPD= 11.2 % for R1234ze(Z)) and mean absolute percentage deviation (MAPD= 17.8% for R1233zd(E) and MAPD= 25.2 % for R1234ze(Z)) between the experimental data and the calculated values.
Furthermore, the experimental data set was assessed several correlations for two-phase pressure drop inside tubes. The classical Friedel (1979) and Muller-Steinhagen and Heck (1986) models satisfactorily predicted the experimental values, as reported in Table 2.

Table 2. Comparison between experimental frictional pressure drops and values calculated according some literature models

-		R1233zd(E)	R1234ze(Z)
Muller-Steinhagen & Heck (1986)	MRPD	22.7	1.6
	MAPD	13.3	12.0
Friedel (1979)	MRPD	26.3	6.3
	MAPD	18.3	15.9

4. CONCLUSIONS

This paper presented some experimental data collected during R1233zd(E) and R1234ze(Z) condensation inside a 4 mm ID horizontal copper smooth tube flux at 40°C of saturation temperature and five different refrigerant mass fluxes, namely G=75, 100, 150, and 200 kg m^{-2} s^{-1}. The effects of refrigerant mass flux and mean vapor quality on heat transfer coefficient and frictional pressure drop were discussed. Following, the experimental data were assessed against several heat transfer coefficient and frictional pressure drop correlations available in the open literature. The Akers et al. (1959) model satisfactorily predicted the forced convection condensation data, while Friedel (1979) and Muller-Steinhagen and Heck (1986) models were able to properly capture the measured frictional pressure drops.

ACKNOWLEDGEMENTS

This research project was partially funded by: CariVerona Foundation, Verona, Italy, Ricerca Scientifica e Tecnologica 2016-2019: “Sostenibilità e autenticazione nutrizionale di filiere lattiero-casearie a tutela del consumatore”.

NOMENCLATURE

A	heat transfer area (m^2)	q	heat flux, $q = Q / A$ ($W.m^{-2}$)
G	refrigerant mass flux ($kg\ m^{-2}s^{-1}$)	Q	heat flow rate (W)
HTC	heat transfer coefficient ($W\ m^{-2}\ K^{-1}$)	T	temperature (°C)
k	coverage factor (-)	X	vapor quality (-)
p	pressure (Pa)	Δ	difference (-)

REFERENCES

Akasaka, R., Higashi, Y., Miyara, A., Koyama, S., 2014. A fundamental equation of state for cis-1,3,3,3-tetrafluoropropene (R1234ze(Z)). Int. J. Refrigeration 44, 168–176.

Akers, W.W., Deans, H.A., Crosser, O.K., 1959. Condensing heat transfer within horizontal tubes. Chem. Eng. Prog. Symp. Series 55, 171–176.

Brown, J.S., Zilio, C., Cavallini, A., 2009. The fluorinated olefin R-1234ze(Z) as a high-temperature heat pumping refrigerant. Int. J. Refrigeration 32, 1412–1422.

Friedel, L., 1979. Improved friction pressure drop correlations for horizontal and vertical two-phase pipe flow. Proceedings of the European Two-Phase Group Meeting, Ispra, Italy, Paper E2.

Giuffrida, A., Pezzuto, D., 2017. Simulation of a scroll expander using R1233zd(E), R1234ze(Z) and their mixtures as drop-in replacements for R245fa. Energy Procedia 129, 301–306.

Hodnebrog, Ø., Etminan, M., Fuglestvedt, J.S., Marston, G., Myhre, G., Nielsen, C.J., Shine, K.P., Wallington, T J., 2013. Global Warming Potentials and Radiative Efficiencies of Halocarbons and Related Compounds: A Comprehensive Review, Reviews of Geophysics 51 (2), 300-378.

Hu, B., Wu, D., Wang, R.Z., 2017. Performance simulation and exergy analysis on multi-stage compression high temperature heat pumps with R1234ze(Z) refrigerant. Proceedings of the 12th IEA heat pump conference, May 15-18, 2017, Rotterdam, The Netherlands.

Kline, S.J., McClintock, F.A., 1953. Describing uncertainties in single-sample experiments. Mech. Eng., 75, 3–8.

Lemmon, E.W., Bell, I.H., Huber, M.L., McLinden, M.O., 2017. NIST Standard Reference Database 23 Beta Version (Aug. 23, 2017): Reference Fluid Thermodynamic and Transport Properties-REFPROP, Version 10.0, National Institute of Standards and Technology, Standard Reference Data Program, Gaithersburg.

Li, L., Ge, Y.T., Luo, X., Tassou, S.A., 2017. Experimental investigations into power generation with low grade waste heat and R245fa Organic Rankine Cycles (ORCs), Applied Thermal Engineering, 115, 815–824.

Longo, G.A., Mancin, S., Righetti, G., Zilio, C., 2017. Saturated vapour condensation of HFC404A inside a 4 mm ID horizontal smooth tube: Comparison with the long-term low GWP substitutes HC290 (Propane) and HC1270 (Propylene). Int. J. Heat and Mass Transf. 108, 2088-2099.

Longo, G.A., Zilio, C., Righetti, G., Brown, J.S., 2014. Experimental assessment of the low GWP refrigerant HFO-1234ze(Z) for high temperature heat pumps. Experimental Thermal and Fluid Science 57, 293–300.

McLinden, M.O., Kazakov, A.F., Brown S., Domanski P.A., 2014. A thermodynamic analysis of refrigerants: Possibilities and tradeoffs for Low-GWP refrigerants, International Journal of Refrigeration, 38, (2014) 80-92.

Műller-Steinhagen, H. Heck, K., 1986. A simple friction pressure drop correlation for two-phase flow in pipes, Chem. Eng. Process ,20, 297–308.

Righetti, G., Longo, G.A., Zilio, C., Akasaka, R., Mancin, S., 2018. R1233zd(E) flow boiling inside a 4.3 mm ID microfin tube, International Journal of Refrigeration, 91, 69-79.

Manuscript ID: 442
DOI: 10.18462/iir.icr.2019.0442

Analysis of the P-T and T-S phase boundary in discriminating suitable low global warming potential and low flammability refrigerants

Moonis R. ALLY[(a)], Vishaldeep SHARMA[(a)], Kashif NAWAZ[(a)]

[(a)]Oak Ridge National Laboratory[1]
Oak Ridge, TN 37831-6070, USA, allymr@ornl.gov

ABSTRACT

Although several alternative low GWP refrigerants including natural have been proposed, the HVAC industry consensus on how to deal with the attendant issues is still evolving. This paper provides a qualitative and quantitative insight into the peculiar phase boundary shapes of refrigerants, essential for understanding their application, and in evaluating existing and future refrigerants. The methodology is firmly grounded in the thermodynamics of phase equilibria and the criteria of positive-definiteness, a direct consequence of the Second Law and the existence of intermolecular forces (IMF). The formal methodology is strikingly easy to implement in practice and explains clearly why certain refrigerants display "re-entrant" behavior while others do not. The paper shows how an evidence-based selection can be made among the 40 refrigerants analyzed in this study.
Keywords: Low GWP, alternate refrigerants, heat pumps, VLE

1. INTRODUCTION

The nocuous environmental impact of human activity on climate demands that low GWP and low ODP refrigerants be identified and used in HVAC and water heating applications. The latest attempt under the Kigali amendment (2016) to the Montreal Protocol emphasized phase-down of hydrofluorocarbons (HFCs). A consequence was the emergence of hydrofluorolefins (HFOs) or unsaturated HFCs which are the fourth generation of fluorine-based refrigerants. HFOs characteristically have zero ODP, low GWP but are classified as mildly flammable (A2L gases). They are also very expensive (Nawaz et al., 2017a,b). In contrast, competing natural refrigerants, ammonia, carbon dioxide, propane are attractive alternatives. Evaluation of potential fluids based on the characteristics of the P-T and T-S phase boundaries as suggested by Morrison (1994) is instructive. The path taken by a refrigerant in a heat pump cycle crosses the saturation boundary and its ultimate effect on systemic performance depends on the shape (skewness) of the T-S boundary and the existence of a "re-entrant" region. A direct consequence is "wet-compression" which can cause mechanical damage to the compressor and loss of efficiency. This paper uses the properties of the phase boundary to screen potential refrigerants. On this basis it recommends attractive natural refrigerants for widespread applications. In a companion paper (DOI: 10.18462/iir.icr.2019.1430) the performance of the selected natural refrigerants in four discrete heat pump cycles is evaluated with one natural refrigerant dominating in performance.

[1] Notice: This manuscript has been authored by UT-Battelle, LLC, under contract DE-AC05-00OR22725 with the US Department of Energy (DOE). The US government retains and the publisher, by accepting the article for publication, acknowledges that the US government retains a nonexclusive, paid-up, irrevocable, worldwide license to publish or reproduce the published form of this manuscript, or allow others to do so, for US government purposes. DOE will provide public access to these results of federally sponsored research in accordance with the DOE Public Access Plan (http://energy.gov/downloads/doe-public-access-plan).

2. P-T SATURATION BOUNDARY

The refrigerants evaluated in this paper are ordered by their respective GWP in **Table *1*** in which the first ten refrigerants have attractively low GWP of interest as alternatives refrigerants. The saturation vapor pressure at the VLE phase boundary plotted in **Figure *1*** as log P vs. T^{-1} yields near linear slope proportional to the latent heat of vaporization of the respective refrigerant as given by the Clausius-Clapeyron equation Eq. (1). The slope of Eq. (1) is essentially constant for the temperature range of interest and becomes zero at the critical point (not shown) where the distinction between vapor and liquid phases disappears.

$$\frac{\partial lnP}{\partial T^{-1}} = \frac{2.303 \partial logP}{\partial (T^{-1})} = \frac{-\Delta H}{R} \qquad \text{Eq. (1)}$$

By treating the log P vs. T^{-1} plot as essentially linear, we are taking an average value of ΔH over the temperature range for each refrigerant. The log P vs. T^{-1} phase defines the operational limits of pressure and temperature over which a refrigerant may operate and the magnitude of ΔH is a measure of the refrigerant charge needed. Most applications would be limited to abscissa values of 0.25-0.4 corresponding to 127°C - 23°C (covering HVAC and water heating applications).The magnitude of ΔH (*molar* basis) is due to the combined effect of molar mass and intermolecular forces (IMF) between the molecules. The IMF includes dipole-dipole, ion-dipole interactions, hydrogen bonding, London dispersion forces, etc. ΔH is determined by the strength of IMF because extra energy must be expended to overcome these interactions. Molecules of high molar mass possess degrees of freedom due to translational, rotational, and vibrational modes of energy that must be overcome during vaporization resulting in higher ΔH_{molar}. These compounds tend to reside on the left side of Figure 1 whereas those with lower ΔH_{molar} tend to reside on the right side. Table 2 lists refrigerants by their ΔH_{molar} and molar mass. Ammonia with a small molar mass has high ΔH_{molar} because of IMF (ion-ion, dipole-dipole interaction from lone electron pairs) requiring extra energy for liquid to vapor phase transition. Both molar mass and IMF contribute to ΔH_{molar}.

Table 1. Refrigerants ordered according by increasing GWP (Strocker et. al. 2013)

No.	Refrigerant	Chemical Composition (Mass Fraction)	Critical Temperature (°C)	Critical Pressure (kPa)	Boiling Point at 101 kPa (°C)	Freezing Point (°C)	Glide (°C)	GWP	Molar Mass (kg/kmol)	Safety Classification
1	ammonia	NH3	132.3	11.33	-33.3	-77.7	-	0	17.03	B2L
2	carbon dioxide	CO2	31	7.38	-78.5	-56.6	-	1	44.01	A1
3	R-1234yf	R1234yf	94.7	3.38	-29.5	-53.2	-	1	114.04	A2L
4	R-1234ze(E)	R1234ze(E)	109.4	3.63	-19	-104.5	-	1	114.04	A2L
5	R-1233zd(E)	R1233zd(E)	166.5	3.62	18.3	-78	-	1	130.5	A1
6	propylene	propylene	91.1	4.56	-47.6	-185.2	-	2	42.08	A3
7	propane	propane	96.7	4.25	-42.1	-187.6	-	3	44.096	A3
8	R-441A	Ethane (0.031), Propane (0.548), isobutane (0.06), butane (0.361)	117.3	4.4	-41.5	-	19.2	3	48.305	A3
9	isobutane	isobutane	134.7	3.63	-11.7	-159.4	-	3	58.122	A3
10	n butane	nbutane	152	3.8	-0.5	-138.3	-	4	58.12	A3
11	R-123	R123	183.7	3.66	27.8	-107.2	-	79	152.93	B1
12	R-451A	R1234yf (0.898), R134a (0.102)	95.4	3.5	-29.6	-	0	133	112.689	A2L
13	R-152a	R152a	113.3	4.52	-24	-118.6	-	138	66.051	A2
14	R-457A	R32 (0.18), R1234yf (0.70), R152a (0.12)	93	4.43	-42.2	-	7.5	139	90.85	A2L
15	R-455A	R744 (0.03), R32 (0.215), R1234yf (0.755)	87.5	4.74	-51.8	-	11.6	146	87.5	A2L
16	R-451B	R1234yf (0.888), R134a (0.112)	95.5	3.52	-29.7	-	0	146	112.558	A2L
17	R-454A	R32 (0.35), R1234yf (0.65)	85.7	4.9	-47.6	-	5.5	238	80.5	A2L
18	AR-M-20b	R32 (0.35), R1234yf (0.55), R152a (0.1)	91.5	4.64	-42.2	-	4.5	251	76.544	A2L
19	R-444B	R32 (0.415), R1234ze(E) (0.485), R152a (0.1)	91.2	5.06	-44.5	-	8.7	295	72.76	A2L
20	AR-M71a	R32 (0.68), R1234yf (0.26), R1234ze(E) (0.06)	83.4	5.31	-48.8	-	4.4	461	62.985	A2L
21	R-446A	R32 (0.68), R1234ze(E) 0.29, butane (0.03)	84.2	5.51	-49.3	-	5.2	461	63.123	A2L
22	R-454B	R32 (0.689), R1234yf (0.311)	80.9	5.51	-50.4	-	1.5	467	62.61	A2L
23	R-450A	R1234ze(E) (0.58), R152a (0.42)	105.6	3.91	-23.4	-	0.6	547	108.67	A1
24	R-447A	R32 (0.68), R125 (0.035), R1234ze(E) (0.285)	82.6	5.41	-49.3	-	4.7	572	63.045	A2L
25	R-513A	R1234yf (0.56), R134a (0.44)	97.7	3.82	-29.3	-	0	573	108.4	A1
26	R-452B	R32 (0.67), R125 (0.07), R1234yf (0.26)	79.7	5.45	-50.6	-	1.3	676	63.525	A2L
27	R-32	R32	78.1	5.78	-51.7	-136.8	-	677	52.024	A2L
28	R-448A	R32 (0.26), R125 (0.26), R1234yf (0.2), R134a (0.21), R1234ze(E) (0.07)	83.7	4.66	-45.9	-	5.7	1273	86.283	A1
29	R-449A	R32 (0.243), R125 (0.247), R1234yf (0.253), R134a (0.257)	83.9	4.63	-45.6	-	5.3	1282	87.213	A1
30	R-134a	R134a	101.1	4.06	-26.1	-103.3	-	1300	102.03	A1
31	R-407C	R32 (0.23), R125 (0.25), R134a (0.52)	86	4.63	-43.6	-	6.2	1624	86.204	A1
32	R-407F	R32 (0.3), R125 (0.3), R134a (0.4)	82.7	4.75	-46.1	-	5.6	1674	82.058	A1
33	R-22	R22	96.1	4.99	-40.8	-157.4	-	1760	86.468	A1
34	R-407A	R32 (0.2), R125 (0.4), R134a (0.4)	82.3	4.52	-45	-	5.6	1923	90.111	A1
35	R-410A	R32 (0.5), R125 (0.5)	71.3	4.9	-51.4	-	0.1	1924	72.585	A1
36	R-452A	R32 (0.11), R125 (0.59), R1234yf (0.3)	75.6	4.04	-46.8	-	3.9	1945	103.5	A1
37	R-125	R125	66	3.62	-48.1	-100.6	-	3170	120.02	A1
38	R-404A	R125 (0.44), R134a (0.04), R143a (0.52)	72	3.73	-46.2	-	0.5	3943	97.604	A1
39	R-507A	R125 (0.5), R143a (0.5)	70.6	3.7	-46.7	-	0	3985	98.859	A1
40	R-143a	R143a	72.7	3.76	-47.2	-111.8	-	4800	84.041	A2

Despite similar ΔH_{molar} values of 23.3 and 22.3.1 kJ·mol^{-1} for ammonia and R1234ze, respectively, the latent heat of vaporization on a mass basis (ΔH) is very different because of the differences between their molar masses. For HVAC, the latent heat per unit of mass (tabulated as ΔH in Table 2) is significant because HVAC charge is quantified gravimetrically. On this basis, the latent heats of NH_3 and R-1234ze are 1369.4 and195.6 kJ·kg^{-1} respectively, making the refrigerant charge for ammonia for a given evaporator duty the lowest among these two refrigerants. Both, molar mass and IMF are important considerations in selecting and discriminating refrigerants with a direct bearing on evaporator and condenser sizing.

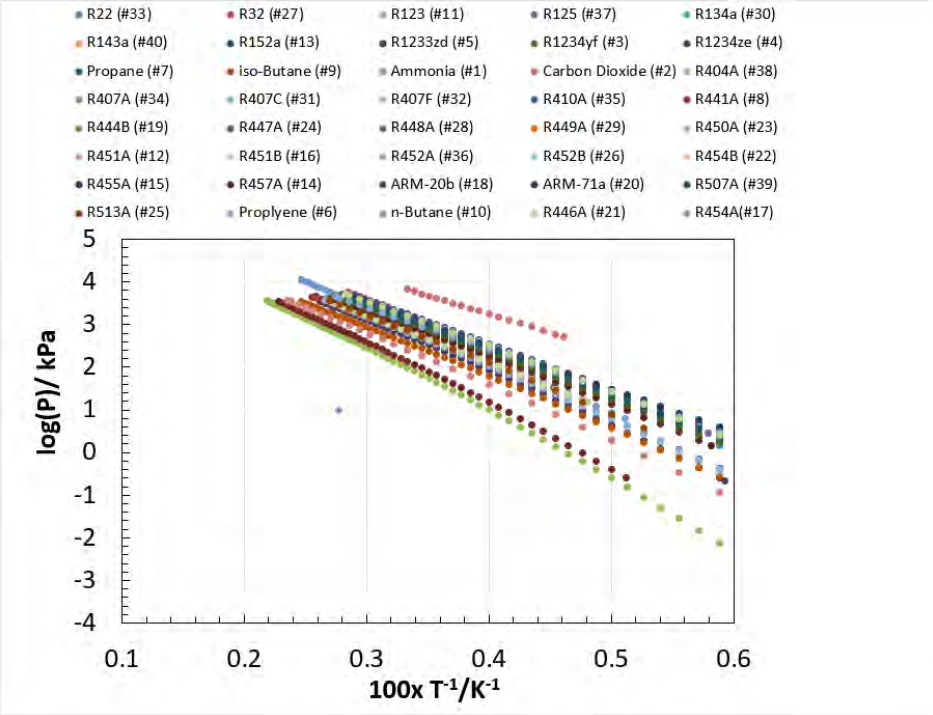

Figure 1: Saturated vapor pressures of refrigerants plotted according to Eq. (1). The slopes of these lines are proportional to the latent heat of vaporization at corresponding saturation temperature. The top most curve (short line) is the VLE for CO_2.The parenthesized number next to the refrigerant in the legend corresponds to the listed number of the refrigerant in Table 1.Data obtained using REFPROP 9.1

3. T-S SATURATION PHASE BOUNDARY

3.1 Qualitative Analysis

Since the T-S phase boundary shape differs markedly from one refrigerant to another, transposition through scaling their temperatures relative to their respective boiling points and their entropies relative to the entropy of vaporization at their respective normal boiling points (Morrison (1994)) puts them on a common comparative basis. Selected refrigerants in Table 1 reveal a peculiar bell-shaped curve for the modified T-S phase boundary as shown in Figure 2. Within the same class of refrigerants for example the HCs, skewness increases with increasing molar mass. Skewness causes a portion of the vapor-liquid branch to have a “re-entrance” region meaning that a line parallel to the ordinate crosses the saturation vapor boundary three times. Skewness is the cause of “wet-compression” occurring towards the end of the compression process, potentially damaging the compressor and lowering cyclic efficiency. Carbon dioxide with ODP=0 and GWP=1 is excluded from Table 2 because at 1 bar, it sublimes and does not possess a npb. Its VLE line is not until its triple point of 5.26 bar. Due to its importance in commercial refrigeration and water heating, it is treated in a separate section below.

Table 2. Properties of refrigerants at their respective nbps. The rightmost column is used to evaluate Eq.(5).

No.	Refrigerant	Molar Mass (kg/kmol)	nbp (°C)	nbp K	C_p $J \cdot mol^{-1} \cdot K^{-1}$	ΔH $kJ \cdot kg^{-1}$	ΔH_{molar} $J \cdot mol^{-1}$	$C_p - \Delta H_{molar}/T_b$ $J \cdot mol^{-1} \cdot K^{-1}$
1	ammonia	17.03	-33.30	239.85	39.12	1369	23322	-58.11
26	R32	52.024	-51.70	221.45	45.50	382	19869	-44.22
21	R454B	62.61	-50.40	222.75	51.33	322	20175	-39.25
25	R452B	63.525	-50.60	222.55	51.91	317	20121	-38.50
23	R447A	63.045	-49.30	223.85	52.01	318	20055	-37.59
19	ARM-71a	62.985	-48.77	224.38	52.03	319	20091	-37.51
20	R446A	63.123	-49.30	223.85	52.30	323	20035	-37.20
32	R22	86.468	-40.80	232.35	52.43	234	20211	-34.56
18	R444B	72.76	-44.50	228.65	59.18	284	20658	-31.17
34	R410A	72.585	-51.40	221.75	58.54	273	19808	-30.79
31	R407F	82.058	-46.10	227.05	62.69	254	20807	-28.96
16	R454A	80.5	-47.60	225.55	63.61	256	20589	-27.67
14	R455A	87.5	-51.80	221.35	66.71	237	20742	-27.00
30	R407C	86.204	-43.60	229.55	65.62	245	21116	-26.37
5	propylene	42.08	-47.60	225.55	56.06	439	18467	-25.82
17	ARM-20b	76.544	-42.20	230.95	62.91	268	20486	-25.79
27	R448A	86.283	-45.90	227.25	66.25	240	20681	-24.76
28	R449A	87.213	-45.60	227.55	66.78	238	20771	-24.50
33	R407A	90.111	-45.00	228.15	67.63	232	20890	-23.94
12	R152a	66.051	-24.00	249.15	64.51	330	21790	-22.95
13	R457A	90.85	-42.20	230.95	70.64	239	20940	-20.02
7	R441A	48.305	-41.50	231.65	68.85	423	20446	-19.41
6	propane	44.096	-42.10	231.05	63.52	426	18766	-17.70
39	R143a	84.041	-47.20	225.95	70.98	227	19044	-13.30
35	R452A	103.5	-46.80	226.35	76.25	195	20174	-12.88
37	R404A	97.604	-46.20	226.95	76.32	200	19566	-9.90
38	R507A	98.859	-46.70	226.45	76.87	197	19467	-9.10
29	R134a	102.03	-26.10	247.05	81.02	217	22139	-8.59
36	R125	120.02	-48.10	225.05	83.67	164	19697	-3.85
24	R513A	108.4	-29.30	243.85	86.93	197	21351	-0.63
22	R450A	108.67	-23.40	249.75	88.44	201	21893	0.78
15	R451B	112.558	-29.70	243.45	91.11	185	20775	5.77
11	R451A	112.689	-29.60	243.55	91.28	184	20751	6.08
3	R1234ze	114.04	-19.00	254.15	94.55	196	22311	6.77
2	R1234yf	114.04	-29.50	243.65	92.69	180	20556	8.32
8	isobutane	58.122	-11.70	261.45	89.91	365	21218	8.75
9	butane	58.12	-0.50	272.65	95.38	386	22419	13.15
4	R1233zd	130.5	18.30	291.45	106.83	195	25492	19.36
10	R123	152.93	27.80	300.95	107.14	170	26029	20.65

The reason for skewness can be found by examining Eq. (2), derived from S=S(T,V). From the extremum principle and stability requirements (Callen (1960)), $\left(\frac{\partial T}{\partial S}\right)_V = \frac{T}{C_V} > 0$, implying that first term on the right side of Eq. (2) is always positive. The value of $\left(\frac{\partial P}{\partial T}\right)_V$ is positive, except for a few substances like water and He-II. The value of $\left.\frac{dV}{dT}\right|_{sat.}$ may be positive or negative depending on the liquid or vapor branch of the phase boundary.

$$\left(\frac{dT}{dS}\right)_{sat.} = \left[\frac{1}{\frac{C_V}{T} + \left(\frac{\partial P}{\partial T}\right)_V \left.\frac{dV}{dT}\right|_{sat.}}\right] \qquad \text{Eq. (2)}$$

Referring to Figure 3, for the liquid branch of the phase boundary, $\left.\frac{dV}{dT}\right|_{sat} > 0$, making both terms of Eq. (2) >0 along the liquid branch approaching the critical point. Nearing the critical point, $\left.\frac{dV}{dT}\right|_{sat} \to \infty$. Both C_v and $\left.\frac{dV}{dT}\right|_{sat}$ while being positive become infinite at the critical point, making $\left.\frac{dT}{dS}\right|_{sat} = 0$ (see Figure 2) from the liquid branch side of the curve. For the vapor branch, the first term, C_V/T, in Eq. (2) is positive. Along the vapor branch, $\left.\frac{dV}{dT}\right|_{sat}$ remains <0 from low temperatures becoming more negative approaching the critical point. At the critical point, $C_v/T \to +\infty$, but the

negative infinity of $\left.\frac{dV}{dT}\right|_{sat}$ is mathematically dominant (Morrison (1994); Sengers (1991)), making the right hand terms of Eq. (2) and $\left.\frac{dT}{dS}\right|_{sat} = 0$ (zero slope at the critical point as indicated in **Figure 2**).

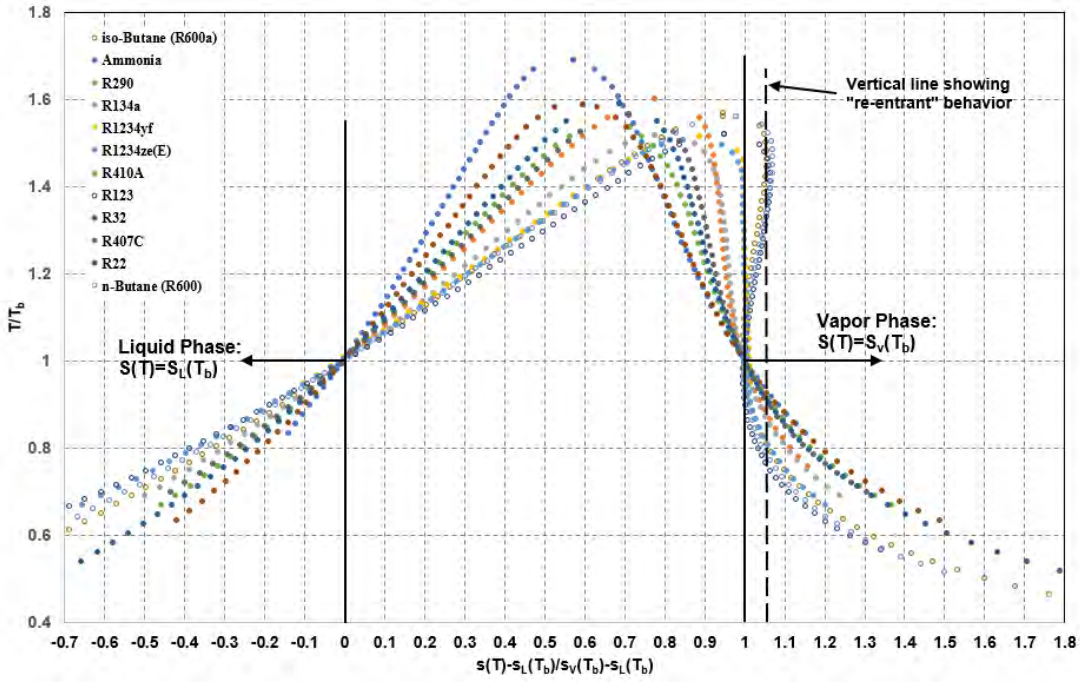

Figure 2: Modified T-S saturation boundaries for select refrigerants where temperatures are normalized relative to the respective boiling points (T/Tb) and entropies are normalized relative to the respective entropy of vaporization at the normal boiling point: $\frac{S(T)-S_L(T_b)}{S_v(T_b)-S_L(T_b)}$. Refrigerants that have a marked skewness display "re-entrant" behavior.

The value of $\left.\frac{dT}{dS}\right|_{sat}$ along the vapor branch goes from a small negative value at low T to zero. It could become >0 along a narrow range in the vapor branch if C_V/T becomes larger than $\left.\frac{dV}{dT}\right|_{sat}$. This can happen with larger molecules whose C_V increases with molecular complexity with many degrees of translational, rotational, and vibration modes of energy (Morrison (1994)).

The origin of the "re-entrant" region is a consequence of a "tug-of-war" between the positive value of C_V/T and the negative value of $\left.\frac{dT}{dS}\right|_{sat}$ over the range of T. "Re-entrant" behavior is expected for refrigerants that display $\left.\frac{dT}{dS}\right|_{sat}$ >0 in the T-S domain of the saturation vapor curve as in Figure 2.

3.2 Quantitative Analysis

A quantitative assessment of the T-S phase boundary is made starting with S=S(T,P) yielding,

$$\left.\frac{dT}{dS}\right|_{sat.} = \frac{1}{\left[\frac{C_P}{T} - \left(\frac{\partial V}{\partial T}\right)_P \left.\frac{dP}{dT}\right|_{sat.}\right]} \qquad \text{Eq. (3)}$$

Assuming modest temperatures and pressures where the ideal gas model reasonably applies to the saturated vapor phase, we obtain Eq. (4) using $PV = RT$ and its derivatives in Eq. (3),

$$\left.\frac{dT}{dS}\right|_{sat.} = \frac{1}{\left[\frac{C_P}{T} + \left.\frac{R\ dlnP}{T^2 dT^{-1}}\right|_{sat.}\right]} = \frac{1}{T^{-1}\left[C_P + \frac{R\,\partial lnP}{T dT^{-1}}\right]} \qquad \text{Eq. (4)}$$

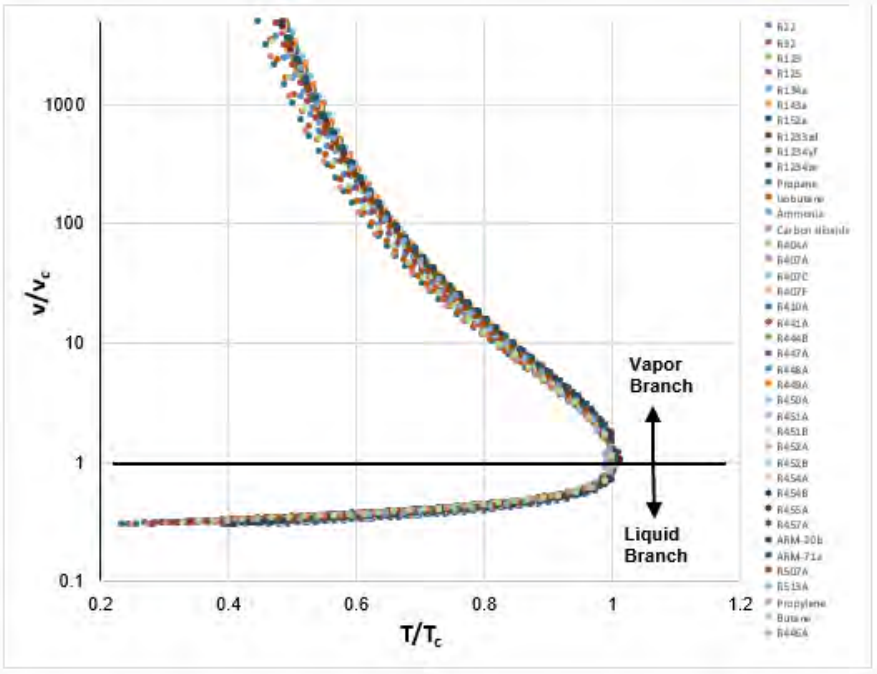

Figure 3: The saturated phase boundaries for various refrigerants with temperatures normalized relative to their respective critical temperatures, and volumes normalized relative to their respective critical volumes

Substituting Eq. (1) in Eq. (4) with slight algebraic manipulation yields Eq.(5)

$$\left.\frac{dT}{dS}\right|_{sat.} = \frac{T}{\left[C_P - \frac{\Delta H_{molar}}{T}\right]} \qquad \text{Eq.(5)}$$

$\left.\frac{dT}{dS}\right|_{sat.}$ may be evaluated anywhere along the T-S saturation boundary, but a convenient point is at the nbp where pressures and temperatures are low enough for the assumptions used in deriving Eq.(5) are valid. The case of CO_2 is treated separately because at 1bar, it sublimes directly from solid to vapor unlike the other refrigerants that undergo liquid to vapor transition. Table 2 lists the two terms involving $C_p, \Delta H_{molar}$, and $T = T_b$ in the denominator of Eq.(5) evaluated at the respective nbps. The rightmost column of Table 2 quantifies the "tug-of-war" between C_P and $\frac{\Delta H_{molar}}{T}$ terms in the denominator of Eq.(5) where both, molar mass, and IMF exert their relative influences to determine their net algebraic sign. Refrigerants with a positive value of $C_P - \frac{\Delta H_{molar}}{T_b}$ must possess re-entrant regions exemplified by R1234ze, R1234yf, isobutane, n-butane, etc. (see Table 2).

3.3 Carbon Dioxide

Various CO_2 subcritical, transcritical and supercritical systems are being utilized in applications such as refrigeration, HVAC, water heating and power generation (Nawaz et al., 2018, Sharma, et. al., 2014, Sharma, et al., 2015; Ahn et. al, 2015; Girotto e. al., 2004; Mazzola, et. al., 2012; Sawalha, 2007) because such systems are competitive with those which currently use refrigerants such as R-404A., R-22, and R-507. Besides performance, leakage rates from 3% to 35% for in-use equipment is not unusual (Sharma, et. al., (2014)). Since CO_2 sublimes at 1 bar and does not exhibit VLE until it reaches saturation at its triple point (5.2 bar, 216.59K) we show (Figure 4) that this fluid has no "re-entrant" characteristic based on its VLE phase boundary relative to the triple point or the critical point, instead of the nbp as done for the other refrigerants (discussed previously).

Besides Figure 4, further confirmation that CO_2 does not have a "re-entrant" region comes from evaluating Eq.(5). From Figure 1 and Eq. (1), ΔH_v obtained graphically is ~15,000J/mole which compares favorably with the value of 14041.4 J/mole at 235K obtained from REFPROP. The value

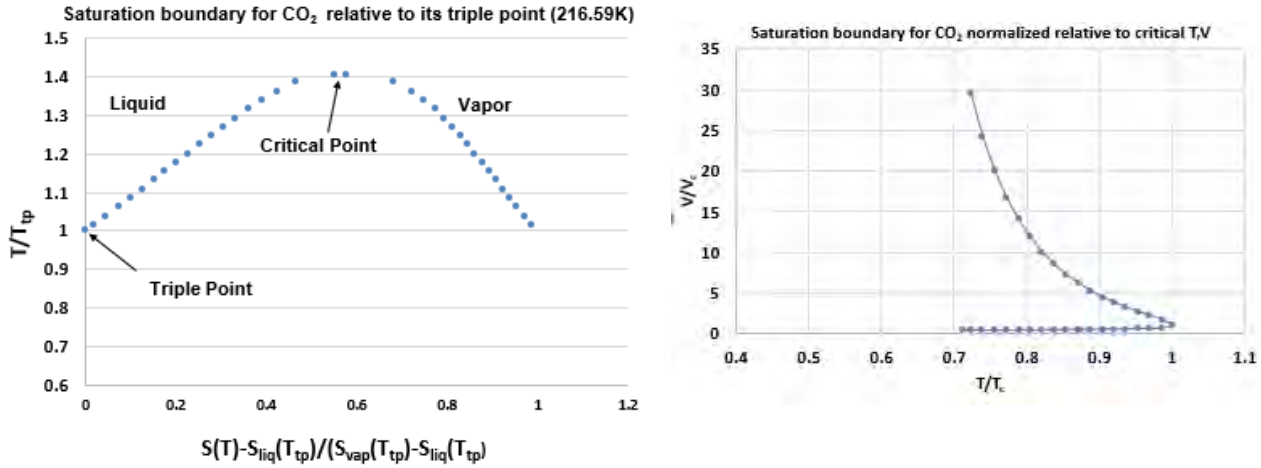

Figure 4: (Left):Modified T-S saturation boundaries for carbon dioxide where temperature is normalized relative to the triple point (T/T_{tp}) and entropy is normalized relative to the entropy of vaporization at the triple boiling point, $\frac{S(T)-S_L(T_{tp})}{S_v(T_{tp})-S_L(T_{tp})}$. (Right): Reduced saturation boundary relative to critical volume and temperature. Values obtained using REFPROP ver. 9.1

of C_p from REFPROP at the same temperature is 46.24 J/mol-K. Substituting these values in Eq.(5) yields -13.51 J/mol-K which is <0 indicating no "re-entrant" region for CO_2.

CONCLUSIONS

The shape of the phase boundary is governed by IMF, the molecular structure and the molar mass of a refrigerant molecule. This paper explains that skewness of the T-S phase boundary quantified by $\left.\frac{dT}{dS}\right|_{sat.}$ explains why some refrigerants exhibit "re-entrant" characteristics while others do not. The P-T phase boundary prescribes appropriate pressure and temperature ranges over which prospective refrigerants may operate as a practical working fluid. Among low GWP (<10) refrigerants, ammonia, CO_2 and propane are leading candidates.

ACKNOWLEDGEMENTS

The authors are grateful to the U.S Department of Energy, Building Technologies Office for supporting this work. We thank Dr. Ayyoub Momen, Dr. Brian Fricke, and Dr. Bo Shen for reviewing the manuscript.

NOMENCLATURE

C_p	specific heat ($kJ{\cdot}mol^{-1}{\cdot}K^{-1}$ or $kJ{\cdot}kg^{-1}{\cdot}K^{-1}$)	HVAC	heating , ventilation, air-conditioning
GWP	global warming potential	ODP	ozone depletion potential
ΔH_v	enthalpy of vaporization ($kJ{\cdot}mol^{-1}$ or $kJ{\cdot}kg^{-1}$)	P	pressure, Pa or bar
		R	gas constant, (8.314×10^{-3} $kJ{\cdot}mol^{-1}{\cdot}K^{-1}$)

S	entropy ($kJ \cdot K^{-1}$)	c	critical point (temperature, volume)
T	temperature (°C or K)		
V	volume (m^3)	molar	per mole, mol^{-1}
VLE	vapor-liquid equilibrium	P	constant pressure
Greek		sat.	saturated state or condition
∂	partial derivative	tp	triple point
subscripts		V	constant volume
b or nbp	normal boiling point		

REFERENCES

Ahn, Y., Bae, S. J., Kim, M., Cho, S. K., Baik, S., Lee, J, I., Cha, J. E., 2015. Review of supercritical CO_2 power cycle technology and current status of research an development. Nuclear Engineering and Technology 47 (2015), pp. 647-661.

Callen, H. B., 1960. Thermodynamics, John Wiley, New York, ISBN 0 471 13035 4, pp.135.

Sengers, J.L., 2017. Thermodynamics of solutions near the solvent's critical point. In *Supercritical Fluid Technology (1991)*(pp. 1-56). CRC Press.

Girotto, S., Minetto, S., Neksa, P., 2004. Commercial refrigeration system using CO_2 as the refrigerant. Int. J. Refrigeration 27, 717-723.

Mazzola, D., Toffolo, A., Orlandi, M., 2012. Supermarket application. CO_2 system with groundwater sink. Model simulation. In: Proceedings of the 10th IIR Gustav Lorentzen Conference on Natural Working Fluids, Delft, The Netherlands, 25-27 June 2012.

Morrison, G, 1994. The shape of the temperature-entropy saturation boundary, Int. J. Refrig. Vol 17 Number 7, 494-504.

Nawaz, K., Shen, B., Elatar, A., Baxter, V., Abdelaziz, O., 2018. Performance Optimization of CO_2 HPWH System, Int. J. Refrigeration, 85, 213-218.

Nawaz, K., Shen, B., Elatar, A., Baxter, V., Abdelaziz, O., 2017. R-290 and R-600a as Natural Refrigerants for Residential Heat Pump Water Heaters, *Applied Thermal Engineering*, 127, 870-883.

Nawaz, K., Shen, B., Elatar, A., Baxter, V., Abdelaziz, O., 2017. R-1234yf and R-1234ze(E) as Low GWP Refrigerants for Residential Heat Pump Water Heaters, Int. J. Refrigeration, 82, 348 365.

Lemmon, E. W., M. L. Huber, and M. O. McLinden. "NIST Standard Reference Database 23: Reference Fluid Thermodynamic and Transport Properties-REFPROP, Version 9.1, National Institute of Standards and Technology, Standard Reference Data Program, Gaithersburg.

Sawalha, S., 2007. Theoretical evaluation of trans-critical CO_2 systems in supermarket refrigeration. Part 1: modeling, simulation and optimization of two system solutions. Int. J. Refrigeration 31, 516-524.

Sharma, V., Fricke, B., Bansal, P., 2014. Supermarket Refrigeration System Charge Reduction Using Cascade Systems. 11th IIR Gustav Lorentzen Conference on Natural Refrigerants (31 Aug- 2 Sept 2014). Hangzhou,China

Sharma, V., Fricke, B., Bansal, P., 2015. Evaluation of a Transcritical CO2 Supermarket Refrigeration System for the USA Market. 6th International Institute of Refrigeration (IIR) Conference on Ammonia and CO2 Refrigeration Technologies (16-18 April, 2015). Ohrid.

T. F. Stocker, D. Qin, G. K. Plattner, M. Tignor, S. K. Allen, J. . Boschung, A. Nauels, Y. Xia, V. Bex, P. M. Midgley, IPCC, Climate Change 2013: The Physical Science Basis. Contribution of Working Group I to the Fifth Assessment Report of the Intergovernmental Panel on Climate Change, Cambridge University Press, Cambridge, UK, 2013.

Manuscript ID: 445
DOI: 10.18462/iir.icr.2019.0445

Simultaneous measurements of flow-induced noise and two-phase flow regime in expansion valves

Yingyue ZHANG [(a)], Stefan ELBEL[(a, b)]

[(a)] Air Conditioning and Refrigeration Center,
Department of Mechanical Science and Engineering,
University of Illinois at Urbana-Champaign,
1206 West Green Street, Urbana, IL 61801, USA, Email: yingyue2@illinois.edu
[(b)] Creative Thermal Solutions, Inc.,
2209 North Willow Road, Urbana, IL 61802, USA, Email: elbel@illinois.edu

ABSTRACT

Flow-induced noise generated by the expansion devices is disturbing to the user because of its high-frequency properties. In the paper, a pumped R134a loop and the simultaneous measurements including the accelerometer, the microphone, the high-speed pressure transducer, and the high-speed camera are utilized. Thus, the flow-induced noise can be related to specific flow movements recorded by the camera. The observed frequency range of the gurgling noise is between 7.5 kHz to 10 kHz, whereas that for the hissing noise is above 10 kHz. The gurgling noise is generated by the flow oscillating movement whereas the hissing noise is caused by the flow-structure interaction. The hissing noise can be enhanced by the structural modes and exists in all kinds of flow regimes. The gurgling noise only exists when TXV inlet has two-phase flow. The acceleration signal matches the microphone signal and the accelerometer can be used to simulate the flow-induced noise.
Keywords: Gurgling noise, Hissing noise, Flow regimes, Flow visualization, Flow-induced noise

1. INTRODUCTION

There are four kinds of noise in HVAC& R systems: the mechanical noise generated by the compressor movement, the flow-induced noise produced by the evaporator, the high-pitched tone generated by the start flow passing the A/C charge port cavity, and the high-frequency noise in expansion devices. The mechanical movement of a compressor usually has low frequency, high amplitude, and appears far from people. The frequency of flow-induced noise in the evaporator is about 500 Hz to 1000 Hz (Thawani et al., 2005), and the high-pitched tone is about 2000 Hz (Thawani and Liu, 2007). The expansion devices' flow-induced noise is more annoying since it is close to the occupants and the frequency is always very high. The frequency of the noise determines the sharpness of the sound. When the sharpness of the sound is high, people will feel more unpleasant. This paper talks about the properties of the unpleasant flow-induced noise in the expansion devices and the relationship between the flow-induced noise and flow regimes. By comparing the simultaneous measurements of the flow-induced noise and flow regimes before and after the expansion devices, the flow mechanism for different types of noise can be explored.

2. SOUND PROPAGATION THEORY AND EXPERIMENTAL SETUP

Noise propagation by the structure is discussed in this section. After the TXV throttles the R134a flow, the internal flow generates an internal traveling sound wave and excites the tube connected to the TXV

into vibration. The internal sound wave that form the acoustic modes has the possibility to couple with the structural modes. The coupling range is discussed here.

2.1 Cut-off Frequency

After being throttled, the internal flow oscillates and generates several sound waves. Some sound waves decay very fast, some sound waves form acoustic modes that can travel along the geometry at certain frequency. As shown in Fig. 1a, ten kinds of acoustic modes are shown (Rodarte et al., 1999). The human audible zone is from 20 Hz to 20 kHz, so that only the first two or three orders of acoustic modes are of interest (Rodarte et al., 1999). The cut-off frequency is the minimum vibrating speed that acoustic modes are formed, which is defined in the Eq. (1) (Rodarte et al., 1999):

$$(f_{co})_{p,q} = \frac{ck_{p,q}(1-M)^{\frac{1}{2}}}{2\pi} \quad \text{Eq. (1)}$$

In the present pumped R134a loop, the velocity of the flow is too small to be taken into consideration compared to the sound speed, so that the Mach number is close to zero. The cut-off frequency of the (1,0) acoustic mode for this tube is about 8.6 kHz.

2.2 Natural Frequency

Tubes have their natural modes of vibration that are called the structural modes. The internal flow vibration excites the tube into vibration. In addition, this tube vibration can further enhance the flow vibration. The natural frequency of the structure is determined by the geometry characteristics. Good coupling between structural modes and acoustic modes amplifies the flow-induced noise. Coupling structural and acoustic modes requires matching the mode order. For instance, (m,1) structural mode can only couple with (1, q) acoustic mode (Fig. 1c). The natural frequencies of the structural modes are shown in Eq. (2) and Eq. (3) (Blevins, 1979):

$$f_{m,n} = \frac{\lambda_{m,n}}{2\pi a_{mi}}\left[\frac{E}{\rho_{ma}(1-v^2)}\right]^{\frac{1}{2}} \quad \text{Eq. (2)}$$

$$\lambda_{m,n} = \frac{\left[(1-v^2)\left(\frac{m\pi a_{mi}}{l}\right)^4 + \left(\frac{h^2}{12a_{mi}^2}\right)\left(n^2+\left(\frac{m\pi a_{mi}}{l}\right)^2\right)^4\right]^{\frac{1}{2}}}{n^2+\left(\frac{m\pi a_{mi}}{l}\right)^2} \quad \text{Eq. (3)}$$

When the tube connected to the noise source is long enough, the geometry natural frequency will not be influenced by the axial mode shapes as shown in Fig. 1b. Since the tube connected to the TXV is also connected to the other parts in the system, the length of the tube connected to the noise source is assumed to be infinite. The thickness of tube wall is 1.245 mm. The natural frequency of the (m,1) structural modes is about 11.7 kHz. When the circumferential mode order is bigger than 1, the natural frequency exceeds the human audible zone. Thus, the cases (n>1) are not of interest in this paper.

2.3 Coupling Range

When the flow oscillates at the speed around the structure's natural frequency, the coupling of the acoustic modes and structural modes happens. The coupling effect that enhances the flow-induced noise is called resonance. The resonance range is defined in Eq. (4) (Blevins and Bressler, 1993):

$$0.8f_{m,n} < (f_{co})_{p,q} < 1.2f_{m,n} \quad \text{Eq. (4)}$$

The coupling effect of the structure happens when the flow oscillates at frequency between 9.4 kHz to 14.1 kHz.

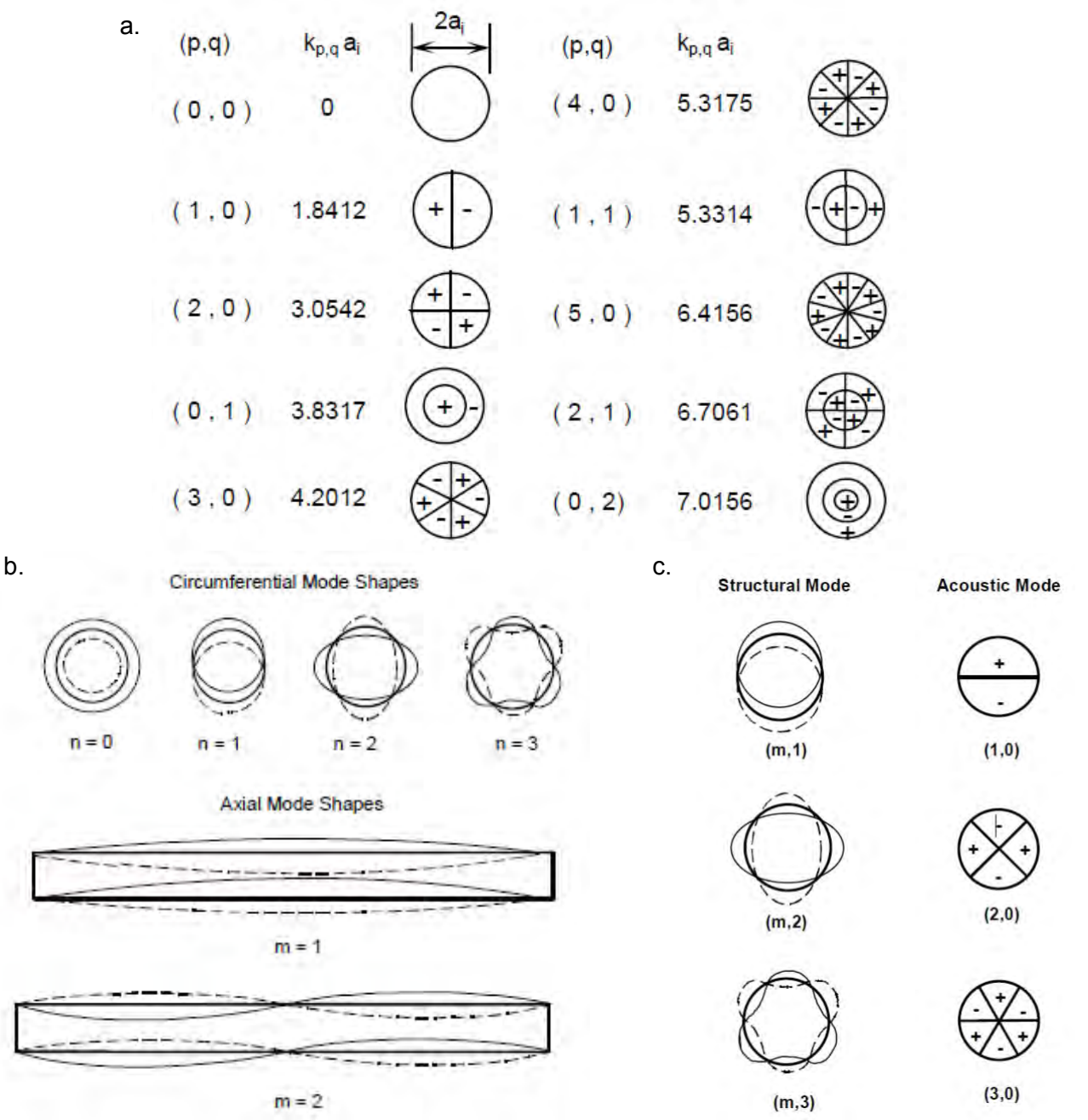

Figure 1: Internal acoustic modes (a) and structural modes (b, c) with sound wave disturbance (Rodarte et al., 1999)

2.4 Experimental Setup

In this experiment, a pumped loop with R134a is used for circulation (as shown in Fig. 2a and Fig. 2b). A water-source evaporator connected to a TXV at the low-pressure side provides the superheat that controls the opening state of the TXV. The constant temperature water tank provides the heat source for the evaporator that maintains the superheat at evaporator outlet. The entire set up is located in a semi-anechoic chamber. The evaporator and TXV are connected using four visualization sections as shown in Fig. 2c: one at the TXV upstream position, two at the TXV's downstream position, and another one at evaporator's downstream position. Therefore, the flow regimes before and after the TXV can be observed. The acceleration of the tube wall indicates the tube's behavior excited by internal flow

oscillations; an accelerometer is installed in the normal direction. The high-speed pressure transducer can record the internal pressure variation which indicates the flow oscillations inside the structure. The flow regimes after being throttled change very fast, so that it is hard to visualize with the bare eye. In this paper, the flow regimes are observed by two high-speed cameras as shown in Fig. 2d. Two high-speed cameras are located in front of the visualization parts to observe the flow regimes at the TXV inlet and outlet. Microphone, accelerometer, pressure transducer, and high-speed cameras are synced in order to compare different data at the same time. The microphone is set up 5 cm from the TXV in a downstream position.

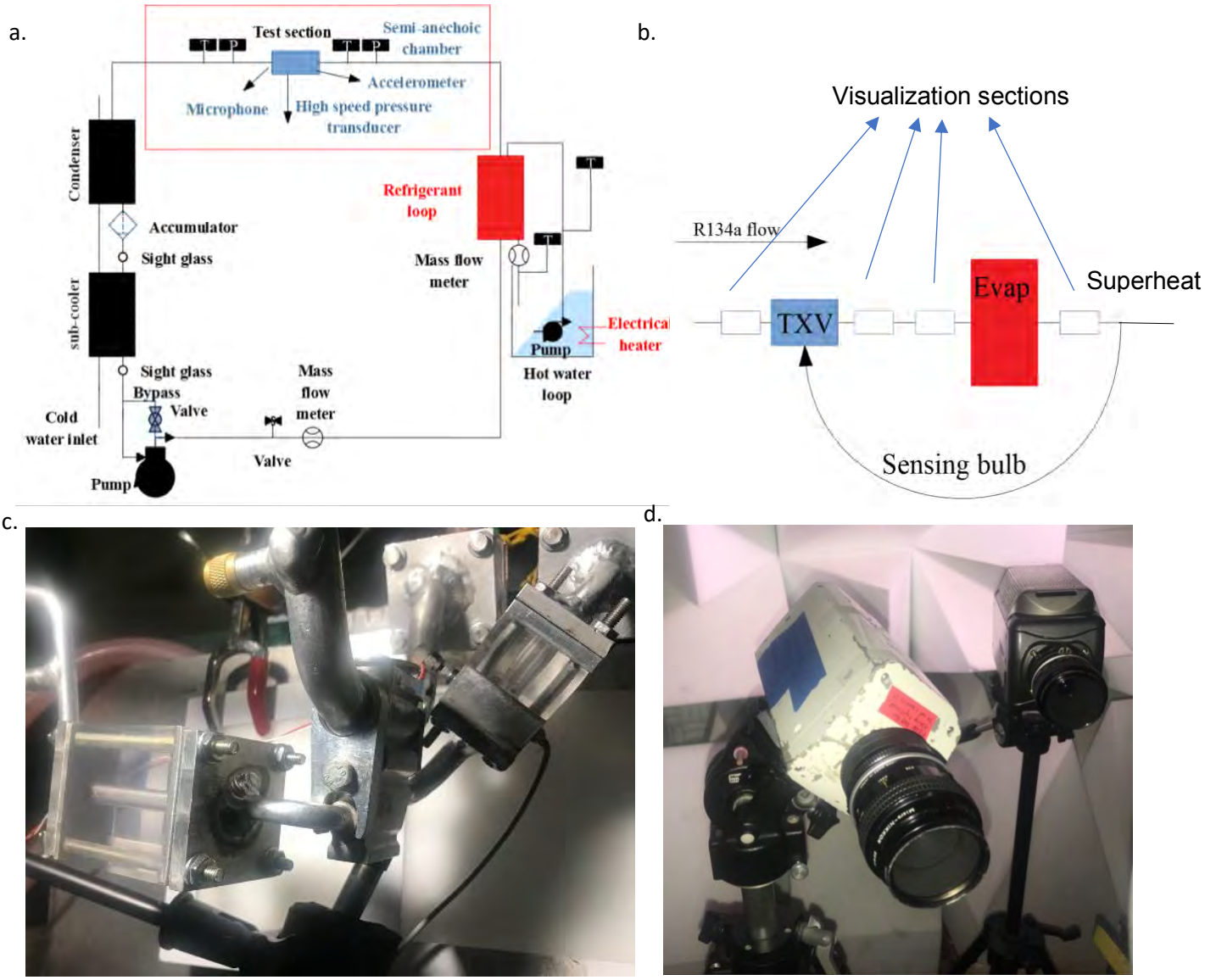

Figure 2: Schematic of the facility (a), arrangement of test component (b), visualization sections (c), and high-speed camera (d)

The sampling rate of the microphone, accelerometer, and the high-speed pressure transducer is set to 44.2 kHz. The human audible zone is from 20 Hz to 20 kHz. A Fast-Fourier-Transform method can transform the data from the time domain to the frequency domain, giving a spectral range from 0 to 22.1 kHz which covers the human audible zone. The testing conditions are listed in Table 1. The case 6 in Table 1 is a comparison test that shows the environmental noise when the system is not working. Five

thermocouples and two mass flow meters are used in the experiment. The uncertainties of the experiments are listed in Table 2.

Table 1. Testing conditions for experimental evaluation

	Case 1	Case 2	Case 3	Case 4	Case 5	Case 6
Low-side pressure (kPa)	600	600	600	600	600	600
Quality (-)	0.02	0.05	0.07	Subcool=1℃	Subcool=1℃	Halt
Mass flow rate (g/s)	10	10	10	8	5	Halt

Table 2. Summary of measured and calculated property uncertainties

Thermocouple reading (℃)	Mass flow rate reading (g/s)	Pressure reading (kPa)	Quality (–)
±0.5	±0.1	±2	±0.01

3. EXPERIMENTAL RESULTS

3.1 The Characteristics and Generation Mechanism of Flow-induced Noise

There are two types of flow-induced noise that can be noticed during the experiment. One of the noise sounds like gurgling, and another sounds like hissing. From Fig. 3 the flow-induced noise that distributes from 7.5 kHz to 10 kHz is called gurgling noise, which is the most noticeable noise generated during the process. The flow-induced noise that distributes over 10 kHz is called hissing noise. The peak of a gurgling noise appears at about 9 kHz while the peak of a hissing noise appears at about 14 kHz. According to the coupling range mentioned in the previous section, both the gurgling noise and the hissing noise can be enhanced as coupling with the structural mode. However, the gurgling noise can only be enhanced when the frequency of noise distributes from 9.4 kHz to 10 kHz. Thus, the coupling effect is more influential on the hissing noise. Noticeable gurgling noise only appears when the TXV has two-phase at the inlet. The gurgling noise is hardly noticeable when the TXV inlet is subcooled flow, so that the hissing noise is the dominant type of noise disturbing occupants. An increase in the amplitude of a gurgling noise is seen in Fig. 3b when higher mass flow rate passing the expansion devices. By comparing Fig. 3a and Fig. 3b, the flow-induced noise is less annoying when the TXV inlet is subcooled. As the quality at TXV inlet increases (Fig. 3a), the gurgling noise becomes more severe and the hissing noise is not obviously influenced.

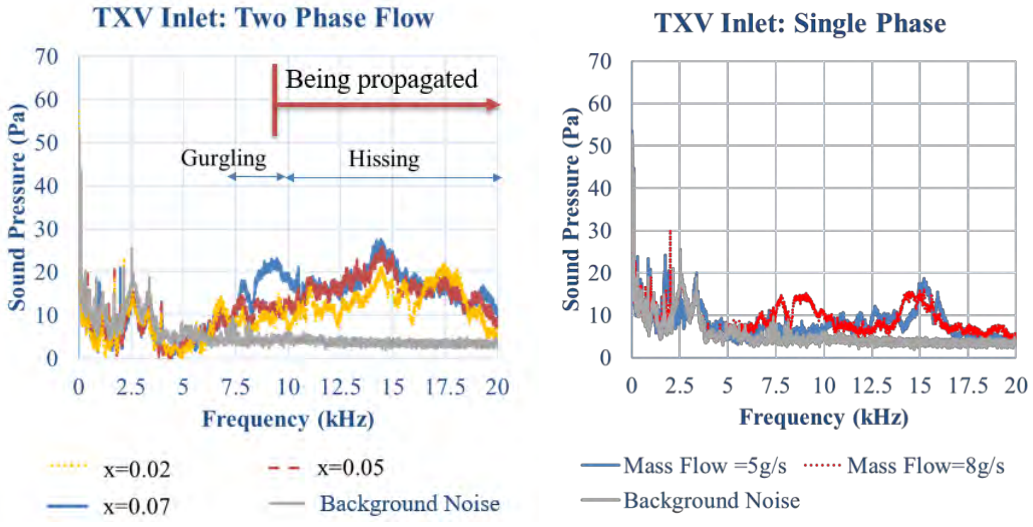

Figure 3: The noise spectra for the flow with different quality (a) and noise spectra when TXV inlet flow is single phase (b)

The existence of vapor is the main reason for the generation of the gurgling noise. As observed from Fig. 4, when the inlet flow at TXV inlet is two-phase with oscillations, the flow regime at TXV outlet becomes more turbulent. Also, more flow oscillations can be seen when a gurgling noise is heard. Because of the existence of vapor phase, more bubbles and unsteady flow appears. From Fig. 4, when gurgling noise appears, the back and forth movement of the flow at TXV outlet can be observed at the TXV inlet. When the proportion of vapor increases, the mean flow becomes more compressible and the flow oscillation becomes more intense. When hissing noise happens, only forward flow and flow stagnation can be seen from the visualization part at TXV outlet. Also, a hissing noise exists under all kinds of TXV inlet flow regimes at TXV inlet including the subcooled flow condition. Due to the fact that the amplitude of hissing noise does not vary as the quality of the flow at TXV inlet changes, a hissing noise is more likely to be caused by the flow and structure interaction, which is influenced by the vibration status of the tube. Also, hissing noise distributes within the range that can be propagated by the structure. The coupling effect of the acoustic modes and structural modes enhance the hissing noise.

Noise type	Hissing noise: above 10 kHz	Gurgling noise: 7.5 kHz to 10 kHz
TXV inlet	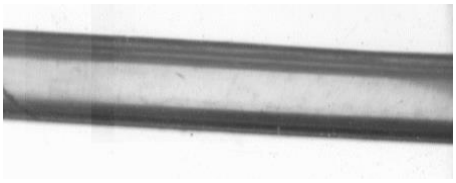	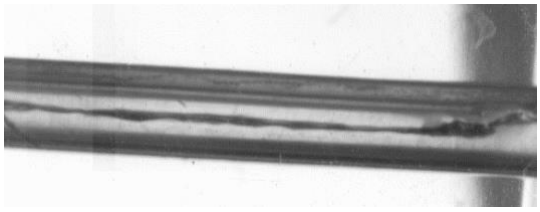
TXV outlet	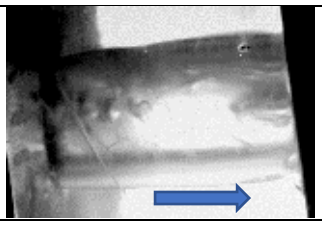	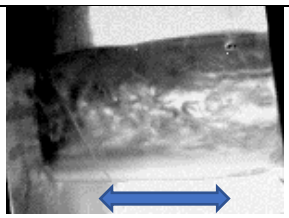
Flow movement description	Forward flow with some stagnation	Forward and reversed flow caused by the two-phase flow upstream

Figure 4: Mechanism for different types of flow-induced noise

3.2 The Comparison of Different Measurements

As shown in Fig. 5, the spectrum of the acceleration of the tube in normal direction matches the microphone spectrum perfectly. The result indicates that the flow and the structure interaction truly exist. The flow inside the tube hits the tube wall and experiences a reaction force which enhances the flow oscillations. The peak at about 1000 Hz is the flow-induced noise generated by the evaporator that is connected to the TXV. The flow-induced noise can be simulated by the acceleration signal. The inflow pressure transducer recognizes obvious oscillations within low frequency range. These oscillations do not show up in the acceleration and microphone spectra. Some of the sound waves without enough acoustic energy tend to decay very fast, some of them can propagates through the system but not being able to couple with the structural vibration. The high-frequency sound waves with enough vibration amplitude form the acoustic modes and resonant with the structural vibration. The microphone spectrum shows that the noise above 10 kHz becomes more intense compared to the acceleration spectrum. This is due to the coupling effect of the structure when the tube's natural frequency and the flow's vibrating frequency matches. With the help with MATLAB, the flow-induced noise can be simulated by the acceleration signal. The simulated noise has similar sound characteristics to the real flow-induced noise recorded by the microphone. Thus, the accelerometer can be used as a replacement of a microphone to study the flow-induced noise.

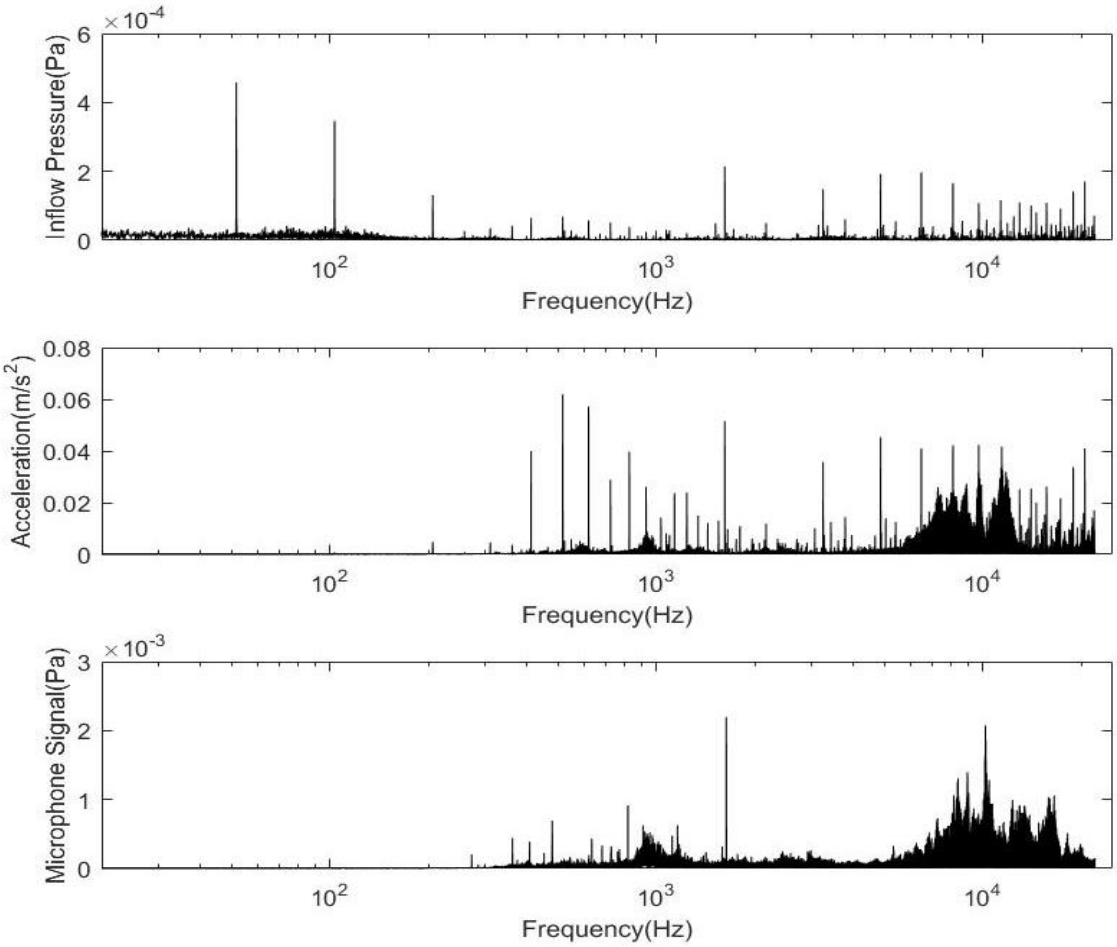

Figure 5: Signal comparison of different measurements

4. CONCLUSIONS

In this paper, simultaneous measurements are used to study the mechanism of the flow-induced noise. The measurements including the microphone, the accelerometer, the high-speed pressure transducer and the high-speed camera are synced in order to visualize the flow regimes and flow-induced noise at the same time. The gurgling noise is distributed within the frequency range from 7.5 kHz to 10 kHz, while the hissing noise is above 10 kHz. With a 12.7 mm aluminum tube, the natural frequency is 11.7 kHz, and the coupling effect between the flow oscillation and the structural vibration will happen when the flow oscillates at frequency between 9.4 kHz and 14.1 kHz. Gurgling noise only appears when TXV inlet is two-phase flow. The flow back and forth oscillation can be observed when the gurgling noise happens. Therefore, the gurgling noise is supposed to be the result of flow oscillations. A hissing noise exists in all kinds of flow regimes and can couple with the first order structural modes. Hissing noise will not change a lot despite the flow regimes at TXV inlet. No obvious flow oscillation at the TXV outlet can be seen when a hissing noise happens. The hissing noise is more likely to be influenced by flow and structure interaction. The acceleration spectrum of the tube in a normal direction matched the microphone spectrum perfectly except for the vibration above 10 kHz. The difference can be explained by the coupling effect of acoustic modes and structural mode: the high-frequency flow oscillation is enhanced by the structure. The accelerometer can be used as a replacement to study flow-induced noise which is much cheaper.

ACKNOWLEDGEMENT

The authors would like to thank the member companies of the Air Conditioning and Refrigeration Center (ACRC) at the University of Illinois at Urbana-Champaign for their financial and technical support and Creative Thermal Solutions, Inc. (CTS) for their technical support.

NOMENCLATURE

Symbols and Abbreviations

a	tube radius [m]
c	speed of sound [m×s^{-1}]
E	modulus of elasticity [N×m^{-2}]
f	frequency [Hz]
h	tube thickness [m]
l	length of the tube [m]
k	wave number [-]
M	Mach number [-]
TXV	thermal expansion valve
v	Poisson's ratio [-]
ρ	density [kg×m^{-3}]
λ	dimensionless parameter associated with a structural natural frequency [-]

Subscripts

co	cut-off
i	interior
ma	material
mi	medium
m	axial mode shape number
n	circumferential mode shape number
o	exterior
p	acoustic circumferential modal number
q	acoustic diametral modal number

REFERENCES

Blevins, R. D., 1979, Formulas for Natural Frequency and Mode Shape, New York: Van Nostrand Reinhold Co.

Blevins, R. D., & Bressler, M. M., 1993, Experiments on Acoustic Resonance in Heat Exchanger Tube Bundles. Journal of Sound and Vibration, 164(3), 503–533. https://doi.org/https://doi.org/10.1006/jsvi.1993.1231

Rodarte, E., Singh, G., Miller, N., and Hrnjak, P., 1999, Refrigerant Expansion Noise Propagation Through Downstream Tube Walls, no. 724. https://doi.org/10.4271/1999-01-1197

Thawani, P., and Liu, Z., 2007. Flow-Induced Tones in Automotive Refrigerant Systems, no. 724. https://doi.org/10.4271/2007-01-2294

Thawani, P., Venkatappa, S., and Liu, Z., 2005, Automotive Refrigerant System Induced Evaporator Hoot, no. 724. https://doi.org/10.4271/2005-01-2509

PAPER ID: 464
DOI: 10.18462/iir.icr.2019.0464

Measurement of Sound Speeds in the Liquid Phase of Hydrochlorofluoroolefins (HCFO)

Takashi NISHIYAMA[(a)], Tomohiro HONDA[(a)], Lei GAO[(a)], Ryo AKASAKA[(b,c)]

[(a)] Fukuoka University
Fukuoka, 814-0180, Japan, tnishiyama@fukuoka-u.ac.jp
[(b)] Kyushu Sangyo University
Fukuoka, 813-8503, Japan
[(c)] Research Center for Next Generation Refrigerant Properties, I2CNER, Kyushu University
Fukuoka, 819-0385, Japan

ABSTRACT

Hydrochlorofluoroolefins (HCFOs) are promising candidates for next-generation refrigerants. Accordingly, more accurate equations of state are desired for this kind of refrigerants. On the other hand, highly accurate speed of sound measurement has been enabled by the advancement of technology, and therefore the speed of sound data of the refrigerant has become one of important thermodynamic properties to improve equations of state. In this study, we aim to measure the speed of sound of HCFOs in liquid-phase. The measurement apparatus is mainly composed of a sound velocity sensor and a standard resistance temperature detector and two pressure transducers. The measurements were conducted in the range of temperature from 300 to 400 K at pressures up to 10 MPa. At first, we measured the liquid-phase speed of sound of difluoromethane to evaluate the accuracy of the apparatus. The consistency was evaluated between speed of sound data obtained in this work and calculated values form available equations of state.
Keywords: Speed of sound, Liquid-phase, Low-GWP, Measurement.

1. INTRODUCTION

Global warming has become one of the most important global problems. In the "Paris Agreement" of 2015, the average temperature rise of the world compared to the pre-industrial should be suppressed to less than 2 °C was suggested. Moreover, "Special report on global warming of 1.5 °C (SR1.5)" reported that the situation deteriorated significantly even at a rise of 1.5 °C. Therefore, further refurbishment of refrigerant is required.

Hydrochlorofluoroolefins (HCFOs) are promising candidates for next-generation refrigerants(Bobbo et al., 2018; Molés et al., 2016), which are characterized by low global warming potential, low ozone depleting potential, and non-flammability. Accordingly, more accurate equations of state are desired for this kind of refrigerants. On the other hand, highly accurate speed of sound measurement has been enabled by the advancement of technology, and therefore the speed of sound data of the refrigerant has become one of important thermodynamic properties to improve equations of state.

In this study, we aim to measure the speed of sound of HCFOs in liquid-phase. At first, we measured the liquid-phase speed of sound of difluoromethane (HFC-32) to evaluate the accuracy of the apparatus. The consistency was evaluated between speed of sound data obtained in this work and calculated values form available equations of state.

2. EXPERIMENT

2.1. Experimental Apparatus

A schematic diagram of the experimental apparatus is shown in Fig. 1. The apparatus consists of a sensing unit of the sound velocity sensor (1), sight-glass (2), a thermostatic water bath (3), two pressure transducers (4), a standard platinum resistance thermometer (5), a leak valve (6), a

connection valve (7), a plunger pump (8), a vacuum pump (9), a control unit (10), a data logger (11), an evaluation unit of the sound velocity sensor (12).
The main loop of the experimental apparatus is built from copper tube. The sensing unit of the sound velocity sensor (L-SONIC6100, Anton Paar GmbH) is mounted at the lowest place of the main loop, and the sight-glass is set about 30 mm higher than the sensing unit of the sound velocity sensor. The sensing unit of the sound velocity sensor and the sight-glass were immersed in the thermostatic water bath (CD20, Lauda), which can control the water temperature at a specified temperature within ±0.02 K. The pressure transducers (PAB-A-2MP and PGR-100KA, Kyowa Electronic Instruments Co., Ltd.) were placed about 300 mm higher than the sensing unit of the sound velocity sensor.
The amount of sample refrigerant charged to the main loop was controlled so that the vapor-liquid interface of the sample appeared inside the sight-glass. Therefore, the temperature at the vapor-liquid interface can be controlled close to the water temperature of the thermostatic bath. The saturation pressure corresponding to the water temperature can be obtained.

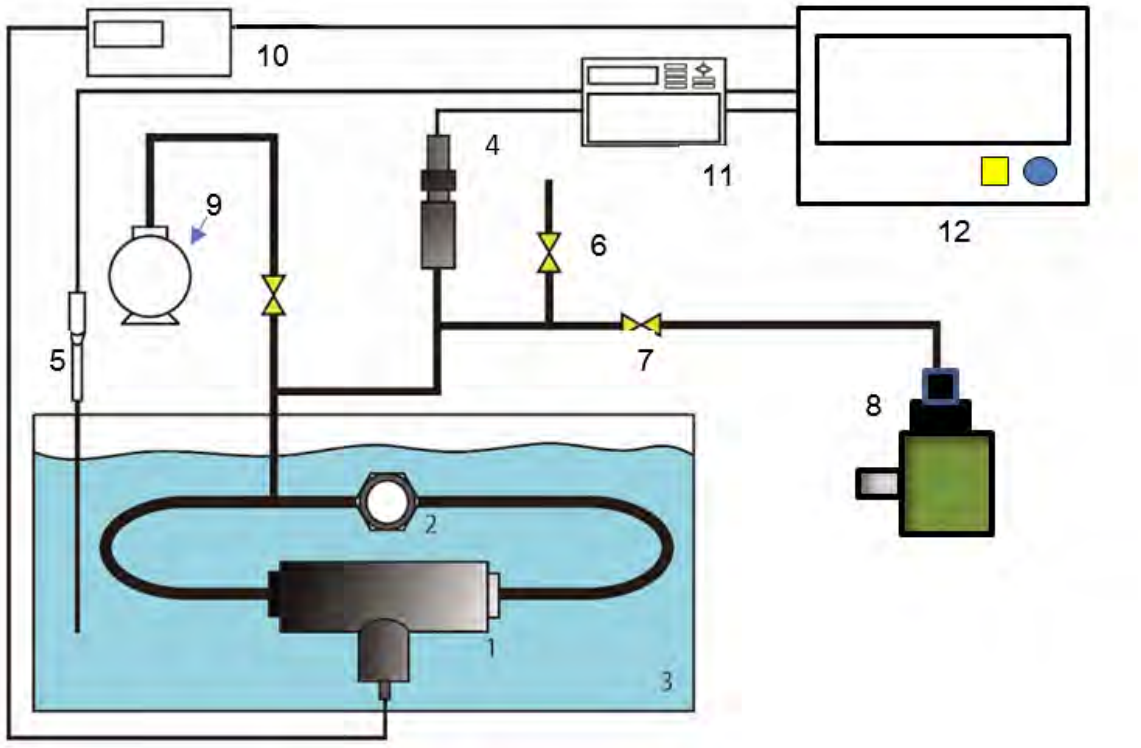

Figure 1: Schematic diagram of experimental apparatus

In the case of the measurement of compressed liquid, the connection valve was opened, and the temperature of the thermostatic water bath (3) was controlled. The amount of sample refrigerant charged to the main loop was supplied by the plunger pump (8). The compressed liquid pressure in the sound velocity sensor was measured by the pressure transducers.
The platinum resistance thermometer equipped in the sound velocity sensor was calibrated with the standard platinum resistance thermometer (NRHS1, CHINO Corporation) in a precision within ±0.03 K.

2.2. Experimental Conditions

To verify the accuracy of the sound velocity sensor, the speed of sound measurement of HFC-32 at a temperature range from 15 to 25 °C was performed. The measurement results were compared with those calculated from REFPROP Version 10.0 (Astina and Sato, 2003; Lemmon et al., 2018; Tillner-Roth and Yokozeki, 1997). The manual of the sound velocity sensor mentions that the accuracy of the speed of sound should be within 0.1 m/s in the velocity range from 200 to 1000 m/s. The extended uncertainties (k = 2) of the speed of sound measured in the previous experiment were estimated to be ±0.062 K for temperature, ±1.1 kPa for pressure and ±0.82 m/s for speed of

sound(Gao et al., 2015). However, configuration of the apparatus was changed and measuring devices were updated, re-evaluation of the accuracy was needed.

3. RESULTS AND DISSCUSION

3.1. Results of HFC-32

Fig. 2 shows the speed of sound data of near saturated liquid of HFC-32 and comparison of the measurement results with those calculated from REFPROP. The solid lines show the speed of sound data calculated from REFPROP at specified temperature and pressure conditions. The speed of sound of HFC-32 tends to increase with pressure at each temperature. Although the measured value is slightly small, it agrees well with the value calculated from REFPROP.

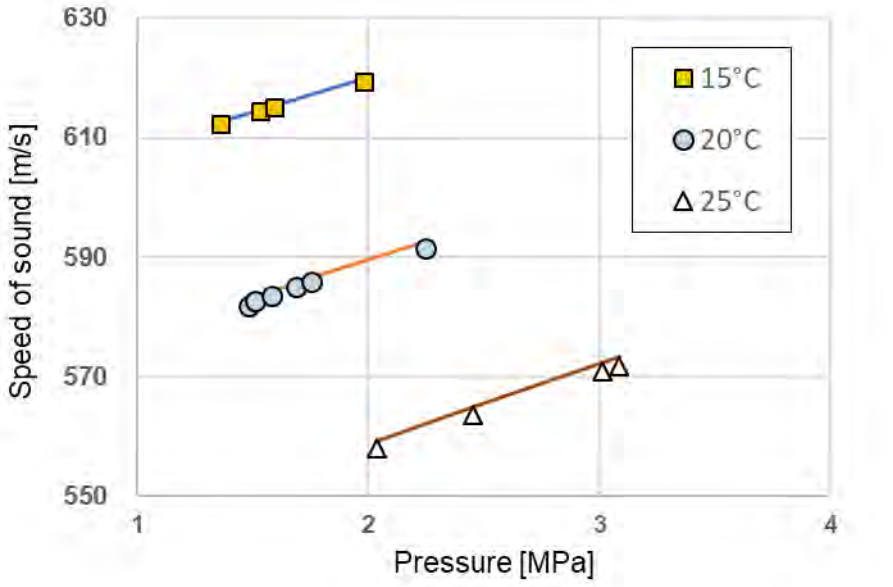

Figure 2. Measurement results of near saturated liquid of HFC-32 and calculation results of REFPROP at each temperature (solid lines)

Fig. 3 shows the deviations between measurement results at the temperature 20 °C for compressed liquid at a pressure range up to 9.04 MPa of HFC-32 and calculation results of REFPROP. The dashed lines show the uncertainty of REFPROP in speed of sound for the liquid phase. All measurement results are within the range of REFPROP uncertainty. Therefore, the measurement results are consistent with those of REFPROP.

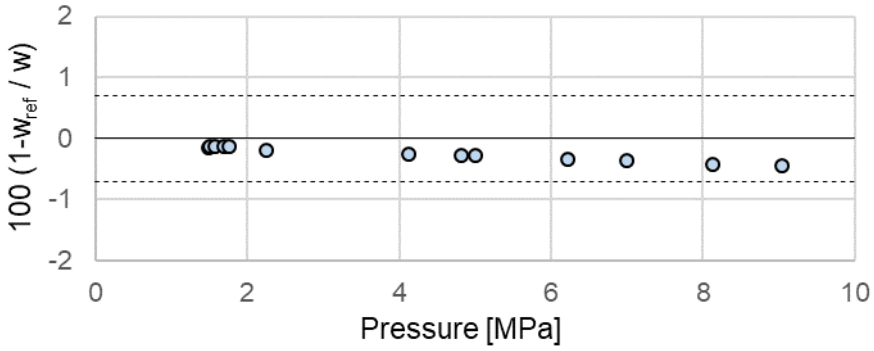

Figure 3. Deviations between speed of sound data and values calculated from REFPROP at the temperature of 20 °C

4. CONCLUSIONS

The speeds of sound of HFC-32 were measured at a temperature range from 15 to 25 °C. The measurement data were compared with the values calculated from REFPROP.

1. The measurement results of near saturated liquid of HFC-32 at a temperature range from 15 to 25 °C are slightly lower than those calculated from REFPROP.
2. The measurement results of compressed liquid of HFC-32 at a pressure range up to 9.04 MPa are slightly lower than those calculated from REFPROP. The speed of sound increases slightly with increasing the pressure at a specified temperature.
3. REFPROP states that speed of sound in HFC-32 liquid phase has an uncertainty of 0.7%. Therefore, the measurement results are consistent with those of REFPROP. The accuracy of updated apparatus is confirmed.
4. Measurement results of HCFO will be reported on the day of the conference.

ACKNOWLEDGEMENTS

We gratefully thank Mr. Takahumi ENDO, Mr. Taito MATANO and other students of Faculty of engineering, Fukuoka University, who conducted the measurement and gave many contributions in this research. We also thank Dr. Hiroyuki ASOU (assistant professor of Faculty of Engineering, Fukuoka University, Japan) for his valuable discussions and support.

REFERENCES

Astina, I.M., Sato, H., 2003. A Rational Helmholtz Fundamental Equation of State for Difluoromethane with an Intermolecular Potential Background. Int. J. Thermophys. 24, 963–990. https://doi.org/10.1023/A:1025096716493

Bobbo, S., Nicola, G. Di, Zilio, C., Brown, J.S., Fedele, L., 2018. Low GWP halocarbon refrigerants: A review of thermophysical properties. Int. J. Refrig. 90, 181–201. https://doi.org/10.1016/j.ijrefrig.2018.03.027

Gao, L., Asou, H., Honda, T., 2015. Speed of Sound Measurements of HFO-1234ze (E) in the Liquid Phase 0–5. https://doi.org/10.18462/iir.icr.2015.0627

Lemmon, E.W., Bell, I.H., Huber, M.L., McLinden, M.O., 2018. NIST Standard Reference Database 23: Reference Fluid Thermodynamic and Transport Properties-REFPROP, Version 10.0, National Institute of Standards and Technology.

Molés, F., Navarro-Esbrí, J., Peris, B., Mota-Babiloni, A., 2016. Experimental evaluation of HCFO-1233zd-E as HFC-245fa replacement in an Organic Rankine Cycle system for low temperature heat sources. Appl. Therm. Eng. 98, 954–961. https://doi.org/10.1016/j.applthermaleng.2016.01.011

Tillner-Roth, R., Yokozeki, A., 1997. An international standard equation of state for difluoromethane (R-32) for temperatures from the triple point at 136.34 K to 435 K and pressures up to 70 MPa. J. Phys. Chem. Ref. Data 26, 1273–1328. https://doi.org/10.1063/1.556002

Manuscript ID: 468
DOI: 10.18462/iir.icr.2019.0468

Pressure drop and void fraction of vertical and horizontal adiabatic two-phase flow in a plate heat exchanger single channel with uniform gas-liquid distribution

Susanne BUSCHER[(a)]

[(a)] Technische Universität Berlin
Berlin, 10587, Germany, susanne.buscher@tu-berlin.de

ABSTRACT

The pressure drop of air-water two-phase flow is studied in a cross-corrugated channel for varying flow directions. Two-phase frictional pressure drop can only be measured for horizontal flow, neglecting acceleration pressure drop. In vertical flow, a void-fraction model is necessary to calculate the pressure drop from a measured pressure difference.
A plate heat exchanger single channel is pivot-mounted to allow horizontal, vertical upward and downward flow. Uniform gas-liquid distribution is obtained injecting both air and water separately into the channel through a number of nozzles.
The experimental dissipation rates of vertical and horizontal two-phase flow are compared to single-phase flow. Thus, homogeneous flow is distinguished from the occurrence of slip caused by buoyancy or annular flow. The validity of the homogenous model is empirically confirmed for volumetric gas flow ratios up to 0.7 and centrifugal Froude numbers above 2 - if a uniform two-phase distribution is achieved. A correlation of the single-phase friction factor is given and found to also be valid for homogeneous flow.
Keywords: Air-Water, Corrugated Surface, Horizontal Plate, Plate Exchanger, Pressure Drop, Two-Phase Flow, Vertical Flow.

1. INTRODUCTION

Plate heat exchangers are widely used because of their compactness, which comes with the price of a high pressure drop. They are in use, inter alia, as evaporators and condensers in high-pressure refrigeration plants. The prediction of two-phase frictional pressure drop, however, is crucial not only to specify the plant, but also to know the evaporation temperature of the refrigerant. To investigate the frictional pressure drop without interference of heat transfer and phase equilibria, adiabatic air-water flow is studied in a cross-corrugated a plate heat exchanger single channel. In contrast to ordinary plate heat exchangers, a uniform two-phase distribution is achieved by separately injecting gas and liquid directly into the channel. To study the influence of buoyancy, measurements of horizontal, vertical upward and downward flow are compared.
Adiabatic two-phase pressure drop in plate heat exchanges has been studied by several authors. Some employed a void fraction correlation for tubes (Kreissig and Müller-Steinhagen, 1992) or correlated the void fraction from measurements (Asano et al., 2004). Other studies assume homogeneous flow to calculate the vertical two-phase pressure drop (Tribbe and Müller-Steinhagen, 2001; Grabenstein et al., 2017; Nilpueng and Wongwises, 2010). Also, correlations of the Lockart-Martinelli two-phase multiplier are given with accuracies of 20-30% (Grabenstein et al., 2017; Nilpueng and Wongwises, 2010; Asano et al., 2004). However, all of the named studies investigated vertically oriented plate heat exchangers, but not horizontal flow. The assumptions about the void fraction in vertical flow influenced the experimental results of frictional pressure drop and the derived correlations. They were not verified by horizontal pressure drop measurements.

2. LAYOUT OF THE EXPERIMENT

A cross-corrugated single channel is pivot-mounted to facilitate experiments in both vertical and horizontal flow direction. The channel consists of two transparent plates made from polycarbonate in which a sinusoidal corrugation profile has been micro-milled. Compressed air of 4 bar(g) in pressure chambers on both sides of the channel prevents deformation and ensures that the wave crests of both plates are in contact. The assembled single channel is shown in Fig. 1. The geometric specifications are given in table 1. The hydraulic diameter and the cross-section are calculated according to Martin (2010).

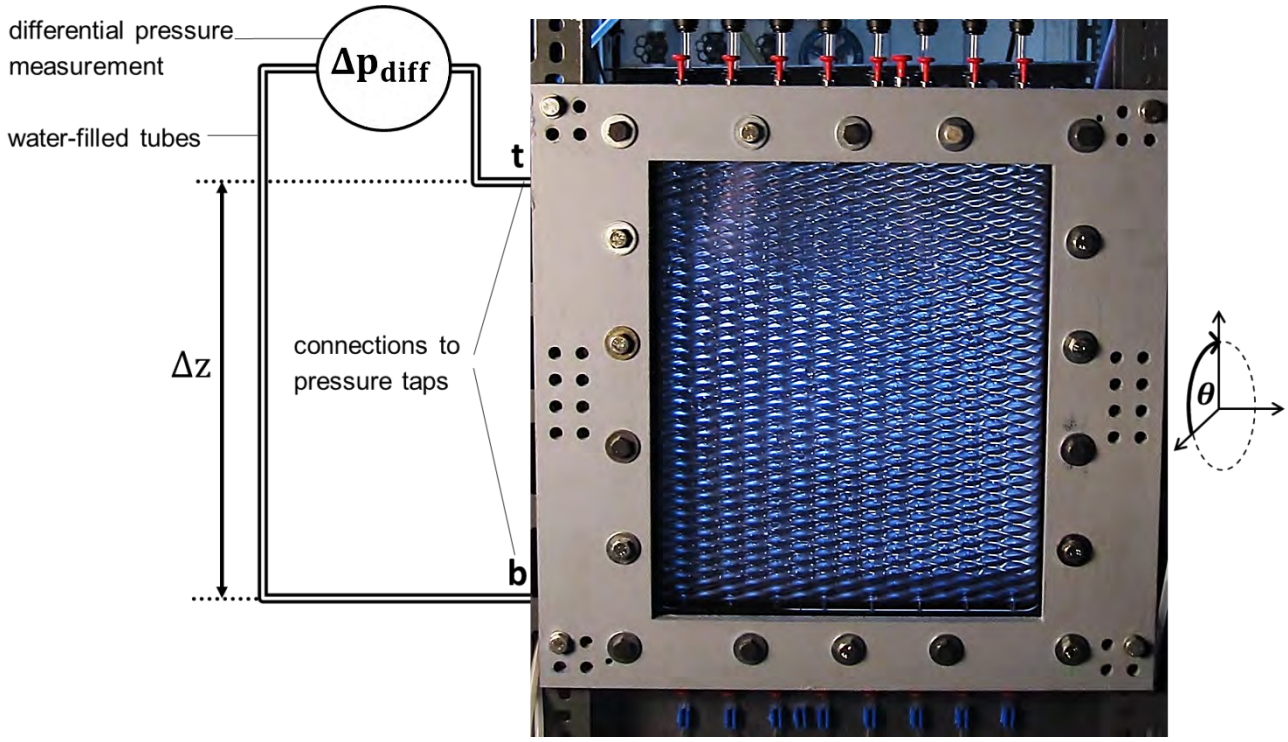

Figure 1: Single Channel and differential pressure measurement

Table 1. Geometric properties of the single channel

Corrugation angle (as to flow direction)	75°	Channel length *L*	326.1 mm
Corrugation depth *a*	1.2 mm	Channel width *B*	278.2 mm
Peak-to-peak amplitude *2a*	2.4 mm	Hydraulic diameter D_h	4.17 mm
Wave number (wave length/ period)	9 mm	Cross-section of the channel *A*	*2a B*

Maldistribution of two-phase flow is likely to occur in most inlet geometries and influences the flow pattern. The responsible phenomena, such as coalescence, slugging, buoyancy, are difficult to eliminate. In order to achieve uniform gas-liquid distribution across the channel width, both phases are injected separately into the channel via 8 nozzles for each phase. The diameter of the liquid nozzles is 3.5 mm, and that of the gas nozzles 0.3 mm, see also Buscher (2019).

Deionized water represents the liquid phase and is re-circulated by a centrifugal pump. Its volumetric flow rate is measured by a nutating disk flowmeter (accuracy 1.5% of reading). Filtered pressurized air represents the gas phase. It is separated from the liquid in the storage tank. The standard volumetric flow rate is measured and controlled by a thermal mass flow meter (accuracy 0.5% of reading plus 0.1% of the upper range set to 0.5 l_n/min, 40 l_n/min or 160 l_n/min).

Orthogonally to the flow direction, pressure taps are inserted to measure gauge pressure and differential pressure (accuracy 0.1% of upper range set to 150 mbar). The pressure taps are bore holes (Ø 0.3 mm) located in wave troughs at the side of the single channel as shown in Fig. 2.

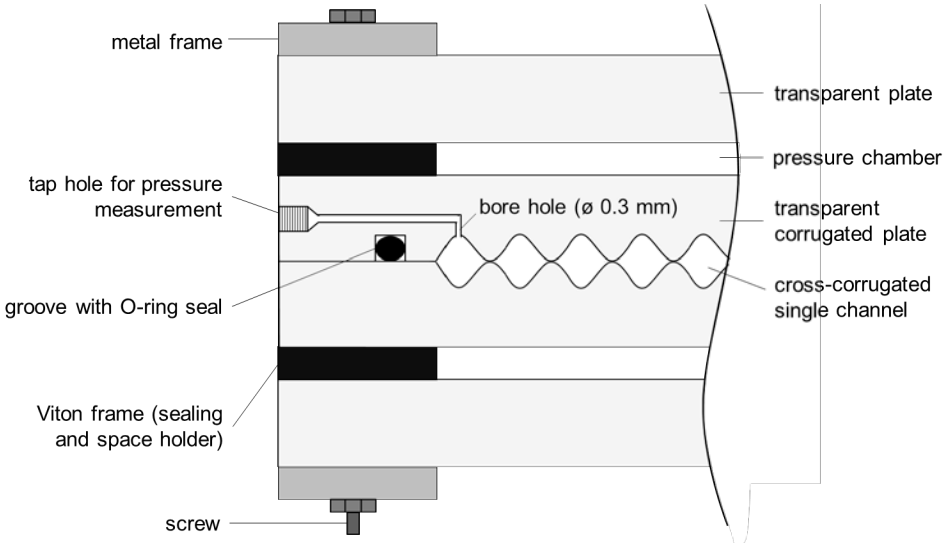

Figure 2: Cross-section of a pressure tap at the side of the single channel

Air bubbles in the flexible tubes connecting the channel and the differential pressure manometer can distort the measurements. After every measurement, therefore, the transparent tubes and connections are inspected, and the air bleed valves of the manometer are opened to check for air bubbles. If bubbles were found they were removed and the measurement was repeated.
The total pressure difference is small compared to the absolute pressure (maximum 13.4% and mean 5.6% with respect to the absolute pressure in the middle of the channel). Therefore, both frictional pressure drop and gas expansion along the main flow direction are presumed to progress linearly. The gauge pressure is measured via a precision manometer (accuracy class 0.25, upper range 1.6 bar) at half of the channel length and is assumed to be the mean gauge pressure. The absolute volumetric flow rate is calculated at the middle of the channel from the downstream temperature and the mean absolute channel pressure, which is derived by adding the ambient pressure to the measured gauge pressure.

3. CALCULATIONS

3.1. Two-Phase Pressure Drop

The total pressure difference in two-phase flow is the sum of frictional pressure drop, hydrostatic pressure difference and pressure drop due to acceleration (see e. g. Thome, 2016):

$$\Delta p_{tot} = \Delta p_{fric} + \sin\theta \; \rho_m \; g \; \Delta z + \Delta p_{acc} \qquad \text{Eq. (1)}$$

$$\rho_m = \rho_{gas} \; \alpha_{\text{hom}} + \rho_{liq} \; (1 - \alpha_{\text{hom}}) \qquad \text{Eq. (2)}$$

$$\alpha_{\text{hom}} = \dot{V}_{gas} / (\dot{V}_{gas} + \dot{V}_{liq}) \qquad \text{Eq. (3)}$$

The mean density ρ_m as given in Eq. (2) assumes homogeneous flow, i. e. that gas and liquid phase move at the same speed without slip. Accordingly, the homogeneous void fraction α_{hom} is given in Eq. (3) where it is calculated from the ratio of gas volumetric flow rate to overall two-phase volumetric flow rate (see e. g. Thome, 2016). The acceleration pressure drop in Eq. (1) is less than 1% of the total pressure drop and, therefore, is neglected.
For single-phase liquid flow, the differential pressure manometer in Fig. 1 does not measure the hydrostatic pressure difference, but only the frictional (and acceleration) pressure drop, assuming the liquid densities to be the same in the channel and the tubes connecting it to the manometer. For two-phase flow, however, the mean densities and, thus, the hydrostatic pressures, differ in the

channel and the tubes. Applying Bernoulli's equation to the experimental setup in Fig. 1 yields the frictional pressure drop from differential pressure measurement by subtracting the difference of the hydrostatic pressures in tubes and channel over the distance between the pressure tabs Δz:

$$\Delta p_{fric} = \Delta p_{diff} + \sin\theta \, \alpha_{\mathrm{hom}} \, (\rho_{liq} - \rho_{gas}) \, g \, \Delta z \qquad \text{Eq. (4)}$$

Eq. (4) is valid for all three flow directions by introducing the orientation angle θ which is defined according to Fig. 1. In the case of horizontal flow, the orientation angle is 0° and, hence, the difference between the hydrostatic pressures in tubes and single channel would be eliminated from Eq. (4). In horizontal two-phase flow, therefore, the frictional pressure drop can be measured directly, without knowledge of the void fraction, and equals the value of the differential pressure – neglecting pressure drop due to acceleration. In the case of single-phase liquid flow, the void fraction is zero and, again, the frictional pressure drop is the same as the measured differential pressure. For two-phase vertical upward and downward flow, however, an assumption about void fraction is necessary to derive the frictional pressure drop from the measured differential pressure.

3.2. Friction Factor and Dissipation Rate

The two-phase Darcy friction factor λ_{2ph} is calculated according to Eq. (5) using the experimental two-phase pressure drop given Eq. (4). The definition is similar to single-phase flow (see e. g. Martin, 2010) but applies the mean density ρ_m from Eq. (2) and the mixture velocity c_{2ph} which equals the individual velocity of each phase in the homogeneous model. In Eq. (6), the homogeneous mixture velocity c_{2ph} is given as the sum of the superficial velocities $c_{S,liq}$ and $c_{S,gas}$ as deduced from the volumetric flux (see e. g. Thome, 2016). The channel length L, the hydraulic diameter D_h and the cross-section A of the channel are given in Table 1.

$$\lambda_{2ph} = 2\Delta p_{fric} \, D_h \, (\rho_m \, {c_{2ph}}^2 \, L)^{-1} \qquad \text{Eq. (5)}$$

$$c_{2ph} = (\dot{V}_{gas} + \dot{V}_{liq}) \, A^{-1} = c_{S,liq} + c_{S,gas} \qquad \text{Eq. (6)}$$

The Reynolds number of the liquid phase in homogeneous two-phase flow is defined in Eq. (7), where ν_{liq} is the liquid kinematic viscosity and c_{2ph} is the velocity of the liquid in two-phase flow, i. e. the homogeneous mixture velocity since gas and liquid are assumed to move at the same speed.

$$\mathrm{Re}_{2ph,liq} = c_{2ph} \, D_h \, {\nu_{liq}}^{-1} \qquad \text{Eq. (7)}$$

The two-phase dissipation rate ε_{2ph} is defined in Eq. (8) as the rate of the dissipated energy per fluid mass in the channel. The rate of the dissipated energy is the product of frictional pressure drop and two-phase volumetric flow rate. The channel volume V_{ch} is length L by cross-section A.

$$\varepsilon_{2ph} = \Delta p_{fric} \, (\dot{V}_{liq} + \dot{V}_{gas}) \, (\rho_m \, V_{ch})^{-1} \qquad \text{Eq. (8)}$$

Induced by the channel corrugations, the centrifugal force has a great impact and often dominates over buoyancy, as described in Buscher (2019). In order to quantify the relation of the centrifugal force to buoyancy, the centrifugal Froude number is defined in Eq. (9). The corrugation depth a, as given in Table 1, is inserted for the characteristic radius R.

$$Fr_c = {c_{2ph}}^2 \, (R \, g)^{-1} \qquad \text{Eq. (9)}$$

The equations Eq. (1) to (9) are also valid for single-phase liquid flow in which void fraction is zero.

3.3. Uncertainty Analysis

Due to error propagation, the extended uncertainties of the friction factor and the centrifugal Froude number are at most 12% which is relatively high compared to the other parameters. In contrast, the dissipation rate has a maximum uncertainty of 7%, the homogeneous mixture velocity a maximum of 3% and the liquid Reynolds number in two-phase flow at most 5%. The uncertainties are calculated for each measurement separately and are usually smaller.

4. RESULTS AND DISCUSSION

4.1. Identifying Homogeneous and Heterogeneous Flow

In Fig. 3, the empirical values almost resemble a straight line in the log-log scale: The dissipation rate according to Eq. (8) is plotted against the homogeneous mixture velocity given in Eq. (6). The values for single-phase liquid flow are indicated as yellow crosses. The yellow line is the predicted dissipation rate of single-phase flow calculated from Eq. (8), Eq. (5) and Eq. (11) below.
The two-phase dissipation rates are displayed in different colors for each flow direction. Different symbols were chosen according to the homogeneous void fraction corresponding to each measurement: If $\alpha_{hom} < 0.7$, a cross is used, and for $\alpha_{hom} > 0.7$ an empty circle is displayed. The centrifugal Froude number given in Eq. (9) is drawn as grey dots underlying the symbols. However, only Froude numbers up to 2 are displayed grey whereas higher values are not displayed.

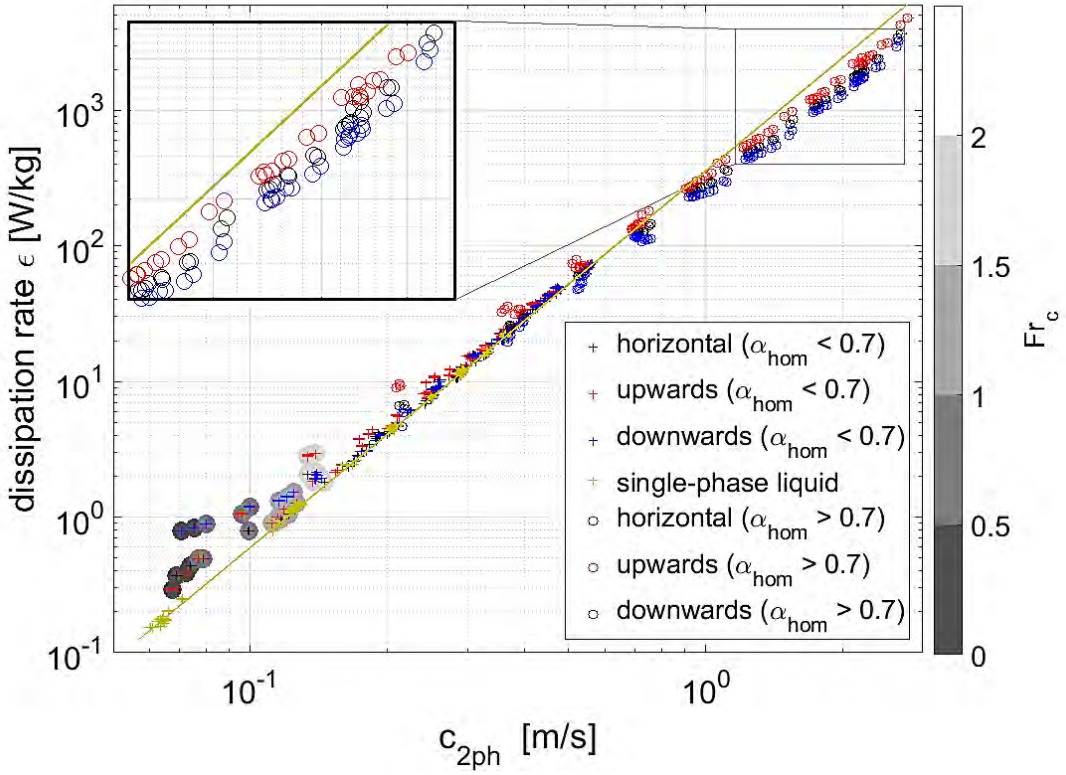

Figure 3: Dissipation rate over homogeneous mixture velocity

The majority of the crosses ($\alpha_{hom} < 0.7$) of all colors (flow directions) are located on the curve of the single-phase liquid dissipation rate. All crosses which are further away from the single-phase curve are plotted on grey dots because their centrifugal Froude numbers are less than 2. In those cases (i. e. $Fr_c < 2$) buoyancy exerts a force which is at least half the value of the centrifugal force due to low mixture velocity. For low Froude numbers, therefore, the buoyancy and, thus, flow direction greatly influences void fraction, pressure drop and dissipation rate. Since slip occurs, the homogeneous model is mostly not valid for $Fr_c < 2$. According to Buscher (2019), the flow patterns

of the three flow directions also differ for $Fr_c < 2$ due to buoyancy, whereas the channel orientation has no impact if the centrifugal force clearly dominates ($Fr_c > 10$).
The crosses without grey dots, falling on the same curve for all flow directions (i. e. $\alpha_{hom} < 0.7$ and $Fr_c > 2$), are identified as homogeneous flow: Since there is no slip, the void fractions and dissipation rates are independent of the flow direction. Buscher (2019) identified the corresponding flow patterns as disperse flow, i. e. mostly bubbly flow. Bigger gas units ("Taylor-like bubbles") were also observed, but were still narrow enough to be subject to the centrifugal forces. In the literature, the homogeneous model is assumed for disperse flow in tubes (e. g. Thome, 2016) and cross-corrugated channels (Grabenstein et al., 2017). Based on the empirical data of this study, the homogeneous model is shown to be actually correct for $\alpha_{hom} < 0.7$ and $Fr_c > 2$, presupposing a uniform gas-liquid distribution. However, bubbly flow at centrifugal Froude numbers lower than 2 is supposed to be strongly influenced by buoyancy and, therefore, not assumed to be homogeneous.
Furthermore, the crosses without the grey dots (i. e. $\alpha_{hom} < 0.7$ and $Fr_c > 2$) fall on the yellow curve of the single-phase flow. This also confirms the validity of the homogeneous model, i. e. that the homogeneous densities and mixture velocities are correct: The mass-specific dissipation rate is expected to be similar for single-phase and homogeneous two-phase flow because it is mostly induced by the contact points of the wave crests where the mass flow is redirected many times. Since the two-phase parameters are very sensitive to void fraction, the calculated two-phase dissipation rate clearly shows even small deviations from the homogeneous model. In the presented data, the mass flow is always dominated by the liquid phase due to the great liquid density: Although the homogeneous void fraction is varied up to 98%, the mass fraction of the gas is always less than 10% of the overall mass flow. Also, the corrugated surface is always wetted.
In Fig. 3, however, the empty circles ($\alpha_{hom} > 0.7$) do not fall either on one curve for different flow directions (colors) or on the yellow single-phase curve. Hence, the homogeneous model is not accurate for void fractions above 0.7. This is not attributed to buoyancy since the centrifugal Froude number is always above 2 in these cases. Instead, the flow patterns which occur for $\alpha_{hom} > 0.7$ are used as explanation: According to Buscher (2019), the gas phase agglomerates to large units constituting regions of local film flow. In contrast to disperse flow, the gas is not obliged to follow the helical flow path and is able to accelerate resulting in slip (Buscher, 2019). Therefore, the mean density increases whereas the velocity of the liquid and the energy dissipation decreases. However, slip only explains the deviations of the empty circles from the single-phase curve, but not the influence of flow direction if buoyancy is to be neglected.
As highlighted by the enlarged section in Fig. 3, the dissipation rates for $\alpha_{hom} > 0.7$ clearly differ with respect to flow direction, i. e. the empty circles of different colors do not fall on one curve. This finding is attributed to the role of the hydrostatic pressure in Eq. (1): The total pressure difference of upward flow is larger compared to downward flow, because the hydrostatic pressure difference is added in the first case and subtracted in the latter, whereas it has no impact on horizontal flow. The higher total pressure drop of upward flow causes the gas to expand more and, probably, to accelerate more resulting in a higher friction at the interface compared to down-flow. Therefore, the friction at the interface friction should not be neglected for $\alpha_{hom} > 0.7$, in contrast to homogeneous flow ($\alpha_{hom} < 0.7$) which has no slip.
In Fig. 4, however, the dissipation rates with $\alpha_{hom} > 0.7$, represented by the empty circles, do neatly fall on one curve, as highlighted by the enlarged section. This is obtained by modifying the frictional pressure drop first given in Eq. (4): Introducing the factor 0.5 to the hydrostatic pressure difference of pure water to two-phase flow yields the modified frictional pressure drop as defined in Eq. (10).

$$\Delta p_{fric,0.5} = \Delta p_{diff} + 0.5 \cdot \sin\theta \, \alpha_{\mathrm{hom}} \, (\rho_{liq} - \rho_{gas}) \, g \, \Delta z \qquad \text{Eq. (10)}$$

Measurement devices, evaluation methods and so forth have been ruled out, of course, to be responsible for this strikingly regular effect. However, only the values denoted by the empty circles (i. e. $\alpha_{hom} > 0.7$ and $Fr_c > 2$) fall together on one curve, whereas the crosses ($\alpha_{hom} < 0.7$) are not affected much or even drawn apart from each other a bit. In both Fig. 3 and 4, the error bars are smaller than the symbols and, therefore, are not visible.

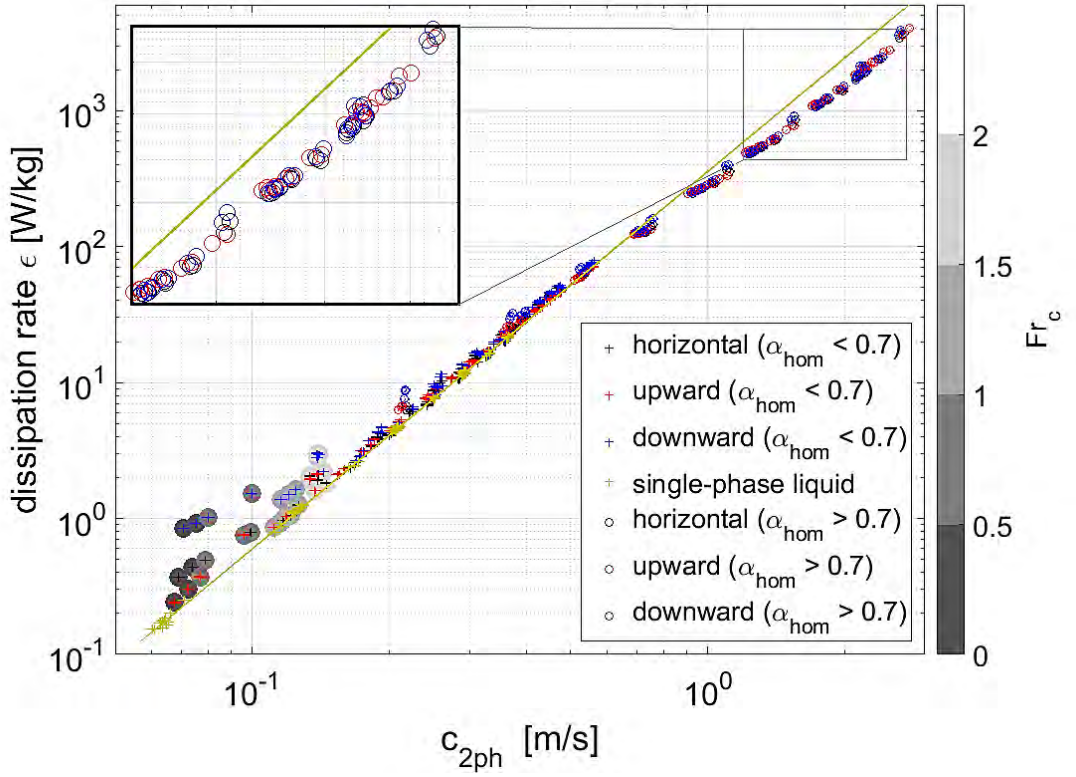

Figure 4: Dissipation rate over homogeneous mixture velocity – modified hydrostatic pressure

4.2. Correlations for Homogeneous and Heterogeneous Friction Factors

In Fig. 5, the two-phase friction factor is plotted over the two-phase Reynolds number of the liquid phase given in Eq. (5) and (7), respectively. As in Fig. 3, the crosses denoting homogeneous flow (α_{hom} < 0.7 and Fr_c > 2) tend to fall on the yellow curve of the single-phase liquid flow. The friction factors with Froude numbers less than 2 or void fractions above 0.7 differ from that curve. Since the friction factor is more sensitive to measurement errors, the effect is not as clear as in Fig. 3, but still visible.

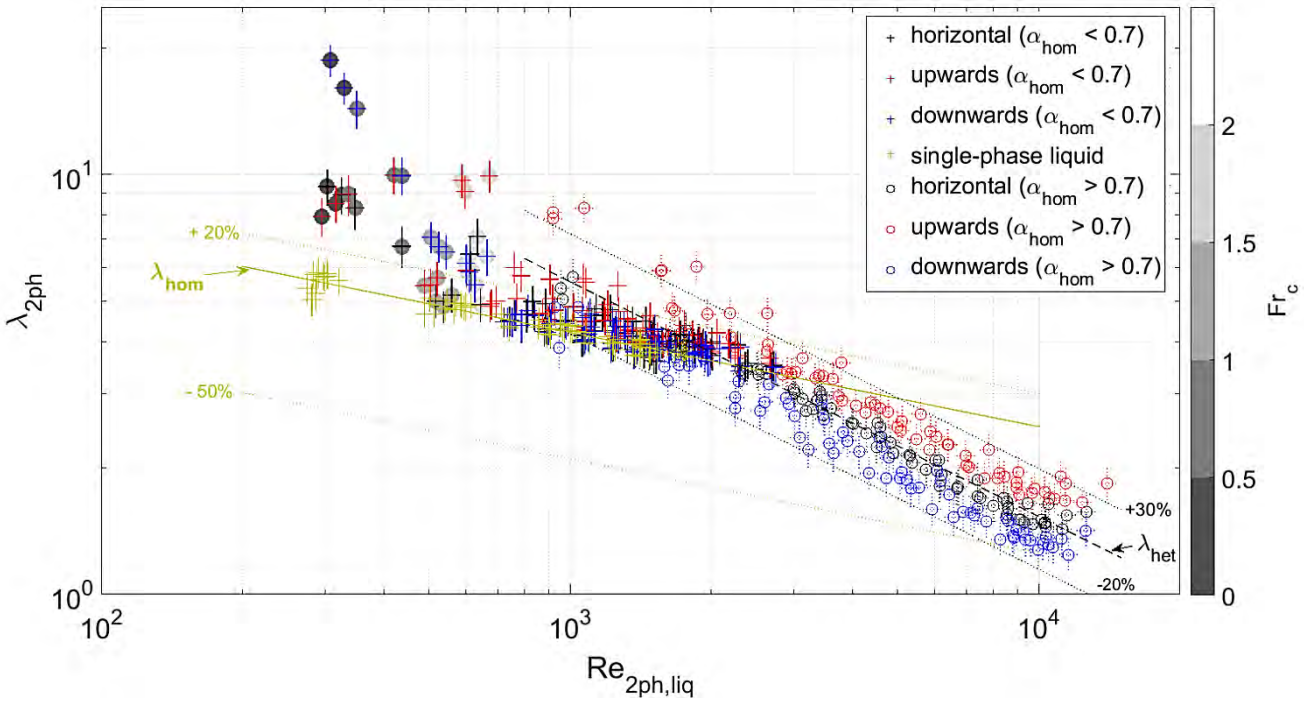

Figure 5: Friction factor over two-phase Reynolds number for the liquid phase

For single-phase measurements, Focke and Knibbe (1986) report turbulent flow for Re>160 in a cross-corrugated channel with a corrugation angle of 80°. Therefore, all measurements presented here are assumed to be turbulent because the Reynolds numbers are well above 200.
The friction factor given in Eq. (11) is fitted to the single-phase measurements and, also, assumed to be valid for the homogeneous flow.

$$\lambda_{\mathrm{hom}} = 19.9\ \mathrm{Re}_{2\,ph,liq}^{-0.225} \qquad \text{Eq. (11)}$$

In Fig. 5, the friction factors of homogeneous two-phase flow, displayed as crosses without grey dots ($\alpha_{hom} < 0.7$ and $Fr_c > 2$), follow the curve given in Eq. (11), mostly deviating less than 20%.
In Eq. (12), a "heterogeneous" friction factor, valid for $\alpha_{hom} > 0.7$, is fitted to horizontal flow which is denoted by the black empty circles. The experimental values with $\alpha_{hom} > 0.7$ are also calculated by the equations given in section 3, although flow is not assumed to be homogeneous. The vertical upward and downward values for $\alpha_{hom} > 0.7$ are within the range of +30% and -20% of Eq. (12) and within -50% below the homogeneous friction factor of Eq. (11).

$$\lambda_{het} = 266\ \mathrm{Re}_{2\,ph,liq}^{-0.56} \qquad \text{Eq. (12)}$$

4.3. Practical Implications

The single-phase friction factor is a means to estimate two-phase pressure drop in a plate heat exchanger – if the liquid is dominant in the total two-phase mass flow, if the Reynolds number is calculated according to Eq. (7), and if the Froude number is above 2. In the case of homogeneous flow, which is valid for bubbly flow and $Fr_c > 2$, this estimation is quite accurate.
In order to test the validity of the homogeneous model in a plate heat exchanger, or to evaluate the gas-liquid distribution, plotting the experimentally derived dissipation rates of liquid flow and two-phase flow over the homogeneous mixture velocity is recommended. Prerequisites are adiabatic two-phase flow, dominance of the liquid mass flow and a high corrugation angle of the plates, i. e. above 60° (Focke and Knibbe, 1986). The homogeneous model is confirmed if the two-phase and single-phase dissipation rates are similar. Furthermore, in the case of absolutely uniform gas-liquid distribution, the two-phase dissipation rate falls on the curve of the single-phase flow for void fractions up to 0.7 and Froude numbers not much above 2. On the other hand, a non-uniform gas-liquid distribution is evident if the two-phase dissipation rate is clearly lower than the single-phase curve for $\alpha_{hom} << 0.7$. This is attributed to early onset of slip due to maldistribution of the gas phase, as is observed in other experiments (yet to be published) in non-uniform gas injection.

5. CONCLUSIONS

The two-phase pressure drop of a cross-corrugated single channel with uniform gas-liquid distribution was investigated for different flow directions. Homogeneous and heterogeneous flow was distinguished by comparing the dissipation rates of two-phase and single-phase flow. Homogeneous flow was found to occur at void fractions below 0.7 and centrifugal Froude numbers above 2. A correlation of the single-phase friction factor was given, being also valid for homogeneous flow, and serving as a rough approximation for pressure drop in heterogeneous flow. Comparing single- and two-phase dissipation rates was proposed as a means of investigating the validity of the homogeneous model or the gas-liquid distribution in a plate heat exchanger.

REFERENCES

Asano, H., Takenaka, N., Fujii, T., 2004. Flow characteristics of gas–liquid two-phase flow in plate heat exchanger (Visualization and void fraction measurement by neutron radiography). Exp. Therm. Fluid Sci. 28, 223–230.

Buscher, S., 2019 (submitted). Flow patterns of vertical and horizontal adiabatic two-phase flow in a plate heat exchanger single channel with uniform gas-liquid distribution. Proceedings of the 25th IIR International Congress of Refrigeration, Montréal, Canada, IIF/IIR, ID 512.

Focke, W., Knibbe, P., 1986. Flow visualization in parallel-plate ducts with corrugated walls. J. Fluid Mech. 165, 73–77.

Grabenstein, V., Polzin, A.-E., Kabelac, S., 2017. Experimental investigation of the flow pattern, pressure drop and void fraction of two-phase flow in the corrugated gap of a plate heat exchanger. Int. J. Multiphase Flow 91, 155-169.

Kreissig, G., Müller-Steinhagen, H.M., 1992. Frictional pressure drop for gas/liquid two-phase flow in plate heat exchangers. Heat Transfer Engineering 13(4), 42–52.

Martin, H., 2010. N6 Pressure drop and heat transfer in plate heat exchangers. In: VDI-GVC (Ed.), VDI Heat Atlas, 2nd ed., Springer-Verlag, Berlin, Heidelberg, 1515-1521.

Nilpueng, K., Wongwises, S., 2010. Two-phase gas–liquid flow characteristics inside a plate heat exchanger. Exp. Therm. Fluid Sci. 34, 1217–1229.

Thome, J. R. (Ed.), 2016. Encyclopedia of two-phase heat transfer and flow I – Fundamentals and methods. World Scientific Publishing, Singapore, 1112 p.

Tribbe, C., Müller-Steinhagen, H., 2001. Gas/liquid flow in plate-and-frame heat exchangers – Part I: Pressure drop measurements. Heat Transfer Eng. 22(1), 5–11.

Manuscript ID: 476
DOI: 10.18462/iir.icr.2019.0476

A fundamental equation of state for lubricant-refrigerant mixtures with optimization based on transport and interfacial properties

Tobias Göpfert[(a)], Christiane Thomas[(a)], Ullrich Hesse[(a)]

(a) Technische Universität Dresden,
BITZER-Chair of Refrigeration, Cryogenics and Compressor Technology
Dresden, 01062, Germany, Tobias.Goepfert@tu-dresden.de

ABSTRACT

For the optimization of refrigeration components the thermophysical properties of the lubricant refrigerant mixtures are needed. Most often semi-empirical equations of state are used which are often developed under strict boundary conditions as more generic equations of state for lubricant refrigerant mixtures are not available.
This paper shows an approach to develop a fundamental equation of state based on the reduced Helmholtz energy to describe the thermodynamic properties of lubricant refrigerant mixtures.
In a new approach, the viscosity and the interfacial tension of the mixtures of lubricant and refrigerant are used for the optimization of the structure and the coefficients of the equations of state. For this purpose the residual entropy viscosity scaling and empirical equations for the interfacial tension are used. Based on this equation also properties like heat capacities of the mixture and the theoretical solubility of the lubricant diluted in the gas phase, which are difficult to measure, can be determined.
Keywords: Lubricant refrigerant mixture, equation of state, entropy scaling, interfacial tension

1. INTRODUCTION

The optimization of refrigeration machines can be achieved by improving the used refrigerant, the refrigeration machine components, the control and feedback control systems and combinations of the mentioned possibilities. Often the used lubricant which circulates in the overall cycle is overlooked. Increasing environmental requirements leads to a reduced number of available refrigerants which means that also other ways for the cycle optimization are needed. One option is to improve the oil management inside the refrigeration cycle. The reduction of friction losses, reduced heat transition by oil deposition in the condenser or evaporator as well as oil deposition in accumulators can improve the overall efficiency of the system. For the optimization process however thermophysical properties of the used lubricant and the refrigerant-oil-solution (ROS) are needed. These data are often not available and several properties for this purpose are also very difficult to measure.
The state of the art shows that the thermodynamic properties of refrigerants and refrigerant mixture can be be calculated very accurately by optimized empirical equations of state (EOS). For this purpose different property measurements of the vapor-liquid-equilibria for each pure fluid and the mixture for different concentrations, heat capacity data, speed of sound data and many more are used. VLE (Vaporl-liquid-equilibria) data are important to create an EOS but are often not available for lubricants since the vapor pressure is very low at moderate temperatures. Additionally the properties at the critical state are often used to produce reduced parameters for the EOS. These properties are also difficult to measure for lubricants and only a few approaches are known like (Skripov et al., 2003) and (Skripov et al., 2007). For the ROS also the critical loci must be calculated which is also difficult to measure. A different concept was shown by (Zhelezny et al., 2003) and (Medvedev et al., 2004) with the backwards calculation of the pseudocritical temperature and density of an ROS based on the VLE data of the ROS itself. This approach is one of the basic ideas for the following algorithm.
Transport properties like the thermal conductivity and viscosity as well as interfacial properties like the boundary tension of pure fluids, the interfacial tension of mixtures and the diffusion coefficient

are calculated by separated equations since these can not be calculated by the derivatives of the EOS. The equations to calculate the properties are nearly always empirical and are fitted to measurement data and the EOS which must be available. Since this is often not the case the empirical equations are mainly based on temperature and pressure. Other discussed approaches like from (Zhelezny et al., 2009) can reduce this problem however they are only useable in a specific range of composition. Approaches based on the residual entropy scaling like from (Novak 2011), (Lötgering-Lin et al., 2015) or (Bell et al., 2016) have the advantage that they correlate the residual entropy directly to the dynamic viscosity. This also means that there is a direct connection of the entropy - which is calculated by derivatives of the EOS - to a transport property. This connection can be used to have a backwards effect in the fitting procedure and so an optimization effect based on transport properties. This is especially interesting since the viscosity data base is mostly better for ROS than the data base of other thermophysical properties.
In this paper a way of fitting an equation of state of an ROS with a further optimization based on transport and interfacial properties is shown. This approach can also be used for other fluid mixtures which are difficult to measure, to produce in high purity or which are unstable in pure form.

2. EMERPICAL EQUATIONS AND FITTING PROCEDURE

2.1. Form of the Equation of State for Lubricants and ROS

The form of the EOS of the lubricant is assumed to be similar to the results of (Alexandrov et al., 2013) which correspond to Eq. (1) to Eq. (3).

$$\alpha(\delta,\tau) = \alpha^o(\delta,\tau) + \alpha^r(\delta,\tau) \qquad \text{Eq. (1)}$$

$$\alpha^o(\delta,\tau) = ln\,\delta + a_1 \cdot ln\,\tau + a_2\tau^{t_2} + \sum_i a_i\, ln[1 - exp(-b_i\tau)] \qquad \text{Eq. (2)}$$

$$\alpha^r = \sum_i n_i \cdot \delta^{d_i} \cdot \tau^{t_i} + \sum_i n_i \cdot \delta^{d_i} \cdot \tau^{t_i} \cdot exp\left(-\delta^{l_i}\right) \qquad \text{Eq. (3)}$$

α is the reduced Helmholtz energy, δ is the reduced density and τ the inverse reduced temperature. The lubricant can be assumed to be a pseudo pure fluid, since the overall concentration and different hydrocarbons are often unknown. The number of the coefficients in Eq. (2) and (3) can be variable or fixed. Since the fitting procedure with variable numbers of coefficients is much more complex and need highly stable solvers and optimization algorithms as discussed in (Span, 2000) a fixed number of variables for the first fitting procedures was used for the description in the present paper. Eq. (1) has to be extended to be used with mixtures as shown in Eq. (4).

$$\alpha(\delta,\tau,\xi) = \alpha^o(\delta[x],\tau[x],x) + \alpha^r(\delta[x],\tau[x],x) + \alpha_{ij}^r(\delta[x],\tau[x]) \qquad \text{Eq. (4)}$$

The concentration vector *x* contains the information about the components and their concentration in the mixture. Details on the calculation of the thermodynamic properties and further equations for the EOS are shown in (Kunz et al., 2007) and (Gernert, 2013). In this paper Eq. (5) was used for the calculation of the interaction Helmholtz energy α_{ij}^r.

$$\begin{aligned}\alpha_{ij}^r(\delta[x],\tau[x]) = &\sum_{k=1}^{N_{pol}} n_{ij,k} \cdot \delta^{d_{ij,k}} \cdot \tau^{t_{ij,k}} + \sum_{k=N_{pol}+1}^{N_{pol}+N_{exp}} n_{ij,k} \cdot \delta^{d_{ij,k}} \cdot \tau^{t_{ij,k}} \cdot exp\left(-\delta^{l_{ij,k}}\right) \\ &+ \sum_{k=N_{pol}+N_{exp}+1}^{N_{pol}+N_{exp}+N_{crit}} n_{ij,k} \cdot \delta^{d_{ij,k}} \cdot \tau^{t_{ij,k}} \cdot exp\left(-\pi_{ij,k} \cdot \left(\delta - \varepsilon_{ij,k}\right)^2 - \beta_{ij,k}\left(\delta - \gamma_{ij,k}\right)\right)\end{aligned} \qquad \text{Eq. (5)}$$

2.2. Calculation of the viscosity based on the residual entropy scaling

The calculation of the dynamic viscosity is based on the entropy scaling shown by (Bell et al., 2016). It has been shown that a lot of fluids can be calculated by a corresponding approach. It can be assumed that the viscosity behaviour of the lubricant can only be poorly well described by refrigerants as reference fluids. In this paper the fitting of the correlation was carried out directly for the lubricant in the fitting procedure. The reduced dynamic viscosity η_r is aa function of the reduced residual entropy χ as shown in Eq. (6), see (Bell et al., 2016).

$$\eta_r = \frac{\eta}{\eta_0} = f(\chi) \quad \text{with} \quad \chi = \frac{s^r}{s_c^r} \qquad \text{Eq. (6)}$$

Where η is the dynamic viscosity, η_0 the ideal gas viscosity, s^r the residual entropy and s_c^r the residual entropy at the critical point which can be calculated from the EOS. The approach of Bell (Bell et al., 2016) does not show results for fluid mixtures so that modifications are needed. The ideal gas viscosity of the fluid mixture can be calculated by the equation of (Wilke, 1950) knowing the ideal gas viscosity of each component calculated by the equation of (Chapman et al., 1970). The generalized reduced viscosity η_r for the saturated liquid phase for each component can be calculated by Eq. (7) and for the mixture by Eq. (8).

$$log_{10}[\eta_{r,i}(\chi)] = \sum_{i=0}^{3} c_i \cdot \chi^i \qquad \text{Eq. (7)}$$

$$log_{10}[\eta_r(\chi, x)] = \sum_{i=1}^{N} x_i \cdot log_{10}(\eta_{r,i}) + \sum_{i=1}^{N-1} \sum_{\substack{j=1 \\ j \neq i}}^{N} x_i \cdot x_j \cdot (A_{ij} + B_{ij} \cdot \chi) \cdot [log_{10}(\eta_{r,i}) \cdot log_{10}(\eta_{r,j})]^{\frac{1}{2}} \qquad \text{Eq. (8)}$$

Where A_{ij} and B_{ij} are the dimensionless interaction parameter and N the number of fluids in the mixture.

2.3. Calculation of the interfacial tension between liquid and vapor phase of ROS

The calculation of the boundary and interfacial tension of the ROS was shown by (Zhelezny et al., 2014). The basic idea is to produce a link between the vapor pressure of the ROS and the boundary tension as shown in Eq. (9).

$$\varphi(T, x) = \frac{\sigma(T, x)}{\sigma_{NBP}(x)} \qquad \pi(T, \xi) = ln\left(\frac{p_c(x)}{p_s(T, x)}\right) \qquad \text{Eq. (9)}$$

Where φ is the reduced boundary tension, σ the boundary tension ,σ_{NBP} is the boundary tension of the ROS at the normal boiling point, π the reduced pressure, p_c the critical pressure of the ROS and p_s the vapor pressure of the ROS as a function of temperature and concentration in MPa. Since the boundary tension corresponds to the vapor pressure of the mixture these equations can be used to have a backwards effect on the fitting procedure. As discussed in (Zhelezny et al., 2014) when using the pendant drop method for measuring the boundary tension, the surface layer is in equilibrium to the gaseous phase. That means the concentration of the layer must be known for further analysis. Since the saturation concentration is easier to measure than the concentration in the boundary between saturated liquid and gas phase, an additional equation as a concentration correction factor is needed as discussed by (Zhelezny et al., 2014).
As shown in former papers like (Göpfert et al., 2016) and (Göpfert et al., 2017) it is much easier to measure the Laplace-coefficient a than the boundary tension itself. For the fitting procedure Eq. (10) was used.

$$a = \sqrt{\frac{\sigma}{\Delta\rho \cdot g}} \qquad \text{Eq. (10)}$$

$\Delta\rho$ the density difference between boiling liquid and saturated dry steam and g is the gravitational acceleration.

2.4. Fitting procedure and boundary conditions

The fitting procedure and the comparison to the state of the art is shown in Fig. 1. In the state of the art the EOS of each fluid has to be fitted at first before the mixture can be fitted. This leads to problems for lubricants or other fluids with very low vapor pressure since they are difficult to measure or can just be pre-calculated by generalized equations. The second step is to fit the data of the critical loci of the mixture since these data are commonly used for calculating the reduced density and reduced temperature. Since they often do not describe the exact critical state they are utilized as reducing parameters. Especially when just a few or no data for the critical loci are available for fitting, it is possible to use a predefined interaction model. By adjusting the parameter of the critical loci the difference between data points and the correlation are minimized. In a third Step the interaction parameters of mixture are fitted, if this is not done in step 2 or not needed.

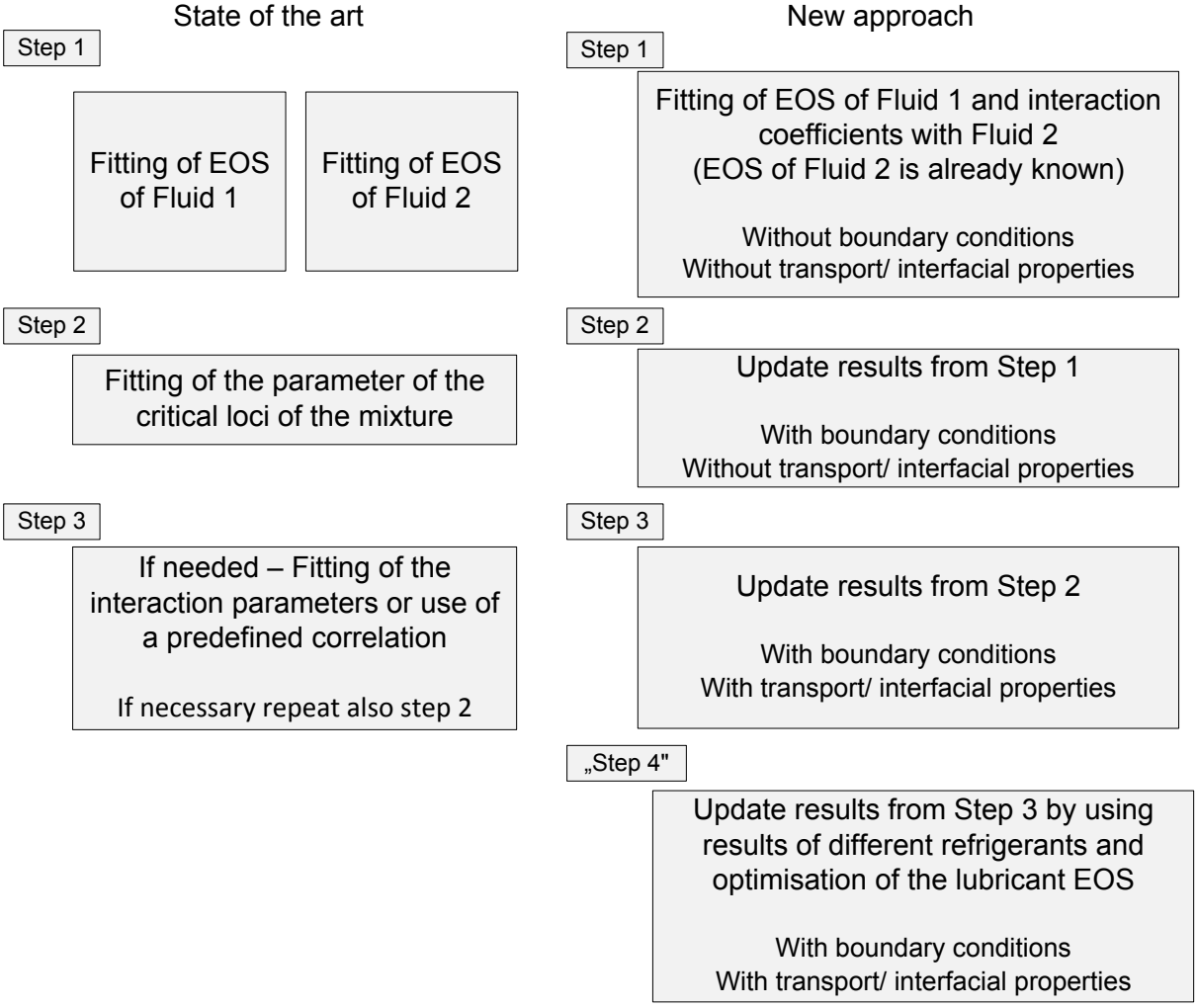

Figure 1: Comparison of fitting procedure to the state of the art

The new approach fits at first the EOS of the lubricant and the interaction with fluid 2 directly. For the first step no transport/interfacial properties and also no boundary conditions are used. This is important to get a first numerically stable solution. In step 2 the results from step 1 are improved relating to the boundary conditions shown in Table 1. The form of the equation changes since after step 1 there are still some boundary conditions which are not satisfied. The algorithm tries to reduce the MSE (Mean Square Error) between measurement points and the fit while reducing the number of not satisfied boundary conditions. In this paper all boundaries must be fulfilled in the fitting procedure, since especially the derivations of the EOS must be numerically stable. In the third step also the transport/interfacial properties are used in the fitting process. This becomes important since there are not always VLE or other thermodynamic properties available for the entire thermodynamic range of interest. Also sometimes the database of viscosity data is much bigger compared to thermodynamic data sets. The interfacial tension has a backwards effect on

the critical temperature and density and changes the overall shape of the EOS. The viscosity is calculated from the residual entropy and has especially an effect on the derivation of the EOS to the inverse reduced temperature which becomes more stable and reasonable. There is the possibility to use a fourth step for a further improvement by using the steps 1 to 3 for different refrigerants with the same lubricant and using the results in a fourth step to achieve a solution with the same lubricant properties.
The fitting procedure becomes much faster and more stable when reducing internal iteration loops while calculating the thermophysical properties. For this purpose data sets of temperature, density and concentration are needed. This is however not always the case and difficult to achieve from an experimental point of view. For the steps 1 and 2 preliminary fittings of simple equations are helpful, like pressure as a function of temperature and concentration for a binary mixture. Following this way a reverse calculation of the concertation for pressure-temperature data sets, is possible. This can also be helpful for binary mixtures to receive the density as a function of pressure and temperature. These pseudo-data sets can be produced for the first and second step of the fitting and should be erased in the last step to reduce uncertainties which come from the preliminary fittings.

Table 1. Boundary Conditions for the fitting procedure in the new approach

Boundary condition	Derivation
Mechanical stability	$p(T,\rho,x) > 0 \;\rightarrow\; (\partial p/\partial\rho)_{T,x} > 0$
Thermal stability	$(\partial T/\partial s)_{\rho,\xi} = c_v > 0$
Chemical stability	$f_i' = f_i''$ for all $i = 1 \ldots N$
Entropy increase by expansion	$(\partial p/\partial T)_{\rho,x} = (\partial s/\partial\rho)_{T,x} > 0$
Positive viscosity	$\eta(T,\rho,x) > 0$

3. FITTING RESULTS AND DISCUSSION

3.1. Fitting Results for a R170 – POE32 – Mixture

For the fitting procedure 308 data points of a mixture of ethane (R170) and a low viscous POE lubricant of the viscosity group 32 was used. The data contained 131 data points of VLE, 19 of isobaric heat capacity of the pure lubricant, 10 points of Liquid-Liquid-Equilibria, 54 points of density, 32 for boundary tension and 62 points for the dynamic viscosity. The experimental results are shown and discussed in (Göpfert et al., 2019). The fitting was carried out in three steps as shown in Fig. 1. Each step was iterated for 1000 generations or a maximum stall generation of 150. The results after each step are shown in Fig. 2 and are discussed in section 3.2.

3.2. Discussion of results

The number of not satisfied boundary conditions decreased from step 1 to 2. At the end of step 2 as well as in step 3 all boundary conditions can be fulfilled. In the program the reduction of the not satisfied boundary conditions is taken priority over the reduction of MSE, which is carried out afterwards. The MSE is low and the number of not satisfied boundaries is high after step 1 which changes with step 2. From step 1 to 2 this was to be expected since the form of the EOS was not restricted so that the polynomial terms tend to swing in step 1. This behavior changes significantly since the derivations in Table 1 tend to reduce the number of density exponents as can be seen in Fig. 2. The distribution of the exponents of the reduced density d_i becomes more uniform in step 2 for the oil and also for the interaction part (Eq. (5)). The same behavior can be seen for the reduced temperature exponents. An interesting effect is, that the uniform distribution of the l_i tend more to the boundary values of 0 and 3 in step 2.
The results after step 3 show a different behavior. The density exponents tend to the boundaries of 0 and 6 which means that the dependence of the equation by the reduced density decreases. On the other hand the dependency on the reduced temperature increases as can be seen in Fig. 2 by the coefficient t_i. The distribution becomes more uniform which results especially from the viscosity data. The reduced entropy in Eq. (6) is calculated by the residual part of reduced Helmholtz energy α^r and the derivation of this part by the inverse reduced temperature τ. The retroactive effect of the

viscosity on the EOS works especially on the temperature dependency. This might lead to an overestimation of the temperature dependency which reduces the density dependency. This effect is also increased by the boundary tension data which have an effect on the critical loci of the ROS and on the reduced temperature dependency of the VLE fitting.

The effect of the overestimation of the temperature dependency might be reduced by using other thermodynamic properties like the speed of sound which have a higher dependency on the reduced density derivations.
The MSE after each step was comparable which means that there was just a small loss on accuracy by improving the boundary conditions. Since the form of the EOS changes dramatically after each step it can be assumed that further boundary conditions must be used in step 3 to decrease the redistribution of the density exponents.

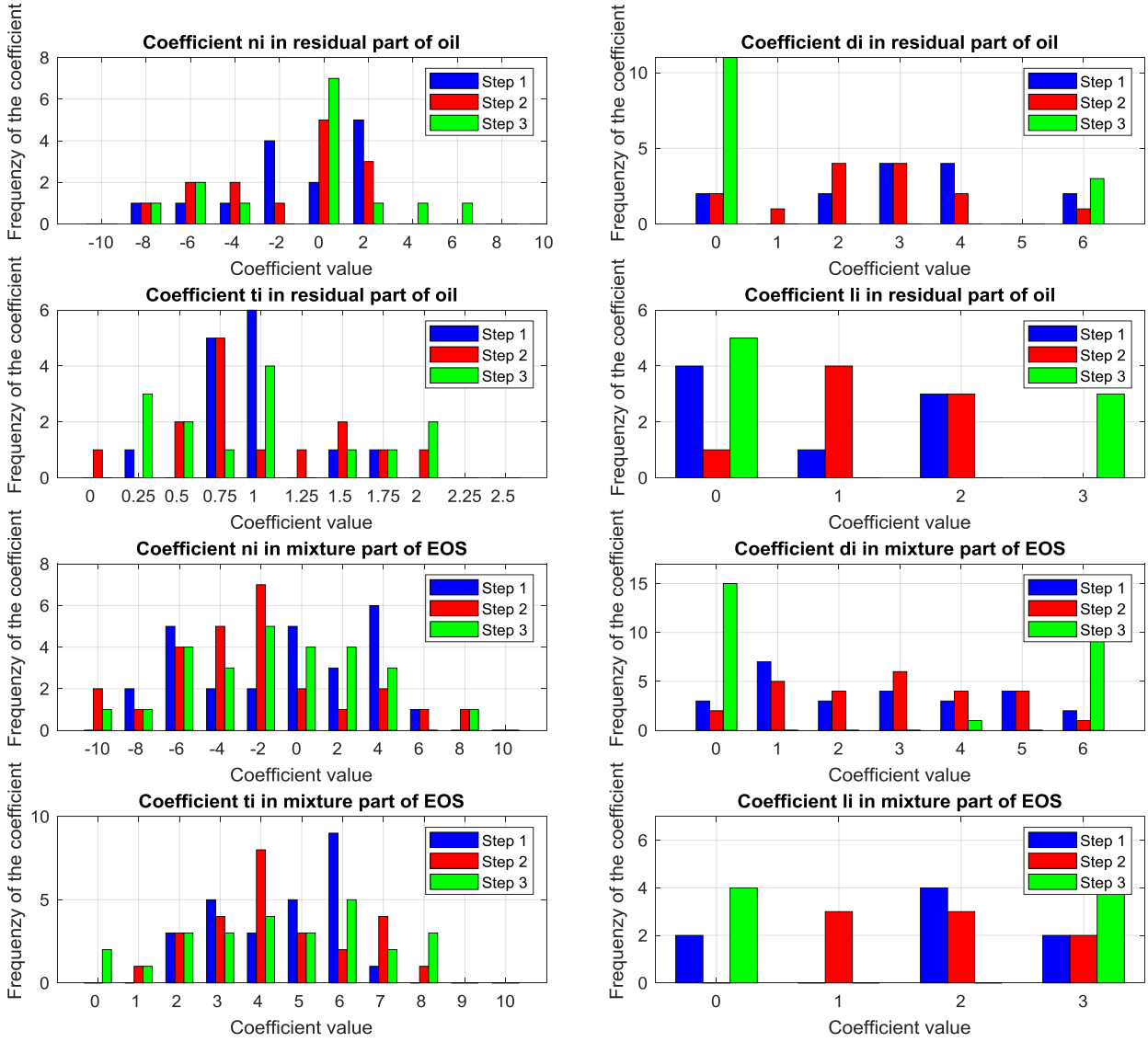

Figure 2: Histograms of the fitting results

4. CONCLUSIONS

The results of the fitting show, that the form and the behaviour of an EOS can be influenced by using transport and boundary properties of fluids and mixtures. The shown algorithm of the EOS fitting by directly fitting the properties of the lubricant and the interaction parameters might be an interesting option also for fluids and mixtures where the fitting of the state of the art procedure is not applicable. Chemically unstable or highly reactive fluids might be such fluids. The temperature dependency of the EOS can be influenced by the viscosity-residual entropy-scaling and the

boundary tension data. But also other properties and mathematical links to the EOS are needed. Another option might be the use of properties like the speed of sound which needs higher derivations to the reduced density. The found EOS shows good results for the boundary conditions but still lacks in term of the reduction of the MSE which is still under development.

NOMENCLATURE

α	Reduced Helmholtz Energy	δ	Reduced density
α^{o}	Ideal gas part of reduced Helmholtz Energy	α^{r}	residual part of reduced Helmholtz Energy
τ	Inverse reduced temperature	x	Concentration vector
η_r	Reduced dynamic viscosity	η	Dynamic viscosity
η_0	Ideal gas dynamic viscosity	s^{r}	Residual entropy
s_c^r	Critical residual entropy	φ	Reduced boundary tension
σ	Boundary tension	σ_{NBP}	Boundary tension at normal boiling point
p_c	Critical pressure	p_s	Vapor pressure of the ROS
$\Delta\rho$	Density difference	a	Laplace coefficient
g	Gravitational acceleration (9.807 m·s^{-2})	A_{ij} B_{ij}	Dimensionless interaction parameter
N	Number of Fluids in the mixture	π	Reduced pressure
T	Absolut temperature	ρ	Density
f	Fugacity		

REFERENCES

Alexandrov, I., Gerasimov, A. and Grigor'ev, B. 2013. Generalized Fundamental equation of state for normal alkaned (C5-C50). s.l.: International Journal of Thermophysics, 34, pp. 1865-1905, 2013.

Bell, Ian and Laesecke, Arno. 2016. Viscosity of refrigerants and other workung fluids from residual entropy scaling. Purdue : 16th International Refrigeration and Air Conditioning Conference at Purdue, 2016.

Chapman, S. and Cowling, T.G. 1970. The mathematical theory of non-uniform gases: an account of the kinetic theory of viscosity, thermal conduction and diffusion in gases. s.l.: Cambridge University Press, 1970.

Gernert, G.J. 2013. A New Helmhotz Energy Model für Humid Gases and CCS Mixtures. Bochum : Ruhr-Universität Bochum, Dissertation, 2013.

Göpfert, T., Thomas, C. and Hesse, U. 2019. Measurement of thermophysical properties of low-viscous polyol ester lubricants in carbon dioxide, ethane and ethylene atmospheres. Montreal : 25th. IIR International Conference of refrigeration ICR, 2019.

Göpfert, T., Thomas, Ch. and Hesse, U. 2017. Effects of temperature and pressure on the surface tension of low viscose lubricants in high pressure atmospheres. Seoul : 5th IIR Conference on Thermophysical Properties and Transfer Processes of Refrigerants, 2017.

Göpfert, T., Thomas, Ch. and Hesse, U. 2016. Surface Tension of Low-viscous Lubricants in High Pressure Carbon Dioxide Atmospheres. West Lafayett: 23rd International Compressor Engineering Conference at Purdue, 2016.

Kunz, O., Klimeck, R., Wagner, W. and Jaeschke, M. 2007. The GERG-2004 Wide Range Equation of State for Natural Gases and Other Mixtures. Düsseldorf : Fortschritt-Berichte VDI, Reihe 6 Nr. 557, 2007.

Lötgering-Lin, O. and Gross, J. 2015. Group Contribution Method for Viscosities Based on Entropy Scaling Using the Peturbed-Chain Polar Statistical Associating Fluid Theory. s.l.: Ind.Eng.Chem.Res, Vol. 54, S. 7942-7652, 2015.

Medvedev, O.O., Zhelezny, P.V. and Zhelezny, V.P. 2004. Prediction of phase equlibria and thermodynamic properties of refrigerant/oil solutions. s.l.: Fluid Phase Equilibria, 215, pp. 29-38, 2004.

Novak, L.T. 2011. Fluid Viscosity-Residual Entropy Correlation. s.l.: International Journal of Chemical Reactor Engineering, 2011. Vol 9, Artikel A107.

Skripov, P.V. et al. 2007. A Method of Controlled Pulse Heating: Applications. s.l.: Journal of Engineering Thermophysics, Vol. 16, No. 3, pp. 155-163, 2007.

Skripov, P.V. et al. 2003. Comparsion of thermophysical properties for oil/refrigerant mixtures by use of the pulse heating method. s.l.: International Journal of Refrigeration, 26, pp. 721-728, 2003.

Span, R. 2000. Multiparameter Equation of State - An Accurate Source of Thermodynamic Property Data. Bochum : Springer-Verlag, 2000. ISBN: 3-540-67311-3.

Wilke, C.R. 1950. A Viscosity Equation for Gas Mixtures . s.l.: The Journal of Chemical Physics, Vol. 18, 517, 1950.

Zhelezny, P.V., Zhelezny, V.P. and Scripov, V.P. 2003. Determination of pseudocritical parameters for refrigerant/oil solutions. s.l.: Fluid Phase Equilibria, 212, pp. 285-302, 2003.

Zhelezny, V.P. et al. 2009. An experimental investigation and modelling of the viscosity refrigerant/oil solutions. s.l.: International Journal of Refrigeration, 32, pp. 1389-1395, 2009.

Zhelezny, V. et al. 2014. Prediction of the surface tension for refrigerants and refrigerant-oil solutions (ROS). s.l.: International Journal of Refrigeration, 40, pp. 241-245, 2014. pp. 241-245.

Manuscript ID: 478
DOI: 10.18462/iir.icr.2019.0478

Measurement of thermophysical properties of low-viscous polyol ester lubricants in carbon dioxide, ethane and ethylene atmospheres

Tobias Göpfert[(a)], Christiane Thomas[(a)], Ullrich Hesse[(a)]

(a) Technische Universität Dresden,
BITZER-Chair of Refrigeration, Cryogenics and Compressor Technology
Dresden, 01062, Germany, Tobias.Goepfert@tu-dresden.de

ABSTRACT

With respect to the increasing ecological requirements on refrigerants and refrigerant mixtures new working fluids especially for temperature applications below 220 K are required. Especially low GWP refrigerants like ethane and ethylene and their binary mixtures with carbon dioxide can be interesting for specific applications were typically low-viscous lubricants are used. However the thermophysical properties of these lubricants with the mentioned refrigerants are often unknown.
This paper shows the experimental results of the measurements of the saturation pressures, miscibility gaps, liquid phase densities, viscosities and interfacial tensions of nine different lubricant refrigerant mixtures.
The results show differences especially in the saturation pressures and the form of the miscibility gaps for the investigated mixtures. For ternary mixtures the effect of refractionation of the refrigerant mixture inside the lubricant is shown by measuring the interfacial tension.
Keywords: Lubricant refrigerant mixture, boundary tension, thermophysical properties, polyol ester lubricants, natural refrigerants, carbon dioxide, R-170, R-1150

1. INTRODUCTION

Increasing environmental requirements leads to a reduced number of available refrigerants for refrigeration cycles. This means that also other ways for the cycle optimization are needed. Especially high-GWP refrigerants have to be replaced by other fluids. One interesting option is to use mixtures of carbon dioxide with other fluids by decreasing the triple point of the mixture and increasing the usable temperature range compared to pure carbon dioxide. As discussed in papers like in example (Di Nicola et al., 2004), (Di Nicola et al., 2007), (Di Nicola et al., 2008), (Di Nicola et al., 2010), (Di Nicola et al., 2011) and (Göpfert et al., 2015) different mixture can be used. However all these publications miss information concerning the properties of refrigerant-oil-solutions (ROS). However these properties are needed for further investigation and experimental research for the application of such mixtures for low temperature refrigeration cascades.

The use of carbon dioxide mixtures is especially interesting in the temperature range from 220 down to 173 K since there are only a few pure refrigerants available. Refrigerants for these temperature ranges are typically used in the second stage of a refrigeration cascade. The lubrication of the used compressor is ensured by using low viscous lubricants, especially POE, and in some few cases dry running machines. Such POE lubricants have a viscosity group equal or lower than 32 cSt at 40 °C, a high viscosity index (VI) and a low pour point. Since typically carbon dioxide is used for higher temperature ranges also higher viscous lubricants are used so that there is an insufficient data situation. As shown by (Göpfert et al., 2015) interesting mixing partners for carbon dioxide are ethane (R170) and ethylene (R1150) since they can form azeotropic mixtures. Similar to carbon dioxide, there is also a lack of data for ethane-POE and ethylene-POE mixtures.
This paper shows experimental results of the thermophysical properties of binary mixtures of 3 different low viscous lubricants from different lubricant suppliers and the refrigerants carbon dioxide, ethane and ethylene.

2. MEASUREMENT DEVICES AND EXPERIMENTAL RESULTS

2.1. Fluids and Experimental Boundary Conditions

Three different commercially available low viscous POE lubricants were analyzed. Oil A and B were from the same and Oil C from another supplier. Oil A and C have the viscosity group 32 and Oil B the viscosity group 22. All lubricants were degassed by heating the oil in a closed vessel up to 70 °C and evacuating it for at least 2 h at a pressure lower than 1 mbar. For the analyses of the lubricant properties the same batch of oil to ensure that there was no influence by analyzing a new product with changed properties. Carbon dioxide with a purity higher than 99.9 % and ethane and ethylene with a purity higher than 99.5 % was used and has been checked periodically by gas chromatography.

2.2. Specific Isobaric Heat Capacity of Lubricants

For the measurement of the isobaric heat capacity of the lubricants a Differential-Scanning-Calorimeter (DSC) in the temperature range from 0 up to 100 °C was applied. Reproduction measurements show an uncertainty of about 4 %. This corresponds to the data sheet of the DSC. Comparing the test results with data from the oil supplier a deviation of about 5 % was exposed. The experimental results and their error band are shown in Fig. 1.

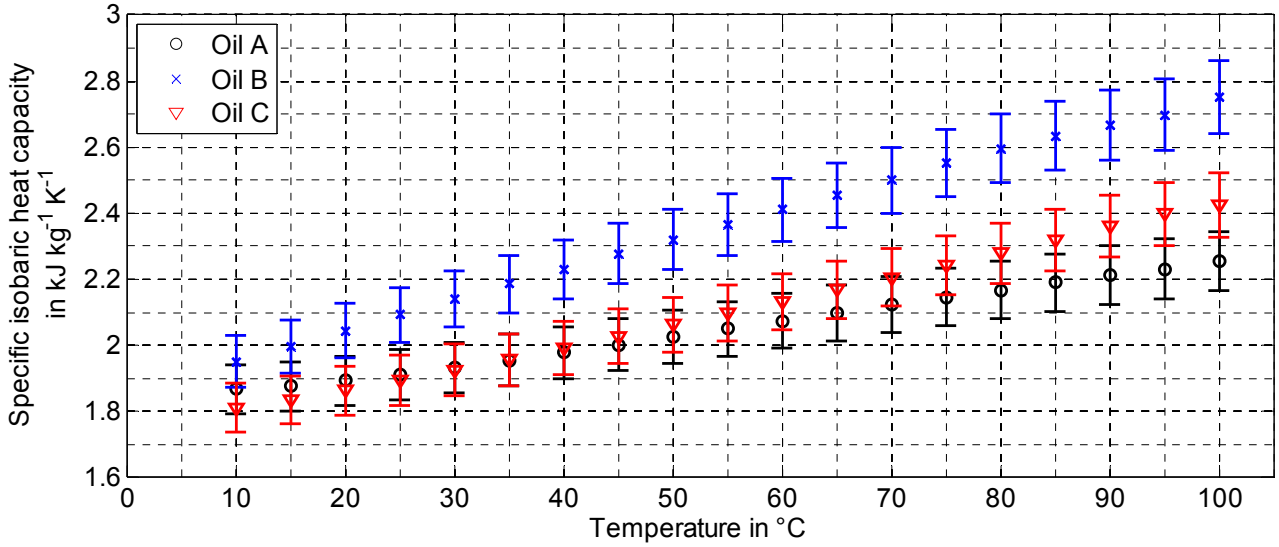

Figure 1: Measurement data of isobaric heat capacity of the lubricants

2.3. Vapor Pressure, Vapor-Liquid-Equilibria (VLE) and Mixing Gaps (LLE) of ROS

For the measurement of the VLE and LLE a new vapor pressure cell made of sapphire glass for pressures up to 150 bar in the temperature range from - 50 up to 80 °C was designed and manufactured. Four cells with different concentrations of oil and refrigerant were analyzed in parallel. Type-T thermocouples with an uncertainty of 0.3 K, pressure sensors with an uncertainty of about 0.2 % (Full-scale) in the pressure range of 0 up to 150 bar have been applied. The relative concentration uncertainty was calculated in the range of 1 up to 5 %. In all cells the pressure, temperature and concentrations were measured while monitoring the phase boundary. When the separation of the liquid phase was detected, the temperature at the beginning of the phase separation was experimentally iterated by in- and decreasing the cell temperature. The results of the LLE are shown in Fig. 2 and of the VLE in Fig. 3. For a better comparison, the results are shown and will be discussed in chapter 3.

2.4. Dynamic and Kinematic Viscosity and Densities of ROS

For the measurement of the dynamic viscosity and the density of the ROS a high pressure double-walled vessel with a viscometer and a density meter was designed. The vessel is temperature controlled by an external device in the temperature region of – 15 up to +80 °C with an uncertainty of the temperature measurement of 0.3 K. The pressure had an uncertainty of about 0.15 %. For

the viscosity measurement an in-Line high pressure process viscometer with a measurement range of 0.1 up to 10.000 mPa·s and an uncertainty of 1 % of the measurement value (but always higher than 0.1 mPa·s) was used. An oscillating fork density meter with a measurement rang of 500 up to 1.500 kg·m^{-3} and an uncertainty of 0.1 % of the measurement value (but always higher than 1 kg·m^{-3}) was implemented in the already described vessel. The experimental results for the viscosity are shown in Fig. 4 and for the density in Fig. 5. To show the relation of the measured values, all results are displayed and discussed in chapter 3.

2.5. Interfacial Tension Mixtures of ROS

The apparatus for the interfacial tension measurement as well as experimental results of the mentioned binary mixtures of refrigerants and lubricants have already been published in (Göpfert et al., 2016) and (Göpfert et al., 2017). In this paper new results of binary refrigerant blends and a lubricant are shown. The overall uncertainty of the measured Laplace constant is about 2.5 %. In addition to the measurements carried out in (Göpfert et al., 2017) the gas phase composition for the ternary mixtures have been analyzed. The uncertainty of the gas chromatography was lower than 1 mole-% which was checked by calibration probes. The experimental results for the ternary mixtures of oil, carbon dioxide and ethane and for carbon dioxide with ethylene are shown in Fig. 6.

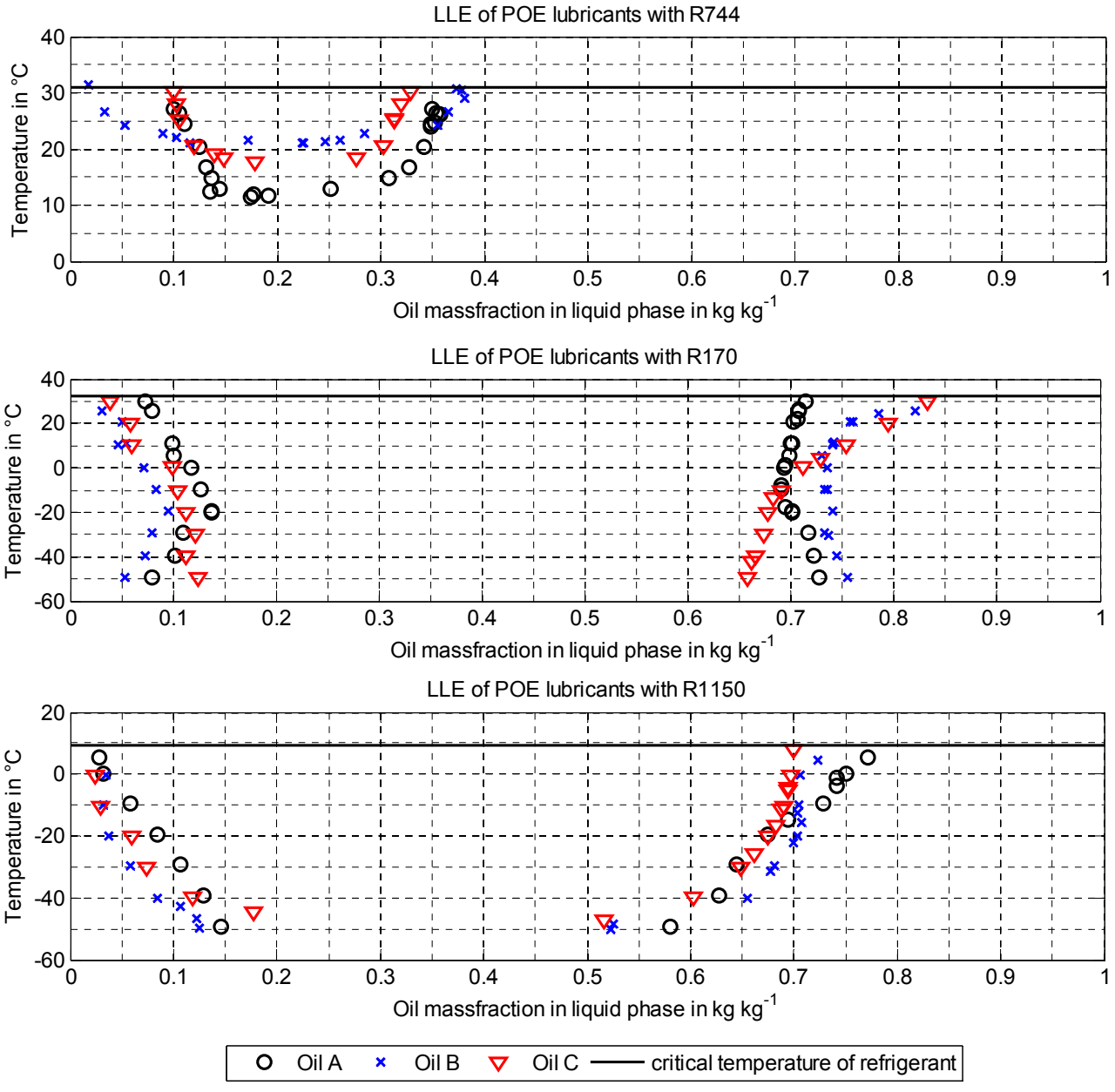

Figure 2: Measurement data of the LLE of the ROS

3. DISCUSSION OF RESULTS

As shown in Fig. 1 there are just small differences between the isobaric heat capacity of oil A and C which have the same viscosity group. Oil C which is a low viscous oil has a higher heat capacity within the entire temperature range. It has not yet been uncovered if this effect derives from the smaller molecules compared to the VG 32 lubricants or types and amount of additives of the lubricant.

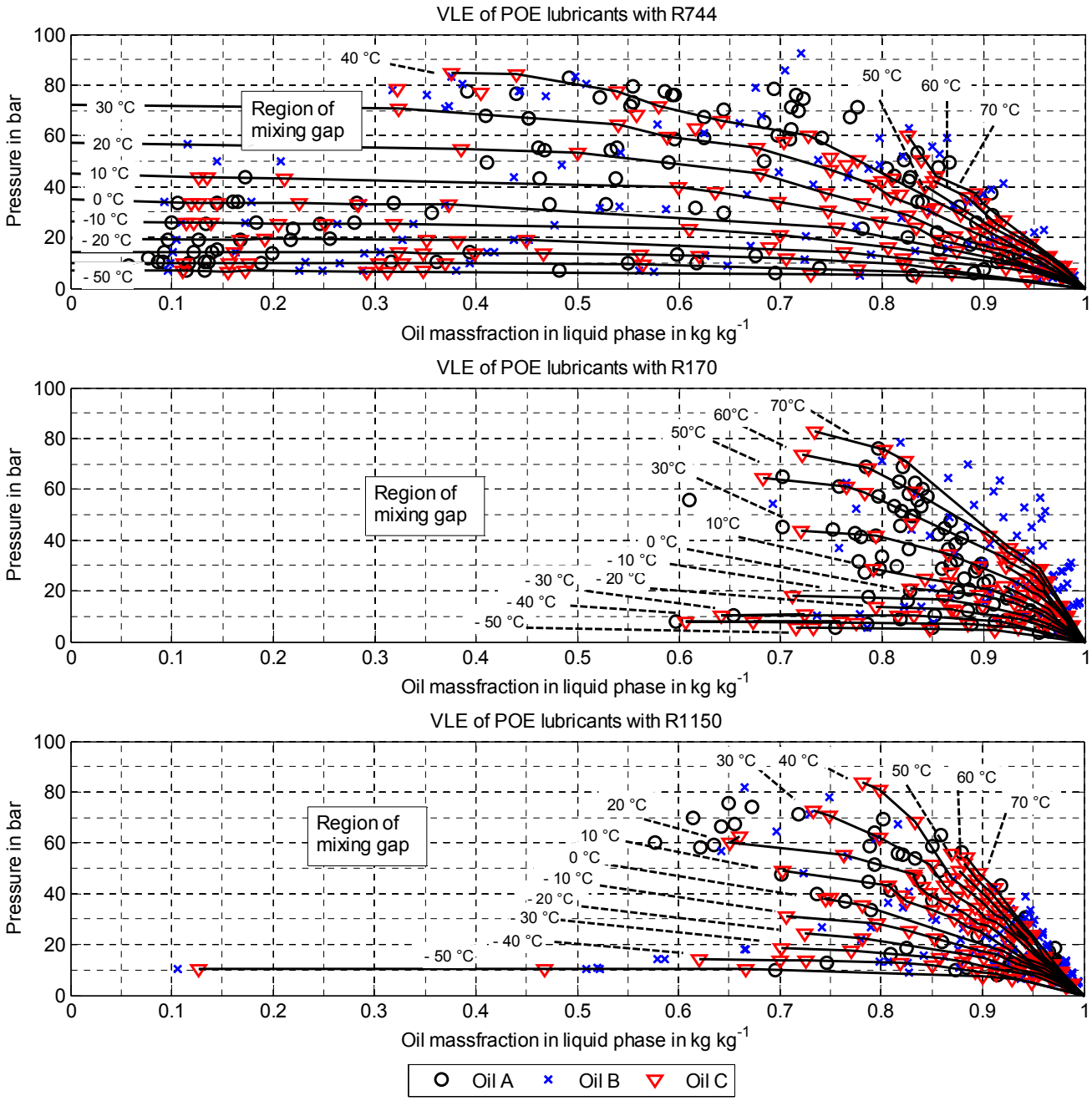

Figure 3: Measurement data of the VLE of the ROS with isotherm of oil C

The LLE in Fig. 2 show a similar behavior of each refrigerant with different lubricants. While the LLE for R744 are in the temperature range of 30 down to 10 °C the other refrigerants show to bigger LLE. The research aims for mixing gaps in the entire concentration range from - 50 °C up to the critical temperature of the refrigerant. This means for the carbon dioxide and ethylene mixtures that there is a possibility of a mixing gap at low temperatures. With R170 the behavior of an hour glass shaped mixing gap is assumed. Especially for Oil C an unexpected behavior was determined. This behavior might result from the very low density differences which have been

observed. This leads to a very slow separation of the liquid phases. In this case the turbidity of the mixture was more difficult to detect compared to the mixtures with carbon dioxide or ethylene.

The differences of the VLE (see Fig. 3) for the different lubricants are small for low temperatures. Especially at temperatures higher than the critical temperature of the refrigerant the differences increase. Oil B has the propensity to higher pressures compared to the other oils. While the difference between Oil A and C is small for carbon dioxide, bigger differences can be found with ethane and ethylene. Oil C has a lower solubility with ethane compared to oil A. This effect can also been seen in the results of the viscosity.

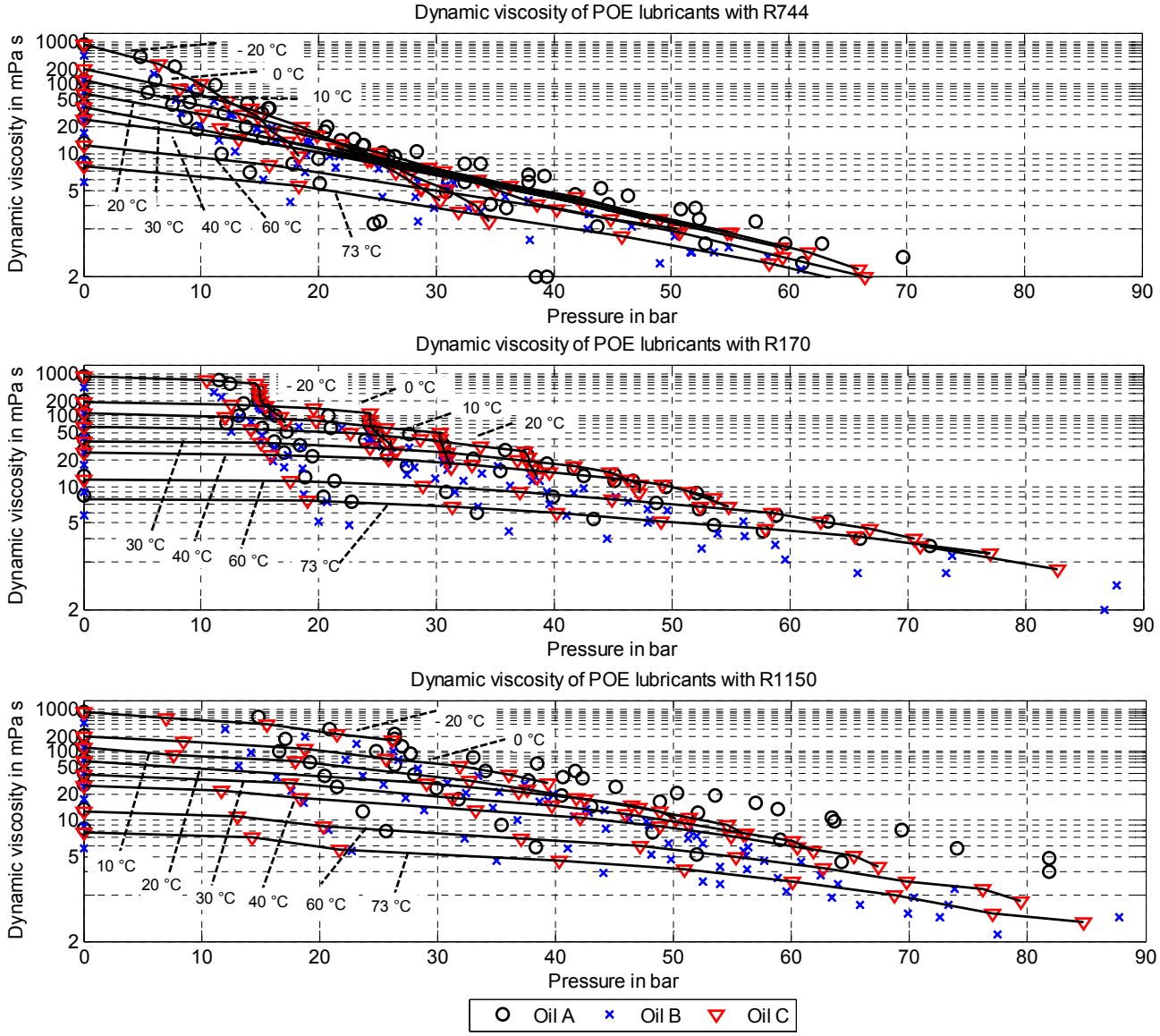

Figure 4: Measurement data of the dynamic viscosity of the ROS with isotherms for oil C

The dynamic viscosity is shown in a viscosity-pressure diagram (Fig. 3), since isothermal data sets were measured. As expected Oil B shows always the lowest viscosity. As seen in Fig. 3 the solubility of the refrigerants is comparable for low temperatures, so that the differences in the range are smaller compared to higher temperatures. The overall differences between oil A and C are small in combination with carbon dioxide but tend to higher differences with ethane and ethylene. Oil C has a lower solubility in ethane. This results in higher viscosities at the same thermodynamic boundary conditions as oil A. The same effect can be seen with ethylene. The solubility of Oil A is lower and it tends to higher viscosities. As discussed for the VLE, this effect increases for higher temperatures.

The density measurement data shown in Fig. 5 fit to the results of the VLE and viscosity measurements. The overall difference between the oils is small for carbon dioxide while Oil A tends to the highest densities. The density reducing effect of the pressure of carbon dioxide is lower compared to ethane and ethylene. This corresponds to the lower liquid densities of ethane and ethylene compared to carbon dioxide.

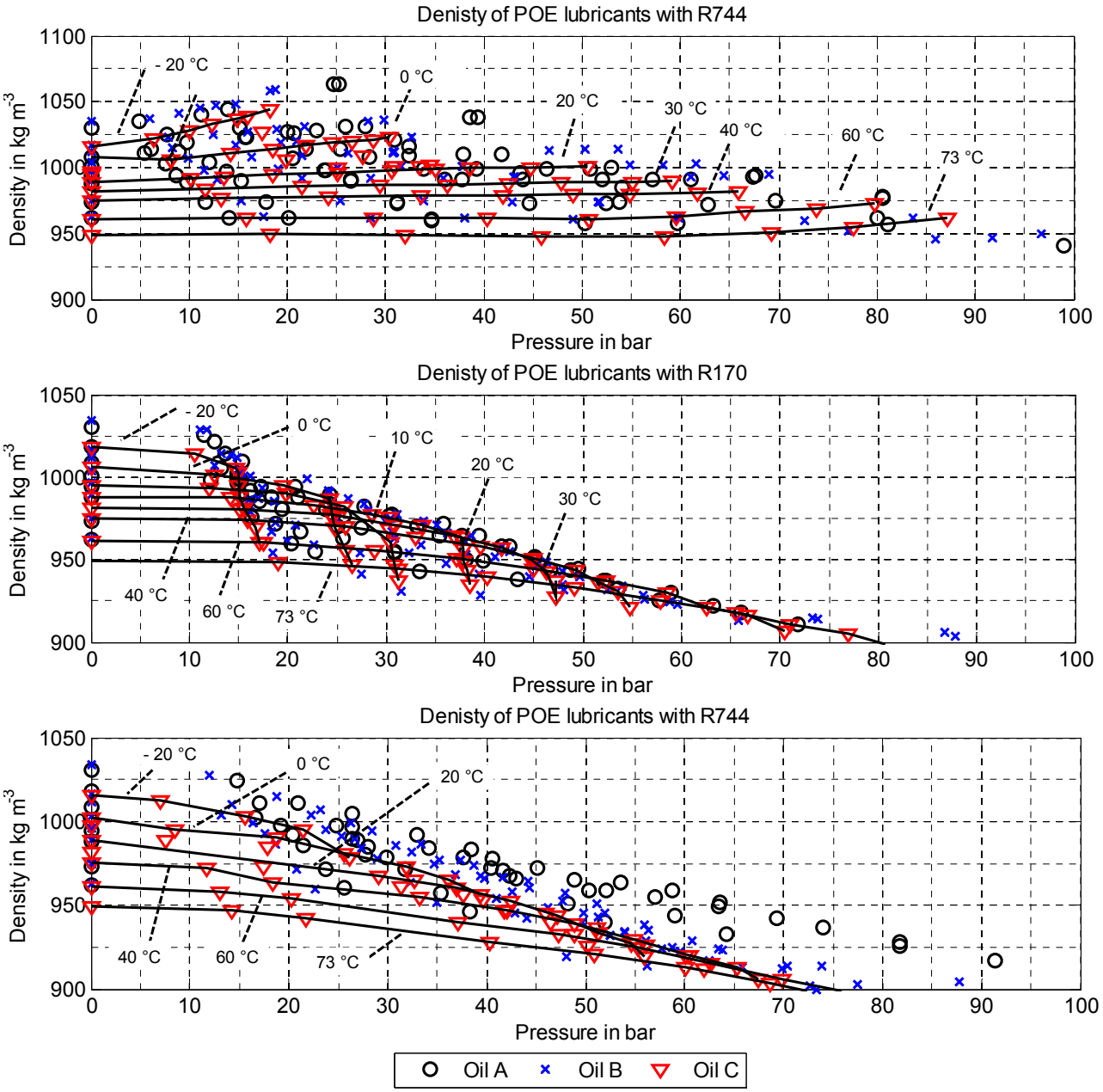

Figure 5: Measurement data of the densities of ROS with isotherm for oil C

Fig. 6 shows the Laplace constant of oil C with a carbon dioxide/ethane and a carbon dioxide/ethylene mixture with different compositions of refrigerants in the gas phase. For the same pressure at the same temperature the Laplace constant changes with variable gas phase composition. The Laplace constant changes monotonically but not linear with the mass or molar fraction of the components. Since carbon dioxide/ethane and carbon dioxide/ethylene are able to produce azeotropes, this derives at least partially from refractionation. Fig. 3 shows that the solubility of carbon dioxide in oil C is higher compared to ethane and ethylene at the same pressure and temperature, especially in the higher temperature region. This means for a gas mixture that carbon dioxide is better soluted in the lubricant and this may lead to a composition change of the refrigerant. This effect is especially interesting for refrigeration machines with low refrigerant charges and high charges of lubricant.

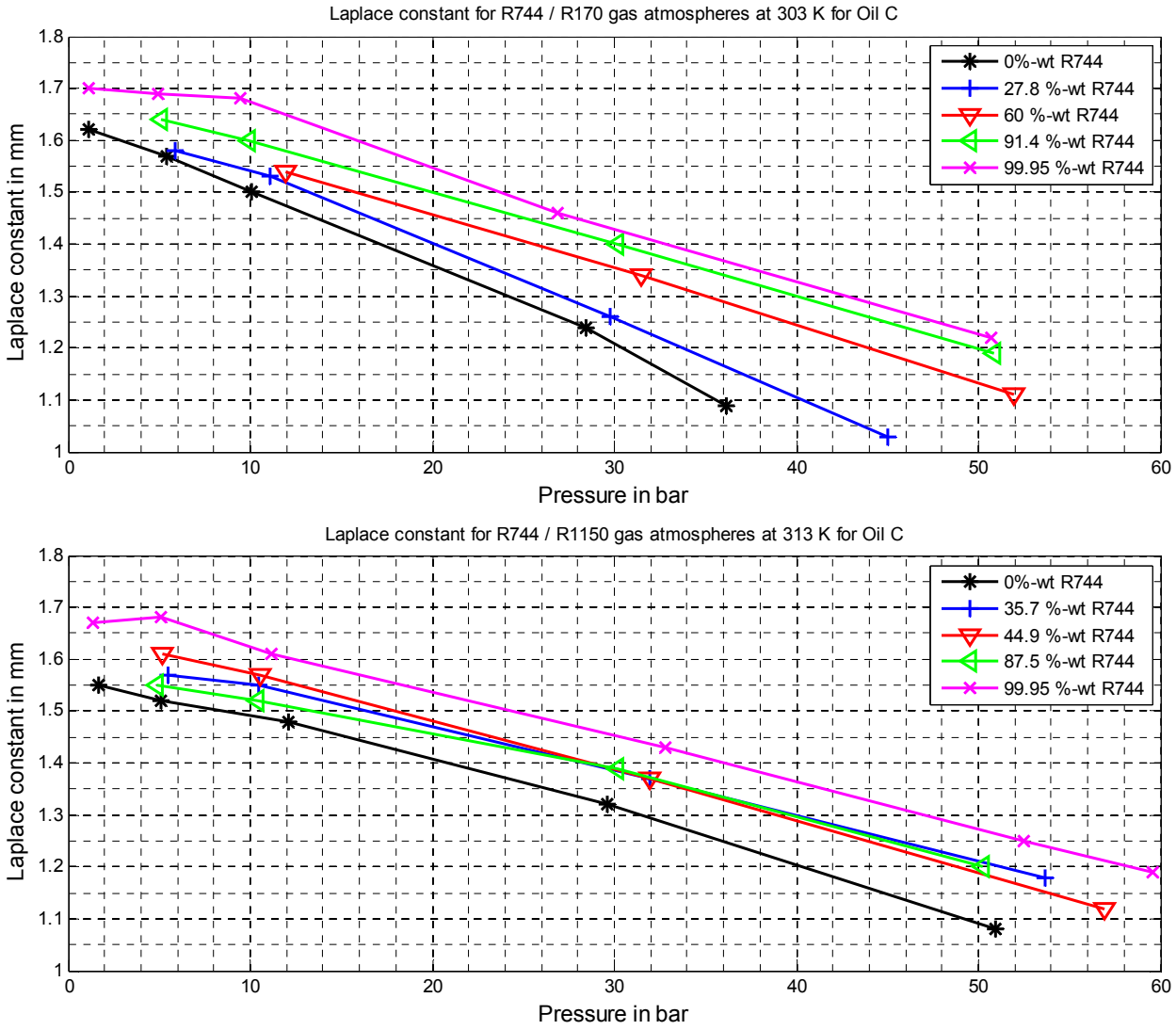

Figure 6: Measurements of the Laplace constant for the ternary mixture of carbon dioxide, ethane and carbon dioxide and ethylene and POE Oil C

4. CONCLUSIONS

The measurement results show the behavior of three different commercially available lubricants with the refrigerants carbon dioxide, ethane and ethylene. The biggest differences can be found for the LLE which differ for each lubricant and also for different refrigerants. Since the phase separation behavior is still difficult to pre-calculate and has a high influence on the equation of state the LLE have always have to be checked by measurements. Especially the VLE, density and viscosity data can be used for the development of an equation of state for lubricant-refrigerant-mixtures, see (Göpfert et al., 2019). The VLE show smaller differences between the researched lubricants, while the lower viscous oil B tends to higher vapor pressures and lower solubility of the refrigerant in the liquid phase. This effect also can be seen for the viscosities and densities. The dilution effect on the density is higher for ethane and ethylene compared to carbon dioxide while the dilution effect on the viscosity is higher for carbon dioxide. This corresponds to its very low viscosity. An interesting approach is the use of the measurement of the Laplace constant to check the ternary fluid mixture of lubricant and a binary refrigerant mixture for the effect on refractionation. This effect can normally just be derived from VLE measurements, which tend to higher experimental effort. The method of the pendant drop as already discussed in (Göpfert et al., 2017) might be an alternative option for property measurement. It is still under research how the effects of the change of the Laplace constant can be used for backwards calculation. In Example is it possible to calculate the vapor pressure of the mixture based on pendant drop measurements.

One possible way might be the algorithm shown by (Zhelezny et al., 2014) which connects the reduced vapor pressure to the reduced boundary tension.

ACKNOWLEDGEMENTS

The authors want to thank the Deutschen Bundesstiftung Umwelt for the financial support of the research project 31263/02.

REFERENCES

Di Nicola, G. et al. 2004. Blends of carbon dioxide and HFCs as working fluids for teh low-temperature circuit in cascade refrigerant systems. s.l.: International Journal of Refrigeration 28, 2004.

Di Nicola, G. et al. 2010. Carbon dioxide + Flouromethane and Nitrous Oxide + Fluoromethane: Solid-Liquid Equilibiria Measurement. s.l.: J.Chem.Eng.Data 55, 5018-5022, 2010.

Di Nicola, G. et al. 2011. Performance of cascade cycles working with blends of CO2 + natural refrigerants. s.l.: International Journal of Refrigeration 34, 2011.

Di Nicola, G. et al. 2008. Solid-Liquid Equilibria for the CO2 + R23 and N2O + R23 Systems. s.l. : Int. J. Thermophysics, 31, 1880-1887, 2008.

Di Nicola, G. et al. 2007. Solid-liquid equilibria for the CO2 + R152a and N2O + R152a systems. s.l.: J.Chem.Eng.Data 52, 2007.

Göpfert, T., Hesse, U. 2015. Survey on nonflammable low GWP refrigerant mixtures based on carbon dioxide for applications below 220 K. 24th. International Conference of Refrigeration, Yokohama : s.n., 2015.

Göpfert, T., Thomas, C., Hesse, U. 2019. A fundamental equation of state for lubricant-refrigerant mixtures with optimization based on transport and interfacial properties. s.l.: International Conference of Refrigeration ICR 2019, Montreal, Canada, 2019.

Göpfert, T., Thomas, C., Hesse, U. 2017. Effects of temperature and pressure on the surface tension of low viscose lubricants in high pressure atmospheres. Seoul: 5th IIR Conference on Thermophysical Properties and Transfer Processes of Refrigerants, 2017.

Göpfert, T., Thomas, C., Hesse, U. 2016. Surface Tension of Low-viscous Lubricants in High Pressure Carbon Dioxide Atmospheres. West Lafayett: 23rd International Compressor Engineering Conference at Purdue, 2016.

Zhelezny, V. et al. 2014. Prediction of the surface tension for refrigerants and refrigerant-oil solutions (ROS). s.l.: International Journal of Refrigeration, 40, pp. 241-245, 2014. pp. 241-245.

Manuscript ID: 502
DOI: 10.18462/iir.icr.2019.0502

Heat transfer model of superheated vapor bubbling in liquid in multi-stage refrigeration systems

Lorenzo CARRIERI[(a)], Gianpiero COLANGELO[(a)], Giuseppe STARACE[(a)]

[(a)] Dept. of Engineering for Innovation, University of Salento
LECCE, 73100, Italy, gianpiero.colangelo@unisalento.it, giuseppe.starace@unisalento.it

ABSTRACT

In low-temperature refrigeration systems, the multi stage approach with inter-cooled compression allows energy demand reduction, increased reliability, financial balance and maintenance costs decrease. An intercooling process between low and high pressure levels, consists of desuperheating the vapor coming from the low-pressure compressor by bubbling it in the saturated liquid intermediate pressure tank towards the saturation conditions.
In this work, a semi-analytical heat transfer model of a single superheated vapor bubble injected in the liquid is proposed by adapting the Fourier equation to defined conditions and by including the effects of sensible and latent heat. The results show trends and highlight the influence of the liquid surface tension, of the injection depth and of the thermal diffusivity of the vapor. The existence of an optimal injection depth can be found, that accounts for the energy transfer at given thermodynamic conditions of the vapor and the injected bubble dimensions.
Keywords: Semi-analytical model, vapor, liquid, bubble, 2-phase heat transfer.

1. INTRODUCTION

In industrial refrigeration applications the reduction of energy demand is made, at a thermodynamic cycle level, through multi-stage intercooled compression techniques. In a 2-stage scheme the low temperature heat sink is obtained internally at an intermediate pressure and is made of the saturated refrigerant expanded after exiting the condenser. In each desuperheating stage, the temperature of the vapor tends to the saturation value, through a heat transfer process, carried out either by injecting liquid into the discharge line of the low-pressure compressor or by bubbling the vapor into the liquid. Due to its characteristics, the bubbling technique is particularly attractive, as it combines economic and energy benefits in a simple technical solution. The main design parameter is the injection depth, that must guarantee the minimum residence time of the vapor, to allow complete desuperheating with the minimum backpressure at the exit of the low-pressure stage. The optimization of the device requires the formulation of a thermal model that considers the complexity of the convective and two-phase heat transfer phenomena occurring. The evolution of a vapor bubble within liquid has been the topic of several studies, limited to the class of pool-type processes. Rayleigh (Farajisarir, 1993) proposes a mechanism for developing the vapor bubble that expands in a superheated, infinitely extended, inviscid and incompressible liquid bath, starting from an initial radius, neglecting the effects of surface tension and considering the growth phenomenon due to differences in pressure across the liquid-vapor interface (inertial model). Bosnjakovic (Farajisarir, 1993) analyzes the phenomenon by considering the thermal and mass exchanges with the liquid on the liquid-vapor frontier (thermal model) as significant for the development of the bubble. Plesset (Plesset, et al., 1954) proposes a model that considers both the inertial and the thermal mechanisms. Solutions to the Plesset model, valid for the transient of the bubble collapse starting from the assigned initial dimension, are provided by Akiyama (Akiyama, 1973) in the hypothesis of inertial collapse and by Florschuetz and Chao (Florschuetz, et al., 1965) for the case of thermal collapse. None of the proposed models can be applied, however, directly to the bubbling analysis since the vapor is injected in superheated conditions and, therefore, far from saturation. In addition, neglecting the vertical floating motions is not possible as they modify the saturation conditions while stimulating convection. In this paper a heat transfer model, based on the Fourier law, that includes the effects

of sensible and latent heat terms, the effects of the liquid surface tension and the vertical floating motions on the convection and on the saturation conditions of the vapor at real operating conditions, is proposed.

2. THE MATHEMATICAL MODEL

The liquid-vapor heat transfer model has been developed with a semi-analytical approach, looking for exact solutions of the fundamental equations in discrete time intervals Δτ. The investigation focused on the cooling of a single bubble, writing the Fourier equation with reference to the operating conditions of the desuperheater and including the effects both of the sensible and latent heat. Hypotheses are the following:

- spherical bubble of radius r_{b}, variable in time and space, starting from a value of r_{b0};
- liquid bath at uniform temperature T_{l} (saturation temperature at the intermediate pressure);
- pressure in the liquid linearly variable with the depth (Stevino's law);
- non-negligible liquid surface tension effects (Laplace equation);
- bubble in vertical motion under gravitational effects and hydrodynamic resistance;
- flow regime with independent bubbles;
- heat transfer in the pure conducting vapor domain ($\mathrm{Ra} < 1000$).

Fig. 1 shows the scheme of the analysed system with the main physical parameters.

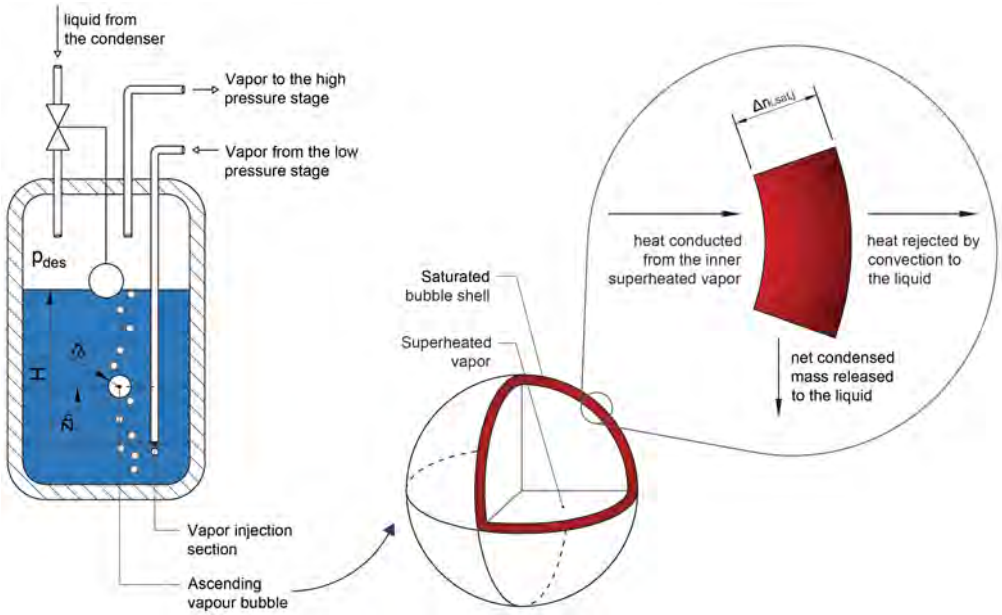

Figure 1: scheme of the analysed system.

2.1. Motion Equations

The analysis of the bubble motion was carried out by considering the only vertical upward component inside the bath as significant for heat transfer phenomenon. With z axis according to the direction of the weight force and positive sign upwards, the fundamental equation of motion written for the time interval j is expressed by Eq. (1) and comes from the translation equilibrium in the z direction.

$$\bar{\rho}_{\mathrm{b},j}\ddot{z}_{\mathrm{b},j}(t) + \frac{3\,\mathrm{sgn}\left[\dot{z}_{\mathrm{b},j}(t)\right]}{8r_{\mathrm{b},j}(t)} C_{\mathrm{D},j}\rho_{\mathrm{l}}\dot{z}^2_{\mathrm{b},j}(t) - g\left[\rho_{\mathrm{l}} - \bar{\rho}_{\mathrm{b},j}\right] = 0 \qquad \text{Eq. (1)}$$

The Eq. (1) is an ordinary non-linear differential equation with non-constant coefficients. Recognizing in Eq. (1) a Riccati equation, the solutions of motion are for the case of an ascending bubble:

$$\begin{cases} z_{\mathrm{b},j}(t) = -\dfrac{1}{G_j}\ln\left\{\dfrac{1}{2}\left[e^{\sqrt{|F_jG_j|}t-G_jz_{0,j}}\left(1-\dfrac{\dot{z}_{0,j}G_j}{\sqrt{|F_jG_j|}}\right)+e^{-\sqrt{|F_jG_j|}t-G_jz_{0,j}}\left(1+\dfrac{\dot{z}_{0,j}G_j}{\sqrt{|F_jG_j|}}\right)\right]\right\} \\ \dot{z}_{\mathrm{b},j}(t) = -\dfrac{\sqrt{|F_jG_j|}e^{-\sqrt{|F_jG_j|}t-G_j[z_{0,j}+z_{\mathrm{b},j}(t)]}}{2G_j}\left[e^{2\sqrt{|F_jG_j|}t}\left(1-\dfrac{\dot{z}_{0,j}G_j}{\sqrt{|F_jG_j|}}\right)-\left(1+\dfrac{\dot{z}_{0,j}G_j}{\sqrt{|F_jG_j|}}\right)\right] \end{cases} \quad \text{Eq. (2)}$$

for the case of a descending bubble:

$$\begin{cases} z_{\mathrm{b},j}(t) = z_{0,j} - \dfrac{1}{G_j}\ln\left[\cos\left(\sqrt{|F_jG_j|}t\right)-\dfrac{G_j\dot{z}_{0,j}}{\sqrt{|F_jG_j|}}\sin\left(\sqrt{|F_jG_j|}t\right)\right] \\ \dot{z}_{\mathrm{b},j}(t) = -\dfrac{1}{G_j}\left[\dfrac{-G_j\dot{z}_{0,j}\cos\left(\sqrt{|F_jG_j|}t\right)-\sqrt{|F_jG_j|}\sin\left(\sqrt{|F_jG_j|}t\right)}{\cos\left(\sqrt{|F_jG_j|}t\right)-\dfrac{G_j\dot{z}_{0,j}}{\sqrt{|F_jG_j|}}\sin\left(\sqrt{|F_jG_j|}t\right)}\right] \end{cases} \quad \text{Eq. (3)}$$

$$\begin{cases} G_j = -\dfrac{3C_{\mathrm{D},j}\rho_{\mathrm{l}}}{8r_{\mathrm{b},j}\bar{\rho}_{\mathrm{b},j}} \\ F_j = -\dfrac{3C_{\mathrm{D},j}\rho_{\mathrm{l}}g\left(\rho_{\mathrm{l}}-\bar{\rho}_{\mathrm{b},j}\right)}{8r_{\mathrm{b},j}\bar{\rho}_{\mathrm{b},j}^2} \end{cases} \quad \text{Eq. (4)}$$

2.2. Heat Transfer Equations

The real cooling process, with variable pressure and geometry, was modelled with a succession of isobar heat transfer equations of duration $\Delta\tau$, written for bubble of constant geometry. With the hypotheses of uniform thermal field around the bubble and of constant Nu at the liquid-vapor interface, a distributed 1-D unsteady heat transfer model has been adopted. The Fourier equation in cylindrical coordinates can be written as a set of M linear differential equations as follows:

$$\begin{cases} \dfrac{1}{r^2}\dfrac{\partial}{\partial r}\left(r^2\dfrac{\partial T_{1,j}}{\partial r}\right) = \dfrac{\rho_{\mathrm{v}1,j}c_{\mathrm{pv}1,j}}{\lambda_{\mathrm{v}1,j}}\dfrac{\partial T_{1,j}}{\partial t} = \dfrac{1}{\alpha_{\mathrm{v}1,j}}\dfrac{\partial T_{1,j}}{\partial t} & 0 \le r \le r_{1,j} \\ \vdots & \\ \dfrac{1}{r^2}\dfrac{\partial}{\partial r}\left(r^2\dfrac{\partial T_{M,j}}{\partial r}\right) = \dfrac{\rho_{\mathrm{v}M,j}c_{\mathrm{pv}M,j}}{\lambda_{\mathrm{v}M,j}}\dfrac{\partial T_{M,j}}{\partial t} = \dfrac{1}{\alpha_{\mathrm{v}M,j}}\dfrac{\partial T_{M,j}}{\partial t} & r_{(M-1),j} \le r \le r_{M,j} \end{cases} \quad \text{Eq. (5)}$$

Eq. 5) is a set of non-linear differential equations with second order partial derivatives in space (r) and with first order in time (t). The spatial and temporal non-linearities introduced by the functions ρ_{v}, c_{pv} and α_{v}, dependent on the variable T (and thus on r and t) at a given pressure, have been relaxed by making a discretization in time and space, assimilating the spherical domain to a system of M concentric shells of thickness Δr_k, each characterized by physical and average thermodynamic properties. $2M$ boundary conditions (valid $\forall t$) and M initial conditions (valid $\forall r \in [r_{k-1}, r_k]$ with $k = 1, \ldots, M$) guarantee a unique solution. The boundary conditions depend on the characteristics of the cooling process: since the surface temperature of the bubble can equal the saturation value, the cases of sensible only and both sensible and latent heat transfer must be distinguished.
In the first case:

$$\begin{cases} \left.\dfrac{\partial T_{1,j}}{\partial r}\right|_{r=0} = 0 \\ \lambda_{\mathrm{v}k,j}\left.\dfrac{\partial T_{k,j}}{\partial r}\right|_{r=r_{k,j}} = \lambda_{\mathrm{v}(k+1),j}\left.\dfrac{\partial T_{(k+1),j}}{\partial r}\right|_{r=r_{k,j}} & \forall k = 1, \dots M-1 \\ T_{k,j}\left(r_{k,j}, t\right) = T_{(k+1),j}\left(r_{k,j}, t\right) & \forall k = 1, \dots M-1 \\ \lambda_{\mathrm{v}k,j}\left.\dfrac{\partial T_{k,j}}{\partial r}\right|_{r=r_{M,j}} = -h_{\mathrm{c},j}\left[T_{k,j}(r,t) - T_l\right]_{r=r_{M,j}} \end{cases} \quad \text{Eq. (6)}$$

while for the second case, based on a constant bubble surface temperature:

$$\begin{cases} \left.\dfrac{\partial T_{1,j}}{\partial r}\right|_{r=0} = 0 \\ \lambda_{\mathrm{v}k,j}\left.\dfrac{\partial T_{k,j}}{\partial r}\right|_{r=r_{k,j}} = \lambda_{\mathrm{v}(k+1),j}\left.\dfrac{\partial T_{(k+1),j}}{\partial r}\right|_{r=r_{k,j}} & \forall k = 1, \dots M-1 \\ T_{k,j}\left(r_{k,j}, t\right) = T_{(k+1),j}\left(r_{k,j}, t\right) & \forall k = 1, \dots M-1 \\ T_{M,j}(r,t)\big|_{r=r_{M,j}} = T_{\mathrm{vsat},j} \end{cases} \quad \text{Eq. (7)}$$

In both cases, the initial conditions guarantee that:

$$T_{k,j}(r,0) = T_{0k,j}(r) \;\; \text{con} \;\; r_{\mathrm{i}k,j} \le r \le r_{\mathrm{e}k,j} \;\; \forall k = 1, \dots, M \quad \text{Eq. (8)}$$

where $T_{0k,\mathrm{j}}(r)$ is the initial temperature field in the k shell for the time interval k. The non-homogeneous problem at the boundary described by the Eq. (6) and Eq. (7) can be brought back to a homogeneous problem with a change in the type of variable shown in Eq. (9), where Ω_j is equal to T_l for the case of sensible-only heat transfer and equal to $T_{vsat,j}$ in the other case.

$$U_{k,j}(r,t) = r[T_{k,j}(r,t) - \Omega_{\mathrm{j}}] \quad \text{Eq. (9)}$$

Separating the variables, the problem can be expressed with the function $U_{k,j}$, that is a Sturm-Liouville problem and the following general solutions can be obtained (Mikhailov et al., 1984):

$$\begin{cases} T_j(r,t) = \bigcup_{k=1}^{M} T_{k,j}(r,t) \\ T_{k,j}(r,t) = \Omega_j + \dfrac{1}{r}\sum_{n=1}^{+\infty} c_{n,j}\Psi_{kn,j}(r)e^{-\beta_{n,j}^2 t} \\ c_{n,j} = \dfrac{\sum_{k=1}^{M}\int_{r_{(k-1),j}}^{r_{k,j}} \rho_{\mathrm{v}k,j}c_{\mathrm{pv}k,j}r\left[T_{0k,j}(r) - T_{\mathrm{l}}\right]\Psi_{kn,j}(r)\mathrm{d}r}{\sum_{k=1}^{M}\int_{r_{(k-1),j}}^{r_{k,j}} \rho_{\mathrm{v}k,j}c_{\mathrm{pv}k,j}\Psi_{kn,j}^2(r)\,\mathrm{d}r} \\ \Psi_{kn,j}(r) = A_{kn,j}\cos\left(\sqrt{\dfrac{\beta_{n,j}^2}{\alpha_{\mathrm{v}k,j}}}r\right) + B_{kn,j}\sin\left(\sqrt{\dfrac{\beta_{n,j}^2}{\alpha_{\mathrm{v}k,j}}}r\right) \end{cases} \quad \text{Eq. (10)}$$

that, in case of average thermodynamic properties in the domain, can be simplified as follows:

$$T_j(r,t) = T_{\mathrm{l}} + \frac{1}{r}\sum_{n=1}^{\infty}\frac{4\beta_{n,j}\int_0^{r_{\mathrm{b},j}} r\left[T_{0,j}(r) - T_{\mathrm{l}}\right]\sin\left(\beta_{n,j}r\right)\mathrm{d}r}{2\beta_{n,j}r_{\mathrm{b},j} - \sin\left(2\beta_{n,j}r_{\mathrm{b},j}\right)}\sin\left(\beta_{n,j}r\right)e^{-\alpha_{\mathrm{v},j}\beta_{n,j}^2 t} \quad \text{Eq. (11)}$$

for the case of sensible-only heat transfer, and:

$$T_j(r,t) = T_{\mathrm{vsat},j} + \frac{1}{r}\sum_{n=1}^{\infty}\frac{2}{r_{\mathrm{b},j}}\sin\left(\beta_{n,j}r\right)e^{-\alpha_{\mathrm{v},j}\beta_{n,j}^2 t}\int_0^{r_{\mathrm{b},j}} r\left[T_{0,j}(r) - T_{\mathrm{vsat},j}\right]\sin\left(\beta_{n,j}r\right)\mathrm{d}r \quad \text{Eq. (12)}$$

for the case of sensible-latent one.
The flow $\dot{m}_{l,j}$, released during the process of vapor condensation, can be estimated by the energy balance on the bubble shell under saturation conditions, under the hypothesis of $\Delta r_{k,\mathrm{sat}} \ll \Delta r_k$:

$$\dot{m}_{\mathrm{l},j} = \frac{4\pi r_{\mathrm{b},j}^2}{h_{\mathrm{vl},j}} \left[\lambda_{\mathrm{v}M} \left. \frac{dT_j}{dr} \right|_{r=r_{\mathrm{b},j}} + h_{\mathrm{c},j} \left(T_{\mathrm{vsat},j} - T_{\mathrm{l}} \right) \right] \qquad \text{Eq. (13)}$$

The first term in brackets is the energy transferred by conduction from the inner layers of the bubble to the saturating shell, while the second one represents the portion transferred by convection.

2.3. Results

2.3.1 Problem initialization

The problem is initialized by providing initial velocity, position, radius and temperature of the bubble, its injection depth and the intermediate pressure. For the validation of the model, a simulation plan was, therefore, formulated, considering a two-stage refrigeration system, with water as refrigerant, operating between the evaporation and condensation temperatures, varying 3 of the 6 degrees of freedom of the model, according to the values reported in Table 1. The thermodynamic and transport properties of water and its vapor were calculated through the correlations of the IAPWS. The average convective heat transfer coefficient on the liquid-vapor frontier surface was evaluated by the Whitaker correlation (Çengel et al., 2009), while for the drag coefficient of the flow the interpolation proposed by Morrison was used (Morrison, 2016). The results of the simulations show the same trends as the thermodynamic injection conditions and the initial radius change. Fig. 2 shows the comparison between velocity and position of the bubble when the initial radius $r_{\mathrm{b}0}$ changes. In all the analyzed cases, the velocity first increases up to a maximum value and then tends to zero, while the cooling process proceeds. The difference in the average densities between liquid and vapor tends to cancel out as the vapor cools down and tends to reach the liquid condition. Comparing the average temperature curves of Fig. 3 to the classic exponentially decreasing cooling trend, 3 different regimes can be observed. The behaviour can be interpreted by looking at the radial thermal profile curves in the vapor (Fig. 4). In the very first moments of the transient cooling (curve 1), the high thermal gradient at the liquid-vapor interface determines the rapid setting up of an area of thermal gradient, where the vapor is affected by the presence of the liquid, by changing its temperature. In this phase the average bubble temperature decreases rapidly over time, until the saturation conditions on the liquid-vapor frontier are reached. The phase change "freezes" the surface ΔT with the liquid, increasing the heat transfer and determining, in relation to the reduced thermal diffusivity of the vapor, the "rigid" translation of the thermal profile towards the center of the bubble (curves 2 and 3). When the amplitude of the transition region equals the instantaneous radius of the bubble (curve 4), even the core of the vapor, that behaves as a thermal reservoir till that moment, is affected by the heat flow and a sudden fall of the average temperature (curve 5) up to the bubble collapse occurs.

Table 1. Parameters of the simulation

Parameter	Value
Desuperheating pressure, p_{des} [MPa]	2.42 x 10^{-3}
Initial velocity, $\dot{z}_0$ [m/s]	0.0
Initial position, z_0 [m]	0.0
Initial radius, $r_{\mathrm{b}0}$ [mm]	{1.0; 5.0; 10.0}
Injection temperature, $T_{\mathrm{b}0}$ [K]	{383.2; 423.2}
Injection depth, H [m]	{0.1; 0.2; 0.3; 0.4; 0.5; 0.6; 0.7}

Assuming the bath at a temperature T_{l}, the injection of vapor at a certain depth, due to the increase in the local pressure and due to the effects of the surface tension of the liquid, implies that the

saturation temperature of the steam is always higher than the that of the surrounding liquid and that its ΔT grows with depth. By increasing the injection depth, it is possible to increase the heat transferred to the liquid, even if this increase is less than proportional to the depth H and tends to saturation for $H \to \infty$ (Fig. 5). To understand this behaviour, it must be considered that the energy released by the vapor during the condensation is proportional to the condensed mass. In this case, the vapor thermal diffusivity plays a fundamental role: as the injection depth increases, the freezing of the ΔT with the liquid at ever higher values increases the convective energy transfer to the bath, but the vapor, as a consequence of its thermal diffusivity, is not able to propagate the thermal front to the innermost layers of the bubble and the effect is an increase of the thermal gradient $\mathrm{d}T/\mathrm{d}r$, calculated on the border surface of the bubble, Eq. (12). The increase in the condensate flow rate, expected with the increase in convection, is, therefore, mitigated by the effects of thermal diffusivity. At given injection conditions, the increase in depth H, on one hand determines the increase of the heat dissipated by the bubble, on the other produces the increase in vapor density and thus, at fixed volume, the increase in the total amount of energy to be removed, down to the saturation conditions. The increase both in heat transferred to the liquid and in the bubble energy as a consequence of the increase of its mass are competing and thus an optimal condition can be found. The curves of the normalized residual energy in Fig. 5 for a bubble with $r_{\mathrm{b0}} = 10\ mm$, show how, when injection depth increases, the energy transfer rate with respect to the total transferable one increases till the maximum value is reached at an optimum depth $H_{opt} = 0.4\ m$ and then decrease again for $H > H_{opt}$. The same behaviour, even if with different optimal depth, can be found when the injection conditions change. The bubble cooling rate depends on the balance between the amount of energy to be removed (proportional to the mass) and the transfer rate, both increasing with the injection depth H. Increasing the injection depth, starting from fixed T_{b0} and r_{b0}, the curves of the normalized bubble residual energy move towards the origin, showing an increase in the bubble cooling rate. In this condition the increase in heat power released to the liquid is preponderant and the result is a reduction in the cooling time. However, it can be observed that equal increases in depth always correspond to ever smaller displacements of the curves, which tend to overlap as $H \to H_{opt}$. By increasing the depth $H > H_{opt}$, the curves tend again to move away from the source, thus demonstrating a reduction in the bubble cooling rate.
In this condition the energy that the vapor must release down to saturation increases with the depth, causing an increase in the cooling time.

2.3.1 Optimal vapor depth of injection

At assigned vapor injection conditions and bubble initial size, an optimal H_{opt} can be therefore found that maximizes the energy release rate towards the bath or minimizes the vapor desuperheating time. The vapor injection at depth H above the optimal value is therefore not convenient since the only effect would be the increase in the discharge conditions of the low-pressure compressor.

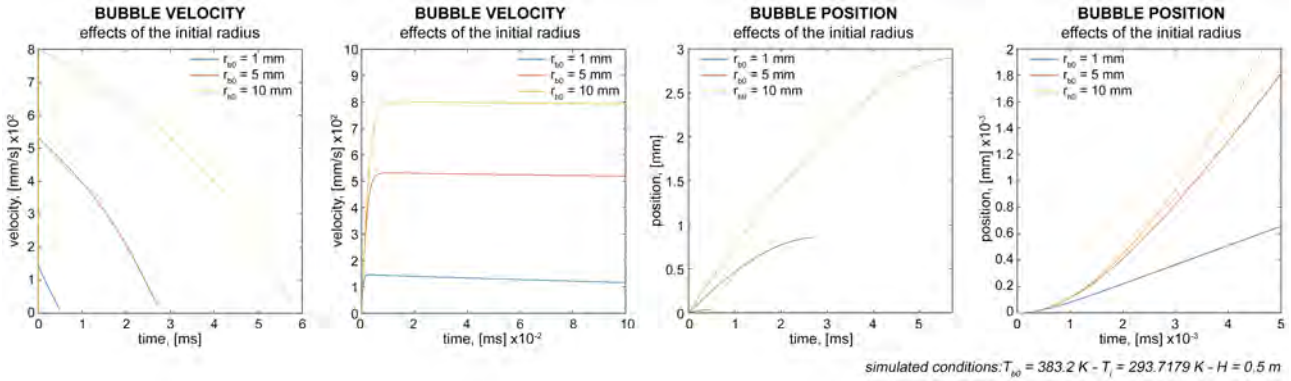

Figure 2: Velocity and position of the bubble.

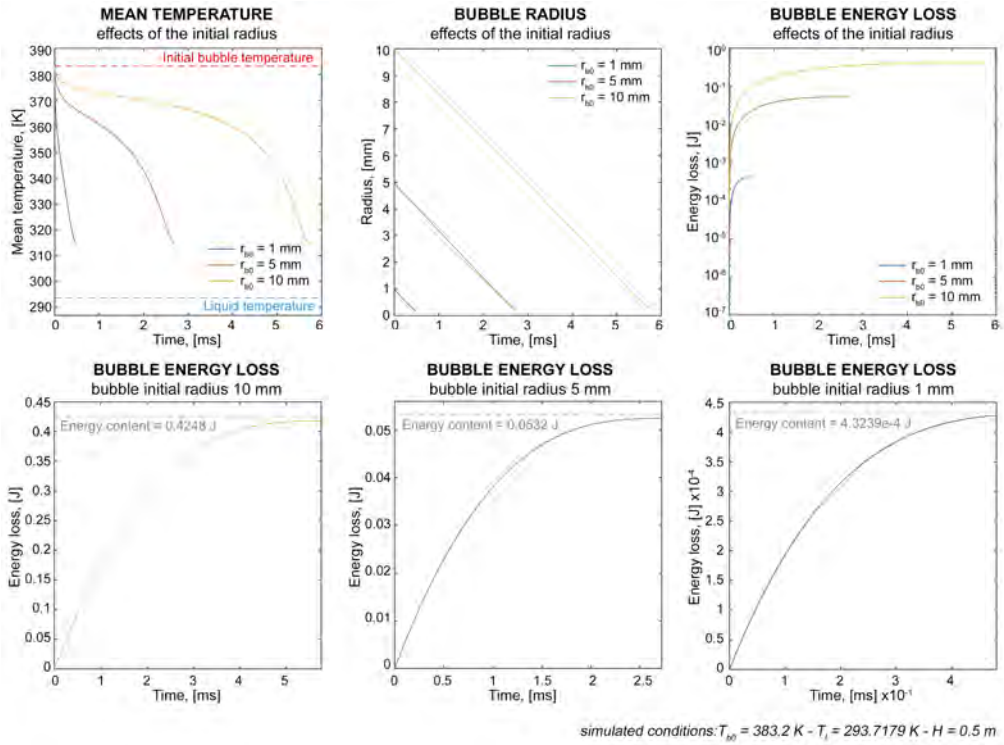

Figure 3: Bubble average temperature, radius and energy losses.

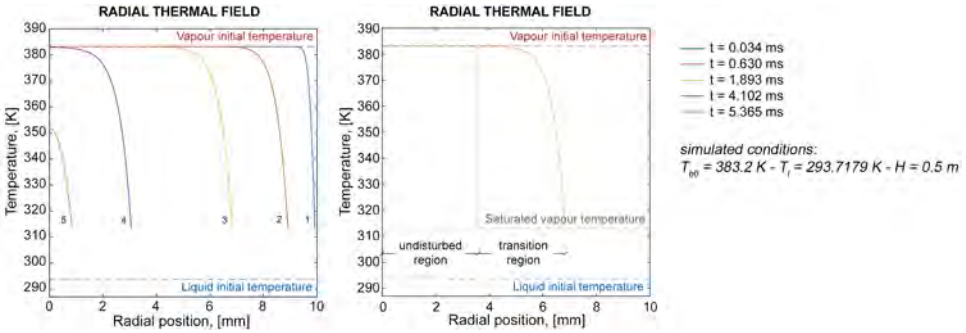

Figure 4: Vapor radial thermal field.

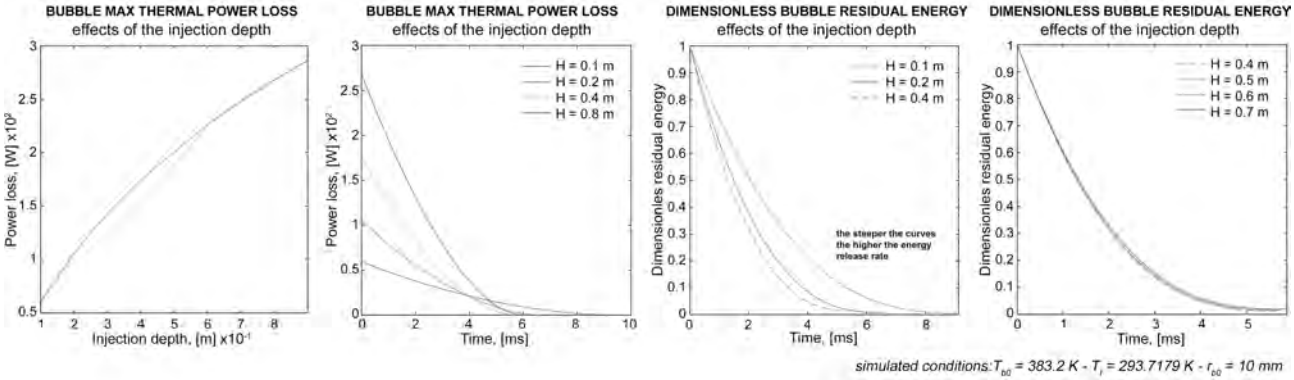

Figure 5: Bubble power loss vs injection depth and residual energy vs time.

3. CONCLUSIONS

A semi-analytical model of heat transfer between liquid and vapor has been proposed, using a single bubble approach, adapting the Fourier thermal equation to real cooling conditions and including the effects of sensible and latent heat. Model appears to be physically consistent and well interpretable

trends can be observed; the liquid surface tension, the injection depth and the thermal diffusivity of the vapor are investigated as antagonistic phenomena in the cooling process. Their effect results in the existence of an optimal injection depth, that optimizes the heat transfer, at given thermodynamic conditions of the vapor entering the desuperheater and of the bubble size. The model can be proposed as a valid tool to help the design of multi-stage systems. Further theoretical and experimental investigations are needed for a full validation of the model and for extension to the general case of multiple bubbles flow.

ACKNOWLEDGEMENTS

The entire work described in this paper was done based on University of Salento funding resources.

NOMENCLATURE

r_{b}	bubble radius (mm)
r	bubble radial coordinate (mm)
t	time (s)
$r_{\mathrm{k},j}$	outer radius of the k-th bubble shell during the j-th time interval (mm)
T_{l}	desuperheater saturated liquid temperature (K)
T	vapor radial thermal field (K)
$T_{0k,j}$	initial temperature field across the k-th bubble shell during the j-th time interval (K)
T_{b0}	vapor injection temperature (K)
$U_{k,j}$	boundary value problem auxiliary variable $(\mathrm{K} \times \mathrm{m})$
$\bar{\rho}_{\mathrm{b}}$	mean vapor density $(\mathrm{kg} \times \mathrm{m}^{-3})$
$\ddot{z}_{\mathrm{b}}$	bubble vertical acceleration $(\mathrm{m} \times \mathrm{s}^{-2})$
g	gravity acceleration $(\mathrm{m} \times \mathrm{s}^{-2})$
$\dot{z}_{\mathrm{b}}$	bubble vertical velocity $(\mathrm{m} \times \mathrm{s}^{-1})$
C_D	flow drag coefficient (dimensionless)
$\lambda_{\mathrm{v}k,j}$	vapor thermal conductivity of the k-th bubble shell during the j-th time interval $(\mathrm{W} \times \mathrm{m}^{-1} \times \mathrm{K}^{-1})$
$z_{0,j}$	initial bubble position at the j-th time (m)
k	bubble shell index
ρ_{v}	vapor local density $(\mathrm{kg} \times \mathrm{m}^{-3})$
c_{pv}	vapor isobaric specific heat $(\mathrm{J} \times \mathrm{kg}^{-1} \times \mathrm{K}^{-1})$
λ_{v}	vapor thermal conductivity $(\mathrm{W} \times \mathrm{m}^{-1} \times \mathrm{K}^{-1})$
α_{v}	vapor thermal diffusivity $(\mathrm{m}^2 \times \mathrm{s}^{-1})$
Δr_k	radial thickness of the k-th bubble shell (m)
V_k	volume of the k-th bubble shell (m^3)
Ω_j	characteristic temperature of the process during the j-th time interval (K)
$\beta_{n,j}$	n-th eigenvalue of the thermal problem during the j-th time interval $(\mathrm{s}^{-1/2})$
$\Psi_{kn,j}$	eigenfunction of the thermal problem associated to the n-th thermal eigenvalue at the j-th time (dimensionless)
r_{b0}	bubble initial radius (mm)
$r_{k-1,j}$	inner radius of the k-th bubble shell in the j-th time interval (mm)
$T_{\mathrm{vsat},}$	saturated vapor temperature in the j-th time interval (K)
T_j	vapor radial thermal field in the j-th time interval (K)
$T_{k,j}$	vapor radial thermal field across the k-th bubble shell in the j-th time interval (K)
ΔT	liquid – vapor temperature difference at the bubble boundary surface (K)
$\bar{\rho}_{\mathrm{b,j}}$	mean vapor density in the j-th time interval $(\mathrm{kg} \times \mathrm{m}^{-3})$
$\ddot{z}_{\mathrm{b,j}}$	bubble vertical acceleration at j-th time $(\mathrm{m} \times \mathrm{s}^{-2})$
$\dot{z}_{\mathrm{b},j}$	bubble vertical velocity at j-th time $(\mathrm{m} \times \mathrm{s}^{-1})$
$C_{D,j}$	flow drag coefficient in the j-th time interval (dimensionless)
ρ_{l}	liquid density $(\mathrm{kg} \times \mathrm{m}^{-3})$
$\rho_{\mathrm{v}1,j}$	vapor density of the k-th bubble shell in the j-th time interval $(\mathrm{kg} \times \mathrm{m}^{-3})$
$c_{\mathrm{pv}k,j}$	vapor isobaric specific heat of the k-th bubble shell during the j-th time interval $(\mathrm{J} \times \mathrm{kg}^{-1} \times \mathrm{K}^{-1})$
j	time interval index
$\alpha_{\mathrm{v}k,j}$	vapor thermal diffusivity of the k-th bubble shell during the j-th time interval $(\mathrm{m}^2 \times \mathrm{s}^{-1})$
$\Delta r_{k,\mathrm{s}}$	radial thickness of the k-th bubble shell in saturated conditions (m)
$\Psi_{kn,j}$	eigenfunction of the thermal problem associated to the n-th thermal eigenvalue during the j-th time interval (dimensionless)
$c_{n,j}$	thermal solution combination constant associated to the n-th thermal eigenvalue during the j-th time interval $(\mathrm{K} \times \mathrm{m})$
H	vapor depth of injection (m)
H_{opt}	optimal vapor depth of injection (m)
$B_{kn,j}$	coefficient of the n-th eigenfunction (dimensionless)

$A_{kn,j}$	coefficient of the n-th eigenfunction (dimensionless)	$h_{c,j}$	liquid – vapor convection heat transfer coefficient during the j-th time interval ($W \times m^2 \times K^{-1}$)
p_{des}	intermediate desuperheating pressure (MPa)	$\dot{m}_{l,j}$	condensed mass flow rate during the j-th time interval ($kg \times s^{-1}$)
$h_{vl,j}$	latent heat of condensation during the j-th time interval ($J \times kg^{-1}$)		

REFERENCES

Akiyama, Mamoru. 1973. Bubble Collapse in Subcooled Boiling. Bulletin of JSME. 1973, Vol. 16, 93, pp. 570 - 575.

Bergman, Theodore L., et al. 2011. Fundamentals of heat and mass transfer. New York: John Wiley & Sons, 2011. p. 1048.

Çengel, Yunus A. and Cirillo, Ettore. 2009. Termodinamica e trasmissione del calore. 3rd ed. Milano: McGraw-Hill, 2009. p. 728.

Farajisarir, Davood. 1993. Growth and collapse of vapour bubbles in convective subcooled boiling of water. Vancouver: University of British Columbia, 1993. Thesis/Dissertation.

Florschuetz, W. and Chao, B. 1965. On the Mechanics of Vapor Bubble Collapse. Journal of Heat Transfer. 1965, pp. 209 - 220.

Hahn, D. W. and Özisik, M. N. 1993. Heat Conduction. 2nd ed. New York: John Wiley & Sons, 1993. p. 692.

Jiji, Latif M. 2009. Heat Conduction. 3rd ed. New York: Springer - Verlag Berlin Heidelberg, 2009. p. 418.

Leighton, T. G. 2007. Derivation of the Rayleigh - Plesset equation in terms of volume. Institute of Sound and Vibration Research, University of Southampton. Southampton: ISVR University of Southampton, 2007. p. 26, Technical Reports.

Mikhailov, M. D. and Özisik, M. N. 1984. Unified analysis and solutions of heat and mass diffusion. 1st ed. s.l.: John Wiley and Sons, 1984. p. 524.

Morrison, Faith A. 2016. Data correlation for drag coefficient for sphere. Department of Chemical Engineering, Michigan Technological University, Houghton, MI. [Online] 2016. www.chem.mtu.edu/~fmorriso/DataCorrelationForSphereDrag2016.pdf.

Plesset, M. S. and Zwick, S. A. 1954. The Growth of Vapor Bubbles in Superheated Liquids. Journal of Applied Physics. 1954, Vol. 25, pp. 493 - 450.

Stoecker, Wilbert F. 1998. Industrial Refrigeration Handbook. 1st ed. s.l.: McGraw-Hill, 1998. p. 800.

Manuscript ID: 508
DOI: 10.18462/iir.icr.2019.0508

Simulation investigation of evaporating tower in heat pump air circulation evaporation separation system for high salinity wastewater

Liang CHEN[(a)], Qingqing LI[(a)], Sumin JIN[(a)]
[(a)] Nanjing Tech University
Nanjing, 211816, China, chen_liang08@163.com

ABSTRACT

The mathematical model of evaporating tower (ET) in heat pump air circulation evaporation separation (HP-ACES) system was built and the effect of inlet solution and air parameters on the heat and mass transfer characteristics of ET was investigated. Results shows that inlet solution parameters have greater effect on the total heat transfer capacity of ET than inlet air parameters. The total heat transfer capacity increases 4.2kW and 3.85 kW with the increase in inlet solution temperature and mass flow, respectively. The inlet solution and air temperatures and solution mass flow are beneficial to the thermal efficiency of ET while inlet solution temperature and dry air mass flow per unit cross-sectional area have negative effect on the concentrating efficiency of ET. Additionally, inlet solution temperature and dry air mass flow have negative effect on the concentrating efficiency.
Keywords: Evaporating Tower, Heat and Mass Transfer, Salinity Wastewater, Mathematical Model.

1. INTRODUCTION

Environmental protection is not only a major socio-economic problem which is the common concern of the people all over the world, but also a great research project in the field of science and technology nowadays. High salinity wastewater are those with the total dissolved solids (TDS) above 3.5%, generated from numerous industries. Supposing that high salinity wastewater was discharged without treatment, it would be greatly harmful to the human health and ecological environment. As high salinity wastewater contains highly concentrated organics and dissolved salt, it is generally difficult to treat(Li et al., 2016). Currently, salinity wastewater treatment, such as membrane distillation, chemical precipitation and coagulation–flocculation (Bella et al., 2014; Lu et al., 2011; Wen et al., 2016), can be classified into physical, chemical, and biological methods.
However, most of these methods do not conform to the idea of “zero liquid discharge” due to sediment harmful to environment as by-product, except thermal evaporation belonging to physical method. Gao et al. (2015) proposed air circulation evaporation separation (ACES) system for high salinity wastewater, as illustrated by Fig. 1.

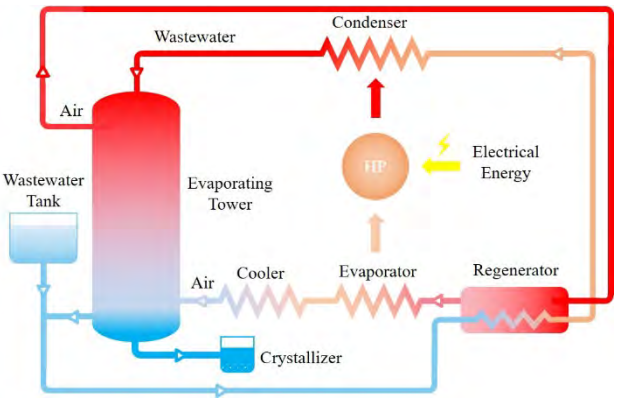

Figure 1: Schematic of ACES system for high salinity wastewater.

It is obvious that ET is the critical component of ACES system. The physical process within ET of ACES system is similar to that within regenerator of liquid desiccant where packed columns are usually utilized (Huang et al., 2018; Zhang et al., 2018). As the heat and mass transfer happens in packed column simultaneously, there is an interrelationship between heat transfer and mass transfer. It was found that all of air flow rate, solution flow rate and inlet solution temperature have positive effect on the evaporation rate of system while both air inlet humidity ratio and inlet solution concentration have negative effect through experiments (Ma et al., 2005; Sultan et al., 2002). Inlet solution temperature, solution flow rate and air flow rate have greater effect on evaporation efficiency of packed column than other parameters (Fumo et al., 2002; Liu et al., 2008). Besides, Alizadeh et al. (2002) explored that environmental conditions are also influential in the performance of regenerator. Furthermore, Kim et al. (2015) derived a model of packed-bed tower which have a wider operating range than an existing model. Haidl et al. (2017) proposed a general mass-transfer model for gas phase in structured packings.

Furthermore, some researchers have focused on the effect of tower's size and packing structure on the heat and mass transfer characteristics. Bassuoni (2011) revealed that an increase in packing density enhances the heat and mass transfer characteristics of tower as heat and mass transfer surface rises. Equally, higher packed tower is beneficial to the evaporating efficiency resulting from the increase in contact time between solution and air (Alizadeh et al., 2002; Zeidan et al., 2011).. Meanwhile, the height of regenerator has a limited value because the direction of heat and mass transfer goes into reverse when the height exceeds the limited value.

Thus far, researchers have made a significant amount of effort to explore and improve the heat and mass transfer characteristics of the packed column which is used as heat exchanger or regenerator, while few studies have focused on the packed column applied in salinity wastewater treatment. The mathematical model of ET in ACES system was built and the effect of inlet parameters of air and solution on the performance of ET was investigated in the paper.

2. HEAT AND MASS TRANSFER MATHEMATICAL MODEL

Liu et al. (2009) revealed that counter-flow configuration has the best mass transfer performance when solution is heat source based on uniform factor analysis of humidity field. Therefore, the counter-flow is chosen as the flow configuration of ET. The schematic of ET is shown in Fig. 2a. The solution flowing into the ET drops from the top by gravity, and the air blown from the bottom contacts with the solution which is distributed over the packing directly. After the heat and mass transfer in the ET, the air and solution are expelled from the top and bottom of ET, respectively. There is a mutual influential and promoting relation between the heat and mass transfer of air and solution. Therefore, heat and mass transfer process cannot be analyzed separately.

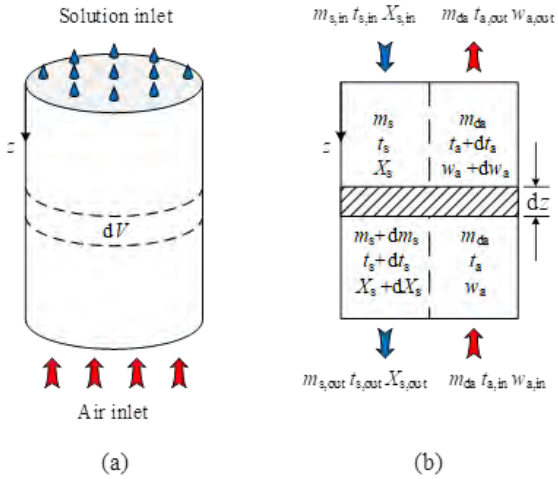

Figure 2: (a) Schematic of ET; (b) Heat and mass transfer model of ET.

Calcium chloride solution and 25mm Pall Rings is utilized in the mathematic model. Besides, in order to calculating the heat and mass transfer characteristics easily, the following approximations for present model are made:

(1) Only the variation of parameters in 1-D direction is consider;

(2) The heat and mass transfer between air and solution is steady and physical parameters are regarded as a constant;
(3) The ET is well insulated;
(4) The heat and mass transfer coefficients are constant throughout the packing.

These assumptions are made on the basis of following reasons.

(1) The states of air and solution have little change in the direction perpendicular to the center line of evaporating tower due to small inner diameter of tower. The calculating speed can increase dramatically while accuracy requirement can be met through using 1-D modeling;
(2) The physical parameters of air and solution have little change, so it is reasonable that they are regarded as constant for a volume of dV;
(3) The evaporating tower will be insulated under realistic operating conditions;
(4) The physical parameters and flow patterns of air and solution are not changed basically.

Heat and mass transfer model of the ET is shown in Fig. 1b, and the ET can be divided into an infinite number of volumes of dV. The decrease of solution mass is equal to the increase of vapor mass in the air based on the conservation of mass, then:

$$\mathrm{d}m_{\mathrm{s}} = m_{\mathrm{da}}\mathrm{d}w_{\mathrm{a}} \qquad \text{Eq. (1)}$$

Because only the water in the solution is evaporated, the mass of solute is constant. It can be expressed by Eq. (2).

$$d\left(m_{\mathrm{s}}X_{\mathrm{s}}\right) = 0 \qquad \text{Eq. (2)}$$

As the ET is well insulated, the enthalpy variation of solution is equal to that of air. It can be expressed by Eq. (3).

$$m_{\mathrm{da}}\mathrm{d}h_{\mathrm{a}} = \mathrm{d}\left(m_{\mathrm{s}}h_{\mathrm{s}}\right) \qquad \text{Eq. (3)}$$

where, dha and dhs can be calculated by Eqs. (4) and (5).

$$\mathrm{d}h_{\mathrm{a}} = \left(Cp_{\mathrm{a}} + Cp_{\mathrm{v}}w_{\mathrm{a}}\right)\mathrm{d}t_{\mathrm{a}} + \left(r_0 + Cp_{\mathrm{v}}t_{\mathrm{a}}\right)\mathrm{d}w_{\mathrm{a}} \qquad \text{Eq. (4)}$$

$$\mathrm{d}h_{\mathrm{s}} = Cp_{\mathrm{s}}\mathrm{d}t_{\mathrm{s}} \qquad \text{Eq. (5)}$$

In the ET, the water vapor pressure gradient affected by air humidity and solution concentration is the driving potential of mass transfer process, while the temperature difference between air and solution is that of heat transfer process. Equivalent humidity ratio which reflects the effect of solution concentration on mass transfer process is introduced in the model for convenient application. Hence, the mass variation of solution and enthalpy variation of air can be calculated by Eqs. (6) and (7), respectively.

$$\mathrm{d}m_{\mathrm{s}} = \beta\left(w_{\mathrm{s}}^{*} - w_{\mathrm{a}}\right)A\mathrm{d}V \qquad \text{Eq. (6)}$$

$$m_{\mathrm{da}}\mathrm{d}h_{\mathrm{a}} = h_{\mathrm{v}}\beta\left(w_{\mathrm{s}}^{*} - w_{\mathrm{a}}\right)A\mathrm{d}V + \alpha\left(t_{\mathrm{s}} - t_{\mathrm{a}}\right)A\mathrm{d}V \qquad \text{Eq. (7)}$$

where equivalent humidity ratio which can be calculated according to the vapor partial pressure of solution related to solution concentration and temperature. It is often expressed as Eq. (8).

$$w_{\mathrm{s}}^{*} = 0.622\frac{P_{\mathrm{v,s}}}{P_0 - P_{\mathrm{v,s}}} \qquad \text{Eq. (8)}$$

According to the definition of Lewis number, Lewis number can be expressed as Eq. (9).

$$\mathrm{Le} = \frac{\alpha}{\beta Cp_{\mathrm{a}}} \qquad \text{Eq. (9)}$$

Through the deduction and simplification, Eq. (10) and Eq. (11) are obtained.

$$\frac{\mathrm{d}t_a}{\mathrm{d}V}=\frac{\beta A\left(t_s-t_a\right)Cp_a\mathrm{Le}}{m_{da}\left(Cp_a+Cp_v w_a\right)} \quad \text{Eq. (10)}$$

$$\frac{\mathrm{d}t_s}{\mathrm{d}V}=\frac{\beta A\left[\left(t_s-t_a\right)Cp_a\mathrm{Le}+\left(r_0+Cp_v t_a-Cp_s t_s\right)\left(w_s^*-w_a\right)\right]}{Cp_s m_s} \quad \text{Eq. (11)}$$

3. PERFORMANCE PARAMETER

The heat transferred from solution to air consists of sensible heat and latent heat in ET, where the former is wasted by air. Latent heat percentage, defined as the ratio of latent heat transfer capacity to total heat transfer capacity, is utilized to evaluate the thermal efficiency of ET. It can be calculated by Eq. (12).

$$\chi=\frac{\left(w_{a,out}-w_{a,in}\right)r_0}{h_{a,out}-h_{a,in}}\times 100\% \quad \text{Eq. (12)}$$

Apart from latent heat percentage, as a vaporization and concentration equipment, the concentrating capacity of ET is a very important evaluation indicator. Hence, concentration efficiency is defined as the ratio of actual humidity variation during evaporation process to ideal humidity variation which is equal to the difference between inlet solution equivalent moisture content and inlet air moisture content. It can be calculated by Eq. (13)

$$\eta=\frac{w_{a,out}-w_{a,in}}{w_{s,in}^*-w_{a,in}} \quad \text{Eq. (13)}$$

4. VALIDATION OF MATHEMATICAL MODEL

The Lewis number of mathematical model equals to 1.06 according to the results in (Chen et al., 2006) and the mass transfer coefficient was obtained on the basis of analysis in (Fumo et al., 2002). The experimental data in (Fumo et al., 2002) were used to verify the validation of mathematical model and results are shown in Table 1. The simulation results of outlet air temperature are in good consistent with the experimental results (relative error is within 4%), which indicates that the mathematical model of ET is accurate.

Table 1. Validation results of mathematical model

No.	m_{da} kg·s^{-1}	$t_{a,in}$ °C	$w_{a,in}$ g·kg^{-1}	m_s kg·s^{-1}	$t_{s,in}$ °C	$X_{s,in}$ %	α W·m^{-2}·°C^{-1}	$t_{a,out}^{exp}$ °C	$t_{a,out}^{sim}$ °C	Δ %
1	1.097	35.1	18	6.348	65.1	33.4	14.2	58.5	57.0	2.6
2	1.102	40	17.8	6.354	65	33.6	14.0	58.9	58.0	1.6
3	1.132	30.2	14.3	6.37	65.2	34	14.3	57.6	55.7	3.3
4	1.116	30.3	18.2	5.185	65.4	34.4	14.1	57.6	55.6	3.4
5	1.097	29.4	21	6.44	65.5	33.6	14.2	58.5	56.7	4.2
6	1.101	29.9	18	7.541	65.2	34.3	14.9	59	56.8	3.8
7	1.111	30	18.7	6.245	60.3	34.4	15.9	55.8	53.7	3.7

5. RESULTS AND DISCUSSION

The effect of inlet parameters of air and solution on the heat transfer capacity, latent heat transfer percentage, capacity of concentrating was investigated under different conditions by simulation. Specific simulation conditions are shown in Table 2.

Table 2. Different simulation conditions

Number	$t_{s,in}$ °C	$X_{s,in}$ %	$q_{s,in}$ kg·m^{-2}·s^{-1}	$t_{a,in}$ °C	$w_{a,in}$ g·kg^{-1}	$q_{a,in}$ kg·m^{-2}·s^{-1}
1	40-70	30	2.21	20	8.73	2.21

2	60	30	1.11-4.42	20	8.73	2.21
3	60	30	2.21	10-35	8.73	2.21
4	60	30	2.21	20	8.73	1.11-4.42

5.1. Inlet Solution Temperature

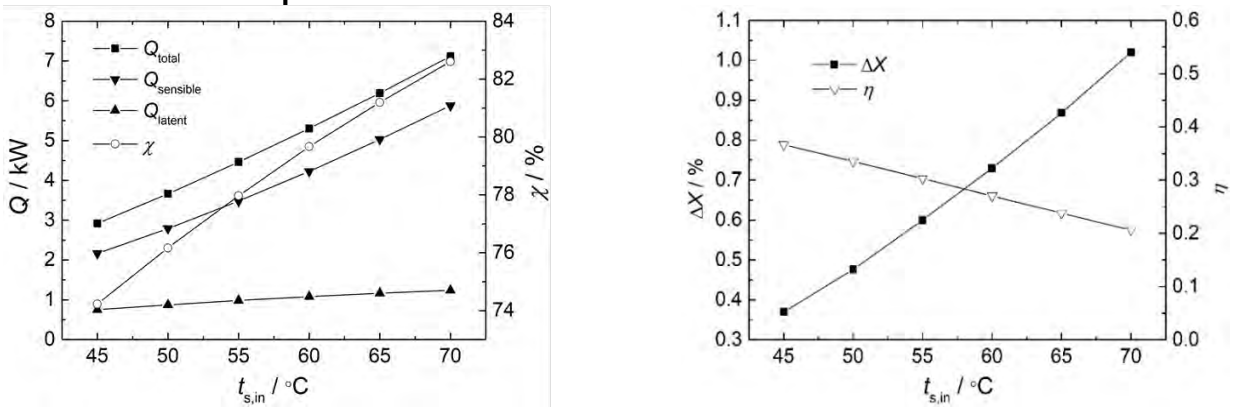

(a) (b)

Figure 3: Effect of inlet solution temperature on the performance of ET: (a) heat exchange; (b) capacity of concentrating

Fig. 3a illustrates the variation of heat exchange of ET with inlet solution temperature. As shown in Fig. 3a, the total heat transfer capacity, sensible heat transfer capacity, latent heat transfer capacity increase 4.2 kW, 0.49 kW and 3.71 kW, when inlet solution temperature varies from 45 °C to 70 °C. it can be explained that not only the heat transfer temperature difference but also the equivalent moisture content of solution increases for higher inlet solution temperature, which reinforces the driving potential of heat and mass transfer. It is remarkable that the latent heat transfer percentage also increases from 72.2% to 82.6%, which means inlet solution temperature has a positive effect on the heat and mass transfer characteristic of ET.

Besides, according to Fig. 3b, the concentration difference increases 0.65%, while the concentration efficiency declines 0.16. The reason is that the increase of the equivalent moisture content of solution for a higher solution temperature results in the enhancement of heat and mass transfer in ET. However, as the increase in the equivalent moisture content of inlet solution is greater than that in outlet air humidity ratio, the concentrating efficiency decreases according to Eq. (13)

5.2 Solution Mass Flow Per Unit Cross-Sectional Area

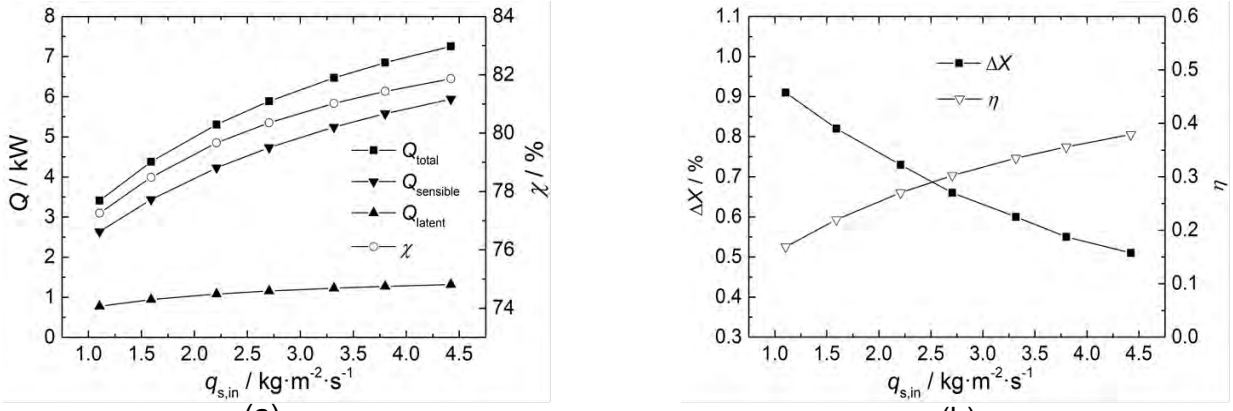

(a) (b)

Figure 4: Effect of solution mass flow per unit cross-sectional area on the performance of ET: (a) heat exchange; (b) capacity of concentrating

The variation of the ET performance with the solution mas flow per unit cross-sectional area is presented in Fig. 4. The total heat transfer capacity, sensible heat transfer capacity, latent heat transfer capacity increase 3.85 kW, 0.55 kW and 2.3 kW, respectively. Larger solution mass flow contributes to faster refresh rate of air and solution film and the reduction of contact thermal

resistance which is the main influencing factor of heat and mass transfer. As latent heat of vaporization largely outweighs the specific heat of solution, the increase in latent heat transfer capacity is larger than that in sensible heat transfer capacity and the latent heat transfer percentage rises 4.6%. Moreover, there is a decrease in the trend growth of sensible heat transfer with the increase in solution mass flow per unit cross-sectional area resulting from the limitation of ET's heat transfer capacity.

Meanwhile, the outlet air temperature increases slightly with the increase in solution mass flow per unit cross-sectional area and the ability of moisture air to carry vapor has little change for a fixed dry air mass flow. Hence, the concentration difference declines 0.4% under simulation conditions. However, from the view-point of air, larger solution mass flow per unit cross-sectional area results in higher outlet air humidity ratio, which means solution mass flow has a positive effect on the concentrating efficiency of ET.

5.3 Inlet Air Temperature

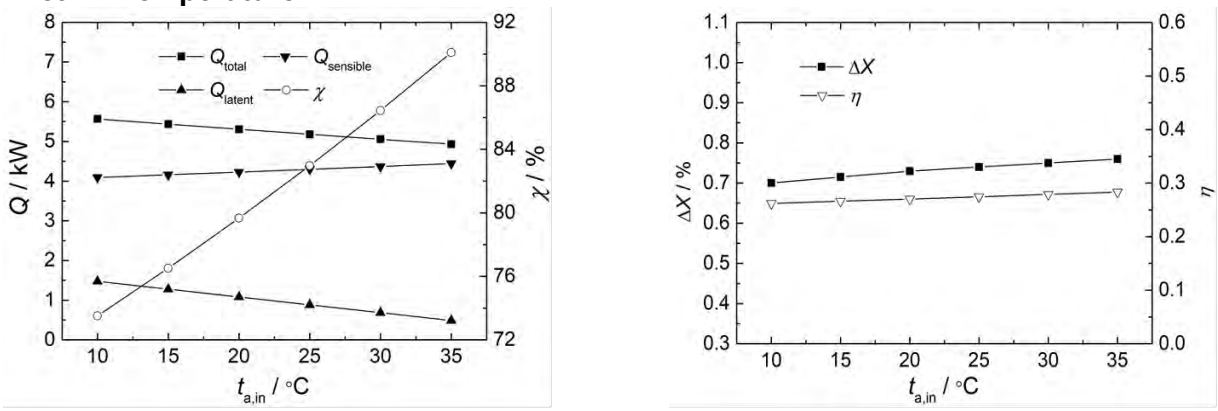

(a) (b)

Figure 5: Effect of inlet air temperature on the performance of ET: (a) heat exchange; (b) capacity of concentrating

The curves in Fig. 5a shows inlet air temperature has negative effect on the sensible heat transfer capacity of ET due to the reduction in heat transfer temperature difference between air and solution. And because of this, the increase in outlet solution temperature leads to higher average equivalent humidity ratio of solution. Hence, the latent heat transfer capacity increases slightly and the latent heat transfer percentage increases from 73.52% to 90.1%. It is noteworthy that the total heat transfer capacity decreases 0.64 kW because the decrease in sensible heat transfer capacity is larger than the increase in latent heat transfer capacity.

As the inlet air temperature enhances the mass transfer process fractionally, the concentration difference of solution increases 0.06 % only. Similarly, both outlet air humidity ratio and inlet solution equivalent humidity ratio rise, thus the concentrating efficiency remains at around 0.27.

5.4 Dry Air Mass Flow Per Unit Cross-Sectional Area

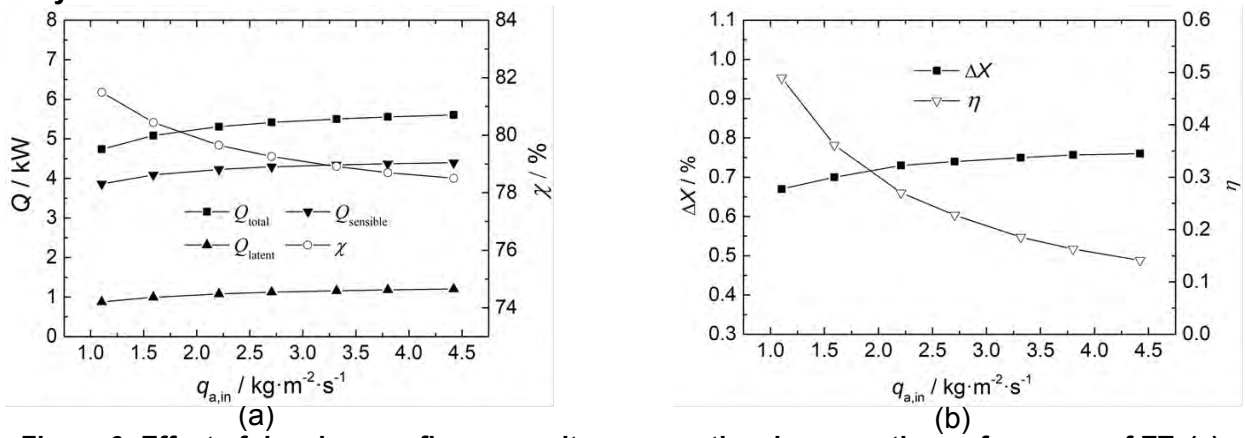

(a) (b)

Figure 6: Effect of dry air mass flow per unit cross-sectional area on the performance of ET: (a) heat exchange; (b) capacity of concentrating

Fig. 6a draws the variation of heat exchange with the dry air mass flow per unit cross-sectional area. The film between air and solution is smaller for larger dry air mass flow, which leads to the reduction of contact thermal resistance. As a consequence, the dry air mass flow as well as solution mass flow, is propitious to strengthen the heat and mass transfer process of ET, and total heat transfer capacity, latent heat transfer capacity, total heat transfer capacity increase 0.32 kW, 0.54 kW and 0.86 kW, respectively. However, the latent heat transfer percentage decreases 2.99%.
As shown in Fig 6b, owing to the enhancement in mass transfer process, the concentration difference increases 0.09 % with the increase in dry air mass flow per unit cross-sectional area. In addition, as outlet air humidity ratio drops, the concentrating efficiency of ET decreases 0.35.

CONCLUSIONS

The mathematical model of ET in ACES system was built and the effect of inlet parameters of air and solution on the heat transfer capacity, latent heat transfer percentage, capacity of concentrating was investigated under different conditions by simulation. The main conclusions are as follows:

1. The heat exchange of ET can be enhanced by increasing the inlet solution temperature, inlet solution mass flow per unit cross-sectional area and dry air mass flow per unit cross-section area. While Inlet solution parameters has greater effect on the heat exchange of ET than inlet air parameter.
2. The thermal efficiency of ET can be improved by increasing inlet solution temperature, inlet solution mass flow per unit cross-sectional area, inlet air temperature.
3. In order to obtain larger concentration difference of solution between inlet and outlet, increasing solution temperature and decreasing inlet solution mass flow per unit cross-sectional area are recommended.
4. Inlet solution temperature and dry air mass flow per unit cross-sectional area have negative effect on the concentrating efficiency, while solution mass flow has positive effect and inlet air temperature almost has no effect.

NOMENCLATURE

Symbols

A	specific surface area ($m^2 \times m^{-3}$)	Cp	specific heat capacity ($kJ \times kg^{-1} \times °C^{-1}$)
h	specific enthalpy ($kJ \times kg^{-1}$)	m	mass flow rate ($kg \times s^{-1}$)
P	pressure (kPa)	P_0	environmental pressure (kPa)
q	mass flow per unit cross-sectional area ($kg \times m^{-2} \times s^{-1}$)	Q	heat transfer capacity (kW)
r_0	water's latent heat of vaporization ($kJ \times kg^{-1}$)	t	temperature (°C)
Δt	temperature difference between air and solution (°C)	V	volume (m^3)
w	humidity ratio ($g \times kg^{-1}$)	w^*	equivalent moisture ($g \times kg^{-1}$)
Δw	humidity ratio difference between air and solution ($g \times kg^{-1}$)	X	concentration (%)

Greek symbols

α	heat transfer coefficient ($W \times m^{-2} \times °C^{-1}$)	β	mass transfer coefficient ($g \times m^{-2} \times s^{-1}$)
η	concentration efficiency	ξ	average error (%)
χ	latent heat transfer percentage (%)		

Subscript

a	moisture air	da	dry air
in	inlet	out	outlet

s	solution	v	vapor
sim	theoretical	exp	experimental

REFERENCES

Alizadeh, S., Saman, W.Y., 2002. An experimental study of a forced flow solar collector/regenerator using liquid desiccant. SOL ENERGY 73(5), 345-362.

Bassuoni, M.M., 2011. An experimental study of structured packing dehumidifier/regenerator operating with liquid desiccant. ENERGY 36(5), 2628-2638.

Bella, D.G., Giustra, M.G., Freni, G., 2014. Optimisation of coagulation/flocculation for pre-treatment of high strength and saline wastewater: Performance analysis with different coagulant doses. CHEM ENG J 254, 283-292.

Chen, X.Y., Li, Z., Jiang, Y., Qu, K.Y., 2006. Analytical solution of adiabatic heat and mass transfer process in packed-type liquid desiccant equipment and its application. SOL ENERGY 80(11), 1509-1516.

Fumo, N., Goswami, D.Y., 2002. Study of an aqueous lithium chloride desiccant system: air dehumidification and desiccant regeneration. SOL ENERGY 72(4), 351-361.

Haidl, J., Rejl, F.J., Valenz, L., Moucha, T., Petříček, R., 2017. General mass-transfer model for gas phase in structured packings. Chemical Engineering Research and Design 126, 45-53.

Hongtai, G., Sumin, J., Liang, C., 2015. Experimental Investigation on the Performance of Heat Pump Evaporation Crystallization Electroplating Wastewater Treatment System. Fluid Machinery 43(10), 7-10.

Huang, S., Lv, Z., Zhang, X., Liang, C., 2018. Experimental investigation on heat and mass transfer in heating tower solution regeneration using packing tower. ENERG BUILDINGS 164(1), 77-86.

Kim, M.H., Park, J.Y., Jeong, J.W., 2015. Simplified model for packed-bed tower regenerator in a liquid desiccant system. APPL THERM ENG 89, 717-726.

Li, H., Wang, H., Liu, Q., Tan, Y., Jiang, N., Lin, Y., 2016. Evaporation process for treating high-salinity industrial wastewater at low temperatures and ambient pressure. DESALIN WATER TREAT 57(56), 1-13.

Liu, C., Zeng, A., Yuan, X., Guocong Yu Kuo Tsung, Y., 2008. Experimental study on mass transfer near gas–liquid interface through quantitative Schlieren method. Chemical Engineering Research and Design 86(2), 201-207.

Liu, X., Yi, X., Chang, X., Jian, Y., 2009. Research on the field uniformity principle in liquid desiccant dehumidifier/regenerator. ACTA ENERGIAE SOLARIS SINICA 30(7), 939-945.

Lu, J., Ma, Y., Liu, Y., Li, M., 2011. Treatment of hypersaline wastewater by a combined neutralization–precipitation with ABR-SBR technique. DESALINATION 277, 321-324.

Ma, Y., Yu, G., Li, H.Z., 2005. Note on the mechanism of interfacial mass transfer of absorption processes. INT J HEAT MASS TRAN 48(16), 3454-3460.

Sultan, G.I., Hamed, A.M., Sultan, A.A., 2002. The effect of inlet parameters on the performance of packed tower-regenerator. RENEW ENERG 26(2), 271-283.

Wen, X., Li, F., Zhao, X., 2016. Removal of nuclides and boron from highly saline radioactive wastewater by direct contact membrane distillation. DESALINATION 394, 101-107.

Zeidan, E.B., Aly, A.A., Hamed, A.M., 2011. Modeling and simulation of solar-powered liquid desiccant regenerator for open absorption cooling cycle. SOL ENERGY 85(11), 2977-2986.

Zhang, L., Liu, X., Wei, H., Zhang, X., 2018. Experimental study and analysis of heat and mass transfer ability of counter-flow packing tower and liquid desiccant dehumidification system. ENERG BUILDINGS 158, 150-161.

Manuscript ID: 512
DOI: 10.18462/iir.icr.2019.0512

Flow patterns of vertical and horizontal adiabatic two-phase flow in a plate heat exchanger single channel with uniform gas-liquid distribution

Susanne BUSCHER[(a)]

[(a)] Technische Universität Berlin
Berlin, 10587, Germany, susanne.buscher@tu-berlin.de

ABSTRACT

Flow patterns of air-water two-phase flow are investigated for various flow directions in a transparent cross-corrugated channel with almost ideal, i. e. uniform, gas-liquid injection. A flow pattern map is derived from visual classification of photographs. Flow directions have little effect on flow patterns. This is attributed to the centrifugal force often dominating over buoyancy in the helical flow path. The ratio of centrifugal to buoyancy force is quantified by the centrifugal Froude number. Bubbly flow patterns are pre-determined by the homogeneous void fraction in the same way as in tubes. However, so-called slug flow is not observed, although being reported for cross-corrugated channels by other authors. Slugging is caused by non-uniform inlet conditions and other oscillating two-phase phenomena in the experimental periphery of the cross-corrugated channel.
Keywords: Air-Water, Corrugated Surface, Distribution, Horizontal Plate, Plate Exchanger, Slugging, Two-Phase Flow, Vertical Flow, Bubbles, Centrifugal Force, Froude Number.

1. INTRODUCTION

Plate heat exchangers can be utilized as evaporators/ condensers or absorbers/ desorbers in refrigeration plants or other processes. For those applications, knowledge of flow pattern is useful in order to estimate pressure drop, heat transfer, and, if required, mass transfer.
In order to investigate flow patterns isolated from the effects of heat or mass transfer, air-water flow is used as a model system. A transparent cross-corrugated single channel has been pivot-mounted to vary flow directions and qualify the impact of buoyancy. The typical inlet region of heat exchanger plates was substituted by separate injection of gas and liquid phase in order to obtain uniform phase distribution. Thus, the flow patterns are certainly induced by the cross-corrugated channel geometry, and not by the distributer.
Flow patterns in plate heat exchangers with air-water mixtures have been investigated by several researchers. Flow direction was either vertical upward or downward, but not horizontal. Some studies compared different corrugation angles (Tribbe and Müller-Steinhagen, 2001; Grabenstein et al., 2017). In most studies, the inlet region of the heat exchanger plate was kept in place (Asano et al., 2004; Nilpueng and Wongwises, 2010; Tribbe and Müller-Steinhagen, 2001; Vlasogiannis et al., 2002). Grabenstein et al. (2017) replaced it by a special mixer design. Yang et al. (2015) changed the location of the gas injector in the inlet region. For some cases, intermittent two-phase flow was reported to occur already in the inlet pipe before the two-phase flow entered the cross-corrugated channel. Thus, the visualized flow patterns were greatly influenced by the inlet conditions (Vlasogiannis, et al. 2002; Asano et al., 2004).

2. LAYOUT OF THE EXPERIMENT

2.1. The Cross-Corrugated Single Channel

The cross-corrugated single channel consists of two transparent polycarbonate plates. A sinusoidal corrugation profile was micro-milled into both plates. The geometric properties of the plates are listed in Table 1. Photographs of both plates are shown in Fig. 1.

Table 1. Geometric properties of the single channel

Corrugation angle (as to flow direction)	75°	Channel length	326.1 mm
Corrugation depth	1.2 mm	Channel width	278.2 mm
Peak-to-peak amplitude	2.4 mm	Hydraulic diameter (acc. Martin, 2010)	4.17 mm
Wave number (wave length/ period)	9 mm	Thickness of transparent plate	20 mm

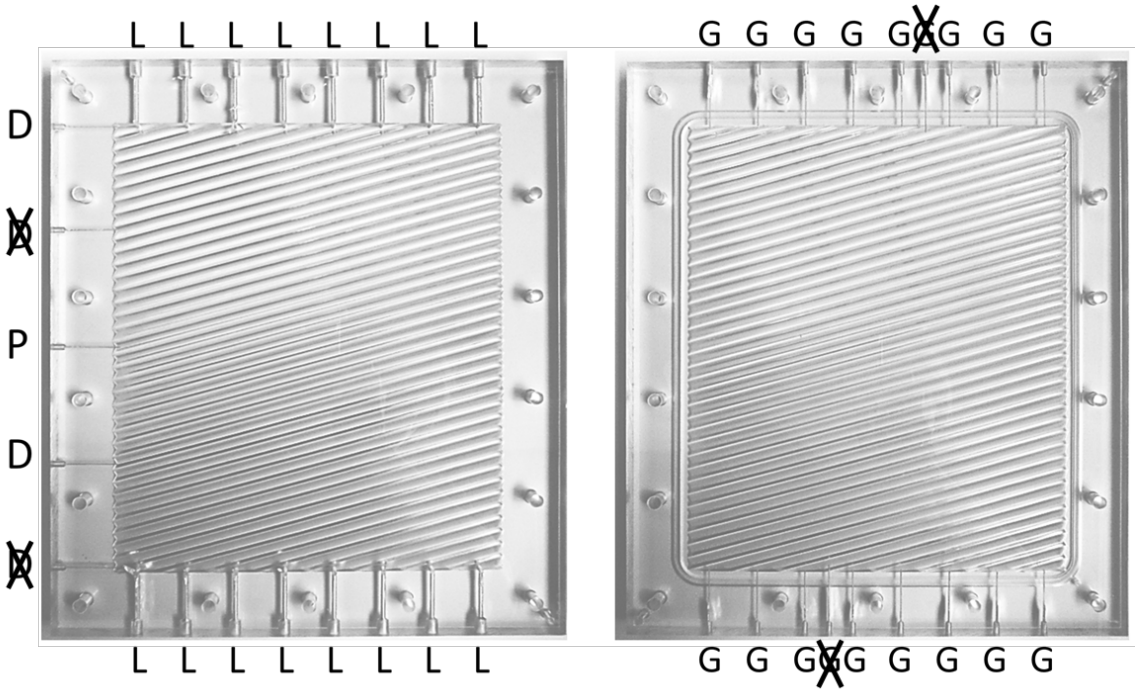

Figure 1: Transparent corrugated plates: tabs marked as liquid (L) and gas (G) inlet / outlet, and for differential (D) and gauge pressure (P) measurement. Crossed: tab closed (damaged / redundant)

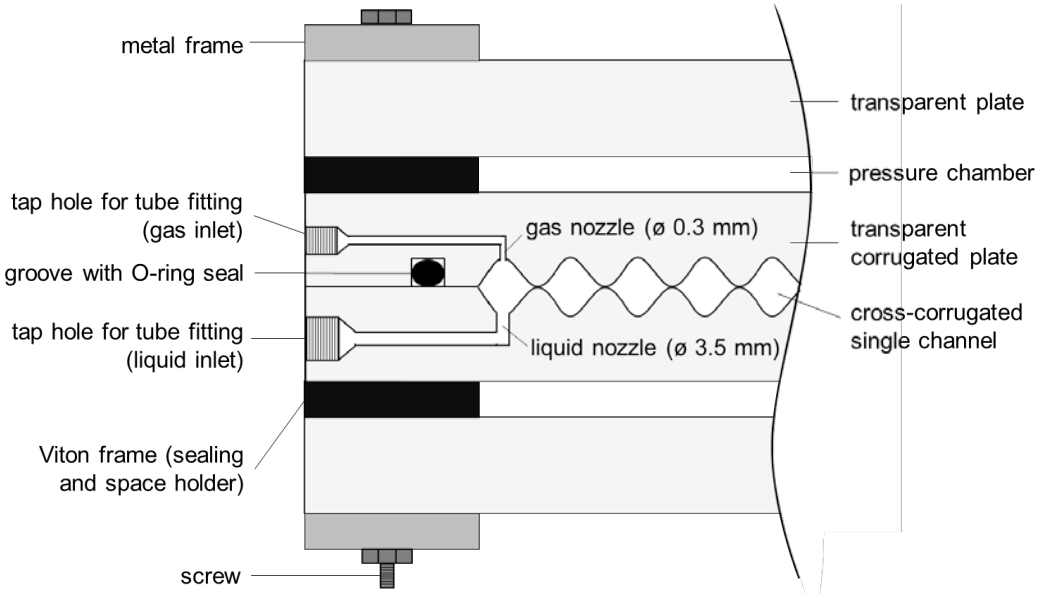

Figure 2: Cross-section of separate gas and liquid inlet nozzles of the single channel

The main objective of the channel design is to obtain a uniform gas-liquid distribution across the channel width. Therefore, both gas and liquid phase are injected separately into the single channel via 8 nozzles. As shown in Fig. 2, each gas jet is facing a liquid jet and vice versa to facilitate intense mixing of the phases. Each jet is located in a wave trough between two wave-crest contact points where both plates touch. However, for gas superficial velocities above 0.3 m/s, the gas has to be injected via T-junctions into the 8 inlet tubes of the liquid phase because of the high pressure drop in the gas jets. This has no negative effect on the gas-liquid distribution.
On both sides of the single channel, pressure chambers are built from additional transparent plates and space holders of Viton sealing (thickness 5 mm), see Fig. 2. They are filled with compressed air of 4 bar(g) to prevent the single channel from deformation.
Orthogonally to the flow direction, pressure taps are inserted for gauge pressure and differential pressure measurements. Presuming linear pressure drop across the channel length, the mean gauge pressure is measured in the middle of the channel length.
A digital camera with high resolution (36 MP) is used to make photographs of the whole single channel which is evenly illuminated by flat-panel LEDs from the back.

2.2. The Test Plant and Pulsating Flow

The deionized water is re-circulated by a centrifugal pump. Filtered pressurized air represents the gas phase and is not re-circulated but separated from the liquid in a storage tank. The standard volumetric flow rate measured is converted to absolute flow rate by means of the temperature, measured in the outlet stream, and the absolute pressure, which is the sum of ambient pressure and the measured gauge pressure.
In preliminary experiments, large pressure oscillations were recorded which in part influenced the flow patterns in the cross-corrugated single channel, particularly for high gas flow. The pulsations were attributed to intermittent flow phenomena in different parts of the test plant, for instance to slug flow in the return tubes and to waves in the storage tank which resulted from intermittent inlet flow and could have affected the flow rate of the pump.
While slug flow cannot be prevented entirely in the test plant, the tube orientation and diameter can influence the onset of slugging. Wu et al. (2017) state that slug flow is unlikely to form in tubes with diameters above 100 mm. Therefore, a long vertical part of the return pipe to the storage tank was replaced by a tube of 100 mm diameter. Barnea (1987) reported that slugging in vertical downward flow occurs less often compared to upward or horizontal flow in the same tube. Therefore, unnecessary horizontal or upward tubes were eliminated from the test plant where possible. In the storage tank, a special inlet design prevents the two-phase return flow from disturbing the water surface. To prohibit interference between mass-flow controller and low-frequent phenomena, the centrifugal pump is only operated at maximum power while the liquid flow is adjusted manually.

2.3. Uncertainty Analysis

The volumetric flowrate of water has a maximum uncertainty of 1.7%. The absolute volumetric flowrate of air (humid) has a maximum uncertainty of 4.8%, as derived from the standard volumetric flowrate, downstream temperature, gauge and atmospheric pressure. For the superficial velocities, the maximum uncertainties include suspected deviations of the corrugation profiles due to fabrication and are assumed for liquid and gas as 3.2%, and 5.5%, respectively. The homogeneous void fraction and the centrifugal Froude number have maximum uncertainties of 4.7%, and 11.6%, respectively. All values are expanded relative uncertainties. For the sake of brevity, only the maximum percentages are given which only emerge at low measurement values.

3. FLOW PATTERN CLASSIFICATION

The flow patterns were defined after a rough preview of all photographs without knowledge of the corresponding superficial velocities. In order to classify the data consistently, the definitions were documented with great detail. However, classification was difficult in some cases because the transitions are gradual. The photographs were not re-classified after the flow pattern maps were complete, because the training effect washed off quickly. To be consistent, re-classifying some cases would make re-evaluation of all photographs necessary. Also, re-classification could be biased by the expectation that boundaries between flow patterns should be clear.

3.1. Bubbly Flow

Bubbly flow was subdivided into predominantly roundish and rather small bubbles (b), and frequently occurring irregular blob-like bubbles (B). Examples of both types are shown in Fig. 3.

3.2. Intermediate Flow

The transition region from bubbly to film flow expands over the biggest part of the flow pattern maps. The intermediate flow patterns are defined to describe the different stages of transition.
Intermediate flow begins when many bubbles combine to form bigger gas units (T), while bubbles are still predominant in the rest of the flow. The big gas units are often several corrugations long and zigzag-shaped. In Fig. 3, the corrugations become apparent as dark shadows at the gas phase. The big gas units are termed “Taylor-like bubbles” because – similar to Taylor bubbles in tubes – their zigzag-shape is determined by the channel geometry, i. e. the corrugations and the distances between the contact-points of the wave crests. The Taylor-like bubbles expand over most of the cross-section between two rows of wave-crest contact points. Focke and Knibbe (1986) have demonstrated that, for cross-corrugated channels with large corrugation angles, the flow stays between those two rows of contact points. This is also true for two-phase flow, as observed both in the presented experiments as well as in other studies (i. e. Tribbe and Müller-Steinhagen, 2001).

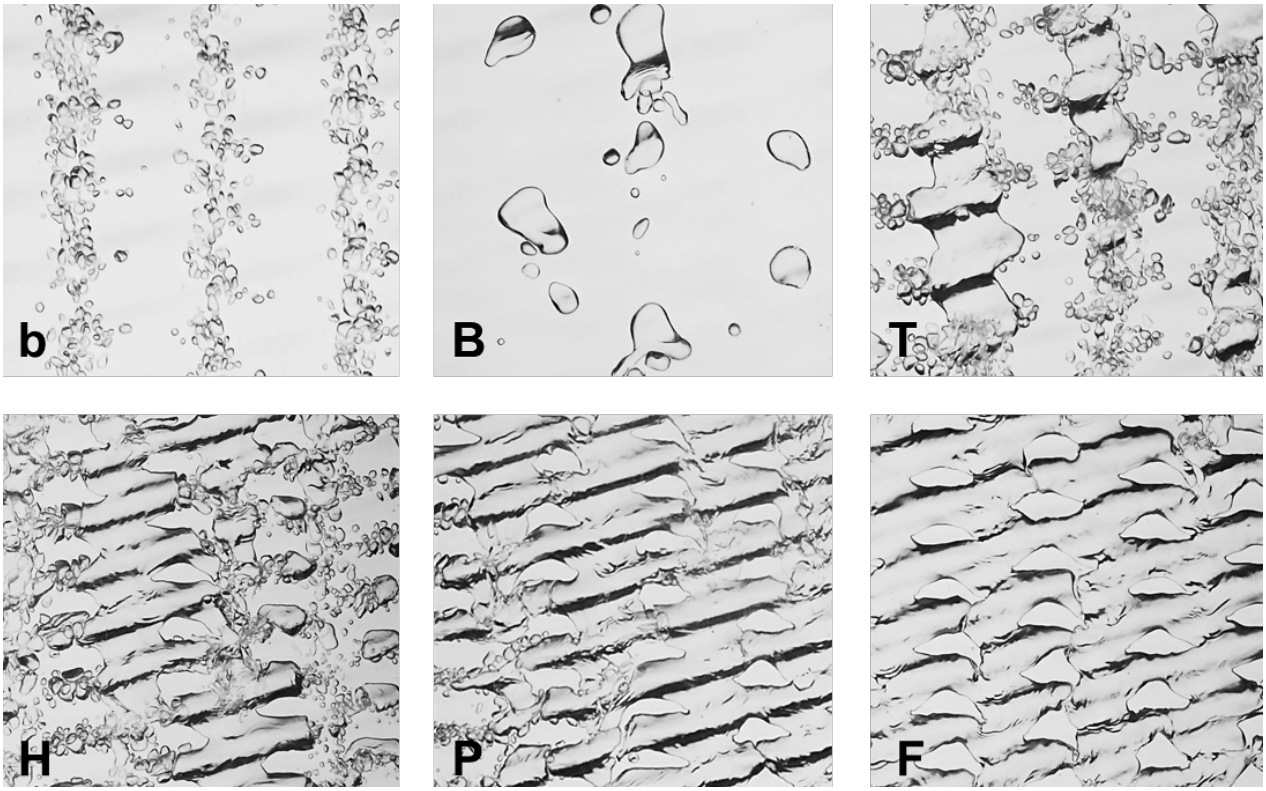

Figure 3: Examples for flow patterns. b: small bubbly, B: blob-like bubbles, T: Taylor-like bubbles, H: heterogeneous flow; P: partial film flow, F: full film flow

If more gas phase is added, the Taylor-like bubbles become bigger and longer. If their combined area extends over about 40% of the projected area of the two-phase flow, it is classified as heterogeneous flow (H). The large gas units start to converge and to extend behind the wave-crest contact points. Thus, the gas units are not considered as separate entities anymore, but as small regions of local film flow. The space around the wave-crest contact points is only filled with liquid. Therefore, their locations are identified in the many bright secluded areas in Fig. 3.
If the local film regions extend in width and, hence, enclose several wave-crest contact points, while some limited regions of bubbly flow are still present, it is classified as partial film flow (P).

3.3. Film Flow

If the local film flow is predominant, it is classified as full film flow (F). However, bubbly flow in less than about 10% of the area may still be found. Those bubbles usually are attached to the local film regions, probably just before coalescing with or after separating from the film.

3.4. Stagnant Gas Phase

One rare flow pattern only occurs at very low gas and liquid flow rates in vertical downward flow: Big stagnant bubbles rest behind the wave-crest contact points while a liquid rivulet (L) slowly flows by, now and then, carrying a few small bubbles. This is shown in the top right picture of Fig. 4.

4. CENTRIFUGAL BUOYANCY

According to the presented experiments and other research (i. e. Tribbe and Müller-Steinhagen, 2001), gas bubbles follow a corkscrew flow path in cross-corrugated channels with large corrugation angles. The two-phase flow is “reflected” close to the wave-crest contact points – just as single-phase flow which was investigated by Focke and Knibbe (1986).
Empirical investigations of two-phase flow in tube bends (Usui et al., 1980; Da Silva Lima and Thome, 2012) show that the centrifugal force causes the lighter phase to be oriented towards the

inner radius of the bend. This effect often is dominant over gravity and has been termed “centrifugal buoyancy” by Wick and Tooby (1977).
Since the two-phase flow in the cross-corrugated channel follows a helical path, centrifugal buoyancy constantly affects both phases. This is evident in the present experiments: In bubbly flow (with or without Taylor-like bubbles), the gas phase concentrates in the middle of the helical path between the wave-crest contact points. The effect is striking for all flow directions, and often seems to dominate over gravity.

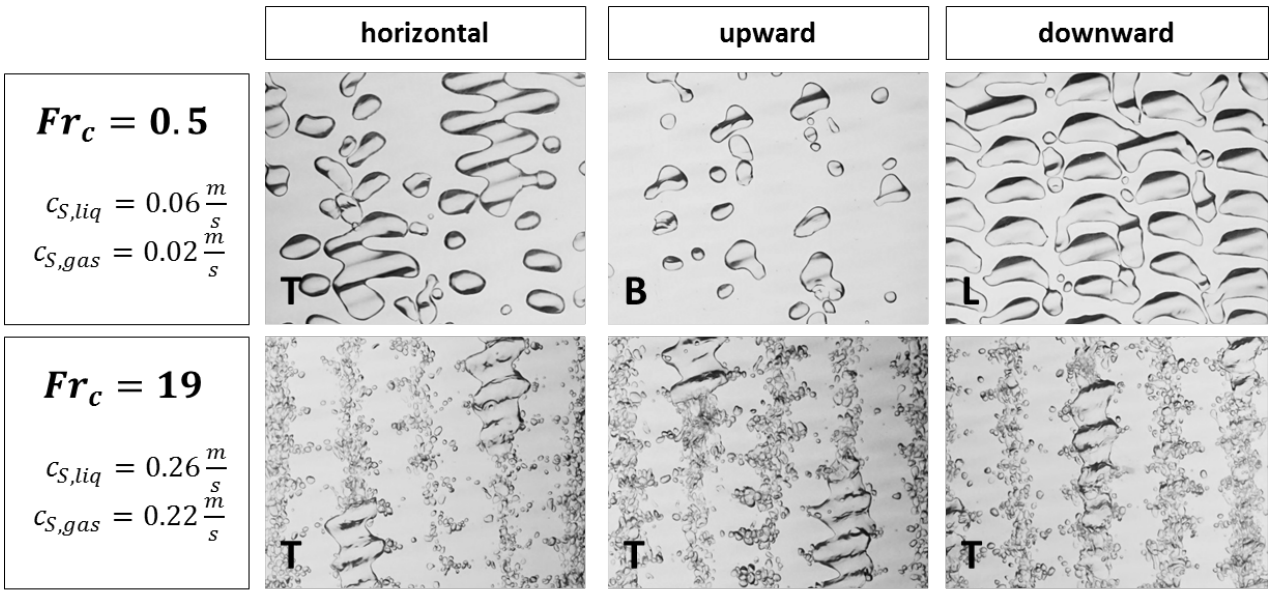

Figure 4: Effect of centrifugal vs. gravitational buoyancy on flow patterns

In order to quantify the impact of the centrifugal force compared to gravity, the centrifugal Froude number is defined in Eq. (1). It contains the gravity *g*, the radius *R* and the homogeneous two-phase velocity, defined as the sum of liquid and gas superficial velocity in Eq. (2).

$$Fr_c = c_{2ph}^{\ 2} \, (R\,g)^{-1} \qquad \text{Eq. (1)}$$

$$c_{2ph} = c_{S,liq} + c_{S,gas} \qquad \text{Eq. (2)}$$

The characteristic radius *R* in Eq. (1) is constant for a given corrugation geometry and is set as half of the peak-to-peak amplitude, i. e. the corrugation depth given in Table 1. This radius has a greater impact on centrifugal force than, for example, the distance between the wave-crest contact points which rather affects the length of the flow path before the flow is coerced to change its direction again circumventing another corrugation.
The centrifugal Froude number given in Eq. (1) is derived from the ratio of centrifugal to gravitational buoyancy. According to Wick and Tooby (1977), the resultant force on a gas bubble in radial direction is given in Eq. (3), where *V* is the bubble volume and *Ω* the angular velocity. The sign of the force becomes negative for bubbles driving them to the pivot point. Since the bubbles are parts of a swarm, the mean density ρ_m of the two-phase flow has to be inserted to represent the surrounding fluid. The resultant force in vertical upward direction is given in Eq. (4). The ratio of radial to vertical force yields the centrifugal Froude number as given in Eq. (1), if the angular velocity in Eq. (5) is calculated with the homogeneous two-phase velocity given in Eq. (2).

$$F_{rad} = V\,(\rho_{gas} - \rho_m)\,\Omega^2\,R \qquad \text{Eq. (3)}$$

$$F_{up} = V\,(\rho_m - \rho_{gas})\,g \qquad \text{Eq. (4)}$$

$$F_{rad} / F_{up} = \Omega^2 R\, g^{-1} = {c_{2\,ph}}^2\, (R\, g)^{-1}$$ Eq. (5)

The impact of centrifugal buoyancy on flow patterns is illustrated in Fig. 4. Photographs of two-phase flow with equal superficial velocities are compared with respect to different directions of flow. If the corresponding Froude number is low the buoyancy and, thus, the flow direction has a significant effect on flow patterns. If the Froude number is high, the direction of flow has no impact.

5. FLOW PATTERN MAPS

5.1. Empirical and Theoretical Boundaries

The results of flow pattern analysis are depicted as flow pattern maps in Fig. 5, presenting each flow direction separately as well as combining all flow directions. The abscissa and ordinate are the gas and liquid superficial velocities, respectively. Contour lines of the centrifugal Froude number and the homogeneous void fraction are also plotted in the flow pattern maps. Since the homogeneous model disregards slip, the homogeneous void fraction is given as:

$$\alpha_{\mathrm{hom}} = c_{S,gas} / (c_{S,gas} + c_{S,liq})$$ Eq. (6)

The empirical flow pattern boundaries, as derived only from horizontal flow, are drawn as thick grey lines in all diagrams of Fig. 5. Each letter represents a point of measurement classified as one of the flow patterns described in section 3. Examples of the flow patterns are shown in Fig. 3 and 4.
For some regions in the diagrams of Fig. 5, different flow patterns were identified for similar superficial velocities of the same flow direction. There, smooth transitions from one flow pattern to another took place which made it difficult to classify the photographs clearly as one type or another. Consequently, the boundary lines are thickened there to indicate the gradual transition.
Strikingly, the flow pattern classification yields very similar results for all flow directions. This is attributed to the centrifugal force which dominates over buoyancy in many cases. Only for low centrifugal Froude numbers, the flow patterns are more likely to differ with respect to flow direction. This is particularly true for Froude numbers below 2, whereas Froude numbers above 10 indicate that flow patterns are definitely independent of flow direction.
Theoretical boundaries are stated by Barnea (1987) for two-phase tube flow: If the gas phase is evenly distributed across the tube cross-section, agglomeration of bubbles is prevented by their distance to each other. Therefore, Barnea assumes dispersed bubbly flow in tubes at void fractions below 0.25, and beginning of Taylor-bubble and liquid-slug formation between 0.25 and 0.52, depending on the turbulent fluctuations. According to Barnea (1987), Taylor bubbles definitely form at void fractions above 0.52 because the maximum packing of bubbles is exceeded.
Both of the theoretical boundaries of Barnea (1987) are confirmed for all flow directions by the results in Fig. 5: If the homogeneous void fraction is less than 0.25, only bubbly flow (b, B) is observed. Between 0.25 and 0.52, both bubbly flow (B) and Taylor-like bubbles (T) are found. Void fractions above 0.52 rule out bubbly flow.
An additional empirical finding with respect to homogeneous void fraction is derived from Fig. 5: The contour lines for the void fractions of 0.7, 0.89 and 0.95 roughly agree with the transitions to heterogeneous flow (H), partial film flow (P), and full film flow (F), respectively.

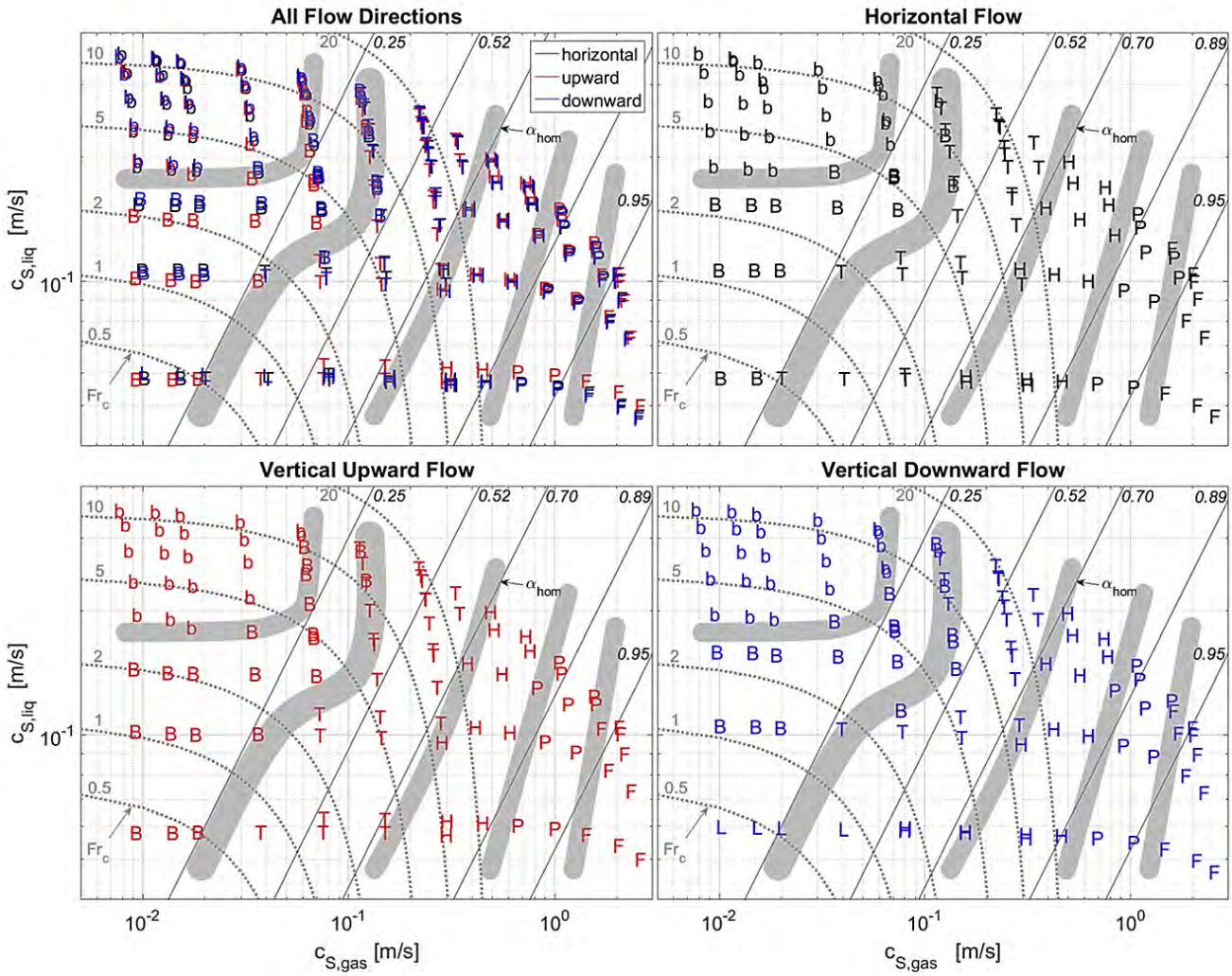

Figure 5: Flow pattern maps – boundaries (thick grey lines) derived from horizontal flow

5.2. The Absence of Slug Flow

In contrast to other studies (Tribbe and Müller-Steinhagen, 2001; Nilpueng and Wongwises, 2010; Vlasogiannis et al., 2002), slug flow was not observed in the presented experiments. They describe slug flow as periodically changing gas-liquid proportion across the whole channel width, i. e. pure or bubbly liquid slugs alternating with large sections of film flow. Since the mentioned studies had tube inlets, the phenomenon can be attributed to intermittent flow in the inlet tube, as also suggested by Vlasogiannis et al. (2002). Grabenstein et al. (2017) installed a mixing section at the entrance of their herringbone-corrugated channel, but also report slug flow. However, intermittent flow responsible for slugging could have been induced by various phenomena in their mixer or the testing facility. This was also encountered in the preliminary experiments to this study, but was reduced to a great extent.

None of the named studies explained why slug flow should occur in a cross-corrugated channel. In slugging pipe flow, the Taylor bubbles are formed by coalescing bubbles which change speed with increasing size and, thus, agglomerate quickly. Therefore, slug flow only emerges after a certain entrance length (Barnea, 1987). Pressure oscillations occur when the liquid slugs between the Taylor bubbles collapse. In cross-corrugated channels, however, bubbles cannot accelerate in the same manner because of their helical flow path, as described in section 4. Pressure does not oscillate if the liquid barriers between Taylor-like bubbles are destroyed because they do not expand over the whole channel cross-section. Consequently, so-called slug flow in plate heat exchangers is attributed to periodic changes of gas-liquid distribution in the inlet tube. Pressure oscillations correspond either to slugging in the inlet or to intermittent phenomena in other parts of the testing facility which also can mutually reinforce each other.

6. CONCLUSIONS

Flow patterns maps are derived for a cross-corrugated channel with uniform gas liquid distribution which is achieved by separate injection of the phases. The variation of flow direction does not affect the flow pattern map in most cases. This is attributed to the centrifugal force which is found to dominate over buoyancy, as quantified by the centrifugal Froude number. Theoretical flow pattern boundaries from the literature, based on homogeneous void fraction, are confirmed by the experiments. In contrast to other studies, slug flow is not observed in the experiments. These findings are attributed to the uniform and steady gas-liquid distribution in the inlet region.
In most plate heat exchanger inlets, however, bubble coalescence, phase separation and periodic changes to the gas-liquid proportion may occur. This maldistribution is responsible for pulsating flow, similar to slug flow in tubes. Also, it influences flow patterns if the flow direction is changed.

REFERENCES

Asano, H., Takenaka, N., Fujii, T., 2004. Flow characteristics of gas–liquid two-phase flow in plate heat exchanger (Visualization and void fraction measurement by neutron radiography). Exp. Therm. Fluid Sci. 28, 223–230.

Barnea, D., 1987. A unified model for predicting flow-pattern transitions for the whole range of pipe inclinations. Int. J. Multiphase Flow 13(1), 1-12.

Da Silva Lima, R.J., Thome, J.R., 2012. Two-phase flow patterns in U-bends and their contiguous straight tubes for different orientations, tube and bend diameters. Int. J. Refrigeration 35, 1439-1454.

Focke, W., Knibbe, P., 1986. Flow visualization in parallel-plate ducts with corrugated walls. J. Fluid Mech. 165, 73–77.

Grabenstein, V., Polzin, A.-E., Kabelac, S., 2017. Experimental investigation of the flow pattern, pressure drop and void fraction of two-phase flow in the corrugated gap of a plate heat exchanger. Int. J. Multiphase Flow 91, 155-169.

Martin, H., 2010. N6 Pressure drop and heat transfer in plate heat exchangers. In: VDI-GVC (Ed.), VDI Heat Atlas, 2nd ed., Springer-Verlag, Berlin, Heidelberg, 1515-1521.

Nilpueng, K., Wongwises, S., 2010. Two-phase gas–liquid flow characteristics inside a plate heat exchanger. Exp. Therm. Fluid Sci. 34, 1217–1229.

Tribbe, C., Müller-Steinhagen, H., 2001. Gas/liquid flow in plate-and-frame heat exchangers - Part II: Two-phase multiplier and flow pattern analysis. Heat Transfer Eng. 22(1), 12–21.

Usui, K., Aoki, S., Inoue, A., 1980. Flow behavior and pressure drop of two-phase flow through C-shaped bend in vertical Plane, (I) Upward flow. J. Nucl. Sci. Technol. 17(12), 875-887.

Vlasogiannis, P., Karagiannis, G., Argyropoulos, P., Bonzozoglou, V., 2002. Air-water two-phase flow and heat transfer in a plate heat exchanger. Int. J. Multiphase Flow 28, 757–772.

Wick, G.L., Tooby, P.F., 1977, Centrifugal buoyancy forces, Am. J. Phys. 45(11), 1074-1076.

Wu, B., Firouzi, M., Mitchell, T., Rufford, T.E., Leonardi, C., Towler, B., 2017. A critical review of flow maps for gas-liquid flows in vertical pipes and annuli. Chem. Eng. J. 326, 350–377.

Yang, C.-Y., Lin, Y-H., Meng, F.-Y., Li, G.-C., 2015. Flow distribution of two-phase refrigerant in plate heat exchangers. Proceedings of the 24th IIR International Congress of Refrigeration, Yokohama, Japan, IIF/IIR, Keynote E1-We-1.

Manuscript ID: 514
DOI: 10.18462/iir.icr.2019.0514

Calibration of a simulation tool for fixed-bed adsorption household refrigerators and determination of optimal design parameters

Mike JÄGER, Kristian HURTIG, Roland KÜHN

Technische Universität Berlin, Marchstr. 18

Berlin, 10587, Germany, mike.jaeger@tu-berlin.de

ABSTRACT

A simulation tool for fixed-bed adsorption household refrigerators, consisting of an evaporator, two adsorption chambers and a condenser, is introduced. The objectives are to calibrate the simulation tool and to identify an optimal adsorber depth.
The fixed-bed adsorbers are cooled by ambient air. The desorption is carried out by hot water flowing through pipes located within the bed. Water is used as refrigerant and silica gel as adsorbent.
One measurement is used to set initial and boundary conditions for the simulation and to adapt the simulation to the measurement results. The simulation results are compared to those of the measurement and they highly comply with each other.
An essential parameter is the refrigeration compartment temperature which can be simulated with a maximum difference of 1 K. Thus, this simulation tool is the basis to determine an optimal adsorber depth.
Keywords: Air-Cooled Adsorption, Fixed-Bed Adsorber, Simulation, Calibration, Refrigerator.

1. INTRODUCTION

Until 2030 the world-wide demand of energy will increase by 60% (Rouhani et al., 2016). Adsorption cooling is a promising alternative to conventional cooling methods by using waste heat, because adsorption works comparatively at low temperatures (Kühn et al., 2018). One possible application is a household refrigerator. According to cost-efficiency it is appropriate to use air-cooled fixed-bed adsorbers to save additional expenses for a cooler and piping. It is beneficial to describe the processes of the adsorption refrigerator mathematically to improve design parameters and thus, achieve a high energy efficiency.
In the paper at hand a simulation tool for an adsorption household refrigerator, operating as two-chamber system, is introduced. For every component the governing thermodynamic, heat and mass transfer equations are solved and coupled to each other. It is then calibrated by using a reference measurement. The objective is to estimate how many pipes are required to regenerate the fixed-bed adsorbers efficiently.

2. THE SIMULATION TOOL

The simulation tool is divided into four parts, one for each main component of the system: two adsorbers, the evaporator and the condenser. Fig. 1 shows a schematic of the adsorption refrigerator with the four parts of the simulation tool and the governing heat and mass flows. The sections 2.1 to 2.4 deal with the mathematical description of the governing energy and mass transport processes in each part referring to Fig. 1. The coupling of the mathematical equations is introduced in section 2.5. Water is used as the refrigerant and silica gel as adsorbent.

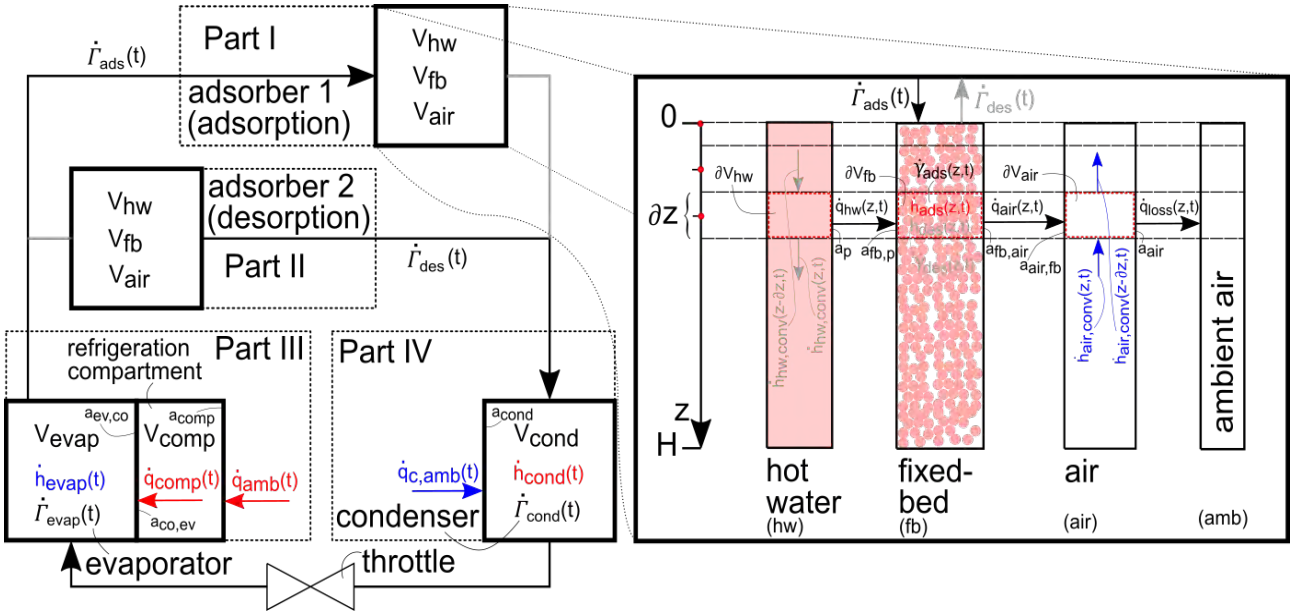

Figure 1: Schematic of the simulation tool of the adsorption refrigerator divided in four parts

On the right side of Fig. 1 the detailed model for one adsorber operated in adsorption phase is shown. During adsorption there is a forced air flow caused by fans (blue enthalpy flows) and a generated adsorption heat source $\dot{h}_{ads}(z,t)$. The grey marked arrows and enthalpy flows mean that they are not active. Part II has the same structure as Part I with the difference that this adsorber is operated in desorption. Thus, the enthalpy flows with the index $hw, conv$ and des are active and those with the index $air, conv$ and ads are inactive. After adsorption adsorber 1 has to be heated up before desorption can start. When desorption is finished the chamber is cooled down and adsorption can start again. The two-chamber system is operated alternating so that each adsorber passes through the adsorption process, while the other is heated up, regenerated (desorption) and cooled down again.

Fig. 2 shows the setup of one adsorber operated in the four phases adsorption, heating up, desorption and cooling down.

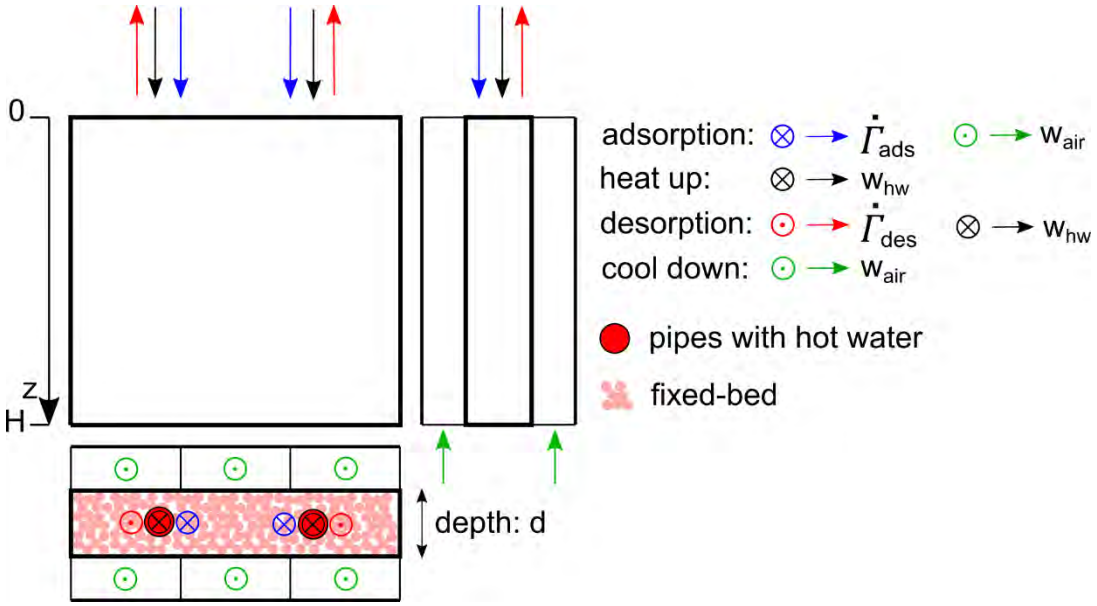

Figure 2: Setup of one adsorber shown in the operation of adsorption, heat up, desorption and cool down

2.1. Adsorber – Part I (Adsorption and Cool Down)

The adsorbers are cuboid chambers filled with spheres of silica gel. The generated heat of adsorption is dissipated through the adsorber walls to a forced air flow caused by fans in an air duct. Thus, the air heats up along the flow direction in the air duct. Therefore, the adsorber model is resolved locally in z-direction (Fig. 1). The adsorber model is subdivided into three subsystems (index hw, fb and air). Within each subsystem differential energy equations in the reference volumes ∂V_i are solved by finite differences.

During adsorption, the adsorbent loading X follows the equilibrium loading X_{eq} which depends on the pressure of the evaporator p_{evap} and the temperature of the fixed-bed in the adsorber $T_{fb}(z,t)$. This process generates an adsorption water mass flow $\dot{\gamma}_{ads}(z,t)$ (Fig. 1) in each differential volume ∂V_{fb} which is described by a Linear-Driving-Force model (Schönbucher, 2002).

$$\dot{\gamma}_{ads}(z,t) = \rho_{Ad}\frac{\partial X(z,t)}{\partial t} = \rho_{Ad}\frac{15D_{eff}}{r^2}\left(X_{eq}\left(p_{evap}(t), T_{fb}(z,t)\right) - X(z,t)\right) \quad \text{Eq. (1)}$$

$\dot{\gamma}_{ads}$ is the generated adsorption mass flow within the differential volume ∂V_{fb}, ρ_{Ad} the apparent density of the adsorbent, D_{eff} a summarized diffusion coefficient containing all mass transfer constraints (Schönbucher, 2002) and r the radius of the spheres. The equilibrium data for X_{eq} are taken from Schawe (Schawe, 1999). To reduce calculation time the pressure drop from evaporator to adsorber is not considered in the simulation ($p_{evap} = p_{fb}$).

The following equations Eqs. (2) to (6) describe the energy transport during the adsorption process for the three subsystems hot water (index hw), fixed-bed (index fb) and air (index air). These equations exemplary apply to the red dash-marked differential system boundaries in Fig. 1.

$$\partial C_{fb}\frac{\partial T_{fb}(z,t)}{\partial t} = \left[\dot{q}_{hw}(z,t) + \dot{h}_{ads}(z,t) - \dot{q}_{air}(z,t)\right]\partial V_{fb} \quad \text{Eq. (2)}$$

$$\partial C_{fb}\frac{\partial T_{fb}(z,t)}{\partial t} = \left[\begin{array}{c} u_p a_{p,fb}\left(T_{hw}(z,t) - T_{fb}(z,t)\right) + (1-\varepsilon)\dot{\gamma}_{ads}(z,t)\Delta h_{Ad}\left(X(z,t)\right) - \\ u_{ads}a_{fb,air}\left(T_{fb}(z,t) - T_{air}(z,t)\right) \end{array}\right]\partial V_{fb} \quad \text{Eq. (3)}$$

$$\partial C_{hw}\frac{\partial T_{hw}(z,t)}{\partial t} = -\dot{q}_{hw}(z,t)\,\partial V_{hw} = -u_p a_p\left(T_{hw}(z,t) - T_{fb}(z,t)\right)\partial V_{hw} \quad \text{Eq. (4)}$$

$$0 = \left[\dot{q}_{air}(z,t) + \dot{h}_{air,conv}(z,t) - \dot{h}_{air,conv}(z-\partial z,t) - \dot{q}_{loss}(z,t)\right]\partial V_{air} \quad \text{Eq. (5)}$$

$$0 = u_{ads}a_{air,fb}\left(T_{fb}(z,t) - T_{air}(z,t)\right) - \rho_{air}c_{p,air}w_{air}\frac{\partial T_{air}(z,t)}{\partial z} - u_{loss,ads}a_{air}\left(T_{air}(z,t) - T_{amb}(z,t)\right) \quad \text{Eq. (6)}$$

∂C_i always defines a heat capacity (J×K^{-1}) which is the product of the specific heat capacity, the density and the considered volume ∂V_i. The index fb contains the volume fractions of silica gel and the metal of the pipes and chamber whereas the index hw only consists of the hot water volume. The parameters C_{fb} and C_{hw} have a constant value for all differential reference volumes ∂V_{fb} and ∂V_{hw}. The first term on the right side of Eq. (3) defines the heat flow from the hot water to the fixed-bed with the thermal transmittance u_p. The hot water temperature T_{hw} is described with an extra equation Eq. (4). The second term of Eq. (3) describes the heat source due to the adsorption process. Δh_{Ad} is the adsorption enthalpy depending on the current loading X (Schnabel, 2009) and ε is the voids fraction of the fixed-bed. The third term in Eq. (3) represents the heat flow from the fixed-bed to the air using the thermal transmittance u_{ads}, including the heat conductivity of the fixed-bed, the heat transfer from the fixed-bed to the wall of the chamber, the heat conductivity of the wall and the heat transfer from the wall to the cooling air in the air duct. $a_{fb,p}$, a_p and $a_{fb,air}$ are constant volume-specific areas. Each is related to the differential volume ∂V which is first in the index of a.

Further theoretical investigations have shown that steady-state equations are sufficient to describe the energy transport of the air flow, Eq. (5) and (6). The first term on the right side in Eq. (6) is the

third term on the right side of Eq. (3) with another volume-specific area $a_{air,fb}$. The second term in Eq. (6) represents the convective heat transfer due to the forced air flow in the air duct with the constant velocity w_{air}. The third term is the heat loss from the air flow to the ambient air with the thermal transmittance $u_{loss,ads}$, including the heat transfer from the air flow to the air duct wall, the heat conductivity of the air duct wall and the heat transfer from the wall to the ambient air. Within the calibration the ambient temperature T_{amb} is a function of the measurement time. The inlet temperature of the cooling air flow equals the ambient temperature ($T_{air}(z = H, t) = T_{amb}$).

2.2. Adsorber – Part II (Desorption and Heat Up)

During desorption, heat is provided to the adsorber through hot water pipes and the adsorbent is regenerated. The heat input leads to a lower equilibrium loading X_{eq} and thus a desorption water vapor mass flow $\dot{\gamma}_{des}(z,t)$ is generated (Fig. 2). Eq. (1) applies also for the desorption, but the pressure of the condenser p_{cond} has to be used to calculate the equilibrium loading. The value for the water vapor flow $\dot{\gamma}_{des}$ becomes negative, because the water is desorbed from the adsorbent.
The energy equations Eq. (2) and (3) are also the same for desorption. The equation for the hot water temperature T_{hw} changes because of a forced water flow within the pipes (Eq. (7) and (8)).

$$\partial C_{hw} \frac{\partial T_{hw}(z,t)}{\partial t} = \left[\dot{h}_{hw,conv}(z-\partial z,t) - \dot{h}_{hw,conv}(z,t) - \dot{q}_{hw}(z,t)\right] \partial V_{hw} \quad \text{Eq. (7)}$$

$$\partial C_{hw} \frac{\partial T_{hw}(z,t)}{\partial t} = \left[\rho_{hw} c_{p,hw} w_{hw} \frac{\partial T_{hw}(z,t)}{\partial z} - u_p a_p \left(T_{hw}(z,t) - T_{fb}(z,t)\right)\right] \partial V_{hw} \quad \text{Eq. (8)}$$

The inlet temperature of the water during heat up and desorption $T_{hw}(z = 0, t)$ is within the calibration a function of the measurement time. There is no forced air flow on the wall of the adsorbers during desorption. This fact leads to a negligence of the enthalpy flow $\dot{h}_{air,conv}(z,t)$ and $\dot{h}_{air,conv}(z-\partial z,t)$ in Eq. (5) and (6) for desorption, but the heat loss $\dot{q}_{loss}(z,t)$ persists. The thermal transmittance within the heat loss during desorption and heat up changes to $u_{loss,des}$.

2.3. Evaporator – Part III

The third part of the simulation tool contains two subsystems. In contrast to the local differentially resolved adsorber model, these subsystems are considered as a lumped model. Eqs. (9) and (10) define the energy equation for the evaporator with a plate design (index $evap$) whereas Eq. (11) represents the energy transport within the refrigeration compartment (index $comp$).

$$C_{evap} \frac{\partial T_{evap}(t)}{\partial t} = \left[\dot{q}_{comp}(t) - \dot{h}_{evap}(t)\right] V_{evap} \quad \text{Eq. (9)}$$

$$C_{evap} \frac{\partial T_{evap}(t)}{\partial t} = \left[u_{evap} a_{ev,co} \left(T_{comp}(t) - T_{evap}(t)\right) - \dot{\Gamma}_{evap}(t) \Delta h_{lv} \left(T_{evap}(t)\right)\right] V_{evap} \quad \text{Eq. (10)}$$

$$C_{comp} \frac{\partial T_{comp}(t)}{\partial t} = \left[u_{comp} a_{comp} \left(T_{amb} - T_{comp}(t)\right) - u_{evap} a_{co,ev} \left(T_{comp}(t) - T_{evap}(t)\right)\right] V_{comp} \quad \text{Eq. (11)}$$

The volumetric heat capacity C_{evap} consists of the volume fractions of liquid and gaseous water within the evaporator. The first term in Eq. (10) on the right side defines the heat input from the refrigeration compartment to the evaporator, with the heat transfer coefficient u_{evap} and the specific surface a_{evap}. The temperature $T_{comp}(t)$ results from an additional equation Eq. (11) using the heat capacity C_{comp} which contains the volume fractions of metal and air located in this refrigeration compartment. The second term of Eq. (10) represents a heat sink due to evaporation of water with the evaporation rate $\dot{\Gamma}_{evap}(t)$. It is assumed that the water vapor is in equilibrium and thus, the calculated pressure $p_{evap}(t)$ is the saturation vapor pressure.

2.4. Condenser – Part IV

The energy equation for the condenser is analogous to Eq. (9) and (10) for the evaporator. The heat capacity C_{cond} consists of the volume fractions of liquid and gaseous water inside of the condenser and the fraction of metal. The heat enthalpy flow $\dot{h}_{cond}(t)$ is a heat source due to condensation process with the condensation rate $\dot{\Gamma}_{cond}(t)$ (see fig. 1). The condenser is cooled down with the ambient heat flow $\dot{q}_{c,amb}(z,t)$ consisting of the heat transfer coefficient u_{cond} and the specific area a_{cond}. It is assumed that the water vapor is in equilibrium and thus, the pressure $p_{cond}(t)$ is calculated by a saturation vapor pressure equation.

2.5. Coupling of the components

In the process the adsorbing adsorber is connected to the evaporator and the desorbing adsorber is connected to the condenser. The coupling condition is expressed by the assumption that the water which is adsorbed in the adsorber is instantaneously evaporated in the evaporator. Consequently, the local integrated adsorption mass flows $\dot{\gamma}_{ads}(z,t)$ in every volume ∂V_{fb} (see Eq. (1)) equal $\dot{\Gamma}_{evap}(t)$ and the vapor mass flow $\dot{\Gamma}_{ads}(t)$ from the evaporator to the adsorber. This condition is defined analogously between adsorber and condenser in the desorption process.

$$\int_{z=H}^{z=0} \dot{\gamma}_{ads}(z,t)\partial z = \dot{\Gamma}_{evap}(t) = \dot{\Gamma}_{ads}(t) \qquad \int_{z=H}^{z=0} \dot{\gamma}_{des}(z,t)\partial z = \dot{\Gamma}_{cond}(t) = \dot{\Gamma}_{des}(t) \quad \text{Eq. (12) and (13)}$$

The recirculation from the condenser to the evaporator is adapted with the help of a condensate storage so that during one cycle the mass of liquid refrigerant in each component is constant.

3. CALIBRATION

To improve consistency between simulation and measurements a calibration of the simulation to measurement results is performed to evaluate the real heat transfer coefficients u_i of the system. To do so a measurement of one periodical steady process cycle is used.
The operation conditions are shown in table 1 and the results of the calibrated thermal transmittances u_i are listed in Table 2. The boundary conditions which incorporate in the simulation tool are the ambient temperature T_{amb}, the hot water inlet temperature $T_{hw,in}(z=0)$ while heat up and desorption, the hot water and air flow velocity w_{hw} and w_{air} and the operation times for adsorption, heat up, desorption and cool down of the adsorbers (t_{ads}, t_{heat}, t_{des}, t_{cool}). T_{amb} and $T_{hw,in}(z=0)$ are functions of time in the measurement and thus, also in the simulation. The initial conditions are taken from the same measurement at the beginning of adsorption of adsorber 1.

Table 1. Boundary and initial conditions for the calibration of the simulation tool

Name	Symbol	Value	Unit
Ambient temperature	T_{amb}	$T_{amb,m}(t) \approx 298.15$	K
Hot water inlet temperature (heat up and desorption)	$T_{hw,in}(z=0)$	$T_{hw,m,in}(t) \approx 333.15$	K
Air flow velocity (cool down and adsorption)	w_{air}	1	$m \times s^{-1}$
Hot water flow velocity (heat up and desorption)	w_{hw}	0.1	$m \times s^{-1}$
Operation times	$t_{ads}/t_{heat}/t_{des}/t_{cool}$	120/5/90/25	min
Initial pressure condenser/evaporator	$p_{cond,i}/p_{evap,i}$	32.7/10.9	mbar
Initial temperature fixed-bed 1/fixed-bed 2	$T_{fb1,i}/T_{fb2,i}$	303/318.4	K
Initial temperature air adsorber 1/adsorber 2	$T_{air1,i}/T_{air2,i}$	$T_{amb,m}(t=0)$	K
Initial temperature hot water adsorber 1/adsorber 2	$T_{hw1,i}/T_{hw2,i}$	303/ $T_{hw,m,in}(t=0)$	K

4. RESULTS

Within the calibration significant pressure curves of the simulation are fitted to those of the measurement. In addition, the refrigeration compartment temperature ϑ_{comp} is compared between simulation and measurement. This temperature is an essential parameter that should be reliably predicted by the simulation for different operation parameters.

The following Fig. 3 shows temporal curves of the pressures of the evaporator p_{evap}, of the condenser p_{cond} and of adsorber 1 p_{fb1} and of the refrigeration comp temperature ϑ_{comp} for simulation (index sim) and measurement (index m) during one steady cycle.

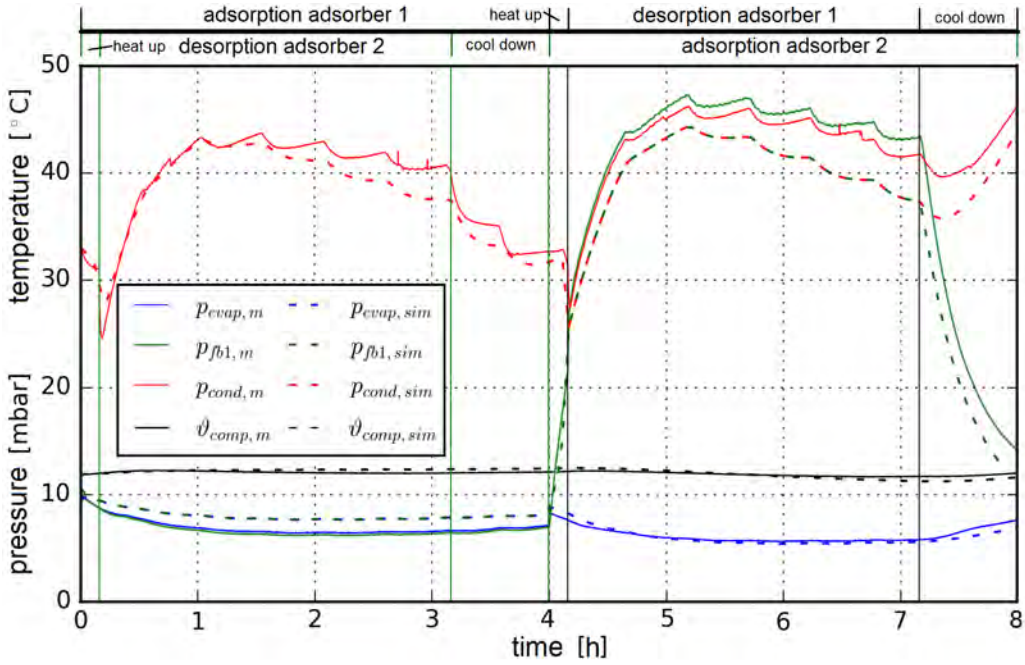

Figure 3: Curves over time of the pressures p_{evap}, p_{cond} and p_{fb1} and of the refrigeration compartment temperature ϑ_{comp} for simulation (sim) and measurement (m)

Qualitatively the curves for simulation and measurement agree to each other. The measurement uncertainty of the pressure is ± 0.25 mbar and for the temperature curve ± 1 K and are not shown in the figure. The slight waves in the curves of $p_{cond,m}$, $p_{cond,sim}$, $p_{fb1,m}$ and $p_{fb1,sim}$ are due to temporal fluctuations of the measured ambient temperature $T_{amb,m}(t)$.

The curve for $p_{evap,sim}$ agrees best with the measurement during the adsorption of adsorber 2 (hours 4 – 8) with an average deviation of 3.4 % whereas during adsorption of adsorber 1 the deviation is 16.3 % (hours 0 – 4). Adsorber 1 copes with a larger pressure interval (10.9 mbar at hour 0 to 6.9 mbar at hour 2) during adsorption than adsorber 2 (8.2 mbar at hour 4 to 6.1 mbar at hour 6). This means that adsorber 1 seems to have a higher adsorption capacity, which the simulation considers by a higher mass of adsorbent. In general, the comparison between these curves illustrates that the equilibrium water vapor approach (end of section 2.3) is useful for the evaporator model.

The condenser pressure $p_{cond,sim}$ agrees best with $p_{cond,m}$ during desorption of adsorber 2, with an average deviation of 2.8 %. While desorption of adsorber 1 this value constitutes 6.3 %. It should be stated that the condenser pressure level for desorption of adsorber 1 is also slightly higher than with adsorber 2, due to the fact that adsorber 1 has a higher adsorption capacity. Analogous to the evaporator, the equilibrium water vapor approach is also useful for the condenser. During desorption there is a higher pressure drop between adsorber and condenser than during adsorption between evaporator and adsorber. This effect is not considered in the simulation but will not lead to significant deviation between simulation and measurement, at least for the adsorption process, where the average pressure drop is below 0.2 mbar. The average deviation of the fixed-bed pressure $p_{fb1,sim}$ and $p_{fb1,m}$ is 15.2 %.

The refrigeration compartment temperature ϑ_{comp} shows a very good agreement between simulation and measurement. Relating to the pressure curves, this curve has no distinctive periodic development over time, thus it is nearly steady-state. The average difference between measurement and simulation within the considered cycle is below 0.5 K.
The heat transfer coefficients u_i resulting from the calibration and the underlying specific areas a_i and volumes V_i are listed in Table 2.

Table 2. Calibrated heat transfer coefficients (u_i), specific surfaces (a_i) and system volumes (V_i)

	Thermal transmittance [W×m^{-2}×K^{-1}]		Specific area [m^{-1}]		Volume [m³×10^{-3}]	
	Symbol	Value	Symbol	Value	Symbol	Value
Hot water pipes – fixed-bed	u_p	30	a_p	883.7	V_p	1.7
			$a_{p,fb}$	39.6		
Fixed-bed – air flow (adsorption and cool down)	u_{ads}	6.3	$a_{fb,air}$	299.4	V_{fb}	37.7
			$a_{air,fb}$	131.3		
Fixed-bed – air (desorption and heat up)	u_{des}	1.9	$a_{fb,air}$	299.4		
			$a_{air,fb}$	131.3		
Air flow – ambient air (adsorption and cool down)	$u_{loss,ads}$	2.1	a_{air}	131.3	V_{air}	86
Air – ambient air (desorption and heat up)	$u_{loss,des}$	1.2				
Refrigeration compartment – evaporator	u_{evap}	1.5	$a_{ev,co}$	250	V_{evap}	7.1
			$a_{co,ev}$	7.1		
Ambient air – refrigeration compartment	u_{comp}	2.05	a_{comp}	4.8	V_{comp}	250
Ambient air – condenser	u_{cond}	5	a_{cond}	2302.1	V_{cond}	1.8

Once the simulation tool is calibrated by one measurement, it is essential to prove its reliability with the parameter set of table 2 at changing operation parameters. Therefore, the hot water inlet temperature $\vartheta_{hw}(z=0)$ as well as the operation times for adsorption, heat up, desorption and cool down ($t_{ads}/t_{heat}/t_{des}/t_{cool}$= 160/7/83/70 min) were changed. Fig. 4 shows the results for the average refrigeration compartment temperature ϑ_{comp} of measurement and simulation for steady cycles at different hot water inlet temperature $\vartheta_{hw}(z=0)$.

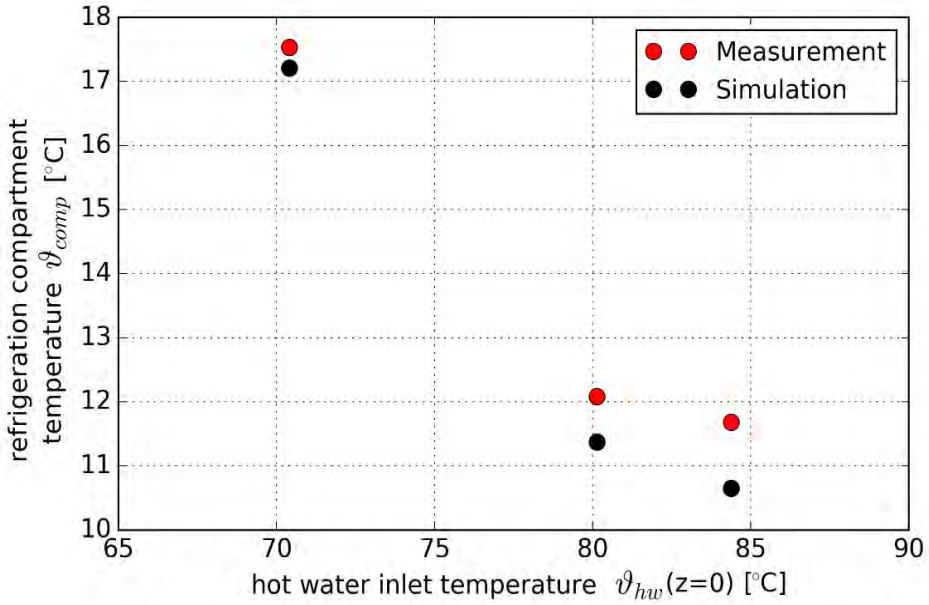

Figure 4: Comparison of average refrigeration compartment temperature ϑ_{comp} in dependency of hot water inlet temperature $\vartheta_{hw}(z=0)$ between measurement and simulation

The simulation results represent the measurement results good with an increasing offset with increasing hot water inlet temperature $\vartheta_{\mathrm{hw}}(\mathrm{z}=0)$. In any case, the simulation calculates a lower refrigeration compartment temperature $\vartheta_{\mathrm{comp}}$ than the measured one. This difference is biggest with 1 K at a hot water inlet temperature of 84.5 °C.
The parameter set of Table 2 is used to improve design parameters such as the adsorber depth d (see Fig. 2). On the one hand, a higher depth leads to more mass of adsorbent, which is beneficial for generating cooling power. On the other hand, the thermal resistance of the fixed-bed is increasing with increasing adsorber depth. This has a negative effect on the efficiency. At an adsorber height of 0.8 m and an adsorption time of 160 min there is an optimal value for the adsorber depth regarding to the coefficient of performance of 0.012 m.

ACKNOWLEDGEMENTS

We hereby thank the Federal Ministry for Economic Affairs and Energy (BMWi) and Projektträger Jülich GmbH for the funding of the research project with the funding number AHA FKZ 03ET1412. We also thank our project partner InvenSor GmbH for their contribution to this research project.

NOMENCLATURE

Symbols

a	specific surface (m^{-1})	
C	heat capacity ($J \times K^{-1}$)	
D	diffusion coefficient ($m \times s^{-2}$)	
d	adsorber depth (m)	
p	pressure (mbar)	
$\dot{\mathrm{q}}$	specific heat flow ($W \times m^{-3}$)	
r	radius (m)	
T	temperature (K)	
t	time (min)	
u	thermal transmittance ($W \times m^{-2} \times K^{-1}$)	
V	volume (m^3)	
w	velocity ($m \times s^{-1}$)	
X	load of adsorbent ($g \times g^{-1}$)	
z	local coordinate (m)	
$\dot{\Gamma}$	specific mass flow ($kg \times s^{-1} \times m^{-3}$)	
$\dot{\gamma}$	specific adsorption mass flow ($kg \times s^{-1} \times m^{-3}$)	
ϑ	temperature (°C)	
ρ	density ($kg \times m^{-3}$)	

Indices

$1, 2$	adsorber 1, 2
Ad	adsorbent
ads	adsorption
amb	ambient air
c	condensation
$\mathrm{co}, \mathrm{comp}$	refrigeration compartment
cond	condenser
conv	convective
des	desorption
eff	effective
eq	equilibrium
$\mathrm{ev}, \mathrm{evap}$	evaporator
fb	fixed-bed
hw	hot water
m	measurement
p	pipes
sim	simulation

REFERENCES

Rouhani, M. et al., 2016. Performance enhancement of an adsorption cooling system with AQSOA FAM-Z02 and low-finned tube evaporator. Proceedings of the IMPRES Conference, Sicily, Italy, 309-310.

Kühn, R. et al., 2018. Comparison of ab- and adsorbents for low temperature heat driven sorption cooling machines. Int. J. Refrigeration Vol. 95, 133-145.

Schönbucher, A., 2002. Thermische Verfahrenstechnik Grundlagen und Berechnungsmethoden für Ausrüstungen und Prozesse, Springer-Verlag, 884 p.

Schawe, D., 1999. Theoretical and Experimental Investigations of an Adsorption Heat Pump with Heat Transfer between two Adsorbers, Dissertation, TU Stuttgart.

Schnabel, L., 2009. Experimentelle und numerische Untersuchung der Adsorptionskinetik von Wasser an Adsorbens-Metallverbundstrukturen, Dissertation, TU Berlin.

Manuscript ID: 515
DOI: 10.18462/iir.icr.2019.0515

Coupling of a two-phase natural circulation cooling system with latent heat storage for aircraft applications

Björn ALBERTSEN[(a)], Gerhard SCHMITZ[(b)]

[(a)] Institute of Engineering Thermodynamics, Hamburg University of Technology
Hamburg, 21073, Germany, bjoern.albertsen@tuhh.de
[(b)] Institute of Engineering Thermodynamics, Hamburg University of Technology
Hamburg, 21073, Germany, schmitz@tuhh.de

ABSTRACT

The progressive electrification of the energy supply in airplanes leads to an increasing demand for innovative cooling technologies. Due to high efficiency and low weight two-phase natural circulation cooling systems provide high potential for this application.
Integration of latent heat storages in such systems using paraffin as phase change material (PCM) is investigated experimentally. The HFO refrigerant R1233zd is used to reach a vaporization temperature in steady-state of 60 °C with a heat load of 700 W (heat flux density: 12,5 W/cm²) and a heat sink temperature of 40 °C (evaporation heat-transfer-coefficient: 6290 W/m²K).
Parameter studies show a strong dependency of the mass flow rate on the heat load and a linear relation between the heat load and recooling temperature with the temperature of the component to be cooled.
In this application PCM is used to dampen heat-load peaks and to compensate lower cooling performances e.g. in disadvantageous flight situations.

Keywords: aircraft, latent heat, low GWP, paraffin, passive cooling, phase-change material, R1233zd(E), two-phase flow

1. INTRODUCTION

In the past years, an increasing number of pneumatic, hydraulic and mechanical systems are replaced by electrical systems in civil aircraft. This concept of a “More Electric Aircraft” (MEA) should lead to a more effective and thus cost-saving energy supply (Wheeler et al., 2012). In comparison to the conventional concept, besides the provision of the thrust, the engine is only used to drive electric generators. As a result, an electrical output of more than 500 kVA per engine can be expected for future on-board power supplies (Abu-Rub et al., 2014).
This results in an increasing number of power electronics to handle the additional effort in control. Depending on the type and dimension of the electric generators and consumers, electronics of different shape and power are used in the distribution system (Abu-Rub et al., 2014). The cooling of such power electronics is currently usually done with air which is conditioned by the air conditioning system accordingly (Chen et al., 2012). With the rising number of modules and the increasing power density, pure air cooling is reaching its limits, so liquid or two-phase cooling systems are becoming the focus of current research. In natural circulation or looped thermosiphon systems, the refrigerant circulates only due to the difference in density between riser and downcomer and the weight, as the crucial parameter, can be additionally reduced. Lohse and Schmitz (2010) were able to demonstrate the suitability of such systems in the aviation sector.
Another option for improved cooling of power electronics exposed to dynamic conditions is the application of phase change materials (PCM). Deployed in a latent heat storage (LHS) these can be used separately or integrated into cooling cycles. In the latter case, load peaks can be compensated by the buffer storage and the cooling system can be downgraded and the weight reduced.

A test rig was developed to perform parameter studies of a natural circulation cooling system in steady-state and investigate the behavior under dynamic conditions that occur in aircraft applications. In addition, the thermal performance is compared to a system with a supplemented latent heat storage placed on the evaporator assembly.

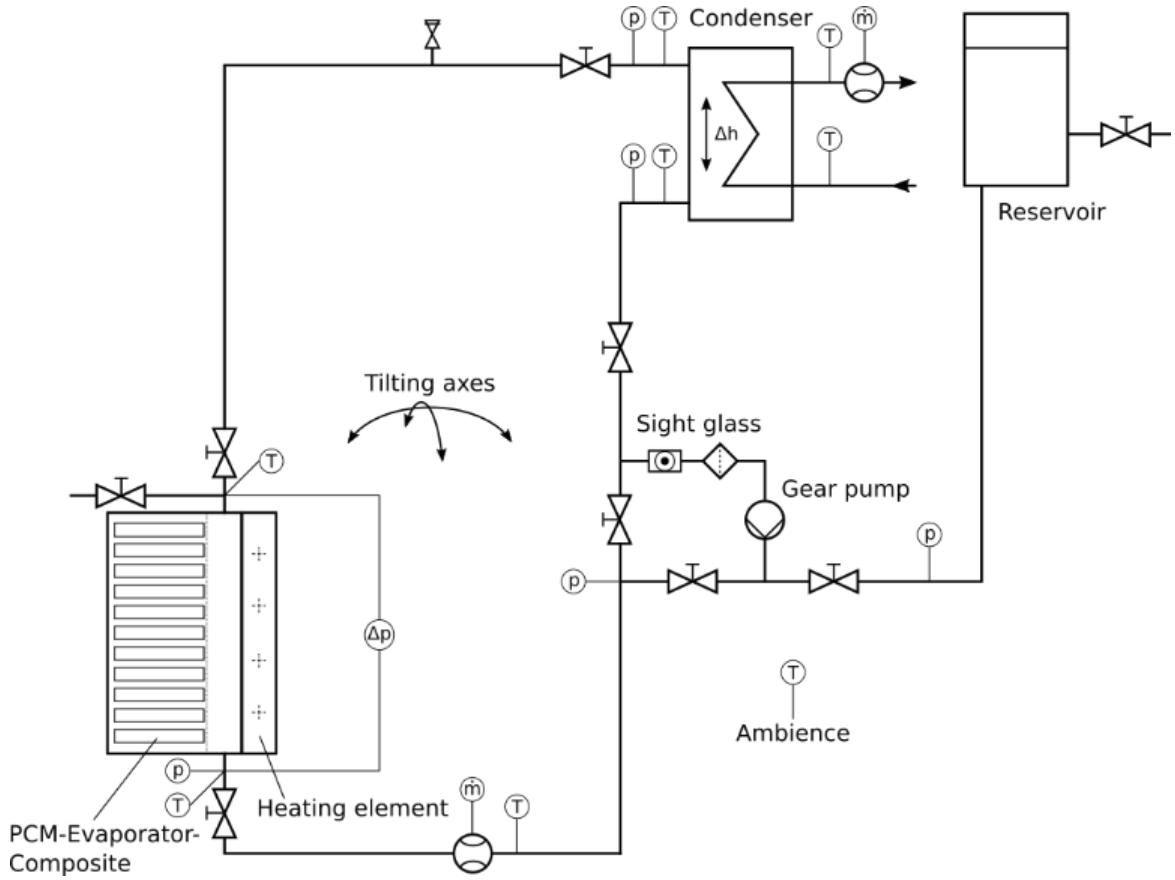

Figure 1: Schematic of the test rig

2. EXPERIMENTAL SETUP

2.1. Test rig

Fig. 1 shows a schematic of the test rig. The focus is on comprehensively measuring the temperatures and pressures at the PCM-evaporator-composite as well as the essential loop parameters, without significantly interfering with the operation of the cooling system. Basically the cycle consists of an evaporator, a riser, a plate heat exchanger as condenser and a downcomer. Transparent tubes are used as riser and downcomer to observe the flow regimes. To carry out tests for the integration of a refrigerant pump into the cooling cycle later in the project, a gear pump is connected in bypass. The remaining components are used for measurement and to fill and empty the system. The entire cycle can be tilted about two axes to simulate different flight situations.

The evaporator assembly shown in Fig. 2 is composed of a heating block with four cartridges (hidden by the isolation), the evaporator with sight glass (a) or PCM storage (b) and a bracing device for setting a uniform contact pressure. The evaporator consists of five parallel refrigerant pipes with a respective cross-sectional area of 18.28 mm², a total surface of 56.03 cm² and is made of aluminum. Several temperature measurement points are placed near the evaporator surface and in the heating block. The latent heat storage is composed of a housing with fins as thermal conductivity enhancer and a paraffin with a melting temperature of 70 °C and a latent heat of about 230 kJ/kg. The total weight is 492 g with a PCM mass fraction of 24,4 % resulting in a storage capacity of 36,2 kJ within a temperature range of 15 K around the melting point.

For the natural circulation, the low-GWP refrigerant R1233zd(E) is used, the essential properties are listed in Table 1. The condenser is recooled by a water propylene glycol cycle. The slightly subcooled refrigerant enters the evaporator from below. Here it is preheated by the heat supply of the heating block and partially evaporated. Subsequently the two-phase mixture passes the riser and enters the

condenser at the top, where it is condensed again and cooled down to the recooling temperature. The ambient temperature is 20 °C during all tests.

Table 1. Properties of R1233zd(E) at room temperature (20 °C) and operating temperature (60 °C)

Property	Temperature in °C	
	20	60
Vapor pressure in bar	1.08	3.90
Enthalpy of vaporisation in kJ/kg	194.5	171.5
Density (liquid) in kg/m³	1275	1173
Specific heat capacity (liquid) in J/kg K	1239	1291

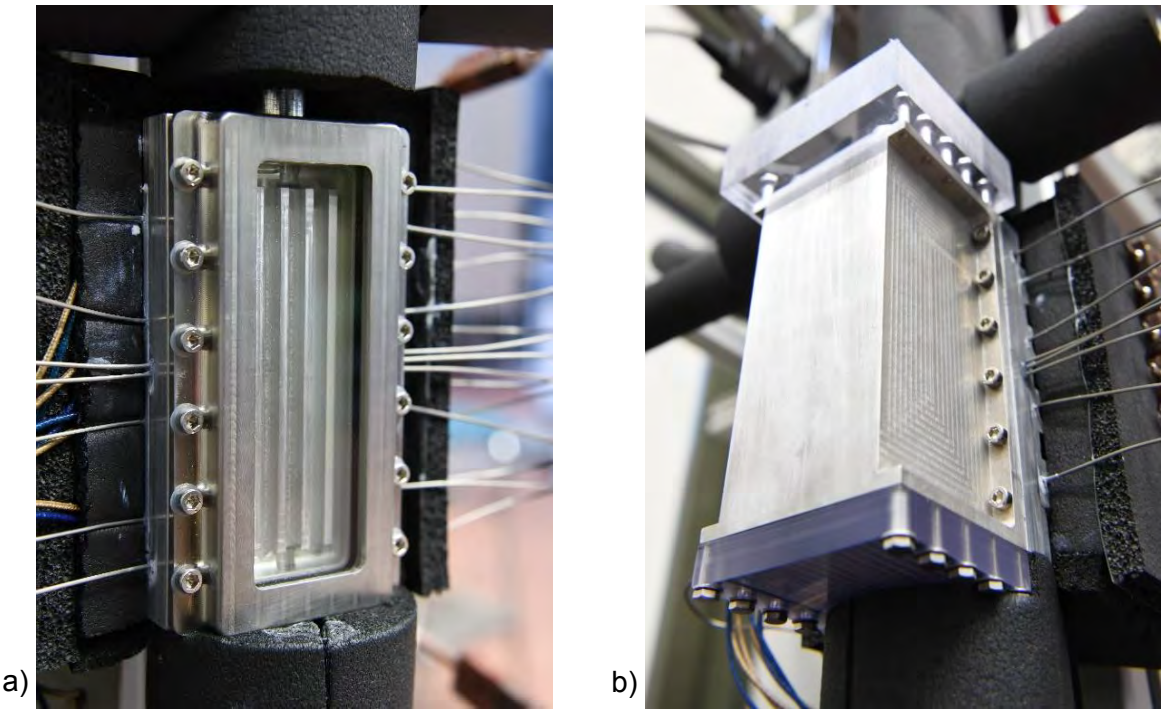

Figure 2: Evaporator assembly with sight glass (a) and PCM storage (b)

3. PARAMETER STUDIES

In this section, results of parameter studies are presented and discussed. In each case, a steady-state is considered and the measurements are recorded every second for a period of 5 minutes, the values are then averaged over time. Besides the varied parameters, the following boundary conditions are implemented:

- Height difference between evaporator outlet and condenser inlet: 100 cm
- Condenser inclined at an angle of 45° to the cycle
- Refrigerant charge: 700 g (complete filling of the downcomer with liquid in operation)

The operating condition in steady state for given geometric boundary conditions is determined by the refrigerant pressure and the current heat load. Due to the lack of a pump or compressor, the pressure varies only slightly within the cooling cycle and is therefore determined mainly by the saturation pressure in the condenser and thus by the recooling temperature. The mass flow rate

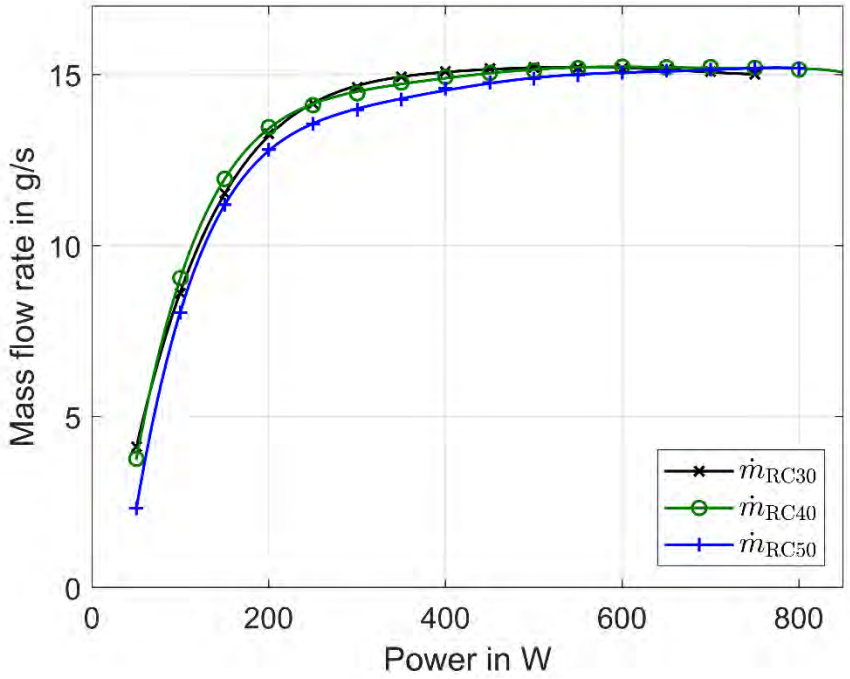

Figure 3: Mass flow rate as a function of the heat flow at different recooling temperatures

finally results from the momentum balance of the driving difference in pressure between the riser and the downcomer and the pressure losses in the loop. Fig. 3 shows the mass flow rate over the heating power for different recooling temperatures. It can be seen that the mass flow rate reaches a maximum after a significant increase in the lower heat load range and remains almost constant with further increasing power. The exact influences of the heat load and recooling temperature on the resulting mass flow rate can be explained based on the momentum balance, which is composed of the pressure differences due to friction (in all parts of the system), acceleration/deceleration (in the evaporator and condenser) and gravitation (in all pipes with height difference):

$$\Delta p_{\mathrm{tot}} = \Delta p_{\mathrm{fric}} + \Delta p_{\mathrm{mom}} + \Delta p_{\mathrm{grav}} \qquad \text{Eq. (1)}$$

The driving pressure difference results from the difference in density between riser and downcomer

$$\Delta p_{\mathrm{drive}} = (\rho_{\mathrm{Downcomer}} - \rho_{\mathrm{Riser}}) \cdot g \cdot \Delta h \qquad \text{Eq. (2)}$$

$$= (\rho_{\mathrm{l}} - (\rho_{\mathrm{l}}(1-\varepsilon) + \rho_{\mathrm{g}} \cdot \varepsilon)) \cdot g \cdot \Delta h \qquad \text{Eq. (3)}$$

where ε is the void fraction in the riser. Since the largest pressure losses occur in the two-phase flow in the evaporator and riser, they are considered in more detail below. In Fig. 4, the measured pressure differences across the downcomer, riser and evaporator are plotted for two different recooling temperatures. The gravitational part of the pressure difference across the downcomer $\Delta p_{Downcomer}$ is the positive part of Δp_{drive}, and remains almost constant for one recooling temperature. As the power increases, the curve decreases slightly, as the mass flow rate and thus the single-phase friction pressure losses increase in the downcomer. The pressure difference across the riser consists of the two-phase friction pressure loss and the gravitational component. The friction pressure loss increases with increasing steam quality and mass flow rate and thus with the power. Simultaneously the hydrostatic pressure drops strongly due to the decreasing mean density in the riser. Overall, this results in a decreasing total pressure difference. In the higher load range, this effect declines as the friction losses progressively dominate. The pressure losses in the evaporator increase according to the power, as here the friction and acceleration dominate. The overall balance

$$\Delta p_{drive}(\varepsilon) = \Delta p_{losses}(\varepsilon, \dot{m}) \qquad \text{Eq. (4)}$$

results in the mass flow rate curve shown in Fig. 3.

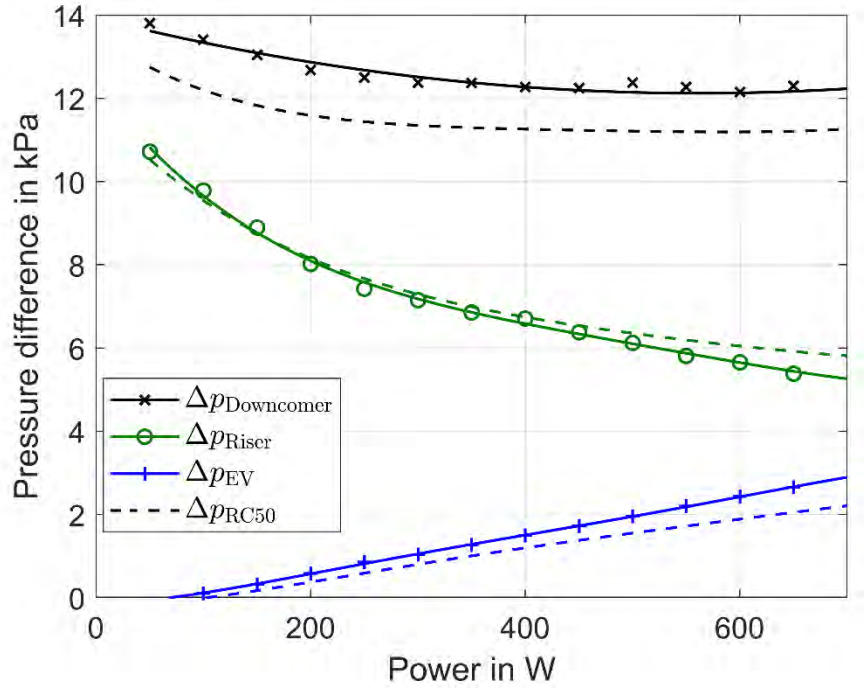

Figure 4: Measured pressure differences across the downcomer, riser and evaporator as a function of the heat load for recooling temperatures of 30 °C and 50 °C

The influence of the recooling temperature on the system performance can also be seen in Fig. 4. The changes are caused by the change in the fluid properties, in particular the refrigerant pressure. At a higher recooling temperature, on the one hand, a lower hydrostatic pressure in the downcomer is revealed due to the reduced liquid density. On the other hand, there are differences in the two-phase flow, where the higher system pressure results in a considerable increase in density of the compressible gas phase. This additionally reduces the volumetric fraction of the gas phase. Overall, the pressure losses due to friction and acceleration are reduced, while the gravitational component increases. Subsequently for a higher recooling temperature of 50 °C, the pressure difference in the evaporator is lower because friction and acceleration dominate. In the riser, the gravitational

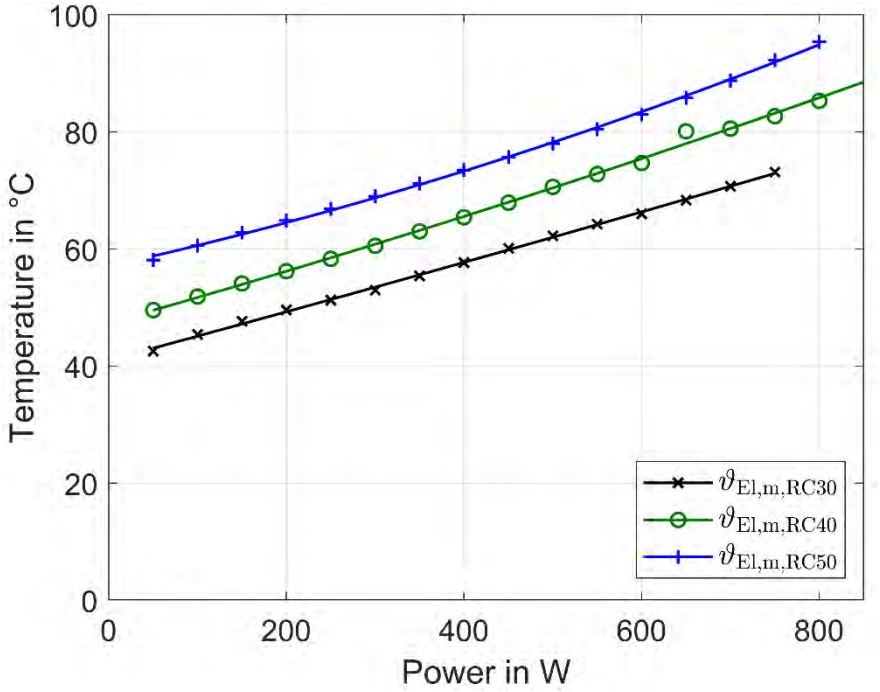

Figure 5: Measured pressure differences across the downcomer, riser and evaporator as a function of the heat load for recooling temperatures of 30 °C and 50 °C

component dominates and a higher pressure difference occurs. For higher recooling temperatures, the overall momentum balance results in slightly lower refrigerant mass flow rates in the predominant power range, as can be seen in Fig. 3.

The influence on the electronics temperature as the main parameter of the cooling system is shown in Fig. 5. The recooling sets the basic level of temperature in the system. The electronics temperature then results from the individual temperature differences between the condenser and evaporator in the loop and within the evaporator assembly. The measurements show an approximately linear curve, in which a power increase of 100 W results in a temperature rise of about 5 K. The electronics temperature increases by about 8 K when the recooling temperature is increased by 10 K, showing a slight improvement in system performance.

4. DYNAMIC TESTS

In contrast to the previous results in steady-state, in this section dynamic tests are considered supplementing the PCM latent heat storage. Besides the heat load, the same boundary conditions as in the parameter studies are applied and the recooling temperature is set to 40 °C.

4.1. Peak load

In the first step, the behavior of the natural circulation system for a heat load profile with a base load of 600 W and a peak load of 1200 W shall be compared to the results adding the latent heat storage. Replacing the sight glass made of borosilicate by the aluminum housing of the storage (see Fig. 2) increases the effective evaporator surface by 34 %, which leads to lower electronics temperatures for the same boundary conditions. During the tests with the LHS, the base load is therefore increased until the mean temperature of the electronics reaches the same level which leads to a base load of 700 W and a peak load of 1300 W. Fig. 6 shows the mean and maximum temperatures on the surface of the electronics over time with and without LHS. To evaluate the thermal performance, the time interval until reaching a certain acceptable temperature is an appropriate criterion. After 100 s the peak load is applied and the mean temperature reaches a value of 90 °C after another 31 s without and after 59 s with latent heat storage. Looking at a temperature level of 95 °C, with values for the time interval of 85 s and 759 s respectively, the difference is even higher and a representative power electronic could be operated about nine times longer at peak load. Besides the average, also the temperature distribution on the surface of the electronics should be considered as one of the

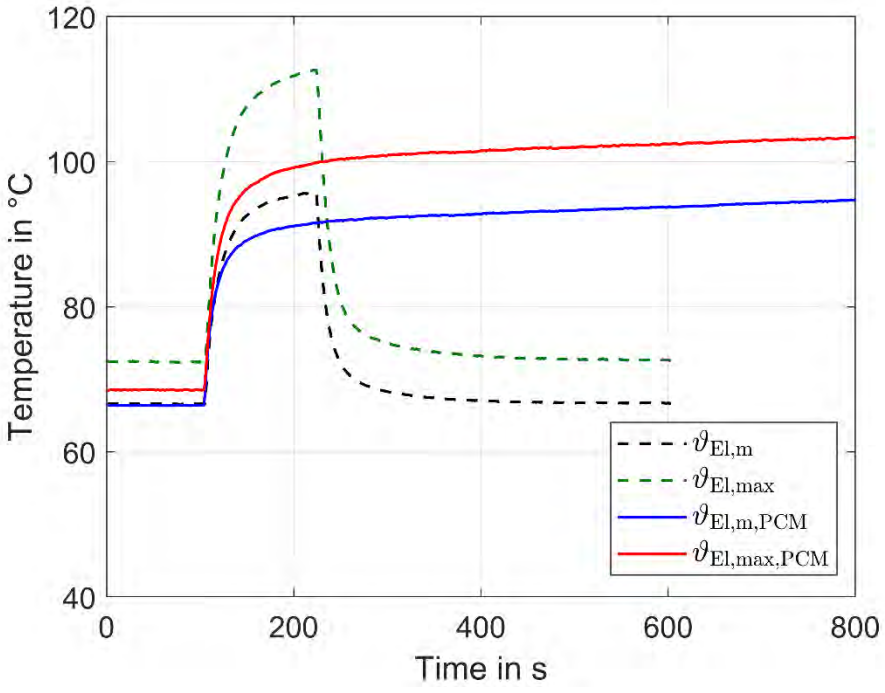

Figure 6: Mean and maximum electronics temperature over time without and with latent heat storage for a peak load

critical design parameters. It can be seen that the difference between the mean and the maximum surface temperature is lower during the entire operation time adding the LHS. As a result, a maximum temperature of 100 °C is reached after 22 s without LHS, whereas it takes a time of 124 s to reach the same value in the system with PCM storage.

4.2. Recooling failure

In a final step, the influence of a latent heat storage in case of a failing recooling system is investigated. This case can also represent a sudden rise of the heat sink temperature, as for example during the landing of the aircraft.

The heat load is set to 800 W and after a time of 100 s, the liquid recooling cycle is switched off. Fig. 7 shows the resulting mean and maximum temperatures of the electronics surface over time with and without LHS. Again, the time interval until reaching a certain temperature is used to evaluate the thermal performance. 141 s after switching off the recooling system the mean temperature reaches

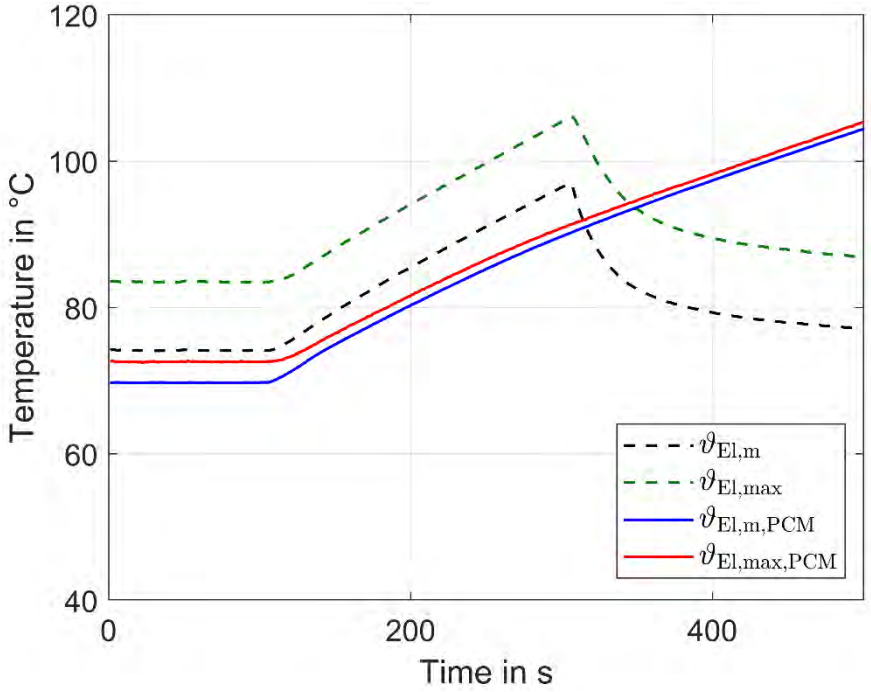

Figure 7: Mean and maximum electronics temperature over time without and with latent heat storage for a switched off recooling cycle

a value of 90 °C without and after 304 s with latent heat storage. Looking at a temperature level of 95 °C, values for the time interval of 187 s and 268 s can be seen. For the maximum temperature, a value of 100 °C is reached after 153 s without and 326 s with LHS. So regarding one of these design criterions, the power electronics could be operated in such a situation about twice as long with the additional latent heat storage as without it. The low differences between the mean and the maximum temperatures in case of the system with LHS during the down time of the recooling cycle is particularly noticeable and an indication of a uniform temperature distribution on the electronics surface.

5. CONCLUSIONS

In this paper, two innovative cooling technologies for power electronics as promising approaches in aircraft applications are investigated. In a first step, experiments on a test rig are carried out to evaluate the thermal performance of a natural circulation cooling system with R1233zd(E) as refrigerant in steady-state. These parameter studies show a strong dependency of the mass flow rate on the heat load, while the recooling temperature has only a minor influence. With rising heat load, the void fraction and thus the driving pressure difference rises and leads to a sharp rise of the mass flow rate in the lower power range, whereas the rising pressure losses due to friction and

acceleration result in a converging mass flow rate for higher heat loads. It can be stated, that there is a linear correlation between the temperature of the electronics with the heat load and also the recooling temperature.

Additionally, in order to investigate the influence of a latent heat storage on such a system as a second cooling approach, dynamic tests are carried out. For a peak load, the electronic temperature can be kept below a critical value of 95 °C about nine times longer using a LHS, if power is increased by 600 W. Furthermore the electronics reaches the same temperature in case of a failing recooling system at a heat load of 800 W after almost twice the time, if the LHS is added.

ACKNOWLEDGEMENTS

The research leading to these results has received funding from the German Federal Ministry for Economic Affairs and Energy.

NOMENCLATURE

g	gravitational constant	Δp_{tot}	total pressure difference (Pa)
Δh	distance evaporator/condenser (m)	p	power (W)
$\dot{m}$	mass flow rate (g×s^{-1})	$\vartheta_{\mathrm{El,m}}$	mean electronics temperature (°C)
$\dot{m}_{\mathrm{RC}}$	mass flow rate for a certain recooling temperature (g×s^{-1})	$\vartheta_{\mathrm{El,max}}$	maximum surface temperature (°C)
$\Delta p_{\mathrm{drive}}$	driving pressure difference (Pa)	$\vartheta_{\mathrm{El,m,PCM}}$	mean electronics temperature under PCM application (°C)
Δp_{EV}	pressure difference across the evaporator (Pa)	$\vartheta_{\mathrm{El,max,PCM}}$	maximum surface temperature und PCM application (°C)
Δp_{fric}	frictional pressure losses (Pa)	$\vartheta_{\mathrm{El,m,RC}}$	mean electronics temperature for a certain recooling temperature (°C)
Δp_{grav}	gravitational pressure difference (Pa)	t	time (s)
$\Delta p_{\mathrm{losses}}$	total pressure losses (Pa)	ε	void fraction
Δp_{mom}	pressure difference due to acceleration (Pa)	ρ	density (kg×m^{-3})

REFERENCES

Abu-Rub, H., Malinowski, M., Al-Haddad, K., 2014. Power electronics for renewable systems, transportation and industrial applications. Lohn Wiley & Sons Ltd., Chichester, 795 p.

Chen, X.Y., Zhao, N., Cai, Y. Z., 2012. Research on a New Cooling System of Airborne Electronic Equipment. Applied Mechanics and Materials 138-139, 117-122.

Lohse, E., Schmitz, G., 2010. Inherently safe looped thermosiphon cooling system for aircraft applications using dielectric fluid H-Galden. Proceedings of the International Refrigeration and Air Conditioning Conference, Purdue, USA, Purdue e-Pubs, 1659.

Wheeler, P.W., Clare, J. C., Trentin, A., 2012. An overview of the more electrical aircraft. J. Aerospace Engineering 227(4), 578-585.

Manuscript ID: 516
DOI: 10.18462/iir.icr.2019.0516

First results of a directly air-cooled fixed-bed adsorber for a refrigerator driven by waste heat

Kristian HURTIG, Karsten DÜWEL, Mike JÄGER, Roland KÜHN

Technische Universität Berlin, Marchstr. 18

Berlin, 10587, Germany, hurtig@tu-berlin.de

ABSTRACT

In the paper at hand first results of testing a directly air-cooled adsorption refrigerator with fixed-bed adsorbers are presented.

The refrigerator utilizes water as refrigerant and silica gel as adsorbent. In contrast to the most common water-cooled adsorbers, the investigated adsorber is cooled with ambient air. The adsorber has a plate geometry with vertical fins. Low power fans are installed to increase the heat transfer. The configuration of the adsorber is introduced, followed by a discussion of its temperature distribution and an outlook on future improvements.The results show that the adsorber's surface temperature varies by up to 10 K over the height. The minimum temperature difference between surface and cooling air occurs at the inlet of the air flow. The temperature difference between inlet and outlet on the surface cannot be induced by the air's temperature increase with flow length only, but is also influenced by the adsorption characteristics.
Keywords: Adsorber, Adsorption, Adsorption system, Air flow, Household refrigerator, Plate-fin Silica gel, Surface temperature, Water (refrigerant)

1. INTRODUCTION

In general, there is an agreement in society that it is important to reduce primary energy consumption significantly. By using waste heat driven sorption cooling machines (Rouhani et al., 2016) conventional electricity driven compression cooling machines can be replaced. Adsorption cooling is a promising alternative to conventional cooling methods by using waste heat, because adsorption works at comparatively low temperatures (Kühn et al., 2018).
Up to now mostly large scale sorption refrigeration systems are developed and implemented. In this work, an adsorption household refrigerator with a small cooling capacity of 25-50 W is investigated. Since the number of household refrigerators is large, the potential to reduce primary energy consumption in this sector is significant.
Most sorption cooling machines on the market are equipped with an additional water circuit for heat rejection. In the case of household refrigerators, this is not practicable and investment costs need to be kept low. Hence, in this work directly air-cooled fixed-bed adsorbers are used. For efficiency a good thermal transmittance from adsorber to the air flow is important. To evaluate the heat transfer processes during the periodical operation of this adsorption refrigerator, temperatures are measured on the surface of one adsorber. Improvement possibilities are derived.
The configuration of the directly air-cooled adsorber is presented in section 2, followed by a discussion of the experimental results showing the temperatures and pressures of the adsorption refrigerator in section 3. Finally, an outlook on future improvements is given in section 4.

2. THE ADSORPTION REFRIGERATOR

In this section the objectives of the research are presented, followed by a description of design and operation of the adsorption refrigerator.

2.1. Objectives

In the research project an adsorption household refrigerator driven by waste heat is developed and investigated. The refrigerator has no freezer compartment. The refrigeration compartment temperature should be between 0 and 8 °C (average 4 °C) at ambient temperatures ranging from 10 to 32 °C (climate class SN). These objectives are to be achieved by using domestic hot water as driving heat and a maximum electrical energy consumption of 1 W.

2.2. Design and Description of the Process

A schematic of the adsorption refrigerator is shown in figure 1. The functional model consists of two adsorption chambers, an evaporator, a condenser and a condensate recirculation. The evaporator is located in the refrigeration compartment and filled with the refrigerant water. The relevant internal valves and sensors are shown in figure 1. The adsorption chambers are designed as cuboid plate adsorbers (see fig. 2). The metallic adsorber casing is filled with an adsorbent bed of spherical silica gel named Siogel (Aristov et al., 2017). The outer surface of the casing is finned to improve the heat transfer from the chamber's surface to the cooling air. The functional model is placed in a climate chamber, which ensures a constant inlet temperature of the forced air flow for heat rejection during adsorption.

In the following, first the adsorption phase is described for adsorber 1 and second the desorption phase for adsorber 2, according to the representation in figure 1.

Adsorption phase: When the pressure in the adsorption chamber 1 is lower than the pressure in the evaporator, valve V1 (figure 1) is opened. Subsequently, refrigerant vapor flows to adsorption chamber 1 and is adsorbed by the adsorbent silica gel. The evaporator's temperature decreases below the temperature of the refrigeration compartment, due to the evaporation process. Thus, heat is dissipated from the refrigeration compartment. The produced adsorption enthalpy in the adsorption chamber is dissipated by a forced air flow on the plate adsorber's surface caused by fans.

Desorption phase: The loaded adsorbent has to be regenerated. Therefore, the adsorber is heated up with hot water flowing through pipes within the fixed bed. Due to the induced temperature increase the refrigerant vapor is released and the pressure in adsorption chamber 2 rises above the condenser's pressure. The desorbed vapor flows through valve V4 into the condenser and condenses while the condensation enthalpy is released to the ambient air. The liquid condensate is returned to the evaporator by a valve.

As soon as adsorber 1 is loaded and adsorber 2 is unloaded, adsorber 1 switches to the desorption phase and adsorber 2 to the adsorption phase, resulting in a cyclic operation with a nearly constant production of cooling power in the refrigeration compartment. At the end of the desorption phase, a cooling must take place until the adsorption can start again. Accordingly, the respective adsorber has to be heated up before the desorption phase starts.

That means that the two adsorbers work alternately as a two-chamber system. While one adsorber adsorbs, the other adsorber performs the heating, desorption and cooling and vice versa.

Table 1 is given to clarify the configuration of the valves etc. during one complete cycle consisting of the four phases, adsorption, heating, desorption and cooling.

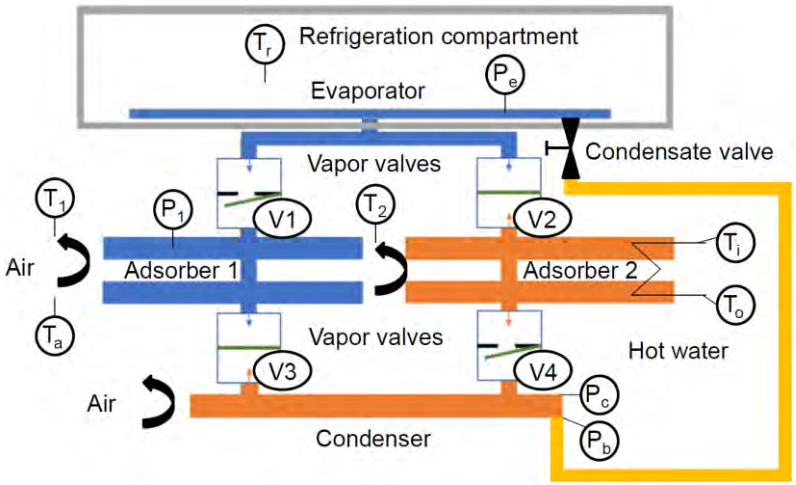

Figure 1: Schematic of the adsorption refrigerator with marked sensors

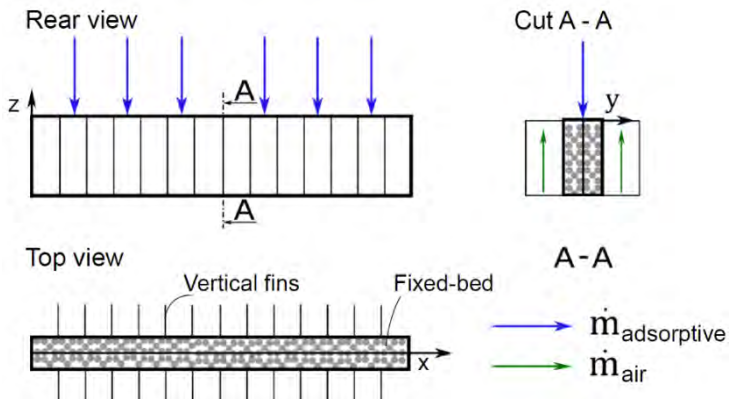

Figure 2: Geometry of the plate adsorber and the fixed-bed

Table 1. Process phases

Adsorber 1	Adsorber 2
Adsorption 180 min, in figure 4 from 0:00 to 3:00 h - Valve V1 open - Valve V3 closed - Adsorber 2 is being cooled by a forced air flow	Heating 10 min, in figure 4 from 0:00 to 0:10 h - Valve V2 and V4 closed - adsorber 2 is heated by hot water
	Desorption 90 min, in figure 4 from 0:10 to 1:40 h - Valve V4 open
	Cooling 80 min, in figure 4 from 1:40 to 3:00 h - Valve 4 closed - Adsorber 2 is cooled by by a forced air flow
Heating 10 min, in figure 4 from 3:00 to 3:10 h - Valve V1 and V3 closed Adsorber I is heated by hot water	Adsorption 180 min, in figure 4 from 3:00 to 6:00 h - Valve V2 open - Valve V4 closed - Adsorber 2 is cooled by a forced air flow
Desorption 90 min, in figure 4 from 3:10 to 4:40 h - Ventil V3 open	
Cooling 80 min, in figure 4 from 4:40 bis 6:00 h - Valve V3 closed - Adsorber 1 is cooled by a forced air flow	

As soon as the level in the condenser has reached a certain value, the condensate recirculation valve between condenser and evaporator is opened for 3 seconds. The accumulated liquid refrigerant is thereby supplied to the evaporator to inhibit dry out. The change from one phase to another is determined by fixed time periods, 10 minutes, 90 minutes and 80 minutes for heating, desorption and cooling. The time periods were determined empirically within the experiments.

2.3. Description of the used temperature and pressure sensors

Pressure and temperature sensors are used for the experimental investigation. The pressure sensors have a measurement uncertainty of 0.25 mbar and are located in the vapor tube of the evaporator (P_e), in the adsorption chamber 1 (P_1), in the head of the condenser (P_c) and at the bottom of the condenser (P_b). Temperature sensors are located in the environment (T_a), in the refrigeration compartment (T_r), at the outlet of the air flow at adsorber 1 (T_1), at the outlet of the air flow at adsorber 2 (T_2), at the hot water inlet (T_i) and at the hot water outlet (T_o). These temperature sensors are calibrated with a measurement uncertainty of 0.04 K. Additionally, nine temperature sensors are positioned on the surface of adsorber 1 in a pattern shown in figure 3. In the paper at hand only the three mean temperatures for each height (T_{s1}, T_{s2} and T_{s3}) are shown. The standard deviation between the sensors and their mean temperature at each height is 1.6 K at the bottom, 0.7 K at the

middle and 1.1 K at the upper position. The temperature sensors on the surface have a measurement uncertainty of 0.35 K.

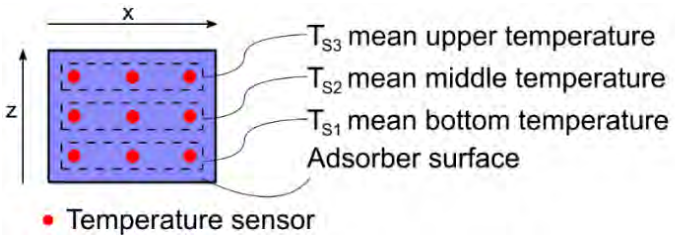

Figure 3: Position of temperature sensors on the adsorber's surface

3. EXPERIMENTAL CHARACTERIZATION

In the following sections the measurement data of temperature and pressure over time is presented and discussed. In the shown measurement interval each adsorber passes through each phase of the adsorption-desorption cycle once. Based on the measurement results improvement potentials for subsequent functional models are presented.

3.1. Discussion of the measured temperatures

Hot water inlet temperatures of 80 °C were used for the first experiments shown below. The ambient temperature is 25 °C. The figures 4 and 5 show measured temperatures over time. The data was collected at two different days to capture all data, because some sensors failed temporarily. Both days show comparable results. The process phases in the headline of the figures refer to adsorber 1, respectively.

Fig. 4 shows the hot water inlet and outlet temperatures (T_i and T_o), the air outlet temperatures of the two adsorbers (T_1 and T_2), the temperature of the climate chamber (T_a) and the refrigeration compartment temperature (T_r). At the beginning of the cycle shown (00:00 h) adsorber 1 performs the adsorption phase and adsorber 2 the heating phase. The air outlet temperature T_1 is approximately 34 °C and decreases during adsorption to below 30 °C. The air outlet temperature T_2 is approximately 39 °C and increases during heating and desorption to approximately 63 °C. At 01:40 h the desorption phase of adsorber 2 ends and is cooled down so that the temperature T_2 is approximately 35 °C at 03:00 h. Thus, the adsorption phase of adsorber 2 can start and the heating of adsorber 1 begins.

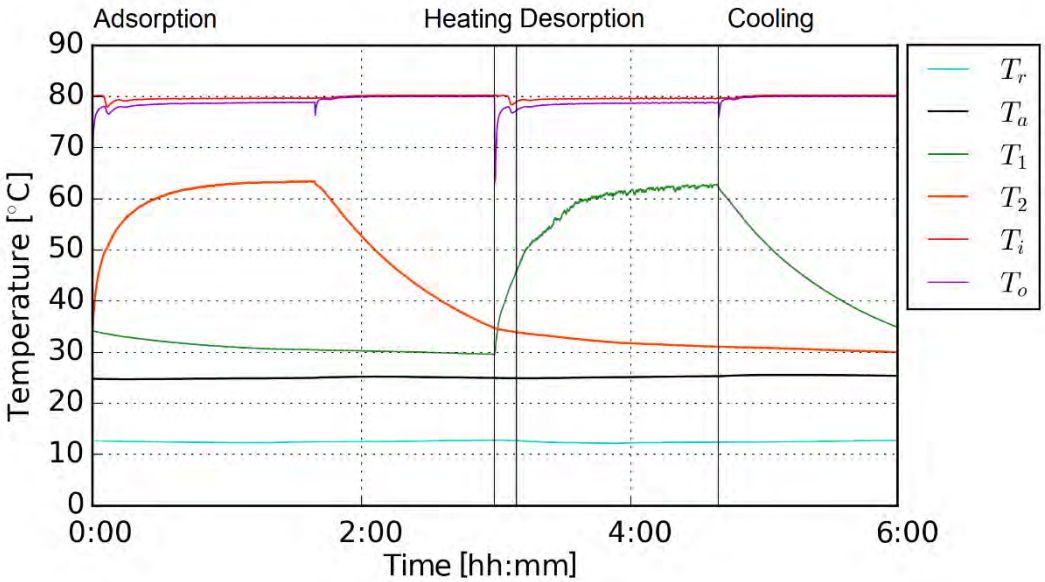

Figure 4: Measured temperatures over time for both adsorbers (data from day 2)

The hot water inlet temperature during the cycle ranges from 78 °C to 80 °C and the hot water outlet temperature from 75 °C to 80 °C. The largest difference between inlet and outlet temperature occurs at the beginning of the heating phase. This is due to the fact, that the adsorber is at its coolest temperature then and the driving temperature difference for the heat flow from the hot water to the adsorber is maximal.

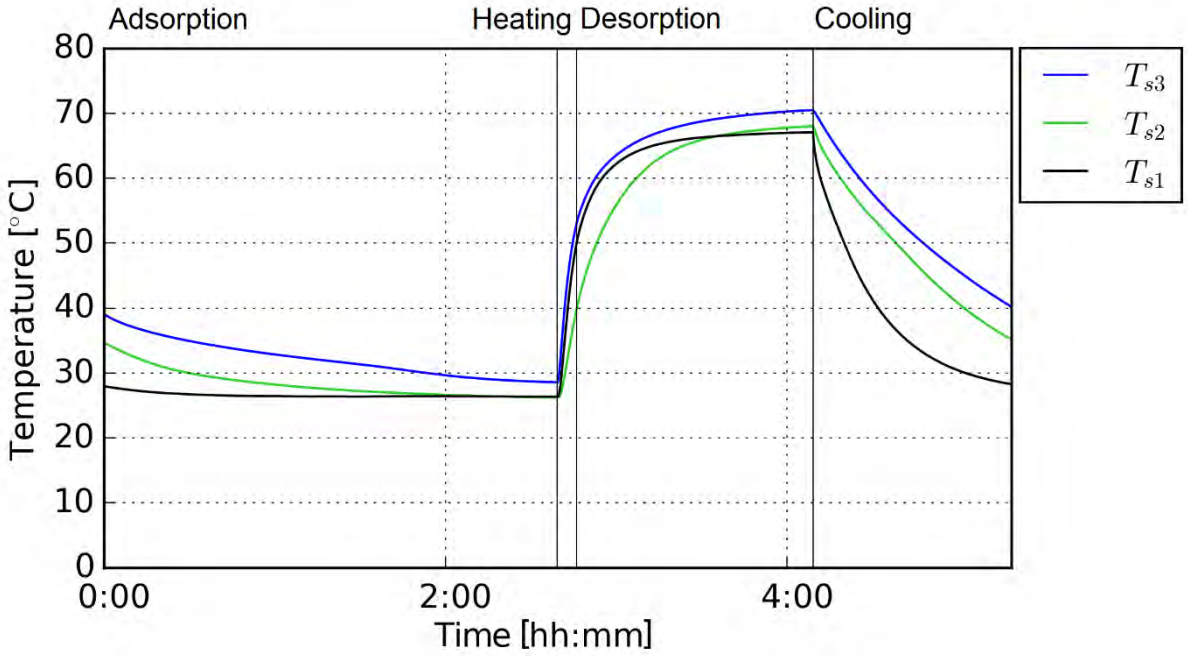

Figure 5: Measured average surface temperatures in different heights over time and the process phases of adsorber 1 (data from day 1)

The climate chamber shows a nearly constant temperature of 25 °C. The temperature in the refrigeration compartment is also nearly constant at 12 °C. This refrigeration compartment temperature is achieved due to the adjustment of the process phases of both adsorbers to provide continuous cooling. One of the chambers is always performing an adsorption phase (see table 1).
As can be seen in table 1 and figures 4 and 5, the cooling phase takes more than an hour (80 minutes). In comparison to the adsorption and desorption phases, the preparing cooling phase is very long. And even after 80 minutes of cooling, the adsorber surface temperatures are up to 15 K above ambient temperature. It can be concluded, that the thermal transmittance from adsorber to the air flow should be improved. The shorter the chosen cycle time will be, the higher the impact of this restriction.
Fig. 5 shows the temperature distribution of the plate adsorber's surface over the height and time. The average surface temperature on each level is illustrated, specifically at bottom T_{s1}, middle T_{s2} and upper position T_{s3}. The temperature decreases during cooling and adsorption phase and increases during heating and desorption phase. Moreover, the surface temperature increases along the flow length of the air flow ($T_{s1} < T_{s2} < T_{s3}$) during cooling and adsorption phase. The surface temperature varies by more than 10K over the height while adsorption takes place, whereas the cooling air temperature difference is below 10K (see figure 4). Additionally, the surface temperature in the middle of the adsorption chamber surface T_{s2} converges to the bottom surface temperature T_{s1}, while the upper temperature T_{s3} remains at an elevated temperature level. Therefore, it can be assumed, that adsorption into the upper part of the fixed-bed is preferred by the vapor.
During the heating and in the beginning of the desorption phase the gradient of T_{s1} and T_{s3} is significantly higher than of T_{s2}. It is assumed that this is due to the fact that there is more metal in the upper and lower part of the adsorption chamber because of the casing. That improves the heat transport from the centre of the adsorber to the surface, leading to a more dynamic temperature development. As the temperature difference to the driving heat source of 80 °C decreases, also the gradient does. At 3:00 h the gradient of T_{s2} is higher than that of T_{s1} and T_{s3}. At 3:30 h the curves of

T_{s1} and T_{s2} intersect and the arrangement of temperatures turns back to the behaviour expected from the adsorption temperature trends ($T_{s1} < T_{s2} < T_{s3}$).
During cooling and adsorption, the temperature of the forced air flow increases with flow length. The same distribution is observed at the end of the desorption phase, due to density differences of the stagnant air. In contrast, during heating and in the beginning of the desorption phase another effect seems to be dominant. The main factor in the development of the surface temperature during heating and desorption is the heat transmittance of the fixed-bed, assuming a nearly homogeneous hot water temperature over the height of the adsorber. On the edges of the plate adsorber there is a higher volumetric fraction of metal than in the middle because of construction reasons. Thus, the thermal bridge created by the metallic cuboid casing of the adsorber seems to increase heat transfer in the bottom and upper position of the adsorber surface compared to the middle position T_{s2}, where the heat transfer is inhibited. Obviously, this heat flow does neither contribute significantly to the heating of the fixed-bed during heating and desorption phase nor to the cooling during cooling and adsorption phase, but causes additional heat losses from the hot water supply.

3.2. Presentation of measured pressures

In fig. 6 the pressures of the evaporator P_e, adsorber P_1 and condenser P_c over a cycle are depicted. A small but measurable pressure difference between the adsorber 1 and the condenser of around 0.6 mbar can be seen during desorption. Evaporator pressure and adsorber pressure almost coincide, which is due to the positioning of the evaporator pressure sensor outside of the evaporator close to the adsorber valves (V1, V2).
Although the pressure in the evaporator drops abruptly at the beginning of the adsorption (00:00 / 03:00 h), no large temperature drops are noticeable in the refrigeration compartment T_r (see fig. 4), staying relatively constant at 12 °C. Probably, the evaporator design does not allow for a greater cooling load. Despite reduced pressure and concomitant reduction of the equilibrium temperature in the evaporator no reduction in the refrigerator temperature occurs. Besides other reasons this is due to a worse heat transfer to the cold air than expected and a disadvantageous design of the evaporator leading to a partial dry out of the evaporator surface and thus, to a significantly reduced active heat transfer surface. Experiments show that approximately half of the evaporator surface is regularly inactive due to inhomogeneous refrigerant distribution.

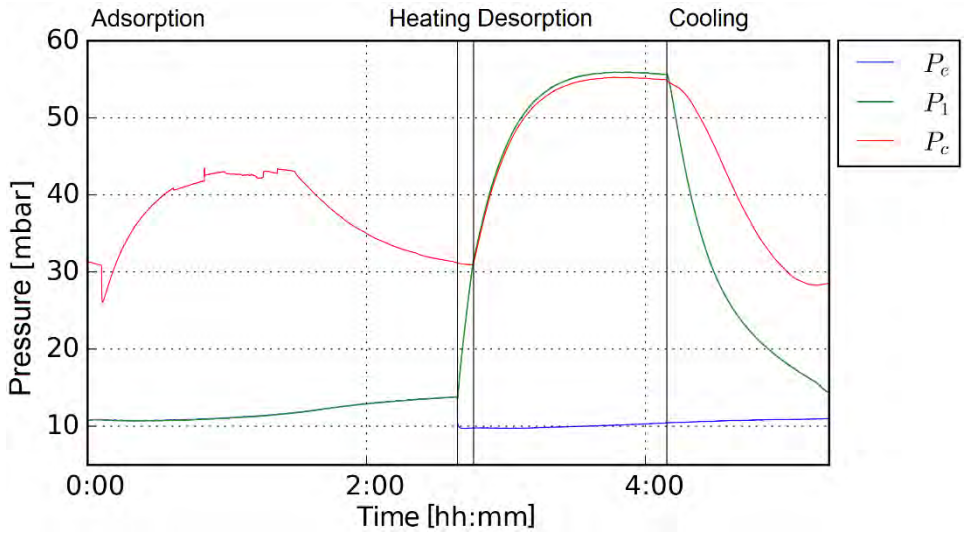

Figure 6: Measured pressures over time (data from day 1)

A prolonged cooling phase with air versus water cooling is to be expected. Thus, the cooling with air should take more time than the heating with water. Accordingly, when looking at the second half cycle (from 03:00 h in figure 6), it is noticeable that the heating phase of the loaded adsorber 1 leads to a pressure increase from 15 mbar to 32 mbar taking only 10 minutes, but in contrast cooling of the unloaded adsorber in the pressure range from 32 mbar to 15 mbar takes over one hour. In steady-state operation this has not been decisive so far, since here the adsorption capacity is acceptable for such long cycles, due to the fact that the bottleneck is currently the evaporator. As

described in section 3.1, in comparison to the adsorption and desorption phases, the adsorption preparing cooling phase is very long. Nevertheless, the adsorber pressure in the cycle from day 1 (figure 6) has not yet fallen below the evaporator pressure at the end of the cooling phase. Thus, a new beginning of the adsorption would have been disadvantageous. This problem can increase in the real application. For example, when the load of new refrigerated goods demands an increased cooling capacity, and the cycle times need to be shortened and especially when the evaporator performance is improved. It should be stated here, that the heat transfer from the adsorber surface to the cooling air flow is even less efficient than expected. Hence, the air cooling should be improved in any case.
During the heating and cooling phases, all valves to the condenser are closed, allowing it to cool down. Accordingly, the condenser pressure drops. It can also be seen in figure 6 that even after separation from the adsorber 1 the condenser remains at a high pressure level before a phase of monotonous, but slow pressure drop begins. Accompanied with the fact that such a high increase in pressure in the condenser and adsorber occurs during desorption, it can be deduced that the condenser capacity is clearly too small to condense the occurring vapor flow in a sufficient time. This adversely affects the load difference over the cycle and, accordingly, the efficiency.

4. CONCLUSIONS AND OUTLOOK

The measurement data leading to the following conclusions reveal the need of improvement for some components. The detected problems are described and it is explained which measurement data has led to the drawn conclusions.
An important result of the first measurements on the functional model of the adsorption refrigerator is that continuous cooling and thus a nearly constant refrigeration compartment temperature have been achieved. The measured refrigeration compartment temperature is 12 °C on average and hereby above the target of 4 °C as well as outside the target range of 0 to 8 °C. In order to achieve the project objective, it is necessary to increase the cooling capacity or to improve the thermal resistance of the refrigerator housing. To increase the cooling capacity, several potential improvements have been identified.
It has been shown that the main components of the cooling machines still work less efficient than expected, especially the evaporator and the condenser.
In addition to the potential of improvement for the heat transfer between refrigeration compartment air and evaporator a better distribution of water in the evaporator is necessary.
The low U-value of the fixed-bed seems to inhibit the heat flow from the fixed-bed to the cooling air. Both the U-value of the fixed-bed and the heat transfer coefficient from the adsorber's surface to the cooling air should be increased. An increased U-value of the fixed bed leads to a decreased desorption time, however, requiring an increased condenser capacity. An increased heat transfer to the cooling air can reduce the necessary time for cooling and increase the adsorption capacity.
The condenser pressure highly increases during desorption and decreases only slowly after desorption. This leads to an increased desorption time and decreased efficiency. In consequence the condenser capacity has to be increased.
From the measurement results described above, some improvement potentials of the functional model can be derived. From the refrigeration compartment temperature and the U-value of the refrigerator a cooling capacity of circa 25 W can be deduced. To achieve the project objective of 4 °C the refrigerator temperature would therefore require circa 50 W of cooling capacity. This cooling capacity could be reduced by an improved refrigerator housing. The results presented form the basis for the design of another adsorption refrigerator within the research project. This functional model 2 should primarily use the potentials identified here in order to achieve the objectives.

5. ACKNOWKLEDGEMENTS

We hereby thank the Federal Ministry for Economic Affairs and Energy and Project Management Jülich GmbH for the funding of the research project with the funding number AHA FKZ 03ET1412. We also thank our project partner InvenSor GmbH for their contribution to the research project.

6. NOMENCLATURE

Symbol		Indices	
COP	Coefficient of Performance $(-)$	1	Adsorber 1
P	Pressure (Pa)	2	Adsorber 2
T	Temperature (°C)	o	Outlet of hot water
U	Thermal transmittance (W/m^{2}K)	i	Inlet of hot water
V1	Vapor valve between evaporator and adsorber 1 $(-)$	c	Condenser
V2	Vapor valve between evaporator and adsorber 2 $(-)$	r	Refrigerator compartment
V3	Vapor valve between condenser and adsorber 1$(-)$	b	Bottom of the condenser
V4	Vapor valve between condenser and adsorber 2 $(-)$	a	Ambient air
$\dot{m}$	Mass flow (kg/s)]	e	Evaporator
x	Coordinate of the height of the adsorber (m)	s1	Surface temperature at the bottom
y	Coordinate of the depth of the adsorber (m)	s2	Surface temperature at the middle position
z	Coordinate of the width of the adsorber (m)	s3	Surface temperature at the upper position

7. LITERATURE

Rouhani, M. et al., 2016. Performance enhancement of an adsorption cooling system with AQSOA FAM-Z02 and low-finned tube evaporator. Proceedings of the IMPRES Conference, Sicily, 309-310.

Kühn, R. et al., 2018. Comparison of ab- and adsorbents for low temperature heat driven sorption cooling machines. International Journal of Refrigeration. November 2018. Pages 133-145.

Aristov, Y., et al., 2017. "Water - Silica Siogel" working pair for adsorption chillers: Adsorption equilibrium and dynamics, Ren. Energy 110, 40-46.

Manuscript ID: 531
DOI: 10.18462/iir.icr.2019.0531

The evaluation of working pairs for single-stage absorption cycle based on excess Gibbs free energy

Yibo FANG[(a)], Jiongliang HUANG[(a)], Yuwen ZHOU[(a)], Kangli BAO[(a)], Xiaogang QIAO[(b)], Xiaohong HAN[(a)], Guangming CHEN[(a)]

[(a)]Key Laboratory of Refrigeration and Cryogenic Technology of Zhejiang Province, Institute of Refrigeration and Cryogenics, Zhejiang University, Hangzhou, 310027, PR China, hanxh66@zju.edu.cn

[(b)]Zhejiang College of Construction, Hangzhou, 311321, PR China, Qiao_xg@163.com

ABSTRACT

The absorption cycle is one of the methods to use the waste heat. There are a series of absorption working pairs. Most researchers thought that the excess Gibbs free energy (G^E) was one of potential scale to evaluate the working pairs. In this work, the published vapor-liquid equilibrium (VLE) data of halohydrocarbon working pairs were collected and tabled. The VLE data were correlated with the NRTL model, and average relative pressure deviations were within 2.51 %. The single-stage absorption cycle model was established, the circulation ratio (*CR*), and exergy efficiency (η) were evaluated. The results showed that the working pairs with negative G^E had a better system performance. And the performance of the system increased with the ratio of extremum G^E at absorbing temperature to extremum G^E at generating temperature. The ratio was a potential scale to evaluate the potential for absorption working pairs.

Keywords: absorption working pairs; single-stage absorption system; performance; Gibbs free energy

1. INTRODUCTION

Absorption system is a great way for making use of the low quality heat sources such as waste heat and solar energy. And more and more researchers focus on the promotion of performance for absorption system or finding a new absorption working pair. There are many working pairs for absorption system, however, there still is not a defined scale to select an optimal working pair for one absorption system. Because it is impossible to evaluate all potential working pairs for absorption system by the experiment method, it is necessary to exhibit a defined scale in theory to select the working pairs. Generally, it is believed that the refrigerant should have a large vaporization latent, low vapor pressure and friendly environmental characteristic (zero ODP, low GWP, etc.). And the absorbent should have a low viscosity, free toxicity, low even zero flammability, etc. For the mixture of refrigerant and absorbent, the solubility of refrigerant in absorbent should be high, and the boiling points of refrigerant and absorbent should have an obvious difference. Those scales are just for the preliminarily evaluation, and not accurate quantitatively.

It was believed that there was some relationship between the absorption system performance and the vapor-liquid equilibria (VLE) characteristic of absorption pair. For example, Elsa and Holland (1987) found that in water + salt absorption heat pump, when the negative deviation from Raoult's law of working pairs was low, the temperature lift from evaporator to condenser was low, and when the negative deviation from Raoult's law of working pairs was high, the generation temperature was high, and they proposed that the absorption system needed the working pairs with negative deviation from Raoult's law, and the optimization of working pairs was to determine the optimal negative deviation value for the actual system. Narodaslawsky et al. (1988) thought that the factors that influenced the coefficient of performance (COP) for absorption heat pump mainly were the vaporization latent at normal boiling point, the value of excess Gibbs free energy (G^E), and the location for extremum excess Gibbs free energy ($G^{E,\ max}$). For an absorption heat pump, COP increased with the vaporization latent at normal boiling point increasing. The $G^{E,\ max}$ should be within (-2000 ~ -1000) J·mol^{-1}, and the location of $G^{E,\ max}$ should at the area that the composition of

refrigerant was more than 0.6. Narodaslawsky et al. (1988) also proposed that there was a linear relationship ($G^E = d \cdot h^E$) between the excess enthalpy h^E and G^E (the value of d should be more than 1 for an absorption heat pump). Kernen et al. (1995) found that for the absorption cycle to work well, G^E should increase sharply with temperature, and the reason was that in the absorber, the vapor pressures, the activity coefficients and G^E for working pairs should be low, but in the generator, G^E should be larger. The results from Zheng et al.'s researches (2001 and 2013) indicated that the value of $G^{E, max}$ had a strong influence on the performance of the system for the working pairs with water as the refrigerant and organic solvents as the absorbents. COP reached the maximum, and circulation ratio CR was at a low level, when the value for $G^{E, max}$ was within (-1500 ~ -1200) J·mol^{-1}. Tufano (1998) observed that the low vapor pressure produced a marked decrease of circulation ratio (*CR*), and the negative h^E produced a comparatively smaller increase of the COP, and he also thought that for a great performance, the absorption working pairs should have a certain negative deviation from the Raoult's law.

In this work, the working pairs with R134a, R32, R152a, and R161 as the refrigerant, respectively, were applied into a single-stage absorption system. And the performance of the system was evaluated. The relationships of the $G^{E, max}$, or the ratio for $G^{E, max}$ at absorbing temperature to $G^{E, max}$ at generating temperature on the performance of system were discussed. The feasibility of applying G^E as one of the scales to evaluate the halohydrocarbon working pairs' potential in the absorption system was analyzed.

2. MODEL

The schematic diagram of the single-grade absorption refrigeration cycle was shown in Fig. 1, and Fig. 2 showed the thermodynamic cycle of the system on *p-T* coordinates. The following assumptions were made for the thermodynamic analysis: (1) the absorption refrigeration system operated at steady state; (2) the pressure changes only occurred in solution pump and throttle valve, and all other flow pressure drop could be neglected; (3) the heat loss in the system could be neglected; (4) the solution streams at the exit of generator (point 4) and absorber (point 2) were at the equilibrium state; (5) the solution streams at the exit of condenser (point 3, *l*) was saturation liquid, and the exit gas stream of evaporator (point 1) was saturation gas; (6) the exit gas stream of generator was pure refrigerant.

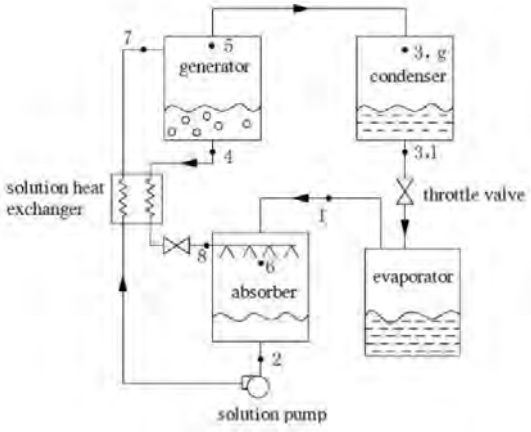

Figure 1: The schematic diagram of the single-stage absorption refrigeration cycle

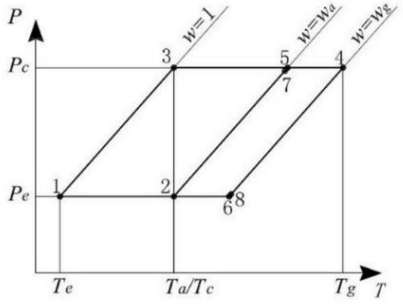

Figure 2: The thermodynamic cycle of the single-stage absorption cycle

The operating pressures of the absorption refrigeration system are determined by the saturation pressures of condenser temperature and evaporator temperature. The temperatures at various state points are shown clearly in Fig. 2. As the exit solution streams of generator and absorber are at the equilibrium condition, the mass fraction of refrigerant in the exit streams of absorber and generator, w_a and w_g, could be calculated by phase equilibrium data of working pairs. Thus, the mass fractions at various state points can also be obtained.
The circulation ratio (*CR*) is determined by Eq. (1).

$$CR = \frac{1 - w_g}{w_a - w_g} \quad \text{Eq. (1)}$$

The power consumption of the solution pump (W_p) is defined by Eq. (2).

$$W_p = \frac{CR \cdot \Delta p \cdot \Phi_e}{\rho \cdot eff \cdot \Delta h} \quad \text{Eq. (2)}$$

The exergy efficiency η is defined as

$$\eta = \frac{\Phi_e}{\Phi_g + W_p} \Big/ \left(\frac{T_g - T_a}{T_g} \cdot \frac{T_e}{T_c - T_e} \right) \quad \text{Eq. (3)}$$

The absorption working pairs are mainly divided into four series (water series, ammonia series, alcohol series, and halogenated hydrocarbon series), according to the different types of refrigerants. In these working pairs, because the amount of halogenated hydrocarbon series is most, and the VLE properties and thermodynamic properties of halogenated hydrocarbon series are comparatively enough, the hydrocarbon series was selected as the working fluids in this work. The fundamental properties of refrigerants and absorbents were listed in Table 1 and Table 2.

Table 1. Fundamental properties of refrigerants

	R134a	R32	R152a	R161
Full name	1,1,1,2-Tetrafluoroethane	Difluoromethane	1,1-Difluoroethane	fluoroethane
Molecule	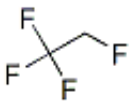			
Cas. No.	811-97-2	75-10-5	75-37-6	353-36-6

Table 2. Fundamental properties of organic absorbents

	DMETrEG	DMAC	DMF	DMEDEG	NMP
Full name	Triethylene glycol dimethyl ether	N,N-dimethylacetamide	N,N-Dimethylformamide	dinthylether diethylene glycol	1-methyl-2-pyrrolidone
Molecule	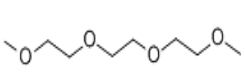		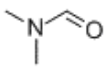	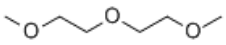	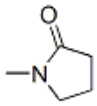
Cas. No.	112-49-2	127-19-5	68-12-2	111-96-6	872-50-4

The VLE data sources of hydrocarbon working pairs were listed in Table 3. For the unification of programming, these published VLE data of hydrocarbon working pairs were recorrelated in this work by the NRTL model (Renon and Prausnitz, 1968). The equations of the NRTL model for binary mixture were as follows.

$$\frac{g^E}{RT} = x_1 x_2 \left(\frac{\tau_{21} G_{21}}{x_1 + x_2 G_{21}} + \frac{\tau_{12} G_{12}}{x_2 + x_1 G_{12}} \right) \quad \text{Eq. (4)}$$

$$\ln \gamma_1 = x_2^2 \left[\tau_{21} \left(\frac{G_{21}}{x_1 + x_2 G_{21}} \right)^2 + \frac{\tau_{12} G_{12}}{\left(x_2 + x_1 G_{12} \right)^2} \right] \quad \text{Eq. (5)}$$

$$\ln \gamma_2 = x_1^2 \left[\tau_{12} \left(\frac{G_{12}}{x_2 + x_1 G_{12}} \right)^2 + \frac{\tau_{21} G_{21}}{\left(x_1 + x_2 G_{21} \right)^2} \right] \quad \text{Eq. (6)}$$

$$G_{12} = \exp(-\alpha \tau_{12}), \quad G_{21} = \exp(-\alpha \tau_{21}) \quad \text{Eq. (7)}$$

$$\tau_{12} = A_0 + A_1 \ln T, \quad \tau_{21} = B_0 + B_1 \ln T \quad \text{Eq. (8)}$$

With the experimental data, the parameters (α, A_0, A_1, B_0, B_1 in Eq. (7) and Eq. (8)) were calculated, which were listed in Table 3. In the process of calculation, the properties of refrigerants were from the Refprop 10.0, and the properties of absorbents were from Aspen Plus v8.4.

Table 3. The data sources and NRTL model parameters for hydrocarbon working pairs

Working pairs	Source	NRTL parameters					ARD%
		α	A_0	A_1	B_0	B_1	
R134a+DMAC	Jing et al., 2013	18.0113	-0.3872	0.4275	1.3769	-0.2601	1.04
R134a+DMEDEG	Zehioua et al., 2010	-0.3146	-7.4361	1.0720	-7.3778	1.3625	1.67
R134a+DMETrEG	Conrnas et al., 2002	-0.4168	-6.3112	0.8749	-6.2444	1.1323	2.02
R134a+DMF	Han et al., 2011	12.6003	3.2156	-0.5415	3.5791	-0.6551	2.04
R32+DMF	Han et al., 2011	4.8359	10.8692	-1.8564	6.3828	-1.1829	2.51
R32+DMAC	Li et al., 2013	17.3682	5.2930	-0.9246	1.1401	-0.2250	1.93
R32+DMEDEG	Li et al., 2013	3.3031	6.6425	-1.0702	5.1794	-0.9781	2.07
R152a+DMETrEG	Fang et al., 2017	0.1529	1.8694	-0.4621	1.9522	-0.2545	1.66
R152a+DMAC	Meng et al., 2013	-0.8928	5.3674	-0.9692	5.3982	-0.8960	1.28
R152a+DMEDEG	Li et al., 2013	2.9766	1.8247	-0.3315	1.8859	-0.3217	1.25
R152a+DMF	Meng et al., 2013	1.4258	2.7234	-0.5496	2.8252	-0.4067	0.91
R161+DMAC	Jing et al., 2013	5.1646	11.3840	-1.8965	6.9151	-1.2748	1.36
R161+DMEDEG	Deng et al., 2014	5.6141	10.3596	-1.5913	6.4691	-1.1938	1.26
R161+DMETrEG	Han et al., 2016	-0.4694	4.8556	-1.3144	8.2862	-1.2970	2.15
R161+DMF	Deng et al., 2014	6.3104	9.4318	-1.0523	6.7219	-1.2132	1.68
R161+NMP	Jing et al., 2013	5.6135	10.2811	1.7137	6.4199	-1.1810	1.34

From Table 3, the average relative pressure deviation (ARD%) for all hydrocarbon working pairs was within 2.51 %. For the four series of working pairs, (R134a series, R32 series, R152a series, and R161 series), the ARD% of R32 series were a little larger than the other series, the reason might be that the R32's vapor pressure was larger than the other refrigerants.

To apply the NRTL model for different working pairs into the single-stage absorption system, it was able to calculate the performance of the system (*CR*, and η) with different working pairs. And the G^E at a certain temperature was also obtained.

3. RESULTS AND DISCUSSIONS

The calculation working conditions were listed in Table 4. The η and *CR* for the system with different working pairs in the generator temperature range were showed in Fig. 3 and Fig. 4, respectively.

Table 4. Simulation working conditions for system

Working condition	T_g (K)	T_a (K)	T_e (K)	T_c (K)	Φ_e (kW)
Range	353.15 ~ 393.15	303.15	273.15	303.15	10

From Fig. 3, it can be seen that the exergy efficiency η for different working pairs increased with the T_g at first but after a certain value of T_g, then it began to decrease with T_g. Therefore, there was an optimal, and its location was different for different working pairs. Comparing to other working pairs, the system with R134a + DMEDEG showed a best exergy efficiency η, and the system R32 + DMF had the lowest exergy efficiency. By comparison, R134a series had a better exergy efficiency than the other series. From Fig. 4, it can be known that the circulation ratio *CR* for all working pairs decreased with the increase of T_g. A low *CR* meant that the mass flow of solution was low. And the system with R134a + DMETrEG and R134a + DMEDEG had the lowest *CR* among T_g = (353.15 ~ 393.15) K. The system with R32 + DMF had a relatively high *CR*. Considering the *CR* and η, the system with R134a series working pairs showed a better performance compared to that with other series working pairs.

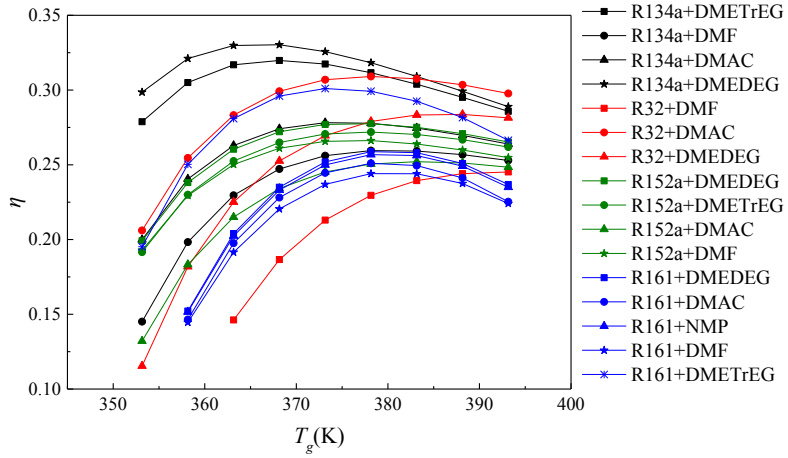

Figure 3: The exergy efficiency η at different generator temperature T_g for different working pairs

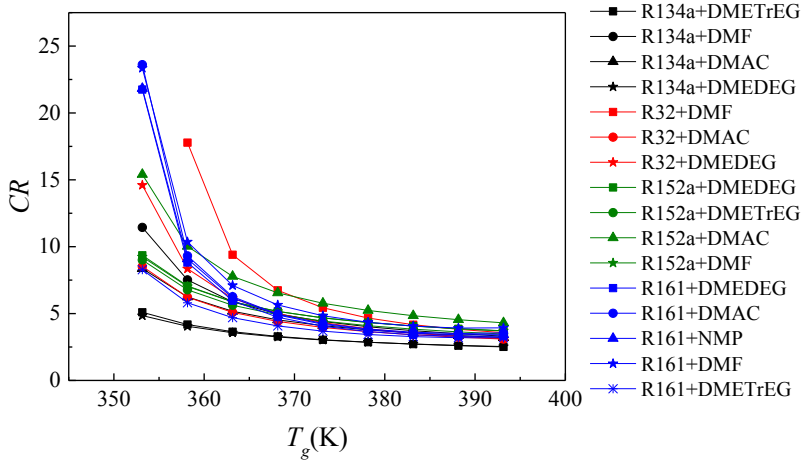

Figure 4: The circulation ration *CR* at different generator temperature T_g for different working pairs

As mentioned at section 1, some researchers believed that there was a strong relationship between the performance of system and the excess Gibbs free energy (G^E), because when G^E was much low than 0, the refrigerant could easily be absorbed by the absorbent, and if G^E was large, the refrigerant could easily be desorbed from absorbent. Narodaslawsky et al. (1988) and Zheng et al. (2001 and 2013) both mentioned that there was a most suitable range of the maximum excess Gibbs free energy ($G^{E,\,max}$) of working fluids for absorption system. It should be emphasized that $G^{E,\,max}$ was the extremum in the curve G^E versus x, which was shown in Fig. 5. For R134 series working pairs, the G^E was negative among x_1 = (0 ~ 1) at absorber temperature (T_a = 303.15 K), and there was an extremum for G^E.

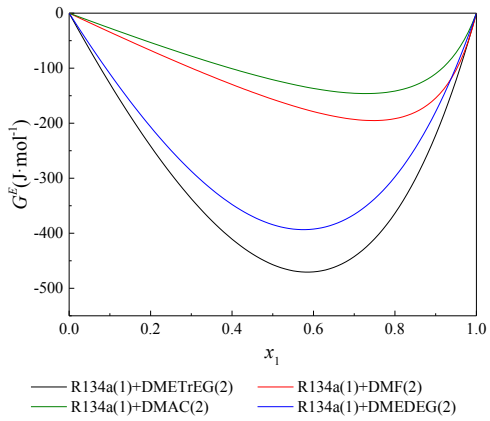

Figure 5: The G^E of R134a series working pairs at T_a = 303.15 K

Fig. 6 showed the influence of $G^{E,\,max}$ on the η and CR at generator temperature T_g = 373.15 K, and the $G^{E,\,max}$ was the extremum value of G^E at absorbing temperature (T_a = 303.15 K). And it was hard to determine any regular rule for $G^{E,\,max}$ influence on these performance parameters. There was not an optimal value for $G^{E,\,max}$ for η and CR. One of the reasons was possibly a little amount of data.

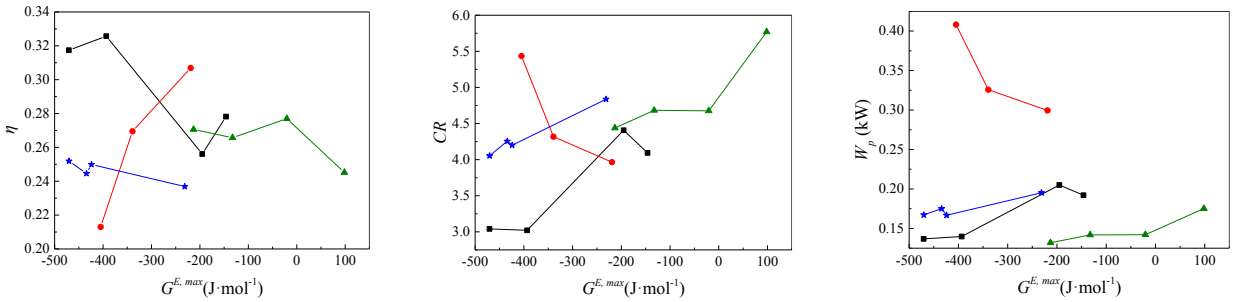

(a). η versus $G^{E,\,max}$. **(b). CR versus $G^{E,\,max}$** **(c) W_p versus $G^{E,\,max}$**

Figure 6: The influence of $G^{E,\,max}$ on the performance of single-stage absorption system for different series working pairs at T_g = 373.15 K (—■—R134a series; —●— R32 series; —▲— R152a series; —★— R161 series)

In Fig. 6, the G^E at absorbing temperature was only considered, however, the desorption process of the refrigerant at generator was also an important process which was involved with the VLE process of working pairs. Therefore, the G^E at generating temperature should also be considered. Fig. 7 showed the results of performance parameters of the system versus the ratio for $G^{E,\,max}$ at T_a = 303.15 K to $G^{E,\,max}$ at T_g = 373.15 K. And it was obviously that the η increased with the ratio increasing, while CR and W_p decreased. Therefore, it was thought that the ratio for $G^{E,\,max}$ at the absorbing temperature to $G^{E,\,max}$ at the generating temperature was a better scale to evaluate the working pairs' potential in a single-stage absorption system. And the performance of the system was getting better while the ratio increased.

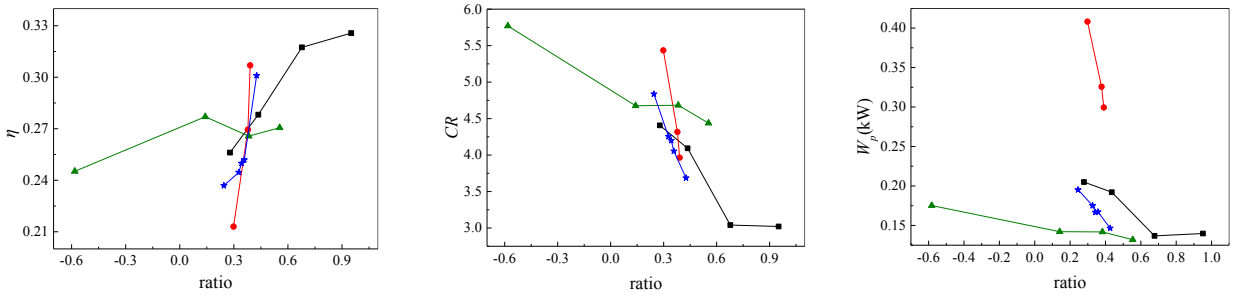

(a).η versus ratio **(b). CR versus ratio** **(c). W_p versus ratio**

Figure 7: The performance parameters (η, CR, and W_p) versus the ratio of $G^{E,\,max}$ at T_a = 303.15 K to $G^{E,\,max}$ at T_g = 373.15 K (—■—R134a series; —●— R32 series; —▲— R152a series; —★— R161 series)

4. CONSLUSIONS

The VLE data of hydrocarbon working pairs were collected and correlated by the NRTL model, and the average relative pressure deviations for all working pairs were within 2.51 %. A single-stage absorption system simulation model was established, and the 16 kinds of working pairs were applied to the model to calculate the performance of the system. Two parameters, *CR* and *η*, were considered to evaluate the performance of the system. The results indicated that the R134a + DMEDEG had the best performance, and R32 + DMF had the worst one. And generally, the R134a series working pairs had a better performance than R32, R152a and R161 series working pairs.

The influence of the excess Gibbs free energy of the working pairs on the single-stage absorption system was discussed. Actually, it was indicated that there was not a definite relationship between the $G^{E,\ max}$, and performance of the system. Because the absorption at the absorber and the desorption at the generator were the two important processes in the absorption system, the ratio of $G^{E,\ max}$ at the absorbing temperature to $G^{E,\ max}$ at the generating temperature was considered. And the result showed that the *η* increased, *CR* and W_p decreased with the ratio increasing. It meant the performance of the system got better while the ratio increased. Therefore, it was thought to adopt the ratio of $G^{E,\ max}$ at T_a to $G^{E,\ max}$ at T_g as the scale to evaluate the potential of working pairs.

ACKNOWLEDGEMENT

This work has been supported by the Nation Natural Science Foundation of China (Grant No. 51576171), and Zhejiang Provincial Natural Science Foundation of China under Grant (Grant No. LZ19E060001).

NOMENCLATURE

A_0, A_1, B_0, B_1	model parameters of NRTL model	Δh	latent heat vaporization of the refrigerant at evaporator temperature ($J \cdot kg^{-1}$)
ARD%	average relative deviation of pressure	*Greek*	
CR	circulation ratio	ρ	density of solution ($kg \cdot m^{-3}$)
eff	efficiency of solution pump (set to 0.5)	Φ	total thermal load (W).
G_{12}, G_{21}	model parameters of NRTL model	η	exergy efficiency
G^E	excess Gibbs free energy ($J \cdot mol^{-1}$)	γ	activity coefficients
$G^{E,max}$	extremum of G^E ($J \cdot mol^{-1}$)	α, τ_{12}, τ_{12},	model parameters of NRTL model
h^E	excess enthalpy ($J \cdot mol^{-1}$)		
T	temperature (K)	*Subscript*	
p	pressure (Pa)	*a*	absorber
w	mass faction of refrigerant	*c*	condenser
W_p	power consumption of solution pump	*e*	evaporator
x	mole fraction	*g*	generator
Δp	the difference of pressure between the inlet and outlet of the solution pump (Pa)	*i*	*i*th component

REFERENCES

Eisa, M. A. R., Holland, F. A., 1987. A study of the optimum interaction between the working fluid and the absorbent in absorption heat pump systems. Heat Recovery Systems 7(2), 107-117.

Narodoslawsky, M., Otter, G., Moser, F., 1988. Thermodynamic criteria for optimal absorption heat pump media. Heat Recovery Systems & CHP 8(3), 221-233.

Narodoslawsky, M., Otter, G., Moser, F., 1988. New working pairs for medium and high temperature industrial absorption heat pumps. Heat Recovery Systems & CHP 8(5), 459-468.

Kernen, M., Lee, L. L., Perez-Blanco, H., 1995. A study of solution properties to optimize absorption cycle COP. Int. J. Refrigeration 18(1), 42-50.
Zheng, D., Ji, P., Qi, J., 2001. Maximum excess Gibbs function of working pairs and absorption cycle performance. Int. J. Refrigeration 24, 834-840.
Zheng, D., Dong, L., Wu, X., 2013. New approach for absorbents species selection with excess Gibbs function. Ind. Eng. Chem. Res. 52, 9480-8489.
Tufano, V., 1998. Simplified criteria for the development of new absorption working pairs. Appl. Therm. Eng. 18, 171-177.
Renon, H., Prausnitz, J. M., 1968. Local compositions in thermodynamic excess functions for liquid mixtures. AIChE J. 14, 135-144.
Jing, X., Deng, R., Zheng, D., 2013. Measurement and correlation of isothermal vapor-liquid equilibrium of fluoroethane + N,N-dimethylacetamide, fluoroethane + N-methyl-2-pyrrolidone, and 1,1,1,2-tetrafluoroethane + N,N-dimethylacetamide systems. J. Chem. Eng. Data 58, 3289-3296.
Zehioua, R., Coquelet, C., Meniai, A., Richon, D., 2010. *p-T-x* measurements for some working fluids for an absorption heat transformer: 1,1,1,2-tetrafluoroethane (R134a) + dimethylether diethylene glycol (DMEDEG) and dimethylether triethylene glycol (DMETrEG). J. Chem. Eng. Data 55, 2769-2775.
Coronas, A., Mainar, M. A., Patil, K. R., Conesa, A., Shen, S., Zhu, S., 2002. Solubility of 1,1,1,2-tetrafluoroethane in triethylene glycol dimethyl ether. J. Chem. Eng. Data 47, 56-58.
Han, X., Gao, Z., Xu, Y., Qiu, Y., Min, X., Cui, X., Chen, G., 2011. Solubility of refrigerant 1,1,1,2-tetrafluoroethane in the N,N-dimethyl formamide in the temperature range from (263.15 to 363.15) K. J. Chem. Eng. Data 56, 1821-1826.
Han, X. H., Xu, Y. J., Gao, Z. J., Wang, Q., Chen, G. M., 2011. Vapor-liquid equilibrium study of an absorption heat transformer working fluid of (HFC-32 + DMF). J. Chem. Eng. Data 56, 1268-1272.
Li, X., Zheng, D., Shen, Y., Meng, X., Li, B., 2013. Vapor-liquid equilibria of difluoromethane + N,N-dimethylacetamide, difluoromethane + dimethylether diethylene glycol and 1,1-difluoroethane + dimethylether diethylene glycol systems. Fluid Phase Equilibria 347, 15-21.
Fang, Y., Guan, W., Hua, C., Wang, Y., Han, X., Chen, G., 2017. Vapor-liquid equilibrium of absorption working pair R152a + DMETrEG. J. Chem. Ind. Eng. (China) 68(11), 4025-4034.
Meng, X., Zheng, D., Li, X., Shen, Y., 2013. Isothermal vapor-liquid equilibrium measurements of 1,1-difluoroethane + N,N-dimethylformamide and N,N-dimethylacetamide. J. Chem. Eng. Data 58, 1078-1085.
Deng, R., Jing, X., Zheng, D., Li, X., 2014. Vapor-liquid equilibrium measurements and assessments of fluoroethane + N,N-dimethylformamide and fluoroethane + dimethylether diethylene glycol systems for the hybrid refrigeration cycle. Int. J. Refrigeration 43, 176-186.
Han, X., Yang, Z., Gao, Z., Guan, W., Chen, G., 2016. Isothermal vapor-liquid equilibrium of HFC-161 + DMETrEG within the temperature range of 293.15-353.15 K and comparison for HFC-161 combined with different absorbents. J. Chem. Eng. Data 61, 1321-1327.

Manuscript ID: 532
DOI: 10.18462/iir.icr.2019.0532

Visual study on the effects of SiO_2/water and CuO/water nanofluids on the start-up and heat transfer performance of pulsating heat pipe

Kangli BAO[(a)], Yibo FANG[(a)], Chenyi XU[(a)], Xiaosheng JI[(a)], Xiaogang QIAO[(b)], Xiaohong HAN[(a)], Guangming CHEN[(a)]

[(a)] Key Laboratory of Refrigeration and Cryogenic Technology of Zhejiang Province, Institute of Refrigeration and Cryogenics, Zhejiang University, Hangzhou 310027, PR China, hanxh66@zju.edu.cn

[(b)] Zhejiang College of Construction, Hangzhou 311321, PR China, Qiao_xg@163.com

ABSTRACT

Visual experiments were conducted to investigate the start-up and heat transfer performance of pulsating heat pipes (PHPs) charged with different volume fractions (0.2 vol %, 0.5 vol %, 0.8 vol % and 1.0 vol %) of CuO/water and SiO_2/water nanofluids. The results showed that the start-up performance of PHPs charged with SiO_2/water nanofluids was worsened compared with distilled water-PHP, while CuO/water nanofluids had less effect on the start-up performance. The thermal resistances of PHPs charged with SiO_2/water nanofluids ((0.2 – 0.8) vol %) and CuO/water nanofluids ((0.2 – 1.0) vol %) were lower than those of distilled water-PHP. However, with high concentration of SiO_2/water nanofluids (1.0 vol %), the heat transfer performance of PHP was worsened at lower heat input (≤ 54.6 W). The optimal concentration of SiO_2/water nanofluids and CuO/water nanofluids were about 0.5 vol % and 0.8 vol %, respectively. In addition, the influence of nanoparticles sedimentation on the heat transfer performance of PHPs was relatively small.

Keywords: Pulsating Heat Pipe, Nanofluids, Visualization, Heat Transfer, Start-up, Thermal Resistance, Nanoparticle Sedimentation

1. INTRODUCTION

With the rapid development of the electronic technology, the power densities of electronic devices have increased sharply in the past few decades (Agostini et al., 2007). It resulted in the increase of heat fluxes of electronic devices. More efficient thermal management is required to match the rising heat fluxes. Pulsating heat pipe (PHP) as a kind of two-phase passive heat transfer device, with excellent heat transfer performance, compact structure and no external power requirement has drawn much attention (Han et al., 2016). A PHP was usually consisted in a capillary tube bended in a planar serpentine manner. It was evacuated and partially filled with working fluid. During the operation, the heat was transferred from evaporation section to condensation section through the motions of the working fluid inside PHP.

PHPs charged with nanofluids were investigated by many researchers because the thermal conductivities of working fluids could be effectively increased by adding small amounts of nanoparticles into base fluids (Godson et al., 2010; Karthikeyan et al., 2014; Nazari et al., 2018). Karthikeyan et al. (2014) found that with silver colloidal nanofluid, the thermal resistance of PHP was decreased and the heat transfer limit was enhanced by 33.3 %. However, when the concentration of nanoparticles was high, the heat transfer performance of PHPs may be worsened. Nazari et al. (2018) found that when the concentrations of 1rapheme oxide/water nanofluids were 0.25 g/lit, 0.5 g/lit and 1.0 g/lit, the thermal resistances of 1rapheme oxide/water nanofluids-PHPs were lower than water-PHP. However, the heat transfer performance of PHP was worsened when the concentration of 1rapheme oxide/water nanofluids was 1.5 g/lit. Therefore, it is significant to investigate the influence of different concentrations of the nanofluids on the heat transfer performance of PHPs.

In addition, to understand the operational mechanism of PHPs including the start-up and heat transfer mechanism, it was of great significance to investigate the relation between the flow motions

of working fluids and the heat transfer of PHPs. For example, Khandekar et al. (2003) conducted a visual experiment on the PHP with R-123 as working fluid. With the increase of input heat flux, a slug-annular flow transition was observed in the PHP. When annular flow developed, convective flow boiling became the dominant phenomenon and the heat transfer coefficient of PHP was increased. For nanofluids-PHPs, when nanofluids were used as working fluids, sedimentations of nanoparticles may exist in PHPs (Godson et al., 2010). Therefore, to understand the operation mechanism of nanofluids-PHPs, it was significant to investigate the flow motions of nanofluids and the dispersion of nanoparticles in PHPs.

In this paper, to give an insight into the influence mechanism of nanofluids, visual experiments were conducted on PHPs charged with SiO_2/water nanofluids and CuO/water nanofluids, respectively. The influence of SiO_2/water nanofluids and CuO/water nanofluids with different concentrations (0.2 vol %, 0.5 vol %, 0.8 vol % and 1.0 vol %) on the start-up performance and heat transfer performance of the PHP were compared and analyzed combined with visual observation. In addition, sedimentation of nanoparticles was observed and the influence of nanoparticles sedimentation on the heat transfer performance of PHP was investigated. The results could be used to better understand the mechanism of heat transfer enhancement of nanofluids on PHPs.

2. EXPERIMENT

2.1 Experimental apparatus

The schematic of the experimental apparatus was shown in Fig. 1. Table 1 showed the summary of experiment parameters of PHP. The PHP was heated by nickel-chrome wire wrapped outside the evaporation section. The power input was controlled by a DC regulated power supply and it was measured by a wattmeter with an accuracy of 0.5 % FS. The condensation section was cooled by cooling water and the inlet temperature of cooling water was set at (20 ± 0.5) °C. Ten T-type thermocouples were used to measure the temperature of evaporation and condensation section and the locations were shown in Fig. 1. Considering both the accuracies of thermocouples and Agilent 34970 A, the uncertainty of the temperature was ± 0.12 °C.

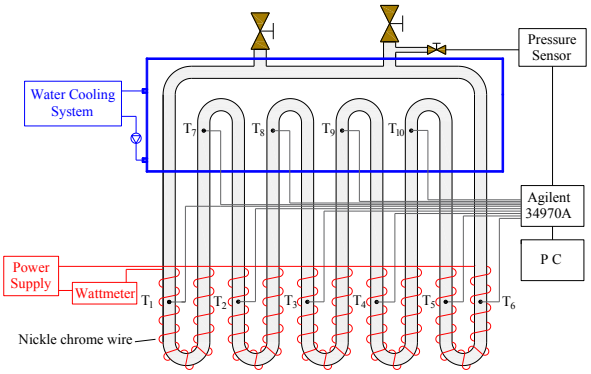

Figure 1: Experimental apparatus

Table 1 Experiment Parameters of PHP

Turns number	Inner/outer diameter (mm)	Length of evaporation section (mm)	Length of adiabatic section (mm)	Length of condensation section (mm)	Filling ratio	Inclination angle (°)
5	2 / 7.5	60	60	65	0.5	90

2.2 Nanofluids preparation

The SiO_2 nanoparticles with a mean diameter of 30 nm and CuO nanoparticles with a mean diameter of 40 nm were used in the experiment. The thermophysical properties of SiO_2 and CuO nanoparticles were shown in Table 2. With distilled water as based fluid, four volume concentrations (0.2 vol %, 0.5 vol %, 0.8 vol% and 1.0 vol %) of CuO/water and SiO_2/water nanofluids were prepared. No surfactant/dispersant additives were added because it might affect the thermophysical properties of nanofluids. The nanofluids were vibrated for 4 h in an ultrasonic bath. Nanoparticles

could disperse well after 24 hours.

Table 2 Thermophysical properties of SiO_2 and CuO nanoparticles (Myers et al., 2016; Touloukian et al., 1970; Hwang et al., 2007)

Nanoparticles	Thermal conductivity (W/m K)	Specific heat (J/g K)	Density (kg/m^3)
SiO_2 nanoparticles (30 nm)	8.3	1.06	2600
CuO nanoparticles (40 nm)	76.5	0.64	6320

2.3 Data processing

The heat transfer performance of PHP could be evaluated by thermal resistance. It is defined as follows:

$$R = (T_e - T_c) / Q \quad \text{Eq. (1)}$$

where T_e was the average temperature of evaporation section, T_c was the average temperature of condensation section and Q was the heat input. T_e and T_c were calculated by:

$$T_e = \left(T_1 + T_2 + T_3 + T_4 + T_5 + T_6\right) / 6 \quad \text{Eq. (2)}$$

$$T_c = \left(T_7 + T_8 + T_9 + T_{10}\right) / 4 \quad \text{Eq. (3)}$$

where T_i represented the temperature of the ith thermocouples. Good insulation was taken outside the evaporation section. However, in order to observe the flow motions of working fluids in the PHP, there was no insulation material wrapped outside the adiabatic section. The heat loss of adiabatic section was estimated to be 9.05 %. The heat input of the PHP could be calculated as:

$$Q = \varphi \times P \quad \text{Eq. (4)}$$

where φ can be taken as 0.91 for all heat input and P was the electrical input power ((20 – 120) W). Through the Eq. 4, the heat input Q was in the range of (18.2 – 109.2) W.
The uncertainty of thermal resistance could be calculated as follows:

$$\delta R = \sqrt{\left(\frac{\partial R}{\partial Q}\delta Q\right)^2 + \left(\frac{\partial R}{\partial T}\delta T\right)^2} \quad \text{Eq. (5)}$$

Through calculation, the maximum uncertainty of the thermal resistance was 6.22 %. The relative uncertainty decreased with the increase of heat input.

3. RESULTS AND DISCUSSIONS

3.1 The effect of nanofluids on the start-up performance of PHP

3.1.1. The effect of different concentrations of SiO_2/water nanofluids on the start-up performance of PHP

According to the visual observation during the experiment, large oscillation amplitudes of evaporation temperatures were related to the stagnation of liquid and vapor plugs in PHPs. At lower heat input, vapor and liquid plugs did not show a continuous pulsating motion, but showed a pulsation-stagnation-pulsation process. Stagnation may last for even dozens of seconds. It was observed that when stagnation happened, the evaporation temperature of positions with liquid plugs continuously rose while the positions with vapor plugs showed a more steady oscillation. When evaporation temperature difference became large enough, the liquid and vapor plugs oscillated again and evaporation temperature sharply decreased. After a pulsation-stagnation-pulsation process, a large peak could be found in the oscillation of evaporation temperature. Take distilled water-PHP as an example, the relation between stagnation and pulsation of liquid and vapor plugs and the oscillation of evaporation temperature was shown in Fig. 2. Thus, from the observation, the oscillation period and amplitude of evaporation temperature at lower heat input showed a strong relation with the stagnation of liquid and vapor plugs. The start-up performance of PHPs charged with nanofluids could be analyzed through the oscillation of evaporation temperature.
The evaporation temperature oscillations of PHPs charged with distilled water and different concentrations of SiO_2/water nanofluids under different heat input during steady operations were

shown in Fig. 2 and Fig. 3, respectively. From Fig. 2 and Fig. 3, it can be found that the oscillation amplitudes of evaporation temperature of PHPs at lower heat input (18.2 W) were commonly larger than those at higher heat input. When the heat input was larger than 36.4 W, the oscillation period and oscillation amplitude of evaporation temperature obviously decreased. It was consistent with the visual observation that stagnation was easily observed at 18.2 W heat input but barely noticed when heat input was larger than 36.4 W. In addition, from Fig. 2 and Fig. 3, it could be found that the oscillation periods and amplitudes of evaporation temperature of SiO_2/water nanofluids-PHPs were much larger than those of distilled-water PHP at heat input of 18.2 W. It was indicated that the stagnation time of SiO_2/water nanofluids-PHPs was longer than that of distilled water-PHP. In addition, the liquid and vapor plugs in PHP charged with 1.0 vol % SiO_2/water nanofluids almost kept stagnation at heat input of 18.2 W. Therefore, the start-up performance of PHPs charged with SiO_2/water nanofluids was deteriorated compared with distilled water-PHP.

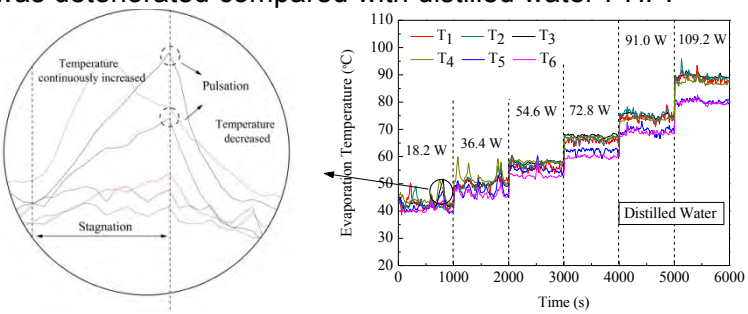

Figure 2: The evaporation temperature oscillation of PHP charged with distilled water

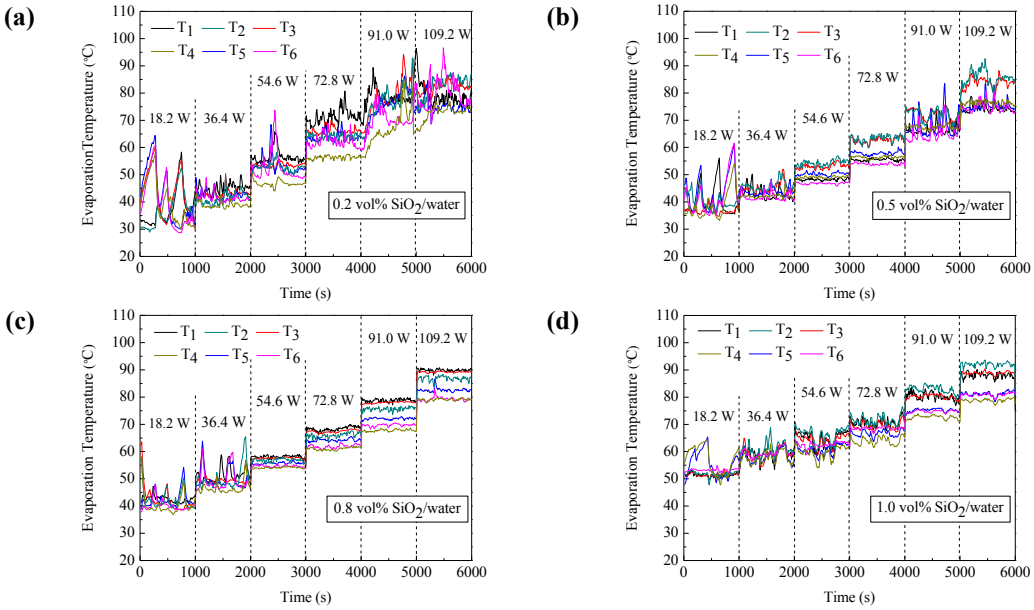

Figure 3: The evaporation temperature oscillation of PHPs charged with SiO_2/water nanofluids with concentration of (a) 0.2 vol %; (b) 0.5 vol %; (c) 0.8 vol %; (d) 1.0 vol %

3.1.2. The effect of different concentrations of CuO/water nanofluids on the start-up performance of PHP

The evaporation temperature oscillations of PHPs charged with different concentrations of CuO/water nanofluids at different heat input were shown in Fig. 4. Stagnation phenomena of liquid and vapor plugs were also observed in the CuO/water nanofluids-PHPs at heat input of 18.2 W. Similar to SiO_2/water nanofluids-PHPs, it can be found that the oscillation amplitudes of evaporation temperature of PHPs charged with different concentrations of CuO/water nanofluids were commonly larger at lower heat input (18.2 W), as shown in Fig. 4.

The evaporation temperature oscillations of CuO/water nanofluids-PHPs and distilled water-PHPs were compared and it was found that the evaporation temperature oscillation amplitudes of CuO/water nanofluids-PHPs were slightly larger than those of distilled water-PHP at lower heat input, as shown in Fig. 2 and Fig. 4.

From the mentioned above, the start-up performance of PHPs were worsened by using SiO_2/water

and CuO/water nanofluids as working fluids. It was attributed to the increase of dynamic viscosity of nanofluids, which increased the flow resistance. In addition, according to the oscillation of evaporation temperature and visual observation, the lasting time of liquid and vapor plugs stagnation of CuO/water nanofluids-PHPs was shorter than that of SiO_2/water nanofluids-PHPs. The start-up performance of CuO/water nanofluids-PHPs was better than SiO_2/water nanofluids-PHPs. It was attributed to higher thermal conductivity of CuO/water nanofluids. Therefore, the deteriorations effects of CuO/water nanofluids on the start-up performance of PHPs were less than that of SiO_2/water nanofluids.

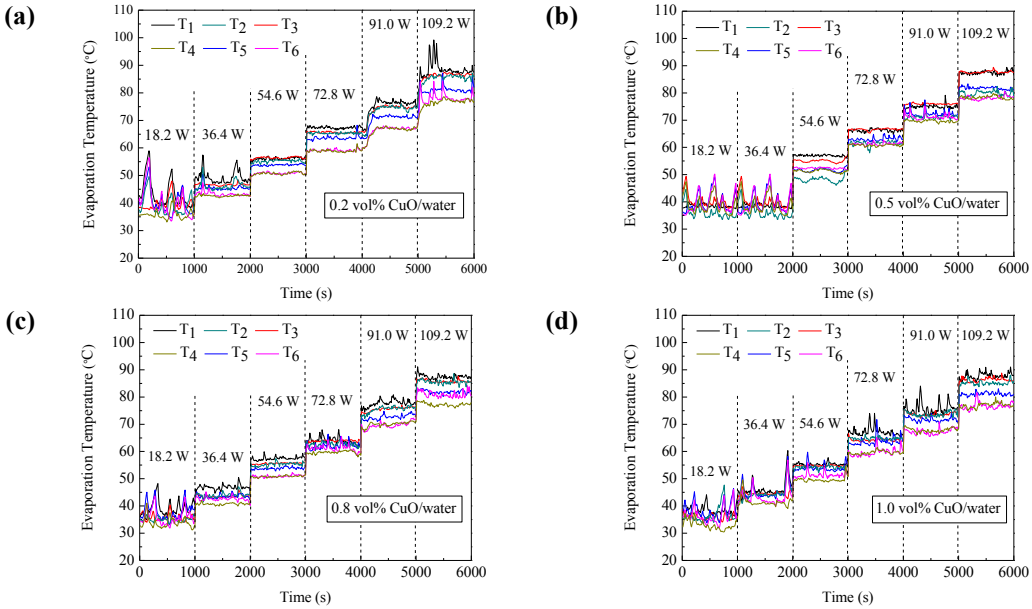

Figure 4: The evaporation temperature oscillation of PHP charged with CuO/water nanofluid (a) 0.2 vol %; (b) 0.5 vol %; (c) 0.8 vol %; (d) 1.0 vol %

3.2. The effect of nanofluids on the heat transfer performance of PHP

Commonly, the PHP with better heat transfer performance has lower thermal resistance (Bergman et al., 2008). In order to investigate the influence of different concentrations of SiO_2/water nanofluids and CuO/water nanofluids on the heat transfer performance of PHP, thermal resistances of PHPs charged with SiO_2/water nanofluids, CuO/water nanofluids and distilled water were calculated and shown in Fig. 5.

3.2.1. The effect of different concentrations of SiO_2/water nanofluids on the heat transfer performance of PHP

According to Fig. 5(a), it could be found that PHPs charged with SiO_2/water nanofluids (0.2 vol %, 0.5 vol % and 0.8 vol %) showed lower thermal resistances compared with distilled water-PHP. However, when the concentration of SiO_2/water nanofluids was 1.0 vol %, the thermal resistances of SiO_2/water nanofluids-PHP was higher than those of distilled water-PHP at lower heat input (≤ 54.6 W) and opposite at higher heat input (> 54.6 W). It could be found that the lowest thermal resistance was achieved when the concentration of SiO_2/water nanofluid was 0.5 vol %. Therefore, the optimal concentration of SiO_2/water nanofluids was about 0.5 vol %.

The main reasons for the improvement or deterioration of heat transfer performance of nanofluids-PHPs were shown as follows: (1) Nucleation sites increased by nanoparticles: The nanoparticles attached to the inner surface of PHP and increased the nucleation sites of the inner surface, which was conducive to the bubble generation. (2) The thermal conductivity of nanofluids: Adding SiO_2 and CuO nanoparticles into distilled water would increase the thermal conductivity and the thermal conductivities of nanofluids increased with volume concentration (Kulkarni et al., 2006). The thermal conductivity of CuO nanoparticles was much higher than that of SiO_2 nanoparticles, as shown in Table 2. Thus, the thermal conductivities of CuO/water nanofluids were higher than that of SiO_2/water nanofluids at same concentration. (3) The dynamic viscosities of nanofluids: The dynamic viscosities of nanofluids increased with volume concentration (Meybodi et al., 2016).

Generally speaking, working fluids with high thermal conductivities and low viscosities are favorable for efficient heat transfer of PHPs.

The influence of nanofluids on the heat transfer performance of PHP was depended on the number of nucleation sites, thermal conductivities and dynamic viscosities of nanofluids. During the experiment, it was visually observed that the main flow pattern in the PHPs was slug flow at lower heat input (≤ 54.6 W). The contribution of sensible heat on the overall heat transfer was dominant in PHP with slug flow pattern as the main flow pattern (Groll and Khadekar, 2004; Khandekar et al., 2003). When the concentration of SiO_2/water nanofluids increased to 1.0 vol %, the dynamic viscosity of SiO_2/water nanofluid was too high and the high flow resistance prevented the motion of liquid and vapor plugs. Thus, the heat transfer performance of PHP with 1.0 vol % SiO_2/water nanofluid was worsened compared with that of distilled water-PHP. When the heat input increased (> 54.6 W), semi-annular and annular flow pattern were developed and visually observed in the experiment. With the increase of heat input, the heat was transferred mostly by evaporation of the liquid film and latent heat became dominant in the heat transfer (Groll and Khadekar, 2004; Khandekar et al., 2003). In this situation, nucleation sites number and thermal conductivities of working fluids were important to the heat transfer performance of PHPs. In addition, the dynamic viscosity of nanofluids decreased with the increase of temperature (Meybodi et al., 2016). The influence of dynamic viscosities weakened at higher heat input. Thus, the thermal resistances of PHP charged with 1.0 vol % SiO_2/water nanofluid was lower than those of distilled water-PHP at higher heat input (> 54.6 W).

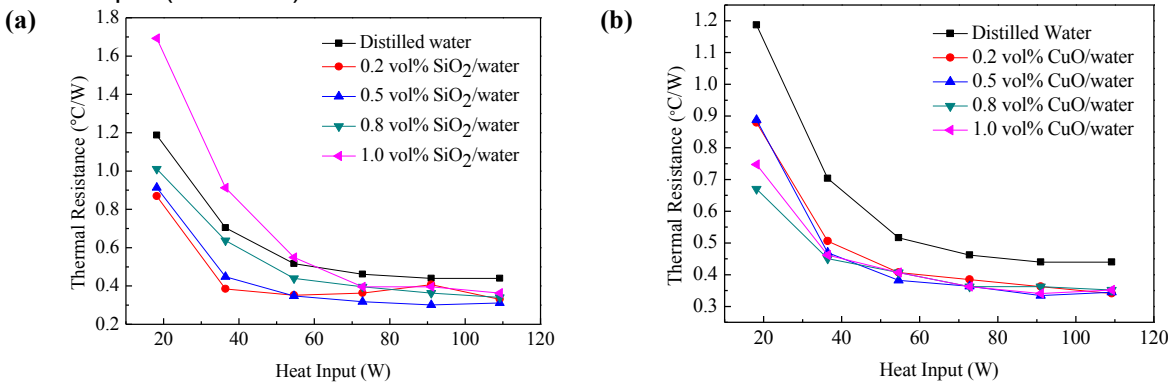

Figure 5: The thermal resistances of PHPs charged with different concentrations of (a) SiO_2/water nanofluids and (b) CuO/water nanofluids

3.2.2. The effect of different concentrations of CuO/water nanofluids on the heat transfer performance of PHP

Fig. 5(b) showed the thermal resistances of PHPs charged with different concentrations of CuO/water nanofluids. According to Fig. 5(b), it could be found that PHPs charged with different concentrations CuO/water nanofluids all showed lower thermal resistances compared with distilled water-PHP. The thermal resistance of CuO/water nanofluids-PHPs decreased with the increase of concentrations in the range of (0.2 - 0.8) vol %. However, the thermal resistances of PHP charged with 1.0 vol% CuO/water nanofluid was higher than those of PHP charged with 0.8 vol % CuO/water nanofluid. Therefore, that the optimal concentration of CuO/water nanofluids was about 0.8 vol %.

In addition, the thermal resistances of CuO/water nanofluids-PHPs and SiO_2/water nanofluids-PHPs were compared and it could be found that the thermal resistances of CuO/water nanofluids-PHPs were lower than those of SiO_2/water nanofluids-PHPs at same concentration because of higher thermal conductivities of CuO/water nanofluids. Therefore, the heat transfer enhancements of CuO/water nanofluids-PHPs were more remarkable.

3.3. The effect of nanoparticles sedimentation on the heat transfer performance of PHP

Sedimentation of nanoparticles was often inevitable in PHPs because of the nanoparticles aggregation. Fig. 6(a) and Fig. 7(a) showed the well dispersed 0.5 vol % SiO_2/water nanofluid and 0.5 vol % CuO/water nanofluids in PHP, respectively. After operation, the nanofluids in PHPs were kept standing for 3 days. Fig. 6(b) and Fig. 7(b) showed the sedimentations of SiO_2 nanoparticles and CuO nanoparticles after 3 days, respectively. As shown in Fig. 6 and Fig. 7, obvious

sedimentation of both SiO_2 nanoparticles and CuO nanoparticles could be seen. It was significant to investigate the influence of nanoparticles sedimentation on PHPs.

Fig. 8(a) and Fig. 8(b) showed the comparison of thermal resistances of PHPs charged with 0.5 vol % SiO_2/water nanofluid and 0.5 vol % CuO/water nanofluids before and after nanoparticles sedimentation, respectively. As can be seen in Fig. 8(a), the thermal resistances of the 0.5 vol % SiO_2/water nanofluid-PHP after nanoparticles sedimentation were slightly higher than those of well dispersed SiO_2/water nanofluid-PHP. The maximum increase of thermal resistance was 0.064 °C/W when heat input was 36.4 W. Similarly, as shown in Fig. 8(b), the thermal resistances of the 0.5 vol % CuO/water nanofluid-PHP after sedimentation were slightly higher than those of well dispersed CuO/water nanofluid-PHP. The maximum increase of thermal resistance was 0.079 °C/W when heat input was 18.2 W. In addition, the thermal resistances of SiO_2/water nanofluid-PHP and CuO/water nanofluid-PHP at concentration of 0.5 vol % were still lower than that of distilled water-PHP after nanoparticles sedimentation. According to the visual observation, the nanoparticles could disperse again in the working fluid after nanoparticles sedimentation except for a few nanoparticles would attach to the inner wall of PHP. Therefore, the influence of nanoparticles sedimentation on the heat transfer performance of PHPs was relatively small.

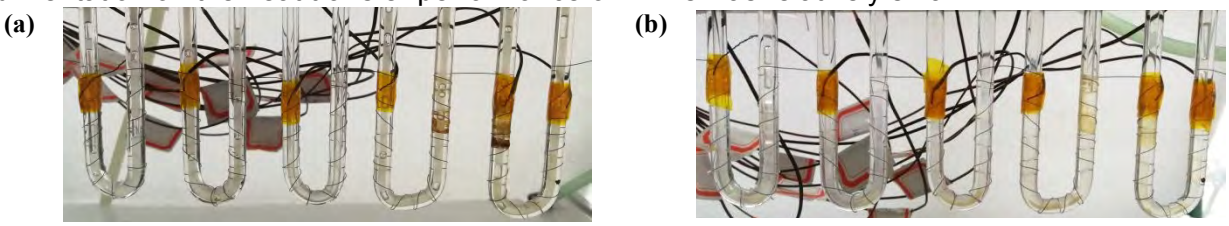

Figure 6: Photographs of 0.5 vol% SiO_2/water nanofluid in PHP (a) just charged; (b) after 3 days

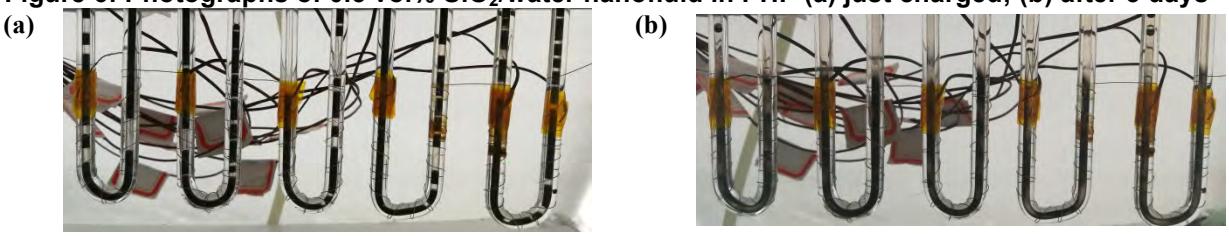

Figure 7: Photographs of 0.5 vol% CuO/water nanofluid in PHP (a) just charged; (b) after 3 days

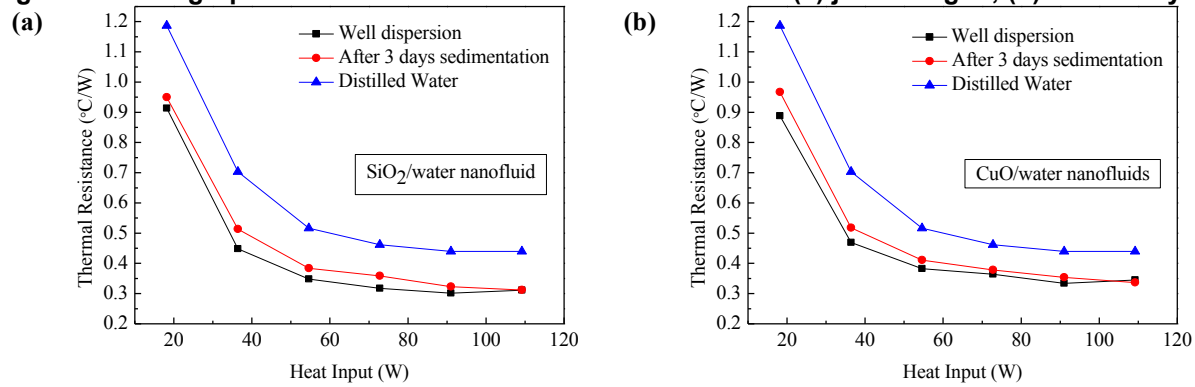

Figure 8: The thermal resistance of PHPs before and after sedimentation of nanoparticles (a) 0.5 vol % SiO_2/water nanofluid and (b) 0.5 vol % CuO/water nanofluid

4. CONCLUSIONS

In this paper, a visual experiment was conducted and the start-up performance and heat transfer performance of PHPs charged with different concentrations of nanofluids (SiO_2/water and CuO/water nanofluids) were compared with distilled water-PHP. The main conclusions were as follows:

(1) The start-up performance of PHPs charged with SiO_2/water nanofluids was worsened compared with that of distilled-water PHP, while CuO/water nanofluids had less effect on the start-up performance of PHP.

(2) PHPs charged with SiO_2/water nanofluids (0.2 vol %, 0.5 vol % and 0.8 vol %) and CuO/water nanofluids (0.2 vol %, 0.5 vol %, 0.8 vol % and 1.0 vol %) showed lower thermal resistances

compared with distilled water-PHP. The heat transfer performance of PHP charged with 1.0 vol % SiO_2/water nanofluids was worsened at lower heat input (≤ 54.6 W) while opposite at higher heat input (> 54.6 W). The influence of nanofluids on the heat transfer performance of PHPs was depended on the influence of nucleation sites, the thermal conductivities and the dynamic viscosities of nanofluids.

(3) The sedimentation of nanoparticles was observed in the experiment. The thermal resistances of PHPs charged with 0.5 vol % SiO_2/water nanofluid and 0.5 vol % CuO/water nanofluids before and after nanoparticles sedimentation were compared. The nanoparticles could disperse again in the nanofluids during the operation of PHPs and the influence of nanoparticles sedimentation on the heat transfer performance of PHP was relatively small.

ACKNOWLEDGEMENTS

This work has been supported by the Nation Natural Science Foundation of China (Grant No. 51576171), and Zhejiang Provincial Natural Science Foundation of China under Grant (Grant No. LZ19E060001).

NOMENCLATURE

P	electrical input power (W)	Subscript Greek symbols	
Q	heat input (W)	e	evaporation section
R	thermal resistance (°C/W)	c	condensation section
T	temperature (°C)		
φ	ratio of heat input to electrical input power		

REFERENCES

Agostini, B et al., 2007. State of the Art of High Heat Flux Cooling Technologies. Heat Transfer Eng., 28(4), 258 - 281.

Bergman, T.L et al., 2008. Fundamentals of Heat and Mass Transfer. 7th ed., John Wiley& Sons, USA, 4-5.

Godson, L et al., 2010. Enhancement of Heat Transfer Using Nanofluids—an Overview. Renewable Sustainable Energy Rev., 14(2), 629-641.

Groll, M et al., 2004. State of the Art on Pulsating Heat Pipe, Proceedings of ICMM. New York, USA, 2318.

Han, X et al., 2016. Review of the Development of Pulsating Heat Pipe for Heat Dissipation. Renewable Sustainable Energy Rev., 59, 692-709.

Hwang, Y et al., 2007. Stability and Thermal Conductivity Characteristics of Nanofluids. THERMOC ACT, 455(1-2), 70-74.

Karthikeyan, V.K., 2014. Effect of Nanofluids on Thermal Performance of Closed Loop Pulsating Heat Pipe. Exp. Therm. Fluid Sci., 54, 171-178.

Khandekar, S et al., 2003. Understanding Operational Regimes of Closed Loop Pulsating Heat Pipes: an Experimental Study. Appl. Therm. Eng., 23, 707-719.

Khandekar, S et al., 2003. Closed Loop Pulsating Heat Pipes Part B: Visualization and semi-empirical Modeling. Applied Thermal Engineering, 23(16), 2021-2033.

Kulkarni, D.P et al., 2006. Temperature Dependent Rheological Property of Copper Oxide Nanoparticles Suspension (Nanofluid). J. Nanosci. Nanotechnol., 6(4), 1150-1154.

Meybodi, M.K et al., 2016. A Novel Correlation Approach for Viscosity Prediction of Water Based Nanofluids of AL2O3, TIO2, SIO2 and CuO. J. Taiwan Inst. Chem. Eng., 58, 19-27.

Myers, P.D et al., 2016. Nitrate Salts Doped With CuO Nanoparticles for Thermal Energy Storage With Improved Heat Transfer. Appl. Energy., 165, 225-233.

Nazari, M.A et al., 2018. Experimental Investigation of Graphene Oxide Nanofluid on Heat Transfer Enhancement of Pulsating Heat Pipe. Int. Commun. Heat Mass Transfer., 91, 90-94.

Touloukian, Y.S et al., 1970. Thermophysical Properties of Matter - the TPRC Data Series. Thermal conductivity: Nonmetallic Solids, Vol. 2. New York, IFI/Plenum.

Manuscript ID: 551
DOI: 10.18462/iir.icr.2019.0551

Direct numerical analysis of pin geometries for magnetocaloric regenerators

Ibai MUGICA[(a)], Sebastien PONCET[(a)], Jonathan BOUCHARD[(b)]

[(a)] Université de Sherbrooke, Sherbrooke, J1K 2R1, Canada, i.mugica@usherbrooke.ca

[(b)] Laboratoire des Technologies de l'Energie, Shawinigan, G9N 7N5, Canada

ABSTRACT

This paper studies the performance of various pin regenerator geometries for rotatory magnetocaloric refrigerators. This is done by directly simulating the fundamental phenomena that takes part in magnetic refrigeration: magnetic, fluid and thermal fields. After a separate analysis, the full 3D Active Magnetic Regenerator (AMR) cycle is simulated for a selected group of geometries. Then, conclusions are drawn taking into consideration the separately computed phenomena and the performance of the AMR. The main conclusion is that an increased tortuosity increases the pressure losses and heat transfer of the surges but decreases the conduction losses. The latter can be directly linked to an increased performance of the AMR.

Keywords: Magnetic refrigeration, direct simulation, Active Magnetocaloric Regenerator, demagnetization, tortuosity.

1. INTRODUCTION

Nowadays commercial refrigeration technology is based on transferring heat by exploiting a liquid-gas phase transition. Magnetic refrigeration presents a relatively new way to transport heat by employing a magnetic phase transition of the refrigerant. The refrigerant of magnetic regenerators is solid, and during its operation is kept in the vicinity of its Curie temperature (T_C). This temperature defines the boundary between ferro- and paramagnetic states and crossing them, suddenly changes the thermodynamic properties of the solid refrigerant. Because the refrigerant is solid (usually a rare earth), there are no issues concerning atmospheric pollutants or noise from the compression-expansion stages. The phase transition of magnetocaloric refrigerants is triggered by an external magnetic field. Paramagnetic states are defined by having an atomic arrangement that produces no resultant remanent magnetic field in the solid crystals. This is due to the relatively random orientation of the atomic magnetic moments. By applying an external magnetic field, the disordered magnetic moments align, and in an adiabatic environment, the entropy associated to the magnetic state becomes thermal entropy (the temperature increases, see Eq. (1)):

$$s_{total} = s_{mangetic} + s_{thermal} \quad \text{Eq. (1)}$$

This happens vice versa, so if a Magneto-Caloric Material (MCM) is ferromagnetic under the influence of and external magnetic field, when the applied magnetic field is retrieved, the MCM cools down. Most published prototypes attempt to introduce this heat exchange in a Brayton-like thermodynamic cycle (see Kitanovski et al. (2015)) with the help of a Heat Transfer Fluid (HTF) to transport the heat to the sink and source. The steps of the thermodynamic cycle have traditionally been the following: 1. Magnetization 2. Fluid surge to the hot sink 3. Demagnetization 4. HTF surge to the cold source. The work that drives the temperature change of the MCM (the Magneto-Caloric effect, MCE), usually comes from the dipole forces of (de)magnetizing the MCM regenerator with a permanent magnet:

$$F_{dipole} = \int (\boldsymbol{M} \cdot \nabla)\boldsymbol{B} dV \qquad \text{Eq. (2)}$$

The relatively low heat exchanged in these magnetic phase transitions, and the large inertia of the required permanent magnets, have led many scientists to develop rotatory refrigerators. These machines have the MCM and the permanent magnet arranged in coaxial cylinders (or disks). That way the frequency of operation can be increased (increasing the power of the machine) and the inertia of the moving part evens out the peaks and valleys of the input torque. A thorough review of the developed rotatory prototypes can be found in Yu et al. (2010).

With a rotatory configuration in mind, it is yet unknown which would be an optimal geometry for the MCM regenerator. Indeed, a relatively high magnetic field is needed to trigger the MCE (1T~2T), and samples suffer from a demagnetization of geometrical origin. This must be coupled with the requirements of a fast heat transfer between the MCM and the HTF, in order to be able to increase the operational frequency. Moreover, the viscous losses are largely influenced by the regenerator geometry. Many authors have numerically investigated the performance of such regenerators by varying global geometrical parameters like the porosity of a particle bed ($\varepsilon = V_{fluid}/V_{solid}$) or the plate thickness and spacing. Most published regenerators are made of plates or packed beds. Generally, when the hydraulic diameter of those porous mediums increases, the cooling power increases in detriment of the efficiency. However, most of these numerical studies have employed averaged correlations to characterize underlaying physical phenomena. This paper tries to tackle the question of optimum performance by directly simulating the three physical phenomena that coexist in a magnetic regenerator: magnetic, flow, and thermal field. In addition, a yet unexplored geometrical parameter is analyzed: the tortuosity of the fluid flow.

2. NUMERICAL CODE

The physical phenomena that takes part in the simulations involved in this study was described and validated in detail by Mugica et al. (2018). The magnetostatic field was computed by a magnetic scalar potential, and different domains had a constant relative magnetic permeability. The fluid flow as computed solving the Navier-Stokes equations with a constant viscosity. The transport of thermal energy was computed with the flow calculated by Navier-Stokes, and a source term in the solid domain that represents the MCE:

$$\mu_0 T \left.\frac{\partial M(H,T)}{\partial T}\right|_H \frac{\partial H}{\partial t} \qquad \text{Eq. (3)}$$

The solver uses the finite volume method to solve the involved partial differential equations. All differential terms were discretized by second order accurate numerical schemes.

3. RESULTS AND DISCUSSION

The regenerators studied in this paper are composed of clusters of pins, oriented parallel to the applied magnetic field, and perpendicular to the HTF flow. This configuration seeks to minimize the shape demagnetization of the MCM. Fig. 1 and Table 1 summarize the dimensions of the cross-sections of those pins.

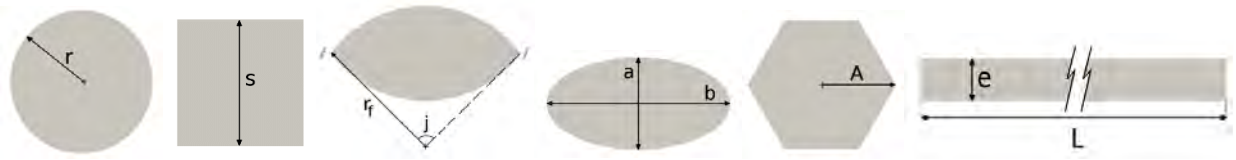

Figure 1: Description of the simulated pin cross-sections. From left to right: circle, square, foil, ellipse, hexagon, and plate.

Table 1. Values of the geometrical parameters of Fig. 1. All pin cross sections are $1mm^2$.

r	0.5642mm	**a**	0.7979mm
s	1mm	**b**	1.5958mm
r_f	1.12mm	**e**	0.25mm
j	106.26deg	**L**	4mm
A	0.6204mm		

In addition to the different cross-sections, two pin arrangements were tested: straight and staggered (see Fig. 2). Straight clusters have the center of the pins aligned to each other in both cartesian directions. Staggered clusters have alternate columns of pins aligned to the interstice of the neighboring pins. The size of the interstices was always the same for both Cartesian directions, for all ε cases.



Figure 2: On the left, straight and staggered arrangements of pins. On the right, schematic view of the tested regenerators. The HTF flows parallel to L.

Table 2. Dimension of the simulated regenerators (see Fig. 2). All regenerators have 24 pins, and H=4mm for all cases.

	W [mm]			L [mm]		
ε	0.5	0.625	0.75	0.5	0.625	0.75
Circle and Square	11.314	13.064	16	4.243	4.899	6
Foil	12.426	14.945	19.22	3.863	4.282	4.995
Ellipse	12.846	15.385	19.686	3.737	4.16	4.877
Hexagon	10.668	12.416	15.349	4.5	5.155	6.255
Straight Plate	12	16	24	4	4	4
Staggered Plate	12.67	13.849	13.849	3.788	4.891	6.932

In the following subsections, the mentioned physical phenomena are simulated and analyzed separately. The final subsection will verse on the 3D direct numerical simulation of some of the presented pin regenerators. All solvers were presented and validated by Mugica et al. (2018).

3.1. Demagnetization

The total demagnetization of the presented geometries (Fig.1 and Table 2) cannot be analytically calculated (Morrish (2001)). Instead, magnetostatic numerical simulations of such pin clusters were ran. Martinez-Huerta et al. (2013) presented Eq. (3), which approximates the total demagnetization

of a porous medium through the demagnetization of its particles (N_{self}) and the macroscopic bed (N_{macro}):

$$N_T \approx N_{self} + (N_{macro} - N_{self})(1 - \varepsilon) \quad \text{Eq. (4)}$$

The simulated clusters were 10mm high, had an applied magnetic field of 1T, and were made infinite by symmetry boundary conditions in the W and L directions (Fig. 2). A Grid Sensitivity Analysis (GSA) determined a minimum surface cell size of $6\mu m$ for the pins. The simulation of isolated pins gave $N_{self} \approx 0.0595$ for all cases.

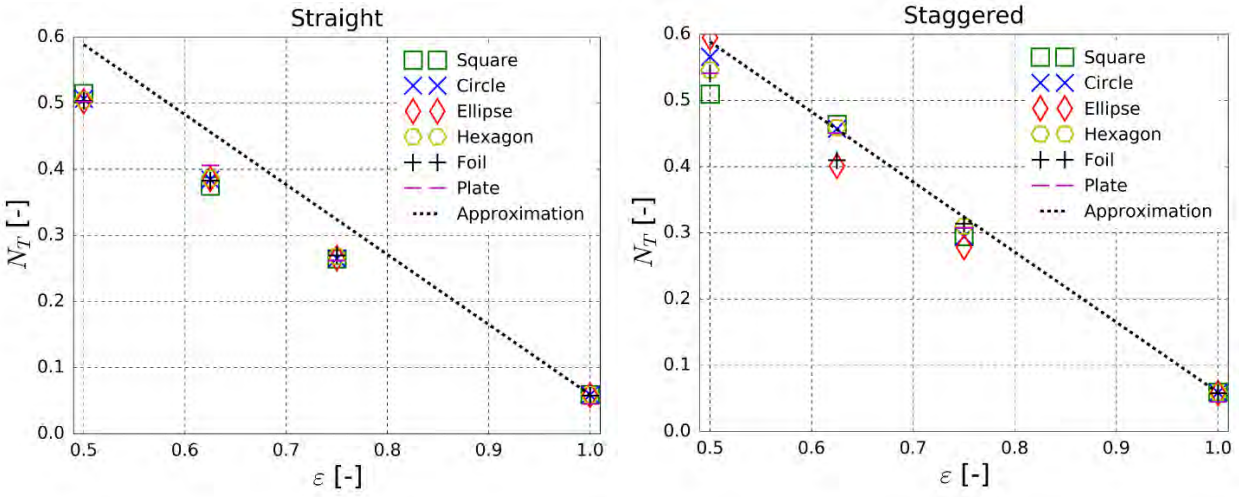

Figure 3: Demagnetization of clusters of 10mm high pins of Fig. 2. The demagnetization of the infinite macroscopic bed was set to $N_{macro} = 1$.

Fig. 3 shows the computed demagnetization of clusters of different ε and $\mu_r = 2$ (which is similar to the one of Gadolinium (Gd), see Mugica et al. (2018)). Staggered clusters show a slightly higher demagnetization. The maximum discrepancy with Eq. (3) is around 0.1 for the straight clusters of $\varepsilon = 0.5$. All in all, the tendency seems quite linear, so Eq. (3) might be a good approximation for packings of high ε and low μ_r.

3.2. Pressure Head

Fig. 4 shows the pressure head of the regenerators presented in Table 2, calculated through a 2D simulation. Fluid velocity and thermal GSA yielded a minimum cell size of $9.375\mu m$ for the fluid domain and $12.5\mu m$ for the solid domain. Fluid and solid domain properties can be found in Table 3.

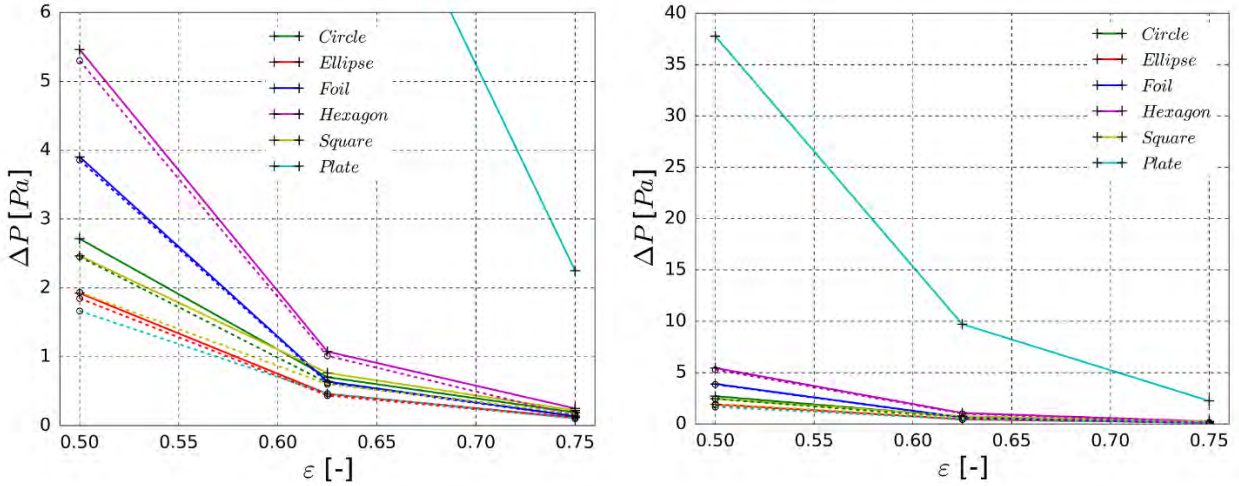

Figure 4: Pressure head of the geometries of Table 2, for the operational point of $f = 1Hz$ and $\varphi = 0.5$. Lines were drawn for a better visualization. Continuous lines refer to staggered cases and discontinuous to straight cases.

Table 3. Physical properties of the simulated fluid and solid domains.

	$\rho\ [kg/m^3]$	$c\ [J/(kg \cdot K)]$	$\lambda\ [W/(m \cdot K)]$	$\mu_f\ [mPa \cdot s]$
Fluid	981	4330	0.52	1.6
Solid	7900	variable, see Mugica et al. (2018)	10.5	-

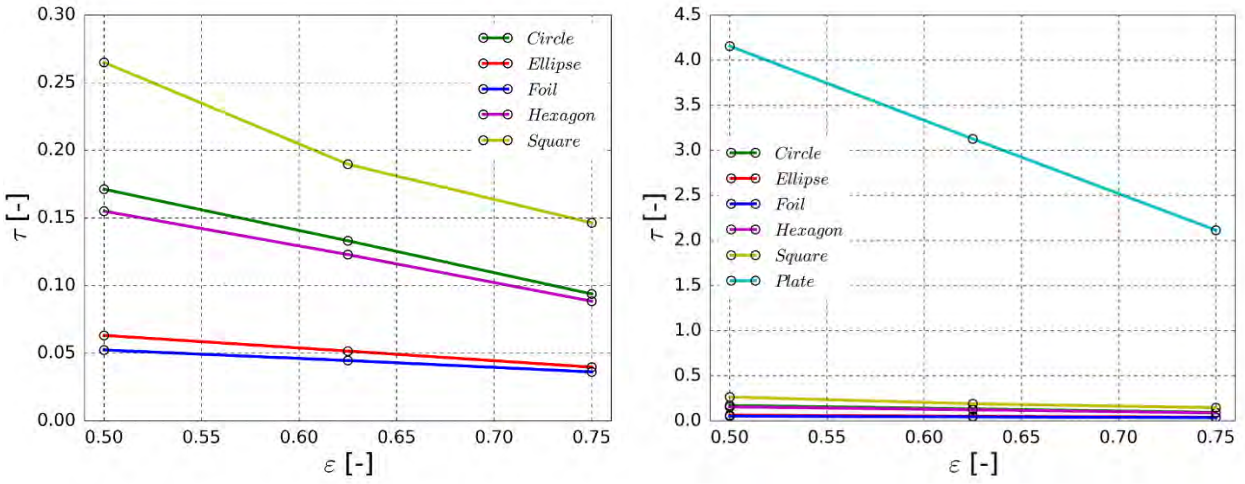

Figure 5: Tortuosity (see Eq. (4)) of the staggered regenerator geometries of Table 2. The left graph shows the lower tortuosity cases of the right side graph.

$$\tau = \frac{\int tr(l)dl}{L} - 1 \qquad \text{Eq. (5)}$$

$$\varphi = \frac{U_{inlet} A_{inlet} \rho_f c_f}{4 f V_s \rho_s c_s} \qquad \text{Eq. (6)}$$

$$f = \frac{1}{4 t_f} \qquad \text{Eq. (7)}$$

Fig. 5 shows the tortuosity (τ, Eq. (4)) of the staggered regenerators of Table 2. The tortuosity was calculated as an average of 10^3 streamlines that were longer than the computational domain (L, see Fig. 2). From Fig. 4 and 5 it can be concluded that the larger the tortuosity, the larger the pressure pressure losses of the staggered configurations.

3.3. Heat transfer

2D thermal simulations of the cases presented in the last section were ran. The initial temperature gradient was linear, and the temperature span was 2K. An additional 1.5K was added to the MCM domain (Gd), to mimic the MCE. The simulations were done in two stages. First one had no HTF flow. The second one started from the temperature field of the first one and had the HTF flow of the last section 2.2. Both stages lasted for 0.25s. Fig. 6 shows the average normal temperature gradient in the fluid flow, for some of the geometries of Fig. 1.

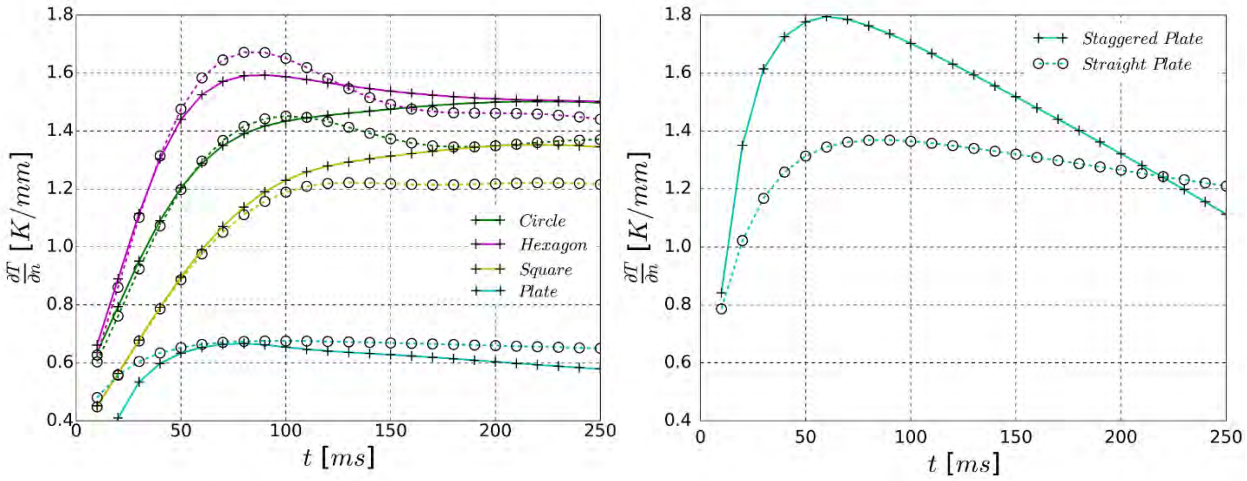

Figure 6: Evolution of the average $\frac{\partial T}{\partial n}$ in the fluid domain at the surface of the pins. Left had $\varphi = 0.5$ and right $\varphi = 1.5$. Continuous lines refer to staggered cases and dashed lines to straight cases.

The heat transfer between phases depicted in Fig. 6 shows some improvement for the staggered cases of higher tortuosity.

Another set of simulations was ran to check the conduction losses of each of the presented geometries. This was like the first stage presented earlier, but without the supplementary 1.5K of the solid domain. Fig. 7 shows how there is not much difference for the staggered cases with low tortuosity. However, the staggered plates (a case with noticeably larger τ) shows a great improvement.

$$S_{cond} = \int \frac{\lambda_f}{T_f^2}\left(\frac{\partial T_f}{\partial x}\right)^2 + \frac{\lambda_s}{T_s^2}\left(\frac{\partial T_s}{\partial x}\right)^2 dt \qquad \text{Eq. (8)}$$

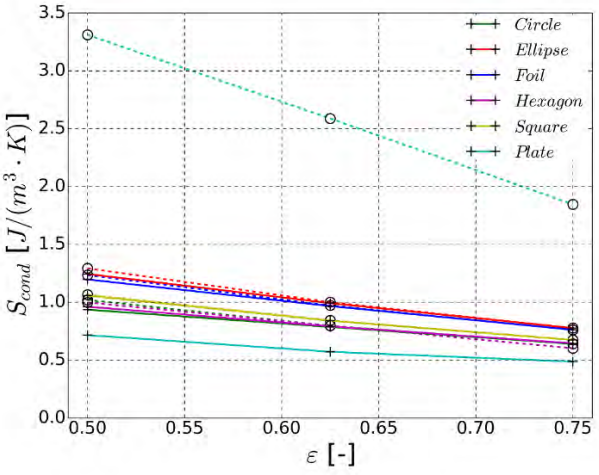

Figure 7: Generated entropy by conduction, see Eq(8).

3.4. AMR simulation

Due to the heavy cost of computation, only the AMR cycle of a selected group of geometries was calculated: staggered plates, staggered circles, and straight plates. The applied magnetic field was 1T at the magnet boundary with an airgap of 2mm. The magnetic field swiped through the positive direction of r (Fig. 8) at constant velocity, determined by the frequency of operation (1Hz). The regenerator of interest (dark) was accompanied by neighboring half regenerators (grey) connected by a periodic boundary condition to mimic the magnetic field of a rotatory regenerator (see Fig. 8).

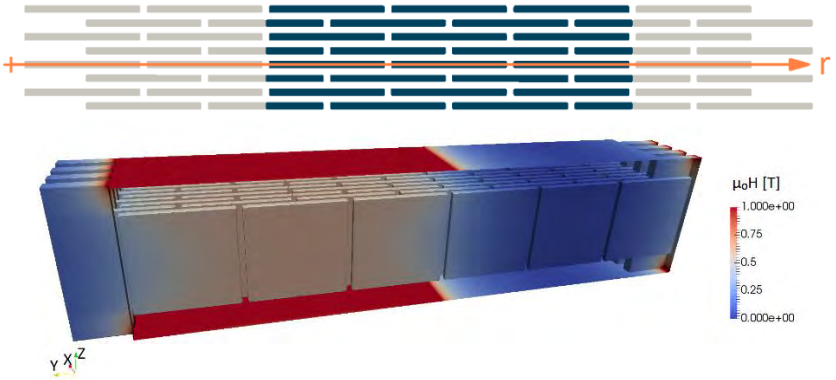

Figure 8: Staggered plate AMR regenerator case of $\varepsilon = 0.5$. Up, dark plates represent the part that takes place in the AMR simulation. Down, applied magnetic field [T].

The radius of the rotatory machine is assumed to be much larger than the height of the pins (4mm), so curvature effects were neglected. Fig. 9 shows the temperature span of the regenerator (ΔT_{reg}), working at zero cooling load, and a constant temperature of 300K at the cold heat exchanger. Staggered plates show the best performance. This is believed to be related to the decreased conduction losses of Fig. 7. Indeed staggered and straight plates have a similar demagnetization (Fig. 3) and similar Nu at $\varphi = 0.5$ (Fig. 6), but very different ΔT_{reg} at $\varphi = 0.5$ in Fig. 9. Staggered circles and straight plates show a decreasing ΔT_{reg} with an increasing ε. This means that, for those cases, the decreased heat transfer of higher porosities overwhelms the decrease in demagentization and conduction losses.

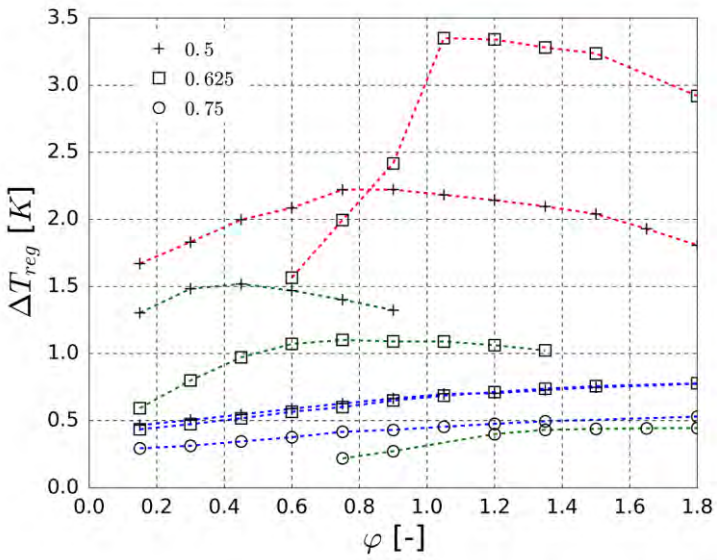

Figure 9: Temperature span of the AMRs at zero cooling load for staggered plates (red), staggered circles (green), and straight plates (blue). Symbols represent different porosities.

4. CONCLUSIONS

Various pin AMR geometries have been studied by directly simulating the physical phenomena they usually undergo. Tortuosity acts like a local velocity multiplier, due to the increased length the fluid needs to travel to get to the other side of the regenerator (at the same mass flowrate). This increases both the pressure head of the regenerator, and the Nusselt number (specially for high φ cases). The highest tortuosity cases also present a distinctly lower conduction losses, which can be directly linked to a higher ΔT_{reg}. Furthermore, higher τ cases favor higher porosities, meaning that the benefit of the reduced demagnetization and conduction losses of high τ and ε cases, outgrows their diminished Nusselt number.

ACKNOWLEDGEMENTS

This work is part of the NSERC chair on industrial energy efficiency established at Université de Sherbrooke in 2014 with the support of Hydro-Québec, Ressources Naturelles Canada (CanmetENERGIE), and Rio Tinto Alcan that are gratefully acknowledged for their financial support. The calculations have been performed on the Mammouth paralléle 2 cluster of Compute Canada, which is also here gratefully acknowledged.

NOMENCLATURE

ε	Porosity (-)	f	Frequency (Hz)
Gd	Gadolinium	*HTF*	Heat Transfer Fluid
N	Demagnetization factor (-)	*Nu*	Nusselt number (-)
MCE	Magneto-Caloric Effect	*MCM*	Magneto-Caloric Material
S	Specific entropy ($J \cdot m^{-3}K^{-1}$)	τ	Tortuosity (-)
T	Temperature (K)	t	Time (s)

REFERENCES

Kitanovski, A., Tušek, J., Tomc, U., Plaznik, U., Ozbolt, M., Poredoš, A., 2015. Magnetocaloric Energy Conversion. Springer, Switzerland.

Martinez-Huerta, J. M., Medina, J. D. L. T., Piraux, L., Encinas, A., 2013. Configuration dependent demagnetizing field in assemblies of interacting magnetic particles. Journal of Physics: Condensed Matter, 25 (22), 226003.

Morrish, A. H., 2001. The Physical Principles of Magnetism. John Wiley & Sons, Massachusetts, USA.

Mugica, I., Poncet, S., Bouchard, J., 2018. An open source DNS solver for the simulation of active magnetocaloric regenerative cycles. Applied Thermal Engineering 141, 600 – 616.

Yu, B., Liu, M., Egolf, P. W., Kitanovski, A., 2010. A review of magnetic refrigerator and heat pump prototypes built before the year 2010. International Journal of Refrigeration 33 (6), 1029 – 1060.

Manuscript ID: 552
DOI: 10.18462/iir.icr.2019.0552

Alternatives to high GWP refrigerants in refrigeration & air-conditioning applications

Thomas MICHINEAU[(a)], Olivier CALMELS[(a)], Stéphanie BARRAULT [(b)], Denis CLODIC[(c)]

[(a)] Cemafroid sas, Fresnes, 94266, France, e-mail : thomas.michineau@cemafroid.fr
[(b)] CITEPA, Paris, 75010, France, e-mail : stephanie.barrault@citepa.org
[(c)] EReIE SAS, Palaiseau, 91120, France, e-mail : denis.clodic@ereie-sas.fr

ABSTRACT

This paper presents an overview of the refrigerants in use in France within the European framework of phase down of HFC quantities put on the European market defined by the F-gas regulation, (UE) 517/2014. Alternative options are analysed by application sector: domestic, Food-industry, retail and tertiary applications, transport refrigeration, mobile air conditioning, chillers and air conditioning equipment. The methodological approach of this study consists first in describing refrigerants used according to the specifications of each application sector. Secondly, authors have summarized applicable regulations and standards which dramatically impact the possible use of available technical options. Authors provide, in a synthetic manner, the most commonly proposed alternatives per application tacking trade-offs between the following key parameters: GWP, flammability and or toxicity, volumetric capacity, cost, availability on the market and energy efficiency. Analyses are based on a literature review but also on end user, equipment manufacturer and refrigerant producer interviews. Finally, the authors present limits and levers to the development of alternatives, focusing on regulatory constraints and need of specific training.
Keywords: Refrigeration, GWP, Alternatives, COP, Energy Efficiency, fluorinated gases, HFC.

1. INTRODUCTION

In the context of the review and the enter into force of the F-Gas European regulation (EU n° 517/2014), a lot of refrigerants have been developed, new technologies have been proposed by producers and manufacturers. How to compare them? GWP is not the only issue. Using low GWP refrigerants can impact the cost of the equipment but also the safety or the energy consumption. Choices are especially difficult for end-users who have to comply with several regulations and need to use efficient equipment, taking into account the costs.
The authors of this paper carried out two studies funded by the AFCE (a French association acting for a sustainable use of refrigerants) in order to assess the alternatives to high GWP HFCs by application for the main refrigeration and air-conditioning sectors, based on literature and expert interviews. They propose to compare, for each referent application, the different alternative solutions by using a six-criteria radar-type indicator. In the second study, the progresses of previously identified options have been analysed. There was also a focus on the impact of refrigerant on the energy efficiency of equipment and on the strong regulatory constraints, which are presented in this paper.

2. OBJECTIVES

The objectives of the study are:

- To list and describe, from a thermodynamic point of view, the available refrigerants, by application, to replace traditionally used high-GWP HFCs: hydrocarbons, ammonia, CO_2, pure HFOs, mixtures composed of HFCs and HFOs or HC;
- To identify the linked technical options but also the technological developments related to the use of these alternatives;
- To analyse the advantages and disadvantages of each option, particularly in terms of energy consumption;
- To explain the standards and regulations linked with the use of the proposed alternatives;

- To make an inventory of existing training courses and identify the needs for the implementation of alternatives.

3. METHODOLOGY

For the purposes of this study we used the segmentation used in the UNEP RTOC reports, based on eight major areas of application: Domestic refrigeration, Commercial refrigeration, Refrigerated transport, Industrial refrigeration (Agri-food Industries), Air conditioning systems, Chillers, Heat pumps and Mobile air conditioning.
A summary sheet has been established for each selected application in the segmentation resulting from the analysis of the user sectors of refrigeration and air conditioning. Each summary sheet consists of 3 parts.
The first part is a description of the reference system. it gives information for each relevant application such as the most commonly used high-GWP HFC, the refrigerant bank in France, a summary of the regulations applicable to the sector in France and in Europe.
The second part presents technical alternatives for new installations. A multicriteria indicator graphically represents 6 technical and economical parameters in order to highlight the advantages and disadvantages of each option.

Table 1. Notation of criterion

Criteria	Indicators						
	0	1	2	3	4	5	6
GWP	Very low (<10)		Low (<150)	Medium (<300)	Quite high (<750)	High (<1500)	Very high (>1500)
Energy Efficiency	Excellent			Medium		Bad	
Safety	Class A1		Classes A2L and B2L		Classes A2 and B2		Classes A3 and B3
Cost	Low			Medium		High	
Availability	Mature option or widely available refrigerant			Several pilots in France or in other countries		Laboratory tests or foreseeable refrigerant shortage	
Volumetric capacity	Sufficient			Medium		Insufficient	



A score of 0 to 6 is assigned to each of the 6 selected technical and economical parameters. The "0" is the best score that can be awarded, and the "6" the lowest. On these "radars" a small surface therefore corresponds to an interesting option. The rating criteria are as follows.

4. REGULATION AND STANDARD STATE OF THE ART

Since its entry into force on January 1st, 2015, the European Regulation (EU) 517/2014 called "F-Gas" has introduced a progressive reduction of the quantities of HFCs authorized to be sold on the European market as well as sectoral bans of use, for new equipment and for the maintenance of refrigeration installations. As a result, the regulation and the use made of their quotas by HFC producers have strongly constrained the market. At the same time, the regulatory and normative framework is evolving rapidly (Figure 2). Ecodesign regulations impose increasingly ambitious

targets, in terms of energy efficiency, for a certain number of equipment in the refrigeration and air conditioning sectors. The “product” standards (60335 series) impose charge limits and warning requirements for flammable refrigerants. The standard EN 378, 2017 version, updates the safety and environmental requirements, integrates the new refrigerant category A2L and introduces new indexes for the calculation of limit charge and the notion of risk analysis throughout the installation lifecycle. Finally, the French regulation concerning fire safety in public buildings prohibits the use of flammable refrigerants to date, which is a limit for the development of low-GWP alternative options.

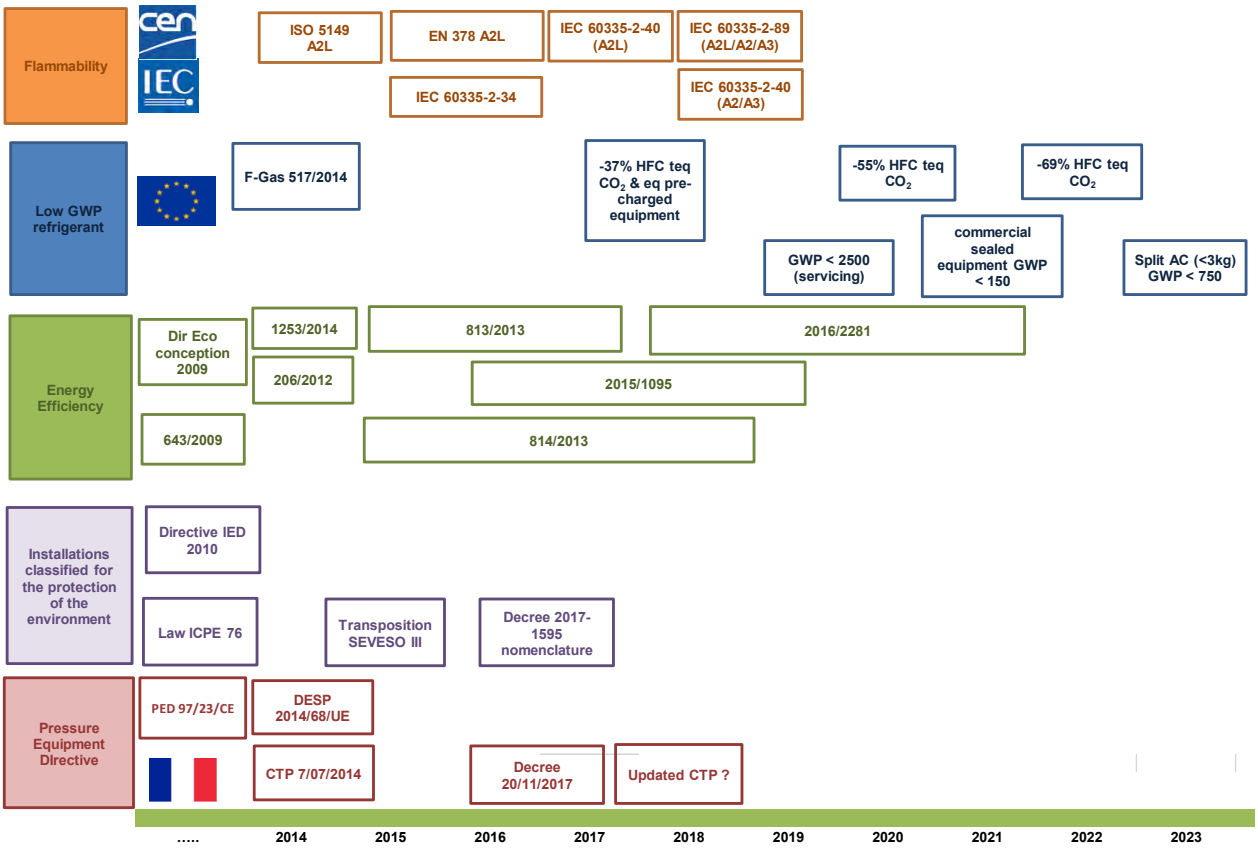

Figure 2. Schedule of entry into force of regulations and standards

5. REFRIGERANT SUBSTITUTES

The study presents the substitutes currently available for each of the 3 main refrigerants (R-134a, R-404A and R-410A) by distinguishing between retrofit substitutes and long-term substitutes for new installations or equipment.
According to the 2016 refrigerant inventory analysis (*Barrault, 2016*), those 3 refrigerants represent more than 85% of the refrigerant bank in France in 2016.

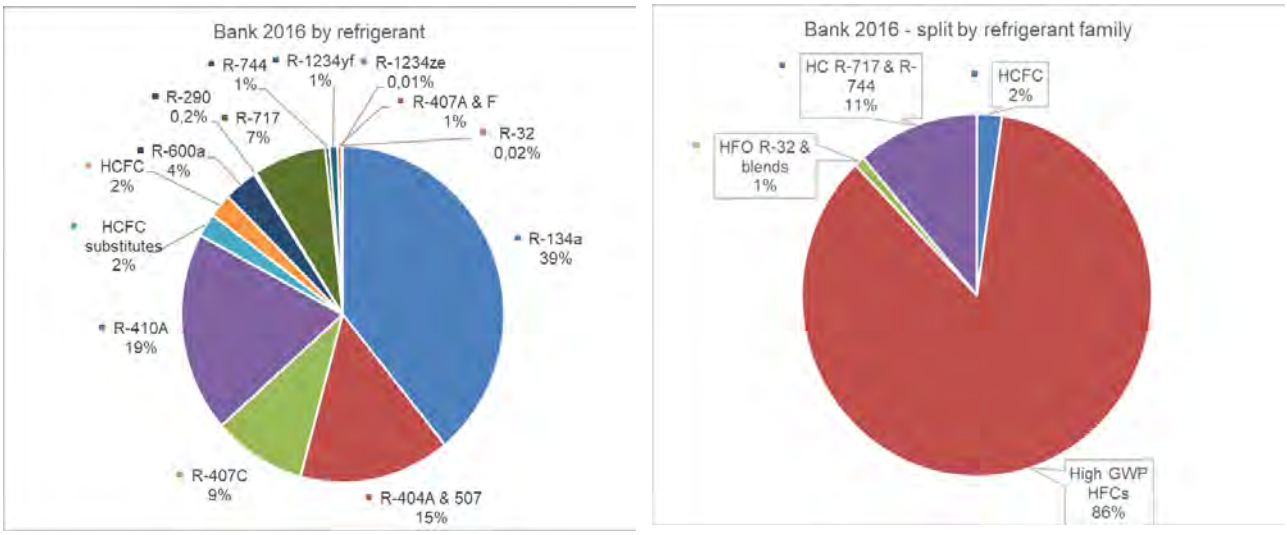

Figure 3. 2016 refrigerant bank – all sectors

5.1. R-134a and its substitutes

R-134a substitutes are different depending on applications and their use started at very different dates.

Table 2. Data on candidates to R-134a replacement

Standardized name	Compositions	GWP	Safety Class	T critical and T normal boiling *(glide)*	Vol. capacity relative to R-134a	COP relative to R-134a COP
R-134a	-	1430	A1	TC = 101°C TNe = -26°C	1	1
R-600a	-	3	A3	TC= 134.6°C TNe =-11°C	1	1,1
R-1234yf	-	4	A2L	Tc = 94.7°C TNe= 29.5°C	0.98	1
R-1234ze(E)	-	7	A2L	TC = 109.6°C TNe= -19°C	0.89	1.07
R-451A et B	R-1234yf / R-134a 89.8 /10.2 et 88.8/11.2	149 164	A2L	TC = 95.3°C TNe=-30.8/ -30.5°C TNe= -31/ -30.6°C	-	-

The replacement of R-134a by isobutane (R-600a) started as soon as 1996 and was extremely fast, once the maximum charge of 150 g and safety measures for domestic refrigeration were taken.
The main application of R-1234yf to replace R-134a is mobile air conditioning. Given the technical difficulties due to the very high CO_2 pressures, the increased costs and the uncertainty of maintenance possibilities in a global market, the choice of R-1234yf which, from the point of view of implementation, required minor adaptations without change of component costs, has been made. Otherwise, for commercial refrigeration applications, R-1234yf is a refrigerant with thermodynamic characteristics and energy performance very close to or even slightly higher than R-134a.
For centrifugal chillers several manufacturers already sell centrifugal units with R-1234ze (E) to replace R-134a. This replacement assumes specific developments since the volumetric cooling capacity of R-1234ze (E) is slightly more than 10% lower than R-134a. Centrifugal unit manufacturers announced gains in energy efficiency of 7 to 10%.

In applications where the equipment value is high and its lifetime long (typically 10 to 20 years), the retrofit of R-134a can be interesting. This is particularly the case of volumetric chillers. R-513A and R-450A are two A1 refrigerants and with GWP values of 631 and 603 respectively. Peer-reviewed publications show that those refrigerants are "drop-in" refrigerants and that the energy performances are superior to those of R 134a.

5.2. R-404A and its substitutes

Several R-404A replacement refrigerants are already on the market.
Propane (R-290) is used by a number of stand-alone display case manufacturers, this equipment is designed with a fully welded circuit. The increased use of R-290 with the higher level of A3 refrigerant charges as defined in EN 378 standard. R-454C blends and R-455A with a GWP lower than 150 are long-term replacements for R-404A. These refrigerants show test results with energy efficiency 10% higher than R-404A on refrigerated cabinets. This has to be confirmed for other applications.
CO_2 (R-744) replaces R-404A either only at the low temperature where it feeds display cases or cold freezing rooms or at both temperature levels (frozen and fresh products); the operation is then in transcritical cycle.
Replacement refrigerants of R-404A used in retrofit are all non-flammable refrigerants (A1). Indeed, it is not possible to retrofit to A3 or A2L flammable refrigerant because the equipment is not designed for. As a result, all intermediate refrigerants include R-125 to neutralize the flammability of A2L components. The GWP of R-125 being 3500, all these refrigerants have a GWP greater than or equal to 1400, which is objectively a GWP gain of more than a factor 2 with respect to R-404A but which is only a transient option to extend the equipment lifetime, in commercial refrigeration, in industrial process refrigeration and in refrigerated transport.

5.3. R-410A and its substitutes

For the replacement of R-410A in air conditioning, replacement refrigerants must meet very strict criteria for both volumetric refrigeration capacity and energy efficiency.
The current trend for large companies is clearly to use replacement refrigerants that have energy performance and volumetric refrigeration capacity equal to or greater than R-410A. As shown in the table below, those candidates are R-32 and mixtures containing more than 65% R-32 (R-452B and R-454B). The first R-32 units are currently marketed in Europe and since 2016 in Japan and Southeast Asia.
From a thermodynamic point of view, R-290 is more a substitute for R-22 than for R-410A, with a volumetric cooling capacity 10% lower. From an energy point of view, the properly implemented R-290 presents an energy efficiency equal to or slightly higher than R-410A. It is marketed in Europe in small "stand-alone" equipment and in individual "splits" air-conditioning systems in China and India; however, due to its high flammability (A3), it is not adopted as an option by major international manufacturers.
The replacement of R-410A by R-32 or mixtures with high R-32 content raises long-term issues because of the R-32 GWP of 675 kg CO_2 eq. The publication of Pham, (*Pham, 2016*) poses the possible tracks. The substitution by CO_2 raises questions of technological developments and costs that seem insurmountable considering the energy penalty that the transcritical cycle represents for the typical conditions of use of air conditioners, that is to say for outdoor temperatures above 25°C and up to 50°C.
The known HFOs (R-1234yf and R 1234ze (E)) cannot be used currently given a volumetric cooling capacity of 40% lower than that of R-410A. Mixtures with GWP <150 limit the R-32 content to about 20%. Developments of new compressors and circuits for such mixtures are needed.
Publications and technological developments will need to be carefully monitored to identify what would be the new routes for the use of GWP<150 refrigerants suitable for stationary air conditioning systems.

6. ALTERNATIVES PER APPLICATION / SEGMENT

The analysis of replacement options is done by application sector and concerns, on the one hand, new installations and, on the other hand, installations in operation for which the retrofit or drop-in options are more limited.
For domestic refrigeration, R-600a is now the only refrigerant used in Europe in refrigerators and freezers, and now achieves the A ++++ label in terms of energy efficiency.

The literature establishing energy comparisons between different options mainly concern, for this sector, the replacement of R-134a by a pure HFO and the replacement of R-404A by an HFC-HFO mixture. The trends are that R-1234yf provides a cooling capacity and an energy efficiency comparable to R-134a (*Sethi, 2016*). R-1234ze (E) requires larger swept volume compressors to achieve the cooling capacity of R-134a, which has no effect on energy performance. For the replacement of R-404A several HFC-HFO blends are developed. According to (*Sethi, 2016--b*), measurements on freezer or cold room equipment using R-448A (GWP 1387) or R-455A (GWP 148) show an improvement in energy efficiency from 4 to 9% compared to R-404A, depending on the case. According to (*Minor*, 2016), the R-454C (GWP = 148) is an energy-saving A2L alternative for small charge equipment, to replace R-404A. The tests show a low energy consumption and a good compatibility of materials and oil used. Alternatives to high-GWP refrigerants exist for condensing units. However, not all products are mature and personnel trained in the use of flammable refrigerants is still scarce. These facts push some manufacturers to choose HFO (R-1234yf or R-1234ze). CO_2 begins to be proposed including by major manufacturers (*Leong, 2017*). Manufacturers also offer R-448A or R-449A as a transition refrigerant to meet immediate demand, but this option is not sustainable.

Different alternatives to direct expansion systems using R-404A are currently available for centralized super and hypermarket installations. The European Commission report of 4 August 2017 (*European Commission, 2017*) makes an initial assessment and shows that on the one hand the R-134a / CO_2 options are energetically efficient and well established in Europe and that, on the other hand, the alternatives "transcritical CO_2" tend to reduce their cost and energy consumption.

Recent technological progress allows transcritical CO_2 installations to improve their energy efficiency and to be considered in a temperate / warm climate, even if the experience feedback needs to be consolidated, for the medium-temperature level (*Sawalha*, *2017, 2015*). The HFC-HFO mixtures with GWP close to 600, prove to be effective substitutes for R-134a in the HFC / CO_2 cascade systems and can be considered, for some, as quasi-drop-in options. Options with GWP below the threshold of 150 exist (R-455A, R454C). Still very scarce in France, indirect systems or cascade systems with ammonia are used in Europe and are very effective, especially in cascade system (*Winter, 2012*).

However, the maintenance needs for commercial refrigeration installations using R-404A remain significant. The proposed replacement refrigerants with GWP around 1300 can reduce energy consumption by 4 to 20% depending on the configurations, in the cases studied in the literature.

The air-conditioning sector massively uses R-410A. For hermetically sealed systems, R-290 is an option but its use is currently limited to hermetic portable units. In split or multi-split systems, the alternative is R-32. According to (*Mota-Babiloni*, *2017*), R-32 presents three advantages over R-410A: A lower GWP, the charge reduction and the energy efficiency improvement. However, its discharge temperature requires technical optimization of the systems. For high-capacity multi-split systems, VRF and Rooftop systems, there is currently no alternative other than R-32 that is proven more efficient than R-410A. The ORNL report (*Abdelaziz, 2016*) on the low-GWP alternatives for rooftops shows that the proposed alternatives, with GWP between 450 and 750, provide better efficiency than R-410A. However, the substitutes studied have a higher GWP than 250.

Heat pumps, which transfer the heat in a water loop, use mainly R-410A. Again, R-32 is offered by several Japanese brands. R-290 is already on the market outside Europe and will probably see its use growing in France, driven by European companies (*Makhnatcha*, *2014*). For both replacement refrigerants, the energy efficiency achieved is equal to or greater than that of R-410A.

For Mobile Air Conditioning, due to the ban of refrigerants with GWP higher than 150 (Directive 2006/40/EC), R-1234yf is the refrigerant chosen by the equipment manufacturers. Studies such as (*Papasavva*, *2014*) have shown that, placed in a global context, R 1234yf is a better alternative than CO_2. The mass production of automotive air conditioning with this refrigerant, whose efficiency compared to R-134a has been demonstrated, is in place.

For centrifugal chillers, the European market is dominated by R-134a. The most common alternative is R-1234ze, which is 5-10% more energy efficient than R134a (*Kasai*, *2013*). R-1233zd, which is an HCFO, has also established itself outside Europe, replacing R-123 (HCFC banned by the Montreal Protocol). By order of decreasing capacity, the alternatives for chillers with volumetric compression are R-290, R-32, ammonia, and R-1234ze for the highest power, alternative options allowing both a gain in GWP and a reduction in energy consumption.

For medium-temperature direct-expansion systems used in industrial processes, ammonia is already widely used as an alternative to R-404A. Other options are R-1234yf or R-1234ze. For low-temperature applications, ammonia is also possible in cascade at both temperature levels. The ammonia / CO_2 cascade remains the option allowing the best gains in terms of energy consumption.

R-404A can also be replaced by R-455A or R-454C, whose measured energy efficiencies are higher than R-404A according to the first feedback. Currently there is no low-GWP mixture and low-temperature glide suitable for flooded installations.
Finally, in the field of refrigerated transport, the alternative to R-404A is, currently, R-452A. CO_2 technology is now available on the market.

7. LIMITS AND LEVERS TO THE DEVELOPMENT OF ALTERNATIVES

The implementation of alternatives to high-GWP HFCs faces two major issues:

- Training programs to acquire specific skills in the use of refrigerant substitutes
- The current regulations leave little space for the use of alternatives.

Forward-looking management of jobs and skills must be a priority of the sector to sustain the profession of refrigeration by relying on existing diplomas, certificates or professional titles and the updating of the Employment / Activities / Competencies Frameworks of the Ministry of Labor.
Modeled on the requirements of the F-Gas, the standards must evolve to integrate the new skills and knowledge required to handle alternative refrigerants.
For obvious safety reasons, refrigeration technicians handling hydrocarbons, which are flammable refrigerants (A3), must acquire knowledge of good handling practices, charge limits (EN 378), drafting of risk analysis (EN 378) and ATEX regulations.
The refrigeration technicians involved in CO_2installations must know the specificities of this high-pressure refrigerant recalled below:

- Thermodynamic properties unsuitable for traditional uses;
- Low-temperature limitation (triple point -56.6°C);
- Critical temperature +31°C; 73.6 bars (for comparison R-404A at 72.1°C, 37.3 bars) so no condensation above the critical point;
- Traditional single and double-stage applications require transcritical compressor operation;
- Very high discharge pressure;
- Component design;
- Problem of oil return.

For refrigerants operating at pressures higher than 85 bars, PED (Pressure Equipment Directive) rules and associated standards and in-service inspections shall be applied when handling CO_2.
Toxicity concerns essentially ammonia. The French Decree of 16 July 1997 requires operators to ensure professional qualification and specific safety training for its personnel. The staff may be assigned to conduct or monitor refrigeration facilities (subject to Item 4735) or likely to operate on them (Article 54). This training includes exercises to become familiar with the wearing of the breathing apparatus and the rules of safety of the installation in case of leakage. In addition, refrigeration technicians must acquire knowledge on risk analysis drafting (EN 378).
Most of low-GWP refrigerants offered are refrigerant mixtures with a higher or lower temperature glide. In particular, the selection of compressors and evaporators is no longer based on the evaporation temperature (at constant pressure) but on the average of the evaporator inlet – and outlet temperatures. In addition, refrigeration technicians must acquire knowledge on risk analysis drafting (EN 378) because of their low flammability.

8. CONCLUSIONS

In conclusion, the study, freely available on the AFCE website, provides the reader with an overall picture of refrigerant alternatives to high GWP HFCs per application. The comparison of the proposed options has been based on the feedback of the owners and operators referred to facilities using these alternatives, on guarantees from equipment manufacturers and on publications submitted to peer review committees.
The safe implementation of alternative options requires special skills for operators handling these refrigerants. A number of European Directives already require adequate training to be provided for personnel working with alternative refrigerants. The lack of a European certification requirement may suggest that there is no binding requirement for training on HFC substitutes, which is not at all the case.

ACKNOWLEDGEMENTS

We thank the members of the AFCE Steering Committee for their contributions.

REFERENCES

Abdelaziz O [and al.] Alternative refrigerant evaluation for high ambient temperature environments: R-22 and R-410A alternatives for rooftop air conditioners [Report]. Oak Ridge National Laboratory for US Department of Energy, 2016.

Barrault S, Zoughaib A and Clodic D. 2016. Inventaire des émissions de fluides frigorigènes – France et DOM COM - Rapport Final [Report].

Clodic D., Michineau T, Devin E, and Barrault S 2013. Alternatives to High GWP HFC in the HVAC&R sector, ADEME. - Rapport Final [Report].

Kasai Kazushige and Johnson Phillip System Drop-in Test of R134a Alternative Fluids R-1234ze(E) and D4Y in a 200 RT Air-Cooled Screw Chiller - 2013 [Report].

Leong CC The first CO_2 refrigerant-based condensing unit to Jaya Grocer in Malaysia [Report]. - Asia Atmosphere, 2017.

Makhnatch P and Khodabandeh R The role of environmental metrics (GWP, TEWI, LCCP) in the selection of low GWP refrigerant. [Report]. The 6th International Conference on Applied Energy – ICAE2014, 2014.

Minor B, Shah S and Simoni L Testing of HFO Refrigerant with less than 150 GWP in a commercial freezer [Report]. - 16th International Refrigeration and Air Conditioning Conference at Purdue, 2016.

Mota-Babiloni A, Makhnatch P and Khodabandeh R Recent investigations in HFCs substitution with lower GWP synthetic alternatives: focus on energetic performance and environmental impact [Report]. International Journal of Refrigeration, 2017.

Pham H. M., Monnier K. Interim And Long-Term Low-GWP Refrigerant Solutions For Air-Conditioning. International Refrigeration and Air Conditioning Conference. Purdue University, 2016.

Papasavva Stella and Moonaw William Comparison between HFC-134a and Alternative Refrigerants in Mobile Air Conditioners using the GREEN-MAC-LCCP© Model [Report]. Purdue University, International Refrigeration and Air Conditioning Conference, 2014.

Report from the Commission of 4.8.2017 assessing the 2022 requirement to avoid highly global warming Hydrofluorocarbons in some commercial refrigeration systems.

Sawalha S [and al.] Field measurements of supermarket refrigeration systems. Part I: Analysis of CO_2 trans-critical refrigeration systems. [Report]. Applied Thermal Engineering 87, 2015. - pp. 633-674.

Sawalha S [and al.] Field measurements of supermarket refrigeration systems. Part II: Analysis of HFC refrigeration systems and comparison to CO_2 trans-critical. [Report]. Applied Thermal Engineering 111, 2017, - pp. 170-182.

Sethi A and Yana Motta S Low GWP Refrigerants for Air Conditioning and Chiller Applications [Report]. Purdue University, International Refrigeration and Air Conditioning Conference, 2016.

Sethi A, Pottker Gérald and Yana Motta S Experimental evaluation and field trial of low global potential R-404A replacements for commercial refrigeration. Science and Technology for the built Environment [Report]. International Journal of Refrigeration, 2016. - pp. 1175-1184.

Sethi A, Vera Becerra E and Yana Motta S Low GWP R-134a replacements for small refrigeration (plug-in) applications [Report]. International Journal of Refrigeration, 2016. - pp. 64-72.

UNEP, 2014 report of the Refrigeration, air conditioning and heat pumps Technical Options Committee, 2014 assessment.

Winter J Success with NH_3/ CO_2Cascade [Report]. - Eurammon symposium, 2012.

Manuscript ID: 569
10.18462/iir.icr.2019.0569

A New Model for Droplets Growth during their Onset of Freezing on Flat Surfaces under Air Forced Convection

Ellyn HARGES[(a)], Lorenzo CREMASCHI[(a)], Burak ADANUR[(a)]

[(a)] Auburn University
Auburn, AL, 36830, USA, lorenzo.cremaschi@auburn.edu

ABSTRACT

Frost formation on the fins of outdoor evaporators of heat pump systems degrades system efficiency. Several experimental and theoretical studies investigated using hydrophobic and hydrophilic surface coatings to inhibit frost formation, with promising results; however, most of the models available consist of empirical correlations.

This paper presented an update to the droplet condensation and growth portion of the comprehensive, three-stage frost model from Harges and Cremaschi (2018b). The updates include a model for droplet coalescence, which seems to have significant impact on droplets that grow larger than 125 μm. It also includes a new freezing time correlation. With these two updates, the model predictions agreed well with new data of large droplets forming on flat aluminum surfaces at high surface temperature from the present work as well as the data of small droplets on low surface temperatures from previously published studies in the literature.

Keywords: Frost, droplet condensation, freezing time, contact angle, heat pump

1. INTRODUCTION

When frost forms on the fins of outdoor evaporators operating within heat pumps, system efficiency is degraded due to the additional thermal resistance of the frost layer as well as to airflow blockage through the fins. Frost growth also leads to the need for defrosting the heat exchangers, and too many defrost cycles significantly reduce the system efficiency of heat pump systems. Several experimental studies investigated surface coatings to inhibit frost growth, and they indicated promising results. A few researchers modeled frost growth with various hydrophilic and hydrophobic coatings but the models are mainly empirical. There is also not a clear distinction among the different stages of frost growth, specifically droplets growth until their freezing, crystal growth on the top of the ice beads, and frost layer growth. Because surface coatings affected the first one of these stages, such distinction is key in order to capture the effect of surface energy on the onset of frost nucleation.

In the range of temperature, humidity, and air speed that are common in heat pump applications, condensation and growth of supercooled liquid water droplets occurs first. Then crystals develop at the top surfaces of the iced droplets – the so-called “crystals growth” phase – and finally a more or less homogeneous frost layer develops on the top of the crystals and penetrates within the voids (Hoke et al., 2000). For the latter phase, frost is typically characterized by average thermodynamic properties. However, surface coatings alter the contact angle of droplets and affect their potential displacements on the surface. Thus, surface energy is a main parameter during the droplets growth period until they freeze. The following phases of crystal growth and frost growth depend on the location, density, and dimensions of the ice beads. Indirectly, one can argue that the effects of coatings are observed in the frost growth phase because of the initial nucleation characteristics. But it is difficult to isolate and

quantify the effects of surface coatings if we do not take into account the initial period of frost nucleation when modeling frost growth. Only a few researchers, according to authors' best knowledge, developed models that included more than one of the three stages of frost growth into a single continuous event. Seki et al. (1985) modeled droplet condensation and growth stages. The droplet model presented in their paper takes into account the contact angle of the surface, but since it lumped frozen droplets into equivalent layers of ice and porous frost, effects of surface energy and contact angle of the supercooled liquid droplets on the subsequent frost growth are not apparent. In the current work, updates are described to the droplet growth phase description of the three-stage model for frost growth presented in the authors' prior work (Harges and Cremaschi, 2018b). The model was improved and validated using data gathered as part of this research as described in detail in the authors' previous paper (Cremaschi et al., 2019). For completeness and clarity, a brief description of the experimental methodology and data reduction are summarized next.

2. EXPERIMENTAL METHODOLOGY

The test facility consisted of a closed-loop wind tunnel that provided airflow at controlled temperature, humidity, and speed. A second smaller wind tunnel, shown in Fig. 1(a), was installed inside the large wind tunnel; this small wind tunnel housed the test section. Two thermoelectric coolers (TECs) and an in-house built stainless steel heat flux meter controlled the surface temperature of the test plate during frosting. An infrared (IR) camera was positioned above the test section and captured images of the test plate through a zinc selenide window built into the top of the small wind tunnel. A High Resolution Charged Couple Device (HR CCD) camera was located at the front or, in repeated tests, at the side of the test plate, as shown in Fig. 1(b). The IR camera measured droplet size during condensation and immediately after freezing, while the HR CCD camera measured droplet size directly after freezing as well as subsequent frost thickness. The sensors shown in Fig. 1(a) measured the time dependent heat flux, air dry bulb and dew point temperatures before and after the test plate, airflow rate, air static pressure, and air pressure drop across the test plate. A nitrogen displacement technique was used to limit the variation of surface temperature during the first few minutes of the test, as well as to prevent condensation before the test plate cooled to the specified set temperature. Further detail on the test apparatus and methodology can be found in Cremaschi et al. (2019).

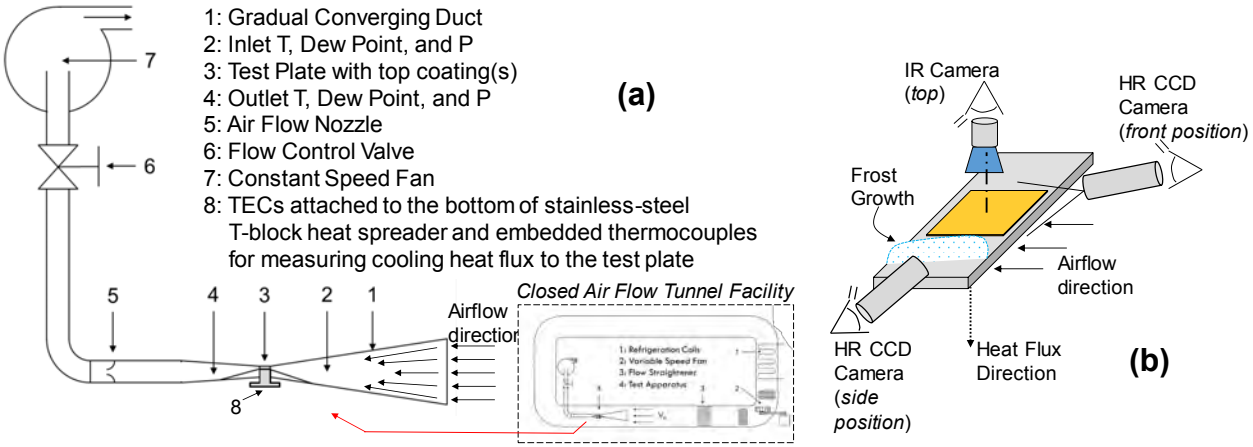

Figure 1: (a) Schematic of main test apparatus, (b) Illustration of the HR CCD camera and IR camera with respect to the test plate

Each test plate was a rectangular, aluminum bar of 25 mm in length (in the airflow direction), 152 mm in width and 6 mm in thickness. The channel above the plate was 4 mm high in order

to mimic a reasonable fin spacing. Haque and Betz (2018) provided a detailed description of the coatings used on the top surfaces of the test plates. The first plate was uncoated aluminum and had a contact angle, θ, of about 75°. The second plate had a super-hydrophobic coating ($\theta \approx$ 110-116°) and the third plate had a super-hydrophilic coating ($\theta \approx$ 19-29°).

Fig. 2 shows some examples of IR images taken of the water droplets on the uncoated aluminum surface at different test conditions. The lighter-colored droplets in Fig. 2(b) were in the midst of freezing and they appeared lighter in color because of their release of latent heat at their instant of freezing. The "freezing duration" was defined as the time it took from the first droplet to the last droplet to freeze. The field of view through the top window was at the center location of the flat plate (see Fig. 1(b)) and the assumption was that this location was a representative region of the entire flat surface. The freezing duration was generally between one and four minutes, with a few exceptions for particular environmental conditions. This freezing duration was used to calculate the "freezing time" for each test, which is defined as indicated in Equation 1 below.

$$t_f = \left(t_{freezing\ onset} - t_{test\ start}\right) + \frac{1}{2} t_{freezing\ duration} \qquad \text{Eq. (1)}$$

Images such as those presented in Fig. 2 were also used to measure the frozen droplet radius for each test. In order to extract the average radius, the images were digitalized and scaled. Individual droplet diameters were measured and an area-weighted average was calculated and considered to be representative of the droplet diameter for each test. The uncertainty on the droplet radius depends on the pixel resolution of the IR camera, the magnification, and the level of fuzziness and focus of the images when droplets developed on the surface. We estimated our uncertainty in the droplet diameter to be ±55 μm during the initial growth phase and until they froze on the surface. After freezing, the variation of their diameter was within the uncertainty of the IR camera and a HR CCD video-scope measured the crystals growth and subsequent frost layer thickness on the top of the droplets. The average droplet diameters for Fig. 2(a), (b), and (c) were 2.14 mm, 1.08 mm, and 0.52 mm, respectively.

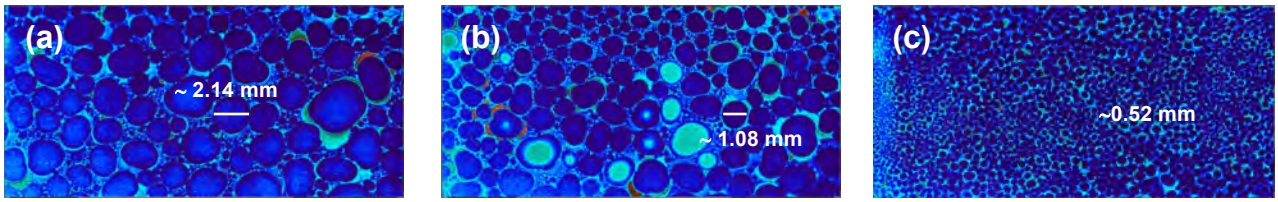

Figure 2: Images from IR camera showing droplet diameter when freezing for (a) T_s = -3°C, air flow @ 3.8 m-s^{-1}, and r_d = 1.07 mm; (b) T_s = -3°C, air flow @ 1.7 m-s^{-1}, r_d = 0.54 mm; and (c) T_s = -6°C, air flow @ 3.8 m-s^{-1}, r_d = 0.26 mm (air at 5°C and 80% R.H)

3. MODEL DEVELOPMENT

3.1. Droplet Radial Growth Rate

The authors' previous work (Harges and Cremaschi, 2018b) provides a detailed description of the methodology used for modeling the radial growth rate of the droplets. For completeness of this paper, the key equations are presented here and summarized next.

The heat transfer rate to an individual droplet was calculated using Equation 2 and an initial guess value of the temperature of the water-humid air interface, T_i. This was based on the resistance between the bulk air stream and the surface of the droplet. The first term in Equation 2 is the rate of sensible heat transfer, while the second represents the latent heat transfer rate.

$$\dot{Q}_d = \pi {r_d}^2 h(T_\infty - T_i) + \frac{1}{AC}\pi {r_d}^2 h_m(\rho_{v,\infty} - \rho_{v,i})H_{fg} \quad \text{Eq. (2)}$$

The model then performed iterative processes to calculate the actual T_i using resistances to heat transfer as outlined in the conventional well-known dropwise condensation theory. Once the interface temperature was estimated, the model calculated the radial growth rate of the liquid droplet by using Equation 3.

$$\frac{dr_d}{dt} = \frac{\frac{1}{AC}h_m(\rho_{v,\infty} - \rho_{v,i})}{\rho_d(1-\cos(\theta))^2(2+\cos(\theta))} \quad \text{Eq. (3)}$$

Finally, the new droplet radius was calculated using Equation 4.

$$r_{d,new} = r_{d,old} + \frac{dr_d}{dt}\,\Delta t \quad \text{Eq. (4)}$$

The model repeated these calculations for every time step until the specified freezing time. At this time the droplets froze and the droplet radius did not change anymore. This is another modeling assumption made based on our experimental observations. Crystals began to develop on the ice beads until a frost layer started to accumulate on the top of the crystals.

3.2. Freezing Time

The freezing time of the droplets on the surface determined the period of droplets growth, and was instrumental in how large they became at the onset of frost nucleation. An equation for the freezing time was developed in Harges and Cremaschi (2018b) using data available in the open literature. However, though the correlation predicted well the droplet freezing times of data available in published literature, our previous correlation did not match the freezing times measured in the experimental portion of the current study. We speculated that the reason was higher surface temperature, lower air temperature, and different surface roughness of our data with respect to those data from which the original freezing time correlation was developed. In other words, the discrepancy was too large and well above the experimental uncertainty and the sensitivity of the correlation to temperature, humidity, and air velocity and we concluded that it was not directly applicable to the test conditions of the current study. A new equation was generated using statistical nonlinear regression techniques and it resulted in a second order polynomial equation. The data used to generate the equation included all the freezing time data used to generate the previous freezing time equation (a total of 96 data points from Tao et al., 1993, Kim et al., 2016, Hoke et al., 2000, and Bryant, 1995) as well as the freezing time data from the current study (a total of 39 data points). The best fit is given by Equation 5 below. In Equation 5, *Ja* is the modified Jakob number as defined in Hermes (2012), except that in this study the latent heat of vaporization is used in place of the latent heat of sublimation. Fig. 3 shows the comparison of the freezing time predicted by the Equation 5 and the data.

$$t_f = (2.42 \times 10^{-7}) \cdot Ja^2 + 10.35513 \cdot {T_s}^2 + 371.804 \cdot T_s + 0.28703 \cdot \theta + 3327.787 \quad \text{Eq. (5)}$$

3.3. Droplet Coalescence

Equation 5 was used with the droplet model from Harges and Cremaschi (2018b) to predict the frozen droplet radii measured. Unfortunately, the model severely under predicted the data points by almost a factor of five times. Furthermore, even when the measured freezing time from our experiment was used as an input to the model (rather than using an equation for

freezing time), the predicted frozen droplet radius was still too small. It should be emphasized here that our model agreed quite well with the data in the literature for which the droplets diameter were less than 125 μm. However, the frozen droplets in our new data were much larger than those observed in the literature (more details are in Harges and Cremaschi, 2018b). Again, we speculated that the discrepancy could have been due to differences in temperatures and surface roughness. Because of low surface temperature, existing droplet freezing models assumed that each individual droplet grew by water vapor condensation and without any interactions with the surrounding droplets. However, our IR data indicated that water droplets coalesced on each other during their growth phase and before they turned into ice beads. It appeared that while droplet coalescence phenomena had small (or negligible) effects for small droplets, when the droplets grow larger than 125 μm, the coalescence phenomenon has to be considered for predicting the droplet diameter at their onset of freezing.

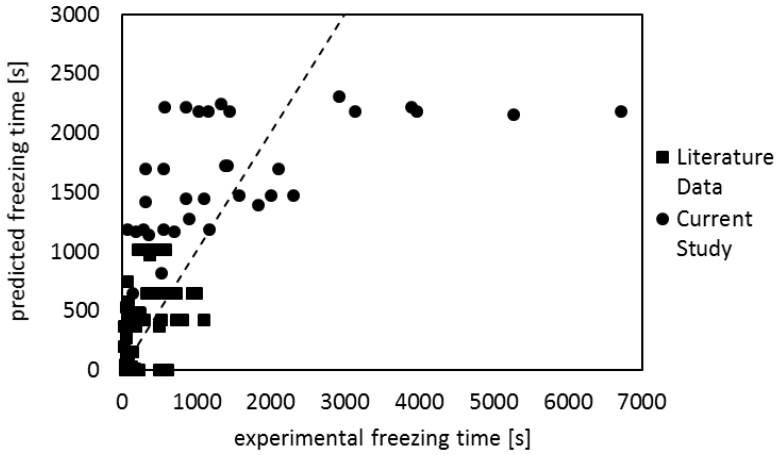

Figure 3: Predicted vs. measured freezing time

To begin the investigation into droplet coalescence, the number and times of droplet coalescence events were determined for each test. This was done by choosing a droplet of average size from the IR camera footage and tracing it backwards until it was smaller than our IR image uncertainty and not distinguishable from the other surrounding droplets in the immediate neighboring region. The times of each coalescence event were recorded and the ratio of droplet size increase due to the coalescence was measured. In the present data, the droplets increased by an average of 33% during each coalescence event; this percent increase was assumed constant in the model and might need to be investigated further in future follow up research. The ratio of increase was embedded in a constant, *C*, to calculate the new droplet radius, as shown in Equations 6 and 7, which replaced Equation 4.

$$r_{d,new} = C \cdot r_{d,old} + \frac{dr_d}{dt}\,\Delta t \qquad \text{Eq. (6)}$$

$$C = \begin{cases} 1 & no\ coalescence \\ 1.33 & with\ coalescence \end{cases} \qquad \text{Eq. (7)}$$

It was also observed that the number of coalescences, *N*, was well described by a logarithmic type expression that was a function of the freezing time only, as given in Equation 8. When used in the model, the freezing time input to Equation 8 was calculated by Equation 5.

$$N = 2.3324 \ln(t_f) - 12.194 \quad \text{Eq. (8)}$$

The model calculated the number of coalescence events before freezing and determined when each coalescence occurred. In the experiments, liquid droplets grew for a certain period before they came close enough to each other to produce a coalescence event. In the present model, an average coalescence time for the first coalescence event was calculated from the present data, and the model placed the first coalescence event at about one fourth of the total freezing time. After the first coalescence event, the next coalescence event occurred after approximately the same length period. In the present model, the representation of the coalescence events were given by Equations 9 and 10,

$$\alpha = \frac{t_f}{4} \quad \text{Eq. (9)}$$

$$\beta = \frac{(t_f - \alpha)}{N} \quad \text{Eq. (10)}$$

in which the coalescence events occurred at times α, $\alpha + \beta$, $\alpha + 2\beta$, and so on. It worth emphasizing in here that the coalescence approach presented in this paper was developed using data for the uncoated aluminum surface and its applicability to other surfaces with super-hydrophilic and super-hydrophobic coatings is part of authors' future work.

4. MODEL VALIDATION

To decouple potential sources of systematic errors, two validations of the model prediction were conducted. First, the actual measured freezing time from the data was entered as direct input to the model. The model then calculated the droplet radius at the onset of freezing with and without taking into consideration the coalescence phenomena.

Fig. 4 shows the predicted versus the measured frozen droplet radius. Fig. 4(a) provides the results of the predicted frozen droplet radius when the coalescence effects were neglected and Fig. 4(b) shows the comparison when the present coalescence model described in section 3.3 was used in conjunction with the measured freezing time from the data. It is obvious that when coalescence effects were not considered, the data points were significantly under predicted. The newly developed coalescence model corrected this discrepancy even though some of the data points were still not predictable.

A second validation of the model was then performed by using the updated freezing time equation as an input to both Equation 8 and the overall droplet condensation and growth model. Fig. 5 below shows the predicted and measured frozen droplet radius for this validation case. The updated droplet condensation and growth model presented in this paper could predict a fairly large range of droplet sizes under a wide variety of test conditions: from small droplets measured in the published studies to large droplet measured in the experimental portion of this work. The model predictions followed the trends of the data and some discrepancies were observed for few points. The reason might be associated to the average values that were used for developing the freezing time correlation and coalescence events model. From this point of view, the discrepancies of a few data points in Fig. 5 highlight that the present average-based value model worked well to capture trends and the order of magnitude of the droplet radius at the onset of freezing. But more specific freezing time and droplet coalescence phenomena models are still needed in order to improve its accuracy for even broader ranges of environmental conditions and for various surface coatings.

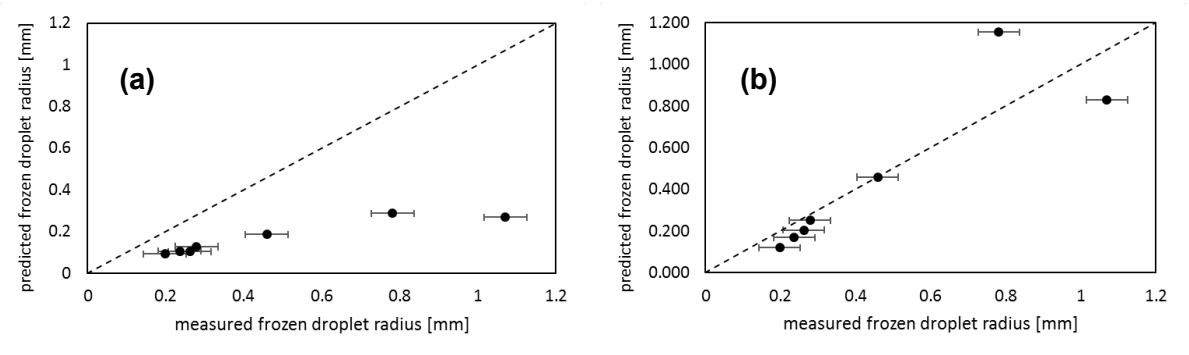

Figure 4: Predicted vs. measured frozen droplet radius (a) without coalescence effects, and (b) with the coalescence model

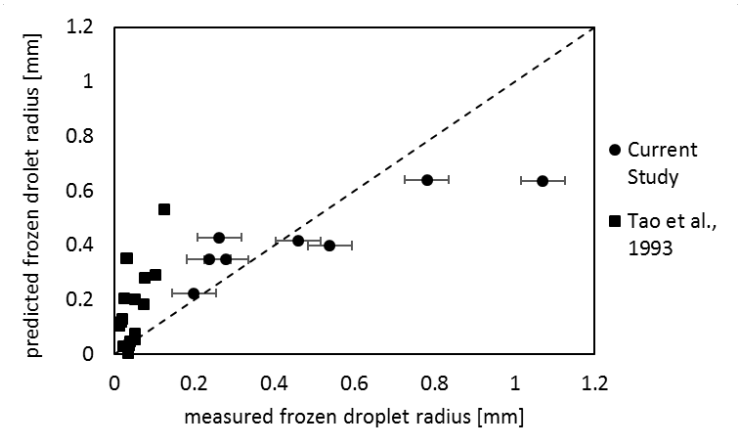

Figure 5: Predicted vs. measured frozen droplet radius

5. CONCLUSIONS

This paper presented updates to the droplet condensation and growth models that were part of the three-stage frost growth model presented in authors' previous work (Harges and Cremaschi, 2018b). These updates reflected the need to be able to model large droplets at their onset of freezing, as shown in the data of authors' previous work (Cremaschi et al., 2019) and for which exiting frost models failed to predict such large diameters. The updates included a model for droplet coalescence phenomena, which appeared to affect droplets when their predicted diameters became larger than 125 μm, and droplets freezing time. The number of coalesce events for a single droplet was given as function of the freezing time, and the size increase for each coalescence event was about 33% in average. With these updates, the present model predicted a fairly large range of droplet sizes under a broad range of test conditions: from small droplets measured in the published studies to large droplets measured in the experimental portion of this work. Future work is needed to investigate freezing time and coalescence events when specific environmental conditions and various surface coatings are adopted.

ACKNOWLEDGEMENTS

The authors would like to acknowledge and thank the National Science Foundation, Chemical, Bioengineering, Environmental, and Transport Systems Division for supporting the present work though Award No. 1604084.

NOMENCLATURE

AC	droplet area coverage (-)	T	dry bulb temperature (K)
C	size increase for coalescence (-)	T_{dew}	dew point temperature (K)
c_p	specific heat ($J \times K^{-1}$)	t_f	freezing time (s)
h	heat transfer coefficient ($W \times m^{-2} \times K^{-1}$)	Δt	time step (s)
H_{fg}	latent heat of vaporization ($J \times kg^{-1}$)	α	constant for t_f calculations (-)
h_m	mass transfer coefficient ($m \times s^{-1}$)	β	constant for t_f calculations (-)
N	number of coalescence events (-)	θ	contact angle (°)
$\dot{Q}$	heat transfer rate (W)	ρ	density ($kg \times m^{-3}$)
r	radius (m)	ω	humidity ratio (kg water × kg dry air)

Subscripts

a	air	sat	saturation
d	droplet	v	vapor
i	water-humid air interface	∞	bulk humid air stream
s	test plate surface		

REFERENCES

Bryant, J.A., 1995. Effects of hydrophobic surface treatments on dropwise condensation and freezing of water. Ph.D. Thesis, Texas A&M University.

Cremaschi, L., Adanur, B., Harges, E., 2019. Effect of humidity and airflow velocity on droplets elapsed time and radius at the onset of freezing and frost nucleation for super-hydrophilic and super-hydrophobic surfaces. Proceedings of the 4th Thermal and Fluids Engineering Conference (TFEC 2019), Las Vegas, NV, April 14-17. Paper TFEC-2019-26880.

Haque, M.R., Betz, A.R., 2018. Frost formation on aluminum and hydrophobic surfaces. Proceedings of the ASME 2018 International Conference on Nanochannels, Microchannels, and Minichannels (ICNMM 2018), June 10-13, Dubrovnik, Croatia. Paper No. ICNMM2018-7609.

Harges, E., Cremaschi, L., 2018. Modeling of frost growth on surfaces with varying contact angle. Proceedings of the 3rd Thermal and Fluids Engineering Conference (TFEC 2018), Ft. Lauderdale, FL, March 4-7. Paper TFEC-2018-20908.

Hermes, C.J.L., 2012. An analytical solution to the problem of frost growth and densification on flat surfaces. Int. J. Heat Mass Transf. 55(23-24), 7346-7351.

Hoke, J.L., Georgiadis, J.G., Jacobi, A.M., 2004. The interaction between the substrate and frost layer through condensate distribution. Air Conditioning and Refrigeration Center, College of Engineering, University of Illinois at Urbana-Champaign.

Kim, H., Kim, D., Jang, H., Kim, D.R., Lee, K.S., 2016. Microscopic observation of frost behaviors at the early stage of frost formation on hydrophobic surfaces. Int. J. Heat Mass Transf., 97, 861-867.

Seki, N., Fukisako, S., Matsuo, K., Uemura, S., 1985. An analysis of incipient frost formation. Wärme- und Stoffübertragung 19(1), pp. 9-18.

Tao, Y.-X., Besant, R.W., Mao, Y., 1993. Characteristics of frost growth on a flat plate during the early growth period. ASHRAE Transactions: Symposia, CH-93-2-2, 746-753.

Manuscript ID: 594
DOI: 10.18462/iir.icr.2019.0594

Thermal performance of a rotary booster driven free-cooling unit for data center

Lianzheng Xue[(a)], Shaocong Li[(a)], Guoyuan Ma, Feng Zhou*[(a)], Fuping Li[(a)], Xianghui Yan[(a)]

[(a)]College of Environmental and Energy Engineering, Beijing University of Technology
Beijing 100124, China

ABSTRACT

A rotary booster driven free-cooling unit using ambient cold was proposed for small and medium sized data center free cooling. The influences of heat exchanging area, refrigerant charging quality and condenser fan frequency on cooling capacity, rotary booster power and energy efficiency ratio (EER) were studied experimentally under different working conditions. Results indicated both the cooling capacity and EER increase with the refrigerant charging quality. With the increase of indoor and outdoor temperature difference Δt, the rotary booster power reduced to about 0.6 kW while the temperature difference was 25℃. And the EER was improved by appropriately reducing the frequency of the condenser fan. When the refrigerant charging quality was 5 kg and condenser fan frequency was 30Hz, the cooling capacity of free-cooling unit with dual heat exchangers was 20.2 kW and the EER was 18.4 when the indoor and outdoor temperature difference was 25℃.
.

Keywords: Free Cooling, Rotary Booster, Data Center, Heat Exchanging Area, Refrigerant Charging Quality.

1. INTRODUCTION

The booming of information technology has given rise to tremendous changes in human life. In recent years, with the advancement of computer and electronic technology, the demand for data processing, data storage and digital communication has increased, and the data center industry has developed rapidly [1-2]. The power consumption of the data center is expected to increase by about 140 billion kWh per year by 2020 [3].

The data center is mainly comprised of three parts: IT equipment, air conditioning system and power supply and distribution system [4]. Cooling equipment is the most important energy-consuming auxiliary facility in the data center, and its energy consumption usually accounts for 30-50% of the total energy consumption [5-7]. The traditional data center cooling system is the computer room air conditioner (CRAC) [8-9]. Conventional cooling system compressors operate year-round even at night or winter when outdoor ambient temperatures are low, resulting in lower energy efficiency [10]. Natural cooling technology, that is, when the outdoor temperature is lower than the indoor temperature, use a natural cold source to cool the data center [11]. Natural cooling in data centers can be divided into three categories: air-type natural cooling, liquid-type natural cooling, and heat pipe-type natural cooling. Among the three types of natural cooling technologies, the heat pipe type natural cooling technology has superior temperature control characteristics, can transfer heat with a small temperature difference, and the heat exchange is safe and reliable, without cross-contamination, and is suitable for natural cooling of the data center, showing great application potential. [12].

When the system is complicated, the separated thermosiphon only relies on gravity, and the heat pipe loop cannot be ensured for work stably. The liquid phase heat pipe driven by the refrigerant pump improves the problem of insufficient driving force of the gravity type split heat pipe. Ma et al [13-14] designed a pump driven two-phase cooling unit for data center by natural cooling. The research shows that when the indoor and outdoor temperature difference is 10 °C, the pump driven two-phase cooling unit COP is 5.88; when the indoor and outdoor temperature difference is 20 °C, the unit COP can reach 10.41. Wang et al [15-16] proposed a power-type split heat pipe refrigeration system. The cooling capacity and COP of the heat pipe module are approximately linear with the indoor and outdoor temperature difference. When the indoor and outdoor temperature difference is

23 °C, the cooling capacity and COP are respectively 31 kW and 14.8, the power-type split heat pipe unit has significant energy saving and emission reduction advantages. Zhou et al [17-18] applied the pump driven two-phase cooling unit to a small data center in Beijing, and studied its operation performance. Based on the engineering application, the pump driven two-phase cooling unit was analyzed to get energy saving rate and investment recovery period in different cities with different climates in China.

The separate heat pipe system driven by the liquid pump addresses the issue of the operational stability of the gravity type separated heat pipe, but the cavitation problem of the liquid pump makes the system unstable. The gas-phase heat pipe driven by the booster improves the above problem. The booster cannot only provide sufficient power for the circulating working medium, but also the pressure increase brought by the driving force can improve the condensation of the working medium in the condenser, and improve the efficiency and stability of the system operation. Chen Dong et al [19] carried out the experiment of air pump drive loop heat pipe, the experimental working medium is R22, and the gas pump adopts a 107 W refrigerator compressor. The experiment is shown that the pressure difference between the front and rear of the driving device is below 0.4 bar, and the heat transfer function can be realized between the cold and heat sources at a long distance. Wei et al [20] proposed applying the gas pump driven loop heat pipe to the data center to achieve energy savings. The experimental analysis of the influence of the relative height of the gas-liquid separator and the evaporator inlet on the system performance. Shi et al [21] proposed a gas-pressurized separation heat pipe circulation technical scheme. The results show that when the indoor and outdoor temperature difference is 20 °C, the gas pressure-separated heat pipe cycle can be used to replace the conventional vapor compression refrigeration cycle and meet the heat dissipation requirements of the machine room. Li et al. [22] proposed a rotary booster driven loop heat pipe cooling unit for small data centers. The study shows that the rotary booster can better utilize the natural cooling source to achieving data center cooling than the standard compressor.

In data center cooling technology, natural cooling technology can effectively reduce cooling power consumption. Heat pipes have attracted considerable attention as devices for effectively utilizing natural cooling sources. For power-type heat pipes, how to optimize system energy efficiency is one of the main tasks. In this paper, a novel rotary booster driven free-cooling unit is proposed. The effects of heat exchange area, refrigerant charging quality and condenser fan frequency on cooling capacity, rotary booster power and energy efficiency ratio (EER) are analyzed.

2. THE ROTARY BOOSTER DRIVEN FREE-COOLING UNIT

The Figure 1 is a schematic diagram of a rotary booster driven free cooling unit. The main components of the unit include rotary booster, condensers, evaporators, gas-liquid separators and throttle valves. The rotary booster that modified rolling rotor compressor powers the working medium with an operating frequency of 50 Hz, a rotational speed of 2880 r/min and a displacement of 36 cm3. Both the evaporator and the condenser are tube-fin type heat exchangers with the same structural specifications, and are equipped with the same type of axial fan. The heat exchanger specifications are shown in Table 1, and the single heat exchanger area is 25.6 m^2. The gas-liquid separator can reduce the pressure pulse at the start of the unit and improve the stability of the system operation.

1, 2, 3, 4 - heat exchanger inlet shut-off valve, 5, 6, 7 8 - three-way valve, 9, 10, 11, 12 - heat exchanger

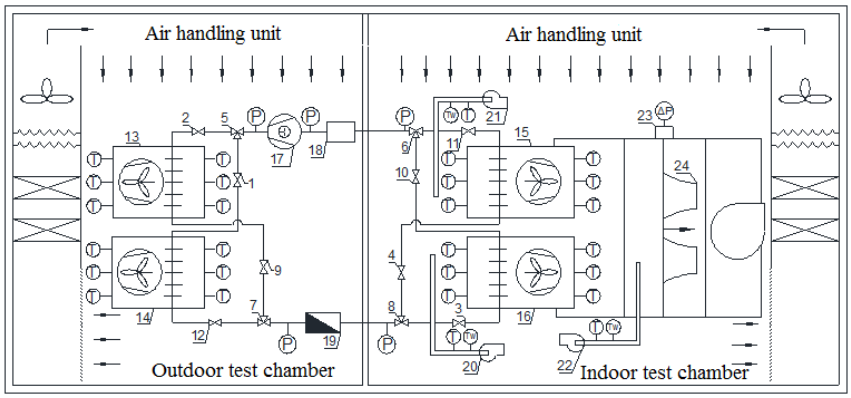

outlet shut-off valve, 13, 14 - condenser, 15, 16 - evaporator, 17- rotary booster, 18-gas-liquid

separator, 19 - mass flow Meter, 20, 21, 22 - sampling fan, 23 - differential pressure measuring point, 24 - nozzle

Fig.1. Experimental setup of rotary booster-driven loop heat pipe energy recovery device

Table. 1 Specifications of the heat exchanger.

Parameter	Value/mm
Copper tube outer diameter d_o	10
Copper tube thickness δ_t	0.5
Copper tube inner diameter d_i	9
Copper tube length l	500
Fin thickness δ_f	0.2
Fin pitch s_f	2.3

3. EXPERIMENTAL METHODS

The experiment is carried out in a enthalpy different laboratory. The rotary booster condenser and gas-liquid separator are arranged in the outdoor simulation test room, and the evaporator is arranged in the indoor simulation test room and connected to the air volume measuring device.In Fig. 1, Ⓣ and Ⓦ respectively indicate the arrangement of the dry bulb temperature and the wet bulb temperature measuring point, and the pressure measuring point arrangement is represented by Ⓟ. The working medium of the unit is R22. According to the "Code for Design of Data Center GB50174-2017", the indoor ambient temperature is set to 25℃, and the outdoor ambient temperature is set to -5 to 20℃. In the experiment, in order to ensure the large air volume of the indoor, the evaporator fan frequency is always 50 Hz.

3.1. Performance factors

Heat exchange area: The unit charge is 4kg, and the condenser fan frequency is 50 Hz. Among them, the single heat exchanger unit experiment, the shut-off valves 1, 3, 10, 12 are closed, open the shut-off valves 2, 4, 9, 11, using the condenser 13 and the evaporator 15; double heat exchanger unit experiment, open the Shut-off valves of the heat exchanger all.

Refrigerant charging quality: Under the condition that the double heat exchanger and the condenser fan frequency are kept at 50 Hz, the system charging quality is changed from 2 to 5kg.

Condenser fan frequency: Under the condition of double heat exchanger and charging quality of 4kg, change the condenser fan frequency. The condenser fan frequency conversion range is 20-50 Hz.

3.2. Performance evaluation parameters

In this experiment, the performance of the unit is mainly evaluated by three performance parameters, namely cooling capacity Q, total unit power Punit and energy efficiency ratio EER.

Table. 2 Main parameters of instruments

Measuring instrument	Precisio	Range	producer	mode
Thermal couple	± 0.2℃	-30~150℃	Omega	T type
Pressure sensor	± 0.2%	0-25bar	Huba	YD512
Coriolis mass flow	± 0.2%	500kg/h	SINCERITY	DMF-1
RTD	±0.1℃	0.00~60.00℃		NRHS3/3wire
Power meter	±0.1%	300V	YOKOGAW	WT230
Data acquisition unit	±0.03%	0–100mA	Agilent	34970A

4. EXPERIMENTAL RESULTS AND DISCUSSION

4.1. Heat exchanger area

As can be seen from Fig. 2, as the indoor and outdoor temperature difference ΔT increases, the power of the rotary booster gradually decreases, and the increase in the number of heat exchanger groups (heat exchange area) increases the power of the rotary booster. When ΔT is 5 °C, the single-heat exchanger rotary booster power is 0.57 kW, and the dual heat exchanger rotary booster power is 1.16 kW. With the increase of indoor and outdoor temperature difference, the difference between the two booster powers is reduced; when the indoor and outdoor temperature difference is 25 °C ~ 30 °C, two kinds The booster power input value is similar under the different heat exchanger area. Under the same indoor and outdoor temperature difference, the heat exchanger area increases and the booster power increases. When the indoor and outdoor temperature difference is between 25 °C and 30 °C, the power curve of the air pump is approaching that the large indoor and outdoor temperature difference weakens the effect of the increase of the heat exchange area and the power input of the rotary booster.

Figure 3 shows the variation of the cooling capacity with the indoor and outdoor temperature difference when the unit is equipped with different heat transfer areas. It can be seen from Fig. 3 that the cooling capacity of the single heat exchanger increases with the increase of the indoor and outdoor temperature difference, and the cooling capacity is stable at 10.4 kW when the indoor and outdoor temperature difference is 25 ° C to 30 ° C. After the area of heat exchangers increases, the cooling capacity is higher than that of single heat exchangers under various indoor and outdoor temperature differences. The cooling capacity increases first and then decreases with the increase of indoor and outdoor temperature difference. The cooling capacity is 20 °C when the temperature difference is 20 °C. It reached a peak of 18.6 kW. Compared with a single heat exchanger, the dual heat exchanger reduces the condensing pressure when the temperature difference between the indoor and outdoor is large, which causes the supply pressure to the evaporator and circulation to decrease, and eventually the cooling capacity increases first and then decreases with the increase of indoor and outdoor temperature difference.

As we can see from Fig. 3. With the increase of indoor and outdoor temperature difference, the EER of a single heat exchanger increases with the increase of indoor and outdoor temperature difference. When the indoor and outdoor temperature difference is between 20 °C and 30 °C, EER of the single heat exchanger tends to be stable at 12.5. The EER of the dual heat exchanger increases first and then decreases with the increase of the indoor and outdoor temperature difference. When the indoor and outdoor temperature difference is 25 °C, the EER of the dual heat exchanger reaches the peak value of 15.2.

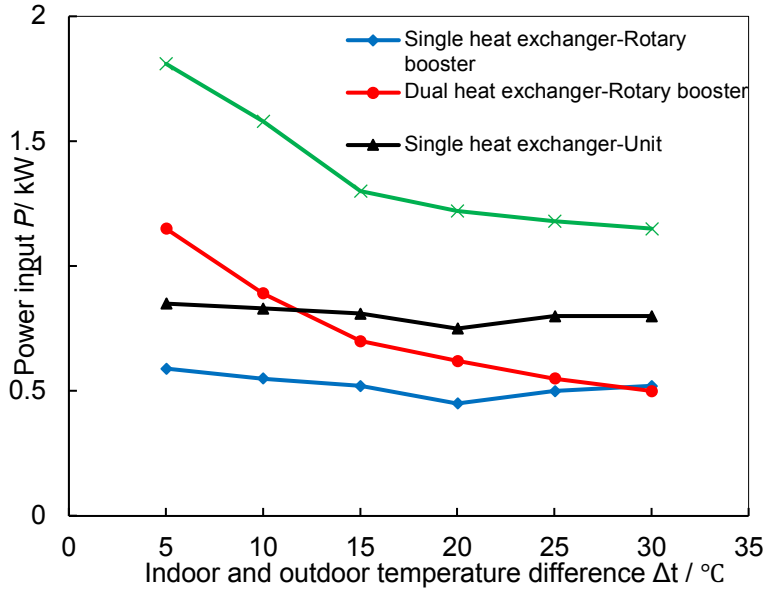

Fig. 2 Variation of power in different heat transfer area

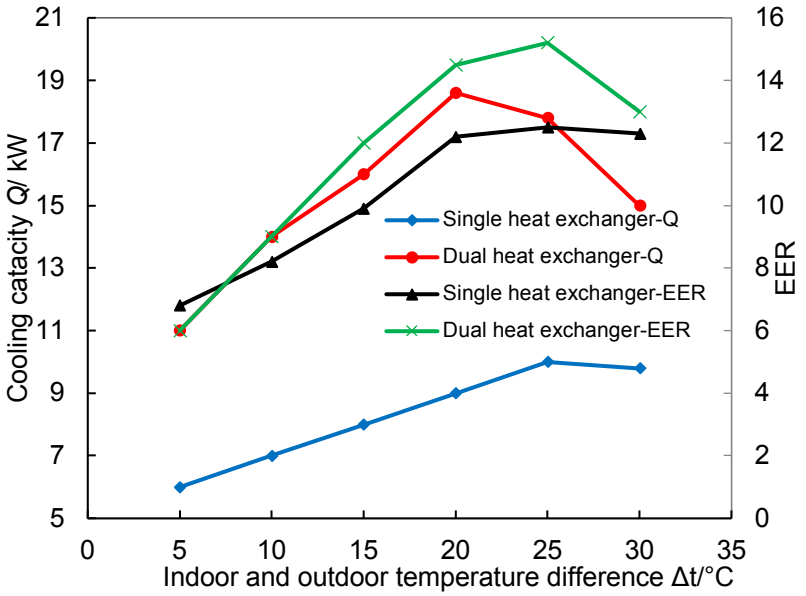

Fig. 3. Variation of cooling capacity and EER in different heat transfer area

4.2. Refrigerant charging quality

The effect of different charge quantities on the performance of the rotary booster driven free cooling unit is shown in Fig. 4-5.

Fig.4 shows the variation of the power under different indoor and outdoor temperature differences. when the indoor and outdoor temperature difference is 5 °C , the rotary booster power increases as the charging quality increases, the minimum power is 1 kW; Δt is greater than 15 °C, the rotary booster power input decreases with the increase of the charge, and the minimum power input of the rotary booster is 5 kg. At the time, the minimum power input is 0.6 kW (Δt = 25 °C). When the indoor and outdoor temperature difference is less than 5 °C, the increase of the charging quality will worsen the condensation condition, and the rotary booster exhaust temperature will increase, resulting in an increase in the booster power input. When the indoor and outdoor temperature difference is larger than 15 °C, the increase of the charging quality improves the problem that the rotary booster is overheated and the specific volume is increased, so the power input of the rotary booster is gradually reduced.

It can be observed from Fig. 5 that the change of the cooling capacity is basically the same with different indoor and outdoor temperature differences as the charging quality is different. When the charging quality is 5 kg, the cooling capacity attains the maximum value under the indoor and outdoor temperature difference. When the indoor and outdoor temperature difference is 20 °C, the cooling capacity reaches 20.4 kW. It can be seen from Fig. 5 that under the same indoor and outdoor temperature difference conditions, The change of EER increases first and then becomes gentle with the increase of charge quality . When the charging quality is 5 kg, the EER attains the maximum value under the indoor and outdoor temperature difference, and the indoor and outdoor temperature difference is 20 °C. The EER reached 15.6.

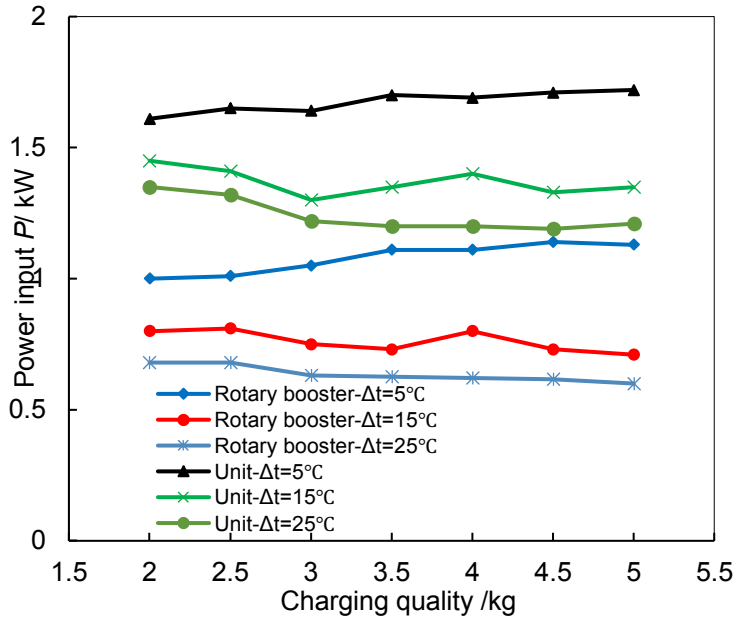

Fig.4. Variation of power with different charging quality

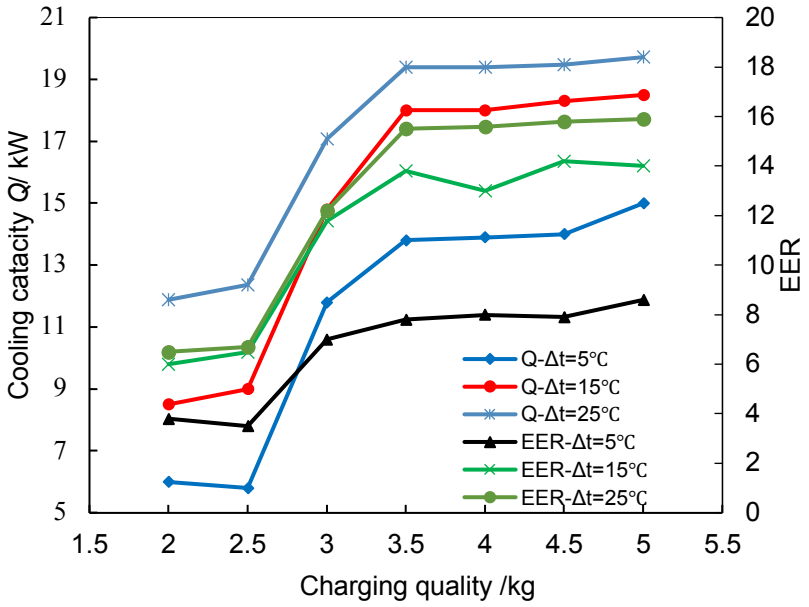

Fig.5. Variation of cooling capacity and EER with different charging quality

4.3. Condenser fan frequency

The effect of different condenser fan frequencies on the performance of the rotary booster driven

free cooling unit is shown in Fig. 6-7.

As shown in Fig. 6, both the rotary booster power input and the total unit power decrease as the indoor and outdoor temperature difference increases. The rotary booster power input increases as the condenser fan frequency increases. The indoor and outdoor temperature difference is 30 °C, the condenser fan frequency is 50 Hz, and the rotary booster power input has a minimum value of 0.56 kW. The total power input of the unit needs to consider the power input of the rotary booster and the axial fan. When the indoor and outdoor temperature difference is 30 °C and the outdoor fan is 30 Hz, the total power input of the unit has a minimum value of 1 kW.

It can be seen from Fig. 7 that no matter how the frequency of the outdoor fan changes, as the temperature difference between indoor and outdoor increases, the cooling capacity increases first and then decreases. The maximum cooling capacity of the unit appears at Δt=25°C, the condenser fan frequency is 30 Hz, and the maximum cooling capacity is 20.2 kW. Properly reducing the frequency of the condenser fan can increase the condensing pressure, ensure the liquid supply pressure of the liquid refrigerant to the evaporator, and improve the problem that the system circulation is reduced owing to the excessive indoor and outdoor temperature difference.

Fig. 7 shows the variation of the EER of the unit with different condenser fan frequencies (50 Hz, 40 Hz, 30 Hz) with the temperature difference between indoor and outdoor. With the increase of indoor and outdoor temperature difference, the EER of the unit increased first and then decreased. Under different indoor and outdoor temperature differences, the maximum EER of the unit: when the indoor and outdoor temperature difference is 5 °C, the EER of the outdoor fan 50Hz is 8.15; when the indoor and outdoor temperature difference is 10 °C, the EER of the outdoor fan 40Hz is 11.1; When the indoor and outdoor temperature difference is 15 °C, the EER of the outdoor fan 40Hz is 14.7; when the indoor and outdoor temperature difference is 20 °C, the EER of the outdoor fan 40Hz is 17.1; when the indoor and outdoor temperature difference is 25 °C, the EER of the outdoor fan 30 Hz reaches all the work. The peak value is 18.9; when the indoor and outdoor temperature difference is 30 °C, the EER of the outdoor fan 30Hz is 17.4; as the indoor and outdoor temperature difference increases, appropriately reducing the condenser fan frequency will increase the EER of the unit.

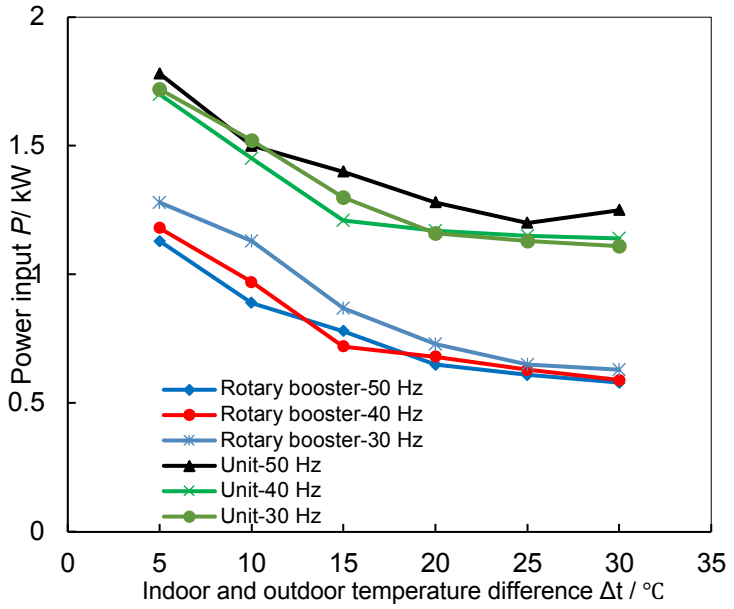

Fig .6. Variation of power with different condenser fan frequency

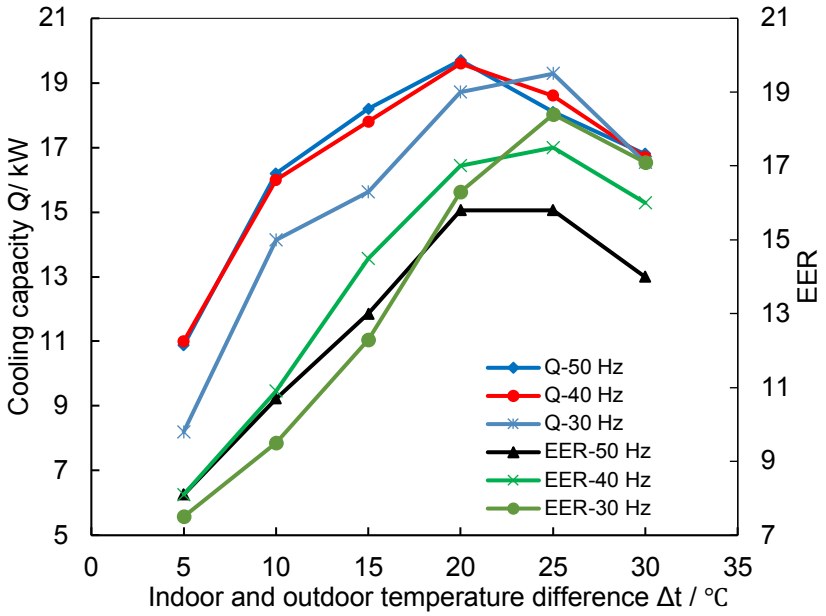

Fig .7. Variation of cooling capacity and EER with different condenser fan frequency

5. CONCLUSIONS

A rotary booster driven free-cooling unit is proposed and designed to analyze the heat exchanging area, refrigerant charging quality and condenser fan frequency to the cooling capacity, rotary booster power and energy efficiency ratio in the outdoor ambient temperature range of -5 °C to 20 °C. The conclusions were drawn as follows.

(1) As the indoor and outdoor temperature difference increases, the rotary booster power decreases. Improving the heat exchanger area increases the cooling capacity of the unit. When the charge is 4 kg and the condenser fan frequency is 50 Hz, the cooling capacity of the unit of the single heat exchanger is 10.4 kW (the indoor and outdoor temperature difference is 25 °C), and the cooling capacity of the unit of the dual heat exchanger is 18.4 kW (indoor and outdoor temperature difference 20 °C). The rotary booster power will increase due to the increase in heat exchange area. When the indoor and outdoor temperature difference is 5 °C, the rotary booster power of the single heat exchanger is 0.57 kW, and the rotary booster power of the dual heat exchanger is 1.16 kW. The EER of the dual heat exchanger unit is higher than that of the single heat exchanger.

(2) When the indoor and outdoor temperature difference is less than 15 °C, the rotary booster power increases with the increase of the charging quantity, and the minimum value of the rotary booster power input is 0.83 kW (charging quantity 3kg); When the indoor and outdoor temperature difference is greater than 15 °C, the rotary booster power input decreases as the charging quantity increases. When the charging quantity is 5kg, the minimum rotary booster power is 0.56 kW (the indoor and outdoor temperature difference is 30 °C). The cooling capacity increases as the amount of charging quantity increases and tends to be flat. When the charging quantity is 5kg, the cooling capacity reaches the maximum value under the indoor and outdoor temperature difference at 20°C, the cooling capacity reaches a peak of 20.2 kW. Increasing the charging quantity can increase the EER of the unit when the temperature difference between the indoor and outdoor is large.

(3) As the indoor and outdoor temperature difference increases, the cooling capacity of the unit can be increased by appropriately reducing the condenser fan frequency, but at the same time, the rotary booster power is also increased. In summarize, when the unit operates at indoor and outdoor temperature difference of 5 ~ 10 ° C, 15 ~ 20 ° C, 25 ~ 30 ° C, in order to make the unit energy efficiency ratio is the best, the condenser fan frequency can be set to 50 Hz, 40 Hz, 30 Hz.

ACKNOWLEDGEMENTS

This research was financially supported by the General Project of Science and Technology Program of Beijing Municipal Education Commission (KM201910005017), and the National Natural Science Foundation of China (51776004).

NOMENCLATURE

Δt	indoor and outdoor temperature difference(℃)	*EER*	energy efficiency ratio
A	heat exchanging area (m^2)	*h*	air enthalpy ($kJ \cdot kg^{-1}$)
m	mass flow rate ($kg \cdot h^{-1}$)	*Q*	heat transfer rate (kW)
P	Power input (kW)	ΔP	pressure difference (Pa)

REFERENCES

[1] Ebrahimi K, Jones GF, Fleischer AS. A review of data center cooling technology, operating conditions and the corresponding low-grade waste heat recovery opportunities. Renew Sustain Energy Rev 2014;31:622–38.

[2] Sevencan S, Lindbergh G, Lagergren C, Alvfors P. Economic feasibility study of a fuel cell-based combined cooling, heating and power system for a data centre. Energy Build 2016;111:218–23.

[3] Whitney J, Delforge P. Data center efficiency assessment. New York: Natural Resources Defense Council; 2014.

[4] European Commission. Code of conduct on data centres energy efficiency version 2.0. Ispra, Italy; November 20; 2009.

[5] Meijer GI. Cooling energy-hungry data centers. Science 2010;328:318–9.

[6] Salim M, Tozer R. Data centers' energy auditing and benchmarking-progress update. Ashrae Trans 2010;116:109–17.

[7] Ni J, Bai X. A review of air conditioning energy performance in data centers. Renew Sustain Energy Rev 2017;67:625–40.

[8] Tian H, He Z, Li Z. A combined cooling solution for high heat density data centers using multi-stage heat pipe loops. Energy Build 2015;94:177–88.

[9] Ling L, Zhang Q, Yu Y, Liao S. Experimental investigation on the thermal performance of water cooled multi-split heat pipe system (MSHPS) for space cooling in modular data centers. Appl Therm Eng 2016;107:591–601.

[10] Ma Y, Ma G, Zhang S, Zhou F. Cooling performance of a pump-driven two phase cooling system for free cooling in data centers. Appl Therm Eng 2015;95:143–9.

[11] Pawlish M, Varde AS. Free cooling: a paradigm shift in datacenters. In: Proceedings of the 5th international conference on information and automation for sustainability held in Colombo, Sri Lanka.

[12] Hainan Zhang, Shuangquan Shao, Hongbo Xu , Huiming Zou, Changqing Tian. Free cooling of data centers: A review[J]. Renewable and Sustainable Energy Reviews 35 (2014) 171–182

[13] ZHANG Shuang, MA Guoyuan, ZHOU Feng, et al. Experimental analysis on function of free cooling unit with a pump-driven loop heat pipe for internet data center[J]. Journal of Civil, Architectural & Environmental Engineering, 2013, 35(4): 145-150.

[14] Zhang S, Ma G, Zhou F. Experimental study on a pump driven loop-heat pipe for data center cooling [J]. Journal of Energy Engineering, 2014, 141(4): 04014054.

[15] Wang T, Wang G, Wang M, Wang J, Zhao S, Liu H, et al. Design and study of composite refrigeration system with heat pipe used in high-performance computer. Cryog Supercond 2013;41(8):63–6, [in Chinese].

[16] Wang F. Design and test of 30 kW dynamic separate type heat pipe. Hefei: Hefei University of Technology; 2014, [in Chinese].

[16] Wang F. Design and test of 30 kW dynamic separate type heat pipe. Hefei: Hefei University of Technology; 2014, [in Chinese].

[17] Feng Zhou, Chuancheng Wei, Guoyuan Ma. Development and analysis of a pump-driven loop heat pipe unit for cooling a small data center[J]. Applied Thermal Engineering 124 (2017) 1169–1175.

[18] Feng Zhou, Cuicui Li, Wanpeng Zhua, Jing Zhoua, Guoyuan Ma, Zhongliang Liu. Energy-saving analysis of a case data center with a pump-driven loop heat pipe system in different climate regions in China[J]. Energy & Buildings 169 (2018) 295–304.

[19] WANG Yue. Study on Mechanically Driven Separate-type Heat Pipe ——Heat Circuit[D]. Tianjin University of Science&Technology, 2000, [in Chinese].

[20] WEI Chuancheng. Cycle Performance study on Vapor pumped Loop Heat Pipe for Cooling in Telecommunication base station[D]. Beijing University of Technology. 2015, [in Chinese].

[21] SHI WenXing, WANG Fei, et al. Develoment of gas pressurized composite air-conditioning unit and annual operation energy efficiency analysis[J]. Refrigeration and Air Conditioning, 2017, 17(2): 11-16, [in Chinese].

[22] Shaocong Li, Guoyuan Ma, Lianzheng Xue, Fuping Li, Xianghui Yan Working characteristics of a rotary booster driven loop cooling unit for a small data center, The 9th Asian Conference on Refrigeration and Air-conditioning,2018,Sapporo, Japan

Manuscript ID: 595
DOI: 10.18462/iir.icr.2019.0595

Heat and mass transfer characteristics of liquid desiccant dehumidification process with microencapsulated phase change material slurry

Yufeng YAN, Xiaofeng NIU, Tao LIU, Guojian SHEN, Dandan WANG, Yue ZHANG

College of Urban Construction, Nanjing Tech University
Nanjing, 210009, China, newfut@gmail.com

ABSTRACT

It is expected that the temperature rise of solution in the liquid desiccant dehumidification process can be restrained by adding microencapsulated phase change materials (MicroPCMs) to the desiccant solution. The heat and mass transfer process of the falling film dehumidification with the microencapsulated phase change material slurry (MPCMS) were simulated. The influences of the concentration of MicroPCMs and the inlet temperature of the slurry on the dehumidification were investigated. The results show that, with the addition of MicroPCMs, the temperature rise in dehumidification process can be restrained. There is an optimum concentration of MicroPCMs to reach the peak value of interfacial mass transfer coefficient. When the concentration of MicroPCMs is 5%, the water condensation rate is 14.2% higher than that of the base fluid. It is recommended that the slurry inlet temperature be close to the onset melting temperature of MicroPCMs.
Keywords: liquid desiccant, microencapsulated phase change material slurry, falling film, heat and mass transfer, simulation.

1. INTRODUCTION

Relative humidity of air is an important factor affecting the thermal comfort of indoor air environment. The liquid desiccant dehumidification technology can utilize the lower surface water vapor partial pressure of the solution to absorb water vapor in the air, and can be regenerated by using low-grade energy sources, such as solar energy and industrial waste heat, which has many advantages over the traditional dehumidification method (Yin et al., 2014). Especially in areas with large humidity loads, it has obvious energy saving potential.

During the dehumidification process, the condensation of water vapor will release a large amount of latent heat, which will cause the temperature rise of the solution and lead to a decline of the mass transfer driving force. In order to solve the problem of solution temperature rise, the internal cooling dehumidifier is an effective option (Liu et al., 2014 and 2016). However, the internal cooling dehumidifiers still consume additional external energy, which weakens the advantages of solution dehumidification technology.

It is expected that the temperature rise of solution in the liquid desiccant dehumidification process can be restrained by adding microencapsulated phase change materials (MicroPCMs) to the desiccant solution (Niu et al., 2017). MicroPCMs has a particle diameter in the range of 1 to 1000 μm (Pania et al., 2015). The microcapsules are dispersed in a base fluid to form stable phase change material microcapsule slurry (MPCMS). MPCMS has been widely studied in recent years due to its high heat storage capacity and good heat transfer characteristics (Delgado et al., 2012). Studies have shown that MPCMS not only has the heat storage capacity of traditional phase change materials, but also has the heat transfer characteristics of micro-nano fluids (Sohn and Chen,1981). At present, most researches on MPCMS focus on its heat transfer characteristics in a circular tube or micro-channel heat exchanger (Zeng et al., 2009; Liu et al., 2016). However, little research has been done on the mass transfer process of MPCMS its application in solution dehumidification. The isothermal endothermic characteristic of MicroPCMs is expected to be utilized to restrain the solution

temperature rise during the dehumidification process. Thus, this "auto-internally cooling" liquid desiccant dehumidifier can overcome the defects of the conventional internal cooling dehumidifier.
The liquid desiccant dehumidification can be considered as a process in which the liquid falling film on the flat plate (or corrugated plate) exchanges heat and mass with the air. An appropriate mathematical model is of great significance for exploring the heat and mass transfer mechanism of the phase change microcapsule slurry dehumidification process. Early scholars used the dual-mode theory to determine the interface mass transfer coefficient, and considered that the mass transfer coefficient has a linear relationship with the diffusion coefficient [9]. In the field of chemical industry, the permeability theory is often employed to determine the mass transfer coefficient [10]. But the effective contact time of gas and liquid in this theory is difficult to determine, which limits its application to some extent. Ren et al. (2016) obtained the analytical solution of the heat and mass transfer coefficient based on the one-dimensional model in the study of the falling film evaporative cooling problem, and can be used to test the numerical results of the two-dimensional model. Luo et al. (2014) used CFD technology, the dynamic characteristics of the heat and mass transfer parameters of the dehumidification process are obtained by simulation.
The purpose of this paper is to investigate the changes in heat and mass transfer characteristics and overall dehumidification performance of MPCMS with LiCl solution as base fluid. A two-dimensional flat film falling film heat and mass transfer model was established. Based on the control of differential equations model, the CFD technology was used to study the heat and mass transfer process of gas-liquid interface and the variation of various phase parameters in the flow field. The calculation of the mass transfer coefficient was different from the previous literature. By calculating the partial pressure of water vapor on the surface of the liquid film, the mass transfer coefficient was calculated by a dynamic boundary condition method. The characteristics of heat and mass transfer in dehumidification process with different concentrations of MicroPCMs and different inlet temperatures of MPCMS were compared.

2. MAIN SECTION

2.1. Physical model

Fig. 1 is the schematic diagram of falling film dehumidification with MPCMS. The phase change microcapsules are uniformly dispersed in the base fluid, and the slurry flows vertically downward along the wall surface of the plate. The humid air flows upward. The water vapor in the air enters the liquid film at the interface, and a complicated heat and mass transfer process occurs. The length of the plate is 300mm.

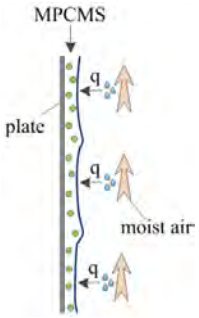

Figure 1: Schematic diagram of falling film dehumidification with MPCMS

The following assumptions were made:
(1) The phase change microcapsules are uniformly and stably dispersed in the base fluid, and the slurry can be regarded as a Newtonian fluid.
(2) Ignore the surface tension of the solution during the falling film flow.
(3) Ignore the interfacial thermal resistance of microcapsules, it is considered that the microcapsule melting time is extremely short, the microcapsule melting process is equivalent to the increase of the specific heat capacity of the slurry, and the specific heat capacity of the slurry is considered to be a single-valued function of temperature.
(4) The water vapor concentration at the vapor-liquid interface is saturated.
(5) Ignore the increase of liquid phase volume caused by slurry moisture absorption.

(6) The final flow field, temperature field and concentration field tend to be stable.
According to previous research literature, for a two-phase flow process with a distinct phase interface, the VOF model can be used to accurately capture the free surface of the liquid film (Luo et al., 2014).

2.2. Mathematical model

2.2.1. Control equation

(1) VOF volume fraction equation
The VOF model solves the governing equation by controlling the volume fraction of the different phases in the body. The model includes the liquid volume fraction rate equation and the gas phase volume fraction equation, and the sum of the gas and liquid volume fractions is 1.0.

$$\frac{\partial \alpha_g}{\partial t} + \vec{u} \cdot \nabla \alpha_g = 0 \qquad \text{Eq. (1-1)}$$

$$\frac{\partial \alpha_l}{\partial t} + \vec{u} \cdot \nabla \alpha_l = 0 \qquad \text{Eq. (1-2)}$$

$$\alpha_g + \alpha_l = 1 \qquad \text{Eq. (1-3)}$$

where α_g and α_l are the volume fractions of the gas phase and the liquid phase in %, respectively.
(2) Mass conservation equation

$$\frac{\partial \rho}{\partial t} + \nabla \cdot \rho \vec{u} = 0 \qquad \text{Eq. (2)}$$

(3) Momentum conservation equation

$$\frac{\partial}{\partial t}(\rho \vec{u}) + \nabla \cdot (\rho \vec{u}\vec{u}) = -\nabla P + \nabla \cdot (\mu(\nabla \vec{u} + \nabla \vec{u}^{\mathrm{T}})) + \rho \vec{g} + \vec{F} \qquad \text{Eq. (3)}$$

where F is the momentum source term.

(4) Energy equation

$$\frac{\partial}{\partial t}(\rho E) + \nabla \cdot (\vec{u}(\rho E + P)) = \nabla \cdot (k_{\mathrm{eff}} \nabla T) + Q \qquad \text{Eq. (4-1)}$$

$$\frac{\partial}{\partial t}(\rho E) + \nabla \cdot (\vec{u}(\rho E + P)) = \nabla \cdot (k_{\mathrm{eff}} \nabla T) + Q \qquad \text{Eq. (4-2)}$$

where Q is the energy source term in $kJ \cdot m^{-2} \cdot s^{-1}$ which is expressed as latent heat transfer due to mass transfer in the dehumidification process. H_l is the latent heat released when water vapor condenses in $kJ \cdot kg^{-1}$.

2.2.2. Initial and boundary conditions

(1) Initial conditions

At the initial moment, it is assumed that there is no liquid phase in the entire watershed, and only a stationary gas phase exists, that is, α_l=0, α_g=1.0.

(2) Boundary conditions

The specific settings of the boundary conditions are shown in Table 1.

Table 1. Boundary conditions

	volume fraction	velocity	thermal	UDS1 (air)	UDS2(liquid)
Liquid inlet	α_l=1，α_g=0	u=$u_{l,in}$	$T_{l,in}$		$\xi_{s,in}$
Liquid outet	α_l=0，α_g=1	pressure outlet	$T_{a,in}$		
Air inlet	α_l=0，α_g=1	u=$u_{g,in}$	$T_{a,in}$	$w_{a,in}$	
Air outlet	α_l=0，α_g=1	pressure outlet	$T_{a,in}$		
Wall		no slip	q_w=0		

2.2.3. Calculation method

The pressure-based solver of Fluent 17.0 was used in the calculation. The pressure-velocity coupling equation used the SIMPLE algorithm, and the Body Force Weighted algorithm was selected for the flow stress term dominated by gravity. The whole calculation process was divided into two parts: firstly the steady-state velocity field and phase distribution field was solved, and then the unsteady temperature field and gas-liquid concentration field was solved simultaneously. For the water vapor concentration equation on air side and the concentration equation on solution side, two UDS equations need to be established separately, while the dynamic boundary conditions and source terms were introduced through the User Defined Function (UDF). In addition, the physical properties of MPCMS in this simulation were also calculated by UDF.

The UDF was created as follows: A DEFINE_ADJUST macro was used to assign the value to the gas-liquid interface grid of 0.5 < C_VOF < 1. The dynamic boundary conditions of the water vapor concentration equation were automatically updated at each iteration step. The concentration gradient at the gas-liquid interface was obtained by using C_UDSI_G, and the mass transfer flux at the interface is calculated. A new temperature field is obtained by introducing the source term into the energy equation through DEFINE_SOURCE macro. The newly calculated solution temperature will affect the surface equilibrium moisture content again.

2.3. Results and Discussion

The effects of mass concentration of MicroPCMs and the inlet temperature of slurry on the dehumidification process were mainly studied. The calculation conditions are shown in Table 2.

Table 2. Calculation condition

Air inlet	$V_{a,in}$ (m·s^{-1})	$T_{a,in}$ (°C)	$w_{a,in}$ (g·kg^{-1})	
	0.5	35	22	
MPCMS inlet	$V_{s,in}$ (m s^{-1})	$T_{s,in}$ (°C)	ξ (%)	c_m (%)
	0.1	23-32 °C	35	1.0~5.0

2.3.1. Effect of MicroPCMs Concentration on Interface Mass Transfer Coefficient

Fig. 2 shows the mass transfer coefficient on the interface along the falling film direction with different MicroPCMs concentrations. It can be found that the interfacial mass transfer coefficient of the MPCMS is significantly higher than that of the base fluid, especially in the air inlet and the central region of falling film. The average interfacial mass transfer coefficient of the MPCMS with only 1% (wt) microcapsules is 19.8% higher than that of the base fluid. There are two reasons for this phenomenon: Firstly, the surface vapor pressure of the slurry decreases after the addition of MicroPCMs, which leads to an increase of the mass transfer potential difference. As a result, the interface mass transfer coefficient is improved to some extent. Secondly, MicroPCMs can restrain the solution temperature rise in the phase change temperature region. Thus a low surface vapor pressure of the slurry can be maintained and the mass transfer coefficient does not decrease rapidly.

It can be also found that when the c_m is 4%, the interface mass transfer coefficients are the highest. When the c_m increases further, the interface mass transfer coefficient decreases. There may be an optimum amount of MicroPCMs added. It can be explained as follows: when the concentration of MicroPCM is increased, the vapor pressure on the surface of the slurry is continuously reduced, which is beneficial to enhance the mass transfer process. However, the viscosity of the MPCMS will also increase, resulting in the weakening of disturbance effect on the interface, and the convective mass transfer effect is deteriorated.

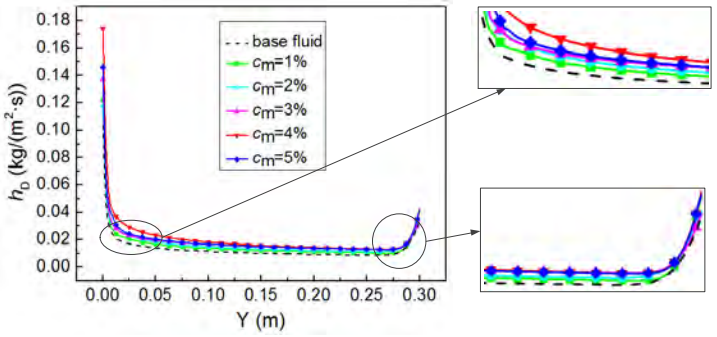

Figure 2: Variation of interfacial mass transfer coefficient with MicroPCMs concentration

2.3.2. Effect of MicroPCMs Concentration on Air Outlet Moisture Content and Overall Mass Transfer Coefficient

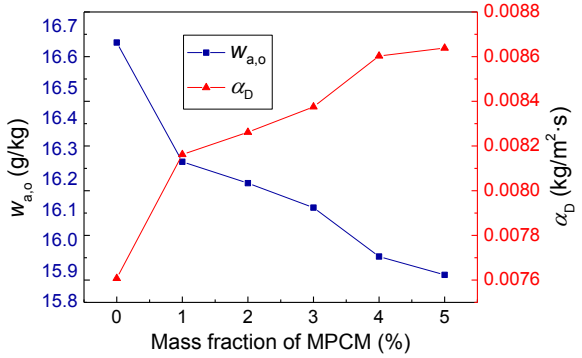

Figure 3: Variation of outlet air moisture content and overall mass transfer coefficient with MicroPCMs concentration

As shown in Fig.3, the addition of microcapsules significantly improves the overall condensation rate. The average moisture content of air after dehumidification with the slurry of c_m=1% decreases by 0.39 g·kg^{-1} compared with the base liquid. When the c_m continues to increase, the improvement on dehumidification is more pronounced. When c_m=5%, the average moisture content of the air outlet reaches 15.89 g·kg^{-1}, which is 0.76 g·kg^{-1} lower than that of the lithium chloride base fluid, and the condensation rate increases by 14.2%.

It can be also seen from the figure that, the overall mass transfer coefficient is obviously improved by adding MicroPCMs. But such improvement effect slows down when the MicroPCMs concentration is further increased. The main reason for this phenomenon is that, the surface vapor pressure of the liquid desiccant solution decreases significantly after the addition of MicroPCMs, but the decrease becomes slower with the increase of MicroPCMs. Moreover, the increase of the amount of microcapsules causes the viscosity of MPCMS to rise, which is not conducive to convective mass transfer.

2.3.3. Effect of MicroPCMs concentration on solution temperature

Fig. 4 shows the change of liquid film temperature with the concentration of micro-CMS. The inlet temperature of solution $t_{s,in}$ in all curves is 27 °C. It can be seen from the figure that, when the concentration of MicroPCMs is 1%, the temperature of the liquid film outlet is higher than the base liquid. While the MicroPCMs concentration is doubled, the temperature rise has been significantly restrained. Moreover, with the increase of MicroPCMs concentration, the temperature rise restraining

effect is more and more significant. When c_m=5%, the slurry outlet temperature is lowered by 0.55 °C than the base liquid. The reason can be explicated as follows: With the addition of MicroPCMs in the solution, the decrease of surface vapor pressure of the slurry leads to the increase of mass transfer and latent heat absorbed by slurry. However, the apparent specific heat capacity of slurry with low MicroPCMs concentration is relatively low, which is insufficient to restrain the temperature rise attributable to more latent heat generated by the increase of mass transfer. When the concentration of MicroPCMs is further increased, the apparent specific heat capacity of the slurry rises sharply in a nearly linear tendency, which is sufficient to restrain the higher temperature rise of the solution caused by the enhanced mass transfer. Therefore, at a higher concentration of MicroPCMs, the restraining effect of solution temperature rise is more significant.

2.3.4. Temperature distribution characteristics of liquid film at different slurry inlet temperatures

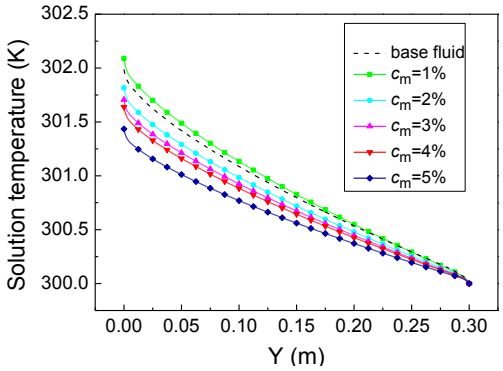

Figure 4: Variation of liquid film temperature with MicroPCMs concentration

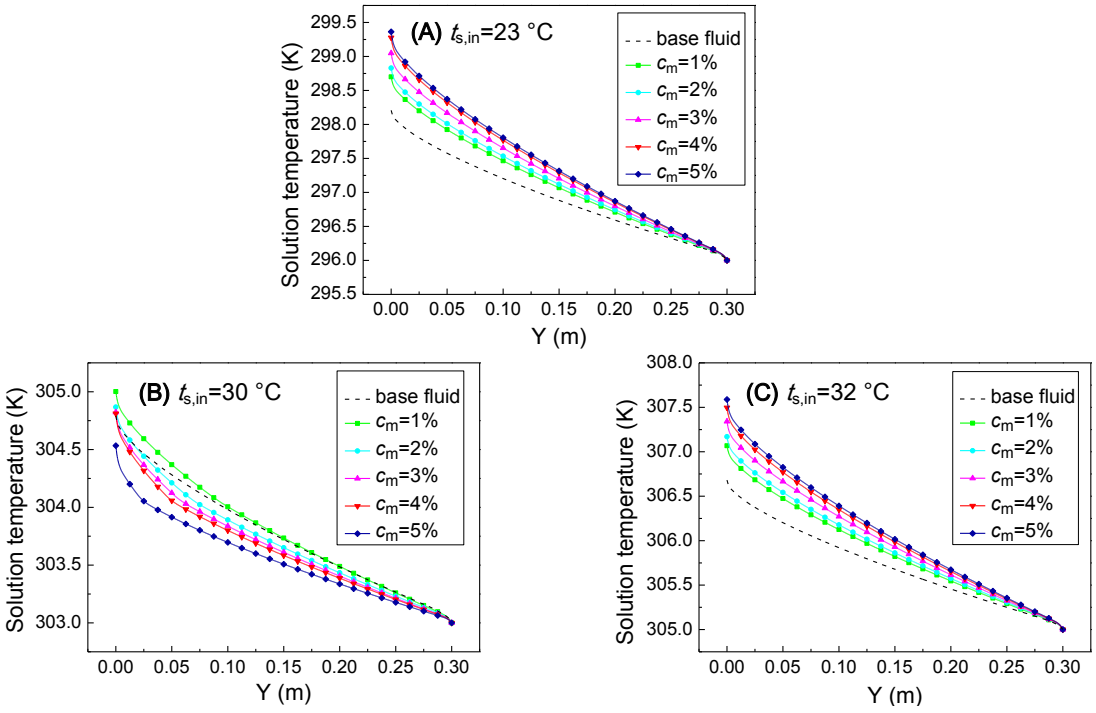

Figure 5: Temperature distribution along falling film direction at different inlet solution temperature and capsule concentration

Four different inlet temperatures of MPCMS were selected to compare the liquid film temperature distributions at different MicroPCMs concentrations (as shown in Fig.4 and Fig.5). It can be seen that, when the inlet temperature of the slurry is beyond the MicroPCMs phase temperature change zone(27~31°C), the temperature rise of the slurry is much higher than that of the base liquid. This is because that, the specific heat capacity of the slurry outside the phase change temperature zone will reduce, while the heat transfer is more intense since the surface vapour pressure is becomes

low, resulting in a significant temperature rise of the slurry. However, when the inlet temperature of the solution is in or close to the MicroPCMs phase change temperature zone, the restraining effect of MicroPCMs on the temperature rise begins to emerge, but the addition of MicroPCMs needs to achieve a certain amount. For example, when $t_{s,\,in}$=27 °C and c_m=1%, the slurry outlet temperature is still higher than the base liquid.

Fig. 6 and Fig. 7 show the changes of the liquid film temperature at different MPCMS inlet temperatures and at different positions, respectively. The concentration of the MicroPCMs is 5%. It can be seen from Fig. 6 that, the temperature of the solution increased along the falling film direction. It should be noted that the temperature rise of the solution outside the phase change temperature zone is more significant. This is because that, the equivalent specific heat capacity of the suspension in the phase change temperature region is about twice that of the base liquid, so the temperature rise restraining effect is obvious. Figure 7 is the liquid film temperature at six different positions in the falling film direction. There is a remarkable feature that at y = 0 to 0.06 m, the temperature rise of the solution is more intense than the rest, because such area is the air inlet region and the mass transfer process is more intense.

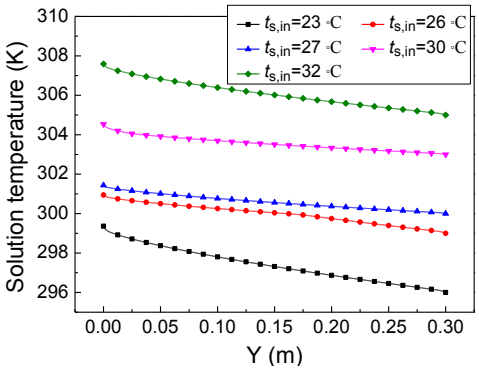

Figure 6: Variation of liquid film temperature with different inlet solution temperature when c_m=5%

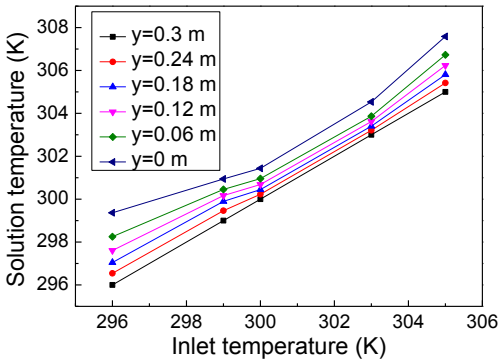

Figure 7: Variation of liquid film temperature at different y values when c_m=5%

3. CONCLUSIONS

In this study, the MicroPCMs with a phase change temperature of 27~31 °C was added to lithium chloride desiccant solution, and the temperature rise of the solution during dehumidification process was expected to be restrained by the isothermal endothermic property of MicroPCMs. A two-dimensional flat film falling film model was established to simulate the heat and mass transfer characteristics of MPCMS falling film dehumidification. The change of the physical properties of the slurry after adding MicroPCMs was considered, and the endothermic effect of the microcapsules was equivalent to the increase of the apparent specific heat capacity. The effects of MPCMS temperature and concentration of MicroPCMs were obtained. The main conclusions are as follows:

(1) The mass transfer coefficient of MPCMS interface after adding microcapsules is significantly higher than that of lithium chloride base fluid, especially in the air inlet and the central region of falling film. There is an optimum MicroPCMs concentration that maximizes the interface mass transfer coefficient.

(2) The addition of MicroPCMs has a significant improvement effect on the dehumidification capacity and the overall mass transfer coefficient. However, with the increase of MicroPCMs concentration, the improvement effect slows down.

(3) Temperature has a great influence on the mass transfer. When the inlet temperature of the MPCMS is 27 °C, the low concentration of MicroPCMs is not enough to restrain the temperature rise. With the increase of MicroPCMs concentration, the temperature rise restraining effect is more significant. When c_m=5%, the liquid outlet temperature is reduced by 0.55 °C compared to the base fluid. While the inlet temperature of the slurry is beyond the MicroPCMs phase temperature change zone (27~31°C), the temperature rise of the slurry is much higher than that of the base liquid.

ACKNOWLEDGEMENTS

This work was supported by the National Key Research and Development Program of China [grant number 2018YFC0704303]; and the National Natural Science Foundation of China [grant number 51406076].

NOMENCLATURE

c_m	mass concentration of MicroPCMs(%)	t	temperature (°C)
α	volume fraction (%)	w	humidity ratio ($g \cdot kg^{-1}$)
ξ	mass concentration of lithium chloride	v,u	flow velocity($m \cdot s^{-1}$)
Subscript:			
a	air	out	outlet
in	inlet	s	slurry

REFERENCES

Delgado, M., Lázaro, A., Mazo, J., et al.,2012. Review on phase change material emulsions and microencapsulated phase change material slurries: Materials, heat transfer studies and applications. Renew. Sust. Energ. Rev. 16(1),253-273.

Liu, J., Liu, X., Zhang, T.,2016. Performance comparison of three typical types of internally-cooled liquid desiccant dehumidifiers. Build. Environ 103,134-145.

Liu, J., Zhang, T., Liu, X., et al.,2015. Experimental analysis of an internally-cooled/heated liquid desiccant dehumidifier/regenerator made of thermally conductive plastic. Energy Build. 99,75-86.

Liu, L., Alva, G., Jia, Y., et al.,2016. Dynamic thermal characteristics analysis of microencapsulated phase change suspensions flowing through rectangular mini-channels for thermal energy storage. Energy Build. 134,37-51.

Luo, Y.M., Yang, H.X., Lv, L.,2014. Liquid desiccant dehumidifier: Development of a new performance predication model based on CFD. Int. J. Heat Mass Tran. 69(2),408-416.

Niu, X..F, Xu, Q., Zhang, Y., et al.,2017. Fabrication and Properties of Micro-Nanoencapsulated Phase Change Materials for Internally-Cooled Liquid Desiccant Dehumidification. Nanomaterials 7(5),96.

Pania, M., Xi, Y., Li, Y.,2012. Utilization of phase change materials and rubber particles to improve thermal and mechanical properties of mortar.Constr. Build. Mater. 28(1),713-721.

Ren, C., Wan, Y.,2016. A new approach to the analysis of heat and mass transfer characteristics for laminar air flow inside vertical plate channels with falling water film evaporation. Int. J. Heat Mass Tran. 103,1017-1028.

Sohn, C.W., Chen. M.M.,1981. Microconvective thermal conductivity in disperse two-phase mixtures as observed in a low velocity couette flow experiment. J. Heat Transfer 103(1),47-51.

Xu, Y.Y., Paschke, S., Repke, J. U., et al.,2009. Computational Approach to Characterize the Mass Transfer between the Counter‐Current Gas‐Liquid Flow.Chem. Eng. Technol. 32(8),1227-1235.

Yin,Y., Qian, J., Zhang, X.,2014.Recent advancements in liquid desiccant dehumidification technology. Renew. Sust. Energ. Rev. 31(31),38-52.

Zeng, R., Wang, X., Chen, B., et al.,2009. Heat transfer characteristics of microencapsulated phase change material slurry in laminar flow under constant heat flux. Appl. Energy 86(12),2661-2670.

Manuscript ID: 607
DOI: 10.18462/iir.icr.2019.0607

Condensation and evaporation of pure refrigerant flowing in small diameter micro-fin tubes

M. Khairul BASHAR[(a)], Keisuke NAKAMURA[(a)], Keishi KARIYA[(b)], Akio MIYARA[(b),(c)]

[(a)] Graduate School of Science and Engineering, Saga University
Saga, 840-8502, Japan, khairul.me08@gmail.com , 18575024@edu.cc.saga-u.ac.jp
[(b)] Department of Mechanical Engineering, Saga University
Saga, 840-8502, Japan, kariya@me.saga-u.ac.jp
[(c)] International Institute for Carbon-Neutral Energy Research, Kyushu University
Fukuoka, 819-0395, Japan, miyara@me.saga-u.ac.jp

ABSTRACT

The heat transfer coefficients were measured for condensation and evaporation of R134a and R1234yf inside smooth and micro-fin tubes. The experiments were performed for a smooth tube of 2.14 mm inner diameter and three micro-fin tubes of 2.17 mm, 2.68 mm and 3.18 mm equivalent diameter respectively. To measure the local heat transfer coefficient, the test section is sub-divided into three sections and having a total of 852 mm working length. The ranges of refrigerant mass flux were from 50 -100 kg m^{-2} s^{-1}, and the saturation temperature was 20 °C for condensation and 13 °C for evaporation. Effects of mass flux, vapour quality, tube diameter and refrigerant properties on heat transfer coefficient were considered. During the evaporation test, the heat transfer coefficient of R1234yf was found to be lower than that of R134a. Microfin tubes are more efficient than smooth tube. Typical correlations were used to predict the measurement.
Keywords: Condensation, Evaporation, Heat Transfer Coefficient, Microfin Tube, R134a, R1234yf.

1. INTRODUCTION

With the approval of the Montreal protocol in August 1987, chlorofluorocarbon (CFC) and hydrochlorofluorocarbon (HCFC) refrigerant like R22, have already been or will be soon phased out since refrigerants like this have a high ozone depleting potential (ODP). Subsequently, the refrigeration, air-conditioning and heat pump systems are switching to hydrofluorocarbon (HFC) refrigerant like R134a as an alternative. However, many HFC refrigerant like R134a have comparatively high global warming potential (GWP) as shown in Fig. 1. Therefore, from an environmental point of view, switching from the high GWP to low GWP refrigerant is one of the most important consideration for refrigeration, air-conditioning and heat pump systems. As a substitute for R134a, new generation refrigerant R1234yf has many environmental benefits such as zero ODP and low GWP, thus, making it a promising refrigerant in future applications. The research regarding R1234yf condensation and evaporation heat transfer in microfin tube is scarce. Some researchers who have investigated different aspects associated with R1234yf are Col et al. (2013), Diani et al. (2015), Han et al. (2013), Kedzierski and Kang (2018), Padilla et al. (2011), Saitoh et al. (2011) and Wang et al. (2012) etc.

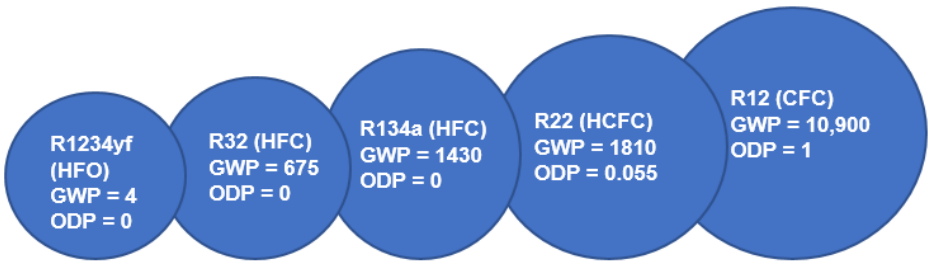

Figure 1: GWP and ODP of the different refrigerants

Presently, many refrigeration and air-conditioning (RAC) industries have highlighted the use of small diameter microfin tubes in RAC applications. Generally, the small diameter microfin tube provides higher heat transfer coefficient than a smooth tube with the same diameter. In addition, small diameter microfin tubes also offer many other advantages such as lower refrigerant charge, less weight, high efficiency, compactness and eco-friendliness. Many researcher who have studied various aspects of small diameter microfin tube (do<5 mm) are Bashar et al. (2018), Dang et al. (2010), Diani et al. (2014), Hirose et al. (2018), Jige et al. (2017) and Mancin et al. (2014) etc.
However, this paper reports some results about R134a and R1234yf condensation and evaporation heat transfer inside smooth and microfin tubes. The results permit to highlight the effects of the mass flux, vapour quality, tube diameter, and refrigerant properties on the heat transfer coefficient of the smooth and microfin tubes. The experimental results were also compared against the values predicted by correlations available in the literature.

2. EXPERIMENTAL APPARATUS

A test facility was established at the Miyara and Kariya Laboratory in the Saga University, Japan to specifically investigate the pressure drop, condensation and evaporation heat transfer coefficients of the refrigerants with horizontal microfin and smooth tubes. A detailed schematic diagram of the test facility with its various components is shown in Fig. 2. The test facility consists of a main refrigerant loop and some auxiliary loops (water baths and cooling/heating water loop), which adjust the desired conditions of the refrigerant in the main loop. Basically, the main loop itself comprises two pumps (one pump is measuring for low mass flux G<100 kg $m^{-2}s^{-1}$ and another one is measuring for high mass flux G<400 kg $m^{-2}s^{-1}$) circulating the refrigerant, a flow control valve for controlling the mass flow of refrigerant, a Coriolis mass flow meter to measure the refrigerant mass fluxes, two pre-heaters, test sections, an accumulator and a cooler. The pre-heaters was employed to pre-heat the liquid refrigerant to the desired condition entering in the test section. The accumulator was used to control the pressure of the system. Moreover, sight glasses were installed at two locations to monitor the refrigerant condition. The entire experimental facility was well insulated so that the outside temperature was not affected. All signals from the measuring devices are collected by a PC using LabVIEW.
Fig.3 shows the schematic diagram of the test section (total length is 852 mm), which consist of a horizontally installed tube, two headers, water channels, three sub-sections (each sub-section length being 248 mm) and total 24 T-type thermocouples on the tube wall for measuring wall temperature. The refrigerant flows inside the test tube, while the counter-current water flows through the water loop, as shown in Fig 3.
The test tube is made of copper. In this study, four types of test tubes were used and their dimensions are listed in Table 1. Photography and schematic view of the test tube is shown in Fig. 4.

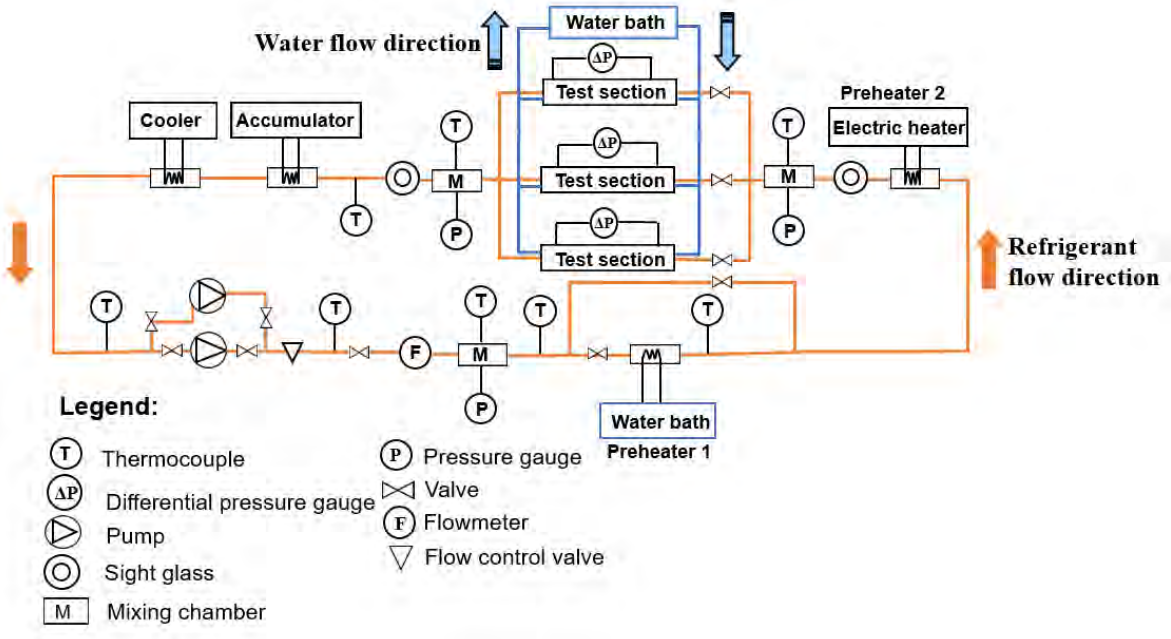

Figure 2: Schematic diagram of the test facility

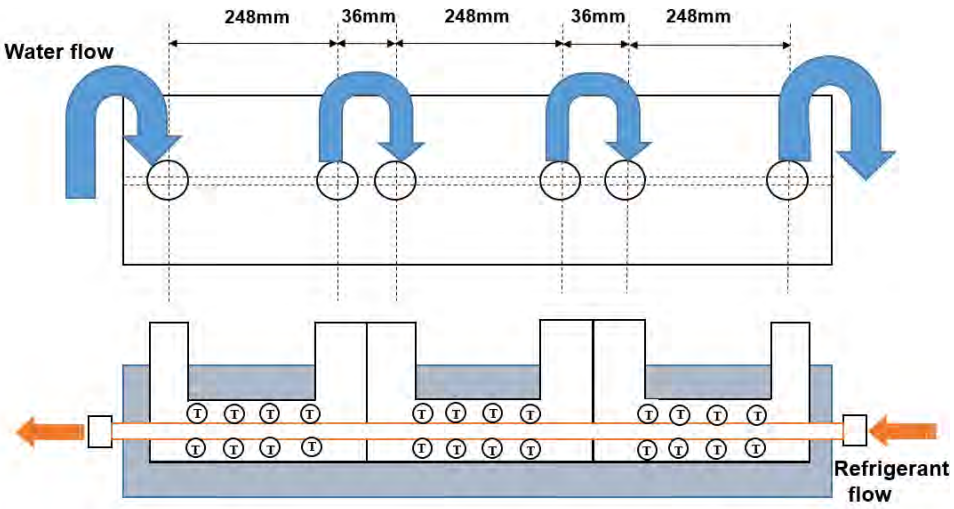

Figure 3: Schematic diagram of the test section

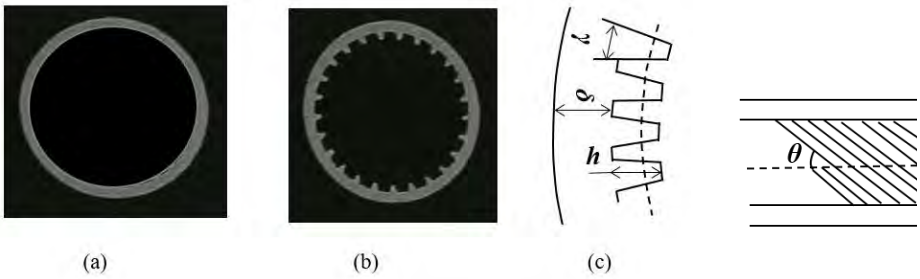

Figure 4: Photography and schematic view of the test tube: (a) smooth tube; (b) microfin tube; and (c) schematic view of the microfin tube

Table 1. Specifications of the test tubes

Parameter (unit)	Type 1 (Smooth tube)	Type 2 (Microfin tube)	Type 3 (Microfin tube)	Type 4 (Microfin tube)
Outside diameter d_o (mm)	2.5	3.5	3.0	2.5
Inner diameter d_i (mm)	2.14	-	-	-
Equivalent diameter d_{eq} (mm)	-	3.18	2.68	2.17
Wall thickness δ (mm)	0.18	0.15	0.15	0.15
Fin height h (mm)	-	0.10	0.10	0.10
Apex angle γ (mm)	-	35	33	31
Helix angle θ (°)	-	10	10	10
Number of fin n (-)	-	25	25	25

3. DATA REDUCTION

The local evaporation and condensation heat transfer coefficient, α, was calculated by Eq (1) and (2) respectively. The inlet vapour quality of refrigerant was calculated by Eq. (3)

$$\alpha = Q_c/\pi d_{eq} L(T_{wi} - T_s) \quad \text{Eq. (1)}$$

$$\alpha = Q_c/\pi d_{eq} L(T_R - T_{wi}) \quad \text{Eq. (2)}$$

$$x = (h_0 - h_l)/(h_v - h_l) \quad \text{Eq. (3)}$$

When the smooth tube d_{eq} was used in the experiment, it was defined by the inner diameter d_i.

4. RESULTS AND DISCUSSION

This section describes the experimental results of R134a and R1234yf in smooth and microfin tubes. For most of the obtained data, the heat balance of the evaporation and condensation heat transfer coefficient was estimated within ± 10%. The heat balance was defined as the ratio of the heat exchange amount on the refrigerant side to the heat exchange amount on the water side.

4.1. Evaporation Test Results

Fig. 5 shows the effect of mass flux and vapour quality on the evaporation heat transfer coefficients. The experiment was carried out in a 2.5 mm outer diameter microfin tube at 13 °C saturation temperature, 50-100 kg $m^{-2}s^{-1}$ mass fluxes and 15 kW m^{-2} heat flux. At 50~100 kg $m^{-2}s^{-1}$, the heat transfer coefficient increases with mass flux. Although, a weak effect of the mass flux was observed on the heat transfer coefficient at low vapour quality region. However, heat transfer coefficient was also increased with vapour quality. In fact, the heat transfer coefficient at x=0.53 is almost double than that measured at 0.1<x<0.2 for mass flux 100 kg $m^{-2}s^{-1}$.

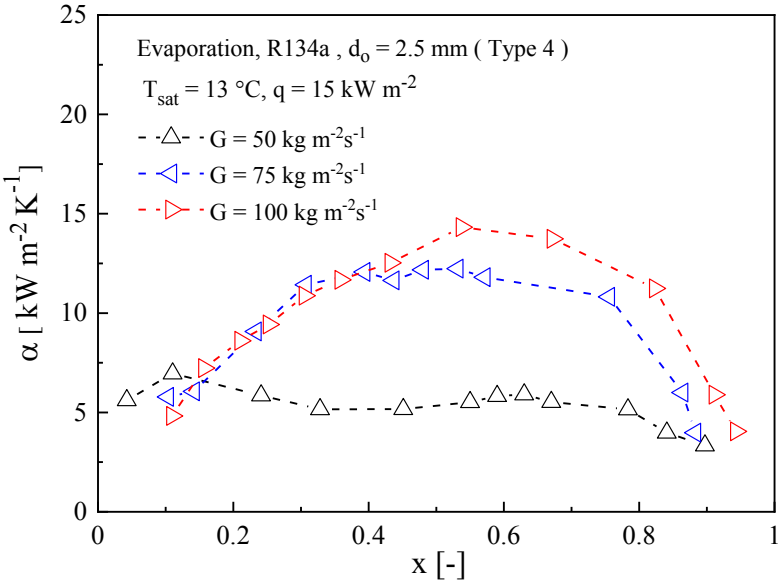

Figure 5: Effect of mass flux and vapour quality on the heat transfer coefficients

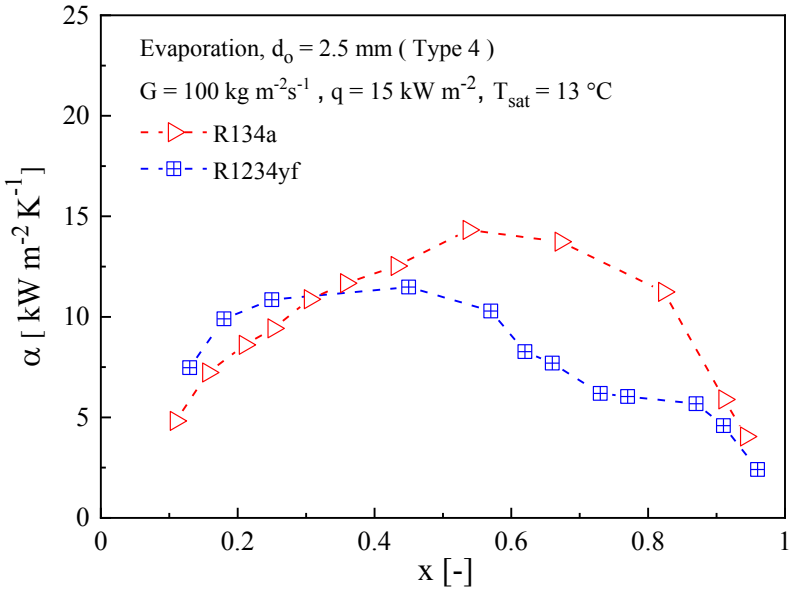

Figure 6: Comparison among the heat transfer coefficient of R134a and R1234yf

As clarified in the introduction, R1234yf has a low GWP compare to the R134a. Thus, R1234yf is one of the potential alternatives for R134a. Hence, a comparison of the evaporation heat transfer coefficient between the two refrigerants at the same experimental condition is proposed and it is shown in Fig.6. It is seen that, R134a shows a higher heat transfer coefficient than that of R1234yf especially at high vapour quality region. It is possible to state that, R134a has a vapour density 5.9% lower than that of R1234yf (see Table 2), and therefore, at fixed mass flux, its vapour velocity is higher, which might imply a higher heat transfer coefficient.

Fig. 7 shows the effect of microfin and tube diameter on the heat transfer coefficient. The working condition includes 13 °C saturation temperature, 50 kg $m^{-2}s^{-1}$ mass flux and 15 kW m^{-2} heat flux. It is seen that, the microfin tube (Type 4) heat transfer coefficient is 1.5 to 2.3 times higher than same outer diameter smooth tube (Type 1). The area expansion ratio for the microfin tube is about 1.5. Consequently, fins provide additional heat transfer area and it may enhance convective heat transfer. As a result, the microfin tube provides a higher heat transfer coefficient than the smooth tube with equal diameter. In addition, the tube diameter is seen to have an effect on the heat transfer coefficient. It is also seen from Fig. 7, that a decrease of the tube diameter could help to improve the heat transfer coefficient particularly at low vapour quality region. While, more experiments under various conditions are needed for confirmation of this trend, generally, when the tube diameter decreases, the effect of shear stress and surface tension increases; this results in a higher heat transfer coefficient.

Furthermore, tube diameter has an effect on dryout quality. Fig.8 shows the effect of the tube's inner diameter on dryout vapour quality. As shown from this Fig.8, the dryout vapour quality X_{dryout} decreased with decreasing inner diameter d_i. Our experimental results are agreeing well with the tendency of experimental results by Saitoh et al. (2005) and Kattan et al. (1998). The calculation method of dryout quality followed by Saitoh et al. (2005).

Table 2. Thermophysical properties of R134a and R1234yf at saturation temperature of 13 °C and 20 °C from REFPROP 9.1 (Lemmon et al. 2013)

Refrigerant	Saturation Temperature(°C)	ρ_L (kg m^{-3})	ρ_v (kg m^{-3})	μ_L (μPa s)	μ_v (μPa s)	Ψ (mN m^{-1})
R134a	13	1251.0	22.18	226.65	11.20	9.65
R1234yf	13	1134.5	26.48	178.31	10.57	7.72
R134a	20	1225.9	27.65	207.75	11.48	8.71
R1234yf	20	1110.4	32.65	164.02	10.86	6.81

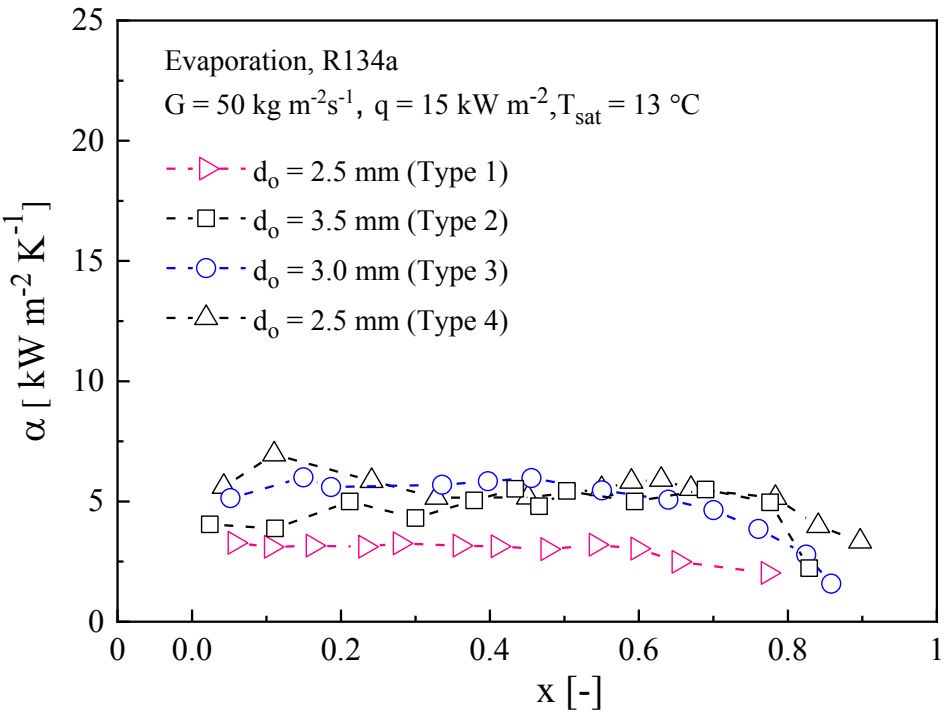

Figure 7: Effect of the microfin and tube diameter on heat transfer coefficient

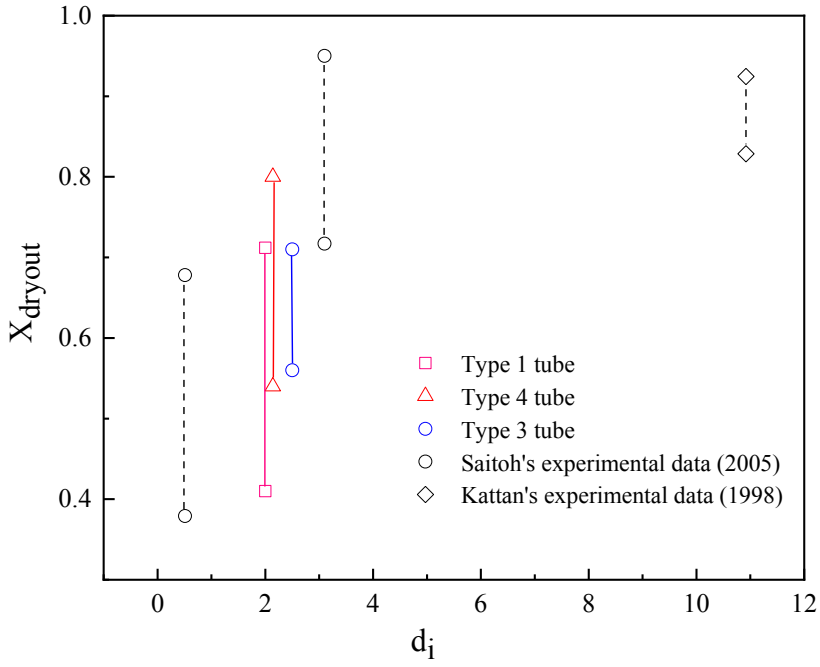

Figure 8: Experimental dryout quality X_{dryout} Vs tube inner diameter d_i

4.2. Condensation Test Results

Fig.9 shows the condensation heat transfer coefficient of R1234yf in 2.5 mm microfin tube at a mass flux and saturation temperature of 100 kg $m^{-2}s^{-1}$ and 20 °C respectively. Results showed that, the heat transfer coefficient decreased as condensation proceeded. The heat transfer coefficient was found to be higher at high vapour quality region because in this region, the velocity of vapour and liquid is high and shear stress increases due to this high velocity. The experimental heat transfer coefficient is compared to the prediction correlations of Koyama and Yonemoto (2006), and Kedzierski and Goncalves (1999) as shown in the Fig.9. The mean deviations of correlation are 19.5% and 64.5% for Koyama and Yonemoto (2006) and Kedzierski and Goncalves (1999) respectively. The correlation for Koyama and Yonemoto was based on data from microfin tubes with different refrigerant and it agrees well with our experimental data.

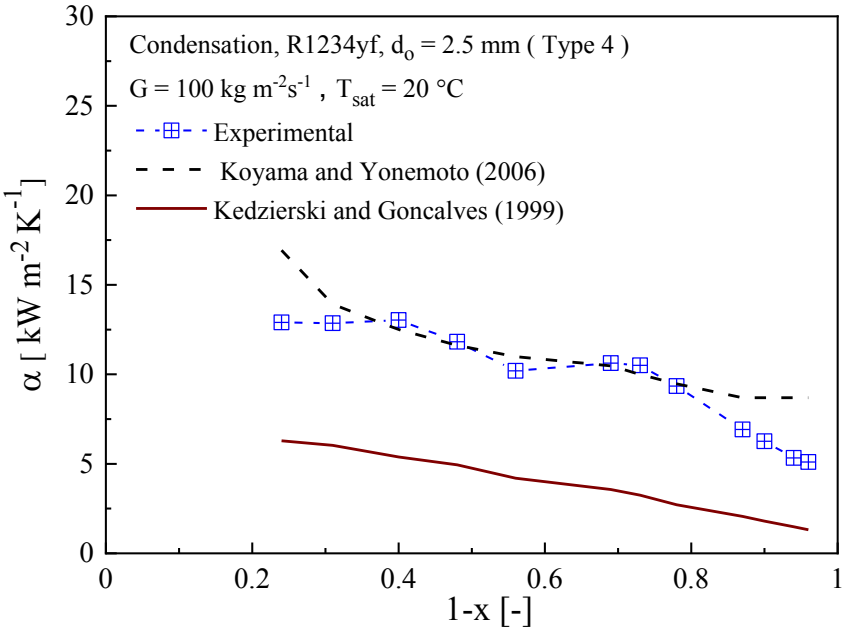

Figure 9: Condensation heat transfer coefficient of R1234yf in microfin tube

5. CONCLUSIONS

This study analysed the R134a and R1234yf condensation and evaporation inside smooth and microfin tubes. It was possible to verify that, the heat transfer coefficient depends on the mass flux, vapour quality, tube diameter and refrigerant properties. From the results of this analysis the following conclusion can be drawn.

1) The increasing of mass flux increased heat transfer coefficient as expected. Increasing mass flux 2 times (50 to 100 kg $m^{-2}s^{-1}$), may increase heat transfer coefficient about 1.2 to 2.5 times.
2) Refrigerant R134a shows better heat transfer performance than R1234yf under the same experimental conditions.
3) During evaporation test, the heat transfer coefficient of the microfin tube (type 4) is approximately 1.5 to 2.3 times greater than that of smooth tube (Type 1) at mass flux 50 kg $m^{-2}s^{-1}$. Decreasing the tube diameter may help improve the heat transfer performance and dryout quality depends on the tube inner diameter.
4) The condensation experimental result compared with correlations and the Koyama and Yonemoto correlation predict a mean deviation of 19.5%.

ACKNOWLEDGEMENTS

The authors would like to thank the Japan Copper Development Association for their financial support.

NOMENCLATURE

AD	average deviation	*d*	diameter (m)
G	mass flux (kg×m^{-2}×s^{-1})	*h*	enthalpy (kJ×kg^{-1})
L	length (m)	*n*	number of fin (-)
q	heat flux (kW×m^{-2})	*T*	temperature (°C)
Q	heat exchange amount (kW)	*α*	heat transfer coefficient (kW×m^{-2}×K^{-1})
x	vapour quality (-)	*γ*	apex angle (mm)
δ	wall thickness (mm)	*μ*	viscosity (μPa s)
ρ	density (kg×m^{-3})	*θ*	helix angle (°)
ψ	surface tension (mN×m^{-1})	*eq*	equivalent (-)
C	coolant	*i*	inner/inlet (-)
l	liquid (-)	*o*	outer/outlet (-)
pre	predicted (-)	*R*	refrigerant (-)
s	saturation (-)	*v*	vapour (-)
wi	inner wall (-)		

REFERENCES

Bashar, M.K., Nakamura, K., Kariya, K., Miyara, A., 2018. Experimental study of condensation heat transfer and pressure drop inside a small diameter microfin and smooth tube at low mass flux condition. Appl. Sci. 8(11), 2146.

Col, D.D., Bortolin, S., Torresin, D., Cavallini, A., 2013. Flow boiling of R1234yf in a 1 mm diameter channel. Int. J. Refrigeration 36(2), 353-362.

Dang, C., Haraguchi, N., Hihara, E., 2010. Flow boiling heat transfer of carbon dioxide inside a small-sized microfin tube. Int. J. Refrigeration 33, 655-663.

Diani, A., Mancin, S., Rossetto, L., 2014. R1234ze (E) flow boiling inside a 3.4 mm ID microfin tube. Int. J. Refrigeration 47, 105-119.

Diani, A., Mancin, S., Rossetto, L., 2015. Flow boiling heat transfer of R1234yf inside a 3.4 mm ID microfin tube. Exp. Therm. Fluid Sci. 66, 127-136.

Han, X., Li, P., Yuan. X., Wang, Q., Chen, G., 2013. The boiling heat transfer characteristics of the mixture HFO-1234yf/oil inside a micro-fin tube. Int. J. Heat Mass Transfer 67, 1122-1130.

Hirose, M., Ichinose, J., Inoue, N., 2018. Development of the general correlation for condensation heat transfer and pressure drop inside horizontal 4 mm small-diameter smooth and microfin tubes. Int. J. Refrigeration 90, 238-248.

Jige, D., Sagawa, K., Inoue, N., 2017. Effect of tube diameter on boiling heat transfer and flow characteristics of refrigerant R32 in horizontal small-diameter tubes. Int. J. Refrigeration 76, 206-218.

Kattan, N., Thome, J.R., Favrat, D., 1998. Flow boiling in horizontal tubes: part 2-new heat transfer data for five refrigerants. J. Heat transfer 120, 148-155.

Kedzierski, M.A., Kang, D., 2018. Horizontal convective boiling of R1234yf, R134a, and R450A within a micro-fin tube. Int. J. Refrigeration 88, 538-551.

Kedzierski, M.A., Goncalves, J.M., 1999. Horizontal convective condensation of alternative refrigerants within a microfin tube. J. Enhanced Heat transfer 6, 161-178.

Koyama, S., Yonemoto, R., 2006. Experimental study on condensation of pure refrigerants in horizontal microfin tube-proposal of correlations for heat transfer coefficient and frictional pressure drop. Proceedings of the Int. Refrig. Air-Cond. Conference, Purdue, USA, R133.

Lemmon, E.W., Huber, M.L., McLinden, M.O., 2013. Reference fluid thermodynamic and transport properties-REFPROF [9.1]; NIST standard database; NIST: Gaithersburg, MD, USA.

Mancin, S., Diani, A., Rossetto, L., 2014. R134a flow boiling heat transfer and pressure drop inside a 3.4 mm ID microfin tube. Energy Procedia 45, 608-615.

Padilla, M., Revellin, R., Haberschill, P., Bensafi, A., Bonjour, J., 2011. Flow regimes and two-phase pressure gradient in horizontal straight tubes: Experimental results for HFO-1234yf, R-134a and R-410A. Exp. Therm. Fluid Sci. 35, 1113-1126.

Saitoh, S., Dang, C., Nakamura, Y., Hihara, E., 2011. Boiling heat transfer of HFO-1234yf flowing in a smooth small-diameter horizontal tube. Int. J. Refrigeration 34, 1846-1853.

Saitoh, S., Daiguji, H., Hihara, E., 2005. Effect of tube diameter on boiling heat transfer of R-134a in horizontal small-diameter tubes. Int. J. Heat Mass Transfer 48, 4973-4984.

Wang, L., Dang, C., Hihara, E., 2012. Experimental study on condensation heat transfer and pressure drop of low GWP refrigerant HFO1234yf in a horizontal tube. Int. J. Refrigeration 35, 1418-1429.

Manuscript ID: 612
DOI: 10.18462/iir.icr.2019.0612

Theoretical analysis of energy efficiency on refrigerants in vapor compression refrigeration cycle under different conditions

Jiongliang HUANG[(a)], Yibo FANG[(a)], Kangli BAO[(a)], Xiaogang QIAO[(b)], Yingjie XU[(c)], Xiaohong HAN[(a)]*, Guangming CHEN[(a)]

[(a)] Key Laboratory of Refrigeration and Cryogenic Technology of Zhejiang Province, Institute of Refrigeration and Cryogenics, Zhejiang University, Hangzhou, 310027, P. R. China, hanxh66@zju.edu.cn
[(b)] Zhejiang College of Construction, Hangzhou, 311231, P. R. China, Qiao_xg@163.com
[(c)] Institute of Process Equipment and Control Engineering, Zhejiang University of Technology, Hangzhou, 310014, P. R. China, xuyingjie@zjut.edu.cn

ABSTRACT

The issue of global warming has aroused our concern of refrigerant replacement. It motivates people to seek appropriate refrigerants to reduce carbon emissions. To evaluate the impact of refrigerants on global warming, refrigerant charge, coefficient of performance (COP), volumetric refrigerating capacity and discharge temperature are required besides the GWP of given refrigerant. Therefore, based on vapor compression refrigeration cycle under different working conditions, theoretical analysis of energy efficiency on a series of refrigerants is carried out in this paper to achieve data needed for evaluation. According to the calculation results, some suggestions are provided for the selection of refrigerants.
Key words: Energy Efficiency, Refrigerants, Vapor Compression Refrigeration Cycle.

1. INTRODUCTION

Global warming is one of the major environmental problems we are facing today. The aggravation of this issue may adversely affect the world, and even damage the ecosystem irreversibly (Zhang et al., 2015). The environmental problem has increasingly aroused social concern. International community has successively formulated and signed a series of documents, including United Nations Framework Convention on Climate Change, Montreal Protocol, Kyoto Protocol and etc. On these conventions, the usage and substitution of environmentally unfriendly refrigerants are planned. As shown in Fig. 1, phase-out schedules of hydrochlorofluorocarbons (HCFCs) and hydrofluorocarbons (HFCs) respectively for China are given according to Kigali Amendment to the Montreal Protocol (Cui et al., 2017). In response to these documents, it is urgent for refrigeration industry to find alternative refrigerants. Environmental indicators are required to quantify the impact of refrigerants to global warming while selecting refrigerants, such as Global Warming Potential (GWP), Total Equivalent Warming Impact (TEWI), Life Cycle Climate Performance (LCCP) (Makhnatch et al., 2014). In recent years, some other indicators are proposed like CO_2 Emissions Reduction Rate (EER), Life Cycle Environmental Performance (LCEP) and Annual Environmental Performance (AEP) (Zhou et al., 2012). Formulas of these indicators are listed in Table 1.

Among all the indicators, GWP is probably the most commonly used. In the Fifth IPCC Assessment, GWP is defined as the time-integrated Radiative Forcing (RF) due to a pulse emission of a given component over a chosen time horizon, relative to that of an equal mass of CO_2 (IPCC, 2013). Although GWP is a practical indicator for comparing refrigerants, many other factors are not included, which might overestimate the benefits of low GWP refrigerants. Zhu et al. argued that simply using GWP was not a comprehensive way to evaluate (Zhu et al., 2011). Even if it is considered from the perspective of direct emissions (DE), the refrigerant charge should not be ignored. Thus, they proposed a new index, EER. On the other hand, devices using refrigerants have energy use during operation, and indirect emissions (IE) are caused by the electricity generated from the combustion of fossil fuels (Harby et al., 2017). GWP cannot reflect this impact. TEWI indicates the overall environmental influence of refrigerants on global warming, but some parameters like refrigerant

charge and COP are needed for calculation. Other indicators require these parameters as well. In addition, volumetric refrigerating capacity might affect the design of compressor size, and high discharge temperature will shorten the lifetime of compressor. These two factors have influence on the values of some indicators like LCEP and AEP. Based on the analysis above, in the process of refrigerant replacement, attention should be paid to not only the GWP values of refrigerants, but also other parameters which can be obtained from efficiency analysis. Therefore, it is necessary to carry out the analysis of energy efficiency on refrigerants in the refrigeration cycle.

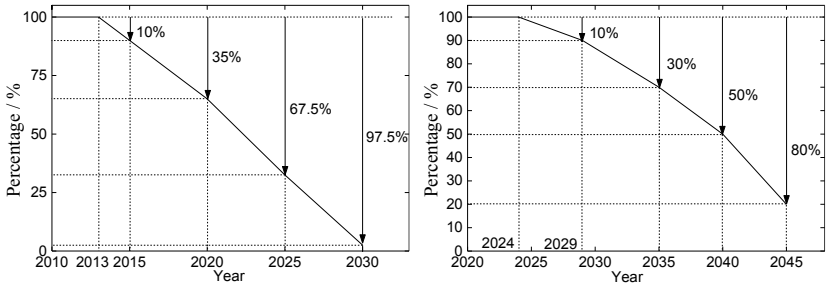

(a) HCFCs **(b) HFCs**

Figure 1: Phase-down schedules of HCFCs and HFCs for China according to Kigali Amendment.

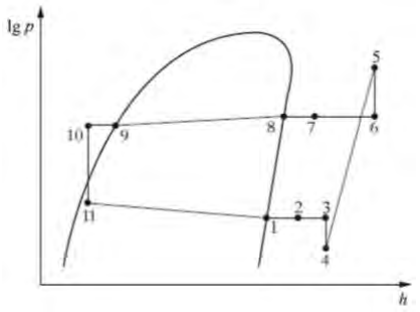

Figure 2: Schematic diagram of the actual cycle.

Table 1. Formulas of indicators for quantifying the impact of refrigerants to global warming

Indicator	Formula
TEWI	$TEWI = IE + DE = \frac{Q}{COP} \times hr \times N \times \beta + GWP \times (L \times N + m_1 \times (1 - \alpha_1))$
LCCP	$LCCP = TEWI + (E_1 + F_1) \times (L \times N + m_1 \times (1 - \alpha_1))$
ERR	$ERR = 1 - \frac{GWP_{substitute} \times m_{substitute}}{GWP_{R22} \times m_{R22}}$
LCEP	$LCEP = LCCP + \frac{ODP}{GWP} \times 10^5 \times DE + \sum_{i=2}^{n} m_i \times [(E_i + F_i) \times (1 - \alpha_i) + G_i \times \alpha_i]$
AEP	$AEP = \frac{LCEP}{Q \times N}$

Vapor compression refrigeration systems are responsible for a large proportion for total world energy use. Although thermally driven cooling systems have been developed to overcome this problem, vapor compression refrigeration systems which have a relatively high COP are still the first choice worldwide, especially in developing countries (Harby et al., 2017). Hence, selection of refrigerants for vapor compression refrigeration systems seems important if their environmental influence needs to be minimized. As previously mentioned, the calculation of different indicators requires the parameters of refrigerant charge, COP, volumetric refrigerating capacity and discharge temperature, so theoretical analysis of energy efficiency on a series of refrigerants in the vapor compression refrigeration cycle under different working conditions is conducted in this paper. It should be explained particularly that the refrigerants calculated in this paper include those which are eliminated already, being phased out gradually and probable to be utilized in the future. The main purpose of this article is to provide a comparative analysis. Without a comparison with refrigerants at different periods of phase out plan, it is difficult to evaluate the potential refrigerants objectively.

2. DESCRIPTION OF THE MODEL

The theoretical analysis of energy efficiency which is conducted in this study is based on an actual vapor compression refrigeration cycle. The cycle on lg P-h diagram is shown in Fig. 2. Process 11-2 represents evaporation of refrigerants in the evaporator. Process 2-4 represents the process of refrigerants flowing from the outlet of evaporator to the compressor before compression happens. Process 4-5 represents compression inside the compressor. Process 5-7 represents the process of refrigerants flowing from the outlet of compressor to the inlet of condenser. Process 7-10 represents condensation of refrigerants in the condenser. Process 10-11 represents the process of refrigerants flowing through the throttling element.

Compared to the ideal vapor compression refrigeration cycle, pressure drop through the evaporator and condenser, pressure drop at both inlet and outlet of the compressor, pressure drop alongside the pipeline, heat gain between the evaporator and the compressor, heat loss between the compressor and the condenser and isentropic efficiency, are considered, which makes the cycle closer to the actual one. The parameters related to pressure drop and temperature variation of the cycle are given in Table 2. Some of them are set according to Shaik's work (Shaik et al., 2017).Furthermore, some assumptions for the analysis are listed as follow:
(1) The system operates under steady-state conditions.
(2) In the evaporator and the condenser, pressure drop only occurs in the two-phase region which is presented as Process 11-1 and Process 8-9 respectively in Fig. 2.
(3) For convenience of calculation, Process 2-4 is divided into an isobaric process and an isenthalpic process. Refrigerants gain heat first and the temperature rises from state point 2 to state point 3. During this process, the pressure remains constant. Then, pressure loss of refrigerants, consisting of pressure drop at the inlet of the compressor and pressure drop alongside the pipeline between the evaporator and the compressor, occurs with the enthalpy unchanged. Process 5-7 is also seen as an isenthalpic process and an isobaric process successively.
(4) The process of refrigerants flowing through the throttling element is isenthalpic.
(5) During the cycle, the state of refrigerants does not reach the critical point.

Table 2. Parameters of the actual vapor compression refrigeration cycle

Parameter	Value
isentropic efficiency	0.75
evaporator pressure drop（kPa）	10
pressure drop alongside the pipeline between the evaporator and the compressor（kPa）	10
pressure drop at the inlet of the compressor（kPa）	20
pressure drop at the outlet of the compressor（kPa）	40
pressure drop alongside the pipeline between the compressor and the condenser（kPa）	10
condenser pressure drop（kPa）	10
increase in temperature due to heat gain（ºC）	10
decrease in temperature due to heat loss（ºC）	10

According to AHRI 540, three different working conditions, as listed in Table 3, are calculated (AHRI, 2004). All the refrigerants involved in this paper are listed in Table 4 (ASHRAE, 2016; IPCC, 2013; Kondo et al., 2002; Sánchez et al., 2017). During the analysis, calculation of refrigerant charge is on the basis of Wang's model (Wang et al., 2003), but it is assumed that heat flux density alongside the heat exchangers is uniform and the internal volumes of both evaporator and condenser are 1000 cm^3. It should be pointed out that these two assumptions may be far from reality, but it can still qualitatively compare the charge amount under the same condition. Besides, COP of the cycle is defined as:

$$\mathrm{COP} = \frac{w}{q} = \frac{h_5 - h_4}{h_2 - h_{11}} \quad \text{Eq. (1)}$$

$$q_v = q_m \times \rho_4 \quad \text{Eq. (2)}$$

$$T_{out} = T_5 \quad \text{Eq. (3)}$$

where w is the energy consumed by the compressor in kg/kW; q_m is the refrigerating capacity per unit mass in kg/kW; q_v is the volumetric refrigerating capacity in kJ/m^3; T_{out} is the discharge temperature in ºC; h is the enthalpy in kg/kW; ρ is the density in kg/m^3; T is the temperature in ºC; the numerical subscripts here represent corresponding state points in Fig. 2.

Table 3. Parameters of different refrigeration cycle

Condition	Evaporation temperature	Degree of superheat	Condensation temperature	Degree of subcooling
High temperature refrigeration	7.2	11.1	54.4	8.3
Medium temperature refrigeration	-6.7	11.1	43.3	0
Low temperature refrigeration	-31.7	11.1	40.6	0

Table 4. Information of refrigerants calculated in this paper

Refrigerant	GWP	Safety classification	Refrigerant	GWP	Safety classification
CFC-12	10200	A1	R404A	3 940	A1
CFC-115	7670	A1	R407C	1 620	A1
HCFC-124	527	A1	R410A	1 920	A1
HCFC-142b	1980	A2	R444A	89	A2L
HCFC-22	1 760	A1	R444B	295	A2L
HFC-32	677	A2L	R447A	572	A2L
HFC-125	3 170	A1	R448A	1273	A1
HFC-134a	1 300	A1	R449A	1291	A1
HFC-143a	4 800	A2L	R450A	547	A1
HFC-152a	138	A2	R454B	467	A2L
HFC-161	4	-	R454C	146	A2L
HFC-227ea	3 350	A1	R455A	146	A2L
HFO-1234yf	< 1	A2L	R463A	1377	A1
HFO-1234ze(E)	< 1	A2L	R500	7 560	A1
HFO-1243zf	< 1	-	R513A	573	A1
HC-290	3	A3	DR-4	298	-
HC-600a	4	A3	DR-33	955	-
HFC-41	116	-			

3. RESULTS AND DISCUSSION

According to Section 2, theoretical calculation results of energy efficiency on different refrigerants under three working conditions are given in Figs. 3 ~ 6. For the convenience of comparison, the order of refrigerants in figures below under the medium and low temperature refrigeration conditions is decided on the basis of the high temperature refrigeration condition.

3.1. Results of Refrigerant Charge

Firstly, the charge of refrigerants is investigated. Fig. 3 shows the results under three working conditions. 34 kinds, 32 kinds and 15 kinds of refrigerants are calculated under high, medium and low temperature refrigeration conditions, respectively. Combining with safety classification of ASHRAE 34, it can be found that some of the flammable pure refrigerants have evidently less charge amount, such as HFC-161(Class 3) and HC-290(Class 3). The charge amount of the rest refrigerants, except for HFC-115 and HFC-125, is close to each other, but the flammable refrigerants generally rank ahead in ascending order, which means their flammability risk is decreased to some extent.

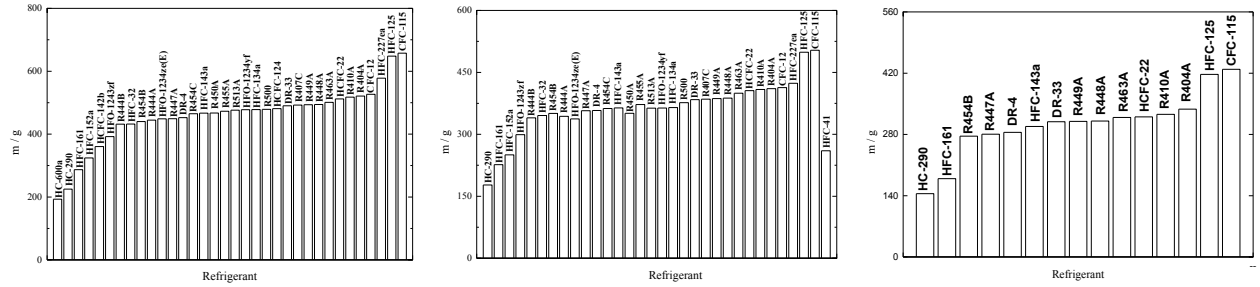

(a) High temperature refrigeration condition **(b) Medium temperature refrigeration condition** **(c) Low temperature refrigeration condition**

Figure 3: Calculation results of refrigerant charge under different conditions.

It is mentioned in Section 1 that some researchers suggest that both GWP and refrigerant charge should be taken into consideration to evaluate more objectively. Thus, high temperature refrigeration condition is taken as an example, and ERR of each refrigerant is obtained (The formula of ERR has been given in Table 1). It shows an approximate linear relationship between ERR and GWP. Here it

is a possible explanation: the maximum charge amount in Fig. 3 (a) is less than four times of the minimum one, however, the difference of GWP among refrigerants is much larger. Hence, the one with lower GWP generally has higher ERR. In summary, although combining GWP with refrigerant charge is more comprehensive, the indicator GWP is enough for comparison when a rough analysis is acceptable. Since it is convenient to obtain GWP value, the selection can be made quickly.

3.2. Results of COP

It can be observed from Fig. 4 that HFC-161, HFC-152a, HCFC-22, CFC-12, HFC-134a and HC-290 are the six pure fluids with the highest COP under high temperature refrigeration condition. Since HCFC-22 is the most widely used refrigerant in China, its COP is set as the baseline (the same below). And refrigerants with COP no less than 95% of the baseline are regarded as being acceptable in this section. The COP values of HFC-161 and HFC-152a are respectively 1.39% and 1.02% higher than the baseline, while CFC-12, HFC-134a and HC-290 have slightly lower COP (-0.03%, -0.90% and -1.04% respectively). These refrigerants keep the IE caused by the energy use of devices low. However, the flammability classification of HFC-152a is Class 2, while that of HFC-161 and HC-290 is Class 3. Three of them are flammable and the others are facing replacement due to environmental problems. Besides, most of the other acceptable pure fluids can be ignited, such as HFO-1234ze(E) (Class A2L, -2.26%), HCFC-142b (Class A2, -3.00%), HC-600a (Class A3, -4.36%), HFO-1234yf (Class A2L, -4.70%) and HFC-32 (Class A2L, -4.73%). HCFC-124, which is being phased out, is the only acceptable pure fluid classified as Class A1 except for HCFC-22, CFC-12 and HFC-134a. Therefore, there are limited refrigerants better than HCFC-22 from the perspective of IE. In addition, 17 mixed refrigerants are calculated. In recent years, tendency to HFO based mixed refrigerants has increased (Devecioğlu et al., 2015; Mota-Babiloni et al., 2015), so several HFC / HFO mixtures are investigated in this article. These 17 refrigerants all have at least one flammable component, but some of them are Class A1 fluids. The mixed refrigerants show similar COP to the baseline (no lower than 90% of it). The COP values of R455A (+1.14%), R444A (+0.77%), R500 (0), R454C (-1.04%), DR-4 (-1.21%) are the highest. And 14 mixtures are acceptable, including 6 Class A1 fluids (R500, R449A, R407C, R513A, R448A and R450A).

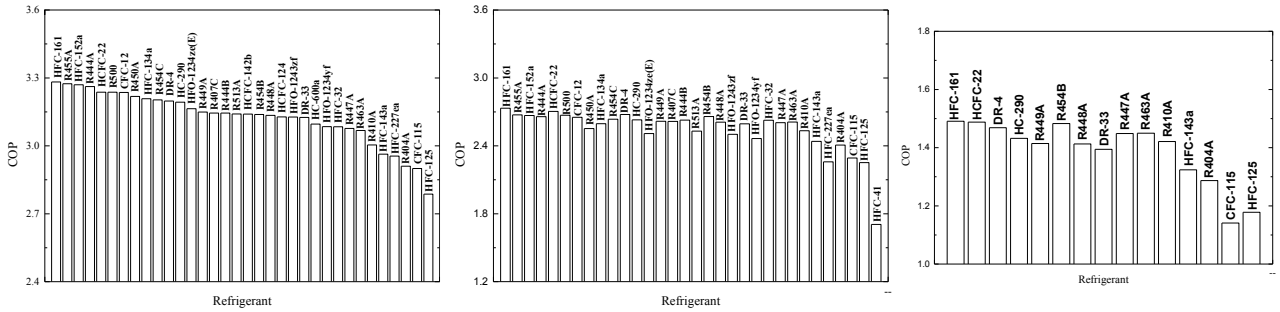

(a) High temperature refrigeration condition **(b) Medium temperature refrigeration condition** **(c) Low temperature refrigeration condition**

Figure 4: Calculation results of COP under different conditions.

Under medium temperature refrigeration condition, the lowest pressure in the cycle of three refrigerants is below atmospheric pressure, so they are not considered. One refrigerant (HFC-41) is added under this condition. The COPs of HFC-161, HFC-152a, HCFC-22, CFC-12 and HC-290 still remain relatively high. The difference to the baseline of each refrigerant is +1.04%, -1.33%, 0, -1.92%, and -2.74%, respectively. DR-4 (-0.98%), R455A (-1.12%), R500 (-1.26%), R454B (-1.66%) and R444A (-1.72%) perform best among all mixed refrigerants. Compared with high temperature refrigeration condition, most refrigerants become further below the baseline, such as R455A (from +1.14% to -1.72%), R444A (from +0.77% to -1.72%), HC-600a (from -4.36% to -10.39%), HFO-1234ze(E) (from -2.26% to -7.21%) etc. There also exist some exceptions. For example, the COP difference between HFC-32 and HCFC-22 rises from -4.73% to -2.88%, and meanwhile the COP of HFC-32 surpasses that of HFC-134a. It indicates that the performance of refrigerants varies under different refrigeration conditions. When it comes to flammability, R500, CFC-12, R449A (-3.19%), R407C (-3.25%) and R463A (-3.46%) are acceptable among all Class A1 refrigerants.

Because the lowest pressure in the cycle of some refrigerants is too low, the number of refrigerants that are calculated under this condition decreases sharply. HFC-161 (+0.20%) still have the best performance. In this case, few refrigerants without flammability meet the acceptable standard.

HCFC-22 is the only acceptable Class A1 pure fluid. In terms of Class A1 mixed refrigerants, there are R463A, R410A and R449A.

3.3. Results of Volumetric Refrigerating Capacity and Discharge Temperature

The calculation results of volumetric refrigerating capacity are shown in Fig. 5. To meet the demand of the same refrigeration capacity, refrigerants with larger volumetric refrigerating capacity needs smaller volume flow. It results in a tinier size of compressor and fewer materials required for manufacturing, which helps reduce the value of LCEP or AEP. Although most of the refrigerants have lower volumetric refrigerating capacity than HCFC-22, some outstanding refrigerants can be easily found. The capacity of HFC-32 is extremely high under the high and medium temperature refrigeration conditions, though it is not suitable to work under low temperature refrigeration condition. The mixed refrigerants, R454B, R463A, R447A and R410A, show high capacity under all conditions.

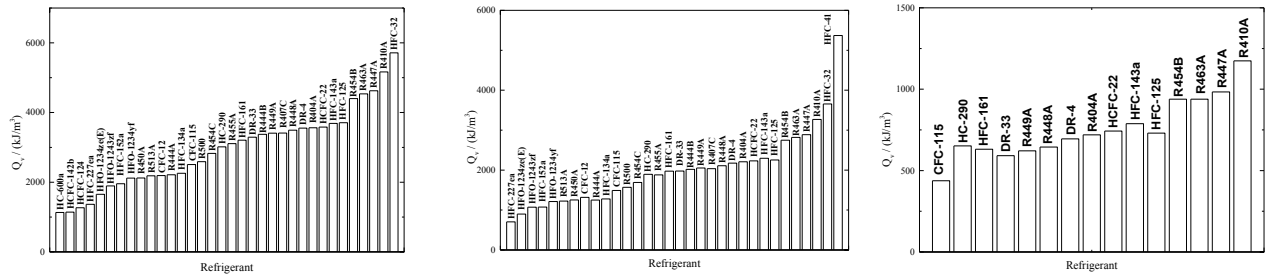

(a) High temperature refrigeration condition **(b) Medium temperature refrigeration condition** **(c) Low temperature refrigeration condition**

Figure 5: Calculation results of volumetric refrigerating capacity under different conditions.

The calculation results of discharge temperature are shown in Fig. 6. High discharge temperature may adversely affect the lifetime of compressor, resulting in a high value of AEP. It is observed that refrigerants showing high capacity in Fig. 5 have high discharge temperature meanwhile. For example, HFC-32 have the highest discharge temperature under the high and medium temperature refrigeration conditions. This situation also occurs when it comes to the mixed refrigerants which are mentioned above.

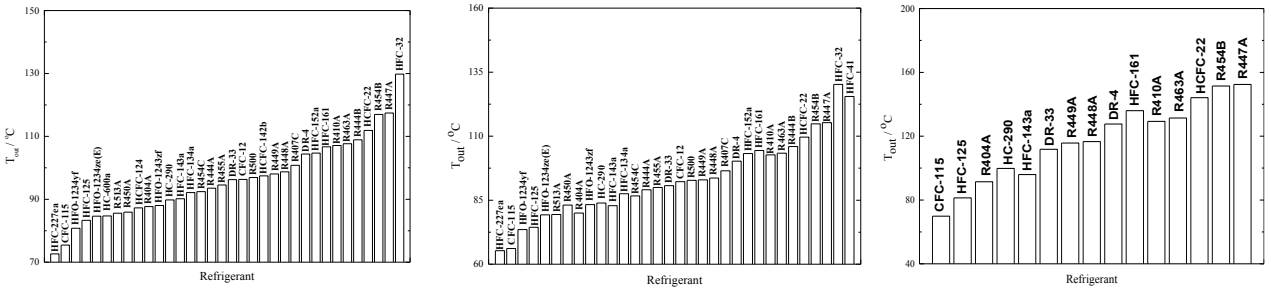

(a) High temperature refrigeration condition **(b) Medium temperature refrigeration condition** **(c) Low temperature refrigeration condition**

Figure 6: Calculation results of discharge temperature under different conditions.

3.4. Discussion

By comparison of calculation results among three working conditions, it can be seen that there is relative performance difference of refrigerants under various conditions, which results in the fluctuation of values, especially in Fig. 4(b) and Fig. 4(c). The compared results indicate that performance analysis under different conditions is indeed needed.

It can be found in Fig. 4 that HFC-161 has higher COP than HCFC-22 under all working conditions, while R455A, HFC-152a and R444A are better only under the high temperature refrigeration condition. However, since HCFC-22 has a relatively high GWP value with large charge amount, the DE of HCFC-22 becomes an important part of its total impact on global warming. Hence, if refrigerants with COP close to that of HCFC-22 have lower DE, carbon emissions might be reduced according to the indicator TEWI. It is assumed that the refrigerants work under high temperature refrigeration condition, and the parameters are listed in Table 5. As pure fluids, the TEWI values of

HFC-161, HFC-152a, HFC-134a, HC-290 and HFO-1234ze(E) are smaller than that of HCFC-22. R455A, R444A, R454C and DR-4 are mixed refrigerants with less carbon emissions. It is noteworthy that almost all of them are capable of igniting. In conclusion, the calculation results indicate that some flammable refrigerants have lower GWP, less refrigerant charge and COP close to that of HCFC-22. If these refrigerants are used carefully, it is an effective manner to reduce carbon emissions. Besides, it is noted that all HFC / HFO mixtures are acceptable or near acceptable. Five of them are Class A1 fluids, which demonstrates special design of composition to solve the problems of flammability without a significant performance cost. GWP value can also be decreased through combining refrigerants with low GWP and refrigerants with high GWP. Using mixed refrigerants is another practical means, and the special designed mixtures are the most possible potential substitute refrigerants.
Analysis of Fig. 5 and Fig. 6 reveals that there is contradiction between high volumetric refrigerating capacity and low discharge temperature to decrease AEP. It needs to be investigated further to balance between these two factors if exactly reducing carbon emissions is required.

Table 5. Parameters of TEWI calculation

Parameter	Value	Parameter	Value
Refrigeration capacity (kW)	2.5	Annual working time (hours·year^{-1})	1500
Annual leakage rate (%)	2	Carbon emission factor (kg_{CO2}·kW^{-1}·h^{-1}	0.86
Life of the system (years)	15	Recovery rate of refrigerant (%)	80

4. CONCLUSIONS

The theoretical analysis of energy efficiency on different refrigerants in the vapor compression refrigeration cycle under three working conditions is theoretically calculated, and the charge amount, COP, volumetric refrigerating capacity and discharge temperature of these refrigerants are obtained. Based on the results, some suggestions for the selection of refrigerants are provided.
(1) Analysis under different conditions is indeed needed because there exists relative performance difference when working conditions change.
(2) When considering the DE of refrigerants, although the indicator ERR is more comprehensive, comparing the GWP value is good enough to distinguish which refrigerant is better. Furthermore, comprehensive indicators are recommended when evaluating refrigerants, because some refrigerants with high COP might cause more carbon emissions eventually.
(3) It should be investigated further to balance between volumetric refrigerating capacity and discharge temperature in order to reduce total carbon emissions.
(4) Some flammable pure refrigerants are suggested due to their relative good performance and environmentally friendly properties. Besides, the use of mixed refrigerants is another reasonable solution. They can maintain good performance as well and even eliminate the risks of flammability.

ACKNOWLEDGEMENTS

This work has been supported by the Nation Natural Science Foundation of China (No. 51576171), and Zhejiang Provincial Natural Science Foundation of China (No. LZ19E060001), and the fund of the State Key Laboratory of Technologies in Space Cryogenic Propellants.

NOMENCLATURE

h	Enthalpy of refrigerants (kJ/kg)	m	mass (kg)
q	refrigerating capacity per unit mass (kg/kW)	G	emissions corresponding to energy required to convert old materials into new ones (kg_{CO2}/kg)
w	energy consumed by compressor (kg/kW)	α	recovery rate (%)
hr	annual working time (hours)	β	carbon emission factor (kg_{CO2}/(kW•h))
E	emissions corresponding to energy required for refrigerant production (kg_{CO2}/kg)		
F	emissions corresponding to energy caused by by-products (kg_{CO2}/kg)		
L	annual leakage amount (kg)	Subscript symbols	
N	life of the system (years)	1	refrigerants

Q refrigeration capacity (kW) i other parts that cause emissions

REFERENCES

ASHRAE, 2016. ANISI/ASHRAE Standard 34, Designation and Safety Classification of Refrigerants.

AHRI, 2004. ANSI/ASHRAE Standard 540, Standard Performance Rating of Positive Displacement Refrigerant Compressors and Compressor Units.

Cui, Q., Sun, Z., Li, Z., Wang, Q., Xie, Z., and Wang, X., 2017. Reanalysis of the Application of Low-Global-Warming-Potential Refrigerants against the Backdrop of the Kigali Amendment. Journal of Refrigeration Technology 40(4), 7-18.

Devecioğlu, A. G., Oruç, V., 2015. Characteristics of Some New Generation Refrigerants with Low GWP. Energy Procedia 75, 1452-1457.

Harby, K., 2017. Hydrocarbons and their Mixtures as Alternatives to Environmental Unfriendly Halogenated Refrigerants: An Updated Overview. Renewable and Sustainable Energy Reviews 73, 1247-1264.

IPCC, 2013. Anthropogenic and Natural Radiative Forcing. Fifth Assessment Report, Climate Change 2013: The Physical Science Basis, Chapter 8.

Kondo, S., Takahashi, A., Tokuhashi, K., and Sekiya, A., 2002. RF Number as a New Index for Assessing Combustion Hazard of Flammable Gases. Journal of Hazardous Materials 93(3), 259-267.

Makhnatch, P., Khodabandeh, R., 2104. The Role of Environmental Metrics (GWP, TEWI, LCCP) in the Selection of Low GWP Refrigerant. Energy Procedia 61, 2460-2463.

Mota-Babiloni, A., Navarro-Esbrí, J., Barragán-Cervera, A., Molés, F., and Peris, B., 2015. Analysis Based on EU Regulation No 517/2014 of New HFC/HFO Mixtures as Alternatives of High GWP Refrigerants in Refrigeration and HVAC Systems. International Journal of Refrigeration 52, 21-31.

Sánchez, D., Cabello, R., Llopis, R., Arauzo, I., Catalán-Gil, J., and Torrella, E., 2017. Energy Performance Evaluation of R1234yf, R1234ze(E), R600a, R290 and R152a as Low-GWP R134a Alternatives. International Journal of Refrigeration 74, 269-282.

Shaik, S. V., Babu, T. P. A., 2017. Theoretical Performance Investigation of Vapour Compression Refrigeration System Using HFC and HC Refrigerant Mixtures as Alternatives to Replace R22. Energy Procedia 109, 235-242.

Wang, J., Zhang, Y., Zhang, Z., 2003. Calculation and Experiment of Charging Quantity for Nature Refrigerant. Fluid Machinery 31(1), 44-47.

Zhang, Z., Chen, J., Gao, Y., Liu, X., 2015. Progress of Refrigerant Substitution in R&AC Industry. Refrigeration and Air-Conditioning 15(1), 1-8.

Zhou. J., 2012. AEP - A New Index Evaluating the Environmental Performance of Refrigeration and Air-Conditioning Equipments. Refrigeration and Air-Conditioning 12(1): 8-11.

Zhu, M., Wang, X., Shi, L., 2011. The Rate of CO_2 Emission Reduction Y - a New Index of Refrigerant Environmental Evaluation. Refrigeration and Air-Conditioning 11(1), 91-94.

Manuscript ID: 631
DOI: 10.18462/iir.icr.2019.0631

CFD research of the counter-flow spray concentration process in solar energy - air evaporating separation saline wastewater treatment system

Jing YU[(a)], Sumin JIN[(a)]

(a) Nanjing Tech University
Nanjing, 211816, China, 18251853848@163.com

ABSTRACT

The spray concentration tower plays an indispensable role in solar energy - air evaporating separation saline wastewater treatment system. The heat and mass transfer performance of the counter-flow spray concentration process is investigated in this paper. The CFD model is established for studying the heat and mass transfer performance of this process under different working conditions and the experiment research is carried out to prove the simulation. The influence of air flow rate and different heating form are also discussed. The results show that the maximum relative errors between the experiment and simulation results of the outlet air temperature, the outlet wastewater temperature and the outlet air relative humidity are 2.58%, 2.92% and 5.94%, respectively. Increasing the temperature of supplied air and spraying brine is beneficial to accelerating the concentration rate. In addition, when wastewater is used as the heat carrier, the evaporation efficiency (EE)becomes higher.
Key words: Air, CFD, Evaporation, Separation, Spray, Waste Water.

1. INTRODUCTION

The rapid development of industrialization promoted the economic boom and facilitated the human life, but some inevitable problems also arose. Water pollution is an important part of these inevitable problems. The improper discharge of industrial waste water has a huge impact on the ecological environment, especially the high-salt wastewater, which contains various elements including some toxic heavy metal ions (Chai et al., 2018).
High-salt wastewater is mainly produced in the chemical production process, including coal chemical processes, dye production, and pesticide production (V. Katheresan et al., 2018). Nowadays, common treatment methods for high-salt wastewater include chemical precipitation (C. Peng et al., 2004), electrochemistry (H.I. Maarof et al., 2017), absorption (X. Huang et al., 2018), membrane separation (Tun et al., 2011) and evaporation. These methods have their own advantages and disadvantages in the treatment of high-salt wastewater. Therefore, in practical industrial application, multiple treatment methods are often combined with each other. In order to achieve the requirement of zero discharge of waste liquid, evaporation method is usually used as the last step of treatment (Wei et al., 2011) leading to the complete separation of water and salt in high-salt wastewater. At present, multi-effect evaporation (MEE) technology (I.S. Al-Mutaz et al., 2014) and mechanical vapor recompression (MVR) technology (M. Ahmadi et al., 2017) are the most widely applied zero emission evaporation treatment technologies in the field of industrial high-salt wastewater. However, these two mature evaporation treatment technologies still have problems of high energy consumption, high system operation cost, frequent equipment maintenance, serious corrosion and scale buildup. Therefore, it is indispensable to develop a new low cost and energy saving evaporation technology for high salinity wastewater treatment.
Spray technology is widely used in the separation of solutions, such as the production of milk powder, chemical fertilizer and powder medicine (S. Wang et al., 2009). Applying spray technology to high salt wastewater treatment can effectively solve the problem of scaling and corrosion of equipment. At the same time, if solar energy is used as a heat source for heating air, it can reduce the

consumption of fossil energy and cut down the operating cost of the system. The spray evaporation technology combined with solar energy is widely used in the research and application of desalination, especially in combination with HDH technology (S.A. El-Agouz et al., 2014). However, there is still a lack of research on high-salt wastewater treatment by this solar spray evaporation technique, as the treatment of high-salt wastewater not only requires the recovery of pure water but also the recycling of salt for reuse. In recent years, there have been some research on treating high-salt wastewater using solar spray evaporation technique, but some unavoidable defects exist in these systems, such as the high temperature of the supply air (Fei et al., 2015) or the need for a certain degree of vacuum in the system (Q. Chen et al., 2018).

Therefore, the method of two-stage treatment is a feasible choice. A novel solar energy air evaporating separation saline wastewater treatment system is proposed in this paper and the system is designed in Fig. 1. The system uses solar energy as the heating source of air and wastewater, and combines the spray concentration tower and the spray separation tower to treat the high-salt wastewater in two stages. By adjusting the air valve, the two towers can operate under different solar energy collection conditions to adapt to the unstable energy input of solar energy. Here, the spray concentration tower is a very important part in this system. Not only is concentrated wastewater more likely to be separated and dried into salt powders, the concentration process inside the spray column consumes most of the heat. Therefore, it is necessary to study heat and mass transfer of the concentration process of spray concentration tower.

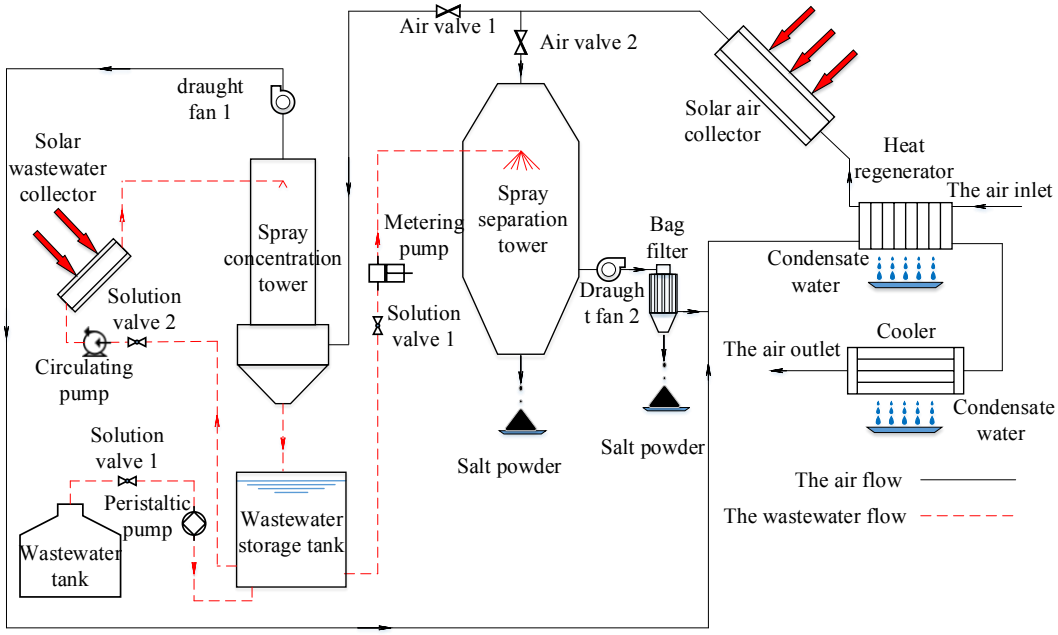

Figure 1 The diagram of the solar energy air evaporating separation saline wastewater treatment system

2. CFD MODEL

In order to study the heat and mass transfer of the two-phase flow in the spray tower that could not be obtained through experiments, a dynamic model is established for the main flow of the spray concentration tower. In this research, ANSYS Fluent 15.0 is used to carry out dynamic simulations of this process.

2.1 Physical model

In order to improve the operation efficiency, the geometry diagram of spray concentration tower given in Fig. 2 is simplified, and a two-dimensional columnar coordinate (axisymmetric) model is established with the center symmetry axis of the tower as the symmetrical interface (an interface used in the simulations). Discrete phase droplets flow in from the top of the simplified model of the tower and out from the bottom, while air comes in from the bottom and comes out from the top. The concentration process in the whole main flow area is counter-flow. Afterwards, the physics model is

meshed using the ICEM software in ANSYS. The grid division is in the form of a rectangular grid, and the grid of the boundary layer on the wall is partially serried. The mesh generation diagram and its local magnification diagram are shown in Fig. 2 and the total number of grids is 162,652.

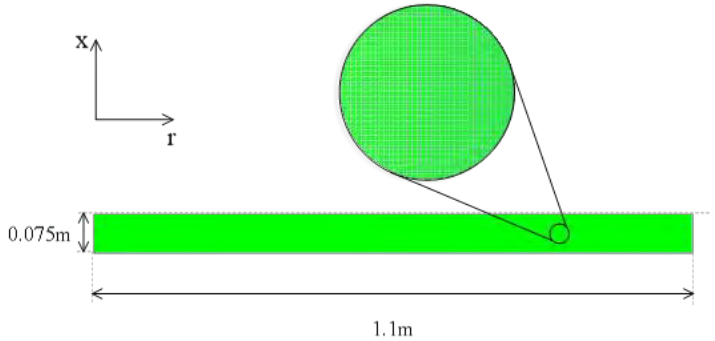

Figure 2 Mesh diagram of main flow area of spray concentration tower

2.2 Continuous phase (air) model

The air flow in the spray concentration tower is a continuous turbulent flow. Therefore, based on the N-S equation, the continuity equation and momentum equation in the case of cylindrical coordinates are expressed in the following form.
Continuity equation:

$$\frac{\partial \rho_a}{\partial t} + \frac{\partial}{\partial x}(\rho_a v_x) + \frac{\partial}{\partial r}(\rho_a v_r) + \frac{\rho_a v_r}{r} = S_m \quad \text{Eq. (1)}$$

Axial momentum equation:

$$\frac{\partial}{\partial t}(\rho_a v_x) + \frac{1}{r}\frac{\partial}{\partial x}(r\rho_a v_x v_x) + \frac{1}{r}\frac{\partial}{\partial r}(r\rho_a v_r v_x) = -\frac{\partial P}{\partial x} + \frac{1}{r}\frac{\partial}{\partial x}\left[r\mu_a\left(\frac{2\partial v_x}{\partial x} - \frac{2}{3}(\nabla \cdot v_a)\right)\right] + \frac{1}{r}\frac{\partial}{\partial r}\left[r\mu_a\left(\frac{\partial v_x}{\partial r} + \frac{\partial v_r}{\partial x}\right)\right] + F_x \quad \text{Eq. (2)}$$

Radial momentum equation:

$$\frac{\partial}{\partial t}(\rho_a v_r) + \frac{1}{r}\frac{\partial}{\partial x}(r\rho_a v_x v_r) + \frac{1}{r}\frac{\partial}{\partial r}(r\rho_a v_r v_r) = -\frac{\partial P}{\partial x} + \frac{1}{r}\frac{\partial}{\partial x}\left[r\mu_a\left(\frac{\partial v_r}{\partial x} + \frac{\partial v_x}{\partial r}\right)\right] + \frac{1}{r}\frac{\partial}{\partial r}\left[r\mu_a\left(\frac{2\partial v_r}{\partial r} - \frac{2}{3}(\nabla \cdot v_a)\right)\right] - 2\mu_a\frac{v_r}{r^2} + \frac{2}{3}\frac{\mu_a}{r}(\nabla \cdot v_a) + F_r \quad \text{Eq. (3)}$$

In these two momentum equations, $\nabla \cdot v_a$ represents the velocity gradient, and its expression is:

$$\nabla \cdot v_a = \frac{\partial v_x}{\partial x} + \frac{\partial v_r}{\partial r} + \frac{v_r}{r} \quad \text{Eq. (4)}$$

The turbulent RNG k-ε model is selected in this simulation research due to its high accuracy and the wall treatment is set up as standard wall function. The turbulent viscosity can be calculated by:

$$\mu_t = C_\mu \rho_a \frac{k^2}{\varepsilon} \quad \text{Eq. (5)}$$

2.3 Discrete phase (solution droplets) model

The liquid phase flow model adopts the discrete phase model (DPM). Meanwhile, the following hypothesis are given for liquid phase spray.
(1) The spray droplets follow the Rosin-Rammler distribution, the droplets are symmetrical spherical and the interactions between the droplets, such as collision and agglomeration, are negligible.
(2) Since the droplets are larger than 10μm in diameter, they are not mesoscopic. Therefore, the effects of Brownian force, basset force and saffman buoyancy are ignored.
(3) The mass and momentum and energy exchange and transmission between gas and liquid are carried out through relative motion of the two-phase flow and heat and mass transfer.
Therefore, discrete phase droplets are affected by its own inertia, gas phase aerodynamic drag force and gravity. According to the combined Euler-Lagrangian approach, the trajectory of droplets can be

obtained by the following force balance equation:

$$\frac{dv_d}{dt} = F_D(v_a - v_d) + \frac{g(\rho_d - \rho_a)}{\rho_d} \quad \text{Eq. (6)}$$

Here F_D can be calculated by:
Eq. (7)

$$F_D = C_D \frac{18\mu_a}{\rho_d d_d^2} \frac{Re_d}{24} \quad \text{Eq. (7)}$$

C_D and Re_d respectively represent the drag coefficient and the liquid drop relative Reynolds number, and their expressions are as follows:

$$C_D = a_1 + \frac{a_2}{Re_d} + \frac{a_3}{Re_d^2} \quad \text{Eq. (8)}$$

$$Re_d = \frac{\rho_a d_d |v_a - v_d|}{\mu_a} \quad \text{Eq. (9)}$$

In the above formula, a_1, a_2 and a_3 are constant and can be obtained from the literature (Morsi S A. et al., 1972). It is assumed that the droplet is spherical, the internal temperature distribution of a single droplet is uniform, and the effect of thermal radiation can be ignored. The heat balance equation of the gas-liquid two-phase flow can be expressed as:

$$m_{dp} C_p \frac{dT_d}{dt} = hA_d(T_\infty - T_d) + \frac{dm_{dp}}{dt} h_{fg} \quad \text{Eq. (10)}$$

The equation of mass transfer process is as follows:

$$\frac{dm_{dp}}{dt} = -k_c A_d (C_s - C_\infty) \quad \text{Eq. (11)}$$

(Sh). The correlation formula is as follows:

$$\mathrm{Nu} = \frac{hd_d}{\lambda_\infty} = 2 + 0.552 Re_d^{\frac{1}{2}} Pr^{\frac{1}{3}} \quad \text{Eq. (12)}$$

$$\mathrm{Sh} = \frac{k_c d_d}{D_m} = 2 + 0.552 Re_d^{\frac{1}{2}} Sc^{\frac{1}{3}} \quad \text{Eq. (13)}$$

2.4 Grid dependence analysis

In order to save the calculation time and improve the calculation accuracy, the grid sensitivity test was carried out for the heat and mass transfer of the model. Under the same inlet boundary conditions ($T_{a\ in}$=323.15, $T_{w\ in}$=323.15, w_{in}=0.01266 and c=20%), the models with different mesh densities are simulated, and the results of the outlet parameters are shown in Table 1. It can be seen from the table that when the grid density reaches 162,652, the calculation error under different mesh densities is already inappreciable. Thus the grid model with a grid number of 162,652 is selected as the model for this simulation research.

Table 1 Comparison of simulation results under different grid densities

Number of grid	Outlet air temperature (K)	Outlet air humidity ratio (kg/kg dry air)	Outlet solution temperature (K)
81,326	317.53848	0.03725083	309.13327
121989	317.39525	0.03737082	308.97401
162,652	317.37936	0.03739971	308.99014

3. EXPERIMENTAL VERIFICATION

To check the CFD model, comparisons between experimental results and simulation results are indicated in this section. As is shown in Fig. 3, the experimental results of the three parameters which

can be obtained directly through experiments are compared with the simulation results.

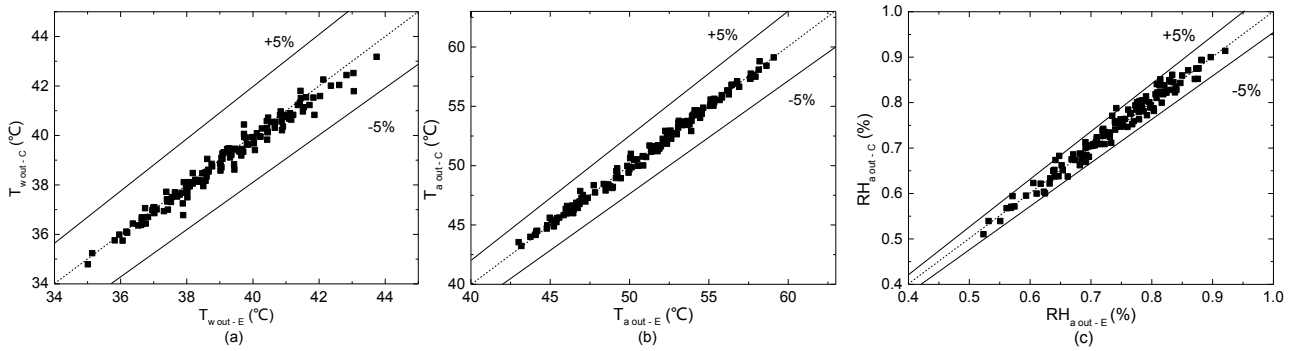

Figure 3 Comparison between experimental results and simulated results.

Here, each point represents an independent working condition, and in each working condition, the simulated initial conditions are set to the same as the inlet results of the spray tower measured in the experiment. It is observed that all outlet solution temperature (Figure 3a) and outlet air temperature (Figure 3b) points fall within the range of ±5%, and the errors of outlet air relative humidity (Figure 3c) are basically less than ±5%, with a few exceptions. Therefore, the model is reliable and it can be used to predict the important parameters in various situations.

4. RESULTS AND DISCUSSION

In this spray concentration tower, the efficiency of the concentration process is directly related to the heat and mass transfer. The 4 main influencing factors (solution inlet temperature, air inlet temperature, air mass flow rate and solution concentration) are involved in this part and the analysis of these factors is proceeded.

4.1 Effects of solution inlet temperature and air inlet temperature

With the case of different solution inlet temperature, the change of solution outlet temperature, air outlet temperature, evaporation rate (m_e) and evaporation efficiency (EE) with air inlet temperature is shown in Fig. 4. Here, the mass flow rate of solution and air is 130kg/h and 83.1kg/h respectively and the solution concentration is 10%.

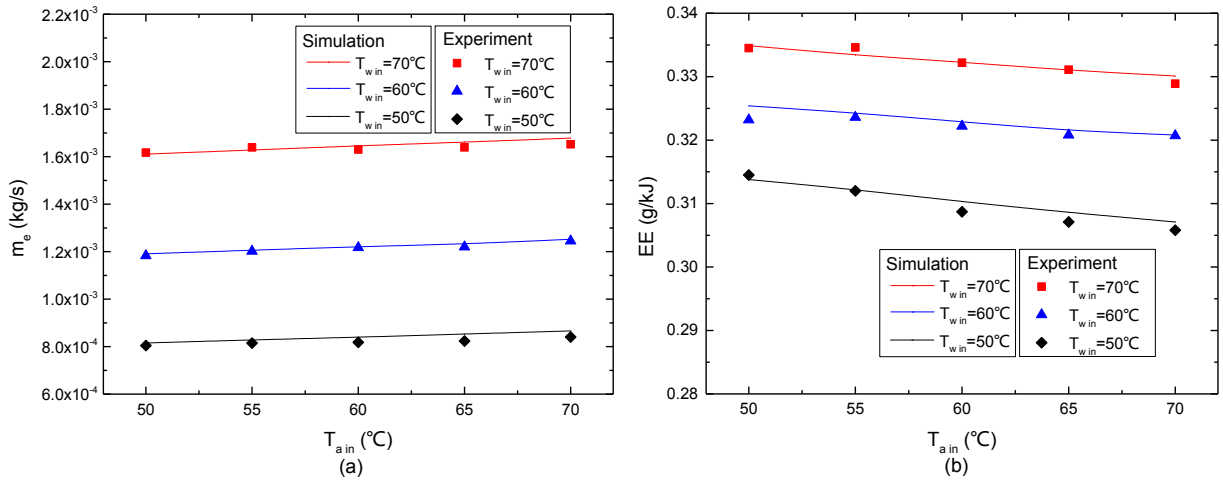

Figure 4 Effects of solution inlet temperature ($T_{w\,in}$) and air inlet temperature ($T_{a\,in}$)

From Fig. 4a, although the evaporation rate increases with the increase of the two fluids inlet temperature, it is clear that the increase of the solution inlet temperature is more effective in increasing the evaporation rate. Meanwhile, when Fig 4b is investigated, increasing the solution inlet temperature can heighten the evaporation efficiency (EE), while the increase of air inlet temperature cannot enhance the evaporation efficiency (EE) and even cause the evaporation efficiency (EE) to go down a little bit. Hence, heating solution is more effective in promoting mass transfer in spray concentration tower than heating air.

4.2 Effects of air mass flow rate

It is well known that the change of flow rate will lead to the change of Reynolds number and also affect the heat and mass transfer of the two phases. In this section, the effects of air mass flow rate on me and EE are illustrated in Fig. 5, with the condition of the solution mass flow rate at 130kg/s, the solution concentration at 10% and the solution inlet temperature at 60˚C. From Fig. 5a, with the increase of air mass flow rate, the evaporation rate of the spray concentration tower positively elevates. However, the increase of air mass flow rate also results in the decrease of evaporation efficiency (EE) shown in Fig. 5b. That is because although the increase of air mass flow rate can make Reynolds number ascend and thus promote the mass transfer process and evaporation rate in the tower, the increase of air flow rate also augments the heat input. The increased heat input has a bigger effect than the enhanced mass transfer, so the evaporation efficiency (EE) decreases gradually.

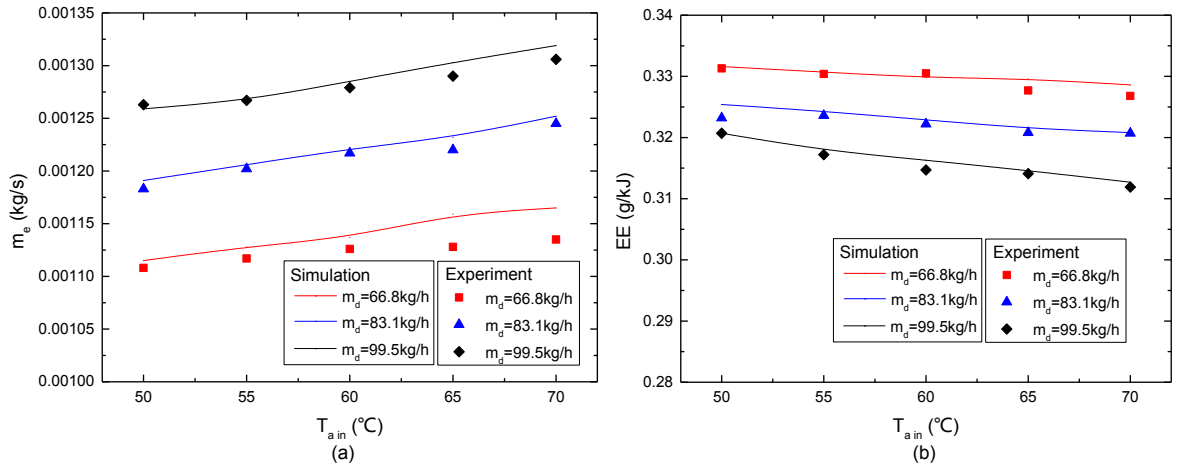

Figure 5 Effects of air mass flow rate (m_d)

4.3 Effects of solution concentration

As is demonstrated in Fig. 6, the effects of solution concentration on m_e and evaporation efficiency (EE) are given, with the condition of the solution mass flow rate at 130kg/s, the air mass flow rate at 83.1kg/s and the solution inlet temperature at 60˚C.

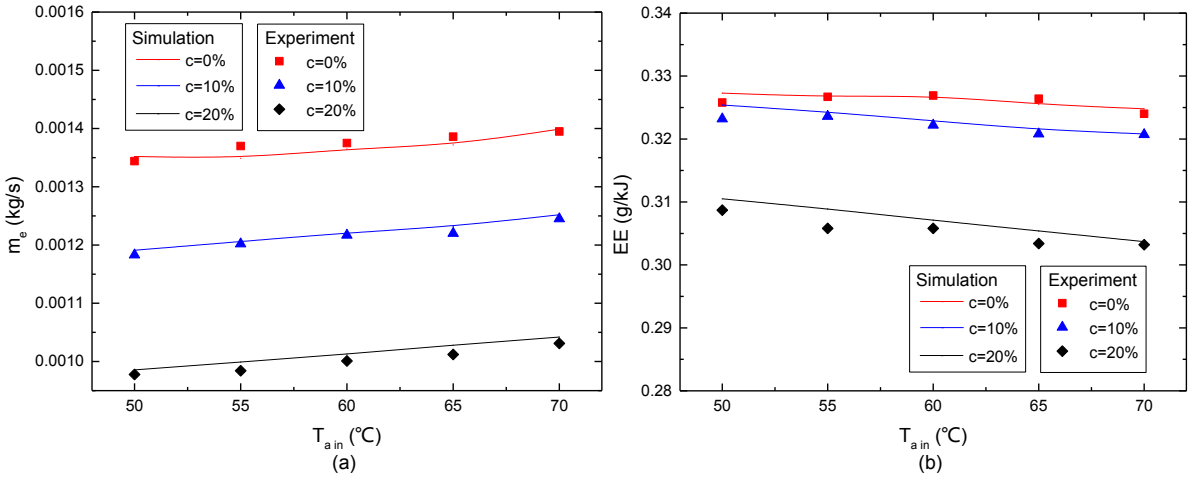

Figure 6 Effects of solution concentration (c)

With the increase of solution concentration, the evaporation rate and evaporation efficiency (EE) both decrease. The increase of solvend undoubtedly worsens the mass transfer effect of the concentration process. There are two reasons for this phenomenon. One is that the increase of solution concentration will change the physical parameters of the solution, such as specific heat capacity and viscosity. The other is that the surface steam partial pressure of the solution increases as the concentration of the solution increases at the same solution temperature.

4.4 Effect of heat distribution

Considering that the influence of temperature would change the heat brought into the concentration process by the two-phase flow, it is not rigorous to make a conclusion only from the change of temperature. Hence, the effect of heat distribution between wastewater carried and air carried is discussed. As is shown in Fig. 7, Both evaporation rate and evaporation efficiency (EE) decrease as the air heating percentage increases and the trend is consistent for different total heat input. That is to say, when wastewater is used as the heat carrier, the concentration process is more high-efficiency.

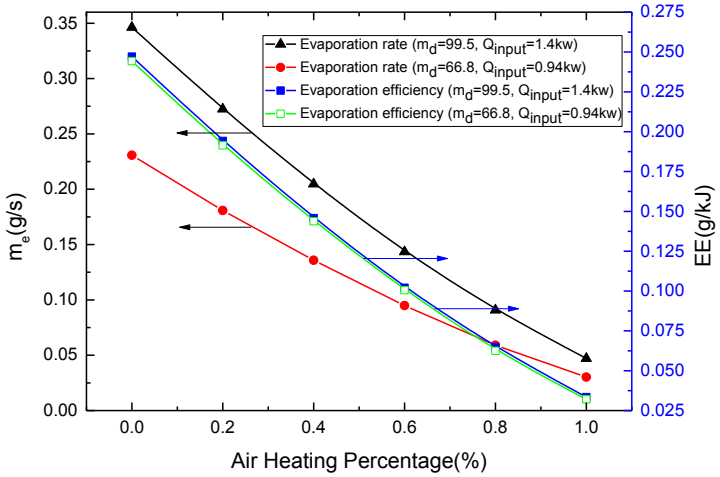

Figure 7 Effects of heat distribution

5. CONCLUSION

The spray concentration process in solar energy air evaporating separation saline wastewater treatment system is investigated using CFD simulation. The research results have been compared with the experimental data, and the errors between are all no more than 6%. Therefore, the numerical model is accurate basically in predicting air temperature, salt solution temperature and air humidity of a spray concentration tower. Simultaneously, the effect of several important factors on the tower performance is investigated.

1 In the concentration process, increasing the inlet temperature of air and solution can effectively promote the evaporation rate,

2, Increasing the temperature of waste water is more effective in increasing the evaporation efficiency (EE) than increasing the temperature of air.

3, The increase of wastewater concentration would result in the decrease of both evaporation rate and evaporation efficiency (EE).

4, Whatever the total input heat, when wastewater is used as the heat carrier, the concentration process is of higher efficiency.

NOMENCLATURE

Symbol	
a_1, a_2 and a_3	Constant parameters for calculation of drag coefficient
A_p	Surface area of the droplet (m^2)
C_D	Drag coefficient
C_p	Heat capacity (J/mol K)
C_s	Moisture concentration at the droplet surface (mol/m^3)
C_∞	Moisture concentration in the bulk gas (mol/m^3)
c	Salt concentration of wastewater
	(%)
d_d	Droplet diameter (m)
EE	Evaporation efficiency (kg/kJ)
F	User-defined-function of additional forces
g	Gravitational acceleration (m/s^2)
h	Convective heat transfer coefficient (W/m^2 K)
h_{fg}	Latent heat (J/kg)
k	Turbulent kinetic energy (m^2/s^2)
k_c	Mass transfer coefficient (m/s^2)

m_{dp}	Mass of droplet (kg)
m_e	Evaporation rate (kg/s)
P	Pressure (Pa)
r	Radius of the tower (m)
RH	Relative humidity (%)
S_m	User-defined mass source
t	Time (s)
v	Velocity (m/s)
T	Temperature (˚C)
T_∞	Gas phase temperature (˚C)
w	humidity ratio (kg/kg dry air)

Greek symbols

ε	Energy dissipation (m^2/s^2)
μ	Viscosity (kg/m s)
μ_t	Turbulent viscosity (kg/m s)
ρ	Density (kg/m^3)
λ_∞	thermal conductivity of the gas phase (W/m K)

Subscripts

a	Air
w	Wastewater
d	Droplet
in	Inlet
out	Outlet
x	Axial direction
r	Radial direction

Non-dimensional number

Nu	Nusselt number
Pr	Prandtl number
Re	Reynolds number
Sc	Schmidt number
Sh	Sherwood number

REFERENCE

Chai L., Li Q., Wang Q., Yan X., 2018. Solid-liquid separation: an emerging issue in heavy metal wastewater treatment. ENVIRON. SCI. POLLUT. R. 25(1), 17250–17267.

C. Peng, S. Song, S. Lu, A. López-Valdivieso, 2004. Electroplating wastewater treatment through chemical precipitation and electro dialysis. EUR. J. MINERAL PROC. ENVIRON. PROT. 4(1), 210-215.

Fei X., Chen L., Dai Y., Ji M., Fu J., 2015. CFD modeling and analysis of brine spray evaporation system integrated with solar collector. DESALINATION 366(1), 139–145.

H.I. Maarof, W. Daud, M.K. Aroua, 2017. Recent trends in removal and recovery of heavy metals from wastewater by electrochemical technologies. REV. CHEM. ENG. 33(1), 359-386.

I.S. Al-Mutaz, I. Wazeer, 2014. Comparative performance evaluation of conventional multi-effect evaporation desalination processes. APPL. THERM. ENG. 73(1), 1194-1203.

M. Ahmadi, E. Baniasadi, H. Ahmadikia, 2017. Process modeling and performance analysis of a productive water recovery system. APPL. THERM. ENG. 112(1), 100-110.

Morsi S A., Alexander A J., 1972. An investigation of particle trajectories in two-phase systems. J. FLUID MECH. 55(1), 193-208.

Q. Chen, M. Kum Ja, Y. Li, K. Chua, 2018. Evaluation of a solar-powered spray-assisted low-temperature desalination technology. APPL. ENERG. 211(1), 997–1008.

S. Wang, T. Langrish, 2009. A review of process simulations and the use of additives in spray drying. FOOD RES. INT. 42(1), 13-25.

S.A. El-Agouz, G.B. Abd El-Aziz, A.M. Awad, 2014. Solar desalination system using spray evaporation. ENERGY 76(1), 276-283.

Tun C M, Groth A M., 2011. Sustainable integrated membrane contactor process for water reclamation, sodium sulfate salt and energy recovery from industrial effluent. DESALINATION 283(1), 187-192.

V. Katheresan, J. Kansedo, S. Y. Lau, 2018. Efficiency of various recent wastewater dye removal methods: A review. J. ENVIRON. CHEM. ENG. 6(1), 4676-4697.

Wei S, Mark B., 2011. Effect of shear rate on fouling in a Vibratory Shear Enhanced Processing (VSEP) RO system. J. MEMBRANE SCI. 366(1), 148-157.

X. Huang, J. Yang, J. Wang, J. Bi, C. Xie, H. Hao, 2018. Design and synthesis of coreeshell Fe3O4@PTMT composite magnetic microspheres for adsorption of heavy metals from high salinity wastewater. CHEMOSPHERE 206(1), 513-521.

Manuscript ID: 635
DOI: 10.18462/iir.icr.2019.0635

Investigation of variable turbulence on heat transfer in packed bed of vegetables

Adam ŁAPIŃSKI[(a)], Jerzy GAGAN[(a)], Kamil ŚMIERCIEW[(a)], Dariusz BUTRYMOWICZ[(a)],

[(a)] Bialystok Technical University,
Wiejska 45C, Bialystok, 15-351, Poland
d.butrymowicz@pb.edu.pl

ABSTRACT

The paper deals with experimental determination of heat transfer coefficient in packed bed of vegetables, using a variable intensity of turbulence in the flowing air stream. The paper presents the results of the influence of turbulence intensity on the heat transfer coefficient in the carrot bed. Correlations for heat transfer coefficient can be found in the literature for calculation of heat transfer, but in most cases, they are developed for elements with simple geometry such as a sphere, cylinder, cone or a flat plate and they are not suitable for packed vegetable beds with very complex geometry. Therefore, the method of single blow technique to determine the heat exchange in the beds consisting of specific vegetables on the example of a carrot bed was applied. The measurements were made with air flow with three different turbulence intensity values as well as longitudinal positioning of the carrot in the bed. The results obtained in this way will allow to create a correlation for heat exchange for a specific type of vegetable.
Keywords: turbulence, single blow, heat transfer, measurements, vegetables, correlations

1. INTRODUCTION

The work concerns the determination of heat exchange in a packed bed of vegetables on the example of a carrot bed. Knowledge of heat exchange parameters and conditions during the cooling or storage of vegetables is important for the effective design of cold rooms. Measurements related to the determination of the heat transfer coefficient in a packed vegetable bed are complicated due to the highly complex geometry of the bed itself, as well as the individual elements of which the bed consists, i.e. vegetables. Due to the highly complex geometry of the bed, it is impossible to use the simplest methods based on direct measurement of the average temperature of the vegetable surface, the temperature distribution of the flowing air, or the heat flux density.

Available dependencies that can be found in the literature, mainly describe the heat exchange in elements with a simple geometry, i.e. a flat plate, a cylinder, a sphere or a cone. In addition, literature can provide information on heat exchange in packed bed, consisting of elements with a simple geometry, ie from the elements listed above. The elements of the bed, which are discussed in the article, i.e. vegetables, usually have intricate geometry themselves in the course of arranging the vegetables in the bed, the geometry is significantly complicated, which makes the available dependencies not useful in such a situation. Due to the lack of knowledge of heat transfer coefficients and methods for prediction of heat transfer in vegetable bed, it was proposed attempt to use the single blow method to determine heat transfer in a packed vegetable bed.

2. METHODOLOGY

In order to determine the average heat transfer coefficient, the work uses the so-called single blow technique, which is considered effective in determining heat exchange in a packed vegetable bed. The average value of the heat transfer coefficient is based on the heat exchange between the

actual surface of the elements filling the bed and the gas flowing through the bed. In the single blast method, the heat transfer coefficient α is determined by comparing the actual air temperature profile (heated before it flows into the bed) measured at the outlet of the tested bed with the predicted temperature profile determined on the basis of the theoretical model. Correct comparison of the temperature profile with the experiment and the predicted theoretical profile depends on the heat transfer coefficient which is used in the theoretical heat exchange model. The measurement approach to the discussed method is presented in Fig. 1.

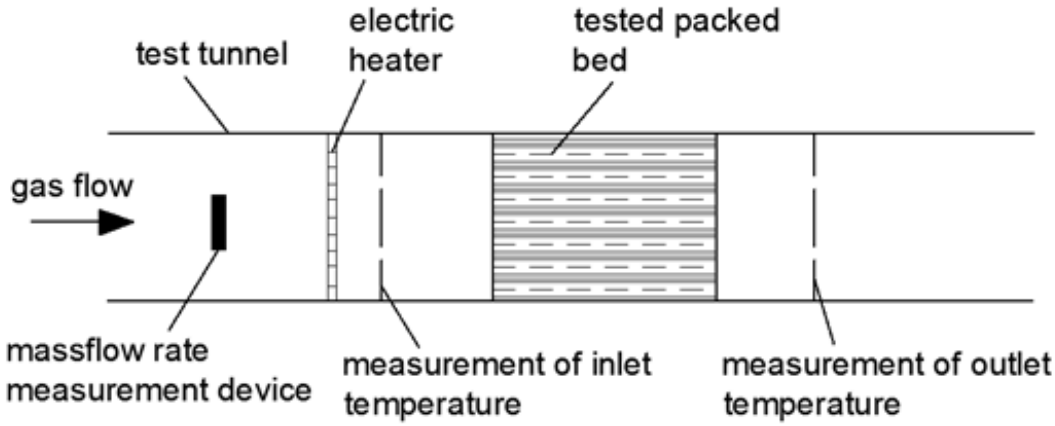

Figure 1: The idea of measuring the heat transfer by mean the single blow technique

The measurement in the single blow method consists in recording the temperature profile of the flowing gas, variable over time, directly at the inlet and outlet of the bed. The change in temperature of the flowing gas is caused by switching the heating element on or off. The following conditions need to be met before the measurement:

- gas flow is steady state (constant velocity);
- the temperature in the measurement section is constant and equal in the axial and radial directions.

Temperature profiles recorded during the single blow technique measurements are used when solving equations modelling heat exchange in the tested packed bed. The measured temperature leap or profile at the inlet to the test section is the boundary condition for the model equations. The measured temperature profile at the outlet of the test section should be predicted on the basis of the model. However, the theoretical and the measured outlet temperature profiles may be compared in several ways that may be thought as equivalent, Butrymowicz et al. (2016).

The most basic one-dimensional model of transient heat transfer between a porous body and a fluid flowing through it is the model proposed by Anzelius (1926). This model became the basis for many further modifications and is still being developed by removing the numerous simplifications assumed by the author in order to obtain analytical solution of the model equations. Anzelius (1926) model is based on the energy balance for a solid body element (porous or perforated packing of the exchanger) in the situation presented in Fig. 2.

One of the reasons for the inaccuracy in determining the heat transfer coefficient by the single

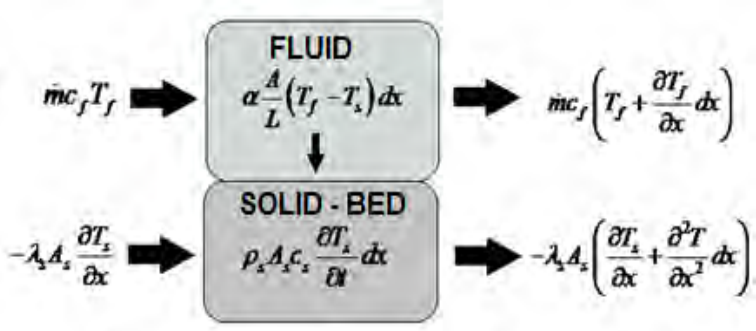

Figure 2: Energy balance between fluid (f) and the packed bed element (s) (Anzelius 1926)

blast method is the difficulty in realizing the temperature jump at the inlet of the exchanger. This state of affairs occurs due to the heat capacity of the heater, i.e. the temperature always rises in a certain time interval. The modifications introduced by Liang and Yang (1975) minimize the problems associated with experimental jump of the temperature at the inlet of the tested deposit. The authors (Liang and Yang 1975) proposed an equation for a dimensionless temperature profile at the bed inlet during turning on or off the heater as an exponential function in the form:

$$\theta_f(t,0) = 1 - e^{-t/\tau^*} \quad \text{Eq. (1)}$$

where τ^* is an experimentally determined dimensionless constant.
In the Anzelius (1926) model, Liang and Yang (1975) included in the balance of liquid energy, its heat capacity, and presented the equation of gas energy equilibrium as follows:

$$\frac{\partial \theta_f}{\partial \tau} + b_1 \frac{\partial \theta_f}{\partial z} = b_2\left(\theta_f - \theta_s\right) \quad \text{Eq. (2)}$$

The thermal conductivity of the solid has been ignored. In dimensionless form, the equation of energy balance for a solid can be presented in the form of:

$$\frac{\partial \theta_s}{\partial \tau} = \theta_f - \theta_s \quad \text{Eq. (3)}$$

The coefficients b_1 and b_2 in Eq. (2) are constants and can be presented in the form:

$$b_1 = b_2 \frac{w_f}{A_{f,\min}}, b_2 = \frac{m_s c_s}{m_f c_f} \quad \text{Eq. (4)}$$

where wf is the volume of fluid (gas) inside the packed bed, while $A_{f,min}$ is the smallest cross-section of the bed through which the fluid flows. To calculate the dimensionless temperature value θ, the temperature of the fluid T_{f1} is required, which will settle at the inlet to the bed after a suitable time from the heater on. Eq. (2) and (3) together with the boundary condition recorded in equation (1) and initial conditions:

$$\theta_s(0,z) = \theta_f(0,z) = 0 \quad \text{Eq. (5)}$$

were solved (Liang and Yang, 1975) with the use of the Laplace transform which gave a set of equations:

$$p\overline{\theta} + b_1 \frac{d\overline{\theta_f}}{dz} = b_2\left(\overline{\theta_s} - \overline{\theta_f}\right) \quad \text{Eq. (6)}$$

$$p\overline{\theta_s} = \overline{\theta_f} - \overline{\theta_s} \quad \text{Eq. (7)}$$

$$\theta_f\left(p,0\right) = \frac{1}{\tau^* p\left(p + \frac{1}{\tau^*}\right)} \quad \text{Eq. (8)}$$

where θ denotes the transform, and p is its argument. The solution to the set of Eq. (6)–(8) in relation to $\overline{\theta}_f$ is as follows (Liang and Yang, 1975):

$$\overline{\theta_f} = \frac{\exp\left(-\frac{p}{b_1}\left(1+\frac{b_2}{1+p}\right)z\right)}{\tau^* p\left(p+\frac{1}{\tau^*}\right)} \qquad \text{Eq. (9)}$$

Finding the inverse Laplace transform for Eq. (9) at z = NTU, the following relationships describing the profile of dimensionless temperature at the packed bed outlet are obtained:
- if $\tau < t^*$ (i.e.: $t < L/w_f$): it is, for the period in which the temperature jump did not reach the bed outlet.

$$\theta_f(\tau, NTU) = 0 \qquad \text{Eq. (10)}$$

- when $\tau \geq t^*$ (i.e. $t \geq L/w_f$): it is obtained the temperature distribution behind the bed

$$\theta_f(\tau, NTU) = \frac{1}{\tau^*}\int_{t^*}^{\tau} e^{-(\tau-\eta)/\tau^* - b_2 t^*}\left\{e^{-(\eta-t^*)} I_0\left(2\sqrt{b_2 t^*(\eta-t^*)}\right) + \int_0^{\eta-t^*} e^{-\xi} I_0\left(2\sqrt{b_2 t^* \xi}\right) d\xi\right\} d\eta \qquad \text{Eq. (11)}$$

where t* denotes dimensionless time defined as follows:

$$t^* = \frac{NTU}{b_1} \qquad \text{Eq. (12)}$$

Provided the relatively high numerical cost connected with the application of more complex mathematical models of heat transfer in regenerators, the authors decided to use the above modified Liang and Yang model (Liang and Yang, 1975). The key element in this model is the consideration of the exponential character of the inlet temperature profile which allows to avoid a considerable error resulting from the impossibility to execute an immediate leap of temperature at the inlet of the tested packed bed. The described model has proved itself useful in the measurement of the average heat transfer coefficient for packed mineral deposits, as presented in the works of Butrymowicz et al. (2016) and Łapiński et al. (2017).

3. TEST APPARATUS

The test tunnel consists of three sections as it is show in Fig. 3. Air flow rate in the tunnel was controlled by means of change of the centrifugal exhaust fan rotational speed. The electric heater capacity was also controlled. The test stand consists of fourth parts:

- the first section - intake, straightening the air stream, and measuring the flow of air;
- the second section, changing the geometry of the tunnel (reducing the tunnel cross-section);
- the third section - measuring section, measurement of individual parameters, place of laying the deposit;
- the fourth section - outlet, with the diffuser inserted and the fan mounted.

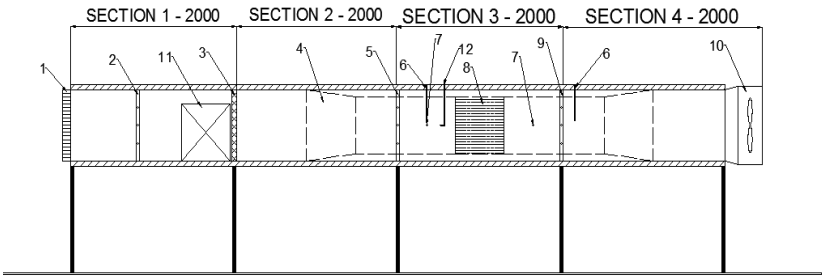

Figure 3: Schematic diagram of the test tunnel: 1 – flow rectifier; 2 – air flow rate and temperature sensors; 3 - electric air heater; 4 – confusor/diffuser; 5 – thermocouples net at the tested bed inlet; 6 – moisture sensors; 7 – pressure gauges; 8 – tested packed bed of vegetables; 9 – thermocouples net at the tested bed outlet; 10 – exhaust fan; 11 - element disrupting the air flow; 12 - measurement of turbulence intensity

The wind tunnel uses an electric heater, which is designed to raise the temperature of flowing air in the tunnel by 5-10 K above the ambient temperature. The electric heater was designed so that the time constant of the temperature rise was as short as possible. This is an important feature from the point of view of the theoretical model that is used to prepare the results of measurements. Simple theoretical models assume an immediate rise in temperature at the inlet of the bed. However, more complicated models use appropriate exponential functions that approximate the actual temperature increase caused by the electric heater. The reported measurements were carried out for the case of carrot. The prepared packed bed of carrot before insertion in the test tunnel were show in Fig. 4.



Figure 4: The packed bed of carrot: on the left a view of the bed inlet; on the right view from the top

Table 1. Parameters of the tested bed of carrot

Range weight (g)	Average mass (g)	Average volume (dm^3)	Average surface area (dm^2)	Amount in bed
60-65	62.3	0.060	1.095	17
65-70	67.7	0.066	1.125	16
70-75	73.3	0.070	1.295	12
75-80	77.7	0.078	1.262	19
80-85	83.0	0.079	1.332	23
85-90	87.6	0.086	1.408	13
90-95	92.2	0.090	1.485	25
95-100	97.2	0.093	1.508	20
100-105	103.0	0.100	1.600	11
105-110	106.4	0.104	1.616	16
110-115	113.2	0.108	1.553	19
115-120	116.8	0.112	1.614	12
120-125	121.6	0.120	1.762	15
125-130	126.8	0.130	1.819	8
130-135	132.6	0.128	1.889	7
135-140	136.4	0.131	1.883	15
140-145	141.8	0.138	1.984	9
145-150	148.0	0.145	1.848	7
150-155	152.2	0.163	1.983	13
155-160	156.4	0.156	1.981	8
160-165	162.2	0.158	2.079	4
165-170	167.2	0.169	2.033	1
170-175	171.8	0.165	2.114	7
175-180	177.6	0.168	2.325	0
180-190	184.4	0.178	2.432	14
190-200	194.4	0.189	2.397	8

Table 2. Summary parameters of the carrot bed

Average mass (kg)	35.69
Average heat transfer surface area (m^2)	5.179
Average volume (m^3)	0.0349
Average density (kg/dm^3)	1.023

A geometry was determined for the carrot bed which in subsequent calculations served to determine the average heat transfer coefficient. In order to determine the geometry of the bed, the carrots were divided into particular weight groups first. Then, in each weight group, the piece with the average weight of the group was selected and the geometrical parameters were determined for the given art. The results of these parameters are listed in Table 1.

The average hydraulic diameter of the packed bed D_h May be assessed on the basis of porosity:

$$d_h = \frac{4A_p}{U_p} = 4\frac{V_p}{A_p} = 4\frac{\varepsilon}{a} \qquad \text{Eq. (13)}$$

In order to create a different degree of turbulence intensity of the flowing air stream, elements disturbing the stable air flow were introduced in the first section of the tunnel (Fig. 3). The boxes were applied as disturbing elements (Fig. 5), which were arranged in such a way that it was possible to reproduce the same turbulent flow conditions for all cases of the tested beds, i.e. for lack of the boxes there is minimum turbulence level, with one empty box the intermediate level of turbulence is produced, and for the combination of boxes that highest turbulence level is achieved.



Figure 5: Elements that disrupt the air flow (on the left: first degree of interference, on the right: second degree of interference)

4. TEST RESULTS

Measurements of the turbulence intensity allowed to determine the turbulence value of the flowing air, in conditions without disturbances and with disturbances. The obtained turbulence intensity results allowed to perform measurements at various flow turbulences, as well as to determine the influence of turbulence intensity on the value of heat transfer coefficient. For undisturbed flow, the turbulence intensity value Tu = 2% was assumed, for the first disturbance stage Tu = 7%, while for the second stage the intensity of turbulence was assumed Tu = 14%.
After processing the results obtained from the measurements using the geometry presented above (Table 2), the results are presented in the table below (Table 3 and Table 4):

Table 3. Results for longitudinal arrangement at turbulence intensity of 2% and 7%

Tu = 2 %						Tu = 7 %					
w (m/s)	Re_{BED}	Re_{iB}	α (W/m^{2}K)	Nu	Pr	w [m/s]	Re_{BED}	Re_{iB}	α (W/m^{2}K)	Nu	Pr
0.108	281.3	1897	7.3	7.138	1.049	0.101	263.4	1776	6.8	6.720	1.061
0.179	463.8	3128	10.5	9.935	1.015	0.176	459.7	3100	10.3	10.738	1.120
0.241	624.5	4211	13.8	13.161	1.023	0.232	602.7	4064	12.6	11.837	1.008
0.277	720.9	4861	14.5	14.950	1.107	0.272	708.8	4780	12.9	14.370	1.197
0.355	922.4	6220	17.4	18.163	1.120	0.343	890.5	6005	15.2	15.608	1.102
0.420	1091	7360	18.0	19.493	1.163	0.458	1188	8012	18.7	18.700	1.140
0.525	1365	9020	21.0	22.166	1.133	0.505	1313	8852	20.0	20.816	1.117
0.612	1591	10730	22.5	23.269	1.110	0.591	1535	10350	23.0	23.839	1.113

Table 4. Results for longitudinal arrangement at turbulence intensity 14%

Tu = 14 %					
w [m/s]	**Re_{BED}**	**Re_{iB}**	**α [W/m^{2}K]**	**Nu**	**Pr**
0.091	236.1	1592	5.8	3.623	1.040
0.180	466.8	3148	10.4	9.919	1.023
0.237	613.9	4140	12.5	11.972	1.027
0.268	695.6	4691	13.3	12.777	1.030
0.328	851.4	5741	14.4	14.836	1.106
0.417	1082	7300	17.8	18.648	1.124
0.511	1329	8961	20.6	21.614	1.126
0.596	1549	10450	22.9	24.176	1.133

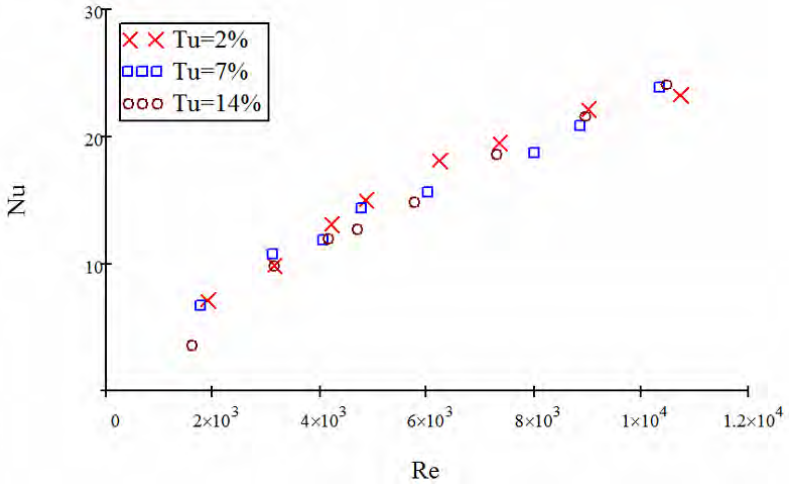

Figure 6: Comparison of results for longitudinal arrangement at three different intensity levels of turbulence

However, it should be known that the Reynolds number (Re) presented in the tables above has values that are calculated in the channels inside the packed carrot bed (Re_{BED}) and the inlet bed (Re_{iB}), while the w value refers to the velocity at the bed inlet. The results presented in the tables above have been graphically presented in the chart below.

The comparison of results from heat exchange in a packed carrot bed at various degrees of turbulence intensity is shown in Fig. 6. As can be seen from the graph in the whole extent Reynolds number, there is no difference in the Nusselt number values for measurements with different turbulence intensity values.

5. CONCLUSIONS

Obtained results of measurements, using a non-invasive method of single blow and made at different intensities of the flowing air stream, allowed to obtain information on the impact of this parameter on the intensity of heat exchange in packed vegetable bed. As can be seen from the graphs above, the value of the Nusselt number, which describes the intensity of heat exchange in the range Reynolds number, does not change as the intensity of turbulence increases, the air stream flowing into the bed inlet. The results allow to conclude that the lack of change in the number of Nusselt with increasing turbulence of the air stream flowing into the bed may be caused by laminarization of the stream which takes place inside the bed. The change in the Reynolds number before and inside the bed is clearly shown in Table 3 and 4. In the further development of work on heat exchange in a packed carrot bed, it is planned to determine the impact of the arrangement of the deposit elements on the heat exchange rate in the bed.

ACKNOWLEDGEMENT

Research financed under the program of the Minister of Science and Higher Education "Regional Initiative of Excellence" in 2019 - 2022 project number 011/RID 2018/19 amount of financing 12,000,000 PLN and partially financed from the project no. 2017/25/N/ST8/02444, from the resources of the National Science Center.

NOMENCLATURE

a	specific surface area (–)	α	heat transfer coefficient ($W \times m^{-2} \times K^{-1}$)
A	transfer area (m^2)	θ	dimensionless temperature (-)
c	specific heat ($J \times kg^{-1} \times K$)	λ	thermal conductivity ($W \times m^{-1} \times K^{-1}$)
d	diameter (m)	ρ	density ($kg \times m^{-3}$)
m	mass (kg)	τ	time (s)
Nu	Nusselt number (-)	τ^*	dimensionless time (-)
NTU	number of heat transfer units (-)	Subscript	
P	Laplace transform variable (-)	a	air
Re	Reynolds number (-)	BED	bed
T	temperature (°C)	f	fluid
Tu	intensity of turbulence (%)	h	hydraulic
U	perimeter (m)	iB	inlet bed
v	volume (m^3)	Min	minimum
w	flow speed ($m \times s^{-1}$)	p	free space
z	length coordinate in flow direction (m)	s	solid
Z	characteristic dimension (m)	t	total

REFERENCES

Anzelius A.,1926, Über Erwärmung vermittels durchströmender Medien. Zeitschrift für Angewandte Mathematik und Mechanik, Vol. 6, No 4, 291–294.

ASHRAE Handbook – Refrigeration., 2010.

Butrymowicz D., Karwacki J., Kwidziński R., Śmierciew K., Gagan J., Przybyliński T., Skiepko T., Łapin M., 2016. Methodology of heat transfer and flow resistance measurement for matrices of rotating regenerative heat exchangers, Chemical and Process Engineering 37 (3), 341-358.

Łapiński A., Butrymowicz D., Kołodziejczyk M. 2017a. Measurement approach of mean heat transfer coefficient for packed bed of vegetables", Acta Mechanica et Automatica, 2017, nr. 39 s. 73-80.

Liang C.Y., Yang. W.-J., 1975. Modified single-blow technique for performance evaluation on heat transfer surfaces. Transactions of the ASME Series C: Journal of Heat Transfer 97, 16-21.

Manuscript ID: 643
DOI: 10.18462/iir.icr.2019.0643

Experiments on boiling heat transfer and pressure drop of refrigerant mixtures R245fa/R1234ze(E) inside horizontal microfin tubes

Yufei LIU[(a)], Kazuhide WATANABE[(b)], Daisuke JIGE[(c)], Norihiro INOUE[(c)]

[(a)] Graduate School of Marine Science and Technology, Tokyo University of Marine Science and Technology, Tokyo, 135-8533, Japan, d172026@edu.kaiyodai.ac.jp
[(b)] Japan Coast Guard Academy, Hiroshima, 717-0832, Japan, watanabe@jcga.ac.jp
[(c)] Tokyo University of Marine Science and Technology, Tokyo, 135-8533, Japan, djige00@kaiyodai.ac.jp, inoue@kaiyodai.ac.jp

ABSTRACT

This study experimentally investigated the boiling heat transfer and pressure drop characteristics of R245fa/R1234ze(E) zeotropic refrigerant mixtures inside horizontal microfin tubes. The test tubes were copper tubes with an outer diameter of 9.52 mm, equivalent inner diameters of 8.9 and 8.7 mm, fin heights of 0.12 and 0.18 mm, and fin numbers of 65 and 85, respectively. The experiments were conducted under mass velocities of 100 and 200 $kgm^{-2}s^{-1}$, mass fractions of 90/10, 80/20, and 65/35 mass% (R245fa/R1234ze(E)), and an average saturation temperature of 40 °C. The measured boiling heat transfer coefficient and frictional pressure drop of the R245fa/R1234ze(E) refrigerant mixture were lower than those of the pure refrigerant R245fa. During the boiling process, the heat transfer coefficient was minimized at a R245fa/R1234ze(E) composition of 65/35 mass%, which had the largest temperature glide. Furthermore, the frictional pressure drops decreased with the mass fraction of R1234ze(E).
Keywords: Boiling, Zeotropic mixtures, Heat transfer, Pressure drop, Microfin tube, R245fa, R1234ze(E), Refrigerant.

1. INTRODUCTION

A heat pump system to generate hot water and high-temperature steam, and a binary organic Rankine cycle generator that utilizes a low-temperature heat source discharged from factories, has attracted research attention among the various efforts focusing on preventing global warming. R245fa has been commercially used in recent years for high-temperature heat pumps and binary generators because of its low working pressure and high critical temperature compared to the refrigerants currently used in refrigeration and air conditioning equipment. However, the capacity of heat pump cycles using R245fa is lower than expected because of its significantly lower volumetric capacity.

To improve the coefficient of performance (COP) and capacity of heat pumps, R245fa is designed to blend R134a to offer a higher volumetric capacity. Guo et al (2016) investigated flow boiling heat transfer of R245fa/R134a mixtures with 18/82 wt% in a smooth tube and compared with the correlations for predicting the heat transfer coefficient. Watanabe et al. (2016) investigated boiling and condensation characteristics of R245fa/R134a inside horizontal microfin tubes.

In the present work, the low GWP R1234ze(E) as an alternative to R134a in ORC systems is carried out. The GWP of the R245fa/R1234ze(E) range from less than 400 to 600, which are still significantly lower than those of R245fa. Furthermore, the refrigerant mixtures have the potential to approach the requirements of the Lorenz cycle depending on the degree to which they match the application glide in both the evaporator and condenser, because they operate at an improved mean temperature than the corresponding pure refrigerant. However, the boiling heat transfer of R245fa/R1234ze(E) inside horizontal microfin tubes has not yet been sufficiently clarified.

In the present study, the boiling heat transfer and frictional pressure drop of R245fa/R1234ze(E) mixtures inside horizontal microfin tubes with an outer diameter of 9.52 mm were experimentally investigated. The effects of the mass velocity, vapor quality, and mass fraction of R1234ze(E) on the boiling heat transfer and pressure drop were clarified and compared to those in previous correlations.

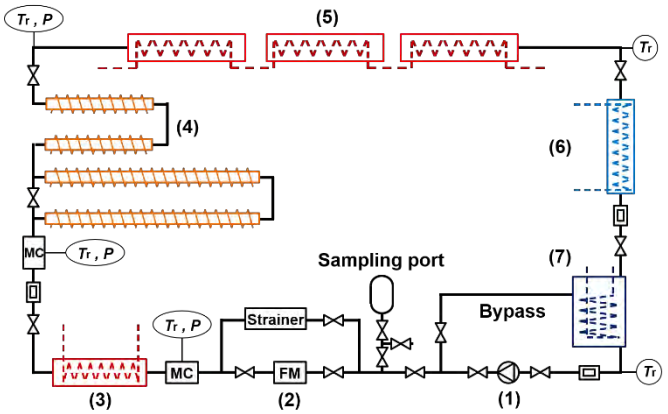

Gear pump
Coriolis-type mass flow meter
Water preheater
Electric preheater
Test section
After-cooler
Receiver tank

Figure 1: Schematic of the test loop

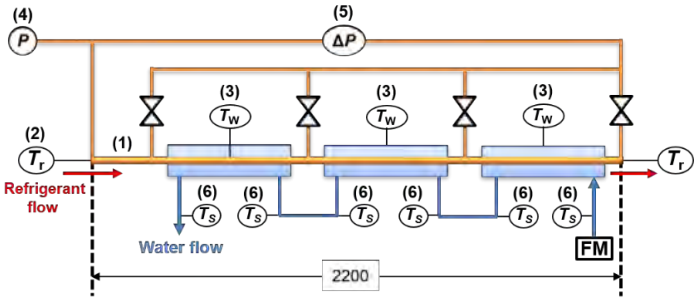

Test tube
Sheathed K-type thermocouple
T-type thermocouple
Absolute pressure transducer
Differential pressure transducer
Pt-resistance thermometer

Figure 2: Detailed view of the test section

2. EXPERIMENTAL APPARATUS AND PROCEDURE

Fig. 1 shows a schematic of the experimental apparatus used for the present study. The refrigerant loop consists of a gear pump (1), Coriolis-type mass flow meter (2), water preheater (3), electric preheater (4), test section (concluding three subsections) (5), cooler (6), and receiver tank (7).
A subcooled refrigerant that is pumped from the gear pump is adjusted to a predetermined vapor quality at the counter-flow-type water preheater and electric preheater, after which it flows into the test section. The refrigerant mass flow rate is controlled by the rotational speed of the pump and the flow-regulating valves of the main and bypass loops. The aftercooler is supplied with cooling or heating water primarily to adjust the refrigerant pressure. The flow rate of the test refrigerant is measured using the Coriolis-type mass flow meter.
Fig. 2 shows details of the test section. The test section is a 2-m-long counter-flow-type double-pipe heat exchanger. In this section, the refrigerant flows through the inner test tube, whilst the heat source water flows through the outer annulus tube, which surrounds the inner tube. The test tube consists of three subsections with total and effective heating lengths of 600 and 557 mm, respectively. The bulk temperatures of the refrigerant at the inlet and outlet of the test section are measured by sheathed K-type thermocouples with a measurement accuracy of ±0.05 K. The outer tube wall temperature is measured using T-type thermocouples that are attached to the top, bottom and sides of the exterior wall at the test tube center. The heat source water temperature is measured by Pt-resistance thermometers that are inserted in the mixing chambers at the inlet and outlet of each subsection. An absolute pressure transducer with an accuracy of ±0.75 kPa measures the refrigerant pressure at the inlet of the test section, while two differential pressure transducers measure the pressure drop between the inlet and outlet of each subsection. The test section and electric preheater are encased with insulation. Table 1 lists the measurement uncertainties for this experiment.
The test tubes are horizontal smooth and microfin copper tubes with an outer diameter of 9.5 mm. The low fin-height (LF) and high fin-height (HF) tubes have an equivalent diameter of 8.9 and 8.7 mm, fin height of 0.12 and 0.18 mm, and fin numbers of 65 and 85, respectively. Details of the test tube are shown in Table 2.

Table 1. Measurement uncertainties

Instrument	Uncertainty
Thermocouples	± 0.05 K
Mass flow meter	± 0.5 %
Absolute pressure transducer	± 0.75 kPa
Differential pressure transducer	± 0.02 kPa

Table 2. Specifications of the test tubes

Tube			ST	LF	HF
Outer diameter	d_o	[mm]	9.52	9.53	9.51
Max. inside diameter	d_i	[mm]	8.32	8.95	8.81
Equivalent diameter	d_{eq}	[mm]	8.32	8.89	8.73
Fin height	h_f	[mm]	-	0.12	0.18
Number of fins	N	[-]	-	65	85
Helix angle	θ	[°]	-	16.5	39.4
Surf. area enlargement	η	[-]	1	1.31	2.09

The test refrigerants were R245fa/R1234ze(E) mixtures. The heat transfer coefficient was measured in a mass velocity range of 50–300 $kgm^{-2}s^{-1}$ and saturation temperature of 40 °C. The thermodynamics properties of the refrigerants and the variation in the temperature glide are shown in Table 3 and Fig. 3. The properties of the refrigerants and heat source water were calculated using Refprop ver.10 (Lemmon et al., 2018).

Table 3. Thermodynamics properties at average saturation temperature of 40 °C

		R245fa	R245fa/R1234ze(E)		
			90/10	80/20	65/35
P	MPa	0.251	0.306	0.356	0.427
ΔT	K	0	6.2	9.1	10.1
Δh_L	$kJkg^{-1}$	182.3	178.7	175.3	170.8
ρ_L	kgm^{-3}	1297	1274	1253	1222
ρ_V	kgm^{-3}	14.01	15.25	16.71	19.44
μ_L	µPas	329.1	298.8	272.9	240.6
μ_V	µPas	10.94	11.10	11.25	11.51
λ_L	$mWm^{-1}K^{-1}$	83.29	81.26	79.37	76.80
λ_V	$mWm^{-1}K^{-1}$	13.95	14.16	14.27	14.43

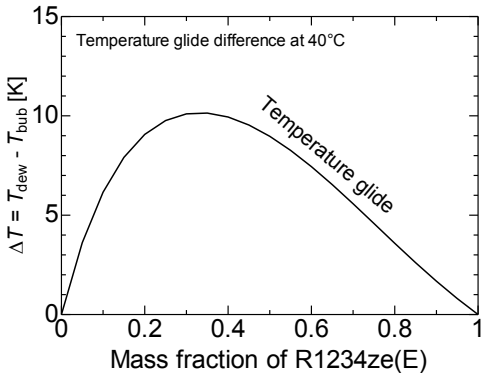

Figure 3: Temperature glide of R245fa/R1234ze(E) mixture

3. DATA REDUCTION

The heat transfer rate Q_s in a subsection is given by

$$Q_s = \dot{m}_s \cdot c_{ps} \cdot \Delta T_s \qquad \text{Eq. (1)}$$

where $\dot{m}_s$ and c_{ps} are the mass flow rate and specific heat capacity of the heat source water, respectively, and ΔT_s is the temperature difference between the inlet and outlet of the heat source water at each subsection. The sectional boiling heat transfer coefficient α is defined by

$$\alpha = q'' / \left(T_{wi} - T_r\right) \qquad \text{Eq. (2)}$$

where q'' is the heat flux based on the actual heat transfer area for each subsection and can be expressed as

$$q'' = Q_s / \left(\pi \cdot d_{eq} \cdot L\right) \qquad \text{Eq. (3)}$$

T_r is the refrigerant temperature, which is calculated from the inlet and outlet temperature at the test section by interpolation for each subsection, and T_{wi} is the inner wall temperature, which can be calculated by Fourier's law from the measured outer wall temperature T_{wo}:

$$T_{wi} = T_{wo} - Q_s / \left(2\pi \cdot \lambda \cdot L\right) \ln\left(d_o / d_{eq}\right) \qquad \text{Eq. (4)}$$

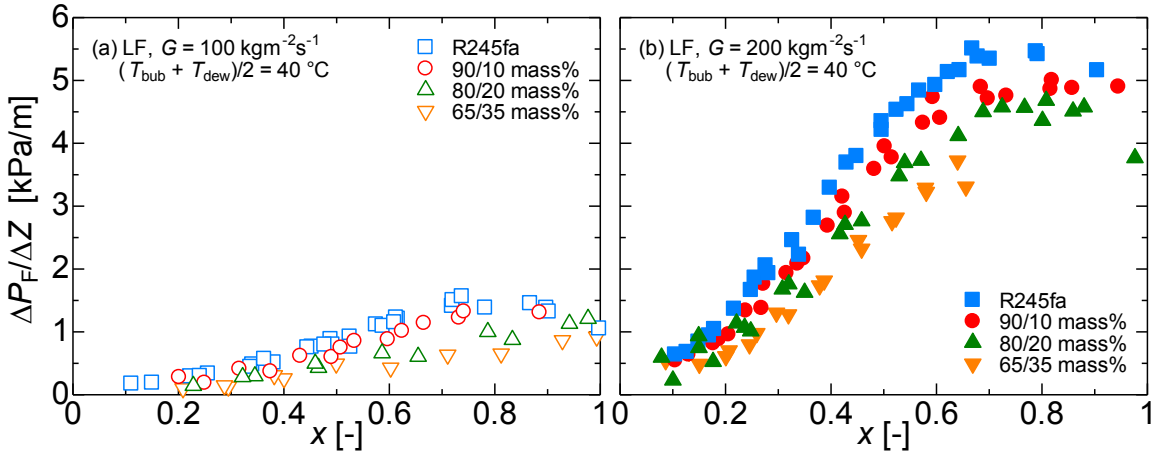

Figure 4: Frictional pressure drops of boiling flow for pure and mixture refrigerants

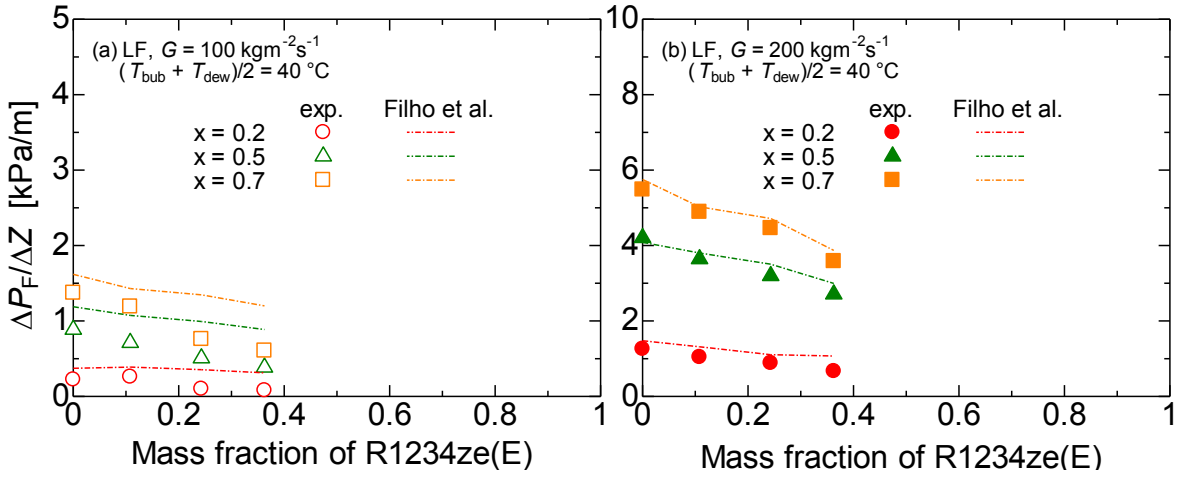

Figure 5: Effect of mass fraction of R1234ze(E) on frictional pressure drops for boiling flow

where λ is the thermal conductivity of the tube wall, L is the effective heating length, and d_o and d_{eq} are respectively the outer and equivalent diameters of the test tubes.
The frictional pressure drop ΔP_F can be expressed as

$$\Delta P_F = \Delta P_{mes} - \Delta P_M \quad \text{Eq. (5)}$$

where ΔP_{mes} is the measured differential pressure in each subsection and ΔP_M is the acceleration pressure drop calculated using the following equation:

$$\Delta P_M = \Delta\left\{G^2 x^2 \Big/ \left(\xi\rho_V\right) + G^2\left(1-x\right)^2 \Big/ \left[\left(1-\xi\right)\rho_L\right]\right\} \quad \text{Eq. (6)}$$

where G is the mass velocity, x is the vapor quality, ρ_V and ρ_L are respectively the vapor and liquid densities, and ξ is the void fraction, which can be calculated using Smith's correlation (Smith, 1969) for a smooth tube:

$$\xi_{Smith} = \left\{1 + \frac{\rho_V}{\rho_L}\left(\frac{1-x}{x}\right)\left(0.4 + 0.6\sqrt{\frac{\frac{\rho_L}{\rho_V} + 0.4\frac{1-x}{x}}{1 + 0.4\frac{1-x}{x}}}\right)\right\}^{-1} \quad \text{Eq. (7)}$$

For a microfin tube, ξ can be calculated using Koyama's correlation (Koyama et al., 2001):

$$\xi_{Koyama} = 0.81\xi_{Smith} + 0.19x^{100(\rho_V/\rho_L)^{0.8}}\xi_{Homo} \quad \text{Eq. (8)}$$

$$\xi_{Homo} = 1/\left\{1 + \left[\left(1-x\right)/x\right]\left(\rho_V/\rho_L\right)\right\} \quad \text{Eq. (9)}$$

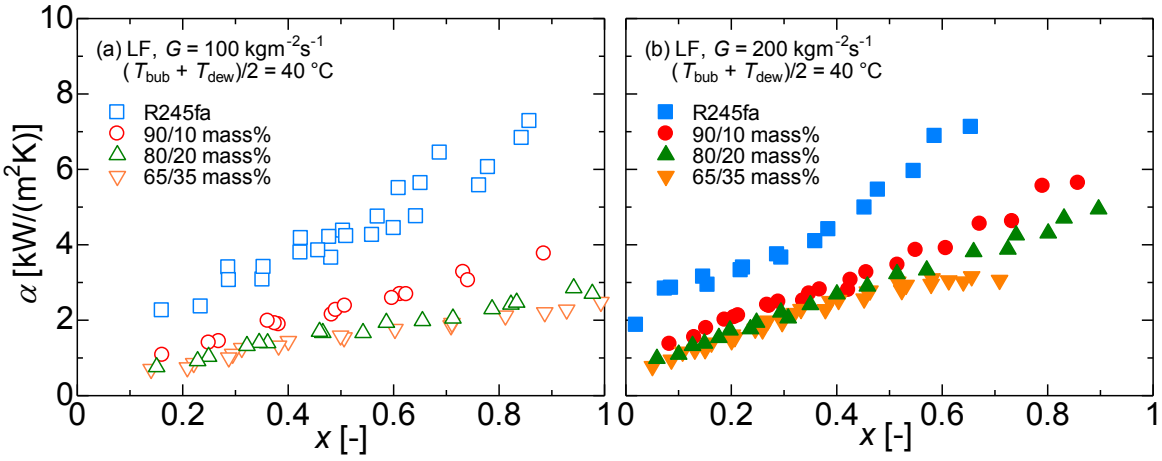

Figure 6: Boiling heat transfer coefficients of pure and mixed refrigerants in the LF tube

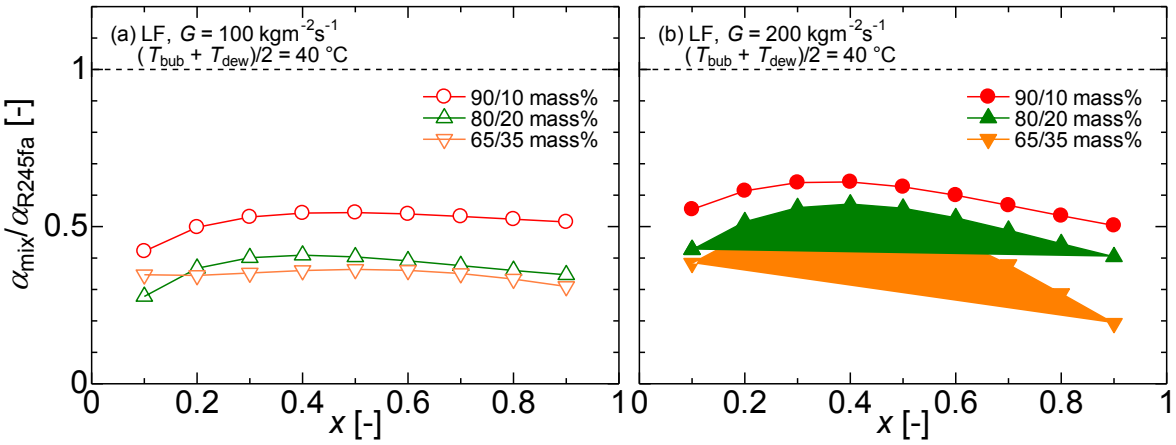

Figure 7: Ratio of the boiling heat transfer coefficients of pure and mixed refrigerants

4. RESULTS AND DISCUSSION

4.1. Frictional Pressure Drop

4.1.1. Experimental Results

Fig. 4 shows the measured frictional pressure drop $(\Delta P_F/\Delta Z)_{exp}$ of the R245fa and R245fa/R1234ze(E) mixtures for boiling flow in the LF tube at a refrigerant temperature of 40 °C with mass velocities of 100 and 200 kgm^{-2}s^{-1}. In this figure, the frictional pressure drops increase with mass velocity and vapor quality for a given mass velocity. It is considered that the increase in the frictional pressure drop is due to the increase in the vapor shear stress with the increase in vapor velocity. In this figure, the frictional pressure drops decrease with the mass fraction of R1234ze(E). It is considered that the decrease in the frictional pressure drop is due to the higher vapor speed because of the smaller vapor density of R1234ze(E).

4.1.2. Comparison to the Predictions of Frictional Pressure Drop

Fig. 5 shows the variation in the frictional pressure drop related to the R1234ze(E) mass fraction at mass velocities of 100 and 200 kgm^{-2}s^{-1} and vapor qualities of 0.2, 0.5, and 0.7. The lines represent the pressure gradient predicted by the correlation of Filho et al. (2004). The experimental results are compared to the selected correlation (Filho et al. 2004). As shown in Fig. 5, the selected correlations reasonably agree with the experimental results. For a mass velocity of 200 kgm^{-2}s^{-1}, Filho correlation agrees well with the experimental results. The correlation proposed for the pure refrigerant predicts the pressure drop for the R245fa/R1234ze(E) mixture well.

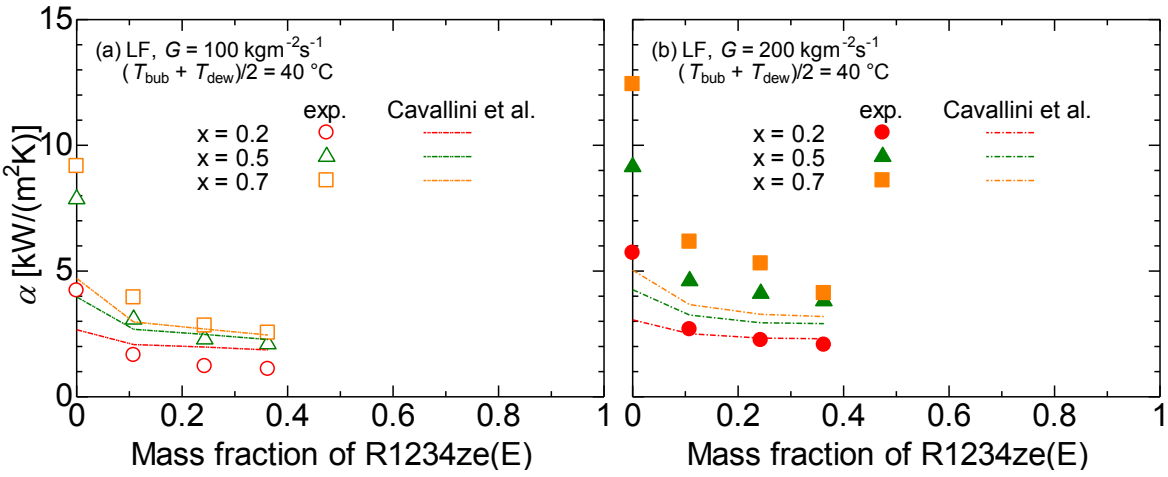

Figure 8: Effect of mass fraction of R1234ze(E) on boiling heat coefficient

4.2. Boiling Heat Transfer

4.2.1. Experimental Results of LF Tube

Fig. 6 shows the measured boiling heat transfer coefficients of pure and mixed refrigerants in the LF tube for mass velocities of 100 and 200 $kgm^{-2}s^{-1}$ with different mass fractions of R1234ze(E). In this figure, the boiling heat transfer coefficient increases with the vapor quality for a given mass velocity and decreases with the mass fraction of R1234ze(E).

Fig. 7 shows the ratio of the boiling heat transfer coefficients of pure and mixed refrigerants related to the R1234ze(E) mass fraction at mass velocities of 100 and 200 $kgm^{-2}s^{-1}$. In comparison to the pure refrigerant, the boiling heat transfer coefficient of the R245fa/R1234ze(E) mixture decreases with the mass fraction of R1234ze(E). It is observed that the heat transfer coefficient zeotropic degradation is not linear for either mass velocity. The heat transfer coefficient decreases considerably at the mass fraction of 90/10 mass%. A sharp decrease in the heat transfer coefficient of approximately 40% is observed for both mass velocities of 100 and 200 $kgm^{-2}s^{-1}$. However, with the increase in the mass fraction of R1234ze(E) from 90/10 to 65/35 mass%, the deterioration ratio of the heat transfer becomes small, which is a result of the fact that the more volatile fluid becomes vapor first and at a higher velocity rate than the less volatile fluid, and as a consequence, the saturated liquid becomes richer in a higher-boiling-point fluid; this change in the liquid fraction composition of the mixture causes an increase in the superheating of the wall for the same heat flux, causing a decrease in the boiling heat transfer coefficient.

4.2.2. Comparison to the Predictions of Boiling Heat Transfer Coefficient

Fig. 8 shows the variation in the boiling heat transfer coefficient related to the R1234ze(E) mass fraction at mass velocities of 100 and 200 $kgm^{-2}s^{-1}$ and vapor qualities of 0.2, 0.5, and 0.7. The lines represent the heat transfer coefficient gradient of zeotropic mixtures predicted by the correlation of Cavallini et al. (1998). In this figure, the boiling heat transfer coefficients decrease with the increase in the mass fraction of R1234ze(E). The Cavallini et al. correlation agrees well with the experimental results at a mass velocity of 100 $kgm^{-2}s^{-1}$. However, the correlation makes a clear overprediction at a mass velocity of 200 $kgm^{-2}s^{-1}$.

4.2.3. Experimental Results of HF Tube

Fig. 9 shows the measured boiling heat transfer coefficients of the mixed refrigerants in the HF tube for mass velocities of 100 and 200 $kgm^{-2}s^{-1}$ with the mass fraction of 90/10 mass% at a saturation temperature of 40 °C. The symbols represent the experimental data with the vertical error bars indicating the measurement uncertainties (Taylor, 1997) and the horizontal error bars indicating the vapor quality change in a subsection. In this figure, similar to the LF tube, the boiling heat transfer coefficient inside the HF tube increases with the vapor quality for a given mass velocity. At a mass velocity of 200 $kgm^{-2}s^{-1}$, a sharp increase in the heat transfer coefficient is observed from the vapor quality of 0.6, owing to the formation of the thin liquid film at the trough between the fins under high vapor qualities and high mass velocity annular flows.

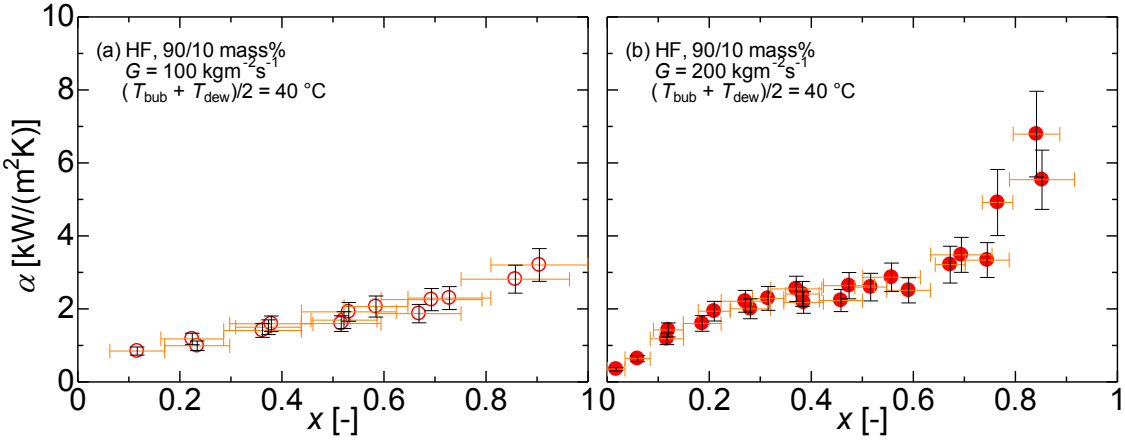

Figure 9: Boiling heat transfer coefficients of the mixed refrigerant in the HF tube

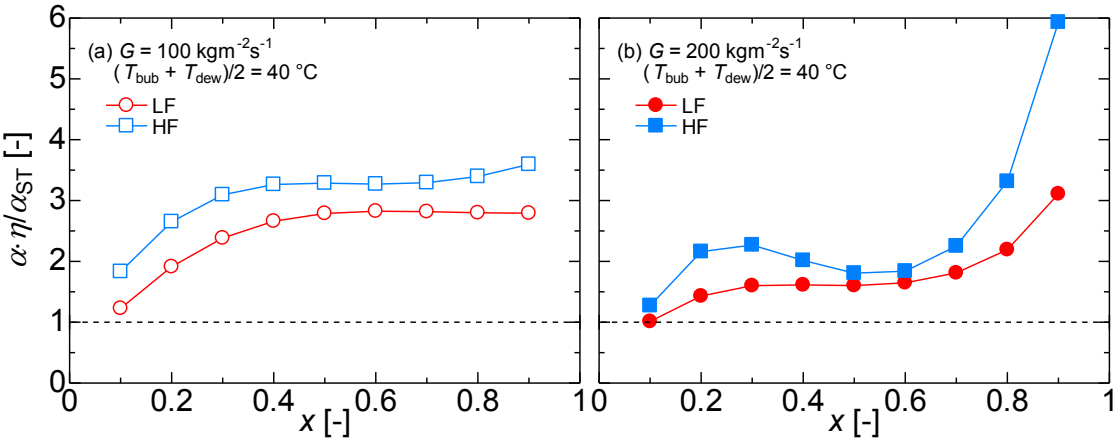

Figure 10: Comparison of boiling heat transfer coefficients between smooth and microfin tubes

4.2.4. Comparison to the Grooved Shape

Fig. 10 shows a comparison of the boiling heat transfer coefficients between the smooth and microfin tubes for mass velocities of 100 and 200 $kgm^{-2}s^{-1}$ with the mass fraction of 90/10 mass%. In this figure, the increase in boiling heat transfer is more pronounced for the HF tube in all vapor quality ranges and mass velocities compared to those for the smooth and LF tubes. This is a result of the high performance (higher fin number, fin height, and helix angle) of the heat transfer enhancement of the HF tube. At the mass velocity of 100 $kgm^{-2}s^{-1}$, these heat transfer enhancements of both microfin tubes exhibit higher values compared to those at the mass velocity of 200 $kgm^{-2}s^{-1}$ for most vapor qualities. Owing to the formation of the thin liquid film, the heat transfer enhancement increases rapidly under a high vapor quality and high mass velocity.

5. CONCLUSIONS

In this study, the boiling heat transfer coefficient and frictional pressure drop of R245fa/R1234ze(E) mixtures inside horizontal microfin tubes with an outside diameter of 9.52 mm were experimentally investigated. The experimental results were compared to the predictions of previously derived correlations, and the following conclusions were drawn based on the findings of the study:

(1) The frictional pressure drop increases with the mass velocity and vapor quality. The frictional pressure drop is dependent on the saturation temperature and decreases with the saturation temperature for a given mass velocity. The experimental results reasonably agree with the correlation by Filho et al. (2004).

(2) The boiling heat transfer coefficient increases with the vapor quality and mass velocity and decreases with the mass fraction of R1234ze(E). A pronounced heat transfer coefficient zeotropic degradation at lower mass fractions of R1234ze(E) than at higher mass fractions was observed. Owing to the formation of the thin liquid film, the increase in boiling heat transfer is more pronounced for the HF tube in high vapor quality range, compared to those for the smooth and LF tubes.

(3) The experimentally determined boiling heat transfer coefficients are approximately ±30% consistent with those predicted by Cavallini et al. (1998); their prediction took into consideration the vapor heat resistance by latent heat variation and nucleate boiling by liquid mass transfer.

ACKNOWLEDGEMENTS

This study was supported by the Mechanical Engineering Laboratory of Kobe Steel, LTD. We would like to express our gratitude here.

NOMENCLATURE

c_p	specific heat capacity, ($Jkg^{-1}K^{-1}$)	ξ	void fraction
d	tube diameter, (m)		
G	mass velocity, ($kgm^{-2}s^{-1}$)	Subscripts	
L	effective heating length, (m)	cal	calculation
q''	heat flux, (Wm^{-2})	exp	experiment
Q	heat transfer rate, (W)	i	inside
T	temperature, (K or °C)	L	liquid
$\dot{m}$	mass flow rate, (kgs^{-1})	o	outside
P	pressure, (Pa)	r	refrigerant
x	vapor quality	s	heat source
ΔZ	length of pressure drop measurement section, (m)	sat	saturation
α	heat transfer coefficient, ($Wm^{-2}K^{-1}$)	V	vapor
λ	thermal conductivity, ($Wm^{-1}K^{-1}$)	w	tube wall
ρ	density, (kgm^{-3})		

REFERENCES

Cavallini, A., Del Col, D., Doretti, L., Longo, G. A., Rossetto, L., 1998. Refrigerant vaporization inside enhanced tubes: a heat transfer model. Proceedings of Heat Transfer in Condensation and Evaporation: Application to Industrial and Environmental Process, Eurotherm Seminar 62, Grenoble, 222-231.

Filho, E. P. B., Jabardo, J. M. S., Barbieri, P. E. L., 2004. Convective boiling pressure drop of refrigerant R-134a in horizontal smooth and microfin tubes. Int. J. Refrigeration, 27(8), 895-903.

Guo, C., Wang J., Du, X., Yang L., 2016. Experimental flow boiling characteristics of R134a/R245fa mixture inside smooth horizontal tube. Applied Thermal Engineering, 103, 901-908.

Kondou, C., Mishima, F., Koyama, S., 2013. Condensation and evaporation of low GWP refrigerant mixture R32/R1234ze(E) in horizontal microfin tubes. Transactions of the Japan Society of Refrigerating and Air Conditioning Engineers 30(4), 61-71. (in Japanese)

Koyama, S., Chen, Y. C., Kitano, R., Kuwahara, K., 2001. Experimental study on void fraction of two-phase flow inside a micro-fin tube. The reports of institute of Advanced Material Study, Kyushu University 15(1), 79-85.

Lemmon, E. W., Bell, I. H., Huber, M. L., McLinden, M.O., 2018. Reference fluid thermodynamic and transport properties-REFPROP Ver. 10.0, National Institute of Standards and Technology, Gaithersburg.

Smith, S. L., 1969. Void fractions in two-phase flow: a correlation based upon an equal velocity head model. Proc. Instn. Mech. Engrs. 184(1)(36), Institution of Mechanical Engineers, 647-664.

Taylor J.T., 1997. An introduction to error analysis, 2nd edition. University science book.

Watanabe, K., Jige D., Inoue N., 2016. Evaporation and condensation characteristics of refrigerant mixtures R245fa/R134a inside horizontal tubes. Transactions of the Japan Society of Refrigerating and Air Conditioning Engineers 33(4), 383-394. (in Japanese)

Manuscript ID: 648
DOI: 10.18462/iir.icr.2019.0648

Generalized COP estimation of heat pump processes for operation off the design point of equipment

Torben OMMEN[(a)], Jonas K. JENSEN[(a)], Wiebke MEESENBURG[(a)], Pernille H. JØRGENSEN[(a)], Henrik PIEPER[(a)], Wiebke B. MARKUSSEN[(a)], Brian ELMEGAARD[(a)]

[(a)] Technical University of Denmark
Kgs. Lyngby, 2800, Denmark, tsom@mek.dtu.dk

ABSTRACT

Heat pumps (HPs) and their individual components experience a significant share of operation away from the design point, due to both sink and source temperature variations as well as operation at part load. In the present study, we expand a generalized HP COP estimation for design conditions to include the performance of conditions within the typical limits for the operating range. The estimation was compared to results based on detailed thermodynamic models of two representative HP installations, of different size and design temperatures. The considered configurations include a 14 kW R134a one-stage cycle and an 800 kW two-stage ammonia heat pump. Based on the design point COP estimation, and five linearized off-design contributions, the performance estimation of COP showed a maximum deviation of 8 %.
Keywords: Heat pumps, Compressors, COP estimation, Performance modelling.

1. INTRODUCTION

The Coefficient of Performance (COP) of a heat pump (HP) is highly dependent on four temperatures defined by the heat source and the heat sink. In addition the load impacts the COP. To obtain an estimation of performance for design conditions, as well as for operation off the design point, performance characteristics may be provided from HP suppliers. However, the detailed information presented in preliminary tenders is in most cases not needed for the first assessment or even for the technical feasibility analysis. The main barrier for HP integration is the operating cost of the system (Ommen et al., 2015). If the performance of a plant depends mainly on external factors (heat source and heat sink) the differences between specific cycle and component choices are of secondary interest. The tender process may thus be seen as a barrier for effortless feasibility analysis which results in fewer successful HP installations.
In a recent paper (Jensen et al., 2018) a generic equation for the COP of a simple one-stage HP cycle was derived analytically for operation between two finite capacity reservoirs. By use of a number of well-established design parameters, the heat pump COP was estimated for design conditions. The presented estimation method required specific information about refrigerant properties. The estimation procedure for COP was included as part of an early assessment tool for evaluating the feasibility of implementing large-scale HPs. In the present study, the COP estimation was expanded to consider conditions within typical limits for the operating range of such installations. The aim of the paper is to present a method for estimation of performance off the design point of equipment. The COP performance estimation is presented and the results are compared to detailed thermodynamic cycle calculations for two specific installations. The point of origin is the method for COP estimation for a design case, and the attempt to use linearized off-design contributions for important parameters and variables.

2. METHODS

In industrial processes, as well as for the case of DH networks, the heat capacity of the reservoirs are finite, in which case the temperature glide may be a significant factor for the competitiveness of

various technologies. In order to evaluate the COP, the analysis addressed five specific parameters of the HP. The parameters were the four temperatures of the finite reservoirs as well as the part load ratio, defined as the load of the unit compared to the design load.
The first subsections address important characteristics of the existing COP estimation for design conditions, and briefly address how the method was modified to estimate the performance of specific cases of HPs in off-design operation. The last section presents the method to obtain detailed thermodynamic cycle calculations used for comparison and verification of the developed method.

2.1. COP estimation of heat pump processes in design conditions

The generic equation for the COP is based on the Second Law of Thermodynamics, from which it is known that the limit to COP can be calculated as a reversible cycle operating between two finite reservoirs (Lorenz, 1894) as shown in Eq (1).

$$\mathrm{COP}_{\mathrm{Lorenz}} = \frac{\bar{T}_H}{\bar{T}_H - \bar{T}_C} = \frac{\bar{T}_H}{\Delta\bar{T}_{\mathrm{lift}}} \qquad \text{Eq. (1)}$$

Constant heat capacities were assumed for the secondary heat sink and heat source processes, in which case the entropic mean temperatures may be calculated as presented in Eq. (2).

$$\Delta\bar{T}_H = \frac{\Delta \mathrm{T}_H}{\ln\left(\frac{T_{H,o}}{T_{H,i}}\right)}, \quad \Delta\bar{T}_C = \frac{\Delta \mathrm{T}_C}{\ln\left(\frac{T_{C,i}}{T_{C,\mathrm{o}}}\right)} \qquad \text{Eq. (2)}$$

To approach real performance of HPs in finite reservoirs, the Lorenz efficiency may be used, given as the ratio between the performance of an actual HP and the Lorenz COP.
A real cycle calculation includes appropriate characteristics of the working fluid and ensures appropriate temperature differences for the heat transfer process. Fig. 1 shows the simple one-stage HP configuration and a simplified temperature versus heat load (T-$\dot{Q}$) diagram for the two heat exchangers. The T-$\dot{Q}$ diagram indicates the temperature differences between the external sink and source streams and the internal processes in case of a sub-critical heat pump cycle for pure fluids and azeotropic mixtures. The minimum temperature difference encountered is referred to as the pinch point temperature difference, ΔT_{PP}. In the condenser, the analysis assumes the fluids will reach the pinch point temperature difference at two occasions, one during the condensation process and again later during the subcooling process. In this way, the degree of subcooling was fixed as a consequence of the sink temperature glide. As shown in the T-$\dot{Q}$ diagram, the temperature difference in the heat exchanger was considered as the sum of two contributions, the pinch point temperature difference, ΔT_{PP}, and the temperature difference imposed by the refrigerant, ΔT_r.
The pressure-enthalpy (*p*-*h*) and temperature-entropy (*T*-*s*) diagrams for the sub-critical heat pump cycle are presented in Fig. 2. Two processes are shown in the diagrams, the internally reversible process (1-2s-3-4s) and the real subcritical vapour compression process (1-2-3-4). The compression work of the compressor was defined based on the isentropic efficiency, $\eta_{\mathrm{is,c}}$, and the heat loss ratio of the compressor, f_Q, which was the ratio between compressor heat loss ($q_c = h_{2w} - h_2$) and com pression work ($\omega_c = h_{2w} - h_1$). Isenthalpic expansion was assumed for the real subcritical vapour compression process.

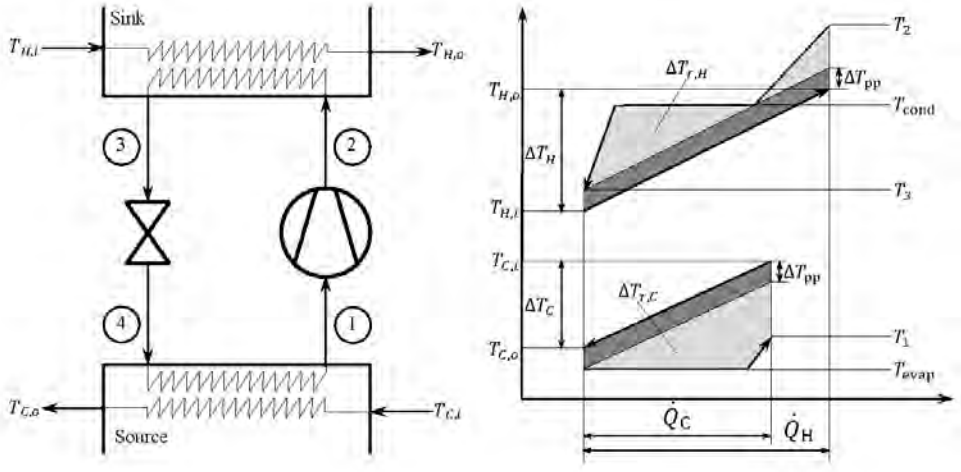

Figure 1: Configuration of a simple one-stage heat pump process and a principle temperature heat load diagram

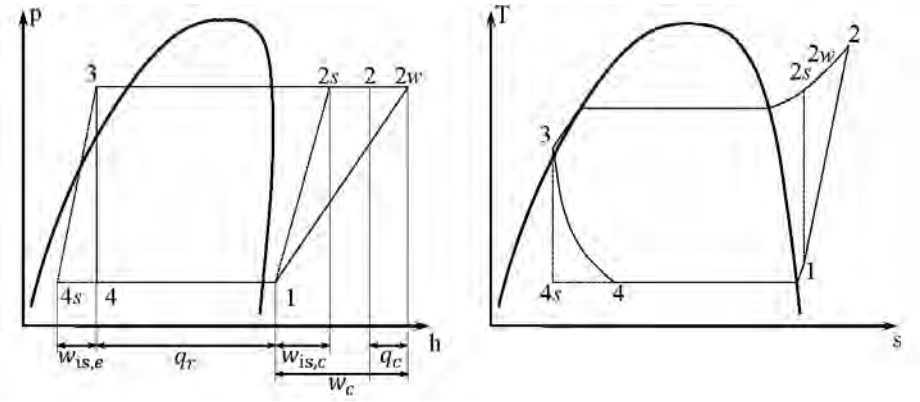

Figure 2: Pressure - enthalpy and temperature - entropy diagram of a simple one-stage heat pump process.

The analytically derived expression for COP (Jensen et al., 2018) is presented as Eq. (3), for a single stage HP cycle, as shown in Fig.1 (superscript 0 denotes design calculation).

$$\mathrm{COP}^0 = \left(\mathrm{COP}_L \frac{1 + \dfrac{\Delta\bar{T}_{r,H} + \Delta\bar{T}_{\mathrm{pp}}}{\bar{T}_H}}{1 + \dfrac{\Delta\bar{T}_{r,H} + \Delta\bar{T}_{r,C} + 2\Delta\bar{T}_{\mathrm{pp}}}{\Delta\bar{T}_{\mathrm{lift}}}} \eta_{\mathrm{is},c} \left(1 - \frac{w_{\mathrm{is},e}}{w_{\mathrm{is},c}}\right) + 1 - \eta_{\mathrm{is},c} - f_Q \right) \qquad \text{Eq. (3)}$$

The variables and parameters needed to evaluate Eq 3. can be divided in three groups. The first group consists of variables dependent on the ***temperatures*** entering and exiting the heat source and heat sink (COP_L, $\bar{T}_H$ and $\Delta\bar{T}_{\mathrm{lift}}$). The second group consists of well-established design ***parameters for specific components*** ($\eta_{\mathrm{is},c}$, f_Q and $\Delta\bar{T}_{\mathrm{pp}}$) and the third group contains variables which are dependent on certain ***characteristics of the refrigerant integration*** with sink and source ($w_{\mathrm{is},e}/w_{\mathrm{is},c}$, $\Delta\bar{T}_{r,H}$, and $\Delta\bar{T}_{r,C}$).

In order to use the analytically derived expression for COP, approximations (or qualified guesses) were required for the third group of variables. In case of limited superheat of the evaporator, the refrigerant-induced temperature difference in the evaporator, was approximated as half of the value of the source temperature difference, $\Delta\bar{T}_{r,C} = 1/2\,\Delta T_C$. The two remaining dependent variables ($w_{\mathrm{is},e}/w_{\mathrm{is},c}$ and $\Delta\bar{T}_{r,H}$) were fitted using simple linear approximations. The approximations were based on simulation results for a wide range of operating conditions (Jensen et al., 2018). The form of the approximations is shown in Eq. 4.

$$\Delta\bar{T}_{r,H} = a\left(T_{H,o} - T_{C,o} + 2\Delta\bar{T}_{\mathrm{pp}}\right) + b\Delta T_H + c, \quad \frac{w_{\mathrm{is},e}}{w_{\mathrm{is},c}} = a\left(T_{H,o} - T_{C,o} + 2\Delta\bar{T}_{\mathrm{pp}}\right) + b\Delta T_H + c \qquad \text{Eq. (4)}$$

For Ammonia and HFC-R134a the coefficients are presented in Table 1.

Table 1. Coefficient for the linear models of $\Delta\bar{T}_{r,H}$ and $\frac{\omega_{\mathrm{is},e}}{\omega_{\mathrm{is},c}}$

	Ammonia			HFC-R134a		
Coefficient	a	b	c	a	b	c
$\Delta\bar{T}_{r,H}$	0.1853	0.1118	-1.0783	-0.0102	0.2647	2.6985
$w_{\mathrm{is},e}/w_{\mathrm{is},c}$	0.0013	-0.0021	0.0306	0.0031	-0.0044	0.0259

2.2. COP performance estimation of heat pump processes in off-design

Based on the COP estimation for design conditions, and a number of linearized contributions, an estimate of the HP performance off the design point of equipment was developed. Such models are sometimes categorized as performance models in literature (Tassou et al., 1983). By refining the estimation to include performance modelling, the applicability of the estimation increases to a point where it could be used for various types of detailed analysis, e.g. to include the hourly variations of performance in the levelized cost of heat, or to evaluate the seasonal impact of specific design considerations.

For models representing specific equipment, a number of changes are required, in order to switch from design calculations to a performance model. The changes include adding details to individual

components such as fixing volumetric capacities, specific characteristics of compression and expansion processes as well as specifying the dimensions and type(s) of heat exchangers.
For a number of specific inputs used for Eq. 3, the magnitude of the parameters and dependent variables may change from the design value, depending on the location of the operation point. On the other hand, if the changes of the values are known in advance, the individual contributions may be used to estimate the COP in both design and performance modes.
Specifically for the input parameters, the different types of contributions were subject to different changes when considering performance modelling. Variables dependent on the case temperatures were included directly "as is" as would be the case in thermodynamic performance modelling. Parameters for specific components were expected to change according to the characteristic information, with the magnitude of such change to be characterized directly based on the information provided by the manufacturer. Depending on the impact of a parameter on the COP, the individual values were chosen to be either fitted, or considered to result in insignificant changes, in which case the parameter was fixed to the design value. Lastly, the characteristics of the refrigerant integration, which were fitted specifically for a design case, was found to require some adjustment. Again, such values were either fitted to obtain changed characteristics, or fixed in case of insignificant impact. Table 2 shows the choice for parameters and variables for COP estimation in performance mode.

Table 2. Changed characteristics to certain parameters and variables for COP estimation

		Change in sink temp (inlet and/or outlet)	Change in source temp (inlet and/or outlet)	Operation in part load
Component specific	$\eta_{\mathrm{is},c}$	Insignificant	Insignificant	Fitted
	f_Q	Insignificant	Insignificant	Fitted
	$\Delta T_{pp,H}$	Fitted	Fitted	Fitted
	$\Delta T_{pp,C}$	Fitted	Fitted	Fitted
Refrigerant integration	$\Delta\bar{T}_{r,H}$	Fitted	Fitted	No change expected
	$\Delta\bar{T}_{r,C}$	Fitted	Fitted	No change expected
	$\frac{w_{\mathrm{is},e}}{w_{\mathrm{is},c}}$	Insignificant	Insignificant	Insignificant

The calculation procedure for COP estimation off the design point of equipment was performed as follows. First, COP was calculated for design conditions, using available information about temperatures and estimation of component specific parameters, as well as the approximations for the characteristics of the refrigerant integration for Eq. 4. Subsequently, the COP estimation for performance mode was considered, which is denoted by a star superscript, as presented in Eq. 5.

$$\mathrm{COP}^* = \left(\mathrm{COP}_L \frac{1 + \frac{\Delta\bar{T}^*_{\mathrm{cond,is}}}{\bar{T}_H}}{1 + \frac{\Delta\bar{T}^*_{\mathrm{cond,is}} + \Delta\bar{T}^*_{\mathrm{evap,is}}}{\Delta\bar{T}_{\mathrm{lift}}}} \eta^*_{\mathrm{is},c} \left(1 - \frac{w_{\mathrm{is},e}}{w_{\mathrm{is},c}}\right) + 1 - \eta^*_{\mathrm{is,c}} - f^*_Q \right) \quad \text{Eq. (5)}$$

where all elements with a star superscript were fitted to obtain an appropriate performance parameter/variable. The fit was performed for each model individually from detailed results derived according to the method presented in subsection 2.3 below. The calculation of the performance model of entropic average temperature differences in condenser and evaporator ($\Delta\bar{T}^*_{\mathrm{cond,is}}$ and $\Delta\bar{T}^*_{\mathrm{evap,is}}$) follows the calculation of Eq. (6) and (7), which uses the value of certain parameters in the design calculation (superscript 0).

$$\Delta\bar{T}^0_{\mathrm{cond,is}} = \Delta\bar{T}^0_{r,H} + \Delta\bar{T}^0_{\mathrm{pp,H}}, \quad \Delta\bar{T}^*_{\mathrm{cond,is}} = \Delta\bar{T}^0_{\mathrm{cond,is}} + \alpha_1(\Delta T_H - \Delta T^0_H) - \alpha_2(1 - r_{\mathrm{PL}}) \quad \text{Eq. (6)}$$

$$\Delta\bar{T}^0_{\mathrm{evap,is}} = \Delta\bar{T}^0_{r,C} + \Delta\bar{T}^0_{\mathrm{pp,C}}, \quad \Delta\bar{T}^*_{\mathrm{evap,is}} = \Delta\bar{T}^0_{\mathrm{evap,is}} + \beta_1(\Delta T_C - \Delta T^0_C) - \beta_2(1 - r_{PL}) \quad \text{Eq. (7)}$$

Where r_{PL} is the load ratio, given as a value between 0 and 1.
The remaining fitted values are presented in Eq. (8) and (9).

$$f^*_Q = f_Q(1/r_{\mathrm{PL}}) \quad \text{Eq. (8)}$$

$$\eta^*_{\mathrm{is},c} = \eta_{\mathrm{is,c}} + \gamma(1 - r_{PL}) \quad \text{Eq. (9)}$$

The values of the individual coefficients for parameters are presented in Table 5 (subsection 3.2).

2.3. Detailed thermodynamic cycle calculations for heat pump processes

Detailed thermodynamic models of two specific heat pumps were used for steady state operation. Both cycle calculations were based on energy, mass and momentum balances.
The models correspond to two different cycle configurations, and represent real plants in two different scales of heat supply. The smallest unit is a simple one-stage cycle operating with HFC-R134a with a condenser capacity at 14 kW in design conditions (Thorsen and Ommen, 2018). The second cycle is a two-stage Ammonia cycle with open intercooler, at a design capacity of 800 kW (Meesenburg et al., 2019). The layout of the second cycle is presented in Fig. 3. The considered design conditions for the thermodynamic cycle calculation are presented in Table 3. The table also contains the feasible ranges of the performance modelling.

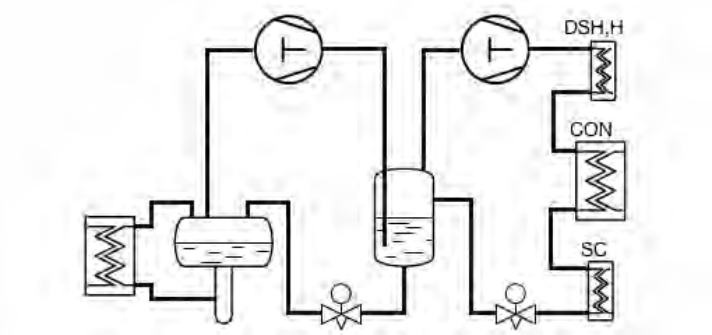

Figure 3: Cycle configuration of two-stage heat pump with open intercooler

Table 3. Design conditions and characteristics of equipment for detailed thermodynamic cycle calculations.

	One-stage HP	Two-stage (open intercooler)
Working fluid	HFC-R134a	R717
Design capacity	14 kW	800 kW
Design temp. in sink	$T_{H,i} = 45$ °C, $T_{H,o} = 60$ °C	$T_{H,i} = 34$ °C, $T_{H,o} = 70$ °C
Design temp. in source	$T_{C,i} = 45$ °C, $T_{C,o} = 25$ °C	$T_{C,i} = 10$ °C, $T_{C,o} = 4$ °C
Software	Engineering Equation Solver	Dymola software with TIL library
Modelled components	4	10
Compressor type(s)	Hermetic scroll	Two open piston compressors
Electric motor(s)	Frequency controlled	Frequency controlled
Compressor $\eta_{\mathrm{is},c}$ and f_Q	Data from manufacturer	Data from manufacturer
Heat exchanger type	Plate heat exchangers	Shell and plate heat exchanger
Heat transfer estimation	Overall heat transfer estimation in part load	Detailed heat transfer correlations
Performance variation sink	$T_{H,i} = \pm 10\ K\ T_{H,o} = \pm 10\ K$	$T_{H,i} = \pm 10\ K\ T_{H,o} = \pm 10\ K$
Performance variation source	$T_{C,i} = \pm 10\ K$, $T_{C,o} = \pm 10\ K$	$T_{C,i} = 9$ °C to16 °C (limitation) $T_{C,o} = 1$ °C to 5 °C (limitation)
Performance variation load	50 % to 100 %	50 % to 100 %

2.4. COP estimation for annual simulations

For evaluating the impact of using the estimation of COP*, the method was compared to the estimation of COP^0 and the assumption of fixed Lorenz efficiency, for an annual simulation. The analysis assumes a DH network as the heat sink, and sea water as the heat source, both according to the case presented in Pieper et al. (2018). All three performance estimates assume similar performance in the design point, which corresponds to operation in February.

3. RESULTS

The first subsection addresses the comparison of model results and the COP estimation for the design case. Following this, the second subsection shows the results of the comparison between

detailed thermodynamic models and the proposed COP estimation in off-design. Finally, the last subsection addresses the differences between three COP estimates for annual operation.

3.1. Comparison of the COP estimation and detailed model results for the design case

Table 4 shows the results of the two COP estimates and two detailed models, all in design conditions. The first four rows present design parameters for specific components. The six following inputs are the values required for the estimation of COP^0. The values of the three fitted parameters were obtained using the coefficients for the linear models from Table 1. Finally, the COP^0 is presented in the last row of the table. The difference presented here is less than 2.5%, which is significantly below the maximum deviation (up to 10 %) suggested by the reference (Jensen et al., 2018). It should furthermore be considered, that not all values are exactly similar to the design, like the pinch temperature difference for the two-stage HP, or the calculation method for heat loss factor.

Table 4. Comparison of the COP estimation and detailed model results for the design case

		Simple one-stage		Two-stage (open intercooler)	
		Estimation	Model	Estimation	Model
$\eta_{\mathrm{is},c}$	(-)	0.70	0.70	0.75	0.71 and 0.79
f_Q	(-)	0.25	0.25	0.11	~0.10
$\Delta T_{pp,H}$	K	4	~4	6	~4 - 8
$\Delta T_{pp,C}$	K	4	~4	2	~2
COP_L	(-)	18.55	18.55	7.27	7.27
$\bar{T}_H$	K	325.6	325.6	324.8	324.8
$\Delta\bar{T}_{\mathrm{lift}}$	K	17.55	17.55	44.68	44.68
$\Delta\bar{T}_{r,H}$	K	6.31	6.63	17,4	Not available
$\Delta\bar{T}_{r,C}$	K	10.0	8.7	3.0	Not available
$\frac{w_{\mathrm{is},e}}{w_{\mathrm{is},c}}$	(-)	0.095	0.1558	0.056	Not available
COP^0	(-)	5.152	5.027	3.512	3.445

3.2. Comparison of the COP performance estimation and detailed performance model

Table 5 presents the coefficients that correspond to the best fit between the detailed cycle calculation and the COP* method for the two examined plants. For α_2 and β_2 it was found that the values correspond to the value of the pinch point temperature difference in design. For γ the difference between the two cases can be explained by the fact that the simple one-stage cycle assumes the compressor polynomial without changes for part load, whereas the two stage cycle employs polynomials that reflect changes with changed rotational speed.

Table 5. Coefficients used for COP performance estimation.

	Simple one-stage	Two-stage (open intercooler)
α_1	0.4	0.4
α_2	$\Delta\bar{T}^0_{\mathrm{pp,H}}$	$\Delta\bar{T}^0_{\mathrm{pp,H}}$
β_1	0.25	0.4
β_2	$\Delta\bar{T}^0_{\mathrm{pp,C}}$	$\Delta\bar{T}^0_{\mathrm{pp,C}}$
γ	0	0.1

Fig. 4 shows the result of a comparison between the detailed thermodynamic model in performance mode (full lines) and the corresponding COP* estimation (dashed lines). The left figure shows results for the simple one-stage cycle, whereas the right figure shows results for the two-stage cycle. The results of Fig. 4 were calculated as relative to COP^0 (from Table 4). Thus, although all four variations in temperature match in the origin, the 2.5% deviation would still be present for the result in terms of COP. It is shown that the proposed coefficients allow an appropriate estimation of COP* for both considered cycle designs, when one variable is varied and all other inputs are equal.

A comparison of the discrepancy for the two estimates (COP^0 and COP*) is presented in Fig. 5, where the plotted deviation is relative to the detailed cycle calculation in performance mode. In both cases the results correspond to the simple one-stage cycle. As shown in the figure, the proposed

estimate for COP* (right) deviates significantly less (2% to 8%) than the COP^0 (left) estimation (-5% to +23 %). This comparison further shows how the constraints imposed by the change from design to the performance mode results in a lower variation in the performance. This is shown as the results of the estimate for COP^0 suggest a significantly higher value (in the range of 20 % deviation) for the configurations with high $T_{C,o}$ and low values of $T_{H,i}$ and $T_{C,i}$.

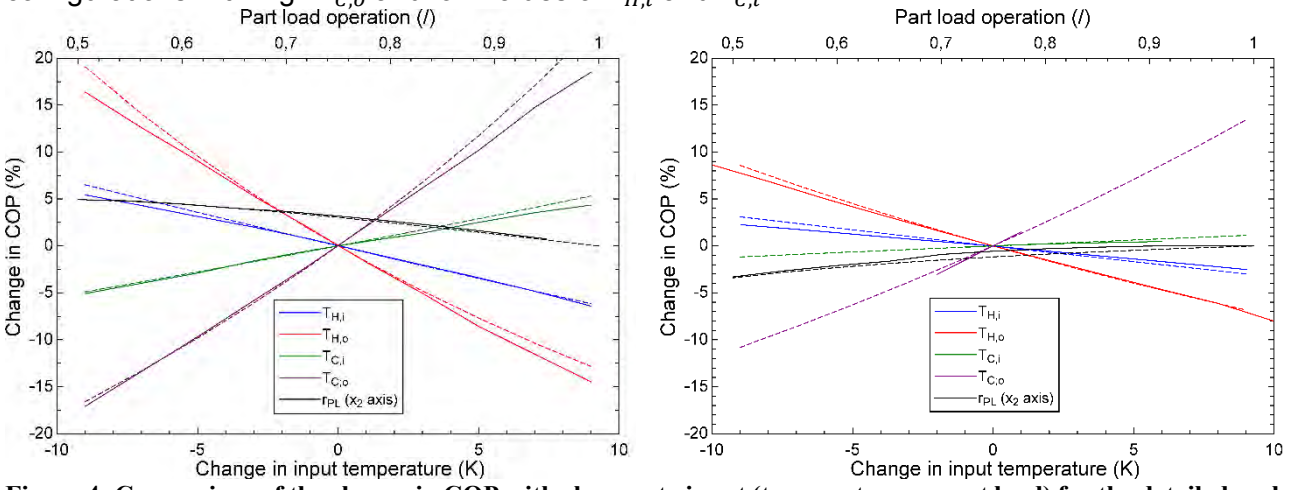

Figure 4: Comparison of the change in COP with changes to input (temperature or part load) for the detailed cycle calculation (full lines) and the proposed COP estimation (dashed line). All results are relative to results presented in Table 4. Left figure shows results for the simple one-stage cycle, two-stage cycle on the right.

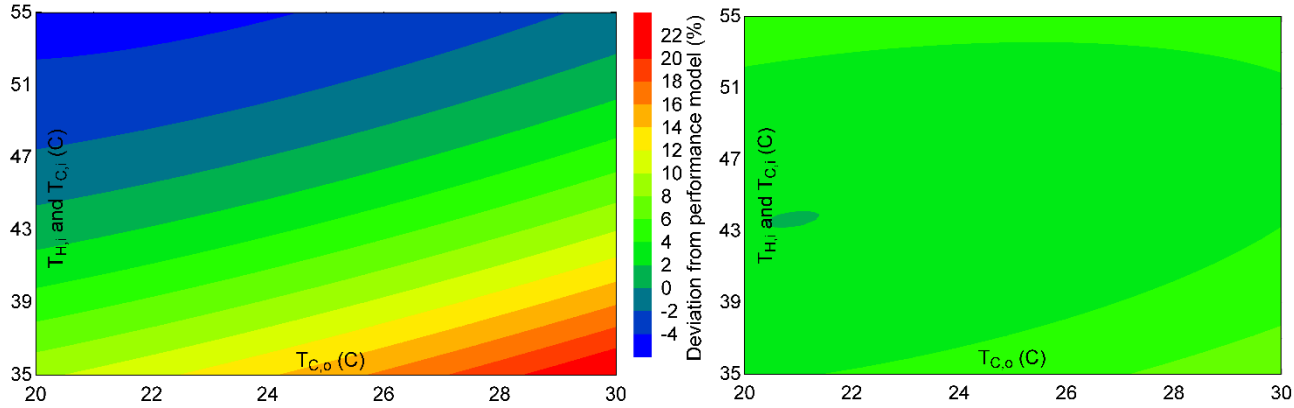

Figure 5: The existing COP estimation for design (left) and the proposed COP performance estimation (right) compared to a detailed cycle calculation in performance mode (Simple one-stage).

3.3. Comparison of various COP estimation for annual simulations

Fig. 6 shows the two COP estimation methods compared to an assumption of fixed Lorenz efficiency for a yearly operation of a DH HP in Copenhagen, Denmark. For conditions similar to the design conditions the deviation between the methods were negligible. However, for significantly changed operating conditions, significant differences were found. For fixed Lorenz efficiency and the estimation for COP* the deviation amount to approximately 11% during the summer period.

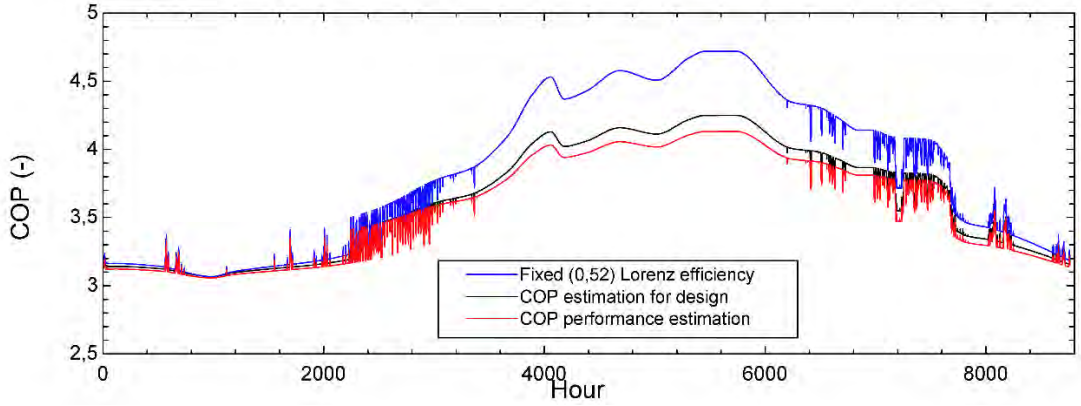

Figure 6: Comparison of three different COP estimation methods.

4. DISCUSSION

This paper presents a first attempt to obtain a generalized performance model for heat pump integration. In the present analysis the coefficients required for estimation of COP* was determined from a detailed cycle calculation in performance mode. This is not a generally applicable method for a wide range of solutions. Thus further analysis on how to obtain such values should be addressed. The method presented here further requires verification and validation by experimental results.
The estimation method for one-stage cycles was shown to fit well with two-stage configurations, which is likely due to the choice regarding subcooling to pinch, which has been observed to even out the performance improvement typically shown for two-stage cycles.

5. CONCLUSIONS

In a recently published paper a COP estimation method was proposed for design conditions. This paper addresses specific options to utilize the estimation method for performance estimation off the design point. The proposed method was shown to estimate the COP of two detailed performance models with low deviation. The results showed that for all considered cases, the estimate deviated less than 8 % from the performance model.

ACKNOWLEDGEMENTS

The research presented in the paper is financially funded by the Danish Energy Agency EUDP (energy technology development and demonstration program). Primarily projects :"EnergyLab Nordhavn - New Urban Energy Infrastructures" (64014-0555) and "Experimental development of electric heat pumps in the Greater Copenhagen DH system - Phase 2" (64015-0571).

NOMENCLATURE

Symbols		*Greek*			
COP	Coefficient of performance (-)	Δ	Difference	*i*	Inlet
f_O	heat loss ratio (-)	η	Efficiency (-)	is	Isentropic
h	Enthalpy ($\mathrm{kJ\,kg^{-1}}$)	*Sub- & superscripts*		o	Outlet
T	Temperature (K)	*c*	Compression	pp	Pinch point
$\bar{T}$	Entropic avg. temperature (K)	*C*	Cold stream (heat source)	*r*	Refrigerant
r_{HP}	Load ratio	*e*	Expansion	0	For design
w	Work ($\mathrm{kJ\,kg^{-1}}$)	*H*	Hot stream (heat sink)	*	Performance

REFERENCES

Jensen, J.K., Ommen, T., Reinholdt, L., Markussen, W.B., Elmegaard, B., 2018. Heat pump COP, part 2: Generalized COP estimation of heat pump processes, in: Proceedings of the13th IIR-Gustav Lorentzen Conference on Natural Refrigerants. IIF/IIR, Valencia.

Lorenz, A., 1894. Contributions to the assessment of cooling machines, in: Z VDI 38. bll 62–68, 98–103, 124–130.

Meesenburg, W., Kofler, R., Ommen, T., Markussen, W.B., Elmegaard, B., 2019. Design considerations for dynamically operated large-scale ammonia heat pumps, in: 25th IIR International Congress of Refrigeration.

Ommen, T., Jensen, J.K., Markussen, W.B., Reinholdt, L., Elmegaard, B., 2015. Technical and economic working domains of industrial heat pumps: Part 1 - single stage vapour compression heat pumps. Int.J.Refrig.

Pieper, H., Ommen, T., Elmegaard, B., Markussen, W., 2018. Assessment of a combination of three heat sources for heat pumps to supply district heating, in: 13th Conference on Sustainable Development of Energy, Water and Environment Systems – SDEWES Conference. Palermo.

Tassou, S.A., Marquand, C.J., Wilson, D.R., 1983. Comparison of the performance of capacity controlled and conventional on/off controlled heat pumps. Appl. Energy 14, 241–256.

Thorsen, J.E., Ommen, T., 2018. Field experience with ULTDH substation for multifamily building. Energy Procedia 149, 197–205. https://doi.org/10.1016/J.EGYPRO.2018.08.184

Manuscript ID: 660
DOI: 10.18462/iir.icr.2019.0660

Experiments on condensation heat transfer and pressure drop of refrigerant mixtures R245fa/R1234ze(E) inside horizontal microfin tubes

Kazuhide WATANABE [(a)], Yufei LIU [(b)], Daisuke JIGE [(c)], Norihiro INOUE [(c)]

[(a)]Japan Coast Guard Academy, Hiroshima, 737-8512, Japan, watanabe@jcga.ac.jp
[(b)] Graduate school of Marine Science and Technology, Tokyo University of Marine Science and Technology, Tokyo, 135-8533, Japan
[(c)]Tokyo University of Marine Science and Technology, Tokyo, 135-8533, Japan, inoue@kaiyodai.ac.jp

ABSTRACT

This study experimentally investigated the condensation heat transfer and pressure drop characteristics of zeotropic refrigerant mixtures R245fa/R1234ze(E) inside horizontal microfin tubes. The test was conducted using copper tubes with an outside diameter of 9.52 mm, equivalent inner diameters of 8.9 and 8.7 mm, fin heights of 0.12 and 0.18 mm, and 65 and 85 fins. The experiments were conducted under mass velocities of 100 and 200 $kg.m^{-2}.s^{-1}$, mass fractions of 90/10, 80/20, and 65/35 mass%, and an average saturation temperature of 60 °C. The measured condensation heat transfer coefficient and frictional pressure drop of the refrigerant mixture R245fa/R1234ze(E) were lower than that of pure refrigerant R245fa. The condensation heat transfer coefficient was minimized with the 65/35 mass% composition R245fa/R1234ze(E) with the largest temperature glide. Furthermore, the frictional pressure drop decreased with an increase in the mass fraction of R1234ze(E).
Keywords: Condensation, Heat transfer, Pressure drop, Refrigerant, Zeotropic mixture, R245fa, R1234ze(E), Microfin tube

1. INTRODUCTION

In recent years, the introduction of high-temperature heat pump equipment has led to its development with the aim of reusing waste heat from factories and the like to generate high-temperature water/steam. For the above equipment, selecting a suitable working fluid for each system temperature level is vital. Watanabe et al. (2016a, 2016b) reported the heat transfer and pressure drop characteristics of the evaporation and condensation flows in a horizontal smooth tube using pure refrigerant R245fa having a low critical pressure and high critical temperature, and a refrigerant mixture R245fa/R134a mixed with R134a having a larger volume capacity and higher critical temperature compared with R245fa. However, owing to the Kigali Amendment to the Montreal Protocol, HFC refrigerants with high greenhouse effect are obliged to gradually reduce its production and consumption. It has been required to switch to alternative refrigerants with lower global warming potential (GWP) values in the future. Because the GWP value of R134a is larger than R245fa, the two-component refrigerant mixture R245fa/R1234ze(E) of the R245fa and hydrofluoroolefins refrigerant R1234ze(E) which is anticipated as an alternative refrigerant. With hardly a few studies on the refrigerant mixture R245fa/R1234ze(E), a quantitative and detailed understanding of the heat transfer and pressure drop characteristics for evaporation and condensation flows of the refrigerant mixture is needed to improve the heat exchanger and cycle performance. In this study, the condensation characteristics of the refrigerant mixture R245fa/R1234ze(E) in the horizontal tubes are experimentally clarified, and the refrigerant composition effect on these characteristics is examined. Because zeotropic refrigerant mixture causes a lowered heat transfer performance compared to pure refrigerant, the evaporator and condenser are required to improve its heat transfer performance. Therefore, a microfin tube is generally used to improve the heat transfer performance on the heat exchanger refrigerant side. To quantitatively understand and verify the inner microfin effect on the heat transfer promotion, experiments of condensation heat transfer and pressure drop inside the two kind of microfin tubes and smooth tube were carried out.

2. EXPERIMENTAL APPARATUS AND PROCEDURE

Fig. 1 shows the experimental apparatus schematic used in this study. The refrigerant pumped from the pump (1) was adjusted to its predetermined vapor quality at the counter-flow-type water preheater (3) and electric preheater (4), after which it flowed into the test section (5). The refrigerant flow rate was adjusted by the pump rotational speed and the test section inlet pressure was maintained constant by adjusting the cooling water temperature at the after-condenser (6). The experiments were conducted under conditions of mass velocity of 100 and 200 $kg.m^{-2}.s^{-1}$ and average saturation temperature of 60 °C. In the refrigerant mixture experiment, the circulating liquid refrigerant was sampled in the vessel at the sampling port (8) provided at the pump outlet, expanded and vaporized in the vessel, and then analyzed by gas chromatography. Composition analysis was conducted three to four times with one sampling and the average value taken as the refrigerant mixture composition. The variation of the composition analysis result by gas chromatograph obtained by one sampling was approximately ±1%. Fig. 2 shows the test section schematic comprised of a counter-flow-type double-pipe heat exchanger. In this section, the refrigerant flowed through the 9.5-mm (outer-diameter) inner copper test tubes, and the heat source water flowed through the annulus around the inner tube. The annulus was divided into three subsections of 600 mm length each. The refrigerant temperatures at the test section inlet and outlet were measured by sheathed K-type thermocouples. The tube wall temperature was measured by T-type thermocouples embedded in the top, bottom, and side of the test tube exterior walls midway its effective heating length of 557 mm. The heat source water temperature was measured by Pt-resistance thermometers installed in the mixing chambers of the heat source water at each subsection inlet and outlet. Pressure ports were bored into the smooth test tube at both ends of each subsection to measure the pressure drop by differential pressure transducers.

Table 1 lists the specifications of the smooth tube and the microfin tubes used in this study. Fig. 3 shows the microfin tube cross-sectional views. Based on Table 1, the microfin tube equivalent diameter is the inner diameter of a smooth tube having a channel cross-sectional area equivalent to the actual microfin tube channel cross-sectional area. The surface area enlargement is the ratio of the actual microfin tube heat transfer area and the equivalent inner diameter heat transfer area taking the helix angle into account.

3. DATA REDUCTION

The frictional pressure drop, ΔP_F, was obtained from the following equation.

$$\Delta P_F = \Delta P_{mes} - \Delta P_M \qquad \text{Eq. (1)}$$

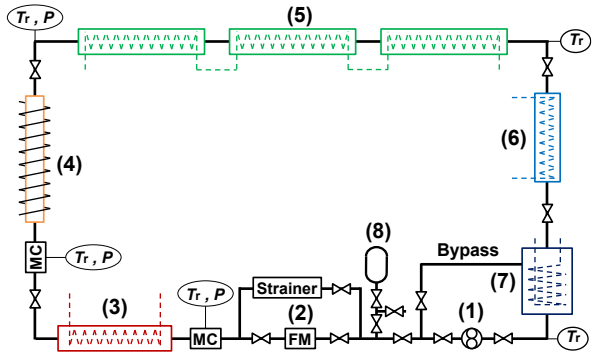

(1) Pump
(2) Mass flow meter
(3) Water preheater
(4) Electric preheater
(5) Test section
(6) After-condenser
(7) Receiver tank
(8) Sampling port

Figure 1. Schematic view of the test loop.

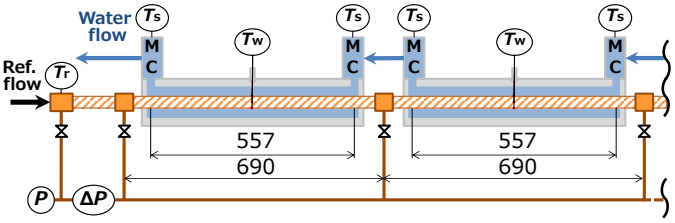

P : Absolute pressure transducer
ΔP : Differential pressure transducer
T_r : Sheathed K-type thermocouple
T_w : T-type thermocouple
T_s : Pt-resistance thermometer

Figure 2. Schematic view of the test section.

where ΔP_{mes} is the measured differential pressure in each subsection. ΔP_M is the acceleration pressure drop calculated using the following equation:

$$\Delta P_M = \Delta\left[\frac{G^2x^2}{\xi\rho_V} + \frac{G^2(1-x)^2}{(1-\xi)\rho_L}\right] \quad \text{Eq. (2)}$$

where G is the mass velocity, x is the vapor quality, ρ_V and ρ_L are respectively the vapor density and liquid density, and ξ is the void fraction was calculated using the correlations of Koyama et al. (2001) for a microfin tube and of Smith (1969) for a smooth tube.

The heat flux, q, of each subsection was obtained from the following equation based on the actual heat transfer area.

$$q = \frac{Q_s}{\pi d_{eq} L\eta} = \frac{W_s c_{ps}\Delta T_s - Q_{loss}}{\pi d_{eq} L\eta} \quad \text{Eq. (3)}$$

where the heat transfer rate, Q_s, is obtained from the heat source water mass flow rate, W_s, .the specific heat capacity, c_{ps}, the temperature difference between the heat source water at each subsection inlet and outlet, ΔT_s, and considering the heat loss, Q_{loss}. The heat transfer coefficient, α, for each subsection is given by

$$\alpha = \frac{q}{T_r - T_{wi}} \quad \text{Eq. (4)}$$

where T_r is the refrigerant temperature. In the case of a pure refrigerant, T_r was obtained from the refrigerant saturation pressure. Whereas for a refrigerant mixture, it was calculated from the refrigerant temperature measured at the test section inlet and outlet by interpolation considering the heat transfer rate of each subsection. The inner tube wall temperature, T_{wi}, is determined from the exterior tube wall temperature by applying the one-dimensional heat equation to the radial direction. The refrigerant mixture physical properties were calculated from the refrigerant composition analyzed by a gas chromatograph and the refrigerant mixture absolute pressure using REFPROP Ver. 10.0. Table 2 summarizes the thermodynamic properties of pure refrigerants R245fa, R1234ze(E), and refrigerant mixtures R245fa/R1234ze(E) (refrigerant composition 80/20 mass% and 65/35 mass%) at an average saturation temperature of 60 °C. Fig. 4 shows the vapor-liquid

Table 1 Specifications of test tubes.

Test Tube			ST	LF	HF
Outer diameter	d_o	[mm]	9.52	9.53	9.51
Wall thickness	t_w	[mm]	0.60	0.29	0.35
Fin height	h_f	[mm]	-	0.12	0.18
Equivalent diameter	d_{eq}	[mm]	8.32	8.89	8.73
Number of fins	N	[-]	-	65	85
Spiral angle	θ	[°]	-	16.5	39.4
Surface area enlargement	η	[-]	1	1.31	2.09

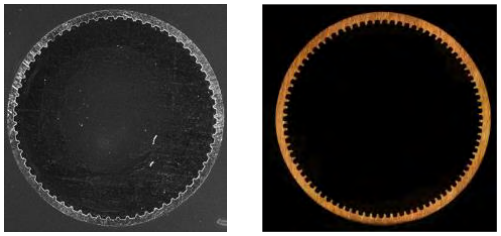

(a) LF **(b) HF**

Figure 3. Microfin tubes cross-sectional views.

Table 2. Thermodynamic properties at the average saturation temperature of 60°C.

		R245fa	R245fa/R1234ze(E)		R1234 ze(E)
			80/20	65/35	
P	MPa	0.462	0.697	0.833	1.277
ΔT	K	0	8.0	8.9	0
Δh_{LV}	kJ×kg^{-1}	169.1	156.1	149.8	135.5
ρ_L	kg×m^{-3}	1236.9	1189.4	1155.9	1032.5
ρ_V	kg×m^{-3}	25.4	37.2	44.4	70.1
μ_L	μPa×s	256.9	213.2	187.7	122.9
μ_V	μPa×s	11.7	12.5	13.0	14.5
λ_L	mW×m^{-1}×K^{-1}	76.9	72.9	70.3	62.8
λ_V	mW×m^{-1}×K^{-1}	15.8	16.3	16.5	17.3

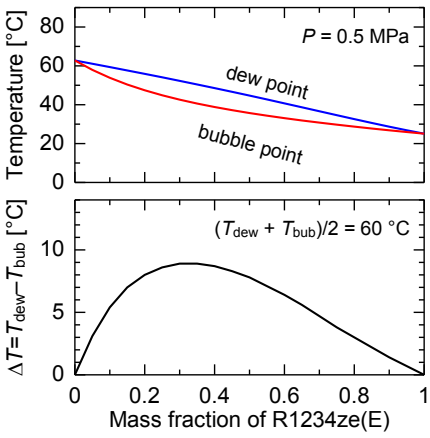

Figure 4. Temperature glide of R245fa/R1234ze(E) mixture.

phase equilibrium diagram and the temperature difference between the dew point and bubble point (hereinafter referred to as temperature glide) of the refrigerant mixture R245fa/R1234ze(E). From Fig. 4, the temperature glide of the refrigerant mixture obtained its maximum value with approximately 65/35 mass% refrigerant composition.

4. RESULTS AND DISCUSSION

4.1. Frictional Pressure Drop

Figs. 5(a) and (b) show the relationship between the frictional pressure drops $(\Delta P_F/\Delta Z)_{exp}$ and the wetness $1–x$ for the pure refrigerant R245fa and refrigerant mixtures R245fa/R1234ze(E) at mass velocities of 100 and 200 kg.m^{-2}.s^{-1}. The frictional pressure drops of the refrigerant mixtures were relatively small compared with that of the pure refrigerant R245fa. Furthermore, the frictional pressure drops were observed to decrease as the mass fraction of R1234ze(E) increases. As shown in Table 2, under the condition of the average saturation temperature of 60 °C, the vapor density of R1234ze(E) is approximately 2.8 times larger than that of R245fa. Under the same mass velocity and wetness condition, the refrigerant mixture vapor velocity decreases as the mass fraction of R1234ze(E) increases. Moreover, because the liquid viscosity is approximately 0.48 times that of R245fa, the vapor shear force decreases. As a result, the frictional pressure drop of R245fa/R1234ze(E) decreased.

4.2. Effect of the Refrigerant Composition on the Frictional Pressure Drop and Comparison with Predictions

Figs. 6(a) and (b) show the change of the frictional pressure drop against the refrigerant composition at the wetness of 0.2, 0.5, and 0.7. The lines in the figure are the frictional pressure drops calculated from the correlations of Chamra et al. (2005) and Inoue et al. (2008), and the refrigerant mixture physical properties of obtained assuming equilibrium of the vapor and liquid on the tube cross-

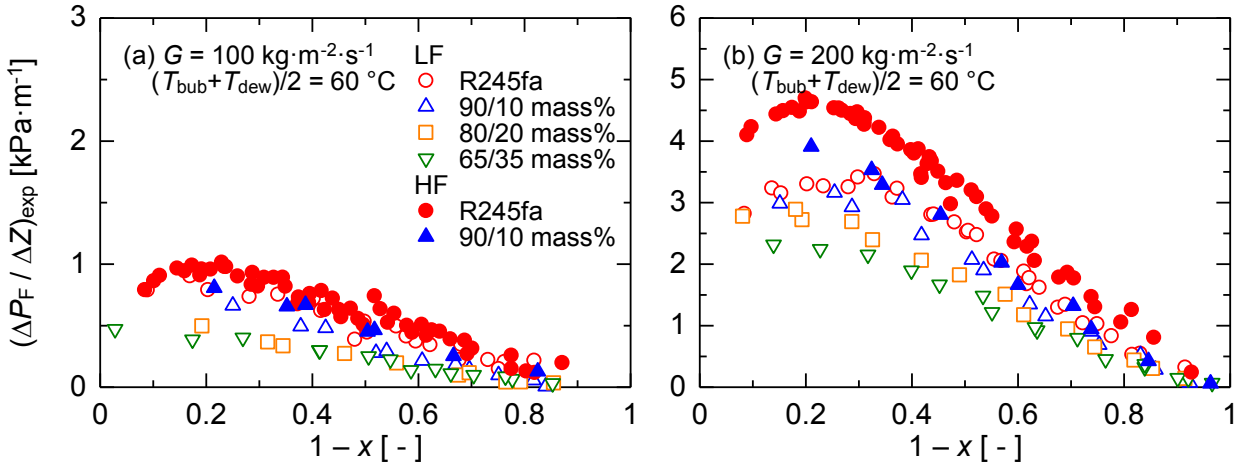

Figure 5. Frictional pressure drops for condensation flow of pure and mixture refrigerants.

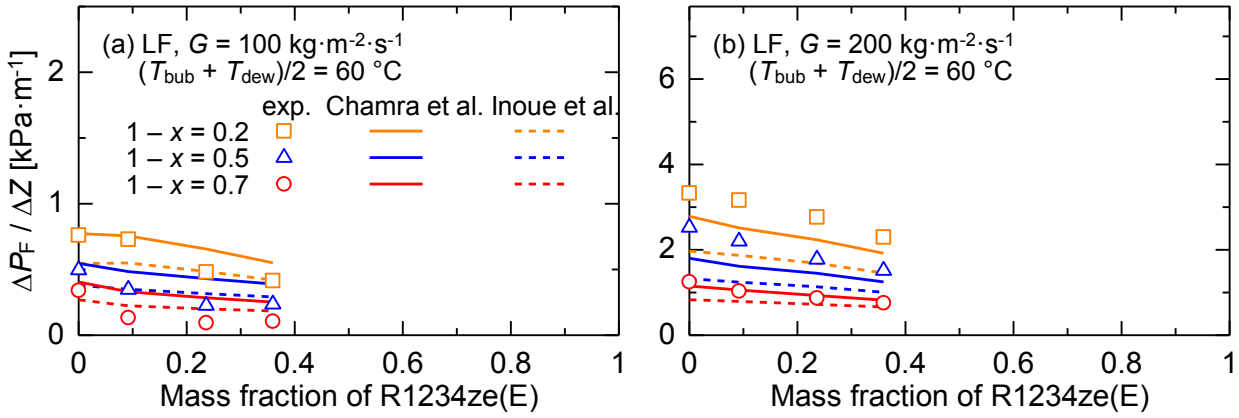

Figure 6. Effects of the mass fraction of R1234ze(E) on the frictional pressure drops for condensation flow.

section. In addition, Figs. 7(a) and (b) compare the measured frictional pressure drops with the values predicted by correlations. With respect to the frictional pressure drops of the refrigerant mixtures in the microfin tube, both conventional correlations of Chamra et al. and Inoue et al. tend to predict excessively more than the experimental values under low mass velocity and high wetness condition. On the other hand, under high mass velocity and low wetness condition, the predictions tend to be lower than the experimental values.

4.3. Condensation Heat Transfer Coefficient

Figs. 8(a) and (b) show the relationship between the condensation heat transfer coefficients, α_{exp}, and the wetness, $1–x$, for the pure refrigerant R245fa and refrigerant mixtures R245fa/R1234ze(E) at mass velocities of 100 and 200 kg.m^{-2}.s^{-1}. Based on the condensation heat transfer coefficient experimental results shown in Figs. 8(a) and (b), the condensation heat transfer coefficients of the pure refrigerant and refrigerant mixtures increase as the mass velocity increases. It then decreases as the wetness increases. Moreover, the condensation heat transfer coefficients of R245fa/R1234ze(E) are smaller than that of the pure refrigerant at any mass velocity and wetness. According to the conventional study, in the zeotropic refrigerant mixture condensation flow, the high-boiling point component of R245fa preferentially condenses, resulting in a concentration distribution owing to the mass transfer resistance formed near the vapor-liquid interface on the vapor side. Subsequently, the low-boiling point component concentration at the vapor-liquid interface increases and the vapor-liquid interface temperature decreases thereby decreasing the temperature difference effective for condensation between the vapor-liquid interface and wall surface. As the condensation progresses, the refrigerant mixture dew point decreases according to the relation of the vapor-liquid phase equilibrium. The refrigerant temperature then decreases in the flow direction. With these factors, the condensation heat transfer coefficients of the zeotropic refrigerant mixtures are assumed to be lower than that of the pure refrigerant.

Based on the condensation heat transfer coefficient ratio of the refrigerant mixtures, α_{mix}, to the pure refrigerant, α_{R245fa}, shown in Figs. 9(a) and (b), the condensation heat transfer coefficient reduction rate of the refrigerant mixture to that of the pure refrigerant did not greatly differ between the

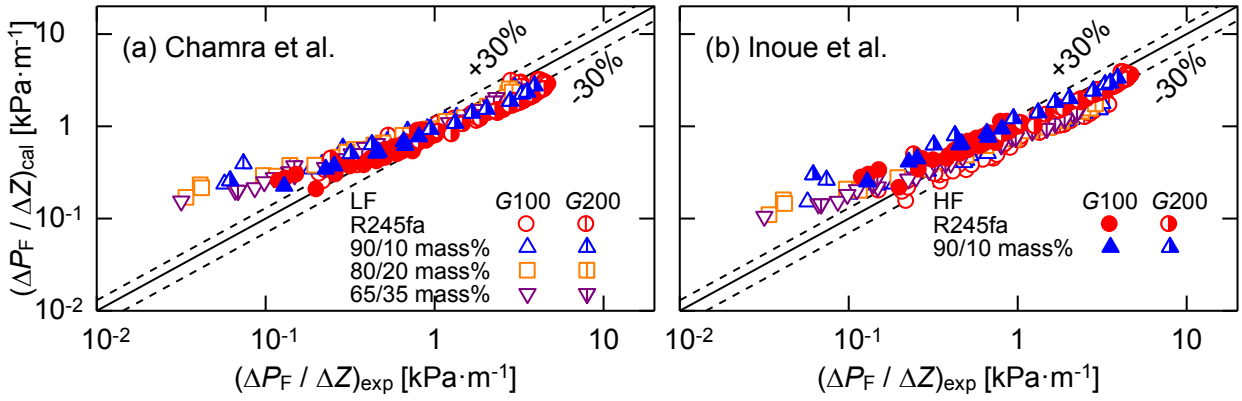

Figure 7. Comparison between measured and predicted frictional pressure drops.

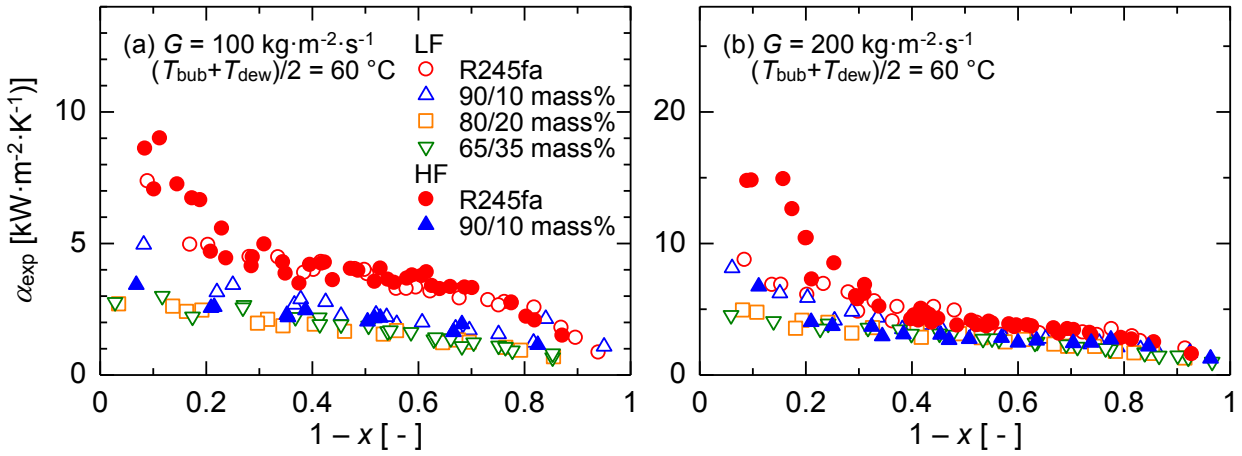

Figure 8. Condensation heat transfer coefficients of pure and mixture refrigerants.

composition ratios of 80/20 mass% and 65/35 mass%; however, the reduction rate is larger than 90/10 mass%. From Table 2 and Fig. 4, the temperature glides, ΔT, of 80/20 mass% and 65/35 mass% are respectively 8.0 K and 8.9 K. These are small differences. Hence, the influence of different temperature glides on the condensation heat transfer coefficient is considered to be minimal. On the other hand, the temperature glide of the 90/10 mass% refrigerant composition ratio was relatively small, with a value of 5.4 K, compared with that of the 80/20 mass% and 65/35 mass% refrigerant composition ratios. Therefore, the condensation heat transfer coefficient reduction rate of the refrigerant composition ratio of 90/10 mass% was reduced. Moreover, the condensation heat transfer coefficients of the refrigerant mixtures were reduced by approximately 30% to 60% compared with the pure refrigerant under the mass velocity condition of 100 $kg.m^{-2}.s^{-1}$. However, with the mass velocity of 200 $kg.m^{-2}.s^{-1}$, the reduction was only approximately 10% to 40%. As the mass velocity decreases, the condensation heat transfer coefficient reduction rate of the refrigerant mixtures was observed to increase. This may be due to the mass transfer promoted by the forced convection as the mass velocity increased and concentration boundary layer near the vapor-liquid interface diffused.

4.4. Effect of the Refrigerant Composition on the Condensation Heat Transfer Coefficient and Comparison with the Prediction

Figs. 10(a) and (b) show the change of the condensation heat transfer coefficient with the refrigerant composition at the wetness of 0.2, 0.5, and 0.7. The lines are the condensation heat transfer coefficient calculated from the correlation of Chamra and Mago (2006) and the refrigerant mixture physical properties obtained assuming equilibrium of the vapor and liquid phase on the tube cross-section. The correlation of Chamra and Mago for the refrigerant mixture was to modify the three constants in the correlation of Chamra at al. (2005) for the pure refrigerant. Fig. 11 compares the measured condensation heat transfer coefficients with the values predicted by correlations. The plot

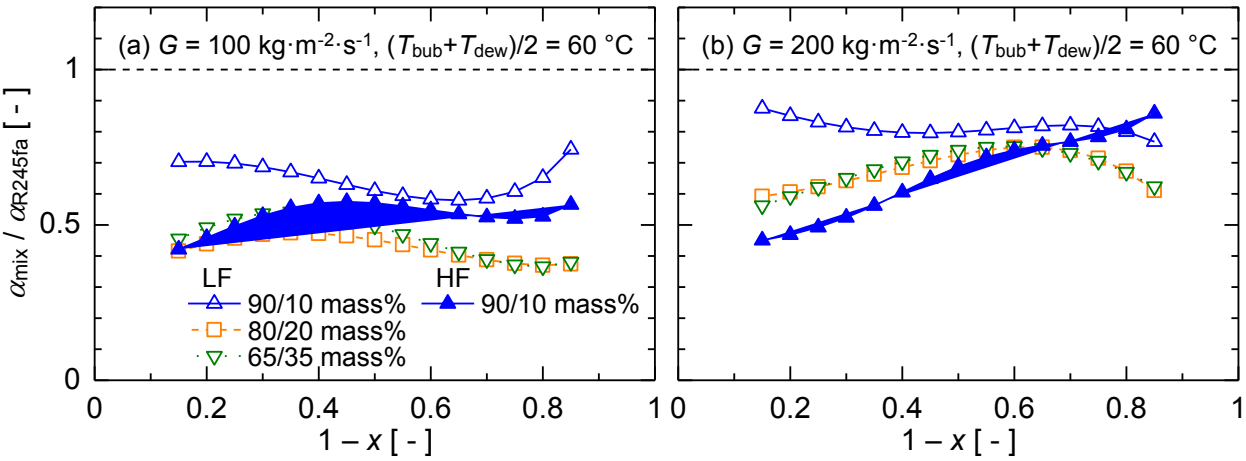

Figure 9. Ratio of the condensation heat transfer coefficients of the pure and mixture refrigerants.

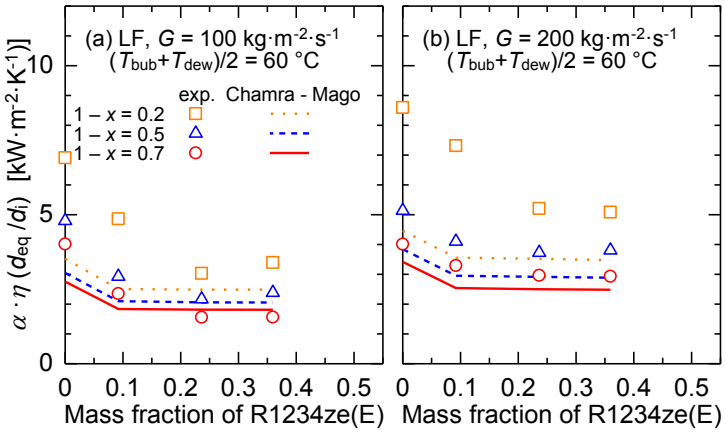

Figure 10. Effects of the mass fraction of R1234ze(E) on the condensation heat transfer coefficients.

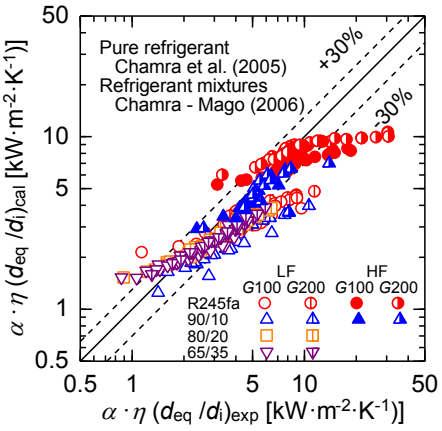

Figure 11. Comparison between measured and predicted HTC.

in the both figures were the heat transfer coefficient definition based on the maximum inside diameter. The predicted values from the correlation of Chamra and Mago tends to predict lower values than the experimental values. When the mass fraction of R1234ze(E) was 0.1 and greater, an almost constant value was observed, and the zeotropic property influence cannot be sufficiently sorted out.

4.5. Heat Transfer Enhancement by Microfin Tubes

Figs. 12(a) and (b) show the condensation heat transfer ratio between the microfin and smooth tube ($\alpha_{MT}\times\eta/\alpha_{ST}$). $\alpha_{MT}\times\eta$ is the microfin tube condensation heat transfer coefficient based on the equivalent inner diameter heat transfer area. The heat transfer enhancement rate in the microfin tube condensation flow was largest in the case of pure refrigerant. Its value was approximately 2.0 times maximum in the case of LF and approximately 5.0 times maximum in the case of HF. Focusing on the refrigerant mixtures, the heat transfer enhancement rate is slightly higher under high mass velocity condition. The heat transfer enhancement effect of LF was approximately 1.3 to 2.0 times at a mass velocity of 100 kg.m^{-2}.s^{-1} and 1.5 to 2.2 times at a mass velocity of 200 kg.m^{-2}.s^{-1}. In the case of HF, a heat transfer enhancement effect of approximately 1.8 to 2.0 times at a mass velocity of 100 kg.m^{-2}.s^{-1} and 2.0 to 2.6 times at a mass velocity of 200 kg.m^{-2}.s^{-1} was obtained. From these, the condensation heat transfer coefficient was confirmed to have a heat transfer enhancement effect by the microfin shape in addition to the surface area contribution enlarging the microfin tube heat transfer area under a high mass velocity condition.

5. CONCLUSIONS

In this study, experiments on the condensing characteristics inside the horizontal smooth and microfin tubes of the refrigerant mixtures R245fa/R1234ze (E) were carried out. The frictional pressure drop and condensation heat transfer coefficient were experimentally clarified. The experimental results were compared with the predictions from previously derived correlations. The following conclusions were drawn based on the findings of the study:

(1) The frictional pressure drops of the condensation flow in the horizontal microfin tubes of the refrigerant mixtures R245fa/R1234ze(E) decrease as the mass fraction of R1234ze(E) increase.

(2) With respect to the frictional pressure drops of the refrigerant mixtures in the microfin tube, previous correlations tend to predict excessively more than experimental values under low mass velocity and high wetness condition. Inversely, under high mass velocity and low wetness conditions, lower experimental values were predicted.

(3) The condensation heat transfer coefficients in the horizontal microfin tubes of the refrigerant mixtures R245fa/R1234ze(E) decreases owing to the temperature glide increase with increasing mass fraction of R1234ze(E) within the range of the refrigerant composition of this study. However, as the mass velocity increases, the mass transfer resistance decreases, thereby decreasing the condensation heat transfer coefficient reduction ratio of the refrigerant mixtures to pure refrigerant.

(4) The condensation heat transfer coefficients in the microfin tubes of the refrigerant mixtures tends are predicted to be excessively smaller than the experimental value from the conventional

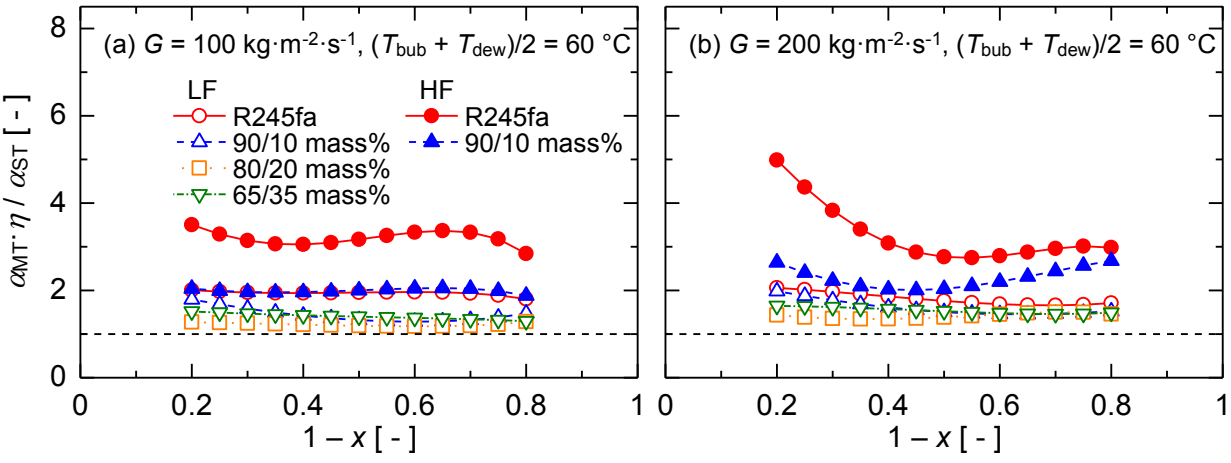

Figure 12. Condensation heat transfer ratio between the microfin and smooth tube.

correlation. When the mass fraction of R1234ze(E) was 0.1 and greater, a nearly constant value was observed, and the zeotropic property influence cannot be sufficiently sorted out.

(5) The microfin tube heat transfer enhancement effect was largest in the case of the pure refrigerant. In the refrigerant mixtures, a slightly higher heat transfer enhancement effect was observed under a high mass velocity condition. The heat transfer enhancement effect of LF and HF was approximately 1.3 to 2.0 times and 1.8 to 2.0 times at a mass velocity of 100 $kg.m^{-2}.s^{-1}$, and 1.5 to 2.2 times and 2.0 to 2.6 times at a mass velocity of 200 $kg.m^{-2}.s^{-1}$.

ACKNOWLEDGEMENTS

This study was supported by the Mechanical Engineering Laboratory of Kobe Steel, LTD. We would like to express our gratitude here.

NOMENCLATURE

c_p	specific heat capacity, $J \times kg^{-1} \times K^{-1}$	ρ	density, $kg \times m^{-3}$
d	tube diameter, m	η	surface area enlargement, -
G	mass velocity, $kg \times m^{-2} \times s^{-1}$		
P	pressure, Pa	Subscripts	
q	heat flux, $W \times m^{-2}$	bub	bubble point
Q	heat transfer rate, W	dew	dew point
T	temperature, K	exp	experiment
W	mass flow rate, $kg \times s^{-1}$	i	inside the tube
L	effective length of heat transfer area, m^2	L	liquid
		mix	refrigerant mixtures
α	heat transfer coefficient, $W \times m^{-2} \times K^{-1}$	MT	microfin tube
Δh_{LV}	latent heat, $J \times kg^{-1}$	r	refrigerant
ΔZ	length pressure drop measurement section, m	s	heat source
		ST	smooth tube
λ	thermal conductivity, $W \times m^{-1} \times K^{-1}$	V	vapor
μ	viscosity, Pa×s	w	tube wall
ξ	void fraction, -		

REFERENCES

Chamra, L. M., Mago, P. J., Tan, M-O., Kung, C-C., 2005. Modeling of condensation heat transfer of pure refrigerants in micro-fin tubes. International Journal of Heat and Mass Transfer 48(7), 1293-1302.

Chamra, L. M., Mago, P. J., 2006. Modeling of Condensation Heat Transfer of Refrigerant Mixture in Micro-Fin Tubes. International Journal of Heat and Mass Tr*ansfer* 49(11-12), 1915-1921.

Inoue, N., Aono, A., Goto, M., Sato, M., Kiyotani, A., Sasaki, N., 2008. Evaluation of prediction method for pressure drop and condensation heat transfer coefficient inside internally helical-grooved horizontal tubes. Journal of the JRICu 47(1), 232-237. (in Japanese)

Koyama, S., Chen, Y. C., Kitano, R., Kuwahara, K., 2001. Experimental study on void fraction of two-phase flow inside a micro-fin tube. The reports of institute of Advanced Material Study, Kyushu University 15(1), 79-85

Lemmon, E. W., Bell, I. H., Huber, M. L., McLinden, M.O., 2018. Reference fluid thermodynamic and transport properties-REFPROP Ver. 10.0, National Institute of Standards and Technology, Gaithersburg.

Smith, S. L., 1969. Void fractions in two-phase flow: a correlation based upon an equal velocity head model. *Proc. Instn. Mech. Engrs.* 184(1)(36), Institution of Mechanical Engineers, 647-664.

Watanabe, K., Jige, D., Inoue, N., 2016. Experimental Study on Evaporation and Condensation Flows of R245fa inside a Horizontal Smooth Tube. Trans. of the JASRAE 33(3), 231-243

Watanabe, K., Jige, D., Inoue, N., 2016. Evaporation and Condensation Characteristics of Refrigerant Mixtures R245fa/R134a inside Horizontal Tubes. Trans. of the JASRAE 33(4), 383-394

Manuscript ID: 673
DOI: 10.18462/iir.icr.2019.0673

Controlling vapor quality of R245fa in a microchannel evaporator

Stanislawa HALON[(a)], Bartosz ZAJACZKOWSKI[(b)], Zbigniew KROLICKI[(b)]

[(a)]Wroclaw University of Science and Technology, Wroclaw, Wybrzeze Wyspianskiego 27, 50-370, Poland, stanislawa.halon@pwr.edu.pl, +48 71 320 27 92
[(b)]Wroclaw University of Science and Technology, Wroclaw, Wybrzeze Wyspianskiego 27, 50-370, Poland

ABSTRACT

Performance of microchannel cooling system depends on, inter alia, vapor quality in the evaporator. Therefore, optimization of evaporation requires precise control of quality at the microchannel inlet (x). Here, we compare three different kinds of preheaters used to adjust x: an immerse heater, a brazed plate heat exchanger (BPHE) and direct current (DC) heater. The study covers critical heat flux (*CHF*), pressure drop, heat transfer coefficient, operating temperature limits imposed by refrigerant, uncertainties in x, and power control. The refrigerant is R245fa and the saturation temperature is 40-90°C. Immerse heaters require liquid immersion and, depending on geometry, are prone to *CHF* occurrence. BPHE requires silicone oil as a heating medium and, consequently, expensive measuring equipment. Compared to BPHE, DC heating offers lower uncertainties, but it is limited by the maximum voltage of the power supply.
Keywords: Heat transfer coefficient, Microchannel, R245fa, Two-phase flow

1. INTRODUCTION

Increasing power of electronic components challenges cooling technology to provide high capacity solutions capable of heat dissipation from limited heat transfer areas. Flow boiling in microchannels is considered to be a promising option due to small channel size and high latent heat of vaporization. As electronic systems are used in a growing number of applications, flow-boiling dynamics, commonly described with heat transfer coefficient (*HTC*), needs to be mastered over a wide range of operating conditions including system temperature t_{sat} and heat fluxes q_w. For constant q_w, t_{sat}, mass flux and channel geometry, *HTC* depends on vapor quality (x) which increases along the microchannel due to vaporization. As shown in Sandler et al. (2018), existing models cannot accurately reproduce this dependence over the entire range of operating conditions. Thus, experimental work spanning from x=0 to x=1 is required to understand heat transfer dynamics. Performing complete vaporization within the microchannel evaporator is difficult due to large pressure drops accompanying two-phase flows. Therefore, the strategy is to employ preheaters to control vapor quality at the microchannel inlet. This paper discusses crucial aspects of preheater design: critical heat flux (*CHF*), pressure drop, heat transfer coefficient, operating temperature limits imposed by the refrigerant, uncertainties in x, and power control. Based on discussed factors, an immerse heater and a direct current (DC) heater are analyzed. Their uncertainties in x are compared with those of a brazed plate heat exchanger (BPHE).

2. PREHEATER DESIGN CONSIDERATIONS

Preheater vaporizes working fluid from the slightly subcooled conditions to the desired vapor quality using supplied heat $\dot{Q}$. Vaporization imposes restrictions on heat exchanger design, as phase-transition from liquid to vapor is prone to *CHF* occurrence. At *CHF,* liquid wall film is replaced with vapor. Because thermal conductivity of vapor is lower than liquid, the heat transfer becomes deteriorated, and the temperatures of the wall and the adjacent working fluid sharply increase. Consequently, there is a risk of preheater burnout and thermal decomposition of working fluid (for

synthetic refrigerants). Prediction models provide information on the maximum heat flux that can be imposed on particular working fluid without the risk of *CHF* occurrence. With the knowledge of *CHF*, the maximum preheater heating power can be determined. However, safe operation depends not only on *CHF*, but also on *HTC* which should be high enough to prevent excessive fluid and wall temperatures.

Two-phase flows are characterized by high pressure drops that impose extra work on the circulating pump and increase the amount of heat that needs to be transferred to fluid $\dot{Q}$. This is because at lower pressure the latent heat of vaporization is higher and more heat is needed to achieve the required *x*. Therefore, high pressure drops should be avoided.

The ease of power adjustment and uncertainty in *x* also need to be considered. Depending on preheater heat source additional control and measurement equipment is required that decides on the accuracy of the obtained vapor quality. This is because *x* is determined based on preheater's energy balance. The cost of the power supply and measurement & control equipment should also be taken into consideration. Summing up, the optimal preheater design is characterized by:

- high values of *CHF* and *HTC* that reduce the risk of preheater burnout or fluid decomposition;
- low pressure drops to avoid unnecessary pump work and heating power;
- reliable power control system allowing precise power adjustment;
- accurate measurement equipment yielding vapor quality of low uncertainty;
- low investment costs.

3. ANALYZED CASE

The analysis concerns a preheater that works in a system of four main components: a circulating pump, a preheater, a microchannel evaporator, and a condenser. The working fluid is a synthetic refrigerant R245fa with thermal decomposition temperature >250ºC. The pressure at the microchannel inlet *p* ranges from 2.5 to 10 bar, which corresponds to saturation temperatures t_{sat} 40-90ºC. Mass flow rates $\dot{m}$ of the working fluid are between 4 and 16 g s^{-1}.

Preheater should evaporate fluid to a point where either the quality at the outlet of microchannel evaporator reaches 1 or the pressure falls below the atmospheric. The latter condition helps to avoid the risk of air coming into the system and pressurizing R245fa. The resulting preheater power at the highest mass flow rate $\dot{m} = 16$ g s^{-1} is 2.5 kW.

The most common preheater design is a DC heater (Fig. 3 a). It consists of a stainless tube connected to a DC power supply and electrically insulated from the rest of the system with dielectric clamps. Design procedure aims at selecting stainless tube diameter, its length and wall thickness at chosen coil diameter (D_{coil}=0.6 m) and pitch (50 mm). The analyzed heater is of helical shape. Because DC preheaters require expensive power supply (especially for high heating powers), we compare it to a simpler AC immerse heater installed inside the refrigerant pipe (Fig. 3 b)). This solution requires an autotransformer to control and a multimeter to measure its heating power. The aim of the immerse heater design procedure is to find refrigerant pipe diameter D_{im} and immerse heater length for heating tubes diameter d = 8 mm. The third analyzed option is a BPHE with a thermostatic bath as a heating source and a silicone oil as a heating medium (as t_{sat} reaches 90ºC). To find its power, measurements of silicone flow rate and its temperatures before and after the BPHE are required. It is worth noting that using silicone may increase the cost of the flow meter. In this article, the main focus of the BPHE analysis is determining the accuracy of the obtained vapor quality.

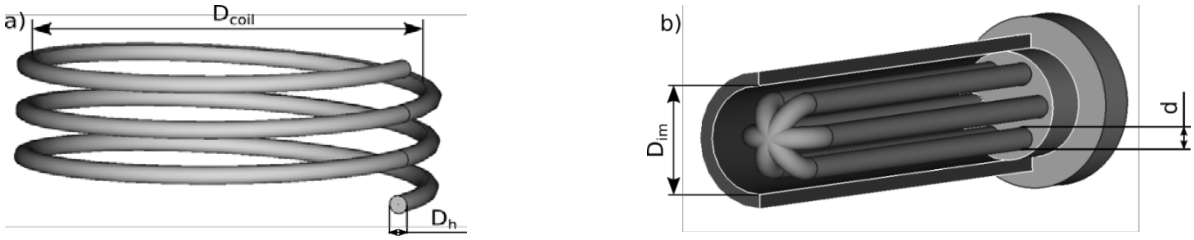

Figure 1: (a) DC heater and (b) immerse heater geometries

The uncertainty in *x* depends on the accuracy of the equipment used to determine preheater power

and R245fa state and flow rate before the preheater. Uncertainties of the measurement equipment are given in Table 1.

Table 1. Specifications of the additional equipment

Preheater type	Equipment	Parameter	Uncertainty, unit
DC preheater	DC power supply Agilent 6681A max. power 5 kW	Voltage U_e Max. 8 V	0.05%reading + 12, mV
		Current I	±(0.1%reading + 400), mA
Immerse preheater	Multimeter UNI-T UT60C	Voltage U_e	±(1% + 5 digit), V
		Current I	±(2% + 5 digits), A
BPHE	Thermostatic bath PolyScience AD15H200	Power max. 2.2 W	
	Flow meter for the heating medium Tecfluid, Covol series	Flow rate $\dot{V}_{hm}$	±0.8%
R245fa state before the preheater	Pressure transducer Wika, A-10	Pressure p	±0.5 FS%
	Thermocouple K	Temperature t	1.5, K
	Flow meter for R245fa KDS-K	Flow rate $\dot{V}$	±3 FS%

4. METHODS

In this section methods for calculation of *CHF, HTC,* pressure drop and uncertainty in *x* are presented. For BPHE only the method for uncertainty in *x* is described as this preheater is selected from manufacturer's catalogue. DC wall thickness is calculated using the following formula:

$$\dot{Q}_{max} = \frac{U_{max}^2 A_e}{L_h \rho_{el}} \quad \text{Eq. (1)}$$

where $\dot{Q}_{max}$ is the required preheater power, U_{max} is the max. voltage of the power supply, ρ_{el} is the resistivity of stainless steel (0.73 Ω·mm^{2}m^{-1}), A_e is the electric current flow cross-section (mm^2). For a given preheater resistance R, U_{max} and the max. power of the power supply limit preheater power.

4.1. Critical Heat Flux (CHF)

CHF was calculated using the method of Katto-Ohno (Katto and Ohno, 1984 cited in Wojtan et al., 2006). In the system of interest R245fa enters the preheater in a subcooled state. For such flow conditions *CHF* is given by:

$$CHF_{sub} = f\left(\frac{L_h}{D_h}; \frac{\sigma \cdot \rho_l}{G^2 L_h}; \frac{\rho_v}{\rho_l}; \frac{h_l - h_{sub}}{h_{lv}}\right) \quad \text{Eq. (2)}$$

According to the experiments of Jayanti and Hewitt, 1991 (cited in Hardik and Prabhu, 2017), in the saturated region ($x > 0$) CHF_{coil} is higher than its straight tube counterpart. In the subcooled region ($x < 0$), CHF_{coil} is lower than CHF_{st} but still higher than $CHF_{coil(x=0)}$. Thus, for helical coils we used Katto-Ohno correlation with $x = 0$. For the immerse heater its diameter D_h was calculated by analogy to the formula used by Qu and Mudawar (2004):

$$D_h = \frac{4 \cdot channel\ crosssectional\ area}{heated\ perimeter} = \frac{4\frac{\pi}{4}\left(D_{im}^2 - 6 \cdot d^2\right)}{6 \cdot \pi \cdot d} \quad \text{Eq. (3)}$$

4.2. Uncertainty in x

Standard error propagation method was used to estimate the absolute uncertainty in *x*. For all the proposed options, the first step was to calculate the uncertainty in working fluid mass flow rate $\dot{m}$ and enthalpy h_{in} before the preheater based on fluid temperature, pressure and volumetric flow rate. It was assumed that subcooling was 10 K. The second step involved calculation of uncertainty in preheater heating power $\dot{Q}$. For DC and immerse heaters $\dot{Q}$ is given by Eq. (4) and for the BPHE by Eq. (5):

$$\dot{Q} = U_e \cdot I \quad \text{Eq. (4)}$$

$$\dot{Q} = \dot{V}_{hm} \cdot \rho_{hm} \cdot c_{P,hm} \cdot \left(t_{hm,in} - t_{hm,out}\right) \quad \text{Eq. (5)}$$

It was assumed that $t_{hm,in} = t_{sat} + 10\text{K}$. Values of $\dot{m}_{hm}$ and $t_{hm,out}$ were calculated by combining Eq. (5) with Eq. (6).

$$\dot{Q} = UA \cdot \frac{\left(t_{hm,in} - t_{hm,out}\right)}{ln\frac{t_{hm,in} - t_{sat}}{t_{hm,out} - t_{sat}}} \quad \text{Eq. (6)}$$

Where *U* is the overall heat transfer coefficient (W m^{-2} K^{-1}) and *A* is the BPHE heat transfer area (m^2). Finally, the uncertainty in *x* was assed using the combination of the following formulas:

$$\dot{Q} = \dot{m} \cdot \left(h_{out} - h_{in}\right) \quad \text{Eq. (7)}$$

$$x = \frac{h_{out} - h_l}{h_{lv}} \quad \text{Eq. (8)}$$

4.3. Pressure Drop, HTC and Wall Temperature Calculation

For a fixed value of *p,* $\dot{m}$ and $\dot{Q}$, calculation procedure is as follows. The heating length is divided into *n* calculation points. Knowing vapor quality at preheater inlet x_{in} its value in the *i*-th point can be determined using Eq. (8) and energy balance equation given by:

$$\dot{Q} \cdot L_{h,i}/L_h = \dot{m} \cdot \left(h_{i,out} - h_{in}\right) \quad \text{Eq. (9)}$$

Then fluid pressure drop is determined as the sum $\Delta p_{fr} + \Delta p_{acc} + \Delta p_{stat}$. For single-phase flows $\Delta p_{acc} = 0$ and for immerse heaters $\Delta p_{stat} = 0$. For two-phase flows, the average pressure drop in the saturated region was calculated first, and then it was assumed that fluid pressure varies linearly with region length. Correlations used for calculation of Δp_{fr} and Δp_{acc} are presented in Fig. 2. If correlations concern only frictional pressure drop, the accelerational term was calculated by the formula presented in Hardik and Prabhu (2018).

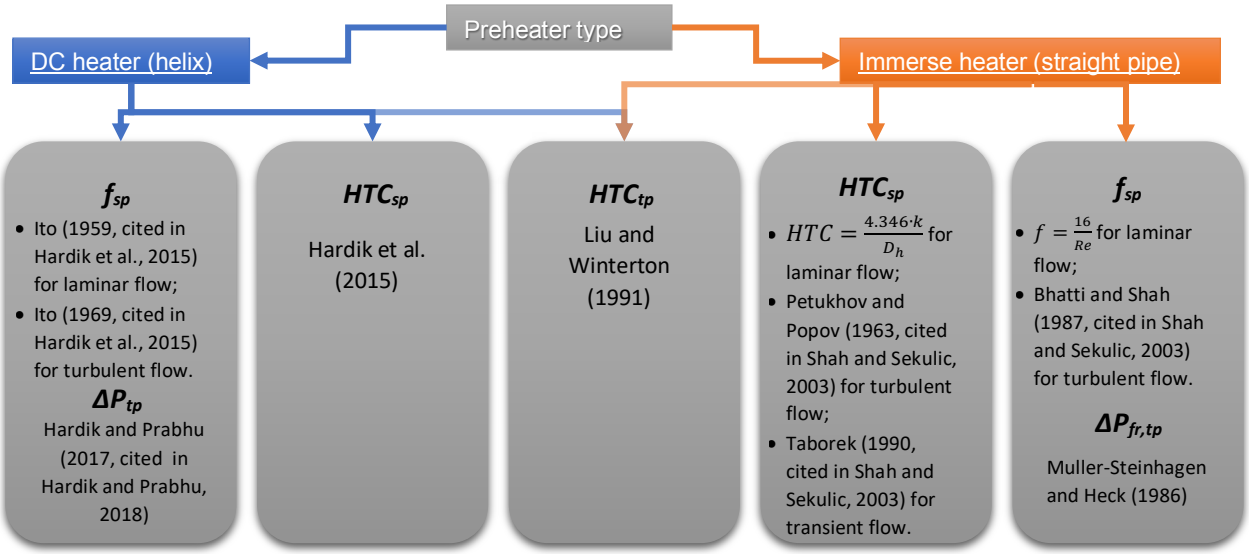

Figure 2: Correlations used for pressure drop and heat transfer coefficient calculations

With the knowledge of fluid pressures and qualities, the value of *HTC* can be determined. Finally, wall temperature is determined as $t_{w,i} = t_{sat,i} + q_w/\text{HTC}_i$. Correlations used to calculate *HTC* depending on preheater type are presented in Fig. 2. In the two-phase flow region *HTC* for both the helical and straight tube was calculated using the same formula of Liu and Winterton (1991)

developed for straight tubes. This is because straight tube formulas can predict heat transfer in helical coils with good accuracy as shown in Zhao et al. (2003).

5. RESULTS OF THE ANALYSIS

Figs. 3 and 4 show results of *CHF* calculations for the DC and immerse heaters together with the maximum power that can be obtained without the risk of *CHF* occurrence as a function of heat exchanger length and diameter.

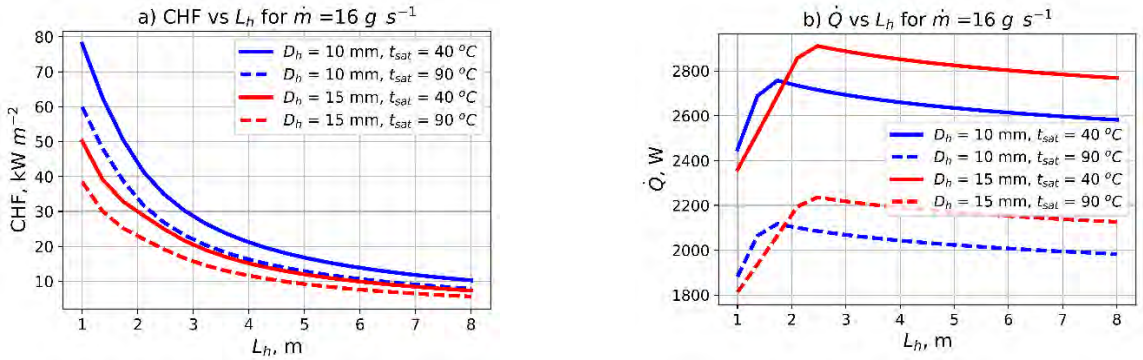

Figure 3: *CHF* and maximum power of a DC heater

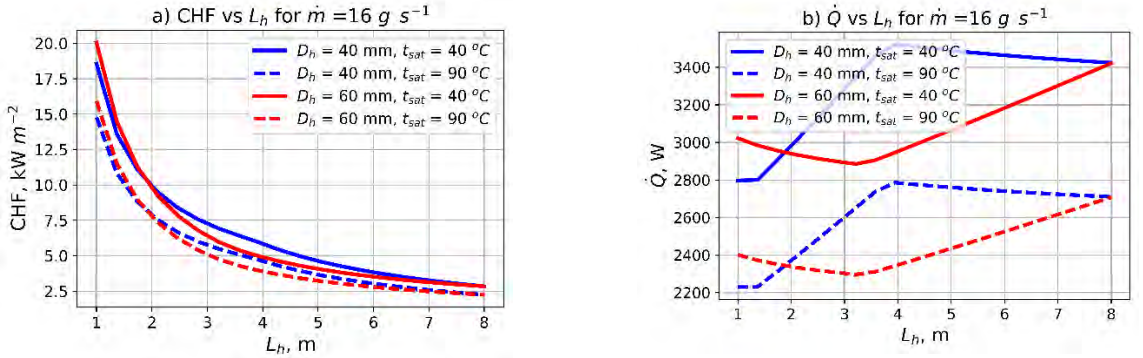

Figure 4: *CHF* and maximum power of a immerse heater

Analysis of the data in Fig. 3 shows that decreasing tube diameter causes the *CHF* to increase. This is because higher fluid velocities restrain the generated vapor from accumulation. As for t_{sat}, its raise promotes bubble nucleation, and thus, *CHF* occurrence. Longer heated length causes *CHF* to fall. Fig. 3b) proves that high *CHF* cannot be treated as a sole indicator of the given geometry power because larger heat transfer area (corresponding to higher L_h and D_h) may make up for the reduced *CHF*. Similar trends can be observed for the immerse heater (see Fig. 4). However, the calculated values of *CHF* are much lower than for the DC heater. The reason is the larger flow area of the immerse heater which yields lower fluid velocity. On the other hand, increased heat transfer area results in higher maximum heating power compared to the DC heater. From the *CHF* management analysis, the recommendable length of a DC heater would be 2.5 m and 4 m for the immerse heater. Fig. 5 and 6 depict the average *HTC* and maximum wall temperature t_w of the DC and immerse heaters for $q_w = \mathrm{CHF}$. Results show that *HTC* rises with lower pipe diameters due to increased fluid velocity. Higher saturation temperatures deteriorate the heat transfer. This might be because increased t_{sat} yields lower *CHF* (translating into lower q_w as the analysis is for $q_w = \mathrm{CHF}$) which diminishes bubble nucleation. The other reason might be lower liquid to vapor density ratio which causes the fluid to experience less acceleration due to phase transition, thus worsening forced convection. Wall temperature shows strong dependence on heated length as t_w follows the *CHF* in trend (see Fig. 5 b)). Immerse heaters give lower *HTC* and consequently higher t_w than the DC heater. Therefore, there is a risk of refrigerant thermal decomposition or preheater burnout.
Fig. 7 shows pressure drop for the DC and immerse heaters as a function of their geometry for $q_w = \mathrm{CHF}$ and $\dot{m}$ = 16 g s^{-1}. Comparing Fig. 7 a) and b) shows that immerse heaters yield lower pressure drops that the DC heater.

Fig. 8 presents the uncertainty in vapor quality of the DC and immerse heaters for $q_w = \mathrm{CHF}$. Comparing the obtained results with the data in Fig. 3 and 4 indicates that the value of *u(x)* follows the behavior of the maximum power $\dot{Q}$: the higher the heating power, the higher uncertainty in *x* can be observed. Comparing the values of uncertainty in *x* of the DC and immerse heaters shows that the former yields lower *u(x)*. For DC heaters it is recommended to use large L_h, while for the immerse heater in the analyzed length range it is more beneficial to use a shorter one ($L_h < 4$ m).

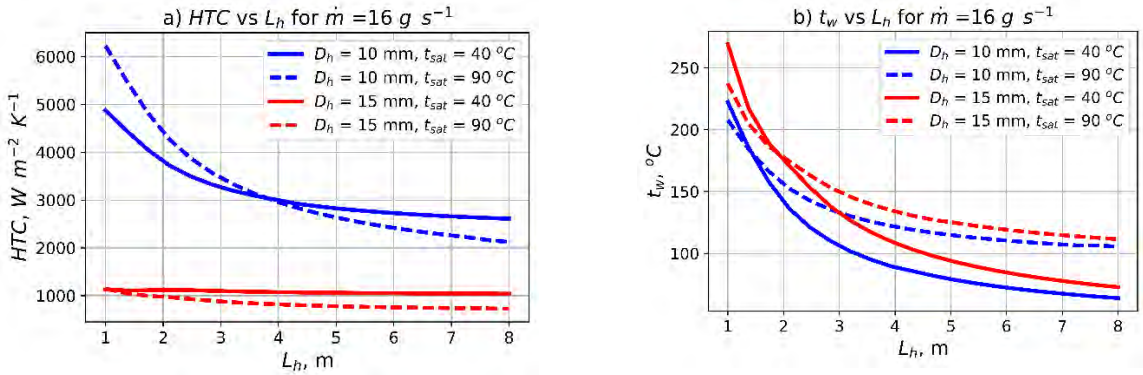

Figure 5: The average HTC and maximum wall temperature of a DC heater.

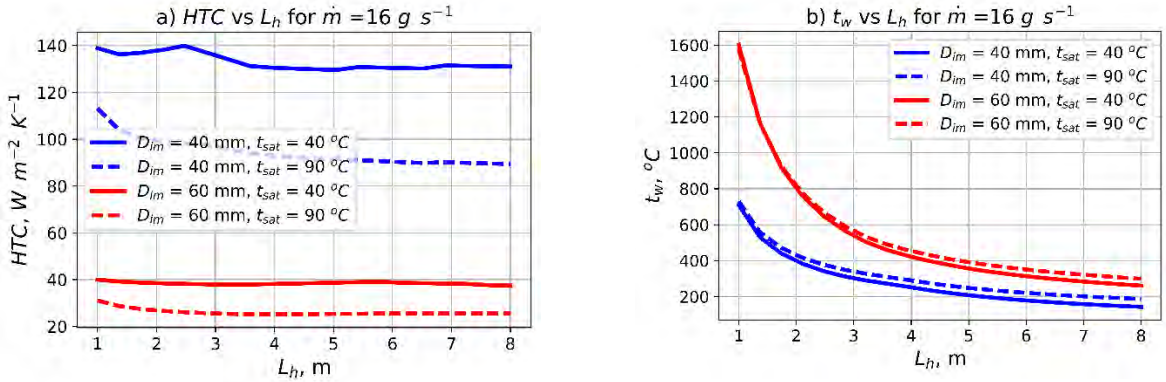

Figure 6: The average HTC and maximum wall temperature of an immerse heater

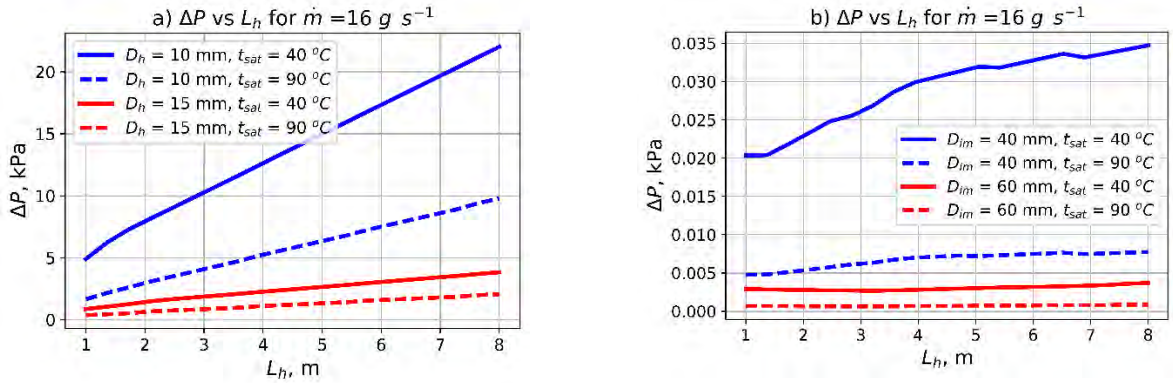

Figure 7: Pressure drop of the (a) DC and (b) immerse heaters

The uncertainty in *x* for the BPHE was calculated for the values of UA in Eq. (6) ranging from 400 to 1000 W K^{-1} assuming that the pressure drop in the heat exchanger is 50 kPa. Heating power was 2500 W. Results are presented in Fig. 9. They show that BPHE yields the highest inaccuracy among the analyzed heaters. Its value decreases with increasing UA due to lower absolute error associated with heating medium flow rate measurement as the flow rate falls with higher UA. Increasing saturation temperature increases the *u(x)* because at higher t_{sat} the absolute inaccuracy associated with determination of fluid enthalpy at preheater inlet rises.

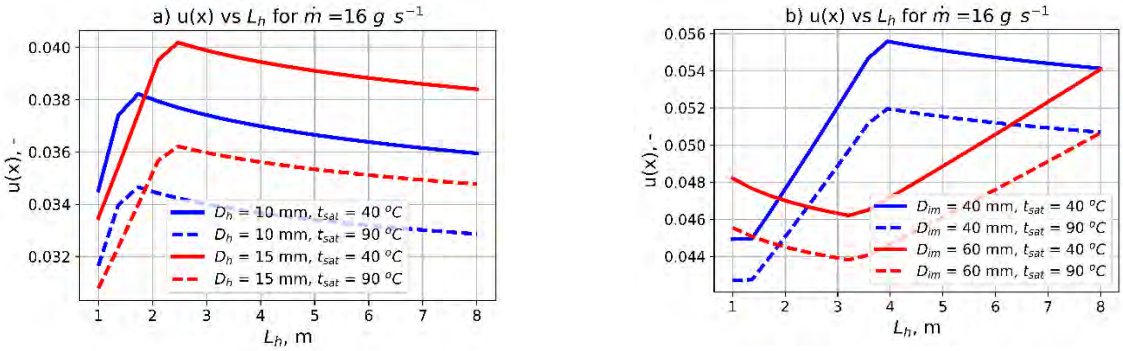

Figure 8: Uncertainty in vapor quality of the (a) DC and (b) immerse heaters.

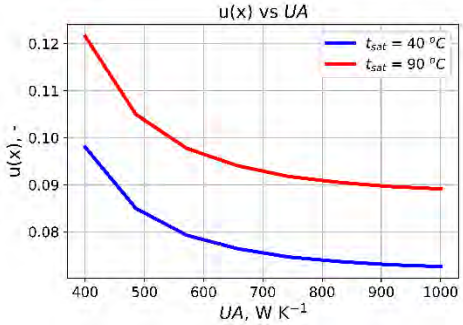

Figure 9. Uncertainty in vapor quality of the BPHE for $\dot{m}$=16 g s^{-1}

6. CONCLUSIONS

In this paper we performed an analysis of a preheater design that includes critical heat flux, heat transfer coefficient, wall temperature, pressure drop and uncertainty in vapor quality considerations. Three types of heat exchangers were analyzed: DC and immerse heaters and a BPHE. Results showed that:

- An immerse heater yields lower pressure drops that the DC heater. On the other hand, it is characterized by lower *CHF* and *HTC*. Thus, its wall temperatures are higher. Moreover, the immerse heater requires full liquid immersion. Consequently, there is a risk of fluid decomposition or preheater burnout.
- The value of *CHF* cannot be considered as the sole indicator of the maximum preheater heating power because large heat transfer area can compensate for lower *CHF*.
- The uncertainty in vapor quality is the lowest for the DC heater and the highest for the BPHE.
- Power control of DC and immerse heaters is easier than for the BPHE because it is based on electric power control instead of the hydraulic one (which may require a trial and error procedure). However, the power of DC heater is limited by its resistance and the power of the power supply. In the case of BPHE, at high saturation temperatures this option requires silicone oil as a heating medium which may increase the cost of the measuring equipment.

Based on the above analysis, a DC heater provides the highest accuracy in vapor quality, easy power control and safe operation in terms of temperature limits. In the analyzed case it is the recommended solution.

ACKNOWLEDGEMENTS

This work was funded by the National Science Centre, Poland [project number 2017/25/N/ST8/01444].
The authors would like to thank Professor Rémi Revellin from Université de Lyon, INSA-Lyon, CETHIL for his support and expert advice on preheater design.

NOMENCLATURE

$\dot{Q}$	heating power (W)
$\dot{V}$	volumetric flow rate (m^3s^{-1})
$\dot{m}$	mass flow rate (kg s^{-1})
Δp	pressure drop (Pa)
CHF	critical heat flux (W m^{-2})
c_P	heat capacity (J kg^{-1} K^{-1})
D	channel diameter (m)
D_h	heated channel diameter (m)
f	Fanning friction factor (-)
G	mass flux density (kg $m^{-2}s^{-1}$)
h	enthalpy (J kg^{-1})
HP	heated perimeter (m)
HTC	heat transfer coefficient (W $m^{-2}K^{-1}$)
I	current (A)
L_h	heated length (m)
p	pressure (Pa)
q	heat flux (Wm^{-2})
R	electric resistance (Ω)
t	temperature (°C)
U	overall thermal conductivity (W $m^{-2}K^{-1}$)
U_e	voltage (V)
x	vapor quality (-)
ρ	density (kg m^{-3})
σ	surface tension (N m^{-1})

Subscripts

acc	accelerational
coil	coil
fr	frictional
hm	heating medium
im	immerse
in	inlet
l	saturated liquid
lv	phase change from liquid from liquid to vapor
out	outlet
sp	single phase
st	straight tube
stat	static
sub	subcooled
tp	two phase
v	saturated vapor
w	wall

REFERENCES

Angelino, G., Invernizzi, C., 2003. Experimental investigation on the thermal stability of some new zero ODP refrigerants. Int. J. Refrigeration 26, 51–58.

Hardik, B. K., Baburajan, P.K., Prabhu, S. V., 2015. Local heat transfer coefficient in helical coils with single phase flow. Int. J. Heat and Mass Transfer 89, 522–538.

Hardik, B. K., Prabhu, S. V., 2017. Critical heat flux in helical coils at low pressure. Appl. Therm. Eng. 112, 1223–1239.

Hardik, B. K., Prabhu, S. V., 2018. Two-phase pressure drop in a helical coil flow boiling system. Heat and Mass Transfer 54 (11), 3231–3251.

Liu, Z., Winterton, R. H.S., 1991. A general correlation for saturated and subcooled flow boiling in tubes and annuli. Int. J. Heat and Mass Transfer 34 (11), 2759–3266.

Muller-Steinhagen, H., Heck, K. 1986. A simple friction pressure drop correlation for two-phase flow in pipes. Chem. Eng. Process. 20, 291-308.

Qu, W., Mudawar, I., 2004. Measurement and correlation of critical heat flux in two-phase micro-channel heat sinks. Int. J. Heat and Mass Transfer 47, 2045–2059

Sandler, S., Zajaczkowski, B., Krolicki, Z., 2018. Review on flow boiling of refrigerants R236fa and R245fa in mini and micro channels. Int. J. Heat and Mass Transfer 126, 591–617.

Shah, R. K., Sekulic, D. P.,2003. Fundamentals of heat exchanger design, John Wiley & Sons, Hoboken, 941 p.

Wojtan, L., Revellin, R., Thome, J. R., 2006. Investigation of saturated critical heat flux in a single, uniformly heated microchannel, Experimental Thermal and Fluid Science 30, 765–774.

Zhao, L., Guo, L., Bai, B., Hou, Y., Zhang, X., 2003. Convective boiling heat transfer and two-phase flow characteristics inside a small horizontal helically coiled tubing once-through steam generator, Int. J. Heat and Mass Transfer 46, 4779–4788.

Manuscript ID: 680
DOI: 10.18462/iir.icr.2019.0680

Water (R718) as a low-GWP alternative

Hans MADSBOLL [a], Alexander C. PACHAI[b]
[a] Danish Technological Institute, Kongsvang Allé 29, DK 8000 Aarhus C, hm@teknologisk.dk
[b] Johnson Controls Denmark Aps, Christian X's Vej 201, DK 8270 Hojbjerg, Alexander.C.Pachai@jci.com

ABSTRACT

The emergence of the first commercial chiller units based on water as refrigerant actualizes the ongoing discussion on the refrigerant for the future – all aspects included.
The paper describes the layout and design of a water vapor-based chiller unit including direct contact heat exchangers and an axial compressor. Field test results for the first two years is presented for the fully automated chiller unit including annual variations and capacity adjustments.
Keywords: Refrigeration, R718, Water, Axial compressor, Evaporators, Energy Efficiency.

INTRODUCTION

Many future low-GWP refrigerants are considered flammable at different levels. A2L, A2, and A3 require the same risk assessment because the released energy in the stoichiometric point will be close to the same as for all the classes. A simple calculation using the gas properties found in ISO 817 shows that a gas with a high LFL is just as dangerous as a gas with a low LFL because there is more of it in the machine room atmosphere. This will not the case when water is used as refrigerant. Water is neither toxic nor flammable. Statistically and as a curiosity, water is, however, dangerous because many people drown every year, you can find dangerous fish in water, and it can fall down from the roof as ice in the winter. As one of the pioneers of the idea of water as refrigerant, Joachim Paul used to say when talking about water as a refrigerant, there is a series of problems with water.

1. REFRIGERANT DISCUSSION

The growing concern about the global warming potential (GWP) of some refrigerants and the safety of the alternatives has made the use of the only non-flammable refrigerant with no GWP, low pressure, and no toxicity - which is 100% natural, i.e. water or R-718, more relevant than ever. In many warm climate zones, the ongoing discussion is which refrigerant to turn to. Some of the most used refrigerants have an ozone depleting potential (ODP), mainly R-22, and others have a GWP, which will come in focus when the Kigali amendment to the Montreal Protocol will apply. The Kigali amendment came in to force on 1 January 2019 in most parts of the world with the exception of a few larger countries, which have chosen to stand outside this landmark agreement. However, for international users, it is a question of whether they can live with the uncertainty of deliveries of a given refrigerant.

Some low-GWP refrigerants are causing concerns in terms of the breakdown of products resulting in the creation of TFA in the ground source water (Wallington et al., 2014). Especially in Germany, there has been a public debate on this concern during the summer 2018. Other refrigerants are causing debate because they contain chlorine, and German politicians believe that these refrigerants should be included in the Montreal Protocol ozone section and be phased out under these regulations.

2. THE CHILLER MARKET

The chillers described in this paper are used for cooling molding machines where the efficiency of the process depends on how quick the molding head can be cooled down after the fluid has been injected in the form. The temperature used is 9 °C leaving temperature and a return temperature at 16 °C. Due to the water quality of the ground water, it is necessary to use a heat exchanger between the molding machines and the chiller, which reduces the efficiency of the chiller by approximately 2%. The warm side is ejecting the heat directly to the ambient, which gives the highest efficiency even with a penalty for the vacuum pumps necessary to keep down the vacuum in the condenser.
The estimated global market value for chillers is about 8,774 Billion US$ (chiller market 2015). The ten largest markets by share are shown in fig. 1. Many other markets are also interesting for water vapor chillers, mainly in the warm climates, because they will draw benefits of being able to run the system at higher evaporating temperatures and thereby also at a higher efficiency.
The efficiency could become the only concern when all refrigerants have extremely low GWPs because the electricity for running the system would become the main obstacle if the system consumes more energy than the refrigerants, it is replacing. Tests have shown that the water vapor compressor used for this project is as efficient as most other refrigerants in chiller applications, but the efficiency increases rapidly as the evaporating temperature increases. Thus, the water vapor compression cycle is especially relevant when it comes to cooling processes in the industrial segment, e.g. computer cooling, molding processes, heat pumps etc.

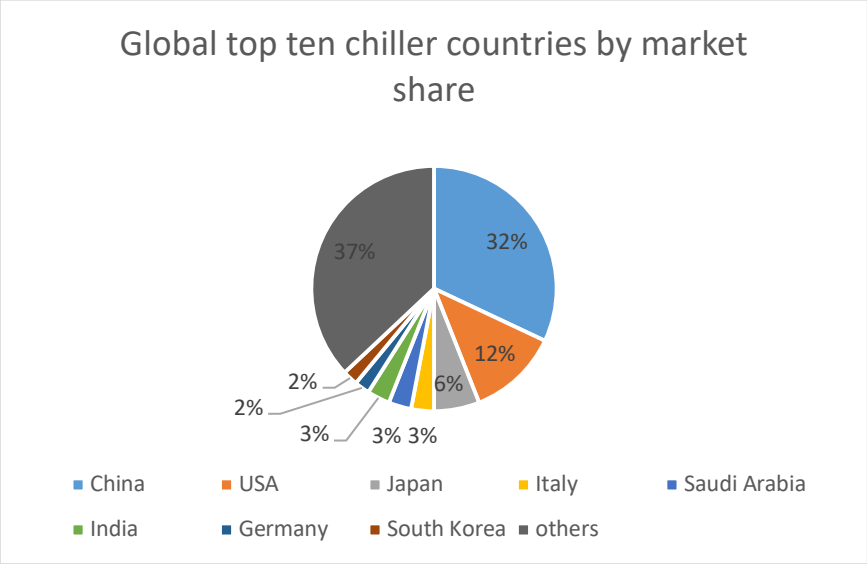

Figure 1: Top 10 chiller markets by share. The global value of chiller market in 2015

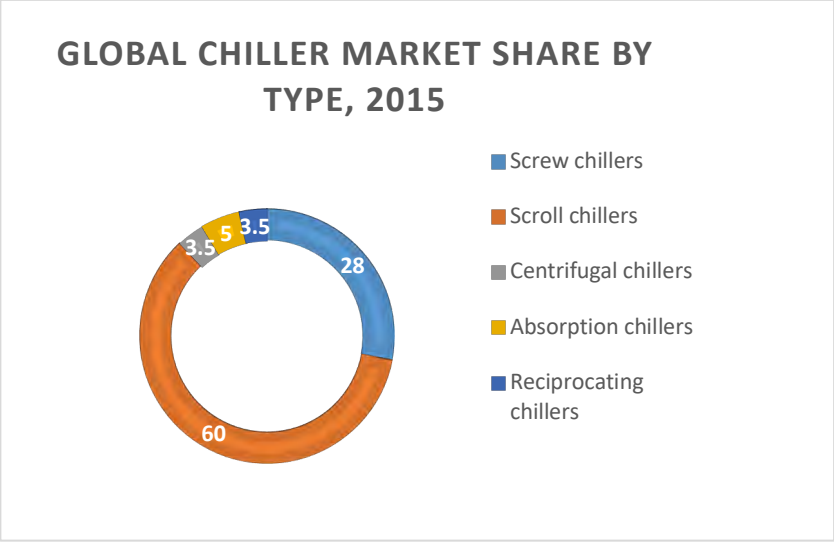

Figure 2 The global chiller market by technology share, 2015

In case of available waste heat, absorption chillers come in to the question as well. Chillers based on reciprocating also play a role, and especially chillers based on ammonia using open type compressors often use reciprocating compressors up to about 1.5 MW. Small type centrifugal compressors (Efficient Energy GmbH) are available on the market with water as the primary refrigerant. Larger types of centrifugal chillers are available at 350 kW by Kawasaki. Market introduction of chillers based on axial compressors using water as the primary refrigerant is under way. This is presented in this paper.

3. ONGOING ACTIVITIES

Steam has been used for decades in processes such as distillation, desalination, mechanical vapor recompression, power plants, etc., which usually are based on Roots type compressors or ejectors. It is relatively new that commercial chillers are available on the market or that they are being developed phase based on R718. A number of companies have activities concerning chillers or heat pumps using water as the fluid. The following list shows a selection of some of them:

IDE Technologies has been on the market for many years with applications i.a. desalination, vacuum ice for mine cooling, and artificial snow generation. The technology is based on large-scale centrifugal compressors with a special design with individual blades. A special direct contact ice generator and drain system has been developed for the vacuum ice applications. The condenser is an indirect type. There are several papers and patents related to the activities, for example (IDE home 2019), (IDE Patents), (Ophir A. 2008).

Johnson Controls Denmark: Cooperates with IDE technologies to establish vacuum ice for district heating and a prototype chiller in the 1980's and the 1990's (Andersen, Boldvig 1987), (Minds G. 1993). Later on, a compressor development project was initiated and resulted in a cooperation to develop a commercial prototype of an axial compressor for chiller applications, the unit in question for this paper (Svarregaard 2001), (Madsboll 2011), (Press Release 2011). A high-temperature heat pump based on a modified turbo-chiller design has also been developed (Larminat P. 2014).

ILK, Dresden: Development of a two-stage centrifugal chiller unit, basically the same type of compressor as IDE Technologies, an indirect evaporator and condenser, which have been commercialized (Wobst, E. et al., 2004**)**. The company now offers the vacuum ice unit with a direct contact ice generator, (ILK Vacuum ice).

Kawasaki Heavy Industries: Offers commercial chiller based on two-stage centrifugal compressor and a specially developed motor in vacuum. The unit has been demonstrated at the factory site. **(**Sakamoto H., 2015), (Kawasaki mizuturbo), (Kawasaki Patent).

Efficient Energy: offers commercial chillers for relatively low capacity and relatively high cooling temperature. The chillers are offered as modules that can be combined, and there are several units in operation in Germany. (Efficient Energy home), (Süss J, 2016).

Kobe Steel (Kobelco): Development of axial compressor and chiller systems for both direct and indirect heat exchanger. Development of screw type high-temperature heat pump system with applications in Japan. (Press Release), (Steam Star).

Rotrex: Development of high-temperature heat pump based on a planetary gear and a centrifugal compressor. The current status is a field test of the latest version in an industrial evaporator (Rotrex home), (Borup J, Jensen J. 2012), (Madsboll H. et al.2015).

F3Snow: Development of system for artificial snow production at a rather low capacity based on two-stage centrifugal compressors. (F3 Snow home).

Black Pine Engineering and Michigan University: Development of a special type of axial compressor modules for relatively high temperature levels. (Qubo L et al, 2011), (Black Pine Engineering home).

Danish Technological Institute: Development center for a number of compressor designs (axial, centrifugal, cycloid), system design etc. for vacuum ice, chiller, and high-temperature heat pump applications. (Nyvad, J., Elefsen, F. 1993), (Madsboll H., 2011), (Madsboll H. et al, 2015).

In addition, some companies have been working in the area of developing systems (Dr. Joachim Paul, EDF among others), and there is also an awareness regarding companies which are in the

process of developing compressors and systems with water as media for various capacities and applications, but they are not ready to go public yet.

4. RESULTS FOR COMMERCIAL CHILLER PROTOTYPE

The main difference between this system and all other refrigeration and AC systems is that it can be designed as an open system. Thus, a part of the refrigerant is evaporated to the ambient without affecting the global climate. In a normal cooling tower system, there is a supply of water in the tower basin, but the supply in the water vapor compression system is the make-up water on the low-pressure side in the evaporator. It is a challenge to do so due to the accumulation of the materials in the evaporator because the vapor does not take impurities, salts etc. through to the condenser. If water is a scarce resource, a dry cooler can be used in the system instead of an open cooling tower. This will have a draw back on the efficiency side as discussed in this paper.
The system uses an axial compressor developed on the basis of the learnings from a series of development projects, which all together have been running for almost 15 years (Press Release), (Madsboll 2011). The final development and field-test are funded by the Danish Energy Agency under the program called EUDP.

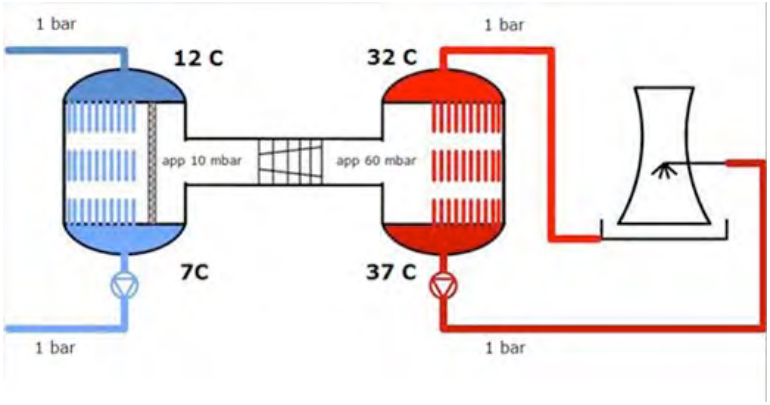

Figure 3 Sketch of chiller unit principle with open evaporator and open condenser – the operating conditions are indicated.

In the current compressor, all bearings are water lubricated, which at times has been a challenge of its own. Water is not a perfect lubricant in all cases, but it was chosen, because it is a way to reduce the mechanical loses to nominal values of about 2-2.5% of the total power consumption due to the low viscosity of the lubricant. The water lubricated bearings allow the compressor to be integrated directly in industrial processes without the risk of oil contamination of for example chemical processes or food industry.

The compressor package is working at the saturation pressures for the water temperatures in question, which is well below the atmospheric pressure. For this reason, vacuum pumps are used on the condenser side to keep the pressure down and to remove the non-condensable gasses. In this refrigeration system, too much air is a killer, which leads to a steep decrease in the heat transfer coefficient and an increase in the compressor performance loss. The air is removed at the high-pressure side of a specially designed deaerator, which is integrated with the condenser, while the pressure at the low-pressure side in the evaporator is kept down by the compressor itself. On this unit, there are two vacuum pumps. One of the methods to keep up the efficiency of this system is to keep the vacuum without using too much power to run the vacuum pumps.

The aerodynamic, mechanical, and rotor dynamic design and test of the compressor have by far been the largest efforts, but from a practical point of view, the water lubricated bearings have been a challenge. They have been in operation in test units since 2007 at Danish Technological Institute (Denmark) and at Kobe Steel (Japan), and they performed excellently from a rotor dynamic

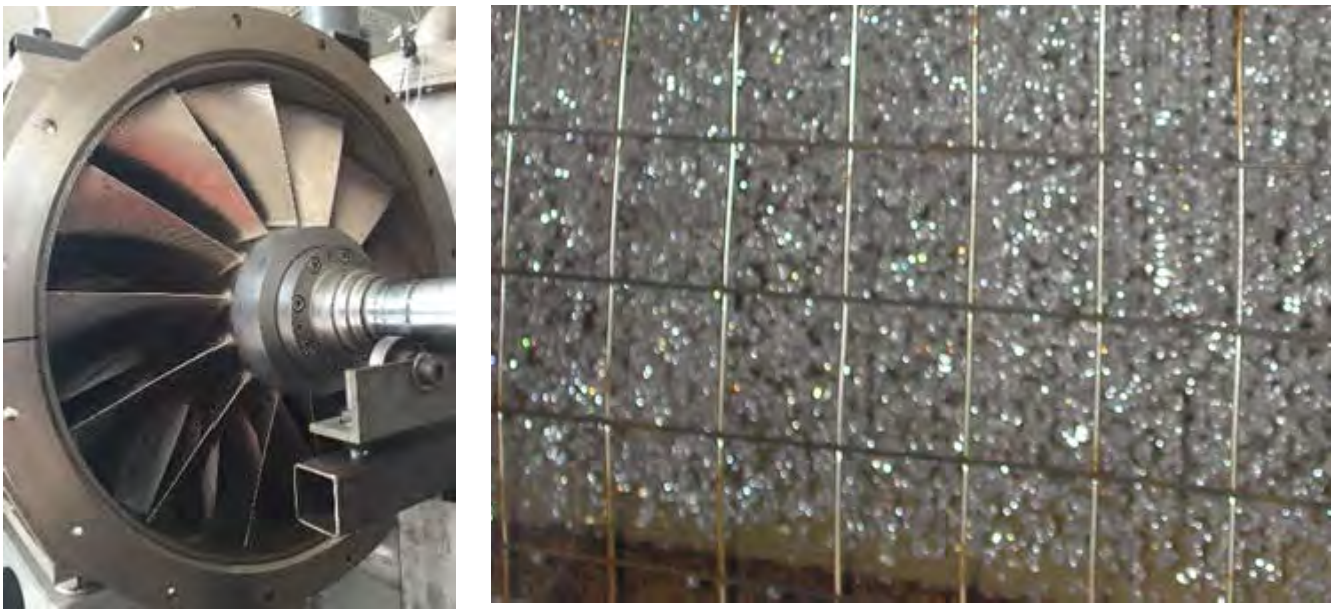

Figure 4 Compressor inlet and direct contact evaporator

perspective. There has been excessive losses from the thrust bearing, which has been redesigned, but not yet implemented in order to meet the target of a total of 2-3 % mechanical losses compared to the total power consumption. Otherwise, the bearings have met the nominal specifications.

Another issue is the water in the evaporator. Water is an excellent solvent, and it will always contain some sort of impurities, salts, minerals, etc. As the water, which evaporates, is pure water vapor, the concentration of these impurities will gradually increase. If the evaporator system is open, this might not be a source of concern, but if one is operating with a closed evaporator system or a small reservoir, this must be dealt with. In practice, it means that the water must be replaced from time to time or additional water must be continuously circulated as is the case for traditional cooling tower operation. On the other hand, this feature can be utilized in a positive way in industrial process integration for the purpose of concentrating various substances, for example juice, chemicals, waste water, etc.

As both the evaporator and the condenser operate at vacuum conditions, the inlet water flow is controlled by valves, while the water must be removed by pumps. This is a well-known situation from other refrigerant pumps, which have to pump a refrigerant close to the boiling point with the risk of cavitation. Right now, the unit is equipped with ordinary low NPSH centrifugal pumps, but it might be a field for future development. Staging could be a solution to increase the pump head if needed and to avoid cavitation. It is the first stage, which in particular is subject to the risk of cavitation, and there are many ways to avoid this, for example a light pre-pressure pump or an inducer.

The compressor is driven directly by a newly developed high-speed induction motor, which is water and air cooled.
The first field test unit has been well-equipped with many points of measurements, only a few of



Figure 5 The compressor and the integrated aearator and condenser

these will be fitted on the final product. The first test unit will be monitored for one year in order to prove that the concept meets the expectations and to gain experience from real-life operation. The gathered data will be used for evaluating running conditions and for the future development of the compressor and chiller unit.

The performance data of the unit at the conditions close to the design values at the demonstration site are listed in table 1. The customer wanted the plant process water to be separated from the direct contact evaporator. Thus, an additional plate heat exchanger has been installed.

Table 1 Test data for water vapor unit at the design point for the demonstration site

Cooling capacity including lubricant cooling	811.6	kW
Compressor shaft power	139.8	kW
Power input to compressor plus vacuum system	153.3	kW
Total power input to unit including water pumps etc.	182.2	kW
Evaporator inlet (plate heat exchanger in)	12 (20)	
Evaporator out, Te (plate heat exchanger out)	7.5 (9.2)	C
Condenser in	25.5	C
Condenser out, Tc	31.2	C
EER (power input to compressor plus vacuum system)	5.29	

The vibration level of the compressor is very low, casing vibrations are less than 1.5 mm/s rms. Thus, it is in the best category for this type of machinery. The compressor has been equipped with proximity sensors close to the bearings in order to monitor shaft vibrations. The results correspond very well to the design.

5. SUMMARY

When considering new low-GWP alternatives, most of these become flammable to some degree and will all require a risk assessment. One thing is the flammability, and another is the break down products of the fluorinated alternatives. Here, the so-called natural refrigerants break down to more innocent products like CO_2 and water whereas the fluorinated compounds result in a variety of products. This can be ventilated away from the machine room and into the atmosphere, which solves the problem for the technician, but in the atmosphere the breakdown products can react with other pollutants already there and form new toxic combinations. Hydrocarbons and ammonia for CO_2 and a bit of H_2O, which can also be ventilated away and cause no problems in nature.

REFERENCES

Andersen K., Boldvig, F.V. 1987. Large capacity heat pump using vacuum ice production as source, 17th International Congress of Refrigeration, pp 694-701, Vienna.

Black Pine Engineering home: http://www.blackpineengineering.com/

Borup J., Jensen J. 2012. Udvikling af Rotrex turbokompressor til vanddamp kompression, Nr. 344-009, PSO Program 2012, Dansk Energi

Chiller Market 2015: https://www.alliedmarketresearch.com/chiller-market

Efficient Energy home: https://efficient-energy.de/

F3 Snow home: http://f3snow.com/

IDE home, https://www.ide-tech.com/en/

IDE Technologies Patents: for example WO2012104787, WO200714833

ILK vacuum ice: https://www.ilkdresden.de/ fileadmin/user_upload/170130_Broschuere_ Vakuumeis _eng_mail.pdf

Kawasaki mizuturbo: https://global.kawasaki.com/en/energy/pdf/mizutorbo.pdf

Kawasaki Patent: for example WO2011JP01906 20110330

Larminat P. et al., 2014, A high temperature heat pump using water as working fluid, 11th IIR Gustav Lorentzen Conference on Natural Refrigerants, pp616 – 624. Hangzhou.

Madsboll H., 2011., Water as refrigerant – development of new type of compact, high efficient and cost effective axial compressor for commercial chillers with water as refrigerant, The 23th IIR ICR, Prague 2011

Madsboll H. et al. (2015). Development of a Water Vapor Compressor for High Temperature Heat Pump Applications, in: Proceedings of International Congress on Refrigeration. IIR, Yokohama, Japan, p. Paper ID 845.

Minds G., Madsboll H,1993. Energy saving in process cooling by use of water as refrigerant.Energy Efficiency in Refrigeration and Global Warming Impact. IIR: Ghent, 75–85 C.,

Nyvad, J., Elefsen, F. 1993, Energy efficient cooling by use of cycloid water vapour compressor IIR Com 1,/2 Gent (1993) 67 74

Ophir A. 2008: Mechanical heat pumps using water as refrigerant for ice production and air conditioning, paper presented to IDEA 99th Annual Convention, Orlando (International District Energy Association: Westborough)

Press Release 2011: http://www.tepco.co.jp/en/press/corp-com/release/11011901-e.html https://www.teknologisk.dk/projekter/vand-erstatter-miljoeskadelige-koelemidler-i-nye-koele-og-airconditionanlaeg/30019

Qubo L. et al., 2011, Design of a novel axial impeller as a part of counter-rotating axial compressor to compress water vapor as Refrigerant, Applied Energy 88 (201) 3156-3168.

Rotrex home: http://www.rotrex.com/Home/OEM_Applications/Industrial/Heat_Pumps

Sakamoto H., ATMO 2015, http://www.atmo.org/media.presentation.php?id=524

Steam Star: http://www.steamstar.jp/index.html

Süss J., 2016., A centrifugal compressor cooling system using water as working fluid. In: 12th IIR-Gustav Lorentzen Natural Working Fluids Conference (GL 2016); 21-24 August; Edinburgh, United Kingdom; 2016. pp. 1178-1184. DOI: 10.18462/iir.gl.2016.1204

Svarregaard C. 2001, Udvikling af vanddampkompressor, EFP95, j.nr. 1743/95-0005, H., 2011,

Wallington, T.J., et al. 2014. Atmospheric chemistry of short-chain haloolefins,Photochemical-ozone creation potentials (POC- Ps), global warming potentials (GWPs), and ozone depletion potentials (ODPs). Chemosphere (2014), http://dx.doi.org/10.1016/

Worbst et al., 2004. "Turbo Water Chiller with Water as Refrigerant" (2004). International Compressor Engineering Conference, Purdue. Paper 1625.

Manuscript ID: 682
DOI: 10.18462/iir.icr.2019.0682

An experimental investigation of the influence of fullerene C_{60} additives in compressor oil on the coefficient of performance of the refrigeration system

Vitaly ZHELEZNY[(a)],Guangming CHEN[(b)], Olga KHLIYEVA[(a)], Mykola LUKIANOV[(a)], Kostyantyn SHESTOPALOV[(a,b)], Serhii KORNIIEVICH[(a)]

[(a)]Institute of refrigeration, cryotechnology and eco-energy, Odessa National Academy of Food Technologies, 112 Kanatnaya str., Odessa, 65039, Ukraine, vzhelezny@mail.ru

[(b)]Ningbo Institute of Technology, Zhejiang University, No 1 QuianHu South Road, Ningbo City, 315100, Zhejiang Province, China, gmchen@zju.edu.cn

ABSTRACT

An application of compressor oil with additives of the fullerenes C_{60} is promising way to increase the energy efficiency of the compression refrigeration machine. The solutions of natural refrigerant R600a with two types of mineral compressor oil (different by the viscosity) and fullerenes C_{60} additives were considered as the working fluids and have been examined. The experimental setup with the small capacity compressor was used for experimental estimation of the cooling capacity, power consumption and coefficient of performance at different flow rate of the working fluids. The experimental data for the energy efficiency parameters of the system operating with different working fluids is presented. The experimental data for the concentration of compressor oil and fullerenes C_{60} in refrigerant before throttle valve at the different flow rates of working fluid is reported. The enhancement of the coefficient of performance is analyzed.

Keywords: compressor refrigeration system, working fluid, fullerenes, coefficient of performance

1. INTRODUCTION

The implementation of the nanorefrigerants (working fluids that contain the refrigerant, compressor oil and nanoparticles) is one of the promising direction to enhancement the energy performance of the vapor compression refrigeration systems (Zhelezny, 2014; Celen et al., 2014; Azmi et al., 2017; Chen et al., 2015; Bi et al., 2008; Bi et al., 2011; Subramani et al., 2011; Jwo et al., 2009; Kumar et al., 2012; Sabareesh et al., 2012; Lukianov et al., 2015; Xing et al., 2014; Jia et al., 2014).

Nowadays there are many experimental studies dedicated to investigation of the thermophysical properties of prospective working fluids for the compression refrigeration systems (solutions of the refrigerant in compressor oil) with additives of the nanoparticles (Celen et al., 2014; Azmi et al., 2017; Zhelezny et al., 2017). The authors found a positive change in the thermophysical properties of the refrigerant-oil solution (ROS) containing the nanoparticles in comparison with properties of the base ROS: i.e. the increase of the thermal conductivity, saturated vapour pressure and decrease of the surface tension. However, adding the nanoparticle additives to liquid leads to increase the viscosity (Celen et al., 2014; Azmi et al., 2017; Zhelezny et al., 2017).The variation in the thermophysical properties of the ROS caused by presence nanoparticles in compressor oil determines the variation in the energy performance of the vapour compression refrigeration system. Moreover, adding the nanoparticles into compressor oil also leads to alteration of the friction losses in compressor (Azmi et al., 2017; Jia et al., 2014; Ku et al., 2010; Lee et al., 2009). It should be mentioned that the energy performance of the vapour compression refrigeration system depends on a large number of factors. Therefore, it is impossible to predict the change of the coefficient of performance of the system operating with working fluid with nanoparticles even in case if data for the thermophysical properties of the ROS containing the nanoparticles is availible.

To our knowledge, there are some papers dedicated to experimental investigation of the energy performance for the compression refrigeration systems operating with working fluids containing nanoparticles of the metal oxide (Chen et al., 2015; Bi et al., 2008; Biet al., 2011; Subramani et al., 2011; Jwo et al., 2009; Kumar et al., 2012; Sabareesh et al., 2012; Lukianov et al., 2015).

At the same time, only one paper dedicated to investigation of the influence of fullerenes C_{60} in the working fluid on the energy performance of the domestic refrigerator (Xing et al., 2014) is published. Authors reported the increase of the COP up to 5.3-5.6 % at using compressor oil containing the 0.003 $g \cdot cm^{-3}$ of fullerenes C_{60}. In addition, (Jia et al., 2014) in paper dedicated to evaluation of the energy performance of the refrigeration system with working fluid containing nanoparticles $MoFe_2O_4$-$NiFe_2O_4$/fullerenes found the increasing of the COP of refrigeration system up to 5.33 % compared to traditional working fluid. It should also be mentioned that using surfactant as additives to the compressor oil is a disadvantage of the technology for preparation of the nano-oil. The presence of surfactant in nano-oil may affect the thermophysical properties of the ROS, friction coefficient in compressor and efficiency of the heat transfer at the ROS boiling in the evaporator.

Thus, addition of nanoparticles to the working fluids leads mainly to enhance in the energy performance of the vapor compression refrigeration systems. However, the positive effects reported in various studies are different. Sometimes, the effects were insignificant or may be compared with experimental uncertainty. However, influence of the nanoparticles additives in compressor oils with different viscosity on the energy performance of the compression refrigeration systems is still poorly investigated.

Therefore, the aim of presented study can be formulated as the evaluation of the energy performance for the refrigeration compressor system operating with working fluid that widespread in domestic refrigerators i.e.- solution of refrigerant R600a (isobutane) in mineral compressor oil with fullerenes C_{60} additives. The choice of the fullerenes C_{60} as the additives to the mineral compressor oil was justified by following reasons: solution mineral oil-fullerenes C_{60} forms the colloidal stable system without using of surfactants (Ku et al., 2010; Lee et al., 2009; Zhelezny et al., 2018); use of the compressor mineral oil with fullerenes C_{60} leads to decrease of the friction loses in compressor (Ku et al., 2010; Lee et al., 2009); additives of the fullerenes C_{60} insignificantly change the base oil viscosity especially in the high temperature range (Ku et al., 2010; Lee et al., 2009; Hwang et al., 2007; Rashidi et al., 2013; Dombek et al., 2014) (contrary to additives of the nanoparticles of metal oxides). In addition, the influence of the compressor oil viscosity on the COP of the compressor refrigeration system has been experimentally investigated.

2. OBJECTS OF STUDY

The following materials have been used in the experiments: commercial mineral compressor oils (information from supplier is presented in Table 1); nanoparticles-fullerenes C_{60} (purchased from Sigma Aldrich, CAS# 99685-96-8, purity 0.999 $kg \cdot kg^{-1}$); isobutane-refrigerant R600a (CAS# 75-28-5) with purity 0.998 $kg \cdot kg^{-1}$.

-ROS1 – solution of the R600a in commercial mineral compressor oil with viscosity 8.0 $mm \cdot s^{-1}$at 40ºC;

- ROS2 – solution of the R600a in commercial mineral compressor oil with viscosity 19.5$mm \cdot s^{-1}$ at 40ºC;

- ROS2**+**C_{60} – ROS2 with additives of 0.0050 $kg \cdot kg^{-1}$ fullerenes C_{60} in oil with viscosity 19.5$mm \cdot s^{-1}$.

The colloidal stability in time of the prepared nanofluid is very important issue for further experiments. Unlike the metal oxides nanoparticles, the fullerenes can exist in solutions both as the individual molecules and as the clusters of molecules with size that determined by the fullerenes concentration, temperature and physical nature of the liquid (Mchedlov-Petrossyan, 2013). The fullerenes solubility in different liquids has been investigated in many studies, for example in (Ruoff et al., 1993). Since molecules of the fullerenes are non-polar, they have high solubility in the non-polar liquids. In addition, the solubility of fullerenes is better when the molecular weight of the base fluid is higher (Ruoff et al., 1993). Thus, the mineral compressor oils are suitable liquids for application the fullerenes as additives considering the nanofluids stability.

For preparation of the solutions of fullerenes in compressor oil, the sonication treatment of samples for 2 hours was used. Ultrasonic bath Codison CD 4800 (frequency 42 kHz, power 0.07 kW) was applied. A light absorbance method was applied to estimate the suspension stability in time. The peak absorbance of fullerene in different solution depends on solvent nature and fullerene concentration as was stated by Mchedlov-Petrossyan (2013). At the same time, Hwang et al. (2007) show that the absorbance peak for the fullerenes in oil-based suspensions appears at wave length 397 nm. Therefore, the stability of nanofluids has been estimated at the wave length 397 nm. For

that purpose, the UV-vis spectrophotometer (Shimadzu UV-120-02, Japan) was applied. The samples of oil were filled into the optical sells with optical path 1.1 mm.

Table 1. Physical-chemical properties of the mineral compressor oil (information from the supplier)

Properties	Oil for ROS1	Oil for ROS2
Kinematic viscosity, $mm^2 \cdot s^{-1}$	8.0 at 40 ºC	19.5 at 40ºC (own data) 16.0-19.0 at 50ºC (information from supplier)
Density at 20 ºC, $kg \cdot m^{-3}$	870 (own measurement)	850-880
Flash point in open crucible (more than), K	426.15	447.0
Solidification temperature (no more than), K	223.15	223.0
Metal corrodibility in compressor oil	Negative	Negative
Content of mechanical additives	Absent	Absent
Water content	Absent	Absent
Acid number(no more than), KOH for 1 g	0.02	0.02

A collection of samples of oil containing the fullerenes $C_{60}$with range of concentration 0.0013 - 0.0050 $kg \cdot kg^{-1}$ have been prepared to study of the colloidal stability. The required quantity of oil and fullerenes were measured using electronic balance Model GR 300 with an instrument uncertainty of 0.5 mg. The image of samples of compressor oil is shown on Fig. 1. It was shown the solutions of C_{60} in oil (viscosity 8.0 $mm \cdot s^{-1}$ at 40 ºC) were transparent at the concentration no more than 0.0020 $kg \cdot kg^{-1}$ at the temperature 20 ºC. But at the concentration higher than 0.0020 $kg \cdot kg^{-1}$ at the temperature 20 ºC the solution oil/C_{60} was turbid probably due to formation of clusters of the C_{60} in oil at the high concentration of fullerenes.

The values of the absorbance for samples of the mineral oil containing fullerenes C_{60} have been measured every 2-5 days for three months. For all oil samples the variation of the absorbance value in time was not observed. So, we can conclude that solutions of the mineral oil with fullerenes demonstrate good colloidal stability.



Figure1: The image of samples of oil (viscosity 8.0 $mm \cdot s^{-1}$ at 40ºC) at temperature 20 ºC: pure oil (left), oil containing 0.0013 $kg \cdot kg^{-1}$ of fullerenes C_{60} (center) and 0.0050 $kg \cdot kg^{-1}$of fullerenes C_{60} (right)

The required amount of the compressor oil containing the 0.0050 $kg \cdot kg^{-1}$of fullerenes C_{60} has been prepared for charging the refrigeration compressor system. The required amount of the refrigerant R600a was charged into refrigeration system after filling into compressor crankcase with oil and evacuation of the system. The composition of the ROS2+C_{60} after charging the refrigeration compressor system was following: compressor oil w_{Oil}=0.7053 $kg \cdot kg^{-1}$, refrigerant w_R=0.2911 $kg \cdot kg^{-1}$, fullerenes $C_{60}$$w_{C60}$=0.0036 $kg \cdot kg^{-1}$.

3. EXPERIMENTAL SETUP

The series of experiment on measurement the cooling capacity and compressor power consumption has been performed to evaluate the expediency of adding the fullerenes C_{60} into working fluid of compressor refrigeration system. For that purpose, the experimental setup has been created. Schematic diagram of the experimental setup is presented in Fig. 2. The test parameters are presented in Table 2.

The method of calorimeter with secondary refrigerant (according to ISO 917-89) has been used for measuring of the cooling capacity for the compressor refrigeration system. The uncertainty of

measurement of the compressor power consumption does not exceed 0.1 %.The cooper-constantan thermocouples with uncertainty no more than 0.2 K have been used to measure the temperature of refrigerant in the different points of refrigeration system and water for cooling of the condenser. For pressure measurement the pressure transmitters WIKA have been installed in the different point of refrigeration system. The pressure measurement uncertainty does not exceed 0.4 %.The flow rate was measured using the calorimetric flow meter 5 (Zhelezny et al., 2014). The series of sampling of the working fluid before the throttle device were performed to estimate the oil concentration in working fluid.

Table 2. The test parameters

Working fluid mass flow rate, $g \cdot s^{-1}$	Evaporation temperature, K	Condensing temperature, K	Superheating in the evaporator (relative to saturation temperature of R600a) ΔT, K
0.202 – 0.404	255.35±0.45 K	300.85±0.15 K	3.0

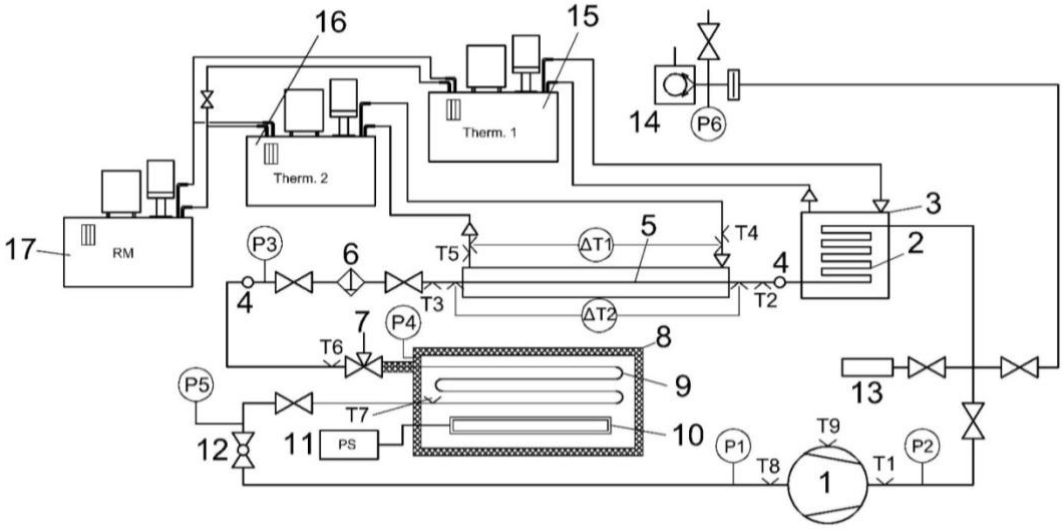

Figure2: Schematic diagram of the experimental setup for the study of the energy performance of the vapor compression refrigeration system: 1 – compressor SKN-150 manufacturer Atlant (volume of cylinders – 10.08 cm^3); 2 – condenser; 3 – heat exchanger of condenser; 4 – sight glass; 5 – calorimetric flow meter; 6 – filter-drier; 7 – throttle valve; 8 – calorimeter with secondary refrigerant R134a; 9 – evaporator of calorimeter; 10 – heater; 11 – power supply; 12 – valve for adjusting the working fluid boiling pressure in evaporator; 13 – charging vessel; 14 – vacuum pump; 15 –thermostat for adjusting the coolant temperature for condenser cooling; 16 – thermostat for adjusting the coolant temperature for cooling the calorimetric flow meter; 17 – refrigeration machine.

The selected test parameters (see Table 2) were adjusted before performing the series of multiply measurement for the estimation of the cooling capacity and compressor power consumption. Following parameters have been examined: the working fluid flow rate, evaporation temperature, condensing temperature, superheating temperature in the evaporator and calorimeter heater power. The instruments reading (power consumption of calorimeter heater 8, thermocouples voltage and readings of pressure transmitters, compressor power consumption) were recorded after obtaining the stable test parameters of the setup.

4. EXPERIMENTAL RESULTS AND ANALYSIS

The experimental values of the cooling capacity and compressor power consumption at the various working fluid mass flow rates are presented in Figs. 3 and 4.

The analysis of trends presented in Fig. 3 shows that decrease in the compressor power consumption of the refrigeration system operating with ROS2 containing the fullerenes was estimated in average as 5 %. However, significant variation of the compressor power consumption using the compressor oil with different viscosity was observed. The increase of the compressor oil viscosity from 8.0 to 19.5 $mm \cdot s^{-1}$ at 40°C leads to increase of the compressor power consumption up to 9-18 %. Considering possibility to use thefullerenes as additives into the ROS it is interesting

to examine the results of experiments reported by Ku et al., 2010. Ku et al. (2010) have shown that decrease in the coefficient of friction losses and anti-wear characteristics due to adding fullerenes into the oil was more significant for oil with low viscosity in comparison to oil with high viscosity. Therefore, for the enhancing energy performance of the compressor refrigeration system the "optimal" choice of the compressor oil is very important no less than the choice of the "optimal" refrigerant.

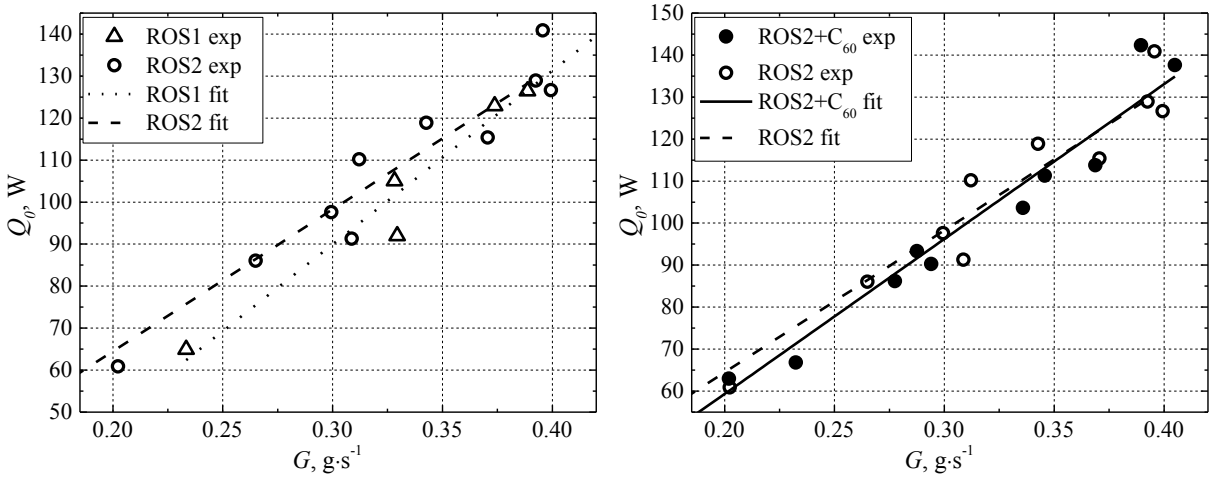

Figure 3: Dependence of the cooling capacity Q_0 from mass flow rate G of the working fluid

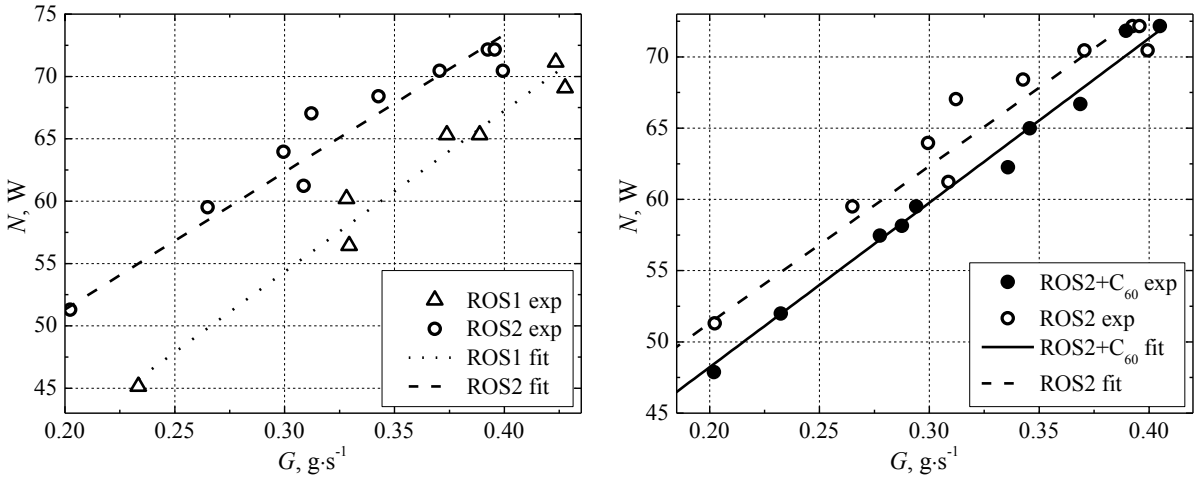

Figure 4: Dependence of the power consumption of compressor N from mass flow rate G of the working fluid

The trends in Fig. 4 allow us to make some conclusions. Firstly, we did not find significant variation of the cooling capacity at the operating of the compressor refrigeration system using ROS2+C60 in comparison with ROS2. Secondly, using of the compressor oils with high viscosity at the low flow rate of the working fluid (consequently, at high oil entrainment from compressor (Zhelezny et al., 2014)) contributed to increase of the cooling capacity. Probably, it can be explained by increasing of the compressor delivery rate. It was also shown that the influence of fullerenes in the ROS on the performance of compressor refrigeration systems is decreased when the working fluid flow rate increases.

The absence of effect of the fullerenes additives in the ROS on the cooling capacity of the compressor refrigeration system can be explained by low concentration of fullerenes in the working fluid and, correspondingly, insignificant effect of C_{60} on the thermophysical properties of the ROS. The fullerenes C_{60} (as any nanoparticles in the ROS) entrainment from compressor with drops of compressor oil. The results of sampling of the ROS before throttle valve at the different values of the mass flow and specified operational parameters were used to determine the mass fractions of the compressor oil and fullerenes in the ROS - see Fig. 5. This information was also used to determine

the mass fraction of the compressor oil and fullerenes in different parts of the compressor refrigeration system - see Fig. 6.

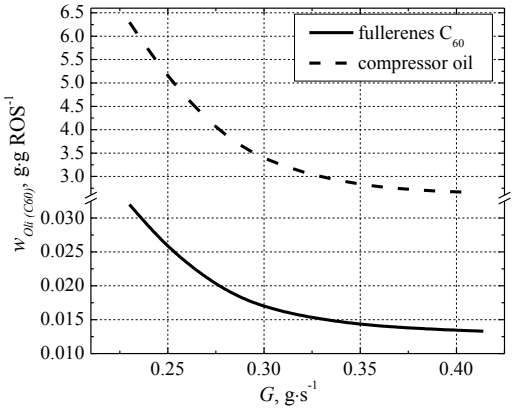

Figure 5: Dependence of the concentration of compressor oil w_{Oil} and fullerenes C_{60} w_{C60} in ROS before the throttle valve from mass flow rate *G* of the working fluid

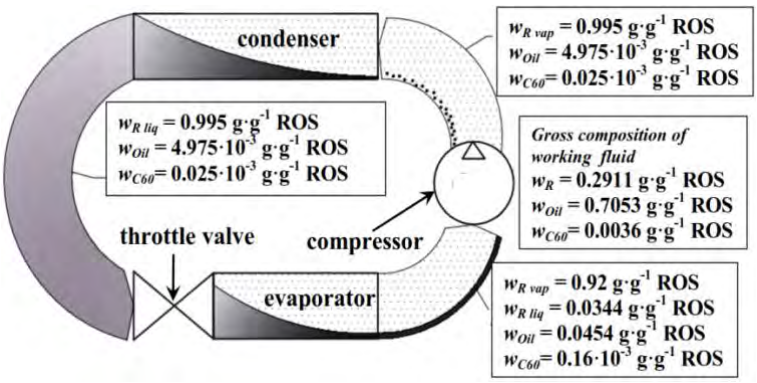

Figure 6: Scheme of circulation of working fluid R600a/compressor oil (viscosity 19.5mm·s^{-1}at 40 ºC)/fullerenes C_{60} in compressor refrigeration system at flow rate 0.252 g·s^{-1}

As can be seen from Fig. 6 the fullerenes circulate in refrigeration compressor system together with liquid phase of the working fluid. As part of the compressor oil drops, the fullerenes are passed from the compressor to the condenser since some amount of the compressor oil always circulates in refrigeration compressor system. Performed studies (Fig. 5) show that the concentrations of oil and fullerenes in the working fluid (in the experimental setup with compressor SKN-150) are insignificant and depended from the mass flow rate of the working fluid. It was shown that the concentration of fullerenes in working fluid in the evaporator is low– 0.025·10^{-3}g·g^{-1} in the ROS. Therefore, such small concentration of fullerenes in the evaporator has no influence on the cooling capacity of the compressor refrigeration system. On the contrary, presence of fullerenes in compressor at the concentration 0.0036 g·g^{-1} in the ROS can lead to significant decreasing of the energy friction losses in compressor.

The COP of the compressor refrigeration system has been calculated using experimental data on the cooling capacity and compressor power consumption (Fig. 7).

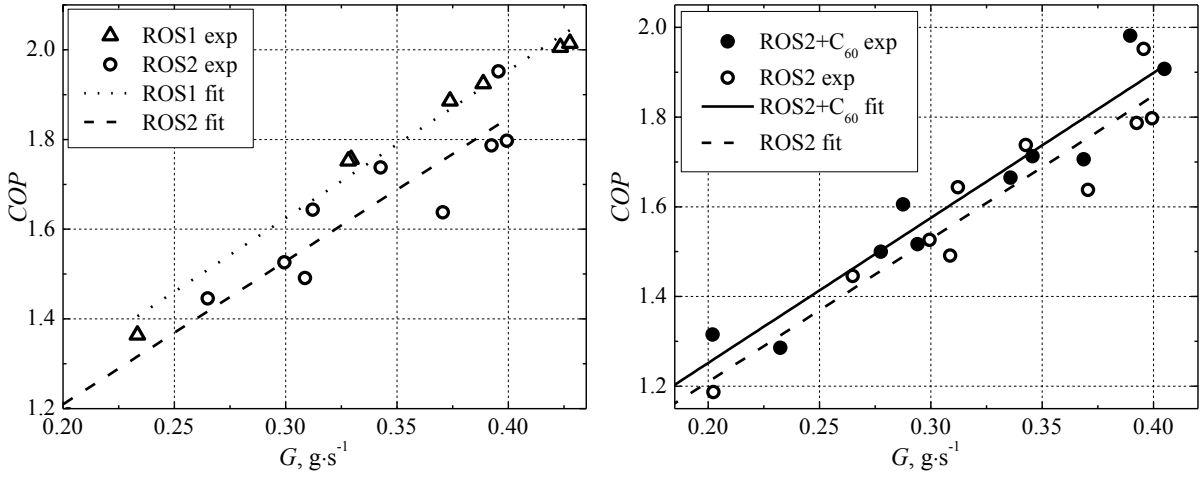

Figure 7: Dependence of the *COP* from mass flow rate *G* of the working fluid

As can be seen from Fig. 7 the coefficient of performance increases up to 4 % in all range of the flow rate of working fluid for the compressor refrigeration system operating with ROS2 with additives of 0.0050kg·kg^{-1}of fullerenes C_{60} in oil. It was shown that using the compressor oil with low viscosity (ROS1) contributes to increase the COP of refrigeration system up to 5-7 % in comparison with more viscous compressor oil (ROS2). Obtained results indicate that enhance of the energy performance

of the compressor refrigeration system can be achieved by decreasing of the friction losses in compressor.

5. CONCLUSIONS

In presented study we have shown that decrease in the compressor power consumption of the refrigeration system operating with ROS containing fullerenes C_{60} in the concentration in oil 0.0050 $kg \cdot kg^{-1}$ was estimated in average up to 5 %.In addition, significant variation of the compressor power consumption using compressor oil with different viscosity was observed. The increase of the compressor oil viscosity from 8.0 to 19.5 $mm \cdot s^{-1}$ at 40°C leads to increase of the compressor power consumption up to 9-18 %.

The variation of the cooling capacity for the compressor refrigeration system with ROS containing fullerenes C_{60} in comparison with ROS without fullerenes did not observed. However, using compressor oil with high viscosity at the low flow rateof the working fluid contribute to increase of the cooling capacity compare with low viscous oil at the same parameters of refrigeration cycle.

The coefficient of performance of the compressor refrigeration system operating with working fluid containing the fullerenes C_{60} increases up to 4 % compared to traditional working fluid in flow rate from 0.202 to 0.404 $g \cdot s^{-1}$. In addition, using the compressor oil with low viscosity contributes to increase the COP of refrigeration system up to 5-7 % in comparison with high viscous oil.

The results of experimental investigation of the concentrations of compressor oil and fullerenes in different parts of the compressor refrigeration system are reported. Obtained effects of the fullerenes additives in working fluids on the cooling capacity and compressor power consumption can be explained by low concentration of fullerenes in evaporator and relatively high concentration of fullerenes in the compressor. It was concluded that “proper” choice of the compressor oil with “optimal” viscosity and fullerenes C_{60} as additives will contribute to enhance the energy efficiency of the compressor refrigeration systems.

ACKNOWLEDGEMENTS

The paper was partly supported by Ministry of Education and Science of Ukraine in framework of projects No. 0118U000238 and No. 0118U000237; as well as by Natural Science Foundation of China (Projects No. 51776187), Zhejiang Province Natural Science Foundation of China (Project No. LY16E060004), and by Ningbo Science and Technology Bureau from the International Cooperation Project No. 2017D10006.

NOMENCLATURE

G	mass flow rate ($g \cdot s^{-1}$)		*Subscripts*
N	compressor power consumption (W)	*exp*	experimental values
Q	cooling capacity (W)	*fit*	fitting values
w	mass concentration ($g \cdot g^{-1}$)	*R*	refrigerant
	Abbreviations	*Oil*	compressor oil
COP	coefficient of performance	*C60*	fullerenes C_{60}
ROS	refrigerant/oil solution		

REFERENCES

Azmi, W. H., Sharif, M. Z., Yusof, T. M., Mamat, R., Redhwan, A. A. M. 2017. Potential of nanorefrigerant and nanolubricant on energy saving in refrigeration system–A review. Renew Sustain Energy Rev. 69. 415-428.

Bi, S., Guo, K., Liu, Z., Wu J. 2011. Performance of a domestic refrigerator using TiO_2-R600a nano-refrigerant as working fluid. Energy Conversion and Management, 52 (1), 733–737.

Bi, S., Shi, L., Zhang, L. 2008. Application of nanoparticles in domestic refrigerators. Appl. Therm. Eng. 28.1834–1843.

Celen, A., Çebi, A., Aktas, M., Mahian, O., Dalkilic, A. S., Wongwises, S. 2014 A review of nanorefrigerants: Flow characteristics and Applications. Int. J. Refrigeration. 44. 125–140.

Chen, G., Zhelezny,V., Shestopalov, K., Lukianov, N., Polyuganich M. 2015. An experimental and theoretical investigation of the compressor oil and nanoparticles admixtures influence on the

performance of the compressor systems. Proc. 24th International Congress of Refrigeration. Yokohama, Japan.
Dombek, G., Nadolny, Z., Przybylek, P. 2014. The study of thermal properties of mineral oil and synthetic ester modified by nanoparticles TiO2 and C60. High Voltage Engineering and Application (ICHVE), 2014 International Conference.
Hwang, Y.j., Lee, J., Lee, C., Jung, Y., Cheong, S., Lee, C., Ku, B., Jang, S. 2007. Stability and thermal conductivity characteristics of nanofluids. Thermochim. Acta. 455. 70–74.
Jia, T., Wang, R., Xu, R. 2014. Performance of $MoFe_2O_4$–$NiFe_2O_4$/Fullerene-added nano-oil applied in the domestic refrigerator compressors. Int. J. Refrigeration. 45. 120-127.
Jwo, C. S., Jeng, L. Y., Teng, T. P., Chang, H. 2009. Effects of nanolubricant on performance of hydrocarbon refrigerant system. Journal of Vacuum Science & Technology B: Microelectronics and Nanometer Structures, 27 (3), 1473–1477.
Ku, B.C., Han, Y.C., Lee, J.E., Lee, J.K., Park, S.H. 2010. Tribological effects of fullerene (C60) nanoparticles added in mineral lubricants according to its viscosity. Int. J. Precis. Eng. Man, 11.607-611.
Kumar, D. S., Elansezhian, R. D. 2012. Experimental Study on Al2O3-R134a Nanorefrigerant in Refrigeration System. Int. J. of Modern Engineering Research, 2 (5), 3927–3929.
Lee, K., Hwang, Y., Cheong, S., Kwon, L., Kim, S., Lee, J. 2009. Performance evaluation of nanolubricantsof fullerene in refrigeration mineral oil. Curr. Appl. Phys., 9(2). 128-131.
Lukianov, M., Khliyeva, O., Zhelezny, V., Semenyuk, Y. 2015. Nanorefrigerants application possibilities study to increase the equipment ecological-energy efficiency. Eastern-European Journal of Enterprise Technologies. 3/5 (75).32–40. (in Russian).
Mchedlov-Petrossyan, N. O. 2013.Fullerenes in liquid media: an unsettling intrusion into the solution chemistry. Chem. rev. 113 (7). 5149-5193.
Rashidi, A., Ahmadi, H., Mohtasebi, S. S., Pourkhalil, M. 2013. Thermal and rheological properties of oil-based nanofluids from different carbon nanostructures. Int. Commun Heat Mass Transfer. 48, 178–182.
Ruoff,R. S, Tse, D. S., Malhotra, R., Lorents, D. C. 1993. Solubility of fullerene (C60) in a variety of solvents.J. Phys. Chem., 97 (13). 3379–3383.
Sabareesh, R. K., Gobinath, N., Sajith, V., Das, S., Sobhan, C. B. 2012. Application of TiO2 nanoparticles as a lubricant-additive for vapor compression refrigeration systems – An experimental investigation. Int. J. Refrigeration. 35 (7), 1989–1996.
Subramani, N., Prakash, M. J. 2011. Experimental studies on a vapour compression system using nanorefrigerant. International Journal of Engineering, Science and Technology, 3(9), 95–102.
Xing, M., Wang, R., Yu, J. 2014. Application of fullerene C60 nano-oil for performance enhancement of domestic refrigerator compressors. Int. J. Refrigeration. 40. 398-403.
Zhelezny, V. P., 2014. An application of nanotechnologies in refrigeration–perspectives and challenges. Proc. 11th IIR Gustav Lorentzen Conference on Natural Refrigerants, IIR Hangzhou, China.
Zhelezny, V. P., Chen, G. M., Shestopalov, K. O., Melnyk, A. V. 2014. Experimental and theoretical investigation of heat transfer coefficient for boiling of the isobutane/compressor oil solution flow in the pipe. Proc. 11th IIR Gustav Lorentzen Conference on Natural Refrigerants, IIR, Hangzhou, China.
Zhelezny, V., Faik, A., Khliyeva, O., Motovoy, I., Ivchenko, D., Grosu, Y., Nikulin, A. 2018. Caloric properties of R600a solutions in compressor oil containing fullerenes C60. Proc. the 13th IIR Gustav Lorentzen Conference on Natural Refrigerants. Valencia, Spain.
Zhelezny, V., Lukianov, N., Khliyeva,O., Nikulina, A., Melnyk, A. 2017. A complex investigation of the nanofluids R600a-mineral oil-Al_2O_3 and R600a-mineral oil-TiO_2. Thermophysical properties. Int. J. Refrigeration. 74. 486-502.

Manuscript ID: 701
DOI: 10.18462/iir.icr.2019.0701

Optimization analysis on the performance of a vapor injection air-source heat pump with single screw compressor

Shanwei LIU[(a)], Yuanwei LU[(a)]*, Yuting WU[(a)], Biao LEI[(a)], Chongfang MA[(a)]

[(a)]Beijing University of Technology, College of Environmental and Energy Engineering, Beijing 100124, China, luyuwei@bjut.edu.cn

ABSTRACT

Adopting an economized vapor injection compressor can improve the heating capacity and energy efficiency ratio of the heat pump system at low environment temperature. In this paper, a kind of new vapor injection port structure located at the surface of slide valve was proposed based on the single screw compressor, so the vapor injection technology also can be used under part load condition and we proposed a new kind of single slide valve structure called compound slide valve to adjust the capacity and internal volume ratio of compressor simultaneously. A new mathematical method was presented to study the vapor injection process. The actual capacity and internal volume ratio at different slide valve working locations can be determined. The pressure, temperature and mass of the working medium in the control volume are calculated in this study. The mathematical expression of the injection region envelope is also presented in this paper.
Keywords: Air source heat pump, Single screw compressor, Slide valve, Vapor injection, Geometric characteristics.

1. INTRODUCTION

Air Source Heat Pump (ASHP) is a kind of energy saving space heating devices. It has two major problems. One is the poor performance at low ambient temperature which has become a primary limitation for further application of ASHP in cold regions (Bin et al., 2018). The other is the drastic change of working conditions, especially the change of pressure ratio, caused by environmental temperatures. In order to solve the problem of poor performance at low environment temperature, many solutions have been proposed such as cascade cycle, two-stage compression, control defrosting, new alternative refrigerant, and adopting an economized vapor injection (EVI). Among these measures, the vapor injection technology (Kang et al., 2018) is an effective method to improve the performance of ASHP. Due to the advantages of simple structure, good stress balance, small vibration, and long bearing life and low noise (Zimmern, 1972), the single screw compressor (SSC) has been widely used in refrigeration and heat pumps industry. Because of the structure of SSC, the application of vapor injection technology can be realized easily, while limited works can be found. According to existing research, only Kamikawa et al. (2016) proposed a kind of circular injection port structure, but no further research on the injection process.

For the problem of the drastic change of working conditions, it is widely believed that the internal volume ratio of compressor should be controlled to meet the needs under different working conditions. Obviously, both the heating capacity and internal volume ratio should be adjusted. The single slide valve is a kind of mature structure and it has been commonly applied to control capacity. In previous investigations, the single slide valve capacity control mechanism was firstly proposed by Zimmern (1983). Wang et al. (2014) presented a mathematical calculation method to study the

working principle of the single slide valve capacity control mechanism. In order to achieve capacity and internal volume ratio regulation simultaneously, VILTER (2010) proposed a double slide valve control mechanism. But the adjustment system also seems to have a complex structure.
In above works, there is still no effective method to adjust the capacity and internal volume ratio simultaneously, except the double slide valve. And there is no research on ASHP based on SSC with vapor injection. Therefore, the research attempts to optimize the parameters of injection port, such as injection port position, injection port structure and injection port size and study the new slide valve structure to adjust the capacity and internal volume ratio simultaneously.

2. GEOMETRIC ANALYSIS

2.1 The vapor injection structure and working principle of the slide valve

As shown in Fig. 1, the single screw compressor includes a screw rotor and two symmetrical gate rotors. The injection port 1 shows the traditional vapor injection port structure designed on the shell. For circular vapor injection port, the diameter of circular cannot greater than the width of the working flank between two adjacent grooves. The vapor injection process through the circular channel which is shown by location 1a can work normally, but the process through the circular channel which is shown by location 1b will be unsuccessful. It is because that the pressure in groove 1 is bigger than the pressure in groove 2 during the compression process. And then the gas will leak from groove 1 to groove 2. For small and medium sized SSC, the circular injection port may get less flow because of the geometric constraint. The most critical question is that the vapor injection port is designed on the shell, so the vapor injection process can work under a certain load only. The problems mentioned above need to be solved.

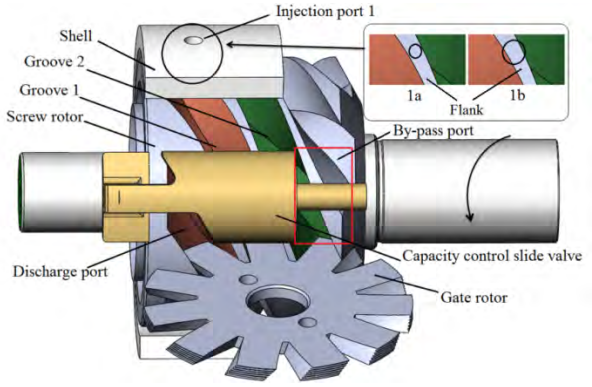

Figure 1: The traditional injection port and capacity control slide valve in SSC

In Fig.1, the single slide valve structure is a traditional slide valve structure used for capacity control and it contacts with the shell. It is shown that the volume of groove 2 has been closed by meshing between screw rotor and gate rotor. By this time, the working fluid in the groove 2 can still go back to the suction tube through the by-pass port, so the compression process has not started. When the by-pass port is closed, the working fluid in the groove 1 begins to be compressed. If the slide valve can move through a kind of driving device, then the capacity of SSC will be controlled. The structure of internal volume ratio slide valve is shown in Fig. 2. It is used to change the discharge port location by moving along with the axis of screw rotor, so the internal volume ratio of SSC can be controlled. In order to adjust the capacity and internal volume ratio simultaneously, both the capacity and internal volume ratio slide valve need to be installed at the same time. Fig. 3 shows the traditional double slide valve system. They are installed parallel and can move by different driving device.
In order to adjust capacity and internal volume ratio using the single slide valve, we designed a kind

of compound slide valve (CSV) structure as shown in Fig. 4 and Fig.5. The CSV contains slide block 1 and slide block 2. When the slide block 1 is bound together with slide block 2 through a mechanical device such as spring as shown in Fig. 4, it can be used as internal volume ratio control slide valve. In this case, slide block 1 and slide block 2 are treated as a whole and move axially by driving device. When the CSV is used as capacity control slide valve, the slide block 2 and slide block 1 are entirely separate as shown in Fig.5. By this time, only the slide block 1 moves axially, while the slide block 2 has been limited to a certain location and the gas in the working chamber such as groove 2 will go back to the low-pressure end through the opened by-pass port.

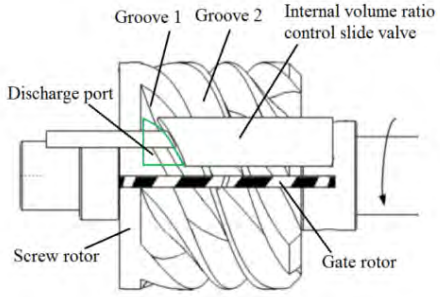

Figure 2:Internal volume ratio slide valve

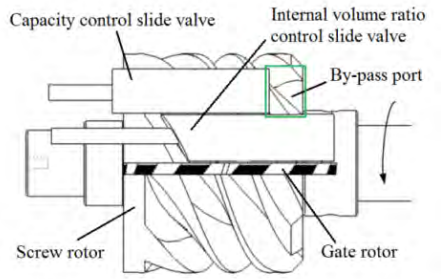

Figure 3:Double slide valve system

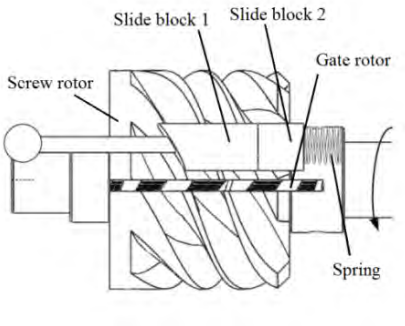

Figure 4:CSV control under full load condition

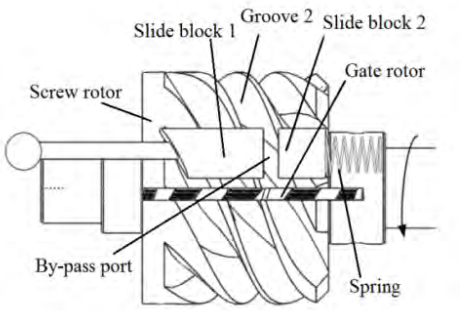

Figure 5:CSV control under part load condition

2.2 Mathematical model

The working chamber is formed by the gate rotor teeth, the screw rotor groove and the shell during the compression process of SSC. In order to facilitate the geometric analysis, the calculation model of a groove of the screw rotor in Fig. 6 was established. The left groove profile is set as *VL* and the right groove profile is set as *VR*. The slide valve structure and screw rotor are expanded in the plane coordinate system. The point *N* which is on the groove profile is the start location where the refrigerant in the working chamber begins to be compressed.

In Fig.6 (b), Δy is the axial distance between the slide block 1 and slide block 2 and *dy* is the axial distance between the slide block 2 and point *N*. When the SSC runs under part load condition and *VL* passes over the point 2, the by-pass port opens to control the capacity and then some refrigerant gas in the compression chamber will go back to the suction tube. The back flow will stop until *VR* passes over the point 1′, At this point, the by-pass port is closed. It is quite clear that the discharge port area will change due to the movement of the slide valve. When *VL* passes over the point 3, the discharge port will open until the discharge process is over. In order to get the effective by-pass area and discharge area, the equation of profile *VL*, *VR* and the four boundary curves of by-pass port should be set up. The calculation method of by-pass area changing with the screw rotation angle can be referred to literature (Wang et al., 2014).

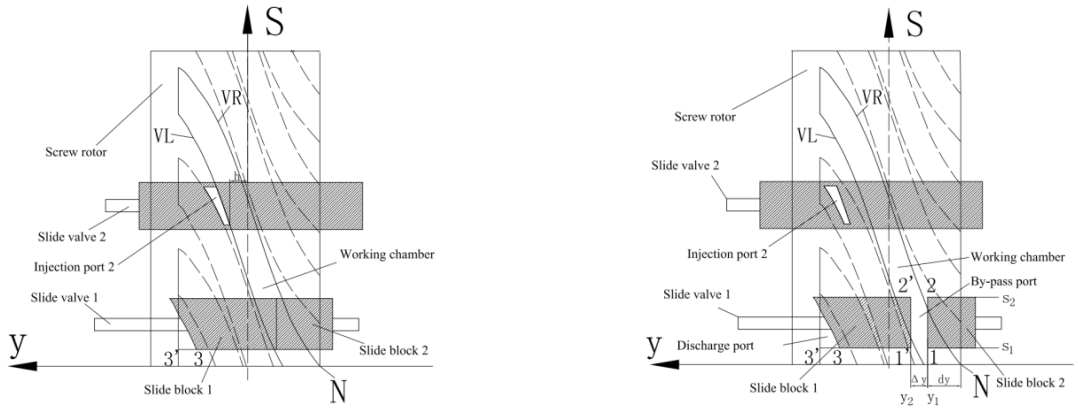

(a) Full load **(b) Part load**

Figure 6: New vapor injection structure and CSV control

2.3 Calculation model of slide valve with vapor injection

Fig. 6 shows that the vapor injection process is concerned with the position of injection port 2 which is indicated by letter *h*. And the effective injection port area under different load condition is also an important factor. The calculation method of injection port area is similar to the method of effective by-pass port area，but there are still differences. The reasons are that the main flow direction of the vapor injection is vertical with the effective injection port. So it is necessary to set up a new plane-coordinate system based on the plane of the injection port projection.

The projection equation of *VL*:

$$f_{TVL}(x_{p1}(\theta), y_{p1}(\theta)): \quad \begin{aligned} y_{p1}(\theta_2) &= a\tan\theta_2 - \frac{b}{2\cos\theta_2} \\ x_{p1}(\theta_1) &= R(1-\cos\theta_1) \end{aligned} \qquad \text{Eq. (1)}$$

The projection equation of *VR*:

$$f_{TVL}(x_{p2}(\theta), y_{p2}(\theta)): \quad \begin{aligned} y_{p2}(\theta_2) &= a\tan\theta_2 - \frac{b}{2\cos\theta_2} \\ x_{p2}(\theta_1) &= R(1-\cos\theta_1) \end{aligned} \qquad \text{Eq. (2)}$$

The *x*-axis is perpendicular to the *y*-axis, *y*-axis is the axial position of screw rotor transmission ratio The effective injection port area $A_T(\theta_2)$ can be expressed by the following equations:

$$A_T(\theta_2) = \begin{cases} 0, & \theta_2 \le \theta_{f_{\min}} \\ Af_{TVL}(\theta_2) - Af_{TVR}(\theta_2), & \theta_{f_{\min}} < \theta_2 < \theta_{b_{\max}} \\ 0, & \theta_2 \ge \theta_{b_{\max}} \end{cases} \qquad \text{Eq. (3)}$$

Where, the effective area $Af_{TVL}(\theta_2)$ is bounded by the projection of *VL* and the injection port, the effective area $Af_{TVR}(\theta_2)$ is bounded by the projection of *VR* and the injection port, the gate rotor angle θ_{fmin} is the minimum value when the injection port and the projection *VL* cross, the θ_{bmax} is the maximum value when the injection port and the projection *VR* cross.

3. THEORETICAL MODEL OF THE VAPOR INJECTION

3.1 Governing equation

In this paper, one screw groove was selected as the control volume which is shown in Fig. 7. Based on the mass balance, the mass changes in the control volume can be expressed as:

$$\frac{dm}{d\theta_1} = \sum \frac{dm_{in}}{d\theta_1} + \sum \frac{dm_s}{d\theta_1} - \sum \frac{dm_{out}}{d\theta_1} \qquad \text{Eq.（4）}$$

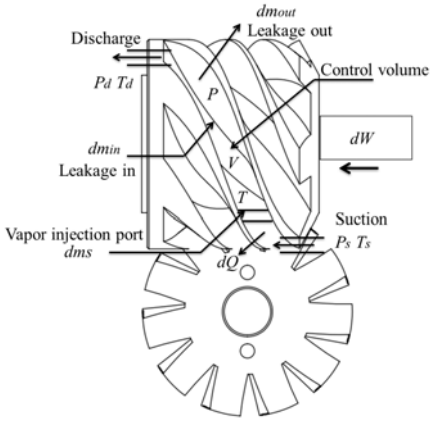

Figure 7: The control volume

The state parameters of the working fluid in the control volume can be obtained as follows:

$$\frac{dp}{\mathrm{d}\theta_1}=\frac{\frac{1}{v}\left[(\frac{\partial h}{\partial v})_T-\frac{(\partial h/\partial T)_v(\partial p/\partial v)_T}{(\partial p/\partial T)_v}\right]\frac{dv}{d\theta}-\frac{1}{V_c}\left[\sum\frac{dm_{in}}{d\theta_1}(h_{in}-h)+\sum\frac{dm_s}{d\theta_1}(h_s-h)-\frac{dQ}{d\theta_1}\right]}{1-\frac{1}{v}\frac{(\partial h/\partial T)_v}{(\partial p/\partial T)_v}} \quad \text{Eq.（5）}$$

$$\frac{dT}{\mathrm{d}\theta_1}=\frac{\left[\frac{1}{v}(\frac{\partial h}{\partial v})_T-(\frac{\partial p}{\partial v})_T\right]\frac{dv}{d\theta_1}-\frac{1}{V_c}\left[\sum\frac{dm_{in}}{d\theta_1}(h_{in}-h)+\sum\frac{dm_s}{d\theta_1}(h_s-h)-\frac{dQ}{d\theta_1}\right]}{(\frac{\partial p}{\partial T})_v-\frac{1}{v}(\frac{\partial h}{\partial T})_v} \quad \text{Eq.（6）}$$

$$\frac{dv}{d\theta_1}=\frac{1}{m}\frac{dV}{d\theta_1}-\frac{V}{m^2}\frac{dm}{d\theta_1} \quad \text{Eq.（7）}$$

The energy conservation law for the control volume can be written as follows:

$$\frac{d(mu)_{\mathrm{cv}}}{\mathrm{d}\theta_1}=\sum\frac{dm_{in}}{\mathrm{d}\theta_1}h_{in}+\sum\frac{dm_s}{\mathrm{d}\theta_1}h_s-\sum\frac{dm_{out}}{\mathrm{d}\theta_1}h_{out}-\frac{dQ}{\mathrm{d}\theta_1}+\frac{dW}{\mathrm{d}\theta_1} \quad \text{Eq.（8）}$$

3.2 Calculation method of the vapor injection process

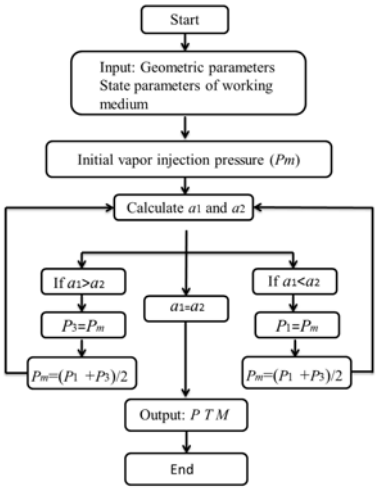

Figure 8: The flowchart of analysis procedure

Fig. 8 shows the flowchart of the analysis procedure. First of all, the geometry parameters of the compressor and operating conditions which are shown in Table 1 should be taken as the initial parameters. Then the governing Eq.(4)~ Eq.(8) can be solved to calculate the state parameters of the working fluid. In order to research the vapor injection process under different vapor injection port

area, the leakage through different leakage paths is negligible in this study. Based on the models, the Runge-Kutta method was used to get the numerical solution of the equations. In Fig.8, a_1 is the vapor injection mass that flow into the compressor and a_2 is the vapor mass that the EVI can provide under the vapor injection pressure. When the value of a_1 is equal to the value of a_2, we can obtain the required state parameters of the working fluid.

Table 1. The main designed geometric parameters

parameters	Value (mm)	parameters	Value
Screw diameter	117	Width of the slide valve 2	20.0 (mm)
Gate rotor diameter	117	Numbers of screw grooves	6
a	35.1	Numbers of gate rotors	11
b	17.15	Rotation speed	2850(rpm)
Length of the slide block 1	36.5	Rated power	27(kW)
Length of the slide block 2	28.0	Theoretical flowing capacity	83.6(m^3/h)
s_1	11.33	Mains frequency	50(HZ)
s_2	45.84	Refrigerant	R22
Length of the slide valve 2	151.0	Lubricating oil	Suniso 4GSD

4. RESULTS AND DISCUSSIONS

4.1 Geometrical relationship

Fig.10 shows the internal volume ratio, pressure ratio and the load control ranges. The axial location of the CSV is marked by the axial distance of the discharge control point 3 on the CSV in Fig. 6. The distance between point 1′ and point 3 is 36.5mm. From Fig.10 (a), we can see that the internal volume ratio and internal pressure ratio tend to increase with the axial distance of slide block 1 increase. And the adjustable ranges of internal volume ratio is 1~8.2 in theory. As shown in Fig.10 (b), the internal volume ratio and capacity adjustment ranges are 1.7~3.0 and 25%-100% respectively. During this process, the internal volume ratio is increasing while the load reduces.

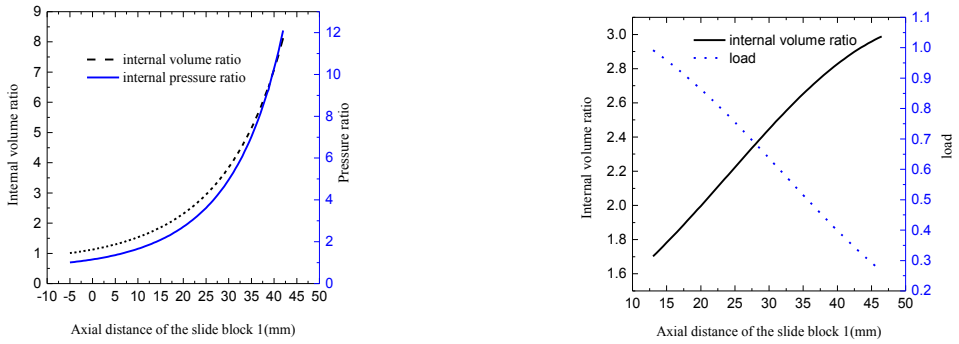

(a) Full load **(b) Part load**

Figure 10: Influence of CSV under full load and part load condition

Fig.11 (a) shows the effective injection port area of different injection port. It can be seen that the vapor injection process of injection port 2 will be longer than other injection port. And the injection port 2 has a higher internal volume ratio which is 1.82. Obviously, the vapor injection technology can also be used under part load condition by moving the slide valve 1 and slide valve 2. The effective areas of injection port 2 which are changing with the gate rotor rotation angle under different load conditions are shown in Fig.11 (b). The vapor injection technology used in part load

condition will improve the performance of ASHP at low environment temperature.

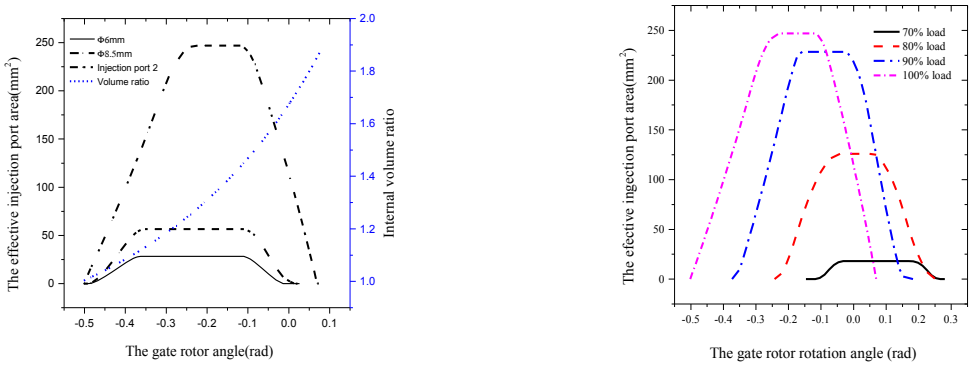

(a) Different injection port **(b) Injection port 2**

Figure 11: Effective injection area changes with the gate rotor rotation angle

4.2 Thermodynamic performances of the vapor injection process

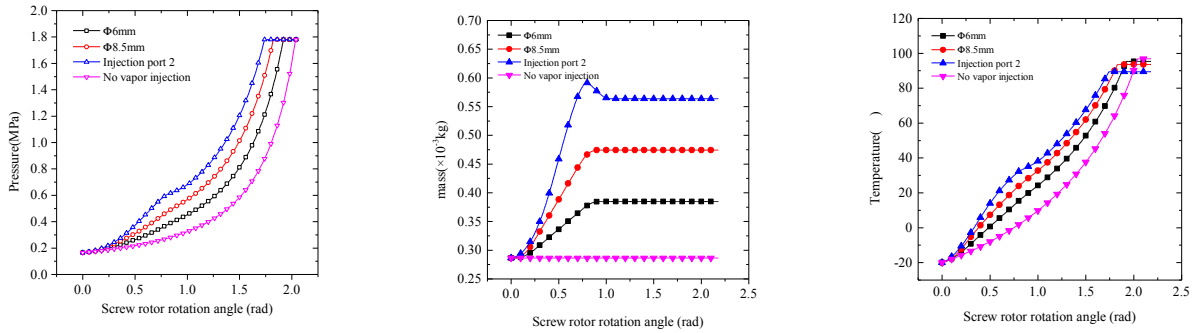

(a) Pressure **(b) Mass** **(c) Temperature**

Figure 12 Main state parameters in the control volume changes with screw rotor rotation angle

Based on the full load condition, the pressure, temperature and mass of the working medium are calculated in this study. From Fig.12, we can see that the pressure will increase with the injection port area increase. Comparing with no vapor injection process, the pressure in the control volume based on the injection port 2 will reach discharge pressure value. The mass flow rate will increase with the injection port area increase. It suggests that the injection port 2 will get more injection flow in a short time and a longer vapor injection process under certain gas pressure. However, the bigger effective injection area might not be good for vapor injection process. It is because that when internal volume ratio is bigger or injection pressure is lower, the pressure in the compression chamber will be higher than that in injection tube, then the gas in the working chamber will go back to the injection tube. So a one-way check valve can be adopted to avoid back-flowing. The discharge temperature based on the injection 2 is lower than other injection port. The results show that vapor injection can decreases the discharge temperature effectively.

5. CONCLUSIONS

The initial angle of the by-pass port when it begins to open is only related to the initial position of slide block 2. When the CSV is used as internal volume ratio control slide valve, the adjustable ranges of internal volume ratio is 1~8.2 in theory. The discharge port initial position has no effect on

the actual capacity of the SSC, but affects the change of the internal volume ratio and the discharge process. The application of the CSV and the new slide valve for vapor injection is advantageous to improve the performance of ASHP based on SSC.

The mass flow rate will increase with the injection port area increase and the discharge temperature of compressor of the vapor injection process can be reduced availability. It is necessary to take further intensive experimental study on the characteristics of the slide valve and vapor injection performance. In general, it is expected that the new structure presented here will be very useful for the investigators to study the ASHP.

ACKNOWLEDGEMENTS

The authors are grateful for the financial support provided by the National Key R&D Program of China (NO.2016YFC0700403), Beijing Municipal Natural Science Foundation (NO.3181001).

NOMENCLATURE

a	central distance between the gate rotor and the screw rotor boundary (mm)	R	radius of the screw and gate rotor (rad)
		m	Mass (kg)
b	tooth width of gate rotor (mm)	Subscripts	
θ_1	the screw rotor angle (rad)	*1*	screw
θ_2	the gate rotor angle (rad)	*2*	Gate rotor
h	specific enthalpy (J/kg)	*cv*	Control volume
P	Pressure (Pa)	*in*	Fluid enter the control volume
T	temperature (℃)	*out*	Fluid leave the control volume
U	internal energy (J)	*s*	Vapor injection

REFERENCES

Bin H, Wang R.Z., 2018. Performance evaluation of different heating terminals used in air source heat pump system. International Journal of Refrigeration, 18, 1-8.

Donghoon Kang, Jihwan Jeong, Byoungjin R, 2018. Heating performance of a VRF heat pump system incorporating double vapor injection in scroll compressor. International Journal of Refrigeration, 96, 50-62.

Wang B, Liu X, Shi W, 2016. Comparative research on air conditioner with gas-injected rotary compressor through injection port on blade. Applied Thermal Engineering,106, 67-75.

Zimmern B and Patel G. C, 1972. Design and operating characters of the zimmern single screw compressors. In: Proceedings of the 1972 Purdue Compressor technology Conference, Purdue University West Lafayette, IN, USA, 17-20, pp. 96-99.

Kamikawa M, Shimoji M, Kouda T, et al., 2016. Screw compressor for refrigerating-cycle apparatus, has economizer port that is formed in auxiliary slide valve and provided to connect compression chamber and economizer gas flow path, and slide valves that are moved separately: WO, 2016046908A1.

Zimmern B and Sur N, 1983. Process to control the delivery of a single screw compressor. Patent 4373866, USA.

Wang Z L, Liu Z, et al., 2014. Research on operating characteristics of single slide valve capacity control mechanism of the single screw refrigeration compressor. Proceedings of the Institution of Mechanical Engineers, Part A: Journal of Power and Energy, 228, 965-977.

Pikute J L, 2010. The compressor with double slide valve. Patent application, CN2007800526.

Manuscript ID: 702
DOI: 10.18462/iir.icr.2019.0702

Heat transfer and pressure drop characteristics of wet air flow in metal foams with different structures and surface wettability during dehumidifying conditions

Haitao Hu, Zhancheng Lai, Guoling DING, Weizhen Han
Institute of Refrigeration and Cryogenics, Shanghai Jiao Tong University,
800 Dongchuan Rd, Shanghai, 200240, China, huhaitao2001@sjtu.edu.cn

ABSTRACT

To optimize the metal foam heat exchangers under dehumidifying conditions, the heat transfer coefficient (HTC) and pressure drop of wet air in metal foams with different structure and surface wettability were obtained experimentally. The pore density of tested metal foams is 5-40 PPI, and the porosity is 0.85-0.95. The wettability includes the hydrophobic, hydrophilic and uncoated surface, with proceeding contact angles from 15.4° to 161.2°. The results show that, the HTC of wet air in metal foams are enhanced by 4%-33% and 2-21% by hydrophobic and hydrophilic coating, respectively; the pressure drops are obviously increased by hydrophobic coating and maximumly decreased by 20% by hydrophilic coating; as PPI increases, the pressure drop in metal foams are increased, while the HTC is firstly increased then decreased at most dehumidifying conditions; as porosity increases, the HTC and pressure drop are both decreased. Considering the comprehensive performance, 20PPI is the best metal foam pore density with best comprehensive performance, while 0.85 and 0.95 are the best porosity for hydrophobic and uncoated metal foams, respectively.
Keywords: Metal foam; Heat transfer; Pressure drop; Surface wettability; Dehumidifying

1. INTRODUCTION

Metal foams have great potential in the heat transfer enhancement under dehumidifying conditions due to its high thermal conductivity and large specific area (Boomsma et al., 2003; Zhao, 2012). In the application of air conditioning systems, the heat exchanger always works at temperature under dew point, and the water vapor in wet air would condense on the cold surface (Hu et al., 2017b). For metal foam heat exchangers under dehumidifying conditions, the interconnection of metal fibers makes the condensate more easily to accumulate in metal foams, resulting in the decrement of heat transfer coefficient and increment of pressure drop (Costa et al., 2014; Mazzei et al., 2005). In order to improve the performance of metal foam heat exchanger, the accumulated condensate should be drained out of the metal foam rapidly.

The key factor for improving the drainage and heat transfer performance in metal foams is the surface wettability of metal fibers (Hu et al., 2017a). The surface wettability determines the condensate model and the adhesive force on the metal fiber surface, which can directly affect the heat transfer and pressure drop characteristics of wet air in metal foams (Liu, 2011; Peng et al., 2015). For the hydrophilic metal foams with large surface wettability, the hydrophilic surface modification could improve the adhesive force of condensate on metal fibers and accelerate the dehumidifying process of wet air (Liu and Jacobi, 2006; Wang et al., 2002), but the increased adhesive force may reduce the drainage performance of metal foam. For the hydrophobic metal foams with small surface wettability, the hydrophobic surface modification could change the condensation model from film wise condensation to dropwise condensation, leading to smaller thermal resistance and larger heat transfer coefficient (Del Col et al., 2017; Rainieri et al., 2009); but the droplet size of condensate is large due to the small wettability (Ganesan et al., 2016), which may block the flow path of wet air in metal foams and increase the pressure drop of wet air in metal foams. In order to quantitative analyze the influence of surface wettability, the influence of surface wettability on the heat transfer and pressure drop characteristics of wet air in metal foams should be known.

For the heat transfer and pressure drop characteristic in metal foams, the existing research mainly focuses on the dry air, and there are only two published papers on wet air in metal foams. The research results on the heat transfer and pressure drop characteristics of dry air show that, both the heat transfer coefficient and pressure drop increase with the increasing PPI (Hwang et al., 2002) and the decreasing porosity (Dukhan, 2006); PPI has a more significant effect on the heat transfer than porosity (Zhao et al., 2004); the optimal porosity based on the balance between pressure drop and heat transfer varies from 0.85 to 0.95 (Zhao et al., 2004). The research results on wet air in metal-foam heat exchangers show that, the heat transfer capacity of copper-foam heat exchanger is enhanced by 56%-196% compared to that of the fin-and-tube heat exchanger (Hu et al., 2016); the heat transfer coefficient under wet condition is slightly higher than that under dry condition (Han et al., 2012). The latent heat transfer and condensate retention make the heat transfer and pressure drop characteristics of wet air in metal foam under dehumidifying conditions much different from that of dry air. Therefore, the existing research results on the dry air cannot be extended to the dehumidifying conditions.

The purpose of the present study is to experimentally investigate the heat transfer and pressure drop characteristics of wet air in metal foams with different wettability under dehumidifying conditions, and to analyze the influence of structure and surface wettability on the performance of metal foams.

2. DESIGN OF EXPERIMENT

2.1. Experimental rig

The experimental apparatus for investigating the heat transfer and pressure drop characteristic of wet air in metal foams with various wettability is shown in Fig. 1. The experimental apparatus consists of wet air side system, cooling water system and data acquisition system. More detail of the experimental apparatus was introduced in the literature (Hu et al., 2016).

The metal foam test sample is composed of copper plate and copper foam. The copper foam and copper plate are welded together by a copper-based amorphous solder at 700°C in a vacuum furnace to reduce the thermal contact resistance. The thermal contact resistance caused by brazing bonding can be neglected, which only accounts for lower than 1% of the total thermal resistance of test sample. In the present study, the PPI (pore number per inch) of tested metal foams is 5-40PPI, and the porosities of tested metal foams are 85%, 90% and 95%, as shown in Fig.2.

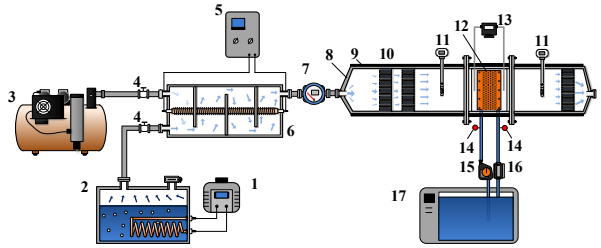

Figure 1: Schematic diagram of experimental rig



Figure 2: Metal foams in the experiment

2.2. Fabrication of hydrophobic and hydrophilic coating

The hydrophilic coating on metal surface was fabricated by the following procedures. Firstly, the copper surface was washed in an ultrasonic cleaner by hydrochloric acid, alcohol and acetone respectively. Secondly, the cleaned copper surface was immersed in an aqueous solution of sodium hydroxide (NaOH) with concentrations of 2.5 mol·L^{-1} and ammonium persulphate ($(NH4)_2S_2O_8$) with concentrations of 0.1 mol·L^{-1} at room temperature for 30 min. Finally, the copper surface is wash by deionized water and dried in nitrogen flow. Then the hydrophilic CuO/$Cu(OH)_2$ micro/nanostructures would be formed on copper surface.

The hydrophobic coating on metal surface was fabricated by the following procedures. Firstly, the fabrication of CuO/Cu(OH)$_2$ micro/nanostructures are conducted on copper surface. Then, the surface with CuO/Cu(OH)$_2$ micro/nanostructures was removed from the solution, washed by deionized water, and then immersed in a 1%wt 1-dodecanethiol/alcohol solution for 15 min. Finally, the surface was removed from the solution, washed by alcohol for 3 min and heated in a vacuum oven at 100 °C for 1 hour.

The metal foams with different wettability (hydrophilic, uncoated and hydrophobic) are shown in Fig. 3. The SEM photos of the coated surfaces are taken to reveal the micro-structures of the hydrophilic and hydrophobic surface, as shown in Fig. 4 (FESEM, Sirion200, FEI Company, USA). The FTIR spectra of hydrophilic and hydrophobic coated surface is used to ensure the formation of coating monolayer because the characteristic bands in FTIR spectra correspond to the vibrations of bonds, as shown in Fig. 5 (Nicolet iN10 MX, Thermo Scientific, USA). The contact angles of metal surface with different surface wettability are measured by optical contact angle measuring device (KINO Industry Co., Ltd., USA). The proceeding and receding contact angles are shown in Table 1.



(a) hydrophilic (b) uncoated (c) hydrophobic
Figure 3: Metal foams with different wettability

Table 1. Contact angles of different samples

Tested sample	Proceeding contact angle (θ_A)	Receding contact angle (θ_R)	Contact angle hysteresis (θ_H)
Hydrophilic	15.4	7.3	8.1
Uncoated	89.2	62.1	27.1
Hydrophobic	163.9	149.1	14.8

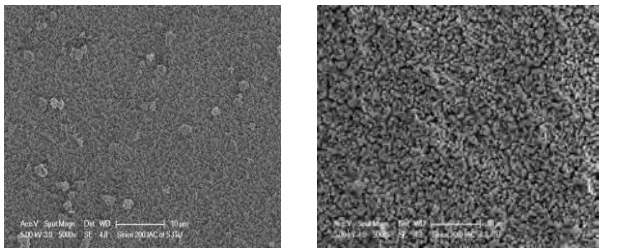

(a) hydrophilic coating (b) hydrophobic coating
Figure 4: SEM photos of different wettability

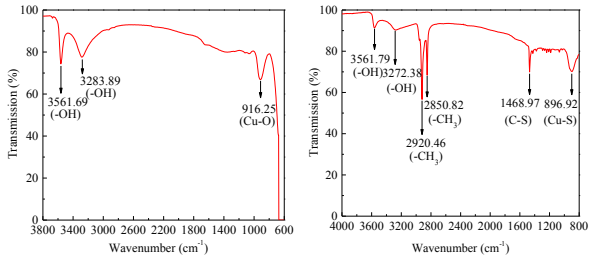

(a) hydrophilic coating (b) hydrophobic coating
Figure 5: FTIR spectra of different wettability

3. DATA REDUCTION AND UNCERTAINTIES

3.1. Data reduction

The heat transfer coefficient h_a for the wet conditions is calculated by the logarithmic mean enthalpy difference (LMED) method is used, as shown in Eqs. (1)-(6):

$$\frac{1}{HA}=\frac{1}{\left(\eta_o h_a A_a / Cp_a\right)_a}+\frac{1}{\left(h_w A_w / b\right)_w}+b\frac{\delta}{kA_w}=\frac{\Delta i_{LM}}{Q} \quad \text{Eq. (1)}$$

$$\Delta i_{LM}=F\frac{\left(i_{a,in}-i_{w,out}\right)-\left(i_{a,out}-i_{w,in}\right)}{ln\left(\frac{i_{a,in}-i_{w,out}}{i_{a,out}-i_{w,in}}\right)} \quad \text{Eq. (2)}$$

$$Q=\frac{1}{2}\left(Q_a+Q_w\right) \quad \text{Eq. (3)}$$

$$Q_a=m_{dehumid}\gamma_w+m_{a,dry}Cp_a\Delta T_a+\left(m_{a,dry}d_{in}-m_{dehumid}\right)Cp_v\Delta T_a+m_{dehumid}Cp_v\left(T_{a,in}-T_{a,dew}\right) \quad \text{Eq. (4)}$$

$$Q_w=m_w Cp_w\left(T_{w,in}-T_{w,out}\right) \quad \text{Eq. (5)}$$

$$m_{\text{dehumid}} = m_{\text{a,dry}} \left(d_{\text{in}} - d_{\text{out}} \right)$$ Eq. (6)

where, HA is the heat transfer coefficient based upon the enthalpy difference, kg·s^{-1}; Δi_{LM} is the logarithmic mean enthalpy difference, kJ·kg^{-1}; F is the flow configuration factor (Incropera, 1985); $i_{\text{a, in}}$, $i_{\text{a, out}}$, $i_{\text{w, in}}$ and $i_{\text{w, out}}$ are the enthalpy of wet air and water at the inlet and outlet of the test section, kJ·kg^{-1}; h_{w} is the water side heat transfer coefficien, W·m^{-2}K^{-1}; k is the thermal conductivity of copper plate, W·m^{-1}K^{-1}; δ is the thickness of copper plate, m; A_{w} is the heat transfer area of water side, A_{a} is heat transfer area of air side and is equal to the base area of copper plate, m^2; b is the slope of saturated enthalpy line evaluated at average water side copper plate temperature, (Zhao et al., 2004); h_{a} is the global heat transfer coefficient on air side, which is calculated based on the heat transfer area on copper plate (Mancin et al., 2012).

The Colburn j factor and friction factor f are calculated by Eqs. (7)-(8):

$$j = \frac{Nu_{\text{a}}}{Re_{\text{a}} \cdot Pr_{\text{a}}^{1/3}}$$ Eq. (7)

$$f = \frac{2\Delta pD}{\rho u^2 L}$$ Eq. (8)

where Nu, Re and Pr are the Nusselt number, Reynolds number and Prandtl number, respectively; u is the wet air velocity, m·s^{-1}; ρ is the density of wet air, kg·m^{-3}; ∆p is the pressure drop of wet air flow, Pa; D is the hydraulic diameter of the flow passage; L is the effective length of metal foam test sample, m.

3.2. Uncertainties

The experimental uncertainties are estimated with the analysis method of error propagation. The maximum uncertainty of heat transfer coefficient, Colburn j factor and friction factor f are ±13.5%, ±14.0% and ±4.8%, respectively. The maximum uncertainty of comprehensive performance index $j \cdot f^{1/3}$ is ±15.6%.

4. EXPERIMENTAL RESULTS AND ANALYSIS

4.1. Effect of pore density on heat transfer and pressure drop characteristics

The heat transfer and pressure drop characteristics of wet air in metal foams with various pore density was shown in Fig. 6.

Fig. 6(a) shows the influence of PPI on heat transfer coefficient of wet air in metal foam is different at various relative humidity. At low relative humidity (30% and 50%), the heat transfer coefficient of wet air always increases as PPI increases; while at high relative humidity (70% and 90%), the heat transfer coefficient of wet air initially increases then decreases as PPI increases, presenting a maximum increment of 16%~21% for 20PPI metal foam. The reason for this phenomenon is explained with the different heat transfer area of metal foams. At low relative humidity (30%, 50%), the heat transfer area always increases as PPI increases, leading to the increment of heat transfer coefficient; while at high humidity (70%, 90%), with the accumulated condensate water in metal foam occupying heat transfer area, the heat transfer area initially increases then decreases as PPI increases from 5 to 40, resulting in the maximum heat transfer coefficient of 20PPI metal foam. The influence of PPI on heat transfer coefficient shows similar tendency at various inlet air temperatures, air velocities, and cooling water temperatures.

Fig. 6(b) shows the influence of PPI on pressure drop of wet air flow in metal foam under various experimental conditions. As PPI increases, the pressure drop always increases, and the maximum increments are within 272%-486% under various conditions. The reason for the increment of pressure drop is explained as follow. Firstly, as PPI increased, the length and diameter of metal fiber is decreased, and the pore size is decreased, resulting in the increase of flow disturbance and resistance. Secondly, with the increase of PPI, the heat transfer area of metal foam is increased and the cell volume of metal foams is decreased, which leads to more accumulated water condense and adhere to the fiber surface, blocking the flow path and resulting in the increment of pressure drop.

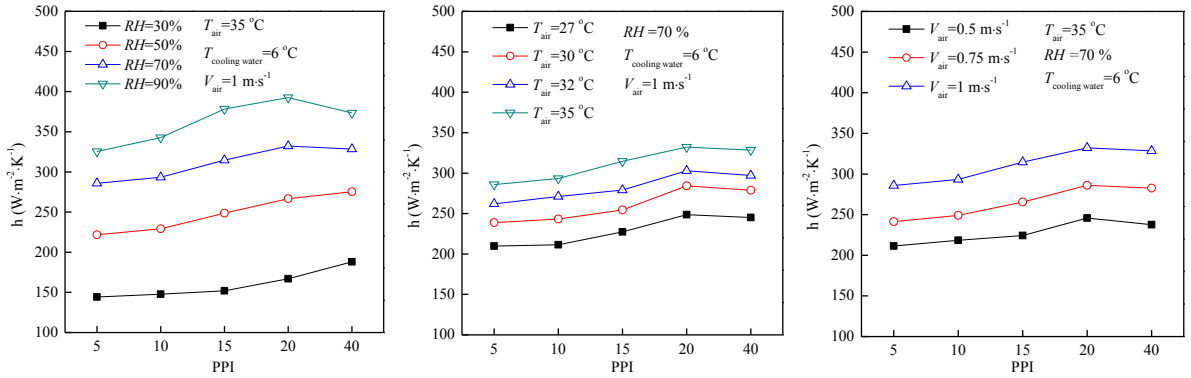

(a) Heat transfer

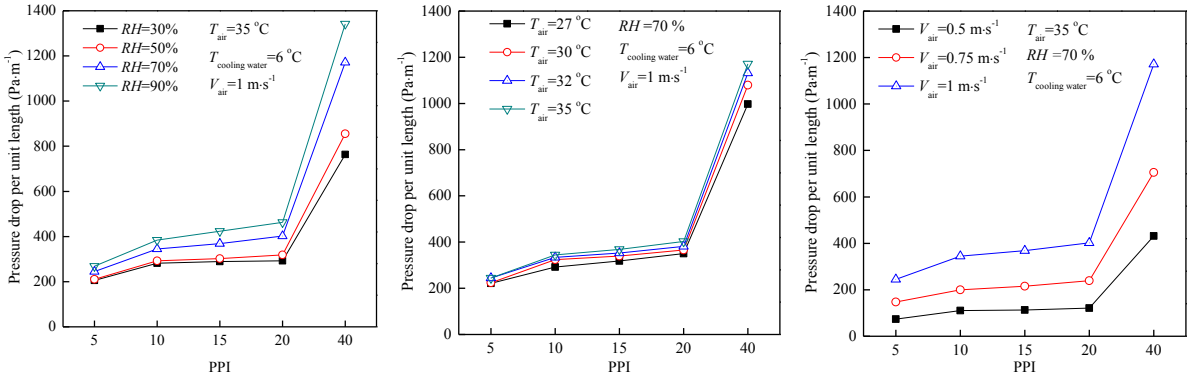

(b) Pressure drop

Figure 6: Effect of pore density on the heat transfer and pressure drop in metal foam

4.2. Effect of porosity on of heat transfer and pressure drop characteristics

Fig. 7 shows the evariation of heat transfer and pressure drop characteristics of wet air in metal foams with virous porosity.

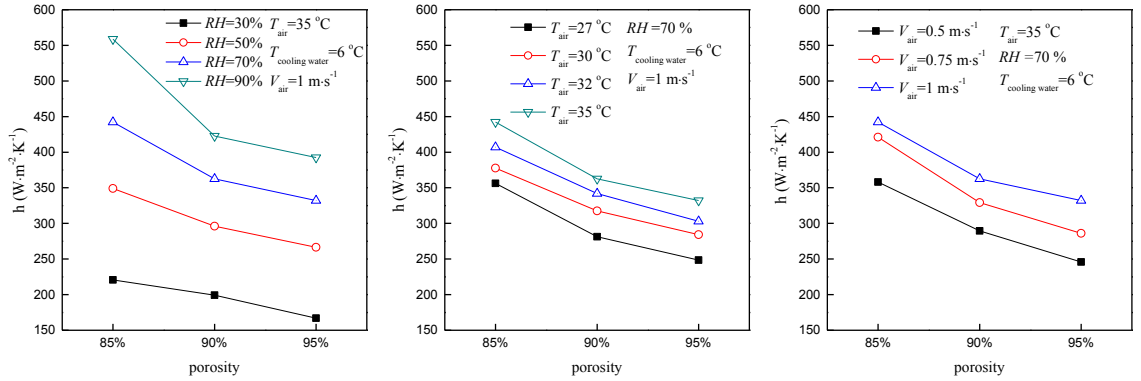

(a) Heat transfer

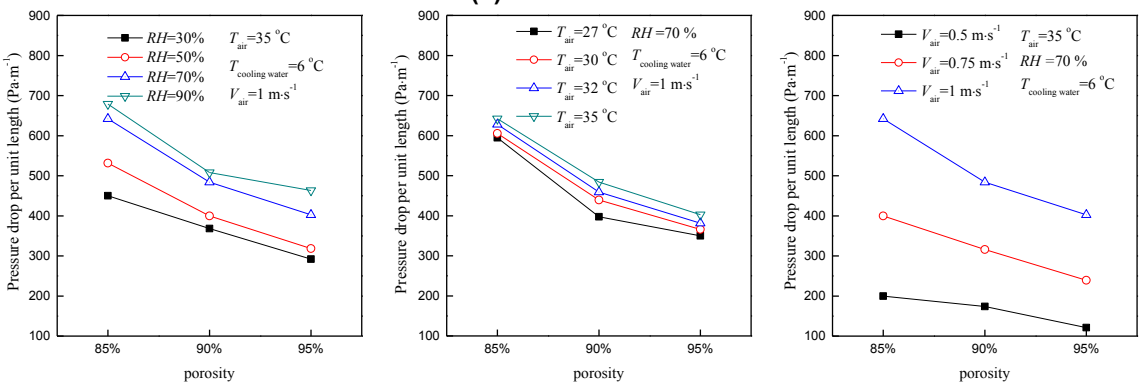

(b) Pressure drop

Figure 7: Effect of porosity on the heat transfer and pressure drop in metal foam

As porosity increases from 85% to 95%, the heat transfer coefficient of wet air is decreased by 22%-32%; with the increment of porosity from 85% to 95%, the heat transfer coefficient of wet air is reduced by 22%, 24%, 25% and 30% at relative humidity of 30%, 50%, 70% and 90%, respectively. The reason for this phenomenon is that the larger fiber diameter and larger specific surface area of metal foam with porosity of 85% leads to better thermal conduction and larger latent heat transfer with more condensate water.

The influence of porosity on the pressure drop of wet air is more obvious at high relative humidity and high air velocity conditions due to the larger condensate water quantity in metal foam; as porosity increases from 85% to 95%, the pressure drop of wet air flow in metal foam decreases by 32%-47%. The reason for this phenomenon is that, as porosity decreases, the fiber diameter is increased, the air volume in metal foam is smaller. The larger cross section area of metal fibers could cause more flow obstruction, which contributes to the larger pressure drop. The increase of copper volume and heat transfer area also enhanced the heat transfer in metal foam, resulting in more condensate and larger pressure drop.

4.3. Effect of surface wettability on heat transfer and pressure drop characteristics

The effect of surface wettability on the heat transfer and pressure drop characteristics of wet air in metal foam is shown in Fig. 8.

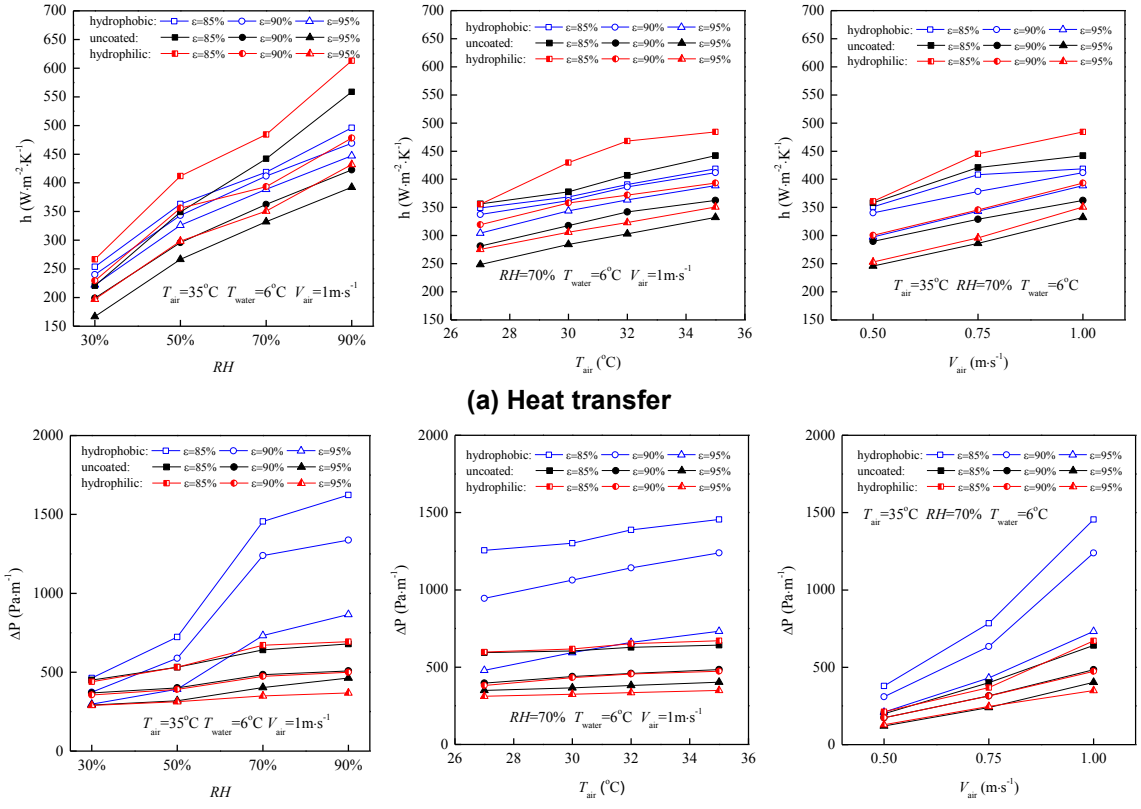

(a) Heat transfer

(b) Pressure drop

Figure 8: Effect of wettability on the heat transfer and pressure drop in metal foam

Compared with uncoated metal foam, the heat transfer coefficient in hydrophilic metal foams is larger, while the heat transfer coefficient in hydrophobic metal foams is larger at most experimental conditions expect for the porosity of 85% and relative humidity of 70%-90%; as relative humidity increases from 30% to 90%, the heat transfer coefficient in metal foams with different wettability are increased by 88%-153%. The heat transfer coefficient in hydrophilic metal foam is larger than that in hydrophobic one at porosity of 85%, while it is smaller than that in hydrophobic metal foam at porosity of 90%-95%.

The pressure drop of wet air in hydrophobic metal foams is larger than that in uncoated metal foams, while the pressure drop in hydrophilic metal foams is smaller than that in uncoated metal foams; as relative humidity increases from 30% to 90%, the pressure drop in hydrophilic and uncoated metal foams is increased by 27%-59%, but the pressure drop in hydrophobic metal foams is increased by

165%-258%. The reason for the more obvious increment of pressure drop in hydrophobic metal foams is that, the larger contact angle of hydrophobic surface leads to the larger condensate droplet size during the dropwise condensation, and the large droplets stay in metal foam and blocks the wet air flow path, resulting in the large increment of pressure drop.

4.4. Comparison of comprehensive performance of metal foams with different wettability

The comprehensive performance index ($j \cdot f^{-1/3}$) of metal foams with different wettability are shown in Fig. 9. As porosity increases, $j \cdot f^{-1/3}$ of uncoated and hydrophilic metal foams are decreased, while $j \cdot f^{-1/3}$ of hydrophobic metal foams are increased. The $j \cdot f^{-1/3}$ of hydrophilic metal foams are larger than those of hydrophobic metal foams. The $j \cdot f^{-1/3}$ of hydrophobic metal foams is larger than that of uncoated metal foam at most experimental conditions except for the porosity of 95% and small condensate quantity conditions.

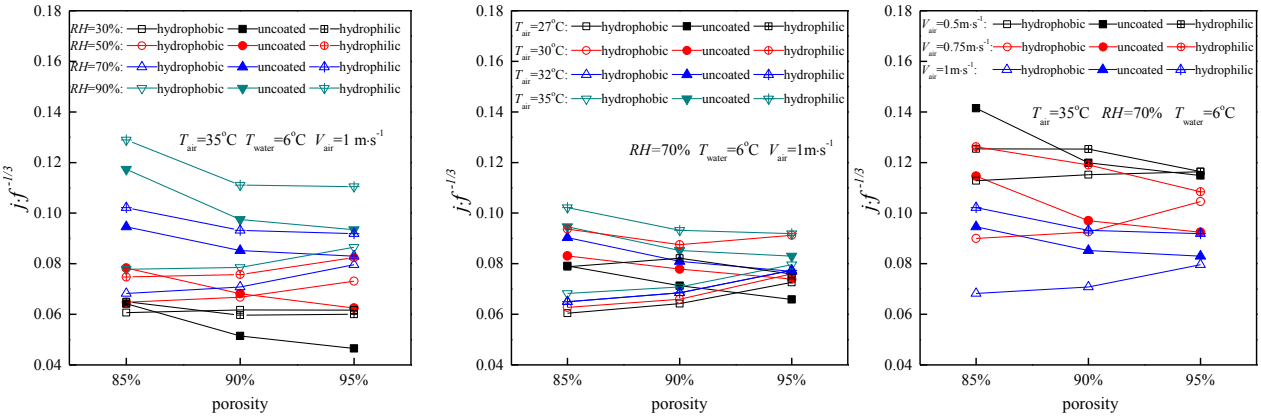

(a) at different relative humidity (b) at different air temperatures (c) at different air velocities

Figure 9: Comprehensive performance index ($j \cdot f^{-1/3}$) of metal foams with different wettability

5. CONCLUSIONS

(1) As PPI increases from 5 to 40, at low relative humidity, the heat transfer coefficient always increases; while at high relative humidity, the heat transfer coefficient initially increases then decreases, presenting a maximum increment of 12%-21% for 20PPI metal foam;

(2) As porosity increases from 85% to 95%, the heat transfer coefficient decreases by 22-32%, and the pressure drop decreases by 32%-47%;

(3) The heat transfer coefficient in hydrophobic and hydrophilic metal foams are larger by 4%-33% and 3-21% than that in uncoated metal foams, respectively;

(4) The pressure drop in hydrophobic metal foams is larger by 3%-139% than that in uncoated metal foams, while the pressure drop in hydrophilic metal foams is smaller by 1%-20% than that in uncoated metal foams;

(5) The comprehensive performance of hydrophilic metal foam under dehumidifying condition is better than that of hydrophobic and uncoated metal foams.

ACKNOWLEDGEMENTS

This study is supported by National Natural Science Foundation of China (No.51576122) and Program of Shanghai Academic Research Leader (No. 16XD1401500).

NOMENCLATURE

A	Area (m^2)	T	Temperature (K)
b	Slope of saturated ehthalpy line ($kJ \cdot kg^{-1}K^{-1}$)	ΔT	Temperature difference (K)
Cp	Specific heat at constant pressure ($kJ \cdot kg^{-1}K^{-1}$)	u	Velocity ($m \cdot s^{-1}$)
D	Hydraulic diameter (m)	L	Length (m)

f	Friction factor, non-dimensional	m	Mass transfer rate ($kg \cdot s^{-1}$)
h	Heat transfer coefficient ($W \cdot m^{-2} \cdot K^{-1}$)	Nu	Nusselt number, non-dimensional
HA	Heat transfer coefficient based upon enthalpy difference ($kg \cdot s^{-1}$)	PPI	Number of pores per inch
i	Enthalpy ($kJ \cdot kg^{-1}$)	Pr	Prandtl number, non-dimensional
j	Colburn j factor, non-dimensional	Δp	Pressure drop (Pa)
k	Thermal conductivity ($W \cdot m \cdot K^{-1}$)	Q	Heat transfer rate (W)

REFERENCES

Boomsma, K., Poulikakos, D., Zwick, F., 2003. Metal foams as compact high performance heat exchangers. Mechanics of Materials 35, 1161-1176.

Costa, C., Miranda, V., Mantelli, M., Da Silva, A., Modenesi, C., Furlan, L., 2014. Experimental study of flexible, unstructured metal foams as condensation structures. Experimental Thermal and Fluid Science 57, 102-110.

Del Col, D., Parin, R., Bisetto, A., Bortolin, S., Martucci, A., 2017. Film condensation of steam flowing on a hydrophobic surface. International Journal of Heat and Mass Transfer 107, 307-318.

Dukhan, N., 2006. Correlations for the pressure drop for flow through metal foam. Experiments in Fluids 41, 665-672.

Ganesan, P., Vanaki, S.M., Thoo, K., Chin, W., 2016. Air-side heat transfer characteristics of hydrophobic and super-hydrophobic fin surfaces in heat exchangers: A review. International Communications in Heat and Mass Transfer 74, 27-35.

Han, X., Kashif, N., Bock, J., Jacobi, A.M., 2012. Open-cell metal foams for use in dehumidifying heat exchangers.

Hu, H., Lai, Z., Ding, G., Zhuang, D., Weng, X., 2017a. Experimental investigation on water drainage characteristics of open-cell metal foams with different wettabilities. International Journal of Refrigeration.

Hu, H., Lai, Z., Weng, X., Ding, G., Zhuang, D., 2017b. Numerical model of dehumidifying process of wet air flow in open-cell metal foam. Applied Thermal Engineering 113, 309-321.

Hu, H., Weng, X., Zhuang, D., Ding, G., Lai, Z., Xu, X., 2016. Heat transfer and pressure drop characteristics of wet air flow in metal foam under dehumidifying conditions. Applied Thermal Engineering 93, 1124-1134.

Hwang, J., Hwang, G., Yeh, R., Chao, C., 2002. Measurement of interstitial convective heat transfer and frictional drag for flow across metal foams. Transactions-American Society Of Mechanical Engineers Journal Of Heat Transfer 124, 120-129.

Incropera, F.P., 1985. Fundamentals of Heat and Mass Transfer. Wiley.

Liu, L., 2011. Effects of air-side surface wettability on the performance of dehumidifying heat exchangers. University of Illinois at Urbana-Champaign.

Liu, L., Jacobi, A.M., 2006. The effects of hydrophilicity on water drainage and condensate retention on air-conditioning evaporators.

Mancin, S., Zilio, C., Diani, A., Rossetto, L., 2012. Experimental air heat transfer and pressure drop through copper foams. Experimental Thermal and Fluid Science 36, 224-232.

Mazzei, P., Minichiello, F., Palma, D., 2005. HVAC dehumidification systems for thermal comfort: a critical review. Applied Thermal Engineering 25, 677-707.

Peng, B., Ma, X., Lan, Z., Xu, W., Wen, R., 2015. Experimental investigation on steam condensation heat transfer enhancement with vertically patterned hydrophobic–hydrophilic hybrid surfaces. International Journal of Heat and Mass Transfer 83, 27-38.

Rainieri, S., Bozzoli, F., Pagliarini, G., 2009. Effect of a hydrophobic coating on the local heat transfer coefficient in forced convection under wet conditions. Experimental Heat Transfer 22, 163-177.

Wang, C.-C., Lee, W.-S., Sheu, W.-J., Chang, Y.-J., 2002. A comparison of the airside performance of the fin-and-tube heat exchangers in wet conditions; with and without hydrophilic coating. Applied Thermal Engineering 22, 267-278.

Zhao, C., 2012. Review on thermal transport in high porosity cellular metal foams with open cells. International Journal of Heat and Mass Transfer 55, 3618-3632.

Zhao, C., Kim, T., Lu, T., Hodson, H., 2004. Thermal transport in high porosity cellular metal foams. Journal of Thermophysics and Heat Transfer 18, 309-317.

Manuscript ID: 725
DOI: 10.18462/iir.icr.2019.0725

Visualization investigation on the expansion state of the primary flow in a transcritical CO_2 two-phase ejector

Yafei LI[(a)], Jianqiang DENG[(a,*)], Li MA[(a)], Yang HE[(a)], Lixing ZHENG[(b)]

[(a)] School of Chemical Engineering and Technology, Xi'an Jiaotong University
Xi'an, 710049, China, lyfxjtu@stu.xjtu.edu.cn, dengjq@mail.xjtu.edu.cn
[(b)] Department of Power Engineering, Shanxi University, Taiyuan, 030006, China,
lxzheng@sxu.edu.cn

ABSTRACT

The expansion state of the primary flow in a two-phase ejector plays an important role in the pressure distribution and phase change position in the primary nozzle. A two-phase CO_2 visualization ejector was designed to investigate the expansion state of the primary flow under various operating conditions and nozzle diverging angles. The results showed that the pressure drop scope in the primary nozzle increased as the secondary flow pressure decreased, and the secondary flow pressure had an insignificant effect on the phase change position in the primary nozzle. With increasing the nozzle diverging angle, the expansion of the primary flow was strengthened resulting in a larger pressure drop in the primary nozzle, and the primary flow shifted from the under-expanded state to the over-expanded state. The study was significant to understand the working mechanism of a two-phase CO_2 ejector and provide a reference for the ejector optimum design.
Keywords: CO_2, Two-phase ejector, Visualization measurement, Expansion.

1. INTRODUCTION

CO_2 is one of the promising environmentally friendly refrigerant (GWP is 1, ODP is 0), which has attracted increasing attention (Bansal, 2012). Due to its low critical temperature, CO_2 refrigeration cycle is inevitably working at transcritical operation state and owning a large throttling loss. In order to improve the coefficient of performance (COP) of a CO_2 refrigeration system, ejector was proposed as an effective method to recover expansion loss (Elbel, 2016). Deng et al. (2007) presented a thermodynamic analysis on a transcritical CO_2 ejector expansion refrigeration cycle (EERC) and showed that the maximum COP was 22.0% better than that of the vapor compression refrigeration cycle, and the cooling capacity could be improved by 11.5%. Ahammed et al. (2014) implemented a numerical simulation on the CO_2 EERC, and their results revealed that the COP enhanced by 21%. The experimental investigation of Elbel and Hrnjak (2008) indicated that the COP of the EERC could be improved by 7%, and the cooling capacity could be enhanced by 8% compared to the conventional CO_2 system. Lucas and Koehler (2012) conducted an experimental comparison between the standard CO_2 expansion valve refrigeration cycle and the ejector refrigeration cycle. Their results claimed that the ejector could improve the COP by 17%.

Geometrical parameters of the ejector play a major role in its performances. Elbel (2011) studied the effect of diffuser angles and mixing section lengths on the CO_2 two-phase ejector performances experimentally. It was found that the smaller diffuser angle and shorter mixing section length generally yielded higher ejector efficiency, entrainment ratio and pressure lift ratio, and the optimum diffuser angle was 5o. Nakagawa et al. (2010) experimentally analyzed the CO_2 two-phase ejector performances for different mixing cross-sectional areas using a rectangular ejector. Their results indicated that smaller mixing cross-sectional area produced higher ejector efficiency due to its higher pressure recovery and entrainment ratio. Nakagawa et al. (2011) also carried out an experiment to determine the effect of mixing length on the performance of the CO_2 two-phase ejector. The results showed that the ejector with the shortest mixing section, 5 mm, yielded the smallest pressure recovery and COP. The middle mixing length of 15 mm provided the highest pressure recovery, entrainment ratio and COP. Palacz et al. (2016) ran a CFD simulation to optimize the mixer length, the mixer diameter and the premixing chamber length of a CO_2 two-phase ejector using the genetic algorithm and the evolutionary algorithm. The results indicated that the mixer diameter had the most crucial influence on the ejector efficiency. Subsequently, Palacz et al. (2017) selected six parameters

containing geometric parameters of ejector mixing section and nozzle for the optimization procedure, and the optimization results showed that the ejector efficiency enhanced by 6%.
Although the ejector owns a simple structure, the flow inside the ejector is complex, such as supersonic, shock wave, turbulent mixing and phase change (Chen et al., 2015). With the development of optical technology, visualization methods are available to capture the flow field inside the ejector. Bouhanguel et al. (2011) experimentally observed the shock structure, mixing process, turbulent structures and flow instability in a supersonic air ejector with laser tomography techniques. Rao and Jagadeesh (2014) employed the time resolved schlieren and laser scattering visualization technique to explore the mixing process of a supersonic air ejector, and their visualization images showed that the non-mixed length was 4.5 to 5.2 times the height of the mixing duct. Little and Garimella (2016) visualized the condensation phenomena in a two-phase R134a ejector using the shadowgraph method. Zhu et al. (2016) used the direct photography method to investigate the primary flow expansion angles in the pre-mixing chamber and the mixing phenomenon in the mixing chamber of a transcritical CO_2 ejector for various operating conditions. Li et al. (2018) utilized the direct photography method to study the phase change phenomena inside the primary nozzle of a transcritical CO_2 ejector under various primary flow operating conditions. The visualization images found that the phase change could start after or before the throat based on the operating conditions. In addition, the phase change position moved upwards when the primary flow inlet pressure and temperature decreased simultaneously.
The primary nozzle is the very crucial component of an ejector, where the primary flow passes through and a rapid expansion occurs. For the transcritical CO_2 two-phase ejector, the investigation on the effect of primary nozzle structures on the expansion state of the primary flow is rare. This present work is intended to assess the effect of the primary nozzle divergent angle and operating conditions on the primary flow expansion state and phase change. In the present study, the direct photography method was used to visualize the flow field inside the CO_2 ejector, and the primary nozzle axial pressure distribution was also measured simultaneously.

2. EXPERIMENTAL SETUP

2.1. Experimental system

The experiment was carried out in a transcritical CO_2 ejector expansion system, as illustrated in Fig. 1. The system mainly contains a compressor, a gas cooler, an ejector, an evaporator, an expansion valve and a gas-liquid separator. The working process can be roughly described as follows: the CO_2 vapor from the separator is sucked into a compressor and compressed to the supercritical state. The supercritical CO_2 is cooled by the gas cooler and then enters the primary nozzle of the ejector. The liquid CO_2 from the separator is evaporated after being throttled by an expansion valve, and then the low-pressure superheated CO_2 vapor is entrained into the ejector and mixed with the primary flow. The mixed flow from the ejector outlet is discharged to the gas-liquid separator with a recovered intermediate pressure.

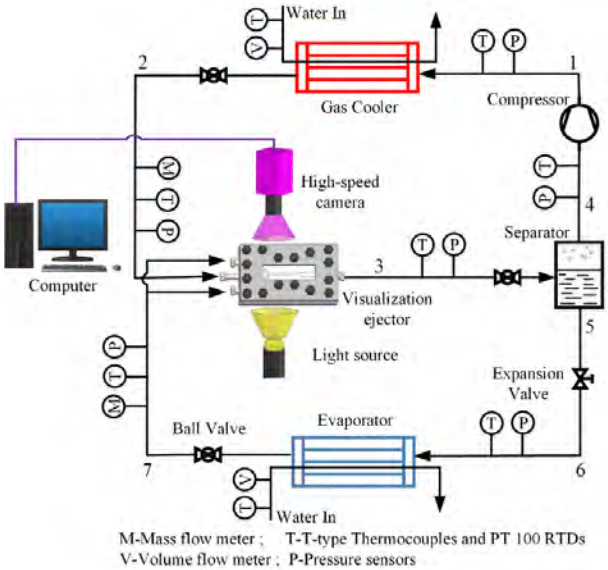

Figure 1: Schematic diagram of the transcritical CO_2 ejector expansion system

The compressor Dorin CD-300H was a prototype semi-hermetic reciprocating type compressor, and an inverter was used to change the compressor frequency. The gas cooler and the evaporator were counter-flow heat exchangers, which were composed of copper and wound into spiral coils. In the heat exchangers, the refrigerant flowed through the inner tubes, and the water flowed through the annulus inversely. The volume of the cylinder separator was 7.4 dm^3. The detailed structure parameters of the experiment components were contained in the reference (Li et al., 2018) and were omitted here.

2.2. Visualization ejector

The visualization ejector was designed with a rectangular cross-section to provide a clear and undistorted optical window, as shown in Fig. 2. It was formed by the stainless steel plate A and B, the transparent PC (polycarbonate) plate A and B, the transparent PET (polyethylene terephthalate) plate A and B with a thickness of 0.5 mm as well as the ejector stainless steel plate. During the test, it was important to keep the surfaces of the transparent material bright and clean. Moreover, all plates should be polished to ensure a good seal when assembled and pressurized. The primary flow inlet, the secondary flow inlet and the outlet were located at the stainless steel plate B, and there were four pressure measurement tubes on the stainless steel plate A to measure the pressure of the primary flow. The stainless steel plate was the core component, which consisted of the primary nozzle, pre-mixing chamber, mixing chamber and diffuser, as illustrated in Fig. 3. Its geometric parameters were marked in Fig. 3 and listed in Table 1. In the experiment, keeping the length of converging section of nozzle invariable and altering the nozzle diverging angle, three ejector stainless steel plates with various nozzle diverging angles were manufactured, and the three nozzle diverging angles were given in Table 1.

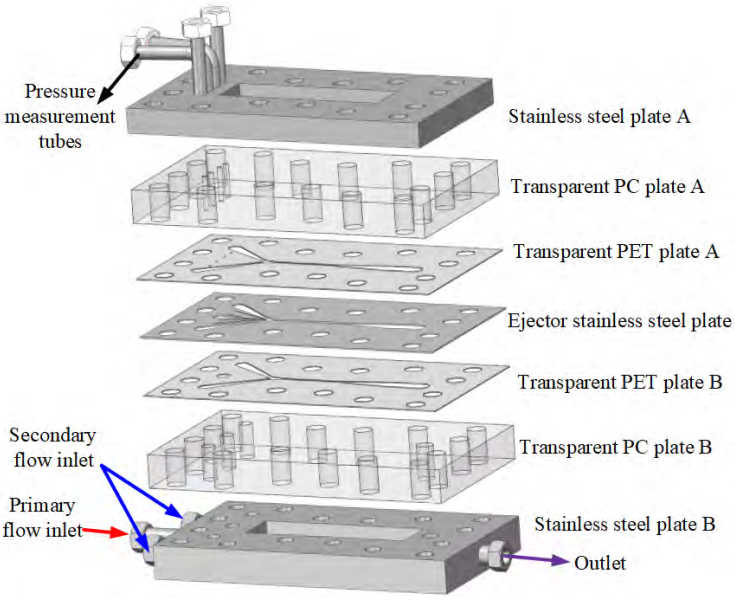

Figure 2: Schematic diagram of the visualization ejector

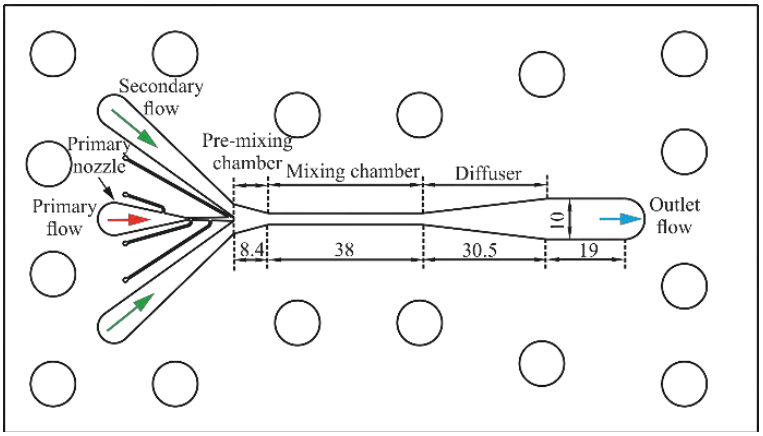

Figure 3: Schematic diagram of the ejector stainless steel plate

Table 1. Main geometric parameters of the ejector stainless steel plate

Parameter	Value	Schematic diagram of nozzle
Width of mixing chamber	2.82 mm	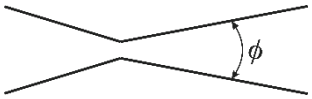
Thickness of ejector stainless steel plate	0.78 mm	
Length of nozzle converging section	17.85 mm	
Width of nozzle inlet	8.00 mm	
Width of nozzle throat	0.49 mm	
Nozzle diverging angle ϕ	2.0°, 3.0°, 4.0°	
Length of nozzle diverging section	11.50 mm	

2.3. Pressure measurement method and visualization method

Four pressure measurement points were cut on the ejector stainless steel plate by the laser, as presented in Fig. 4. The pressure measurement points were connected to the nozzle by four spindly channels with a width of 0.4 mm. The measurement point A was located at the converging section of the nozzle, and the axial distance from the throat was 5.75 mm. The measurement point B was used to obtain the throat pressure. The measurement point C was situated in the diverging section of nozzle, and the axial distance from the throat was 5.75 mm. The measurement point D was set to gain the nozzle exit pressure.

The direct photography method was utilized to visualize the two-phase flow in a transcritical CO_2 ejector. The visualization test platform was mainly formed by a high-speed camera, a visualization ejector and a light source, as depicted in Fig. 5. The camera was used to capture images with a constant frame rate of 1000 frames per second and connected to a computer with an Ethernet cable. A LED lamp was used to provide a light source for the camera with constant lightness.

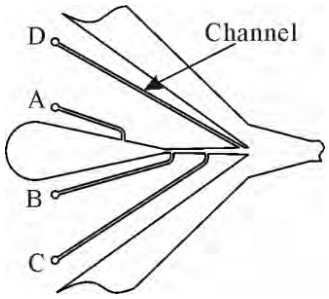

Figure 4: Position of pressure measurement points

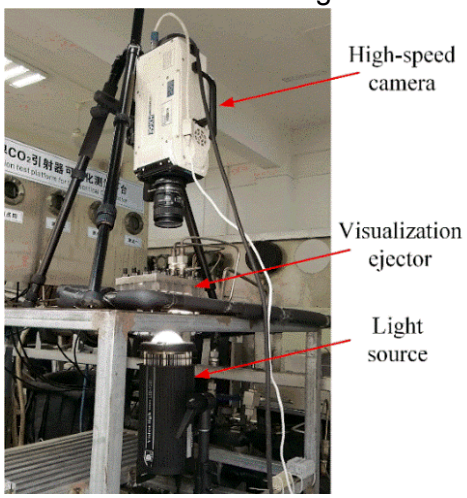

Figure 5: Photography of the visualization test platform

3. RESULTS AND DISCUSSION

During the test, the primary flow pressure P_p was maintained at 9.50 MPa, and the primary flow temperature T_p was kept as stable as possible. The secondary flow pressure P_s was varied by adjusting the opening of the expansion valve. In the experiment, the primary nozzle axial pressure distribution and visualization images under various secondary flow pressure and nozzle diverging angles were obtained. The results were discussed as follows.

3.1. Expansion state of primary flow

The nozzle axial pressure distribution of different nozzle diverging angles was shown in Fig. 6~8. The results showed that the pressure of the nozzle diverging section decreased with the decrease of the secondary flow pressure correspondingly, and the nozzle throat pressure remained almost unchanged. As a result, the pressure difference of the nozzle diverging section increased gradually with decreasing the secondary flow pressure. The reason was that the expansion degree of the primary flow increased as the nozzle exit back pressure decreased, which resulted in the increase of the pressure drop in the nozzle diverging section.

As shown in Fig. 6, the nozzle pressure continued decreasing along the nozzle axis when the nozzle diverging angles was 2.0°, indicating that the primary flow was under-expanded. When the nozzle diverging angles was 4.0°, it was apparent from the Fig. 8 that the nozzle exit pressure was higher than the pressure of measuring point C, which was the emblem of the shock wave, meaning that the primary flow was over-expended. When the nozzle diverging angle was 3.0°, it could be seen that the pressure of measuring point C was slightly greater than the nozzle exit pressure when the secondary flow pressure was higher than 3.90 MPa. Inversely, when the secondary flow pressure was lower than 3.90 MPa, the nozzle exit pressure was slightly greater than the pressure of measuring point C. Consequently, the results disclosed that the expansion state of the primary flow was transformed from under-expanded state to over-expanded state with the decrease of the secondary flow pressure in the angle.
The nozzle axial pressure distribution at different nozzle diverging angles was compared in Fig. 9. It could be noted that the effect of the nozzle diverging angle on the nozzle pressure distribution was more significant. The result revealed that the pressure drop gradient of the nozzle diverging section increased notably as the nozzle diverging angles increased, and the expansion state of the primary flow changed from the under-expanded state to the over-expanded state.

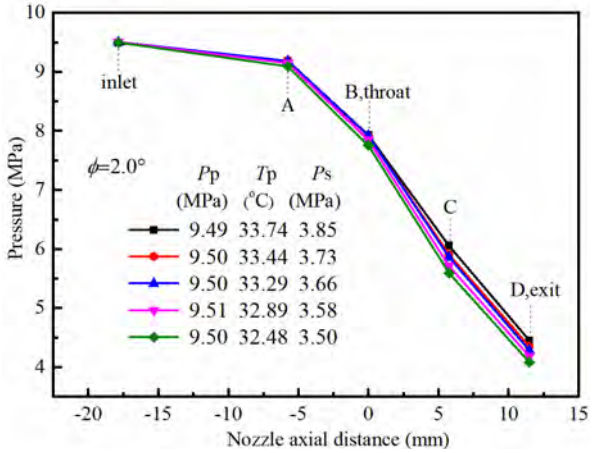

Figure 6: Nozzle axial pressure distribution when nozzle diverging angle ϕ was 2.0°

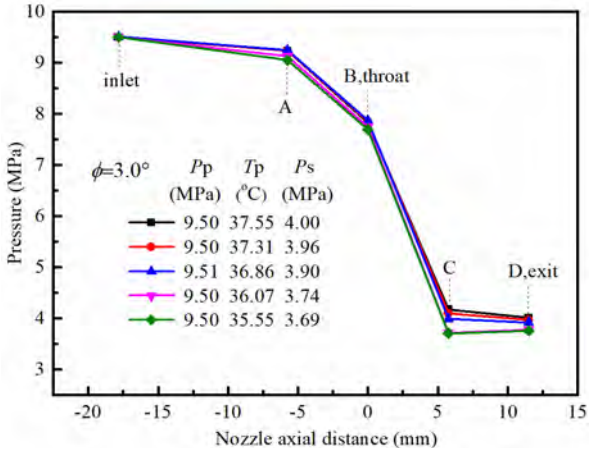

Figure 7: Nozzle axial pressure distribution when nozzle diverging angle ϕ was 3.0°

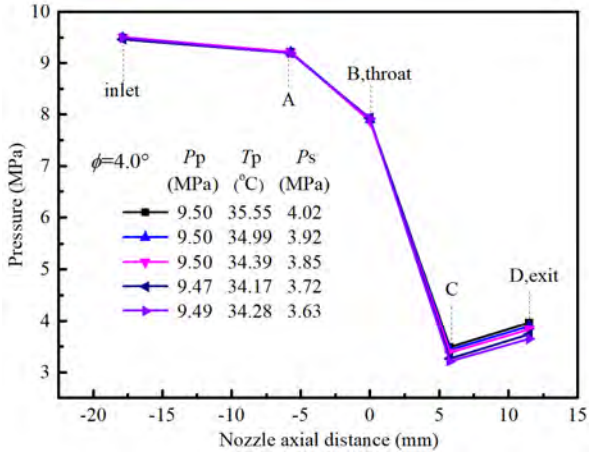

Figure 8: Nozzle axial pressure distribution when nozzle diverging angle ϕ was 4.0°

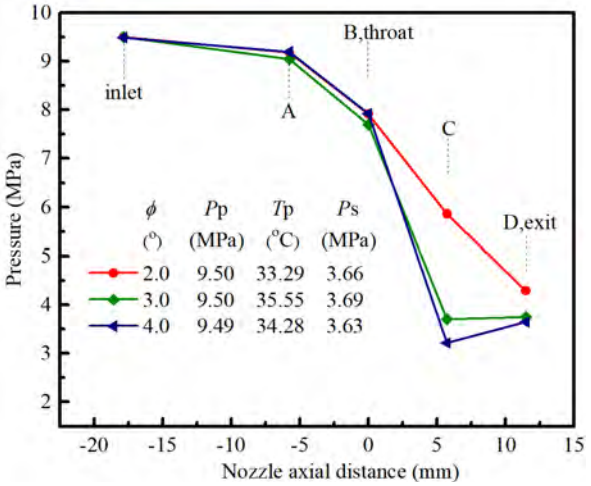

Figure 9: Nozzle axial pressure distribution under different nozzle diverging angles

3.2. Phase change

When the supercritical CO_2 flowed through a converging-diverging nozzle, the CO_2 was expanded rapidly to two-phase region, causing the phase change occurred in the nozzle. In order to explore the effect of the expansion state of the primary flow on the phase change, visualization images of different nozzle diverging angles were obtained, as illustrated in Fig. 10~12. Owing to the visualization principle, the dark region in the images refers to the two-phase flow, and the light region is the single-phase region. As a result, the interface of the dark region and light region refers to the

phase change position. It was noticed that the effect of secondary flow pressure on phase change was weak in all nozzle diverging angles, as shown by dotted line P. That was, the phase change position varied slimly with decreasing the secondary flow pressure. It was ascribed to the fact that the nozzle throat pressure remained almost unchanged as the secondary flow pressure decreased, as presented in Fig. 6~8. The comparison of images under different nozzle diverging angles was presented in Fig. 13. The results revealed that no significant difference of the phase change position was found in the three angles, as shown by dotted line M. This result may be explained by the fact that the pressure of the nozzle throat was almost same under the three angles, and the flashing was induced near the throat of the converging-diverging nozzles.

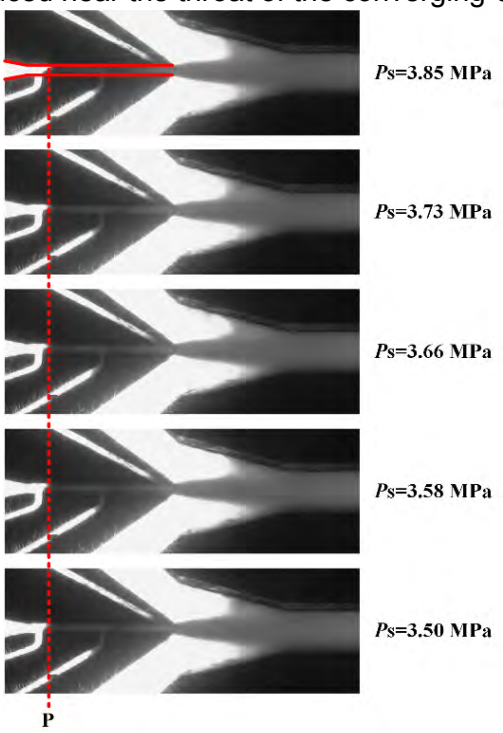

Figure 10: Visualization images when nozzle diverging angle ϕ was 2.0°

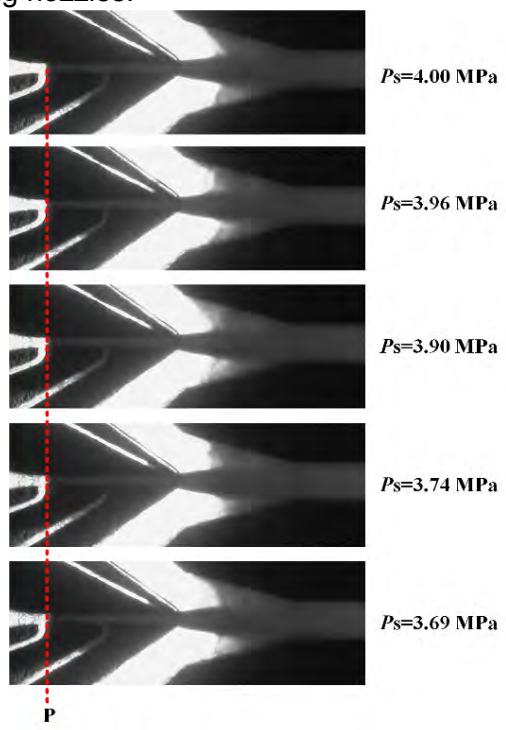

Figure 11: Visualization images when nozzle diverging angle ϕ was 3.0°

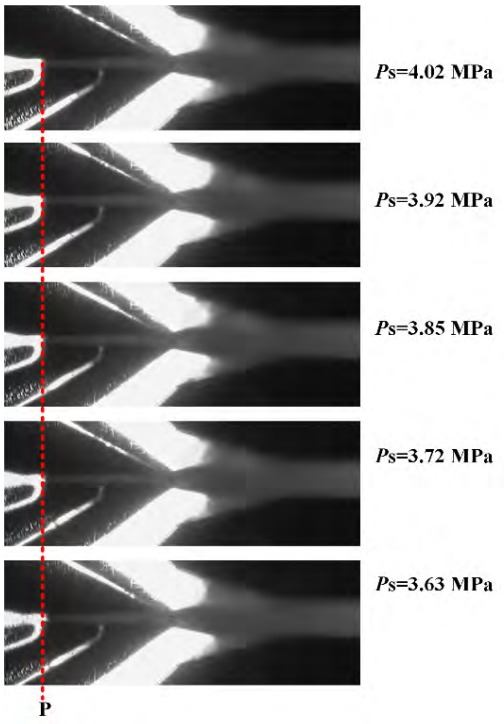

Figure 12: Visualization images when nozzle diverging angle ϕ was 4.0°

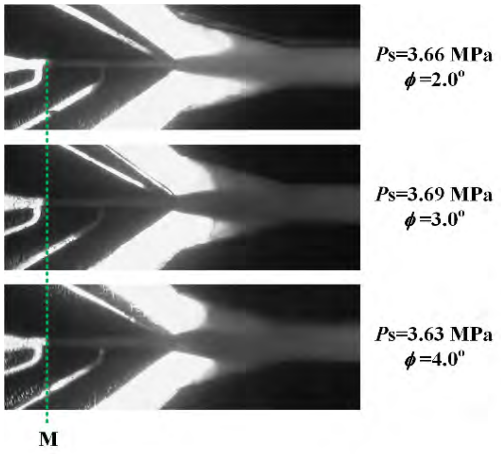

Figure 13: Comparison of images under different nozzle diverging angles

4. CONCLUSIONS

The influence of the secondary flow pressure and nozzle diverging angles on the expansion state and phase change of the primary flow was explored using visualization measurement method. The results showed that the pressure drop in the nozzle diverging section increased as the secondary flow pressure decreased. In addition, when the nozzle diverging angle was 3.0°, the expansion state of the primary flow shifted from under-expanded state to over-expanded state as the secondary flow pressure decreased. The expansion state of primary flow was more sensitive to the nozzle diverging angles, and the primary flow was transformed from the under-expanded state to over-expanded state with increasing the nozzle diverging angle. The visualization images revealed that the effect of secondary flow pressure and the tested nozzle diverging angles on the phase change position was small and could be neglected. The findings provided an important opportunity to advance the understanding of the expansion characteristic of the primary flow in a transcritical CO_2 two-phase ejector.

ACKNOWLEDGEMENTS

This work was supported by the National Natural Science Foundation of China (Grant No. 51676148).

REFERENCES

Bansal, P., 2012. A review–Status of CO_2 as a low temperature refrigerant: Fundamentals and R&D opportunities. Appl. Therm. Eng. 41, 18-29.

Elbel, S., 2016. Lawrence N. Review of recent developments in advanced ejector technology. Int. J. Refrig. 62, 1-18.

Deng, J.Q., Jiang, P.X., Lu, T., 2007. Lu, W., Particular characteristics of transcritical CO_2 refrigeration cycle with an ejector. Appl. Therm. Eng. 27(2-3), 381-388.

Ahammed, M.E., Bhattacharyya, S., Ramgopal, M., 2014. Thermodynamic design and simulation of a CO_2 based transcritical vapour compression refrigeration system with an ejector. Int. J. Refrig. 45, 177-188.

Elbel, S., Hrnjak, P., 2008. Experimental validation of a prototype ejector designed to reduce throttling losses encountered in transcritical R744 system operation. Int. J. Refrig. 31(3), 411-422.

Lucas, C., Koehler, J., 2012. Experimental investigation of the COP improvement of a refrigeration cycle by use of an ejector. Int. J. Refrig. 35(6), 1595-1603.

Elbel, S., 2011. Historical and present developments of ejector refrigeration systems with emphasis on transcritical carbon dioxide air-conditioning applications. Int. J. Refrig. 34(7), 1545-1561.

Nakagawa, M., Marasigan, A.R., Matsukawa, T., 2010. Experimental analysis of two-phase ejector system with varying mixing cross-sectional area using natural refrigerant CO_2. Int. J. Air-Conditioning and Refrigeration 18(4), 297-307.

Nakagawa, M., Marasigan, A.R., Matsukawa, T., Kurashina, A., 2011. Experimental investigation on the effect of mixing length on the performance of two-phase ejector for CO_2 refrigeration cycle with and without heat exchanger. Int. J. Refrig. 34(7), 1604-1613.

Palacz, M., Smolka, J., Kus, W., Fic, A., Bulinski, Z., Nowak, A.J., et al., 2016. CFD-based shape optimisation of a CO_2 two-phase ejector mixing section. Appl. Therm. Eng. 95, 62-69.

Palacz, M., Smolka, J., Nowak, A.J., Banasiak, K., Hafner, A., 2017. Shape optimisation of a two-phase ejector for CO_2 refrigeration systems. Int. J. Refrig. 74, 212-223.

Chen, J.Y., Jarall, S., Havtun, H., Palm, B., 2015. A review on versatile ejector applications in refrigeration systems. Renew. Sustain. Energy Rev. 49, 67-90.

Bouhanguel, A., Desevaux, P., Gavignet, E., 2011. Flow visualization in supersonic ejectors using laser tomography techniques. Int. J. Refrig. 34(7), 1633-1640.

Rao, S.M.V., Jagadeesh, G., 2014. Observations on the non-mixed length and unsteady shock motion in a two dimensional supersonic ejector. Phys. Fluids 26(3), 243-247.

Little, A.B., Garimella, S., 2016. Shadowgraph visualization of condensing R134a flow through ejectors. Int. J. Refrig. 68, 118-129.

Zhu, Y.H., Wang, Z.C., Yang, Y.P., Jiang, P.X., 2016. Flow visualization of supersonic two-phase transcritical flow of CO_2 in an ejector of a refrigeration system. Int. J. Refrig. 74, 354-361.

Li, Y.F., Deng, J.Q., Ma, L., Zhang, Y.Z., 2018. Visualization of two-phase flow in primary nozzle of a transcritical CO_2 ejector. Energy Convers. Manage. 171, 729-741.

Manuscript ID: 726
DOI: 10.18462/iir.icr.2019.0726

Increasing the performances of a CO_2 refrigeration system using cool thermal energy storage for subcooling: a supermarket application

Benedicte BALLOT-MIGUET[(a)], Gilles DEJARDINS, Bastien QUARO, Amaury DEFRUIT[(b)], David ROUSSET

[(a)] EDF R&D
Avenue des Renardières, Moret sur Loing, F-77250, France, benedicte.ballot-miguet@edf.fr
[(b)]DALKIA FROID SOLUTIONS
Saint-Sylvain d'Anjou, F-49484, France, amaury.defruit@dalkiafroidsolutions.com

ABSTRACT

The electricity consumption of a supermarket refrigerating plant situated in the south of France has been measured during 8 months. A cool thermal energy storage (CTES) and a CO_2 subcooler were added to the full CO_2 refrigerating plant. The plant is described, as well as the charge/discharge/subcooling schedule strategy. The objectives of the work were to quantify the energy saving obtained thanks to the CTES and the subcooling. We obtained 23 kWh electricity saving and 2 k€ financial saving, which represents 6% of the annual electricity bill dedicated to medium temperature refrigeration production. The strategy depends on a lot of parameters (supermarket opening hours, outside temperature, electricity tariffs), and the tests showed it is important to review the control (schedule and set points).
Keywords: Supermarket, Refrigeration, Carbon Dioxide, Cool Thermal Energy Storage, CTES, Subcooling, Energy Efficiency, Electricity

1. INTRODUCTION

Statistic studies (Ceren, 2014) conducted by EDF show that the electricity consumption, dedicated to food refrigeration in the commercial sector in France, represents 20% of the total electricity consumption of the sector. The refrigeration daily load curve of a supermarket shows that the electricity for refrigeration is mainly consumed during the opening hours of the supermarket (Rasmussen et al., 2016). Moreover, the efficiency of the refrigerating system is outside-temperature sensitive (Acha et al., 2016), which is emphasised if the working fluid is transcritical CO_2 (Kauf, 1999). Advantages and disadvantages of cool thermal energy storage (CTES) have been previously described (see for example Kosi et al, 2015). CTES is not often used in commercial sector in France, because of the high reliability of the electricity supply, as well as the low price of electricity. The most common technologies used to store cool energy are chilled water (sensible heat energy storage) and ice or Phase-Change Material (PCM) (latent heat energy storage) (Fang et al., 2016). Subcooling is a well-known solution to increase the cooling capacity as well as the Coefficient Of Performance (COP) of a refrigerating plant (Zubair, 1990; Dai et al., 2017).
Considering all these facts, a CTES added to the refrigerating plant and used to subcool it, is expected to lower the electricity consumption, partially transfer the opening hours electricity consumption to closed hours, increase the Coefficient of Performance of the refrigerating plant, and reduce or optimise costs and energy impacts. In a previous work, Quaro (2016) described the two main CTES technologies as well as CTES design and operating strategies. The aim of his work was to develop and evaluate a software tool for sizing and optimising CTES solution under various electricity tariff schemes. The case study of a supermarket using CO_2 as a working fluid was presented.

Following this previous work, EDF and DALKIA FROID SOLUTIONS had the opportunity to patent (Quaro et al., 2018) and install a CTES in a customer's supermarket. In the present paper, we will describe the refrigerating plant of the supermarket. We will then describe the control strategy, the measurements and the results. We will be able to compare the energy consumption of the plant with and without the use of the subcooling allowed by the CTES. The conclusion of the work will suggest improvements on the system regulation.

2. THE PLANT

The idea consists in adding a Cool Thermal Energy Storage (CTES) to a full CO_2 refrigerating plant, and discharge the CTES to subcool the CO_2.

2.1. Main Part of the Plant

The supermarket is situated in the south of France. It is approximately 2 600 m^2. The refrigerating plant is composed of a transcritical CO_2 refrigerating plant and a subcritical CO_2 refrigerating plant, both of them connected with a glycol water loop. The display cabinets for chilled food are connected to the glycol water loop, as well as the condenser of the subcritical CO_2 refrigerating plant. The frozen food cabinets are supplied with CO_2 in direct expansion from the subcritical CO_2 refrigerating plant. The glycol water loop temperatures are -7°C/-3°C. Low temperature cabinets are closed. Medium temperature opened cabinets are in rooms closed with plastic strip curtains.

2.2. Addition of a CTES

To this main part of the supermarket refrigerating plant, a CTES has been added. It is connected to the glycol water loop. The CTES is composed of a tank, filled with tap water and a heat exchanger network immersed in the tap water. The glycol water circulates inside the heat exchanger network, allowing the formation of ice on the external surface of the immerged heat exchanger network. The CTES is completely loaded when 95% of the water is frozen. This CTES is called "internal melt" because the discharge is done by the circulation of the glycol water, which is inside the tubes of the heat exchanger network. The floor surface used by the CTES is 20 m^2. Its dimensions are 3245 mm length, 1595 mm width and 3020 mm height. Its maximum capacity is 499 kWh, corresponding to the formation of 95 vol% of ice. The total charge lasts for roughly 6 hours. It is settled outside the buildings, on the car park. Figure 1 shows the CTES connected to the main part of the refrigerating plant.

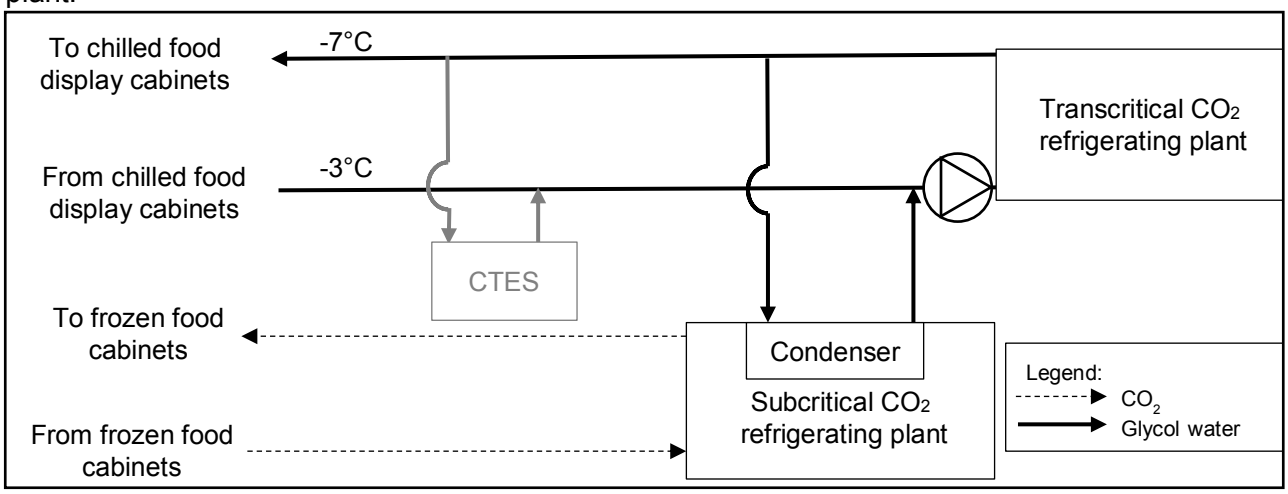

Figure 1: Black: main part of the transcritical and subcritical CO_2 supermarket refrigerating plant. Grey: addition of the cool thermal energy storage

2.3. Addition of the subcooling

Finally, a subcooler is added to the CO_2 transcritical plant, just after the dry gascooler. This subcooler is a CO_2/glycol water heat exchanger. It is connected to the CTES via the glycol water loop. The CTES discharge is used to subcool the CO_2. The temperature of the glycol water coming out from the CTES is about 5°C, and the temperature of the glycol water going back to the CTES is about

10°C. The CO_2 outlet temperature from the subcooler is about 15°C. Figure 2 shows the global architecture of the refrigerating plant, including the CTES and the CO_2 subcooler.

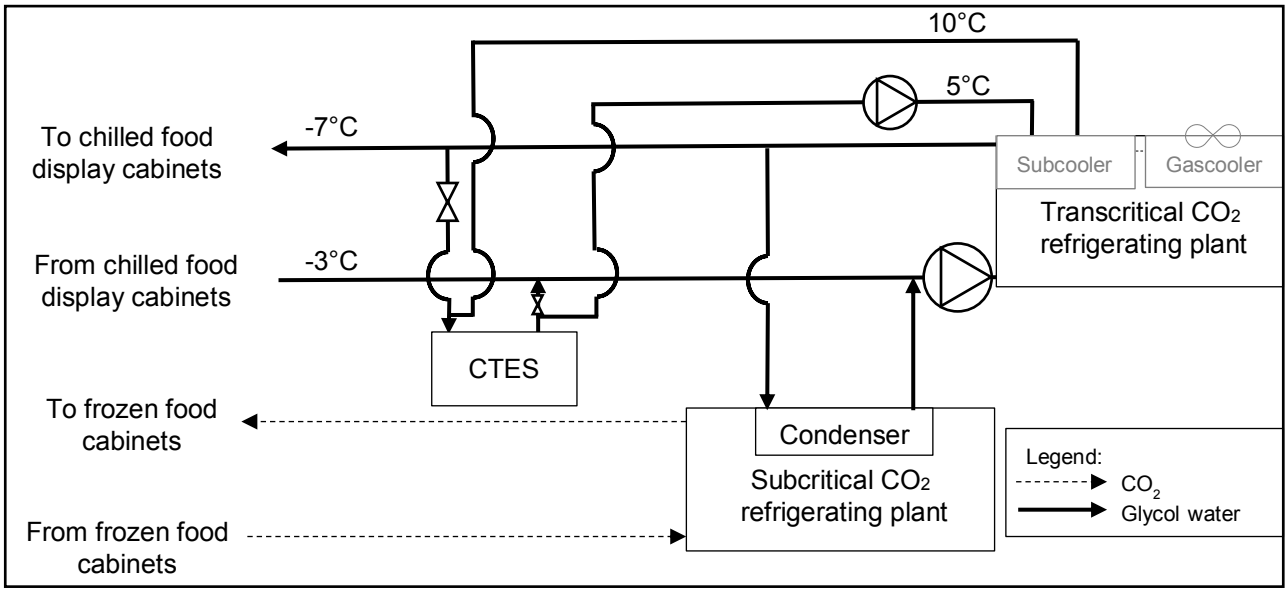

Figure 2: Use of the cool thermal energy storage to subcool the transcritical CO_2

2.4. Thermodynamics

Three states (Figure 3) are defined: State 1 (transcritical, no subcooling, no CTES charge), State 2 (transcritical, subcooling, no CTES charge), State 3 (subcritical (or transcritical with lower outlet gas temperature than states 1 and 2), no subcooling, CTES charge).

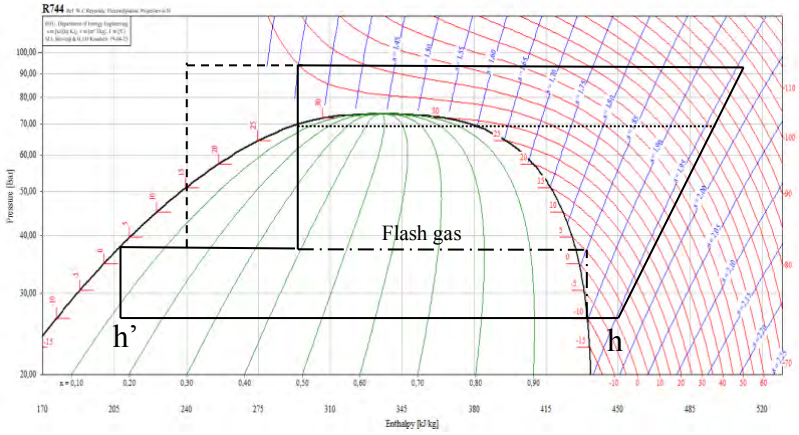

Figure 3: state 1 (bold), 2 (dashed line) and 3 (dotted line)

Comparing states 1 and 2, the subcooling induces a reduction on the flash gas mass flow, and thus an increase of the CO_2 mass flow in the evaporators as shown in Eq. (1). For the same compressor rotating speed in states 1 and 2, Eq. (2) to (4) define the cooling capacities, and lead to Eq. (5).

$$m_2 > m_1 \quad \text{Eq. (1)}$$
$$Q_1 = m_1 (h-h') \quad \text{Eq. (2)}$$
$$Q_2 = m_2 (h-h') \quad \text{Eq. (3)}$$
$$Q_2 > Q_1 \quad \text{Eq. (4)}$$
$$EER_2 > EER_1 \quad \text{Eq. (5)}$$

On state 1, Q_1 is only dedicated to the display cabinets (Eq. (6)), while on state 3, Q_3 is dedicated to the display cabinets and the CTES (Eq. (7)). State 3 occurs by night so Q_{3dc} is lower than Q_{1dc}, which allows to charge the CTES. Assuming that Q_1 equals Q_3, and as the high pressure in state 3 (night) is lower than in state 1 (day), this leads to Eq. (8).

$$Q_1 = Q_{1dc} \quad \text{Eq.(6)}$$

$$Q_3 = Q_{3dc} + Q_{3CTES} \quad \text{Eq. (7)}$$

$$\text{For } Q_1 = Q_3,\ EER_3 > EER_1 \quad \text{Eq. (8)}$$

Considering Eq. (5) and (8), the plant should work as much as possible on state 2 and 3, and use state 1 when the electricity price is at its lowest.

2.5. Control and Strategy

The charge/discharge/subcooling strategy has been chosen based on the following:

- During opening hours of the supermarket, the cooling demand is high, so the charge is avoided;
- By night, when the outside temperature is low, the performances of the refrigerating plant are high, and the cooling demand of the cabinets is low, so the charge is ON;
- Around noon, the outside temperature is high, so the subcooling (discharge) is ON to increase de performances of the transcritical CO_2 plant;
- When the electricity tariffs are high (see below), charge is OFF and subcooling is ON.

The refrigerating plant works 24 hours a day. The cabinets are cool fed continuously.
On the contrary, the CTES is charging during a few hours every night. During the charging mode, the refrigerating plant provides cooling to the CTES and to the cabinets. During the CTES charge, there is no subcooling.
The subcooling occurs while the CTES is discharged. The discharge and the subcooling occur during the hottest hours of the day.
After several weeks of tests, the best schedule has been defined as follows:

- Winter time:
  - The CTES is charged from 10 pm to 6 am on week days. Thus, it is discharged from 6 am to 10pm.
  - On weekends, the CTES is kept loaded: no discharge during 48 hours.
- Summer time:
  - The CTES is charged from 10 pm to 10 am. Thus, it is discharged from 10 am to 10 pm. This applies for both weekdays and weekends.

Remark regarding the winter weekends: keeping a loaded CTES during the weekends is not efficient, because of the thermal losses. But, by the time of the tests, the automatic control did not allow keeping a completely unloaded CTES without turning OFF the subcooler pumps, which was not efficient either. We chose to keep the CTES loaded, and the pumps OFF.
The CO_2 outlet subcooling temperature is controlled with a three-way valve on the glycol water loop. The set point is 13°C in summer, so that the CTES doesn't discharge too fast. It is 1°C in winter, so that the CTES is completely unloaded every weekday.

3. ELECTRICITY TARIFFS

French electricity tariffs have been widely characterised in Quaro, 2016. We remind here that French electricity tariffs have 3 components:

- a "supply" component, which corresponds to the energy consumed by the customer;
- a "transmission and distribution network use" which is a contribution to the operation, the development and the maintenance of the French electrical network;
- taxes.

The supply component is proportional to the electricity consumption in kWh, but depends on the season and the hour of the day.
There are 2 seasons:

- winter electricity tariff season, from November the 1st to March the 31st;
- summer electricity tariff season, from April the 1st to October the 31st.

During the winter electricity season, there are 3 tariffs: rush hour tariff (from 9 am to 11 am and from 6 pm to 8 pm), off-peak hour tariff (from 10 pm to 6 am, and 48 hours weekends) and peak hour tariff. During the summer season, there are only peak (from 6 am to 10 pm) and off-peak (from 10 pm to 6 am during weekdays and 48 hour weekends) hour tariffs.
At first, the CO_2 outlet subcooling temperature set point was lower during rush hours than during

peak hours. But it finally remained constant during all the discharge phase, to allow a better understanding of the subcooling effect.
The supply component has a subscribed electrical capacity part, which is proportional to the instant power absorbed by the customer. CTES is a good way to reduce this part of the electricity invoice, by levelling the electricity load curve.

4. MEASUREMENTS AND RESULTS

4.1. Charge/discharge cycle

Figure 4 represents a summer week data recording. The CTES is charged and discharged on a daily base, except during the weekend. We can see that the discharge and the subcooling occur when the outside temperature is at its highest, so on those periods, the CO_2 subcooled temperature is at its lowest and is lower than the outside temperature, thanks to the use of the CTES. When there is no subcooling (charging phase), the CO_2 outlet subcooler temperature follows the outside temperature.
In winter, it has first been observed that the minimum ice level was around 40% with a CO_2 outlet subcooler temperature set point of 6°C during rush hours and 15°C during peak hours. In order to completely unload the CTES every day, the set point has been lowered to 1°C during all discharging hours.

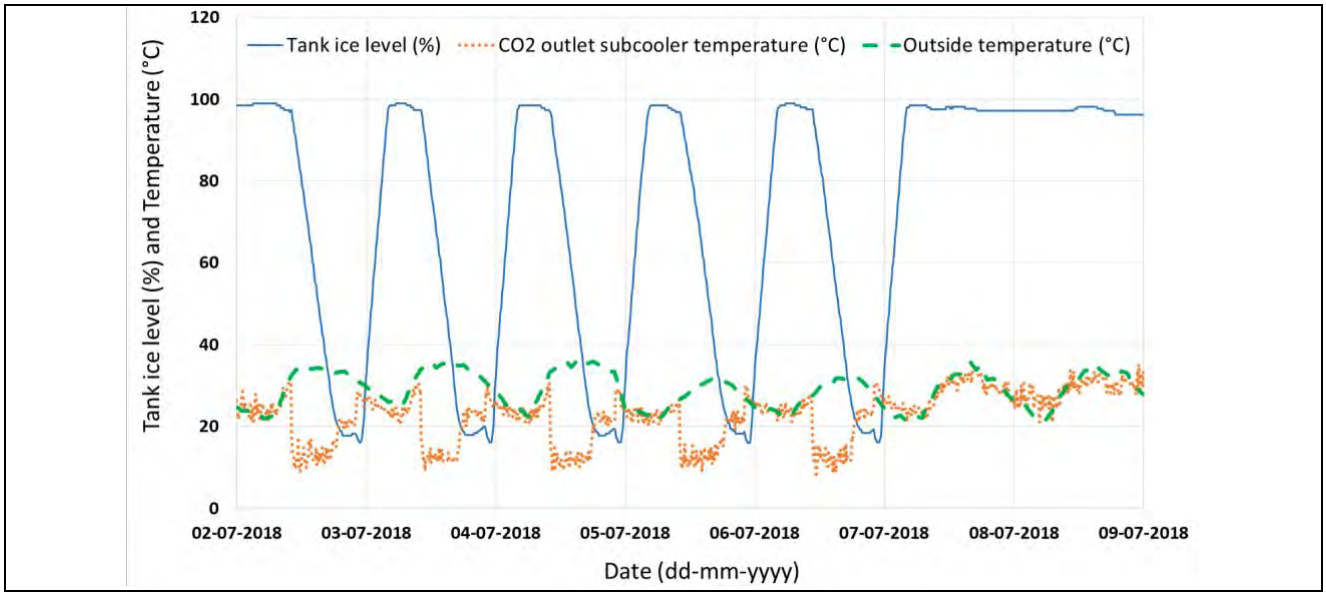

Figure 4: One summer week data recording: remaining cooling capacity in the CTES, CO_2 outlet subcooling measured temperature, and outside temperature

4.2. Plant Refrigeration Output

Measurements have been recorded during three summer weeks, during which the CTES, as well as the CO_2 subcooling, were OFF. Over those 3 weeks, the plant refrigeration output has been averaged on the 3 Sundays, on the 3 Saturdays, and on the 15 weekdays.
Figure 5 shows the medium temperature refrigeration average output. On weekdays, the supermarket is open all day. On Saturdays, the supermarket closes at midday. On Sunday, the supermarket is closed, with no employees working; the refrigeration production only allows the compensation of the thermal losses. Figure 5 illustrates that the plant refrigeration output depends on the opening hours of the supermarket.
Measurements have been recorded during height summer weeks, during which the CTES was on charge and as well as the CO_2 subcooling was in use. Over those height weeks, the plant refrigeration output has been averaged on the 8 Sundays, on the 8 Saturdays, and on the 40 weekdays. Figure 6 shows the medium temperature refrigeration average output. The 10 pm peak is due to the beginning of the CTES charge. It has not been investigated whether or not it is more efficient to i) completely freeze the CTES in the shortest time (so the refrigerating plant works at its best performances, but then thermal losses occur during the time period between the end of the

charge and the beginning of the discharge), or ii) charge the CTES gradually along the 12 charging hours (this mode minimises the thermal losses, but lowers the refrigerating plant performances). Programming the refrigerating plant to reach the full CTES capacity just before 10 am, within the shortest time of charge, would certainly be the more energy efficient mode. Nevertheless, as peak refrigeration production means peak electricity consumption, there is a risk to exceed the site subscribed electrical capacity.

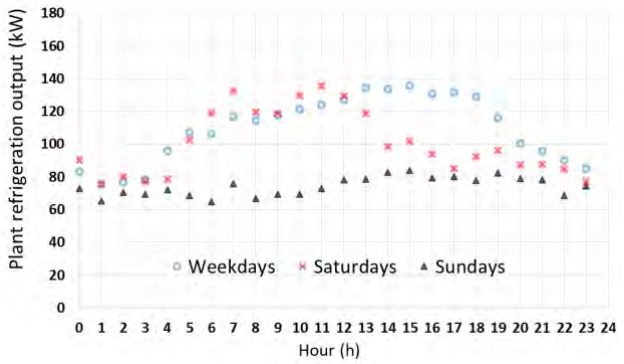

Figure 5: High-pressure stage average refrigeration output, without cool storage nor CO_2 subcooling, summer time

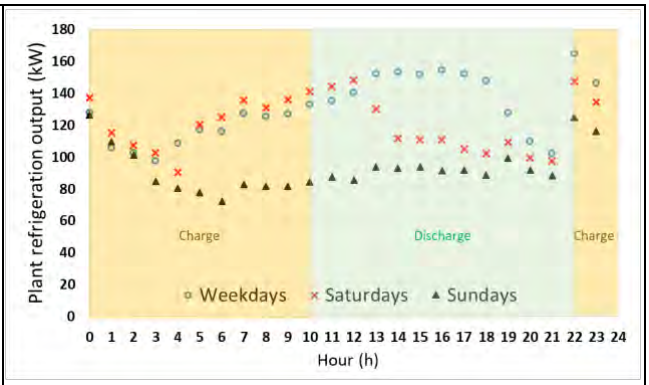

Figure 6: Plant high-pressure stage average refrigeration output, with cool storage and CO_2 subcooling, summer time

4.3. Electricity consumption

Figure 7 compares the electricity consumption of the whole supermarket, during two weeks in summer: during one week, the CTES and the subcooling were on use, and during one week, they were not. During the discharge and CO_2 subcooling hours, the total absorbed electrical capacity of the supermarket is lower during the week with CTES and subcooling. During the CTES charging hours (by night), the contrary is observed. The gap between the curves during the night corresponds to the electricity needed to charge the CTES. Every weekday, a peak occurs around 10 pm, which is the beginning hour of the charge. The peaks are due to the very important electricity demand of the high pressure (HP) compressors, as it can be seen on Figure 8. This figure represents the electricity consumption of the whole supermarket and the electricity consumption of the HP CO_2 compressors, during the same week. On this figure, the everyday 10 pm peak electricity demand, on the supermarket curve, corresponds exactly to the HP compressors curve. The slight difference between the peaks heights can be attributed to the auxiliaries like gascooler fans and glycol water pump. The 10 pm peaks may occur an overshoot of the subscribed electrical capacity (thus an additional cost for the electricity end user), which is against the load levelling targeted by CTES. In the future, the control should be modified so that the peak electricity consumption is distributed all over the night.

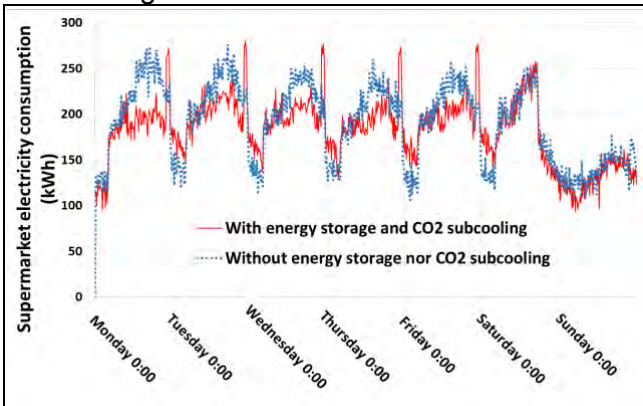

Figure 7: Whole supermarket electricity consumption with and without cool storage and CO_2 subcooling. Summer time

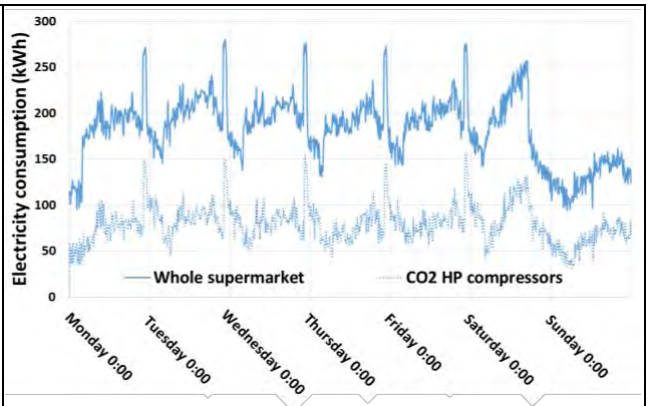

Figure 8: Electricity consumption of the whole supermarket and of the high-pressure CO_2 compressors. Summer week with cool storage ON and CO_2 subcooling ON

Electricity consumption has been measured from December Monday the 18th 2017 to March Sunday

the 11th 2018. It has been measured that, during winter time, the use of CTES and CO_2 subcooling during weekends end up to an electricity overconsumption. This is due to the very low cooling need during weekends. By extrapolating the measurements over the all winter electricity tariff season (108 weekdays), the CO_2 subcooling combined to the CTES yields to 920 kWh electricity saving.
Electricity consumption measurements from July Monday the 18th 2018 to July Sunday the 15th 2018 show that, during summer time, the use of CTES and CO_2 subcooling end up to an electricity saving, if used during both weekdays and weekends. By extrapolating the measurements over the all summer electricity tariff season, the CO_2 subcooling combined to the CTES yields to 21 930 kWh electricity saving.
The orders of magnitude of the electricity consumption, sorted by season, with and without using CTES and CO_2 subcooling, are indicated in Table 1. The electricity consumption dedicated to the refrigeration production gathers the gascooler fans, all the glycol water pumps, and all the compressors (HP and BP) of the refrigerating unit.
An estimation of the financial saving is shown on Table 2. It takes into account the electricity tariffs versus hour of the day and season. The saving is of 2 k€ per year, which represents 6% of the annual electricity bill dedicated to medium temperature refrigeration production.

Table 1: Orders of magnitude of annual extrapolating electricity savings (MWh)

		Winter electricity tariff season (151 days)	Summer electricity tariff season (214 days)	Annual Total (365 days)	Annual Saving
Whole supermarket electricity consumption	Without cool storage nor CO_2 subcooling	410	687	1097	
	With cool storage and CO_2 subcooling	409	665	1074	23
Electricity consumption dedicated to refrigeration (fans, pumps, CO_2 trans and subcritical compressors)	Without cool storage nor CO_2 subcooling	106	294	400	
	With cool storage and CO_2 subcooling	105	272	377	23

Table 2. Financial savings estimated from the measurements done in 2017 and 2018 (€uros)

Electricity tariff component	Estimated financial saving during winter electricity tariff season (151 days)	Estimated financial saving during summer electricity tariff season (214 days)	Total (€)
Energy saving on the supply component	102	1 043	1 145
Energy saving on the transmission and distribution network use component	52	222	274
Energy saving on the taxes component	21	493	514
TOTAL	**175**	**1 758**	**1 933**

5. CONCLUSION AND FUTURE WORK

A full CO_2 refrigerating plant has been installed in a supermarket by EDF and DALKIA FROID

SOLUTIONS. The plant was equipped with a CTES as well as a CO_2 subcooler. When discharged, the CTES provides the subcooling. The charge/discharge strategy takes into account the external temperature, the supermarket opening hours and the electricity tariffs. The annual electricity saving is 23 MWh, and 2 k€.
The results showed that the control and the charge/discharge strategy are very important to optimise the use of the CTES as well of the subcooling. As an example, we understood that the strategy should be different during the weekends depending on the season. We suggest to improve the control as follows:

- Lowering the CO_2 outlet subcooler temperature set point and increase the discharge duration so that the CTES is totally discharged in winter.
- Investigating whether or not the CTES strategy should be different between Saturdays and Sundays.
- Levelling the charge all over the night to avoid an electricity consumption peak at 10 pm.

6. NOMENCLATURE

m	CO_2 mass flow in evaporators ($kg.s^{-1}$)	Q	Cooling capacity (kW)
h	Enthalpy ($kJ.kg^{-1}$)	EER	Energy Efficiency Ratio (-)
dc	Display Cabinets		

REFERENCES

Acha, S., Du, Y., Shah, N., 2016. Enhancing energy efficiency in supermarket refrigeration systems through a robust energy performance indicator. Int. J. Refrigeration, 64, 40-50

Ceren (Centre d'Etudes et de Recherches Economiques sur l'Energie – French economic studies and research center on energy), 2014. Les consommations d'électricité spécifique par usage – année 2012. Study financed by EDF and ADEME, private communication.

Dai, B., Liu, S., Ma, Y., 2017. Thermodynamic Performance Analysis of CO2 transcritical refrigeration cycle assisted with mechanical subcooling. Energy Procedia, 105, 2033-2038.

Fang, G., Tang, F., Cao, L., 2016. Dynamic characteristics of cool thermal energy storage systems – a review. Int. J. Green Energy, 13, (1), 1-13.

Kauf, F., 1999. Determination of the optimum high pressure for transcritical CO2 refrigeration cycles. Int. J. Therm. Sci, 38, 325-330.

Kosi, F., Zivkovic, B., Komatina, M., Antonijevic, D., Galil, M., Milovancevic, U., 2015. Cold Thermal Energy Storage. In: Gaspar, P., da Silva, P., Handbook of Research on Advances and Applications in Refrigeration Systemes and Technologies, Engineering Science Reference, Hershey USA, 752-783.

Quaro, B., 2016. Cold storage, a flexibility and energy efficiency solution. 4th IIR International Conference on Sustainability and the Cold Chain. Proceedings: Auckland, New Zealand, April 7-9.

Quaro, B., Fraisse, Ph., Girard, S., 2018. Installation Frigorifique. French Patent FR3063539 (A1), filed 2017-03-03, application for patent invention 2018-09-07.

Rasmussen, L., Bacher, P., Madsen, H., Nielsen, H., Heerup, C., Green, T., 2016. Load forecasting of supermarket refrigeration. Applied Energy, 163, 32-40.

Zubair, S., 1990. Improvement of refrigeration/air-conditioning performance with mechanical sub-cooling. Energy, 15, (5), 427-433.

Manuscript ID: 727
DOI: 10.18462/iir.icr.2019.0727

Condensation heat transfer and pressure drop of NH_3 and NH_3/H_2O within a plate heat exchanger

Xuan TAO[(a)], Elias DAHLGREN[(a)], Carlos INFANTE FERREIRA[(a)]

[(a)] Delft University of Technology, Process and Energy Department
Delft, 2628 CB, the Netherlands, x.tao@tudelft.nl

ABSTRACT

The heat transfer coefficients (HTCs) of NH_3 are higher than of HFCs and hydrocarbons during the condensation within plate heat exchangers (PHEs) mainly due to its favorable transport properties. NH_3/H_2O has a large temperature glide, and its heat transfer is dependent on mass transfer. Few models have been specifically developed for NH_3 and NH_3/H_2O condensation in PHEs. This paper presents heat transfer and pressure drop experiments for partial condensation. The calculation method for condensation HTCs and frictional pressure drop is introduced. The working fluids are pure NH_3 and NH_3/H_2O with a weight concentration of 96%. For a mass flux of 62 $kgm^{-2}s^{-1}$, the HTCs of NH_3 increase from 10 to 20 $kWm^{-2}K^{-1}$ with vapor quality. The apparent HTCs of NH_3/H_2O are significantly lower than NH_3 at high vapor qualities because of mass transfer resistance. Condensation pressure level has a slight influence on HTCs and frictional pressure drop.
Keywords: Plate heat exchanger, Condensation, Absorption, Heat transfer, Pressure drop, NH_3 and NH_3/H_2O.

1. INTRODUCTION

Plate heat exchangers (PHEs) are a type of compact heat exchangers and are widely used in industry. PHEs are composed of multiple plates that are stacked together. These plates are corrugated and form periodic flow channels. On the one hand, the corrugated plates provide larger heat transfer areas; on the other hand, the flow is disturbed and secondary flow is introduced, which enhances the thermal performance. PHEs have large heat transfer areas per volume and small hydraulic diameters. The small flow passage area reduces the charge of working fluid. Hot and cold fluids flow alternately and counter-currently in the channels, what makes it easy to adjust heat transfer areas by changing the number of plates. The knowledge of evaporation and condensation within PHEs is limited despite the growing application. Researches of condensation are especially needed (Tao et al., 2018a).

PHEs are promising candidates for NH_3 systems because of large capacity and compact structure. The fluid properties of NH_3 are distinct from HFCs or hydrocarbons with larger latent heat and surface tension. Heat transfer correlations derived from other refrigerants are unlikely to be applicable for NH_3, but NH_3 condensation in PHEs is not reported in detail by open literature (Tao et al., 2018b). The condensation of NH_3/H_2O mixture is characterized by a large temperature glide and simultaneous heat and mass transfer. This process is also referred to as absorption. NH_3/H_2O condensation within PHEs has been analysed both experimentally and numerically, but is still not fully understood (Kang et al., 2000; Cerezo et al., 2010; Triché et al., 2017). This paper experimentally investigates the condensation of NH_3 and high concentration NH_3/H_2O within a PHE.

2. EXPERIMENTAL SETUP

More detailed descriptions of the experimental setup and test section are given in a previous paper (Tao et al., 2018b). Fig. 1 shows the system diagram. The operation of NH_3 and NH_3/H_2O is similar. For NH_3/H_2O, a two-phase mixture flows into a separator after being heated and partially vaporized in an evaporator. Liquid of relatively low NH_3 concentration flows through a recuperator and an expansion valve, while high concentration vapor flows through an expansion valve and mixes up with liquid at the inlet of the test section. The vapor and liquid are controlled to be at the same

pressure before mixing. NH_3/H_2O flows from the top to the bottom of the test section, and is cooled by cold water that flows upward. NH_3/H_2O then flows through an after cooler, a buffer tank, a working fluid pump, the recuperator, and flows back to the evaporator. During NH_3 operation, the flow is also separated into vapor and liquid at the separator and mixes up before the test section. But it is pure fluid everywhere. Temperature, pressure, mass flow rate and density are measured at the locations indicated in Fig.1. Cold water is used to remove the heat from the test section and from the after cooler, while hot water flows into the evaporator. The test section is a gasketed plate heat exchanger with three plates in total and one plate effective for heat transfer. It has a hydraulic diameter of 2.99 mm and a chevron angle of 63° (Tao et al., 2018b).

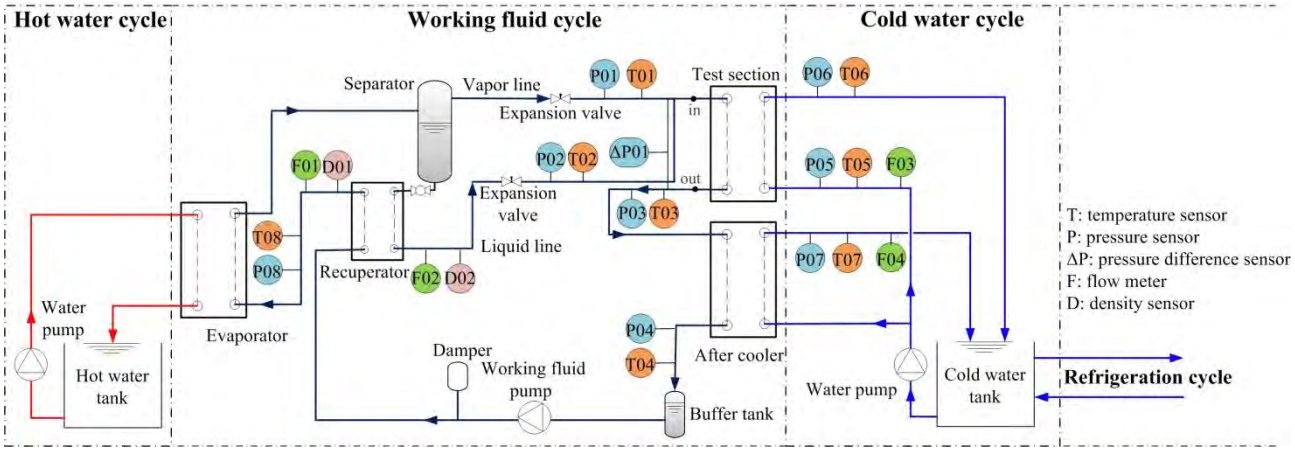

Figure 1: Experimental setup diagram including the working fluid cycle, the cold water cycle and the hot water cycle

3. DATA REDUCTION

3.1. H_2O-H_2O experiments

H_2O-H_2O experiments were carried out to obtain the single-phase HTCs and Fanning friction factors. The single-phase HTCs of PHEs, α_w, are generally accepted to have the form of Eq. (1) (García-Cascales et al., 2007). Θ_1 and Θ_2 depend on the geometry of PHEs, and can be calculated by Wilson-plot method (Fernández-Seara et al., 2007). During experiments, the mass flow rate of hot water was kept constant while the mass flow rate of cold water was varied. Θ_2 is determined to be 0.7 by best fitting. Fig. 2 presents the results of Wilson-plot method obtained by curve fitting. U is the overall HTC, and d_p/λ_{wall} is the wall thermal resistance. The resulting correlation is given in Eq. (2).

$$Nu_w = \frac{\alpha_w d_h}{\lambda_w} = \theta_1 Re_w^{\theta_2} Pr_w^{1/3} \quad \text{Eq. (1)}$$

$$Nu_w = \frac{\alpha_w d_h}{\lambda_w} = 0.275 Re_w^{0.7} Pr_w^{1/3} \qquad 320 \le Re_w \le 2600 \quad \text{Eq. (2)}$$

$\Delta P_{exp,w}$ is the measured pressure drop. Eqs. (3)-(5) calculate the water frictional pressure drop, $\Delta P_{fri,w}$, the pressure drops of inlet and outlet ports, $\Delta P_{in\ port,w}$, $\Delta P_{out\ port,w}$, and elevation pressure decrease, $\Delta P_{ele,w}$ (Shah and Focke, 1988).

$$\Delta P_{fri,w} = \Delta P_{exp,w} - \Delta P_{in\,port,w} - \Delta P_{out\,port,w} - \Delta P_{ele,w} \quad \text{Eq. (3)}$$

$$\Delta P_{port,w} = 1.5 G_w^2 / (2\rho_w) \quad \text{Eq. (4)}$$

$$\Delta P_{ele,w} = \rho_w g L_p \quad \text{Eq. (5)}$$

Eq. (6) defines the single-phase Fanning friction factor, f_w, which is needed to discuss two-phase frictional pressure drop using the Lockhart-Martinelli model. It is correlated in Eq. (7), and the results are presented in Fig. 3. The pressure drop experiments were conducted at the same operating conditions as heat transfer experiments, but the ranges of the pressure sensors were limited and the data at larger mass fluxes cannot be obtained. So Eq. (7) has a narrower range of Reynolds number compared with Eq. (2). The flow is expected to transit from laminar to turbulent flow with the increase of mass fluxes. The transition of PHEs takes place at smaller Reynolds number than for tubes (Sarraf et al., 2015; Focke et al., 1985). In the tested range, Eq. (7) considers the flow as turbulent, and is only valid for the present measurement.

$$\Delta P_{fri,w} = 2 f_w \frac{G_w^2}{\rho_w} \frac{L_p}{d_h} \qquad \text{Eq. (6)}$$

$$f_w = 4.608 Re_w^{-0.287} \qquad 400 \le Re_w \le 2500 \qquad \text{Eq. (7)}$$

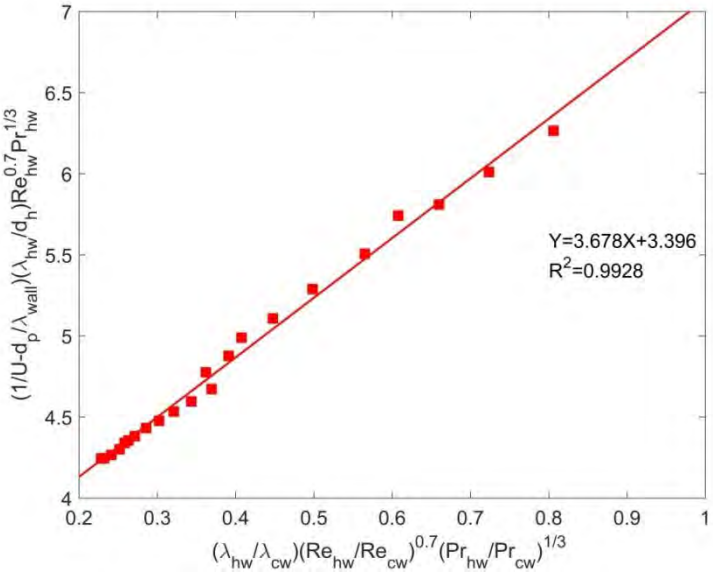

Figure 2: Results of Wilson-plot method for H_2O-H_2O experiments

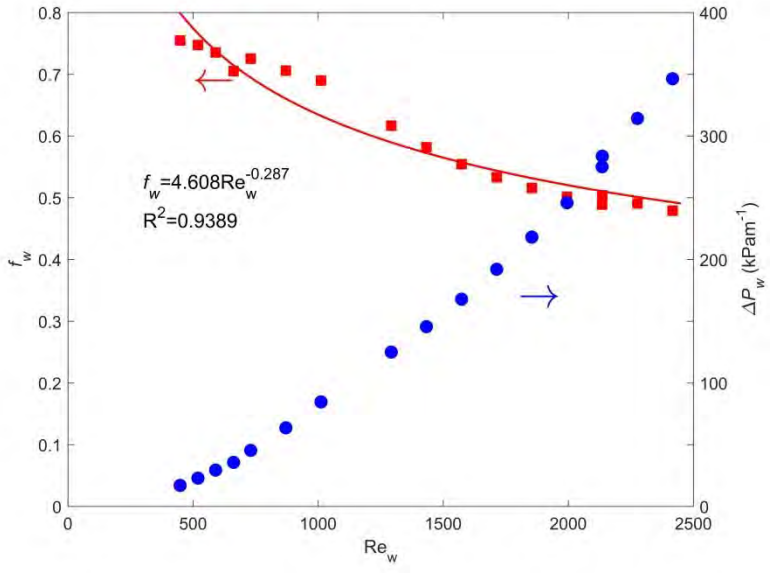

Figure 3: The correlation of single-phase Fanning friction factor and experimental data

3.2. HTCs of NH_3

To reduce the experimental data of NH_3, Eqs. (8)-(9) calculate the energy balances of the after cooler and test section. $h_{a,out}$ and $h_{a,in}$ are the NH_3 enthalpy at the outlet and inlet of the test section, which are used to determine the corresponding vapor qualities (Lemmon et al., 2013). $h_{a,04}$ is the enthalpy at the outlet of the after cooler and is determined by the measured temperature and pressure. Q is the heat transfer rate, and $\dot{m}$ is the mass flow rate. $c_{p,w}$ is the specific heat capacity of water. T_w is the water temperature.

$$h_{a,out} = h_{a,04} + \frac{Q_{after}}{\dot{m}_{a,01}} = h_{a,04} + \frac{c_{p,w}\dot{m}_{w,04}\left(T_{w,07} - T_{w,05}\right)}{\dot{m}_{a,01}} \quad \text{Eq. (8)}$$

$$h_{a,in} = h_{a,out} + \frac{Q_{test}}{\dot{m}_{a,01}} = h_{a,out} + \frac{c_{p,w}\dot{m}_{w,03}\left(T_{w,06} - T_{w,05}\right)}{\dot{m}_{a,01}} \quad \text{Eq. (9)}$$

Eq. (10) determines the condensation HTCs, α_a, where U is the overall HTC and is the combination of water HTC, α_w, wall thermal resistances, d_p/λ_{wall}, and NH_3 HTC, α_a. T_a is the NH_3 temperature and is constant in the test section.

$$\begin{aligned} Q_{test} &= \dot{m}_{w,03}c_{p,w}\left(T_{w,06} - T_{w,05}\right) = \dot{m}_{a,01}\left(h_{a,in} - h_{a,out}\right) \\ &= UA\frac{\left(T_{a,in} - T_{w,06}\right) - \left(T_{a,out} - T_{w,05}\right)}{\ln\dfrac{T_{a,in} - T_{w,06}}{T_{a,out} - T_{w,05}}} = \frac{A}{\dfrac{1}{\alpha_a} + \dfrac{d_p}{\lambda_{wall}} + \dfrac{1}{\alpha_w}}\frac{\left(T_{a,in} - T_{w,06}\right) - \left(T_{a,out} - T_{w,05}\right)}{\ln\dfrac{T_{a,in} - T_{w,06}}{T_{a,out} - T_{w,05}}} \end{aligned} \quad \text{Eq. (10)}$$

3.3. Apparent HTCs of NH_3/H_2O

The data reduction of NH_3/H_2O takes place in a similar way as for NH_3, while the bulk NH_3 concentration is needed to determine the thermodynamic state. The masses of the charged NH_3 and H_2O are first measured, and the global concentration is calculated. During experiments, the density of the NH_3/H_2O liquid is measured by D01 shown in Fig. 1 and is used to determine the bulk NH_3 concentration together with the temperature and pressure measured by T08 and P07 at the same position. The bulk NH_3 concentration of the overall flow is constant, while the separated liquid phase has lower concentration and vapor phase has higher concentration. Fluid properties are calculated with the database of Refprop and M. Conde Engineering (Lemmon et al., 2013; M. Conde Engineering, 2006).

Eqs. (8)-(10) are also used to calculate the condensation HTCs of NH_3/H_2O with the additional input of bulk NH_3 concentration, where T_a is the mixture equilibrium temperature and depends on the vapor qualities. α_a is the apparent HTC of NH_3/H_2O and considers the deterioration of heat transfer due to mass transfer, but the mass transfer resistance is not calculated directly. Apparent HTC takes the mixture effect into account and is more relevant for high concentration NH_3/H_2O, which is comparable with NH_3 (Fronk and Garimella, 2016).

3.4. Frictional pressure drop

As shown in Eq. (11), the condensation frictional pressure drop, $\Delta P_{fri,a}$, is calculated by subtracting the other components from the measured pressure drop, $\Delta P_{exp,a}$, including: the pressure drop of inlet and outlet ports, $\Delta P_{in\ port,a}$, $\Delta P_{out\ port,a}$, mixing pressure drop, $\Delta P_{mix,a}$, deceleration pressure rise, $\Delta P_{de,a}$, and elevation pressure rise, $\Delta P_{ele,a}$.

$$\Delta P_{fri,a} = \Delta P_{exp,a} - \Delta P_{in\,port,a} - \Delta P_{out\,port,a} - \Delta P_{mix,a} + \Delta P_{de,a} + \Delta P_{ele,a} \quad \text{Eq. (11)}$$

In Eqs. (12)-(13), $\Delta P_{in\ port,a}$ and $\Delta P_{out\ port,a}$ are treated as sudden enlargement and sudden contraction of two-phase flow, respectively. G_{tube} is the mass flux in the connection tubes. A_{tube} and A_{port} are the flow areas of tubes and ports. v_L and v_G are the specific volume of liquid and vapor. x is the vapor quality. 0.591 is an empirical parameter and is determined by the ratio of A_{tube} to A_{port} (Collier and Thome, 1994).

$$\Delta P_{in\ port,a} = G_{tube}^2 v_L \frac{A_{tube}}{A_{port}}\left(1 - \frac{A_{tube}}{A_{port}}\right)\left(1 + \frac{v_G - v_L}{v_L}x\right) \quad \text{Eq. (12)}$$

$$\Delta P_{out\ port,a} = \frac{G_{tube}^2 v_L}{2}\left(\frac{1}{0.591}-1\right)^2\left(1+\frac{v_G - v_L}{v_L}x\right) \quad \text{Eq. (13)}$$

In Eqs. (14)-(16), $\Delta P_{de,a}$ and $\Delta P_{ele,a}$ are calculated using the homogeneous two-phase model, which considers the two-phase flow as a single fluid. G is the mass flux at the flow channel of the PHE. The averaged density is calculated at the averaged vapor quality (Collier and Thome, 1994).

$$\Delta P_{de,a} = G^2\left(v_G - v_L\right)\left(x_{in} - x_{out}\right) \quad \text{Eq. (14)}$$

$$\Delta P_{ele,a} = \rho_{av} g L_p \quad \text{Eq. (15)}$$

$$\frac{1}{\rho_{av}} = \frac{1-x_{av}}{\rho_L} + \frac{x_{av}}{\rho_G} \quad \text{Eq. (16)}$$

At the inlet of the test section, liquid is sprayed into vapor through orifices. The pressure drop of flowing through orifices is composed of sharp-edged effects at the entrance and exit regions, as well as the frictional component through finite-thickness (Jankowski et al., 2008; Ushida et al., 2014). This pressure drop is calculated in Eqs. (17)-(20). u_{ori} is the liquid velocity at the orifices. d_{ori} and d_{tube} are the diameters of the orifices and inlet tube. f_{com} is a combined friction factor, and includes sharp-edged term and frictional term in Eq. (18), respectively. $Re_{L,ori}$ is based on orifice diameter and velocity (Jankowski et al., 2008).

$$\Delta P_{mix,a} = 0.5 u_{ori}^2 \rho_L \left[1-\left(\frac{d_{ori}}{d_{tube}}\right)^4\right] f_{com} \quad \text{Eq. (17)}$$

$$f_{com} = \frac{25}{9}\left[1+e^{-0.12\sqrt{Re_{L,ori}}} - 2.16e^{-0.26\sqrt{Re_{L,ori}}} + 0.16\left(1-\frac{\sqrt{Re_{L,ori}}}{1+\sqrt{Re_{L,ori}}}\right)\right]^{-2} + \frac{4}{Re_{L,ori}}\frac{L_{ori}}{d_{ori}}\left(\frac{3.44}{\sqrt{\xi}} + \frac{16+0.3125\xi^{-1}-3.44/\sqrt{\xi}}{1+2.12\times10^{-4}\xi^{-2}}\right) \quad \text{Eq. (18)}$$

$$Re_{L,ori} = \rho_L u_{ori} d_{ori} / \mu_L \quad \text{Eq. (19)}$$

$$\xi = L_{ori} / \left(d_{ori}\, Re_{L,ori}\right) \quad \text{Eq. (20)}$$

4. RESULTS AND DISCUSSION

Condensation experiments of NH_3 and NH_3/H_2O were carried out to collect the data of heat transfer and pressure drop. The mass fluxes of the cold water were maintained to be the maximum value allowed by the setup, so this heat transfer resistance is restricted. As a consequence, the heat transfer resistance of the condensation side is larger than of the water side. The weight concentration of NH_3/H_2O is 96% ± 1%, and the concentration increases slightly with vapor qualities during operation. The mass fluxes were kept almost the same for NH_3 and NH_3/H_2O, and were 62 $kgm^{-2}s^{-1}$ and 60 $kgm^{-2}s^{-1}$, respectively. So the experimental results can be compared. The condensation pressures were 630 and 770 kPa for NH_3 and 650 kPa for NH_3/H_2O. Since the latent heat of the working fluids is large and the cooling capacity of the setup is limited to around 6 kW at 10 °C, high vapor quality cannot be obtained and the changes of the vapor quality are smaller than 0.2.

In Fig. 4, HTCs increase sharply with vapor qualities. The HTCs of NH_3 double when the vapor qualities rise from 0.2 to 0.4, while the apparent HTCs of NH_3/H_2O increase 1.5 times in the same range. NH_3 and NH_3/H_2O have large two-phase density difference. The thickness of condensate film decreases with vapor quality. NH_3 and NH_3/H_2O have stronger sensitivities to vapor quality than other refrigerants such as R134a and R410A (Yan et al., 1999; Kuo et al., 2005). NH_3 yields larger HTCs than NH_3/H_2O especially at higher vapor qualities as a result of mass transfer resistance. NH_3/H_2O has a large temperature glide, and mass transfer resistance deteriorates the heat transfer distinctly even the weight concentration is as high as 96%. Being the less volatile component, H_2O tends to condense first at higher vapor qualities, where the mass transfer resistance is stronger. At lower vapor qualities, the vapor phase is almost pure NH_3 since most of

the H_2O has already been condensed, so the HTCs are consistent with purity (Fronk and Garimella, 2016). For NH_3, higher condensation pressure slightly reduces the HTCs, since the two-phase density ratio is closer to 1, and the shear force at the interface is restricted.

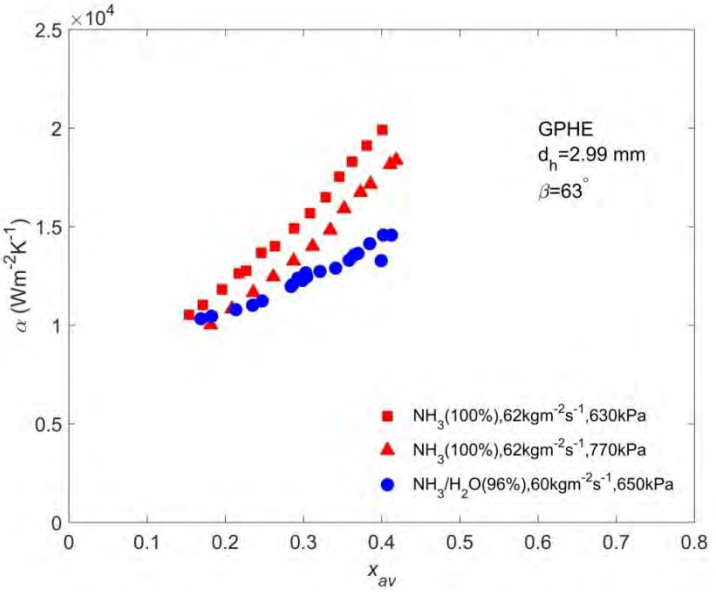

Figure 4: Condensation HTCs of NH_3 and NH_3/H_2O with varying averaged vapor quality and condensation pressure

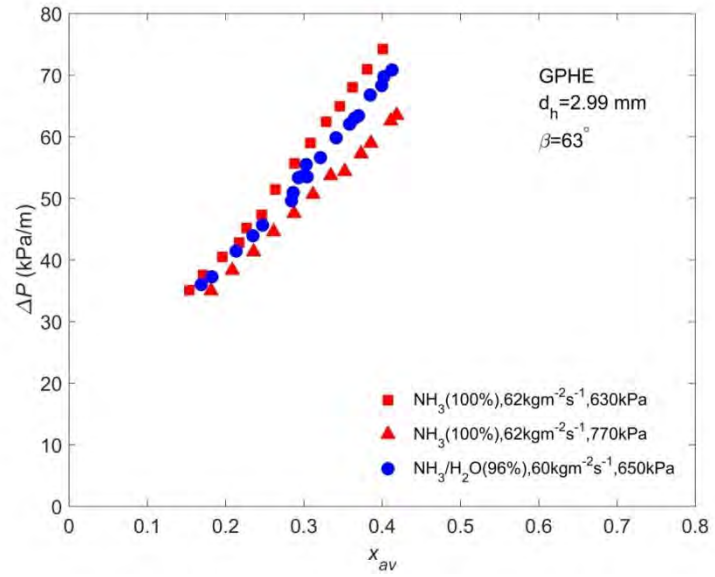

Figure 5: Frictional pressure drop of NH_3 and NH_3/H_2O with varying averaged vapor quality and condensation pressure

Fig. 5 presents the frictional pressure drop under the same operating conditions as Fig. 4. The data were calculated as described in Section 3.4. The pressure losses or gains contributed by flow area change, velocity change, mixing, etc. are minor, and are smaller than one tenth of the frictional pressure drop. Vapor qualities have a significant influence on the frictional pressure drop. It can be attributed to the large density difference of the fluids. The rise of the vapor quality increases the volume flux and shear force at the two-phase interface. The mixture effect can be neglected, and the data of NH_3/H_2O are almost the same as NH_3 under similar mass fluxes and condensation pressure. The pressure drop also decreases with increasing condensation pressure, and the difference is more noticeable at higher vapor qualities. As the pressure increases, the two-phase density difference reduces, as well as the shear force. This is similar to the results of Fig. 4.

5. CONCLUSIONS

This paper describes condensation experiments of NH_3 and NH_3/H_2O with a weight concentration of 96% in a PHE. H_2O-H_2O experiments were first conducted to determine the single-phase HTCs and Fanning friction factors, which were needed to analyse condensation. Additionally, the data reduction methods are provided to determine condensation HTCs and frictional pressure drop.
For a mass flux of 62 $kgm^{-2}s^{-1}$, the condensation HTCs of NH_3 vary from 10 to 20 $kWm^{-2}K^{-1}$, while the apparent HTCs of NH_3/H_2O are in the range of 10-15 $kWm^{-2}K^{-1}$ for 60 $kgm^{-2}s^{-1}$. The HTCs of both working fluids are similar for low vapor qualities, but the mass transfer resistance deteriorates the heat transfer noticeably for higher vapor qualities. On the other hand, the mixture effect is negligible for the frictional pressure drop. Higher condensation pressure mainly affects the two-phase density, and slightly reduces the HTCs and frictional pressure drop.

ACKNOWLEDGEMENTS

This project has been developed in cooperation with Bluerise BV. X.T. and C.A.I.F. acknowledge the financial support from the China Scholarship Council and from the Koude Groep Delft / Wageningen.

NOMENCLATURE

Symbols

A	actual heat transfer area (m^2)
c_p	specific heat capacity ($J.kg^{-1}.K^{-1}$)
d	diameter (m)
d_h	hydraulic diameter (m)
d_p	plate thickness (m)
f	friction factor (-)
g	gravitational constant (ms^{-2})
G	mass flux ($kgm^{-2}s^{-1}$)
h	enthalpy ($J.kg^{-1}$)
L_p	port-to-port plate length (m)
$\dot{m}$	mass flow rate ($kg.s^{-1}$)
Nu	Nusselt number (-)
P	pressure (Pa)
Pr	Prandtl number (-)
Q	heat flow rate (W)
Re	Reynolds number (-)
T	temperature (K)
u	velocity (ms^{-1})
U	overall heat transfer coefficient ($W.m^{-2}.K^{-1}$)
v	specific volume (m^3kg^{-1})
x	vapor quality (-)

Greek symbols

α	heat transfer coefficient ($W.m^{-2}.K^{-1}$)
β	chevron angle to flow direction (°)
Δ	difference
ξ	parameter in eq. (20) (-)
ρ	density (kgm^{-3})
Θ_i	parameters in eq. (1) (-)
λ	thermal conductivity ($W.m^{-1}.K^{-1}$)
μ	dynamic viscosity (Pas)

Subscripts

a	ammonia or ammonia water
after	after cooler
av	averaged
com	combined value
cw	cold water
de	deceleration
ele	elevation
exp	measured value
fri	frictional pressure drop
G	gas or vapor
hw	hot water
in	inlet of test section
L	liquid
mix	mixing process
ori	orifice
out	outlet of test section
port	ports of test section
test	test section
tube	connected tube
w	water
wall	plate wall

REFERENCES

Cerezo, J., Best, R., Bourouis, M., Coronas, A., 2010. Comparison of numerical and experimental performance criteria of an ammonia–water bubble absorber using plate heat exchangers. Int. J. Heat Mass Transf. 53, 3379-3386.

Collier, J. G., Thome J. R., 1994. Convective boiling and condensation, Clarendon Press, Oxford.

Conde Engineering, M., 2006. Thermophysical properties of ammonia-water mixtures for the industrial design of absorption refrigeration equipment.

Fernández-Seara, J., Uhía, F. J., Sieres, J., Campo, A., 2007. A general review of the Wilson plot method and its modifications to determine convection coefficients in heat exchange devices. Appl. Therm. Eng. 27, 2745-2757.

Focke, W. W., Zachariades, J., Olivier, I., 1985. The effect of the corrugation inclination angle on the thermohydraulic performance of plate heat exchangers. Int. J. Heat Mass Transf. 28, 1469-1479.

Fronk, B.M., Garimella, S., 2016. Condensation of ammonia and high-temperature-glide ammonia/water zeotropic mixtures in minichannels–Part I: Measurements. Int. J. Heat Mass Transf. 101, 1343-1356.

García-Cascales, J. R., Vera-García, F., Corberán-Salvador, J. M., Gonzálvez-Maciá, J., 2007. Assessment of boiling and condensation heat transfer correlations in the modelling of plate heat exchangers. Int. J. Refrig. 30, 1029-1041.

Jankowski, T. A., Schmierer, E. N., Prenger, F. C., Ashworth, S. P., 2008. A series pressure drop representation for flow through orifice tubes. J. Fluids Eng. 130(5), 051204.

Kang, Y. T., Akisawa, A., Kashiwagi, T., 2000. Analytical investigation of two different absorption modes: falling film and bubble types. Int. J. Refrigeration. 23, 430-443.

Kuo, W. S., Lie, Y. M., Hsieh, Y. Y., Lin, T. F., 2005. Condensation heat transfer and pressure drop of refrigerant R-410A flow in a vertical plate heat exchanger. Int. J. Heat Mass Transf 48, 5205-5220.

Lemmon, E. W., Huber, M. L., McLinden, M. O., 2013. NIST Standard Reference Database 23: Reference Fluid Thermodynamic and Transport Properties-REFPROP, Version 9.1, National Institute of Standards and Technology, Standard Reference Data Program, Gaithersburg.

Sarraf, K., Launay, S., Tadrist, L., 2015. Complex 3D-flow analysis and corrugation angle effect in plate heat exchangers. Int. J. Therm Sci. 94, 126-138.

Shah R.K., Focke W.W., 1988. Plate heat exchangers and their design theory, in: Shah R.K., Subbarao E.C., Mashelkar R.K. (Eds.), Heat Transfer Equipment Design, Hemisphere, Washington DC, 227-254.

Tao, X., Nuijten, M., Infante Ferreira, C., 2018a. Two-phase vertical downward flow in plate heat exchangers: Flow patterns and condensation mechanisms. Int. J. Refrigeration. 85: 489-510.

Tao, X., Dahlgren, E., Infante Ferreira, C., 2018b. Local NH_3 condensation in a plate heat exchanger. 13th IIR Gustav Lorentzen Conference On Natural Refrigerants. Valencia, Spain.

Triché, D., Bonnot, S., Perier-Muzet, M. Boudéhenn, F. Demasles, H. Caney, N., 2017. Experimental and numerical study of a falling film absorber in an ammonia-water absorption chiller. Int. J. Heat Mass Transf. 111, 374-385.

Ushida, A., Hasegawa, T., Narumi, T., 2014. Anomalous phenomena in pressure drops of water flows through micro-orifices. Microfluid Nanofluidics 17(5), 863-870.

Yan, Y.-Y., Lio, H.-C., Lin, T.-F., 1999. Condensation heat transfer and pressure drop of refrigerant R-134a in a plate heat exchanger. Int. J. Heat Mass Transf. 42, 993-1006.

Manuscript ID: 738
DOI: 10.18462/iir.icr.2019.0738

Performance analysis of a thermoelectric assisted indirect evaporative cooling system considering condensation from primary air

Ming GAO[(a)], Yuanyuan ZHOU[(a)], Jianlin YU[(b)], Yanshun YU[(a)]

[(a)] School of Energy and Power Engineering, Nanjing University of Science & Technology,

Nanjing 210094, China, fax: 86-25-84315476, email: zhouyy@njust.edu.cn

[(b)] Department of Refrigeration & Cryogenic Engineering, School of Energy and Power Engineering,

Xi'an Jiaotong University, Xi'an 710049, China

Abstract

This paper proposes a thermoelectric assisted indirect evaporative cooling (TIEC) system, in which thermoelectric cooling modules are sandwiched between channels of a plate-fin indirect evaporative cooler operated in a countercurrent flow mode. As the moisture content of fresh air is high, condensation may occur in the dry channels. A mathematical model of this novel system is developed with taking the condensation from primary air into consideration. Performance analysis of the TIEC system with condensation is conducted in detail. Analytical results show that the condensation from primary air weakens the performance of system by reducing the values of the coefficient of performance and dew point effectiveness. The effects of main operating conditions, such as the electrical current and number of the thermoelectric cooling modules, inlet temperature, humidity ratio and velocity of the primary air are also investigated.
Keywords: Thermoelectric, Indirect evaporative cooling, Condensation, Dew point effectiveness, coefficient of performance.

1. INTRODUCTION

Building energy consumption has increased globally for past decades, which accounts for about 40% of total primary energy requirement (Yang et al., 2014). The urgency of environment protection and energy conservation attracts worldwide study to reduce the high energy cost of HAVC (heating, ventilating, and air-conditioning) systems in buildings. Indirect evaporative cooler (IEC) is an environmentally friendly cooling device which uses water as the refrigerant, and could reduce much more energy consumption (Porumb et al., 2016). However, the ambient air condition has a significant influence on IEC system's performance which makes IEC systems inefficient to be applied independently in wet regions. (Riangvilaikul and Kumar, 2010).

In order to enhance the performance and adaptability to the environment of the IEC systems, many numerical analysis and experimental study have been conducted. The theory of heat and mass exchange calculation for IEC systems has always been the emphasis of evaporative cooling

technology (Chua et al., 2016). Maclaine-Cross and Banks (1981) studied the basic theory of heat exchanger with wet surface. Kettleborough and Hsieh (1983) proposed the plate humidity parameters to improve the mathematical model for heat transfer of counter-flow and cross-flow IEC systems. Stoitchkov and Dimitrov (1988) improved the Maclaine-Cross and Banks model and established a two-dimensional mathematical model based on flowing liquid film. Various indirect evaporative cooler configurations have been investigated over the past decades (Mahmood et al., 2016., Zhan et al. 2011., Demis et al. 2017). In recent years, several researches also proposed novel hybrid evaporative cooling system (Heidarinejad et al., 2010., Kim et al., 2015., Gao et al., 2015.), allowing the system able to achieve a thermal comfort condition in humid regions. In a previous study by the authors (Zhou et al., 2018), a novel thermoelectric assisted indirect evaporative cooling (TIEC) system was developed by combining the thermoelectric cooling technology and the indirect evaporative cooling technology. The simulation results show that the proposed system is able to cool primary air to a temperature much lower than inlet air wet bulb temperature, even dew point temperature.

Although most of the previous studies focused on the wet channel and only considered the sensible heat transfer from primary air, some researchers also conducted numerical and experimental studies to investigate and prove the impact of the condensation from primary air on performance of IEC system (Yang et al. 2006., Chen et al., 2016., Meng et al., 2018., Li et al., 2018). Considering the ignorance of the influence of condensation from primary air in the previous study (Zhou et al., 2018), a novel mathematical model of a thermoelectric assisted indirect evaporative cooling system considering the condensation from primary air is developed in this paper. The influence of condensation on COP and cooling effectiveness is investigated under various operating parameters, including the electrical current and number of thermoelectric modules, inlet temperature, humidity ratio and velocity of the primary air.

2. MAIN SECTION

2.1. System description

Figure 1(a) shows schematic diagrams of the TIEC system. The TEC modules are inserted inside the intermediate plate between dry and wet channels of the cooler. The hot side is connected to the wet channel and the cold side to the dry channel. Offset strip fins are arranged in the wet channel. Figure 1(b) shows schematic diagram of the plate-fin counter-flow indirect evaporative cooler with TEC modules. The base plate and fin surfaces in wet channel are covered by the water film sprayed from the top by nozzles. As the water flows down, it absorbs heat released by the hot side of the TEC modules and exchanges heat and mass with the secondary air.

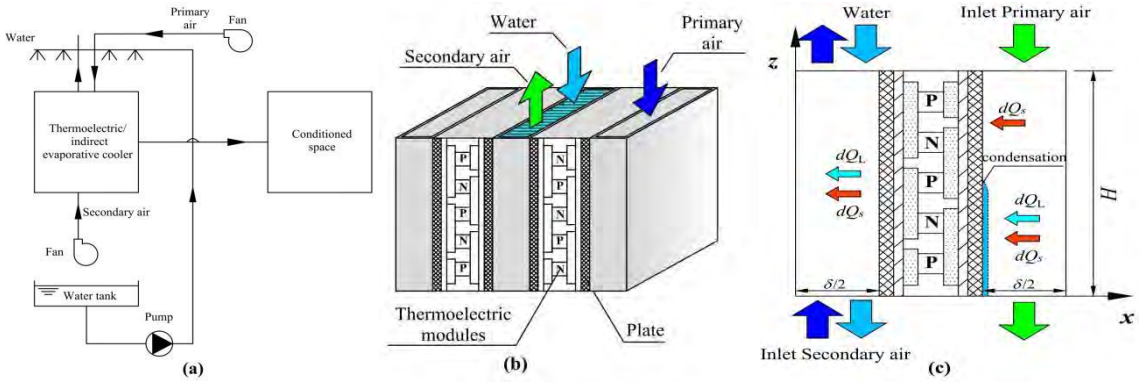

Figure 1: (a) Schematic diagram of the TIEC system; (a) Schematic diagram of a flat plate counter flow thermoelectric/indirect evaporative cooler; (c) Control volume of a thermoelectric/indirect evaporative cooler.

2.2. Mathematic model

Figure 1(c) demonstrates the control volume of a thermoelectric/indirect evaporative cooler, including the half dry channel and half wet channel filled with fins. Primary air and secondary air flow in a parallel flow pattern, and secondary air and water flow in a countercurrent flow pattern. The control volume finite difference method is used for heat and mass transfer process in wet channel and the lumped parameter method is used in the dry channel. Some necessary assumptions are made to simply the model (Liu et al., 2013., Shourideha et al., 2018). Only the important equations will be presented here.

According to the standard equations of TEC performance, the heat absorbed and released for TEC modules, Q_c and Q_h, can be given by (Zhou and Yu, 2012),

$$Q_{\mathrm{c}} = n\left[\alpha_0 I T_{\mathrm{c}} - K_0(T_{\mathrm{h}} - T_{\mathrm{c}}) - \frac{1}{2}R_0 I^2\right] \quad \text{Eq. (1)}$$

$$Q_{\mathrm{h}} = n\left[\alpha_0 I T_{\mathrm{h}} - K_0(T_{\mathrm{h}} - T_{\mathrm{c}}) + \frac{1}{2}R_0 I^2\right] \quad \text{Eq. (2)}$$

T_h and T_c are the individual cold and hot junction temperatures of the TEC module.

The heat released and the heat absorbed by TEC modules for each segment of the wet and dry channel, dQ_h and dQ_c can be given by,

$$dQ_{\mathrm{h}} = \frac{Q_h}{H}dz = K_{\mathrm{h}}dA_{\mathrm{h}}(T_{\mathrm{h}} - T_{\mathrm{h,w}}) \quad \text{Eq. (3)}$$

$$dQ_{\mathrm{c}} = \frac{Q_c}{H}dz = K_{\mathrm{c}}dA_{\mathrm{c}}(T_{\mathrm{c}} - T_{\mathrm{c,w}}) \quad \text{Eq. (4)}$$

$T_{h,w}$ is the wall temperature in wet channel. $T_{c,w}$ is the wall temperature in dry channel.

The heat balance per unit height of the wet channel can be expressed by the following equations,

$$dQ_{\mathrm{h}} = dQ_{\mathrm{a}} + dQ_{\mathrm{w}} \quad \text{Eq. (5)}$$

$$dQ_{\mathrm{a}} = dQ_{\mathrm{s}} + dQ_{\mathrm{l}} = [h_{\mathrm{a}}(T_{\mathrm{w}} - T_{\mathrm{a}}) + r_{\mathrm{w}}k_{\mathrm{d,a}}(W_{\mathrm{w}} - W_{\mathrm{a}})\beta](L_{\mathrm{f}} \cdot \eta_{\mathrm{f}} + L_{\mathrm{b}})dz \quad \text{Eq. (6)}$$

η_f is local fin efficiency in wet channel, which can be estimated by (Zhou et al., 2014),

$$\eta_{\mathrm{f}} = \frac{\tanh(mb)}{mb}, b = H_{\mathrm{f}}/2, m = \left(\frac{2h_{\mathrm{f}}}{\lambda_{\mathrm{w}}\delta_{\mathrm{f}}}\right)^{1/2} \quad \text{Eq. (7)}$$

β is the surface wettability factor, and is set as 0.8 for analysis (Duan, 2011). The appearance of condensation leads to sensible and latent heat transfer in dry channel. When condensation occurs, the latent heat transfer $dQ_{p,l}$ should be considered as (Li et al., 2018),

$$dQ_{\mathrm{p,l}} = r_{\mathrm{w}} k_{\mathrm{p,d}} (W_{\mathrm{p,w}} - W_{\mathrm{p}}) \beta \sigma L dz \qquad \text{Eq. (8)}$$

Condensation factor ϭ was chosen to describe condensation situations of dry channel in equations, the value equals 1 while condensation exists, and equals 0 while there exist no condensation.
When recirculating water is used, no heat is taken or given by the water, thus,

$$\int_0^H dQ_{\mathrm{w}} = 0 \qquad \text{Eq. (9)}$$

In order to evaluate the overall performance of the system, dew-point effectiveness ε_{db} and coefficient of performance (COP) for the proposed system need to be calculated as,

$$\varepsilon_{\mathrm{db}} = \frac{T_{\mathrm{p1}} - T_{\mathrm{p2}}}{T_{\mathrm{p1}} - T_{\mathrm{pd}}} \qquad \text{Eq. (10)}$$

$$\mathrm{COP} = \frac{Q_{\mathrm{c}}}{N} \qquad \text{Eq. (11)}$$

2.3. Results and discussions

The performances of the proposed TIEC system with and without considering the condensation from primary air are analyzed based on the established mathematical model. The commercial Bi_2Te_3 based semiconductors are selected as thermoelectric materials (Zhou and Yu, 2012). In this paper, the inlet secondary air temperature is set as 28˚C, relative humidity as 50% and the velocity as 3 m/s. The length and width of the channel are all 0.4 meters, and the width of channel is 5mm. The pitch of fin in wet channel is 10mm and the thickness is 0.2mm.
Figure 2 shows the variations of COP and dew point effectiveness ε_{db} with the working electric current I and number n of TEC modules with inlet temperature of primary air (T_{p1}) as 35˚C and three different relative humidity of primary air RH_p. It can be seen that larger I and n could result in lower COP but higher ε_{db}. Figure 2 also shows that without considering the condensation from primary air, COP is independent of the RH_p, however, ε_{db} increases when the RH_p increases due to the increase of the dew point temperature. In Figure 2 (a), with considering the condensation, and the RH_p as 20%, the condensation occurs in dry channel when I bigger than 1.6A. With the RH_p as 40%, the condensation occurs when I is bigger than 0.6A. And With the RH_p as 60%, the condensation occurs when I is smaller than 0.5A. The condensation from the primary air would decrease both COP and ε_{db}. The reason is that the condensation in dry channel increases the thermal load at the cold side of the thermoelectric modules, resulting in a reduction in the total cooling capacity. Figure 2 (b) further shows both the COP and ε_{db} decrease once condensation occurs when the n is bigger than 10 with RH_p as 40% and I as 0.5A. As RH_p increases to 60%, the amount of condensation increases dramatically which leads to a remarkable influence on COP and ε_{db}.

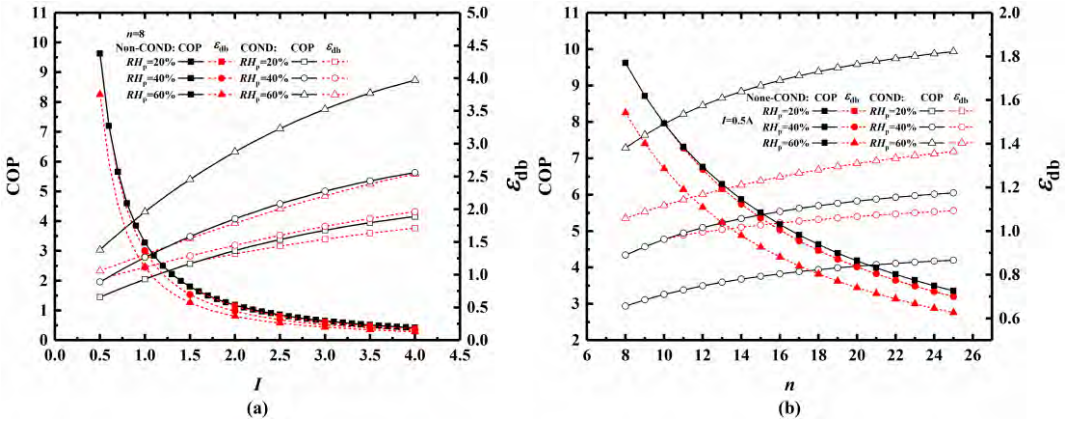

Figure 2: (a) COP and ε_{db} versus the I under different RH_p; (b) COP and ε_{db} versus the n under different RH_p.

Figure 3 presents the influence of RH_p on COP and ε_{db}. In Figure 3, condensation occurs when RH_p reach 40.4% with n as 10 and I as 0.5A. With n as 15 and I as 0.5A, condensation occurs when RH_p is larger than 36.2%. And when n is 10 and I is 1A, condensation occurs while RH_p smaller than 30%. Figure 3(a) shows that without condensation, COP remains constant with varying RH_p. The turning point of RH_p from non-condensation to condensation state decreases with the increase of I and n. This is because higher the I and n are, faster the cold side temperature of TEC module will decrease down to below the dew point temperature of primary air which makes condensation occur in lower RH_p. Figure 3(b) indicates that ε_{db} increase monotonously with the increase of RH_p. Addtionally, the effect of condensation on COP and ε_{db} gradually increases as the RH_p increases.

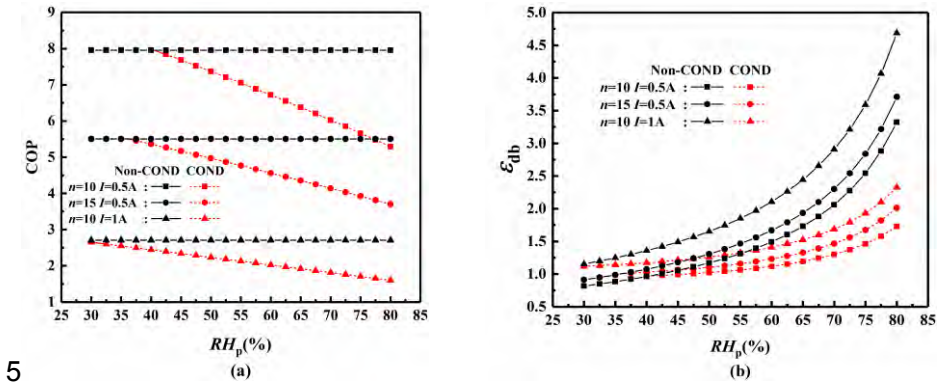

Figure 3: (a) COP versus the RH_p; (b) ε_{db} versus the RH_p.

Figure 4 depicts the variation curves of COP and ε_{db} versus the T_{p1}. When the T_{p1} increases from 25˚C to 45˚C under given n and I, the temperature difference between primary air and wall increases, leading to the increase of COP and ε_{db}. In Figure 4(a), when RH_p is 40%, condensation occurs with T_{p1} higher than 35˚C. And with RH_p as 60%, condensation already occurs while T_{p1} is smaller than 25˚C. Figure 4(b) further shows that the upward trend of ε_{db} gradually becomes flatter and eventually changes little with T_{p1} under condensation state. The reason is that the latent heat released by condensation water results in the increase of wall temperature in dry channel as well as outlet air temperature T_{p2}.

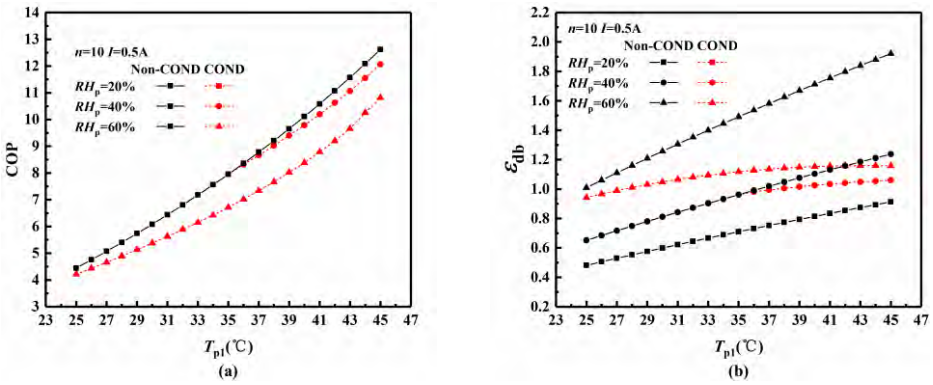

Figure 4: (a) COP versus the T_{p1}; (b) ε_{db} versus the T_{p1}.

Figure 5 presents the variation curves of COP and ε_{db} versus inlet velocity of primary air V_p. In Figure 5(a), COP increases with the increase of V_p under given condition. That can be explained by the fact that while keeping the size of heat exchanger unchanged, the increase of V_p would result in a higher mass flow rate, leading to a larger cooling capacity. It can be observed that with RH_p as 40%, condensation occurs when V_p is higher than 2.75 m/s. And with RH_p as 60%, condensation already occurs while V_p is smaller than 0.5 m/s. The reason is that the increase of V_p weakens the heat transfer while the parameters of secondary air keep constant. Figure 5(b) further shows that the appearance of condensation reduces the value of ε_{db} due to the increase of T_{p2}. Moreover, Figure 5 also shows that with RH_p as 60%, there exist a maximum reduction of COP and ε_{db} considering condensation when V_p is 4m/s and 1.25m/s respectively.

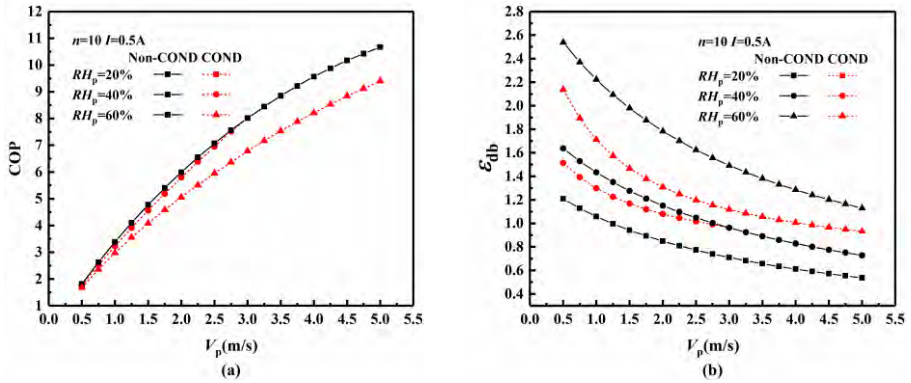

Figure 5: (a) COP versus the V_p; (b) Ɛdb versus the V_p.

3. CONCLUSIONS

A novel numerical model of thermoelectric assisted IEC system considering condensation from primary air has been established. The performance of the system is theoretically investigated under non-condensation state and condensation state. The highlighted results can be concluded as follows: (1) Condensation occurs in dry channel when primary air temperature decreases lower than saturated temperature, which would risie the wall temperature in dry channel and weakens the performance of system by reducing the COP and ε_{db} values. (2) The influence of condensation on COP and ε_{db} would rise dramatically with the increase of RH_p. Thus, it is important to take condensation from primary air into consideration when designing a thermoelectric assisted indirect evaporative cooling system. (3) Influences of temperature and inlet velocity of primary air, Tp_1 and V_p, on COP and ε_{db} between non-condensation and condensation state also have been analyzed.

Compared with COP, the influence of condensation on ε_{db} is more obvious when Tp_1 increases. And the variation of V_p would cause a maximum reduction of COP and ε_{db} while condensation occurs.

ACKNOWLEDGEMENTS

This work was supported by the National Natural Science Foundation of China (NSFC) [grant No.51706099] and Postgraduate Research & Practice Innovation Program of Jiangsu Province [grant No.SJCX18_0154]. The authors would like to express sincere thanks for the sponsorship.

NOMENCLATURE

A	area (m^2)	b	base plate (m)
c_p	specific heat (J/kg·K)	H	height of the heat exchanger (m)
h	heat transfer coefficient ($W/m^2·K$)	I	electrical current (A)
k_d	mass transfer coefficient ($kg/m^2·s$)	K	total heat transfer coefficient ($W/m^2·K$)
K_0	total thermal conductance of TEC module (W/K)	L	length of the heat exchanger (m)
n	number of TEC modules	N	power consumption (W)
Q	heat transfer rate (W)	r_w	specific enthalpy of water vapor (J/kg)
R_0	total electrical resistance (Ω)	RH	relative humidity(%)
T	temperature (K)	W	humidity ratio of air (kg/kg)
V	velocity (m/s)	δ	thickness(m)
p	primary air	α_0	seebeck coefficient (V/K)
η_f	fin efficiency	a	secondary air
β	surface wettability factor	ε_{db}	dew point effectiveness
s	sensible	λ	thermal conductivity (W/m K)
l	latent	w	water

REFERENCES

Chua, K., Xu, J., Cui, X., Ng, KC., Islam, M., 2016. Numerical heat and mass transfer analysis of a cross‐flow indirect evaporative cooler with plates and flat tubes. Heat Mass Transfer 52, 1765-1777.

Chen, Y., Yang, H., Luo, Y., 2016. Indirect evaporative cooler considering condensation from primary air: Model development and parameter analysis. Building and Environment 95, 330-345.

Duan, Z. Investigation of a novel dew point indirect evaporative air conditioning system for buildings. University of Nottingham, 2011.

Gao, W., Worek, W., Konduru, V., Adensin, K., 2015. Numerical study on performance of a desiccant cooling system with indirect evaporative cooler. Energy and Buildings 86, 16-24.

Heidarinejad, G., Khalajzadeh, V., Delfani, S., 2010. Performance analysis of a ground-assisted direct evaporative cooling air conditioner. Build. Environ 45 (11), 2421-2429.

Kim, M.H., Park, J.Y. Ham, S.W., Jeong, J.W., 2015. Energy conservation benefit of water-side free cooling in a liquid desiccant and evaporative cooling-assisted 100% outdoor air system, Energy Build 104, 302-315.

Kettleborough, C., Hsieh, C., 1983. The thermal performance of the wet plastic plate heat exchanger used as an indirect evaporative cooler. ASME Journal of Heat Transfer 105, 366-373.

Liu, Z., Allen, W., Modera, M., 2013. Simplified thermal modeling of indirect evaporative heat exchangers. HVAC R Res 19(3), 257-67.

Li, W., Li, Y., Zeng, L., Lu, J., 2018. Comparative study of vertical and horizontal indirect evaporative cooling heat recovery exchangers. International Journal of Heat and Mass Transfer 124, 1245-1261.

Meng, D., Lv, J., Chen, Y., Li, H., Ma, X., 2018. Visualized experimental investigation on cross-flow indirect evaporative cooler with condensation. Applied Thermal Engineering 145, 165-173.

Maclaine-cross, I., Banks, P., 1981. .A general theory of wet surface heat exchangers and its application to regenerative evaporative cooling. ASME Journal of Heat transfer 103, 579-585.

Mahmood, MH., Sultan, M., Miyazaki, T., 2016. Overview of the Maisotsenko cycle - a way towards dew point evaporative cooling. Renew Sustain Energy Rev 66(C), 537-55.

Pandelidis, D., Anisimov, S., Rajski, K., Rajski, K., Sidorczk, M., 2017. Performance comparison of the advanced indirect evaporative air coolers. Energy 135, 138-152.

Porumb, B., Ungureşan, P., Tutunaru, L., Şerban, A., Bălan, M., 2016. A review of indirect evaporative cooling technology. Energy Procedia 85, 461-471.

Riangvilaikul, B., Kumar, S., 2010. An experimental study of a novel dew point evaporative cooling system. Energy Build 42, 637-644.

Shourideha, A., Ajrama, W., Lamia, J., Haggaga, S., Mansourib, A., 2018. A comprehensive study of an atmospheric water generator using Peltier effect. Thermal Science and Engineering Progress 6, 14-26.

Stoitchkov, N., Dimitrov, G., 1998. Effectiveness of cross-flow plate heat exchanger for indirect evaporative cooling. Int J.Refrig 21(6), 463-471.

Yang, H., Ren, C., Cui, P., 2006. Study on Performance Correlations of an Indirect Evaporative Cooler with Condensation from Primary Airflow. HVAC&R RESEARCH 12.

Yang, L., Yan, H, Lam, J., 2014. Thermal comfort and building energy consumption implications - A review. Applied Energy 115, 164-173.

Zhan, C., Duan, Z., Zhao, X., Smith, H., Jin, S., 2011. Comparative study of the performance of the M-cycle counter-flow and cross-flow heat exchangers for indirect evaporative cooling - paving the path toward sustainable cooling of buildings, Energy 36 (12) 6790 – 6805.

Zhou, Y., Yu, J., 2012. Design optimization of thermoelectric cooling system for applications in electronic devices. Int. J. Refrigeration 35(4), 1139-44.

Zhou, Y., Zhang, T., Wang, F., Yu, Y., 2018. Performance analysis of a novel thermoelectric assisted indirect evaporative cooling system. Energy 162, 299-308.

Zhou, Y., Zhu, L., Yu, J., L, Y., 2014. Optimization of plate-fin heat exchangers by minimizing specific entropy generation rate. International Journal of Heat and Mass Transfer 78, 942-946.

Manuscript ID: 742
DOI: 10.18462/iir.icr.2019.0742

Examining low global warming potential hydrofluoroolefin-hydrofluorocarbon blends as alternatives to R-404A

Stephen SPLETZER[(a)], Jethro MEDINA, Joshua HUGHES

[(a)]The Chemours Company
974 Centre Road, Wilmington, DE, 19805, USA,
stephen.spletzer@chemours.com

ABSTRACT

Reducing the impact of refrigeration systems is crucial to environmental sustainability. Therefore, lower global warming potential (GWP < 250) refrigerants are a priority. As R-404A is a higher GWP mainstream refrigerant, characterization of mildly flammable (class A2L) potential replacements was performed for this study. Examination of system properties, such as pressures, capacities, COPs, and mass flow rates was completed. Soft-optimized testing was also conducted, including minor equipment changes.

Results are given for XL40 (R-454A), XL20 (R-454C), R-455A, and R-459B. Equipment testing in a commercial refrigerator shows that A2Ls are viable alternatives to R-404A, with similar-to-better performance achieved with relatively minor system changes. Lubricant effects on compressor performance were also examined.

Safety considerations for use of A2Ls in new ACR equipment is also discussed, with regards to recently developed / in-process international standards work.

Keywords: A2L, Compressor, COP, Energy, Freezer, GWP, HFC, HFO, LFL, Lubricant, R-454A, R-454C, R-455A, R-459B, Refrigerant, XL20, XL40.

1. INTRODUCTION

Regulatory directives are leading ACR systems towards lower GWP refrigerants. Given R-404A's relatively high GWP, many blends have been formulated to replace it. The use of nonflammable products, such as XP40 (R-449A) (Minor 2015) and XP44 (R-452A), are growing globally. Yet still lower GWP options are needed to meet certain regulations (e.g. EU F-Gas 2014). Mildly flammable (A2L Safety Rating - ANSI / ASHRAE Standard 34-2016) HFO-based blends offer very low GWP solutions for self-contained equipment. These refrigerants allow for larger charge sizes than the highly flammable (A3 Safety Rating) hydrocarbons. As such, more equipment types may consider A2Ls as replacements. Design compatibility with R-404A equipment is also highly desirable for system OEMs, as this may help reduce the cost of implementing future refrigerant options.

Four mildly flammable (A2L) refrigerants were tested - XL40, XL20, R-455A, and R-459B. XL40 and XL20 are binary blends of R-32 / R-1234yf, while R-455A also uses CO_2, and the R-459B blend uses R-1234ze(E). Basic information on these refrigerants is listed in Table 1. Refrigerant performance was characterized using soft-optimized system testing in an upright two-door R-404A freezer. The results of these tests were then compared to the R-404A baseline data. Lubricant considerations were also examined for all four replacements. Implementation of A2Ls, through certain international safety standards, is also discussed.

Table 1: Refrigerant Blend Compositions, GWPs, & Safety Ratings

Product	Nominal Blend Composition (by weight %)	$GWP_{100\ Yr.}$ (AR4 / AR5)	Safety Rating
R-404A	44.0% R-125 / 52.0% R-143a / 4.0% R-134a	3,922 / 3,943	A1
XL40	35.0% R-32 / 65.0% R-1234yf	239 / 238	A2L
XL20	21.5% R-32 / 78.5% R-1234yf	148 / 146	A2L
R-455A	3.0% CO_2 / 21.5% R-32 / 75.5% R-1234yf	148 / 145	A2L
R-459B	21.0% R-32 / 69.0% R-1234yf / 10.0% R-1234ze(E)	144 / 143	A2L

2. THERMODYNAMIC PROPERTIES & THEORETICAL PERFORMANCE

Close operating properties are vital for replacement refrigerants, as this may allow OEMs to minimize equipment redesign. Thermophysical properties of all five refrigerants are shown in Table 2. Normal boiling points are similar for XL20, XL40, and R-459B, but slightly lower for R-455A. This can be attributed to R-455A's CO_2 content. Critical points are higher for the alternatives, which may contribute to better high ambient performance. XL20 and R-459B have lower pressures than R-404A, while the pressures of XL40 are close. Liquid densities of the replacements are close to those of R-404A, while vapor densities are all significantly lower. This would likely result in lower mass flow rates for the alternatives, relative to R-404A.

Table 2: Refrigerant Thermophysical Properties

	R-404A	XL40	XL20	R-455A	R-459B
Normal Boiling Point (°C)	-46	-48	-46	-52	-45
Critical Point Temp. (°C)	72	82	86	84	87
Liquid Pressure @ 25°C (kPa)	1255	1344	1191	1393	1163
Vapor Pressure @ 25°C (kPa)	1241	1164	977	1044	948
Liquid Density @ 25°C (kg/m^3)	1044	1021	1042	1035	1051
Vapor Density @ 25°C (kg/m^3)	65.3	48.1	44.5	45.8	43.0

Idealized thermodynamic cycle simulations were performed for all five refrigerants. Relative performance was estimated for a low temperature application at 35°C / -28°C Condenser / Evaporator temperatures, 13.3K / 3.9K Subcooling / Superheat, and 70% compressor isentropic efficiency (see Table 3). These conditions were selected using the last minute of pull-down for the R-404A freezer baseline test runs. XL40 showed higher capacity than R-404A, while R-455A was similar, and XL20 and R-459B were both lower. All replacements showed slightly higher COPs than R-404A. XL40 was a close pressure match to R-404A, while the other alternatives showed lower operating pressures. Discharge temperatures were higher for all replacements. For XL20 and R-459B, the differences are small enough that discharge temperature mitigation may not be required in certain low temperature applications. However, for XL40 and R-455A, discharge temperature control may be required, particularly for higher ambient conditions. R-455A also produced the largest temperature glides.

Table 3: Thermodynamic Cycle Performance Comparison

	R-404A	XL40	XL20	R-455A	R-459B
Capacity (Relative to R-404A - %)	100	106	89	98	86
COP (Relative to R-404A - %)	100	103	104	103	104
Mass Flow Rate (Relative to R-404A - %)	100	73	81	78	80
Suction Pressure Δ (from R-404A – kPa)	N/A	-10	-45	-26	-53
Discharge Pressure Δ (from R-404A – kPa)	N/A	14	-208	-52	-250
Discharge Temperature Δ (from R-404A – K)	N/A	19.5	10.1	14.7	10.7
Evaporator Temperature Glide (K)	0.5	4.7	5.6	7.4	6.1
Condenser Temperature Glide (K)	0.4	5.1	7.0	10.2	7.5

3. EQUIPMENT TEST SETUP

Refrigerant performance was evaluated in an R-404A double-door standalone upright reach-in freezer, with a top-mounted refrigeration skid. The freezer was instrumented and placed in a controlled constant temperature room. Internal volume of the refrigerated box was 1.5 m^3. The refrigeration circuit used a reciprocating compressor and adjustable TXVs feeding a dual evaporator assembly. Factory charge was 1.05 kg of R-404A / 1.15 kg of ISO 32 grade POE.

Instrumentation used for this study included thermocouples, pressure transducers, a Coriolis mass flow meter, and a digital power meter. A photograph of the equipment and diagrams of the experimental setup are included in Figure 1. Seven thermocouples were used to measure condenser temperatures, while five thermocouples were used on each evaporator assembly.

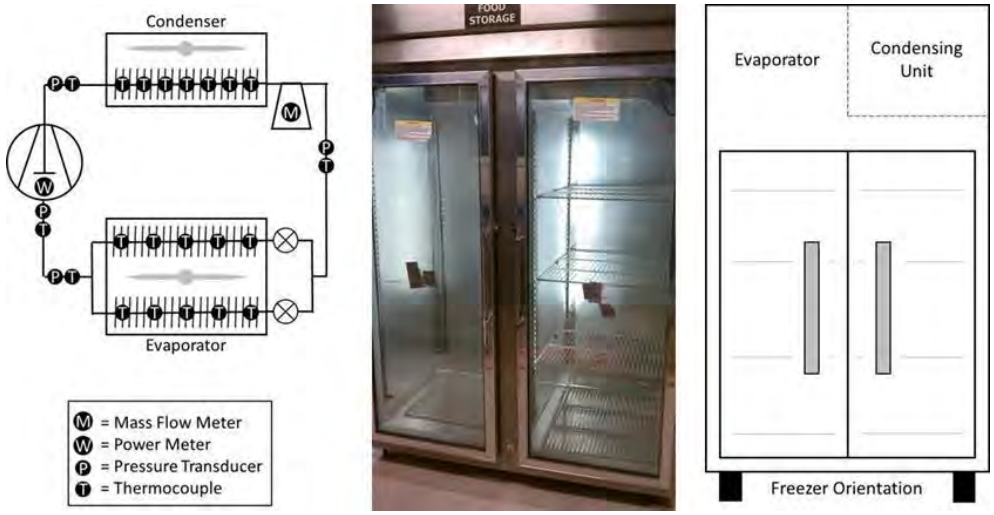

Figure 1: Equipment test setup

4. TEST PROCEDURES

Baseline system performance was established with R-404A. Test runs were conducted for a target evaporator temperature of -30°C, per OEM instructions, with ambient temperatures of 23.9°C and 32.2°C, in line with conditions used in ANSI/AHRI Standard 1200 (2013 version) and AHAM HRF-1 (2016 version), respectively. Refrigerant temperatures, pressures, and flow rates were captured throughout the system, as were compressor run times, system run cycles, defrost times, and energy consumption. System tests were duplicated for repeatability.
After the R-404A baseline was established, the refrigerant was recovered and the system was pulled into a deep vacuum (< 500 microns). The system was recharged with an alternative

refrigerant, and tests were run to optimize refrigerant charge for energy consumption at the 32.2°C ambient temperature. This process was repeated for each new refrigerant candidate. TXV settings were also optimized for each replacement. Since the alternatives are higher glide blends, performance was evaluated after adjusting the TXVs to match the average evaporator temperature of R-404A for both ambient conditions. To produce equivalent test conditions for each of the alternatives, matched average evaporator temperatures were obtained by adjusting superheats at the suction inlet of the compressor. Results of these tests are shown in section 5.

5. EXPERIMENTAL RESULTS

As part of the soft-optimization, charge size / TXV positions were adjusted for each refrigerant. Results of these adjustments are given in Table 4. XL40 had the highest system charge (9.1% higher than R-404A), followed by R-455A and R-459B with 4.4% higher. XL20 used 5.1% less. TXV adjustments shown in Table 5, are the average of both TXVs. In general, TXV superheat setting screws were adjusted inward, relative to R-404A. This is expected, as the alternatives use significantly lower flow rates. XL20 required the least adjustment, overall.

Table 4: System Charge & Thermostatic Expansion Valve (TXV) Adjustments

	System Charge (g)	# Turns Adjusted
R-404A Baseline (@ 23.9°C / 32.2°C)	1,054	+0 / +0
XL40 Equivalent Average Evaporator (@ 23.9°C / 32.2°C)	1,150	-½ / -⅛
XL20 Equivalent Average Evaporator (@ 23.9°C / 32.2°C)	1,000	+0 / +0
R-455A Equivalent Average Evaporator (@ 23.9°C / 32.2°C)	1,100	-⅝ / -½
R-459B Equivalent Average Evaporator (@ 23.9°C / 32.2°C)	1,100	-2½ / -2

Operating properties, captured for each refrigerant, are listed in Tables 5 and 6. Values shown in these tables are averaged data from multiple test runs. When comparing operating pressures, R-459B had the lowest suction and discharge pressures. The differences in values shown for the 23.9°C ambient are similar to the simulated differences shown in Table 3 for this blend. XL40 had the closest suction pressures while R-455A had the closest discharge pressures. All the alternatives produced higher compression ratios than R-404A. R-459B had the lowest values of the replacements, while R-455A had the highest. Discharge temperatures were higher for all alternatives, and were the lowest for R-459B and the highest for XL40. This again is consistent with the trends shown in Table 3. Mass flow rates of all the alternatives were much lower than those of R-404A. Differences in mass flow rates are close in magnitude to the differences in vapor densities of these products, as shown previously in Table 2.

Table 5: Refrigerant Operating Properties – 23.9°C Ambient

	R-404A	XL40	XL20	R-455A	R-459B
Suction Pressure (kPa)	208.2	192.4	162.7	179.3	148.8
Discharge Pressure (kPa)	1662	1770	1427	1707	1298
Compression Ratio	7.98	9.20	8.77	9.52	8.72
Discharge Temperature (°C)	79.1	94.5	86.4	93.6	82.4
Mass Flow Rate (kg/hr)	50.2	35.1	32.7	34.1	29.7

Table 6: Refrigerant Operating Properties – 32.2°C Ambient

	R-404A	XL40	XL20	R-455A	R-459B
Suction Pressure (kPa)	222.0	197.9	160.0	188.2	155.8
Discharge Pressure (kPa)	2072	2101	1693	2016	1536
Compression Ratio	9.33	10.62	10.59	10.71	9.86
Discharge Temperature (°C)	94.3	109.6	101.5	107.8	95.1
Mass Flow Rate (kg/hr)	47.0	32.2	33.7	36.1	27.5

Freezer performance data is given in Table 7. Test runs with XL40 produced similar pull-down times to R-404A. This is not surprising, given their similarity in capacity. However, XL20, R-455A, and R-459B all produced longer pull-down times. This is expected for XL20 and R-459B, as these are lower capacity blends. However, while R-455A is theoretically similar in capacity to R-404A, its pull-down times were closer to those of XL20. As such, it appears that R-455A's CO_2 content has little overall impact on evaporator capacity.

Table 7: Freezer Performance

	R-404A	XL40	XL20	R-455A	R-459B
Pull-Down Time @ 23.9°C (min)	2.0	2.9	3.8	3.4	5.0
Relative to R-404A (%)	100.0	145.0	190.0	170.0	250.0
Pull-Down Time @ 32.2°C (min)	5.1	5.2	16.1	11.7	21.5
Relative to R-404A (%)	100.0	102.0	315.7	229.4	422.9
Energy Consumption (kWhr/day) @ 23.9°C	25.70	25.9	26.78	28.08	27.58
Relative to R-404A (%)	100.0	100.8	104.2	109.3	107.3
Energy Consumption (kWhr/day) @ 32.2°C	34.17	32.11	35.63	36.51	35.33
Relative to R-404A (%)	100.0	94.0	104.3	106.8	103.4
Compressor Run Time @ 23.9°C (%)	43.20	46.18	54.56	54.52	62.68
Compressor Run Time @ 32.2°C (%)	65.44	64.99	83.36	83.23	85.70

Daily energy consumption for XL40 was lower than R-404A overall (2.6% lower on average). XL20 consumed 4.2% more energy, while average energy consumption of R-459B and R-455A was 5.3% and 8.1% higher, respectively. While pull-down times for XL20, R-455A, and R-459B were much longer than R-404A's and XL40's, the freezer ran for fewer cycles each day with these blends. An overview of energy consumption is shown below in Figure 2.

While theoretically, all the replacements are more energy efficient than R-404A, only XL40 showed lower energy consumption during testing. However, this does not consider testing of refrigerants in a system that is only optimized for R-404A. Modifying the system design to better match the properties of each individual refrigerant would likely lead to improved efficiencies for all the low GWP alternatives.

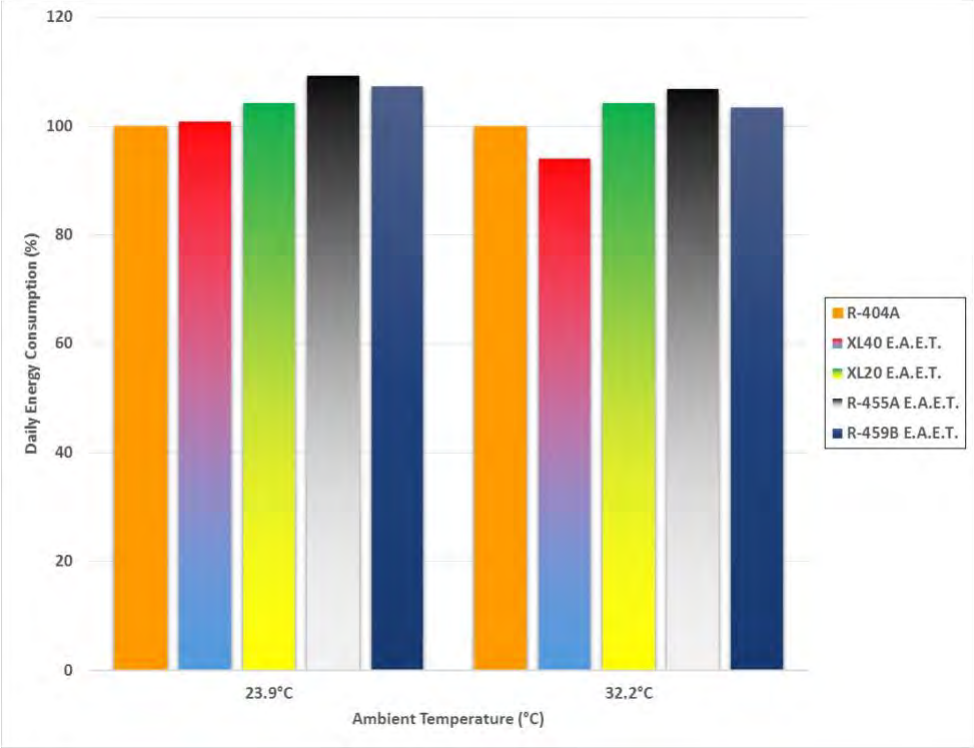

Figure 2: Energy consumption vs. ambient temperature of R-404A alternatives

6. COMPRESSOR LUBRICATION

Overall impact of the HFO-based blends on lubrication was also examined. Oil sump conditions were approximated using Pressure-Temperature measurements at the compressor inlet. Daniel plots were developed for the alternative refrigerants with ISO 32 grade POE oil. Kinematic viscosities were then determined for compressor inlet or sump conditions. Sample results are shown in Table 8.

Results show similar working kinematic viscosities of R-404A and XL20. However, the viscosities of XL40 and R-459B are roughly 10% lower, while for R-455A, 27% higher. These changes in viscosity may impact compressor drag, potentially contributing to higher efficiencies for XL40 and worsening performance for R-455A. Given the closeness of R-455A and XL20, the higher viscosity may be attributed, in large part, to R-455A's CO_2 content.

Table 8: Lubricant Properties

	R-404A	XL40	XL20	R-455A	R-459B
Suction Pressure (kPa)	208.2	192.4	162.7	178.6	152.3
Suction Temperature (°C)	-6.1	-4.5	-4.4	-3.8	-8.0
Kinematic Viscosity (cSt)	98.6	89.6	102.5	125.3	87.7
Relative to R-404A (%)	100	90.9	104.0	127.1	88.9

7. INDUSTRY ACTIVITIES & IMPLICATIONS FOR CODES & STANDARDS

Industry research continues to focus on enabling the safe use of flammable refrigerants in a wide range of ACR applications, and understanding practical differences between the different refrigerant safety groups (e.g. A2L vs A3). Results of this research help to inform and shape safety standards and codes. Many of these learnings will help determine allowable refrigerant

charge sizes and help specify safety mitigation requirements needed to reduce the risks associated with refrigerant leaks.

ISO 5149 (2014), an international, general safety standard for ACR systems, has considered the relative safety of the different types of flammable refrigerants. Increasing charge caps (m_1, m_2, & m_3), have been established for flammables, based upon their LFLs (Lower Flammability Limits), in conjunction with increasing mitigation requirements. For class 2L refrigerants, these caps are increased by a factor of 1.5, as opposed to those for class 2 and 3, "in recognition of the lower burning velocity of these refrigerants, which lead to a reduced risk of ignition and impact". Table 5 shows examples of charge sizes for different flammability classes, based upon the limits established in ISO 5149-1. The charge limits of the A2L are ≈ 3.5 times larger than the A2 and 11.5 times larger than the A3. A number of other safety standards are also establishing refrigerant charge limits, based upon the LFLs of refrigerants. This will allow for larger applications to be designed using A2Ls, as opposed to A2s and A3s.

Table 9: Examples of Refrigerant Charge Limit Caps Based on ISO 5149 (2014)

ASHRAE #	XL20 (R-454C)	R-152a	R-290
Safety Group	A2L	A2	A3
m_1 (kg)	1.746	0.520	0.152
m_2 (kg)	11.349	3.380	0.988
m_3 (kg)	56.745	16.900	4.940

A recent AHRI study (AHRI Report No. 8017 - 2017) reported on testing of A2Ls with residential ignition sources. One of the findings from this study is that many common ignition sources will not ignite A2Ls. Safety standards, such as IEC 60335-2-40 (2018) are differentiating what are ignition sources for A2Ls vs. A2s and A3s, based on flame arrest enclosures, quenching effect, opening size, and electrical switch load levels. Since many ignition sources for A2s and A3s may not be ignition sources for A2Ls, this may allow for easier integration of electrical components by OEMs into system designs with A2Ls.

IEC SC61C is also in the process of updating the IEC 60335-2-89 standard to allow for larger charge sizes of flammable refrigerants in self-contained commercial refrigerating appliances. While this standard is still in the developmental stages, the proposed changes would potentially allow for more applications to incorporate the use of flammable refrigerants.

8. CONCLUSIONS

Four mildly flammable, very low GWP refrigerants were tested and compared to R-404A in a low temperature reach-in freezer. XL40 was designed to closely match R-404A's performance, while XL20, R-455A, and R-459B are lower GWP, falling under the <150 GWP limit imposed by certain regional climate legislation. Of the four alternatives, XL40 produced the closest performance match to R-404A. Pull-down times were close to those of R-404A, with lower overall energy consumption (2.6% lower, on average). Pressures were also close. However, for the XL20, R-455A, and R-459B blends, longer pull-down times and higher energy consumption (4.2, 8.3, and 5.1%, on average, respectively) were observed. Equipment redesign to match a replacement's properties has the potential to improve performance.

Similar oil viscosities were observed for R-404A and XL20. R-455A had higher kinematic viscosity, which could be a contributing factor to its higher energy consumption levels. XL40 and R-459B had slightly lower kinematic viscosities, which might facilitate improved efficiencies. However, these viscosities do not appear to be low enough to detrimentally impact compressor lubrication. XL20 produced close working viscosities to R-404A.

Given the theoretical properties of these blends, an opportunity exists for improving energy efficiency and LCCP, relative to R-404A, using very low GWP alternatives. Ongoing research and updates to safety standards are helping to pave the way to greater use and acceptance of these products within the ACR industry.

NOMENCLATURE

A1	lower toxicity, no flame propagation	COP	coefficient of performance
A2L	lower toxicity, lower flammability, burning velocity ≤ 10 cm/s	E.A.E.T.	equivalent average evaporator temperature
A3	lower toxicity, higher flammability	GWP	global warming potential
ACR	air-conditioning / refrigeration	HFC	hydrofluorocarbon
AHAM	Association of Home Appliance Manufacturers	HFO	hydrofluoroolefin
ANSI	American National Standards Institute	ISO	International Organization for Standardization
AHRI	Air-Conditioning, Heating, & Refrigeration Institute	LCCP	life cycle climate performance
AR4	IPCC Fourth Assessment Report	LFL	lower flammability limit
AR5	IPCC Fifth Assessment Report	POE	polyolester
ASHRAE	American Society of Heating, Refrigerating, and Air-Conditioning Engineers	TXV	thermostatic expansion valve

REFERENCES

AHAM HRF-1-2016. (2016). Energy and Internal Volume of Refrigerating Appliances. *Association of Home Appliance Manufacturers (AHAM)*. Washington, DC.

ANSI/ASHRAE Standard 34-2016. (2016). Designation and Safety Classification of Refrigerants. *American Society of Heating, Refrigerating and Air-Conditioning Engineers (ASHRAE).* Atlanta, GA.

ANSI/AHRI Standard 1200. (2013). Performance Rating of Commercial Refrigerated Display Merchandisers and Storage Cabinets. *Air-Conditioning, Heating, & Refrigeration Institute (AHRI).* Arlington, VA.

IEC 60335-2-40, Sixth Edition. (2018). Household and Similar Electrical Appliances – Safety – Part 2-40: Particular requirements for electrical heat pumps, air-conditioners, and dehumidifiers. *International Electrotechnical Commission (IEC)*. Geneva, Switzerland.

ISO 5149-1. (2014). Refrigerating systems and heat pumps – Safety and environmental requirements. *International Organization for Standardization (ISO)*. Geneva, Switzerland.

Minor, B. & J. Hughes. (2015). HFO Refrigerants in Stationary: From Concept to Reality. *Proceedings for the AIRAH 2015 Refrigeration Conference.* Sydney, Australia.

Manuscript ID: 746
DOI: 10.18462/iir.icr.2019.0746

Flow visualization of ammonia inside a Gasketed Plate Heat Exchanger condenser

Maaike LEICHSENRING[(a)], Xuan TAO[(a)], Carlos INFANTE FERREIRA[(a)], Joost KIRKENIER[(b)]

[(a)] Delft University of Technology
Delft, 2628CB 39, Netherlands, X.Tao@tudelft.nl
[(b)] Bluerise B.V.
Delft, 2612PA 6, Netherlands, j.kirkenier@bluerise.nl

ABSTRACT

Most of the previously published flow pattern maps for plate heat exchangers have been based on air-water experiments. In this study, vertical downward flow of condensing ammonia in a gasketed plate heat exchanger is visualized. Polystyrene is tested on its chemical compatibility to liquid ammonia and proven to be resistant for several days. A 25 mm thick transparent plate has been machined from Polystyrene and Polymethylmethacrylaat with the same corrugation profile as the stainless steel heat transfer plates. The study distinguishes between partial film and film flow and the influence of mass flux and vapor quality is observed. The experimental operational conditions are compared to a flow pattern map of air/water two-phase flow in plate heat exchangers and film transition lines in mini-tubes. The results show that more visualization studies are required to extend the applicability of the flow pattern map for different condensing fluids inside gasketed plate heat exchangers.
Keywords: Two-phase flow, vertical downward flow, flow patterns, plate heat exchangers, flow visualization, ammonia, condensation

1. INTRODUCTION

Plate heat exchangers (PHEs) have a wide range of applications due to their superior performance in relation to favourable heat transfer coefficients (HTCs), compactness, design flexibility and thermal effectiveness (Thulukannam, 2013). However, the two-phase behaviour inside the PHEs is yet not fully understood, resulting in over- or underestimating by several published heat transfer and pressure drop correlations, which are limited by the range of conditions they cover (Amalfi et al., 2016). Tao et al. (2018) conclude that better predictions of flow patterns in plate heat exchangers will improve the calculation of heat transfer and pressure drop. Flow patterns are determined visually by an experimental setup where the flow is observed through a transparent plate. Flow patterns are defined by the geometric configurations of vapor and liquid and are classified into four main flow patterns: bubbly, slug, churn and film flow. The sequence of occurrence is based on the increase of the vapor mass flux. Al-Zaidi et al. (2017), Arima et al. (2008) and Arima et al. (2011) conclude that the average vapor quality also plays a significant role, as it is observed that a low vapor quality corresponds to bubbly flow and a high vapor quality to film flow. It is expected that the various flow patterns relate to different forms of heat transfer inside condensers. Vlasiogannis et al. (2001) conclude that film flow shows particularly favourable heat transfer enhancement as compared to the other flow regimes. Al-Zaidi et al. (2017) compared the flow patterns to the local condensation heat transfer coefficient and concluded that for film flow the heat transfer coefficient (HTC) is largest. A flow pattern map helps distinguish the various regimes in a graphical way. Tao et al. (2018) created a flow pattern map for two-phase vertical downward flow in plate heat exchangers including the property modifying group Λ, see Eq. (1), that enables the inclusion of fluid properties into the flow pattern map.

$$\Lambda = \mu_L \mu_w^{-1} \rho_L^{-1/4} \rho_w^{1/4} \sigma_L^{-3/4} \sigma_w^{3/4} \quad \text{Eq. (1)}$$

The axes of the flow pattern map make use of dimensionless groups: the liquid Reynolds number Re_L, and the two-phase Froude number Fr_{TP}, see Eq. (2) and Eq. (3).

$$\mathrm{Re}_L = G(1-x)d_h\mu_L^{-1} \qquad \text{Eq. (2)}$$

$$\mathrm{Fr}_{TP} = xG\left(gd_h\,\rho_G\,(\rho_L-\rho_G)\right)^{-0.5} \qquad \text{Eq. (3)}$$

Flow visualization of pure ammonia condensing flow inside a corrugated vertical plate heat exchanger has not been investigated previously. This study compares the results of pure ammonia flow visualization in a vertical downward PHE to the flow pattern map constructed by Tao et al. (2018). Section 2 explains the experimental setup and the performed research to enable the construction of a durable transparent test plate. Section 3 explains the test procedure and section 4 discusses the results of the visualization experiments.

2. EXPERIMENTAL SETUP

2.1. Experimental Apparatus and Procedure

In cooperation with the Delft University of Technology, Bluerise B.V. constructed a small scale OTEC-plant to test the performance of the OTEC-cycle and optimize its outputs. The 100 W OTEC demo consists of an Organic Rankine cycle using pure ammonia as the working fluid. Figure 1 shows a schematic representation of the experimental setup.

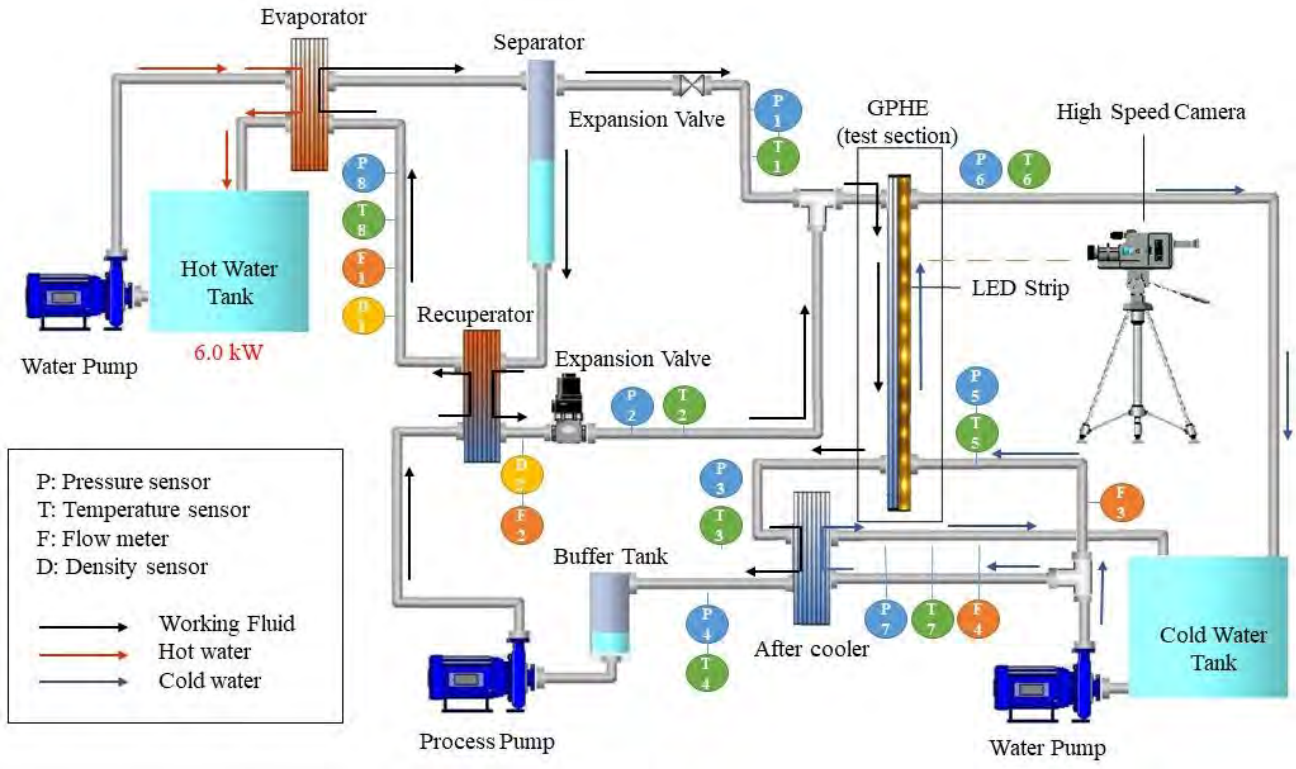

Figure 1: Experimental setup diagram of OTEC demo cycle

Pure ammonia is vaporized while flowing through the evaporator due to the counter current hot water flow. The separator splits the remaining liquid ammonia from the vapor and sends it to the recuperator, which acts as a preheater for the ammonia that is to be heated. The pure ammonia vapor is sent through a turbine and is reunited with the ammonia liquid right before the test section. The two-phase working fluid is condensed in the Gasketed Plate Heat Exchanger (GPHE) by a cold water stream from the cold water tank. A sub-cooler and buffer tank are placed to guarantee that all vapor in the working fluid flow is fully condensed by the time it reaches the process pump. The hot water tank is heated by a heating coil and the cold water tank is connected to a refrigeration system.

2.2. Test Section for Visualization

The test section is a GPHE, containing a cold water channel and a working fluid channel. Table 1 gives the detailed geometric parameters of the stainless-steel plate used for heat transfer. Figure 2 shows its schematic diagram.

Table 1: Geometric parameters of the heat transfer plates

Channel gap d_g	1.72 (mm)	Plate length $\mathrm{L_v}$	0.668 (m)
Chevron angle β	63 (°)	Plate pitch p_{cp}	2.3 (mm)
Corrugation pitch p	7.5 (mm)	Plate thickness d_p	0.58 (m)
Corrugation wavelength Λ_{wave}	6.67 (mm)	Plate width L_h	0.06 (m)
Effective heat transfer area A_e	0.537($\mathrm{m^2}$)	Port diameter D_p	0.035 (m)
Effective width heat transfer L_w	0.095 (m)	Thermal conductivity κ	16.3 (W.m $^{-1}$K $^{-1}$)

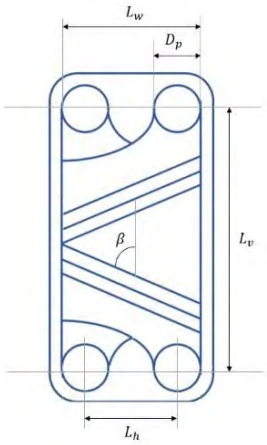

Figure 2: Schematic representation of the corrugated heat transfer plates of the GPHE

The PHE includes a 95 cm x 12.5 cm transparent corrugated polymer plate that enables visualization of the condensing ammonia on the working fluid side. This visualization plate has the same geometric specifications as the heat transfer plate except for the plate thickness, which is 25 mm. The plate is illuminated by a 500 cm LED strip including 300 LED's that encircles the plate from its sides twice. A 3000 fps high speed camera is placed in front of the visualization plate to capture the flow patterns under varying operating conditions. Figure 3 shows the transparent polymer plate, the visualization section including pressure plate and illumination and the placement of the camera.



Figure 3: Left) Corrugated visualization plate. Middle) Visualization section including illumination and pressure plate. Right) Visualization section and high speed camera

2.3. Material Selection of Visualization Plate

The challenge is finding a material that meets the following criteria: Chemically compatible to ammonia, transparency, high strength (able to withstand an operational pressure up to 12 bar) and machinable into the corrugation patterns. Arima et al. (2011) and Xue et al. (2013) use glass in front of a flat plate. However, machining a brittle material such as glass into a corrugation pattern contains

large risks on mechanical performance due its brittle structure (Lutgendorf, 2014). The latter stresses the importance of finding a polymer (as is used by Al-Zaidi et al. (2017), Grabenstein et al. (2016), Jassim et al. (2006), Tribbe & Muller-Steinhagen (2001) and Vlasiogannis et al. (2001)) that meets the requirements. According to the material database CES Edupack (2018), Polystyrene (PS) is a polymer that meets the optical, mechanical and machinability criteria. Generally, it is stated that this material is chemically compatible to ammonia (CES Edupack, 2018) but it is not mentioned for which experimental conditions this applies such as phase, temperature, pressure and the ammonia being a pure fluid or a diluted mixture. Woishnis and Ebjesajjad (2012) show an extensive research on PS stating that PS is highly compatible to an aqueous solution with 25% ammonia at room temperature for years, but no data is found for pure ammonia. Therefore, several samples are placed in a pressure vessel filled with pure, liquid ammonia at a pressure of 8 bar absolute and ambient temperature for four days. The samples are machined into the desired corrugated pattern, compressed onto each other by two stainless steel clamps.



Figure 4: Left) Samples before test. Middle) Frontal view samples after test. Right) Top view samples after test

Fig. 4 shows the clamped corrugated samples before and after the test. The material shows a slight bend and tiny damages on the locations of contact between the samples, but it did not reduce the transparency significantly. A sheet of PS has a maximum thickness of 4.75 mm, onto which the corrugated pattern is machined by a CNC-machine. The corrugated PS sheet is glued with a UV light curing adhesive onto a PMMA plate of 20 mm thickness to benefit from the superior mechanical properties that PMMA has relative to PS.

3. TEST PROCEDURE

The ammonia mass flux G_a is determined by Eq. (4). The ammonia mass flow $\dot{m}_a$ is measured by flow meter F1, see Figure 1. The flow passage area A_f is calculated by multiplying L_w, the effective heat transfer width with d_g, the channel gap.

$$G_a = \dot{m}_a A_f^{-1} \qquad \text{Eq. (4)}$$

The single phase condition at the outlet of the after cooler is used to determine the enthalpy of the liquid ammonia. The average quality $\bar{x}$ inside the GPHE is determined by Eq. (5). An energy balance is used to determine the two-phase enthalpy at the inlet of the after cooler, which is assumed to be the same as the enthalpy at the outlet x_{out} of the GPHE. A second energy balance determines the enthalpy of the ammonia at the inlet of the GPHE x_{in} which is determined by Eq. (6). $h_{L,sat}$ and $h_{V,sat}$ represent the saturated liquid and vapour phase enthalpy of the ammonia at the inlet conditions of the condenser.

$$\bar{x} = 0.5(x_{in} + x_{out}) \qquad \text{Eq. (5)}$$

$$x_{in} = (h_{in} - h_{L,sat})\left(h_{V,sat} - h_{L,sat}\right)^{-1} \qquad \text{Eq. (6)}$$

Experiments are performed where the mass flux G_a is kept constant and the vapor quality x_{in} is increased. Both the influence of the mass flux and inlet quality on the flow configurations are recorded for the top, middle and bottom windows.

4. EXPERIMENTAL RESULTS

For all recorded conditions, a framerate of 3000 fps with a resolution of 1024 x 1024 pixels is used. The transparent plate remained intact for 7 days, but on the 8th day of performing experiments degradation in the material was visible in the form of small cracks in the PS surface and crystal shaped spots between the PS and PMMA layer that grew in size over time. It is concluded that PS has a limited durability when in contact with pure ammonia.

4.1. Flow Pattern and Path over the Length of the Heat Transfer Plate

For all performed experiments, no bubbles, slugs or churns were detected and only film flow and partial film flow are observed. The path of the flow remained similar under the various circumstances. Figure 5 shows the path of the flow over the different windows. Due to the shapes of the distribution zone at the inlet, the liquid flow is pushed to the left which causes most of the liquid flow to disperse turbulently over the left upper diagonal of the window. It is expected that in that zone also vapor is present, but less than in the lower diagonal.

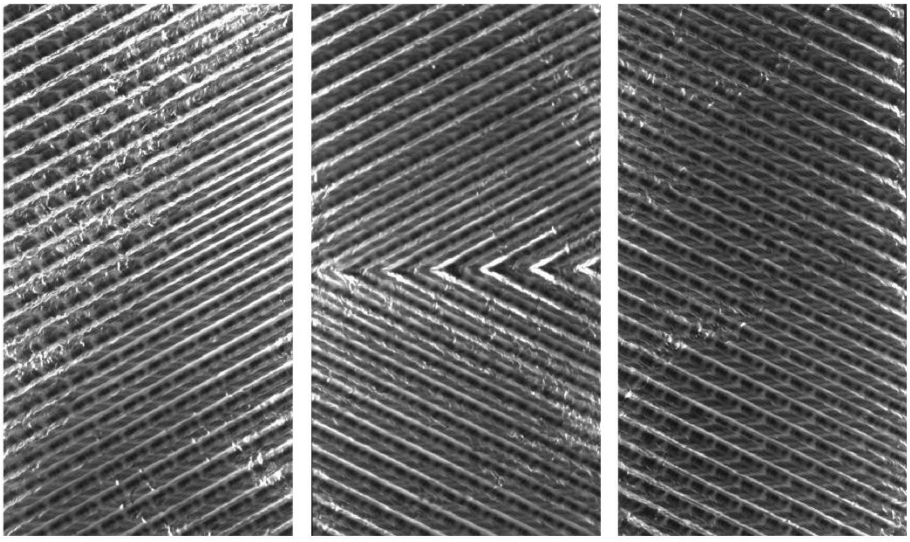

Figure 5: G = 92 kg/m^{2}s, $\bar{x}$ = 0.27. Left) Top window. Middle) Middle window. Right) Bottom window

The area of the upper diagonal covered by mainly liquid decreases for smaller mass fluxes. This area is indicated by the zones that reflect light in various directions. Most of the vapor flows at the lower diagonal of the top window, indicated by a still image. In the middle window the corrugation direction switches and this sudden change in flow direction causes the liquid to evenly distribute over the corrugations in the lower part of the middle window. Less vapor is detected. The bottom window is mostly covered in liquid and shows more laminar characteristics than the top window.

4.2. Influence of Vapor Quality and Mass flux on flow configuration

A distinction can be made between film flow and partial film flow, see
Figure 6. Film flow includes a liquid layer on both plates while partial film flow leaves dry patches when the amount of liquid film is limited and unable to cover the entire plate. If partial film flow occurs in the GPHE and dry patches are present on the transparent plate, an opaque surface will be visible.

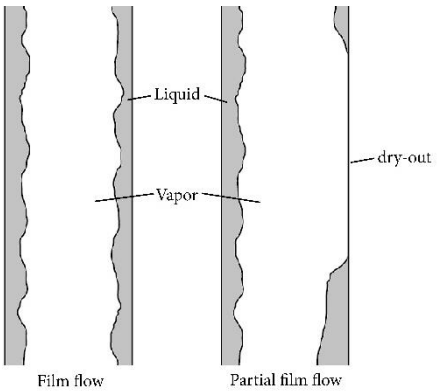

Figure 6: Schematic representation of film flow and partial film flow inside the channel (side view of GPHE)

The distribution of the vapor phase and liquid phases differs at varying circumstances, see Figure 7. Only the top window is represented in the figure since this window shows the varying configurations most clearly.

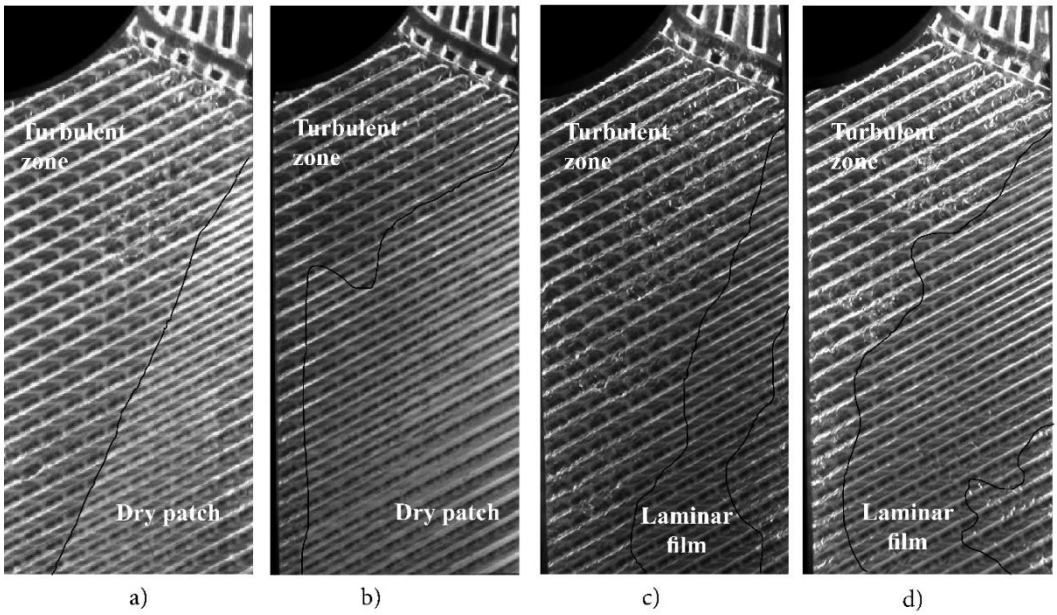

Figure 7: a) G = 42 kg/m²s, x_{in} = 0.26. b) G = 42 kg/m²s, x_{in}= 0.69. c) G = 80 kg/m²s, x_{in}= 0.19. d) G = 80 kg/m²s, x_{in}= 0.34

From Figure 7 a, b, at a constant mass flux but increasing vapor quality the vapor contact area increases. With a lower mass flux, the contact between the transparent plate and vapor turns the surface opaque, indicating a zone of dry-out, i.e. partial film flow. With a higher mass flux, Figure 7 c, d shows an enhanced turbulent flow of the upper diagonal, in the figure indicated by the higher amount of light reflectance. The lower diagonal shows a clear surface, even when the vapor quality is increased, indicating film flow. An increased liquid entrainment in the lower diagonal wets the surface of the transparent plate that causes the clarity of that area. The lower diagonal shows no light reflectance indicating a film flow with laminar characteristics, see Figure 7 c, d.

4.3. Comparison of Results to Flow Pattern Map by Tao et al. (2018)

The operating conditions of the experiments are represented in Fig. 8. Fig. 8 shows a flow pattern map constructed by Tao et al. (2018) for plate heat exchangers that makes use of the dimensionless quantities Re_L and Fr_{TP} which account for gravity, viscous forces, inertia and fluid properties. This construction is based on results from previous visualization experiments for two-phase vertical downward flow of mainly air-water mixtures in plate heat exchangers. The viscosity, surface tension and vapour-liquid density ratio of ammonia locate its operating conditions at high values of the y-axis. In this operating range also Tribbe & Muller-Steinhagen (2001) have identified film and partial film flow conditions. Fig. 8 also shows the film and film-slug transition lines which apply for mini-tubes

(see Tao et al., 2018). This indicates that the film transition line, most probably, is located at higher values of Re_L than expected from the air-water experiments. More visualization studies with a wider range of experimental conditions on condensing flow of pure ammonia in vertical PHE's are required to accurately describe the flow pattern behaviour of pure ammonia in this type of heat exchangers and extend the applicability of the flow pattern map for different fluids.

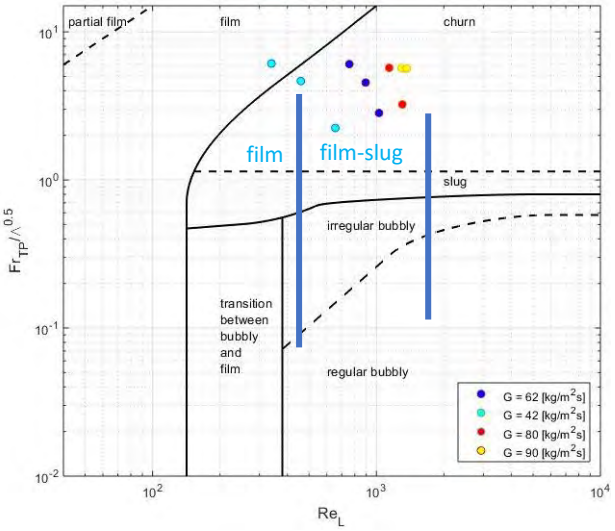

Figure 8: Experimental operating conditions shown in simplified flow pattern map of two-phase flow in PHEs by Tao et al. (2018) based on air/water data, including the film transition lines in mini-tubes (indicated with blue lines) reported by Tao et al. (2018)

5. CONCLUSIONS

The flow morphology of pure ammonia in a vertical downward GPHE has been captured. A corrugated visualization plate is produced from transparent PS by a CNC-machine and has proven to be chemically compatible to pure ammonia for several days and mechanically resistant to a condensation pressure up to 7 bar absolute. For all conditions introduced, film flow and partial film flow is observed. The flow patterns were most visible on the top window, where most of the liquid phase covers the left upper diagonal and most of the vapor the lower diagonal of the window. An increased vapor quality increases the area of dry-out (partial film flow) on the visualization plate. Increasing the mass flux enhances the turbulence of both phases, creating more liquid entrainment in the lower diagonal resulting in film flow. The operating conditions during the performed ammonia condensation experiments (liquid Reynolds number and two-phase Froude number) have been indicated in the flow pattern map constructed by Tao et al. (2018). The results indicate that the film flow and partial film flow transition line needs to be moved to higher values of the Re_L than indicated in the flow pattern map which is mainly based on air-water experiments. More visualization studies are required to extend the applicability of the flow pattern map for different condensing fluids inside GPHE's.

ACKNOWLEDGEMENTS

The authors would like to acknowledge the financial support from the China Scholarship Council and Koudegroep Delft-Wageningen.

NOMENCLATURE

Abbreviations			
GPHE	Gasketed plate heat exchanger	p	Corrugation pitch [mm]
HTC	Heat transfer coefficient	p_{cp}	plate pitch [mm]
LED	Light emitting diode	Re	Reynolds number [-]
		x	Vapor quality [-]

OTEC	Ocean thermal energy conversion	$\bar{x}$	Average vapor quality [-]
PHE	Plate heat exchanger	*Greek*	
PMMA	Polymethylmethacrylaat	β	Chevron angle [°]
PS	Polystyrene	Λ	Property modifying parameter [-]
Symbols		Λ_{wave}	Corrugation wavelength [mm]
A_e	Effective heat transfer area [m^2]	κ	Thermal conductivity [$\mathrm{Wm^{-1}K^{-1}}$]
A_f	Flow passage area [m^2]	μ	Dynamic viscosity [Pas]
d_g	Channel gap [mm]	ρ	Density [$\mathrm{kgm^{-3}}$]
d_h	Hydraulic diameter [m]	σ	Surface tension [$\mathrm{Nm^{-1}}$]
d_p	Plate thickness [mm]	*Subscripts*	
D_p	Port Diameter [m]	a	Ammonia
Fr	Froude number [-]	G	Gas
g	Gravitational constant [$\mathrm{ms^{-2}}$]	in	Inlet conditions
G	Mass flux [$\mathrm{kgs^{-1}m^{-2}}$]	L	Liquid
h	Enthalpy [$\mathrm{Jkg^{-1}}$]	out	Outlet conditions
L_h	Plate width [m]	*sat*	Saturated
L_v	Plate length [m]	*TP*	Two-phase
L_w	Effective heat transfer width [m]	V	Vapor
$\dot{m}$	Mass flow [$\mathrm{kgs^{-1}}$]	w	Water

REFERENCES

Al-Zaidi, A., Mahmoud, M. & Karayiannis, T., 2017. Condensation flow patterns and heat transfer in horizontal microchannels. Experimental Thermal and Fluid Science 90, 153-173.

Amalfi, R., Vakili-Farahani, F. & Thome, J., 2016. Flow boiling and frictional pressure gradients in plate heat exchangers. International Journal of Refrigeration 61,166-184.

CES Edupack 2018, Granta Design Limited.

Arima, H., Kim, J., Okamoto, A. & Ikegami, Y., 2008. Local boiling heat transfer characteristics of ammonia in a vertical plate evaporator. International Journal of Refrigeration 33, 359-370.

Arima, H., Okamoto, A. & Ikegami, Y., 2011. Local boiling heat transfer characteristics of ammonia/water binary mixture in a vertical plate evaporator. International Journal of Refrigeration 34, 648-657.

Grabenstein, V., Plzin, A. & Kabelac, S., 2016. Experimental investigation of the flow pattern, pressure drop and void fraction of two-phase flow in the corrugated gap of a plate heat exchanger. International Journal of Multiphase Flow 91, 155-169.

Jassim, E., Newell, T. & Chato, J., 2006. Two-phase flow visualization in chevron and bumpy style flat plate heat exchangers. Heat transfer Engineering 27, 20.

Kim, H., Liebenberg, L. & Jacobi, A., 2018. Flow Visualization of Two-Phase R-245fa at Low Mass Flux in a plate Heate Exchanger near the Micro-Macroscale Transition. Proceedings of the 17th International Refrigeration and Air Conditioning Conference, Indiana, U.S.

Lutgendorf, J., 2014. Structural design of glass geometries, Delft: Delft University of Technology.

Tao, X., Nuijten, M. & Infante Ferreira, C., 2018. Two-phase vertical downward flow in plate heat exchangers: Flow patterns and condensation mechanisms. International Journal of Refrigeration 85, 489-510.

Thulukannam, K., 2013. Heat Exchanger Design Handbook. Taylor & Francis Inc., Boca Raton

Tribbe, C. & Muller-Steinhagen, M., 2001. Gas/Liquid flow in plate-and-frame heat exchangers - Part II: Two-phase multiplier and flow pattern analysis. Heat transfer engineering 22, 12-21.

Vlasiogiannis, P., Karagiannis, G., Argyropoulos, P. & Bontozoglou, B., 2001. Air-water two-phase flow and heat transfer in plate heat exchanger. International Journal of Multiphase Flow 28, 757-772.

Woishnis, W. A. & Ebnesajjad, S., 2012. Chemical Resistance of Thermoplastics. William Andrew Publishing, Norwich.

Xue, Z., Qu, W. & Xie, M., 2013. Full visualization and startup performance of an ammonia pulsating heat pipe. Propulsion and power research 2(4), 263-268.

Manuscript ID: 751
DOI: 10.18462/iir.icr.2019.0751

Performance simulations of heat and mass transfer of a novel compound absorber

Weixing Yuan[(a)], Yu Li[(b)], Yuxue Guo[(a)], BoYang[(a)]

[(a)]Laboratory of Ergonomics and Environmental Control, School of Aeronautic Science and Engineering, Beihang University
Beijing 100191, China, yuanwx@buaa.edu.cn
[(b)]Institute of Aircraft Pneumatic Energy Engineering, Shanghai Aircraft Design and Research Institute, Commercial Aircraft Corporation of China Ltd
Shanghai 201210, China, liyu6578@163.com

ABSTRACT

The miniaturization of absorption heat pump is mainly restricted by the conventional shell-and-tube absorber which requires large heat and mass transfer area. This paper proposed a novel type of plate-fin flat heat pipe absorber (PFFHPA) with compact structure and low metal consumption. In this paper, by building the mass balance equations, energy balance equations, phase equilibrium equations of ammonia-water and heat and mass transfer characteristic equations, a two-dimensional numerical model is developed to simulate the heat and mass transfer process of the absorber. The model takes account of the distribution of liquid-phase temperature and concentration, heat transfer coefficient and absorption rate. A parametric analysis is also conducted to assess the effect of inlet conditions and pressures on the absorption performance. As expected, the novel structure is conducive to a great volume reduction of the absorber by 70% and thereby the entire volume of absorption heat pump system can be greatly reduced in comparison with the conventional heat pump with shell-and-tube absorber.
Keywords: Absorber, Compact, Absorption, Mass transfer

1. INTRODUCTION

Heat driven absorption cycle has attracted much attention in heating field in recent years, which provides a possibility of generating power in an environment-friendly way. However, due to its large size and complicated piping layout, traditional large-scale heat pump is difficult to be widely promoted in common residential buildings, office buildings and villas. Therefore, the miniaturization of the unit has great application prospects in the heating field. In the absorption system, the absorber conventionally accounts for the largest heat transfer area, so the compactness of the absorber is the key to the system miniaturization.

In order to achieve the compactness of absorber, much research has been done on enhancing the heat and mass transfer in the absorption process at home and abroad. Yang et al. developed computational models and conducted numerical simulation on the heat-pipe falling film absorber [J.C. Yang, 1997]. Zheng and Chen designed an air-cooled LiBr absorber with precooling adiabatic absorption, and conducted an experimental study on the mass transfer performance of the adiabatic falling film absorption outside smooth tube [F. Zheng, 2002]. Bie et al. designed a LiBr absorption refrigerator consisting of plate-fin heat exchangers, whose volume was only 42% of the conventional shell-and-tube system [S.J. Bie, 2002]. Chen and Li proposed double dimensional cross wave surface plate lithium bromide aqueous falling film absorber. Compared with common wave surface plate, the overall heat transfer coefficient could be increased by 30% [Y.P. Chen, 2002]. Cui et al. proposed a plate falling film absorber with film inverting configuration, the special design of the flow channel of solution can timely cool the high-temperature surface of the solution [X.Y. Cui, 2005]. Chen et al. proposed to destroy and regenerate liquid film by installing stainless steel corrugated gauze structured packing in order to enhance mass transfer process [L. Wang, 2006]. Shang proposed an air-cooled falling film absorber with louvered fins and analyzed the influence of the structural parameters of the fin on the system performance by developing computational models [R. Shang, 2008]. Zhang et al. proposed a plate-and-fin absorber with wire-meshed fins, the heat and mass transfer area is effectively expanded [N. Zhang, 2011]. Fang and Wang investigated a heat pipe absorber with a

transverse groove, whose heat and mass transfer coefficients were about 2-3 times and twice of the smooth tube absorber [S.Q. Fang, 2012]. Yan et al. proposed applied ultrasound technology to adiabatic absorber, combining the advantages of both ejector and ultrasonic wave, realized the small-scale air-cooled and high efficiency of solar absorption chiller [X.n. Yan, 2017]. Bassols et al. produced an ammonia absorption refrigerator all consisting of plate-fin heat exchangers. The 1 MW unit had only 1/24 the volume of the common absorption refrigerator [Bassols J, 1995]. Flamensbeck et al. designed an absorber based on liquid-liquid plate-type heat exchange and adiabatic jet absorption, whose heat transfer coefficient achieved as high as 2-2.7kW/(m2K) while the area was only half of common falling film absorber [Flamensbeck M, 1998]. Islam et al. proposed a tubular falling film absorber whose absorption rate was increased by 100% compared with traditional absorber under testing conditions [Islam Md R, 2003]. Meacham and Garimella vertically stacked a number of horizontal tubes with micro-channels inside which the coolant flew and designed a perforated drip dispenser for solution. The refrigeration capacity was 1.5kW when the heat transfer area was 1.456m2 [Meacham J. M, 2004]. Goel and Goswami designed a kind of metallic mesh to optimize the distribution of the solution and the wetness degree of the coolant pipe surface. The heat transfer coefficient was increased by nearly 50% compared with no mesh. Simulation results showed that 25% of the volume can be saved under the same refrigeration capacity [Goel N, 2005]. Faisal et al. performed a steady-state heat and mass transfer analysis of a water-lithium bromide membrane based absorber, where the solution film thickness and velocity could be controlled independently. Simulation results showed that the absorption rate was increased by three times when the solution film thickness was reduced from 2 mm to 0.5 mm [Asfand F, 2015].

In this paper, a novel plate-fin flat heat pipe absorber is designed and studied, as shown in Fig. 1. A set of flat plate heat pipes (4) are arranged as shown in Fig. 2, with the evaporation ends as the absorption section (1) of the absorber and the condensation ends as the cooling section (2). Absorption section fins (3) are installed between adjacent flat heat pipes as shown in Fig. 3. Weak ammonia water solution enters from (5-1), falls along the wall of the rectangular channels formed by the flat heat pipes and the fins, and flows out of (7) after absorbing ammonia vapor coming from (6) in counter-current pattern. The absorption heat is transferred to the cooling section via the flat heat pipes and is taken away by the cooling fluid coming from (8). The absorber takes advantage of the thermal homogeneity between the evaporation side and condensing side of the flat heat pipe to release plenty of absorption heat, while the fins greatly increase heat and mass exchange area. This novel structure brings about the advantages of small size, excellent heat and mass transfer performance, low metal consumption and thereby low cost. The dimension parameters of flat heat pipes and fins are shown as Table 1.

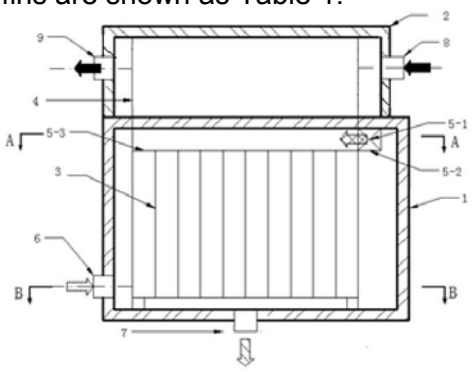

1: Absorption section
2: Cooling section
3: Absorption section fin
4: Flat heat pipe
5-1: Weak solution entrance
5-2: Weak solution channel
5-3: Mental head
6 : Ammonia vapor entrance
7 : Concentrated solution exit
8 : Cooling liquid entrance
9 : Cooling liquid exit

Figure 1: Plate-fin flat heat pipe absorber profile

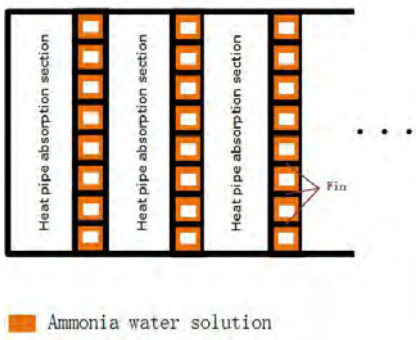

Figure 2: The top cutaway view of absorption section

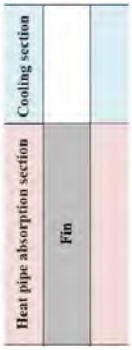

Figure 3: The left cutaway view of absorber

Table 1. Dimension parameters of flat heat pipes and fins

Structural parameters	Value	Structural parameters	Value
Width of flat heat pipe (m)	1.2	Distance between flat heat pipes(mm)	5
Height of the absorption section(m)	1	Spacing of fins(mm)	2.86
Height of the cooling section(m)	0.4	Thickness of fins(mm)	0.2
Thickness of flat heat pipe(mm)	3.2	Number of flow channels	21

2. MATHEMATICAL MODEL

In order to simplify the simulation without affecting the modeling accuracy much, following assumptions are made:

1. System pressure is constant, and the absorption process is assumed to be in steady state.
2. Thermodynamic equilibrium exists at the liquid-vapor interface.
3. The heat transfer surface is completely wet.
4. Heat losses to the environment are negligible.
5. Heat of convection between vapor and interface is negligible.
6. Water vapor and non-absorbable gases in ammonia vapor are ignored.
7. Neglecting the entrance effect, the concentration, temperature and velocity of solution are uniformly distributed along the circumferential direction at the entrance.

The mathematic model of two-dimensional steady heat and mass transfer is set up by the following differential equations:

Energy conservation equation of cooling liquid:

$$\Delta(m_c H_c) = \frac{T_l - T_c}{R \cdot L_1 L_2}, \quad R = \frac{1}{h_1^*} + \frac{\delta^*}{\lambda} + \frac{\delta}{\lambda} + \frac{1}{h_2^*} \qquad \text{Eq.(1)}$$

Mass conservation equation of solution:

$$\Delta m_l = \dot{m} \qquad \text{Eq.(2)}$$

Component mass conservation equation of solution:

$$\Delta(m_l \cdot x_l) = \dot{m} \qquad \text{Eq.(3)}$$

Energy conservation equation of solution:

$$\Delta(m_l H_l) = \frac{T_l - T_c}{R \cdot L_1 L_2} + L_1 L_2 \cdot h_{li}(T_i - T_l) + \dot{m} H_{li} \qquad \text{Eq.(4)}$$

Energy conservation equation of liquid-vapor interface:

$$\dot{m} H_v = L_1 L_2 \cdot h_{li}(T_i - T_l) + \dot{m} H_{li} \qquad \text{Eq.(5)}$$

Mass conservation equation of ammonia vapor:

$$\Delta m_v = -\dot{m} \qquad \text{Eq.(6)}$$

Energy conservation equation of ammonia vapor:

$$\Delta(m_v H_v) = -\dot{m} H_v \qquad \text{Eq.(7)}$$

The heat transfer coefficient between cooling liquid and flat heat pipe [D. Azbel, 1984]:

$$h_l = 0.026\left(\frac{\lambda_c}{s_p}\right) \mathrm{Re}_c^{0.82} \, \mathrm{Pr}_c^{0.32} \qquad \text{Eq.(8)}$$

The heat transfer coefficient between solution and flat heat pipe [W. Wilke, 1969]:

$$h_2 = 1.88\left(\frac{\lambda_l}{\delta_l}\right) \qquad \text{Eq.(9)}$$

The thickness of solution film can be expressed as[Yih S.M, 1987]:

$$\delta_l = 0.91 \mathrm{Re}_l^{\frac{1}{3}} \left(\frac{\nu_l^2}{g}\right)^{\frac{1}{3}} \qquad \text{Eq.(10)}$$

The liquid-side mass transfer correlation can be expressed as [Eremisinoff I, 1986]:

$$K_{li} = 0.1099\,\mathrm{Re}_l^{0.3955}\, Sc_l^{0.5} D_{aw} (\frac{g}{\nu_l^2})^{\frac{1}{3}} \quad \text{Eq.(11)}$$

The similarity between heat and mass transfer processes can be utilized to deduce the analogous heat and mass transfer coefficients [T.H. Chilton, 1934]:

$$h_3 = C_p \cdot M \cdot (\frac{Sc_l}{\mathrm{Pr}_l})^{\frac{2}{3}} \cdot K_{li} \quad \text{Eq.(12)}$$

For steady state, the mass flow of the vapor absorbed by the weak solution is given by:

$$\dot{m} = K_{li}(x_i - x_l) \quad \text{Eq.(13)}$$

Boundary conditions：

$$t_l(1,j) = t_{l0};\ x_l(1,j) = x_{l0};\ m_l(1,j) = m_{l0}\ t_v(m,j) = t_{v0};\ m_v(m,j) = m_{v0};\ t_c(i,n) = t_{c0} \quad \text{Eq.(14)}$$

The mathematical model involves seven unknown quantities: temperature of cooling fluid t_c, temperature of solution t_l, concentration of solution x_l, mass flow rate of solution m_l, temperature of liquid-vapor interface t_i, mass flow rate of ammonia vapour m_v and temperature of ammonia vapour t_v. Taking into account the phase equilibrium, the enthalpy of liquid-vapor interface is a function of pressure and temperature, while the enthalpy of liquid film requires pressure, temperature and concentration to be jointly determined. Totally implicit difference scheme is used to discretize the equations in the calculation. The numerical solutions are obtained by Newton's iterative method.

3. CONCLUSIONS, RESULTS AND DISCUSSION

By solving the model of plate-fin flat heat pipe, the field distribution of each physical quantity on the two-dimensional plane of flat heat pipe under rated working conditions is obtained. The numerical solutions of can visually show the distribution of temperature and concentration field distributionof the absorber under stable working conditions, while mass transfer rate characterizes the mass transfer effect of the absorber, and thermal resistance characterizes the heat transfer effect between coolant and solution.

Table 2. Rated working conditions

System parameters	Value	System parameters	Value
Pressure(bar)	3.3	Mass flow rate of ammonia vapor(kg/s)	0.33
Mass flow rate of solution(kg/s)	1.2	Inlet temperature of ammonia vapor (℃)	14
Inlet temperature of solution (℃)	58	Mass flow rate of coolant(kg/s)	30
Inlet concentration of solution(kg/kg)	0.15	Inlet temperature of coolant (℃)	43

3.1. Analysis of Temperature and Concentration Field Results

Figs. 4 to 5 are two-dimensional temperature nephograms of coolant and solution. It can be seen intuitively from the figure that the temperature of the coolant has obvious changes along the both directions. The temperature of the coolant increases along its flow direction, and the temperature near the inlet of the diluted solution is higher than that at the outlet of the concentrated solution. This is because the solution absorbs ammonia vapor and emits a large amount of heat, which causes the temperature of the solution to rise. Since the coolant takes away this heat, the overall temperature of the solution decreases, that is, the outlet temperature of solution is lower than the inlet temperature. Therefore, the coolant temperature near the outlet of solution is also lower. The temperature of the solution decrease along the flow direction of the falling film, and the decreasing rate increases gradually. The reason is that the concentration of the solution increases with the increase of ammonia absorption, that is, the mass transfer impetus in the inlet section is greater than that in the outlet section. Therefore, the absorption of the solution in the entrance section is intense, so a large amount of absorption heat released. The latent heat (i.e. absorption heat) cannot be removed by coolant in time, resulting in a slow temperature drop of the solution in the entrance section. With the decrease of the absorption rate, the latent heat load gradually decreases, the solution can be cooled more quickly by the coolant, so the solution temperature decreases quickly as well as the liquid-vapor interface temperature. As the temperature of the solution decreases continuously, the temperature difference between the solution and the coolant

gradually decreases and thereby the heat transfer rate decreases, so the declining rate of the temperature decreases gradually.

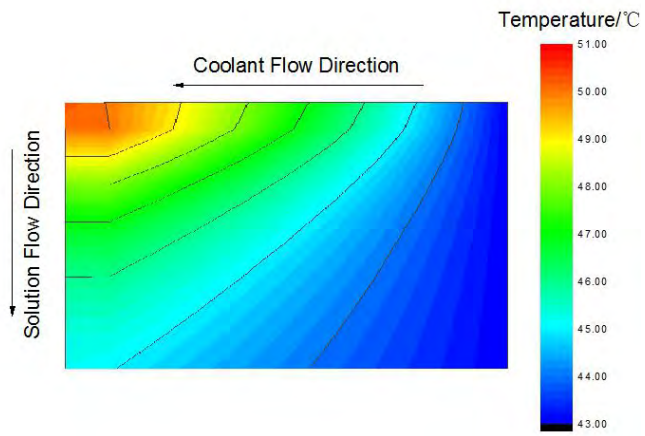

Figure 4: Nephogram of coolant temperature field

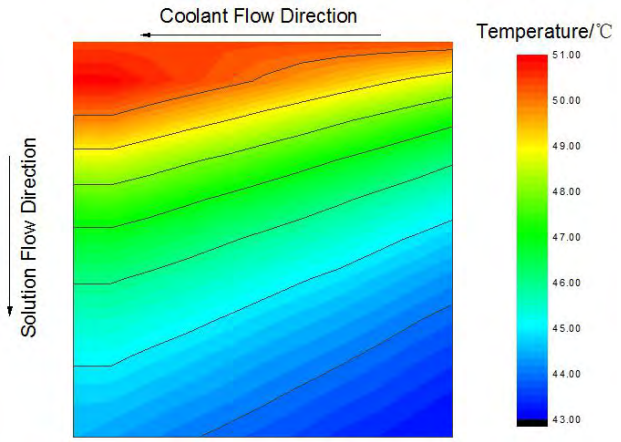

Figure 5: Nephogram of solution temperature field

The simulation results show that the absorber can generate 590 kW heat in a volume of 0.295 m3, and its effective heat and mass transfer area volume ratio can reach 212m2/m3. Compared with other literatures and experiments of the same heating capacity, the tube type can save 43% of the volume and realize the compactness of the absorber.

3.2. Effect of Pressure on the Performance of Absorber

Absorption pressure is an important factor affecting the absorption effect, which directly affects the saturated concentration of ammonia components at the liquid-vapor interface, that is, the mass transfer driving force. The effect of pressure on mass transfer is analyzed in detail. Figs. 6-7 shows the effect of pressure on mass transfer.

Fig. 6 shows that with the increase of the pressure, the mass transfer coefficient affected by viscosity and density increases, and the concentration difference of mass transfer also increase. This is because the saturation concentration of ammonia at the liquid-vapor interface is higher than low pressure. Therefore, as shown in Fig. 7, the increase of the pressure leads to the increase of mass transfer rate and the enhancement of the absorption process, which is conducive to the miniaturization of the absorber.

However, it should be noted that this conclusion is only for absorber components. If the absorber is placed in the whole heat pump system, the increase of the absorption pressure means the increase of the evaporation temperature, so the temperature of the solution entering the absorber rises, which is not conducive to the absorption process. Without considering the inlet temperature change of the solution, the increase of the pressure is beneficial to strengthen the absorption process of absorber and increase its heating capacity.

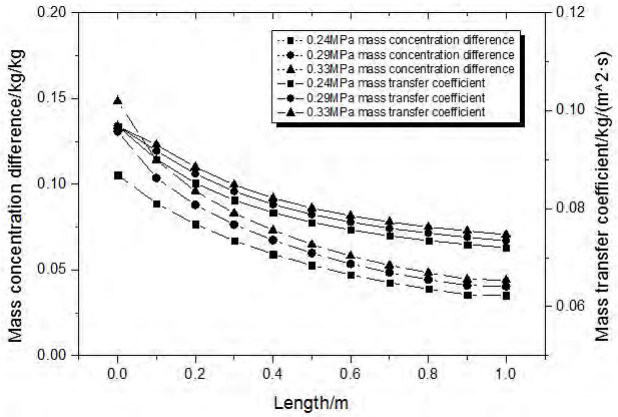

Figure 6: Variation of mass concentration difference and transfer coefficient along the absorber length at various pressure

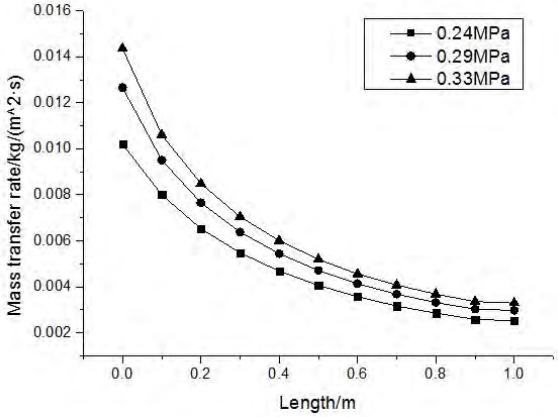

Figure 7: Variation of mass transfer rate along the absorber length at various pressure

3.3. Effect of Inlet Cooling Conditions on the Performance of Absorber

There is a lot of latent heat released in the absorber, and the key to enhance the absorption process is to take the latent heat away in time. Therefore, the cooling capacity of coolant directly affects the performance of the absorber. Fig. 8 shows the effect of the coolant inlet temperature on mass transfer.

With the increase of the inlet temperature of coolant, the mass transfer driving force decreases. The reason is the increase of the solution temperature caused by the decrease of the heat transfer temperature difference between the coolant and the solution. At a certain pressure, the increase of solution temperature leads to the decrease of saturated concentration of ammonia components at liquid-vapor interface and the decrease of mass transfer concentration difference. Therefore, variation of mass transfer rate at various inlet temperature of coolant is drawn as shown in Fig. 8. It can be seen that the absorption effect decreases with the increase of the inlet temperature of the coolant. Therefore, as shown in Fig. 9, with the increase of the inlet temperature of the coolant, the heating capacity of the absorber decreases due to the weakening of the absorption effect.

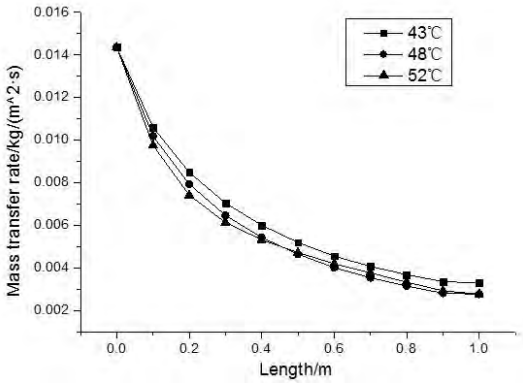

Figure 8: Variation of mass transfer rate along the absorber length at various inlet temperature of coolant

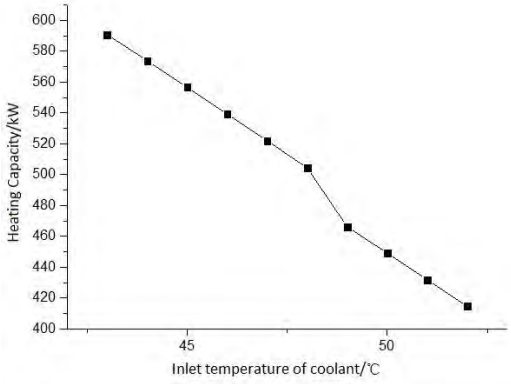

Figure 9: Variation of heating capacity at various inlet temperature of coolant

3.4. Effect of Inlet Conditions of Solution on the Performance of Absorber

The inlet condition of the solution is one of the important factors affecting the performance of the absorber. With the increase of the inlet temperature of the solution, the mass transfer rate only decreases with the increase of solution inlet temperature in the entrance section, and then remains basically unchanged. However, the difference of heat transfer temperature in the absorber increases, and the heat transfer effect is greatly enhanced. Therefore, as shown in Fig. 10, with the increase of the inlet temperature of solution, the heating capacity of the absorber increases.

As shown in Fig. 11, with the increase of the inlet concentration of the solution, the absorption effect is significantly weakened. Therefore, the heating capacity of the absorber decreases with the increase of the inlet concentration of solution.

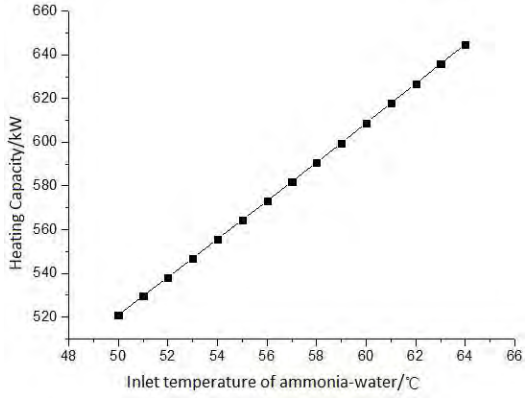

Figure 10: Variation of heating capacity at various inlet temperature of solution

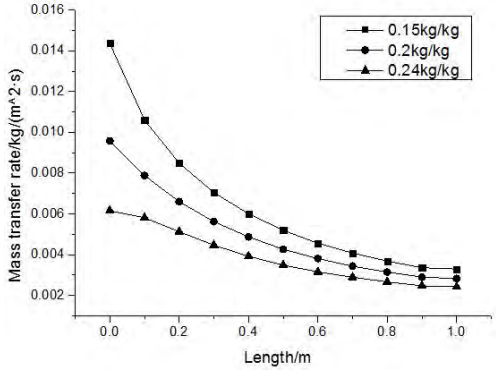

Figure 11: Variation of mass transfer rate along the absorber length at various inlet concentration of solution

4. CONCLUSIONS

In this paper, the working performance of a novel plate-fin flat-plate heat pipe absorber is simulated. The simulation results show that: in order to improve the heat and mass transfer effect of the absorber, the absorption pressure can be increased appropriately; the inlet temperature of the coolant should be reduced or the mass flow rate of the coolant should be increased; the inlet temperature of the solution should be increased or the inlet concentration of the solution be reduced. In order to evaluate the compactness of the absorber, the concept of compactness is introduced: f/V, f is the effective heat transfer area of heat exchanger, V is the volume of heat exchanger. In order to characterize both compact structure and heat transfer performance, the concept of heat transfer compactness is introduced: kf/V, which is the result of heat transfer coefficient times compactness. The compactness f/V of the new absorber can reach 212 m2/m3 and kf/V can reach 371 kW/(K·m3). Compared with the traditional tubular absorber (f/V:127 m2/m3 and kf/V:177 kW/(K·m3))[Zhuoming B C , 2003], the new absorber has much miniaturization application value.

NOMENCLATURE

C_p	Specific heat, J/(kg·K)	T	Temperature,℃
D_{aw}	volumetric diffusivity, m2/s	x	Mass fraction of ammonia
g	Acceleration due to gravity, m/s2	μ	Dynamic viscosity, Pa·s
h	Heat transfer coefficient, kW/(K·m2)	υ	Kinematic viscosity, m2/s
H	Enthalpy, kJ//kg	λ	Coefficient of thermal conductivity, kW/(K·m)
K	Mass transfer coefficient, kg/(m2·s)	δ	Thickness,m
L_1	Length of ammonia water solution flow, m	**Subscripts:**	
L_2	Length of coolant flow, m	*0*	Entrance status
m	Mass flow rate, kg/s	*1*	Flat heat pipe cooling section
M	Molecular weight, kg/kmol	*2*	Flat heat pipe absorption section
$\dot{m}$	Ammonia mass flow rate absorbed per area, kg/(m2·s)	*c*	Coolant/cooling fluid
Pr	Prandtl number	*v*	Ammonia vapor
R	Thermal resistance, (K·m2) /kW	*i*	Liquid-vapor interface
Re	Reynolds number for falling film	*l*	Liquid film
Sc	Schmidt number		

REFERENCES

J.C. Yang, G.X. Zhang, J.X. Dang. Heat and Mass Transfer Process in Heat-Pipe Type Falling Film Absorber[J]. Journal of Chemical Engineering of Chinese Universities, 1997(02): 15-19.

F. Zheng, G.M. Chen. Experimental Study on Lithium-Bromide Aqueous Solution Adiabatic Absorption Process [J]. Acta Energiae Solaris Sinica, 2002(02): 166-170.

S.J. Bie, M. Lu, M.L. Li. A New Type LiBr Absorption Chiller System Used Plate-fin Heat Exchanger [J]. Fluid Machinery, 2002(01):62-64.

Y.P. Chen, Y.B. Li. Experimental Study Of Double Dimensional Cross Wave Surface Plate Lithium Bromide Aqueous Falling Film Absorber[C]. Proceedings Of the Annual Conference On Heat and Mass Transfer . Shanghai the Chinese Engineering Thermodynamics Committee 2002, 921-924.

X.Y. Cui, C. Tang, M. L. Li. Design and Performance Study of Plate Falling Film Absorber with a Film-inverting Configuration[J]. Journal of Refrigeration,2005, 26(3): 47-52.

L. Wang. Study on Key Technology of Air-Cooled Adiabatic Absorption Refrigeration[D]. ZheJiang University, 2006.

R. Shang. Performance Analysis of Air-cooled Absorption refrigeration System and Structural Optimization of Absorber[D]. Huazhong University of Science and Technology, 2008.

N. Zhang. Study on Heat and Mass Transfer in Plate-Fin Falling Film Absorber with Wire-meshed Fins [D].Nanjing: Southeast University,2011.

S.Q. Fang, J. Guo, R.Y. Wang. Experimental Study on Heat and Mass Transfer in Heat Pipe-Type Absorber[J]. Journal of Zhengzhou University (Engineering Science), 2012, 33(03): 99-102.

X.n. Yan, L. Wang, Y.Y. Tan. et al. A Review of Developments in Small Size Air-Cooled Absorption Refrigeration [J]. Refrigeration, 2017, 45(04): 82-86.

Bassols J, Langreck R, Schneider R, Kuckelkorn B ,Veelken H. Absorption cooling machine based On compact plate-fin heat exchangers[C]. Proceedings of the 19th International Congress Of Refrigeration. Hague Netherlands 1995, 240-245.

Flamensbeck M, Summerer F, Riesch P Ziegler G. A Cost Effective Absorption Chiller with Plate Heat Exchangers Using Water and Hydroxides[J]. A lied thermal engineering. 1998(18) 413-425.

Islam Md R, Wijeysundera N E. Performance Study of A Falling Film Absorber with A Film-Inverting Configuration[J] .Int. J. Refrigeration 2003(2) 909-917.

Meacham J. M, Garimella S. Ammonia-Water Absorption Heat and Mass Transfer in Micro-Channel Absorbers with Visual Confirmation[J]. Ashrae Transactions, 2004, 110:525-532.

Goel N, Goswami D. Y. A Compact Falling Film Absorber[J]. Journal of Heat Transfer, 2005, 127(9):957-965.

Asfand F, Stiriba Y , Bourouis M . CFD simulation to investigate heat and mass transfer processes in a membrane-based absorber for water-LiBr absorption cooling systems[J]. Energy, 2015, 91:517-530.

D. Azbel. Fundamentals of Heat Transfer for Process Engineering, Noyes Publications, Park Ridge, NJ, 1984,382

W. Wilke, Warmeubergang an Rieselfilme, VDI-Fors-chungsheft 490 (1969) B28

Yih S.M. Modeling heat and mass transfer in wavy and turbulent falling liquid films[J]. Wärme-und Stoffübertragung, 1987, 21: 373-381

Eremisinoff I, Bucgilas P. Handbook of heat and mass transfer V.2. Mass transfer and reactor design, Gulf Publishing Company, Texas, 1986

T.H. Chilton, A.P. Colburn, Mass transfer (absorption) coefficients, Ind. Eng. Chem. 26 (1934) 1183-1187

Zhuoming B C , Meiling L . Structure and performance study of LiBr absorption chiller based on whole-plate-fin heat-exchanger[J]. Refrigeration Journal, 2003.

Manuscript ID: 758
DOI: 10.18462/iir.icr.2019.0758

Experimental study of the impact of crystallization parameters on properties of modified and reinforced ice structures intended for sports facilities and the Arctic

Vyacheslav M. BUZNIK[(a)], Galina Yu. GONCHAROVA[(c)], Nikolay D. Razomasov[(b)], Georgy A. Nuzhny[(a)]

[(a)]Federal state unitary enterprise "All-Russian scientific research institute of aviation materials"
Moscow, 105005, Russian Federation, lab30@viam.ru
[(b)]GP "Refrigerating - Engineering Center"
Moscow, 127422, Russian Federation, ice4sport@gmail.com
[(c)]Moscow State Technical University n.a. N.E. Bauman
Moscow, 105005, Russian Federation, galinagoncharova@mail.ru

ABSTRACT

The paper presents the results of experimental studies confirming the impact of crystallization parameters and water chemical composition on distribution of modifiers introduced into the ice massif. Criteria of choice of compounds to modify the ice properties to be applied at sport and arctic facilities are offered, the mechanism of further compounds migration depending on direction of heat removal and operation conditions is given. The possibility to increase the ice strength properties by introduction of microdoses of modifying compounds was proved experimentally as well as appropriateness of additional reinforcement using up-to-date high-strength fibers. The ice structure obtained was visualized. Examples of testing of the technology developed to form ice covering in sports facilities are cited; the perspectives of their application in arctic regions were estimated too.
Keywords: Ice, Crystalline Structure, Modifying Compounds, Strength, Choice Criteria

1. INTRODUCTION

The structure and macro properties of water ice depend on many factors the majors of which are as follows: water chemical composition, crystallization rate, mode of the ice massif formation and heat removal from the crystallization front, ice age as well. The current work investigates the method of impact of high-molecular compounds-modifiers introduced into water for ice covering. It agrees well with the basic ideas of crystallography and makes it possible to change natural ice properties purposefully due to creation of a regular structure in which the compounds introduced are distributed in the intercrystalline space and play the role of damper and so, reduce the intensity of intercrystalline interactions (Arkharov and Goncharova, 2010).The relationship between the structure of the solid phase and solidification conditions has been actively studied in metallurgy. However, the fundamental difference of the current problem is that products made of metals are operated at temperatures substantially lower than their melting point; but the water ice structure has to "work" at temperatures close to the melting temperature. Therefore, in metals, the distribution of alloying additives occurs in the process of alloy crystallization and remains almost unchanged; but in the ice there is a redistribution of the compounds introduced under the impact of temperature and concentration gradients. This is of great importance for sports facilities as, during operation, ice is cut and filled with clean hot water, which activates the diffusion process and contributes to the redistribution of the compounds introduced. Therefore, in the process of research, the factors were first identified that determine the initial distribution of the modifying compounds introduced over the depth of the ice massif, and then the patterns of their subsequent redistribution during operation.The task of using ice as a construction material for construction was relevant for countries with large areas in the cold climate zone. Canada and Russia have many years of experience in operating ice structures created from ice due to natural cold. However, the main obstacle to more extensive use of ice has always been its insufficient strength and high fragility. And so, research in the field of

hardening of ice structures and the creation on their basis of composite building materials are relevant and in demand, especially in the Arctic region. In the world of professional sports, most records in ice sports are directly linked with the artificial reduction of the friction coefficient between skate and ice. A significant improvement in sliding as a result of the introduction of structurizing additives is described in the works **(**Kietzig, 2010) and is used by many leading sports countries. These countries actively make use of fundamental and engineering science achievements to obtain new national and world records. Therefore the Congress of International Skating Union (ISU) held in Budapest (Hungary) in 2006 accepted a resolution on requirements of observance of equal conditions for all competitors.

2. EXPERIMENTAL STUDY OF PHYSICAL AND MECHANICAL PROPERTIES OF MODIFIED AND REINFORCED ICE STRUCTURES

The paper submits the visualization of the crystalline structure of modified ice and results of study of its mechanical properties. The study was carried out in laboratory and at real sports facilities.

2.1. Selection of chemical compounds groups to improve strength and tribological ice properties

2.1.1. Criteria of selection of chemical compounds groups to improve strength and tribological ice properties

Chemical compounds were chosen using V.A. Kargin principle that established the interaction between the configuration of macromolecules of modifiers introduced into ice and expected parameters of ice created: strength, elasticity, plasticity. On this basis considering the stereochemistry of water molecules hydrogen bonds we offered the criteria that might be symbolically divided into two groups. The first group represents criteria that are general for all types of engineering problems, the second one - criteria that are different for sports facilities and the Arctic considering particularities of ice formation and modified ice operation. It is proposed to consider the following criteria as general:

1. Environment and human safety.
2. Chemical inertness. At simultaneous introduction of several compounds of different functional purposes, the mixture components should not enter into chemical interaction - the principle of “a passive neighbor”.
3. Low temperature of crystallization or “vitrifying”. During the crystallization of solutions, pure water first freezes out, and the introduced compounds are dislocated in the intercrystalline space, creating a damping substance. Therefore, the solidification temperatures of the compounds introduced that form the eutectic should be below minus 8-10° C at sports facilities and ambient temperatures in the Arctic region (down to minus 60-70°C).
4. Minimum viscosity maintained over the entire operating temperature range.
5. The flexibility of the molecular chain, which determines the ability of the macromolecule to change the shape and linear dimensions without breaking the valence bonds of the polymer chain. The structure of water with tetrahedral symmetry is the most rigid, acting as “scaffolding” in which the molecules of the introduced compounds should be embedded.
6. Similarity of selected compounds to the structure of natural biopolymers. This approach is justified by the fact that the systems of living nature are necessarily hydrated, and the orientation of their free H-bonds coincides with the direction of free H-bonds of water, through which the connection takes place. This criterion is the final common criterion for the tasks of sport and the Arctic. Criteria relating only to sports ice are designated by the letter S, and to the Arctic tasks - by the letter A. The reduction of resistance to sliding on ice may be achieved by reducing the deformation component of friction F_{def} as a result of the appearance of a liquid film in the contact zone and the adhesive component F_{adh} by decreasing the surface tension of this film. Therefore, the additional criteria for sports tasks are as follows:
7.S. High surface activity. The compounds introduced into the ice structure must belong to the group of surface-active substances (SAS), be pushed to the surface as the water layer crystallizes and reduces the surface energy of the liquid formed in the contact zone.
8.S. High molecular mass of a polymer. For organic compounds according to the Traube’s rule and the Shishkovsky equation, the surface activity increases as their molecular mass increases.
9.S. Anti-friction properties to reduce sliding friction.

For the northern regions, the main task is to enhance the strength properties of ice when exposed to different loads of various types. Therefore, the criterion of Arctic tasks is as follows:

7.A. Surface inactivity of the compounds introduced which interact with water more actively than between themselves. As a result, most of the molecules are entrained in the volume of water and the modifying compounds are captured by the crystallization front and remain inside the ice after freezing, reducing the intensity of intercrystalline interactions, they do not rise to the surface.

The above criteria allowed a systematic approach to the selection of compounds for the modification of ice and move away from the unproductive search of polymers based on general and intuitive considerations.

2.1.2. Results of criterion selection and visualization of ice structures obtained

In accordance with the listed criteria and functional purpose, the following groups of modifying compounds were formed. The first group – compounds for reducing the resistance to sliding and minimizing the dry friction zone. For this purpose the organic silicon compounds were chosen, in particular, the organic silicon liquids (OSL) (oils). The pour point of most OSL is minus 60 - 80°C and below. They have physical and chemical inertness, hydrophobicity, high compressibility and minimal dependence of viscosity on temperature, as well as a flexible and mobile basic molecular chain. The second group, functionally designed to reduce the adhesion component of friction, mainly includes fluorine-containing compounds. They are distinguished by high cold and heat resistance, surface activity, the best anti-adhesive properties. However, fluoroplastic is insoluble in water, therefore, to modify the properties of ice, it was proposed to use fine (0.05-0.1 μm) aqueous suspensions of polytetrafluoroethylene (PTFE), stabilized by surface-active substances. An additional advantage of PTFE is maintaining the minimum coefficient of friction at low temperatures. Microemulsions based on the mixture of fluoride-organic silicon and organic silicon SAS of different structure are also included in the second group. Whereupon all compounds introduced in micro doses are chemically stable, safe for a human organism, and the fluoroplastic of brand marks applied is accepted to be used in medicine. For the Arctic region, the most important is to reduce brittleness and increase the strength properties of bending, compression and shock loads. So, the third group includes polymers with rubber-like properties and surface inactivity: organic silicon rubbers with phenyl groups at necessary freeze resistance (to minus 130° C), high strength properties and the linear expansion coefficient close to ice. To confirm the hypothesis put forward about the localization of introduced compounds in the intercrystalline space, the structure of modified ice was studied using Quanta 3DFEG and Quanta 250 multifunctional raster cryoelectronic microscopes (manufactured by FEI Company). Fig. 1.b shows an image of an ice sample modified with PTFE at a magnification of 1000 x, in which the crystal boundaries are clearly visible; and Fig.1.a shows separate ramified fragments of macromolecules PTFE that are well seen at a magnification of 5000 x. The presence of fluorine in the area of white ramified particles was defined by energy-dispersion analysis (as illustrated in Fig. 2.a). The analysis showed the expressed peaks in the areas F and C in the result window as the main elements included in the PTFE molecules. For comparison Fig.2.b shows the result of analysis of the dark area free from particles of foreign substances. There are no pronounced peaks, except the peak in the zone responsible for the oxygen content, in accordance with the composition of the water molecule. Lately leading sports countries actively make use of fundamental and engineering science achievements to obtain new national and world records. With this the Congress of International Skating Union (ISU) held in Budapest (Hungary) in 2006 accepted a resolution on requirements of observance of equal conditions for all competitors.

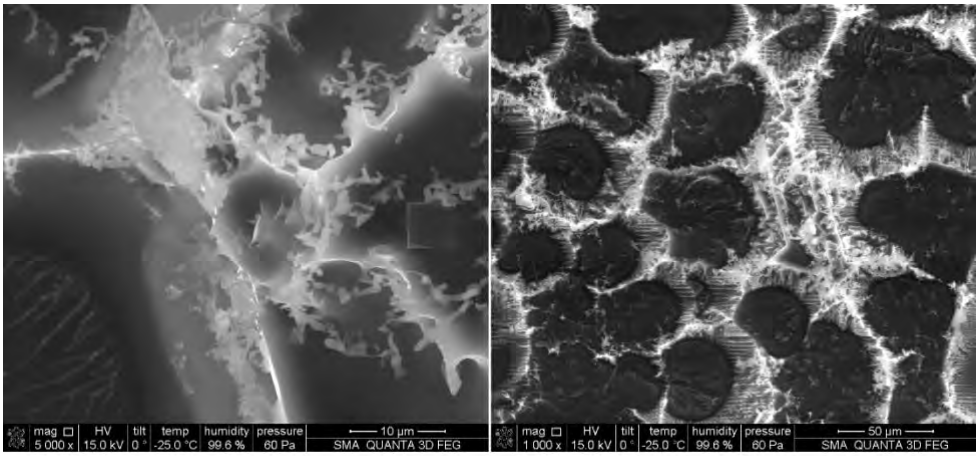

Figure1: Image of the ice sample surface from above

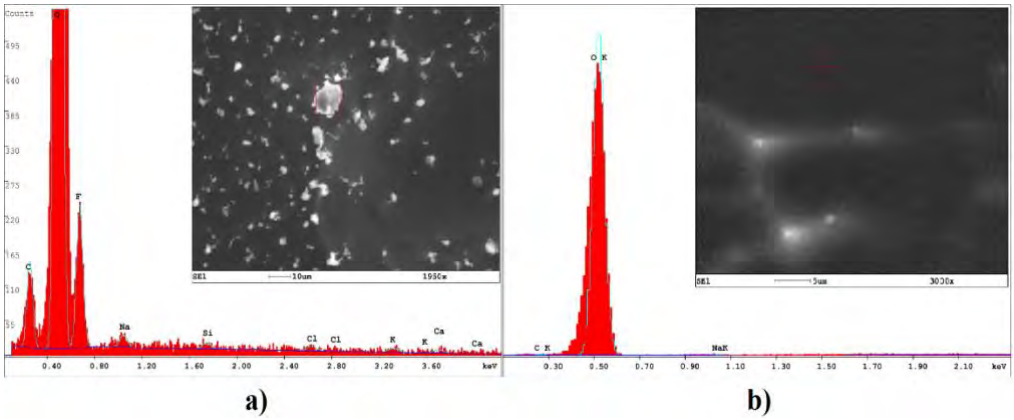

Figure 2: Results of energy dispersed analysis of ice samples different zones

2.2. The effect of crystallization rate on the distribution of modifiers in the ice massif.

The results of basic research on the effect of water crystallization rate on the ice structure obtained are correlated: the lower the speed the more gaseous inclusions and defects of the crystal lattice have time to relax and go to the surface (Shavlov et al., 2007). However, when modifiers are introduced into water, their initial distribution through the depth of the ice massif also depends on the properties of the compounds themselves: surface activity, molecular configuration, length of the main chain and molecular mass. Thanks to chemical passivity and significant differences in the molecular structure they do not form a united diffusing medium and migrate in the ice “body” at different intensity.

Thus, the molecules of organic silicon compounds at a molecular mass not exceeding10^3 a. u. are most likely to rise to the surface, and the heaviest PTFE macromolecules at 10^6 – 10^7 a. u. are captured by the crystallization front and fixed in the ice layer formed. Further at periodical cutting and pouring with pure hot water their concentration in the surface layer decreases. It leads to redistribution of compounds in the ice massif under action of thermal and concentration components of diffusion. The connection of the processes of the simultaneous heat and mass transfer may be established by Onsager theorem (reciprocity theorem) (Beckman, 2016). The velocity of these processes is adopted proportional to the concentration gradient (for mass transfer) and temperature gradient (for heat transfer). In the one-dimensional problem and for each of the components of the mixture, the following system of differential equations takes place:

$$\frac{\partial C}{\partial t} = D_m \cdot \frac{\partial^2 C}{\partial x^2} + D_m \frac{k_T}{T} \frac{\partial^2 T}{\partial x^2} \quad \textbf{Eq. (1)}$$

$$\frac{\partial T}{\partial t} = a \cdot \frac{\partial^2 T}{\partial x^2} + D_T \frac{Q}{C_p} \frac{\partial^2 C}{\partial x^2}, \quad \textbf{Eq. (2)}$$

where C is concentration of diffusing substance; a is the coefficient of temperature conductivity; D_m is the coefficient of molecular diffusion; D_t is the coefficient of thermal diffusion; Q is a specific heat of isothermal transfer; $k_T=D_t/D_m$; Cp is heat capacity.

In the absence of a mathematically formalized description of the geometry of the intercrystalline space, which determines the values of the thermal diffusion coefficients included in the equations, it is impossible to describe analytically the migration of the components of the diffusant, which is a complex system of various chemical compounds. Hence, in the present work a mathematical model of heat and mass transfer was not created, but precision modeling and experimental study of the effect of crystallization rate and mixture composition on the distribution of modifiers in the ice mass and strength characteristics of ice obtained were carried out. Below are cited the results of experimental investigations of modifiers distribution through the ice depth at one-dimensional removal of heat to coolant circulating in the flagstone. The investigations were carried out in laboratory. After freezing the ice massif obtained was mechanically divided into layers 1mm thick using a precision cutter. Then, the concentration of modifiers using a permanganate oxidation index in each melt was defined. This index characterizes the total organic phase content. To more accuracy of data the melts composition was analyzed by conductometric and spectroscopic methods of element analysis. The results of studies conducted by the authors earlier (Goncharova et al., 2015) showed that the compositions of the mixtures, and the optimum concentration range of the compounds introduced, are determined by the character, method of application of the loads and the duration of their action.

In speed skating the total water concentration of modifiers should not exceed 20 ppm; at load increasing and shock loading (figure skating, bobsleigh) the concentration may reach 150-200 ppm. Fig.3.A illustrates the initial modifiers distribution in the ice layer 15 mm thick at concentration of the water mixture introduced ξ_{mi} = 20 ppm and 150 ppm at the same rate of crystallization. It is seen that both curves are identical for mixtures without PTFE: practically invariable concentration of modifiers in inner ice layers with abrupt increasing up to the ice surface. But the concentration ratio on the surface and in the massif remained invariable at different concentrations in poured out water and was about 5 to 1. For PTFE mixtures (green curve) the dependence is different: most of ingredients remained in the ice massif which was a consequence of the significantly large size of macromolecules. Besides, exactly the crystallization rate regulated by coolants temperature exerted a considerable impact on modifiers distribution as shown in Fig. 3.B. The higher the crystallization rate, the greater the number of molecules captured by the crystallization front and fixed in the inner layers of ice. And vice versa, at low rate the surface activity of macromolecules introduced allowed them going to the surface and staying in the upper ice layer. Hence, the freezing rate is the main instrument to regulate the modifiers distribution in the ice massif.

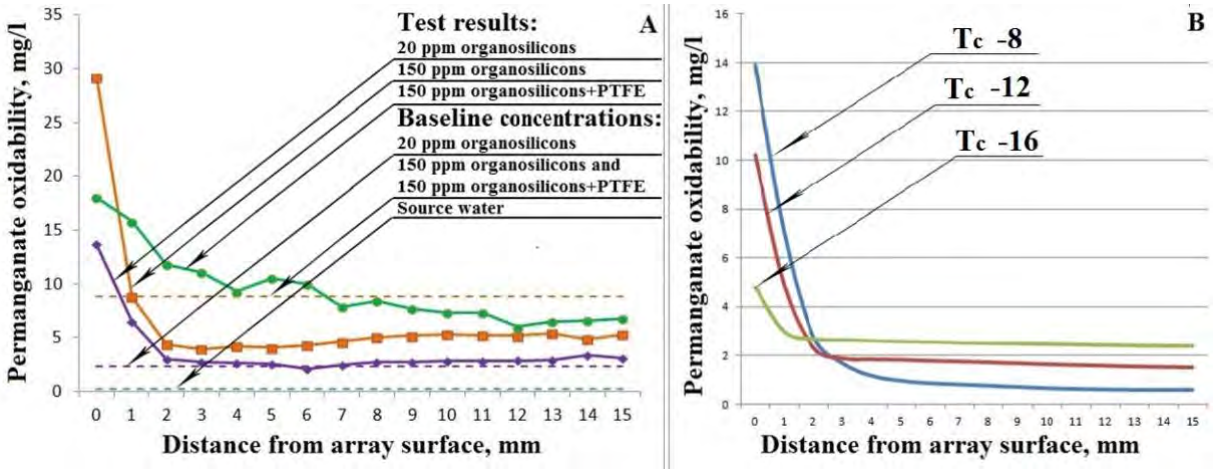

Figure 3: Modified substances distribution to the massif depth

2.3. Laboratory tests of strength properties of modified and reinforced ice

2.3.1. Research methods

The recommendations of the International Association of Hydrologic Studies (IAHS) were taken into account when developing the test program on bending and selection of geometrical ratios of ice samples. The samples were parallelepipeds at 150 mm x 50 mm x 25 mm sides and were frozen under identical conditions. The study of the strength properties of ice samples was carried out on the plant Zwick / Roell Z050, allowing to change the rate of the load application to the sample in the range from 1 to 100 mm per minute and to maintain a constant temperature in the test chamber. The measurements error was not higher 0.25% of load measured and not more 0.2 μm at measuring the sample deformation (Buznik et al., 2018).

2.3.2. Results of studies of strength on bending of modified ice samples

In the process of testing, the maximum loads for samples of PTFE modified and two types of organic silicon microemulsions were determined experimentally. Water was poured by layers of 1-1.2 mm and frozen at one-dimensional heat removal. The concentrations ranged from 20 to 500 ppm at individual compounds introduction and to 10000 ppm at introduction of mixtures on the basis of these compounds. The analysis of experiments resulted in following conclusions:

-greater effect is achieved when modifiers are introduced in the mixture but not individuall**y;**

-mixture introduction into water allowed increasing strength characteristics at three-point bending 2.1-2.2 times, and deformation to destruction 1.6-1.8 times as shown in Fig. 4a.

-dependence of strength properties on concentration is of extreme character and the interval of concentrations recommended is ~150-300 ppм as shown in Fig. 4b.

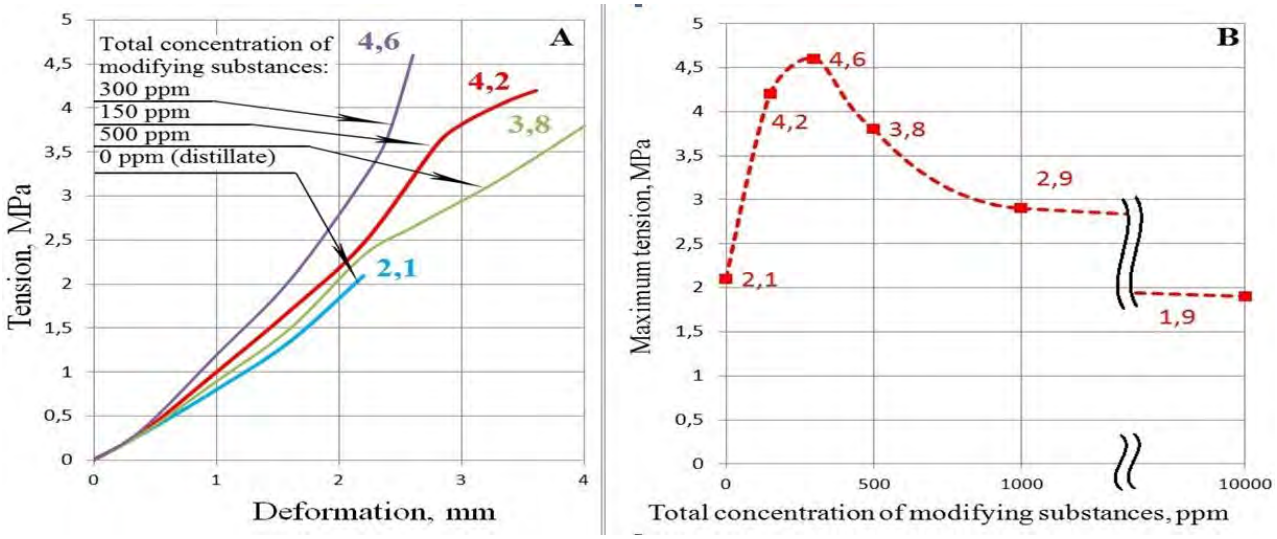

Figure 4: Dependence of strength characteristics on total concentration of modified substances

2.3.3. Results of studies of modified ice samples reinforced by fibers

The same equipment was used to conduct the experiments on strength of ice samples with the mixture of modifiers and basalt reinforced by fibers; ice samples were placed at different level from the bottom, the aim was to study a synergic impact of both factors. The most promising results obtained for samples reinforced by basalt fibers at 2 mm level from the lower border of the sample are shown in Fig. 5.A. The blue line shows the tension deformation of the sample frozen of distilled water. And the red line presents the tension deformation of the sample modified by PTFE mixture, organic silicon oils and emulsions at ratio 1:1:1. Fig.5.B demonstrates an external view of the sample during the test and after the load is removed. The reinforcing by basalt fibers leads to a significant increase of maximal strength (from 2.5 to 8.4 MPa) at bending σ^{b}_{max} fixed during the test of the distillate sample; the sample conserves its integrity up to linear deformation of 22-23 mm. The same reinforcing using basalt and introduction of modified mixture contributes to increasing σ^{b}_{max} value to 10 MPa and keeping carrying capacity of the sample at higher level of 8 MPa at deformations of 25-30 mm. A reciprocal disposition of curves makes it possible to suppose that modified compounds introduction stops the cracks development at the expense of damping substance in the intercrystalline space and the fibers contribute to keeping the sample integrity even after a partial destruction.

2.4. Comparative tests of ice strength properties of sports ice coverings

During natural experiments we compared a short-time shock impact of a sportsman skate on modified ice coverings and coverings with frozen pure water. For this purpose we developed a plant imitating a touchdown of a sportsman after jumping as illustrated by Fig. 6.A. It consists of a metal acceleration trestle and a heavy shock element made on the basis of the figure skate blade as shown in Fig. 6.B.

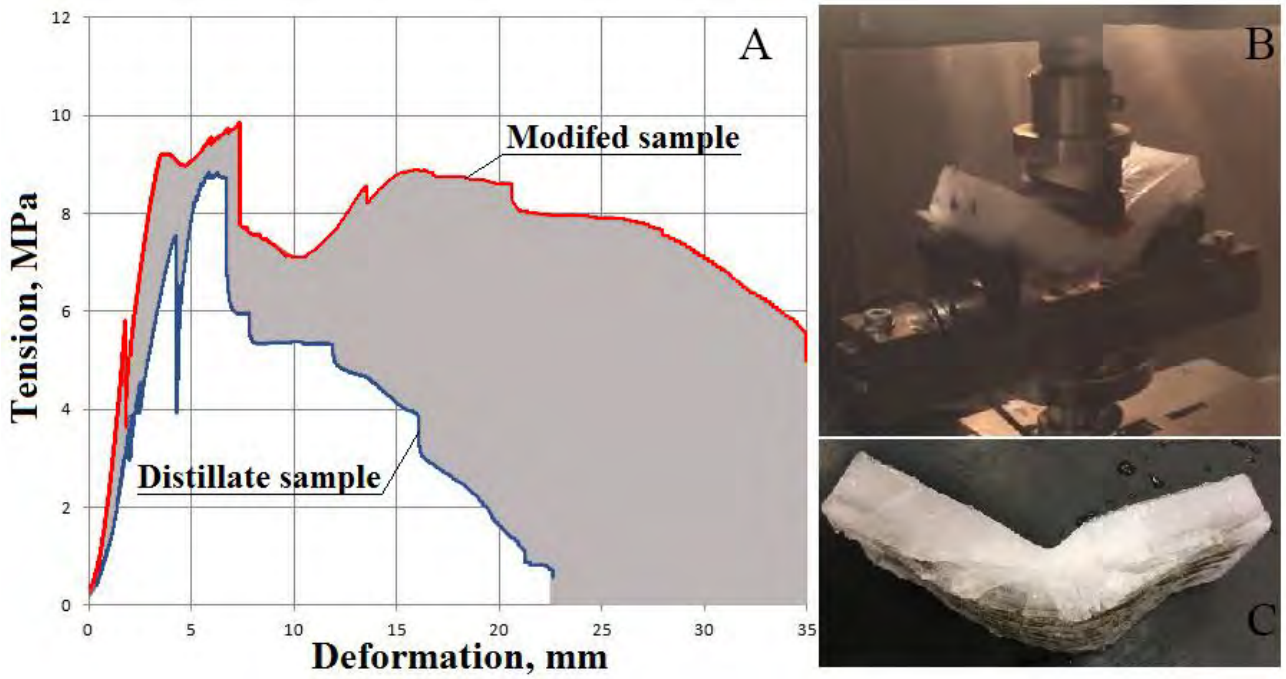

Figure 5: Study of ice samples reinforced by basalt fibers

Besides the visualization estimation of ice destruction, a quantitative evaluation of the volume of the emerged crack was realized. The crack was fully filled with water by a syringe and then the liquid volume was defined. Fig.6. C shows the result of the first experiments. The torn borders of the skate trace and significant volume of destructions of the ice massif are well seen: 1.6-1.8 ml liquid. After deposition of 3 layers of ice ~ 1,5 mm thick, modified with PTFE mixture, organic silicon oils and microemulsions at total concentration of 10 ppm, the trace left by the imitator after touchdown is not deep, crack borders are even, crumbs are practically absent (as shown in Fig. 6.D); the average volume of ice break doesn't exceed 0.8 ml that is almost half as much as on pure ice.



Figure 6: Plant imitated the shock at a sportsman touchdown (A, B), damages of ice massif (C, D)

Natural tests of modified ice confirmed qualitatively and quantitatively the effect of strengthening the ice structure during shock impact. Hence, at shock impact on modified ice the cracks development is stopped due to a liquid substance in the intercrystalline space that later contributes to regelation and crack healing of ice layers destroyed.

3. CONCLUSIONS

1. Introduction of modified mixtures in water for pouring ice covering increases significantly the maximum strength at three-point bending up to 2.1-2.2 times and deformation to destruction 1.6-1.8 times.
2. In combination with reinforcing, modified ice may support loads exceeding the strength of distillate, keep integrity after cracks emerged, and it may be used as a construction material in the Arctic region.
3. Criteria formulated may be applied for selection of groups of chemical compounds in order to purposeful changing the properties of natural ice depending on its function.
4. Efficiency of use of ice modifiers in sports ice facilities when short-time destructive impact occurs was proved experimentally.
5. It was shown that the freezing rate and mixtures composition were the main instruments to impact on modifiers distribution in ice as well as on its physical and mechanical properties

REFERENCES

Arkharov, I.A., Goncharova, G.Yu. 2010. Experimental study of ice structures modified with polymers. Refrigeration technique 11, 23-32.

Anne-Marie Kietzig, 2010. Microscopic ice friction, The University Of British Columbia, April

Shavlov, A.V., Ryabtseva, A.A., Shavlova, V.A. 2007. "Superslippery" ice for skating. Earth cryosphere (2), 49-59.

Beckman I.N., 2016. Math of diffusion: study guide. Publishing house "OntoPrint", Moscow, 400 p.

Buznik, V.M., Cherepanin, R.N., Nuzhnyi, G.A., Razomasov, N.D., Goncharova, G.Y.. 2018. Physicomechanical Properties of Glacial Composite Materials Reinforced by Rusar-S Fibers. Inorganic Materials: Applied Research 9(1), 114-120.

Goncharova G.Yu, Nikiforova I.G., Ustugova T.G., Razomasov N.D., 2015. Investigation of the possibility of reducing frictional interaction in a "blade-ice" pair by modifying the structure of both contacting surfaces. RFBR Journal 3, 45-53

Manuscript ID: 767
DOI: 10.18462/iir.icr.2019.0767

Safety related properties of low-GWP refrigerants

Enis ASKAR[(a)], Volkmar SCHRÖDER[(a)], Tobias GÖPFERT[(b)], Ullrich HESSE[(b)], Erik WINTERLEITNER[(c)], Michael SCHWARZE[(c)]

[(a)] BAM Bundesanstalt für Materialforschung und -prüfung
12205 Berlin, Germany, enis.askar@bam.de
[(b)] Technische Universität Dresden
01062 Dresden, Germany
[(c)] Technische Universität Berlin
10623 Berlin, Germany

ABSTRACT

Most fluorinated hydrocarbons that shall replace refrigerants with high GWP, like R134a, are flammable. For evaluating inertization measures for explosion protection, flammability of low-GWP refrigerants R1234yf, R32 and R1132a blended with carbon dioxide, nitrogen and argon were studied experimentally in a closed autoclave at atmospheric conditions. Furthermore, a calculation method was adapted to reduce the experimental costs for flammability studies on these gas mixtures. For igniting R1234yf in the closed autoclave a newly developed ignition system was used that allows generating electric arcs with high ignition energy. Gas mixtures containing the mildly flammable R1234yf and R32 could be inerted by adding much less inert gas than mixtures containing R1132a, which is more similar to unfluorinated hydrocarbons regarding the explosion regions. By using the adapted model of constant adiabatic flame temperature profiles estimating the explosion limits of fluorinated hydrocarbons was possible with similar accuracy as for unfluorinated hydrocarbons.
Keywords: Explosion Protection, Inertization, Flammability, HFOs, HFC,.R1234yf, R32, R1132a.

1. INTRODUCTION

Because of new environmental regulations related to existing international agreements, including the Montreal and Kyoto Protocols to avert stratospheric ozone depletion and global climate change, the need for a new generation of refrigerants is increased over the past years (Calm, 2008). Especially substitutes for R134a, one of the most common refrigerants are demanded. The gradual phase-out of R134a or R134a-based refrigerants like R410A, is motivated because of its high global warming potential (GWP).

The hydrofluoroolefine (HFO) R1234yf and the hydrofluorocarbon (HFC) R32 are considered promising next generation refrigerants with low GWP for different applications. One of the main issues of using these refrigerants, however, is their flammability. Both refrigerants are classified as mildly flammable (class 2L according to ANSI/ASHRAE 34, 2016) to distinguish them from highly flammable substances like hydrocarbons. However, flammability must be considered for safety evaluation, if R1234yf or R32 are used, which is not necessary in case of using R134a, which is not flammable. One possible approach to avoid flammable atmospheres when using mildly flammable refrigerants is inertization by adding inert gases. However, experimental determination of explosion regions in ternary systems of fuel gas, inert gas and air is quite elaborate and therefore, only few data is available in literature.

In this work, the inertization of gas atmospheres containing the mildly flammable low GWP refrigerants R1234yf and R32 and the flammable R1132a (class 2 according to ANSI/ASHRAE 34, 2016) by adding different inert gases should be studied. For this purpose, the explosion regions for ternary systems containing refrigerant, inert gas and air were determined experimentally with different inert gases in a closed vessel in accordance with EN 1839 (2017) -bomb method. Then, the applicability of the model of constant adiabatic flame temperature profiles (CAFTP) should be

studied for calculating the explosion regions of these substances (Askar et al., 2010). Semi empirical calculation methods based on adiabatic flame temperature calculations like the CAFTP model are very appropriate for calculating the explosion limits of hydrocarbons as already shown in several works (e.g., Giurcan et al., 2013; Ma, 2013; Mashuga and Crowl, 1999; Thiel-Böhm, 1991). The high experimental effort for explosion limit determination could be reduced significantly by using the models also for estimating the explosion limits of fluorinated hydrocarbons.

2. EXPERIMENTAL PROCEDURE AND CALCULATION METHOD

2.1. Experimental Set-up and Test Procedure

For the experiments a test set-up in accordance with EN 1839 -bomb method (2017) was used. The ignitions were carried out in a closed spherical autoclave made of stainless steel with an inner volume of 14 dm^3. The autoclave was heated to the test temperature with heating sleeves. An exploding wire igniter was used as described in EN 1839 (2017). A 0.12 mm nichrome wire was used, which was soldered over the tips of two isolated brass electrodes in a distance of 5 mm. The electrical power was supplied by an isolating transformer generating the electrical arc with ignition energy between 10 J and 20 J. The ignition energy induced into the gas system is calculated by measuring the current and voltage development during the ignition process. Only in the tests with R1234yf, the electrical power was provided by a newly developed capacitor ignition device that allows generating electrical arcs with higher ignition energy (Askar et al., 2018). The ignition energy was between 950 J – 1150 J in these tests. As shown in previous works, R1234yf is difficult to ignite in closed systems with the usual ignition energy of 10 J – 20 J (Davis et al., 2017; Kondo et al., 2011).

Temperature was measured near the center of the autoclave with 1,5-mm-thermocouple, type K, class 1. Pressure was measured with piezoresistive pressure transducers (company: Keller, type: PA-10). The measuring uncertainty of the pressure sensors is better than 0.2% full scale (FS). For measuring the explosion pressure, a pressure sensor with a measuring range up to 10 bar was used. For mixture preparation a pressure sensor with a measuring range up to 2 bar was used. For measuring the vacuum pressure, a Pirani Gauge was used with a measuring uncertainty of 15% (company: Edwards, type: APG-M). The test apparatus as a whole was calibrated by determining the explosion limits of methane as reference substance as specified in EN 1839 (2017).

All test substances used in the ignition test had a purity of minimum 99.5%. The compressed air used in the tests was dry and free from oil. The mixtures were prepared directly in the spherical autoclave before each ignition according to the partial pressure method. For that the heated autoclave was first evacuated until the pressure was less than 1 mbar. Afterwards, the test mixture was prepared by adding the single components of the ternary mixture according to their accordant partial pressures. It was assumed that the partial pressure fractions of the components are equal to the molar fractions (ideal gas). As shown by Kondo (2011) the deviation for atmospheric pressure is less than 0.1 % in relative values for the tested substances. Since the explosion regions of R1234yf are slightly enlarged at high humidity (JSRAE, 2017), initially water vapor was added up to a partial pressure of 10 mbar (i.e. 1 mol%) in all ignition tests with R1234yf. The test temperature for the tests with R1234yf was increased to 60 °C. In all other tests, the test temperature was 40 °C and no water vapor was added.

The test mixtures were homogenized by a PC-fan that was installed inside the autoclave for at least three minutes. Finally, the PC-fan was turned off and after another waiting time of at least 30 s the ignition was triggered in the quiescent mixture. Simultaneously data acquisition was started. The measuring frequency was 20,000 Hz in the first 10 ms for calculating the ignition energy. Then, it was switched to 2,000 Hz for recording the following pressure development. In accordance to EN 1839 (2017) an explosion was defined as pressure rise of at least 5% after triggering the ignition source (pressure rise criterion). Because of the much higher ignition energy in the tests with R1234yf, the pressure threshold for detecting explosions was increased to 50% plus the pressure rise of 16% caused by the ignition source itself, when it is triggered in the same ignition vessel with pure air yielding to a pressure rise criterion of 66% (Askar et al., 2018). After each ignition, the test apparatus was purged with air or nitrogen for several minutes.

The mixture composition was varied from test to test in steps of 0.5 mol%. Until the lowest and the highest fuel gas fractions were found, at which no explosions are observed. These compositions were validated by four repetition tests respectively. The apex of the explosion region in the ternary diagram was determined by varying the fuel gas and the air fraction systematically according to the short method described in EN 1839 (2017).

2.2. Calculation Method

The explosion limits were calculated according to the semi-empirical model of constant adiabatic flame temperature profiles as described in (Askar et al., 2010). According to this model, it is assumed that a gas mixture can be ignited if the calculated adiabatic flame temperature of this mixture exceeds a certain threshold temperature. This threshold temperature is independent from the type of inert gas and the initial temperature (Burgess and Wheeler, 1911). The adiabatic flame temperatures for the compositions at the experimentally determined explosion limits in the ternary systems of refrigerant, nitrogen and air were calculated first. So, the threshold temperatures for each refrigerant in dependence from the inert gas concentrations were obtained. Then, these temperature profiles were used as reference to calculate the explosion limits for ternary gas mixtures with other types of inert gas (i.e. carbon dioxide or argon) by finding compositions with calculated adiabatic flame temperatures equal to the corresponding reference flame temperature of the combustible-nitrogen-air-system.

Flame temperature calculation was carried out by using the software GasEq (Morley, 2019). For the thermodynamic calculations the main product species formed during the combustion of the fluorinated hydrocarbons identified by Magnusson et al. (2016) were considered additionally to the product species formed during the combustion of usual hydrocarbons. The thermodynamic parameters of these species were obtained from the standard database of the software GasEq, NASA thermodynamic data sets and the Database of New NASA Polynomials (Morley, 2019; Gordon and McBride,1994; Goos et al., 2018). The following species were considered products for flame temperature calculation:

C, CH_4, CO, C_2H_6, C_3H_8, C_2H_4O, CH_3, CH_2O, H, H_2, OH, O, O_2, CH_3CHO, HCO, CH, CH_2, CO_2, H_2O, N_2, CN, NH_3, NO, NH_2, NH, N, C_8H_2, Ar, $C_3H_2F_4$, COF_2, HF, F_2, F, CF_4, CF, CH_2F_2, C_2F_4, C_2F_6, C_2H_2, C_6H_6, FO, FO_2, C_2H_4, $C_2H_2F_2$.

For calculating the apex of each system, it was assumed that the ratio of combustible and air is similar at the apex for all systems independent from the type of inert gas. Thus, the apex was calculated by fixing the combustible/air-ratio and finding the inert gas concentration, at which the calculated flame temperature was similar to the previously calculated flame temperature for the mixture at the apex of the reference system.

Explosion limit calculation was carried out with an VBA algorithm using an Excel-macro and by using a GasEq-interface for the flame temperature calculations (Askar et al., 2010).

3. RESULTS

3.1. Test Results

In Fig. 1 the explosion regions of R1234yf, R32, R1132a and the highly flammable R290 (propane) adding the inert gases nitrogen, argon and carbon dioxide are shown in ternary diagrams. The explosion regions of R290 were taken from Molnarne (2008). The other explosion regions were completely determined experimentally in this work except for the upper explosion limit of R1132a in air without inert gas, which was taken from CHEMSAFE (2016). In Table 1 safety characteristics that can be derived from the ternary diagrams are summarized. The maximum oxidizing gas concentration (MOC) is the largest oxygen fraction in a certain ternary system of flammable gas, inert gas and air, for which the gas mixture cannot become explosible irrespective of the amount of flammable gas being added (Molnarne, 2008). The MOC usually corresponds to the apex of the explosion region in the ternary diagram. The maximum permissible flammable gas concentration (MXC) in a flammable gas/inert gas mixture is the largest fraction of the flammable gas for which this gas mixture cannot become explosible irrespective of the amount of oxidizer added (Molnarne, 2008). The MXC were determined by calculating the intersection point of the tangent of the

explosion regions that cut the 100% inert gas concentration point in the triangular diagrams with the inert gas axis.

R1234yf and R32 have the smallest explosion regions of the four refrigerants. Thus, the least amounts of inert gas are needed to inertize atmospheres. The explosion range of R1234yf in air without inert gas complies very well with the explosion range of 4.8 mol% - 15.0 mol% determined according to the ASHRAE method (ASHRAE, 2016) in other works (JSRAE, 2017) at similar conditions considering that the test set-up was very different, and a much stronger ignition source was used in this work. With the same type of inert gas, the MOC of R32 is only slightly lower than the MOC of R1234yf, but the range between the lower and upper explosion limit is much larger than for R1234yf. R32 has the highest lower explosion limits of all four refrigerants. Thus, a much higher amount of R32 compared to the other refrigerants must be released until explosible mixtures can be formed at all. Therefore, also the MXC value of R32 is the lowest, i.e. less of an inert component must be added to R32, to obtain mixtures that cannot become explosible if released in the atmosphere. The MXC for R32 determined in this work comply with the similar fuel inertization points (FIP) determined by the JSRAE (2017). The FIP of R32 determined by the JSRAE (2017) vary between 47 mol% and 42 mol% with nitrogen as inert gas and between 66 mol% and 55 mol% with carbon dioxide as inert gas depending on the test method applied; the ASHRAE method (ASHRAE, 2016) using spherical glass vessel or the HPGSA-A (JSRAE, 2017) method using 2-liter pressure-tight spherical metal vessel. The explosion regions of R1132a are even larger than the explosion regions of R290, though the MOCs of R290 are still lower than the MOCs of R1132a. Altogether the extent of the explosion regions of 1132a are more similar to the explosion regions of highly flammable hydrocarbons than to R32 or R1234yf.

Comparing the three inert gases, it is obvious that adding carbon dioxide has the strongest inertization effect, because of the high molar heat capacity of carbon dioxide. Argon, which has a very low molar heat capacity, is the least effective inert gas.

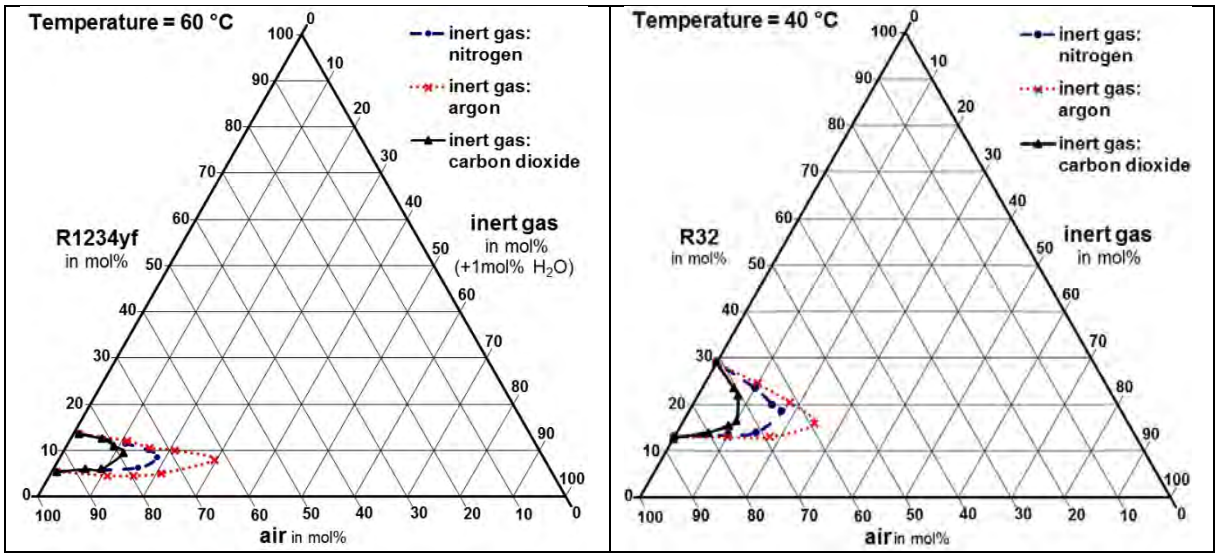

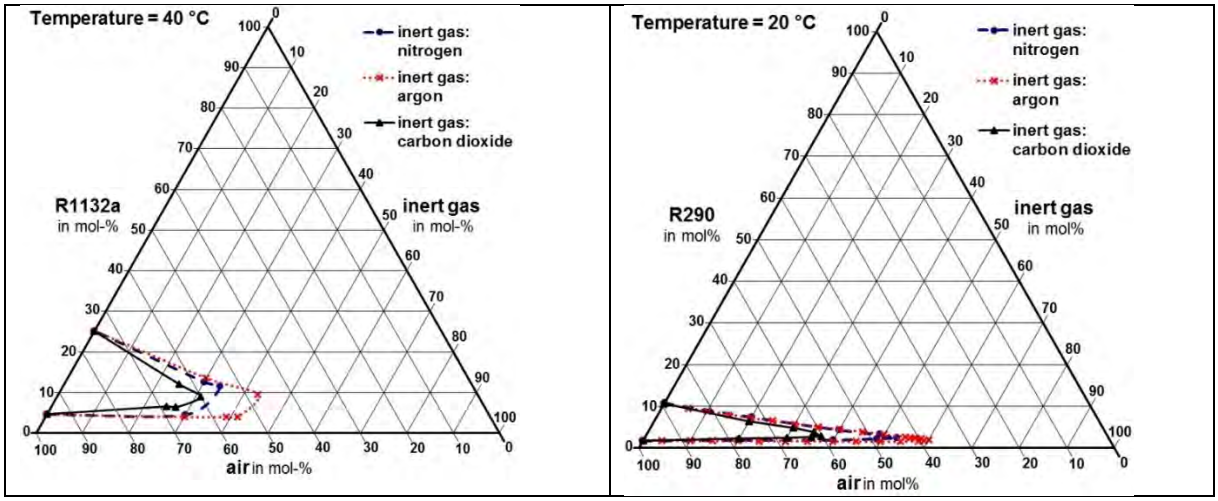

Figure 1: Explosion regions of the refrigerants R1234yf, R32, R32 and R290

Table 1. safety characteristics of the refrigerants R1234yf, R32, R32 and R290 that can be derived from the ternary diagrams

-	Inert gas	R1234yf	R32	R1132a	R290**
LEL in air	Without inert gas	5.4	13.0	4.6	1.8
UEL in air	Without inert gas	13.6	29.0	25.1*	10.6
MOC	Nitrogen	15.2	13.4	11.4	9,3
	Argon	13.0	12.3	9.9	8,0
	Carbon dioxide	16.5	14.7	12.5	12,6
MXC	Nitrogen	27	48	13	4
	Argon	19	39	8	2
	Carbon dioxide	40	62	18	6

* from CHEMSAFE (2016) measured in an open glass tube similar to EN 1839 (2017)
** from Molnarne (2008) measured in an open glass tube (tube method) according to EN 1839 (2017)

3.2. Calculation Results

In Fig. 2 the calculation results for the explosion regions of R1234yf, R32 and R1132a with inert gases argon and carbon dioxide, respectively are compared to the experimental results.

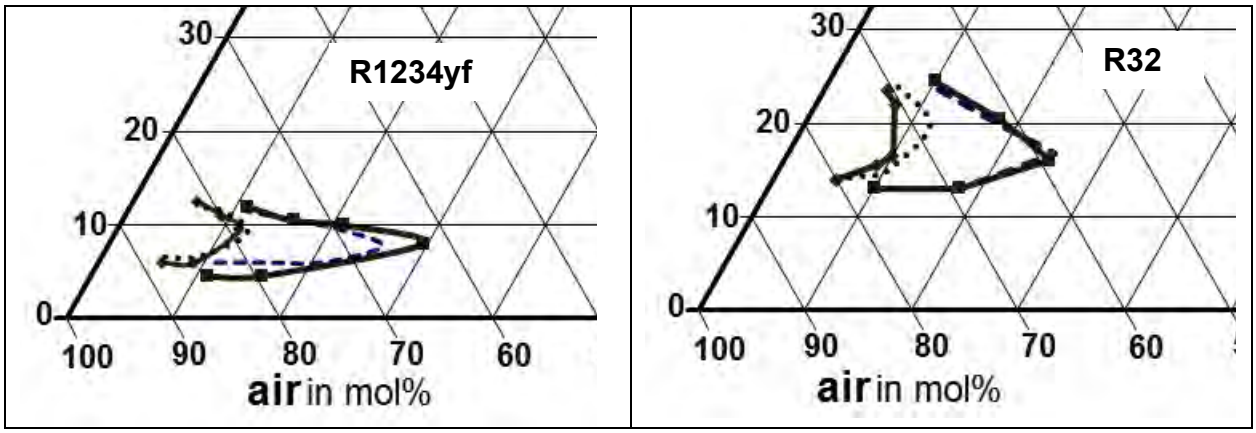

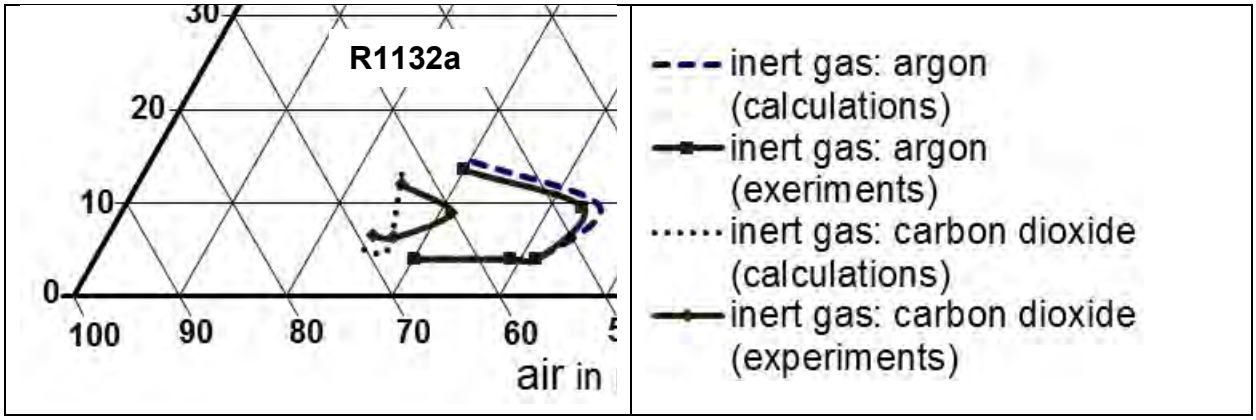

Figure 2: Calculated explosion regions of the refrigerants R1234yf, R32 and R32 compared to the experimental results

The explosion regions with nitrogen as inert gas were taken as reference for the calculations. In Table 2 the average and the maximum absolute deviations between the calculations and the experiments are summarized related to the air and the oxygen fraction at the apex and related to the fuel gas concentration for all other explosion limits. The largest deviations occur at the apex of the explosion regions in the ternary diagram, which is not unusual for the calculation of explosion regions (Mashuga and Crowl, 1999; Thiel-Böhm, 1991; Askar, 2010) and which can be attributed mainly to the poorest experimental reproducibility at the apex (Molnarne, 2008). Altogether the accuracy of the calculations is very similar to the accuracy of the analogue calculation for hydrocarbons. Considering the maximum absolute deviation of 4 mol% air at the apex and 2 mol% for all other explosion limits and considering a measuring uncertainty of one step size in the experiments (i.e. 0,5 mol%), the calculation method seems to be adequate not only for the estimation of explosion limits of hydrocarbons, but also of fluorinated hydrocarbons.

Table 2. maximum and average absolute deviations of the calculated explosion limits from the experimental results

-	Fuel gas fraction at the explosion limits (without apex)	Air fraction at the apex	Oxygen fraction at the apex
Average deviation	0.7 mol%	2.0 mol%	0.4 mol%
Maximum deviation	2.0 mol%	4.0 mol%	0.8 mol%

4. CONCLUSIONS

Safety related properties for the inertization of gas atmospheres containing the low-GWP-refrigerants R1234yf, R32 and R1132a by adding nitrogen, carbon dioxide or argon were determined experimentally in this work. The experiments were carried out in a closed 14dm^3-autoclave in accordance with the European standard EN 1839-bomb method (2017). Because of the high lower explosion limit, the maximum permissible flammable gas concentration (MXC) of R32 in a flammable gas/inert gas mixture to avoid explosible mixtures is the highest compared to the other two refrigerants. Also, the amount of R32 to be released, until explosible mixtures can be formed in air is clearly the highest. The maximum oxidizing gas concentration (MOC), at which the gas mixtures cannot become explosible is lowest for R1234yf. Altogether, the safety related properties for inertization of R32 and R1234yf are similar, whereas R1132a is more similar to the hydrocarbon propane in this regard. Finally, it was shown that the model of constant adiabatic flame temperature profiles, that was used to calculate the explosion limits of hydrocarbons in previous works, is also a good instrument for estimating the explosion limits of fluorinated hydrocarbons and olefins. Thus, the high experimental costs could be reduced significantly, even if the experiments cannot be replaced completely.

REFERENCES

ANSI/ASHRAE Standard 34-2016, Designation and safety classification of refrigerants, American Society of Heating, Refrigerating and Air-conditioning Engineers, Inc.

Askar, E., Schröder, V., Steinbach, J., 2010. Calculation of Explosion Regions of Gas Mixtures. Proceedings of the 13th International Symposium on Loss Prevention, Brugge, Belgium, Vol. 2, 141-149.

Askar, E., Schröder, V., Schmid, T., Schwarze, M., 2018. Explosion characteristics of mildly flammable refrigerants ignited with high-energy ignition sources in closed systems. Int. J. Refrigeration 90, 249-256.

Burgess, M.J., Wheeler, R.V., 1911. The lower limit of inflammation of mixtures of the paraffin hydrocarbons with air. J. Chem. Soc. Trans. 99, 2013 - 2030.

Calm, J.M., 2008. The next generation of refrigerants – Historical review, considerations, and outlook. Int. J. Refrigeration 31(7), 1123-1133.

CHEMSAFE, 2016. Database for Recommended Safety Characteristics of Flammable Gases and Gas Mixtures. DECHEMA, BAM, PTB, Karlsruhe.

Davis, S.G., Pagliaro, J.L., Debold, T.F., van Wingerden, M., van Wingerden, K., 2017. Flammability and explosion characteristics of mildly flammable refrigerants. J. Loss Prev. Proc. 49, 662–674.

EN 1839:2017-04, Determination of the explosion limits and the limiting oxygen concentration (LOC) for flammable gases and vapours, European Committee for Standardisation, Brussels, Belgium.

Giurcan, V., Razus, D., Mitu, M., Schroder, V., 2013. Limiting oxygen concentration and minimum inert concentration of fuel-air-inert gaseous mixtures evaluation by means of adiabatic flame temperatures and measured fuel-air lower flammability limits. Rev. De Chim. 14, 1445 - 1453.

Goos, E., Burcat, A., Ruscic, B., 2016. Extended Third Millennium Thermodynamic Database of New NASA Polynomials with Active Thermochemical Tables update. Report ANL 05/20 TAE 960. Online in: http://burcat.technion.ac.il/dir (January 9, 2019)

Gordon, S., McBride, B.J., 1994. Computer Program for Calculation of Complex Chemical Equilibrium Compositions and Applications. NASA Reference Publication, 1311

JSRAE The Japan Society of Refrigerating and Air Conditioning Engineers 2017. Risk Assessment of Mildly Flammable Refrigerants. Final Report 2016, JSRAE The Japan Society of Refrigerating and Air Conditioning Engineers.

Kondo, S., Takahashi, A., Takizawa, K., Tokuhashi, K., 2011. On the pressure dependence of flammability limits of CH2CFCF3, CH2F2 and methane. Fire Safety J. 46, 289–293.

Ma, T., 2013. Using critical flame temperature for estimating lower flammable limits of a mixture. Process Saf. Prog. 32, 387 - 392.

Magnusson, R., Hägglund, L., Gustafsson, A., Bergström, U., Lejon, C., 2016. Identifcation and brief toxicological assessment of combustion products of the refrigerant HFO-1234yf. FOI-R--4285—SE, FOI, Swedish Defence Research Agency

Mashuga, C.V., Crowl, D.A., 1999. Flammability zone prediction using calculated adiabatic flame temperatures. Process Saf. Prog. 18, 127 - 134.

Molnarne, M., Schendler, T., Schröder, V., 2008. Safety Characteristic Data Volume 2: Explosion Regions of Gas Mixtures, 2nd revised and extended edition, Wirtschaftsverlag NW, Verlag für neue Wissenschaft GmbH; Bremerhaven,

Morley, C., 2019. GASEQ - a Chemical Equilibrium Program for Windows. http://www.gaseq.co.uk (January 9, 2019)

Thiel-Böhm, A, 1991. Explosionsgrenzen methanhaltiger Brenngasgemische - Experimentelle Bestimmung und Simulation. Fortschritt-Berichte VDI, Reihe 3, Nr.258; VDI-Verlag GmbH, Düsseldorf

Manuscript ID: 773
DOI: 10.18462/iir.icr.2019.0773

A magnetic refrigeration prototype operating with a rare-earth-free magnetic field source

Urban TOMC[(a)], Katja KLINAR[(a)], Simon NOSAN[(a)], Franc MAJDIČ[(a)], Joško VALENTINČIČ[(a)], Jure MENCINGER[(b)], Andrej LJUBENKO[(b)], Dejan DREN[(b)], Andrej KITANOVSKI[(a)]

[(a)] Faculty of mechanical engineering, University of Ljubljana, Ljubljana, Slovenia, andrej.kitanovski@fs.uni-lj.si
[(b)] Gorenje d.d., Velenje, Slovenia

ABSTRACT

This article presents a new magnetic refrigeration prototype that operates with a rare-earth-free magnetic field source. Its main novelty, in comparison to existing state-of-the-art magnetic prototypes, is the application of a static electromagnet assembly that can regenerate magnetic energy and enables a rapid alternation of the magnetic field, which is one of the crucial operating parameters that could lead towards the future miniaturization of magnetocaloric devices. The presented prototype consists of two electromagnetic assemblies, each containing a packed-bed active magnetic regenerator (AMR) that consists of 30 g of single-layered Gd magnetocaloric material (MCM) in the form of spheres. The prototype was experimentally tested for its performance in terms of temperature span and cooling power. For instance, operating with a single-layered Gd AMR at 4-Hz operating frequency, the prototype produced 114 Wkg^{-1} of specific cooling power (per MCM mass), while maintaining a temperature span of 5 K below ambient conditions.
Keywords: electromagnetism, magnetic refrigeration, magnetic refrigerator, magnetocaloric material, regeneration, regenerator

1. INTRODUCTION

In recent years, magnetic refrigeration has shown the potential to be applied as an alternative to vapour-compression technology. It should be noted that there were several comparative studies reported in recent years on alternative cooling technologies, such as Goetzler et al. (2014), Qian et al. (2016) and Choi et al. (2019). Their common conclusion was that magnetic refrigeration is one of the most promising alternative refrigeration technologies for the future. Since the early 2000s there has been a significant increase in research and development activities to bring this technology to the market, as described in Kitanovski et al. (2015). However, despite the substantial progress made in the field of magnetic refrigeration, there are still many issues that need to be resolved. Mostly, these challenges relate to the use of rare-earth materials (Tura and Rowe, 2016), energy efficiency (Kitanovski et al., 2015) and the cost of potential future devices (Bjørk et al., 2016). Recently, a research paper by Klinar et al. (2019) presented a novel concept for an electromagnetic field source with magnetic energy recovery that could be applied for the purposes of magnetic refrigeration. The new electromagnet does not use any rare-earth materials, is completely static, regenerates a certain amount of magnetic energy and enables the rapid alternation of the magnetic field. Moreover, in comparison with existing electromagnetic field sources the energy efficiency was substantially improved, which was numerically and experimentally proven. This article presents the progress made in an ongoing project to develop a first-generation magnetic prototype by implementing a novel electromagnetic assembly with

magnetic energy recovery. The following sections present the design of the individual components of the magnetic prototype, as well as the operation of the prototype at the end.

2. MAGNETOCALORIC PROTOTYPE DESIGN

In this section the main components designed for the magnetocaloric prototype are presented, each in its own subsection. Overall, the prototype comprises two electromagnetic assemblies (with an electronic control circuit for the regeneration of the magnetic energy), each containing one AMR, a refrigerated cabinet (to impose the cooling load) containing one (cold) heat exchanger and a (hot) heat exchanger to reject the heat to the ambient. Furthermore, a hydraulic system connects all these components by maintaining the oscillation of the fluid through the AMRs and a uni-directional continuous flow through the heat exchangers by means of a pump and a set of electromagnetic valves and check valves. Moreover, at the end of the section the results of the experimental testing of the prototype are presented with regards to the temperature span and the cooling power.

2.1. Electromagnet with Magnetic Energy Recovery

In this section the new concept of the electromagnet with magnetic energy regeneration is presented, which was implemented in the magnetocaloric refrigeration prototype. Detailed analyses of the electromagnet's parametric design and the experimental validation are explained in Klinar (2017) and Klinar et al. (2019). The results of those studies led to the development of the electromagnet presented in Fig. 1. The overall dimensions of the electromagnet are 240×194×55 mm^3, while the air gap dimensions are 55×40×4 mm^3. Furthermore, the mass of the core is 12.8 kg and the coil is 15.2 kg. The coil is divided into two parts (below and above the air gap) connected in series and its electrical characteristics are listed in Table 1. Rapid alternation of the magnetic field inside the air gap is controlled by the electronic circuit in Fig. 1 (left), which consists of a voltage power source, diodes, transistors and a 100-μF capacitor.

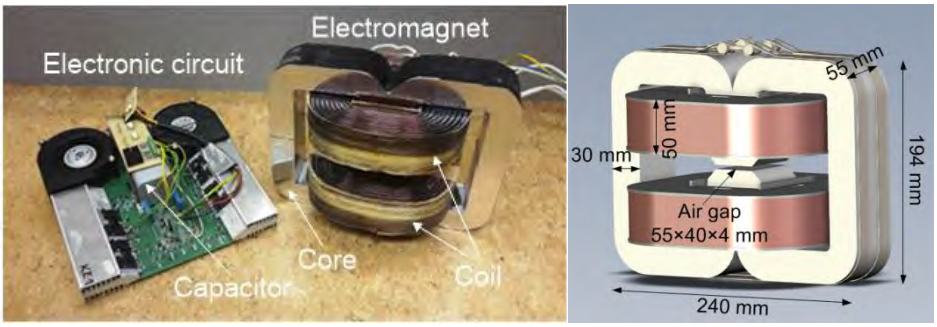

Figure 1: Photography of electromagnet and electronic control circuit (left) and 3D model of the electromagnet (right)

Table 1: Electrical characteristics of the capacitor and coil

Capacitor capacitance	100 μF
Number of turns in the coil	446
Eelctrical resistance of the coil	0.4 Ω
Inductance of the coil	0.29 H
Eelctric current (mag. field 1 T)	7.38 A
Time response (0 – 1 T, 1 – 0 T)	10 ms

The connection between the coil and the capacitor enables the regeneration of magnetic energy, as follows. During the phase of the demagnetisation process the energy in the coil is released to the capacitor, where it is stored. Thereafter, in the phase of the magnetization process this stored energy is then released back to the coil. In this manner a substantial amount of the energy needed

for the magnetization process is usefully regenerated. With the existing electronic circuit elements we were able to recover more than 93% of the available energy from the demagnetisation process. On the other hand, such magnetic energy regeneration also enables rapid magnetisation or demagnetisation processes. In order to establish a magnetic field change of 1 T, the presented electromagnet with respective electronics took 10 ms. Fig. 2 shows the measured and theoretically calculated magnetic fields inside the air gap in relation to the electric current in the coil (left) and the time-dependent magnetic field change during the operation at different operating frequencies (right). In Fig. 2 (left) the static magnetic field in the middle of the air gap was measured with a Hall probe FH 54, while the electric current was provided by the power supply Velleman LABPS3020. The experimental results are compared to the analytically calculated required electric currents for a certain magnetic field in the air gap utilizing Ampere's law:

$$B = \frac{\mu_0 \cdot N \cdot I}{d}, \qquad \text{Eq. (1)}$$

where B is the magnetic field in T, μ_0 is the vacuum permeability in mA^{-1}, N is number of turns in the coil, I is the electric current in the coil in A, and d is the thickness of the air gap in m.
In Fig. 2 (right) the time-dependent magnetic field was indirectly measured using the electric current flowing through the coil using a National Instruments cDAQ 9174 and a NI 9207 with a high sampling rate and calculating it using Eq. (1). The alternation of the magnetic field was measured for two operating frequencies of 1 and 5 Hz. The operating frequency is defined as

$$f = \left(t_{mag} + t_{HField} + t_{demag} + t_{LField}\right)^{-1}, \qquad \text{Eq. (2)}$$

where t_{mag} and t_{demag} represent the time of (de)magnetisation (10 ms), while t_{HField} and t_{LField} represent the times of the high magnetic field (1 T) and the low magnetic field (0 T).

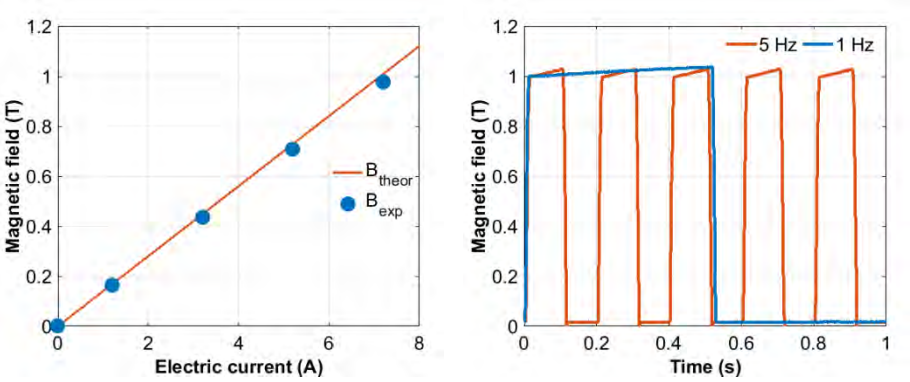

Figure 2: Calculated and measured magnetic field (in the air gap) in relation to the electric current applied to the coil (left) and the time-dependent magnetic field in the air gap for operating frequencies of 1 and 5 Hz (right)

2.2. Active Magnetic Regenerator

The geometrical characteristics of each AMR implemented in the prototype are given in Table 2. Each AMR was made of gadolinium spheres, 100–300 µm in diameter. Furthermore, the overall geometry of one AMR was 55×40×3 mm^3, which contributed approximately 30 g in mass. The heat-transfer fluid applied was a mixture of distilled water and glycol (70/30). The AMR was fitted into the casing shown in Fig. 3, which was built with a stereolithographic (SLA) 3D printing process. Fig. 3 (above) shows a photograph of one fully assembled AMR. Each side of the AMR casing has one inlet and one outlet, with special manifolds that hold inserts for the thermocouples. Fig. 3 (below) shows a cross-sectional view of the AMR casing 3D model. Special consideration was given to the design of the flanges (flow distributors). As we can see, sets of pins were designed right before the AMR enclosure that have three purposes. First, they hold a thin mesh before the AMR enclosure to keep the MC spheres in place. Second, they reduce the dead volume between

the AMR and the check valves, which can severely decrease the AMR performance, as shown in Lozano et al. (2016). And third, a unique design of pins and inlets/outlets placement together in the center of the flange (rather than two separate placements for the inlet and outlet) lead to a more uniform distribution of the fluid flow to the AMR. The simulation of the fluid flow through the flow distributors and the packed-bed structure from Table 2 was performed with the software Ansys Fluent. The results are presented in Fig. 4. The diagram shows the fluid-velocity distribution at the entrance, in the middle and at the exit of the AMR. We can see that the flow is evenly distributed throughout the whole packed-bed regenerator, without any high- or low-velocity regions.

Table 2: AMR geometrical characteristics

Magnteocaloric material	Gadolinium spheres
Overall AMR dimensions	55×40×3 mm
Sphere diameter	100 – 300 μm
AMR porosity	~0.40
AMR mass	30 g
Heat transfer fluid	70% distilled water, 30% glycol

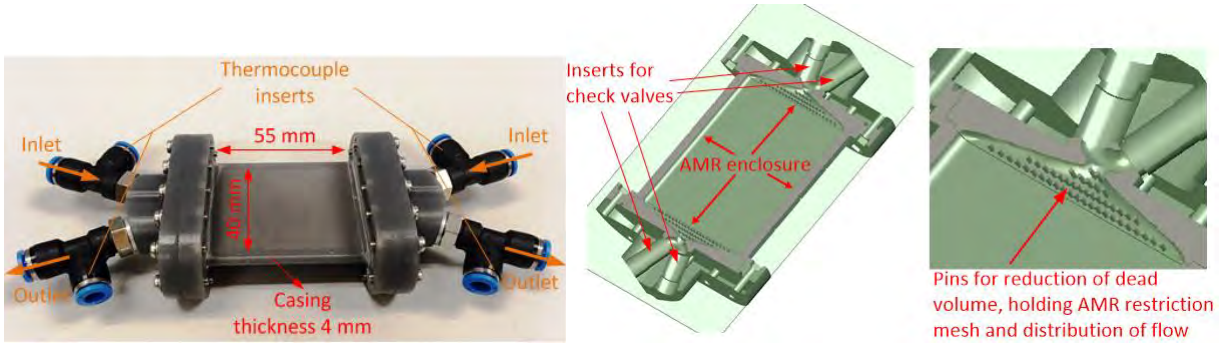

Figure 3: Photograph of the fully assembled AMR (casing, flanges, MCM, manifolds) and cross-sectional view of the AMR casing 3D model

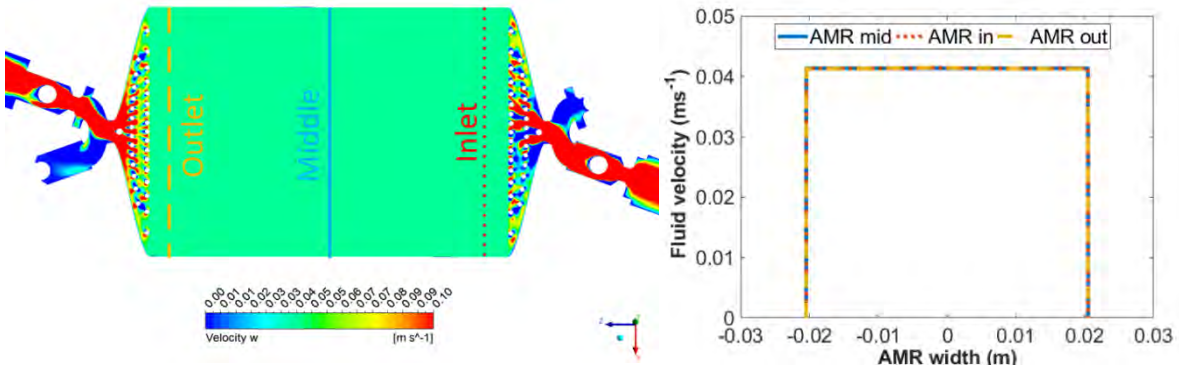

Figure 4: Simulated fluid velocity through packed-bed AMR (left) and fluid-velocity distribution at the inlet, middle and outlet of the AMR

2.3. Refrigerated Cabinet

To apply a cooling load during the operation of the presented magnetocaloric refrigeration prototype a refrigerated cabinet was implemented in the system. The cabinet was originally applied as a part of a wine cooler based on a vapour-compression refrigeration system (Gorenje, model VC1667). The characteristics of the wine cabinet are presented in Table 3, while the geometrical specifications and pictures of the cabinet (real and model) are shown in Fig. 5. The volume of the cabinet is 136 l, while the envelope of the cabinet is insulated with 10-mm-thick vacuum panels. In the cross-sectional view of the 3D model in Fig. 5 (middle) we can see a fin on the tube heat

exchanger with a fan mounted in the back wall of the cabinet. Such a heat exchanger was connected to the cold side of the magnetocaloric prototype to absorb the heat from the cabinet.

Table 3: Refrigerated cabinet characteristics

Total volume	136 l
Dimensions	600×580×868 mm
Characteristics	capacity 42 wine bottles, 1 chamber, 1 temperature
Thermal insulation	Vacuum panels, thickness 10 mm
Heat exchanger (cold and hot)	Aluminium fin on tube, with fan

The cabinet was tested for its cooling load in a so-called Reverse Heat Leakage Test (RHLT) (Tao and Sun, 2001). The cabinet was put into a climate chamber with a predefined temperature of approximately 5°C and the cooling system was turned on to maintain the temperature. On the other hand, an electric heater inside the cabinet maintained the inside temperature at 25°C, while operating with 27.3 W of heating power. Utilizing a known relation between the thermal resistance, the temperature difference and the heat flow ($R = \Delta T / \dot{Q}$) we can derive the thermal resistance of the envelope of the cabinet to be 0.73 KW^{-1}. Based on the findings from the RHLT we can define the cooling power needed for the refrigerated wine cabinet to maintain a certain inside temperature with respect to the ambient temperature, which is shown in Fig. 5 (right). For instance, to maintain the cabinet temperature at 10°C (T_{amb}=25°C), the magnetic refrigeration prototype would need to produce approximately 20 W of cooling power.

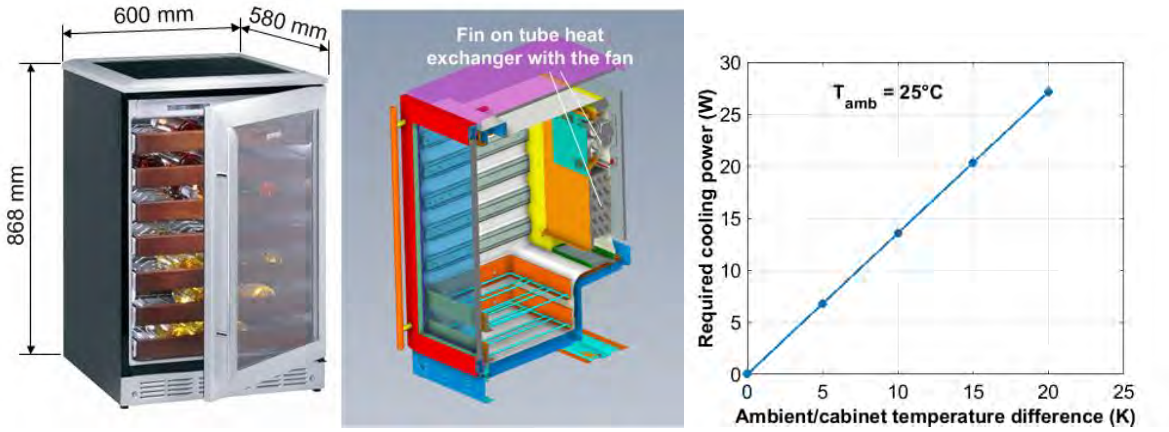

Figure 5: Picture of the refrigeration cabinet (left), a cross-sectional view of a 3D model (middle) and required cooling power to the cabinet with regards to the temperature difference between the ambient and the cabinet derived from the reverse-heat-leakage test (right)

2.4. Hydraulic System

As stated at the beginning of this section the hydraulic system applied in this magnetocaloric prototype connects all the components into a single device, where the performances of all the components are interdependent of each other. Thus, the placement of this subsection at the end seems like an appropriate round up of the whole prototype presentation. The fluid flow in the prototype was managed by one uni-directional gear pump, four electromagnetic valves (EMV) and a set of check valves. All are listed with respect to their characteristics in Table 4. A schematic of the full hydraulic system of the prototype is presented in Fig. 6, where it shows one phase of the operation (AMR1 demagnetised, AMR2 magnetised). In this way the fluid-flow path is as follows. The gear pump pumps the heat-transfer fluid (distilled water + glycol) from the container through the hot heat exchanger (HHEX), where the heat is transferred to the ambient. From HHEX the fluid flows through the open EMV A (EMV D closed) through the demagnetised AMR1. Furthermore, the fluid exits AMR1 through the check valve, flowing directly through the cold heat exchanger (CHEX)

(absorbing heat from the wine cabinet) and then on through the check valve into the magnetized AMR2. On the hot side of AMR2 the fluid exits through the check valve and the open EMV C (EMV B closed) to the fluid container. When the phase of operation changes to AMR1 being magnetised and AMR 2 demagnetised, the change in the flow direction through the AMRs is managed by EMVs B and D being open, while EMVs A and C are closed. The EMVs control the oscillation of the fluid only through the AMRs, while the check valves secure the uni-directional flow through both HHEX and CHEX. The operation of the EMVs is synchronised with the alternating operation of the electromagnets via the control electronic circuit run by the Arduino mega 2560. Moreover, the EMVs are PWM controlled in a manner to establish fast ON/OFF switching with a time response of 10 ms (the same as the electromagnets) and to reduce the electric input power during ON time as shown in Fig 7. (left) and explained in detail in Nosan et al. (2018). On the other hand, the change in the flow direction through the AMRs can be seen in Fig. 7 (right). The diagram shows time-dependent pressures measured at the inlets of the AMRs' hot sides, operating at a frequency of 3 Hz. An abrupt change in the pressure suggests a rapid change in the flow direction as well as the rapid establishment of the fluid flow rate.

Table 4: Hydraulic system management components and their characteristics

Gear pump	TCS Micropumps, MG2000S, U_{max}=24 V, p_{max}=10 bar
Electromagnetic valves	Jakša, D221 NC 24VDC TM35, p_{max}=80bar
Check valves	Koenig, BR660080024, reverse flow, no spring, d=8 mm
Pressure sensor	Shen Zhen Le Fei Electronics Co., PT 2300, 0-15 bar
Thermocouples	*AMR*: Omega type T, d=0.13 mm *HEXs, cabinet, ambient*: Omega type T, d=0.51 mm

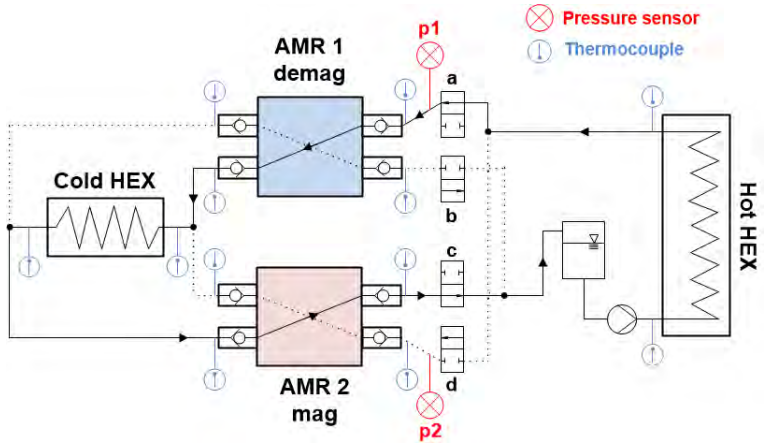

Figure 6: Hydraulic schematic of the magnetocaloric prototype in one phase of operation (AMR1 demagnetised, AMR2 magnetised)

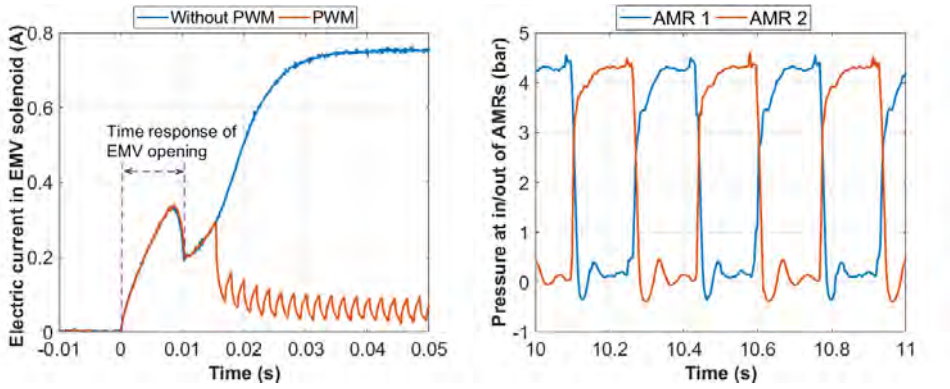

Figure 7: Measured EMV's opening time response (left) and pressure on the hot sides of both AMRs (p1 and p2) during operation at an operating frequency of 3 Hz (right).

2.5. Experimental Results

This subsection presents the results of the experimental tests performed on the magnetocaloric refrigeration prototype described in the previous sections. Fig. 8 (left) shows the measured, no-load temperature span established on one of the AMRs operating at 2 Hz of operating frequency. In this case the refrigerated cabinet was not connected to the prototype. In particular, the fluid from the outlets on the cold side of the AMRs was by-passed directly back to the inlets. In such a manner the AMR's cold-side temperature settled at 10°C, while the hot side topped out at approximately 23.5°C, altogether establishing 13.5 K of temperature span along the AMR. On the other hand, Fig. 8 (right) presents the actual specific cooling power (per MCM mass) produced by the prototype, while also establishing a certain temperature difference between the insides of the refrigerated cabinet and the ambient environment. The ambient temperature was varying between 22 and 24°C. Four operating frequencies were tested, ranging from 1 to 4 Hz. At each operating frequency a set of different fluid-flow rates were tested to find the maximum temperature difference (ambient/cabinet) with a respective cooling power. From this perspective, the results in Fig. 8 (right) show only the maximum temperature differences established at the given operating frequencies. What is interesting is that the prototype increases its performance with an increase of the operating frequency. That being the case, operating at a frequency of 1 Hz, the prototype establishes a temperature difference of only approximately 1.5 K, while producing approximately 37 Wkg^{-1} of specific cooling power, while at 4 Hz the temperature difference increases up to 4.8 K and the specific cooling power up to 114 Wkg^{-1}. Experiments above an operating frequency of 4 Hz could not be performed at this moment, since the AMR casings cracked due to the rapid oscillation of the relatively high pressure (approx. 5 bar).

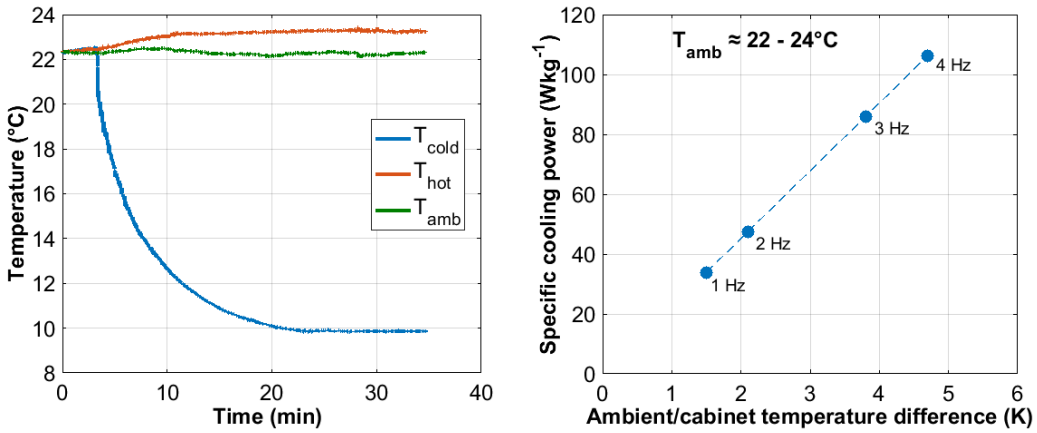

Figure 8: Measured no-load temperature span between hot/cold side of one AMR operating at 2 Hz (left) and the produced specific cooling power at different ambient/cabinet temperature differences and for different operating frequencies (right)

3. CONCLUSIONS

This article presented the work done so far in an ongoing project to develop a magnetic wine cooler operating with a rare-earth-free magnetic field source. As such, a first-generation prototype utilizing two electromagnetic assemblies with magnetic energy recovery was developed and tested for its viability. Different components of the prototype, such as the electromagnet, the AMRs, the refrigerated cabinet and the hydraulic system, were designed and individually evaluated, before incorporating them together into the magnetic refrigeration device. Until now the prototype was able to operate with a maximum specific cooling power of 114 Wkg^{-1}, while maintaining approximately 5 K of a temperature difference between the refrigerated cabinet and the ambient conditions.

Even though certain shortcomings in the operation were identified, the results are definitely not conclusive and the ongoing work in the research project to develop a second-generation prototype is as follows:

- Investigation of operation at higher frequencies (>4 HZ);
- Application of graded AMR (instead of single-layer Gd AMR) with additional MCM layers;
- Optimization of peripheral elements, such as valves, pump and other hydraulic connections
- Minimization of the thermal losses due to the operation of the pump, valves and electromagnet

ACKNOWLEDGEMENTS

This research project is co-financed by the Republic of Slovenia and the European Union under the European Regional Development Fund, as the part of the IQ HOME program (Intelligent home on the new generation design on smart appliances and wood).

REFERENCES

Bjørk, R., Bahl, C.R.H., Nielsen, K.K., 2016. The lifetime cost of a magnetic refrigerator. Int. J. Refrig. 63, 48-62.

Choi, S., Han, U., Cho, H., Lee, H., 2018. Review: recent advances in household refrigerator cycle technologies. Appl. Therm. Eng. 132, 560-574.

Goetzler, W., Zogg, R., Young, J., Johnson, C., 2014. Alternatives to vapor compression HVAC technology. ASHRAE J., 12-23.

Kitanovski, A., Tušek, J., Tomc, U., Plaznik, U., Ožbolt, M., Poredoš, A., 2015. Magnetocaloric energy conversion: from theory to applications. Springer.

Klinar, K., Tomc, U., Jelenc, B., Nosan, S., Kitanovski, A., 2019. New frontiers in magnetic refrigeration with high oscillation energy-efficient electromagnets. Appl. Energy 236, 1062-1077.

Klinar, K, 2017. Thermo-magnetic analysis and design of a magnet assembly with the magnetocaloric regenerator. Master Thesis, University of Ljubljana, Faculty of mechanical engineering.

Kitanovski, A., Plaznik, U., Tomc, U., Poredoš, A., 2015. Present and future caloric refrigeration and heat-pump technologies. Int. J. Refrig. 57, 288-298.

Nosan, S., Tomc, U., Klinar, K., Vončina, D., Kitanovski, A., 2018. Heat loss reduction of an electromagnetic valve. Proceedings of the Twenty-seventh International Electrotechnical and Computer Science Conference, Portorož, Slovenia, IEEE, 265-268.

Qian, S., Nasuta, D., Rhoads, A., Wang, Y., Geng, Y., Hwang, Y, Radermacher, R., Takeuchi, I., 2016. Not-in-kind cooling technologies: A quantitative comparison of refrigerants and system performace. Int. J. Refrig. 62, 177-192.

Tura, A., Rowe, A., 2014. Concentric Halbach cylinder magnetic refrigerator cost optimization. Int. J. Refrig. 37, 106-116.

Tao, W.H., Sun, J.Y., 2001. Simulation and experimental study on the air flow and heat loads of different refrigerator cabinet designs. Chem. Eng. Commun. 186, 171-182.

Trevizoli, P.V., Peixer, G.F., Nakashima, A.T., Capovilla, M.S., Lozano, J.A., Barbosa Jr., J.R., 2018. Influence of inlet flow maldistribution and carryover losses on the performance of thermal regenerators. Appl. Therm. Eng. 133, 472-482.

Manuscript ID: 804
DOI: 10.18462/iir.icr.2019.0804

Comparison of R-404a, R-448A and R-452A as drop-in replacements for R-218 in special applications

Martin Doubek, Václav Vacek

Czech Technical University Faculty of Mechanical Engineering, Prague, Czech Republic,
martin.doubek@cern.ch, vaclav.vacek@cern.ch

ABSTRACT

We present a comparison of the R-404A, R-448A and R-452A as drop-in replacements for R-218 refrigerant in high-tech electronics cooling. The tests were carried out in an oil-less experimental circuit originally designed for cooling of silicon chips with R-218. The circuit is equipped with tens of temperature, pressure and flow sensors and precise liquid and vapour pressure control. The same capillary was used for all the tested refrigerants providing mass flow of 1.2 g/s. Two-stage compression allowed to test suction pressures from 0.5-1 bar absolute. The aim was to evaluate the possibility of replacing the rarely used, expensive and environment unfriendly R-218 by more ecological blends while achieving lower evaporation temperature and without hardware modifications to the existing circuit layout. The results are applicable to low temperature systems with commercial two-stage reciprocating compressors that are being converted from R-404a to ecological alternatives R-448A/R-449A or R-452A.
Keywords: refrigerants, blends, R-218, R-404A, R-448A, R-452A, low temperature, two-stage

1. INTRODUCTION

Cooling systems with two-stage compressors can provide low evaporation temperatures even with ecological non-flammable low-GWP refrigerants. Typical refrigerant currently used in such systems is the R404A. The system with two-stage compression and low suction pressures are often employed as blast freezers and many other applications including laboratory chillers for cooling of high-tech electronics. The disadvantages of systems with low suction pressure are often outweighed by their simplicity. The cooling capacity of the two-stage systems is relatively low when compared to the low-temperature cascade systems but they require less components and the controls are simpler. We have focused on evaluation of the R-448A and R-452A as drop-in replacements for the R-404A and the somewhat exotic R-218 that is used in the field of high-tech electronics and particle physics.
There are three ways to achieve low temperature cooling:
One can use common one-stage refrigeration loop with air condenser and evaporation slightly above atmospheric pressure and select a fluid with low normal boiling point. The R-32 could be a good choice since it has low normal boiling point of -51.7°C. The R-32 has GWP of 675 but it is mildly flammable (A2L classification). The flammability should be a concern due to risk of diesel explosion when the refrigerant is mixed with air due to leaks in suction line during pump down or when the system is used in closed spaces (small laboratories etc.). Unfortunately, the widely used non-flammable refrigerants cannot achieve very low temperatures; common refrigerants have following normal boiling points: R-134A -26.3 °C, R-125 -48.5 °C, the R-404A -46.2°C, R-1234yf -30 °C.
Other option of how to achieve low temperature are cascade systems. The systems are usually designed so that the low stage refrigerant condenses in the cascade condenser at temperatures between -20°C and -10°C and it evaporators are pressure above 0.1 MPa. This allows using very-low temperature refrigerants such is the R-23, R-508, R-170 (Ethane) or R-1150 (Ethylene). The cascade systems are relatively complex in terms of both construction and control. An expansion volume might be required for the low stage fluid during the off periods since their critical point is below ambient conditions. The R-23 is typical very-low temperature refrigerant for temperature down

to -80°C. Unfortunately, it has very high GWP (14800). The replacement R-508B is only slightly better (GWP of 13396). The natural refrigerants R-170 and R-1150 are extremely flammable which can be acceptable for industrial applications where the chiller can be located outside of the building but it is a major drawback for most of the applications in laboratories.
The third option for low temperature refrigeration are systems with evaporation pressure below atmospheric pressure. These systems often utilize two-stage compression with low pressure and high-pressure pistons in one compressor body to achieve the low (vacuum) suction pressures. Large selection of two-stage piston compressors is commercially available from multiple brands. The highest cooling capacity per compressor reaches approximately 8 kW at -60°C. The technology is well proven although it might be difficult to run multiple compressor in parallel due to oil balancing issues. The reason is that the crankcase of the compressors is at the intermediate pressure that is slightly different for each compressor. The R-404A (GWP of 3922, non-flammable) is typically used in these systems but it is being replaced by more ecological alternatives due to the F-gas Directive 517/2014, which bans the commercial use of refrigerants with GWP above 2500 by the year 2020. The R-448A and R-449A are two similar substitutes that both offer significantly improved GWP of 1387 and 1397 respectively. The availability of these two blends is good and the price is acceptable. This will likely remain the case also in the future since two different producers manufacture these two blends and several large supermarket chains have adopted them. Both blends have following disadvantages: lower cooling capacity than R-404A, high discharge temperatures and very high glide. The R-452A is another blend designed to replace the R-404A, it offers much lower glide and cooling capacity very close to the R-404A at an expense of GWP of 2141, which is just below the limit of the F-gas Directive 517/2014. All three replacement blends discussed above are non-flammable in contrast with the other similar blends R-454 and R-455A. It should be mentioned that from our experience the availability of the R-452A in Europe is not very good.
The R-218, included in this comparison as a base line, is a pure fluid used in some special cooling application namely in cooling of electronic equipment in laboratories. The fluid has high GWP of 8830 but due to its special properties, it is sometimes favored over much more ecological options. Its normal boiling point is -36°C therefore; it is not a refrigerant for particularly low temperatures. The R-116, which is similar molecule to R-218 only with lower carbon number, offers much lower boiling point of -78°C but in its pure form it, is suitable only for cascade systems. Some applications can use blends of R-116 and R-218 to achieve lower evaporation temperature (Bates et al. 2015), (Doubek et al., 2017) and (Doubek et al., 2016). The main advantages of the R-218 and R-116 are the excellent dielectric properties, nontoxicity, non-flammability and radiation hardness. Especially the resistance to the irradiation is a property that cannot be offered by the modern ecological fluids with molecules that quickly brake down in the atmosphere. In other words, the R-218 cannot be replaced by any of the above-mentioned blends in application with radiation such is the cooling of particle detectors. There are other applications (without radiation) where the existing R-218 system can switch to these blends and that would benefit from lower evaporation temperatures. Some of these applications include commissioning of particle detectors (without irradiation) and testing of electronic components such as chips and sensors at low temperatures.

2. TESTED REFRIGERANTS

The presented comparison between the R-218, R-404A, R-448A and R-452A aims to demonstrate the differences between the R-448A and R-452A that are used as replacement for R-404A and that can be used also as drop-in replacement for R-218 in systems where there is no exposure of the refrigerant to radiation (as discussed above). The properties of the tested fluids are compared at three different temperatures down to -50°C in Table 1. Particular attention should be paid to the glide of the blends.

Table 1. Fluid properties

	R-218	R-404A	R-448A	R-452A	
Fluid type	Pure	Blend	Blend	Blend	
Molecular mass	188.02	97.604	189.9	103.5	g/mol
Normal. Boiling point (mean)	-36.79	-46.22	-42.9	-47.0	°C
Critical temperature	71.9	72.1	83.7	74.9	°C
Critical pressure	2.64	3.74	4.66	4.00	MPa
Mean saturated pressure[x]					
+20°C	0.76	1.10	1.05	1.09	MPa
-20°C	0.21	0.31	0.23	0.30	MPa
-50°C	0.053	0.084	0.075	0.072	MPa
Heat of vaporization[*]					
+20°C	79	145	185	142	kJ/kg
-20°C	99	181	224	176	kJ/kg
-50°C	110	202	246	195	kJ/kg
Saturated vapor density[+]					
+20°C	73.9	56.3	45.8	55.2	kg/m3
-20°C	20.0	15.4	12.3	14.8	kg/m3
-50°C	5.6	4.4	3.6	4.1	kg/m3
Glide					
+20°C	0	0.43	5.3	3.9	°C
-20°C	0	0.61	5.9	3.7	°C
-50°C	0	0.78	6.2	3.7	°C

Mean temperatures were used to calculate the properties of blends

[x]At equilibrium; [+]Bubble and dew point at the same composition; *At the same composition

The R-218 (C_3F_8) is a saturated fluorocarbon, extremely stable molecule with only C-F and C=C bonds which results in extremely high atmospheric lifetimes and high GWP (8830). The fluid is used as a component in few blends, namely in the R-403 and R-412. It is a popular fluid for cooling applications in particle physics since it is not affected by radiation (i.e. it is radiation hard). There are still several systems employing R-218 refrigerant with charges ranging from tens of kilograms to 1.5 tons. These systems are running at particle physics laboratories, namely at CERN in Switzerland (Attree et al., 2008), (Hallewell et al. 2017) and (Anelli et al. 2018).

The R-404A is widely used in many household and industrial systems. The fluid is being phased out and there is a great effort to replace it with other carefully formulated blends. The R-404A is a nearly azeotropic blend of 52wt% R143a, 44wt% R125 and 4wt% R134a. Unfortunately, the proposed replacement blends are usually strongly zeotropic and their properties can be thus relatively far off in certain aspects. For example, the R-404A exhibits only small glides: even at very low evaporation pressures (vacuum), see Table 1. The nearly azeotropic behavior also means that the vapor composition is very close to the liquid: at an equilibrium at 20°C the vapor composition is 51.6wt% R143a, 45.8wt% R125 and 2.6wt% R134a.

The R-448A is a low GWP replacement for R-404A, its behavior is very close to the other (competing) replacement R-449A. It is a quite complex zeotropic blend of 26wt% R-32, 26wt% R-125, 21wt% R-134a, 7wt% R-1234ze and 20wt% R-1234yf. At an equilibrium at 20°C the vapor phase composition is 35.0% R-32, 30.0% R-125, 13.5% R-134a, 0.04% R-1234ze and 17.3% R-1234yf. The fluid exhibits large glide, which can reach more than 6°C at very low evaporation pressures (vacuum). The lower vapor density, which results in lower mass-flow through the same compressor in comparison with the R-404A, is compensated by the higher enthalpy of evaporation; see the values in Table 1.

The R-452A blend was develop to have properties as close as possible to the R-404A while keeping the GWP just below the 2500 limit imposed by the European directive. It is a blend of 11.0%wt R-32, 59.0% R-125 and 30.0% R-1234yf. The blend is inflammable and exhibits only moderate glides even at low evaporation pressures, Table 1. At an equilibrium at 20°C the vapor phase composition is 15%wt R-32, 60% R-125 and 22% R-1234yf. Table 1 also reveals that the vapor density and enthalpy of evaporation are very close to the R-404A.

3. TEST EQUIPMENT

The performance of the all four refrigerants was tested in a special oil-less cooling circuit with two-stage compression, Figs. 1 and 2. The circuit is highly versatile allowing to test all sort of conditions; it is equipped with liquid pressure regulator and vapor backpressure regulator, three types of flowmeters (Coriolis, turbine and volumetric). The circuit contains sub-cooling and super-heating exchangers that allow to precisely control temperature of the liquid and vapor. On the top of that numerous temperature and pressure sensors monitor the liquid and vapor state at any important location in the circuit. The circuit operates with fairly low mass flows from 1 g/s to 3 g/s depending on the installed capillary and the liquid pressure. The first stage compressor is a membrane type capable of operating with vacuum suction pressures; the second stage compressor is piston oil-less type with one cylinder, Figure 2. More detailed description of the test circuit can be found in (Vacek et al. 2011).

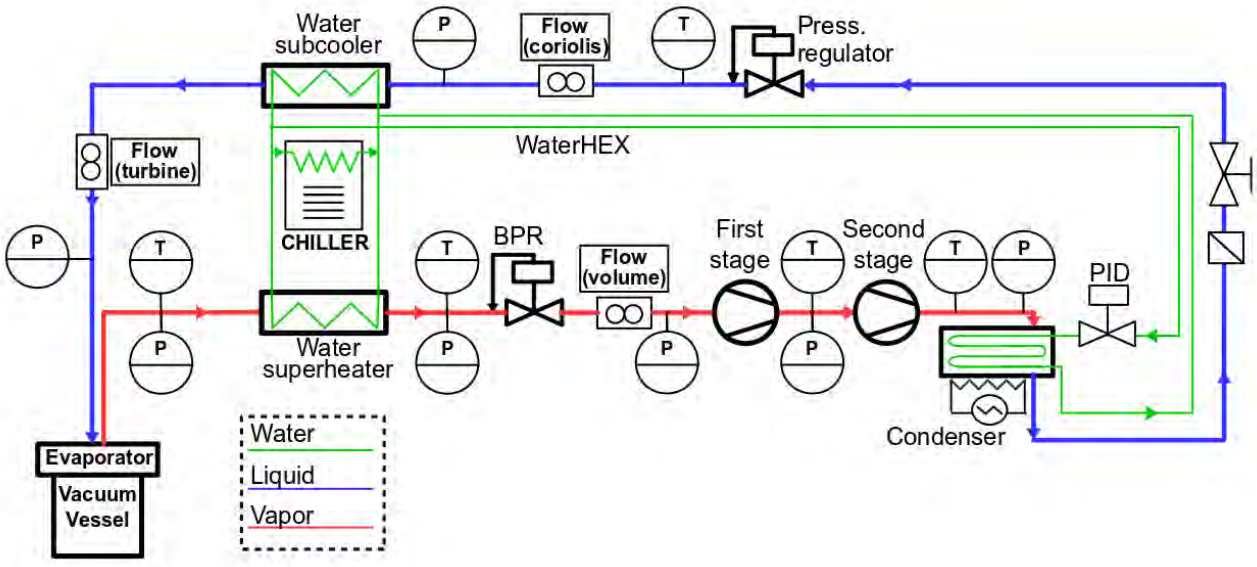

Figure 1: Simplified P&ID diagram of the test circuit

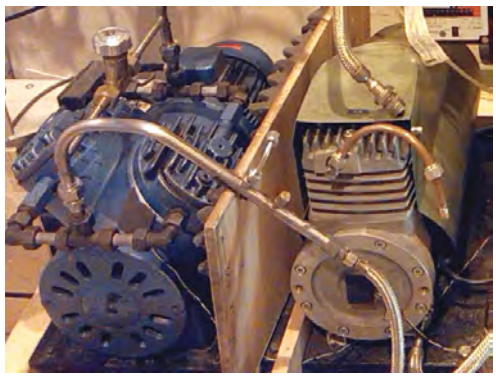

Figure 2: The first stage membrane compressor (on the left) and the second stage piston compressor (on the right)

An electric dummy-load on the evaporator simulates the heat load. The whole assembly of capillaries, evaporators and the dummy load is installed inside a stainless steel vacuum chamber in order to prevent condensation, icing and heat loses, Figure 3. The evaporator and dummy load are equipped with twenty temperature sensors that enable us to evaluate the temperature profile (gradient) along the evaporator. This installation is used to evaluate thermal performance of Roman Pot particle detectors of TOTEM experiment at CERN, Switzerland (Anelli et al., 2018) and (Oriunno et al., 2007).

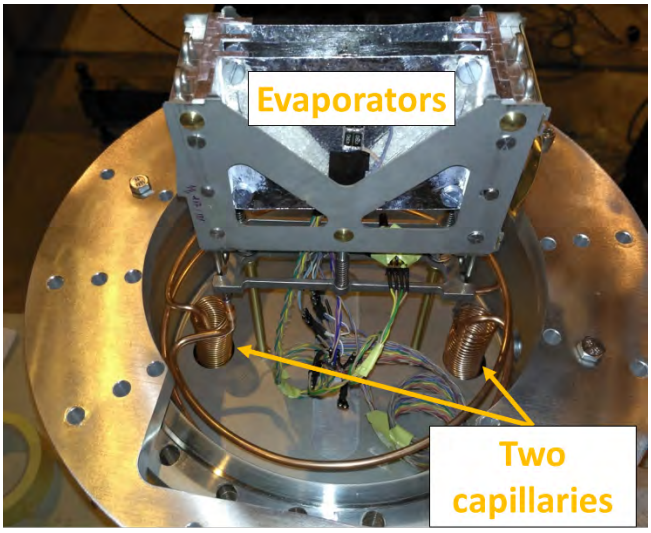

Figure 3: The capillaries and the evaporator + dummy load

The parameters of the tests are listed in Table 2. The test circuit was operated with the lowest possible condenser/liquid pressure that allowed for stable circulation (bubble free liquid before capillaries at 20°C). For this reason, the liquid pressure of the R-218 is significantly lower than pressure of the other refrigerants. The 0.85 MPa liquid pressure corresponds to the standard value used in the R-218 cooling circuit during commissioning of the TOTEM Roman Pot detectors (Vacek et al. 2011). Such pressure ensures sufficient safety margin in terms of boiling in the ambient-temperature liquid lines as the R-218 saturation pressure is 0.76 MPa at 20°C. The R-452A required higher liquid pressure than the R-404A and R-448A to prevent it from boiling. Our liquid circuit exhibited instability of the mass flow when the R-452A liquid pressure was set below 1.20 MPa. This result is not surprising since the R-452A liquid pressure at 20°C is 1.147 MPa which is the highest from all the tested fluids.

Table 2. Test parameters

	R-218	R-404A	R-448A	R-452A	
Condenser pressure	0.85	1.10	1.08	1.23	MPa
Liquid pressure	0.85	1.10	1.08	1.23	MPa
Mass flow	1.19	1.29	1.22	1.28	g/s
Compressor suction	0.028	0.041	0.036	0.040	MPa (abs)

The compressor discharge temperatures were one of the studied characteristics, Figure 4. The observed temperatures were low in comparison with usual industrial systems with higher mass flows. Most of the heat was dissipated through the compressor body and head before the refrigerant reached the temperature sensor at the discharge line in our system. Nevertheless, the differences between the fluids are clearly visible. The R-404A exhibits the lowest discharge temperature in comparison with the other blends and relatively close to the R-218. The R-452A and the R-448A discharge temperatures after the first stage were the same but the R-452A exhibited higher discharge temperature after the second stage; the higher condenser (head) pressure needed to ensure stable operation of the cooling circuit with the R-452A caused this. In all cases, the discharge temperatures were acceptable and did not disqualify any of the tested blends as potential drop-in replacement for the R-218 in systems with low mass flows.

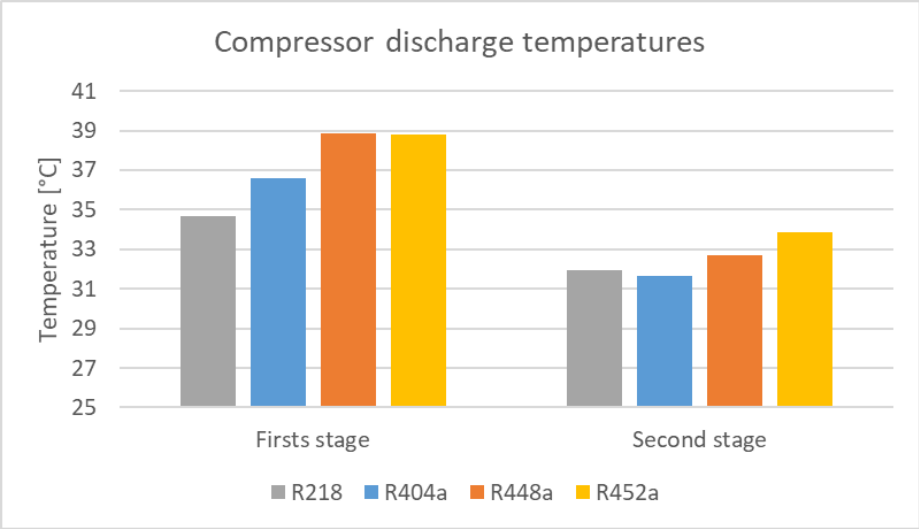

Figure 4: Discharge temperatures

Three tests with three different settings of the backpressure valves were carried out. The pressure before the backpressure was set to 0.10, 0.075 and 0.05 MPa. The actual evaporation temperatures in the evaporator were affected by the pressure drop of the vapor line and the super-heater heat exchanger. The mean evaporation temperatures from the 0.05 MPa test are show in in Figure 5 with and without dissipated heat load. The R-452A clearly achieves the lowest temperatures (-41°C without load and -35°C with load), while the R-448A is the closest to the R-218 (-35°C without load and -30°C with load). One should notice that the R-452A achieved the lowest temperatures despite slightly higher mass flow, which increased the pressure drop in the vapor line.

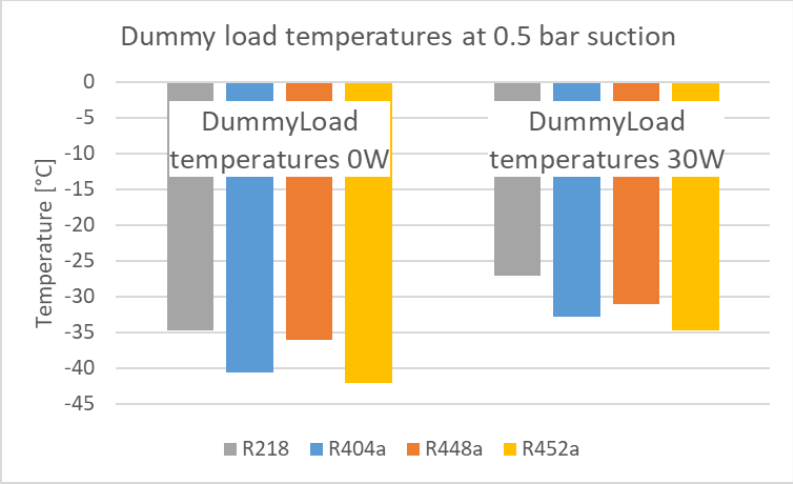

Figure 5: Lowest achieved average temperatures

The differences between the evaporator inlet and outlet temperature at three different backpressure settings are shown in the Fig. 6. This difference is affected by the evaporator pressure drop and by the glide of the zeotropic blends. The evaluated difference is positive with the R-218, which is pure fluid, and with the nearly azeotropic R-404A, In other words, the temperature at evaporator outlet was lower than at the inlet due to the evaporator pressure drop. The R-452A and R-448A blends can exhibit lower temperature at the evaporator inlet due the large glide of these blends. It is also apparent from the Figure 6 that with certain dissipated heat and certain suction pressure one can achieve uniform temperature along the evaporator (zero temperature difference in the Fig. 6.). The uniform temperature can be desirable for certain applications especially in electronics cooling. The plot in Figure 6 also allows an assessment of vapor return line pressure drop. The settings of the backpressure valve on the compressor suctions were exactly the same for the three data-points on each line in the plot. The horizontal position of the data-points represents the actual pressure at the outlet of the evaporator and it is therefore directly related to the vapor line pressure drop.

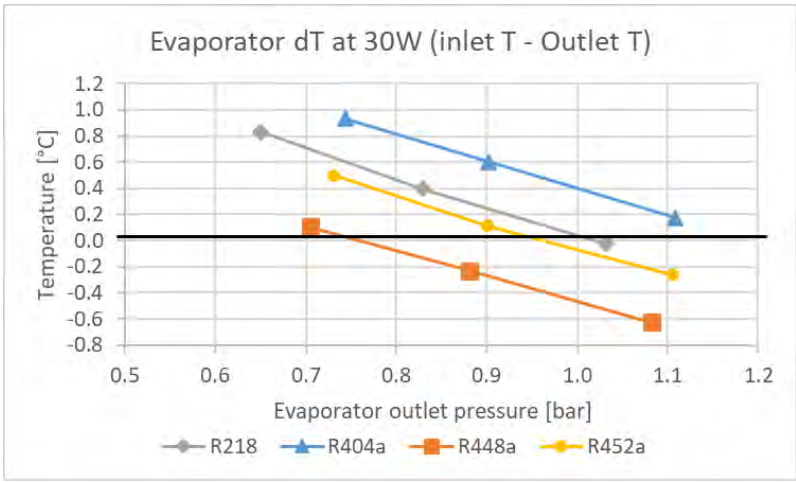

Figure 6: Temperature distribution on the evaporator at 30W dissipated load

4. CONCLUSIONS

The performance of three refrigerant blends R-404A, R-448A and R-452A was tested against reference R-218 refrigerant in a special oil-less low-flow cooling circuit with two-stage compression. The study was carried out in order to evaluate the blends as drop-in replacements for the R-218. The R-218 dominated the cooling of high-tech electronics and particle physics detectors in the past but it has a very high GWP and its availability is becoming problematic. We have proven that it can be replaced in the remaining applications where there is no exposure to radiation with the R-448A

or the R-452A (the R-404A is not recommended due to its GWP above 2500). The only condition is that the cooling circuit must be able to operate at slightly elevated condensing and liquid pressure (1.1 to 1.2 MPa) to prevent boiling in the liquid lines. The lower evaporation temperatures of the replacement blends are significant advantage for most applications in this filed, nevertheless, backpressure regulator can help to maintain similar temperatures to R-218 if needed. We have observed that the R-448A can provide uniform evaporation temperature along the evaporator at -30°C with 30W load in our system at mass flow of 1.2 g/s. The R-452A delivered average temperature of -35°C at the same pressure but with 0.4°C difference along the evaporator. The large glide of the R-448A blend compensated the drop of evaporation temperature due to the evaporator pressure drop. Many applications can benefit from this effect, as it is often desirable to maintain the same temperature over the whole length of the evaporator, for example, when multiple silicon chips are in contact with a cold bar that is in fact one long evaporator tube.

ACKNOWLEDGEMENTS

Authors would like to express their gratitude to support provided through the following grants LM2015058, LTT17018 and European Regional Development Fund – Project ”Center for Advanced Applied Science” (No.CZ.02.1.01/0.0/0.0/16-019/0000778).

REFERENCES

Anelli G., Antchev G., Aspell P. et al, 2008, The TOTEM Experiment at the CERN Large Hadron Collider, J Instrum. 3 (S08007).

Attree, D., Anderson, B., Anderssen E. C. et al. 2008, The evaporative cooling system for the ATLAS inner detector, J Instrum., Volume 3

Bates, R., Battistin, M., Berry, S. et al. 2015, The cooling capabilities of C2F6/C3F8 saturated fluorocarbon blends for the ATLAS silicon tracker, J Instrum.10, 03027

Doubek, M., Haubner, M., Vacek, V., 2017, Measurement of heat transfer coefficient in two phase flows of radiation-resistant zeotropic C2F6/C3F8 blends, Int. J. Heat Mass Transf. 113, 246-256

Doubek, M., Vacek, V., 2016, Speed of Sound Data in Pure Refrigerants R-116 and R-218 and Their Mixtures: Experiment and Modeling, J. Chem. Eng. Data, 61 (12), 4046–4056

Hallewell G., Battistin M., Berry, S. et al., 2017, The use of a 90 metre thermosiphon cooling plant and associated custom ultrasonic instrumentation in the cooling of the ATLAS inner silicon tracker, ICALEPCS, Barcelona, Spain, pp.THPHA193

Oriunno M., Battistin M., David E. et al. 2007, Design and Prototype Studies of the TOTEM Roman Pot Detectors, Nuclear Instruments and Methods in Physics Research, Section A, Accelerators, Spectrometers, Detectors and Associated Equipment. 581 , 499-503

Vacek, V., Vítek, M., Janda, M., Oriunno, M.: 2011, Versatile refrigeration circuit developed for the particle detector commissioning, 23rd IIR international congress of refrigeration, Book Series: Congress International du Froid-International Congress of Refrigeration 23, 3376-3385

Manuscript ID: 809
DOI: 10.18462/iir.icr.2019.0809

Void fraction and flow regime of in-tube condensation in a vapor-compression system

Jiange XIAO[(a)], Pega HRNJAK[(a)(b)]

[(a)] [1]University of Illinois at Urbana-Champaign, Department of Science and Engineering,

Urbana, IL, 61820, USA, jxiao10@illinois.edu

[(b)] Creative Thermal Solutions,

Urbana, IL, 61802, USA, pega@illinois.edu

ABSTRACT

In vapor-compression systems, superheated vapor condenses with temperature gradient. A "3-zone" (superheated, two-phase and subcooled) approach is not fully representative of the process because condensation happens earlier and later than bulk quality 1 and 0 respectively.
The new approach, which is "5-zone" (additional condensing superheated and condensing subcooled), addresses those issues by capturing the non-equilibrium effects.
Void fraction and flow regime measured in 4 and 6 mm smooth horizontal round tubes are used to validate the new approach in the range: mass flux from 50 to 400 kg m^{-2} s^{-1}; heat flux 5 to 15 kW m^{-2}; condensing temperatures 30 and 50°C. The refrigerants explored are R32, R134a, R1234ze(E), R245fa and R1233zd(E).
Comparing to the "3-zone" approach, the new void fraction correlation and flow regime map expend the prediction range by finding the real onset and end of condensation, providing grounds for new heat transfer and pressure drop models.
Keywords: Vapor-Compression System, Void Fraction, Flow Regime Map, Non-Equilibrium, Condensing Superheated Region.

1. INTRODUCTION

When the superheated refrigerant vapor comes out of the compressor and enters the condenser, usually the refrigerant does not condense right away, and in addition to the two-phase (TP) region, there are regions where single-phase refrigerant is present. In a conventional way of modelling, a 3-zone approach is taken, where the TP region is preceded by the superheated (SH) region, and followed by the subcooled (SC) region. The first droplet forms at thermodynamic (bulk) quality 1 and the last vapor disappears at bulk quality 0. However, according to the works by Minkowycz and Sparrow (1969), Fujii et al. (1978), Webb (1998), Kondou and Hrnjak (2011, 2012), Agarwal and Hrnjak (2015), Meyer and Hrnjak (2016), condensation happens before the specific enthalpy of the flow reaches that of the bulk quality 1. This means there could be 5 different regions during a condensation process, with another two regions called the condensing superheated (CSH) region and condensing subcooled (CSC) region. As a matter of fact, as soon as the wall temperature drops to the saturation temperature, the liquid film forms and condensation begins. This phenomenon has pronounced impact on the condensation process and its effect (the non-equilibrium effect) is characterized by Xiao and Hrnjak (2016, 2017a, 2017b, 2018a, 2018b, 2018c, 2018d). This paper will talk about the effect of non-equilibrium on two of the most important parameters in the modeling of a two-phase flow—void fraction and flow regime, in a vapor-compression system.

2. VOID FRACTION AND CORRELATIONS

Film thickness measurements have been conducted with a non-intrusive method and during the condensation process in facility, both of which are introduced by Xiao and Hrnjak (2017). Fig. 1 is a schematic of the method. Basically, a LED light is shined upon a glass tube whose outer wall is wrapped by the duct tape. The function of the duct tape is diffusion so that the pointed light source

can be assumed to be facing each different directions. There is one angle called “critical angle” that any light trying to across the liquid-vapor interface will be reflected back, and it depends on the refractive indices of refrigerant and glass. This phenomenon is called “total reflection”. As long as total reflection happens, the brightness of the light increases because the energy loss through refraction is minimum, and it created a light pattern that looks like an ellipse in Fig. 1. Because the size of the ellipse is directly related to the film thickness, with careful calibration, it is possible to measure the running film inside a glass tube non-intrusively. Fig. 2 illustrated the results of the film thickness measurements. It is obvious that liquid film starts to be condensed on the tube wall before the specific enthalpy drops to that of bulk quality 1. Hence, the void fraction has to be lower than 1 at and even before bulk quality 1. A brief comparison horizontally and vertically demonstrates the development of the liquid film as condensation proceeds and the effect of mass flux on the film distribution. Due to the pulling from the gravity, the film starts to be drawn to the bottom of the tube once it gets thicker. Because the shear force from the vapor core tends to spread the film along the tube circumference, the higher the mass flux, the more uniform the film distribution is. Fig. 3 shows the void fractions converted from the film thickness measurements against specific enthalpies and the comparisons with some correlations using bulk qualities. Apparently none of the curves in Fig. 3 fit the experimental data, and this is expected. When bulk quality is used, it is automatically assumed that the temperature profile is uniform inside the tube. The fact that non-equilibrium effects exist during an operation in a vapor-compression system makes it impossible for bulk quality to represent the actual temperature of the refrigerant. In order to have a more accurate definition of “quality”, which is technically the ratio between the vapor mass flow rate and total mass flow rate for a two-phase flow, “superficial quality” is proposed by Xiao and Hrnjak (2016), where the specific enthalpy is used to find the onset and end of condensation. The onset and end of condensation are calculated by Eq. (1-2). Both equations require iteration to find the temperature or specific enthalpy, and the single-phase HTC correlation could be any that fit into the application. For example, correlations by Gnielinski (1976) or Dittus-Boelter equation are recommended. The criteria for the onset of condensation is that the wall temperature becomes the saturation temperature; the criteria for the end of condensation is that the highest temperature inside the tube becomes the saturation temperature (note that an empirical constant 0.33 is needed here to match the experimental observations). Then the superficial quality is defined in Eq. (3). Then if we apply the superficial quality instead of bulk quality into a correlation such as the one developed by El Hajal et al. (2003), a better fit can be realized in Fig. 4 because the non-equilibrium effects have been taken into consideration. It is worth mentioning here that even though the authors decided to employ superficial quality on the specific correlation by El Hajal et al. (2003), it could be used in other correlations when required by the applications. As long as the onset and end of condensation do not happen at bulk quality 1 and 0, which is probably true for any heat transfer process, superficial quality can better reflect the mass fraction of vapor inside the tube, thus improves the predictability of not only void fraction correlations, but also the relevant correlations such as those for the heat transfer and pressure drop.

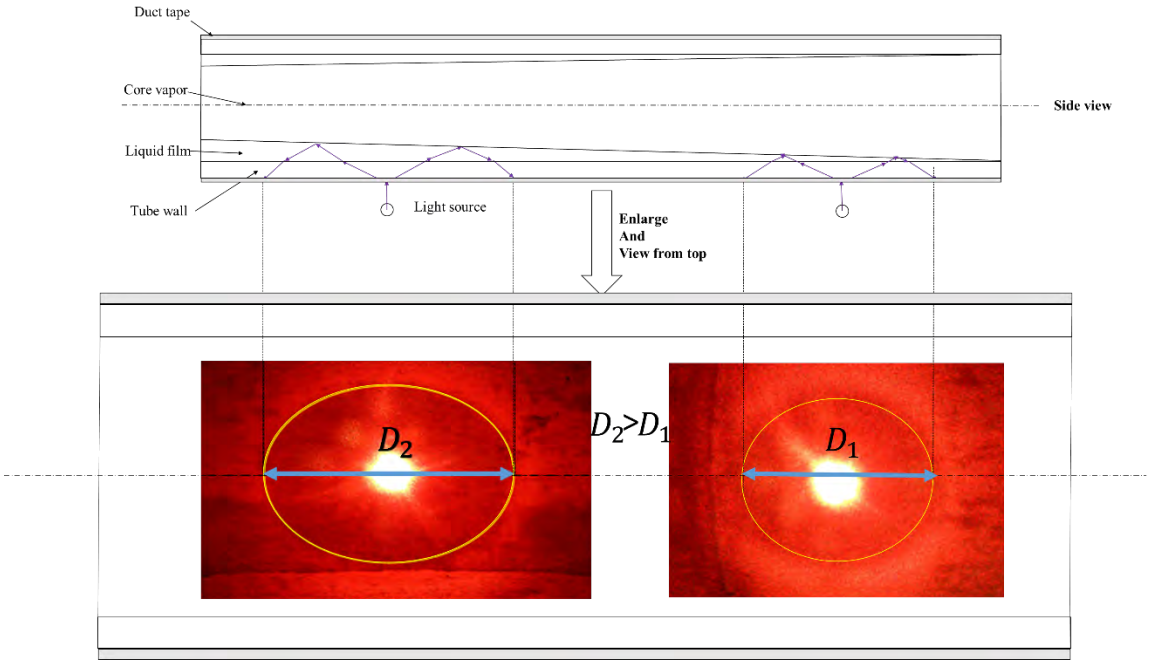

Figure 1: The principle of using total reflection to measure the film thickness

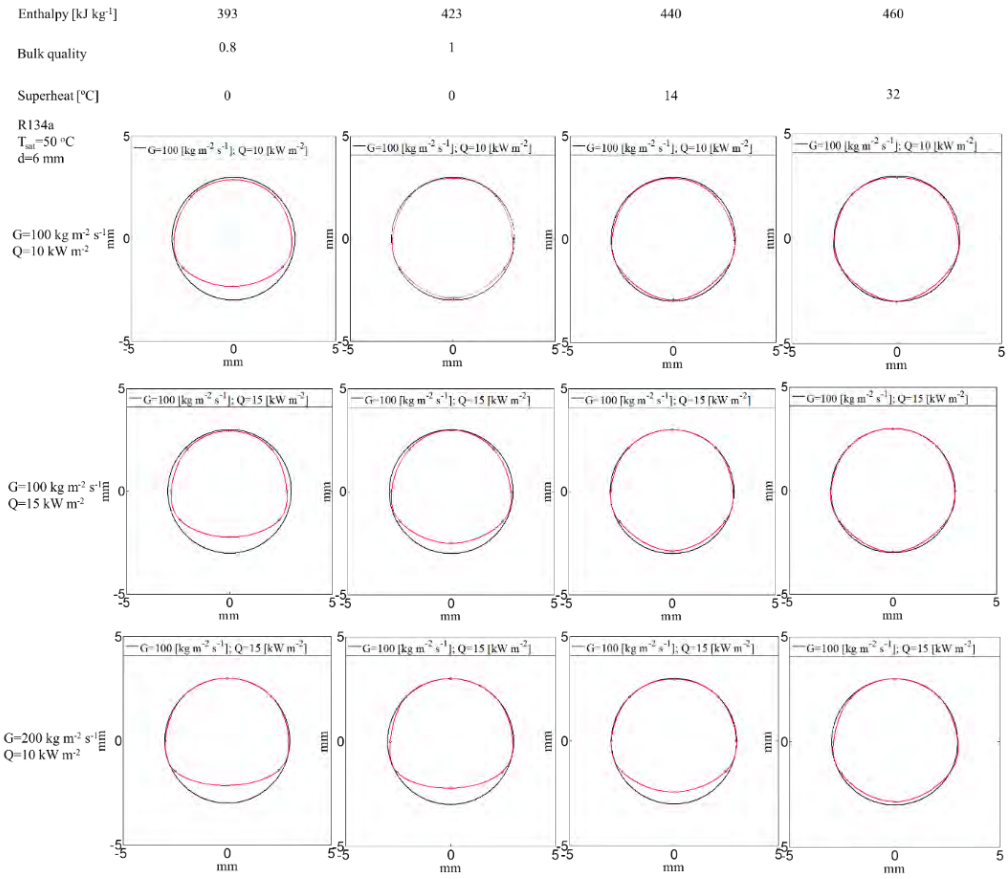

Figure 2: Film thickness measurements at 4 specific enthalpies under 3 mass fluxes

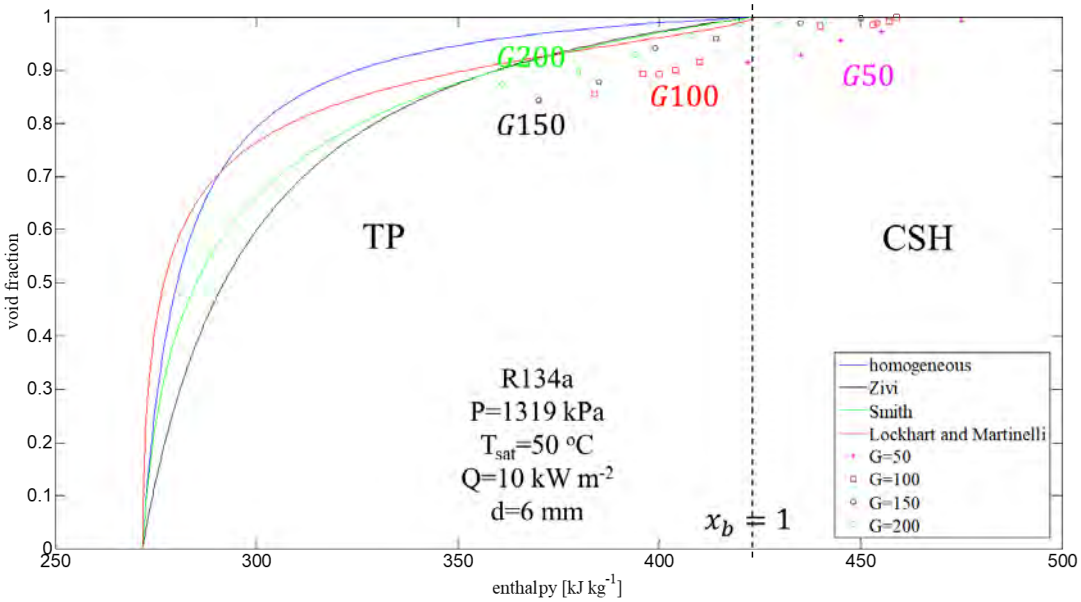

Figure 3: Void fractions of R134a condensing at 50 °C in a 6 mm tube under 3 mass fluxes

$$T_{b,onset} = T_{sat} + \frac{Q}{HTC_{onset}} \quad \text{Eq. (1)}$$

$$T_{b,end} = T_{sat} - 0.33\frac{Q}{HTC_{end}} \quad \text{Eq. (2)}$$

$$x_{sup} = \frac{h - h_{end}}{h_{onset} - h_{end}} \quad \text{Eq. (3)}$$

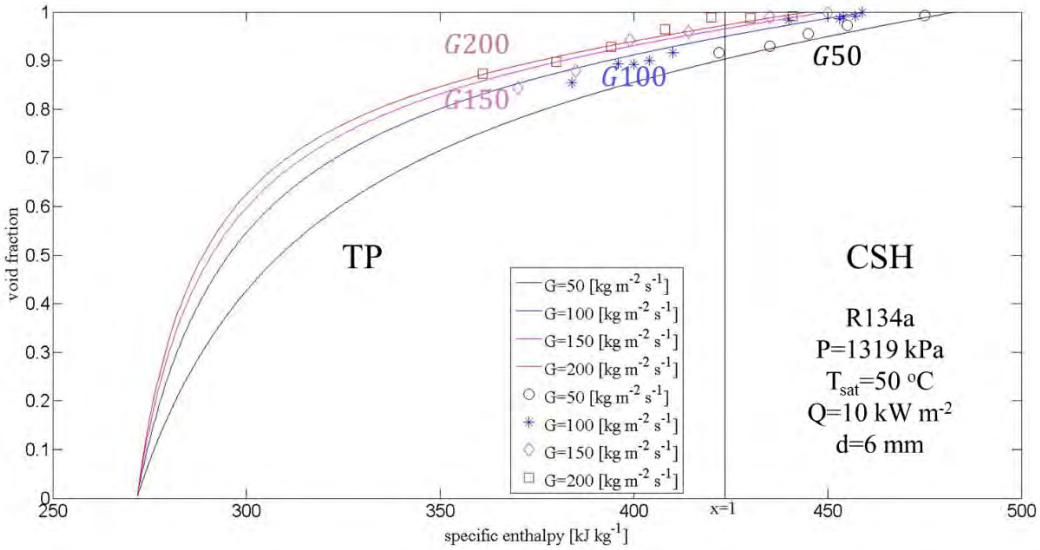

Figure 4: Experimental data are better predicted by using superficial quality instead of bulk quality

3. FLOW REGIME AND FLOW REGIME MAP

Flow regimes are defined differently by different researchers. For the two-phase flow during condensation, four different types of flow regimes—annular, intermittent, stratified-wavy, and fully-stratified—are most commonly referred to. Annular flow has an annular liquid ring around the circumference of the wall and core vapor at the center. The film thickness is usually assumed to be uniform but not necessarily so in reality. Annular flow is always the first flow regime to be observed during a condensation process. When the wall temperature becomes the saturation temperature,

the entire tube circumference is covered with liquid. Due to the high void fraction at the beginning of the condensation, the film is too thin to be pulled down by the gravity force, or be peeled off by the wall by the shear force, or form stable liquid slug, thus annular flow is the only possible option right after the onset of condensation. Stratified-wavy flow comes after the annular flow when the gravity dominates over the shear force and surface tension. The gravity pulls some of the condensate from the upper part of the tube down to the bottom and form a liquid pool there. The film thickness at the bottom is greater than other parts of the tube for a stratified-wavy flow due to the presence of the liquid pool. The wavy structure comes from two instabilities. One is the Kelvin-Helmholtz instability that is triggered by the velocity difference between vapor and liquid. For horizontal tube, vapor velocity is always greater than liquid velocity because of the lower density of the vapor and the fact that liquid first forms at the tube wall, which is stationary. The other source of wave generation is the Rayleigh-Taylor instability, created directly by the density difference between liquid and vapor. When the annular flow forms, some liquid is on top of the vapor, which is less dense than the liquid, and so generates the Rayleigh-Taylor instability in the form of waves. When the flow velocity decreases, the interface becomes calmer as the instability becomes less significant. Eventually, the liquid-vapor interface, especially the interface of the liquid pool at the bottom of the tube, becomes smooth, and the stratified-wavy flow transitions to the fully-stratified flow. Fully-stratified flow is also affected by the dominant gravity, but the waves essentially die down and the interactions between liquid and vapor grows weaker. Fully-stratified flow usually happens at the low superficial qualities by the end of the condensation. Intermittent flow also follows annular flow, but unlike transitions to the stratified-wavy flow, it happens at high mass fluxes. When the mass flux is low, the shear force cannot overcome gravity and liquid pool forms. When the mass flux is high, the shear force is high and spreads the liquid film to counter the gravitational effect. Meanwhile, because of the large difference between liquid and vapor velocities, the Kelvin-Helmholtz instability is significant and the waves are frequent and high. When the void fraction becomes low, there could be sufficient liquid and waves to form stable liquid slugs that are the signature of the intermittent flow. Intermittent flow also tends to occur at low superficial qualities or small tubes where surface tension counters the gravity effects along with the spreading force from the shear. Fig. 6 includes all four different type of flow regimes with the screen shots from the high-speed videos during condensation processes under 4 different mass fluxes.

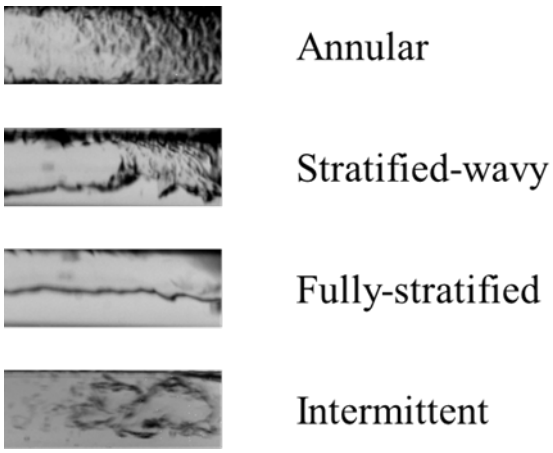

Figure 5: Four different types of flow regimes during condensation

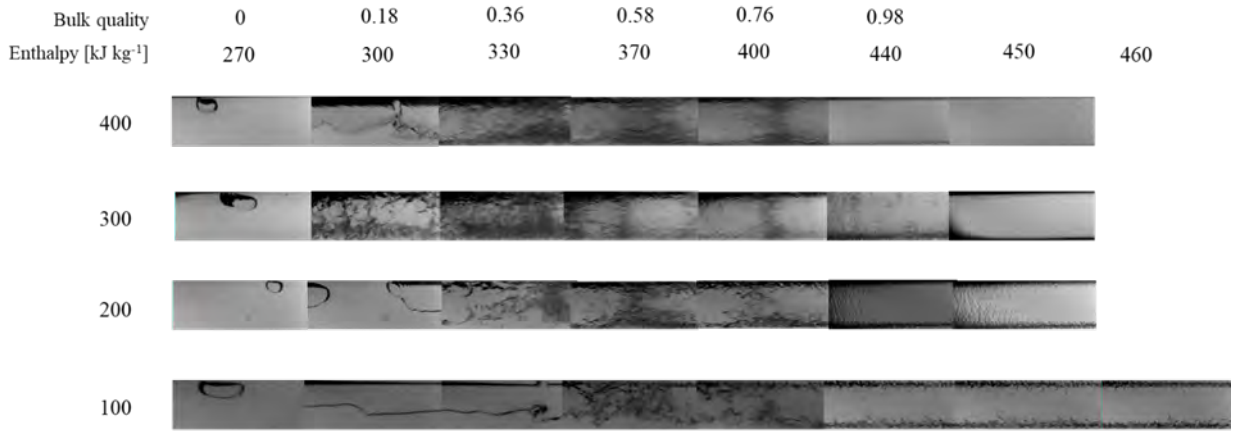

Figure 6: Flow regimes during complete condensation processes under 4 different mass fluxes

The transition between annular flow and stratified-wavy flow is expressed in Eq. (4), where the gravity is completely countered by the surface tension and shear force. By plotting the Eq. (4) under a specific condition in Fig. 7, it can be seen that the higher the mass flux, the longer the annular flow persists. The transition line between stratified-wavy and fully-stratified flow can be plotted from Eq. (6), which indicates the condition where Kelvin-Helmholtz instability vanishes. When Eq. (5) is plotted in Fig. 8, it can be seen that the higher the mass flux, the longer the stratified-wavy flow. The transition line between the annular flow and intermittent flow can be plotted in Fig. 9 using Eq. (6). It can be seen that the higher the mass flux, the more likely there will be intermittent flow. If the three transition lines are overlaid on the same chart, Fig. 10 can be obtained, which can already be used as a flow regime map. To make sure that the flow regimes in each region of the flow regime map are exclusive in that region, some simplifications are made on Fig. 10 in the circled regions to attain Fig. 11, which is the final version of the flow regime map. In Fig. 12 demonstrates how the flow regime map can extends to the applications in microchannels by including the impact of surface tension. When the tube is a conventional round tube, all four flow regimes are present. However, when the tube size becomes smaller, so do the regions affected by stratification. This is because the surface tension becomes more and more important compared to the gravity as the tube diameter decreases. Eventually gravity will be completely overwhelmed by surface tension, and the stratification disappears. Therefore, microchannels are the tubes where only annular and intermittent flow can be observed.

$$G_{AW} = \{2\,[\rho_l g r^2(1-\varepsilon^{0.5}) - 0.005\sigma]\rho_v \frac{1}{0.25 f_v r}\}^{0.5} \quad \text{Eq. (4)}$$

$$G_{WS} = \left[226.3^2 A_{ld} A_{vd}^2\, \rho_v(\rho_l - \rho_v)\mu_l g\right]^{\frac{1}{3}}\left[x_{sup}^2(1-x_{sup})\pi^3\right]^{-\frac{1}{3}} + 20 - 40x_{sup}^2 \quad \text{Eq. (5)}$$

$$G_{AI} = C_3 u_c \left[\frac{x_{sup}}{\rho_v \varepsilon} - \frac{1-x_{sup}}{\rho_l(1-\varepsilon)}\right]^{-1} (d-2\delta)^m \frac{\delta_m^{n-m}}{\delta^n} \quad \text{Eq. (6)}$$

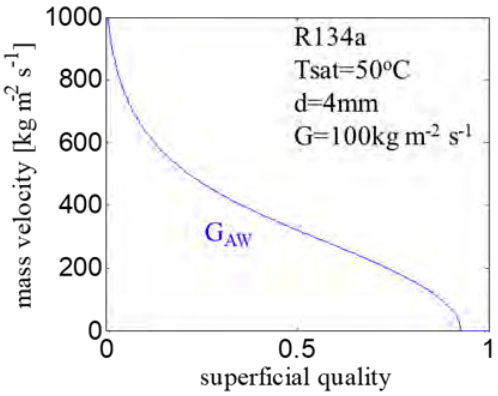

Figure 7: Transition line between the annular flow and stratified-wavy flow

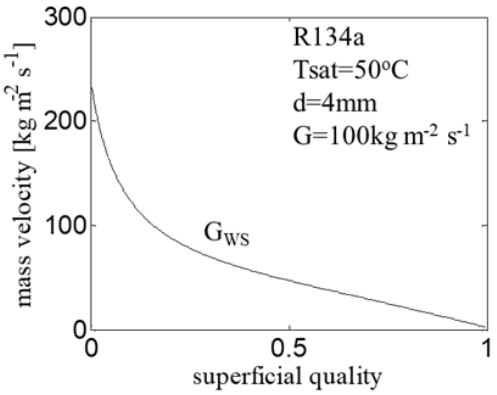

Figure 8: Transition line between the stratified-wavy flow and fully-stratified flow

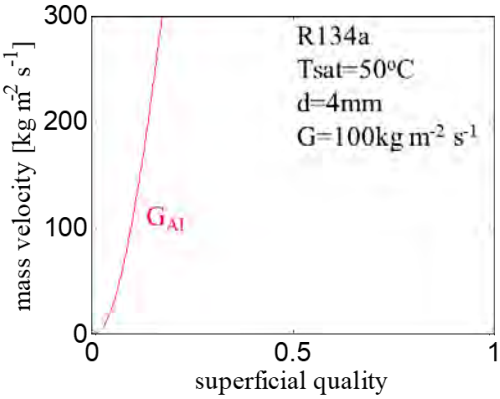

Figure 9: Transition line between the annular flow and intermittent flow

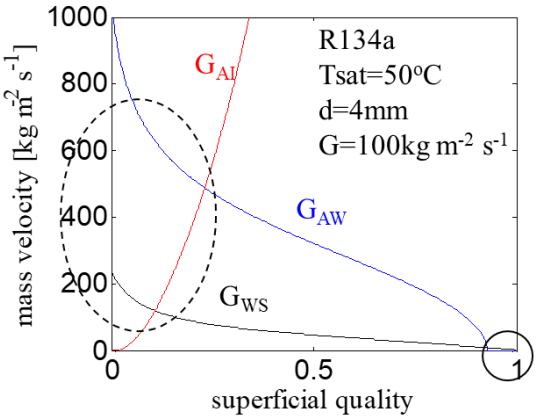

Figure 10: Plotting the three transition lines on the same chart

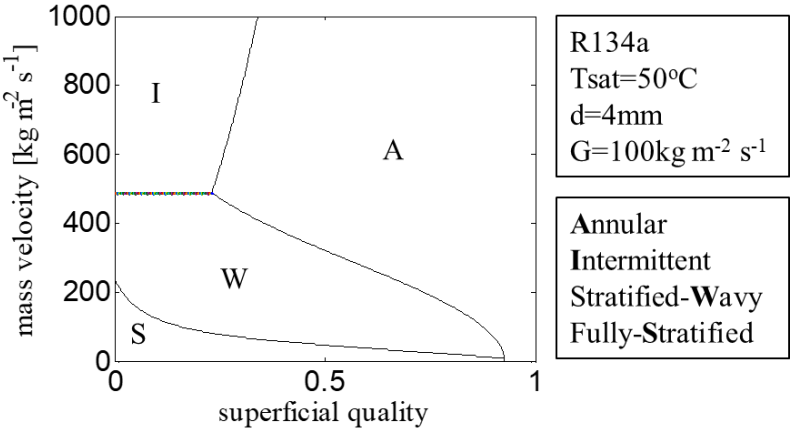

Figure 11: Fig. 10 simplified to be the flow regime map

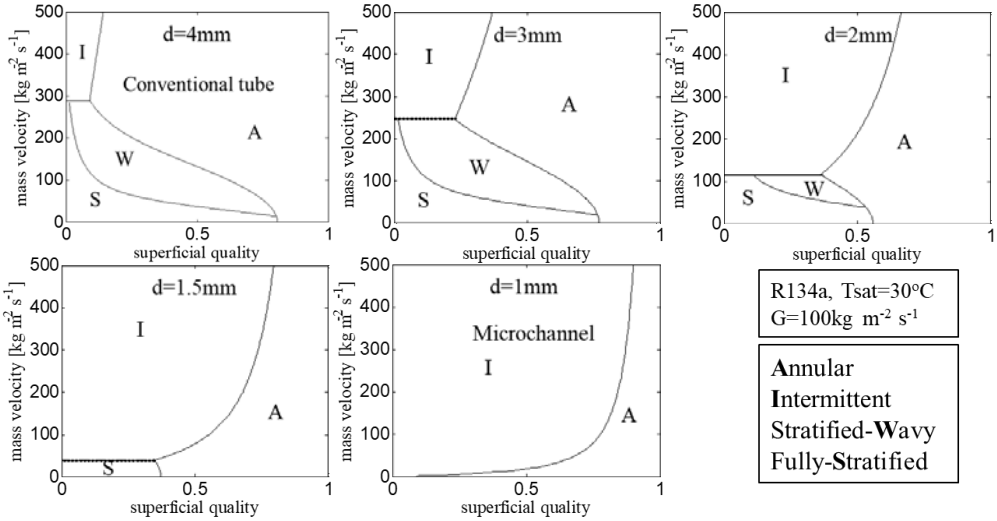

Figure 12: Flow regime maps from conventional tubes to microchannels

4. CONCLUSIONS

Due to the temperature gradient inside the tube during condensation, the onset and end of condensation is advanced and delayed. Therefore, void fraction drops below 1 before the specific enthalpy drops to that of the bulk quality 1. Assuming equilibrium two-phase flow cannot give accurate predictions of the void fraction. This can be corrected by using the superficial quality instead. In addition to the void fraction, flow regimes during the condensation process in a vapor-compression system need to be reconsidered because of the non-equilibrium effect. The first flow regime during the condensation process is always annular and three other flow regimes typically follow the annular flow. The transition between annular flow and stratified-wavy flow is due to the growing magnitude of gravity as condensate accumulates. The transition between stratified-wavy flow and fully-stratified flow is because of the disappearance of Kelvin-Helmholtz instability. The transition between the annular flow and intermittent flow is the result of growing waves and formation of stable liquid slugs. A new flow regime map is proposed using superficial quality, and its prediction range extends to the microchannels.

ACKNOWLEDGEMENTS

The authors thankfully acknowledge the support provided by the Air Conditioning and Refrigeration Center at the University of Illinois at Urbana-Champaign, and technical support from Creative Thermal Solutions, Inc. (CTS).

NOMENCLATURE

P	Pressure (Pa)	d	Tube inner diameter (m)
T	Temperature (K)	G	Mass flux (kg m^{-2} s^{-1})
Q	Heat flux (W m^{-2})	HTC	Heat transfer coefficient (W K^{-1} m^{-2})
δ	Film thickness (m)	ε	Void fraction
r	Tube radius (m)	u	Velocity (m s^{-1})
x	Quality	ρ	Density (kg m^{-3})
σ	Surface tension (N m^{-1})	g	Gravitational acceleration (m s^{-2})
μ	Dynamic viscosity (kg m^{-1} s^{-1})		

REFERENCES

Agarwal, R., Hrnjak, P., 2015. Condensation in two phase and desuperheating zone for R1234ze(E), R134a and R32 in horizontal smooth tubes, Int. J. Refrigeration 50, 172-183.

Churchill, S.W., 1977. Friction-factor equation spans all fluid-flow regimes. Chem. Eng. 7, 91–92.

El Hajal, J., Thome, J.R., Cavallini, A., 2003. Condensation in horizontal tubes, Part 1: Two-phase flow pattern map, Int. J. Heat Mass Transfer 46(18), 3349–3363.

Friedel, L., 1979. Improved friction pressure drop correlation for horizontal and vertical two phase flow, 3R Int. 18(7), 485–491.

Fujii, T., Honda, H., Nozu, S., Nakarai, S., 1978. Condensation of superheated vapor inside horizontal tube, Heat Transfer- Japanese Research 4(3), 1-48.

Gnielinski, V., 2976. New equation of heat and mass transfer in turbulent pipe and channel flow, Int. Chem. Eng 16 359-367.

Kondou, C., Hrnjak, P., 2011a. Heat rejection from R744 flow under uniform temperature cooling in a horizontal smooth tube around the critical point, Int. J. Refrigeration 34(3), 719-731.

Kondou, C., Hrnjak, P., 2012. Condensation from superheated vapor flow of R744 and R410A at subcritical pressures in a horizontal smooth tube, Int. J. Heat Mass Transfer 55, 2779-2791.

Meyer, M., Hrnjak, P., 2017. Flow regimes during condensation in superheated zone, Int. J. Refrigeration 84, 336-343.

Minkowycz, W.J., Sparrow, E.M., 1969. The effect of superheating on condensation heat transfer in a forced convection boundary layer flow, Int. J. Heat Mass Transfer 12, 147–154.

Webb, R.L., 1998. Convective condensation of superheated vapor. Trans ASME J. Heat Transfer 120, 418-420.

Xiao, J., Hrnjak, P., 2016. Heat transfer and pressure drop of condensation from superheated vapor to subcooled liquid. Int. J. Heat Mass Transfer 103, 1327-1334.

Xiao, J., Hrnjak, P., 2017a. A new flow regime map and void fraction model based on the flow characterization of condensation, Int. J. Heat Mass Transfer 108, 443-452.

Xiao, J., Hrnjak, P., 2017b. A heat transfer model for condensation accounting for non-equilibrium effects, Int. J. Heat Mass Transfer 111, 201-210.

Xiao, J., Hrnjak, P., 2018a. Pressure drop of R134a, R32 and R1233zd(E) in diabatic conditions during condensation from superheated vapor, Int. J. Heat Mass Transfer 122, 442-450.

Xiao, J., Hrnjak, P., 2018b. A pressure drop model for condensation accounting for non-equilibrium effects, Int. J. Heat Mass Transfer 122, 442-450.

Xiao, J., Hrnjak, P., 2018c. Flow regimes during condensation from superheated vapor, Int. J. Heat Mass Transfer 132, 301-308.

Xiao, J., Hrnjak, P., 2018d. A flow regime map for condensation in macro and micro tubes with non-equilibrium effects taken into account, Int. J. Heat Mass Transfer 130, 893-900.

Manuscript ID: 812
DOI: 10.18462/iir.icr.2019.0812

Heat transfer and pressure drop model of in-tube condensation in a vapor-compression system

Jiange XIAO[(a)], Pega HRNJAK[(a)(b)]

[(a)] [1]University of Illinois at Urbana-Champaign, Department of Science and Engineering, Urbana, IL, 61820, USA, jxiao10@illinois.edu

[(b)] Creative Thermal Solutions, Urbana, IL, 61802, USA, pega@illinois.edu

ABSTRACT

A typical "3-zone" models assume uniform temperature in the cross section of the tube during condensation. The first droplet occurs when the bulk quality is 1. However, as soon as wall temperature drops to the saturation, condensation begins regardless of what the bulk temperature is.

The new heat transfer and pressure drop models use "5-zone" approach, seeking to capture the two-phase mechanisms in the condensing superheated (CSH) and condensing subcooled (CSC) regions.

Heat transfer coefficient and pressure drop measured in 4 and 6 mm tubes are used to validate the new approach in the range: mass flux from 50 to 400 kg m^{-2} s^{-1}; heat flux 5 to 15 kW m^{-2}; condensing temperatures 30 and 50°C. The refrigerants explored are R744, R32, R410A, R134a, and R1233zd(E).

The new models are more physical and better fit the experimental data than the conventional models, especially in the CSH region. This is because the latent heat and vapor-liquid interaction are present even though the bulk temperature indicates otherwise.

.

Keywords: Vapor-compression system, Heat transfer, Pressure drop, Non-equilibrium, Condensing superheated region

1. INTRODUCTION

Due to the temperature gradient, liquid film forms before the thermodynamic (bulk) quality becomes 1. Because of the interactions between the liquid and wave, especially in the form of waves at the liquid-vapor interface, the heat transfer coefficient and pressure drop tends to be higher than predicted by a single-phase correlation. The phenomenon was introduced by Minkowycz and Sparrow (1969), Fujii et al. (1978), Webb (1998), Kondou and Hrnjak (2011, 2012), Agarwal and Hrnjak (2015), Meyer and Hrnjak (2016), where some heat transfer correlations were proposed with limited range of applications, and no pressure drop developed. The non-equilibrium effect has been extensively characterized by Xiao and Hrnjak (2016, 2017a, 2017b, 2018a, 2018b, 2018c, 2018d). This paper will talk about the effect of non-equilibrium on probably the most important parameters when designing a condenser—heat transfer and pressure drop, in a vapor-compression system.

2. A MECHANISTIC HEAT TRANSFER MODEL

During the condensation process, usually the heat transfer coefficient (HTC) is considered to be monotonically dropping, which makes sense because as more condensate is generated, the density of the flow increases, thus the flow velocity deceases, causing the convective heat transfer to be weaker. However, as the previous studies mentioned in section 1 mentioned, in the CSH region, HTC could increase instead of decrease due to the presence of liquid film, namely latent heat, during the heat transfer process. The seemingly counterintuitive trend was explained by Xiao and Hrnjak (2016). A new definition for heat transfer coefficient, "film HTC", was proposed, reasoned by the positive correlation between film thickness and thermal resistance through the liquid film. The definitions of bulk HTC and film HTC are listed in Eq. (1-2). It is obvious that in the two-phase (TP) region, the two definition collapses into one, but in the CSH and CSC regions, bulk

HTC measures the heat transfer behaviour through the entire two-phase flow, while film HTC only characterizes the heat transfer capability through the liquid film. Because both HTCs talk about the same process but from different angles, a mechanistic heat transfer model could be built upon the film HTC so that it can be linked to the film thickness (which can be determined knowing the void fraction and flow regime). Then the film HTC can be converted into the bulk HTC so that the definition in CSC, CSH and TP is consistent with that in the superheated (SH) and subcooled (SC) regions. Eq. (3) can be used to make the conversion.

$$HTC_{bulk} = \frac{Q}{T_{bulk} - T_{wall}} \quad \text{Eq. (1)}$$

$$HTC_{film} = \frac{Q}{T_{sat} - T_{wall}} \quad \text{Eq. (2)}$$

$$HTC_{bulk} = HTC_{film}\frac{T_{sat} - T_{wall}}{T_{bulk} - T_{wa;;}} = \frac{Q}{T_{bulk} - T_{sat} + \frac{Q}{HTC_{film}}} \quad \text{Eq. (3)}$$

A typical condensation process is demonstrated with Fig. 1. Superheated vapor enters the condensation, whose HTC can be calculated using correlations by Gnielinski (1976) or Dittus-Boelter equation. Then with the heat transfer known, the model marches segment by segment until the wall temperature becomes the saturation temperature, indicating the onset of condensation. The onset of condensation can be calculated with Eq. (4). According to the flow regime map by Xiao and Hrnjak (2018b), the first flow regime has to be annular, where the film distribution can be assumed to be uniform. Using the void fraction correlation by Xiao and Hrnjak (2017a), the void fraction of condensation from superheated vapor can be determined, which in turn can be used to find the film thickness by Eq. (5). Eq. (6) is then used to find the film HTC for the annular flow, where K_i is the wave-enhancement factor calculated by Eq. (7). The superficial liquid and vapor velocities in Eq. (7) are calculated by Eq. (8-9). The film Reynolds number in Eq. (6) is defined by Eq. (10). The transition from annular flow to the stratified-wavy flow can be found using the flow regime map mentioned above. The intermittent flow is combined into the stratified-wavy flow for simplicity. For stratified-wavy flow, the stratification angle, which is calculated from iterations using Eq. (11), is used to represent the proportion of film flow at the upper part of the flow in relation to the entire tube. Because the upper and lower part of the tube have different film thickness, the film thickness for the upper part of the tube is assumed to be the film thickness at the transition between annular flow and stratified-wavy flow. Thus the film HTC at the upper part of the tube can be determined by the same equation for annular flow, which is Eq. (6). The film thickness at the bottom of the tube can be determined from the stratification angle using Eq. (12). The overall film HTC is calculated using Eq. (13). Then the film HTC at the bottom part of the tube can also be determined by Eq. (6), but using a different film thickness. The end of condensation is calculated in a similar manner as the onset of condensation in Eq. (14). After the end of the condensation, the HTC goes back to being determined by single-phase correlations.

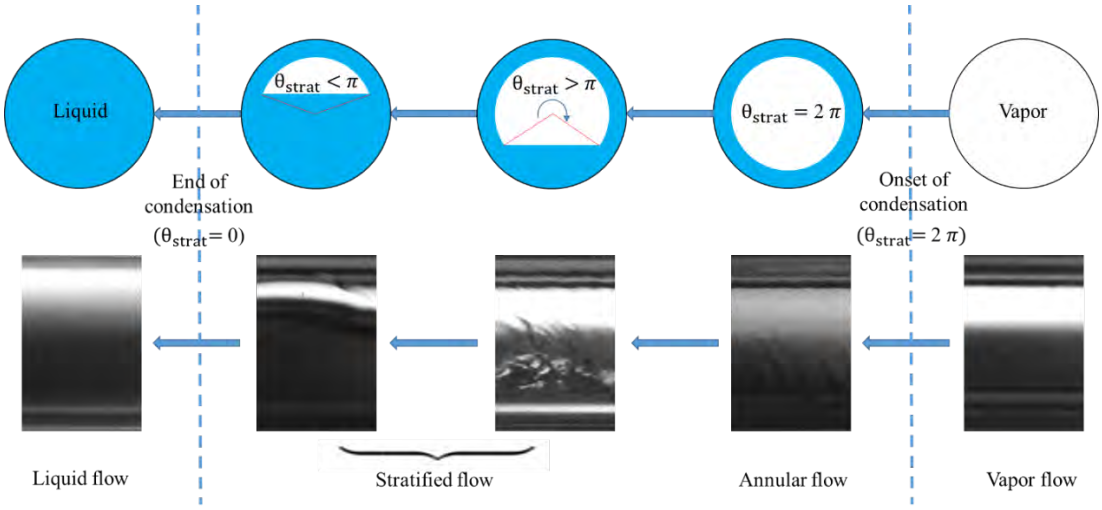

Figure 1: A typical process of condensation in a vapor-compression system

$$T_{b,onset} = T_{sat} + \frac{Q}{HTC_{onset}} \quad \text{Eq. (4)}$$

$$\delta = 0.5d(1 - \varepsilon^{0.5}) \quad \text{Eq. (5)}$$

$$HTC_{film,annular} = 0.023\, Re_f^{0.8}\, Pr_l^{0.3} \frac{k_l}{d}\left(\frac{d}{2\delta}\right)^{0.94} K_i \quad \text{Eq. (6)}$$

$$K_i = 1 + \left(\frac{u_v}{u_l}\right)^{0.5}\left[\frac{(\rho_l - \rho_v)g\delta^2}{\sigma}\right]^{0.34} x_{sup}^{0.1} \quad \text{Eq. (7)}$$

$$u_v = \frac{Gx_{sup}}{\rho_v \varepsilon} \quad \text{Eq. (8)}$$

$$u_l = \frac{G(1 - x_{\text{sup}})}{\rho_l(1 - \varepsilon)} \quad \text{Eq. (9)}$$

$$Re_f = \frac{2G(1 - x_{sup})\delta}{(1 - \varepsilon)\mu_l} \quad \text{Eq. (10)}$$

$$\frac{\pi d^2(1 - \varepsilon)}{4} = \frac{d^2}{8}[(2\pi - \theta_{strat}) - \sin(2\pi - \theta_{strat}) + \theta_{strat}(1 - \varepsilon_{trans})] \quad \text{Eq. (11)}$$

$$\delta_{lower} = 0.5d[1 - \frac{\sin(2\pi - \theta_{strat})}{2\pi - \theta}] \quad \text{Eq. (12)}$$

$$HTC_{f,total} = HTC_{f,upper}\frac{\theta_{strat}}{2\pi} + HTC_{f,lower}\frac{2\pi - \theta_{strat}}{2\pi} \quad \text{Eq. (13)}$$

$$T_{b,end} = T_{sat} - 0.33\frac{Q}{HTC_{end}} \quad \text{Eq. (14)}$$

A comparison between the predictions from a 3-zone approach and a 5-zone approach is shown in Fig. 2. Apparently the experimental data by Xiao and Hrnjak (2016) is better predicted by the current model, especially in the CSH and CSC region. This is because in those two regions, even though the specific enthalpy indicates single-phase flow inside the tube, it is actually two-phase flow because of the non-equilibrium effect. The 5-zone approach, which is the current mechanistic model captures this phenomenon, hence the higher HTC due to the presence of the latent heat is predicted to a satisfactory level. Fig. 3 provides the comparison between predictions from the current model and experimental data from Xiao and Hrnjak (2016). Most predictions are within 15% from the experimental data on R134a, R32, R1234ze(E), R410A, as well as R744 under mass flux from 100 to 200 kg m^{-2} s^{-1} and heat flux from 5 to 25 kW m^{-2} in a 6 mm tube. New experiments on mixtures and microchannels are on the way.

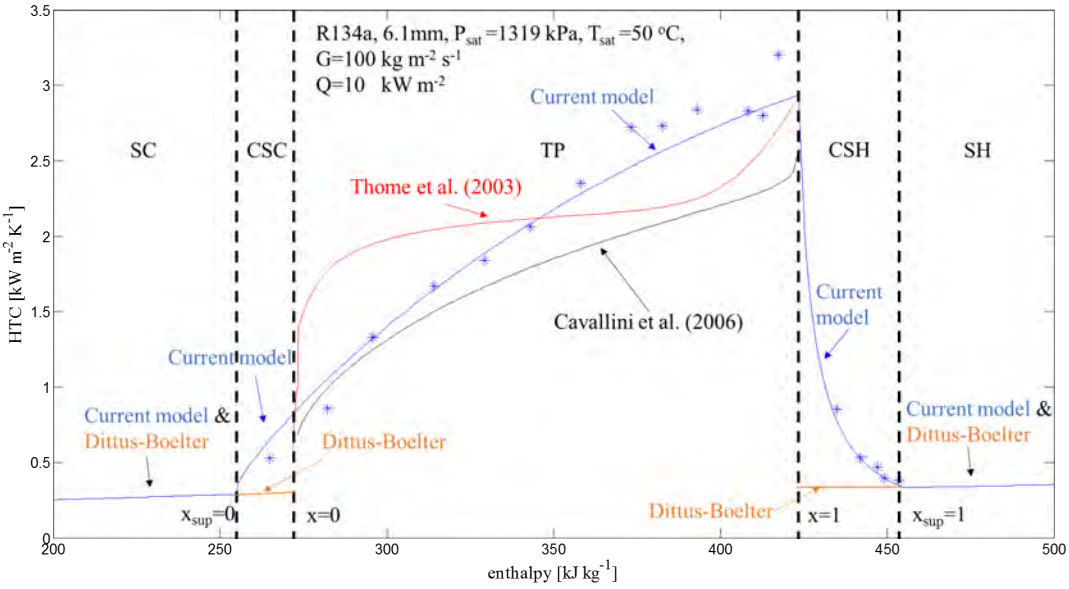

Figure 2: Comparison between the current model and other models, and with experimental data

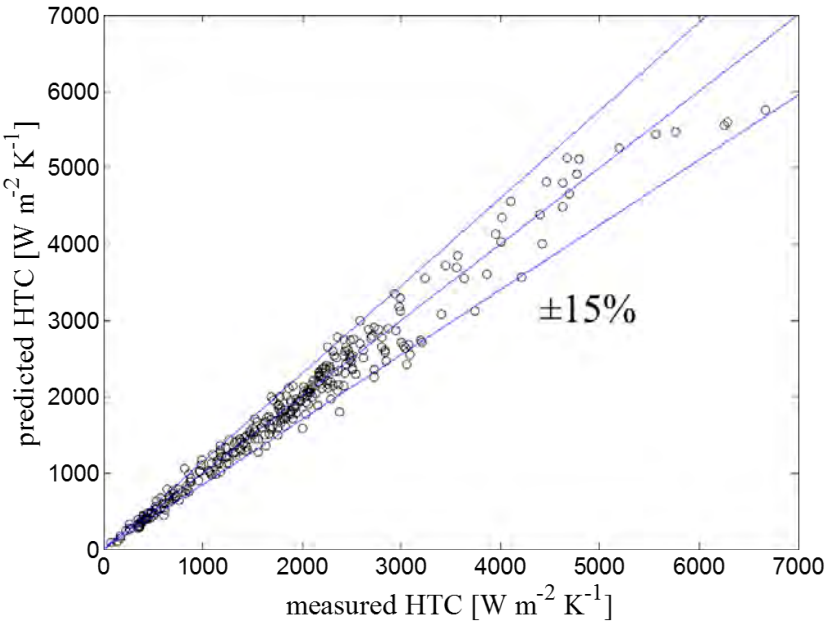

Figure 3: Most experimental data are predicted within a discrepancy of 15%

3. A MECHANISTIC PRESSURE DROP MODEL

Due to the heat and momentum analogy, it is expected that when the HTC starts to increase in the CSH region, the pressure drop increases, too. It is indeed the case according to Xiao and Hrnjak (2018), where pressure drop during condensation of R32, R134a and R1233zd(E) in 6 and 4 mm tubes were measured under different mass fluxes. For instance, in Fig. 4 pressure drop first decreases in the SH region because the density of the flow increases and the velocity of the flow decreases. However, even though the velocity of the flow keeps decreasing during the entire condensation process, pressure drop increases after the onset of condensation, suggesting another mechanism that increases pressure drop. According to the visualizations by Xiao and Hrnjak (2017), it is obvious that right after the onset of condensation, liquid film forms on the tube wall, and because of the instabilities, waves form on the liquid-vapor interface. The waves create longer and rougher path for the vapor to flow through compared to the smooth tube wall, thus more energy is dissipated during the process, which is manifested in the form of higher pressure drop. To account for this effect, using a similar method as the mechanistic heat transfer model introduced in Section 2, a mechanistic pressure drop model is also possible, knowing the void fraction and flow regime. First of all, the effect of the waves on pressure drop needs to be mathematically determined. The wave-enhancement factor is used to do the job. As mentioned in the last section, waves form due to the Kelvin-Helmholtz instability and the Rayleigh-Taylor instability. The minimum velocity difference required to trigger the Kelvin-Helmholtz instability is expressed in Eq. (15). The most dangerous wavelength of the Rayleigh-Taylor instability is expressed in Eq. (16). The higher the velocity difference between the liquid and vapor, the more likely Kelvin-Helmholtz instability creates waves, thus the ratio between the difference between liquid and vapor superficial velocities and the minimum velocity difference required represent the frequency and strength of waves created by the Kelvin-Helmholtz instability. Meanwhile, the more liquid there is, the more likely that the falling film forms waves at the interface due to the Rayleigh-Taylor instability. Hence, the ratio between film thickness, which can be calculated using Eq. (5), and the most dangerous wavelength is used here to represent the frequency and strength of the waves generated because of the Rayleigh-Taylor instability. The wave-enhancement factor for pressure drop is then defined as Eq. (17). Note that the wave-enhancement factor for pressure drop in Eq. (17) is slightly different than that for heat transfer in Eq. (7). There are two different paths the refrigerant can take. One is “annular-intermittent”; the other is “annular-stratified (wavy)”, both of which are shown in Fig. 5. The two-phase flow pressure drop starts after the onset of condensation. The pressure drop for the annular flow can be determined using Eq. (18). The bulk

density in Eq. (18) can be calculated using Eq. (19). The correlation by Churchill (1977) is selected to find the single-phase pressure drop. When the transition from annular flow to the intermittent flow, β, which is calculated using Eq. (20), is used to characterize the length of the tube that is occupied by the liquid slugs. In Eq. (20), the transitional void fraction is the void fraction calculated at the transition between annular flow and intermittent flow. Similar to the heat transfer model, the pressure drop of the liquid slug is modelled by Churchill correlation, and the rest of the flow remained to be modelled by the annular flow model, which is Eq. (18). The film thickness of the liquid annulus in intermittent flow is assumed to be the film thickness at the transition between the annular flow and the intermittent flow. The overall pressure drop of an intermittent flow is calculated using Eq. (21). If the mass flux is sufficiently low that stratified (wavy) instead of intermittent flow is present, the tube should then be divided vertically rather than longitudinally because the film is thicker at the bottom than the top. Under such circumstances, Eq. (22) is used to calculate the overall pressure drop of the flow. The upper part of tube is still modelled as annular flow by Eq. (18), whose film thickness is assumed to be the same as the film thickness at the transition between annular and stratified (wavy) flow. The lower part of the tube is also modelled as annular flow but the film thickness is calculated by Eq. (12), and the stratification angle is calculated using Eq. (11). It can be easily seen that when the stratification angle α or β becomes 2π or 0, condensation stops and the correlation reduces to Churchill correlation.

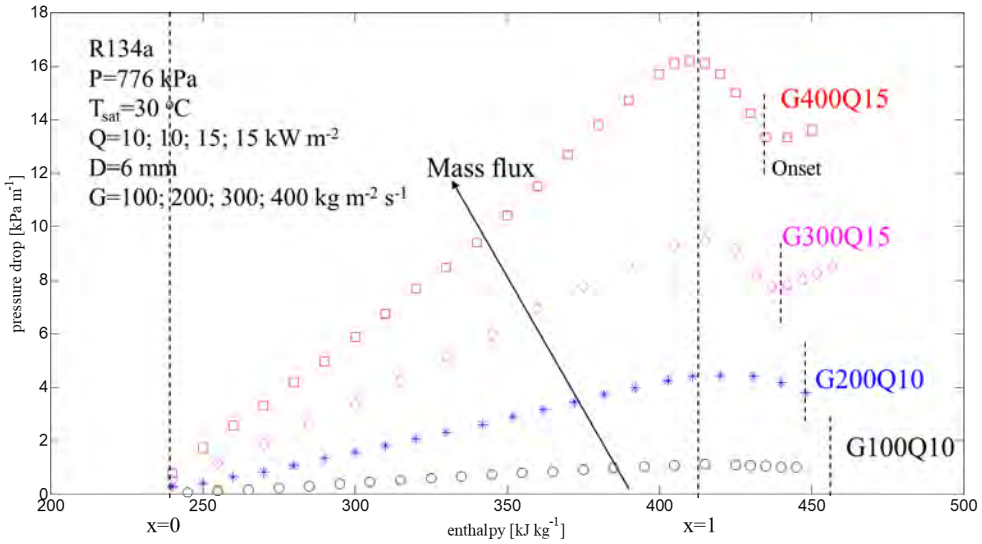

Figure 4: Pressure drop during R134a condensing in 6 mm tube at 30 °C under 4 mass fluxes

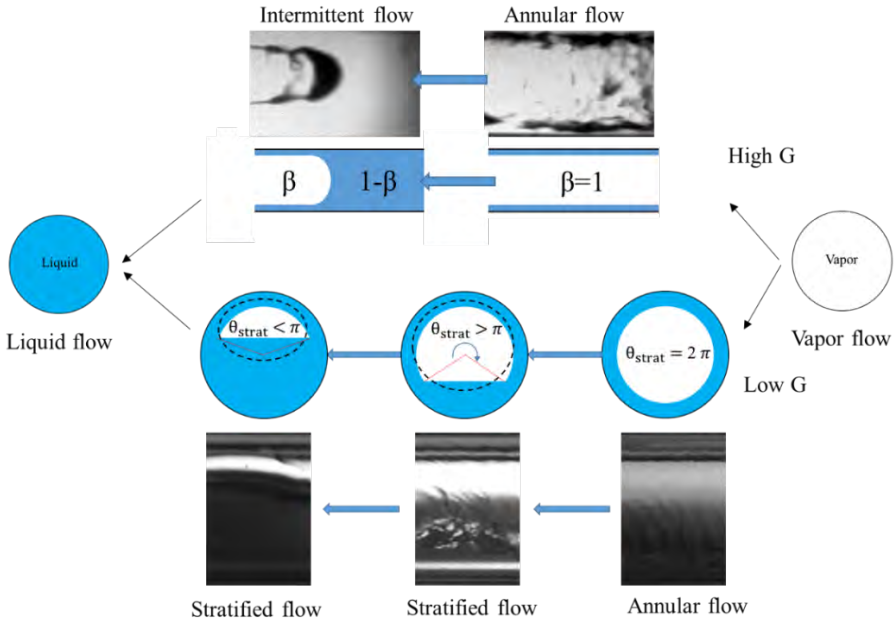

Figure 5: Two different path refrigerant can take during condensation from superheated vapor

$$u_{min} = \left[\frac{2(\rho_l - \rho_v)}{\rho_l}\right]^{0.5} \left[\frac{\sigma(\rho_l - \rho_v)g}{\rho_v^2}\right]^{0.25} \quad \text{Eq. (15)}$$

$$\delta_m = 2\pi \left[\frac{\sigma g}{\rho_l - \rho_v}\right]^{0.5} \quad \text{Eq. (16)}$$

$$K_i = 1 + C \left(\frac{u_v - u_l}{u_{min}}\right)^p \left(\frac{\delta}{\delta_{crit}}\right)^q \quad \text{Eq. (17)}$$

$$\frac{PD}{\rho} = PD_v * K_i \frac{x_{sup}}{\rho_v} + PD_l * K_i \frac{1 - x_{sup}}{\rho_l} \quad \text{Eq. (18)}$$

$$\rho = \left(\frac{x_{sup}}{\rho_v} + \frac{1 - x_{sup}}{\rho_l}\right)^{-1} \quad \text{Eq. (19)}$$

$$\beta = \frac{\varepsilon}{\varepsilon_{trans}} \quad \text{Eq. (20)}$$

$$PD = \beta PD_{annular} + (1 - \beta) PD_{liquid} \quad \text{Eq. (21)}$$

$$PD = PD_{upper} \frac{\theta_{strat}}{2\pi} + PD_{lower} \frac{2\pi - \theta_{strat}}{2\pi} \quad \text{Eq. (22)}$$

A comparison between the predictions from a 3-zone approach and a 5-zone approach is shown in Fig. 6. For the 3-zone approach, Churchill correlation and correlation by Friedel (1979) are used. There is obvious underprediction in the CSH region due to the neglect of liquid-vapor interaction, which is the waves mentioned above. Using the 5-zone approach in this section, the underprediction is corrected and the overall accuracy of the model prediction improves. The 5-zone approach also creates a seamless line throughout all 5 regions, which is hardly achieved by the 3 zone approaches. The seemingly continuous curve in Fig. 6 with the 3-zone approach is artificially created by using Churchill instead of Blasius equation in the Friedel correlation. In this way the effect of surface roughness can be consistence in SH, TP and SC regions. Fig. 7 shows the comparison between the predictions by the 5-zone approach and the experimental data, which is from the condensation of R32, R134a and R1233zd(E) at 30 ^{o}C in 4 and 6 mm tubes under mass fluxes ranged from 100 to 400 kg m^{-2} s^{-1}. The model predictions have a difference smaller than 10% with the experimental data, most of which are in the lower magnitude region. This is probably due to the systematic error when the pressure drop is small. New experiments on mixtures and microchannels are on the way.

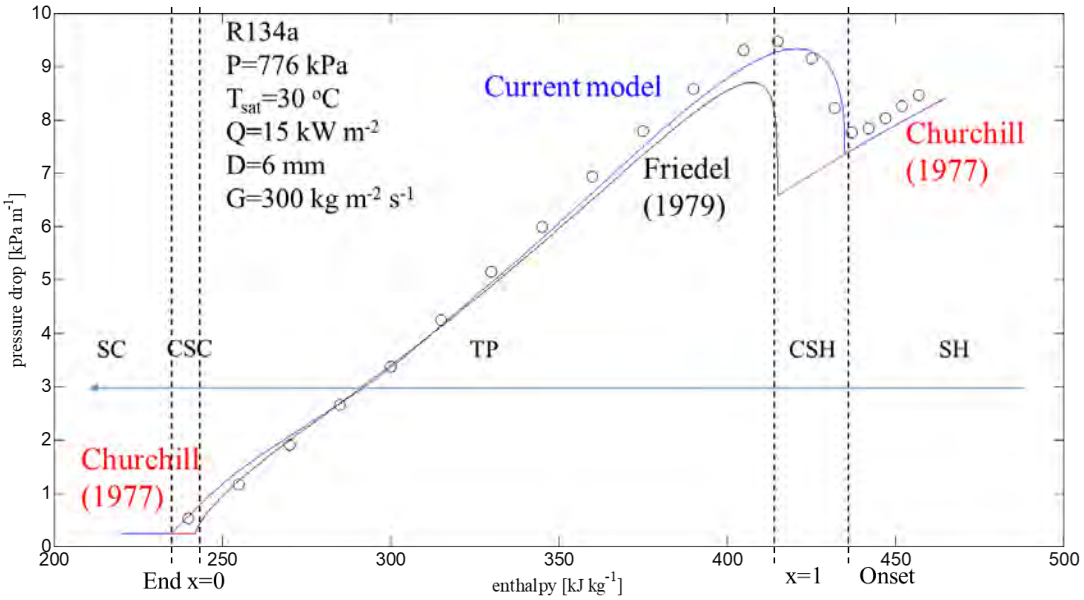

Figure 6: Comparison between the current model and other models, and with experimental data

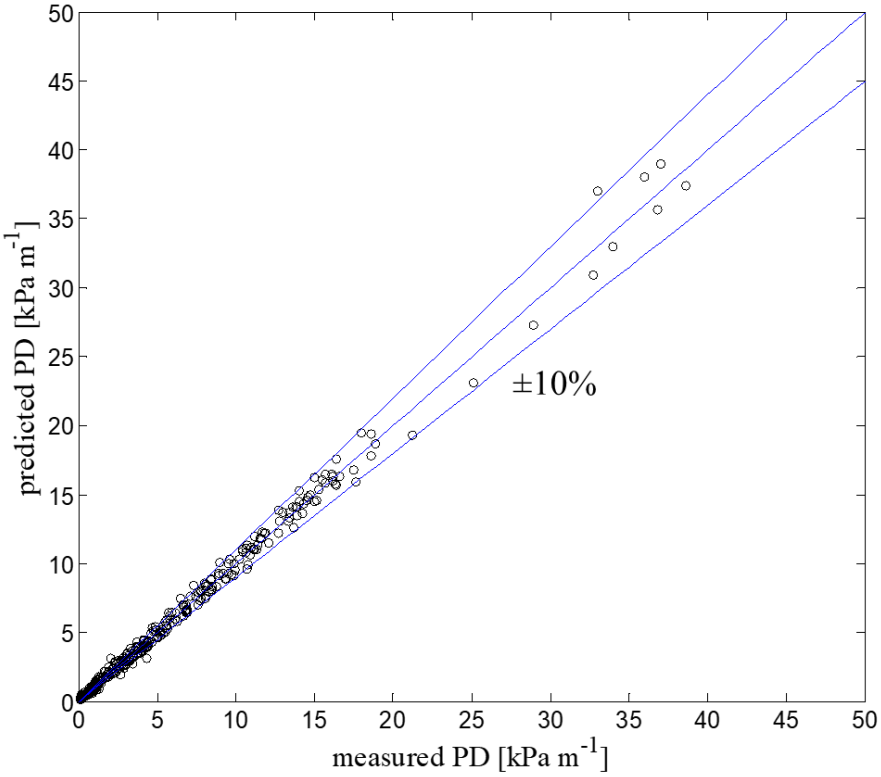

Figure 7: Most experimental data are predicted within a discrepancy of 10%

4. CONCLUSIONS

A mechanistic model for heat transfer and pressure drop is described in this paper. For heat transfer in a vapor-compression system, as soon as the wall temperature drops to the saturation temperature, condensation begins. The liquid film brings latent heat into the picture and heat transfer coefficient increases as a result. The superficial quality is used in order to better

characterize the fraction of vapor mass flow rate inside the tube. Film heat transfer coefficient is first modelled by connecting the heat transfer coefficient with the film thickness, flow regime, and single-phase heat transfer correlation. Then the film heat transfer coefficient is converted back to the bulk heat transfer coefficient so that the definition of the heat transfer coefficient is consistent for single-phase and two-phase regions. As for the pressure drop, after the onset of condensation, due to the presence of liquid film, waves form at the liquid-vapor interface. The interfacial film dissipates more energy and the pressure drop increases rather than decreases in the CSH region. However, as the flow velocity decreases as condensation proceeds, eventually the pressure drop decreases again. The pressure drop is modelled in a similar way as the heat transfer model. Wave-enhancement factor indicates the relationship between waves and instabilities, and provide the mathematical interpretation of the effects of waves on pressure drop. Both heat transfer and pressure drop models are compared to the experimental data and good agreements are achieved.

ACKNOWLEDGEMENTS

The authors thankfully acknowledge the support provided by the Air Conditioning and Refrigeration Center at the University of Illinois at Urbana-Champaign, and technical support from Creative Thermal Solutions, Inc. (CTS).

NOMENCLATURE [Ref, Nom, Ack Heading]

P	Pressure (Pa)	d	Tube inner diameter (m)
T	Temperature (K)	G	Mass flux (kg m^{-2} s^{-1})
Q	Heat flux (W m^{-2})	HTC	Heat transfer coefficient (W K^{-1} m^{-2})
δ	Film thickness (m)	ε	Void fraction
k	Conductivity (W K^{-1} m^{-1})	u	Velocity (m s^{-1})
x	Quality	ρ	Density (kg m^{-3})
σ	Surface tension (N m^{-1})	g	Gravitational acceleration (m s^{-2})
μ	Dynamic viscosity (kg m^{-1} s^{-1})	Θ	Angle (rad)
PD	Pressure drop (Pa m^{-1})		

REFERENCES

Agarwal, R., Hrnjak, P., 2015. Condensation in two phase and desuperheating zone for R1234ze(E), R134a and R32 in horizontal smooth tubes, Int. J. Refrigeration 50, 172-183.

Churchill, S.W., 1977. Friction-factor equation spans all fluid-flow regimes. Chem. Eng. 7, 91–92.

Friedel, L., 1979. Improved friction pressure drop correlation for horizontal and vertical two phase flow, 3R Int. 18(7), 485–491.

Fujii, T., Honda, H., Nozu, S., Nakarai, S., 1978. Condensation of superheated vapor inside horizontal tube, Heat Transfer- Japanese Research 4(3), 1-48.

Gnielinski, V., 2976. New equation of heat and mass transfer in turbulent pipe and channel flow, Int. Chem. Eng 16 359-367.

Kondou, C., Hrnjak, P., 2011a. Heat rejection from R744 flow under uniform temperature cooling in a horizontal smooth tube around the critical point, Int. J. Refrigeration 34(3), 719-731.

Kondou, C., Hrnjak, P., 2012. Condensation from superheated vapor flow of R744 and R410A at subcritical pressures in a horizontal smooth tube, Int. J. Heat Mass Transfer 55, 2779-2791.

Meyer, M., Hrnjak, P., 2017. Flow regimes during condensation in superheated zone, Int. J. Refrigeration 84, 336-343.

Minkowycz, W.J., Sparrow, E.M., 1969. The effect of superheating on condensation heat transfer in a forced convection boundary layer flow, Int. J. Heat Mass Transfer 12, 147–154.

Webb, R.L., 1998. Convective condensation of superheated vapor. Trans ASME J. Heat Transfer 120, 418-420.

Xiao, J., Hrnjak, P., 2016. Heat transfer and pressure drop of condensation from superheated vapor to subcooled liquid. Int. J. Heat Mass Transfer 103, 1327-1334.

Xiao, J., Hrnjak, P., 2017a. A new flow regime map and void fraction model based on the flow characterization of condensation, Int. J. Heat Mass Transfer 108, 443-452.

Xiao, J., Hrnjak, P., 2017b. A heat transfer model for condensation accounting for non-equilibrium effects, Int. J. Heat Mass Transfer 111, 201-210.

Xiao, J., Hrnjak, P., 2018a. Pressure drop of R134a, R32 and R1233zd(E) in diabatic conditions during condensation from superheated vapor, Int. J. Heat Mass Transfer 122, 442-450.

Xiao, J., Hrnjak, P., 2018b. A pressure drop model for condensation accounting for non-equilibrium effects, Int. J. Heat Mass Transfer 122, 442-450.

Xiao, J., Hrnjak, P., 2018c. Flow regimes during condensation from superheated vapor, Int. J. Heat Mass Transfer 132, 301-308.

Xiao, J., Hrnjak, P., 2018d. A flow regime map for condensation in macro and micro tubes with non-equilibrium effects taken into account, Int. J. Heat Mass Transfer 130, 893-900.

Manuscript ID: 818
DOI: 10.18462/iir.icr.2019.0818

Co-current upward vaporization of binary mixtures in finned compact heat exchangers with offset strip fins

Ines BEN EL MEKKI[(a, b)], Marine ANDRICH[(a)], Florine GIRAUD[(b)], Brice TREMEAC[(b)], Pascal TOBALY[(b)]

[(a)] Centre de recherche Paris-Saclay, Air Liquide, 1, chemin de la Porte des Loges – BP 126 – 78354 Jouy en Josas – France, ines.benelmekki@airliquide.com
[(b)] Laboratoire du Froid, des Systèmes Energétiques et Thermiques (LaFSET), Cnam, HESAM Université, 292 rue Saint-Martin 75003 Paris, France

ABSTRACT

Although flow boiling in small channels was intensively investigated, the influence of binary mixture composition on flow boiling in microscale has not been widely studied so far.
The aim of this study is to investigate heat transfer to binary mixtures in finned compact evaporators. Three coupled physical phenomena are examined: thermodynamic (mixture vaporization), hydrodynamic (two-phase upward flow) and interphase mass and heat transfer.
An experimental rig is being designed to study the upward vaporization of binary mixtures. The fluids tested are either HFC (mixture of R-134a and R-245fa) or hydrocarbons. The test section is an electrically-heated passage with serrated fins which allows flow regimes visualization.
In this paper, a review about flow boiling of mixtures will be presented as well as the description of the experimental apparatus and the goals behind this study.
Keywords: Flow boiling, Binary mixtures, Offset strip fins, Upward two-phase flow, Micro-channels

1. INTRODUCTION

Natural gas is having nowadays a bigger place in the energy mix. Due to political, technical and market flexibility purposes, it is increasingly liquefied for storage and shipping. Within this context, finned compact evaporators such as brazed Aluminum heat exchangers are intensively used in order to cool natural gas to -160°C using a refrigerant mixture. This mixture undergoes a vertical upward vaporization since the liquefied natural gas is easily recovered by gravity at the bottom of the heat exchanger and a counter-current heat exchange is always recommended in order to achieve high heat exchange efficiencies. Thus, the main goal of this paper is to investigate this upward vaporization of mixtures in confined geometries such as offset strip fins (rectangular finned channels with $D_h \sim 1.75\,mm$). The hydrodynamic two-phase flow, the vaporization of mixture and the interphase mass and heat transfer will be studied. The important results found in literature dealing with this subject will be shown as well as the experimental rig dedicated to this study.

2. UPWARD TWO-PHASE FLOW

2.1. Flow Regimes and Flow Maps

Although there is a big disparity between different authors to define flow regimes, they all agree that the interface between vapor and liquid phases adopt specific shapes depending on liquid and gas velocities. In co-current upward flow, the major flow patterns encountered in literature are presented in Fig. 1. We find mainly:

- Bubbly flow: a gas phase present as discrete bubbles within a volume mainly occupied by liquid.
- Slug flow: the bubbles coalesce and form vapor slugs, which have the cross-section limited by the channel geometry. A liquid continuum is trapped between these vapor slugs and contain smaller bubbles.
- Churn flow: the vapor slugs present some instabilities as the gas velocity increases. It results in a big oscillatory flow pattern characterized by a chaotic liquid-vapor interface.
- Annular flow: a vapor continuum is trapped between the liquid films present on the channel wall. It is the more stable flow regime.
- Mist flow: the liquid film on the channel is interrupted and the “dry-out” regime is observed. It is characterized by the presence of some liquid droplets in a volume mainly occupied by the gas phase.

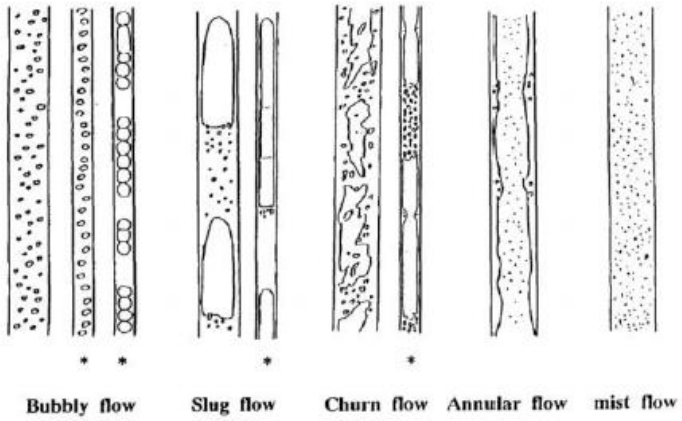

Figure 1: Different flow regimes in co-current upward two-phase flow (Mishima and Hibiki, 1996)

The identification of flow patterns during upward vaporization study is important as long as the investigation of heat transfer mechanisms require significant information about the flow configurations. Hence, a flow map of the studied two-phase system in the corresponding geometry has to be established to analyze properly in which conditions a flow regime can appear. Usually, flow maps are shown in liquid and gas superficial coordinates:

Gas superficial velocity: $$u_G = \frac{xG}{\rho_v}$$ Eq. (1)

Liquid superficial velocity: $$u_L = \frac{(1-x)G}{\rho_L}$$ Eq. (2)

It is requisite to point out that between these different flow regimes, there are transition zones, which depend on the fluid used and the geometry considered. In fact, flow patterns in narrow channels might be significantly different from those in large ones. From a hydraulic point of view, Wang (2014) explains this deviation with a possible change in the dominant forces such as surface tension (capillary forces) which become much stronger when reducing the channel size while gravitational forces are usually weakened. Therefore, a transition criterion is needed to mark the distinction between microscale and macroscale. However, several transition limits have been proposed in literature and no universal criterion has been established so far. Table 1 gives an overview about some transition limits, some of them are based on geometric considerations (e.g. hydraulic diameter) and others are based on the fluid used (e.g. confinement number) and flow characteristics (e.g. Reynolds number).

Table 1: Some definitions of transition criteria between micro and macroscale

Author	Transition criterion	Remarks
Kandlikar (2002)	Micro heat exchanger: D_h = 1 - 100 µm Meso heat exchanger: D_h = 100 µm - 1 mm Compact heat exchangers: D_h = 1 - 6 mm Conventional heat exchangers: D_h > 6 mm	Based only on hydraulic diameter
Suo and Griffith (1964)	$\lambda/D_h > 0.5$: Micro-channels	Based on fluid characteristics and hydraulic diameter
Zhang (2009)	$Co > 0.5$: Micro-channels	Based on fluid characteristics and hydraulic diameter
Li (2010)	$Bo\sqrt{Re} < 200$: Micro-channels	Takes into account all the present forces; viscous, gravitational, inertia and surface tension

Carey and Mandrusiak (1985) studied upward two-phase flow of water, methanol and n-butanol in vertical channels containing serrated fins. The hydraulic diameter of this specific geometry based on wetted perimeter is 5.15 mm. The mass flux was ranging from 3 to 100 $kg.m^{-2}.s^{-1}$ and vapor quality from 0.05 to 0.7. They postulated that a rapid transition from bubbly, slug and churn to annular flow was observed. A possible interpretation of this observation is that offset strip fins create sufficient pressure drop able to stabilize the flow. Thus, according to them, a more stable flow regime is rapidly set up when using serrated fins.

2.2. Pressure Drop

Generally, two-phase pressure gradient in flow boiling is composed mainly of three terms (Eq. (3)). The first one is due to the effect of gravity. The second one is related to inertia and acceleration of the two phases and the last one is the impact of friction between liquid and gas phases.

$$\left(\frac{dP}{dz}\right)_{Total} = \left(\frac{dP}{dz}\right)_{Acceleration} + \left(\frac{dP}{dz}\right)_{Gravitationnal} + \left(\frac{dP}{dz}\right)_{Frictional} \quad \text{Eq. (3)}$$

The gravitational and the acceleration terms are generally considered as negligible for vertical flow boiling. Moreover, when considering the separated model flow, the two-phase frictional pressure drop may be given by Eq. (4):

$$\left(\frac{dP}{dz}\right)_{Frictional} = (\Phi_V)^2 \left(\frac{dP}{dz}\right)_V = (\Phi_L)^2 \left(\frac{dP}{dz}\right)_L \quad \text{Eq. (4)}$$

Kim and Sohn (2006) focused on pressure drop in offset strip fins while investigating flow boiling of R-113. Their hydraulic diameter was around 2.84 mm. In order to predict pressure drop they used the correlation of Lockhart and Martinelli (1949) given by Eq. (5) and Eq. (6).

$$\Phi_L^2 = 1 + \frac{C}{\chi} + \frac{1}{\chi^2} \quad \text{Eq. (5)}$$

$$\chi^2 = \frac{\left(\frac{dP}{dz}\right)_L}{\left(\frac{dP}{dz}\right)_V} = \frac{f_L}{f_V}\frac{\rho_V}{\rho_L}\frac{(1-x)^2}{x^2} \quad \text{Eq. (6)}$$

The deviation between this correlation and experimental results was about 20%. However, the authors postulated that Martinelli parameter is not suitable to study pressure drop in serrated fins since the correlation of two-phase flow for serrated fins has to take into consideration both wall friction and fin form drag.

3. MASS AND HEAT TRANSFER

3.1. Definitions

While heating a subcooled liquid in vertical upward flow configuration, thermodynamic phase-change involves two main mechanisms of heat transfer from the wall to the fluid:

- Nucleate boiling (NB): which manifests itself by the formation of bubbles on a heated wall. Many authors agree that heat transfer mechanism is characterized by a big dependence on only heat flux input. Mass flux and vapor quality do not have a significant influence on heat transfer coefficient in this specific mode of heat transfer, which is present especially in bubbly, slug and churn flows.
- Convective evaporative boiling (CB): which corresponds to liquid vaporization at the vapor-liquid interface. This mode of heat transfer is characterized by a bid dependence upon mass flux and vapor quality. Heat flux has little impact on heat transfer coefficient in this configuration present mainly in annular flow.

3.2. Flow Boiling of Binary Mixtures

Jung and Radermacher (1992) studied the effect of composition and mixtures on flow boiling and heat transfer coefficient. They reported that nucleate boiling is suppressed for all mixtures used at vapor qualities greater than 20%. They concluded that convective boiling is thereby the main mode of heat transfer for all the mixtures investigated. Moreover, a very important result has been reported in their paper, which consists in the reduction of heat transfer of about 55% when using mixtures with large volatility difference comparing to the results obtained using pure fluids. They explained this observation with three main reasons: the presence of an additional mass transfer resistance, a possible degradation of fluid properties when using mixtures and finally the reduction of mass flow rates leading to the reduction of heat transfer coefficient. Fig. 2 shows the results of heat transfer coefficient found by these authors for different heat fluxes. The graph depicts two main distinct regions. The first one is called partial boiling regime characterized by a big dependence on heat fluxes at low vapor qualities (NB). For the second region observed for high vapor qualities, annular flow is being set up, the liquid film present on the wall becomes thinner as the vapor quality increases. Hence, the heat transfer resistance decreases and the superheat between the wall temperature and the saturation temperature is no longer able to sustain bubble formation on the wall. Therefore, the nucleate boiling region is suppressed and convective boiling is the major mode of heat transfer. The vapor quality at which this transition occurs is called “suppression of nucleate boiling” (XSNB).

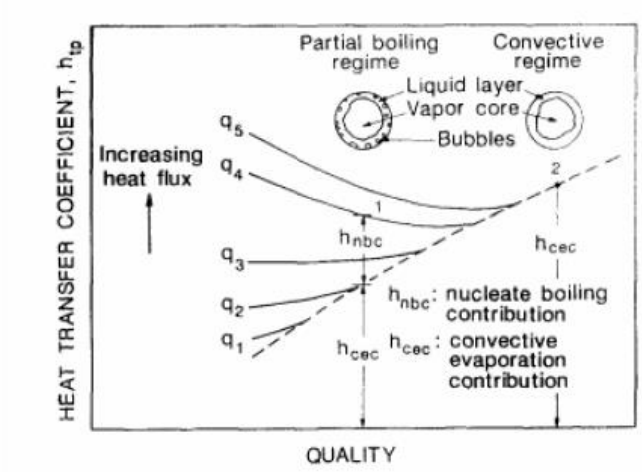

Figure 2: Heat transfer coefficient as a function of vapor quality for different heat fluxes, mixtures used (R-12/R-152a and R-22/R-114), D_h = 9.1 mm, q=10-45 $kW.m^{-2}$ (Jung and Radermacher, 1992)

Jung and Radermacher (1992) observed that XSNB is much lower for mixtures than for pure fluids in the same conditions. This might be explained by two main mechanisms proper to binary mixtures. The first possible explanation is related to the internal process of local bubble dynamics. If we consider, a single-component system, the only limitation for the bubble growth is the diffusion of the latent heat of vaporization through the liquid-vapor interface. However, for binary mixtures, another additional limitation appears. In fact, the volatility difference between the lightest and heaviest components leads to a stripping of the most volatile component from the liquid phase to the vapor core. A local concentration gradient is thereby established and the lightest component diffuse in the vapor core of the bubble. Eventually, this leads to an additional mass transfer resistance to heat transfer mechanism. The more the volatility difference between the two components is large, the more this additional limitation is apparent and the less XSNB would be.

The second explanation is that bubble growth mechanism is directly related to the wall superheat ($\mathbf{T_w} - \mathbf{T_{sat}}$). Fig. 3 gives the equilibrium diagram of the zeotropic mixture used by Jung and Radermacher (1992). Initially, $\mathbf{X_b}$ is the composition of the most volatile component. Thus, the superheat is equal to ($\mathbf{T_w} - \mathbf{T_b}$) (see Fig. 3). However, locally, at the interface of the bubble, and since the lightest component is diffusing into the vapor core, the liquid is depleted of the most volatile component. Therefore, locally, the bubble temperature of the liquid near the interface would increase from $\mathbf{T_b}$ to $\mathbf{T_i}$. Thus, the superheat is reduced to $\mathbf{\Delta T_{eff}}$ .Hence, this mechanism is responsible for slower growing bubbles. Consequently, nucleate boiling is rapidly suppressed when dealing with binary mixtures comparing to pure fluids.

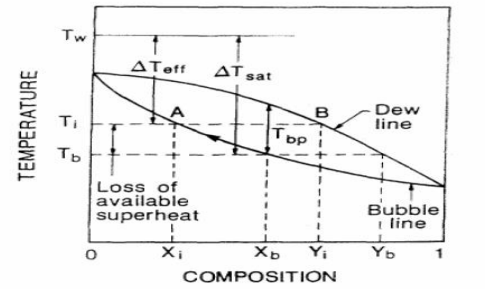

Figure 3: Two-phase equilibrium diagram for zeotropic mixtures, the mechanism of reducing superheat at liquid and vapor interface (Jung and Radermacher, 1992)

Abadi *et al*. (2015) investigated flow boiling of R-134a and R-245fa mixtures in a 3 mm-diameter tube. They concluded from the results shown in Fig. 4 that heat transfer coefficient of mixtures is under the straight ideal line connecting heat transfer coefficients of pure fluids. If A and B are the two components

of the binary mixture with $\bar{x}$ is the molar concentration of A, then the ideal heat transfer coefficient would be:

$$\frac{1}{h_{id}} = \frac{\bar{x}}{h_A} + \frac{1-\bar{x}}{h_B} \quad (7)$$

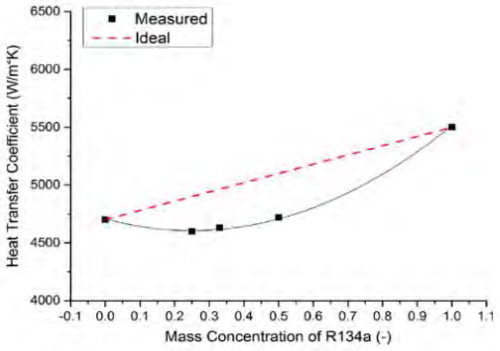

Figure 4: Heat transfer coefficient of mixtures and difference from ideal straight line. Results found for G=300 $kg.m^{-2}.s^{-1}$, x=0.48 - 0.51 (Abadi *et al.*, 2015)

This reduction in heat transfer coefficient is due to interphase mass transfer.

4. EXPERIMENTAL APPARATUS

In order to investigate upward vaporization of mixtures, an experimental bench presented in Fig. 5 is being designed. The test section is an electrically heated vertical single fin passage covered with a transparent plate allowing the visualization of two-phase flow and bubbles shape. The fins used within this passage are serrated ($D_h \sim 1.75\ mm$). The opposite side of the passage will be electrically heated. The fluids tested are hydrocarbons (mixtures of n-butane/n-hexane; isobutane/n-hexane) and hydrofluorocarbons (mixtures of R-134a and R-245fa) which are zeotropic mixtures. The measurement rig contains a circulation pump. A pre-heater is used in order to reach the bubble point temperature at the vaporizer inlet. The fluid leaves the test section in a superheated state. Then it enters a condenser designed in order to subcool the fluid before entering the liquid buffer capacity. The operating pressure in the test section is ranging from 2 to 5 bar absolute and the mass flux used is around 40 $kg.m^{-2}.s^{-1}$.

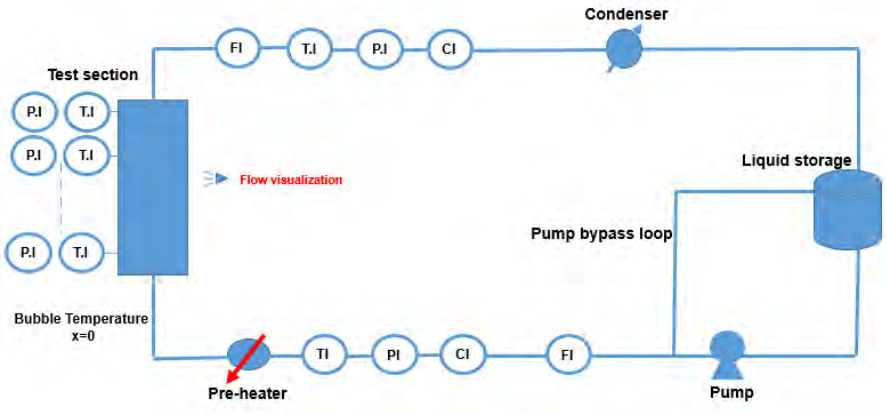

Figure 5: Schematic view of the experimental loop

A section across the thickness of the vaporizer (the test section) is presented in Fig. 6. Heating resistances are inserted into thick aluminum blocks able to homogenize the heat input at the wall channel. A Nitrogen “layer” is pressurized at 6 bar absolute (above the operating pressure in the finned

passage). It avoids a possible bypass between the glass plate and the serrated fins. Along with the polycarbonate plates, this layer reduces the heat losses. The glass and the polycarbonate plates allow the visualization of the upward two-phase flow and the bubble formation. The overall test section, while using hydrocarbons is contained in a Nitrogen airtight box to avoid explosive atmosphere.

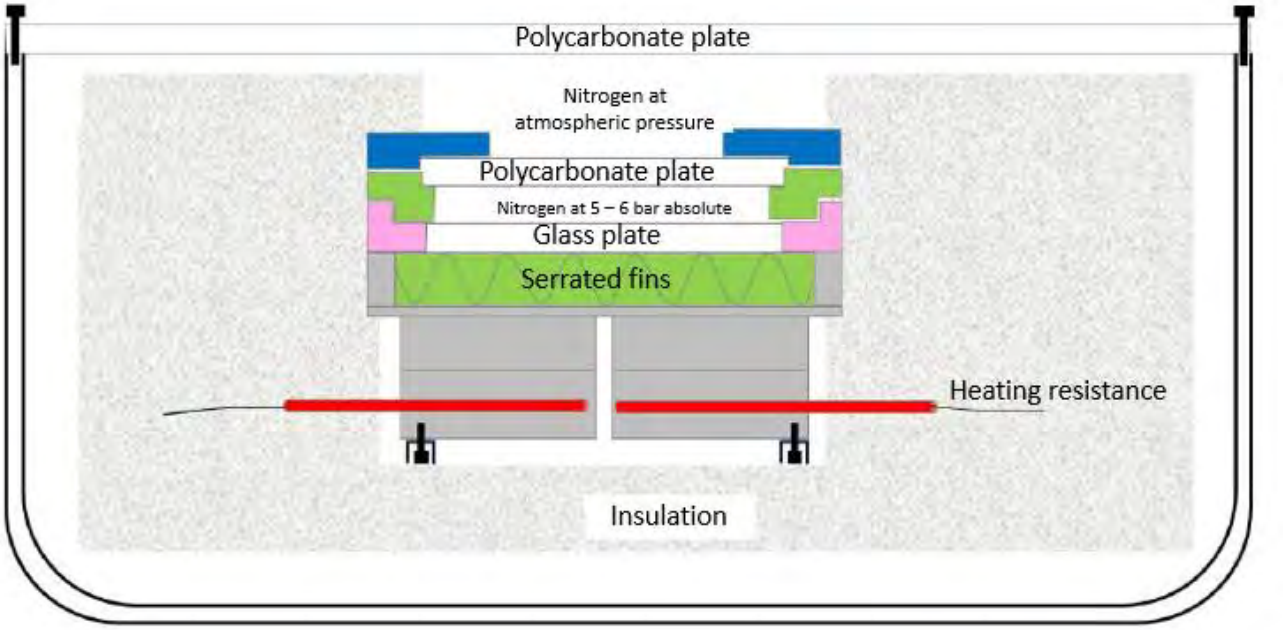

Figure 6: Schematic view of the test section

Throughout the exploitation of this experimental bench, series of measurements of the heat transfer coefficient and the pressure drop will be carried out by varying the operating parameters (temperature, pressure, flowrates, heat input, and composition of the binary mixtures). On this purpose, temperatures and pressure indicators are inserted into the test section. Moreover, thanks to flow visualization, flow patterns will be set up along with the study of hydrodynamic instabilities. Finally, the impact of binary mixtures and mass transfer on heat transfer efficiency will be investigated.

5. CONCLUSIONS

In this present paper, a state-of art has been presented regarding flow boiling of binary mixtures in compact and confined finned evaporators. As a conclusion, the use of binary mixtures may reduce the heat transfer coefficient comparing to the values obtained with pure fluids. However, mixed refrigerants are used in LNG liquefaction processes in order to limit the entropy generation and improve the performance of evaporators.
In order to study the three coupled physical phenomena governing the internal process of flow boiling in microscale, an experimental bench is being designed. The design of this measurement rig is ongoing; the first results will be obtained by June 2019.

NOMENCLATURE

$\bar{x}$	Molar concentration of the component A ($mol.mol^{-1}$)	Re	Reynolds number = $\frac{GD_h}{\mu_L}$
D_h	Hydraulic diameter (m)	q	Heat flux ($kW.m^{-2}$)
u_G, u_L	Superficial velocity of vapor or liquid phases ($m.s^{-1}$)	T_w	Wall temperature (K)
ρ_V, ρ_L	Density of the vapor or liquid phases ($kg.m^{-3}$)	h_A, h_B	Heat transfer coefficient of the component A or B $(W.m^{-2}.K^{-1})$
Co	Confinement Number = $\frac{1}{D_h}\sqrt{\frac{\sigma_L}{(\rho_L-\rho_V)g}}$	λ	Laplace constant = $\sqrt{\frac{\sigma_L}{(\rho_L-\rho_V)g}}$
dP/dz	Pressure gradient ($Pa.m^{-1}$)	T_{sat}	saturation temperature (K)
G	Mass flux $(kg.m^{-2}.s^{-1})$	Bo	Bond number = $\frac{(\rho_L-\rho_V)gD_h{}^2}{\sigma}$
x	Vapor quality	f_v, f_L	Friction factors for vapor or liquid phases
α	Void fraction	ΔT	Superheat (K)
σ	Surface tension ($N.m^{-1}$)	Φ_V, Φ_L	Liquid or vapor two-phase multipliers
χ	Martinelli Parameter	μ_L	Liquid viscosity (Pa.s)
g	Gravitational constant ($m.s^{-2}$)	h_{id}	Ideal heat transfer coefficient $(W.m^{-2}.K^{-1})$
PI	Pressure indicator	FI	Flow indicator
TI	Temperature indicator	CI	Binary composition indicator

REFERENCES

Abadi, G.B., Yun, E., Kim, K.C., 2015. Flow boiling characteristics of R134a and R245fa mixtures in a vertical circular tube. Exp. Therm. Fluid. Sci. (72), 112-124

Carey, V.P., Mandrusiak, G.D., 1985. Annular film-flow boiling of liquids in a partially heated vertical channel with offset strip fins. Int. j. of Heat and Mass Transfer (29), 927-939

Jung, D.S., Radermacher, R., 1992. Prediction of evaporation heat transfer coefficient and pressure drop of refrigerant mixtures. Int. J. Refrig. 1993. 16 (5), 330-338

Kandlikar, S.G., 2002. Fundamental issues related to flow boiling in mini-channels and micro-channels. Exp. Therm. Fluid Sci. (26), 38-47

Kim, B., Sohn, B., 2006. An experimental study of flow boiling in a rectangular channel with offset strip fins. Int. J. of Heat and Fluid flow (27), 514-521

Li, W., Wu, Z., 2010. A general criterion for evaporative heat transfer in micro/mini-channels. Int. J. of Heat and Mass Transfer (53), 1967-1976

Lockhart, R.W., Martinelli, R.C., 1949. Proposed correlation of data for isothermal two-phase two-component flow in pipes. Chemical Engineering Progress (45), 39-48

Mishima, K., Hibiki, T., 1996. Some characteristics of air-water two-phase flow in small diameter vertical tubes. Int. J. of Multiphase Flow (22), 703-712

Suo, M., Griffith, P., 1964. Two-phase flow in capillary tubes. J. Basic Eng. (86), 576-582

Wang, Y., Wang, Z.G., 2014. An overview of liquid-vapor phase change, flow and heat transfer in mini and micro-channels. Int. J. of Thermal Sciences (86), 227-245

Zhang, P., Fu, X., 2009. Two-phase flow characteristics of liquid Nitrogen in vertically upward 0.5 and 1.0 mm micro-channels. Int. J. of Multiphase flow (36), 60-70

Manuscript ID: 821
DOI: 10.18462/iir.icr.2019.0821

Effect of lubricating oil on flow boiling heat transfer of low-GWP refrigerants in extruded multi-port tubes

Eiji HIHARA[(a)], Shizuo SAITOH[(a)], Chaobin DANG[(a)]

[(a)]The University of Tokyo
5-1-5 Kashiwanoha, Kashiwa, 277-0882, Japan, hihara@edu.k.u-tokyo.ac.jp

ABSTRACT

The effects of lubricating oil on flow boiling of low Global Warming Potential refrigerants (R-290, R-1234yf, and R-32) in extruded multiport tubes with 18 mini-channels with a square cross-section (0.9 × 0.9 mm) were experimentally investigated. In the experiments, local heat transfer coefficients, flow visualization, and pressure drops were measured, and the effect of lubricating oil was investigated. The experiments were conducted at oil circulation rates of 0–5.4 wt%, inlet quality of 0–0.25, mass flux of 25–200 $kg \cdot m^{-2} \cdot s^{-1}$, heat flux of 2.1–8.1 $kW \cdot m^{-2}$, and evaporation temperature of 15 °C. Polyolester oil was used. The addition of a small amount of oil increased the heat transfer coefficient, but as the amount of oil increased, the heat transfer coefficient decreased. The pressure drop increased proportionally with the oil circulation rate; the pressure drops of R290, R-1234yf, and R32 were also compared.
Keywords: Lubricating Oil, Flow Boiling Heat transfer, Extruded Multi-Port Tubes.

1. INTRODUCTION

High efficiency and compact heat exchangers are attracting increased attention, and research and development are being conducted for energy efficient refrigeration and air conditioning equipment. In general, it is possible to increase the heat transfer area per unit mass flow rate of fluid as the tube diameter is decreased, and thus enhancing heat transfer inside the pipe. Therefore, to circulate the refrigerant at the flow rate required for heat exchange while suppressing the rise in the pressure loss, a multiport tube-type heat exchange is used.

Recently, many studies on boiling heat transfer in a pipe using low Global Warming Potential (GWP) refrigerants have been reported to reduce the environment impact of high-efficiency heat exchangers. Zhu et al. (2017) examined the heat transfer coefficient and pressure drop of R32 flow boiling in horizontal tubes with inner diameters of 1 mm and 2 mm, and showed that the heat transfer coefficient increased with decreasing tube size and increasing saturation temperature, mass flux, or heat flux. Many studies have been conducted on the influence of lubricating oil on flow boiling heat transfer and pressure drop. Filho et al. (2009) reviewed the flow boiling characteristics of refrigerant/oil mixtures based on a large amount of open literature, and reported that according to the results of numerous studies, increasing oil concentration increased pressure drop but had no effect on heat transfer coefficient. Although there are only few studies on the influence of oil on flow boiling heat transfer inside a small tube with a hydraulic inner diameter of 1 mm or less, Saitoh et al. (2018) experimentally investigated the effect of oil on flow boiling of propane/oil mixture in mini-channel multiport tubes with 18 paths of square cross-section (0.9 mm × 0.9 mm). They reported that when the heat flux was low, the heat transfer coefficient tended to decrease almost uniformly as oil concentration increased; however, when the heat flux was high, the heat transfer coefficient increased with the addition of oil.

The purpose of this study is to investigate the effect of lubricating oil on the characteristics of flow boiling heat transfer of low GWP refrigerants (R32, R1234yf, and R290) in mini-channel multiport

tubes. The pressure drop was also investigated.

2. EXPERIMENTAL APPARATUS AND PROCEDURE

Fig. 1 shows a schematic diagram of the experimental setup that consists of a “test loop” and an “oil loop.” The “test loop” consists of a gear pump, Coriolis-type flow meter, equipment for quality adjustment (subcooler and preheater), mixer, test section, and condenser; this is the main circulation flow path of the refrigerant. The refrigerant flow rate is controlled by the frequency of the gear pump; the evaporating temperature of the evaporator was adjusted by changing the temperature of the condenser; and the inlet vapor quality of the evaporator was controlled by quality control equipment. The “oil loop” consists of a plunger pump, oil flow meter, part of the test loop, and oil separator (oil separation efficiency 99.9%). The oil flow rate was adjusted by changing the pump frequency. Figure 2 shows a flow rectifying device, which suppresses intermittent flow and enables equal flow distribution to multiport tubes. Figure 3 shows two types of test parts: (a) extruded multiport aluminum tubes for the heat transfer experiment, and (b) multiport channels for visualization. The visualization multichannels are equipped with a transparent glass plate on one side of the flow channels. Heating of multiport tubes in (a) was done by Joule heating using DC power supply, while heating in (b) was done by a rubber heater attached to the opposite surface of copper multiport channels. The multiport channels (a) and (b) with the same square cross-section (0.9 mm × 0.9 mm) have 18 and 16 paths, respectively. The outer wall temperature of the multiport tubes was measured by thermocouples (0.1 mm OD, T-type), and the measuring points were the intersections of the a, b, c lines, and the i lines (i = 1 to 10) in Fig. 3(a). Refrigerant temperature and pressure at the inlet of the multiport tubes were measured with a sheath thermocouple (1.6 mm OD, T-type) and pressure transmitter (PAA-35X, accuracy 0.05% FS, manufactured by KELLER), respectively. All thermocouples were calibrated and had an accuracy of 0.1 °C. Tables 1 and 2 list the properties of the refrigerant and oil, and the experimental conditions, respectively. Heat transfer and visualization experiments were carried out under a step-wise rise with oil circulation rate of 0–5 wt%. Experimental data was recorded on a personal computer for various refrigerant temperature, pressure, flow rates (oil and refrigerant) and stable flow conditions. Flow patterns were observed using a high-speed video camera. Flow is vertical upflow.

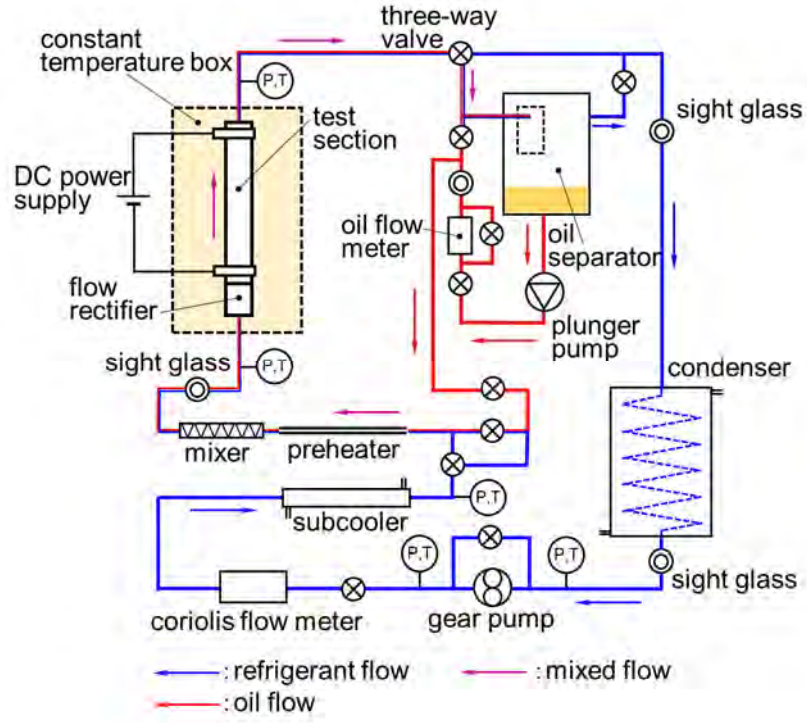

Figure 1: Schematic diagram of experimental apparatus

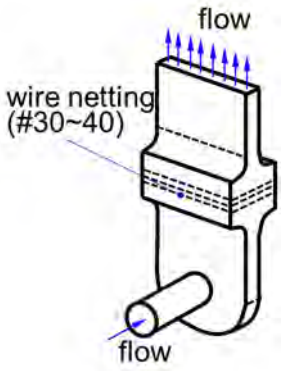

Figure 2: Flow-rectifying device

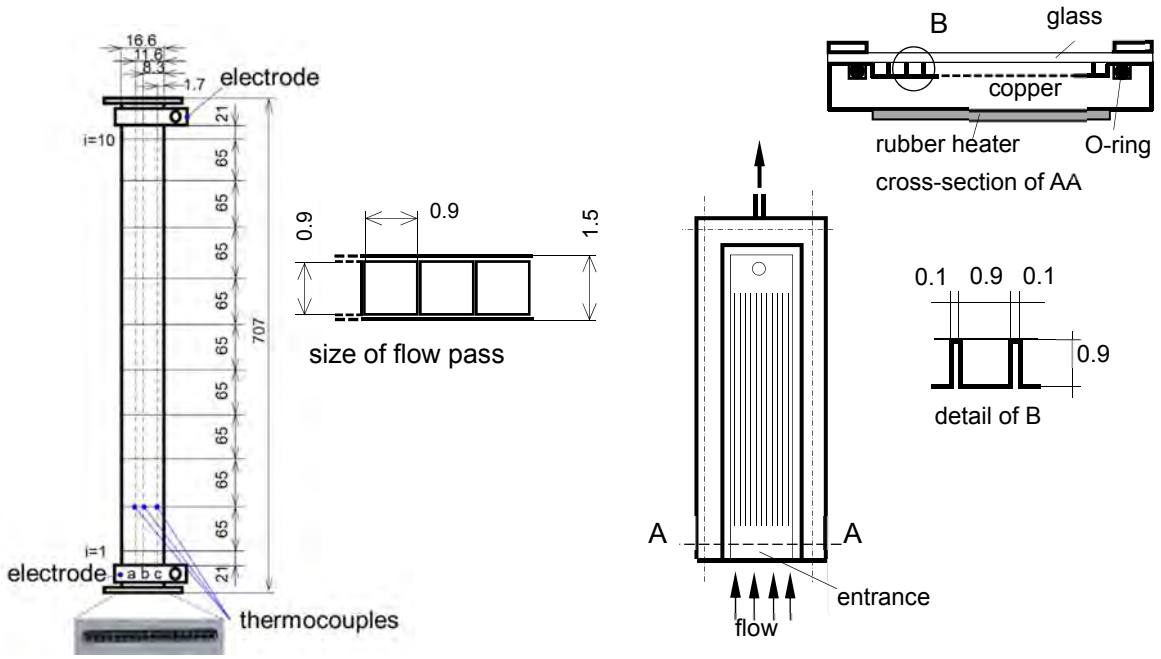

(a) Extruded multiport aluminum tubes **(b) Multiport channels for visualization**

Figure 3: Evaporators for test section

Table 1. Properties of refrigerants and oil

Substance	R32	R290	R1234yf	POE(VG68)
Purity (%)	99.9	>99.5	99.5	
Density (liq. at 15 °C) (kg m^{-3})	1000.9	507.5	1127.2	960
Viscosity (liq. at 15 °C) (μPa s)	127.3	107.7	173.8	
Surface tension at 15 °C (mN m^{-1})	8.42	8.24	7.44	
Heat of evaporation at 15 °C (kJ kg^{-1})	290	352	153	
Thermal conductivity (liq. at 15 °C) (W m^{-1} K^{-1})	0.133	0.098	0.067	0.135

Table 2. Experimental conditions

Experiment	Heat transfer	Visualization
Test section	Aluminum multi-port extruded tube (18 paths, 0.9 mm × 9.0 mm cross section, *L*=627 mm heated section)	Copper multi-port channel (16 paths, 0.9 mm × 9.0 mm cross section, *L*=355 mm heated section)
Inlet temperature (°C)	15	15
Inlet quality (-)	0.01−0.25	0−0.1
Outlet quality (-)	0.88−1.11	0.78−0.87
Heat flux (kW m^{-2})	2.1−8.1	7.1−14.4
Mass flux (kg m^{-2} s^{-2})	25−200	25−131
Oil (base oil)	POE (VG68)	POE (VG68)
Oil circulation rate, C_O (wt%)	0−5.4	0−5.2

3. RESULTS AND DISCUSSION

The local heat transfer coefficient (*h*) was calculated by

$$h = \frac{q}{(T_w - T_{bub})} \qquad \text{Eq. (1)}$$

where *q*, T_w, and T_{bub} are the heat flux, temperature at the inner wall, and boiling point of the

refrigerant/oil mixture, respectively. We assumed that $T_{bub} = T_{sat}$, where T_{sat} is the saturation temperature of the refrigerant corresponding to the local pressure interpolated from pressures at the inlet and outlet of the tube. The difference in surface temperature between the inner and outer walls was negligible. Assuming that the outer wall temperature distribution is symmetrical with respect to the center line b, the wall temperature at the i-th point $T_{w,i}$ was obtained from the following equation:

$$T_{W,i} = \frac{1}{5}\left(2T_{a,i} + T_{b,i} + 2T_{c,i}\right) \quad \text{Eq. (2)}$$

where $T_{a,i}$, $T_{b,i}$, and $T_{c,i}$ are the temperatures of the outer wall. The oil circulation rate (C_o) is defined by

$$C_o = 100\frac{m_o}{m_r + m_o} \quad \text{Eq. (3)}$$

where m_o and m_r are the mass flow rate of oil and refrigerant, respectively. Vapor quality (x) was calculated as:

$$x = \frac{m_{r,v}}{m_r} \quad \text{Eq. (4)}$$

where $m_{r,v}$ is the mass flow rate of refrigerant vapor. The mass flux of the refrigerant is denoted as G.

3.1. Characteristic Aspects

As the pipe diameter decreases, the influence of surface tension increases, and the liquid becomes uneven in the rectangular channel. In the cross-section of the channel, the amount of liquid is large at the corner and small at the flat portion. Boiling occurs at the corner of the channel while liquid film evaporation occurs at the flat part. The liquid film heat transfer remains good as the liquid film becomes thinner, but when the liquid film disappears (called a dry patch), the heat transfer deteriorates. Fig. 4 shows the boiling bubbles at the corner, the liquid film, and dry patch at the flat portion. Since dry patches are more likely to occur as the heat flux increases, we considered that when the heat flux is low, liquid film rupture hardly occurs and heat transfer remains high. Figure 5 shows the heat transfer coefficient (h) without oil; and for a wide range of vapor quality (x), the lower the heat flux, the higher the heat transfer coefficient and the h, which supports the above. Since it is known that the effect of mass flux (G) on the h is small from the experiment, the tendency of the h in Fig. 5 shows the effect of heat flux.

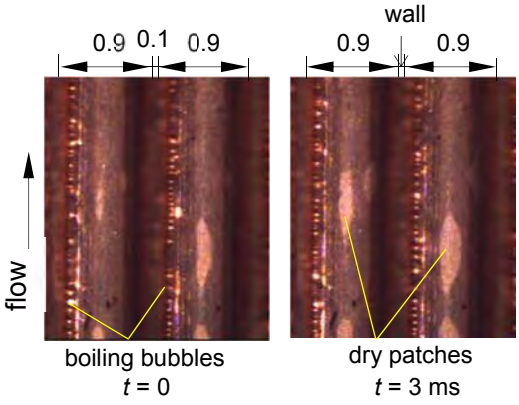

Figure 4: Dry patch

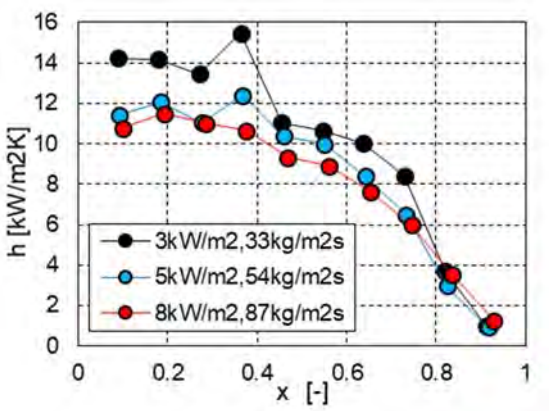

Figure 5: Heat transfer coefficient for R32 with C_0 = 0 wt%

3.2. Effect of Oil on Flow Pattern

It is known that foaming occurs when oil is mixed with refrigerant. In this experiment, the causes of foaming are boiling and vapor-liquid mixing. Figs. 6(a) and (b) for x = 0.2 and x = 0.8, respectively, show the flow patterns due to the differences in heat flux (q) and in oil circulation rate (C_0). The main flow regimes were slag flow (Fig. 6(a)-1) and annular flow (Fig. 6(b)-1). When heated, bubbles appeared in the liquid slag (Fig.6 (a)-2), and small bubbles were observed in the liquid slag

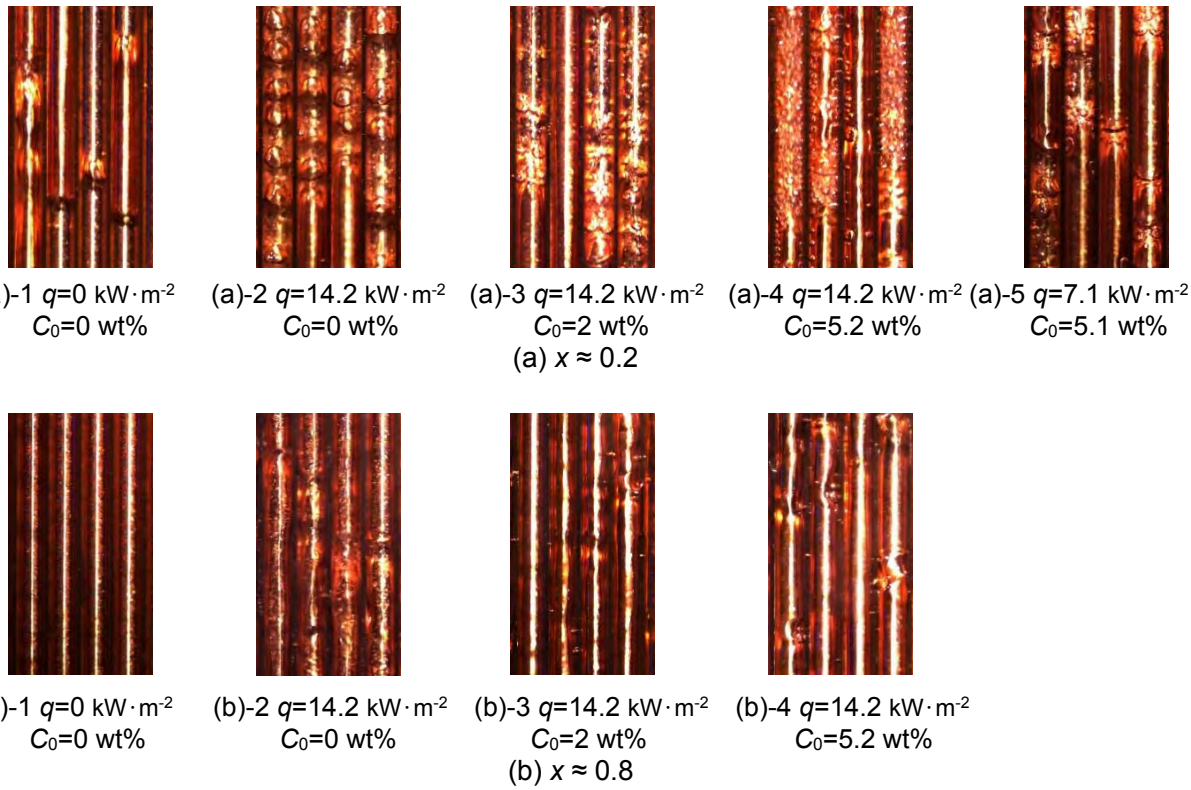

Figure 6: Flow patterns

when oil was added (Fig. 6(a)-3). Increasing C_0 increased small bubbles (foaming, Fig. 6(a)-4), and decreasing q decreased bubbles (comparison between Fig. 6(a)-4 and 5). Therefore, foaming is greatly affected by the q. On the other hand, the flow pattern of x = 0.8 is an annular flow and foaming was not observed. Foaming occurs in the area where nucleate boiling dominates (low vapor quality area), and disappears in the high-quality area. The addition of oil tended to delay the transition from slug flow to annular flow.

3.3. Effect of Oil on Heat Transfer Coefficient

The lubricating oil and refrigerant R32 are partially immiscible in the liquid (see Fig. A. 1), but the refrigerants R1234yf and R290 are miscible. Fig. 7 shows the influence of the oil on heat transfer coefficient (h) for R32. When the heat flux (q) is low (Fig. 7(a)), the h with small amount of oil (C_0 = 0.3 wt%) is larger than the h without oil; when C_0 = 1.1 wt% or more, the h decreases monotonically as oil increases. When the q is increased, the h is higher than the h without oil until C_0 = 1 wt% (Fig. 7(b)). These tendencies are the same in the heat transfer experiments for R1234yf and R290. The addition of oil increases the viscosity and surface tension of the mixture. Moderate increase in viscosity and surface tension due to small amount of oil and foaming suppressed the occurrence of dry patches. Moreover, the thermal conductivity of the oil is higher than that of the refrigerants. It is thought that these improved the h. When the q is large, many dry patches occurred; in order to suppress these, more oil is required. As the oil increases further, the viscosity of the refrigerant/oil mixture increases, the increase in mass diffusion resistance in liquid suppresses the evaporation of liquid film, and the h decreases. When the vapor quality is 0.8 or less, the h obtained from Eq. (1) using the boiling point of the refrigerant/oil mixture shows that the h values of R32 and R1234yf increased by up to 8% while that of R290 increased by 86%. The increase in R290 is large because the boiling point increase was greater than the others.

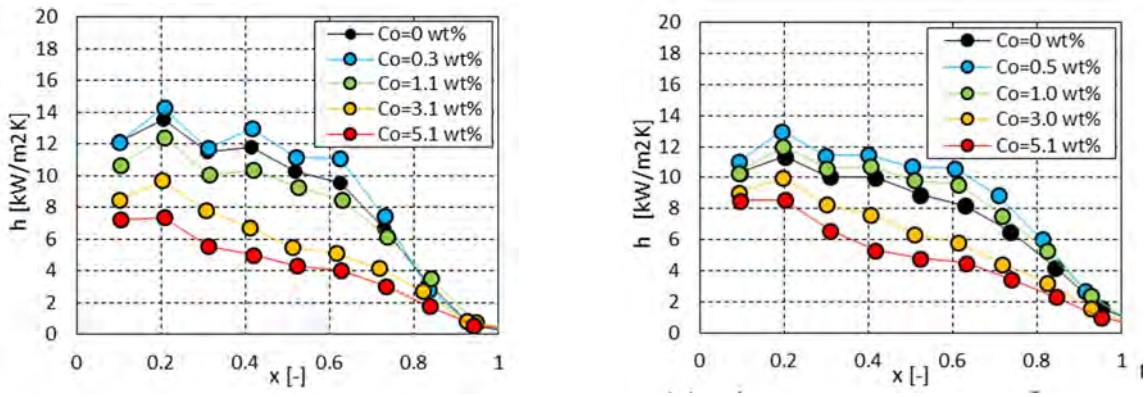

Figure 7: Effect of oil on heat transfer coefficient for R32

3.4. Pressure Drop

Fig. 8 shows the ratio of the pressure drop (ΔP) to the pressure drop ($\Delta P_{Co=0}$) without oil with respect to the oil circulation rate (C_0). ΔP is the pressure difference between the inlet and outlet of the multiport tube; the inlet and outlet vapor quality are x_{in} = 0–0.16, x_{out} = 0.95–1, respectively. ΔP linearly increases with respect to C_0, and the rates of increase of R32, R1234yf, and R290 are 0.2, 0.24, and 0.1 [wt%$^{-1}$], respectively. ΔP is greatly influenced by the density and viscosity of the refrigerant; the ΔP of R1234yf with large density and viscosity is large, whereas ΔP of R290 with small density and viscosity is small. When C_0 is 5 wt%, the pressure drops of R290, R32, and R1234yf are 1.5, 2, and 2.2 times, respectively, compared with that without oil.

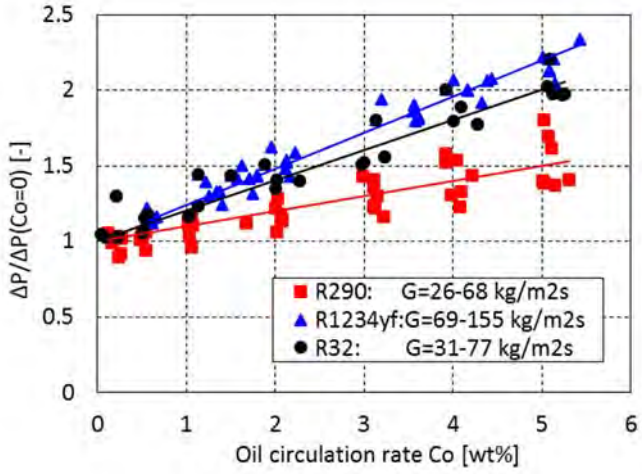

Figure 8: Pressure drop

4. CONCLUSIONS

Flow boiling heat transfer and visualization of low GWP refrigerant/oil mixtures were investigated experimentally in multiport tubes. The results are summarized as follows.

(1) In mini-channel tubes with square cross-section, the heat transfer coefficient increases at low heat flux because a thin liquid film formed on the flat part owing to the influence of surface tension. The effect of evaporative heat transfer from the thin liquid film is significant.

(2) When oil was added, foaming occurred. Foaming is greatly influenced by oil concentration and heat flux, and it is strong in the low vapor quality range where nucleate boiling dominates. The addition of oil delayed the transition from slug flow to annular flow.

(3) The addition of a small amount of oil prevented the occurrence of dry patches and increased the heat transfer coefficient; however, with increasing amount of oil, the heat transfer coefficient decreased owing to an increase in the mass diffusion resistance of liquid.

(4) The pressure loss increased proportionally with the oil circulation rate. When C_0 is 5 wt%, the pressure drops of R290, R32, and R1234yf are 1.5, 2, and 2.2 times, respectively, compared with that without oil.

REFERENCES

Zhu, Y., Wu, X., Zhao, R., 2017, R32 flow boiling in horizontal mini channels: Part II Flow-pattern based prediction methods for heat transfer and pressure drop, Int. J. Heat Mass Transf. 115(A), 1233-1244.

Filho, B., E.P., Cheng, L., Thome, J.R., 2009. Flow boiling characteristics and flow pattern visualization of refrigerant/lubricant oil mixtures. Int. J. Refrig. 32, 185–202.

Saitoh. S., Dang, C., Hihara, E., 2018, Effect of lubricating oil on flow boiling heat transfer of propane in extruded multiport tubes, DOI:10.18462/iir.gl.2018.1182.
Thome J. R.: Wolverine Engineering Data Book III (2006)

Appendix: Boiling point of R32 / oil mixture

The boiling point of R32/oil mixture was measured and the data was organized as

$$\ln(P_{sat}) = \frac{A}{T_{bub}} + B \qquad \text{Eq. (A-1)}$$

where P_{sat} is the saturation pressure. A and B are defined by the following equations:

$$A = a_0 + a_1 c + a_2 c^3 + a_3 c^5 + a_4 c^7$$
$$B = b_0 + b_1 c + b_2 c^3 + b_3 c^5 + b_4 c^7 \qquad \text{Eq. (A-2)}$$

where c and $a_{0\sim4}$, $b_{0\sim4}$ are the mass fraction of oil and coefficients, respectively. The coefficient values were determined from Thome's method and experimental data. The following equation shows the relationship between vapor quality (x) and oil mass fraction (c).

$$c = \frac{C_0}{(1-x)(100-C_0)+C_0} \qquad \text{Eq. (A-3)}$$

Figure A-1 shows the measured values of vapor pressure against the mass fraction of R32 in the R32/oil (POE (VG68)) mixture. The white symbols indicate that phase separation occurred in the mixed solution, and the others are in miscible state. Table A-1 shows the coefficients obtained by fitting the experimental values using Eq. (A-1). Figure A-2 shows the relationship between the oil concentration c and the rise in the boiling point ($\Delta T = T_{bub} - T_{sat}$) of the R32/oil mixture using Eq. (A-1) and (A-3). When the vapor quality is x = 0.5 with oil circulation rate of 5 wt%, the oil mass fraction c is 0.095, and the ΔT becomes 0.01 K for R32 (red arrow in Fig. A-2).

Table A-1. Coefficients of Eq. (A-2)

a_0	-2380	b_0	8.508
a_1	212.1	b_1	-0.736
a_2	-801.6	b_2	2.356
a_3	4523	b_3	-13.76
a_4	-5995	b_4	17.6

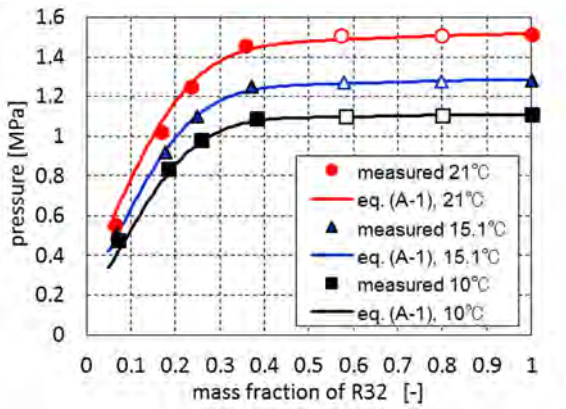

Figure A-1: Relationship between vapor pressure and mass fraction of R32

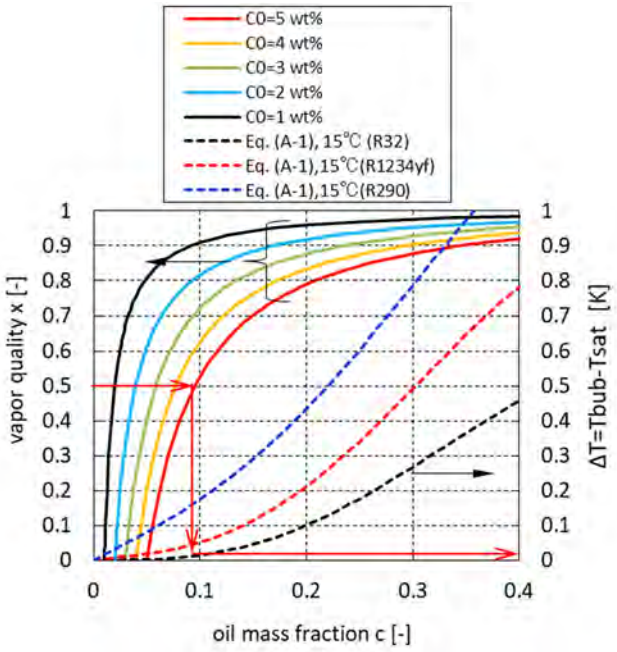

Figure A-2: Relationship between c and $\Delta T = (T_{bub}-T_{sat})$

Manuscript ID: 822
DOI: 10.18462/iir.icr.2019.0822

Disproportionation Reaction of HFO-1123 Refrigerant

Makoto Ito, Zhihua Zhang, Chaobin Dang, Eiji Hihara
Dept. of Human & Engineered Environmental Studies, University of Tokyo
Kashiwa, 277-0882, Japan, hihara@edu.k.u-tokyo.ac.jp

ABSTRACT

Hydrofluoroolefin (HFO) -1123 has very low GWP and ODP and is proposed as a next-generation refrigerant in the fields of refrigeration and air conditioning. However, HFO-1123 may cause a disproportionation reaction under high temperature and pressure conditions. Therefore, in order to develop the practical applications of HFO-1123, it is necessary to first develop a technology that suppresses the disproportionation reaction. In this study, we investigated the boundary between various pressure and temperature conditions at which the disproportionation reaction propagates. Disproportionation experiments were carried out under various temperature and pressure conditions using a metallic pressure vessel having a capacity of 0.65 L, and changes in pressure, temperature, and input energy were recorded. The disproportionation reaction was photographed with a high-speed camera, and the maximum temperature was determined by analyzing the video by the two-color temperature radiometry method (H & B method). Immediately after the disproportionation reaction, qualitative analysis was performed by GC-MS (Gas chromatography–mass spectrometry) and the composition of the sampling gas was examined.
Keywords: Refrigeration, HFO-1123, GC-MS, Disproportionation reaction.

1. INTRUDUCTION

In the field of refrigeration and air conditioning, the development of next generation refrigerants has been studied in order to prevent depletion of the stratospheric ozone layer due to the use of chlorofluorocarbons and hydrochlorofluorocarbons as refrigerants. HFC (Hydrofluorocarbon) refrigerants have a low ozone depletion potential (ODP), but a high global warming potential (GWP) which is a serious problem. Since the Kigali amendment to the Montreal Protocol was approved, United Nations member countries are requesting to switch to low GWP refrigerants such as hydrofluoroolefins (HFO) and natural refrigerants.
Substances with a low GWP have a short lifetime in the atmosphere and are easily decomposed. This means that they are highly reactive in the atmosphere. Therefore, in many cases, the compounds expected to appear as new low-GWP refrigerants have the disadvantage of having a higher reactivity than conventional refrigerants. In addition, these compounds are highly flammable and may undergo disproportionation reactions. Instability of refrigerants is a problem in converting to low-GWP substances. Therefore, we need to evaluate these risks.
HFO-1123 (CF_2=CHF) is a hydrofluoroolefin (HFO) and has no risk of ozone layer destruction. Since this HFO contains a carbon-carbon double bond, it has low chemical stability and a short atmospheric lifetime. Therefore, HFO-1123 has a much smaller GWP than the HFC refrigerants HFC-410A and HFC-32 currently used for domestic air conditioners. As shown in Table 1, HFO-1123 has very low GWP and ODP, and should be appropriate as a next-generation refrigerant in the field of refrigeration and air conditioning.

Table 1. Properties of typical refrigerants

	HFC-410A	HFC-32	HFO-1123
ODP	0	0	0.0
GWP	2090	675	0.3

However, HFO-1123 may undergo a disproportionation reaction as shown in Eq. (1) under high temperature and high pressure conditions even without the presence of an oxidizing agent such as oxygen (Lisochkin and Poznyak, 2006). This is a disproportionation reaction accompanied by a marked rise in pressure and temperature. Thus it poses a danger that cannot be ignored considering its practical use as a refrigerant for air conditioners.

$$CF_2{=}CHF \rightarrow \frac{1}{2}CF_4 + \frac{3}{2}C + HF + 250\,kJ \qquad \text{Eq. (1)}$$

Therefore, in order to put HFO-1123 into practical use, it is necessary first to develop a technology to suppress the disproportionation reaction. The disproportionation of HFO-1123 is influenced not only by its activation energy but also by its temperature and pressure. In this study, we investigated the boundary between various pressure and temperature conditions at which the disproportionation reaction occurs.

According to previous studies, it was found that the disproportionation of HFO-1123 was suppressed by mixing R32 refrigerant with HFO-1123 (Otsuka et al., 2018). In this research, we aimed to evaluate HFO-1123 as a refrigerant in air-conditioning equipment, and we studied its disproportionation reaction which presents an obstacle for this purpose. Experiments were conducted, using a metal pressure vessel, to study the effect of admixing substances to HFO-1123 on suppressing the disproportionation reaction.

2. EXPERIMENTAL METHOD

2.1. Schematic Diagram of the Experiment

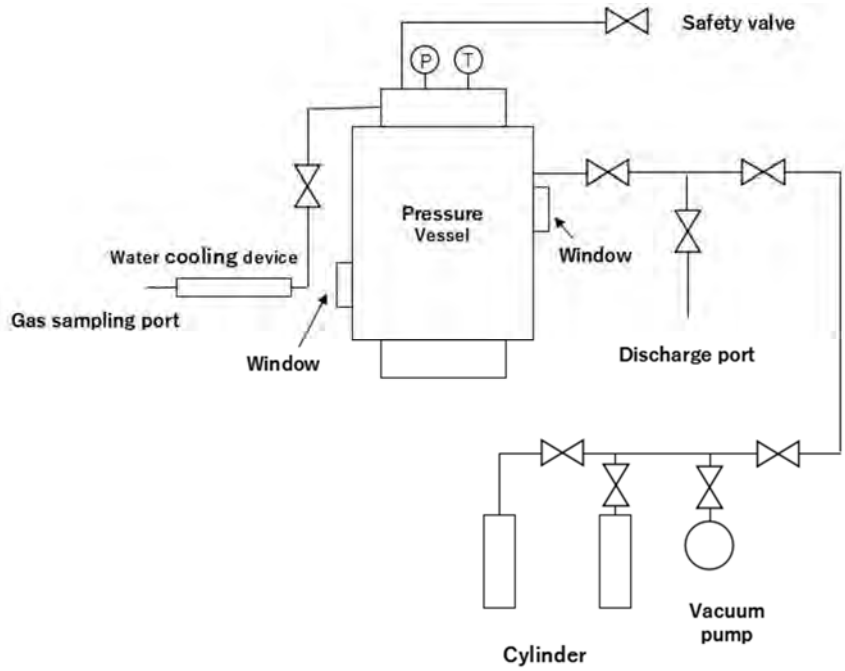

Figure 1: Schematic diagram of the experimental apparatus

Experimental equipment for observing the disproportionation reaction of HFO-1123 and investigating boundary lines of disproportionation reaction conditions in the experiments is depicted in Fig. 1. The experimental equipment includes stainless steel pressure vessels, vacuum pumps, a refrigerant cylinder, pipes, valves, safety valves and a water cooling device. Energy is applied by melting a molybdenum wire to change pressure and temperature conditions. It was observed from the upper and lower windows in the experimental vessel whether the disproportionation reaction started and propagated.

2.2. Experimental Apparatus

The refrigerant was introduced into a stainless steel vessel (Figure 2) having a pressure resistance of 29 MPa and a temperature resistance of 200 °C. The inside of the vessel was cylindrical with a diameter of 75 mm and a height of 148 mm; the internal volume of the vessel was 0.65 L. To observe the reaction, there were two circular quartz glass windows with a diameter of 20 mm, on the side of the vessel at heights of 54 mm and 94 mm from the bottom of the interior of the vessel. Four 300 W cartridge heaters were inserted in the side wall of the vessel to control the gas temperature inside

the vessel and the temperature of the vessel itself, between ambient temperature and 200 °C. Two round copper electrodes with diameters of 3 mm, spaced 45 mm apart, were inserted into the vessel at a height of 40 mm from the bottom of the inside the vessel (Figure 3) in order to impart energy to the gas inside.



Figure 2: Stainless steel vessel

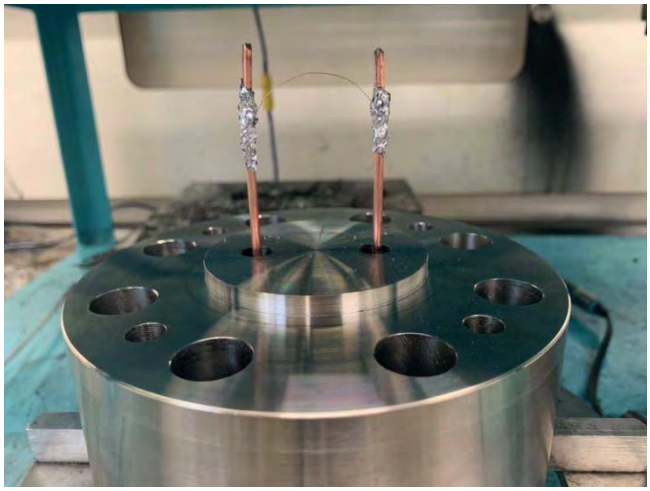

Figure 3: Bottom view of vessel

2.3. Discharged Energy

In this experiment, energy input at the start of the experiment was carried out by melting a Mo wire. By connecting the copper electrodes with the molybdenum wire in the vessel and applying a high voltage with a power supply device, the molybdenum wire was heated and melted, supplying the activation energy necessary for initiation of the disproportionation reaction.
Fig. 4 shows the relationship between the length and the discharged energy, allowing measurement of the amount of energy discharged.

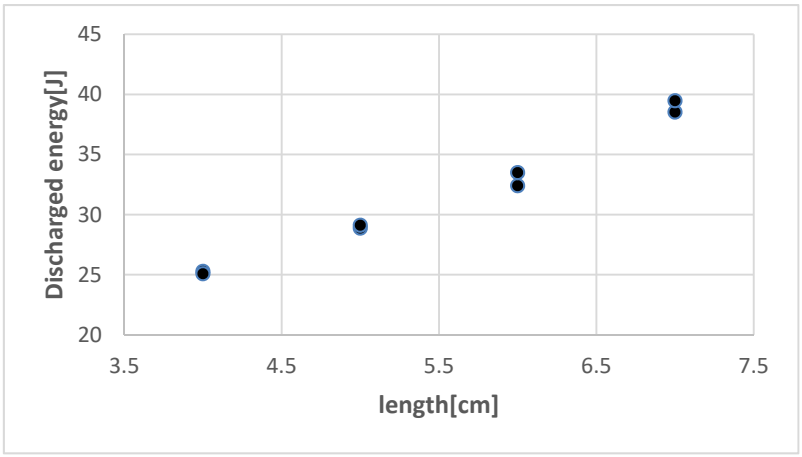

Figure 4: Relationship between the Mo wire length melted and the discharged energy

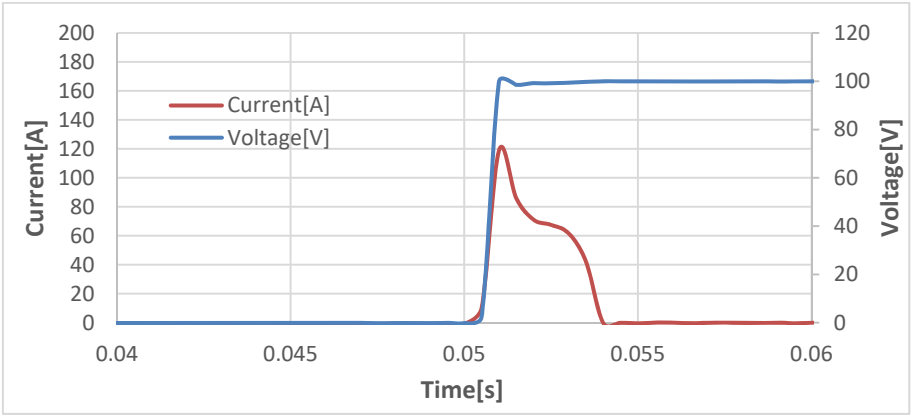

Figure 5: Current and voltage change after melting

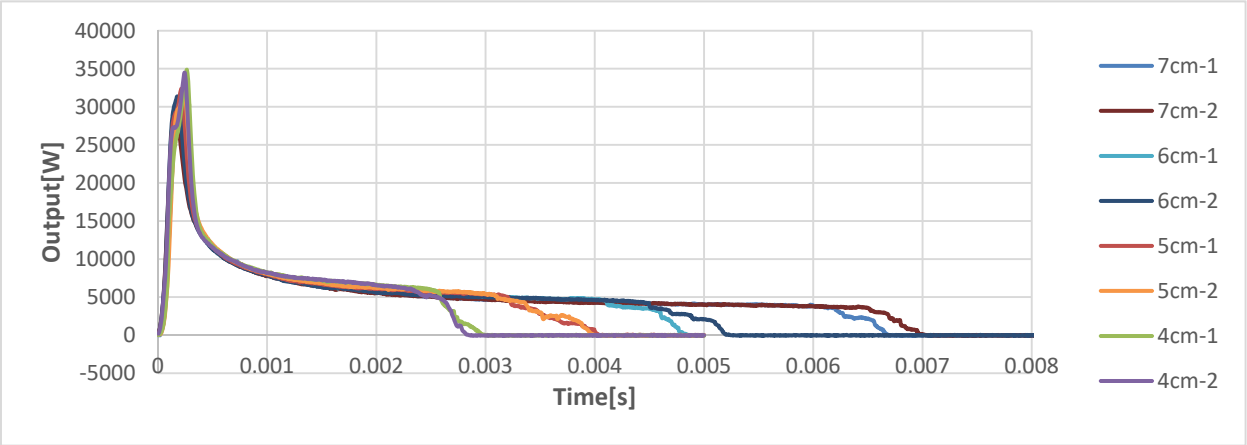

Figure 6: Output changes over time

Increasing the length of the wire also increased the input energy. As a result, it was found that by increasing the length of the molybdenum wire, the charging energy could be controlled in the range of 25 to 40 J. Changes over time of the current and voltage when the molybdenum wire melted are shown in Fig. 5. Voltage application began 0.005 s after the start of measurement. Looking at the value of the current over time, the current sharply increases when voltage is applied, and then it decreases smoothly to 0.0054 s shortly thereafter. This is because the heat generated by the current flowing through the molybdenum wire raises the temperature and resistance of the molybdenum wire. It was estimated that the current sharply decreased after 0.0054 s, at which point molybdenum wire melting occurred. It was confirmed that the voltage value was stable at 100 V. Fig. 6 shows how the power output changed over time, and we find that it has almost the same peak for all lengths of Mo wire, when the length changed it only extended the time required to melt the Mo wire. The amount of energy input due to melting of the molybdenum wire was calculated by integrating the product of current and voltage over time.

2.4. Experimental Procedure

The experiments were carried out following the procedure described below:

1. After confirming that no short circuit is occurring between the electrode and the lower lid, connect the electrodes with a molybdenum wire.
2. Tighten the lower lid with a hexagon head bolt.
3. After evacuation with a vacuum pump, HFO-1123 is heated to reach the target pressure after heating.
4. Heat to the target temperature with a heater embedded in the wall of the container.
5. Energy is injected into the container by melting molybdenum wire at 100 V DC.
6. Disproportionation reaction is observed from the window with a high-speed camera already focused.
7. After the reaction, sample gas is collected, a qualitative analysis is performed with GC-MS, and then the gas in the container is evacuated.

2.5. Experimental Conditions

To clarify the influence of pressure and temperature at the energy input time on propagation of the HFO-1123 disproportionation reaction, experimental conditions are presented in Table 3.

Table 3. The experimental conditions

Volume of the vessel	0.65 L
Diameter of the molybdenum wire	0.2 mm
Length of the molybdenum wire	50 mm
Voltage	100 V
Operation time	10 s
Gas temperature	100–170 ºC
Gas pressure	0.70–1.10 MPa
Input energy	19.9-35.9 J

3. HFO-1123 DISPROPORTIONATION EXPERIMENT

The experiments to investigate the reaction were conducted under the conditions given in Table 4.

Table 4. HFO-1123 Disproportionation experimental conditions

Test	Temperature [°C]	Pressure [MPa]	Discharged energy [J]	Propagation of Disproportionation reaction
1	170.0	0.986	26.8	Yes
2	170.8	1.012	23.3	Yes
3	170.5	0.976	19.9	Yes
4	170.5	0.770	27.8	Yes
5	170.7	0.706	35.9	Yes
6	170.8	0.704	23.3	Yes
7	169.6	0.672	30.3	No
8	170.6	0.670	27.3	No
9	170.2	0.694	30.5	No
10	149.8	0.764	23.7	No
11	149.7	0.776	23.3	No
12	150.6	0.770	29.6	No
13	150.0	0.780	26.4	Yes
14	149.9	0.784	29.0	Yes
15	129.9	0.782	29.9	Yes
16	130.9	0.736	24.0	No
17	130.3	0.766	23.2	No
18	101.1	0.814	23.6	Yes

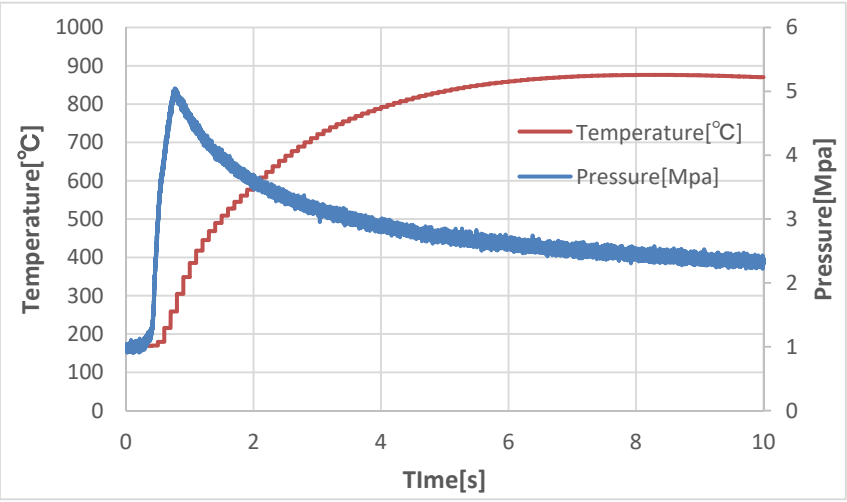

Figure 7: Changes in pressure and temperature (No. 4)

Figure 7 shows how the pressure and temperature changed under the condition of test no. 4. Supply of current to the electrodes was started 0.005 s after the start of measurement. At the same time, energy input to the gas inside the pressure vessel was started. In both cases, it was confirmed from the current waveform that the molybdenum wire was melted within about 0.0004 s after energy was discharged, but the application of voltage was continued for 10 s thereafter although no current flow was detected. During test No. 4 (Table 4), the pressure increased to 5 MPa after energy was discharged into the vessel, and the temperature rose to about 900 °C (Figure 7). However, as a result of analyzing the flame video with software based on the two-color temperature radiometry method (H & B method), the maximum temperature was over 2439 °C (Figure 8). When the disproportionation reaction was found not to propagate (as indicated in Table 4), only a small amount of soot was produced, and this was evidence that the disproportionation reaction did not propagate. When the disproportionation reaction of Table 4 did propagate, a large amount of soot was produced, as shown in Figure 9. How the temperature and the pressure influenced the HFO-1123 disproportionation reaction is shown in Figure 10.

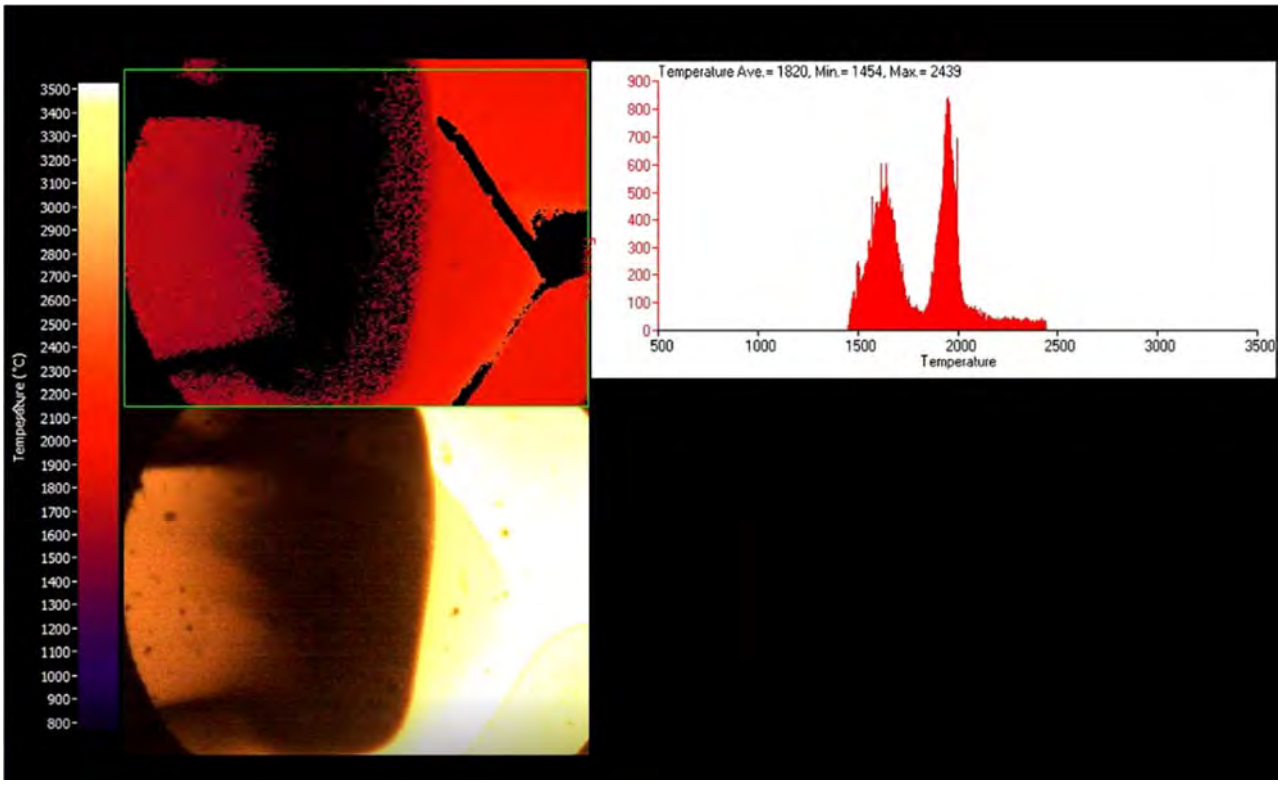

Figure 8: Analysis of flame video with the two-color temperature radiometry method (H & B method)

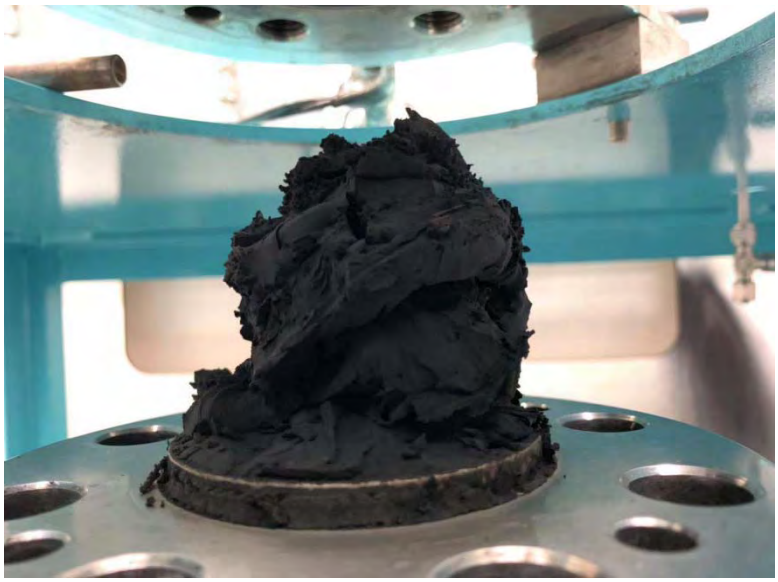

Figure 9: Image of a large amount of soot

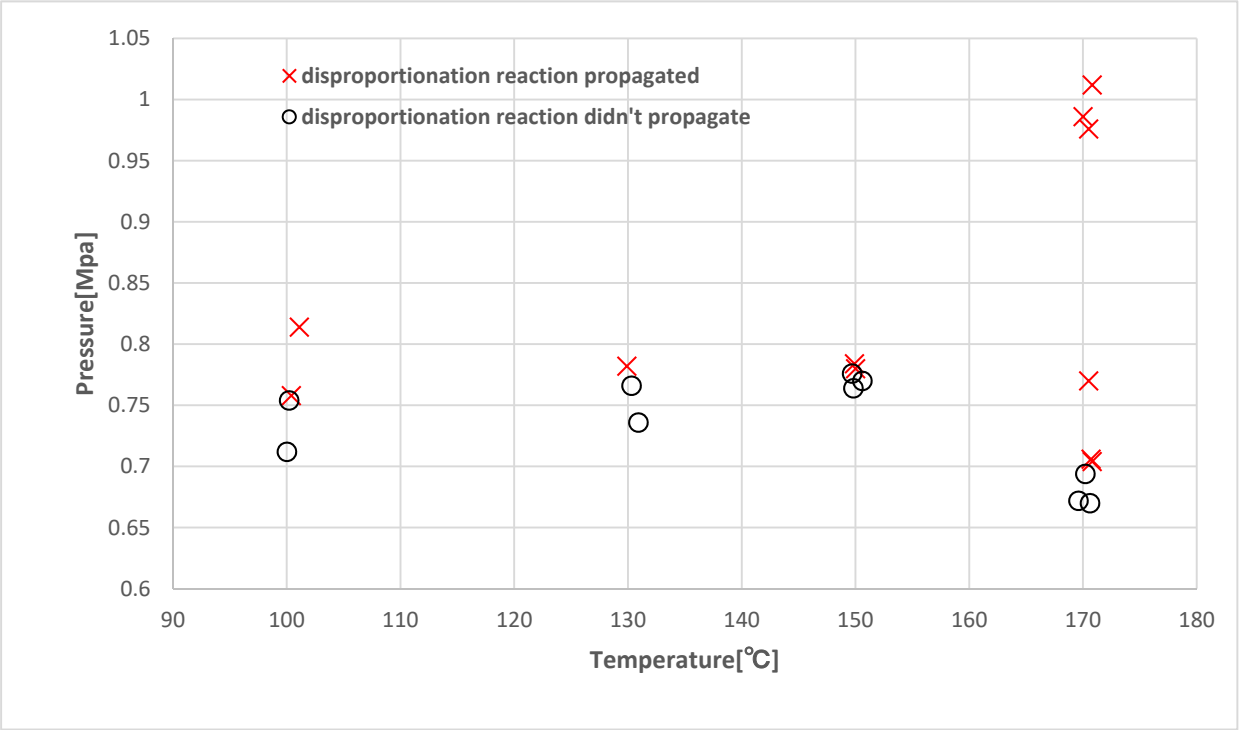

Figure 10: Influence of temperature and pressure on the disproportionation reaction

The results of the qualitative analysis by GC-MS of gas sampled immediately after the disproportionation reaction propagation are shown in Figure 11. As a result of GC-MS analysis, it was clarified that C_2H_6, C_2F_6 and CHF_3 are produced from the disproportionation reaction as intermediate products.

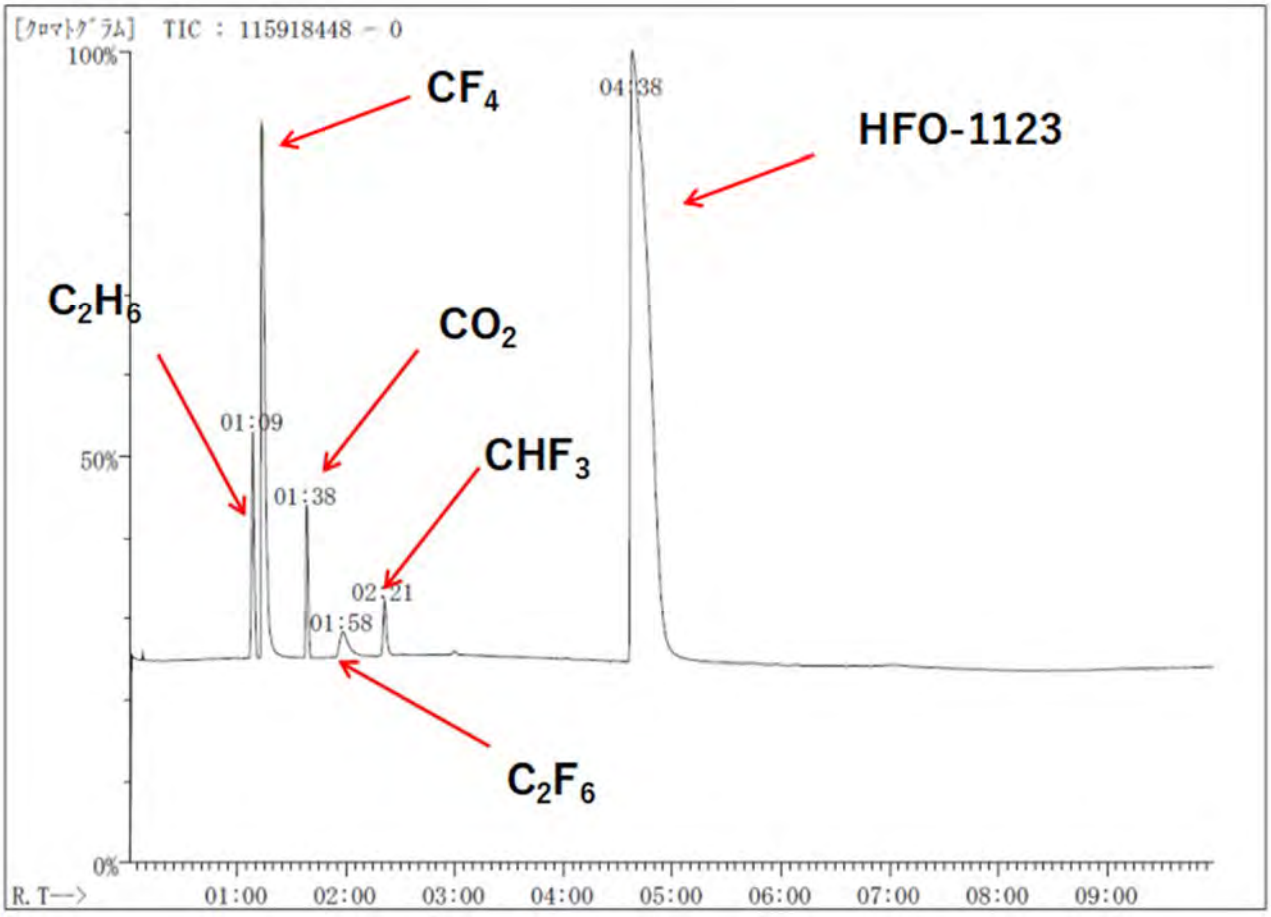

Figure 11: Result of GC-MS analysis of the sampled gas

4. CONCLUSION

Experiments with varying experimental conditions allowed us to determine the boundary conditions under which the disproportionation reaction propagates in pure HFO-1123 within the range from 100 to 170 °C. The qualitative analysis by GC-MS allowed us to clarify the intermediate products of the disproportionation reaction. Moreover, since it was possible to determine the maximum temperature achieved, this will contribute to an understanding of the combustion model.

ACKNOWLEDGEMENT

The authors wish to express their gratitude to the New Energy and Industrial Technology Development Organization (NEDO) for financial support of this study.

REFERENCES

Otsuka, T., Ueno, K., Okamoto, H., Ippommatsu, M., & Dobashi, R., 2018. Analysis of disproportionation process of trifluoroethylene mixtures. Journal of Loss Prevention in the Process Industries, 54(June 2017), 179–182.

Fukaya, H.,Hayakawa, Y.,Okamoto, H.,Ueno, K.,Otsuka, T., 2017.Theoretical study of disproportionation reaction of fluorinated ethylenes. Journal of Fluorine Chemistry 200(2017), 133-141.

Otsuka, T., Ueno, K., Okamoto, H., Ippommatsu, M., & Dobashi, R., 2018. Analysis of disproportionation process of trifluoroethylene using high power spark ignitions over 5 J. Journal of Loss Prevention in the Process Industries,51(2018),36-41.

Lisochkin, Y. A., & Poznyak, V. I., 2006. Explosive-hazard estimates for several fluorine-containing monomers and their mixtures, based on the minimum ignition pressure with a fixed igniter energy. Combustion, Explosion and Shock Waves, 42(2), 140–14.

Manuscript ID:824
DOI: 10.18462/iir.icr.2019.0824

Experimental study of method for charge composition determining for Joule–Thomson multicomponent mixed-refrigerant refrigerator

Eugeny BYCHKOV[(a)], Anatoly ZHERDEV[(a)], Boris MAKAROV[(b)], Yaroslav SAMOKHVALOV[(a)]

[(a)] Bauman Moscow State Technical University
Moscow, 105005, Russia, bychkov.eg@bmstu.ru
[(b)] CSRI «Kurs»
Moscow, 105187, Russia

ABSTRACT

One of the main practical problem of creating low-temperature equipment based on real Joule–Thomson refrigerators operating mixed refrigerant is the difficulty in determining charge composition. The existing methods in the literature mainly solve the problem of determining and correcting the theoretical values of the mixed refrigerant component mass concentrations in certain scheme of refrigerator at steady state operating mode due to their changing in relation to charged. This article represents approach of experimental approving of developed numerical method. The method allows determining mixed refrigerant temperature distribution along working cycle of refrigerator and composition of refrigerant charge with given geometry of refrigeration circuit and composition of circulating mixed refrigerant. Practical value of the method is ability to determine charge of refrigerant for specified refrigeration circuit, as consequence, reducing test duration of developed equipment. Developed test bench for suggested method approving is presented.
Keywords: Joule–Thomson, Mixed system, Refrigerant charge, Cryopreservation.

1. INTRODUCTION

Developing of new types of refrigeration systems, which provide cryostatting of cooled objects (maintenance of constant temperature or glide in range of 5K) with temperature in range of minus 160°C to minus 90°C, applying throttling low-temperature machines (TLTM), working on Joule-Thomson cycle, is currently central. According to Arkharov et al. (2016a), Arkharov et al. (2016b), Gareeva and Lavrov (2016), Arkharov and Semenov (2016) efficiency improvement for these machines, working on closed cycle, can be achieved by reducing losses in main elements – compressor, heat exchangers and so on, or by increasing efficiency of throttling cycle, applying multicomponent mixed refrigerant (MMR) as a working fluid. Studies of Brodyanski and Semenov (1980), Lavrenchenko (1985), Boyarski et al. (1990), Brodyanski and Grezin (1973), Lavrenchenko et al. (1983) and others started in 70-80s, show that using of MMR significantly improve energy and weight-size parameters of TLTM, reduce cost of equipment, decrease start time of these systems by higher volume refrigeration capacity of working fluid and intensification of heat transfer from cooled objects. Krotov (2011) showed that TLTM working on MMR has efficiency close to efficiency of gas refrigerators.

2. THEORETICAL MODEL AND LITERATURE REVIEW

One of the main practical problems in process of developing low-temperature equipment, based on TLTM on MMR working in Joule-Tomson cycle, is determining composition profile of charged MMR components. This involves an increase in volume of tests leading to time and money spending.
Amount of MMR to charge is calculated by integral along refrigerator working circuit (continuous closed circuit of structural elements - heat exchangers, throttling device, connecting pipelines, which are closed to compressor that provides MMR circulation), as shown in Eq. 1:

$$M_a = \oint \frac{S(l)}{\vartheta} dl \quad \text{Eq. (1)}$$

where S(l) is current value of clear area of TLTM working circuit, l – dimension coordinate in the line of flow, ϑ – specific volume of liquid-vapour mixture, calculated by Eq. 2:

$$\vartheta = (1 - \mathrm{X})\vartheta' + X\vartheta'' \quad \text{Eq. (2)}$$

where ϑ'' - specific volume of vapour fraction, ϑ' - specific volume of liquid fraction, X – mass vapour fraction.

Mass of each component of MMR is calculated as sum of two integrals, as shown in Eq. 3

$$M_i = \oint \frac{X y_i}{\vartheta} S(l) dl + \oint \frac{(1-X) x_i}{\vartheta} S(l) dl \quad \text{Eq. (3)}$$

where y_i and x_i are mass fractions of MMR components in vapour and liquid phase respectively, i – subscript for MMR component.

Eq. 1 and Eq. 3 show connection between composition of circulating MMR and composition profile of charged MMR.

Evaluation of these equations is connected with solving set of equations: MMR temperature changing along working circuit equation, equation of state for liquid and vapour phases, vapour-liquid equilibrium equation for mixed refrigerant. Therein, MMR flow characteristics are evaluated by set of equations, which include principles of conservation for mass (continuity equation), impulse (motion equation), energy, and equations of state.

From these considerations, and supposing that vapour-liquid fraction of MMR is in equilibrium at medium temperature for this section profile during steady regime (TLTM working regime with nearly constant parameters, beginning after start regime), in work of Bychkov et al. (2019) calculation were made for cycle parameters and zeotropic MMR flow characteristics with nitrogen-methane-ethane-propane-isobuthane composition, refrigerating at minus 150°C temperature level.

Calculation was made considering that working circle is closed-loop, no end volumes along circle, solubility of components in compressor oil was not taken in account. In this case, mass flux is constant in all profiles (compressor mass flow is constant) in steady regime. Also, calculated “charged” composition (composition, which is calculated considering geometry of circuit and “circulating” composition. It differs from “circulating” composition because of assumptions made in calculation method) differs from “circulating” composition (composition, which is determined as a result of evaluations and optimization of refrigerator parameters (mass fractions of MMR components), providing required cryostatting temperature achieving maximum effectiveness objective) in approximation of thermodynamic characteristics of isobars of high and low pressures of “circulating” MMR error, but composition is constant all along working circle (components’ mass concentrations of MMR in any phase condition are constant in all profiles of circuit). In addition, TLTM parameters and “circulating” MMR composition were optimized by non-linear programming method with global solution search described by Yakovlev et al (2016). Pang et al (2016) and Smorodin and Parshin (2018) mention other optimization methods for such systems.

One of the main characteristics in application of zeotropic MMR as a working fluid in real TLTM, influencing refrigerator energy parameters, is mismatch between MMR composition circulating in steady regime and “charged” composition.

This problem was researched by Gong et al. (2002), Gong et al. (2007a), Gong et al. (2007b), Narasimhan and Venkatarathnam (2010), Sreenivas (2017), Bao and Zhao (2016), Pang et al. (2016). However, some conclusions and experimental data required additional experimental research and validation. For example, mentioned authors analyze steady regime of refrigerator stating that the main reason of MMR composition changing is phase “glide” in two-phase region, because of different velocities of vapour and liquid phases.

From our perspective, in consequence of heat transfer from external sources and between flows of working fluid temperature, pressures, vapour fraction, MMR components’ concentration profiles are built up during starting operation of TLTM working on MMR. Meanwhile, intensity of heat transfer processes depends on concentrations and temperature gradient. During steady regime, these processes also become steady. Amount of liquid phase in every heat exchanger element is constant

and defined by vapour fraction, which means it does not depend on velocities of liquid and vapour phases. Taking this into account, phase "glide" does not influence on MMR components' concentrations. In other words, total composition of MMR in every profile of the circuit is constant during steady working regime of TLTM.
In addition, in other studies no criteria for steady working regime is given and uncertainty in test conditions is presented.
According to Babakin and Babakin (2017), it is also important to note that solubility of MMR components in lubrication oil significantly depends on thermodynamical properties of MMR flow: pressure, temperature and types of lubrication oil and MMR components. Firstly, temperature and suction pressure influence on solubility in these types of machines. Solubility rate of vapour MMR components in compressor discharge line and oil separator is calculated by Henry's law. In case of significant amount of oil circulating in working circuit, which is carried over from oil separator, oil should consider as a component of MMR.
In our opinion, the main possible reasons of difference between circulating MMR composition in steady regime and "charged" composition are: 1)inexactness in calculation of geometry of real TLTM, at which point, it leads to error in amount of charged MMR (as consequence, insufficient or extra amount of MMR charge); 2)working circuit design features, end volumes of compressor or heat exchanger and relative space configuration of elements; 3) separation of significant amount of high-boiling components of MMR because of their solubility in lubrication compressor oil.
As a part of the independent experimental studies by Narasimhan and Venkatarathnam (2010), Sreenivas (2017) and Pang et al. (2016) of this process in real TLTM with different designs and different MMR compositions, it was determined that circulating composition of MMR in steady regime depends linear on "charged" MMR composition (Eq. 4, Eq.5):

$$x_i = A_{xi} x_i' + B_{xi} \quad \text{Eq. (4)}$$

$$y_i = A_{yi} y_i' + B_{yi} \quad \text{Eq. (5)}$$

Where y_i' and x_i' - mass concentrations of MMR components in vapour and liquid phases respectively, circulating in working circuit in steady working regime of real TLTM, A_{xi}, B_{xi}, A_{yi}, B_{yi} – experimental constants for steady working regime of TLTM, which depend on factors 1)-3) mentioned previously.
As a result, corrected mass of every component of MMR is calculated as a sum of two integrals (Eq. 6):

$$M_i' = \oint \frac{X(A_{yi} y_i' + B_{yi})}{\vartheta} S(l) dl + \oint \frac{(1-X)(A_{xi} x_i' + B_{xi})}{\vartheta} S(l) dl \quad \text{Eq. (6)}$$

Taking in consideration the above, design chain for low-temperature machines based on TLTM working on MMR includes:

a) Choice of throttling refrigerator scheme, which is capable of cooling and cryostatting objects at certain temperature and certain cooling capacity, analyzed by Bychkov et al. (2016);
b) Choice of equation of state for MMR and determining thermodynamical properties as a function of pressure and temperature;
c) Calculation of specific cycle parameters (compression work, refrigeration capacity, heat exchangers' duty);
d) Cycle's parameters optimization with known optimization objective, determining "circulating" composition of MMR;
e) Design of refrigerator;
f) Determining amount of "charged" MMR depending on TLTM circuit geometry;
g) Experimental research for "corrected charge" of MMR (calculated composition of MMR, by correction of "charge" composition in reliance on test data, accounting real TLTM geometry) for certain TLTM design.

Authors developed and made test bench for experimental validation of suggested design chain, which allows determining temperature of mixed refrigerant along working circuit of TLTM and with

known geometry to evaluate composition of “charge” with given “circulating” composition and evaluate “corrected charge” in real TLTM, accounting influencing factors.

3. EXPERIMENTAL SETUP

Test bench, shown on Fig. 1, consists of thermally insulated body with two calorimeters, low-temperature refrigerator, which provides cooling and cryostatting, and control system. Lower stage cold section is situated in thermally insulated body. Type of body insulation – frosted polyurethane system Elastopor H2120/80/2 is used to reduce the radiation heat leak to the cold section. Detailed description of design and parameters of low-temperature refrigerator is given by Yakovlev et al. (2016), Bychkov et al. (2017). The main refrigeration system parts and control system are placed in machinery space. Low-temperature refrigerator includes two stages: upper stage – the single stage J-T refrigerator operating with azeotropic mixture – R404a; lower stage - J-T refrigerator operating with zeotropic mixtures. It consists of a hermetic single-acting reciprocating compressor (cylinder capacity 24.2 cm^3) with polyester oil (charge amount 890 cm^3) as lubricant, double-threaded fin-tube after cooler, thermal expansion valve and plate heat exchanger as evaporator in upper stage. Hot section of lower stage is comprised of a hermetic single-acting reciprocating compressor (cylinder capacity 34,4 cm^3) lubricated by polyester oil (charge amount 890 cm^3), double-threaded fin-tube after cooler, dehydration filter and float type oil separator with a reservoir volume of 2 liters. Cold section of lower stage consists of multi tubular heat exchanger of length 5.5 meters coiled in serpentinous shape, electronic expansion valve with step engine and two calorimeters for flexible evaporator capacity control. Calorimeters represent a copper tube bent into coils, with flexible heating tape ENGL-1-0,33 which are fixed by hold-down elements. Low-temperature temperature sensors are fixed and isolated on straight sections of the calorimeters tubes. Heating tape braided from woven ribbon of glass yarn, based on eight heating wires of nichrome. Outside, the heaters are covered with a waterproof silicone rubber sheath. End crimps are made of the same rubber. Total maximum power of each heat tape – 300 W. There is a power control system of heat tape to ensure any load in the specified range. The pressure difference at the inlet and outlet of the calorimeters is measured by the pressure-difference transducer Aplisens APR-2000. In multi tubular heat exchanger the high pressure refrigerant flows through eight capillary tubes with an internal diameter of 3.15 mm each, while the low pressure refrigerant flows on the shell side (internal diameter of 19 mm). The electrical tape is installed on the suction line and connected to the controller for ensuring a constant suction temperature while conducting experimental studies and comparing the results. Thus, due to the possibility of regulating the suction and discharge pressures, as well as the temperature at the suction, it becomes possible to ensure the invariance of external conditions during the experiments.

Resistant thermometers Elemer TS-1388B/Pt-100, calibrated on liquid nitrogen temperature level, measure the temperature of the working refrigerant in cold section. The pressure transducers of Emerson evaluate discharge and suction pressure of the compressors. In this test bench, the flow rate of the working refrigerant is indirect measured by Coriolis flowmeter Promass 83A. Compressors power is measured separately using an electronic power meter - Mercury 230. Refrigerant samples would be extracted during steady state operation from the several points (1-7) and the composition of the mixture in circulation is determined using a gas chromatograph with thermal conductivity detector (TCD) and flame-ionization detector (FID) (Chromos GC-1000). The gas chromatograph (GC) is calibrated against standard mixtures and the uncertainty in the determination of composition was estimated to be ±0.2%. Method used in GC makes it possible to determine refrigerants on simultaneously sample injection in capillary and packed column. Whereby N2, C1 are determined on TCD channel with packed column NaX and eight-port valve with backpurging function, and C2, C3, C4 and repeated C1 on FID channel with capillary column St -PLOT/Si (50m x 0.32mm x 3.0μm) with six-port injection valve. For sample injection additional bench with expansion tanks and fine oil filters is installed. Carrier gases perform GC gas supply: helium for TCD column, nitrogen for FID column, hydrogen and air.

The Elemer 5104 and 5122 meters are used to collect experimental data, which took 30 seconds to scan all the system variables. SCADA system was developed for a visual illustration of the processes and graphs of variable values.

Apparatus construction of test bench and its connection elements are designed to eliminate end volumes. It is achieved by application of tube and plate heat exchangers, minimization of connection tube lengths and optimization of their diameters to compressor capacity. As a result, high mass flux in working circuit is achieved.
Additionally, amount of high-boiling MMR components saluted lubricating oil during steady working regime is estimated. Solubility of components is calculated considering suction pressure and compressor's cylinder inlet temperature, according to Minashkin (2005).
Taken together, the main instruments and their measuring range and accuracy presented in Table 1.

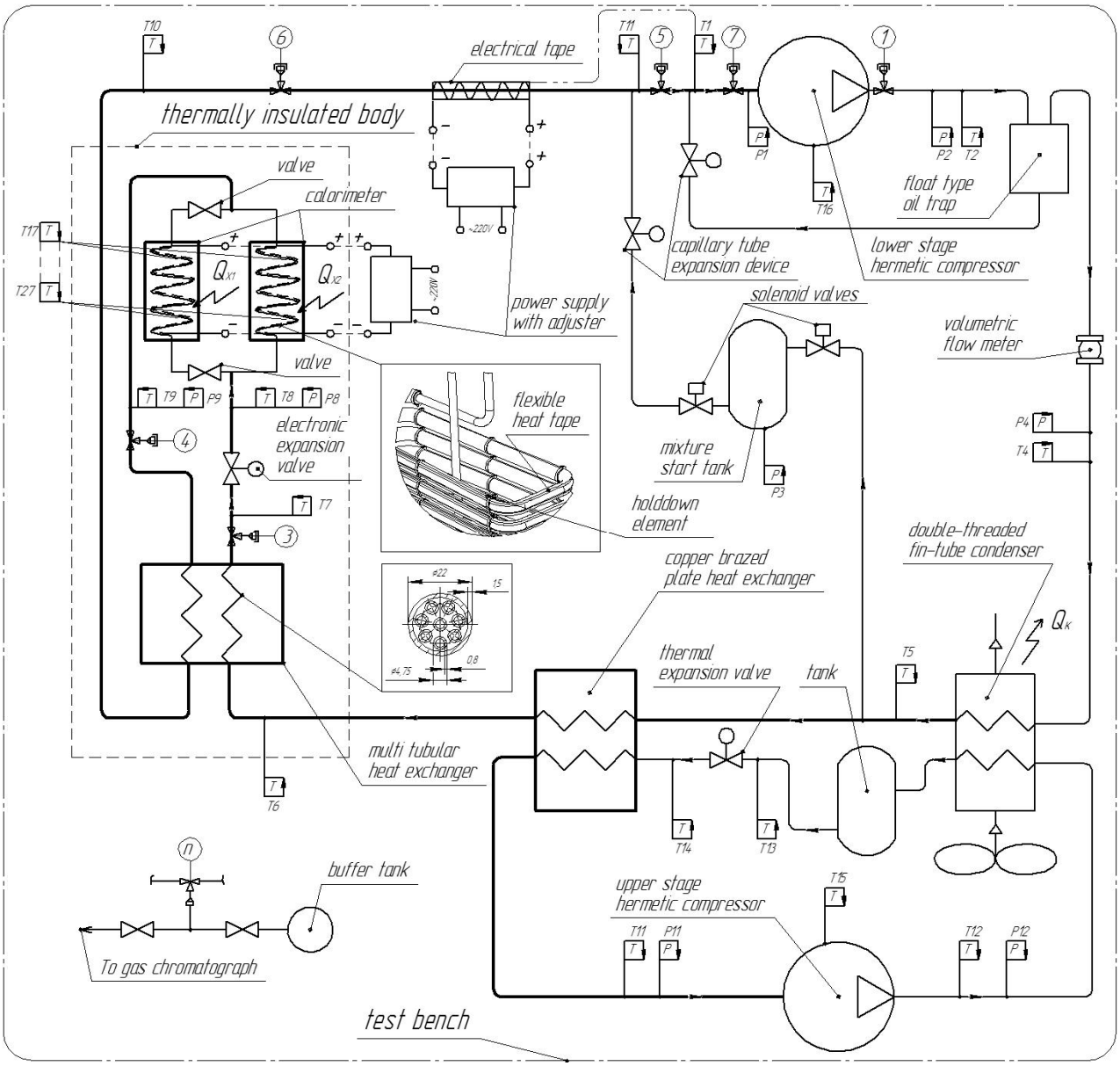

Figure 1: Test bench circuit diagram, T1-T27 и P1-P11 indicate measuring points for temperature and pressure respectively, the numbers from 1 to 7 indicate different sampling points

Experimental procedure is carried out as follows. Upper and lower stages of the test bench circuit were initially flushed with dry nitrogen gas. The compressor oil was heated to a temperature of about 80°C to remove all dissolved gases. A vacuum pump was used to evacuate the desorbed mixture components before charging refrigerants. The required quantity of each of the components was charged, starting from the highest boiling point component to the lowest boiling point component. At the same time, each component charge mass is measured by changing the mass of the cylinder without connected flexible pipes. At a steady state operation samples of the circulating stream were

extracted and analyzed in a gas chromatograph to measure the concentration in circulation. All measuring parameters were recorded in SCADA system. Constant ambient conditions where test bench is placed are provided with room air conditioning system.

Table 1. Main instruments and their measuring properties

Parameters	Instruments	Measuring range	Accuracy
Temperature (cold section)	Elemer TS-1388B (Pt-100)	-196 – 200°C	0.3+0.005*|t|%
Temperature (hot section)	Elemer TS-1388 (Pt-100)	-50 – 200°C	
High pressure	Emerson PT5-30M	0 – 30 bar	≤±1%
Low Pressure	Emerson PT5-07M	-0.5 – 7 bar	≤±1%
Pressure difference	Aplisens APR-2000	0 – 3000 Pa	0.075%
Mass flow rate	E&H Promass 83A	0–45 kg/h	2‰
Density	E&H Promass 83A	0–2000 kg/m3	±0.5 kg/m3
Power	Mercury 230 ART02	0 – 10 A	1%
Weighing balance	CAS SWII-05	0.02-5 kg	e=d=1g
Chromatography	Chromos GC-1000	–	0.2%

4. CONCLUSIONS AND DIRECTION OF EXPERIMENTAL RESEARCH

System method is required for designing new types of machines based on TLTM working on MMR, which provide cryostatting of cooled objects (maintenance of constant temperature or glide in range of 5K) at temperatures in range of minus 160°C to minus 90°C.

Despite of wide range of theoretical methods of calculation and optimization for characteristics of the refrigeration systems, the main practical problem is definition of charge amount of every MMR component. In addition, for every new design of TLTM with new geometry, starting-up and charge adjustment are carried out using step-by-step method, it takes very long time and demands expenses on refrigerants. It should be noted that, there is discrepancy between MMR composition circulating in real TLTM working in steady regime and “charged” composition, suggesting that correction for charge calculation method is required. Analyzing results of previous works, there is need in additional experimental research and validation of factors, defining the discrepancy. For that purpose, the authors developed and made test bench, based on cascade TLTM working on five-component MMR on lower cascade.

Experimental research will include:

1. Defining MMR composition circulating in real TLTM at steady regime with different heat load on evaporator. Comparison of that composition with “charge” composition, which was calculated with suggested method, calculation of “corrected charge” composition. During all experiments suction temperature and pressure, discharge pressure should be constant, steady regime is confirmed by long-time working with fixed ambient conditions.
2. Comparison of parameters (components, mass of charge, evaporator volume) of TLTM working on different composition of MMR in relation to “corrected charge” composition.
3. Experiment data analysis of contribution of every factor, which influence on circulating in real TLTM at steady regime MMR composition mismatch.
4. Error estimation and results analysis

This and next research will be helpful in understanding the work mechanism of this type MRTR and will be useful in the design of similar systems.

REFERENCES

Arkharov, A.M., Semenov, V.Y., 2016. Analysis of Thermodynamic Efficiency of Small-Scale Natural Gas Liquefying Plant Operating on Medium-Pressure Cycle. Chemical and Petroleum Engineering, 51 (9-10), 656-664.

Arkharov, A.M., Semenov, V.Y., Krasnonosova, S.D., 2016. Methodology of Statistical Entropy Analysis of Small-Scale Natural Gas Liquefiers. Chemical and Petroleum Engineering, 51 (9-10), 665-673.

Arkharov, A.M., Semenov, V.Y., Krasnonosova, S.D., Lebedev, S.Y., Kul'byakin, V.P., 2016. Statistical Entropy Analysis and Experimental Study of LNG Plant with Precooling at -70°C. Chemical and Petroleum Engineering, 52 (7-8), 468-475.

Babakin, B.S., Babakin, S.B., 2017. Refrigerants and refrigeration oils (In Russian). Deli plus, Moscow, 390 p.

Bao, J., Zhao, L., 2016. Experimental research on the influence of system parameters on the composition shift for zeotropic mixture (isobutane/pentane) in a system occurring phase change. Energy Conversion and Management, 113**,** 1-15.

Boyarski, M.Y., Lunin, A.I., Mogorychnyi, V.I., 1990. Characteristics of Cryogenic Systems When Functioning with Mixtures (in Russian), edited by V. M. Brodyanski. Moscow Energy Institute, Moscow.

Brodyanski, V.M. and Semenov, A.M., 1980. Thermodynamic Foundations of Cryogenic Technology (in Russian). Energiya, Moscow.

Brodyanski, V.M., Grezin, A.K., 1973. Increasing the efficiency of low-temperature refrigeration machines (In Russian). Kholod. Tekhnika, 3, 1-6.

Bychkov, E. G., Makarov, B. A., Zherdev, A. A., 2019. Development of a Method of Determining the Component Composition of the Working Fluid of Low-Temperature Throttling Refrigeration Machines Operating with Multicomponent Mixtures of Coolants. Chemical and Petroleum Engineering, Article in Press.

Bychkov, E., Kovalev, A., Samokhvalov, Y., Starostin, S., 2016. Theoretical research and designing of small-scale mixed refrigerant systems for constant-temperature processes at 180..120K (In Russian). Problems of Ship Armament and Vessel Radioelectroic Equipment Development, 1(10), 49-54.

Bychkov, E.G., Samokhvalov, Y.V., Makarov, B.A., Yakovlev, V.I., 2017. Experimental research of low-temperature throttling refrigerator for cryoconservation of medical and biological objects. Journal of Physics: Conference Series, 891(1), article №012109.

Gareeva, D.T., Lavrov, N.A., 2016. Entropy production and exergy loss during mixing of gases. Chemical and Petroleum Engineering, 51 (11-12), 759-764.

Gong, M., Deng, Z., Wu, J., 2007. Composition shift of a mixed-gas Joule–Thomson refrigerator driven by an oil-free compressor. Cryocoolers, 14, 453-458.

Gong, M., Zhou, W., Wu, J., 2007. Composition shifts due to different solubility in the lubricant oil for multicomponent mixtures. Cryocoolers, 14**,** 459-467.

Gong, M.Q., Wu, J.F., Luo, E.C., Qi, Y.F., Hu, Q.G., Zhou, Y., 2002. Research on the change of mixture compositions in mixed-refrigerant Joule-Thomson cryocoolers. AIP Conference Proceedings, 613(1), 881-886.

Krotov, A.S., 2011. An Investigation of the Dynamic Characteristics of Steam Compressor Refrigerating Machines Functioning with Multicomponent Mixtures of Coolants (In Russian). Dissertation for the Degree of Candidate of Technical Sciences. Bauman Moscow State Technical University.

Lavrenchenko, G.K., 1985. Development of Efficient Multicomponent Working Fluids and the Creation of Throttling Compressor Refrigerating Systems Based on These Working Fluids (in Russian). Author's Summary of Dissertation for the Degree of Doctor of Technical Sciences. OIIMF, Odessa.

Lavrenchenko, G.K., Kotenko, S.V., Zubrilin, S.A., 1988. Features of the energy characteristics of throttling compression cooling systems for cryostatic control over a broad range of temperatures (In Russian). Kholod. Tekhnika I Tekhnologiya, 46, 23-28.

Minashkin, M.G., 2005. Improved calculation method of hermetic compressor based on test of dimethyl ether as refrigerant (In Russian). Dissertation for the Degree of Candidate of Technical Sciences. Bauman Moscow State Technical University.

Narasimhan, N.L., Venkatarathnam G., 2010. A method for estimating the composition of the mixture to be charged to get the desired composition in circulation in a single stage JT refrigerator operating with mixtures. Cryogenics, 50(2), 93-101.

Pang, W., Liu, J., Xu, X., 2016. A strategy to optimize the charge amount of the mixed refrigerant for the Joule–Thomson cooler. International Journal of Refrigeration, 69**,** 466-479.

Smorodin, A.I., Parshin, S.A., 2018. Optimization of Refrigerant Composition of Low-Temperature Stage of Dual Mixed Refrigerant Cycle. Chemical and Petroleum Engineering, 54 (7-8), 493-498.

Sreenivas, B., Nayak, H.G., Venkatarathnam, G., 2017. Relationship between composition of mixture charged and that in circulation in an auto refrigerant cascade and a JT refrigerator operating in liquid refrigerant supply mode. Cryogenics, 81, 42-46.

Yakovlev, V.I., Bychkov, E.G., Makarov, B.A., Samokhvalov, Y.V., 2016. Results of theoretical and experimental investigations of a refrigeration machine for an ultra-low-temperature medical freezer for maintaining cryoconservation and long-term storage of medical and biological compounds (In Russian). Probl. Razvitiya Korabel. Vooruzh. I Sudov. Radioelek. Oborudovaniya, 3(8), 51-59.

Manuscript ID: 831
DOI: 18462/iir.icr.2019.0831

Combining HFO Refrigerants with different System Architectures to Reduce Energy Use and CO_2 Emissions in Supermarket Refrigeration

Nilesh PUROHIT, Gustavo POTTKER[1*], Samuel F. YANA MOTTA, Ankit SETHI

[1]Honeywell Buffalo Research Laboratory
Buffalo, NY 14210, USA
gustavo.pottker@honeywell.com

ABSTRACT

Commercial refrigeration systems worldwide predominantly use high global warming potential (GWP) refrigerants such as R404A. However, these refrigerants are under an agressive phase out process in several countries through strict CO_2 regulations. One widely implemented strategy to reduce CO_2 emissions is to retrofit existing systems to lower GWP refrigerants such as R448A, while improving the system efficiency at same time. For new installations, there is opportunity to further reduce CO_2 emissions by designing system architectures that enable the use of very low-GWP refrigerants. In this paper, two new concepts of distributed system architectures using ultra-low GWP fluids are proposed. In the first concept system, refrigeration at both low and medium temperature levels is provided using R1234yf based hermetic self-contained units while a two phase heat transfer fluid based secondary loop in combination with R1234ze(E) based chiller removes the heat from self-contained units to ambient. In the second concept, a low-GWP refrigerant is used in both medium temperature cases and to provide cooling to low-temperature self-contained cases through cascade heat exchangers. We will show that both new systems can signifanctly reduce emissions and energy consumption.
Keywords: HFO-Refrigerants, LCCP, Commercial Refrigeration, Supermarkets

1. INTRODUCTION

A common strategy to reduce CO_2 emissions in existing supermarket refrigeration systems is to retrofit the currently used high GWP refrigerants with low GWP alternatives. R448A (GWP of 1273) is one such non-flammable retrofit option for existing R404A systems leading to reduction in direct emissions and about 11% improvement in energy efficiency (Abdelaziz and Fricke, 2014). Baba and Yamagushi (2014) showed that in comparison to R404A adoption of R448A in both low and medium temperature condensing units can yield up to 16% higher coefficient of performance (COP) and a near match in refrigeration capacity. Alternatively, Petersen et al., 2018 revealed that the system with refrigerant having lowest GWP does not automatically lead to the lowest emissions. Rather, overall emissions of refrigeration system depend on energy efficiency as well as on GWP of refrigerant. Hence, a new holistic approach is required to design and modify the existing system architectures to enable the adoption of low GWP fluids.

In the first section, the thermodynamic performance of low-GWP refrigerants such as R1234yf, R1234ze(E) and R515A are compared to the baseline refrigerant R134a. In the following step two new distributed system architectures using R1234yf, R1234ze(E) and R515A are proposed and their performance in terms of energy efficiency and CO_2 emissions is compared with those of traditional systems as well as with current retrofit and other low-GWP alternative systems. Using a comprehensive analysis approach, the proposed new distributed system architectures with low GWP refrigerants R1234yf, R1234ze(E) and R515A are shown to be energy efficient leading to a significant reduction in both direct and indirect emissions compared to other systems.

2. LOW GWP ALTERNATIVES

In this session we will briefly describe three low-GWP refrigerants, R1234yf, R1234ze(E) and R515A, that are used in the new system architectures proposed in this paper. All three refrigerants are known to be “R134-like”, with lower pressures and around 40-50% lower volumetric capacity than R404A. Thermodynamic analysis is carried out to compare the performance of these three low GWP alternatives in contrast to R134a in terms of cooling capacity and COP. The analysis is conducted at evaporation temperature of -7°C, evaporator superheat of 5.5°C, condensing temperature of 40.5°C, condenser sub cooling of 5.5°C, compressor isentropic efficiency of 65% and compressor volumetric efficiency of 100%. Table 1 summarizes the results obtained using thermodynamic data from the NIST property database REFPROP 9.1 (Lemmon et al., 2013). In comparison to R134a, all three alternatives show a close match in efficiency as well as reduced compressor discharge temperatures. R1234yf also has similar capacity. The reduction in capacity for R1234ze(E) and R515A in comparison to R134a can be compensated in new system architectures by increasing the compressor displacement.

Table 1 Comparison of thermodynamic properties of R134a with low GWP alternatives.

Refrigerants	R134a	R1234yf	R1234ze(E)	R515A
ASHRAE Safety Classification	A1	A2L	A2L	A1
Composition	R134a (100%)	R1234yf (100%)	R1234ze(E) (100%)	R1234ze(E)/ R227ea (88%/12%)
GWP (AR5)	1300	<1	<1	402
Capacity [% of R134a]	100%	96%	74%	73%
Efficiency [% of R134a]	100%	96%	100%	100%
Suction pressure [kPa]	225	247	166	166
Discharge pressure [kPa]	1017	1018	767	767
Pressure ratio [% of R134a]	100%	91%	102%	102%
Difference in compressor discharge temperature vs. R134a [K]	0.0	-13	-8.8	-10

3. NEW AND EXISTING SYSTEM ARCHITECTURES FOR SUPERMARKETS

The R404A centralized Direct Expansion (DX) system is the most common architecture used in supermarket refrigeration. It has a centralized machine room consisting of compressor racks for both medium and low temperature cases. Its long reftrigerant lines typically require large refrigerant charge and lead to higher refrigerant emissions due to higher leak rates associated with more connections. Long connecting lines also yield higher pressure drop and heat gains which cause increase in compressor suction temperature.

In contrast to centralized systems, distributed refrigeration architectures are gaining popularity in recent years. In these systems, refrigerant tubing lenght is significantly reduced owing to adoption of distributed compressor racks located closer to both medium and low temperature cases, typically located in the back room of the supermarket, rather than in a remote machine room. In addition, condensers are typically located in the roof immediately above the racks, reducing the lenght of liquid lines. This leads to reduction in refrigerant charge and losses due to shorter connecting lines, which leads to higher efficiency, lower leak rates and consequently lower CO_2 emissions.

New system architectures facilitate adoption of low GWP alternatives. One example is the R744 booster system which is essentially a two-stage system. R744 booster system can achieve comparable energy efficiency to R404A centralized systems at low ambient temperature operation. However, owing to the low critical temperature (31°C), the booster system operates in a trans-critical mode at ambient conditions above around 25°C, which leads to significant drop in energy efficiency. Adoption of parallel compressor (Karampour and Sawalha, 2016) and dedicated mechanical sub-cooling (Llopis et al., 2016) are two prominent modification strategies to improve performance of R744 booster system in high ambient conditions.

Fig. 1 introduces the first new low-GWP system architecture, called micro-cascade refrigeration system. This configuration uses R515A in medium temperature stage and R1234yf in the low

temperature stage. R515A being non-flammable is employed in a traditional DX configuration to satisfy medium temperature load in store as well as to remove heat from the low temperature self-contained systems, using multiple cascade heat exchangers. R1234yf, although being mildly flammable, can be employed safely in low temperature stage owing to use of multiple low refrigerant charge hermetic units, as shown in Fig. 1. The choice of R1234yf in low temperature stage is favored over the highly flammable A3 refrigerants such as R290 which has lower allowable refrigerant charge.

The second proposed system architecture, called micro-distributed system, is show in Fig. 2. In this configuration, R1234yf is used in both low and medium temperature self-contained hermetic units, while a two phase Heat Transfer Fluid (HTF) secondary loop, in conjunction with a R1234ze(E) based chiller, removes the heat from all self-contained stages to outside ambient. Here, the choice of a two-phase HTF reduces the temperature difference in the cascade heat exchangers in comparison to single-phase heat transfer fluids such as water or water/glycol mixtures, improving consequently energy efficiency. The three-way valve, as shown in Fig. 2, allows use of free cooling of HTF in low ambient temperature operation, in which the R1234ze(E) Chiller would not be turned off. Thermodynamic optimization based on cooling temperature of two phase HTF and onset of free cooling depending on ambient temperature is therefore required for best performance. Another distributed configuration investigated is R290/water micro-cascade system which is being adopted in supermarkets in recent years. In this architecture, R290 is employed in self-contained low temperature and medium temperature cases. Water is used as secondary fluid to remove the heat from the self-contained units, while heat from water can be removed either directly to the outside ambient or by using a chiller.

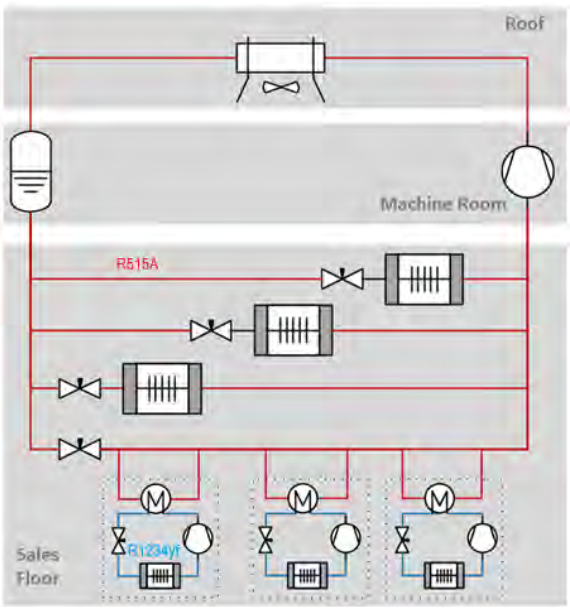

Figure 1: R515A/R1234yf Micro Cascade Refrigeration System

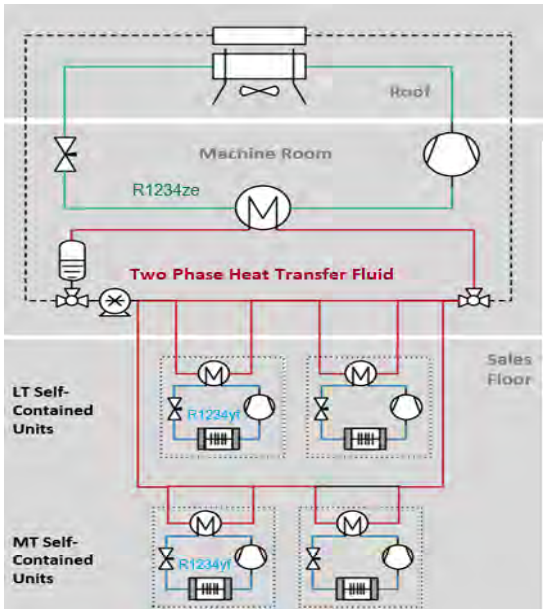

Figure 2: R1234ze/HTF/R1234yf Micro Distributed Refrigeration System with a two-phase HTF

The energy efficiency and emissions of all abovementioned system architectures were simulated assuming a typical store size of 4180 m^2. The various assumptions made for the analysis are listed in Table 2. The refrigeration load is modelled as a function of ambient temperature derived from the actual refrigeration case data as shown in Fig. 3. The design refrigeration load for medium temperature and low temperature is 138 [kW] and 87 [kW], respectively. A higher evaporation temperature is assumed for R744 in comparison to R404A and R448A due to its better heat transfer properties. Due to short connecting lines, self-contained units are assumed to operate at higher evaporation temperature owing to lower suction line pressure drop, and lower suction superheat due to fewer heat transfer infiltration losses. The compressor isentropic and volumetric efficiencies of R290 are comparatively inferior owing to reduced size of piston-displacement compressors in self-

contained units. The adoption of electronic expansion valves in booster, micro-cascade and micro-distributed configurations enables lower minimum condensing temperature.

Table 1 Refrigeration System Assumptions

Description	Unit	R404A Centralized	R448A Distributed	R744 booster	Micro-Cascade R515A/ R1234yf	Micro-Distributed R1234ze/ HTF/ R1234yf	R290/ Water cooled
Global Warming Potential (AR5)	[-]	3943	1273	1	402/<1	<1	3
Refrigerant charge	[kg]	1450	750	1000	750	750	750
Leak rate	[%]	15%	10%	15%	10%	10%	10%
MT Evaporation temperature	[°C]	-6.7	-6.7	-6.1	-6.7	-5.5	-5.5
LT Evaporation temperature	[°C]	-28.9	-28.9	-28.3	-27.8	-27.8	-27.8
LT/MT Cooling Load (Design Load)	[kW]	87/138					
Evaporator superheat MT/LT	[°C]	5.5					
Suction superheat LT	[°C]	27.7	22.2	22.2	5.5	5.5	5.5
Suction superheat MT	[°C]	13.8	8.3	8.3	5.5	5.5	5.5
Isentropic efficiency LT	[-]	0.67			0.6	0.6	0.52
Isentropic efficiency MT		0.70					0.55
Volumetric efficiency LT/MT		0.95					0.90
Approach temperature Cascade Condenser	[K]	-	-	-	5.5	5.5	6.6
Approach temperature Condenser	[K]	5.5	5.5	5.5 SC, 2.8 TC	5.5	5.5	5.5
Minimum condensing temperature	[°C]	21.1	21.1	10	15.5	15.5	15.5

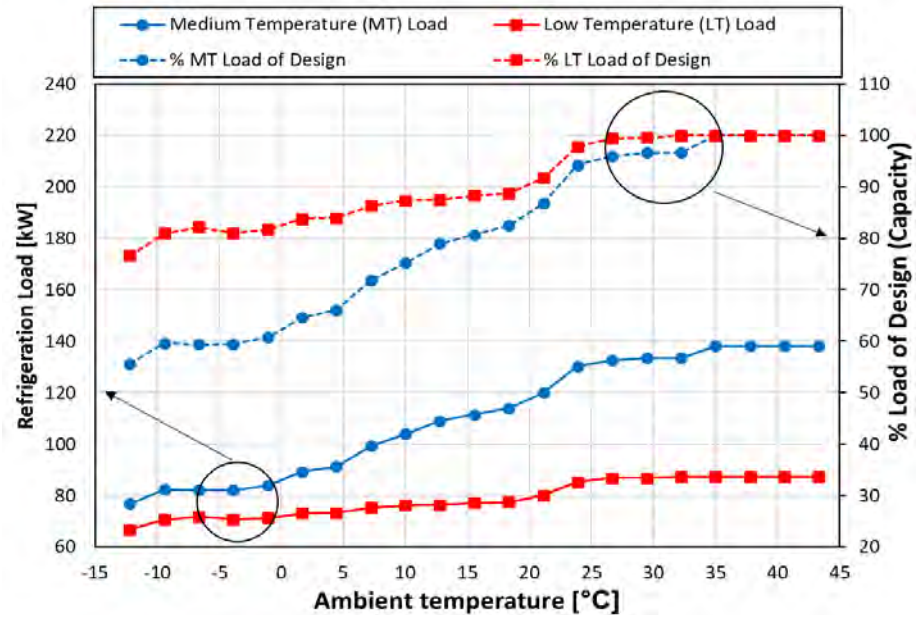

Figure 3: Refrigeration Load [kW] vs Ambient Temperature

4. ENERGY EFFICIENCY ANALYSIS

In this section, we carry out a comparison of all above mentioned system architectures in terms of energy efficiency, for different ambient temperatures and geographical locations.
In the proposed micro-distributed system, the two-phase HTF, removes the heat from the self-contained units either directly to the ambient, as “free cooling”, or to a R1234ze chiller dependent on the ambient temperature conditions. The power consumption of self-contained units increases with increase in temperature of HTF in the secondary loop while the power consumed by R1234ze chiller is reduced. Likewise, the power consumed by self-contained units decreases while that of R1234ze chiller increases with decrease in secondary loop HTF temperature. This leads to a trade-off and an operating temperature of 4.4°C is found optimal which maximizes the energy efficiency for different ambient temperatures. Further, the availability of free cooling depending on ambient condition provides additional advantage. Fig. 4 depicts the optimization of the operation of micro-distributed configuration with respect to availability of free cooling. The dotted green line represents the operation of cycle with fixed HTF temperature of 4.4°C. While, the solid green line depicts the optimized operation of cycle with respect to availability of free cooling where the HTF temperature floats with the ambient temperature when the free cooling operation increases the overall energy efficiency. Use of two phase HTF in place of single phase (liquid) HTF such as water or ethylene glycol in the secondary loop leads to reduction in the temperature difference for a given cascade heat exchanger heat transfer area. In addition, the lower bulk density of two phase HTF and the higher enthalpy difference across the cascade heat exchanger offers lower pressure drop and pumping power.

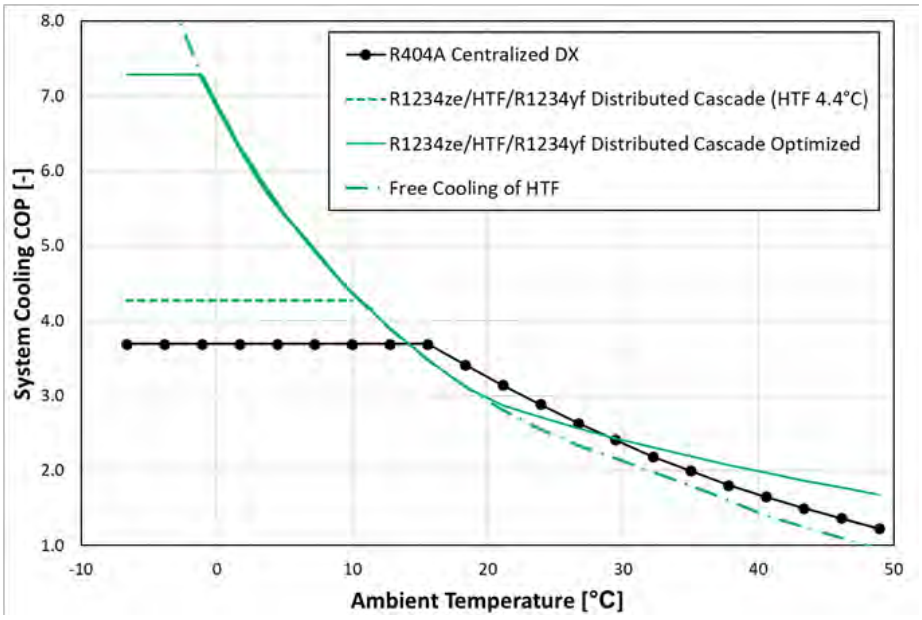

Figure 4: Cooling COP at different ambient temperatures for micro-distributed configuration

Fig. 5 presents the comparison of cooling COP of various investigated supermarket configurations at different outside ambient temperatures. At high ambient operation above 40°C, R1234ze/HTF/R1234yf micro-distributed, followed by R515A/R1234yf micro-cascade and R448A distributed systems show higher cooling COPs than systems with natural refrigerants such as R290 and R744 as well as baseline R404A centralized configuration. At ambient temperature range from 10°C to 40°C, R515A/R1234yf micro-cascade followed by R448A distributed and R1234ze/HTF/R1234yf micro-distributed systems show superior performance. At ambient temperature conditions below 10°C, the R1234ze/HTF/R1234yf micro-distributed configuration followed by R515A/R1234yf micro cascade, R744 booster and R290/water cooled configurations show higher energy efficiency (COP). This is attributed to the use of free cooling in the micro-distributed and R290/water cooled systems. The lower minimum condensing temperature in micro-cascade and R744 booster configurations also make these systems more energy efficient than R404A. At higher ambient conditions the trans-critical operation of R744 configurations leads to increased losses penalizing the system performance even with adoption of parallel compressor and

dedicated mechanical sub-cooler. Adoption of electronic expansion valve in R448A distributed DX configuration would lead to further improvement in energy efficiency, especially at low ambient, owing to reduction in minimum condensing temperature.

The annual weighted COP of all investigated configurations is calculated for ten different geographical locations (Table 2a and 2b). The annual weighted COP is determined based on the BIN temperatures for the locations over the course of one year. For comparatively warm locations such as Atlanta, Shanghai, Sau Paulo, New Delhi, Seville, Teheran and Athens, the R515A/R1234yf micro cascade configuration followed by R448A distributed and R1234ze/HTF/R1234yf micro-distributed configurations show the highest annual efficiency. While the annual weighted COP is highest for R515A/R1234yf micro cascade configuration followed by R1234ze/HTF/R1234yf micro-distributed and R448A distributed configurations for comparatively colder locations such as Milan and Frankfurt. The annual weighted COP for R1234ze/HTF/R1234yf micro-distributed configuration is found like that of R515A/R1234yf micro cascade configuration for operation in extreme cold climate like Oslo due to use of free cooling. The annual weighted COP for R744 booster configurations is found inferior to R404A centralized DX configuration, except for operation in extreme cold climate condition such as in Oslo.

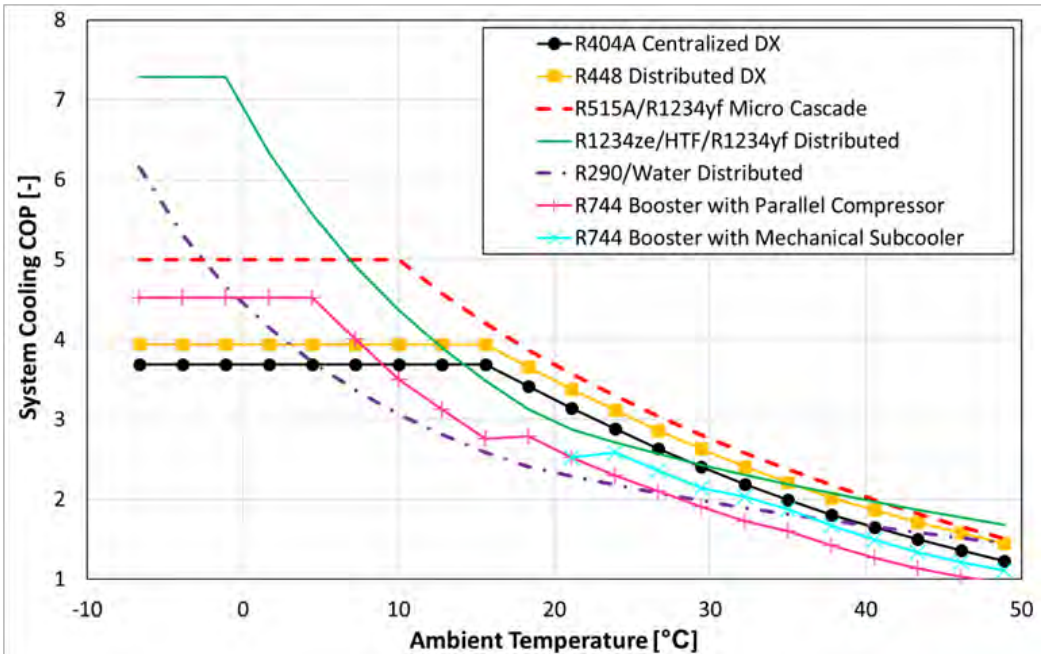

Figure 5: Cooling COP at different ambient temperatures for investigated configurations

Table 2a: Annual Weighted COP of investigated configurations

Location	Yearly Avg. Temp. [°C]	R404A Centralized	R448A Distributed	Micro-Cascade R515A/ R1234yf	Micro-Distributed R1234ze/ HTF/ R1234yf	R744 with sub-cooler	R744 with parallel comp.	R290/ Water Cooled
Atlanta, USA	16.1	3.14	3.38	3.73	3.22	2.79	2.65	2.49
Shanghai, China	17.8	2.99	3.23	3.56	3.09	2.68	2.50	2.40
SaoPaulo, Brazil	21.6	2.99	3.23	3.43	2.84	2.54	2.38	2.25
New Delhi, India	24.8	2.57	2.80	3.01	2.61	2.29	2.05	2.10
Teheran, Iran	16.8	2.94	3.18	3.52	3.12	2.69	2.49	2.42
Seville, Spain	18.1	3.07	3.32	3.65	3.11	2.68	2.53	2.40
Milan, Italy	10.3	3.47	3.71	4.30	3.92	3.24	3.18	2.89
Frankfurt, Germany	8.7	3.57	3.82	4.52	4.25	3.43	3.41	3.06
Athens, Greece	16.5	3.21	3.45	3.82	3.24	2.80	2.67	2.48
Oslo, Norway	5.7	3.64	3.89	4.69	4.70	3.65	3.65	3.35

Table 2b: Annual Weighted COP of investigated configurations relative to R404A centralized Configuration

Location	Yearly Avg. Temp. [°C]	R404A Centralized	R448A Distributed	Micro-Cascade R515A/ R1234yf	Micro-Distributed R1234ze/ HTF/ R1234yf	R744 with sub-cooler	R744 with parallel comp.	R290/ Water Cooled
Atlanta, USA	16.1	100%	108%	119%	103%	89%	84%	79%
Shanghai, China	17.8	100%	108%	119%	103%	90%	84%	80%
Sau Paulo, Brazil	21.6	100%	108%	115%	95%	85%	80%	75%
New Delhi, India	24.8	100%	109%	117%	102%	89%	80%	82%
Teheran, Iran	16.8	100%	108%	120%	106%	92%	85%	83%
Seville, Spain	18.1	100%	108%	119%	101%	87%	82%	78%
Milan, Italy	10.3	100%	107%	124%	113%	94%	92%	83%
Frankfurt, Germany	8.7	100%	107%	126%	119%	96%	95%	86%
Athens, Greece	16.5	100%	108%	119%	101%	87%	83%	77%
Oslo, Norway	5.7	100%	107%	129%	129%	100%	100%	92%

5. LCCP ANALYSIS

Life Cycle Climate Performance (LCCP) is a powerful tool to conduct environmental impact analysis in which comparison of the overall equivalent carbon dioxide emissions of the refrigeration systems over its lifetime is carried out (Purohit et al. 2016). Both the direct and indirect emissions along with the emissions due to manufacturing and disposal of the system are evaluated. The direct emissions are based on the leaking refrigerant over the lifetime of the equipment. The indirect emissions are caused by the carbon dioxide that is emitted to produce the energy that is consumed over the lifetime of the equipment. The environmental impact of the investigated systems for a 15-year lifetime is determined for ten global locations.

The local electricity emission factors for different geographical locations are derived from (MCT, 2014; eGRID, 2016; IEA, 2017). The simulated direct and indirect emissions as well as average COPs for all investigated configurations operating in four locations in Frankfurt, Germany, Atlanta, USA, Shanghai, China and Sau Paulo, Brazil are shown in Figure 6. The R404A centralized system has the largest overall emissions due to the high GWP and leak rate. With a R448A distributed system, there is a significant reduction in direct emissions due to the 68% lower GWP as well as the reduced refrigerant charge amount and leakage rates of distributed systems, compared to centralized configuration. In addition, an improvement of energy efficiency due to refrigerant and system effects effectively reduces the indirect emissions. Overall emission reduction from R404A can be achieved for R448A between 79% and 53% for Sao Paulo and Shanghai respectively. The R448A distributed system achieves similar emissions compared to R744 and R290 in all four locations, due to its superior energy efficiency (lower indirect emissions), even though its GWP and direct emissions are higher. Besides CO_2 emissions, the energy efficiency is especially important for the user of the equipment since it contributes directly to the energy cost. R448A shows hereby better performance than R404A centralized, R744 booster and R290/water cooled system effectively reducing the operating cost. The R744 booster system has the lowest GWP of the four investigated solutions. However, the efficiency penalty it experiences due to trans-critical operation leads to higher indirect emissions. Figure 7 shows the estimated total global CO_2 emissions for all investigated configurations. The total global emissions were calculated by multiplying the number of supermarkets in each of the 10 countries considered by the CO_2 emissions per system, for a representative city (Table 2a) in each country. R515A/R1234yf micro-cascade and R1234ze/HTF/R1234yf micro-distributed configurations are found to have lowest global emissions. In comparison to R404A system, those two new configurations reduce the environmental emissions by about 75%, respectively. While in comparison to R744 booster configuration with mechanical sub-cooler, the emissions are reduced by about 20% for the two new configurations. Total global CO_2 emissions for R448 distributed DX configurations are found similar to both R744 booster and R290/water distributed cascade configurations.

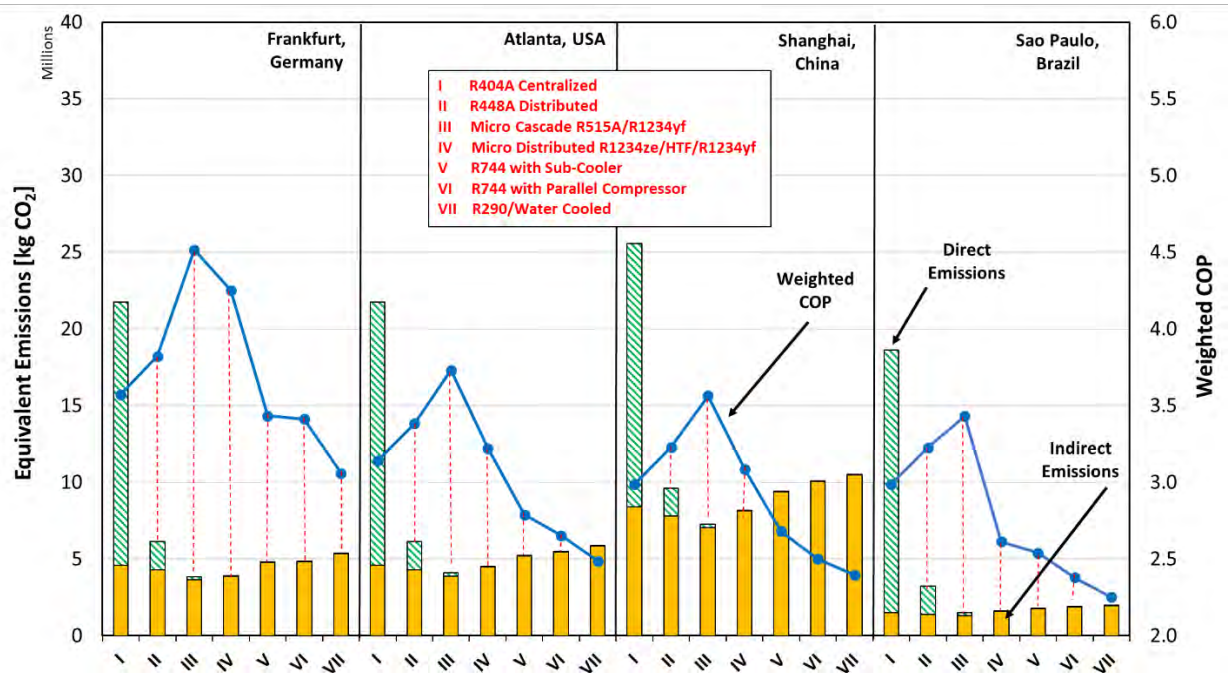

Figure 6: Direct and Indirect Carbon Dioxide Equivalent Emissions

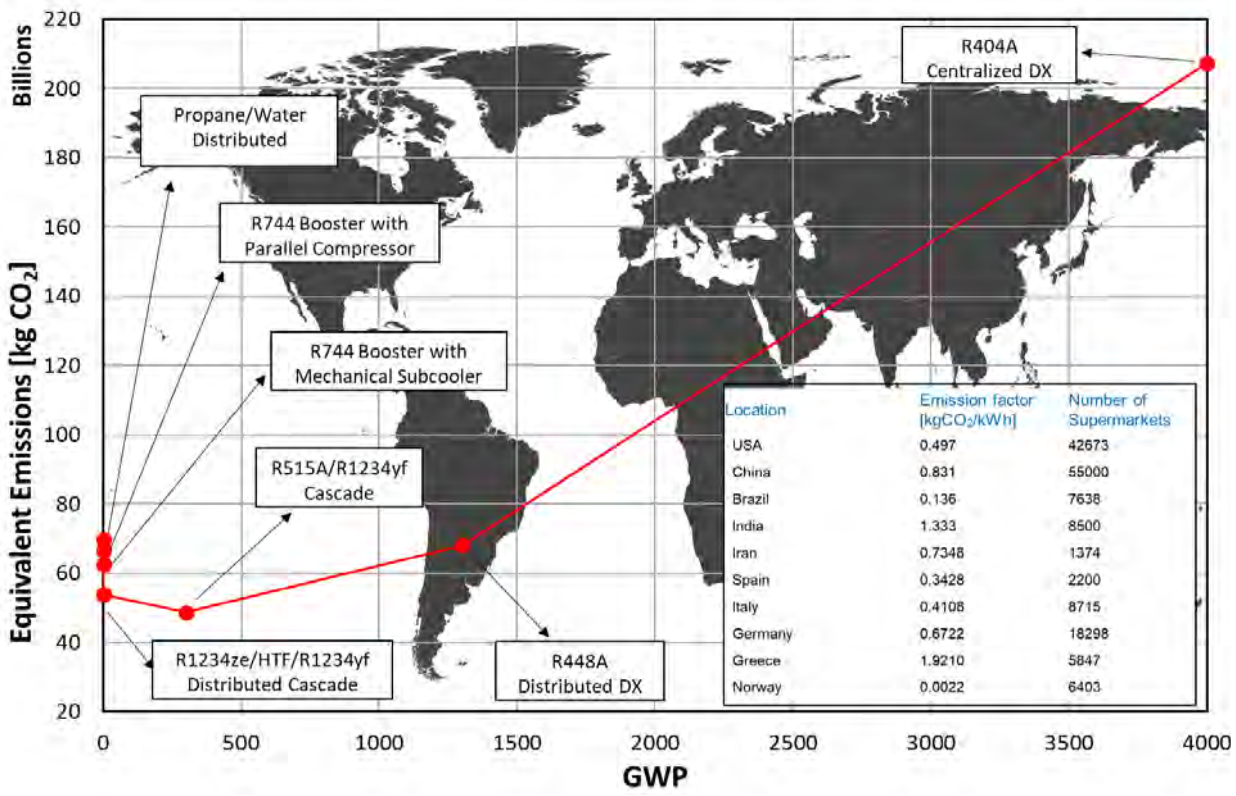

Figure 7: Global Emissions for investigated refrigeration systems

6. CONCLUSIONS

Two new refrigeration system architectures that significantly reduce CO_2 emissions and increase energy efficiency were proposed and compared to existing systems. The new systems use low-GWP refrigerants such as R515A, R1234ze and R1234yf. Both micro-cascade and micro-distributed systems show superior energy efficiency and environmental performance in several different

geographical locations, both cold and warm weather, in comparison with “natural refrigerants” system configurations such as CO_2 booster and water cooled with R290. In comparison to R744 and R290 systems, the R448A distributed configuration also shows higher energy efficiency with comparable global emissions, even though it has a higher GWP.
Finally, this paper demonstrates that the use of very low GWP “natural refrigerants” such as R744 and R290 does not necessarily mean lower CO_2 emissions since energy efficiency plays a key role to achieve environmental performance.

NOMENCLATURE

DX	Direct Expansion	MT	Medium Temperature
GWP	Global Warming Potential	SC	Subcritical
LCCP	Life Cycle Climate Performance	TC	Transcritical
LT	Low Temperature		

REFERENCES

Abdelaziz, O., Fricke, B., Working Fluids: Low Global Warming Potential Refrigerants, 2014 Building Technologies Office Peer Review - US Department of Energy, Oak Ridge National Laboratory, Arlington-VA.

Baba, A., Yamaguchi, H., 2014, Performance evaluation of condensing unit using low GWP refrigerants., JRAIA, Symposium on New Refrigerants and Environmental Technology, Kobe, Japan.

eGRID- Emissions & Generation Resource Integrated Database, 2016, Environmental Protection Agency

IEA (2017). Statistics. IPCC (2006). Revised IPCC Guidelines for National Greenhouse Gas Inventories: Reference Manual. Intergovernmental Panel on Climate Change. Cambridge University Press, Cambridge.

Karampour, M. and Sawalha, S., 2015, August. Theoretical analysis of CO2 trans-critical system with parallel compression for heat recovery and air conditioning in supermarkets. In 24th IIR Refrigeration Congress of Refrigeration. IIF/IIR, Yokohama, Japan.

Lemmon, E.W., Huber, M.L., McLinden, M.O., 2013, Reference Fluid Thermodynamic and Transport Properties - REFPROP Ver. 9.1., NIST, Boulder, Colorado, USA.

Llopis, R., Nebot-Andrés, L., Cabello, R., Sánchez, D. and Catalán-Gil, J., 2016. Experimental evaluation of a CO_2 transcritical refrigeration plant with dedicated mechanical subcooling. International Journal of Refrigeration, 69, pp.361-368.

MCT (2014). Arquivos dos Fatores de Emissão. Ministério da Ciência e Tecnologia.

Petersen, M., Pottker, G., Sethi, A., Yana Motta, S. 2018, Refrigerants with Low Environmental Impact for Refrigeration Systems, 17th International Refrigeration and Air Conditioning Conference at Purdue.

Purohit, N., Sharma, V., Sawalha, S., Fricke, B., Llopis, R. and Dasgupta, M.S., 2018. Integrated supermarket refrigeration for very high ambient temperature. Energy, 165, pp.572-590.

UNEP, 2016, The Kigali Amendment to the Montreal Protocol: HFC phase-down, OzonAction.

DISCLAIMER
Although all statements and information contained herein are believed to be accurate and reliable, they are presented without guarantee or warranty of any kind, expressed or implied. Information provided herein does not relieve the user from the responsibility of carrying out its own tests and experiments, and the user assumes all risks and liability for use of the information and results obtained. Statements or suggestions concerning the use of materials and processes are made without representation or warranty that any such use is free of patent infringement and are not recommendations to infringe on any patents. The user should not assume that all toxicity data and safety measures are indicated herein or that other measures may not be required.

Manuscript ID: 838
DOI: 10.18462/iir.icr.2019.0838

Flow boiling heat transfer and pressure drop of hydrocarbons R600a and R290 in a multiport minichannel tube

Jacqueline B. COPETTI[(a*)], Mario H. MACAGNAN[(a)], Jeferson D. OLIVEIRA[(b)] and Priscila F. SILVA

(a) Mechanical Engineering Graduate Program, Universidade do Vale do Rio dos Sinos-UNISINOS, Unisinos Av., 950, São Leopoldo, RS, Brazil
[(*)]jcopetti@unisinos.br
(b) Mechanical Engineering - Faculdade da Serra Gaúcha - FSG, Rua Os Dezoito do Forte, 2366, Caxias do Sul, RS, Brazil

ABSTRACT

The design of compact evaporators for refrigeration systems has motivated the research in flow boiling for better understanding of heat transfer, pressure drop and modelling improvement. This work presents the results of experimental studies of flow boiling of R600a and R290 in a multiport tube with 1.47 mm ID. The effects of heat (q"=5-20 kW/m²) and mass flux (G=35-170 kg/m²s) on heat transfer coefficient, h, and pressure drop, Δp, were studied for T_{sat}=20 ºC. The h reached values up to 18 and 9 kW/m²K for R290 and R600a, respectively. The influence of G on Δp was observed, and the highest loss for R600a. The flow patterns during the tests were plug, slug and annular, but with differences in minichannels. The patterns for R600a evolved to annular faster than R290.
Keywords: Flow boiling, R600a, R290, Multi-port extruded tubes, Heat transfer coefficient, Pressure drop, Flow patterns

1. INTRODUCTION

Compact heat exchangers characterized by high-performance using micro channels have been developed for several applications, including automobile air conditioning and heat pumps, electronic cooling, power generation (Khan and Fartaj, 2011). Many studies with multiport extruded aluminum tube (MPE) have focused characteristics of heat transfer and pressure drop during condensation (López-Belchí et al., 2016; Pham et al., 2015) to apply for condensers. The studies of boiling for evaporators are more limited, mainly with hydrocarbons. Huai et al. (2004) analyzed the heat transfer coefficient and pressure drop in boiling of CO_2 in a MPE aluminum channels with 10 channels and 1.31 mm ID over mass flux range of 131-399 kg/m²s, heat fluxes from 10.1 to 20.1 kW/m². The authors reported that the heat transfer is increased in the two-phase region when compared to single-phase condition, both mass and heat fluxes have significant effects, and pressure drop is very small. Yun et al. (2006) investigated the flow boiling of R410A in a MPE tubes with 8 channels, hydraulic diameter from 1.36 to 1.44 mm, heat fluxes from 10 to 20 kW/m², mass fluxes from 200 to 400 kg/m²s, and saturation temperatures at 0, 5 and 10 °C. The heat transfer coefficients were higher than those in large and small single channels at similar conditions. They found significant effects of saturation temperature, heat flux and mass flux on heat transfer coefficient only after dryout vapor quality and they observed that the pressure drop presented the same trends that in large diameter tubes. The effects of low mass fluxes on heat transfer of R134a and R1234yf in minichannels were performed by Mortada et al. (2012). It was used a 6-rectangular channel tube with 1.1 mm ID with mass flux of 20-100 kg/m²s and heat flux of 2-15 kW/m². As result, it was observed that the convective boiling was the dominant regime during the tests. Vakili-Farahani et al. (2013) tested R245fa and R1234ze (E) in a vertical MPE with 7 channels of 1.4 mm ID and observed a non-uniform distribution of heat throughout the test section. The heat transfer coefficient was constant or presented small reductions after the start of boiling with the establishment of bubbles, after that the coefficient gradually

increased with the predominance of annular pattern. The coefficient also increased with increasing saturation temperature, heat flux and mass velocity. Characteristics of heat transfer and pressure drop during vertical up-flow boiling of R1234yf in two different MPE with 16 channels and one with 40 channels were investigated by Li et al. (2017). The experiments were carried out under saturation temperature of 15 °C, mass flux of 60-240 kg/m²s and heat flux of 3-16 kW/m². According to the results, the heat transfer coefficient decreases linearly with increasing vapor quality. Besides, it was also observed that both heat transfer coefficient and pressure drop were not well predicted by existing correlations.

In literature of flow boiling in MPE using hydrocarbons few experimental studies are reported. Then this work aims to present the experimental results of the refrigerants R600a and propane R290 analyzing the flow pattern, heat transfer coefficient and pressure drop in a rectangular aluminum multiport tube in order to gather new data for heat exchanger design. The effects of mass velocity, heat flux and vapor quality will be presented besides the visualization of flow patterns in different conditions.

2. EXPERIMENTS AND PROCEDURES

2.1. Experimental Facility

An experimental facility was developed to investigate the flow boiling and pressure drop in a multiport minichannels and is schematically shown in Fig. 1a. The system consists of a loop that provides controlled mass flux, and it was designed to test different fluids under a wide range of flow conditions. The main part of the circuit has a pre-heater (PH), the test section (TS) and a visualization section (VS). The secondary part consists of a condenser, a refrigerant reservoir, a liquid refrigerant vessel, a magnetic driven micro gear pump and a subcooler.

The PH (horizontal stainless steel tube with 4.4 mm ID, 500 mm length) is uniformly heated by Joule effect and establishes the experimental conditions entering in the TS just downstream. The refrigerant enters in the PH as subcooled liquid and reaches the saturation condition to the exit. This condition sets vapor quality at the inlet of TS and varies according to the heat flux imposed on the PH. The TS consists of an extruded aluminum tube with 7 parallel rectangular channels with 300 mm length and 1,47mm average diameter of channels. The TS is heated by an electrical tape resistance wrapped around its surface to guarantee a uniform heat flux, as shown in Fig.1b. Both the PH and TS are thermally insulated. Downstream of the TS there is a VS with 32 mm length (Fig. 1c). It consists of the multiport tube, open, and mounted in a polycarbonate structure to allow visualizing the flow pattern. A high speed camera was used to capture images during the tests. c

The pressure and temperature measurements at the inlet and outlet of the PH are carried out by two absolute pressure transducers and T-thermocouples, in direct contact with the refrigerant. On the upper outer wall 15 T-thermocouples were fixed at 5 positions along the tube, and there are 3 per position distributed on the channels (Fig. 1b). This configuration allow verifying the temperature distribution in the channels and along the length of TS, moreover the heat transfer coefficient is a function of wall temperature. The confinement effect of vapor-phase observed on minichannels in horizontal flow avoids variation in thickness of liquid film, thus ensuring the same heat transfer effect in both bottom and top sides. The outlet pressure was determined through the differential pressure. Tests were carried out to verify the effect of mass flux, G, heat flux, q”, and vapor quality on flow patterns, heat transfer coefficient and pressure drop. For a fixed G, tests are performed for different q" in the TS. In each test, q" is set and the heat rate applied to the PH is increased by varying the quality, x, at the inlet of TS. The variation on the parameters were: G = 35 to 170 kg/m²s and q”= 5 to 20 kW/m², for the saturation temperature of 20 ºC. This temperature is an intermediate condition between various applications (refrigerators, air conditioners and cooling of electronic components), and is the lowest temperature where conditions remained stable during all tests performed. The parameters of the thermal-hydraulic analysis were calculated from measured data of refrigerant temperatures, wall temperatures, pressures, flow rate, heat flux, and geometrical parameters. Single-phase tests were performed in order to determine thermal losses for both the PH and TS. In all cases, the losses are lower than 5%, and they were considered in the calculus.

2.2. Data Reduction

The heat flux is calculated considering the electrical power supplied, the internal surface area and the number of channels, for heated length. The mass flux considering the channel flow area, as follow:

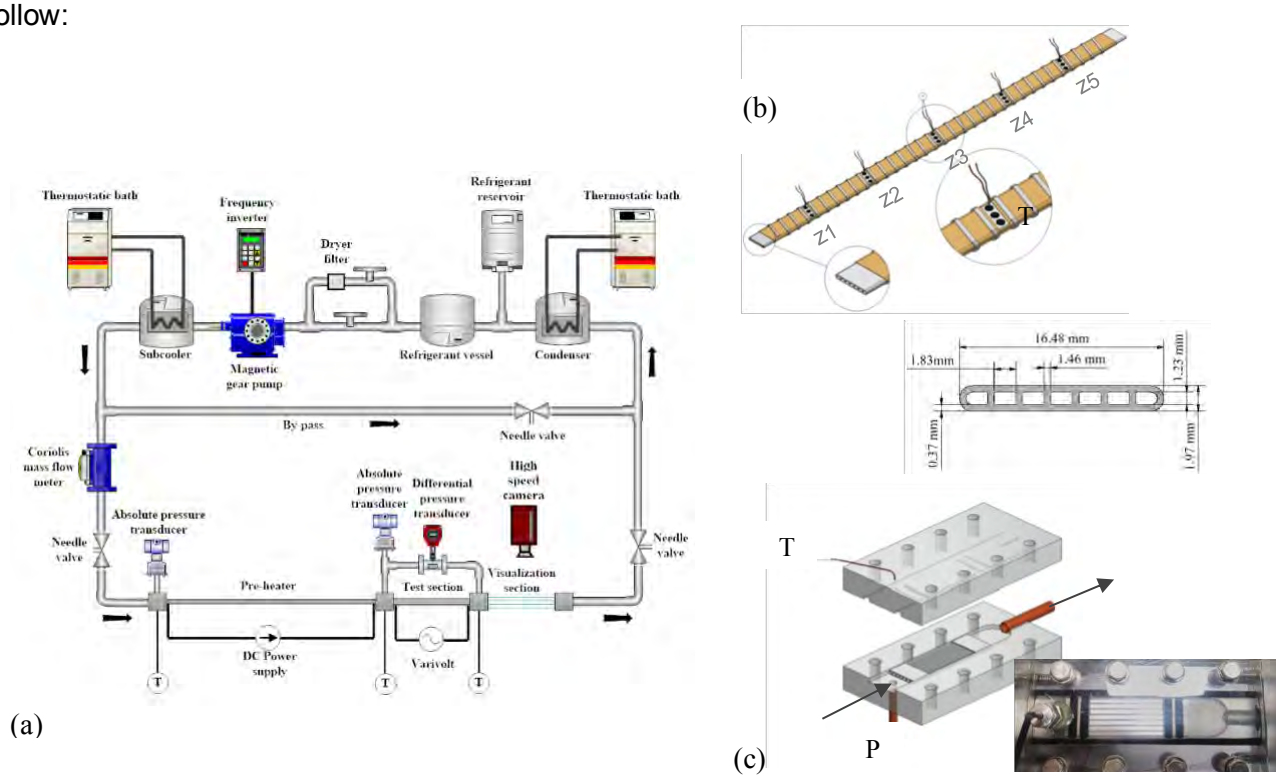

Figure 1: (a) Schematic view of the experimental facility; (b) Test section, TS – multiport minichannels and dimensions and (c) Visualization section, VS

$$q'' = \frac{q}{NA_{is}} \quad \text{and} \quad G = \frac{\dot{m}}{NA_c} \qquad \text{Eq. (1)}$$

The local heat transfer coefficient, h_z, is determined as follows:

$$h_z = \frac{q''}{(T_{wi,z} - T_{sat,z})} \qquad \text{Eq. (2)}$$

The internal wall temperature was calculated assuming radial conduction through the wall as given by:

$$T_{iw} = T_{ew} - \frac{qe}{kA_{es}} \qquad \text{Eq. (3)}$$

For each axial location *z* along the test tube (Fig. 1b), the external wall temperature was assumed to be the average of three measured top wall temperatures. The local saturation temperature, $T_{sat,z}$, is obtained as a function of local saturation pressure, $p_{sat,z}$, considering the pressure drop as being linear along the tube.

The vapor quality in test section inlet, $x_{i\text{-}TS}$, was calculated from energy balance in PH, or:

$$i_{i-TS} = i_{o-PH} = \frac{q_{PH}}{\dot{m}} + i_{i-PH} \quad \text{and} \quad x_{i-TS} = \frac{i_{i-TS} - i_l}{i_{lv}} \qquad \text{Eq. (4)}$$

The enthalpies were estimated by pressure and temperature measurements downstream and upstream the section. The local enthalpy and vapor quality in the test section were estimated as in the PH section.

The total two-phase flow pressure drop was measured in the TS for different G and q", and is the sum of friction and acceleration contributions. The minor losses related to entrance and exit head losses (sudden contraction and sudden enlargement pressure drop) were neglected ($\Delta p_{i-o} \approx 0$).

$$\Delta p_{tot} = \Delta p_f + \Delta p_{ac} + \Delta p_{i-o} \quad \text{Eq. (5)}$$

The acceleration or momentum component, Δp_{ac}, results from flow acceleration due to specific volume enhancement during evaporation. Between generic points *i* and *o*, this pressure drop is given by Eq. (6), and the simplest assumption of homogenous flow was used to calculate the void fraction, α. The frictional pressure drop component was obtained by subtracting the acceleration component from the measured total pressure drop.

$$\Delta p_{ac} = G^2 \left\{ \left[\frac{(1-x)^2}{\rho_l (1-\alpha)} + \frac{x^2}{\alpha \rho_v} \right]_o - \left[\frac{(1-x)^2}{\rho_l (1-\alpha)} + \frac{x^2}{\alpha \rho_v} \right]_i \right\} \quad \text{Eq. (6)}$$

The relative uncertainties of measured parameters for various experimental conditions were calculated using the method of expanded uncertainty. The maximum uncertainties of temperature is 0.3 ºC, the local pressure 1.3 %, mass flux 0.17%, heat flux 2%, vapor quality 4.5%, frictional pressure drop 2.5% and heat transfer coefficient 9.1%.

3. RESULTS AND DISCUSSION

3.1. Flow patterns

Some images of flow patterns in different conditions are shown in Fig. 2. The patterns plug/slug, intermittent (churn/wavy annular) and annular were identified, considering the predominant pattern among parallel channels. It is possible to note the influence of G and q" and different patterns in parallel channels at the same conditions, probably associated to the flow and heat maldistribution into the channels and the transient thin-film evaporation mechanism. Isolated and elongated bubbles were observed in specific conditions, as high G and low q", for low x. Intermittent and annular flow patterns were observed in different conditions, and sometimes in a low x, G and q", and can be considered predominant patterns in the tests. Fig. 3 presents the flow patterns maps for the refrigerants. The flow patterns of the R600a evolve faster to the annular pattern, compared to R290. This is due to the surface tension effects that are more dominant for R600a (10.7 mN/m and R290 7.63 mN/m) and therefore the more confinement between the two fluids (Co_{R600a}=0.96 and Co_{R290}= 0.86) and leads to the transition from the elongated bubble to the annular flow in lower vapor quality, x. It can also be observed that as G increases, it becomes more difficult to classify the transition from churn, annular wavy and annular, which tends to occur at lower, x (convective boiling domain, CB).

3.2. Heat Transfer Coefficient

3.2.1 Effect of mass flux, G

Fig. 4 shows the variation of local heat transfer coefficient, hz, with vapor quality, x, and mass flux, G, for R290 (a and b) and R600a (c and d), for heat fluxes of q" = 5 e 15 kW/m², respectively. For R290 the coefficient hz increases with G, but this effect is more evident as the quality, x, increases and for a higher heat flux, q" (Fig. 4b). For higher values of G, the values of coefficient increases at lower x. The effect of G is minimal at low x, where the bubble pattern was identified and the values of hz represent the beginning of nucleated boiling (NB).

3.2.2. Effect of heat flux, q"

For R290 and lower G (Fig. 5a) one can see the influence of q" up to a certain quality (x ~ 0.8), hz increases with increasing q". For larger x the coefficient increases, but independent of the q". In Fig. 5b for a larger G, hz increases regardless from q", reaching the value around 18 kW/m²K for x of 0.05 to 0.87. This behavior also occurs for R600a, but for larger G (Fig. 5d). The hz reached values

close to 9 kW/m²K. For the lowest G, the decrease of hz, and the little influence of q" for the entire range of x, can be verified.
Comparing the behavior of the coefficient hz for the fluids in Fig. 6, it is verified that for low values of x the behavior is similar. With the increase of x, R290 has the highest coefficient and it continues to increase with x. As for the R600a, the hz stabilizes and subsequently tends to decrease, reaching in this condition the dry-out. The predominant patterns observed for this condition were the plug and slug for the R290 and the annular for the R600a. The main differences are related to different refrigerant properties, like conductivity, viscosity and enthalpy of vaporization.

Propane - R290	Isobutane - R600a
Isolated Bubbles q"=5kW/m², G=170 kg/m²s, $x_{o\text{-}TS}$=0.09	Isolated Bubbles
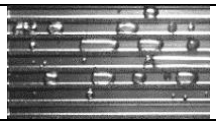	Not observed
Plug and Slug q"=10kW/m², G=70 kg/m²s, $x_{o\text{-}TS}$=0.43	Plug and Slug q"=5kW/m², G=35 kg/m²s, $x_{o\text{-}TS}$=0.29
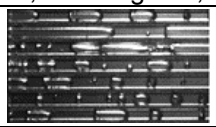	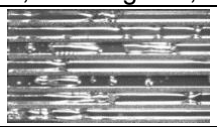
Churn q"=5kW/m², G=100 kg/m²s,$x_{o\text{-}TS}$=0.41	Churn q"=16kW/m², G=100 kg/m²s,$x_{o\text{-}TS}$=0.3
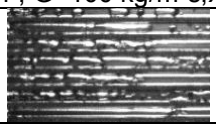	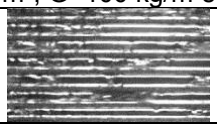
Wave Annular q"=20kW/m², G=70 kg/m²s,$x_{o\text{-}TS}$=0.98	Wave Annular q"=15 kW/m², G=60 kg/m²s,$x_{o\text{-}TS}$=0.56
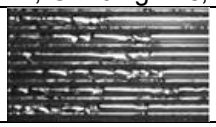	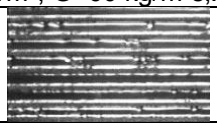
Annular q"=15 kW/m², G=55 kg/m²s,$x_{o\text{-}TS}$=0.98	Annular q"=10kW/m², G=55 kg/m²s,$x_{o\text{-}TS}$=0.81
	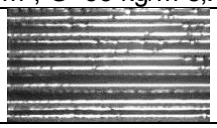

Figure 2: Images of flow patterns observed for refrigerants R290 and R600a

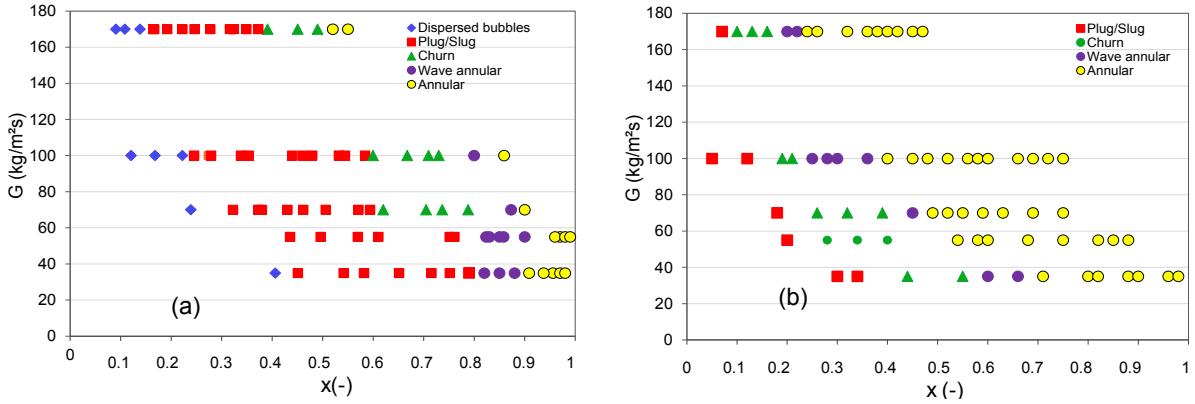

Figure 3: Maps of flow patterns: (a) R290 and (b) R600a

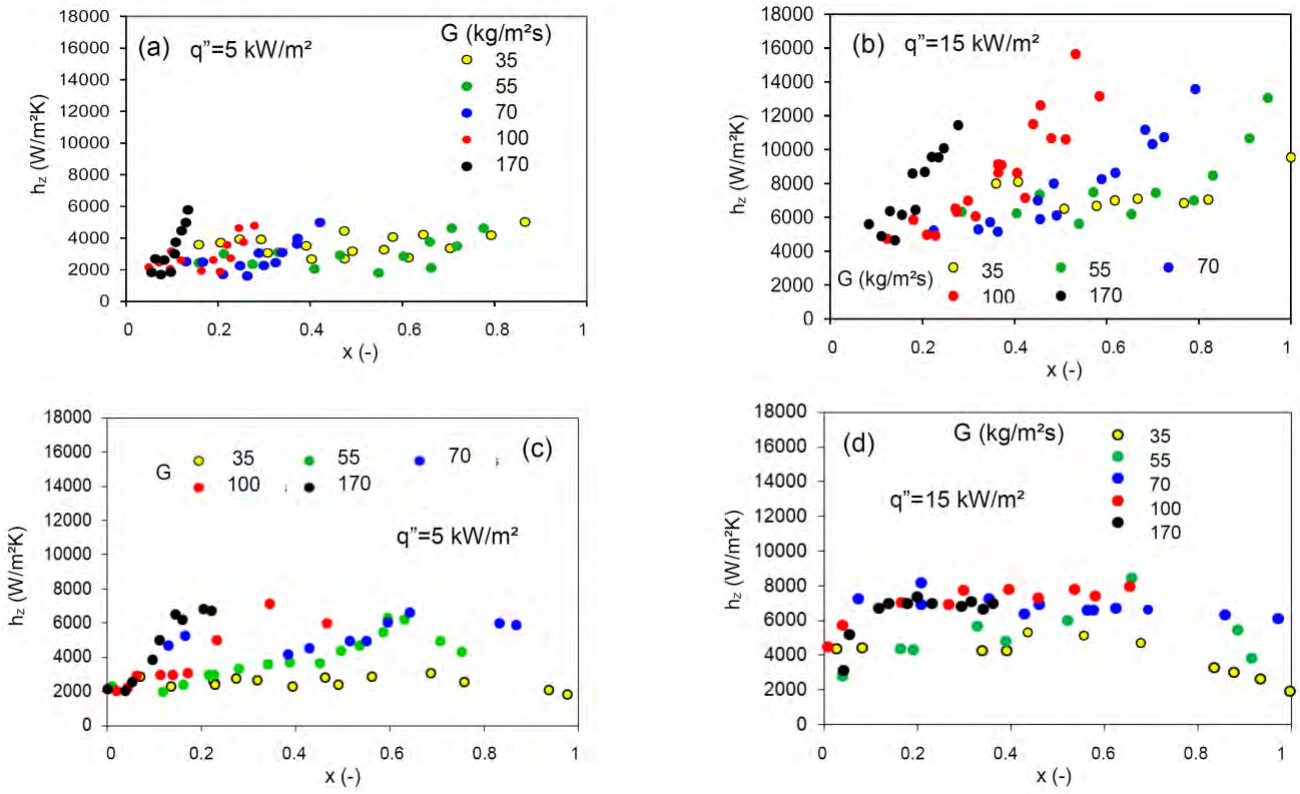

Figure 4: Local heat transfer coefficient for R290 (a) - (b) and R600a (c) - (d) for heat fluxes of q"= 5 kW/m² and q"= 15 kW/m²

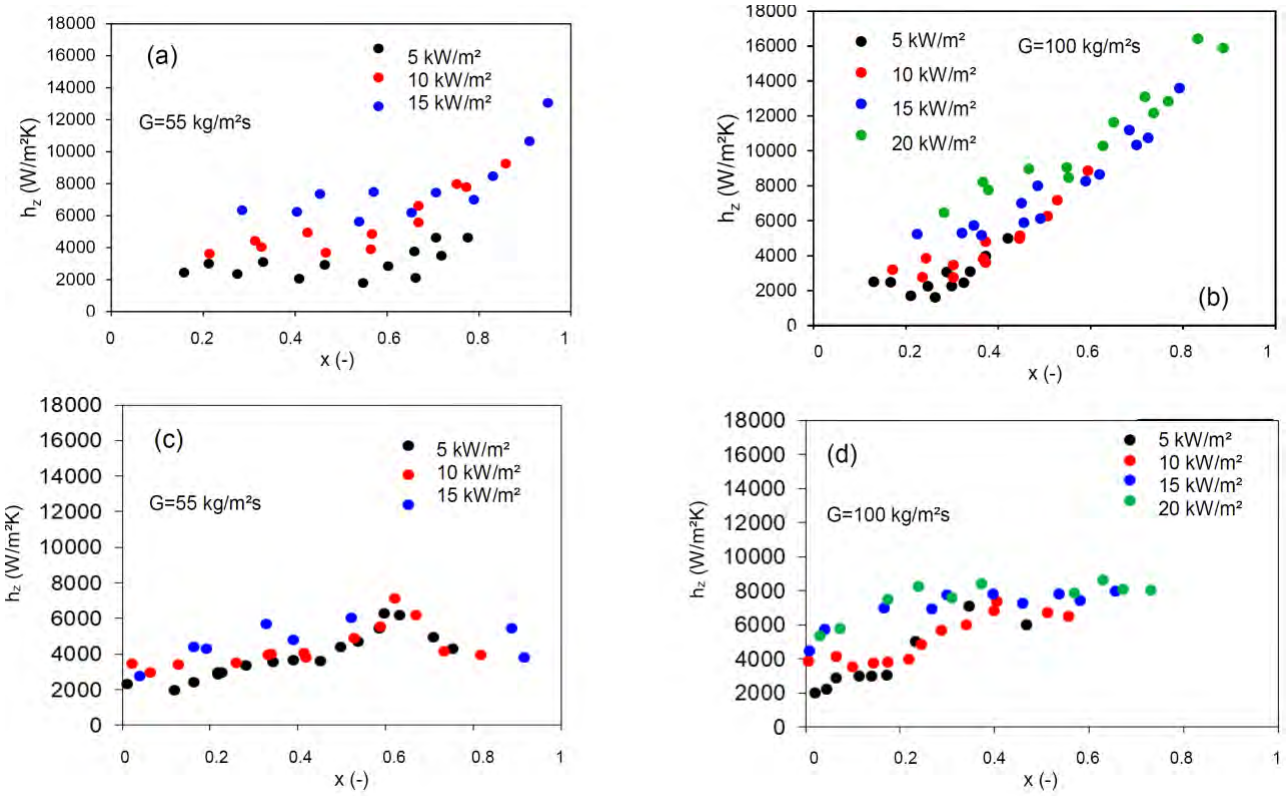

Figure 5: Local heat transfer coefficient for R290 (a) - (b) and R600a (c) - (d) for mass flux of G=55 kg/m²s and G=100 kg/m²s

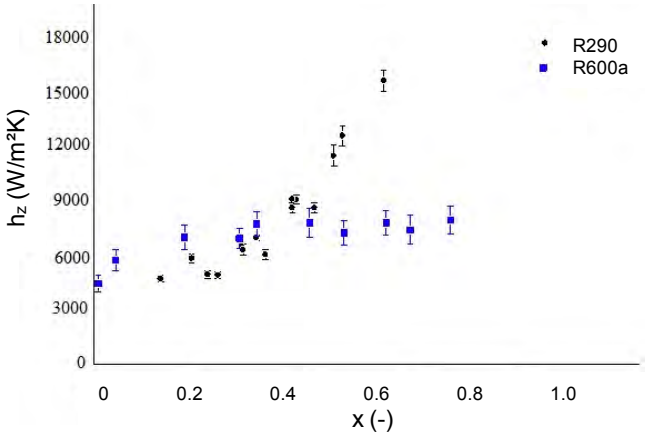

Figure 6: Heat transfer coefficient of R290 and R600a comparison for q"=15 kW/m² and G=100 kg/m²s

3.3 Pressure drop

The acceleration, or momentum pressure, represents a very low percentage of the total pressure drop (around 4% for low G and 9% for higher G). In Fig. 7 is shown the effect of G on frictional pressure gradient, dp/dz_f, for R290 (Fig. 7a) and R600a (Fig. 7b). Most notably, as G increases, pressure drop increases and nearly linearly for most of the quality range. An increase in the friction pressure gradient with the vapor quality is observed as G increases, and this effect is more evident for R600a. The lower G the gradient practically independent of quality. The R290 has lower pressure drop than R600a (8 kPa/m and 18 kPa/m, respectively). This is justified because the propane has higher vapor density, higher density ratio and lower viscosity of the liquid, besides the higher saturation pressure (840 kPa in relation to 303 kPa for the isobutane).
The increase in pressure drop with G is related to the velocity difference between the liquid and vapor phases and the flow regime, because the larger the G, the greater the variation of the slip velocity between the phases and consequently, and the predominant pattern is annular.

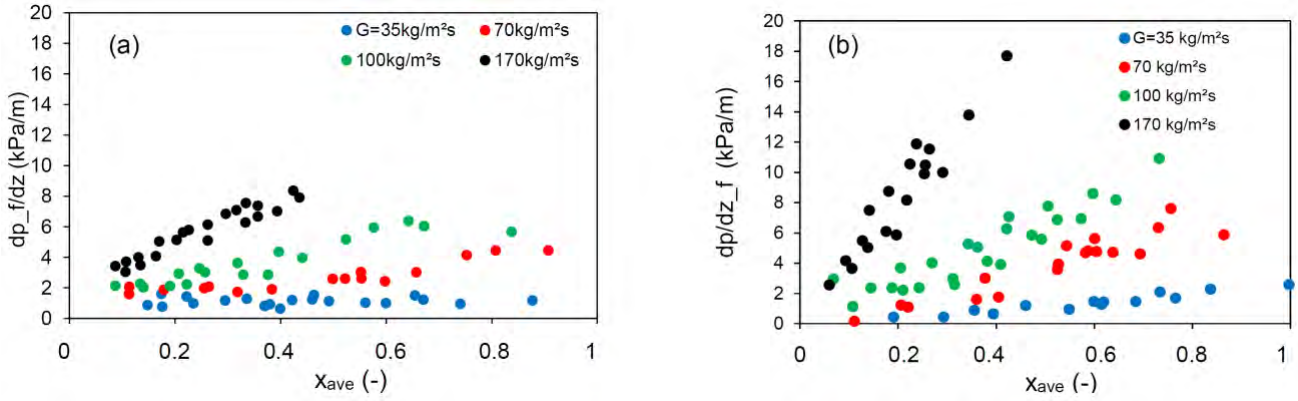

Figure 7: Frictional pressure drop variation for different mass flux for R290 (a) and R600a (b)

4. CONCLUSIONS

Experimental results during flow boiling of R290 and R600a in a horizontal MPE tube, under variations in the mass flux, G, heat flux, q", and vapor quality, x, were presented. The behavior of heat transfer coefficient, h, and pressure drop gradient, dp/dz, for different conditions were investigated and the flow patterns were identified. Some observations could be made from this study:
- The HT coefficient, h, increases with q", for both fluids, especially for low vapor qualities. The effect of increasing G on h is greater for larger qualities and is almost negligible for smaller ones.

For R600a for smaller values of G, the h is almost independent of x and, different from R290, for larger G there is a decrease of h. In the comparison between R290 and R600a, the coefficient h for the propane, is practically 50% higher;
- The frictional pressure losses increase with increasing G and the quality, and the relation with the evolution of the flow patterns is observed. The R600a has a higher pressure loss than R290, and this effect is more evident for larger G;
-The main flow patterns observed for both fluids were plug/slug, intermittent (churn, annular waviness) and annular, and heat and mass flux have significant effect on the patterns and the transition; different flow patterns in parallel minichannels have been verified. It has also been found that the flow patterns for R600a evolve faster to the annular pattern, relative to R290.

ACKNOWLEDGEMENTS

The authors gratefully acknowledge support of this work by Brazilian National Council of Research (CNPq), and to Capes/Ministry of Education.

NOMENCLATURE

		Subscripts	
A	area [m^2]	*ac*	acceleration
e	wall thickness [m]	*c*	cross section
G	mass flux [kg/m^2s]	*es*	external surface
h	heat transfer coefficient [W/m^2K]	*ew*	external wall
i	enthalpy [kJ/kg]	*f*	frictional
k	thermal conductivity [W/mK]	*i*	inlet
L	length [m]	*is*	Internal surface
$\dot{m}$	mass flow rate [kg/s]	*l*	liquid
N	number of channels	*lv*	liquid-vapor
p	pressure [kPa]	*o*	outlet
Δp	pressure drop [kPa]	*PH*	pre-heater
q	electrical power, heat rate [W]	*s*	superficial
q"	heat flux [kW/m^2]	*sat*	saturation
T	temperature [ºC]	*tot*	total
x	vapor quality [-]	*TS*	test section
ρ	density [kg/m^3]	*v*	vapor
α	void fraction [-]	*z*	axial location/local

REFERENCES

Huai, X., et al., 2004, An experimental study of flow boiling characteristics of carbon dioxide in multiport mini channels. *Applied Thermal Eng.* 24: 1443–1463.

Khan, M. G., Fartaj, A. 2011, A review on microchannel heat exchangers and potential applications. *Int. J. of Energy Resources*, 35(7): 553-582.

López-Belchí, et al., F. 2016. Condensing two-phase pressure drop and heat transfer coefficient of propane in a horizontal multiport mini-channel tube: Experimental measurements. *Int. J. of Refrigeration*, 68:59-75.

Mortada, S., et al., D. 2012. Boiling heat transfer and pressure drop of R-134a and R-1234yf in minichannels for low mass fluxes. *Int. J. of Refrig*. 35: 962-973.

Pham, Q.V., Choi, K-Il, Oh, J.-T., Cho H., Kim T., Kim J., Choi J. 2015. An experimental study of condensation heat transfer using R410A in a multiport extruded tube. In: ICR 2015, August 16 - 22 - Yokohama, Japan.

Vakili-Farahani, F., Agostini, B, Thome, J. R., 2013, Experimental study on flow boiling heat transfer of multiport tubes with R245fa and R1234ze(E). *Int. J. of Refrig.* 36: 335 – 352.

Yun, R., Heo, J.H., Kim, Y., 2006, Evaporative heat transfer and pressure drop of R410A in microchannels. *Int. J. of Refrig.* 29: 92–100.

Manuscript ID: 839
DOI: 10.18462/iir.icr.2019.0839

Signal analysis and mass measurement based calibration of capacitive sensors for void fraction and flow regimes in horizontal and vertical round tubes using R134a

Hongliang QIAN[(a)], Pega HRNJAK[(a,b)*]

[(a)] Air Conditioning and Refrigeration Center, University of Illinois at Urbana-Champaign, 1206 West Green Street, Urbana, IL 61801, USA
[(b)] Creative Thermal Solutions, 2209 Willow Rd., Urbana, IL, USA
[(*)] Corresponding author

ABSTRACT

Flow patterns and void fraction are crucial descriptors of two-phase flows. This paper presents flow pattern identification and void fraction measurement with a non-intrusive method by a new capacitive sensor.
In addition, this paper presents characterization of flow patterns with the capacitive sensor, correlated to visualization results obtained by a high-speed camera in horizontal and vertical round tubes (D=7mm) with R134a in developed adiabatic conditions. The sensor can characterize flow patterns observed within the test conditions. The sensor was calibrated based on mass measurements. After this calibration, the capacitive sensor can be directly used to measure void fraction in further studies. Three different axial lengths of electrodes in the sensor are built to explore the potential of application of this sensor in various HVAC&R systems. The comparison of signals from each of them shows that the signals are independent of axial length in the range explored.

1. INTRODUCTION

A non-intrusive way to characterize flow regimes and void fractions has many potential benefits over classical methods. Keska *et al.* (1999) claimed that capacitive signals showed very good potential to recognize flow patterns. Different capacitance sensors for void fraction and flow regimes were designed and presented by various authors (Abouelwafa and Kendall, 1980, Ahmed and Ismail, 2008, Canière, T'Joen*, et al.*, 2007, Canière *et al.*, 2008, Elkow and Rezkallah, 1996, Geraets and Borst, 1988, Jaworek and Krupa, 2004, 2010, Kendoush and Sarkis, 1995). Some typical electrodes configurations for a capacitance sensor are shown in Fig. 1. In the work presented in this paper, we used an original, newly developed sensors by the authors (Qian and Hrnjak, 2018), having configuration with two concave plates (Fig. 1(a)) which has the potential to measure cross-sectional void fraction by reducing axial length of electrodes. In former studies, the axial length of electrodes was commonly set to be equal to one or more than one inner diameter. We studied three axial lengths to see whether it can be reduced and thus be used in various HVAC&R systems that require more compact design.

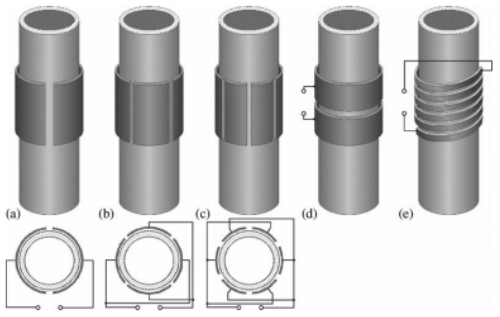

Figure 1: Some typical electrode configurations: (a) Two concave plates. (b) Four concave plates. (c) Six concave plates. (d) Rings. (e) Double helix. (Jaworek and Krupa, 2004)

2. DESIGN OF CAPACITANCE SENSOR

Two concave electrodes do not provide uniform electric field. That means the capacitive signals of two-phase mixture within the sensor depends on both two phase distribution and dielectric constant of the mixture. That strengthens the need of the calibration procedure in real conditions, not based on void fraction correlations.

We used R134a as the working fluid which has very high volume resistivity. At 25ºC, dielectric constant for liquid phase is 9.87 and for vapor phase is 1.0125 (ASHRAE, 2013). The dielectric constant difference between two phases will be the signal for the flow patterns and void fraction. The sensor must have the capability to measure small capacitive signals (in pF) to be utilized in HFC systems. Also, the dielectric constant is a temperature dependent property. For R134a, researches (Feja, 2012, Sedrez and Barbosa, 2015) reported dielectric constant decreased as temperature increased. However, if the temperature is kept constant when refergeant is in the two-phase zone, the effect can be neglected. dos Reis and Goldstein (2005) developed a procedure to correct the effect of variation of fluid flow temperatures and it can be used in this sensor when needed.

The capacitance sensor in this paper has similarity to the one developed by Canière, T'Joen*, et al.* (2007). To utilize this sensor in more situations other than only horizontal tubes, some modifications and further developments are made. Fig. 2 shows the cross-sectional and side view of the sensor. Fig. 3 shows configuration of the electrodes in the sensor. Detailed description of this sensor can be found in the earlier publication (Qian and Hrnjak, 2018). Seven pairs of electrodes (1-7) with three different axial lengths locate in a row with the gap between each pair of electrodes of half inner diameter of the tube (D/2). First three pairs from the left (1-3) have the axial length of one diameter (D). Axial length of two pairs of electrodes (4 and 5) is 2D/3 and of the last two pairs (6 and 7) is D/2. Four pairs of electrodes (1, 3, 5 and 7) are connected to the ground as guarding electrodes to let the electric field be kept within the electrodes. The other three pairs with different axial lengths measure the capacitive signals within the electric field. We have used a commercially available transmitter which can directly measure capacitive signals from custom sensors. It is capable to read such small capacitive signals and provide relative good resolution (approx. 0.001 pF).

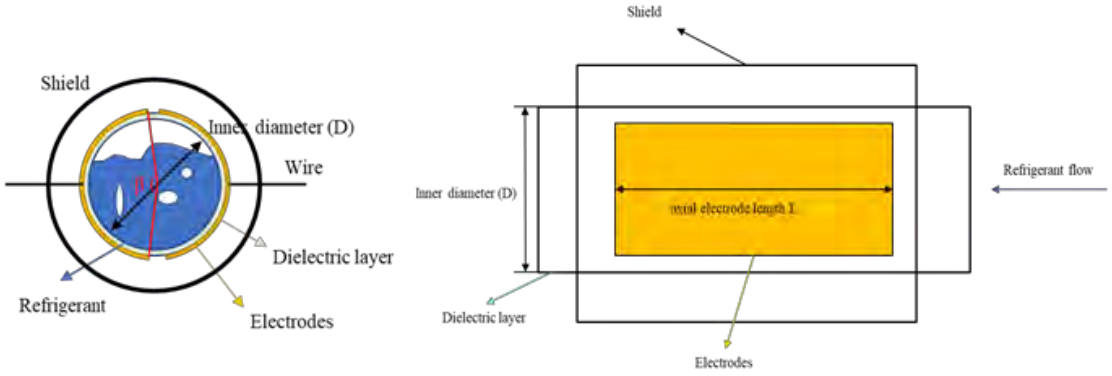

Figure 2: Cross-sectional and side view of the capacitance sensor

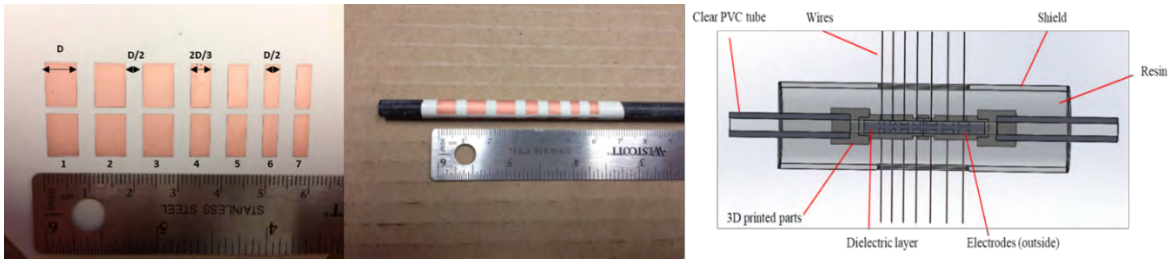

Figure 3: Configuration of the electrodes in the sensor

3. FACILITY

The schematic drawing of the calibration facility is shown in Fig. 4. Detailed description of the facility can be found in (Qian and Hrnjak, 2018). Basically, it is a gear pump facility without oil. Refrigerant is first heated into superheat vapor and then condensed to desired quality. Quality is determined by measuring temperature and mass flow rate of the secondary fluid. In the test section, two quick-closing valves are used to measured void fraction. A high-speed camera is used to capture high-speed video of flow regimes with resolution 512x512 and speed of 2200 frames per second. The sensor is located right after the visualization part. The experimental conditions are listed in Tab. 1.

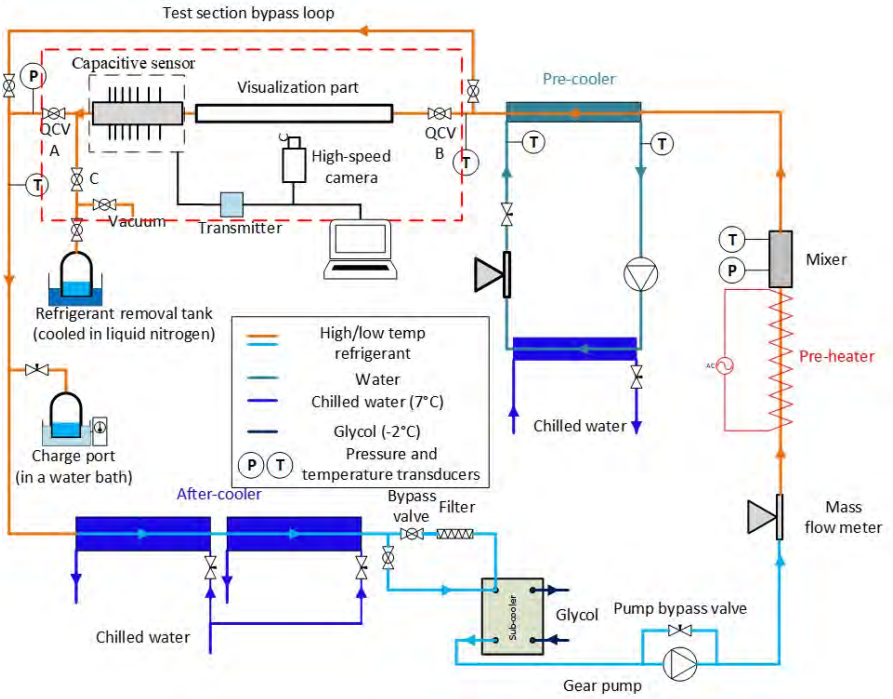

Figure 4: Schematic drawing of experimental facility, test section in the red box

Table 1. Experimental conditions

Working media	R134a
Refrigerant temperature (T_r)	33ºC
Test section orientation	Horizontal and vertical
Test section length	Horizontal: 1500 mm (~214 dia.) Vertical: 750 mm (~107 diameters)
Mass flux	Horizontal: 40, 80 and 115 kg/m2s Vertical: 65, 80 and 115 kg/m2s

4. RESULTS

For a certain mass flux and flow direction, the capacitive signals are read by a PC in pF directly. Capacitive signals for two base points are measured before each set of experiment was conducted: signals for fully liquid phase (C_{Liquid}) and fully vapor phase (C_{Vapor}). C_{Liquid} is determined for 33 ºC, which is equal to T_r. Olivier *et al.* (2015) indicate that dielectric constant of refrigerant vapor phase is not dependent on temperature. Hence, C_{Vapor} is measured at room temperature. After the two base points are measured, the capacitive signals for other test conditions ($C_{Measured}$) is then obtained. The normalized capacitance is then defined as following:

$$C_{norm} = \frac{C_{measured} - C_{Vapor}}{C_{Liquid} - C_{Vapor}} \qquad \text{Eq. (1)}$$

Though C_{Liquid} and C_{Vapor} may shift among different sets of experiments, $\Delta C_{L\text{-}V}$ ($\Delta C_{L\text{-}V} = C_{Liquid} - C_{Vapor}$, denominator of Eq. (1), the entire range of signal change from two base points) keeps quite

constant for all three axial lengths (Table 2) as the test temperature keeps constant. For a certain quality the numerator shows how much is the value larger than the value for the vapor condition (x = 1). Hence, the normalized signals are typically from 0 to 1. Though the base points shift among different sets of experiments, De Kerpel *et al.* (2013) proposed that normalized calibration curves would not be affected if $\Delta C_{L\text{-}V}$ remained the same.

Table 2. Range of $\Delta C_{L\text{-}V}$ for different sets of experiments for horizontal and vertical configurations, axial length of L=D/2, 2D/3 and D

$\Delta C_{L\text{-}V}$ (pF)	L=D/2	L=2D/3	L=D
Horizontal	1.1186±0.057	1.2241±0.0492	1.7972±0.069
Vertical	1.3190±0.011	1.3629±0.0174	1.8532±0.0085

4.1. Capacitive signal characteristics for various flow patterns

4.1.1. Horizontal flow regimes

Two major flow regimes are observed within the given mass flux range: slug/stratified-wavy flow and stratified-wavy flow. Fig. 5(a) and (b) show visualization results and schematic drawings. For slug/stratified-wavy flow, vapor slug appears in the upper portion of the tube periodically with liquid bridges in the middle. Boundary between upper vapor and lower liquid is wavy. When the vapor quality increases, liquid flow at the bottom and vapor stays in the upper portion of the tube with a wavy boundary.



Figure 5: (a) Slug/stratified-wavy flow (R134a, 80 kg/m2s, x=0.1, T=33ºC), (b) Stratified-way flow (R134a, 115 kg/m2s, x=0.6, T=33ºC)

Fig. 6(a) shows the normalized signals of slug/stratified-wavy flow (x=0.1), stratified-wavy flow (x=0.5) and two reference quality: fully liquid (x=0) and fully vapor (x=1) for the mass flux of G=80 kg/m^{2}s. When the quality x = 0.1 (slug/stratified-wavy flow), normalized signals show two major concentrations: one is at the top and the other is in the middle. This is because that when the vapor slugs goes into the sensor, capacitive signals stay at the middle level. When liquid bridges enter the sensor (all the cross-sectional area within the sensor is filled with liquid phase refrigerant), signals move up to the top. For the quality of 0.5 (stratified-wavy flow), no liquid bridges appeared in the visualization results. Vapor and liquid phase are separated by a wavy boundary. The signals show only one major concentration with relatively small oscillation amplitude. Fig. 6(b) shows the probability density estimate (PDE) results for both x=0.1 and 0.5. PDE which is to estimate the probability density in a non-parametric way is used to obtain signal amplitude distributions. As expected, for x = 0.1, two peaks representing two dominant levels (around 1 and 0.65) show up in the PDE diagram. For PDE results of x=0.5, only one steep peak presents. Combining Fig. 6(a) and (b), the major flow regimes appeared within tested mass flux range can be characterized by the capacitive signals.

Fig. 7(a) and (b) show the comparison among electrodes with different axial lengths. Two qualities representing two flow regimes which are discussed above are shown here. In both conditions, all of the three pairs of electrodes can give signals with same patterns. The comparison results are similar to qualities and mass fluxes. Besides, results from PDE diagram are also similar. They are not shown here due to the space limitation. Hence, for horizontal flows, D/2 electrodes can give similar results as larger electrodes does.

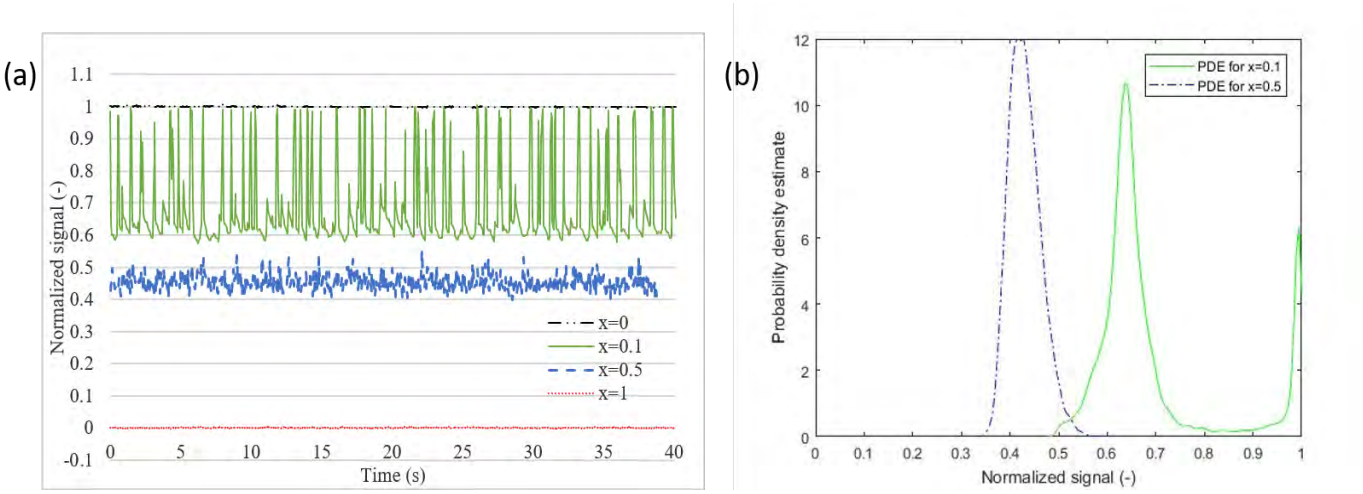

Figure 6: (a) Normalized signals for x=0.1, x=0.5 and two base points, G=80 kg/m²s, horizontal (b) PDE for x=0.1 and x=0.5, G=80 kg/m²s, horizontal

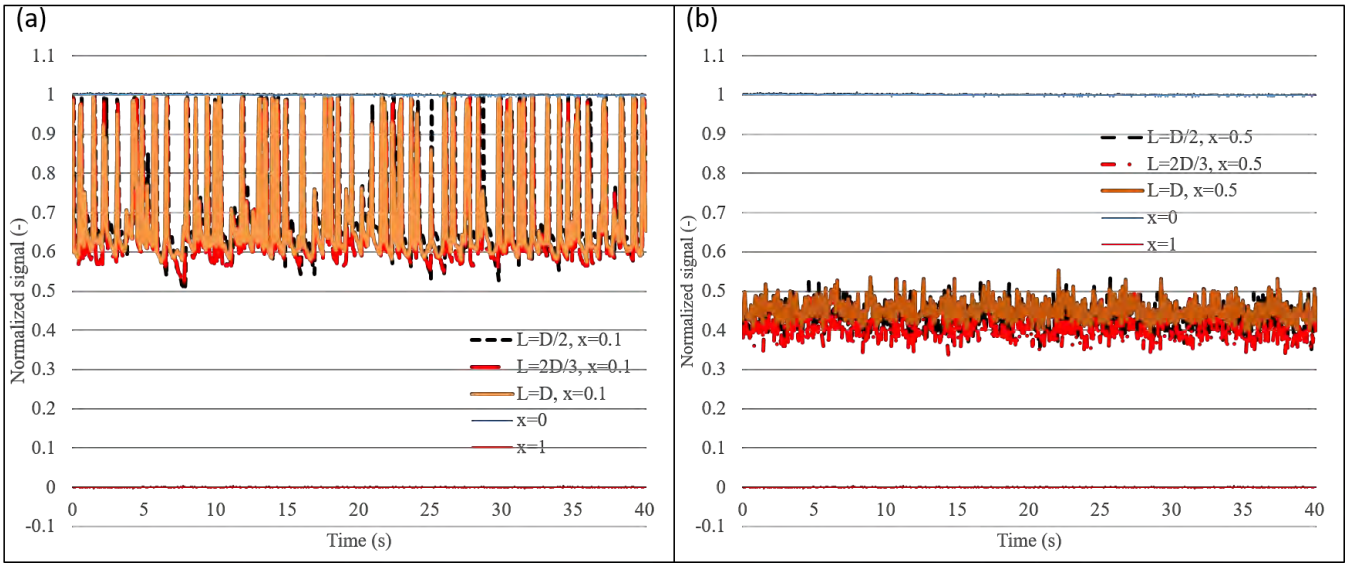

Figure 7: Signals comparison among electrodes with axial length of D, 2D/3, D/2 (a) x=0.1, G=80 kg/m²s, horizontal, (b) x=0.5, G=80 kg/m²s, horizontal

4.1.2. Vertical upward flow regimes

In this mass flux range, we observed slug, churn and annular flows. Fig. 8(a)-(c) shows the visualization results and schematic drawings. Slug flow is observed when quality is small. Vapor slugs appear periodically with liquid bridge in the middle. The slugs are in the middle of the tube and filling almost the entire cross section due to the direction of gravity is opposite of the flow. For high qualities, annular flow appears when liquid flows along the wall of the tube with vapor in the central core. It is relatively stable though the interface between liquid and vapor core is wavy. Churn flow which is in the middle quality range is highly agitated and the interface between liquid and vapor is hard to locate.

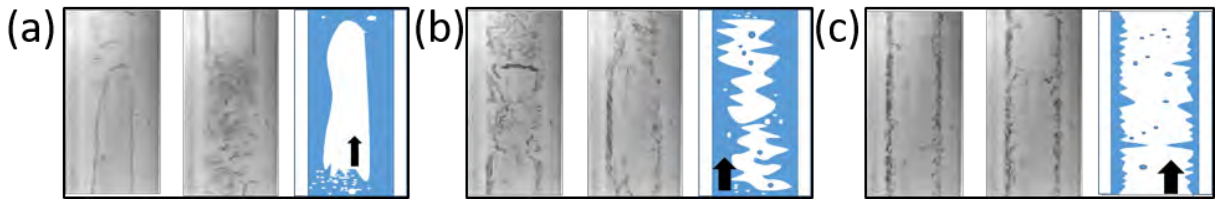

Figure 8: (a) Slug flow (R134a, 80 kg/m²s, x=0.1, T=33°C), (b) Churn flow (R134a, 80 kg/m²s, x=0.5, T=33°C), (c) Annular flow (R134a, 115 kg/m²s, x=0.9, T=33°C)

Similar to flow regimes in horizontal tubes, normalized signals and PDE results for different flow regimes are shown in Fig. 9(a) and (b). We selected x=0.1 (slug flow), x=0.4 (churn flow), x=0.8 (annular flow) and two reference conditions: x=0 and x=1 for mass flux equals to G=80 kg/m^{2}s as an example to show the characterization procedure. For slug flow, the signal pattern is similar to slug flows in horizontal tubes. Signals concentrate at two major lever depending on whether vapor slug or liquid is in the sensor. For annular flows, the signals concentrate at one major level. Signals fluctuate at a relatively suitable state and no huge oscillations are observed. Signals for churn flows are relatively more unstable compared to annular flows. The amplitude of oscillation is bigger. In Fig. 9(b), two peaks which represent dominant signal values are shown for slug flows. Only one peak which represents the dominant signal value is shown for annular flows. The peak in the diagram has a very small span, which shows the possibility of signals appears closely around the major value is much higher than other ranges. For churn flows, only one peak shows in the diagram as well. However, the span of the peak is bigger than that of annular flow, which means signals appear in a wider range.

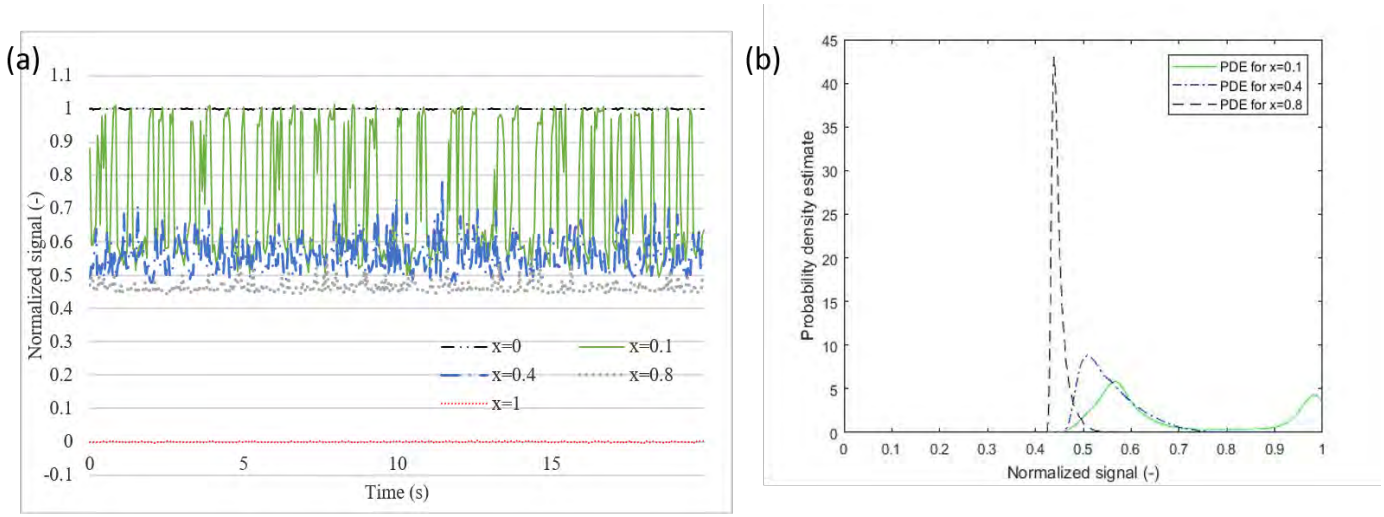

Figure 9: (a) Normalized signals for x=0.1, x=0.4, x=0.8 and two base points, G=80 kg/m^{2}s, vertical (b) PDE for x=0.1, x=0.4 and x=0.8, G=80 kg/m^{2}s, vertical

Fig. 10(a) to (c) show the comparison of signals among electrodes with different axial length. The three qualities discussed above which represent three different flow regimes are shown here. Signals from electrodes with different axial length give similar patterns and PDE results. Hence, for vertical upward flows, D/2 electrodes can give similar results as larger electrodes.

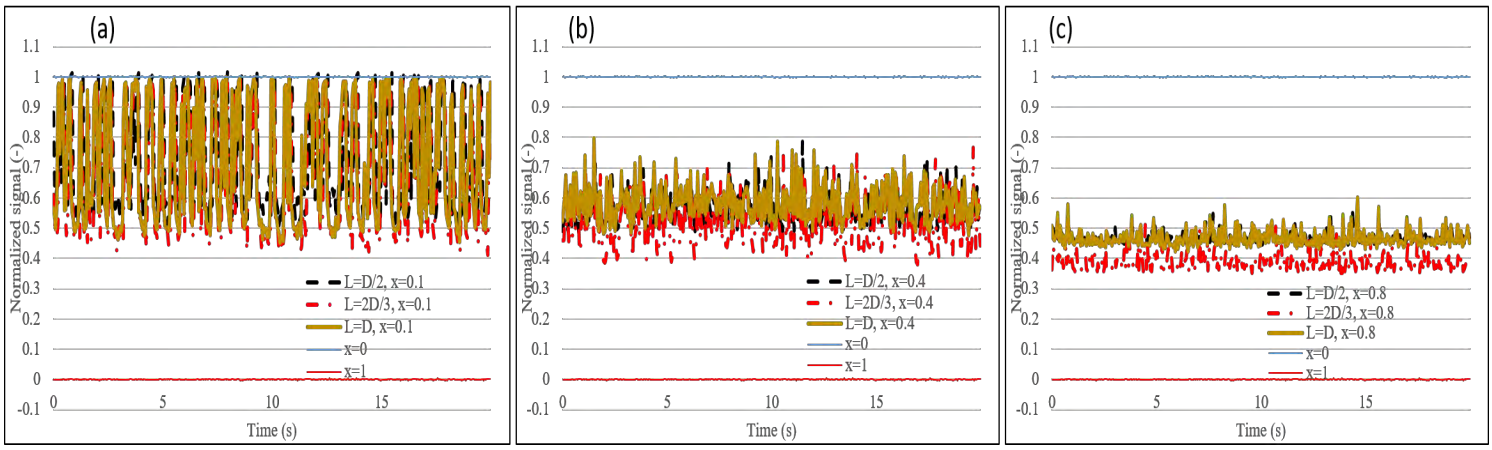

Figure 10: Signals comparison among electrodes with axial length of D, 2D/3, D/2 (a) x=0.1, G=80 kg/m^{2}s, vertical, (b) x=0.4, G=80 kg/m^{2}s, vertical, (c) x=0.8, G=80 kg/m^{2}s, vertical

4.2. Calibrated correlations for signals vs. void fraction based on mass measurements in smooth tubes

As mentioned above, the electric field is not uniform due to the configuration of electrodes. This results for the relationship between void fraction and capacitive signals is not linear. The calibration procedure is necessary before using this sensor to measure void fraction. Detailed calibration procedure can be found in (Qian and Hrnjak, 2018) and the results are shown in Fig 11(a) and (b). With these graphs (equations), sensors can be directly utilized to measure void fraction in horizontal and vertical upward flows with R134a in this mass flux range.

Fig 12(a) to (c) show the comparison of signals obtained from electrodes with different axial length corresponding to the measured void fraction for horizontal flows. All three mass flux conditions are compared. Three series of signals have the same trend. When the electrodes with different axial lengths measure the same void fraction and flow regime, the values of normalized time-averaged singles are nearly the same among these three pairs of electrodes. The signal values from electrodes with length of D/2 are overlapping those of D. However, the signal valves of electrodes with length of 2D/3 are a little bit smaller than those from the other two pairs. This may due to the configuration of the electrodes or instrumental errors. The pair of electrodes with 2D/3 axial length locates in the middle, where more guarding electrodes that are connected to the ground on both sides. This may reduce the values of signals. The normalized time-averaged signals are independent of void fraction and flow regimes and can be used to measure void fraction. Results for vertical upward flows are similar and not shown here due to the space limitation.

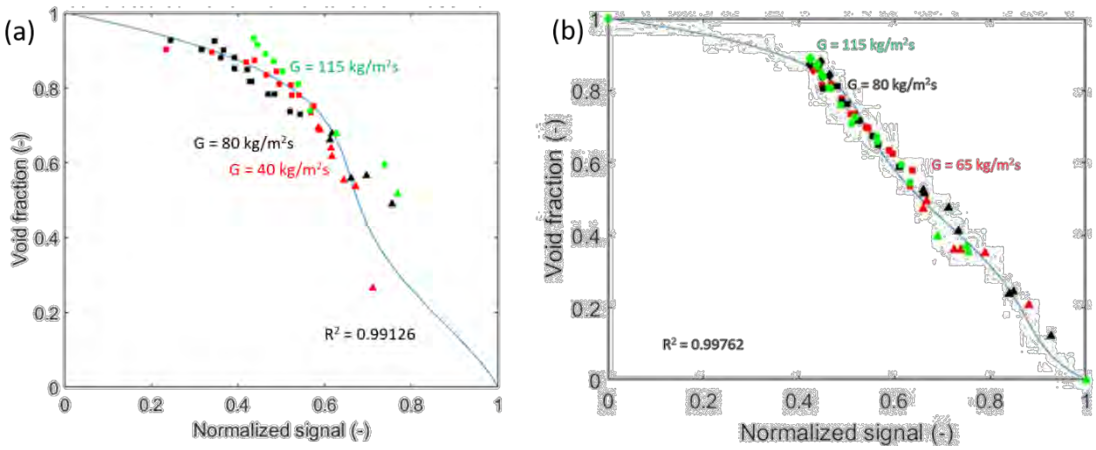

Figure 11: Calibrated relationship for capacitance sensor: measured void fraction by extraction vs. normalized signal at low mass flux, R134a, 33°C. (a) horizontal flows; (b) vertical upward flows

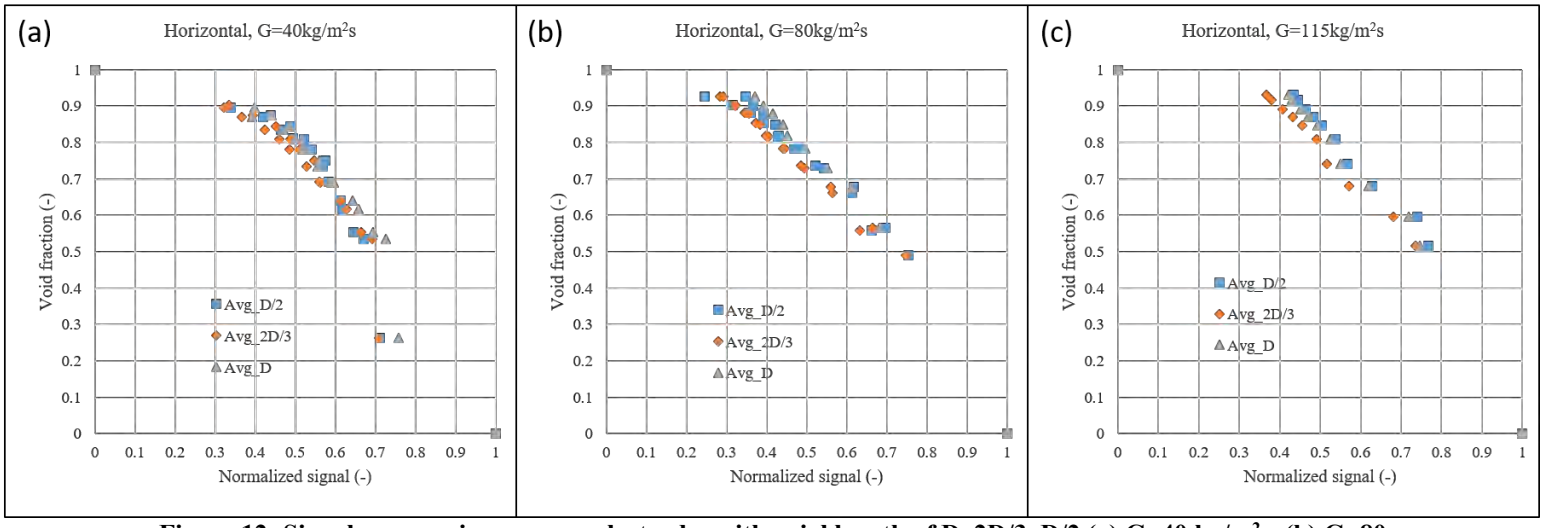

Figure 12: Signals comparison among electrodes with axial length of D, 2D/3, D/2 (a) G=40 kg/m²s, (b) G=80 kg/m²s, (c) G=115 kg/m²s

5. SUMMARY AND CONCLUSIONS

A new capacitance sensor is developed to characterize flow regimes in non-transparent tubes and measure void fraction for horizontal and vertical upward flows in smooth tubes.
Mass measurement method (extraction) is used to calibrate the sensor for void fraction.
Comparison of signals among electrodes with different axial lengths shows that all three lengths of electrodes have similar capabilities when characterizing flow regimes and measuring void fraction. The length can be reduced to at least half of inner tube diameter from one when using this sensor in more compact applications.

REFERENCES

Abouelwafa, M. S. A., & Kendall, E. J. M. (1980). The use of capacitance sensors for phase percentage determination in multiphase pipelines. *IEEE Transactions on Instrumentation and measurement, 29*(1), 24-27.

Ahmed, W. H., & Ismail, B. I. (2008). Innovative techniques for two-phase flow measurements. *Recent Patents on Electrical & Electronic Engineering (Formerly Recent Patents on Electrical Engineering), 1*(1), 1-13.

ASHRAE. (2013). 2013 ASHRAE Handbook - Fundamentals (I-P Edition). In: American Society of Heating, Refrigerating and Air-Conditioning Engineers, Inc.

Canière, H., T'Joen, C., Willockx, A., De Paepe, M., Christians, M., Van Rooyen, E., . . . Meyer, J. (2007). Horizontal two-phase flow characterization for small diameter tubes with a capacitance sensor. *Measurement Science and Technology, 18*(9), 2898.

Canière, H., T'Joen, C., Willockx, A., & De Paepe, M. (2007). *Capacitance Sensor Design For Refrigerant Two-Phase Flow Characterization.* Paper presented at the AIP Conference Proceedings.

Canière, H., T'Joen, C., Willockx, A., & De Paepe, M. (2008). Capacitance signal analysis of horizontal two-phase flow in a small diameter tube. *Experimental Thermal and Fluid Science, 32*(3), 892-904.

De Kerpel, K., Ameel, B., T'Joen, C., Canière, H., & De Paepe, M. (2013). Flow regime based calibration of a capacitive void fraction sensor for small diameter tubes. *International Journal of Refrigeration, 36*(2), 390-401.

dos Reis, E., & Goldstein, L. (2005). A procedure for correcting for the effect of fluid flow temperature variation on the response of capacitive void fraction meters. *Flow Measurement and Instrumentation, 16*(4), 267-274.

Elkow, K. J., & Rezkallah, K. S. (1996). Void fraction measurements in gas-liquid flows using capacitance sensors. *Measurement Science and Technology, 7*(8), 1153.

Feja, S. (2012). Measurement of electrical properties of refrigerants and refrigerant–oil mixtures. *International Journal of Refrigeration, 35*(5), 1367-1371. doi:https://doi.org/10.1016/j.ijrefrig.2012.03.011

Geraets, J., & Borst, J. (1988). A capacitance sensor for two-phase void fraction measurement and flow pattern identification. *International Journal of Multiphase Flow, 14*(3), 305-320.

Jaworek, A., & Krupa, A. (2004). Gas/liquid ratio measurements by rf resonance capacitance sensor. *Sensors and Actuators A: Physical, 113*(2), 133-139.

Jaworek, A., & Krupa, A. (2010). Phase-shift detection for capacitance sensor measuring void fraction in two-phase flow. *Sensors and Actuators A: Physical, 160*(1), 78-86.

Kendoush, A. A., & Sarkis, Z. A. (1995). Improving the accuracy of the capacitance method for void fraction measurement. *Experimental Thermal and Fluid Science, 11*(4), 321-326.

Keska, J. K., Smith, M. D., & Williams, B. E. (1999). Comparison study of a cluster of four dynamic flow pattern discrimination techniques for multi-phase flow. *Flow Measurement and Instrumentation, 10*(2), 65-77.

Olivier, S., Meyer, J., Elton, L., Müller, C., Martin, S. J., Huisseune, H., . . . Marzo, S. (2015). Measured void fraction and heat transfer coefficients during condensation. *Sort, 100*, 250.

Qian, H., & Hrnjak, P. (2018). Void Fraction and Flow Regimes Determined by Visualization, Mass Measurement and New Capacitance Sensor. *in: Proceedings of 17th International Refrigeration and Air Conditioning Conference at Purdue, Paper # 2223, 2018*.

Sedrez, P. C., & Barbosa, J. R. (2015). Relative permittivity of mixtures of R-134a and R-1234yf and a polyol ester lubricating oil. *International Journal of Refrigeration, 49*(Supplement C), 141-150. doi:https://doi.org/10.1016/j.ijrefrig.2014.09.019

Manuscript ID: 840
DOI: 10.18462/iir.icr.2019.0840

Visualization of two-phase flow through distributors and effect on performance of evaporators

Yufang YAO[(a)], Raghu KONEPUDI[(b)], Pega HRNJAK[(a,c)*]

[(a)] Air Conditioning and Refrigeration Center, University of Illinois at Urbana-Champaign
Urbana, 61801, USA, yufangy@illinois.edu
[(b)] Parker Hannifin
Washington, 98944, USA, raghujit.kunapuli@parker.com
[(c)] Creative Thermal Solutions
Urbana, 61820, USA, pega@illinois.edu
[(*)] Corresponding author

ABSTRACT

Proper operation of refrigerant distributors is essential for full utilization of evaporators with multiple circuits. The most common principle to first generate fully homogeneous flow after expansion valve and then distribute fluid into numbers of “feeder” tubes. Imperfect selection of the parameters can affect the uniformity of distribution.
This paper presents experimental evaluation of distribution with visualization of the flow through distributor and feeder tubes. The entire line between expansion valve and evaporator (distributor and feeder tubes) are all transparent.
The operation in this research was conducted in real 4-5 kW R134a system. The mass flow rate and inlet quality for each evaporator circuit are measured under same superheat, which represent the uniformity of distribution. Combining this quantitative mal-distribution with the visualization result, it offers a deeper insight into the mechanism of distributor performance.
Keywords: Distributor, Two Phase, Evaporator, Visualization, Geometry, Quality, Mass Flow Rate, Orientation

1. INTRODUCTION

Refrigerant distributors are commonly used on multi-circuits evaporators to separate liquid and vapor refrigerant evenly to each circuit and reduce pressure drop through evaporators. It is well known that distribution of two-phase refrigerant in distributor is significant to the performance of evaporator and system efficiency. Fay and Hrnjak (2012) investigated the effect of maldistribution of a conical distributor on capacity and system COP in a commercial air conditioning system. They found that an improvement of 4% in COP and 5% in capacity could be obtained when uniform distribution was achieved by adjusting distribution by needle valves installed in each circuit. There are many factors influencing the performance of distributor, such as mass flow rate, quality, inclination angle, distributor type and geometries. Several researches have been done to get more understanding about distributor and explore possible ways to improve its performance. Nakayama *et al*. (2000) found that the maximum cooling capacity difference among each circuit was higher at lower vapor quality. However, mass flow rate had nearly no effect on this parameter. This indicated that two-phase flow was mixed well inside the distributor. The influence of orientation depends on both the distributor type and working conditions. Zhang *et al.* (2014) demonstrated that reservoir type distributor could keep good performance when the inclination angle deviating from vertical direction was less than 10°. However, its performance would become much worse when the distributor was installed horizontally. For a good conical type distributor, Fay and Hrnjak (2012) found there was almost no difference in superheat patterns when the distributor was installed vertically or inclined with an angle of 45°. Li *et al.* (2005) indicated that the shape of distributor base and the position of orifice with respect to the distributor base had a significant effect on distribution by CFD simulation. The connections between distributor and expansion device also influence the uniformity of distribution. Bowers *et al*. (2014) indicated that by using an expansion device which integrated the distributor into the valve body, distributions of mass flow rate and superheat among each circuit became more uniform than the traditional valve and distributor assembly.

Visualization through a transparent distributor with a high-speed camera is a good option to get a deeper insight of how the refrigerant two-phase flow is mixed and then separated into each circuit. Aziz *et al*. (2012) conducted experiments to visualize air and water two-phase flow in an acrylic resin distributor. They found that the two-phase distribution was more uniform at high superficial velocities of vapor and liquid. Flow patterns at the inlet of the distributor observed in their study were in good agreement with Mandhane-Baker and Sekohuchi flow map for horizontal flow and vertical flow. Yoshioka *et al*. (2008) visualized R410A two-phase flow in a cylinder type distributor made of poly-carbonate resin. It was observed that liquid remained at the bottom of the distributor and part of it was dragged by the inlet flow unevenly into each circuit. This was because the inlet flow tended to incline in a certain direction.
In this study, several factors influencing the performance of refrigerant distributor were investigated. A 3D-printed transparent distributor is built with the same inner geometry of a distributor from Parker Hannifin. A high-speed camera was used to visualize the refrigerant two-phase flow in the transparent distributor and in the tube between distributor and expansion device.

2. EXPERIMENT

2.1. Facility

The operation in this research is conducted in a real 4-5 kW R134a system (shown in Fig. 1). It consists of two parts: the condensing unit and the test section. The condensing unit includes a compressor, an air-cooled condenser and a brazed plate heat exchanger as a sub-cooler. The test section is composed of a thermostatic expansion valve (TEV), a distributor and an electrical-heated evaporator. The TEV and the distributor are provided by Parker Hannifin. Four electrical heaters are controlled by variacs individually so that the same superheat can be achieved at evaporator exits. Four watt-transducers are used to measure the heating power of each electrical heater. Superheat at evaporator exit is obtained by measuring both pressure and temperature of the refrigerant. Four Micro Motions are installed downstream of the evaporator to get the mass flow rate of each circuit. Another one is installed before TEV to get the total mass flow rate. After passing through Micro Motions, four circuits converge into one tube connected to compressor, which is lubricated with POE 32 oil. All the four circuits have the same tube length with similar configuration to reduce the influence of facility on refrigerant distribution. The test section and the condensing unit are connected by flexible hoses. Hence, the test section can be set at different orientations with the connection between TEV and distributor not changing.
To visualize refrigerant two-phase flow in distributors, a transparent one is built based on the geometry of a distributor form Sporlan by 3D-printing. As shown in figure 2, the transparent distributor is connected to TEV directly by bolts and sealed with O-ring. Clear PFA tubes are glued to distributor outlets as feeder tubes. It is possible to visualize the flow patterns in any part between TEV and evaporator in this facility.

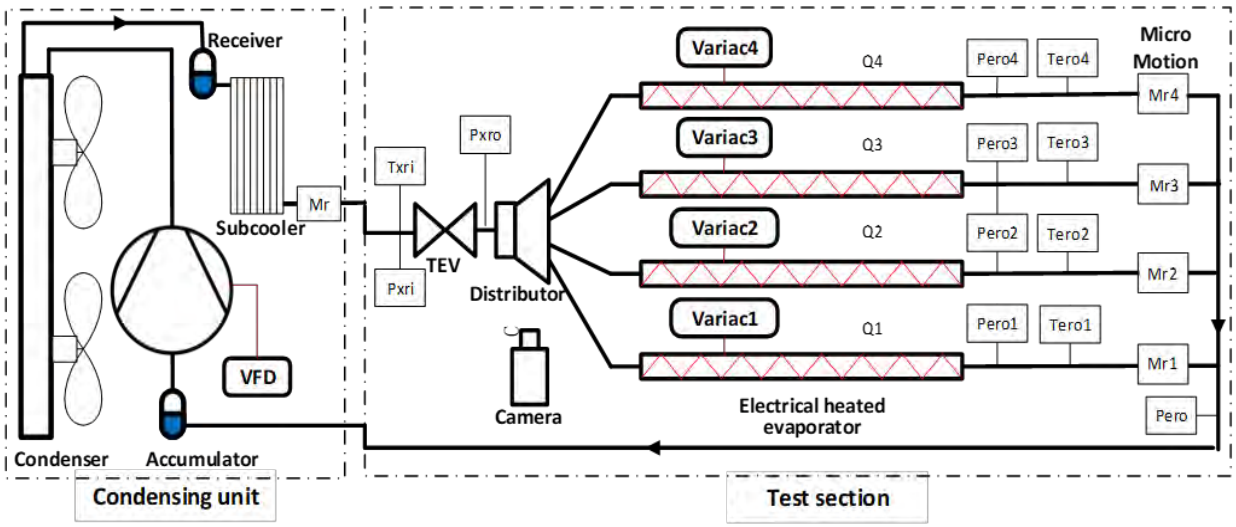

Figure 1: Schematics of experimental facility

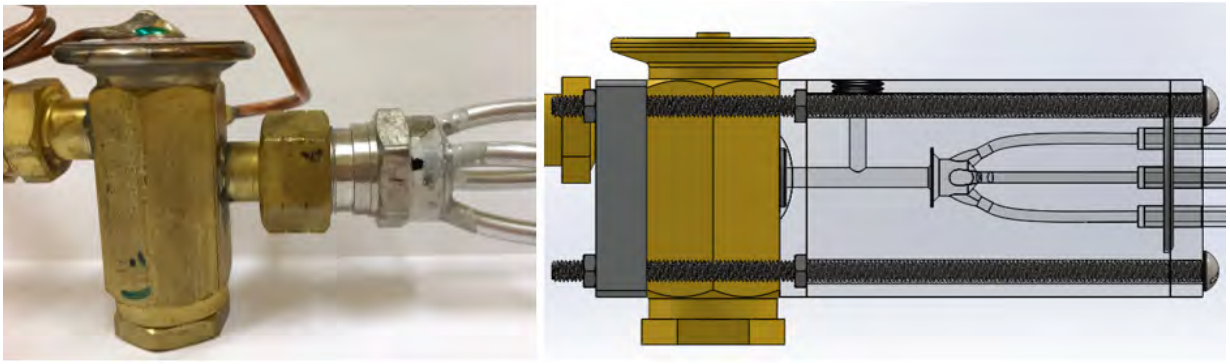

Figure 2: TEV and distributor assembly

2.2. Operating conditions and data reduction

This study investigates the effect of mass flow rates, vapor qualities at the distributor inlet and orientations on distribution characteristics. Refrigerant mass flow rates are controlled by changing the compressor frequency with a VFD. Vapor qualities at the distributor inlet are adjusted by changing the flow rate of chilling water in the sub-cooler. For each combination of mass flow rate and distributor inlet quality, three flow orientations (horizontal, vertical upward and vertical downward) are studied (Table 1). Figure 3 shows the test section at horizontal orientation.



Figure 3: Test section at horizontal orientation

Table 1. Experiment conditions

Conditions	Mass flow rate [g/s]	Quality [-]
1	15	0.23
2	20	0.23
3	25	0.23
4	25	0.15
5	25	0.09

Distributor performance is evaluated by the uniformity of refrigerant mass flow rates, vapor qualities at distributor outlets and heat loads among each circuit. Since the superheat at evaporator exit is controlled to be the same for all circuits, the heat load is proportional to the amount of liquid phase refrigerant. Mass flow rates and heat loads are measured by micromotions and watt transducers directly, while qualities are calculated by the following equations:

$$h_{ero,i} = f(T_{ero,i}, P_{ero,i}) \quad \text{Eq. (1)}$$

$$h_{l,i} = f(P_{ero,i}) \quad \text{Eq. (2)}$$

$$h_{g,i} = f(P_{ero,i}) \quad \text{Eq. (3)}$$

$$h_{eri,i} = h_{ero,i} - Q_i/m_i \quad \text{Eq. (4)}$$

$$x_i = \frac{(h_{eri,i} - h_{l,i})}{(h_{g,i} - h_{l,i})} \quad \text{Eq. (5)}$$

Where i represents each circuit (i=1-4). T_{ero} and P_{ero} are the temperature and pressure at evaporator outlet; h_{ero} and h_{eri} are the specific enthalpy of refrigerant at the evaporator outlet and inlet; h_l and h_g are the specific enthalpy of saturated liquid and gas at evaporating pressure; Q is heat load providing to each circuit; m is refrigerant mass flow rate; and x is vapor quality of each circuit at distributor outlet. The specific enthalpies are obtained by REFPROP.

3. RESULTS AND DISCUSSION

3.1. Influence of Mass Flow Rate

To compare distributor performance under different working conditions in one figure, non-dimensional mass flow rates ($m_i{}^*$,), qualities ($x_i{}^*$) and heat loads ($Q_i{}^*$) are defined by equations 6-8:

$$m_i{}^* = \frac{m_i}{(\sum_{i=1}^{4} m_i)/4} \quad \text{Eq. (6)}$$

$$x_i{}^* = \frac{x_i}{(\sum_{i=1}^{4} x_i)/4} \quad \text{Eq. (7)}$$

$$Q_i{}^* = \frac{Q_i}{(\sum_{i=1}^{4} Q_i)/4} \quad \text{Eq. (8)}$$

where m_i, x_i, and Q_i are mass flow rate, quality (distributor outlet), and heat load of circuit i (i=1 to 4). Figure 4 shows the distributions of $m_i{}^*$, $x_i{}^*$ and $Q_i{}^*$ at horizontal orientation with total mass flow rates varying from 15 to 25 g/s. Figure 4(a) and 4(b) illustrate that circuits with higher mass flow rates are corresponding to lower qualities. This is because flow resistance in each circuit is the same. Therefore, the combination of lower vapor quality and higher mass flow rate (or higher vapor quality and lower mass flow rate) is a logical result to produce the same pressure drop. Figure 4(c) shows more heat loads are applied on circuits 1 and 4 than circuits 2 and 3 to achieve the same superheat. This indicates more liquid phase refrigerant is divided into circuits 1 and 4. Distributions of the non-dimensional parameters show similar patterns when distributor is installed vertically.

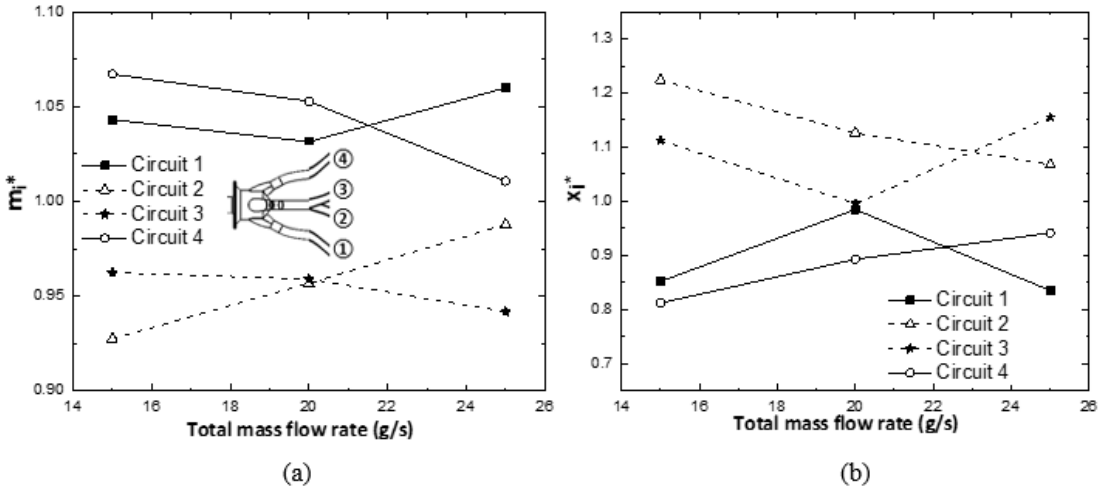

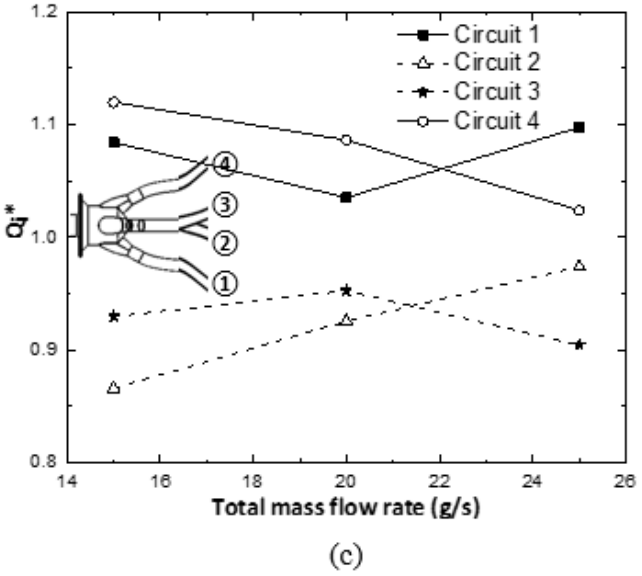

(c)

Figure 4: Distributions of non-dimensional (a) mass flow rates, (b) qualities, and (c) heat loads of each circuit as a function of total mass flow rate (distributor inlet quality is fixed at 0.23)

When total mass flow rates increase, all the non-dimensional parameters are closer to 1 indicating more uniform distribution. As flow velocity for both liquid and vapor increases when mass flow rates are increased, the inertial force is stronger. On the other hand, as two-phase flow develops along the tube between TEV and distributor, flow velocity in the region right after TEV is decreased. The decrease of velocity for liquid phase is not as large as vapor because liquid phase is more affected by inertia and inclined to resist the change in velocity. As a result, the velocity difference between liquid and vapor in the distributor inlet tube is smaller and the two-phase flow is more homogeneous. It is also observed that gravity does not influence refrigerant distribution because circuit at the top position (circuit 4) gets more liquid refrigerant than circuits at the middle (circuits 2 and 3). This indicates for all the tested mass flow rates (15–25 g/s), inertia prevails over gravity.

3.2. Influence of Distributor Inlet Quality

Figure 5 shows the distributions of m_i^*, x_i^* and Q_i^* as a function of the distributor inlet quality at vertical downward orientation. In figure 5(a), it shows that distribution of mass flow rates becomes more uniform at lower inlet quality. However, distribution of qualities shows an opposite trend. In this case, distribution of heat loads is more decisive because majority of the cooling capacity in the evaporator depends on liquid phase refrigerant. According to figure 5(c), heat loads applied on each circuit are more uniform as inlet quality decreases. A contrary conclusion was obtained by Nakayama *et al.* (2000). They found the cooling capacity difference among each circuit is larger at low quality. This indicates that the influence of inlet quality on distribution characteristic may be determined by two opposing factors at the same time. Slip ratio, defined by Equation 9, is used here to explain this phenomenon. Smaller slip ratio means more homogeneous flow and can contribute to more uniform distribution.

According to Ahmed *et al.* (2008), void fraction in both developing and developed region is smaller for lower vapor quality. Thus, when distributor inlet quality is decreased, the first term on the right side of Equation 9 is decreased, while the second term is increased. The third term is a constant when temperature and pressure are not changed. Consequently, the slip ratio may increase or decrease depending on which term is dominant. This may be a possible reason for the contrary conclusion between this study and Nakayama *et al.* (2000).

$$S = \frac{u_g}{u_l} = \frac{x}{1-x}\,\frac{1-\alpha}{\alpha}\,\frac{\rho_l}{\rho_g} \qquad \text{Eq. (9)}$$

Where u_g and u_l are flow velocity of vapor and liquid phase; ρ is density; x is distributor inlet quality; and α is void fraction.

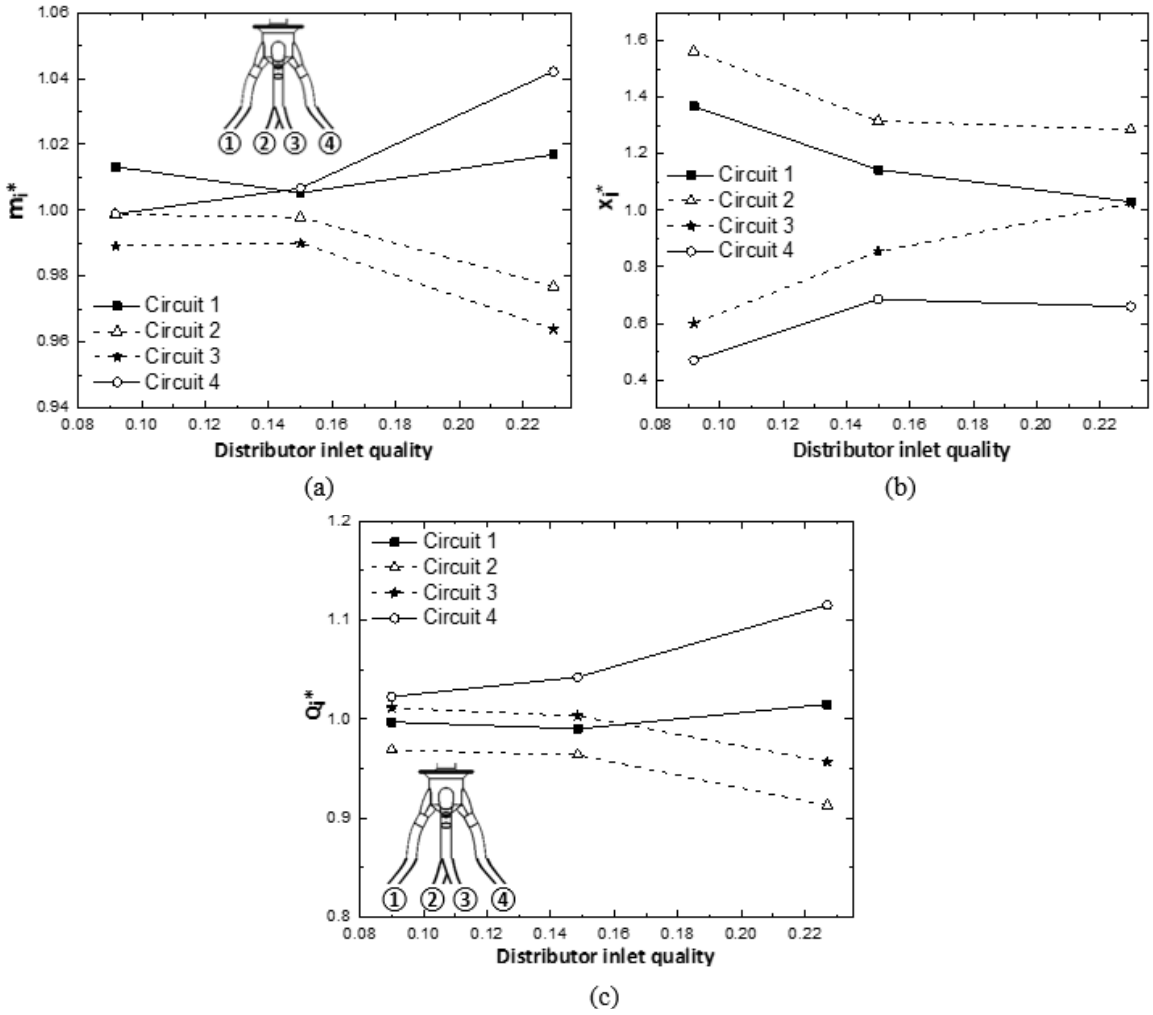

Figure 5: Distributions of (a) mass flow rates, (b) qualities, and (c) heat loads of each circuit as a function of distributor inlet quality (mass flow rate is fixed at 25 g/s)

3.3. Influence of Orientation

Standard deviation which reflects the relative scatter with respect to the mean value can be used to indicate the distributor performance of a certain working condition concisely (Han *et al*., 2014). Equations 10 and 11 show the definition of standard deviation of mass flow rates and heat loads.

$$STD_m = \sqrt{\frac{\sum_{i=1}^{4}(m_i{}^* - 1)^2}{4}} \quad \text{Eq. (10)}$$

$$STD_Q = \sqrt{\frac{\sum_{i=1}^{4}(Q_i{}^* - 1)^2}{4}} \quad \text{Eq. (11)}$$

where $m_i{}^*$ and $Q_i{}^*$ are non-dimensional mass flow rate and heat load of circuit i (i=1 to 4).
Figure 6 illustrates the standard deviation of mass flow rates (dash lines) and heat loads (solid lines) at three orientations with different mass flow rates (Fig. 6a) and different distributor inlet quality (Fig. 6b). It was noticed that the difference in standard deviations at three orientations is almost negligible. That is to say this distributor can be installed at any orientations and keep similar performance. A possible reason for this phenomenon is the distance between the TEV and distributor is very short (about 25 mm). The two-phase flow is still at developing region and phase separation is not happened.

On the other hand, both STD_m and STD_Q get smaller as mass flow rate increases (Fig. 6a) or distributor inlet quality decreases (Fig. 6b). This is consistent to the conclusions in Section 3.1 and 3.2.

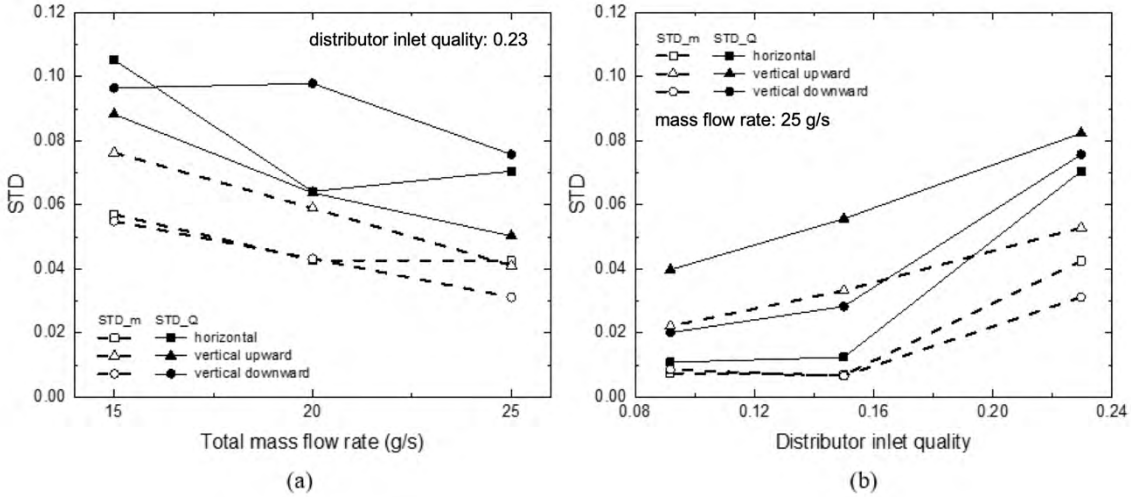

Figure 6: Standard deviations as a function of (a) total mass flow rates and (b) distributor inlet qualities

4. VISUALIZATION

To get a better understanding about maldistribution of refrigerant two-phase flow in distributors and the tubes before it, a transparent distributor made by 3D-printing is used for visualization. Figure 7 illustrates the visualization results with different mass flow rates at horizontal orientation. When mass flow rate is 3.5 g/s, the flow regime before the distributor is annular flow. Liquid at the bottom of the tube is thicker than that at the top. It can be predicted that circuit at the bottom will get more liquid than other circuits in this case. As mass flow rate increases to 8 g/s, it is still annular flow. However, the liquid layer thickness at the bottom is quite close to that at top. When mass flow rates are within the range of 15 to 25 g/s (the tested working conditions in this study), the two-phase flow becomes more uniform in the inlet tube and inside the distributor. It seems that a gradual transition from annular flow to homogeneous flow happens as mass flow rates increase. As shown previously in figure 4, circuits at the bottom did not get more liquid when mass flow rates are among 15 to 25 g/s. This also indicates that phase separation due to the effect of gravity is not observed in this study.

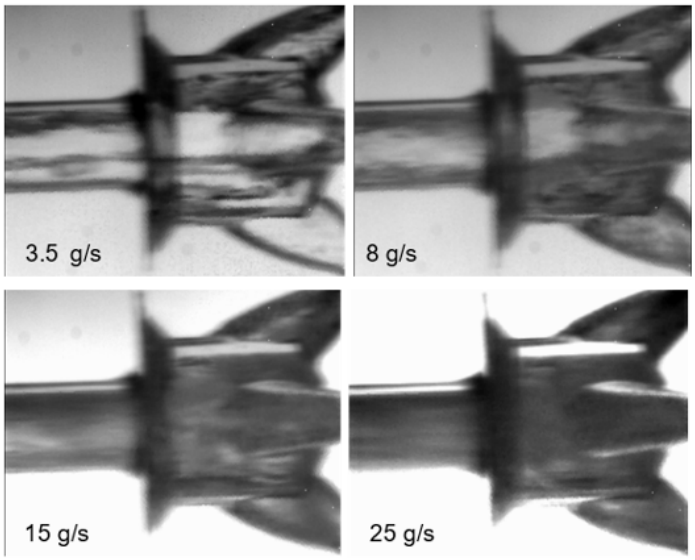

Figure 7: Visualization of two-phase flow in distributor

The nominal cooling capacity for this distributor is 4-5 kW. If using R134a as working fluid, the mass flow rate should be about 25 to 30 g/s. Both the visualization and experimental results show that

when mass flow rate is above 55% of the nominal flow rate (larger than 15 g/s), the influence of gravity on flow distribution is negligible.

5. SUMMARY AND CONCLUSIONS

Some possible factors influencing the performance of refrigerant distributor were investigated in a R134a system. It was found that higher mass flow rate and lower distributor inlet quality can result in more uniform distribution, while the effect of orientation (or gravity) is negligible. Phase separation due to gravity is not happened in visualization results for the tested working conditions. But at extremely low flow rates, the effect of gravity is observed.

ACKNOWLEDGEMENTS

The authors would like to acknowledge Parker Hannifin - Sporlan Division for their support of this work and the devices they provided.

NOMENCLATURE

h	specific enthalpy (kJ/kg)	m	mass flow rate (g/s)
P	pressure (kPa)	Q	heat load (W)
T	temperature (K)	x	vapor quality (-)
S	slip ratio (-)	STD	standard deviation (-)
ρ	density (kg/m^3)	α	void fraction (-)

SUBSCRIPTS

eri	evaporator refrigerant inlet	ero	evaporator refrigerant outlet
g	saturated gas	i	i circuit
l	saturated liquid		

REFERENCES

Ahmed, W. H., Ching, C. Y., & Shoukri, M. (2008). Development of two-phase flow downstream of a horizontal sudden expansion. International Journal of Heat and Fluid Flow, 29(1), 194-206.

Aziz, A. Z., Miyara, A. K., & Sugino, F. U., 2012. Distribution of two-phase flow in a distributor. J. Eng. Sci. Technol, 7(1), 41-55.

Bowers, C. D., Wrocklage, D., Elbel, S., & Hrnjak, P. S., 2014. Improvements in Refrigerant Flow Distribution Using an Expansion Valve with Integrated Distributor. Proceedings of International Refrigeration and Air Conditioning Conference at Purdue, Paper # 1458.

Fay, M. A., 2012. Effect of conical distributors on evaporator and system performance (Doctoral dissertation).

Han, Q., Zhang, C., & Chen, J., 2014. Experimental and CFD investigation of R410a distributors for air conditioner. International Journal of Air-Conditioning and Refrigeration, 22(02), 1440002.

Li, G., Frankel, S., Braun, J. E., & Groll, E. A., 2005. Application of CFD models to two-phase flow in refrigerant distributors. HVAC&R Research, 11(1), 45-62.

Nakayama, M., Sumida, Y., Hirakuni, S., & Mochizuki, A., 2000. Development of a refrigerant two-phase flow distributor for a room air conditioner. Proceedings of International Refrigeration and Air Conditioning Conference at Purdue, Paper # 497.

Yoshioka, S., Kim, H., & Kasai, K., 2008. Performance evaluation and optimization of a refrigerant distributor for air conditioner. Journal of Thermal Science and Technology. Technology, 3(1).

Zhang, C., Wang, Y., & Chen, J., 2014. Optimization of the reserve-type distributor for R410a air conditioner. International Journal of Air-Conditioning and Refrigeration, 22(04), 1450022.

Manuscript ID: 844
DOI: 10.18462/iir.icr.2019.0844

Flow patterns and pressure drop of vertical upward flows in a tube with header-like protrusions with R134a

Hongliang QIAN[(a)], Pega HRNJAK[(a,b)*]

[(a)] Air Conditioning and Refrigeration Center, University of Illinois at Urbana-Champaign, 1206 West Green Street, Urbana, IL 61801, USA
[(b)] Creative Thermal Solutions, 2209 Willow Rd., Urbana, IL, USA
[(*)] Corresponding author

ABSTRACT

Flow patterns and pressure drop in a vertical tube with header-like protrusions in adiabatic conditions are presented. Three major flow patterns are observed with a high-speed camera in the mass flow rate range studied in this paper: slug flow, churn flow and annular flow. The flow pattern map is proposed.
As the distance between two measurement ports along the tube decreases, pressure drop of refrigerant flows in the tube with protrusions decreases for all vapor qualities and mass flow rates. The relation is close to linear. However, the relation between pressure drop between two certain ports and quality is not linear. For relatively larger mass flow rate, as the quality increases from 0, pressure drop decreases first and then increases. There is a smallest pressure drop at moderate quality. The smallest pressure drop among all the qualities between two certain ports happens decrease from x=1 to x=0.6 as mass flow rate increase from 3 g/s to 7.5 g/s. If the quality is kept to be constant, DP is smaller for higher mass flow rate for relatively small qualities. However, in the high-quality range, DP is larger for higher mass flow rate.
Keywords: R134a, Pressure drop, Vertical flow, Refrigerant

1. INTRODUCTION

Pressure drop and flow patterns are some of crucial information in two-phase flows. Void fraction, heat transfer coefficient and refrigerant charge are highly related to those two parameters. This paper shows the transitional study from round tubes to headers of microchannel heat exchangers. In former studies, Qian and Hrnjak (2019) visualized flow patterns and measured void fraction for vertical upwards flow in round tubes. Yang and Hrnjak (2018) studied the pressure drop for two-phase flow within both smooth tubes and microfin tubes. Li and Hrnjak (2018) used the correlation of Friedel (1979) to model the two-phase frictional pressure drop in a header because of the large data bank that Friedel used. However, how accurate Friedel's correlation is for headers requires more experimental validation.

A capacitance sensor used to measure void fraction and characterize flow patterns in horizontal and vertical round tubes was developed in Qian and Hrnjak (2018). Before utilizing this sensor in headers to measure void fraction, applying it to a tube with header-like protrusions as a further calibration procedure is necessary. Void fraction, pressure drop, flow patterns and capacitive signals for tubes with protrusions are going to be correlated together to calibrate the sensor for real headers. After these studies, this test section will be converted into a header with 5 inlets and 5 outlets. Flow patterns and void fraction along the headers will be studied.

2. FACILITY

The schematic drawing of the facility is shown in Fig. 1. Subcooled liquid refrigerant (R134a) is pumped through a mass flow meter with a gear pump without oil. Enthalpy is obtained from refrigerant pressure and temperature before the heater. The flow is then heated by an electric heater and the power is measured by a watt transducer. With the measured power, mass flow rate and inlet enthalpy, vapor quality after the heater is determined. After refrigerant is mixed in the mixer, it flows into the test section which includes a visualization part and ten pressure measurement ports. The

details of the test section will be shown later in this section. The model of pressure transducers is Sensotec's TJE and the differential pressure sensor is Rosemount. T-type thermocouples are used to measure temperature. All the pressure transducers, differential pressure transducer and thermocouples are calibrated before being applied in the facility and the uncertainties are listed in Table 1. Upstream of the visualization section, a piece of 500 mm of 9.25mm PFA tube is utilized to ensure the flow is fully developed. A high-speed camera is used to capture videos of the flow with resolution of 512x512 and speed of 2200 frames per second (fps). Phantom CV 2.8 from Vision Research Inc. is used to process the video. After refrigerant passes the test section, refrigerant flows into two coolers whose secondary liquid is glycol then subcooled into liquid condition. The subcooled liquid is fed into the gear pump to finish the loop.

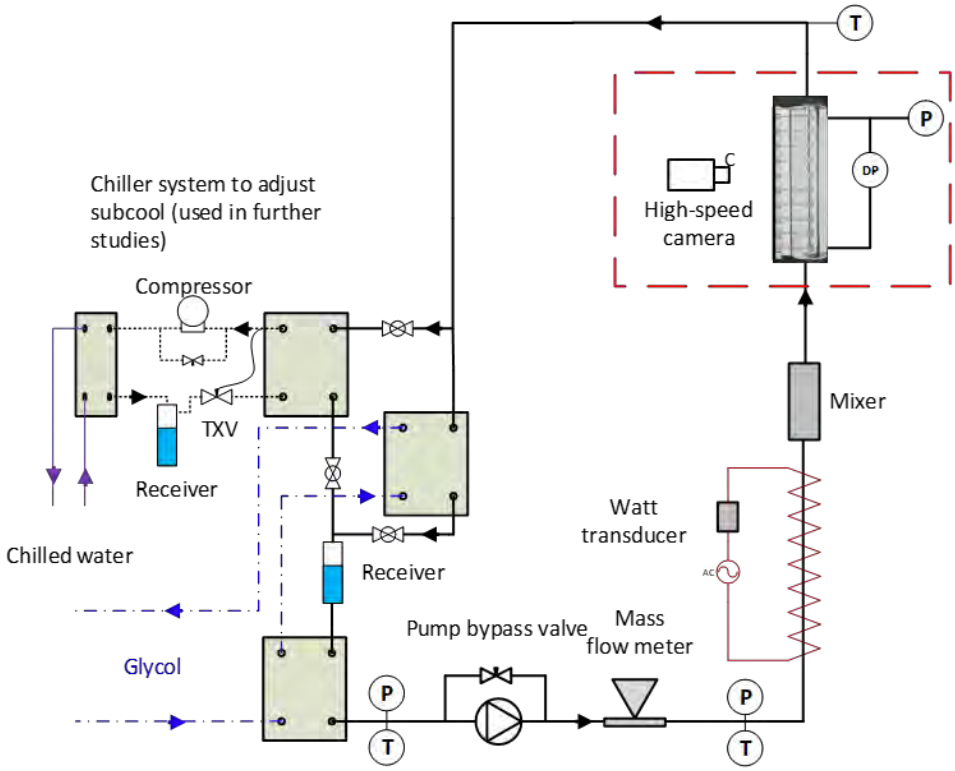

Figure 1: Schematic drawing of experimental facility, test section in the red box

Table 1. Instrument uncertainties

Instrument	Uncertainty	Instrument	Uncertainty
Sensotec's THE pressure transducer	±1% FS	Rosemount 0 to 30 inH2O DP transmitter	±0.2% FS
T-type thermocouple	±0.5 ºC	Ohio Semitronics GW5-024CX5 watt transducer	±0.2% FS

Fig. 2 and 3 show the details of the test section. It is a 3D printed, transparent tube with header-like protrusions. It contains ten protrusions and ten pressure measurement ports. Each protrusion with a thickness of 3 mm has 6 microchannels. The pitch between two protrusions is 15.8 mm which is the same as the inner tube diameter without protrusions. The other end of each protrusion which is sealed has a socket (shown by Fig. 3). It can be easily connected to an aluminum microchannel tube if necessary for following studies. The total length of this test section is 173.8 mm and each end of the section is connected to a steel structure then a PFA tube.

Pressure measurement ports are named 1 to 10 from low to high. To measure the pressure difference when single-phase or two-phase refrigerants flowing along the test section, port number 10 (assumed to be the lowest pressure port) is chosen to be the pressure baseline (connected to the low end of the DP sensor). All other 9 ports are connected to the high end of the DP sensor by switching in a ball-valve system. By this method, the instrumental uncertainties from using multiple DP sensors can be reduced.

Table 2 lists the experimental conditions that have been tested.

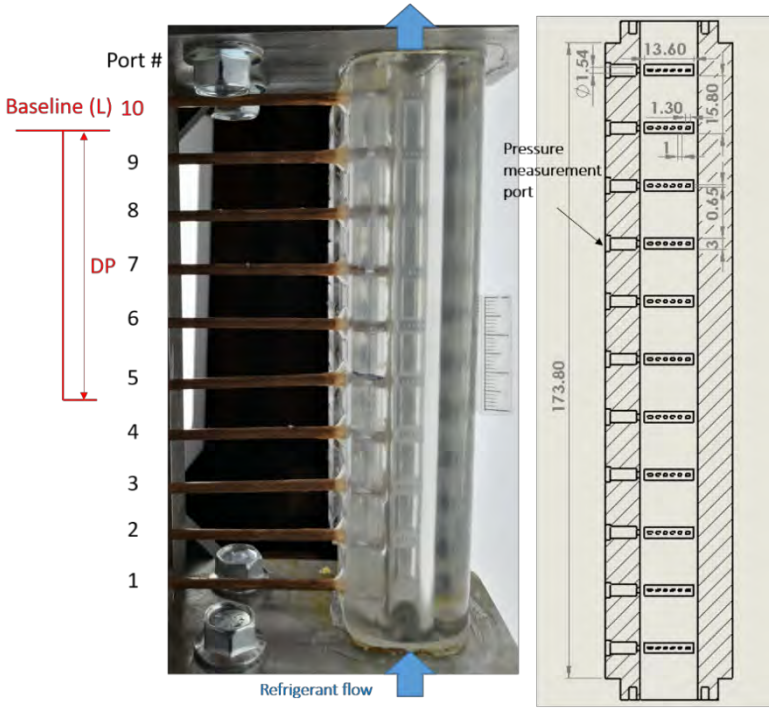

Figure 2: Structure and dimension of the test section

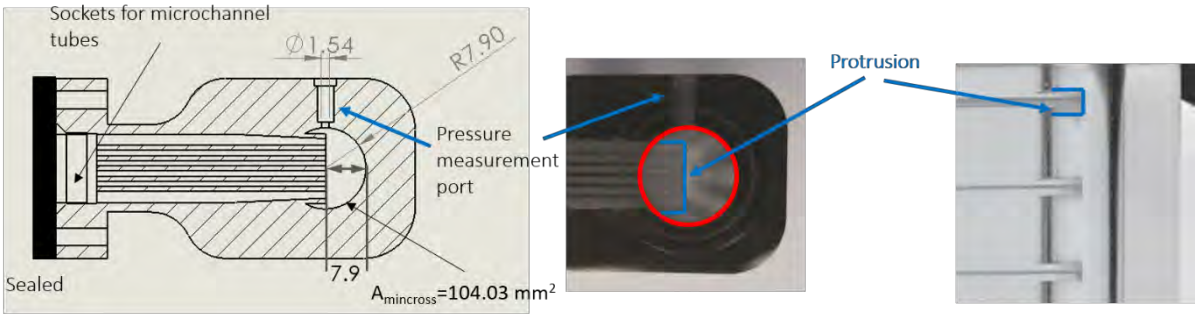

Figure 3: Cross-section of the test section

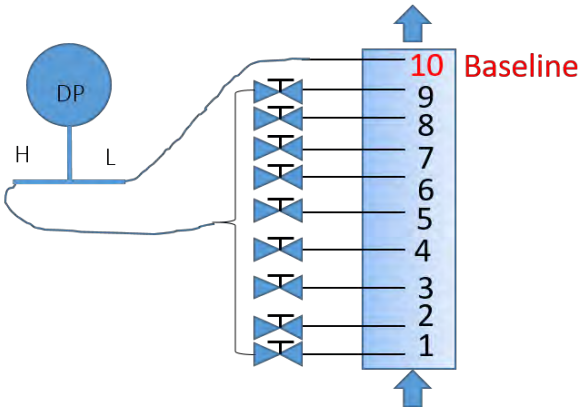

Figure 4: Pressure drop measurement method

Table 1. Experimental conditions

Working media	R134a	Mass flow rate	3, 4.5, 6 and 7.5 g/s
Refrigerant temperature	14.5 ºC	Vapor quality	Subcooled liquid, 0.1-0.9 and superheat vapor

3. RESULTS

3.1. Flow patterns

Refrigerant is controlled to flow into the test section from subcooled liquid to two-phase, and lastly to superheated vapor condition with a quality increment of 0.1. In the mass flow rate explored in this paper, we observed three major flow patterns: slug flow, churn flow and annular flow. The criterion for each flow pattern is listed below (Fig. 5):

Slug flow: Vapor slugs appear periodically with liquid bridge in the middle. The slugs which are disturbed by protrusions are followed by some small bubbles.

Churn flow: The total effect combined of shear on interface, pressure gradient and gravity on a droplet is not constant upwards. Also, due to the disturbance of the protrusions, flow structures are very chaotic. Liquid may go up and down intermittently though the mean velocity of the two-phase mixture going up. This flow pattern is highly agitated and the interface between liquid and vapor is constantly changing.

Annular flow: Liquid flows along the wall of the tube with vapor in the central core. Though the appearance of the protrusions disturbs the liquid film along the tube wall, it is relatively more stable and less chaotic than churn flow. The interface between liquid and vapor core is wavy.

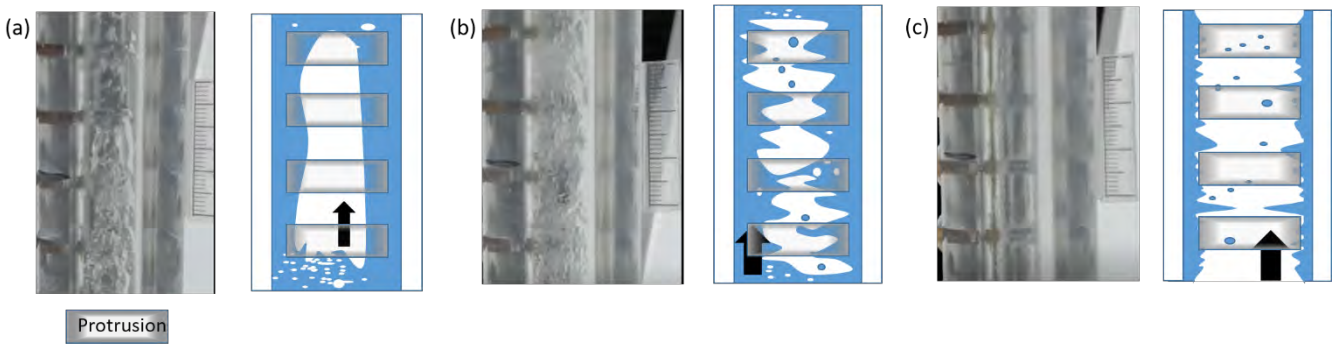

Figure 5: Flow pattern definition: (a) slug flow, (b) churn flow and (c) annular flow

Visualization classification of flow patterns is shown in Fig. 6. Flow patterns presented are for mass flow rate ranging from 3 to 7.5 g/s and saturation temperature of 14.5ºC. When protrusions are present, mass flux defined by the smallest cross-section area is more representative (Bowers *et al.*, 2006). Hence, to convert from mass flow rate to mass flux, the smallest cross-section area is used (Fig. 3). Data are shown in dots with three different symbols that represent different flow patterns: ▲-slug, ■-churn, and ♦-annular flow. Due to the limitation of experimental instruments, vapor qualities lower than 0.05 cannot be obtained in steady state. Hence, bubbly flows which are supposed to be observed before slug flows are not captured by the high-speed camera. When the vapor quality and mass flow rate are relatively low, vapor slugs followed by small bubbles periodically appear in the test section. As the quality and mass flow rate increase, the flow pattern becomes much more chaotic. The existence of the protrusions has a further disturbance of the two-phase flow. When the vapor quality approaches to 1, the flow pattern becomes more stable. Vapor flows in the central core of the tube with liquid along the wall. As the vapor quality increases to 1, no liquid exists in the test section.

.

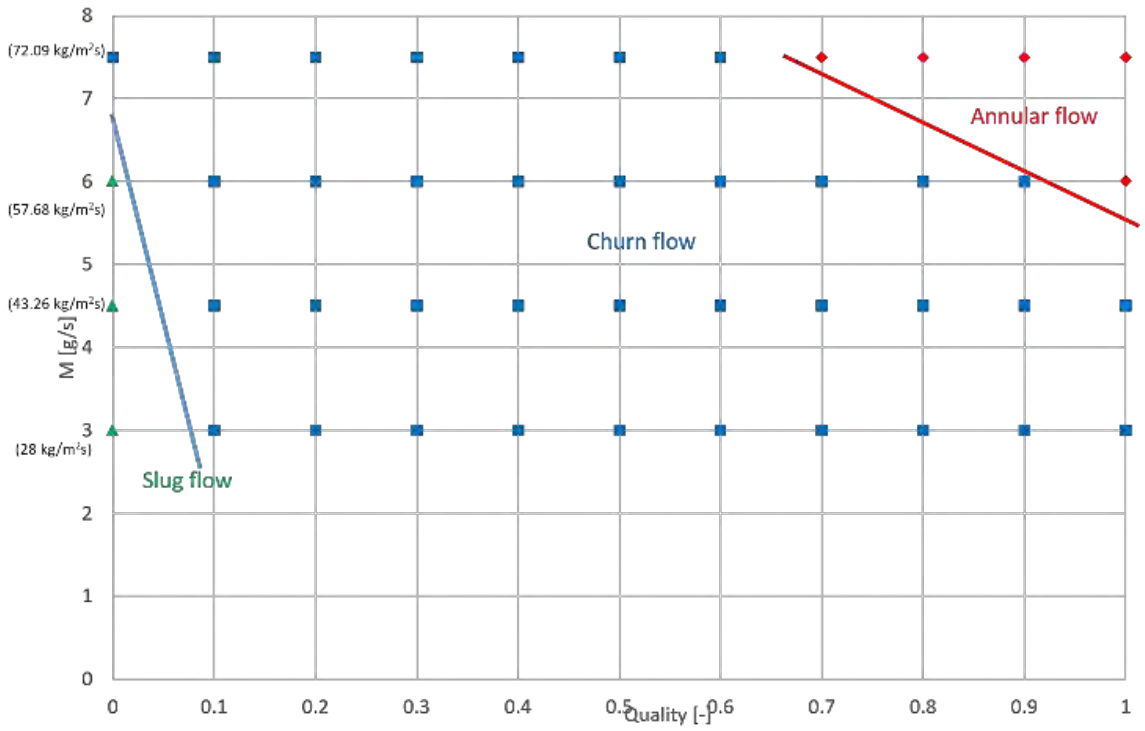

Figure 6: Flow patterns for vertical upwards flows in a tube with header-like protrusions. ▲-slug, ■-churn, and ♦-annular flow

3.2. Pressure drop

For the ten pressure measurement ports in the test section, port number 10 is selected to be the baseline which is connected to the lower-pressure end of the differential pressure sensor. The measured overall pressure drop includes three major components in this study: $\Delta P_{gravity}$, $\Delta P_{friction}$ and ΔP_{local} (due to protrosions). The results of pressure drop vs the port number (height) for all mass flow rates and vapor qualities are discussed first. After that, the relation between pressure drop and vapor qualities for all ports are shown. Finally, for a certain vapor quality, the influence of mass flow rate on pressure drop is discussed.

3.2.1. Pressure drop for different ports

Fig. 7 (a) to (d) show the pressure difference between #th port and the 10th port. For all the four mass flow rate conditions, as the port number (height) increases, the pressure difference becomes smaller for all qualities. When the distance between two measured ports becomes smaller, the influence of gravity, friction as well as protrusions decrease. This will result in smaller pressure drop. And the relation between distance of two measured ports and pressure drop is almost linear. When the mass flow rate is small (3 g/s), pressure drop for higher vapor qualities is smaller compared that of lower quality conditions. However, for the higher mass flow rates (6 and 7.5 g/s), higher qualities may have a higher pressure drop. This trend will be shown in detail in next section.

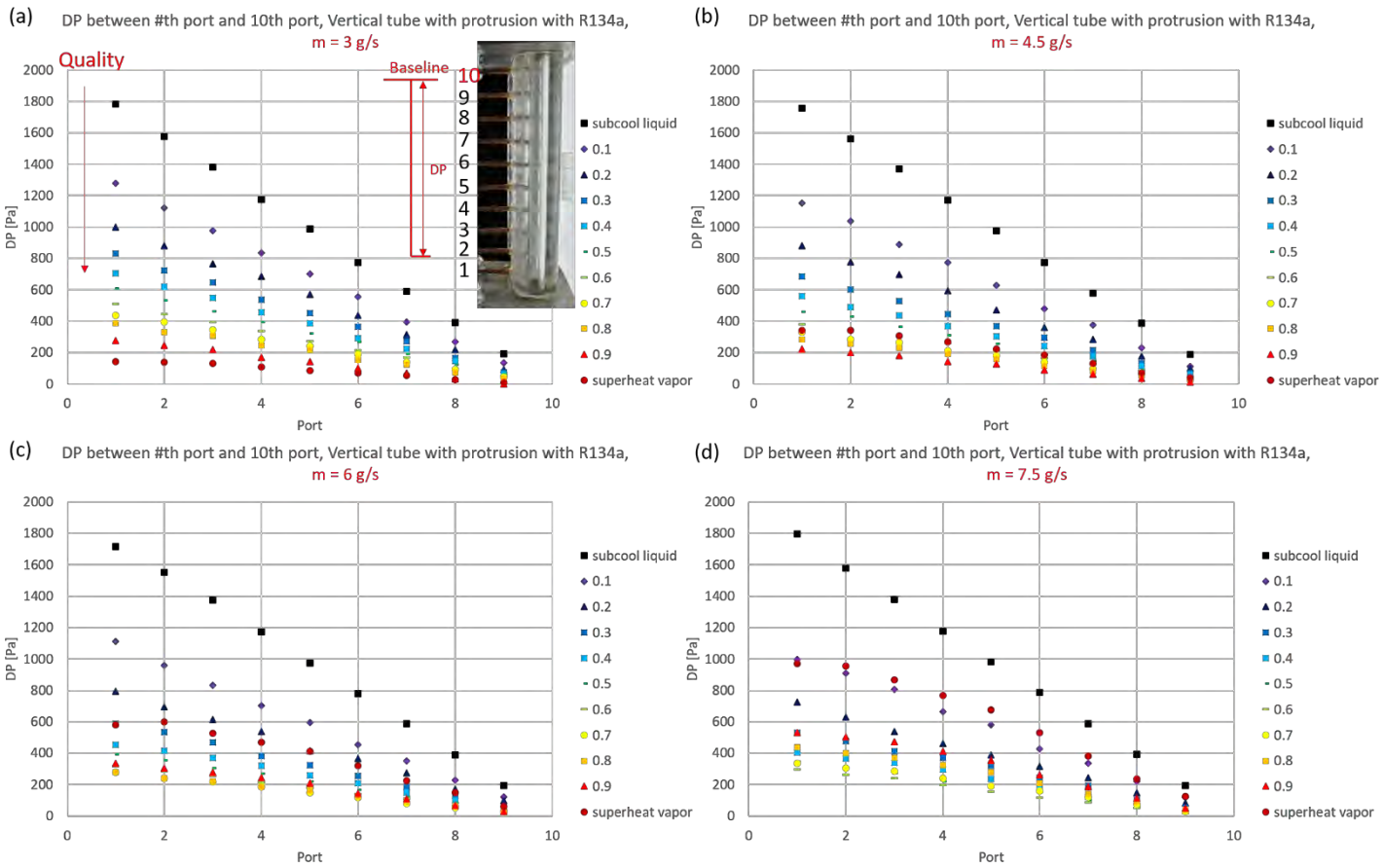

Figure 7: Pressure drop between #th port and 10th port for all qualities: (a) m=3 g/s, (b) m=4.5 g/s (c) m=6 g/s (d) m=7.5 g/s

3.2.2. Pressure drop for different qualities

Fig. 8 (a) to (d) show the pressure drop vs quality for all mass flow rate and ports. As mentioned above, as the port number increase, the pressure drop will decrease at the same quality. The relation between pressure drop and vapor quality is not linear. As the mass flow rate increases, the quality for the smallest pressure drop becomes smaller. When the mass flow rate is relatively large (4.5 – 7.5 g/s), the smallest DP for different qualities does not happen when it has highest quality (0.9 or superheated vapor). Void fraction increases dramatically as the quality increases in low quality range. In this range, as the quality increases, less liquid with larger density exists in the test section. This results in $\Delta P_{gravity}$ which is dominant at low qualities reducing dramatically. The overall pressure drop decreases.

In the higher quality range, void fraction is almost one and does not change much. The effect of $\Delta P_{gravity}$ becomes less significant. High velocity of vapor phase will result in higher $\Delta P_{friction}$ and ΔP_{local}. Hence, the $\Delta P_{friction}$ and ΔP_{local} will dominant the overall pressure drop. As the quality increase, the overall pressure drop thus increases as well.

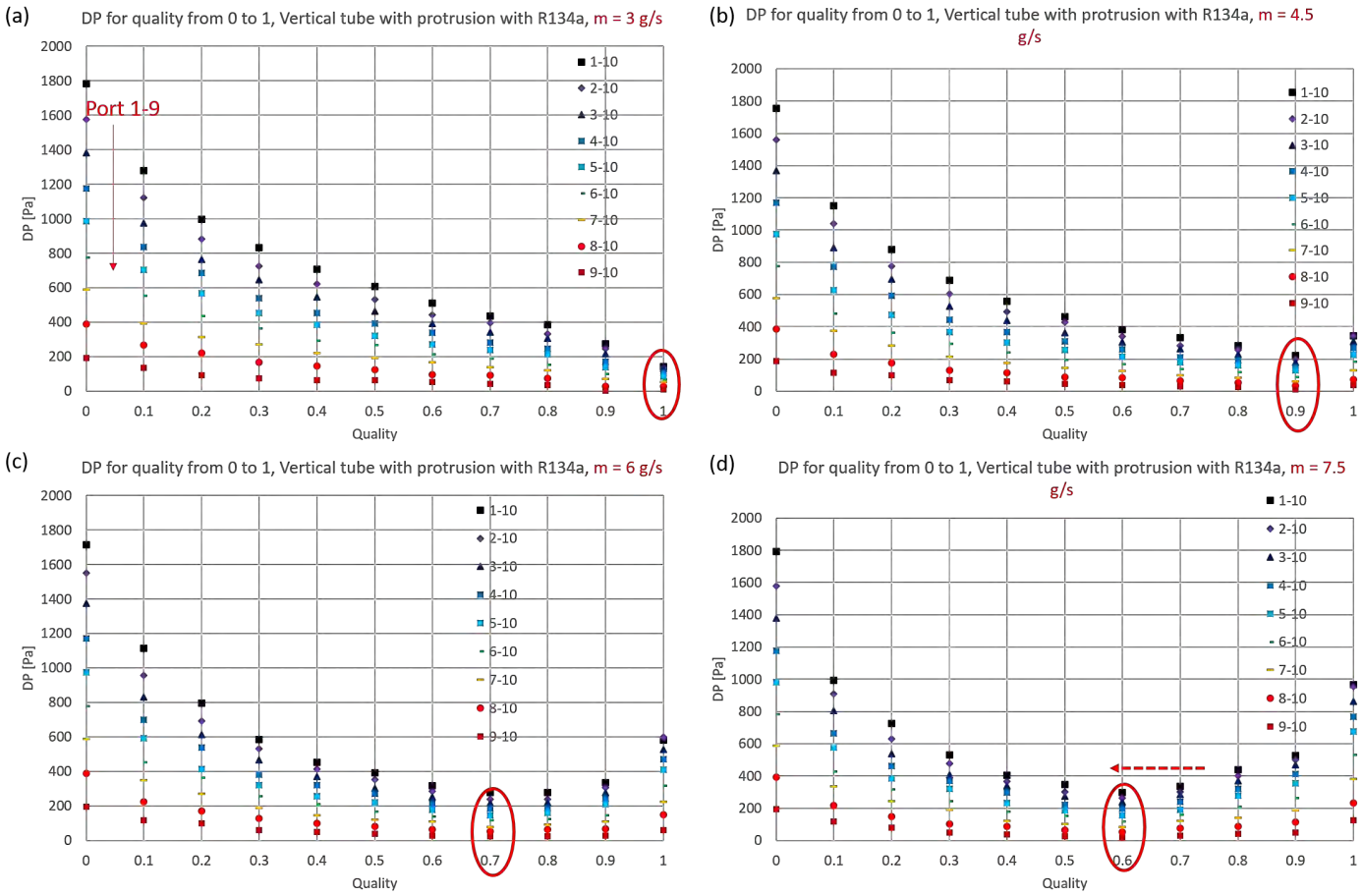

Figure 8: Pressure drop between two certain ports for all qualities: (a) m=3 g/s, (b) m=4.5 g/s (c) m=6 g/s (d) m=7.5 g/s

3.2.3. Influence of mass flow rate on pressure drop

Fig. 9 shows the effect of mass flow rate on the overall pressure drop between two certain ports. Pressure drop between port 5 and 10 is chosen as an example and pressure drop between other locations are similar. For lower-range qualities, pressure drop is smaller when mass flow is higher at constant quality. But in the higher-quality range, this trend reversed. The reasons are following.

Qian and Hrnjak (2019) claimed that for a certain vapor quality, void fraction for a higher mass flux is larger for vertical upward flows in smooth tubes. In this paper, the vertical upward flow is in a tube with protrusions, but the relation between void fraction and mass flux may remain similar. Hence, in the low-quality range, void fraction increases more dramatically for high mass flow rates than in high-quality range. More liquid exists in the test section for smaller mass flow rate and the $\Delta P_{gravity}$ dominates the overall pressure drop. As the quality increases, void fraction is close to 1 and vapor velocity increases. So, the friction pressure drop and the protrusion pressure drop become more significant than hydrostatic pressure drop especially for higher mass flow rates.

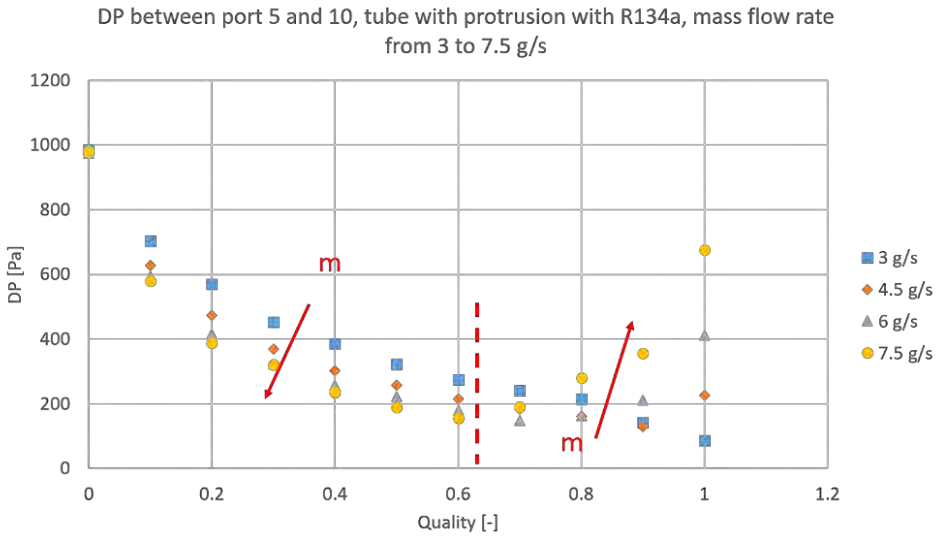

Figure 9: Pressure drop between port 5 and 10 for all mass flow rates

4. SUMMARY AND CONCLUSIONS

Flow patterns and pressure drop in a vertical tube with header-like protrusions in adiabatic conditions are presented. Three major flow patterns are observed in the test section: slug flow, churn flow and annular flow. A flow regime map for R134a is proposed (Fig. 6).

Following conclusions on pressure drop of an upward flow in a tube with protrusions are obtained:

- As the distance between two measured ports decreases, there is an almost linear relation between the pressure drop and the distance. Pressure drop decreases for all vapor qualities and mass flow rates.
- The relation between pressure drop and quality is not linear. The smallest pressure drop may happen at a moderate quality. As mass flow rate increases, smallest pressure happens at a smaller quality
- If the quality is kept to be constant, pressure drop is smaller for higher mass flow rate at relatively lower qualities. However, in the high-quality range, pressure drop is larger for higher mass flow rate.

REFERENCES

Bowers, C. D., Newell, T., & Hrnjak, P. (2006). *Experimental investigation of two-phase refrigerant distribution in a microchannel manifold*. Air Conditioning and Refrigeration Center. College of Engineering. University of Illinois at Urbana-Champaign: http://hdl.handle.net/2142/12356

Friedel, L. (1979). Improved friction pressure drop correlation for horizontal and vertical two-phase pipe flow. *Proc. of European Two-Phase Flow Group Meet., Ispra, Italy, 1979*.

Li, J., & Hrnjak, P. (2018). *Phase Separation in Vertical Header of Microchannel Condensers: A Mechanistic Model.* Paper presented at the ASME 2018 5th Joint US-European Fluids Engineering Division Summer Meeting.

Qian, H., & Hrnjak, P. (2018). Void Fraction and Flow Regimes Determined by Visualization, Mass Measurement and New Capacitance Sensor. *in: Proceedings of 17th International Refrigeration and Air Conditioning Conference at Purdue, Paper # 2223, 2018*.

Qian, H., & Hrnjak, P. (2019). Void Fraction Measurement and Flow Regimes Visualization of R134a in Horizontal and Vertical ID 7 mm Circular Tubes. *International Journal of Refrigeration*. doi:https://doi.org/10.1016/j.ijrefrig.2019.04.018

Yang, C.-M., & Hrnjak, P. (2018). Effect of straight micro fins on heat transfer and pressure drop of R410A during evaporation in round tubes. *International Journal of Heat and Mass Transfer, 117*, 924-939.

Manuscript ID: 857
DOI: 10.18462/iir.icr.2019.0857

Modified flow pattern maps for flow boiling in horizontal micro-finned tubes considering the effect of helix angle

Cheng-Min YANG[(a)], Pega HRNJAK[(a),(b)]

[(a)] ACRC, University of Illinois at Urbana-Champaign
Urbana, 61801, USA, cyang73@illinois.edu
[(b)] Creative Thermal Solutions, Inc.
Urbana, 61802, USA, pega@illinois.edu

ABSTRACT

The existed flow pattern map of flow boiling are mainly developed for horizontal smooth tubes, which are not suitable for predicting the flow patterns in micro-finned tubes. This paper presents an improved flow pattern map for flow boiling in horizontal micro-finned tubes considering the effect of helix angle. Visualization of R410A flow boiling was carried out through the transparent smooth and micro-finned tubes with 0°, 10° and 18° helix angle. The result shows that the flow pattern map for micro-finned tube with 0° helix angle is generally similar to that in the smooth tube. For the tube with 10° and 18° helix angle, the annular flow occurs at lower vapor quality and lower mass flux. A modified model accounting for the early transition to annular flow in the micro-finned tubes is built.
Keywords: Flow pattern map, Micro-fin, Helix angle, Visualization, Flow boiling.

1. INTRODUCTION

The simultaneous motion of liquid and vapor phases in the condensing or evaporative channel leads to several configurations known as flow patterns, which influence the wetting characteristic and the heat transfer mechanism in the channel. Two-phase flow pattern map is a model including various transition criteria to predict the local flow pattern under a certain condition. In the earlier research, the flow pattern maps were built with air-water systems such as Alves (1954), Baker (1955), Taitel and Dukler (1976). However, most of these studies were confined to the air-water system and did not consider the effect of fluid properties and the thermal interactions on the flow. Diabatic flow pattern maps, directly for the in-tube evaporation or condensation of a fluid, was developed and studied. In this type of map, the local flow pattern was usually observed through a sight glass at the exit of the evaporator or condenser tube. Kattan et al. (1998) built up a diabatic flow regime map for evaporation considering the effect of heat flux and dry-out phenomenon at high vapor quality conditions. Many researchers such as Zürcher et al. (2001), Thome and El-Hajal (2003), Wojtan et al. (2005), and Mastrullo et al. (2012) improved Kattan et al.'s map (1998) and extended it to cover different refrigerants.

Internally micro-finned tubes are believed to increase heat transfer performance in two-phase flow because of the increasing heat transfer area and wetting characteristics. In order to further know the mechanism for heat transfer enhancement, flow patterns in internally micro-finned tubes were investigated by numerous researchers such as Yu et al. (2002), Hatamipour and Akhavan-Behabadi (2012), Colombo et al. (2012). They found that the annular flow in the helical micro-finned tubes occurs at lower mass flux and vapor quality than in the smooth tubes. Therefore, the existed flow pattern map models developed for smooth tubes were not able to predict the flow pattern in the micro-finned tube correctly. Sharar et al. (2013) considered the early transition to annular flow due to the geometry effect and built up a map for micro-finned tubes. They modified the Wojtan et al. (2005) flow pattern map originally developed for smooth tubes by adjusting the empirical constant based on the flow visualization data in the 18° helical micro-finned tubes published by Yu et al.(2002) and Hatamipour and Akhavan-Behabadi (2012). Rollmann and Spindler (2015) developed a flow pattern map for flow boiling in the micro-finned tube with 18° helix angle. They derived the equations for the transition curve based on their experimental data of R134a flow boiling. However, the above two maps were only developed for the micro-finned tube with 18° helix angle, and did not consider the effect of helix angle.

The present work aims at building up a flow pattern map for micro-finned tubes considering the effect of helix angle. The experiments of R410A flow boiling were conducted and the details of the experimental setup was presented in Yang and Hrnjak's work (2018) & (2019). Visualization of two-phase flow was carried out through the 3D printed smooth and micro-finned tubes with 0°, 10° and 18° helix angle. Wojtan et al. (2005) flow pattern map was used as a basis for the proposed flow pattern map. The transition of stratified-wavy to wavy-annular flow (SW-WA) and the transition of intermittent to annular or stratified-wavy flow (I-A or I-S) were modified and the transition of wavy-annular to fully annular flow (WA-A) was added.

2. DESCRIPTION OF FLOW PATEERN MAP

The new flow pattern map for micro-finned tubes is modified from Wojtan et al. (2005) flow pattern map developed for horizontal flow boiling inside smooth tubes. The observed flow patterns in the transparent micro-finned tube with 18° helix angle from the present study are depicted on the Wojtan et al. (2005)'s map, as shown in Fig. 1(a). The solid and hollow symbols are the visualization data in our experiments and the black solid lines are the transition curves from the equations in Wojtan's paper. Note that the slug flow, slug+SW, and intermittent flow are not separated in our experimental data and all of them are marked as intermittent flow (I). It is found that there are two discrepancies between our experimental data and Wojtan et al.'s map: (1) The SW-W/A transition occurs at earlier vapor quality and mass flux conditions due to the internal helical micro-fins;(2) The I-A and or I-S transition in Wojtan et al.'s map is a vertical line (constant vapor quality), which could not predict the intermittent flow in our experiment properly. After the modification, it is seen from the Fig. 1(b) that the new model has a better prediction for the flow patterns in the micro-finned tube. The following subsections describe the details of the flow regime transitions in the flow pattern map.

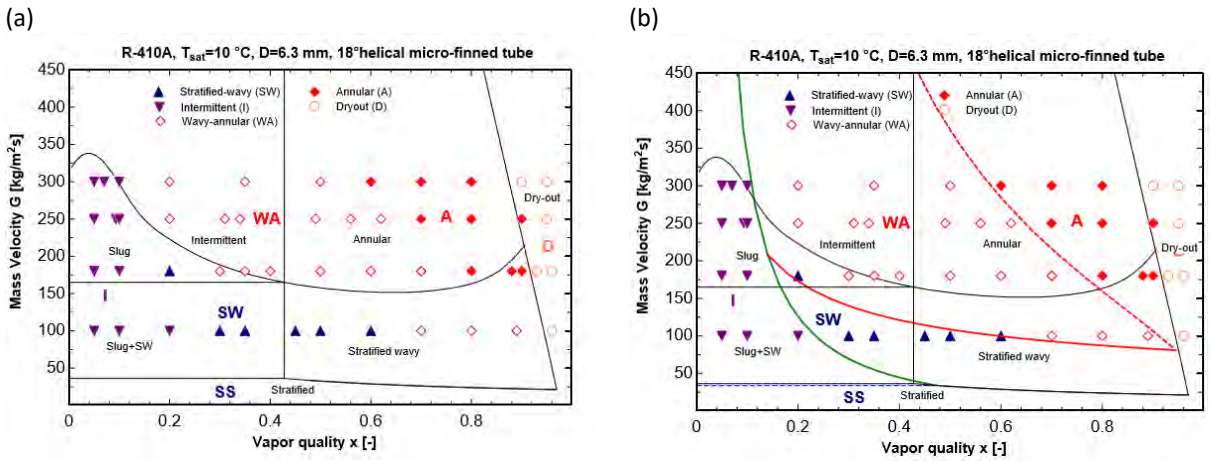

Figure 1: Comparison of the experimental data in 18° helical micro-finned tube with (a) original Wojtan et al.'s (2005) flow pattern map and (b) modified map

2.1. Transition of Stratified-wavy Flow (SW) to Wavy-annular Flow (W/A)

For the low mass flux or low vapor quality condition, the momentum of the flow in the evaporator tube is low, and the liquid and vapor are naturally separated into two layers due to gravity. As the increase of the vapor quality or mass flux, the higher gas velocity extends the interfacial waves around the circumference and leads the liquid to climb up the wall to form annular flow. The SW-W/A transition is derived from the force balance method similar to Xiao and Hrnjak (2018)'s work. Centrifugal force induced by the helical micro-finned geometry (swirling term) is added to consider the micro-fin effect. As the annular flow is formed, the gravity, surface tension, shear, and centrifugal force is balanced in the control volume, as demonstrated in Fig. 2(a). The transition between the stratified wavy and wavy annular flow is obtained with the force balance and presented in Eq. (1). C_1 and C_2 are two empirical constants to represent the vertical portion of the forces. C_1 is between 0 and 2, which represents the horizontal and vertical liquid-vapor interface, respectively. C_2 is between 0 and 1, which means that the direction of the shear force is horizontal and vertical, respectively. C_3 depends on the tube geometry: C_3=0 for smooth tube and C_3=1 for micro-finned tube.

$$\rho_l g\delta D + C_1\sigma = C_2 D f_v \rho_v u_v^2 + C_3(\rho_l \delta D)u_\theta^2 / D \qquad \text{Eq. (1)}$$

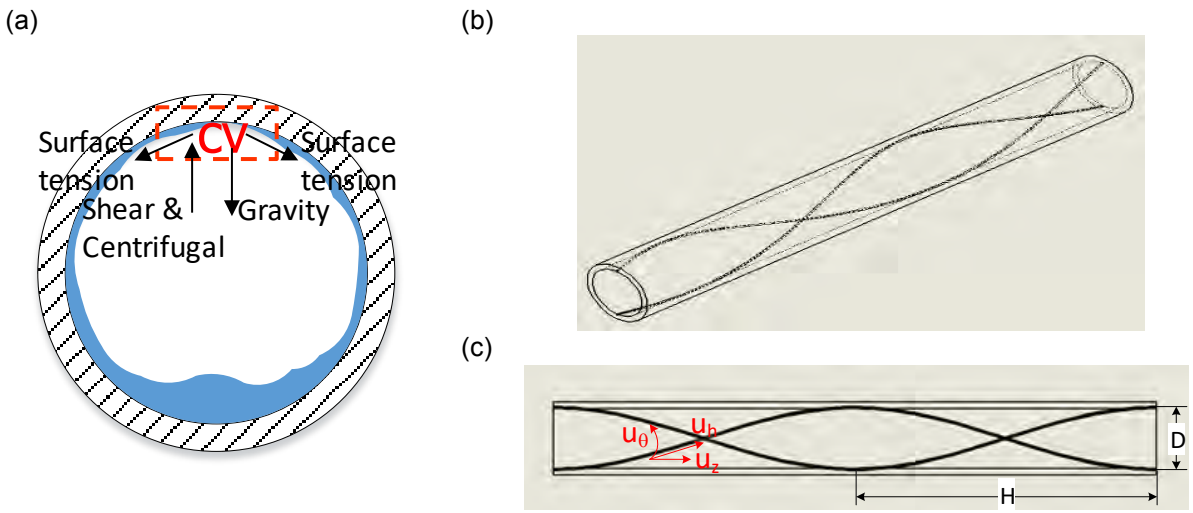

Figure 2: Schematic views for helical micro-finned tubes: (a) force balance in the control volume, (b) demonstration of the internal spiral grooves, and (c) geometrical characteristics

The film thickness δ at the top of the tube used here is the average value of the film thickness measured by Xiao and Hrnjak (2015), which is 0.03617 mm.
The interfacial shear stress can be expressed in terms of friction factor, which is calculated with the Blasius equation.

$$f_v = 0.079\,\mathrm{Re}_v^{-0.25} \qquad \text{Eq. (2)}$$

The superficial velocity of the vapor is calculated by Eq. (3)

$$u_v = \frac{Gx}{\rho_v \varepsilon} \qquad \text{Eq. (3)}$$

where ε is the void fraction calculated with the Steiner (1993) version of the Rouhani-Axelsson drift flux model.

$$\varepsilon = \left(\frac{x}{\rho_v}\right)\left\{\left(1+0.12(1-x)\right)\left(\frac{x}{\rho_v}+\frac{1-x}{\rho_l}\right)+\frac{1.18(1-x)\left[g\sigma(\rho_l-\rho_v)\right]^{0.25}}{G\rho_l^{0.5}}\right\}^{-1} \qquad \text{Eq. (4)}$$

The second term of the right hand side in Eq.(1) represents the centrifugal force due to the micro-fin geometry. For demonstration of the helical grooves inside the round tube, the isometric schematic view of the micro-finned tube with two grooves is shown in Fig. 2(b) and the geometry features of the micro-finned tube are described in Fig. 2(c). H is the longitudinal distance that the groove twists 180°, and D is the root diameter of the tube.

$$H = \frac{D\pi}{2\tan\beta} \qquad \text{Eq. (5)}$$

The liquid refrigerant flowing inside the helical groove is assumed to rotate around the tube axis with a constant angular speed. The fluid helical velocity is resolved into an axial component and tangential component as shown in Fig. 2(b).

$$u_h = \sqrt{u_z^2 + u_\theta^2} \qquad \text{Eq. (6)}$$

$$u_z = \frac{G(1-x)}{\rho_l(1-\varepsilon)} \quad \text{Eq. (7)}$$

$$u_\theta = \left(\frac{l_\theta}{l_z}\right)u_z = \left(\frac{\pi D}{2H}\right)u_z \quad \text{Eq. (8)}$$

Substituting Eq.(2), (3), (4) and (8) into Eq. (1) yields the SW-W/A transition.

$$G_{SA} = \left[\left(\rho_l g\delta D + 0.05\sigma\right)\left(\frac{0.8 f_v D x^2}{\rho_v \varepsilon^2} + 2\delta\left(\tan\beta\right)^2\left(\frac{(1-x)^2}{\rho_l(1-\varepsilon)^2}\right)\right)^{-1}\right]^{0.5} \quad \text{Eq. (9)}$$

2.2. Transition of Wavy Annular Flow (W/A) to Annular Flow (A)

As the liquid film begins to wet all the tube periphery in the evaporative tube, the liquid film thickness is not uniform due to gravity. This W/A flow pattern presents a thicker film thickness at the bottom of the tube. As the vapor velocity is increased, W/A flow becomes fully annular flow (A), and the film thickness is thinner and more uniform around the tube. As the liquid film at the top is too thick, the surface tension and interfacial shear cannot hold it. The gravitational force pulls the condensate from the upper part of tube to the bottom. The W/A-A transition is calculated by the transition of annular flow to stratified flow in condensation proposed by Xiao and Hrnjak (2019). The transition from the wavy-annular flow to annular flow is determined through the balance between the three different forces: gravity, surface tension and interfacial shear as shown in Eq.(10). C_1 and C_2 are two empirical constants, which are the same as that in Eq. (1).

$$\rho_l g\delta D + C_1\sigma = C_2 D f_v \rho_v u_v^2 \quad \text{Eq. (10)}$$

where δ is the film thickness with the assumption of uniform distribution and is calculated by the void fraction correlation by Xiao and Hrnjak (2017).

$$\delta = \frac{D}{2}\left(1-\varepsilon^{0.5}\right) \quad \text{Eq. (11)}$$

The W-A transition is calculated by

$$G_{WA} = \left[\frac{\left(\rho_l g\delta D + 0.05\sigma\right)\rho_v\varepsilon^2}{0.8 f_v D x^2}\right]^{0.5} \quad \text{Eq. (12)}$$

2.3. Transition of Stratified Wavy Flow (SW) or Annular Flow (A) to Intermittent Flow (I)

In the Kattan et al. (1998) and Wojtan et al.(2005) maps, the IA or IS transition has been kept at a fixed Martinelli's parameter of 0.34. Barbieri et al. (2008) argued that the transition did not occur at a constant vapor quality (related to a single value of the Martinelli parameter) and found that the transition vapor quality diminishes with the mass velocity increases and increases with the tube diameter. They proposed that the transition can be presented and correlated with liquid Froude number, Fr_l, and Martinelli's number, X_{tt}, defined as the following:

$$Fr_l = \frac{\left(G(1-x)\right)^2}{\rho_l^2 gD} \quad \text{Eq. (13)}$$

$$X_{tt} = \left((1-x)/x\right)^{0.9} \left(\rho_v/\rho_l\right)^{0.5} \left(\mu_l/\mu_v\right)^{0.1} \quad \text{Eq. (14)}$$

The transition of intermittent to stratified or annular flow is correlated following the above non-dimensional groups with the experimental data and presented in Eq. (15).

$$G_{IS} = \left[\frac{0.2\rho_l^2 gD}{(1-x)^2} \left(\frac{1-x}{x}\right)^{2.7} \left(\frac{\rho_v}{\rho_l}\right)^{1.5} \left(\frac{\mu_l}{\mu_v}\right)^{0.3} \right]^{0.5} \quad \text{Eq. (15)}$$

2.4. Transition of Stratified Smooth Flow (SS) to Stratified Wavy Flow (SW)

In the stratified flow, the flow can be further subdivided into two regions: stratified-smooth (SS) and stratified-wavy (SW). The SS flow pattern occurs when the liquid and vapor velocity are low enough that the interface remains relatively smooth. As the vapor velocity increases, the wave is initiated because the pressure and shear work on a wave overcome the viscous dissipation in the wave. The S-SW transition is the same in the Wojtan et al. (2005) map and is calculated from the original version of the Kattan et al. (1998) boundary:

$$G_{sw} = \left[\frac{226.3^2 A_{LD} A_{VD}^2 \rho_v (\rho_l - \rho_v) g \mu_l}{x^2 (1-x) \pi^3} \right]^{1/3} \quad \text{Eq. (16)}$$

Where

$$A_{LD} = \frac{A_L}{D^2} \quad \text{Eq. (17)}$$

$$A_{VD} = \frac{A_V}{D^2} \quad \text{Eq. (18)}$$

and $G_{SW}=G_{SW}(x_{IS})$ for $x<x_{IS}$.
Note that X_{IS} is the vapor quality for the intersection point of G_{SW} and G_{IS}.

2.5. Transition of Annular Flow (A) to Annular Flow with Partial Dry-out (D)

For the annular flow in evaporation, the continuous liquid film around the tube eventually dries out as heated. When the partial dry-out phenomenon occurs, the wall temperature rises abruptly. Thus, the heat transfer coefficient drops drastically. The A-D transition is calculated from the Wojtan et al. (2005) boundary, which was based on their measurements of heat transfer coefficient :

$$G_{AD} = \left[\left(\frac{1}{0.235}\right) \left[\ln\left(\frac{0.58}{x}\right) + 0.52 \right] \left(\frac{D}{\rho_v \sigma}\right)^{-0.17} \left[\frac{1}{gD\rho_v(\rho_l - \rho_v)} \right]^{-0.37} \left(\frac{\rho_v}{\rho_l}\right)^{-0.25} \left(\frac{\dot{q}}{\dot{q}_c}\right)^{-0.70} \right]^{0.926} \quad \text{Eq. (19)}$$

Where q_c is the critical heat flux and is calculated with the model of Kutateladze (1948):

$$\dot{q}_c = 0.131 \rho_v^{0.5} h_{fg} \left[g\sigma(\rho_l - \rho_v) \right]^{0.25} \quad \text{Eq. (20)}$$

Where h_{fg} is the latent heat of the refrigerant.

3. RESULTS AND DISSCUSSION

Fig. 4(a) and (b) show the experimental data of the visualization inside the smooth and axial micro-finned (0°helix angle) tubes plotted on the predicted flow pattern maps. In Fig. 4(a) and (b), the solid and hollow symbols are the visualization data and the black solid lines are the transition curves from the equations described in the previous section. Comparing our experimental data inside the smooth tube and axial micro-finned tubes, it is seen that there is no significant difference of the transitions. Axial micro-fins (0° helix angle) do not provide additional force to lift up the liquid in the round tube,

that is to say the annular flow pattern does not occur earlier (at low vapor quality or mass flux conditions) than in the smooth tube. In addition, the predicted flow pattern maps show good agreement with experimental results in both cases.

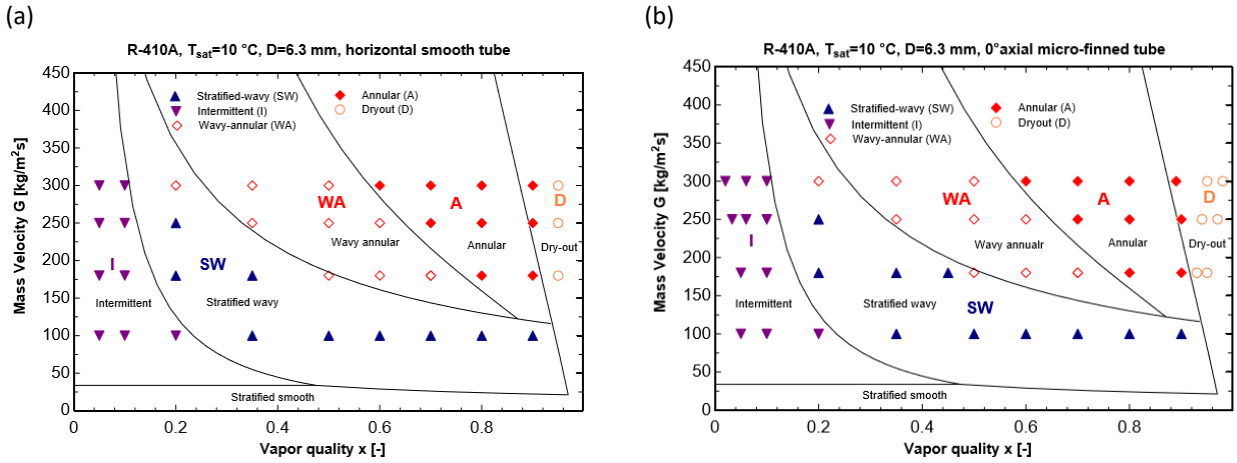

Figure 4: Flow pattern map in (a) smooth and (b) axial micro-finned (0°helix angle) tubes

Fig. 5(a) and (b) show the experimental data of the visualization inside the helical micro-finned tubes with different helix angles (18° and 10°) plotted on the corresponding flow pattern maps. The solid and hollow symbols are the visualization data and the black solid lines are the transition curves from the equations described in the previous section. In the helical micro-finned tubes, the transition of the intermittent flow to stratified wavy or wavy annular flow is same as that in the smooth or axial micro-finned tubes. The intermittent flow take places as the roll wave at the liquid vapor interface triggered by the K-H instability is strong enough as well as a sufficient liquid level, which is more related to the tube geometry (diameter) rather than inner micro-fins. In addition, the helical micro-grooves provide additional centrifugal force such that the liquid refrigerant is easier to climb to the top of the tube and forms annular flow. Therefore, the annular flow in the helical micro-finned tubes occurs at lower vapor quality and lower mass flux than the smooth or axial micro-finned tube. The transition of stratified wavy to wavy annular flow in the helical micro-finned tube is shifted down. Compared to our experimental data inside the helical micro-finned tubes, the predicted flow pattern maps show good agreements with experimental results.

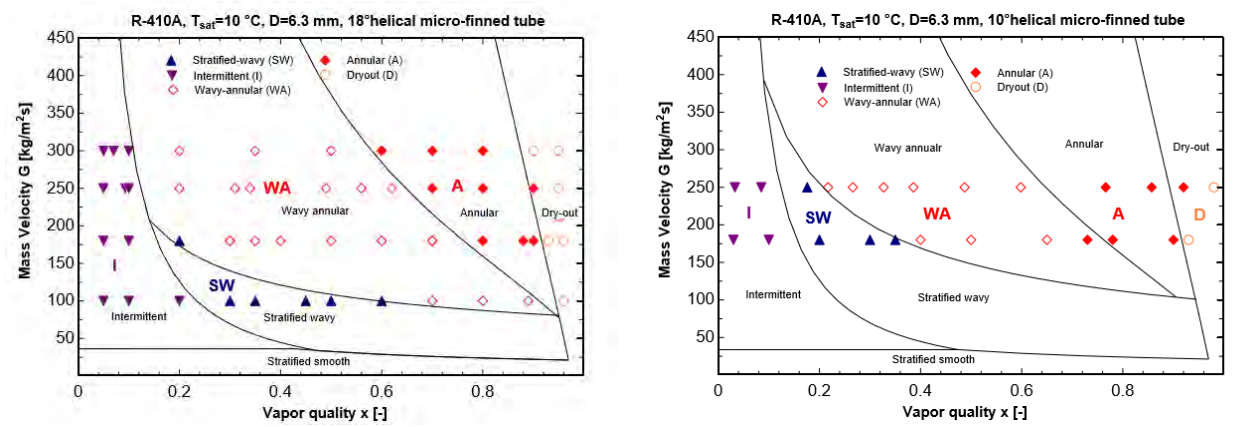

Figure 5: Flow pattern map in helical micro-finned tubes with (a) 18° helix angle and (b) 10° helix angle

Helical micro-grooves in the round tubes influence the transition of stratified wavy flow to annular flow, and this transition boundary is related to the helix angle. Fig. 6(a)-(c) shows the flow patterns captured inside the micro-finned tubes with different helix angles under the same conditions (T_{sat}=10°C, G=180 kg×s^{-1}×m^{-2}, and x=0.35). The flow regime in the tube with 0° helix angle is stratified wavy flow, and the axial groove structure does not change the height of the wave. In the tube with 10° helix angle, it is found that some liquid waves reach to higher location of the tube but only part of the upper tube is wetted. For the 18° helix angle, liquid waves have enough momentum to reach to the top and all the tube is wetted. The SW-W/A transition in Fig. 6(d) reflects this trend, and the transition boundary shifts down with the increase of helix angle. However, the flow pattern

map is built and validated with the current experimental data. More experimental data in different helix angles is needed to expand the availability of the flow pattern map.

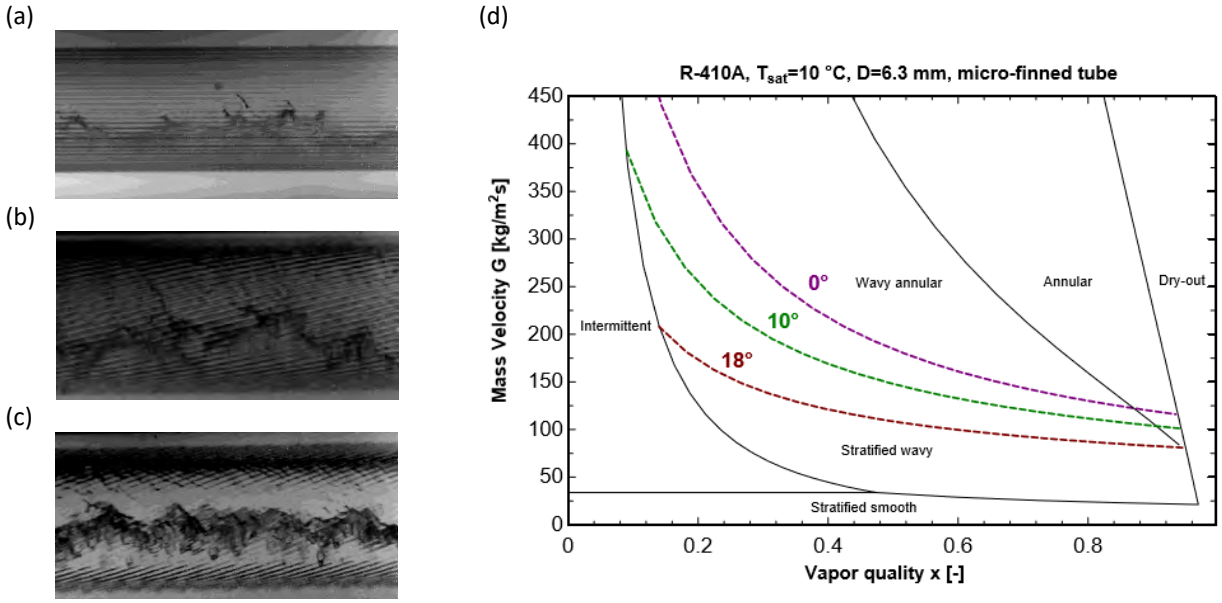

Figure 6: Visualization of two-phase flow in the micro-finned tubes with different helix angles: (a) 0 °, (b) 10 ° and (c) 18 °, and the related SW-W/A transitions in the flow map

4. CONCLUSIONS

Visualization of R410A flow boiling was conducted through the clear smooth and micro-finned tubes with 0°, 10° and 18° helix angle. The result shows that the flow pattern map for a micro-finned tube with 0° helix angle is generally similar to that in the smooth tube. For the tube with 18° helix angle, the annular flow occurs at lower vapor quality and mass flux. A modified flow pattern model accounting for the early transition to annular flow in the micro-finned tubes is built. The comparison between experimental data and the flow regime map shows good agreement.

ACKNOWLEDGEMENTS

This study is supported by the Air-Conditioning and Refrigeration Center (ACRC) at the University of Illinois at Urbana-Champaign (UIUC). The authors would like to acknowledge the technical support from Creative Thermal Solutions Inc. (CTS). The authors are also grateful to MechSE RP Lab at UIUC for manufacturing 3D-printed tubes.

NOMENCLATURE

A	area (m^2)	σ	Surface tension ($N \times m^{-1}$)
D	Inner diameter (m)	β	helix angle (°)
G	mass flux ($kg \times s^{-1} \times m^{-2}$)	***Subscripts***	
HTC	heat transfer coefficient ($W \times K^{-1} \times m^{-2}$)	l	liquid
P	pressure (kPa)	v	vapor
q	heat flux ($W \times m^{-2}$)	SA	stratified wavy to wavy annular
T	temperature (°C)	SI	stratified wavy to intermittent
u	velocity ($m^2 \times s^{-1}$)	AD	annular to annular with partial dry-out
x	vapor quality (-)	SW	stratified smooth to stratified wavy
ρ	density ($kg \times m^{-3}$)	sat	saturated

REFERENCES

Alves, G., 1954. Concurrent liquid-gas flow in a pipe-line contactor. Chem. Eng. Prog. 50(9), 449-456.

Baker, O., 1954. Design of pipe lines for simultaneous flow of oil and gas. Oil and Gas Journal 53(12), 185-195.

Barbieri, P., Jabardo, J., Bandarra Filho, E., 2008. Flow patterns in convective boiling of refrigerant R134a in smooth tubes of several diameters. 5th European Thermal-Science Conference, The Netherlands.

Colombo, L., Lucchini, A., Muzzio, A., 2012. Flow patterns, heat transfer and pressure drop for evaporation and condensation of R134a in microfin tubes. International Journal of Refrigeration 35, 2150-2165.

Hatamipour, V., Akhavan-Behabadi, M., 2012. Visual study on flow patterns and heat transfer during convective boiling inside horizontal smooth and micro-fin tubes. World Academy of Science, Engineering, and Technology 69, 700-706.

Kattan, N., Thome, J., Favrat, D., 1998. Flow boiling in horizontal tubes: Part 1-development of a diabatic two-phase flow pattern map. Journal of Heat Transfer 120(1), 140-147.

Kutateladze, S., 1948. On the transition on film boiling under natural convection. Kotloturbostroenie 3(10).

Mastrullo, R., Mauro, A., Thome, J., Toto, D., Vanoli, G., 2012. Flow pattern maps for convective boiling of CO 2 and R410A in a horizontal smooth tube: Experiments and new correlations analyzing the effect of the reduced pressure. International Journal of Heat and Mass Transfer 55 (5-6), 1519-1528.

Rollmann, P., Spindler, K., 2015. A new flow pattern for flow boiling in microfin tubes. International Journal of Multiphase Flow 72, 181-187.

Sharar, D. J., Jankowski, N. R., Bar-Cohen, A., 2013. Modified model for improved flow regime prediction in internally grooved tubes. Proceedings of the ASME 2013 International Technical Conference and Exhibition on Packaging and Integration of Electronic and Photonic Microsystems, Burlingame, CA, USA.

Steiner, D., 1993. Heat transfer to boiling saturated liquids, in: VDI Heat Atlas.

Taitel, Y., Dukler, A.,1976. A model for predicting flow transitions in horizontal and near horizontal gas-liquid flow. AIChE J. 22(1), 47-55.

Thome, J., El Hajal, J., 2003. Two-phase flow pattern map for evaporation in horizontal tubes: Latest version. Heat Transfer Engineering 24(6), 3-10.

Wojtan, L., Ursenbacher, T., Thome, J. R., 2005. Investigation of flow boiling in horizontal tubes: Part I-A new diabatic two-phase flow pattern map. International Journal of Heat and Mass Transfer 48 (14), 2955-2969.

Xiao, J., Hrnjak, P., 2015. Condensation in horizontal smooth round tube. ACRC Report No. TR-321.

Xiao, J., Hrnjak, P., 2017. A new flow regime map and void fraction model based on the flow characterization of condensation. International Journal of Heat and Mass Transfer 108, 443-452.

Xiao, J., Hrnjak, P., 2019. A flow regime map for condensation in macro and micro tubes with non-equilibrium effects taken into account. International Journal of Heat and Mass Transfer 130, 893-900.

Yang, C.-M., Hrnjak, P., 2018. Effect of straight micro fins on heat transfer and pressure drop of R410A during evaporation in round tubes. International Journal of Heat and Mass Transfer 117, 924-939.

Yang, C.-M., Hrnjak, P., 2019. Visualization of two-phase flow of R410A in horizontal smooth and axial micro-finned tubes. International Journal of Heat and Mass Transfer 138, 49-58.

Yu, M.-H., Lin, T.-K., Tseng, C.-C, 2002. Heat transfer and flow pattern during two-phase flow boiling of R-134a in horizontal smooth and microfin tubes. International Journal of Refrigeration 25, 789-798.

Zürcher, O., Favrat, D., Thome, J., 2001. Development of a diabetic two-phase flow pattern map for horizontal flow boiling. International Journal of Heat and Mass Transfer 45(2), 291-301.

Manuscript ID: 858
DOI: 10.18462/iir.icr.2019.0858

Analysis and quantification of generated bubbles for flow boiling through diabatic visualization

Cheng-Min YANG[(a)], Pega HRNJAK[(a),(b)]

[(a)] ACRC, University of Illinois at Urbana-Champaign
Urbana, 61801, USA, cyang73@illinois.edu
[(b)] Creative Thermal Solutions, Inc.
Urbana, 61802, USA, pega@illinois.edu

ABSTRACT

This paper aims at presenting the heat transfer analysis of flow boiling in horizontal smooth and micro-finned tubes through visualization in diabatic conditions. Visualization of R410A flow boiling experiments were conducted in a transparent concentric heat exchanger. 3D printed clear resin tubes with different geometries are placed in an outer glass tube with annular water flow for visualizing the flow during evaporation. Parameters of generated bubble such as departure diameter and frequency are quantified based on visualization using high-speed camera and video processing techniques. Heat transfer in the test section is analyzed through the temperature measurements and estimated bubble parameters. Two regions of incipience of boiling are found in the current experiments. As the superheat is insufficient to reach the onset point of nucleate boiling, the heat transfer is governed by forced convection. At a higher heat flux, the heat transfer is by the mechanisms of the forced convection and surface nucleate boiling.
Keywords: Visualization, Diabatic condition, Micro-fin, 3D printed, Flow boiling.

1. INTRODUCTION

Micro-finned tubes are widely used for evaporators and condensers in refrigeration and air-conditioning systems. It was found that the micro-fin geometry significantly enhanced the heat transfer coefficient in round tubes with a minor additional pressure drop penalty. Investigating the two-phase flow behavior in the micro-finned tube provides some evidences for the mechanism of heat transfer enhancement. A number of experimental studies concerned with the flow regimes of two-phase flow in micro-finned tubes have been reported. The most common way is using a sight glass for visualization at the exit of the tested micro-finned tube such as Fujii et al. (1995), Yu et al. (2002), Schael and Kind (2005), Chen et al. (2006), Olivier et al. (2007), Rollmann and Spindler (2015), and Sharar and Bar-Cohen (2016). However, these glass tubes do not have internal micro-fin geometry. In addition, the flow regime is visualized without heating or cooling, which is near adiabatic condition. Yang and Hrnjak (2018 a) have earlier presented a new technique to visualize the two phase flow in clear smooth and micro-finned tubes under diabatic conditions. Compared to the traditional adiabatic visualization technique, the more realistic evaporative condition is simulated and the developing evaporation process can be captured. In order to further understand the physics behind, the objective of this paper is to quantify the bubble parameters and analyze the heat transfer mechanisms for flow boiling in horizontal smooth and micro-finned tubes through visualization under diabatic conditions.

2. EXPERIMENTS

In order to understand the heat transfer mechanism in round tubes with different geometries during flow boiling, a diabatic visualization section with 3D printed micro-finned tubes developed by Yang and Hrnjak (2018 a) is used. With this technique, the geometry effect of micro-fin on flow is investigated and the more realistic evaporative condition than the typical adiabatic one is simulated. As shown in Fig. 1(a) and (b), the visualization section consists of two concentric tubes. The outer tube is a 10 cm long glass tube, whose inner and outer diameter are 15.75 mm and 19.05 mm, respectively. The inner tube is a 21 cm clear resin tube with different internal geometries. Refrigerant flows in the inner resin tube, while the water flows between the inner resin tube and the outer glass tube. For the refrigerant side, R410A without oil is used and the vapor quality condition is controlled

through the calorimeter. The secondary fluid, water, is heated by a cartridge heater and injected into the visualization section via circular manifold. The heat flux for the evaporative tube is provided by the water flowing through the transparent concentric tubes and is determined with the measurement of the inlet and outlet water temperature as well as the water mass flow rate. The details of flow loops and instruments are described in Yang and Hrnjak's previous work (2018 b & 2019).
The transparent resin tubes with and without internal micro-fin geometry are manufactured by a SLA 3D printer (stereolithography system). The SLA used here provides a beam diameter of 0.075±0.015 mm with a minimum feature size of 0.02 mm in High Resolution (HR) mode. The printed material is WaterClear Ultra 10122, a type of optically clear resin with ABS-like properties. The 3D printed tubes reproduce the inner diameter and fin geometry in the aluminum tubes used in the heat transfer test section, but the wall is thicken for maintaining a factor of safety over the burst pressure. For the 3D printed smooth tube (Fig. 1(c)), the inner and outer diameter are 6.32 mm and 9.525 mm respectively. The 3D printed micro-finned tube (Fig. 1(d)) has 58 fins with outer diameter of 9.525 mm and fin-tip diameter of 6.08 mm.

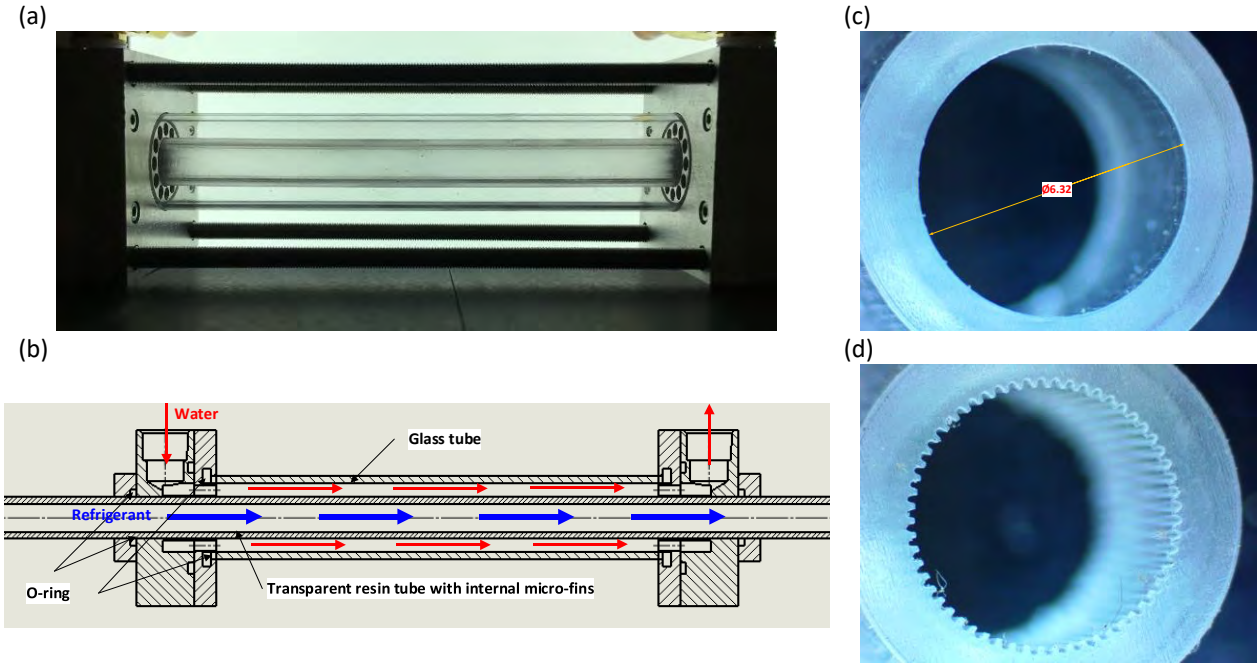

Figure 1: (a) photographic and (b) schematic views of the diabatic visualization section. Transparent resin tubes (c) without and (d) with internal micro-fins

3. HEAT TRANSFER ANALYSIS THROUGH VISUALIZATION

Fig. 2(a) and (b) show the top view and side view of the two phase flow during the subcooled flow boiling. The experiment was conducted in the transparent smooth tube at G = 180 kg/m^{2}s, T_{sat} = 10°C and q=1.92 kW/m^2. It is seen that some bubbles are generated from the tube wall and then detached from the wall. Then, the detached bubbles grow as the flowing liquid and merge with the nearby bubbles to form a vapor plug at the top center of the tube. The related schematic view for explanation of mechanisms is demonstrated in Fig 2(c). At the inlet of the visualization section, the bulk fluid temperature is lower than its saturation temperature. As the wall temperature of the tube is raised above the saturation temperature and beyond the onset of the boiling, some of the nucleation sites on the tube wall are activated. Since the mechanism of convection plays an important role under moderate heat flux condition (incipient boiling or partial boiling region), the bulk fluid is superheated and causes the detached bubbles to grow. The wall heat flux is transferred to the refrigerant through the bubble generation, bubble growth, and forced convection. Through the captured videos, different heat transfer mechanisms during the subcooled flow boiling can be further analysed and quantified. The details of the parameters quantification and the analysis of different heat transfer mechanisms are described in the following subsections.

(a)



(b)



(c)

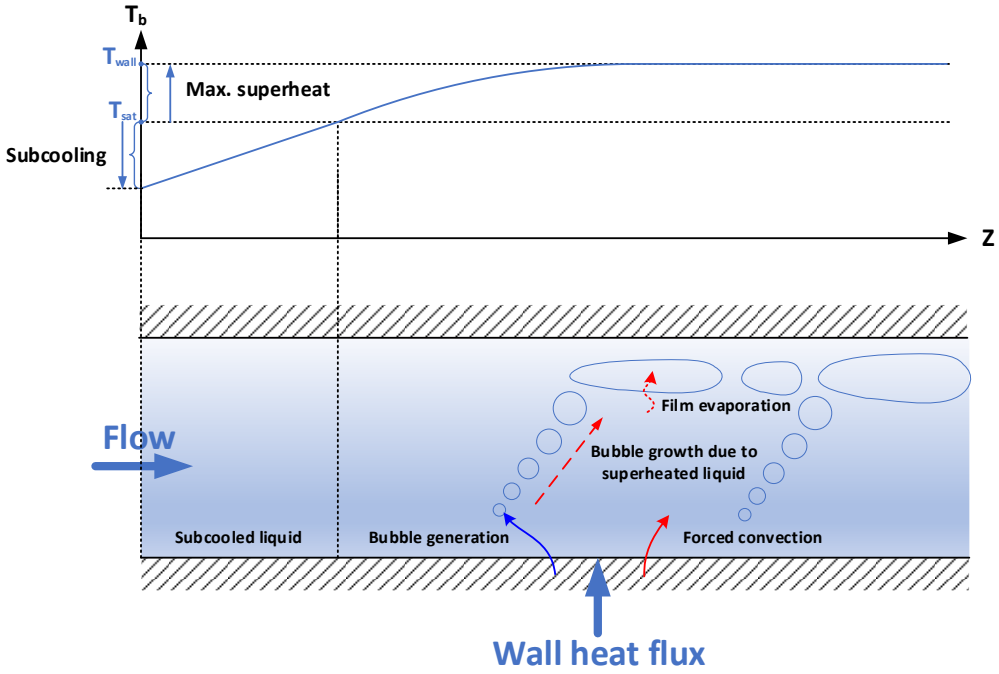

Figure 2: (a) top view, (b)side view, and (c) schematic illustration of the flow boiling at vapor quality around zero

3.1. Quantification of the parameters

In order to determine the quantity of the heat transferred from the tube wall to the refrigerant through evaporation (bubble generation), the parameters such as bubble generation frequency (f), bubble departure diameter (D_d), and the activated nucleation site density (N) should be quantified. The bubble generation frequency for a nucleation site was determined by measuring how much time it takes to generate 50 bubbles. The bubble departure diameter is measured at the moment when the bubble begin to slide and the diameter is determined by counting the pixels of the bubble boundary in the photo.

To estimate the activated nucleation site density, it is important know the real area that is accounted for in the viewing area (captured photo). As demonstrated in Fig. 3, the video of the two-phase flow is captured from the side of the tube and the video control volume only represents a small part of the whole tube. Since the object in the video is a curved surface, the projection area (h×w) cannot reflect viewing area (P×w). In addition, the depth of field, a third dimension of the control volume for in-focus zone, influences the projected viewing area.

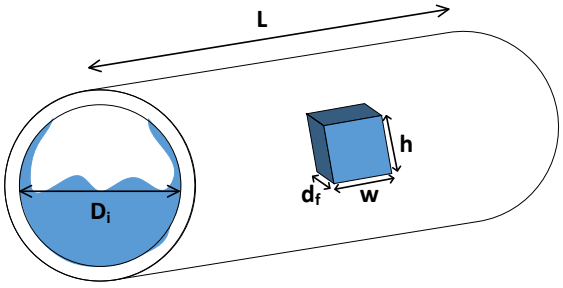

Figure 3: Schematic view of the video control volume in the visualized tube

There are two situations for calculating the viewing area as illustrated in Fig. 4. In the first case, the depth of field is larger than t_r, and the details of the calculation are shown in the following equations,

$$A_{viewing} = p \times w = R_i \theta \times w = 2R_i w \sin^{-1}(h/2R_i) \quad \text{Eq. (1)}$$

In the second case, the depth of field is smaller than t_r, and the viewing area is calculated with Eq. (2)

$$A_{viewing} = p_f \times w = R_i \theta_f \times w = 2R_i w \cos^{-1}((R_i - d_f)/R_i) \quad \text{Eq. (2)}$$

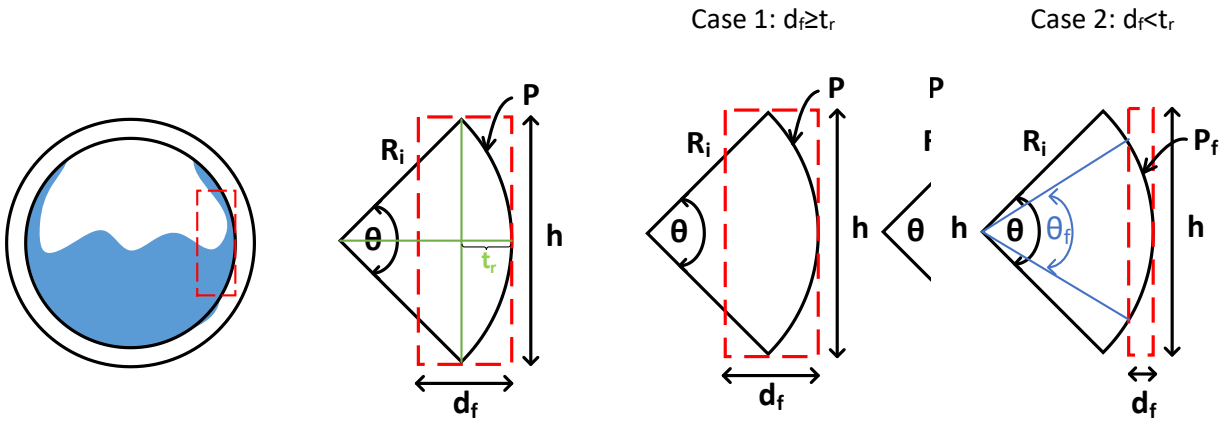

Figure 4: Illustration of viewing area calculation

As the above discussion, the depth of field is needed for calculating the viewing area. Depth of field is the distance between the two extreme axial points where an image is judged to be in focus, as illustrated in Fig. 5(a). In other words, the image captured by the camera will be blurry when the camera is too close to or too far away from the object. In order to estimate the depth of field for the corresponding lens in our visualization set-up, an in-focus calibration test is performed. As shown in Fig. 5(b), a known size particle is placed at the center of the tube (visualization section) and the high speed camera is placed on an adjustable optic platform, which is used to provide the precise adjustment of horizontal position of the camera. The resolution of position adjustment is 0.1 mm. The photos captured from far to close (camera position) are analyzed through the image processing to determine if they are in focus. The images are first converted into pixel values, which describe the brightness of the pixel. The pixel values ranges from 0 to 255 (i.e., 8-bit), where 0 is a fully black pixel and 255 is a white pixel. A pixel with grayness is given a pixel value between 0 to 255 and is proportional to its light intensity. The critical grayscale gradient indicator ($GI_{critical}$), proposed by Koh et al. (2001) is used as the in-focus criterion. The details of the in-focus calculation are described in Xu and Hrnjak's work (2017). With the in-focus criterion, the depth of field for the corresponding lens can be estimated.

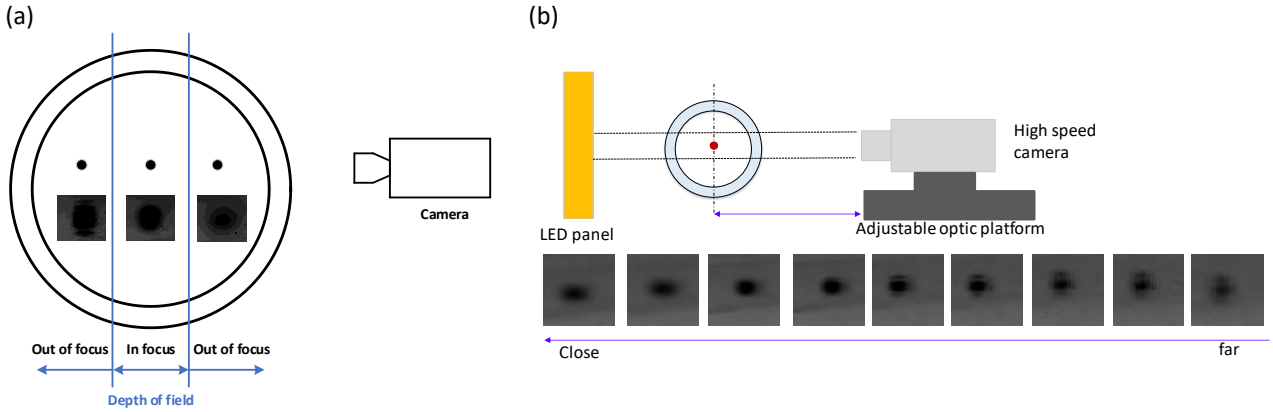

Figure 5: Schematic diagram of (a) image of single particle at different focal distance (b) calibration test of the depth of field

3.2. Total Wall Heat Flux

In the diabatic visualization section, the wall heat flux to the refrigerant is provided by the water flowing through the transparent concentric tubes. The heat transfer to the refrigerant is based on the heat transfer from the water minus the heat loss to the ambient. The heat transfer from the water is estimated through the water temperature difference between the inlet and outlet of the visualization section times the mass flow rate. The heat loss to the ambient is estimated through a calibration test. The total wall heat flux is calculated by the following equation,

$$q_w = \frac{(Q_w - Q_{amb})}{(\pi D_i L)\zeta} = \frac{(\dot{m}C_p)_w (T_{w,vis,i} - T_{w,vis,o}) - \dot{Q}_{amb,vis}}{(\pi D_i L)\zeta} \quad \text{Eq. (3)}$$

3.3. Different Heat Transfer Mechanisms

3.3.1. Nucleate boiling (bubble generation)

The heat flux for bubble generation is computed as the latent heat carried away through the bubbles departed from the heated wall. The evaporative heat flux is given by

$$q_{evap} = (f \cdot \rho_g \cdot \tfrac{4}{3}\pi(\tfrac{D_d}{2})^3) h_{fg} \cdot N \quad \text{Eq. (4)}$$

3.3.2. Convection

The other heat transfer mechanism from the wall to the fluid is through convection (single-phase heat transfer), which is the other part of the wall heat flux and is estimated by Eq. (5).

$$q_{conv} = q_w - q_{evap} \quad \text{Eq. (5)}$$

The heat can be further transferred from the liquid to the bubbles or to the liquid vapor interface (ex: film boiling at the interface of the stratified flow).

1) Bubble growth

Under the heat flux conditions in our experiments (relatively low heat flux), the single phase convection mechanism plays an important role, and the liquid refrigerant in the visualization is superheated. The heat coming from the superheated liquid causes the departed bubbles to grow. The liquid nearby the bubble is evaporated (vapor expansion), and the interfacial heat flux is calculated through film boiling.

$$q_{bubblegrowth} = \left(\frac{\dot{m}_{fg} h_{fg}}{A}\right) = \left(\frac{\rho_v}{A}\frac{dV}{dt}\right) h_{fg} \quad \text{Eq. (6)}$$

The volume change rate is estimated from the dimeter change of the growing bubble in the viewing area as demonstrated in Fig. 6 (a) and (b). The value of Δt is the time taken as the diameter changes from D_1 to D_9, which is known from the captured high speed video.

$$\frac{dV}{dt} \simeq \frac{\Delta V}{\Delta t} = \frac{4\pi/3\,((D_9/2)^3 - (D_1/2)^3)}{\Delta t} \quad \text{Eq. (7)}$$

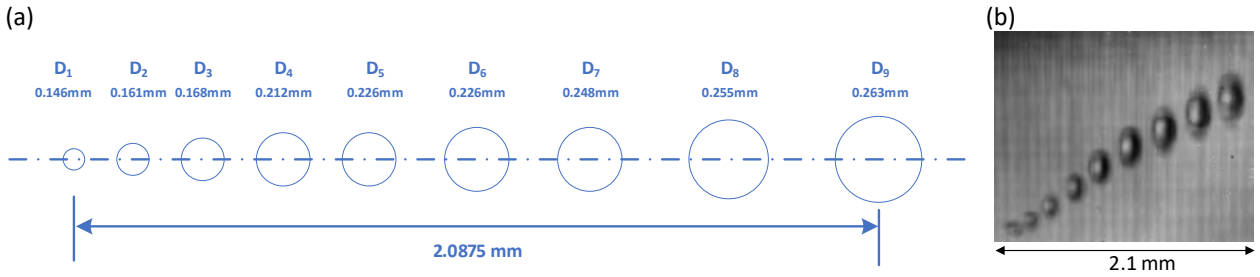

Figure 6: A growing bubble train in a superheated liquid within the viewing area:(a) schematic and (b) photographic views

2) Other mechanisms

In addition to the bubble growth, the remaining part of the convective heat flux contributes to the film evaporation at the liquid-vapor interface and the increase of the liquid temperature.

$$q_{conv,other} = q_{conv} - q_{bubblegrowth} \qquad \text{Eq. (8)}$$

4. RESULTS AND DISSCUSSION

In the flow boiling, three distinct regions with different mechanisms were found and explained by Bergles and Rohsenow (1964), as demonstrated with the schematic view in Fig. 7. In the forced convection region (low wall superheat), the heat transfer is governed by forced convection. In the incipient boiling region (moderate wall superheat), relatively few nucleation sites are activated and a proportion of heat from the wall is transferred to the fluid through single-phase process. The heat transfer is determined by the combined effects of forced convection and surface nucleate boiling. As the heat flux increases, the activated sites increases and the convection portion decreases. Finally the effect of forced convection seems to disappear in the fully developed boiling region (high wall superheat). In our visualization experiment, the provided heat flux condition is limited because of the tube material. Returning to Fig. 1(a), the 3D printed evaporative tube is made of optically clear resin, and its thermal conductivity is around 0.21 W m^{-1} K^{-1}, which is only 0.1% of aluminium. Besides, the hard resin becomes viscous or rubbery when the water (secondary fluid) temperature is over 40°C. Then, the resin tube could not hold the high pressure any more. Thus, the heat flux to the refrigerant is relatively lower than that in normal metal evaporative tube and not enough to reach the fully developed boiling region. In other words, the captured videos in our work are in the forced convection region and incipient boiling region.

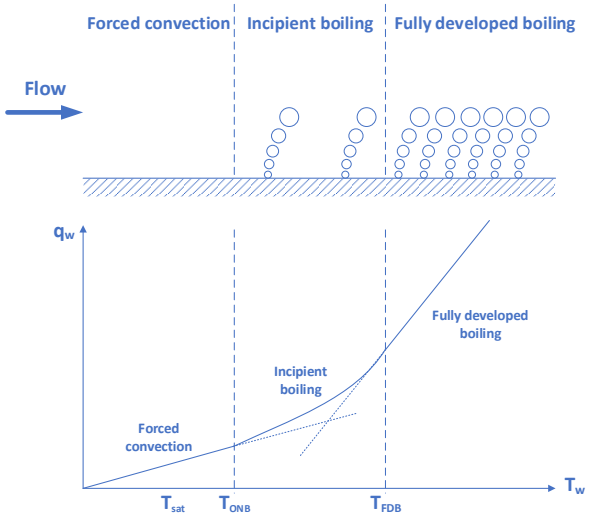

Figure 7: Illustration of three regions in flow boiling (Bergles and Rohsenow, 1964)

The flow behavior of R410A during flow boiling at vapor quality near zero in the smooth tube, axial micro-finned (0° helix angle), and 10° helical micro-finned tubes under diabatic condition was captured through the high speed camera with a microscope lens, as shown in Fig. 8(a)-(c). Each

image in Fig. 8 consists of 512×512 pixels, and the corresponding image size is about 6.63 mm×6.63 mm. The heat transfer mechanisms in the different tubes and conditions were analyzed with the method described in Section 3.3 and summarized in Table 1. It is found that the proportion of the evaporative heat flux (for bubble generation) depends on the heat flux conditions. The heat is transferred through forced convection mechanism thoroughly as the heat flux is low. As the heat flux increases, the proportion of evaporative mechanism becomes important. However, the evaporative heat flux only accounts for up to 5.67% of the total heat flux in our experiments due to the limit of our heat flux conditions. In addition, it is found that the axial micro-fins and helical micro-fins do not influence the proportion of the evaporative heat flux significantly. Take the case of the axial micro-fins as an example. The heat flux condition (total wall heat flux) is 2.307 $kW \times m^{-2}$, and the heat flux transferred to the refrigerant through evaporation accounts for 1.72%. The proportion of the evaporative heat flux is between the second case (1.55%) and the third case (5.67%) in the smooth tube because the heat flux condition is also in between. As a result, the proportion of the heat transfer mechanisms mainly depends on heat flux condition. Experiments for the flow boiling will be improved and more heat flux conditions are needed for further investigation of the mechanisms.

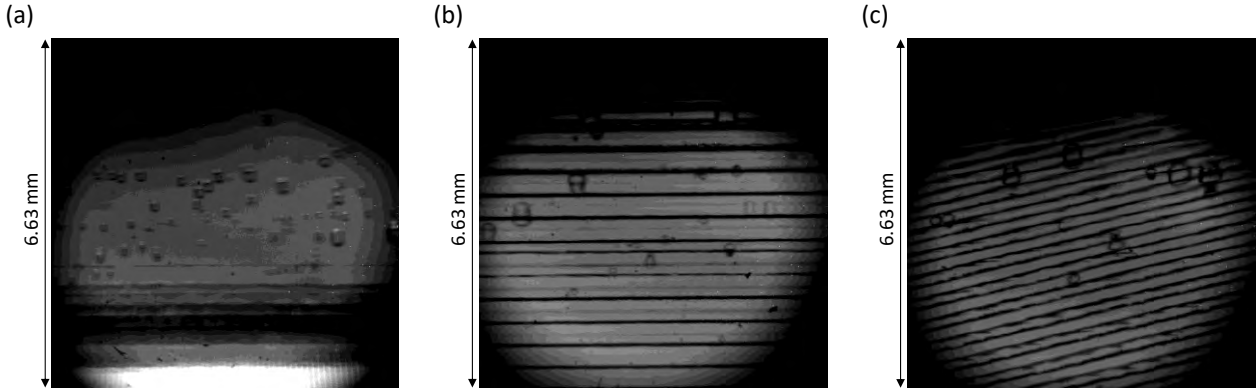

Figure 8: Captured images of flow boiling in (a) smooth, (b) axial micro-finned, (c) and helical micro-finned tubes

Table 1. Proportion of different heat transfer mechanisms of the total wall heat flux

Geometry	q_w ($kW \times m^{-2}$)	q_{evap} ($kW \times m^{-2}$)	$q_{bubblegrowth}$ ($kW \times m^{-2}$)	$q_{conv.other}$ ($kW \times m^{-2}$)
Smooth	1.450	0(0%)	0(0%)	1.450(100%)
Smooth	1.920	0.0298(1.55%)	0.277(14.43%)	1.655(84.02%)
Smooth	2.700	0.1532(5.67%)	0.449(16.63%)	2.098(77.7%)
Axial micro-fin	2.307	0.0397(1.72%)	0.295(12.79%)	1.972(85.49%)
Helical micro-fin	1.890	0.0093(0.5%)	0.3119(16.5%)	1.569(83.0%)

5. CONCLUSIONS

This paper presents the heat transfer analysis for flow boiling in horizontal smooth and micro-finned tubes through visualization under diabatic conditions. R410A flow boiling experiments were conducted in different tube geometries. Parameters of generated bubble such as departure diameter and frequency are quantified. Details for analyzing different heat transfer mechanisms in the visualized two-phase flow are described. Two regions of flow boiling are found in the current experiments. As the superheat is not enough to reach the onset of boiling, the heat transfer is governed by forced convection. At a higher heat flux, the heat is transfer by the mechanisms of the forced convection and surface nucleate boiling. Since the limit of the heat flux condition in our visualization section, the evaporative heat flux only accounts for a small proportion of the total heat flux.

ACKNOWLEDGEMENTS

This study is supported by the Air-Conditioning and Refrigeration Center (ACRC) at the University of Illinois at Urbana-Champaign (UIUC). The authors would like to acknowledge the technical support

from Creative Thermal Solutions Inc. (CTS). The authors are also grateful to MechSE RP Lab at UIUC for manufacturing 3D-printed tubes.

NOMENCLATURE

C_p	specific heat (KJ×kg^{-1}×K^{-1})	ρ	Density (kg×m^{-1})
D_d	bubble departure diameter (m)		
D_i	inner diameter (m)	*Subscript*	
f	bubble generation frequency (Hz)	*amb*	ambient
G	mass flux (kg×m^{-2}×s^{-1})	*b*	bulk
$GI_{critical}$	critical gradient indicator	*conv*	convection
h_{fg}	latent heat (kJ×kg^{-1})	*evap*	evaporation
L	length of the tube (m)	*FDB*	fully developed nucleate boiling
m	mass flow rate (kg×s^{-1})	*i*	inlet
N	nucleation site density (sites×m^{-2})	*o*	outlet
Q	heat transfer rate (kW)	*ONB*	onset of nucleate boiling
q	heat flux (kW×m^{-2})	*r*	refrigerant
T	Temperature (°C)	*vis*	visualization section
x	Vapor quality (-)	*w*	wall
ζ	area enhancement ratio due to micro-fin geometry (-)		

REFERENCES

Bergles, A., Rohsenow, W., 1964. The Determination of Forced-Convection Surface-Boiling Heat Transfer. Journal of Heat Transfer, 365-372.

Chen, Q., Amano, R., Xin, M., 2006. Experimental study of flow patterns and regime of condensation in horizontal three-dimensional micro-fin tubes. Heat Mass Transfer 43, 201-206.

Fujii, T., Koyama, S., Inoue, N., Kuwahara, K., Hirakuni, S., 1995. An experimental study of evaporation heat trasnfer of refrigerant HCFC22 inside an internally grooved horizontal tube. JSME International Journal 38(4), 618-627.

Koh, K., Kim, J., Lee, S., 2001. Determination of in-focus criteria and depth of field in image processing of spray particles. Atomization and Sprays 11(4), 317-333.

Olivier, J. A., Liebenberg, L., Thome, J. R., Meyer, J. P., 2007. Heat transfer, pressure drop, and flow pattern recognition during condensation inside smooth, helical micro-fin, and herringbone tubes. International Journal of Refrigeration 30, 609-623.

Rollmann, P., Spindler, K., 2015. A new flow pattern for flow boiling in microfin tubes. International Journal of Multiphase Flow 72, 181-187.

Schael, A., Kind, M., 2005. Flow pattern and heat transfer characteristics during flow boiling of CO_2 in a horizontal micro fin tube and comparison with smooth tube data. International Journal of Refrigeration 28 , 1186-1195.

Sharar, D. J., Bar-Cohen, A., 2016. Flow regimes and evaporative heat transfer coefficients for flow boiling in smooth and internally-grooved tubes. 15th IEEE ITHERM Conference.

Xu, J., Hrnjak, P., 2017. Quantification of flow and retention of oil in compressor discharge pipe. International Journal of Refrigeration 80, 252-263.

Yang, C.-M., Hrnjak, P., 2018. Visualization of R410A flow boiling in diabatic conditions inside horizontal round tubes. 17th International Refrigeration and Air Conditioning Conference at Purdue.

Yang, C.-M., Hrnjak, P., 2018. Effect of straight micro fins on heat transfer and pressure drop of R410A during evaporation in round tubes. International Journal of Heat and Mass Transfer 117, 924-939.

Yang, C.-M., Hrnjak, P., 2019. Visualization of two-phase flow of R410A in horizontal smooth and axial micro-finned tubes. International Journal of Heat and Mass Transfer 138, 49-58.

Yu, M.-H., Lin, T.-K., Tseng, C.-C., 2002. Heat transfer and flow pattern during two-phase flow boiling of R-134a in horizontal smooth and microfin tubes. International Journal of Refrigeration 25, 789-798.

Manuscript ID: 871
DOI: 10.18462/iir.icr.2019.0871

Experiments on boiling/condensation heat transfer and pressure drop of refrigerant HFO1336mzz(E) and the mixture inside a horizontal microfin tube

Norihiro INOUE[(a)], Yufei LIU[(b)], Kazuhide WATANABE[(c)], Daisuke JIGE[(a)]

[(a)] Tokyo University of Marine Science and Technology, Tokyo, 135-8533, Japan, inoue@kaiyodai.ac.jp, djige00@kaiyodai.ac.jp

[(b)] Graduate School of Marine Science and Technology, Tokyo University of Marine Science and Technology, Tokyo, 135-8533, Japan, d172026@edu.kaiyodai.ac.jp

[(c)] Japan Coast Guard Academy, 737-0832, Hiroshima, Japan, watanabe@jcga.ac.jp

ABSTRACT

This study experimentally investigated the boiling/condensation heat transfer and pressure drop characteristics of HFO1336mzz(E) and a mixture of HFO1336mzz(E) and HFO1336mzz(Z), inside a horizontal microfin tube. The test tube was copper, with an outside diameter of 9.52 mm, an equivalent inner diameter of 8.95 mm, fin heights of 0.12 mm, a helix angle of 16.5°, and 65 fins. The experiments were conducted under a mass velocity range from 50 to 300 $kgm^{-2}s^{-1}$ at boiling and condensation saturated temperatures of 40 °C and 60 °C. The relationship between heat transfer coefficient/frictional pressure drop and vapor quality in boiling and condensation processes were clarified. The boiling/condensation heat transfer coefficient of HFO1336mzz(E) was lower than that of R245fa, however the pressure drop of HFO1336mzz(E) was lower than that of R245fa.
Keywords: Boiling, Condensation, Zeotropic mixtures, Heat Transfer, HFO, Pressure Drop, R245fa

1. INTRODUCTION

As part of efforts to combat global warming, significant research has been directed towards heat pump systems that generate hot water and high-temperature steam, and binary organic Rankine cycle (ORC) generators that utilize a low-temperature heat source discharged from factories. In recent years, R245fa, which has a high critical temperature and a low working pressure, has been commercially used as working fluid for both high-temperature heat pump systems and binary generators. However, when used as a hydrofluorocarbon (HFC) refrigerant, it has a high global warming potential (GWP). To comply with the Kigali Amendment of the Montreal Protocol, therefore, HFO1336mzz(E) and HFO1336mzz(Z) are attracting attention as drop-in refrigerant replacements for R245fa; they have low GWP and are non-flammable. Juhasz (2017) reported the fluid characteristics, thermal stability, metal compatibility, material compatibility, and cycle performance of HFC1336mzz(E), and evaluated the coefficient of performance (COP) of heat pump systems using HFO1336mzz(E), HFO1336mzz(Z), R245fa, and others. They concluded that R1336mzz(E) could be a viable working fluid in waste heat recovery applications, such as high temperature heat pumps and low temperature ORC applications.

Though necessary to design the heat exchangers for heat pump systems, research to clarify the boiling/condensation heat transfer and pressure drop characteristics of HFO1336mzz(E) and HFO1336mzz(Z) is limited. Moreover, mixtures of HFO1336mzz(E) and HFO1336mzz(Z) could also replace R245fa, because the operation pressure of HFO1336mzz(E) is higher than that of R245fa, whereas that of HFO1336mzz(Z) is lower than R245fa; when combined they could have the same pressure level as R245fa. However, to date there has been no research into the boiling/condensation heat transfer and pressure drop characteristics of such a mixture.

This study experimentally investigated the boiling/condensation heat transfer and pressure drop characteristics of pure refrigerants HFO1336mzz(E) and HFO1336mzz(Z), and a HFO1336mzz(E)/HFO1336mzz(Z) mixture, inside a horizontal microfin tube with an outer diameter of 9.5 mm. The boiling/condensation heat transfer coefficient and pressure drop of pure refrigerants and those mixtures were compared under mass velocities of 50–300 $kgm^{-2}s^{-1}$, and the relationship between the heat transfer coefficient and the frictional pressure drop in boiling and condensation

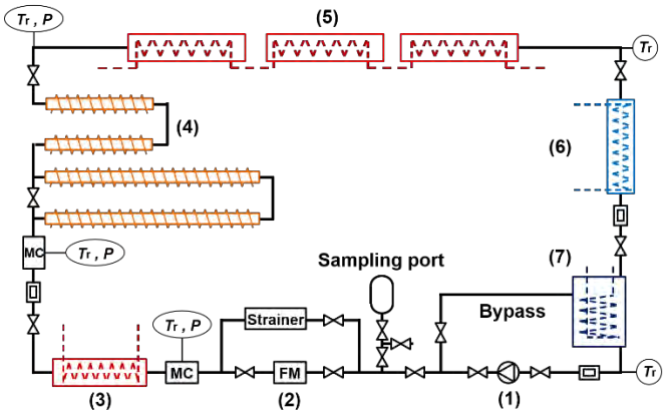

(1) Gear pump
(2) Coriolis-type mass flow meter
(3) Water preheater
(4) Electric preheater
(5) Test section
(6) After-cooler
(7) Receiver tank

Figure 1: Schematic diagram of the test loop

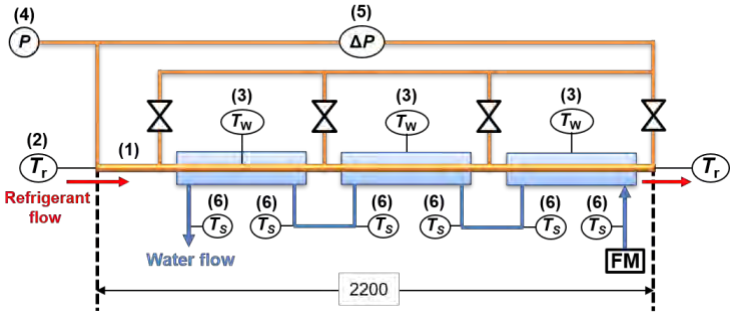

(1) Test tube
(2) Sheathed K-type thermocouple
(3) T-type thermocouple
(4) Absolute pressure transducer
(5) Differential pressure transducer
(6) Pt-resistance thermometer

Figure 2: Detail of the test section

processes were clarified. Moreover, the heat transfer coefficient and frictional pressure drop of HFO1336mzz(E) and the mixture were compared with those of pure R245fa.

2. EXPERIMENTAL APPARATUS AND PROCEDURE

Figure 1 shows a schematic view of the experimental apparatus used for the study. The refrigerant loop consists of a gear pump (1), a Coriolis-type mass flow meter (2), a water preheater (3), an electric preheater (4), a test section (concluding three subsections) (5), a cooler (6), and a receiver tank (7).

A subcooled refrigerant that was pumped from the gear pump was adjusted to a predetermined vapor quality at the counter-flow-type water preheater and electric preheater, after which it flowed into the test section. The refrigerant mass flow rate is controlled by the rotational speed of the pump and the flow-regulating valves of the main and bypass loops. The aftercooler was supplied with cooling or heating water to adjust the refrigerant pressure primarily. The flow rate of the test refrigerant was measured using the Coriolis-type mass flow meter.

Figure 2 shows the details of the test section. The test section was a two-meter-long counter-flow-type double-pipe heat exchanger. In this section, the refrigerant flowed through the inner test tube, whilst the heat source water flowed through the outer annulus tube, which surrounds the inner tube. The test tube consisted of three subsections with total and effective heating lengths of 600 mm and 557 mm, respectively. The bulk temperatures of the refrigerant at the inlet and outlet of the test section were measured by sheathed K-type thermocouples with a measurement accuracy of ±0.05 K. The outer tube wall temperature was measured using T-type thermocouples that was attached to the top, bottom and sides of the exterior wall at the test tube center. The heat source water temperature was measured by Pt-resistance thermometers that were inserted in the mixing chambers at the inlet and outlet of each subsection. An absolute pressure transducer with an accuracy of ±0.75 kPa measured the refrigerant pressure at the inlet of the test section. Two differential pressure transducers measured the pressure drop between the inlet and outlet of each subsection. The test section and electric preheater were encased with insulation.

Table 1. Specifications of the test tube.

Tube			LF
Outer diameter	d_o	[mm]	9.53
Maximum inside diameter	d_i	[mm]	8.95
Equivalent diameter	d_{eq}	[mm]	8.89
Fin height	h_f	[mm]	0.12
Number of fins	N	[-]	65
Helix angle	θ	[°]	16.5
Surface area enlargement	η	[-]	1.31

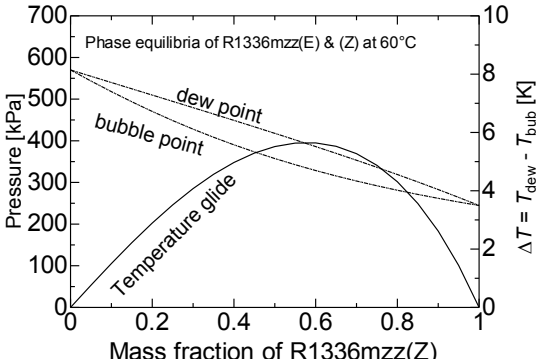

Figure 3: Temperature glide of R1336mzz(E)/(Z) refrigerant mixture with mass fraction

Table 2. The typical thermophysical and transport properties of refrigerants at saturation temperature of 60 °C

Refrigerant			R245fa	R1336mzz(E)	(E) / (Z) 70 / 30	R1336mzz(Z)
Pressure		kPa	462.46	570.03	453.72	244.67
Temperature glide		K	0.0	0.0	4.1	0.0
Latent heat		kJ/kg	169.12	126.42	132.91	151.33
Vapor	Density	kg/m^3	25.45	39.65	28.91	16.02
Liquid			1236.9	1351.4	1315.2	1268.4
Vapor	Viscosity	μPa s	11.68	16.08	14.69	11.37
Liquid			256.94	200.01	206.73	245.10
Vapor	Thermal conductivity	mW/(m K)	15.77	18.00	16.60	14.12
Liquid			76.87	61.19	61.39	65.05
Vapor	Specific heat	kJ/(kg K)	0.906	0.855	0.892	0.976
Liquid			0.982	1.244	1.243	1.296
Surface tension		mN/m	9.24	6.87	8.11	11.08

The test tube was a horizontal microfin copper tube with an outer diameter of 9.5 mm. The Low fin-height tube (LF) had an equivalent diameter of 8.9 mm, a fin height of 0.12 mm, and had 65 fins. The details of the test tube are shown in Table 1.

The test refrigerants were R1336mzz(E), and a mixture of R1336mzz(E) and (Z) (herein referred to as the "E/Z mixture." The heat transfer coefficient was measured across a mass velocity range of 50–300 kgm^{-2}s^{-1}, at saturation temperatures of 40 °C and 60 °C. The typical thermophysical and transport properties of refrigerants at a saturation temperature of 60 °C, and the variation of the temperature glide, are shown in Table 2 and Figure 3. The thermophysical and transport properties of the refrigerants and the heat source water were calculated using Refprop ver.10 (Lemmon, 2018); the R1336mzz(E) fluid file was provided by the Chemours Company.

3. DATA REDUCTION

The heat transfer rate Q_s in a subsection is given by

$$Q_s = W_s \cdot c_{ps} \cdot \Delta T_s \qquad \text{Eq. (1)}$$

where W_s and c_{ps} are the mass flow rate and specific heat capacity of the heat source water, and ΔT_s is the temperature difference between the inlet and outlet of the heat source water at each subsection.

The boiling and condensation heat transfer coefficient α for each subsection is defined by

$$\alpha = q/\left(\pm T_{wi} \mp T_r\right) \qquad \text{Eq. (2)}$$

where, q is the heat flux based on the actual heat transfer area for each subsection is given by

$$q = Q_s / (\pi \cdot d_i \cdot \ell) \quad \text{Eq. (3)}$$

T_r is the refrigerant temperature, which is calculated from the inlet and outlet temperature at test section by Interpolation for each subsection, and the T_{wi} is the inner wall temperature which is calculated by Fourier's law from measured outer wall temperature T_{wo}:

$$T_{wi} = T_{wo} \mp Q_s / (2\pi \cdot \lambda \cdot \ell) \ln(d_o / d_i) \quad \text{Eq. (4)}$$

where λ is the thermal conductivity of the tube wall, ℓ is the effective heating length, d_o and d_i are respectively the outer and inner diameters of the test tubes.
where T_r is the refrigerant temperature, which is calculated from the saturation pressure.
The frictional pressure drop ΔP_F is given by

$$\Delta P_F = \Delta P_{mes} \mp \Delta P_M \quad \text{Eq. (5)}$$

where ΔP_{mes} is the measured differential pressure in each subsection, and ΔP_M is the acceleration pressure drop calculated using the following equation:

$$\Delta P_M = \Delta \left\{ G^2 x^2 / (\xi \rho_V) + G^2 (1-x)^2 / \left[(1-\xi) \rho_L \right] \right\} \quad \text{Eq. (6)}$$

where G is the mass velocity, x is the vapor quality, ρ_V and ρ_L are respectively the vapor and liquid density, and ξ is the void fraction, which was calculated using Smith's correlation (Smith, 1969) for a smooth tube:

$$\xi_{Smith} = \left\{ 1 + \frac{\rho_V}{\rho_L} \left(\frac{1-x}{x} \right) \left(0.4 + 0.6 \sqrt{\frac{\frac{\rho_L}{\rho_V} + 0.4\frac{1-x}{x}}{1 + 0.4\frac{1-x}{x}}} \right) \right\}^{-1} \quad \text{Eq. (7)}$$

for a microfin tube, ξ was calculated using Koyama's correlation (Koyama, 2001):

$$\xi_{Koyama} = 0.81 \xi_{Smith} + 0.19 x^{100(\rho_V/\rho_L)^{0.8}} \xi_{Homo} \quad \text{Eq. (8)}$$

$$\xi_{Homo} = 1 / \left\{ 1 + \left[(1-x)/x \right] (\rho_V / \rho_L) \right\} \quad \text{Eq. (9)}$$

4. RESULTS AND DISCUSSION

4.1. Characteristics of R1336mzz(E)

4.1.1. Boiling/Condensation Heat Transfer Coefficients

Figure 4 shows the boiling and condensation heat transfer coefficients of R1336mzz(E) at refrigerant saturated temperatures of 40 °C and 60 °C, with mass velocities from 50 to 300 kg/(m^{2}s). The boiling heat transfer coefficient increased with increasing mass velocity, for mass velocities from 50 to 200 kg/(m^{2}s). In the case of mass velocities of 200-300 kg/(m^{2}s), however, there is no large difference in the forced convection effect, because the flow pattern is annular at mass velocities of >200 kg/(m^{2}s). The condensation heat transfer coefficient at mass velocities of 50-300 kg/(m^{2}s) showed only a small difference due to the forced convection effect.

4.1.2. Pressure Drops

Figure 5 shows the frictional pressure drops of R1336mzz(E) during the boiling and condensation processes. The pressure drop increased with increasing vapor quality during boiling, whereas it decreased with increasing wetness during condensation. As mass velocity increased, the ratio of pressure drop increased.

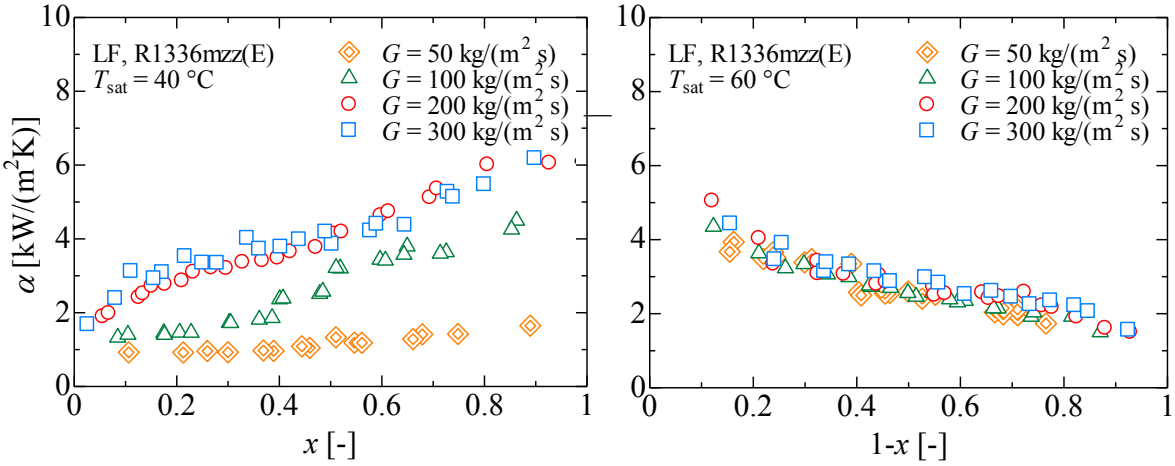

Figure 4: Boiling / Condensation heat transfer coefficients of R1336mzz(E)

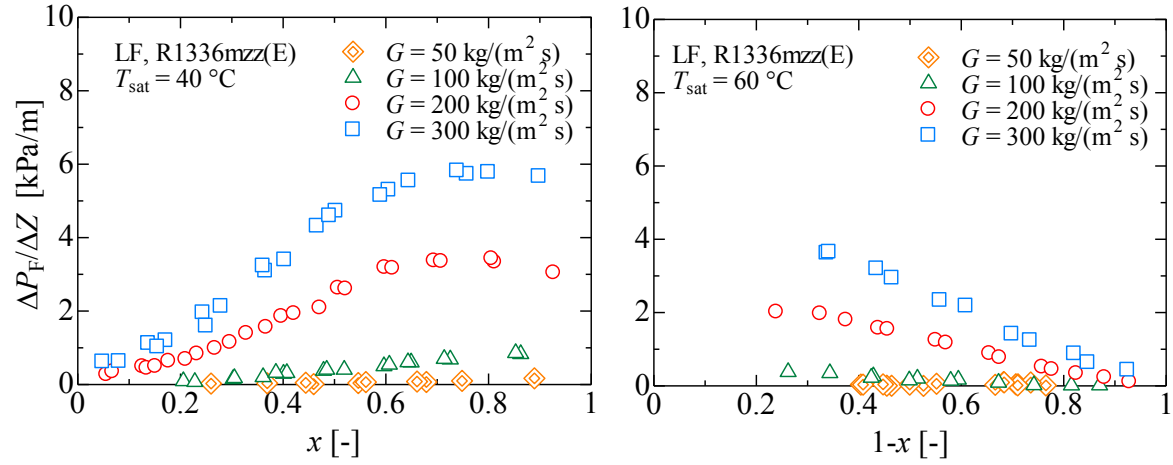

Figure 5: Pressure Drops of R1336mzz(E)

4.2. Characteristics of the 70/30 mass% mixture of R1336mzz(E) and (Z)

4.2.1. Boiling/Condensation Heat Transfer Coefficients

Figure 6 shows the boiling and condensation heat transfer coefficients of the E/Z mixture, at refrigerant saturated temperatures of 40 °C and 60 °C, and with a mass velocity range of 50 to 300 kg/(m^{2}s). The boiling heat transfer increased with increasing mass velocity for all vapor qualities, due to the forced convection effect. The condensation heat transfer coefficient also increased, due to both the forced convection effect and the reduction in thermal resistance caused by diffusion of the liquid film, which occurred due to the increase in mass velocity for the E/Z mixture refrigerant.

4.2.2. Pressure Drops

Figure 7 shows the frictional pressure drop of the E/Z mixture during the boiling and condensation processes. Similarly to pure refrigerant R1336mzz(E), the pressure drop increased with increasing vapor quality during boiling, and the pressure drop decreased with increasing wetness during condensation. The ratio of the pressure drop also increased with increasing mass velocity.

4.3. Comparison with R245fa

4.3.1. Boiling and Condensation Heat Transfer Coefficients

Figures 8 and 9 compare the boiling and condensation heat transfer coefficients between R1336mzz(E), the E/Z mixture, and R245fa, for mass velocities of 100 kg/(m^{2}s) and 200 kg/(m^{2}s) and at saturation temperatures of 40 °C and 60 °C. The boiling heat transfer coefficient of R1336mzz(E) were 0.43-0.73 times smaller than those of R245fa, across the mass velocity range.

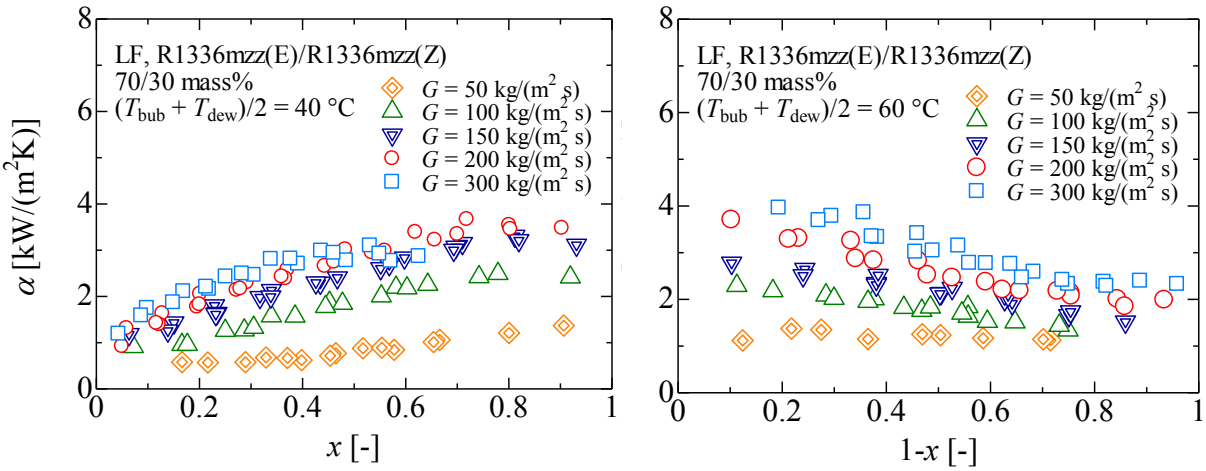

Figure 6: Boiling / Condensation heat transfer coefficients of the mixture 70/30 mass% of R1336mzz(E) and (Z)

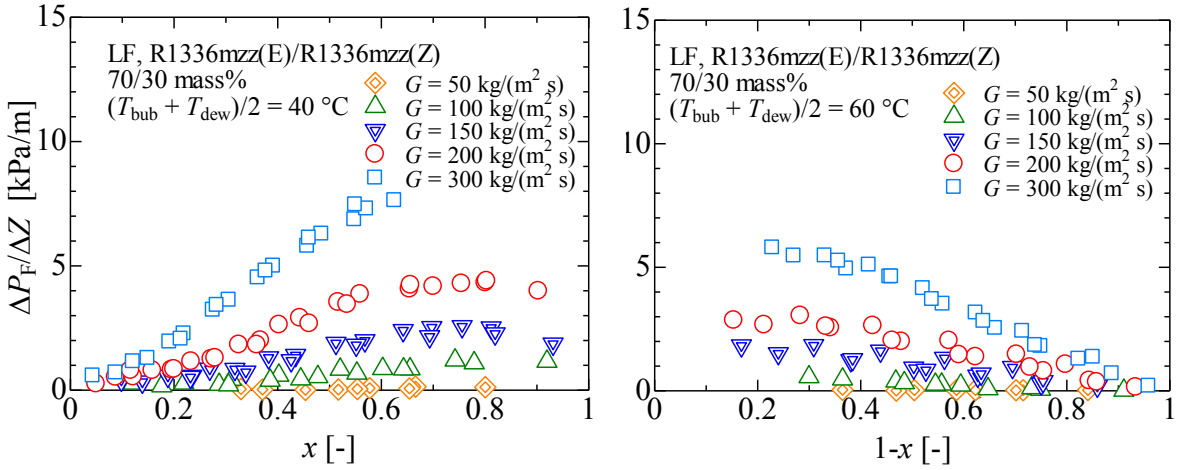

Figure 7: Pressure Drops of the mixture 70/30 mass% of R1336mzz(E) and (Z)

The condensation heat transfer coefficient of R1336mzz(E) were 0.61-0.79 times smaller than those of R245fa. It should be noted that the vapor density of R1336mzz(E) is about 1.6 time larger than that of R245fa. Therefore, the influence of forced convection becomes small. One further factor is the fact that the liquid thermal conductivity of R 1336mmz(E) is about 0.8 times smaller than that of R245fa. The boiling and condensation heat transfer coefficients of the E/Z mixture is smaller than those of R1336mzz(E) because the E/Z mixture has a temperature glide, meaning that the heat transfer performance did not improve.

4.3.2. Pressure Drops of Boiling and Condensation processes

Figures 10 and 11 compare the frictional pressure drop of R1336mzz(E), the E/Z mixture, and R245fa, for mass velocities of 100 and 200 kg/(m^{2}s) during boiling and condensation processes. The pressure drops of R1336mzz(E) are lower than those of R245fa and the E/Z mixture, and the pressure drops of the E/Z mixture are lower than those of R245fa. This meant that the vapor density of R1336mzz(Z) was about 0.4 times smaller than that of R1336mzz (E), and the vapor velocity increased. In addition, one further factor is the fact that the liquid viscosity of R1336mmz(Z) is about 1.2 times larger than that of R1336mmz(E).

5. CONCLUSIONS

In this study, the boiling and condensation heat transfer coefficients and frictional pressure drop of R1336mzz(E), a R1336mzz(E)/(Z) mixture, and R245fa tube were experimentally investigated. The experimental results were obtained as followed:

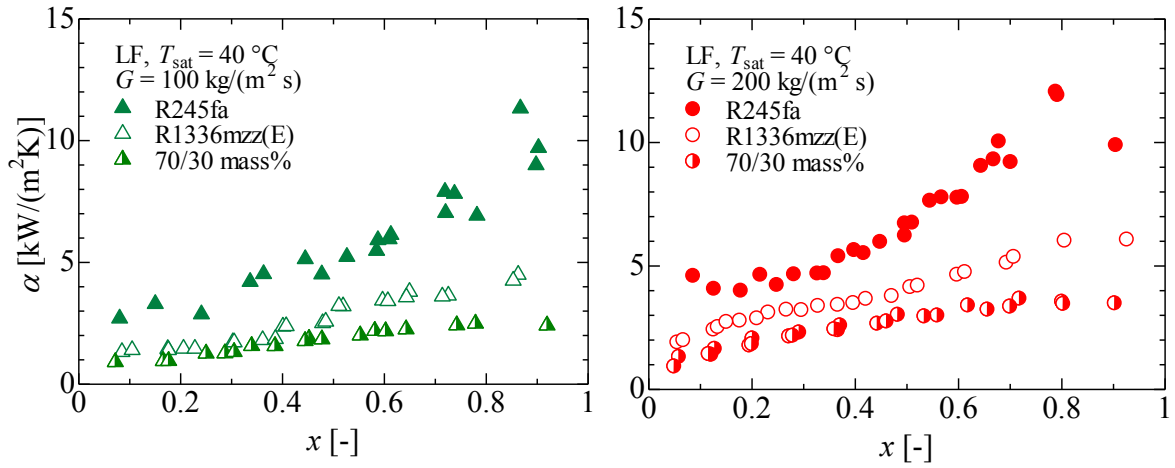

Figure 8: Comparison of boiling heat transfer coefficients between R1336mzz(E) / the E/Z mixtures and R245fa

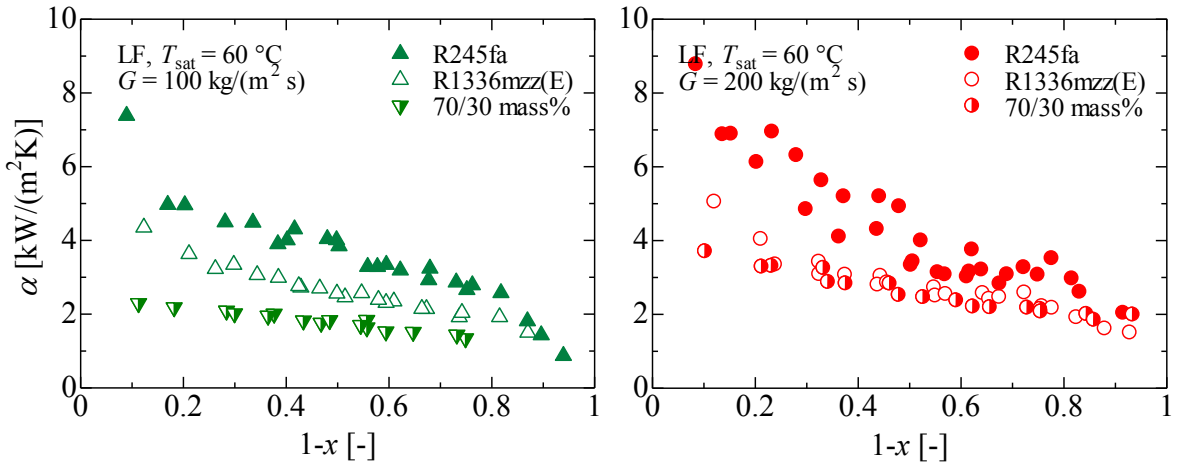

Figure 9: Comparison of condensation heat transfer coefficients between R1336mzz(E) / the E/Z mixtures and R245fa

(1) The boiling and condensation heat transfer coefficients of R1336mzz(E) and the E/Z mixture, which are the next generation low GWP refrigerants, were related to vapor quality and mass velocity.
(2) The frictional pressure drops of R1336mzz(E) and the E/Z mixture were shown to be related to vapor quality and mass velocity.
(3) The boiling/condensation heat transfer coefficients of HFO1336mzz(E) are lower than R245fa, however the pressure drops of HFO1336mzz(E) are lower than R245fa.

ACKNOWLEDGEMENTS

This study was supported by the Mechanical Engineering Laboratory of Kobe Steel, LTD. and the Chemours Company. We would like to express our gratitude here.

NOMENCLATURE

c_p	specific heat capacity, J/(kgK)
d	tube diameter, m
G	mass velocity, kg/(m^{2}s)
ℓ	effective heating length, m
q	heat flux, W/m^2
Q	heat transfer rate, W
T	temperature, K
W	mass flow rate, kg/s

Subscripts

bub	bubble point
cal	calculation
dew	dew point
exp	experiment
F	frictional
i	inside
L	liquid

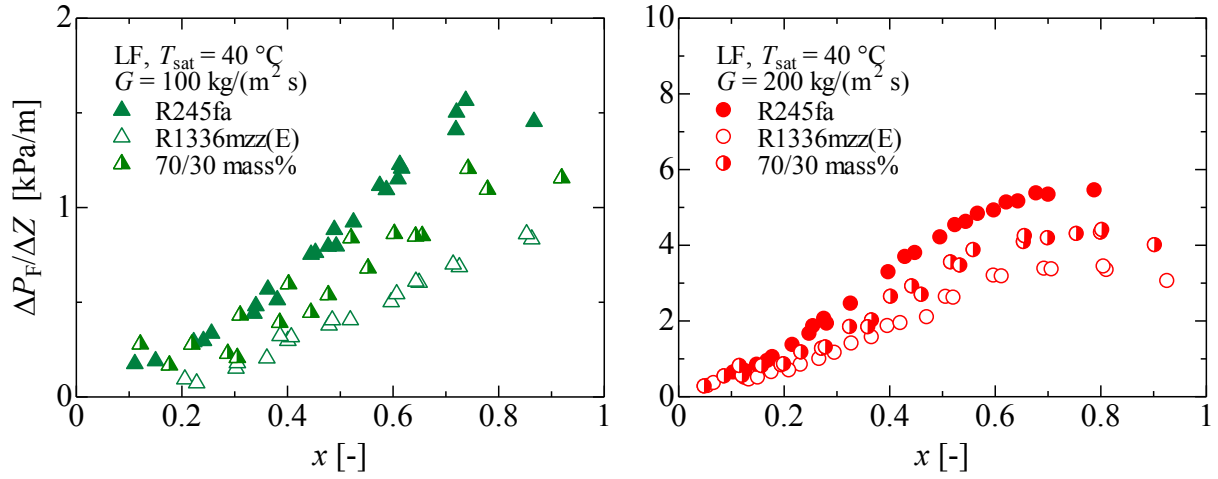

Figure 10: Comparison of pressure drops of boiling process between R1336mzz(E) / the mixtures and R245fa

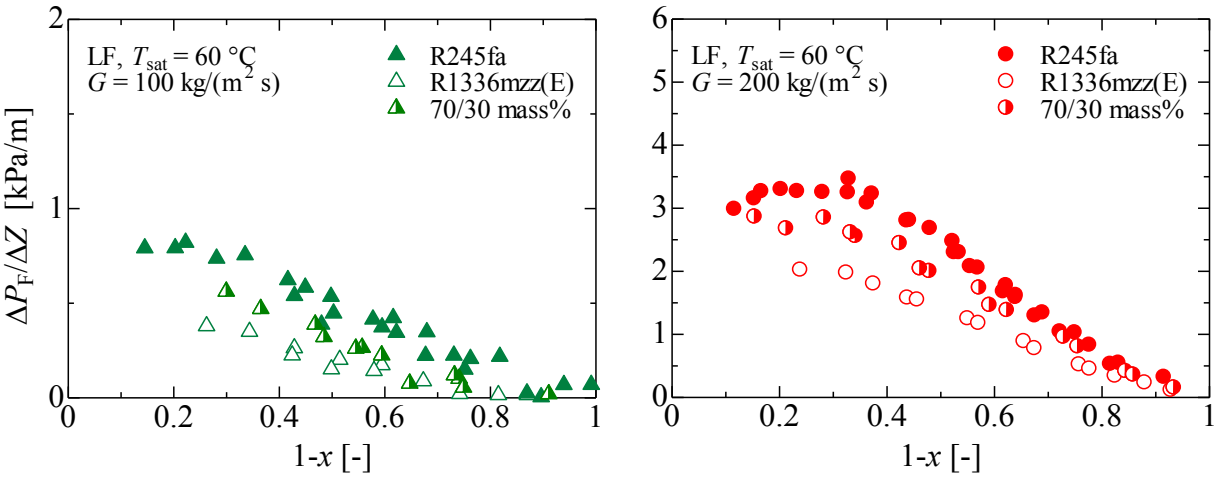

Figure 11: Comparison of pressure drops of condensation process between R1336mzz(E) / the mixtures and R245fa

x	vapor quality	M	momentum
P	pressure, Pa	mes	measure
ΔP	pressure difference, Pa	o	outside
ΔZ	length of pressure drop measurement section, m	r	refrigerant
α	heat transfer coefficient, W/(m^{2}K)	s	heat source
λ	thermal conductivity, W/(mK)	sat	saturation
ρ	density, kg/m^3	V	vapor
ξ	void fraction	w	tube wall

REFERENCES

Juhasz, Jason R., 2017. Novel Working Fluid, HFO-1336mzz(E), for Use in Waste Heat Recovery Application. 12th IEA Heat Pump Conference 2017.

Koyama, S., Chen, Y. C., Kitano, R., Kuwahara, K., 2001. Experimental study on void fraction of two-phase flow inside a micro-fin tube. The reports of institute of Advanced Material Study, Kyushu University 15(1), 79-85. (in Japanese)

Lemmon, E. W., Bell, I. H., Huber, M. L., McLinden, M.O., 2018. Reference fluid thermodynamic and transport properties-REFPROP Ver. 10.0, National Institute of Standards and Technology, Gaithersburg.

Smith, S. L., 1969. Void fractions in two-phase flow: a correlation based upon an equal velocity head model. Proc. Instn. Mech. Engrs. 184(1)(36), Institution of Mechanical Engineers, 647-664.

Manuscript ID: 875
DOI: 10.18462/iir.icr.2019.0875

Experimental study on falling film evaporation heat transfer of ammonia on horizontal tubes

Ikuro Akada[(a)], Kenichi Obata[(a)], Masashi Kato[(a)], Kosaku Nishida[(a)], Norihiro Inoue[(b)]

[(a)] R and D Center, MAYEKAWA MFG. CO., LTD.
2000 Tatsuzawa, Moriya City, Ibaraki, 302-0118, Japan, ikurou-akada@mayekawa.co.jp
[(b)] Tokyo University of Marine Science and Technology
2-1-6 Etchujima, Koto-ku,Tokyo, 135-8533, Japan, inoue@kaiyodai.ac.jp

ABSTRACT

The present study experimentally investigated falling film evaporation heat transfer characteristics of ammonia on horizontal stainless smooth tubes. Test tubes with diameters of 60.5mm and 42.7mm respectively and an effective heat transfer length of 300mm ware tested. Experiments were conducted using the ammonia as the refrigerant at a saturation temperature of -5 °C, heat flux range of 3 to 20 kWm^{-2} and film Reynolds number of 100 to 500. Falling film evaporation heat transfer coefficients increased with increasing heat flux and decreased with increasing film Reynolds numbers. Measured heat transfer coefficients were 4 times higher than values calculated by pool boiling heat transfer equations when heat flux was 10 kWm^{-2}. Measured heat transfer coefficients were compared with predicted values calculated by previous correlations and found to be lower than the predicted ones.
Keywords: Ammonia, Evaporator, Falling Film, Heat Transfer Coefficient.

1. INTRODUCTION

Global environmental issues require many countries to reduce greenhouse gases among their approaches. In the industrial sector, high-efficiencies and energy-saving technologies are urgently required. For reduction of the environmental load, natural refrigerants are attracting attention as refrigerants for use in refrigeration systems. Ammonia, one of the natural refrigerants, has been widely used in refrigeration systems for a long time. Shell-and-tube falling film evaporators are one of the heat exchangers mainly used for OTEC and refrigeration systems. Falling film evaporators have attracted attention because they have higher evaporation heat transfer coefficients and much less refrigerant charge than flooded evaporators.
Fernández-Seara et al. (2016) carried out experiments on spray evaporation and pool boiling heat transfer of ammonia on plane titanium pipe and compared both processes. Zhao et al. (2016) carried out experiments on falling film evaporation heat transfer of R134a on a single horizontal smooth tube and investigated the effect of the tube diameter, saturation temperature, film flow rate and heat flux. However, in all these studies, data on heat transfer characteristics of ammonia is insufficient and there are few detail studies on falling film heat transfer. The present study experimentally investigated falling film evaporation heat transfer characteristics of ammonia on horizontal smooth stainless tubes. Test tubes with diameters of 60.5mm and 42.7mm and an effective heat transfer length of 300mm were tested. Measured heat transfer coefficients are compared with predicted values calculated by previous correlations.

2. EXPERIMENTAL APPARATUS AND PROCEDURE

Fig. 1 shows the schematic diagram of the experimental apparatus. The experimental apparatus is a pump loop where liquid refrigerant is circulated. It mainly comprises of an evaporator (test section), a condenser, a receiver, a sub-cooler, and a refrigerant pump. Brine is use in the condenser and sub-cooler as the heat sink. The condenser adjusts temperature and pressure in the test section while the sub-cooler adjusts temperature in the test loop. Liquid refrigerant in the receiver is sub-cooled by the sub-cooler before it is pumped to the test section by the refrigerant pump. The liquid refrigerant flow rate is adjusted by control valves in the main and by-pass loops and measured by a

volumetric flow meter. The evaporated refrigerant in the test section flows to the condenser where it is condensed and returns to the receiver while the falling liquid refrigerant in the test section returns from the bottom of the test section to the receiver.
Figure 2 shows details of the test section. The test section consists of a pressure vessel, a refrigerant liquid distributor, a dummy tube and two heat transfer tubes in line row arrangement. All materials are made of stainless steel because ammonia is used as the refrigerant. Sight glasses are provided on the outside surface of the pressure vessel in parallel with the heat transfer and dummy tubes.
The liquid distributor supplies the liquid refrigerant to the dummy tube and a liquid film forms on the tube surface of the dummy tube. The refrigerant liquid is then supplied to the upper heat transfer tube (No.1) and to the lower heat transfer tube (No.2). Cartridge heaters are inserted in both tubes No.1 and No.2 and an alloy is melted in between the heat transfer tubes and the cartridge heaters in order to generate uniform the heat flux on the tube surface. Heat flux in the test heat transfer tubes is predetermined by adjusting the heating load in the cartridge heater and the heat generated is exchanged with the liquid film on the tube surface. T-type thermocouples are attached to the inner walls of the test heat transfer tubes at the top, sides and bottom in the circumferential direction of the tubes, and the tube wall temperature at the central part of the heat transfer tube is measured. In order to eliminate the influence of sub cooling and liquid film thickness on heat transfer due to liquid distribution, wall temperatures of tube No.2 were measured. Two heat transfer tubes with different outside tube diameters of 42.7 mm and 60.5 mm were used in this experiment. Both heat transfer tubes are smooth surface, and the surface of the tubes was cleaned by acid pickling. The tests tubes are separated by a distance 1.65 times of the ratio between the central axis of the heat transfer tubes to the tube outside diameters P/D.
Falling film evaporation heat transfer experiments were conducted using ammonia as the test fluid at a saturation temperature of -5 °C, film flow rate range of Re_f 100 - 500, and heat flux range of 3 - 25 kWm^{-2}. Falling film heat transfer coefficients were measured and liquid film flows were observed in all the experiment ranges.

3. DATA REDUCTION

The surface temperature of the outside tube wall T_{o_wall} is defined as follows:

$$T_{in\_wall} = \left(T_{in\_wall\_t} + T_{in\_wall\_b} + T_{in\_wall\_l} + T_{in\_wall\_r}\right)/4 \quad \text{Eq. (1)}$$

$$T_{o\_wall} = T_{in\_wall} - Q(1/\lambda_{sus}) \ln(D_o/D_{in})/2\pi l \quad \text{Eq. (2)}$$

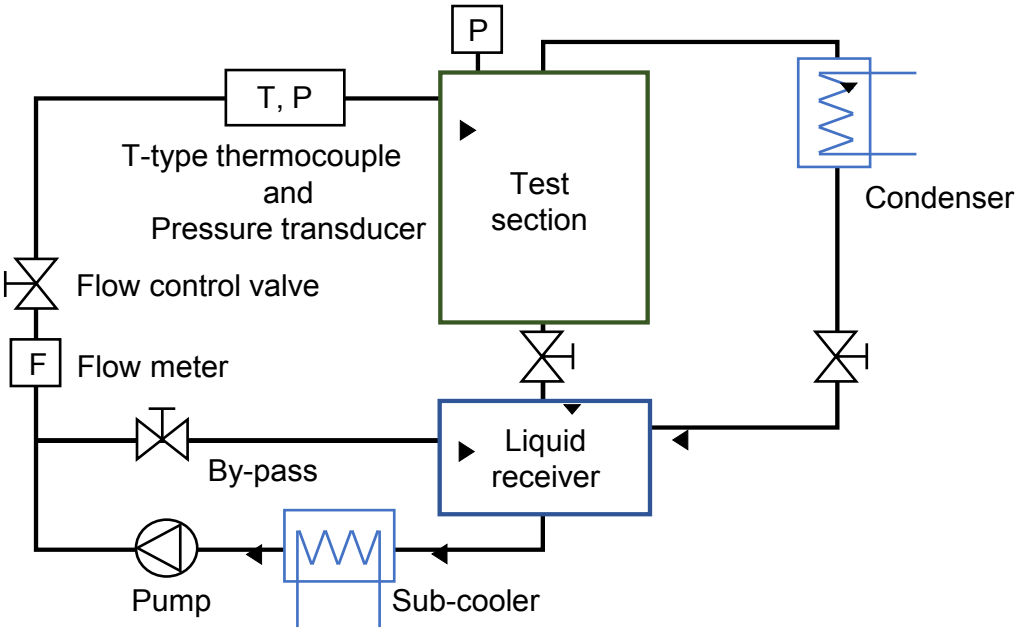

Figure 1: Schematic diagram of experimental apparatus

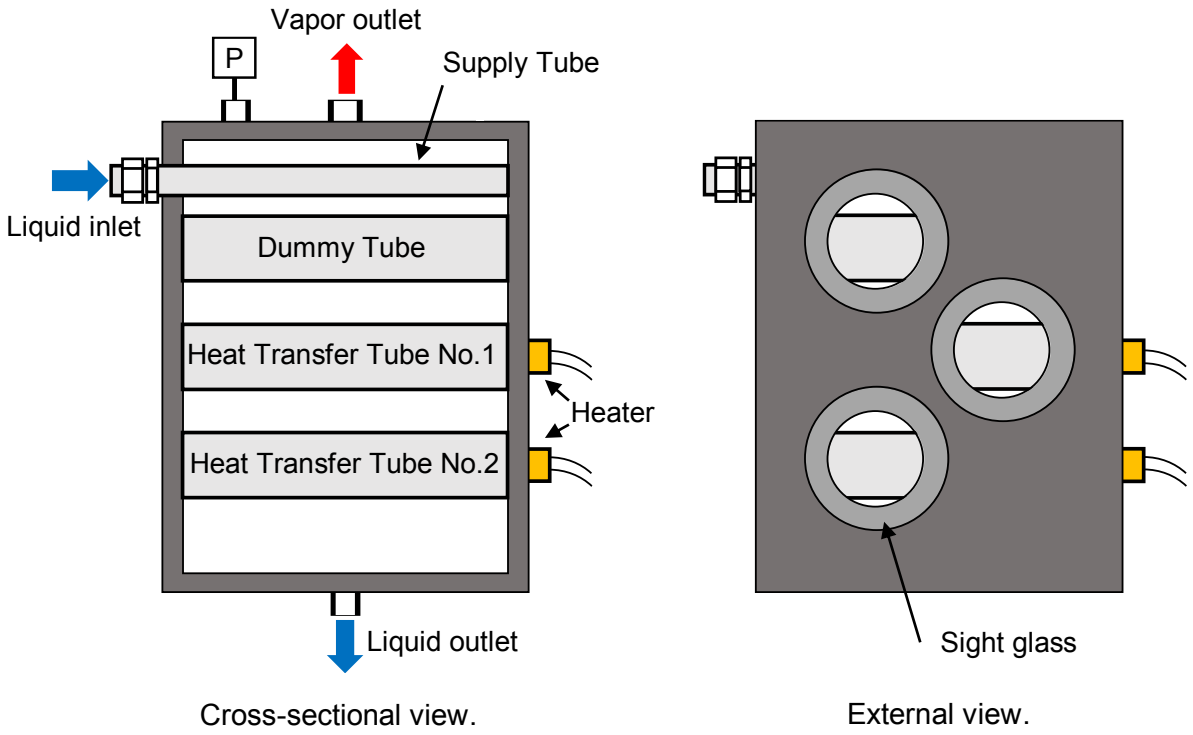

Figure 2: Detail of test section

where $T_{\text{in\_wall}}$ is the temperature of the inside tube wall. Q is the heat transfer rate, λ_{SUS} is the thermal conductivity of the stainless tube. D_{o} and D_{in} is the tube outside and inside diameter.
The heat transfer coefficient α (HTC) is defined as follows:

$$\alpha = q/\left(T_{\text{o\_wall}} - T_{\text{sat}}\right) \qquad \text{Eq. (3)}$$

where q is the heat flux, T_{sat} is the saturation temperature of the refrigerant is determined form the measured pressure in the test section.
The Nusselt number Nu and the film Reynolds number Re_{f} are defined as follows:

$$\text{Nu} = \alpha({\nu_{\text{L}}}^2/g)^{1/3}/\,\lambda_{\text{L}} \qquad \text{Eq. (4)}$$

$$\text{Re}_{\text{f}} = 4\Gamma/\mu_{\text{L}} = 4m/(2l\mu_{\text{L}}) \qquad \text{Eq. (5)}$$

where ν_{L}, μ_{L}, and λ_{L} are the kinematic viscosity, viscosity, and thermal conductivity of the saturation liquid, g is the gravitational acceleration, l is the effective heat transfer length, and m is the refrigerant mass flow rate.

4. RESULTS AND DISCUSSION

4.1. Flow Characteristics of Falling Film Evaporation

Fig. 3 shows the flow characteristics of falling film evaporation of ammonia observed. They were taken from the heat transfer tube No.2 for both outside diameters of 42.7 mm and 60.5 mm by a digital high speed camera. The photographs were taken at a saturation temperature of -5 °C, heat flux of 10kw m^{-2} and film Reynolds number of 100 to 500. Typical flow patterns of falling film are classified into three types: Droplet, Column, and Sheet mode. The Droplet mode was observed when the film flow rate was small. Falling liquid film around the tube combine at the tube bottom as the flow rate increases the droplet mode shifts to column and finally to the Sheet mode. In the range of this experiment, only Droplet mode was observed regardless of the outside tube diameter and dry patches were not observed on the surface of the tubes. Bubble nucleation did not occur at the top

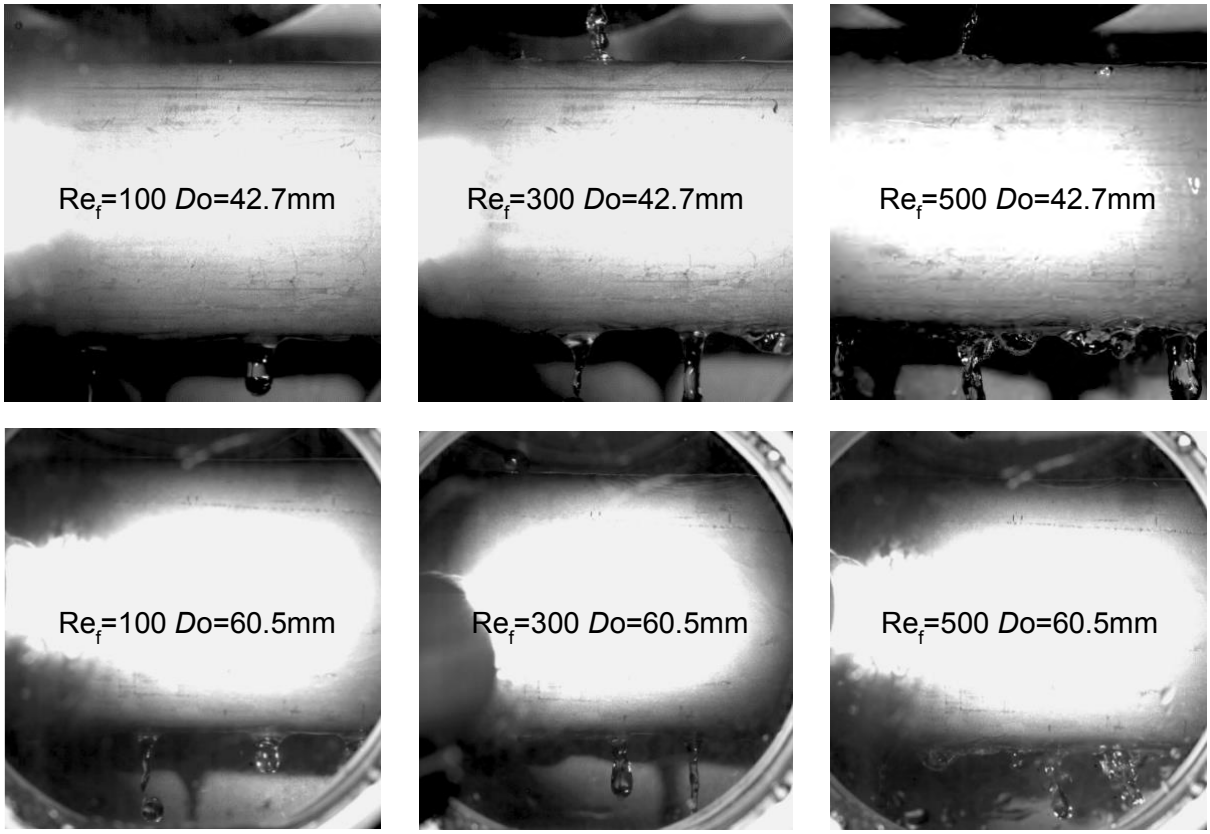

Figure 3: Flow characteristics of the test tubes. (q = 10 kW.m^{-2})

and sides of the tubes. However, bubble nucleation was slightly observed in the liquid film at the bottom of the tubes and increased as the heat flux increased. This is because the falling liquid film around the tube combine at the bottom and the liquid film is thickest at the bottom. As it can be seen in figure 3, droplets falling from the bottom of the tubes increased in frequency as film flow rate Re_f increased. When the film flow rate is more than 400, more falling liquid film combines at the tube bottom, and droplets are larger.

4.2. Pool Boiling Heat Transfer

The same experimental apparatus was also used for pool boiling heat transfer tests. During pool boiling tests the valve below the test section connecting to the receiver was closed. Condensed refrigerant collected in the receiver was pumped by the refrigerant pump to the test section and the liquid level in the test section was held so that heat transfer tube No.2 was sufficiently immersed. Fig. 4 shows measured pool boiling heat transfer coefficients versus heat flux at a saturation temperature of -5 °C for heat transfer tube No.2 with an outside diameter of 60.5 mm. For comparison, lines in the figure show boiling heat transfer coefficients calculated by correlations of Jung et al. (2003) and Stephan-Abdelsalam (1980).

As shown in the figure, boiling heat transfer coefficients increase as the heat flux increases. Measured heat transfer coefficients are higher than values of Stephan-Abdelsalam correlation and are about 2.5 times higher in the heat flux range of 10 kWm^{-2} to 20 kWm^{-2}. For the same heat flux of 10 kWm^{-2} to 20 kWm^{-2}, measured heat transfer coefficients compare well with the values of the Jung et al. correlation. However, for heat flux of 3 kWm^{-2} to 5 kWm^{-2}, measured values are higher than Jung et al. correlation. This is presumed to be affected by the convection of the refrigerant liquid. It can be noted from the figure that the Jung et al. correlation shows closer agreement with the experimental values than the Stephan-Abdelsalam correlation.

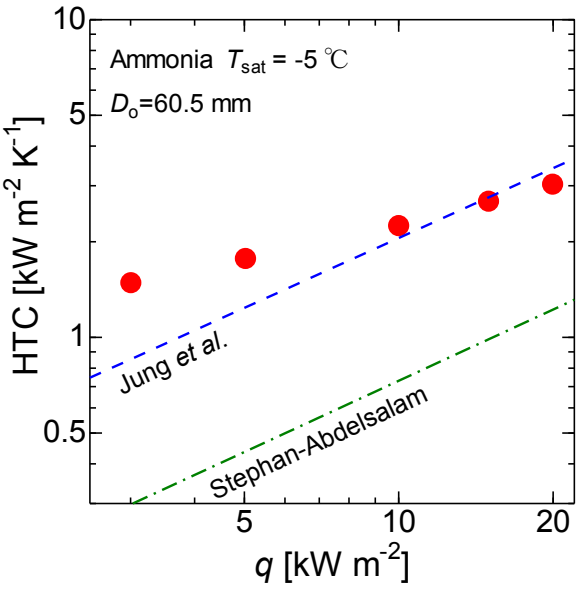

Figure 4: Relation between pool boiling heat transfer coefficient and heat flux

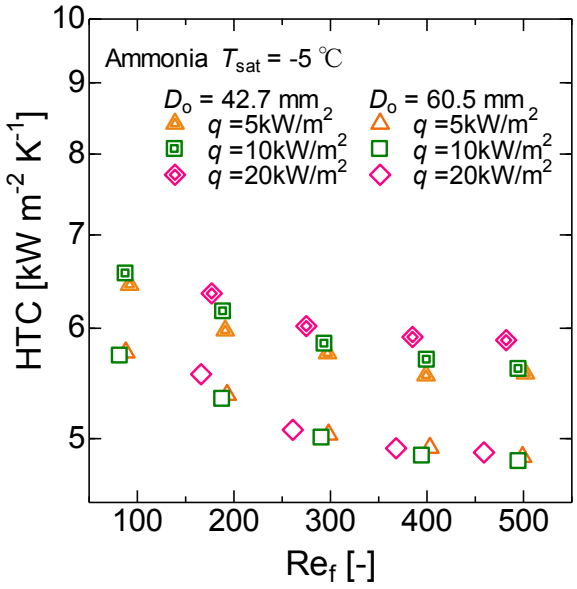

Figure 5: Relation between falling film heat transfer coefficient and film Reynolds number

4.3. Falling Film Evaporation Heat Transfer

Fig. 5 shows falling film heat transfer coefficients versus film Reynolds number for both tubes of outside diameter 42.7 mm and 60.5 mm respectively. For film Reynolds Numbers less than 400, falling film heat transfer coefficients decrease as the film Reynolds number increases. It is considered that the liquid film flow is presumed to be in laminar region, the heat transfer coefficients decrease as the liquid film becomes thick. For film Reynolds Numbers larger than 400, heat transfer coefficients approach constant values independent of the film Reynolds number. It is considered that the liquid film flow is presumed to be in transition region, it does not significantly affect the heat transfer coefficients as the liquid film becomes thick. It can be note from the figure that heat transfer coefficients of a tube with an outside diameter of 42.7 mm are 20% higher than that of a 60.5 mm tube. Stagnation, impingement flow and thermal developing regions have higher heat transfer coefficients than a fully developed region. It is considered a tube with a smaller diameter has a larger surface area ratio thus high heat transfer coefficients.

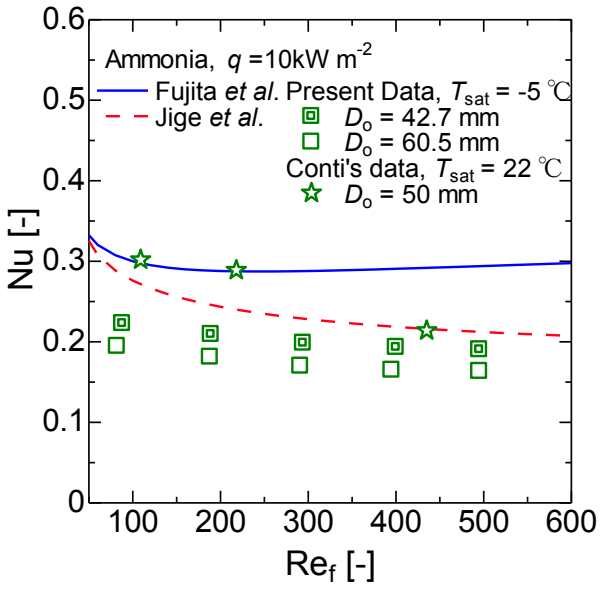

Figure 6: Comparison between measured and predicted values. (Re_f - Nu)

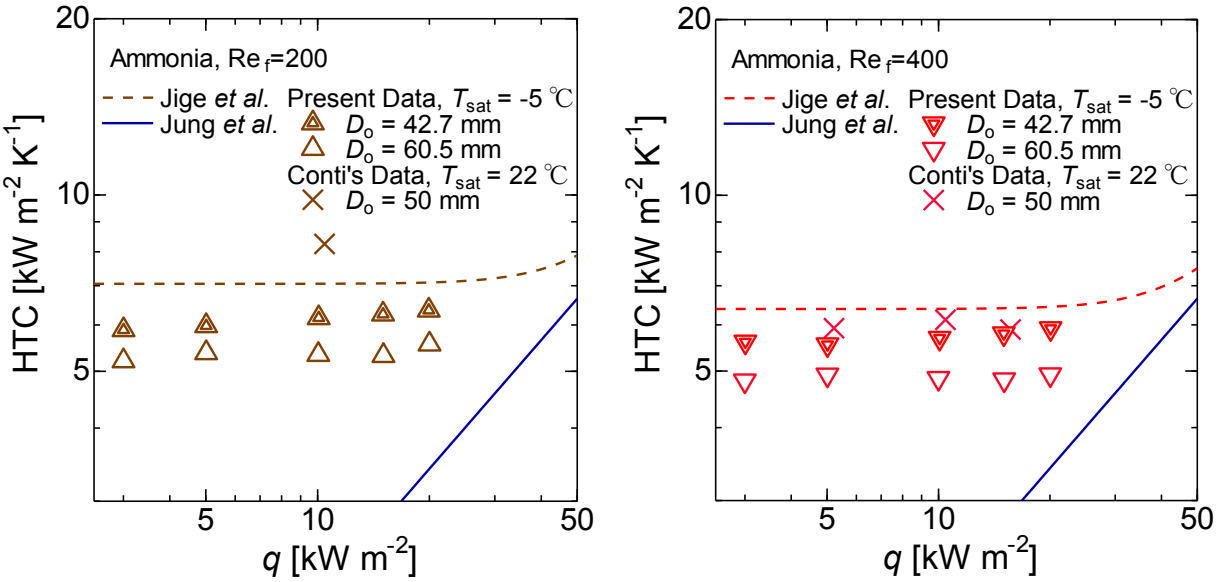

(a) Re_f=200 (b) Re_f=400

Figure 7: Comparison between measured and predicted values. (*q* - HTC)

4.4. Comparison between Measured and Predicted Values

Fig. 6 shows the Nusselt number versus the film Reynolds number for both tubes with heat flux of 10kWm^{-2}. For comparison, experimental values of Conti (1978), predicted values of falling film heat transfer coefficient from correlations of Fujita and Tsutsui (1994) and Jige et al. (2018) are also shown. Conti's data is for falling film heat transfer coefficient of ammonia at a saturation temperature T_{sat} = 22 °C using stainless heat transfer steel tubes with outside diameters of 50 mm. The correlation of Fujita and Tsutsui is for falling film heat transfer coefficient of a single heat transfer tube with outside diameters of 25 mm using R11 as the refrigerant. The correlation of Jige et al. is for falling film heat transfer coefficient of single heat transfer tube using R1234ze(E) as the refrigerant and the correlation was adapted to ammonia data of Conti. For film Reynolds number Re_f = 100 to 200, measured experimental values are lower than the values of Conti by about 30% and for film Reynolds numbers larger than Re_f = 300 measured heat transfer coefficients slightly lower. Fujita

and Tsutsui predicted values are 35% higher than the experimental values at Re_f = 100, and more than 40% at Re_f = 500. The Jige et al. predicted values are relatively close to the measured Nusselt numbers however, they are 20% higher regardless of the film Reynolds number.
Fig. 7 shows heat flux versus falling film heat transfer coefficients for both tubes of outside diameter of 42.7 mm and 60.5 mm. (a) and (B) show heat transfer coefficient versus heat flux at Re_f = 200 and Re_f = 400.These figures show that measured falling film heat transfer coefficients are higher than pool boiling heat transfer coefficients of the correlation of Jung et al. These also shows that measured values are lower than the predicted values of Jige et al. Fig. 7 (a) shows that experimental values of the tube with an outside diameter of 42.7 mm are lower than the experiment value of Conti. The experimental values gradually approaches the values predicted by Jige et al. correlation as the heat flux increases. Values predicted by Jige et al. correlation are about 15% higher than experimental values of the tube with outside diameter of 42.7 mm and are about 25% higher than those of the tube with outside diameter of 60.5 mm. A comparison of measured heat transfer coefficients of both tubes shows that values of the 42.7 mm tube are about 15% higher than those of the 60.5 mm tube. Fig. 7 (b) shows that experimental values of the tube with an outside diameter of 42.7 mm are in close agreement with those of Conti. Values predicted by Jige et al. correlation are 10% higher than experimental values of the tube with outside diameter of 42.7 mm and are 25% higher than those of the tube with outside diameter of 60.5 mm. A comparison of measured heat transfer coefficients of both tubes shows that values of the 42.7 mm tube are about 20% higher than those of the 60.5 mm tube.
From these results, necessary to include outside tube diameter as a parameter in order to derive a precise correlation for falling film heat transfer coefficient.

5. CONCLUSIONS

Experiments on falling film and pool boiling heat transfer were carried out using ammonia as the refrigerant and tubes with outside diameters of 60.5 mm and 42.7 mm respectively.
The conclusions reached with respect to flow observation, pool boiling and falling film heat transfer are summarized as follows:
(1) The Droplet mode was the only flow pattern observed during observations of the flow characteristics and no dry patches were observed on the surface of the tubes in the flow range of this experiment.
(2) Measured boiling heat transfer coefficients are more in close agreement with the Jung et al. correlation than that of Stephan-Abdelsalam.
(3) For film Reynolds Numbers less than 400, falling film heat transfer coefficients decrease as the film Reynolds number increases, the film flow in this range is presumed to be laminar. For film Reynolds Numbers larger than 400, heat transfer coefficients approach constant values independent of the film Reynolds number, the liquid film flow is presumed to be in transition region.
(4) Heat transfer coefficients measured in this experiment are lower than those of Conti. Predicted values from Fujita and Tsutsui correlation are 35% higher while the Jige et al values are close to the experimental values. The Jige et al values are about 20% higher than the experiment values regardless of the film Reynolds number.
(5) Heat transfer coefficients of a tube with an outside diameter of 42.7 mm are 20% higher than that of a 60.5 mm tube. It is necessary to include outside tube diameter as a parameter in order to derive a precise correlation for falling film heat transfer coefficient.

NOMENCLATURE

D	Tube diameter (m)	g	Gravitational acceleration (ms^{-2})
l	Effective heat transfer length (m)	m	Mass flow rate (kgs^{-1})
Nu	Nusselt number (-)	Q	Heat transfer rate (W)
q	Heat flux (Wm^{-2})	Re_f	Film Reynolds number (-)
T	Temperature (°C)		
Greek			
α	Heat transfer coefficient ($Wm^{-2}K^{-1}$)	λ	Thermal conductivity ($Wm^{-1}K^{-1}$)
ν	Kinematic viscosity (m^2s^{-1})	μ	Viscosity ($kgm^{-1}s^{-1}$)
Subscript			
b	Bottom	in	Inside

L	Liquid refrigerant	l	Left
o	Outside	r	Right
sat	Saturation	sus	Stainless
t	Top	wall	Wall

REFERENCES

Conti, RJ., 1978. Experimental investigation of horizontal-tube ammonia film evaporation with small temperature differentials. Proceedings of the 5th Ocean Thermal Energy Conversion Conference, Miami Beach, Florida, 161-180.

Fernandez-Seara, J., Pardinas, AA., Diz, R., 2016. Experimental heat transfer coefficients of pool boiling and spray evaporation of ammonia on a horizontal plain tube. Int. J. Refrigeration 67, 259-270.

Fujita, Y., Tsutsui, M., 1998. Evaporation heat transfer of falling films on horizontal tube. Part 2: Experimental study. *Heat Transfer - Japanese Research* 27(8), 609-618.

Jige, D., Miyata, H., Inoue, N., 2018. Evaporation heat transfer of falling liquid film outside a horizontal smooth tube, Proceedings of the 55th National Heat Transfer Symposium of Japan, Sapporo, Hokkaido, 33-144.

Jung, D., Kim, Y., Ko, Y., Song, K., 2003. Nucleate boiling heat transfer coefficients of pure halogenated refrigerants. Int. J. Refrigeration 26, 240-248.

Stephan, K., Abdelsalam, M., 1980. Heat-transfer correlations for natural convection boiling. Int. J. Heat Mass Transfer 23 (1), 73–87.

Zhao, CY., Ji, WT., Jin, PH., Tao, WQ., 2016. Heat transfer correlation of the falling film evaporation on a single horizontal smooth tube. Applied Thermal Engineering 103(25), 177-186.

Manuscript ID: 898

DOI: 10.18462/iir.icr.2019.0898

Steam condensation heat transfer coefficient in large, flattened-tube steam condensers

William A. DAVIES III [(a)], Pega HRNJAK [(a, b*)]

[(a)] Air Conditioning and Refrigeration Center (ACRC), Department of Mechanical Science and Engineering, University of Illinois at Urbana-Champaign, Urbana, IL, USA, daviesi2@illinois.edu, pega@illinois.edu

[(b)] CTS – Creative Thermal Solutions, Inc., Urbana, IL, USA, pega@illinois.edu

ABSTRACT

Steam condensation heat transfer coefficient (HTC) in a large, flattened tube with variable heat flux, wall temperature and inclination angle is determined experimentally. The condenser tube is that used in air-cooled condensers for power plants. The steel tube has an elongated-slot cross section with inner dimensions of 216 x 16 mm. Vapor and liquid flow concurrently through a 5.7 m long air-cooled conditioning section, and HTC is determined in a 0.12 m long water-cooled test section. Tube inclination angle is varied from 0 – 25° downwards. The long conditioning section creates conditions in the test section that mimic the conditions in an operating condenser – allowing for realistic development of flow regime and void fraction. HTC is then determined in the water-cooled section. Quality in this section ranges from 0 – 0.75. A visualization section allows determination of flow regime and void fraction. The flow is found to be stratified for all conditions. HTC is found to increase by 6-10 times along the condenser height.

1. INTRODUCTION

Large, flattened-tube steam condensers are commonly found in air-cooled condensers (ACC) for power-plants (Kröger, 2004). It has been previously shown that the flow regime in this type of condenser tube with large diameter and high aspect ratio is predominantly stratified (Kang et al., 2017). In addition, it has been shown that the condensation heat transfer coefficient (HTC) can vary over two orders of magnitude in one tube cross section (Abadi *et al.*, 2019; William A Davies III *et al.*, 2019). In addition, HTC has been shown to be affected by parameters such as inclination and condensation temperature (Davies III & Hrnjak, 2019 (In press); William A. Davies III *et al.*, 2019). In order to provide further insight into the condenser physics, and to aid in the improvement of the condenser design, this paper presents experimental results for local condensation heat transfer coefficient under the realistic conditions of varying heat flux and wall temperature in this high-aspect-ratio large-diameter condenser tube.

In-tube convective condensation has been well studied (Cavallini *et al.*, 2003; Dalkilic & Wongwises, 2009; Liebenberg & Meyer, 2008) in varying tube geometries and conditions, and several correlations for HTC are in wide use. However, the majority of the investigations of HTC have focused on small tubes and refrigerants. Several aspects of the ACC make it difficult to apply previous correlations with reasonable certainty. The ACC tubes are inclined, with large diameter and an elongated-slot cross-section, with HTC, heat flux, and temperatures varying circumferentially around the tube.

The correlations for condensation have generally agreed on the existence of two regimes of condensation: the gravity-driven regime and the shear-driven regime (Dobson & Chato, 1998). Only the gravity-driven regime has been found in this experiment. The gravity-driven regime occurs during low mass flux, and includes stratified and stratified-wavy flow. In this regime, the predominant heat

transfer mechanism is through the liquid film along the walls, and the HTC depends on ΔT between the vapor and wall, but not on Reynolds number of the flow. The correlations for this regime are all based on the theory of Nusselt (1916) for condensation on a flat plate under natural convection and require knowledge of ΔT. Therefore, they are difficult to apply in an engineering situation with non-linear variation in wall temperature and heat flux, where ΔT is unknown. The one exception is the correlation of Kröger (2004), which is purely analytical and provides no supporting data.
This study determines condensation HTC for a large-diameter, flattened-tube steam condenser while maintaining the non-uniform temperature and heat flux conditions in an operating condenser. The ultimate goal is to develop a correlation that can be applied to an ACC with ΔT varying and unknown.

2. FACILITY

2.1 Overview

The facility used in this study is similar to that used in (Davies III & Hrnjak, 2019 (In press)), although with several modifications. A schematic of the experimental setup is presented in Figure 1. The setup contains two consecutive test sections: an air-cooled condenser tube of 5.7 m length, and a water-cooled condenser tube of 0.12 m length. Steam is generated by two boilers (24 kW and 45 kW), from where it passes through a pre-heater into the air-cooled test section. At the outlet of the air-cooled section, the collected steam and condensate flow directly into the water-cooled test section. These tubes are connected directly via flange in order to assure that no disruption is made to the flow regime. After these two test sections, the collected condensate passes through a Micromotion CMF025 coriolis mass flow meter and into a condensate receiver for return to the boilers. The remaining steam passes to a secondary condenser, where it is condensed completely. This secondary condensate is pumped back into the boilers via a CMF010 coriolis mass flow meter.

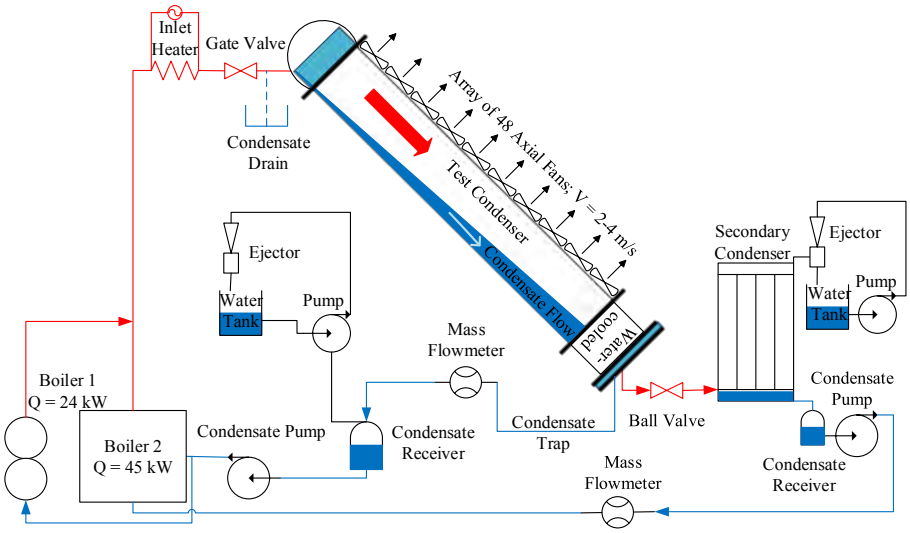

Figure 1: Diagram of condenser test facility

2.2 Test Tube

The condenser tube in this experiment is 0.216 m in inner height and 0.016 m in inner width, as seen in Figure 2. The tube is steel with aluminum cladding on the outside, and the wavy fins are aluminum. The fins are 200 mm x 19 mm, with a thickness of 0.25 mm. The tube is installed in an air duct, with crossflowing air pulled upwards through the fins. The water-cooled tube has the same geometry, but the fins are not present.

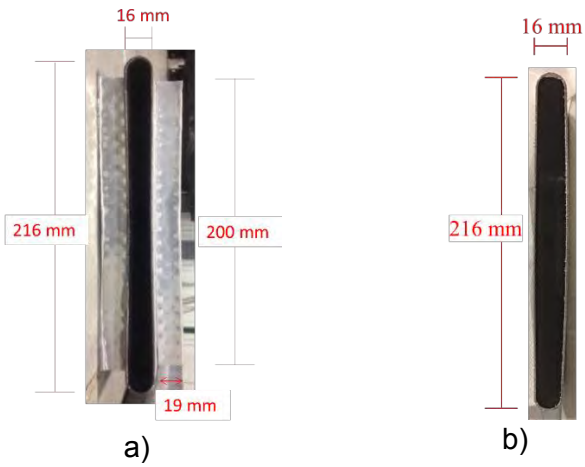

Figure 2: Condenser tube cross-section views: a) air-cooled tube; b) water-cooled tube (no fins)

2.3 Air-Cooled Test Section

Air-side capacity is determined in the air-cooled test section, along with steam temperature and pressure. Air inlet and outlet temperatures are measured at 0.5 m intervals along the test tube with T-type thermocouples. Temperature of the stratified condensate layer is also measured at Z = 2 m and Z = 4 m along the tube. Air velocity is measured by a handheld hot-wire anemometer at 360 points along the tube. Gauge pressure is measured at condenser inlet and outlet with differential pressure sensors. Atmospheric pressure is measured locally with a barometer.

2.4 Water-Cooled Test Section

The water-cooled test section is cooled via a polycarbonate water jacket that was manufactured using fused deposition modeling. A diagram of the water-cooling loop is presented in Figure 3.

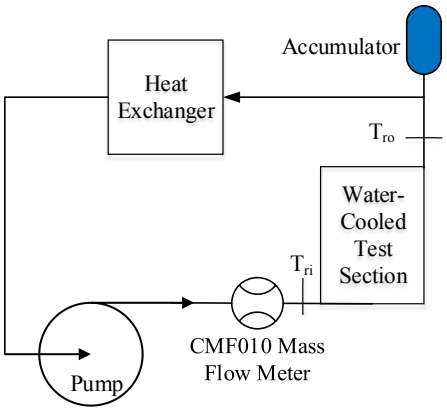

Figure 3: Diagram of water-cooling loop

The water-cooled tube is attached via flange to the air-cooled section in to ensure continuous development of flow regime. A schematic of the test section is presented in Figure 4. The polycarbonate water jacket is presented in Figure 5.

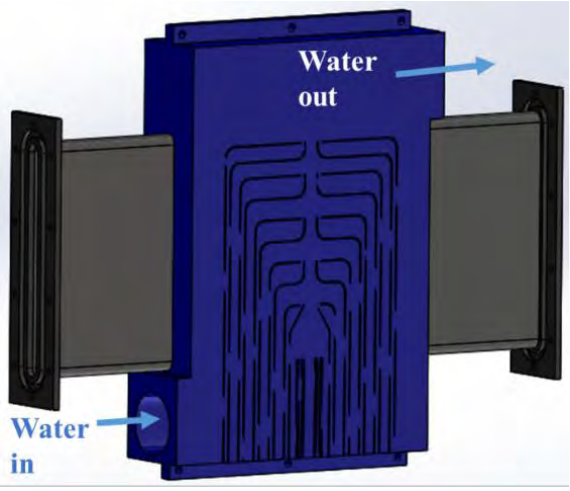

Figure 4: Diagram of water-cooled test section, with water jacket covering tube

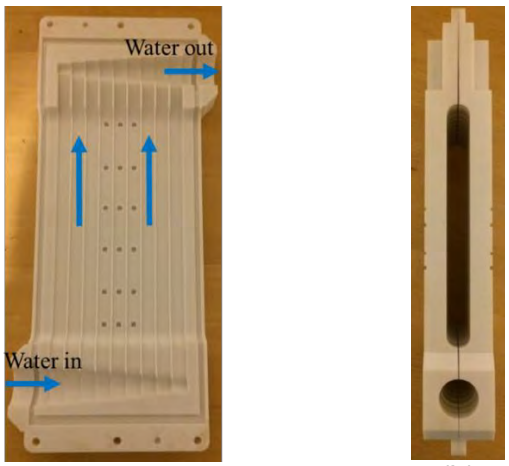

Figure 5: Polycarbonate water jacket, (a) View of inside one half of the jacket. Recesses for Tr thermocouples can be seen in the middle three channels. (b) End view showing water inlet and space for tube; notches on sides are for thermocouple wires

The water jacket and test tube form a single-pass counter-flow heat exchanger. The water jacket channels are designed to mimic the large temperature glide present in an air-cooled condenser (William A Davies III et al., 2019). The steam-side flow is in the stratified regime, so the condensation HTC depends on wall-steam temperature difference. Therefore, it is important to mimic the ACC conditions in order to develop a useful HTC correlation.

Channel geometry and instrumentation are shown in Figure 6. Water temperature is measured at the inlet and outlet to the jacket, as well as at six locations in each of the three middle channels, on each side of the condenser tube. The thermocouples along each channel are positioned in recesses directly above the water channels, in order to measure the water temperature at the top of the channel. In order to determine the mixing-cup temperature of the water flow, a CFD simulation was performed, and results were compared to the temperature measurements. The decision to measure the unmixed water temperatures along the channels was an intentional one. The water-cooling system was designed with the goal of matching the temperature glide of air through the fins in the air-cooled test section. Due to the high heat capacity of water in comparison to air, this requirement compelled the use of thin (1.4 mm height) water channels. These channels were too thin to build a polycarbonate mixing structure along the length of the channel. An alternative option would be to pull the water away from the tube into separate mixing chambers before each temperature measurement. However, this would interrupt the thermal boundary layer and expose the tube to intermittent doses of cooler water – once again failing in the requirement to match the temperature glide of the air-cooled section. Therefore, a combined experimental and CFD approach was chosen to maintain this uninterrupted temperature glide. This method introduces increased uncertainty in the determination of water temperatures along the channel, and therefore in the determination of local condensation HTC. However, the mixing-cup temperatures of the inlet and outlet water were measured directly, so the uncertainty of the mean HTC is unaffected.

In following the water temperature measurements, wall temperature is measured in six locations at each of the three middle channels on both sides of the tube. The thermocouples are embedded in the 1.7 mm-thick steel wall of the tube. The thermocouple beads are covered with Omegabond 101 high thermal conductivity epoxy (published thermal conductivity of 1.0 W m^{-1} K^{-1}) before insertion to ensure proper thermal contact with the wall. In addition, the channels for the wires are filled with this thermal epoxy after insertion in order to affix the thermocouples and ensure proper heat conduction through the wall. The wall thermocouples after installation are shown in Figure 7. All temperatures are measured with T-type thermocouples.

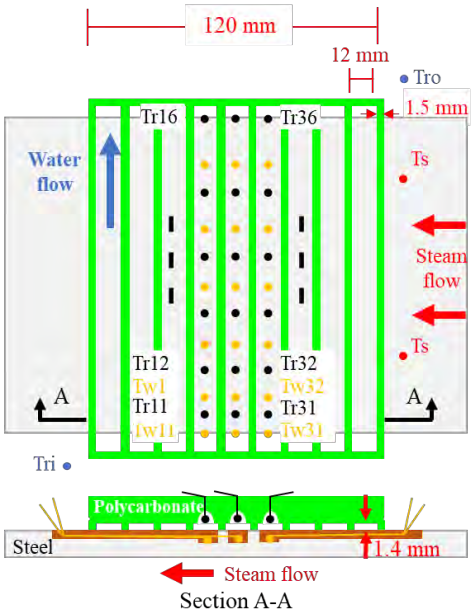

Figure 6: Diagram of water-cooled section; Wall (Tw_{jk}) and water (Tr_{jk}) temperatures are measured in the three center channels along the channel length

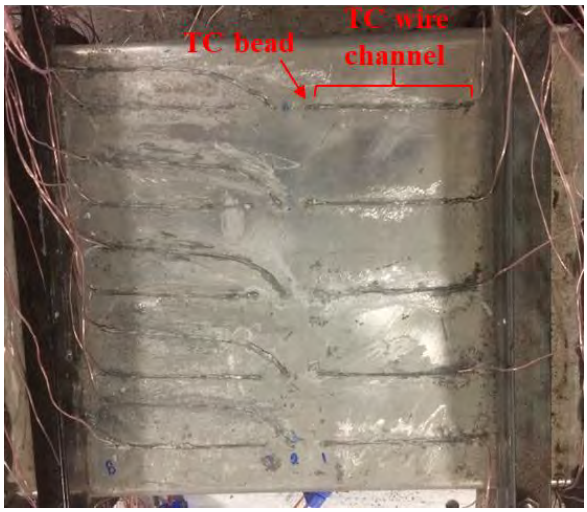

Figure 7: Water-cooled test section with wall thermocouples installed. TC are installed in three adjacent channels on each side of the tube. The TC wires run through channels cut into the steel wall perpendicularly to the channel direction. TC are affixed with Omegabond 101 high-conductivity thermal epoxy

3. METHOD

3.1 Data Reduction

Total steam mass flow rate is the sum of the condensate mass flow rates leaving each of the water-cooled test section and the secondary condenser.

$$\dot{m}_s = \dot{m}_{c1} + \dot{m}_{c2} \qquad \text{Eq. (1)}$$

Steam mass flux is the total steam mass flow rate divided by the inner cross-sectional area of the condenser tube:

$$G_s = \frac{\dot{m}_s}{A_{cs}} \qquad \text{Eq. (2)}$$

Steam quality at the inlet to the water-cooled test section is determined by two methods. For the first method, condensate generated by the water-cooled section is subtracted from mass flow rate of condensate leaving the primary condenser. The result is divided by the system mass flow rate.

$$x_{r,method1} = \frac{\dot{m}_{c1} - Q_r / i_{lv}}{\dot{m}_s} \qquad \text{Eq. (3)}$$

Capacity of the water-cooled test section, Q_r, is determined by equation (4):

$$Q_r = \dot{m}_r \left(T_{ro} c_{p,ro} - T_{ri} c_{p,ri} \right) \qquad \text{Eq. (4)}$$

The second method to determine quality is by using the capacity of the air-cooled test section, measured via heat transferred to the cooling air (equation (5)):

$$x_{r,method2} = \frac{Q_a / i_{lv}}{\dot{m}_s} \qquad \text{Eq. (5)}$$

Air-side capacity, Q_a, is determined via air velocity and air-side temperature difference. A complete description of this determination is available in Davies and Hrnjak (Davies III & Hrnjak, 2019 (In press)).

Final steam quality is determined by an uncertainty-weighted average, as described by Park et al. (Park et al., 2010):

$$x_r = \frac{\left(\frac{1}{u_{method1}^{\ 2}}\right)x_{r,method1} + \left(\frac{1}{u_{method2}^{\ 2}}\right)x_{r,method2}}{\frac{1}{u_{method1}^{\ 2}} + \frac{1}{u_{method2}^{\ 2}}} \quad \text{Eq. (6)}$$

Equation (7) shows that heat flux of the water-cooled section is determined by water-cooled capacity divided by the total steam-side heat transfer area of the water-cooled section, which totals 0.0547 m^2:

$$q''_r = \frac{Q_r}{A_{s,r}} \quad \text{Eq. (7)}$$

Local capacity of the water-cooled section is determined from change in local water temperature in each channel, as in equation (8):

$$Q_{r,jk} = \frac{\dot{m}_r}{\#\,\text{of channels}}\left(T_{r,j,k+1}c_{pr,j,k+1} - T_{r,j,k}c_{pr,j,k}\right) \quad \text{Eq. (8)}$$

The local water mass flow rate is determined by assuming equivalent mass flow rate in each of the 18 channels. This was achieved through careful design – maintaining higher pressure drop through the channels than in the header – and verified by comparing temperature measurements in adjacent and opposing channels.

Local heat flux is then determined by the local water-side heat transfer area, with the subscripts j and k in equations (8) and (9) denoting the channel number (1-9) and axial location along the channel (1-6) respectively:

$$q''_{r,j,\mathrm{k}} = \frac{Q_{r,j,k}}{A_{s,r,k}} \quad \text{Eq. (9)}$$

The local condensation heat transfer coefficient is then determined by local heat flux and temperature difference between the steam and the wall, and then accounting for the heat transfer resistance of the wall (equations (10) and (11)):

$$h_{j,k} = \frac{q''_{r,j,k}}{T_s - T_{w,j,k}} \quad \text{Eq. (10)}$$

$$h_{s,j,\mathrm{k}} = \left(\frac{1}{h_{j,k}} - \frac{t_w}{k_w}\right)^{-1} \quad \text{Eq. (11)}$$

4. RESULTS AND DISCUSSION

Figure 8 shows the measured wall, steam, inlet water and outlet water temperatures, as well as the local water temperatures determined using CFD for one experimental point. These are compared to modeled temperatures, determined using the equation of Dhir and Lienhard (1971) to determine condensation HTC for points 2-6, and that of Dobson and Chato (1998) to determine HTC at point 1 at the bottom of the tube. The experiment finds equivalent wall temperatures to the model, but greater

water temperature for all points. This indicates higher heat transfer and higher heat transfer coefficient than that predicted by the experiment.

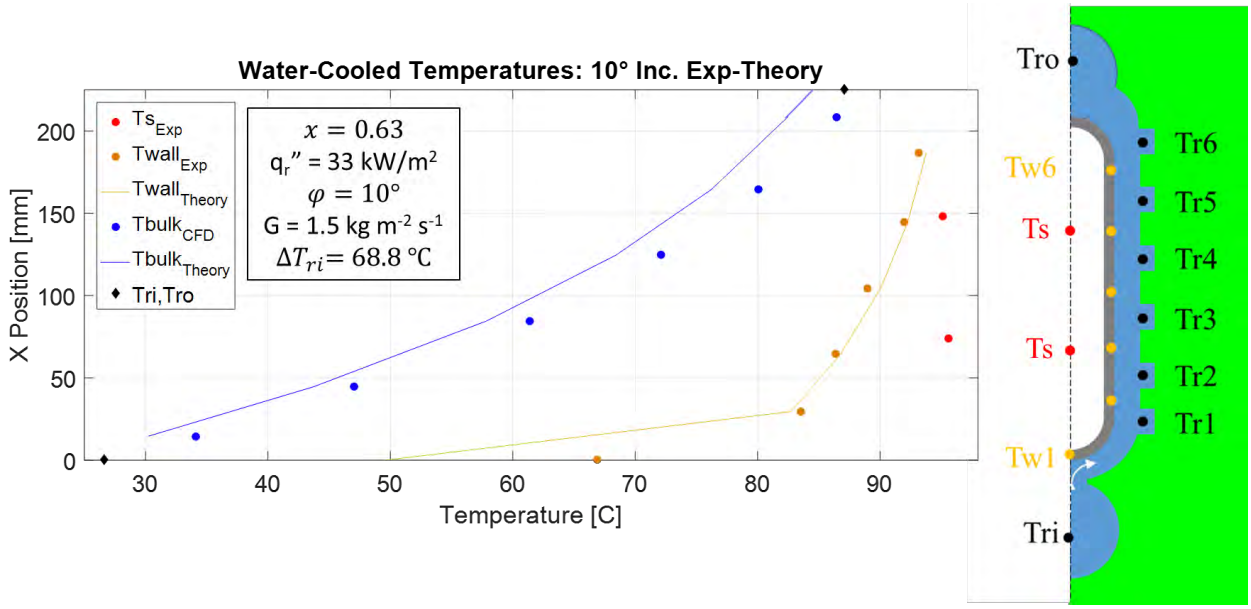

Figure 8: Measured and CFD temperatures vs. theoretical temperatures determined using the Dhir & Lienhard (1971) and Dobson and Chato (1998) correlations for HTC

Figure 9 displays local HTC for the same experimental point. The HTC is lowest at the tube bottom, as expected due to the build-up of condensate at the tube bottom. Condensation HTC then increases along the tube height due to the smaller film thickness at the higher position. Measured HTC agrees well with the natural-convection correlation of Dhir and Lienhard (1971) for all points.

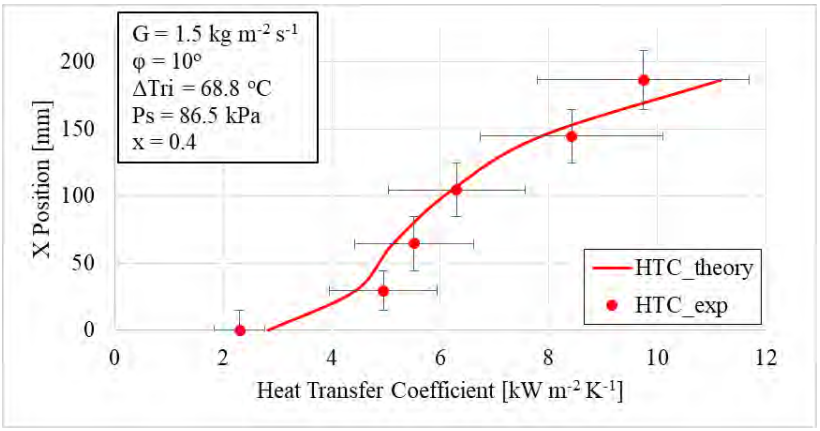

Figure 9: Local condensation HTC for one data point, compared to analytical HTC from Dhir & Lienhard (1971)

5. CONCLUSIONS

The method of determining condensation heat transfer coefficient while maintaining the varying heat flux and wall temperature of an operating air-cooled condenser has been shown to be accurate. In addition, condensation heat transfer coefficient has been shown to increase along the condenser height by over five times in magnitude.

ACKNOWLEDGEMENTS

The authors acknowledge the technical support provided by the Air Conditioning and Refrigeration Center (ACRC) at the University of Illinois at Urbana-Champaign, and by Creative Thermal Solutions, Inc. that provided the experimental apparatus, laboratory space and support.

NOMENCLATURE

A	Area	m^2
c_p	Specific heat at constant pressure	J kg^{-1} K^{-1}
G	Mass flux	kg m^{-2} s^{-1}
h	Heat transfer coefficient	W m^{-2} K^{-1}
i	Specific enthalpy	J kg^{-1}
i_{lv}	Specific enthalpy of vaporization	J kg^{-1}
k	Thermal conductivity	W m^{-1} K^{-1}
$\dot{m}$	Mass flow rate	kg s^{-1}
Q	Heat transferred	W
q''	Heat flux	W m^{-2}
t	Thickness	m
T	Temperature	^oC
T_{bulk}	Bulk water temperature	^oC
u	Uncertainty	
x	Vapor quality	
X	Position along wall height	m
Z	Axial position	m

Subscripts

a	Air
b	Back of the tube
$c1$	Primary condenser (consisting of air and water-cooled test sections)
$c2$	Secondary condenser
cs	Cross-section
f	Front of the tube
i	Inlet
j	Channel number
k	Index of position along X-direction
l	liquid
o	Outlet
r	Water-cooling loop
s	Steam
v	Vapor
w	Wall

Greek Symbols

φ	Inclination angle	^{o}

REFERENCES

Abadi, S. M. A. N. R., Davies, W. A., Hrnjak, P., & Meyer, J. P. (2019). Numerical study of steam condensation inside a long inclined flattened channel. *International Journal of Heat and Mass Transfer, 134*, 450-467. doi:https://doi.org/10.1016/j.ijheatmasstransfer.2019.01.063

Cavallini, A., Censi, G., Del Col, D., Doretti, L., Longo, G., Rossetto, L., & Zilio, C. (2003). Condensation inside and outside smooth and enhanced tubes—a review of recent research. *International journal of refrigeration, 26*(4), 373-392.

Dalkilic, A., & Wongwises, S. (2009). Intensive literature review of condensation inside smooth and enhanced tubes. *International Journal of Heat and Mass Transfer, 52*(15-16), 3409-3426.

Davies III, W. A., & Hrnjak, P. (2019 (In press)). Heat transfer in a large, inclined, flattened-tube steam condenser. *Heat Transfer Engineering, 41*(19).

Davies III, W. A., Kang, Y., Hrnjak, P., & Jacobi, A. M. (2019). Effect of inclination on heat transfer and flow regimes in large flattened-tube steam condensers. *Applied Thermal Engineering, 148*, 999-1006. doi:https://doi.org/10.1016/j.applthermaleng.2018.11.078

Davies III, W. A., Kang, Y., Hrnjak, P., & Jacobi, A. M. (2019). Heat transfer and flow regimes in large flattened-tube steam condensers. *Applied Thermal Engineering, 148*, 722-733. doi:10.1016/j.applthermaleng.2018.11.079

Dhir, V., & Lienhard, J. (1971). Laminar film condensation on plane and axisymmetric bodies in nonuniform gravity. *Journal of Heat Transfer, 93*(1), 97-100.

Dobson, M., & Chato, J. (1998). Condensation in smooth horizontal tubes. *Journal of Heat Transfer, 120*(1), 193-213.

Kang, Y., Davies III, W. A., Hrnjak, P., & Jacobi, A. M. (2017). Effect of inclination on pressure drop and flow regimes in large flattened-tube steam condensers. *Applied Thermal Engineering, 123*, 498-513. doi:10.1016/j.applthermaleng.2017.05.062

Kröger, D. G. (2004). *Air-cooled heat exchangers and cooling towers* (Vol. 1). USA: PennWell Books.

Liebenberg, L., & Meyer, J. P. (2008). A review of flow pattern-based predictive correlations during refrigerant condensation in horizontally smooth and enhanced tubes. *Heat Transfer Engineering, 29*(1), 3-19.

Nusselt, W. (1916). Die Oberflachenkondesation des Wasserdamffes the surface condensation of water. *Zetrschr. Ver. Deutch. Ing., 60*, 541-546.

Park, Y.-G., Liu, L., & Jacobi, A. M. (2010). Rational approaches for combining redundant, independent measurements to minimize combined experimental uncertainty. *Experimental Thermal and Fluid Science, 34*(6), 720-724.

Manuscript ID: 906
DOI: 10.18462/iir.icr.2019.0906

Pressure drop in large flattened-tube steam condensers

William A. DAVIES III [(a)], Pega HRNJAK [(a, b)]

[(a)] Air Conditioning and Refrigeration Center (ACRC), Department of Mechanical Science and Engineering, University of Illinois at Urbana-Champaign, Urbana, IL, USA, daviesi2@illinois.edu, pega@illinois.edu

[(b)] CTS – Creative Thermal Solutions, Inc., Urbana, IL, USA, pega@illinois.edu

ABSTRACT

Pressure drop during steam condensation is measured experimentally in a large, flattened-tube air-cooled condenser. The steel tube is 5.7 m long, with an elongated-slot cross section with inner dimensions of 216 x 16 mm. Cooling air is provided by 48 axial fans of 120 mm diameter, providing air velocity from 2 – 2.7 m s^{-1}. Tube inclination angle is varied from 0 – 49° downwards, and condensation pressure is varied from 70 – 105 kPa.

Pressure drop is measured in two 2.85 m sections along the tube. Pressure drop for the full tube is also measured by difference between inlet and outlet gauge pressure. Pressure drop is found to be very small (<100 Pa) for all test conditions due to the low mass flux (< 5 kg m^{-2} s^{-1}). Frictional pressure drop is found to increase as mass flux increases, and total pressure drop is found to decrease as inclination increases.

1. INTRODUCTION

This paper examines the effect of condenser pressure, mass flux, and tube inclination on steam-side pressure drop for a power-plant air-cooled condenser (ACC). Condensation pressure is an important system-level parameter. Decreasing condensation pressure improves power-plant performance by increasing the Carnot efficiency, as shown by O'Donovan and Grimes (2014). Only a few previous experimental parametric studies of ACC performance have been performed. Of the previous studies, O'Donovan and Grimes (2015) found that steam-side frictional pressure drop in an ACC bundle increases as inlet vapor velocity increases. However, they also found that momentum recovery also increases, so total pressure drop only increases slightly. They found the correlation of Lockhart and Martinelli (1949) for frictional pressure drop most closely matched their experimental data. However, this correlation was developed for small round tubes with high mass flux. In another experimental study, Kang *et al.* (2017) studied pressure drop in inclined, flattened-tube ACCs. They found that steam-side pressure drop decreases as tube inclination increases due to improved drainage of condensate and increased gravitational pressure recovery. In addition, they found a hydraulic roughness of 0.3 mm during condensation in this tube.

Although many condensation pressure drop correlations exist for small, round-tube condensers, only a few exist for the case of large, flattened tubes. For this specific case with low mass flux, Groenewald and Kröger (1995) numerically developed and experimentally validated a correlation for pressure drop that accounts for the suction rate of vapor towards the condensing wall, which affects the friction factor. Their model also finds that the effect of interfacial waviness is negligible due to the high aspect ratio and low mass flux of the tubes. For condensation in inclined tubes, S. Lips and J. Meyer (2012) presented a pressure-drop model based on the correlation of Taitel and Dukler (1976). Developed based on experimental results in small-diameter round tubes, their model takes into account the curved shape of the vapor-liquid interface.

2. FACILITY

2.1 Overview

The facility used in this study is identical to that used in (Davies III & Hrnjak, 2019 (In press)). A schematic of the experimental setup is presented in Fig. 1. Steam is generated by two boilers (24 kW and 45 kW), from where it passes through a pre-heater into an air-cooled test section. The test section is 5.7 m in length, and is cooled by 48 axial fans with 120 mm diameter. The steam enters in a slightly-superheated state, and is completely condensed in this test section, so that only condensate flows through the Micromotion CMF025 coriolis mass flow meter and into a condensate receiver for return to the boilers.

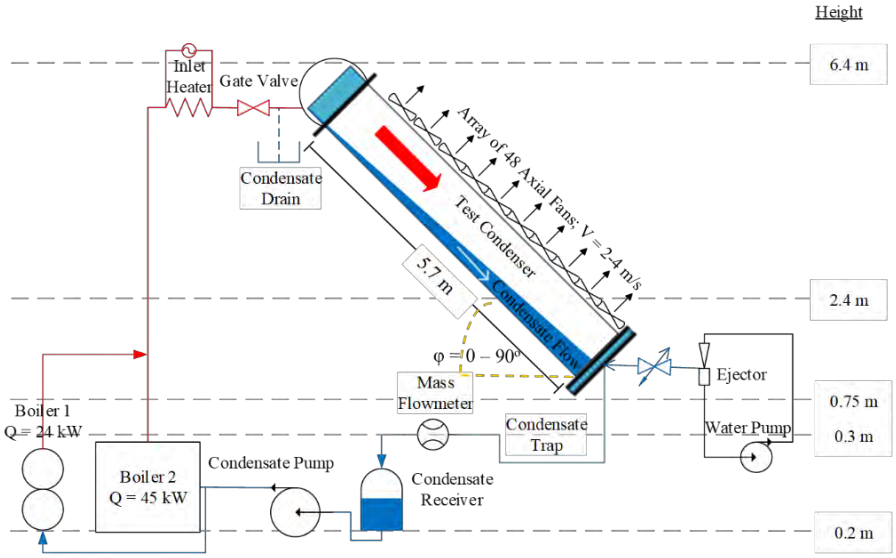

Figure 1: Diagram of condenser test facility

2.2 Test Tube

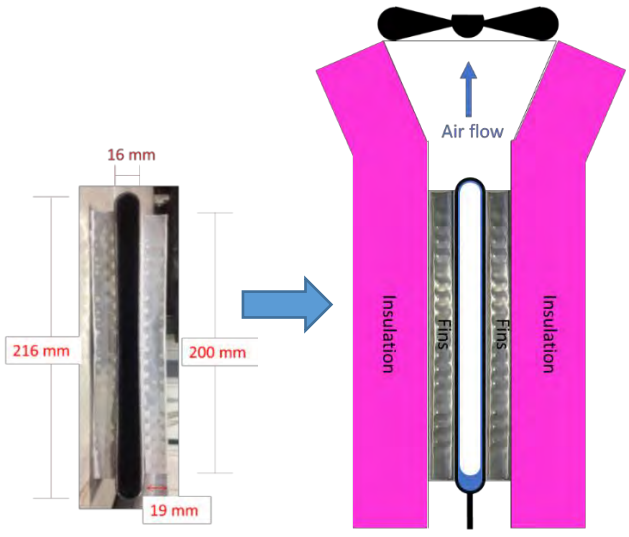

(a) (b)

Figure 2: Condenser tube (a) stand-alone and (b) installed in air duct

The condenser tube is 0.216 m in inner height and 0.016 m in inner width, as seen in Figure 2. The tube has a cross-sectional area of 34 cm^2 and a hydraulic diameter of 3 cm. The tube is steel of 1.8 mm thickness, with aluminum cladding on the outside, and the wavy fins are aluminum. The fins are 200 mm x 19 mm, with a thickness of 0.25 mm and fin pitch of 2.3 mm. The tube is installed in a

specially-designed air duct, in order to maintain uniform air flow rate along the tube length. This crossflowing air is pulled upwards through the fins.

2.3 Test Section Instrumentation

Temperatures and pressures are measured along the test section at the points shown in Figure 3. Air inlet and outlet temperatures are measured at 0.5 m intervals along the test tube with T-type thermocouples. Air velocity is measured by a handheld hot-wire anemometer at 360 points along the tube. There is significant local variation in air velocity due to small variations in the fins and non-uniform fan flow rate along each individual fan. Gauge pressure is measured at the condenser inlet and outlet with differential pressure sensors. Pressure drop is measured in two 2.85 m sections along the tube length. Positive gauge pressure is measured by sensors with a maximum range of 7.47 kPa. When gauge pressure is negative, a sensor with a range of 124 kPa is used. The sectional pressure drops are measured by sensors with ranges of 498 Pa for positive pressure drop and 249 Pa for negative pressure drop. Pressure drop is occasionally negative due to pressure gain from deceleration and from decrease in elevation. Atmospheric pressure is measured locally with a barometer.

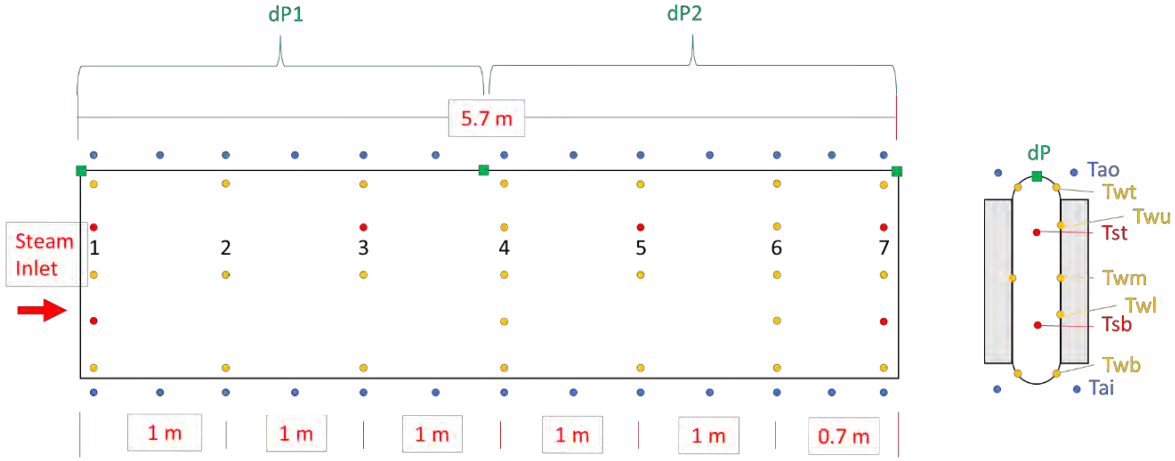

Figure 3: Measurement points along condenser test section

3. METHOD

3.1 Data Reduction

Pressure drop is determined by two methods. The pressure drop of the individual 2.85 m sections issummed to find pressure drop along the entire tube length shown by Eq. (1):

$$\Delta P_{tot,sum} = \Delta P_1 + \Delta P_2 \qquad \text{Eq. (1)}$$

As a second method, the difference between inlet and outlet gauge pressure is found by equation (2). This method is only valid for positive gauge pressures. For negative gauge pressures, the range of the sensors is too large to provide an accurate measurement of the small pressure drop.

$$\Delta P_{tot,\mathrm{diff}} = P_i - P_o \qquad \text{Eq. (2)}$$

The two methods are combined by Eq. (3) using the method of Park and Jacobi (2010) in order to reduce uncertainty:

$$\Delta P_{tot} = \frac{\left(\frac{1}{u_{sum}^{\ 2}}\right)\Delta P_{total,sum} + \left(\frac{1}{u_{diff}^{\ 2}}\right)\Delta P_{tot,diff}}{\frac{1}{u_{sum}^{\ 2}} + \frac{1}{u_{diff}^{\ 2}}} \quad \text{Eq. (3)}$$

Once obtained, the total pressure drop can be divided into three components: the gravitational, momentum and frictional pressure drops, as in Eq. (4):

$$\Delta P_{tot} = \Delta P_g + \Delta P_m + \Delta P_f \quad \text{Eq. (4)}$$

As explained by Taitel and Dukler (1976), for stratified flow, the pressure drop between the vapor and liquid phases will be equal. Therefore, in calculating the components of the total pressure drop, it is possible to consider the pressure drop in the vapor phase, only. The gravitational pressure drop is then the hydrostatic pressure in the vapor phase Eq. (5):

$$\Delta P_g = \rho_v g L \sin(\varphi) \quad \text{Eq. (5)}$$

The gravitational pressure drop will be negative for a downwardly-inclined tube, indicating an increase in pressure along the tube length. In condensation, momentum pressure drop also increases the pressure. It is the result of the deceleration of the vapor flow, and is calculated by Eq. (6):

$$\Delta P_m = \frac{1}{2}\left[\left(\rho_v v_v^2\right)_o - \left(\rho_v v_v^2\right)_i\right] \quad \text{Eq. (6)}$$

Only condensate exits the tube, so the outlet vapor velocity is zero. In the experiment, mass flow rate of condensate is measured directly. The inlet quality and void fraction are approximately equal to one, so the inlet vapor velocity can be determined by Eq. (7):

$$v_{g,\mathrm{i}} = \frac{\dot{m}_s}{\rho_v A_{cs}} \quad \text{Eq. (7)}$$

Frictional pressure drop is then determined by subtracting the momentum and gravitational pressure drops from the measured total pressure drop.

Total mass flux is also determined from the measured condensate mass flow rate:

$$G = \frac{\dot{m}_s}{A_{cs}} \quad \text{Eq. (8)}$$

Inlet vapor Reynolds number is then determined from the mass flux and fluid properties:

$$\mathrm{Re}_{vi} = \frac{GD_h}{\mu_v} \quad \text{Eq. (9)}$$

Due to the stratified flow throughout the tube length, and the constant heat flux leading to linear variation in vapor velocity (Davies III *et al.*, 2019), a model for single-phase pressure drop in the vapor can be assumed, and the pressure drop can be discretized along the length to determine an interfacial friction factor:

$$f_{\text{int}} = \frac{2\Delta P_f D_h}{\Delta Z v_v^2 \rho_v} \quad \text{Eq. (10)}$$

Interfacial roughness, ε_{int}, can be determined by fitting Churchill's (1977) model for friction factor to the results for friction factor as a function of vapor Reynolds number:

$$f_{\text{int}} = 8\left[\left(\frac{8}{\text{Re}_v}\right)^{12} + \frac{1}{\left(B_1 + B_2\right)^{1.5}}\right]^{1/12} \quad \text{Eq. (11)}$$

$$B_1 = \left[-2.457 \ln\left(\left(\frac{7}{\text{Re}_v}\right)^{0.9} + \frac{0.27\varepsilon_{\text{int}}}{D_h}\right)\right]^{16} \quad \text{Eq. (12)}$$

$$B_2 = \left(\frac{37530}{\text{Re}_v}\right)^{16} \quad \text{Eq. (13)}$$

3.2 Uncertainty

There are two main causes of uncertainty of the pressure drop measurement: uncertainty of the pressure sensors and uncertainty caused by fluctuations in the system pressure. The published sensor uncertainty is 0.2% of the sensor range. Therefore, the instrument uncertainty is 1 Pa when measuring positive pressure drop, and 0.5 Pa when measuring a negative pressure drop. However, significant uncertainty is added by the boiling process. The generation of steam is unsteady, so the condenser pressure undergoes significant variation with time. Taking the standard error of the measurements at the 95% confidence level, and combining with the instrument uncertainty, the final uncertainty of pressure drop over the full tube length is 10 Pa.

Uncertainty of the interfacial roughness depends on the uncertainty of the friction factor, as well as the uncertainty of fitting Churchill's model to the results. The uncertainty of the interfacial roughness is 20%.

4. RESULTS AND DISCUSSION

4.1 Overall Pressure Drop

Frictional pressure drop in the tube is compared to the models of S. Lips and J. P. Meyer (2012), Groenewald and Kröger (1995) and Kang et al. (2017) in Figure 4. In addition, the interfacial roughness is derived from the current experimental results, and Churchill's (1977) model is plotted with this interfacial roughness. Frictional pressure drop is very small in magnitude, so there is significant experimental error. However, the experimental results exceed the predictions of all three models, with closest agreement to the models of S. Lips and J. P. Meyer (2012) and Kang et al. (2017). Despite this under-prediction, the experimental results follows the trend of all three models in increasing frictional pressure drop as inlet vapor Reynolds number increases. This is the result of the increased vapor velocity increasing interfacial shear stress. Figure 5 shows the momentum and frictional components of pressure drop. These results are for a horizontal tube, so the gravitational pressure gain is zero. The increase in overall pressure drop with inlet vapor Reynolds number is shown to be due to an increase in frictional pressure drop, which is partially offset by an increase in

the momentum pressure recovery. As with frictional pressure drop the experimental data follows the trend of the model, but exceeds the result predicted by the model. Figure 6 shows a very similar trend for the higher condensing pressure of 100 kPa. It can also be seen that frictional pressure drop is lower for a given Reynolds number at the higher condensing pressure. This agrees with the prediction of the model.

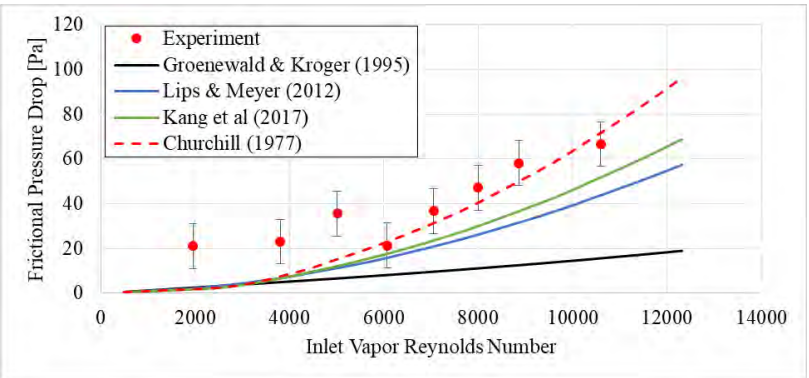

Figure 4: Experimental frictional pressure drop compared to the models of Kang et al. (2017), Groenewald and Kröger (1995), S. Lips and J. P. Meyer (2012) for a horizontally-inclined tube. The model of Churchill (1977) uses the roughness derived in the current experiment of 0.94 mm

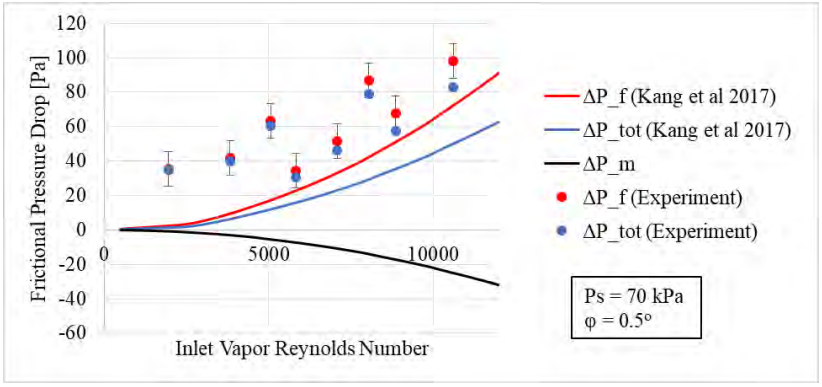

Figure 5: Pressure drop vs. mass flux, with experimental results compared to the frictional pressure drop model of Kang et al. (2017) for Ps = 70 kPa

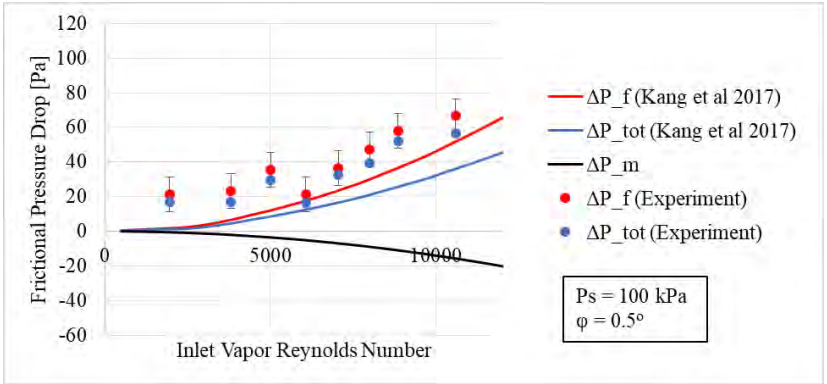

Figure 6: Pressure drop vs. mass flux, with experimental results compared to the frictional pressure drop model of Kang et al. (2017) for Ps = 100 kPa

Figure 7 shows the total pressure drop as tube inclination changes. It can be seen that pressure drop decreases as inclination increases. This is a result of increased gravitational pressure recovery. Friction also decreases slightly with inclination. Previous experimental results (Kang et al., 2017) have shown that frictional pressure drop can decrease with increasing inclination due to improved condensate drainage. This experiment confirms this result.

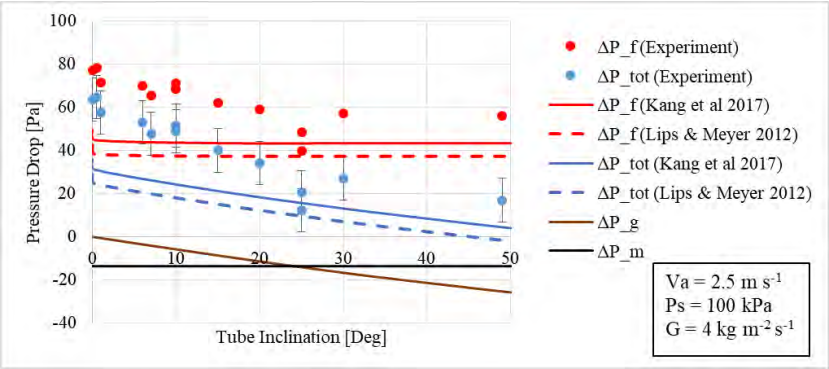

Figure 7: Total pressure drop vs. tube inclination angle, with experimental results compared to the models of S. Lips and J. P. Meyer (2012) and Kang et al. (2017)

Figure 8 shows friction factor compared to that of several models over a range of local Reynolds numbers. The results show that the experimentally-determined friction factor exceeds that of all the models, with a greater discrepancy in the laminar region. In this high-aspect-ratio tube, the transition Reynolds number is approximately 2800 (Hanks & Ruo, 1966). Applying Churchill's model to the results, the interfacial roughness is derived, yielding a result of 0.94 mm.

Figure 9 shows the decrease in frictional pressure drop as quality decreases. This is mainly the result of the decreased velocity as the two-phase density increases.

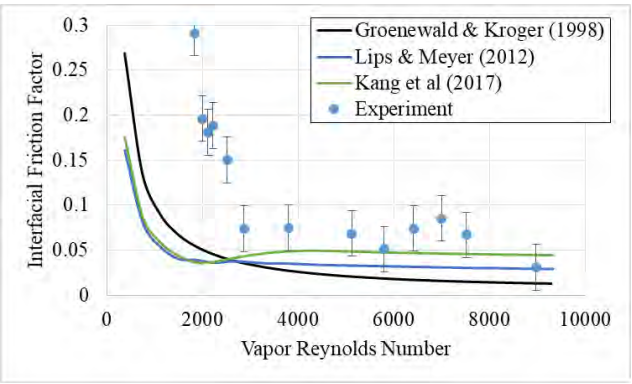

Figure 8: Experimental friction factor exceeds that of relevant models

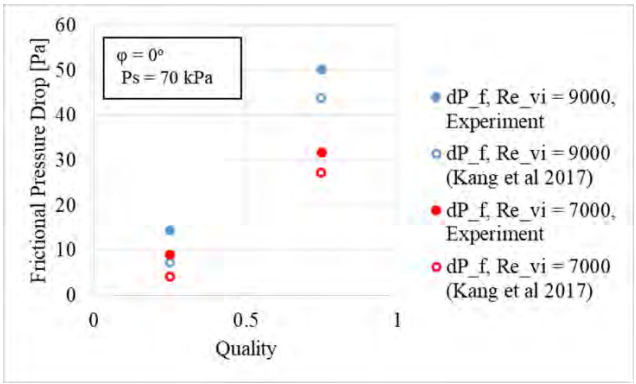

Figure 9: Frictional pressure drop vs. vapor quality

5. CONCLUSIONS

Pressure drop has been measured during condensation of steam in a 5.7 m flattened tube. Pressure drop has been found to decrease as downward tube inclination increases due to an increase in gravitational pressure recovery. Frictional pressure drop has been found to decrease as well with increasing inclination. Pressure drop has also been found to increase as inlet vapor Reynolds number increases, and as condensation pressure decreases. Total pressure drop is very low in magnitude, due to the low mass flux.

ACKNOWLEDGEMENTS

The authors acknowledge the technical support provided by the Air Conditioning and Refrigeration Center (ACRC) at the University of Illinois at Urbana-Champaign, and by Creative Thermal Solutions, Inc. that provided the experimental apparatus, laboratory space and support.

NOMENCLATURE

A	Area	m^2
D_h	Hydraulic diameter	m
f	Friction factor	
G	Mass flux	kg m^{-2} s^{-1}
g	Gravitational acceleration	m s^{-2}
L	Length	m
$\dot{m}$	Mass flow rate	kg s^{-1}
P	Pressure	kPa
Q	Heat transferred	W
Re	Reynolds number	
T	Temperature	°C
u	Uncertainty	
v	Velocity	m s^{-1}
x	Vapor quality	
Z	Axial position	m

Subscripts

1	Measurement section 1
a	Air
cs	Cross-section
diff	Pressure drop determined by difference between inlet and outlet gauge pressure
f	Frictional
g	Gravitational
i	Inlet
int	Interfacial
l	liquid
m	Momentum
o	Outlet
s	Steam
sum	Pressure drop measured as sum of pressure drop in each measurement section
tot	Total pressure drop
v	Vapor
w	Wall

Greek Symbols

ΔP	Pressure drop	Pa
ε	Roughness	m
μ	Viscosity	Pa s
ρ	Density	kg m^{-3}
φ	Inclination angle	°

REFERENCES

Churchill, S. W. (1977). Friction-factor equation spans all fluid-flow regimes. *Chemical engineering, 84*(24), 91-92.

Davies III, W. A., & Hrnjak, P. (2019 (In press)). Heat transfer in a large, inclined, flattened-tube steam condenser. *Heat Transfer Engineering, 41*(19).

Davies III, W. A., Kang, Y., Hrnjak, P., & Jacobi, A. M. (2019). Heat transfer and flow regimes in large flattened-tube steam condensers. *Applied Thermal Engineering, 148*, 722-733. doi:10.1016/j.applthermaleng.2018.11.079

Groenewald, W., & Kröger, D. G. (1995). Effect of mass transfer on turbulent friction during condensation inside ducts. *International Journal of Heat and Mass Transfer, 38*(18), 3385-3392. doi:https://doi.org/10.1016/0017-9310(95)00092-N

Hanks, R. W., & Ruo, H. C. (1966). Laminar-Turbulent Transition in Ducts of Rectangular Cross Section. *Industrial & Engineering Chemistry Fundamentals, 5*(4), 558-561. doi:10.1021/i160020a022

Kang, Y., Davies III, W. A., Hrnjak, P., & Jacobi, A. M. (2017). Effect of inclination on pressure drop and flow regimes in large flattened-tube steam condensers. *Applied Thermal Engineering, 123*, 498-513. doi:10.1016/j.applthermaleng.2017.05.062

Lips, S., & Meyer, J. (2012). Experimental study of convective condensation in an inclined smooth tube. Part II: inclination effect on pressure drop and void fraction. *International Journal of Heat and Mass Transfer, 55*, 405-412.

Lips, S., & Meyer, J. P. (2012). Stratified flow model for convective condensation in an inclined tube. *International Journal of Heat and fluid flow, 36*, 83-91.

Lockhart, R., & Martinelli, R. (1949). Proposed correlation of data for isothermal two-phase, two-component flow in pipes. *Chem. Eng. Prog, 45*(1), 39-48.

O'Donovan, A., & Grimes, R. (2014). A theoretical and experimental investigation into the thermodynamic performance of a 50 MW power plant with a novel modular air-cooled condenser. *Applied Thermal Engineering, 71*(1), 119-129.

O'Donovan, A., & Grimes, R. (2015). Pressure drop analysis of steam condensation in air-cooled circular tube bundles. *Applied Thermal Engineering, 87*, 106-116.

Park, Y.-G., Liu, L., & Jacobi, A. M. (2010). Rational approaches for combining redundant, independent measurements to minimize combined experimental uncertainty. *Experimental Thermal and Fluid Science, 34*(6), 720-724.

Taitel, Y., & Dukler, A. (1976). A model for predicting flow regime transitions in horizontal and near horizontal gas-liquid flow. *AIChE Journal, 22*(1), 47-55.

Manuscript ID: 907
DOI: 10.18462/iir.icr.2019.0907

Heat transfer and flow characteristics of condensing flow in a quadrilobed tube

Tomonori ASANO[(a)], Hitoshi ASANO[(b)], Hitoshi HARA[(a)]

[(a)] Noritz Corporation
5 Mninamifuami, Futami-cho, Akashi-shi, 674-0093, Japan, t-asano@noritz.co.jp
[(b)] Department of Mechanical Engineering, Kobe University
1-1, Rokkodai, Nada, Kobe, 657-8501, Japan, asano@mech.kobe-u.ac.jp

ABSTRACT

A double tube heat exchanger is usually used in heat pump water heater to obtain large water temperature rise. Condensing heat transfer coefficient decreases with decreasing vapor quality due to increase in liquid film thickness. Non-circular small diameter tube has possibility to improve the condensing heat transfer, because liquid film thickness becomes non-uniform by surface tension. This study deals with condensing heat transfer of HFC-134a in quadrilobed tube with the cross-section consisting of four leaves and core. Condensing heat transfer and pressure loss in horizontal tubes were experimentally evaluated. From the results, it was confirmed that deterioration in the condensing heat transfer coefficient was suppressed under moderate wetness for the low refrigerant mass flux less than 300 $kg \times m^{-2} \times s^{-1}$, because condensed liquid might be accumulated in the narrow part by the surface tension. However, pressure loss increased due to maldistribution of refrigerant flow.

Keywords: Condensation, Horizontal tube, Pressure drop, R134a, Surface tension, Two-phase flow.

1. INTRODUCTION

Heat pump water heater using CO_2 is widely used in Japanese households for energy saving. When a refrigerant with high critical point was used for heat pump to decrease the operation pressure or to improve the COP, the refrigerant will flow as a condensing flow in the water heater. Many researchers have studied condensing heat transfer for various refrigerant and tube configurations, such as triangular or rectangular channels. Koyama et al. (2003) investigated condensing heat transfer in multi-port extruded tubes having multiple mini rectangular channels. They reported that condensing heat transfer strongly depended on the tube configuration and flow conditions of the refrigerant. Especially, in heat transfer coefficient under low quality condition deterioration in heat transfer coefficient could be suppressed, because the condensate was accumulated at the corner by surface tension. Del Col et al. (2011) measured condensation heat transfer coefficients in a single square cross section minichannel with the 1.18 mm side length, during condensation of refrigerant R134a at 40 ºC saturation temperature, at mass flux ranging from between 200 to 800 $kg \times m^{-2} \times s^{-1}$. They found a heat transfer enhancement at the lowest mass flux in the square cross section channel compared to the circular channel with the same hydraulic diameter by the effect of surface tension. Wang and Rose (2006 and 2011) proposed a theoretical model to predict condensation heat transfer in horizontal square and triangular microchannels considering the effects of interfacial shear stress, gravity and surface tension force on the liquid film structure.

In this present work, condensing heat transfer characteristics in quadrilobed tube with a clearance in the heat transfer wall for leak detection used for a heat pump water heater were experimentally investigated. The effects of the tube configuration and flow condition of the refrigerant are discussed.

2. EXPERIMENTAL APPARATUS AND CONDITIONS

2.1. Experimental apparatus

Fig. 1 shows the schematic diagram of the experimental apparatus. HFC-134a was used as the refrigerant. The test loop consists of a gear pump, an evaporator, a test section and sub-cooler. To absorb a volume increase with a phase change of the refrigerant an accumulator is connected to the branch pipe at the upstream of the pump. The mass flow rate was measured by a Coriolis mass flow meter. The refrigerant was heated and vaporized in the evaporator. Wet vapor was supplied to the test section and condensed by heat exchange with water in the test section. The refrigerant from the test section was further cooled at the sub-cooler to keep the subcooling degree for the gear pump. The pressure of the test loop is maintained by changing the temperature of the accumulator. The test section consists of a quadrilobed tube and a transparent acrylic resin cover. The tube configuration and channel cross-section are shown in Fig. 2. The quadrilobed tube has a cross-section shaped like four leaves and core as shown in Fig. 2 (b). Specification of the tested quadrilobed tube is summarized in Table 1. The length of the heat transfer section was 200 mm of the 720 mm length quadrilobed tube. A 1/4 inch circular tube with 60 mm in length was connected at each end for the connection. The tested tube has double wall for leak detection. The tested tube was gently twisted with the pitch of 400 mm as shown in Fig. 3. The flow direction of the refrigerant and water was a counter flow as shown in Fig. 2 (a). In order to evaluate wall temperature at the middle of the test section, four 0.1 mm K-type thermocouples were mounted on the top and bottom convex parts and root parts.

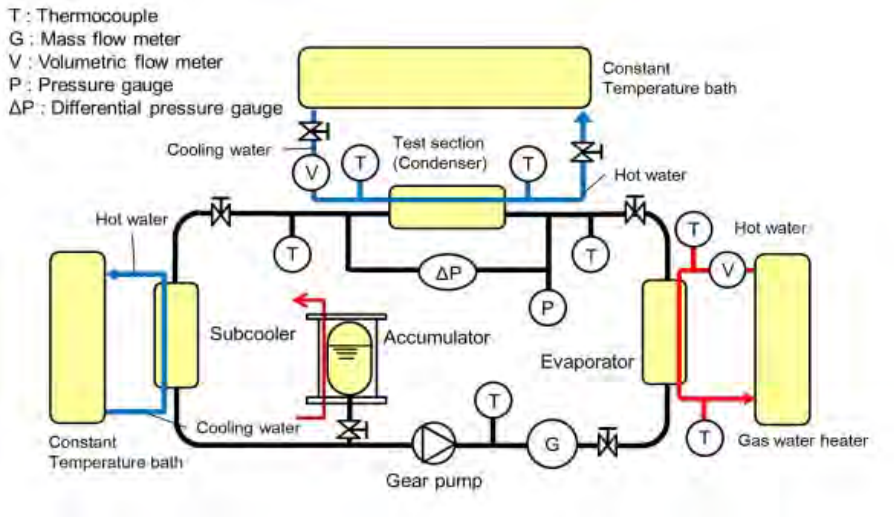

Figure 1: Schematic diagram of experimental apparatus

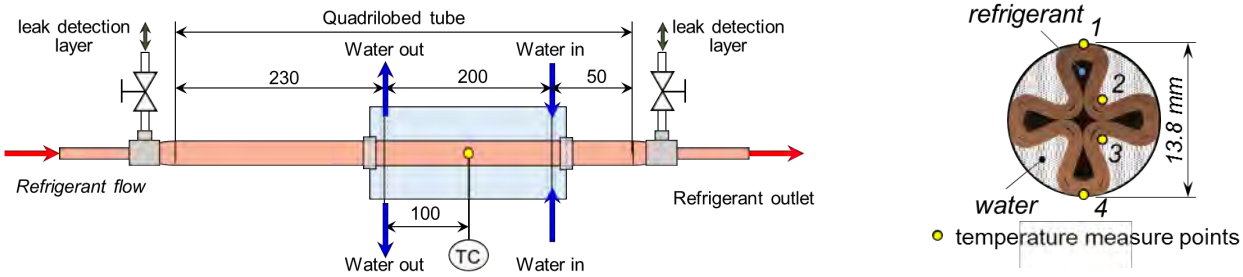

(a) Configuration (b) Cross-section shape

Figure 2: Schematic drawing of the test section

Table 1. Specifications of quadrilobed tube

Maximum diameter	13.8 mm
Cross-section area	16.65 mm^2
Wetted perimeter (inside)	44.85 mm
Wetted perimeter (outside)	58.32 mm
Thickness	1.3~1.6 mm
Hydraulic diameter	1.48 mm



Figure 3: Appearance of quadrilobed tube

2.2. Experimental conditions and methods

The experimental conditions are summarized in Table 2. The refrigerant mass flux is varied in the range of G = 200 to 900 kg×m^{-2}×s^{-1} in single phase experiments and G = 200 to 400 kg×m^{-2}×s^{-1} in condensation experiments. The pressure of test section was kept constant at 1.77 MPa. The volumetric flow rate and inlet temperature of water were also kept at 0.66 L×min^{-1} and 35 ºC, respectively. To evaluate the effect of the clearance for leak detection on the thermal resistance, heat transfer performance of single-phase flow was evaluated by changing the enclosed gas with different thermal conductivity, such as dry air and helium.

Table 2. Experimental conditions

(a) Single phase flow and condensing heat transfer experiments

	Single-phase experiments	Condensation experiments
Inlet temperature [ºC]	60	~64
Inlet quality [-]	-	0.2 to 1.0
Mass flux [kg×m^{-2}×s^{-1}]	200 to 900	200 to 400
Pressure [MPa]	1.77	

(b) Evaluation of the effect of the clearance for leak detection

Material	Thermal conductivity [W×m^{-1}×K^{-1}]
Air	0.025
He	0.15

3. EXPERIMENTAL RESULTS AND DISCUSSION

3.1. Liquid single-phase flow heat transfer experiments

Experimental results of overall heat transfer coefficient of refrigerant single-phase flow are plotted against the refrigerant Reynolds number in Fig. 4. Water overall heat transfer coefficient increased with increasing refrigerant Reynolds number. The overall heat transfer coefficient K in W×m^{-2}×K^{-1} can be expressed by Eq. (1).

$$\frac{1}{K}=\frac{1}{\alpha_{ave,r}}+\frac{1}{\alpha_w} \qquad \text{Eq. (1)}$$

where $\alpha_{ave,r}$ and α_w are refrigerant and water heat transfer coefficient and in W×m^{-2}×K^{-1}. We assumed the refrigerant heat transfer rate $\alpha_{ave,r}$ is proportional to the 0.8th power of refrigerant Reynolds number like turbulent flows in circular channels. Since the water heat transfer coefficient is constant for the same flow rate and inlet temperature, water average heat transfer coefficient was measured by curve fitting by least squares method. The obtained results are shown in Table 3. In this case, thermal resistance of heat transfer wall is included in the heat transfer coefficient of water flows.

Table 3. Estimated results of water and refrigerant single-phase flow heat transfer coefficient

Refrigerant side $\alpha_{ave,r}$ [W×m^{-2}×K^{-1}]	Water side α_w [W×m^{-2}×K^{-1}]
$1.74\times Re^{0.8}$	2.21×10^3

Refrigerant local heat transfer coefficients in single phase flows are shown in Fig. 5. Black line indicates the refrigerant average heat transfer coefficient calculated by Table 3. Also red line shows the heat transfer coefficient calculated by Dittus-Bölter for turbulent flow heat transfer coefficient. These results show single phase heat transfer in quadrilobed tube can be estimated by previous correlation for circular channels. The reason why the local heat transfer coefficient includes thermal resistance of the heat transfer wall. The effect of measure position was a little. The pipe friction factor of refrigerant liquid single-phase flows in the quadrilobed tube is shown in Fig. 6. Theoretical values for laminar flow and those by Blasius equation for turbulent flows are plotted solid lines. Although the measured results were a little bit larger than those by Blasius equation, the results showed the same tendency against Reynolds number.

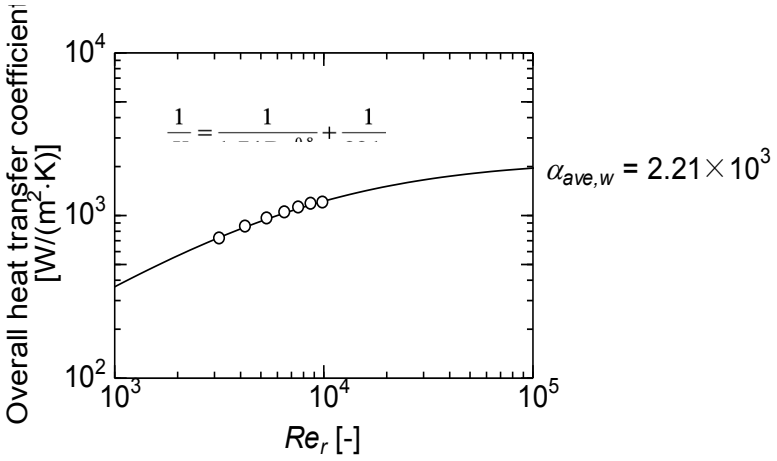

Figure 4: Overall heat transfer coefficient and estimated water heat transfer coefficient

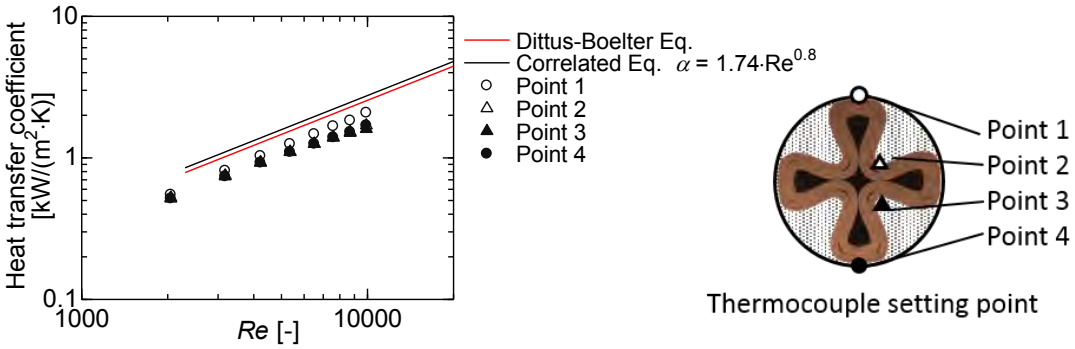

Figure 5: Local heat transfer coefficient of liquid refrigerant flow

Overall heat transfer coefficients for refrigerant liquid single-phase flows with changing the enclosed gas into the clearance for leak detection are plotted against Reynolds number in Fig. 7. Overall heat transfer coefficients using helium gas were larger than those using air, and the difference became larger with increasing Reynolds number, because the total thermal resistance became smaller. If the heat transfer wall is single copper wall, heat transfer rate would be able to be improved.

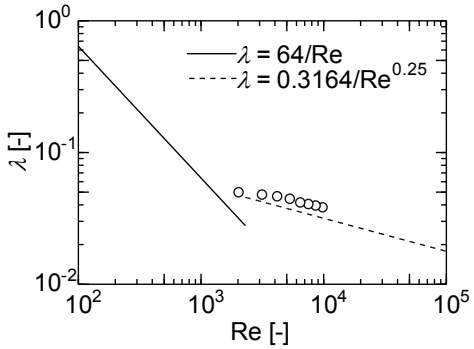

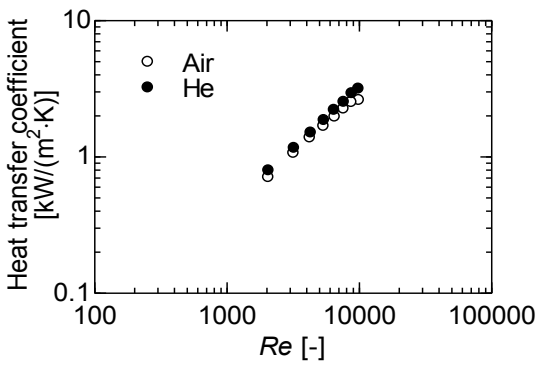

Figure 6: Pipe friction factor of refrigerant liquid single-phase flow

Figure 7: Effect of the clearance for leak detection on overall heat transfer coefficient

3.2. Two-phase flow condensate heat transfer experiment

Local condensing heat transfer coefficients at the center of test section are plotted against wetness in Fig. 8 (a) to (c) for each mass flux, respectively. The same symbols with those in Fig. 5 are used. The thermodynamically equilibrium quality x at the measure point was estimated by Eq. (2).

$$x = \frac{h_{meas} - h_{L,sat}}{h_{G,sat} - h_{L,sat}} \qquad \text{Eq. (2)}$$

where h_{meas} is average specific enthalpy of the inlet and outlet of the test section in J×kg^{-1}, and $h_{G,sat}$ and $h_{L,sat}$ are specific enthalpy of saturation vapor and liquid in J×kg^{-1}, respectively. The position effect on heat transfer coefficients were confirmed in low wetness condition for high refrigerant mass flux. The value at the top convex part was the highest, those at the bottom convex and root part were almost the same, and were higher than those at the top root part. The difference might be caused by maldistribution of refrigerant and water flows, the thermal resistance of the clearance, and condensate liquid film distribution. Local heat transfer coefficients decreased with increasing wetness. The degree of deterioration was larger under higher mass flux condition.

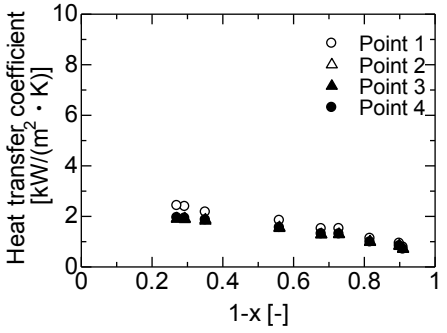

(a) Mass flux G = 200 kg×m^{-2}×s^{-1}

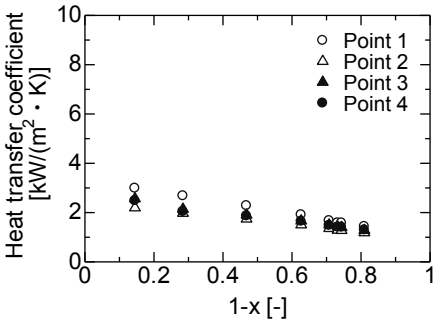

(b) Mass flux G = 300 kg×m^{-2}×s^{-1}

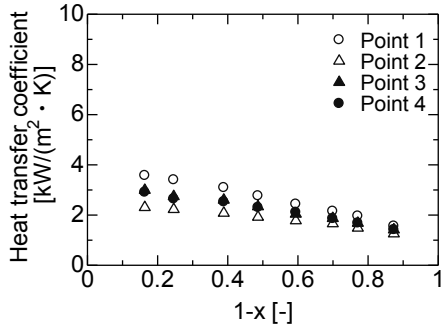

(c) Mass flux G = 400 kg×m^{-2}×s^{-1}

Figure 8: Local heat transfer coefficient of refrigerant condensing flows including the thermal resistance through the heat transfer wall

The overall heat transfer coefficients in condensing experiments are plotted against wetness in Fig. 9. Since thermal resistance in water flow and heat transfer wall could be estimated to be constant, the decrease with increasing refrigerant wetness was caused by deterioration in condensing heat transfer coefficient. Average heat transfer coefficients of condensing flows are shown in Fig. 10. While those for G= 300 kg×m^{-2}×s^{-1} became lower than those for 400 kg×m^{-2}×s^{-1}, the difference between G = 300 and 200 kg×m^{-2}×s^{-1} was a little. The deterioration in condensing heat transfer coefficients was suppressed under lower mass flux condition.

Measured data of differential pressure through the test section are shown in Fig. 11. The values are pressure difference between the static pressure ports at the inlet and outlet of the test section as shown in Fig. 1, therefore the values included the acceleration loss due to the phase change. The pressure loss decreased with increasing wetness for each mass flux, due to deceleration of liquid

flow. Although the effect of mass flux on condensing heat transfer coefficient was a little, especially under the lower mass flux condition, differential pressure quite increased with increasing mass flux. The larger differential pressure might be caused by maldistribution of refrigerant flow. Large amount of vapor might be flowing through the core channel along the center axis, because thermal resistance from water is larger than leaf channels.

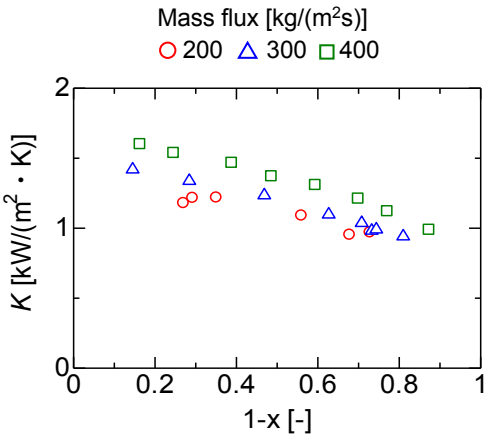

Figure 9: Overall heat transfer coefficient in condensing experiments

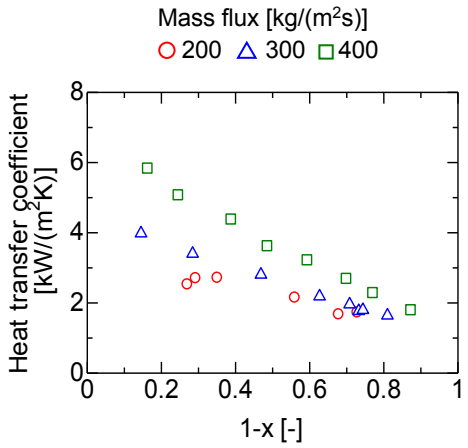

Figure 10: Average heat transfer coefficient of condensing refrigerant flow

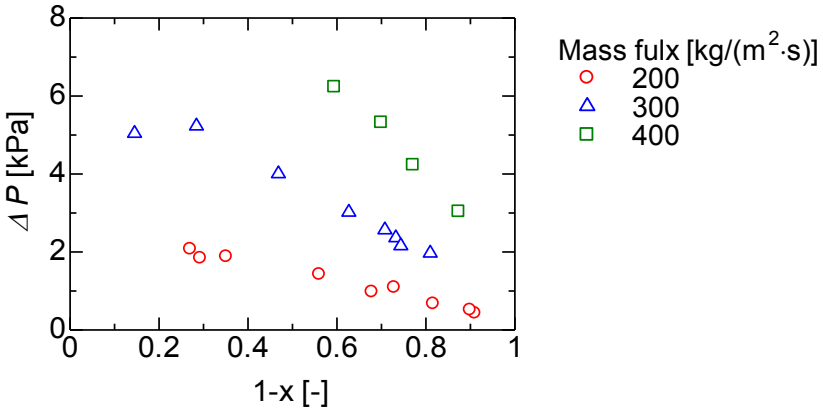

Figure 11: Pressure drop of condensing refrigerant flow

Various heat transfer prediction models taking account of the size and configuration of channels, thermophysical properties of refrigerant and refrigerant flow conditions have been proposed. Prediction correlation equation for condensing heat transfer coefficient in rectangular microchannel proposed by Jige et al. (2012) was applied and compared to the experimental results. Nusselt numbers are plotted with calculated results in Fig. 12. Calculated results were agreed well with the experimental results, especially under the lower mass flux conditions less than 300 kg×m^{-2}×s^{-1}. For G= 400 kg×m^{-2}×s^{-1}, the difference becomes larger with decreasing wetness. It can be said surface tension effect is well taken into account in Jige's model.

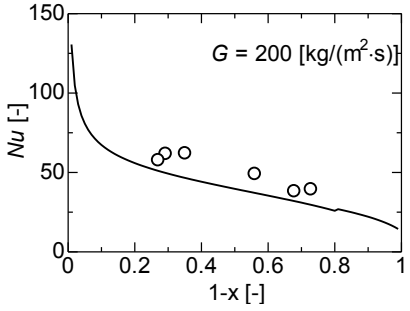

(a) Mass flux 200 kg×m^{-2}×s^{-1}

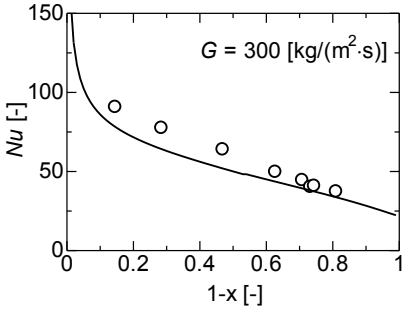

(b) Mass flux 300 kg×m^{-2}×s^{-1}

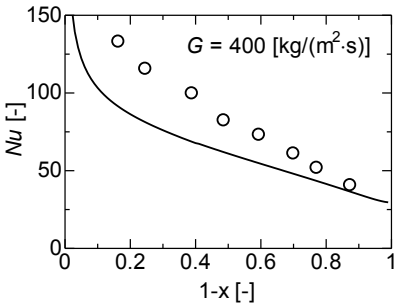

(c) Mass flux 400 kg×m^{-2}×s^{-1}

Figure 12: Comparison of experimental results of Nusselt number of condensing heat transfer with those of calculated results by Jige's correlation equation.

4. CONCLUSIONS

Condensing heat transfer characteristics in a horizontal quadrilobed tube with double heat transfer wall for leak detection was experimentally investigated using R134a as the refrigerant. The deterioration of the heat transfer coefficient was suppressed under medium wetness condition in the lower mass flux conditions less than 300 kg×m^{-2}×s^{-1} due to the effect of the surface tension. However, the pressure loss quite increased due to the maldistribution of the refrigerant flow. The improvement of heat transfer coefficient couldn't be seen in the high mass flux conditions because the inertia force was dominant. The effect of the clearance for the leak detection increased with decreasing thermal resistance. The fraction to total thermal resistance was up to 10.4 %.

ACKNOWLEDGEMENTS

The authors sincerely thank Mr. Taihei Kawaguchi who was a graduate student of those days of the Kobe University for his experimental cooperation. This study is financially supported by Noritz Corp. (5 Minamifutami, Futami-cho, Akashi-shi, Hyogo, Japan)

NOMENCLATURE

h	specific enthalpy (kJ×kg^{-1})	subscript	
m	mass flow rate (kg×s^{-1})	*r*	refrigerant
K	overall heat transfer coefficient (kW×m^{-2}×K^{-1})	*ave*	average
Re	Reynolds number (-)	*meas*	measurement
G	mass flux (kg×m^{-2}×s^{-1})		
Nu	Nusselt number (-)	*w*	water
α	Heat transfer rate (kW×m^{-2}×K^{-1})	*G*	Gas phase
λ	pipe friction factor (-)	*L*	Liquid phase
x	vapor quality (-)	*sat*	Saturated condition

REFERENCES

Del Col, D., Bortolin, S., Cavallini, A., Matkovic M., 2011. Effect of cross sectional shape during condensation in a single square minichannel. Int. J. Heat Mass Transfer 54. 3909-3920.

Jige, D., Inoue, N., Koyama, S., 2016, Condensation of refrigerants in a multiport tube with rectangular minichannels, I. J. Refrigeration, 67, 202-213.

Jige, D., Koyama, S., 2012, Condensation of HFC and HFO Refrigerants in Horizontal Mini-Channels : Prediction Model of Heat transfer in Rectangular Channels, Trans. of JSRAE, 29(4), 421-432. (in Japanese)

Koyama, S., Kuwahara, K., Nakashita, K., Yamamoto, K., 2003. An experimental study on condensation of refrigerant R134a in a multi-port extruded tube, Int. J. Refrigeration 24(4), 425-432.

Wang, H.S., Rose, J. W., 2006. Film condensation in horizontal microchannels: Effect of channel shape. Int. J. Thermal Sciences. 45, 1205-1212.

Wang, H.S., Rose, J. W., 2011. Theory of heat transfer during condensation in microchannels, Int. J. Heat Mass Transfer 54, 2525-2534.

Manuscript ID: 909
DOI: 10.18462/iir.icr.2019.0909

Air-water two-phase flow distribution in a manifold having four indoor-unit connections of a VRF system

Seongkwan HAM, Siyoung CHOI, Ji Hwan JEONG*

School of mechanical engineering, Pusan national university, 2,
Busandaehak-ro 63beon-gil, Geumjeong-gu, Busan, 46241, Republic of Korea
*: Corresponding Author, E-mail: jihwan@pusan.ac.kr

ABSTRACT

In case of a Variable refrigerant flow(VRF) system, the refrigerant is supplied from one outdoor unit to a number of indoor units through manifold-shaped distributors. As the height difference between the distributors increases, the refrigerant may enter the distributor in two-phase state due to the pressure drop. Therefore, this study experimentally investigated the flow distribution characteristics in a distributor with four branches using air-water as a working fluid. Most of the literature deals only with the case where the working fluid is supplied from one inlet. However, for a VRF system depending on the mode of the indoor unit, the working fluid is supplied from both the inlet and branch. Therefore, the characteristics of two-phase flow distribution were investigated through three experimental cases considered in the flow arrangements varied by operation mode of the indoor unit. The experimental data of the two-phase flow distribution were obtained by varying void fraction, mass flow rate, and downstream flow resistance in the branch for each case. The unevenness of the distribution was suggested by the difference of liquid fraction where the liquid was most distributed and where it was least distributed.
Keywords: Distribution, Two-phase flow, Air-water, Parallel flow.

1. INTRODUCTION

Variable refrigerant flow(VRF) system air conditioner is a system that allows cooling and heating in an individual space by connecting several indoor units to one outdoor unit. In the VRF system air conditioner the refrigerant is supplied to several indoor units through a refrigerant distributor. The refrigerant flow in the refrigerant distributor is shown in Fig. 1. The refrigerant distributor consists of a liquid pipe, a high-pressure gas pipe, and a low-pressure gas pipe. These are manifold shaped and are connected to the indoor units in the respective air conditioning spaces. When the indoor unit is in the cooling mode, the liquid refrigerant in the liquid pipe is distributed to each indoor unit, and after heat exchange in the indoor unit, the refrigerant in gaseous state flows to the low-pressure gas pipe. When the indoor unit is in the heating mode, the gas refrigerant in the high-pressure gas pipe is distributed to the indoor unit, where it transitions into the liquid state after heat exchange, and flows to the liquid pipe. The condensed refrigerant is again distributed to the cooling mode indoor unit. The distribution in the liquid pipe should consider not only the fluid supplied from the inlet but also the condensed fluid coming from the branch tube. The refrigerant distributor can be connected to the indoor unit as well as to other refrigerant distributors. This flow arrangement is different from the distribution in a common manifold where refrigerant is supplied from only inlet. As the height difference between the refrigerant distributors becomes larger, not only the pressure drop in the long pipe, but static pressure difference increases as well. As a result, the two-phase refrigerant can be supplied due to the pressure difference between refrigerant distributors. When the two-phase refrigerant flows into the distributor, some problem in maldistribution occurs. Many studies related to two-phase flow maldistribution have been conducted in parallel-flow mini channel heat exchangers. Draio et al. (2013) summarized the factors affecting the two-phase flow distribution. The factors affecting the distribution are divided into geometrical factors, fluid properties, and operating conditions. Vist and Pettersen (2004) experimentally investigated the distribution tendency according to varying the geometrical factor (diameter of header) and operating conditions (quality, mass flow rate). Kim and Han (2008) also experimentally investigated the distribution tendency according to varying the geometrical factor (intrusion depth) and operating conditions (quality, mass flux).

Experimental results showed that geometrical factors and flow conditions affect the two-phase flow distribution in manifolds. The geometry of the refrigerant distributor differs from the conventional parallel heat exchanger. It has a double pipe heat exchanger inserted at the center of the header for subcooling. It is difficult to find the previous research related to the two-phase flow distribution that reflects the geometry and flow arrangement of the refrigerant distributor. Therefore, the characteristics of two-phase flow distribution were investigated through experiments reflecting flow arrangements and the geometry with a double pipe inserted at the center of the header. The experimental cases considered in the flow arrangements varied by operation mode of the indoor unit. There are three experimental cases as shown in Fig. 2. In the first case, only air-water is supplied from the inlet. In the second case, air-water is supplied to the inlet, and the liquid is supplied from the branch closest to the inlet. In the third case, air-water is supplied to the inlet, and the liquid is supplied from the farthest branch. The experimental data of the two-phase flow distribution were obtained by varying void fraction, mass flow rate, and downstream flow resistance on branch for each case. The unevenness of the distribution was suggested by the difference of liquid fraction where the liquid was most distributed and where it was least distributed.

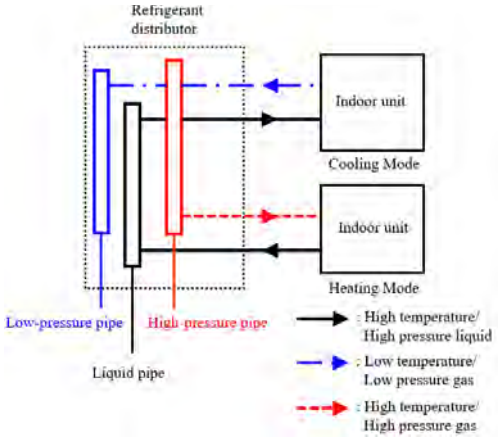

Figure 1: Refrigerant flow in distributor

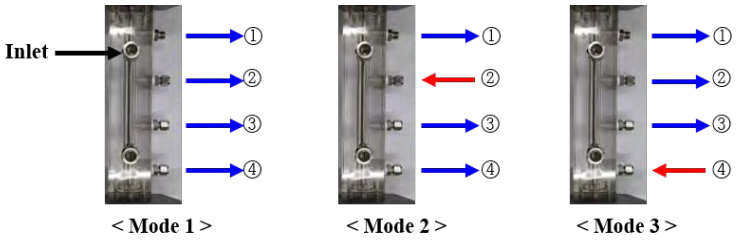

Figure 2: Experimental modes

2. EXPERIMENTAL APPARATUS

The test section was made of acrylic glass for flow visualization with same scale as the liquid pipe of the refrigerant distributor and is shown in Fig. 3. A stainless steel tube is inserted at the center of the header for simulating a double pipe heat exchanger. The inlet of the header is perpendicular to the header and is located between the first branch tube and second branch tube. Schematic diagram of the experimental apparatus is shown in Fig. 4. In order to measure the flow rate of four branches using one magnetic flow meter, flow measurement section was made as shown in Fig. 4. Experimental apparatus is shown in Fig. 5. The path that circulates inside the system without measuring the flow rate is referred as path 1, and the path that bypasses working fluid to measure the flow rate is referred as path 2. When the flow path changes from path 1 to path 2 to measure the flow rate, the flow resistance of the flow path is changed. If the flow resistance of the flow path is different, the flow rate which is distributed to each branch tube is different. To prevent it, the differential pressure is measured from the inlet of the header to just before bypassing. The two-phase pressure drop is a function of flow rate and quality. Therefore, differential pressure was maintained the same by controlling the valve in bypass line (path 2). During the test, pressure

fluctuation occurred due to the characteristic of two-phase flow. Therefore, the boundary of fluctuation was recorded after the observation until it was stable when the fluid flowed to path 1. As fluid flowed into path 2, the valve attached in path 2 was adjusted so that the fluctuation of the differential pressure had the same boundary. A separator was needed to measure the flow rate of the gas and liquids distributed into the branch tube. When the two-phase fluid is separated by density difference, the flow rate should be measured while maintaining a constant water level in the separator. The differential pressure was measured so that the water level in the separator was known. The electric signal (4~20mA) of the differential pressure gauge was transmitted to the inverter of the pump, and the rotation speed of the pump was controlled by feedback control to maintain a constant water level in the separator. The liquid flow rate was measured by the magnetic flow meter after passing through the separator. The gas flow rate was measured by a mass flow meter (MFM). Despite feedback control, there was a fluctuation in the measured flow rate. As the amount of gas phase increased, the fluctuation increased by up to ±20% of average value. To minimize the effect of fluctuations, data were taken more than 10 minutes after the system was at steady state. Experimental uncertainties are listed in Table 1. To maintain the similarity of the experiment with the actual system in the case of the liquid phase, the flow rate of water equal to the Reynolds number of the refrigerant was set as the experimental condition. Mode 2 and 3 assume that the flow rate of the water supplied from the branch tube to the header is about 1/4 of the total flow rate. In the case of two-phase flow, it has different flow characteristics depending on the flow pattern. To maintain similarities to the flow of two-phase refrigerant and the air-water, the void fraction which is associated with the flow pattern was kept the same. When the quality of the refrigerant was between 0 and 0.1, the void fraction was calculated assuming a slip ratio (S) of 1. Eq. (1) is an expression representing the definition of S and can be summarized as a function of the flow quality and the void fraction.

$$S = \frac{U_g}{U_l} = \frac{\dot{m}_g/(\rho_g A_g)}{\dot{m}_l/(\rho_l A_l)} = \left(\frac{x}{1-x}\right)\left(\frac{\rho_l}{\rho_g}\right)\left(\frac{1-\alpha}{\alpha}\right) \quad \text{Eq. (1)}$$

When air-water was supplied, mass flow rate was controlled. By rearranging Eq. (1), it is possible to calculate flow quality of air-water.

$$x = \frac{1}{\left(\frac{\rho_l}{\rho_g}\right)\left(\frac{1-\alpha}{\alpha}\right)\left(\frac{1}{S}\right)+1} \quad \text{Eq. (2)}$$

It is assumed that S=1. The temperature of the water and the air was obtained by using the supplied temperature value and the pressure was arbitrarily assumed. Then, ρ_g and ρ_l were obtained using the above values. All properties were obtained using REFPROP, version 9.1. Using the calculated flow quality, the mass flow rate of liquid and gas were obtained. Pressure at the inlet of test section in the actual flow was measured. ρ_g and ρ_l were obtained by re-entering the measured pressure value and corrected air and water mass flow rate. Repeating this process to find the mass flow rate of the air and water at which the input pressure and the actually measured pressure were equal. A needle valve was installed to investigate the distribution tendency according to the change of the flow resistance of the branch tube. The flow resistance of the valve is expressed using the flow coefficient. The flow coefficient is expressed by Eq. (3).

$$C_v = \frac{5}{12} \cdot Q \cdot \sqrt{\frac{SG}{\Delta P}} \quad \text{Eq. (3)}$$

The openness of the valve was adjusted so that the flow coefficient was 1.61, 1.31, 1.07, 0.64.

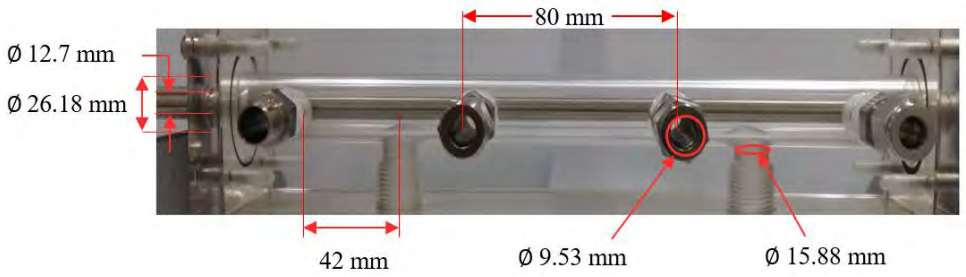

Figure 3: Test section

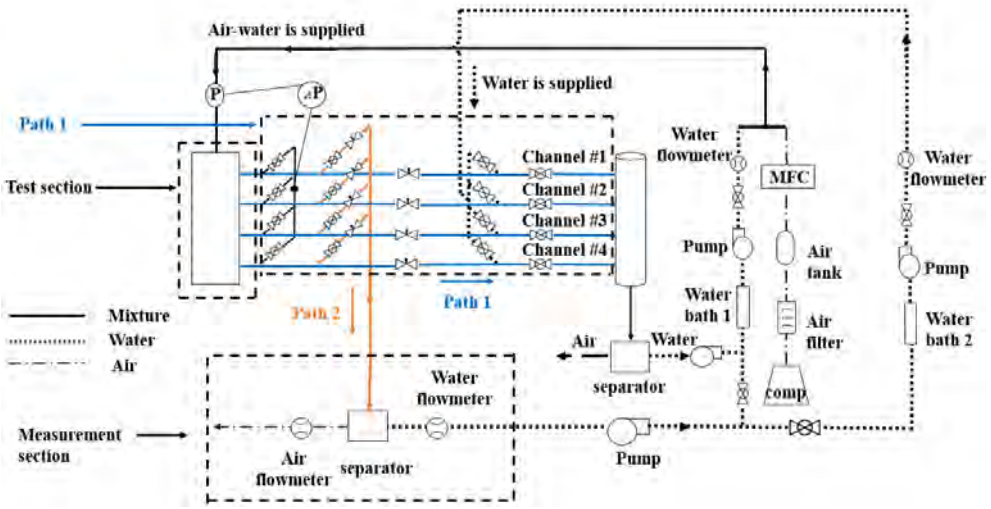

Figure 4: Schematic diagram of the experimental apparatus

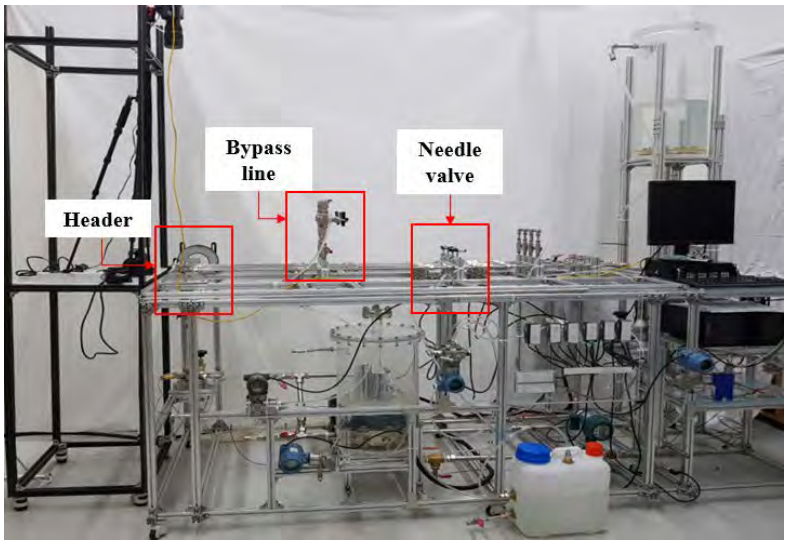

Figure 5: Photograph of the experimental apparatus

Table 1. Experimental uncertainties

Measured parameter	Uncertainty
Differential pressure	±0.055% of span
Water flow meter	±0.35% of reading
Air flow meter	±1% of full scale

3. RESULT AND DISCUSSION

3.1. Configuration of Flow and Effect of Void Fraction

Two-phase flow was recorded at 2000 frames per second and the flow images of various modes are shown in Fig. 6. The fluid supplied at the inlet swirled along the inserted stainless steel tube as if it was competing with each other. When the void fraction was small, dispersed bubbly flow was observed, but as the void fraction increased, Taylor bubbles were observed. As the fluid passes the branch tube inserted in header, a vortex occurred at the wake and the velocity of the bubble decreases. It coalesced with the bubbles coming from the upstream. Mode 1 is the case where two-phase (air-water) flow is supplied only at the header inlet. As Azzorpardi and Whalley (1982) reported, the gas phase which has relatively small momentum was better distributed than liquid phase to the branch tube in the T-junction. Therefore, most of the gas phase was already distributed before reaching the rear part of the header. After the liquid phase was already distributed to the front part of the header, the drag force of the liquid phase became smaller. The bubble stagnation occurred

due to the reduction of drag force and the liquid phase flowing backward from the end portion. This phenomenon was more visible at the last branch, far from the inlet. The stagnant bubbles combine to form larger bubbles and a rotating flow was formed along the stainless steel tube. The total mass flow rate was 0.26 kg/s, and the flow coefficient (C_v) of the needle valve in each branch tube is fixed at 1.61. The larger the void fraction at a constant mass flow rate, the faster the average velocity of the working fluid and the greater the momentum. As a result, more liquid phase reached the rear part of the header. In addition to the momentum difference, physically the differential pressure from the header inlet to the header outlet must be the same for any branch tube. Therefore, the gas phase was distributed less in the branch tube where much of the liquid phase was distributed. Mode 2 is the case where only two-phase (air-water) flow was supplied at the header inlet and the water entered from the branch closest to the inlet. The liquid phase supplied at the branch closest to the inlet acts as flow resistance and prevents the gas phase from flowing to the rear part of the header. The gas phase slowed down and coalesced to form larger bubbles. Because of the same reason as in mode 1, air stagnation occurred at the end portion of the header. The larger the void fraction at a constant mass flow rate, the faster the average velocity of the working fluid and the greater the momentum. As the momentum of the fluid supplied from the inlet became larger, the liquid phase supplied from the branch tube was distributed at the rear end of the header. Mode 3 is the case where two-phase (water-air) flow is supplied at the header inlet and the water entered from the branch farthest to the inlet. Similar to mode 2, the liquid phase supplied at the branch farthest to the inlet acted as flow resistance and prevented the gas phase from flowing to the rear part of the header. As the momentum of the fluid supplied from the inlet became larger, more liquid phase supplied from the branch tube was distributed to the next branch tube. The distribution unevenness due to the variation of the void fraction is shown in Table 2 as the maximum difference of the liquid fraction between the branch tubes.

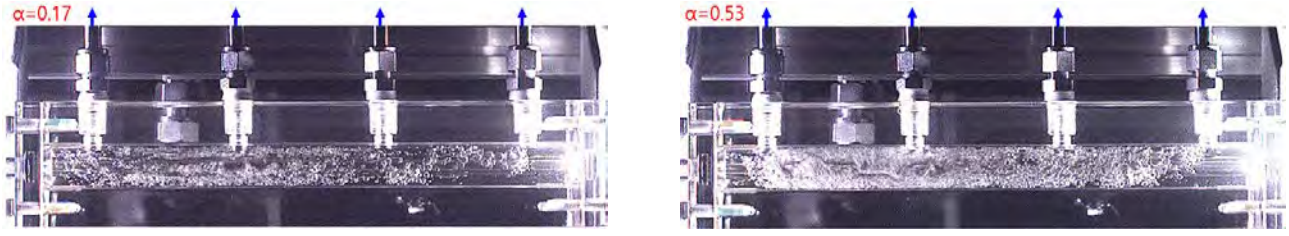

(a) Flow configuration of mode 1

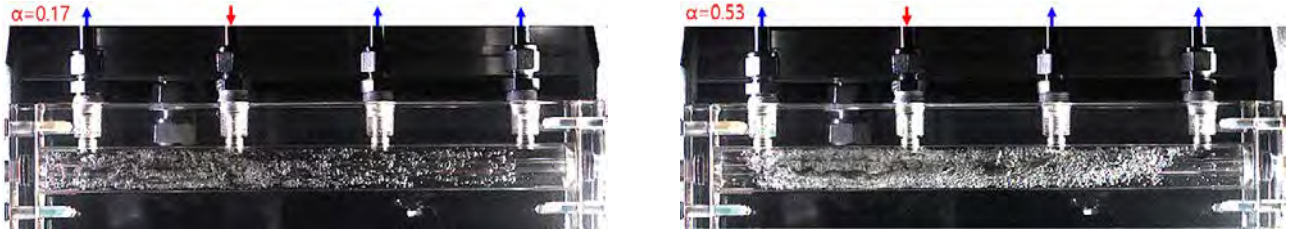

(b) Flow configuration of mode 2

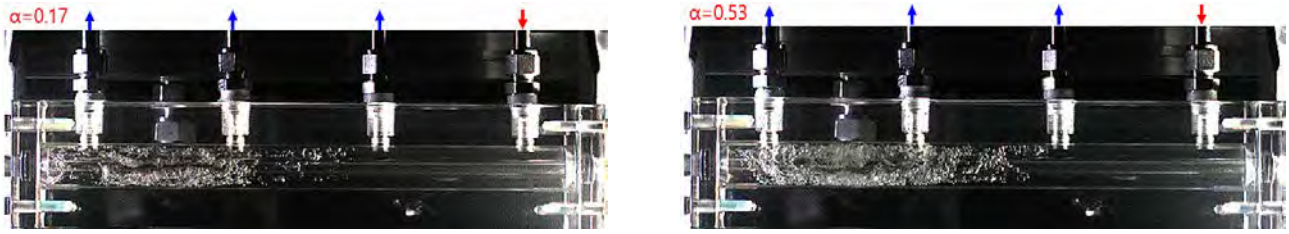

(c) Flow configuration of mode 3

Figure 6: Flow configuration

Table 2. Maximum difference in the liquid fraction between channels due to the variation of void fraction

	Single phase	Two phase ($\alpha = 0.17$)	Two phase ($\alpha = 0.53$)
Mode 1	2 %	1 %	8 %
Mode 2	1 %	5 %	10 %
Mode 3	1 %	5 %	12 %

3.2. Effect of Mass Flow Rate

The void fraction was 0.53, and the flow coefficient (C_v) of the needle valve attached to each branch tube was fixed at 1.61 and the total mass flow rate was varied as 0.16, 0.21, 0.26 kg/s. By decreasing the total mass flow rate, the momentum of the liquid phase decreased and the drag force became weaker. The momentum of the fluid flowing backward at the end portion of the header was also decreased. Therefore, the distribution of gas phase in the first branch was increased. When the gas phase was much distributed, the liquid phase was less distributed, because the differential pressure from the header inlet to the header outlet must be the same for any branch tube. Mode 2 and 3 are experiments in which the water supplied from the branch tube is assumed to be 1/4 of the total mass flow rate. By decreasing the total mass flow, the momentum difference between the two-phase supplied from the inlet and the water supplied from the branch tube decreased. Therefore, the flow resistance of the liquid phase coming from the branch tube increased. Also, in the case of mode 2, the gas phase was much distributed to the first branch due to the flow resistance effect. Conversely, the liquid phase was less distributed to the first branch. In the case of mode 3, the water supplied from the fourth branch was more distributed to the second branch than the third branch by decreasing the momentum difference. The distribution unevenness due to the variation of the mass flow rate is shown in Table 3 as the maximum difference of the liquid fraction between the branch tubes.

Table 3. Maximum difference in the liquid fraction between channels due to the variation of mass flow rate

	Two phase ($\dot{m}_{tot} = 0.16kg/s$)	Two phase ($\dot{m}_{tot} = 0.26kg/s$)
Mode 1	8 %	8 %
Mode 2	11 %	10 %
Mode 3	9 %	12 %

3.3. Effect of Flow Resistance

The Electronic expansion valve (EEV) is installed between the indoor unit and the refrigerant distributor. It is used to control the flow rate of refrigerant distributed to the indoor unit. When a single phase is distributed in a manifold. The manifold shape and pressure drop across the branch tube dominate the distribution. However, in two-phase flow distribution, not only the flow distribution but also the phase separation occurs. Because it is not known how the pressure drop in the branch tube affects phase separation, it is difficult to predict the two-phase flow distribution using only the information of the pressure drop in the branch tube. Therefore, it is necessary to investigate how the change in the flow resistance of the branch tube affects the two-phase flow distribution. The distribution tendency according to the change of the flow resistance is investigated by controlling the flow resistance of the branch tube where the liquid phase was most distributed. In order to investigate how the reduced liquid phase is distributed to the other branch tubes when the flow resistance of the branch tube where the liquid phase was most distributed is increased, the total mass flow rate was fixed at 0.26 kg/s, the void fraction was fixed at 0.53, and the flow coefficient (C_v) of the needle valve was changed to 1.61, 1.31, 1.07, and 0.64. The change of the flow rate due to the change of the flow resistance was not much. Also the liquid fraction in the branch tube, where the most gas phase is distributed showed little change. In the experiment of Watanabe et al. (1996), the pressure drop from the branch tube had a greater effect on the distribution when the branch tubes were heated. However, there was almost no variation of the distribution tendency according to the changes in heating load on branch tube in the experiment of Vist and Pettersen (2004). This is because the pressure drop due to the heat load of the branch has small effect on the distribution in the header. In the present study, the variation of the downstream flow resistance in the branch tube was not sufficient to affect the distribution in the header.

3.4. Comparison of Experimental Data and Previous Correlations

Experimental correlations that can predict the phase distribution have been developed in previous studies, and can be divided into two types. The first type requires iterative calculations both for the upstream and the downstream. The second type is a correlation which can be easily used only by upstream information. In this study, the liquid fraction acquired from experiment was compared with prediction data calculated by the second type correlations. The inlet of the test section used in the experiment was connected in perpendicular to the header between the first branch tube and second

branch tube. To apply the correlation developed in the previous research, it was assumed that the header inlet was parallel to the header. Only the experimental results of mode 1, which is the same as the existing flow arrangement, were compared with the predicted data by correlations. The form of the correlation that predicts the distribution is expressed as a function of the gas Reynolds number. Using the correlation, the flow rate distributed to the branch tube from upstream of the branch tube was obtained, and the remaining flow was calculated to be the upstream of the other branch tube. The graph comparing the calculation results with the experimental data is shown in Fig. 7. As a result, it can be seen that conventional experimental correlations did not satisfactorily predict the two-phase flow distribution in the refrigerant distributor. The reason for this difference is because the geometry and flow conditions of present and previous studies were different. In the present study, the header was inserted with a stainless steel tube simulating a double-pipe heat exchanger, and the position of the inlet was also different from the previous studies. In addition, the header/branch diameter ratio (D/d) in present study (D/d = 1.8), which affects the two-phase flow distribution, was significantly different from previous studies (D/d = 12.9 for Byun and Kim, and D/d = 29.7 for Zou and Hrnjak). Previous studies were conducted with a mass flux of less than 300kg/m^2s, while the present study was conducted in the range of 1000~2000kg/m^2s. There was also difference in flow patterns. In the present study, mainly dispersed bubbly flow was observed. Previous studies observed churn flow and separated flow (stratified flow or annular flow). According to Azzorpardi and Whalley (1982), the phase distributions in the annular flow were strongly influenced by the velocity of the gas phase. Refrigerant correlations that predict distribution in many manifolds have also been developed in the separated flow (stratified flow, annular flow). In the separated flow, information of the upstream gas phase is important because there is friction at the interface between liquid phase and gas phase, but other parameter should be considered in other flow pattern. Also, In the present study, air-water is used as a working fluid. However, previous study used refrigerant R134a, and R410A. According to Zou and Hrnjak (2014), the flow property affects the results of two-phase distribution in the same experimental conditions. Therefore, the working fluid should be considered while comparing with the experimental correlation. In addition, since the VRF system has different distances from the refrigerant distributor to the individual spaces, the flow resistance of downstream is different. In order to predict the refrigerant distribution in the VRF system, it is necessary to develop a simulation that reflects not only upstream but downstream information as well.

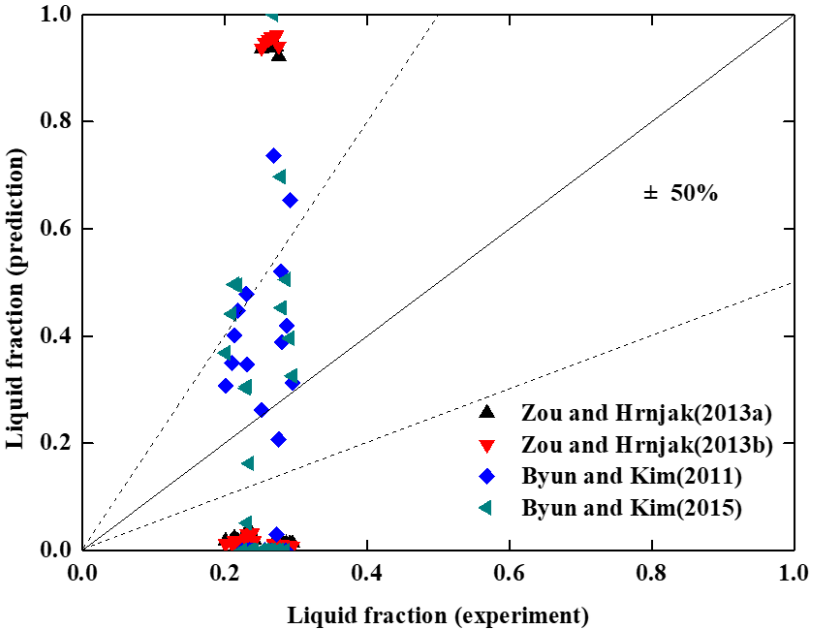

Figure 7: Comparison of experimental data with correlations

4. CONCLUSION

The present study experimentally investigated the two-phase flow distribution characteristics in a refrigerant distributor of a VRF system using air-water. The test section was made of acrylic for flow visualization and the flow was recorded at 2000 frames per second. Experiments were conducted in horizontal header. The experiment was divided into three experimental modes according to the flow

arrangement. Two-phase (air-water) flow distribution characteristics were investigated according to variation of void fraction, mass flow rate, and flow resistance. The two-phase flow maldistribution increased as the void fraction increased. As the void fraction increased, a large amount of gas phase was distributed in the branch tube near the inlet, and the liquid phase was distributed in the rear part of the header. As the mass flow rate decreased, the drag force of the liquid also decreased, so that the gas phase was distributed to the front part of the header. The change of the void fraction influenced the distribution more than the change of mass flow rate in the experimental range. Conventional experimental correlation could not predict the two-phase flow distribution in the refrigerant distributor due to differences in geometry and flow condition between the present study and previous studies.

NOMENCLATURE

Q	Volumetric flow rate ($m^3 s^{-1}$)	Re	Reynolds number
$\dot{m}$	Mass flow rate ($kg\ s^{-1}$)	S	Slip ratio
ΔP	Pressure drop (pa)	D	Hydraulic inner diameter of header (m)
C_v	Flow coefficient	d	Inner diameter of branch tube (m)
SG	Specific gravity	U	Velocity ($m\ s^{-1}$)
Greek letters			
α	Void fraction	ρ	Density ($kg\ m^{-3}$)
Subscripts			
g	Gas	l	Liquid
us	Upstream	br	Branch
i	I-th channel	tot	Total

REFERENCES

B.J. Azzopardi, P. B. Whalley, 1982. The effect of flow patterns on two-phase flow in a T junction. Int. J. Multiphase Flow 8(5), 491-507.

M. Watanabe, M. Katsuta, K. Nagata, 1995. Two-phase flow distribution in multi-pass tube modeling serpentine type evaporator, ASME/JSME Thermal Eng. Conf. 2, 35-42.

S. Vist, J. Pettersen, 2004. Two-Phase Flow Distribution in Compact Heat Exchanger Manifolds, Exp. Thermal Fluid Sci. 28, 209-215.

N.-H. Kim, S.-P. Han, 2008. Distribution of air-water annular flow in a header of a parallel flow heat exchanger. Int. J. Heat Mass Transfer 51, 977-992.

Dario, E., Tadrist, L., Passos, J., 2013. Review on two-phase flow distribution in parallel channels with macro and micro hydraulic diameters: Main results, analyses, trends. Appl. Thermal Eng. 59, 316-335.

Y. Zou, P. Hrnjak, 2013. Experiment and visualization on R134a upward flow in the vertical header of microchannel heat exchanger and its effect on distribution, Int. J. Int. J. Heat Mass Transfer 62, 2196-2208.

Y. Zou, P. Hrnjak, 2013. Refrigerant distribution in the vertical header of the micro-channel heat exchanger-Measurement and visualization of R410A flow. Int. J. Refrig. 36, 2196-2208.

Y. Zou, P. Hrnjak, 2014. Effects of fluid properties on two-phase flow and refrigerant distribution in the vertical header of a reversible microchannel heat exchanger – Comparing R345fa, R134a, R410A, and R32. Appl. Thermal Eng. 70, 966-976

H.-W. Byun, N.-H. Kim, 2011. Refrigerant distribution a parallel flow heat exchanger having vertical header and heated horizontal tubes, Exp. Thermal Fluid Sci. 35, 920-932.

H.-W. Byun, N.-H. Kim, 2015. Two-phase refrigerant distribution in an intermediate header of a parallel flow minichannel heat exchanger, Int. J. Refrig. 59, 14-28.

Manuscript ID: 952
DOI: 10.18462/iir.icr.2019.0952

Flow Boiling Heat Transfer and Pressure Drop for R134a and RL32H in Multi-channel Tube

Xiu-Wei YIN[a,b], Wen WANG [a]*, Vikas PATNAIK [b], Jin-Sheng ZHOU [b], Xiang-Chao HUANG [b], Raymond RITE [b]

[a] Institute of Refrigerant and Cryogenics, School of Mechanical Engineering, Shanghai Jiao Tong University, Shanghai 200240, China, wenwang@sjtu.edu.cn
[b] Engineering&Technology Center, Ingersoll Rand, Tyler, TX 75709, US, xwyin@trane.com

ABSTRACT

Experimental data for pure R134a, R134a and lubricant RL32H mixture heat transfer and pressure drop in flow boiling for micro-channels is presented and analyzed. Inlet vapor quality of test section was changing at 0.2, 0.4, 0.6 to 0.8 with 0.2 quality increase along the tube, mass fraction of lubricant was changing from 0%, 0.65%, 2.2% to 3.7%, and mass velocity of the pure and mixture varied from 391 to 652 kg s^{-1} m^{-2}. The experiments have been conducted for average saturation temperature at 5 ºC to 20 ºC. Literatures on two-phase flow boiling heat transfer and pressure drop for both pure refrigerant and refrigerant with lubricant are carefully reviewed, popular published correlations are used in this study to evaluate test data. New two-phase flow boiling heat transfer and pressure drop correlations for pure refrigerant and mixtures inside multi micro-channel tube are proposed.
Key words: R134a, RL32H, Flow Boiling, Heat Transfer, Pressure Drop, Multi-channel, Refrigerant and Lubricant Mixture, Micro-Channel.

1. INTRODUCTION

The implementation of microchannel heat exchangers has increased in automotive and building air conditioning systems during the past few decades, due to smaller volume, compact structure, smaller heat resistance, and smaller refrigerant charge inventory.
Due to the flow distribution among the paralleled channels, the investigation on single mini/micro-channel tube could be very different with multi-channels. The flow inside single channel is more stable and uniform compare to that of multi-channels. Issues like flow instabilities, back flow, possibly early or delayed critical heat flux, were often found in multichannel study only (Bergles and Kandlikar, 2005; Agostini et al., 2008, Zhu et al. 2017, Wen et al. 2018). Therefore, the study in multi micro-channels is necessary to understand the thermal dynamics of flow boiling with interactions among parallel channels. There are many researcher worked in flow boiling pressure drop testing in multiple parallel channels for pure refrigerant (Webb, 1996; Monroe, 2003, Newell et al., 2003; Qu and Mudawa, 2003; Lee and Mudawa, 2005; Cavallini et al., 2005; Zhang et al. 2017). There are also many flow boiling pressure drop correlations have been developed (Tran, 1999; Lee and Lee, 2001; Li and Wu, 2011). Recently, Kim and Mudawar (2013) did a critical review on most of the test data and correlations, and then proposed a universal pressure drop model for pure refrigerant in mini/micro channels.
In most of current vapor compression processes, the presence of oil is intrinsic and unavoidable since the oil is required to lubricate the moving part of compressor. The amount of lubricant oil circulating in the system can vary from 0.1% to 8.0% by weight in the refrigerant flow. In the open literature, a large amount of papers are involved in the discussion of impaction of oil in refrigerant system for macro tubes (Shen and Groll, 2003; Pierre et al., 1964; Choi et al., 2001; Hu et al., 2008; Schlager et al., 1990; Eckels et al., 1994). Although the present of the oil might result in improve heat transfer at a certain oil concentration and deteriorate heat transfer at most of conditions, however, the pressure drop results showed an increased when oil becomes part of the flow fluid.

R134a is widely used in air conditioning systems in both chiller and unitary units. RL32H is an ISO VG 32 synthetic polyol ester lubricant formulated specifically for air-conditioning compressors. A test facility was set up to evaluate heat transfer and pressure drop for both flow boiling and condensation inside mini and micro-channels. In this study, the flow boiling tests were conduct for pure R134a and R134a with RL32H in multiple rectangular micro-channels. With comparing with existing correlations, new correlations are recommended for both pure refrigerant and refrigerant lubricant mixture to match the test data.

2. EXPERIMENTAL APPARATUS

2.1. Flow Loop

The test facility used in this study shows in Fig. 1. The cycle drives by a refrigerant gear pump, subcooled liquid refrigerant flows through the pre-heater to heat up to a desired quality, and then flows through evaporator with certain quality rise, then enters post-heater to become superheated gas before entering pre-condenser. The refrigerant is pre-cooled to a desired quality at entering of condenser with constant temperature cooling water or glycol bath, refrigerant is then cooled down to subcooled liquid flow by post-condenser before a Coriolis mass flow meter and the pump. The pre-heater, evaporator and post-heater are electronic heaters, and the pre-condenser, condenser and post-condensers are constant temperature water/glycol bath.

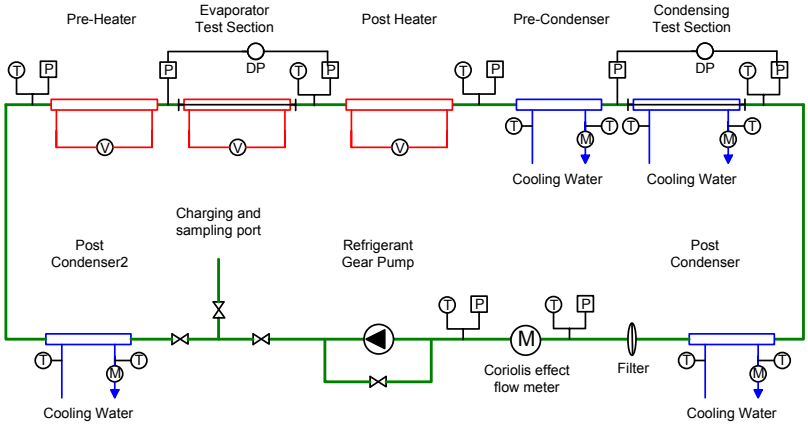

Figure 1: Schematic of test loop

2.2. Test Section

Fig. 2 shows the detail of the transient connection which is well shaped from round tube to micro-channel tubes. The purpose of the design is to improve the universal flow of the two-phase and control the flow pattern. The pressure drop of the transient connection is also conducted separately in the data reduction process.

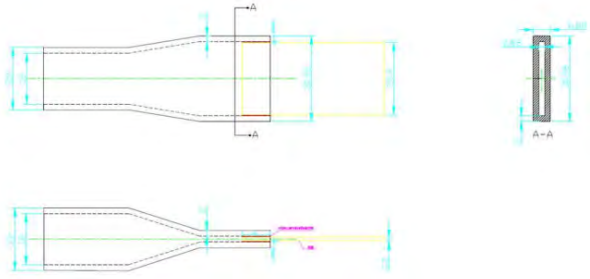

Figure 2: Transient tube

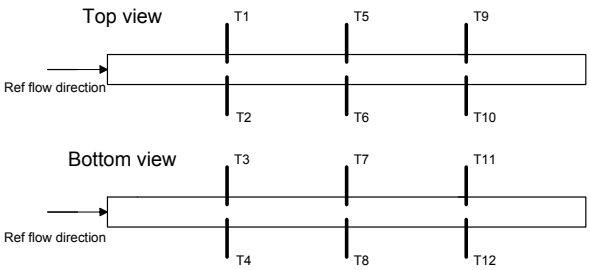

Figure 3: RTD location on flat tube

There are twelve platinum resistance thermometers attached on the surface of the each test tube as showing in Fig. 3, with six of them on the top of the tube and six on the bottom side. They are used to identify surface temperature for heat transfer coefficient reduction, and help to observe the distribution of refrigerant flow inside multi-channels. The accuracy of the platinum resistance

thermometers is better than ±0.1 °C. Fig. 4 shows the cross section detail geometry information of the 26 ports micro-channel with around 0.6 mm as channel width and 0.7mm as channel height. The length of the test section is 0.43 m.

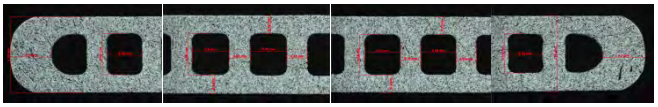

Figure 4: Enlarged image of the multiple channel rectangular tube

2.3. Operating Conditions and Measurement Accuracy

Heat loss from the overall boiling section including pre-heater, evaporator and post-heater is estimated less than 3.0%, as well as condensing section. The accuracy of the flow rate was better than 0.5%. The saturated evaporating temperature is within 5 °C to 20 °C, the mass flux of the fluid is within 100 to 600 kg m^{-2} s^{-1}, the entering quality of the evaporating test section changes from 0.2, 0.4, 0.6 to 0.8 with a changing quality of 0.2 across test section.
Oil concentrations is measured in the mixture used sample analysis refer to ASHRAE 41.4. The sample is taken between pump and pre-heater that the liquid flow through. The pipe from pre-heater until evaporator is straight pipe and a turbulent was installed ahead of evaporator to pre-mix the refrigerant and lubricant mixture to improve the flow at the entrance of the microchannel tube. The oil mass concentration in the mixture was controlled to be 0.43%, 2.84% and 4.20%.
The pressure sensors are installed in the system before and after each heaters and condensers with error less than ±0.5%, five platinum resistance thermometers type of temperature sensors are inserted into the tubes at: entering pre-heater, leaving evaporator, leaving pre-heater (entering pre-condenser), entering mass flow meter and entering gear pump, the error is smaller than ±0.1°C. The other temperature sensors are attached to the surface of the pipes with error smaller than ±0.5°C. There is also a pressure difference transducer installed across evaporator and condenser section with error smaller than ±206 Pa.

3. DATA REDUCTION PROCESS

3.1. Heat Transfer Coefficient

Refer to single tube with rectangular multiple channel, the heat transfer coefficients for pure refrigerant and refrigerant with lubricant are listed in equations below.

$$\alpha_{r,tp} = \frac{q\times((N+1)\times(W_{ch}+W_s)-W_{ch})}{(T_w-T_{sat})\times(2\eta(N+1)H_{ch}+NW_{ch})} \quad \text{Eq. (1)}$$

$$\alpha_{r,o,tp} = \frac{q\times((N+1)\times(W_{ch}+W_s)-W_{ch})}{(T_w-T_{bub,r,o})\times(2\eta(N+1)H_{ch}+NW_{ch})} \quad \text{Eq. (2)}$$

Where q is heat flux in W/m^2. N is number of channels. W_{ch} is single channel width in meter. W_s is single channel wall thickness in meter. H_{ch} is single channel height in meter. η is channel inner fin efficiency. Tw is inner wall temperature of test channel in °C. T_{sat} is saturated refrigerant temperature flow inside channel in °C. $T_{bub,r,o}$ is the bulb temperature of refrigerant and lubricant mixture in °C. The fin efficiency is calculated in following: $\eta = \frac{tanh(mH_{ch})}{mH_{ch}}$, $m = \sqrt{\frac{2\alpha_{r,tp}}{k_s W_s}}$. Where K_s is conductivity of aluminum channel in W/(m*K). The mixture properties are calculated in following: $T_{bub,r,o} = \frac{A}{\ln(P_{sat})-B}$, $A = a_0 + a_1\omega_{loc} + a_2\omega_{loc}^3 + a_3\omega_{loc}^5 + a_4\omega_{loc}^7$, $B = b_0 + b_1\omega_{loc} + b_2\omega_{loc}^3 + b_3\omega_{loc}^5 + b_4\omega_{loc}^7$. Where P_{sat} is the mixture saturated pressure in kPa, ω_{loc} is local lubricant mass concentration in mixture and calculated in equation 3. For different refrigerant and lubricant mixtures, a_1- a_4, b_1- b_4 would not change. When no lubricant exist in refrigerant, properties is calculated by pure

refrigerant for a_0 and b_0. For R134a and lubricant mixture, a_0 - a_4 is -2665.2，182.52，-724.21，3868.0，-5268.9, and b_0- b_4 are 8.53257，-0.72212，2.3914，-13.779，17.066。

$$\omega_{loc} = \frac{\omega_{no}}{1-x} \quad \text{Eq. (3)}$$

Where *x* is gas refrigerant mass fraction in mixture, ω_{no} is lubricant mass fraction in mixture, which can get from chemical test.

$$T_w = T_{wi} \approx T_{wo} \quad \text{Eq. (4)}$$

Where T_{w} is tube wall temperature in °C, T_{wi} is inner tube wall temperature in °C and T_{wo} is outer tube wall temperature in °C. Since the tube wall thickness is 0.3mm, the inner and outer tube-wall temperature difference is less than 0.05 °C based on thermal conductivity calculation, which is smaller than the measurement accuracy of RTDs. Therefore, this study consider the temperature at inner wall is very close to outer wall of the average of test temperature from point 5, 6, 7, 8.

3.2. Pressure Drop

Total pressure drop is presented as equation 5, which including pressure drops: constriction from transfer connection to microchannel tube ΔP_c, expansion from microchannel tube to transfer connection ΔP_e, channel ΔP_{ch}, entering and leaving transfer connection ΔP_{restr}.

$$\Delta P_T = \Delta P_e + \Delta p_{restr} + \Delta P_{ch} + \Delta P_c \quad \text{Eq. (5)}$$

$$\Delta P_c = \frac{G^2 v_f}{2}\left[\left(\frac{1}{C_c}-1\right)^2 + (1-\sigma_c^2)\right](1+\frac{v_{fg}x_{in}}{v_f}) \quad \text{Eq. (6)}$$

$$\Delta P_e = G^2 v_f \sigma_c(\sigma_c - 1)(1+\frac{\mathrm{v_{fg}x_{out}}}{\mathrm{v_f}}) \quad \text{Eq. (7)}$$

Where, the coefficient C_c comes from the study of Geiger, and mass flux G_{ch} is calculated based on homogenies flow in each channel presented as: $C_c = 1 - \frac{1-\sigma_c}{2.08(1-\sigma_c)+0.5371}$, $G_{ch} = \frac{M}{NW_{ch}H_{ch}}$.

The pressure drop in microchannel including friction part and acceleration part:

$$\Delta P_{\mathrm{ch}} = \Delta P_{tp,f} + \Delta P_{tp,a} \quad \text{Eq. (8)}$$

Where, used Lockhart and Martinelli (1949) void fraction model to calculate acceleration part:

$$\Delta P_{tp,a} = G^2 v_f\left[\frac{x_{e,out}^2}{\alpha_{out}}\left(\frac{v_g}{v_f}\right) + \frac{(1-x_{out})^2}{1-\alpha_{out}} - 1\right] \quad \text{Eq. (9)}$$

$$\alpha_{out} = \frac{1}{1+\frac{1-x_{out}}{x_{out}}\left(\frac{v_f}{v_g}\right)^{2/3}} \quad \text{Eq. (10)}$$

Applying water into transaction header for testing, use Churchill (1978) pressure drop correlation to calculate single phase part, and the rest pressure drop is presented as: $\Delta p_{restr} = \frac{G^2}{2\rho_l}\zeta$.

4. TEST DATA ALALYSIS

4.1. Test Points on Flow Pattern Map

The test points for both pure R134a and R134a with RL32H are plotted on two different flow pattern maps on Figs. 5 and 6, which shows most of the points fall into annual flow region. The present of lubricant in refrigerant contribute to move the flow pattern towards annual flow.

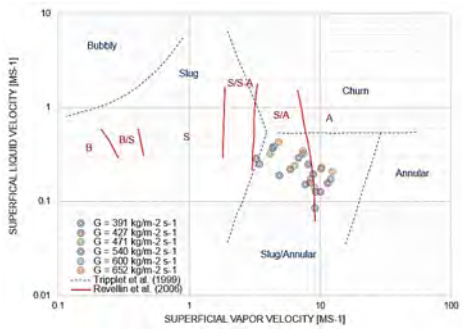

a) Triplett et al. (1990) and Revellin et al. (2006)

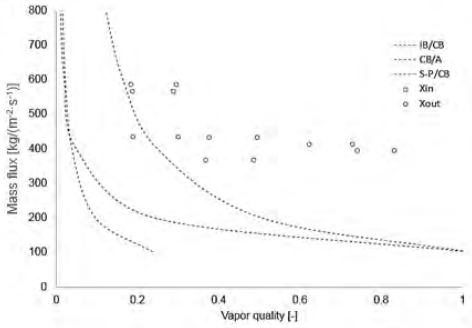

b) Ong and Thome (2010a)

Figure 5: Test point of pure R134a on flow pattern maps

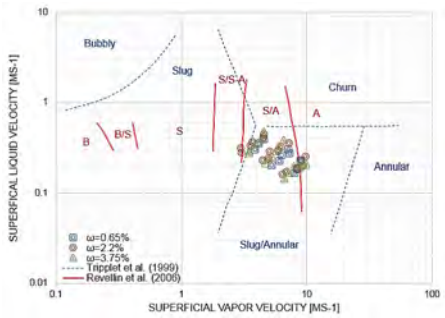

a) Triplett et al. (1990) and Revellin et al. (2006)

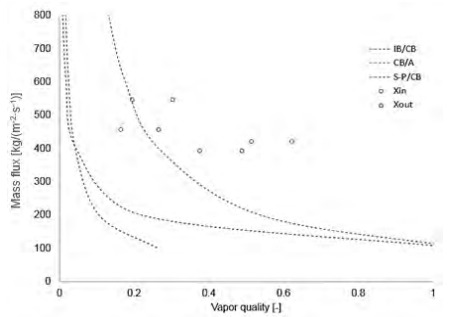

b) Ong and Thome (2010a)

Figure 6: Test point of R134a and RL32H on flow pattern maps

4.2. Frictional Pressure Drop for Pure R134a

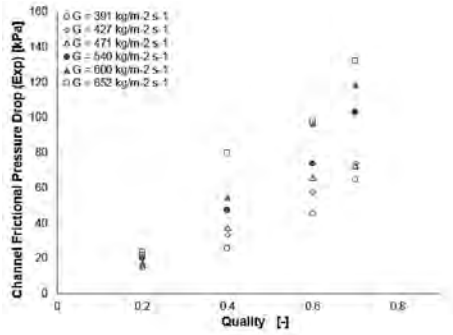

a) Channel frictional pressure drop

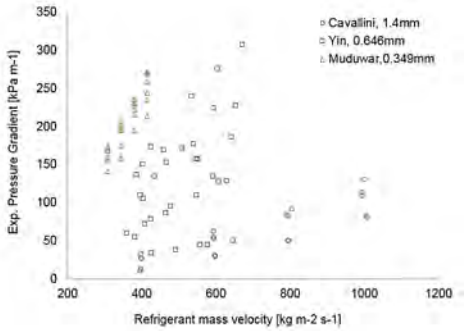

b) Compare with literatures

Figure 7: Frictional pressure drop test points for pure R134a

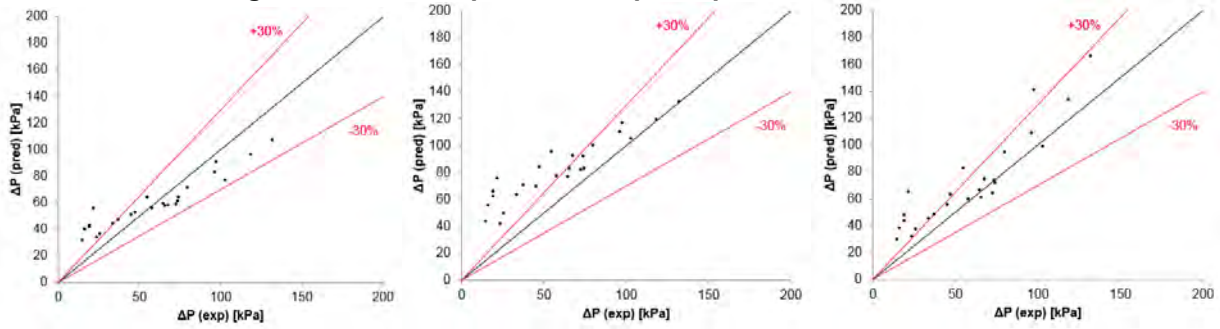

a) Friedel(1979) b) Lockhard and Martinelli(1949) c) Li and Wu(2011)

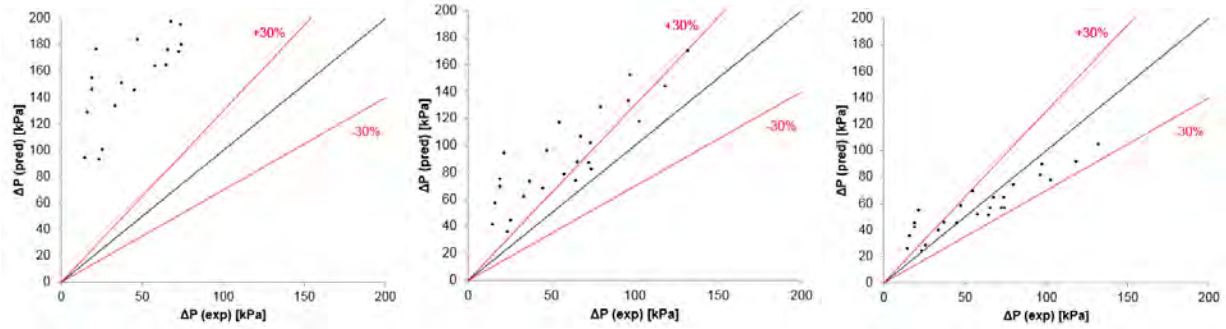

d) Tran(1999) **e) Lee and Lee(2001)** **f) Kim and Mudawar(2013)**

Figure 8: Friction factor correlation comparison

The microchannel friction pressure drop changing with entering quality and mass flux is presented in Fig. 7-a, and comparison with other published literature data in different channel size in Figure 7-b shows the test data is in a reasonable range.

Apply different two-phase friction factor correlations in the test condition and compare with test data are presented in Fig. 8, where Kim and Mudawar (2013) correlation shows the best match with test data and the author decided to use the same correlation for pure R134a in this study.

4.3. Heat Transfer for Pure R134a

The pure R134a heat transfer coefficients changing with entering quality at different mass flux and heat flux level are presented in Figure 9. Based on the test data, the dry-out happens very clearly after entering quality higher than 0.6.



a) Different mass flux **b) Different heat flux**

Figure 9: Heat Transfer Coefficients change with mass and heat flux

4.3.1 Dry-out for Pure R134a

There are several researchers studied the boundary of dry-ut in the two-phase refrigerant flow. Via applying these correlations to the test conditions in this study and compare to test data, the results are presented in Figure 10 as following:

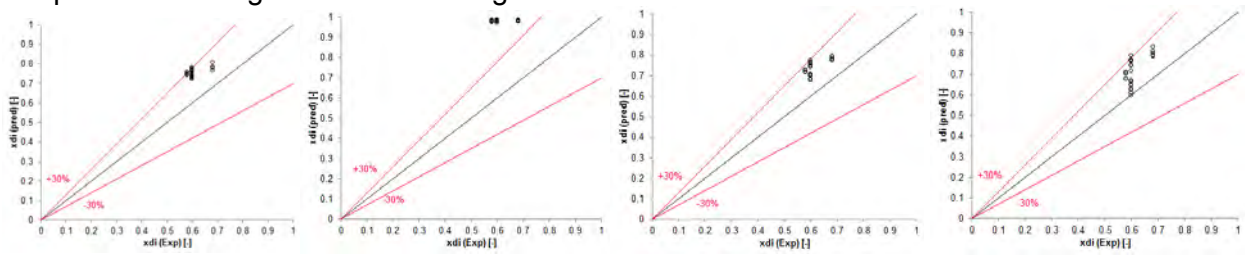

a) Kim and Mudawar(2013) **b) Du(2010)** **c) Cheng(2008)** **d) Cheng(2006)**

Figure 10: Correlation Comparison for Dry-out Conditions

Due to the poor alignment with existing dry-out prediction correlations, the author proposed a new correlation to address test points as equation 11 and 12 below. Here, h_M is mist flow heat transfer coefficient and equal to gas phase heat transfer coefficient.

$$x_{di} = 0.50exp\left[0.52 - 0.67We_g^{0.17}Fr_{g,Mori}^{0.348}\left(\frac{\rho_g}{\rho_f}\right)^{0.25}\left(\frac{q''_H}{q''_{crit}}\right)^{0.70}\right] \quad \text{Eq. (11)}$$

$$h_{dryout} = h_{tp}(x_{di}) - \frac{x - x_{di}}{1.0 - x_{di}}(h_{tp}(x_{di}) - h_M) \quad \text{Eq. (12)}$$

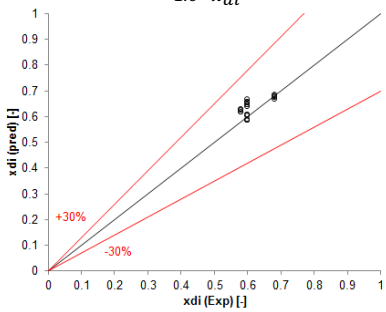

Figure 11: New Proposed Correlation for Dry-out Conditions

4.3.2 Heat Transfer Correlation for Pre dry-out conditions for Pure R134a

For pre dry-out condition, there are many researchers proposed correlations for heat transfer, apply them to current test data and present comparison results in Figure 12. There is no well match with current test data, so the author proposed a new correlation in equation 13-15.

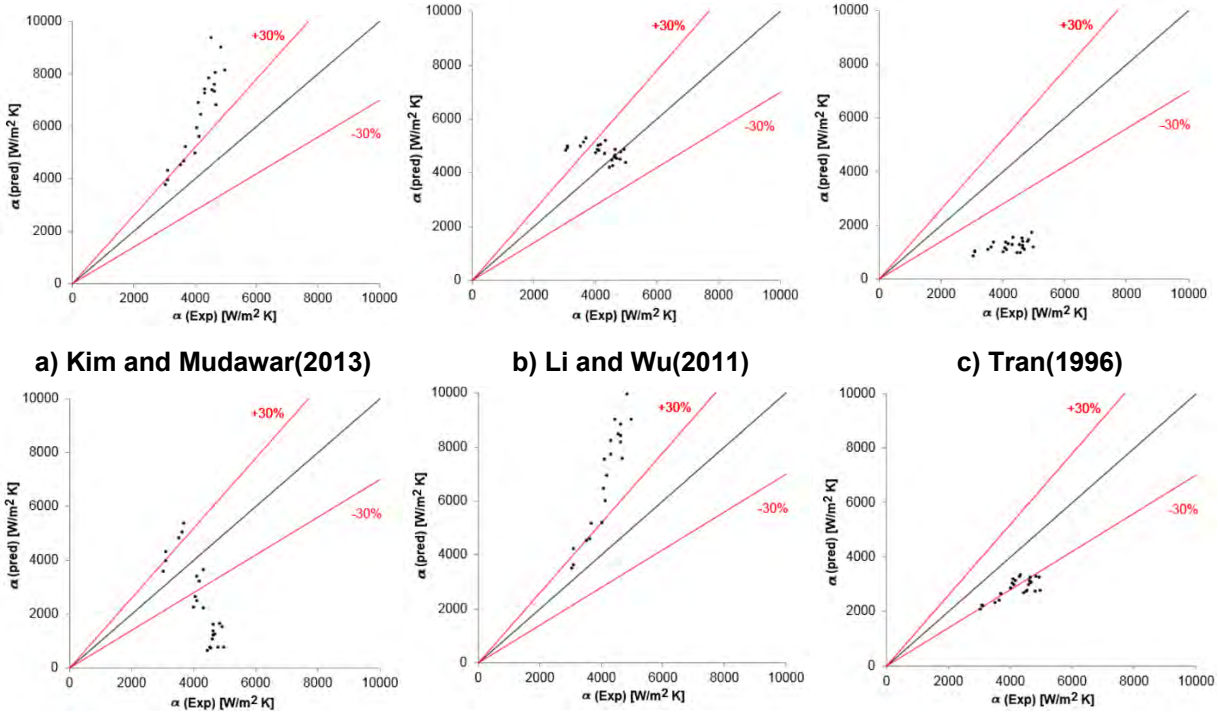

a) Kim and Mudawar(2013) **b) Li and Wu(2011)** **c) Tran(1996)**

d) Warrier(2002) **e) Oh and Son(2011)** **f) Bertsch(2009)**

Figure 12: Heat Transfer Correlation Comparison for Pre Dry-out Conditions

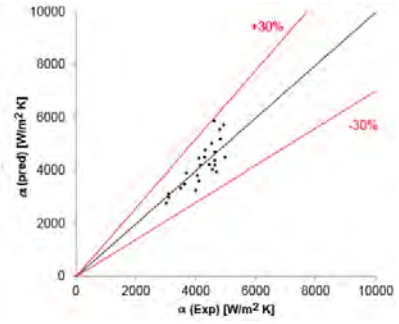

Figure 13: Proposed Heat Transfer Correlation Prediction Compared with Test Data

$$h_{tp} = (h_{nb}^2 + h_{cb}^2)^{0.5} \quad \text{Eq. (13)}$$

$$h_{nb} = [2500.0(Bo)^{0.70} P_R^{0.38}(1-x)^{-0.51}]\left(0.023 Re_f^{0.8} Pr_f^{0.4} \frac{k_f}{D_h}\right) \quad \text{Eq. (14)}$$

$$h_{cb} = \left[5.2(Bo)^{0.08} We_{fo}^{-0.54} + 2.6\left(\frac{1}{X_{tt}}\right)^{0.85}\left(\frac{\rho_g}{\rho_f}\right)^{0.3}\right]\left(0.023 Re_f^{0.8} Pr_f^{0.4} \frac{k_f}{D_h}\right) \quad \text{Eq. (15)}$$

Where, $\text{Bo} = \frac{q''_H}{Gh_{fg}}, P_R = \frac{P}{P_{crit}}, Re_f = \frac{G(1-x)D_h}{\mu_f}, We_{fo} = \frac{G^2 D_h}{\rho_f \sigma}, X_{tt} = \left(\frac{\mu_f}{\mu_g}\right)^{0.1}\left(\frac{1-x}{x}\right)^{0.9}\left(\frac{\rho_g}{\rho_f}\right)^{0.5}$. The comparison of test data and new correlation is present in Figure 13.

4.4. Channel Frictional Pressure Drop for R134a and RL32H

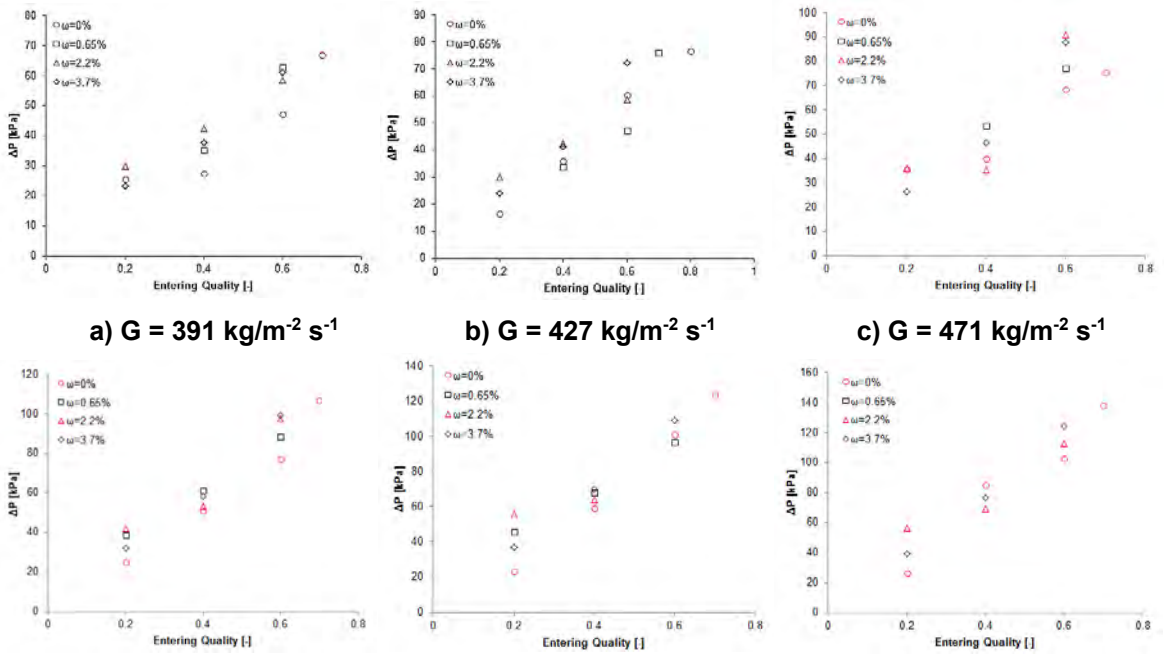

a) G = 391 kg/m^{-2} s^{-1} **b) G = 427 kg/m^{-2} s^{-1}** **c) G = 471 kg/m^{-2} s^{-1}**

d) G = 540 kg/m^{-2} s^{-1} **e) G = 600 kg/m^{-2} s^{-1}** **f) G = 652 kg/m^{-2} s^{-1}**

Figure 14: Channel Pressure Drop Change with Variant Parameters

The author proposed a new frictional pressure drop correlation as presented in Equation 16.

$$\left(\frac{dP}{dz}\right)_F = \left(\frac{dP}{dz}\right)_f \emptyset_f^2 \quad \text{Eq. (16)}$$

Where, $-\left(\frac{dP}{dz}\right)_f = \frac{2f_{f,oil} v_{f,oil} G^2(1-x)^2}{D_h}, -\left(\frac{dP}{dz}\right)_g = \frac{2f_g v_g G^2(1-x)^2}{D_h}, f_k = 16Re_k^{-1}$ for $Re_k < 2000$, $f_k = 0.079Re_k^{-0.25}$ for $2000 \le Re_k < 2000$, $f_k = 0.046Re_k^{-0.2}$ for $Re_k \ge 20000$. For laminar flow in rectangular channel, $f_k Re_k = 24(1 - 1.3553\beta + 1.9467\beta^2 - 1.7012\beta^3 + 0.9564\beta^4 - 0.2537\beta^5)$. Here, subscript k represent pure liquid or gas. $Re_{f,oil} = \frac{G(1-x)D_h}{\mu_{f,oil}}, Re_g = \frac{GxD_h}{\mu_g}, Re_{fo,oil} = \frac{GD_h}{\mu_{f,oil}}, Su_{go} = \frac{\rho_g \sigma D_h}{\mu_g^2}, We_{fo,oil} = \frac{G^2 D_h}{\rho_{f,oil}\sigma_{r,oil}}, Bo = \frac{q''_H}{GH_{fg}}$. The comparison of prediction of correlation and test data is shown in Figure 15.

	$C_{non-boiling}$
$Re_f \ge 2000, Re_g \ge 2000\ (tt)$	$0.39Re_{fo}^{0.03} Su_{go}^{0.10}\left(\frac{\rho_f}{\rho_g}\right)^{0.35}$
$Re_f \ge 2000, Re_g < 2000\ (tv)$	$8.7 \times 10^{-4} Re_{fo}^{0.17} Su_{go}^{0.50}\left(\frac{\rho_f}{\rho_g}\right)^{0.14}$
$Re_f < 2000, Re_g \ge 2000\ (vt)$	$0.0015Re_{fo}^{0.59} Su_{go}^{0.19}\left(\frac{\rho_f}{\rho_g}\right)^{0.36}$
$Re_f < 2000, Re_g < 2000\ (vv)$	$3.9 \times 10^{-5} Re_{fo}^{0.44} Su_{go}^{0.50}\left(\frac{\rho_f}{\rho_g}\right)^{0.48}$

	C
$Re_f \ge 2000$	$C_{non-boiling}[1 + 60We_{fo}^{0.32}\left(Bo\frac{P_H}{P_f}\right)^{0.78}]$
$Re_f < 2000$	$C_{non-boiling}[1 + 530We_{fo}^{0.52}\left(Bo\frac{P_H}{P_f}\right)^{1.09}]$

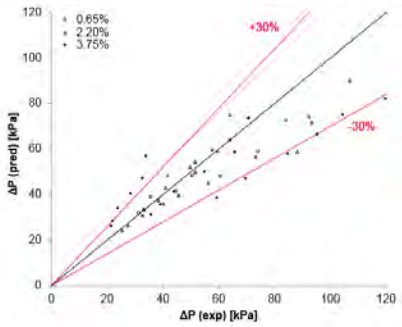

Figure 15: Channel Pressure Drop Correlation Prediction Compare to Test Data

4.5. Heat Transfer for R134a and RL32H

The author proposed a new heat transfer correlation presented in Equation 17-19. And the comparison between prediction from the new correlation and test data is present in Fig. 17.

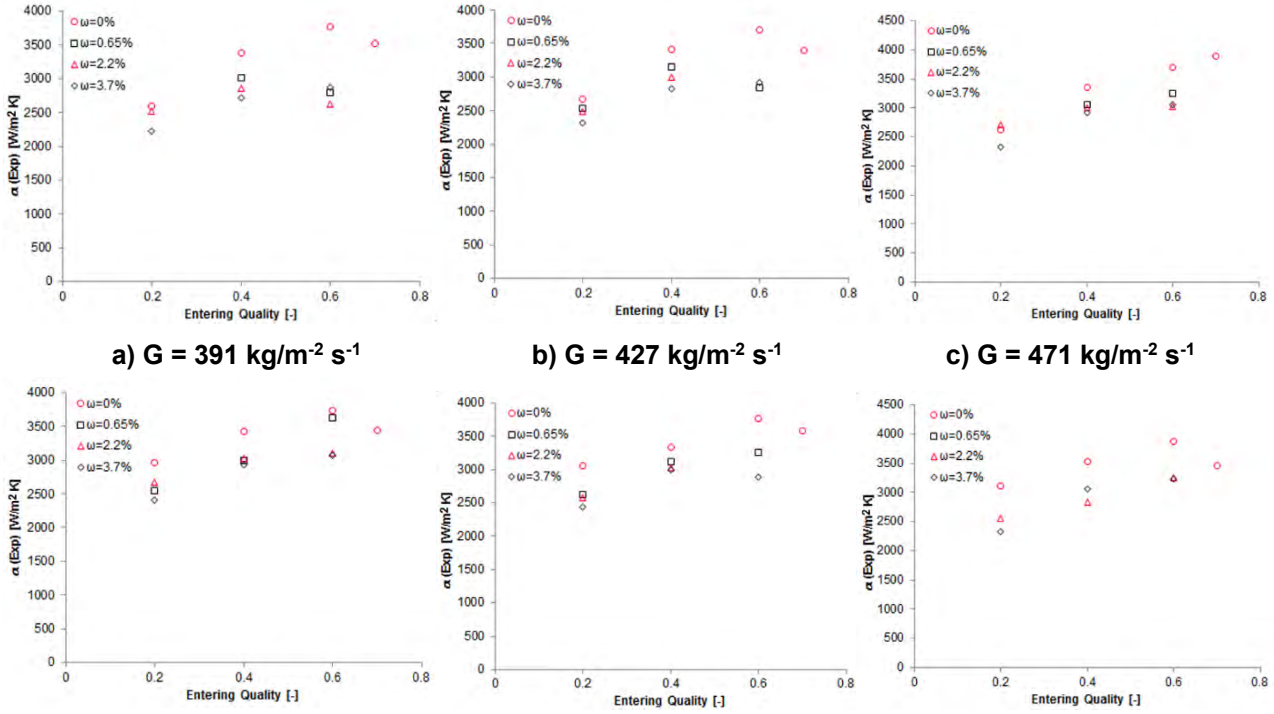

a) G = 391 kg/m^{-2} s^{-1} b) G = 427 kg/m^{-2} s^{-1} c) G = 471 kg/m^{-2} s^{-1}

d) G = 540 kg/m^{-2} s^{-1} e) G = 600 kg/m^{-2} s^{-1} f) G = 652 kg/m^{-2} s^{-1}

Figure 16: Heat Transfer Coefficient Change with Variant Parameters

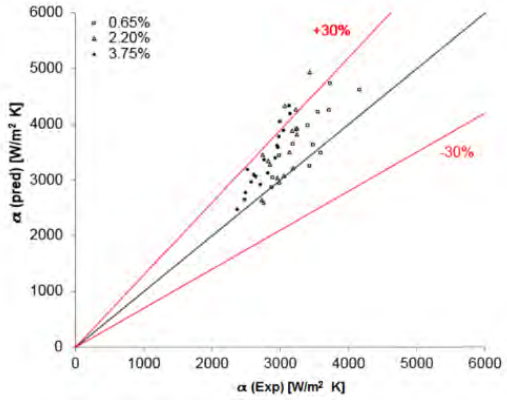

Figure 17: Heat Transfer Correlation Prediction Compare to Test Data

$$h_{tp} = (h_{nb}^2 + h_{cb}^2)^{0.5} \quad \text{Eq. (17)}$$

$$h_{nb} = [2500.0(Bo)^{0.70} P_R^{0.38} (1-x)^{-0.51}] \left(0.023 Re_{f,oil}^{0.8} Pr_f^{0.4} \frac{k_f}{D_h}\right) \quad \text{Eq. (18)}$$

$$h_{cb} = \left[5.2(Bo)^{0.08} We_{fo,oil}^{-0.54} + 2.6 \left(\frac{1}{X_{tt,oil}}\right)^{0.85} \left(\frac{\rho_g}{\rho_f}\right)^{0.3}\right] \left(0.023 Re_{f,oil}^{0.8} Pr_f^{0.4} \frac{k_f}{D_h}\right) \quad \text{Eq. (19)}$$

Here, $\text{Bo} = \frac{q_H^{"}}{G h_{fg}}, P_R = \frac{P}{P_{crit}}, Re_{f,oil} = \frac{G(1-x)D_h}{\mu_{f,oil}}, We_{fo,oil} = \frac{G^2 D_h}{\rho_{f,oil}\sigma_{r,oil}}, X_{tt,oil} = \left(\frac{\mu_{f,oil}}{\mu_g}\right)^{0.1} \left(\frac{1-x}{x}\right)^{0.9} \left(\frac{\rho_g}{\rho_{f,oil}}\right)^{0.5}$.

5. CONCLUSIONS

The author proposed heat transfer correlations for both pure R134a and R134a with RL32H, as well as frictional pressure drop for R134a and RL32H in this study, and the predicted data matches well with test data in this study.

NOMENCLATURE

Parameters:

A	Area, m^2	Q	Heat Transfer, W
Bd	Bond Number	R	Heat Resistance, m^2 K W^{-1}
Bo	Boiling Number	Re	Reynolds Number
C	Lockhart-Martinelli Coefficient，Capacity rate (W K^{-1})	Re_f	Liquid Surface Reynold Number, $\text{Re}_f = \text{G}(1-\text{x})\,\text{D}_h/\mu_f$
C_p	Specific Heat, J kg^{-1} K^{-1}	Re_{fo}	Reynolds Number based on pure liquid property, $\text{Re}_{fo} = \text{G}\,\text{D}_h/\mu_f$
D	Diameter, m	Re_g	Gas Surface Reynolds Number, $\text{Re}_g = \text{Gx}\,\text{D}_h/\mu_g$
Dh	Hydronic diameter, m	S	Split ratio between refrigerant liquid and gas
f	Fanning friction factor	Su	Suratman Number
Ft	Froude Number	T	Temperature, ºC
G	Mass flux, kg m^{-2} s	We	Weber Number
g	Gravity Acceleration, m s^{-2}	x	Quality, Average Quality
h	Specific Enthalpy, kJ kg-1	X	Non-dimensional Coefficient
h_{LG}	Latent heat, kJ kg^{-1}	X_{tt}	Lockhart-Martinelli Coefficent
L	Length, m	α	Heat Transfer Coefficient，W m^{-2} K^{-1}
m	Mass flow rate, kg/s	e	Void Faction Factor
Nconf	Confinement Number	ρ	Density, kg m^{-1}
p	Pressure, Pa	ξ	Refrigerant concentration in mixture，%
p_{sat}	Saturated Pressure, Pa	ζ	Pressure drop coefficient
ΔP	Pressure Drop, Pa	λ	Heat Conductivity, W m^{-2} K^{-1}
$q_H^{"}$	Heat Flux, W m^{-2}	Δ	Difference

Subscript:

a	Air, acceleration	oil	Lubricant, oil
ann	Annual flow	restr	Restriction
c	Constriction	rest	Rest in the system

ch	Channel	s	Slag flow
e	Entrance	strat	Stratified flow
f	Fluid, friction	ref	Refrigerant
g	Gas	tp	Two Phase
gas	Refrigerant gas	tt	Liquid turbulent – Gas turbulent flow
in	Inlet	tv	Liquid turbulent – Gas laminar flow
it	Inlet tube	v	Refrigerant gas
k	Liquid (f) or gas (g)	vo	Refrigerant gas only
l	Leaving, Refrigerant liquid	vap	Vapor Flow Patten
liq	Liquid Flow Patten	vt	Liquid laminar– Gas turbulent flow
lo	Local	vv	Liquid laminar– Gas laminar flow
no	Nominal	w	Wall

REFERENCES

Agostini, B., Thome, J. R., Fabbri, M., Michel, B., Calmi, D., Kloter. U., 2008. High heat flux flow boiling in silicon multi-microchannels – Part I: Heat transfer characteristics of refrigerant R236fa. International Journal of Heat and Mass Transfer 51 (2008) 5400–5414.

Beattie, D.H., Whalley, P.B., 1982. Simple two-phase frictional pressure drop calculation method, International Journal of Multiphase Flow 8 (1982) 83–87.

Bergles, A.E., Kandlikar, S.G., 2005. On the nature of critical heat flux in microchannels, J. Heat Transfer 127 (2005) 101–107.

Bertsch, S.S., Groll, E.A., Garimella, S.V., 2009. A composite heat transfer correlation for saturated flow boiling in small channels[J], Int. J. Heat Mass Transfer, 2009, 52:2110-2118.

Cavallini, A., Col, D.D., Doretti, L., Matkovic, M., Rossetto, L., Zilio, C., 2005. Two-phase frictional pressure gradient of R236ea, R134a and R410A inside multi-port mini-channels, Experimental Thermal and Fluid Science 29 (2005) 861–870.

Cheng, L. , Ribatski, G., Wojtan, L., 2006. New flow boiling heat transfer model and flow pattern map for carbon dioxide evaporating inside horizontal tubes[J], Int. J. Heat Mass Transfer, 2006, 49:4082-4094.

Cheng, L., Ribatski, G., Quibén, J.M., 2008. New prediction methods for CO2 evaporation inside tubes: part I – a two-phase flow pattern map and a flow pattern based phenomenological model for two-phase flow frictional pressure drops [J], Int. J. Heat Mass Transfer, 2008, 51: 111-124.

Choi, J.Y., Kedzierski, M.A., Domanski, P.A., 2001. Generalized pressure drop correlation for evaporation and condensation in smooth and micro-fin tubes, In: Proc. Of IIF-IIR Commision B1, Paderborn, Germany, B4 (2001) 9-16

Collier, J.G., Thome, J.R., 1994. Convective Boiling and Condensation. Third ed., Oxford University Press, New York.

Ducoulombier, M., 2010. Ébullition convective du dioxyde de carbone – étude expérimentale en micro-canal[D], Institut National des Sciences Appliquées (INSA) de Lyon, France.

Eckels, S.J., Doerr, T.M., Pate, M.B., 1998. A comparison of the heat transfer and pressure drop performance of R134a-lubricant mixtures in different diameter smooth tubes and micro-fin tubes, ASHRAE Trans., 104(1A) (1998) 376-386.

Enio, P. F., Chen, L., Thome, J.R., 2009. Flow boiling characteristics and flow pattern visualization of refrigerant/lubricant oil mixture. International journal of refrigeration 32 (2009) 185-202.

Etienne, C-P, Jonathan, O., Bogdan, A. N., Bruno, M., John, R.T., 2011. Two-phase flow of refrigerants in 85 μm-wide multi-microchannels: Part I – Pressure drop. Heat and Fluid Flow 32 (2011) 451-463.

Friedel, L., 1979. Improved friction pressure drop correlations for horizontal and vertical two-phase pipe flow, in: European Two-phase Group Meeting, Ispra, Italy, 1979, Paper E2.

Geiger, G.E., 1964. Sudden contraction losses in single and two-phase flow, Ph.D. Thesis, University of Pittsburgh, PA.

Hu. H., Ding, G., Wei, W., Wang, Z., Wang, K., 2008. Heat transfer characteristics of R410A-oil mixture flow boiling inside a 7mm straight smooth tube. Exp. Therm. Fluid Sci. 32 (3), 857 869.

Incropera, F.P., Dewitt, D.P., 2002. Fundamentals of Heat and Mass Transfer, fifth ed., Wiley, New York.

Kim. S. M., Mudawar. I., 2013. Universal approach to predicting two-phase frictional pressure drop for mini/micro-channel saturated flow boiling, Int. J. of Heat and Mass Transfer 58 (2013) 718-734.

Lee, H.J., Lee, S.Y., 2001. Pressure drop correlations for two-phase flow within horizontal rectangular channels with small heights[J], Int. J. Multiphase Flow, 2001, 27(5):783-796

Lee, J., Mudawar, I., 2005. Two-phase flow in high-heat-flux micro-channel heat sink for refrigeration cooling applications: Part I – pressure drop characteristics, Int. J. Heat Mass Transfer 48 (2005) 928–940.

Li, W., Wu, Z., 2011. Generalized adiabatic pressure drop correlations in evaporative micro/mini channels, Exp. Therm. Fluid Sci. 35 (2011) 866–872.

Lockhart, R. W., Martinelli, R. C., 1949. Proposed Correlation of Data for Isothermal Two-Phase, Two-Component Flow in Pipes, Chemical Engineering Progress, 1949, 45(1):39-48. Churchill, SW., 1977. Friction-factor equation spans all fluid flow regimes. Chem Engng 1977,7:91–2.S.-M.

Monroe, C.A., Newell, T.A., Chato, J.C., 2003. An experimental investigation of pressure drop and heat transfer in internally enhanced aluminum microchannels, Report No. ACRC TR-213, Air Conditioning and Refrigeration Center, University of Illinois at Urbana-Champaign.

Oh, H.K., Son, C.H., 2011. Evaporation flow pattern and heat transfer of R-22 and R-134a in small diameter tubes[J], Int. J. Heat Mass Transfer, 2011, 47:703-717.

Ong, C.L., Thome, J.R. 2011. Macro-to-microchannel transition in two-phase flow: part 1: two phase flow patterns and film thickness measurements[J]. Exp. Therm. Fluid Sci. 2011a, 35: 37-47.

Pierre, B., 1964. Flow resistance with boiling refrigerant-part I, ASHRAE J 6(9) (1964) 58-65.

Qu, W., Mudawar, I., 2003. Measurement and prediction of pressure drop in twophase micro channel heat sinks, Int. J. Heat Mass Transfer 46 (2003) 2737–2753.

Revellin, R., Thome, J.R., 2007. A new type of diabatic flow pattern map for boiling heat transfer in microchannels[J]. J. Micromech. Microeng. 2007a, 17:788-796.

Schlager, L. M., Pate, M.B., Bergles, A.E., 1989. Heat transfer and pressure drop performance of smooth and internally finned tubes with oil and refrigerant 22 mixtures, ASHRAE Trans., 95(2) (1989) 160-169.

Shah, R.K., London, A.L., 1978. Laminar Flow Forced Convection in Ducts: A Source Book of Compact Heat Exchanger Analytical Data, Academic Press, New York, 1978 (Suppl.1).

Shen, B., Groll, E. A., 2005. A Critical Review of the influence of lubricants on the heat transfer and pressure drop of refrigerant, Part I: Lubricant influence on pool and flow boiling. HVAC & R research, 2005, 11,3.
Thome, J.R., 2004. Engineering Data Book III. Wolverine Tube Inc. (Chapters 15 and 16), 2004.
Tran, T., Chyu, M-C., Wambsganss, M., 1999. Two-phase pressure drop of refrigerants during flow boiling insmall channels: an experimental investigation and correlation development[C]. In: Shah RK, editor. Compact heat exchangers and enhancement technology for the process industries. New York: Begell House, 1999:293-302.
Tran, T.N., Chyu, M.C., Wambsganss, M.W., France, D.M., 2000. Two-phase pressure drop of refrigerants during flow boiling in small channels: an experimental investigation and correlation development, Int. J. multiphase Flow 26 (2000) 1739–1754.
Triplett, K.A., Ghiaasiaan, S.M., Abdel-Khalik, S.I., 1999. Gaseliquid two-phase flow in microchannels part I: two-phase flow patterns[J]. Int. J. Multiphase Flow, 1999a, 25:377-394.
Warrier, G.R., Dhir, V.K., Momoda, L.A., 2002. Heat transfer and pressure drop in narrow rectangular channels, Exp. Therm[J]. Fluid Sci., 2002, 26:53-64.
Wen, T., Zhan, H.b., Lu, L., Zhang, D.l., Experimental Investigation and Development of New Correlation for Flow Boiling Heat Transfer in Mini-channel. International Journal of Thermal Sciences. 2018.
Yang, C.R., Webb, R.L., 1996. Friction pressure drop of R-12 in small hydraulic diameter extruded aluminum tubes with and without micro-fins, International Journal of Heat and Mass Transfer 39 (1996) 801–809.
Zhang, B., Wang, Y., Zhang, J.q., Li, Q.L., Experimental research on pressure drop fluctuation of two-phase flow in signle horizontal mini-channels. Exprimental Thermal and Fluid Science. 2017. 160-170.
Zhu, Y., Wu, X.m., Zhao, R. R32 flow boiling in horizontal mini channels: Part II. Flow-pattern based reduction method for heat transfer and pressure drop. International Journal of Heat and Mass Transfer. 2017, 1233-1244.

Manuscript ID: 954
DOI: 10.18462/iir.icr.2019.0954

Experimental investigation on the super-cooling effect of fluids confined in non-metallic vessels using pure water and silicon carbide

Gund SEBASTIAN[(a)], Kauffeld MICHAEL[(a)]

(a) University of Applied Sciences Karlsruhe
Karlsruhe, 76133, Germany, sebastian.gund@hs-karlsruhe.de

ABSTRACT

One of the main challenges of ice slurry application is its production. Research with special focus on energy efficient production of ice slurries leads to the application of the supercooling phenomenon where a liquid is cooled below its freezing point without crystallization in the heat exchanger. The key parameter, that needs to be improved for a high applicability of this technology, is the degree of supercooling. Crystallization theory states, that the interface between a crystallizing fluid and a substrate has great impact on the achievable amount of supercooling. Silicon carbide seems to offer ideal properties as wall material. Pure water is confined in a vessel made of silicon carbide and cooled until crystallization occurs. As reference, the same experiment is done simultaneously with pure water confined in a glass and a copper vessel. The results of this study show the influence of the surface material on the degree of supercooling.
Keywords: ice slurry, supercooling, material, silicon carbide, water.

1. INTRODUCTION

The research on renewable energies is more present than ever before and shows an increasing trend. In order to fully utilize the potential of renewable energies, energy storage systems are needed due to the naturally occurring fluctuations in wind and solar energy. This leads to thermal energy storage for refrigeration applications. A good argument for energy storage is the decoupling of production and consumption.
In addition to increasing overall stability, this enables the production of cold energy at night, when the ambient temperature drops and energy prices are lower. A good side effect can be the peak load reduction of cooling systems during short periods of high demand. If large amounts of energy need to be stored without increasing the size of the storage tank, phase change materials (PCMs) can be chosen, using the latent heat of fusion and not just the sensible heat alone.
A relatively cheap and non-toxic PCM that is often used is ice. Pure ice storage systems have one disadvantage - a low output due to limited heat transfer through the ice. Only a relatively small heat exchanger surface can be exposed to the ice. In order to counteract these problems, ice slurry can be used. Since ice slurry is a mixture of many ice particles with a diameter of 0.1 mm to 1 mm and a carrier liquid, the effective total surface area is larger than that of pure ice. This results in a higher discharge performance and also allows the ice to be pumped instead of serving as a stationary storage material alone. By changing the carrier fluid, the usable temperature range of the ice slurry can be adjusted. (Egolf and Kauffeld, 2005; Kauffeld et al., 2005)
Although ice slurry has a better performance than solid ice, it has the disadvantage of initial production. In the past, many production methods for ice slurry have been developed. (Chibana et al., 2002; Fumoto et al., 2015; Fumoto et al., 2013) A selection: Direct contact evaporation (Wijeysundera et al., 2004), vacuum freezing of water (Safarik M. et al., 2016) or the use of inductive heating to remove ice from a heat exchanger surface (Schaaf and Kauffeld, 2018). The most common method for producing ice slurry are scraped surface evaporators (Stamatiou et al., 2005).
An energy-efficient process for the production of ice slurry is to cool water below its freezing temperature, whereby it initially remains liquid without crystallizing. (Inaba et al., 1994) Crystallization is then initiated in a crystallizer. Because of the heat of fusion induced in the remaining liquid, the water does not freeze completely and ice slurry forms directly from the supercooled liquid. The energetic advantage of this method is that relatively high evaporation temperatures can be used compared to scrapers. In addition to pumps and a refrigeration system, which are also necessary for

all other production methods, no other moving parts are involved in the production of ice slurry with the supercooling method. The disadvantage of the supercooling method is that crystallization follows a statistical process. Crystallisation can take place at any time as long as the temperature of the liquid remains below the freezing temperature. This also includes the heat exchanger in which the water is subcooled. This leads to blocking of the supercooler, which then has to be defrosted.
The stability of this process has numerous influencing factors. (Hozumi et al., 2002; Inaba et al., 1998; Liu et al., 2015) One of them is the interface between the brine and the heat exchanger wall. In order to increase the stability of the process and to equate the method of supercooled brine with scraped surface evaporators, it is important to investigate exactly this interface. The aim of this study is to find a suitable wall material for heat exchangers that reduces the probability of crystallization by using a material with a different crystal structure than ice. For a first study, silicon carbide is selected and compared to copper.

2. SUPERCOOLING EFFECT IN FLUIDS

All fluids undergo supercooling before solidification (nucleation). The supercooling of a fluid can be expressed by the degree of supercooling ΔT, where $\Delta T = T_s - T$, with the melting temperature T_s and the current temperature of the fluid T.
A distinction can be made between homogeneous and heterogeneous nucleation. Homogeneous nucleation describes the solidification of the pure fluid within itself. In heterogeneous nucleation, a substrate is always present whose surface favors nucleation. For this reason, the maximum achievable degrees of supercooling for homogeneous and heterogeneous nucleation differ greatly from each other. For pure water, the thermodynamically calculated maximum supercooling is about $\Delta T_{max} = 42$ K. A homogeneous nucleation can be excluded in real applications, therefore the achieved supercooling degrees are significantly lower. For a technical process, an achievable supercooling of $\Delta T_{tech} = 4$ K can be assumed. (Bédécarrats et al., 2010; Wang et al., 2016).
The supercooled state is not a thermodynamic equilibrium state but a metastable state which the fluid must leave to solidify. However, every thermodynamic system strives to achieve a state of equilibrium and thus minimise its system energy. For the investigation of nucleation in an isobaric and isothermal state, it is useful to describe the change in system energy with the change in Gibbs energy ΔG. (Fisher et al., 1948) Assuming that random ice-like structures (germs) permanently form in the supercooled fluid due to fluctuation, which have a sphere-like shape with radius r, the change of the Gibbs energy of the system can be expressed as follows:

$$\Delta G(r) = 4\pi r^2 \sigma - \frac{4}{3}\pi r^3 \Delta G_v \qquad \text{Eq. (1)}$$

σ is the interfacial energy between fluid and the forming crystal and ΔG_v is the energy change through the formation of a crystal, which can be expressed by the heat of fusion L_f as follows:

$$\Delta G_v = \frac{L_f}{T}\Delta T \qquad \text{Eq. (2)}$$

For germs with a small radius, the positive first term of Eq. (1) prevails, which would result in an increase of the system energy. This counteracts the efforts of the system to reach an energy minimum. The result is that the germ decays again.
Only if by chance a germ is formed which is large enough, the second term in Eq. (1) predominates and the change of the system energy becomes negative. Then it is thermodynamically more favourable for the germ to continue growing.
By differentiation from Eq. (1) to r the critical radius r^* of a germ can be found. With the critical radius and Eq. (1) the Nucleation barrier ΔG^* is given by:

$$\Delta G^* = \frac{16\pi\sigma^3 T_s}{3L_f \Delta T^2} \qquad \text{Eq. (3)}$$

The relationships mentioned above initially refer only to homogeneous crystallization. To describe a heterogeneous crystallization, Eq. (1) must be supplemented by the portion caused by the influence of the surface. A selection of surface mechanisms that can have an influence on crystallization is shown in Fig. 1.
Case a) in Fig. 1 schematically illustrates the influence of surface roughness. Water molecules can be seen which come together to form an ice crystal which begins to grow in a notch on the surface. There are investigations that establish a connection between surface roughness and supercooling,

but only consider the macroscopic case. (Ernst and Kauffeld, 2016; Faucheux et al., 2006) In a microscopic case, the notch opening angle is of great importance. (Campbell et al., 2015) Due to an inappropriate notch angle, the water molecules cannot arrange themselves in a regular ice structure and thus crystallization is inhibited. Case b) shows the crystal structure of the surface and the ice crystal. If these are congruent, crystallization is promoted. There are studies for this mainly from meteorology. For example, silver iodide can be used to trigger a crystallization. Case c) shows an inappropriate crystal structure which inhibits the tendency to crystallize. As the molecules of substrate and ice crystal do not fit together, a mechanical stress is induced in the ice crystal during crystallization, which has to be overcome in addition to the (homogeneous) nucleation barrier. (Okawa et al., 2006) Vonnegut showed this as early as 1947. This allows the Gibbs energy to be extended by the term for the induced stress in the ice crystal and leads to it:

$$\Delta G(r) = 4\pi r^2\sigma - \frac{4}{3}\pi r^3 \Delta G_v + \Delta G_s \qquad \text{Eq. (4)}$$

ΔG_s is the part caused by the plastic deformation of the ice crystal during crystallization. In the search for materials which have both sufficient deviation of their crystal structure from ice and a similar heat conduction as common materials used for heat exchangers, a first selection fell on silicon carbide.

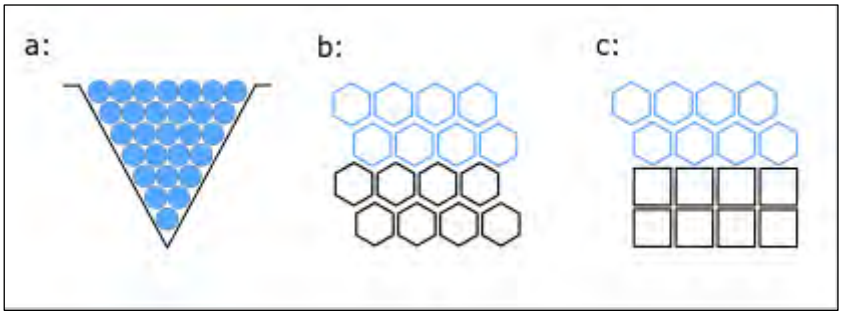

Figure 1: Influence mechanisms on the crystallization tendency of supercooled fluids: a) roughness, b) suitable crystal structure, c) unsuitable crystal structure

3. TEST SETUP AND EXECUTION

The experimental setup (Fig. 2) consists of a specimen holder immersed in a circulating thermostat. The sample holder consists of two parallel polyvinyl chloride plates with a thickness of 12 mm, which can be clamped against each other with four screws. In the sample holder, two pieces of silicon carbide, copper and glass tube are clamped, sealed from above and below and stand vertically in the temperature bath. The samples have an outer diameter of 14 mm, a length of 100 mm and a wall thickness of 2 mm. In the upper side of the sample holder there is a hole through which temperature sensors can be inserted exactly in the middle of the tube, as well as a second hole which allows the expansion of the water during crystallization.
Initially, only one of the two samples was fitted with an internal temperature sensor and the internal temperature of the sample was determined from the reference sample by measuring and comparing the external wall temperature. In this way it can be made sure that the surface of a temperature sensor mounted in the tube has no influence on the crystallization.
It can also be excluded that a possible crystallization starts at the upper side of the sample cover, because, as can be seen in Fig. 2, this is located outside the cold bath and therefore does not experience any cooling. Crystallization cannot take place at the bottom of the sample holder either, because in preliminary tests the temperature in the polyvinyl plate was determined over the duration of the test and was above the freezing point.
For the experiments, all samples are cleaned with acetone and rinsed with pure water, clamped in the sample holder, filled with 7 ml pure deionized water and equipped with temperature sensors. The temperature bath is tempered to 10 °C and the sample holder is inserted so that the liquid filling of the bath ends 1 cm below the upper sample cover.
The following cycles are run 33 times:

1. Cooling down to -10 °C, -6 °C, -4 °C
2. 600 s maintaining the temperature
3. Heating to 10 °C
4. 600 s maintaining the temperature

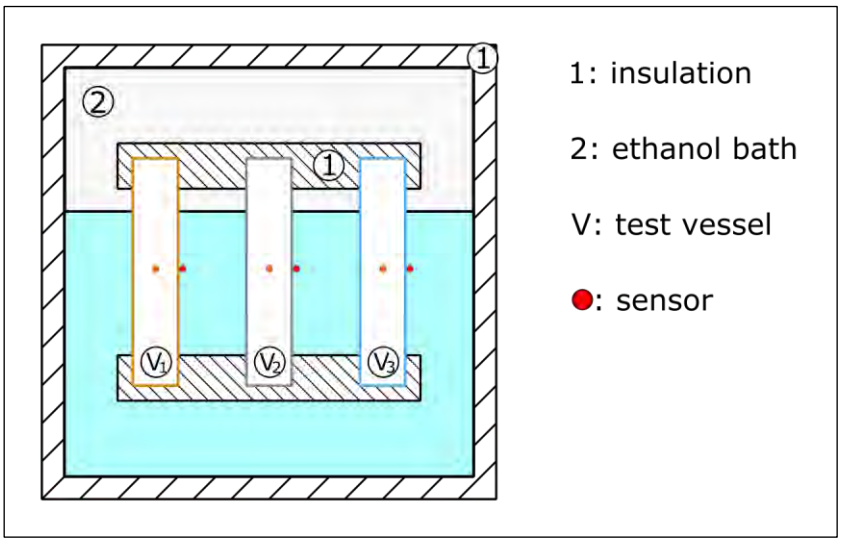

Figure 2: Schematic representation of the experimental setup for determining the crystallization tendency of various pipe samples in a temperature bath

A cycle always starts at 10 °C. To ensure that all samples are ice-free, this temperature is maintained for 600 s. After the upper holding time, the cooling phase begins. Three different cooling temperatures are investigated (-10 °C, -6 °C and -4 °C). The cooling rate is 0.5 K/min in all test series and all cycles. After the cooling phase, the lower holding time of also 600 s begins, followed by the warm-up phase until the initial temperature of 10 °C is reached again and the next cycle begins.
PT100 resistance thermometers are used to measure the temperatures. The measuring section is calibrated to ±0.1 K with a Fluke block calibrator. The resistance values are measured with an Agilent 34980A data acquisition device.

4. RESULTS AND DISCUSSION

Fig. 3 shows an example of a temperature curve of the samples in the cold bath over a cycle at a cooling temperature of -10 °C. It can be seen that the samples are completely defrosted when a bath temperature of 10 °C is reached. The curve for the sample SiC_2 shows that the sample only thaws completely after about 400 s, because then the temperature of the sample begins to rise and adapt to the bath temperature. After 3100 s it is clearly visible that the sample crystallizes and its temperature jumps to the freezing point.

Fig. 4 shows the crystallization events of the series of measurements with cooling temperatures of -4 °C and -6 °C. Two copper, two glass and two silicon carbide samples were examined. During the cooling phase, no samples crystallized. Only during the holding time crystallization events could be detected.

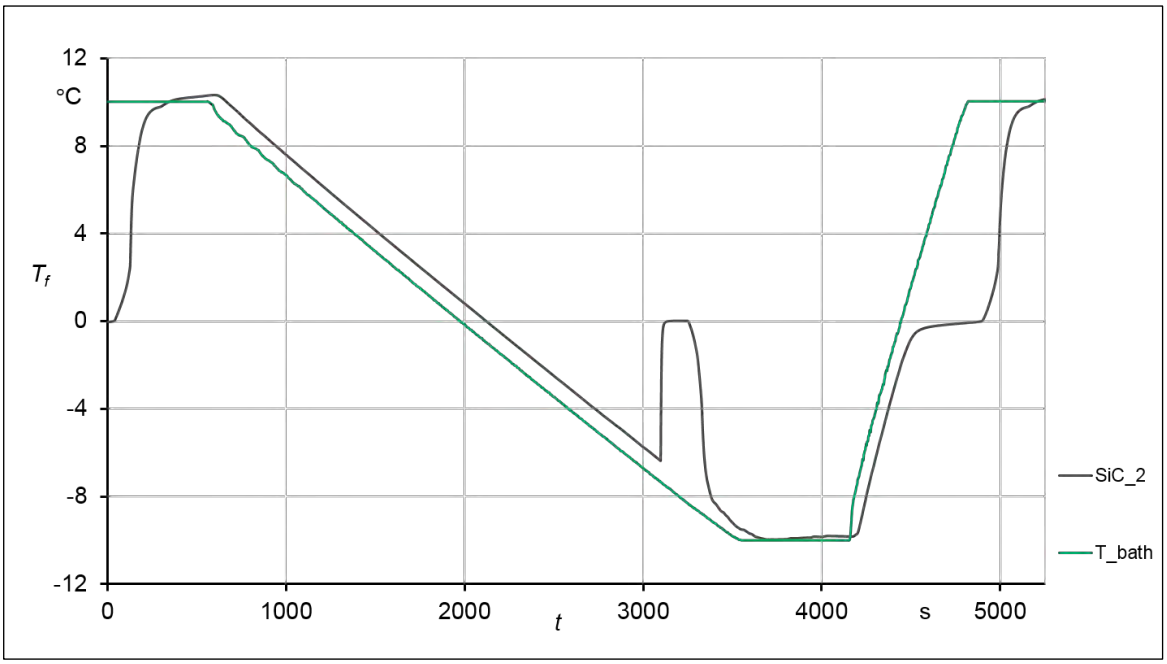

Figure 3: Cooling curves of the sample tubes in the cooling bath over 4700 s, figure corresponds to one cycle

Measuring series -4 °C:
The sample Cu_1 crystallized in the fourth cycle. For the remaining samples, no crystallization could be detected in any cycle.
Measurement series -6 °C:
In the Cu_2 sample, crystallization was observed in the tenth and fourteenth cycles. The remaining samples remained crystallization-free.
Fig. 5 shows the series of measurements with a cooling temperature of -10 °C. None of the samples crystallized during the lower holding time, all samples crystallized during the cooling process in each cycle. The figure shows the averaged crystallization temperatures of the samples. The error bars correspond to the respective standard deviations. It can be seen that the samples SiC_1 and SiC_2 crystallize at a lower temperature than the samples for copper and show a lower scattering.
There are therefore indications that the thesis that a changed crystal structure has a positive effect on supercooling can be confirmed. However, a comparison with the literature is difficult because comparative data are missing or the experimental conditions of these sources are not sufficiently described. (Gorbenko et al., 2002; Ronceray and Harrowell, 2017; Vonnegut, 1947) However, the same tendency can always be observed that initiated the experiments with silicon carbide.

5. CONCLUSION

This work deals with the influence of the surface material on the supercooling of pure water. Three different materials (copper, glass and silicon carbide) were tested. In this thesis the surface roughness was not considered. Due to the lower dispersion of the crystallization events of silicon carbide at low cooling temperatures and the lower crystallization tendency at higher cooling temperatures, it could be confirmed that the surface structure also has an influence on supercooling and that silicon carbide is a good alternative to copper. As follow up further investigation especially considering the microscopic structure of the chosen specimen is needed.

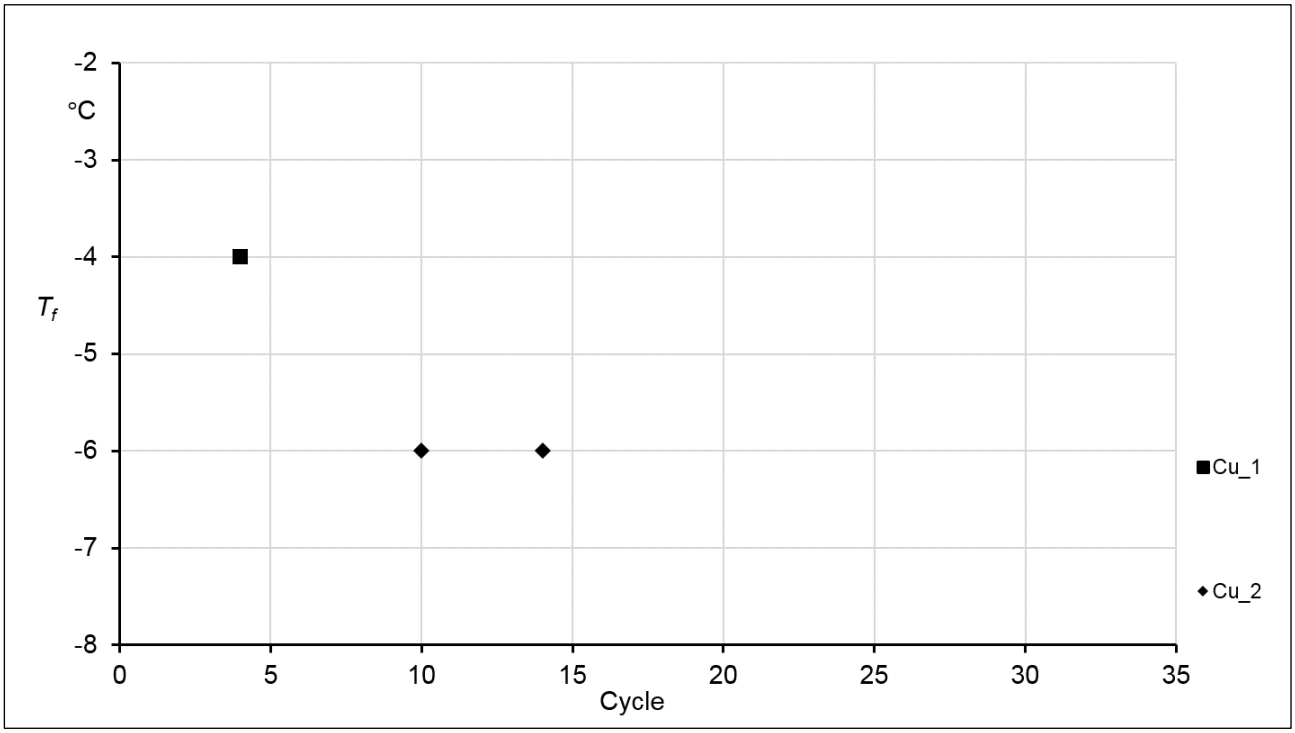

Figure 4: Crystallization temperatures of pure water in two test tubes each of copper and silicon carbide, 33 cycles. 10 °C and 600 s holding time, cooled down to -4 °C or -6 °C and 600 s holding time

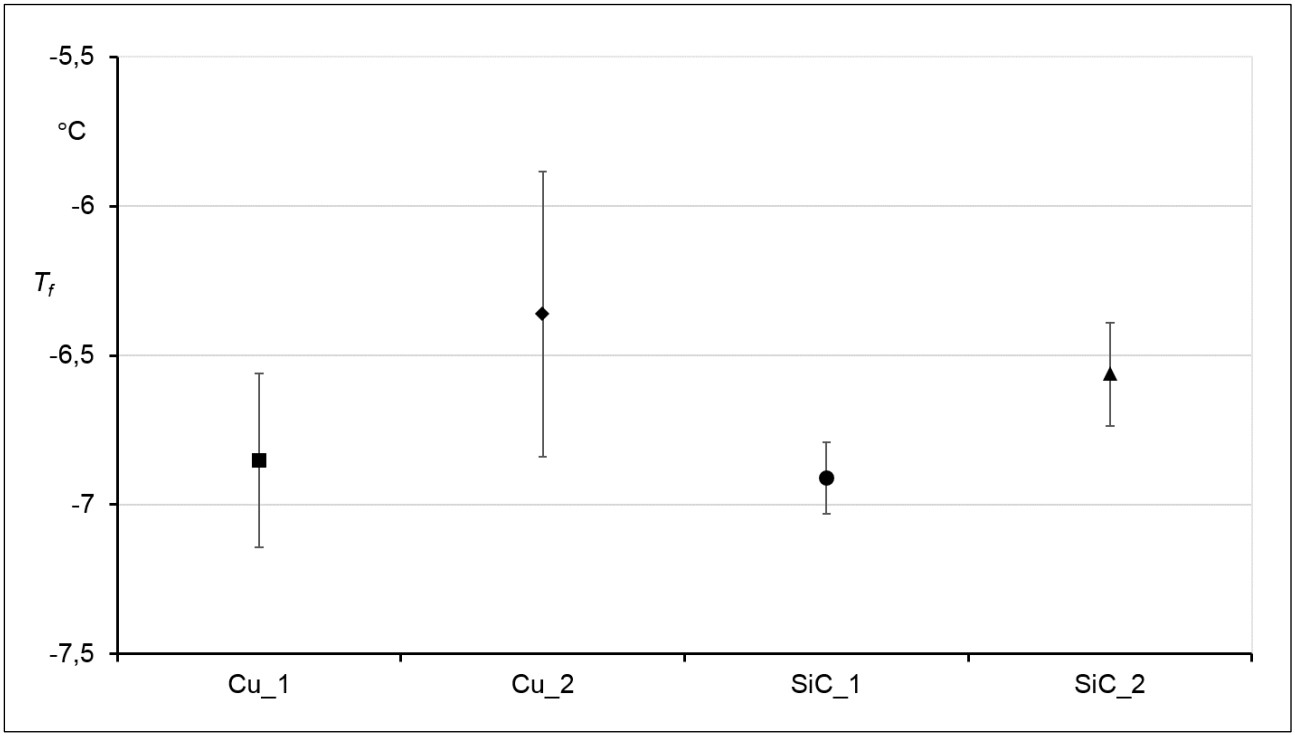

Figure 5: Crystallization temperatures of pure water in two test tubes each of copper and silicon carbide, 33 cycles. 10 °C and 600 s holding time, cooled down to -10 °C and 600 s holding time

NOMENCLATURE

G Gibbs energy (J)
σ interfacial energy (J·m^2)
L heat of fusion (J)
r Radius (m)
T Temperature (K)

REFERENCES

Bédécarrats, J.-P., David, T., Castaing-Lasvignottes, J., 2010. Ice slurry production using supercooling phenomenon. International Journal of Refrigeration 33, 196–204.

Campbell, J.M., Meldrum, F.C., Christenson, H.K., 2015. Is Ice Nucleation from Supercooled Water Insensitive to Surface Roughness? J. Phys. Chem. C 119, 1164–1169.

Chibana, K., Kang, C., Okada, M., Matsumoto, K., Kawagoe, T., 2002. Continuous formation of slurry ice by cooling water–oil emulsion in a tube. International Journal of Refrigeration 25, 259–266.

Egolf, P.W., Kauffeld, M., 2005. From physical properties of ice slurries to industrial ice slurry applications. International Journal of Refrigeration 28, 4–12.

Ernst, G., Kauffeld, M., 2016. Influence of the wall surface roughness on the supercooling degree of water flowing inside a heat exchanger.

Faucheux, M., Muller, G., Havet, M., LeBail, A., 2006. Influence of surface roughness on the supercooling degree: Case of selected water/ethanol solutions frozen on aluminium surfaces. International Journal of Refrigeration 29, 1218–1224.

Fisher, J.C., Hollomon, J.H., Turnbull, D., 1948. Nucleation. Journal of Applied Physics 19, 775–784.

Fumoto, K., Kawanami T., Inamura T., 2015. Study on generator for ice slurry using the pressure shift feezing method.

Fumoto, K., Sato, T., Kawanami, T., Inamura, T., Shirota, M., 2013. Ice slurry generator using freezing-point depression by pressurization – Case of low-concentration NaCl aqueous solution. International Journal of Refrigeration 36, 795–800.

Gorbenko, O.Y., Samoilenkov, S.V., Graboy, I.E., Kaul, A.R., 2002. Epitaxial Stabilization of Oxides in Thin Films. Chem. Mater. 14, 4026–4043.

Hozumi, T., Saito, A., Okawa, S., Matsui, T., 2002. Freezing phenomena of supercooled water under impacts of ultrasonic waves. International Journal of Refrigeration 25, 948–953.

Inaba, H., Lee, D.W., Horibe, A., 1998. Study on the critical conditions of ice formation for a continuous ice making system in a cooling pipe. Heat Trans. Jpn. Res. 27, 74–83.

Inaba, H., Takeya, K., Nozu, S., 1994. Fundamental Study on Continuous Ice Making Using Flowing Supercooled Water. JSME international journal. Ser. B, Fluids and thermal engineering 37, 385–393.

Kauffeld, M., Kawaji, M., Egolf, P.W., 2005. Handbook on ice slurries: Fundamentals and engineering. International Institute of Refrigeration, Paris, 360 S., 1 CD-ROM.

Liu, S., Hao, L., Guo, X., Rao, Z., 2015. Experimental Study on Crystallization Process and Freezing Properties of Ice Slurry Generation Based Sodium Chloride Solution. Energy Procedia 75, 1445–1451.

Okawa, S., Saito, A., Matsui, T., 2006. Nucleation of supercooled water on solid surfaces. International Journal of Refrigeration 29, 134–141.

Ronceray, P., Harrowell, P., 2017. Suppression of crystalline fluctuations by competing structures in a supercooled liquid. Physical review. E 96, 42602.

Safarik M., Honke M., Steffan C., et al., 2016. Applications of the direct evaporation vacuum freezing technology.

Schaaf, J., Kauffeld, M., 2018. Ice aluminum debonding with induction heating. Journal of Adhesion Science and Technology 32, 2111–2127.

Stamatiou, E., Meewisse, J.W., Kawaji, M., 2005. Ice slurry generation involving moving parts. International Journal of Refrigeration 28, 60–72.

Vonnegut, B., 1947. The Nucleation of Ice Formation by Silver Iodide. Journal of Applied Physics 18, 593–595.

Wang, H., Feng, R., Duan, H., Chen, A., 2016. Investigation into the ice generator with double supercooled heat exchangers. Applied Thermal Engineering 98, 380–386.

Wijeysundera, N.E., Hawlader, M., Andy, C.W.B., Hossain, M., 2004. Ice-slurry production using direct contact heat transfer. International Journal of Refrigeration 27, 511–519.

Manuscript ID: 990
DOI: 10.18462/iir.icr.2019.0990

Study on air conditioner with dense membrane

Hyunjeong LIM[(a)], Sangmi CHOI[(a)], Soyeon KIM[(a)], Min Gyu JUNG[(b)], Jinwook LEE[(b)], Minsung KIM[(b)]

[(a)] Department of Energy Systems Engineering, Chung-Ang University
Seoul, 06974, Republic of Korea, lhj5967@cau.ac.kr
[(b)] School of Energy Systems Engineering, Chung-Ang University
Seoul, 06974, Republic of Korea, minsungk@cau.ac.kr

ABSTRACT

As the cooling load increases due to global warming, it is necessary to develop technologies that can replace the conventional vapor compression cycle. One alternative is a membrane heat pump. In this paper, we studied about vacuum membrane dehumidification (VMD) systems which can separate only vapor from humid air. Dehumidification COP of each typical VMD systems are calculated and compared, respectively. After this, unconventional air conditioning system which latent heat removal part and sensible heat removal part are separated is constructed. Because the latent heat is removed first with dehumidification, the energy consumption for cooling is reduced so it is more efficient than conventional air conditioner. From the simulation, COP of air conditioner with dense membrane is calculated as 8.59. The simulation process and result can help construct the proper air conditioner with dense membrane, in reality.
Keywords: Membrane, Vacuum Membrane Dehumidification, Vacuum Compressor, Dehumidification COP, Air Conditioning.

1. INTRODUCTION

Most widely used technology for cooling was vapor compression cycle about 100 years. In vapor compression cycle, the refrigerant moves heat by compressing, condensing, expanding and evaporating. It can supply space cooling to maintain a comfortable environment within buildings. Since vapor compression cycle was started to use for artificial cooling, many researchers tried to improve its efficiency and it contributed greatly to energy savings so far.

However, it is not enough to satisfy increasing cooling demand due to the improvement of a standard of living. Heating, ventilation and air conditioning (HVAC) system is regarded as an important technology and it accounts for almost 40% of global energy consumption (Ben (2011)). Moreover, conventional refrigerants used in vapor compression cycles cause global climate change and the ozone layer depletion when they are released to the atmosphere.

Some alternative refrigerants have low global warming potential, but they still have toxicity, low efficiency, and high equipment cost. To approach this problem by the new way, alternative systems are considered to replace classical vapor compression cycle.

Building Technologies Office in U.S Department of Energy starts to find alternative technologies for vapor compression (US Department of Energy (2014)). They selected 17 candidate technologies and evaluated them by technical energy saving potential, installation and operational cost, system complexity and realization possibility, etc. Among them, the membrane heat pump, which was ranked second, provides cooling and dehumidification by transferring moisture across the membrane. It can be applicable to cooling for residential and commercial buildings in all climate regions but needs additional study yet.

In this study, three types of vacuum membrane dehumidification are studied and their dehumidification COP was simulated under several conditions. Simulation results were analysed and compared, respectively. Moreover, the air conditioner was constructed by combining the vacuum membrane dehumidification system and cooling cycle, and the performance was analyzed, too.

2. MEMBRANE THEORY

A membrane, selective barrier used to separate one species from another, is classified by the existence of pores (Woods (2014)). The porous membrane consists of approximated 0.1 μm pores. A typical hydrophobic porous membrane is usually made of polymer and utilized to separate gas out of liquid-gas mixture since the membrane only allows gas to pass through owing to the hydrophobic characteristic. On the contrary, dense membrane consists of ion nanochannels without actual pores, so only selected gas can pass through those channels from gas-gas mixture. The driving force for transferring the water vapor through the membrane is the vapor pressure difference between the each side of membrane (feed side and permeate side). Even if permeate side's absolute pressure is higher than feed side's, water vapor can move along ions from the feed side to permeate side when the vapor pressure of feed side is higher than permeate side.

When specific material is separated continuously, the concentration polarization phenomenon that the concentration of the material near the membrane becomes lower than the initial state occurs. In the water vapor separation process, there is not concentration polarization on the permeate side because only vapor can pass through the membrane. At first, the water vapor distributes evenly but the concentration near the surface gradually decreases as the separation takes place. As a result, the concentration gradient to transfer the material disappears and separation performance is degraded. The lowered concentration area is called the boundary layer and it acts as the resistance to the separation. The polarization problem can be solved when this layer should be minimized. However, it can be assumed that the concentration polarization has less effect during the gas separation process because the gas has a high diffusion coefficient (Baker (2013)). This problem can also be controlled when the flow rate near the membrane surface is increased.

3. VACUUM MEMBRANE DEHUMIDIFICATION

The dense membrane which is hydrophilic as mentioned above can be applied to HVAC, and a vacuum membrane dehumidification (VMD) is an one example. In this system, a vacuum compressor which is on one side of a dense membrane creates low pressure. There are three types of the system, direct compression, bypass compression, and water vapor compression. A direct type is the most basic structure and it is represented in Fig. 1 (Woods (2014)). The water vapor in the humid air is separated when the air enters and passes the feed side of membrane, so dehumidified air can be supplied. However, compressor outlet temperature reaches 700℃ in this type because of high compression ratio, then some modifications are needed.

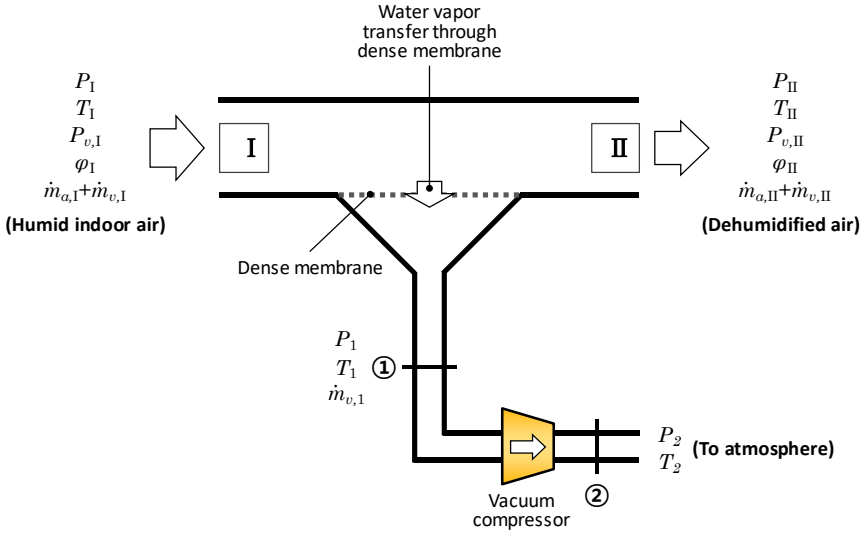

Figure 1: Schematic diagram of direct compression vacuum membrane dehumidification system

One of modified model is bypass compression type (Scovazzo, 2013). As shown in Fig. 2, some dehumidified air is bypassed to the permeate side of the membrane. Therefore, the vapor pressure of the permeate side can be low and the absolute pressure is higher than direct compression type. The compression ratio becomes around 5, but vacuum compressor consumes a lot of energy because the flow rate through the compressor is high.

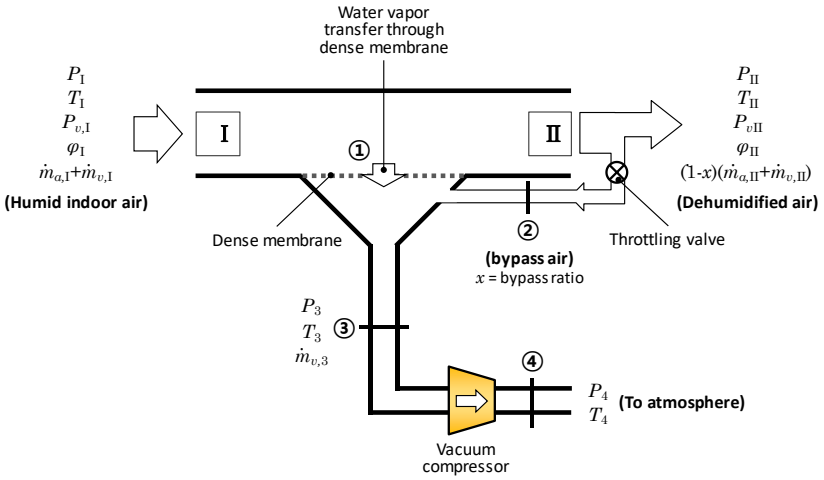

Figure 2: Schematic diagram of bypass compression vacuum membrane dehumidification system

A water vapor compression type (Dais, 2014) is another modified type, and it is represented in Fig. 3. In this model, one more membrane is installed at the compressor outlet and the air from the outdoor flows at the permeate side of this membrane. This structure helps to discharge the water vapor with a low compression ratio of the vacuum compressor. As mentioned above, the driving force of a membrane is the vapor pressure gradient, so the vapor can be discharged if the vacuum compressor makes the pressure of the vapor to be higher than the outdoor air vapor partial pressure. As a result, the compression ratio becomes around 3 and the compressor consumes less energy than before cases because the flow rate is the smallest. Moreover, the discharge temperature becomes lower, too. Therefore, this type is the most effective among the three types of vacuum membrane dehumidification systems.

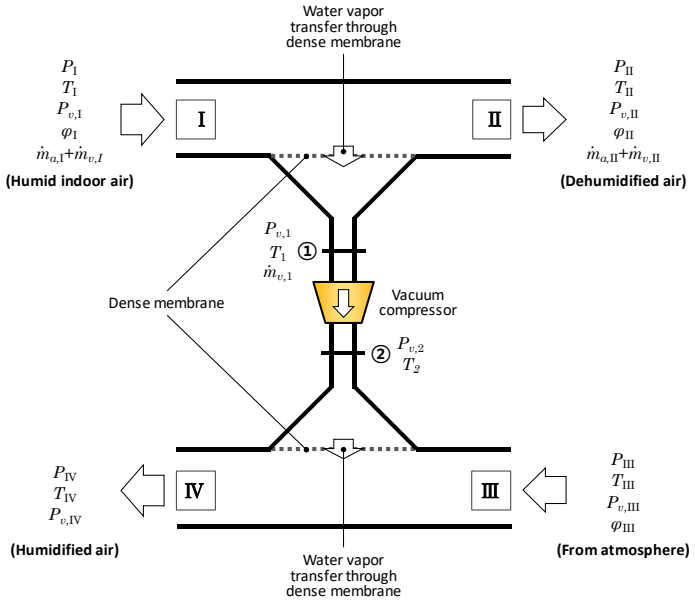

Figure 3: Schematic diagram of water vapor compression vacuum membrane dehumidification system

4. PERFORMANCE ANALYSIS OF VACUUM MEMBRANE DEHUMIDIFICATION SYSTEMS

Dehumidification COP(COP_{DH})s of two modified VMD systems, bypass compression and water vapor compression type, are calculated under ISO 5151 conditions. The indoor air (T_I=27℃, φ_I=46.94 %) is flowing into the VMD. To meet the defined condition, some water vapor is separated from the air. For bypass compression type, bypass ratio (x) is varied from 5% to 50% and permeate

side pressure (P_3) is controlled between 5 and 30 kPa. In the water vapor compression type, the outdoor air conditions are set as T_{III}=35℃, φ_{III}=40.28 % based on ISO 5151.
When the mass flow rate of indoor air (m_I) is assumed as 0.05 kg/s, the latent heat of this air ($\dot{Q}_{lh}$) can be calculated by multiplying the vaporization enthalpy and the vapor flow rate which separated through the membrane. Work rate of the vacuum compressor consumes ($\dot{W}_{vc}$) is can be calculated by using flow rate through the compressor and the enthalpy difference between inlet and outlet side. Finally, COP_{DH} can be calculated like the below equation.

$$\mathrm{COP_{DH}} = \frac{\dot{Q}_{lh}}{\dot{W}_{lh}} \qquad \text{Eq. (1)}$$

COP_{DH} of bypass compression type is represented like Fig. 4. When the bypass ratio is getting higher, COP_{DH} is decreased due to the increase of flow rate. As shown in the Fig. 4, there are some empty points. This is because there is no driving force through the membrane because the vapor pressure of permeate side becomes higher than the feed side in those cases.

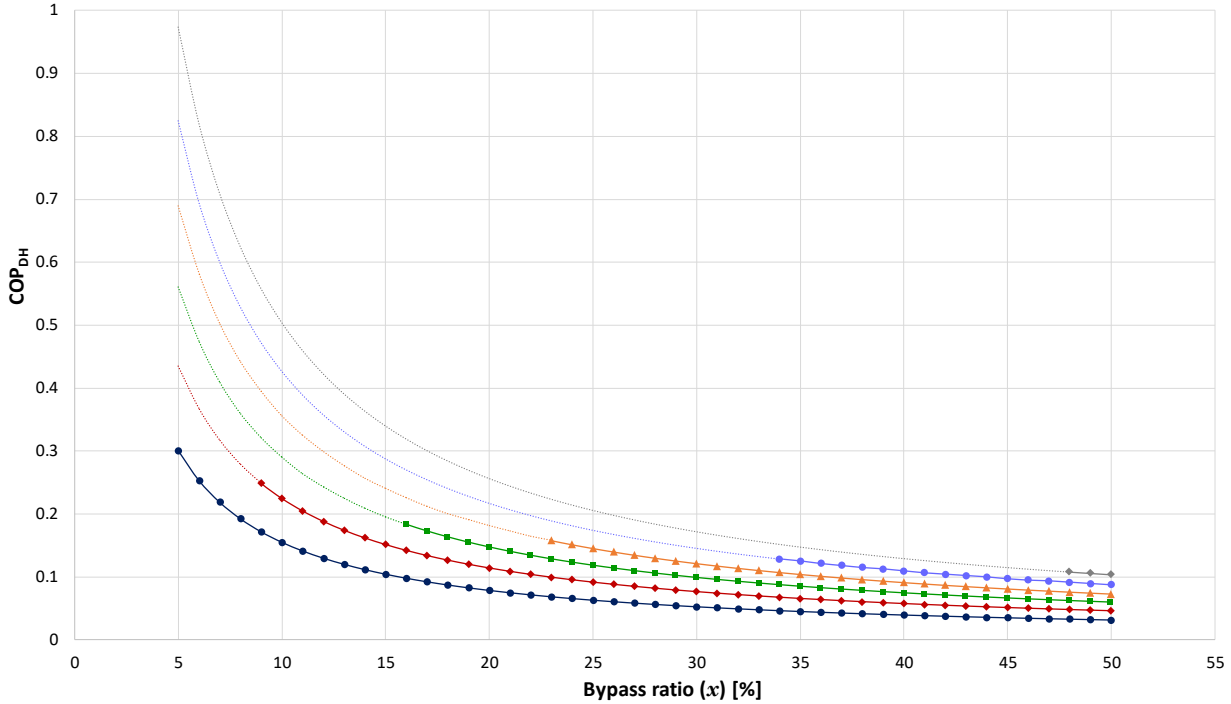

Figure 4: Simulation results of bypass compression vacuum membrane dehumidification system under ISO 5151 conditions

COP_{DH} of water vapor compression type is calculated as 7.1488, and this value is much higher than COP_{DH} of bypass compression type. Because the mixture of dry air and water vapor is flowing together through the vacuum compressor of bypass compression type VMD, the flow rate of this type is higher about 85 times than water vapor compression type VMD. This leads the big difference of COP_{DH} between two types.

5. AIR CONDITIONER WITH VACUUM MEMBRANE DEHUMIDIFICATION SYSTEM

By combining vacuum membrane dehumidification system and cooling cycle, an air conditioner can be constructed. In this paper, water vapor compression type VMD is used because it has the largest COP_{DH}. Fig. 5 show the schematic diagram of an air conditioner which using the dense membrane which has high selectivity to water vapor. The system is different from a conventional vapor compression cycle where the dehumidification and cooling process are separated. The air conditioner consists of air circulation part and water circulation part. The indoor air is driven into the air conditioner through the point I and passes point II and V.
In the air circulation part, water vapor compression VMD, the absolute humidity (w) of the indoor air is removed and the latent heat of the air is eliminated at the same time. The water circulation part of the air conditioner removes the sensible heat. The temperature of the water inside in the cycle stays about 12℃ and the pressure is set as saturated pressure corresponding to that temperature. There

are water cycle, sensible heat exchanger, evaporative cooling heat exchanger, dense membrane, and vacuum compressor. The saturated water inside the cycle is circulating and this water changes to vapor when the temperature increases slightly after exchanging the sensible heat with the air. The temperature of water becomes low again and the vapor formed in this process is discharged when it passes the evaporative cooling heat exchanger which is connected with the dense membrane and vacuum compressor.

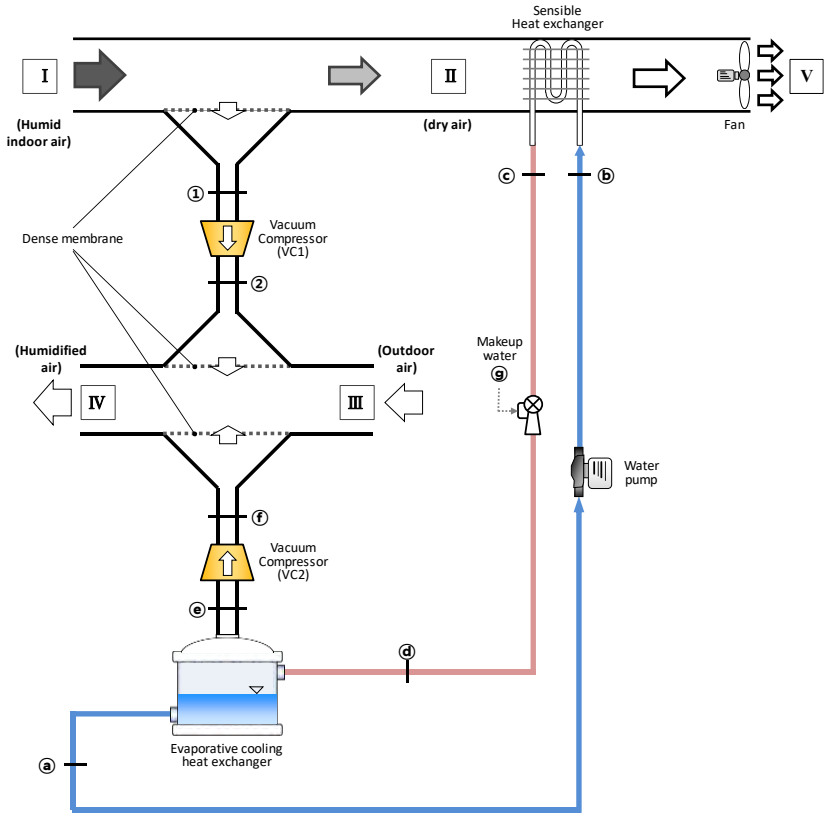

Figure 5: Schematic diagram of air conditioner with dense membrane

There are two vacuum compressors and water pump. Therefore, the overall COP of this air conditioner can be calculated like below and the result is 8.5943 when using ISO 5151 conditions.

$$\mathrm{COP} = \frac{\dot{Q}_{tot}}{\dot{W}_{tot}} = \frac{\dot{Q}_{lh} + \dot{Q}_{sh}}{\dot{W}_{vc1} + \dot{W}_{vc2} + \dot{W}_{pu}} \qquad \text{Eq. (2)}$$

By using the 2018 summer climate data from June to September in Seoul, Korea as an outdoor condition in the same simulation, COP is distributed as shown in Fig. 6. In July and August, it is simulated that the air conditioner was most frequently operated because average temperature and humidity were high.

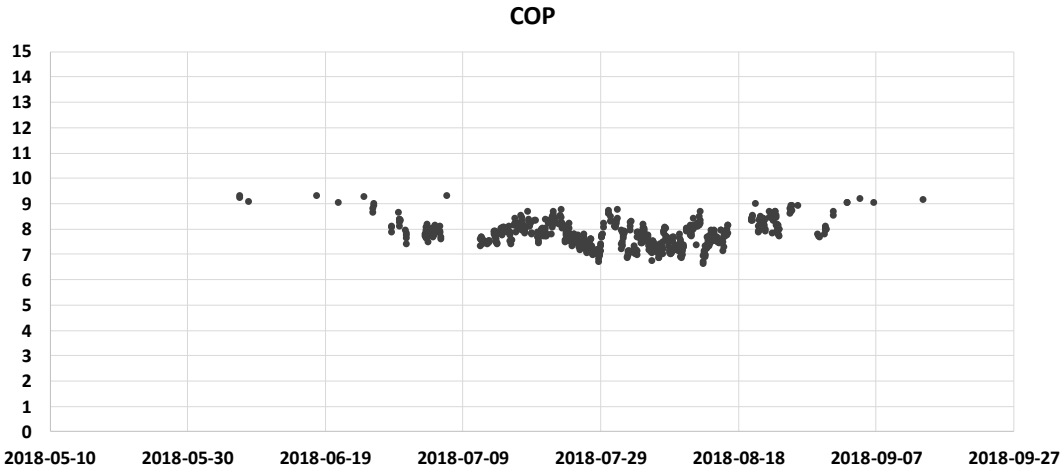

Figure 6: COP variation when using dry bulb temperature and relative humidity data of Seoul in 2018

The COP is distributed between 6 and 10. At the various weather conditions, the air conditioner with the vacuum membrane dehumidification system has still high COP than the conventional air conditioner.

6. CONCLUSIONS

In this paper, characteristics of vacuum membrane dehumidification systems are studied and the dehumidification COPs of bypass compression and water compression VMD are calculated. Because the flow rate through the vacuum compressor is very different between the two types, COP_{DH} is different greatly, too.

By combining the water vapor compression vacuum membrane dehumidification system and the cooling cycle, the unconventional air conditioner is constructed. Because dehumidification and cooling process are separated, it consumes less energy than other air conditioners. From the simulation, overall COP is calculated as 8.5943. When the outdoor air conditions are various, COP is still high.

To realize the new type of air conditioner, it is needed to be done the continuous study on the membrane and vacuum compressor.

ACKNOWLEDGEMENTS

This paper is jointly supported by Korea Institute of Energy Technology Evaluation and Planning (KETEP) of the Republic of Korea (No. 20168510011420 and No. 20161120200090) and by Korea Institute of Energy Research (KIER) (No. 20190064).

NOMENCLATURE

P	pressure (kPa)	x	bypass ratio (%)
T	temperature (℃)	φ	relative humidity (%)
$\dot{m}$	mass flow rate (kg/s)	$\dot{Q}_{lh}$	latent heat (kW/s)
$\dot{W}_{vc}$	work of vacuum compressor (kW/s)	COP_{DH}	dehumidification COP (-)
w	Absolute humidity (kgv/kga)		

REFERENCES

Ben, H., 2011. A review of sustainable cooling technologies in buildings, Renewable and Sustainable Energy Reviews 15, 3112-3120.

US Department of Energy, 2014. Energy Savings Potential and RD&D Opportunities for Non-Vapor Compression HVAC Technologies, Building Technology Office Report.

Baker, R.W., 2013. Membrane Technology and Applications. Wiley.

Woods, J., 2014. Membrane Processes of Heating, Ventilation and Air Conditioning, Renewable and Sustainable Energy Reviews 33, 290-304.

Scovazzo, P., 2013. Isothermal dehumidification or gas drying using vacuum sweep dehumidification, Applied Thermal Engineering 50, 225-233.

Dais, 2014. NanoAir, Dais Analytic Inc.

ISO 5151, 2017. Non-ducted Air Conditioners and Heat Pumps.

Manuscript ID: 1011
DOI: 10.18462/iir.icr.2019.1011

Measurements of isobaric heat capacity of gaseous R 1234yf

Noboru KAGAWA [(a)], Atsushi MATSUGUCHI [(a)], Koichi WATANABE [(b)]

[(a)] Department of Mechanical Systems Engineering, National Defense Academy
Yokosuka, Kanagawa 239-8686 Japan, kagawa@nda.ac.jp
[(b)] Department of System Design Engineering, Faculty of Science and Technology, Keio University
Yokohama, Kanagawa 223-8522 Japan, ttn8j8y233@mx9.ttcn.ne.jp

ABSTRACT

The specific isobaric heat capacity (c_p) in the gas phase was measured for R1234yf (2,3,3,3-tetrafluoropropene). Twenty-two measurements for R1234yf were carefully measured at temperatures from 315 K to 353 K and at pressures from 0.5 MPa to 2.2 MPa. The expanded uncertainty (k=2) of the temperature measurements is estimated to be less than 27 mK, and that of the pressure measurements should be less than 9 kPa. The expanded uncertainty for c_p is calculated to range from 15 to 35 $J \cdot kg^{-1} \cdot K^{-1}$. The measurements were compared with two published equations of state.

Keywords: Heat capacity, R1234yf, Gas, Calorimeter.

1. INTRODUCTION

R1234yf (2,3,3,3-tetrafluoropropene, CH_2=CFCF) is used as an alternative refrigerant of R134a because of its environmentally friendly properties, e.g., zero ozone depletion potential (ODP) and a lower global warming potential (GWP). To replace other conventional refrigerants with the alternative refrigerant, there are many proposals of refrigerant mixtures with R1234yf. To calculate thermodynamic properties of R1234yf and its mixtures for equipment design, a reliable equation of state (EOS) is required. In order to formulate a more reliable EOS for a fluid, it will be recommended to refer various thermodynamic property measurements of the target fluid. During formulating equations of state (EOSs), isobaric heat capacity (c_p) measurements in the gas phase is useful to confirm the caloric properties and the second derivative of the specific volume with respect to temperature. Therefore, c_p information is available to formulate EOSs but is challenging to measure due to its small heat capacity of low density gas. However, calorimetric property data for R1234yf in the gas phase are very limited. Kano et al. (2010) reported speed of sound of gaseous R1234yf at temperatures from 273 K to 353 K and at pressures from 0.025 MPa to 0.4 MPa.

By using a flow calorimeter, Mukoyama et al. (1998) and Yasumoto and Watanabe (2002) obtained gaseous c_p measurements of R134a (1,1,1,2-tetrafluoroethane, CF_3CH_2F) and R143a (1,1,1-trifluoroethane, CF_3CH_3). An additional 10 data and the previous 17 those of c_p for R143a were evaluated with available EOSs (Kagawa et al., 2007). Furthermore, c_p data in the gas phase of six materials: HFE-347pcf2(1,1,2,2-tetrafluoroethyl-2,2,2-trifluoroethylether, $CHF_2CF_2OCH_2CF_3$) (Kagawa et al., 2009a), R134a, carbon dioxide (CO_2) (Kagawa et al., 2009b), R125 (pentafluoroethane, $CH_2F_2CF_3$) (Kagawa et al., 2011a, Matsugchi et al.,2019), and R1234ze(E) (trans-1,3,3,3-tetrafluoropropene, trans-CHF=$CHCF_3$) (Kagawa et al., 2011b), R32 (difluoromethane, CH_2F_2) (Kagawa et al., 2012, 2013) were obtained and were compared with some published EOSs, respectively.

In this work, c_p for R1234yf in the gas phase was obtained using the flow calorimeter. 22 measurements are obtained at temperatures from 303 K to 353 K and at pressures from 0.5 MPa to 2.2 MPa. Two published EOSs are evaluated by these measurements.

2. MEASUREMENTS

2.1. Experimental Procedure

A flow calorimeter (D in Fig. 1) was used for this study; it has been introduced in detail by Mukoyama et al. (1998) and Kagawa et al. (2009b). A steady sample flow is stabilized at the calorimeter tube inlet of the heating section, and an inserted microheater produces a feat flux. The calorimeter is inserted in an evacuated thermal shield, and the tube and shield are put in a well-stirred water bath whose temperature is kept at constant within ±10 mK. Apparently specific isobaric heat $c_{p,\mathrm{app}}$ is obtained by the temperature increment at the heating section, $\triangle T$, and mass flow rate, $\dot{m}$, of R1234yf.

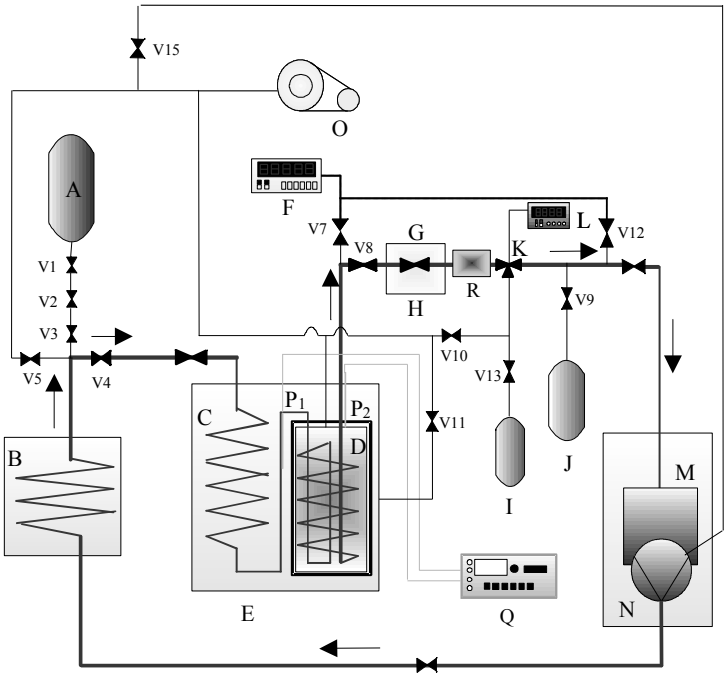

Figure 1: Apparatus

To measure $\triangle T$, two calibrated standard platinum resistance thermometers (PRTs) (P_1,P_2) are located at both ends of the heating section. For $\dot{m}$, a three-way solenoid valve (K) controlled by a timer (L) and a sampling cylinder (I) were inserted. During one minute, the sample flowed into the cylinder cooled by liquefied nitrogen. An electronic balance with an uncertainty of 0.1 mg measures the cylinder.

To establish a stable sample flow in the calorimeter tube during the measurements, a condenser (M) with a liquid pump (N), an evaporator (B), and a nozzle (needle valve) (G) are used for the apparatus. The liquid pump is a bellows type reciprocated by a DC motor. The fluctuations of the sample mass flow ($\dot{m}_{\mathrm{fluc}}$ / $\dot{m}$) were usually less than ±0.5 %, but the maximum one reached ±2 %. A mass flow meter (R) can observe the flow conditions after the expansion valve. The mass flow can be adjusted by the needle valve (G). The sample pressure at the calorimeter outlet was measured with a quartz crystal pressure transducer (F).

By measuring the heat input to the heating element, $\dot{Q}$, and mass flow rate, $\dot{m}$, experimental values of $c_{p,\mathrm{app}}$ are obtained from

$$c_{p,\mathrm{app}} = \frac{\dot{Q}}{\dot{m}\Delta T} = \frac{\dot{Q}_{\mathrm{R}}}{\dot{m}\Delta T} + \frac{\dot{Q}_{\mathrm{L}}}{\dot{m}\Delta T} = c_p + \frac{\dot{Q}_{\mathrm{L}}}{\dot{m}\Delta T} \tag{1}$$

Part of the heating energy, $\dot{Q}_{\mathrm{L}}$, is released from the sample and the calorimeter to the surroundings even though the calorimeter is thermally shielded. In order to determine the value of $\dot{Q}_{\mathrm{L}}$, more than

five $c_{p,app}$ data were measured by changing the mass flow rate from 2.7 to 4.2 g·min^{-1} with $\triangle T$ = 2 K at the same temperature and pressure. By plotting a $c_{p,app}$ curve versus $\dot{m}^{-1}$ and extrapolating the curve to $\dot{m}^{-1} \rightarrow 0$, the actual c_p can be determined. For example, the points at 0.5 MPa and 1.5 MPa both at 333.15 K were determined as shown in Fig. 2. Vertical error bars in the figure indicate the expanded uncertainty (a coverage factor, k=2) of the experimental data.

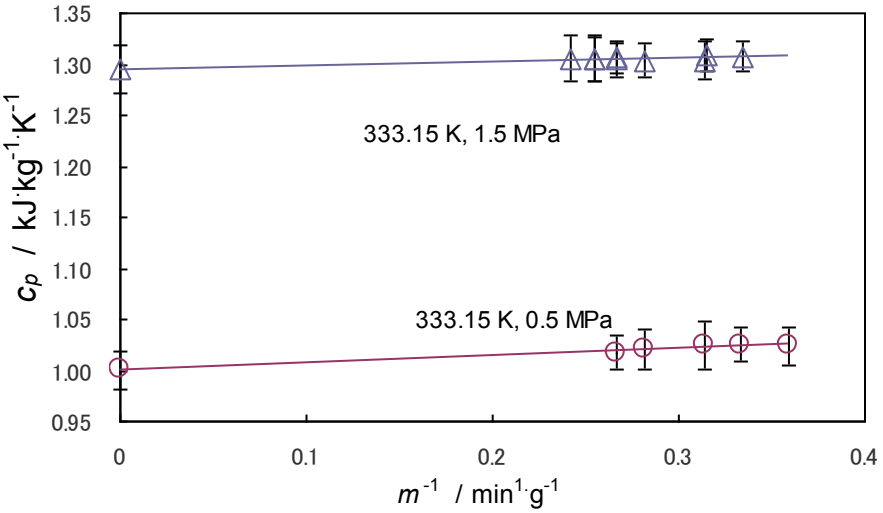

Figure 2: The relation between c_p, $c_{p,app}$ and $\dot{m}^{-1}$ for 333.15 K, 0.5 MPa and 333.15 K, 1.5 MPa. Vertical error bars in the figure indicate the uncertainties of the experimental data

2.2. Materials

The R1234yf was certified by the manufacturer to have a minimum purity of 99.95 mass% by gas chromatographic analysis. The sample fluid in a sample cylinder was transferred into the evaporator of the apparatus. About 1 kg mass of the sample was transferred. The sample purity of remaining in the sample cylinder was identified using a gas chromatography in our laboratory. The purity was more than 99.99 mass%

2.3. Assessment of Uncertainties

The experimental expanded uncertainty has been described previously in detail (Kagawa et al. (2009a)). The experimental expanded uncertainty according to the ISO/IEC guideline (ISO/IEC (2008)) (with k = 2) of the temperature measurement is from 13 mK to 27 mK, by considering the calibration test of the PRTs (the expanded uncertainty is 3.5 mK), the temperature distribution in the calorimeter (< 27 mK), and the accuracy of each instrument. That of the pressure measurement is less 23 kPa, based on the pressure transducer's specifications (0.6 kPa) and pressure fluctuations (< 3.5 kPa). The expanded uncertainty of c_p data is estimated from a combination of the standard uncertainty of the mass flow rate for 1 minute (< 0.62 mg·s^{-1}), that of the supplied heat quantity (< 22 mW), and that of the temperature increment (< 32 mK). The resulting expanded uncertainty (k=2) of c_p ranges from 13 to 27 J·kg^{-1}·K^{-1} depending on the condition of each measurement.

3. Results

Figure 3 shows a c_p -T diagram for the present measurements for R1234yf. Vertical error bars in the figure indicate the estimated uncertainties of the experimental data. It shows the data behavior seems to be reasonable. The c_p values with the expanded uncertainties are arranged in Table 1. The behavior of isobars and the saturation curve calculated by the available EOSs, which have been formulated by Akasaka (2011) and Richter et al. (2011) referring experimental thermodynamic property data, are also depicted in Fig. 3.

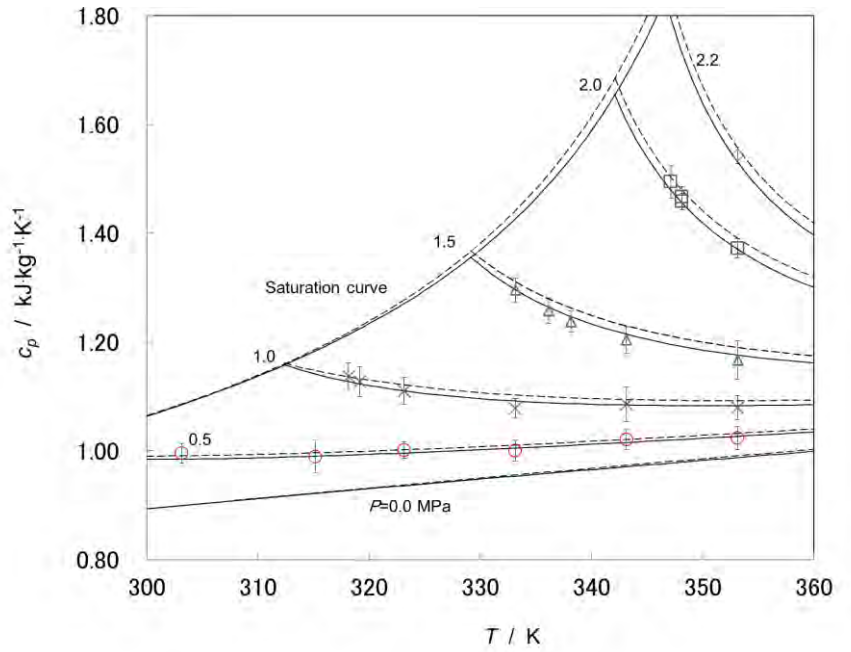

Figure 3: Experimental data (points) compared to several EOSs (lines); ○ : 0.5 MPa, ×:1.0 MPa, △: 1.5 MPa, □: 2.0 MPa, ◇:2.2 MPa, , _____: Akasaka (2011), _ _ _ _ _: Richter et al. (2011)

Table 1. Experimental cp results for R1234yf

T (K)	p (kPa)	c_p (J·kg^{-1}·K^{-1})	Expanded uncertainty (k = 2)			
			T (mK)	p (kPa)	c_p (J·kg^{-1}·K^{-1})	[%]
303.15	500	996	26	3.8	18	1.81
315.15	500	989	27	2.4	30	3.03
323.15	500	1001	20	4.2	15	1.50
333.15	500	1000	23	2.3	19	1.90
343.15	500	1020	19	4.2	18	1.76
353.15	500	1023	22	2.5	21	2.05
318.15	1000	1137	25	3.0	25	2.19
319.15	1000	1127	19	3.0	27	2.40
323.15	1000	1110	24	8.9	25	2.25
333.15	1000	1078	19	1.9	18	1.67
343.15	1000	1086	23	5.9	32	2.95
353.15	1000	1070	22	2.6	22	2.06
333.15	1500	1295	18	3.0	23	1.78
336.15	1500	1258	12	2.2	23	1.83
338.15	1500	1238	13	1.8	19	1.54
343.15	1500	1204	23	9.2	24	1.99
353.15	1500	1167	23	7.1	35	3.00
347.15	2000	1495	23	2.8	23	1.54
348.15	2000	1458	17	5.3	32	2.19
348.15	2000	1467	23	2.8	29	1.98
353.15	2000	1372	24	2.7	27	1.97
353.15	2200	1543	20	2.9	26	1.68

Evaluations of the present c_p measurements were made with values calculated with the available EOSs developed by Akasaka (2011) and Richter et al. (2011). They did not have access to the present measurements. Therefore, these equations were developed with the limited experimental information of the gaseous caloric properties, only speed of sound measured by Kano et al. Figures 4 and 5 show the relative deviations of the calculated values from the present measurements.

Figure 4 shows the c_p deviations of a Helmholtz-type EOS developed by Akasaka. The equation represents present data between -1.1 % and +1.2 %. In the measuring range, the systematic deviations are almost constant.

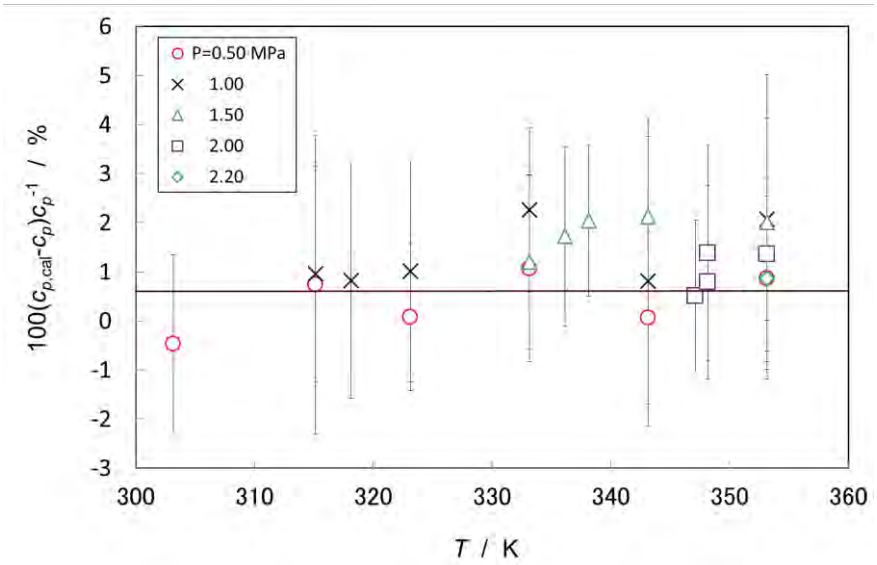

Figure 4: Deviations of calculated c_p values with an EOS by Akasaka (2011) for R1234yf from the experimental c_p data

Figure 5 shows the c_p deviations of a Helmholtz-type EOS developed by Richter et al. The present data are represented between -0.46 % and +2.3 %. Most of them are within the measurement uncertainties. The systematic deviations increase as the saturation curve is disengaged, especially at higher isobars more than 1.5 MPa.

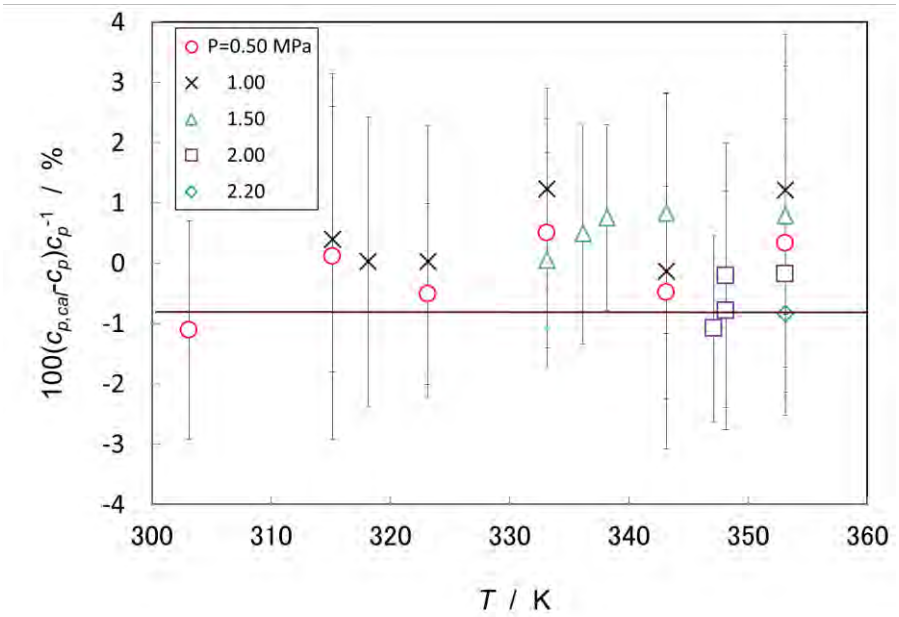

Figure 5: Deviations of calculated c_p values with an EOS by Richter et al. (2011) for R1234yf from the experimental c_p data

4. Discussons

Table 2 shows the systematic and absolute c_p deviations of two available EOSs from the present 19 data. For R1234yf, the EOS proposed by Akasaka represents the data sufficiently. Among the two available equations, the best agreements with the present c_p data are obtained by the Helmholtz equation by Akasaka. Considering the comparisons for the other fluids reported by authors, however, the differences are not so significant. The reason may be the weak polar characteristics, small dipole moment and large molecule size, of R1234yf. Also, the speed of sound was only available as reliable caloric property information in the gas phase when the EOSs were formulated. In the higher temperature and pressure areas, EOS by Richter et al. shows slightly larger discrepancy of +2.1%. If the present data were available, both equations might be arranged to represent the caloric properties much better.

Table 2. Bias and average absolute deviations (AAD) with calculated data from available EOSs ($c_{p,\mathrm{cal}}$) and present 19 data points (c_p)

EOS	$\mathrm{Bias} = 100\frac{1}{N}\sum_{i=1}^{N}\frac{(c_{p,\mathrm{cal}}-c_p)}{c_p}$ (%)	$\mathrm{AAD} = 100\frac{1}{N}\sum_{i=1}^{N}\frac{\lvert c_{p,\mathrm{cal}}-c_p\rvert}{c_p}$ (%)
Akasaka (2011)[*a]	0.067	0.55
Richter, McLinden and Lemmon (2011)[*a]	1.10	1.15

5. CONCLUSIONS

Twenty-two measurements of c_p were reported for R1234yf in the gas phase. The available EOSs can represent the observed behavior at most conditions sufficiently. The calculations by the Helmholtz-type EOSs deviate from the c_p measurements by less than 2.3 %.

The authors gratefully acknowledge Kenichi Tamura, National Defense Academy, for his help with the c_p measurements.

NOMENCLATURE

c_p	specific heat capacity ($J \cdot g^{-1} \cdot K^{-1}$)	Δ	differential
k	coverage factor	*Subscript*	
$\dot{m}$	mass flow rate ($g \cdot s^{-1}$)	*0*	ideal
N	number of data	*app*	appearance
p	pressure (Pa)	*fluc*	fluctuation
T	temperature (K)	*L*	loss
$\dot{Q}$	heat input (J)	*R*	actual

REFERENCES

Akasaka, R., 2011. New Fundamental Equations of State with a Common Functional Form for 2,3,3,3-Tetrafluoropropene (R-1234yf) and Trans-1,3,3,3-Tetrafluoropropene (R-1234ze(E)), Int. J. Thermophy., 32, 1125-1147.

ISO/IEC, 2008. Uncertainty of Measurement. Part 3: Guide to the Expression of Uncertainty in Measurement (GUM:1995), ISO/IEC Guide 98-3.

Kagawa, N., Matsuguchi, A., Watanabe, K., 2007. Measurements of Specific Heat Capacity of Gaseous R 143a Using a Flow Calorimeter, Int. J. Thermophys., 28, 481-489.

Kagawa, N., Matsuguchi, A., Watanabe, K., 2009a. Measurements of Specific Heat Capacity of Gaseous HFE-347pcf2 Using a Flow Calorimeter, Proc. 4th ACRA, TSHRAE, Paper No.150.

Kagawa, N., Matsuguchi, A., Watanabe, K., 2009b. Measurement of Isobaric Heat Capacity for R 134a and Carbon Dioxide by Using a Flow Calorimeter, Trans. JSME, 75 B, 1491-1496 (in Japanese).

Kagawa, N., Matsuguchi, A., Watanabe, K., 2011a, Measurement of Isobaric Heat Capacity of R125, Int. J. Refrig. 34, 275-279.

Kagawa, N., Matsuguchi, A., Watanabe, K., 2011b. Measurements of Isobaric Heat Capacity of Gaseous Trans-1,3,3,3-tetrafluoropropene (HFO 1234ze(E)), Trans. JSRAE, 28, 71-76.

Kagawa, N., Matsuguchi, K. Yamaya, A., Watanabe, K., 2012. Measurements of isobaric heat capacity of R32, Int. J. Refrig. 35, 1014-1020.

Kagawa, N., Matsuguchi, A., Watanabe, K., 2013. Behavior of isobaric heat capacity of R 32 in the gas phase, Int. J. Refrig. 36, 2216-2222.

Kano, Y., Kayukawa Y., Fujii K., Sato H., 2010. Ideal-gas heat capacity for 2,3,3,3-tetrafluoropropene (HFO-1234yf) determined from speed-of-sound measurements, Int. J. Thermophys., 31, 2051-2058

Matsuguchi, A., Kagawa, N., Watanabe, K., 2013. Behavior of Isobaric Heat Capacity of Pentafluoroethane in the Gas Phase, J. Chem. Eng. Data 63, 3727-3732.

Mukoyama, K., Sato, H., Watanabe, K., 1998. Measurements of Gaseous Isobaric Specific Heat Capacity of R-134a and R-143a, Proc. Int. Conf. High Press. Sci. Tech., M. Nakaiwa, ed., 158-164.

Richter, M., McLinden, M.O., and Lemmon, E.W., 2011. Thermodynamic Properties of 2,3,3,3-Tetrafluoroprop-1-ene (R1234yf): Vapor Pressure and p-rho-T Measurements and an Equation of State, J. Chem. Eng. Data, 56, 3254-3264.

Yasumoto, K., Watanabe, K., 2002. Specific Isobaric Heat Capacity Measurements for Gaseous R-143a (1,1,1-Trifluoroethane), Proc. 16th European Conf. Thermophys. Props., London. CD-ROM.

Manuscript ID: 1014
DOI: 10.18462/iir.icr.2019.1014

Investigation into low viscosity refrigeration oil for refrigerators

Yohei SHONO, Fumiyuki NARA, Takeshi OKIDO, Kiyomi SAKAMOTO
JXTG Nippon Oil & Energy Corporation
Yokohama, 231-0815, Japan, shono.yohei@jxtg.com

ABSTRACT

As with automotive lubricants, the trend in refrigeration oils for refrigerators is toward lower viscosities, in pursuit of higher energy efficiency. A viscosity grade (VG) of 32 was once common for refrigeration oils. Recently, however, we have developed an extremely low viscosity refrigeration oil (VG3) for refrigerators that use R600a. In this presentation, we will discuss the technical difficulties (e.g. anti-wear properties) that are caused by lowering the viscosity of refrigeration oils and how to solve them.
Keywords: Efficiency, Low GWP, Lubricant, Mineral Oil, R600a, Refrigerator, Viscosity, Wear.

1. INTRODUCTION

Manufacturers are working to develop lower viscosity lubricating oils, especially for automobiles, in order to improve energy efficiency in an effort to reduce global warming. Similarly, lower viscosity refrigeration oils can play a role in improving efficiency. In particular, the viscosity of refrigeration oils for household refrigerators has been trending downward (Matsumoto and Kaimai, 2010).
Since most of the energy needed to run a refrigerator or other refrigeration equipment is used by the compressor, the idea of lowering the viscosity of the refrigeration oil has been advanced as a means of reducing energy consumption in the reciprocating compressors of household refrigerators. By lowering the viscosity, it is possible to reduce churning in the oil, which can result lower energy use. The viscosity of a lubricant is typically expressed as its viscosity grade (VG), which is the viscosity of the lubricant at 40 °C. Ester oils and mineral oils of VG32 and VG22 had been used as refrigeration oils for refrigerators in the past. Refrigeration oils of VG10 came into use around the year 2000, and refrigeration oils of VG8 and VG7 have since become mainstream. In the 2010s, VG5 refrigeration oils also came into use. There has been a push to develop even lower viscosity VG3 refrigeration oils. This has yet to be achieved using mineral oils, however, due to the low flash point of these oils and their inability to adequately protect the moving parts of the equipment.
In this study, our aim was to develop a mineral oil-based VG3 refrigeration oil for household refrigerators that use R600a. Here we will describe the technical hurdles involved and their solutions.

2. STUDY ON BASE OIL FORMULATION

As mentioned above, reducing the base oil viscosity can lower the flash point. Generally speaking, lower viscosity oils will have a lower flash point. Our current refrigeration oils of VG5 and higher are made using paraffinic mineral oil, which has a higher flash point than naphthenic mineral oil. However, at around VG3, the flash point is very low even with paraffinic mineral oil, falling below 120 °C. From a safety standpoint, the flash point must be higher, so we took another look at the base oil formulation. To create a VG3 mineral oil with a higher flash point, we reduced the amount of light fractions. As Fig. 1 shows, the newly developed base oil has a higher flash point than the conventional paraffinic mineral oil even at VG3.

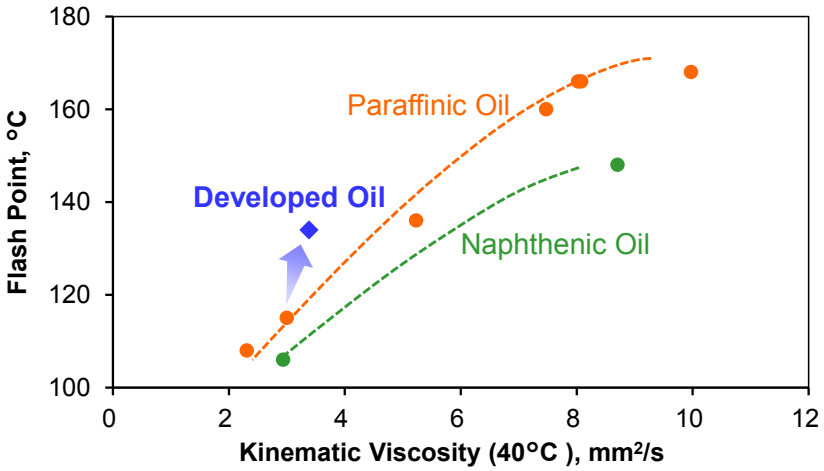

Figure 1: Flash point of developed base oil

3. FRICTION STUDY ON LOW VISCOSITY OIL

MTM (Mini traction machine) tests were performed to compare the frictional characteristics of the developed VG3 base oil and a conventional VG5 base oil. In the MTM test, a disk test piece and ball test piece are brought into contact and rotated simultaneously, allowing us to measure the coefficient of friction in a mixture of rolling and sliding conditions. Friction coefficients were measured using a standard disk test piece (SUJ 2) and ball test piece (SUJ 2), at a test temperature of 40 °C, a load of 10 N, a sliding rate of 30%, and sliding speeds from 0.02 $m \cdot s^{-1}$ to 2 $m \cdot s^{-1}$. The results are shown in Fig. 2. As the viscosity of the base oil decreased from VG8 to VG3, the friction coefficient at high sliding speeds (0.2 to 2 $m \cdot s^{-1}$) decreased. This is thought to be due to a decrease in the viscous resistance of the fluid, which was the result of lowering its viscosity. On the other hand, we know that as the sliding speed decreases, the oil film thickness also decreases, leading to increased boundary lubrication, in which there is direct metal-to-metal contact, and the friction coefficient tends to increase. This tendency is more pronounced when the viscosity is lower, such that the VG3 base oil had a higher friction coefficient than the VG8 base oil at low sliding speeds (0.02 $m \cdot s^{-1}$ to 0.2 $m \cdot s^{-1}$). Therefore, if the VG3 base oil were used, there could be increased wear in mixed and boundary lubrication regimes at low sliding speeds.

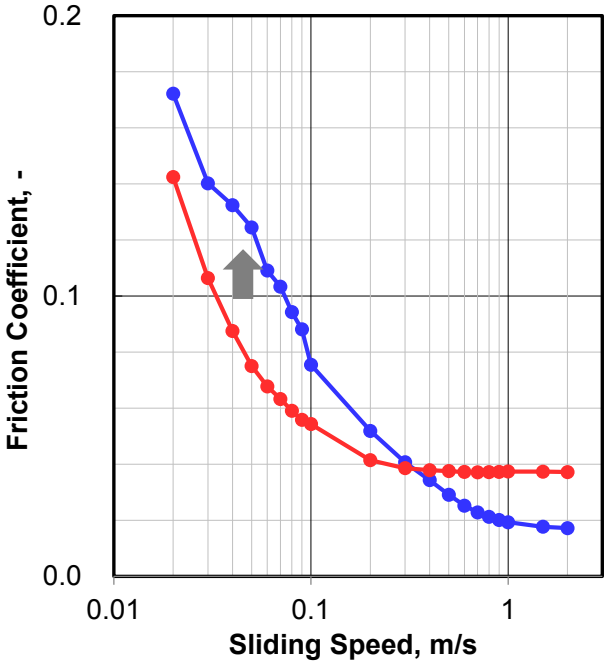

Figure 2: Comparison of the friction coefficient between VG8 and VG3

4. STUDY ON ANTI-WEAR ADDITIVES

Additives are generally effective at controlling wear in boundary lubrication regimes, in which there is some contact between metal surfaces. We thus looked at using anti-wear additives to improve the anti-wear properties of the lubricant in mixed and boundary lubrication regimes. The wear characteristics were evaluated using SRV (Schwingungs Reihungund und Verschleiss) tests. Tests were performed using a ball (SUJ2) with a diameter of 10 mm and a disk (SUJ2) with a thickness of 7.9 mm. The ball was pressed down on the disk and moved in a reciprocating sliding motion for 30 min at a test temperature of 80 °C, an amplitude of 1 mm, a frequency of 50 Hz, and a load of 300 N. After the tests, the diameters of the wear scars on the balls were measured. Low-viscosity refrigeration oils for refrigerators are typically formulated with anti-wear agents to ensure sufficient anti-wear properties. A commonly used anti-wear additive is the phosphorus-based TCP (Tri-cresyl phosphate). In this study, SRV tests were performed using the VG8 oil and the VG3 oil, to which was added TCP. After testing, it was found that the wear scar diameter was larger with the VG3 oil than with the VG8. This is because the lubrication conditions were more severe with the lower viscosity oil, and TCP alone was not enough to give the VG3 oil sufficient anti-wear properties.

Normally, phosphorus anti-wear additives such as TCP adsorb on oxide films on metal surfaces and react to form anti-wear films. In the case of the low viscosity oil, the oxide film may have been broken due to metal-to-metal contact, such that the phosphorus anti-wear additives could not be sufficiently effective. We therefore turned our attention to an anti-wear additive containing sulfur and phosphorus (SP anti-wear additive) that might be capable of providing an anti-wear effect even in severe lubrication conditions. Fig. 3 shows the wear scar diameters of the balls after SRV tests with VG3 prepared with TCP and VG3 prepared with the SP additive and TCP. The wear scar was smaller with the oil prepared with both TCP and the SP additive, and was the same size as that with a VG8 base oil prepared with TCP, which is representative of a conventional oil. Thus, by optimizing the anti-wear additives in a VG3 base oil, we developed an oil with anti-wear properties equivalent to that of a conventional VG8 oil.

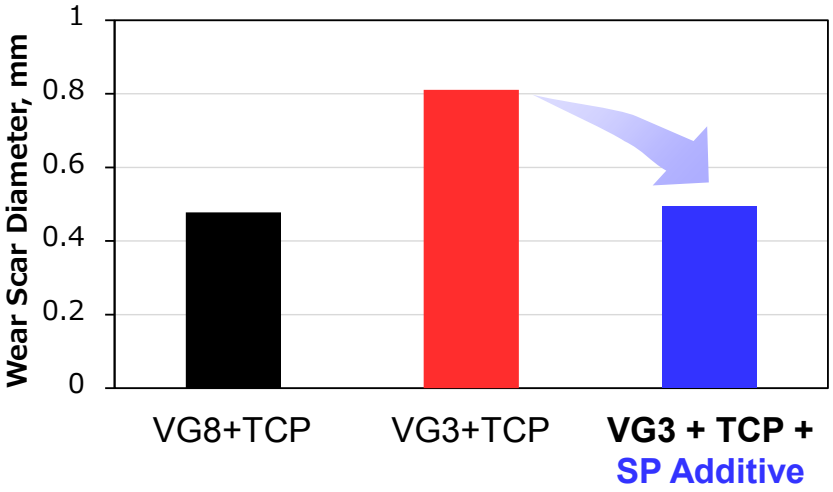

Figure 3: Wear scar diameters after SRV tests for VG8 & VG3 oils with anti-wear additives

5. STUDY ON THE FRICTION PROPERTIES OF DEVELOPED OIL

The compressors in home refrigerators will operate at a range of speeds from low to high. For the refrigerator to run more efficiently, it is therefore important that the refrigeration oil have friction-reducing effects in a wide range of lubrication conditions. We thus used MTM tests to evaluate the friction characteristics of the newly developed oil to see whether it would be able to help improve the efficiency of refrigerators. The results are shown in Fig. 4. With the VG8 oil, the addition of TCP had little effect on the friction characteristics. By contrast, the VG3 oil tended to show slightly lower friction coefficients in the low speed range, even with TCP alone. It may be that, whereas the VG8 oil forms an oil film even in low speed conditions and it can maintain some degree of lubricity, the effect of the anti-wear additive is more pronounced with the VG3 oil because the oil films are thinner. Moreover, the oil prepared with a combination of TCP and SP anti-wear additives showed lower friction coefficients at low speeds of 0.1 $m \cdot s^{-1}$ and below than did the oil prepared with TCP alone. These results suggest that the SP additive is effective in low speed sliding conditions, in which the oil films are easily broken, such that good lubrication is maintained. This newly developed oil, formulated with a VG3 base oil and a combination of TCP and SP additives, exhibits friction characteristics equivalent to a VG8 oil even in the low speed range, and shows excellent friction properties over a wide range of speeds from low to high. This suggests it could help improve the efficiency of refrigerators used in the home.

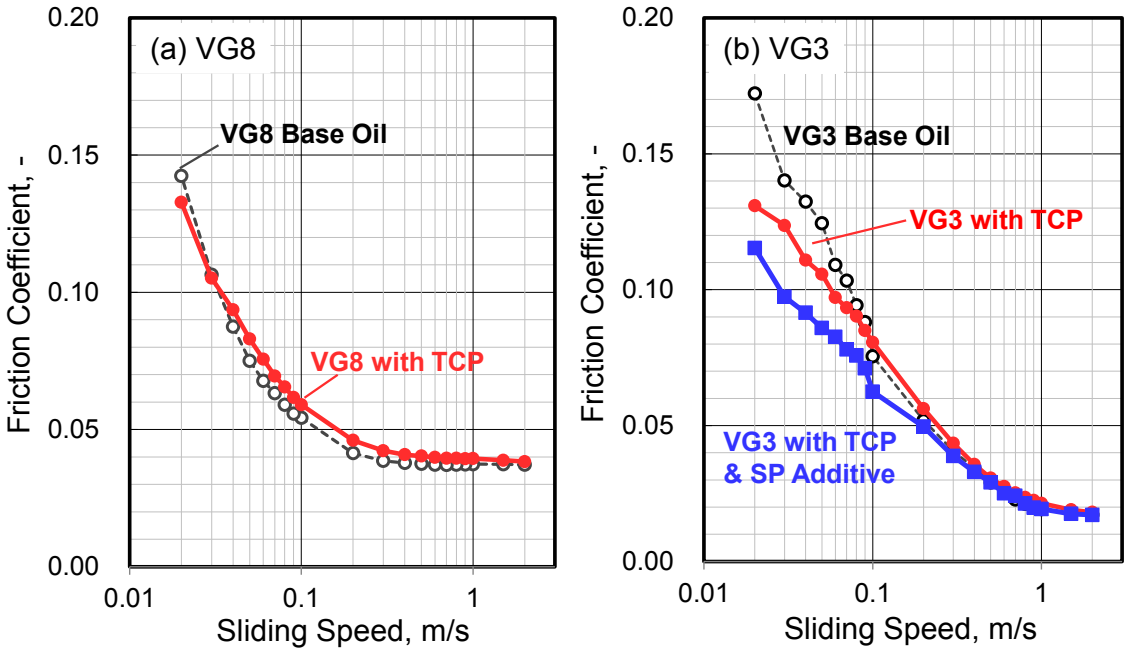

Figure 4: Friction coefficient of (a) VG8, (b) VG3 with anti-wear additives

6. SURFACE ANALYSIS OF SLIDING SURFACES AND ACTION MECHANISM OF ANTI-WEAR ADDITIVES

As discussed above, it was determined that good lubrication can be maintained even in boundary lubrication regimes by using TCP and SP additives. To better understand the action mechanism of the anti-wear additives, we carried out surface analysis on the sliding part of the balls used in the SRV tests. EPMA was used for the surface analysis, with an acceleration voltage of 15 kB, an irradiation current of 1×10^{-7} A, and an observation magnification of 100x. The phosphorus, oxygen, and sulfur detected from the sliding parts are shown in element maps in Fig. 5. Large amounts of phosphorus and oxygen were detected from the sliding part of the ball tested with the VG3 oil prepared with TCP alone, suggesting that an iron phosphate film had formed on the sliding surface. Meanwhile, phosphorus and oxygen were detected in the sliding part of the ball tested with the oil prepared with TCP and the SP additive in combination, along with sulfur. Although the amount of sulfur detected was small compared to that of phosphorus and oxygen, it was mainly detected at the edge of the wear scar, where the sliding was most severe.

These results suggest that the SP additive acts locally under severe sliding conditions and prevents wear from progressing.

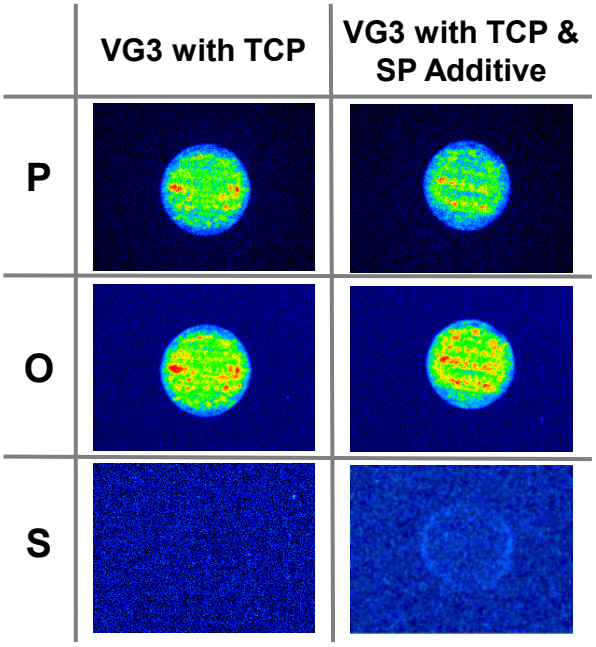

Figure 5: Elemental mapping of EPMA analysis for VG3 oil with anti-wear additives

7. CONCLUSION

We studied low viscosity refrigeration oil for refrigerators with the aim of making refrigerators more energy efficient. Although the flash point drops when the viscosity is lowered, we were able to ensure a high flash point even when the viscosity was lowered to VG3 by reducing the proportion of light fractions. Compared to a more conventional VG8 refrigeration oil, the VG3 oil showed lower friction coefficients in fluid-film and elastohydrodynamic lubrication regimes due to reduced viscous drag, but may provide inadequate lubrication in boundary and mixed lubrication regimes because oil films cannot properly form. We thus studied the anti-wear agents and found it was possible to achieve sufficient anti-wear properties in boundary lubrication regimes and excellent friction characteristics with a VG3 oil formulated with a combination of TCP an SP anti-wear additives. It is thought that with the newly developed oil, an iron sulfide film forms even under severe sliding conditions, preventing the deterioration of wear and friction characteristics.

REFERENCE

Matsumoto, T., Kaimai, T., 2010. New Demands for Refrigeration Oil Extreme Low Viscosity Oil. Proceedings of the 13th International Refrigeration and Air Conditioning Conference at Purdue, July 12-15.

Manuscript ID:1033
DOI: 10.18462/iir.icr.2019.1033

Comparative analysis of ionic liquids as sorptive media for absorption cooling systems

Hifni M. Ariyadi[(a)], Niccolò GIANNETTI[(b)], Seiichi YAMAGUCHI[(a),(c)] and Kiyoshi SAITO[(a),(c)]

[(a)]Department of Applied Mechanics and Aerospace Engineering, Waseda University, Tokyo, 169-8555, Japan, e-mail: hifni.ariyadi@aoni.waseda.jp
[(b)]Waseda Institute for Advanced Study, Waseda University, Tokyo, 169-8050, Japan, e-mail: niccolo@aoni.waseda.jp
[(c)]Interdisciplinary Institute for Thermal Energy Conversion Engineering and Mathematics, Waseda University, Tokyo, 169-8555, Japan, e-mail: sei_yamaguchi@aoni.waseda.jp

ABSTRACT

Ionic liquids have been widely introduced in various engineering applications, including absorption cooling systems. The use of ionic liquids as sorptive media in absorption systems is intended to improve the system performances by removing the disadvantages of conventional working fluids.
Although theoretical investigations based on solubility of refrigerant/ionic liquid mixtures show a competitive performance, heat transfer and mass absorption performance, which is also an important key of system, remains open.
This paper theoretically studies the absorption process of refrigerant in ionic liquid to obtain the most prominent ionic liquids for absorption machines, both in terms of thermodynamic and heat and mass transfer performance.
The results are analyzed, and the performances are compared with conventional working fluid. For instance, in the case of water/[dmim][DMP], the heat transfer performance is higher, but its lower solubility and diffusivity gives less absorption rate than water/LiBr working fluid.
Keywords: Ionic Liquids, Sorptive Media, Absorption.

1. INTRODUCTION

The global energy demand for air-cooling and refrigeration significantly increases in the past decades together with the rapid growth of human population and economic, particularly in populated and dense countries and meanwhile, the energy supply to date is still predominantly generated from non-renewable fossil fuel combustion.
Absorption cooling system is a thermal-driven heat pump technology operating based on absorption-desorption processes of refrigerant in the absorbent which, with high potential of renewable and green energy available in the world, can be adopted to solve the need of refrigeration and heating/cooling demands while reducing the fossil fuel-based energy consumptions and gas emissions by utilizing renewable energy or waste heat.
The absorption cooling systems commonly work using ammonia/water and water/lithium bromide mixtures, where the latter is the most common working pair for cooling/heating systems as it cannot produce cold below 0°C. This working pair, where water works as refrigerant and aqueous LiBr solution works as absorbent, are limited by corrosion and solidification of LiBr salt at certain operative conditions. Many attempts have been addressed to eliminate these limitations, such as using multicomponent salts absorbent (Bourouis et al., 2005), adding surfactants and additives (Kim et al., 2006), and applying novel absorbent such as ionic liquids (IL) (Kim et al., 2012). The latter application in absorption cooling systems can give several advantages as ionic liquids have liquid phase in wide range of temperature, near-zero vapor pressure, high solubility with most of natural refrigerants, non-corrosive, non-toxic, and thermally stable (Kim et al., 2012). In addition, the thermophysical properties of ionic liquids can be adjusted by combining the cation and anion pair (Popp et al., 2015).
Studies on the applications of water/ionic liquid working pairs as working fluid for absorption cooling systems are growing in number. Recent studies on the thermodynamic performance of absorption cooling systems using water/ionic liquid working pairs have been published in open literatures,

introducing some ionic liquids such as 1,3-dimethyl-imidazolium dimethylphosphate ([dmim] [DMP]), 1-ethyl-3-methyl-imidazolium dimethylphosphate ([emim] [DMP]), 1-ethyl-3-methyl-imidazolium ethylsulfate ([emim] [$EtSO_4$]), etc (Kim et al., 2012, Popp et al., 2015, Ariyadi and Coronas, 2016, Yokozeki and Shiflett, 2010). Based on theoretical thermodynamic calculation using solubility data, the coefficient of performance (COP) of single-stage absorption cooling systems using water/ionic liquid fluids is quite competitive in comparison with conventional water/LiBr working fluid (Yokozeki and Shiflett, 2010) considering the above-mentioned advantages of ionic liquids over conventional aqueous LiBr solution although the solution circulation ratio is higher than water/LiBr systems.
Although studies on the theoretical performance of absorption cooling systems using water/ionic liquid working pairs can be found in many sources (Kim et al., 2012, Popp et al., 2015, Ariyadi and Coronas, 2016, Yokozeki and Shiflett, 2010), wider and more comprehensive studies of these new working pairs remain incomplete. In actual conditions the efficiency and performance of an absorption machine are not only characterized solely by coefficient of performance and solution circulation ratio, but also determined by system design and size, initial cost and the operating cost of the system, which are strongly dependent on the working fluid properties. Screening of new working fluid for absorption system therefore should be properly and extensively carried out, considering not only solubility (vapor-liquid equilibria) of refrigerant in the absorbent, but also transport properties of the working fluid mixtures which have great influence on the heat and mass transfer performance, such as viscosity, thermal conductivity, and diffusivity. This study aims to extensively examine the ability of ionic liquids as sorptive media in absorption in order to obtain the suitable ionic liquids with not only optimum thermal performance but also optimum heat and mass transfer performance, which is also an important parameter in absorption cooling machines, particularly in terms of system design and costs.

2. MATHEMATICAL MODEL

In this work, two imidazolium based ionic liquids, namely 1-ethyl-3-methyl-imidazolium ethyl sulphate [emim][$EtSO_4$] and 1,3-dimethyl-imidazolium dimethyl phosphate [dmim][DMP] are chosen as absorbent for water refrigerant.
Heat and mass transfer characteristics of water/ionic liquid working fluids in the absorber is evaluated using a model consisting of energy and mass balance equations, derived from the absorption process taking place in an infinitesimal area of a vertical tube absorber as schematically shown in Fig. 1. Detail of mathematical description of the model is explained in Tsai and Perez-Blanco (1998).

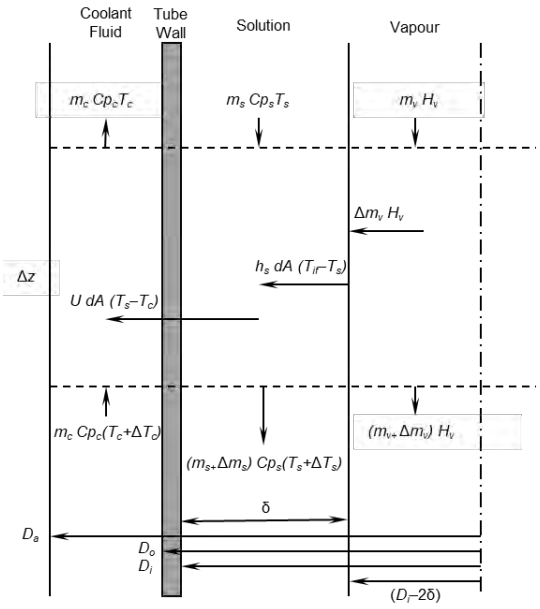

Figure 1: The schematic diagram of water vapor absorption process in vertical tube falling film absorber.

The high ionic liquid concentration of absorbent-refrigerant solution enters from the top of the tube, downwards through the inner wall as a falling film. At the same time, the water vapor enters from the top of the vertical tube and be absorbed by the solution. The solution with low ionic liquid concentration then leaves the absorber through the bottom of the tube.
The coolant fluid flows from the bottom of the absorber trough tube annulus space to remove the heat generated during the absorption process, transferred from the solution to the cooling water while mass transfer process occurs in the vapor-solution surface.
Assuming that the vapor-solution interface is always in saturation condition and the bulk solution is perfectly mixed along the tube, the amount of water vapor absorbed by the solution can be calculated using following equation

$$\frac{dm_s}{dz} = k_s(\pi\, Di)\left(c_{w,\mathrm{int}} - c_w\right) \qquad \text{Eq. (1)}$$

Moreover, with assumptions that the heat transfer only occurs in horizontal direction, and there is no heat loss in the absorber, from the energy balance at the solution side, the solution temperature at a control volume can be written as follows

$$\frac{dT_s}{dz} = \frac{H_v - Cp_s T_s}{m_s Cp_s}\frac{dm_s}{dz} - \frac{U\pi Di(T_s - T_c)}{m_s Cp_s} \qquad \text{Eq. (2)}$$

Furthermore, the cooling water temperature at a control volume can be written as follows

$$\frac{dT_c}{dz} = \frac{U\pi Di(T_s - T_c)}{m_c Cp_c} \qquad \text{Eq. (3)}$$

3. THERMOPHYSICAL PROPERTIES

Solubility. In absorption technologies, the performance of the systems may be reflected from the solubility of refrigerant in the absorbent and can be roughly estimated from the concentration lines in a Dühring diagram. A good working fluid for absorption system must be well soluble in the absorbent under the conditions in which absorption takes place. High solubility and affinity of refrigerant in the absorbent reduce the amount of absorbent needed to circulate the refrigerant at certain cooling capacity, thus decreasing pumping power and reducing heat exchangers size.
Solubility data of water in [dmim][DMP] and [emim][$EtSO_4$] were obtained and correlated using Non-Random Two-Liquids (NRTL) model from Zhao et al. (2006) and Wang et al. (2007). Pressure-temperature-concentration (*PTX*) diagrams of water solubility in [dmim][DMP] and [emim][$EtSO_4$] mixtures are shown in Fig 2 (a) and (b), respectively. Although both solutions present significant negative deviation to ideal Raoult's law, these two ionic liquids have considerably lower solubility than LiBr salt in terms of mass concentration.

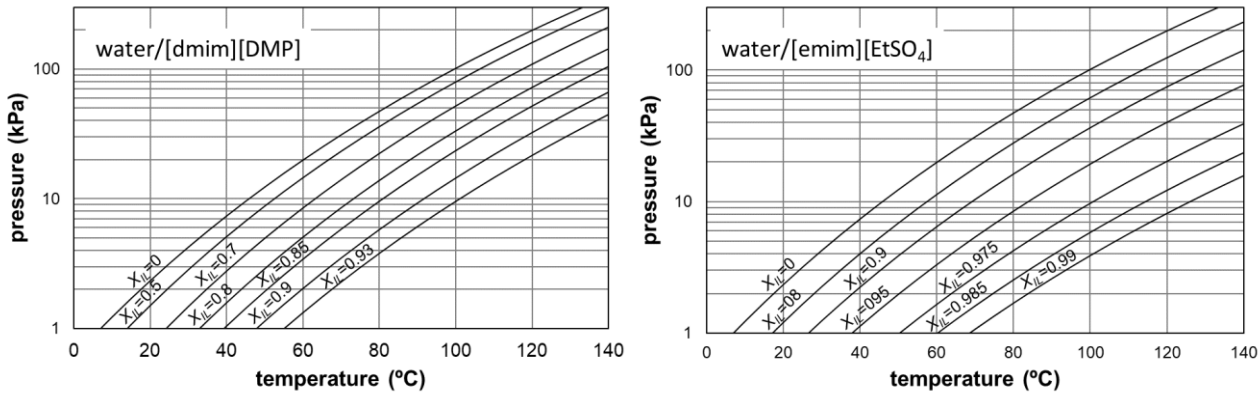

Figure 2: *PTX* diagram of water/[dmim][DMP] (a) and water/[emim][$EtSO_4$] (b)

From *PTX* diagrams in Fig 2 one can see that at the same pressure and temperature conditions, working fluid mixtures with wider concentration distribution will have more refrigerant mass concentration in absorber-generator loop. Therefore, the working fluid mixtures with wider concentration lines distribution have lower solution flow rates as it has higher concentration difference between strong and weak solution.

Apart of that, it also can be seen that the solubility of water in [dmim][DMP] is higher than in [emim][$EtSO_4$]. An example of the concentration (both weak and strong solution) of studied ionic liquid in comparison with LiBr solution at different typical operative conditions (T_{abs}=T_{cond}=30~40 ºC, T_{evap}=5~10 ºC, T_{gen}=80~90 ºC) is summarized in Table 1.

Table 1. Saturation absorbent concentration at various operative conditions

T_{evap} (ºC)	X_{abs}					
	T_{abs}= 30 ºC			T_{abs}= 40 ºC		
	[dmim][DMP]	[emim][$EtSO_4$]	LiBr	[dmim][DMP]	[emim][$EtSO_4$]	LiBr
5	79.07	93.01	52.57	86.84	96.14	57.81
8	75.93	91.38	50.57	84.71	95.27	56.08
10	73.62	90.08	49.13	83.16	94.58	54.90
T_{gen} (ºC)	X_{gen}					
	T_{cond}= 30 ºC			T_{cond}= 40 ºC		
	[dmim][DMP]	[emim][$EtSO_4$]	LiBr	[dmim][DMP]	[emim][$EtSO_4$]	LiBr
80	92.25	97.50	62.94	87.79	95.65	57.62
85	93.72	97.99	65.20	89.94	96.50	59.91
90	94.92	98.37	67.45	91.72	97.17	62.15

Dynamic viscosity. One of the most common issues in ionic liquids that may lead to a significant drawback is their high viscosity. Very viscous absorbent may cause significant pressure drops in the solution circulation loop, which can lead to the increase of pumping power and system size. The viscosity data of water/[dmim][DMP] and water/[emim][$EtSO_4$] solutions were taken and correlated from He et al. (2010) and Bhattacharjee et al. (2012), respectively.

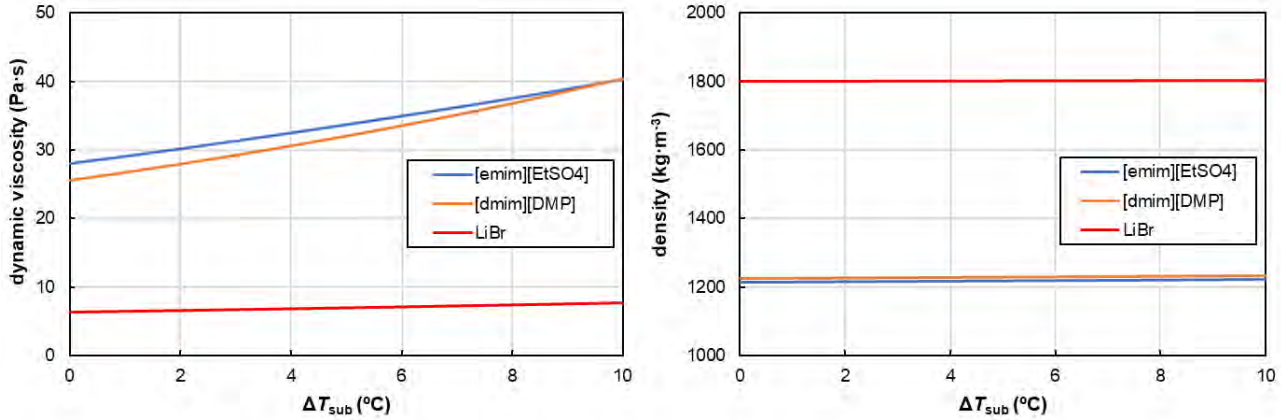

Figure 3: Viscosity (a) and density (b) of water/ionic liquid and water/LiBr mixtures leaving from the generator (T_{gen}=90 °C, T_{cond}=30 °C) at different subcooled temperature (T_{evap}=5 ºC)

The viscosity of water/ionic liquid mixtures at different subcooled temperature (T_{evap}=5 ºC) are shown in Fig 3 (a). As it can be seen in Fig. 3 (a), the viscosity of water/[emim][$EtSO_4$] is higher than water/[dmim][DMP] and water/LiBr.

Density. The density data of water/[dmim][DMP] and water/[emim][$EtSO_4$] were taken and correlated from He et al. (2010) and Bhattacharjee et al. (2012), respectively. The density of water/ionic liquid mixtures at different subcooled temperature (T_{evap}=5 ºC) is shown in Fig 3 (b) with the density of water/ionic liquid solutions are almost similar, being the water/LiBr is much higher than ionic liquids.

Heat capacity. Heat capacity is also one of the most important property used to analyse both thermal performance and heat transfer characteristic of a system. Several experimental data of heat capacities of the studied working fluids were taken from literatures (He et al.,2010, García-Miaja et al., 2009).

Fig 4 (a) illustrates the heat capacity of studied solutions at various degree of subcooling in a typical entrance absorber condition. The solution concentration is determined from a condition where the solution is saturated when leaving the generator at temperature of 90 °C and pressure of 4.25 kPa

(corresponds to T_{cond}=30 °C). This condition is used to plot the heat capacity over absorber temperature as the heat transfer phenomena in the absorption process starts taking place at the entrance of absorber. The correlation based on experimental data shows that the heat capacity of aqueous ionic liquid solutions is higher than that of water/LiBr solution, being that of water/[dmim][DMP] is the highest (see Fig 4 (a)).

Mass diffusivity. Mass diffusivity is an important property to evaluate mass transfer characteristic particularly in the absorber. Although this property is important, to the best of our knowledge there is no available data or correlation of mass diffusivity of water in studied ionic liquids and thus, to estimate the mass diffusivity of water in ionic liquids a method suggested by Krannich et al. (2016) is used.

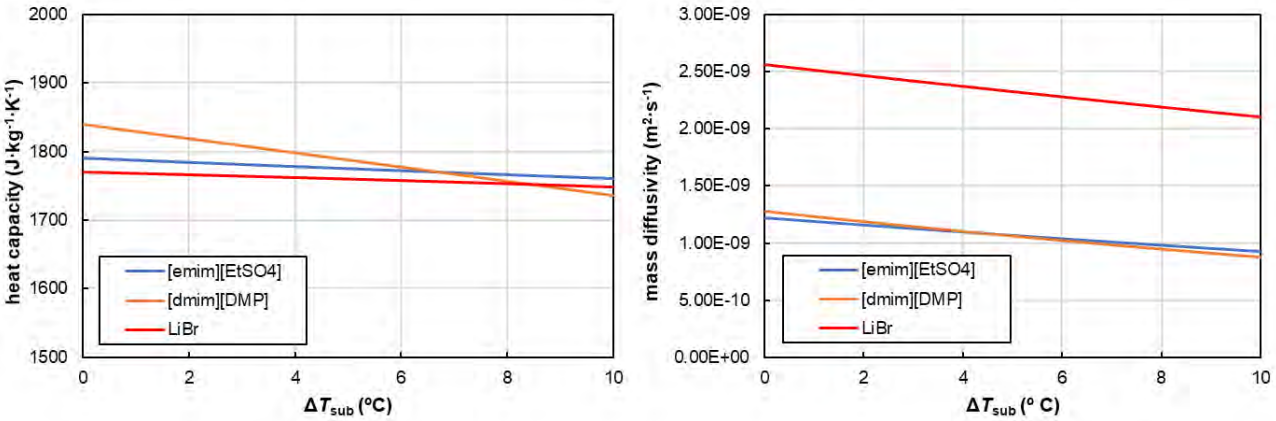

Figure 4: Heat capacity (a) and mass diffusivity (b) of water/ionic liquid and water/LiBr mixtures at saturation condition leaving from the generator (T_{gen}=90 °C, T_{cond}=30 °C) and different subcooled absorber temperature (T_{evap}=5 °C)

Using similar condition to Fig 4 (a), the mass diffusivity of water in studied solutions at typical entrance absorber conditions at various degree of subcooling is then plotted in Fig 4 (b). In this figure, it shows that the mass diffusivity of studied ionic liquids is much lower in comparison with conventional aqueous LiBr solution, being [emim][$EtSO_4$] is the lowest among three studied working fluids. This low mass diffusivity will significantly affect to the mass transfer behaviour, as will be discussed later.

4. RESULTS AND DISCUSSIONS

4.1. Model Validation

Before being applied to water/ionic liquid mixtures, the model is validated using experimental data from literature (Takamatsu et al., 2003) using water/LiBr as the working fluid for an absorber with the same dimensions and operation conditions of the experiments. The comparison between calculated and experimental results is shown in Table 2 and it shows acceptable results.

Table 2. Comparison of the model and experimental data.

Parameters	Unit	Present Simulation	Takamatsu et al. (2003)
Re_s		60.8	
ΔT_{sub}	°C	0.1	
P_{abs}	kPa	1.338	
$T_{s,in}$	°C	39.1	
$T_{s,out}$	°C	27.5	24.1
$T_{c,in}$	°C	22.8	
$T_{c,out}$	°C	23.6	23.7
Heat flux	$kW \cdot m^{-2}$	6.167	7.267
Mass flux	$g \cdot m^{-2} \cdot s^{-1}$	1.71	1.33

4.2. Effect of Solution Reynolds Number

In order to get more understanding on the comparison of the performance of ionic liquids in absorption process, heat and mass transfer characteristics of absorption process of water vapor in ionic liquid solutions is theoretically studied, using absorber configuration and operation conditions similar to the one studied by Ariyadi et al. (2018).

Mass and heat flux of water/[dmim][DMP] and water/[emim][$EtSO_4$] working fluids in comparison with water/LiBr working fluid are presented in Fig. 5 (a) and (b), respectively, with solution Reynolds number varies up to 400. In Fig. 5 (a) it can be explained that the mass flux of all studied working fluids increases with the increase of solution Reynolds number until reaches its optimum value then decreases with the increase of solution Reynolds number. This phenomenon happens because at low solution Reynolds number (i.e. Re_s < 20 in the case of [dmim][DMP]), with an assumption that solution-vapor interface is always in equilibrium condition along the tube, the heat due to absorption process can be transferred out at higher rate, making the temperature difference between solution interface and bulk is low, hence the mass absorption rate increases. At higher solution Reynolds number, with the same assumption of equilibrium condition at solution-vapor interface, the heat due to absorption process cannot be moved out at higher rate, creating high the temperature difference between solution interface and bulk, thus the increase of solution Reynolds number will not improve the absorption rate and the absorption mass flux will decrease with the increase of solution Reynolds number. Generally, the mass flux and its optimum values follow an order of water/LiBr > water/[dmim][DMP] > water/[emim][$EtSO_4$], following diffusivity and solubility values of water in the absorbent as the main influencing properties. The optimum mass flux is reached at low solution Reynolds number in the case of ionic liquids system as the Reynolds number of water/ionic liquid solutions at the same mass flow rate is lower than that of water/LiBr solution due to the high viscosity of water/ionic liquid solutions.

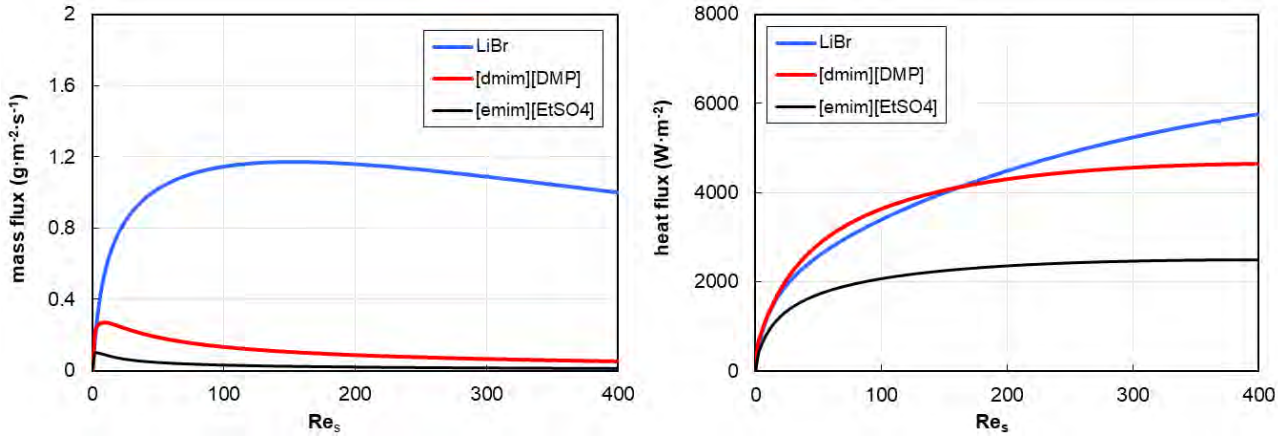

Figure 5. Mass flux (a) and heat flux (b) vs solution Reynolds number of water/LiBr and water/ionic liquid solutions.

Although mass flux of water/[dmim][DMP] solution is lower than that of water/LiBr solution, at the same absorber configuration and operation conditions, the heat flux of that water/[dmim][DMP] working fluid is slightly higher than that of water/LiBr working fluid at lower solution Reynolds number and the heat flux of that water/[emim][$EtSO_4$] working fluid remain the lowest as its low heat capacity and low heat of absorption. The heat flux increases with the increase of solution Reynolds number even when the absorption rate decreases, as shown in Figure 5(b).

4.3. Effect of Solution Degree Subcooling

The effect of solution degree subcooling (from 0°C to 8°C) on the mass flux and mass flux of water/[dmim][DMP] and water/[emim][$EtSO_4$] working fluids in comparison with conventional water/LiBr working fluid are shown in Fig. 6 (a) and (b), respectively.

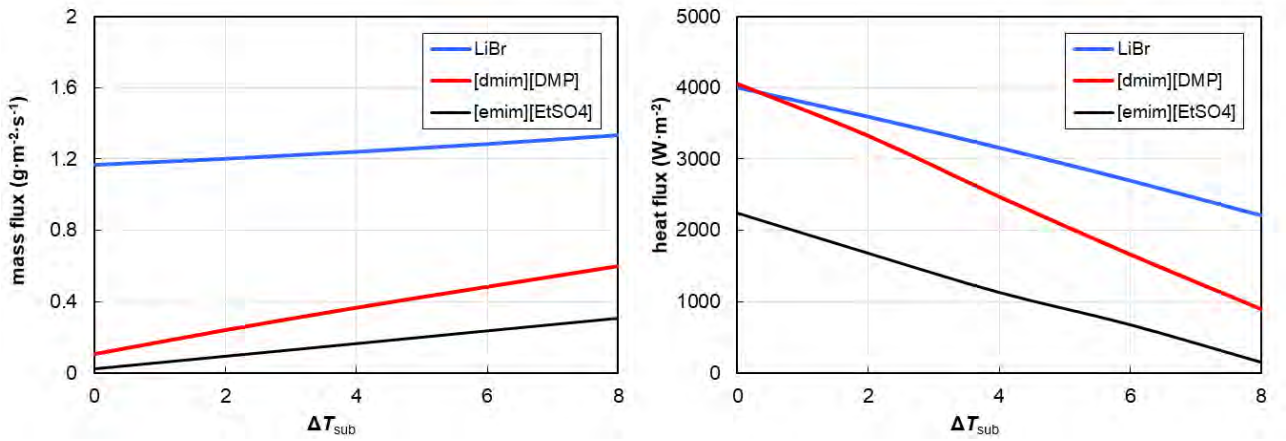

Figure 6. Mass flux (a) and heat flux (b) vs solution degree subcooling of water/LiBr and water/ionic liquid solutions.

Although mass flux of all studied solution increase with the increase of solution degree subcooling, the heat flux of all studied working fluids decrease when the solution degree subcooling increases (see Fig. 6 (b)). This is because at higher solution degree subcooling, at the same inlet coolant temperature, the temperature difference between solution and coolant water is lower thus reducing the heat transfer rate from the solution to the coolant fluid.

5. CONCLUSIONS

Two imidazolium based ionic liquids for water absorbent has been comprehensively studied to examine their suitability as absorbent for water refrigerant to replace LiBr salt by analyzing their thermophysical properties and their heat and mass transfer characteristics on absorption process in a vertical tube absorber. It is clear that the performances of a refrigerant/absorbent working pairs do not only depend on the vapor-liquid equilibrium or solubility but is also highly influenced by its thermal and transport properties. Between two studied ionic liquids, generally, [dmim][DMP] provides better properties than [emim][$EtSO_4$]. [dmim][DMP] provides better properties, such as high heat capacity, low density, and no solidification risk in comparison with conventional water/LiBr solution which can make this ionic liquid as better alternative absorbent to aqueous LiBr solution. However, it still has undesirable properties that can make significance decrease in the system performance, such as low solubility and diffusivity, and high viscosity. In terms of heat and mass transfer, the conventional water/LiBr working fluids still shows better performance than the studied ionic liquids in any operative conditions far from its crystallization zone. Theoretically, the thermophysical properties of ionic liquids can be tuned by combining the cation and anion pair. However, in practice, finding the best combination of cation and anion of ionic liquids to have good properties for absorption application is not an easy task. Considering the high potential application of ionic liquids as an absorbent in absorption application, further study on prominent ionic liquids which have better properties for absorption cooling applications remains necessary.

NOMENCLATURE

c	concentration ($kg \cdot m^{-3}$)	**Subscript**	
Cp	constant pressure heat capacity ($kJ \cdot kg^{-1} \cdot K^{-1}$)	abs	absorber
		c	coolant fluid
Di	inside diameter (m)	cond	condenser
H	enthalpy ($kJ \cdot kg^{-1}$)	evap	evaporator
k	mass transfer coefficient ($m \cdot s^{-1}$)	gen	generator
L	tube length (m)	int	vapor-solution interface
m	mass flowrate ($kg \cdot s^{-1}$)	s	solution
P	pressure (kPa)	sub	subcooled
Re	Reynolds number	v	vapor
T	temperature (ºC)	w	water

U overall heat transfer coefficient ($kW \cdot m^{-2} \cdot K^{-1}$)

X solution concentration (% mass of absorbent)

REFERENCES

Ariyadi, H. M., Coronas, A., 2016. Absorption Capacity of Ammonia into Ionic Liquids for Absorption Refrigeration Applications, J. Phys.: Conf. Ser., 745 032105

Ariyadi, H. M., Giannetti, N., Yamaguchi, S., Saito., K, 2018. Modelling of Water Vapor Absorption by Aqueous Ionic Liquid Fluids in a Vertical-Tube Falling Film Absorber, Proc. Grand Renew. Energy 2018, Yokohama, Japan, June 18-22, 2018

Bhattacharjee, A., Varanda, C., Freire, M. G., Matted., S., Santos, L. M. N. B. F., Marrucho, I. M., Coutinho, J. A. P., 2012. Density and Viscosity Data for Binary Mixtures of 1-Alkyl-3-methylimidazolium Alkylsulfates + Water, J. Chem. Eng. Data, 57, pp. 3473−3482.

Bourouis, M., Vallès, M., Medrano, M., Coronas, A., 2005. Absorption of water vapour in the falling film of water– (LiBr+LiI+LiNO3+LiCl) in a vertical tube at air-cooling thermal conditions, Int. J. Therm. Sci., 44, pp. 491–498.

García-Miaja, G., Troncoso, J., Romaní, 2009. Excess enthalpy, density, and heat capacity for binary systems of alkylimidazolium-based ionic liquids + water, J. Chem. Thermodynamics, 41, pp. 161–166.

He, Z., Zhao, Z., Zhang, X., Feng, H., 2010. Thermodynamic properties of new heat pump working pairs: 1,3-Dimethylimidazolium dimethylphosphate and water, ethanol and methanol, Fluid Phase Equilibria, 298, pp. 83–91

Kim, J.K., Jung, J.Y., Kang, Y.T., 2006. The effect of nano-particles on the bubble absorption performance in a binary nanofluid, Int. J. Refrigeration, 29, pp. 22–29.

Kim, Y. J., Kim, S., Joshi, Y. K., Fedorov, A. G., Kohl, P. A., 2012. Thermodynamic analysis of an absorption refrigeration system with ionic-liquid/refrigerant mixture as a working fluid, Energy 44, pp. 1005–1016.

Krannich, M., Heym, F., Jess, A., 2016. Characterization of Six Hygroscopic Ionic Liquids with Regard to Their Suitability for Gas Dehydration: Density, Viscosity, Thermal and Oxidative Stability, Vapor Pressure, Diffusion Coefficient, and Activity Coefficient of Water, J. Chem. Eng. Data, 61, pp. 1162−1176.

Popp, S., Bösmann, A., Wölfel, R., Wasserscheid, P., 2015. Screening of Ionic Liquid/H2O Working Pairs for Application in Low Temperature Driven Sorption Heat Pump Systems, ACS Sustainable Chem. Eng. 3, pp. 750−757.

Takamatsu, H., Yamashiro, H., Takata, N., Honda, H., 2003. Vapor absorption by LiBr aqueous solution in vertical smooth tubes, Int. J. Refrigeration, 26, pp 659–666.

Tsai, B. B. and Perez-Blanco, H., 1998. Limits of mass transfer enhancement in lithium bromide-water absorbers by active techniques, Int. J. Heat Mass Transfer, 41 (15), pp. 240–2416.

Wang, J. F., Li, C. X., Wang, Z. H., 2007. Measurement and Prediction of Vapor Pressure of Binary and Ternary Systems Containing 1-Ethyl-3-methylimidazolium Ethyl Sulfate, J. Chem. Eng. Data, 52, pp. 1307-1312

Yokozeki, A., and Shiflett, M. B., 2010. Water Solubility in Ionic Liquids and Application to Absorption Cycles, Ind. Eng. Chem. Res. 49, pp. 9496–9503.

Zhao, J., Jiang, X.C., Li, C.X., Wang, Z.H., 2006. Vapor pressure measurement for binary and ternary systems containing a phosphoric ionic liquid, Fluid Phase Equilibria 247 (2006) 190–198.

Manuscript ID: 1034
DOI: 10.18462/iir.icr.2019.1034

Overview on experimental techniques for heat flux and heat transfer estimations, during non-dropwise condensation

Marie-Adélaïde CREMIEUX[a, b], Florine GIRAUD[b], Jacopo SEIWERT[a], Frédéric CRAYSSAC[a], Marc WAGNER[a], Christophe MARVILLET[b], Brice TREMEAC[b]

[a] Paris Innovation Campus, Air Liquide, 1, chemin de la Porte des Loges – BP 126 – 78354 Jouy en Josas – France, marie-adelaide.cremieux@airliquide.com
[b] Laboratoire du Froid, des Systèmes Energétiques et Thermiques (LaFSET), Cnam, HESAM Université, 292 rue Saint-Martin 75003 Paris, France

ABSTRACT

This review gives an overview of experimental techniques for the measurement and estimation of heat flux and heat transfer coefficients, during filmwise condensation.
It is shown that heat flux can be estimated either from measurements in the solid medium, from boundary conditions, or from a global balance on the condensing fluid. Some advice is given in order to reduce measurement uncertainties. The choice of the measurement method does not depend on the value of the heat flux or heat transfer coefficient, but relies on experimental constraints, specific to each study (for example imposed subcooling of the solid medium).
The heat transfer coefficient is then deduced from the heat flux and either from measurements or estimation of the wall and fluid temperatures, or from estimations of the secondary fluid heat transfer coefficient.
Keywords: Condensation, Experimentation, Heat Flux, Heat Transfer Coefficient, Review.

1. INTRODUCTION

Several reviews have been published in the field of filmwise condensation (for example Cavallini et al., 2003; Dalkilic and Wongwises, 2009; Huang et al., 2015). They take into account various aspects of the condensation (presence of non-condensable gases, geometry and orientation of the condenser, smoothness of the condensing wall, nature of the refrigerant, test conditions …). However, none of them present in detail the experimental methods implemented in the articles they reviewed to estimate the heat flux and the heat transfer coefficient (named thereafter HTC). That is why this review aims at giving an overview as general as possible of the different experimental techniques that can be used to estimate the heat flux and the HTC during filmwise condensation. To conduct this review, published papers dealing with experimental filmwise condensation, heat flux and HTC measurements were searched for. Due to space constraints, only few papers will be discussed here.
A HTC being the ratio of the heat flux to the difference of temperature between the wall and the fluid, methods to estimate heat fluxes will first be presented. The paper will then focus on the estimation of the temperature difference between the wall and the fluid. Another method to estimate the HTC will then be introduced before concluding the paper.

2. ESTIMATION OF THE HEAT FLUX

The methods used to estimate the heat flux in heat exchangers can be classified in two categories: estimation of the wall heat flux or estimation of the heat flux from boundary conditions. A global balance on the condensing fluid can also be used (for example Oh and Revankar, 2005; Ohira, 2001) or coupled with one of the local heat transfer estimation method described hereafter (for example Yadav et al., 2018). For a matter of concision, this last method will not be developed here.

2.1. Estimation of the Heat Flux in the Wall

2.1.1. Using heat flux sensors (HFS)

The most direct way to measure a local heat flux is to use HFSs, usually embedded in the solid medium dividing the two fluids in a heat exchanger (Koyama et al., 2003; Singh et al., 2017). It is extremely important to choose carefully the location of the HFS. Indeed, its presence can affect the local heat flux and hence induce an error in the measurement. As explained by Trethowen (1986), the characteristics of heat flux around a HFS depend on both the distribution of heat flows within the measured structure and the surface heat transfer conditions around and over the sensor. Some evaluations of the errors in heat flux measurements induced by the presence of a HFS are summed up in Table 1. The errors are mainly due to the heat flowing preferably around the sensor than through it due to a higher thermal resistance of the sensor than heat conduction medium (Singh et al., 2017; Yadav et al., 2018). They are also due to the fact that a portion of the flux within the sensor spills around its edges and is therefore not measured. Different parameters, such as the thickness of the HFS, also have an impact.
Trethowen (1986) thus proposed various general methods to reduce and stabilize measurement errors. It is possible, for example, to increase the size of the sensor or the thermal resistance of the wall under test. Singh et al. (2017) also proposed to use HFS with an impedance similar to that of the heat conduction medium, in order to reduce intrusion effects.

Table 1. Some evaluations of the errors in heat flux measurements induced by the presence of a HFS

Author	Estimation of error	Causes of errors	Remarks
Singh et al. (2017)	1. From its bibliographic review. Evaluation from Wright *et al.*, (1983): ~ 25%	Various contact thermal resistances.	No indication on the heat flux
	2. From its own study. Decrease of wall heat flux along the thickness of the plate, due to the presence of the HFS: - From 0 to 60 % (HFS flush-mounted at the front surface) - From 0 to 100% (HFS flush-mounted at the rear surface)	- Uncalibrated HFS - Ratio of the thickness of the conduction medium to the thickness of the HFS - Nature of the heat conduction medium	Numerical simulation Heat flux of 90 $kW \cdot m^{-2}$
Trethowen (1986)	Predicted measurement errors (for surface-mounted HFS without edge guards) from 0.66% to 88%	- Various thermal resistances (surface resistance, total thermal resistance of structure, …) - Conductivity and thickness of top substrate layer - Length of HFS	Numerical simulation Heat flux of 4-70 $W \cdot m^{-2}$

According to a recent study conducted by Singh et al. (2017), it is better to have a flush-mounted HFS situated at the rear of the plate (other side compared to the fluid of interest - Fig. 1). Flush mounting limits the impact of the sensor on the flow (creation of flow field disturbances, turbulence and eddies), but cannot eliminate the contact resistance. The effect of flush-mounted HFS on the boundary conditions is more important for laminar than for turbulent flow. Indeed, the latter is more rapidly changing and chaotic. However, the mounting of the HFS at the rear of the wall induces delay in the time response. It is due to its remote location from the area of interest, which must be added to the time constant of the sensor itself. Therefore, it can only be used for quasi steady-state measurements. It is also to be noted, that a mounting of the HFS at the rear of the plate induces a greater reduction in heat flux along the thickness of the plate. It implies an increase of heat flux measurements' errors (Table 1).
A solution that could improve both the efficiency and the accuracy of the sensor is a calibration of the latter in the experimental conditions (Singh et al., 2017; Yadav et al., 2018). Unfortunately, in these papers, no estimation of the errors reduction due to such a calibration is given.
In any case, it is worth noting that a HFS measures only unidirectional heat fluxes.

In the papers presented in this section, the measured heat flux varies from 20 to 88 kW·m^{-2}, and the estimated HTC from 12 to 15 kW·m^{-2}K^{-1}.

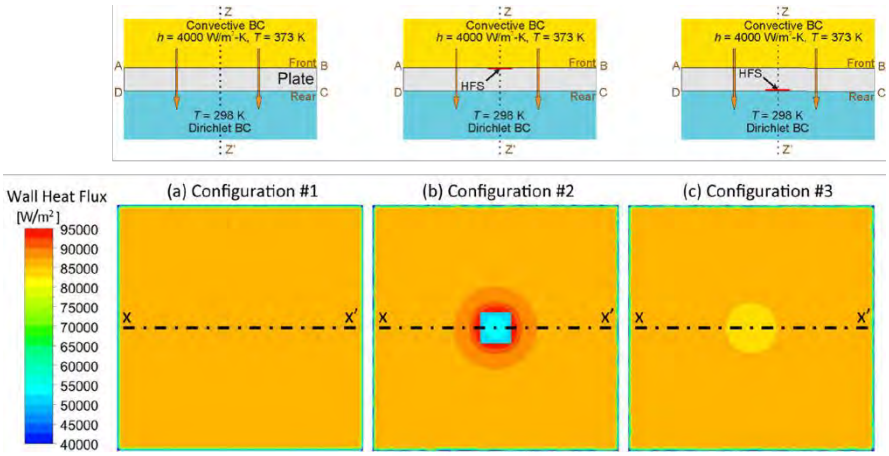

Figure 1: Top: three different set-ups of Singh *et al.* (2017), with no sensor (a), a flush mounted HFS on the front surface (b), a flush mounted HFS on the rear surface (c). Bottom: view from top of the steel plate, with a color scale presenting the wall heat flux at the front of the plate in the three mountings presented above. Numerical study results

2.1.2. Using temperature sensors

Another method to estimate the heat flux consists in first measuring the temperature of the wall in one or several points (usually with thermocouples). The heat flux is then deduced from these data by an inverse heat conduction method coupled with several hypotheses depending on the study. These studies are divided in two main categories: those making the approximation of a steady-state phenomenon and those measuring a transient local heat flux.

In the papers presented in this section, the estimated heat flux varies from 4 to 1000 kW·m^{-2} (the highest heat fluxes are obtained in micro channels), with uncertainties from ± 3.8% to ± 16%. And the estimated HTC varies from 0.5 to 27 kW·m^{-2}K^{-1} (with uncertainties ± 3.6% to ± 21%).

a) Steady-state local heat flux measurements

When observing a well-established phenomenon of filmwise condensation, most authors assume a steady state phenomenon in order to determine the heat flux from temperature measurements, using simplified steady-state heat conduction equations (for example Akaki et al., 1995; Al-Zaidi et al., 2018, Lee et al., 2006). This hypothesis implies several experimental precautions and especially requires a waiting time for the test conditions to reach a steady state (for example, 5 mn for fluctuations of less than 5% of measured value in the study of Xu et al., 2016). However, this precaution does not prevent local unstable phenomena. The hypothesis of a one dimensional heat transfer is always made in the simplified cases presented in the papers. The heat flux is then deduced from the thermal conductivity of the material, its thickness, and the gradient of temperature.

In order to estimate the gradient of temperature, even if it might not lead to the lowest uncertainties, the most common solution consists in measuring the difference of temperature between pairs of thermocouples. Several authors, like Al-Zaidi et al. (2018), use a simple arrangement with thermocouples inserted in two rows (Fig. 2).

According to Wu and Vierow (2006) and Akaki et al. (1995), the errors on the estimated heat flux mainly come from errors on the temperature measurements. Ensuring an efficient thermal contact between the wall and the temperature sensors is therefore necessary. That is why these authors proposed each a solution. The first one consists in using thermocouples with a plug design and filling the gap with silver epoxy. The other one consists in using stainless steel bands to hold the thermocouples, and defining an effective thermal resistivity of the wall to compensate for the residual contact resistance. Another conclusion that could be drawn from the initial remark is that this “steady state local heat flux estimation”

solution is especially fitted for experiments where it is possible to implement a significant sub cooling of the wall. Indeed, for low sub cooling, the impact of the sensors uncertainties will not be negligible.
Shin and Kim (2004) adopted an entirely new technique to estimate in tube condensation heat transfer for very low heat dissipation rate and mass flow rates. Their set-up uses two parallel copper tubes, both cooled by the same fluid. In the first one, the condensing refrigerant flows horizontally. In the second one, the authors placed a variable power supplied heater, experimentally adjusted to exchange the same heat flux as the refrigerant (by temperature comparison). It allows a very simple control of the heat flux, which does not necessitate any information on the secondary fluid and which enables very small dissipation rates (as low as 0.75 W). This method is also very accurate. A preliminary test, where another heater replaced the refrigerant, gave a maximum error of 2.6 % between the value of the second heater and the value calculated using the described method.

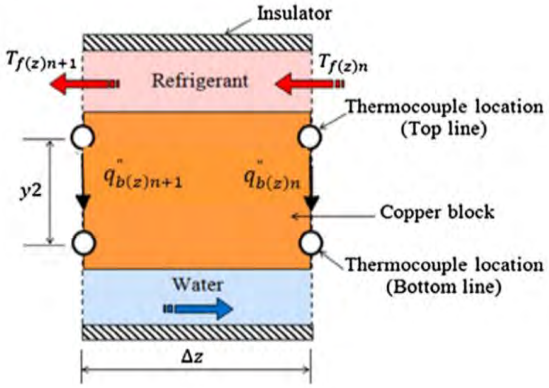

Figure 2: Typical scheme of the heat flux measurement inside the solid medium, using two thermocouple lines (Al-Zaidi et al., 2018)

b) Transient local heat flux measurements

Understanding the behavior of a system during transient phenomena represents an essential step in its global comprehension and can shed light on the physical processes at stake. The transient heat flux can be estimated, using data from one or two thermocouples and an inversion algorithm (Inverse Heat Conduction Method). Yadav et al. (2018) presents three different models. The first one uses data from one thermocouple embedded inside the wall, with known boundary conditions. The second one uses one thermocouple for the inversion process, and boundary conditions deduced from another thermocouple's data history. The last model models the solid as a semi-infinite medium and uses data from at least one thermocouple. They showed that the results obtained for the two thermocouples method are more accurate than for the one-thermocouple method. Indeed, the one thermocouple model is dependent on the assumption of constant temperature at rear boundary, hypothesis which is not verified in their experiment. According to the authors, the two thermocouples model is also much more robust and versatile. Since they compared their results with results obtained from a HFS positioned on the rear surface of the condensing plate, it is worth noting another of their conclusions: a rear-mounted HFS must not be used to capture transient behaviours. Indeed, they observed a delay during the establishment of the steady-state.

2.2. Estimation of the Heat Flux from Boundary Conditions

2.2.1. Using thermoelectric coolers

In order to control the heat flux passed onto the condensing fluid, several authors used thermoelectric coolers (Baird et al., 2003; Tiwari, 2011). In this solution, the heat flux is controlled by the electrical power supplied to the cooler (conceptually equivalent to the use of electric heaters in the studies on vaporization). One challenge is to evacuate the heat flux produced by the cooler on the hot side of the device. One solution is to employ a heat sink, which offers several advantages. It enables the control of the hot side temperature, and thus the control of the heat flux (Tiwari, 2011). It also improves the efficiency of the cooler, by minimising the temperature difference between its two faces (Baird et al., 2003). On the cold side, a heat sink is not necessary, as condensation is one of the best solution to

dissipate heat. However, it can be appropriate to homogenise the temperature, using for example an aluminium plate (Tiwari, 2011), or a copper block (Baird et al., 2003).
Baird et al. (2003) underlined a limitation of this solution. When the temperature difference between their two faces increases, thermoelectric coolers efficiency decreases. For a given thermoelectric cooler, there is a limit temperature difference, above which it does not produce the needed heat flux. In their study conducted at constant heat flux, because of the low HTCs in the area near complete condensation (mass fraction of vapour less than 0.2 in the study), the required wall temperatures were below the available thermoelectric device sink temperature. Therefore, the wall heat flux was lower than needed. Another limitation is that, if this solution is experimentally interesting at small scales, it is less fitted for large scales, due to low heat transfer capacities per cooler (around 100 W).
The uncertainty associated with the thermoelectric cooler's calibration in the study of Baird et al. (2003) is less than 5 %. It gives an uncertainty in the local heat flux estimation of less than 10 %, for a range of heat flux from 15 to 110 kW/m^2.

2.2.2. Balance on the secondary fluid

Using a single-phase secondary fluid can be a sufficient solution for an easy measurement of the heat flux. In fact, heat transfers in the case of monophasic fluids are usually well known and the heat flux measurement can therefore be readily implemented. The general idea of this method is to measure the flow rate of the secondary fluid, as well as its inlet and outlet temperatures. Knowing its heat capacity, it is then possible to calculate the heat flux. This method can be used to measure mean heat flux on the whole condensing section (temperature known only at the inlet and outlet of the section - Dalkilic et al., 2009; Fan et al., 2018; Han et al., 2003; Longo et al., 2004), mean heat flux on subsections of the heat exchanger (temperature known at several axial locations - Rahman et al., 2018; Sarraf et al., 2015), and local heat flux (temperature known at every axial location of the condensing section - Matkovic et al., 2009; Peterson et al., 1997). Due to high latent heat in condensation, the needed secondary fluid mass flux is usually high. For this reason, this method is not applicable to all experimental cases.
In the papers presented in this section, the estimated heat flux varies from 4.7 to 110 $kW \cdot m^{-2}$(with uncertainties from ± 4% to ± 10%) and the estimated HTC from 0.7 to 30 $kW \cdot m^{-2}K^{-1}$(with uncertainties from 4.3% to 27%).
Park et al. (2011) underline one limit of this method. If the difference of temperature between the inlet and outlet of the coolant section is low, large errors are made on the estimation of the heat flux, due to the increased ratio of measurement errors to measurement values.
Sarraf et al. (2015) used this method, estimating the temperature of the coolant in several locations. Unlike most of the other studies, they did not use thermocouples, but instead used infrareds. The raw heat flux is then calculated multiplying the mass flow with the difference of enthalpy between the inlet and outlet of the section (the section corresponds to the area comprised between two consecutive temperature sensors). Rahman et al. (2018) determined for example the enthalpy with an iterative method. Some authors, like Rahman et al. (2018), also took into account the thermal losses in their calculation of the heat flux. The local heat flux is weighted by the ratio of the heat release of refrigerant to the sensible heat gain of the coolant on the whole condenser. An estimated heat dissipation can also be subtracted to the section heat flux.
The authors interested in obtaining local heat flux (for example: Matkovic et al., 2009; Peterson et al., 1997) used a slightly different method. They interpolated the temperature of the coolant from measurements made at several positions with thermocouples. Some, like Matkovic et al. (2009), interpolated it with a polynomial function, while Peterson et al. (1997) implemented a more refined method, with temperature profile factors depending on temperatures and flow rates. The authors were then able to calculate the local heat flux at every axial location of the tube.

3. ESTIMATION OF THE HEAT TRANSFER COEFFICIENT (HTC)

Once the heat flux has been estimated using one of the methods presented above, the condensation HTC can then be deduced from these data and either from measurements or estimation of the wall and fluid temperatures, or from estimations of the secondary fluid HTC.

3.1. Measurement of Wall and Fluid Temperatures

3.1.1. Measurement of fluid temperature

Three different methods have been implemented by the authors to measure the fluid temperature: direct measurement in the condensing channel (Akaki et al., 1995; Lee et al., 2006; Rahman et al., 2018); estimation from pressure measurements (Al-Zaidi et al., 2018; Matkovic et al., 2009; Oh and Revankar, 2005; Ohira, 2001); or estimation from the bulk vapour mass fraction if the gas flow rate is considered as constant (Peterson et al., 1997).

While using direct measurements, precautions, such as locating the thermometer upstream to the condenser, must be taken in order not to disturb the vapour flow (Ohira, 2001). Taking a local value for the bulk temperature also potentially implies large errors if flow temperature and properties vary significantly (Peterson et al., 1997). Thus, some authors (Fan et al., 2018; Koyama et al., 2003) took a mean value of the fluid temperature, using the measured value at the inlet and at the outlet of the section, and possibly those measured along the condenser section.

The saturation pressure is often just measured at the inlet and outlet of the condenser and estimated in-between, generally with usual correlations. These correlations take into account the pressure loss due to sudden condensation, the momentum pressure drop, and the frictional pressure drop. Void fraction can be calculated using, for example, Rouhani & Axelsson equations and the friction pressure drop can be deduced from the Lockhart-Martinelli equation.

3.1.2. Measurement of wall temperature

The wall temperature can be measured directly at the wall surface, in one or several locations (for example Fan et al., 2018). However, in order not to disturb the flow on the condensation side, the condensation side wall temperature is often deduced from the other side wall temperature measurements, or from measurements inside the wall (Al Zaidi et al., 2018; Matkovic et al., 2009; Rahman et al., 2018). The heat flux is deduced from previous estimations. Authors generally assume a one-dimensional steady state heat conduction through the wall.

It is worth noting that, in their study, Akaki et al. (1995) presented a method to obtain very accurate estimations of the temperature. They applied it to a condensation case, with a 5.5 mm-thick stainless steel wall. Thermocouples with a diameter of 0.65 mm were inserted in grooves on the inner and outer walls. The authors corrected the measured values, accounting for the dispersion of the thermocouples in the grooves at each level.

3.2. HTC of the Secondary Fluid Known

For mean HTC estimation, another method using the overall HTC of the exchanger and the HTC of the secondary fluid is often implemented. This overall HTC is defined as the product of the heat transfer with the logarithmic mean temperature difference. This simplified method implies significant hypotheses: heat losses are supposed negligible, specific heat capacity of the fluid and HTCs are supposed constant along the test section.

The overall HTC accounts for different heat transfers: the one between the wall and the secondary fluid, the heat conduction inside the wall and the condensation heat transfer. The fouling resistances are usually assumed negligible and are therefore not considered. The thermal resistance of the wall depends on its thickness and thermal conductivity. It is sometimes assumed negligible compared to convection (Han et al., 2003).

The HTC on the side of the secondary fluid is estimated using either correlations obtained from the literature (for example, the Kutateladze correlation, used by Ewald and Perroud, 1971); or previous correlations from experimental data (Oh and Revankar, 2005). For example, Han et al. (2003) used results obtained for single-phase pre-tests. Several authors, like Longo et al. (2004), also opted for the Wilson plot method running specific experimental tests beforehand. Longo et al. (2004) even used a modified Wilson plot technique accounting for variable fluid property effects.

It is interesting to note that, according to Ewald and Perroud (1971), if the HTC of the secondary fluid is much greater than the overall coefficient, which is the case in their study (boiling secondary fluid), an error in the secondary fluid HTC will have a reduce impact on the primary fluid HTC.

4. CONCLUSIONS

Heat flux can be determined from the measurement of a temperature difference inside the solid medium, but also from boundary conditions or a global balance on the whole test section. The choice of the measurement method does not depend on the value of the heat flux or HTC, but relies on experimental constraints specific to each study (for example imposed subcooling of the wall). Condensation HTCs are then deduced from the heat flux and else, wall and fluid temperatures, or, secondary fluid HTC. The most precise method is the one where wall and fluid temperatures are directly measured.
Practical steps can be taken in order to reduce measurement uncertainties. Some have been presented all along this review. Among them ensuring an efficient thermal contact between the wall and the temperature sensors, using HFSs with an impedance similar to that of the heat conduction medium or, having flush-mounted HFSs at the rear of the plate. Other methods to reduce uncertainties can be cited, including an on-site calibration of thermocouples, a check of temperature and pressure under saturated conditions and a check of thermal balance in the test section (Matkovic et al., 2009). It is also worth noting, although it is evident, that the largest uncertainties will be found at low mass flux (Dalkilic et al., 2009) and low difference of temperature between the wall and the fluid (Oh and Revankar, 2006), or low value of the logarithmic mean temperature difference. These parameters thus may be set at a sufficient value to reduce these uncertainties.

REFERENCES

Akaki, H., Kataoka, Y., Murase, M., 1995. Measurement of Condensation Heat Transfer Coefficient inside a Vertical Tube in the Presence of Noncondensable Gas, J. Nucl. Sci. Technol. 32(6), 517-526.

Al-Zaidi, A.H., Mahmoud, M.M., Karayiannis, T.G., 2018. Condensation flow patterns and heat transfer in horizontal microchannels, Exp. Therm. Fluid Sci 90, 153-173.

Baird, J.R., Fletcher, D.F., Haynes, B.S., 2003. Local condensation heat transfer rates in fine passages, Int. J. Heat Mass Transf. 46, 4453–4466.

Cavallini, A., Censi, G., Del Col, D., Doretti, L., Longo, G.A., Rossetto, L., Zilio, C., 2003. Condensation inside and outside smooth and enhanced tubes — a review of recent research, Int. J. Refrigeration 26(4), 373-392.

Dalkilic, A.S., Wongwises, S., 2009. Intensive literature review of condensation inside smooth and enhanced tubes, Int. J. Heat Mass Transf. 52(15-16), 3409-3426.

Dalkilic, A.S., Yildiz, S., Wongwises, S., 2009. Experimental investigation of convective heat transfer coefficient during downward laminar flow condensation of R134a in a vertical smooth tube, Int. J. Heat Mass Transf. 52, 142–150.

Ewald, R., Perroud, P., 1971. Measurements of film-condensation heat transfer on vertical tubes for nitrogen, hydrogen, and deuterium, In: Advances in Cryogenic Engineering, Springer, 475-481.

Fan, G., Tong, P., Sun, Z., Chen, Y., 2018. Development of a new empirical correlation for steam condensation rates in the presence of air outside vertical smooth tube, Ann. Nucl. Energy 113, 139–146.

Han, D.H., Lee, K.J., Kim, Y.H., 2003. The Characteristics of Condensation in Brazed Plate Heat Exchangers with Different Chevron Angles, J. Korean Phys. Soc. 43(1), 66-73.

Huang, J., Zhang, J., Wang, L., 2015. Review of vapor condensation heat and mass transfer in the presence of non-condensable gas, Appl. Therm. Eng. 89, 469-484.

Koyama, S., Kuwahara, K., Nakashita, K., Yamamoto, K., 2003. An experimental study on condensation of refrigerant R134a in a multi-port extruded tube, Int. J. Refrigeration 26(4), 425-432.

Lee, K.W., Cheon No, H., Chu, I.C., Moon, Y.M., Chun, M.H., 2006. Local heat transfer during reflux condensation mode in a U-tube with and without noncondensable gases, Int. J. Heat Mass Transf. 49, 1813–1819.

Longo, G.A., Gasparella, A., Sartori, R., 2004. Experimental heat transfer coefficients during refrigerant vaporisation and condensation inside herringbone-type plate heat exchangers with enhanced surfaces", Int. J. Heat Mass Transf. 47, 4125–4136.

Matkovic, M., Cavallini, A., Del Col, D., Rosetto, L., 2009. Experimental study on condensation heat transfer inside a single circular minichannel, Int. J. Heat Mass Transf. 52, 2311–2323.

Oh, S., Revankar, S.T., 2005. Effect of noncondensable gas in a vertical tube condenser, Nucl. Eng. Des. 235, 1699–1712.

Oh, S., Revankar, S.T., 2006. Experimental and theoretical investigation of film condensation with noncondensable gas, Int. J. Heat Mass Transf. 49, 2523–2534.

Ohira, K., 2001. Laminar Film Condensation Heat Transfer of Hydrogen and Nitrogen Inside a Vertical Tube, Heat Tran. Asian Res. 30(7), 542-560.

Park, J.E., Vakili-Farahani, F., Consolini, L., Thome, J.R., 2011. Experimental study on condensation heat transfer in vertical minichannels for new refrigerant R1234ze (E) versus R134a and R236fa, Exp. Therm. Fluid Sci. 35, 442–454.

Peterson, P.F., Schrock, V.E., Kuhn, S.Z., 1997. Recent experiments for laminar and turbulent film heat transfer in vertical tubes, Nucl. Eng. Des. 175, 157–166.

Rahman, M.M., Kariya, K., Miyara, A., 2018. An experimental study and development of new correlation for condensation heat transfer coefficient of refrigerant inside a multiport minichannel with and without fins", Int. J. Heat Mass Transf. 116, 50–60.

Sarraf, K., Launay, S., El Achkar, G., Tadrist, L., 2015. Echangeur à plaques corruguées en mode condenseur : étude locale des transferts thermo-hydrauliques », Proceedings of the 22ème Congrès Français de Mécanique, Lyon, France.

Shin, J.S., Kim, M.H., 2004. An experimental study of condensation heat transfer inside a mini-channel with a new measurement technique, Int. J. Multiph. Flow 30, 311–325.

Singh, S.K., Yadav, M.K., Khandekar, S., 2017. Measurement issues associated with surface mounting of thermopile heat flux sensors, Appl. Therm. Eng. 114, 1105-1113.

Tiwari, A., 2011. Characterization of mass transfer by condensation on a horizontal plate, PhD thesis Université Blaise Pascal, Clermont-Ferrand II, France, 284p.

Trethowen, H., 1986. Measurement errors with surface-mounted heat flux sensors, Build. Env. 21(1), 41-56.

Wright Jr., R.E., Kantsios, A.G., Henley, W.C., 1983. Effect of Mounting on the Performance of Surface Heat Flow Meters Used to Evaluate Building Heat Losses, Thermal Insulation, Materials and System for Energy Conservation in 80s, ASTM 789, 293-317.

Wu, T., Vierow, K., 2006. Local heat transfer measurements of steam/air mixtures in horizontal condenser tubes, Int. J. Heat Mass Transf. 49, 2491–2501.

Xu, H., Sun, Z., Gu, H., Li, H., 2016. Experimental study on the effect of wall-subcooling on condensation heat transfer in the presence of noncondensable gases in a horizontal tube", Ann. Nucl. Energy 90, 9-21.

Yadav, M.K., Singh, S.K., Parwez, A., Khandekar, S., 2018. Inverse models for transient wall heat flux estimation based on single and multi-point temperature measurements, Int. J. Therm. Sci. 124, 307-317.

Manuscript ID: 1052
DOI: 10.18462/iir.icr.2019.1052

Ammonia/ionic liquid absorption in a plate heat exchanger: a theoretical study and an experimental setup

Meng WANG*, Carlos A. INFANTE FERREIRA

Process & Energy Department, Delft University of Technology
Leeghwaterstraat 39, 2628 CB Delft, M.Wang-2020@outlook.com

ABSTRACT

Negative transport properties have always been pointed out as the key factors that hinder the application of ammonia/ionic liquids (NH_3/ILs) in the absorption cycles, while heat and mass transfer of these new fluids in components have been rarely reported. The authors selected corrugated plate heat exchangers as the geometry to explore the absorption of the proposed working fluids. In this paper, a modeling method and a continuous absorption-desorption setup are introduced. Absorption process is modeled with the two-resistance theory by introducing a gas-liquid interface. Analytical heat transfer results and mass transfer from penetration theory are applied. With the model, distribution of local parameters and overall heat and mass transfer characteristics of an absorber in a cooling application are obtained. The overall heat transfer coefficient of an absorber for a refrigeration application is around 1350 W/(m^2K) for the studied NH_3/IL working fluids. An experimental setup is developed for further model improvement.
Keywords: Ammonia, Ionic liquid, Absorption, Plate Heat Exchanger, Heat Pumps, Heat/Mass Transfer.

1. INTRODUCTION

Thermally driven vapor absorption heat pumps and refrigeration systems provide energy-efficient ways of heating and cooling for the industry, agriculture, residential and transport sectors. Recently investigations have been carried out to explore the application of ionic liquids (ILs), a type of room-temperature molten salts, as absorbents in vapor absorption systems, to prevent the risks of corrosion and crystallization of H_2O/LiBr pair and weaknesses of low efficiency and complexity of systems with NH_3/H_2O pair. In particular, working pairs of NH_3/ILs have been proposed as working fluids in absorption cycles to remove rectification and distillation sections, and to improve cycles' thermal efficiency (Wang et al., 2018; Wang and Infante Ferreira, 2017).

To study the absorption process of NH_3 into NH_3/ILs solution, a theoretical model is proposed to describe the heat and mass transfer performance of the vapor absorption inside corrugated plate heat exchangers (PHX), which combines the two-resistance theory with a gas-liquid interface, void-fraction for a prediction of the liquid film thickness, and Chilton-Colburn analogy to couple the heat and mass transfer. Additionally, an experimental setup is developed for further improvement of the model. In this paper, the use of the proposed model in a cooling application is presented. The work with the setup is not finished yet. Nevertheless, the setup is also introduced to show the continuous process and the key components and instruments in the testing section. With these efforts, heat and mass transfer performances are investigated during NH_3 absorption by different NH_3/IL fluids inside the PHX.

2. HEAT AND MASS TRANSFER MODEL

As shown in Fig. 1, taking advantage of the symmetry feature of the plate heat exchanger, only a plate with its surrounding two streams are studied in this model. Distribution of parameters is considered by numerically dividing the plate heat exchanger into small control volumes along the bulk streams (the length of the plates). The heat and mass transfer of the three streams, i.e., the cooling water, the solution and the NH_3 vapor, are studied in each control volume. Regarding the vapor absorption, the two-resistance theory with an interface is applied to describe the heat and

mass transport between the vapor-liquid interface with its surroundings (the vapor and solution bulk streams, respectively). Heat and mass transfer fluxes are calculated using empirical correlations.

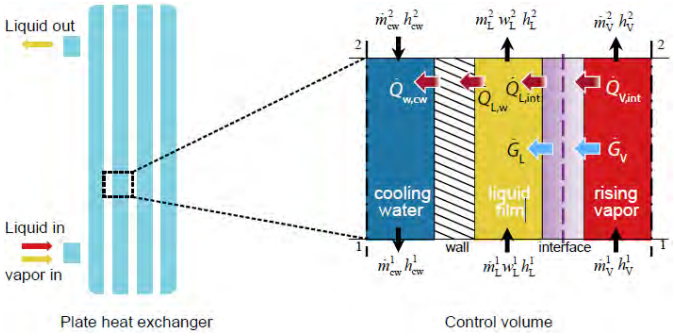

(a) (b)

Figure 1: Schematic diagram of the modeled absorber (a), and the split control volume (b) The corrugated surface of plates is not shown

Simplifications are adopted to develop the heat and mass transfer model of absorption:

- Absorption is assumed at a steady state.
- The liquid film is assumed to have a symmetrical thin feature contacting with plates.
- Interface is in equilibrium at saturated conditions.
- The distribution along the width of plates is taken as uniform.
- Properties and conditions at the inlet of a control volume are used to represent the local ones.
- Absorbents are regarded as non-volatile, thus no mass transfer of it occurs in the vapor phase.
- Thermal boundary layers between the two-phase and single-phase regions smoothly transit.
- Heat conduction along the thickness of plates is negligible.
- Longitudinal conduction of plates and fluids are negligible.
- No heat loss to the environment.

In this study, the calculation is carried out from the bottom of the plate heat exchanger to its top. Control volumes are discretized according to their lengths, which are identical in the current setting. For each control volume, conditions (flow, temperature, pressure and composition) at the inlet are taken as the input. Sub-routines for obtaining other thermophysical properties, film thicknesses and dimensionless numbers are also implemented. An iteration is carried out based on the heat and mass balances to obtain the local interface temperature, T_{int}.
Calculated results are heat and mass transfer properties and the outlet parameters. The latter ones will be used as the input for the next control volume.

2.1. Fluids and Properties

The fluids in this study include $NH_3/LiNO_3$ and NH_3/[emim][SCN] (1-ethyl-3-methylimidazoliumthiocyanate). The properties of pure NH_3 are from NIST database Refprop 9.1 (Lemmon et al., 2013). The required properties of $NH_3/LiNO_3$ are vapor-liquid equilibrium (Libotean et al., 2007), density, heat capacity, enthalpy (Infante Ferreira, 1984), viscosity (Libotean et al., 2008), thermal conductivity (Cuenca et al., 2014) and diffusivity (Venegas et al., 2004). Thermodynamic properties, such as vapor-liquid equilibria, densities, heat capacities and enthalpies regarding NH_3/[emim][SCN] mixture are provided by Wang et al. (2018) and Wang and Infante Ferreira (2017). Required transport properties are introduced by Wang (2019).

2.2. Film Thickness

Symmetrical thin films on plates can be used to represent the liquid flow of various flow patterns, such as film and slug flow, for vapor-liquid two phase flow in PHXs. In this study, the solution streams are also simplified as liquid films. The thickness of the liquid film is obtained with the help of the void-fraction. NH_3 vapor is assumed surrounded with liquid films between plates, as shown in Fig. 1. The

void-fraction is applied to estimate the fraction of the channel cross-sectional area that is occupied by the gas phase. With it, the film thickness is expressed as,

$$\delta_{\mathrm{f}}=\left(1-\varepsilon\right)\frac{L_{\mathrm{g}}}{2} \qquad \text{Eq. (1)}$$

where, L_{g} is the gap between plates. The void-fraction, ε, is obtained via Eq. 2 (Zivi, 1964):

$$\frac{1}{\varepsilon}=1+\left(\frac{1-q}{q}\right)\left(\frac{\rho_{\mathrm{V}}}{\rho_{\mathrm{L}}}\right)^{2/3} \qquad \text{Eq. (2)}$$

2.3. Pressure Drop

The frictional pressure drop of a stream along a channel is estimated using Eq. 3:

$$\frac{\mathrm{d}P}{\mathrm{d}L}=\xi\frac{\rho\bar{v}^{2}}{2d_{\mathrm{h}}} \qquad \text{Eq. (3)}$$

For the studied plate heat exchanger, the friction factor, ξ, is obtained from the experimental data of Amaris Castilla (2013) as reported by Wang (2019),

$$\xi=23050\cdot\mathrm{Re}_{\mathrm{L}}^{-1.69} \qquad \text{Eq. (4)}$$

2.4. Heat Transfer

Heat transfer characteristics of the two single-phase flows: cooling water, and NH_3 vapor (heat transfer to the interface), are described using the following two correlations, respectively.

$$\mathrm{Nu}_{\mathrm{cw}}=0.858\,\mathrm{Re}^{0.555}\,\mathrm{Pr}^{1/3} \qquad \text{Eq. (5)}$$

$$\mathrm{Nu}_{\mathrm{V}}=8.23 \qquad \text{Eq. (6)}$$

Characteristic lengths of the dimensionless numbers are the hydraulic diameters for both cases.

The interface which is introduced for a convenience to study absorption problems does not naturally exist. The heat and mass transfer related to it cannot be practically detected. In this work, with the help of the proposed model, the Nusselt numbers of the liquid film, $\mathrm{Nu}_{\mathrm{L,w}}$ and $\mathrm{Nu}_{\mathrm{L,int}}$, are determined using the experimental data from Amaris Castilla (2013) as reported by Wang (2019),

$$\mathrm{Nu}_{\mathrm{L,w}}=0.1372\cdot\mathrm{Re}_{\mathrm{L}}^{0.6139}\cdot\mathrm{Pr}^{1/3} \qquad \text{Eq. (7)}$$

$$\mathrm{Nu}_{\mathrm{L,int}}=0.9077\cdot\mathrm{Re}_{\mathrm{L}}^{0.8381}\cdot\mathrm{Pr}^{1/3} \qquad \text{Eq. (8)}$$

2.5. Mass Transfer

In the studied problem with absorption controlled by the liquid phase, the only mass transfer takes place from the interface to the solution bulk stream. The Chilton-Colburn analogy is applied to obtain the mass transfer coefficient between them, which is based on the boundary layers analogy:

$$\frac{\mathrm{Sh}}{\mathrm{Nu}_{\mathrm{L,int}}}\approx\left(\frac{\mathrm{Sc}}{\mathrm{Pr}}\right)^{1/3} \qquad \text{Eq. (9)}$$

The characteristic lengths of the dimensionless numbers for the liquid film in the two-phase region are selected as the film thickness.

3. EXPERIMENTAL SETUP

A continuous absorption-desorption section is designed and constructed in the authors' lab. Compared with an absorption heat pump system, the setup has no evaporator or no condenser. The focus of experiment with the setup is on the absorption process. The process diagram of the set-up is shown in Fig. 2.

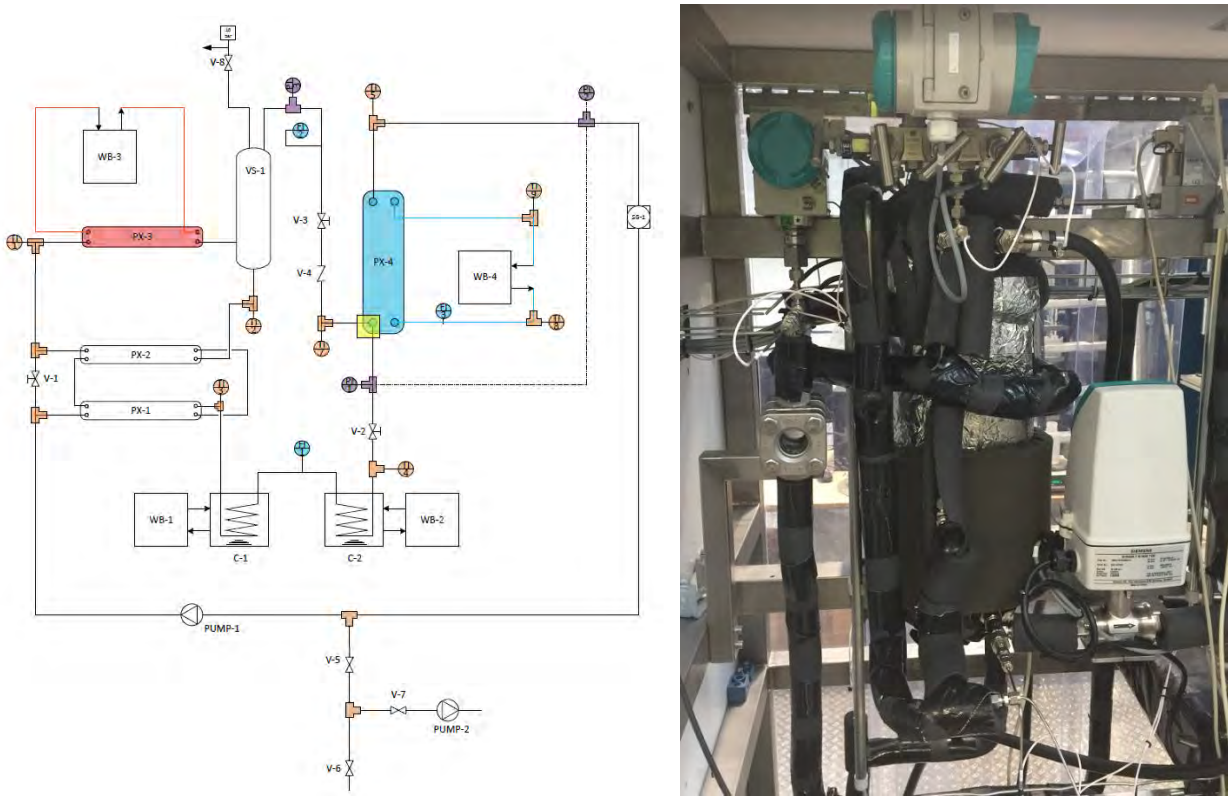

(a) (b)

Figure 2: Process flow diagram of the experimental absorber setup in (a) and the absorber test section in (b)

The setup consists of four sections: a heating loop with a thermostatic bath WB-3 (with an internal pump) and a PHX PX-3, a cooling loop with a thermostatic bath WB-4 (with an internal pump) and PHX PX-4 (the absorber), a working fluids loop, and some auxiliary lines (such as pressure relief valve for safety, and fluids charging lines).

As the main section, the working fluids loop is constructed with a plenty of components and instruments. As a part of it, the PHX PX-4 provides the geometry for NH_3 vapor - solution absorption. Vapor and weak solution streams enter the PX-4 from the bottom. The strong solution stream leaves it from the top and is pumped to the separation section which consists of PX-3 and separator VS-1. The cooling water enters the other side of the PX-4 from the top.

Inlet and outlet temperature signals of the working fluids and cooling water are detected by the PT100 sensors TI-4, TI-5 and TI-8, TI-9 (systematic uncertainty of ±0.03°C). The pressure drop and the outlet pressure in the working fluid side are detected using a pressure difference transmitter PI-1 (accuracy ± 0.8 kPa) and a pressure transmitter PI-2 (accuracy ±8 kPa). Flow rates are recorded by the flowmeters FI-1 (accuracy ±0.15% of measured flow), 2 (accuracy ±0.5% of measured flow) and 3 (accuracy 0.25% of measured flow) for the weak solution stream, vapor stream and cooling water stream, respectively. Meanwhile, FI-1 also records the density of the solution stream (accuracy ±0.5 kg /m^3).

The pump PUMP-1 is used to circulate the weak solution stream. The silicon oil flow inside the other side of the PX-3 provides heat to boil the NH_3 off from the strong solution stream. Separated weak solution will be precooled in the thermostatic baths WB-1 and WB-2 with coils C-1 and C-2 before

entering the absorber. Also two PHXs PX-1 and PX-2 are applied as internal heat exchangers between the hot weak solution and cold strong one to save loads of thermostatic baths.
A check valve V-4 is used to prevent the back flow in the vapor line. Sight glass SG-1 is provided to confirm full absorption. Apart from the PT-100 sensors used in streams of the testing heat exchanger, there are some extra to monitor the temperature in different parts of the process.
For safety issues, a pressure switch PI-3 is applied to stop the setup, and a pressure relief valve V-8 will release vapor, when pressure is too high inside the working fluid loop.

4. SIMULATION RESULTS

Currently, only simulation work has been carried out.

4.1. Cooling Cycle Performance

The exploration of heat and mass transfer performance of NH_3/ILs absorption is based on the application of NH_3 absorption refrigeration system in an operation condition of $T_{gen}/T_{con}/T_{abs}/T_{eva}$ = 120/35/35/-5 °C (Wang and Infante Ferreira, 2017). The case of $NH_3/LiNO_3$ is also studied for reference purposes.

Table 1. Inlet conditions of the NH_3-based working fluids side of the absorber

	$\dot{m}_L^{in} / \dot{m}_V^{in}$ [-]	w_L^{in} [kg/kg]	$\dot{T}_L^{in}$ [°C]	$\dot{T}_V^{in}$ [°C]	*COP* [-]
[emim][SCN]	40.57	0.036	40.4	-5.0	0.660
$LiNO_3$	4.18	0.344	40.0	-5.0	0.619

The inlet conditions of these fluids are listed in Table 1, together with the predicted *COP*. For an easy comparison, the vapor flow and cooling water inlet conditions are kept the same for all cases, which are $\dot{m}_V$ = 4.32×10^{-4} kg/s, T_{cw}^{in} = 30 °C and $\dot{m}_{cw}$ = 1.28×10^{-2} kg/s.

4.2. Distribution of Parameters during Absorption

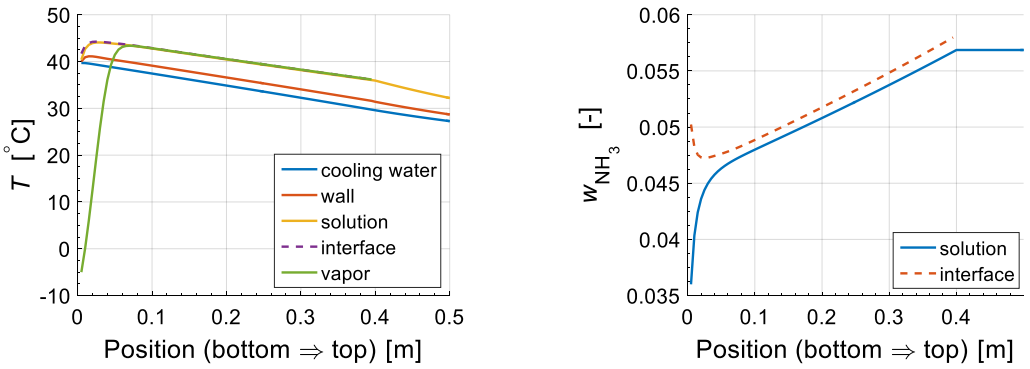

Figure 3: Distributions of (a) temperatures and (b) NH_3 mass fractions for the NH_3 absorption case with fluid NH_3/[emim][SCN]

For the case of NH_3 absorption by the fluid NH_3/[emim][SCN] as shown in Fig. 3a, temperature of NH_3 vapor increases rapidly at the beginning of the absorption. Then it reaches peak which is at a comparable level with the local temperature of the solution, and drops until it is completely absorbed. The temperature of interface is close to that of the liquid, since the heat resistance between them is lower. On the other hand, the NH_3 fraction difference between them is larger at the entrance (as shown in Fig. 3b). It drives a high rate of NH_3 mass transfer from the interface to the liquid. The high transfer of mass also leads to a large amount of absorption heat release, which in turn increases the

liquid temperature. An increase of interface temperature causes the equilibrium fraction of NH_3 to drop, thus the absorption rate reduces. In the no-absorption region, since no absorption heat is released, the drop of solution temperature is sharper.

For the reference case of $NH_3/LiNO_3$, the aforementioned vapor flow is too large to be fully absorbed with the proposed geometric and external conditions. To keep the absorption area in this case the same as that of NH_3/IL case, the vapor flow is $\dot{m}_V$ = 2.42×10^{-4} kg/s (Note that the solution flow is determined making use of the corresponding circulation ratio from cycle calculations). The temperature and concentration distributions are shown in Fig. 4.

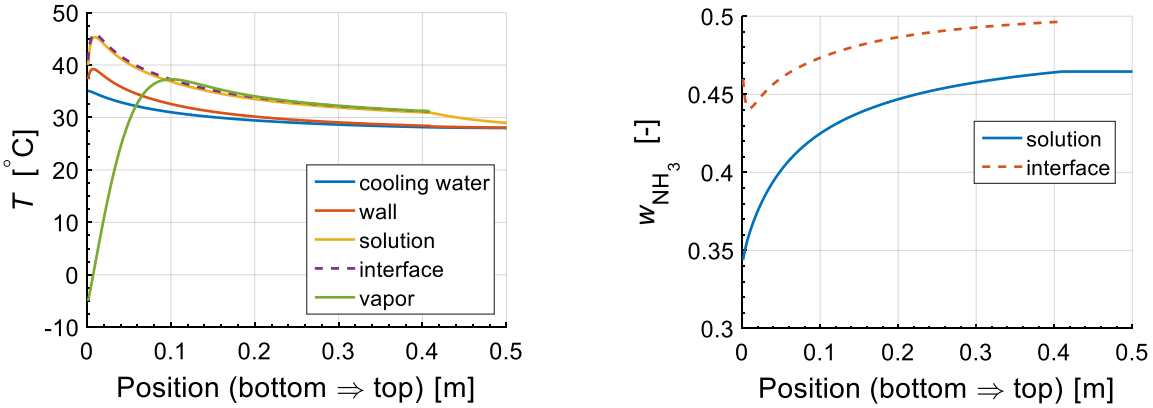

(a) (b)

Figure 4: Distributions of (a) temperatures and (b) NH_3 mass fractions for the NH_3 absorption case with reference fluid $NH_3/LiNO_3$

Compared with the ILs case, the reference case shows a less rapid increasing of vapor temperature. The temperature rise of the solution stream is more obvious at the entrance. Compared with the IL case, the reference case has a higher level of NH_3 fractions. The levels of interface NH_3 fractions reflect the absorbents' solubilities of NH_3. Because it has a significantly smaller solution flow, see Table 1, the increase of NH_3 fraction in the $NH_3/LiNO_3$ solution is also larger than that of the NH_3/IL case.

4.3. Overall Performance during Absorption

Parameters concerning the heat transfer, mass transfer and pressure drop are summarized to evaluate the overall performance of the studied fluids in the PHX absorber. Results of these parameters are obtained and listed in Table 2.

Table 2. Overall performance of the studied PHX absorber with NH3-based fluids

-	A_{mt}/A [-]	$\dot{Q}/A$ [kW/m^2]	$LMTD$ [K]	U [W/(m^{2}K)]	$\dot{G}$ [g/(m^{2}s)]	P_{out} [kPa]
[emim][SCN]	0.8	6.63	4.90	1353.0	5.40	356.0
$LiNO_3$	0.8	3.77	2.44	1545.5	3.02	348.1

The term $\dot{Q}/A$ is the heat transfer flux across the plate. Using the logarithmic mean temperature difference, defined in Eq. 10, the overall heat transfer coefficient, U, can be obtained to evaluate the heat transfer performance of different fluids in the studied PHX.

$$LMTD = \frac{\left(T_L^{out} - T_{cw}^{in}\right) - \left(T_L^{in} - T_{cw}^{out}\right)}{\ln\left[\left(T_L^{out} - T_{cw}^{in}\right) / \left(T_L^{in} - T_{cw}^{out}\right)\right]} \qquad \text{Eq. (10)}$$

$$U = \frac{\dot{Q} / A}{LMTD}$$ Eq. (11)

The reference fluid, $NH_3/LiNO_3$ shows a better heat transfer performance than the studied NH_3/IL fluid. However, mass transfer performance of it is significantly worse than the IL-based case.

5. CONCLUSIONS

This work discusses the performance of the absorber of IL-based absorption systems. Heat and mass transfer during the absorption of NH_3 into NH_3/non-volatile salts solutions inside corrugated plate heat exchangers has been modeled. Heat transfer coefficients of NH_3/[emim][SCN] fluid are estimated around 1350 W/m^{2}K with the studied geometry and in the studied condition for an absorption refrigeration application. The overall heat transfer coefficient of NH_3/[emim][SCN] is lower than that of the reference fluid $NH_3/LiNO_3$. However its mass transfer performance is significantly better.

ACKNOWLEDGEMENTS

The authors would like to acknowledge the financial support from the China Scholarship Council and Koudegroep Delft-Wageningen.

NOMENCLATURE

A	Area [m^2]	C_p	Heat capacity [J/(kg K)]
D	Mass diffusivity [m^2/s]	d	Diameter [m]
$\dot{G}$	Mass flux [kg/(m^2 s)]	h	Enthalpy [J/kg]
L	Length [m]	$LMTD$	Logarithmic mean temperature difference [K]
$\dot{m}$	Mass flow rate [kg/s]	P	pressure [kPa]
$\dot{Q}$	Heat flow [W]	q	Vapor quality [kg/kg]
T	Temperature [°C]	U	Overall heat transfer coefficient [W/(m^2 K)]
v	Velocity [m/s]	w	Mass fraction [kg/kg]
	Greek letter		
α	Heat transfer coefficient [W/(m^2 K)]	β	Mass transfer coefficient [m/s]
δ	Thickness [m]	ε	Void-fraction [m^3/m^3]
λ	Thermal conductivity [W/(m K)]	μ	Viscosity [Pa s]
ρ	Density [kg/m^3]	ξ	Frictional factor [-]
	Subscript and superscript		
1,2	Inlet/outlet of control volumes	abs	Absorber
ave	Average	c	Characteristic (length)
con	Condenser	cw	Cooling water
eva	Evaporator	f	Film
g	gap	gen	Generator
h	Hydraulic (diameter)	in	Inlet
int	Interface	L	Liquid
mt	Mass transfer	NH_3	NH_3 component
out	Outlet	V	Vapor
w	Wall		

Dimensionless numbers

$\mathrm{Nu} = \frac{\alpha L_c}{\lambda}$	Nusselt number	$\mathrm{Pr} = \frac{c_p \mu}{\lambda}$	Prandtl number
$\mathrm{Re} = \frac{\rho v L_c}{\mu}$	Reynolds number	$\mathrm{Sc} = \frac{\mu}{\rho D}$	Schmidt number

$\mathrm{Sh} = \frac{\beta L_c}{D}$ Schmidt number

REFERENCES

Amaris Castilla, C.F., 2013. Intensification of NH3 bubble absorption process using advanced surfaces and carbon nanotubes for NH3/LINO3 absorption chillers. Universitat Rovira i Virgili.

Cuenca, Y., Salavera, D., Vernet, A., Teja, A.S., Vallès, M., 2014. Thermal conductivity of ammonia + lithium nitrate and ammonia + lithium nitrate + water solutions over a wide range of concentrations and temperatures. Int. J. Refrig. 38, 333–340. https://doi.org/10.1016/j.ijrefrig.2013.08.010

Infante Ferreira, C.A., 1984. Thermodynamic and physical property data equations for ammonia-lithium nitrate and ammonia-sodium thiocyanate solutions. Sol. Energy 32, 231–236. https://doi.org/10.1016/S0038-092X(84)80040-7

Lemmon, E.W., Huber, M.L., McLinden, M.O., 2013. NIST reference fluid thermodynamic and transport properties–REFPROP.

Libotean, S., Martín, A., Salavera, D., Valles, M., Esteve, X., Coronas, A., 2008. Densities, Viscosities, and Heat Capacities of Ammonia + Lithium Nitrate and Ammonia + Lithium Nitrate + Water Solutions between (293.15 and 353.15) K. J. Chem. Eng. Data 53, 2383–2388. https://doi.org/10.1021/je8003035

Libotean, S., Salavera, D., Valles, M., Esteve, X., Coronas, A., 2007. Vapor−Liquid Equilibrium of Ammonia + Lithium Nitrate + Water and Ammonia + Lithium Nitrate Solutions from (293.15 to 353.15) K. J. Chem. Eng. Data 52, 1050–1055. https://doi.org/10.1021/je7000045

Venegas, M., Izquierdo, M., Rodríguez, P., Lecuona, A., 2004. Heat and mass transfer during absorption of ammonia vapour by LiNO3–NH3 solution droplets. Int. J. Heat Mass Transf. 47, 2653–2667. https://doi.org/10.1016/j.ijheatmasstransfer.2003.12.014

Wang, M., 2019. Highly efficient absorption heat pump and refrigeration systems based on ionic liquids. PhD. Thesis. Delft University of Technology.

Wang, M., Becker, T.M., Schouten, B.A., Vlugt, T.J.H., Infante Ferreira, C.A., 2018. Ammonia/ionic liquid based double-effect vapor absorption refrigeration cycles driven by waste heat for cooling in fishing vessels. Energy Convers. Manag. 174, 824–843. https://doi.org/10.1016/j.enconman.2018.08.060

Wang, M., Infante Ferreira, C.A., 2017. Absorption heat pump cycle with NH3 - ionic liquid working pairs. Appl. Energy 204, 819–830. https://doi.org/10.1016/j.apenergy.2017.07.074

Zivi, S.M., 1964. Estimation of Steady-State Steam Void-Fraction by Means of the Principle of Minimum Entropy Production. J. Heat Transfer 86, 247–251. https://doi.org/10.1115/1.3687113

Manuscript ID: 1075
DOI: 10.18462/iir.icr.2019.1075

A study on the operating parameter optimization of solid desiccant heat pump based on a real-time algorithm

Lingji HUA[(a)], Tianshu GE[(a)], Ruzhu WANG[(a)]

[(a)])Institute of refrigeration and cryogenics, Shanghai Jiao Tong University,
800 Dongchuan road. Minhang District, Shanghai 200240, China, rzwang@sjtu.edu.cn

ABSTRACT

Solid desiccant heat pump (SDHP) is a promising household air-conditioning. As mentioned in former publication, it features periodic switchover and weakly-coupled temperature and humidity control. The switchover period is typically no more than ten minutes and, to prevent the transient shock right after the switchover, the refrigerant flow rate should also be altered regularly. Furthermore, the sensible and latent heat handling capacity of the device has to be balanced and real-time self-tuning is imperative to adapt the system to changing outdoor air condition and indoor requirement. That is, system control strategies of the SDHP are more complicated than normal vapor compression (VC) system. In this paper, a real-time control algorithm is proposed to optimize the system operating parameters, such as switchover period, compressor frequency and valve opening. According to calculation, real system incorporated with the control algorithm can achieve higher COP and provides air of higher comfort level and stability.
Keywords: Solid Desiccant Heat Pump, Weakly-Coupled Temperature and Humidity Control, A Real-Time Control Algorithm, Operating Parameters Optimization

1. INTRODUCTION

With the rising standards of living and diminishing resources, nowadays there is an urgent need for high-efficient methods of air quality adjustment and energy recovery. In the field regarding humidity control, solid desiccant has arisen wide attention, for its advantages like feasibility, adaptability, energy conservation and environment protection (Zheng et al., 2014). The desiccant rotary wheel is the most typical system taking advantages of solid adsorbent. However, the device features increasing adsorption temperature and thus decaying dehumidification capacity along with high regeneration temperature, due to the inherently positive adsorption heat of the material. Recent studies on rotary wheel focus on developing isothermal dehumidification (Ge et al., 2009), which can be realized by directing air alternatively through infinite desiccant wheels and intercoolers(Zhang and Niu, 1998). Multistage rotary setups with intercooler(s) are then built based on the above hypothesis (Ge et al., 2008), more effective in moisture removal but rather complex in structure. The liquid desiccant dehumidification is also a promising alternative, since the inner cooling is more likely in a liquid system (Ge et al., 2008). However, it has the drawback of corrosion(Ge et al., 2008). Further research has been done to rule out above side effects. These endeavors accelerate the advent of desiccant-coated heat exchangers (DCHEs).

DCHE is processed by coating solid desiccant on the outer surface of a conventional heat exchanger (HE) (Jiang et al., 2015). Unsaturated desiccant is highly affinitive with water vapor, so mass transfer occurs when humid air flows through. The cold fluid in the tubes facilitates the process, by removing the adsorption heat and maintaining the desiccation ability. The regeneration step, conversely, is aided with hot fluid flow. In order to treat the latent load continuously, two DCHEs work alternatively between the two modes. When the cooling or heating capacity of the medium in tubes is redundant, the device can also handle sensible heat load.

Single-phase fluid is potential candidate of the heat transfer medium, and the studies regarding the DCHEs facilitated by the single-phase refrigerant (normally water), both numerically and experimentally, are now extensive (Saeed and Al-Alili, 2017). Utilizing solar energy (or industrial waste heat) as the heat source, DCHEs have been successfully adopted in the field of solar driven desiccant cooling system (Park et al., 2016; Zhao et al., 2014; Zhao et al., 2016). Typical features of such systems include periodical switchover, effective dehumidification but poor control of the

temperature. Thus, a supplementary device like evaporative cooling or heat pump is needed in practical application to overcome the indoor sensible load.
Two-phase refrigerant, however, is also an alternative. Since a compressor is commonly adopted in temperature regulation of two-phase refrigerants, the solid desiccant heat pump (SDHP) is then proposed to combine a VC system with DCHE (transforming to DCE/DCC). When incorporated in heat pumps (Tolga et al., 2008; Tolga et al., 2010; Tu et al., 2017), the function of DCHEs would be further extended, that is, realizing weakly-coupled temperature and humidity control both in the cooling and heating modes. Several experimental studies have been published based on it, mainly to clarify the concept, validate the practicality and show its energy saving potential. Detailed research, aiming to explain mechanism and optimize the system design, are lacked both experimentally and theoretically.
To investigate the novel heat pump system SDHPs, a dynamic mathematical model is imperative, in order to facilitate the component selection, the parameter optimization and the performance evaluation. In this paper, a real-time control algorithm is proposed to optimize the system operating parameters, such as switchover period, compressor frequency and valve opening. According to calculation, real system incorporated with the control algorithm can achieve higher COP and provides air of higher comfort level and stability.

MATHEMATICAL MODEL

1.1. System Description

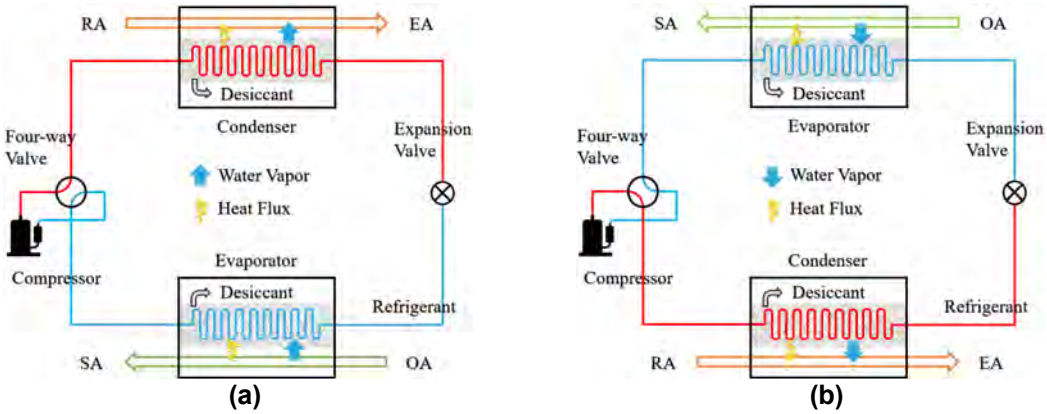

Figure 1: The schematic of SDHP and its working principle

The solid desiccant heat pump (SDHP) system can be taken as a combination and revision of the traditional VC system and the solid desiccant material. In this system, the sensible heat exchangers (including an evaporator and a condenser) within the VC cycle are replaced by the desiccant coated heat exchangers.
Same as the conventional VC system, the refrigerant in the SDHP operates as shown in Fig.1: after absorbing the heat in the evaporator, the refrigerant vapor is compressed in the compressor, condenses in the condenser and expands through the throttling device, then the cold refrigerant goes to the evaporator again. The evaporator/condenser in this system, different from traditional HX, would adsorb/desorb heat and moisture to/from the air simultaneously if facilitated by the cold/hot fluid. Then, when the evaporator/condenser is saturated/dried up, it is time to switch over the four-way reversing valve, exchanging the position between the evaporator and the condenser. Thus, the SDHP features a process of periodic switchover of the evaporator and condenser. The air duct should also be re-constructed, to persistently guide the cooling air into the condenser.

1.2. Mathematical Model of the DCEs/DCCs

Fig. 2 demonstrates the configuration of an example DCE/DCC and the fluids (air & refrigerant) flowing through it. The structure confined in the cuboid (length: L_x; width: L_y; height: L_z), with the repetitive unit shown in Fig. 2(c), is our object to conduct heat and mass transfer analysis. To implement governing equation derivation in the air side, a Cartesian coordinate is defined as shown in Fig. 2(a), with its origin coinciding with one of cuboid vertexes. While the refrigerant and DCE/DCC

temperature calculation is conducted along the refrigerant mainstream direction, denoted as y_2-axis. This axis firstly points inward the tube at the inlet of the evaporator/condenser, and then reverses its orientation once encountering a bend tube. Since the moisture content in desiccant varies throughout the desiccant coating thickness, another n-axis (Fig. 2(d) and 2(e)) is also imperative.
The governing Eq. (1)-(4) of the DCE/DCCs, which respectively describe the transfer process in air-side, desiccant side, HX side and refrigerant side, are then derived to analyze the component quantitatively.

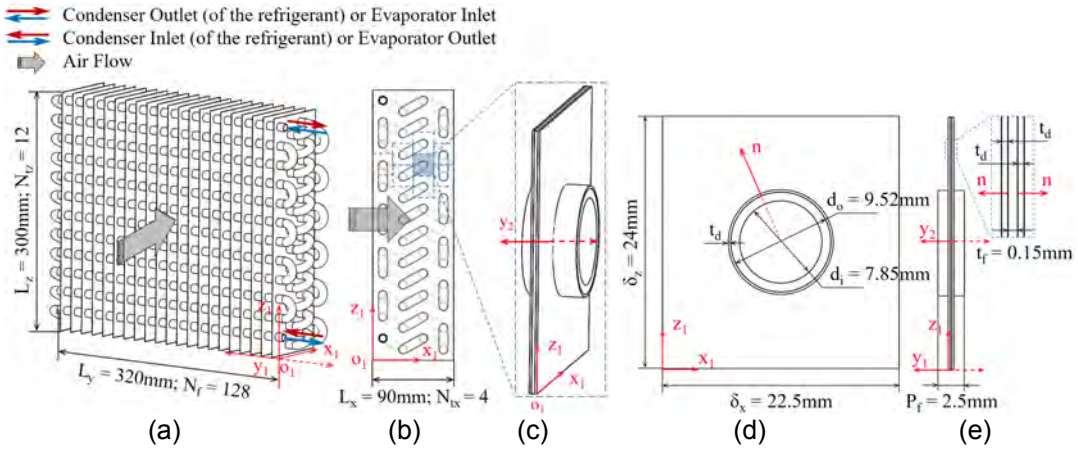

Figure 2: Detailed configuration of the example DCHE and its corresponding dimension (a) the schematic diagram of the example DCHE (b)the left view of the DCHE (c)the repeating unit of the DCHE (d)the left view of the repeating unit (e)the front view of the repeating unit

$$\begin{cases} \dfrac{\partial(\rho_a Y_a)}{\partial t}+\dfrac{\partial(\rho_a u_a Y_a)}{\partial x_1}=\dfrac{1}{l_a}K_y\left(Y_{da}\big|_{n=t_d}-Y_a\right) \\ \dfrac{\partial\left[\rho_a\left(c_{pa}+c_{pv}Y_a\right)T_a\right]}{\partial t}+\dfrac{\partial\left[\rho_a u_a\left(c_{pa}+c_{pv}Y_a\right)T_a\right]}{\partial x_1}=\dfrac{1}{l_a}K_y c_{pv}\left(Y_{da}\big|_{n=t_d}-Y_a\right)T_s+\dfrac{1}{l_a}h_a\left(T_{HX}-T_a\right), T_s=\begin{cases}T_a, adsorption\\ T_{HX}, desorption\end{cases} \end{cases}$$

Eq. (1)

$$\frac{\partial(\rho_d W_d)}{\partial t}-\frac{\partial}{\partial n}\left[D_S\frac{\partial(\rho_d W_d)}{\partial n}\right]=0$$

Eq. (2)

$$\frac{\partial\left[\left(\sum_{j=d,f,t}\rho_j\varepsilon_j c_j+\rho_d\varepsilon_d c_{pv}W_d^*\right)T_{HX}\right]}{\partial t}-\frac{\partial}{\partial y_2}\left(\varepsilon_t\lambda_t\frac{\partial T_{HX}}{\partial y_2}\right)$$

$$=\frac{1}{l_{aHX}}K_y\left(Y_a-Y_{da}\big|_{n=\delta_d}\right)\left(q_{st}+c_{pv}T_s\right)+\frac{1}{l_{aHX}}h_a\left(T_a-T_{HX}\right)+\frac{1}{l_{rHX}}h_r\left(T_r-T_{HX}\right), T_s=\begin{cases}T_a, adsorption\\ T_{HX}, desorption\end{cases}$$

Eq. (3)

$$\begin{cases} \dfrac{\partial\rho_r}{\partial t}+\dfrac{\partial(\rho_r v_r)}{\partial y_2}=0 \\ \dfrac{\partial(\rho_r v_r)}{\partial t}+\dfrac{\partial\left(\rho_r v_r^{\,2}\right)}{\partial y_2}=-\dfrac{\partial p_r}{\partial y_2}-f_r(single-phase)/\dfrac{\partial}{\partial y_2}\left\{p_r+\left(\rho_r v_r\right)^2\left[\dfrac{\left(1-x_r\right)^2}{\rho_{rl}\left(1-\alpha_r\right)}+\dfrac{x_r^{\,2}}{\rho_{rg}\alpha_r}\right]\right\}=-\dfrac{\partial(\rho_r v_r)}{\partial t}-f_r^{TP}(two-phase) \\ \dfrac{\partial(\rho_r i_r)}{\partial t}+\dfrac{\partial(\rho_r v_r i_r)}{\partial y_2}=\dfrac{\partial p_r}{\partial t}+\dfrac{1}{l_r}h_r\left(T_{HX}-T_r\right) \end{cases}$$

Eq. (4)

1.3. Mathematical Model of the Compressor and the Throttling Valve

To supply indoor with comfort air and maintain high efficiency, the evaporation/condensation pressure and the mass flow rate of the refrigerant in a heat pump should be compatible with its air

handling requirements. As the pressure controllers and mass flow rate regulators of the two-phase refrigerant, the compressor and the throttling valve are thus essential components in a SDHP.
A simplified model based on a variable-frequency rotor compressor is applied to the system simulation. The basic governing equations (Eq. (5)) indicate that, given the evaporation pressure $p_{r,E}$, the outlet refrigerant enthalpy $i_{r,Eout}$ of the DCE and the condensation pressure $p_{r,C}$, the significant parameters of the compressor (the mass flow rate $m_{r,CM}$, the electricity consumption P_{CM} and the outlet refrigerant enthalpy $i_{r,Cin}$) can then be obtained.

$$\begin{cases} m_{r,CM} = N_{CM} V_{CM} \rho_{r,Eout} \eta_v, \eta_v = 1 + c_r - c_r \left(\dfrac{p_{r,C}}{p_{r,E}} \right)^{c_{v,Eout}/c_{p,Eout}} \\ i_{r,Cin} = \dfrac{\left(i_{r,iso-entropy} - i_{r,Eout} \right)}{\eta_s} + i_{r,Eout}, \eta_s = 0.85 \\ P_{CM} = \dfrac{m_{r,CM} \left(i_{r,Cin} - i_{r,Eout} \right)}{\eta_e}, \eta_e = 0.9 \end{cases} \quad \text{Eq. (5)}$$

While the mass flow rate $m_{r,VL}$ and outlet enthalpy $i_{r,Ein}$ of the throttling valve are governed by the pressure difference ($p_{r,C}$-$p_{r,E}$) and the outlet refrigerant conditions $i_{r,Cout}$ of the DCC.

$$\begin{cases} m_{r,VL} = K \sqrt{\left(p_{r,C} - p_{r,E} \right) \rho_{r,Cout}} \\ i_{r,Ein} = i_{r,Cout} \end{cases} \quad \text{Eq. (6)}$$

As the throttling valve and the compressor are both assumed to have very small thermal inertia and charge amount, the steady state models are applied for these component. In this case, the temperature variation and the disparities of mass flow rate from inlet to outlet of the compressor and throttling valve are omitted.

2. THE DYNAMIC SIMULATION OF SDHP

2.1. Framework of the System Simulation

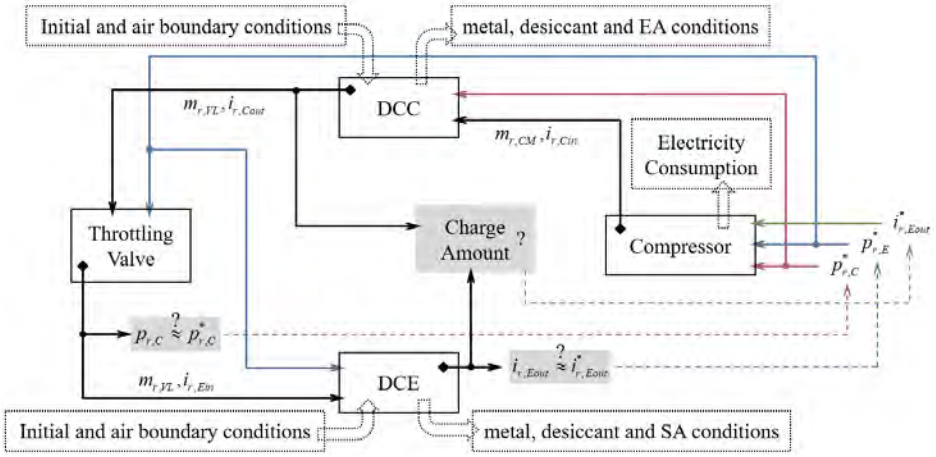

Figure 3: Framework of the system simulation of the SDHP

Fig.3 illustrates the calculation algorithm of the numerical study on the SDHP (equation (1)-(6)) consisting of four basic components, namely, a compressor (equation (5)), a throttling valve (equation (6)), a DCE (equation (1)-(4)) and a DCC (equation (1)-(4)). The process shown in Fig.3 is repeated every time step with the updated initial conditions from one time step before. With the assumed evaporation pressure $p^*_{r,E}$, evaporator outlet refrigerant enthalpy $i^*_{r,Eout}$ and condensation pressure $p^*_{r,C}$, the refrigerant conditions flowing through the compressor, DCC, throttling valve and DCE can be successively derived. The obtained value of condensation pressure $p_{r,C}$, as an output of throttling model, then can be used to supplement the assumed value of $p^*_{r,C}$ iteratively, until they are almost equal. Similarly, the value of evaporation pressure $p^*_{r,E}$/refrigerant enthalpy $i^*_{r,Eout}$ at

evaporator outlet is estimated at first and amend repeatedly until the calculated enthalpy $i_{r,Eout}$/charge amount equals with the assumed/practical one.
When the above system encounters a sudden switchover, the status of the DCC/DCE (the spatial distribution of the air temperature, the air humidity, the desiccant temperature, the desiccant moisture ratio and the metal temperature) right before the switchover should be logged and then inputted as initial conditions to the new DCE/DCC after the switchover. Apart from the refrigerant conditions, the transient electricity consumption, the metal temperature, the desiccant moisture content and the air output conditions can also be obtained during the process.

2.2. Characteristics and Performance of the SDHP

Table 1. Main parameters adopted in the numerical study of SDHP

Component Parameters		Operating parameters	
Compressor volume (m^3)	9.8e-6	Air velocity of the OA(m/s)	0.8
Compressor clearance Ratio	0.08	*Air conditions of the OA	35°C,21g/kg
Compressor isentropic efficiency	0.85	Air velocity of the RA(m/s)	1.2
Compressor electricity efficiency	0.9	*Air conditions of the RA	25°C,10g/kg
Characteristic Constant of throttling valve	6e-7	System charge amount	980

Table 1 summarizes the important parameters adopted in the system simulation. The component parameters of the compressor are empirical ones of rotor compressors commonly used in household air conditioning. While the characteristic constant of throttling valve and the system charge amount are chosen to match the compressor capacity. The DCE and DCC of the SDHP are in the same size, to facilitate the frequent role exchange between the evaporator and condenser. To dissipate the condensation heat in time and thus maintain an appropriate evaporation temperature in SDHP, the air velocity through the condenser should be larger than the evaporator.
The switchover poses negative effects on SDHP system. In detail, an ideal regeneration cycle completely warms up the DCC. Then, when it is transferred into the DCE, it needs to be pre-cooled to regain the dehumidification capacity. Such process of alternative cooling and heating would waste energy. Therefore, the heat load of the DCE can then be divided into three categories: latent heat, sensible heat and transient heat, as defined in Eq. (7).

$$\begin{cases} Q_{latent} = m_{a,E} q_{st} \left(Y_{a,Ein} - Y_{a,Eout} \right) \\ Q_{sensible} = m_{a,E} \left(i_{a,Ein} - i_{a,Eout} \right) - Q_{latent}, i_a = c_{pa} T_a + \left(q_{st} + c_{pv} T_a \right) Y_a \\ Q_{trasient} = m_{r,CM} \left(i_{r,Eout} - i_{r,Ein} \right) - Q_{latent} - Q_{sensible} \end{cases} \quad \text{Eq. (7)}$$

The system COP can be calculated both in the refrigerant side and in the air side, as defined in Eq. (8), namely, the enthalpy change of the refrigerant/air in the DCE divided by the electricity consumption of the compressor.

$$\begin{cases} \mathrm{COP}_r = \dfrac{m_{r,CM} \left(i_{r,Eout} - i_{r,Ein} \right)}{P_{CM}} \\ \mathrm{COP}_a = \dfrac{m_a \left(i_{a,Ein} - i_{a,Eout} \right)}{P_{CM}} \end{cases} \quad \text{Eq. (8)}$$

The numerical study shows that, after several minutes of fluctuation and quick self-regulation, the SDHP features periodical performance given arbitrary initial conditions. Fig. 4(a) then depicts the outlet air conditions, along with the system evaporation and condensation temperature, of the second and third calculated cycles, showing repeatable patterns. Within one cycle, the evaporation temperature fluctuates between 16°C and 19°C, while the condensation temperature gradually increasing from 38°C to 52°C. It also reveals that the humidity removal/regeneration in DCEs/DCCs happens together with the temperature reduction/recover, and thus validates the possibility of the simultaneous handling of sensible and latent load in such system. Some specific features of the mass and heat transfer in DCEs/DCCs are worth mentioning here. The solid material of DCEs/DCCs is dried off/wetted out but not cold/warm enough after the sudden switchover from DCCs/DCEs. The

moisture removal/recover, promoted both by the low/high temperature and dry/wet material, obtains a maximum during the cycle, usually quite near the onset when the DCEs/DCCs are partially cooled/heated but still almost unsaturated/saturated. The sensible heat transfer at air-side increases monotonically and then reaches a plateau within one cycle, due to the abundant latent heat and the temperature hysteresis of DCEs/DCCs in the beginning. The averaged supply air condition is 23 °C, 9g/kg.

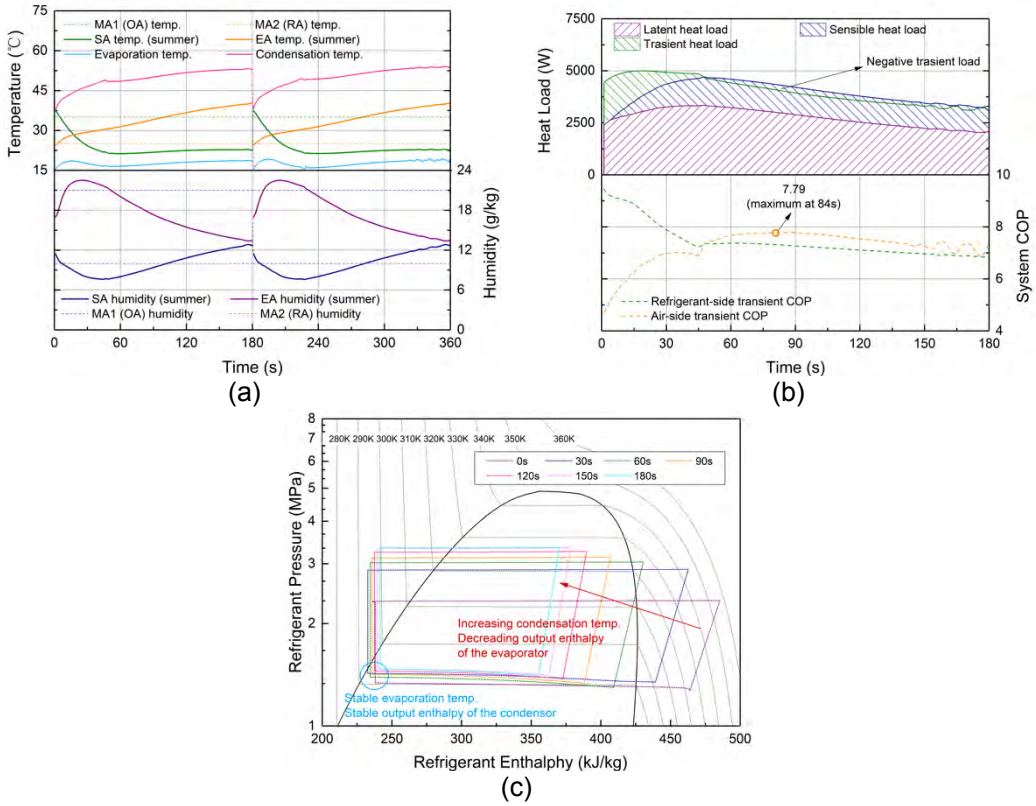

Figure 4: The characteristics and performance of the different elements of the SDHP (a) outlet air and refrigerant conditions (b) heat load and estimated COP (c) refrigerant cycle

Fig. 4(b) shows the transient load of the DCE due to the unstable operation, altogether with the sensible and the latent heat load for comparison. Definition of the above three terms are shown in Eq. (7). The heat waste is relatively small (8.3% for adsorption process), but not negligible, according to the figure. The enthalpy increase of the refrigerant in SDHP does not equal the enthalpy decrease of the air, due to the existence of the transient heat load. The air-side value is deemed more reasonable. The COP calculated at the air-side, as shown in Fig. 4(b) obtains a maximum of 7.79 at 84s with the averaged value of 7.19. Refrigerant cycle shown in Fig. 4(c) reveals that, without any control strategy, the refrigerant at compressor entrance is in two-phase region after around 1 min.

3. OPERATIONAL PARAMETER OPTIMIZATION BASED ON A REAL-TIME CONTROL ALGORITHM

According to Fig. 4(b), the total heat load of the SDHP would decay with the elongated switchover period. The switchover period is typically no more than ten minutes and, to prevent two-phase phenomena at compressor inlet, the refrigerant flow rate should also be altered regularly by changing the frequency of compressor and the characteristic constant of throttling valve. In this paper, a real-time algorithm is proposed, via incorporating a negative feedback control (Eq. (9)) in the dynamic simulation model, to optimize the system operating parameters, such as switchover period, compressor frequency and valve opening. According to calculation, real system incorporated with the control algorithm can achieve higher COP and provides air of higher comfort level and stability. The comparison is shown in the Fig. 5. To be specific, the COP is nearly doubled by the negative feedback control with improved temperature control performance (by 14%) and slightly subdued humidity control performance (by 4%).

$$\left(m_{r,CM}\right)_{NOW}=\frac{\left(i_{r,Eout}-i_{r,Ein}\right)_{BFR}}{\left(i_{rG,E}-i_{rL,E}\right)_{NOW}}\left(m_{r,CM}\right)_{BFR} \quad \text{Eq. (9)}$$

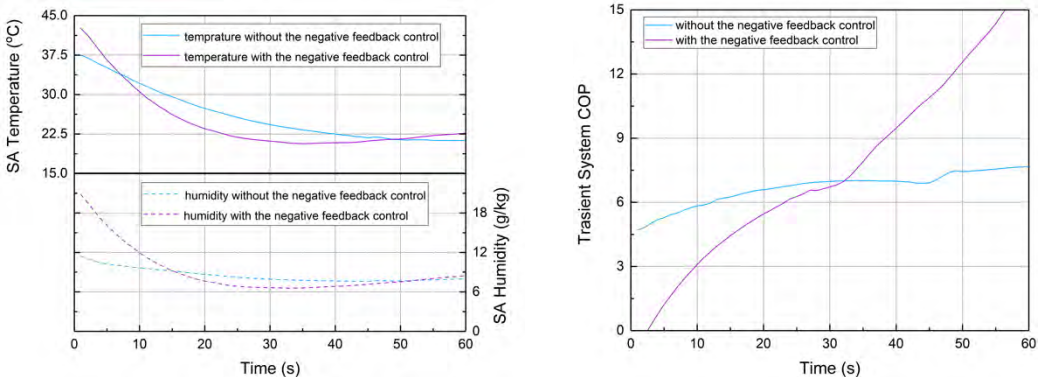

(a) (b)

Figure 5 The performance of the SDHP with and without the negative feedback control

4. CONCLUSIONS

In this paper, the SDHP, containing DCEs/DCCs as core components, is evaluated by a numerical study. Afterwards, a real-time algorithm is proposed, via incorporating a negative feedback control in the dynamic simulation model, to optimize the system operating parameters, such as switchover period, compressor frequency and valve opening. According to calculation, real system incorporated with the control algorithm can achieve higher COP and provides air of higher comfort level and stability.

ACKNOWLEDGEMENTS

This research work was founded by Key Program of National Natural Science Foundation of China [No.51336004] and also the Foundation for Innovative Research Groups of the National Natural Science Foundation of China [No. 51521004]

NOMENCLATURE

c	specific heat ($J\times kg^{-1}\times K^{-1}$)	T	temperature (°C)
c_p	specific heat (isobaric) ($J\times kg^{-1}\times K^{-1}$)	u/v	Velocity along the x/y direction ($m\times s^{-1}$)
f	friction ($N\times m^{-3}$)	V	volume (m^3)
h	convective heat transfer coefficient ($W\times m^{-2}\times K^{-1}$)	W	moisture content of the material (g/g)
i	specific enthalpy ($J\times kg^{-1}$)	x	quality
m	mass flow rate ($kg\times s^{-1}$)	Y	air humidity ratio (g/kg)
M	coating amount (kg)	t	thickness(m)
N	rotation frequency (Hz)	α	void fraction
p	pressure (Pa)	φ	relative humidity
P	electricity consumption (W)	λ	conductivity ($W\times m^{-1}\times K^{-1}$)
t	thickness(m)	ρ	density ($kg\times m^{-3}$)

Subscripts

a	air flowing freely on the desiccant surface	*HX*	DCHE (including the coated desiccant)
ad	adsorption	*r*	refrigerant
C	condenser	*TP*	the two-phase refrigerant
CM	compressor	*rg*	saturated gas of the refrigerant
d	porous desiccant coating	*rl*	saturated liquid of the refrigerant
da	air confined in the desiccant pores	*t*	tube
E	evaporator	*v*	water vapor
f	fin	*VL*	throttling valve

Nomenclature (with specific definition)

c_r compressor clearance ratio

D_s surface diffusivity of the liquid water adsorbed by the desiccant ($m^2 \times s^{-1}$)

k_y convective mass transfer coefficient ($kg \times m^{-2} \times s^{-1}$)

K characteristic constant of the expansion device

q_{st} specific sorption heat of the desiccant ($J \times kg^{-1}$)

W_d^* $W_d^* = \int_0^{t_d} W_d(n,t)dn \Big/ t_d$ moisture content (whose gradient along the desiccant thickness is omitted) (kg water×kg dry material)

REFERENCES

Aynur, T. N., Hwang, Y., Radermacher, R., 2010. Field performance measurements of a heat pump desiccant unit in heating and humidification mode. Energy and Buildings 42(5), 678-683.

Aynur, T. N., Hwang, Y., Radermacher, R., 2010. Integration of variable refrigerant flow and heat pump desiccant systems for the cooling season. Energy and Buildings 42(4), 468-476.

Ge, T. S., Dai, Y. J., Wang, R. Z., Li, Y, 2008. Experimental investigation on a one-rotor two-stage rotary desiccant cooling system. Energy 33(12), 1807-1815.

Ge, T. S., Li, Y., Wang, R. Z., Dai, Y. J., 2009. Experimental study on a two-stage rotary desiccant cooling system. International Journal of Refrigeration 32(3), 498-508.

Jiang, Y., Ge, T. S., Wang, R. Z., Hu, L. M., 2015. Experimental investigation and analysis of composite silica-gel coated fin-tube heat exchangers. International Journal of Refrigeration 51, 169-179.

Park, B., Lee, S., & Kato, S., 2016. Technical feasibility study of a compact desiccant-based outdoor air system using cogenerated hot water. Applied Thermal Engineering 106, 968-980.

Saeed, A., Al-Alili, A., 2017, A review on desiccant coated heat exchangers. HVAC&R Research 23(1), 15.

Tu, Y. D., Wang, R. Z., Ge, T. S., Zheng, X., 2017. Comfortable, high-efficiency heat pump with desiccant-coated, water-sorbing heat exchangers. Scientific Repots 7(2), 40437.

Zhang, H., Niu, J., 1998. A two stage desiccant cooling system using low temperature heat. International Journal of Refrigeration 20(2), 51-55.

Zhao, Y., Ge, T. S., Dai, Y. J., Wang, R. Z., 2014. Experimental investigation on a desiccant dehumidification unit using fin-tube heat exchanger with silica gel coating. Applied Tnermal Engineering 63(1), 52-58.

Zhao, Y., Dai, Y. J., Ge, T. S., Wang, H. H., Wang, R. Z., 2016. A high performance desiccant dehumidification unit using solid desiccant coated heat exchanger with heat recovery. Energy and Buildings 116, 583-592.

Zheng, X., Ge, T. S., Wang, R. Z., 2014. Recent progress on desiccant materials for solid desiccant cooling systems. Energy 74(1), 280-294.

Manuscript ID: 1083
DOI: 10.18462/iir.icr.2019.1083

Performance characteristics of a plate fin heat exchanger

Mohammad Sultan MAHMUD[(a)], Emamul KABIR[(b)]

(a) Department of Mechanical Engineering, Khulna University of Engineering & Technology, Khulna-9203, Bangladesh, sultan@me.kuet.ac.bd

(b) Department of Mechanical Engineering, Khulna University of Engineering & Technology, Khulna-9203, Bangladesh, emamulkabir.96@gmail.com

ABSTRACT

This study presents the numerical simulation results for thermal performance analysis, flow visualization, and heat transfer characteristic in a plate fin heat exchanger (PFHE). Rectangular and perforated baffles are used to increase the heat transfer rates. The performances of a plate fin with and without baffles show effective comparison in cooling. When the heat exchanger is equipped with baffles, the efficiency of two configurations can be compared easily: a baffle with and without perforation. It concerns three cases (only a channel without baffle, with rectangular baffle and baffles with slot type perforation). A commercial CFD (computational fluid dynamics) program is used for the numerical simulation. Mesh independence test is carried out to check the accuracy of results. Validation of numerical results with the available experimental data from the literature shows satisfactorily. The flow field has been studied for different Reynolds number for the range 500 to 1800 to validate the results. Results were obtained finally in terms of generalized Reynolds number for the range 2 to 20. It increases the heat transfer substantially but with an additional energy cost. Nusselt number is increased 59% to case 2 from case 1 and 77.3% to case 3 from case 2. On the other hand pressure drop is highly increased at case 2 due to rectangular baffles which is 34.3% greater than case 1 and due to slot type perforation in case 3, pressure drop is decreased by 5.8% based on generalized Reynolds number. So that from thermodynamic point of view this numerical simulation is very much important.

Keywords: Plate-Fin, Heat Exchanger, Numerical Simulation, Nusselt Number, Pressure Drop, CFD, Heat Transfer, Baffle.

1. INTRODUCTION

Heat transfer is the area that deals with the mechanism responsible for transferring energy from one place to another when temperature difference exists. Forced convection is the practical method of cooling and heating. In a channel complex flow structures is often introduced. Therefore, it is important to understand the heat transfer characteristics and fluid flow phenomena in a channel.

The analysis of heat transfer characteristics in a plate fin heat exchanger becomes a popular subject of research in present time. Plate fin heat exchangers are widely encountered in several industrial processes such as in refrigeration, heating, air conditioning, radiator of vehicles and other areas. They are used for its small size, low cost and high performance. From the different types of fins cited previously, the plain plate is the widely used for its durability, simplicity, versatility in applications and lower pressure drop.

The cooling of mechanical or electronic devices has ever growing importance due to the wide spread introduction of microelectronics together with increasing demands up on functionally and reliability. Heat is trapped in thermal devices for various reasons. Due to lack of efficient cooling of heat entrapped in the thermal devices, they can under-perform or even breakdown under certain condition. The ever increasing miniaturization, packaging density, quality demands and reduction in life cost will put ever increasing pressure on the solution of these problems. The solution of such heat transfer depends on successfully solving Momentum equation along with Energy equation.

With experiments, Chamoli (2015) showed the great heat transfer enhancement for a rectangular channel equipped with V-down perforated baffles. The number of holes influences highly on the flow fields and heat transfer rates, and two perforated baffles perform better that one baffle, as reported by Ary (2012).

Khoshvaght-Aliabadi et al. (2015) studied the effect of delta-winglets under different arrangements. For the plain tube and at the transitional flow, they observed a good prediction of Nusselt number by

the Notter Rouse equation than the Gnielinski equation. Compared to the plain tube, they found a maximum PEC (performance evaluation criterion) of 1.41 with this VG at Re=8715.
The recirculation flow formed in the downstream zone of vortex generators creates hot points in this area. This great issue may be solved by using perforated baffles. This great issue may be solved by using perforated baffles (Ma et al., 2017).
A comprehensive review of studies on the vortex-generator applications has been recently conducted by (Ahmed et al., 2012). The literature shows that the studies on heat transfer characteristics of vortex-generators inside the plate fin heat exchangers are scarce.
Akcayoglu (2011) performed an investigation about the heat transfer enhancement in a plate fin heat exchanger with triangular fins as insert using a winglet pair of vortex generator. It was confirmed that the average Nusselt number increases with an increase in the angle of attack and Reynolds number.
Zeng et al. (2010) investigated the thermal performance in a plate fins channel using the four basic types of vortex-generators. They pointed out that the mixing effect between wing cascades improves the heat transfer characteristics, as the inclination angle of winglet increases.
Khoshvaght-Aliabadi et al. (2014) assessed experiments on the thermo hydraulic performance of copper–water nano fluid flow through various plate-fin channels, including: pin, vortex generator, offset strip, wavy, louvered, plain and perforated. Their results showed an enhancement in heat transfer coefficients and pressure drop with the rise of nano particles weight fraction. They reported also that the vortex generator channels have given the appropriate thermal–hydraulic performance.
In the noted literature, there are few studies in detailed analysis of heat transfer enhancement by the plate fin heat exchanger with baffles, when liquids are applied as working media. In this study, the flow dynamics and heat transfer characteristics of a plate fin heat exchanger are investigated numerically. The physical model for the numerical analysis is made using the plate fin heat exchanger with buffles used in the experimental studies of Karima-Boukhadia et al. (2018). Based on the numerical results, a detailed description of the heat transfer characteristics, pressure drop and flow distribution are discussed.

2. PHYSICAL MODEL OF COMPUTATIONAL DOMAIN

There is a rectangular channel without baffles shown in left of Fig. 1. The length of the channel is 300 mm and its width and height is 12 mm. A channel with rectangular baffles is shown in right of Fig. 1. The length and width of each baffle is 5 mm and thickness of each one is 1 mm. Six ranges of baffles are inserted and distance between two consecutive ranges is 20 mm. One perforated baffle is considered here which is slot type perforation shown in right of Fig. 1 and 2. The left of Fig. 2 presents the arrangement of rectangular baffles without perforation in a rectangular channel.

3. GOVERNING EQUATION

All investigations were performed via numerical simulations. The working fluid has a shear thinning behavior (the flow behavior index n = 0.69 and the density is ρ = 997 (kg m^{-3}), modeled by the Otwald law (power law) as follow, Azevedo (1995)

$$\tau = \mu_a \gamma^n \qquad \text{Eq. (1)}$$

Where, μ_a is the apparent viscosity and $\gamma\cdot$ is the shear rate.

$$\mu_a = k\gamma^{n-1} \qquad \text{Eq. (2)}$$

where *k* is the consistency index.
On the basis of these assumptions, the governing equations for the mathematical model are written as follows:
- Conservation of mass for fluid:

$$\frac{d}{dx_i}(\rho u_i) = 0 \qquad \text{Eq. (3)}$$

- Conservation of momentum for fluid:

$$\frac{d}{dx_i}(\rho u_i) = \frac{d}{dx_i}\left(\frac{k_f}{C_p}\frac{dT}{dx_i}\right) \qquad \text{Eq. (4)}$$

where C_p is the specific heat of working fluids.

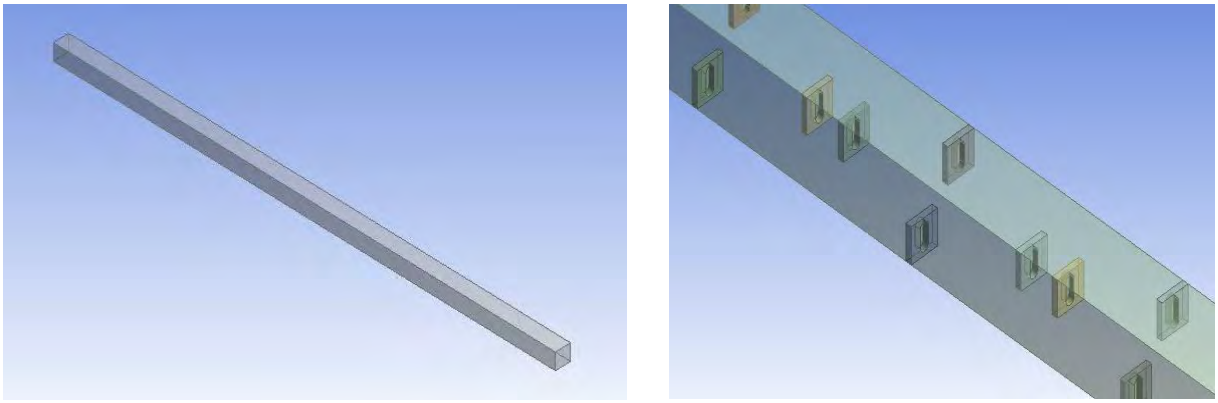

Figure 1: Rectangular channel without baffle (case 1) and with rectangular baffles (case 2 and 3).

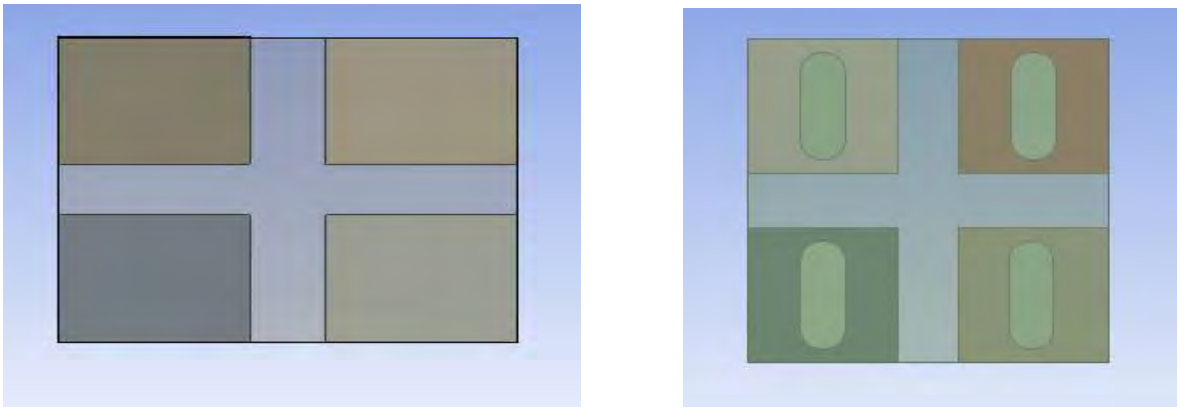

Figure 2: Rectangular baffles without slot (case 2) and with slot type perforation (case 3).

h is the convective heat transfer coefficient, given by:

$$h = \frac{Q_{CONV}}{A_t(T_w - T_b)_{LMTD}} \quad \text{Eq. (5)}$$

where A_t is the total heat transfer area and Q_{CONV} is the convective heat transfer rate expressed as follows:

$$Q_{CONV} = mC_p\left(T_{b,out} - T_{b,in}\right) \quad \text{Eq. (6)}$$

where *m* is the mass flow rate, $T_{b,in}$ and $T_{b,out}$ are the average temperature of fluid at the inlet and outlet of test section respectively. $(T_w - T_b)_{LMTD}$ is the log mean temperature difference given by:

$$(T_w - T_b)_{LMTD} = \frac{\left(\Delta T_{w-b,in} - \Delta T_{w-b,out}\right)}{log\left(\frac{\Delta T_{w-b,in}}{\Delta T_{w-b,out}}\right)} \quad \text{Eq. (7)}$$

Where $\Delta T_{w\text{-}b,in}$ and $\Delta T_{w\text{-}b,out}$ denote the differences between the wall temperature and the bulk fluid temperature at the inlet and outlet of heat transfer section. The Δp is the pressure difference between inlet and outlet defined as:

$$\Delta p = \left(P_{avg,in} - P_{avg,out}\right) \quad \text{Eq. (8)}$$

where subscripts '*avg, in*' and '*avg, out*' refer to the average pressure values at the inlet and outlet cross sections. The generalized Reynolds number (Re_g) for a shear thinning fluid is given by:

$$Re_g = \frac{u_{in}^{2-n}}{k} D_h^n \rho \quad \text{Eq. (9)}$$

$$D_h = \frac{4LA_c}{A_t} \quad \text{Eq. (10)}$$

Where A_c is the minimum cross-sectional flow area.

4. BOUNDARY CONDITION

The different boundary conditions taken to carry out the simulation are described below.
At the inlet of the channel (inlet condition):

$$u_y = u_z = 0;\ u_x = u_{in} = constant;\ T = T_{in} = 52℃ \quad \text{Eq. (11)}$$

where *u* is the velocity and *T* is the temperature of fluid.
Lower and upper surface (wall condition):

$$u_x = u_y = u_z = 0;\ T = T_{wall} = 6.5℃;\ \frac{dT}{dz} = 0; \quad \text{Eq. (12)}$$

Right and left sides (symmetry condition):

$$u_x = u_y = u_z = 0;\ \frac{dT}{dx} = 0; \quad \text{Eq. (13)}$$

Exit of channel (outlet condition):

$$\frac{du_x}{dx} = \frac{du_y}{dy} = \frac{du_z}{dz} = 0;\ \frac{dT}{dx} = 0; \quad \text{Eq. (14)}$$

Baffles: adiabatic wall.

5. MESH GENERATION AND SOLUTION METHODS

The ANSYS computer tool was used to make the geometry and to mesh the computational domain. Tetrahedral mesh type was adopted. ANSYS Fluent was employed to achieve all simulations. The increased mesh density was created near the baffles and walls of channel in order to capture the details of boundary layer flow. A sufficient number of nodes defining the curvature of the perforation in baffles was made on the baffle edge, which resulted in a very refined mesh (Fig. 3. The used computer code is based on the finite volume method (FVM) to solve the governing equations. For the pressure-velocity coupling, the SIMPLE (Semi Implicit Method for Pressure Linked Equation) algorithm was employed. In the momentum and energy equations, first and second order upwind scheme was used which gives a stable solution. Also, a second order upwind scheme was adopted for the discretization of convection terms. The above mentioned governing equations were solved by a segregated implicit iterative scheme. The under-relaxation factors were 0.3, 0.7, and 0.8 for the pressure, momentum and energy, respectively. We remind that these factors are used to ensure the computational convergence. The residual target for the continuity, momentum and energy equations was 10^{-7}. The governing equations were iteratively solved until the set residuals were obtained or when they stabilized at constant values. Most simulations required about 500 – 600 iterations.

6. MESH INDEPENDENCE TEST AND NUMERICAL MODEL VALIDATION

In order to check the variation of the simulation results with the number of elements, the model is tested with settings employing different number of elements. In this way, results from eleven different settings with gradually increasing number of elements were compared (Fig. 4). The results from last two settings (490010 and 508023 elements respectively) are very close to each other and Nusselt number differences are around 0.49 percent. So the setting employing 490010 elements is used in the simulation for greater accuracy.
The computational domain of this research is validated with the main aim to assure that the numerical result has reliability and high accuracy. In order to validate the present numerical model is valid for the plate fine heat exchanger, a rectangular channel with rectangular baffle without perforation is chosen. For different values of Reynolds number, the variation of pressure drop and heat transfer coefficient through the channel are predicted. Fig. 5 and Fig. 6 present the validations of the plate

fine heat exchanger with respect to the heat transfer coefficient and pressure drop respectively. The working fluid considered in this case same as Karima-Boukhadia et al. (2018) is Newtonian (water, Pr = 7). The validation is performed in the Re from 500 to 1800 in the laminar regime. A good agreement is observed when comparing the predicted results with those obtained by Karima-Boukhadia et al. (2018).

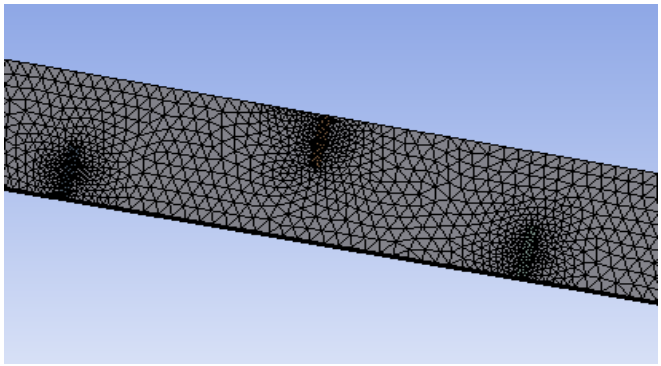

Figure 3: Mesh grids (tetrahedral elements).

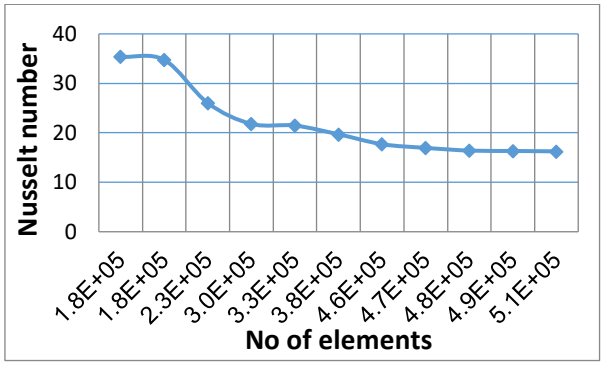

Figure 4: Results for mesh independence study.

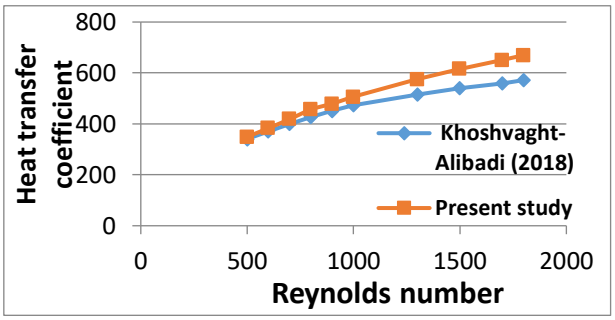

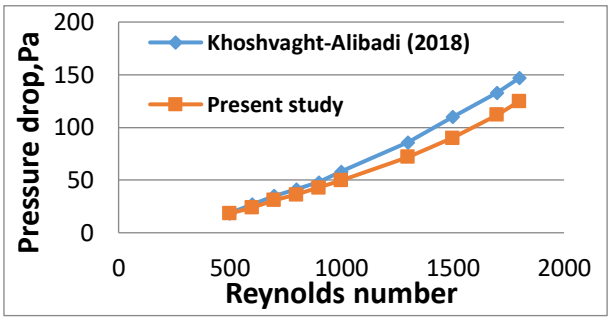

Figure 5: Variation of heat transfer coefficient with Re. Figure 6: Variation of pressure drop with Re.

7. RESULTS AND DISCUSSION

Generally, the increase in heat transfer by the baffling technique produces pressure losses. The effects perforated baffle on the pressure drop values are represented on Fig. 7 in terms of Generalized Reynolds number (Re_g). This figure shows the variation of pressure drop which tends to raise with the rise of the Reynolds number. In fact, the baffled channels with or without perforation in baffles yield higher pressure drop than the unbaffled channel.

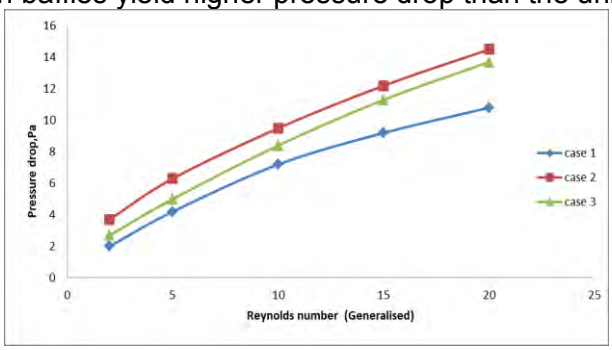

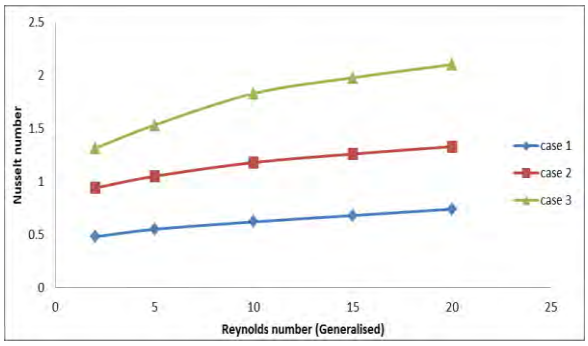

Figure 7: Variation of pressure drop with Re_g. **Figure 8: Variation of Nusselt number with Re_g.**

Fig. 7 shows the pressure drop for the three case. Perforated baffle yield lower pressure drop than the baffle without perforation .This is because of the surface of cut in baffle. For the unbaffled channel (Case 1), the cooling of fluid needs a long distance. However, the heat transfer is greatly increased with the presence of baffles. The variation of Nusselt number (Nu) for various Reynolds numbers ranging from 2 to 20 for all geometrical configurations is presented in Fig. 8. It is clear that the values

of Nusselt number tend to increase with the rise of Reynolds numbers, which induces an enhancement in the heat transfer in the Plate fin heat exchanger. The first reason of the heat transfer enhancement in this system is the perforation shape in baffle, which increases the mixing by separating the boundary layer in the channel. And the second reason becomes the repeated operation of growth and wake destruction of boundary layers

It is clear that the presence of baffle increases the cooling of the shear thinning fluid. Also, the presence of perforation in baffles allows further reduction in the temperature along the heat exchanger. Consequently, the perforated baffle with slot shape merits to be realized in the conception of the plate fin heat exchanger. Nusselt number is increased 59% to case 2 from case 1 and 77.3% to case 3 from case 2. On the other hand pressure drop is highly increased at case 2 due to rectangular baffles which is 34.3% greater than case 1 and due to slot type perforation in case 3, pressure drop is decreased by 5.8% based on generalized Reynolds number. So that from thermodynamic point of view this numerical simulation is very much important. The Contour of velocity of three different cases 1, 2 and 3 at Re_g 20 are presented in Fig 9.

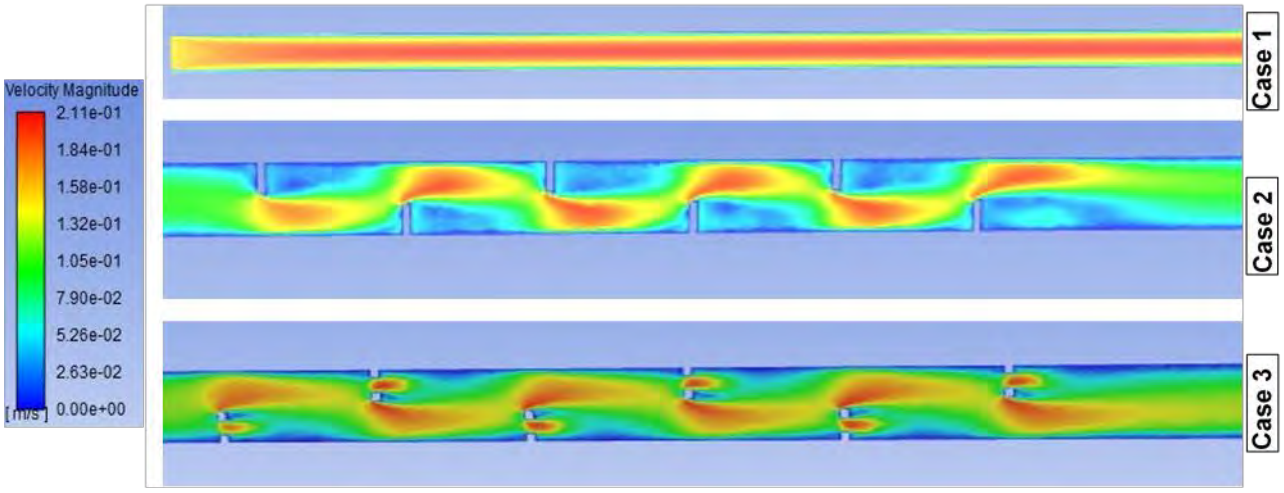

Figure 9: Contour of velocity of three different cases at Re_g 20 at 0.003 m from left wall.

In case 1, color contour is same along the length of the channel which indicates the flow is fully developed. But in another cases color variation shows the velocity changes. At the top of the each baffle high red color region indicates the velocity fluctuation where velocity is highly increased. Behind the each baffle blue region indicates the velocity reduction which is at an intense in case 2. Velocity reduces from top of the baffle to the lower and upper surface gradually that can be easily anticipated by the color variation shown Fig. 9.

The fluid flow movements are described by arrow in the contour of velocity vector in Figs. 10, 11, 12 respectively. In the case 1, the fluid flow is being uniform where the fluid particles have straight ward movement and they are parallel to each other and there is simply high and low velocity region shown in Fig. 10. When fluid flows through rectangular baffle, fluid velocity is increased at the top of the baffle due to obstruction, pressure is decreased and flow separation occurs. It is called zone of reattachment and due to flow separation, flow recirculates at a higher rate. Vortex generation occurs just behind the baffle which is shown in Fig. 11. At the closest behind the baffle velocity approximately becomes zero. Turbulent intensity and velocity fluctuation are shown in Fig. 11 at the top of the baffle. Perforation technique (case 3) is actually done to reduce pressure drop as it minimizes formation of zone of recirculation. No vortex is generated, no recirculation having with straight fluid particles moving behind the perforated space increasing fluid flow due to surface cut in baffle and taking active part in the heat transfer improvement shown in Fig. 12.

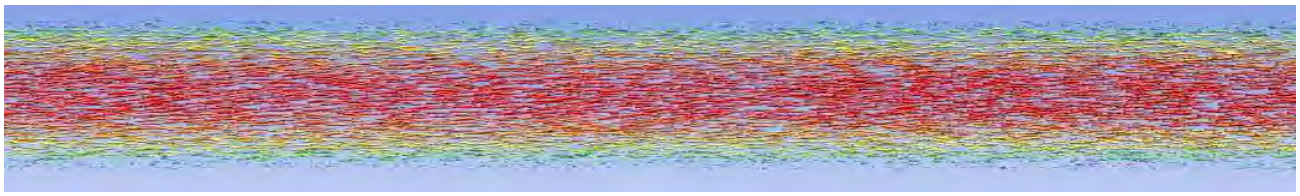

Figure 10: Contour of velocity vector of rectangular channel without baffles (case 1).

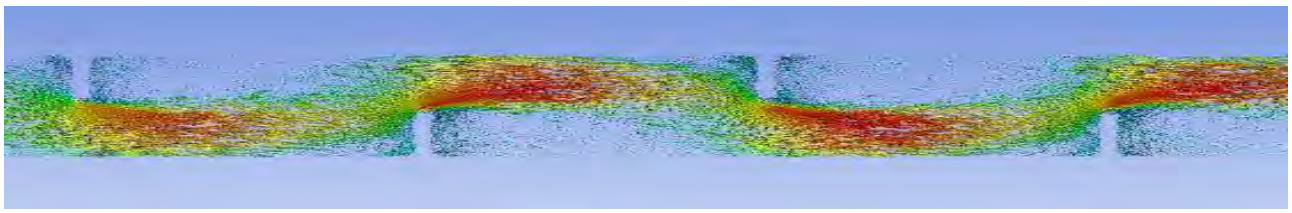

Figure 11: Contour of velocity vector of rectangular channel with baffles without perforation (case 2).

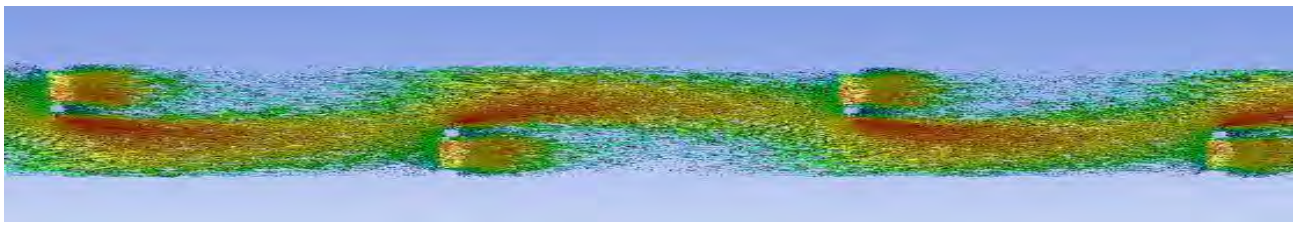

Figure 12: Velocity vector of rectangular channel with baffles with slot type perforation (Case 3).

In the temperature profiles captured in Fig. 13 actually show the evidence of heat transfer enhancement. In case 1 temperature is decreasing very slowly through the length of the channel. But from case 2 to case 3, temperature is decreasing very sharply at a lower distance from inlet due to turbulence and flow disturbances. As upper and lower wall is constant temperature which is lower than fluid temperature at inlet and forced convection occurs by baffling technique and heat is transferred more from fluid to solid at a higher rate.

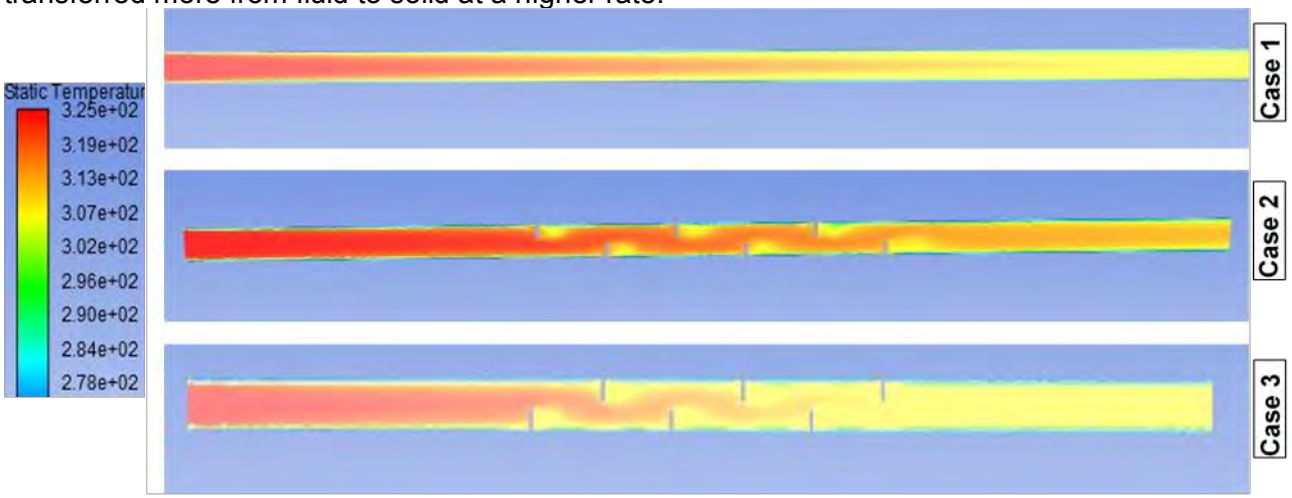

Figure 13: Temperature contour of three different cases at Reg 20 at 0.003 m from left wall.

In the Fig. 14, contour of pressure shows the normal pressure drop in case 1. But at case 2, due to flow disturbances and sudden contraction in flow area, velocity is highly increased and pressure is reduced greatly. But pressure drop is minimized by perforation technique minimizing the second zone of flow recirculation in cases 3 though pressure drop is higher than case 1. Fig. 14 shows behind each baffle throughout the channel color contour is changed which signifies the pressure reduction throughout the length of the channel.

8. CONCLUSIONS

A numerical method was applied to investigate the performance of plate fin heat exchangers. The effects of perforation in the baffles were investigated. Also, the dominance of perforation shape (slot) on the heat transfer characteristics was investigated. The main conclusions are described as follows: (i) The presence of baffles (with or without perforations) increases the heat transfer, but with an extra energy cost. (ii) The perforated baffles have showed a great improvement in heat transfer comparing to the channel heat exchanger without perforated baffles. (iii) The value of Nusselt number increases

with perforation of baffles which is much higher than rectangular baffle without perforation and without baffles. Nusselt number is increased 59% to case 2 from case 1 and 77.3% to case 3 from case 2. (iv) Pressure drop enhances with the presence of baffles and decreases with the rise of the surface of cut in baffles. pressure drop is highly increased at case 2 due to rectangular baffles which is 34.3% greater than case 1. However at low Reynolds number, the difference in pressure drop is slight between the non-perforated baffles and slot type of perforation. Due to slot type perforation in case 3, pressure drop is decreased by 5.8% based on generalized Reynolds number.

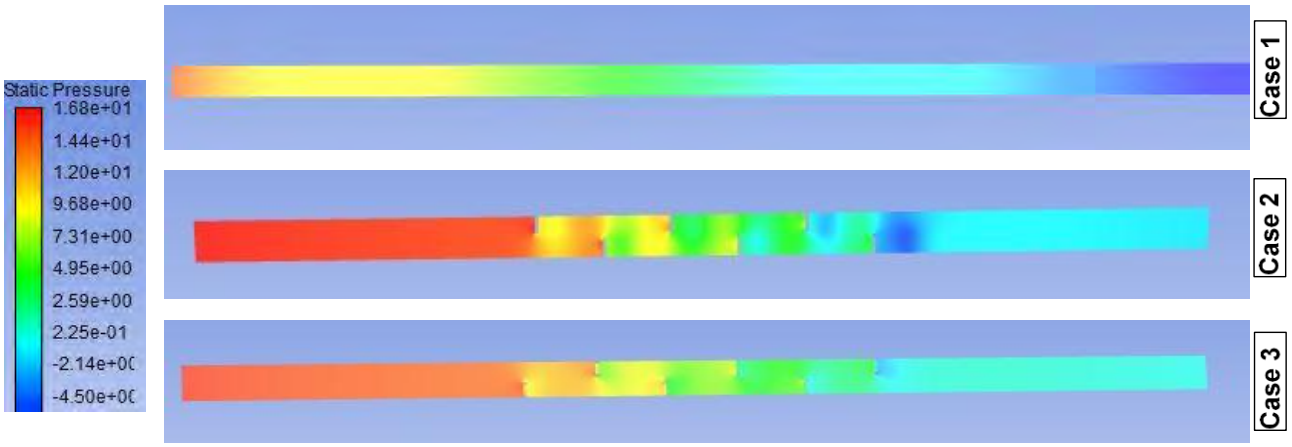

Figure 14: Contour of pressure of three different cases at Reg 20 at 0.003 m from left wall.

REFERENCES

Ahmed, H. E., Mohammed, H. A., Yusoff, M. Z., 2012. An overview on heat transfer augmentation using vortex generators and nanofluids: approaches and applications, Renewable Sustainable Energy Rev. 16, 5951-5993.

Akcayoglu, A., 2011. Flow past confined delta-wing type vortex generators. Exp Therm Fluid Sci 35, 112– 120.

Ary, B.K.P., Lee, M.S., Ahn, S.W., Lee, D.H., 2012. The effect of the inclined perforated baffle on heat transfer and flow patterns in the channel, Int Commun Heat Mass Transfer 39, 1578–1583. Int Commun Heat Mass Transfer 39, 1578–1583.

Azevedo, I., Lebouche, M., Devienne, R., 1995. Laminar cooling of pseudoplastic fluids flowing through cylindrical horizontal pipes. Int. J. Heat Fluid Flow 16, 125–130.

Chamoli, S., 2015. Hybrid FAHP (fuzzy analytical hierarchy process)- FTOPSIS (fuzzy technique for order preference by similarity of an ideal solution) approach for performance evaluation of the V down perforated baffle roughened rectangular channel. Energy 84, 432-442.

Karima Boukhadiaa, Houari Ameura, Djamel Sahelc, Mohamed Bozitb, 2018. Effect of the perforation design on the fluid flow and heat transfer characteristics of a plate fin heat exchanger. International Journal of Thermal Sciences 126, 172- 180.

Khoshvaght-Aliabadi, M., Hormozi, F., Zamzamian, A., 2014. Experimental analysis of thermal-hydraulic performance of copper- water nano fluid flow in different plate-fin channels. Exp Therm Fluid Sci 52, 248–258.

Khoshvaght-Aliabadi, M., Sartipzadeh, O., Alizadeh, A., 2015. An experimental study on vortex-generator insert with different arrangements of delta-winglets. Energy 82, 629–639.

Ma, T., Lu, X., Pandit, J., Ekkad, S.V., Huxtable, S.T., Deshpande, S., Wang, Q., 2017. Numerical study on thermoelectric–hydraulic performance of a thermoelectric power generator with a plate-fin heat exchanger with longitudinal vortex generators. Applied Energy 185, 1343-1354.

Zeng, M., Tang, L., Lin, M., Wang, Q.W., 2010. Optimization of heat exchangers with vortex-generator fin by Taguchi method. Appl. Therm. Eng. 30, 1775–1783.

Manuscript ID: 1095
DOI: 10.18462/iir.icr.2019.1095

Void fraction characteristics of adiabatic one-component vertically upward two-phase flows in circular and non-circular small diameter tubes

Hitoshi ASANO[(a)], Hideki MURAKAWA[(a)], Tomonori ASANO[(b)]

[(a)] Department of Mechanical Engineering, Kobe University
1-1, Rokkodai, Nada, Kobe, 657-8501, Japan, asano@mech.kobe-u.ac.jp
[(b)] Noritz Corporation
5 Mninamifuami, Futami-cho, Akashi-shi, 674-0093, Japan, t-asano@noritz.co.jp

ABSTRACT

Evaporating and condensing heat transfer and pressure loss characteristics strongly depend on interfacial structure of gas-liquid two-phase flows. Cross-sectional average void fraction is important parameter on the one-dimensional analysis. Recently, since channel diameter becomes smaller, the effect of surface tension on the flow behaviors would become stronger. This study deals with void fraction characteristics of adiabatic two-phase flows using FC-72 as the working fluid. Cross-sectional average void fraction was measured by capacitance sensor. Circular, square and triangular tubes with the hydraulic diameter of 2 mm were used. Vertically upward flow was selected to evaluate for axially symmetric phase distribution. From the results, it was confirmed that for the square and triangular tube, void fraction became lower than the circular tube because liquid was accumulated in the corner by surface tension. Although the lower void fraction leads to larger slip velocity, the gas-liquid interface of liquid film became smoother.
Keywords: Two-Phase Flow, Surface Tension, Void Fraction, Square Tube, Triangular Tube, Capacitance Sensor.

1. INTRODUCTION

Reduction in channel diameter of refrigerant heat exchanger is effective to reduce refrigerant charge amount and to increase heat transfer area density. Recently, compact heat exchangers using multiport aluminum tubes whose diameter is less than 1 mm are developed and applied to air-conditioners. Heat transfer and pressure loss characteristics of evaporating and condensing flows strongly depend on interfacial structure of gas-liquid two-phase flows. Several forces are acting on two-phase flows, such as, gravitational force, inertia force and surface tension force. When channel diameter becomes smaller, the effect of surface tension will become relatively larger than gravity. For example, we can easily image that the meniscus of water in a capillary tube is not affected by gravity. When gas-liquid interface structure is dominated by surface tension, the heat transfer and pressure loss characteristics of vertically upward flows will be the same with those of vertically downward and horizontal flows. The effect of channel orientation will become little.

Mishima and Hibiki (1996) had investigated the effect of channel diameter on void fraction characteristics of air-water flows. Measured void fractions were arranged based on the drift flux model. They showed that for bubbly and slug flows, the distribution parameter increased with decreasing channel diameter in the diameter range less than 4 mm. Since refrigerant used in refrigerating and heat pump system has lower surface tension than water, the transition diameter where the surface tension effect appears will become smaller. Ong and Thome (2011a, 2011b) had investigated the effect of properties, mass flux, and heat flux on flow pattern and heat transfer characteristics in small diameter channel with the diameter less than 3 mm using three kinds of refrigerants. They introduced confinement number as a non-dimensional number of the ratio of surface tension to gravity. It was concluded that the surface tension effect appears at the confinement number larger than 0.3-0.4. Baba et al. (2012) had investigated the effect of gravity on heat transfer characteristics for small diameter channel of 0.13 and 0.51 mm using FC-72 with the similar surface tension of HFC refrigerants. They introduced Bond number defined as the ratio of gravity to surface tension force. In their results, the effect of gravity on boiling heat transfer was not observed for the Bond number of 0.18, and that was observed for the Bond number of 0.71. The

Bond number of 0.71 is equivalent to the confinement number of 1.19. Gomyo and Asano (2016) had investigated the effect of channel diameter of vertical upward two-phase flows on flow pattern transition and void fraction characteristics using FC-72 as the working fluid. In their results, gas volumetric flux at the flow pattern transition boundary to annular flow was affected by channel diameter less than 2.0 mm, while that for 4.0 mm channel was agreed well with the previous transition model proposed by Mishima and Ishii. For the two-phase flow in 2.0 mm channel Bond number and confinement number is 8.5 and 0.34, respectively. It can be estimated that the surface tension effect appears on gas-liquid interface structure of FC-72 two-phase flows in 2.0 mm channel. The definitions of confinement number and Bond number are shown in Eq. (1) and (2).

$$Co = \frac{1}{D}\sqrt{\frac{\sigma}{(\rho_L - \rho_G)g}} = \frac{1}{\sqrt{Bo}} \quad \text{Eq. (1)}$$

$$Bo = \frac{(\rho_L - \rho_G)gD^2}{\sigma} \quad \text{Eq. (2)}$$

where σ is surface tension in N×m^{-1}, D is channel diameter in m, ρ_L and ρ_G are liquid and gas densities in kg×m^3, respectively, and g is gravitational acceleration in m×s^{-2}.

When the channel shape is non-circular, liquid film distribution on the wall will be affected by the surface tension. For rectangular or triangular channels the liquid film thickness at the side will become thinner due to liquid accumulation in the corner. The effect has a possibility to improve the heat transfer and flow characteristics.

Jige and Koyama (2011) had investigated condensing heat transfer characteristics in horizontal multiport tubes consisting of rectangular channels with the hydraulic diameter of 0.85 mm. It was reported that the condensing heat transfer coefficient could be kept constant in the quality range of 0.3 to 0.8 due to the surface tension effect on liquid film thickness. Enoki et al. (2013) had performed a detail observation of flow patterns of one-component gas-liquid two-phase mixture flowing vertically upward and downward, and horizontally in circular and noncircular (square and equilateral triangular) channels with the hydraulic diameter of about 1 mm. They showed that the liquid film structure and flow pattern transition were affected by the channel cross-sectional shape under the condition with the mass flux less than 100 kg·(m^{-2}s^{-1}). Wang and Rose (2006 and 2011) proposed a theoretical model to predict condensation heat transfer in horizontal square and triangular microchannels considering the effects of interfacial shear stress, gravity and surface tension force on the liquid film structure.

In a one-dimensional analysis of gas-liquid two-phase flows, for example two-fluid model, void fraction is important to estimate the slip velocity between gas and liquid phases. Information on void fraction characteristics in small diameter non-circular tubes is not enough to understand the phenomena. In this report, vertical upward one-component gas-liquid two-phase flows of FC-72 in circular, square, and triangular channels with the hydraulic diameter of 2 mm were examined. Cross-sectional average void fractions were measured by an electrostatic capacitance sensor. The effect of the cross-sectional shape on void fraction characteristics was considered with flow characteristics observed by a high frame rate camera simultaneously.

2. EXPERIMENTAL APPARATUS AND CONDITIONS

Schematic diagram of the experimental apparatus is shown in Fig. 1. Deaerated FC-72 (boiling point: 56.7 °C, surface tension: 8.35 mN·m^{-1} at the boiling point) was used as the working fluid. Simple pumped loop was used. The system configuration is the same with that in previous studies (Gomyo et al., 2014, and Gomyo and Asano, 2016). Subcooled liquid with certain subcooling degree was heated and evaporated in the main-heater by a direct AC current Joule heating. The main-heater is a circular tube with the inner diameter of 2 mm. The wet vapor was supplied to the test section directly connected to the main heater. The refrigerant from the test section was condensed in a condenser and returned to the tank. A schematic drawing of the test section is shown in Fig. 2. Three types of channels with the different cross-section as shown in Fig. 3 were used. A PYREX glass tube with the 2 mm in inner diameter was used as the circular channel. The square and triangular channels were made by a stack of thin transparent acrylic resin plates. The hydraulic diameter for each tube was 2 mm. Cross-sectional average void fraction at the middle of the test section was measured by an electrostatic capacitance sensor. A plate-type electrode was applied. The electrode

consists of a sensing electrode with the sensing area of 16 mm in width and 8 mm in length, guard electrode, and earth electrode. The flow behaviors in the sensing area can be observed in the direction parallel to the electrodes by a high frame rate camera simultaneously.

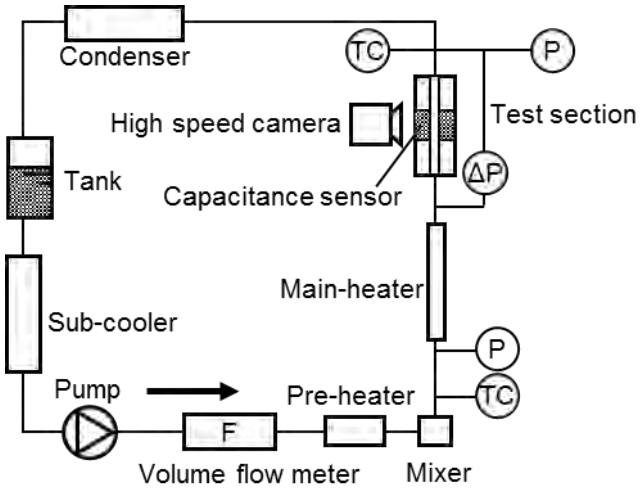

Figure 1: Schematic diagram of experimental apparatus

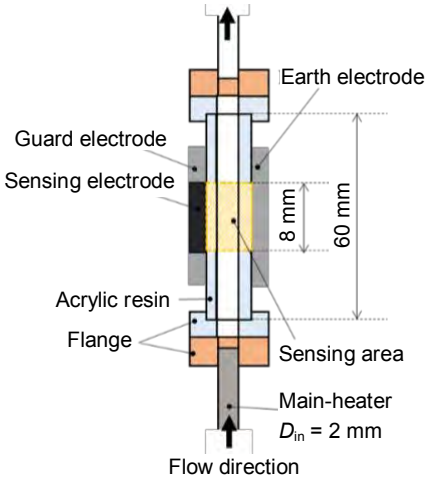

Figure 2: Test section

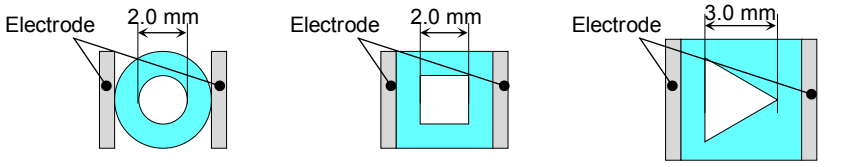

(a) Circular channel (b) Square channel (c) Triangular channel

Figure 3: Cross-sectional shape of tested channel

Volumetric average void fraction α in the sensing area can be measured from the capacitance, *C*, by the following equation.

$$\alpha = 1 - \frac{C - C_G}{C_L - C_G} \qquad \text{Eq. (3)}$$

where, C_G and C_L are the capacitance of vapor and liquid single-phase, respectively.
The experiments were carried out at the system pressure at about 100 kPa for varied vapor quality with four mass fluxes at 50, 100, 150, 200 $kg \cdot m^{-2} \cdot s^{-1}$. Capacitance was measured by a high sensitivity capacitance meter (Type HC-102 produced by Yamamoto Electric Instrument, Co. Ltd.,) with the sensing resolution of 10^{-4} pF and sampling frequency of 1 kHz. Temperature and pressure were recorded with sampling frequency of 100 Hz. Flow behaviors were observed with 1000 fps and the exposure time of 100 μs.

3. EXPERIMENTAL RESULTS AND DISCUSSION

3.1. Flow Behaviours

Flow behaviours at the capacitance sensor were observed from the horizontal direction parallel to the electrode. Example images obtained by the high frame rate camera for circular, square, and triangular channels are shown in Figs. 4a to 4c, respectively. Mass flux was 100 $kg \cdot m^2 \cdot s^{-1}$. For low quality of 0.06 to 0.10 shown in Fig. 4c, i, long slug bubbles were flowing for each channel. Bubble interface in the square channel seemed to be smoother than that in the circular channel. For the triangular channel, it was clearly seen that the area in the corner was filled with liquid. For high quality of 0.52 to 0.6, flow pattern was annular flow with gas core flow. The corner area of triangular channel was filled with liquid. The gas-liquid interface in the triangular channel was largely undulated.

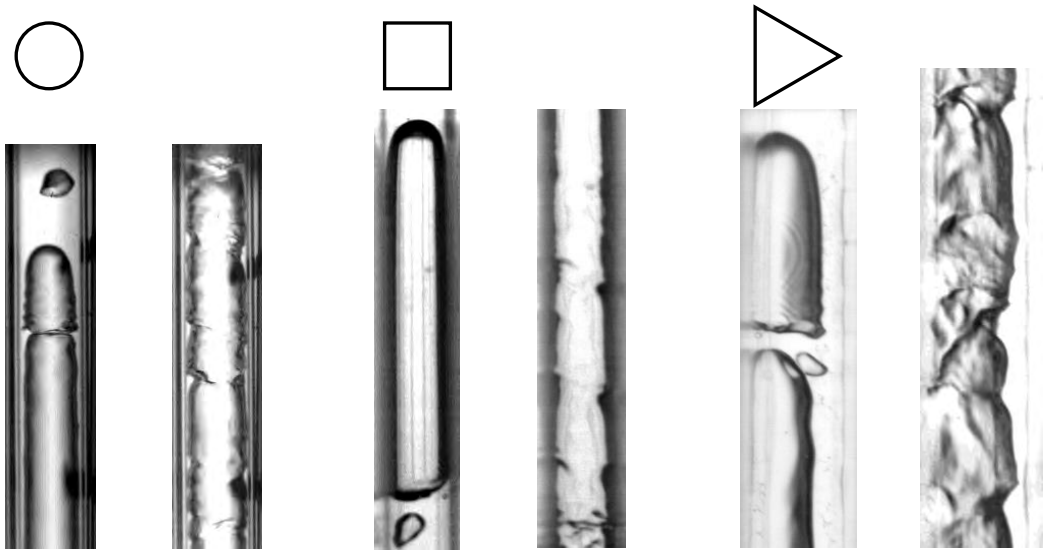

(i) x = 0.09 (ii) x = 0.52 (i) x = 0.10 (ii) x = 0.60 (i) x = 0.06 (ii) x = 0.53

(a) Circular channel (b) Square channel (c) Triangular channel

Figure 4: Observed flow behaviors at the void fraction measurement section (G=100 kg×m^{-2}×s^{-1})

3.2. Flow Pattern

Observed flow patterns were classified into bubbly, slug, churn, semi-annular and annular flows. In a bubbly flow vapor bubbles smaller than the tube diameter were flowing in the channel. In a slug flow vapor was flowing as large bullet-shaped bubbles. Some small vapor bubbles existed in the wake of the large bubbles. Churn flow was highly unstable flow with intermittent liquid reverse flows due to gravity and many vapor bubbles were included in liquid slugs. Semi-annular flow was similar to churn flow, but there was no intermittent liquid reverse flows. In annular flow liquid travelled partly as a liquid film on the channel walls and partly as fine drops distributed in the vapor core. Partial thick liquid film was considered as disturbance waves generated by interfacial shear stress between the liquid film and vapor core flows.

Flow patterns for circular, square, and triangular channels are plotted on j_L-j_G diagram in Fig. 5a to 5c with Mishima-Ishii's flow pattern transition boundaries (Mishima and Ishii, 1984), respectively.

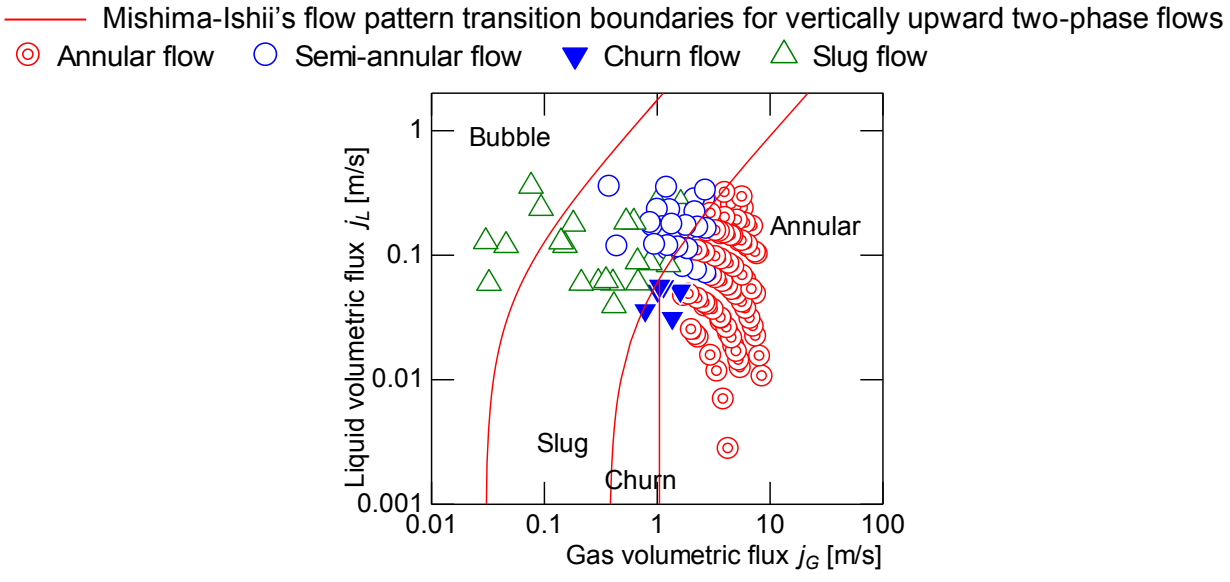

(a) Circular channel

Figure 5: Flow patter map of one-component vertically upward two-phase flows in various shaped channel with the hydraulic diameter of 2 mm

Mishima-Ishii's flow pattern transition boundaries for vertically upward two-phase flows

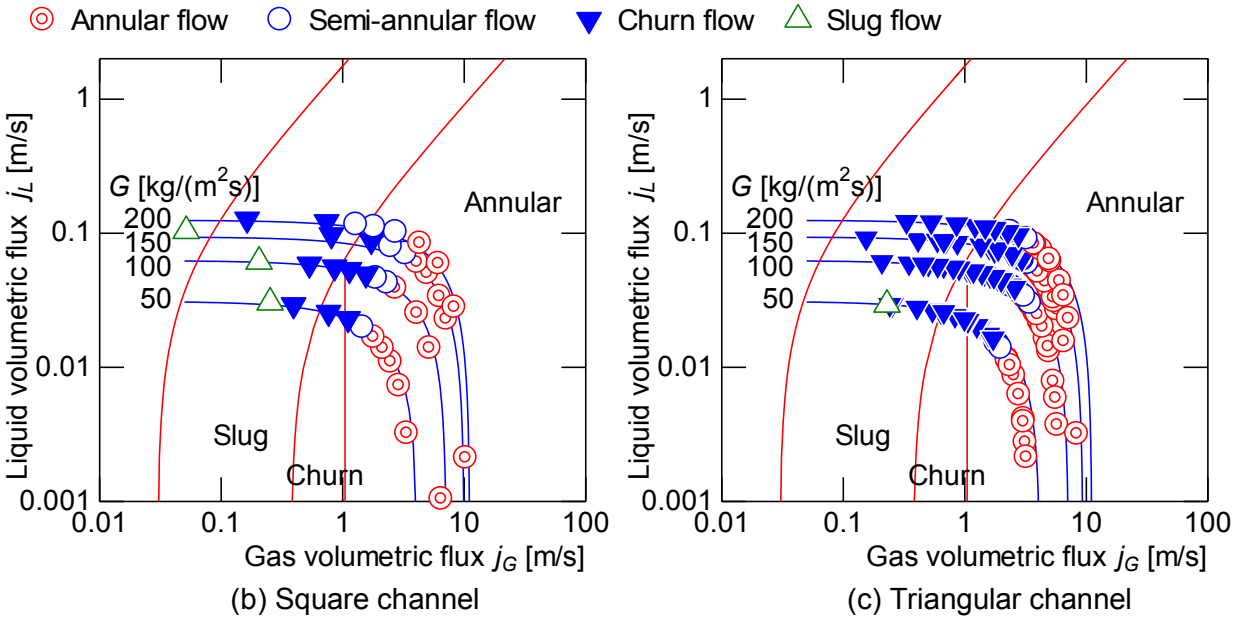

(b) Square channel (c) Triangular channel

Figure 5: Flow patter map of one-component vertically upward two-phase flows in various shaped channel with the hydraulic diameter of 2 mm

Gomyo and Asano (2016) reported that gas volumetric flux at the flow pattern transition to annular flow became higher with decreasing the channel diameter for vertically upward flows in small diameter channel, while the transition boundary for 4 mm channel was agreed well with Mishima Ishii's transition boundary. For the square channel (Fig. 5b), the transition boundary to annular flow was almost the same with that for the circular channel. Churn flow was observed in the wide range with low gas volumetric flux. For the triangular channel (Fig. 5c), the transition boundary to annular flow became higher gas volumetric flux. Since liquid accumulated in the corner due to surface tension, liquid film thickness became thicker. The thicker liquid film might cause easy formation of intermittent liquid reverse flow due to gravity. On the other hand, for the triangular tube, the area with churn flow spread to the lower gas volumetric flux. The reason was on the bubble behavior. Since bubbles in the triangular tube tended to flow along the center axis, void fraction at the center became higher. The behavior might lead to gas core formation. However, under the lower gas volumetric flux, interfacial shear stress was not enough to keep the thicker liquid film. Therefore, churn flow was observed in the wider range for the triangular channel.

3.3. Void Fraction

Comparisons in void fraction fluctuations are shown in Figs. 6a and 6b. Figs. 6a and 6b show the comparison of the square and triangular channel with the circular channel, respectively. The flow conditions with the vapor quality around 0.5 were selected. The flow pattern was annular flow. Instantaneous drop of void fraction means passing of disturbance wave. Different tendency depending on mass flux was observed. For the higher mass flux over 100 $kg \cdot m^2 \cdot s^{-1}$, average void fraction for non-circular channel became lower, and the passing frequency of disturbance waves became lower. Although lower void fraction means larger velocity difference between gas and liquid, liquid film in the noncircular channels became smoother. The fact might be caused by thicker liquid film thickness in the corners. The interface velocity might be higher in the non-circular channels. So, gas-liquid interface became smoother.

On the other hand, for the lowest mass flux of 50 $kg \cdot m^{-2} s^{-1}$, the magnitude of void fraction fluctuation became quite larger for the non-circular channel. The thicker liquid film could not be kept by the low gas velocity.

Time average void fractions are plotted against quality with the calculated results by correlation equations in Fig. 7. The solid and bold lines show the calculation results of homogeneous model and Cioncolini and Thome's model (Cioncolini and Thome, 2012), respectively. The condition with negative quality means subcooled boiling. It could be clearly seen that void fraction in the square channel was smaller than in the circular channel. In the comparison between the square and triangular channels, void fraction in the triangular channel was slightly lower. Under the middle range

of quality condition, void fraction in the square and triangular channels decreased with decreasing mass flux, while the effect of mass flux was small for the circular tube.

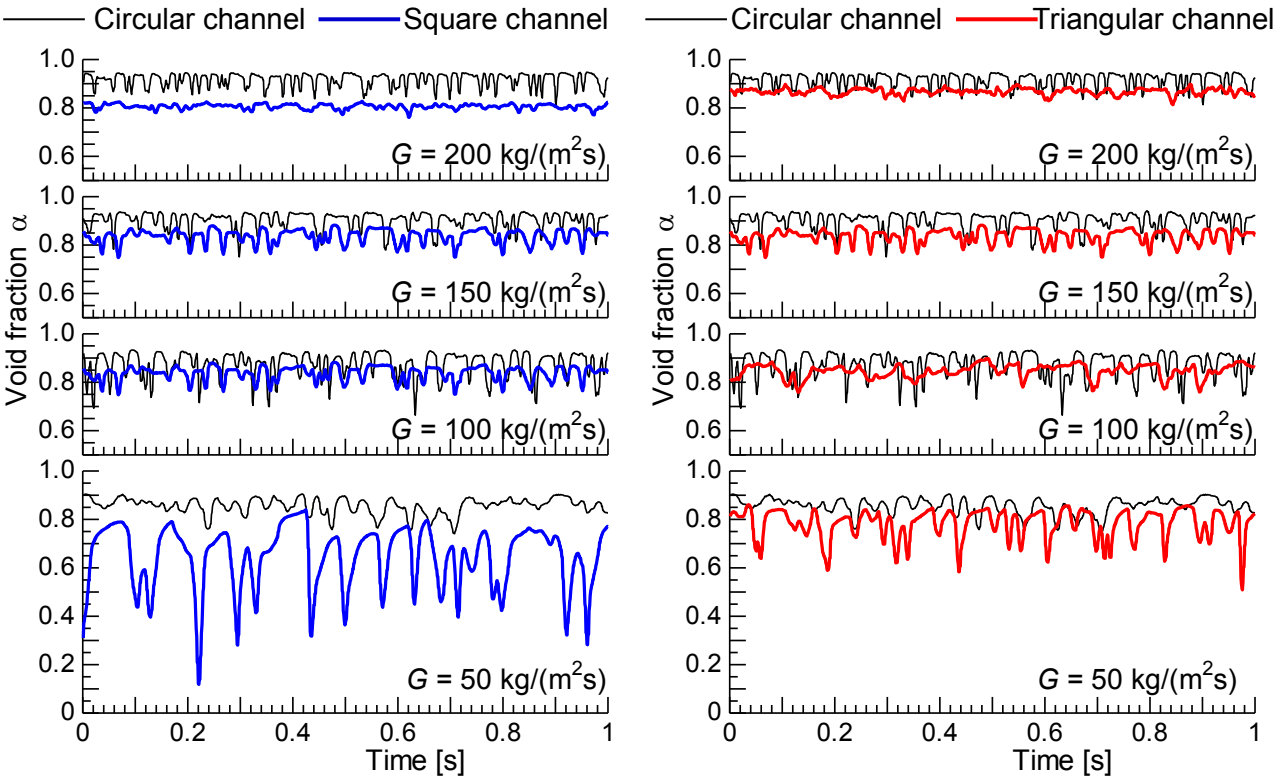

(a) Circular and square channel (b) Circular and triangular channel

Figure 6: Void fraction fluctuations of annular flows with vapor quality of about 0.5

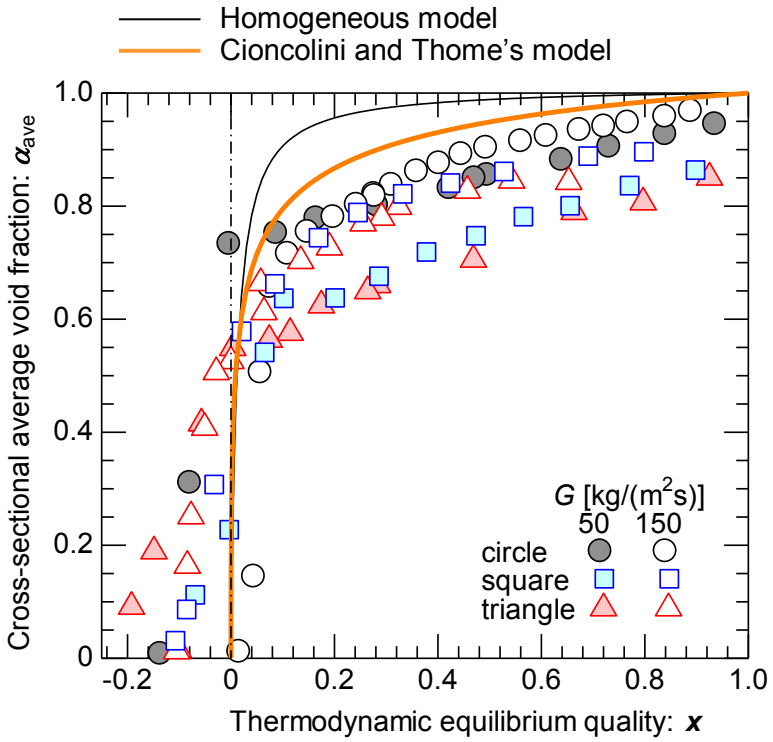

Figure 7: Average void fraction characteristics

4. CONCLUSIONS

The effect of the cross-sectional shape on one-component vertically upward two-phase flows in small diameter channel was examined based on the measured results of void fraction. Three kind of channels, such as circular, square, and triangular channels, with the hydraulic diameter of 2 mm were used. The obtained results are summarized as the followings.

Flow pattern transition boundary from churn to annular flow for the square channel was almost the same with the circular channel. On the other hand, the gas volumetric flux at the transition for the triangular channel became higher, and the range with churn flow became wider gas volumetric flux range.

Average void fractions in the square and triangular channels were lower than those in the circular channel, because liquid might be accumulated in the corner by the surface tension and the formation of disturbance waves was suppressed.

Although the void fractions for the noncircular channels were lower than those for the circular channel, gas-liquid interface of liquid film in annular flows was smoother for the noncircular tube. Since liquid was accumulated in the corner, thick liquid film thickness might make interfacial velocity higher.

NOMENCLATURE

Bo	Bond number
C	electrostatic capacitance (pF)
Co	confinement number
D	hydraulic diameter (m)
g	gravitational acceleration ($m \times s^{-2}$)
G	mass flux ($kg \times m^{-2} \times s^{-1}$)
j	volumetric flux ($m \times s^{-1}$)
x	thermodynamic equilibrium quality (-)
α	void fraction (-)
ρ	density ($kg \times m^{-3}$)
σ	surface tension ($N \times m^{-1}$)

subscript

ave	time average
G	vapor phase
L	liquid phase

REFERENCES

Baba S., Ohtani N., Kawanami O., Inoue K., Ohta H., 2012. Experiments on Dominant Force Regimes in Flow Boiling Using Mini-Tubes, Frontiers in Heat and Mass Transfer 3, 043002.

Cioncolini A. and Thome J.R., 2012. Void Fraction Prediction in Annular Two-Phase Flow, Int. J. of Multiphase Flow 43, 72–84.

Enoki K., Mori H., Miyata K., Hamamoto Y., 2013. Flow Patterns of the Vapor-liquid Two-phase Flow in Small Tubes, Transaction of the JSRAE, 30(2), 155–167 (in Japanese).

Gomyo T., Asano H., Ohta H., Shinmoto Y., Kawanami O., Kurimoto T., Komasaki M., Matsumoto S., 2014.Void Fraction Characteristics and Flow Patterns of One-Component Gas-Liquid Two-Phase Flow, Japanese J. of Multiphase Flow 27(5), 547–554 (in Japanese).

Gomyo T. and Asano H., 2016. Void Fraction Characteristics of One-Component Gas-Liquid Two-Phase Flow in Small Diameter Tube, Interfacial Phenomena and Heat Transfer 4(1), 1–18.

Jige D., Koyama S., 2011. Experiments on Condensation of R1234ze(E) in a Multi-port Extruded Tube, Transaction of the JSRAE 28(3), 225–232 (in Japanese).

Mishima K. and Ishii M., 1984. Flow Regime Transition Criteria for Upward Two-Phase Flow in Vertical Tubes, Int. J. Heat Mass Transfer 27, 723–737.

Mishima K. and Hibiki T., 1996. Some Characteristics of Air-Water Two-Phase Flow in Small Diameter Vertical Tubes, Int. J. of Multiphase Flow 22(4), 703–712.

Ong C.L. and Thome J.R., 2011a. Macro-to-Microchannel Transition in Two-phase Flow: Part 1 – Two-phase flow patterns and film thickness measurements, Experimental Thermal and Fluid Science 35, 37–47.

Ong C.L. and Thome J.R., 2011b. Macro-to-Microchannel Transition in Two-phase Flow: Part 2 – Flow boiling heat transfer and critical heat flux, Experimental Thermal and Fluid Science 35, 873–886.

Wang H.S., Rose J. W., 2006. Film condensation in horizontal microchannels: Effect of channel shape. Int. J. Thermal Sciences 45, 1205–1212.

Wang H.S., Rose J. W., 2011. Theory of heat transfer during condensation in microchannels, Int. J. Heat Mass Transfer 54, 2525–2534.

Manuscript ID: 1107
DOI: 10.18462/iir.icr.2019.1107

Solar driven Organic Rankine Cycle – ab/adsorption cogeneration systems

Tryfonas C. ROUMPEDAKIS [(a)], Carlos A. INFANTE FERREIRA [(a)]

[(a)] Delft University of Technology, Section Engineering Thermodynamics
Leeghwaterstraat 39, 2628 CB Delft, The Netherlands, c.a.infanteferreira@tudelft.nl

ABSTRACT

Solar-based poly-generation systems with thermally driven sorption heat pump / chillers use the condensation heat of ORC to cover heating and cooling loads of buildings. In the present study the performance of such systems when used in buildings in the Netherlands and Greece is investigated taking both exergy efficiency and economic aspects into account. The alternative of using PV-panels and electrically driven vapour compression heat pumps / chillers is also investigated. The performance of the systems is compared to the performance of conventional heating and cooling systems. Higher exergy efficiencies can be attained with the ORC sorption systems only for unacceptably long payback times. Optimum systems will have low exergy efficiency (8 %) compared to the exergy efficiency of conventional systems (16 %) and still long payback times (longer than 19 years). PV – panel vapour compression heat pump / chiller systems have generally acceptable payback times smaller than 10 years.
Keywords: Poly-generation, solar thermal, absorption chiller, adsorption chiller, vapour compression cycle.

1. INTRODUCTION

Combined heat and power (CHP) systems have demonstrated the advantages of using the “waste” streams of energy systems for other purposes. In 2015, in the European Union CHP contributed to 10% of the total energy mix and, for instance, in the Netherlands it covered even about 28% of the energy mix. In recent years the idea of further cascading systems to create extra value has been exploited by a large number of researchers. Roumpedakis (2018) lists 28 recent (since 2011) studies on poly-generation systems in which the “waste” heat from organic Rankine cycles (ORC) was used to drive sorption refrigeration / heat pump cycles. Most of the investigated systems make use of concentrating solar collectors to operate ORCs. Sorption chillers, mostly LiBr-H_2O absorption chillers, use the heat rejected at the condenser of the ORC at about 90 ^oC, to create a chilling effect slightly above 0 ^oC. Studies report exergy efficiencies between 8 and 30% when the exergy of the solar energy entering the system is taken into account (Roumpedakis 2018); the reported pay-back times from similar studies range between 3 and 17 years. The exergetic and economic potential of these poly-generation systems seems to be very dependent on the assumptions made and the irreversibility losses which are taken into account. These studies do not further clarify if adsorption systems requiring lower driving temperatures result in advantages in comparison to liquid absorption systems, see Fig. 1.
In the present study the authors investigate the potential of ORC-sorption chiller poly-generation systems for the cases of Netherlands (Amsterdam) and Greece (Athens). In the winter the chillers are used as heat pumps which make use of the ab(d)sorption heat plus condensation heat. In this way, the systems could substitute the current heating and cooling methods which are based on natural gas combustion (heating) and electrically driven vapour compression chillers (cooling). The performance of the conventional methods of heating and cooling is used as reference to evaluate the advantages and disadvantages of the poly-generation systems. Since Infante Ferreira and Kim (2014) have identified the use of vapour compression systems based on PV solar collector electricity as competitive, also this option is compared to the present heating and cooling methods.

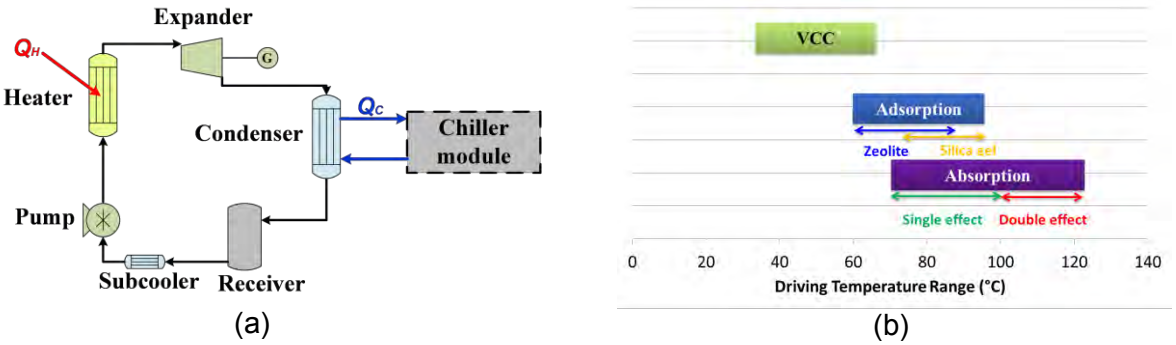

Figure 1: (a) Schematic of the ORC coupling with a chiller module (b) Driving temperature range for the available heat pump / cooling technologies. Data source: Fahrenheit (2018)

Main goal of this study is to investigate from technical as well as economical points of view the potential coupling of ORCs and sorption chillers and identify the level of competitiveness of the proposed hybrid system for decentralized applications. For each of the main components of the system separate models have been developed taking into account that the final goal is to predict the system performance for a whole year. Each of these models will be first shortly introduced in separate sections. Finally in section 5 the system performance of the conventional system is discussed and compared with the performance of the PV – vapour compression chiller and the ORC – sorption poly-generation solutions.

2. SOLAR COLLECTORS AND THERMAL STORAGE

The poly-generation systems considered here are powered by solar collectors. The application of sorption chillers / heat pumps requires driving temperatures in the range of 70-90 °C as illustrated in Figure 1. Thus, the condensation temperature of the ORC systems needs to be slightly higher. As it will be discussed in section 3 the optimum evaporating temperatures are in the range 200-210 °C so that the solar collectors must deliver heat at a slightly higher temperature. This requires the use of concentrating solar collectors which show low heat losses and can reach this range of temperatures (Jradi and Riffat, 2014).

The variations of solar radiation and the mismatch between the availability of solar excess and the heat consumption make the use of a storage option a necessity for applications utilizing solar energy (Morofsky, 2007; Alva et al., 2018). Furthermore, the implementation of a storage option between the ORC and the solar collectors is necessary to absorb the energy spikes relevant to the local weather and provide a more stable input to the evaporator of the ORC.

The solar thermal collector efficiencies have been estimated using the empirical polynomials proposed by Infante Ferreira and Kim (2014). Only CPTC (concentrated parabolic trough collectors) and CPDC (concentrated parabolic dish collectors) can deliver the temperatures required to drive the tri-generation systems (130 to 210 °C) at an acceptable efficiency.

Fig. 2 shows schematically how the solar collectors are connected to the storage tank and the evaporator of the ORC. When there is no solar radiation, the solar collectors are decoupled from the storage tank. On the other hand, when solar energy is available the heat transfer fluid of the solar collector circulates and heats the storage tank. A threshold temperature of 130 °C has been selected above which the circulation pump starts to supply hot fluid to the ORC evaporator.

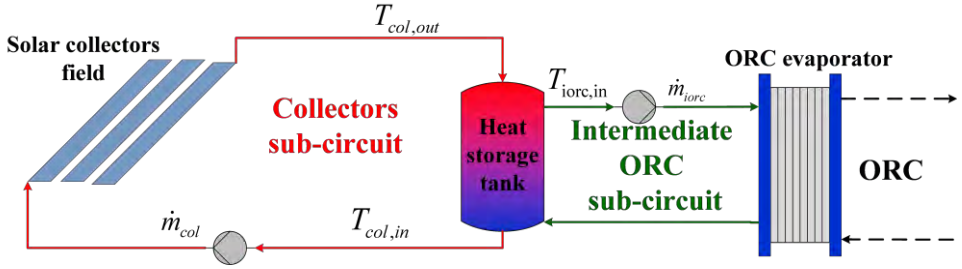

Figure 2: Schematic of the coupled solar collectors-storage tank-intermediate ORC sub-circuit system

For the modelling of the PV modules the procedure proposed by Bellia et al. (2014) was used. For a set of ambient temperature and solar radiation the corresponding output currents are estimated by applying a set of different values for the voltage from 0 up to the open circuit voltage.
Fig. 3 presents the results of a yearly simulation for the performance of PV panels with an area of 93 m^2 installed in the considered locations. The performance of the PV is comparable for both regions because the excess of solar radiation in Athens is counterbalanced by the increase in the cell's temperature which leads to increased losses. These results are mainly explained by the right hand side of the figure. The higher ambient temperatures and higher values of the solar radiation as well as the lower wind velocities in Athens result in significantly higher cell temperatures, harming the efficiency of the PV modules and finally, leading to comparable operation in Amsterdam. In an annual basis the net efficiency in Athens is 14.9% and the respective value for Amsterdam is 14.1%.

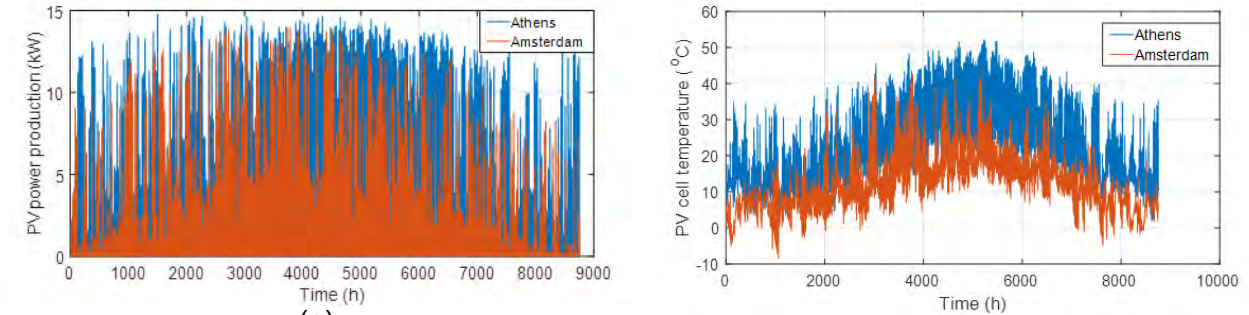

Figure 3: (a) Overview of the power production for a PV array for the two considered cities throughout a year. (b) Overview of the cell's temperature for a PV module for the two considered cities throughout a year simulation

3. ORGANIC RANKINE CYCLE

The large temperature difference between the inlet of the ORC's evaporator and the exit from the expanders provides sufficient driving force for a recuperator. When a single stage expander is used, its pressure ratio limitation prevents high evaporation temperatures (pressures) and limits the maximum obtained thermal efficiency. In order to allow for higher evaporation temperatures a second expander is implemented in series with the first expander. The final layout of the ORC considered in this study is shown in Fig. 4.

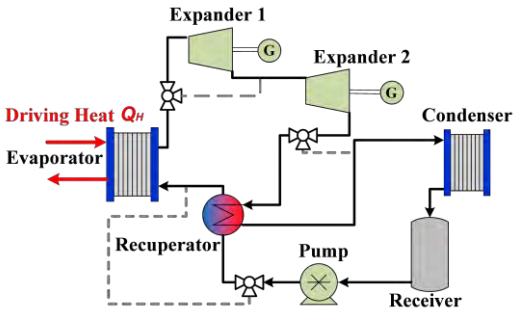

Figure 4: Schematic of an ORC with two-stage expansion and internal heat recovery by a recuperator

3.1. Performance Indicators

To measure the performance of the considered cycles some performance parameters have to be introduced for the ORC. The thermal efficiency for the ORC is obtained from (Lecompte et al., 2014):

$$\eta_{th,ORC} = \frac{\dot{W}_{el,\exp} - \dot{W}_{el,pump}}{\dot{Q}_{in,ORC}} \quad \text{Eq. (1)}$$

The second law efficiency for the ORC system is calculated from the following expression (Maraver et al., 2014):

$$\eta_{ex,ORC} = \frac{(\dot{W}_{el,\exp} - \dot{W}_{el,pump}) + \dot{E}x_w}{\dot{E}x_{HTF,in} - \dot{E}x_{HTF,out}} \quad \text{Eq. (2)}$$

The exergy rate increase of the condenser water stream is useful as it is used to drive the sorption chiller. It is obtained with Eq. (3).

$$\dot{E}x_w = \dot{E}x_{w,out} - \dot{E}x_{w,in} = \dot{m}_w[h_{w,out} - h_{w,in} - T_0(s_{w,out} - s_{w,in})] \quad \text{Eq. (3)}$$

with T_0 = 298.15 K. The exergy input to the system is calculated with Eq. (4).

$$\dot{E}x_{HTF} = \dot{E}x_{HTF,out} - \dot{E}x_{HTF,in} = \dot{m}_{HTF}[h_{HTF,out} - h_{HTF,in} - T_0(s_{HTF,out} - s_{HTF,in})] \quad \text{Eq. (4)}$$

The subscript HTF refers to the properties of the stream flowing between the heat storage tank and the evaporator of the ORC. The internal exergy efficiency is defined in relation to the Carnot efficiency of the cycle:

$$\eta_{ex,ORC\_Carnot} = \frac{\eta_{th,ORC}}{1 - \frac{T_{low}}{T_{high}}} \quad \text{Eq. (5)}$$

with

$$T_{low} = \frac{T_{w,out} - T_{w,in}}{\ln(T_{w,out} / T_{w,in})}; T_{high} = \frac{T_{HTF,in} - T_{HTF,out}}{\ln(T_{HTF,in} / T_{HTF,out})} \quad \text{Eq. (6)}$$

3.2. ORC Optimization Results

Table 1 lists the optimal operating conditions for the considered working fluids. The largest performance indicators are marked in yellow.

Table 1. Optimized design points for all the considered working fluids for maximum efficiency HTF mass flow rate=0.5 kg/s

Fluid	Cyclo hexane	Heptane	Toluene	Isohexane	Cyclo pentane
Thermal efficiency (%)	14.03	13.77	13.31	13.59	13.05
Exergy efficiency ORC (%)	51.67	50.17	52.68	48.81	48.71
Exergy efficiency Carnot based (%)	52.08	53.49	51.64	52.32	49.32
Expander efficiency (%)	76.91	74.87	76.76	77.49	77.78
Pump efficiency (%)	64.22	71.28	42.74	73.09	74.02
Net power output (kW)	4.58	3.92	3.52	4.03	4.32
Heat input (kW)	32.63	28.44	26.46	29.68	33.13
Recuperator heat duty (kW)	6.07	5.63	3.48	7.38	3.56
Condensation temperature (°C)	87.8	87. 6	88.2	87.6	89.8
Evaporation temperature (°C)	205.2	207.7	204.1	205.9	209.1
Level of superheating (K)	10.3	9.5	8.6	13.9	6.7

Cyclohexane, heptane and toluene show the most attractive solutions. Cyclohexane maximizes both the thermal efficiency and the net power output. For this reason it has been selected as the working fluid of the installation in all upcoming calculations. Notice that the highest performance is obtained for evaporating temperatures in the range 204 to 209 °C.

4. COOLING CYCLES

Recently Roumpedakis et al. (2018) investigated the performance of a 10 kW zeolite-water adsorption chiller / heat pump. They developed a model which allows for the identification of the

relation between the inlet temperatures of the three external flows and the performance of the machine. These are the heat source temperature, the heat rejection temperature and the chilled water temperature. The results of this model have been implemented in table form in the ORC – adsorption system model allowing for the performance prediction both for operation as chiller and as heat pump. Different data sets of cooling water and chilled water temperatures for a given heat source temperature allow to predict the performance over a wide range of conditions.
The model used to predict the absorption chiller's performance is based on the approach proposed by Kim and Infante Ferreira (2008). The model was calibrated for a LiBr-H_2O single-effect absorption chiller. The nominal mass flowrate of the solution was set to be equal to 0.0556 kg/s. The mass flows of the secondary streams of generator, absorber and evaporator have been set at 1 kg/s while the mass flow of external fluid through the condenser has been taken as 1.5 kg/s.
The considered vapour compression chiller (VCC) was selected to operate with a typical working fluid, R410A, without any optimization procedures to define the optimal fluid. Both the nominal and the off-design performance of the VCC have been determined by cubic interpolations of actual data provided by a chiller manufacturer. This model is also used in combination with the PV panels as an all-electric solution.

5. PERFORMANCE OF THE POLY-GENERATION SYSTEMS

Two types of buildings have been evaluated: a residential building with a total surface of 100 m² and a utility building of 639 m². The heating and cooling requirements of the two building types have been evaluated for both Amsterdam and Athens. The calculations have been conducted in the environment of EnergyPlus. The buildings are reasonably well insulated. For instance the windows are double glazed windows with an overall heat transfer coefficient equal to 3.8 $Wm^{-2}K^{-1}$.
For the specification of the buildings' thermal loads a central air conditioner with a COP of 3.28 has been selected to cover the cooling loads, while the heating demands (including water heating) were covered by a gas fired boiler with a thermal efficiency of 95%. For the residential buildings the heating set point was selected to be 21.1 °C, while the cooling set point was set at 24.4 °C. For the case of the utility buildings the same setpoints were considered but only for working hours (9 am-5 pm).
Table 2 presents, the total annual consumption to cover the thermal demands of the considered buildings using conventional systems. The exergy input in annual basis consists of two parts, the exergy of the natural gas and the total electrical consumption for the central air conditioner. The specific exergy (kJ kg^{-1}) of natural gas is equal to the lower heating value of natural gas multiplied by a factor of 1.04 (Oliveira Júnior, 2013).

Table 2. Overview of conventional systems consumption, costs and exergy efficiencies

-	Residential Athens	Residential Amsterdam	Utility Athens	Utility Amsterdam
Annual heating demand (kWh)	1,897.6	9,576.7	5,753.9	30,719.3
Annual cooling demand (kWh)	5,481.4	457.3	9,968.9	245.7
Annual electricity consumption for cooling (kWh)	1,669.9	139.4	3,037.1	74.9
Annual costs for cooling and heating (€)	394.3	802.2	524.2	832.1
Annual exergy input (kWh)	3643.4	10099.1	9021.2	32023.0
Annual exergy output (kWh)	656.8	1,602.7	1,295.2	3,899.6
Average annual exergy efficiency (%)	18.03	15.87	14.36	12.18

Table 2 shows that the exergy efficiency of the conventional systems is in the range 12 to 18%. Huangfu et al. (2007) report a maximum exergy efficiency of 26% for an internal combustion engine combined with an adsorption system and a payback time of 3 years. Al-Sulaiman et al. (2011) report a similar exergy efficiency (27.5%) for a biomass fired ORC combined with absorption. These results indicate that the ORC combined with adsorption or absorption systems might be competitive.

5.1. PV-Heat Pump/Chiller Configuration

In order to, in terms of exergy efficiency and cost competitiveness, determine the optimum number of PV panels coupled with the vapour compression system a loop has been implemented which evaluated all possible number of modules from a single PV module to covering the whole roof of the given buildings. The maximum number of PV panels that could be installed in the considered

buildings was determined by considering the gross surface of a single panel to be 25% larger than the net surface (which is equal to 1.66 m²).
The capital cost of the chiller / heat pump has been determined using a cost correlation while the capital cost of the PV panels has been taken as 1400 €/kW$_p$ (Huld et al., 2014). The annual savings from the operation of the PV panels combined with the chiller / heat pump have been obtained by comparing the annual costs with the annual costs of the reference case listed in Table 2. From these savings the payback time for the considered PV-heat pump system has been obtained. For what concerns the electricity produced from the PV panels, net metering was considered to be applied with no feed-in tariff. The results for the cost optimization are presented in Fig. 5 for the residential (left) and the utility building (right), respectively. For the case of Athens and for a PV surface larger than 8.3 m², the payback period is less than 10 years, making the investment quite competitive. For the residential case of Amsterdam, the payback period is below 10 years for all the considered values of the PV surface. This is justified by the fact that the heat pump is operating mostly for heating in Amsterdam, resulting in an overall higher efficiency and thus lower operating costs. The slight increase in the payback period for the utility case of Amsterdam for small PV surfaces is observed due to the lower solar radiation which results in low return in comparison to the purchase costs of the PVs.

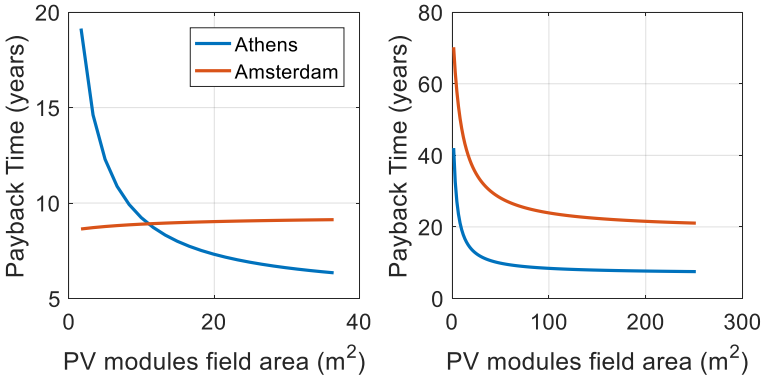

Figure 5: Payback time of PV-heat pump systems for the considered utility (right) and residential buildings (left)

The exergy input to these systems is the exergy corresponding to the solar energy given in Eq. (7).

$$\dot{E}x_{sol} = \left(1 - \frac{T_o}{T_{sol}}\right) I_{sol} A_{pv} \qquad \text{Eq. (7)}$$

where T_{sol} is the temperature of the sun (5770 K, Kalogirou et al. (2016)), I_{sol} is the solar radiation and A_{pv} is the solar panel surface. The large exergy losses in the PV panels lead to low exergy efficiencies when large solar collector areas are installed. For instance in Amsterdam areas above 10 m^2 (residential) and 30 m^2 (utility) lead to exergy efficiencies lower than 10%.

5.2. Solar Thermally Driven ORC-Sorption Systems with a Backup Boiler

In case the ORC is not supplying sufficient heat to the sorption heat pump / chiller, the model calculates the additional heat input that is required to cover the heating / cooling loads of the building. This additional exergy input is added to the solar exergy input to the solar collectors when calculating the exergy efficiency of the systems.
For the evaluation of these systems a genetic algorithm has been used with objective functions to maximize the exergy efficiency while minimizing the payback time. Since the best performance is obtained with concentrated parabolic dish collectors only the results for these collectors will be discussed. Fig. shows the optimization results for the ORC combined with sorption heat pump / chiller systems. On the left hand side the results for the absorption systems and the right side for the adsorption systems. Adsorption systems show an inferior performance when compared to the absorption systems.

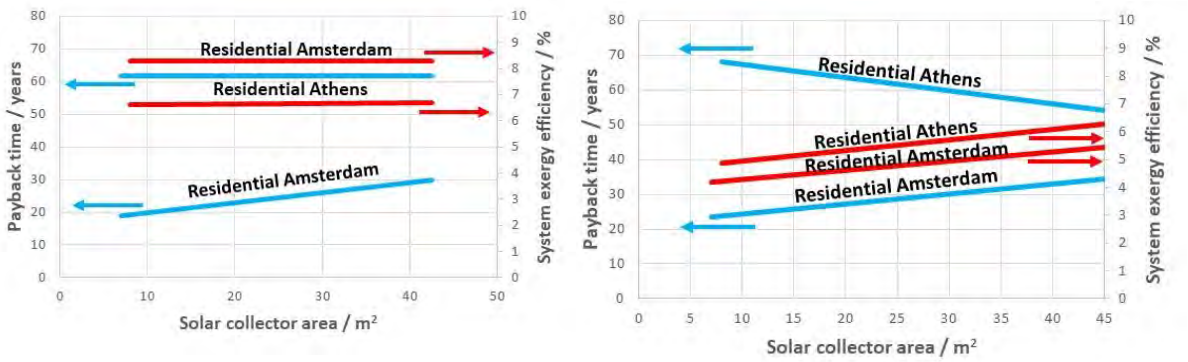

Figure 6: Payback time and exergy efficiency of ORC-sorption heat pump systems for the considered residential buildings when combined with absorption (left) and adsorption (right) systems

Fig. 6 shows that the exergy efficiency of these systems is comparable to the exergy efficiency of the PV – VCC systems. The solar exergy input is high while the solar thermal collectors, the storage buffer and the ORC introduce large amounts of irreversibilities. The auxiliary boiler with its low exergy efficiency also contributes to the low value of the exergy efficiency. With payback times larger than 20 years, these systems cannot compete with the conventional systems.
The genetic algorithm results have confirmed that the ORC combined with an absorption heat pump can attain system exergy efficiencies up to 20% but that this is only possible with very long payback times. Better economic performance leads to systems with low exergy efficiency.

6. CONCLUSIONS

In this study the authors have investigated the potential of solar driven ORC with a sorption heat pump / chiller coupled to the condenser of the ORC. The performance of such systems has been investigated for applications both in Amsterdam and Athens. From this study the following conclusions can be drawn:
Solar energy can be converted into electricity with PV panel and the electricity can then be used to operate a heat pump / chiller for heating / cooling purposes. The average PV panel area of 12 m^2, generally used in residential buildings in the Netherlands, leads to system payback times of 9 years and system exergy efficiency of 8%. This efficiency is lower than the efficiency of the conventional system (16%).
When adsorption heat pumps / chillers are used in combination with the solar driven ORC the payback times become unacceptably high (lowest value being 23 years) and the exergy efficiency remains low around 8%. When absorption heat pumps / chillers are used in combination with the solar driven ORC the payback times are comparably better (lowest value being 19 years) while the exergy efficiency remains at a similar level of 8%.

NOMENCLATURE

	Roman symbols		el	electrical
A	area	m^2	exp	expander
$\dot{E}x$	exergy flow	kW	high	high temperature side
h	specific enthalpy	$kJkg^{-1}$	HTF	heat transfer fluid
I	solar radiation	Wm^{-2}	in	inlet
$\dot{m}$	mass flow	Kgs^{-1}	low	low temperature side
$\dot{Q}$	heat flow	kW	ORC	organic Rankine cycle
s	entropy	$kJkg^{-1}K^{-1}$	out	outlet
T	temperature	K	pv	PV panel
$\dot{W}$	mechanical power	kW	sol	solar / sun
			th	thermal

	Greek symbols			
η	efficiency	-	w	water stream
	Subscripts			
0	reference state			

REFERENCES

Al-Sulaiman, F.A., Hamdullahpur, F., Dincer, I., 2011. Greenhouse gas emission and exergy assessments of an integrated organic Rankine cycle with a biomass combustor for combined cooling, heating and power production. Appl. Therm. Eng. 31(4), 439-446.

Alva, G., Lin, Y., Fang, G., 2018. An overview of thermal energy storage systems. Energy 144, 341-378.

Bellia, H., Youcef, R., Fatima, M., 2014. A detailed modeling of photovoltaic module using MATLAB. NRIAG Journal of Astronomy and Geophysics 3(1), 53-61.

Fahrenheit©. 2018. Fahrenheit: eZea. accessed January 2018. https://fahrenheit.cool/en/zeo/.

Huangfu, Y., Wu, J.Y., Wang, R.Z., Kong, X.Q., Wei, B.H., 2007. Evaluation and analysis of novel micro-scale combined cooling, heating and power (MCCHP) system. Energy Convers. Manage. 48(5), 1703-1709.

Huld, T., Jäger Waldau, A., Ossenbrink, H., Szabo, S., Dunlop, E., Taylor, N., 2014. Cost Maps for Unsubsidised Photovoltaic Electricity In JRC 91937.

Infante Ferreira, C., Kim, D.-S., 2014. Techno-economic review of solar cooling technologies based on location-specific data. Int. J. Refrigeration 39 (Supplement C), 23-37.

Jradi, M., Riffat, S., 2014. Medium temperature concentrators for solar thermal applications. International Journal of Low-Carbon Technologies 9(3), 214-224.

Kalogirou, S.A., Karellas, S., Braimakis, K., Stanciu, C., Badescu, V., 2016. Exergy analysis of solar thermal collectors and processes. Prog. Energy Combust. Sci. 56, 106-137.

Kim, D.S., Infante Ferreira, C.A., 2008. Analytic modelling of steady state single-effect absorption cycles. Int. J. Refrigeration 31(6), 1012-1020.

Lecompte, S., Ameel, B., Ziviani, D., van den Broek, M., De Paepe, M., 2014. Exergy analysis of zeotropic mixtures as working fluids in Organic Rankine Cycles. Energy Convers. Manage. 85, 727-739.

Maraver, D., Royo, J., Lemort, V., Quoilin, S., 2014. Systematic optimization of subcritical and transcritical organic Rankine cycles (ORCs) constrained by technical parameters in multiple applications. Appl. Energy 117, 11-29

Morofsky, E. 2007. History of thermal energy storage. In Thermal Energy Storage for Sustainable Energy Consumption. Edited by H. O. Paksoy. NATO Science Series Vol. 234. Springer, Dordrecht, The Netherlands, pp. 3-22..

Oliveira Júnior, S.d., 2013. Exergy : production, cost and renewability. 1 online resource (xiv, 336 pages) : illustrations (some color). vols. London Springer.

Roumpedakis, T.C. 2018. Techno-economic investigations of a solar driven ORC-sorption system for combined cooling, heating and power. MSc thesis. Process & Energy. Delft University of Technology.

Roumpedakis, T.C., Christou, T., Braimakis, K., Varvagiannis, E., Karellas, S., 2018. Integrated ORC-Adsorption cycle: A first and second law analysis of potential configurations. ECOS 2018, Guimaraes, Portugal, 17-22 June.

Manuscript ID: 1108
DOI: 10.18462/iir.icr.2019.1108

Characteristics of refrigerant leaks from small HVAC&R systems

Viral K. PATEL, Ahmad ABU-HEIBA, William MILLER, Van BAXTER

Oak Ridge National Laboratory[1]
Oak Ridge, TN 37831, USA
patelvk@ornl.gov, abuheibaag@ornl.gov, wmille17@utk.edu, baxtervd@ornl.gov

ABSTRACT

Reduced use of high global warming potential (GWP) hydrofluorocarbon (HFC) refrigerants is desired. However, many lower-GWP alternatives are flammable, some of higher flammability levels, or A3, and others of lower flammability (A2 or A2L).
Safety standards for A2 and A3 flammable refrigerants, including the International Electrotechnical Commission (IEC) standard IEC 60335-2-40 calculate maximum flammable refrigerant charge limits using a fixed 4-minute leak time based on the time to leak 150 g of CO_2 through a capillary tube.
Actual refrigerant leak times depend on the equipment type, leak location, leak orifice diameter and equipment operation condition (on or off).
Five systems were installed in test chambers with leak quantities and rates measured by tracking total system weight during the leak event. Among the major results were that almost all of the system charge was shown to escape the units, >80% within the first 10 minutes.
Keywords: refrigerants, flammable, leak rate measurements, air-conditioning, refrigeration

1. INTRODUCTION

Under the Montréal Protocol a global phase-out of chlorofluorocarbon (CFCs) has been completed and phase-out of hydrochlorofluorocarbon (HCFCs) is in final stages. Hydrofluorocarbons (HFCs) like R-410A and R-134a have been used as alternatives to HCFCs for many HVAC&R applications but have relatively high global warming potential (GWP). In October 2016, the Kigali Amendment to the Montréal Protocol was adopted to phase-down the use of HFCs (UNEP, 2016). Proposed lower-GWP alternatives to replace high-GWP HFCs include low-GWP HFCs, hydrofluoroolefins (HFO), hydrochlorofluoroolefins (HCFO), hydrocarbons (HC), ammonia (R-717), CO_2 (R-744), or blends containing low-GWP HFCs and other low-GWP fluids. Most of the lower toxicity (class A) low-GWP alternatives are flammable to some degree according to Addendum g to ANSI/ASHRAE 34 (ASHRAE, 2016a) and ISO 817:2014 (ISO, 2014a), which designate toxicity and flammability of refrigerants.
Refrigerant flammability introduces challenges to the usage of low-GWP refrigerants in real life applications. Those challenges are centered around the deflagration risk associated with their use and its implications on personal and property safety. Standards have been developed to systematically set maximum allowable flammable refrigerant charges to ensure safety in case of refrigerant leakage. These standards were initially based on limited testing and numerical analyses of refrigerant leakage into confined spaces (Clodic and Cai, 1996, Kataoka et al., 1999, Kataoka et al., 2000). Currently published general safety standards include International Standards Organization (ISO) 5149 (ISO, 2014b), and its relative counterpart ANSI/ASHRAE 15 (ASHRAE, 2016b). Equipment standards include those by the International Electrotechnical Commission (e.g. (IEC, 2016, 2018)) and Underwriter's Laboratories (e.g. (UL, 2017)).

[1] This manuscript has been authored by UT-Battelle, LLC under Contract No. DE-AC05-00OR22725 with the U.S. Department of Energy. The United States Government retains and the publisher, by accepting the article for publication, acknowledges that the United States Government retains a non-exclusive, paid-up, irrevocable, world-wide license to publish or reproduce the published form of this manuscript, or allow others to do so, for United States Government purposes. The Department of Energy will provide public access to these results of federally sponsored research in accordance with the DOE Public Access Plan (http://energy.gov/downloads/doe-public-access-plan).

Most low-GWP refrigerant options are either class A2L (lower flammability) or A3 (higher flammability). While expanded use of such refrigerants is generally seen as a key to reducing the global environmental impact of HVAC&R equipment and systems, current codes significantly restrict the use of all flammable refrigerants, including lower flammability A2L types. There is, therefore, a need to revise the relevant safety standards and codes to facilitate wider use of low-GWP but flammable refrigerant alternatives; especially A2L refrigerants.

Calculations of maximum flammable refrigerant charge limits in standards such as IEC 60335-2-40 (IEC, 2016) have generally assumed a fixed leak time of 4 minutes. This was originally meant to represent a catastrophic leak and was based on the time taken to leak 150 g of CO_2 through a capillary tube (about 3.5 minutes), defined (at that time) in IEC 60335-2-24 (IEC, 1997). As such, the 4-minute leak time is embedded into the global IEC standard and into all subsequent standards which are based on it. Although the above assumptions were reasonable and necessary at the time, the actual leak rate and duration for new and existing flammable refrigerants in HVAC&R systems is known to depend strongly on the equipment type, leak location (e.g. evaporator or condenser leak), refrigerant type (i.e. lower- or higher-pressure), leak orifice diameter and equipment operation condition (i.e. on or off). For these reasons, it is imperative to quantify the actual leak rates and duration for various pieces of equipment and account for slow, medium, rapid and catastrophic leaks.

The objectives of the current project are to conduct refrigerant leak testing under conditions representative of those seen by actual equipment to document the pressure decay rate, the mass flow rate of leaked refrigerant, and the quality (vapor versus liquid) of the leaking refrigerant as a function of time. When liquid remains in the leaking refrigerant after the initial process of flashing to atmospheric pressure, a determination of the amount of liquid that “rains out” versus the small droplets that remain suspended (as a fog) as a function of time is also of interest as these phenomena will affect refrigerant concentration profiles. It is also important to know what fraction of the total charge remains in the equipment due to self-chilling from system pressure reduction. This could have implications for calculation of maximum allowable charge in systems with A2L refrigerants.

This project was intended to simulate massive failures resulting in much more rapid charge releases than the more typical, much slower rates seen in practice that would take days, weeks, or months to empty a system of its entire charge. Thus, the high leak rates chosen were meant to simulate a “maximum possible” worst case refrigerant release scenario (e.g., full line break or other rupture resulting in an orifice diameter equal to the liquid line of the system under test). For the low leak rate cases, the intent was to simulate a refrigerant leak (or release) rate that would result in a total loss of system charge in “roughly” four minutes. The choice of the 4-minute rate was intended to represent a “reasonable” worst case release scenario to match the refrigerant leak rate assumption used in IEC 60335-2-40 (IEC, 2016).

The results of this work will be used to help update the safety standards and will be part of the national and international research effort to enable the widespread use of environmentally preferred, higher-efficiency refrigerants for different applications. This paper describes the scope, tasks, and relevant results of the project. Section 2 provides a general description of the test approach along with descriptions of the test equipment. Section 3 provides a discussion of key results from tests of the various units. Finally, the project conclusions and summary are given in Section 4. This work is also part of a larger effort which is summarized in detail in (Baxter et al., 2019).

2. GENERAL APPROACH AND SETUP

2.1 Test Matrix and Equipment

The project involved imposing refrigerant leaks on five systems and conducting tests to obtain data to meet the project objectives. Systems chosen covered three air-conditioning (AC) applications (packaged terminal AC or PTAC, 10.6 kW (3-ton) residential split system AC, and 17.6 kW (5-ton) packaged rooftop AC) and two refrigeration applications (split system unit cooler, and standalone display case), as shown in Figure 1.

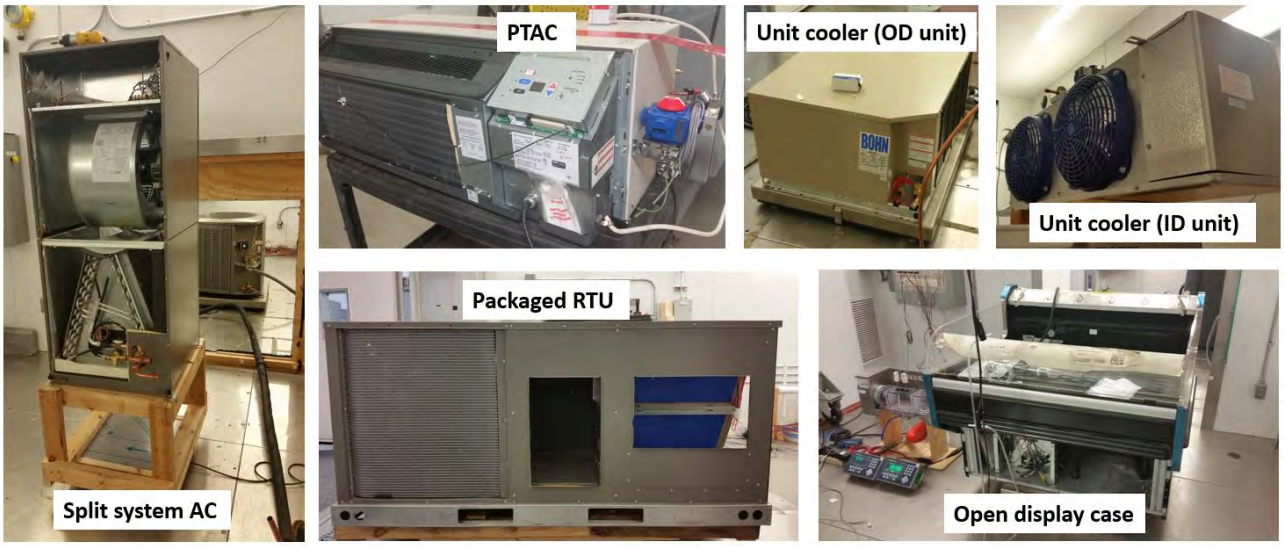

Figure 1: Equipment tested

Table 1 below shows the test matrix for each system. All systems utilized a vapor-compression cycle; refrigerants used for the testing program were R-410A for the AC systems and R-404A for the refrigeration systems. The "low-side" refers to leaks originating at the point after the evaporator outlet, prior to the compressor suction. The "high-side" refers to leaks originating at the point after the condenser outlet, prior to the expansion device.

Table 1. Test matrix for each system

Test #	Low leak rate	High leak rate	Equipment on	Equipment off	Low-side leak	High-side leak
1	×		×		×	
2	×		×			×
3	×			×	×	
4	×			×		×
5		×	×		×	
6		×	×			×
7		×		×	×	
8		×		×		×

For the high-side leaks at "high leak rate," a tube the size of the test system's liquid line with no restriction was used for the release point. For "low leak rate," the original plan was to use a release area that was ½ the cross-sectional area of the release tube. However, after reviewing results of the first system tested (split AC) this was changed to use an orifice diameter for the other four units to closely approach a total leak time (for 99% of the total refrigerant released to exit the unit) of about 4 minutes for the "equipment off," and "low-side leak" test cases.

2.2 Test Setup and Instrumentation

Figure 2 illustrates the general test chamber setup arrangement as used for the split AC unit and illustrates the approximate positioning of equipment on top of scales, the leak release apparatus, leak visualization, refrigerant concentration, and space temperature instrumentation. This positioning was basically similar for all the test units. The equipment was installed in environmental chambers so that ambient temperature and relative humidity could be kept uniform from test to test, as well as to simulate actual indoor and outdoor conditions.

The leak release apparatus consisted of a pneumatically-operated, fast-acting, full-port ball valve which was controlled by the data acquisition (DAQ) system through a computer. Two hand-operated ball valves were installed prior to the release valve to enable the test operator to select the high- or low-side leak point as required for each test.

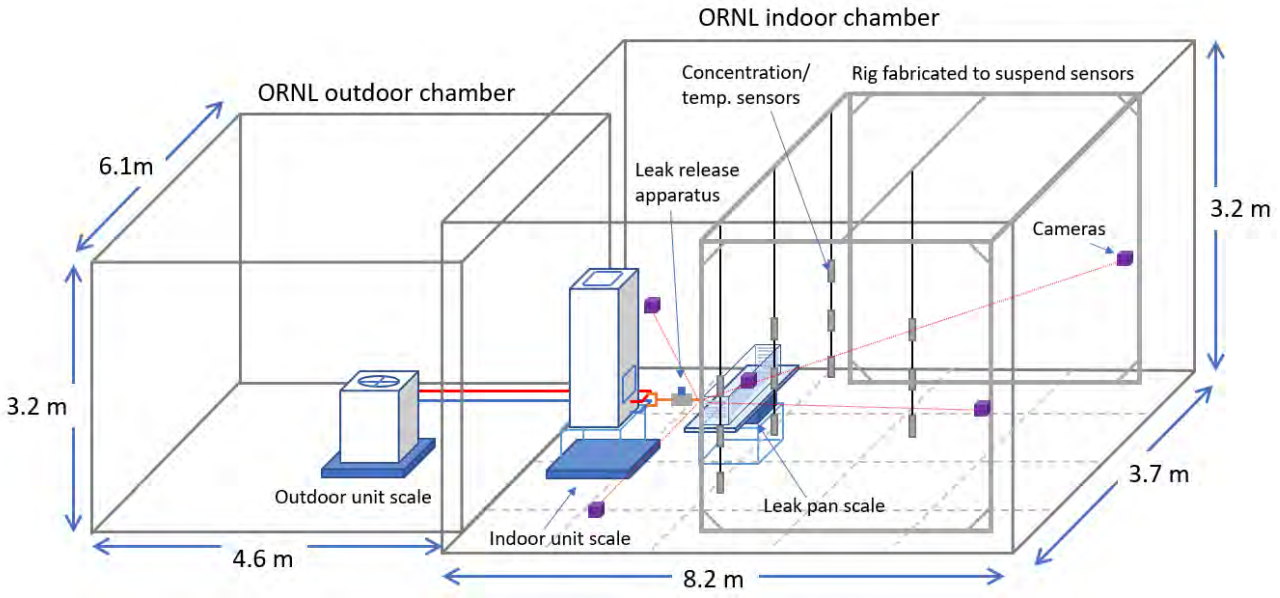

Figure 2: Split AC test unit setup in test chamber (not to scale)

To record video of the refrigerant releases, five GoPro HERO5 Session™ cameras were used for each system (positioned just under, above, to left of, to right of, and looking directly at the leak release point). To measure refrigerant concentration as a function of time, 12 Apogee® SO-220 O_2 sensors were arrayed in the room (sensing oxygen concentration as surrogate for refrigerant concentration). These sensors also had 12 built-in type K thermocouples for measurement of air temperature. To record the decay of refrigerant pressure within the high and low-pressure sides of the equipment, high-accuracy pressure transducers were located just upstream of the leak location. Type T thermocouples were co-located with each pressure sensor and a third TC was located at the leak release point.

To quantify the mass flow rate of the released refrigerant, the equipment was placed on high-capacity, high-precision scales to track unit mass vs. time. Two scales were used for the split-AC and unit cooler systems and one scale used for all other systems. The capacity of the larger outdoor unit scale was 300 kg with a readability of ±5 g. The capacity of the indoor unit scale was 120 kg, with a readability of ±2 g. Finally, the capacity of the leak pan scale was 30 kg, with a readability of ± 2 g.

Some test systems (e.g., split-AC) included means (sight glass or external refrigerant/oil level tube) for direct monitoring of compressor sump oil level, but not all. A leak “capture” box was fabricated and mounted on a separate weigh scale. Refrigerant releases were directed into this box to obtain a secondary estimate of any oil and/or liquid refrigerant release during the leak tests. The box would also be able to record any liquid refrigerant droplets collected in the drip pan during leak tests.

2.3 Test Conditions and Procedure

Prior to the start of all tests, the air in the environmental chambers was first conditioned. Ambient temperature conditions of 35 ± 1.1°C (95 ± 2°F) for the “outdoor portion” and 23.9 ± 1.1°C (75 ± 2°F) for the “indoor portion” of the equipment were specified for the AC test units. While the standard indoor temperature for rating ACs in the US is 26.7°C (80°F), 23.9°C was specified for these tests as being more representative of the set points actually used in service. For the display case unit, a 23.9 ± 1.1°C (75 ± 2°F) operating condition was specified. For the split unit cooler, ambient temperature conditions of 35 ± 1.1°C (95°F ± 2°F) for the “outdoor portion” and (-6.67 ± 1.1°C (20 ± 2°F) for the “indoor portion” of the equipment were specified.

For all equipment “on” tests, the systems were allowed to reach steady operation at the noted conditions prior to initiating a refrigerant leak event – approximately 20 minutes. This ensured that refrigerant was distributed throughout the system under normal conditions. Compressor and unit power were measured during each “on” test to provide a direct indication of compressor shut off during the test (e.g., due to low pressure cut out or other system safety controls). For all equipment

"off" tests, the systems were initially run until steady-state operation was reached, after which they were turned off prior to the leak event.
When the chambers were conditioned and the equipment was ready, a leak event was initiated by opening the pneumatically-actuated valve. This caused refrigerant to be immediately discharged into the chamber, reducing the system mass accordingly. All measurements of mass, temperature, pressure and concentration were recorded as a function of time by the DAQ at a sampling frequency of 10 Hz. Video was recorded from five different angles during the leak event. The data collection continued for 20 min, after which the test chambers were evacuated, and the system was prepared for the next test.

3. TEST RESULTS

To illustrate the typical data acquired for each equipment during a leak event, Figure 3 shows results from a test on the PTAC unit, which had a high-side leak through a 1.04 mm orifice with the equipment off. The dotted vertical line indicates the start of the leak event.

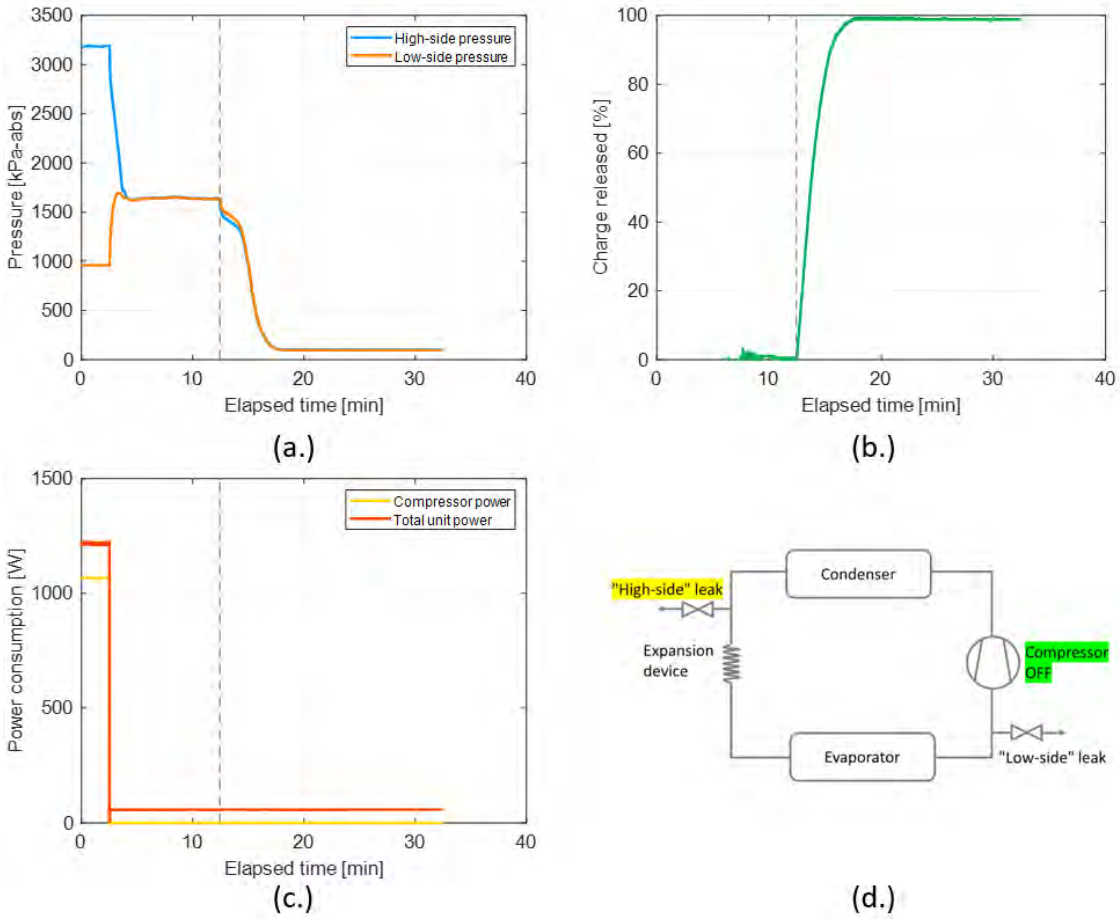

Figure 3. Typical experimental data for PTAC unit with 1.04 mm orifice, equipment off, high-side leak: (a.) High- and low-side pressure decay, (b.) percent charge released (c.) power consumption and (d.) system diagram

As shown above, nearly all (~99%) of the system charge was released for this case. As noted in the previous section, for the equipment off tests, the system was initially run until it reached steady-state operation, after which it was turned off. When this occurred, the system pressure equalized (Figure 3a) and the compressor power consumption was 0 W (Figure 3c). The unit fan continued to operate, resulting in the total unit power consumption to be nonzero.
A summary of the pertinent experimental data regarding the system charge and leak rate is provided in Table 2 for all systems. The test number sequence corresponds to that in Table 1. For example, test 119 is the third test in the package RTU test series. As indicated in Table 1, the third test in the series was conducted with a low leak rate, with equipment off and the leak occurred on the low-side of the system.

Table 2. Summary of experimental results for all systems tested

Test #	Equipment	Refrigerant	System charge [kg]	Total charge released [kg]	Collector pan mass change [kg]	Time to release 80% of total charge [s]	Average leak rate for 80% release [kg/min]
101	PTAC	R-410A	0.936	0.865	-0.001	549.00	0.08
102	PTAC	R-410A	0.936	0.895	-0.001	74.50	0.60
103	PTAC	R-410A	0.936	0.955	-0.005	116.60	0.39
104	PTAC	R-410A	0.936	0.925	0.000	146.10	0.31
105	PTAC	R-410A	0.936	0.945	0.000	132.50	0.34
106	PTAC	R-410A	0.936	0.935	-0.003	15.70	2.86
107	PTAC	R-410A	0.936	0.965	-0.008	19.20	2.34
108	PTAC	R-410A	0.936	0.955	0.000	32.80	1.37
109	Split-AC	R-410A	3.799	3.775	-0.004	102.40	1.77
110	Split-AC	R-410A	3.799	3.735	-0.007	35.40	5.15
111	Split-AC	R-410A	3.799	3.675	0.002	86.60	2.11
112	Split-AC	R-410A	3.799	3.705	-0.002	45.58	4.00
113	Split-AC	R-410A	3.799	3.925	-0.011	73.35	2.57
114	Split-AC	R-410A	3.799	3.670	0.003	27.70	6.35
115	Split-AC	R-410A	3.799	3.750	0.077	29.70	6.06
116	Split-AC	R-410A	3.799	3.775	-0.002	34.40	5.26
117	RTU	R-410A	1.790	1.713	N/A	92.90	0.92
118	RTU	R-410A	1.790	1.573	N/A	30.50	2.82
119	RTU	R-410A	1.790	1.675	N/A	51.10	1.68
120	RTU	R-410A	1.790	1.670	N/A	33.40	2.57
121	RTU	R-410A	1.790	1.578	N/A	48.70	1.76
122	RTU	R-410A	1.790	1.613	N/A	18.00	4.77
123	RTU	R-410A	1.790	1.730	N/A	26.00	3.30
124	RTU	R-410A	1.790	1.715	N/A	19.40	4.43
125	Display case	R-404A	1.497	1.425	-0.007	379.80	0.19
126	Display case	R-404A	1.497	1.510	-0.003	111.70	0.64
127	Display case	R-404A	1.497	1.465	-0.014	210.80	0.34
128	Display case	R-404A	1.497	1.430	0.000	256.40	0.28
129	Display case	R-404A	1.497	1.425	-0.010	227.00	0.32
130	Display case	R-404A	1.497	1.500	-0.001	96.70	0.74
131	Display case	R-404A	1.497	1.450	-0.016	135.60	0.53
132	Display case	R-404A	1.497	1.425	0.000	191.10	0.38
133	Unit cooler	R-404A	2.268	2.160	-0.004	294.70	0.37
134	Unit cooler	R-404A	2.268	2.240	-0.001	23.60	4.61
135	Unit cooler	R-404A	2.268	0.090	-0.007	-	-
136	Unit cooler	R-404A	2.268	2.190	-0.001	19.30	5.64
137	Unit cooler	R-404A	2.268	2.185	0.000	193.20	0.56
138	Unit cooler	R-404A	2.268	2.285	0.010	14.80	7.36
139	Unit cooler	R-404A	2.268	0.135	0.002	-	-
140	Unit cooler	R-404A	2.268	2.245	-0.001	14.20	7.67

Based on the information above, for all systems (with the exception of the unit cooler), the compressor on, high side release, larger orifice generally showed the fastest leak flow rate (i.e. tests PTAC-106, split-AC-114, packaged-RTU-122 and display-case-130). The compressor on, low side release, smaller orifice showed the slowest leak flow rate (i.e. tests PTAC-101, split-AC-109, packaged-RTU-117 and display-case-125). In general - with compressor on the high-side leak rates are greater than the low-side rates (higher pressure and density at the leak location); with the compressor off high-side leak rates are lesser than the low-side rates (larger line size, less flow resistance to leak location on compressor suction line).

In the unit cooler system, test result trends were different. The refrigeration circuit for this system included a normally closed solenoid valve in the liquid line upstream of the thermostatic expansion valve (TXV). When the room temperature control thermostat is satisfied this valve closes, isolating the evaporator from the condensing unit. The system also uses a pump down cycle at thermostat shut down to move most of the refrigerant in the evaporator to the condensing unit. As a result, low-side leaks with the unit off (i.e. tests unit-cooler-135 and unit-cooler-139) resulted in only very small refrigerant loss (4% of the charge for the low leak rate or smaller orifice case and 6% for the high leak rate case).

For the high-side leak tests, rates with compressor off are somewhat greater than for compressor on, opposite the trend seen with the other units tested. For compressor off cases, the liquid line solenoid valve is closed and the system pump down cycle had moved most of the refrigerant to the condensing unit; in the compressor on cases, the solenoid valve remained open and no pump down cycle occurred before the leak.

Other important highlights from the tests are given below in Table 3 for each equipment type.

Table 3. Additional test highlights for each equipment type

Equipment type	Additional highlights
PTAC	• ~100% of charge was released for all tests except the two compressor on tests with the smaller orifice size (for the low and high side leak locations, the PTAC retained ~8% and ~4% of the charge, respectively) • There was no measurable oil release during any of the tests
Split-AC	• Nearly all of the system charge was released (96-100%) for all eight test scenarios • For the compressor off, higher leak rate and low side leak test (test 115) about 0.077 kg of oil is estimated to have been ejected with the refrigerant; there was no measurable oil leakage for any of the other tests.
Packaged-RTU	• No significant oil release observed during any of the tests (oil catch/weigh system not used for the RTU tests) • All of RTU test results showed some refrigerant retention at the end of the 20-min test period, ranging from 3.3% to 12.1%; generally, for the compressor “on,” more refrigerant remained in the RTU at test end than for the corresponding compressor “off” tests (low side leak, lower rate tests (117 and 119) being the sole exception). • No measurable oil release during any of the tests
Display case	• The only test condition to show 100% charge release was the compressor on, high-side leak • All other tests showed 2-5% charge retention • There was no measurable oil release during any of the tests
Unit cooler	• No measurable oil release during any of the tests

4. CONCLUSIONS

Based on results from the leak tests for the split AC, PTAC, standalone display case, and RTU AC systems, the compressor on, high side release, larger orifice showed the fastest leak flow rate. The compressor on, low side release, smaller orifice showed the slowest leak flow. In general - with compressor on the high side leak rates are greater than the low side rates (higher pressure and density at the leak location); with the compressor off, high side leak rates are lesser than the low

side rates (larger line size, less flow resistance to leak location on compressor suction line). For the unit cooler system, the general test result trends were different due to the presence of a solenoid valve upstream of the TXV. Low side leaks with the unit compressor off resulted in only very small refrigerant loss (4% of the charge for the low leak rate or smaller orifice case and 6% for the high leak rate case).

ACKNOWLEDGEMENTS

This work was sponsored by the U. S. Department of Energy's Building Technologies Office under Contract No. DE-AC05-00OR22725 with UT-Battelle, LLC. The authors would also like to acknowledge Mr. Antonio Bouza, Technology Manager – HVAC&R, Water Heating, and Appliance, U.S. Department of Energy Building Technologies Office.

REFERENCES

ASHRAE, 2016a. ASHRAE 34-2016 - Designation and Classification of Refrigerants, American Society of Heating, Refrigerating and Air-Conditioning Engineers.

ASHRAE, 2016b. ASHRAE 15-2016 - Safety Standard for Refrigeration Systems, American Society of Heating, Refrigerating and Air-Conditioning Engineers.

Baxter, V., V. K. Patel, A. Abu-Heiba, W. A. Miller, R. Linkous and G. Ormston, 2019. Experimental Evaluation of Refrigerant Leak Characteristics for Different HVAC&R Equipment Types - ORNL/TM-2018/1058. Oak Ridge, TN, Oak Ridge National Laboratory.

Clodic, D. and W. Cai, 1996. Tests and Simulations of Diffusion of Various Hydrocarbons in Rooms from Air-Conditioners and Refrigerators. IIF - IIR Gustav Lorentzen Conference on Natural Working Fluids - Applications for Natural Refrigerants, Commissions B1, B2, E1 & E2, Aarhus, Denmark.

IEC, 1997. IEC 60335-2-24:1997 Safety of Household and Similar Electrical Appliances - Part 2: Particular Requirements for Refrigerating Appliances and Ice makers, International Electrotechnical Commission.

IEC, 2016. IEC 60335-2-40:2016 Household and similar electrical appliances - Safety - Part 2-40: Particular requirements for electrical heat pumps, air-conditioners and dehumidifiers. Geneva, Switzerland, International Electrotechnical Commission.

IEC, 2018. IEC 60335-2-40:2018 Household and Similar Electrical Appliances - Safety - Part 2-40: Particular Requirements for Electrical Heat Pumps, Air-conditioners and Dehumidifiers. Geneva, Switzerland, International Electrotechnical Commission.

ISO, 2014a. ISO 817:2014 Refrigerants - Designation and Safety Classification. Geneva, Switzerland, International Organization for Standardization: 73.

ISO, 2014b. ISO 5149 Refrigerating Systems and Heat Pumps: Safety and Environmental Requirements. Geneva, Switzerland, International Organization for Standardization.

Kataoka, O., S. Ishida, T. Hirakawa and M. Yoshizawa, 1999. Experimental and numerical analyses of refrigerant leaks in a closed room. ASHRAE transactions, SE-99-19-02: 1151.

Kataoka, O., M. Yoshizawa and T. Hirakawa, 2000. Allowable charge calculation method for flammable refrigerants. International Refrigeration and Air Conditioning Conference, Purdue University, West Lafayette, IN.

UL, 2017. UL 60335-2-40:2017 Household and Similar Electrical Appliances - Safety - Part 2-40: Particular Requirements for Electrical Heat Pumps, Air-conditioners and Dehumidifiers, Underwriters Laboratories.

UNEP, 2016. The Kigali Amendment to the Montreal Protocol: HFC Phase-down, United Nations Environment Program OzonAction Fact Sheet, http://multimedia.3m.com/mws/media/1365924O/unep-fact-sheet-kigali-amendment-to-mp.pdf.

Manuscript ID: 1129
DOI 10.18462/iir.icr.2019.1129

Aqua ammonia as secondary refrigerant in ice rink applications

J. ROGSTAM[(a)], S. BOLTEAU[(a)], J. POMERANCEVS[(a)], C. GRÖNQVIST[(a)]

[(a)] Energi & Kylanalys AB, Prästgårdsgränd 4
Älvsjö 125 44, Sweden
jorgen.rogstam@ekanalys.se, simon.bolteau@ekanalys.se,
juris.pomerancevs@ekanalys.se, cajus.gronqvist@ekanalys.se

ABSTRACT

Ice rink refrigeration systems are often designed as indirect systems to reduce the refrigerant charge. Therefore, these systems require a secondary refrigerant which inevitably will impose an extra temperature difference and require pump energy. The associated pumping energy in practice use to correspond to 10-20% of the total refrigeration system energy usage depending on fluid used and pump control strategy. Aqueous solutions with ethylene glycol or different kind of salts are the most commonly used fluids but they have less favourable thermophysical properties implying higher pump power demand. There is a growing interest in using aqua ammonia (ammonia-water) as secondary refrigerant in ice rinks for both new construction and retrofit. This is an environmentally friendly and very energy efficient fluid which offers low corrosivity and very low pumping power. Material compatibility and safety must be considered when designing the systems. Aqua ammonia theoretically uses 55% less pumping power compared with ethylene glycol at -10°C fluid temperature. Current field measurements show that systems using aqua ammonia may reduce the pumping power as a share of in the total energy usage to 1-3%. Reference systems which are about 10 years old using calcium chloride would use about 10% of the total refrigeration system energy. In Sweden the first rink floor system was retrofitted in 2007 and it is still in operation with good results. Today the number of indoor hockey rinks using aqua ammonia is 34 and rapidly growing. One reason being the increasing interest for CO2 as primary refrigerant which benefit due to a considerably lower evaporator cost when aqua ammonia is used as secondary refrigerant.
Keywords: Ice Rink, Secondary Refrigerant, Aqua Ammonia, Pressure Drop, Retrofit, Pump Energy, Safety.

1. INTRODUCTION

Sweden currently has 368 indoor ice rinks with the ambition to further grow the number. The cost of operation, however, is a challenge for many arena owners, which has brought the arena energy usage in focus. There are many ways to reduce the energy usage but it is evident that the refrigeration system is a major contributor. When it comes to the environmental impact one may state that it stems from primarily two factors; the amount energy used and the type of refrigerant. Statistics from Sweden show that a typical single ice sheet indoor rink uses about 1 000 000 kWh purchased energy annually, with the refrigeration system accounting for about 43% and heating for about 26%. (Rogstam, 2010). As far as refrigerants are concerned there are essentially two groups available; synthetic and natural. In the synthetic group the most commonly used refrigerants are found, the so-called fluorinated hydrocarbons. Most of these are potent greenhouse gases and in order to reduce emissions from fluorinated greenhouse gases (F-gases), the European Union updated the F-gas Regulation in 2015, where refrigerants with high global warming potential (GWP) are to be gradually phased out and replaced by substances that fulfil the environmental requirements. A group of refrigerants highly affected by the F-gas Regulation are the hydrofluorocarbons (HFCs), which have been very popular over the last decades and to some extent also used in ice rink refrigeration systems. This means that many existing facilities will be facing renovations and retrofits in the near future. The alternative to synthetic refrigerant is the natural alternatives which are limited to; ammonia, hydrocarbons and carbon dioxide where the two first are poisonous and/or flammable. This implies that refrigeration systems using those will inevitably be

indirect i.e., using a secondary refrigerant in the rink floor. CO2 being an exception since it is not poisonous and/or flammable may therefore be used directly in the rink floor (Rogstam & Bolteau 2015). It, however, poses certain requirements on the pipes in the floor due to higher pressure which prevents a direct retrofit. Having that said, most newly built and future retrofits in ice rinks will imply so called indirect refrigeration systems which will require a secondary refrigerant.

1.1. Indirect Refrigeration Systems

Indirect systems may be separated into fully or partly indirect systems where the first refers to a system with a liquid connection on both cold and warm side, and the latter just on the cold side. A partly indirect system is illustrated in the principle figure below (Fig. 1) which has been a common way to build ice rinks refrigeration systems in recent times.

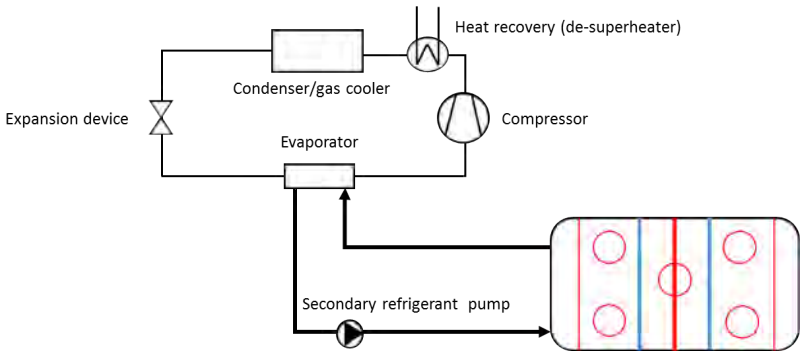

Figure 1: A partly indirect ice rink refrigeration systems

An indirect solution will reduce the refrigerant charge and a fully indirect solution even more so. As pointed out, the advantage being a reduced refrigerant charge but the disadvantage being an extra temperature difference imposed by the heat exchanger which will decrease the evaporation temperature. Further, the distribution of the fluid in the rink floor will also require a pump and the associated electrical pump energy.

A typical ice hockey rink floor in Europe (60x30m) requires around 20 km of tubing provided the tube pitch is 80-100mm which is considered standard practice today. The length of the distribution system and considering that the typical temperature of the fluid is in the range of -15 to -5°C, sets the expectations as far as pump energy is concerned. To put the distribution energy usage into perspective, Rogstam (2010) presented the energy data from 19 ice rinks with fully indirect refrigeration systems. All motors had frequency converters, which enabled the energy usage to be recorded. The systems represented reasonably well-designed refrigeration systems with a majority ammonia systems and $CaCl_2$ or Freezium as secondary refrigerant.

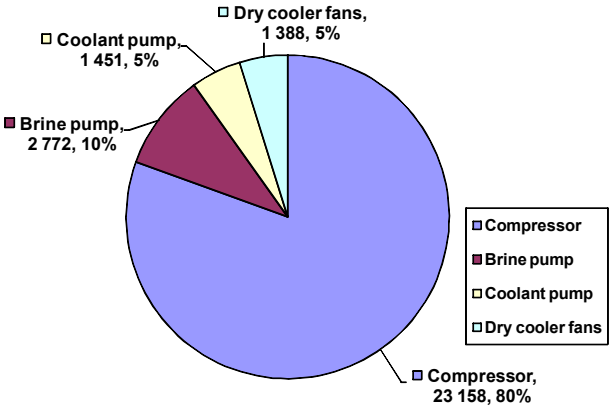

Figure 2: Monthly energy usage for 19 indirect ice rink refrigeration systems (Rogstam, 2010)

The conclusion from Fig. 1 is that the total distribution energy is about 20% of total refrigeration system

energy input, and that the secondary refrigerant pumps account for about 10% on average. It should be emphasised that these systems controls the capacity of the brine pumps to the refrigeration need to avoid excessive pump energy usage, although the exact control strategy is not known.

2. AMMONIA WATER AS SECONDARY REFRIGERANT

The term secondary refrigerant refers to the working media transferring the heat from the rink floor to the evaporator in an indirect system. It circulates in the secondary loop; being both a heat sink for the ice rink floor and a heat source for the evaporation process. Phase-changing secondary fluids, such as CO2, have an advantage over the single-phase ones due to the high latent heat during the phase change process. The single-phase solutions are a mix between water and a freezing point depressant mixture with additives (e.g. corrosion inhibitors) (Mazzotti, 2013).

2.1. Aqua Ammonia / Ammonia Water – Literature Study

A literature study on aqua-ammonia has been conducted to see what the scientific interest in this fluid has been recently. There are seemingly no recent published papers on the subject of the use of aqua ammonia in (ice rink) refrigeration systems. A search for published articles generally related to aqua ammonia gave diverse results. Most of the recent literature about aqua ammonia with respect to refrigeration either justifies the use of the mixture in an absorption cooler analyses its use in absorption coolers powered by solar energy or incorporates an absorption cooler into a polygeneration system. Only one study found, experimented to find the thermodynamic properties of aqua ammonia. Ganesh & Srinivas, 2017 found correlations between the temperature, specific volume, enthalpy, entropy, and exergy at different solution concentrations at varying pressures.
One of very few references on refrigeration applications is Gibert (2007), which presents practical aspects of ammonia water and he claims about 50 installations with “alkali” in France in 2007. He primarily uses mono-ethylene glycol as reference and shows that ammonia water “allow to reduce drastically the electrical consumption of the refrigeration installation designed with a secondary loop, and especially at low temperature”.

2.2. Environmental and Safety Aspects of Ammonia Water

Ammonia water (Ammonium hydroxide, NH4OH) is a solution of ammonia in water which is mainly used as a cleanser and in manufacturing plastics, rubber, fertilizer and textiles. It's a colorless, clear liquid with a pungent-to-faint ammonia odor. Stable under normal temperatures and pressures, heating it produces ammonia gas. It is incompatible with acids, hypochlorites, halogens, sodium hydroxide, galvanized surfaces and strong oxidizing agents, plus metals and their alloys (Lab Safety Supply, 2009).
Contact with eyes may result in ulceration of the conjunctiva and cornea, eye burns and temporary loss of sight. It causes skin irritation; contact can lead to severe irritation and burns. Ingestion can cause vomiting, nausea, gastric irritation and, in severe cases, perforation, central nervous system depression, shock, convulsions and pulmonary edema. If inhaled, mild exposure can cause nose irritation (sneezing, coughing). Exposure to high concentrations may cause pulmonary edema, shock, convulsions, cyanosis or central nervous system depression. Chronic exposure may cause bronchitis, conjunctivitis or dermatitis. Engineering controls should provide local fume exhaust and/or general dilution ventilation (Lab Safety Supply, 2009).

2.2.1 Personal Protective Equipment

Wear splash-proof safety goggles. Install an emergency eye wash unit in the immediate area. Do not wear contact lenses when working with ammonium hydroxide. Wear appropriate gloves and protective clothing to prevent skin contact. No respiratory protection is required when working with this chemical under an appropriate fume hood. If the ammonium hydroxide airborne concentration is 300 ppm or higher, wear a self-contained breathing apparatus (SCBA) with full facepiece. Store the chemical in capped, glass or plastic containers protected from heat and incompatible substances. Thoroughly wash after handling. Avoid breathing dust, vapor, mist or gas.

2.2.2 Fire fighting measures

If possible, move the storage container away from fire. Ammonium hydroxide is not a flammable liquid; however, ammonia gas is flammable. The gas is an eye, skin and respiratory irritant. For small fires, use dry chemical, carbon dioxide, water spray or alcohol-resistant foam extinguishers. Wear appropriate protective clothing to prevent contact with skin and eyes (Lab Safety Supply 2009).

2.3. Thermophysical Properties as Secondary Refrigerants

When comparing secondary fluids in terms of the heat transfer, pressure drop and freezing protection, the following thermo-physical properties are typically of interest: freezing point, viscosity, thermal conductivity, specific heat capacity and density. For other concerns, like the thermal vessel design, the thermal volume expansion, the boiling point and the surface tension may be relevant properties to consider (Mazzotti, 2013).
There are many secondary refrigerants to choose from but in ice rink applications, $CaCl_2$ has been dominating at least the Swedish market. Due to corrosion issues, some markets prefer to go in the direction of ethylene glycol, EG, which is easier to handle but has less favorable properties. A rather new candidate in this context, that has attracted some interest lately, is ammonia-water.

Table 1. Properties of different secondary refrigerants at -10°C, freezing point -20°C (SecCool)

-	Dynamic Viscosity (cP)	Conductivity ($W.m^{-1}K^{-1}$)	Specific heat ($kJ.kg^{-1}K^{-1}$)	Density ($kg.m^{-3}$)
H2O + $CaCl_2$	4.523	0.5293	2.984	1199
H20 + EG	8.024	0.4148	3.487	1058
H2O + NH3	2.754	0.4591	4.241	954
CO_2	0.1097	0.122	2.241	983

Table 1 lists the thermophysical properties of 4 candidates where $CaCl_2$ represents the traditional solution with inherent drawbacks such as corrosivity, and still requiring a rather high pumping power. Ammonia-water has similar or better properties across the range and is therefore considered a better candidate with lower required pump power and better heat transfer properties.

2.4. Secondary Refrigerants Performance Comparison

Mazzotti 2013 evaluated the performance of different secondary refrigerant in an ice rink application using typical pipe geometries, pumps and heat exchangers. To illustrate the relative impact of the heat transfer properties and the resulting convection temperature difference in the pipes vs. the rink floor, Mazzotti produced the graph below. This analysis is carried out with the following assumptions: cooling capacity 150 kW, Δt_{SR} 1.5 K and freezing point -30°C. It is shown in Fig. 3 that EG almost always remain in the laminar flow regime, even for higher loads and lower temperature difference. This also highlights the poor heat transfer properties associated with the laminar flow. Indeed, all secondary fluids presenting a large convection share are in the laminar flow regime, for these conditions. As shown, PG, EG, EA and K-acetate have a much higher ice/secondary fluid temperature difference than $CaCl_2$, NH_3 and K-formate which are in turbulent flow range.

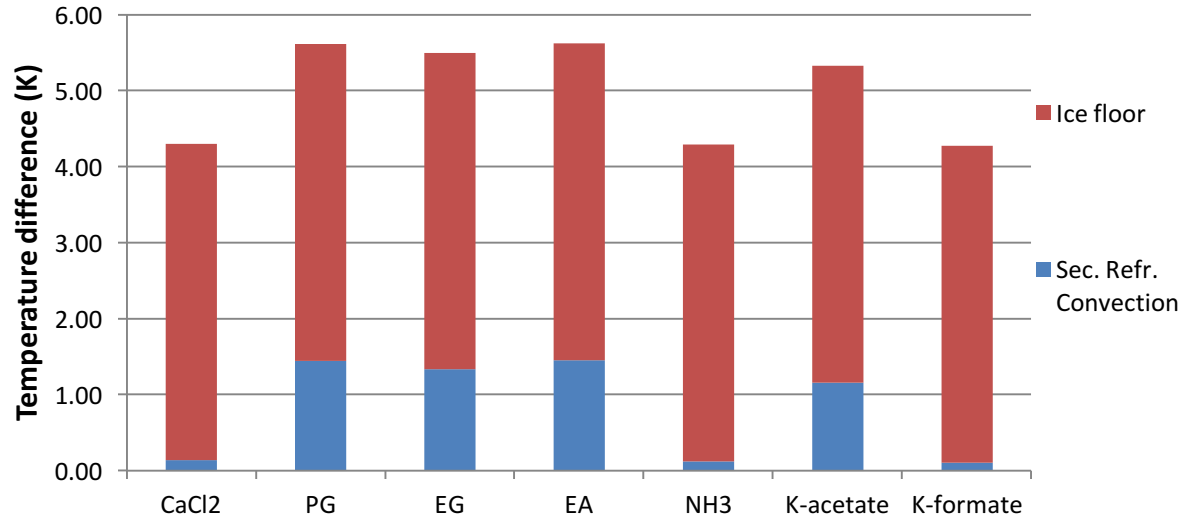

Figure 3: Temperature differences (CC = 150 kW; Fp = -30 °C; ΔT = 1,5 K; T_{ice} = -3,5 °C) (Mazzotti, 2013)

Fig. 4 shows the pumping power for the chosen secondary refrigerants versus their average operational temperature. This analysis is carried out with the following assumptions: cooling capacity 200 kW, Δt = 2 K and freezing point -30°C. Ammonia water has low pressure drop and the lowest pumping power. The pumping power is varying between 2 and 7 kW which is rather low due to the fact that the assumption of variable speed pump was made. Once again, the discontinuities that may be observed in the curves are due to the flow regime change. The laminar flow may lead to lower pumping power than turbulent flow but on the other hand the heat transfer coefficients decrease radically.

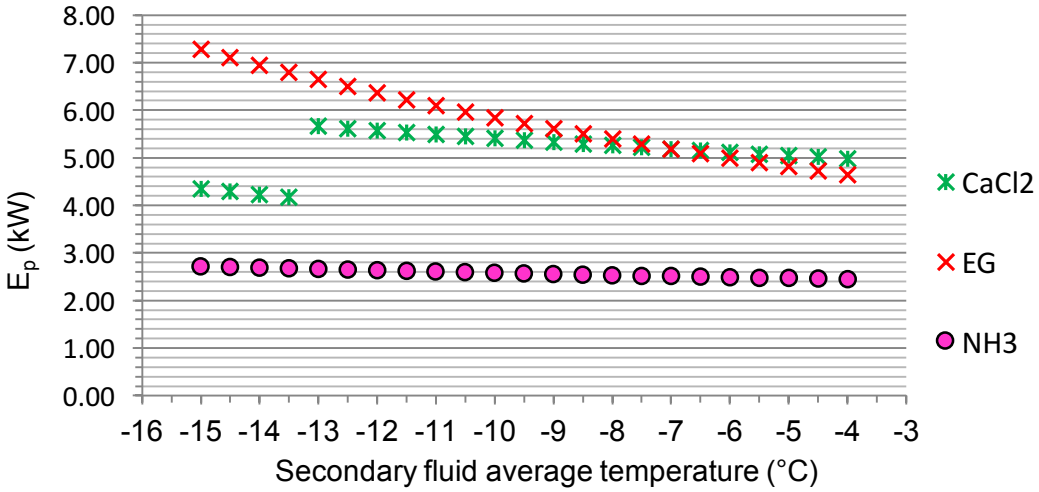

Figure 4 Pumping power versus Tav (C_C = 200 kW; Fp = -30 °C; ΔT = 2 K) (Mazzotti, 2013)

Provided the thermophysical properties and their impact on the energy usage it can be concluded that ammonia water has a significant advantage. Firstly, the heat transfer properties which contribute to a smaller heat transfer temperature differences will increase the evaporation temperatures compared to the traditional ice rink fluids. The total gain in the rink pipes may be about 1 K. Secondly, the pump power may be significantly reduced, and the Fig. 4 above shows a reduction compared to EG with 54% (NH_3; 2.6 kW vs EG; 5.6 kW). Overall these theoretical results support and explains the good practical results obtained with ammonia water in the field.

3. AMMONIA WATER MARKET DEVELOPMENT

The Swedish ice rink market has, as far as secondary refrigerants is concerned, been dominated by calcium chloride. A few other alternatives have been tested like Freezium (potassium formate) or Tyfoxit (potassium acetate), which have similar or slightly better properties than $CaCl_2$. They all have in common that they are highly corrosive and CaCl2 to the extent that it requires titanium alloy in the evaporator which drives the cost. Ethylene glycol has never gained traction in Swedish permanent ice rinks which is probably due to it poisonous and poorer thermophysical properties - especially at lower temperatures. Having that said, in a Swedish perspective $CaCl_2$ is the main reference when referring to properties and potential gain with alternatives

3.1. Early Swedish Ammonia Water Installations

The first ammonia water installation in a Swedish ice rink was done already in 2007 in the Nittorp ice rink. This project was well documented in an article by Bache & Stenhede (2008). The existing steel pipe was originally designed for DX ammonia and thus had way too small diameter (½" pipes). Since the system was converted from DX ammonia to $CaCl_2$ in 1985 it had suffered problems related to flow distribution problems which is obvious given the small pipe diameter. After the retrofit to ammonia water the freezing process was reported to work significantly better and the pump speed could be reduced. Unfortunately, there was no energy measurement carried out on the pumps before and after. Since ammonia water is a very good cleaning solution there was plenty of sludge found in the filters. No corrosion problems with pumps or pipes has been experienced. This system is still in operation in 2019. Asplund (2011) presented experiences from the retrofit of the indoor ice rink Pinbackshallen which was retrofitted from CaCl2 to ammonia water. As an argument for the retrofit Asplund emphasized the potential issues with $CaCl_2$ such as corrosion and occasional foaming which blocks the pipes and causes uneven flow. After the retrofit he reported vast amounts of dirt which called for frequent filter replacement/cleaning. The ammonia water system appeared to be easier to de-air compared to the previously used $CaCl_2$ although the pipework was exactly the same. Due to the cleaning properties of the ammonia water the heat transfer seemed to be improved. On average the evaporation temperature was 1.5 K higher after the retrofit which resulted in a 4.8% reduced average motor power to the compressors. This saved 19 670 kWh during the first season of operation.

3.2. Ammonia Water Ice Rink Installations in Sweden

As reported above the first ice rink installation with ammonia water in Sweden took place in 2007 and in 2018 there are at least 34 installations in indoor ice hockey ice rinks. There are even more installations when other ice arenas and outdoor rinks are included but the numbers are not fully known. As can be seen below the total number indoor ice hockey rinks in Sweden is today about 368. Most of these still use us $CaCl_2$ but the trend is clearly going direction CO2 and ammonia-water with 6 respectively 34 installations each. Most likely the number of ammonia water installations is even higher, but these are the ones publicly known.

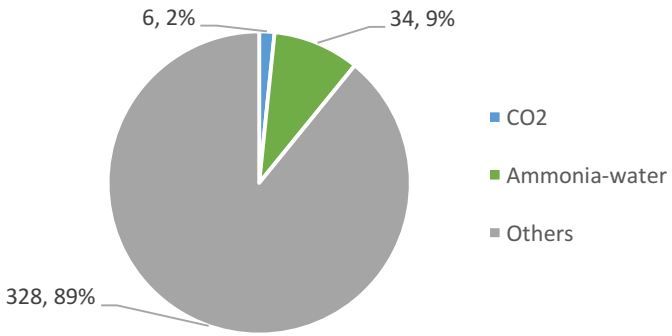

Figure 5: Installed secondary refrigerants in Swedish indoor ice hockey rinks

The reason why the number of installations is growing rapidly is primarily the good experience from the

first installations reported above. Also, the mentioned issues with $CaCl_2$ has motivated the market to look at alternatives, and ammonia-water does offer practical advantages as well as disadvantages. A further reason is the rapid growth in using CO2 as primary refrigerant (Rogstam et al., 2017). To use CO2 as refrigerant with its high operating pressures in combination with a titanium alloy evaporator drives the cost of the evaporator and consequently of the whole unit. If ammonia water is being used, normal stainless steel can be used in the evaporator thus saving ±10 000 Euro. This cost offsets the secondary refrigerant retrofit cost which is of the same order of magnitude – typically 10 000 – 20 000 Euro. Consequently, the retrofit is "paid" by the cheaper evaporator and then the system has half the pump power for the rest of its technical life.

4. FIELD MEASUREMENTS AND RESULTS

Although there are quite a few systems in operation it is challenging to come across quality field measurement data. The aim of this study was to present data on a similar format like the reference data in section 1. For the time being there were only two installations available with comparable data but there should come up more soon. The ice rinks in Table 2 are both refrigeration units using CO2 as primary refrigerant and ammonia water as secondary refrigerant. Ice rink 1 has been in operation for about two years and it is a semi enclosed hockey rink with three walls and a roof. Ice rink 2 is now on its fourth season and it includes an indoor hockey rink and a curling rink. Due to the two ice sheets it has a somewhat longer and more complex supply arrangement than normal, which may explain the slightly higher pump work. Both systems have Δt-control on the pumps which is typically set to 2-3 K. If the compressors stop the pumps will continue operating as lowest possible speed.

Table 2. Refrigeration system energy data from two ice rinks

-	Compressors		Gas cooler		NH3-Water Pump	
Unit	kWh	%	kWh	%	kWh	%
Ice rink 1	302 460	97.7%	3 491	1.1%	3 638	1.2%
Ice rink 2	934 822	95.4%	14 393	1.5%	31 031	3.2%

When looking into the details to compare with the reference data in section 1 there are some differences to consider. These CO2 systems operate in heat recovery mode most of the time which increases the compressor energy usage and reduces the gas cooler fan energy. The latter since the rejected heat is to a large extent recovered and does not require much work by the gas cooler fans. This, however, makes the compressor energy a larger share in these systems compared to ones which does not operate with elevated head pressure for heat recovery reasons. Consequently, the pump share will become smaller, but nevertheless it can be concluded that the pump energy share for ice rinks 1 and 2 is very low. Table 2 suggests that for it is only between 1.2 and 3.2%, whereas the reference systems from 2010 used about 10% of the total refrigeration system energy for secondary refrigerant distribution.

5. CONCLUSIONS

Ice rink refrigeration systems are often designed as indirect systems to reduce the refrigerant charge. Therefore, these systems require a secondary refrigerant which inevitably will impose an extra temperature difference and require pump energy. The associated pumping energy in practice use to correspond to 10-20% of the total refrigeration system energy usage depending on fluid used and pump control strategy. Aqueous solutions with ethylene glycol or different kind of salts are the most commonly used fluids in ice rinks. Especially ethylene glycol has less favourable thermophysical properties implying a high pump power demand. In Sweden there is a growing interest in using ammonia-water as secondary refrigerant in ice rinks for both new construction and retrofit projects.

This is an environmentally friendly and very energy efficient fluid which offers low corrosivity and very low pumping power. Material compatibility and safety must be considered when designing the systems. Aqua ammonia theoretically uses 55% less pumping power compared with ethylene glycol at -10°C fluid temperature. Current field measurements show that systems using aqua ammonia may reduce the

pumping power as a share of in the total refrigeration system energy usage to 1-3%. Reference systems which are about 10 years old using calcium chloride would use about 10% of the total refrigeration system energy.
In Sweden the first rink floor system was retrofitted to ammonia water in 2007 and it is still in operation with good results. Experiences from retrofits in general reports a significant cleaning effect with vast amounts of dirt coming out of the system requiring good filter arrangements. As a result, the improved the heat transfer has increased the evaporation temperature. This will contribute to energy savings through better operating conditions and lower pump power. Today there are 34 of indoor hockey rinks using aqua ammonia and continues to grow rapidly. One reason being the increasing interest for CO2 as primary refrigerant which benefit due to a ±10 000 Euro lower evaporator cost when aqua ammonia is used as secondary refrigerant.

NOMENCLATURE

COP	Coefficient of performance (-)	NH_3	Ammonia (-water)
Q_c	Cooling capacity (kW)	CO_2	Carbon dioxide
$CaCl_2$	Calcium chloride	EG	Ethylene Glycol
EA	Ethyl Alcohol	PG	Propylene glycol
K-acetate	Potassium acetate	K-formate	Potassium formate
Fp	Freezing point (°C)	E_p	Pump power (kW)
Δt_{SR}	Temperature difference (K)		

REFERENCES

Rogstam, J., 2010. Energy usage statistics and saving potential in ice rinks. 2nd IIR Workshop on Refrigerant Charge Reduction in Refrigerating Systems: Stockholm.

Rogstam J., 2010. Ice rinks using carbon dioxide as secondary refrigerant. IIR Sustainable Refrigeration and Heat Pump Technology, Stockholm, Sweden, 2010.

Rogstam, J., Bolteau, S., 2015. Ice rink of the future - evaluation of energy and system solutions. EKA, www.ekanalys.se.

Rogstam, J., Bolteau, S., Grönqvist, C. 2017. Cooling and heating ice rinks with CO2. ASHRAE Journal, 59(8).

Ganesh & Srinivas, 2017. Development of thermo-physical properties of aqua ammonia for Kalina cycle system. International Journal of Materials and Product Technology 55(1/2/3):113

Gibert, V., 2007. Ammonia water solution as secondary refrigerant, advantages and drawbacks. IIR Conference: Ammonia Refrigeration Technology for Today and Tomorrow, Ohrid, 2007.

Mazzotti, W., 2013. Secondary Fluids Impact on Ice Rink Refrigeration System Performance. Master of Science Thesis, School of Industrial Engineering and Management, KTH, STOCKHOLM.

Lab Safety Supply, 2009 Working with Ammonium Hydroxide. (www.labmanager.com/lab-health-and-safety/2009/09/working-with-ammonium-hydroxide#.XFLOplxKhaQ).

Bache, A., Stenhede, C., 2008. Ammonium hydroxide in ice rinks. ScanRef. No. 5. November 2008.

Asplund, T,. 2011. Presentation at the conference Arenadagarna 2011.

Manuscript ID: 1134
DOI: 10.18462/iir.icr.2019.1134

Methodology to estimate vapor quality of refrigerant leaks

William MILLER, Viral K. PATEL, Ahmad ABU-HEIBA, Van BAXTER

Oak Ridge National Laboratory[1]
Oak Ridge, TN 37831, USA, patelvk@ornl.gov, abuheibaag@ornl.gov, baxtervd@ornl.gov
Univ. TN, Knoxville, 37916, USA, wmille17@utk.edu

ABSTRACT

The US Department of Energy (DOE) Building Technology Office (BTO) and the Air-conditioning, Heating & Refrigeration Technology Institute (AHRTI) are sponsoring an experimental study of refrigerant leak characteristics. The objectives are to conduct refrigerant leak tests on several heating, ventilating, air conditioning and refrigeration (HVAC&R) systems under operating conditions representative of actual applications to document the pressure decay rate and the mass flow rate of leaked refrigerant as a function of time. Another aspect of the study was to formulate and document a procedure for estimating the quality (vapor versus liquid) of the leaking refrigerant and oil escaping from the high- and low-pressure sides with the unit energized and with the unit turned off. Refrigerant quality was estimated by tracking total system weight of a packaged air-conditioning (AC) unit and the total weight of a large container used to capture the refrigerant leakage escaping the packaged unit.

1. INTRODUCTION

The Montréal Protocol established refrigerant guidelines because of the damaging effect of chlorofluorocarbons (CFCs) and hydrochlorofluorocarbons (HCFCs) on stratospheric ozone. CFCs were phased out in 2010, and directives are in effect to eliminate the use of HCFCs by 2030. Hydrofluorocarbons (HFCs) like R-410A and R-134a were suitable alternatives to HCFCs for many HVAC&R applications but have relatively high global warming potentials (GWP). Low-GWP HFCs, hydrofluoroolefins (HFO), hydrochlorofluoroolefins (HCFO), hydrocarbons (HC), ammonia (R-717), CO_2 (R-744), or blends containing low-GWP HFCs with lower GWP are promising alternatives. However, most of the lower toxicity (class A) low-GWP alternatives have some degree of flammability according to Addendum g to ANSI/ASHRAE 34 (2016) and ISO 817:2014.

Walter (2000) and Walter et al. (2002) reported that in the United States, codes and regulations prohibit the use of flammable refrigerants in occupied spaces because of the safety need to protect building occupants. Therefore, the goal of our exploratory study was to determine the refrigerant quality of a leak. If the leak has a low-quality (predominantly liquid) then there is indeed a safety concern because of the liquid pooling of a highly concentrated volatile and flammable refrigerant. If the leak has a high-quality then as a vapor leak the refrigerant will disperse rapidly and pose less threat for the occurrence of an uncontrolled and unwanted fire.

2. PRELIMINARY PROOF OF CONCEPT TESTS

Preliminary tests were conducted to help formulate and validate a testing procedure and an algorithm for estimating the quality of a refrigerant leak. A refrigerant charging cylinder containing R-134a served as the refrigerant source. A 1.041 m^3 (275-gallon) capacity, rigid plastic tank container held

[1] This manuscript has been authored by UT-Battelle, LLC under Contract No. DE-AC05-00OR22725 with the U.S. Department of Energy. The United States Government retains and the publisher, by accepting the article for publication, acknowledges that the United States Government retains a non-exclusive, paid-up, irrevocable, world-wide license to publish or reproduce the published form of this manuscript, or allow others to do so, for United States Government purposes. The Department of Energy will provide public access to these results of federally sponsored research in accordance with the DOE Public Access Plan (http://energy.gov/downloads/doe-public-access-plan).

the leaked refrigerant while maintaining near atmospheric pressure. The container was instrumented with temperature and pressure sensors. Type T copper-constantan thermocouples were used to measure the refrigerant temperatures at several locations in the container. A sensor was placed mid-height in the container directly in line with the 1 mm orifice used to spray leaked refrigerant in the container. Other thermocouples were also placed mid-height to the left and right side and to the back of the container. These 4 measures were averaged to yield a bulk refrigerant temperature inside the container. Another thermocouple was placed on the container floor for detecting liquid refrigerant that might pool if the leak were primarily liquid. Two absolute pressure transducers were installed on the container. One measured the absolute pressure of the container and had a pressure measurement range of 0 to 344.7 kPa (0 to 50 psia). The second measured refrigerant pressure upstream the 1 mm orifice, sensing pressure for both high-side and low-side leaks and had a pressure measurement range of 0 to 3447.4 kPa (0 to 500 psia). A video device was used to observe the leak flow leaving the 1 mm diameter orifice. A flexible elastomeric thermal insulation was attached to all exterior surfaces of the container to retard heat gain and prevent condensation of water vapor in air near the exterior surfaces of the container. The refrigerant charging cylinder was placed on an electronic weigh scale to measure the amount of refrigerant manually leaked into the container for a leak flow rate of 0.5 g-s^{-1} (4 lb-h^{-1}). Calculation of the refrigerant enthalpy upstream the needle valve was based on computed P-v-T relations for the mixture of air, an ideal gas, and for R-134a, a real gas captured by the container. A refrigerant quality in the container was also computed from the mass of captured air and R-134a and P-v-T relationships to estimate the amounts of leaked liquid and vapor. An energy balance for flow entering the container was used to compute the enthalpy upstream the needle valve. The computed enthalpy is compared to the saturated liquid and vapor enthalpy of refrigerant in the weigh cylinder, Fig. 1. The results show that the computed enthalpy based on P-v-T relationships for the container and a 1st Law energy balance is consistent with thermodynamic principals for constant enthalpy (isenthalpic) flow.

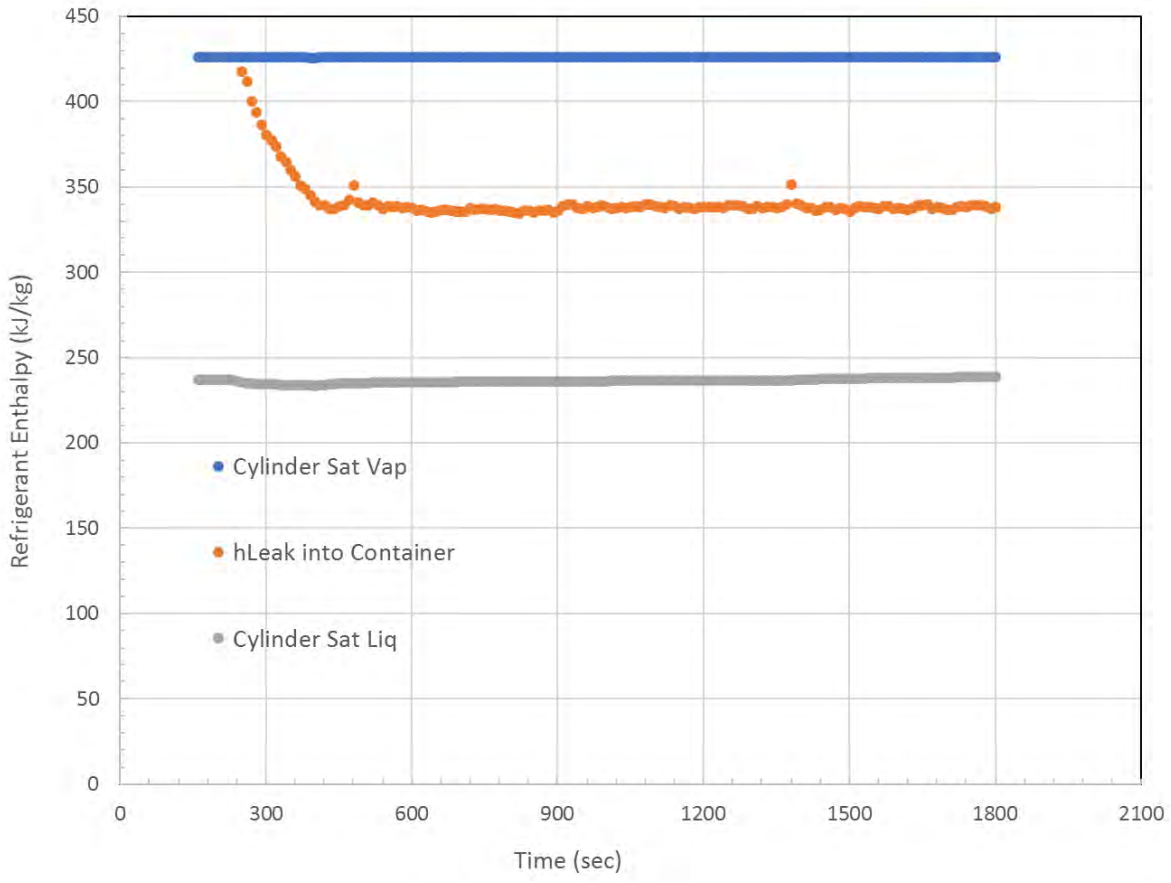

Figure 1: Leak quality estimates (in plastic container and refrigerant cylinder) for 0.5 g/s leak

The refrigerant enthalpy in the container falls between the saturated vapor and saturated liquid states in the refrigerant cylinder, which is consistent with an isenthalpic throttling process. Visual inspection of the leak showed it to start as a high-pressure vapor flow which transitioned more to a sputtering two-phase liquid and vapor flow. The data was reduced further for computing the refrigerant quality [$x(t)_{ref}$] upstream the leak near the refrigerant cylinder, Fig. 2. At leak start the quality of the refrigerant is high, near a value of one, and gradually drops over the 1800 s duration of the test. There is also seen an overall increase in the quality of refrigerant within the container. For this test, liquid refrigerant was observed pooled on the bottom of the container. Measurement of the pooled liquid would be difficult. Therefore, an alternative approach using computed partial pressure of refrigerant and air was attempted for estimating the amount of saturated liquid refrigerant and vapor accumulating in the container. The computation for internal energy change in the container was based on quality estimates in the container, and bulk refrigerant temperature and pressure in the container. The enthalpy entering the container was computed from an energy balance for the enclosed container. The overall pressure of the plastic container rose slightly from 98.6 to 99.97 MPa (14.3 to 14.5 psia) over the 1800 s test period. Therefore, the results were promising enough to attempt additional tests on a packaged 17.6 kW (5-ton) rooftop AC unit (RTU).

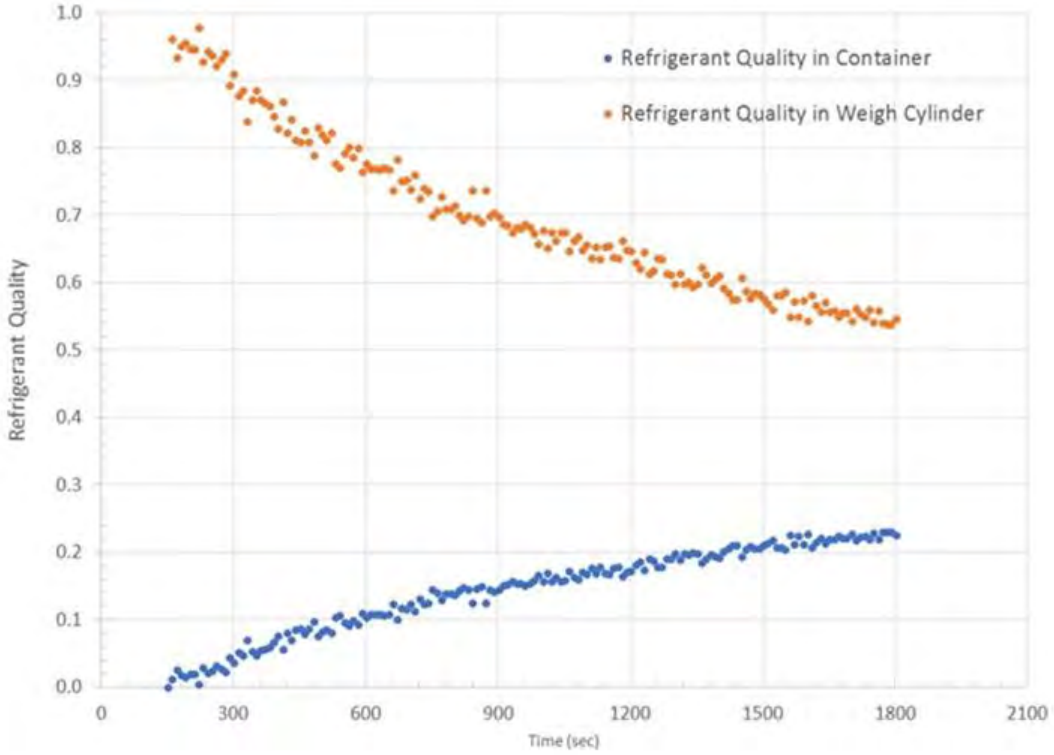

Figure 2: Leak quality estimates (in plastic container and refrigerant cylinder) for 0.5 g/s leak

3. FORMULATION AND VALIDATION OF PROCEDURE

The RTU used here is the same unit tested by Patel et al (2019) and testing followed the logic used by Baxter et al (2019). Therefore, the existing setup and the existing manifold for liquid and suction lines at the evaporator were used as reported by Baxter et al. (2019). The exception being that refrigerant released from the RTU was captured inside the rigid plastic tank container rather then released to the surrounding ambient, Fig. 3. Also, a smaller orifice of 1 mm was used to allow more time to observe the leakage of R-410A refrigerant while limiting the pressure increase in the 1.041 m^3 container. It was important to maintain near atmospheric pressure in the container to best simulate a leak to the surrounding ambient. Leaks were initiated on the high-side (liquid line upstream expansion valve) and on the low-side (vapor line between evaporator and compressor suction). Leaking refrigerant from the low-side yielded a refrigerant quality of 1 for tests with the unit running. The refrigerant leaving the evaporator is superheated vapor and a reduction in refrigerant pressure across the orifice would cause the refrigerant state to remain outside and to the lower right

side of the saturated refrigerant dome for R-410A. Therefore, the leak would remain a vapor with a quality of 1.

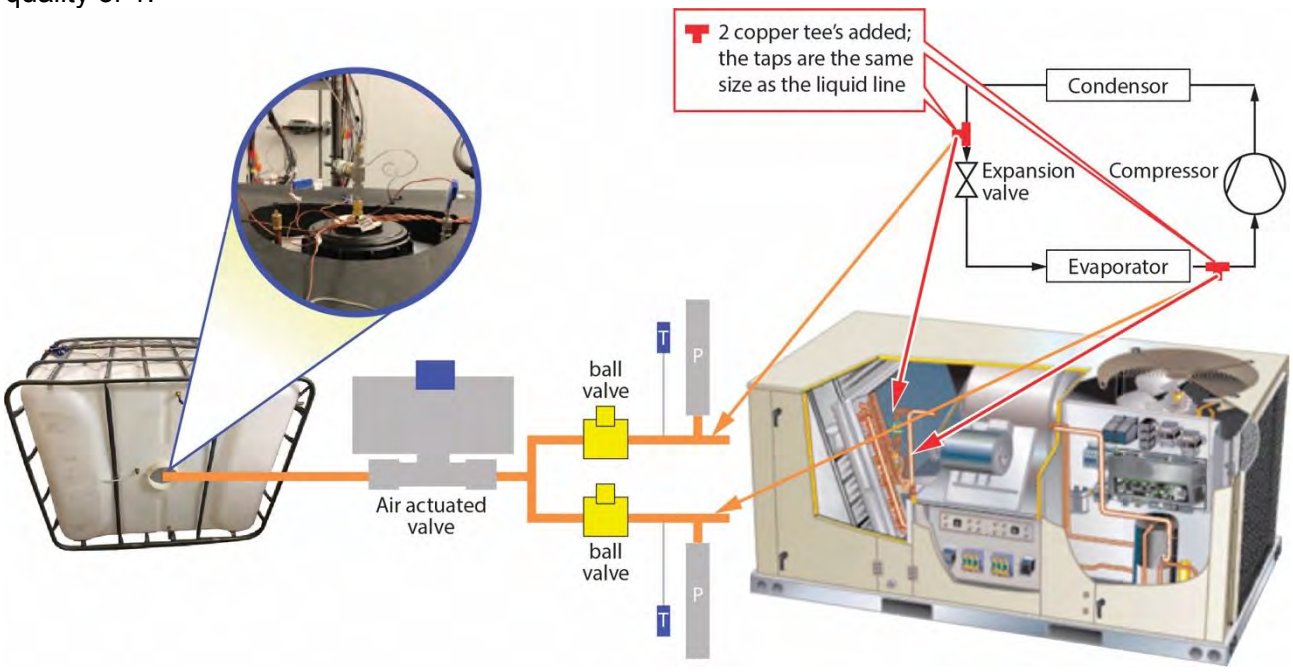

Figure 3: Schematic illustrating the setup for high- and low-side refrigerant leaks from the RTU into the 1.041 m^3 container.

Quality tests used two high-precision floor weight scales to record the total mass of the RTU test unit and the plastic container as function of time during a refrigerant leakage. The change in mass was correlated directly with the movement of refrigerant. Baxter et al (2019) provides relevant specifications for the scales. The “outdoor unit” scale was used to weigh the RTU. The “indoor unit” scale was used to weigh the rigid plastic container.

A vacuum pump was attached to the plastic container to remove any R-410A from previous testing and to bring the container pressure down to slightly below atmospheric pressure; surrounding atmospheric pressure being about 98.6 kPa (14.3 psia). Afterwards, the vacuum pump was shut-off from the container by closing a ball valve.

3.1 Formulation of Algorithm and Testing Procedure

The RTU was operated in the environmental chambers under steady-state conditions for about 30 min and was then de-energized prior to the release of a high-side refrigerant leak. About 90 s passed to allow the weigh scales to steady before opening the leak port (air actuated valve, Fig. 3). Note that several seconds of container pressure and bulk temperature data were used after the RTU de-energized and the leak not energized to compute the mass of air held by the container. The mass of air remained fixed during the leakage period. The number of moles of air were computed and added to the number of moles of R-410A as it leaked into the container. On command, the data acquisition system (DAS) initiated the leak and monitored all data at a 0.1 s interval. Over the leak interval the weigh scale for the RTU showed a refrigerant loss of 0.73 kg (1.6 lb) while the container weight scale showed a refrigerant gain of 0.82 kg (1.8 lb), Fig. 4. The difference is most likely due to differing thrust effects on the scale readings. The weight measure used to compute quality estimates differed depending on the operating state of the RTU. If the RTU was on, the container measurement was felt to be more accurate (less subject to thrust noise). Some thrust effect is transmitted across the flexible leak line attached to the container. However, with the RTU off, and the blowers to the environmental chamber off the RTU scale was felt to be more accurate so it was used.

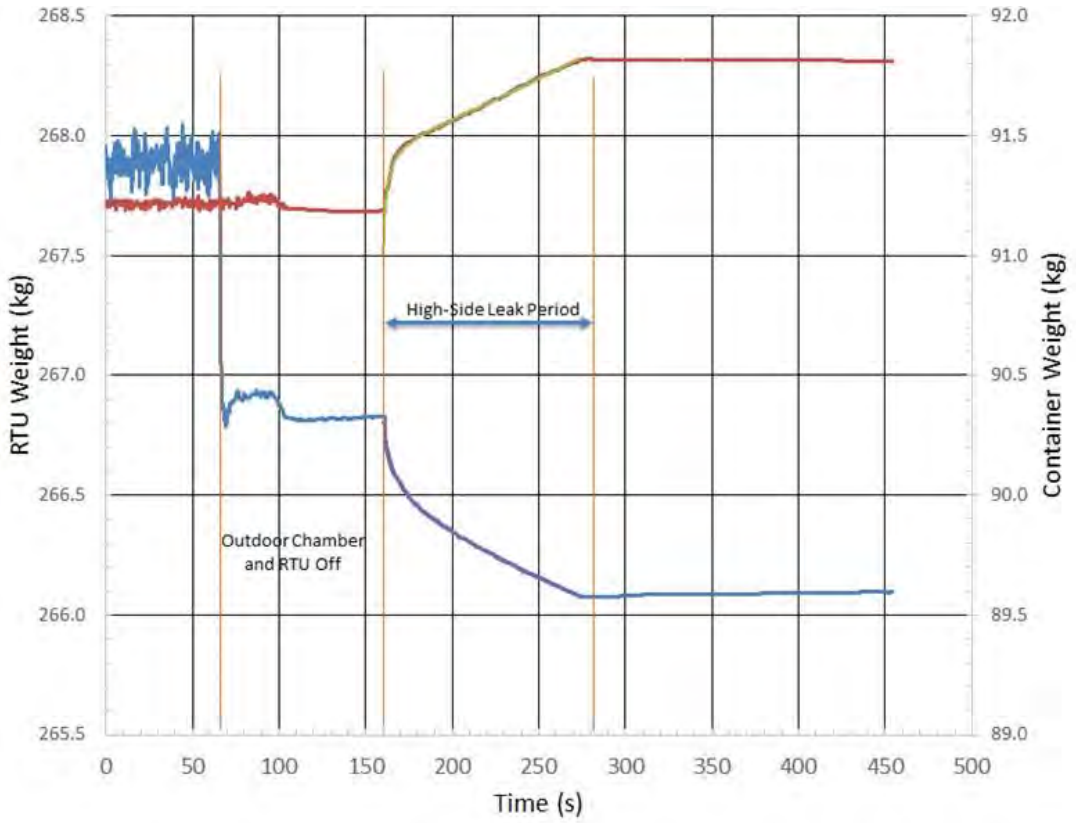

Figure 4: Container (red & green lines) and RTU (blue & purple lines) weights measured during refrigerant leaking from the high-side with the RTU deenergized 90 s after operating under steady-state conditions

Both Dalton's Law of Additive pressures and Amagat's law of additive volumes (Moran and Shapiro, 1992) were used with the molar mass fraction to compute the partial pressures and partial volumes of R-410A and air in the container. Given these values the bulk density of R-410A was computed from Equation 1 as:

$$\bar{\rho}_{ref} = \frac{m_{ref}}{[y_{ref} \cdot Vol_{cont}]} \qquad \text{Eq. (1)}$$

where:

$$y_{ref} = \frac{\eta_{ref}}{\eta_{ref} + \eta_{air}}$$

is the mole fraction of refrigerant in the refrigerant and air mixture. A relationship derived by Miller (1987) was used for the quality of refrigerant in the container which takes the form:

$$x(t)_{cont} = \frac{\rho_v}{(\rho_v - \rho_L)} - \frac{\rho_v}{\bar{\rho}_{ref}}\left[\frac{\rho_L}{\rho_v - \rho_L}\right] \qquad \text{Eq. (2)}$$

If the saturated liquid density is much greater than the saturated vapor density, then to first order the quality simplifies to: $x(t)_{cont} = \frac{\rho_v}{\bar{\rho}_{ref}}$. Calculation of the container quality (Eq. 2) allows one to estimate the liquid and vapor content of the refrigerant released through the orifice. Measuring the amount of liquid pooling on the bottom of the container is too difficult and intrusive on the container and most likely leading to greater error than observed using Eq. 2. The approach using the quality in the container was selected because of its simplicity leading hopefully to better accuracy of the quality estimate. Next an energy balance for the container was formulated much like the charging of a vessel.

The balance takes the form:

$$h_{Leak} = \frac{(U)_2 - (U)_1}{(m_2 - m_1)} - \frac{\dot{Q}_{cv} \cdot \Delta t}{(m_2 - m_1)} \quad \text{Eq. (3)}$$

where:

internal energy U_1 at time t	$U_1 = \left[m_{f\,vap} \cdot u_{vap} + m_{f\,liq} \cdot u_{liq}\right]_1$
internal energy U_2 at time t+dt	$U_2 = \left[m_{f\,vap} \cdot u_{vap} + m_{f\,liq} \cdot u_{liq}\right]_2$
mass of refrigerant in container at time t	m_1
mass of refrigerant in container at time t+dt	m_2
heat transfer due to flashing of refrigerant	$\dot{Q}_{cv} = \dot{m}_{ref} \cdot h_{fg}$
mass flow of refrigerant entering container	$\dot{m}_{ref} = \frac{m_2 - m_1}{\Delta t}$

The throttling process is assumed isenthalpic with minimal heat loss across the orifice and therefore the enthalpy h_{Leak} represents the enthalpy upstream the throttle. It can be used in Equation 4 to compute the quality of the refrigerant as:

$$x(t)_{ref} = \frac{[h_{Leak} - h_{sat\,liq}]}{h_{fg}} \quad \text{Eq. (4)}$$

where:

$h_{sat\,liq}$	enthalpy based on pressure of R-410A measured in the RTU
h_{fg}	change in enthalpy saturated vapor to saturated liquid based on pressure in the RTU

Computations using Eqs. 1 through 4 are displayed in Fig. 5. Refrigerant weight measurement for this test came from the RTU scale because the unit was powered off and there was some thrust effect being transmitted across the flexible leak line to the container. The leakage line has about 0.914 m (3 ft) of travel from the RTU's evaporator coil to the 1 mm orifice in the container. This line is open to the atmosphere of the container until the solenoid energizes and allows the flow of refrigerant through the line to the orifice. Quality starts at 1 (all vapor) but within 1 s drops to 0.8 and in less than a min becomes all liquid (i.e., quality of 0).

As the leak progressed the container pressure was closely monitored so that the container would not exceed atmospheric conditions. A pressure relief valve on the container was set at 110 kPa (16 psia) as a safety. Baxter et al (2019) shows the change in container pressure caused by a refrigerant leak introduced from the high-side with the RTU running. The container pressure rose from 100 to 107.4 kPa (14.5 to 15.6 psia). After the solenoid valve closed, the container pressure remained steady for about 3 min showing the container leak tight.

Testing continued with refrigerant again leaked from the high-side of the RTU. However, for this test the RTU remained energized. Quality estimates were similar for a high-side leak whether the RTU was on or off. Fig. 6 shows the weights and redistribution of refrigerant once the leak is initiated with the RTU running. After about 60 s of refrigerant leakage the compressor started to cycle on/off as low-side pressure dropped. A low-side pressure switch stopped the unit, but the compressor and condenser fan attempted to restart as observed in Fig. 6. The weight of the container was not affected by the cycling and allowed some measure of quality.

The refrigerant quality starts at 1 but drops within seconds as liquid refrigerant is released from the high-side liquid line. Within about 35 s the quality drops from 1 to 0 as liquid refrigerant fills the leak line and is released into the container, Fig. 7. As stated earlier, similar quality trends occur for leakage from the high-side with the unit turned off. During the test the container pressure rose from 100 kPa to 107 kPa and remained constant for the duration of the test showing the container to be leak tight.

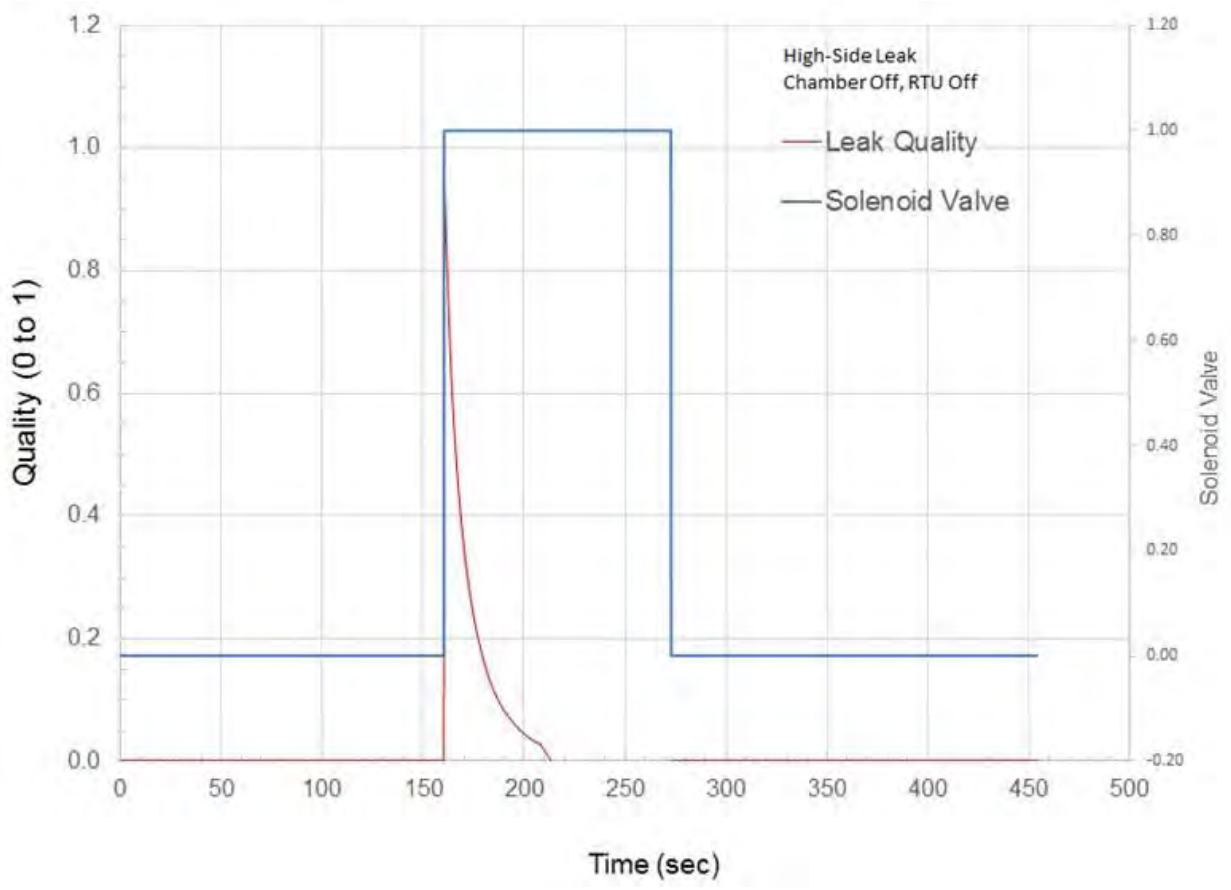

Figure 5: Refrigerant quality computed upstream the orifice during refrigerant leaking from the high-side with the RTU de-energized

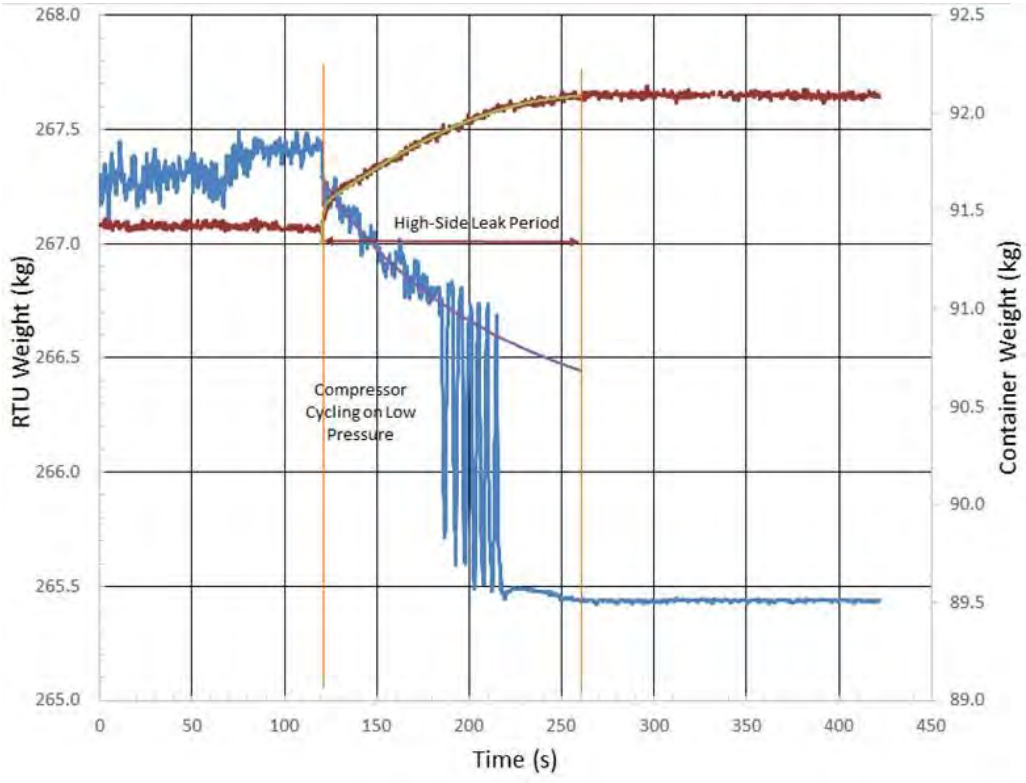

Figure 6: RTU (blue & purple lines) and container (red & green lines) weights showing the movement of refrigerant during the high-side leak with the unit running

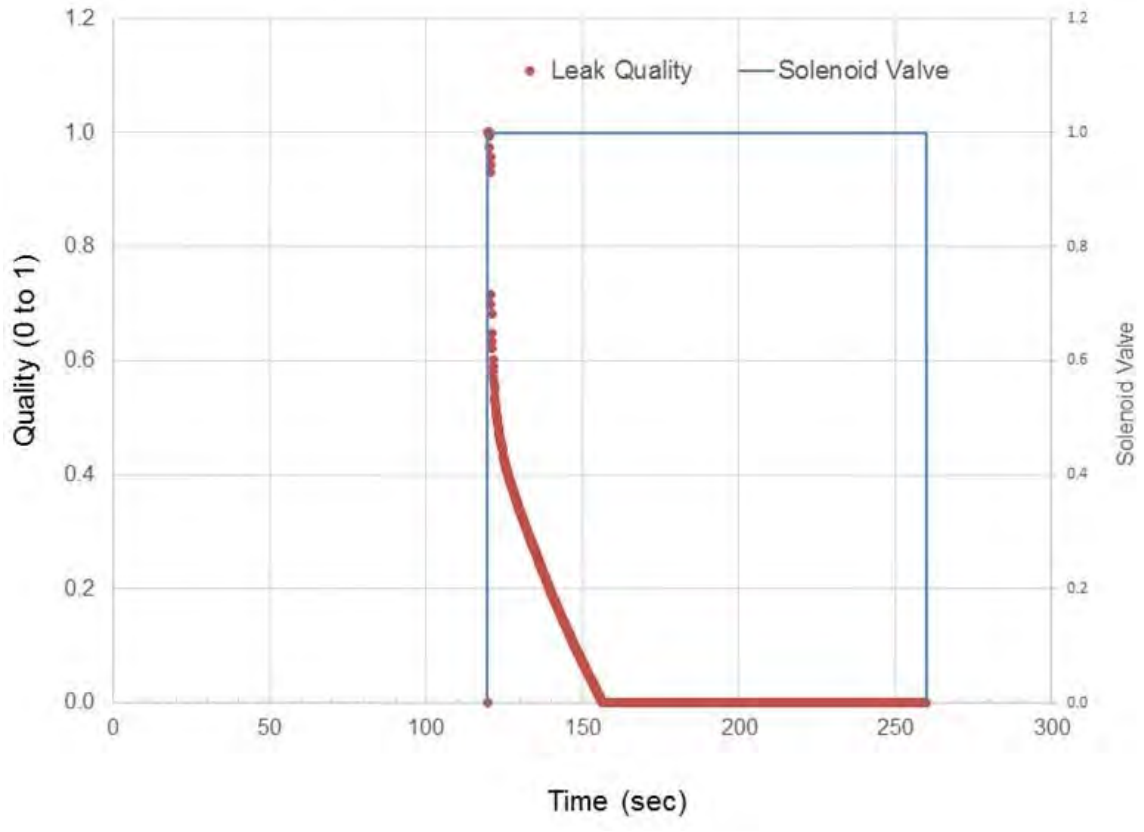

Figure 7: Leak quality estimates for high-side tests of the RTU running at steady-state.

Table 1 lists a brief synopsis of results for the quality estimation tests. The "Total Pressure Drop" columns in Table 1 represent the change in high-side pressure (drop) and low-side pressure (rise) inside the unit during the refrigerant release period. A leak orifice diameter of ~1mm was used to prevent pressure inside the container from rising too quickly during the test.

Table 1. Salient results of quality estimation test

Test	Leak period	Total pressure change in RTU		Container pressure at end of leakage	Cont. R-410A weight increase	RTU R-410A weight decrease	Leak quality
		High-side drop	Low-side rise				
	sec	kPa	kPa	kPa	kg	kg	0 to 1
Low-side,Off	180	1452.9	793.5	101.94	0.49	0.65	~0.85
Low-side,On	180	124.2	270.2	100.36	0.22	0.36	1.0
High-side,Off	112.6	1375.6	363.4	107.44	0.82	0.73	~1 to 0.0 in ~55s
High-side,On	140.0	2116.9	383.5	106.9	0.75	0.85	~1 to 0.0 in ~35s

4. CONCLUSIONS

A testing procedure was developed, and an algorithm formulated that estimates the quality of a refrigerant leak upstream the point of leakage. Tests conducted on a 17.6 kW rooftop AC unit operating under conventional ambient conditions and with ~1mm diameter leak orifice showed the following results:

- Low-side leak, unit on — Vapor leak, quality (x) = 1
- Low-side leak, unit off — Two-phase leak, x ~0.85
- High-side leak, unit on — Leak quality drops from 1 to 0 in ~35s
- High-side leak, unit off — Leak quality drops from 1 to 0 in ~55s

ACKNOWLEDGEMENTS

This work was sponsored by the U. S. Department of Energy's Building Technologies Office under Contract No. DE-AC05-00OR22725 with UT-Battelle, LLC.

REFERENCES

ASHRAE, 2016, ASHRAE 34-2016. Designation and Classification of Refrigerants, American Society of Heating, Refrigerating and Air-Conditioning Engineers.

ISO, 2014, ISO 817:2014. Refrigerants - Designation and Safety Classification, International Organization for Standardization. References.

Walter, William, Furuhama, Kokichi, Shizuoka-Ken., 2002. Refrigerant Flammability an International Perspective, May.

Walter, W. F., 2000. Designation and safety classification of refrigerants – proposed changes to ISO Standard 817, IEA Heat Pump Newsletter 18(3).

Patel, V.K., Abu-Heiba Ahmad, Baxter, V., Miller, W., 2019. Characteristics of refrigerant leaks from small HVAC&R systems. In Proceedings of the 25th IIR International Conference of Refrigeration, June.

Baxter, V., Patel, V.K., Abu-Heiba Ahmad, Miller, W., Linkous, R. Ormston, G., 2019. Experimental evaluation of refrigerant leak characteristics for different HVAC&R equipment types, ORNL/TM-2018/1058, February.

Moran, M. J. and Shapiro, H. N. 1992, Fundamentals of Engineering Thermodynamics, 2nd Edition, John Wiley & Sons, Inc, USA, p. 542-543.

Miller et. al. 1987, "Method and Apparatus for Measuring Steam Quality," United States Patent #4,679,947, July 14.

Manuscript ID: 1150
DOI: 10.18462/iir.icr.2019.1150

Reduced-order model to estimate safe flammable refrigerant charge limits for a one-room air conditioner

K. Dean EDWARDS, Ahmad ABU-HEIBA, Miroslav K. STOYANOV, Mingkan ZHANG, Ahmed F. ELATAR, Viral K. PATEL, Van D. BAXTER, Charles E.A. FINNEY, Omar ABDELAZIZ

Oak Ridge National Laboratory
Oak Ridge, TN 37831, USA
edwardskd@ornl.gov, abuheibaag@ornl.gov, stoyanovmk@ornl.gov, zhangm1@ornl.gov, elataraf@ornl.gov, patelvk@ornl.gov, baxtervd@ornl.gov, finneyc@ornl.gov, abdelazizoa@ornl.gov

ABSTRACT

The Heating, Ventilation, Air-Conditioning and Refrigeration (HVAC&R) industry is currently transitioning away from high global warming potential (GWP) hydrofluorocarbon (HFC) refrigerants. However, many lower-GWP alternatives are flammable. Current safety codes restrict use of all flammable refrigerants; revision of the codes is needed to facilitate wider use of flammable alternatives. Hence, information is needed to enable reliable estimates of safe charge limits for flammable refrigerant options for different HVAC&R applications. A reduced-order model (ROM) was developed and validated to help estimate safe charge limits based on computational fluid dynamics (CFD) simulations of refrigerant releases in a single room for a range of parameters. Validation of the ROM vs. the CFD results showed good general agreement for mean refrigerant concentration. The normalized mean bias error (NMBE) was 0.67% with a maximum error of 15%.
Keywords: Refrigerants, Flammable, lower-GWP, Charge Limits

1. INTRODUCTION

The HVAC&R industry is working to move to lower-GWP refrigerants. Proposed lower-GWP refrigerants include hydrocarbons (HC, e.g., propane (R-290)), ammonia (R-717), CO_2 (R-744), hydrofluoroolefins (HFO), or blends of low-GWP HFCs with other low-GWP fluids. Most of the viable alternatives are flammable to some degree according to Addendum g to ASHRAE standard 34 (2016) and ISO standard 817 (2014), which designate toxicity and flammability of refrigerants as follows:

Table 1. Safety classification of refrigerants as outlined in ISO 817 and ASHRAE 34

	Safety group	
Higher flammability	A3	B3
Flammable	A2	B2
Lower flammability	A2L	B2L
No flame propagation	A1	B1
	Lower toxicity	Higher toxicity

Refrigerant flammability introduces challenges that are centered around deflagration risk. Standards have been developed to systematically set maximum allowable refrigerant charges to ensure safety in case of refrigerant leakage (i.e. the International Electrotechnical Commission (IEC) standard IEC

(2016), Underwriter's Laboratories (2017)). These standards were based on numerical analyses of refrigerant leakage into confined spaces as well as risk analyses of associated ignition events. A2L refrigerants are treated at the same risk level as those in the A2 category in many standards (and the same as A3 refrigerants in some). Therefore, there is a need to revise the relevant safety standards and codes to facilitate wider use of flammable low-GWP A2L refrigerant. However, the bodies responsible for maintaining and updating these standards and codes must have credible, publicly available, science-based knowledge about the safe use of these refrigerants. In 2016, Oak Ridge National Laboratory (ORNL) began a project to investigate a systematic approach to setting safe charge size limits for various types of equipment employing flammable refrigerants. The primary objective of the project was to develop a reduced-order model (ROM) that correlates various information regarding the evolution of refrigerant concentration in a room to the most significant parameters of an application. The ROM was developed using a Computational Fluid Dynamics (CFD) campaign.

The ROM is intended to be simple tool that can provide a quick estimate of refrigerant concentration evolution based on the CFD parametric study. The study focuses on refrigerant releases in a single room for a range of parameters including refrigerant type, refrigerant release rate, quantity, release height, outdoor air ventilation rate, and room floor area.

2. ROM DEVELOPMENT APPROACH

The ROM is a multi-dimensional response fit of the CFD outputs of interest based on the input parameters. Figure 1 shows the overall approach for developing the ROM.

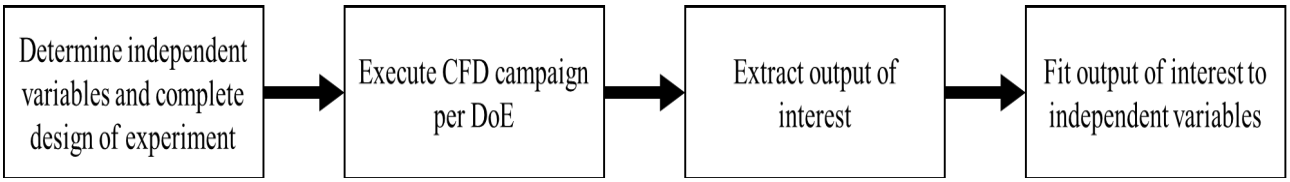

Figure 1. ROM development workflow

2.1 Parameter Domain and Design of Experiments

The parameter domain includes all the independent variables that significantly affect the dispersion of the released refrigerant into the room. For the purpose of developing the ROM, all releases were assumed to be in vapor phase from a wall-mounted air conditioner (AC). The following eight parameters were assumed to fully describe the evolution of the temporal and spatial distribution of released refrigerant vapor into the room: AC indoor air fan (on or off), room size (volume), refrigerant release height, room openings, ventilation rate, charge amount, release flow rate, and refrigerant molecular weight.

Operation status of the unit fan during a refrigerant leak event has an extreme impact on how the refrigerant enters, mixes within, and is dispersed into the room. With the fan on, refrigerant is more readily mixed with the circulating air and more widely distributed throughout the room. With the fan off, mixing and distribution is more heavily dependent on release flow rate. It was decided that separate ROMs would be needed for the "fan on" and "fan off" cases. This paper describes only the "fan off" ROM case; the "fan on" ROM will be covered in a subsequent publication. The room used as the basis for the CFD simulations had a floorplan aspect ratio of 3:4 and a height of 2.44 m (8 ft) as shown in Figure 2.

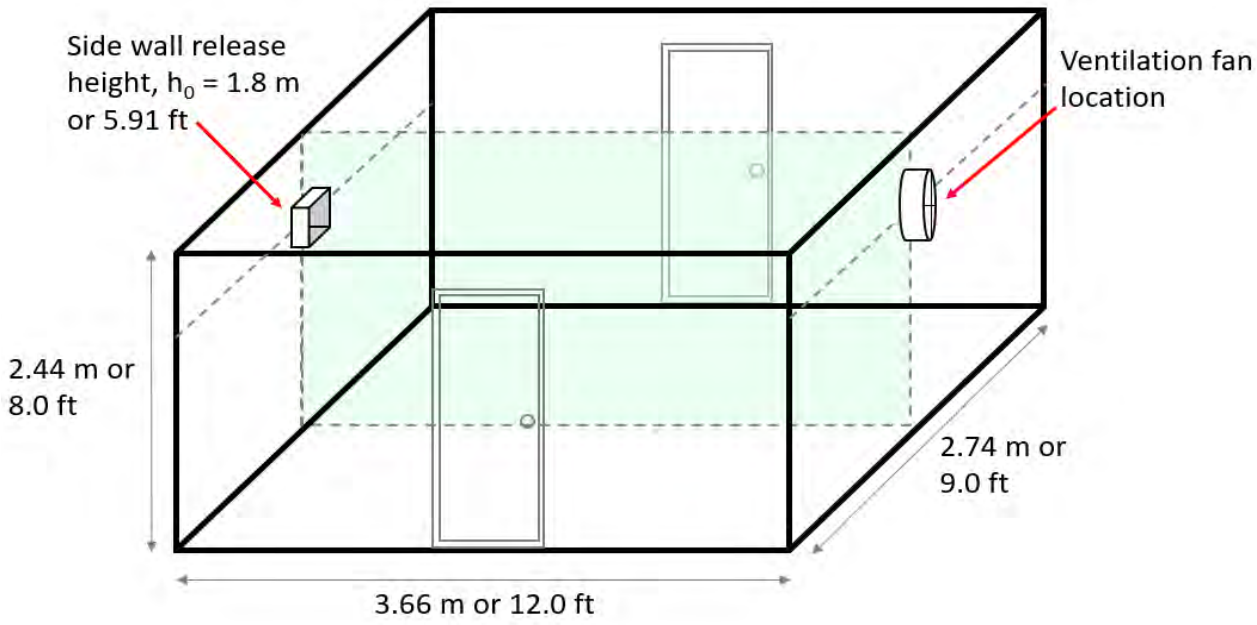

Figure 2. Geometry of room used for ROM CFD simulations. Dimensions shown are for the smallest room floorplan; one of five release locations from Table 2 shown

The Design of Experiments (DoE), and subsequently the regression analysis, were performed in Tasmanian (Toolkit for Adaptive Stochastic Modeling And Non-Intrusive ApproximatioN) (Stoyanov 2018a, 2018b). Learnings from previous simulation efforts (Baxter et al, 2018) and results from a small subset of initial simulations were used to obtain an estimate of the sensitivity and functionality of the model response (as indicated by mean refrigerant concentration in the room) to each input parameter. This information was used with the sparse grids sampling tools within Tasmanian to determine the required number of sample points for each parameter as well as the functionality of the fit. Table 2 summarizes the range and number of levels chosen for each parameter with additional detail provided below. The resulting DoE contained 586 CFD cases.

Table 2. ROM parameters and their ranges

Parameter #	Parameter	Number of levels	Levels
1	Unit circulation fan	2 (discrete)	Off, On
2	Room floorplan area	3	5, 10, 20 m^2
3	Leak release height	5	0, 0.616, 1.219, 1.822, 2.438 m
4	Room openings	3	0.0116, 0.988, 1.964 m^2
5	Ventilation	6	0, 1.0, 4.1, 8.2, 9.2, 16.3 m^3/min
6	Charge amount	5	0.1, 3.825, 7.55, 11.275, 15 kg
7	Leak rate	5	1.875, 12.656, 23.43, 34.219, 45 kg/min
8	Molecular weight	5	44, 69, 94, 119, 144 kg/kmole

2.2 CFD Model

A commercial software platform, CONVERGE, was used for the CFD simulations (Convergent Science, 2018). To reduce computational requirements, the cases were set up to take advantage of symmetry so that only half the domain needed to be modeled. Common simulation parameters used for all simulated cases are listed in Table 3. An adaptive mesh refinement (AMR) tool was used to allow for the use of a coarser base grid which is only refined in areas where high sub-grid property gradients are predicted. Specifically, a cubic base grid of 0.1 m was used to model the room spaces,

resulting in base mesh sizes of approximately 14,000, 30,000, and 54,000 cells for the three floor areas. Whenever velocity or refrigerant concentration are predicted to vary across a cell by more than the specified AMR sub-grid tolerances, CONVERGE will automatically sub-divide that cell into smaller cells until either the tolerances are no longer exceeded, or the minimum cell size is reached. This approach provides a more accurate tracking of the mixing front with less numerical diffusion than the coarse mesh alone and less computational requirements than a refined mesh across the full domain.

Table 3. CFD simulation setup parameters common to all cases

Equation of state	**Ideal gas**
Solver	Transient
Gas Flow Solver	Compressible
Body Force (m/s^2)	9.81
Turbulence Model	Standard $k-\varepsilon$
Pressure-Velocity Coupling	Pressure implicit with splitting of operators (PISO)
Initial Time Step (s)	1×10^{-5}
Minimum Time Step (s)	1×10^{-7}
Maximum Time Step (s)	0.5
Total Simulation Time (s)	600

2.3 Outputs of Interest

Each CFD simulation produced an output file at every second of the simulation containing the location, volume, composition, and thermophysical conditions (temperature, pressure, etc.) of every computational cell in the model domain. For generation of the ROM, MATLAB (Mathworks, 2018) scripts were used to extract the spatial and temporal concentration data for each cell from the raw CFD results and to calculate the following 396 outputs of interest:

- Refrigerant concentration: maximum and spatiotemporal mean across entire room plus min, mean, and max temporal profiles at 5, 10, 20, 50, 100, 200, 300, 400, 500, and 600 seconds
- Flammable volume fraction (FVF) and accumulated fuel volume fraction (AFV)
    - FVF is the fraction of the total room volume that has a concentration between the LFL and UFL at any time divided by the total volume of the room. FVF provides an indication of the likelihood of an ignition event. Values range from 0 to 1.
    - AFV is the fraction of the total room volume that has a concentration greater than the LFL at any time divided by the total volume of the room. AFV provides an indication of the severity of an ignition event. Values range from 0 to 1.
    - The following statistics were calculated:
        - Temporal maximum and mean of FVF and AFV
        - Total time duration for some FVF and AFV
        - FVF and AFV temporal profile at 5, 10, 20, 50, 100, 200, 300, 400, 500, and 600 seconds

3. CONSTRUCTING THE ROM

The ROM was developed using the sparse grids approximation techniques implemented in Tasmanian, specifically the hierarchical methods that use a linear piece-wise polynomial basis (Stoyanov, 2018b). Given the complex CFD model and the set of input parameters with corresponding ranges, Tasmanian was used to generate a grid that consists of combinations of values for the inputs. CFD model simulations were performed with the corresponding inputs and the results (outputs) of the simulation were then input to Tasmanian. The output data were analyzed and compiled into a Tasmanian grid file that was used to infer model outputs for any arbitrary values of the input parameters. The computational cost of this approximate (surrogate) model is negligible compared to the full CFD — thus thousands of samples can be computed, and rigorous statistical

analysis can be performed. Results of the initial test runs were analyzed to gain early insight to impact of the input parameters on mean refrigerant concentration within the room. Based on this information, a bias was introduced in the sparse grids construction, so that the final surrogate will deliver more accurate results with the same number of full CFD model simulations. First, a nonlinear transformation was used for the room height, ventilation rate, and leak height parameters; as a result, more samples were collected for small room sizes and ventilation rates, and the leak heights. Then, CFD simulations were performed with inputs from a sparse coarse grid and a subset of a much denser grid. Performing all CFD simulations on the denser grid was prohibitively expensive, and the subset was chosen with expert opinion, focusing on areas where the highest gradients in mean refrigerant concentration were noted in the initial scoping runs. The CFD simulation data were then projected on the entire denser grid using the least-squares method described by Stoyanov (2018b). Effectively, the projection removed any missing or redundant points in the grid and minimized the size of the Tasmanian grid file while preserving the accuracy of the surrogate model.

4. RESULTS

In constructing the ROM, Tasmanian minimizes the residual error at the sample points. The test of its accuracy is determined by how well the fit predicts the response at points that lie between the sample points. To provide an initial assessment of the ROM accuracy, 11 test cases, shown in Table 4, were run with both the CFD model and the ROM. The input values for these validation cases were specifically chosen to align with parameter sweeps in the training data to evaluate the accuracy of the ROM at locations between sample points where high sensitivity and higher-order functionality were observed and largest errors might be expected.

Table 4. Input parameters for the test cases. The highlighted cells are values that were not used in training the ROM

Case number	Floor area m^2	Leak height m	Open door area m^2	Ventilation rate m^3/min	Total charge kg	Leak rate kg/min	MW kg/kmole
1	5	1.822	0.0116	2.8	15	1.875	44
2	5	1.822	0.0116	5.7	15	1.875	44
3	5	1.822	0.0116	9.9	15	1.875	44
4	10	1.219	0.988	4.1	7.55	23.43	57
5	10	1.219	0.988	4.1	7.55	23.43	84
6	10	1.219	0.988	4.1	1	23.43	94
7	10	1.219	0.988	4.1	5.5	23.43	94
8	10	1.219	0.988	4.1	7.55	4	94
9	10	1.219	0.988	4.1	7.55	6	94
10	10	1.219	0.988	4.1	7.55	8	94
11	10	1.219	0.988	4.1	7.55	28	94

The ROM was found to do well predicting the mean refrigerant concentration vs. ventilation rate for the 11 test cases. Figure 3 provides a qualitative measure of goodness of fit for five of the ROM outputs (mean concentration at 20, 100, 200, 300, and 400 s). This figure includes CFD and ROM results for test cases 1–3 which were chosen to coincide with areas of high sensitivity and higher-order functionality in the model response. The ROM agrees well with the CFD results for these cases, capturing both the functionality and sensitivity of the output trends between sample points. Quantitively, the absolute values of mean concentration show an NMBE of 0.67% but is relatively high at some points, especially those at later times in the simulations (e.g., maximum error of 15% occurring for the 20-s output value with a ventilation rate of 9.9 m^3/min). Note: Figures 3 and 5-7 are all for the case of unit fan off, door closed, refrigerant with MW=44 kg/kmole, 15 kg charge leaked at 1.875 kg/min from a location 1.822 m above room floor.

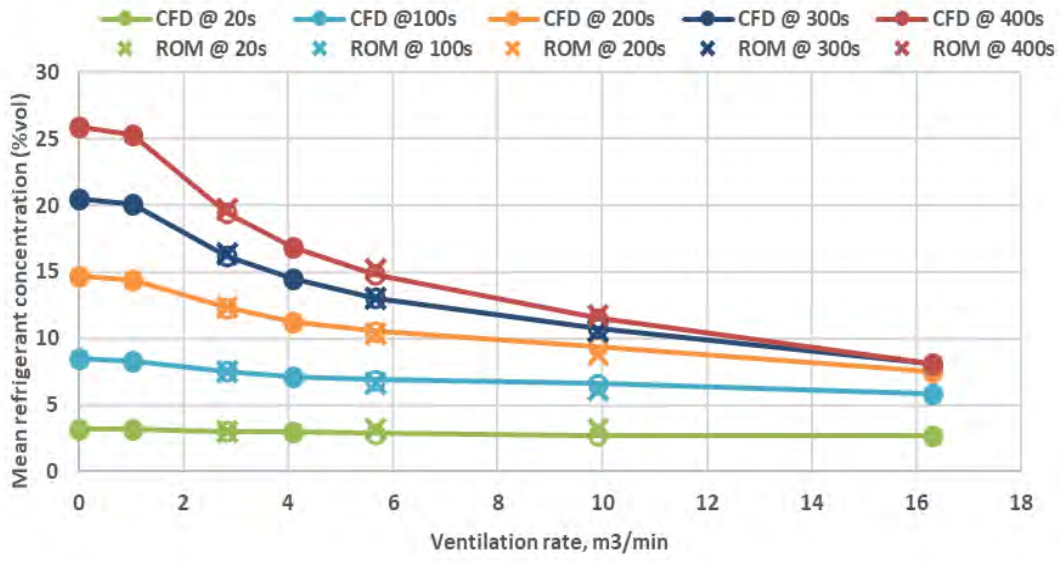

Figure 3. Comparison of predicted mean refrigerant concentration with the CFD model (○) and ROM (×) at three test points selected to fall within high sensitivity response regions with limited sampling in CFD training cases (●).

The current ROM does less well at predicting many of the other target output parameters. For the eleven test cases, the maximum absolute error in the maximum FVF was 1.32% and the maximum absolute error in the duration of FVF was 205.64 seconds. The NMBE of those two outputs for the eleven cases were 0.5% and 77.74 seconds, respectively. Figure 4 shows the NMBE of the maximum refrigerant concentration in the space (% v/v) for all test cases for each of the 10 simulation time steps that the ROM outputs. The maximum absolute error in the maximum refrigerant concentration was 71% for case number 8.

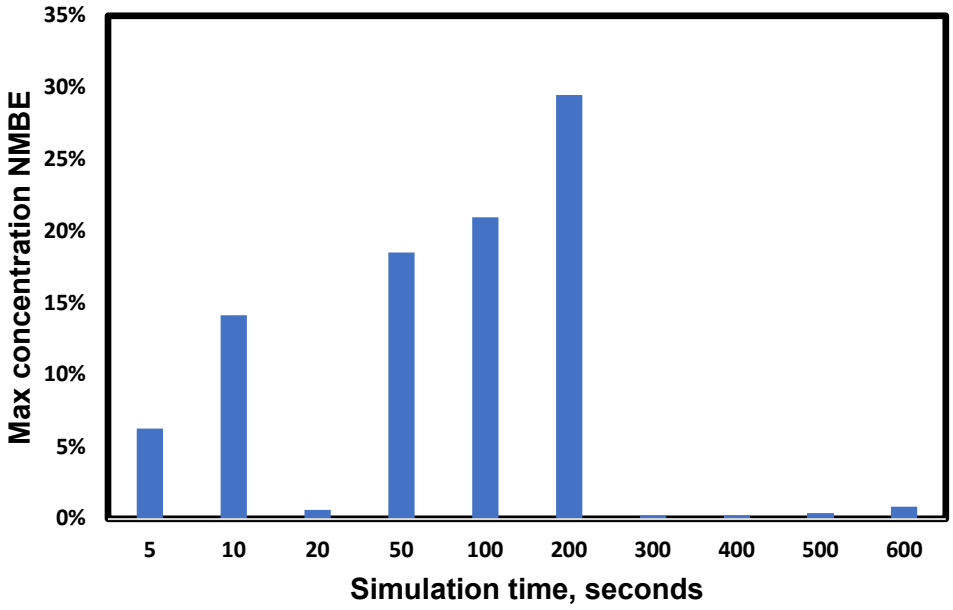

Figure 4. NMBE of maximum refrigerant concentration in the room space at different simulation times

Figures 5-7 show the predicted outputs during a parametric sweep of ventilation rate for five of the ROM output parameters: the temporally averaged FVF in the room, the duration with some FVF in the room, and the spatially averaged FVF at 200, 300, and 400s (all calculated based on the flammability range of R-32). Most of these output parameters show a high-order functionality with

highest sensitivity occurring in the large sampling gap between 4.1 and 15.2 m^3/min. As a result, the ROM does a poor job predicting the outputs in those areas. The skewed distribution of sampling points for the ventilation rate input parameter was chosen to capture the high sensitivity of mean refrigerant concentration at low ventilation rates as shown in Figure 3; the ROM performs well for this parameter. Similarly, the output variable for spatially averaged mean FVF at 200 s shows greatest sensitivity at lower ventilation rates (Figure 7), and as a result the ROM also predicts this parameter well. While this discussion has focused on differences in the response of the output parameters to changes in ventilation rate, similar trends are observed for the other input parameters.

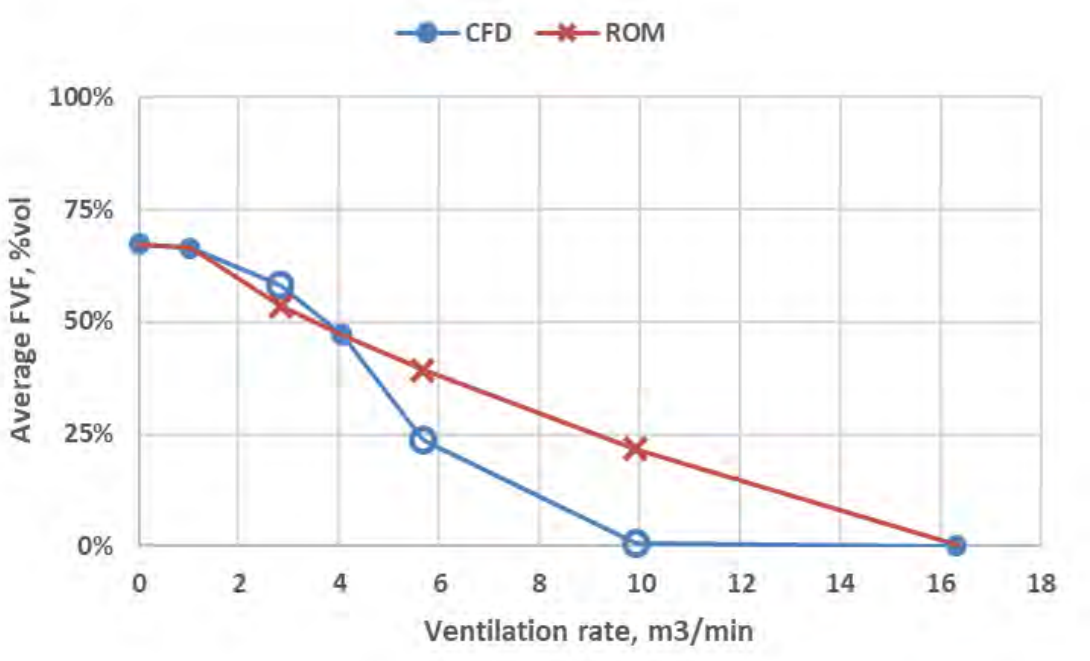

Figure 5. Comparison of predicted temporal mean of FVF using CFD model (○) and ROM (×) at three test points falling between training samples (●).

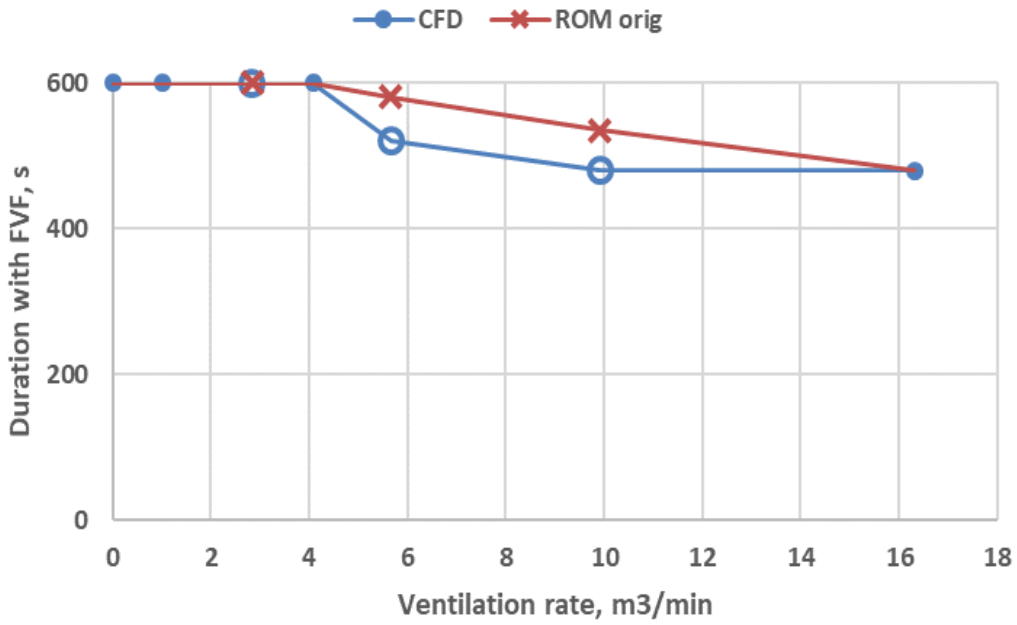

Figure 6. Comparison of predicted FVF duration in the room using CFD model (○) and ROM (×) at three test points falling between training samples (●).

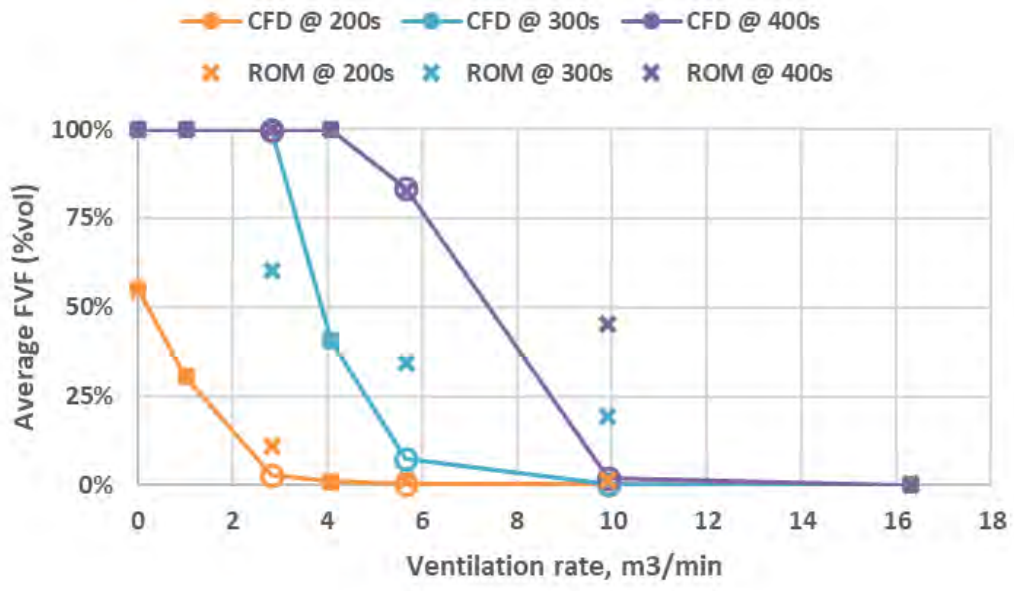

Figure 7. Comparison of predicted FVF at selected times using CFD model (○) and ROM (×) at three test points falling between training samples (●).

5. CONCLUSIONS

The density of the sampling grid was intentionally skewed toward regions of the parameter space where large gradients in mean refrigerant concentration were noted in the initial scoping study. As a result, the ROM does a reasonable job in accurately predicting mean refrigerant concentration. This indicates that the overall methodology is promising, in concert with adaptive refinement of the sampling grid to accurately handle higher-order responses. Accuracy is reduced when the ROM is extended to evaluate output parameters (such as FVF and AVF) which were not considered when constructing the sampling grid and which show greatest sensitivity in sparsely sampled regions of the parameter space. CFD results from additional training cases would be necessary to develop a refined, more accurate ROM for other variables of interest.

ACKNOWLEDGEMENTS

This work was sponsored by the U.S. Department of Energy's Building Technologies Office under Contract No. DE-AC05-00OR22725 with UT-Battelle, LLC. The authors would also like to acknowledge Mr. Antonio Bouza, Technology Manager – HVAC&R, Water Heating, and Appliance, U.S. Department of Energy Building Technologies Office and members of the AHRTI advisory group for the project. This manuscript has been authored by UT-Battelle, LLC under Contract No. DE-AC05-00OR22725 with the U.S. Department of Energy. The United States Government retains and the publisher, by accepting the article for publication, acknowledges that the United States Government retains a non-exclusive, paid-up, irrevocable, world-wide license to publish or reproduce the published form of this manuscript, or allow others to do so, for United States Government purposes. The Department of Energy will provide public access to these results of federally sponsored research in accordance with the DOE Public Access Plan (http://energy.gov/downloads/doe-public-access-plan).

REFERENCES

ASHRAE (2016). ASHRAE 34-2016 - Designation and Safety Classification of Refrigerants, American Society of Heating, Refrigerating and Air-Conditioning Engineers.

ISO (2014). ISO 817:2014 Refrigerants - Designation and Safety Classification. Geneva, Switzerland, International Organization for Standardization: 73.

IEC (2016). IEC 60335-2-40:2016 Household and similar electrical appliances - Safety - Part 2-40: Particular requirements for electrical heat pumps, air-conditioners and dehumidifiers. Geneva, Switzerland, International Electrotechnical Commission.

UL (2017). UL 60335-2-40:2017 Household and Similar Electrical Appliances - Safety - Part 2-40: Particular Requirements for Electrical Heat Pumps, Air-conditioners and Dehumidifiers, Underwriters Laboratories.

Stoyanov M. (2018a). User Manual: Toolkit for Adaptive Stochastic Modeling and Non-Intrusive Approximation, version 6.0, ORNL/TM-2015/596.

Stoyanov M. (2018b). "Adaptive Sparse Grid Construction in a Context of Local Anisotropy and Multiple Hierarchical Parents," Proc. Sparse Grids and Applications, Miami, FL, Springer International Publishing, pp. 175-199.

Baxter V.D., Abdelaziz O., Abu-Heiba A., Edwards K.D., Elatar A.F., Finney C.E.A., Patel V.K., Zhang M. (2018), “Milestone Report BTO 3.2.2.25 – Methodology for Estimating Safe Charge Limits of Flammable Refrigerants in HVAC&R Applications – Part 1”, ORNL Report ORNL/TM-2018/804.

Convergent Science, Inc (2018). CONVERGE CFD Software, Madison, Wisconsin, USA.

Mathworks, Inc. (2018). MATLAB software, Natick, Massachusetts, USA.

Manuscript ID: 1164
DOI: 10.18462/iir.icr.2019.1164

Screening of surface active agents to enhance absorption in ammonia-water systems

Girish KINI[(a)], Srinivas GARIMELLA[(a)]

(a) GWW School of Mechanical Engineering, Georgia Institute of Technology
Atlanta, 30318, USA, e-mail:sgarimella@gatech.edu

ABSTRACT

Surface active agents have the potential to substantially enhance heat and mass transfer in ammonia-water absorption by reducing the surface tension of the working fluid. The enhancement is caused by improved interactions at the vapor-liquid interface that result from surface tension gradients. A screening analysis is performed based on the value of surface tension and critical concentration. Surface tension measurements are made by a goniometer with and without surface active agents using the pendant drop method. Different concentrations of ammonia and additives that span the range of conditions encountered in the operation of an absorption heat pump are considered. Based on these assessments, surface active agents and their ideal concentrations for the enhancement of ammonia-water absorption are recommended.
Keywords: Additive, Ammonia-Water, Surface Tension, Surfactant.

1. INTRODUCTION

With an increasing emphasis on the reduction of electricity consumption and the eventual phasing out of commonly used refrigerants, there is renewed interest in non-vapor compression technologies for space cooling. Advances in miniaturization of heat exchangers have led to development of compact vapor absorption systems as viable alternatives to vapor compression systems (Determan and Garimella, 2012;Garimella, 2003;Hoysall and Garimella, 2019;Nagavarapu and Garimella, 2011)The use of an ammonia-water mixture as the working fluid allows for cooling below freezing temperatures, thereby overcoming the limitations of a water-lithium bromide absorption system. The low specific volume of ammonia vapor and the development of heat exchangers with microscale geometries have enabled the miniaturization of these systems. The small size of these microchannel based absorption systems broadens the range of potential applications to include residential and other small-scale applications. The versatility of these systems in terms of heat source coupling has been demonstrated by Garimella et al. (2016) and Goyal et al. (2017) by developing natural gas driven and waste-heat driven systems, respectively, with standalone control systems for autonomous operation. A direct, gas-coupled absorption system was developed by Staedter and Garimella (2018). The absorber is often the bottleneck of these absorption systems: the performance of the absorber limits the performance of the overall system as observed in Goyal et al. (2017). The absorber can often also be the largest component in the system and dictates system size. Thus, enhancement of absorption will directly translate to more efficient and compact systems.

Absorption of ammonia vapor into a dilute ammonia-water solution is a coupled heat and mass transfer process, typically limited by the high mass transfer resistance on the liquid side in microscale geometries (Hoysall and Garimella, 2019). The high mass transfer resistance can be attributed to the low diffusivity of ammonia and low circulation velocity in microscale geometries. The addition of surface active agents or surfactants to the working fluid could lead to increased interfacial turbulence and better absorption. The interfacial turbulence is induced by surface tension gradients, also known as the Marangoni effect. Although surfactants have been studied well for water-LiBr absorption systems, their effect on ammonia-water systems is not well understood. Kang and Kashiwagi (2002) reported that the addition of surfactants such as 2-ethyl-1-hexanol enhanced ammonia absorption in a bubble type absorber by 3 - 4.6 times. However, the lack of understanding of the underlying phenomena has prevented the development of surfactant

enhanced ammonia water absorption systems. In the present study, surface tension values for ammonia-water solutions with various surfactants added in different concentrations are measured. The results from this study will lead to an understanding of the pertinent enhancement mechanisms and the eventual development of efficient and compact absorbers for vapor absorption systems.

2. LITERATURE REVIEW

Surfactants have been widely used and studied for water-LiBr absorption systems. The enhancement caused by surfactants was first reported by Kashiwagi (1985). Based on experimental evidence from three enhancement additives, Beutler et al. (1996) concluded that 2-ethyl-1-hexanol (2E1H) had the best enhancement by a factor of 1.5. However, they concluded that the reduction in surface tension cannot be the only reason for enhancement, as the addition of 1-decanol reduced surface tension but did not enhance performance. Hoffmann et al. (1996) investigated the effect of surfactants on a horizontal falling-film water-LiBr absorber and suggested that the improvement in performance was due to the combined effect of surface tension reduction and change in droplet characteristics. Kulankara and Herold (2000) studied the effect of surfactants on falling-films over vertical tubes, and developed the so-called vapor surfactant theory. Möller and Knoche (1996) were the first to conduct experiments on the ammonia-water working fluid and concluded that 50 PPM of 1-octanol resulted in the best enhancement in a bubble absorber. Kim et al. (2006) visually investigated the effect of surfactants and confirmed that Marangoni convection played a role in the enhancement of performance. They suggest using 700 PPM of 2-ethyl-1-hexanol to maximize absorption rates in the bubble mode. Kim et al. (2007) show enhancement in ammonia-water bubble absorbers by adding copper nanoparticles. It must be noted that all ammonia-water studies, except Hoysall and Garimella (2019), are conducted on the bubble mode of ammonia-water absorption. There is a need to study the effect of these additives in convective flow and falling-film absorbers. Excepting Marlon-A, an anionic tenside, all studies employed various hydrocarbon alcohols as the additive. Figure 1 summarizes the magnitude of enhancement caused by various additives reported in the literature.

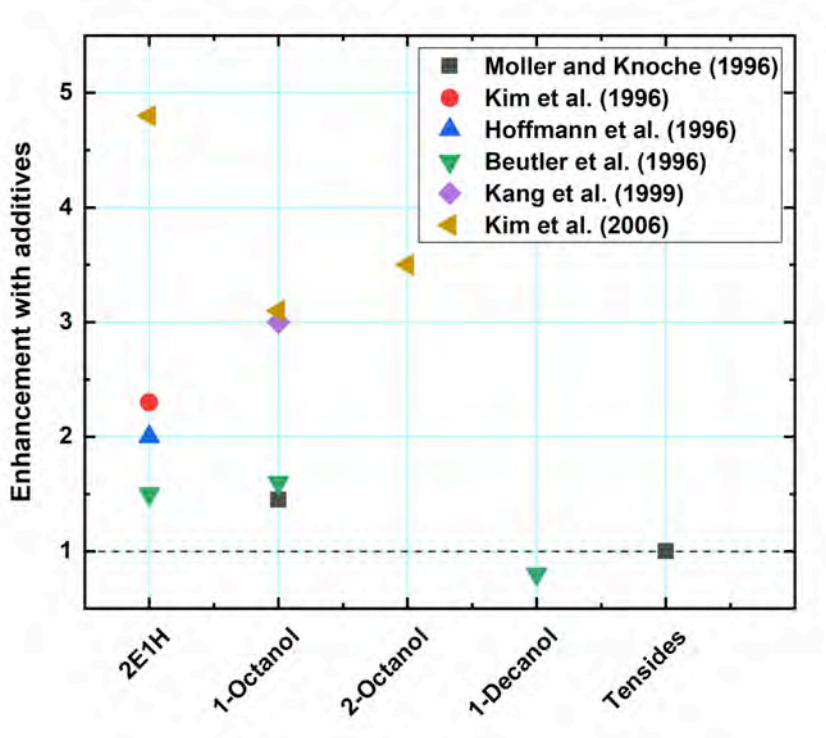

Figure 1: Magnitude of enhancement by additives

Fluorinated surfactants are another class of surfactants that have been observed to reduce surface tension of water very effectively. However, there are no studies that characterize their impact on absorption. Inoue et al. (2004) investigated the enhancement of pool boiling in water and water/ethanol mixtures using perfluoroalkyl surfactants. The exceptional thermal and chemical stability of this class of surfactants has led to its accumulation in groundwater and blood samples and has raised environmental concerns. Alternatives including synthetic organic surfactants like sodium dodecyl sulfate (SDS) that are used in household cleaning products have been declared safe with regard to human and environmental toxicity concerns. Therefore, SDS is evaluated in this study.

A few different theories have been proposed to explain the mechanism of enhancement. Kashiwagi (1988) explained the enhancement in water-LiBr on the basis of Marangoni convection. He proposed that the presence of droplets or islands of additive on the surface is required to induce Marangoni convection. It is thus referred to as the island theory. The strong gradients of surface tension around these islands during absorption results in Marangoni convection. According to this model, the additive concentration should exceed the solubility limit and thus be able to form droplets on the surface. However, many studies have reported the presence of islands is not a necessary condition for enhancement.

According to the radical out effect, additive molecules dissociate in the solution with one part dissolving in the bulk solution and the other part adsorbing on the surface. For instance, 1-octanol dissociates into $C_8H_{17}^+$ and OH^-. The OH^- ion bonds with NH_4^+ allowing the $C_8H_{17}^+$ ions to diffuse to the interface and reduce local surface tension in various regions, resulting in interfacial turbulence (Kim et al., 2006). Kulankara and Herold (2000) proposed the vapor surfactant theory to explain the enhancement caused by surfactants in water-LiBr absorption chillers. This theory also attributes the enhancement to Marangoni convection but differs from other theories in how the instability is induced. According to this theory, some of the alcohol vaporizes and travels in the vapor phase and condenses on the vapor-liquid surface leading to secondary flows.

3. EXPERIMENTAL METHOD

Force measurement and optical methods are most commonly used to measure surface and interfacial tension. Force tensiometry is basically the measurement of forces exerted on a probe that is positioned at the liquid-gas or liquid-liquid interface. The forces measured by the balance as the probe interacts with the surface of the liquid are used to calculate surface tension. The Du-Nouy ring and Wilhelmy plate methods are examples of force tensiometry. Surfactant-based solutions, however, pose a challenge. The use of the ring method, where the interface is stretched during measurements means that the equilibrium state is not achieved, because new surface area for surfactants to move to is constantly created. The measured surface tension values are higher than the actual value. On the other hand, the equilibrium state can be achieved with the Wilhelmy plate method as the plate can be kept stationary. However, the change in wettability of the plate due to unwanted adsorption of surfactants can affect the measured values. It is for these reasons that the pendant drop optical technique is best suited for surfactant-based solutions. It must also be ensured that the needle tip does not influence the drop shape. For the present study, the Dataphysics OCA 25 goniometer with drop shape analysis capability is used. A schematic of the system setup is shown in Figure 2.

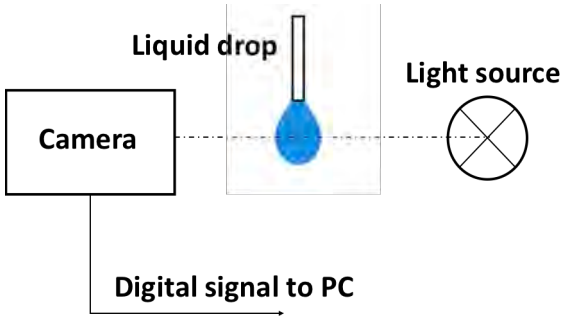

Figure 2: Schematic of experimental apparatus

The shape of the drop is governed by the Young-Laplace equation given by Eq. (1). It is determined by the combination of surface tension force that tends to create a spherical drop and gravitational forces that stretch the drop, leading to the typical pear or pendant shaped drop. The shape of the drop is extracted by image analysis and the method elucidated by Stauffer (1965) is used to calculate the value of surface tension.

$$\Delta P_t = \Delta P_0 \pm \Delta\rho g z = \sigma\left(\frac{1}{R_1} + \frac{1}{R_2}\right) \quad \text{Eq. (1)}$$

Four different surfactants are investigated in this study. A summary of test conditions is provided in Table 1.

Table 1: Experimental conditions

Base solution	Ammonia-water solution
Concentration of ammonia (x)	0%; 15%; 28% (percentage of ammonia)
Surfactant	1-octanol; 2-ethyl-1-hexanol; 1-decanol and sodium dodecyl sulfate
Concentration of surfactant (C)	0; 100; 200; 500; 1000 (PPM of surfactant)
Ambient temperature	23 °C
Needle	24 gauge
Dosing volume	~ 50 µL
Instrument uncertainty	$10^{-3}\,\mathrm{Nm^{-1}}$

The surface tension values obtained from the experiment are averaged over ten readings, and validated by comparing them with values reported in the literature, as shown in Table 2. There is high degree of agreement between measured and reported values.

Table 2: Comparison of measured and reported values

Working fluid	Surface tension from current study $(10^{-3}\,\mathrm{Nm^{-1}})$	Surface tension from literature $(10^{-3}\,\mathrm{Nm^{-1}})$	Reference
Pure water	73.53	72.44	Harkins (1952)
15% ammonia-water solution	61.13	61.98	Ware (1928)

4. RESULTS

Surface tension measurements with additives are made for water and ammonia-water solution. The shape of the drop, analyzed using the Dataphysics SCA 22 module is shown for two cases in Figure 3. On the left is a drop of pure water with no surfactant, while on the right is a drop with 1000 PPM of 1-octanol. It is observed that with addition of surfactant, the size of the drop decreases and it assumes a stretched oval shape.



Figure 3: Shape of water droplet with 1-octanol with C = 0 PPM (left), and C = 1000 PPM (right)

Figure 4 shows the variation of surface tension of ammonia-water solution with the addition of 1-octanol. As little as 100 PPM of the additive causes a 30% change in surface tension. It is also seen that 500 PPM is the critical concentration of the 1-octanol, beyond which there is no appreciable reduction in surface tension.

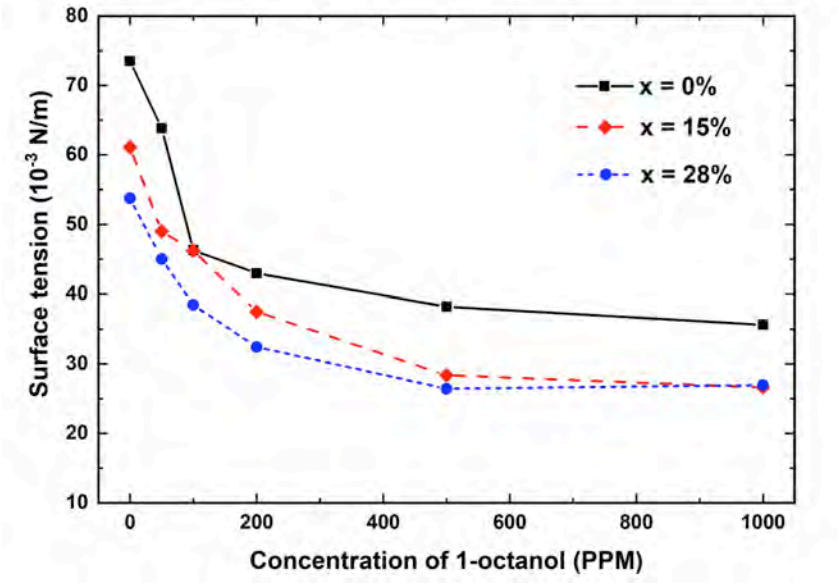

Figure 4: Surface tension of ammonia-water solution with 1-octanol

There is ambiguity in the literature about the variation of surface tension of ammonia-water solution with increasing concentration of ammonia in the presence of surfactants. Some studies including Kang et al. (1999) show an increase in surface tension as the ammonia concentration increases in the presence of 1-octanol. In the present study, it is observed that surface tension decreases with increase in ammonia concentration in the presence of surfactants. Figure 5 shows data for 1-octanol as the additive. It is, however, observed that as the concentration of surfactant is

increased, the slope of the surface tension curve decreases. For instance, with 100 PPM of 1-octanol, the change in surface tension is more than the case with 1000 PPM of the surfactant. These data will help understand the magnitude of enhancement at different sections of the absorber.

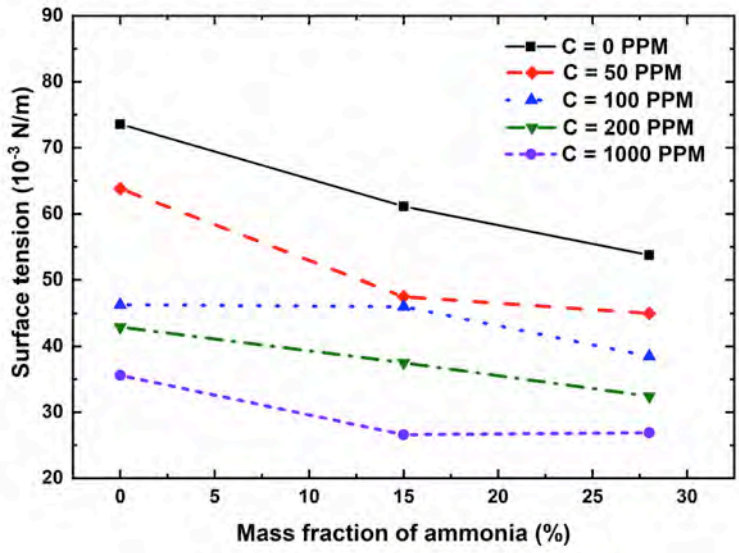

Figure 5: Surface tension versus mass fraction of ammonia

Figure 6 shows measured surface tension values for various surfactants in 15% ammonia-water solution. A critical concentration of about 500 PPM is again observed for all the hydrocarbon alcohols. The plateau value of surface tension for 1-decanol is $33.4\times10^{-3}\,\mathrm{Nm^{-1}}$ while the values for 1-octanol and 2-ethyl-1-hexanol are slightly lower than $28\times10^{-3}\,\mathrm{Nm^{-1}}$. Sodium dodecyl sulfate performs poorly in comparison, reducing the surface tension only to $40.2\times10^{-3}\,\mathrm{Nm^{-1}}$. Islands of the additive are observed in the solution when the concentration is above 100 PPM in the case of 1-octanol, 2-ethyl-1-hexanol and 1-decanol, indicating very low solubility for these additives. SDS is however completely soluble in water and ammonia-water solution.

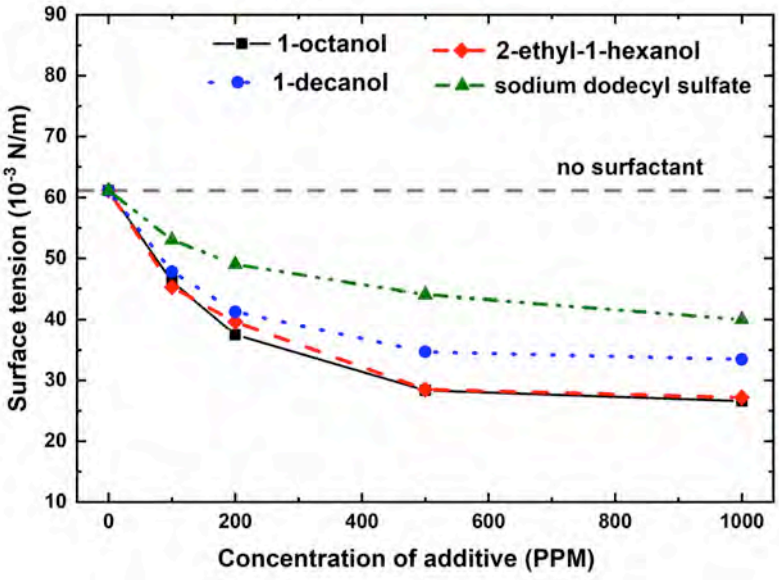

Figure 6: Surface tension with four additives

Surfactants have very low diffusivity in ammonia-water due to the large size of their molecules. If a small amount of surfactant is added during absorption, the surfactant molecules which are dispersed randomly reduce the local surface tension. However, the surface tension in the bulk of ammonia-water solution is still high. This gradient in surface tension is the driving force for a secondary flow. Many such secondary flow patterns are initiated in the vicinity of surfactant molecules that increase interfacial interactions and enhances performance. In addition, the increase in wettability due to lower surface tension ensures better use of heat transfer area and potentially reduces maldistribution in the headers of microchannel heat exchangers.

5. CONCLUSIONS

This study provides surface tension data for ammonia-water solution with various surfactants. Up to 57% reduction in surface tension is observed with the addition of surfactants, which allows for Marangoni convection flows to be initiated. Based on the plateau value of surface tension, 500 PPM of 1-octanol and 2-ethyl-1-hexanol are the preferred additives. This work contributes towards understanding the enhancement mechanism in ammonia vapor absorption in the presence of surfactants, eventually leading to development of efficient and compact absorbers.

ACKNOWLEDGEMENTS

The authors acknowledge assistance from the Tribology and Surface Engineering Lab of Prof. Michael Varenberg at Georgia Institute of Technology in conducting the surface tension measurements. Help from Ye Qi is also acknowledged.

NOMENCLATURE

C	additive concentration by mass (PPM)	g	gravitational acceleration ($m \cdot s^{-2}$)
P_0	Laplace pressure (kPa)	P_t	total pressure (kPa)
R	principal radius of curvature (m)	x	ammonia concentration by mass (%)
z	height from reference (m)	Δ	difference (-)
ρ	density ($kg \cdot m^{-3}$)	σ	surface tension ($N \cdot m^{-1}$)

REFERENCES

Beutler, A., Greiter, I., Wagner, A., Hoffman, L., Schreier, S., Alefeld, G., 1996. Surfactants and fluid properties. International Journal of Refrigeration 19(5), 342-346.

Determan, M.D., Garimella, S., 2012. Design, fabrication, and experimental demonstration of a microscale monolithic modular absorption heat pump. Applied Thermal Engineering 47, 119-125.

Garimella, S., 2003. Innovations in energy efficient and environmentally friendly space-conditioning systems. Energy 28(15), 1593-1614.

Garimella, S., Keinath, C.M., Delahanty, J.C., Hoysall, D.C., Staedter, M.A., Goyal, A., Garrabrant, M.A., 2016. Development and demonstration of a compact ammonia–water absorption heat pump prototype with microscale features for space-conditioning applications. Applied Thermal Engineering 102, 557-564.

Goyal, A., Staedter, M.A., Hoysall, D.C., Ponkala, M.J., Garimella, S., 2017. Experimental evaluation of a small-capacity, waste-heat driven ammonia-water absorption chiller. International Journal of Refrigeration 79, 89-100.

Harkins, W., 1952. The Physical Chemistry of Surface Films. New York, Reinhold Pub.

Hoffmann, L., Greiter, I., Wagner, A., Weiss, V., Alefeld, G., 1996. Experimental investigation of heat transfer in a horizontal tube falling film absorber with aqueous solutions of LiBr with and without surfactants. International Journal of Refrigeration 19(5), 331-341.

Hoysall, D.C., Garimella, S., 2019. Investigation of a microchannel heat and mass exchanger for absorption systems. Applied Thermal Engineering 148, 650-661.

Inoue, T., Teruya, Y., Monde, M., 2004. Enhancement of pool boiling heat transfer in water and ethanol/water mixtures with surface-active agent. International Journal of Heat and Mass Transfer 47(25), 5555-5563.

Kang, Y.T., Akisawa, A., Kashiwagi, T., 1999. Visualization and model development of Marangoni convection in NH3–H2O system. International Journal of Refrigeration 22(8), 640-649.

Kang, Y.T., Kashiwagi, T., 2002. Heat transfer enhancement by Marangoni convection in the NH3–H2O absorption process. International Journal of Refrigeration 25(6), 780-788.

Kashiwagi, T., 1985. THe activity of surfactant in high performance absorber and absorption enhancement. Refrigeration 60, 72-79.

Kashiwagi, T., 1988. Basic mechanism of absorption heat and mass transfer enhancement by the Marangoni effect. Newsletter IEA Heat Pupm Center 6(4), 2-6.

Kim, J.-K., Jung, J.Y., Kim, J.H., Kim, M.-G., Kashiwagi, T., Kang, Y.T., 2006. The effect of chemical surfactants on the absorption performance during NH3/H2O bubble absorption process. International Journal of Refrigeration 29(2), 170-177.

Kim, J.-K., Jung, J.Y., Kang, Y.T., 2007. Absorption performance enhancement by nano-particles and chemical surfactants in binary nanofluids. International Journal of Refrigeration 30(1), 50-57.

Kim, K.J., Berman, N.S., Wood, B.D., 1996. The interfacial turbulence in falling film absorption: effects of additives. International Journal of Refrigeration 19(5), 322-330.

Kulankara, S., Herold, K.E., 2000. Theory of Heat/Mass Transfer Additives in Absorption Chillers. HVAC&R Research 6(4), 369-380.

Möller, R., Knoche, K.F., 1996. Surfactants with NH_3-H_2O. International Journal of Refrigeration 19(5), 317-321.

Nagavarapu, A.K., Garimella, S., 2011. Design of Microscale Heat and Mass Exchangers for Absorption Space Conditioning Applications. Journal of Thermal Science and Engineering Applications 3(2), 021005-021005-021009.

Staedter, M.A., Garimella, S., 2018. Direct-coupled desorption for small capacity ammonia-water absorption systems. International Journal of Heat and Mass Transfer 127, 196-205.

Stauffer, C.E., 1965. The Measurement of Surface Tension by the Pendant Drop Technique. The Journal of Physical Chemistry 69(6), 1933-1938.

Ware, G., 1928. Surface tension of liquid ammonia and adsorption studies at its liquid vapor interface, Kansas State Agricultural College.

Manuscript ID: 1174
DOI: 10.18462/iir.icr.2019.1174

Boiling heat transfer of new zeotropic mixtures

Arianna BERTO[(a)], Costantino GUZZARDI[(a)], Marco AZZOLIN[(a)], Stefano BORTOLIN[(a)], Davide DEL COL[(a)]

[(a)] University of Padova – Department of Industrial Engineering
Padova, 35131, Italy, davide.delcol@unipd.it

ABSTRACT

The aim of the present work is to investigate the heat transfer performance of non-azeotropic ternary low global warming potential (GWP) mixtures when vaporizing inside two channels: a 8,0 mm inner diameter tube and a 0,96 mm inner diameter channel. The tested mixtures are R455A, which is a ternary blend of R32, R1234yf and R744 (21,5/75,5/3,0% by mass composition), and R452B, which is a ternary blend of R32, R1234yf and R125 (67,0/26,0/7,0% by mass composition). While R455A presents a GWP value equal to 146 and a temperature glide of about 10 K, R452B is characterized by higher GWP (equal to 676) but lower temperature glide (about 1 K). Results demonstrate that an increased temperature glide leads to higher mass transfer resistance which penalizes the heat transfer of the zeotropic mixtures during vaporization and must be taken into account when extending available correlations developed for pure fluids to non-azeotropic blends.
Keywords: Boiling, Heat Transfer Coefficient, Low GWP, Zeotropic Mixture.

1. INTRODUCTION

In recent years, refrigeration and air-conditioning industries have been strongly affected by national and international regulations on environmental protection and global warming. The F-gas Regulation (EU) No 517/2014 imposed the gradual phase-down of hydrofluorocarbons (HFCs), leading to a 80% cut of HFCs sales within 2030. The 28th Meeting of the Parties to the Montreal Protocol held in Kigali (Rwanda) established HFCs phase-out targets by 2040s. In order to find suitable replacement refrigerants, increasing attention has been addressed to mixtures of hydrofluoroolefins (HFOs, such as R1234ze(E) and R1234yf) and hydrofluorocarbons (HFCs).
Experimental works carried out with the aim to investigate the flow boiling characteristics of non-azeotropic mixtures of HFCs and HFOs are limited in the literature. Lillo et al. (2018) recently investigated the flow boiling heat transfer performance of R452A, which is a ternary non-azeotropic blend of R32, R125 and R1234yf at 11,0/59,0/39,0% by mass composition with a temperature glide of about 3 K, inside a 6,0 mm inner diameter channel. The heat transfer coefficients of the mixture were found to be dependent on heat flux and mass velocity. Azzolin et al. (2016) carried out experimental vaporization tests using a R32/R1234ze(E) mixture at 50,0/50,0% mass composition inside a 0,96 mm minichannel. The tested mixture displayed lower heat transfer coefficients with respect to pure fluids due to the additional mass transfer resistance caused by the different volatility of the components. This heat transfer degradation was also shown by the work of Li et al. (2012), who experimentally investigated the flow boiling heat transfer performance of binary mixtures of R32 and R1234yf at two different mass compositions (80,0/20,0% and 50,0/50,0%) inside a 2,0 mm inner diameter tube. The heat transfer coefficients of the blends at the two concentrations were found to be respectively 20-50% lower than those of pure fluid R32. Kondou et al. (2013) experimentally and theoretically studied the flow boiling of R32/R1234ze(E) blends inside a horizontal microfin tube of 5,21 mm inner diameter. A predicting correlation that considers the thermal resistance in the vapor phase due to the temperature glide and the boiling heat transfer degradation caused by the decrease in the effective superheat was proposed by the authors, showing good agreement with experimental data. Local heat transfer measurements during flow boiling of three low GWP HFOs/HFCs mixtures inside a horizontal microfin tube of hydraulic diameter equal to 5,45 mm were performed by Kedzierski and Kang (2016). They tested the mixtures R448A (R32/R125/R134a/R1234ze/R1234yf at 26,0/26,0/21,0/7,0/20,0%), R449A (R32/R125/R134a/R1234yf at 24,3/24,7/25,7/25,3%) and R452B (R32/R125/R1234yf at 67,0/7,0/26,0%). Mixture R452B exhibited the highest heat transfer

coefficient, due to the smaller temperature glide. An existing flow boiling correlation was modified for multi-component mixtures, predicting 98% of the measurements within ±20%.
The present study aims at investigating the flow boiling heat transfer performance of two ternary low-GWP non-azeotropic mixtures, named R455A and R452B, when vaporizing inside a 8,0 mm and a 0,96 mm inner diameter channels. The effect of vapor quality, heat flux, mass velocity, mean saturation temperature, mass composition and channel diameter on the heat transfer coefficient of the blends is investigated. The present experimental database is then compared against some correlations available in the literature.

2. EXPERIMENTAL APPARATUS

Experimental tests have been performed on two distinct test sections available at the Two-phase Heat Transfer Laboratory of the University of Padova and designed respectively for heat transfer measurements in a 8,0 mm and in a 0,96 diameter channel. Due to the different mass flow rate involved, each test section is installed in a dedicated experimental apparatus and consists of two tube-in-tube heat exchangers: the pre-conditioning sector and the measuring sector where the heat transfer coefficient is measured. Both the facilities present a similar layout consisting of a primary refrigerant loop and three auxiliary water loops (Fig. 1). In the primary loop, the subcooled refrigerant is sent by a magnetic-driven gear pump to the test section where it is heated and vaporized using hot water as secondary fluid. After the test section, the refrigerant enters in the post-condenser, where it is fully condensed and subcooled.

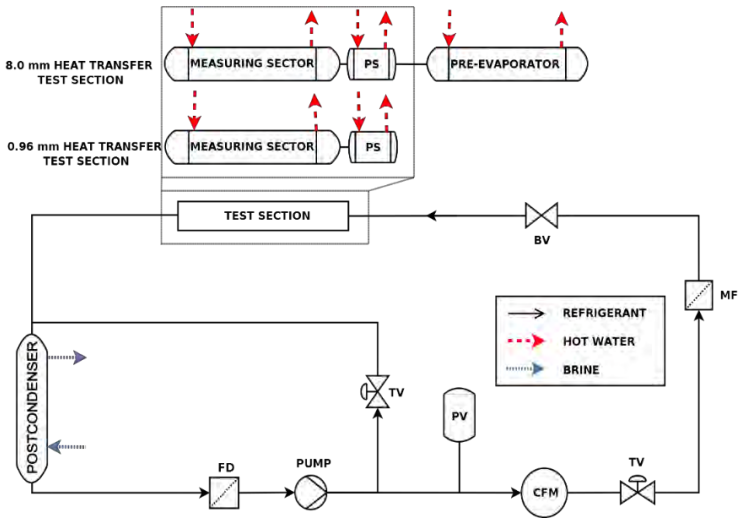

Figure 1: Layout of the two experimental test rigs: PS pre-conditioning sector, PV pressure vessel, MF mechanical filter, TV valve, CFM Coriolis-effect mass flow meter, FD filter drier, BV ball valve

In the case of the setup for the 8,0 mm diameter channel, a tube-in-tube pre-evaporator is employed to set the thermodynamic conditions (i.e. the vapor quality) at the inlet of the test section. The refrigerant loop is provided with a Coriolis-effect mass flow meter, while magnetic type flow meters are employed in the hot water circuits to measure the mass flow rates. The water temperature differences in the different sections are determined using triple junction copper-constantan thermopiles inserted into the corresponding mixing chambers while the inlet water temperatures are measured with copper-constantan (type T) thermocouples. Two pressure transducers (absolute and differential) are connected to manometric taps to measure the vapor pressure upstream and downstream of the test section. The heat transfer coefficient is obtained by measuring the heat flow rate exchanged (from the water side), the refrigerant temperatures at the inlet and outlet of the test section (by means of thermocouples inserted into the refrigerant flow, located in adiabatic sectors) and the wall temperatures at the inlet and outlet of the vaporization sector (by means of T-type thermocouples embedded in the tube wall at the two ends of the test section). Detailed description of the experimental apparatus and data reduction procedure is reported in Del Col (2010).
In the case of the 0,96 mm channel, the test section has been designed to allow precise measurements of the water temperature profile (by means of fifteen thermocouples) which is in turn

used for the determination of local heat flux and, hence, of the local heat transfer coefficient. Coriolis-effect mass flow meters are employed for both the refrigerant and the hot water loops. In the hot water circuits, copper-constantan thermocouples and triple junction thermopiles are used to measure the water inlet temperatures and the temperature differences. Wall temperatures are directly measured along the test section through thirteen T-type thermocouples embedded in the tube wall, while refrigerant temperatures are determined from the local pressure and the local specific enthalpy. Along the measuring section, the local pressure is obtained starting from the pressure measured at the inlet and outlet of the test section, as reported in Azzolin et al. (2016). The local vapor quality is obtained from the local pressure and the specific enthalpy. A complete description of the setup and data reduction can be found in Azzolin et al. (2016).
For the presented experimental database, the average experimental uncertainty of the heat transfer coefficient is equal to 4,7%. A complete description of the followed procedure is reported in Azzolin et al. (2016).

3. MIXTURE COMPOSITION

Flow boiling tests have been performed with the ternary low $GWP_{100\text{-years}}$ non-azeotropic mixtures R455A and R452B. R455A is a blend of R1234yf, R32 and R744 at 75,5/21,5/3,0% by mass composition and can be employed for commercial refrigeration in low temperature applications for replacing R404A due to comparable volumetric cooling capacity. R452B is composed of R1234yf, R32 and R125 at 26,0/67,0/7,0% by mass composition and is suitable for air conditioning and heat pump applications as substitute for R410A. Both these blends belong to the ANSI/ASHRAE A2L class. In Table 1, thermodynamic and transport properties of the tested refrigerant blends are reported and compared to those of the main pure fluid components R32, R1234yf and R125. Properties are computed using NIST Refprop 9.1 (Lemmon et al., 2013).

Table 1. Properties of saturated R32, R1234yf, R125, R455A and R452B calculated using Refprop 9.1 (Lemmon et al., 2013) at pressure corresponding to 10,5 °C mean saturation temperature.

Fluid	R32	R1234yf	R125	R455A	R452B
$GWP_{100\text{-years}}$	677	<1	3170	146	676
$p_{saturation}$ (bar)	11,23	4,44	9,22	8,1	10,4
ρ_l (kg m^{-3})	1017,8	1142,4	1268,9	1111,8	1055,2
ρ_g (kg m^{-3})	30,7	24,65	58,46	35,16	34,61
ρ_l/ρ_g (-)	33,15	46,34	21,71	31,62	30,49
μ_l (μPa s)	133,88	183,41	175,23	162,27	137,17
λ_l (W m^{-1} K^{-1})	0,137	0,068	0,065	0,086	0,113
T_{bubble} (°C)	-	-	-	4,78	9,93
Glide (K)	-	-	-	11,49	1,15

The ternary mixture R455A is characterized by low $GWP_{100\text{-years}}$ value (equal to 146), but high temperature difference between the dew and the bubble point (equal to about 11,5 K). Instead, the mixture R452B presents $GWP_{100\text{-years}}$ value equal to 676 and a temperature glide of 1,15 K.

4. FLOW BOILING RESULTS

In Figs. 2 and 3 the heat transfer coefficients measured inside the 8,0 mm inner diameter tube with R455A and R452B are reported at two different mean saturation temperatures, for mass velocity G = 200 kg m^{-2} s^{-1} and heat flux q' within the range 14-17 kW m^{-2}. The heat transfer performance of the two blends is not significantly affected by the saturation temperature variations. This can be due to the competition between nucleate boiling, which may be enhanced by the higher saturation temperature, and the convective boiling contribution, which increases at lower temperature and higher vapour quality.
In Fig. 4 the heat transfer coefficients of mixtures R455A and R452B measured inside the 8,0 mm channel are reported versus vapour quality at mass velocities G equal to 200 and 400 kg m^{-2} s^{-1}, mean saturation temperature equal to 10,5 °C and heat flux between 14 and 17 kW m^{-2}. The heat transfer coefficients of both R455A and R452B become higher when increasing the mass velocity.

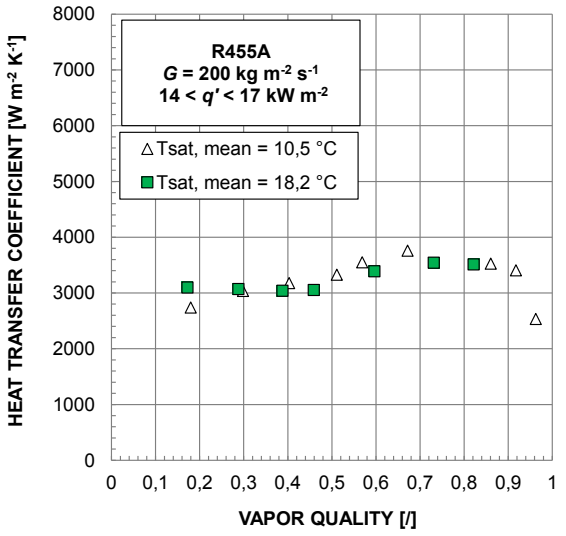

Figure 2: Experimental heat transfer coefficients of R455A inside the 8 mm channel, at G = 200 kg m^{-2} s^{-1}, heat flux 14 < q' < 17 kW m^{-2} and mean saturation temperatures equal to 10,5 and 18,2 °C

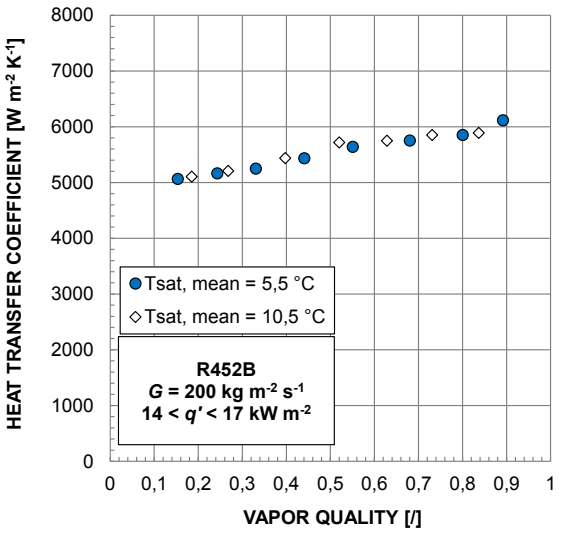

Figure 3: Experimental heat transfer coefficients of R452B inside the 8 mm channel, at G = 200 kg m^{-2} s^{-1}, heat flux 14 < q' < 17 kW m^{-2} and mean saturation temperatures equal to 5,5 and 10,5 °C

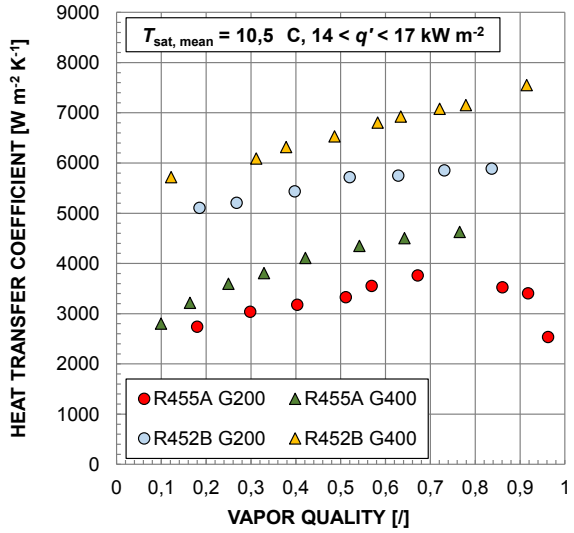

Figure 4: Experimental heat transfer coefficients of R455A and R452B inside the 8 mm channel, at mass velocity G = 200-400 kg m^{-2} s^{-1}, heat flux 14 < q' < 17 kW m^{-2} and mean saturation temperature equal to 10,5 °C

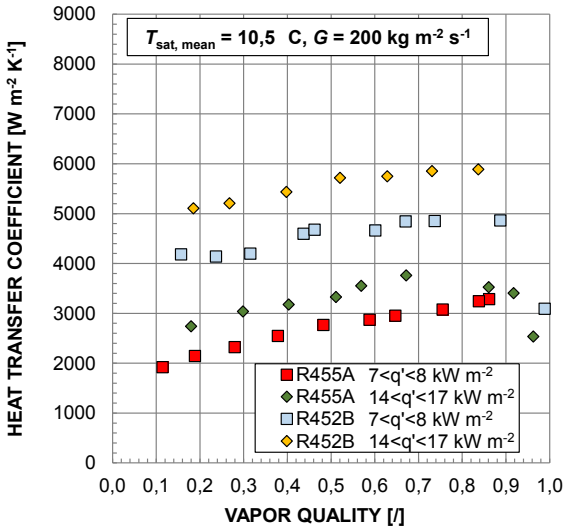

Figure 5: Experimental heat transfer coefficients of R455A and R452B inside the 8 mm channel, at mass velocity G = 200 kg m^{-2} s^{-1}, mean saturation temperature equal to 10,5 °C and heat flux 14 < q' < 17 kW m^{-2}

Comparing the performance of the two blends, R452B displays higher heat transfer coefficients due to the greater fraction of R32, which leads to an increase in the liquid thermal conductivity. It is also worth pointing out that R452B is characterized by a lower temperature glide compared with R455A. Fig. 5 reports the heat transfer coefficients of mixtures R455A and R452B measured inside the 8,0 mm channel at two different heat fluxes, mass velocity G equal to 200 kg m^{-2} s^{-1} and mean saturation temperature equal to 10,5 °C. The effect of the heat flux on the heat transfer coefficient is higher for the mixture R452B compared to R455A. This can be explained considering the physical phenomena which characterize the flow boiling heat transfer with non-azeotropic mixtures. As the blend is heated, the more volatile component (for both the mixtures, R32) evaporates faster than the less volatile one (R1234yf). This leads to a change in the composition of the liquid and vapor phases, introduces a concentration gradient at the interface and rises the bubble point. Furthermore heat has

to be supplied for sensible heating of the liquid and vapor phases in addition to the heat for evaporation. The high-temperature glide mixture, due to the mass diffusion resistance and to the greater sensible heat, shows a reduced increase of the heat transfer coefficient with heat flux, if compared to the low-temperature glide mixture. It is also interesting to notice that for both the blends the dry-out inception is delayed at the lower heat fluxes.

In Fig. 6 experimental heat transfer coefficients of ternary mixture R455A inside the 0,96 mm and the 8,0 mm inner diameter channels are compared at fixed heat flux, 30 °C mean saturation temperature and mass velocity G = 300 kg m^{-2} s^{-1}. For vapor quality lower than 0,5, the heat transfer coefficient in the small diameter channel is higher than the one measured in the 8,0 mm channel. It tends to decrease with vapor quality: this behaviour was found also for a R32/R1234ze(E) blend by Azzolin et al. (2016). In the 8,0 mm test section, the heat transfer coefficient of R455A is approximately constant for all vapor quality range. This is probably due to the fact that nucleate boiling is the dominant heat transfer mechanism in these conditions. In Fig. 7 the heat transfer coefficients measured inside the 0,96 mm diameter minichannel with R455A and pure fluid components R1234yf and R32 are reported against heat flux, at mean saturation temperature equal to 30 °C and vapor quality x between 0,15 and 0,25. The heat transfer coefficient of R1234yf and R32 increases significantly with the heat flux; for R455A the heat transfer coefficient rises with heat flux but to a lower extent compared to pure components. From Fig. 7, it can also be noticed that, at a fixed heat flux, R455A shows the lowest heat transfer coefficients compared to pure fluids components and this must be due to the high temperature glide (about 11 K) and the associated mass transfer resistance during flow boiling.

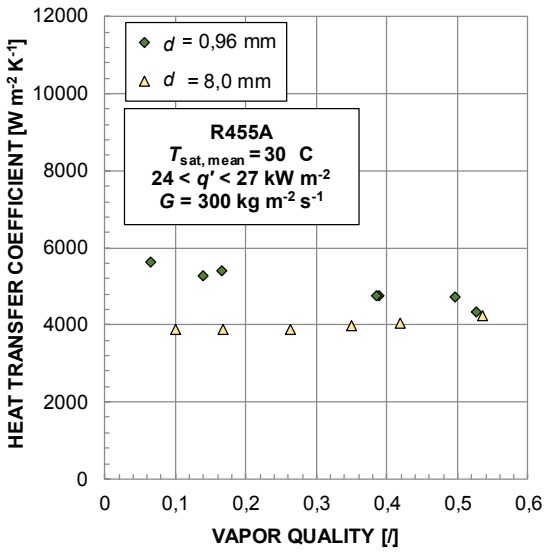

Figure 6: Heat transfer coefficients of R455A in the 0,96 mm and 8 mm diameter channels at mean saturation temperature equal to 30 °C, heat flux 24 < *q'* < 27 kW m^{-2} and mass velocity *G* = 300 kg m^{-2} s^{-1}

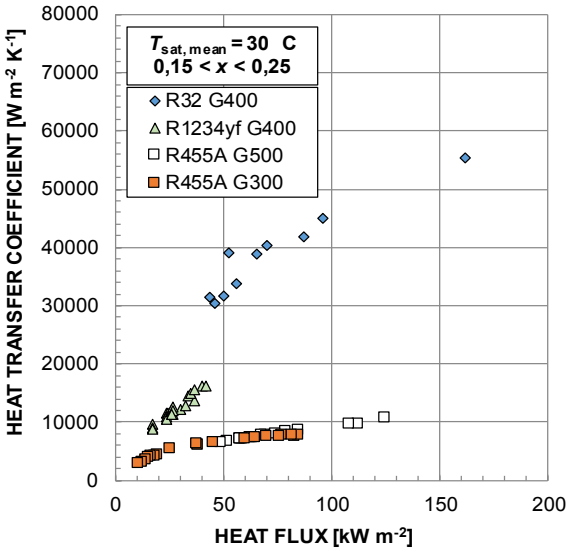

Figure 7: Heat transfer coefficients of R455A and its components R32 and R1234yf inside the 0,96 mm diameter channel at different mass velocities *G*, mean saturation temperature equal to 30 °C and vapour quality *x* between 0,15 and 0,25

5. COMPARISON AGAINST MODELS

Experimental data of mixtures R455A and R452B taken inside the 8.0 mm diameter channel have been compared against predictions from the Gungor and Winterton (1986) and the Sun and Mishima (2009) correlations. The Gungor and Winterton (1986) model was developed for saturated boiling in horizontal and vertical tubes with internal diameter between 2.95 and 32 mm. The heat transfer coefficient evaluated with the correlation (Eq. 1) is the sum of the pool boiling term, multiplied by a suppression factor S, and the heat transfer coefficient of the liquid phase flowing alone in the tube multiplied by an enhancement factor E.

$$\alpha = \alpha_{nb} S + \alpha_l E \qquad \text{Eq. (1)}$$

This correlation predicts the present experimental database with a mean absolute deviation equal to 16,6% and a standard deviation equal to 24,3% (for R455A e_{AB} = 23,1% and σ_N =33,8%, for R452B e_{AB} = 10,0% and σ_N = 14,8%).
Sun and Mishima (2009) assumed that nucleate boiling is the dominant mechanism but introduced also the dependence of heat transfer coefficient on the Weber number for the liquid phase, developing a flow boiling correlation for horizontal and vertical channels (Eq. 2).

$$\alpha = \frac{6\,\mathrm{Re}_{lo}^{1.05}\,\mathrm{Bo}^{0.54}}{\mathrm{We}_{lo}^{0.191}\left(\frac{\rho_l}{\rho_g}\right)^{0.142}}\frac{\lambda_l}{d} \qquad \text{Eq. (2)}$$

On the whole, the Sun and Mishima (2009) equation overestimates the present experimental database with a mean absolute deviation equal to 23,4% and a standard deviation equal to 29,3% (for R455A e_{AB} = 36,8% and σ_N = 37,3%, for R452B e_{AB} = 9,9% and σ_N =21,3%).
The previous correlations have been developed for pure fluids or near azeotropic mixtures. In this paper, they are applied to mixtures R452B and R455A employing the thermodynamic and transport properties of the mixtures but neglecting the additional mass transfer resistance. As previously stated, this leads to general inaccurate predictions of the heat transfer coefficient. To improve the predictions of the considered correlations, the degradation of the heat transfer coefficient due to the additional mass transfer resistance should be properly accounted for. The Gungor and Winterton (1986) model can be modified following the method by Shah (2014), applying two well-known correction factors, one for pool boiling in the nucleate boiling region and the other one for the convective boiling region. To account for the effect of the mass transfer resistance on bubble nucleation, the Thome and Shakir (1987) factor F_c is employed:

$$F_c = \left[1+\left(\frac{\alpha_{fb}\,\Delta T_{GL}}{q'}\right)\left(1-e^{-\left(\frac{Bq'}{\rho_l \Delta h_m \beta_l}\right)}\right)\right] \qquad \text{Eq. (3)}$$

where α_{fb} is calculated using the Cooper (1984) correlation for pool boiling. The heat transfer during convective boiling of blends involves sensible heating of the mixture and mass transfer resistance in the liquid and vapor. Due to the fact that the convective phenomena involved during condensation and flow boiling are similar, the Bell and Ghaly (1973) correction can be applied to flow boiling models as reported in Eq. (4):

$$\alpha_m = \left(\frac{1}{\alpha_f} + \frac{\partial q_{sg}/\partial q_t}{\alpha_g}\right)^{-1} \qquad \text{Eq. (4)}$$

where α_f is the heat transfer coefficient calculated from a flow boiling equation, α_g is the convective heat transfer coefficient of the vapor phase, $\partial q_{sg}/\partial q_t$ is the ratio between the sensible heat flow rate heating the vapor and the total heat flow rate. This ratio can be approximated as:

$$\frac{\partial q_{sg}}{\partial q_t} \approx x\,c_{pg}\,\frac{\Delta T_{GL}}{\Delta h_m} \qquad \text{Eq. (5)}$$

The correction terms proposed by Shah (2014) for non-azeotropic mixtures are applied to Gungor and Winterton (1986) model as indicated in the following equation:

$$\alpha_m = F_c\alpha_{nb}S + \left(\frac{1}{\alpha_l E} + \frac{\partial q_{sg}/\partial q_t}{\alpha_g}\right)^{-1} \qquad \text{Eq. (6)}$$

For the Sun and Mishima (2009) model, which considers only the nucleate boiling contribution, the heat transfer coefficient can be calculated applying only the Thome and Shakir (1973) correction to the boiling number Bo in Eq. (2).

The heat transfer coefficients evaluated with the two correlations corrected for blends are reported in Figs. 8 and 9. An improvement in the prediction accuracy has been found for both the models: the Sun and Mishima (2009) correlation is able to predict the whole presented experimental database with a mean absolute deviation e_{AB} = 10,9% and a standard deviation σ_N = 23,9% (for R455A e_{AB} = 13,0% and σ_N = 27,2%, for R452B e_{AB} = 8,7% and σ_N = 20,6%). For the Gungor and Winterton (1986) model, the mean absolute deviation is equal to 14,0%, with a standard deviation of 22,6% (for R455A e_{AB} = 14,9% and σ_N = 30,5%, for R452B e_{AB} = 13,1% and σ_N = 14,7%). In particular, the effect of the correction is more appreciable for mixture R455A due to the dependence of F_c and of the Bell and Ghaly (1973) correction on the temperature glide of the mixture, which is high (around 11 K).

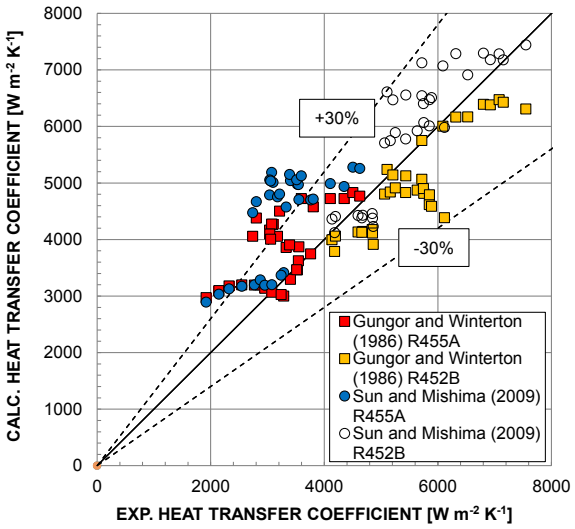

Figure 8: Experimental data compared to Gungor and Winterton (1986) and Sun and Mishima (2009) models, without correction for blends

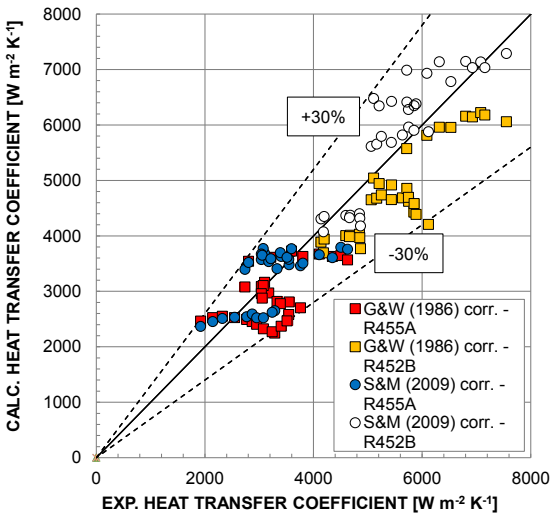

Figure 9: Experimental data compared to Gungor and Winterton (1986) and Sun and Mishima (2009) models, corrected for blends

6. CONCLUSIONS

In the present paper, the flow boiling heat transfer performance of two low-GWP non-azeotropic mixtures inside a 8,0 mm and a 0,96 mm inner diameter channels is investigated. The tested fluids are R455A, ternary blend of R32, R1234yf and R744 at 21,5/75,5/3,0% by mass composition, and R452B, mixture of R32, R1234yf and R125 at 67,0/26,0/7,0% by mass composition. For both the blends the heat transfer coefficients are found to increase with heat flux and mass velocity, while the effect of the mean saturation temperature is negligible. The heat transfer coefficients of R452B are higher in comparison with those of R455A due to the lower temperature glide and higher liquid thermal conductivity. The Sun and Mishima (2009) and Gungor and Winterton (1986) flow boiling models, developed for pure fluids, are selected for comparing their predictions with experimental data. The penalization of the heat transfer coefficient due to the additional mass transfer resistance is important only for the high temperature glide mixture (R455A) and it can be accounted for by applying the Bell and Ghaly (1973) correction together with the Thome and Shakir (1987) correction factor for nucleate boiling F_c, as suggested by Shah (2014). The Sun and Mishima (2009) and the Gungor and Winterton (1986) correlations, corrected for blends, are able to predict the present experimental database with a mean absolute deviation of about 10,9% and 14,0%, respectively.

ACKNOWLEDGEMENTS

The authors acknowledge the financial support of the MIUR through the PRIN 2015 project “Clean Heating and Cooling Technologies for an Energy Efficient Smart Grid”.

NOMENCLATURE

B	scaling factor in Eq. (3) (-)	p	pressure (bar)
Bo	boiling number (-)	q	heat flow rate (W)

c_p	isobaric specific heat (J kg^{-1} K^{-1})	q'	heat flux (W m^{-2})
d	hydraulic diameter (m)	Re	Reynolds number (-)
E	enhancement factor in Eq. (1) (-)	S	suppression factor in Eq. (1) (-)
e_{AB}	absolute deviation (%)	T	temperature (°C)
F_c	mixture correction factor (-)	We	Weber number (-)
G	mass velocity (kg m^{-2} s^{-1})	x	thermodynamic vapor quality (-)

Greek symbols

α	heat transfer coefficient (W m^{-2} K^{-1})	λ	thermal conductivity (W m^{-1} K^{-1})
β	mass transfer coefficient (m s^{-1})	μ	dynamic viscosity (Pa s)
Δh	enthalpy difference (J kg^{-1})	ρ	density (kg m^{-3})
ΔT	temperature difference (K)	σ_N	standard deviation (%)

Subscripts

f	film	*m*	mixture
fb	flow boiling	*nb*	nucleate boiling
g	vapor	*s*	sensible
GL	glide	*sat*	saturation
l	liquid	*t*	total
lo	liquid only		

REFERENCES

Azzolin, M., Bortolin, S., Del Col, D., 2016. Flow boiling heat transfer of a zeotropic binary mixture of new refrigerants inside a single microchannel. Int. J. Thermal Sciences 110, 83-95.

Bell, K.J., Ghaly, M.A., 1973. An approximate generalized design method for multicomponent/partial condenser. AIChE Symposium Series 69, 72-79.

Cooper, M.G., 1984. Heat flow rates in saturated nucleate pool boiling - A wide ranging examination using reduced properties. Advances in Heat Transfer 16, 157-239.

Del Col, D., 2010. Flow boiling of halogenated refrigerants at high saturation temperature in a horizontal smooth tube. Exp. Thermal and Fluid Science 34, 234-245.

Gungor, K.E., Winterton, R.H.S., 1986. A general correlation for flow boiling in tubes and annuli. Int. J. Heat and Mass Transfer 29(3), 351-358.

Kedzierski, M.A., Kang, D., 2016. Horizontal convective flow boiling of R448A, R449A, and R452B within a micro-fin tube. Science and Technology for the Built Environment 22(8), 1090-1103.

Kondou, C., BaBa, D., Mishima, F., Koyama, S., 2013. Flow boiling of non-azeotropic mixture R32/R1234ze(E) in horizontal microfin tubes. Int. J. of Refrigeration 36, 2366-2378.

Lemmon, E.W., Huber, M.L., McLinden, M.O., 2013. NIST Standard Reference Database 23: Reference Fluid Thermodynamic and Transport Properties – REFPROP, Version 9.1, Gaithersburg.

Li, M., Dang, C., Hihara, E., 2012. Flow boiling heat transfer of HFO1234yf and R32 refrigerant mixtures in a smooth horizontal tube: Part I. Experimental investigation. Int. J. Heat and Mass Transfer 55, 3437-3446.

Lillo, G., Mastrullo, R., Mauro, W.A., Viscito, L., 2018. Flow boiling data of R452A. Energy Procedia 148, 1034-1041.

Shah, M.M., 2014. Evaluation of a method for predicting heat transfer during boiling of mixtures in plain tubes. Proceedings of the 15th International Heat Transfer Conference, Kyoto, Japan.

Sun, L., Mishima, K., 2009. An evaluation of prediction methods for saturated flow boiling heat transfer in mini-channels. Int. J. Heat and Mass Transfer 52(23-24), 5323-5329.

Thome, J.R., Shakir, S., 1987. A new correlation for nucleate boiling of aqueous mixtures. AIChE Symposium Series 83(257), 46-57.

Manuscript ID: 1178
DOI: 10.18462/iir.icr.2019.1178

A multilayer desiccant dehumidification system

Hirofumi DAIGUJI[(a)], Jubair A. SHAMIM[(a)], Wei-Lun HSU[(a)], Soumyadeep PAUL[(a)]

[(a)]Department of Mechanical Engineering, The University of Tokyo
Tokyo, 113-8656, Japan, daiguji@thml.t.u-tokyo.ac.jp

ABSTRACT

A multilayer sheet type solid desiccant dehumidifier was constructed performing distinguished adsorption capacity and water removal efficiency. Micro sphere silica gel (M. S. Gel) with a pore diameter of 2.7 nm manufactured by AGC Si-Tech. Co., Ltd., Japan, was adopted as adsorbent that the characterized regeneration temperature was below 60 degree Celsius. The micron-sized desiccant particles were confined between metal mesh sheets without polymer binder elevating the water uptake capability. Instead of conventional honeycomb structure of the flow channels, the multilayered slit bed effectively lowered the fan power required to operate the process air. The device performance is evaluated by analyzing the dynamic heat and mass transfer characteristics during the adsorption and regeneration processes at various supply air conditions and desiccant bed thicknesses, demonstrating itself as a competitive alternative to existing solid desiccant dehumidifiers.
Keywords: Multilayer Desiccant Dehumidifier, Heat and Mass Transfer, Adsorption, Desorption.

1. INTRODUCTION

The building sector accounts for approximately 30% of the total electricity consumption in the world (Ürge-Vorsatz et al., 2015). The fraction is estimated to increase by 60% in 2050 compared to that in 2007 (Tanaka, 2011). As a mutual target across the globe, recently the concept of Net Zero Energy Building (NZEB) has emerged rapidly worldwide (Wells et al., 2018) for reducing the overall electricity consumption by the buildings. A next step toward the realization of the NZEB will be the development of highly efficient heat pump system, since space cooling or heating is one of the highest consumers of electricity in the buildings globally. Among plenty of proposed energy efficient heat pump systems in the literature, the desiccant based evaporative cooling (DEC), also known as hybrid air-conditioning when combined with a traditional vapor compression system, was ranked within the top five by the U.S. Department of Energy (DoE) based on its energy saving potential (Goetzler et al., 2014). Consequently, significant efforts have been made by the researchers in the past decade to advance this technology for both solid and liquid desiccant dehumidifiers.

Solid desiccant dehumidifiers can be briefly classified into the following four categories: (i) packed bed, (ii) fluidized bed, (iii) rotary desiccant wheel, and (iv) desiccant coated heat exchanger (DCHE). However, rotary desiccant wheels gained much attention over both the packed bed and fluidized bed dehumidifiers owing to its relatively lower pressure drop, excellent dehumidification capacity and their ability to provide uniform outlet humidity as well as continuous cycle operation without changing cycles between the adsorption and desorption processes. Despite that the rotary desiccant wheels have showed much improved performance compared to their ancestors, two major drawbacks deteriorating in this system are (Li et al., 2015): (i) they cannot be operated in an isothermal manner that the outlet air temperature rises by the release of heat of adsorption limiting the dehumidification capacity and (ii) irreversibility and high heat loss occurring during the heat transfer from the high temperature regeneration air to desiccant particles. Being as a prospective solution to overcome these limitations, the concept of DCHE has been proposed and investigated (Vivekh et al., 2018), where the desiccant particles can be directly cooled or heated more efficiently by flowing cold or hot water though the desiccant particles coated fin tubes.

Albeit significant improvements have been achieved in terms of performance by both rotary desiccant wheel and DCHE systems, major concerns remained related to their engineering design, being (Shamim et al., 2019): (i) the airflow retardation caused by the presence of complex honeycomb structure in rotary wheel and by the densely spaced fin tubes (fin pitch 1.5 mm to 2.0 mm) in DCHE; (ii) the pore blockage originated from the polymer binders used to fix the desiccant particles onto the honeycomb structure or the fin tubes; (iii) the application of liquid solvents and high temperature, prolonged re-drying of desiccants during coating; (iv) the amount of desiccants that can be accommodated per unit volume, which is directly related to the large physical dimension and less compactness of the system.

In order to overcome the above criticalities of the existing solid desiccant systems, the concept of a multilayer fixed-bed, binder-free desiccant dehumidifier (MFBDD) was previously proposed by the authors and the transient heat and mass transfer characteristics of the device were evaluated experimentally for both adsorption (Shamim et al., 2018) and regeneration (Shamim et al., 2019) processes. In this study we summarize the key findings in these experimental results, presenting in a sequential order in section 4 and section 5. The dynamic heat and mass transfer characteristics of the MFBDD system during both adsorption and desorption were evaluated experimentally by varying inlet air conditions and desiccant bed thicknesses. The comparison of the pressure drop and dehumidification capacity between MFBDD system and other typical desiccant systems are shown in Table 1 and Table 2, respectively.

Table 1. Comparison of pressure drop between MFBDD system and other typical desiccant systems (Shamim et al., 2019)

Pressure drop, ΔP (Pa m^{-1})				
Desiccant Wheel	DCHE (air flow velocity approx. 1.1 m s^{-1} and fin pitch 2.0 mm)	Packed Bed	Fluidized Bed	MFBDD (air flow velocity 0.9 m s^{-1} and bed thickness 1.0 mm)
770 (approx. 154 Pa for 0.2 m wheel dia)	66 (approx. 20 Pa for 0.3 m fin length)	12897.70	8849.52	20 (approx. 4 Pa for 0.2 m sheet length)

Table 2. Comparison of average dehumidification capacity between MFBDD system, a typical rotary desiccant wheel and DCHEs (Shamim et al., 2019)

Parameters	MFBDD	Rotary Wheel	DCHE 1	DCHE 2
System dimension (mm)	length = 200 width = 10 height = 30	wheel dia = 350 wheel thk = 200	length = 380 width = 127.8 height = 380	length = 200 width = 150 tube dia = 9.525
Cycle duration (s)	600	Not applicable	599	543
Specific humidity of inlet air (g kg_{DA}^{-1})	16.5	16.2	16.37	-
Relative humidity of inlet air (%)	70-73%	Not mentioned	55.56% (at 31.99 °C)	75%
Approximated average dehumidification capacity (g kg_{DA}^{-1})	7.07 (8.67 for 300 s cycle duration)	5.2	5.12	5.0
Approximated maximum dehumidification capacity (g kg_{DA}^{-1})	12.0	Not applicable	7.08	13.0

2. EXPERIMENTAL

2.1. Multilayer Fixed-bed, Binder-free Desiccant Dehumidifier

In the MFBDD system, sheet-type desiccant beds (200 mm × 10 mm × 1 mm) were fabricated using stainless steel frame. Two stainless steel mesh having square voids of 72 μm × 72 μm were glued

to the steel frame. Since the average particle diameter was larger than the void size, desiccant particles could be dispersed between the two steel meshes without an adhesive. As a result, the dehumidification capacity was improved. Furthermore, the relatively large gap of 5.0 mm between two parallel desiccant sheets reduces the airflow restriction resulting in significantly lower pressure drop. The test facility including the MFBDD prototype that was developed at the University of Tokyo as shown in Fig. 1. The key components of the test facility are: a humidity controller to supply inlet air at desired humidity and temperature, air heater to supply hot air during regeneration, flow control valve and flow meter, humidity sensors, differential pressure gauge, thermocouples (K-type) and a constant temperature oven. The purpose of using the oven was twofold: (i) to control the ambient temperature of the test section and the desiccant particles; (ii) to minimize the heat loss from the hot regeneration air to the surroundings.

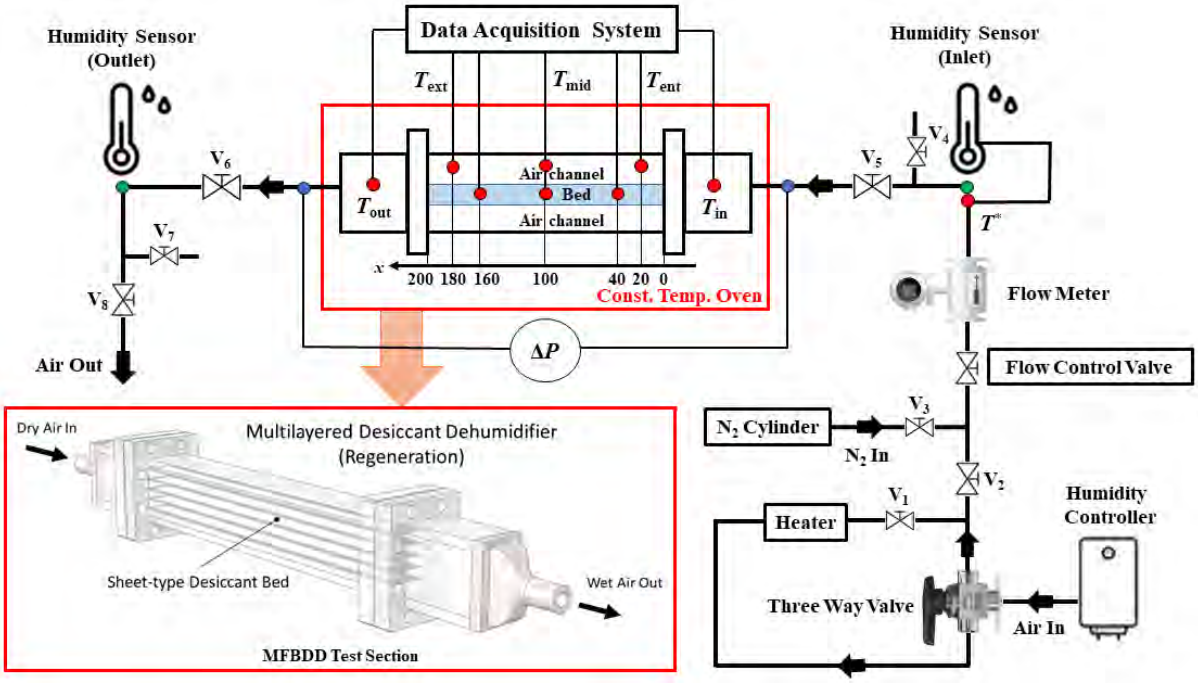

Figure1: Test facility constructed at The University of Tokyo (dimensions in mm) (Shamim et al., 2019).

2.2. Adsorption

The adsorption experiments were carried out at room temperature and in two steps (i.e. drying by N_2 and adsorption). At first the dry N_2 gas (relative humidity (RH) 0.0%) was passed over the desiccant beds and the RH of the N_2 gas at the outlet was monitored. At the beginning of drying, the RH at the outlet reached to as high as 40% due to transfer of water vapor from desiccant beds to dry N_2 gas. However, with time the amount of water in the beds was reduced and after one hour, the RH of N_2 gas at the outlet was dropped below 1.5%. At this condition, the desiccant beds were reasonably dry and adsorption was started by supplying humid air from the humidity controller.

2.3. Regeneration

The regeneration process was investigated separately involving six steps (i.e. drying by N_2, 1st adsorption, heating of desiccant particles in the oven, regeneration by hot air, cooling to the room temperature and 2nd adsorption). At first the desiccant beds were dried with N_2 gas (as described in section 2.2) and adsorption was carried out (1st adsorption) for 30 min. After the 1st adsorption approximately 2.0 g of water was accumulated in the beds, however the bed temperature was approached to the room temperature at the end of adsorption. Therefore, the convection oven was turned on to heat the desiccant particles and the bed temperature was raised to the same level of regeneration air temperature. During this period, there was no airflow in the test section. Simultaneously, the temperature of regeneration air was raised by the air heater. When the temperature of desiccant beds and hot air temperature reached to the desired value, regeneration was started. After that, the desiccant beds were cooled down to room temperature again and another

adsorption cycle was carried out (2nd adsorption) to understand how regeneration of the desiccant beds under different temperatures could affect the adsorption performance of the device in the following cycle.

3. PERFORMANCE INDICATORS

Dehumidification Capacity (ΔX_{ads}) / Moisture Gain (ΔX_{reg}): The dehumidification capacity and moisture gain during adsorption and desorption respectively $\Delta X_{ads/reg}$ were calculated as follows:

$$\Delta X_{\text{ads/reg}} = \left| X_{\text{out}} - X_{\text{in}} \right|_{\text{ads/reg}} \quad \text{Eq. (1)}$$

Here, X_{out} and X_{in} are the absolute humidity (g kg_{DA}^{-1}) measured by the humidity sensor at the outlet and inlet of MFBDD test section during experiments.

Degree of Bed Temperature Reduction during Regeneration (ΔT_{mid}^{bed}): The degree of bed temperature reduction at the middle (°C) with respect of regeneration air temperature was calculated as follows:

$$\Delta T_{\text{mid}}^{\text{bed}} = T_{\text{mid}}^{\text{bed}} - T_{\text{in(reg)}} \quad \text{Eq. (2)}$$

Here, T_{mid}^{bed} is the desiccant bed temperature (°C) recorded exactly at the middle of the desiccant sheet and $T_{in(reg)}$ is the temperature of regeneration air at the inlet (°C) of the test section.

Regeneration specific heat input (*RSHI*): *RSHI*, expressed in kJ kg^{-1}, is a measure of energy efficiency, and it can be calculated as follows (Shamim et al., 2019):

$$RSHI = \frac{C_{p,\text{air}}}{\Delta X_{\text{ads}}} \frac{\dot{m}_{\text{reg}}}{\dot{m}_{\text{ads}}} \left(T_{\text{in (reg)}} - T_{\text{room}} \right) \quad \text{Eq. (3)}$$

In the above equation, $C_{p,air}$ is the specific heat capacity of air, taken as 1.005 kJ kg^{-1} K^{-1}; $\dot{m}_{reg}/\dot{m}_{ads}$ is the ratio of the mass flow rate during the regeneration process to that during the adsorption process; ΔX_{ads} (kg kg_{DA}^{-1}) is the dehumidification capacity of the device in the subsequent adsorption cycle after regeneration; $T_{in(reg)}$ (°C) is the inlet air temperature of the regeneration process; and T_{room} (°C) is the temperature of room air that was heated and used for regeneration. Since, $\dot{m}_{reg}/\dot{m}_{ads}$ was equal to 1.0 in our experiment, the above equation represents the ratio of regeneration heat input to the dehumidification capacity achieved after regeneration. Thus, a lower value of *RSHI* indicates a higher dehumidification capacity obtained by lower regeneration heat input.

4. ADSORPTION EXPERIMENTS

The adsorption experiments were performed by varying the inlet air flow velocity, inlet air humidity, and desiccant bed thickness. The adsorption-desorption isotherm of M. S. Gel desiccants obtained by gravimetric measurement at 298.0 K is shown in Fig. 2(a). Note that, the M. S. Gel has a prone S-shape isotherm and the equilibrium water uptake capacity of M. S. Gel at 80% RH was close to 0.7 g g^{-1}, which is much higher compared to traditional silica gel or zeolite desiccants. The dehumidification capacity of the MFBDD prototype under varying inlet air flow velocity, inlet air humidity, and desiccant bed thickness are shown in Fig. 2(b) to (d) respectively. In Fig. 2(b) and (c), when the inlet air conditions were varied, where the desiccant bed thickness was kept constant at 1.0 mm. In Fig. 2(d), when the bed thickness was altered with consistent inlet air conditions.

It is indicated that a higher dehumidification capacity was obtained (i) when the flow velocity of inlet air became lower, (ii) when the humidity of inlet air increased and (iii) when the desiccant bed became thicker. At low velocity, the inlet air had longer residence time and thus better contact with the desiccant particles. At high humidity, the partial vapor pressure difference between the desiccant surface and flowing air was increased. Thus, in both cases the average dehumidification capacity of the device increased. However, in a thicker bed, it can be seen that the increment of dehumidification capacity was not linear. Specifically, when the bed thickness was increased from 1.0 mm to 2.0 mm, the dehumidification capacity did not improve that much compared to the case when the bed thickness was increased from 0.2 mm to 1.0 mm, indicating that, in a thicker bed, the adsorption at

the bottom layers was slower and did not contribute much towards the enhancement of overall dehumidification capacity. Thus, the thickness of the desiccant bed can be a parameter of optimization depending on how much dehumidification is required.

The transient change of desiccant bed and air temperature at different locations from inlet to outlet during the adsorption process is depicted in Fig. 2(e) and (f) respectively. It can be seen that due to adsorption heat release, both the desiccant bed and air temperature were increased, reached to a peak, and with time as the desiccant beds became soaked with water, these temperatures became minimal too. However, a gradual shift of peak bed temperature was observed with time (Fig. 2(e)), which implies that the mass transfer zone also shifted from inlet towards outlet as the adsorption progressed. The air temperature was maximum at the outlet, as the air flowed from inlet towards outlet, it carried out more heat from the desiccant bed by convection.

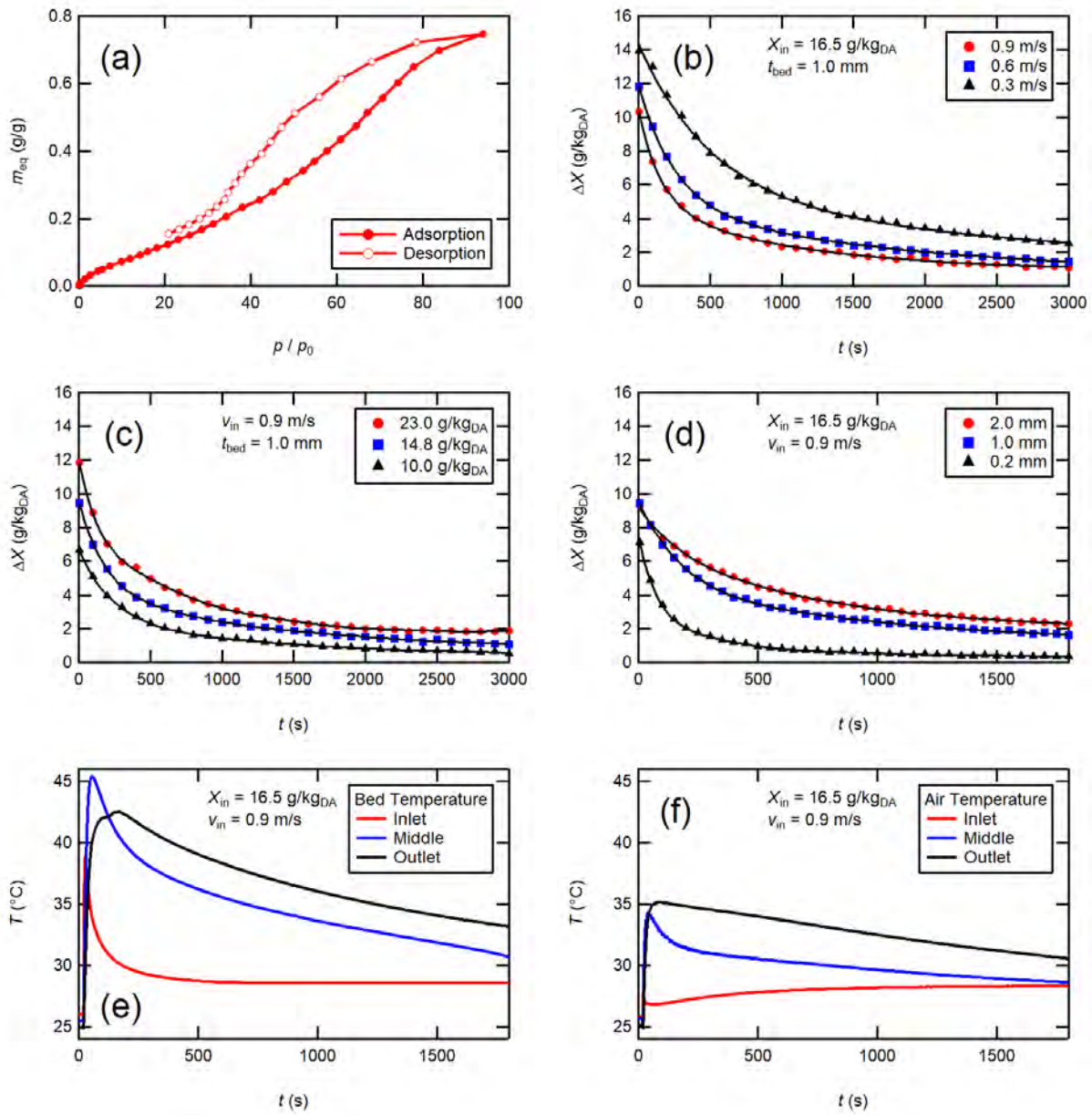

Figure 2: (a) Adsorption-desorption isotherm of M. S. Gel at 298.0 K. Transient change of dehumidification capacity with variation of (b) inlet air velocity; (c) inlet air humidity; (d) desiccant bed thickness. Transient change of temperature during adsorption from inlet towards outlet within (e) the desiccant bed; (f) airflow channel.

5. REGENERATION EXPERIMENTS

During regeneration, the enthalpy of hot air was consumed by the desiccant particles and as a result, both the desiccant bed and the air temperature at all locations from inlet towards outlet were decreased as shown in Fig. 3(a) and (b) respectively. Also note that like adsorption, the peak of reduced bed temperature shifted from inlet towards outlet during regeneration too due to the shifting of mass transfer zone with time. Once majority of the water from the beds were regenerated, consumption of enthalpy became smaller and both the bed and air temperature increased sharply. The slope of such sharp increment of bed and air temperature also varied from inlet towards outlet according to the mass of remaining water in different parts of the bed.

The moisture gain, degree of bed temperature reduction, subsequent dehumidification capacity during 2nd adsorption and regeneration specific heat input were also assessed under the influence of varying regeneration air temperature as shown in Fig. 3(c) to (f) respectively. An increase in regeneration air temperature led to a higher moisture gain (as more water could be desorbed) and higher degree of reduction of the desiccant bed temperature (Fig. 3(c) and (d) respectively). As a result, it was feasible to achieve a higher dehumidification capacity during the 2nd adsorption when the beds were regenerated at high temperatures (Fig. 3(e)). At temperature above 50 °C, the RH of regeneration air became significantly lower. This resulted in an increase in the partial vapor pressure difference between the desiccant bed and the flowing air, which in turn augmented the desorption from the desiccant bed. At such a high temperature, the moisture gain after 600 s of regeneration decreased sharply indicating a rapid decrease in the desorption after this period. This phenomenon is also evident from the bed temperature profile as shown in Fig. 3(d), where after 600 s a sharp increase in bed temperature is observed. Thus, at high temperature, most of the desorption occurred within first 600 s of regeneration.

The time course of *RSHI* as defined by Eq. (3) for different regeneration temperature is shown in Fig. 3(f). In the calculation of *RSHI*, the room temperature was assumed to be 27.5 °C. Note that with an increase in regeneration temperature, the *RSHI* also became higher owing to an increase in regeneration heat input. However, until first 200 s, *RSHI* for 52.0 °C increased slightly compared to *RSHI* for 45.8 °C, as the 2nd dehumidification capacity at 52.0 °C was much larger than that at 45.8 °C until this period (Fig. 3(e)). After that the 2nd dehumidification capacity at 52.0 °C decreased sharply and in turn *RSHI* also became higher. Although *RSHI* for 41.4 °C was the lowest (as the heat input was smallest in this case), but the 2nd dehumidification capacity for this temperature was also significantly lower. These results suggest that the *RSHI* can be used as a parameter to optimize the regeneration temperature and regeneration period for a specific demand for dehumidification to maximize the energy efficiency.

The influences of regeneration air humidity and flow velocity on moisture gain are depicted in Fig. 3(g) and (h) respectively. It is clearly seen that when the RH of the regeneration air was increased, a smaller amount of water vapor was desorbed from the desiccant bed (Fig. 3(g)) owing to a decrease in the partial vapor pressure difference between the desiccant bed and the regeneration air. Thus, if the RH in the outdoor air is too high, a higher temperature will be required for regeneration.

The effects of varying flow velocity of the regeneration air on the moisture gain were assessed over a wide range of inlet velocities (0.6–0.9 m s^{-1}); the results are shown in Fig. 3(h). When the flow velocity was decreased, slightly larger moisture gain was obtained owing to a longer residence time of the regeneration air within the test section. However, at a reduced regeneration air flow velocity, the mass of desorbed water also became smaller and therefore, it was expected that the dehumidification capacity of the device during the 2nd adsorption would also become lower in such case.

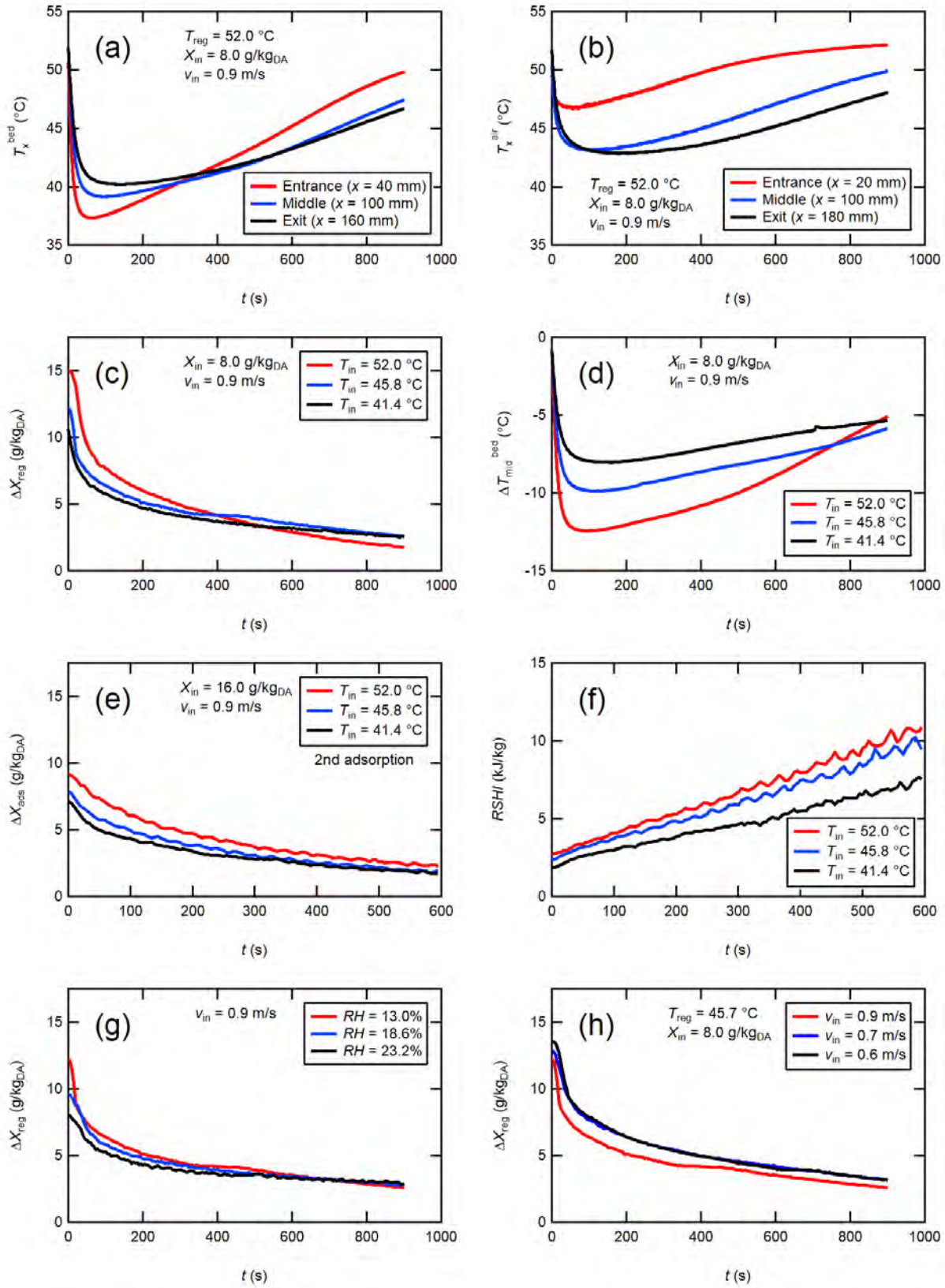

Figure 3: Transient change of temperature during regeneraation from inlet towards outlet within (a) the desiccant bed; (b) airflow channel. Tranisent change of (c) moisture gain; (d) degree of bed temperature reduction at X = 100 mm; (e) dehumidification capacity during 2nd adsorption and (f) regeneration specific heat input under varying regeneration air temperature. Transient change of moisture gain under varying regeneration air (g) humidity (T_{reg} = 45.8 °C; X_{in} = 8.0, 11.4, and 14.3 g kg$_{DA}^{-1}$ at RH = 13.0%, 18.6%, and 23.2%, respectively) and (h) velocity.

6. CONCLUSIONS

In conclusion, the concept of a new multilayer sheet-type desiccant dehumidifier was proposed where the desiccant particles could be enclosed without using polymer binder. As a result, the new device was able to demonstrate higher dehumidification capacity compared to existing solid desiccant systems. The multilayer sheet-type arrangement of desiccant beds reduced the airflow restriction and thus, the pressure drop could be effectively reduced. In addition, the transient heat and mass transfer characteristics of the device were evaluated experimentally under varying inlet air conditions and desiccant bed thickness during both adsorption and regeneration process. The authors anticipate that the outcomes of this study will be helpful for the HVAC designers to better understand the underlying physics of adsorption-desorption in a multilayer device as well as to design highly efficient dehumidifiers for next generation solid desiccant technology.

ACKNOWLEDGEMENTS

This work was financed by AGC Inc., Japan, and partly supported by JST-CREST Grant Number JPMJCR17I3, Japan.

NOMENCLATURE

t_{bed}	thickness of desiccant bed (mm)	v_{in}	velocity of inlet air (m s^{-1})
T_{reg}	temperature of regeneration air (°C)	X_{in}	specific humidity of inlet air (g kg_{DA}^{-1})

REFERENCES

Goetzler, W., Zogg, R., Young, J., Johnson, C., 2014. Energy savings potential and RD&D opportunities for non-vapor-compression HVAC technologies. Navigant Consulting Inc.

Shamim, J. A., Hsu, W. -L., Kitaoka, K., Paul, S., Daiguji, H., 2018. Design and performance evaluation of a multilayer fixed-bed binder-free desiccant dehumidifier for hybrid air-conditioning systems: Part I–experimental. Int. J. Heat Mass Transfer 116, 1361-1369.

Shamim, J. A., Paul, S., Hsu, W. -L., Kitaoka, K., Daiguji, H., 2019. Theoretical analysis of transient heat and mass transfer during regeneration in multilayer fixed-bed binder-free desiccant dehumidifier: Model validation and parametric study. Int. J. Heat Mass Transfer 134, 1024-1040.

Shamim, J. A., Paul, S., Kitaoka, K., Hsu, W. -L., Daiguji, H., 2019. Experimental evaluation of transient heat and mass transfer during regeneration in multilayer fixed-bed binder-free desiccant dehumidifier. Int. J. Heat Mass Transfer 128, 623-633.

Tanaka, N., 2019. Technology Roadmaps Energy-efficient buildings: heating and cooling equipment; (https://www.iea.org/publications/freepublications/publication/buildings_roadmap.pdf).

Ürge-Vorsatz, D., Cabeza, L.F., Serrano, S., Barreneche, C., Petrichenko, K., 2015. Heating and cooling energy trends and drivers in buildings. Renew. Sust. Energ. Rev. 41, 85-98.

Vivekh, P., Kumja, M., Bui, D., Chua, K., 2018. Recent developments in solid desiccant coated heat exchangers–A review. Appl. Energy 229, 778-803.

Wells, L., Rismanchi, B., Aye, L., 2018. A review of Net Zero Energy Buildings with reflections on the Australian context. Energy Buildings 158, 616-628.

Zhang, L., Saikawa, M., Fujinawa, T., 2015. Experimental study on heat and mass transfer characteristics for a desiccant-coated fin-tube heat exchanger. Int. J. Heat Mass Transfer 89, 641-651.

Manuscript ID: 1188
DOI: 10.18462/iir.icr.2019.1188

Gas to liquid transfer enhancement during hydrate crystallization: Case study of CO_2 hydrate for cold storage and transport

Véronique OSSWALD[(a)], Amokrane BOUFARES[(a,b)], Pascal CLAIN[(a,c)], Elise PROVOST[(b)], Didier DALMAZZONE[(b)],Hong Minh HOANG[(a)], Laurence FOURNAISON[(a)], Anthony DELAHAYE[(a)]

[(a)] GPAN Irstea
ANTONY, 92761, France
[(b)] UCP, ENSTA Paristech
PALAISEAU, 91120, France
[(C)] DRVC Pôle Universitaire
PARIS – LA DEFENSE, 92916, France

ABSTRACT

Secondary refrigerants, like ice slurries, are already used for industrial application, but their generation requires mechanical processes (scraping or brushing surface exchangers). CO_2 hydrates slurries were classically obtained in a stirred reactor, by gaseous CO_2 dissolution inside liquid water and cooling process.
In the present work, an original set up was developed in order to measure in real time and in situ the dissolved CO_2 amount in the liquid phase during crystallization process thanks to the FTIR-ATR measurements.
Results on this device allowed to quantify crystallization driving force, related to supersaturation, and to focus on the crystallization limiting step, in particular to determine whether or not it is gas to liquid diffusion. Some parameters were tested as stirrer type (propeller, Rushton turbine with and without hollow shaft) or stirring speeds. The increase of stirring speed or hollow shaft stirrer choice enhanced significatively gas/liquid transfer and thus strongly attenuated or even eliminated under certain conditions the limiting factor at the vapor-liquid interface.
Keywords: Secondary Refrigeration, CO_2 Hydrate, Phase Change Material, FTIR-ATR, Mass and Heat Transfer.

1. INTRODUCTION

Clathrate hydrates are crystalline compounds formed from cages of water molecules, also called host molecule. Various molecules can be a guest molecule; commonly it is gases like methane or carbon dioxide. Hydrates formation have been considered for a long time as a key problem in oil and gas industry, especially for flow assurance in petroleum pipeline. But since the last twenty years plenty of friendly applications appeared like gases treatment, seawater desalination or secondary refrigeration process. Secondary refrigeration is one way to reduce environmental impact of primary refrigerant and consists in reducing fluid quantity, confining it in a primary refrigeration loop and using a secondary refrigeration loop for storage and cold distribution. CO_2 hydrates, have been investigated as secondary refrigerant, due to their high dissociation enthalpy (around 500 $kJ.kg^{-1}$water, higher than that of ice i.e. 333 $kJ.kg^{-1}$) (Fournaison et al., 2004; Fukushima et al., 1999). While CO_2 hydrates thermodynamic properties are now well established, knowledge of crystallization kinetics phenomena is always a challenge (Warrier et al., 2016). Trying to understand and control gas hydrates formation is a key factor since discovery of hydrates as pipeline plugs by Hammerschmidt (Hammerschmidt, 1934).
Most of hydrate reactors at laboratory scale are equipped with pressure and temperature recorders, and kinetic model are based on assumptions. In pharmaceutical or chemical research, process analytical tools (PAT) were used for a long time to monitor crystallization, like particle size

distribution probe ((Zhao et al., 2012) or Raman or Infrared spectroscopy (Togkalidou et al., 2001). In hydrates research field, ATR FTIR measurement was only performed to characterize solid phase (Kumar et al., 2009), and liquid phase composition was unusually characterized by sampling inside the reactor and then analysed (Servio and Englezos, 2001). Recently a new validated method to quantify dissolved CO_2 in liquid water in-situ and in-line during hydrate formation has been developed by Irstea and Ensta (Boufares et al., 2018). The aim of this study is to apply ATR-FTIR protocol previously validated and to determine the limiting transfer for hydrate crystallization at different mixing rates (same impeller), for two different impellers.

2. MATERIAL AND METHOD

2.1. Raw Material Specifications

A CO_2 cylinder tank was purchased from Air Liquide (purity 99.995% in volume) and deionized water was used for the experiments.

2.2. Equipment

Fig. 1 presents the setup used for those experiments. The device is composed of four parts: CO_2 feed, an external refrigerating unit, a magnetic drive coupling motor agitator and a customized high pressure stainless steel reactor. The autoclave, with an internal volume of 382 mL, was equipped with a calibrated PT100 temperature probe (uncertainty ± 0.1 K) and a calibrated pressure sensor supplied by Drück (in the range 0 – 3000 kPa, uncertainty ± 1 kPa). Temperature and pressure measurements were recorded by a data acquisition unit each second. The temperature set point was controlled by a thermostatic bath. Inside the reactor, liquid and gas phases were stirred. For the liquid phase, two different types of stirrer were compared: on one hand, a classical propeller, and on the other hand, a Dispersimax hollow gas-induction impeller, intended to provide efficient vapor-liquid mixing. The stirring velocity could be regulated from 0 to 1200 rpm, three set point velocities were tested: 400, 600 and 800 rpm.

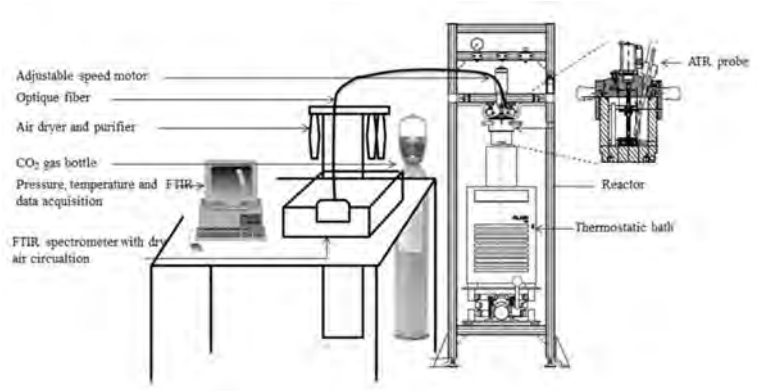

Figure 1: Experimental set-up for measurement of CO_2 in the liquid phase during the hydrate formation process

.

A diamond ATR probe was fixed on the lid and connected via optical fiber to an FTIR spectroscopy analyzer (HTS-XT-Tensor 27, Bruker Optics GmbH, Ettlingen, Germany). FTIR spectra were obtained in the absorption mode (OPUS v6.5, Bruker Optics GmbH, Ettlingen, Germany) in the spectral region 400 - 4000 cm-1, with a spectral resolution of 4 cm-1 and taking 32 scans. The ATR probe was in contact with the liquid to determine the concentration of dissolved CO_2. A FTIR spectrum was recorded each 10 seconds. In order to avoid any interference from atmospheric CO_2, dry and purified air was allowed to circulate inside the spectrometer during all experiments.

2.3. Experimental Protocol

2.3.1. CO_2 concentration measurement in the liquid – FTIR spectroscopy device calibration

Thanks to a specific protocol, already detailed in a previous work (Boufares et al., 2018), based on the infrared radiation due to the C=O bond vibration of CO_2 dissolved in water solution, a

calibration were established and peak height measurement correlated to CO_2 concentration. This calibration protocol was achieved for a range of temperature between 272.2 and 283.2 K and a set of pressure from 1.0 to 2.5 MPa, at a stirring rate of 600 rpm, without hydrate phase.

2.3.2. CO_2 hydrates formation / dissociation

All experiments were conducted in a batch reactor with an initial liquid/gas volume ratio of 1:1. Empty reactor was filled with pure water (191±0.1 g) and then residual air was removed under vacuum. Reactor stirring rate were set-up to fixed value and thermostatic bath set at initial temperature of 283.2 K. Then reactor was fully immersed in thermostatic bath. Desired quantity of CO_2 gas was injected at a fixed set pressure CO_2. When liquid vapor equilibrium was reached, then temperature of thermostatic bath was set up to 272.2 K. After cooling and crystallization occurred, CO_2 hydrates formation was completed when pressure and temperature stabilized with no further drop. Then thermostatic bath temperature was set up to 283.2 K to dissociate hydrates.

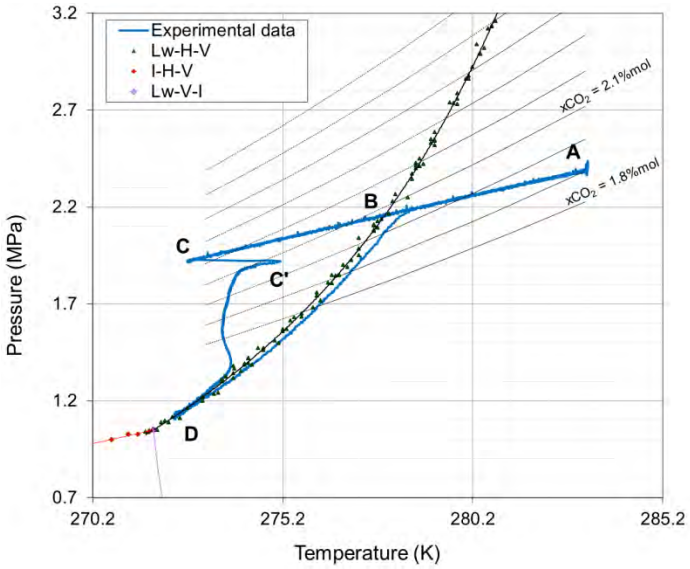

Figure 2: Experimental protocol description – Results of reference case (Dispersimax 600rpm)

3. RESULTS AND DISCUSSION

As previously mentioned, the originality of this study is based on in-situ and real time CO_2 dissolved concentration measurement during CO_2 hydrates formation and dissociation in order to determine kinetics limiting factors. Thanks to this new way to monitor CO_2 hydrate formation, different stirring rates and stirrer types have been tested to enhance CO_2 hydrates crystallization. To determine the effect of each parameter, only one parameter was changed for each new test, and compared to a reference case.

3.1. Reference Case

The reference case was obtained with the Dispersimax hollow gas-induction impeller at 600 rpm. Fig. 3 showed the evolution of pressure, temperature and CO_2 concentration inside the reactor during the test. The reference time value was the beginning of the crystallization, just for a better understanding and comparison with the other cases, because spontaneous crystallization is a stochastic phenomenon. In Figure 3, different steps were clearly identified:

- Injection (from -7000 to -5000 s): when CO_2 is injected within the system, an increase in pressure and CO_2 concentration was observed (in the vapor and liquid phases respectively). Moreover, temperature increases due to CO_2 dissolution which is an exothermal phenomenon.
- Stabilization (from -5000 to -1800 s): after the CO_2 dissolution step, pressure, temperature and CO_2 concentration reached steady state.

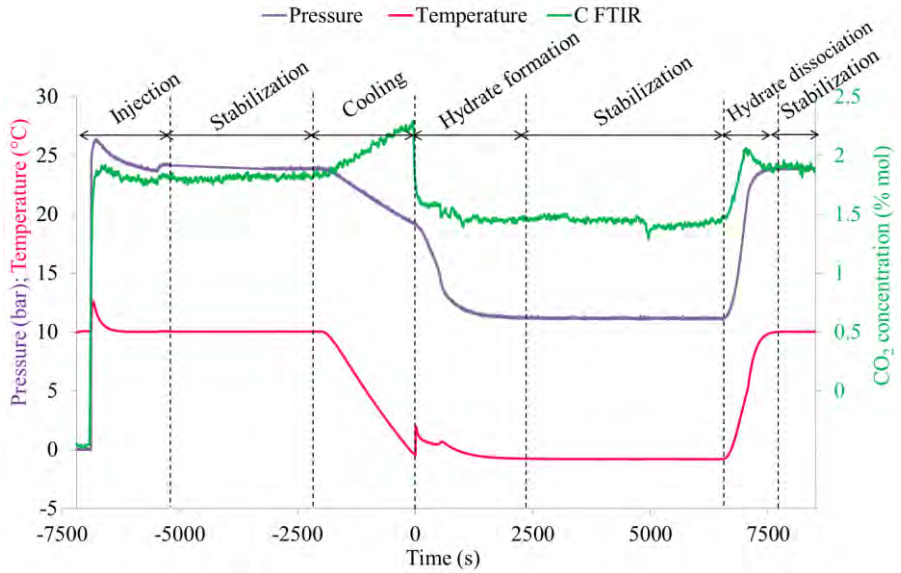

Figure 3: Pressure, temperature and CO_2 concentration curves versus time

• Cooling and supercooling (from -1800 to 0 s): once the system has reached equilibrium, the solution was cooled down in order to form CO_2 hydrates. During this stage, pressure and temperature decreased and CO_2 concentration in the liquid phase increases, because of a CO_2 mass transfer from the vapor phase to the liquid phase. In other words, solubility of CO_2 in liquid water increases with temperature decrease as expected. At point B (see Fig. 2), thermodynamically conditions were reached to crystallize CO_2 hydrates (HL_wVE curve). Nevertheless, the pressure and temperature conditions followed firstly the same linear trend in this theoretical two-phase field H-L_W than in the L_W-V field. Consequently, the system was in a metastable Liquid-Vapor equilibrium without hydrate. At the same time, the CO_2 concentration in the liquid phase continued to increase which lead to supersaturation conditions favorable for CO_2 hydrate crystallization.

• Crystallization: at 0 s (points C – C' (see Fig. 2), a sudden decrease of CO_2 concentration was observed which is related to a consumption of dissolved CO_2 in the liquid phase due to hydrate formation. At the same time, a decrease in reactor pressure (feeding of the liquid phase because CO_2 dissolved is consumed by hydrates) and an increase in temperature (exothermal reaction) were also observed corresponding to hydrate crystallization.

After these sudden variations, temperature, pressure and CO_2 concentration values decreased slowly until 2000 s corresponding to the beginning of a new stable zone where the system contains CO_2 in three phases (CO_2 gas, CO_2 dissolved and CO_2 hydrates).

• Dissociation: After stabilization, the bath temperature was set to 10 °C to dissociate CO_2 hydrates. The reactor was maintained under agitation during the whole dissociation process. Once heating started, an increase in CO_2 concentration in the liquid phase was observed, related to the release of CO_2 entrapped inside hydrate crystals during CO_2 hydrate melting. Simultaneously, an increase of reactor pressure was noticed due to both temperature increase and CO_2 release during hydrate dissociation. Once the temperature inside the reactor reached 10 °C, the system tended the L_wVE conditions and a new stabilization stage took place.

In order to characterize the mechanisms governing CO_2 hydrate formation, real-time CO_2 concentration obtained by FTIR method was compared with predicted data of CO_2 concentrations in liquid water. In order to define limiting factors in the system during hydrate formation it is important to understand whether experimental FTIR concentrations are relevant to equilibrium or non-equilibrium data. Before hydrate crystallization, the CO_2 concentration in the liquid phase was calculated from L_wVE equation based on experimental (p,T) measured during dissolution and supercooling. After crystallization, CO_2 concentration in the liquid phase was predicted based on two different methods:

- The first method consists of estimating the CO_2 concentration in the liquid phase from L_wVE at experimental pressure and temperature. To express this equilibrium, the equality of the

fugacities and chemical potentials between CO_2 in vapor and liquid phase were used and taking the infinite dilution as a reference state for dissolved CO_2, Eq. Eq. (**1**) was developed as:

$$\varphi_{CO_2} y_{CO_2} p = \gamma_{CO_2} x_{CO_2} H_{CO_2} \times \exp\left(\int_0^p \frac{v^*_{CO_2}}{RT} dp \right) \quad \text{Eq. (1)}$$

Pressure range is moderate, then we assumed that liquid and vapor phases are ideal. Due to this hypothesis fugacity and activity coefficients were set to 1.We also neglected pressure effect on the behavior of the liquid phase, thus the poynting factor was set to 1 as well.

$$p = x_{CO_2} H_{CO_2} \quad \text{Eq. (2)}$$

Where the Henry's constant (H_{CO2}) was calculated as mentioned in (Holder et al., 1988).

- The second method consists of estimating the CO_2 concentration in the liquid phase at HL_wVE pressure corresponding to the experimental temperature. (p,T) values of HL_wVE curve were used to estimate the CO_2 concentration using Eq. (2) and a correlation of the CO_2 concentration as a function of T has been deduced and is given by Eq. (3). :

$$x_{CO_2} = 1.528 + 9.661.10^{-2} * T + 1.634.10^{-3} * T^2 + 6.403.10^{-4} * T^3 - 4.120.10^{-5} * T^4 \quad \text{Eq. (3)}$$

Figure 4 shows the comparison between experimental value and equilibrium calculations. Before hydrate formation, experimental CO_2 (FTIR measurements) and L_wVE prediction concentration are in good agreement, even in supersaturated conditions. However, at the moment of hydrate formation, a sharp decrease of CO_2 concentration in the liquid phase was observed via FTIR measurements, but was not observed on CO_2 concentration predicted by L_wVE prediction. Experimental CO_2 concentration was temporarily much lower than predicted assuming L_wVE, showing a limitation of CO_2 transfer from the vapor to the liquid phase, which does not however prevent hydrates from forming quickly by consuming the dissolved gas.
Measured CO_2 concentrations were compared also to those predicted by the HL_wVE (Eq. (3)) considering (p_{eq},T) when the CO_2 hydrate crystallizes and a good agreement was observed between both curves. It was noted that the measured CO_2 concentration had the same trend as the concentration given for (p_{eq},T) couple on the HL_wVE. The results showed that at the beginning of hydrate formation, equilibrium (in the condensed phase) may be assumed close to the liquid and hydrate equilibrium. When crystallization occurred, CO_2 concentration drops quickly which means that hydrates consume the dissolved CO_2 in the surrounding liquid at a high rate and act as a "CO_2 sponge" for aqueous phase. CO_2 concentration in the liquid phase, calculated via Eq. (3), was related to experimental reactor temperature and not to reactor pressure (HL_wVE pressure at the experimental temperature). This result confirmed the limitation of the mass transfer from the vapor to the liquid phase during CO_2 hydrate crystallization and that the "local" equilibrium between the liquid and hydrate phases depends only on the experimental temperature.

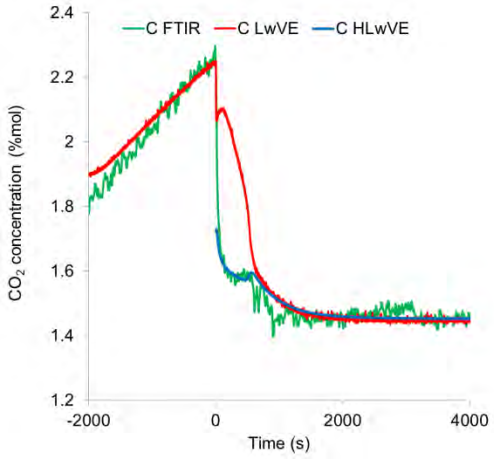

Figure 4: Comparison between CO_2 experimental concentration and theoretical equilibrium concentration (L_wVE and HL_wVE) – Reference case

3.2. Effect of the Stirring Rate

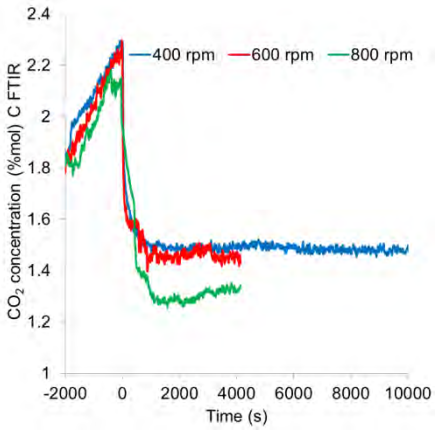

Figure 5: Comparison between 400, 600 and 800 RPM of CO_2 experimental concentration versus time

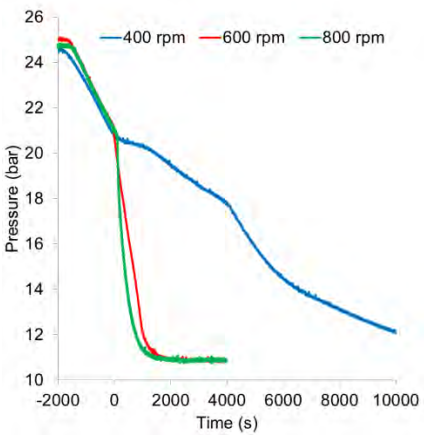

Figure 6: Comparison between 400, 600 and 800 RPM of reactor pressure versus time

One way to improve vapor to liquid transfer consists to increase vapor liquid interface. Three stirring rate were tested. Figure 5 shows the evolution of CO_2 concentration in the liquid phase and Figure 6 reactor pressure evolution for different stirring rate under the same operating conditions (water amount, initial pressure and temperature) as reference case.

According to Figure 5, it is obvious that the rotational speed has almost no effect either on CO_2 consumption in the liquid phase during cooling and CO_2 hydrate crystallization steps. The small deviation between the three experiments is due to small difference in crystallization temperature. At the hydrate formation point, the strong impoverishment of CO_2 in the liquid phase was identified for all velocities, meaning that this impoverishment is mainly governed by hydrate crystallization.

The reactor pressure evolution in Figure 5 is the same during the cooling stage, showing a good thermal transfer between the cooling bath and the reactor which is independent of the rotational stirrer. However, from the crystallization to the end of stabilization, the pressure profile depends on the stirring rate. For both 600 rpm and 800 rpm, the pressure profiles were almost the same noting that at 800 rpm the pressure drop is faster than that at 600 rpm. At 400 rpm the decrease in pressure was significantly slower than at 600 and 800 rpm. This indicates that the mass transfer resistance between the vapor and liquid phases was more significant at this stirring speed.

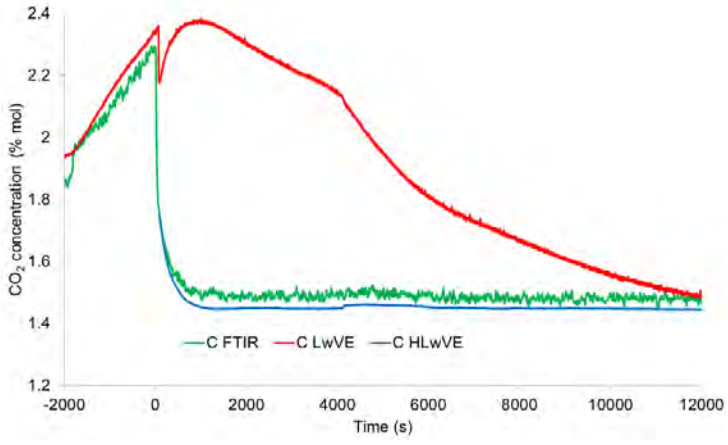

Figure 7: Comparison between CO_2 experimental concentration and theoretical equilibrium concentration (L_wVE and HL_wVE) – 400 RPM

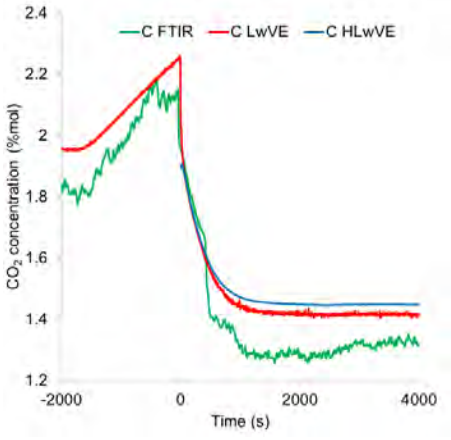

Figure 8: Comparison between CO_2 experimental concentration and theoretical equilibrium concentration (L_wVE and HL_wVE) – 800 RPM

As for reference case, results obtained for the CO_2 concentrations measurements in the liquid phase were compared to L_wVE predicted concentrations (Eq. (2)) and considering the (p_{eq},T) couple conditions (Eq. (3)) when the crystallization took place (see Fig. 4, Figure 7 and Figure 8). In the cooling stage, from -2000 to 0 s, for this stage the measured and L_wVE predicted concentrations fit very well for rotational speeds of 600 rpm and 400 rpm. The measured

concentration is lower than LwVE curve for 800 rpm probably due to the turbulences that can take place.
At the crystallization, comparing the measured concentration to that projected on the HL_wVE curve at (p_{eq},T) (Eq. (3)) these results confirm our previous observations (see reference case). The results showed differences by comparing the measured and L_wVE prediction concentration. This gap was more important for 400 rpm than that at 600 rpm and vanished for the 800 rpm. This can be explained by the fact that for 400 rpm and 600 rpm the mass transfer resistance is significantly higher whereas for **800 rpm it can be neglected**.

3.3. Effect of the Impeller Type

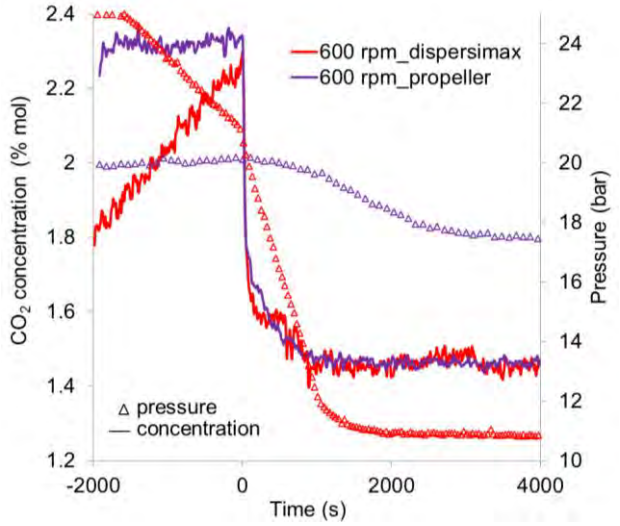

Figure 9: Comparison between Dispersimax and propeller at 600 RPM of CO_2 experimental concentrations and pressure versus time

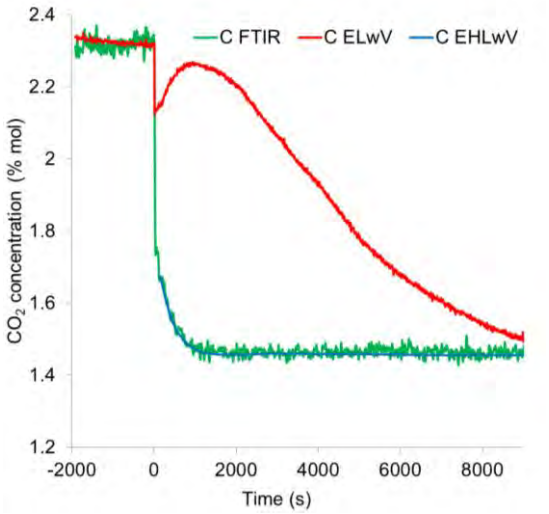

Figure 10: Comparison between CO_2 experimental concentration and theoretical equilibrium concentration (L_wVE and HL_wVE) – 600 RPM propeller

In experiments comparing the effect of impeller type, crystallization did not occur at the same step for both cases: during cooling step for Dispersimax and after cooling during stabilization step at low temperature for propeller, due to the stochastic crystallization phenomenon. This fact explain why even if we performed tests in same initial operating conditions, reactor pressure before crystallization was at 2.0 MPa for propeller and at 2.5 MPa for Dispersimax. Nevertheless concentration profiles during crystallization were similar, despite of pressure profiles (see Fig. 9). In the same way, the comparison between CO_2 concentration measurement and L_wVE (Eq. (2)) and HL_wVE (p_{eq},T) predicted concentrations (see Fig. 10) are very similar comparing to the reference case (good agreement with L_wVE before crystallization, very close to HL_wVE profile after crystallization). As for reference case, the transfer was limited at the vapor - liquid interface. Thanks to these two experiments the effect of gas recirculation (with Dispersimax) was highlighted, increasing liquid – vapor contacting area and enhanced significantly mass and thermal transfer.

4. CONCLUSION

A protocol allows in situ and real-time measurement of CO_2 concentration in liquid phase during the CO_2 hydrate formation/dissociation process. Two mechanism steps took place:
1. Rapid consumption of dissolved CO_2 during hydrate formation leading to crystal growth limitation
2. Gas transfer from vapor to liquid phase, which governs the pursuit of the process.
Thanks to these results, CO_2 transfer at the vapor/liquid interface was identifying as the limiting step of the crystallization process after the first rapid step. The effect of the stirring speeds and impeller type was tested and showed that an increase of stirring rate speed or a gas recirculation improves the gas/liquid contacting area and enhances gas transfer from vapor to liquid phase, reducing the limiting factor at the vapor liquid interface.

ACKNOWLEDGEMENTS

This work was supported by the French National Research Agency under the program Crisalhyd (ANR-14-CE05-0045) and the different project's partners.

NOMENCLATURE

L_wVE	Liquid-Vapor Equilibrium	p	Pressure (Pa)
HL_wVE	Hydrate-Liquid-Vapor Equilibrium	p_{eq}	Equilibrium pressure (Pa)
HL_wE	Hydrate-Liquid Equilibrium	T	Temperature (K)
φ_{CO_2}	Fugacity coefficient	R	Universal gas constant
γ_{CO_2}	Activity coefficient	H_{CO_2}	Henry's constant

REFERENCES

Boufares, A., Provost, E., Dalmazzone, D., Osswald, V., Clain, P., Delahaye, A., Fournaison, L., 2018. Kinetic study of CO_2 hydrates crystallization: Characterization using FTIR/ATR spectroscopy and contribution modeling of equilibrium/non-equilibrium phase-behavior. Chem. Eng. Sci. 192, 371-379.

Fournaison, L., Delahaye, A., Chatti, I., Petitet, J.-P., 2004. CO_2 hydrates in refrigeration processes. Ind. Eng. Chem. Res. 43, 6521-6526.

Fukushima, S., Takao, S., Ogoshi, H., Ida, H., Matsumoto, S., Akiyama, T., Otsuka, T., 1999. Development of high-density cold latent heat with clathrate hydrate. NKK Technical Report 166, 65-70.

Hammerschmidt, E.G., 1934. Formation of Gas Hydrates in Natural Gas Transmission Lines. Ind. Eng. Chem. 26, 851-855.

Holder, G.D., Zetts, S.P., Pradhan, N., 1988. Phase Behavior in Systems Containing Clathrate Hydrates: A Review. Rev. Chem. Eng. 5, 1-4.

Kumar, R., Lang, S., Englezos, P., Ripmeester, J., 2009. Application of the ATR-IR Spectroscopic Technique to the Characterization of Hydrates Formed by CO_2, CO_2/H_2 and $CO_2/H_2/C_3H_8$. J. Phys. Chem. A. 113, 6308-6313.

Servio, P., Englezos, P., 2001. Effect of temperature and pressure on the solubility of carbon dioxide in water in the presence of gas hydrate. Fluid Phase Equilib. 190, 127-134.

Togkalidou, T., Fujiwara, M., Patel, S., Braatz, R.D., 2001. Solute concentration prediction using chemometrics and ATR-FTIR spectroscopy. J. Cryst. Growth 231, 534-543.

Warrier, P., Khan, M.N., Srivastava, V., Maupin, C.M., Koh, C.A., 2016. Overview: Nucleation of clathrate hydrates. J. Chem. Phys. 145.

Zhao, Y., Yuan, J., Ji, Z., Wang, J., Rohani, S., 2012. Combined Application of in Situ FBRM, ATR-FTIR, and Raman on Polymorphism Transformation Monitoring During the Cooling Crystallization. Ind. Eng. Chem. Res. 51, 12530-12536.

Manuscript ID: 1197
DOI: 10.18462/iir.icr.2019.1197

Heat transfer mechanisms during refrigerant condensation when varying inclination

Marco AZZOLIN[(a)], Stefano BORTOLIN[(a)], Arianna BERTO[(a)], Pascal LAVIEILLE[(b)], Marc MISCEVIC[(b)], Davide DEL COL[(a)]

[(a)] University of Padova – Department of Industrial Engineering
Padova, 35131, Italy, davide.delcol@unipd.it
[(b)] Université Paul Sabatier - Laboratoire Plasma et Conversion d'Energie,
118 Route de Narbonne, Toulouse, France, pascal.lavieille@laplace.univ-tlse.fr

ABSTRACT

Capacity control in chillers and heat pumps is done more and more by adopting variable speed compressors. In such a case, at partial loads, the refrigerant flow rate running in the equipment is reduced and this is a strong reason for studying convective condensation at low mass flux.
Here, the mechanisms of condensation inside a tube with an internal diameter equal to 3.4 mm are investigated. The test section allows to perform flow pattern visualizations, measurements of the heat transfer coefficient and of the liquid film thickness. Experiments have been conducted with R134a and R245fa in horizontal and vertical downward flow at mass velocity equal to 50 and 100 kg m^{-2} s^{-1} at 40°C saturation temperature. The visualized flow patterns provide fundamental information to understand the effect of channel inclination. The liquid film thickness during vertical downflow condensation has been measured with a confocal sensor.
Keywords: Two-Phase Flow, Heat Transfer Coefficient, Inclined Tube, Liquid Film Thickness.

1. INTRODUCTION

Three quantities can be identified as main actors governing convective condensation inside channels: vapor shear stress, gravity force, surface tension. Their mutual influence, together with fluid properties, is responsible of the development of different flow regimes (e.g. annular, stratified, plug-slug…), the laminar-to-turbulent transition in the liquid film, the presence of interface instabilities (waves) and liquid entrainment in the vapor core. At relatively high values of mass velocity (e.g. G > 300 kg m^{-2} s^{-1}) several data taken during in-tube condensation of refrigerants are available in the literature and the correlations usually well predict experimental data and they can be applied down to 1 mm diameter channel (Del Col et al. 2015, Matkovic et al. 2009). Instead, when reducing the mass velocity, vapor shear stress, gravity force and (in small diameter channels) surface tension becomes similar making the prediction of the heat transfer more difficult. Toninelli et al. (2018) investigated by means of VOF (Volume Of Fluid) numerical simulations the relative importance of shear, gravity and surface tension during condensation of R134a in two channels (internal diameters equal to 1 mm and 3.4 mm) and they showed that the presence of waves at the vapor-liquid interface leads to an enhancement of the heat transfer coefficient. From the application perspective, low mass velocities are very interesting because of the adoption of inverter-driven compressors with variable speed leads often the system to work far from its design conditions and thus the condenser can be found to operate at low values of mass velocity. Beside this, at low mass velocity, due to the increase role of gravity over vapor shear stress, the channel inclination becomes an important factor to be considered in the design of heat exchangers. The number of studies dealing with condensation in small diameter channels (e.g below 4 mm) and those investigating the effect of the channel inclination is very limited. Even less are the available works that, in these working conditions, correlate the condensation heat transfer with the corresponding two-phase flow pattern. Ewim et al. (2018) studied the effect of channel inclination on heat transfer coefficients and flow patterns during R134a condensation inside a 8.38 mm diameter tube at 40°C saturation temperature. Condensation experiments were conducted at different inclination angles ranging from -90° (vertically downwards) to +90° (vertically upwards), at mass fluxes of 50, 75, and 100 kg $m^{-2}s^{-1}$. They reported that channel inclination significantly influences the flow patterns and the heat transfer coefficients; in particular, the inclination effect is more evident for downwards flows than upwards flows, with an optimal angle

between -30° and -15°. Recently, Azzolin et al. (2018) studied convective condensation inside a 3.4 mm diameter channel in microgravity: in microgravity conditions the penalization of the heat transfer coefficient with respect to the horizontal channel in normal gravity condition was found to vary between 10% and 24% at mass velocity G = 70 - 100 kg m^{-2} s^{-1} and vapor quality from 0.8 to 0.5.
From one side, heat transfer coefficient data coupled with flow pattern visualizations provide enough information for the development and assessment of heat transfer correlations but, from a more fundamental point of view, the knowledge of the evolution of the liquid film thickness in condensation is very important because during annular condensation, the leading thermal resistance is due to the liquid film thickness at the wall. Most of the studies dealing with liquid film thickness measurements available in the literature concern relatively big channels (e.g. 20-30 mm diameter) and air-water mixtures (Cioncolini et al. 2013). There is a lack of data taken with refrigerants in saturated conditions and inside small channels. Different techniques can be used such as laser induced fluorescence, optical techniques, conductance technique and ultrasonic method. A comprehensive review of the methods employed in micro-scale for the liquid film thickness measurement and related literature is provided by Tibiriçá et al. (2010). Among the optical techniques, Mederic et al. (2006) performed measurements of local liquid film thickness and local void fraction by means of image analysis during condensation of *n*-pentane inside a borosilicate tube with inner diameter equal to 0.56 mm. Han et al. (2015) measured annular liquid film thickness by laser confocal displacement meter using degassed water and air in glass tubes with inner diameters of 0.3, 0.5 and 1.0 mm. Inside the 1.0 mm tube, the mean liquid film thickness decreases from about 55 μm to 5 μm at G=100 kg m^{-2} s^{-1} and from 30 μm to 5 μm at G=500 kg m^{-2} s^{-1} in the vapor quality range x = 0.10÷1. None of these works address refrigerants.
In the present paper, the effect of gravity during R134a condensation in a horizontal and vertical tube (3.4 mm internal diameter) is investigated by heat transfer measurements and flow visualizations. Furthermore, with the aim to study the effect of fluid properties, data taken with R134a have been compared with R245fa data in vertical downflow covering heat transfer coefficients and liquid film thickness.

2. EXPERIMENTAL TEST SECTION

The layout of the test rig used for condensation tests is reported in Fig. 1a. It consists of a primary refrigerant loop and three auxiliary water loops. In the refrigerant loop, a post-condenser is used to keep the refrigerant subcooled before it enters a magnetic driven gear pump. The refrigerant mass flow rate is measured by Coriolis-effect mass flow meter and a tube-in-tube heat exchanger is used to vaporize and superheat the fluid. After the evaporator, the refrigerant enters in the heat transfer test section in which is partially or fully condensed using distilled water as secondary fluid.
The experimental test section is composed of three parts: two counter-current heat exchangers for heat transfer measurements and a glass window for flow pattern visualization and liquid film thickness measurement (Fig. 1b). Each heat exchanger is divided respectively in three and two sub-sectors: the refrigerant flows in the internal circular channel (3.4 mm diameter), beside water flows in the external annulus. A finned geometry has been machined on the water coolant side with the aim to decrease the water side heat transfer resistance and to accommodate wall thermocouples (in each sub-sector six thermocouples are embedded in the copper wall). On the water side, two thermocouples and a triple junction thermopile are used to double check the temperature difference of the flowing water at the inlet and outlet of each sub-sector. Two Coriolis effect mass flow meters are employed to measure the water mass flow rate. The refrigerant temperatures at the inlet and outlet of the test section are measured with two T-type thermocouples immersed in the fluid flow and the pressure is measured at the inlet of the first heat exchanger by means of a relative pressure transducers, whereas two differential pressure transducers with different full scale are employed to measure the pressure drop along the test section.
Between the two heat exchangers, a borosilicate glass tube has been placed for the visualization of the flow pattern. The glass tube has an internal diameter equal to 3.4 mm and is 40 mm long. The external side of the glass has been designed and machined to obtain a lens for better detection of the liquid film.

2.1. Data Reduction

During the heat transfer tests the heat flow rate between the refrigerant and the water for each sub-sector is evaluated as:

$$q_{\text{water,i}} = \dot{m}_{\text{water,i}}\, c_{\text{water}}\, \Delta T_{\text{water,i}} \qquad \text{Eq. (1)}$$

where $\Delta T_{\text{water,i}}$ is the water temperature difference measured by the *i*-th thermopile.
The heat transfer coefficient in the *i*-th sub-sector can be then obtained as:

$$\alpha_i = \frac{q_{\text{water,i}}}{A \cdot \left(T_{\text{sat}} - T_{\text{w,m}}\right)_{\text{i}}} \qquad \text{Eq. (2)}$$

where T_{sat} and $T_{\text{w,m}}$ are respectively the saturation and mean wall temperature. In each sub-sector the wall temperatures are measured with 6 thermocouples in different positions. The heat transfer coefficient (Eq. 2) can be calculated using the mean wall temperature ($T_{\text{w,m}}$).
The enthalpy at the outlet of each sub-sector $h_{\text{out,i}}$ can be determined from the heat flow rate, the mass flow rate and the inlet enthalpy of the condensing fluid:

$$h_{\text{out,i}} = h_{\text{in,i}} - \frac{q_{\text{water,i}}}{\dot{m}_{\text{ref}}} \qquad \text{Eq. (3)}$$

where the enthalpy at the inlet of the test section is evaluated from the measured temperature and pressure using REFPROP 9.1 (Lemmon et al. 2013) and the outlet enthalpy from one sub-sector is considered as the inlet value of the following sub-sector. The thermodynamic vapor quality at the outlet of a sub-sector (and at inlet of the following one) can be calculated using the outlet enthalpy (Eq. 3). The mean vapor quality for each sub-sector is calculated from the inlet and outlet values.
To complete the data reduction, the following contributions are considered: dissipated heat flow rate (the mean dissipated heat flow rate was about 1 W per sub-sector with a temperature difference of 10 K between the water and the external ambient); effect of the wall thermocouples positioning (the effective wall temperature measurement is located 0.6 mm from the internal channel surface and thus the measured temperature can be corrected to account for the conduction resistance in the thin copper wall); effect of the axial conduction (this effect may promote heat transfer from water to the condensing refrigerant between the sub-sectors).

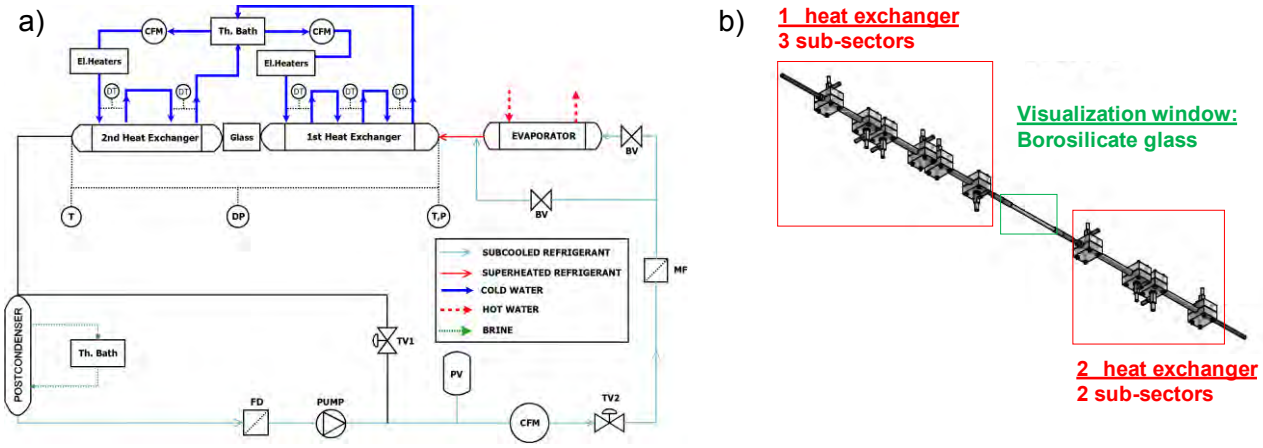

Figure 1: a) Experimental test rig: FD (filter dryer); PV (pressure vessel); CFM (Coriolis mass flow meter); TV (throttling valve); MF (mechanical filter); BV (ball valve); P (pressure transducer); DP (differential pressure transducer); T (thermocouple); DT (thermopile). b) Detail of the test section

3. EFFECT OF CHANNEL ORIENTATION

The main objective of this work is to investigate the effect of channel orientation during condensation at low mass flux, when gravity has bigger effect. Tests with R134a have been done at mass flux equal to 100 and 50 kg m^{-2} s^{-1} in horizontal and vertical configuration. The condensation heat transfer coefficient has been measured in the five sub-sectors with the exception of the first one where the working fluid enters the test section as superheated vapor and thus part of the first sub-sector serves to desuperheat the fluid and achieve the thermodynamic conditions at the inlet of the following sub-

sector. Between the 3rd and the 4th sub-sector, the visualization window allows to record the flow pattern using a high speed camera.
The experimental heat transfer coefficients of R134a are plotted versus vapor quality in Fig. 2a. As expected for forced convective condensation inside pipes, the heat transfer coefficient decreases as the condensation process is moving forward and the vapor quality decreases in the channel. Beside, the heat transfer coefficient depends on the mass velocity, due to the effect of the shear stress. At G=50 kg m^{-2} s^{-1}, the effect of the saturation-to-wall temperature difference is evident; at the same vapor quality, at lower saturation-to-wall temperature difference the heat transfer coefficient results higher.
The visualized flow patterns are the following (Fig. 2b):
- at G=100 kg m^{-2} s^{-1} the stratified wavy flow pattern can be recognized in a wide range of vapor qualities. The waves intensity and amplitude changes with quality but the liquid-vapor interface is always clearly distinguishable. At x=0.27 the interface is smooth with some waves appearing from time to time;
- at the mass velocity equal to 50 kg m^{-2} s^{-1} the flow pattern is smooth stratified for vapor quality higher than 0.45. When decreasing the vapor quality the thickness of the liquid film increases gradually. For vapor qualities equal to 0.26, intermittent flow can be recognized.

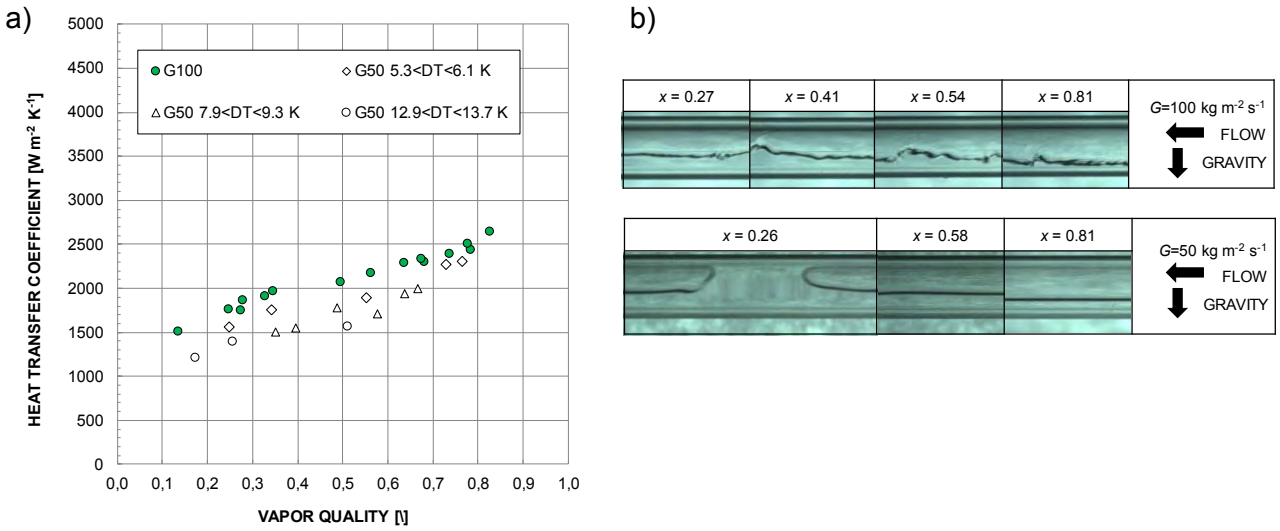

Figure 2: Condensation of R134a at 40°C temperature in a 3.4 mm diameter tube in horizontal configuration. a) Experimental heat transfer coefficient versus vapor quality. b) Flow pattern at different vapor qualities

At these two mass velocities, in vertical downward configuration, the flow pattern is annular for the whole range of vapor qualities (Fig. 3). During vertical annular flow, the liquid film forms a uniform continuous film around the internal perimeter of the tube and the heat transfer coefficient depends on the interface shear stress and the liquid film thickness. The interface, depending on the vapor quality, is disturbed by waves with different amplitude.

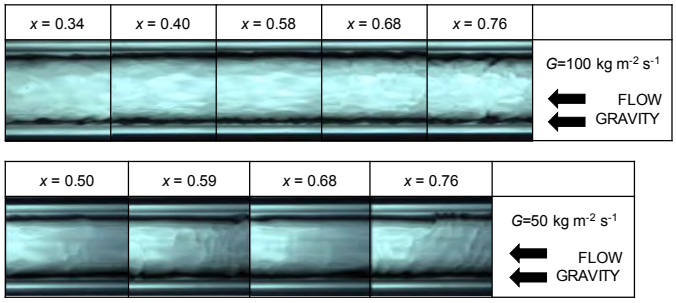

Figure 3: Flow pattern, at different vapor qualities, during vertical downward condensation of R134a at 40 °C saturation temperature in a 3.4 mm internal diameter tube

Fig. 4a compares the heat transfer coefficient between the two channel inclinations (when considering G=50 kg m^{-2} s^{-1} and horizontal configuration the saturation-to-wall temperature difference has been limited between 12.9 K and 7.9 K). For both mass velocities, the flow pattern is annular in the vertical configuration and stratified-wavy (for G=100 kg m^{-2} s^{-1}) or smooth stratified (for G=50 kg m^{-2} s^{-1}) in the horizontal configuration. The difference in the flow pattern between the vertical and the horizontal configuration produces a decrease of the heat transfer coefficient during vertical downflow. In horizontal configuration, due to gravity, the liquid film thickness is thinned at the top and in the middle of the tube while it becomes thicker at the bottom. This leads to an average higher heat transfer coefficient in the horizontal configuration compared to the vertical configuration in which the flow is annular. Toninelli et al. (2018) have shown, with numerical simulations by means of the VOF method, that 85% of the heat transfer is exchanged in the upper part of the tube where the liquid film thickness is thinner. The ratio between the heat transfer coefficient in horizontal and that in vertical configuration can reach 0.45 at x=0.5 and 0.58 at x=0.7 for G=100 kg m^{-2} s^{-1}.
While in the literature there are various correlations able to predict the condensation heat transfer coefficient in horizontal configuration, very few models are available for vertical flow. In the present case, the experimental data were compared against the predictions of the Shah (2016) correlation which was developed for convective condensation inside tubes considering both the horizontal and vertical configurations (Fig. 4b). When only the horizontal configuration is considered, the mean absolute deviation of the Shah (2016) correlation is 12.9% and the standard deviation is equal to 8.4%. When the vertical configuration is considered, the predicted values from the correlation largely deviates from the experimental ones: on average, the mean absolute deviation is equal to 52.4% and the standard deviations equal to 14.7%.

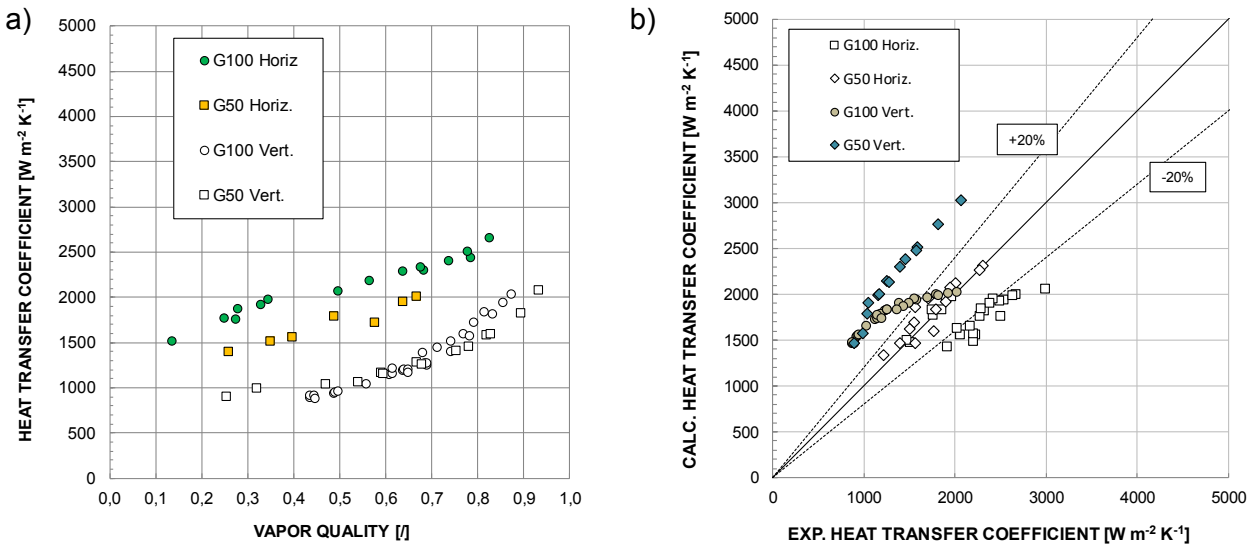

Figure 4: Horizontal and vertical downflow condensation of R134a at T_{sat}=40 °C in a tube with internal diameter equal to 3.4 mm. a) Experimental heat transfer coefficient versus vapor quality. b) Predictions of the heat transfer coefficient with the Shah (2016) model

4. EFFECT OF THE FLUID PROPERTIES AND LIQUID FILM THICKNESS MEASUREMENTS

4.1. Effect of the Fluid Properties

The results obtained during vertical downflow condensation of R134a have been compared with those obtained with R245fa in Figure 5a. Thermophysical properties of the two fluids are reported in Table 1. In this section, the comparison is done to investigate the effect of the fluid properties on the heat transfer coefficient and not to compare the performance of the two fluids in a condenser.
At the same mass velocity and saturation temperature, R245fa displays a higher heat transfer coefficient: at x=0.5 the heat transfer coefficient of R245fa is 52% higher than that of R134a at G=50 kg m^{-2} s^{-1} and at G=100 kg m^{-2} s^{-1} is two times that of R134a. This is due to the liquid thermal conductivity: R245fa has a higher liquid thermal conductivity compared to R134a. Moreover R245fa

displays lower vapor density and thus higher vapor phase velocity, which increases the vapor shear stress on the liquid film thickness. This causes a higher effect of the mass velocity on the heat transfer coefficient compared to R134a.
A complete comparison between the two fluids should clearly account for the pressure drops, but this is out of the scope of the present paper.

Table 1. Properties of saturated R134a and R245fa at 40°C saturation temperature computed with REFPROP 9.1 (Lemmon et al. 2013)

	p_{sat} [bar]	ρ_L [kg m^{-3}]	ρ_G [kg m^{-3}]	μ_L [μPa s]	μ_G [μPa s]	λ_L [W m^{-1} K^{-1}]
R134a	10.17	1146.7	50.1	161.4	12.4	74.7
R245fa	2.5	1296.7	14.1	328.6	10.9	83.6

4.2. Liquid Film Thickness Measurements

The liquid film thickness is one of the most important parameters in modeling the condensation heat transfer phenomena. Although many studies on liquid film thickness have been carried out, quantitative data of annular liquid film especially in small channels are limited due to the technical difficulties in measuring it. The confocal interferometry technique used in this study allows to detect liquid film thickness in the range 20 μm to 300 μm without disturbing the two-phase flow.
Fig. 5b reports the heat transfer coefficient and the mean liquid film thickness measured during vertical downflow condensation of R245fa at 40°C saturation temperature. The heat transfer coefficients are those measured in the five sub-sectors of the test section while the liquid film thickness is the one measured with the confocal probe at a certain axial position in the glass tube. To get the values of the liquid film thickness at different vapor qualities, the heat flux in the first three sub-sectors is changed varying water temperature and water flow rate. The liquid film thickness measurements and the flow pattern visualizations are done simultaneously with the confocal sensor and the high speed camera. The data from the confocal sensor are acquired for seven seconds.

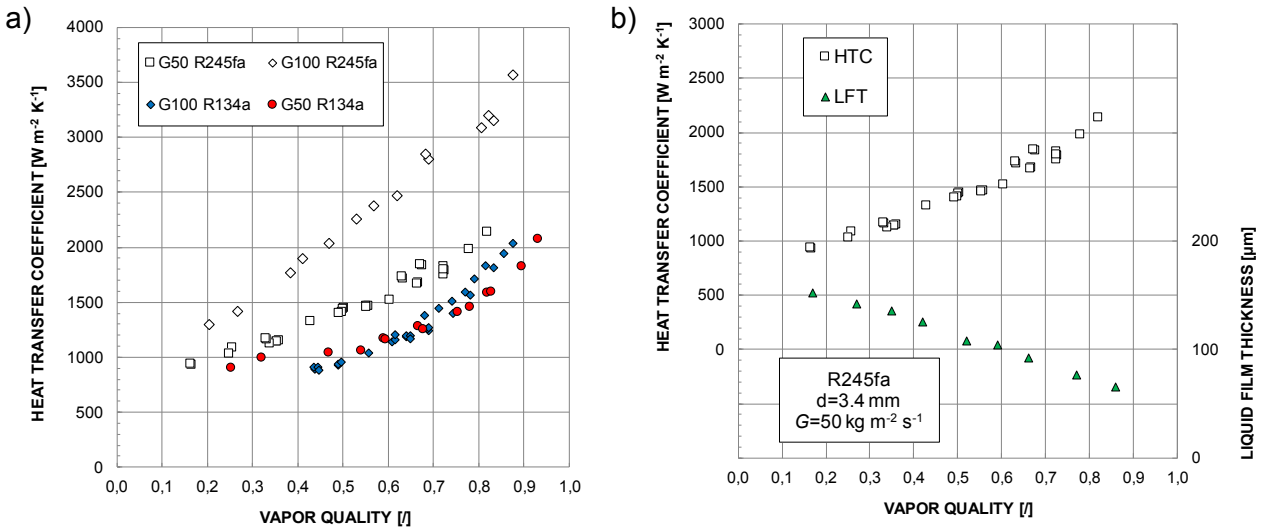

Figure 5: Vertical downflow condensation of R134a and R245fa in a 3.4 mm diameter tube at 40°C saturation temperature. a) Experimental heat transfer coefficient versus vapor quality of R134a and R245fa. b) Experimental heat transfer coefficient and mean liquid film thickness for R245fa at G=50 kg m^{-2} s^{-1}

Fig. 6 reports the first 0.2 seconds of the confocal data acquisition (Fig. 6a) and four images of the flow pattern acquired at 0.07, 0.08, 0.09 and 0.1 seconds (Fig. 6b) for R245fa at G=50 kg m^{-2} s^{-1} and x=0.52. In Fig. 6a, the white points are the instantaneous measurements of the local film thickness while the green line represents the mean liquid film thickness during the seven seconds. At this working condition, the liquid film thickness keeps changing due to the waves in the flow pattern, as can be seen in Fig. 6b looking at the liquid film in the correspondence of the confocal sensor measurement line. The mean value of the liquid film thickness is equal to 108 μm. The measured values of the mean liquid film thickness varying the vapor quality can be seen in Figure 5b. It has an

opposite trend compared to the heat transfer coefficient: the mean liquid film thickness decreases with the vapor quality while the heat transfer coefficient increases. This emphasis the important correlation between the heat transfer coefficient and the liquid film thickness showing that during vertical condensation of R245fa at G=50 kg m^{-2} s^{-1} the heat transfer coefficient is given by heat conduction and convection across the liquid film.

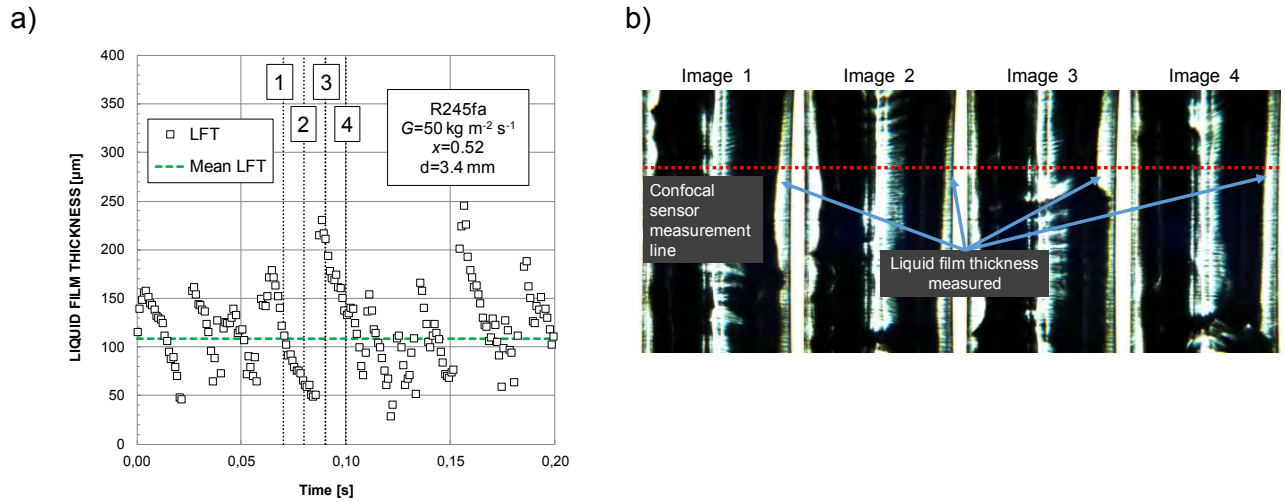

Figure 6: Temporal evolution of the liquid film thickness during vertical downflow condensation of R245fa at 40°C saturation temperature in a 3.4 mm internal diameter tube (G=50 kg m^{-2} s^{-1} and x=0.52). a) Liquid film thickness measurements. b) Images of the flow pattern

5. CONCLUSIONS

The purpose of this work was to present the condensation heat transfer mechanisms at low mass velocities which are less studied but often encountered when the refrigeration equipment works at partial loads. The condensation heat transfer coefficient of R134a was measured in horizontal and vertical downflow configuration at mass velocity equal to 50 and 100 kg m^{-2} s^{-1} and 40°C saturation temperature. In horizontal configuration, the gravity force pushes the liquid to the lower part of the tube thinning the liquid film at the top compared to the vertical case. The visualization of the flow pattern clearly shows that in horizontal configuration the flow is stratified-wavy and stratified smooth while in vertical it is always annular. This difference in the flow pattern leads to a higher heat transfer coefficient, at the same working conditions, when the tube is in horizontal. The ratio of heat transfer coefficient in vertical downflow to that in horizontal can be as low as 0.45 at G=100 kg m^{-2} s^{-1} and x=0.5. During vertical downflow the heat transfer coefficient has been measured also with R245fa. In this case besides the heat transfer coefficient and flow pattern visualizations, the liquid film thickness has also been measured using a confocal sensor placed in correspondence of a glass tube. This technique allows to measure the liquid film thickness without disturbing the two-phase flow. For R245fa during vertical downflow condensation at G=50 kg m^{-2} s^{-1} and x=0.52, the mean value of the liquid film thickness is equal to 108 µm and the heat transfer coefficient decreases as the film thickness increases.
Unfortunately, although available correlations can predict pretty well the heat transfer coefficient in horizontal channels, the accuracy in vertical configuration is not satisfactory. The simultaneous knowledge of heat transfer coefficient, flow pattern and liquid film thickness can lead to more accurate design models in this case.

ACKNOWLEDGEMENTS

The authors acknowledge the financial support of the MIUR through the program PRIN 2015 (Grant Number 2015M8S2PA) and of the Department of Industrial Engineering of the University of Padova through the project BIRD160582/16. The support of the European Space Agency through the MAP Condensation program ENCOM-3 (AO-2204-096) is also acknowledged.

NOMENCLATURE

A	exchange surface area (m^2)	LFT	liquid film thickness (μm)
c	specific heat (J kg^{-1} K^{-1})	$\dot{m}$	mass flow rate (kg s^{-1})
d	hydraulic diameter (m)	p	pressure (Pa)
G	mass velocity (kg m^{-2} s^{-1})	q	heat flow rate (W)
h	specific enthalpy (J kg^{-1})	T	temperature (K)
HTC	heat transfer coefficient (W m^{-2} K^{-1})	x	thermodynamic vapor quality (-)

Greek symbols

α	heat transfer coefficient (W m^{-2} K^{-1})	μ	dynamic viscosity (μPa s)
ΔT	temperature difference (K)	ρ	density (kg m^{-3})
λ	thermal conductivity (W m^{-1} K^{-1})		

Subscripts

G	vapor	m	mean
i	i-th element	out	outlet
in	inlet	ref	refrigerant
L	liquid	sat	saturation
		w	wall

REFERENCES

Azzolin, M., Bortolin, S., Le Nguyen, L.P., Lavieille, P., Glushchuk, A., Queeckers, P., Miscevic, M., Iorio, C.S., Del Col, D., 2018. Experimental investigation of in-tube condensation in microgravity. Int. Communications in Heat and Mass Transfer, 96, 69-79.

Cioncolini, A., Thome, J.R., 2013. Liquid film circumferential asymmetry prediction in horizontal two-phase flow. Int. J. Multiph. Flow 51, 44-54.

Del Col, D., Bortolato, M., Azzolin, M., Bortolin, S., 2015. Condensation heat transfer and two-phase frictional pressure drop in a single minichannel with R1234ze(E) and other refrigerants. Int. J. Ref. 50, 87-103.

Ewim, D.R.E., Meyer, J.P., Noori Rahim Abadi, S.M.A., 2018. Condensation heat transfer coefficients in an inclined smooth tube at low mass fluxes. Int. J. Heat Mass Transf. 123, 455-467.

Han, Y., Hiroshi, K., Ahn, Y.-J., Shikazono, N., 2015. Measurement of liquid film thickness in micro tube annular flow. Int. J. Multiphase Flow 73, 264–274.

Lemmon, E. W., Huber, M. L., McLinden, M. O., 2013. NIST Standard Reference Database 23: Reference Fluid Thermodynamic and Transport Properties-REFPROP, Version 9.1, National Institute of Standards and Technology, Gaithersburg

Matkovic, M., Cavallini, A., Del Col, D., Rossetto, L., 2009. Experimental study on condensation heat transfer inside a single circular minichannel. Int. J. Heat Mass Transf. 52, 2311-2323.

Mederic, B., Lavieille, P., Miscevic, M., 2006. Heat transfer analysis according to condensation flow structures in a minichannel. Exp. Therm. Fluid Science 30, 785-793.

Shah, M.M., 2016. Comprehensive correlations for heat transfer during condensation in conventional and mini/micro channels in all orientations. Int. J. Refrig. 67, 22–41.

Tibiriçá, C.B., do Nascimento, F.J., Ribatski, G., 2010. Film thickness measurement techniques applied to micro-scale two-phase flow systems. Exp. Therm. Fluid Science 34, 463-473.

Toninelli, P., Bortolin, S., Azzolin, M., Del Col, D., 2018. Visualization and Numerical Simulations of Condensing Flow in Small Diameter Channels. Heat Transf. Eng., in press.

Manuscript ID: 1209
DOI: 10.18462/iir.icr.2019.1209

Experimental analysis of transcritical CO_2 booster refrigeration system with heat recovery and ejector expansion

Kundan KUMAR[1], Simarpreet SINGH[2], Pramod KUMAR[1], M.P. MAIYA[2], Armin HAFNER[3], Krzysztof BANASIAK[4], Petter NEKSA[4]

[1]Department of Mechanical Engineering, Indian Institute of Science, Bangalore -560012, India
Kundank466@gmail.com, pramod@iisc.ac.in
[2]Department of Mechanical Engineering, Indian Institute of Technology Madras, Chennai - 600036, India
[3]NTNU Trondheim - 7034, Norway
[4]SINTEF Energy Research Trondheim -7034, Norway

ABSTRACT

The growing environmental concerns and advanced technologies are convincing researchers to revisit CO_2 refrigeration. Due to a low critical temperature of CO_2, the refrigeration system work in the transcritical cycle for high ambient temperature conditions. It is important to identify the optimum gas-cooler pressure above the critical point to obtain the maximum COP. This paper presents the experimental analysis of the performance of two-stage cooling, low temperature (-31 °C) and medium temperature (-8 to -4 °C) with a booster system and heat recovery. The experimental setup is designed for optimum gas cooler pressure and equipped with a multi-ejector rack to reduce the throttling losses. The effect of gas cooler temperature, receiver pressure and internal heat exchanger (IHEX) on the performance of CO_2 refrigeration system are experimentally investigated. It is observed that an optimum receiver pressure exists where the COP is maximum and the system with IHEX has better performance.

Keywords: Transcritical, CO_2, Ejector, Heat Recovery

1. INTRODUCTION

Environmental issues mainly global warming and stringent environmental regulation have turned the attention of the researchers towards the natural working fluids such as carbon dioxide, propane and other hydrocarbons in the refrigeration and air-conditioning systems. Among these natural refrigerants, CO_2 has gained more attention in refrigeration and air-conditioning because CO_2 is a non-toxic, non-flammable refrigerant and have excellent heat transfer and transport properties (Lorentzen and Pettersen, 1993). These properties include a higher density, latent heat, and volumetric cooling capacity, and lower viscosity. Due to the low critical temperature of CO_2 (31.1°C), CO_2 system operates in a transcritical region at high ambient temperature and heat rejection takes place by cooling the compressed CO_2 in supercritical region, while heat absorption in the evaporator remains subcritical. In the supercritical region temperature and pressure are independent to each other and slope of isotherms becomes almost flat near the critical point and become stepper with increasing pressure, hence an optimum discharge pressure exists where COP of the system becomes maximum (Kauf, 1998). The high-pressure side of the CO_2 refrigeration system is in the supercritical region because of that throttling losses are more, and ejector can be used to reduce these losses (Sumeru et.al. 2012). Throttling losses can also be reduced using internal heat exchangers in the transcritical CO_2 refrigeration systems by reducing the optimum discharge pressure but internal heat exchangers have an adverse effect on some others the refrigerants system such as R22 (Kim et al., 2004). Li and Groll (2005) investigated theoretically the performance of transcritical CO_2 refrigeration cycle with ejector as an expansion device. They found that the ejector expansion cycle has a 16% higher COP than the standard cycle. Yari and Siriousazar (2007) investigated the performance of transcritical CO_2 refrigeration cycle with ejector as an expansion device based on the second law of thermodynamics. They found that the ejector cycle has 24.8% more second law efficiency compared with the standard CO_2 cycle and 16% compared with the internal heat exchanger system. Domanski (1995) found that the ejector efficiency also affects the

performance of the ejector expansion refrigeration cycle. Parallel compression is proposed by Hafner et al. (2012) to improve the performance of CO_2 booster refrigeration system in warmer climates. Chesi et al. (2014) had done thermodynamic analysis to find out the effect of compressor volumetric flow ratio and separator efficiency on CO_2 system performance with the parallel compression CO_2 cycle. Sarkar and Agrawal (2010) investigated that a parallel compressor can improve the performance up to 47.3% compared with standard gas-bypass system and had done thermodynamics analysis of CO_2 refrigeration system and found that the optimum heat rejection pressure depends on the gas-cooler outlet temperature evaporator temperature and the performance of the compressor.
In this paper, the performance of two-stage cooling, medium temperature (-8°C to -4°C) and low temperature (-31°C) with booster system and heat recovery is experimentally analysed for different environmental temperatures. The evaporators capacities are 3 and 15 kW for low and medium temperature applications respectively. The experimental setup is designed for optimum gas-cooler pressure and equipped with an auxiliary compressor and a multi-ejector rack to reduce the load on the main compressor. In this study, the effect of gas-cooler temperature, Intermediate receiver pressure and Internal heat exchangers on the performance of CO_2 refrigeration system are experimentally investigated.

2. EXPERIMENTAL SETUP AND SYSTEM DESCRIPTION

Fig. 1 shows a parallel compression booster system with heat recovery and multi-ejector rack. The multi ejector rack, contains 4 vapour ejectors having capacities 6 kW, 12 kW, 25 kW and 50 kW and 2 liquid ejectors all are fixed geometry ejectors of different throat diameter, connected parallel to each other. Fig. 2 shows the model of Danfoss vapour ejector which is used in this system. A high-pressure control valve (tv-1) is also mounted on the skid parallel to the vapour ejector. This control valve works only when any ejector primary nozzle throat is not chocked otherwise it is in off condition.

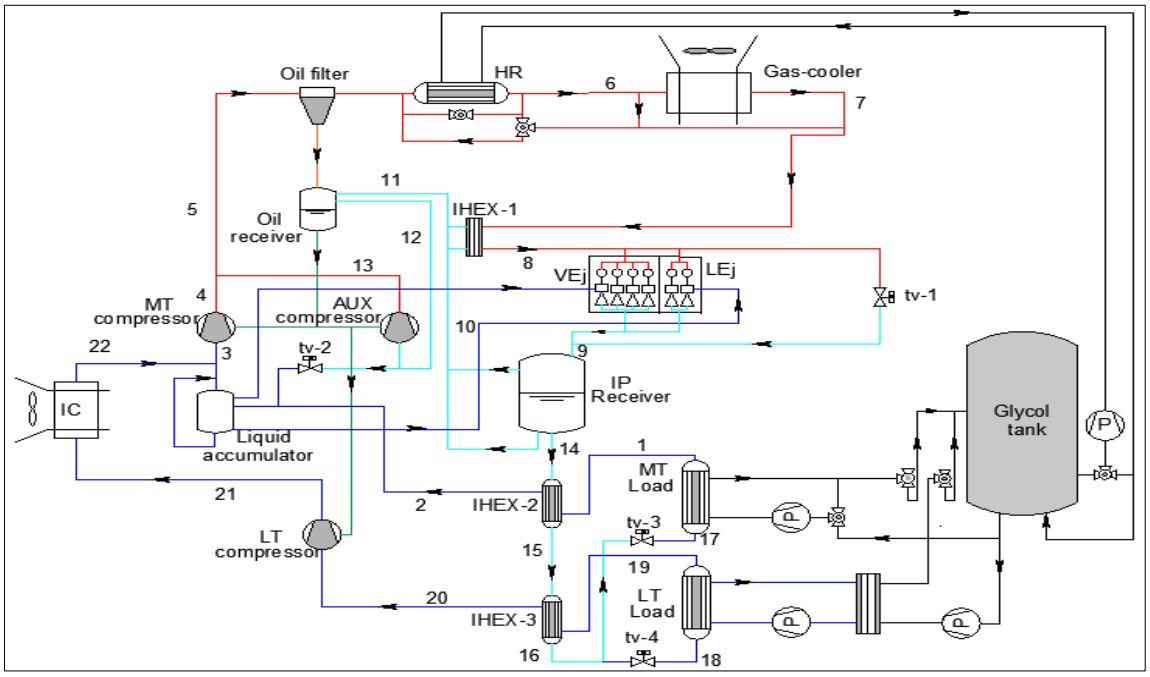

Figure 1: Schematic of the experimental setup.

The vapour ejector uses the energy of high-pressure refrigerant coming from the gas-cooler and entrained some of the vapour from the liquid accumulator and send it to the IP receiver. This reduces the load of the medium temperature (MT) compressor and total power consumption.
Solenoid valves are mounted on the motive side of the ejector to match the required capacities with changing the ejector combination by switching on or off the necessary ejector. The liquid ejector (LEj) is used to pump the liquid from liquid accumulator to the IP receiver and it starts working only

when MT evaporator starts flooding and the liquid in the accumulator reaches the specified level. The liquid accumulator is used to providing superheated or saturated vapour at the suction of the MT compressor and secondary side of the ejector and IP receiver is used as a flash tank to sperate the two-phase refrigerants into liquid and vapour at an intermediate pressure. The vapour from IP receiver first passes through IHEX-1, exchange the heat and gain some superheat then passes through oil receiver to cool the high-temperature oil before supplying to compressors.
An auxiliary compressor is used to draw the vapour from the intermediate pressure (IP) receiver (Flash Tank) generated after the expansion of high-pressure fluid coming from gas-cooler. Thus, the vapour is compressed from intermediate pressure to the high pressure, allowing the system to reduce energy consumption. If the amount of flash gas is lower than the minimum volume flow rate of the auxiliary compressor, all flashed vapour is throttled by throttling valve (tv-2) and send it to the liquid accumulator and if the amount of flashed vapour is more than the maximum volume flow rate of the auxiliary compressor then extra flashed vapour is throttled by throttling valve (tv-2) and send it to the liquid accumulator so it maintains constant pressure in the IP receiver. The pressure at MT and LT evaporator is maintained using Danfoss electronic expansion valve tv-3 and tv-4 respectively. An intercooler is used at the exit of low temperature (LT) compressor to desuperheat the refrigerant before mixing at the suction of the MT compressor to reduce the suction superheat and save power consumption. Three internal heat exchangers are used in this system to provide subcooling, one at the exit of gas-cooler and the other two at the common liquid line coming from IP receiver. Two types of test are conducted on this system to know the effect of IHEX after the gas-cooler on the system performance. In test-1 all IHEX is used but in test-2 IHEX-1 is bypassed, but other two IHEX-2 and IHEX-3 is always in the flow line.

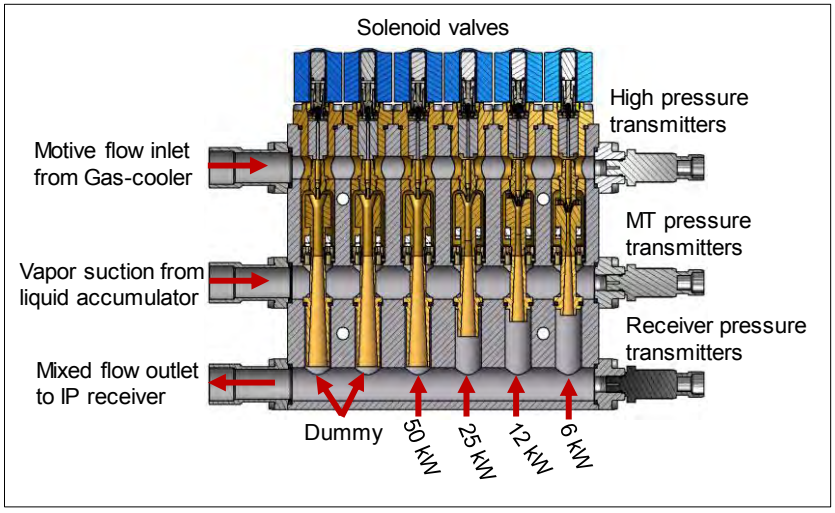

Figure 2: Schematic of vapour ejector (Danfoss Data Sheet).

A heat recovery unit is also accommodated in the system before the gas-cooler to utilize the waste heat after the compression process of the refrigerant and the extra heat rejected to the environment using gas-cooler. A glycol tank is employed, contains propylene glycol and water mixture with a concentration of 50% to extract the heat from heat recovery and maintain the load of MT evaporator. A secondary glycol loop with 55% concentration of propylene glycol is also employed to exchange the heat from LT evaporator. In the experimental setup, Dorin semi-hermetic compressors of different models are used. Auxiliary compressor (CD-1300H), MT compressor (CD-700H), and LT compressor (CD-300H) having a volumetric flow rate of 8.92, 4.34 and 1.46 $\mathrm{m^3 hr^{-1}}$ respectively at 50 Hz.

3. SYSTEM PERFORMANCE CALCULATIONS

In this paper, all results are analysed for steady state conditions. For steady state condition, cooling capacities of both the evaporator and heat recovery are calculated using energy balance across the heat exchangers because of both mass flow rate and temperatures across heat exchangers were measured on the glycol loop. Flow meters are mounted on the propylene glycol loop to reduce the

pressure losses in the CO_2 system. Temperature and pressure transducers are attached at inlet and outlet of every component. LT and MT evaporator capacities are calculated using equation 1.

$$\dot{Q}_{evap} = \dot{m}_{g,evap} * \left[C_{p,g,in} * \left(t_{in,g} + 273.15\right) - C_{p,g,out} * \left(t_{out,g} + 273.15\right)\right] \quad \text{Eq. (1)}$$

where C_p is the specific heat capacity of the glycol and calculated using Engineering Equation Solver (EES) and found that it is a linear function of temperature.

$C_p = 0.0038t_i + 3.4531$, for 50% glycol concentration in MT evaporator and heat recovery loop.

$C_p = 0.0042t_i + 3.3522$, for 55% glycol concentration in LT evaporator loop.

where C_p is in $(kJkg^{-1}K^{-1})$ and t_i is in $°C$
The mass flow rate of CO_2 in the evaporators are calculated by energy balance across the evaporators.

$$\dot{m}_{CO_2} = \dot{Q}_{evap} * (h_{out} - h_{in})^{-1} \quad \text{Eq. (2)}$$

Waste heat recovery after the compression of the refrigerants is calculated using equation 3.

$$\dot{Q}_{HR} = \dot{m}_{g,evap} * \left[C_{p,g,out} * \left(t_{out,g} + 273.15\right) - C_{p,g,in} * \left(t_{in,g} + 273.15\right)\right] \quad \text{Eq. (3)}$$

Cooling coefficient of performance is calculated by using equation 4.

$$COP(R) = \left(\dot{Q}_{LT} + \dot{Q}_{MT}\right) * \left(\dot{W}_{LT} + \dot{W}_{MT} + \dot{W}_{AUX}\right)^{-1} \quad \text{Eq. (4)}$$

System coefficient of performance with cooling and heating is calculated by using equation 5.

$$COP_{(R+H)} = \left(\dot{Q}_{LT} + \dot{Q}_{MT} + \dot{Q}_{HR}\right) * \left(\dot{W}_{LT} + \dot{W}_{MT} + \dot{W}_{AUX}\right)^{-1} \quad \text{Eq. (5)}$$

The performance of ejector is measured with three parameters pressure ratio, entrainment ratio and ejector efficiency.
Pressure ratio (P_r): It is defined as the ratio of outlet pressure of ejector to the suction (secondary fluid) pressure and for this refrigeration system it is expressed as

$$P_r = P_{IP} * P_{evap,MT}^{-1} \quad \text{Eq. (6)}$$

Entrainment ratio (ω): It is defined as the ratio of secondary (entrained) mass flow rate to motive mass flow rate and it is expressed as

$$\omega = \dot{m}_{entrainment} * \dot{m}_{motive}^{-1} \quad \text{Eq. (7)}$$

Ejector efficiency $(\eta_{ejector})$: It is defined as the ratio of the amount of expansion work recovered to the maximum potential to recover the expansion work by the ejector (Elbel and Hrnjak, 2008)

$$\eta_{ejector} = \omega * [h_c(s_{suction}, P_{out}) - h_D(s_{suction}, P_{suction})] * [h_A(s_{motive}, P_{out}) - h_B(s_{motive}, P_{out})]^{-1} \quad \text{Eq. (8)}$$

4. RESULTS AND DISCUSSIONS

To assure that the system is operating at the optimum gas-cooler pressure and meet the load requirement, the controller that simultaneously adjusts the speed of the compressors and the opening of the throttling valve when it is required. While conducting the experiments receiver pressure is varied from 42 to 48 bar and LT evaporator temperature is kept at -31°C and MT evaporator temperature is varied from -8 to -4 °C. All the data are taken from the system manager during the experiment, only when the system reaches steady state condition at the step size of 5 seconds and a total of 30 minutes for every input condition. Initially, when the system is started it takes around 1 hour to reach the steady state, where the fluctuation of pressure and temperature is about ±0.5 bar and ±1°C respectively. Temperature and pressure transducers are attached at inlet and outlet of every component. Fig. 3 shows the process flow of the transcritical CO_2 refrigeration system with ejector expansion and internal heat exchangers on the p-h chart. There is an optimum gas-cooler pressure in transcritical CO_2 refrigeration system where the system has maximum COP for a given gas-cooler exit temperature. The experimental setup used for performance analysis automatically controls the optimum gas-cooler pressure for a given gas-cooler exit temperature.

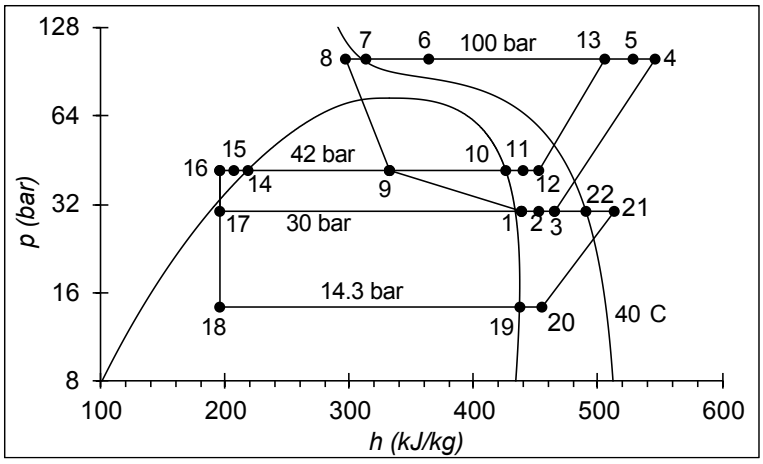

Figure 3: p-h chart of the system with IHEX.

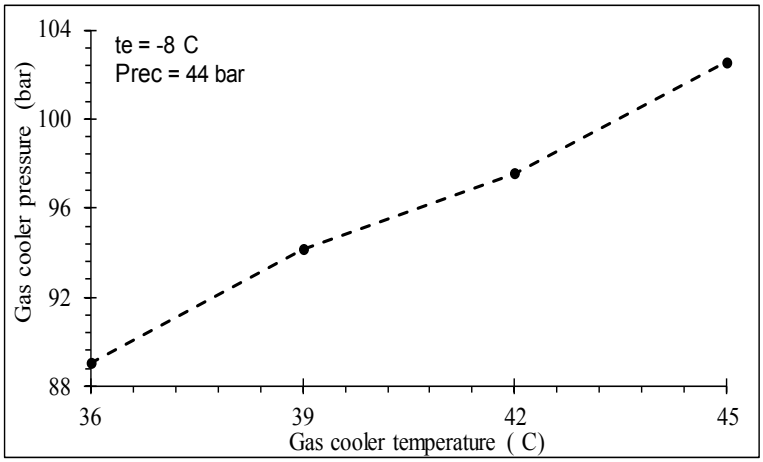

Figure 4: Effect of gas-cooler temperature on optimum gas-cooler pressure.

As the gas-cooler exit temperature increases the optimum gas-cooler pressure also increases and it is an almost linear function of gas-cooler temperature as shown in the Fig. 4 this is because the isothermal line becomes almost flat near the critical point and then it became almost steeper as shown in the Fig. 3. Fig. 5 shows that the variation of cooling COP with gas-cooler outlet temperature. An almost linear relationship is observed between the gas-cooler temperature and COP. COP of the system starts decreasing as the gas-cooler temperature increases for a specific evaporator temperature. This is because the optimum gas-cooler pressure increases with an increase in gas-

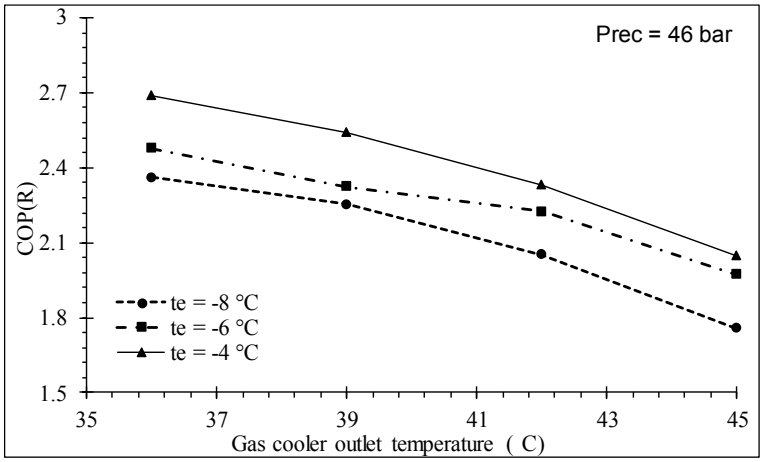

Figure 5: Effect of gas-cooler temperature on cooling COP.

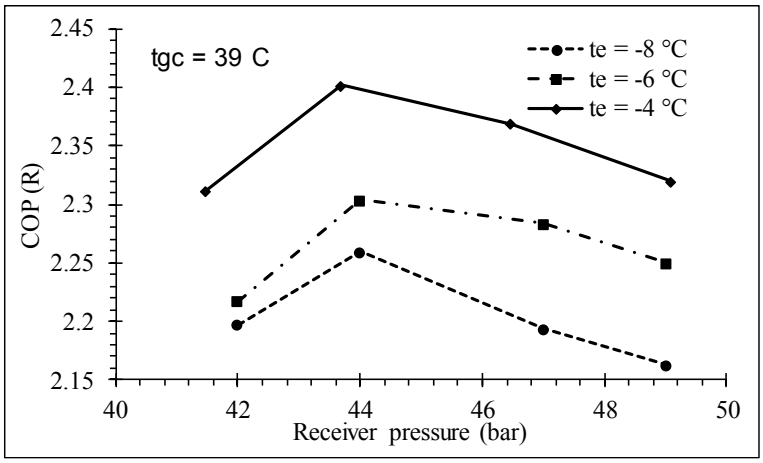

Figure 6: Effect of receiver pressure on cooling COP.

cooler temperature causes the increase in pressure ratio and power consumption of the compressor. Fig. 5 also shows that with increases in MT evaporator temperature COP also increases because the suction pressure of the MT compressor is more for higher evaporating temperature. Fig. 6 shows the variation of COP with receiver pressure. COP first increases and achieve maximum COP near receiver pressure of 44 bar then start decreasing with an increase in receiver pressure. This is because the pressure lift of secondary fluid in the ejector is increased with increase in receiver pressure cause deterioration in the performance of the ejector i.e. ejector will suck less vapour from the liquid accumulator and load on MT compressor increases cause an increase in power consumption.

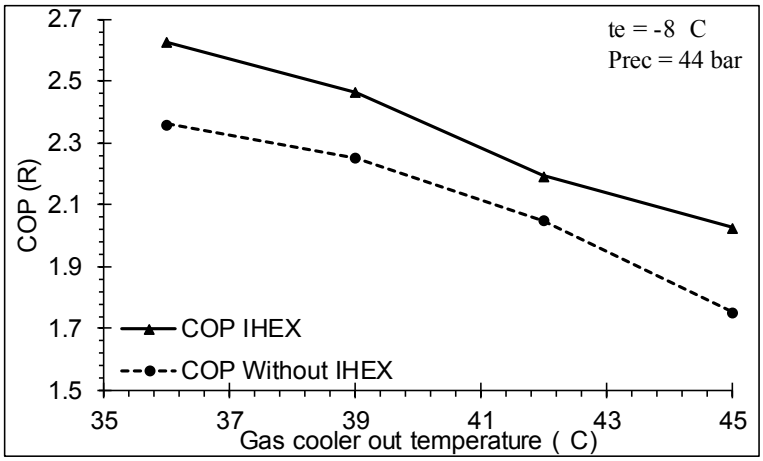

Figure 7: Comparison of cooling COP of the system with and without IHEX.

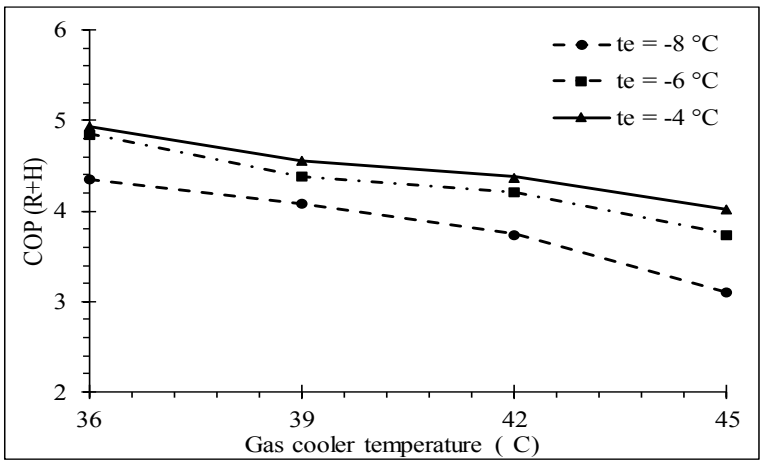

Figure 8: Effect of gas-cooler temperature on combined heating and cooling COP.

Fig. 7 shows that the system with IHEX-1 is higher COP than the without IHEX-1. This is because with the use of IHEX-1, not only subcooled the high-pressure fluid coming from gas-cooler but also reduce the optimum compressor discharge pressure. Due to less pressure ratio volumetric efficiency of compressor increases because of this mass flow rate also increases. Because of subcooling of high-pressure fluid, the specific enthalpy difference across the evaporator increases and combined effect increase the cooling capacity but subsequently, it adds superheat to flashed vapour cause increment in the auxiliary compressor work consumption, but the overall effect causes the increment in COP. In this system, 2 to 5°C Subcooling is achieved for high-pressure fluid and 3 to 10% COP improvement is seen in his system. With this analysis, it can be said that 1-2% improvement in COP can be achieved using internal heat exchangers for per 1°C subcooling.

CO_2 system has high potential to recover the waste heat after the compression process. Due to the higher isentropic exponent of CO_2, temperature after the compression process reached beyond 130°C. This recovered heat can be utilized for domestic water heating and underfloor heating in the stores according to the seasonal demand. Fig. 8 shows that effect gas cooler temperature on combined cooling and heating COP of the system. It can be clearly seen from fig.8 the combined COP of the system decreases with increase in gas-cooler temperature, this is because of increases in gas-cooler pressure, the optimum compressor discharge pressure increases cause an increment in power consumption

5. CONCLUSIONS

The analysis shows that the optimum gas-cooler pressure mainly depends on the gas-cooler outlet temperature. To assure that the system is operating at the optimum gas-cooler pressure and meet the load requirement, the controller will simultaneously adjust the opening of the high-pressure regulating valve and speed of the compressors. System performance is deteriorating when the gas-cooler temperature increases and system performance also depends on the receiver pressure. 5-10% improvement in COP can be achieved with the addition of IHEX in the transcritical CO_2 refrigeration systems. If we use CO_2 refrigeration system for both cooling and heating simultaneously then system performance is comparable with the synthetic refrigerants.

ACKNOWLEDGEMENTS

The authors wish to thank IIT Madras for providing test facility to conduct the experiment and wish to thank Ministry of external affairs, Government of Norway for providing the fully funded experimental setup at IIT Madras through NTNU and SINTEF, Norway.

NOMENCLATURE

$\dot{W}$	Compressor work (kW)	T	Temperature (°C)
$\dot{m}$	Mass flow rate (kgs^{-1})	h	Enthalpy (kJ/kg)
$\dot{Q}$	Capacity of heat exchanger (kW)	C	Specific heat (kJ/kg K)

Subscript

LT	Low temperature	MT	Medium temperature
MT	Medium temperature	AUX	Auxiliary
g	Glycol	e	Evaporator
tv	Throttling valve	HR	Heat recovery
p	Pressure	gc	Gas-cooler

REFERENCES

Chesi, A., Esposito, F., Ferrara, G., 2014. Experimental analysis of R744 parallel compression cycle. Appl. Energy 135, 274–85.

Elbel, S., Hrnjak, P., 2008. Experimental validation of a prototype ejector designed to reduce throttling losses encountered in transcritical R744 system operation. Int. J. Refrigeration 31, 411–422.

Kauf, F., 1999. Determination of the optimum high pressure for transcritical CO_2 refrigeration cycle. Int. J. Therm. Sci. 38, 325-330.

Hafner, A., Poppi, S., Neksa, P., Minetto, S., Eikevik, T.M., 2012. Development of commercial refrigeration systems with heat recovery for supermarket building. In Proceedings of the 10th IIR Gustav Lorentzen Conference on Natural Refrigerants, 25th – 27th June, Delft, The Netherlands. Paper ID: 192.

Sarkar, J., Agrawal N., 2010. Performance optimization of transcritical CO_2 cycle with parallel compression economization. International Journal of Thermal Sciences 49, 838-843.

Kim, M. H., Pettersen, J., Bullard, C. W., 2004. Fundamental process and system design issues in CO_2 vapour compression systems. Progress in Energy and Combustion Science 30, 19–174.

Li, D, Groll, A., 2005. Transcritical CO_2 refrigeration cycle with ejector-expansion device. International Journal of Refrigeration 28, 766–773.

Lorentzen, G., Pettersen, J., 1993. A new, efficient and environmentally benign system for car air-conditioning. Int. J. of Refrigeration 16(1), 4-12.

Domanski, P.A., 1995. Theoretical evaluation of the vapour compression cycle with a liquid-line/suction-line heat exchanger, economizer, and ejector, NISTIR-5606, National Institute of Standards and Technology.

Sumeru, K., Nasution, H., Ani, F.N., 2012. A review on two-phase ejector as an expansion device in the vapor compression refrigeration cycle. Renewable and Sustainable Energy Reviews 16, 4927–4937.

Yari, M, Sirousazar, M., 2007. Thermodynamic analysis on transcritical CO_2 refrigeration cycle with ejector-expansion device. In Proceedings of the Fifteenth Annual International Conference on Mechanical Engineering – ISME, Amirkabir University of Technology, Tehran, Iran, 15–17 May 1–12.

Manuscript ID: 1223
DOI: 10.18462/iir.icr.2019.1223

Online composition measurements of refrigerant mixtures by optical fibres and infrared spectroscopy

Pascal TOBALY[(a)], Marie-France TERRIER[(a)]

[(a)]Laboratoire du Froid, des Systèmes Energétiques et Thermiques (LaFSET)
Conservatoire National des Arts et Métiers, HESAM Université, Paris, France
Paris, 75003, France, pascal.tobaly@lecnam.net

ABSTRACT

As refrigeration and heat pump industries use more and more mixtures as refrigerants it is useful to measure the composition of the fluid at different locations in the machine. For our own research purposes on mixture based cycles, we have implemented an online non-intrusive technique based on infrared spectroscopy.
This paper describes the apparatus used and also the data treatment that allows to extract valuable information from the recorded spectra. The calibration of the method for a given mixture is obtained by recording spectra with known concentrations, pressure and temperature. Partial least squares (PLS) or principal component regression (PCR) statistical methods are used to build a model. Then compositions can be determined for unknown mixtures.
Results are presented for CO2+Propane mixtures. The sensitivity of the method to baseline treatment is tested. The best accuracy obtained so far is of the order of 2%
The method is well tested and can be applied to other mixtures.
Keywords: Refrigerant Mixtures, CO2, Propane, Spectroscopy, Composition Measurement.

1. INTRODUCTION

International regulations on the use of working fluids in the refrigeration and heat pump industry become more restrictive. Therefore, industries are considering the use of natural fluids including CO2 (R744). However, CO2 has some drawbacks like its low critical temperature and high working pressures (Ma et al. 2004). We are investigating in our laboratory the possibility to use a mixture of CO2 with another compound to improve the performances. As part of this work, we have implemented a heat pump with composition measurements at different positions in the loop (Bouteiller, 2017). The present article will describe the composition measurement technique that is used and the tests of the accuracy.

2. EXPERIMENTAL SETUP

The test heat pump is described on Fig. 1. It is a classical one stage loop with a scroll compressor, two plate heat exchangers for the evaporator and the gas cooler, an electronic expansion valve and also an internal heat exchanger. The test loop is equipped with all needed instrumentation, temperature and pressure sensors and mass flow meters. The latter are also used to measure the density of the fluid, which as we shall see is necessary for our composition measurements. At different places in the loop, optical cells are inserted in the circuit so that light can pass through the fluid to perform our measurement. The light generated by a source in the spectrometer is routed to the cell by an optical fiber. The light transmitted by the cell is then returned to a detector in the spectrometer.
An optical multiplexer is used to choose between the different optical cells to be analyzed.
Then, the signal is treated to yield an absorption spectrum specifying the amount of absorbed light for each wavelength λ (or its reciprocal, the wavenumber $\sigma = \lambda^{-1}$). The treatment of the signal to extract valuable information (namely compositions) will be described in the next section.

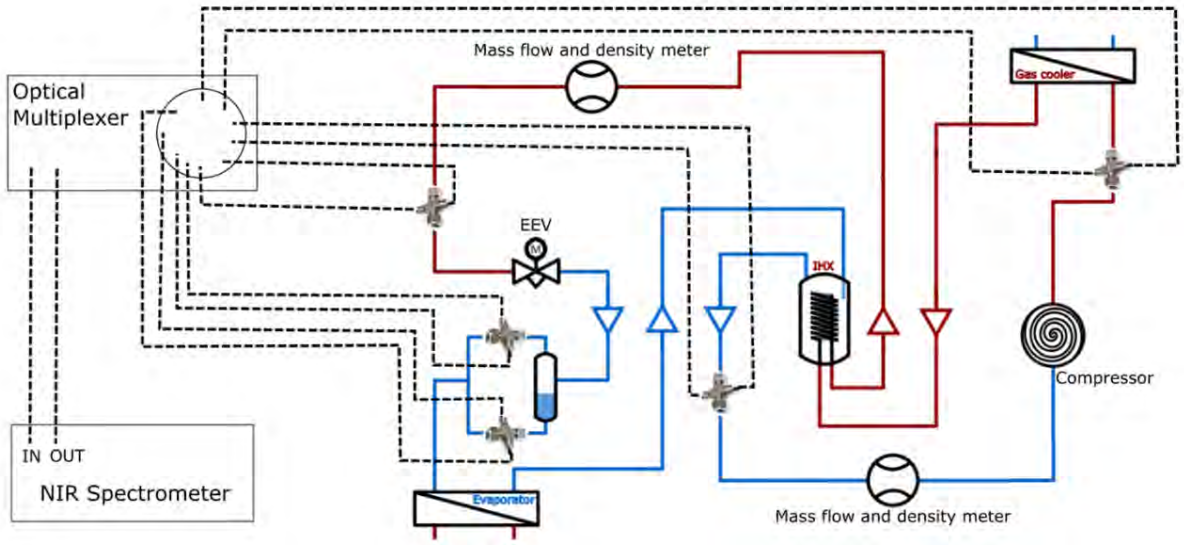

Figure 1: Experimental setup (dotted lines are optical fibres)

3. DATA TREATMENT

An example of a mixture spectrum compared to spectra of the pure species is shown on Fig. 2. It can be seen on this figure that the peaks of the spectra of the pure species are also present in the mixture spectrum. In principle, the absorbance should be proportional to the concentration of the species (Beer-lambert law). However, the peaks are distorted, widened and lowered by different physical phenomena. Hence, in practice, it is difficult to relate the concentration to absorption in a simple way. Therefore, we rely on a statistical treatment of a large number of absorption values. In this case, our spectra are recorded in the range $4500 - 10000\,cm^{-1}$ with a resolution of $1\,cm^{-1}$ which means one spectrum consists in 5500 absorption values.

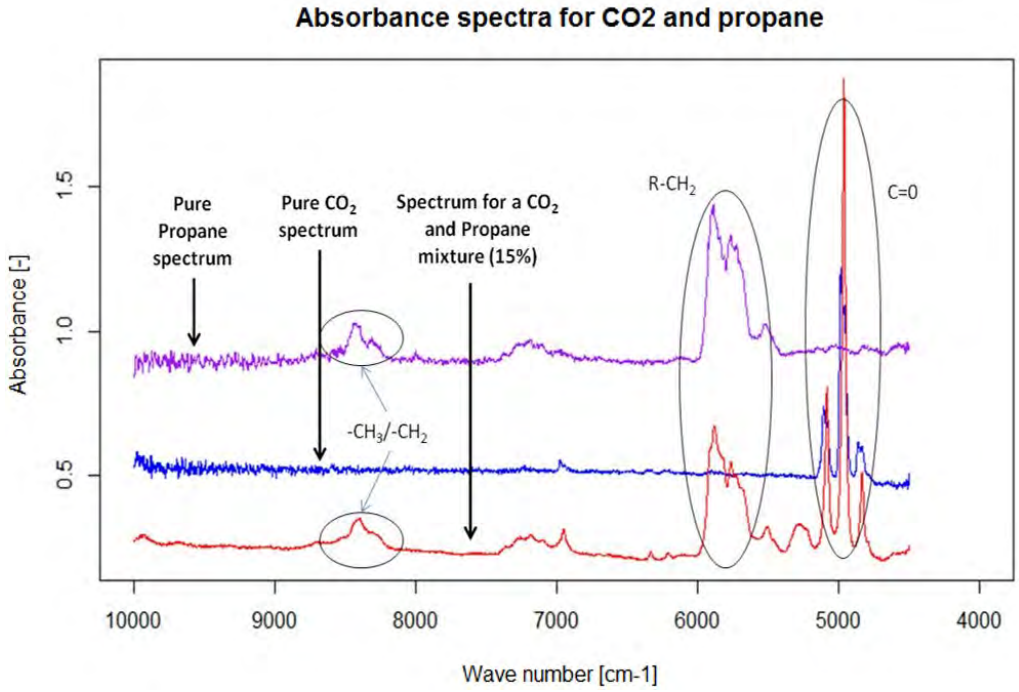

Figure 2: Spectra of pure CO2 and propane along with mixture spectrum. The mixture spectrum exhibits structures found on both spectra of the pure species

Chemometric methods have been developed in the last decades for these purposes. Also known as multivariate calibration, these are statistical methods used to relate some physical or chemical properties to the spectra (Martens and Naes, 1989; Varmuza and Filzmoser; 2009, Wehrens, 2011).

3.1. Principal Component Regression (PCR)

The principle of the method is to reduce the dimension of the space of variables to only the most significant ones. Here, we have 5500 variables i.e. a vector space with 5500 dimensions where absorption data for each wavenumber are the coordinates. The idea is to find the few (less than 10) principal directions of this space (those which retain the most significant coordinates) and then to project the data to this little subspace. It is then easy to solve the problem in this reduced space. An example is shown in two dimensions to visualize the concept on Fig. 3. Here two coordinates x, y describe the data but if they are projected to the oblique axis, we end up with only one coordinate that retains the most significant characterization of the data and the coordinate in the orthogonal direction may be considered as noise. Technically, this corresponds to the highest eigen values of the covariance matrix of the original data.

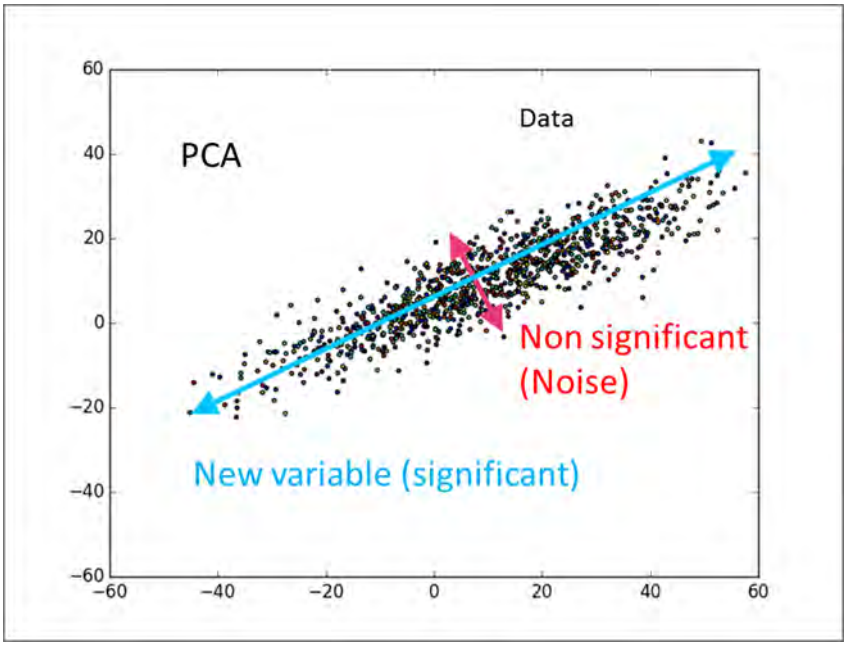

Figure 3: Projection on principal axis of a set of data (example in two dimensions)

3.2. Calibration

The principal components are defined by an analysis of the data for a given set of spectra named the calibration or the training set. In this case it is a collection of n spectra for which the composition is known (here the concentration of CO2 and propane in the mixture). We want to relate the concentrations Y to the spectra X by a linear relationship of the form:

$$Y = XB^t$$

Where Y is a matrix (n rows x 2 columns) containing the concentration data for the n calibration spectra and X is a matrix (n rows x 5500 columns) containing the n spectra. B^t is the transpose of B which is a big matrix with too many coefficients. The system is underdetermined because we have far less than 5500 calibration spectra.
This is where principal components analysis comes into play. The data are projected on a small subspace with only a few dimensions and we end up in the new space with a reduced system of the form:

$$Y = UA^t$$

Where U is the matrix of the data in the new coordinates and A the matrix of the coefficients of the relation in the new space. Since we have here more spectra than variables, a least squares fit is possible to determine the coefficients. This is what PCR calibration does.
Once the coefficients are determined, it is easy to treat a new spectrum with unknown concentration by projecting the data in the new space and then solving for Y. (i. e. the concentrations that we want to determine)

3.3. Calibration data

It is necessary to collect the concentrations of CO_2 and propane for the calibration spectra in order to determine the coefficients of the model.
In order to do that, we have implemented micro samplers on the experimental loop and use gas chromatography to measure the composition of the fluid. However, spectra are related to the concentration of each species in the mixtures while gas chromatography can only measure the mole fractions. Hence, it is necessary to measure the overall density ρ_{mix} of the fluid in order to determine the concentrations as:

$$c_i = \frac{x_i \rho_{mix}}{x_1 M_1 + x_2 M_2} \qquad \text{Eq. (1)}$$

Where x_i are the molar fractions of the species and M_i are the molar masses. Note that molar concentrations c_i are defined as the number of moles per unit volume i.e.

$$c_i = \frac{n_i}{V}$$

Where n_i are the number of moles in the volume V.

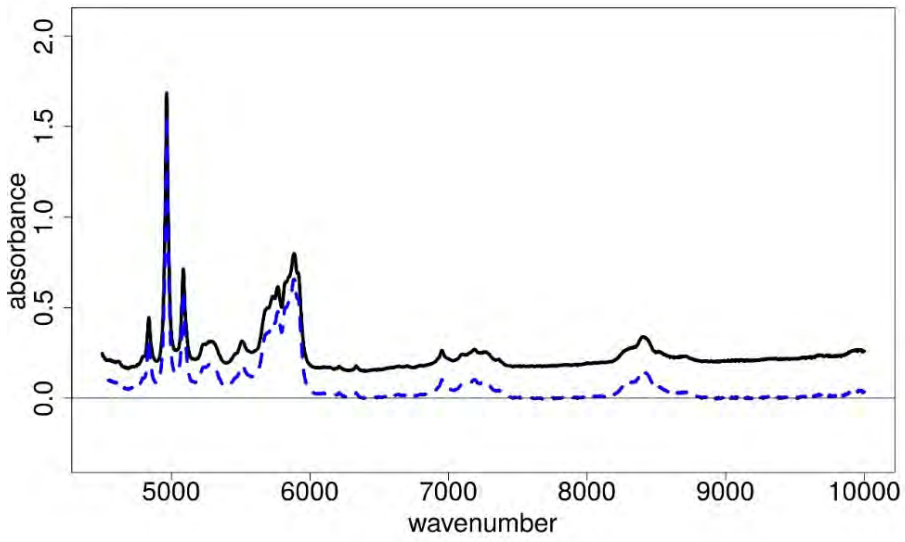

Figure 4: Baseline correction (original spectrum: solid line; corrected: dotted line)

3.4. Partial Least Squares (PLS)

Partial least squares is similar except that unlike for PCR, the data in Y (i.e. here concentrations) are also used in the process of determination of the principal axes. Technically, the covariance of data in Y and X are also taken into account. The principal axes are slightly different and generally, so are the prediction results. We shall see later that in our case, it does not make a big difference on the predicted concentrations. There are different algorithms giving nearly identical results (Wold et al.,1984; Geladi, 1986; de Jong , 1993; Dayal, 1997). We used here the so called kernel algorithm (Dayal, 1997).

3.5. Cross Validation

In order to test the validity of the model during the calibration process, it is customary to divide the calibration set in a number of segments, exclude one segment from the calibration process and then test the prediction on the segment spectra. This is repeated for each segment and the prediction errors are evaluated to validate (or not) the model (Wehrens,2011). In the following we used a 10 segments cross validation procedure. Technically, the root mean squared error of prediction (RMSEP) is used. The latter is defined as:

$$RMSEP = \frac{1}{n}\sqrt{\sum_{i=1}^{n}\left(y_i^p - y_i^m\right)^2} \qquad \text{Eq. (2)}$$

Where y_i^p are the predicted values and y_i^m are the measured ones.

3.6. Baseline Correction

Due to different physical phenomena (reflection on cell interfaces, refraction index of the fluid …), the recorded spectrum is usually shifted from its baseline as can be seen on figure 4. It is customary to correct the spectrum to set its value to zero in regions where no absorption occurs. This was done here by fitting a straight line to the “no absorption” zones and then subtracting it to the spectrum. On figure 4, the solid line is the original spectrum and the corrected one is the dotted curve.

4. RESULTS AND DISCUSSION

An example of the results will be presented here. A total of 121 spectra were used in this case. They were recorded at the inlet of the expansion valve in the circuit of the heat pump. 71 spectra were randomly chosen among these to build the training set. The remaining 50 spectra were used to test the predictive value of the final model generated with the whole set of calibration spectra.

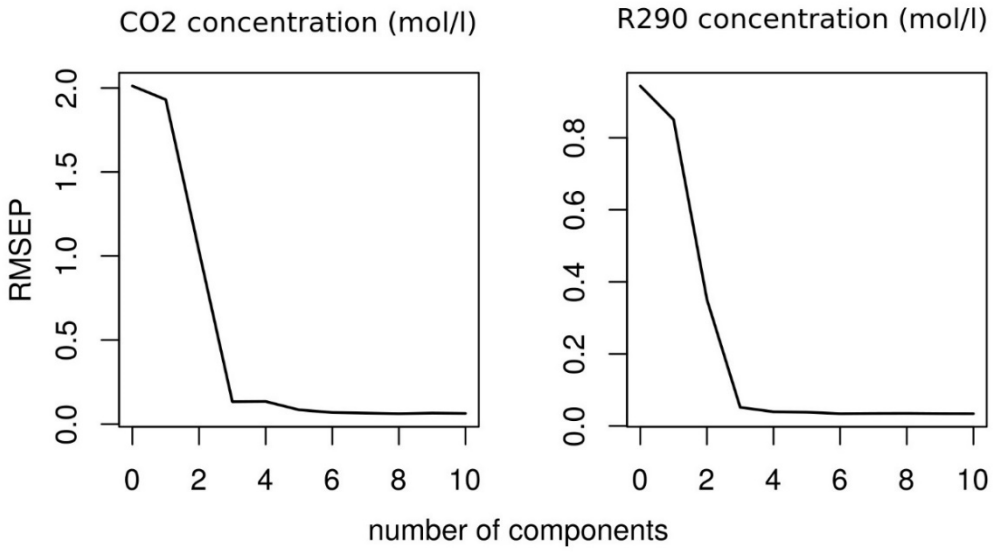

Figure 5: Root mean Squared error of prediction as function of number of principal components used

We tried different strategies in order to evaluate the best one for our purposes.
Here the results of a typical run of the data treatment are presented in some detail, then they will be compared with a few others.
We use here, the whole spectrum without selecting specific spectral bands. Also, no baseline correction was performed in this case. The algorithm used was PLS and a cross validation test is performed with 10 random samples.
Figure 5 shows plots of the Root Mean Squared Error of Prediction (RMSEP, Eq. (2)) estimated by the cross-validation algorithm as a function of the number of principal components used. This is used to determine how many of those components will be used to achieve a sufficient accuracy. It is clear here that using 6 principal components is a good choice as the precision is not much improved when using more.

The prediction of the final model has then been tested against the 50 spectra in the validation set. The mean relative error and the maximum relative error are reported in table 1 (as %).

The values reported in the table are: $100.Mean\left(\left|\frac{y_i^p - y_i^m}{y_i^m}\right|\right)$ and $100.Max\left(\left|\frac{y_i^p - y_i^m}{y_i^m}\right|\right)$

Fig. 6 shows the predicted concentration versus the measured one for both fluids. It appears that the model gives a better prediction accuracy for CO2 than for propane.

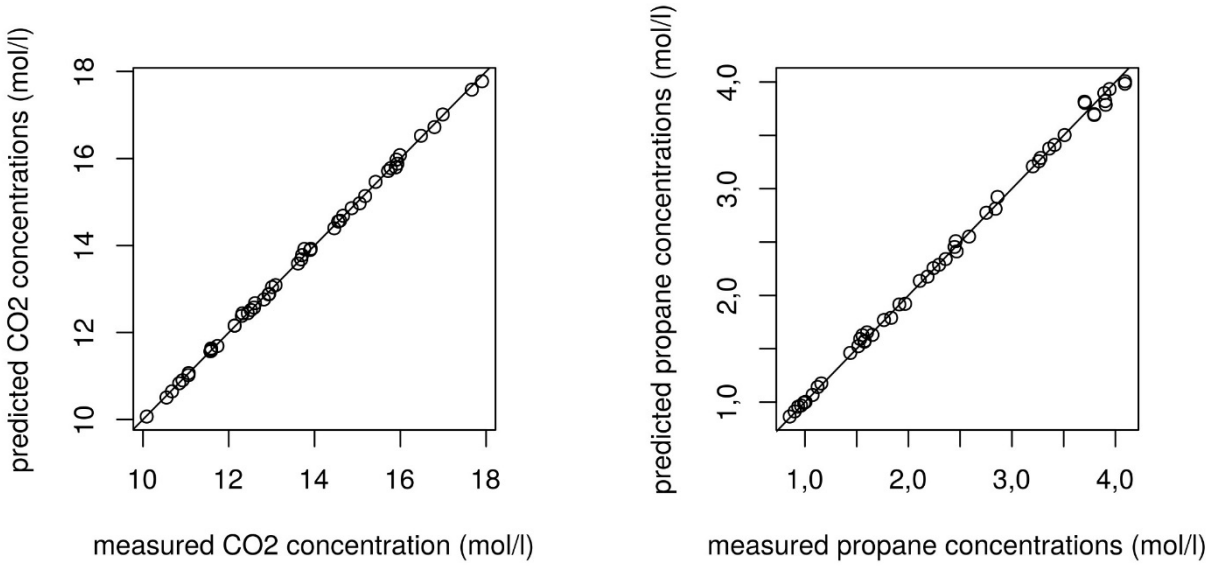

Figure 6: Predictions for propane and CO2 concentrations on validation set

The deviation plot shown on figure 7 also shows how the errors are distributed for the different points. As can be seen on these figures, most of the deviations lie below 0.6% for propane concentrations and below 3% for propane concentrations.
As a further test of the consistence of the model, the density of the mixture was calculated from the predicted values of the concentration:

$$\rho_{mix} = M_1 c_1 + M_2 c_2 \qquad \text{Eq. (3)}$$

Where M_i stand for molar mass of chemical component i and c_i stand for molar concentration of species i.
Most surprisingly, such calculated densities match the measured ones better than predicted concentrations (at least for propane) as may be seen in table 1 where the mean and maximum deviations are reported for correlated data and predicted data.
This is perhaps because those 3 parameters are correlated and also perhaps because the accuracy of our measurements on densities is better than our mole fractions measurements (mostly on propane). Remember here that the concentrations were calculated by equation (1) which uses both densities and molar fractions (and also molar masses, but those are constants).
When density data are considered in the calibration process, the precision is not always improved
Also, in some cases, the density calculated from the predicted concentrations may be slightly more accurate. However, all these errors are of the same order.
When PCR is used, adding the density data in the calibration procedure doesn't change at all the prediction on other parameters as if each parameter was predicted independently.
Baseline correction doesn't seem to make a big difference. It doesn't always improve the accuracy. This is perhaps because all spectra here were recorded with the same optical cell with the same optical path and fibers. It remains to be seen if it would have been the same with different optical cells where the baseline may have a different shape. This will be tested in future work.

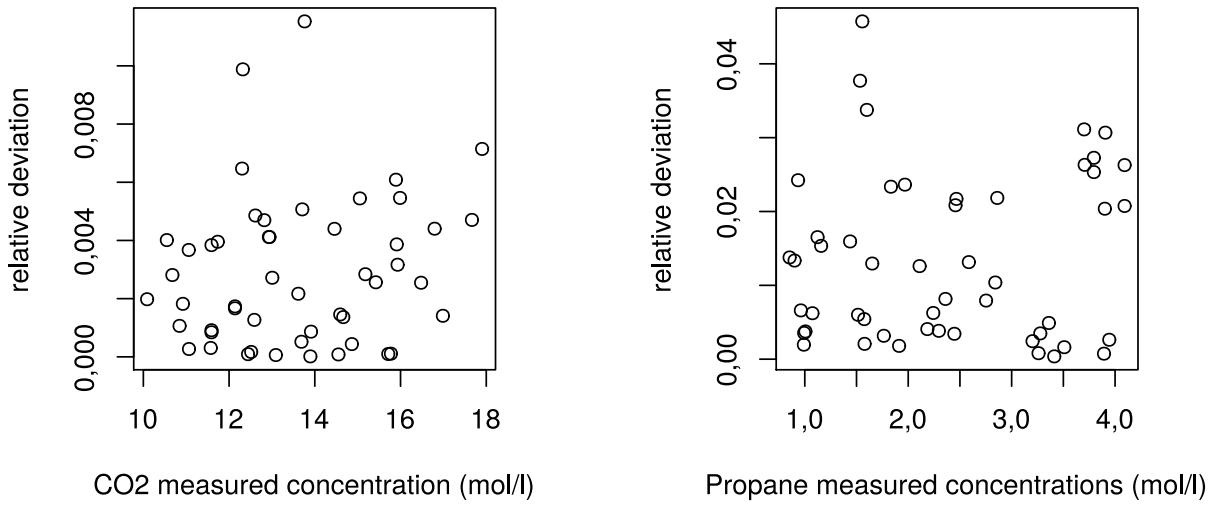

Figure 7: Relative prediction errors distribution

It is interesting to see if including the densities in the calibration process would improve the prediction. To this end, we performed such tests with 3 variables, mixture density and both concentrations for CO2 and propane. The results are similar and the deviations have been reported in Table 1.

Table 1. Relative deviations (%) on calculated properties (correlation data for spectra in the calibration set, used in the calibration process) and prediction errors (calculated for spectra in the validation set, not used in the calibration)

Correlation data									
CO2 concentration		R290 concentrattion		Measured Density		Calculated density			
Mean error	Max error	Mean error	Max error	Mean error	Max error	Mean error	Max error	Baseline correction	Algorithm
0,32	1,06	1,27	4,48	NA	NA	0,26	1,19	NO	PLS
0,25	0,82	1,32	6,12	NA	NA	0,21	0,97	YES	PLS
0,48	1,53	1,49	5,20	NA	NA	0,49	1,65	NO	PCR
0,54	1,50	1,60	6,03	NA	NA	0,54	1,76	YES	PCR
0,35	1,07	1,19	4,48	0,26	1,18	0,26	1,18	NO	PLS
0,27	0,86	1,27	5,66	0,20	0,87	0,19	0,88	YES	PLS
0,48	1,53	1,49	5,20	0,48	1,64	0,49	1,65	NO	PCR
0,54	1,50	1,60	6,03	0,53	1,77	0,54	1,76	YES	PCR
Prediction data									
0,29	1,15	1,35	4,57	NA	NA	0,23	0,80	NO	PLS
0,30	1,03	1,45	4,41	NA	NA	0,22	0,80	YES	PLS
0,35	1,26	1,58	5,20	NA	NA	0,39	1,21	NO	PCR
0,40	1,17	1,56	4,02	NA	NA	0,43	1,07	YES	PCR
0,33	1,15	1,30	4,64	0,23	0,67	0,22	0,72	NO	PLS
0,31	0,99	1,43	4,09	0,21	0,83	0,20	0,79	YES	PLS
0,35	1,26	1,58	5,20	0,39	1,25	0,39	1,21	NO	PCR
0,40	1,17	1,56	4,02	0,44	1,15	0,43	1,07	YES	PCR

Here, errors on concentrations are reported because the spectral method is sensitive to concentrations, not mole or mass fractions. However, mole fractions can be calculated easily from concentrations and then compared to values measured by chromatography. This has been done for the 50 spectra in the prediction test set. The average relative deviation on mole fractions is 1.3% for propane and 0.25% for CO2. The maximum observed relative deviations are 4.3% for propane and 1% for CO2. These values are consistent with those reported for concentrations in table 1. They are also consistent with, the uncertainties of mole fractions measured by chromatography that were estimated as 4% for propane and 2% for CO2.
Note also that in this particular case, mass fractions are the same as mole fractions because both fluids have the same molar mass (i.e. 44 g/mol).

5. CONCLUSIONS

A method for measurements of concentrations of species in refrigerant mixtures by spectroscopy and statistical chemometry procedures was presented and tested on a CO2+propane experimental heat pump. Different treatments of the recorded spectra were presented and compared. The uncertainty in the calculated concentrations is similar in most cases. It is of the order of 1% of the measured value for CO2 concentrations and 3% of the measured value for propane concentrations. It is also shown that the overall density can be predicted by this kind of methods with an accuracy of the order of 0.5%. It seems that the precision on concentrations can be improved if the data used for calibration are more accurate. This will be investigated in future work.

REFERENCES

Bouteiller P., 2017. Etude expérimentale de cycles de pompe à chaleur utilisant des mélanges à base de CO2. PhD Thesis 2017 CNAM Paris France, 197p

Dayal B. S. and Mac Gregor J .F., 1997. Improved pls algorithms. Journal of Chemometrics 11(1), 73–85,

De Jong S., 1993. SIMPLS: an alternative approach to partial least squares regression. Chemometrics and Intelligent Laboratory Systems, 18, 251–263, 1993.

Geladi, P., and Kowalski B. R., 1986. “Partial Least-Squares Regression: A Tutorial.” Analytica Chimica Acta 185 (C): 1–17.

Kim, M., Pettersen J., Bullard and C.W., 2004. Fundamental Process and System Design Issues in CO2 Vapor Compression Systems. Progress in Energy and Combustion Science. 30(2) 119-174

Ma Y., Liu Z., and Tian H. 2013. “A Review of Transcritical Carbon Dioxide Heat Pump and Refrigeration Cycles.” Energy 55 (2013). Elsevier Ltd: 156–72.

Martens H. and Næs T. Multivariate Calibration. Wiley, Chichester, 1989.

Varmuza K., Filzmoser P. Introduction to multivariate statistical analysis in chemometrics. [s.l.] : [s.n.], 2009. 321 p.

Wehrens, R. 2011. Use R! Chemometrics with R: Multivariate Data Analysis in the Natural Sciences and Life Sciences. Edited by Springer 267p

Wold, S., Ruhe, A. Wold, H. and Dunn W.J., 1984. “The Collinearity Problem in Linear Regression. The Partial Least Squares (PLS) Approach to Generalized Inverses.” J. Sci. and Stat. Comput. 5 (3), 735–43.

Manuscript ID: 1234
DOI: 10.18462/iir.icr.2019.1234

Influence of thermophysical properties in nucleate boiling

Niklas BUCHHOLZ, Andrea LUKE

University of Kassel, Institute of Technical Thermodynamics,
34125 Kassel, Germany, ttk@uni-kassel.de

ABSTRACT

The heat transfer coefficient in nucleate boiling is mainly determined by the heat flux, the saturation pressure, the thermophysical properties of the liquid and the properties of the material and the structure of the heating surface. However, new prediction methods for the heat and mass transfer in boiling will be required in future to replace the empirical correlations used until now, since they are inexact for many cases. Recently, new correlations have been established to describe the influence of the physical properties in nucleate boiling. In this context, the heat transfer for different hydrocarbons boiling on the outside of a horizontal tube (mainly of copper) with defined surface properties will be presented and compared to the new correlations from literature. The results show that the equation developed recently is only valid for limited applications of pure fluids and within certain boundary conditions. A proposal for the modification of the correlation is presented.
Keywords: pool boiling, cavity, evaporation, heat transfer

1. INTRODUCTION

Evaporation in free convection, so-called pool boiling, is used in refrigeration, e.g. in the evaporation of a refrigerant on the outside of the heat transferring surfaces of tube bundles in heat exchangers. In the case of evaporation, in particular in nucleate boiling, high heat fluxes are transmitted very efficiently at low temperature gradients. It is important to make all components and their interaction more efficient, i.e. to minimize the exergetic losses, for the optimization of the entire refrigeration process. Therefore the design of the heat exchanger is an essential part of reducing costs and increasing the efficiency of the entire system.
The design of flooded evaporators is usually done with empirical correlations, which are based on more or less accurate experimental data. Hence an accurate calculation of the heat transfer is only allowed for very specific (or even unknown) secondary conditions. Any errors in the correlations are compensated by high safety factors in the calculation of the heat transferring surfaces, which results in higher pressure losses, higher material costs and an increased amount of refrigerant. The overall efficiency of such systems decreases. A further development of present calculation methods is necessary.
Previous methods to calculate the two-phase heat transfer disregard many phenomena proven already by research or consider them inadequately. The influences on the heat transfer are usually considered separately in the pool boiling regime and interactions between the influencing variables are mainly neglected, e.g. the correlation according to Gorenflo (1997) for the calculation of the two-phase heat transfer coefficient α during pool boiling

$$\frac{\alpha}{\alpha_0} = F_q \cdot F_{p^*} \cdot F_w, \qquad \text{Eq. (1)}$$

in which the influencing factors on the heat transfer are taken into account by dimensionless factors. F_q represents the influence of the heat flux density, F_p* the influence of the reduced pressure and F_w the influence of the heating surface material and the surface structure. The influence of the fluid properties on the heat transfer is taken into account only by the normalization

value α_0, which is the heat transfer coefficient of the fluid at the reference values $p^* = p_s / p_c = 0.1$, $\dot{q}_0 = 20$ kW / m^2 and $P_{a,0} = 0.4$ µm with copper as the heating surface.
The normalization value α_0 directly affects α in Eq. (1). Errors with respect to this value affect the calculated heat transfer coefficient α and thus the designed apparatus. α_0 is calculated according to Stephan and Abdelsalam (1978) for water, hydrocarbons, cryogenic fluids and refrigerants based on a dimensional analysis from the dimensionless Nusselt number

$$Nu = \frac{\alpha d_A}{\lambda'} = 0.23 \left(\frac{q_0 d_A}{\lambda' T_s}\right)^{0.674} \left(\frac{\rho''}{\rho'}\right)^{0.297} \left(\frac{\Delta h_v d_A^2}{a'^2}\right)^{0.371} \left(\frac{\rho' - \rho''}{\rho'}\right)^{-1.73} \left(\frac{a'^2 \rho'}{\sigma d_A}\right)^{0.35} \quad \text{Eq. (2)}$$

with the thermal conductivity of the fluid λ', the boiling temperature T_s, the densities ρ'' and ρ' of the gaseous and liquid phases, the enthalpy of vaporization Δh_v, the thermal diffusivity a' of the liquid phase and the surface tension σ. The bubble departure diameter d_A according to Fritz (1935) is used as the characteristic length. A variety of authors published further correlations for calculating the bubble departure diameter, e.g. Weckesser (1990), Schömann (1994) and Luke (2000). All corrections have very high deviations in comparison with measured values, so that an exact calculation of the bubble departure diameter is not possible. Also the distribution of the bubble departure diameter is not detected at constant heat flux and constant reduced pressure.
Stephan and Preußer (1979) fit Eq. (2) to other measuring data that gives a good representation of the heat transfer coefficient for water at ambient pressure but shows large deviations for organic refrigerants. The Nusselt number results in

$$Nu = 0.1 \left(\frac{q_0 d_A}{\lambda' T_s}\right)^{0.674} \left(\frac{\rho''}{\rho'}\right)^{0.156} \left(\frac{\Delta h_v d_A^2}{a'^2}\right)^{0.371} \left(\frac{a'^2 \rho'}{\sigma d_A}\right)^{0.35} \left(\frac{\eta' c_p'}{\lambda'}\right)^{-0.16} \quad \text{Eq. (3)}$$

with the dynamic viscosity η 'and the specific heat capacity c_p' of the liquid. The influence of the reduced pressure is represented in Eq. (2) and (3) only by a variety of physical properties, so that the pressure dependence of the heat transfer coefficient is not sufficiently considered in both equations. For most refrigerants the ambient pressure is approximately $p^* = 0.03$ (Gorenflo, 1997). With F_p^* (s. Eq. (1))

$$F_{p^*} = 1.2\, p^{*0,27} + \left(2.5 + \frac{1}{1 - p^*}\right) p^* \quad \text{Eq. (1a)}$$

the influence of pressure is considered in Eq. (3) according to Gorenflo (1997). In recent works (Gorenflo, 2013), the factors in Eq. (1a) are adapted to further data, resulting in a steeper slope of the heat transfer coefficient as a function of reduced pressure.
Kotthoff (2014) proposes the calculation of the heat transfer coefficient α_0 based on fluid parameter P_f, which Bier et al. (1973) postulates as the pressure dependence of the heat transfer coefficient of a vapor bubble in equilibrium. By adaptation to measured data results

$$\alpha_0 = 3.58 \cdot P_f^{0,6} = 3.58 \cdot \left(\frac{(dp/dT)_{vpk}}{\sigma}\right)^{0,6} \quad \text{Eq. (4)}$$

with the slope of the vapor pressure curve $(dp / dT)_{vpk}$ and the surface tension σ at $p^* = 0.1$, P_f in (µm K)$^{-1}$ and α_0 in kW(m^2 K)$^{-1}$.
The heat transfer coefficient is shown in Figure 1 as crosses for n-pentane according to Eq. (2), (3) and (4) in comparison to measurements by Wengler (2018), Buljina (2010) and Siebert (1987). In addition, the pressure influence is represented with Eq. (1a) in Figure 1, starting from the three differently calculated values of α_0. The calculated values deviate considerably from the measured ones at $p^* = 0.1$, s. Table 1. In addition, measurements from Wengler (2018) show positive deviations from the heat transfer coefficient and measured values of Buljina (2010) and Siebert (1987) show negative deviations compared to the frequently used Eq. (3).

Table 1: Comparison of calculated and measured heat transfer coefficients (at the reduced pressure $p^* = 0.1$, $\dot{q} = 20$ kW/m^2 of a copper heating surface with $P_{a0} = 0.61$ - 0.66 µm

$(\alpha_{exp} - \alpha_{calc}) / \alpha_{calc}$	Stephan, Abdelsalam [Eq. (2)]	Stephan, Preußer [Eq. (3)]	Kotthoff [Eq. (4)]
Siebert (1987)	-37.23 %	-12.72 %	-21.97 %
Buljina (2010)	-27.15 %	1.31 %	-9.43 %
Wengler (2018)	11.20 %	54.64 %	38.24 %

A more detailed description of the thermophysical relationships in pool boiling will be obtained by considering interactions between the different parameters in Eq. (1). Luke (1996) takes the interaction between the arithmetic mean roughness and the reduced pressure into account, based on Eq. (1), and adjusts the slope of the heat transfer coefficient as function of the heat flux density for various roughness.

All of the equations listed above for the calculation of the heat transfer coefficient are valid for fluid values in equilibrium between the vapor bubbles and the boiling liquid. The wetting of the surface is usually not taken into account. In the following an approach is presented based on Luke (1996) which describes the mechanism of vapor bubble formation at activated nucleation sites, i.e. in cavities in the surface, converted into a mathematical notation, which enters into a correlation to describe the heat transfer at pool boiling. A theoretical approach is presented in which the nucleation and wetting of the solid surface are described only on the basis of fluid data of the refrigerant and the roughness profile of the surface. The methodology is going to be validated with experimental data. Finally, the experimental setup for generating the data is presented.

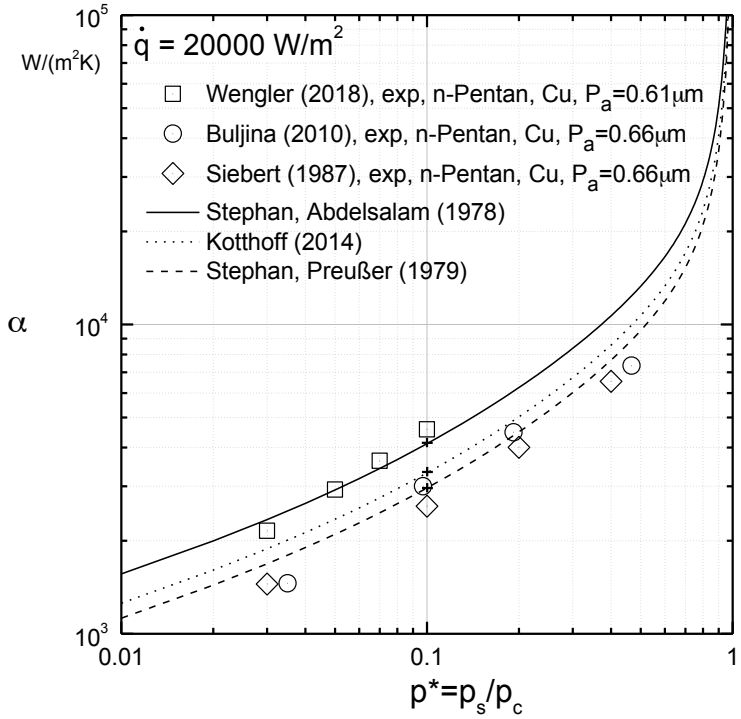

Figure 1: Comparison of calculated and measured heat transfer coefficients of copper as function of the reduced pressure for n-pentane (α_0 shown as crosses)

2. MODELLING

The heterogeneous nucleation, i.e. the formation of vapor bubbles on a solid surface, must be taken into account by considering the influence of fluid properties on the two-phase heat transfer, since these are decisive for the integral heat transfer coefficient. Previous approaches only consider the influence of fluid properties and the influence of surface roughness separately. The influence of surface roughness resp. topography shown in Eq. (1) is described only by the standard arithmetic mean roughness value. The shape of one single nucleation site is essential for the

activation of the bubbles, their growth, bubble departure diameter and frequency. An integral roughness parameter (such as P_a) is not suitable for describing the mechanism of nucleation because the shape of the cavity and the wetting of the surface are not considered.
For modelling of the nucleation site and its influence on the heat transfer a parameter is to be found, which takes into account the cavity in the surface, the wetting of the surface and the properties of the fluid. Salem (1979), Knabe (1984) and Blöchl (1986) already define cavity parameters, which Schömann (1994) assigns to the envelope method. A ball with variable rolling radius R_K is pushed over the roughness profile of a surface in the envelope method to obtain the cavity parameter. The centers of the sphere form a trajectory, which is pushed onto the actual profile of the surface. The cavity parameters are calculated from the profile of the surface and the envelope. The definitions of the various parameters are given by Schömann (1994). Luke (1996) extends Schömann's (1994) cavity parameters by the parameter characteristic for a single cavity

$$P_5^* = \sqrt[3]{V_K} \qquad \text{Eq. (5)}$$

with the volume V_k of a sphere of diameter d as the maximum distance between the surface profile and the envelope. The critical nucleation radius of a viable bubble is given with the Thomson equation and the Clausius-Clapeyron equation

$$r_c = \frac{2\sigma T_s}{\rho'' \Delta h_v \Delta T} \qquad \text{Eq. (6)}$$

for high enough boiling temperatures with the surface tension σ, the boiling temperature T_s, the gas density ρ'', the enthalpy of vaporization Δh_v and the superheating ΔT at which a vapor bubble is viable. The critical nucleation radius decreases for higher reduced pressures, s. Figure 2. More and smaller nucleation sites are activated at the same superheating for increasing pressures. The pressure dependence of the activated nucleation sites and thus the heat transfer is given with the choice of the spherical radius R_K. Fewer but larger nucleation sites are found with larger spherical radii, s. the cumulative distribution of the parameters P_5* in Figure 3. Similarly, the wetting of the surface by the boiling liquid influences the spherical radius or the resulting cumulative distribution of P_5*. For each reduced pressure is derived a characteristic size of P_5* from the cumulative distribution

$$P_5^* = f(p^*, \Theta) \qquad \text{Eq. (7)}$$

with the contact angle Θ. A new parameter is defined to account for the interaction between the surface and the boiling fluid for the calculation of heat transfer for different fluids, based on Eq. (1).

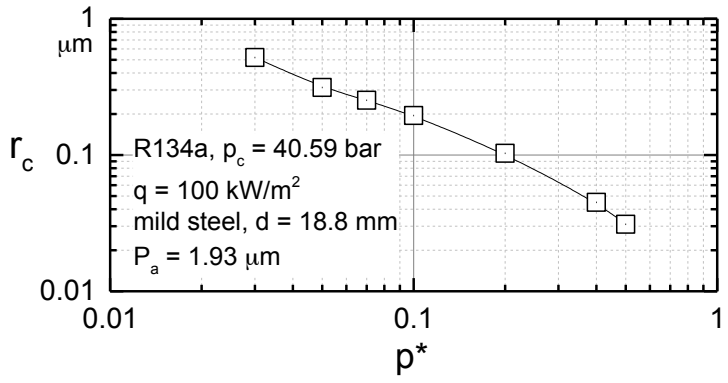

Figure 2: Critical nucleation radius as a function of the reduced pressure on the basis of experimental data from Müller (2019) for R134a at a constant heat flux density

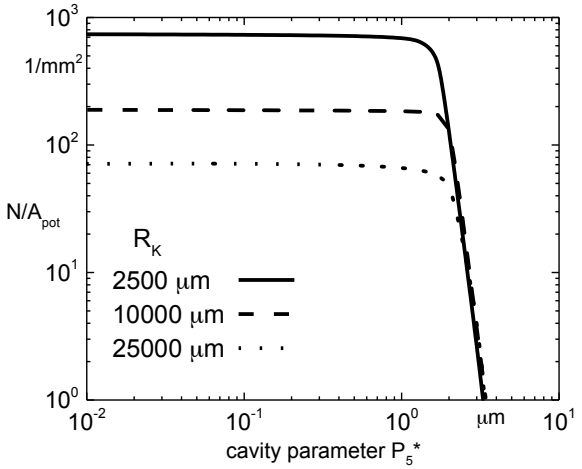

Figure 3: Exemplary representation of the cumulative distribution of the cavity parameter P_5* for a fine sandblasted copper tube (P_a = 0.25 µm) according to Luke (2002)

The interactions between the fluid properties and the surface structure are given by the bond number and P_f in Eq. (4). The Bond number *Bo* is the ratio of bulk forces to surface forces, in the case of ascending vapor bubbles, the ratio of buoyancy force to force due to the surface tension

$$Bo = \frac{\Delta\rho g l^2}{\sigma} \qquad \text{Eq. (8)}$$

with the difference between the liquid and gas density $\Delta\rho$, the gravitational acceleration g, the characteristic length l and the surface tension σ. A function resp. an averaged value of the cavity parameter P_5^* becomes apparent

$$l = f(P_5^*) \qquad \text{Eq. (9)}$$

and is used as a characteristic length in Eq. (8) to take account of the interaction between fluid properties and nucleation size and distribution. The course of the reciprocal of the product of bond number and P_f, based on a reference value (Gorenflo (2013)) for dimensionless representation in Figure 4, tends to reflect the course of a potentially higher heat flux density with a smaller cavity parameter at constant reduced pressure. Small nucleation sites are activated for high heat flux densities, increasing the evaporation rate and the heat transfer coefficient. Heat transfer measurements are carried out on a newly constructed standard-boiling apparatus according to Goetz (1980) to adapt Eq. (7) and Eq. (9) to experimental data and to create the parameter from P_f and *Bo* for use in Eq. (1). The experimental tube consists of a heating conductor wound on a copper helix, which is brazed into an outer cladding tube made of copper in contrast to many previous designs by Müller (2019), Fath (1986) and Sokol (1994). It is soldered in a vacuum

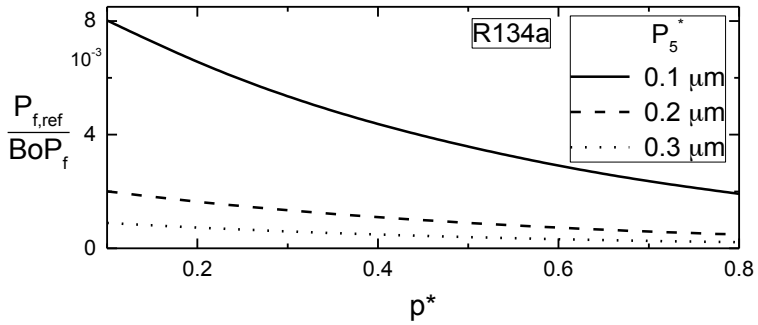

Figure 4: Product of bond number and dimensionless parameter P_f for different values of P_5* as function of the reduced pressure

furnace to prevent cavities in the solder layer, which impede a uniform distribution of the heat flow in the experimental tube. The overheating is measured with twelve azimuthally distributed thermocouples connected to comparative thermocouples in the boiling liquid. The thermocouples are located in eroded holes 1.5 mm below the surface. The innovative experimental tube construction is described in detail by Wengler (2018). Wengler (2018) uses no vacuum furnace in contrast to this work, so cavities in Wengler (2018) work cannot be completely excluded.

3. SURFACE TREATMENT AND ANALYSIS

The test tube surface for the heat transfer measurements should have a stochastic distribution of cavities, so that the activated nucleation sites are evenly distributed on the surface and the critical radius can be reduced to a characteristic cavity. Therefore, the surface is fine sandblasted. Roughness measurements are carried out with a mechanical stylus system (Fa. Hommelwerke, T8000) and an ultrasonic stylus (Fa. Jenoptik, Nanoswing 100) to determine the cavity parameters. A controller keeps the stylus at a constant distance above the surface by means of a motor during the measurement. The measuring principle is described in detail by Luke (2002) and Müller (2019). The roughness measurements are taken at several azimuthally distributed positions each above the thermocouple tips. The results of the surface analysis according to DIN EN 4287 (07.2010) are shown in Table 2 and Figure 5.

The arithmetic mean roughness value P_a of the surface is 0.51 µm with a standard deviation of 0.05 µm, s. Table 2. The stochastic distribution of cavities becomes apparent in the exemplary profile (bottom) in Figure 5 and the topography (top left) in Figure 5. At the top right of Figure 5, the frequency distribution of P_a is shown for the fine sandblasted surface. The topographies are evaluated according to the above-mentioned enveloping surface method to calculate the cavity parameters and potential nucleation sites, s. the envelopes of the surfaces for different values of R_k in Figure 6. Many and small nucleation sites can be found for the envelope surfaces with a small value of R_k, for larger radii few and large nucleation sites while comparing the envelopes with the topographic representation of the surface in Figure 5. The next step is the statistical analysis and evaluation of the cavity parameters and the relation to the heat transfer.

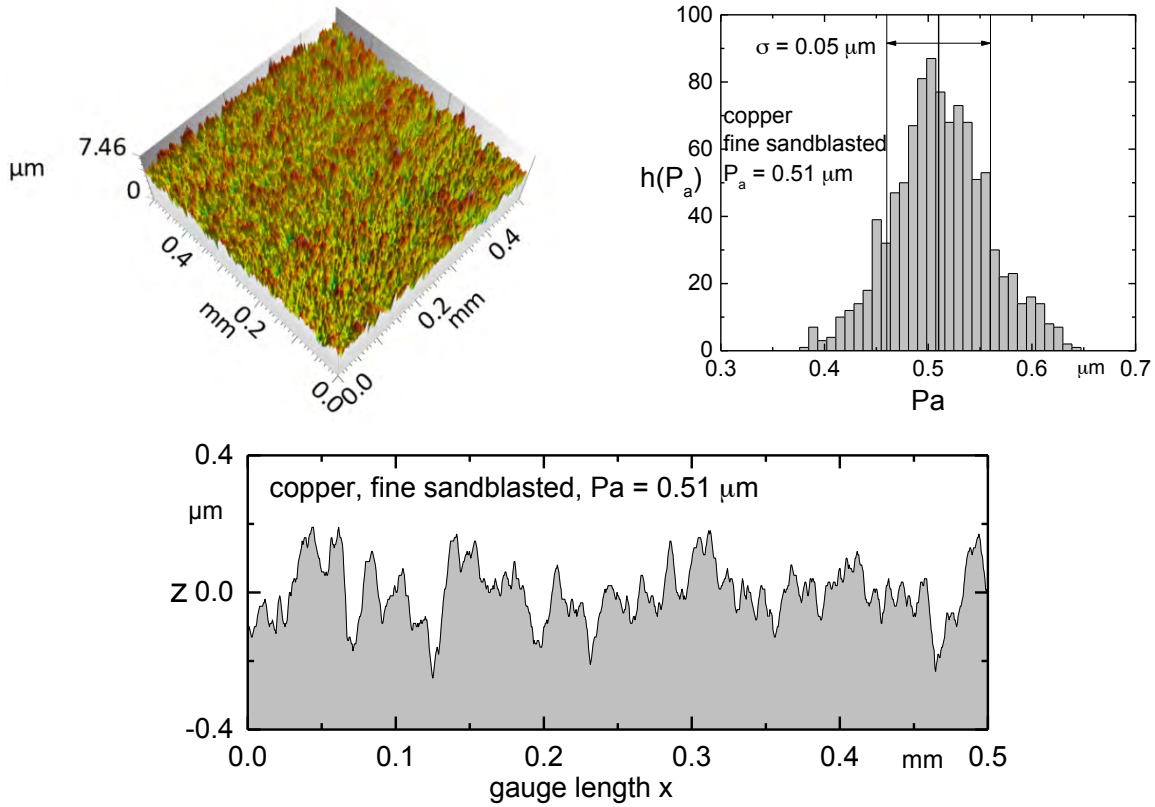

Figure 5: Isometric view (top left), frequency distribution of P_a (top right) and representative profile (bottom) of the sandblasted test tube surface made of copper

Table 2: Roughness parameters of the sandblasted test tube surface for a measuring length of 500 µm (DIN EN ISO 4287 (07.2010))

		Pa [µm]	*Pq* [µm]	*Pp* [µm]	*Pt* [µm]	*Pz* [µm]	Measured profiles
cooper, *D* = 19.05 mm, fine sandblasted	mid	0.51	0.65	2.05	4.18	4.18	2002
	max	0.65	0.83	3.63	6.71	6.71	
	min	0.38	0.49	0.99	2.76	2.76	
	σ	0.05	0.06	0.46	0.60	0.60	

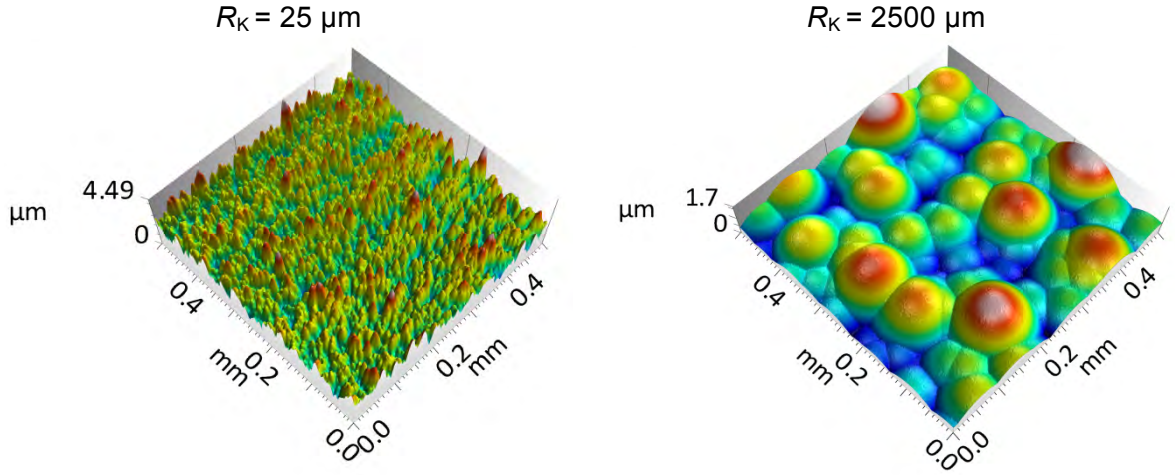

Figure 6: Envelope areas calculated for the topography in Figure 5 for different R_K

5. CONCLUSION

In the present work, the influence of the material properties in interaction with the microstructure of the heating surface on the heat transfer during pool boiling is described by a new theoretical approach, to be included into a correlation for the calculation of the heat transfer coefficient. The interaction between fluid and microstructure of the heating surface or vapor bubble formation at nucleation sites is taken into account by the bond number and the fluid parameter P_f. For this purpose, the cavity parameter P_5* is introduced in connection with the wetting of the heating surface by the contact angle. The approach corresponds to the theoretical concept of a lower critical nucleation radius with better heat transfer at lower superheat. Heat transfer measurements are made with various refrigerants in a standard boiling apparatus to validate the approach. The sandblasted tube surface has a stochastic distribution of cavities and is thus suitable for determining the activated nucleation sites for each heat flux density and each reduced pressure. Further heat transfer measurements are carried out with a new test tube surface and different cavity sizes to take into account different cavity sizes in the heating surface.

NOMENCLATURE

a	thermal diffusivity (m^2s^{-1})	$\dot{q}$	heat flux density (Wm^{-2})
A	surface (m^2)	r_c	critical nucleation radius (µm)
c_p	specific heat capacity ($kJ(kgK)^{-1}$)	R_K	rolling radius (µm)
D	tube diameter (mm)	T	temperature (K)
d_A	bubble departure diameter (µm)	V_K	ball volume (µm)
F	factor (-)	x	gauge length (mm)
g	gravitational acceleration (ms^{-2})	z	profile height (µm)
h	frequency (-)	α	heat transfer coefficient ($kW(m^2K)^{-1}$)
l	characteristic length (m)	Δh_v	heat of vaporization ($kJkg^{-1}$)

N	quantity (-)	η	dynamic viscosity (Pas)
p	pressure (bar)	Θ	contact angle (°)
p^*	reduced pressure (-)	λ	heat conductivity ($W(mK)^{-1}$)
P_5^*	cavity parameter (µm)	ρ	density (kgm^{-3})
P_f	fluid parameter $(mK)^{-1}$	σ	standard deviation (µm)
P	roughness parameters acc. to DIN EN ISO 4287 (µm)	σ	surface tension (Nm^{-1})

REFERENCES

Bier, K., Gorenflo, D., Wickenhäuser, G., 1973. Zum Wärmeübergang beim Blasensieden in einem weiten Druckbereich; Chem.-Ing.-Techn. 45, 935-942.

Blöchl, R., 1986. Zum Einfluss der Oberflächenstruktur unterschiedlich bearbeiteter Heizflächen auf die Wärmeübertragung beim Blasensieden, Diss., University Karlsruhe.

Buljina, I. 2010. Entwicklung und Aufbau zweier Siedeapparaturen zur Untersuchung des Wärmeübergangs weitsiedender binärer niedrig- und hochviskoser Gemische, Diss., University Bochum.

DIN EN ISO 4287 (07.2010) Oberflächenbeschaffenheit: Tastschnittverfahren, Benennungen, Definitionen und Kenngrößen der Oberflächenbeschaffenheit.

Fath, W., 1986. Wärmeübergangsmessungen an Glatt- und Rippenrohren in einer Standardapparatur für Siedeversuche, Diss., University Paderborn.

Fritz, W., 1935. Über den Verdampfungsvorgang nach kinematischen Aufnahmen an Dampfblasen, Phys. Z. 37, 391-401.

Goetz, J., 1980. Entwicklung und Erprobung einer Normapparatur zur Messung des Wärmeübergangs beim Blasensieden; Diss., University Karlsruhe.

Gorenflo, D., 1997. Hab, VDI-Wärmeatlas, Springer-Verlag, Berlin, Heidelberg, New York.

Gorenflo, D., 2013. H2, VDI-Wärmeatlas, Springer-Verlag, Berlin, Heidelberg, New York.

Knabe, V., 1984. Zum Einfluss der Heizflächenrauhigkeit auf den Wärmeübergang und die maximale Wärmestromdichte beim Blasensieden, Diss., University Paderborn.

Kotthoff, S., 2014. Zum Einfluss von Fluid- und Heizflächeneigenschaften auf Wärmeübergang und Blasenbildung beim Sieden, Diss., University Paderborn.

Luke, A., 1996. Beitrag zum Einfluss der Mikrostruktur von Heizflächen auf den Wärmeübergang beim Blasensieden, Diss., University Paderborn.

Luke, A., 2002. Thermo- und Fluiddynamik beim Sieden: Zusammenhänge zwischen Heizflächenstruktur, Verdampfung und Wärmeübergang, Habil, University Paderborn.

Luke, A., Gorenflo, D., 2000. Heat Transfer and Size Distribution of Active Nucleation Sites in Boiling Propane outside a Tube; Int. J. Therm. Sci. 39, 919-930.

Müller, B., 2019. Bewertung mikrostrukturierter Verdampferrohre hinsichtlich des Wärmeübergangs, Diss., University Kassel, in press

Salem, M. I., 1979. Wärmeübergang beim Blasensieden und Größenverteilung von stabilen Blasenkeimen sowie von Rauhigkeitsvertiefungen der Heizfläche, Diss., University Karlsruhe.

Schömann, H., 1994. Beitrag zum Einfluss der Heizflächenrauhigkeit auf den Wärmeübergang beim Blasensieden, Diss., University Paderborn.

Siebert, M., 1987. Untersuchung zum Einfluss des Wandmaterials und des Rohrdurchmessers auf den Wärmeübergang von horizontalen Rohren an siedende Flüssigkeiten, Diss., University Karlsruhe.

Sokol, P., 1994. Untersuchungen zum Wärmeübergang beim Blasensieden an Glatt- und Rippenrohren mit großem Außendurchmesser, Diss., University Paderborn.

Stephan, K., Abdelsalam, M., 1978. Heat-Transfer correlations for natural convection boiling, Int. J. Heat Mass Transfer 23, 73-87.

Stephan, K., Preußer, P., 1979. Wärmeübergang und maximale Wärmestromdichte beim Behältersieden binärer und ternärer Flüssigkeitsgemische; Chem.-Ing.-Techn. 51, 37 .

Weckesser, M., 1990. Untersuchung zur Blasenbildung beim Sieden in freier Konvektion, Diss., TH Karlsruhe.

Wengler, C., 2018. Einfluss des Heizwandmaterials auf den Wärmeübergang beim Blasensieden, Diss., University Kassel.

GEFÖRDERT VOM

Bundesministerium für Bildung und Forschung

Manuscript ID: 1252
DOI: 10.18462/iir.icr.2019.1252

Flow patterns of some new low GWP refrigerants during evaporation in small tube

Houpei LI[(a)], Pega HRNJAK[(a) (b)]

[(a)] Air Conditioning and Refrigeration Center, Department of Mechanical Engineering, University of Illinois at Urbana Champaign, 1206 West Green Street, Urbana, IL 61801, USA, hli84@illinois.edu
[(b)] CTS, 2209 Willow Rd., Urbana IL, USA, pega@illinois.edu

ABSTRACT

This paper reports visualization results of two-phase flow of R1233zd(E) and R1336mzz(Z) in a 24-port microchannel tube. The tube has an averaged hydraulic diameter of 0.643 mm. Mass flux is in the range from 50 to 200 kg-m^{-2}s^{-1}. Flow patterns are classified as plug/slug, transitional, and annular flow. In plug/slug flow, a clear interface between liquid slug and vapor plug is observed. In transitional flow, the interface between vapor plug and liquid slug is broken and becomes a thick liquid ring and vapor bridge. In annular flow, only liquid film is observed in the tube. Both mass flux and vapor density strong affect the flow pattern because they affect the flow velocity. The results are compared to other fluids tested on the same facility: R32, R134a, R1234ze(E), and R1234yf. R134a, R1234ze(E), and R1234yf have similar flow patterns at the same condition. Both R1233zd(E) and R1336mzz(Z) also have similar flow patterns because they have similar properties.
Keywords: Refrigerant, visualization, flow pattern, microchannel, HFO

1. INTRODUCTION

A new type of experimental facility for evaluation of heat transfer and hydraulic behavior in microchannel used in this work has been introduced in Li and Hrnjak (2017). In the original facility, six heat transfer coefficient and six pressure drop measurements at different vapor qualities are measured simultaneously in the six test sections. One evaporator and five conditioning sections adjust the inlet quality of the test sections. Visualization sections have been made and installed in the facility for flow characteristic research (Li and Hrnjak, 2019a, 2019b). Six visualization sections are placed after the six test sections. The evaporator and conditioning sections are still used as quality controllers for the test sections.

The new facility provides relatively efficient experiments but more importantly, the vapor quality of refrigerant is changed continually in one pass. The flow in the channels is closer to a realistic heat exchanger in a vapor-compression system, especially for refrigerant-oil mixtures or refrigerant blends because this design maintains realistic concentrations in the liquid structures close to the wall.

There are two methods of generation of two-phase flow: the mix method and the heat transfer method. In the first one, liquid and gas are mixed in the required flow rates before entering the visualization section, such as in Nino et al. (2002) and Triplett et al. (1993). In the heat transfer method, which is adopted here, liquid is heated, (or vapor is cooled in condensation experiments) from single phase to a two-phase state of desired quality before entering the test and visualization sections. The start from single phase assures uniformity of distribution among channels assuming uniform heating of the channels.

Table 1 listed the properties of tested fluids evaluated at 30 °C except R1336mzz(Z). The reason that the property of R1336mzz(Z) is evaluated at 50 °C is that the experiment was done at higher temperature than other fluids. R1233zd(E) and R1336mzz(Z) are low pressure fluids compare the other fluids listed. The two low pressure fluids have very low vapor density, which results in a very high vapor velocity and therefore the two-phase flow velocity. With higher velocity, the occurrence of flow pattern transitioning will advance to lower quality. The two low pressure fluids also have higher liquid viscosity and high surface tension. With higher surface tension, the surface force can conquer the gravity so stratify flow will not be observed when tube diameter is small.

Figure 1 shows the flow pattern concluded from the previous research (Li and Hrnjak 2019a, 2019b). Flow is classified as: plug/slug, transitional, and annular flows.

The plug/slug flow is like the bubbly flow, intermittent flow, or slug flow named in the literature. We always observe confined bubbles in the images. In plug/slug flow, a clear vapor plug can be seen in the video. In-between two clear vapor boundaries is the liquid slug. Sometimes bubbles can be seen at low quality or even in the thermally subcooled region. At high vapor quality but low mass flux, a liquid slug is still in the tube and the vapor plug is very long. A significant characteristic of this flow pattern is that the flow is homogeneous. Vapor plugs and liquid slugs are moving at the same velocity. Velocity of the liquid film is not determined due to the limitations of the visualization technique, but it is assumed that the film has lower velocity than the vapor plug.

In the transitional flow, vapor plug head and tail are not clear. This flow pattern is a transition from plug/slug flow to annular flow. This is similar to the churn flow, liquid-ring flow, or slug-annular flow in literature. A darker region can be observed in between the blurry boundary of vapor plugs and it is a liquid ring with a vapor bridge at the center. At higher quality or mass flux, we see waves and droplets in the vapor zone, making it similar to churn flow in literature.

In the annular flow, we see liquid film in the channel and at the center must be a vapor core when mass flux is lower and quality is higher. A liquid film with waves is observed at higher mass fluxes.

Table 1. Properties of tested fluids evaluated at 30 or 50 °C.

Property	Unit	R32	R1234yf	R134a	R1234ze(E)	R1233zd (E)	R1336mzz (Z)
$P_{sat}(T_{sat})$	[kPa(°C)]	1927(30)	784(30)	770(30)	578(30)	154.7(30)	178.6(50)
P_R	-	0.333	0.232	0.190	0.159	0.0427	0.0615
σ	[mN m^{-1}]	5.988	5.563	7.417	8.209	13.91	10.73
H_{lv}	[kJ kg^{-1}]	260.4	141.2	173.1	163.1	188.5	157.6
ρ_l	[kg m^{-3}]	939.6	1073	1187	1146	1251	1300
ρ_v	[kg m^{-3}]	54.78	42.73	37.54	30.5	8.512	11.73
μ_l	[kg $m^{-1}s^{-1}$ $\times 10^{-4}$]	1.072	1.453	1.831	1.880	4.403	2.935
μ_v	[kg $m^{-1}s^{-1}$ $\times 10^{-4}$]	0.1313	0.1135	0.1191	0.1246	0.1125	0.1671

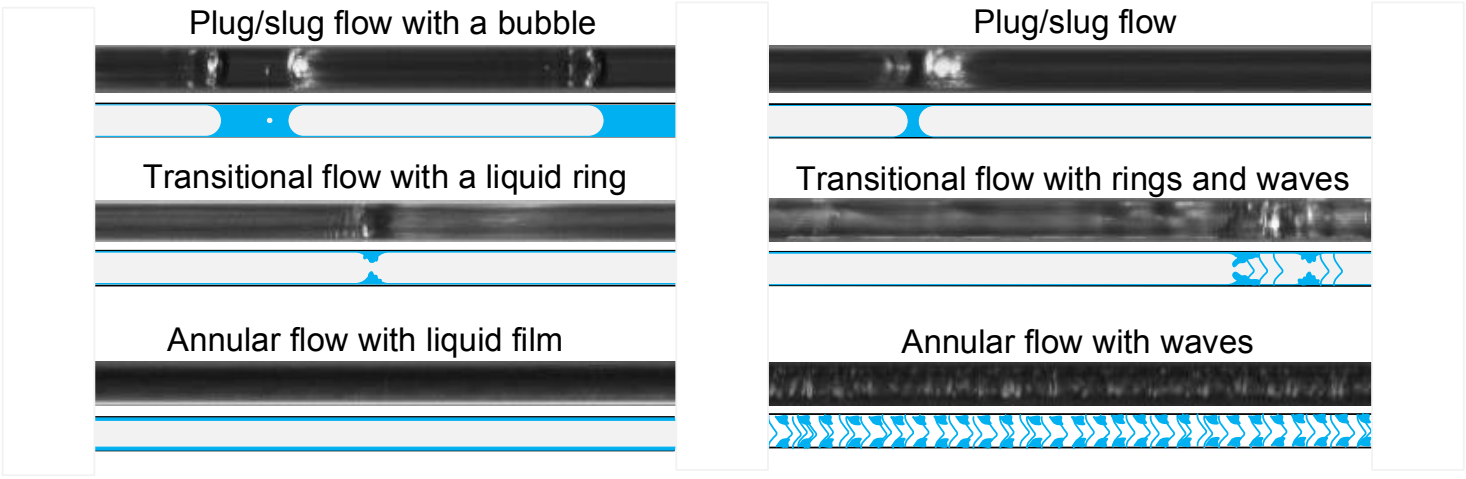

Figure 1. There are three flow patterns: plug/slug, transitional, and annular flow.

2. FACILITY AND CALIBRATION

The experimental facility has been introduced in Li and Hrnjak (2017, 2018) to study heat transfer and pressure gradient of fluids in the microchannel tube. The facility can measure heat transfer coefficient for a given heat flux, mass flux, and wall temperature. Simultaneously, diabatic pressure drop and flow regime at the exit of each test section can be collected. Adiabatic pressure drop can be measured separately without heat load. The facility is made of three loops: a refrigerant loop, a coolant (water) loop, and a chiller (glycol) loop, as Figure 2 shows. The detail of facility description

and calibration can be found in the mentioned references and the Thesis (Li 2016). The facility was upgraded in (Li and Hrnjak 2019a, 2019b) for further research in flow patterns by adding visualization sections.

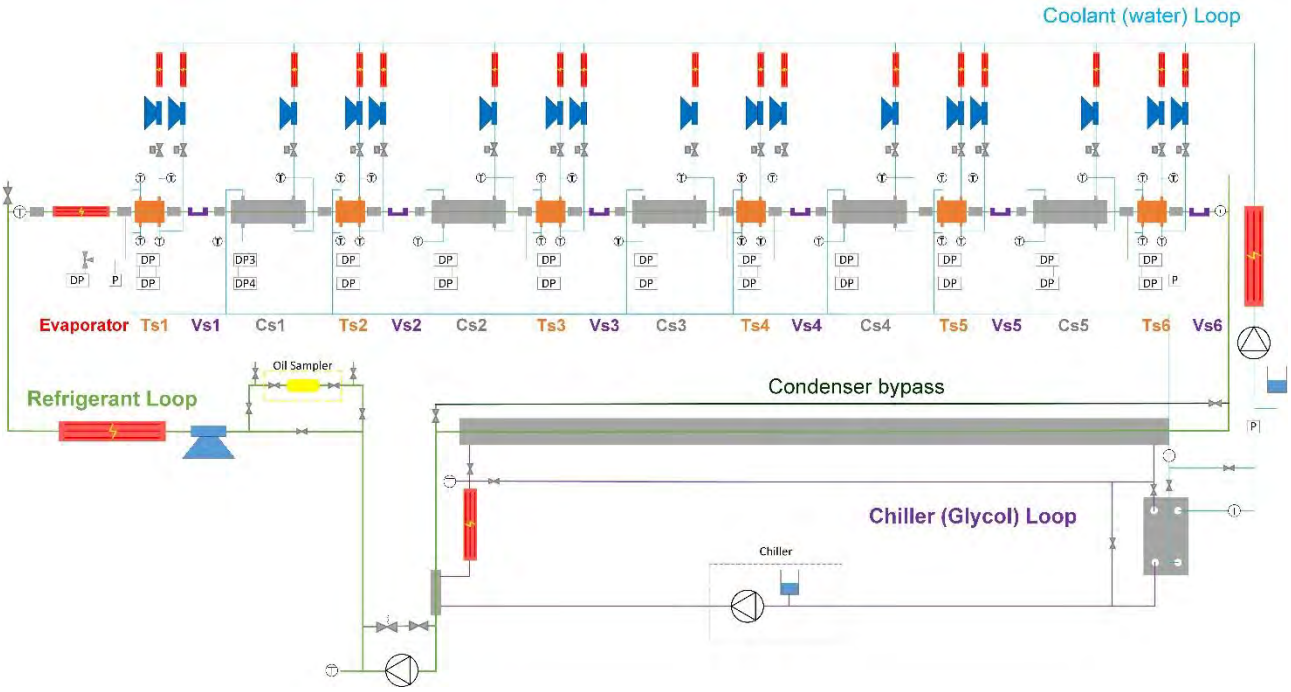

Figure 2. Schematic of the facility with refrigerant loop (green), coolant loop (blue), and chiller loop (purple).

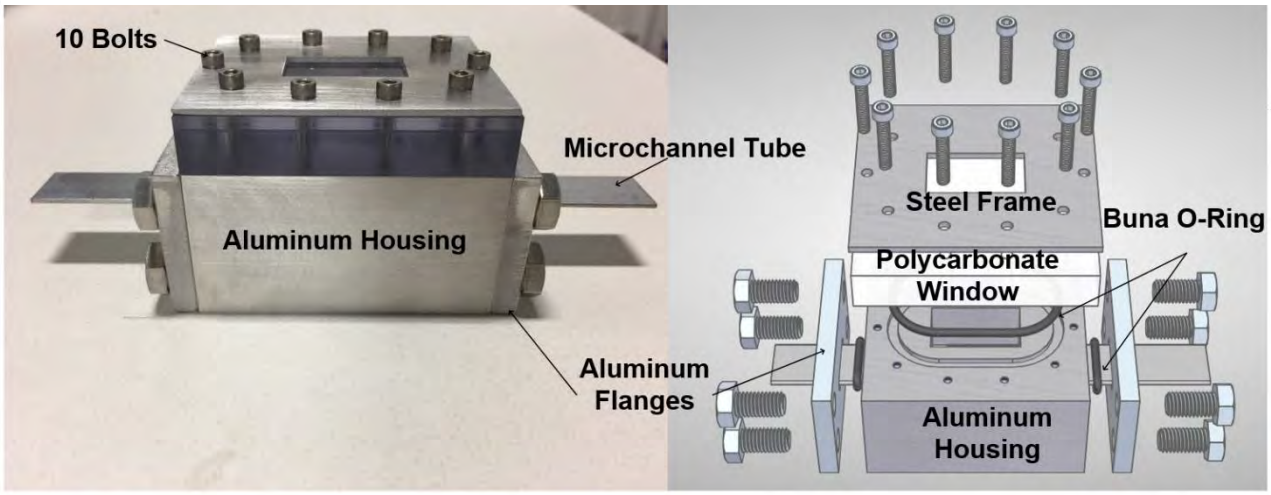

Figure 3. Visualization section consists of a steel frame, a polycarbonate window, an aluminum housing, a microchannel tube with top wall removed, two aluminum flanges and three O-Rings.

The design of visualization sections is presented in Figure 3. The visualization section which consists of an aluminum housing, a polycarbonate window, a steel frame, two aluminum flanges, a microchannel tube with top-wall removed, three O-rings, and multiple bolts. The top wall of the tube in the visualization section has been removed by EDM (Electrical Discharge Machining). That created a 30 mm long window in the center of the 167 mm long tube. The machining is done carefully to make sure that only the top wall is removed while channel cross-sectional area stays unchanged. Obviously that can be done when channels are square and the tube used is very close to that case. The T-shape polycarbonate window replaces the top wall, and the refrigerant is sealed by an O-ring made of Buna. The window only reaches to the position of the top inner wall of the microchannel tube when inserted into the housing to make sure it does not interrupt the flow. Ten bolts fix the frame and window over the top flange to the housing and compress the O-ring. On the left and right sides, aluminum flanges and Buna O-rings seal the refrigerant. During recording, a high-speed

camera (Phantom V9.1) is fixed above the top of the section to a separate stand and takes video from there. An 1100 lumen LED flashlight provides the necessary light without significant heat input. The overall uncertainty (εR) of a result (R) with a known function F of n variables x_i with known uncertainties (εx_i) is expressed in equation 1 based on NIST technical Note 1297 (Taylor and Kuyatt, 1994). This equation is under the assumptions that all variables are independent, repeated measurements show Gaussian distribution, and all uncertainties of variables are in the same level of confidence. In this paper, the level of confidence is 95%.

Table 2. Uncertainties of instruments.

εP	1.25 kPa
εDP	0.0015 to 0.04 kPa
εT	0.07 to 0.2 °C
εm	0.1% to 0.15% of rate
ερ	0.0005 g-cm^{-3}

$$\varepsilon R = \sqrt{\sum_{i=1}^{n} \left(\frac{\partial F}{\partial x_i} \varepsilon x_i \right)^2} \quad (1)$$

Instruments are calibrated to ensure the accuracy of the measurements. The overall uncertainties of instruments are listed in Table 2. Ambient heat loss is measured and heat transfer rate is corrected. The contact resistance between the heat transfer block and the microchannel tube is measured and the value is 0.0086 K W^{-1}. Tube channel size is measured by Mitutoyo WF microscope. The average diameter is 0.643 mm, and the standard deviation of diameters is 0.0232 mm. The detailed calibration process can be found in the previous studies (Li, 2016, Li and Hrnjak, 2017).
In this paper, the flow pattern map will be presented as a function of mass flux and vapor quality, and as a function of superficial velocities. Total mass flow rate is measured by mass flow meter and the flow cross-sectional area is measured by microscope. Vapor quality is determined by enthalpy. The inlet enthalpy (h_{in}) of the test line is determined by pressure and temperature measurements. Enthalpy of each test section is determined by adding or removing energy as equation 2 shows.

$$x_i = \frac{h_{in} + \frac{\sum_{n=1}^{i} Q}{\dot{m}} - h_l}{h_{lv}} \quad (2)$$

3. FLOW PATTERNS

3.1. Flow pattern of R1233zd(E) at 30 °C

Figure 4 shows the flow patterns of R1233zd(E) and R1336mzz(Z) in the 0.643 mm microchannel tube. For R1233zd(E), the experiment was done at constant saturation temperature of 30 °C.
When mass flux is 200 kg-m^{-2}s^{-1}, the experiment is stopped at quality of 0.6 due to the high pressure drop of this fluid exceeds the limit of the facility. It is believed that when quality is higher than 0.6, it should always be annular flow. The flow reaches transitional flow at quality of 0.2 and annular flow at 0.38. As mass flux decreases, the occurrence of transitional flow and annular flow delays to higher quality. This is because when mass flux decreases, the quality needs to be higher to reach a high flow velocity. At lower mass flux (25 and 50 kg-m^{-2}s^{-1}), there is no transitional flow observed. When quality reaches about 0.85, the flow changes from plug/slug flow to annular flow at mass flux of 25 kg-m^{-2}s^{-1}. One possible reason is that the transitional flow happens very shortly between quality 0.8 and 0.85. The other reason is that R1233zd(E) has very high surface tension (Table 1). When mass flux is low, it is easier to form a liquid slug in the tube than a thick liquid ring.

3.2. Flow pattern of R1336mzz(Z) at 50 °C

The experiment of R1336mzz(Z) was conducted under constant saturation temperature of 50 °C. When mass flux is high (150 kg-m^{-2}s^{-1}), the transitional flow starts at quality of 0.35 and annular flow starts at 0.5. As mass flux decreases, the transitioning delays to higher quality. This is because the velocity of two-phase flow is proportional to both mass flux and quality. As same as R1233zd(E), no transitional flow was observed for lower mass flux (25 and 50 kg-m^{-2}s^{-1}). R1336mzz(Z) also has high surface tension so the liquid slug is easier to be formed than liquid ring in a small tube.

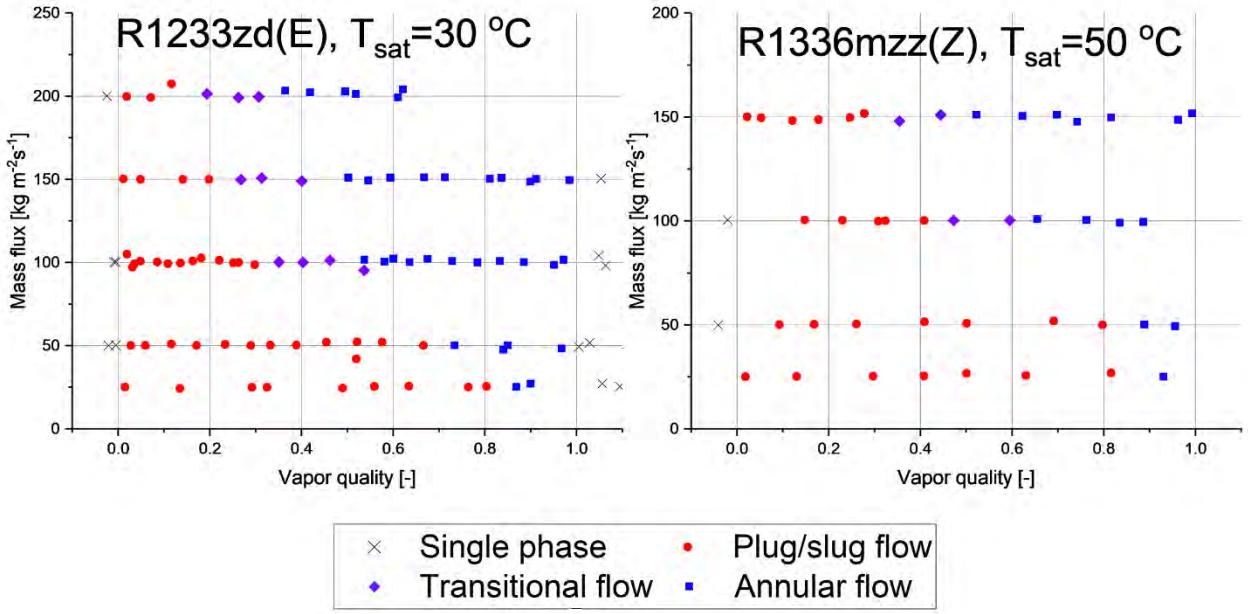

Figure 4. Flow patterns of R1233zd(E) and R1336mzz(Z) at constant saturation temperature.

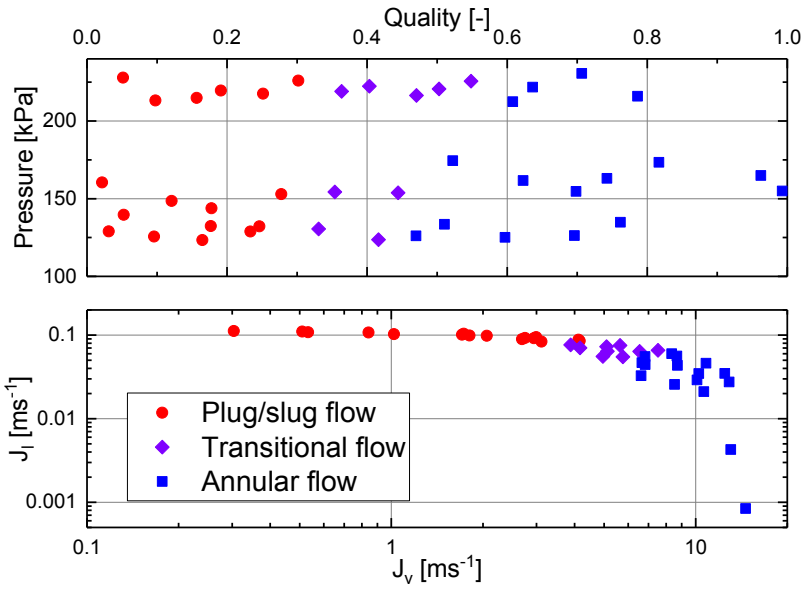

Figure 5. Flow pattern is affected by saturation pressure for R1336mzz(Z) at constant mass flux 150 kg-m^{-2}s^{-1}.

3.3. Flow pattern of R1336mzz(Z) at 150 kg-m^{-2}s^{-1}

Figure 5 shows the flow pattern of R1336mzz(Z) at constant mass flux (150 kg-m^{-2}s^{-1}) at varies saturation temperature/pressure (40 to 60 °C, or 125 to 225 kPa). The upper plot is the experimental

results using pressure and vapor quality as coordinates. The plot was remade in the bottom plot of Figure 5 which uses superficial velocities J as coordinates.
When the temperature is 40 ºC and pressure is low (about 125 kPa), the fluid enters transitional flow at quality of 0.3 and annular flow at 0.45. As pressure increases, the boundary of two flow patterns delays. When the temperature is 60 ºC (pressure is about 225 kPa), the transitional flow starts at quality of 0.35 and annular flow starts at 0.6. This is mainly because when pressure increases, the vapor density increases, thus the velocity decreases. The two-phase flow will have the same velocity at a higher quality, if the vapor density is higher.
In the bottom plot of Figure 5, flow is in plug/slug when vapor superficial velocity is lower than 4 m-s^{-1}. When vapor velocity is higher than 6 to 8 m-s^{-1} and liquid velocity is lower than about 0.06 to 0.08 m-s^{-1}, flow is in annular. Both Figures 4 and 5 show that the flow pattern is a strong function of velocity. Flow velocity is affected by mass flux and vapor density.

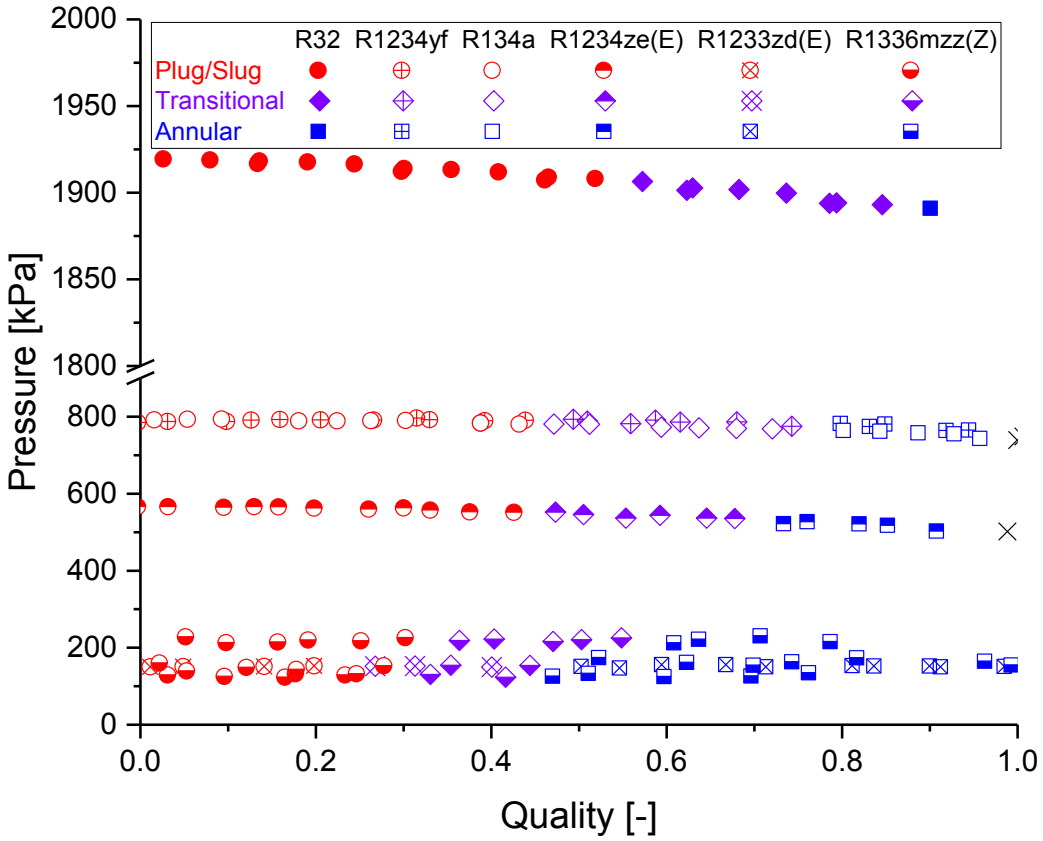

Figure 6. Flow patterns of six fluids obtained on the same facility at the same mass flux (150 kg-m^{-2}s^{-1}). R134a, R1234yf, and R1234ze(E) have similar flow patterns. R1233zd(E) and R1336mzz(Z) have similar flow patterns.

3.4. The flow pattern of six fluids

Figure 6 shows the flow patterns of six fluids: R32, R1234yf, R134a, R1234ze(E), R1233zd(E), and R1336mzz(Z) at the same mass flux (150 kg-m^{-2}s^{-1}). Most of them are at the same saturation temperature (30 ºC) except R1336mzz(Z) is at 40 to 60 ºC. When testing higher pressure (R32) and moderate pressure fluids (R134a, R1234yf, R1234ze(E)), the experiment was done in one pass, so the real pressure of each data point is decreasing as quality increases. For low pressure fluids (R1233zd(E) and R1336mzz(Z)), the experiment was done on one visualization section only, thus the pressure is constant.
R32 has the highest saturation pressure and the highest vapor density. R32 should have the lowest velocity than other fluids at the same mass flux and quality. It has the annular flow starts at the highest quality, which is about 0.9.
R134a and R1234yf have almost the same saturation pressure. R1234ze(E) has slightly lower pressure than R134a. Since both R1234ze(E) and R1234yf are hydrofluoroolefins (HFOs), they have

unity global warming potential (IPCC, 2014). Both HFOs are considered as substitute of R134a because they are more environmental friendly. These three fluids have very similar flow patterns at the same condition. All of them start transitional flow at quality about 0.45. For R134a and R1234yf, the annular flow starts at quality of 0.8. For R1234ze(E), the annular flow starts earlier, where quality is about 0.72. The reason is that R1234ze(E) has low vapor density than the other two fluids, thus it has higher flow velocity at the same quality.

R1233zd(E) and R1336mzz(Z) have similar flow patterns. For R1336mzz(Z), the flow pattern is affected by saturation pressure, which has been discussed previously in this paper. R1233zd(E) enters transitional flow at slightly lower quality than R1336mzz(Z) at the same saturation pressure (about 155 kPa). Both fluids enter annular flow at quality of 0.5 at this pressure.

Figure 6 shows that the properties of fluids strongly affect flow pattern. The most important property is probably the vapor density, which affects vapor-phase velocity. Other properties such as surface tension, viscosity, etc. also has effect on the flow patterns.

4. CONCLUSIONS

The definition of flow patterns is adopted from the previous work (Li and Hrnjak 2019a). Flow patterns of two-phase flow in the 0.643 mm microchannel tube is classified as: plug/slug, transitional, and annular flows.

Figure 3 shows the design of the visualization section used in this work. The section consists of a steel frame, a polycarbonate window, an aluminium housing, as microchannel tube with top wall removed, two aluminium flanges, and three O-Rings.

The flow patterns of R1233zd(E) and R1336mzz(Z) at constant saturation temperature/pressure are presented in Figure 4. As mass flux decreases, the transitioning delays to higher quality due to changes in velocity. The transitional flow absents in lower mass flux due to the higher surface tension of the two fluids.

The saturation pressure affects the flow patterns as well (Figure 5). As pressure increases, the starting quality of annular flow increases. This is mainly caused by the change of vapor density as pressure changes.

Figure 6 shows a comparison of six fluids: R32, R1234yf, R134a, R1234ze(E), R1233zd(E), and R1336mzz(Z). R32 has the highest pressure and the annular flow starts at the highest quality (0.9). R1234yf, R134a, and R1234ze(E) have similar flow patterns. R1233zd(E) and R1336mzz(Z) have similar flow patterns.

ACKNOWLEDGEMENTS

This paper is a result of a project that was financially supported by the Air Conditioning and Refrigeration Center at the University of Illinois and its 30 member companies. CTS (Creative Thermal Solutions Inc.) provided the material, instrumentation and previous 3 m long facility as a basis for the new, improved facility used to get presented data.

NOMENCLATURE

H_{lv}	*vaporization enthalpy (kJ-kg^{-1})*	J_l	*liquid superficial velocity(m-s^{-1})*
J_v	*vapor superficial velocity (m-s^{-1})*	P	*pressure (kPa)*
P_R	*reduced pressure (-)*	T	*temperature (^{o}C)*
μ_l	*liquid dynamic viscosity (kg-m^{-1}s^{-1})*	μ_v	*vapor dynamic viscosity (kg-m^{-1}s^{-1})*
ρ_l	*Liquid density (kg-m^{-3})*	ρ_v	*vapor density (kg-m^{-3})*
σ	*Surface tension (mN-m^{-1})*		

REFERENCES

IPCC, 2014, Climate Change 2014: Synthesis Report, Contribution of Working Groups I, II and III to the Fifth Assessment Report of the Intergovernmental Panel on Climate Change, Geneva, Switzerland.

Li, H., 2016, An experimental Facility for Microchannel Research and Evaporating R134a in Microchannel Tube, M.S. Thesis, University of Illinois.

Li, H., Hrnjak, P., 2017, Measurement of heat transfer coefficient and pressure drop during evaporation of R134a in new type facility with one pass flow through microchannel tube, Int. J. Heat and Mass Transfer, 115, 502-512.

Li, H., Hrnjak, P., 2018, Heat transfer and pressure drop of R32 evaporating in one pass microchannel tube with parallel channels, Int. J. Heat and Mass Transfer, 127, 526-540.

Li, H., Hrnjak, P., 2019a, Flow visualization of R32 in parallel-port microchannel tube, Int. J. Heat and Mass Transfer, 128, 1-11.

Li, H., Hrnjak, P., 2019b, Flow patterns and plug/slug flow characteristic of R134a in a microchannel tube, Int. J. Heat and Mass Transfer, 132, 1062-1073.

Nino, V., Hrnjak, P., Newell, T., 2002, Characterization of Two-Phase Flow in Microchannels, Air Conditioning and Refrigeration Center TR-202, Urbana, IL.

Taylor, B., Kuyatt, C., 1994, Guidelines for Evaluating and Expressing the Uncertainty of NIST Measurement Results. NIST Technical Note 1297.

Triplett, K., Chiaasiaan, S., Abdel-Khalik, S., Sadowski, D., 1993, Gas-liquid two-phase flow in microchannels Part I: two-phase flow patterns, Int. J. Multiphase Flow 25, 377-394.

Manuscript ID: 1255
DOI: 10.18462/iir.icr.2019.1255

Heat transfer coefficient, pressure drop, and flow visualization for some new low GWP refrigerants during evaporation in small tube

Houpei LI[(a)], Pega HRNJAK[(a) (b)]

[(a)] Air Conditioning and Refrigeration Center, Department of Mechanical Engineering, University of Illinois at Urbana Champaign, 1206 West Green Street, Urbana, IL 61801, USA, hli84@illinois.edu
[(b)] CTS, 2209 Willow Rd., Urbana IL, USA, pega@illinois.edu

ABSTRACT

This paper shows comprehensive data and analysis for low GWP refrigerants evaporation in a microchannel tube with a hydraulic diameter of 0.643 mm. Measurements over the entire range of qualities are completed in one pass to have conditions similar to a real heat exchanger. Six heat transfer coefficients, six diabatic pressure drops, and six visualizations at exits are obtained simultaneously. This is especially important when testing mixtures where the local concentration of fluid (specifically in the liquid next to the wall) is changing as quality changes along the channel. Data are presented in an actual, non-isobaric condition due to pressure drop along the tube. Results presented and compared for different experimental condition (mass flux, heat flux, saturation temperature, etc.). Discussion of results is enhanced with video captures presenting flow patterns. Refrigerants R1233zd(E), R1336mzz(Z), and mixture R448A are under evaluation in this paper.
Keywords: Refrigerant, Microchannel, Heat transfer, Pressure drop, Visualization, Evaporation.

1. INTRODUCTION

A new type of facility for evaluation of heat transfer and hydraulic behavior in microchannels has been used in this paper and has been firstly introduced in Li and Hrnjak (2017). Heat transfer coefficients and pressure drops are measured in six test sections simultaneously, in only one pass. Experiments are conducted with a given heat flux, mass flux, and wall temperature at each test section. Uniform heat flux conditions at both top and bottom of the microchannel tube are assured by controlling heaters and valves before each thermal block. Each test section has one upper and one lower block. Between tests sections are conditioning sections that adjust quality difference to the required value.

Later the facility is updated with six visualization sections install at the exits of the six test sections (Li and Hrnjak, 2018). While the six heat transfer coefficients and six pressure drops are measured, the flow patterns at exit of each data point are recorded.

The new facility provides relatively efficient experiments with the six test sections. More important – since the vapor quality of refrigerant is changed continually in one pass – flow patterns and the situation in the liquid film (concentration of oil if any or components if blend) in the experimental condition is closer to a realistic heat exchanger in a vapor-compression system, especially for refrigerant-oil mixtures or refrigerants blends. The R448A is tested in this method so the mass transfer resistance in liquid film is closer to a realistic heat exchange application.

For low pressure fluids such as R1336mzz(Z) and R1233zd(E), the measurements are done in only one test section. Due to the low vapor density of these fluids, the total pressure drop will be too large if the fluid is evaporating over the length of six test sections. Therefore while dealing with them, the first test section and visualization was used for measurement, and all other test section and conditioning sections are used as condenser to reduce the total pressure drop in the system. When measuring the heat transfer coefficient and pressure gradient in this method, the pressure can be controlled to be constant (isobaric condition).

2. FACILITYN

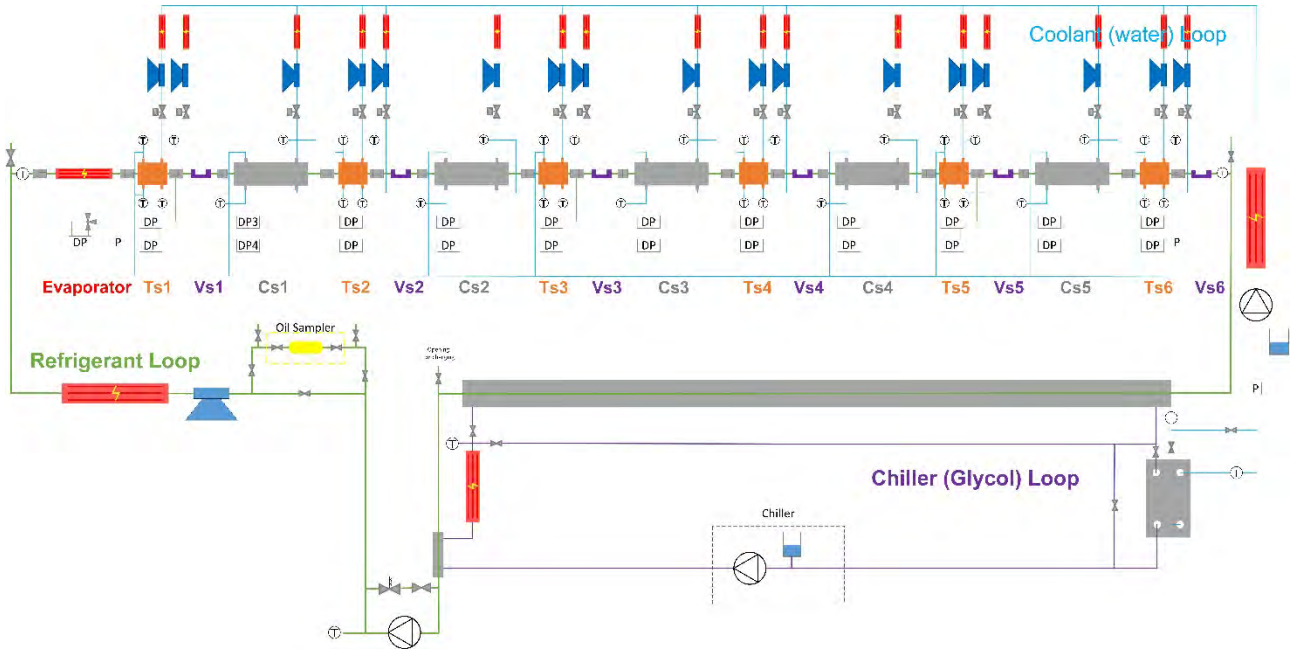

Figure 1. Schematic of the facility with refrigerant loop (green), coolant loop (blue), and chiller loop (purple).

The experimental facility has been introduced in Li and Hrnjak (2017) to study heat transfer and hydraulic behavior of refrigerants in microchannel tubes. The facility can measure heat transfer coefficient for a given heat flux, mass flux, and wall temperature. Simultaneously, diabatic pressure gradient and flow regime at the exit of each test section can be collected. Adiabatic pressure gradient can be measured separately without heat load. The facility is made of three loops: a refrigerant loop, a coolant (water) loop, and a chiller (glycol) loop, as shown in Figure 1. A heat transfer block is 152.4 mm long and with a water channel inside for the coolant loop. Two blocks sandwich a microchannel tube and the wall temperature is measured by six thermocouple probes inserted in wells near the tube in each block. The two blocks are tightened by four long bolts with nuts with the same torque (7.6 N-m). Between the blocks and microchannel, the surface cavities are filled with thermal paste with reported thermal conductivity of 0.75 $W\text{-}m^{-1}K^{-1}$ (Lubritech, 2007). In each test section, the microchannel tube is 181.8 mm long, combining with the heated length (152.4 mm) and the connectors. After the test section, refrigerant goes through a visualization section and a conditioning section. The conditioning section has the same design as the test section but is longer (400 mm), without wall temperature TC wells.

The heat transfer rate of the test or conditioning section is determined by the flow rate of coolant into the heat transfer block and the temperature difference of coolant at the outlet and inlet of the block. In the test sections, the top and bottom blocks have different controls to make sure the conditions on the top and bottom sides of the microchannel tube are the same. As Figure 2 shows, two water sub-loops control the top and bottom heat transfer blocks individually. A water sub-loop is made of a flow meter, an electrical control valve, a heater, thermocouples, and tube.

Heat transfer rate combined with refrigerant mass flow rate and pressure determines the increase in vapor quality within the conditioning section. Saturation pressure or temperature is determined by adding (or subtracting) pressure drop in each section. On each pressure measurement point, there are two pressure transducers with different range and accuracy for measurement. The two-pressure-sensor design provides excellent and needed accuracy of both absolute and differential pressure measurements over a range of operation wider than the range of a single sensor. On one test section, a pair of Rosemount 1151 DP3 (range = 2 kPa, εDP = 0.002 kPa) and DP4 (range = 15 kPa, εDP = 0.015 kPa) differential pressure transducers are installed. When the measured pressure is higher than the limit of the sensor with the lower range, measurement from the sensor with the higher range is adopted. When all pressure drops are added together, it should be equal to the difference between the readings of the pressure transducers at the inlet and outlet of the test line, within the accuracy. Pressures at the inlet and the outlet are measured by Rosemount 3051S1 pressure transducers with 0.04% FS accuracy (Rosemount, 2008).

With proper control, six measurement conditions encompassing the required qualities are taken simultaneously over the full range of qualities from 0 to 1, at the same mass flux and adjusted to be the same heat flux. So, six heat transfer coefficients and pressure drops are measured at the same time.

After the test line, a lab-made coaxial (microchannel in a round tube) heat exchanger and a shell-and-tube sub-cooler is used to condense the refrigerant. The openings located at the inlet and outlet of the test line are for charging and evacuation. An external receiver is used to help set up the system pressure. The oil sampler is by-passed at this stage since a pure refrigerant is being tested. The oil sampler will be used to measure oil circulation rate when testing refrigerant-oil mixtures in the future.

Distilled water in the coolant loop is pumped to a heater. When a lower temperature is needed, water in the coolant loop is replaced by ethanol or a glycol mixture. A pump with a VFD controller is used to pump the fluid. A reservoir tank is installed at the suction of the pump in order to maintain a minimum suction pressure. The pressure at the discharge is measured by a pressure sensor and this signal is used to adjust the pump speed to maintain discharge pressure. Fluid is supplied to an inlet header, where it then goes to each test/conditioning section. The fluid temperature at the inlet to the test or conditioning section is adjusted by a 530 W heater while the flow rate is adjusted by a stepper motor valve. The mass flow rate is measured by two CMF010 elite mass flow meters (Emerson, 2017) per test section (heat transfer in upper and lower blocks are measured independently) and one DS006 mass flow meter per conditioning section. Temperature measurements are done by T-type thermocouples inserted into the coolant tube. Coolant from test sections and conditioning sections returns to the outlet header. A plate heat exchanger and a 1.5 kW heater are installed after the header to adjust coolant temperature supplied to the pump.

The chiller loop provides cooling to the refrigerant sub-cooler, refrigerant condenser, and brazed-plate heat exchanger in the coolant loop. The chiller loop consists of a chiller with pump and reservoir tank and now is running with a 50%-50% ethylene-glycol water mixture. After the pump, glycol flows to a sub-cooler which sub-cools the refrigerant to make sure that liquid refrigerant flows into the gear pump. A 1.5 kW heater is used to adjust the condenser inlet temperature of glycol. A bypass has been made for the condenser to reduce pressure drop when the system is in condensation mode. A plate heat exchanger is used for glycol (coolant loop).

The visualization section consists of an aluminum housing, a polycarbonate window, a steel frame, two aluminum flanges, a microchannel tube with top-wall removed, three O-rings, and multiple bolts. The top wall of the tube in the visualization section has been removed by EDM (Electrical Discharge Machining). That created a 30 mm long window in the center of the 167 mm long tube. The machining is done carefully to make sure that only the top wall is removed while channel cross-sectional area stays unchanged. Obviously that can be done when channels are square. The T-shape polycarbonate window replaces the top wall, and the refrigerant is sealed by an O-ring made of Buna. The window only reaches to the position of the top inner wall of the microchannel tube when inserted into the housing to make sure it does not interrupt the flow. Ten bolts fix the frame and window over the top flange to the housing and compress the O-ring. On the left and right sides, aluminum flanges and Buna O-rings seal the refrigerant. During recording, a high-speed camera (Phantom V9.1) is fixed above the top of the section to a separate stand and takes video from there. An 1100 lumen LED flashlight provides the necessary light without significant heat input.

The detailed introduction of the facility and calibration can be found in Li and Hrnjak (2017, 2018) and the thesis (Li, 2016). Details and drawings of the visualization can be found in Li and Hrnjak (2019a, 2019b).

3. RESULTS AND DISCUSSION

3.1. Single-phase friction factor of low GWP refrigerants

Figure 2 shows the single-phase friction factor of R32, R1234yf, and R1336mzz(Z). The results are plotted against the single-phase Reynold's number (Re) and compared to Churchill equation (1977). The Re is defined in Eq. (1).

$$Re = \frac{\rho v D}{\mu} \qquad \text{Eq. (1)}$$

The Churchill equation is defined in Eq. (2).

$$f = \left[\left(\frac{8}{Re}\right)^{12} + \frac{1}{(A+B)^{1.5}}\right]^{\frac{1}{12}},\ A = \left[2.457 \ln\left(\frac{1}{\left(\frac{7}{Re}\right)^{0.9} + \frac{0.27\epsilon}{D}}\right)\right]^{16},\ B = \left(\frac{37{,}350}{Re}\right)^{16} \qquad \text{Eq. (2)}$$

In Figure 2, when Re less than 1700, flow is in laminar regime and the friction factor agrees to theoretical value involved in the Churchill equation ($f \times Re = 64$). It shows that the measurement of this tube diameter (0.643mm) is accurate and the tube has hydraulic behaviour as same as a round tube. In the transition regime (1700<Re<3000), the calculated friction factor from Churchill always underpredict the measurements. When the Re is larger than 3000, the measurements are used to fit the roughness parameter (ϵ/D) in the Churchill equation. For different fluids, different parameter obtained by experiment: for R32, ϵ/D=0.0027, for R1234ze(E), ϵ/D=0.0041, and for R1336mzz(Z), ϵ/D=0.0051. One explanation of the difference in roughness parameter could be the Churchill equation is not valid in small tube. The original concept of the roughness parameter (ϵ/D) is the grain size in tube. This parameter is not directly related to roughness parameters measured such as Rp or Ra. The other reason for the difference in roughness could come from the accuracies of properties calculation of these fluids. The properties such as liquid and vapor phases densities and viscosities are used to calculate friction factor and Reynolds number.

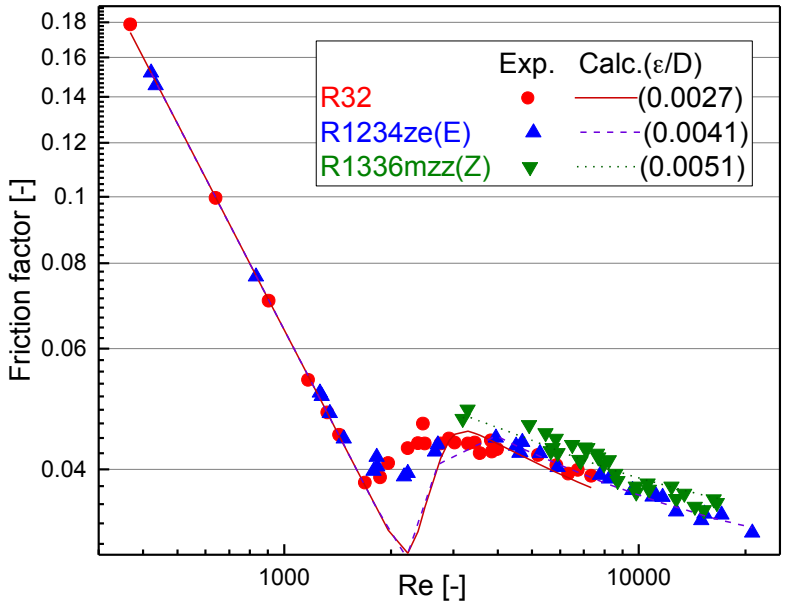

Figure 2. The single-phase friction factor of three fluids shows different roughness parameter when fit to Churchill (1977).

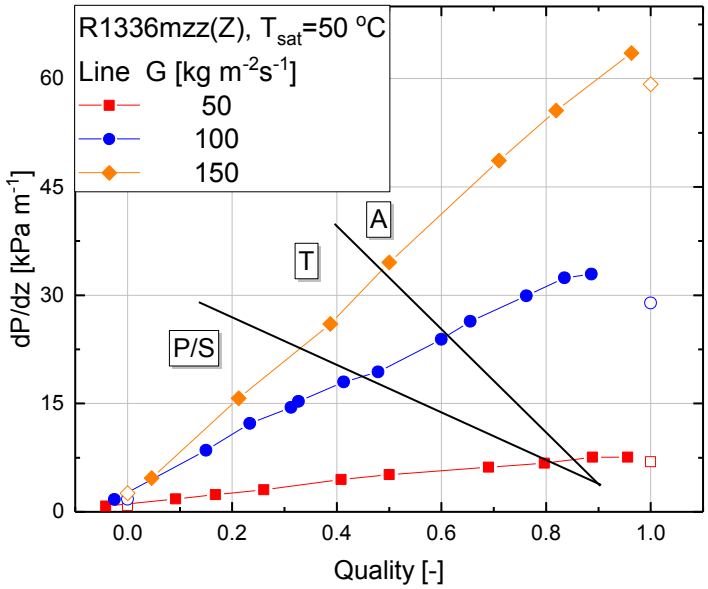

Figure 3. The adiabatic pressure gradient of R1336mzz(Z). There are three flow patterns observed: plug/slug (P/S), transitional (T), and annular (A).

The difference of roughness used in Churchill equation between R1336mzz(Z) and R32 is 47%. However, the difference between calculated friction factor is much smaller. For example, when Re=6000, f=0.04247 (ϵ/D=0.0051) or 0.03936 (ϵ/D=0.0027). The difference in friction factor is only 7.8%. Even the roughness is affecting the in-tube pressure drop, the mass flux and property may have more significant effect than roughness in the experiment conditions.

3.2. Two-phase pressure gradient and flow patterns of R1336mzz(Z)

Figure 3 shows the adiabatic pressure gradient in two-phase of R1336mzz(Z) and the corresponding flow pattern observed at exist of each data point. The black boundary line in Figure 3 only indicates the flow pattern type of each data point and it is not a flow pattern mapping. The flow pattern is defined as plug/slug (P/S), transitional (T), and annular (A) flows. The detail of definition of flow pattern can be found in Li and Hrnjak (2019a). The experiments are done with only one test section to maintain a constant pressure due to the limitation of total pressure drop of the system.

As vapor quality increases, the pressure gradient increases almost linearly, as the solid symbols show in Figure 3. The empty symbols are calculated single-phase pressure gradient based on Churchill equation with fitted roughens parameter (ϵ/D=0.0051). They show the asymptote trend of the two-phase pressure gradient. As mass flux increases, the pressure gradient increases dramatically. From mass flux 50 to 150 kg-m^{-2}s^{-1}, the mass velocity is tripled and the pressure gradient is nine times. This is because pressure drop is proportional to the square of velocity. The flow patterns show that as quality increases, the flow is firstly in plug/slug, then transitional, and lastly annular flow. When mass flux is 150 kg-m^{-2}s^{-1}, the transitional flow starts when quality reaches 0.4, and annular flow starts when quality reaches 0.5. As quality decreases, the occurrence of annular flow and transitional flow delayed to higher quality. When mass flux is 50 kg-m^{-2}s^{-1}, there is no transitional flow observed. There is not a clear trend that flow pattern is affecting the pressure gradient. It seems that both flow pattern and pressure gradient are strongly affected by the mass flux and quality.

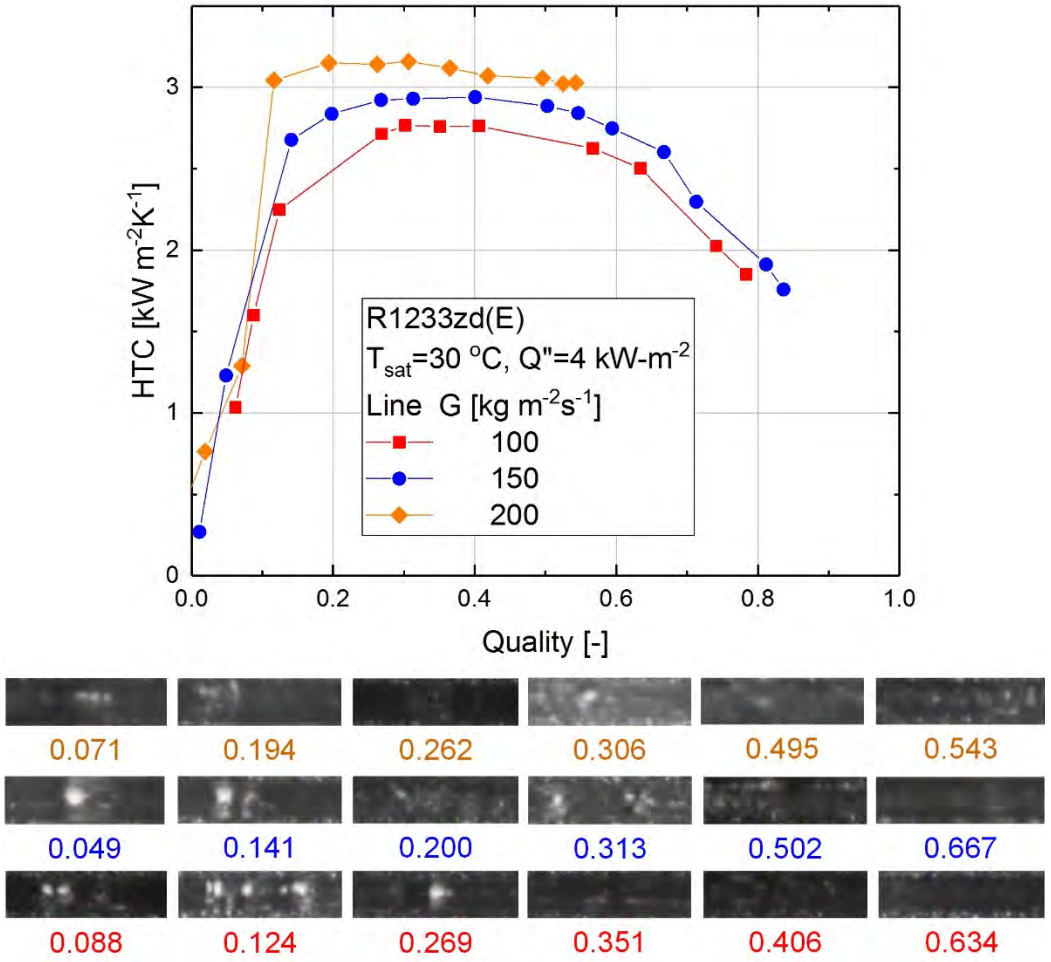

Figure 4. Heat transfer coefficient and flow patterns of R1233zd(E) at varies mass flux.

3.3. Heat transfer coefficient and flow patterns of R1233zd(E)

Figure 4 shows the heat transfer coefficient of R1233zd(E) at constant saturation temperature of 30 ^{o}C, constant heat flux of 4 kW-m^{-2}, and varies mass flux from 100 to 200 kg-m^{-2}s^{-1}. The flow patterns of data points observed at the exit of test section are presented at the bottom part of the figure. The experiments are done within only one test section for a constant pressure conditions.

The heat transfer coefficient of R1233zd(E) firstly increases as vapor quality increases. And then the HTC maintain at local maximum from low quality (about 0.1) to moderate quality (about 0.4). When quality is higher than 0.5 there is a clear trend that the HTC is dropping as quality increases. As vapor quality increases, the flow is firstly in plug/slug flow, then transitional flow, and at last annular flow. When mass flux is 100 kg-m^{-2}s^{-1}, the flow pattern is in plug/slug flow for quality 0.088 and 0.124. In plug/slug flow, the clear boundary between liquid slug and vapor plug is observed. When quality is higher than 0.269 (where the exit quality is about 0.361), the flow is in transitional where a dark region is observed which represent a thick liquid ring or wave. When quality is higher than 0.406 (where exit quality is about 0.505), the flow is in wavy annular. When mass flux increases, the boundary between two flow patterns advances to low quality. This is because of that for a certain flow velocity, the quality is lower when mass flux is higher. When mass flux is 150 kg-m^{-2}s^{-1}, the flow reaches transitional when quality is 0.200 (exit quality is 0.263), and annular flow at 0.502 (exit 0.572). When mass flux is 200 kg-m^{-2}s^{-1}, the flow reaches transitional when quality is 0.262 (exit quality is 0.311), and annular flow at 0.306 (exit 0.413).

It seems that when mass flux is higher, the reduction in HTC is earlier. When mass flux is 100 kg-m^{-2}s^{-1}, the HTC drops when quality is higher than 0.4. When mass flux is 200, the HTC drops at 0.3. This is because that the flow enters annular flow in lower quality when mass flux is higher. In annular flow, the thin liquid film cannot provide enough liquid for nucleate boiling. In plug/slug and transitional flow, there is always liquid slug or thick liquid ring flow though the tube to wet the wall. Therefore, in the plug/slug and transitional flows, local dry-out does not occur as much as in annular flow.

3.4. Heat transfer coefficient and diabatic pressure gradient of R448A and its component fluids

Heat transfer coefficient and pressure drop of R134a, R32, R1234ze(E), and R1234yf have been measured on the same facility and reported in the previous research (Li and Hrnjak, 2017, 2018). This subsection focuses on the heat transfer coefficient and diabatic pressure gradient of the mixture R448A.

Table 1. Properties evaluated at 20 ^{o}C for R448A and its component fluids.

Property	Unit	R32	R125	R1234yf	R134a	R1234ze(E)	R448A
P_{sat}	kPa	1475	1205	591.7	572.1	427.4	1153/1019
P_R	-	0.255	0.333	0.175	0.141	0.118	0.238/0.211
σ	mN m^{-1}	7.594	4.419	6.798	8.688	9.500	7.165
H_{lv}	kJ kg^{-1}	280.8	115.6	149.29	182.3	170.5	176.4
k_l	W m^{-1}K^{-1}	0.128	0.615	0.0651	0.0856	0.0761	0.0808
k_v	W m^{-1}K^{-1}	0.0167	0.0147	0.0134	0.0141	0.0132	0.0141
Cp_l	kJ kg^{-1}K^{-1}	1.886	1.367	1.369	1.405	1.366	1.528
Cp_v	kJ kg^{-1}K^{-1}	1.514	1.023	1.024	1.001	0.959	1.140
ρ_l	kg m^{-3}	981.4	1218	1110	1225	1179	1106
ρ_v	kg m^{-3}	40.9	78.0	32.8	27.8	22.6	45.0
μ_l	kg m^{-1}s^{-1} ×10^{-4}	1.246	1.522	1.637	2.068	2.116	1.144
μ_v	kg m^{-1}s^{-1} ×10^{-4}	0.1249	0.1310	0.1087	0.1175	0.1202	0.1254
Pr_l	-	1.843	3.384	3.445	3.393	3.796	2.731
Pr_v	-	1.134	0.913	0.832	0.836	0.875	1.017

R1234ze(E) and R1234yf are hydrofluoroolefin (HFO) with very short life span and unity GWP100 (100 years global warming potential). They are considered as a substitute of R134a because of similar properties. But they are much more environmentally friendly (lower GWP and 0 ODP). R448A is a refrigerant mixture with five components: 26% R32, 26% R125, 21% R134a, 7% R1234ze(E), and 20%R1234yf. By including high pressure fluids such as R32 and low pressure fluids such as R1234ze(E), this mixture has high temperature glide while evaporating. The property evaluated at

20 °C of R448A and its component fluids are listed in table 1. The properties of the pure fluids and mixture are evaluated in REFPROP 9.

R32 and R125 are high pressure fluids with higher reduced pressure. R1234yf and R1234ze(E) are new substitute of R134a with similar properties and saturation pressure. R125 and R1234yf has relatively low surface tension which is good for nucleate boiling. R32 has high vaporization enthalpy which results in a high Boiling number. The high vaporization enthalpy also results in a lower mass flow rate in a heat exchanger for a certain heat capacity. R32 has the highest liquid conductivity which makes it has the strongest film conduction in the microchannel tube. R125 has very high vapor density which makes a lower velocity at a given mass flux, thus lowest pressure gradient. Except R32, the other four pure fluids have high liquid Prandtl number and lower vapor Prandtl number. R1234yf, R1234ze(E), and R134a have similar properties and they are expected to have similar heat transfer performance. R1234ze(E) should have the higher pressure gradient among the five pure fluids since the vapor density is the lowest. R448A is a mixture with the five fluids so the properties are basically within the range of the components. However, due to the high temperature glide and mass transfer resistance in liquid phase, R448A may have lower heat transfer coefficient than its components'.

The heat transfer coefficient and diabatic pressure gradient of R448A is measured and presented in Figure 5. The measurements are done in six test section in one pass, so there is a real pressure drop as quality increases. R448A is a mixture of five fluids and four of the component fluids are tested on the same facility and shown in the figure. R448A has evaporating pressure lower than R32 but higher than the HFOs. Due to the high vapor density of R125, R448A has relatively high vapor density. Therefore, R448A has low vapor velocity and thus a low pressure gradient compare to the HFOs and R134a. R448A has relatively higher heat transfer coefficient than the HFOs and R134a when quality is lower than 0.2. This is because both R32 and R125 are more volatile fluids in the mixture and they have very high HTC. As quality increases, the HTC of the mixture decreases. When quality is higher than 0.4, the measured HTC of the mixture is even lower than its component fluids which is caused by the mass transfer resistance in the liquid film.

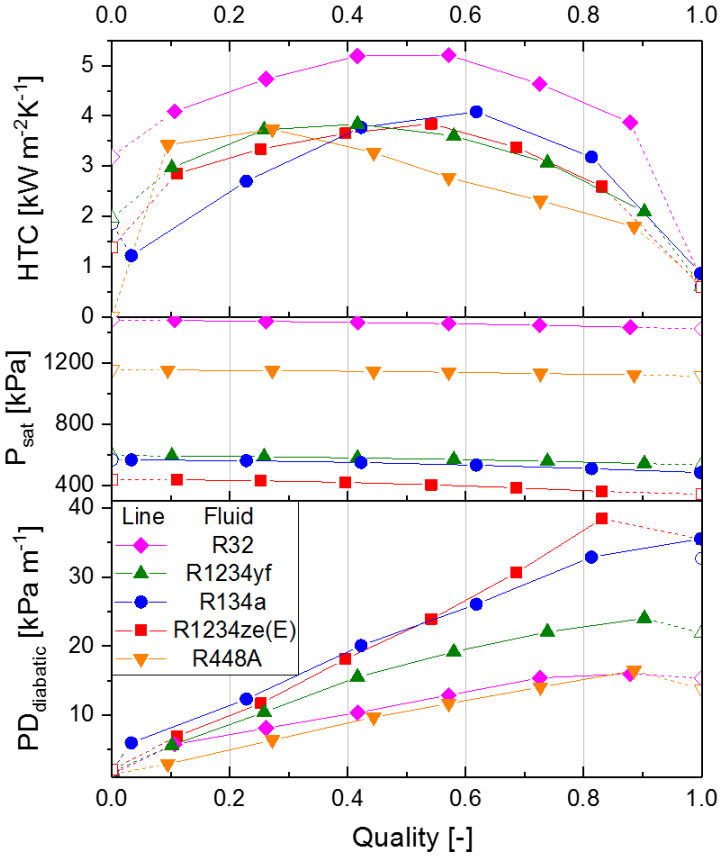

Figure 5. Heat transfer coefficient and diabatic pressure gradient of R448A and its component fluids.

4. CONCLUSIONS

This paper presented the result of experiments of some low Global Warming Potential fluids.
The single-phase friction factor proves the accuracy of tube diameter measurements (Figure 1). The measured friction factor of R32, R1234ze(E), and R1336mzz(Z) results in different roughness parameter in the Churchill equations (1977). This is probably due to the validity of Churchill equations in microchannel tube or the accuracy of properties of these fluids.
The adiabatic two-phase pressure gradient of R1336mzz(Z) is a strong function of mass flux and vapor quality (Figure 3). There are three flow pattern observed in tube: plug/slug, transitional, and annular flow. The heat transfer coefficient of R1233zd(E) is affected by both mass flux and vapor quality (Figure 4). The flow pattern shows that the HTC reaches local maximum when flow is in plug/slug or transitional flow. The HTC of R448A shows that the HTC of R448A is lower than all of its component fluids when quality is higher than 0.4 due to the mass transfer resistance in liquid film.

ACKNOWLEDGEMENTS

This paper is a result of a project that was financially supported by the Air Conditioning and Refrigeration Center at the University of Illinois and its 30 member companies. CTS (Creative Thermal Solutions Inc.) provided the material, instrumentation and previous 3 m long facility as a basis for the new, improved facility used to get presented data.

NOMENCLATURE

D	diameter (m)	f	friction factor (-)
P	pressure (kPa)	Re	Reynolds number (-)
T	temperature (^{o}C)	v	velocity (-)
μ	*dynamic viscosity (kg-m^{-1}s^{-1})*	ρ	*density (kg-m^{-3})*

REFERENCES

Churchill, S., 1977, Friction-factor equation spans all fluid-flow regimes, Chemical Engineering,

Emerson, 2017, Micro Motion® ELITE® Coriolis Flow and Density Meters, Product Data Sheet PS-00374, Rev. AE

Lemmon, E., Hube, M., Mclinden, M., Physics and Chemical Properties Division, REFPROP 9.0, NIST Standard Reference Database

Li, H., 2016, An experimental Facility for Microchannel Research and Evaporating R134a in Microchannel Tube, University of Illinois.

Li, H., Hrnjak, P., 2017, Measurement of heat transfer coefficient and pressure drop during evaporation of R134a in new type facility with one pass flow through microchannel tube, Int. J. Heat and Mass Transfer, 115, 502-512.

Li, H., Hrnjak, P., 2018, Heat transfer and pressure drop of R32 evaporating in one pass microchannel tube with parallel channels, Int. J. Heat and Mass Transfer, 127, 526-540.

Li, H., Hrnjak, P., 2019a, Flow visualization of R32 in parallel-port microchannel tube, Int. J. Heat and Mass Transfer, 128, 1-11.

Li, H., Hrnjak, P., 2019b, Flow patterns and plug/slug flow characteristic of R134a in a microchannel tube, Int. J. Heat and Mass Transfer, 132, 1062-1073.

Lubritech, 2007, CHEMPLEX® 1381 Product Information

Rosemount, 2008, Rosemount 1151 Pressure Transmitter, Reference Manual 00809-0100-4360

Manuscript ID: 1256
DOI: 10.18462/iir.icr.2019.1256

Droplet injection at the diffuser outlet in an ejector-based refrigeration cycle working with R245fa

Mehdi BENCHARIF[(a)], Sébastien PONCET[(b)], Hakim NESREDDINE[(c)], Said ZID [(a)]

[(a)] Département de génie climatique, Université des frères Mentouri, Constantine 1, Algeria
mehdi.bencharif@umc.edu.dz
[(b)] Mechanical Engineering Department, Université de Sherbrooke, Sherbrooke (QC), Canada
Sebastien.Poncet@USherbrooke.ca
[(b)] Laboratoire des technologies de l'énergie, Hydro-Québec, Shawinigan (QC), Canada
nesreddine.hakim@ireq.ca

ABSTRACT

This work presents a combined experimental and thermodynamic approach used to investigate the influence of droplet injection on the performance of an ejector-based refrigeration cycle developed for Heating, Ventilation and Air-Conditioning applications. A thermodynamic model has been developed within Matlab for each component of the cycle with a particular emphasis on the ejector modeling, which is based on the constant pressure mixing assumption. It is validated against the experimental data obtained on the Hydro-Québec's test rig working with R245fa. The numerical model agrees fairly well with the experiments. The results show that injecting R245fa droplets at the end of the ejector diffuser at the condensing temperature has a significant impact on the performance of the ejector itself and of the whole cycle. It reduces especially and significantly the temperature of the overheated vapors at the outlet of the ejector leading to a significant improvement of the Coefficient of Performance (COP).
Keywords: Ejector, Refrigeration system, COP, R245fa, Droplet.

1. INTRODUCTION

The major challenge of the last decade aims at reducing the energy consumption of cooling and air-conditioning systems which accounts for 20 % of the total energy consumed worldwide while using more environmentally friendly refrigerants. The ejector refrigeration system is an interesting alternative to conventional refrigeration systems. It can be powered by solar energy, waste and exhaust heat (Sumeru et al., 2012). Also, they can operate with a new range of refrigerants harmless to the environment (Chen, 2015). Such a system offers several other advantages like a simple construction with a low cost, long life, and no maintenance. Moreover, different configurations of these systems can be realized depending on the role of the ejector in the cycle (Besagni et al., 2016). Several kinds of research on ejector systems have been realized, both theoretical and experimental using a wide variety of working fluids (Gil and Kasperski, 2015), considering the influence of geometrical parameters like the nozzle, mixing chamber and area ratio (Banasiak et al., 2012; Tang et al., 2017), or for particular applications like low temperature driven ejector (Smierciew et al., 2014).

An ejector refrigeration system is driven by thermal energy and consists of an ejector, three heat exchangers (generator, condenser, and evaporator), a pump, and finally a throttling device. The working principle of the system is generalized as follows. The high-pressure vapor is delivered from the generator named primary flow or propellant, this flow enters into the supersonic nozzle and draws low-pressure vapor from the evaporator, which is named the secondary flow. The two flows undergo mixing at constant pressure and leave the ejector after a pressure recovery in the diffuser. The mixed flow is then fed into the condenser. The liquid coming out of the condenser is divided into two parts. One goes through the expansion device to the evaporator. The remaining part is pumped back to the generator by the pump, and completes the cycle.

The performances of the Ejector Refrigeration System (ERS) and the ejector may be characterized by:

- Entrainment ratio ω defined as the ratio of the mass flow rate of the secondary($\dot{m}_s$) fluid to that of the primary fluid ($\dot{m}_p$) :

$$\omega = \frac{\dot{m}s}{\dot{m}p} \qquad \text{Eq. (1)}$$

- Pressure ratio P_{CR} representing the ratio of the condensing pressure (P_c) to the evaporating pressure (P_e) given by:

$$P_{cr} = \frac{P_c}{P_e} \qquad \text{Eq. (2)}$$

- Thermodynamic Coefficient Of Performance (COP) COP_{th}, which is the ratio of the refrigerating capacity produced in the evaporator to the sum of the heat supplied to the generator and the power consumed by the pump:

$$COP_{th} = \frac{Q_e}{Q_{ge} + W_{pump}} \qquad \text{Eq. (3)}$$

- Mechanical COP_m defined as being the ratio of the useful cooling generated by the evaporator over the energy consumed by the pump. The energy input to the generator is not taken into account as it is considered as a free source of energy. It is given by:

$$COP_m = \frac{Q_e}{W_{pump}} \qquad \text{Eq. (4)}$$

In this present work, droplet injection is made at the outlet of the ejector (diffuser). Droplets come directly from the circulation pump in red on Fig.1 at high pressure and condensation temperature. Note that the power of the pump has been significantly increased so as not to alter the functioning of the system. The droplets affect the main flow by extracting heat and so modifying the thermodynamic properties of the main flow. One expects that it has the effect of reducing the temperature of the superheated vapor at the outlet of the ejector before entering the condenser and of improving the condenser performance and that of the entire system.

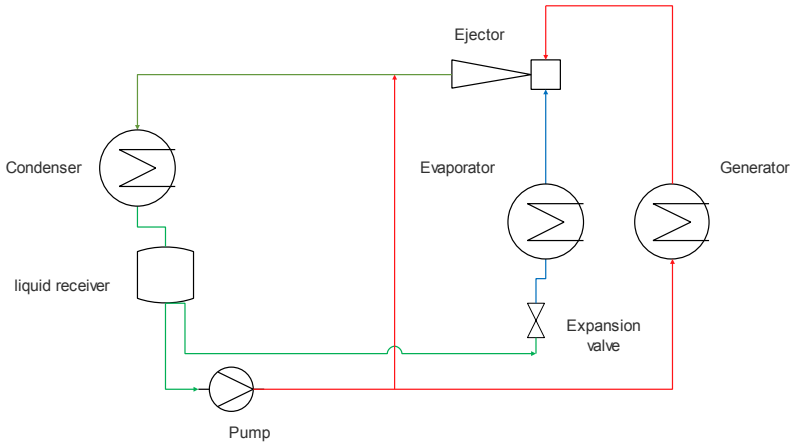

Figure 1: Schematic view of the Ejector Refrigeration System with droplet injection at the ejector's outlet

2. EXPERIMENTAL AND NUMERICAL METHODS

2.1. Experimental set-up

More than a hundred tests were carried out at the Institute for Research of Hydro-Québec in Shawinigan, Canada. The nominal cooling capacity of the prototype is 35 kW using R245fa as the working fluid. The tests were realized by varying the primary flow rate as well as the temperatures of the heat transfer fluids at the inlet of the boiler, the condenser, and the evaporator. It should be noted that these parameters are very dependent on each other. The experimental set-up consists of an ERS and three auxiliary utility circuits: a heating loop, a cooling loop, and a thermal load loop fully described in (Hamzaoui et al., 2018).

The heating loop consists of a 250 kW electric boiler that delivers thermal energy to the ERS vapor generator in order to simulate a waste heat source. Propylene glycol (50/50) used as a thermal fluid is pumped by means of a centrifugal pump. At the vapor generator inlet, the temperature is finely adjusted by the boiler PID controller (deviation of ±0.1°C).

The cooling loop consists of a cooling tower with a rated capacity of 400 kW, to which the ERS condenser is connected. The heat transfer fluid used in this loop is propylene glycol (20/80). The temperature at the inlet of the condenser is controlled by means of a three-way mixing valve with a deviation of ±0.5 °C while the flow rate is adjusted through a variable frequency driver on the corresponding pump. Finally, the thermal load loop simulates the cooling load: the ERS evaporator extracts the heat input provided by a 45 kW electric cartridge heater and carried through by the thermal fluid ethylene glycol (50/50). Similarly, to the cooling loop, the flow rate is manually controlled by the use of a variable frequency driver to adjust the rotational speed of the circulating pump.

The type of ejector is based on the design of the nozzle exit position (Keenan et al., 1950) through the so-called constant pressure mixing (CPM) assumption. The nozzle exit is located within the converging part of the suction chamber and the mixing occurs at constant pressure (Chen et al., 2016). The dimensions of the ejector are given in Fig.2.

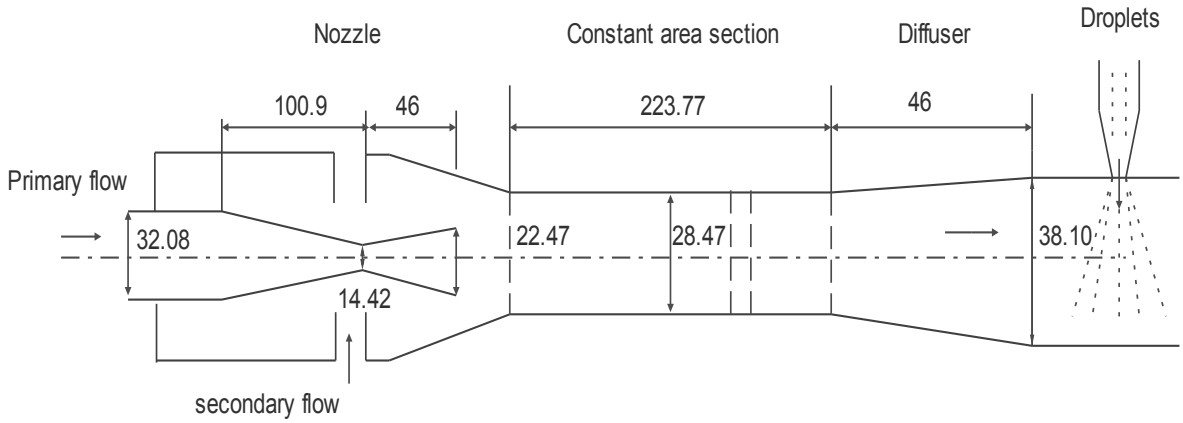

Figure 2: Schematic view of the supersonic ejector with relevant dimensions

2.2. Numerical method

The thermodynamic model developed using MATLAB (R2017b) determines the performance of the ejector refrigeration system with and without droplet injection. Some hypotheses are necessary for the development of the thermodynamic model:

For the ejector model (Croquer et al., 2017):

- The flow inside the ejector is steady state and one-dimensional,
- The secondary flow throat (effective area) occurs at the entrance of the constant area section,
- The pressure at the entrance of the constant area section maximizes the secondary flow,
- A normal shock occurs before the diffuser inlet,
- Irreversibilities in the ejector are taken into account by using polytropic efficiencies (Haghparast et al., 2018).

For the droplet injection:

- The chemical component of the droplets is the same as the gas phase used in the primary flow,
- The flow of the injected drops is $\dot{m}_i$ = 0.08 kg/s,
- The pressure at the input of the generator is the same with the injection of drops,
- The temperature at the injection is equal to the condenser temperature,
- Coalescence and droplet deformation effects are neglected.

For the heat exchangers, the models of the generator, condenser and evaporator are steady state.

2.3. Calculation procedure

For the ejector, the conservation principles of mass, momentum, and energy are applied with two inlets and one outlet as follows:

Conservation of mass:

$$\rho_{in,1} V_{in,1} A_{in,1} + \rho_{in,2} V_{in,2} A_{in,2} = \rho_{out} V_{out} A_{out} \quad \text{Eq. (5)}$$

Conservation of momentum:

$$[P_{in,1} V_{in,1} + \dot{m}_{in,1}] + [P_{in,2} V_{in,2} + \dot{m}_{in,2}] = [P_{out} V_{out} + \dot{m}_{out}] \quad \text{Eq. (6)}$$

Conservation of energy:

$$\dot{m}_{in,1}[h_{in,1} + \frac{1}{2} V_{in,1}^2] + \dot{m}_{in,2}[h_{in,2} + \frac{1}{2} V_{in,2}^2] = \dot{m}_{out}[h_{out} + \frac{1}{2} V_{out}^2] \quad \text{Eq. (7)}$$

where ρ is the fluid density, V is the flow velocity, A is the cross sectional area, P is the pressure, ṁ is the mass flow rate and h is the specific enthalpy.

Polytropic efficiencies are used to account for friction losses within the ejector. A polytropic efficiency is defined as the isentropic efficiency of an element process. It takes into account the elemental

pressure ratio and the irreversibility occurring during the acceleration and deceleration processes, unlike the isentropic efficiency for primary and secondary flows (Haghparast et al., 2018):

$$\eta_{pol,p,or,s} = \frac{h_j - h_{j+1}}{h_j - h_{j+1,is}} \quad \text{Eq. (8)}$$

In the diffuser:

$$\eta_{pol,D} = \frac{h_j - h_{j+1,is}}{h_j - h_{j+1}} \quad \text{Eq. (9)}$$

Droplets injected after the diffuser are expected to affect the main flow by extracting energy for the breakup and by altering thermodynamic properties. The terms related to the breakup energy of droplet are described as following:

The surface energy of a droplet can be defined as the product of its surface area S_d by its surface tension σ (Adika et al., 2009).

$$E_s = S_d \sigma \quad \text{Eq. (10)}$$

The Weber number represents the breakup mechanism and resulting droplet size:

$$We = \frac{\rho_g V_s D_d}{\sigma_d} \quad \text{Eq. (11)}$$

where ρ_g is the surrounding gas density and V_S is the relative velocity. No breakup is expected for local Weber numbers lower thanr a critical value We_c (Pilch et al., 1987);

$$We_c = 12(1 + 1.077 Oh^{1.6}) \quad \text{Eq. (12)}$$

where *Oh* is the Ohnesorge number, which relates the viscous to the inertial and surface tension forces in a droplet (Chauvin et al., 2016). The total breakup energy writes:

$$\Delta E_{br,i} = \frac{6.\sigma.\dot{m}_i}{\rho_i D_i}\left(\frac{D_i}{D_d} - 1\right) \quad \text{Eq. (13)}$$

where $\dot{m}_i$ is the mass flow rate of the droplets, D_I the diameter of the droplets, D_d the diameter of the diffuser and ρ_i is the density of droplets.

For the three heat exchangers, the powers write:

Generator $$Q_{ge} = \dot{m}_p(\Delta h) \quad \text{Eq. (14)}$$

Condenser $$Q_c = (\dot{m}_s + \dot{m}_p)(\Delta h) \quad \text{Eq. (15)}$$

Evaporator $$Q_e = \dot{m}_s(\Delta h) \quad \text{Eq. (16)}$$

3. RESULTS AND DISCUSSION

The effect of the droplet injection at the exit of the ejector is analyzed. A comparison between the thermodynamic model and the experimental data is performed as well as a comprehensive comparison between the cases with and without droplet injection to quantify their effect on the performance of the system. The main results can be summarized as follows:

- The results displayed in Figure 3 show that the relative errors between the numerical model and experimental data are less than 5% for the primary mass flow rate and 12% for the entrainment ratio for both cases with and without injection. This fairly good agreement

between the numerical and experimental results confirms the validity of the present and new thermodynamic model.

- Figure 4 illustrates the variations of the refrigerant temperature according to the condenser mass flow rate as well as the variations of the condenser pressure against the condenser mass flow rate and this for different values of the glycol temperature within the range [20°C-26°C]. Injecting droplets results in a slight pressure decrease, by about 3%. Regarding the temperature, the effect of droplet injection is more pronounced with a decrease from 69.58°C to 30.17°C at the condenser inlet.
- Figure 5 displays the influence of the entrainment ratio on both coefficients of performance (COP), the thermodynamic and mechanical ones, as a function of the coolant temperature in the heat exchanger. These two coefficients of performance increase by increasing the entrainment ratio with and without droplets. It is worth mentioning that with droplet injection, the coefficient COP_{th} may be increased by up to 35%. At the same time, the COP_m decreases as the consumption of the circulation pump increases with the injection of droplets not to alter the primary flow that enters the generator and ensuring the operation of the cycle.

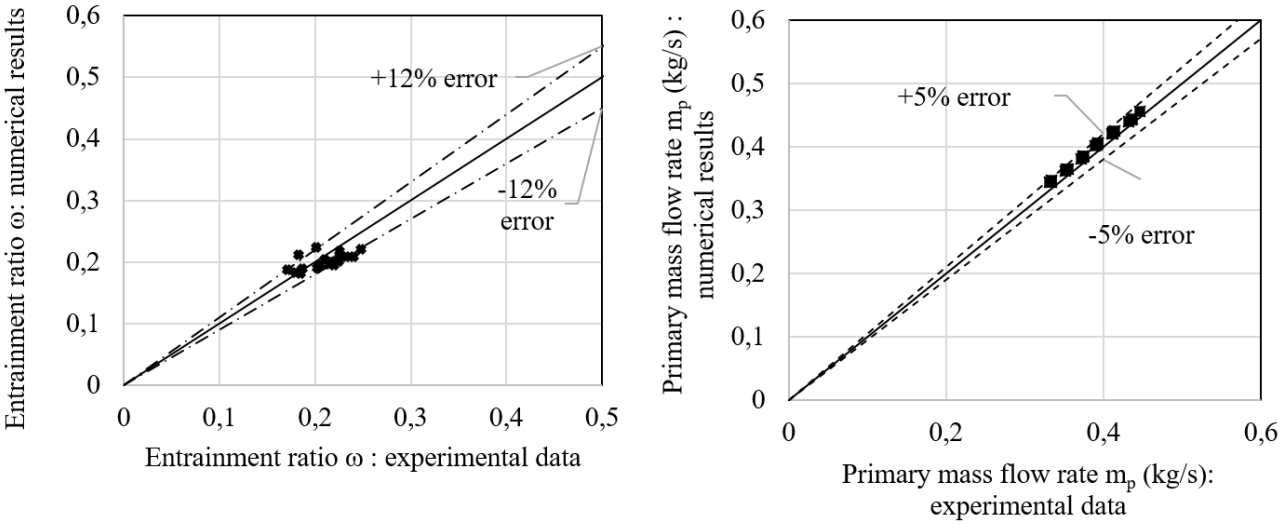

Figure 3: Comparison between the thermodynamic model and the experimental data in terms of entrainment ratio (left) and primary mass flowrate (right) with injection.

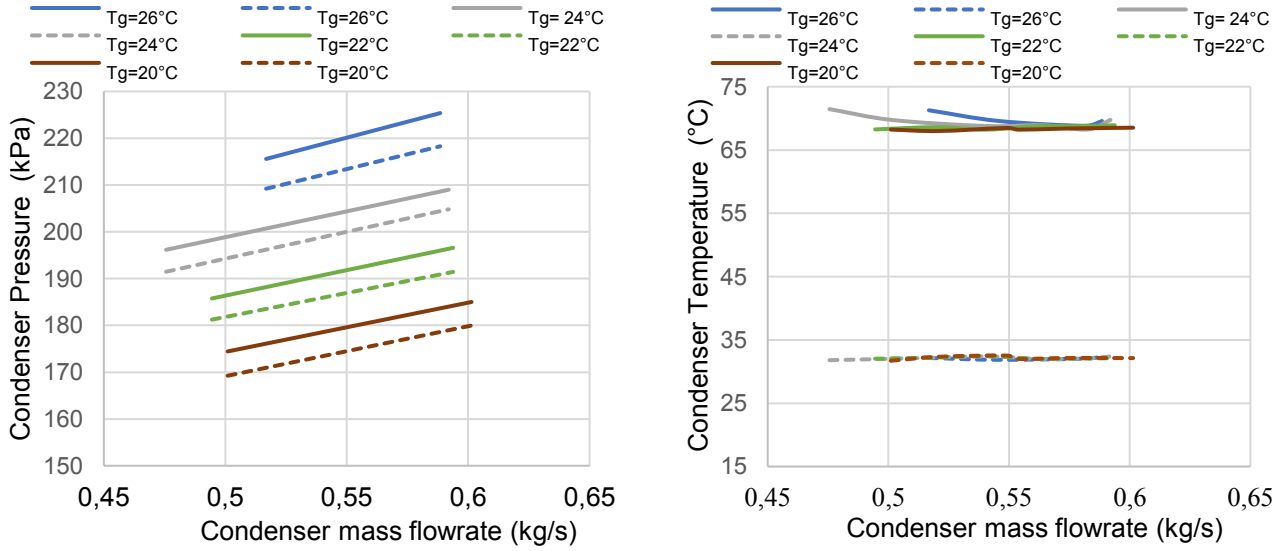

Figure 4: Influence of the condenser mass flowrate in the condenser temperature and pressure for four generator temperatures. Comparison between the cases with (solid lines) and without (dashed lines) droplets.

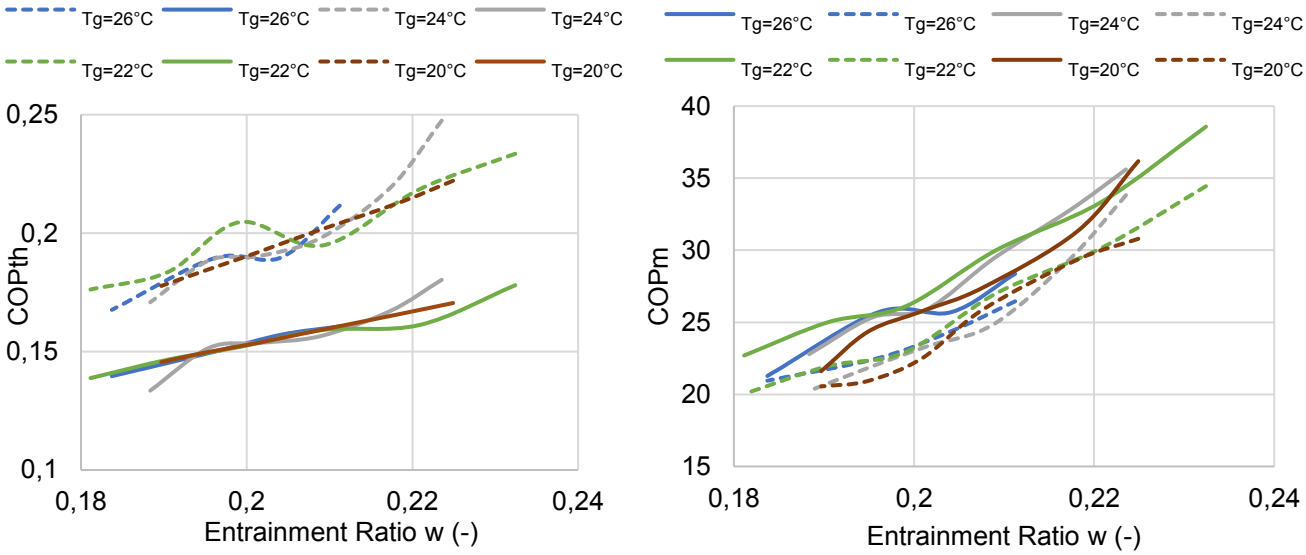

Figure 5: Influence of the entrainment ratio on the thermal (left) and mechanical COP. Comparison between the cases with (solid lines) and without (dashed lines) droplets.

4. CONCLUSIONS

A thermodynamic model based on polytropic efficiencies has been developed and validated against extensive experimental data to predict the entrainment ratio and the outlet temperature of a supersonic ejector with and without droplet injection. The performance of the ejector-based refrigeration system has been quantified and the results show first that there is a fairly good agreement between the two approaches. Second, the most important impact of droplet injection is the reduction of the temperature at the outlet of the diffuser. The thermodynamic COP may be increased by up to 35% by injecting liquid droplets.

ACKNOWLEDGEMENTS

This project is a part of the collaboration between Université de Sherbrooke Canada and Génie Climatique Laboratory at the University of Constantine. The authors would like to thank the Hydro-Québec research laboratory for its support offered during the experiments.

NOMENCLATURE

A	cross section area (mm^2)	ω	entrainment ratio
S	section (mm^2)	ρ	density ($kg.m^{-3}$)
Cp	specific heat ($J.kg^{-1}.K^{-1}$)	*σ*	surface tension ($N.m^{-1}$)
D	diameter (mm)		Subscripts
h	specific enthalpy ($kJ.kg^{-1}$)	g	glycol
ṁ	mass flow rate ($kg.s^{-1}$)	*ge*	generator
p	pressure (kPa)	*c*	condenser
P_{cr}	pressure ratio	*e*	evaporator
T	temperature (°C)	*t*	total
V	velocity ($m.s^{-1}$)	*th*	Ejector throat
Q	rate of heat flow (kW)		Acronyms
W	power (kW)	CPM	constant pressure mixing
	Greek symbols	ERS	Ejector refrigeration system

REFERENCES

Adiga, K.; Willauer, H.D.; Ananth, R.; Williams, F.W., 2009 Implications of droplet breakup and formation of ultra fine mist in blast mitigation. Fire Saf. J., 44, 363–369.

Banasiak, K., Hafner, A., Andresen, T., 2012. Experimental and numerical investigation of the influence of the two phase ejector geometry on the performance of the R744 heat pump, Int. J. Refrigeration 35, 1617-1625.

Besagni, G., Mereu, R., Inzoli F., 2016. Ejector refrigeration: A comprehensive review, Renew. Sust. Energ. Rev. 53, 373–407.

Chauvin, A., Daniel, E.,ChinnayyaJ, A.,Massoni,J., Jourdan.,G 2016. Shock waves in sprays: numerical study of secondary atomization and experimental comparison, Shock Waves 26, 403–415.

Chen, J., 2015. A review on versatile ejector applications in refrigeration systems, Int. J. Refrigeration 49, 67–90.

Chen, W., Shi, C., Zhang, S., Chen, H., Chong, D., Yan, J., 2016. Theoretical analysis of ejector refrigeration system performance under overall modes, Applied Energy 185 (2), 2074-2084.

Croquer, S., Poncet, S., Aidoun Z., 2017. Thermodynamic Modelling of Supersonic Gas Ejector with Droplets, Entropy 19 (579), 1-21.

Gil, B., Kasperski, J., 2015. Efficiency analysis of alternative refrigerants for ejector cooling cycles, Energ. Convers. Manage. 94, 12-18.

Haghparast, P., Sorin, M.V., Nesreddine, H., 2018. Effects of component polytropic efficiencies on the dimensions of monophasic ejectors, Energ. Convers. Manage. 162, 251-263.

Hamzaoui, M., Nesreddine, H., Aidoun, Z., Balistrou, M., 2018. Experimental study of a low grade heat driven ejector cooling system using the working fluid R245fa, Int. J. Refrigeration 86, 388-400.

Keenan, J.H., Neumann, E.P., Lustwerk, F**.,** 1950. An investigation of ejector design by analysis and experiment, J. Appl. Mech. 72, 299–309.

Pilch, M.; Erdman, C., 1987. Use of breakup time data and velocity history data to predict the maximum size of stable fragments for acceleration-induced breakup of a liquid drop. Int. J. Multiph. Flow, 13, 741–757.

Smierciew, K., Gagan, J., Butrymowicz, D., Karwacki, J., 2014. Experimental investigations of solar driven ejector air-conditioning system, Energy & Buildings 80, 260-267.

Sumeru, K., Nasution, H., Ani, F., 2012. A review on two-phase ejector as an expansion device in vapor compression refrigeration cycle, Renew. Sust. Energ. Rev. 16, 4927–4937.

Tang, Y., Liu, Z., Li, Y., Shi, C., Wu, H**.,** 2017. Performance improvement of steam ejectors under designed parameters with auxiliary entrainment and structure optimization for high energy efficiency, Energ. Convers. Manage. 153, 12-21.

Manuscript ID: 1267
DOI: 10.18462/iir.icr.2019.1267

Two-phase flow distribution in dual-compartment microchannel heat exchanger header

Mark Anthony REDO[(a)], Jongsoo JEONG[(a)], Seiichi YAMAGUCHI[(a),(b)], Kiyoshi SAITO[(a),(b)], Hyunyoung KIM[(c)]

[(a)] Department of Applied Mechanics and Aerospace Engineering, Waseda University
Tokyo, 169-8555, Japan, mark.redo@aoni.waseda.jp
[(b)] Interdisciplinary Institute for Thermal Energy Conversion Engineering and Mathematics,
Waseda University, Tokyo, 169-8555, Japan, sei_yamaguchi@aoni.waseda.jp
[(c)] Samsung Research and Development Institute Japan
Osaka, 562-0036, Japan, hyunyoung1.kim@samsung.com

ABSTRACT

With the inherent flow maldistribution problem within the microchannel heat exchanger header, which degrades the heat transfer performance, new microchannel heat exchanger header was designed and tested to improve this flow distribution performance, specifically for R410A. It features dual-compartment made of multiple layers consisting of the main section, baffle and hole seat, and rear section. Twenty flat tubes containing microchannels were inserted at 50% protrusion. Experiments and visualizations were conducted at 50, 100, and 200 $kg \cdot h^{-1}$ of mass flow rate (equivalent mass flux of 220.5, 441, and 882 $kg \cdot m^{-2}s^{-1}$), which were at partial to full loading capacity. Inlet vapor quality was fixed at 0.2 and evaporating temperature at 15 ºC, for evaporator application of air-conditioning system. Considering the same microchannel element, flow distribution enhancement was achieved when compared to the conventional header data. Liquid flow distribution was improved by around 65% at part-load conditions based on the relative standard deviation.
Keywords: Dual-Compartment Header, Microchannel, Heat Exchanger, Flow Distribution, Two-Phase Flow.

1. INTRODUCTION

Heat exchange devices are indispensable element applied in a variety of applications such as electronics, industries, power plants, and air-conditioning and refrigeration systems. High-performing heat exchangers contribute to the overall system efficiency and productivity (Dixit and Ghosh, 2015). The recent development of microfluidic technologies has led to the production of microchannel heat exchangers (MCHX), where small channels or passages serve as conduits for accomplishing an efficient heat and mass transfer processes (Kandlikar et al., 2006). This cutting edge technology offers both thermal energy savings and compactness. The latter gives flexibility to a wider scale of applications, material and space saving, and lesser refrigerant charge. However, the current structure and design adopted specifically for air-conditioning operative conditions face an on-going challenge of two-phase flow maldistribution inside the manifold or header (Anbumeenakshi and Thansekhar, 2016), where the microchannels are connected into, for evaporation process. This non-uniform flow distribution results to dry-out channels leading to about 20% evaporating capacity degradation as reported by Kulkarni et al. (2004). Among the factors that affect the distribution characteristics are the (i) operating conditions, including the mass flowrate, mass flux and vapour quality at the inlet of the header; (ii) the working fluid properties, particularly the thermodynamic and transport properties; and (iii) the MCHX structural and geometric design including the header and microchannel orientation, channel protrusion depth into the header, inlet flow alignment, and the inside of the header such as its shape and cross-section (Mueller and Chiou,

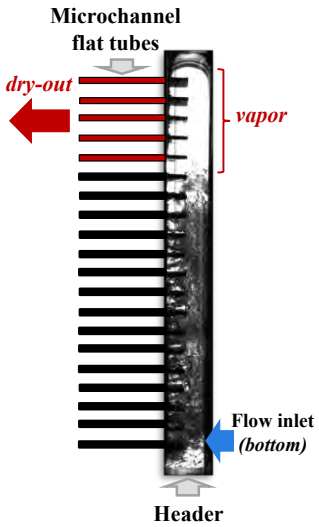

Figure 1: Flow maldistribution in conventional header

1988 and Kitto and Robertson, 1988). Many studies have tried to understand each of these factors. Siddiqui and Zubbair (2017) in their comprehensive review about MCHX, have concluded that the proper design of the header is one crucial aspect in achieving a well distributed flow because its profile defines how the fluid gets distributed.

Several works attempted to seek solutions in achieving a better flow distribution. Ahmad et al. (2009) with their goal to homogenize the separated two-phase flow at the inlet of the header, used additional expansion devices such as atomization orifice and splashing grid. The latter was able to improve the flow distribution but was compromised by a very large pressure drop. Kim et al. (2013) used insertion devices inside the header such as wire mesh and perforated plate, yet only the perforated tube was able to significantly enhance the flow distribution, but carried the same problem of having a high pressure drop increase by about 80%, from without insert. Additionally, most of these researches, particularly the experimental investigations, focused on small sized MCHX having small capacities limited to automobile air-conditioning applications. Redo et al. (2019) designed and constructed an experimental setup with test section representing an actual heat exchanger size and capacity of air-conditioners operating at bigger capacities. At a wider range of operating conditions, they have summarized the effect of inlet mass flux, vapour quality, tube protrusion depth, and evaporating temperature on the flow distribution characteristics. The findings were used to design a new header for enhancing the flow distribution. Therefore, the current paper reports the design of a dual-compartment header and the experiment test results when the inlet mass flowrate was at 50, 100, and 200 $kg \cdot h^{-1}$, vapour quality at 0.2 and 10 ºC evaporating temperature. Experiments and visualizations were conducted, with results being presented in metrics that highlighted the flow distribution enhancement when compared to conventional header.

2. EXPERIMENT FACILITY AND METHODS

The experimental setup was designed and constructed with an aim to investigate the flow distribution behaviour that represents an actual size evaporation heat exchanger of an air-conditioning system. Its schematic diagram is shown in Fig. 2, where the elements enclosed in red dashed lines comprise the test section, while the remaining components are under the condition-generating section. The test section consists mainly of the front vertical header and multiple horizontal flat tubes with microchannels in them. The major components of the condition-generating section are the refrigerant pump, liquid flowmeter, pre-heaters, condenser, sub-cooler and brine cooling system.

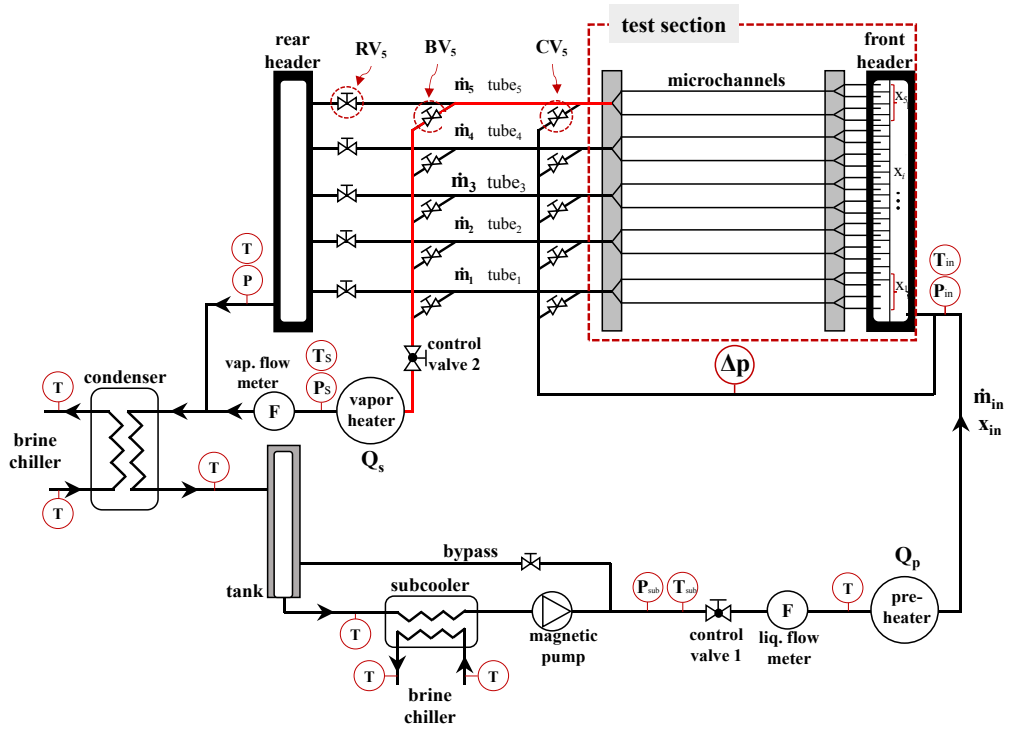

Figure 2: Experiment setup schematic diagram

2.1. Test Section

The current work presents the comparison of two headers, but utilizing exactly the same microchannel elements. There were 20 microchannel flat tubes connected into the header, but owing to a challenging flow measurement, they were purposely paired together through Y-connectors, thereby producing 10 flat tubes. The merging is shown in Fig. 3 (left side), as well as the profile and dimensions of the microchannels for each of these flat tubes. While on the right side of Fig. 3, the header part portraying the conventional and dual-compartment header photos are shown.

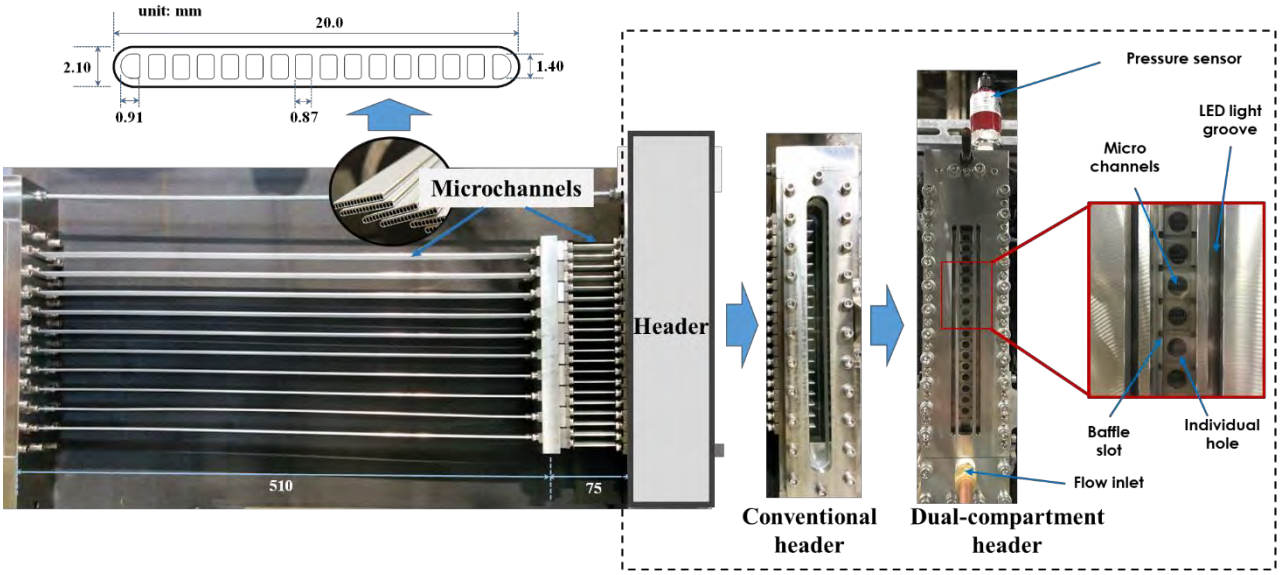

Figure 3: Microchannels, conventional and dual-compartment headers

The previous header, which is conventional in its form, features a typical MCHX structure, with bigger dimensions, and having single compartment. Once the fluid enters the inlet, it directly flows through the branching parallel flat tubes or microchannels, as illustrated in Fig. 4.

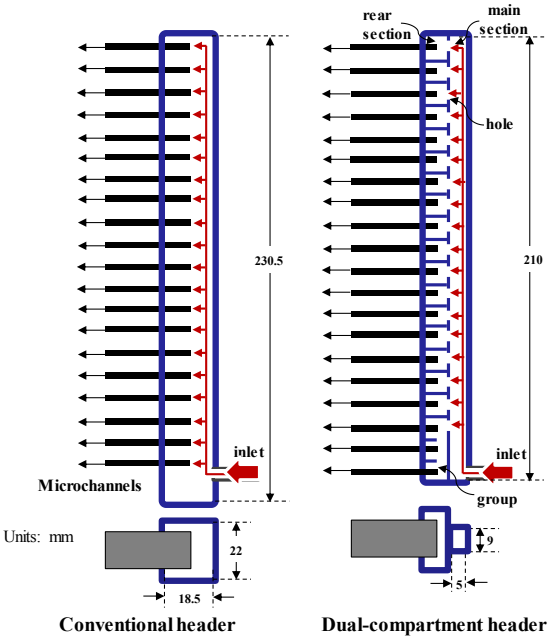

Figure 4: Schematics of both headers

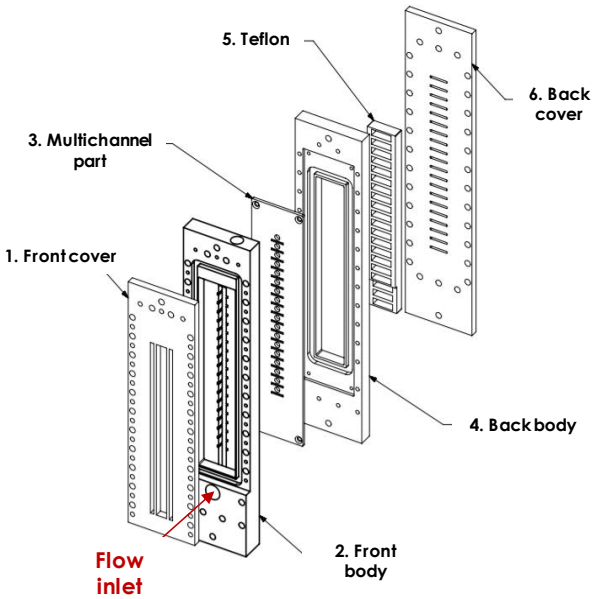

Figure 5: Dual-compartment header components

On the contrary, the latter has smaller header hydraulic diameter to facilitate liquid flow boosting towards the top portion of the header. It is built with multiple layers (Fig. 5) assembling a dual-compartment header. The main section is where the flow stream goes first prior to reaching the rear

section that houses the parallel flat tubes. There are eighteen 10 mm diameter holes on the separating wall that serve as the flow passageway. Three flat tubes at the bottom are grouped together with one connecting hole to the main section. It was purposively done to regulate the flow, since a lot of liquid exits at the bottom channels for low loading capacity within the conventional MCHX header (Redo et al., 2017). For the purpose of visualization, the multi-layered components of the header contributed difficulty for the glass to be similarly installed at the sides like the conventional header. It was then situated at the front side, which became the visualization window of the flow in the main section. Providing a better lighting was a challenge, nevertheless, the high speed camera was able to capture fair quality videos.

2.2. Measurement Procedures

After the condensation, the fluid entered the sub-cooler and was circulated by means of a magnetically driven centrifugal pump capable of delivering up to 28 l/min of fluid. This main flow ($\dot{m}_{in}$) was regulated through the control valve 1 and bypass valve until the desired flowrate was achieved at a stable state with reference to the flowrate reading at the liquid Coriolis flowmeter. It was subsequently heated as it passed through a set of cartridge preheaters with a maximum heating capacity of 9 kW, where the power volume was controlled until the vapour quality (x_{in}) was obtained. The two-phase flow liquid entered at the bottom of the header and the total flow was distributed into the branching microchannels. The distribution tests and measurements were successively conducted. The superheated flow exiting at the measurement path and the flow from the rear header both entered the condenser, where brine was used as a coolant. Then the cycle continued.
Referring back to Fig. 2, the 10 flat tubes were then paired again, yielding 5 measurement tubes. Therefore, there were 5 sets of mass flowrates ($\dot{m}_i$) and vapour qualities (x_i) being measured and calculated, as represented in Fig. 6. This was done by foremost measuring the pressure drop (Δp) between the inlet of the header and the outlet of the flat tube for each of the 5 measurement tubes by opening the corresponding control valve (CV) at a time. Each of this pressure drop was used as a reference when measuring the individual flowrate ($\dot{m}_1$ to $\dot{m}_5$). Shown in a red line path in Fig. 2, the mass flowrate for tube 5 ($\dot{m}_5$) was measured by opening its bypass valve (BV_5), while its rear valve (RV_5) was closed. The flow was superheated as it passes through the vapour heater and the control valve 2 was adjusted until the same Δp_5 was obtained. The $\dot{m}_5$ was then measured through the vapour Coriolis flowmeter. The procedures were repeated for the rest of the measurement tubes ($\dot{m}_4$ to $\dot{m}_1$).

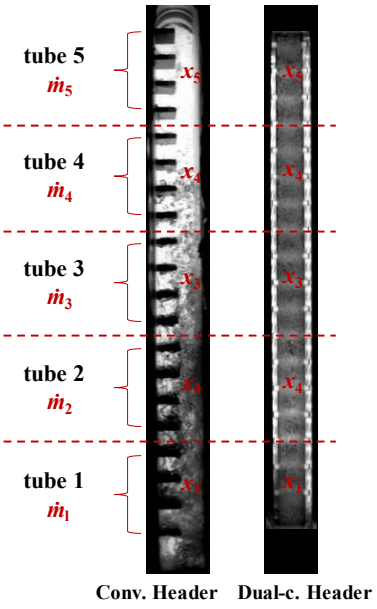

Figure 6: Data representation

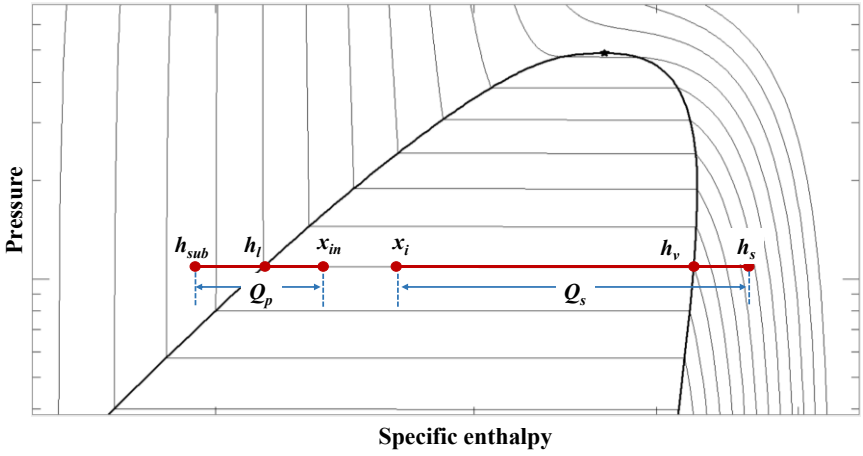

Figure 7: P-h Diagram of R410A

The individual quality (x_i) expressed in Eq. (1) was calculated given the measured individual mass flowrate and the properties of the refrigerant, as illustrated on the P-h graph in Fig. 7. The heat input

at the vapour heater (Q_s) with the corresponding temperature (T_s) and pressure (P_s) were measured, so the enthalpy of the superheated vapour ($h_s = f(T_s, P_s)$) for R410a was therefore known.

$$x_i = \frac{\dot{m}_i (h_s - h_l) - Q_s}{\dot{m}_i (h_v - h_l)} \quad \text{Eq. (1)}$$

3. RESULTS AND DISCUSSIONS

The parameters and ranges of experiment conditions are summarized in Table 1. The variation was mostly focused on the inlet mass flowrate, in which the corresponding mass fluxes inside the two headers are different because of the difference in their cross-sectional areas.

Table 1. Parameters and condition ranges

$\dot{m}_{in}$ [kg·h^{-1}]	$G_{conventional}$ [kg·m^{-2}·s^{-1}]	$G_{dual\text{-}compartment}$ [kg·m^{-2}·s^{-1}]	x_{in} [-]	T_{eva} [°C]	Tube protrusion [%]
50, 100, 200	63, 125, 250	220.5, 441, 882	0.2	15	50

Metrics were adopted to compare the flow distribution performance of both headers. With the individual mass flowrates ($\dot{m}_i$) and individual vapor qualities (x_i) previously defined, the amount of the liquid and the vapor measured in five measurement tubes (Fig. 6) are presented in terms of the liquid flow ratio ($FR_{l,i}$) and the vapor flow ratio ($FR_{l,i}$) expressed in Eq. (2) and Eq. (3), respectively. A uniform flow is indicated by a flow ratio equal to one or unity. Additionally, the relative standard deviation (RSD) shown in Eq. (4) is adopted, which is the standard deviation ratio to the mean. The flow distribution gets better as the RSD value approaches zero.

$$FR_{l,i} = \frac{\dot{m}_{l,i}}{\bar{m}_l} \quad \text{Eq. (2)}$$

$$FR_{v,i} = \frac{\dot{m}_{v,i}}{\bar{m}_v} \quad \text{Eq. (3)}$$

$$RSD = \frac{SD}{\bar{m}} = \frac{\sqrt{\frac{1}{n}\sum_{1}^{n}(\dot{m}_i - \bar{m})^2}}{\bar{m}} \quad \text{Eq. (4)}$$

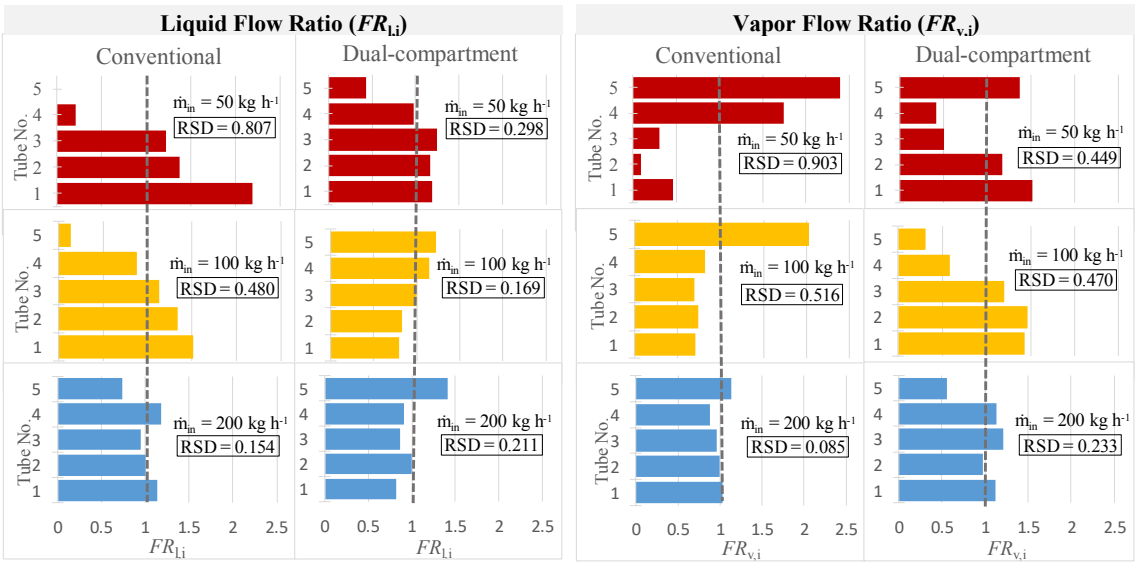

Figure 8: Flow distribution profiles

Illustrated in Fig. 8 are the flow distribution profiles for the two headers with the inlet mass flowrates ($\dot{m}_{in}$) arranged incrementally in a vertical manner. At 50 kg·h^{-1}, there is no liquid at the top of the header and only vapour exits at topmost tube (tube 5), for the conventional header. Subsequently, as the $\dot{m}_{in}$ increases, the better the flow distribution becomes, with a large difference of RSD of the liquid flowrate jumping from 0.807 to 0.154 for 50 kg·h^{-1} and 200 kg·h^{-1}, respectively. This is resulted by the increase of the liquid flow level observed simultaneously from the visualization snapshots in Fig. 9.

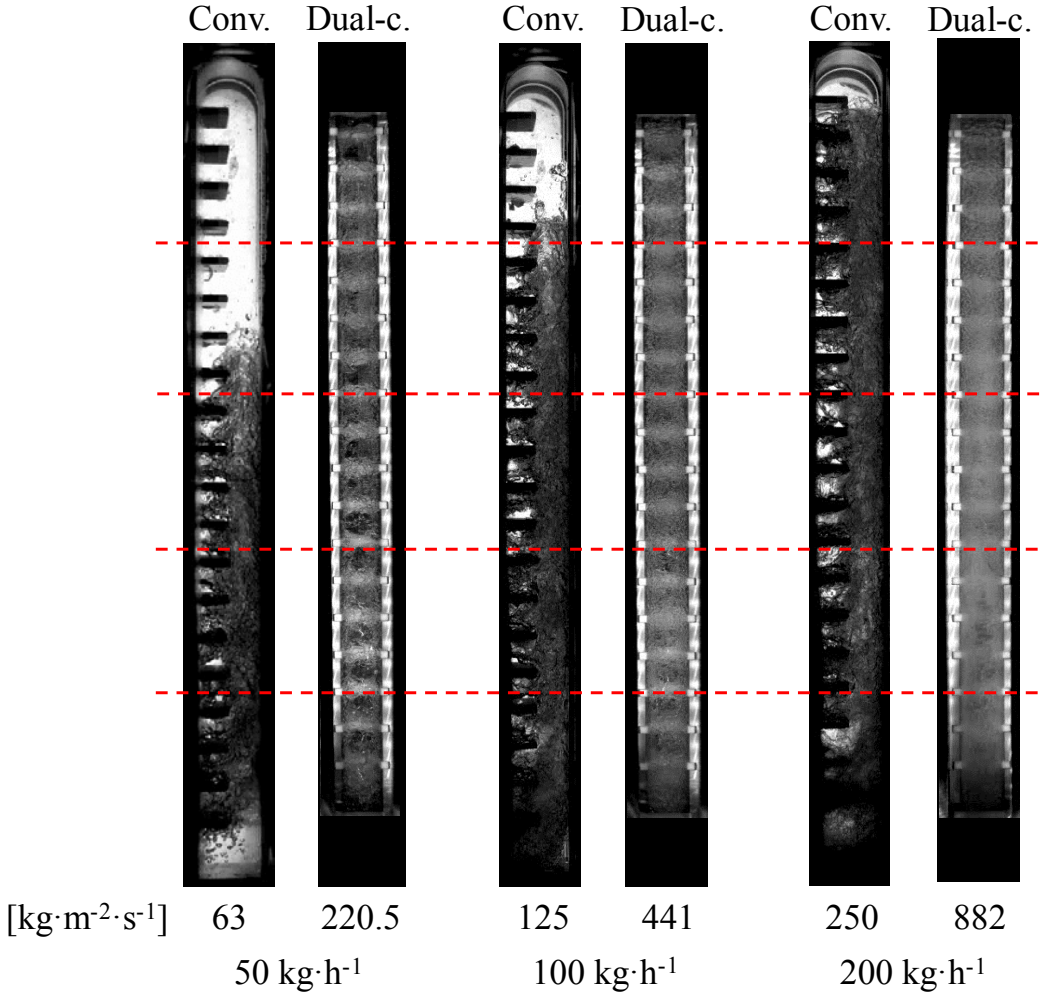

Figure 9: Visualization snapshots

Carrying in the results for the dual-compartment header, there was liquid flowing out from the top tubes at 50 kg·h^{-1}. When compared with the conventional data, liquid flow distribution enhancement was obtained by about 65% for both the 50 and 100 kg·h^{-1} based on the liquid flow. As shown in Fig. 10, the RSD is closely the same for all the tested inlet mass flowrates, but as the $\dot{m}_{in}$ further increases from 100 kg·h^{-1}, more liquid flows out from the top tubes as compared to the bottom tubes, which reverses the distribution trend. This is mostly caused by the increase of inertial force that pushes more liquid towards the top, and was evident by the flow velocity increase when referred to the visualization videos. There is around 25% liquid flow distribution deterioration when header was shifted to dual-compartment from conventional one for 200 kg·h^{-1} based on RSD. This might require an additional improvement, but in most actual air-conditioning cases, the high and full-load capacities do not occur as frequent as that of the low or part-load conditions.

Although the present investigation focused on an evaporation case, where the pressure drop (Δp) does not directly affect the system performance, when it is applied for condensation, it has to be considered. Shown in Fig. 11 is the average Δp obtained for both the headers, when assumed to be relatively similar for condenser case, the 20% increase in average Δp for the new header is actually small compared to what the previous studies have obtained.

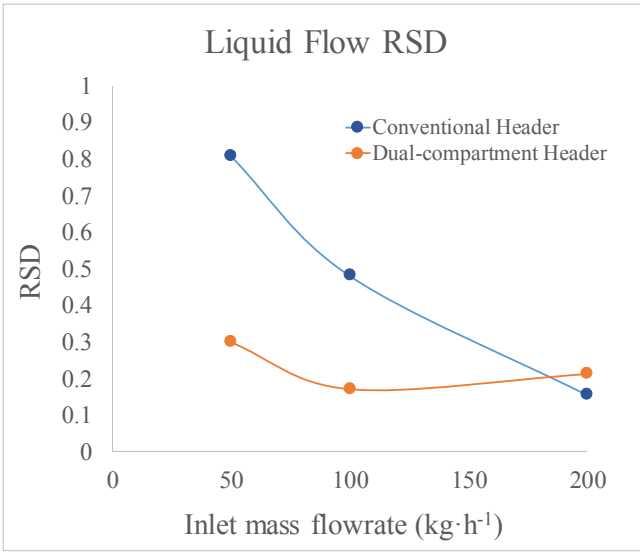

Figure 10: Liquid Flow RSD

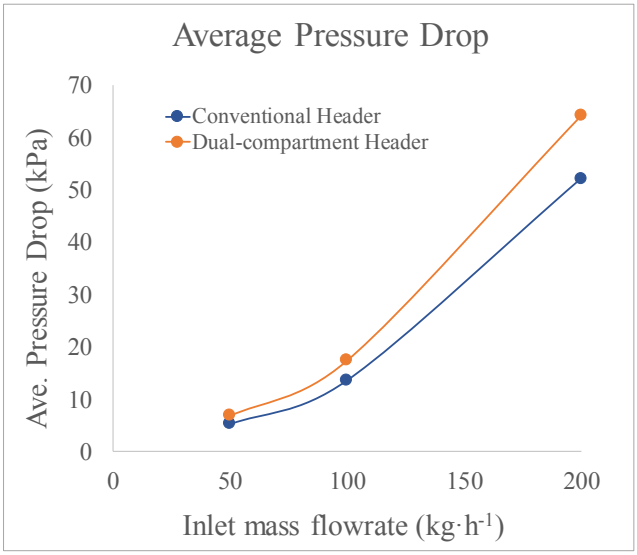

Figure 11: Average pressure drop

4. CONCLUSIONS

An experiment setup covering an evaporator microchannel heat exchanger test section for an actual size air-conditioning system was designed and constructed. Conventional and dual-compartment headers were installed and tested individually, keeping the same microchannel elements. The former header has a typical structure having one-compartment, while the latter is a dual-compartment header composed of multiple layers.

Experiment data have shown that the liquid flow distribution has improved for the dual-compartment header when compared to the conventional one, by about 65% based on the RSD, for part-load at $\dot{m}_{in}$ 50 and 100 kg·h^{-1}. As the $\dot{m}_{in}$ approaches 200 kg·h^{-1}, a trend reversal happens where most liquid flows at the top than the bottom tubes for the dual-compartment header, caused by an increase inertial force, observed also from the velocity increase through the visualization clips. Although this led to around 25% flow distribution deterioration in reference to the conventional header, the condition was at full-load, which is not the common occurrence for an air-conditioning system. Despite that the focus of the work was on an evaporator application, the average Δp was compared for its possibility of application to condensation case, where the parameter is considered significant for perforamance determination. Around 20% increase in Δp was obtained for each of the inlet mass flowrate for the dual-compartment header when compared to the conventional one, which is not as significantly large when related to other studies.

NOMENCLATURE

G	mass flux (kg×m^{-2}×s^{-1})		Subscripts
h	specific enthalpy (J×kg^{-1})	i	Individual, index
$\dot{m}$	mass flowrate (kg×h^{-1})	in	inlet
p	pressure (kPa)	l	liquid
Q	heat (kW)	s	superheated
T	temperature (K)	v	vapor
x	vapour quality		

REFERENCES

Ahmad, M., Berthoud, G., Mercier, P., 2009. General characteristics of two-phase flow distribution in a compact heat exchanger. Int. J. of Heat and Mass Trans. 52, 442-450.

Anbumeenakshi, C., Thansekhar, M.R., 2016. Experimental investigation of header shape and inlet configuration on flow maldistribution in microchannel. Exp. Therm. and Fluid Sci. 75, 156-161.

Dixit, T., Ghosh, I., 2015. Review of micro- and mini-channel heat sinks and heat exchangers for single phase fluids. Renewable and Sustainable Energy Reviews. 41, 1298-1311.

Kandlikar, S., Garimella, S., Li, D., Colin, S., King, M., 2006. Heat Transfer and Fluid Flow in Minichannels and Microchannels. Butterworth-Heinemann Publications, Massachusetts, 555 p.

Kim, N.H., Lee, E.J., Byun, H.W., 2013. Improvement of two-phase refrigerant distribution in a parallel flow minichannel heat exchanger using insertion devices. Appl. Therm. Eng. 59, 116-130.

Kitto Jr., J.B., Robertson, J.M., 1988. Effects of maldistribution of flow on heat transfer equipment performance. Heat Transfer Eng. 10, 18–25.

Kulkarni, T., Bullard, C.W., Cho, K., 2004. Header design tradeoffs in microchannel evaporators. Appl. Therm. Eng. 24, 759–776.

Mueller, A.C., Chiou, J.P., 1988. Review of various types of flow maldistribution in heat exchangers. Heat Transfer Eng. 9, 36–50.

Redo, M.A., Jeong, J., Giannetti, N., Enoki, J., Yamaguchi, S., Saito, K., Kim, H., 2019. Characterization of two-phase flow distribution in microchannel heat exchanger header for air-conditioning system. Exp. Therm. And Fluid Sci. 10.1016/j.expthermflusci.2019.04.021.

Redo, M.A., Giannetti, N., Jeong, J., Enoki, K., Ota, I., Saito, K., Kim, H., 2017. Experiment and visualization of R410A flow distribution within the vertical header of microchannel heat exchanger. Proceedings of the IIR-TPTPR Conference, Seoul, South Korea.

Siddiqui, O., Zubair, S., 2017. Efficient energy utilization through proper design of microchannel heat exchanger manifolds: a comprehensive review. Renew. Sustain. Energy Rev. 74, 969-1002.

Manuscript ID: 1269
DOI: 10.18462/iir.icr.2019.1269

Numerical study of heat and mass transfer absorption processes using a horizontal flooded-liquid film in ammonia-water mixtures

Beethoven NARVÁEZ-ROMO, José R. SIMÕES-MOREIRA

SISEA – Alternative Energy Systems Lab., Mechanical Engineering Department
Escola Politécnica, University of São Paulo, Brazil
betonarmo@usp.br , jrsimoes@usp.br

ABSTRACT

This paper presents a numerical study of the heat and mass transfer (HMT) absorption process using ammonia-water solution in a new configuration of horizontal flooded-liquid film, in which the total surface wettability is reached. The absorber is composed of several plates placed in the vertical position. Each one of these plates have a spiral cooling tube, in which the coolant flows and the liquid solution flows over and around the tube. The plate depth guarantees a one-millimeter liquid film of the ammonia-water solution. A mathematical model based on the overall balance of mass, ammonia species, and energy equations was carried out. These equations were solved for a set of control volumes discretized by the finite difference method, and with the HMT correlations. A parametric study of the absorption process was performed: surface temperature, plates number, and liquid film thickness.
Keywords: Absorption Process, Heat and Mass Transfer, Ammonia-Water, Flooded Tubes, Falling-Film, Total Wettability, Absorption Refrigeration Cycle.

1. INTRODUCTION

An ARC, absorption refrigeration cycle, operates at two pressure levels (Fig. 1). The high pressure is established by the condensing pressure imposed by the environmental temperature, and the low pressure follows the saturation pressure at the designed evaporating temperature. Low pressure at very high ammonia concentration vapor (pure ammonia vapor in theory) leaves the evaporator ($\dot{Q}_{eva}$) and then flows into the absorber. At the same time a low ammonia concentration liquid solution comes from the EV-2 (weak solution) to absorb that ammonia vapor to become a high ammonia concentration liquid solution (strong solution) by heat rejection ($\dot{Q}_{abs}$) to a cooling liquid. The pump drives the liquid solution to the high-pressure level.
At high pressure, the strong solution is driven to a heat exchanger, where it undergoes a pre-heating process in a counter flow configuration before entering the generator. At the generator, a heat source ($\dot{Q}_{gen}$) provides heat to the liquid solution and part of it evaporates giving rise to a vapor mixture as it occurs in a typical distillation process as studied by Zavaleta-Aguilar and Simões-Moreira (2012).

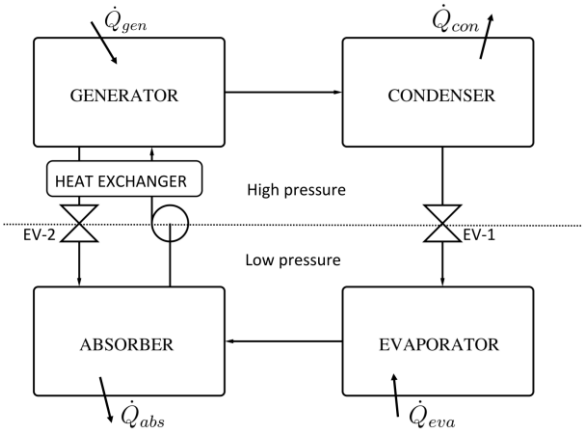

Figure 1: Absorption refrigeration cycle diagram

The weak liquid solution flows down to the absorber after being pre-cooled in the counter flow heat exchanger and then flows through EV-2 decreasing its pressure. The vapor mixture that leaves the generator is still wet and, consequently, is driven to a rectification zone to achieve a high ammonia concentration by rejecting heat to the environment. It is worth mentioning that both the absorber and the generator are the main components of the absorption system because that there is a simultaneous heat and mass transfer process, and those components are characterized by low values rates of heat and mass transfer (Castro et al., 2009). Moreover, all most of those components employ the falling film technology, in which it shows advantageous of heat and mass transfer as compared from flooded evaporator. According to falling film technology, several studies have been developed, for instance, Thome (1999) carried out a review of falling film evaporation on both smooth and enhanced tubes focusing on working fluids as alternative refrigerants including ammonia; he found that the falling film technology provides a higher heat transfer coefficient than flooded evaporators. Ribatski and Jacobi (2005) carried out a critical review of falling film evaporation process over horizontal tubes (single and tube bundles), covering hydrodynamic studies and the heat transfer coefficient affected by several operation conditions on smooth and enhanced tubes. They pointed out that the falling film technology presents inconveniences due the liquid film maldistribution and wettability problems. Narváez-Romo and Simões-Moreira (2017) found the same difficulties to achieve a good liquid film distribution. Zavaleta-Aguilar and Simões-Moreira (2015) study the wettability behavior in the generation process using horizontal tube bundle falling film. Narváez-Romo et al. (2017) carried out a critical review of falling film technology focused to study the heat and mass transfer correlations applied in absorption process for both working fluids; ammonia-water and lithium bromide-water. All these reviews show a common care of the falling film technology; for instance, wettability behavior. Thus, the current research studies the heat and mass transfer absorption process in a novel configuration, using a horizontal flooded-liquid film in ammonia-water mixtures to reach a total wettability.

2. MODELING OF THE ABSORPTION PROCESS

Arbitrary operational conditions are defined to analyze the absorption process and the inlet parameters for the absorber are fixed by ARC modeling; thermal load of 1 TR, vaporization temperature of -10°C, condensation temperature of 40°C. Hence, these conditions established the boundary conditions in the flooded-liquid film configuration for ammonia-water such as;

- Liquid phase inlet mass flow: 0.020kg/s or liquid flow rate per unit of plate width: γ_L=0.010 kg/m.s;
- Inlet liquid phase ammonia mass fraction: 0.358;
- Inlet liquid phase temperature: 313.0 K (saturation temperature for *x*=0.408 and *P*=2.91bar);
- Inlet vapor phase mass flow: 0.0033 kg/s;
- Inlet vapor phase ammonia mass fraction: 1.0;
- Inlet vapor phase temperature: 263.0K;
- Circular plate wall temperature: 298.0K;
- OD circular plate: 0.172m;

Fig. 2a shows the new proposal technology, in which weak solution coming from generator enters to the absorber to absorb the ammonia vapor coming from the evaporator, obtaining a strong solution at the exit of absorption equipment. It is projected of several spiral heat exchanger as is shown in that Fig. (2a). Fig. (2b) represents the flooded-liquid film absorption process. A spiral heat exchanger is used as coolant secondary circuit, and it is mounted over a 3D printed circular plate. The weak solution moves over the heat exchanger, allowing the contact between the ammonia vapor and the solution over it. As absorption process occurs, heat of absorption is transferred to the coolant fluid. Total wettability is guaranteed by flooded phenomenon as shown in Fig. 3.

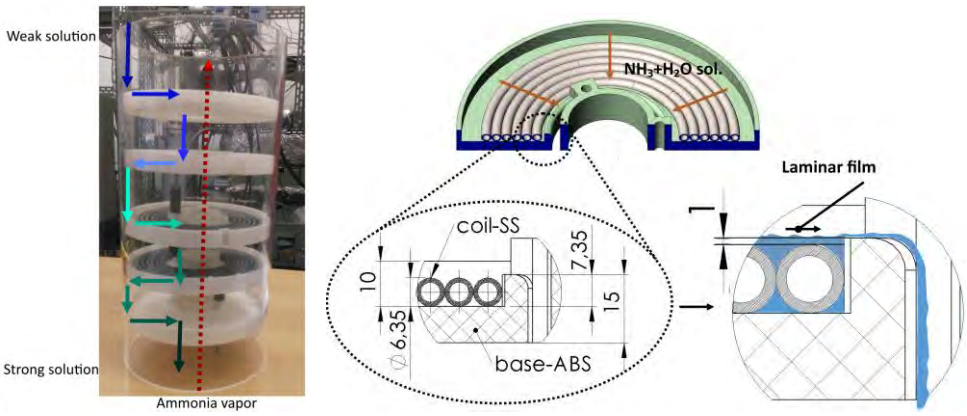

Figure 2: a) Horizontal flooded-liquid film absorber, b) schematic representation of the flooded-liquid film absorption process for each spiral heat exchanger



Figure 3: Total wettability on the plate using water

2.1. Discretized equations

Concerning the discretized equations in ammonia-water absorption process using falling film technology, Fernández-Seara et al., (2005) performed one of the first thermal modeling studies including the vapor phase property variation. They used the finite difference technique, applying the laws of conservation of mass, species of ammonia, and energy for each discrete control volume: liquid, vapor, and linked by the interface. This section discussed the discretized equations, in which the liquid-vapor interfacial phenomenon is also considered. The liquid-vapor interface can be represented as a control volume in which both phases coexist in thermodynamic equilibrium (Fig. 4). As the ammonia and water mass flux across the interface must be conserved, they can be calculated using Colburn and Drew (1937) equations relating the mass transfer coefficients with the interfacial properties.

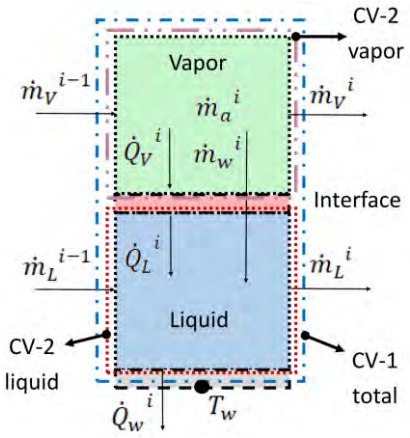

Figure 4: Representation of heat and mass transfers in control volumes 1, 2, and 3

The ammonia mass flux transfer through interface can be calculated by Eq. (1).

$$\dot{m}_a = z.h_{mV}.\rho_V.A_{int}.\ln\left(\frac{z-y_{int}}{z-y}\right) \quad \text{Eq. (1)}$$

The same ammonia mass fraction from the liquid phase side is given by Eq. (2).

$$\dot{m}_a = z.h_{mL}.\rho_L.A_{int}.\ln\left(\frac{z-x}{z-x_{int}}\right) \quad \text{Eq. (2)}$$

where,

$$z = \frac{\dot{m}_a}{\dot{m}_a + \dot{m}_w} \quad \text{Eq. (3)}$$

Energy balance across the interface must take into account the heat flow across the interface by convection on either side of the interface as well as the condensation or vaporization enthalpy. This is explicit in the energy balance given by Eq (4).

$$\dot{Q}_V + (\dot{m}_a + \dot{m}_w).H_{Vint} = \dot{Q}_L + (\dot{m}_a + \dot{m}_w).H_{Lint} \quad \text{Eq. (4)}$$

The heat transfer to each or from each phase is given by convection alone. Eqs. (5-6) give the heat flow to the liquid and vapor phase, respectively,

$$\dot{Q}_L = h_L^*.A_{int}.(T_{int} - T_L) \quad \text{Eq. (5)}$$

$$\dot{Q}_V = h_V^*.A_{int}.(T_V - T_{int}) \quad \text{Eq. (6)}$$

In previous expressions, the superscript * indicates that the heat transfer coefficient is corrected for simultaneous heat and mass transfer by the expression proposed by Treybal (1999). The convective heat flow to the surface is given by Eq. (7).

$$\dot{Q}_s = h_L.A_{int}.(T_L - T_s) \quad \text{Eq. (7)}$$

To compute the heat transfer coefficient, therefore, heat and mass transfer coefficients for the ammonia-water absorption process were calculated by Churchill and Ozoe's (1973) correlation (Eq. 8),

$$\mathrm{Nu} = \frac{0.3387 Pr^{1/3} Re^{0.5}}{\left(1+\left(\frac{0.0468}{Pr}\right)^{2/3}\right)^{0.5}} \quad \text{Eq. (8)}$$

The above equations are now applied to a 1-D cell. First, an individual cell is split into three control volumes as depicted in Fig. (3). Control volume 1 (CV-1) is the whole volume of the cell, including both liquid and vapor phases; control volume 2 (CV-2) envelopes only the liquid phase (liquid film); and control volume 3 (CV-3) encompasses the vapor phase. The balances of total mass, ammonia mass, and energy in CV-1 are given by the set of Eqs. (9-11)

$$\dot{m}_L^{i-1} + \dot{m}_V^{i-1} = \dot{m}_L^i + \dot{m}_V^i \quad \text{Eq. (9)}$$

$$\dot{m}_L^{i-1}.x^{i-1} + \dot{m}_V^{i-1}.y^{i-1} = \dot{m}_L^i.x^i + \dot{m}_V^i.y^i \quad \text{Eq. (10)}$$

$$\dot{m}_L^{i-1}.H_L^{i-1} + \dot{m}_V^{i-1}.H_V^{i-1} = \dot{m}_L^i.H_L^i + \dot{m}_V^i.H_V^i + \dot{Q}_s^i \quad \text{Eq. (11)}$$

The balances of total mass, ammonia mass, and energy in CV-2 are given by the set of Eqs. (12-14).

$$\dot{m}_L^{i-1} + \dot{m}_a^i + \dot{m}_w^i = \dot{m}_L^i \quad \text{Eq. (12)}$$

$$\dot{m}_L^{i-1}.x^{i-1} + \dot{m}_a^i = \dot{m}_L^i.x^i \quad \text{Eq. (13)}$$

$$\dot{m}_L^{i-1}.H_L^{i-1} + (\dot{m}_a^i + \dot{m}_w^i.)H_{Lint}^i + \dot{Q}_L^i = \dot{m}_L^i.H_L^i + \dot{Q}_s^i \quad \text{Eq. (14)}$$

The energy balance at the liquid-vapor interface is given by Eq. (15).

$$\dot{Q}_V^i + (\dot{m}_a^i + \dot{m}_w^i).H_{Vint}^i = \dot{Q}_L^i + (\dot{m}_a^i + \dot{m}_w^i).H_{Lint}^i \quad \text{Eq. (15)}$$

The heat flow on the surface is given by Eq. (16).

$$\dot{Q}_s^i = h_L.A_{int}.(T_L^i - T_s^i) \quad \text{Eq. (16)}$$

The heat flows across the interface are given by Eqs. (17) and (18) for liquid and vapor sides, respectively.

$$\dot{Q}_L^i = h_L^*.A_{int}.(T_{int}^i - T_L^i) \quad \text{Eq. (17)}$$

$$\dot{Q}_V^i = h_V^*.A_{int}.(T_V^i - T_{int}^i) \quad \text{Eq. (18)}$$

The mass flows across the interface are given by the set of eqs. (19) and (20).

$$\dot{m}_a^i = z^i.h_{mV}.\rho_V.A_{int}.\ln\left(\frac{z^i - y_{int}^i}{z^i - y^i}\right) \quad \text{Eq. (19)}$$

$$\dot{m}_a^i = z^i.h_{mL}.\rho_L.A_{int}.\ln\left(\frac{z^i - x^i}{z^i - x_{int}^i}\right) \quad \text{Eq. (20)}$$

$$z^i = \frac{\dot{m}_a^i}{\dot{m}_a^i + \dot{m}_w^i} \quad \text{Eq. (21)}$$

Liquid film thickness δ_f was defined as geometrical parameter. For this work, the liquid film thickness was of 0.001m. The liquid phase Reynolds number is given by Eq. (22)

$$\mathrm{Re} = \frac{4\Gamma}{\mu_l} \quad \text{Eq. (22)}$$

3. RESULTS AND ANALYSIS

3.1. Global Absorber Behavior

Fig. 5 shows the temperature behavior as a function of the equivalent length in the absorption process; T_v is the vapor temperature, T_s is the surface temperature, T_{int} is the interface temperature, and T_l is the liquid temperature. Inlet conditions are given at L=0. As readily noticed, all the three values converge to the surface temperature at 298K, in which the coolant temperature is assumed constant. The thermal resistance over the wall tube is neglected. The liquid phase temperature strictly decreases along the plate while the vapor phase temperature rises first to a peak and then decreases to reach the surface temperature. Absorption process is an exothermic phenomenon resulting in a great amount of heat released at the interface, in which high driving forces are present at the plate beginning.

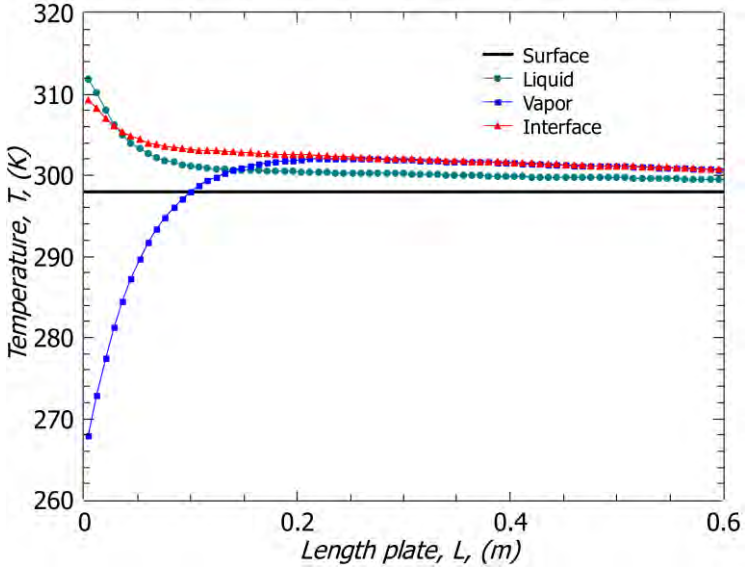

Figure 5: Temperature distribution along equivalent length

Fig. 6 shows the heat flow along the plate length to or from each phase and to the plate surface. It is clearly shown that the heat flow in the liquid phase is larger than the heat flow in the vapor phase. That can be explained because a higher thermal resistance occurs on the vapor phase. The negative flow in the vapor phase indicates that the direction is from the interface to the vapor phase, because there is a range in which the interface temperature is higher than the temperature of the vapor phase. For a 1TR, the absorber test rig should achieve an area of 0.108 m^2, allowing to reach an outlet temperature of T_{ss}=299.5K and an outlet concentration of 0.452. By ARC modeling, for these operational conditions, the strong solution should achieve 0.4657 in ammonia-water concentration at 298.2K.

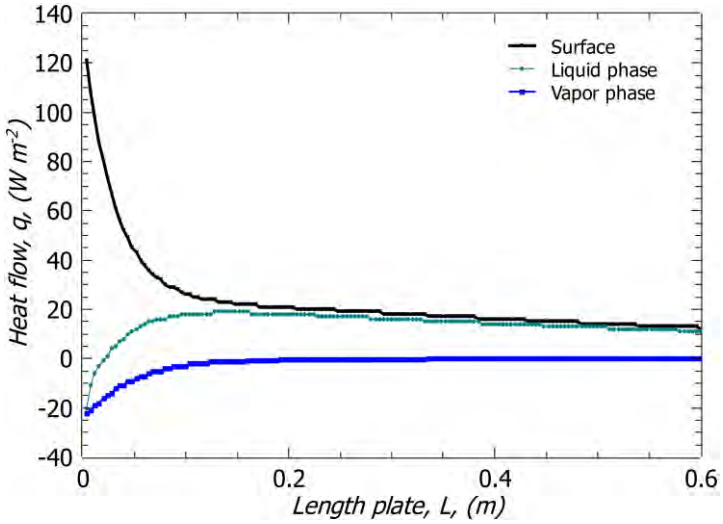

Figure 6. Heat flow along equivalent length

The temperature of the liquid phase reached 91.1% from the surface temperature, and 77.4% from the required concentration at the outlet for 0.6*m* length. The plate length should be 0.76 *m* to achieve 90% from the required concentration at the outlet. It is worthwhile to mention that the saturated concentration allowed for 298*K* is 0.4895.

3.2. Individual Plate Heat Exchanger

It's worthwhile to mention the absorbed heat rate of each plate is different although the surface temperature is kept constant. Heat and mass transfer processes are prominent in the beginning of the absorber. In Fig. 7, plate heat exchanger labeled with "1" is referenced to the first position and "7" as the lowest plate into the absorber. That figure also shows the absorption heat rejection decreases as a function of the position into the absorber, whose first plate absorbed about 30% of the total heat of absorption.

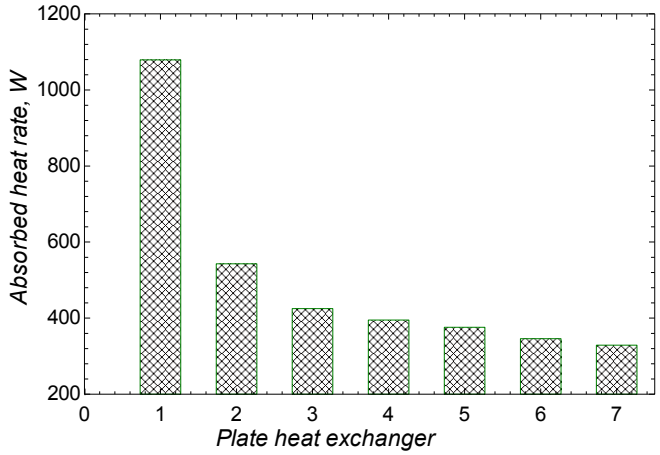

Figure 7: Absorbed heat rate as a function of the plate position into the absorber; 1 is the position and 7 the lowest position

Absorption process is an exothermic reaction in which all the heat is released at the liquid-vapor interface. Fig. (8) shows that behavior for the plate "3"; the vapor temperature overcomes the liquid interface as a result of the heat of absorption, but all the temperatures will converge at the surface temperature as shown in Fig. 5.

3.3. Liquid film thickness and surface temperature

The first plate is fixed to analyze the heat and mass transfer behavior as function of the liquid film thickness and the surface temperature.

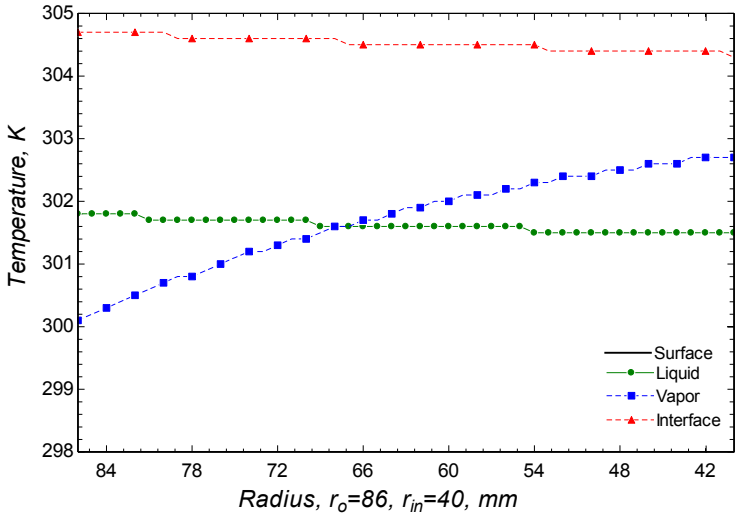

Figure 8: Absorption process for the "3" plate

Fig. 9 shows the heat of the absorption as a function of the surface temperature (lower axe) and the liquid film thickness (upper axe). Higher heat rates are obtained in lower surface temperatures and lower liquid film thickness due to film thickening increases the thermal resistance.

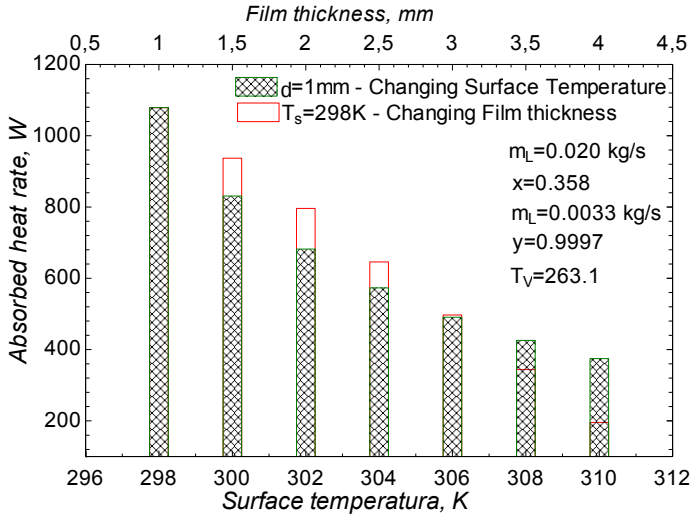

Figure 9. Absorbed heat rate as a function of the surface temperature and the liquid film thickness

4. CONCLUSIONS AND FUTURE WORK

The numerical study of the heat and mass transfer absorption process in a novel configuration was analyzed. It employed a horizontal flooded-liquid film configuration using ammonia-water mixtures as working fluid and in which the total wettability is reached. Absorption process is an exothermic phenomenon resulting in a great amount of heat released at the interface, in which high driving forces are prominent at the first plate. Moreover, absorber heat rate was improved by using lowest surface temperature and lowest liquid film thickness. Experimental studies are underway in the laboratory in order to obtain experimental results and it will be subject of a future publication.

ACKNOWLEDGEMENTS

The first and the second author thanks São Paulo Research Foundation (FAPESP), grant No. 2016/09509-1 for the project financial support. First author would like to thank National Research Council (CNPq) and the Administrative Department do Science, Technology and Innovation (COLCIENCIAS) for the personal support. The second author thanks CNPq for the research scholarship.

NOMENCLATURE

A	area (m²)
ARC	Absorption Refrigeration Cycle
CV	control volume
EV	expansion valve
h	heat transfer coefficient ($W.m^{-2}.K^{-1}$)
h^*	corrected heat transfer coefficient ($W m^{-2}.K^{-1}$)
h_m	mass transfer coefficient ($m.s^{-1}$)
H	specific enthalpy per unit of mixture ($J. kg^{-1}$)
k	thermal conductivity ($W.m^{-1}.K^{-1}$)
L	plate length (m)
ln	neperian logarithm
$\dot{m}$	mass flow rate ($kg.s^{-1}$)
Nu	Nusselt number
P	pressure (kPa)
$\dot{Q}$	heat flow (kW)
Re	Reynolds number
T	temperature (*K*)
TR	ton of refrigeration
x	liquid phase ammonia mass fraction
y	vapor phase ammonia mass fraction
z	ratio between ammonia flow and total flow through interface

Greek Symbols

δ_f	film thickness (m)
μ	dynamic viscosity (Pa.s)
v	kinematic viscosity ($m.s^{-2}$)
ρ	density ($kg.m^{-3}$)
Γ	mass flow rate per unit of plate width ($kg.m^{-1}. s^{-1}$)

Subscripts

a	ammonia
abs	absorption
f	film
int	interface
L	liquid
s	surface
ss	strong solution
V	vapor
w	water
ws	weak solution

Superscripts

i	i-element

REFERENCES

Castro, J., Oliet, C., Rodríguez, I., Oliva, A., 2009. Comparison of the performance of falling film and bubble absorbers for air-cooled absorption systems. Int. J. Thermal Sciences, 48(7), 1355–1366.

Churchill, S. W., Ozoe, H., 1973. Correlations for laminar forced convection with uniform heating in flow over a plate and in developing and fully developed flow in a tube. J. of Heat Transfer, 95(1), 78-84.

Colburn, A.P., Drew, T. B., 1937. The condensation of mixed vapors. American Institute of Chemical Engineers.

Fernández-Seara, J., Sieres, J., Rodríguez, C., Vázquez, M., 2005. Ammonia–water absorption in vertical tubular absorbers. Int. J. Thermal Sciences, 44(3), 277-288.

Narváez-Romo, B., Chhay, M., Zavaleta-Aguilar, E. W., Simões-Moreira, J. R., 2017. A critical review of heat and mass transfer correlations for LiBr-H2O and NH3-H2O absorption refrigeration machines using falling liquid film technology. Applied Thermal Engineering, 123, 1079-1095.

Narváez-Romo, B., Simões-Moreira, J. R., 2017. Falling liquid film evaporation in subcooled and saturated water over horizontal heated tubes. Heat Transfer Engineering, 38(3), 361-376.

Ribatski, G., Jacobi, A. M., 2005. Falling-film evaporation on horizontal tubes - A critical review. Int. J. Refrigeration, 28(5), 635–653.

Thome, J. R., 1999. Falling film evaporation: state-of-the-art review of recent work. J. of Enhanced Heat Transfer, 6, 263–278.

Zavaleta-Aguilar, E. W., Simões-Moreira, J. R., 2012. Thermal design of a tray-type distillation column of an ammonia/water absorption refrigeration cycle. Applied Thermal Engineering, 41, 52-60.

Zavaleta-Aguilar, E. W., Simões-Moreira, J. R., 2015. Horizontal tube bundle falling film distiller for ammonia–water mixtures. International Journal of Refrigeration, (59), 304-316.

Manuscript ID: 1276
DOI: 10.18462/iir.icr.2019. 1276

Mapping of Coefficient of Performance for large-scale ammonia heat pumps for district heating systems

Pernille Hartmund JØRGENSEN*[(a)], Torben OMMEN[(a)], Wiebke Brix MARKUSSEN[(a)] , Brian ELMEGAARD[(a)]

[(a)] Technical University of Denmark
Kgs. Lyngby, 2800, Denmark, *phaj@mek.dtu.dk

ABSTRACT

Many system configurations of large-scale heat pumps (HP) are applicable to a district heating system, and choosing the right HP technology may be a challenge. In this study, thermodynamic models of eight different HP configurations are used to compare the Coefficient of Performance (COP) and Lorenz efficiency, for a range of sink and source outlet temperatures. Furthermore, for a specific case the total volume flow rate for each configuration was compared. The results revealed that a configuration with two two-stage cycles with low stage desuperheat heat exchangers in most operating conditions was superior in terms of COP. However, for all considered operating conditions at least three configurations obtained a COP which was less than 3 % lower than the best one. Comparing the volume flow rates among the configurations a combination of a one-stage cycle and a two-stage cycle with low stage desuperheat heat exchanger holds the lowest needed volume flow rate.
Keywords: Large-scale heat pumps, District heating, Natural refrigerant, COP

1. INTRODUCTION

Electric-driven large-scale heat pumps are expected to play an import role in the transition towards electrification of the district heating (DH) system (Annex-47, 2018). The DH network is well established in Denmark and covers 64 % of the heating demand for households, and hence also a big share of the CO_2 emissions related to the heating sector. By integrating large-scale heat pumps as production units in the system, the heating sector can benefit from the increasing share of electricity produced by renewable resources, and thereby reduce the CO2 emissions of the sector. The HP technology is well known from the refrigeration industry, the application in the DH network, however, yields other temperature levels and operation constraints, with other design considerations as a consequence. Since large-scale HPs are introduced as a new technology in the DH sector, there is a need for generalized information for many of the industry's stakeholders. This will contribute to a clarification of expectations to the technology and facilitating collaboration between utility companies, consulting engineering companies, and HP suppliers. Decision-making on the best solution for a HP installation includes both a technical and economic investigation in order to find the solution with the lowest cost of heat. From a general perspective, the design considerations for a specific case includes among others, choice of refrigerant, compressor technology, cycle, and system configuration.

In Ommen, et al, (2015) both the technical and economic feasibility of industrial HPs in serial configuration was investigated. Here the results revealed an increase in COP and decrease in NPV for the series connection of up to three one stage ammonia HPs, compared to a reference system with only one HP. Furthermore, it was found that the technically feasible working domain was expanded when more HPs were connected in series, due to a lower discharge temperature. This paper presents eight different vapour compression HP configurations, all utilizing the natural refrigerant Ammonia using reciprocating compressors. The analysis focuses on the impact of the HP configuration on the COP and the needed volume flow rate. A comparison of the COP was done for a combination of 12 different design conditions in terms of sink temperatures and range of different source outlet temperatures. The needed volume flow in the different configurations was analysed for

one specific design condition with supply temperature of 80 °C, sink inlet temperature of 50 °C and source outlet temperature of 5 °C.

2. METHOD

This section presents the eight different HP configurations evaluated (Sec 2.1), the considered design conditions (Sec. 2.2), the thermodynamic cycle calculations (Sec.2.3) and an outline of the evaluated performance indicators (sec. 2.4). The comparisons were based on thermodynamic models for each HP configuration, implemented in the software Engineering Equation Solver, f-chart (1992).

2.1. HP Configurations

The evaluated HP configurations and numbering are shown in T able 1. Configurations 4 to 8 use combinations of the first three: 1) a one-stage cycle, 2) a two-stage cycle with open intercooler or 3) a two-stage cycle with a desuperheater after the low stage compressor. Configurations 4 to 8 consider two heat pumps connected in series with the heat sink, and in parallel regarding the heat source. The configurations were analysed for a heating capacity of 1 MW, and in cases with two HP cycles in the configuration a load share of 50 % was assumed.

Table 1: principle sketch, number and designation of the eight different configurations.

Configuration 1 One-stage	Configuration 2 Two-stage	Configuration 3 Two-stage, with low stage DSH
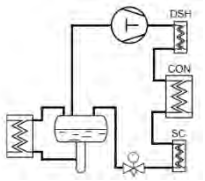	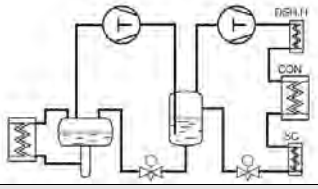	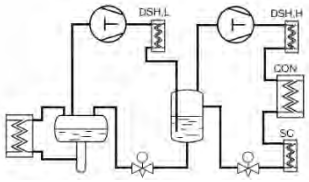
Configuration 4 Two one-stage	**Configuration 5** Two two-stage	**Configuration 6** Two two-stage, with low stage DSH
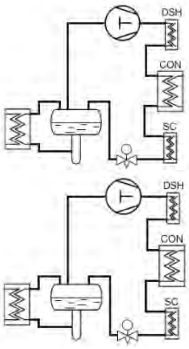	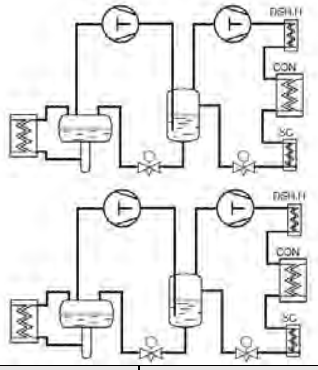	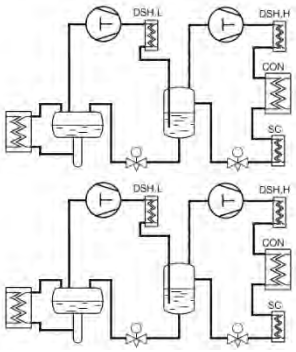
Configuration 7 one one-stage + one two-stage	**Configuration 8** one one-stage + one two-stage with low stage DSH	
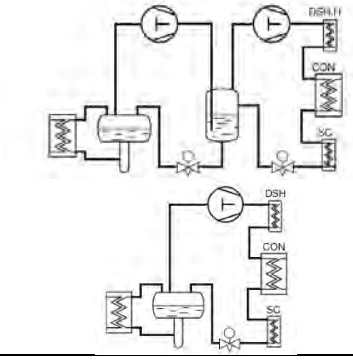	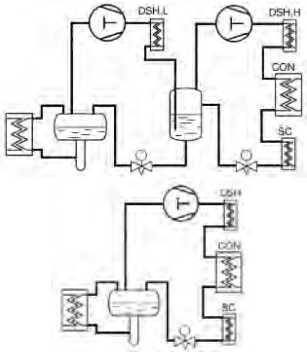	

2.2. Temperature levels of heat sink and source

The supply temperature from the heat pump was assumed to be 70 °C, 75 °C or 80 °C, The return temperature from the network of was assumed to be 35 °C, 40 °C, 45 °C or 50 °C. In total this amounts to 12 different sink temperature sets. The investigated sink temperatures represent relevant temperature levels in an arbitrary DH network in a Danish context, as presented by the Danish District Heating Association (2017).

Due to the choice of parallel evaporator design, the inlet temperature of the source is not required to fix the conditions in the heat pump cycle, and it could in principle be any temperature higher than then considered source outlet temperature. For a system consideration, the glide of the source will have an impact on the needed power to create a given flow of the source, as well as an impact on the heat transfer conditions, heat transfer area and heat output. The outlet temperature of the heat source was varied between 30 °C and 1 °C. The source temperatures were selected to represent low-temperature heat sources, natural as well as industrial.

2.3. Thermodynamic cycle calculations and technical constraints

The assumptions regarding the specific components follows the assumptions presented in Table 2 and the calculation procedure indicated below. For configurations utilising a single stage cycle, the efficiencies for a high stage compressor was applied.

Table 2: Assumptions used for the thermodynamic modelling of the compressors.

Designation	Value	Unit
Isentropic efficiency, low stage	0.70	-
Isentropic efficiency, high stage	0.72	-
Volumetric efficiency, low stage	0.85	-
Volumetric efficiency, high stage	0.80	-
Heat loss	10	%
Load share	50	%

The compressor work was calculated as in Eq. (1)

$$\dot{W}_{\mathrm{comp}} = \dot{m}_{\mathrm{ref}}(h_{\mathrm{out,w}} - h_{\mathrm{in}}), \quad \text{Eq. (1)}$$

where the enthalpy out of the compressor, $h_{\mathrm{out},w}$ was found by Eq. (2) by taking the isentropic efficiency (η_{is}) into account

$$h_{\mathrm{out,w}} = h_{\mathrm{in}} + \frac{h_{\mathrm{out,is}} - h_{\mathrm{in}}}{\eta_{\mathrm{is}}} \quad \text{Eq. (2)}$$

The outlet condition from the compressors was found by Eq. (3) by taking the heat loss factor (f_Q) into account.

$$h_{\mathrm{out}} = h_{\mathrm{out,w}} - f_Q\left(h_{\mathrm{out,w}} - h_{\mathrm{in}}\right) \quad \text{Eq. (3)}$$

The maximum allowed temperature out of a compressor was 190 °C. In case of discharge temperature above 190 °C, the specific configuration was excluded from the comparisons.

The heat transferred in each heat exchanger between the refrigerant and the DH network was calculated by energy balances and a pinch temperature difference of 2.5 K for all heat exchangers. The condensation temperature was found by the pinch temperature difference between the DH water temperature out of the condenser section (CON, in table 1) and the ammonia at the condition of saturated vapour. The amount of subcooling was maximized for each cycle, by reaching the pinch temperature difference between the inlet temperature of the DH water into the subcooler, and the outlet of the subcooled refrigerant. A temperature heat load diagram, where the method described above is illustrated, is shown in Sec. 3.1.

The evaporators were assumed to be flooded with an outlet quality of 0.7, such that no superheating was assumed at the compressor inlet. A pinch temperature difference between the outlet temperature of the source and the inlet condition of the ammonia defined the evaporation temperature.

The intermediate pressure between the low stage and high stage compression in a heat pump cycle was either set by Eq. (6) or by a technical constraint of maximum 43 °C evaporation temperature for the high stage compressors

$$p_{int} = \sqrt{p_L p_H} \quad \text{Eq. (6)}$$

The temperature of the superheated ammonia at the outlet of the desuperheater ($T_{\mathrm{DSH,L,OUT}}$) after the low stage compression (present in configuration 3, configuration 6 and configuration 8) was either set by the heat transfer using the pinch temperature difference, or by assuming 0.1 K superheating at the intermediate pressure (p_{int}). This constraint was implemented, to avoid condensation in this heat exchanger.

2.4. Evaluation of performance

The configurations were compared on basis of the COP, as defined in Eq. (6),

$$\mathrm{COP} = \frac{\dot{Q}_{\mathrm{heat}}}{\sum \dot{W}_{\mathrm{comp}}}, \quad \text{Eq. (6)}$$

where the heat output, $\dot{Q}_{\mathrm{heat}}$, represents the total heat delivered from the HP to the DH network (1 MW), and the sum of the compressor power $\sum \dot{W}_{\mathrm{comp}}$, calculated individually by Eq. (1).

Furthermore, the Lorenz efficiency η_{L}, for a special case of the Lorenz COP, was calculated using Eq. (7) and Eq. (8), as introduced by Lorenz, H (1895).

$$\eta_{\mathrm{L}} = \frac{\mathrm{COP}}{\left(\frac{\bar{T}_{\mathrm{lm,h}}}{\bar{T}_{\mathrm{lm,h}} - T_{\mathrm{source,out}}}\right)} \qquad \text{Eq. (7)}$$

$$\bar{T}_{\mathrm{lm,h}} = \frac{T_{\mathrm{DH,supply}} - T_{\mathrm{DH,return}}}{\ln\left(\frac{T_{\mathrm{DH,supply}}}{T_{\mathrm{DH,return}}}\right)} \qquad \text{Eq. (8)}$$

where Eq. (8) is the logarithmic mean temperature of the sink, and the denominator in Eq. (7) is the maximum performance of a reversible heat pump working between a finite capacity heat sink and infinite capacity heat source.
Based on the evaluation of the COP of each configuration, the configuration with the highest COP was presented as the benchmark, together with its corresponding η_{L}. As the difference in the calculated COP among the eight configurations was found to be relatively small for some cases, it was also indicated if a configuration had a COP within 3% from the maximum calculated COP.

In order to extend the evaluation of the different configurations, the needed volume flow, indicating the needed size of a compressor, was evaluated for a specific temperature case. The volume flow in m^3/h was calculated for each compressor by Eq. (9),

$$V = \frac{\dot{m}_{\mathrm{ref}} \cdot \upsilon \cdot 3600}{\eta_v}, \qquad \text{Eq. (9)}$$

where υ was the specific volume evaluated at the inlet conditions, $\dot{m}_{\mathrm{ref}}$ was the mass flow rate of refrigerant through the compressors and η_v the volumetric efficiency. For configurations utilising a single stage cycle, the volume flow of the compressor was assumed to correspond to a high stage compressor.

3. RESULTS

3.1. Cycle verification

A log P-h diagram and a temperature heat load diagram for configuration 6 (two two-stage cycles with low pressure DSH) are shown in Figure 1. The diagrams are shown for a case with the sink temperatures 80 °C as supply temperature and 50 °C as return temperature, and a source outlet temperature of 5 °C. In the temperature heat load diagram, it can be seen how a pinch temperature difference determined both the amount of DSH after the low stage compression (first stream for both cycles), and the amount of subcooling as well as the condensing temperature (second stream for both cycles).

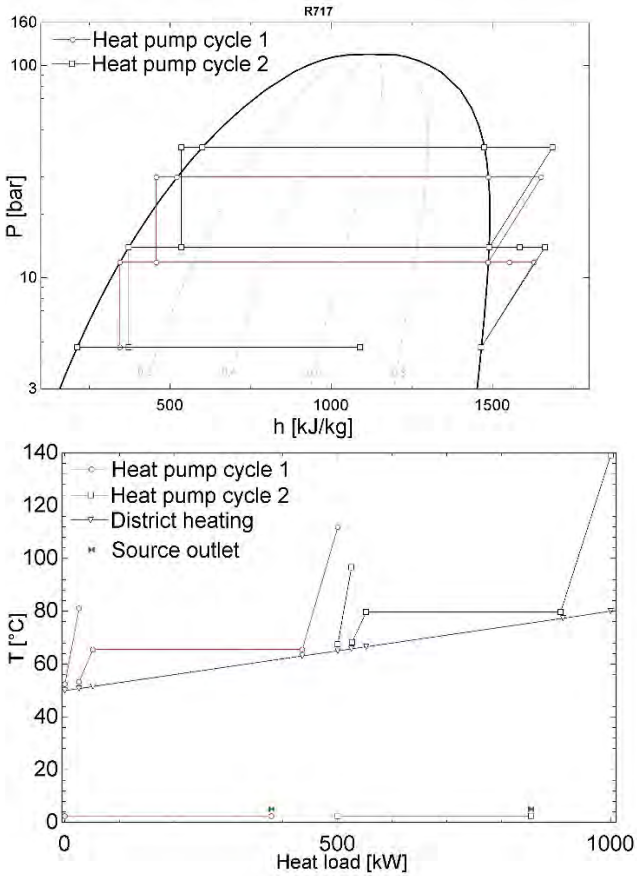

Figure 1: A log P h diagram (left) and a temperature heat load diagram (right) for configuration 6, with sink temperatures of 80 °C / 50 °C and a source outlet temperature of 5 °C

3.2. Maximum COP and η_{L}

The maximum calculated COP among the eight different configurations and the corresponding η_{L} are shown in Figure 2, for the range of temperatures of sink and source. The colour of a cell indicates for which configuration the benchmark COP was found, according to the colour bar below the table. Analysing the trends of the COP shown in Figure 2, it can be seen that the benchmark COP increases for all sink temperatures with an increasing source outlet temperature. Furthermore, for a given return temperature of the DH water, the COP increases with a decreasing supply temperature. This is in general due to the decreasing temperature lift needed, and consequently lower pressure ratios of compression.

Comparing the COP for a constant supply temperature and decreasing return temperatures, it can be seen that the COP increases with a larger sink temperature glide $(T_{\mathrm{DH,supply}} - T_{\mathrm{DH,return}})$. A lower return temperature increased the capacity of the subcooler, which affected both the needed mass flow rate of refrigerant and the condensing temperature positively.

$T_{DH,supply}$:		70 °C				75 °C				80 °C			
$T_{DH,return}$:		35 °C	40 °C	45 °C	50 °C	35 °C	40 °C	45 °C	50 °C	35 °C	40 °C	45 °C	50 °C
$T_{source,out}$:	1	3.7 / 58	3.6 / 59	3.5 / 60	3.4 / 61	3.6 / 58	3.5 / 59	3.4 / 60	3.3 / 61	3.4 / 58	3.4 / 59	3.3 / 60	3.2 / 60
	2	3.8 / 58	3.7 / 59	3.6 / 60	3.5 / 61	3.6 / 58	3.5 / 59	3.4 / 60	3.4 / 60	3.5 / 58	3.4 / 59	3.3 / 60	3.2 / 60
	3	3.8 / 58	3.7 / 59	3.6 / 60	3.5 / 60	3.7 / 58	3.6 / 59	3.5 / 60	3.4 / 60	3.6 / 58	3.5 / 59	3.4 / 60	3.3 / 60
	4	3.9 / 58	3.8 / 59	3.7 / 60	3.6 / 60	3.7 / 58	3.6 / 59	3.6 / 59	3.5 / 60	3.6 / 58	3.5 / 59	3.4 / 59	3.3 / 60
	5	4.0 / 58	3.9 / 59	3.8 / 59	3.6 / 60	3.8 / 58	3.7 / 59	3.6 / 59	3.5 / 60	3.7 / 58	3.6 / 58	3.5 / 59	3.4 / 60
	6	4.0 / 57	3.9 / 58	3.8 / 59	3.7 / 60	3.9 / 57	3.8 / 58	3.7 / 59	3.6 / 60	3.7 / 57	3.6 / 58	3.5 / 59	3.4 / 60
	7	4.1 / 57	4.0 / 58	3.9 / 59	3.8 / 60	3.9 / 57	3.8 / 58	3.7 / 59	3.6 / 60	3.8 / 57	3.7 / 58	3.6 / 59	3.5 / 60
	8	4.2 / 57	4.1 / 58	3.9 / 59	3.8 / 60	4.0 / 57	3.9 / 58	3.8 / 59	3.7 / 59	3.8 / 57	3.7 / 58	3.6 / 59	3.5 / 59
	9	4.3 / 56	4.1 / 58	4.0 / 59	3.9 / 59	4.1 / 57	3.9 / 58	3.8 / 59	3.7 / 59	3.9 / 57	3.8 / 58	3.7 / 58	3.6 / 59
	10	4.3 / 56	4.2 / 57	4.1 / 58	4.0 / 59	4.1 / 56	4.0 / 57	3.9 / 58	3.8 / 59	4.0 / 56	3.8 / 57	3.7 / 58	3.6 / 59
	11	4.4 / 56	4.3 / 57	4.2 / 58	4.0 / 59	4.2 / 56	4.1 / 57	4.0 / 58	3.9 / 59	4.0 / 56	3.9 / 57	3.8 / 58	3.7 / 59
	12	4.5 / 56	4.4 / 57	4.2 / 58	4.1 / 59	4.3 / 56	4.2 / 57	4.0 / 58	3.9 / 59	4.1 / 56	4.0 / 57	3.9 / 58	3.8 / 59
	13	4.6 / 55	4.4 / 57	4.3 / 58	4.2 / 59	4.4 / 55	4.2 / 57	4.1 / 58	4.0 / 59	4.2 / 55	4.0 / 57	3.9 / 58	3.8 / 58
	14	4.7 / 55	4.5 / 56	4.4 / 57	4.2 / 59	4.4 / 55	4.3 / 56	4.2 / 57	4.1 / 58	4.2 / 55	4.1 / 56	4.0 / 57	3.9 / 58
	15	4.8 / 55	4.6 / 56	4.5 / 57	4.3 / 58	4.5 / 55	4.4 / 56	4.3 / 57	4.1 / 58	4.3 / 55	4.2 / 56	4.1 / 57	3.9 / 58
	16	4.9 / 54	4.7 / 56	4.6 / 57	4.4 / 58	4.6 / 54	4.5 / 56	4.3 / 57	4.2 / 58	4.4 / 54	4.3 / 56	4.1 / 57	4.0 / 58
	17	5.0 / 54	4.8 / 55	4.6 / 57	4.5 / 58	4.7 / 54	4.6 / 55	4.4 / 57	4.3 / 58	4.5 / 54	4.3 / 55	4.2 / 57	4.1 / 58
	18	5.1 / 53	4.9 / 55	4.7 / 56	4.6 / 58	4.8 / 54	4.6 / 55	4.5 / 56	4.3 / 57	4.6 / 54	4.4 / 55	4.3 / 56	4.1 / 57
	19	5.2 / 53	5.0 / 55	4.8 / 56	4.7 / 57	4.9 / 53	4.7 / 55	4.6 / 56	4.4 / 57	4.6 / 53	4.5 / 55	4.4 / 56	4.2 / 57
	20	5.3 / 52	5.1 / 54	4.9 / 56	4.8 / 57	5.0 / 53	4.8 / 54	4.7 / 56	4.5 / 57	4.7 / 53	4.6 / 54	4.4 / 56	4.3 / 57
	21	5.4 / 52	5.2 / 54	5.0 / 55	4.9 / 57	5.1 / 52	4.9 / 54	4.8 / 55	4.6 / 57	4.8 / 53	4.7 / 54	4.5 / 55	4.4 / 57
	22	5.6 / 52	5.3 / 53	5.2 / 55	5.0 / 57	5.2 / 52	5.0 / 54	4.9 / 55	4.7 / 56	4.9 / 52	4.8 / 54	4.6 / 55	4.4 / 56
	23	5.7 / 51	5.5 / 53	5.3 / 55	5.1 / 56	5.3 / 51	5.1 / 53	5.0 / 55	4.8 / 56	5.0 / 52	4.8 / 53	4.7 / 55	4.5 / 56
	24	5.8 / 50	5.6 / 53	5.4 / 54	5.2 / 56	5.4 / 51	5.2 / 53	5.1 / 54	4.9 / 56	5.1 / 51	4.9 / 53	4.8 / 54	4.6 / 56
	25	6.0 / 50	5.7 / 52	5.5 / 54	5.3 / 56	5.6 / 50	5.4 / 52	5.2 / 54	5.0 / 55	5.2 / 51	5.0 / 52	4.9 / 54	4.7 / 55
	26	6.1 / 49	5.9 / 52	5.6 / 54	5.4 / 55	5.7 / 50	5.5 / 52	5.3 / 54	5.1 / 55	5.4 / 50	5.1 / 52	5.0 / 54	4.8 / 55
	27	6.3 / 49	6.0 / 51	5.8 / 53	5.6 / 55	5.9 / 49	5.6 / 51	5.4 / 53	5.2 / 55	5.5 / 50	5.3 / 52	5.1 / 53	4.9 / 55
	28	6.5 / 48	6.2 / 50	5.9 / 53	5.7 / 54	6.0 / 49	5.7 / 51	5.5 / 53	5.3 / 54	5.6 / 49	5.4 / 51	5.2 / 53	5.0 / 54
	29	6.7 / 47	6.3 / 50	6.1 / 52	5.8 / 54	6.2 / 48	5.9 / 50	5.6 / 52	5.4 / 54	5.7 / 49	5.5 / 51	5.3 / 52	5.1 / 54
	30	6.8 / 47	6.5 / 49	6.2 / 52	6.0 / 54	6.3 / 47	6.0 / 50	5.8 / 52	5.5 / 53	5.9 / 48	5.6 / 50	5.4 / 52	5.2 / 53

Configuration 6 | Configuration 8

Figure 2: The maximal calculated COP and the corresponding Lorenz efficiency (η_L) for each sink temperature set and outlet source temperature. The colors indicate the configuration with the highest COP.

Considering the calculated Lorenz efficiency also listed in Figure 2, the highest efficiency was found at the lowest outlet source temperature. It decreases by approximately 10 % at the highest outlet temperature. This indicates that the investigated heat pump configurations performed closer to the theoretical maximum at the lowest source outlet temperatures. To further interpret this, it is important to be aware of that the theoretical maximum performance (Lorenz COP, described as the denominator in Eq. (7)) increased from e.g. 6.4 to 17 from a source outlet temperature of 1 °C to 33 °C (sink: 35 °C /70 °C).
In general, the theoretical maximum performance follows the same trend as the maximum calculated COP, meaning an increase for a higher source outlet temperature, lower return temperatures as well as lower supply temperatures.
From the colours in Figure 2, it can be seen that configuration 6 reaches the highest COP for almost all investigated conditions. The trend was only interfered at higher source outlet temperatures and low return temperatures, where the highest COP was found for configuration 7. This was due to a very low compression ratio in the first heat pump cycle of the configuration, where a benefit of one stage of compression exceeded the benefits from a two-stage compression.

However, analysing the COP for all eight configurations revealed that the difference in COP in some cases was relatively small. This is illustrated in Figure 3, where a presence of a coloured line indicates the investigated configuration to be within the limit of 3 % from the benchmark COP. The configuration holding the benchmark COP is also indicated in Figure 3. For all conditions, at least three other configurations had a COP within the 3 % limit, however with a complete absence of configuration 1 (one one-stage HP) and 2 (one two-stage HP).

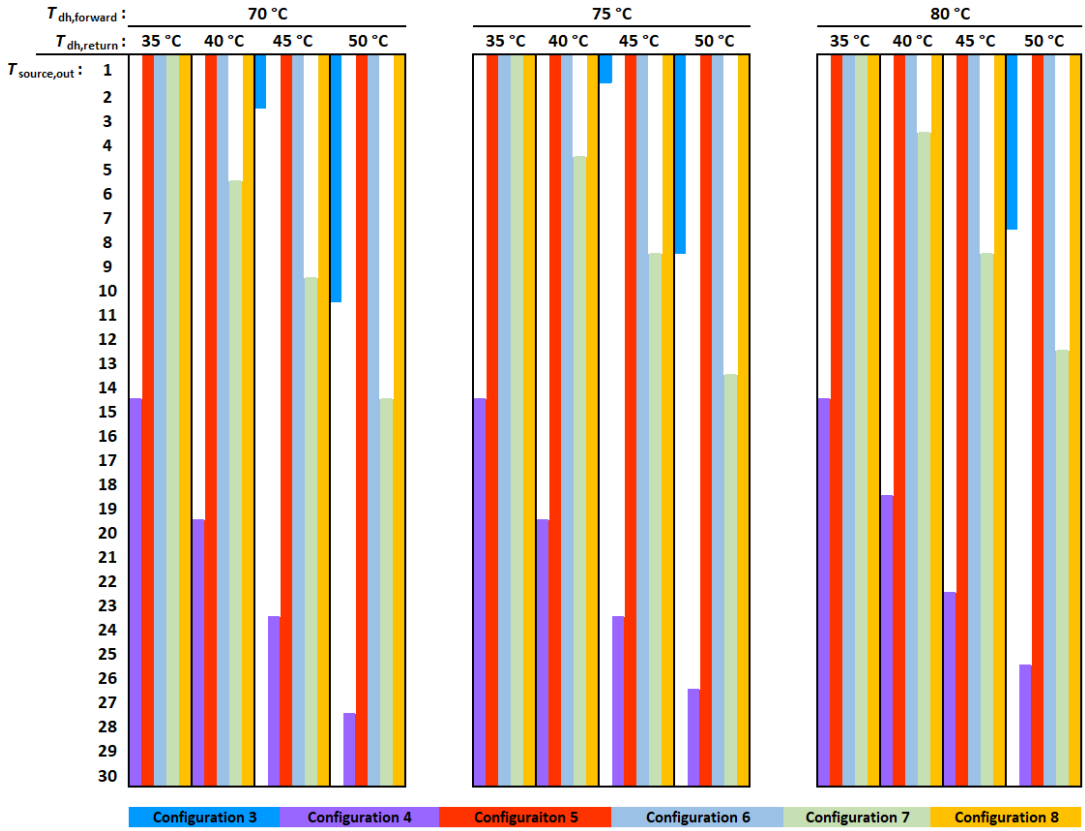

Figure 3: The presence of a coloured line indicates that the configuration, for a given set of heat sink temperatures and source outlet temperatures, holds a COP within a limit of 3 % from the benchmark COP.

Configuration 5 and configuration 6 are within this limit for all conditions. Knowing from Figure 2, that configuration 6 holds the highest COP, the desuperheater after the low stage compressor, must for all conditions have a positive impact on the COP. The positive impact can also be noted when comparing configuration 7 and configuration 8, where configuration 8 was highlighted in Figure 2, and in general present for all conditions in Figure 3.
Configuration 4 seems to benefit from higher source outlet temperatures, and low temperature lifts, while configuration 3 was present only for low source outlet temperatures and high return temperatures, which also could be expected as beneficial conditions for a two-stage compression.

3.3. Volume flow

Another evaluation parameter when choosing among different heat pump configurations is the needed volume flow rate to reach the heating capacity of 1 MW.
The volumetric flow translates to the size of the needed compressor, which to some extent is correlated to the investment cost. However, in relation to the investment cost, it is important to distinguish between whether the flow relates to a high stage or a low stage compressor.
In Table 3 the COP, Lorenz efficiency, and needed volume flow for the eight different configurations are presented for a case with the sink temperatures 80 °C as supply temperature and 50 °C as return temperature, and a source outlet temperature of 5 °C. The volume flow is presented as the needed flow for the low stage compression, the high stage compression, and the total volume flow as the sum of the two. If two HP cycles were present in the configuration, the presented low stage flow was a sum of both low stage compressors. The same is the case for the high stage compressor.
Configurations 1, 2, 4, and 7 (first four columns in Table 3) were omitted from the comparison below, either because of too high discharge temperature or a COP more than 3 % away from the benchmark.
Considering the total amount of needed volume flow, Configuration 8 had the smallest amount of flow of 975 m^3/h. However, from an investment point of view, it could be expected that there will be

a price difference in high and low pressure compressors, and also a higher cost if more compressors are used.

Table 3: Performance indicators and cycle specifications at the heat sink temperatures (supply/return): 80 °C /50 °C and source temperature outlet: 5 °C.

	Config 1	Config 2	Config 4	Config 7	Config 3	Config 5	Config 6	Config 8
COP (% from max COP)	3.16 (6.6 %)	3.20 (5.5 %)	3.18 (6.1 %)	3.26 (3.6 %)	3.129 (2.7 %)	3.31 (2.2 %)	3.38 (-)	3.30 (2.4%)
η_L	55.9	56.6	56.2	57.7	58.2	58.5	59.9	58.4
V (m^3/h) Low stage	-	734	-	361	743	737	743	364
V (m^3/h) High stage	842	349	878	620	324	385	366	611
V (m^3/h) Total	842	1083	878	980	1066	1123	1110	975
T_{dis}, (°C)								
Low HP 1	-	94.1	-	-	94.5	81.0	81.2	-
High HP1	193.6	131.0	167.5	167.5	131.5	111.8	111.9	167.5
Low HP 2	-	-	-	96.5	-	96.5	96.6	96.6
High HP 2	-	-	202.7	134.5	-	134.5	134.7	134.7

Considering the needed volume flow from low pressure compressors, configuration 3, 5 and 6 needed double the volume flow, compared to configuration 8. This is due to the fact that HP 1 in configuration 8 was a one stage cycle, with a high pressure compressor (condensing temperature: 63.9 °C). This is also why configuration 8 needed approximately 1.7 times higher flow than configuration 3, 5 and 6 in the high stage compressors.
Analysing the numbers from an investment point of view, configuration 3 would have an advantage in terms of only two compressors needed, while configuration 5 and 6 both needed four compressors. Comparing configuration 3 with configuration 8, the numbers of compressors was 2 vs 3.

4. DISCUSSION

The COP of the presented heat pump systems was in general highly sensitive to the input parameters, listed in Table 2 and hence the assumptions made. Input parameters like the pinch temperature difference and the load share relate to the design of components and system, and could for each configuration be subject for optimization. The efficiencies and the compressor heat loss will depend on the chosen compressor at the specific operating conditions. As the compressor operating conditions, such as the pressure ratio, suction gas temperature, and speed changed for the different configurations for the same sink and source conditions, a variation in the efficiencies and heat loss could be expected. For simplicity and generality, this aspect was not included in the current study.
As mentioned the decrease in Lorenz efficiency with increasing source outlet temperature, as shown in Figure 2, came from a large increase in the Lorenz COP. This means that there is a greater potential for high performance at higher source outlet temperatures. However, in order to reach the potential, it would be necessary either to increase the number of HPs in serial connection or to optimize the components in terms of pinch temperature difference, isentropic efficiency, load share or heat loss.
Comparing the configurations for a specific case in Table 3 illustrated a difference in the volumetric flow rate needed. This indicates the possibility of a trade-off between the COP and the needed volume flow rate. Further to this, the same possibility for a trade-off could be expected for the needed heat transfer area of the HEX connected to the heat sink. How these trade-offs, as well as the number of components needed, affects the optimal choice of configuration, can be further analysed with a more comprehensive analysis of the investment cost and the lifetime economy.

5. CONCLUSION

Eight different heat pump configurations were compared by their COP and Lorenz efficiency, for 12 sets of sink temperatures and 30 different source outlet temperatures. It was found that configuration 6, utilising two two-stage cycles with low stage DSH heat exchanger, for most of the considered operating conditions obtained the highest COP. Only at low return temperatures and high source outlet temperatures, configuration 8, comprising of one one-stage cycle and one two-stage cycle with low stage DSH, obtained a higher COP. However, it was also found that at least three other configurations at all operating conditions obtained a COP within a limit of 3 % less than the highest found. For a source outlet temperature of 5 °C and sink temperatures of 50 °C /80 °C, the needed volume flow rate for each configuration was compared. Between the best candidates, configuration 8 holds the lowest needed volume flow rate, however with approximately 1.7 times higher flow rate for high stage compressors. Further analysis may be needed to distinguish COP and needed volume flow rate for achieving the lowest levelized cost of heat.

ACKNOWLEDGEMENTS

This research project was supported by EUDP (Energy Technology Development and Demonstration). “Experimental development of electric heat pumps in the Greater Copenhagen DH system – Phase 2”, project number: 64015 – 0571.

NOMENCLATURE

Symbols		*h*	high
f	heat loss (-)	is	isentropic
h	enthalpy (kJ/kg)	*l*	low
$\dot{m}$	mass flow rate (kg/s)	*L*	Lorentz
p	pressure (bar)	lm	logarithmic mean temperature
$\dot{Q}$	heating capacity (kW)	ref	refrigerant
T	temperature (°C)	*v*	volumetric
V	volumetric flow rate (m^3/h)	***Abbreviations***	
$\dot{W}$	power (kW)	COP	coefficient of performance
Greek		DSH	desuperheater
η	efficiency (-)	CON	condenser
υ	specific volume (m^3/kg)	SC	subcooler
Subscripts		HP	heat pump
comp	compressor	DH	district heating
dis	discharge		

REFERENCES

Annex-47, 2018. Heat pumps in District Heating and Cooling systems. IEA Heat Pumping Technologies (HPT).

Ommen, T., Jensen, J. K., Markussen, W. B., Elmegaard, B., 2015. Enhanced technical and economic working domains of industrial heat pumps operated in series. Proceedings of the 24th IIR International Congress of Refrigeration, Refrigeration Science and Technology (2015), Pages 3463–3470.

F-chart, Klein, S. A., 1992. Engineering Equation Solver, http://www.fchart.com/ees/ (accessed 19.12.2018).

Danish District Heating Association, Danish District Heating Association’s Annual statistics 2017, https://www.danskfjernvarme.dk/viden/statistik-subsection/aarsstatistik/statistik-2017 (accessed 20.07.2018)

Lorenz, H, 1895. Die ermittelung der grenzwerte der thermodynamischen energieumwandlung. Zeitschrift für die gesammte Kälte-Industrie, 2(1-3, 6-12).

Manuscript ID: 1278
DOI: 10.18462/iir.icr.2019.1278

Flow boiling heat transfer of refrigerants HFO-1234yf and HFC-134a in a chevron plate heat exchanger

Kuan-Ting CHEN, Chien-Yuh YANG

National Central University
Jhongli, Taoyuan 32001, Taiwan, cyyang@ncu.edu.tw

ABSTRACT

HFO-1234yf has similar thermodynamic properties to HFC-134a but much lower GWP value. It is expected as a good candidate to replace the refrigerant HFC-134a in the near future. However, only very few papers have been published in the past years regarding to this new refrigerant in plate heat exchangers. This study provides an experimental comparison of refrigerants HFO-1234yf and HFC-134a flow boiling in a 6 plates chevron brazed plate heat exchanger. The effects of mass fluxes and vapor qualities was discussed. The test results show that at the lowest mass flux, liquid thermal conductivity dominate the heat transfer mechanism and therefore the heat transfer coefficients of HFC-134a are that those of HFO-1234yf. For higher mass fluxes, in addition to the liquid thermal conductivity, liquid and vapor viscosity are also important for heat transfer process. The interaction of these two effects caused the heat transfer coefficients of these two refrigerants are very close.

Keywords: HFO-1234yf, HFC-134a, flow boiling, plate heat exchanger, heat transfer

1. INTRODUCTION

Owing to the global warming effect consideration, the EU has banned the use of refrigerants with Global Warming Potential (GWP) value higher than 150 in all new Domestic refrigerators and freezers, Refrigerators and freezers for commercial use and passenger cars starting from 1 January 2015 and 2020 respectively [EU directive 2014/517/EN (2014)]. The study on the replacement of high GWP refrigerant such as HFC-134a is an important and urgent issue in the coming years. Recently, a new refrigerant, HFO-1234yf has been developed with similar thermodynamic properties to HFC-134a but much lower GWP value (GWP equals to 4 in comparing to 1,430 of HFC-134a). It is expected as a good candidate to replace the refrigerant HFC-134a in the near future. However, most of the heat transfer and flow performances of HFO-1234yf are still not very clear up-to-date. Only very few papers have been published in the past years regarding to the flow boiling heat transfer performance of this new refrigerant. Some of their results are still not in consistent with each other.

Yang et al. (2018) experimentally compared the flow boiling of refrigerants HFO-1234yf and HFC-134a in a 4.0 mm circular tube. The test results show that both pressure drop and heat transfer performance depend on the fluid properties, flow conditions and flow patterns. The major controlling properties on pressure drops and heat transfer coefficients of flow boiling is strongly depending on their two-phase flow pattern at various flow conditions. The flow pattern analysis is able to explain the inconsistency between the test results in the previous published literatures on flow boiling heat transfer and pressure of refrigerants HFC-134a and HFO-1234yf adequately.

Plate heat exchanger is one of the most common heat exchangers in air condition and refrigeration systems. It has the advantages of high heat transfer performance and high compactness in comparing to other heat exchangers. Longo (2012) measured the heat transfer coefficients and pressure drop during vaporisation of the refrigerant HFO-1234yf inside a Brazed Plate Heat Exchanger (BPHE). The heat transfer coefficients show great sensitivity to heat flux and outlet conditions and weak sensitivity to saturation temperature. The tested boiling heat transfer coefficients are reasonable agree with those predicted by Cooper (1984) and Gorenflo (1993). The author compared the results to his previous study for HFC-134a. HFO-1234yf exhibits heat transfer coefficients slightly lower (6-10%) and frictional pressure drop lower (10-18%) than those of HFC-134a. Kim et al. (2018) measured the flow boiling heat transfer characteristics of HFO-1234ze(E) and HFC-134a in plate heat exchangers with different Chevron angles. For a Chevron angle of 60°, the average heat transfer coefficient of HFO-1234ze(E) is on average 4.7% higher than that of HFC-134a and the average pressure drop of HFO-1234ze(E) is also higher than that of HFC-134a

Owing to the corrugate flow passages inside the late heat exchangers, the flow patterns are much complicate than those in other heat exchangers. However, there are very few studies regarding to HFO refrigerants in these heat exchangers have been published in the past years. The heat transfer mechanism of refrigerant HFO-1234yf in the plate heat exchangers is still not clear. This study provides an experimental investigation on the flow boiling heat transfer and pressure drop of refrigerants HFO-1234yf and HFC-134a in 6 plates brazed plate heat exchanger. It is aimed to further understand the difference on heat transfer characteristics of these two refrigerants in plate heat exchangers.

2. EXPERIMENTAL METHOD

2.1 Test section

The test section used in the present study is a brazed plate heat exchanger shown in Fig. 1. It consists of 6 chevron corrugation plates with length 194 mm and width 154 mm. The total height of the test section is 80 mm. The chevron angle of the corrugation in the plate heat exchanger is 65° with an amplitude of 2.0 mm. Table 1 lists the detail geometrical parameters of the test section.

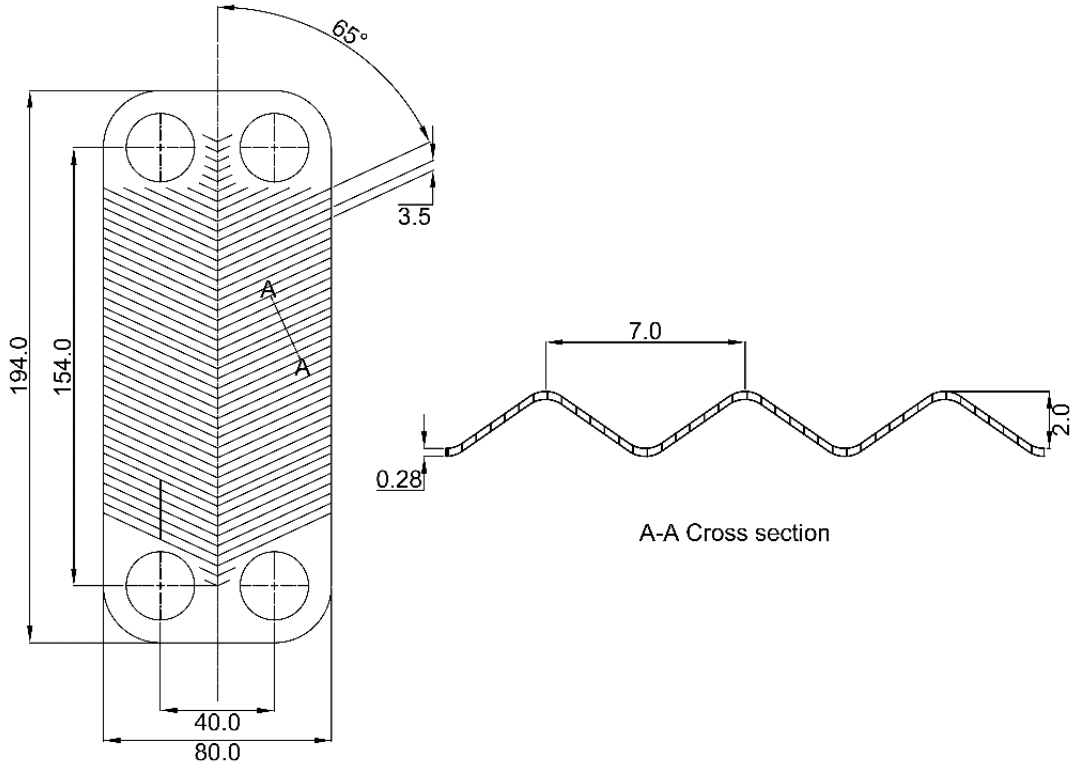

Figure 1: Geometric parameters of the test plates

Table 1. Geometrical characteristics of the plate heat exchanger

Plate Length, L (mm)	194
Plate width, W (mm)	80
Plate spacing, s (mm)	2.0
Plate thickness, t (mm)	0.28
Corrugation type	Chevron
Angle of corrugation (°)	65
Corrugation amplitude (mm)	2
Corrugation pitch (mm)	7
Heat transfer area of a plate (m^2)	0.0117
Number of plates	6

2.2 Experimental system

The schematic diagram of the experimental system is shown in Figure 2. It consists of a refrigerant loop, a heating water loop, a pre-heating water loop and a sub-cooling water loop.

2.2.1 Refrigerant loop

As shown in Figure 2, liquid refrigerant was moved from the receiver by a gear pump, through a flow meter and entered the preheater. It was heated in the preheater to the required test vapor quality and flowed into the test section. The two-phase refrigerant was evaporated in the test section by the heating water provided from the heating water loop. The two-phase refrigerant out of the test section flowed through a sub-cooler to completely condensed to liquid and flowed into the receiver to complete a refrigerant cycle.

The refrigerant flow rate was controlled by a variable speed gear pump. A Coriolis type mass flow meter was placed prior to the preheater to measure liquid refrigerant flow rate. The saturation temperature of the two-phase refrigerant in the test tube was controlled by the sub-cooler and the heat transfer rate was adjusted by the temperature and flow rate of the heating water. Thus, the test saturation temperature, inlet vapor quality, mass flow rate, and heat transfer rate in the test tube were independently controlled. The saturation temperature of the refrigerant was kept at 30 ^{o}C for all tests.

Two Pt-100 RTDs were setup at the inlet and exit ports of the test section to measure the refrigerant side inlet and exit temperatures. A pressure transducer was setup prior to the test section to measure the refrigerant saturation pressure for properties evaluation. The pressure drop through the test section was measured by a differential pressure transducer installed between the inlet and exit port of the test section.

2.2.2 Heating water loop

The heating water for the test section of the refrigerant system was provided by a thermostat reservoir. The temperature-controlled heating water was pumped from that reservoir to the test section. It transferred heat to the two-phase refrigerant and then flowed back to the reservoir to complete a close cycle. A gear type flowmeter was placed after pump to measure the heating water flow rate. The temperatures at the inlet and exit of the test section were measured by two RTDs. The total heat transfer rate to the refrigerant in the test section was evaluated by using the energy balance between the water and the refrigerant sides.

2.2.3 Preheating water loop

A thermostat reservoir was used to provide the heating water for the preheater. The temperature at the inlet and exit of the preheater and the flow rate of heating water were measured by two RTDs and a gear type flow meter. The total heat transfer rate to the refrigerant in the preheater was evaluated by using the energy balance between the water and the refrigerant sides.

2.2.4 Sub-cooling water loop

A thermostat reservoir was used to provide the cooling water for the sub-cooler. The temperature at the exit of the sub-cooler was measured by an RTD to make sure the refrigerant flowing into the receiver is subcooled.

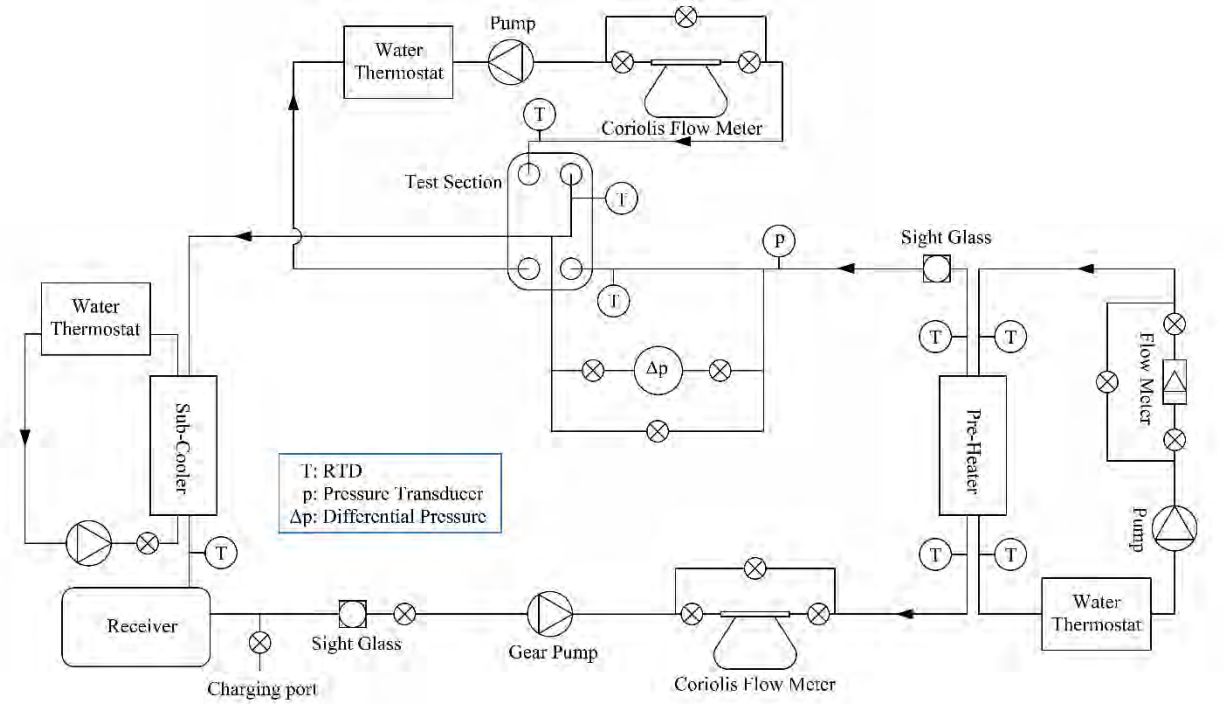

Figure 1: Schematic of the experimental setup

2.3 Data reduction

The heat transfer rate in the preheater, q_{pre} was obtained by measuring the heating water flow rate, $\dot{m}_{pre}$ and temperature difference between the inlet and exit of the preheater, T_{prei}-T_{preo}.

$$q_{pre} = \dot{m}_{pre} \cdot c_{pw} \cdot \left(T_{prei} - T_{preo}\right) \quad \text{Eq. (1)}$$

From the energy balance between the refrigerant and the water sides, the heat transfer rate to the refrigerant equals to q_{pre}. It consists of two components, sensible heat, q_{sen} and latent heat, q_{lat}. The vapor quality of the refrigerant leaving the preheater, was calculated from equation (5).

$$q_{pre} = q_{sen} + q_{lat} = \dot{m}_r \cdot c_{pr} \cdot \left(T_{rsat} - T_{ri}\right) + \dot{m}_r \cdot i_{lv} \cdot x_i \quad \text{Eq. (2)}$$

Where T_{rsat} is the saturation temperature of the refrigerant and T_{ri} is the inlet refrigerant temperature. Since the piping between the preheater and the inlet of the test section was well isolated, the vapor quality leaving the preheater equals to the vapor quality entering the test section.

The total heat transfer rate in the test section was determined from an energy balance on the heating water flow in the test section.

$$q_r = q_w = \dot{m}_w \cdot c_{Pw} \cdot \left(T_{wi} - T_{wo}\right) \quad \text{Eq. (3)}$$

Where $\dot{m}_w$, T_{wi} and T_{wo} are mass flow rate, inlet and exit temperatures of heating water respectively. The heat transferred into the refrigerant caused vapor quality changed in the test section.

$$q_r = \dot{m}_r \cdot i_{lv} \cdot \Delta x = \dot{m}_r \cdot i_{lv} \cdot \left(x_o - x_i\right) \quad \text{Eq. (4)}$$

Where Δx is the vapor quality change in the test section and x_0 is the exit vapor quality from the test section. The vapor quality changes from inlet to outlet was kept at approximately 0.2 for each test. The average vapor quality x_{ave} was defined as the average of the inlet and exit vapor qualities.

$$x_{ave} = \frac{1}{2}\left(x_i + x_o\right) \quad \text{Eq. (5)}$$

By using the LMTD method, the total thermal resistance (*1/UA*) was calculated by the logarithmic mean temperature difference of the refrigerant and water temperatures through the test section per unit heat transfer rate.

$$\frac{1}{UA} = \frac{\Delta T_{lm}}{q_r} \quad \text{Eq. (6)}$$

$$\Delta T_{lm} = \frac{\left(T_{wi} - T_{ro}\right) - \left(T_{wo} - T_{ri}\right)}{\ln\left(\frac{\left(T_{wi} - T_{ro}\right)}{\left(T_{wo} - T_{ri}\right)}\right)} \quad \text{Eq. (7)}$$

Where T_{ro} and T_{ri} are the inlet and exit temperatures of the refrigerant respectively.

The total thermal resistance is the summation of the water side, refrigerant side and the plate wall thermal resistances.

$$\frac{1}{UA} = \frac{1}{h_w A_w} + R_{wall} + \frac{1}{h_r A_r} \quad \text{Eq. (8)}$$

Where the h_w, h_r, A_w, A_r and R_{wall} are the water side, refrigerant side heat transfer coefficients, heat transfer areas and plate wall thermal resistance respectively. The modified Wilson plot method as described by Briggs and Young (1969) was used to evaluate the water side heat transfer coefficient. By neglecting the plate wall thermal resistance, the refrigerant side heat transfer coefficient was determined from the overall heat transfer coefficient and the evaluated water side heat transfer coefficient in equations (6)-(8).

The single-phase refrigerant Nusselt number, Nu_d was defined as:

$$Nu_d = \frac{h_r d_h}{k} \quad \text{Eq. (9)}$$

Where d_h is the hydraulic diameter of the plate heat exchanger which defined as twice of the plate spacing $d_h = 2s$. Refrigerant Reynolds number, Re_d was defined as:

$$Re_d = \frac{G d_h}{\mu} \quad \text{Eq. (10)}$$

All fluids properties were evaluated from the REFPROP 9.1 by NIST (2013). Table 2 compares selected properties those related to the present study of these two refrigerants at saturation temperature of 30 °C. Detail test conditions which including mass flux rate, heat flux and vapor quality changed in the test section are listed in Table 3. Uncertainties of the measured and derived parameters are listed in Table 4.

Table 2. HFC-134a and HFO-1234yf properties (at T_{sat}=30°C)

Properties	Units	HFO-1234yf	HFC-134a
Latent heat	kJ/kg	141.4	173.2
Liquid viscosity	10^{-6} N/m^2·s	145.6	183.5
Vapor viscosity	10^{-6} N/m^2·s	11.3	11.9
Liquid Density	kg/m^3	1073.9	1188.0
Vapor Density	kg/m^3	43.5	37.4
Prandtl number	dimensionless	3.3	3.4
Liquid thermal conductivity	10^{-3} W/m·K	62.0	79.1
Vapor thermal conductivity	10^{-3} W/m·K	14.4	14.3
Liquid specific heat	J/kg·K	1415.9	1445.8
Vapor specific heat	J/kg·K	1085.4	1064.4
Surface Tension	10^{-3} N/m	5.6	7.4

Table 3. Test condition for flow boiling experiment

Mass flux (kg/m^{2}s)		Heat flux (kW/m^2)		Δx
Marked	Range	Marked	Range	range
10	9.1-10.8	2.3	2.2-2.4	HFC-134a: 0.194-0.208 HFO-1234yf: 0.238-0.255
20	19.9-20.9	4.5	4.3-4.8	
30	29.4-31.1	6.9	6.8-7.1	
40	39.8-41.0	9.0	8.8-9.3	

Table 4. Uncertainties of apparatus and derived parameters

Apparatuses	**Uncertainty**	**Calibration range**
Temperature (RTD)	±0.1 K	0-100 °C
Water flow meter	±0.1 %	2,180 kg/h
Refrigerant mass flow meter	±0.1 %	30 g/s
Pressure transducer	±0.25 %	3,500 kPa
Differential pressure transducer	±0.065%	10 kPa
Derived parameters		
Mass flux, G (kg/m^{2}s)	±0.2%-1%	
Vapor quality, x	±5.9%-9.1%	
Heat flux, q" (W/m^2)	±5.8%-8.1%	
Refrigerant heat transfer coefficient, h_r (W/m^{2}s)	±6.3%-9.5%	

3. RESULTS AND DISCUSSIONS

3.1 Single-phase heat transfer coefficients

Fig. 3 compares the single-phase Nusselt number of refrigerants HFO-1234yf and HFC-134a. The result shows that heat transfer coefficients of HFC-134a are approximately from 1.0-9.3% higher than those of HFO-1234yf respectively. Those are within the experimental uncertainties range.

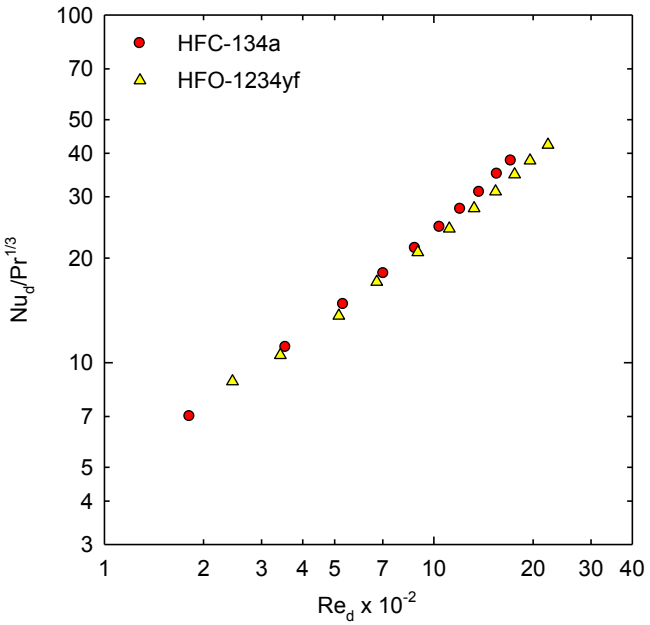

Figure 3: Single-phase Nusselt number of refrigerants HFO-1234yf and HFC-134a

3.2 Boiling heat transfer coefficients

Fig. 4 compares the flow boiling heat transfer coefficient of HFO-1234yf and HFC-134a at mass flux of G=10, 20, 30 and 40 kg/m^{2}s. The flow boiling heat transfer coefficients increase with increasing mass fluxes and vapor qualities until it reached the dry out condition. Fig. 5(a) shows the heat transfer coefficient of the HFO-1234yf is around 15% lower than HFC-134a at the lowest mass flux G=10 kg/m^{2}s. Since at the lowest mass flux condition, inertia force was overcome by the surface tension force, most of the liquid was drained at the intersection of chevron flow passages. There was only a thin liquid film attach on the plate surface especially for the higher surface tension refrigerant, HFC-134a. As proposed by Yang et al. (2018), liquid thermal conductivity dominate the heat transfer mechanism at this condition. Since the conductivity of HFC-134a is higher than that of HFO-1234yf, this caused the heat transfer coefficients of HFC-134a are that those of HFO-1234yf.

For higher mass fluxes, G=20, 30 and 40 kg/m^{2}s, owing to the extremely complicate flow paths in the chevron plate heat exchanger, the flow is at highly turbulent condition. Liquid and vapor flow mixed together. In addition to the liquid thermal conductivity, liquid and vapor viscosity are also important for heat transfer process. Since the liquid viscosity of HFC-134a is much higher than that of HFO-1234yf, the high liquid viscosity retarded the liquid flow and degrade heat transfer performance. The interaction of these two effects caused the heat transfer coefficients of these two refrigerants are very close.

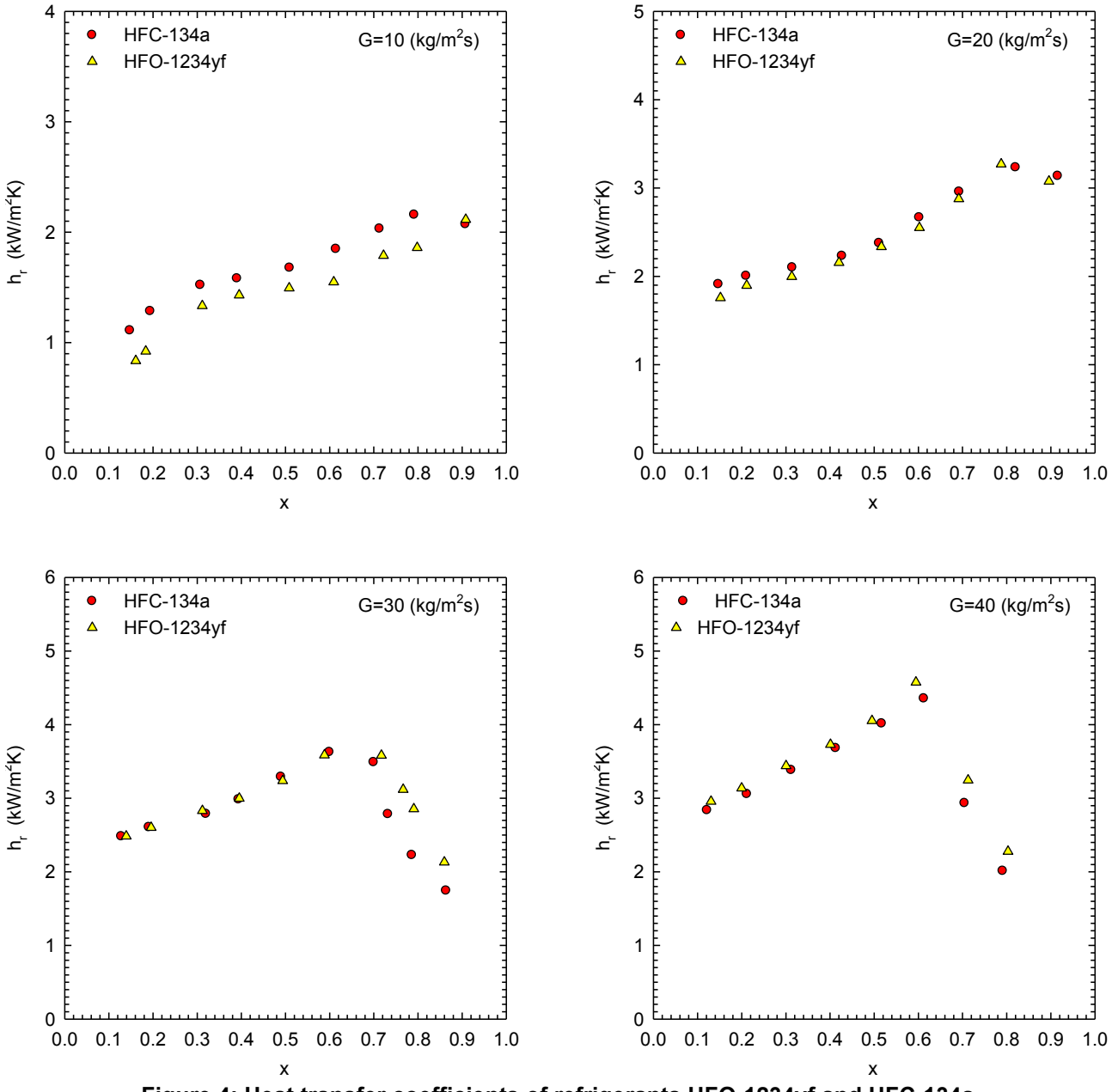

Figure 4: Heat transfer coefficients of refrigerants HFO-1234yf and HFC-134a

CONCLUSIONS

This study provides an experimental comparison of refrigerants HFO-1234yf and HFC-134a flow boiling in a chevron brazed plate heat exchanger. The effects of mass fluxes and vapor qualities was discussed. The test results show that at the lowest mass flux, inertia force was overcome by the surface tension force, most of the liquid was drained at the intersection of chevron flow passages. There was only a thin liquid film attach on the plate surface especially for the higher surface tension refrigerant, HFC-134a. Liquid thermal conductivity dominate the heat transfer mechanism and therefore the heat transfer coefficients of HFC-134a are higher than that those of HFO-1234yf. For higher mass fluxes, in addition to the liquid thermal conductivity, liquid and vapor viscosity are also important for heat transfer process. The interaction of these two effects caused the heat transfer coefficients of these two refrigerants are very close.

NOMENCLATURE

A	Heat transfer area (m^2)	c_p	Specific heat (J/kgK)
d_h	Hydraulic diameter (m^2)	f	Friction factor
G	Mass flux (kg/m^2s)	h	Heat transfer coefficient (W/m^2s)
i_{lv}	Enthalpy of evaporation (kJ/kg)	k	Thermal conductivity (W/mK)
L	Plate heat exchanger length (m)	$\dot{m}$	Mass flow rate (kg/s)
Nu	Nusselt number	Re	Reynolds number
q	Heat transfer rate (W)	R	Thermal resistance (K/W)
T	Temperature (K)	U	Overall heat transfer coefficient (W/m^2K)
x	Vapor quality	x_{avg}	Average vapor quality
μ	Dynamic Viscosity (Ns/m^2)	ΔT_{lm}	Log mean temperature difference (K)
ρ	Density (kg/m^3)		
subscript		i	Inlet
l	Liquid	o	Exit
r	Refrigerant	w	Water

REFERENCES

Briggs, D, Young, E.H., 1969. Modified Wilson plot techniques for obtaining heat transfer correlations for shell and tube heat exchangers. Chemical Engineering Progress Symposium Series, AIChE, New York, 35-45.

Cooper, M.G., 1984. Saturation Nucleate Pool Boiling - A Simple Correlation, International Chemical Engineering Symposium Series. 86 785-792.

EU directive 2014/517/EN, 2014. Regulation 2014/517/EN of the council of the European union of 16 April 2014 on fluorinated greenhouse gases and repealing Regulation (EC) No 842/2006. Official Journal of the European Union, L161, 12-18.

Gorenflo, D., 1993. Pool boiling. VDI Heat Atlas, Dusseldorf, Germany, Ha1-25.

Kays, W.M., London, A.L., 1984. Compact Heat Exchangers. McGraw-Hill, New York, 335.

Kim, DW, Lee, DC, Jang, DS, Jeon, YS, Kim, YC,2018. Comparative evaluation of flow boiling heat transfer characteristics of R-1234ze (E) and R-134a in plate heat exchangers with different Chevron angles. Applied Thermal Engineering 132, 719-729.

Lemmon, E, Huber, M., McLinden, M., 2013. REFPROP 9.1, NIST Standard Reference Database, 23.

Longo, G. A., 2012. Vaporisation of the low GWP refrigerant HFO1234yf inside a brazed plate heat exchanger. Int. J. Refrigeration, 35(4), 952-961.

Yang, C. Y., Nalbandian, H., & Lin, F. C., 2018. Flow boiling heat transfer and pressure drop of refrigerants HFO-1234yf and HFC-134a in small circular tube. Int. J. Heat and Mass Transfer, 121, 726-735.

Manuscript ID: 1282
DOI: 10.18462/iir.icr.2019.1282

New low global warming halogenated olefin working fluids for use in two-phase cooling

Jason R. JUHASZ[(a)], Luke D. SIMONI[(b)]

[(a)] Chemours Company
Wilmington, 19805, USA, jason.r.juhasz@chemours.com
[(b)] Chemours Company
Wilmington, 19805, USA, luke.s.simoni@chemours.com

ABSTRACT

Two-phase cooling solutions address thermal management for large heat density electronic applications, such as power electronics, electric vehicles and server systems. Passive two-phase cooling systems rely on latent heat of liquid vaporization to displace heat without moving components. Traditionally, fluids like saturated halogenated carbons potentially with ethers and ketones, as well as water, have been used. Although water is an excellent working fluid for such applications due to its large heat of vaporization and surface tension, isolation from electrical components for cooling is necessary. Even in a heat pipe, where the working fluid is sequestered, there is the potential for leaks, which could ruin the electronic components. Furthermore, the push towards lower global warming potential (GWP) working fluids has motivated a search for halogenated olefins for passive two-phase cooling.

The newly developed halogenated olefins can offer effective heat removal with improved reliability and a smaller footprint than traditional cooling systems. These halogenated olefins are being developed with characteristics on both excellent safety and environmental attributes, where GWP is less than 10. Having non-flammable, non-conductive and higher boiling points than traditional refrigerants which is ideal in applications where excessive pressure buildup is a concern. Their fluid properties allow for direct contact, or immersion, with electronic components as they possess high resistivity, dielectric constant and breakdown voltage.

Keywords: Dielectric Property, Electric Vehicle, Electronics, Heat Pipe, HFOs, Immersion, Low GWP, Refrigerant and Two-Phase Coolant.

1. INTRODUCTION

Traditional heat removal techniques involving natural or forced convection are more complicated and less effective than employing a two-phase passive solution. The system's footprint can also be substantially reduced by removing both extra components and weight, and enable higher heat density loads with direct contact by using dielectric coolants. These dielectric coolants are more commonly being evaluated based on their potential to simplify the cooling aspect in many electronic applications. Advantages of the fluorinated fluids are safety in use and sustainability from an environmental perspective. Having the characteristics of being non-flammable and having low dielectric constants, low GWP, no ODP and favorable toxicity profiles are some of the elements that make them suitable for use in these challenging applications.

With the focus on finding ideal candidates for a wide range of applications, understanding the basis for evaluating whether a particular fluid has the right characteristics for pool boiling at a working temperature range is critical to performance. For purpose of this paper, a methodology, Figure of Merit (FOM), was adopted to screen fluid behavior based on their thermophysical properties which is independent of fluid flow and geometry. Specifically, two FOMs are used to determine potential performance: 1) a FOM for incipience boiling and 2) a FOM for critical heat flux. These FOMs determine if a fluid will fall in the nucleate boiling region, critical for pool boiling heat transfer. Fluorinated fluids, SF30, SF33, SF50, Vertrel™ XF, SF70 and SF10 were selected and their vapor pressures, surface tensions, heats of vaporization, vapor density and liquid density in the working temperature range of interest (20 to 120 °C) along with the resultant FOMs are presented. Out of these fluorinated fluids, only the Vertrel™ XF is not a newly developed hydrofluoroolefin and as such has a high GWP. However, it is being used a comparative fluid as it already exists in insulated-gate bipolar transistor (IGBT) applications and has shown exceptional performance to date.

2. FLUID SELECTION BASIS

It is conventional to screen fluid candidates for two-phase passive cooling by evaluating appropriate FOMs for the system, which are functions of their thermophysical properties and independent of system geometry and flow patterns. This section describes the parameters needed to assess a fluid's capability for nucleate boiling by adopting FOMs based on bubble incipience and the critical heat flux (CHF) that are relevant for pool boiling on a flat surface. Six halogenated carbon fluids where selected for investigation of their relative attributes for use in these types of applications.

2.1. Derivation of FOM from Thermophysical Properties

Figure of Merit (FOM) is a metric that is independent of the system geometry and fluid flow. It is a metric of the fluid itself based on its thermophysical properties. While the specific heat transfer to the boiling process and from the condensation process are vital to determining an overall performance, a figure of merit can screen fluids by using the intrinsic thermophysical properties of the fluid. In practice, the figure of merit contains only fluid property information and can be factored out of the overall critical heat flux expression. While the exact expression of the FOM can vary from application to application, in general it is proportional to fluid's heat of vaporization, surface tension, heat capacity, density, and thermal conductivity. It is inversely proportional to the fluids viscosity.

In the case of passive two phase cooling, the phenomenon of pool boiling is the mechanism that transfers heat from the heat source. As such, the boiling domain is dependent degrees of super heat is between the heated surface and the bulk fluid, ΔT_s. Nucleate boiling is the region where bubbles are formed on the hot surface from a minimum ΔT_s at incipience to a maximum ΔT_s at the critical heat flux, CHF.

In the case of pool boiling with only natural convection, the incipient lower bound is driven by the surface tension of the fluid, σ. The incipience mechanism is the creation of gas-liquid embryos that can separate liquid from vapor. The greater the surface tension, the more likely these bubbles are to form small and early. Nucleation cannot occur on a wetted surface. Therefore, the closer the wall temperature is to the saturation temperature of the boiling fluid, the more effective the heat transfer is away from the heat source via the vaporization process. A mechanical force balance on the gas/liquid interface of an incipient bubble cavity can be derived such that the excess vapor pressure required to activate a nucleation cavity, and has been reported by Saylor et al. (1988), and is reproduced below.

$$P^{sat}(T_w) - P^{sat}\left(T_{liq}\right) = \frac{2\sigma(T_w)}{r_{bubble}} \qquad \text{Eq. (1)}$$

where P^{sat} is the vapor pressure, T_w is the temperature of the heated surface, T_{liq} is the temperature of the bulk liquid, σ is the surface tension and r_{bubble} is the radius of the bubble, which is a function of the contact angle and conical angle of concavity, 2φ. Expressions for the bubble radius have been developed by Tong et al. (1990), where the following was geometrically derived for a bubble embryo activated in a microcavity and is adopted here.

$$r_{\text{bubble}} = R_0 \left[\frac{(\beta - 2\varphi)^{1/2}\beta^{-1/2}}{1 + \varphi(2 - 3(\beta - \varphi) + (\beta - \varphi)^3)}\right]^{1/3} \qquad \text{Eq. (2)}$$

where R_0 is the cavity radius at the surface, the top of the conical cavity. In Eq. 2, It is assumed that there is no contact angle hysteresis, such that the static contact angle and dynamic contact angle are taken to be the same, β. The incipience superheat required can effectively be determined numerically from Eq. 1 and 2. The smaller the incipience superheat the greater the FOM for nucleate incipience. That is, fluids can be ranked by the following for incipience.

$$FOM_{\text{incipience}} = \left(\Delta T_{\text{s,incipience}}\right)^{-1} \qquad \text{Eq. (3)}$$

where $\Delta T_{\text{s,incipience}}$ is the incipience super heat.

At the latter end of the nucleate boiling region, at the maximum ΔT_s of the nucleate region, the heat transfer from wall to boiling liquid breaks down as vapor blankets the surface. The CHF is when the surface tension is overcome and a film of gas separates the liquid from the hot surface to the detriment of the heat transfer coefficient. At this point, there is a maximum in the heat flux, which is known as the critical heat flux (CHF). From the CHF, further increases in ΔT_s result in a dramatic drop-off of the heat flux. In this regime, the heat of vaporization is the dominate property variable of the fluid, followed by the vapor density (Saylor et al., 1988). The heat of vaporization is the amount of heat the fluid can acquire

do to vaporization. Additionally, the surface tension directly affects the amount of superheat a fluid can withstand before the CHF is reached. For the purpose of screening and comparing fluids for two-phase passive cooling, the boiling process can be approximated by pool boiling on a large flat surface. As shown by Zuber et al. (1963), the CHF can be approximated by the following.

$$CHF = \frac{\pi}{24}\sqrt{\rho_{\mathrm{g}}}\Delta h_{\mathrm{vap}}\left(\sigma g\left(\rho_{\mathrm{liq}} - \rho_{\mathrm{g}}\right)\right)^{1/4} \quad \text{Eq. (4)}$$

where Δh_{vap} is the latent heat of vaporization, ρ_i is the density of the fluid in phase i, and g is the acceleration due to gravity. Once can see that the critical heat flux on a flat surface is directly proportional to the fluid's Δh_{vap} and $\sqrt{\rho_{\mathrm{g}}}$. These are the primary and secondary drivers for the CHF. Since Eq. 3 is dependent on fluid properties alone, it can also be used as a FOM for the CHF. That is,

$$FOM_{\mathrm{CHF}} = \frac{CHF}{\pi/24} \quad \text{Eq. (5)}$$

In summary the smaller the $\Delta T_{\mathrm{s,incipience}}$ and the larger the CHF, the more promising the fluid for two-phase cooling.

2.2. Fluid Screening Results

Although two-phase passive cooling is not a new technology, new low global warming potential dielectric working fluids are sought to meet the demands of new electronic devices with large heat densities. New halogenated olefins and provide these requirements, however, most working fluids in this class are highly wetting as they have low surface tensions, a challenge to overcome. In this contribution we evaluate the properties, both measured and predicted, of six fluids, five of which being halogenated olefins. These fluids are presented in Table 1 along with their basic properties. Figs. 1 through 5 are plots of their vapor pressures, surface tensions, heats of vaporization, vapor density and liquid density in the working temperature range of interest, 20 to 120 °C.

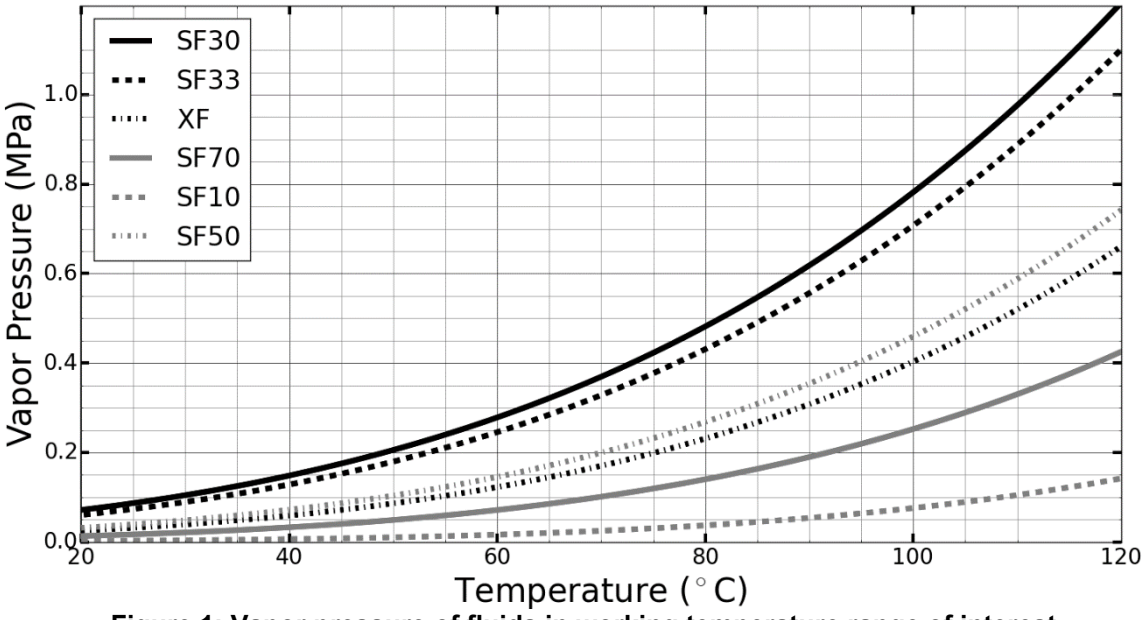

Figure 1: Vapor pressure of fluids in working temperature range of interest

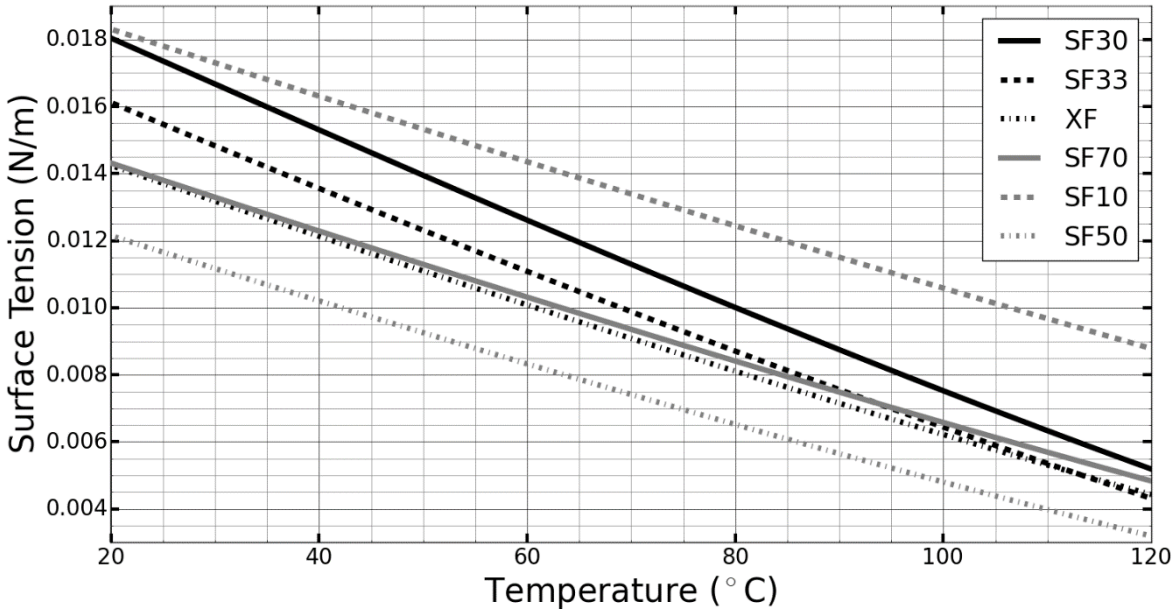

Figure 2: Surface tension of fluids in working temperature range of interest

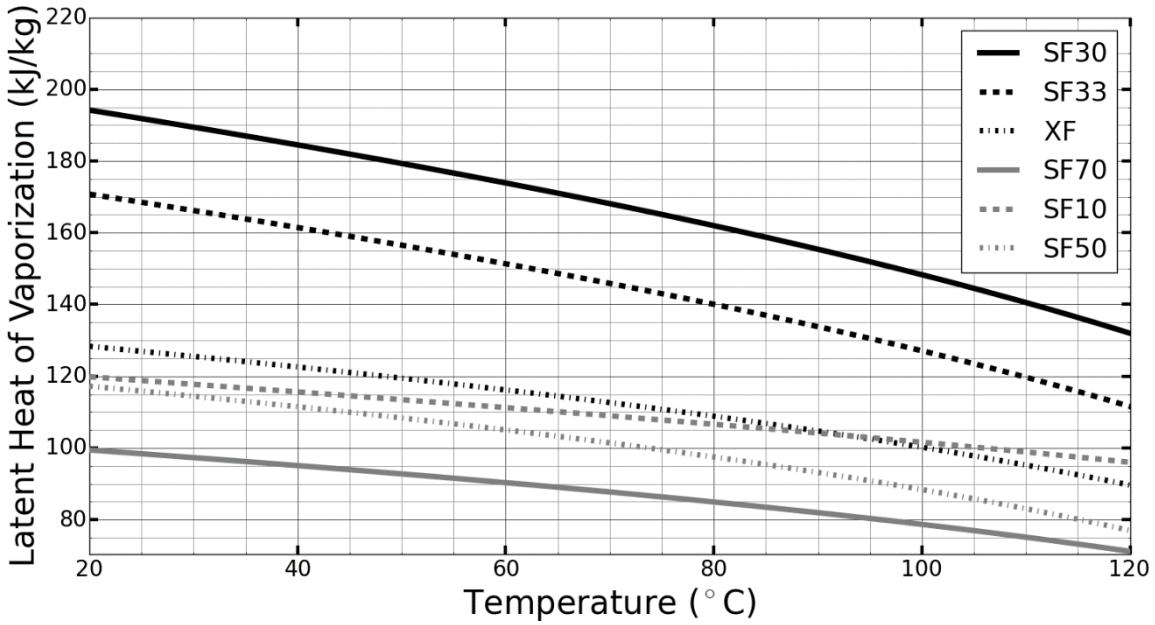

Figure 3: Heat of vaporization of fluids in working temperature range of interest

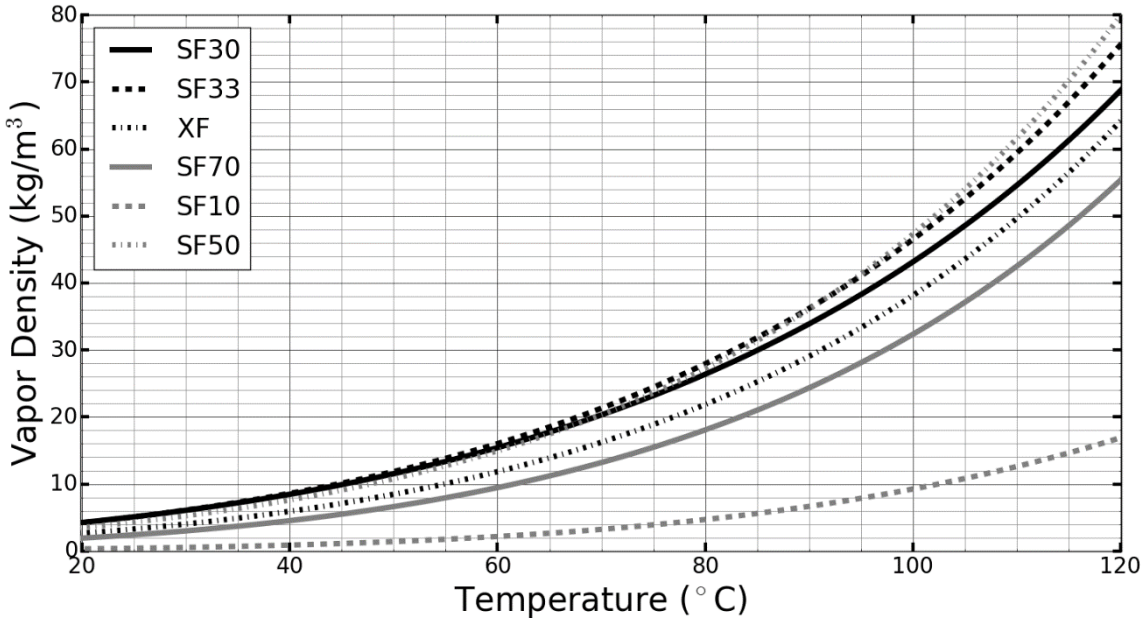

Figure 4: Vapor density of fluids in working temperature range of interest

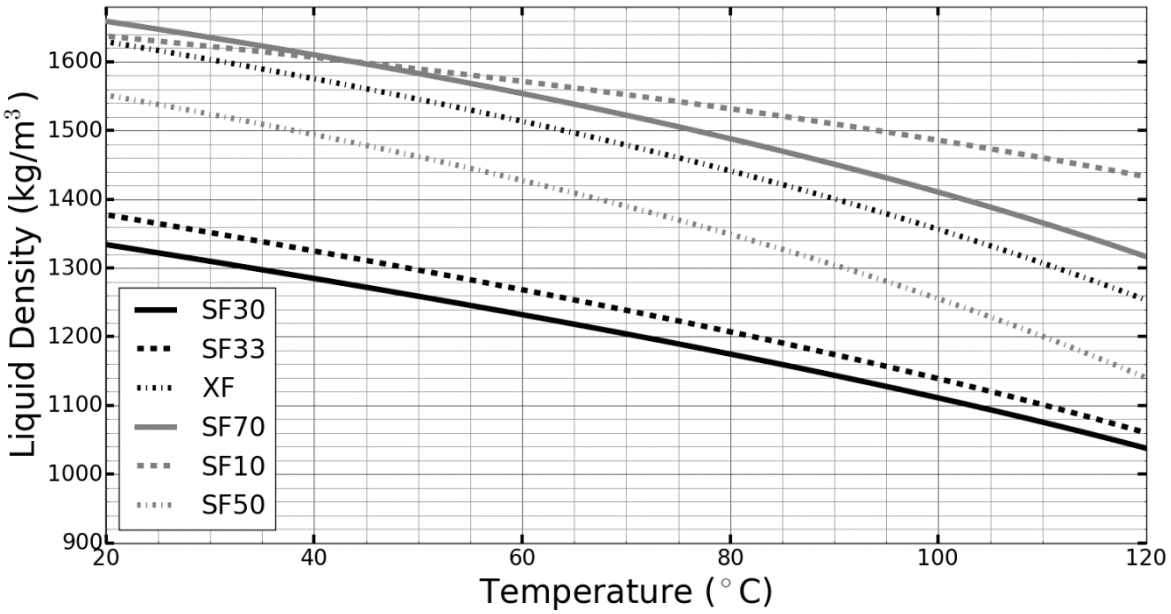

Figure 5: Liquid density of fluids in working temperature range of interest

First, we consider the case of incipience pool boiling, to determine the minimum amount of superheat needed for the fluid to reach the nucleate boiling regime. As is shown in Eq. 1 and 2, the amount of superheat, $\Delta T_{\mathrm{s,incipience}}$ is dependent on the fluids vapor pressure, surface tension, contact angle, cavity conical angle and the conical cavity radius at the surface. In Saylor et al. (1988), $\beta = 2.0°$, $2\varphi = 1.0°$ and $R_0 = 5\mathrm{e}-7\ \mathrm{m}$ are deemed reasonable values, which have been adopted here. For highly wetting fluids, the incipient bubble radius is less than the cavity radius, where a large super heat vapor pressure is needed to create the bubble. Fig. 6 depicts the $\mathrm{FOM}_{\mathrm{incipience}}$ as a function of temperature over the working temperature range for the 6 fluids.

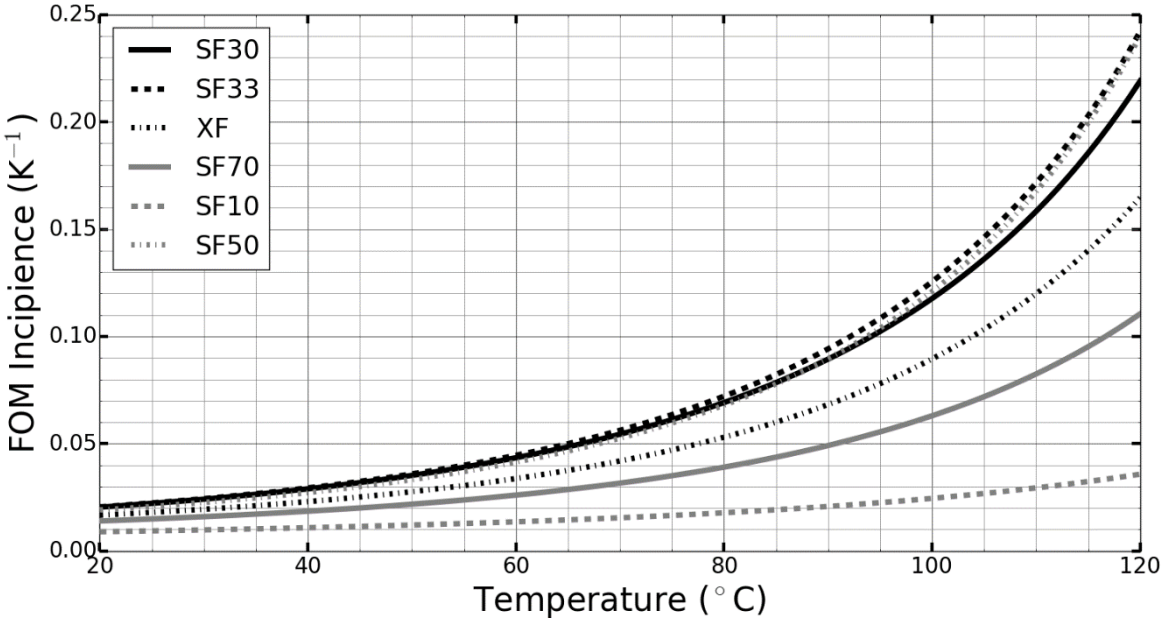

Figure 6: $FOM_{incipience}$ of fluids in working temperature range of interest

One can see from Fig. 6 that SF33, SF50 and SF30 appear to be the most promising in terms of the super heat needed in order for incipience boiling to occur. Interestingly, SF10, which has the largest surface tension requires the most about of superheat for bubbles to spontaneously occur in microcavities. This is because its vapor pressure is so small in this region.

Next, we evaluate the fluids in terms of the other side of the nucleate boiling region, denoted by the CHF in Eqs. 4 and 5. As discussed, the CHF figure of merit is directly proportional to the CHF for boiling on a large flat surface. The larger the CHF the more superheat can be tolerated before a blanket of vapor insulates the heated surface. Fig. 7 is a plot of the FOM_{CHF} for the 6 fluids over the working temperature range.

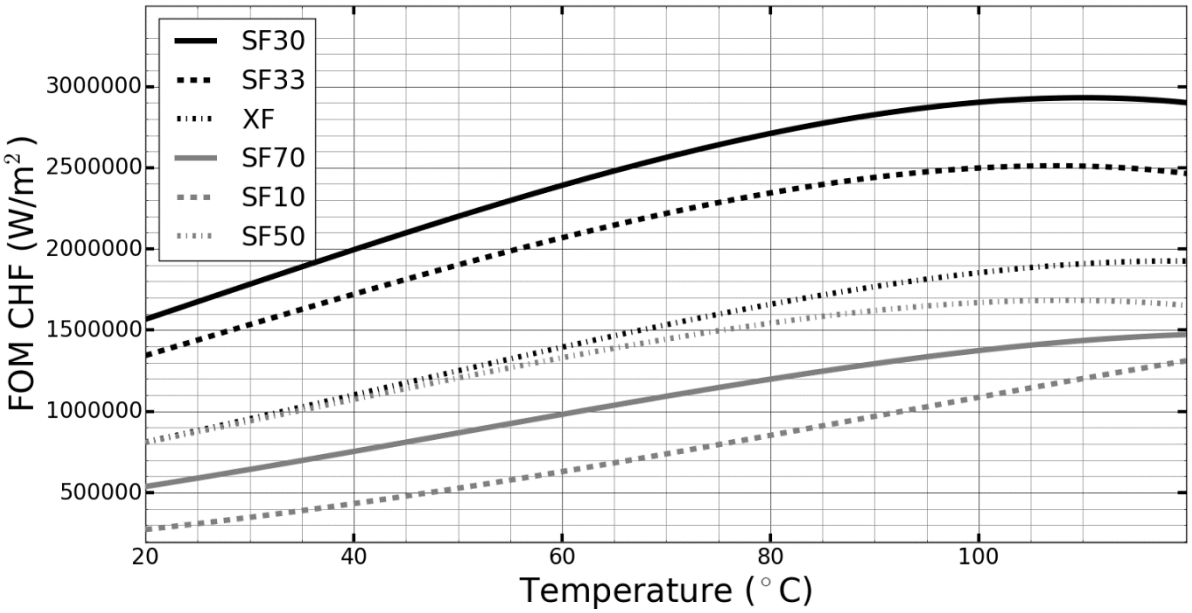

Figure 7: FOM_{CHF} of fluids in working temperature range of interest

Clearly the heat of vaporization drives this metric, followed by vapor density. In fact, one can see that the trend in FOM_{CHF} is amount the same as the heat of vaporization. The exception to this is SF10. SF10 has a relatively small vapor density. That said, most of the fluid properties are model predictions based on preliminary data. Never the less, SF30 and SF33 are clearly strong candidates for passive two-phase cooling.

Table 1. Table for selected working fluids

Property	Units	Opteon™ SF30	Opteon™ SF33	Opteon™ SF50	Vetrel™ XF	Opteon™ SF70	Opteon™ SF10
Molecular Weight	g/mol	140	164	264	252	350	362
Boiling Point	°C	29.2	33.4	49.5	55	70.6	110
Freeze Point	°C	<-80	<-80	<-80	<-80	<-80	< -80
Critical Temperature	°C	179	171	170	181	189	240
Critical Pressure	MPa	3.5	2.9	2	2.3	1.8	1.7
Density @ 25°C	kg/m^3	1320	1370	1540	1620	1650	1630
Viscosity @ 25°C	cP	0.34	0.39	0.67	0.59	0.77	0.66
Vapor Pressure @ 25°C	MPa	0.0868	0.0737	0.0394	0.0316	0.0168	0.0027
Surface Tension @ 25°C	N/m	0.017	0.013	0.012	0.014	0.014	0.018
Heat of Vaporization @ BP	kJ/kg	192	169	116	127	98.4	119
Liquid Thermal Conductivity	W/m-K	0.087	0.077	0.073	0.077	0.089	0.072
Liquid Specific Heat @ 25°C	kJ/kg-K	1.12	1.23	1.03	1.09	0.961	1.02
Coefficient of Expansion	1/K	0.0018	0.0019	0.0018	0.0013	0.0014	0.0015
Flash Point, CC ASTM D56		None	None	None	None	none	None
Dielectric Strength, 0.1" gap	kV	TBD (1)	11.5	TBD(1)	32	37	29
Volume Resistivity	Ohm-cm	TBD (1)	5.8E8	TBD(1)	3.8E10	2.1E15	2.2E11
Dielectric Constant		TBD (1)	32	TBD(1)	7.1	1.8	5.16
Occupational Exposure Limit	ppm	425	500	TBD(1)	200	TBD (1)	500
Ozone Depletion Potential (ODP)		0	0	0	0	0	0
Global Warming Potential (GWP)		2	2	<10 TBD (1)	1650	< 20 TBD (1)	2.5

TBD (1) - To be determined

From Table 1 provided above, an overall perspective of each fluid is captured. This table only gives the thermophysical properties at 25 °C where Figs. 1 through 7 assess them across a broader temperature range. Other important characteristics of the fluids are described such as dielectric strength, volume resistivity and dielectric constant which are important aspects in dielectric cooling. Some of the working fluids are newly developed and have not been fully evaluated, but are expected to be exceptional fluids in this regard. Also in this table, flash point, occupational exposure and global warming potential are also key elements which help to address safety and sustainability of the fluid for use in these applications.

3. CONCLUSIONS

The results of this study yielded some interesting learnings for the selection of a working fluid in a two-phase cooling application. The latent heat of vaporization has the greatest influence on the FOM_{CHF} numbers, whereas the surface tension and vapor pressure drive $FOM_{incipience}$, both of which are indicative of the performance on a relative basis for heat removal in a specified area, where all other parameters involving the surface morphology are held constant. The results of this fluid analysis suggest that SF30

and SF33 would be best candidates followed by Vertrel™ XF and SF50. Obviously, there are other considerations, which have an important influence in selection the working fluid such as the dielectric properties. Clearly, there would be concern about the electrical insulating ability of SF30 and SF33. Although this is part of a preliminary fluid screening, it is apparent these newly developed HFOs are going to play a key role in the future especially as dielectric coolants based on their key value proposition.

NOMENCLATURE

GWP	global warming potential	Δh_{vap}	heat of vaporization (kJ/kg)
ODP	ozone depletion potential	P^{sat}	vapor pressure (MPa)
HFO	hydrofluoroolefin	σ	surface tension (N/m)
FOM	figure of merit	ρ	density (kg/m^3)
IGBT	insulted-gate bipolar transistor	g	gravity (9.8 m/s^2)
ΔT_s	degrees of superheat (K)	T_w	wall temperature (°C)
CFH	critical heat flux (W/m^2)	T_{liq}	liquid temperature (°C)

REFERENCES

ASHRAE 2016. ANSI/ASHRAE Standard 34-2016: Designation and Safety Classification of Refrigerants. Atlanta, American Society of Hearting Refrigeration and Air Conditioning Engineers, Inc.

Myhre, G. and Shindell, G. *et al*. Ed. 2013, IPCC, Climate Change 2013: The Physical Science Basis, the Fifth Assessment report Ch. 8 WG1 – *Anthropogenic and Natural Radiative Forcing*, IPCC.org. Cambridge University Press, Cambridge UK and New York, NY.

Saylor, J. R., Bar-Cohen, A., Lee, T. Y., Simon, T. W., Tong, W., Wu, P. S., 1988. Fluid selection and property effects in single- and two-phase immersion cooling. IEEE 11(4), 557-565.

Tong, W., Bar-Cohen, A., Simon, T. W., You, S. M., 1990. Contact angle effects on boiling incipience of highly-wetting liquids. Int. J. Heat Mass Transfer 33(1), 91-103.

Zuber, N., Tribius, M., Westwater, J. W., 1963. The hydrodynamic crisis in pool boiling of saturated and subcooled liquid. Int. Devel. In Heat Transfer 27,220-236.

Manuscript ID: 1283
DOI: 10.18462/iir.icr.2019.1283

Pool boiling heat transfer measurements on a horizontal plate with a low global warming potential refrigerant

Ilya T'JOLLYN[(a,b)], Jasper NONNEMAN[(a,b)], Michel DE PAEPE[(a,b)]

[(a)] Department of Flow, Heat and Combustion Mechanics; Ghent University
Ghent, 9000, Belgium, ilya.tjollyn@ugent.be
[(b)] Flanders Make; Core lab UGent-EEDT
Leuven, 3000, Belgium

ABSTRACT

Pool boiling is a space efficient method with high heat transfer coefficients for cooling of several applications, for example power electronics. In previous studies, refrigerants such asFC72 and R113 have been used, which have a high GWP (global warming potential). In this study, the refrigerant used is 1,1,1,2,2,4,5,5,5-nonafluoro-4-(trifluoromethyl)-3-pentanone or also known by its trade name Novec 649. It has similar thermal properties as FC-72 and R-113, but has a very low GWP of 1. An experimental setup is constructed to measure pool boiling heat transfer on a horizontal plate. The measured boiling curve corresponds to reported measurements of other authors for similar refrigerants. The measurements are compared with three available correlations from literature on pool boiling. None of the correlations represent the boiling measurement data with adequate accuracy.
Keywords: Electronics, Heat Transfer, Low GWP, Pool Boiling.

1. INTRODUCTION

The power density of power electronics is swiftly increasing, due to the need for higher powers while lowering the weight and volume, for example drivetrains in electric vehicles (Emadi et al., 2008). Because of the higher power density, the heat dissipation is also increased, resulting in high heat fluxes. To allow for efficient and safe operation of power electronics, the devices have to be cooled by means of a very effective heat transfer mechanism. Current state of the art in power electronics cooling is forced liquid cooling, which features rather large heat sinks and for which cooling performance can be limited by the thermal interface resistances in the heat transfer path from the power electronics to the cooling fluid (Chu, 2004). Direct immersion cooling with dielectric fluids can be an alternative, with reduced size and no thermal interface resistances. Furthermore, two-phase or boiling immersion cooling features high heat transfer coefficients without having the requirements of utilizing large heat sinks.

Direct immersion cooling with dielectric fluids has been researched since the 1960's (Chu, 2004). However, most measurements in literature report of measurements with water (non-dielectric) and refrigerants such as FC-72 (perfluorohexane) and R-113 (1,1,1-trichlorotrifluoroethane) which pose risks to the global climate, due to their high global warming potential (GWP). In recent years, new refrigerants with very low GWP have been introduced in the market as alternatives for these refrigerants. Data on the pool boiling performance of these refrigerants is very scarce, and it is not clear if the proposed correlations based on measurement data with other refrigerants are suitable to predict the heat transfer performance of these refrigerants.

The refrigerant chosen for measurements in this paper is a fluorinated ketone, known by its trade name Novec 649. It has a very low GWP equal to 1 and a boiling point of 49°C at atmospheric pressure, making it an interesting alternative for pool boiling cooling of power electronics. One study reports on the pool boiling heat transfer of Novec 649 from a heated wire, where similar performance has been found when compared to FC-72 (Forrest et al., 2009). This paper presents measurements of pool boiling on a horizontal plate with dimensions representative of a power electronics (IGBT) module. The boiling curve is measured at different saturation temperatures and compared to three commonly used correlations from literature.

2. EXPERIMENTAL SETUP

2.1. Overview

A schematic overview of the setup is shown in Fig. 1. A sealed reservoir, filled with a two-phase refrigerant mixture, is heated from the bottom plate, where boiling occurs on a horizontal plane. At the top, in the vapour phase, the refrigerant is cooled down and condensed on a helical coil in which a water-glycol mixture is circulated. A chiller is used to decrease the temperature of the water-glycol mixture at the inlet of the cooling coil to the desired setpoint.

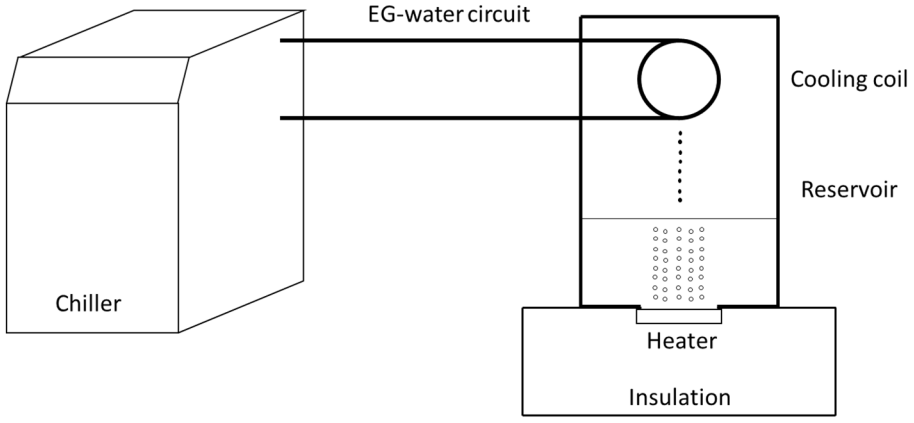

Figure 1: Schematic overview of immersion boiling setup

A 3D and a cross-sectional view of the reservoir is shown in Fig. 2. The reservoir has a length of 176mm, a width of 213mm and a height of 330mm and is made of stainless steel plates with a thickness of 8mm. Two polycarbonate windows are utilized to be able to visually observe the boiling phenomena. The bottom plate is made of a PMMA plate with a thickness of 10mm which has a rectangular opening of 108mm by 47mm. Attached to this opening is an aluminium plate on which the boiling occurs. This plate has a thickness of 10mm and the aluminium used has a thermal conductivity of 167W/(mK). The dimensions are chosen in accordance to the dimensions of the base plate of an inverter used in electric vehicles. The reservoir is made leak tight by welding the stainless steel plate, bolting the polycarbonate and PMMA plate with silicon sealing mats between the junctions and applying silicon mastic at the outside of the junctions.
Heating is supplied by a rectangular ceramic heater (150 x 87 x 15.3mm). Since the heated surface is smaller than the surface of the heater, an aluminium heat spreader is used to conduct the heat from the larger heater surface to the smaller boiling surface. At the interface of the heater and the heat spreader and the interface of the heat spreader and the heated plate, thermal paste with a thermal conductivity of 4W/(mK) is used to decrease the thermal interface resistance. The power dissipation in the heater can be set from 0W to 875W, resulting in heat fluxes up to 172kW/m². To minimize the heat losses from the heater to the environment, the reservoir and heater are supported on a 150mm-thick layer of foam glass insulation (0.05W/(mK)), which can withstand temperatures up to 430°C. The area surrounding the heater and the heat spreader is insulated with a layer of ceramic fibre insulation (0.21W/(mK)) with a minimum thickness of 31.5mm, withstanding temperatures up to 1250°C.
The refrigerant chosen for the boiling measurements in this paper is 1,1,1,2,2,4,5,5,5-nonafluoro-4-(trifluoromethyl)-3-pentanone (trade name Novec-649). This refrigerant was chosen because of its low global warming potential (GWP = 1) compared to refrigerant with similar properties, non-flammability and non-toxicity and because of its low boiling point at atmospheric pressure (49°C).

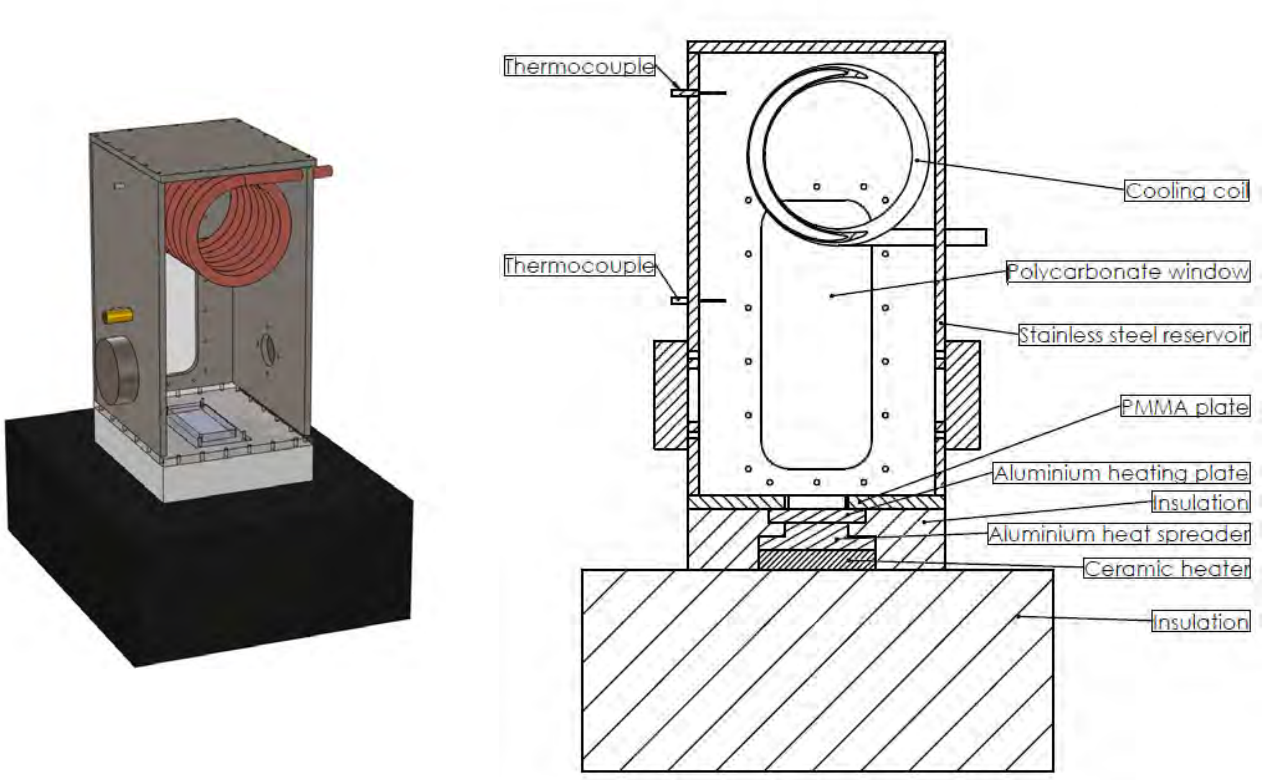

Figure 2: 3D view of the reservoir with front plate and window removed (left) and cross-sectional view of the reservoir(right)

2.2. Setup control and measurements

Power is supplied to the heating element by a variable DC source, which can supply a voltage ranging from 0-360V. The heating element is a resistor with a resistance of approximately 61Ω. The power supply measures the voltage and the current with a respective accuracy of ±0.72V and ±0.06A.

The temperature of the refrigerant in the reservoir is measured at two locations, as shown in Fig. 2. Two type T mineral insulated thermocouples with a diameter of 1mm are used for the refrigerant temperature measurements. Due to the heating by the heating plate and the cooling by the cooling coil, thermal gradients exist in the refrigerant reservoir. For some conditions, the saturation temperature is not accurately represented by the thermocouple measurements in the reservoir. A pressure transducer with an accuracy of ±450Pa is implemented to measure the saturation pressure, which is recalculated to the saturation temperature using the refrigerant properties. This temperature is used for the measurement analysis. For one set of measurements, the saturation temperature and pressure is kept constant while varying the heat flux from the heated plate. The desired value for the saturation temperature is maintained within ±1°C by controlling the inlet temperature of the water-glycol mixture entering the cooling coil.

The temperature of the heated aluminium plate is measured at the interface between the heat spreader and the heated plate. Five type K mineral insulated thermocouples with a diameter of 0.5mm are used. To fix the thermocouple, 0.5mm wide and deep grooves are milled in the surface. The temperature is measured at the middle of the heating plate and at five locations equally distributed over the length. To determine the temperature at the interface of the heating plate and the refrigerant, the temperature difference over the heated plate is estimated using the dimensions and the thermal conductivity of the used aluminium. All thermocouples are calibrated in-house, resulting in a temperature measurement with an accuracy of ±0.1°C.

2.3. Measurement uncertainty analysis

To analyse the heat transfer behaviour of the pool boiling process, the heat flux from the surface is analysed in function of the temperature difference between the surface of the heated plate and the

refrigerant (surface superheat temperature). The heat flux q is determined from the measured voltage V and current I, divided by the heat transfer surface area A:

$$q = \frac{VI}{A} \qquad \text{Eq. (1)}$$

The error on the derived heat flux can be calculated from the errors on the voltage and current measurement as:

$$\delta q = \frac{\sqrt{(\delta V\ I)^2 + (V\ \delta I)^2}}{A} \qquad \text{Eq. (2)}$$

In this equation, δq, δV and δI are the respective error on the heat flux, voltage and current. The average temperature at the wall in contact with the refrigerant is determined from the average temperature at the outside of the heated plate and the temperature drop due to conduction through the plate:

$$T_w = \frac{\sum_i T_{TC,i}}{5} - q\frac{t}{k} \qquad \text{Eq. (3)}$$

In this equation, T_w is the average wall temperature, $T_{TC,i}$ is the measured thermocouple temperature, t is the thickness of the aluminium heated plate and k is the thermal conductivity of the heated plate. The error on the determination of the surface superheat temperature can be determined as:

$$\delta(T_w - T_{sat}) = \sqrt{5\left(\frac{\delta T_{TC}}{5}\right)^2 + \left(\delta q\frac{t}{k}\right)^2 + \delta T_{sat}^2} = \sqrt{\frac{\delta T^2}{5} + \left(\frac{t}{k}\right)^2 \delta q^2 + \left(\frac{\partial T_{sat}}{\partial p_{sat}}\right)^2 \delta p_{sat}^2} \qquad \text{Eq. (4)}$$

The liquid saturation temperature T_{sat} is determined from the saturation pressure p_{sat}. The maximal errors on the heat flux and temperature difference are respectively 2.1kW/m² and 0.24°C.

3. RESULTS AND DISCUSSION

The boiling curve is shown in Fig. 3 for a saturation temperature of 35°C. All measurements shown are of nucleate boiling, measurement points of natural convection are omitted. The measured boiling curve exhibits similar features as those measured by El-Genk & Bostanci (2003) for saturation pool boiling of another Novec fluid, HFE-7100. Three different regions with a quasi-linear relation between

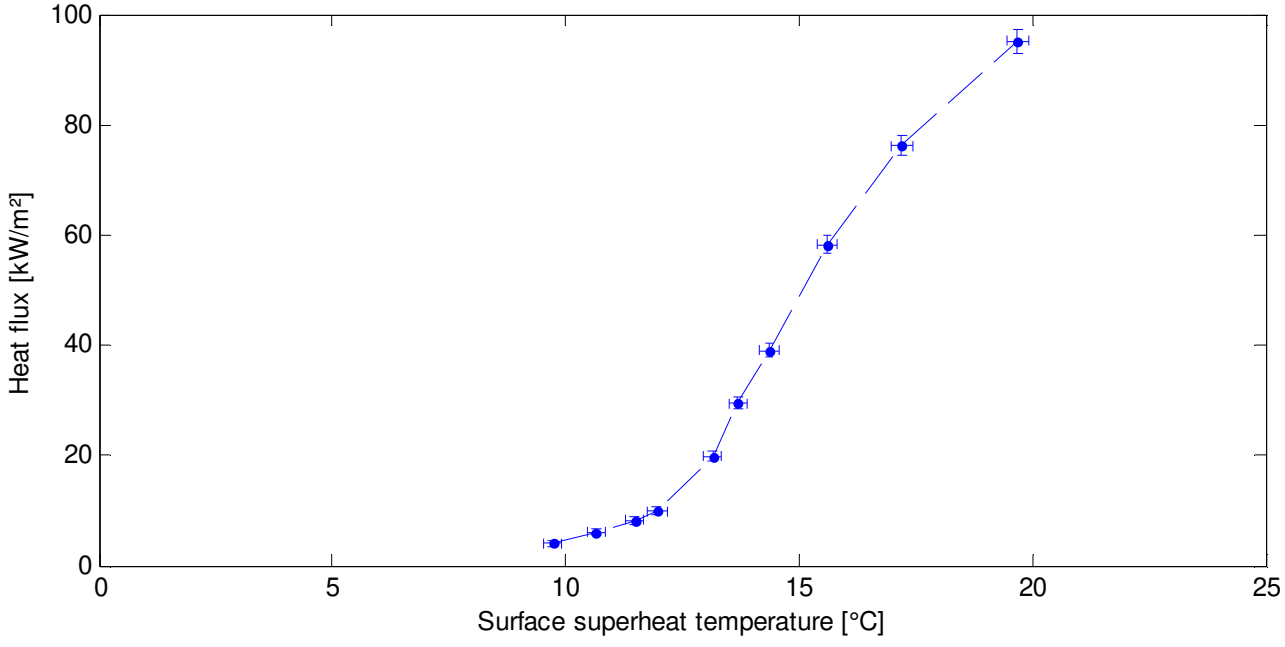

Figure 3: Heat flux as a function of surface superheat temperature for a constant liquid saturation temperature of 35°C

surface superheat temperature and heat flux can be perceived. These different regions with different slopes of the boiling curve can be interpreted by the visual observations of the boiling phenomenon. In the first region at low heat fluxes, the slope is lowest due to a smaller amount of active nucleation sites at the surface. In the second region where the slope is highest, nearly all nucleation sites are active and high heat fluxes can be transferred. With even higher heat fluxes and surface superheat temperatures, the slope decreases again. This can be explained by the accumulation of larger vapour bubbles near the surface, obstructing the heat transfer.
The influence of the saturation temperature on the boiling curve is shown in Fig. 4, where boiling curves are shown for two saturation temperatures: 30°C and 35°C. The measurements indicate that heat transfer is enhanced by increasing the saturation temperature, which is consistent with previous measurements reported in literature.

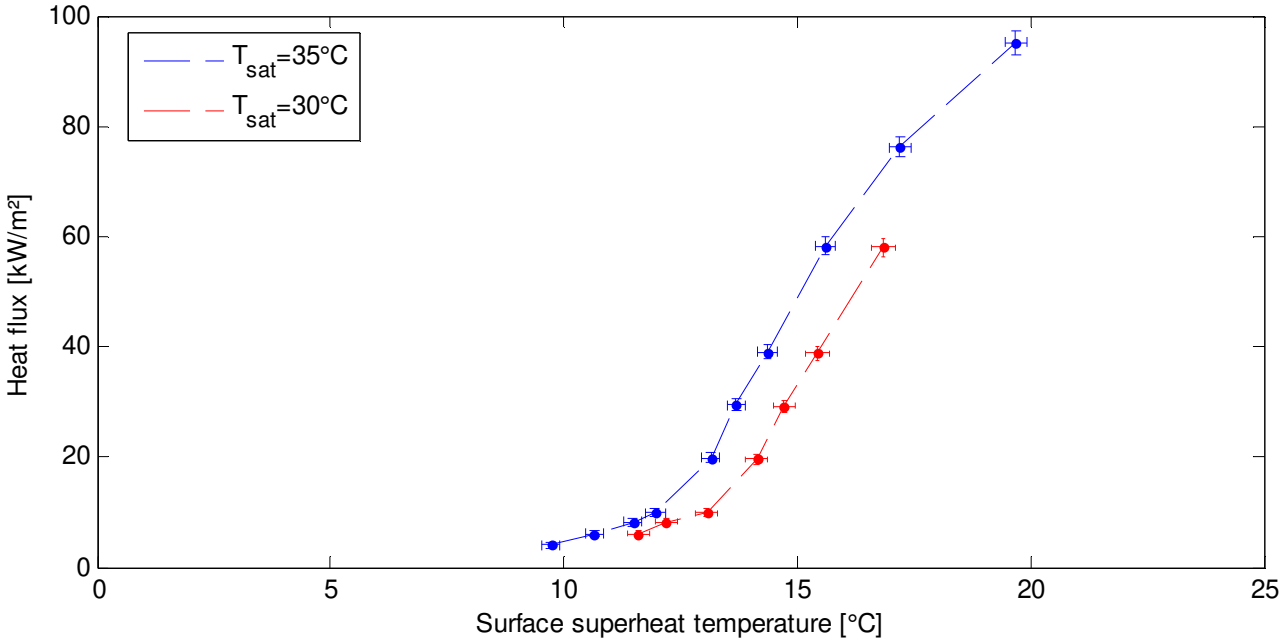

Figure 4: Heat flux as a function of surface superheat temperature for two liquid saturation temperatures, 30°C and 35°C

The measured boiling curve for a saturation temperature of 35°C is compared to those predicted by three widely used but distinctly different correlations for pool boiling: the Rohsenow (1952), Cooper (1984) and Stephan & Abdelsalam (1980) correlations. For the Rohsenow correlation, the constants determined by Pioro (1999) for a surface-fluid combination of aluminium and refrigerant R-113 are used, since no data is available on the constants for the refrigerant used in this study. In the Cooper correlation, a surface roughness of 5µm is used, which is representative for the boiling surface used in the experiments. Stephan and Abdelsalam proposed four different correlations for different groups of fluids, the proposed correlation for refrigerants is used in this comparison. Fig. 5 shows the comparison of the correlations and the measurement data. Since all correlations predict the relation between surface superheat and heat flux function with a constant power, none of the correlations predict a trend corresponding to the measurements. The order of magnitude of the heat transfer coefficient is predicted fairly by the Rohsenow and Cooper correlations, while it is overestimated by the Stephan & Abdelsalam correlation. Overall, none of the correlations are able to predict the heat transfer performance with adequate accuracy.

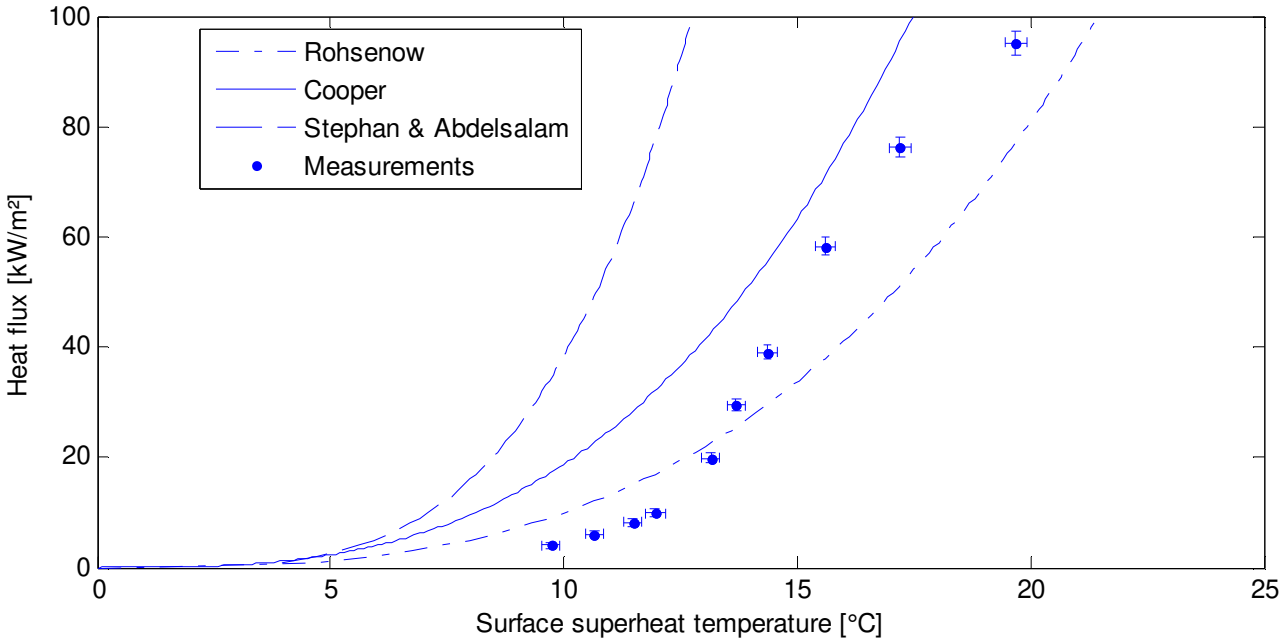

Figure 5: Comparison of the measured boiling curve with the boiling curves predicted by the Rohsenow (1952), Cooper (1984) and Stephan & Abdelsalam (1980) correlation

4. CONCLUSIONS

Pool boiling measurements have been done on a horizontal plate with representative dimensions for a power electronics module in contact with a low-GWP refrigerant. A sealed reservoir is used to be able to change the saturation temperature and pressure. The boiling curve is measured and this corresponds to other measurements found in literature. A higher saturation temperature results in a higher heat transfer coefficient.

A comparison between measurements and three different correlations from literature is made. The measurements show a trend of three regions with different slopes in the boiling curve at low, moderate and high heat fluxes, which is not predicted by any of the correlations. The Cooper and Rohsenow correlation do predict heat transfer coefficients in the correct order of magnitude, while the correlation of Stephan & Abdelsalam overestimates the heat transfer coefficient. In general, no correlation was found to be able to predict the boiling curve with a high degree of accuracy.

ACKNOWLEDGEMENTS

This research was supported by Flanders Make, the strategic research centre for the manufacturing industry, and the HERMESFONDS in the framework of the Hipercool project (HBC.2016.0463).

NOMENCLATURE

A	heat transfer surface (m²)	T_{sat}	saturation temperature (°C)
I	heater current (A)	T_{TC}	temperature measured by thermocouple (°C)
k	thermal conductivity (W/(mK))	T_w	wall temperature (°C)
p_{sat}	saturation pressure (Pa)	V	heater voltage (V)
q	heat flux (W/m²)	δ	measurement error (-)
t	heating plate thickness (m)		

REFERENCES

Chu, R.C., 2004. The challenges of electronic cooling: past, current and future. *J. Electro. packaging 126*(4), 491-500.

Cooper, M.G., 1984. Heat flow rates in saturated nucleate pool boiling-a wide-ranging examination using reduced properties. *Advances in heat transfer* 16, 157-239.

El-Genk, M.S., Bostanci, H., 2003. Saturation boiling of HFE-7100 from a copper surface, simulating a microelectronic chip. *Int. J. Heat Mass Tran. 46*(10), 1841-1854.

Emadi, A., Lee, Y.J. and Rajashekara, K., 2008. Power electronics and motor drives in electric, hybrid electric, and plug-in hybrid electric vehicles. *IEEE T. Ind. Electron. 55*(6), 2237-2245.

Forrest, E., Buongiorno, J., McKrell, T. and Hu, L.W., 2009. Pool boiling performance of Novec TM 649 engineered fluid. Proceedings of the ECI International Conference on Boiling Heat Transfer, Florianópolis, Brazil.

Pioro, I.L., 1999. Experimental evaluation of constants for the Rohsenow pool boiling correlation. *Int. J. Heat Mass Tran. 42*(11), 2003-2013.

Rohsenow, W.M., 1952. *A method of correlating heat transfer data for surface boiling of liquids*. T. ASME 74, 969-976.

Stephan, K., Abdelsalam, M., 1980. Heat-transfer correlations for natural convection boiling. *Int. J. Heat Mass Tran. 23*(1), 73-87.

Manuscript ID: 1290
DOI: 10.18462/iir.icr.2019.1290

Performance measurement of a two stage CO_2 refrigerator and SEPR comparison with low-GWP alternative

Biagio CITARELLA[(a)], Rita MASTRULLO[(a)], Alfonso W.MAURO[(a) (*)], Massimiliano SFRAGARA[(b)], Marcello TAMMARO[(b)]

[(a)] Federico II University of Naples, Dept. of Industrial Engineering
P.leTecchio 80 Napoli, 80125,Italy, email: wmauro@unina.it[(*)]
[(b)] Zanotti SpAVia M.L. King 30Pegognaga, 46030, Italy

ABSTRACT

CO_2 is a natural refrigerant whose use agrees with GWP limitations imposed by recent environmental regulations in Europe. The energy performance indexes may not fulfil the limits imposed by Ecodesign rules especially in transcritical operation. In this paper, a condensing unit working with R744 is considered. The target application is the cooling of rooms and convenience stores. It is a two-stage system working with inverter-driven rotary compressor, liquid receiver, intercooler and intermediate pressure flash gas extraction. Its cooling capacity is up to 13 kW at an evaporating temperature of -10 °C and ambient temperature of 32 °C. Energy performance is measured according to EN13215 regulation; its seasonal energy performance ratio (*SEPR*) is over the threshold value of 2.3 applied since 2018. In this work we report the effect on energy performance of intercooler, thermodynamic analysis of main factors of influence and a comparison of seasonal performance with a unit designed for the same application employing a low-GWP class A1 synthetic refrigerant.
Keywords: Refrigeration, CO_2, Condensing unit, Two stage, Inverter, Intercooler, SEPR, design choices, low-GWP.

1. INTRODUCTION

The refrigeration industry is facing in these years significant change, which is necessary to reduce its impact on global warming. While its indirect contribution to global warming depends on the technologies adopted, its direct contribution is due to the refrigerant. The F-Gas Regulation (European Parliament, 2014) and the Kigali Amendment to the Montreal Protocol (UNEP, 2016), which entered into force on 1/1/2019, are pushing towards substitution of refrigerants with high GWP (global warming potential). The push is two-fold: some high GWP substances are banned altogether (depending on the sector), some are disfavoured proportionally to their GWP value. The result is a quick transition, in progress, towards refrigerants with lower GWP. The definitive solution will be the adoption of very low GWP or natural refrigerants.
Cooling of fresh products in small shops or restaurants and cold rooms is achieved, often, with single (split-type or self-contained) refrigerators. For this application, flammability of the refrigerant, even when limited (such as in A2L blends (ANSI/ASHRAE, 2016)), entails a risk, which needs to be handled. Low GWP A1 blends and CO_2 are not flammable and have large market acceptance even though, in the case of CO_2, a complete redesign of the system is needed with price increase for the customer.
Among recent studies on this topic, Domanski et al. (2017) explains the trade-off between flammability, low GWP, volumetric capacity and *COP* in R-404A replacements; Mota-Babiloni et al. (2015) discuss how commercial refrigeration units need modifications to improve system efficiency; Mota-Babiloni et al. (2017) show that the transition to new refrigerants favours CO_2 and new blends which must be tailored on the specific application, as discussed also in drop-in tests by Olson (2015) and Urbieta (2015) as part of the AHRI Low-GWP ARE program.

Considering cooling of fresh products in small shops/cold rooms, the purpose of this study is to evaluate Seasonal Energy Performance Ratio *SEPR* (European Parliament, 2009) of a two-stage, CO_2 condensing unit with an analysis of the main factors of influence and a comparison with a unit designed for the same application employing a low GWP A1 refrigerant, R-449A.

2. METHOD

The refrigerator tested is composed of an evaporator (not under evaluation) and a condensing unit that use R744 (CO_2) as a refrigerant. The piping diagram and measurement instruments layout are shown in Fig. 1. The condensing unit is equipped with a hermetic, inverter-driven, two stage rolling piston compressor, two fin-and-tube heat exchangers, a receiver (REC), high pressure valve (HPV) and flash gas valve (FGV). The compressor's speed can be varied between 30 and 60 RPS while fans speed is fixed. Both heat exchangers are cross counter flow and they are in series with regards to air flow. Air passes gascooler first and then intercooler (IC). It is possible to bypass the intercooler refrigerant side by closing ball valves V_1 and V_2 and opening ball valve BPV. However, BPV is closed while V_1 and V_2 are opened unless otherwise specified. FGV is an electronic back pressure valve that regulates its opening in order to maintain the set receiver pressure. HPV is an electronic back pressure valve that regulates its opening in order to maintain the optimal gascooler pressure depending on temperature and pressure measurement at gascooler outlet. During the tests shown in this work, the FGV is always forced to be fully open unless otherwise specified. The receiver and lines are insulated with 9 mm thick rubber except for discharge lines connecting the compressor with the intercooler and the gascooler. The EEV is the electronic expansion valve that regulates its opening in order to maintain the set superheat depending on temperature and pressure measured at evaporator (EV) outlet. The tests are carried out with dry calorimeter method used by Tammaro et al. (2018) and described in EN13771-2. The refrigerant side thermocouples are fixed to the copper pipes with insulating tape and insulated with rubber.

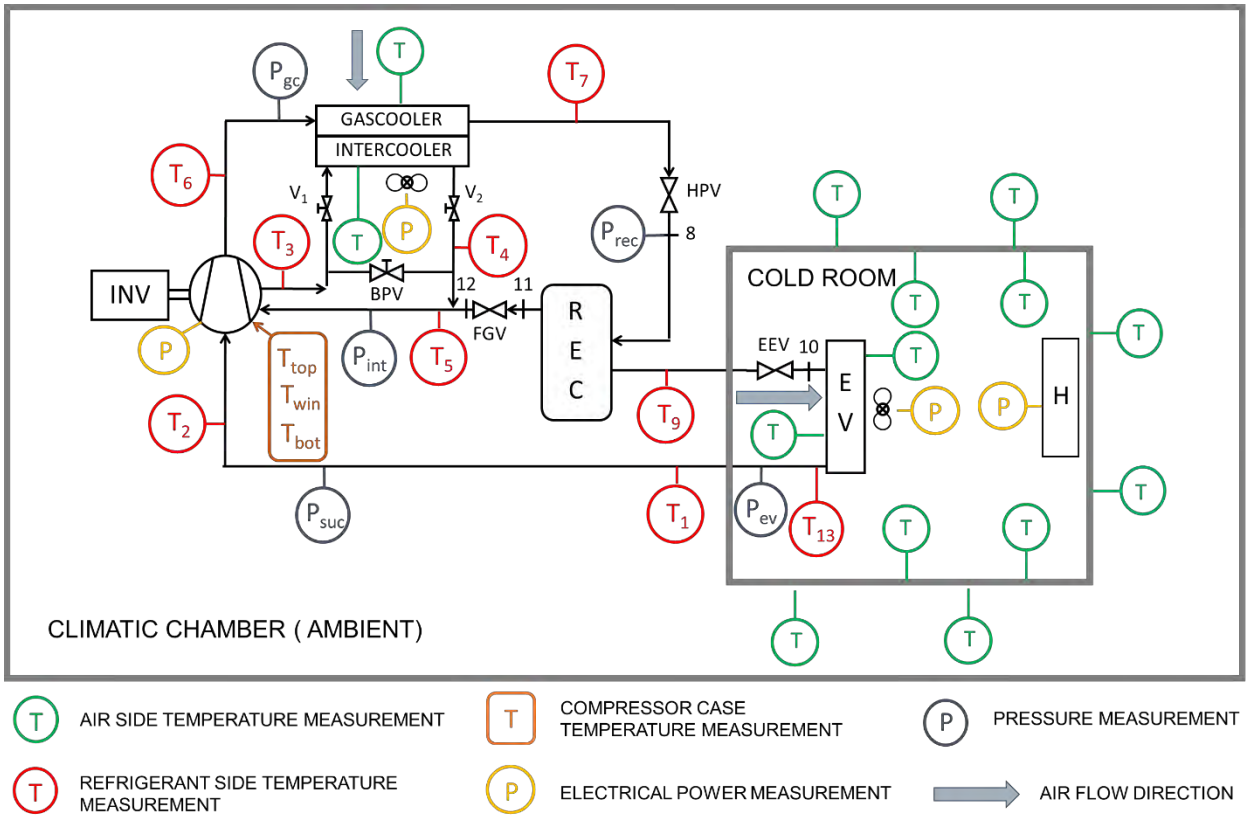

Figure 1: Piping diagram and instrument layout

The air side thermocouples are disposed at a 30mm distance from the surface of the heat exchanger (air inlet) or fan protective cover (air outlet). 6 thermocouples are located on the external and 4 on internal cold room surfaces in order to measure, respectively, T_{amb} and T_c as mean values. They measure air temperature at 10 mm distance from the cold room surface. 3 temperature measurements are made on top (T_{top}), middle and bottom (T_{bot}) of compressor case. The middle point is representative of the motor winding (T_{win}) temperature.
In each test, ambient temperature (T_{amb}), evaporating temperature (T_{ev}), position of BPV and compressor speed *n* are fixed. At the beginning of each test, the climatic chamber's HVAC system is turned on in order to reach the set T_{amb} and then the condensing unit is turned on at fixed compressor speed *n*. In a first phase the cold room temperature T_c is pulled down to reach a lower T_{ev} than the desired value. In a second phase a variable capacity heater (H) positioned inside the cold room is turned on. Its power is varied at 100 W steps until the steady state conditions are reached at the desired T_{amb} and T_{ev}. The steady state conditions are recorded for at least 30 minutes and during this phase the allowable fluctuations of ambient and cold room temperature stay within ±1°C and ±0.5°C, while the power absorbed by heaters varies within ±1%. After each test, the mean value of all measurements is calculated during the steady state period. The cooling capacity (Q_{ev}) of condensing unit balances, during the steady state period, the heat furnished by heaters (P_{heater}) and the heat exchanged between cold room at T_c and climatic chamber at T_{amb} as in Eq. (1).

$$Q_{ev} = P_{heater} + UA\,(T_{amb} - T_c) \qquad \text{Eq. (1)}$$

The heat leakage factor *UA* [W K^{-1}] is determined with a calibration test according to EN13771-2 prior to the tests shown in this work. *COP* is evaluated using Eq. (2).

$$COP = Q_{ev} P_{el}^{-1} \qquad \text{Eq. (2)}$$

Cooling capacity (Q_{ev}), electrical consumption of the unit (P_{el}) and *COP* are measured with a maximum uncertainty of 1.1% on *COP* (Moffat, 1988).
According to EN13215, Q_{ev} and *COP* must be measured in 4 different conditions (named A, B, C and D) and results must be corrected considering enthalpy (*h*) and density (ρ) with 10K superheat at the condensing unit inlet (point 1 in Fig. 1), in order to present performance data and evaluate the *SEPR*. $Q_{ev,cor}$ and COP_{cor} are calculated with the Eq. (3) and Eq. (4) respectively.

$$Q_{ev,cor} = Q_{ev}\rho_{1,cor}\left(h_{1,cor} - h_9\right)[\rho_1(h_1 - h_9)]^{-1} \qquad \text{Eq. (3)}$$

$$COP_{cor} = Q_{ev,cor} P_{el}^{-1} \qquad \text{Eq. (4)}$$

Once the tests at conditions A, B, C and D are carried out, the *SEPR* is evaluated with the Eq. (5) according to EN13215. $Q_{dm,MT}$ is the cooling demand [W]; the symbol *d* is the duration of each binned ambient temperature *j*, measured in hours. To each ambient temperature corresponds its *COP*, indicated by $COP_{cor,SEPR,j}$.

$$SEPR = \sum_{j=1}^{58}\left(Q_{dm,MT\ j} d_j\right)\left\{\sum_{j=1}^{58}\left[Q_{dm,MT\ j} d_j \left(COP_{cor,SEPR,j}\right)^{-1}\right]\right\}^{-1} \qquad \text{Eq. (5)}$$

3. RESULTS

12 tests are carried out with different ambient temperatures, evaporating temperatures, compressor speeds and intercooler usages in order to analyse the influence of each variation on

thermodynamic cycle and to evaluate the *SEPR*. In Table 1 all tests are listed and divided in different “analyses” for a simpler discussion.

3.1. Thermodynamic analysis

To compare the effect of ambient temperature on the unit performances, tests #1, 5, 8, 9, 10, 11 and 12 are considered; they are carried out at different evaporating temperatures (three at T_{ev}= -10°C and three at T_{ev} = -20°C) with n = 60Hz and IC = yes.
In Fig. 2 thermodynamic cycles of the considered tests are shown, with test numbers reported in the key.

Table 1. Test matrix

Analysis					#	T_{amb} [°C]	T_{ev} [°C]	n [Hz]	Intercooler
T_{ev}	T_{amb}			SEPR	1	32	-10	60	Active (Yes)
		Intercooler effect			2	25	-10	51	yes
					3	5	-10	36	yes
			n		4	15	-10	44	yes
T_{ev}	T_{amb}				5	15	-10	60	yes
					6	15	-10	30	yes
		Intercooler effect			7	25	-10	51	Bypassed (no)
T_{ev}					8	25	-10	60	yes
					9	25	-20	60	yes
	T_{amb}				10	5	-20	60	yes
T_{ev}					11	32	-20	60	yes
					12	15	-20	60	yes

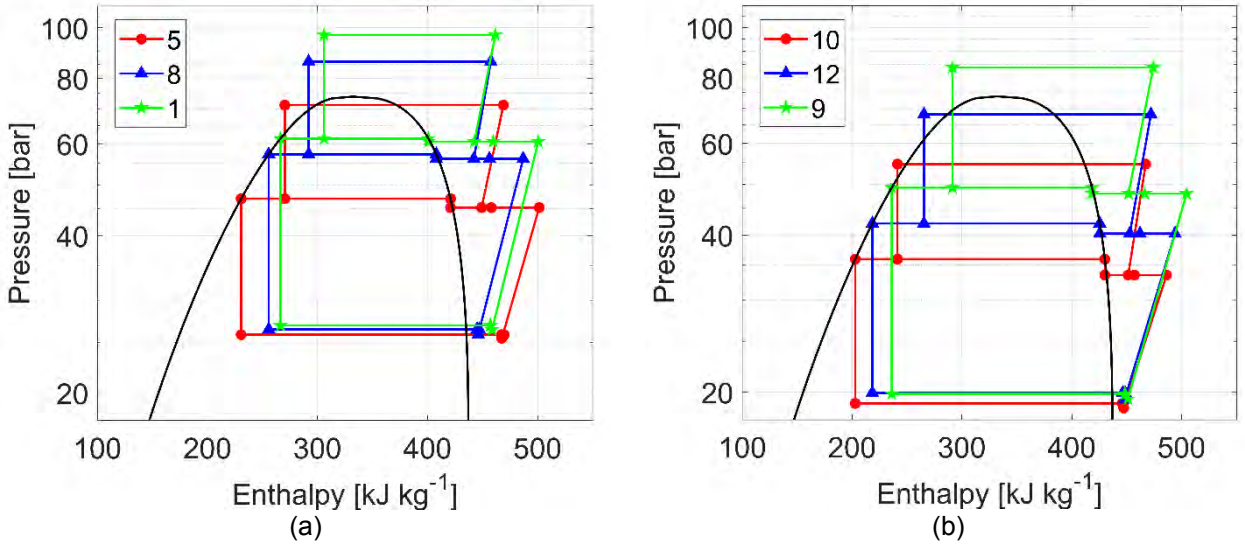

Figure 2: Thermodynamic cycle on p-h diagram of tests at different ambient temperature T_{amb}(a) T_{ev}= -10°C IC = yes n = 60Hz (b) T_{ev}= -20°C IC = yes and n = 60Hz

For T_{amb} below 15°C the thermodynamic cycle is subcritical while for T_{amb} equal to 25°C and 32°C it is transcritical; this is due to CO_2 critical temperature and pressure of 31°C and 73.77 bar respectively. At a fixed T_{ev} the evaporator inlet quality increases with the increase of T_{amb}, because of the higher pressure at the inlet of EEV. In transcritical tests the temperature difference between ambient and gas cooler refrigerant outlet (T_7-T_{amb}) ranges from 5 to 7.5K: lower values allow higher temperature of evaporation with advantages both on capacity and COP. Discharge temperatures of first and second compressor stage (T_3 and T_6) increase both with ambient temperature; this is due to higher pressure ratio. The desuperheating effect between the first stage discharge (point 3 on Fig. 1) and the second stage suction (point 5 on Fig. 1) is obtained with intercooler and flash gas injection (FGV) effects. In fact, the mass flow rate at compressor first stage discharge goes to intercooler where it is cooled by ambient air; afterwards, it mixes with colder vapour at receiver pressure p_{rec}, extracted from receiver through FGV. The difference between intermediate pressure p_{int} and p_{rec} is within 2 bar in all tests. Considering as a reference test 5, which is characterized by maximum cooling capacity ($Q_{ev,max}$) and *COP*, in Fig.3 dimensionless Q_{ev} and *COP* are shown for the same tests considered in Fig.2. The test number (see Table 1) is displayed at the top of each point. The highest cooling capacity and *COP* are found at the highest T_{ev} and lowest T_{amb}.

Cooling capacity at each T_{ev}, decreases of about 20% from the maximum value (test 5 to test 1 and test 12 to test 11) with ambient temperature increase; this is due to the higher vapour quality at evaporator inlet and lower compressor volumetric efficiency for higher pressure ratio. Test 10 to 12 is an exception, partly due to 1.4K lower evaporating temperature in test 10 compared to test 12 (Fig.2b).While cooling capacity does not show a linear behaviour, *COP* decreases with ambient temperature increase reaching, in test #1, 57% of the reference test's value at T_{ev}= -10°C, while from test 10 to test 11, *COP* decrease is about 50%. In Fig. 4 pressure vs enthalpy thermodynamic diagrams of tests 8 and 9 are shown to compare evaporating temperature effect on thermodynamic cycle.

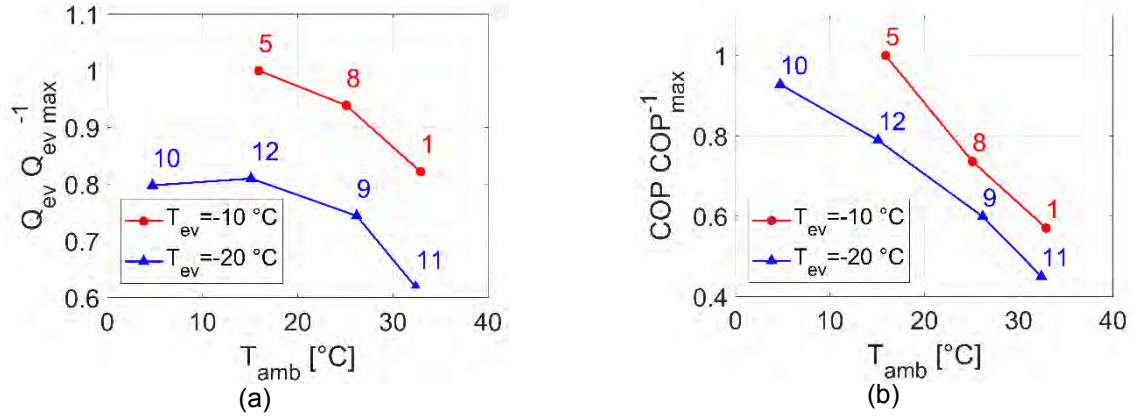

Figure 3: Dimensionless cooling capacity (a) and COP (b) vs T_{amb} with IC=yes and *n*=60Hz.

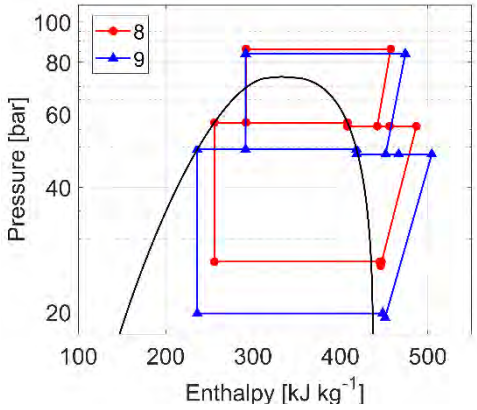

Figure 4: Thermodynamic cycle on p-h diagram of tests 8, 9 at different evaporating temperatures T_{ev} with T_{amb}=25°C, IC=yes and *n*=60Hz.

For lower T_{ev} the discharge temperatures from both compressor stages (T_3 and T_6) are higher, this is due to the higher pressure ratios and lower suction density at both compression stages. Receiver pressure p_{rec} is lower at T_{ev}= -20°C. This leads to a lower quality at the evaporator inlet and, at the same time, an increase of evaporator enthalpy variation; nevertheless, the decrease of evaporator mass flow rate caused by lower density at compressor inlet and lower volumetric efficiency leads to a lower cooling capacity in test 9.
Compressor speed effect can be analysed considering tests #4, 5 and 6; they are carried out at T_{amb}= 15°C, T_{ev}= -10°C, IC = yes. In Fig.5a a pressure vs enthalpy thermodynamic diagram of considered tests is shown.

During these tests, unit works in subcritical state. An increase of compressor speed leads to an increase of cooling capacity because of the increase of mass flow rate. In test 5, compressor suction temperature T_2 is higher than in tests 4 and 6, which leads to higher discharge temperature values T_3 also because of the higher pressure ratio. In subcritical tests, HPV regulates its opening in order to maintain the set subcooling (4K) at gascooler outlet; at the same time the heat exchanged in gascooler increases with the compressor speed which leads to a higher gascooler pressure.

In Fig. 5b dimensionless Q_{ev}, P_{el} and *COP* are shown versus dimensionless compressor speed$n\,n_{max}^{-1}$. *COP* decreases from maximum value COP_{max} at $n\,n_{max}^{-1}$= 0.5 to 90% of COP_{max} at $n\,n_{max}^{-1}$= 1, this means that the increase of P_{el} with speed is higher than Q_{ev} increase due to lower mechanical efficiency of the compressor. Compressor case temperatures increase with speed because of higher P_{el} and refrigerant temperatures at suction and discharge of both compressor stages. To analyse the effect of the intercooler presence on unit's performances, tests 2 and 7 are chosen; they are carried out at T_{amb}=25°C, T_{ev}=-10°C and n=51Hz. In test 7, the intercooler is excluded opening BPV and closing ball valves V_1 and V_2. Thermodynamic cycle of considered tests on pressure vs enthalpy diagram is shown in Fig.6.In test 7 the discharge temperatures from both compressor's stages are higher than that measured in test 2. In the first stage the higher value of discharge temperature T_3 is caused mainly by the higher value of p_{int} without intercooler; while second stage discharge temperature T_6 is higher due to the lower density at suction due to the absence of intercooler. This leads to higher compressor's case temperatures without intercooler.

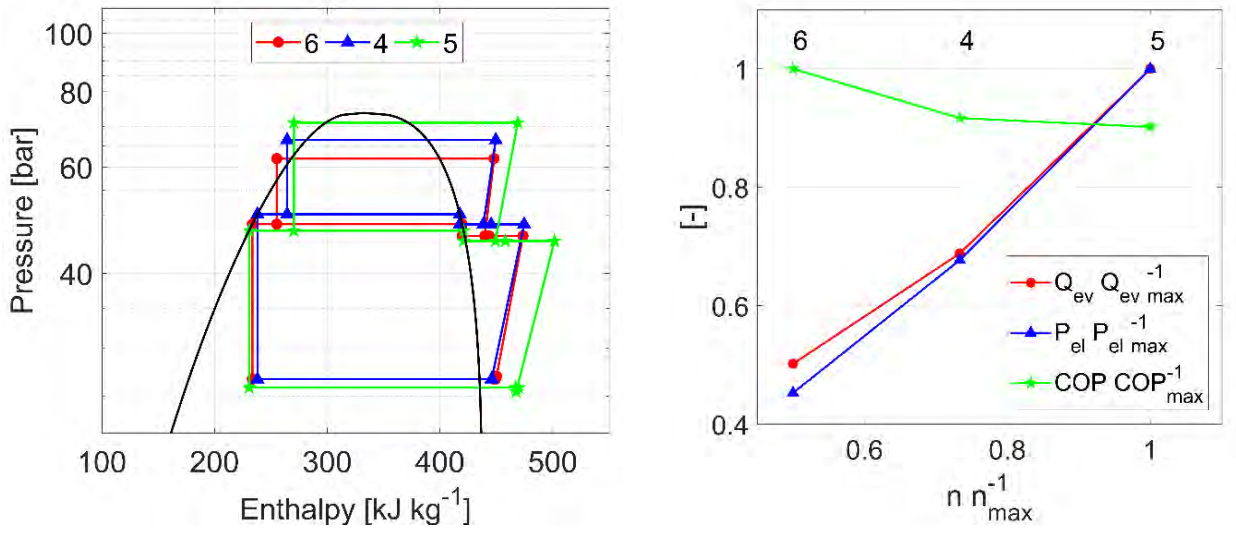

Figure 5: Thermodynamic cycle on p-h diagram (a) and dimensionless cooling capacity ($Q_{ev}\,Q_{ev\,max}^{-1}$), power input ($P_{el}P_{el\,max}^{-1}$) and COP vs $n\,n_{max}^{-1}$(b) of tests 4, 5 and 6at different compressor speeds n with T_{amb}= 15°C, T_{ev}= -10°C and IC = yes.

Receiver pressure (p_{rec}) in test 7 is higher than in test 2, this is caused by the absence of the intercooler volume which leads to accumulation of charge in the receiver; higher receiver pressure leads to a higher quality at evaporator inlet causing a decrease of evaporator enthalpy variation. This, coupled with a lower volumetric efficiency, caused by higher first stage pressure ratio in test 7, causes a reduction of cooling capacity of 9% with the same power consumption.

3.2. SEPR comparison

In this section the tests at rating point A, B, C and D according to EN13215 (1, 2, 3 and 4 from Table 1) of the CO_2 (GWP = 1) condensing unit, that will be called “unit 1”, are compared to the same tests carried out on a single stage condensing unit equipped with R449A (an HFC/HFO blend with GWP = 1397), following called “unit 2”. The main features of both units are listed in Table 2.

The *SEPR* is evaluated with Eq.(5) and it is similar for both units (less than 2% higher for the CO_2 unit which scores 3.07). This means that the CO_2 unit has same efficiency of the low GWP unit but with a more complex architecture.

4. CONCLUSIONS

In this work an experimental campaign of a two stage CO_2 condensing unit was presented. The unit was equipped with intercooler, a hermetic rolling piston compressor with inverter. Following the test method indicated in EN13771-2, 12 tests were carried out with different combinations of T_{ev}, T_{amb}, compressor speed and intercooler usages. First, it was found that the cooling capacity and COP decreased with ambient temperature increase, up to 20% and 57% respectively. Then, compressor speed influence was studied; *COP* decreased with compressor speed increase.

About intercooler influence, it was found that cooling capacity without intercooler was 9% lower than with intercooler. Finally, *SEPR* was evaluated according to EN13215 and compared to another unit designed for the same application that employs low-GWP refrigerant R-449A. The unit used for comparison had a single stage, fixed speed semi-hermetic reciprocating compressor. It was found that *SEPR* values were similar for both units, although this conclusion cannot be reduced to the different refrigerants employed. In fact, the CO_2 unit has a more complex and more expensive architecture than the other equipped with R-449A. On the other hand, the CO_2 unit has more longevity because, being a natural refrigerant with GWP = 1, it represents a refrigerant choice not subject to any restriction by current and foreseeable future legislation.

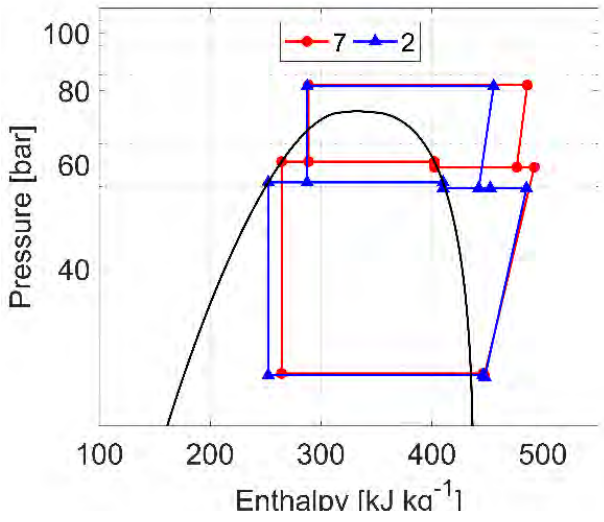

Figure 6: Thermodynamic cycle on p-h diagram of tests with T_{amb}=25°C, T_{ev}=-10°C and n=51Hz

Table 2. Characteristics of compared units

	Unit 1	Unit 2
Refrigerant	CO_2	R449A
Compressor type	Hermetic rolling piston double stage (20.8 and 14.6 cm^3)	Semi-hermetic reciprocating single stage (475 cm^3)
Capacity control	Stepless (with inverter)	Fixed (no inverter)
Intercooler	Yes	No

REFERENCES

ANSI/ASHRAE 34, 2016, “Designation and Safety Classification of Refrigerants”.

CEN (EUROPEAN COMMITTEE FOR STANDARDIZATION), 2016, EN13215:2016 Condensing units for refrigeration - Rating conditions, tolerances and presentation of manufacturer’s performance data

CEN (EUROPEAN COMMITTEE FOR STANDARDIZATION), 2017, EN13771-2:2017, Compressors and condensing units for refrigeration- Performance testing and test methods- Part 2: Condensing units

Domanski, P.A., Brignoli, R., Brown, J. S., Kazakov, A. F., McLinden, M. O., 2017. Low-GWP refrigerants for medium and hig-pressure applications. Int. J. of Refrigeration 84, 198–209.

European Parliament, 2009, EcoDesign Directive (2009/125/EC).

European Parliament, 2014, EU Regulation 517/2014 on fluorinated greenhouse gases.

Moffat, R.J., 1982. Describing the uncertainties in experimental results, Experimental Thermal Fluid Science 1, 3-17.

Mota-Babiloni, A., Navarro-Esbrì, J., Barragan-Cervera, A., Moles, F., Peris, B., Verdù, G., 2015. Commercial refrigeration – An overview of current status. Int. J. of Refrigeration 57, 186-196.

Mota-Babiloni, A., Makhnatch, P., Khodabandeh, R., 2017. Recent investigations in HFCs substitution with lower GWP synthetic alternatives: Focus on energetic performance and environmental impact. Int. J. of Refrigeration 82, 288-301.

Olson, W., 2015. System drop-in test of refrigerant blends ARM-20b and N-40c (R-448A) in automatic commercial ice maker designed for R-404A. Test Report #45 of AHRI Low-GWP AREP.

Tammaro, M., Mastrullo, R., Mauro, A.W., Sfragara, M., 2018. Experimental comparison of cooling capacity and EER in a positive temperature monoblock after replacement of R404A with R407H and soft-optimization of components, International Conference on Cryogenics and Refrigeration (ICCR), Shanghai.

UNEP, 2016. Multilateral Treaties Deposited with the Secretary-General, Chapter XXVII 2.f. Amendment to the Montreal Protocol on Substances that Deplete the Ozone Layer. Kigali, 15 October 2016

Urbieta, H., 2015. System drop-in tests of refrigerants N-40 and L-20 in a R-404A ice machine. Test Report #48 of AHRI Low-GWP AREP.

Manuscript ID: 1292
DOI: 10.18462/iir.icr.2019.1292

Long term viability of R-513A in a stationary refrigeration system

Jethro MEDINA[(a)], Joshua HUGHES[(b)], Ryan COOMBS[(c)]

[(a)] The Chemours Company, Fluoroproducts
Wilmington, DE, 19805 USA, jethro.medina@chemours.com
[(b)] The Chemours Company, Fluoroproducts
Wilmington, DE, 19805 USA, joshua.hughes@chemours.com
[(c)] The Chemours Company, Fluoroproducts
Wilmington, DE, 19805 USA, ryan.coombs@chemours.com

ABSTRACT

HFO-1234yf has been functioning as a low global warming potential (GWP) replacement for HFC-134a in refrigeration and air conditioning applications. Its viability has been proven as a pure fluid and in refrigerant blends. Once such blend is R-513A, an azeotropic blend of HFC-134a and HFO-1234yf. A long term, continuous study on a commercial stationary refrigerator was conducted with R-513A refrigerant. The original HFC-134a refrigerant was replaced with R-513A in a 2-door commercial reach-in refrigerator and operated continuously for over 6 years. Energy usage and system parameters were continuously measured and compared to the original baseline operation with R-134a. The refrigerant and lubricant samples were collected for chemical and physical analyses and the compressor was removed for visual and metrology analysis. This paper reports the results of the longest continuous known test to date for R-513A in a refrigeration system, which will be used to validate the long-term viability of HFO refrigerants and R-513A in stationary refrigeration applications.

Keywords: Chemical Analysis, Commercial Refrigerator, Compressor, Energy Consumption, Lubricant, Performance, Polyolester, R-1234yf, R-513A, Refrigerant, Stability

1. INTRODUCTION

The phase-out of CFC and HCFC refrigerants, such as R-12 and R-22, has been completed or in progress under the Montreal Protocol. The subsequent transition to HFC refrigerants, such as HFC-134a, has led to non-ozone depleting refrigerants. To satisfy new environmental regulations now requiring refrigerants with a lower Global Warming Potential (GWP), HFO refrigerants such as HFO-1234yf can offer comparable performance to the incumbent HFCs with reduced environmental impact. With a very low GWP value <1, R-1234yf and subsequent refrigerant blends offer large GWP reductions. One such commercial refrigerant, R-513A, is an HFO-1234yf / HFC-134a, nonflammable refrigerant blend. This refrigerant offers a 56% reduction in GWP from R-134a from 1300 to 573.
Recently, R-1234yf and R-513A have been successfully installed in numerous HVACR systems worldwide. To study the long-term performance and stability of R-513A in a system, a commercial R-134a stationary refrigerator was tested with R-134a, R-1234yf, and R-513A and evaluated for performance. Following this study, the refrigerator was continuously operated for 6 years using R-513A refrigerant. Energy usage and dry bulb temperature data was monitored during operation. The refrigerator was recently shut down, the refrigerant and oil were recovered for physical and chemical analyses, and the compressor was removed for wear analysis.

2. SYSTEM CONVERSION AND DECOMMISSIONING

2.1. System Conversion

A McCall refrigerator, Model #2-2045GD, was installed in the lab space of the Chemours Refrigerants Testing Center in Wilmington, DE. Lower GWP R-134a replacement refrigerants were tested to evaluate performance in the refrigerator including R-1234yf and R-513A. Physical and chemical properties of R-134a, R-1234yf, and R-513A are given below in Table 1.

Table 1: Physical and chemical properties for R-134a, R-1234yf, and R-513A

	R-134a	R-1234yf	R-513A
Name	1,1,1,2 Tetrafluoro ethane	2,3,3,3 Tetrafluoro prop-1-ene	R-1234yf / R-134a
Chemical Formula / Composition	CF3CFH2	CH2=CFCF3	56.0 / 44.0
Molecular Weight	102	114	108.4
Normal Boiling Point,°C	-26.1	-29.4	-29.2
Sat Vap Pres (kPa) @ 20 °C	571.7	591.7	616.8
Sat Vap Pres (kPa) @ 60 °C	1682	1642	1743
Critical Temperature, °C	101.1	94.7	96.5
GWP (AR5) CO2 = 1.0	1300	<1	573

Standard industry guidelines were followed in the system conversion from R-134a to all testing fluids. Refrigerant and oil was evacuated from the system, then charged with new refrigerant. System modifications were minimal, which included temperature, pressure, and energy consumption monitoring and an oil level sight glass on the compressor. Following completion of performance testing, the refrigerator operated continuously with R-513A refrigerant for 6 years. The refrigerator operated indoors with the surrounding room temperature subject to normal building indoor climate control.

2.2. System Decommissioning and Refrigerant, Lubricant, and Compressor Analysis

Upon shutting down of the test unit after 6 years of operation, refrigerant and oil were recovered. Samples of each fluid were evaluated by chemical analysis. Condition analysis of the compressor was performed by an external engineering service company with expertise in evaluating compressors of this type.

3. RESULTS AND DISCUSSION

3.1. System Performance

Thermodynamic cycle analyses were completed for R-134a and R-513A, the results are shown in Table 2. Cycle conditions for both fluids matched the operating conditions for R-134a. The following were used in cycle analyses: -2.6°C evaporator, 2.2K superheat, 43.3°C condenser, 2.9K subcooling, 70% compressor isentropic efficiency.

Table 2: Thermodynamic cycle analyses for R-134a and R-513A

	COP	COP to R-134a	CAP (kJ/m^3)	CAP to R-134a	P_{suct} (kPa)	P_{dis} (kPa)	T_{dis} (°C)	T_{glide} (°C)
R-134a	3.308	100%	1852	100%	267	1111	62	0
R-513A	3.213	97%	1878	101%	294	1164	56	0

At these operating conditions R-513A was modeled to have 3% lower COP and 1% greater volumetric capacity than R-134a. Both suction and discharge pressures for R-513A were slightly greater than those of R-134a. Being an azeotropic mixture of R-134a and R-1234yf, R-513A exhibits 0°C glide. Operating and performance data from the refrigerator is shown below in Table 3.

Table 3: Operating and performance of R-134a and R-513A

	EC (kWh/day)	EC to R-134a	Mass Flow (kg/s)	P_{suct} (kPa)	P_{dis} (kPa)	CR	T_{dis} (°C)
R-134a	13.57	100%	7.36E-03	234	1202	5.1	79
R-513A	14.03	103%	8.72E-03	260	1281	4.9	76

The information above was collected in a constant temperature room set to a 32.2°C dry bulb temperature. As in the thermodynamic cycle analysis, the suction and discharge pressures for R-513A were slightly greater than those of R-134a. The energy consumption was similar, with about 3% higher energy consumption for R-513A. Operating discharge temperatures were similar as well. R-513A offers a non-flammable, low GWP replacement to R-134a with similar operating parameters and performance.

Following refrigerant testing at 32.2 °C, the test unit was moved to an open lab space subject to building temperature control changes. The refrigerator was in continuous operation with R-513A for about 6 years between 2013 and 2019. Fig. 1 below shows daily energy consumption comparing periods in 2015 and 2018.

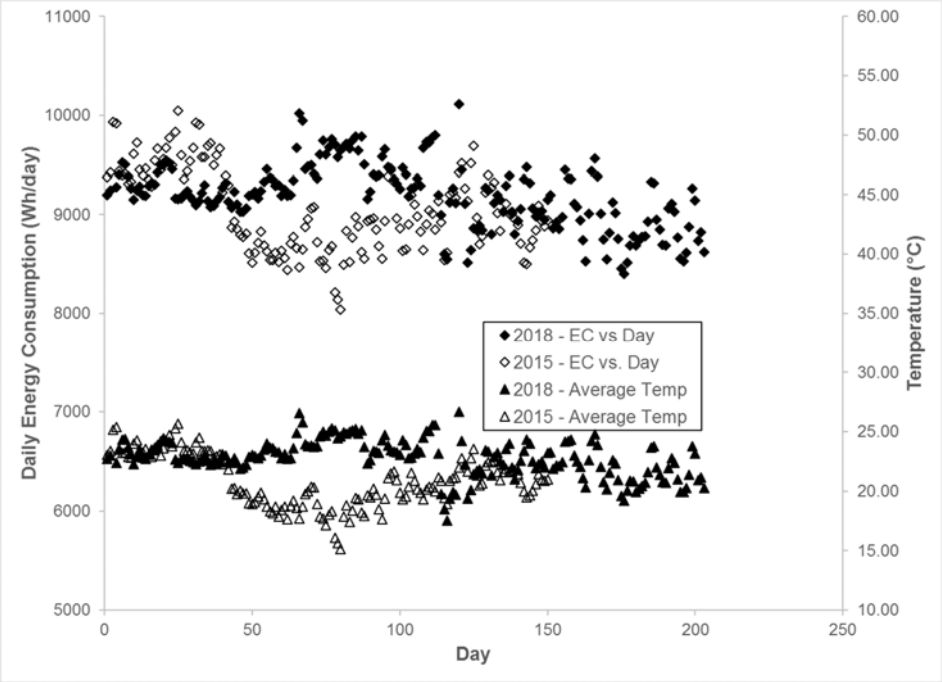

Figure 1: Daily energy consumption using R-513A, 2015 and 2018

In both 2015 and 2018, there was a correlation between daily energy consumption and dry bulb temperature of the space; as dry bulb temperature increased and decreased, energy use increased and decreased as well. Furthermore, energy use was similar between both of these sampling periods; average energy consumptions differing by less than 2%. Average dry bulb temperatures for 2015 and 2018 differed by about 1.8 °C. Continuous, long-term refrigerator operation with R-513A produced consistent performance.

3.2. Recovered Refrigerant and Lubricant Analysis

Following 6 years of operation, the refrigerant and lubricant were recovered. An impurity analysis of the recovered R-513A refrigerant is reported in Table 4. The analysis was performed on a gas chromatography/flame ionization detector/mass spectrometry (GC-FID/MS).

Table 4: Impurities of recovered R-513A by GC-FID/MS after 6 years

Impurity in Recovered XP10	ppm, wt
HFC-32 & HFC125	3
HFC-143a	58
HFC-134	583
HFC-152a	36
HFO-1225ye(Z)	4
HFC-161	7
HFO-1243zf	1
HCFC-22	131
HCFC-124	1
HCFC-31	2
Isobutane	2
Isobutene	3
Unknowns/Small Others	8
R-513A Purity	99.916%

R-513A purity composition was measured on a gas chromatography/thermal conductivity detector (GC/TCD), with results in Table 5 below.

Table 5: Composition of recovered R-513A by GC/TCD after 6 years

R-134a	R-1234yf
44.63%	55.37%

GC-FID/MS analysis (Table 4) showed overall purity of R-513A after 6 years of continuous running to still be quite high with less than 0.09% of total impurities observed. R-513A impurities are consistent with normally observed byproducts of HFO-1234yf and HFC-134a, indicating low decomposition occurring. Slight amounts of hydrocarbons were detected due to the presence of oil in the system. The refrigerator was utilized in testing programs with many refrigerant candidates prior to R-134a / R-1234yf. Such test refrigerants may not have been completely removed in the evacuation process, which could have contributed to other HFC and HCFC impurity levels that were measured.

A normalized breakdown of the R-513A composition by GC/TCD (Table 5) after recovery displayed very little component change, an indication of refrigerant stability. The ASHRAE Standard 34 composition tolerances for R-513A are 56.0% / 44.0% (±1.0% / ±1.0%), which were satisfied by the GC/TCD results.

Table 6 contains the analysis of R-513A and recovered polyol ester (POE) lubricant for acidity by acid titration, as well as fluoride and chloride levels by ion chromatography (IC). Virgin oil was also analyzed to compare with used lubricant.

Table 6: Recovered R-513A with oil and acidity concentration after 6 years

			Acidity	
	Anion, ppm [a]		HCL eq [b]	TAN [c]
Sample	F-	Cl-	ppm	mm KOH/g
Recovered R-513A	<MDL	1.08	0.51	
Virgin POE Oil	<MDL	<MDL		<MDL
Recovered oil from R-513A system	<MDL	3.43		0.11

[a] Anion MDLs: Fluoride, Chloride = 0.20 ppm, 0.30 ppm

[b] HCL eq MDL: 0.16 ppm (blank)

[c] TAN MDL: 0.08 mg KOH/g

The lubricant was observed to have a slight yellowish color as compared to the clear virgin POE although transparency was still high indicative of low turbidity (Fig. 2). Both refrigerant and recovered lubricant decompositions were minimal, displaying only low levels of chloride ions and very low

acidity consistent with standard operation of the compressor and other system components compared to controls.

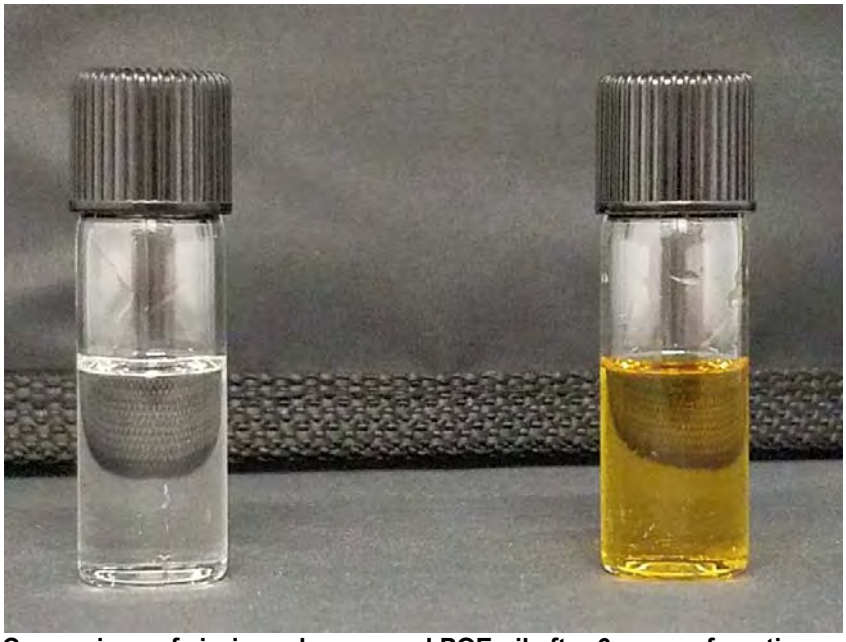

Figure 2: Comparison of virgin and recovered POE oil after 6 years of continuous running

To analyze compressor wear in the hermetic refrigeration system, the lubricant was submitted for trace metal analysis by inductively coupled plasma optical emission spectroscopy (ICP-OES). Results are presented in Table 7.

Table 7: Analysis of recovered POE oil using ICP-OES

ICP-OES Analysis for Trace Metals					
	Virgin POE Oil (ppm)	Recovered Oil (ppm)		Virgin POE Oil (ppm)	Recovered Oil (ppm)
Al	17.1	<1	Na	<1	<1
As	<1	<1	Nb	<1	<1
B	<1	<1	Ni	<1	<1
Ba	<1	<1	P	7.23	<1
Bi	<1	<1	Pb	<1	12.2
Ca	9.25	1.11	Sb	<1	<1
Cd	<1	<1	Si	<1	<1
Co	<1	<1	Sn	<1	<1
Cr	<1	<1	Sr	<1	<1
Cu	<1	1.69	Ta	<1	<1
Fe	1.32	1.11	Ti	<1	<1
K	<1	<1	V	<1	<1
Li	<1	<1	W	<1	<1
Mg	19.9	<1	Zn	<1	<1
Mn	<1	<1	Zr	<1	<1
Mo	<1	<1			

All values were low and consistent with standard operation of the compressor and other system components. Trace metal content from the lubricant used in the system for 6+ years was comparable to that found in virgin oil of similar type and gave no indication of significant compressor wear, metallurgic, or lubrication issues.

3.3. Compressor Tear Down Analysis

3.3.1. Overall engineering firm conclusion

"In NES engineer's opinion, using R-513A refrigerant for six+ years does not appear to have an adverse effect on all of the different materials used in the manufacture of the EMBRACO ASPERA compressor. In our opinion, the use of R-513A refrigerant has a similar effect on compressor wear when compared to compressors using R-134a refrigerant."

3.3.2. Tear down analysis – running conditions and procedural details

As mentioned prior, the refrigerator was operated in a controlled temperature environment for performance data collection. Running conditions for R-513A at the 32.2 °C dry bulb temperature are given below in Table 8.

Table 8: R-513A running conditions, 32.2°C DBT

Discharge Pressure, kPa	1093 - 1325
Discharge Temperature, °C	45.7 - 78.3
Suction Pressure, kPa	228.5 - 384.2
Suction Temperature, °C	9.4 - 46.1
Superheat, °C	14.7 - 42.9
Refrigerator Box Temp, °C	0.8-5.6

Operating conditions during the continuous 6-year run time were subject to normal indoor building temperatures. Data acquisition for the 6-year operation included energy consumption, compressor discharge temperature, and dry bulb temperature measurement. Temperature ranges were as follows: 15.1 – 26.7 °C dry bulb temperatures, 31.4 – 48.0 °C discharge temperatures.

Upon refrigerator decommissioning, the OEM compressor, Embraco Aspera model T6217Z, was removed and sent to an engineering firm for tear down analysis. The compressor was cut open and separated into components. Each component underwent microscopic analysis. Observations of each wear surface were completed from 0.5X to 50X magnification. Images of the crankcase and piston assembly are shown in Fig. 3.



Figure 3: Compressor crankcase bore - 10X (left), piston - 10X (middle), crankshaft - 2X (right)

3.4. Summary of Visual and Metrology Analysis

- The roundness and surface finish measurements performed on the used EMBRACO ASPERA Compressor, S/N T6217Z, found no significant wear issues. The compressor components appear in very good condition with light wear found on the plain bearings contact surfaces. No corrosion or surface degradation are observed on any of the compressor components.
- Compressor cast iron case had no notable corrosion or degradation. Gasket material in motor housing, along with wires and connectors, were in good condition.
- Crankcase, which houses the piston bore and piston, were in good condition with no significant degradation. Bore surfaces show no significant wear from lubricant.
- The connecting rod assembly showed light wear and minor scratches and a slightly aged, darker color on the copper portion. The aluminum portion of the plain bearing showed similar wear with no notable corrosion or degradation. Fine contamination particles, including some welding bead particles, caused slight scratching of the bushing material.

- Wrist pin showed minor scratches as well.
- Crankshaft had light rub and wear. No significant wear found on wrist pin and crankshaft.

4. CONCLUSIONS

R-513A has been shown to be a viable replacement for R-134a in refrigeration systems. Energy consumption was measured to be within 3% of R-134a, while offering a non-flammable alternative that achieves a 56% GWP reduction from 1300 for R-134a to 573. The 6-year study displayed sustained performance over long-term operation. Refrigerant and lubricant analysis showed no significant signs of refrigerant breakdown or contamination. Compressor wear analysis concluded no significant degradation or unusual wear.

With the continuing transition of HVACR systems to HFO refrigerants and blends, it is imperative to understand long-term operational effects on these systems. These refrigerants balance performance, environmental sustainability, and safety. R-513A is one example of how extended HFO blend use can reduce environmental impact while maintaining comparable performance in a long running system.

NOMENCLATURE

CAP	Volumetric cooling capacity; the amount of heat transferred respectively at the evaporator or condenser (including the compressed vapour superheat and liquid sub-cooling) per unit volume of the working fluid entering the compressor	*COP*	Coefficient of Performance for cooling; ratio of the heat absorbed at the evaporator or condenser (including the compressed vapor superheat and the liquid sub-cooling) and the work of the compression
CFC	Chlorofluorocarbon	*CR*	Compression ratio
DBT	Dry-Bulb Temperature (°C)	*EC*	Daily energy consumption (Wh/day)
GWP	Global Warming Potential	*HCFC*	Hydrochlorofluorocarbon
HFC	Hydrofluorocarbon	*MDL*	Minimum detection limit
P_{dis}	Compressor discharge pressure (kPa)	P_{suct}	Compressor suction pressure (kPa)
T_{dis}	Compressor discharge temperature (°C)		

REFERENCES

AHAM 2008. ANSI/AHAM HRF-1-2008: Energy and Internal Volume of Refrigerating Appliances. Washington D.C., Association of Home Appliance Manufacturers.

ASHRAE 2016. ANSI/ASHRAE Standard 34-2016: Designation and Safety Classification of Refrigerants. Atlanta, American Society of Hearting Refrigeration and Air Conditioning Engineers, Inc.

ANSI/AHRI 2013. ANSI/AHRI Standard 1200: Performance Rating of Commercial Refrigerated Display Merchandisers and Storage Cabinets. Air-Conditioning, Heating, & Refrigeration Institute (AHRI). Arlington, VA.

Allgood, C.C., et al., 2014. Long Term Viability of HFO-1234yf in Stationary Refrigeration Systems – Multi-Year Evaluation of Refrigerant, Lubricant, and Compressor Performance in a Domestic Freezer. 15th International Refrigeration and Air Conditioning Conference at Purdue University, West Lafayette, IN, 1-8.

Lemmon, E.W., Huber, M.L., McLinden, M.O., 2018. NIST Standard Reference Database 23: Reference Fluid Thermodynamic and Transport Properties-REFPROP, Version 10.0. National Institute of Standards and Technology, Standard Reference Data Program, Gaithersburg, MD.

Myhre, G. and Shindell, G. et al. Ed. 2013, IPCC, Climate Change 2013: The Physical Science Basis, the Fifth Assessment report Ch. 8 WG1 – Anthropogenic and Natural Radiative Forcing, IPCC.org. Cambridge University Press, Cambridge UK and New York, NY.

Manuscript ID: 1297
DOI: 10.18462/iir.icr.2019.1297

Experimental data during flow boiling of refrigerants R448A and R452A

Gianluca LILLO, Rita MASTRULLO, Alfonso William MAURO, Luca VISCITO

Department of Industrial Engineering, Federico II University of Naples
Naples, 80125, Italy, wmauro@unina.it

ABSTRACT

Refrigerators and heat pump systems represent a significant contribution to the global warming phenomenon, due to direct greenhouse gas emissions in case of leakages and plants dismantlement. For this reason, there is an increasing interest from the scientific community and the manufacturers towards low-GWP refrigerants. Among them, R448A and R452A are two attractive solutions for the next future as possible replacements of R404A. However, few data on two-phase heat transfer and pressure drop are currently available in open literature. This paper therefore presents flow boiling heat transfer and pressure drop experimental data of refrigerants R448A and R452A in a horizontal stainless-steel tube with an internal diameter of 6.0 mm. The effect of the operating parameters in terms of mass flux (from 150 to 600 kg $m^{-2}s^{-1}$), heat flux (from 10 to 40 kW m^{-2}) and saturation temperature (from 25 to 55 °C) are presented and discussed.

Keywords: Two-phase flow, heat transfer coefficient, R452A, R448A.

1. INTRODUCTION

The presence and stability of harmful substances such as volatile organic compounds, chlorofluorocarbons (CFCs), and hydro-chlorofluorocarbons (HCFCs) in the lower atmosphere has increasingly threatened the environment, as well as people's health and safety, over the last two centuries. This is mainly the result of the leakage of refrigerants, industrial and vehicular exhaust gases, and aerosols into the atmosphere. The role of the refrigerants is of primary importance. The recent European F-Gas Regulation (Regulation (EU) No 517/2014) has been issued with the aim to achieve a consistent reduction of the greenhouse gas emissions and to promote the utilization of eco-friendly refrigerants, imposing more and more stringent limits on the use of HFC refrigerants, attaining a limit in 2030 equal to 21% of the current equivalent CO_2 emissions. Apart from natural refrigerants as ammonia, carbon dioxide and hydrocarbons, the chemical industry proposes different alternative low-GWP fluids. In particular, new blends R452A and R448A are developed to be a drop-in substitute of R404A in air-cooled applications as well as for on-road applications. R452A is an HFC/HFO mixture (R32/R125/R1234yf, with 11%/59%/39% as weight composition), and is non-toxic and non-flammable, having the same classification (A1) as R404A, having a GWP equal to 2140 over a 100-year time span. R448A is composed of R32/R125/R134a/R1234yf/R1234ze(E) (26/26/20/21/7 in % mass), resulting non-flammable and GWP of 1205.

As suggested by Li (2017), R452A, is an alternative to R404A also in food-transport refrigeration systems. Due to its low GWP the use of R452A can reduce carbon emissions by between 5% and 15%. Thanks to its thermodynamic characteristic, experimental investigations and on-field studies have shown that vapor compression cycles using R452A for on-road and marine refrigeration units provide similar capacities and performances when compared to conventional systems employing R404A (Kujak et al., 2015). Furthermore, when used as drop-in of R404A, R452A is able to avoid a complete redesign of the compressor and other principal cycle components (Zgliczynski and Sedliak, 2015).

As shown by recent theorical and experimental studies, R448A can substitute usefully R404A in various kind of applications. Mota-Babiloni et al. (2014) theoretically analyzed six R404A

alternatives considering different configurations of vapor compression cycles obtaining higher system efficiency with R448A. Better efficiency with respect to R404A results also in the research of Yana Motta et al. (2014) in which R448A is the working fluid of 2.2 kW semi-hermetic condensing unit with evaporator for walk-in freezer/cooler. At the same capacity an increase in terms of system efficiency equal to 6% is obtained. Direct expansion systems using a scroll compressor centralized obtained lower energy consumption for R448A (from 3% to 8%) as shown by Rajendran (2013). Abdelaziz and Fricke (2014), in a test facility that uses reciprocating compressors and two separate temperature/humidity controlled rooms, found that refrigerant R448A average energy efficiency was 11.6% higher than that obtained with R404A.

With this scenario, flow boiling heat transfer of R452A and R448A can be very useful for a proper design of evaporators. However, to the authors' knowledge, experimental data on boiling of R452A in tubes are not available in scientific literature so far meanwhile just few experimental data for R448A are found (Mendoza-Miranda et al., 2015), (Kedzierski and Kang, 2016). The aim of the current paper is therefore to present new two-phase heat transfer coefficient data of mixtures R452A and R448A in a horizontal stainless-steel tube having an internal diameter of 6.0 mm. Tests have been carried out from the onset of boiling up to the dry-out condition, by analyzing the effect of the operating parameters in terms of mass flux (from 150 to 600 kg $m^{-2}s^{-1}$), heat flux (from 10 to 40 kW m^{-2}) and saturation temperature (from 25 to 55 °C).

2. EXPERIMENTAL FACILITY AND TEST SECTION

A schematic lay-out of the test facility for the flow boiling heat transfer experiments is shown in Fig. 1, in which the black lines represent the refrigerant loop while the blue ones the water-cooling loop. A photograph of the test rig is shown instead in Fig. 2.

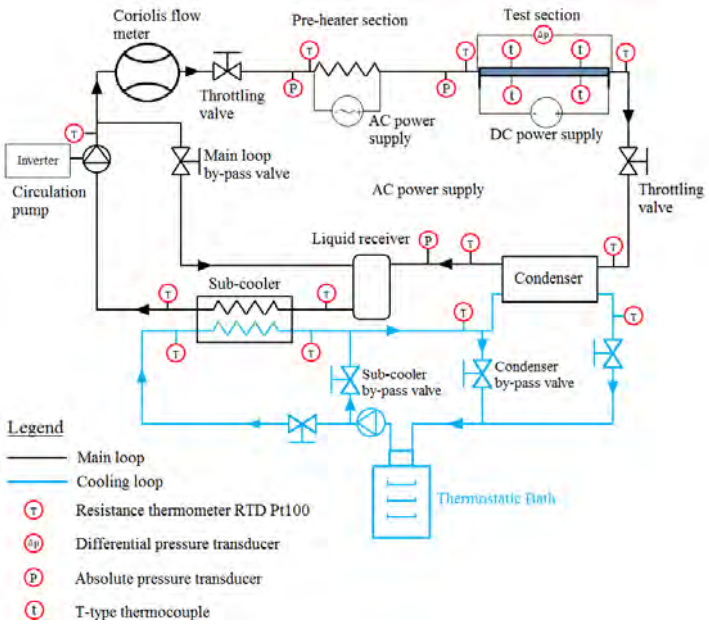

Figure 1: Schematic description of the experimental facility

The refrigerant in sub-cooled condition flows through a magnetic gear pump, which is able to provide volumetric flow rates within a range of 1.3-2.5 dm^3 min^{-1} by changing its rotating speed. A Coriolis flow meter measures the liquid mass flow rate before the preheater section, which is made up of a copper tube where the heat is provided by four fiberglass heating tapes (each one with a nominal heat power of 900 W at 25 °C and 240 V). A solid-state relay is used to modulate the applied heat at the preheater section in order to obtain a specific local vapor quality at the test section inlet

A 40 cm adiabatic horizontal stainless-steel tube before the test section is given to ensure the condition of fully developed flow before the test section inlet. The working fluid in saturated

conditions is condensed and sub-cooled in the following plate heat exchanger and tube-in-tube heat exchanger before the pump suction head that closes the loop. Two different throttling valves are positioned on the liquid and vapor lines, respectively, and a bypass circuit is provided at the pump outlet in order to have multiple mass flow rate control options. Demineralized water is used as cooling fluid, whose temperature is controlled by a thermostatic bath. Two dedicated bypass circuits are able to independently exclude from the water flow both the tube-in-tube and the plate heat exchangers.

2.1. Test section

All the flow boiling experiments have been conducted in a smooth, horizontal, circular stainless steel (AISI SS316) tube having an internal diameter of 6.00±0.05 mm and an external diameter of 8.00±0.05 mm. The heat flux is obtained through Joule effect provided by a DC power supply unit (within the range 0-8 V and 0-300 A) connected to the test section with two shorts copper wires clamped on copper electrodes welded on the tube surface at a distance of 193.7±0.79 mm representing the total measured heated length. At a distance of 237.5±0.91 mm, two pressure taps are provided for the measurement of the inlet absolute pressure and of the pressure drop across the test section. The local heat transfer coefficient is measured at a distance of 146.7 ±0.64 mm from the inlet section. In this point, four T-type thermocouples are glued on the tube external surface with a high-conductivity epoxy resin, whereas a Kapton thin adhesive layer guarantees the electrical insulation from the heated channel. The DC voltage for the evaluation of the imposed heat flux is measured between two points at a distance of 101.6 ±0.41 mm in order to avoid locally concentrated tension drops in the electrodes proximity. Different layers of synthetic foam (with a thermal conductivity of λ= 0.040 W $m^{-1}K^{-1}$) are used for the insulation of the test section and of the entire test facility, with the exception of the preheater section, which has been firstly covered with two layers of mineral wool (λ = 0.070 W $m^{-1}K^{-1}$) due to the higher temperatures reached during the experimental procedure. More details can be found in some authors' previous works (Lillo et al., 2018a, 2019a-b, Mastrullo et al., 2018).



Figure 2. Photograph of the test rig

2.2. Measurement instrumentation

In order to measure the working and cooling fluid temperatures, several RTDs are placed along the main and secondary loops, carrying an overall uncertainty of ±0.180 °C. Instead, four T-type thermocouples, calibrated in-situ with two resistance thermometers and a thermostatic bath, ensure the wall temperature measurements for the evaluation of the heat transfer coefficients. For these sensors, an overall uncertainty of ±0.1 °C is estimated. Also, the residual errors of the calibration curve are considered. An absolute pressure transducer having a measuring range of 0-35 bar and an overall uncertainty of ±0.5% of the read value is used to measure the absolute

pressure at the test section inlet. The pressure drop is instead estimated with a differential pressure transducer, calibrated in-situ with a water liquid column and a yardstick. The instrumental uncertainty is estimated to be ±0.06 kPa. A Coriolis flow meter, calibrated up to 2% of the full scale, gives the value of the mass flow rate, with a maximum uncertainty of ±1% of the measurement. A digital wattmeter provides the heat applied to the preheater section, by separately measuring the voltage (100 mV-500 V) and current (1 mA-16 A). Its uncertainty is ±1.0% of the reading, as provided by the manufacturer.

The heat flux applied to the test section requires the measurement of the DC voltage (electrical voltage transducer within 0-5 V and an uncertainty of ±0.03% of the reading) and the DC current (directly measured by the DC power unit within 0-300 A and an uncertainty of ±1.0%).

2.3. Experimental procedure

The operating parameters in terms of mass flux, saturation temperature and heat flux are fixed at the beginning of each experiment, which starts from the onset of boiling and proceeds with increasing vapor quality up to the occurrence of dry-out regulating the AC voltage applied to the fiberglass heating tapes of the preheater section. Once the dry-out heat transfer is established and wide wall temperature fluctuations occur, the high-quality experimental data are not guaranteed and the test is stopped. The saturation temperature of the system is controlled by a thermostatic bath. In this case, being the investigated refrigerants mixtures having a not negligible temperature glide, the test is carried-out keeping constant the saturation pressure. The corresponding bubble temperature is used as reference in the experimental results. The inverter frequency of the electrical motor coupled with the magnetic gear pump changes the mass flow rate. Further mass flow rate regulations can be obtained by using the bypass circuit and/or the throttling valves on the liquid and vapor lines. Finally, the heat flux is imposed by setting the desired voltage of the DC power supply unit. All the data are obtained in steady state conditions (with the exception of the dry-out points in which the phenomenon itself is time-dependent), with a recording frequency of 1.0 Hz. The nominal values of each sample are the arithmetic average of the measured quantities over a recording time of 90 s. The system is considered at steady state conditions when the calculated deviation of the mass velocity and saturation pressure are below ±2% within the acquisition time.

3. EXPERIMENTAL METHOD

3.1. Data reduction

The local heat transfer coefficient and the imposed heat flux are evaluated by using Eq. (1) and Eq. (2), respectively.

$$h = \frac{q}{T_{wall} - T_{sat}} \quad \text{Eq. (1)}$$

$$q = \frac{V_{BD} \cdot I}{\pi d \overline{BD}} \quad \text{Eq. (2)}$$

The subscripts *wall* and *sat* refer to the inner wall temperature and the saturation temperature, respectively. V_{BD} is the voltage applied in the section BD, I is the DC current flowing in the test tube and d is the channel internal diameter. The fluid saturation temperature at the measurement point is obtained by considering a linear pressure drop profile from the tube inlet. The wall temperature is instead evaluated from the measured wall outer temperature T_{th} by considering 1-D heat transfer and uniform generation in the metal tube having λ_{tube} (16.26 W m^{-1}K^{-1}) as thermal conductivity and D as external diameter by using the following Eq. (3).

$$T_{wall} = T_{th} + \frac{V_{BD} \cdot I}{4\pi\lambda_{tube} \overline{BD}} \cdot \left[\left(D/d \right)^2 \cdot \left(1 - \ln\left(\left(D/d \right)^2 \right) \right) - 1 \right] \cdot \left[\left(D/d \right)^2 - 1 \right]^{-1} \quad \text{Eq. (3)}$$

The local enthalpy, needed to evaluate the local vapour quality at the measurement point is computable by an energy balance applied to the test section, as reported in Eq. (4), where *G* is the refrigerant mass flux.

$$i = i_{in} + \frac{4 \cdot \overline{AC} \cdot q}{G \cdot d} \quad \text{Eq. (4)}$$

The value of the test section inlet enthalpy i_{in} is obtained from an energy balance applied to the preheater section, in which $i_{in,preh}$ is the preheater inlet enthalpy of the sub-cooled liquid, Q_{preh} is the preheater load and *m* is the measured refrigerant mass flow rate, as showed in Eq. (5).

$$i_{in} = i_{in,preh} + \frac{\dot{Q}_{preh}}{\dot{m}} \quad \text{Eq. (5)}$$

All refrigerant thermodynamic properties are evaluated with the software REFPROP (Lemmon et al., 2009) 9.0, whereas the whole data reduction is carried out with MATLAB software.

3.2. Uncertainty analysis and validation

The standard deviation evaluated in the recording time for all the measured parameters compose the instrumental B-type uncertainties. The uncertainty analysis of the derived results is then carried out by using the law of propagation of errors as reported in Moffat (1982) and Moffat (1985). To estimate the maximum uncertainties the dry-out occurrence is considered due to taking into account the higher fluctuations of the measured parameters. Lower uncertainty results during stable boiling. The maximum and the average recorded uncertainty for the main operating parameters and results are summarized in Table 1. In order to ensure the preheater and test section insulation as well as the correct behavior of the whole experimental apparatus, liquid single-phase experiments by using refrigerant R134a has been carried-out. Through two energy balances on the heated sections, the electrical power (from 220 to 1460 W in the preheater section and from 10 to 150 W in the test section) is compared to the heat absorbed by the sub-cooled refrigerant. In all tests, the wall and ambient temperatures reached similar values than those obtained during the flow boiling experiments. The liquid single-phase heat transfer coefficients for refrigerant R134a are also evaluated and compared to the well-known Dittus-Boelter prediction method (Dittus and Boelter, 1930). Further detailed information on the validation procedure and results can be obtained from previous works of the same authors with the same test facility (Lillo et al., 2018b, Mastrullo et al., 2017).

Table 1. Results of the uncertainty analysis

Parameter	Average uncertainty	Maximum uncertainty
Saturation temperature T_{sat}	±0.05°C	±0.17°C
Mass flux *G*	±1.1%	±2.1%
Heat flux *q*	±0.71%	±0.76%
Mean heat transfer coefficient h_{mean}	±4.7%	±20.8%

4. RESULTS

4.1. Effect of operating parameters

In this experimental campaign, R448A and R452A are employed as working fluids. Mass fluxes between 150 and 600 kg $m^{-2}s^{-1}$, heat fluxes from 10 to 40 kW m^{-2} and saturation temperatures between 25 to 55 °C have been investigated and the effect of their variation on the local heat transfer coefficients is discussed in the following diagrams. The heat transfer coefficients points presented in this section are intended to be averaged over the four measurement points (top, bottom, left and right sides of the tube). The parameters and their uncertainties for all the titles and legends in the following diagrams are averaged over all the corresponding represented data. Fig. 3 shows the effect of the mass flux on the heat transfer coefficient. Fig. 3a refers to refrigerant

R448A and Fig. 3b refers to R452A with an imposed heat flux of 10 kW m^{-2} and a saturation temperature of 25 °C. Regarding the R448A, the trends of the heat transfer coefficient seems to be convective for all the investigated mass fluxes with higher gradient at 601 $kgm^{-2}s^{-1}$ due to the high flow velocity. There is not difference at low values of the local vapor quality. The heat transfer coefficient reaches the maximum values for the same vapor quality (about 0.5), not dependent on the mass flux. However, increasing the mass flux from 152 to 601 $kgm^{-2}s^{-1}$ the heat transfer coefficient reaches a value of 10.11 kW $m^{-2}K^{-1}$ with a percentage increase equal to 95.9%. After the local vapor quality corresponding to the maximum value, the heat transfer coefficient decreases slightly due to a possible intermittent dry-out. When considering R452A (Figure 3b), the heat transfer coefficient has a convective trend with a lower slope with respect to R448A due to the higher value of the reduced pressure in case of R452A, resulting in a higher values of the ratio between the vapor density and the liquid density (0.054 for R452A and 0.042 for R448A at a saturation temperature of 25 °C). Differently from R448A, the dry-out occurs at high values of vapor quality (approximately 0.9) with an abrupt decrease of the heat transfer coefficient. This latter consideration is not valid for the experiment with mass flux of 149 kg $m^{-2}s^{-1}$ in which the heat transfer coefficient assumes low values, decreasing with the vapor quality due to a possible stratified flow. The effect of the imposed heat flux on the average heat transfer coefficients of R448A and R452A is shown in Fig. 4a-b, respectively. For each investigated mixture, the nucleative contribution assumes a greater weight with respect to the convective contribution passing from heat flux of 10 kW m^{-2} to 40 kW m^{-2}, with more evident difference at low values of the vapor quality: in case of R448A and at vapor quality of 0.2, the heat transfer coefficient increases from 4.9 kW $m^{-2}K^{-1}$ up to 9.4 kW $m^{-2}K^{-1}$. The convective contribution assumes relevant weight with the ongoing evaporation up to a vapor quality approximately equal to 0.8 when the heat transfer coefficient assumes the same values between 10 kW m^{-2} and 40 kW m^{-2}, when the dry-out occurs. The same consideration seems to be valid for both of fluids and for different values of saturation temperature and mass flux, as indicated in Fig. 4a-b.

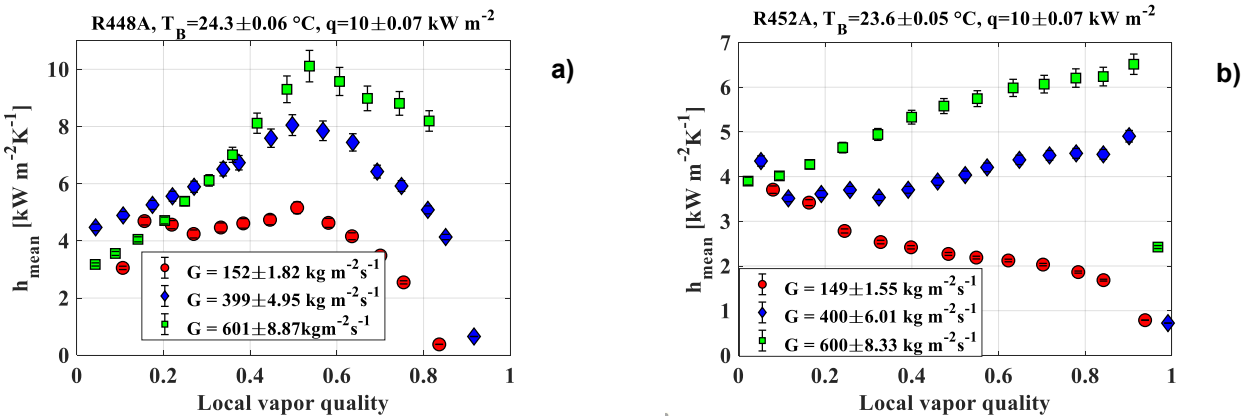

Figure 3: Effect of the mass flux on the mean heat transfer coefficient at different conditions. (a) R448A; (b) R452A

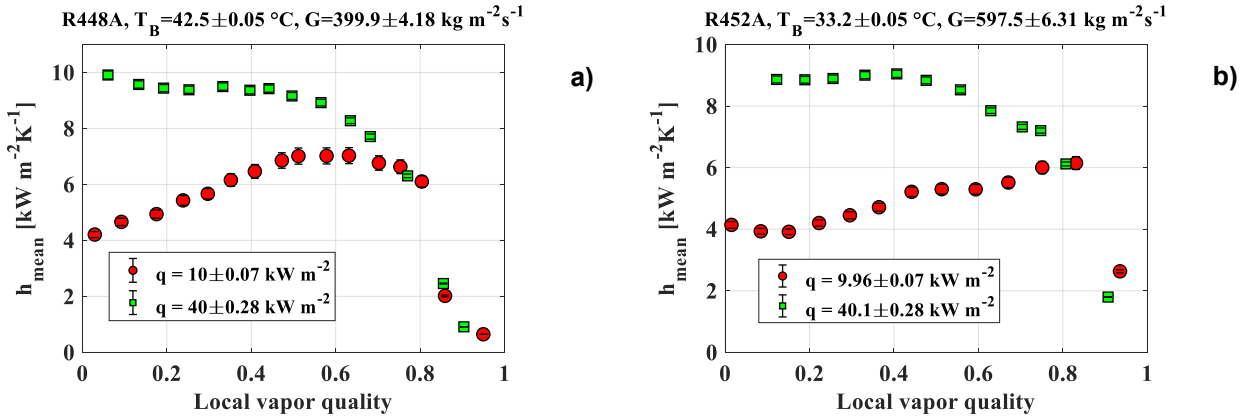

Figure 4: Effect of the heat flux on the mean heat transfer coefficient at different conditions. (a) R448A; (b) R452A

4.2. Comparison between R448A and R452A

The comparison between heat transfer coefficient experimental data of R448A and R452A are shown in Fig. 5a-b at different mass flux and saturation temperature for an imposed heat flux equal to 10 kW m^{-2}. Fig. 5a shows the comparison between the investigated fluids at mass flux and saturation temperature respectively equal to 150 kg $m^{-2}s^{-1}$ and 23.7°C. When considering R452A, the heat transfer coefficient decreases with the vapor quality whereas R448A is characterized by an increasing up to a vapor quality of 0.5 where the dry-out occurs. This significant difference in the heat transfer coefficient trend can be explained with a possible stratified flow for R448A due to lower value of the surface tension at the same saturation temperature (at 25°C, R448A and R452A have a surface tension of 0.0063 N m^{-1} and 0.0049 N m^{-1} respectively). In Fig. 5b, when high mass flux and high saturation temperature are considered, the convective contribution seems to be relevant for both of fluids, with higher slope of the R448A experimental data due to the lower reduced pressure with respect to the R452A one. Furthermore, at the saturation temperature of 43.5°C, the vapor density is 104.6 kg m^{-3} and 79.1 kg m^{-3} for R452A and R448A, respectively, resulting in high speed flow when considering R448A.

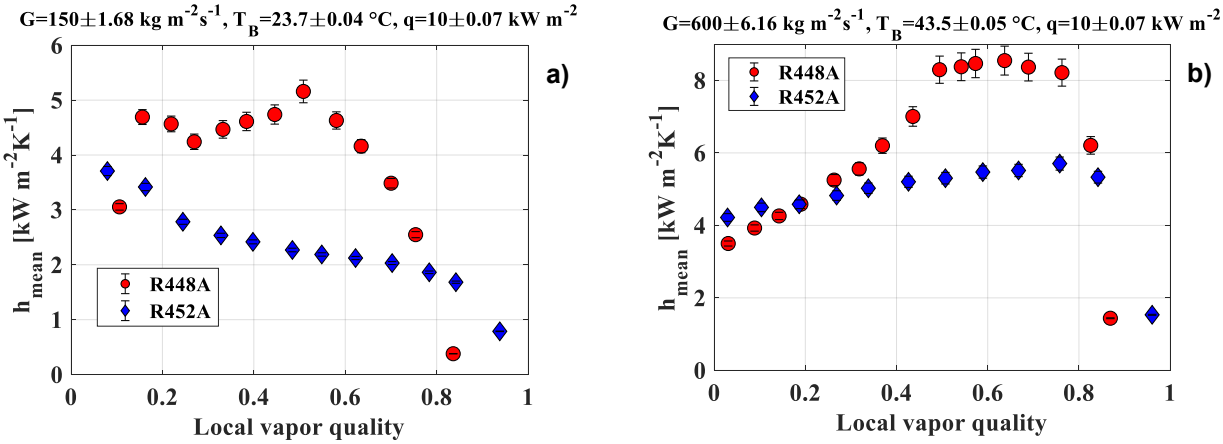

Figure 5: Effect of the fluid on the mean heat transfer coefficient at the conditions on the top of the figure.

5. CONCLUSION

New experimental data on local two-phase heat transfer coefficients for blends R448A and R452A at different operating conditions are obtained for a horizontal stainless-steel tube of 6.0 mm internal diameter. The effects of the heat flux (from 10 to 40 kW m^{-2}), mass flux (from 150 to 600 kg $m^{-2}s^{-1}$) and liquid saturation temperature (from 25 to 55 °C) on the heat transfer coefficient are investigated. The main conclusions may be summarized as follows:

- For both fluids, the mass flux increases the heat transfer coefficient at medium-high vapor qualities. Dry-out vapor quality does not seem to be affected by increasing mass flux and it assumes higher values for R452A.
- For both fluids, the heat flux increases the heat transfer coefficient at low-medium vapor qualities, and a slight reduction of the dry-out vapor quality is seen with increasing heat flux.
- Especially for higher vapor qualities, higher heat transfer coefficient values are observed for the refrigerant R448A, both for low and high mass fluxes.

ACKNOWLEDGEMENTS

Luca Viscito received a grant at Federico II University funded by “Ministero dell'Istruzione dell'Università e della Ricerca”, via the project PRIN2015 “Clean Heating and Cooling Technologies For An Energy Efficient Smart Grid”, which is gratefully acknowledged.

REFERENCES

Abdelaziz, O., Fricke, B., 2014. Working Fluids: Low Global Warming Potential Refrigerants. Building Technologies Office Peer Review - US Dept of Energy, Oak Ridge National Laboratory, Arlington, VA.

Dittus, F. W., Boelter, L.M.K., 1930. Heat Transfer in Automobile Radiators of the Tubular Type. Univ. Calif. Publ. Engin. 2, 443-461.

Kedzierski, M.A., Kang, D., 2016. Horizontal convective boiling of R448A, R449A, and R452B within a micro-fin tube. Science and technology for the built environment. 22, 1090-1103.

Kujak, S., Kolda, M., Berge, J., Majurin, J., 2015. Assessment of Next Generation Refrigerant R452A to Replace R404A for Transport Refrigeration Products. ASHRAE Transactions.121, 1YY.

Lemmon, E.W., Huber, M.L., McLinden, M.O., 2009. REFPROP, NIST Standard Reference Database 23, Version 9.0.

Li, G., 2017. Comprehensive investigation of transport refrigeration life cycle climate performance. Sustain. Energy Technol. Assess. 21, 33-49.

Lillo, G., Mastrullo, R., Mauro, A.W., Viscito, L., 2018. Flow boiling heat transfer, dry-out vapor quality and pressure drop of propane (R290): Experiments and assessment of predictive methods. Int. J. Heat Mass Tr. 126, 1236-1252.

Lillo, G., Mastrullo, R., Mauro, A.W., Viscito, L., 2018. Flow boiling data of R452A, Energy Procedia 148, 1034-1041.

Lillo, G., Mastrullo, R., Mauro, A.W., Viscito, L., 2019. Flow boiling of R1233zd(E) in a horizontal tube: Experiments, assessment and correlation for asymmetric annular flow. Int. J. Heat Mass Tr. 129, 547-561.

Lillo, G., Mastrullo, R., Mauro, A.W., Viscito, L., 2019. Flow boiling of R32 in a horizontal stainless steel tube with 6.00 mm ID. Experiments, assessment of correlations and comparison with refrigerant R410A. Int. J. Refrig. 97, 143-156.

Mastrullo, R., Mauro, A. W., Viscito, L., 2017. Flow boiling of R32 in a horizontal smooth tube of 6.0 mm internal diameter: heat transfer coefficient and pressure drop. J. Phys.: Conf. Series. 923, 12-15.

Mastrullo, R., Mauro, A.W., Revellin, R., Viscito, L., 2018. Flow boiling heat transfer and pressure drop of pure ethanol (99.8%) in a horizontal stainless steel tube at low reduced pressures. Appl Therm Eng. 145, 251-263

MATLAB Release, 2017. Natick, Massachussets, United States, The MathWorks, Inc

Mendoza-Miranda, J. M., Mota-Babiloni, A., Navarro-Esbrí, J., 2016. Evaluation of R448A and R450A as low-GWP alternatives for R404A and R134a using a micro-fin tube evaporator model. Appl. Therm. En. 98, 330-339.

Moffat, R. J., 1982. Trans. ASME: J. Fl. Eng. 104, 250-260.

Moffat, R. J., 1985. Trans. ASME: J. Fl. Eng. 107, 173-178.

Mota-Babiloni, A., Navarro-Esbri, J., Barragan, A., Moles, F., Peris, B., 2014. Theoretical comparison of low GWP alternatives for different refrigeration configurations taking R404A as baseline. Int. J. Refrig. 44, 81–90.

Regulation (EU) No 517/2014 of the European Parliament and the Council of 16 April 2014 fluorinated greenhouse gases and repealing Regulation (EC) No 842/2006. Off. J. Union. 2014.

Yana Motta, S.F., Spatz, M.W., Pottker, G., Smith, G.L., 2014. Refrigerants with Low Environmental Impact for Refrigeration Applications. International Refrigeration and Air Conditioning Conference, 1554.

Zgliczynski, M., Sedliak, J., 2015. F-Gases EU Regulation: R404A Replacement Refrigerants–Compressor Manufacturer Experience.

Manuscript ID: 1303
DOI: 10.18462/iir.icr.2019.1303

Experiments on condensation heat transfer and visualization of flow pattern with R1234ze(E) inside horizontal 4mm small-diameter microfin tubes

Masataka HIROSE[(a)], Daisuke JIGE[(b)], Norihiro INOUE[(c)]

[(a)] Graduate School of Marine Science and Technology, Tokyo University of Marine Science and Technology, Tokyo, 135-8533, Japan,
hirose-m@toba-cmt.ac.jp
[(b)] Tokyo University of Marine Science and Technology, Tokyo, 135-8533, Japan,
djige00@kaiyodai.ac.jp
[(c)] Tokyo University of Marine Science and Technology, Tokyo, 135-8533, Japan,
inoue@kaiyodai.ac.jp

ABSTRACT

In this study, we investigate the visualization of flow pattern of R1234ze(E) at the outlet of three types of horizontal microfin tubes, each with an outer diameter of 4 mm. The flow patterns observed during condensation were classified into three types, namely, annular, wavy, and slug flows. The annular flow was not observed at a mass velocity of 50 $kgm^{-2}s^{-1}$ in any of the test tubes. The difference of the transition line for annular-wavy flows was small for all the tubes, and the effect of fin geometry on flow pattern transition was small. Moreover, we propose a new correlation for the condensation heat transfer coefficient considering the effects of fin geometries and flow pattern on the condensation heat transfer. The proposed correlation agreed well with the measured heat transfer coefficient of R1234ze(E) within ±30%.
Keywords: Condensation Flow, Visualization, R1234ze(E), Heat Transfer Correlation.

1. INTRODUCTION

In the field of refrigeration and air-conditioning, microfin tubes with an outer diameter of 5 mm or less have been developed to increase energy savings by improving the performance of the heat exchanger and reduce the charge amount of the refrigerant by downsizing the heat exchanger. Microfin tubes with 4 mm outer diameter have been utilized in only some practical applications.
There are many existing studies on flow pattern visualization in horizontal smooth tubes. However, there are few studies on flow pattern visualization in microfin tubes. Nozu et al. (1996) investigated the condensation flow pattern of R11 inside microfin tubes of 8.4 and 8.8 mm maximum diameters at a saturation temperature of 40 °C and a mass velocity range of 95–460 $kgm^{-2}s^{-1}$. Cavallini et al. (2009) investigated the condensation flow pattern of R236ea, R134a, and R410A in a 7.7 mm fin-tip diameter microfin tube at a saturation temperature 40 °C and a mass velocity range of 100–800 $kgm^{-2}s^{-1}$. Cavallini et al. proposed the flow pattern map, which was classified as two types, namely, ΔT-independent regime associated to annular flow and ΔT-dependent flow associated to stratified-wavy flow. As a study targeting microfin tubes of smaller diameters, Jige et al. (2018) observed the adiabatic two-phase flow of R32 in a 3.6 mm maximum diameter microfin tube at a saturation temperature of 15 °C and a mass velocity range of 50–400 $kgm^{-2}s^{-1}$, and proposed a modified flow pattern map of Cavallini et al. (2009). However, studies on flow pattern visualization during condensation in small-diameter microfin tubes with an outer diameter of 4 mm or less are limited.
Therefore, in this study, we visualize the condensation flow pattern of R1234ze(E) inside three types of horizontal small-diameter microfin tubes of 3.6 mm maximum diameter and 4.0 mm outer diameter with different fin geometries. Furthermore, we propose a new heat transfer correlation considering the effects of fin geometries and flow pattern on the condensation heat transfer.

2. EXPERIMENTAL APPARATUS AND EXPERIMENT METHOD

Fig. 1 shows the schematic view of the experimental apparatus, which is a vapor compression heat pump system. The refrigerant loop comprises the following components: compressor, oil separator, pre-condenser, heat transfer test section, visualization section, rear condenser, receiver, mass flow meter, expansion valve, and evaporator. The refrigerant flow rate is measured using the Coriolis mass flow meter. The pre-condenser, test section, rear condenser, and evaporator consist of double-tube type heat exchangers. The bulk temperatures of the cooling water are measured by Pt-resistance thermometers inserted at the inlets and outlets of the pre-condenser and evaporator. The heat transfer test section was discussed in detail in a previous study (Inoue et al. 2018).
Fig. 2 shows the schematic view of the visualization section, which consists of a glass tube and microfin tube. To observe the flow pattern at the outlet of microfin tube, the test tube is cut at an angle of 45º. The flow pattern was observed from the horizontal direction using a digital camera and halogen light.
Table 1 summarizes the specifications of the three test microfin tubes, namely, LF50L, LF50S, and HF40, used in the experiment. These test microfin tubes are copper tubes each with outer diameter of 4.0 mm. Figure 3 shows the schematic view of a test microfin tube, which has a maximum diameter of 3.6 mm.
R1234ze(E) was used as the test refrigerant and its flow pattern was visualized at a mass velocity range of 50–400 $kgm^{-2}s^{-1}$ and saturation temperature of 35 °C.

3. DATA REDUCTION

In the visualization section, the vapor quality at the microfin tube outlet x_{out} is obtained by

$$x_{out} = \frac{h_{out} - h_L}{h_V - h_L} \qquad \text{Eq. (1)}$$

where h_V and h_L are the enthalpies of vapor and liquid in the saturation state and h_{out} is the enthalpy of the visualization point at the outlet of microfin test tube. h_V and h_L are determined using the measured refrigerant pressure. The enthalpy of the visualization point h_{out} is defined as follows:

$$h_{out} = h_{pre} - \frac{Q_{pre} + Q_{TS}}{m_r} \qquad \text{Eq. (2)}$$

where, h_{pre} is the enthalpy of superheated vapor refrigerant at the inlet of the pre-condenser and Q_{pre} and Q_{TS} are the heat transfer rates in the pre-condenser and test section, respectively. m_r is the flow rate of the refrigerant. h_{pre} is the enthalpy of the pre-condenser inlet determined using the refrigerant pressure and temperature at the pre-condenser inlet. The refrigerant properties were evaluated by REFPROP (Lemon et al., 2018). The heat transfer rates in the pre-condenser and test section, Q_{pre} and Q_{TS}, respectively, are determined using the flow rate of cooling water, isobaric specific heat of cooling water, temperature of cooling water at the inlets and outlets of pre-condenser and test section.

$$Q_{TS} = m_{WTS} c_{PW} \left(T_{WTSout} - T_{WTSin} \right) \qquad \text{Eq. (3)}$$

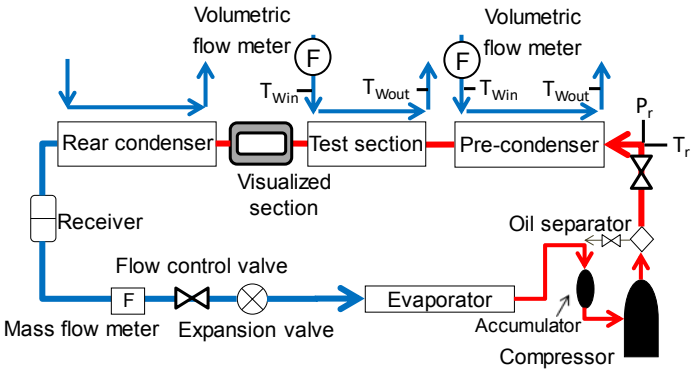

Figure 1: Schematic view of the experimental apparatus

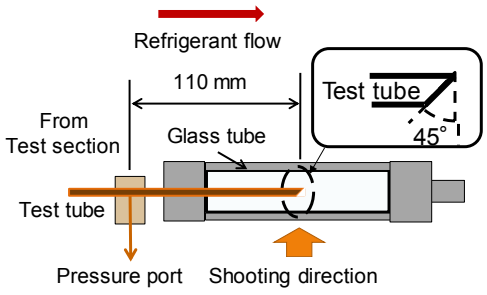

Figure 2 : Schematic view of the visualization section

Table 1: Specifications of the microfin tubes

Tube name	HF40	LF50S	LF50L
Outer diameter d_o [mm]	4.03	4.00	4.00
Equivalent ID d_{eq} [mm]	3.48	3.46	3.44
Wall thickness δ [mm]	0.21	0.22	0.22
Fin height h [mm]	0.18	0.13	0.15
Helix angle θ [deg.]	17	25	12
Number of fins n [-]	40	50	50
Area enlargement ratio η [-]	2.13	1.90	1.94

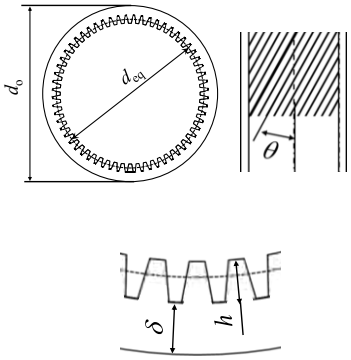

Figure 3: Schematic view of the microfin tube

$$Q_{\mathrm{Pr}e} = m_{\mathrm{WPre}} c_{P\mathrm{W}} \left(T_{\mathrm{WPreout}} - T_{\mathrm{WPrein}} \right) \quad \text{Eq. (4)}$$

The reliability of the experimental apparatus confirmed that the heat balance agrees within 10% between the refrigerant and cooling water sides. The accuracy of the calculation of quality is within ±0.05.

4. RESULTS AND DISCUSSION

4.1. Visualization of Flow Pattern with R1234ze(E)

Fig. 4 shows the visualization results of flow pattern at the outlet of the microfin tube (HF40). The flow pattern was classified into annular, wavy and slug flows. Figs. 4(a), (b) and (c) illustrate the observed flow patterns of the annular flow. The annular flow was observed at low wetness and high mass velocity conditions. In the annular flow, the liquid thickness became uniform around the circumferential direction and a vapor phase flowed in the center of the tube. The vapor and liquid phases flow continuously, whereas there is turbulence at the gas-liquid interface. The annular liquid film swirled along the direction of the grooves. As condensation progressed, the wetness increased, and the flow pattern transited from annular flow to wavy flow at mass velocities of 100 $\mathrm{kgm^{-2}s^{-1}}$ or higher. The wavy flow, wherein the vapor and liquid flow separately due to gravity, was observed at middle to high wetness regions, as shown in Figure 4(d). As the liquid flow rate increased, the wetness increased, and the liquid film at the bottom of the tube became thicker. The condensate liquid film was observed at the top of the tube. Figure 4(e) shows the wavy-slug flow. This flow pattern was observed the transition for wavy to slug flow. Slug flow was observed in the lower mass velocity and high wetness regions and was characterized by an intermittent flow pattern, wherein a bubble-shaped vapor plug and liquid slug filled the channel flowing alternately, as shown in Figure 4 (f).
Figs. 5(a), (b), and (c) show the classified flow pattern map of HF40, LF50S, and LF50L, respectively, for different mass velocities and wetness. The annular flow was not observed at a mass velocity of 50 $\mathrm{kgm^{-2}s^{-1}}$ in any of the test tubes. The wavy flow cannot be observed at the highest mass velocity region in HF40. However, the difference of fin geometry has a small effect on the flow pattern transition line for annular-wavy flows.

4.2. Comparison of Visualization Results and Previous Flow Pattern Map

Fig. 6 shows that the comparison between the visualization results and flow pattern map proposed by Cavallini et al. (2009) and Jige et al. (2018). The vertical axis represents the dimensionless vapor velocity J_V and the horizontal axis represents the Lockhart-Martinelli parameter X_{tt}. The dimensionless vapor velocity J_V is defined as:

$$J_{\mathrm{V}} = xG \Big/ \sqrt{gd\rho_{\mathrm{V}}(\rho_{\mathrm{L}} - \rho_{\mathrm{V}})} \quad \text{Eq. (5)}$$

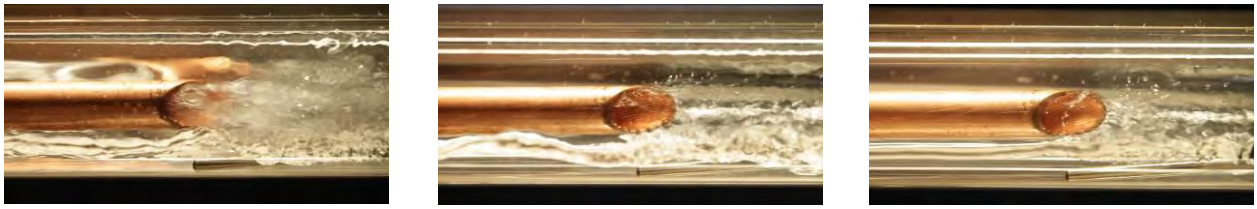

(a)G=400 kgm^{-2}s^{-1} 1-x = 0.60 Annular flow

(b)G=200 kgm^{-2}s^{-1} 1-x = 0.15 Annular flow

(c)G=100 kgm^{-2}s^{-1} 1-x = 0.14 Annular flow

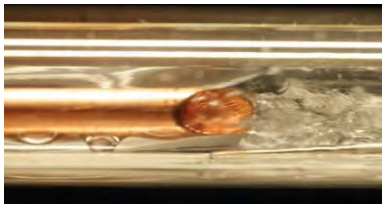

(d)G=200 kgm^{-2}s^{-1} 1-x = 0.73 Wavy flow

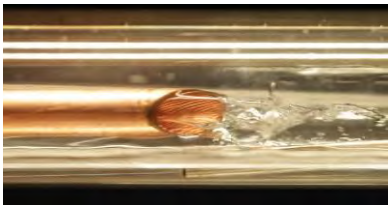

(e)G=100 kgm^{-2}s^{-1} 1-x = 0.70 Wavy-slug flow

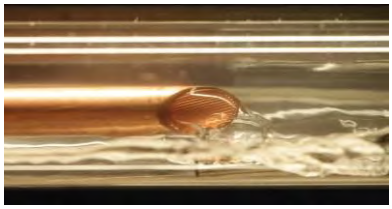

(f)G=50 kgm^{-2}s^{-1} 1-x = 0.73 Slug flow

Figure 4 : Typical flow pattern of R1234ze(E) at the outlet of HF40

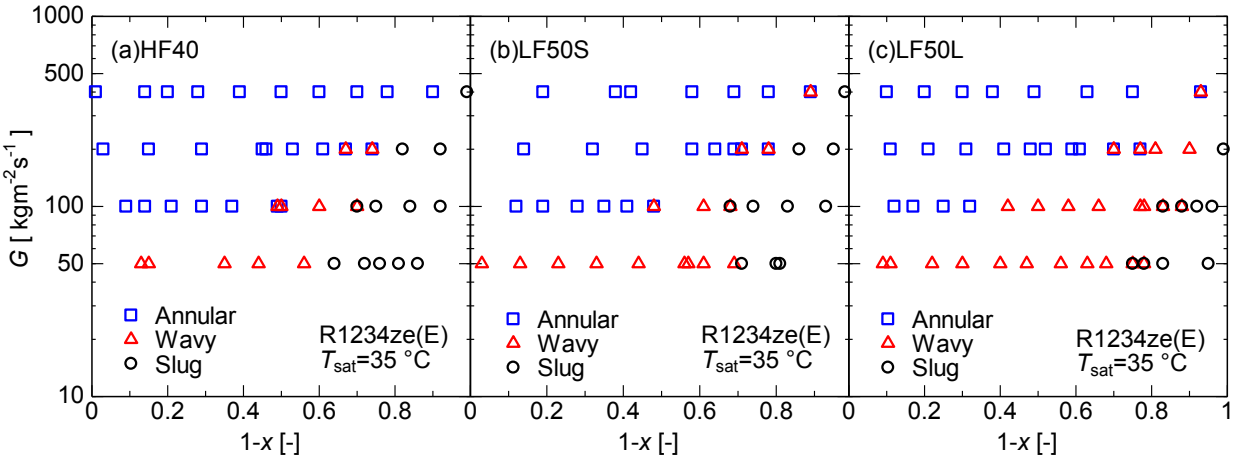

Figure 5 : Flow pattern map of R1234ze(E) for microfin tubes

The Lockhart-Martinelli parameter X_{tt} is defined as:

$$X_{tt} = \{(1-x)/x\}^{0.9} (\rho_V/\rho_L)^{0.5} (\mu_L/\mu_V)^{0.1} \quad \text{Eq. (6)}$$

The Cavallini et al. (2009) transition line for annular to wavy-slug is defined as:

$$J_V^* = 0.6\left[\left\{7.5/\left(4.3X_{tt}^{1.111}+1\right)\right\}^{-3} + 2.6^{-3}\right]^{-1/3} \quad \text{Eq. (7)}$$

The Jige et al. (2018) transition line for annular to wavy-slug is defined as:

$$J_V^* = 0.6\left[\left\{30/\left(4.3X_{tt}^{1.111}+1\right)\right\}^{-3} + 2.6^{-3}\right]^{-1/3} \quad \text{Eq. (8)}$$

Although, the flow pattern map of Jige et al. was proposed based on the observation results of R32 in a 4 mm outer diameter microfin tube at a saturation temperature of 15 ºC under adiabatic condition, the transition line from annular flow to wavy-slug flow for each test tube can be estimated.

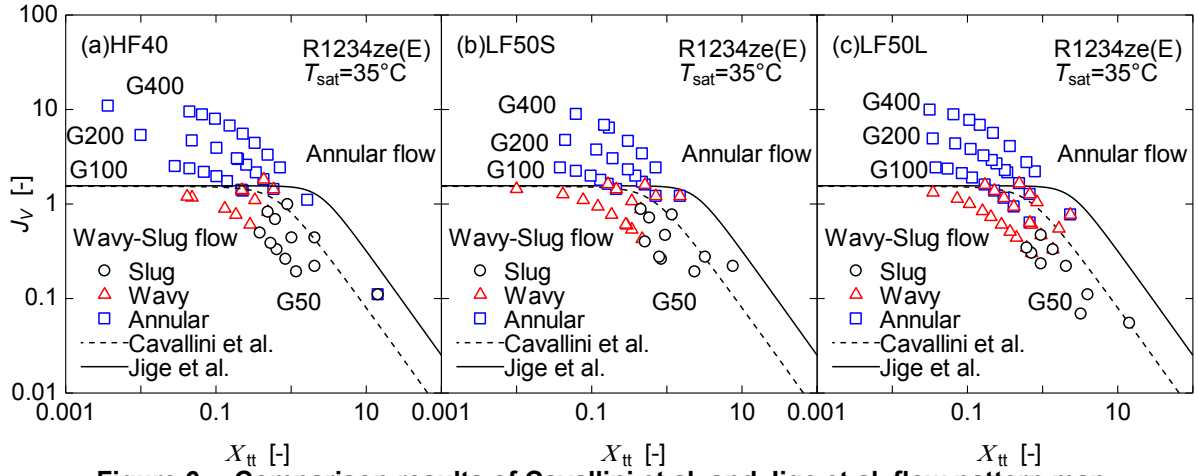

Figure 6 : Comparison results of Cavallini et al. and Jige et al. flow pattern map

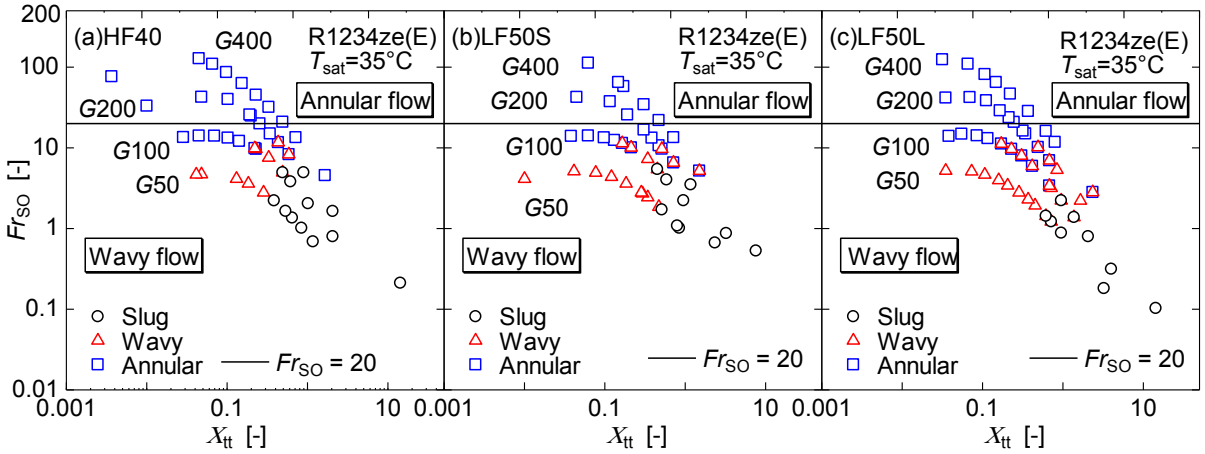

Figure 7 : Relation between Froude number Fr_{SO} and Lockhart-Martinelli parameter X_{tt}

4.3. New Heat Transfer Correlation based on Flow Observation Results

Hirose et al. (2018) proposed the heat transfer coefficient correlation, which consists of forced and free convections for annular and wavy flows. The flow pattern was classified used Soliman's modified Froude number for smooth tubes. The Soliman's modified Froude number Fr_{SO} is defined as:

$$Fr_{so} = 0.025 Re_L^{1.59} \left\{ \left(1 + 1.09 X_{tt}^{0.039}\right) / X_{tt} \right\}^{1.5} / Ga^{0.5} \quad \text{For } (Re_L \le 1250) \qquad \text{Eq. (9)}$$

$$Fr_{so} = 1.26 Re_L^{1.04} \left\{ \left(1 + 1.09 X_{tt}^{0.039}\right) / X_{tt} \right\}^{1.5} / Ga^{0.5} \quad \text{For } (Re_L > 1250) \qquad \text{Eq. (10)}$$

Figure 7 shows the relation between Soliman's modified Froude number Fr_{SO} and Lockhart-Martinelli parameter X_{tt}. The flow pattern was classified at Fr_{SO} = 20 (Hirose et al., 2018). The observed transition lines of flow pattern in the test microfin tubes were different from that of the smooth tubes. Therefore, we tried to improve the condensation heat transfer correlation proposed by Hirose et al. (2018) to predict the heat transfer coefficient of R1234ze(E) reported by Inoue et al. (2018). Nusselt number is determined using the measured heat transfer coefficients α.

$$Nu = \frac{\alpha d_{max}}{\lambda_L} \qquad \text{Eq. (11)}$$

where, d_{max} is maximum diameter, λ_L is thermal conductivity. Figure 8 shows the classified heat transfer coefficient for annular and wavy-slug flows using the transition line proposed by Jige et al.

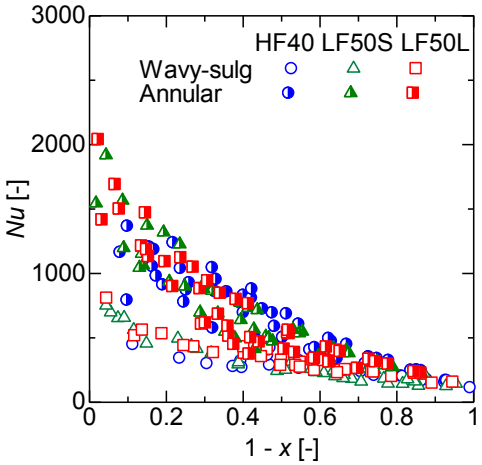

Figure 8 : Classified Nusselt number for annular and wavy-slug flows

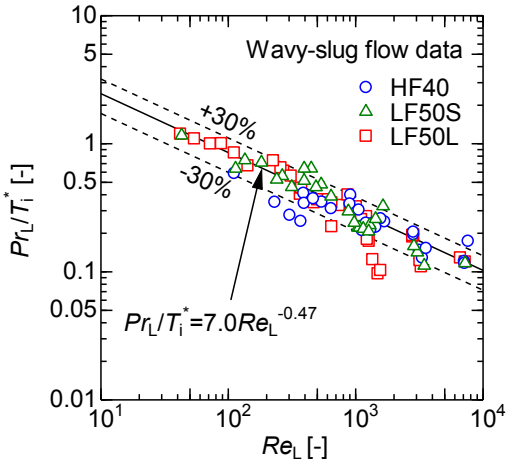

Figure 9 : Relation between Re_L and (Pr/Ti^*) at wavy-slug flow

(2018). It can be confirmed that the heat transfer characteristics were different between annular and wavy-slug flows. Nusselt number can be defined as:

$$Nu = \sqrt{Nu_F^2 + Nu_B^2} \qquad \text{Eq. (12)}$$

where Nu_F and Nu_B are forced and free convection Nusselt numbers. The forced convection Nusselt number is defined as:

$$Nu_F = \sqrt{0.5 f_V}\, Re_L \Phi_V \left(\rho_L / \rho_V\right)^{0.5} \left\{x/(1-x)\right\}\left(Pr_L / T_i^*\right) \qquad \text{Eq. (13)}$$

where f_V and Φ_V are the friction factor and two-phase pressure drop multiplier. The f_V and Φ_V are determined by the following equation from Hirose et al. (2018).

$$f_V = 0.26 Re_V^{-0.38} \eta^{0.95} \left(\cos\theta\right)^{-2.8} \qquad \text{Eq. (14)}$$

$$\Phi_V = 1 + 1.55 X_{tt}^{0.4} \qquad \text{Eq. (15)}$$

The dimensionless temperature difference (Pr_L/T_i^*) is defined as:

$$\left(Pr_L / T_i^*\right) = \frac{\left(Nu^2 - Nu_B{}^2\right)^{0.5}}{\sqrt{0.5 f_V}\, Re_L \Phi_V \left(\rho_L / \rho_V\right)^{0.5} \left\{x/(1-x)\right\}} \qquad \text{Eq. (16)}$$

The free convection Nusselt number Nu_B was obtained by Hirose et al. correlation (2018):

$$Nu_B = 1.60 \eta^{-0.25} Bo^{-0.20} H(\xi) \left(GaPr_L / Ph_L\right)^{0.25} \qquad \text{Eq. (17)}$$

$$H(\xi) = \xi + \left\{10(1-\xi)^{0.1} - 8\right\}\sqrt{\xi}(1-\xi) \qquad \text{Eq. (18)}$$

The void fraction is calculated by the correlation of Smith (1969).

$$\xi = \left[1 + \left(\rho_V/\rho_L\right)\left(\frac{1-x}{x}\right)\left(0.4 + 0.6\sqrt{\frac{\left(\rho_L/\rho_V\right) + 0.4(1-x)/x}{1 + 0.4(1-x)/x}}\right)\right]^{-1} \qquad \text{Eq. (19)}$$

4.3.1. The heat transfer correlation for wavy-slug flow

In the wavy-slug flow region ($J_V/J_V^*<1$), figure 9 shows that the relation between (Pr/Ti^*) and Re_L. The following correlation was obtained within $\pm 30\%$.

$$\left(Pr_L / T_i^*\right) = 7.0 Re_L^{-0.47} \qquad \text{Eq. (20)}$$

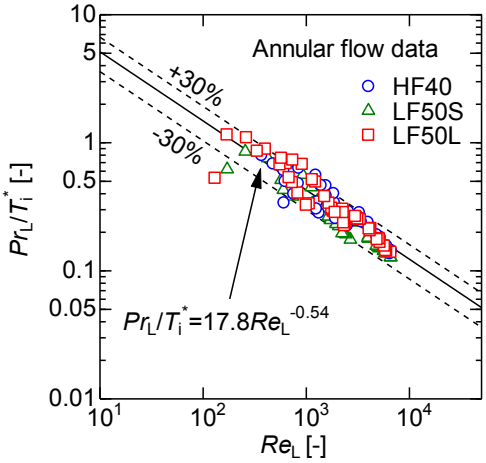

Figure 10 : Relation between Re_L and (Pr/Ti^*) at annular flow

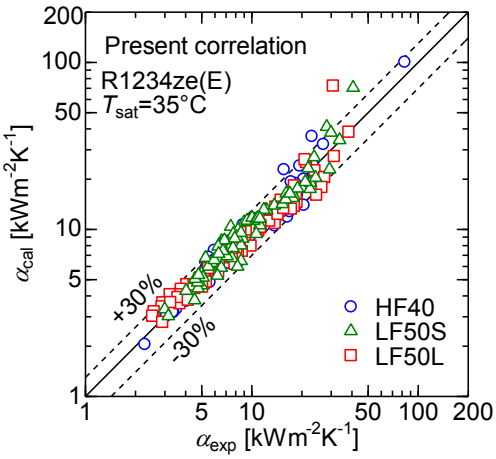

Figure 11 : Comparison result of experimental value and calculation value

Therefore, the new correlation of forced convection Nusselt number Nu_F is defined by the following equation.

$$Nu_F = 4.96\sqrt{f_V}\Phi_V\left(\rho_L/\rho_V\right)^{0.5}\left\{x/(1-x)\right\}Re_L^{0.53} \qquad \text{Eq. (21)}$$

4.3.2. The heat transfer coefficient correlation for annular flow

In the annular flow region, figure 10 shows the relation between (Pr/Ti^*) and Re_L. The following correlation was obtained within approximately ±30%.

$$\left(Pr_L/T_i^*\right)=17.8Re_L^{-0.54} \qquad \text{Eq. (22)}$$

Therefore, the new correlation of forced convection Nusselt number Nu_F is defined by the following equation.

$$Nu_F = 12.6\sqrt{f_V}\Phi_V\left(\rho_L/\rho_V\right)^{0.5}\left\{x/(1-x)\right\}Re_L^{0.46} \qquad \text{Eq. (23)}$$

If $J_V/J_V^* < 1$ (wavy-slug flow region), then the Nu number is obtained using Eq. (12), (17) and Eq. (21). If $J_V/J_V^* \geqq 1$ (annular flow region), then the Nu number is obtained using Eq. (12), (17) and Eq. (23).

Figure 11 shows the comparison between the new correlations and measured data of R1234ze(E) in HF40, LF50S, and LF50L microfin tubes. From the figure, it is observed that the new correlation agrees well the measured data within about ±30%.

5. CONCLUSIONS

We investigated the condensation flow pattern of R1234ze(E) inside three horizontal 4.0 mm outer diameter microfin tubes with different fin geometries. We classified the flow pattern into three types, namely, annular, wavy, and slug. The previous correlations can estimate the transition line from annular flow to wavy-slug flow observation results of each small-diameter microfin tube. Based on the visualization results of R1234ze(E), we proposed a new heat transfer correlation, which agrees well with the measured data within ±30%.

ACKNOWLEDGEMENTS

This study was supported by the Research & Development Section, Technical Department, Kobelco & Material Copper Tube, Ltd. and the Japan Copper Development Association. We would like to express our gratitude for the support provided.

NOMENCLATURE

Bo	Bond number = $(\rho_L - \rho_V) g d_{max}^2 / \sigma$ (-)
c_P	isobaric specific heat (Jkg^{-1}K^{-1})
d	diameter (m)
f_V	friction factor (-)
Fr_{SO}	Soliman's modified Froude number (-)
G	mass velocity (kgm^{-2}s^{-1})
G_{max}	*G* based on maximum diameter = $4m_r / \pi d_{max}^2$ (kgm^{-2}s^{-1})
g	gravity acceleration (ms^{-2})
Ga	Galileo number = $g d_{max}^3 \rho_L^2 / \mu_L^2$ (-)
h	enthalpy (Jkg^{-1})
J_V	dimensionless vapor velocity (-)
m	mass flow rate (kgs^{-1})
Nu	Nusselt number (-)
Nu_B	free convection Nusselt number (-)
Nu_F	forced convection Nusselt number (-)
P	pressure (Pa)
Ph	phase change number = $c_P (T_{sat} - T_{wall}) / \Delta h$ (-)
Pr	Prandtl number (-)
Q	heat transfer rate (W)
Re_L	liquid phase Reynolds number= $G_{max}(1-x) d_{max} / \mu_L$ (-)
Re_V	vapor phase Reynolds number= $G_{max} x d_{max} / \mu_V$ (-)
T	temperature (℃)
T_i^*	dimensionless temperature difference (-)
x	vapor quality (-)

Greek symbols

α	heat transfer coefficient (Wm^{-2}K^{-1})
Δh	latent heat (Jkg^{-1})
η	area enlargement ratio (-)
Θ	helix angle of microfin (deg.)
λ	thermal conductivity (Wm^{-1}K^{-1})
μ	viscosity (Pa s)
ξ	void fraction (-)
ρ	density (kgm^{-3})
σ	surface tension (Nm^{-1})
Φ	two-phase pressure drop multiplier (-)
X_{tt}	Lockhart-Martinelli parameter (-)

Subscripts

eq	equivalent
max	maximum
sat	saturation
W	water
L	liquid
r	refrigerant
V	vapor

REFERENCES

Cavallini A, Del Col D, Rossetto L, Mancin S. 2009. Condensation of pure and near-azeotropic refrigerants in microfin tubes A new computational procedure, *Int. J. Refrig*. 32: 162-174.

Lemmon E.W., Bell I.H., Huber M.L. and McLinden M.O., 2018. NIST reference fluid thermodynamic and transport properties database (REFPROP): Version 10.

Hirose M, Ichinose J, Inoue N, 2018. Development of the general correlation for condensation heat transfer and pressure drop inside horizontal 4 mm small-diameter smooth and microfin tubes, *Int. J. Refrig*. 95: 72-83.

Inoue N, Hirose M, Jige D., 2018. Effect of fin geometries on condensation heat transfer and pressure drop inside horizontal small-diameter 4 mm microfin tubes, Proc. of the 17th International Refrigeration and Air Conditioning Conference, Purdue, ID 2511.

Jige D, Sagawa K, Iizuka S and Inoue N, 2018. Boiling heat transfer and flow characteristic of R32 inside a horizontal small-diameter microfin tube, *Int. J. Refrig*. 90: 238-248.

Nozu S. Katayama H, Nakata H and Honda H, 1996. Condensation of refrigerant CFC11 in horizontal microfin tubes (Proposal of a correlation equation for frictional pressure gradient), Journal of the Japan Society of Mechanical Engineering (B). 62(601): 155-162. (in Japanese).

Manuscript ID: 1316
DOI: 10.18462/iir.icr.2019.1316

Use of diamond/POE nanolubricant in a refrigeration system operating with R410A and R32

David F. Marcucci Pico[(a)], Luiz Freitas Pereira[(a)], Enio P. Bandarra Filho[(a)]

[(a)] School of Mechanical Engineering, Federal University of Uberlandia (UFU)
Uberlandia, 38400-902, Brazil, bandarra@ufu.br

ABSTRACT

The present study deals with the use of a nanolubricant based on synthetic lubricant polyol ester (POE) and diamond nanoparticles in a refrigeration system. An experimental refrigeration bench was developed in order to evaluate the refrigeration capacity, the power consumption by the compressor, the coefficient of performance (COP), the discharge temperature of the compressor and, finally, the performance of the nanolubricants at the mass fractions of 0.0%, 0.1% and 0.5% of diamond nanoparticles. Tests were performed with R410A and R32 refrigerants in the evaporation temperature range between -7 and 7 °C, varying the operating frequency of the compressor from 45 to 60 Hz and maintaining the condensation temperature constant at 41 °C. According to the results of R410A, it was possible to conclude that, with the use of nanolubricant, there was an increase in both the refrigeration capacity and the coefficient of performance. The compressor's discharge temperature decreased. In contrast, for R32, the use of nanolubricants under the evaluated conditions did not show significant improvements in the refrigeration system in terms of refrigeration capacity and discharge temperature.
Keywords: COP, Nanolubricant, Nanoparticle, COP, R32, R410A.

1. INTRODUCTION

Due to the high utilization of cooling systems, it is important to constantly improve them, always aimed at better efficiency and lower energy consumption. In this sense, researchers have proposed different alternatives to achieve this objective, of which the use of nanoparticles as lubricating additives is presented as an alternative that aims improvements in the thermophysical and tribological properties of conventional lubricants. The dispersion of nanoparticles within a base fluid is referred to as nanofluid (Choi and Eastman, 1995) and more specifically, when the base fluid is a lubricating oil, it is called nanolubricant (Rasheed et al., 2016).

Nanoparticles, when applied in refrigeration systems, can improve their performance by increasing the heat transfer or reducing the energy consumption. Bi et al. (2008) found reductions of up to 26% in the energy consumption of a domestic refrigerator operating with R134a and nanolubricants composed of mineral oil (MO) and TiO_2 nanoparticles. Using the same nanoparticle and oil, Hussen (2014) found a COP increase of 12% and a reduction of up to 13% in the power consumption by the compressor. Xing et al. (2014) found a maximum reduction in the power consumption of 4.5% and an increase in the COP of 6% when adding fullerenes (C_{60}) in a system operating with R600a. Similarly, with the same refrigerant and system type, Lou et al. (2015), using graphite nanoparticles, found increases in cooling speed and a reduction of up to 4.6% in energy consumption. Recently, Sharif et al.(2017) found gains of up to 3.3% in refrigeration capacity and reductions in compressor-specific work in an automotive air conditioning system using SiO_2 nanoparticles. Additionally, they reported that at high concentrations the specific work of the compressor tends to be increased, which was also reported by Ohunakin et al. (2018). On the other hand, Fedele et al. (2014) and Wang et al. (2017) did not find significant gains in terms of the cooling capacity and the energy consumption of the system, when using nanoparticles of different compositions.

Finally, this work presents an experimental evaluation of the use of nanolubricants, diamond nanoparticles and POE oil in a refrigeration system.

2. METHODOLOGY

The nanolubricants used in this present work were produced by the two-step method. The first step is to obtain the nanoparticles separately and the second one corresponds to the dispersion of nanoparticles in the base fluid at the desired concentration. For this, the diamond nanoparticles were obtained from the company *Nanostructured & Amorphous Material, Inc.*, in powder, without any superficial treatment, with spherical morphology, diameter between 3 - 6 nm and purity above 97%. In order to improve the stability of the nanolubricants, the diamond nanoparticles were capped with oleic acid according to the following procedure: firstly, the nanoparticles were dispersed in oleic acid using an ultrasonic vibrator for approximately 30 min, then, the dispersion was separated using a centrifugal separator for 10 min at 8000 RPM. Further, the capped diamond nanoparticles were weighted with a semi-analytical balance at the desired mass concentrations. Finally, the nanoparticles were immersed in the POE oil by ultrasonic vibration until a good dispersion was achieved. The samples were dispersed until homogeneous dispersion was achieved for approximately one hour. It was observed that 15 days after this procedure, nanolubricants showed visible sedimentation of the nanoparticles, especially at high concentrations. To evaluate the effect of the concentration, three samples were produced with mass concentrations of 0.1%, 0.5% and 1.0%.

An experimental bench was developed for the analysis of the refrigeration system operating with nanolubricants. Fig. 1 shows the schematic diagram of the experimental facility used in the present work.

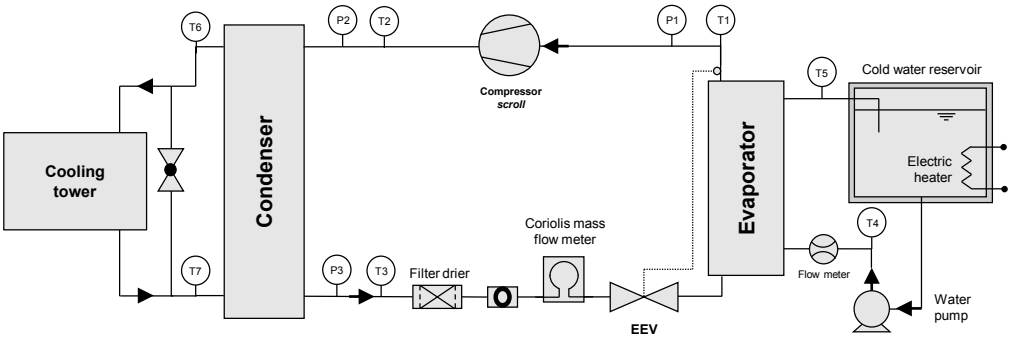

Figure 1: Schematic diagram of the experimental facility

The experimental bench is composed by three circuits: the refrigerant circuit (basic refrigeration cycle), the cold water loop and the condensation water circuit. The refrigerant circuit consists of: compressor, brazed plate heat exchangers (evaporator and condenser), electronic expansion valve, drying filter, liquid sight glass and Coriolis flow meter. The cold water loop is in charge of simulating the thermal load required for the operation of the refrigeration system. This circuit consists of a circulation pump, a turbine flow meter, a cold water reservoir and electrical heaters, which controls the temperature of the water at the evaporator inlet. The condensing water circuit is responsible for rejecting the heat of the cooling system and consists of circulation pumps, a condenser and a cooling tower.

The experimental bench temperatures were measured using PT-100 type temperature sensors. System pressures were measured using piezoresistive pressure transducers. The mass flow rate of the refrigeration system was measured using a Coriolis type mass flowmeter. The power consumption by the compressor was measured using a power analyser. The measuring points of the instruments used are shown in Fig. 1.

The tests were carried out in steady-state condition for the nanoparticles' concentrations of 0.0%, 0.1 and 0.5%, the evaporation temperature from -7 to 7 °C, rotation speed of the compressor of 45 up to 60 Hz. The experimental data for R410A can be found at Marcucci Pico et al. (2018).

Table 1 summarizes the experimental uncertainties of the measured variables calculated according to Abernethy and Thompson (1973). The uncertainties of the calculated variables from the measured

data are listed in Table 2 and were estimated using an EES routine that is in accordance with the Taylor and Kuyatt (1994) methodology.

Table 1. Experimental uncertainties

Measured variable	Sensor	Range	Uncertainty
Refrigerant temperature	PT-100	-20 – 100 °C	±0.3 °C
Compressor temperatures	Type t thermocouple	15 – 150 °C	±0.5 °C
Evaporation pressure	Piezoresistive transmitter	0 – 10 bar	±0.25%
Condensation pressure	Piezoresistive transmitter	0 – 25 bar	±0.25%
Refrigerant mass flow	Coriolis mass flow meter	0.2 – 150 g/s	±0.15%
Compressor input power	Power analyser	0 – 20 A 0 – 250 V	±1.0%

Table 2. Propagated uncertainties of the calculated variables

Calculated variable	Uncertainty
Evaporation temperature	±0.2 °C
Condensation temperatures	±0.2 °C
Cooling capacity	±1.0%
Coefficient of performance	±3.3%
Isentropic efficiency	±3.5%

3. RESULTS

Fig. 2 shows the results obtained for the cooling capacity of the system operating with R410A and R32 and nanolubricants at different concentrations. Based on Fig. 2a and Fig. 2b, the cooling capacity of the system operating with nanolubricants presented a tendency to increase in relation to the system operating with pure POE. In addition, when comparing both figures, it is noted that the increases in cooling capacity of the system, when compared to the system operating with pure lubricant under the same conditions, tended to be higher with increasing diamond concentration. The maximum increase in this property found for R410A at a concentration of 0.1% was 4.2%, evaporating at -7 °C and with a rotation of 45 Hz, whereas, at the concentration of 0.5%, the maximum increase was found to be ~ 7% under the same test conditions, -7 °C and 45 Hz. For R32, at the concentration of 0.1%, a maximum increase of 4% in cooling capacity was found with the system evaporating at - 7 °C and with the rotation frequency of 45 Hz. The mass concentration of 0.5% reached a maximum increase of 2% under the conditions of 1 °C and 45 Hz. Although some gains in this parameter of the system with R32 were found for some conditions, mainly at low frequency and evaporation temperature, these were found in few operating conditions.
In relation to the power consumption by the compressor, it was possible to identify that there was no significant variation in this property, reaching maximum variations of 0.4% and 3.0% for R410A and

R32, respectively. Similar results in which the compressor consumption was not sensitive by the addition of nanoparticles were found by Fedele et al. (2014) and Wang et al. (2017).

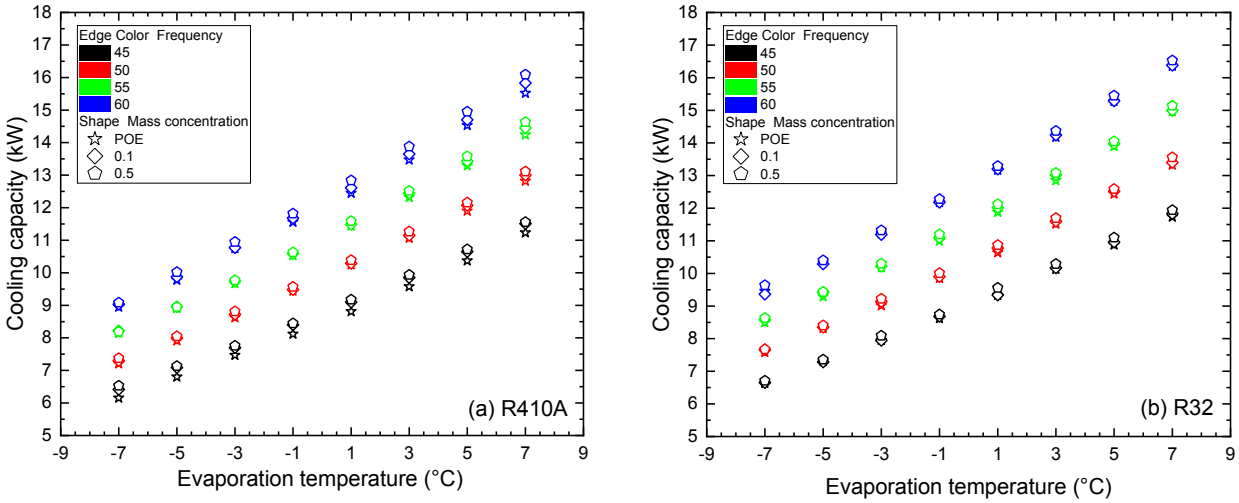

Figure 2: Cooling capacity of the system operating with (a) R410A and (b) R32

Once the cooling capacity and the power consumption of the compressor were measured, for the system operating with the nanolubricants, it was possible to calculate the COP, which is presented by Fig. 3 (a) e Fig. 3b, for the R410A and the R32, respectively. For the system operating with R410A and nanolubricants, it is possible to conclude that the addition of nanoparticles increased the performance of the system, with maximum increments in the range of 4% and 8% for lubricants containing 0.1% and 0.5% respectively. In this sense, it is possible to conclude that there is a tendency of performance gain with the accretion in the concentration of nanoparticles. For the R32 refrigerant when operating with diamond nanolubricant, maximum increments of 2.0% and 5.0% were found for concentrations of 0.1% and 0.5%, respectively. In addition, in Fig. 3 (a) and (b) it can be seen that the system COP is reduced by decreasing the evaporation temperature and the rotation frequency of the compressor. This can be explained from the fact that when the compressor frequency is reduced, the leaks between the compression volutes are increased as a consequence of the increased compression time of each fluid volume (Cui and Sauls, 2008).

Figs. 4a and 4b show the compressor discharge temperature results for the system operating with fluids (a) R410A and (b) R32, respectively. In the figures, it is observed that the discharge temperature is decreased with the use of nanolubricants. For R410A, a maximum reduction of 3 and 4°C in the compressor discharge temperature was found with the mass concentrations of 0.1% and 0.5% of diamond, respectively. Discharge temperature tends to decrease with increasing concentration of diamond nanoparticles. As for R32, as can be seen in Fig. 4b, the discharge temperature can be reduced by up to 1 and 2°C with the use of diamond nanolubricants in the compressor at concentrations of 0.1% and 0.5%, respectively.

For both fluids, it is possible to observe in Figs. 4a and 4b that the reduction was more pronounced at low frequency, since at the frequencies of 60 and 55 Hz the discharge temperature remained approximately constant.

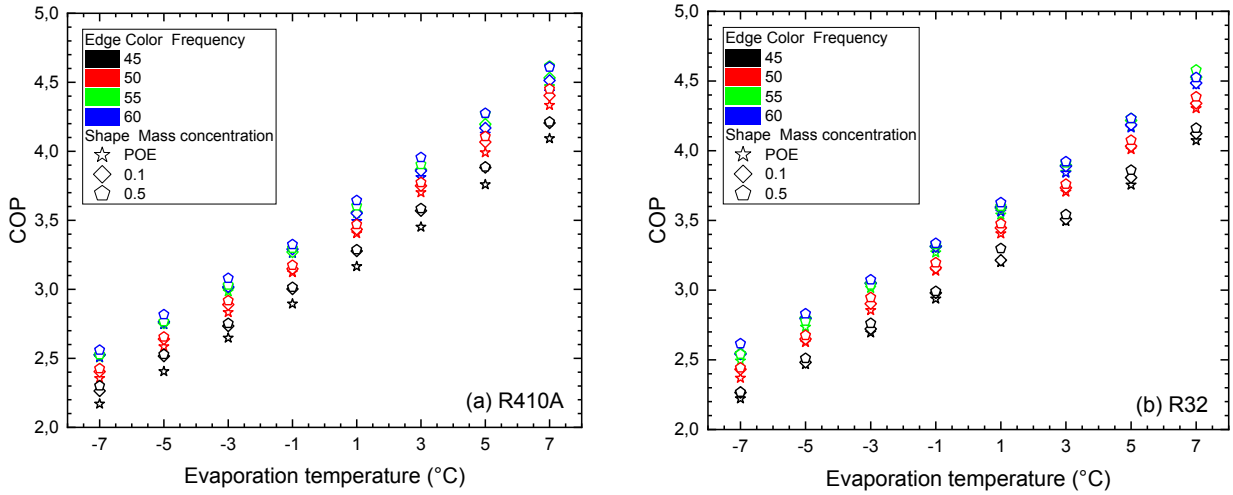

Figure 3: Coefficient of Performance of the system operating with (a) R410A and (b) R32

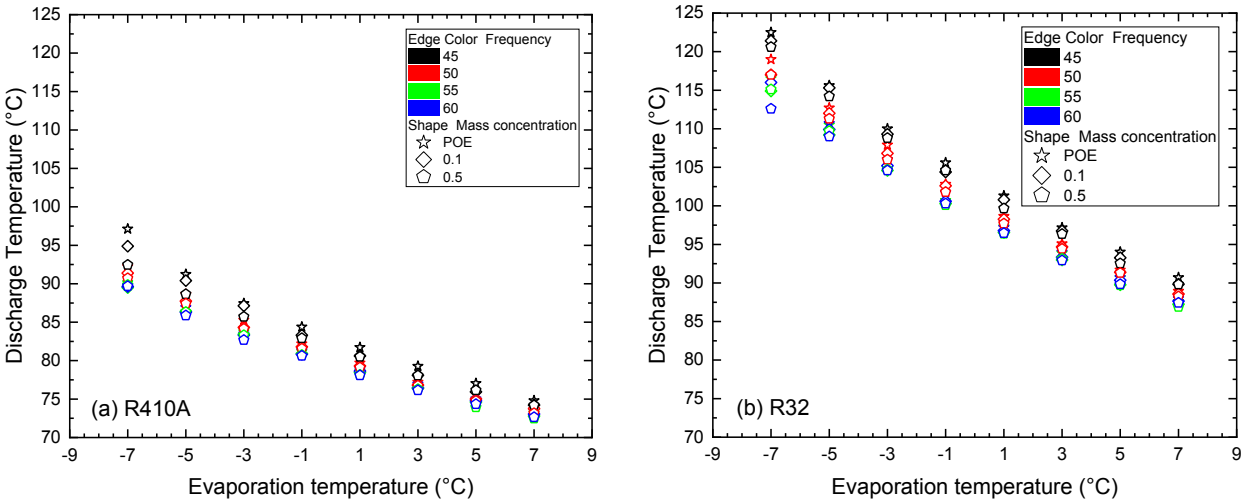

Figure 4: Compressor discharge temperature operating with (a) R410A e (b) R32

4. CONCLUSIONS

In this work, the effect of using Diamond/POE nanolubricants in a refrigeration system was evaluated, taking into account the R410A and R32 refrigerants. Maximum gains of 7% and 4% were found in the cooling capacity of the system operating with R410A and R32, respectively. It was found that the use of nanodiamond/POE lubricant does not significantly influence the power consumption of the compressor. Therefore, the enhancements obtained for the COP were attributed, mainly, to the increase in the refrigeration capacity.

On the other hand, it has been found that the discharge temperature of the compressor, when operating with R410A, can be reduced. However, when operating with R32, the reductions in this property were less relevant.

When comparing the increases caused by the addition of nanoparticles between the two evaluated refrigerants, R410A and R32, it can be stated that they were higher for R410A. This is because R32 operates at very high temperatures relative to R410A, which worsens the stability of nanolubricants. In this perspective, the use of diamond nanoparticles dispersed in the synthetic lubricant POE does not encourage the drop-in process of R410A by the R32.

ACKNOWLEDGEMENTS

The authors thank the Post Graduate Program in Mechanical Engineering at the Federal University of Uberlândia, CAPES, CNPq and FAPEMIG for financial support.

REFERENCES

Abernethy, R.B., Thompson, J.W., 1973. Uncertainty in Gas Turbine Measurements, AEDC-TR-73. ed. AD 75535.

Bi, S., Shi, L., Zhang, L., 2008. Application of nanoparticles in domestic refrigerators. Appl. Therm. Eng. 28, 1834–1843. https://doi.org/10.1016/j.applthermaleng.2007.11.018

Choi, S.U.S., Eastman, J.A., 1995. Enhancing thermal conductivity of fluids with nanoparticles. ASME Int. Mech. Eng. Congr. Expo. 66, 99–105. https://doi.org/10.1115/1.1532008

Cui, M.M., Sauls, J., 2008. Impact of Power Frequency on the Performance of a Scroll Compressor, in: International Compressor Engineering Conference. Purdue University, West Lafaye, IN, USA, p. Paper 1903.

Fedele, L., Colla, L., Bellomare, F., Bobbo, S., 2014. Nanofluids Application as Nanolubricants in Heat Pumps Systems.

Hussen, H.A., 2014. Experimental Investigation for TiO2 nanoparticles as a Lubricant- Additive for a Compressor of Window Type Air-Conditioner System 20.

Lou, J. -f., Zhang, H., Wang, R., 2015. Experimental investigation of graphite nanolubricant used in a domestic refrigerator. Adv. Mech. Eng. 7, 1687814015571011. https://doi.org/10.1177/1687814015571011

Marcucci Pico, da Silva, L.R.R., Schneider, P.S., Filho, E.P.B., 2019. Performance evaluation of diamond nanolubricants applied to a refrigeration system. Int. J. Refrig. 100, 104–112. https://doi.org/10.1016/j.ijrefrig.2018.12.009

Ohunakin, O.S., Adelekan, D.S., Gill, J., Atayero, A.A., Atiba, O.E., Okokpujie, I.P., Abam, F.I., 2018. Performance of a hydrocarbon driven domestic refrigerator based on varying concentration of SiO_2 nano-lubricant. Int. J. Refrig. 94, 59–70. https://doi.org/10.1016/j.ijrefrig.2018.07.022

Rasheed, A.K., Khalid, M., Rashmi, W., Gupta, T.C.S.M., Chan, A., 2016. Graphene based nanofluids and nanolubricants - Review of recent developments. Renew. Sustain. Energy Rev. 63, 346–362. https://doi.org/10.1016/j.rser.2016.04.072

Sharif, M.Z., Azmi, W.H., Redhwan, A.A.M., Mamat, R., Yusof, T.M., 2017. Performance analysis of SiO2/PAG nanolubricant in automotive air conditioning system. Int. J. Refrig. https://doi.org/10.1016/j.ijrefrig.2017.01.004

Taylor, B.N., Kuyatt, C.E., 1994. Guidelines for Evaluating and Expressing the Uncertainty of NIST Measurement Results. https://doi.org/10.6028/nist.tn.1297

Wang, R., Zhang, Y., Liao, Y., 2017. Performance of rolling piston type rotary compressor using fullerenes (C70) and NiFe2O4 nanocomposites as lubricants additives. Front. Energy 1–5. https://doi.org/10.1007/s11708-017-0453-y

Xing, M., Wang, R., Yu, J., 2014. Application of fullerene C_{60} nano-oil for performance enhancement of domestic refrigerator compressors. Int. J. Refrig. 40, 398–403. https://doi.org/10.1016/j.ijrefrig.2013.12.004

Manuscript ID: 1320
DOI: 10.18462/iir.icr.2019.1320

Two-Phase refrigerant distribution of vertical header with insertion structure of branch pipe for multi type air conditioner

Yoji ONAKA[(a)], Takashi MATSUMOTO[(b)], Hiroyuki OKANO[(c)]

[(a)] Advanced Technology R&D Center, Mitsubishi Electric Corporation, Amagasaki, Hyogo, 661-8661, Japan, Onaka.Yoji@db.MitsubishiElectric.co.jp
[(b)] Advanced Technology R&D Center, Mitsubishi Electric Corporation, Amagasaki, Hyogo, 661-8661, Japan, Matsumoto.Takashi@dy.MitsubishiElectric.co.jp
[(c)] Air-Conditioning and Refrigeration Works, Mitsubishi Electric Corporation, Wakayama, 152-0033, Japan, Okano.Hiroyuki@da.MitsubishiElectric.co.jp

ABSTRACT

In order to reduce refrigerant charge, tube size of heat exchanger is reduced, the number of heat exchanger paths of refrigerants have increased. Therefore, the design technologies of vertical headers are recently getting strongly attention. Many researchers are now devoting their energies to develop vertical header for equal refrigerant distribution to improve evaporation performance of heat exchanger. Some header has been suggested for equal distribution. However, air flow rate is non-uniform in some multi type air conditioner system of out-door unit. In this study, a vertical header distributor of the new structure with the branch pipe inserted in the main pipe is installed in heat exchanger and applied to the out-door unit of the top flow type multi air conditioner for building. The evaporation performance of heat exchanger can be improved by about 10% is confirmed by experiment.
Keywords: Heat Exchanger, Distribution, Vertical Header, Evaporator, Refrigerant, Heat Pump.

1. INTRODUCTION

The regulation of fluorocarbon refrigerant is promoted due to global warming problem partly due to effect of air conditioning. Reduction of refrigerant charge for air conditioning system is seen as potential to partly. Especially, tubes of heat exchanger are becoming smaller to reduce refrigerant amount in heat exchanger. In order to suppress pressure drop, the number of tube of heat exchanger increase. Therefore, the design technologies of vertical headers are recently getting strongly attention. Many researchers are now devoting their energies to develop vertical header for equal refrigerant distribution to improve evaporation performance of heat exchanger (Lee 2006, Zou and Hrnjak, 2014, Ekawa at al. 2018). Generally, an out-door unit of the building multi type air conditioner adopts a structure in which a blower is provided in the upper part of the housing. In this case, the flow of air passing through the heat exchanger is not uniform, and the air volume is increased at the upper part of the heat exchanger close to the blower as shown Fig. 1.

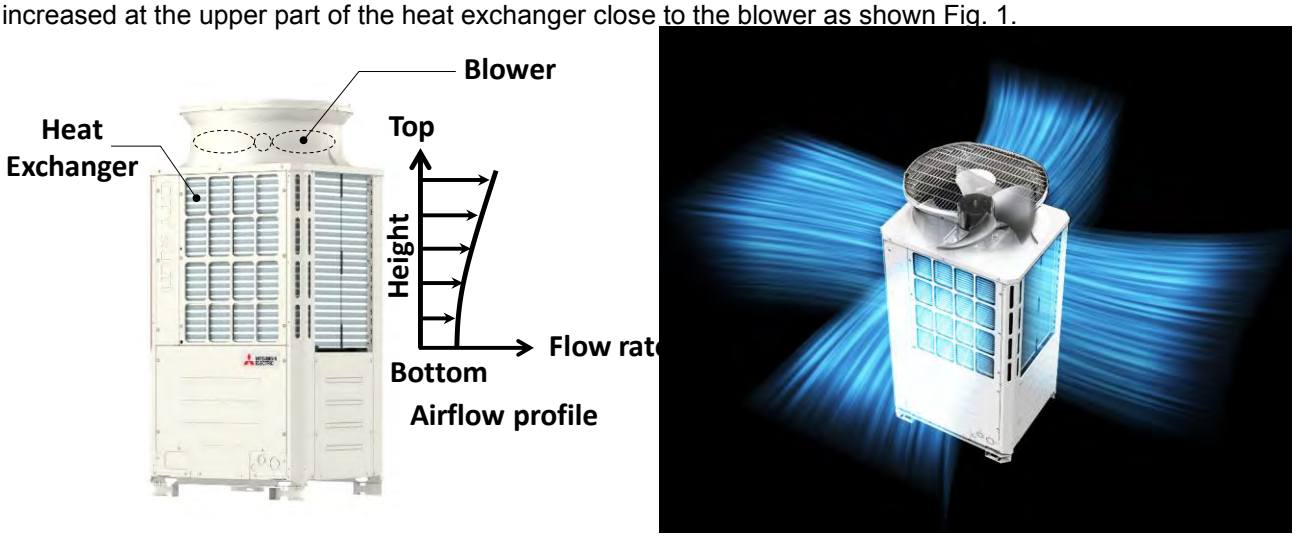

Fig. 1 Out-door unit of the building multi type air conditioner

In this case, ideal refrigerant distribution is a distribution of refrigerant similar to the airflow distribution rather than the uniform distribution, and it was difficult to design the refrigerant distribution of the vertical header. In this study, we have carried out experimental study on a new structure of a vertical header which realize refrigerant distribution, matching a top flow type out-door unit in which the airflow profile of heat exchanger.

2. EXPERIMENTAL METHOD

2.1. New Header Structure and Distribution Mechanism

In the vertical header, the refrigerant flow vertically upward in the main pipe and is distributed by the branch pipe. It is confirmed by visualization that the gas-liquid two-phase refrigerant flow in the main pipe is a flow in which the gas phase is distributed more in the vicinity of the center of main pipe according to previous study by the authors (Onaka et al., 2017). As a result, there was a tendency for the liquid refrigerant to flow relatively more in the lower part of the header in conventional header.

Fig.2 shows a new schematic diagram of vertical header. A conventional general vertical header has a structure in which a branch pipe is inserted to a position along the main pipe wall, but in the new structure, it is inserted to the center of main pipe.

Fig.3 compares the schematic diagram of the conventional structure with the refrigerant flow of the new structure. In the new vertical header, it is possible to selectively distribute the gas refrigerant distributed in the central part of the main pipe as shown by Fig.3. As a result, the refrigerant flowing through the main pipe becomes thicker in the upper part of the header, and more liquid refrigerant is distributed by inserted branch pipes. It has been possible to change the characteristics of the liquid refrigerant distribution, which was conventionally changed depending on the mass velocity, which was difficult to control.

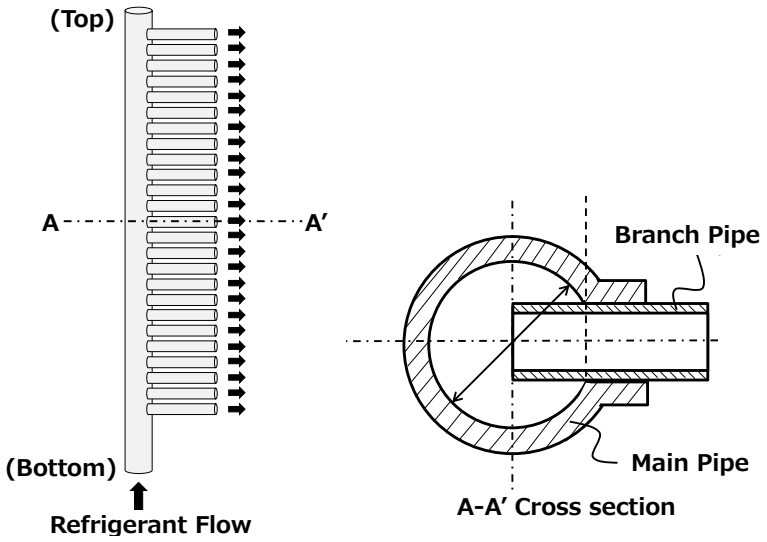

Fig. 2 Schematic of a new structure of vertical header

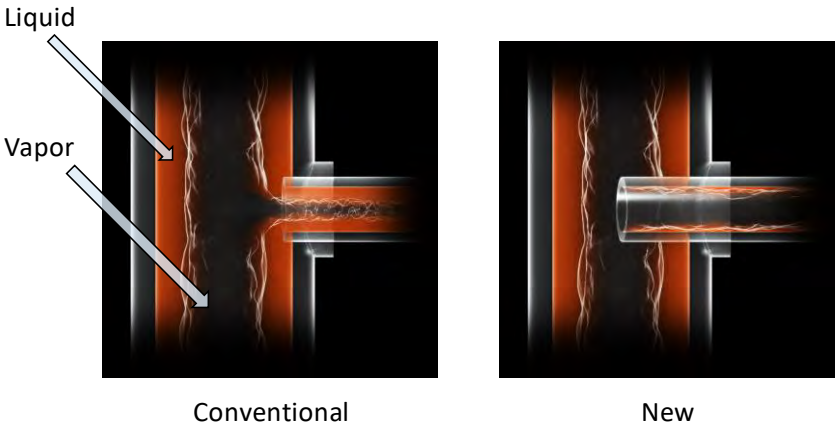

Fig.3 Schematic diagram of the conventional structure and new structure with the refrigerant flow

2.2. Experimental Apparatus

Fig. 4 shows the schematic diagram of experimental apparatus. The experimental apparatus is a header distribution apparatus composed of a refrigeration cycle, a header, switching valves and a measurement circuit. A header is connected downstream of a refrigeration cycle apparatus that supplies refrigerant of arbitrary mass flow rate and vapor quality.

Each branch pipe is provided with a needle valve to control the pressure loss coefficient downstream of the header. In addition, a switching valve is connected to each branch pipe, which is an adiabatic experimental system that can be switched and connected to measurement circuit.

The measuring circuit consists of a heater, a watt meter, a needle valve, and a Coriolis refrigerant mass flowmeter to measure liquid mass flow rate and vapor quality by total mass flow rate and heating rate. The accuracy of liquid refrigerant flow rate ±3% has been verified by preliminary experiment. In order to confirm the flow of the refrigerant, a sight glass (not shown by Fig. 4) is provided on the downstream side of the needle valve. This makes it possible to confirm the branch flow path by visual inspection at a portion where the liquid refrigerant is not flowing.

Table 1 shows the list of measuring instruments of the experiment.

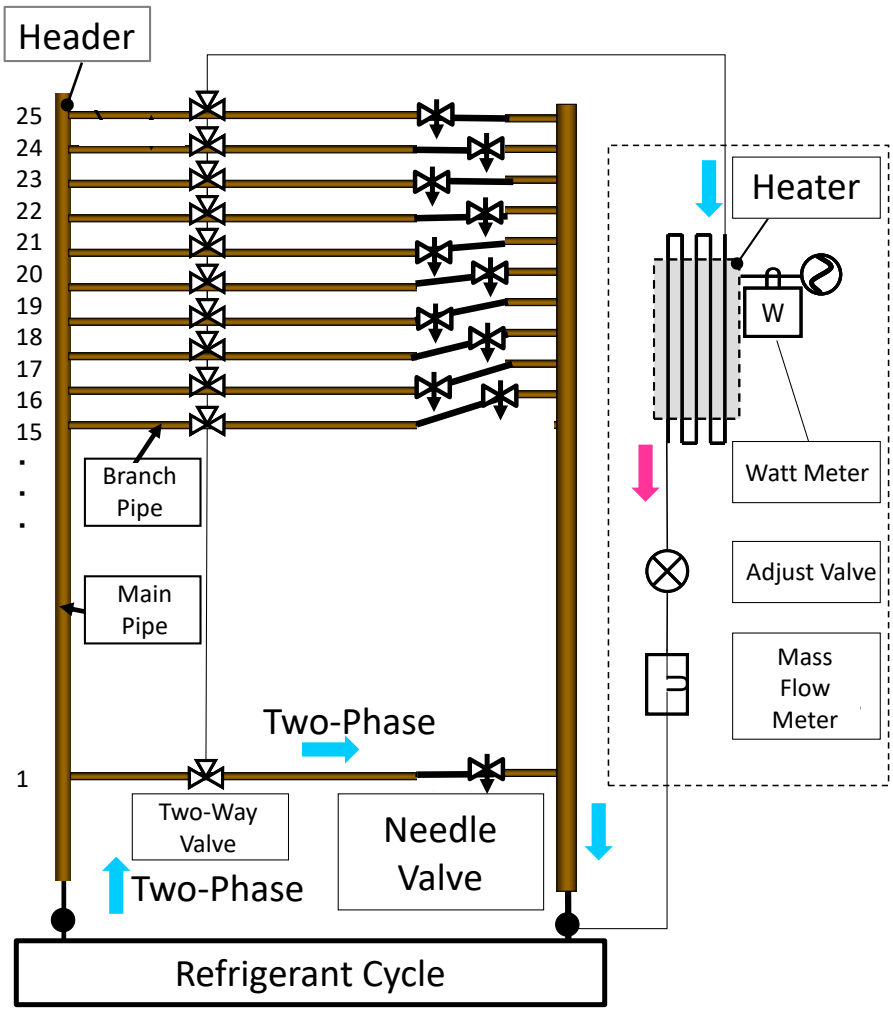

Table 1. Measuring instruments

Parameter	Model	Accuracy
Q[W]	Yokogawa UPM-100	±0.5% FS
M[kg/h]	Micro motion CFM-010	±0.01%
P_{in}[Pa]	Yokogawa FP101A-D21-C20A	±0.25%

3. RESULT AND DISCUSSION

Fig. 5 shows compares between the experimental results of the liquid distribution characteristics of the conventional structure and the new structure for vertical header of 25 branch pipes. The solid line in the Fig. 5 shows the ideal liquid refrigerant distribution characteristics calculated from the air volume distribution of building outdoor unit in which a blower is provided in the upper part of the housing.

In the conventional structure, more liquid-phase refrigerant is distributed in the lower part of the header, so it was difficult to flow liquid refrigerant to the upper part of the heat exchanger with large air volume. In the new structure, it is confirmed that the distribution of the liquid refrigerant to lower part of the heat exchanger with smaller air volume is suppressed and the liquid refrigerant can be distributed more to upper part of the heat exchanger. As a result, it is confirmed experimentally that the evaporation performance of the heat exchanger can be improved by about 10%.

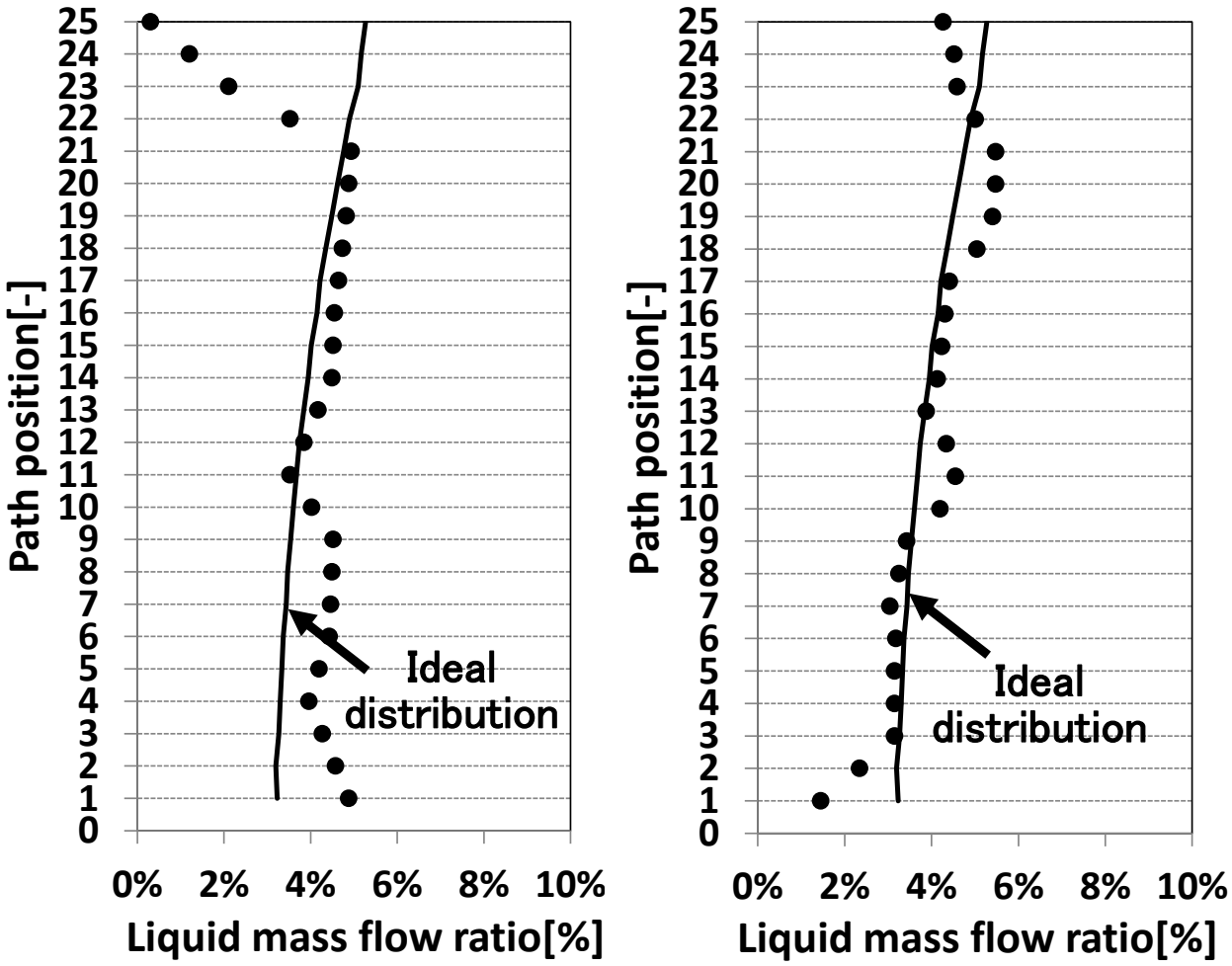

(a) Conventional header (no insertion)

(b) New developed header

Fig. 5 The comparison of liquid distribution profile between conventional header and new header

4. CONCLUSION

The vertical header of the new structure with the branch pipes inserted in the main pipe is installed in the heat exchanger and applied to the out-door unit of the top flow type multi air conditioner for building, the evaporation performance of the heat exchanger can be improved by about 10% because of improved distribution characteristics as shown Fig. 6.

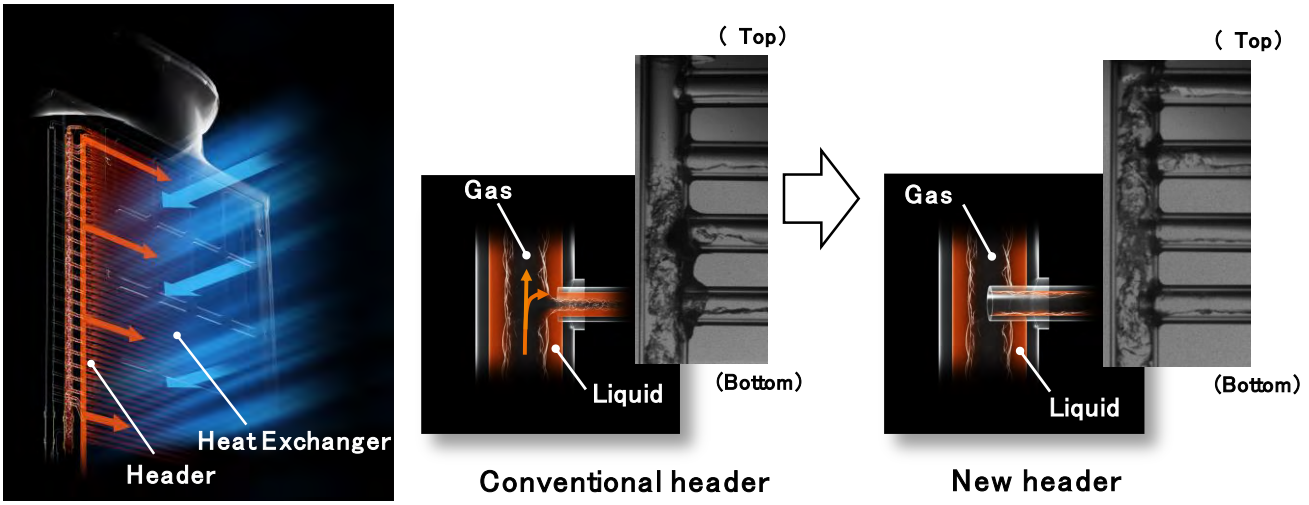

Fig. 6 The effect of new vertical header

NOMENCLATURE

M	Mass flow rate (kg/h)	*P*	Pressure (Pa)
Q	Heating rate (W)		

REFERENCES

Ekawa, A., Hirota, M., Hatada, T., Onodera A., 2018., Gas-Liquid Distributions of Refrigerant Flow in Multi-Pass Channel with Vertical Headers, Proceedings of Thermal Engineering Conference, Toyama, Japan, A214.

Onaka, Y., Li J., Matsumoto T., Hrnjak P., 2017., The Experimental Study of Two-Phase Flow Distribution in Vertical Header, Proceedings of 5th IIR International Conference on Thermophysical properties and Transfer Processes of Refrigerants, Seoul, South Korea, No.105.

Lee, S.Y., 2006., Flow distribution behaviour in condensers and evaporators, Proceedings of the 13th International Heat Transfer Conference, Sydney, Australia, KN-08.

Zou, Y., Hrnjak P.S., 2014., Effects of fluid properties on two-phase flow and refrigerant distribution in the vertical header of a reversible microchannel heat exchanger – Comparing R245fa, R134a, R410A, and R32. Applied Thermal Engineering 70, 966-976.

Manuscript ID: 1323
DOI: 10.18462/iir.icr.2019. 1323

Numerical simulation on buoyancy-induced deterioration of supercritical heat transfer

Jiacheng HE, Chaobin DANG, Eiji HIHARA

The University of Tokyo
5-1-5, Kashiwanoha, Kashiwa, 277-8563, Japan, palmhe@hee.k.u-tokyo.ac.jp

ABSTRACT

The unique characteristics of thermo-physical properties of a fluid under supercritical pressures have profound effect on the heat transfer. The buoyancy effect that is induced by the severe variation of density in radial direction would cause the heat transfer deterioration. In this study, numerical simulation is conducted with R245fa at 4MPa to investigate the mechanism on the heat transfer deterioration phenomena. Low-Re turbulence model is adopted for the simulation. Results show that the flow field is significantly distorted due to the effect of buoyancy, leading to suppression of the turbulence production. Agreement is achieved between the previous theoretical study and present simulation investigation in terms of the location of salient points of velocity profiles. Simulation with the density-modified R245fa is conducted as well. Results show that the heat transfer deterioration is improved with a smaller density difference between liquid-like and gas-like region, suggesting the density difference has profound effect on heat transfer under supercritical pressures.
Keywords: Supercritical Heat Transfer, Buoyancy, R245fa, Numerical Simulation.

1. INTRODUCTION

Heat transfer of a fluid at supercritical pressure is involved in a number of industrial applications, such as supercritical water-cooled nuclear reactor (Mokry et al., 2011) , heat pump (Dang and Hihara, 2004) , and organic Rankine cycle (He et al., 2018a, b) . Owing to the severe variation of the thermo-physical properties under supercritical pressure, the heat transfer exhibits unique characteristics compared to those fluids with constant thermos-physical properties. Experimental investigation with different working fluid and different heat transfer geometries are used to study the novel heat transfer phenomenon. Some consistent conclusions can be drawn from the experiment, for example, the working fluid experiences heat transfer deterioration under moderate ratio of heat flux and mass flux in the case of upward flow, while it behaves normally in the downward flow. Researchers proposed theories from different perspectives to analyze the unique phenomenon, such as the effect of buoyancy owning to the density change in radials and acceleration owning to the density change in axials. However, experimental investigation can hardly look into the flow field because of the harsh working conditions under supercritical pressure, the numerical simulation, therefore, are adopted to obtain such information for further investigation.

A numerical analysis with Jones-Launder k-ε model was carried out to investigate the deteriorated heat transfer in a vertical pipe (Koshizuka et al., 1995). The simulation results concluded that thicker viscous sublayer leads to monotonic heat transfer deterioration at high flow rates. At low flow rates, the buoyancy was concluded as predominant factor for the deterioration.

He et al. (2004) conducted the simulation of turbulent mixed convection heat transfer with carbon dioxide. Five low-Reynolds k-ε models including Launder and Sharma (LS), Chien (CH), Lam and Bremhorst (LB), Abe, Kondoh and Nagano (AKN) and Myong and Kasagi (MK) and a k–ω model Wilcox (WI) were employed in the simulation. The results showed that all the models examined were able to some extent to reproduce the observed effects of buoyancy on heat transfer. However, the performance of the models varied significantly from one to another in terms of the predicted onset and magnitude of such effects. A comprehensive comparison between a series of turbulence models and DNS data was conducted subsequently (Kim et al., 2008). It was concluded that the low-Reynolds k-ε models of Launder-Sharma, Cotton–Kirwin, Abe–Kondoh–Nagano, Yang–Shih and a k–ε–v^2–f model of Durbin can predict the buoyancy-induced impairment of heat transfer reasonably

well. The distortion of the mean flow field resulting from the influence of buoyancy was proved the predominant reason for the heat transfer impairment. Later, another comparison between turbulence models and DNS on the forced and mixed convection was presented (He et al., 2008) . The supercritical carbon dioxide was used as working fluid. The results showed that the low-Reynolds *k-ε* models of Launder and Sharma, Yang-Shih, Abe, Kondoh and Nagano, Chien and Myong and Kasagi over-predicted the mixed convection with strong buoyancy.

In the upward heating flow of supercritical fluid, the fluid near wall decreases significantly when local fluid temperature is close to the pseudocritical temperature. The local fluid velocity, as a result, will be accelerated compared to the velocity of the fluid in the tube center. The velocity profile is characterized as the so-called M-shaped velocity profile. Such a velocity profile has been verified by the numerical simulations. The M-shaped velocity profile generated with buoyancy accompanies with the heat transfer deterioration and recovery. The gradient of velocity profile associated with turbulence production near the wall varies with magnitude of buoyancy. This process is characterized with change in location of salient point of velocity profile. In the previous study of the author, a theoretical model based on the force balance between buoyancy and wall shear stress is proposed (He et al., 2018c). The results showed that the location of salient point has significant effect on turbulence production and thus heat transfer. In this study, a numerical simulation is conducted to demonstrate the theoretical model.

2. DETAILS OF NUMERICAL SIMULATION

The commercial code ANSYS Fluent 16/18 are employed to conduct the numerical simulation. The LS low-Reynolds *k-ε* model is adopted to conduct the simulation. Table 1 summarizes the features of the selected model.

Table 1. Constants and damping function of LS low-Reynolds *k-ε* model

Parameters	Functions	Parameters	Functions
C_μ	0.09	f_μ	$\exp\left[\frac{-3.4}{(1+Re_t/50)^2}\right]$
C_1	1.44	f_1	1.0
C_2	1.92	f_2	$1-0.3\exp(-Re_t^2)$
σ_k	1.0	D	$2\nu\left(\partial\sqrt{k}/\partial y\right)^2$
σ_ε	1.3	E	$2\nu\nu_t\left(\partial^2 U/\partial y^2\right)^2$

3. RESULTS AND DISCUSSION

The simulation was conducted with R245fa at 4MPa, 400kg/m^{2}s and 40 kW/m^2. Distributions of wall temperature and bulk fluid temperatures along the tube are illustrated in Fig.1. In the location of 200 mm behind the inlet, the wall temperature increases more dramatically compared with the upstream, and decreases when bulk fluid temperature approaches pseudocritical temperature. Velocity profiles of cross-sections are shown in Fig. 2. A clear picture shows the evolution of the shape of velocity profile as well as the location of salient point. In order to further confirm the location of salient points in M-shaped velocity profile in the recovery region, part of the region behind 400 mm is considered as well. The entire analysis region is indicated as the arrow shows. Three sections, A, B and C shown in Fig. 1, are selected for further analysis.

The numerical results will be presented in two groups, i.e. the mean quantities and turbulence quantities. In the first group, the quantities including shear stress, velocity, dimensionless velocity and temperature will be illustrated. In the second group, the turbulence intensity and turbulence production will be presented.

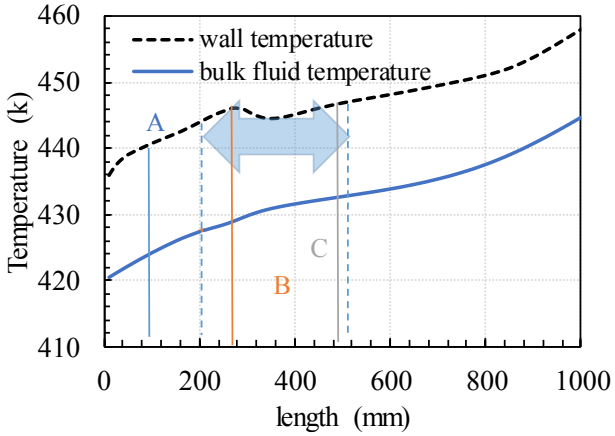

Figure 1: Wall temperature and bulk fluid temperatures

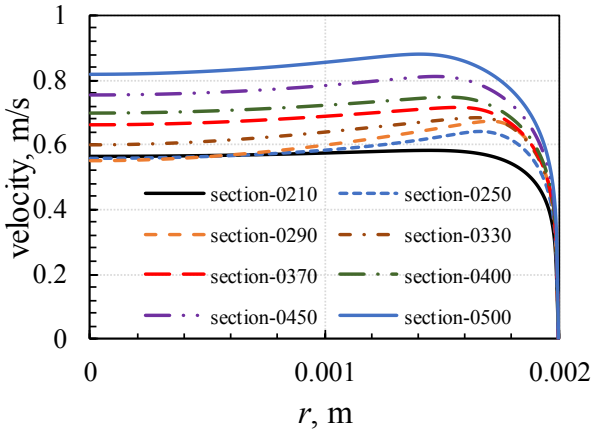

Figure 2: Velocity profiles of cross-section

3.1 Mean Quantities

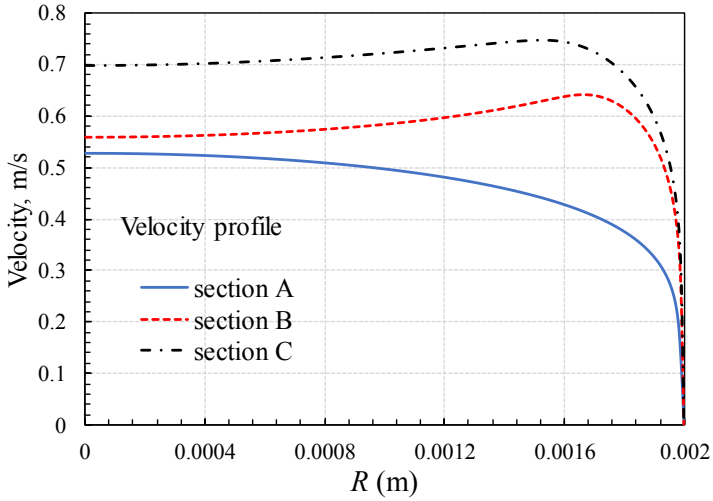

Figure 3: Velocity profiles of three sections

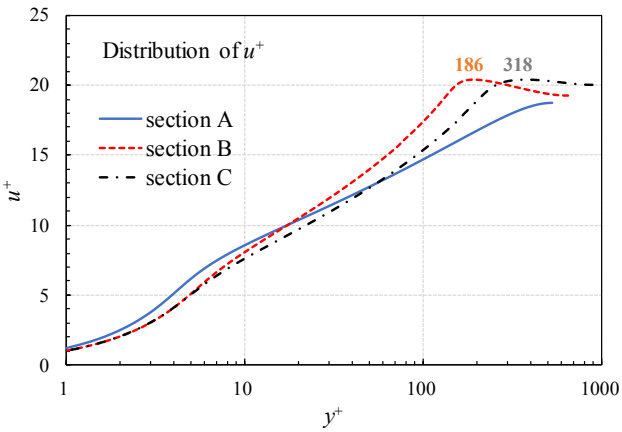

Figure 4: u^+ distributions

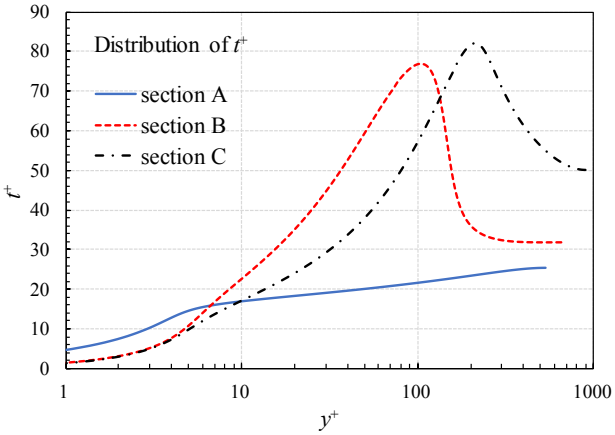

Figure 5: t^+ distributions

In Fig. 3, velocity profiles of each section are shown. In section A that belongs to the region ahead of deterioration, a velocity profile that fits the power law is obtained. In section B and C, on the other hand, the M-shaped velocity profiles occur because of the buoyancy effect. The salient point in section B locates closer to the wall than the one in section C. A clear picture is shown in Fig. 4 in dimensionless form. The maximum u^+ of section B and C lie in y^+ of 186 and 318, respectively. Fig. 5 shows the t^+ versus y^+. The peak in the profile of section C takes place in a larger y^+ than section B.

Fig. 6 shows the shear stress distributions against both the tube radius and y^+. The shear stresses of section B and C are strongly influenced by the buoyancy effect, resulting in a zero point in radius direction other that the center point of the tube. The zero point in section C, again, locates closer to the canter line than that of section B. Since section B and C respectively belong to deterioration and recovery region, it can be concluded that the M-shaped velocity profile exists in both working conditions.

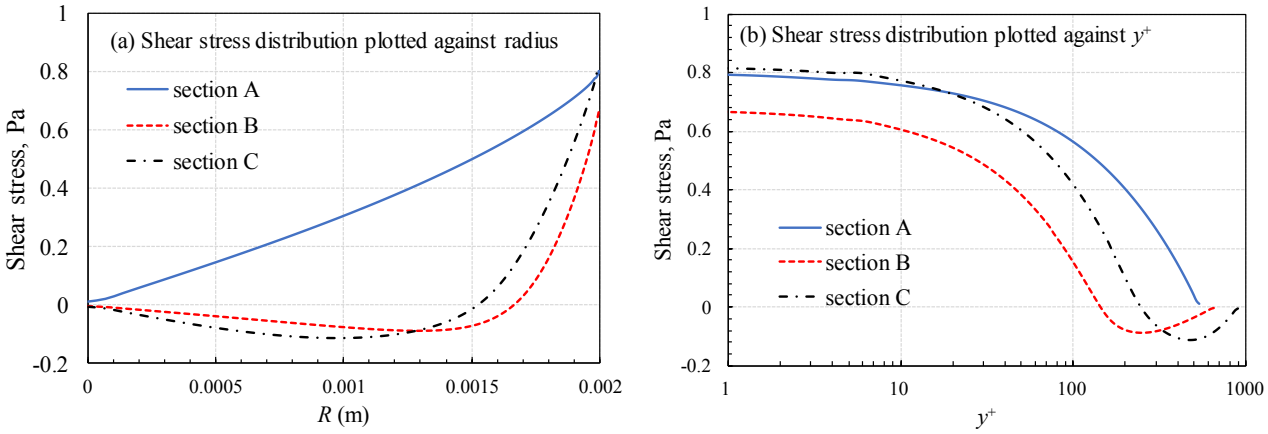

Figure 6: Shear stress distributions

3.2 Turbulence Quantities

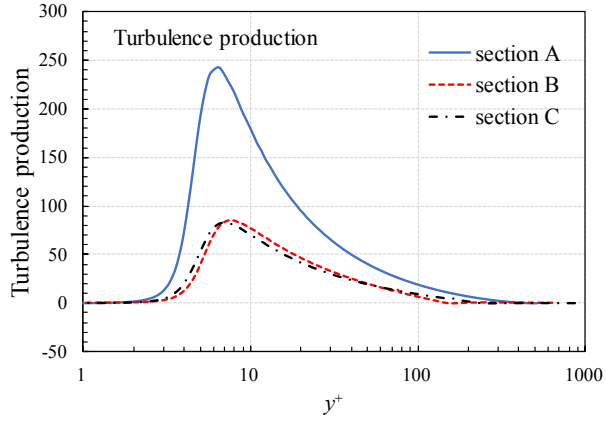

Figure 7: Turbulence production of section

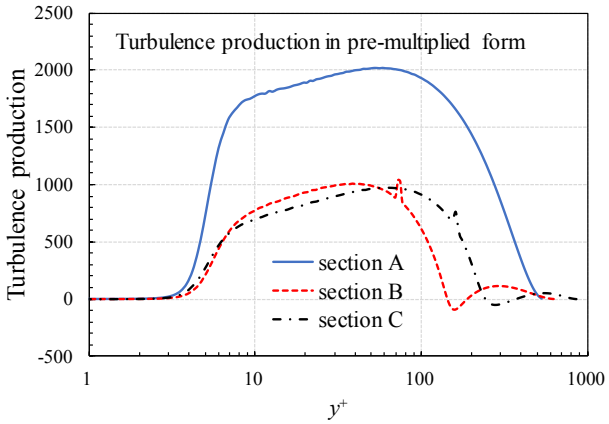

Figure 8: Turbulence production of each each section in pre-multiplied form

In order to further identify the relation between salient point in velocity profile and heat transfer deterioration, the variation of turbulence production are shown in Figs. 7 and 8 of different form. In Fig. 7, for section B and C, the turbulence production is much less than that of section A; however, it is hardly to distinguish it between them. In Fig. 8, on the contrary, a significant difference in the location of zero point in terms of pre-multiplied form in section B and C can be observed. The zero point in section B is much closer to the wall compared to that of section C. To visualize the variation of this process, a more detailed results of the considered region are shown in Fig. 9. The cross-sections 450 and 500 locate in the recovery region while the others belong to deterioration region. Section 210 is illustrated as a reference since it locates ahead of deterioration. At the early stage of deterioration, the zero point of turbulence production exists in small y^+. The zero points in the turbulence production profiles moves towards a higher y^+ in the deterioration process. In recovery region, the zero points exist at y^+ greater than 300. As discussed in previous section, the M-shaped velocity profile accompanies the deterioration and recovery region, which coincides with the conclusions in this section.

In Fig. 10, comparison of the location of salient points is conducted between numerical simulation and theoretical model. The simulation results coincide with the results of theoretical model for various

working fluids under different deteriorated working conditions. For the numerical simulation, the deterioration takes place at a friction Reynolds number greater then 1800, while the theoretical model gives a much smaller friction Reynolds number for the deterioration onset. Such a difference might attribute to the poor prediction of the onset of deterioration of the turbulence model.

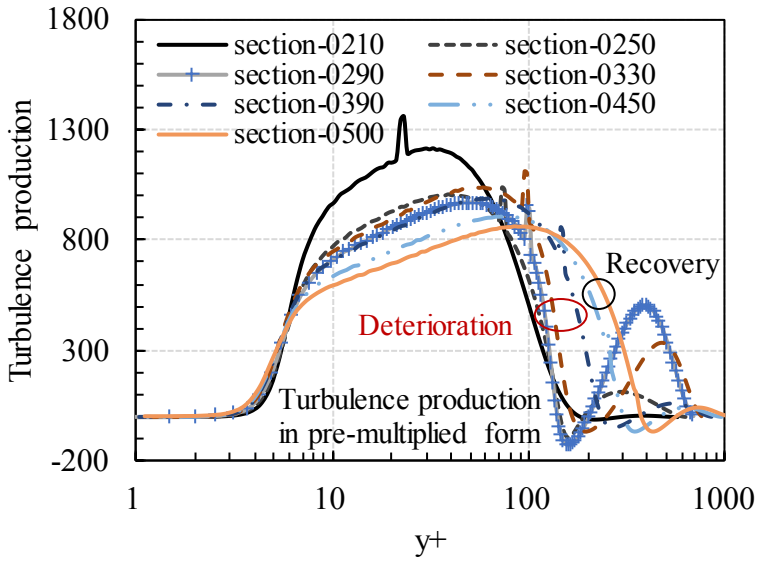

Figure 9: Turbulence production of the considered region in pre-multiplied form

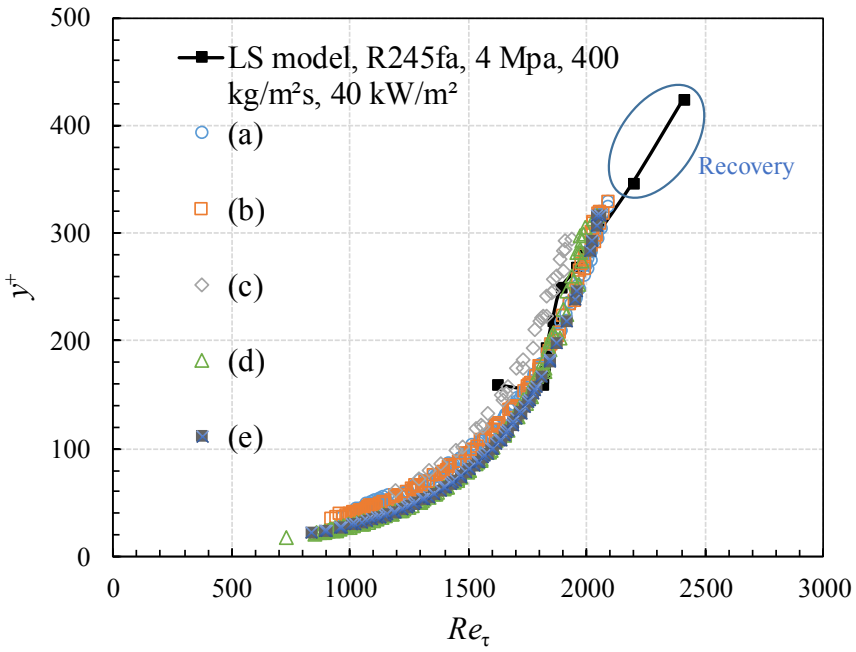

(a) R245fa, d = 4 mm, P = 4 MPa, G = 400 kg/m²s, q = 30 kW/m²;

(b) R245fa, d = 4 mm, P = 4MPa, G = 400 kg/m²s, q = 40 kW/m²;

(c) R245fa, d = 4 mm, P = 4.5 MPa, G = 400 kg/m²s, q = 30 kW/m²;

(d) R22, d = 4.4 mm, P = 5.5 MPa, G = 400 kg/m²s, q = 24.9 kW/m²;

(e) CO_2, d = 4.4 mm, P = 8.12 MPa, G = 400 kg/m²s, q = 30 kW/m²;

Figure 10: Comparison of the location of salient points between numerical simulation and theoretical model

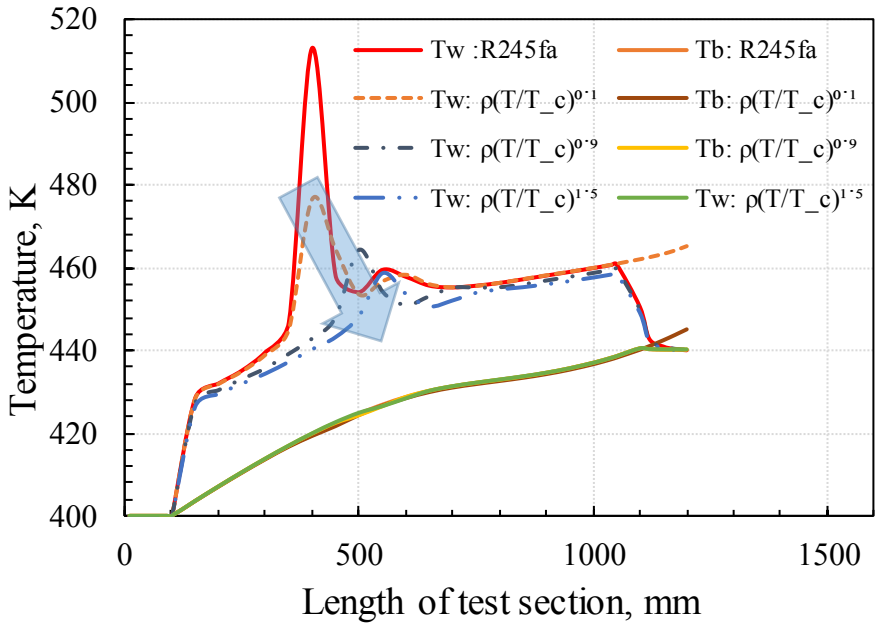

Figure 11: Simulation results of the cases with modified densities

3.3 Further Demonstration by Modifying Density

Since the forces equilibrium plays a key role in the buoyancy-induced deterioration condition, thus a smaller buoyancy, if possible, is expected to improve the heat transfer. Given that the buoyancy is generated owing to the density difference of the fluid near wall and in the tube center, a smaller density difference could certainly result in a smaller buoyancy. Therefore, the density of R245fa is modified by multiplying a corrected factor to conduct the simulation.

$$\rho_{modified} = \left(\frac{T}{T_{pc}}\right)^{n} \rho \qquad \text{Eq. (1)}$$

The exponent n of the corrected factor varies from 0.1 to 1.5. Simulation results in terms of fluid temperature and wall temperature are shown in Fig. 11. In general, the temperature peaks in the wall are significantly minimized by decreasing the density difference, indicating that a improvement is obtained by modifying the density of R245fa. Over 30 ℃ decrease in the peak wall temperature was obtained with a minor modification in density, suggesting the buoyancy resulted from density gradient in radius is greatly reduced. Moreover, the onset of the deterioration moves to a higher bulk fluid temperature.

4. CONCLUSIONS

A numerical study was conducted to provide the flow field characteristics. The LS low-Reynolds *k-ε* model is adopted for the simulation. Results of the simulation showed the M-shaped velocity profile is generated and exists in the deterioration as well as recovery process. The location of salient point in velocity profile has significant effect on turbulence production and thus heat transfer. The location of salient point of simulation results were compared to the results of the model, good agreement was achieved, which suggested the validation of the theoretical model. In addition, the simulation results of R245fa with modified density demonstrates the significance of force equilibrium in the buoyancy-induced heat transfer deterioration.

ACKNOWLEDGEMENTS

The project is supported by the New Energy and Industrial Technology Development Organization (NEDO).

NOMENCLATURE

d	diameter (m)	G	mass flux (400 kg/m²s)
p	pressure (MPa)	q	heat flux (kW/m²)
T	temperature (K)	u^+	dimensionless velocity
y^+	dimensionless distance to wall	ρ	density (kg/m^3)

REFERENCES

Dang, C., and E. Hihara, 2004. In-tube cooling heat transfer of supercritical carbon dioxide. Part 1. Experimental measurement. Int. J. Refrigeration 27, 736-747.

He, J., C. Dang, and E. Hihara, 2018. Experimental investigation of heat transfer to supercritical R245fa flowing vertically upward in a circular tube. Int. J. Heat and Mass Transfer 127, 286-295.

He, J., C. Dang, and E. Hihara, 2018. Supercritical heat transfer characteristics of R1233zd(E) in vertically upward flow. Int. J. Heat and Mass Transfer 127, 497-505.

He, J., C. Dang, and E. Hihara, 2018. Theoretical model for buoyancy-Induced heat transfer deterioration under supercritical pressure. Proceedings of the International Refrigeration and Air Conditioning Conference, West Lafayette, IN, USA.

He, S., W. S. Kim, P. X. Jiang, and J. D. Jackson, 2004. Simulation of mixed convection heat transfer to carbon dioxide at supercritical pressure: Proceedings of the Institution of Mechanical Engineers, Part C: Journal of Mechanical Engineering Science, v. 218, p. 1281-1296.

He, S., W. S. Kim, and J. H. Bae, 2008. Assessment of performance of turbulence models in predicting supercritical pressure heat transfer in a vertical tube. Int. J. Heat and Mass Transfer 51, 4659-4675.

Kim, W. S., S. He, and J. D. Jackson, 2008. Assessment by comparison with DNS data of turbulence models used in simulations of mixed convection. Int. J. Heat and Mass Transfer 51, 1293-1312.

Koshizuka, S., N. Takano, and Y. Oka, 1995. Numerical analysis of deterioration phenomena in heat transfer to supercritical water: Int. J. Heat and Mass Transfer 38, 3077-3084.

Mokry, S., I. Pioro, A. Farah, K. King, S. Gupta, W. Peiman, and P. Kirillov, 2011. Development of supercritical water heat-transfer correlation for vertical bare tubes. Nuclear Engineering and Design 241, 1126-1136.

Manuscript ID: 1327
DOI: 10.18462/iir.icr.2019. 1327

Permeability of PTFE flat-type membrane for absorption chiller

Jiacheng HE, Chaobin DANG, Eiji HIHARA

The University of Tokyo
5-1-5, Kashiwanoha, Kashiwa, 277-8563, Japan, palmhe@hee.k.u-tokyo.ac.jp

ABSTRACT

Applying the hydrophobic membrane into the absorber and generator of the absorption chiller can significantly downsize the absorption system. In this study, the permeability of the hydrophobic membrane is evaluated using CO_2 prior to the system test. The PTFE flat-type membrane with three nominal pope sizes of 0.1, 0.45 and 1 micron were tested for both flow directions. Results show that the permeability decreases with imposed pressure when the pressure is relatively small, and then tends to be constant. The mass transport mechanism differs for the membrane samples, and higher permeability was obtained with larger pore sizes. The variation of the permeability can be qualitatively explained with the pore size distribution.
Keywords: Permeability, Membrane, Hydrophobic, PTFE, Absorption Chiller.

1. INTRODUCTION

Absorption chiller, which can be driven by the low-grade heat source, is appealing more and more attention owing to the continuous efforts made on the energy conservation in refrigeration system. However, it should be admitted that the large scale of the absorption system restricts its application. In this study, the hydrophobic membrane is attempted to apply in the absorber and generator to replace the usual ones. In general, the membrane has high specific surface area, which allows much more interface compared with the traditional absorber and generator. The hydrophobicity of the membrane prevents the passage of the liquid solution across the membrane layer by a large capillary action, while refrigerant vapor is allowed to pass through the membrane pores.

A flat sheet membrane-based absorption refrigeration system was built and examined both the desorption and absorption characteristics in terms of the height of the microchannel (Nasr Isfahani et al., 2013; Nasr Isfahani and Moghaddam, 2013). In order to enhance the absorption rate, microstructure (Nasr Isfahani et al., 2015) and iso-thermal unit (Asfand and Bourouis, 2015) were proposed. The results showed that the absorption rate was significantly improved. The adiabatic and non-adiabatic flat-type membrane based absorber were evaluated as well (Venegas et al., 2017). Besides, the hollow-fiber-membrane-based absorber and generator were investigated by simulation and experiment (Hong et al., 2018, 2016; Wang et al., 2009).

Prior to investigate the performance of the membrane-based absorber, the permeability test using gas is conducted to understand the mass transport mechanism in the membrane by excluding the influence of solution and interface. Therefore, in this study, the permeability of CO_2 in the PTFE flat-type membrane with different pore size is tested.

2. EXPERIMENT DETAILS

The experimental setup is shown in Fig. 1. The test membrane sample is fixed inside a holder made of stainless steel. The gas, CO_2 in this research, is introduced to the holder and passes through the membrane at a certain pressure. The flow rate of gas will then measured in the downsream with an air flow meter. In the experiment, the pressure difference (measured by the model Setra 230) and flow rate (measured by the model TOKYO KEISO TF-5330) of the membrane are measured. By changing the pressure difference, a series of flow rates can be obtained, which allows evaluating the permeability performance of the membrane. For each membrane sample, the measurement was conducted for both sides, as indicated in Fig. 1. In addition, for each side, the pressure was changed in both ascending and descending order.

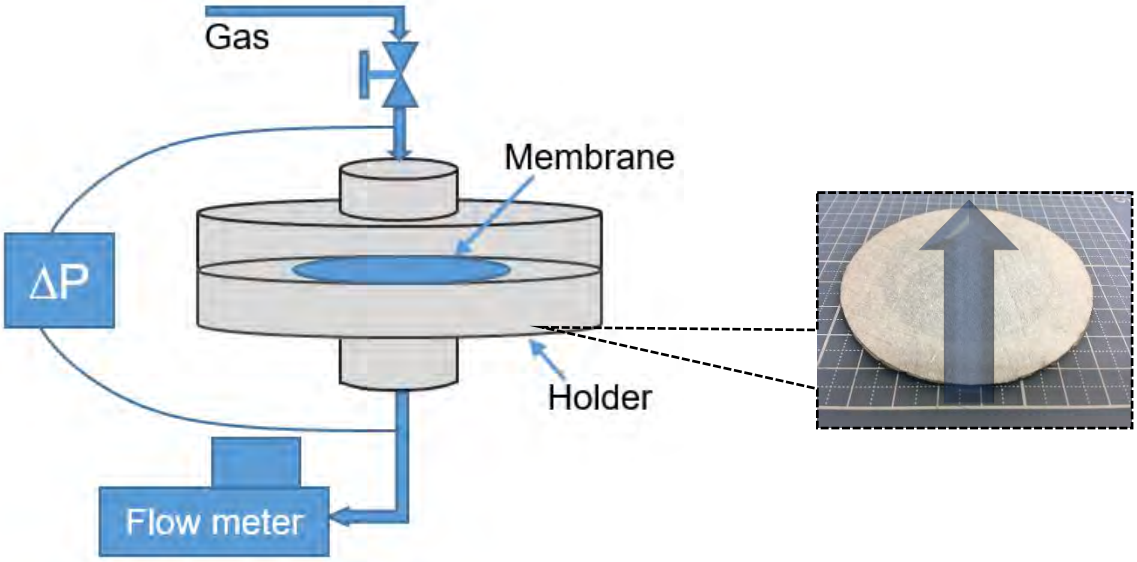

Figure 1: schematic of the experimental setup

The morphology of the membrane is shown in Fig. 2.

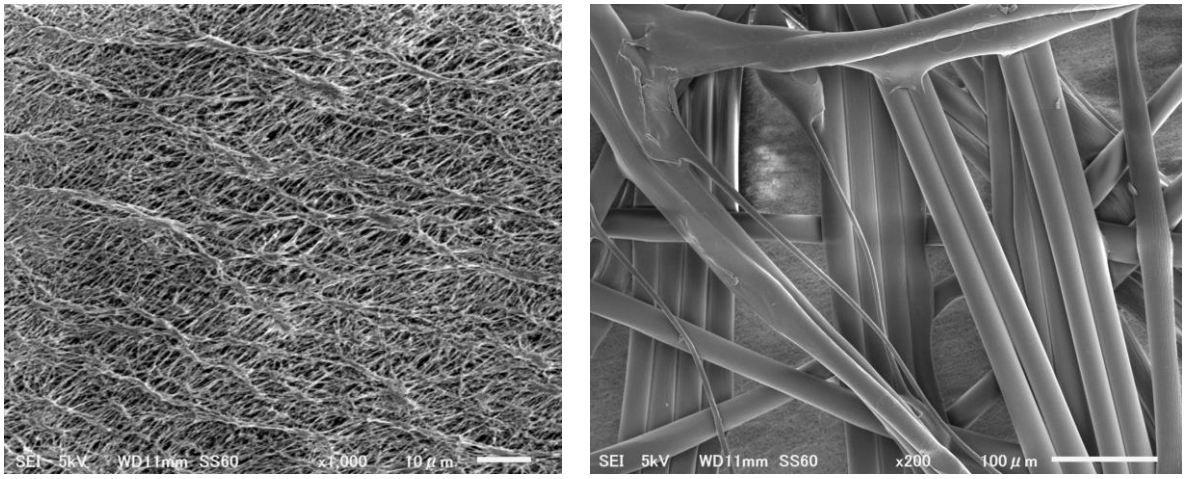

Figure 2: Morphology of the membrane sample (1 micron)

Table 1: Details of the flat-type membrane samples

	1st sample	2nd sample	3rd sample
Material		PTFE	
Pore size (μm)	0.1	0.45	1
Thickness (mm)		0.15	

3. RESULTS AND DISCUSSION

The transport of gas through porous media has been studied with the proposed mechanisms based on the kinetic theories. The Knudsen number, which is defined as the ratio of mean free path of gas to the pore size ($Kn = \lambda / d_p$), determines the transport mechanism of the gas inside a given pore under certain conditions. In general, if $Kn > 1$ or $d_p < \lambda$, the molecular-wall collisions are dominant over the molecular-molecular collisions, thus the Knudsen diffusion is used to describe the mass

transport. The permeability is evaluated using the following expression.

$$B_m^K = \frac{2\pi}{3}\frac{M}{RT}\sqrt{\frac{8RT}{\pi M}}\frac{r^3}{\tau\delta} \quad \text{Eq. (1)}$$

where *M* is the molecular weight of CO_2, *R* is the universal gas constant, *T* is the mean temperature in the pores, *r* is radius of the pore, τ is the tortuosity and δ is thickness of the membrane.

If $Kn < 0.01$ or $d_p > 100\lambda$, on the other hand, the molecular diffusion is dominant and the mass transfer coefficient is calculated with Eq. (2)

$$B_m^V = \frac{M}{\delta}\left(\frac{p}{RT\mu}\frac{d^2\varepsilon}{32\tau}\right) \quad \text{Eq. (2)}$$

A transitional flow regime exists if $0.01 < Kn < 1$ and according to the Dusty-Gas model, the mass transfer through a membrane consists of both Knudsen diffusion and viscous fluxes:

$$B_m^{trans} = \frac{M}{\delta}\left(\frac{2\pi}{3}\frac{1}{RT}\sqrt{\frac{8RT}{\pi M}}\frac{r^3}{\tau} + \frac{p}{RT\mu}\frac{d^2\varepsilon}{32\tau}\right) \quad \text{Eq. (3)}$$

The mean free path of gas is calculated using the following equation,

$$\lambda = \frac{k_B T}{\sqrt{2}\pi\bar{p}\sigma^2} \quad \text{Eq. (4)}$$

Where σ is the collision diameter (3.76 $\mathring{A}$ for CO_2), k_B is the Boltzmann constant, $\bar{p}$ the mean pressure within the membrane pores and *T* the absolute temperature. Under the experimental conditions, the mean free path of CO_2 is 0.13 micron, resulting in the Knudsen number ranging from approximately 1 to 0.1. Therefore, the transport mechanism will differs with the tested membranes under such conditions.

Figs. 3 to 5 show the measurement results of in terms of the permeability and pressure difference for both sides of each membrane sample. Fig. 3 is the measurement results of the membrane sample with nominal pore size of 0.1 micron. The permeability decreases with pressure when the pressure is relatively small. It might be attributed to the non-rigid nature of this material since it would be deformed under the imposed pressure. The pore size will be reduced when the pressure acts on the membrane, leading to smaller permeability for both Knudsen and molecular diffusion indicated by Eqs. (1) and (2). As pressure increase, the deformation is less owing to the small thickness of the membrane. The permeability tends to be constant with pressure for both diffusion direction. The measurement is less accurate in the conditions of small pressure difference owing to the large uncertainty in the measurement of flow rate. For the membrane sample with pore size of 0.45 and 1 micron, similar results were obtained as shown in Figs. 4 and 5.

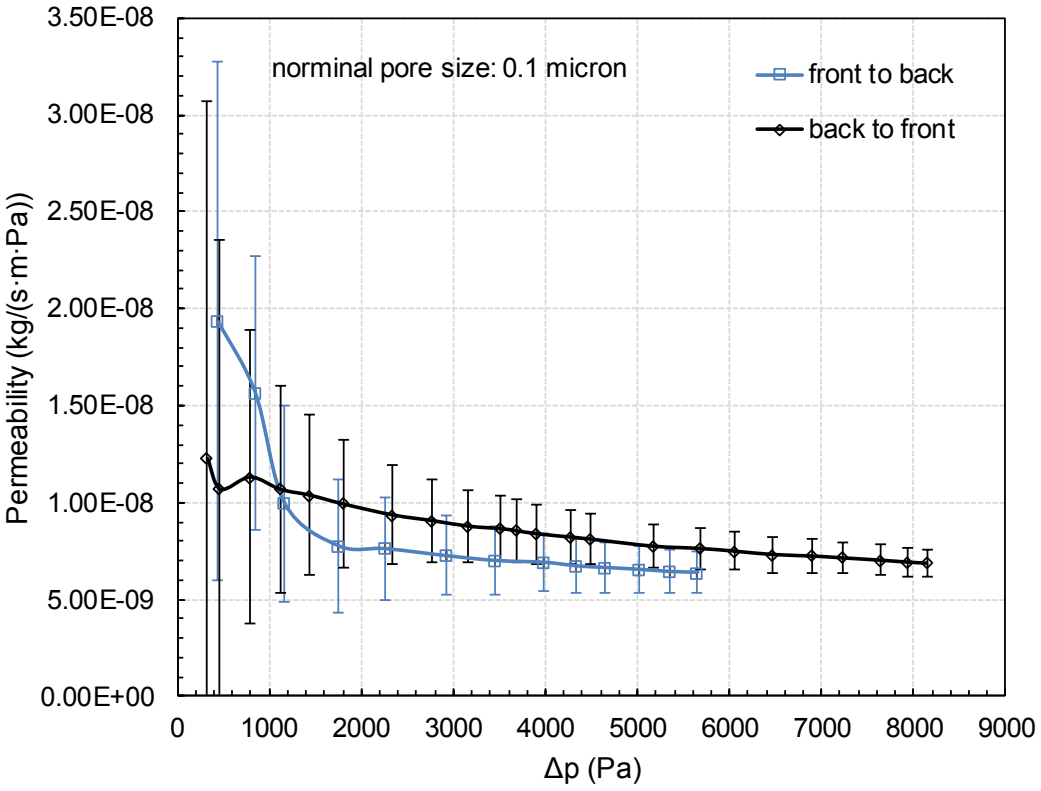

Figure 3: Permeability of membrane with pore size of 0.1 micron

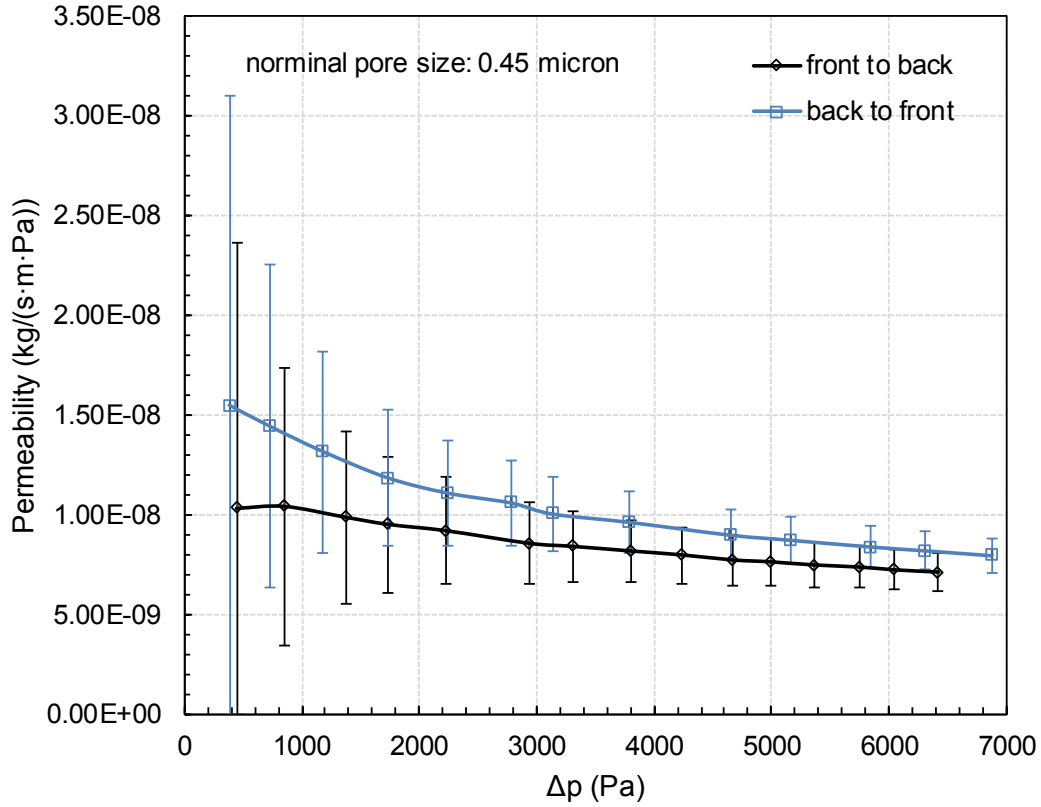

Figure 4: Permeability of membrane with pore size of 0.45 micron

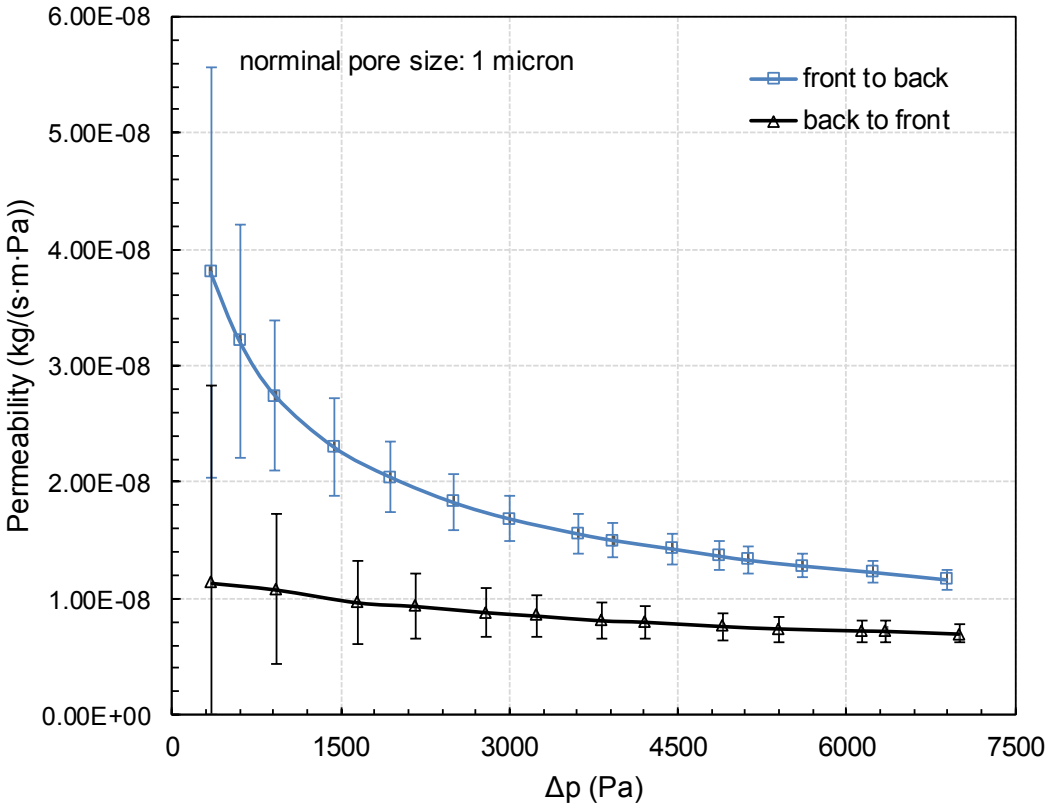

Figure 5: Permeability of membrane with pore size of 1 micron

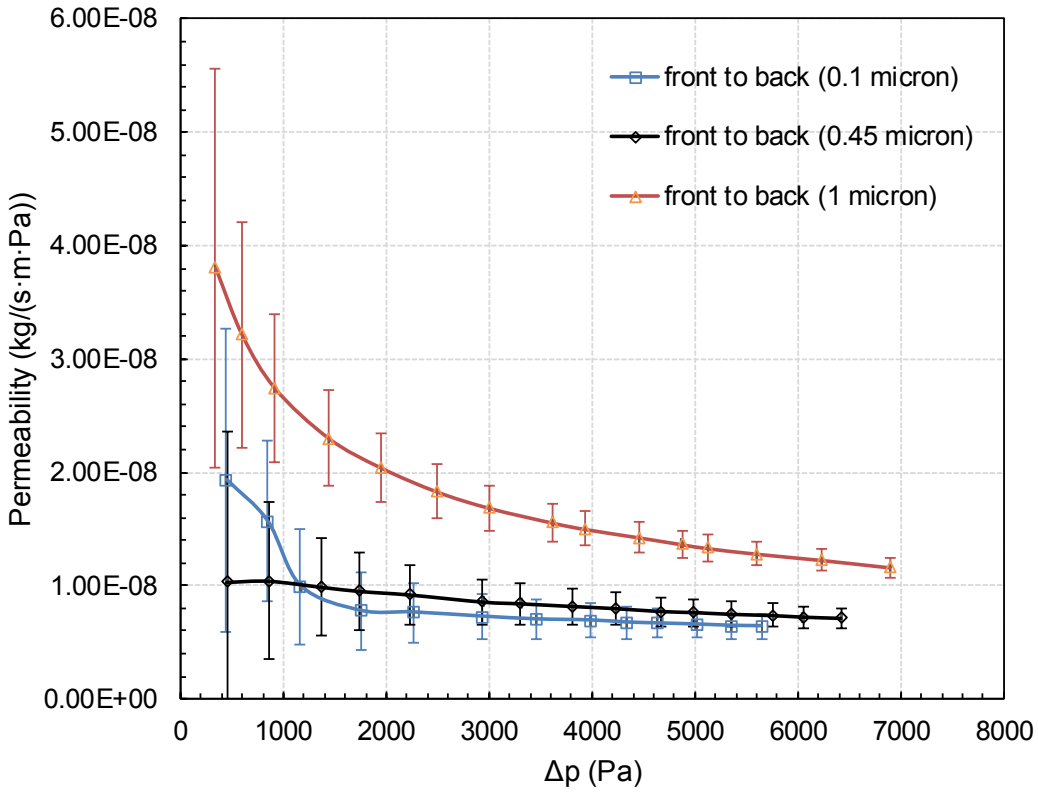

Figure 6: Comparison of the permeability of membrane samples

Fig. 6 shows the comparison of the permeability of all the samples. Except for the conditions of small

pressure difference with relatively large uncertainties, the permeability increases with pore size. Knudsen number is greater than 1 for membrane with pore size of 0.1 micron and about 0.2 and 0.1 for membrane with pore size of 0.45 and 1 micron, respectively. The corresponding mass transfer, therefore, is govern by different mechanism. The contribution of the Knudsen diffusion and molecular diffusion varies with *Kn* (Woods et al., 2011), leading to a greater permeability for the membrane with larger pore size.

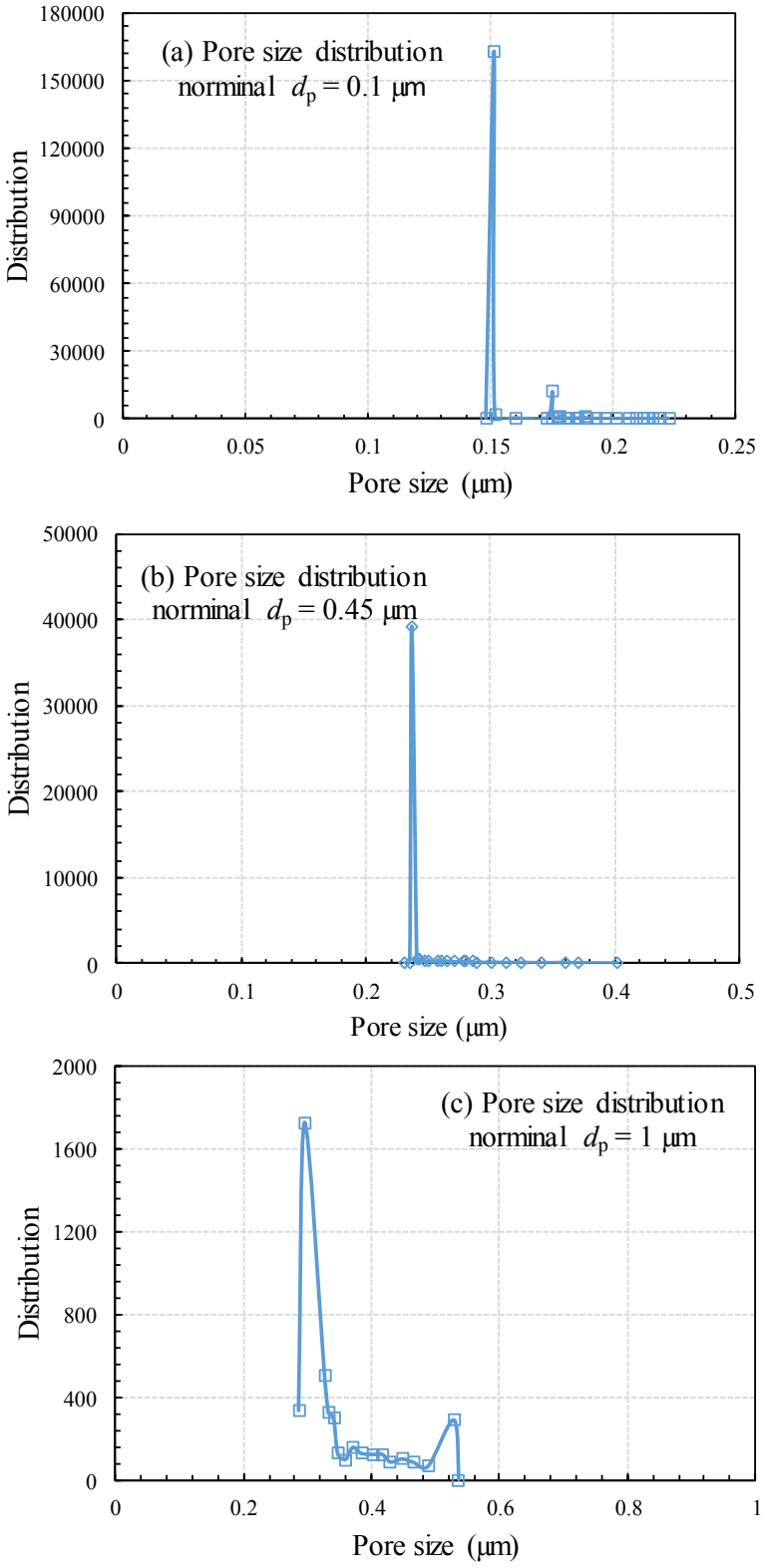

Figure 7: Pore size distribution of the membrane samples

The pore size distribution of the membrane samples were measured as well by the capillary flow porosimetry (CFP-1200-AEL, Porous Materials Inc., U.S.A.). The membrane sample was completely wetted with a certain fluid that has small surface tension, and measured the flow rate of air as well as the imposed pressure. This measurement was also conducted under dry conditions. The pore size can be calculated via the information of flow and pressure. Results are shown in Fig. 7. The vast majority of the pores of the membrane sample that has nominal pore size of 0.1 and 0.45 micron locate near its nominal value, however, for the membrane that has nominal pore size of 1 micron, the pore size distributes much less than the nominal value. For the measured results in Fig. 6, the variation of permeability can be qualitatively explained with the pore size distribution. A quantitative description will be developed in the following research.

4. CONCLUSIONS

In order to obtain the mass transport performance of flat-type membrane, a gas permeability test was conducted on the PTFE membrane with different pore size using CO_2. It was found that the permeability for all the test membrane decreases when the imposed pressure is small and tends to be constant with pressure. The membrane with larger pore size has greater permeability compared with those with smaller pores, which can be contributed to the great proportion of molecular diffusion for larger pores. The permeability of gas can provides fundamental information on the mass transport in the membrane, which would help better understand the mass transport in the condition with a solution.

ACKNOWLEDGEMENTS

The project is commissioned by the New Energy and Industrial Technology Development Organization (NEDO)

NOMENCLATURE

B_m	permeability ()	d_p	pore size (μm)
k_B	Boltzmann constant	Kn	Knudsen number
M	molecular weight (kg/kmol)	$\bar{p}$	pressure inside pore (Pa)
R	universal gas constant	r	radius of pore (m)
T	temperature (K)	σ	collision diameter of gas
τ	membrane tortuosity	δ	thickness of the membrane
ε	membrane porosity	μ	viscousity (Pa·s)

REFERENCES

Asfand, F., Bourouis, M., 2015. A review of membrane contactors applied in absorption refrigeration systems. Renew. Sust. Energ. Rev, 45, 173-191.

Hong, S. J., E. Hihara, and C. Dang, 2016. Novel absorption refrigeration system with a hollow fiber membrane-based generator. Int. J. Refrigeration 67, 418-432.

Hong, S. J., E. Hihara, C. Dang, 2018. Analysis of adiabatic heat and mass transfer of microporous hydrophobic hollow fiber membrane-based generator in vapor absorption refrigeration system. J. Membr. Sci. 564, 415-427.

Nasr Isfahani, R., K. Sampath, S. Moghaddam, 2013. Nanofibrous membrane-based absorption refrigeration system. Int. J. Refrigeration 36, 2297-2307.

Nasr Isfahani, R., S. Bigham, M. Mortazavi, X. Wei, S. Moghaddam, 2015. Impact of micromixing on performance of a membrane-based absorber. Energy 90, 997-1004.

Nasr Isfahani, R., and S. Moghaddam, 2013. Absorption characteristics of lithium bromide (LiBr) solution constrained by superhydrophobic nanofibrous structures. Int. J. Heat and Mass Transfer 63, 82-90.

Venegas, M., M. de Vega, N. García-Hernando, U. Ruiz-Rivas, 2017. Adiabatic vs non-adiabatic membrane-based rectangular micro-absorbers for H2O-LiBr absorption chillers. Energy 134, 757-766.
Wang, Z., Z. Gu, S. Feng, Y. Li, 2009. Application of vacuum membrane distillation to lithium bromide absorption refrigeration system. Int. J. Refrigeration 32, 1587-1596.
Woods, J., J. Pellegrino, J. Burch, 2011. Generalized guidance for considering pore-size distribution in membrane distillation. J. Membr. Sci. 368, 124-133.

Manuscript ID: 1328
DOI: 10.18462/iir.icr.2019.1328

The developing of lower GWP refrigerants

Shun OHKUBO[(a)], Felix FLOHR[(b)], Kenji GOBOH[(a)], Tatsumi TSUCHIYA[(a)], Hitomi ARIMOTO[(c)], Yuzo KOMATSU[(a)]

[(a)] Daikin Industries, Ltd.
Osaka, 566-8585, Japan, shun.ohkubo@daikin.co.jp
[(b)] Daikin Chemical Europe GmbH
Hannover, 30173, Germany, felix.flohr@daikinchem.de
[(c)] Daikin U.S. Corporation
Washington DC, 20005, USA, hitomi.arimoto@daikinus.com

ABSTRACT

Many lower global warming potential (GWP) refrigerants were developed as R404A alternatives to reduce environmental impact. In order to adapt to global regulation, many development options are necessary; New to market R468A was developed as a slightly flammable ultra-low GWP option with a GWP 146. Physical properties of R468A are comparable to R404A. Flammability and stability of the HFO blended option R468A should be considered, however it demonstrates a lower flammable limit (LFL) and burning velocity are similar to widely adopted for automotive use R1234yf and the thermal stability is also comparable to that of R1234yf. Since coefficient of properties (COP) of R468A is better than R404A in both medium temp (MT) and low temp (LT) condition, R468A is considered to be one potential option for R404A replacement to contribute reducing environmental impact for the earth in direct and indirect CO2 emission.
Keywords: Environment,, Low GWP, , Physical Propertity, R404A,Refrigerant. .

1. INTRODUCTION

Lower GWP refrigerants are required by regulation in all over the world to reduce environmental impact. In particular, R404A which has been widely used for all type of commercial refrigeration systems has a high GWP (3922), and is a target of reduction and phase down. Currently some non-flammable lower GWP refrigerants with GWP less than 1500 such as R407H are proposed as alternative for R404A. However, to further reduce GWP levels in order to comply with regional HFC regulation and "the Kigali Amendment to the Montreal Protocol" we have to reduce the total CO_2 Equivalent impact of refrigerants (GWP × amount) below 15 to 21% of baseline. European F-gas Regulation and the recent California proposal require refrigeration units to have GWP below 150. Therefore, development of much lower GWP refrigerant is necessary. This development necessitates the trade-off between the GWP of refrigerant and its flammability. R468A, a new refrigerant with the GWP of 146, is evaluated from following four viewpoints; Safety, Environmental impact, Energy-efficiency and Cost-effectiveness.

2. PHYSICAL PROPERTIES

2.1. Basic Properties

A core consideration in refrigerant choice is its environmental impact. Ozone depleting potential (ODP) and global warming potential (GWP) should be considered; a refrigerant should have zero ODP. Lower GWP value would have smaller environmental impact. In the viewpoint of recycle and reuse of refrigerants, the number of refrigerant component gasses is the smaller the better.
Basic properties of candidate refrigerants are shown in Table 1. ODP of alternative refrigerants are 0 and GWP of them are much lower than that of R404A. R407H is non-flammable alternative with the GWP of 1378. As R407H is R407 series, it consists of common components R32/R125/R134a, which are widely used in refrigerants. R468A is 3 components mixture, consists of R32, R1234yf

and R1132a. R1132a is widely used as a monomer for fluoro-elastomer manufacture and it is one of the latest refrigerant components classified as A2 in ASHRAE. R468A is slightly flammable, however, its GWP is below 150; 96% lower than R404A. R454A consists of R32/R1234yf and its GWP is below 300. Physical properties such as Boiling point of these alternatives are similar to R404A. Saturated pressures of these refrigerants were shown in Figure 1. Pressures were calculated by Refprop 9.1 and they were very close to each other. R407H, R454A and R468A can be potentially used with traditional R404A equipment and components without significant alternations.

Table 1. Physical properties of candidate refrigerants

Refrigerant	R404A	R407H	R454A	R468A
Composition	R125/R143a/R134a (44.0/52.0/4.0)	R32/R125/R134a (32.5/15.0/52.5)	R32/R1234yf (35/65)	R1132a/R32/R1234yf (3.5/21.5/75.0)
Molecular mass	97.6	79.1	80.5	88.8
Boiling point (101.3 kPa)	-46.2°C	-44.6°C	-47.4°C	-51.2°C
Critical temperature	72.0°C	86.5°C	86.2°C	83.9°C
Critical pressure	3.73 MPa	4.85 MPa	4.95 MPa	4.46 MPa
Pressure (25°C)	1.25 MPa	1.24 MPa	1.34 MPa	1.33 MPa
ODP	0	0	0	0
GWP AR5(AR4)	3943 (3922)	1378 (1495)	238 (239)	146 (148)
ASHRAE safety class	A1	A1	A2L	A2L

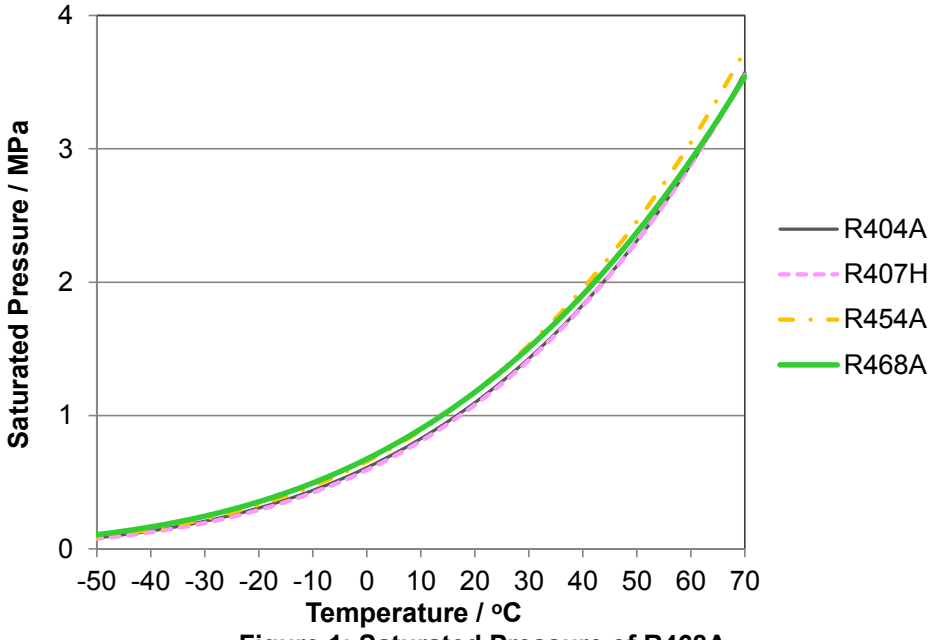

Figure 1: Saturated Pressure of R468A.

2.2. Energy Efficiency

Energy Efficiency affects indirect CO_2 emission. It is an important consideration as energy consumption for cooling, heating and refrigeration has a substantial impact on the total energy consumption of buildings and countries.

The theoretical cycle performance was simulated based on REFPROP 9.1. Calculation condition was shown in Table 2. Condensing temperature was determined as mid-point between dew point of refrigerant and outlet of condenser. Evaporated temperature was determined as mid-point between inlet of evaporator and dew point of refrigerant.

COP of all candidate refrigerants were better than that of R404A. COP of R407H was the highest of all the candidates and Capacity of R454A was the highest of all candidates. COP of R468A was 7% higher than that of R404A in LT and 5% high than that of R404A. Capacity of R468A was similar to that of R404A. Both COP and Capacity of R454A was better than R404A, however, its GWP is higher than 150.

Table 2. Calculation condition

Conditions	Low temperature (LT)	Medium temperature (MT)
Condensing temperature	40°C	45°C
Evaporating temperature	-40°C	-10°C
Superheat	20 K	20 K
Subcooling	0 K	0 K

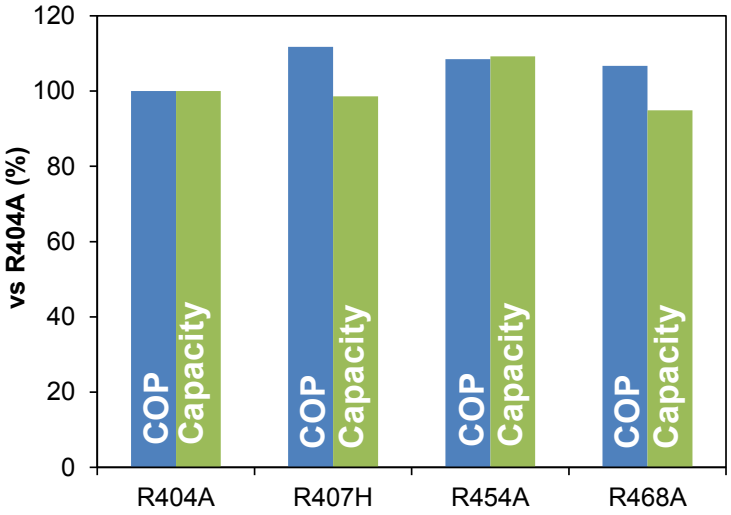

Figure 2: Cycle Simulation in LT Condition (Te = -40°C).

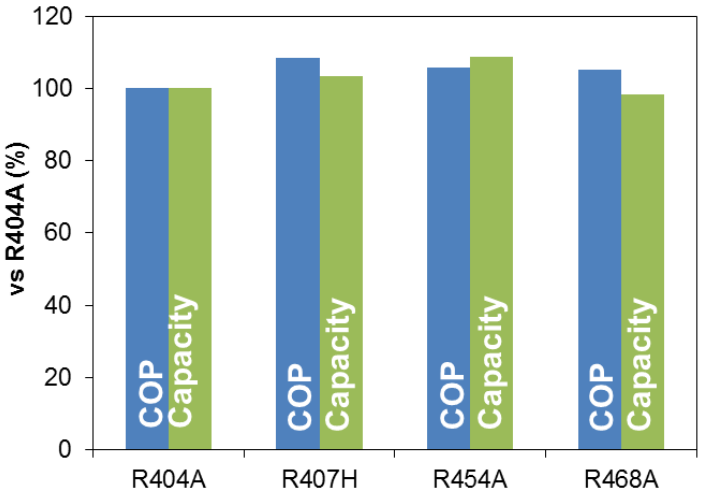

Figure 3: Cycle Simulation in MT Condition (Te = -10°C).

2.3. Thermal Stability

Thermal stability of lubricants and refrigerants mixture was evaluated with sealed tube test, based on ASHRAE Standard 97-2007. Each tube contained 2 grams of lubricant and metal coupons of steel, aluminium and copper. The refrigerant was added in an amount such that the internal pressure was 3 MPa at 175°C. Prior to its addition into the sealed tube, moisture of the lubricant sample was measured by Karl Fischer method. The moisture level was then adjusted to the experimental value by adding liquid deionized water. The lubricant was added to each tube with a syringe. The tube was evacuated followed by charging of refrigerant through condensation while the tube was submerged

in liquid nitrogen. The sealed tubes were aged at 175°C for 14 days. After aging, the tube contents were also analysed for Total Acid Number (TAN). Polyvinyl Ether (PVE) type lubricant was used for both HFC and HFO based refrigerants. The method for measuring TAN was based on ASTM D664 with some modifications to accommodate small sample sizes. 0.5 grams of the lubricant was dissolved in 5 grams titration solvent containing toluene, 2-propanol and a small amount of water and titrated with 2-propanol solution of potassium hydroxide at room temperature using p-naphthol benzene as an indicator. The 2-propanol solution of potassium hydroxide was adjusted to 0.01 $mol \cdot l^{-1}$.

Total acid number of each test was shown in Fig. 4. In the case of R407H, TAN was very small in all tests, even in the test with air and moisture. It indicates that HFCs can be used with both PVE oil because HFCs is very stable. In the case of R468A and R1234yf, even when PVE oil for HFCs used as lubricant, there was no significant increase of TAN after tested without air and moisture. However, TAN was increased when tested HFOs with lubricants for HFCs, air and moisture. When PVE oil for HFOs used as lubricant, there was no significant increase of TAN after tested with HFOs, air and moisture. When using HFOs, air and moisture should be managed and it is recommended for HFOs to use with lubricants for HFCs.

Table 3. Conditions of thermal stability test

Conditions	Test 1 (Without air and moisture)	Test 2 (With air and moisture)
Temperature (°C)	175	175
Test term (days)	14	14
Water content (ppm)	< 50	500
Air pressure (ppm)	< 10	6000
Catalyst	Fe / Cu / Al	Fe / Cu / Al
Oil	PVE for HFCs or HFOs	PVE for HFCs or HFOs

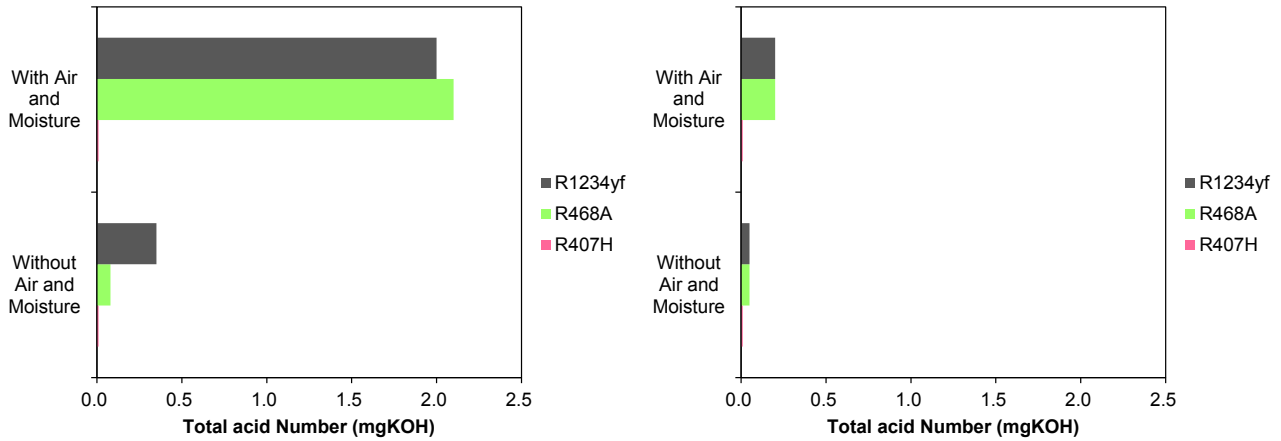

Figure 4: Thermal Stability of Refrigerants (Left: PVE for HFCs, Right: PVE for HFOs).

2.4. Flammability

Safety should take first priority to any other points. Refrigerants must be safe to use through the entire lifecycle of the equipment. In the case of R468A, it includes R1132a whose flammability categorized as not A2L but A2. Therefore, flammability of R468A should be cautiously evaluated.

LFL and Burning Velocity of refrigerants were tested. The LFL test apparatus and procedure were according to ASTM E681-2009 and Appendix B1 to ASHRAE Standard 34-2016. Burning velocities were measured by the closed-vessel method.

The flammability results of R454A and R468A are shown in Table 1. LFL of R454A and R468A were higher than R1234yf and burning velocity of them were slower than R32. Therefore, R454A and R468A are classified as A2L by ASHRAE Safety Classification and they can be used as well as R32, R1234yf and other A2L refrigerants.

Table 4. Flammability Test Results of Refrigerants

-	GWP (AR5)	LFL (vol%)	Burning velocity ($cm \cdot s^{-1}$)	ASHRAE safety class
R407H	1378	Non-flammable	-	A1
R32	677	14.4	6.7	A2L
R1234yf	<1	6.2	1.5	A2L
R454A	238	8.4	1.5	A2L
R468A	146	7.3	2.1	A2L

3. CONCLUSIONS

Several refrigerants were evaluated as R404A alternatives for refrigeration. Physical properties of R407H, R454A and R468A were similar to R404A and their theoretical COPs were better than R404A by 12%, 9%, 5% respectively. GWP of non-flammable refrigerant should be considered, however, its safety is as well as R404A. GWP of R468A is below 150 and it will suit for global HFC regulations. When HFOs are used with current equipment, we should consider its flammability and stability. Flammability of R468A is similar to R1234yf. The result of thermal stability tests indicates that lubricants for HFOs are useful for HFO blends including R468A. All in all R468A offers a well-balanced solution considering safety, environmental impact and total cost of ownership. Further studies on R468A will follow to give the full pictures about its technical characteristic. In addition, further studies on developing much lower refrigerant will be contributed to reduce environmental impact.

NOMENCLATURE

ODP	Ozone Depleting Potential (R11 = 1)	GWP	Global Warming Potential (CO_2 = 1)
COP	Coefficient Of Performance	LFL	Lower Flammability Limit (vol%)
MT	Medium Temperature	LT	Low Temperature
TAN	Total Acid Number	PVE	Polyvinyl Ether type Lubricant

REFERENCES

ANSI/ASHRAE 34-2016, Designation and Safety Classification of Refrigerants www.ashrae.org

IPCC 5th Edition: Intergovernmental Panel on Climate Change http://www.ipcc.ch/

Shibanuma, T., 2016. Steps Toward the Practical Use of Lower GWP Refrigerants for Refrigeration. The international Symposium on New Refrigerants and Environmental Technology, p. 317.

Ohkubo, S., 2018. The Evaluation of Low GWP Non-flammable Refrigerant R407H for Refrigeration as R404A Alternative. Proceedings of the 5th IIR Conference on Sustainability and the Cold Chain, Beijing China.

Rydkin, I., 2018. Laboratory Evaluation of R407H for Commercial Refrigeration. 17th International Refrigeration and Air Conditioning Conference at Purdue, p. 2603.

Low, R., 2018. Evaluation of Potential Use of R-1132a as a Refrigerant Blend Component. 1st IIR International Conference on the Application of HFO Refrigerants, Birmingham, UK, 1150.

Matsumoto, T., 2018. Evaluations of PVE Lubricants for Refrigeration Systems with the Low GWP Refrigerants. The international Symposium on New Refrigerants and Environmental Technology, p. 227.

Manuscript ID: 1338
DOI: 10.18462/iir.icr.2019.1338

Improvement of CO_2 hydrate slurry transportation in flow loop: Effect of anti-agglomerant additive on rheological properties

Pascal CLAIN[(a, c)], Amokrane BOUFARES[(a, b)], Fatima BENMESBAH[(a, d)], Amira ZENNOUNE[(a)], Véronique OSSWALD[(a)], Hong Minh HOANG[(a)], Didier DALMAZZONE[(b)], Anthony DELAHAYE[(a)], Laurence FOURNAISON[(a)]

[(a)] GPAN Irstea
ANTONY, 92761, France
[(b)] UCP, ENSTA Paristech
PALAISEAU, 91120, France
[(C)] DVRC Pôle Universitaire
PARIS – LA DEFENSE, 92916, France
[(d)] IFREMER
BREST, 29280, France

ABSTRACT

Previous studies showed that CO_2 hydrate slurries are potentially one of the top PCM slurries used as a secondary refrigerant, due to high dissociation enthalpy. However, crystal agglomeration phenomenon observed with solid-rich slurry that can lead to pipe plugging is a real limitation for an industrial application, and use of additives could be a way to prevent it.
Experimental rheological behaviour of CO_2 hydrate suspensions with a rheology modifier additive in various concentrations was studied in a dynamic flow loop using gaseous CO_2 injection in a pre-cooled water to crystallize CO_2 hydrates and to measure pressure drops as a function of volume flow rate for various solid particle fractions. The Herschel-Bulkley model was used to characterize the laminar flow regime and a shear-thinning behaviour was obtained. A FBRM probe was used to characterise chord length distributions of CO_2 hydrates and exhibited a threshold effect for this additive for the slurry.
The results showed that the use of the additive avoids slurry agglomeration phenomenon, bring a threshold to the slurry and improves their flow properties due to the affinity of additive to CO_2 hydrates.
Keywords: Gas Hydrates, Carbon Dioxide, Rheology, Anti-Agglomerant, Secondary Refrigeration.

1. INTRODUCTION

Secondary refrigeration is a method using a neutral fluid for cold distribution in order to confine primary refrigerants and reduce their quantities and thus their direct greenhouse effect due to gas emissions. Two-phase refrigerants (solid-liquid) are relevant for this method since their energy density is higher than a single phase secondary refrigerant because of the melting latent heat of the solid. Ice slurries are already used but their generation requires mechanical processes increasing exergy losses (Guilpart et al., 2006). Hydrate slurries composed of a suspension of hydrate crystals in aqueous solution can also be used as secondary refrigerants and have the advantage of being able to form without mechanical processes. CO_2 hydrate can be a suitable possibility for secondary refrigeration applications because of its high dissociation enthalpy 500 kJ/kg. As a result, CO_2 hydrate slurries can contain and carry large energy quantities (Fournaison et al., 2004; Marinhas et al., 2006). However, the use of CO_2 hydrates in cooling systems requires formation pressure higher than 1 MPa.

Previous studies in a dynamic loop performed at Irstea have shown that CO_2 hydrates in aqueous liquid phase can agglomerate (Delahaye et al. 2008, Delahaye et al. 2011, Jerbi et al., 2013), and even form plugs as in pipelines. Depending on whether the loop system studied does or does not have a stirred-tank reactor, hydrates can agglomerate and form plugs from a high hydrate fraction of 20 vol.% (with a stirred tank reactor) (Jerbi et al., 2013) or from a low hydrate fraction of 5-10 vol.% (Delahaye et al., 2008).

The addition of chemical promoters, as quaternary salts (TBAB, TBPB, TBPF…) (Clain et al., 2012; Fukushima et al., 1999; Hashimoto et al., 2011) or Sodium Dodecyl Sulfate (SDS) (Oignet et al., 2017) is a solution to reduce the agglomeration. Previous results show that SDS used at concentrations of 1,500 to 2,000 ppm significantly decreases agglomeration and improves the flow properties of the slurry. Moreover, SDS helps decreasing the viscosity of CO_2-hydrate slurry at high fraction (> 10 vol.%) and therefore could be suitable for use in industrial applications such as secondary refrigeration, in which hydrate slurries must be easy to handle (see Table 1).

This work presents a rheological study of CO_2 hydrate slurry in the presence of a chemical additive named AA_A carried out in a dynamic flow loop in order to observe the effect of this additive on slurry viscosity and agglomeration. This behaviour is characterized in the present work by applying the capillary viscometer method (based on pressure drop vs. flow measurements), and the Herschel-Bulkley model is used in a first approach to represent the apparent viscosity of the slurry. In hydrate field, particle size analysis is usually used for experimental studies of hydrate growth and agglomeration (Clain et al., 2015; Clarke and Bishnoi, 2005; Greaves et al., 2008; Leba et al., 2010). The work of Clarke and Bishnoi on the kinetics of CO_2 hydrate formation in water showed that the FBRM probe could detect hydrate nucleation, i.e. the total number of particle counts increasing sharply, corresponding to a sudden rise of temperature. Then hydrate particle growth could be observed by an increasing of the number of large chord length and agglomeration could be seen as a sudden drop in the total number of particles (Greaves et al., 2008) studied the reliability of FBRM probe by measurement tests such as THF hydrate, ice and different glass particle size. They found that the FBRM can detect with a high accuracy the system changes. Nevertheless, they remarked that the measured chord length distribution can be distorted and a calibration specific need required for the particle size. Moreover, in bimodal system, large particles often diminish the ability of the FBRM to measure and count small particles.

Table 1. Summary of rheological studies performed on different hydrate slurries. OdW: Ostwald-de Waele; S-Thin.: Shear thinning; S-Thicken.: Shear thickening; HB: Herschel-Bulkley

Reference	Hydrate	Solution	Viscometer	ϕ_s	Behaviour
Fukushima et al. (1999)	TBAB	Aqueous	Capillary	0.22-0.31	OdW S-Thin.: μ_{app}: 30-2000 mPa.s
Andersson and Gudmundsson, (2000)	CH_4	Aqueous	Capillary	0.01-0.1	Bingham: k: 1-3.5 mPa.s
Darbouret et al. (2005)	TBAB	Aqueous	Capillary	0.04-0.53	Bingham: k: 8-170 mPa.s
Delahaye et al. (2008)	CO_2	Aqueous	Capillary	0.04-0.1 0.1-0.2	OdW S-Thicken. HB S-Thin.: μ_{app}: 4-42 mPa.s (at 400 s^{-1})
Delahaye et al. (2011)	CO_2	Aqueous + TA	Capillary	0.04-0.1	Newtonian: μ_{app}: 3.3-16.6 mPa.s
Clain et al. (2012)	TBPB	Aqueous	Capillary	0-0.28	OdW S-Thin.: μ_{app}: 4-41 mPa.s
Jerbi et al. (2013)	CO_2	Aqueous	Capillary	0-0.21	OdW S-Thin. : μ_{app}: 3-10 mPa.s
Waycuilis et al. (2011)	CH_4	Aqueous	Capillary	0-0.12	Non-Newtonian: μ_{app}: 1.26-4.8 mPa.s
Oignet et al. (2017)	CO_2	Aqueous +SDS	Capillary	0-0.155	OdW S-Thin.: μ_{app}: 8-15 mPa.s

2. MATERIAL AND METHOD

2.1. Materials

A CO_2 cylinder was purchased from Air Liquide (99.995 % in volume) and deionized water was used for the experiments. AA_A additive is a hydrophobic-modified alkali-swellable emulsion (HASE) polymer. It was used to at two mass concentrations of 0.3 and 0.5 wt%.

2.2. Equipment and Protocol

A dynamic loop, described in previous works, is used to produce CO_2 hydrate slurry and to characterize its rheological properties. The loop is mainly composed of stainless steel pipes with an internal diameter of 8 mm (external diameter of 10 mm) and a total length of 2 m. A scheme of the apparatus is shown in Fig. 1. The total volume of the loop is 2.65 10^{-4} m^3. The loop is located in a cold room (6 m^3) whose temperature is controlled by PID. Temperature and pressure are maintained within the range of 268 – 293 K and up to 3.5 MPa respectively. The dynamic loop is also composed of a glass tube (with an inner volume of around 3.10^{-5} m^3) for detecting the formation of hydrate particles and visualizing hydrate slurry flow. The loop is equipped with a differential pressure gauge (ABB 265 DS, up to 0.02 MPa, ± 0.04 %) to measure the pressure drops caused by fluid flow on a straight line of the loop (0.5 m), and with a pump (AxFlow GC-M25, maximum flow rate = 0.17 $m^3.h^{-1}$) and an electromagnetic flowmeter (IFM6080K-type Variflux, ± 0.5 %) to control and measure fluid flow. The device is equipped with 6 T-type thermocouples (± 0.3 K) and 2 pressure gauges (range: 0-5 MPa, accuracy 0.05 %). Finally, a FBRM probe can be used for chord length study in the loop during the rheology experiments.

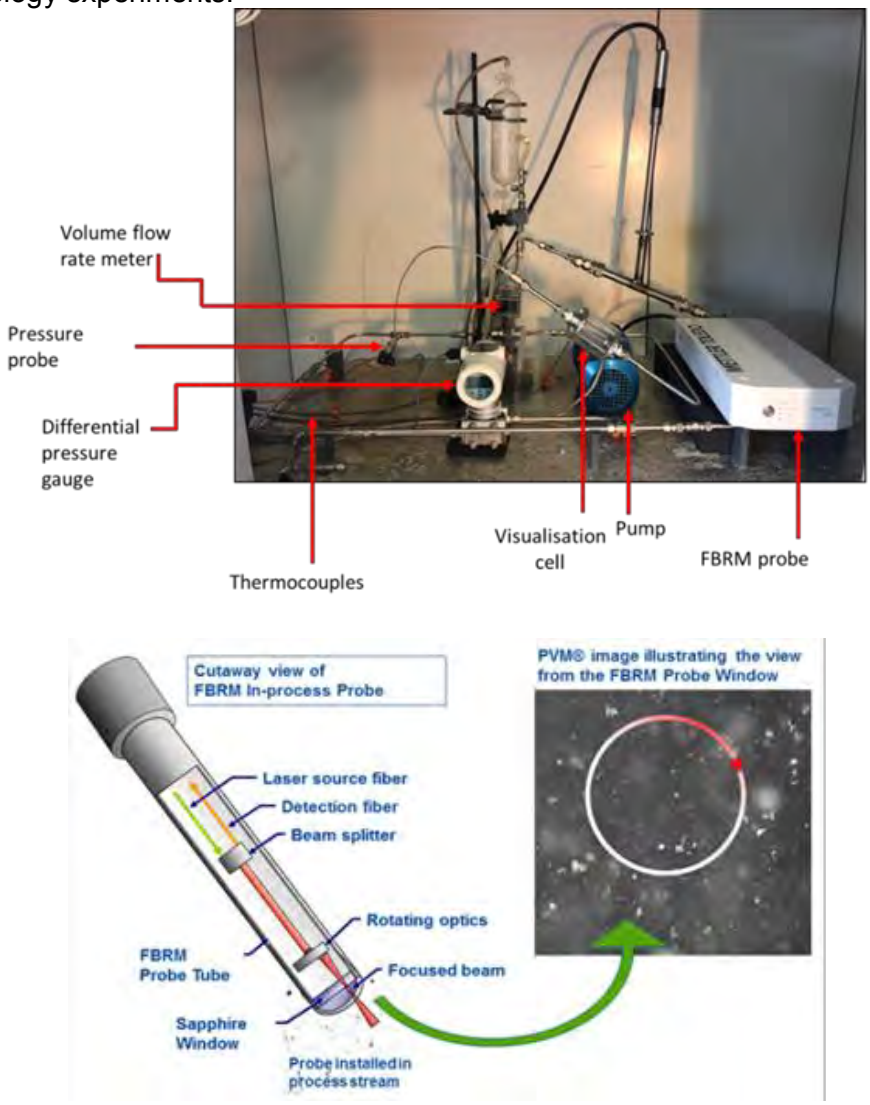

Figure 1: Rheology flow loop and FBRM probe

After the introduction of water in the loop, the cooling stage starts with the cold unit of the box until reaching a set temperature. At this moment, the gas injection starts. The injection is refrigerated and calibrated through the syringe pump (1000D ISCO) placed outside the box. As the injection takes place, the gas dissolves in the liquid phase until it reaches the equilibrium HLV curve. During this phase, the cooling continues in the system until the set temperature is reached. At the equilibrium temperature, the gas injection continues until the water starts to trouble and quickly reaches the HLV equilibrium curve. This moment is a sign that the hydrates begin to form in the system. Gas is still injected to the amount required to form the desired hydrate solid fraction.

Once the hydrates are formed and the equilibrium established in the loop, the rheological study is carried out by varying the flow rate and measuring the corresponding pressure drop as shown in Fig. 2. We realized two phases of measurement: a downward phase where we decrease the volume flow rate of higher to lower flow rate values and an upward phase where we increase the volume flow rate of the lower to higher flow rate values. Each level is labelled as illustrated in Fig. 2 (levels D2 and U1 are the same volume flow rate value in the downward and upward phase respectively, 50 $l.h^{-1}$, D1 and U2 are at 70 $l.h^{-1}$ for this example and so on for the others levels).

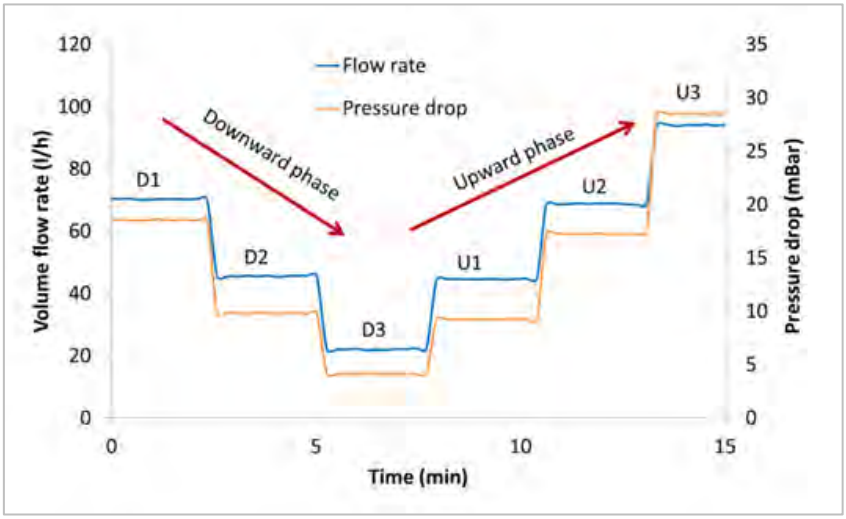

Figure 2: Evolution of pressure drop at various flow rate

The capillary viscometer method used to evaluate hydrate slurry rheology is based on various assumptions. In a first approximation, CO_2 hydrate slurry can be considered as a pseudo-homogeneous fluid, circulating in laminar regime and without wall slip in the cylindrical pipe. Flow rate, shear stress, shear rate can thus be represented at the wall by the Rabinowitsch-Mooney's equation:

$$\frac{Q}{\pi R^3} = \frac{1}{4}\left(\frac{8U}{D}\right) = \frac{1}{\tau_w^{\,3}}\int_0^{\tau_w} \tau^2 \dot{\gamma}\, \mathrm{d}\tau \qquad \text{Eq. (1)}$$

Where τ_w is the shear stress at the wall in Pa, related to regular pressure drops ΔP in Pa due to a pipe of length L in m and diameter D in m. After derivation of the expression of Rabinowitsch-Mooney, a differential equation is solved and an expression of the shear rate at the wall is obtained and n is the behaviour index defined as:

$$\tau_w = \frac{D\,\Delta P}{4\,L} \qquad \text{Eq. (2)}$$

$$\dot{\gamma}_w = \frac{8U}{D}\frac{(3n+1)}{4n} \qquad \text{Eq. (3)}$$

$$n = \frac{\mathrm{d}\ln \tau_w}{\mathrm{d}\ln \frac{8u}{D}} \qquad \text{Eq. (4)}$$

Thus, measurements of pressure drop ΔP and flow velocity allow the rheological behaviour of the fluid to be established according to Herschel-Bulkley's model:

$$\tau_w = \tau_0 + k\,\dot{\gamma}_w^n \qquad \text{Eq. (5)}$$

Hydrate size analyses were performed thanks to a Focused Beam Reflectance method (FBRM), which is an in-situ method of counting and sizing particles and aggregates. The technology uses a probe where a revolving laser beam is projected through a sapphire window at a wavelength of 780 nm and highly focused just outside the window surface. The focused beam rotates at a high rate of speed about 2 $m.s^{-1}$, so that particle motion is insignificant to the measurement. As particles pass by the window surface, the focused beam intersects the edge of a particle. The particle then begins to backscatter laser light until the focused beam reaches the particle's opposite edge as showed in Fig. 1. The backscattered light is collected by the FBRM optics and converted into an electronic signal. The particle backscattering time is multiplied by the scan speed and the result is a chord length. A chord length is a straight line between any two points on the edge of a particle or particle structure. During a specified measurement time, measured chord lengths are recorded and a chord length distribution (CLD) is returned. The measured CLD depends on both the particle size distribution (PSD) and the shape of the particle, so it can be used to represent the characteristics of a particulate system. The FBRM instrument is composed of a measurement probe, an electronic measurement unit and a computer for data acquisition and analysis. For CLD analysis, the probe is inserted into the flow loop with an inclination of 70° using a dedicated stand. The data analysis software gives the counts number n_i per second for each selected size class *i* of chord length c_i.

3. RESULTS AND DISCUSSION

3.1. Impact of Anti-Agglomerant Additives on CO_2 Hydrate Slurries

Fig. 3 shows the volume flow rate and pressure drop variations at various hydrate fractions (10 and 12 vol%) and additive concentrations of 0.3 and 0.5 wt% and a CLD distribution for CO_2 + AA_A at 0,3 wt% for a flow rate stage of 80 $l.h^{-1}$. As we can see on the results, pressure drop varies with the imposed volume flow rate, more or less regularly depending on the operating conditions. On Fig. 3.a, the flow behaviour of CO_2 hydrate slurry with a solid fraction of 10 vol% without additive is presented. Two different periods can be observed. First, during downward stage, pressure drop and flow rate evolved regularly between 0 and 80 min. Pressure drops levels are not constant like the flow rate levels but continue to increase slightly. This might indicate either a plugging within the pressure drop gauge pipes or a phenomenon increasing the pressure drop at given flow rate like agglomeration. From 80 min, when the upward stage started, pressure drop values did not stabilize quickly which indicates strong disturbances in the system. It is also noted that the pressure drop is more important for U1 level than D3 level. This can be related to a change in the slurry composition. We can consider the appearance of possible agglomerates that disturb slurry flow and increase pressure drop. Beyond this level, there is unstable pressure drop behaviour with a continuous decrease. This denoted at least a partial plugging in the pipe. The same behaviours have also been observed for larger solid hydrate fractions (higher than 10 vol%). On Figs. 3b and 3c, we presented the flow behaviour of CO_2 + AA_A hydrate slurry for two mass concentrations, 0.3 and 0.5 wt%, and solid hydrate fraction, 12 and 10 vol% respectively.

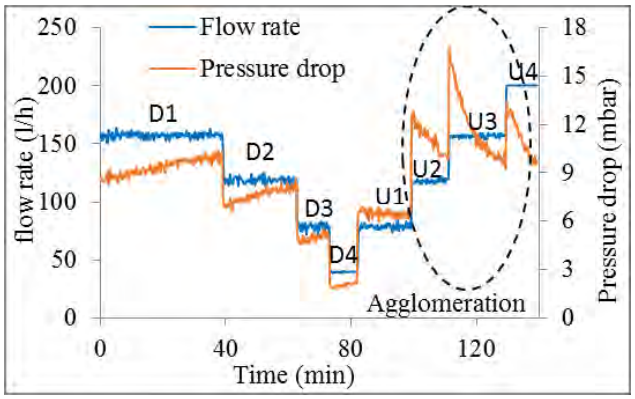

3.a: CO_2; hydrate fraction = 10 vol%

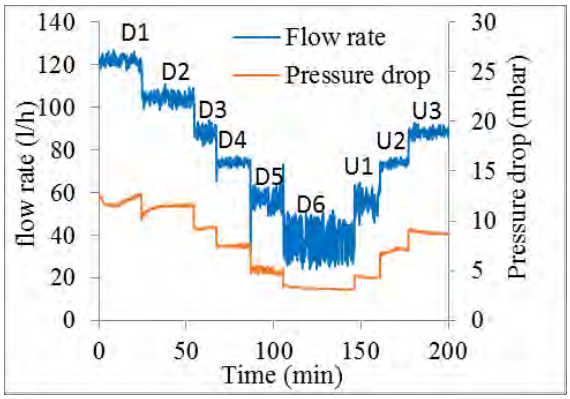

3.b: CO_2+AA_ A at 0.3 wt%; hydrate fraction = 12 vol%

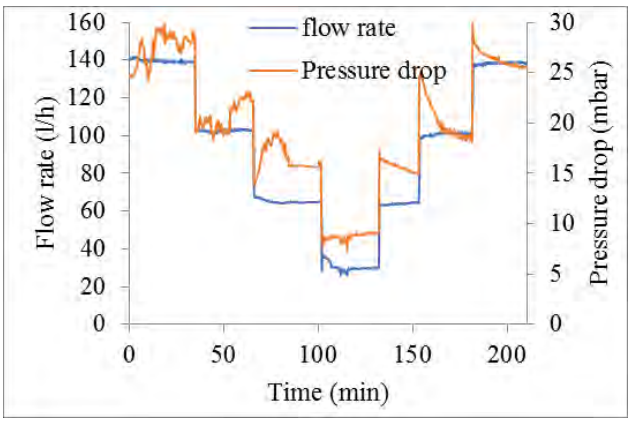

3.c: CO_2+AA_ A at 0.5 wt%; hydrate fraction = 10 vol%

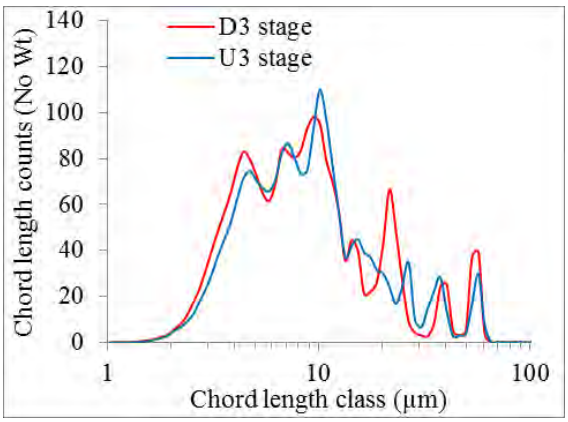

3.d: CLD for CO_2+AA_A at 0,3 wt%; hydrate fraction = 12 vol%

Figure 3: Volume flow rate and pressure drop variations at various hydrate fractions, two AA_A additive concentrations. CLD distribution for CO_2 + AA_A at 0,3 wt% and 80 l.h^{-1}

First, we note that the variation of the pressure drop is globally proportional to the flow rate variation. We observe that CO_2 hydrate slurry with AA_A pressure drop is more stable than single CO_2 hydrate slurry. It can be observed that the pressure drop seems to have difficulties stabilizing on the different levels during the downward phase but displays similar values for the upward and downward phases. This effect suggests that the AA_A additive acts as an anti-agglomerant agent. However, it can be noted that the flow rates are more stable at a mass concentration of 0.5 wt% than at 0.3 wt%. On the other hand, it can be noted that the pressure drop has higher perturbations at 0.5 wt% than at 0.3 wt% although flow rate stage are in steady conditions. This would indicate a better stability of the fluid flow at the lowest additive concentration. Finally, the pressure drop value is higher for the concentration at 0.5 wt% than at 0.3 wt% which can be attributed to the increase in the viscosity of the carrier solution in the presence of additive. Indeed, during the preparation of the solution, it was observed that it became more and more viscous with the presence of this additive. This first qualitative observation has to be check with a CLD characterization of CO_2 hydrate crystals for confirming the assumption. On Fig. 3.d, we present CLD distributions at level U3 and D3 (flow rate = 80 l.h^{-1}) for the same experiment of Fig. 3.b. We observe that neither the count nor the chords length changes significantly during the CO_2 hydrate slurries rheological characterization. A threshold effect has been identified in the presence of this additive and seems interesting for the intended application because the pressure drop is not too high. The threshold effect is the ability of additives bind to the hydrate particles by chemical bonds, in order to maintain them in the solution without sedimentation or agglomeration.

In order to verify the relevance of the present results, it is interesting to compare them with literature data as seen in Fig. 4. This figure proposes comparisons between various viscosities obtained for CO_2 hydrate slurries with and without stirred tank reactor used to homogenize the slurry inside the vessel and prevent formation of hydrate agglomerates for a constant shear rate at 400 s^{-1}, as described in previous works (Delahaye et al., 2008; Jerbi et al. 2013; Oignet et al. 2017). Concerning the evolution of apparent viscosity as a function of shear rate, it can be seen that CO_2 hydrate slurry in the presence of the additive has a shear-thinning behaviour. Finally, as shown in literature for hydrate slurries, the apparent viscosity increases with solid fraction, which is an expected result. Indeed, it varies between 4.1 mPa.s at 6.2 vol% and 6.7 mPa.s at 12 vol% for AA_A for a shear rate of 400 s^{-1}. Single CO_2 hydrate slurries have also a shear-thinning behaviour (see Table 1). Nevertheless, according to the studied system, viscosity values differ. We observed that the apparent viscosities for CO_2 hydrate slurry with AA_A are quite low in comparison with other literature data. We saw that this additive used in this work have an impressive impact on the apparent viscosity close to the results obtained by Jerbi et al. 2013. In their work, the presence of a stirred tank reactor associated to the loop allows hydrate slurry viscosity to be relatively low. This result can be explained by the rheological behaviour of hydrate slurries. Indeed, stirring action in the tank increases shear rate, which consequently may result in a decrease in the viscosity of the slurry in the loop due to its shear-thinning behaviour. AA_A additive used to in this work is able to have the same effect on apparent viscosity without mechanical stirring, which could be very interesting for energy efficiency of cooling applications.

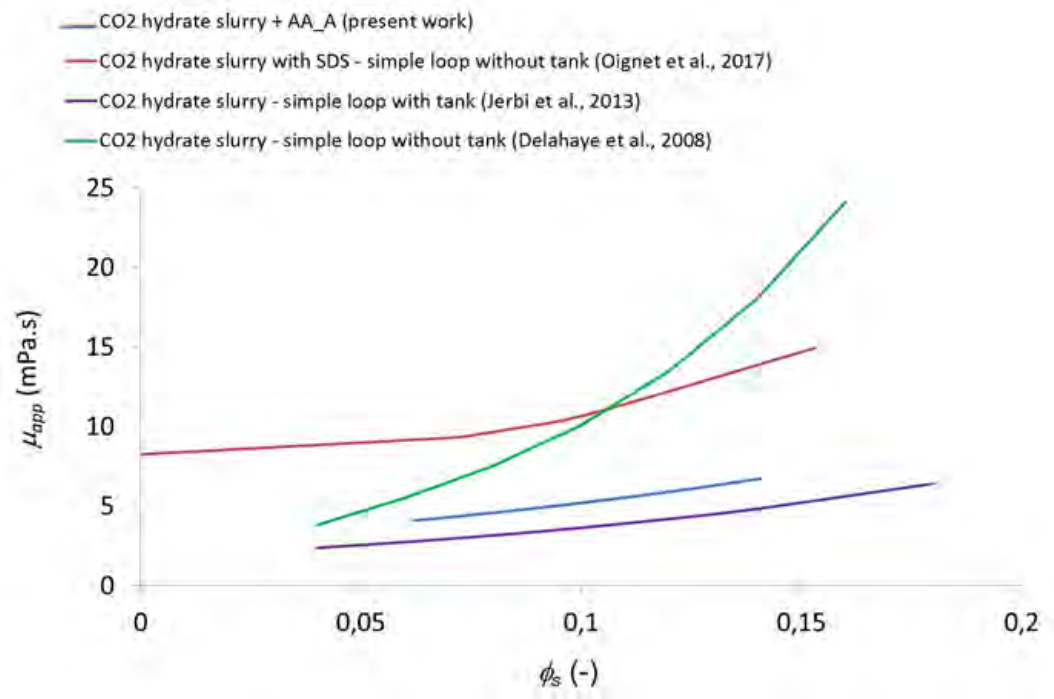

Figure 4: Comparison between hydrate slurry viscosities and literature data at 400 s^{-1}

4. CONCLUSION

In this work, we examined the effect of a HASE additive on rheological properties of CO_2 hydrate slurries in a dynamic loop for hydrates fractions between 6 and 12 vol%. The Ostwald (capillary) viscometer method was used to show that CO_2 hydrate slurries with additive have a shear-thinning behaviour. This non-Newtonian behaviour is generally observed in studies on hydrate slurries. Apparent viscosities obtained for this additive are quite low and close to the results of Jerbi which use a mechanical stirring. We were also able to highlight the properties of anti-agglomeration and threshold of this additive on the CO_2 hydrate slurry. Others experiments have to be run at various mass concentrations and types additives for evaluate their impact on the CO_2 hydrate slurries flow. In the same time, particle size distribution study will be carrying out to develop a better comprehension on the mechanisms of anti-agglomeration of theses additives.

ACKNOWLEDGEMENTS

This work was supported by the French National Research Agency under the program Crisalhyd (ANR-14-CE05-0045) and the different project's partners.

NOMENCLATURE

c	Chord length class	U	Fluid velocity ($m.s^{-1}$)
D	Pipe diameter (m)	ΔP	pressure drop (Pa)
k	Consistency index ($Pa.s^n$)	$\dot{\gamma}_w$	shear rate at the wall (s^{-1})
L	Tube length (m)	ϕ_s	volume fraction of hydrate
n	Behaviour index ; count number	τ_0	minimal shear or yield stress (Pa)
Q	Volume flow rate ($m^3.s^{-1}$)	τ_w	shear stress at the wall (Pa)

R Pipe radius (m) μ_{app} apparent viscosity (Pa.s)

REFERENCES

Andersson, V., Gudmundsson, J.S., 2000. Flow properties of hydrate-in-water slurries. Annals of the New York Academy of Sciences 912, 322-329.

Clain, P., Delahaye, A., Fournaison, L., Mayoufi, N., Dalmazzone, D., Fürst, W., 2012. Rheological properties of tetra-n-butylphosphonium bromide hydrate slurry flow. Chem. Eng. J. 193-194, 112-122.

Clain, P., Ndoye, F.T., Delahaye, A., Fournaison, L., Lin, W., Dalmazzone, D., 2015. Particle size distribution of TBPB hydrates by focused beam reflectance measurement (FBRM) for secondary refrigeration application. Int. J. Refrig. 50, 19-31.

Clarke, M.A., Bishnoi, P.R., 2005. Determination of the intrinsic kinetics of CO_2 gas hydrate formation using in situ particle size analysis. Chem. Eng. Sci. 60, 695-709.

Darbouret, M., Cournil, M., Herri, J.M., 2005. Rheological study of TBAB hydrate slurries as secondary two-phase refrigerants. Int. J. Refrig. 28, 663-671.

Delahaye, A., Fournaison, L., Jerbi, S., Mayoufi, N., 2011. Rheological Properties of CO_2 Hydrate Slurry Flow in the Presence of Additives. Ind Eng Chem Res 50, 8344-8353.

Delahaye, A., Fournaison, L., Marinhas, S., Martinez, M.C., 2008. Rheological study of CO_2 hydrate slurry in a dynamic loop applied to secondary refrigeration. Chem. Eng. Sci. 63, 3551-3559.

Fournaison, L., Delahaye, A., Chatti, I., Petitet, J.P., 2004. CO_2 hydrates in refrigeration processes. Ind. Eng. Chem. Res 43, 6521-6526.

Fukushima, S., Takao, S., Ogoshi, H., Ida, H., Matsumoto, S., Akiyama, T., Otsuka, T., 1999. Development of high-density cold latent heat with clathrate hydrate. NKK Technical Report 166, 65-70.

Greaves, D., Boxall, J., Mulligan, J., Montesi, A., Creek, J., Sloan, E.D., Koh, C.A., 2008. Measuring the particle size of a known distribution using the focused beam reflectance measurement technique. Chem. Eng. Sci. 63, 5410-5419.

Guilpart, J., Stamatiou, E., Delahaye, A., Fournaison, L., 2006. Comparison of the performance of different ice slurry types depending on the application temperature. Int. J. Refrig. 29, 781-788.

Hashimoto, S., Kawamura, K., Ito, H., Nobeoka, M., Ohgaki, K., Inoue, Y., 2011. Rheological study on tetra-n-butyl ammonium salt semi-clathrate hydrate slurries, 7th International Conference on Gas Hydrates, Edinburgh, Scotland, United Kingdom.

Jerbi, S., Delahaye, A., Oignet, J., Fournaison, L., Haberschill, P., 2013. Rheological properties of CO_2 hydrate slurry produced in a stirred tank reactor and a secondary refrigeration loop. Int. J. Refrig. 36, 1294–1301.

Leba, H., Cameirao, A., Herri, J.-M., Darbouret, M., Peytavy, J.-L., Glénat, P., 2010. Chord length distributions measurements during crystallization and agglomeration of gas hydrate in a water-in-oil emulsion: Simulation and experimentation. Chem. Eng. Sci. 65, 1185-1200.

Marinhas, S., Delahaye, A., Fournaison, L., Dalmazzone, D., Furst, W., Petitet, J.P., 2006. Modelling of the available latent heat of a CO_2 hydrate slurry in an experimental loop applied to secondary refrigeration. Chem. Eng. Process. 45, 184-192.

Oignet, J., Delahaye, A., Torré, J.-P., Dicharry, C., Hoang, H.M., Clain, P., Osswald, V., Youssef, Z., Fournaison, L., 2017. Rheological study of CO_2 hydrate slurry in the presence of Sodium Dodecyl Sulfate in a secondary refrigeration loop. Chem. Eng. Sci. 158, 294-303.

Waycuilis, J., Sirajuddin, H., Rensing, P., 2011. A novel approach to production of hydrate slurries at high process intensity and conceptual applications, ICGH, Edinburgh.

Manuscript ID: 1347
DOI: 10.18462/iir.icr.2019.1347

The R744 vapour compression test rig designed for visualisation of two-phase flow inside ejectors

Michal HAIDA[(a)], Rafal FINGAS[(a)], Wojciech SZWAJNOCH[(a)], Jakub BODYS[(a)], Michal PALACZ[(a)], Jacek SMOLKA[(a)], Andrzej J. NOWAK[(a)]

[(a)] Institute of Thermal Technology, Silesian University of Technology
Gliwice, 44-100, Poland, michal.haida@polsl.pl

ABSTRACT

Use of advanced experimental technique for the R744 two-phase flow observation inside the ejector is required to find a possibility of the ejector efficiency improvement. Hence, the CO2 refrigeration test facility dedicated to visualise the flow behaviour inside the ejector is presented. The test rig is designed and installed for operation analysis of freezers through air conditioning applications. The R744 vapour compression rack is equipped with the transparent ejector designed for the flow visualisation investigation. The ejector section was prepared in order to perform flow velocity and mixing process analyses using the Particle Image Velocimetry system and high-speed camera. The designed system let to investigate various shapes of the ejector cross-sections due to modular construction as well as another expansion devices, e.g., a capillary tube. The performance and main characteristics of the test rig was analysed on the basis of the coefficient of performance and the first-law analysis with and without the ejector.
Keywords: Refrigeration, Carbon Dioxide, Ejectors, COP, Energy Efficiency.

1. INTRODUCTION

The carbon dioxide (denoted as R744) is an one of the most promising natural refrigerant and competitive when compared to the synthetic refrigerant. The recent regulations presented in Kigali Amendment (United Nations Environment Programme, 2016) and in the European F-gas regulations (Parliament and of the European Union, 2014) forced to phase out common synthetic refrigerants from the market, i.e., R410A or R22 due to the high global warming potential (GWP) index.

The number of the installed refrigeration units based on the natural refrigerants, especially R744 ones in supermarkets, significantly increased as the result of the system improvements (Shecco, 2013). However, the R744-based refrigeration units obtained much lower coefficient of performance (COP) at hot and tropical climates when compared to the cold and moderate climates due to the low critical temperature of 31.1°C and high critical pressure of 73.8 bar. The very high pressure differences in the expansion and compression sections caused an increase in the energy loss and a decrease in COP (Kim et al., 2004). For this reason, COP of the R744 refrigeration system must be improved by implementation of the well-designed components that reduce the energy and exergy losses (Bansal, 2012).

The high thermodynamic losses that appeared in the expansion valve led to introduce more complex device to recover some potentially expansion work (Elbel and Hrnjak, 2008). Moreover, the possibility to utilise the evaporator in the flooded mode allowed for the COP improvement which required a recirculation of the liquid phase from the evaporator. One of the solutions is to use a two-phase ejector as a main expansion device in the R744 refrigeration system. The main aim of the ejector is to expand the motive flow from the discharge section through the converging-diverging nozzle, entrain the suction stream outside from the evaporator and compress the mixed flow through the diffuser to the intermediate pressure level. The ejector can be utilised to entrain either the vapour flow from the evaporator outlet or the liquid flow for the overfeed evaporator (Li et al., 2014).

The numerical investigation of the R744 ejector-based system obtained a significant COP improvement compared to the standard direct expansion system or R744 booster system with flash

gas bypass concept (Li and Groll, 2005). The authors stated that the COP improvement was more than 16% when compared to the basic transcritical R744 cycle for air-conditioning operating conditions. The similar improvement was observed for the R744 ejector-based system with the internal heat exchanger (Deng et al., 2007). Surprisingly, the prototype ejector implemented to the R744 transcritical cycle improved COP up to 7%, whereas the COP improvement of the ejector-based system should be approximately 18% based on the theoretical results (Elbel and Hrnjak, 2008). Therefore, the design process of the two-phase ejector has to be done using more accurate complex mathematical approach such as computational fluid dynamics (CFD) model.

The defined two-phase fluid flow assumption in the CFD model of the two-phase ejector allowed for the evaluation of the flow behaviour inside the ejector. The most common approach used in the numerical investigation was the homogenous equilibrium model (HEM), which assumed mechanical and thermodynamic equilibrium between both phases (Lucas et al., 2014). The application range of HEM for R744 two-phase ejector based on the mass flow rate predictions was defined close to the critical point and in transcritical conditions (Palacz et al., 2015). The accuracy improvement of the CFD ejector model at the subcritical conditions was done when the modified homogeneous relaxation model (HRM) was used for evaluation of the metastable effect during expansion process (Haida et al., 2017). The further improvement of the accuracy of CFD R744 ejector model can be attained by use of the mixture fluid flow assumption (Giacomelli et al., 2018).

The CFD model allowed for the accurate prediction of the two-phase flow inside the R744 ejector. However, the implementation of the aforementioned CFD models in dynamic simulation is impossible due to the computation time for a single operating point. The theoretical analysis of the R744 ejector-based cycle were mostly performed using zero-dimensional homogeneous equilibrium model (Kornhauser, 1990). The approach let to evaluate ejector performance based on the equilibrium state of both phases and assumed efficiency of each ejector part. The efficiencies of ejector parts were defined as a constant value for selected operating regimes (Liu et al., 2012). The aforementioned assumption caused high discrepancy of the motive and suction mass flow rates predictions given by theoretical model when compared to the experimental results. Therefore, the low-order and fast mathematical approach built by use of the complex computational fluid dynamic (CFD) model results and experimental data allows to predict ejector performance at high accuracy for very wide operating regime. One of the solutions is to implement the reduced-order model (ROM) of the designed two-phase ejector into the dynamic simulations of the R744 transcritical cycle based on the proper orthogonal decomposition (POD) approximation basis (Ostrowski et al., 2008).

The most important advantage of ROM for the approximation base is its optimality, i.e., there is no other approximation base with smaller error. Due to this property, the ROM constructed using the full CFD model of two-phase flow is characterised by very high accuracy, while the computational time is decreased significantly. To generate ROM as a continuous function of the input parameters, the radial basis function (RBF) interpolation method was implemented for the POD-ROM (Ostrowski et al., 2008). The POD-RBF model of the R744 two-phase ejector based on the CFD results was developed for ejector performance evaluation (Haida et al., 2018b). The ROM was built based on the HEM results for transcritical conditions and the accuracy of ROM was similar to the CFD results compared to the experimental data. Moreover, the hybrid combination of the CFD results and experimental data were used to build the hybrid ROM of the R744 ejectors (Haida et al., 2018a). The previously discussed model was used to generate maps of ejectors performances installed in the multi-ejector module (Banasiak et al., 2015) for R744 supermarket system.

The motive nozzle and suction nozzle mass flow rates accuracy of the each ROM was within ±10% for operating conditions typical for supermarket application. One of the reason of the specified model prediction is the parameters selected for model validation. The validation procedure of the R744 two-phase ejector numerical model were performed to define the model accuracy based on the pressure distribution (Nakagawa et al., 2011), motive nozzle and suction nozzle mass flow rates (Haida et al., 2017), and temperature of the ejector walls (Haida et al., 2018). Each method let to evaluate the global flow parameters as well as at defined local point. Therefore, the investigation of the flow behaviour, especially in the mixing section, can be done by visualisation of the two-phase flow to build more advanced and accurate mathematical model. The flow visualisation by use of the particle image velocimetry method (PIV) allowed the authors to perform numerical investigation of the CFD model with different turbulent models (Little and Garimella,

2016). The visualisation of the R744 two-phase ejector with a rectangular cross-section was performed (Zhu et al., 2017).The authors used the light film and a single-lens reflex camera to observe the liquid and vapour flow together with the expansion angle in the mixing chamber. Based on the experimental results given by (Zhu et al., 2017), the evaporation line in the mixing section was presented and the flow quality was approximated based on the captured snapshots.
The main aim of this paper is to present the R744 vapour compression test rig equipped with the R744 two-phase ejector designed for flow visualisation inside the ejector using PIV method. The test rig was defined to investigate the ejector performance at refrigeration, air-conditioning and heat pump applications. At first, the system layout was presented with the detailed description of the R744 circuit, oil loop and auxiliary loops. Then, the design concept of the ejector with transparent walls was shown. Finally, the first-law analysis was done to define COP improvement of the test rig working with the utilised ejector compared to the system working in the reference booster mode. The energy performance analysis was performed using OpenModelica software with implemented hybrid ROM of the R744 two-phase ejector to evaluate COP of the system equipped with the designed ejector.

2. THE R744 VAPOUR COMPRESSION TEST RIG EQUIPPED WITH THE TRANSPARENT EJECTOR

The test rig was designed to carry out the experimental investigation of the R744 two-phase ejector based on the two-phase flow visualisation inside the ejector. The PIV method was employed for mixing process observation and validation of the CFD R744 ejector model with different turbulence approaches. Moreover, the test campaigns were defined for different applications and different climate zones. Therefore, the R744 loop with all components and measurements was shown in Fig. 1. The test rig was designed as a standard booster system with flash gas bypass and additional liquid receiver. The semi-hermetic compressor Dorin CD 1400H was used to compress the vapour flow from evaporator pressure level. Moreover, the aforementioned compressor was connected to the inverter to control the capacity by frequency modification.

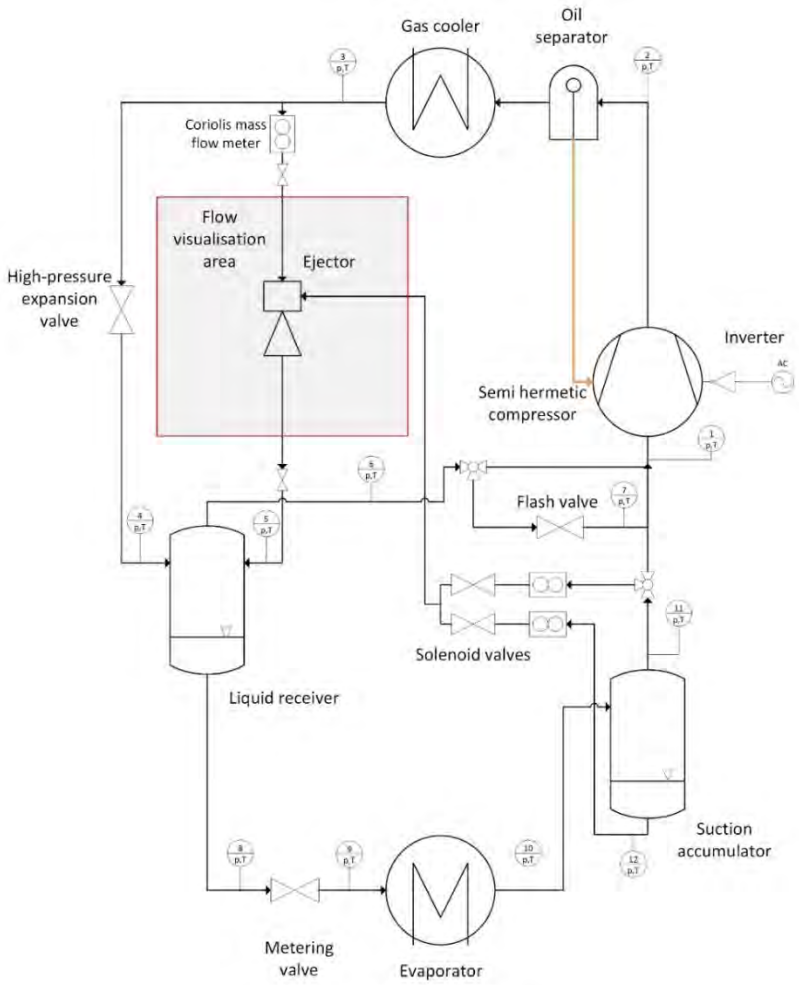

Figure 1: The P&ID diagram of the R744 circuit with oil recovery

The oil recovery loop with oil separator was designed to ensure the proper level of the lubricant in the compressor and avoid the performance degradation of the other components. The heat rejection in discharge line was controlled using the SWEP brazed plate-type heat exchanger as a gas cooler. The outlet conditions of the gas cooler are strongly related to the expansion process in the ejector and high-pressure expansion valve. The Danfoss CCTM-8 electronic expansion valves were used to throttle the R744 flow between the gas cooler and the liquid receiver as well as between the liquid receiver and the evaporator pressure level. Similarly to the gas cooler, the SWEP brazed plate-type heat exchanger was used to absorb the heat from the secondary loop for different application. The additional separator was installed outside the evaporator to accumulate the liquid flow that can be entrained by the ejector, which let to utilise the evaporator in a flooded mode and avoid any liquid droplet in the compressor suction port. Finally, the ejector was installed with the defined space for installation of the PIV instruments. The Swagelok type connectors were selected to easily integrate the various manufactured ejector as well as different expansion devices such as the capillary tube.

The heat transfer in the gas cooler and the evaporator was controlled by installation of the secondary loops in the proposed test rig, which was shown in Fig. 2. The secondary fluid was defined as a mixture of water with glycol at specific concentration. The auxiliary loops were divided into the heat absorption from the R744 flow in the gas cooler and heat rejection from the R744 flow in the evaporator. Both loops consisted of the pump connected to the inverter and the glycol tank. Moreover, the additional internal heat exchanger was used to minimise the total power consumption of the test rig. Finally, the dry cooler was located at the building wall to reject heat into the air outside from the laboratory.

Fig. 3 presents the design concept of the R744 two-phase ejector for the flow visualisation experiments based on the PIV method. The designed shape was defined similarly to the ejector used for the previously performed heat transfer analysis (Haida et al., 2018). The assembly consisted of four parts: motive nozzle made of stainless steel, suction nozzle made of brass,

transparent mixing section and diffuser part again from brass. The borosilicate glass was used to visualise flow inside the ejector due to the optical clarity. The rectangular cross-section of the mixer part outer walls was designed to avoid any deformation of the laser beams on curved external surfaces. The inner wall surface of the mixer part was defined as a axisymmetric to evaluate mixing process in real ejector shape. The laser source was set on the top to emit laser sheet along the ejector axis and the speed camera was located to record snapshots perpendicularly to the laser source.

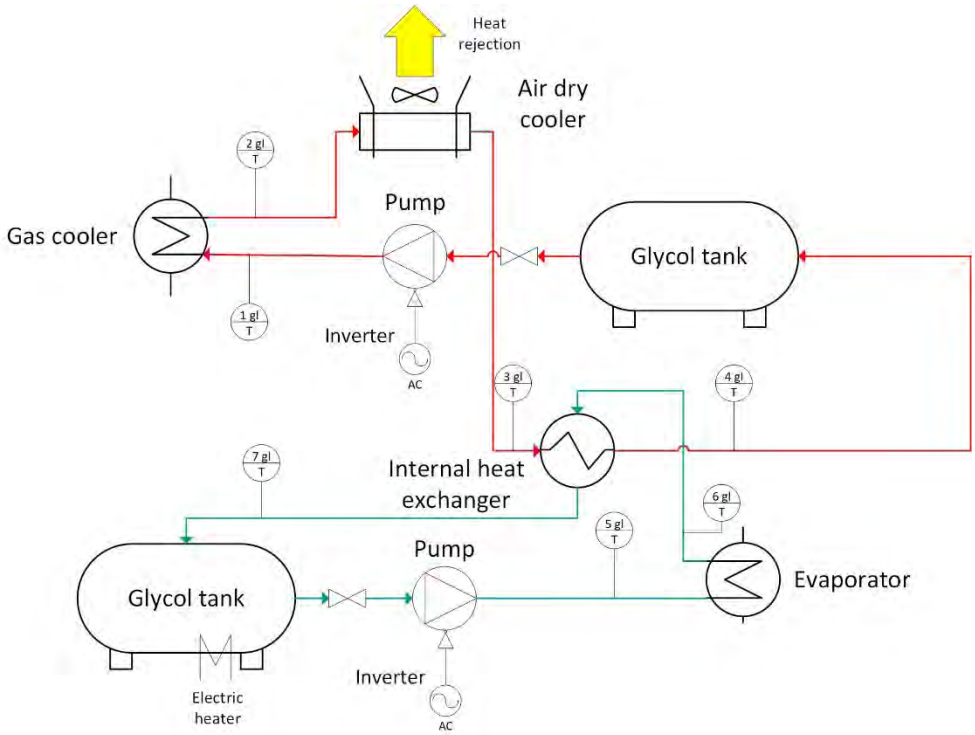

Figure 2: The P&ID diagram of the auxiliary loops

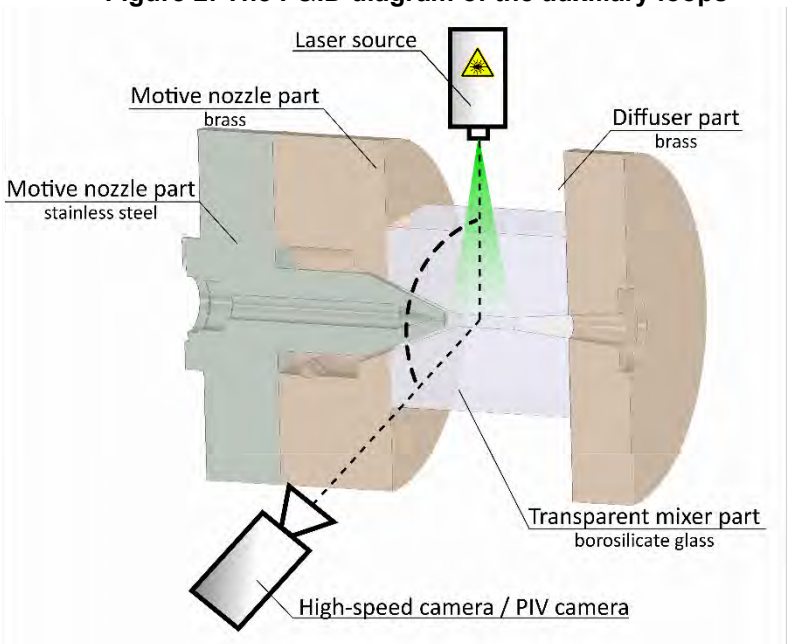

Figure 3: The R744 ejector with transparent mixing section during flow visualisation

3. FIRST LAW ANALYSIS OF THE R744 VAPOUR COMPRESSION TEST RIG

The proposed R744 vapour compression test rig for flow visualisation inside the ejector was defined to perform test campaign in the subcritical conditions with different sub-cooling degree and transcritical conditions at various outlet gas cooler pressure and temperature. Moreover, different

evaporation temperature as well as the superheat degree was considered during experiments. Therefore, the information about the system energy performance as well as ejector performance let to evaluate the COP improvement of the test rig working with the aforementioned ejector when compared to the reference booster mode. The first law analysis was done by use of the OpenModelica software due to the possibility of dynamic simulations performance based on the object-oriented modelling (Richter, 2008). The investigation was performed to define the system COP of the cooling mode calculated as follows:

$$COP = \frac{\dot{Q}_{evap}}{\dot{W}_{comp}} = \frac{\dot{m}_{evap}(h_9 - h_{10})}{\dot{m}_{comp}(h_2 - h_1)} \quad \textit{Eq. (1)}$$

where $\dot{Q}_{evap}$ is the evaporation heat rate in kW, $\dot{W}_{comp}$ is the power consumption, $\dot{m}$ is the mass flow rate in kg/s, and h is the specific enthalpy in kJ/kg. The COP improvement was defined as follows:

$$COP_{improvement} = \frac{COP_{ejector}}{COP_{booster}} - 1 \quad \textit{Eq. (2)}$$

Each component of the proposed test rig was defined based on the datasheet and information given by the manufactures. The fluid properties of R744 were given from CoolProp libraries (Bell et al., 2014). The two-phase ejector was simulated based on the hybrid ROM, which was implemented to the OpenModelica software as the external C-code function. The developed object-oriented model of the R744 two-phase ejector based on the hybrid ROM allowed for the evaluation of the designed two-phase ejector at very high accuracy in steady-state conditions or in transient simulations. Moreover, the application range of the hybrid ROM was defined for the R744 HVAC&R integrated system, which covered operating conditions considered in this investigation. The ejector performance of the R744 two-phase ejector was calculated based on the thermodynamic definition proposed in (Elbel and Hrnjak, 2008):

$$\eta_{ej} = \frac{\dot{m}_{evap}}{\dot{m}_{comp}} \cdot \frac{h|_{s=SN\ p=p_{out}} - h_{SN}}{h_{MN} - h|_{s=MN\ p=p_{out}}} \quad \textit{Eq. (3)}$$

where *s* is the specific entropy in J/(kg·K), and subscripts “MN” and “SN “defined the motive nozzle and the suction nozzle. The R744 test rig was controlled by set of the outlet gas cooler parameters, pressure level in the liquid receiver and evaporation temperature with the defined superheat. The gas cooler conditions were set according to the approximation curve in terms of the ambient temperature defined for supermarket system (Gullo et al., 2017). The pressure level in the liquid receiver was set to 40 bar and the evaporation temperature was varied between 2°C and 6°C with the superheat degree of 10 K.

4. RESULTS

Fig. 5 presents a comparison of COP between the R744 vapour compression test rig equipped with the ejector and test rig working as a reference booster system. Moreover, the analysis was done for different gas cooler pressure range from approximately 65 bar to over 100 bar that was related to the different climate zones. It was found that running the test rig at both operating modes, COP decreased from approximately 4.8 to 2.5 during increase of the gas cooler pressure. The ejector-based system obtained higher COP when compared to the booster system for all investigated points. Therefore, the utilisation of the ejector let to reduce the total power consumption and improve the energy performance of the system.

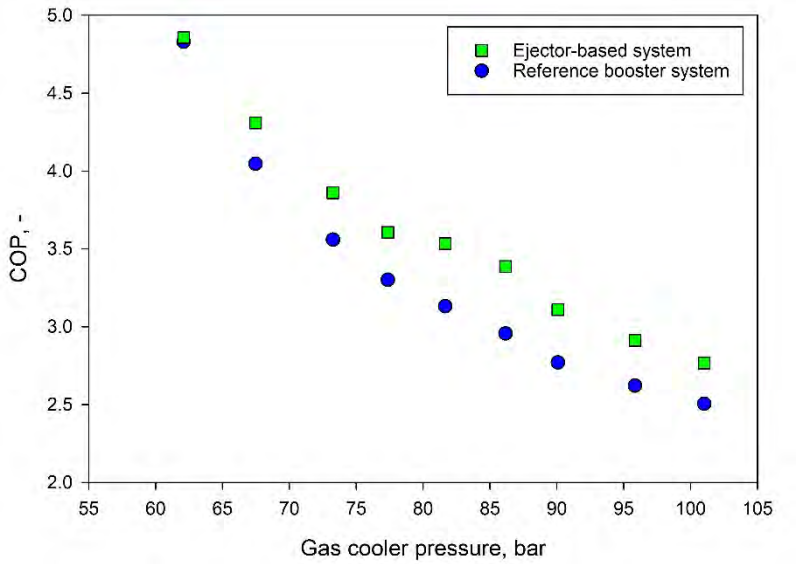

Figure 5: COP of the R744 vapour compression test rig at different operating mode in terms of the gas cooler pressure

The comparison between the two operating modes of the R744 vapour compression test rig confirmed improvement of the system energy performance as a result of the designed two-phase ejector. Fig. 6 presents the ejector efficiency of the designed ejector and the COP improvement of the ejector-based system in terms of the gas cooler pressure from over 60 bar up to approximately 100 bar. At transcritical conditions, the ejector reached efficiency of approximately 0.3, which resulted on the highest COP improvement. The ejector efficiency significantly dropped close to the critical point and in the subcritical conditions due to the fixed pressure difference between the outlet and the suction port. The COP improvement was varied from 5% up to approximately 11% for the gas cooler pressure above 65 bar. The smallest COP improvement was obtained for gas cooler pressure of approximately 62 bar due to the small value of the ejector efficiency. The highest COP improvement was obtained for the best ejector efficiency of approximately 30%. Therefore, the possibility to increase the efficiency of the ejector work improved the system energy performance. In other hand, the evaluation of the sub-cooling degree of the gas cooler section as well as the defined superheating would increase the COP value of the R744 refrigeration system equipped with the designed ejector.

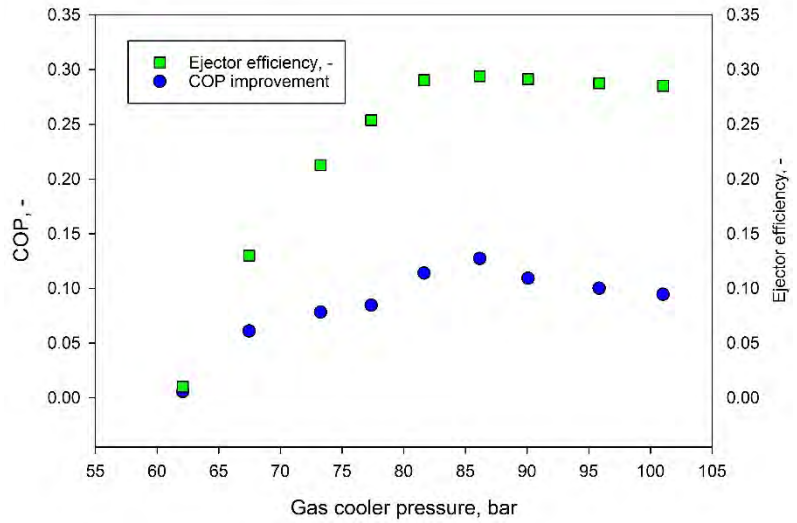

Figure 7: The ejector efficiency and COP improvement of the ejector-based system in terms of the gas cooler pressure

5. CONCLUSIONS

The R744 vapour compression test rig for the two-phase flow visualisation inside the ejector was proposed. The R744 circuit and auxiliary loops were designed for the ejector work evaluation at different cooling capacity and ambient conditions from subcritical conditions to transcritical conditions. The R744 two-phase ejector was designed for the flow visualisation in the mixing section based on the PIV method. The first law analysis was performed based on the object-oriented modelling in OpenModelica software. Moreover, the ejector hybrid ROM was implemented to evaluate ejector performance at high accuracy. The COP improvement was obtained for all the investigated points at different gas cooler conditions due to the ejector utilisation at high efficiency. However, the searching of the proper operating conditions let to improve COP of the system, especially by modifying the liquid receiver pressure and sub-cooling degree in the gas cooler.

ACKNOWLEDGEMENTS

The authors gratefully acknowledge the financial support of the National Science Centre through project No. 2017/27/B/ST8/00945.

REFERENCES

Banasiak, K., Hafner, A., Kriezi, E.E., Madsen, K.B., Birkelund, M., Fredslund, K., Olsson, R., 2015. Development and performance mapping of a multi-ejector expansion work recovery pack for R744 vapour compression units. Int. J. Refrig. 57, 265–276.

Bansal, P., 2012. A review – Status of CO2 as a low temperature refrigerant: Fundamentals and R&D opportunities. Appl. Therm. Eng. 41, 18–29.

Bell, I., Wronski, J., Quoilin, S., Lemort, V., 2014. Pure and Pseudo-pure Fluid Thermophysical Property Evaluation and the Open-Source Thermophysical Property Library CoolProp. Ind. Eng. Chem. Res. 5, 2498–2508.

Deng, J. q, Jiang, P. x, Lu, T., Lu, W., 2007. Particular characteristics of transcritical CO2 refrigeration cycle with an ejector. Appl. Therm. Eng. 27, 381–388.

Elbel, S., Hrnjak, P., 2008. Experimental validation of a prototype ejector designed to reduce throttling losses encountered in transcritical R744 system operation. Int. J. Refrig. Int. Du Froid 31, 411–422.

Giacomelli, F., Mazzelli, F., Milazzo, A., 2018. A novel CFD approach for the computation of R744 flashing nozzles in compressible and metastable conditions. Energy 162, 1092–1105.

Gullo, P., Hafner, A., Cortella, G., 2017. Multi-ejector R744 booster refrigerating plant and air conditioning system integration – A theoretical evaluation of energy benefits for supermarket applications. Int. J. Refrig. 75, 164–176.

Haida, M., Smolka, J., Hafner, A., Mastrowski, M., Palacz, M., Madsen, K.B., Nowak, A.J., Banasiak, K., 2018. Numerical investigation of heat transfer in a CO2 two-phase ejector. Energy 163, 682–698.

Haida, M., Smolka, J., Hafner, A., Palacz, M., Banasiak, K., Nowak, A.J., 2017. Modified homogeneous relaxation model for the R744 trans-critical flow in a two-phase ejector. Int. J. Refrig.

Haida, Smolka, J., Hafner, A., Ostrowski, Z., Palacz, M., Madsen, K.B., Försterling, S., Nowak, A.J., Banasiak, K., 2018a. Performance mapping of the R744 ejectors for refrigeration and air conditioning supermarket application: A hybrid reduced-order model. Energy 153.

Haida, Smolka, J., Hafner, A., Ostrowski, Z., Palacz, M., Nowak, A.J., Banasiak, K., 2018b. System model derivation of the CO2 two-phase ejector based on the CFD-based reduced-order model. Energy 144, 941–956.

Kim, M.H., Pettersen, J., Bullard, C.W., 2004. Fundamental process and system design issues in CO2 vapor compression systems. Prog. Energy Combust. Sci. 30, 119–174.

Kornhauser, A.A., 1990. The use of an ejector as a refrigerant expander, in: International Refrigeration and Air Conditioning Conference. Purdue ePubs, The address of the publisher, pp. 1–11.

Li, D., Groll, E.A., 2005. Transcritical CO2 refrigeration cycle with ejector-expansion device. Int. J. Refrig. 28, 766–773.

Li, Y., Tan, L., Zhang, X., Du, K., 2014. Experimental evaluation of an ejector as liquid re-circulator in a falling-film water chiller. Int. J. Refrig.

Little, A.B., Garimella, S., 2016. Shadowgraph visualization of condensing R134a flow through ejectors. Int. J. Refrig. 68, 118–129.

Liu, F., Groll, E.A., Li, D., 2012. Investigation on performance of variable geometry ejectors for CO2 refrigeration cycles. Energy 45, 829–839.

Lucas, C., Rusche, H., Schroeder, A., Koehler, J., 2014. Numerical investigation of a two-phase CO2 ejector. Int. J. Refrig.

Nakagawa, M., Marasigan, A.R., Matsukawa, T., Kurashina, A., 2011. Experimental investigation on the effect of mixing length on the performance of two-phase ejector for CO2 refrigeration cycle with and without heat exchanger. Int. J. Refrig. 34, 1604–1613.

Ostrowski, Z., Białecki, R.A., Kassab, A.J., 2008. Solving inverse heat conduction problems using trained POD-RBF network inverse method. Inverse Probl. Sci. Eng. 16, 39–54.

Palacz, M., Smolka, J., Fic, A., Bulinski, Z., Nowak, A.J., Banasiak, K., Hafner, A., 2015. Application range of the HEM approach for CO2 expansion inside two-phase ejectors for supermarket refrigeration systems. Int. J. Refrig. 59, 251–258.

Parliament, E., of the European Union, C., 2014. Regulation (EU) No 517/2014 of the European Parliament and of the Council of 16 April 2014 on fluorinated greenhouse gases and repealing Regulation (EC) No 842/2006 Text with EEA relevance.

Richter, C., 2008. Proposal of new object-oriented equation-based model libraries for thermodynamic systems. Braunschweig University of Technology.

Shecco, 2013. Natural Refrigerant Market Trends.

United Nations Environment Programme, 2016. Kigali Amendment to Montreal Protocol.

Zhu, Y., Wang, Z., Yang, Y., Jiang, P.X., 2017. Visualisation d'un écoulement transcritique diphasique supersonique de CO2 dans un éjecteur d'un système frigorifique. Int. J. Refrig. 74, 352–359.

Manuscript ID: 1363
DOI: 10.18462/iir.icr.2019.1363

Condensation and evaporation heat transfer characteristics of pure and binary-mixture HFO refrigerants inside a plate heat exchanger

Keishi KARIYA [(a)], Akio MIYARA[(a)]

[(a)] Saga university
Saga, 840-8502, Japan, kariya@me.saga-u.ac.jp

ABSTRACT

In the present study, condensation and evaporation local heat transfer coefficients and pressure drop of the pure and binary-mixture HFO refrigerants inside a brazed plate heat exchanger were investigated by using a test section which is combined with two grooved stainless steel plates. In the test section, wall temperature distribution was measured for local heat transfer coefficient. In order to measure local heat transfer and temperature distribution, five thermocouples were set on flow direction for each wall temperature measurement of the refrigerant side and heat source water side. Local heat transfer coefficient were calculated from local wall temperature of refrigerant side, saturation temperature and local heat flux obtained by temperature gradient between heat transfer surface of refrigerant side and heat source side.
Keywords: Condensation, Evaporation, Plate Heat Exchanger.

1. INTRODUCTION

In the technical field of refrigeration and air-conditioning, plate heat exchangers are getting attention due to their compactness and high thermal efficiency. Although these were mainly designed for liquid single-phase heat exchanger, its application was extended to two phase heat exchangers such as condensers and evaporators. Condensation and evaporation heat transfer coefficients in plate heat exchangers have been studied by many researchers. Most of the existing literatures discussed mainly overall heat transfer characteristics (Longo et al., 2010, Yan et al., 1999). Some recent studies are described about local heat transfer characteristics. For example, Shikichi et al. (2018), Jin and Hrnjak (2017) investigated heat transfer characteristics by both observation using IR camera and heat transfer experiment. However, local heat transfer behavior has not been clarified sufficiently. Because of the effects on global warming by the refrigerants used in the present heat pump/refrigeration systems, new synthetic refrigerants, hydrofluoroolefins (HFOs), which have low global warming potential (GWP) are recently getting attention as next generation refrigerants (Miyara et al., 2012; Kariya et al., 2016; Zhang et al., 2017). Many of HFOs has low flammability and expensive. Therefore, systems in which small amount of refrigerant is charged are required. When the plate heat exchangers are used as evaporator and/or condenser, maldistribution of refrigerant flow occurs in channels between the plates and headers to distribute it to the channels. This maldistribution deteriorates the heat exchanger performance. And local heat transfer coefficient may vary at flow direction and width direction in plate heat exchangers. It is important to investigate flow characteristics for understanding the heat transfer characteristic and for enhancing the heat transfer. Void fraction distributions in the plate heat exchanger were also measured. Arima et al. (2012) carried out flow observations and void fraction measurements on evaporation of ammonia flowing in parallel plates instead of an actual channel of plate heat exchangers. Experiments on condensation and evaporation heat transfer of low GWP refrigerants, R1234yf, in a plate heat exchanger have been carried out by Longo et al. (2012). Heat transfer coefficients and pressure drops in the condensation and evaporation of R1234ze(E) and R1234yf were measured and effects of saturation temperature, refrigerant mass flux and vapour super-heating are discussed. The data have been obtained from overall heat transfer performance and there is no sufficient discussion about local heat transfer characteristics. The local heat transfer coefficient varies not only flow direction but also width direction by gas-liquid distribution. In order to further understand the heat transfer characteristics, information about the local heat transfer is necessary. But measurements of local wall temperatures and heat fluxes are difficult because of the complicated structure of the PHE. In the present study, a

specially designed test section has been constructed for the measurement of local heat transfer coefficient. Experiments on condensation and evaporation heat transfer of a low GWP refrigerant, pure refrigerant R32 and binary mixture R1123/R32 40:60 mass% were carried out and local heat transfer characteristics were discussed.

2. EXPERIMENTAL APPARATUS AND DATA REDUCTION

2.1. Refrigerant Flow Loop

Fig. 1 shows experimental flow loop of refrigerant. The apparatus is same as our previous study (Kariya et al., 2018). It mainly consists of magnet pump, pre-heater, test section and after condenser. After the refrigerant flows from magnet pump, mass flow rate is measured by Coriolis flow meter. Then the refrigerant is heated by the pre-heater to set a designated enthalpy condition at the inlet of test section. After the refrigerant flows out through the test section, it is cooled by the after condenser to keep a certain sub-cooling. And the subcooled liquid comes back to the magnet pump. Mixing chambers are installed at inlet of the pre-heater and inlet and outlet of the test section to obtain the bulk enthalpy from measured refrigerant pressure and temperature at the mixing chamber. The refrigerant is heated or cooled by water of which temperature is controlled by thermostatic bath. The flow rate of refrigerant is controlled by the flow control valve and the rotation speed of magnet pump and needle valve set after the magnet pump.

2.2. Test Section

For the measurement of local heat transfer characteristics of plate heat exchanger, a specially designed test section has been produced same as our previous study (Kariya et al., 2016). Fig. 2 shows the schematic of test section and the installed points of thermocouples with the photograph. Chevron shape grooved are dug over a stainless steel plate of which length, width and thickness are

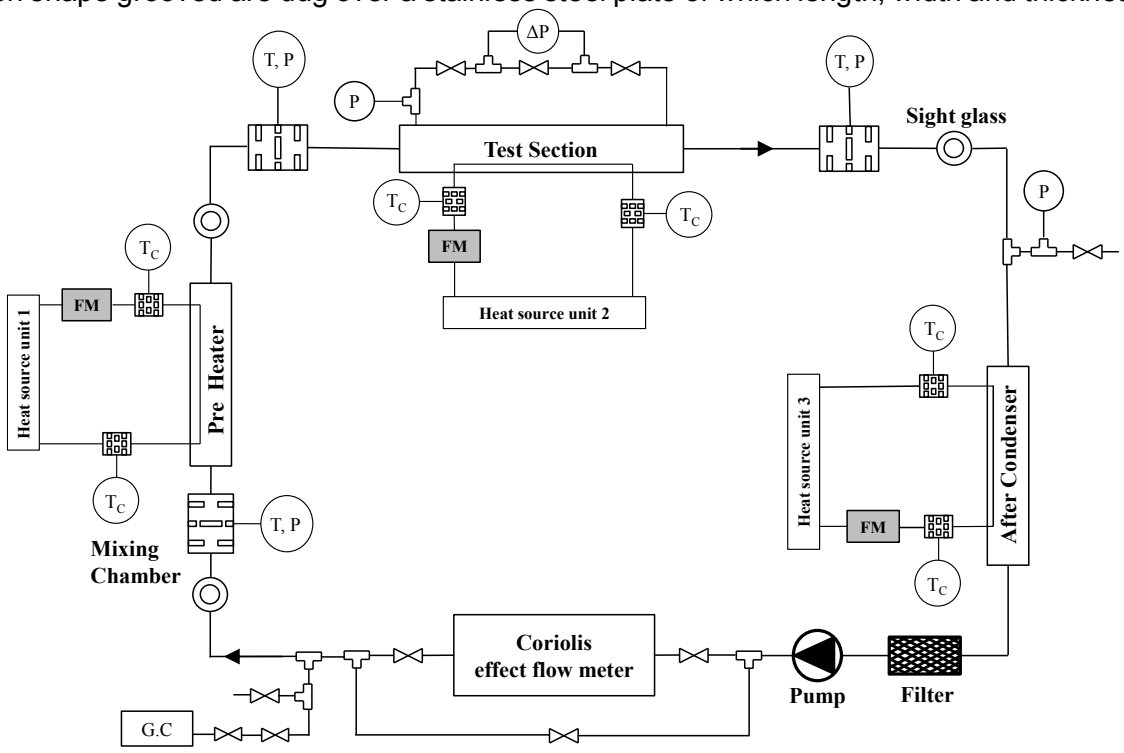

Figure 1: Refrigerant loop.

186 mm, 84 mm and 5 mm, respectively. The pitch and depth are 5.6 mm and 1.5 mm, respectively. A channel of the plate heat exchanger where the refrigerant flows is constructed by facing two grooved plats. Next of the grooved plates, flat plates are set to measure heat flux. Plates for the water channel are set outside of the flat plates. Whole of the test section is constructed with eight different kinds of plates which are brazed each other. The chevron directions of each plates which make a refrigerant flow channel are reversely assembled so that heat transfer enhance. The flat plates with 10mm in thickness have holes of 1.6mm in diameter on both sides where wire T-type thermocouples are installed and temperatures are measured. Positions of the temperature

measurement are set at 4, 12, 20, 28, 36, 44, 52, 60 and 64 mm from end face of the cross section of the channel. Position of the inlet and outlet of refrigerant are 20 mm. Temperatures of local heat transfer surface at refrigerant and water sides are estimated from the measured temperature as explained later. The temperatures are also used to calculate the heat flux and heat transfer coefficient. The water channels consist of flat plates and the channel height is 5mm. Water flows into the channels from both sides of the test section, front and back. It should be noted, surface which have the inlet/outlet ports of refrigerant is called as inlet side and another side is call as opposite side. In addition, the centre region is set for temperature measurement between the inlet and the opposite side, as shown in Fig. 2. The geometrical characteristics of the test section are listed in Table 1.

Table 1. Geometrical characteristics of the test section

Fluid flow plate length (mm)	117.5
Plate width (mm)	64
Area of the plate (m^2)	0.75
Corrugation type	Chevron
Angle of the corrugation (°)	60
Corrugation pitch (mm)	5.6
Number of plates	8
Number of channels on refrigerant side	1
Number of channels on water side	2

2.3. Data Reduction Method

By assuming the steady sate one-dimensional heat conduction, the local heat flux q_x ($kW.m^{-2}$) in test section can be calculated from the temperatures measured at both sides of 10mm thick flat plates as below:

$$q_x = \frac{T_{w,ref} - T_{w,water}}{l_1}\lambda \qquad \text{Eq. (1)}$$

Where $T_{w,ref,}$ (K) is temperature of measurement place of refrigerant side, $T_{w,\,water}$ (K) is temperature of measurement place of water side, l_1 (m) is distance between each K-type thermocouples, λ ($kw.m^{-1}.K^{-1}$) is the thermal conductivity of the stainless steel plate. Wall surface temperature of refrigerant side is calculated with the following equation where the linear temperature distribution is assumed and the temperature is extrapolated to the representative of surface of refrigerant side. l_2 (m) in the equation is the distance between the K-type thermocouple and the average surface of the refrigerant side:

$$T_{wall,x} = T_{w.ref} \pm \frac{q_x l_2}{\lambda} \qquad \text{Eq. (2)}$$

The plus-minus sign means the plus for condensation experiment, and the minus for evaporation experiment.

The local heat transfer coefficient, h_x ($kW.m^{-2}$) is defined with the following equation:

$$h_x = \frac{q_x}{T_{wall,x} - T_{sat}} \qquad \text{Eq. (3)}$$

Where T_{sat} (K) is the saturation temperature of refrigerant which is calculated from measured pressure. In the experiment of binary mixture refrigerant, the local thermodynamic equivalent quality x and saturation temperature (boiling point) T_{sat} (K) in the plate channel are varying along the flow channel depending on the composition of refrigerants in each gas and liquid phase. Quality and saturation temperature can be obtained from mass balance of low-boiling point component Eq. (5) and correlation of saturation temperature obtained by thermodynamic properties measurement (Higashi and Akasaka, 2016) as below:

$$x = \frac{m_V}{m} \qquad \text{Eq. (4)}$$

$$w_L = \frac{w_b}{1 + x\left(\frac{w_V}{w_L} - 1\right)} \quad \text{Eq. (5)}$$

$$T_{sat} = f(w_L, P) \quad \text{Eq. (6)}$$

Where w_L, w_V, w_b indicate liquid, vapour and bulk mass concentration, respectively. Finally, the local specific enthalpy in the test section is calculated from mass flow rate $\dot{m}$ and the heat transfer rate from the inlet to a certain point which is obtained by integrating the heat flux, as expressed with the following equation(7).

$$i_x = i_{in} + \frac{1}{\dot{m}} \int_0^{A_x} q dA \quad \text{Eq. (7)}$$

Frictional pressure drop Δp_f (kPa) of the test section is calculated by measured pressure drop in the adiabatic condition Δp_{exp} (kPa) and pressure drop due a change in elevation between inlet and outlet of the test section Δp_g (kPa) using following equation (8).

$$\Delta p_f = \Delta p_{exp} \pm \Delta p_g \quad \text{Eq. (8)}$$

3. RESULTS AND DISCUSSION

3.1. Experimental Conditions

Table 1 shows conditions of heat transfer experiment. Refrigerant tested is R1123/R32 40/60 mass % binary mixture which is one of the promising candidates of the next generation refrigerants and has the low GWP. Pure R32 measurement was also conducted for comparison with the binary mixture. Flow direction of the refrigerant is the downward for condensation test and the upward for evaporation test. Saturated temperature are 20 °C and 10 °C for condensation and evaporation tests, respectively. Mass flux conditions are 10 and 20 ($kg.m^{-2}.s^{-1}$) in both experiments. In the case of mass flux 10 ($kg.m^{-2}.s^{-1}$) conditions for both condensation and evaporation experiment, temperature of cooling water (heat source at the test section) is controlled in order that the refrigerant flows into the test section as nearly saturated vapor (condensation) or liquid (evaporation) state and flows out as nearly saturated liquid (condensation) or vapor (evaporation). In the condition of mass flux 20 ($kg.m^{-2}.s^{-1}$), both condensation and evaporation experiment are carried out in two inlet conditions in order to measure large quality region. In the condensation and evaporation experiment, inlet conditions are nearly saturated vapor (condensation) or saturated liquid (condensation) and x = 0.5 (condensation and evaporation) with the same heat flux condition of mass flux 10 ($kg.m^{-2}.s^{-1}$).
Table 2 shows experimental conditions of pressure drop. Pressure drop is measured both upward and downward flow at adiabatic conditions in saturation temperature 30 °C and mass velocity 10, 20, 50, 100 and 150 ($kg.m^{-2}.s^{-1}$) using pure R32.

Table 1. Experimental conditions of heat transfer experiment

	Refrigerant	Flow direction	T_{sat} (°C)	G ($kg.m^{-2}.s^{-1}$)
Condensation	Pure R32 R1123/R32 40/60 mass% mixture	Downward	20	10 and 20
Evaporation	Pure R32 R1123/R32 40/60 mass% mixture	Upward	10	10 and 20

Table 2. Experimental conditions of pressure drop experiment

	Refrigerant	Flow direction	T_{sat} (°C)	G ($kg.m^{-2}.s^{-1}$)
Adiabatic	Pure R32	Downward and upward	30	10 - 150

3.2. Local Heat Transfer Characteristics

Figs. 3 (a) and (b) show local heat transfer coefficient distribution in the case of the binary mixture of the evaporation experiment at x = 0.11, 0.62 with mass flux G = 10 ($kg.m^{-2}.s^{-1}$), respectively. Fig. 3 (c) and (d) respectively shows the results of pure R32 at x=0.14 and 0.50 with mass flux 10. Pure R32 data are re-measured from our previous study (Kariya et al., 2018). As shown in figures, the

position indicating maximum value of heat transfer coefficient is about 20 mm due to the inlet refrigerant effect and heat transfer coefficient represent the minimum value at the end face of the channel. Compared with binary mixture and pure refrigerant, heat transfer coefficients of pure R32 are higher than that of binary mixture at any quality conditions.

Figs. 4 (a) and (b) show local heat transfer coefficient distribution in the case of the binary mixture of the condensation experiment at x = 0.93, 0.57 with mass flux G = 10 ($kg.m^{-2}.s^{-1}$), respectively. Figs. 4 (c) and (d) respectively show the results of pure R32 at x=0.92 and 0.41 with mass flux 10. Pure R32 condensation data are also re-measured from our previous study (Kariya et al., 2018). It is also found that local condensation heat transfer coefficient at 20 mm is the highest due to the inlet effect at any conditions and. Compared with the results of the mixture and pure refrigerants, condensation heat transfer coefficient indicate almost same value.

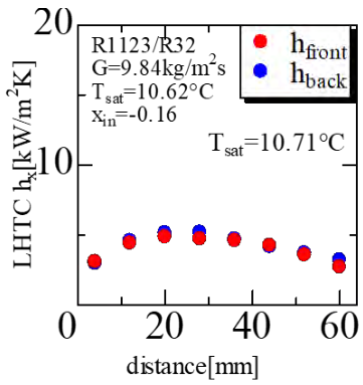

(a) Mixture, x = 0.11

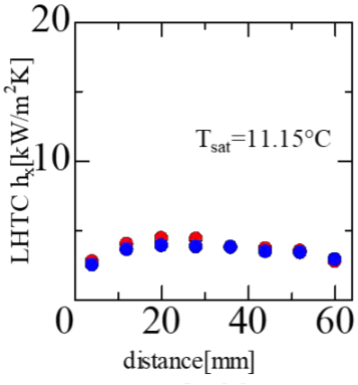

(b) Mixture, x = 0.62

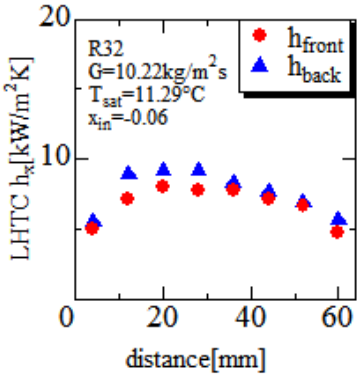

(c) Pure R32, x = 0.14

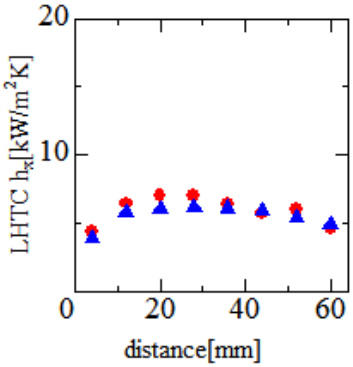

(d) Pure R32, x = 0.50

Figure 3 Local heat transfer coefficient (evaporation).

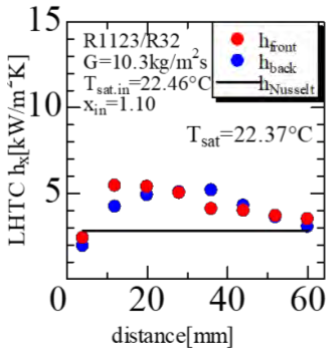

(a) Mixture, x = 0.93

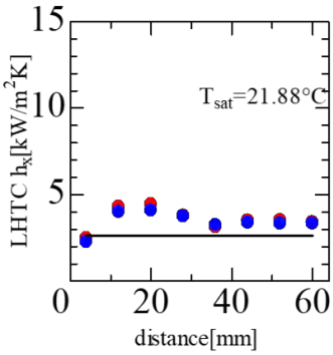

(b) Mixture, x = 0.57

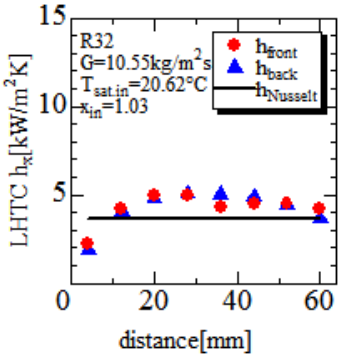

(c) Pure R32, x = 0.92

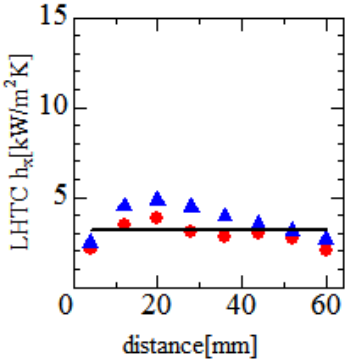

(d) Pure R32, x = 0.41

Figure 4 Local heat transfer coefficient (condensation).

3.3. Pressure Drop

Fig. 5 shows frictional pressure drop of test channel. At mass velocity higher than 50 ($kg.m^{-2}.s^{-1}$) conditions, frictional pressure drop increases with increasing quality as recognized. However, at mass velocity lower than 20 kg/m^2s, frictional pressure drop decreases with increasing quality both upward and downward condition. At low mass flux condition, flow pattern is not homogeneous according to observation of flow inside plate heat exchanger (Kariya et al., 2018). Relationship between flow pattern and frictional pressure drop in a plate heat exchanger channels should be clarified in future.

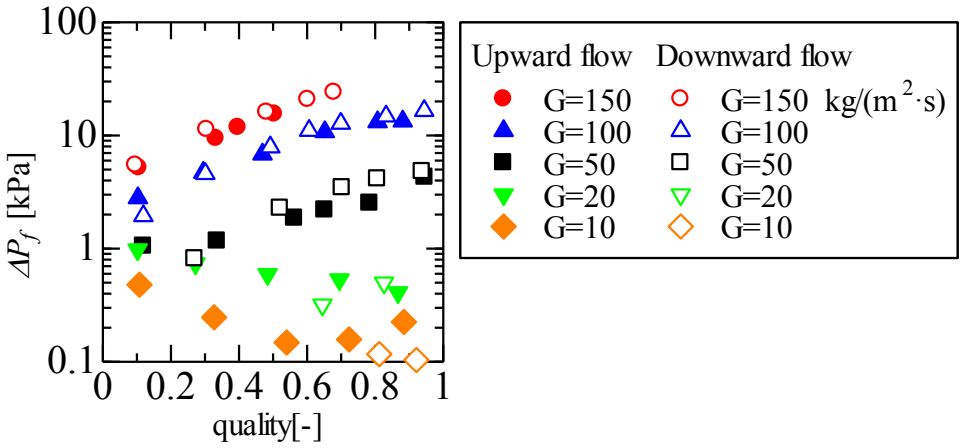

Figure 5 Frictional pressure drop of upward and downward flow (adiabatic).

4. CONCLUSIONS

In order to obtain local heat transfer coefficient during condensation and evaporation of pure and binary mixture in a plate heat exchanger, a special test section has been produced where the channel is formed with two stainless steel plate having chevron grooves. Experiments on condensation and evaporation of R1123/R32 40/60 mass% binary mixture and pure R32 have been carried out and frictional pressure drop also measured in the test section. The following results were obtained:

(1) In evaporation experiment, local heat transfer coefficient indicates maximum value near refrigerants inlet position and minimum value at end face position of cross section of the channel.
(2) Values of evaporation heat transfer coefficient of R1123/R32 binary mixture are lower than that of pure R32.
(3) In condensation experiment, local heat transfer coefficient indicates maximum value near refrigerants inlet position and minimum value at end face position of cross section of the channel.
(4) Values of condensation heat transfer coefficient of R1123/R32 binary mixture are similar to that of pure R32.
(5) Frictional pressure drop of pure R32 in the test plates increases with increasing quality at mass velocity higher than 50 ($kg.m^{-2}.s^{-1}$).
(6) Frictional pressure drop of pure R32 in the test plates decreases with increasing quality at mass velocity lower than 20 ($kg.m^{-2}.s^{-1}$).

ACKNOWLEDGEMENTS

This study was sponsored by New Energy and Industrial Technology Development Organization (NEDO), Japan.

REFERENCES

Arima, H., Mishima, F., Koyama, K., Fukunami, K., Ikegami Y., 2012. Study on void fraction measurement of ammonia boiling heat transfer in plate evaporator, Proc. 49th NHTS, NHTS: A232 (in Japanese).

Higashi, Y., Akasaka, R., 2016. Measurement of Thermodynamic properties for R1123 and R1123+R32 Mixture. Proc.16th Int. Ref. and Air Conditioning Conference (2016 Purdue conference), No. 2283.

Jin, S., Hrnjak P., 2017. Effect of end plates on heat transfer of plate heat exchanger. Int. J. Heat and Mass Transfer 108(Part A), 740-748.

Kariya, K., Mahmud, M. S., Kawazoe A.,Miyara A., 2016. Local heat transfer characteristics of the R1234ze(E) two phase flow inside a plate heat exchanger. Proc.16th Int. Ref. and Air Conditioning Conference (2016 Purdue conference), No. 2600.

Kariya, K., Sonoda K., Wakasugi S.,Miyara A., 2018. Condensation and evaporation local heat transfer characteristics of the refrigerant mixture of R1123 and R32 inside a plate heat exchanger. Proc. 17th Int. Ref. and Air Conditioning Conference (2018 Purdue conference), No. 2565.

Longo, G.A., 2010. Heat transfer and pressure drop during HFC refrigerant saturated vapour condensation inside a brazed plate heat exchanger. Int. J. Heat and Mass Transfer 53(5-6), 1079-1087.

Longo, G.A., 2012. Vaporisation of the low GWP refrigerant HFO1234yf inside a brazed plate heat exchanger. Int. J. Refrigeration 35, 952-961.

Longo, G.A., 2012. Condensation of the low GWP refrigerant HFO1234yf inside a brazed plate heat exchanger. Int. J. Refrigeration 36, 612-621

Miyara, A., Onaka, Y.,Koyama, S., 2012. Ways of next generation refrigerants and heat pump/refrigeration systems, Int. J. Air-Conditioning and Refrigeration 20(1), 1130002.

Shikichi, K., Minoura K.,Asano H., 2018. Effect of Flow Direction of Heating Medium on Boiling Heat Transfer Characteristics in a Single-Channel Plate-Fin Heat Exchanger. Proc. 17th International Refrigeration and Air Conditioning Conference at Purdue, No. 2416.

Yan, Y-Y., Lio, H.C., Lin, T.F., 1999. Condensation heat transfer and pressure drop of refrigerant R-134a in a plate heat exchanger. Proc. Int. J. Heat and Mass Transfer 42, 993-1006.

Zhang, J., Desideri, A., Kærna, M., R., Ommen, T., S., Wronski, J., Haglind, F., 2017. Flow boiling heat transfer and pressure drop characteristics of R134a, R1234yf and R1234ze in a plate heat exchanger for organic Rankine cycle units, Int. J. Heat and Mass Transfer 108, 1787-1801.

Manuscript ID: 1376
DOI: 10.18462/iir.icr.2019.1376

Experiment study on spreading and horizontal motions of Lithium Bromide solution droplets on horizontal tubes

Yueting YANG [(a)], Xiaoyun XIE[(a)], Yi JIANG[(a)]

[(a)] Tsinghua University
Beijing, 100084, China, xiexiaoyun@tsinghua.edu.cn

ABSTRACT

Uniform distribution of liquid film on horizontal tubes influences falling film heat and mass transfer efficiency. Droplets spreading and horizontal motions at tube bottoms directly influence liquid distribution on the next row. This paper studies Lithium bromide aqueous solution droplets spreading and horizontal motions on horizontal tubes. A vacuum experimental section is built. The tube diameters and spacing are 16mm. The liquid spray density is 0.05~0.10 $kg \cdot m^{-1} \cdot s^{-1}$. Droplets horizontal motions are caused by disturbance at tube bottom, which includes different falling film times of adjacent droplets, uneven tube roughness, or non-uniform velocity distribution in the falling film regime. The horizontal motion distance of pre-wetting tubes are larger than that of no pre-wetting tubes. When the orifice spacing is 1.5cm, droplets horizontal motion distance on a 16mm diameter smoother copper tube is 0.45-0.83cm under liquid spray density of 0.05-0.10 $kg \cdot m^{-1} \cdot s^{-1}$, and it decreases when liquid spray density rises.
Keywords: Enhancement, Falling film, Heat Transfer, Horizontal Cylinder.

1. INTRODUCTION

Falling film is widely applied in heat and mass transfer processes, especially in absorption heat pumps and absorption heat exchangers (Yung et al., 1980; Parken et al, 1990; Ribatski et al., 2005). Liquid distribution of falling film directly influences heat and mass transfer processes. Two liquid distribution phenomena are discovered in falling film on horizontal tube bundles: one is dry spots on the liquid film, and the other is the droplets horizontal motions at horizontal tube bottoms. Fig.1 and Fig.2 show pictures of the two phenomena. Dry spots reduces efficient heat and mass transfer areas, while horizontal motions at tube bottoms lead to redistribution of droplets on the next row. These two flow phenomena directly affect the effective heat and mass transfer processes of liquid film on horizontal tubes.

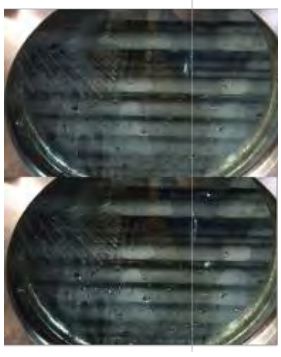

Figure 1: Dry spots during falling film absorption



Figure 2: Horizontal motions of LiBr-H2O droplets

Researches on liquid distribution on horizontal tubes have been focusing mostly on flow transition of falling film (droplets, jets and sheets), droplets formation and spreading on horizontal tubes. Depending on different Re numbers, falling flow regime is divided into droplets, jets, and sheets (Mitrovic, 1995), as shown in Fig. 3. Hu and Jacobi (1996,1998) described the transitions between falling film modes in terms of competing flow mechanisms: the sheet mode is dominated by gravity, while the droplet mode is dominated by gravity or surface-tension. In the droplet and jet modes, the liquid falls from the tube bottom at different sites, and distances between adjacent are the same, λ, which is named as the “departure site spacing”. The departure site spacing is related to the Taylor instability, and the equations are given in related to the liquid density, surface tension, and local gravity acceleration. Following researches focus on the improvement of the wavelengths equations (Lienhard et al., 1964; Bellman et al., 1953). Falling film experiments results were compared with solution results to confirm the accuracy of formulas (Wang and Jacobi, 2014).

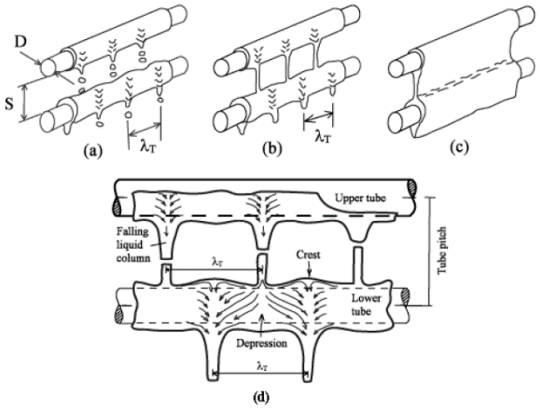

Figure 3: Falling film regimes (a, b, c, d represent the droplet mode, the jet mode, the sheet mode, and the front view of falling film)

Droplets spreading on flat plats and horizontal tubes is a widely discussed problem in liquid flow researches. Subramaniam and Garimella (2009) and Wang (2010) conducted researches on droplets spreading on horizontal tubes. Saddle-shaped ripples were observed during droplet spreading. A circumferential liquid ring with fixed axes will appear when two saddle waves meet on the tube (Subramaniam, 2013). When the propagation width is larger than the distance between droplets, adjacent saddle-shaped liquid film merge with each other (Jeong and Garimella, 2015; Wang, 2010).

Droplets formation at tube bottoms are related to Reynold instability, and gravity and surface tension act together. Gravity is the main driving force for droplets formation. The gravitational potential energy of satellite droplets is partly transformed into elastic potential energy to stretch the liquid column. When droplets fall off, the upper part of the liquid column will rebound back to the tube bottom, and wait for the next droplet (Wang, 2007).

Killion and Garimella (2003) described for the first time the phenomenon of droplets horizontal motions at tube bottoms, as shown in Fig. 4. Wang (2010) believed the droplets horizontal motions are caused by the transportation of unstable waves in the liquid film, and the new departure site spacing between two adjacent droplets would no longer agree with the wave length under stable conditions.

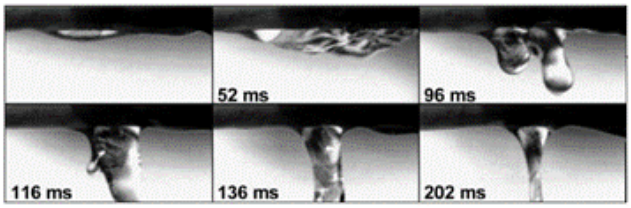

Figure 4: Droplets horizontal motions at tube bottoms

Above all, researches on falling film flow have been focusing on falling film regimes, droplets formation and spreading, and observations of horizontal motions. There are little research focusing on the principle of falling film, and principle of droplets horizontal motions at tube bottoms. This paper is going to study the liquid spreading and horizontal motions of aqueous Lithium Bromide solution on falling film horizontal tube bundles. Experiments are carried out on a vacuum test bench. Falling film experiments are conducted to observe droplets spreading and horizontal motions, and to investigate the principle of droplets spreading, and horizontal motions.

2. METHODS

2.1. Falling Film Experiments

Fig. 5 shows the vacuum absorption-evaporation experiment section. The experiment section is built to reproduce the phenomena of droplet spreading and horizontal motions. In the absorber, the LiBr aqueous solution flows through an orifice plate liquid dispenser, and falls on the first row of the horizontal tube bundle. Both the liquid dispenser and the tube bundles in the absorber are replaceable so that orifice diameters, orifice spacing, tube diameters and tube spacing are changeable. Sight windows are set to observe phenomenon of falling film flow and liquid level in the liquid dispenser. Solution and refrigerant water temperatures inside the section are measured by T type thermocouples. Thermocouples in the vacuum section are connected to an aviation connector, so that the temperature data inside the section can be collected by a data collector. A pressure sensor (0-200torr) is set in the evaporator to measure evaporation pressure during the experiment. Fig.6 shows the vacuum experiment system. The system is based on a massive vacuum test bench. The test bench provides adequate solution, maintains solution temperature, and keeps perfect vacuity inside the experimental section.

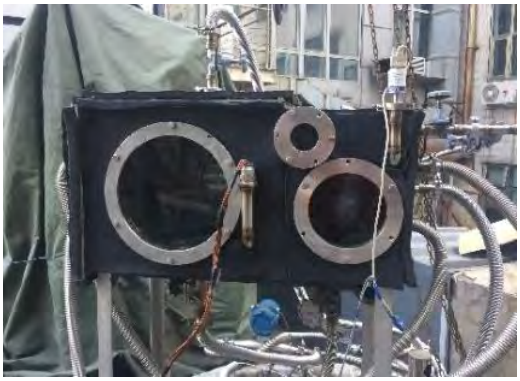

Figure 5: Vacuum experiment section: absorption-evaporation

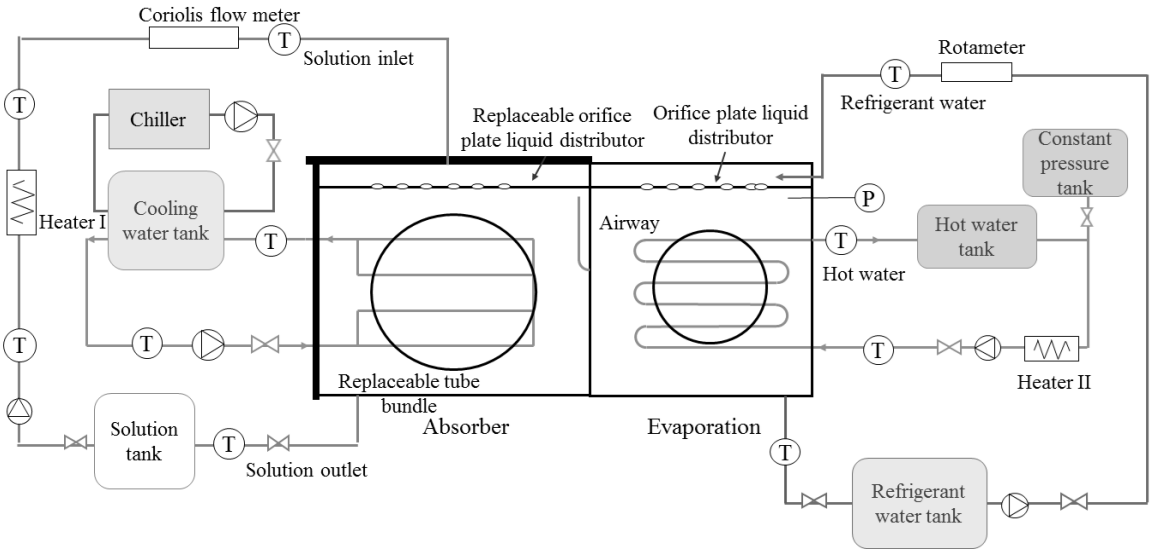

Figure 6: The vacuum experiment system

The falling flow experiments are conducted using smooth copper tubes. The diameter of the holes in the orifice is 1.5 mm. A tube bundle with four vertical rows is placed under the orifice. Test tubes are 16×1 mm in diameter and thickness, and the tube length is 30 cm, and the spacing between tubes is 16 mm. Images and films of horizontal motions of droplets are collected by a high speed camera. Falling film experiments on droplets horizontal motions include influence of tube pre-wetting, liquid spray density, and solution surface tension. During the experiment on the influence of tube pre-wetting, the tube is firstly covered with solution before the falling film experiments.

2.2. Falling Film Phenomena

2.2.1. Droplets spreading on horizontal tubes

Fig. 7 shows spreading shapes of LiBr solution on cooper tubes and steel tubes. The falling film flow rate are shown in Table 1. For the spreading process of droplets, the droplets spread axially on the top of the tube and flow downward the tube. The wetting area is larger on the top of the tube than the bottom. Finally, the droplets form at the bottom of the horizontal tube and fall to the next row. Since the wetting shape of droplet spreading are similar, the spreading width of droplets on top of horizontal tubes are used to represent spreading areas of droplets. Table 1 presents the experimental conditions during the experiment. The spreading width are calculated using image processing tool.

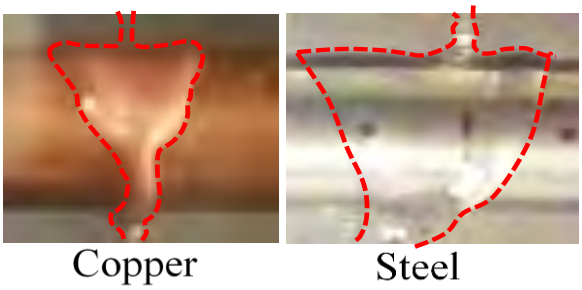

Figure 7: Droplets spreading on a copper tube and a steel tube

Table 1. Experimental conditions of copper tube experiment

Flow rate ($kg \cdot h^{-1}$)	Tube length (m)	Liquid spray density ($kg \cdot m^{-1} \cdot s^{-1}$)	Re	$Ga^{0.25}$	Flow mode
75.36	0.3	0.07	41.51	157.0	Droplets

2.2.2. Droplets horizontal motions

Fig. 8 shows pictures of the process of a droplet horizontal motion at tube bottom before it jumps off to the next tube row. When focused on the first tube row, the horizontal motion of a single droplet is described clearly. Firstly, the droplet forms from a breaking liquid bridge. After the bridge breaks, the droplet jumps off to the next tube. At this time, the residual liquid at tube bottom is not enough to produce another droplet immediately, and the waves at the tube bottom push the next droplet to form at another site near the first droplet. There is a horizontal distance between the two continuous droplets jumping off sites. This process lasts less than one second, and is very hard to recognize with naked eyes. It is so fast that it seems to be a “horizontal motion” of droplets.

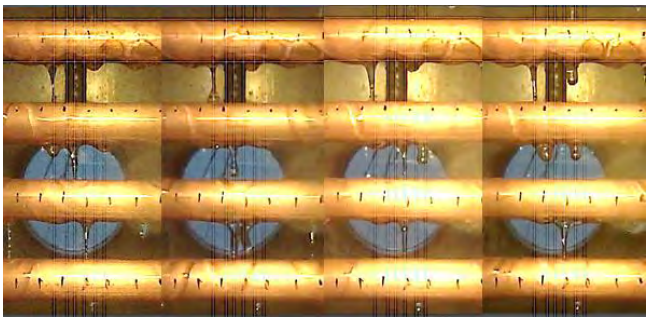

Figure 8: Droplets horizontal motions

Therefore, the definition of horizontal motion distance is explained in Eq. (1):

$$d_{hm} = x_{t(\mathrm{i})} - x_{t(i-1)} \qquad \text{Eq. (1)}$$

where d_{hm} is the horizontal motion distance in cm, $t_{(i)}$ is the droplet jumping off time, and x is the droplet jumping off site at the tube bottom in cm.

The droplets horizontal motion distances are measured on the first row of the tube bundle. In order to analyse the principle of droplet horizontal motions, experiments are conducted on single droplets and fully wetted falling film. For single droplets, no horizontal motion is observed at the first tube bottom. As for fully wetted film, droplets horizontal motions are observed at the first tube bottom. During the observation, waves caused by disturbance in the falling film process are also essential prerequisites of droplets horizontal motions. The disturbance includes different falling film times of adjacent droplets, uneven tube roughness, or non-uniform velocity distribution in the falling film regime. The disturbance influences film waves at tube bottoms, and changes the liquid amount of different sites at the tube bottom. Therefore, droplets jump off the tube bottom at different times and different sites.

2.3. Discussion

2.3.1. Droplets spreading

Fig. 9 shows droplets spreading widths on different horizontal rows. The spreading widths of the lower rows are generally wider than those of upper rows. However, as the solution goes down

several rows, spreading lengths tend to be stable. It turns out that under the experiment conditions, in which the tube diameter and tube spacing are 16mm, row numbers would limit the spreading of the liquid film. The droplets spreading limit leads to the dry spots on the tube bundle. In order to find a higher wetting ratio, it is important to find out a best row number for a tube bundle.

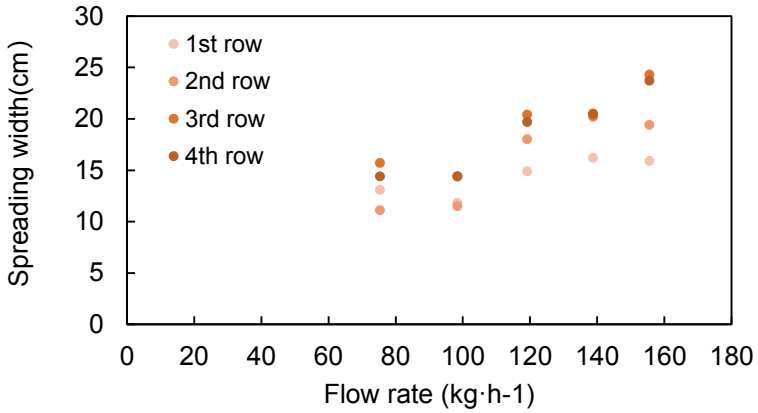

Figure 9: Total spreading width droplets on different rows

2.3.2. Droplets horizontal motions

Fig. 10 shows droplet horizontal motions on pre-wetting copper cubes and no pre-wetting tubes. The horizontal motion distances of pre-wetting tubes are larger than that of no pre-wetting tubes. The horizontal motion distances are on the same magnitude of droplet departure site spacing. Fig. 11 shows droplet horizontal motion distances under different liquid spray densities. As solution mass flow rate rises, liquid spray density rises, and droplet horizontal motion distances decrease. This trend is relatively easy to explain that as flow rate rises, Re number rises, and falling film regime tends to transfer to jets mode. In the jets mode, gravity dominates the falling film regime, and there are seldom any horizontal motions.

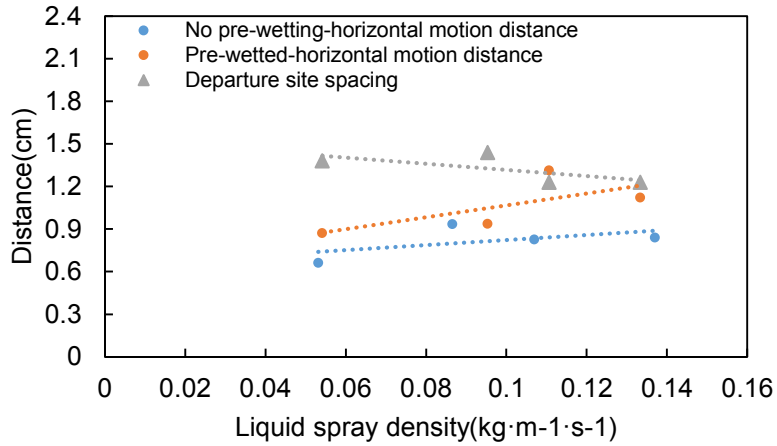

Figure 10: Horizontal motion distances with pre-wetting and no pre-wetting tubes

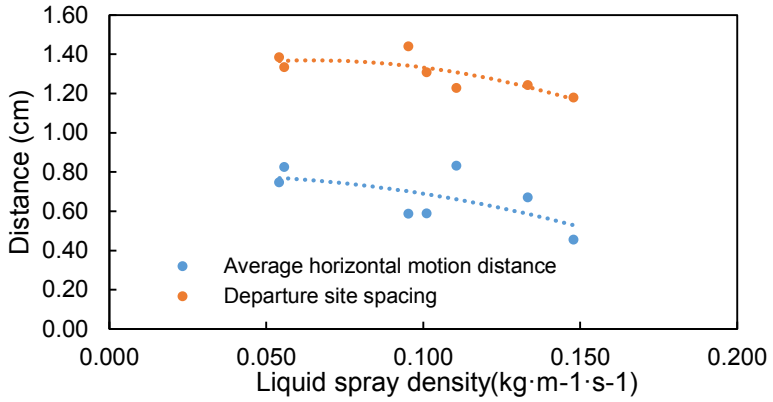

Figure 11: Horizontal motion distances under different liquid spray densities

Figs. 12 and 13 show droplets horizontal motion distances of two liquid spray density ranges under different surface tension. Under spray density around 0.050-0.0.057 kg·m^{-1}·s^{-1}, the falling film is in droplet mode, and horizontal motion distances varies with surface tension. Under spray density around 0.095-0.100 kg·m^{-1}·s^{-1}, the falling film is in jets mode, and the horizontal motion distances seldom changes with surface tension. Fig. 14 shows pictures of horizontal motions under the two spray density ranges. The frequency of horizontal motions decreases with the rise of liquid spray density.

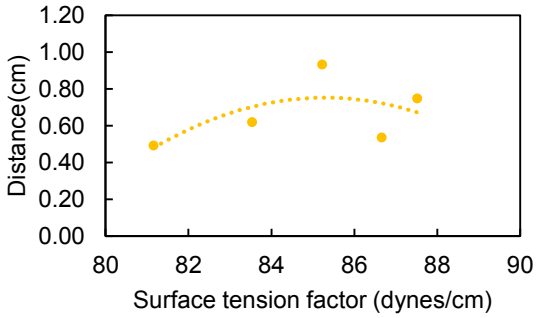

Figure12: Horizontal motion distances under spray density: 0.050-0.0.057 kg·m^{-1}·s^{-1}

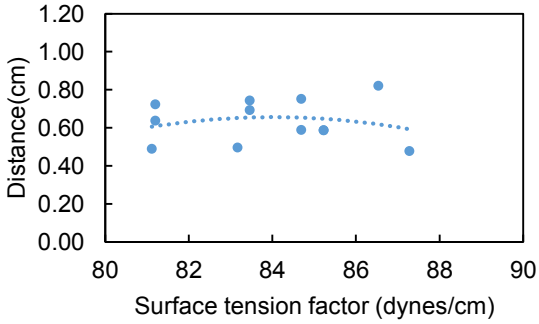

Figure13: Horizontal motions distance under spray density: 0.095-0.100 kg·m^{-1}·s^{-1}

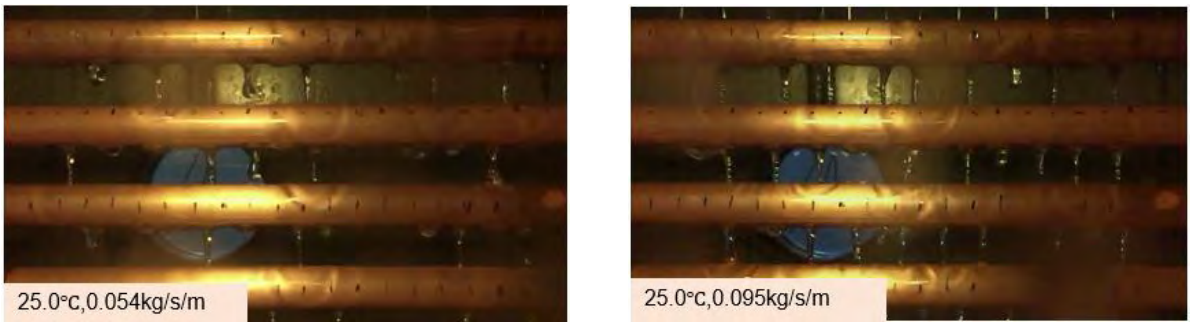

Figure14: Horizontal motions under different spray densities

3. CONCLUSIONS

Falling film LiBr flow experiments are conducted on droplets spreading and horizontal motions. The conclusions are as follows:

1) The spreading length of the lower row generally rises at the first several tube rows. However, the spreading length tend to be stable on the rest rows;
2) Droplets horizontal motions are caused by disturbance at tube bottom, which includes different falling film times of adjacent droplets, uneven tube roughness, or non-uniform velocity distribution in the falling film regime;
3) Horizontal motion distances of pre-wetting tubes are larger than that of no pre-wetting tubes;
4) When the orifice spacing is 1.5cm, LiBr aqueous solution droplets horizontal motion distances on a 16mm diameter smoother copper tube are 0.45-0.83cm under liquid spray density of 0.05-0.10 $kg \cdot m^{-1} \cdot s^{-1}$, and it decreases when liquid spray density rises;

Therefore, further researches are still necessary on influence of different tube and liquid distribution characteristics on droplets horizontal motions. More data are needed for further researches on the principle of droplets horizontal motions, and their effects on heat and mass transfer processes of falling film horizontal tubes.

ACKNOWLEDGEMENTS

The authors gratefully acknowledge the support from the National Natural Science Foundation of China (Grant number 51306098, 51138005), the innovative Research Groups of National Natural Science Foundation of China (Grant number 51521005), and the Tsinghua University Initiative Scientific Research Program (No. 20151080470).

NOMENCLATURE

d_{hm}	Horizontal motions distance (cm)	x	Droplet jumping off site (cm)
t	Droplet jumping off time (s)	i	Number of droplet
p	pressure (kPa)	ρ	solution density ($kg\times m^{-3}$)
T_w	Water temperature (℃)	T_s	Solution temperature (℃)
Re	Reynolds number	Ga	Galileo number

REFERENCES

Bellman, R., Pennington, H., 1953. Effects of surface tension and viscosity on Taylor instability. Q. Appl. Math. 12(2), 151-162.

Yung, D., Lorenz, J., Ganic, N., 1980. Vapor/liquid interaction and entrainment in falling film evaporators. J. Heat Transfer 102(1), 20-25

Hu, X., Jacobi, M., et al., 1996. The intertube falling film: part 2—mode effects on sensible heat transfer to a falling liquid film. J. Heat Transfer 118(3), 626-633.

Hu, X., Jacobi, M., 1998. Departure-site spacing for liquid droplets and jets falling between horizontal circular tubes. Exp. Therm. Fluid. Sci. 16(4), 322–331.

Killion, J., Garimella, S., 2003. A review of experimental investigations of absorption of water vapor in liquid films falling over horizontal tubes. Hvac & R Research 9(2), 111-136.

Jeong, S., Garimella, S., 2005. Optimal design of compact horizontal tube libr/water absorbers. HVAC&R Research 11(1), 27-44.

Lienhard, H., Wong, Y., 1964. The dominant unstable wavelength and minimum heat flux during film boiling on a horizontal cylinder. J. Heat Transfer 86(2), 220-225.

Mitrovic, J., Ricoeur, A., Fluid dynamics and condensation-heating of capillary liquid jets. Int. J. Heat and Mass Transfer, 1995, 38(8):1483-1494.

Parken, H., Fletcher, S., et al., 1990. Heat transfer through falling film evaporation and boiling on horizontal tubes. J. Heat Transfer, 112(3), 744.

Ribatski, G., Jacobi, M., 2005, Falling-film evaporation on horizontal tubes—a critical review. Int. J. Refrigeration 28(5), 635-653.

Subramaniam, V., Garimella, S., 2009. From measurements of hydrodynamics to computation of species transport in falling films. Int. J. Refrigeration 32(4), 607-626.

Subramaniam, V., Garimella, S., 2013. Numerical study of heat and mass transfer in lithium bromide-water falling films and droplets. Int. J. Refrigeration 40(3), 211-226.

Wang, L., You, S., Wang, S., 2010. Analysis of dropwise falling film flow of lithium bromide solution between horizontal tubes. J. Tianjin Univ. (Natural Science and Engineering Edition) 43 (1): 37-42.

Wang, S., Study on falling film dynamics and interfacial absorption performance of horizontal tube bundles, 2007, Tsinghua University, Beijing, 136p.

Wang, X., Jacobi, M., 2014. A thermodynamic basis for predicting falling-film mode transitions. Int. J. Refrigeration 43(4), 123-132.

Manuscript ID: 1402
DOI: 10.18462/iir.icr.2019.1402

Thermodynamic cycle analysis and experimental investigation on a three-stage vapor Injection air source heat pump

Huan ZHAO[(a)], Peiyu LEI[(a)], Yujie HUANG[(a)], Youlin ZHANG[(a)], Jun SHEN[(a)]

[(a)] Refrigeration Institute, Gree Electric Appliances, Inc. of Zhuhai,
789 Jinji Road, Qianshan, Zhuhai, Guangdong, 519070, P.R. China
407509978@qq.com

ABSTRACT

For the air source heat pump of R-410A, when the ambient temperature is low, the heating performance of the two-stage compression system is not perfect. In this paper, the heating performance coefficients of four three-stage compression heating cycles were theoretically deduced and analyzed, and the experimental prototype of the three-stage compression heat pump system was constructed to compare the heating performance of the two-stage compression heat pump system under the same working conditions. It was concluded that for these four three-stage compression cycles the calculated coefficient of performance (COP) of the three-stage compression with two flash tanks cycle is better than that of other three cycles. The experimental result shows that the COP of the three-stage compression system was 0.5%~3% higher than that of the two-stage compression system at the indoor temperature of 20℃ and the outdoor temperature of -20℃~7℃, and comparing with the two-stage compression system, the three-stage compression system has no obvious advantages.
Keywords: Air Source Heat Pump, Three-stage Compression, Low Ambient Temperature, COP.

1. INTRODUCTION

In recent years, air source heat pump units have received extensive attention due to their energy-efficient features. However, conventional single-stage heat pump systems have problems such as large compression ratio, excessive discharge temperature, low COP and difficulty in starting-up at low temperature, which restricts their application in cold regions (Bertsch et al., 2008).
In order to solve the applicability and low COP of air source heat pump in cold climate, many scholars have carried out many technical studies, such as scroll compressor vapor injection quasi-secondary compression technology (Chen et al., 2010), two-stage vapor injection compression with the flash tank technology(Xu et al., 2014; Huang et al.,2016), using a fuel heater to heat up the evaporator at low outdoor temperature(Horiuchi N., 1997). Among them, the two-stage compression system is an optimal solution for air source heat pump, but its COP is not perfect at low temperature. Therefore, in order to further reduce the compression ratio and the power consumption of the compressor, and improve the COP of the system, this paper proposed a three-stage compression cycle system. In this paper, the COP of four three-stage compression heating cycles with different throttling patterns were theoretically deduced and analyzed. Based on this, a prototype of a three-stage compression heat pump system was constructed. The test compared the heating performance of the two-stage compression system and the three-stage compression system under the same working conditions, summarized the key influence factors and control methods of the three-stage compression system, and provided a reference for studying of the three-stage compression air source heat pump system at low-temperature.

2. THEORETICAL ANALYSIS AND EXPERIMENTAL RESEARCH OF THREE - STAGE COMPRESSION HEAT PUMP SYSTEM

2.1. Theoretical Derivation for Four Modes of Three-Stage Compression Heating Cycle

According to different throttling types, the three-stage compression heat pump system can be divided into four cycling modes. The P-h diagrams of these four cycling modes are shown in Fig. 1, respectively.

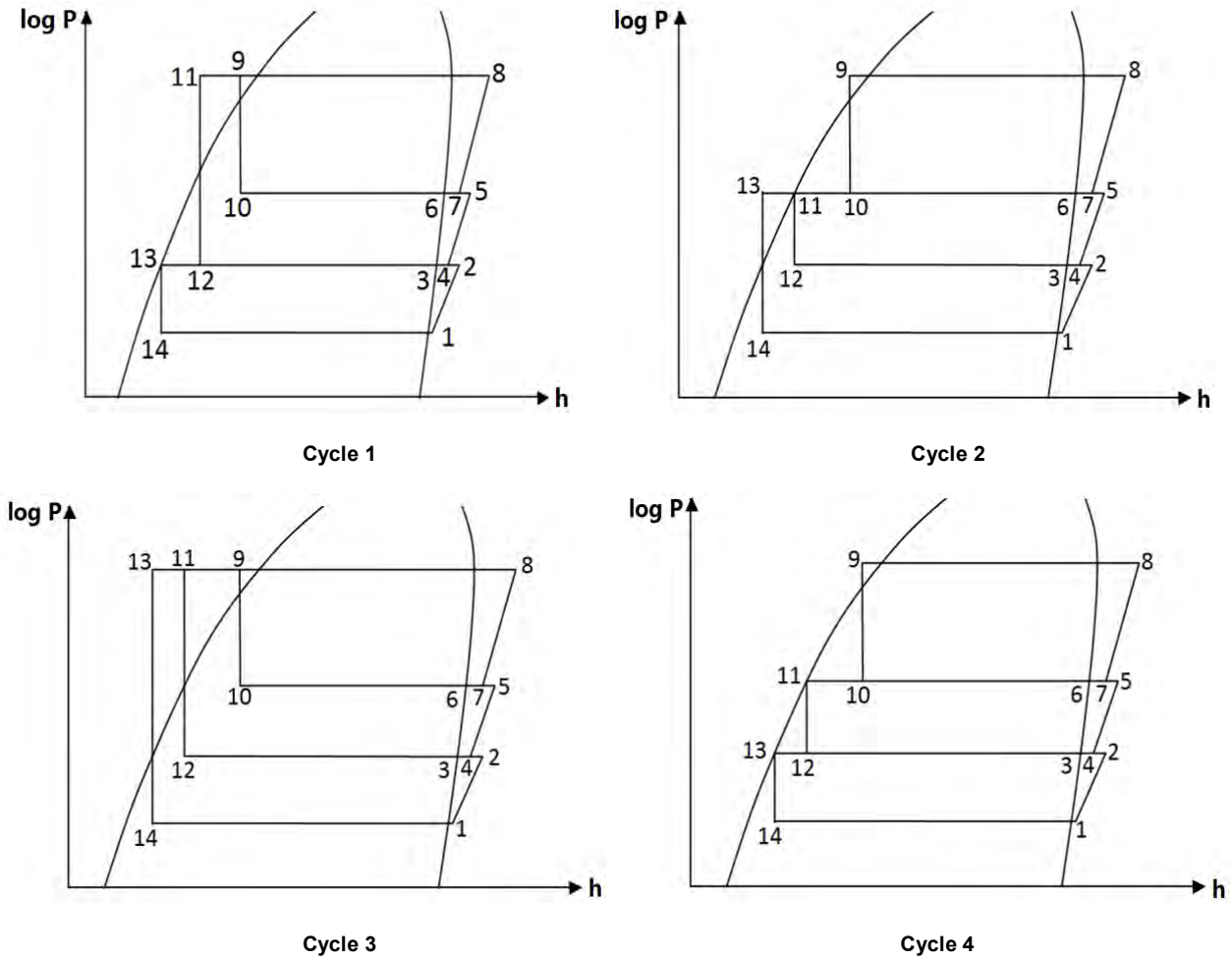

Figure 1: The P-h diagram for four cycles

In order to simplify the calculation, the following assumptions are made: under the same working conditions, the four cycles have the same condensation pressure P_c and evaporation pressure P_e; the flow pressure drop in the condenser, evaporator and tube is not considered; when the refrigerant flows through the throttling device, there is no heat exchange with the external environment. So the heating capacity Q_c and the COP are calculated as:

$$Q_c = m_c \cdot (h_8 - h_9) \quad \text{Eq. (1)}$$

$$W_{LS} = m_e \cdot (h_2 - h_1) \quad \text{Eq. (2)}$$

$$W_{MS} = m_M \cdot (h_5 - h_4) \quad \text{Eq. (3)}$$

$$W_{HS} = m_c \cdot (h_8 - h_7) \quad \text{Eq. (4)}$$

$$m_c \cdot h_9 = (m_c - m_M) \cdot h_6 + m_M \cdot h_{11} \quad \text{Eq. (5)}$$

$$m_M \cdot h_{12} = (m_M - m_e) \cdot h_3 + m_e \cdot h_{13} \quad \text{Eq. (6)}$$

$$COP = \frac{(h_8 - h_9)\cdot(h_{11} - h_6)}{\frac{(h_9 - h_6)\cdot(h_{11} - h_3)\cdot(h_2 - h_1)}{(h_{13} - h_3)} + (h_9 - h_6)\cdot(h_5 - h_4) + (h_{11} - h_6)\cdot(h_8 - h_7)} \quad \text{Eq. (7)}$$

Where m_c, m_M, m_e are the mass flow of the evaporator, middle-stage compressor and condenser respectively, and W_{HS}, W_{MS}, W_{LS} refers to the power consumption of the high-stage, middle-stage and low-stage compressor respectively.

2.2. The Theory Calculation of Three-Stage Compression Heating Cycle

According to the above-mentioned energy balance relation and the thermodynamics parameter of R-410A, the EES software is used to solve the corresponding mathematical models of the four circulation modes. By changing the values of the two intermediate temperatures, the optimal COP and its corresponding two optimal intermediate temperatures are obtained. Working conditions for theory calculation are given in Table 1. The assumptions of calculation parameters are as follows: the isentropic efficiency of the compressor is 0.7; the subcooling degree at the outlet of the condenser and the superheating degree at the outlet of the evaporator are both 5℃; In each working condition, the condensation temperature T_c is 45℃, and the evaporation temperature T_e is 10 ℃ lower than the outdoor ambient temperature. Fig. 2 shows the variation of COP of four cycles with different working conditions.

Table 1. Experiment and simulation condition

-	Inside room	Outside room	
Dry bulb temperature (℃)	20	-20, -15, -7	7
Wet bulb temperature (℃)	-	-	6

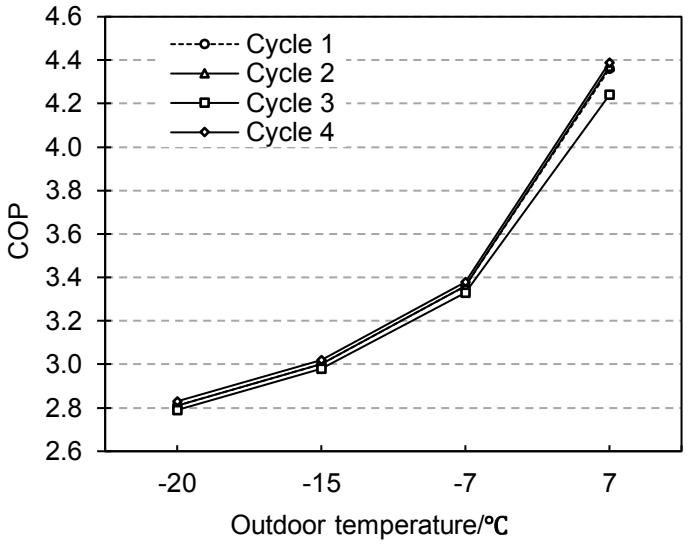

Figure 2: Variation of COP with different conditions

Under the same working condition, the COP of cycle 4 is higher than that of the other three cycles, which is 0.6 % ~ 0.7 %, 0.5 % ~ 0.7 % and 1.3 % ~ 3.5 % higher than that of cycle 1, cycle 2 and cycle 3, respectively. Therefore, the three-stage compression with two flash tanks cycle 4 is selected for subsequent tests.

2.3. The Theory Calculation Analysis for Three-Stage Compression with Two Flash Tanks and Two-Stage Compression with Flash Tank Heat Pump System

Similarly, the EES software is also used to solve the heating performance for the two-stage compression, and the COP comparison of the two cycles is shown in Fig. 3.

Under the same conditions, the COP of the three-stage compression with two flash tanks cycle is 1.62%-2.54% higher than that of the two-stage compression with flash tank system, and the relative difference increases with the outdoor temperature decreasing.

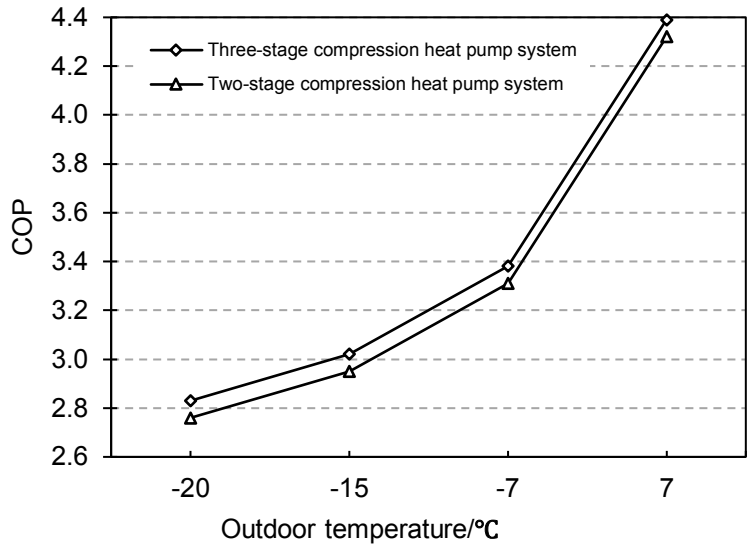

Figure 3: Variation of COP with different conditions between three-stage compression system and two-stage compression system

2.4. Experimental Validation

The side outlet low-temperature air source multi-connected heat pump units using three-stage compression with two flash tanks system and two-stage compression system with flash tank are taken as examples to perform performance comparison analysis. In 16kW heating capacity, the parameters of these two models are exactly the same, such as indoor and outdoor heat exchanger (area, heat pipe size, fins, etc.) and circulating air volume, except the compressor and heat pump cycle mode are different.

The test prototype of the three-stage compression with two flash tanks heat pump system was constructed by connecting a single-stage compressor and a two-stage compressor in series, which main configuration parameters is shown in Table 2. The system diagram is shown in Fig. 4a. And to compare with two-stage compression system under the same working conditions (shown in Table 1), a test prototype of the two-stage compression heat pump system was constructed, and the system diagram is shown in Fig. 4b.

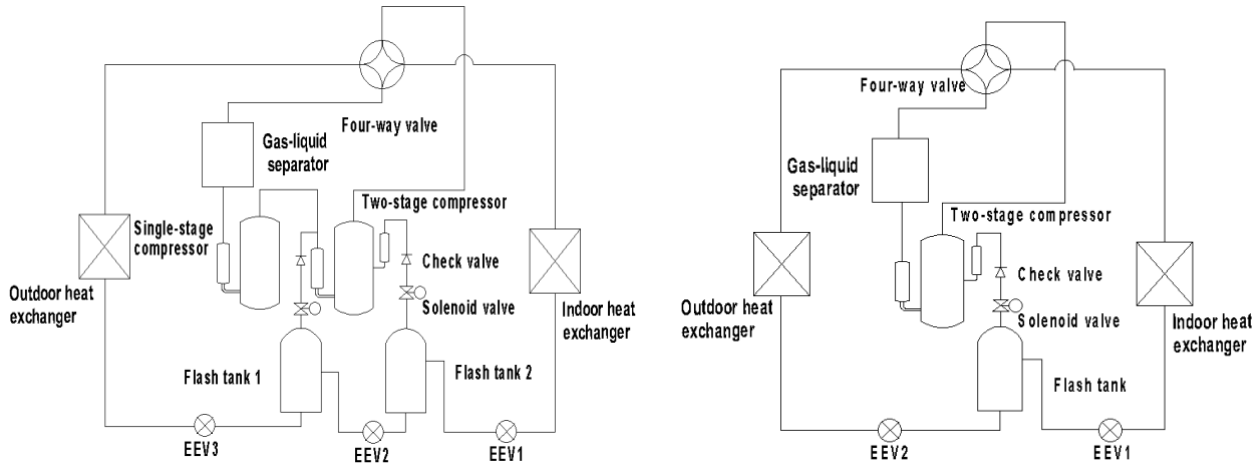

Figure 4:Schematic diagram for two-stage compression with flash tank system and three-stage compression with two flash tanks system

Table 2. Main configuration parameters of the test prototype

Item	Specification
Outdoor heat exchanger	Length × Height × Thickness: 1012 mm×1320 mm×38 mm

Single-stage compressor	Cylinder volume: 51.8 cm^3
Two-stage compressor	Low-stage cylinder volume: 51.8 cm^3
	High-stage cylinder volume: 31.6 cm^3
Electronic expansion valve	Seat: φ 3.2 mm
Refrigerant	R-410A

Through the experimental research, the key influence factors and control methods of the three-stage compression system are mainly analyzed. The results are as follows:

① According to the theoretical calculation, it can be seen that the COP of the system is the highest when the suction state of the two-stage and three-stage compressors is saturated, which is also evident in the experiment. The superheat degree of the compressor suction should be reduced as far as possible under the condition that the compressor suction does not contain liquid, so that the discharge temperature of the compressor can be reduced and the COP of the system can be improved.

② It is found through experimental research that the openings of the three electronic expansion valves (EEV) have influence on the suction and discharge temperature of the compressor. The opening of EEV2 has greatest influence on the tertiary discharge temperature. The tertiary discharge temperature decreases, the heating capacity increases, and the COP increases with EEV2 opening reducing. The opening of EEV1 mainly affects subcooling degree and the tertiary discharge temperature. The subcooling degree and the tertiary discharge temperature decreases with EEV1 opening increasing. The opening of EEV3 mainly affects the suction and discharge temperature of the first-stage compressor. The suction and discharge temperature decreases with EEV3 opening increasing.

③ From the liquid level observation of the flash tank, the flash tank 2 is almost full of liquid under all working conditions, but the flash tank 1 has no liquid. Due to the volumes of the two flash tanks in the system are same, so we can deduce that the design of the flash tank volume may has some problem, or the amount of refrigerant charge is not enough for the system. This result needs to be further verified.

In this paper, the experimental results of the three-stage compression heat pump system and the two-stage compression heat pump system are compared under different working conditions. The heating capacity and COP results are respectively shown in Fig. 5 and Fig. 6.

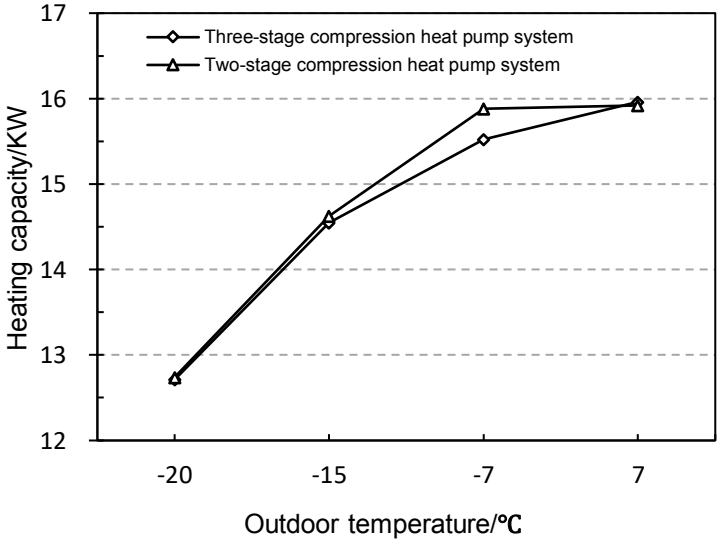

Figure 5 Variation of heating capacity with different conditions between three-stage compression system and two-stage compression system

It can be seen from the Fig. 5 that the heating capacity of three-stage compression system is smaller than that of two-stage compression system. And it can be seen from the Fig. 6 that the experimental result is basically consistent with the theoretical calculation trend. Under the same working conditions and heating capability, the energy efficiency value of the three-stage compression system is 0.5%~3%

higher than that of the two-stage compression system, which has some difference to the theoretical calculation results. The main reason for this difference is the pressure loss of the two supplemental solenoid valves in the system. Due to the structure of three-stage compression system is more complex than that of the two-stage compression system, the long-term reliability of the three-stage compression system is more difficult to guarantee, and the cost will be greatly increased. Therefore, in terms of economy and reliability, when the ambient temperature above -20℃, the three-stage compression system is not better than the two-stage compression system.

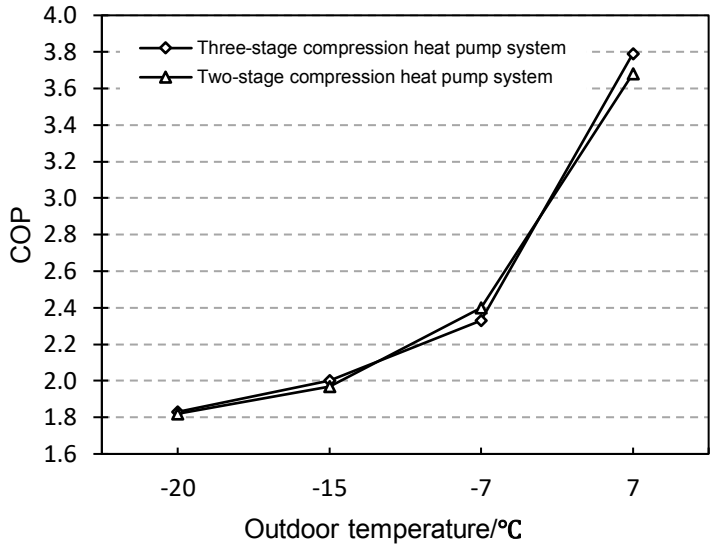

Figure 6 Variation of COP with different conditions between three-stage compression system and two-stage compression system

3. CONCLUSIONS

In this paper, the theoretical and experimental analyses of the three-stage and two-stage compression system are carried out, and the conclusions can be summarized as follows:

(1) According to theoretical analysis for four three-stage compression cycles, the COP of the three-stage compression with two flash tanks cycle is better than the other three cycles.

(2) The key factor affecting the heating performance of the three-stage compression system is the control of the two middle temperatures and the suction superheat degree of the secondary and tertiary compressors.

(3) The experimental result shows that the COP of the three-stage compression system is 0.5% to 3% higher than that of the two-stage compression heat pump system under the same working conditions. But in terms of economy and reliability, when the ambient temperature is above -20℃, the three-stage compression system is not better than two-stage compression system.

NOMENCLATURE

Q	Heat(W)	Subscript	
h	Specific enthalpy (kJ×kg^{-1})	*c*	Condenser
m	Mass flow rate (kg×s^{-1})	*e*	Evaporator
COP	Coefficient of performance	*HS*	High compression stage
		MS	Middle compression stage
		LS	Low compression stage

REFERENCES

Bertsch, Stefan S , and Groll E. A., 2008. Two-stage air-source heat pump for residential heating and cooling applications in northern U.S. climates. International Journal of Refrigeration 31(7), 1282-1292.

Chen J.J., Yang C.Y., Cai B.M., 2010. Experiment of low temperature heat-flash type air source heat pump water heater. Fluid Machinery 38(1), 72-75.

Xu S.X., Ma G.Y., 2014. Experimental study on two-stage compression refrigeration/heat pump system with dual-cylinder rolling piston compressor. Applied Thermal Engineering 62(2), 803-808.

Huang H., Liang X.F., Zhen B., Huang B.L., Fang J.S., Zhuang R., 2016. Thermodynamic cycle analysis and experimental investigate on a two-stage vapor injection low temperature air source heat pump with a variable displacement ratio rotary compressor, 16th International Refrigeration and Air Conditioning Conference at Purdue, Purdue University, 1746-1754.

Horiuchi N., 1997. Development of package air conditioner for cold regions. Refrigeration, 72(7), 72-83.

Manuscript ID: 1412
DOI: 10.18462/iir.icr.2019.1412

The preparation of paraffin/EVA/graphene phase change materials and its thermal properties analysis

Changling WANG [(a) (b)], Xiaosong ZHANG [(a) (b)], Zhenghao LIU [(a) (b)]

[(a)] School of Energy and Environment, Southeast University, Nanjing, 210000, People's Republic of China, wzdup@seu.edu.cn

[(b)] Shenzhen Research Institute of Southeast University
Shenzhen, 518116, People's Republic of China, 712315016@qq.com

ABSTRACT

In this paper, graphene/paraffin/EVA PCMs (GrPrE) was prepared by melting, blending and ultrasonic dispersion method with a series of graphene mass fraction of 0.05%,0.1%,0.25%, and 0.5%. The physical properties of GrPrE were characterized by SEM, DSC, and Hot-Disk. The experimental equipment of heat storage tester was built to test the thermal efficiency and performance of GrPrE during the energy storage process. The result showed that the GrPrE had a good performance in dispersion and stability. The temperature and latent heat of phase transition had no significant change. The thermal conductivity increased with the increasing of graphene mass fraction. In the thermal storage test, the heat transfer rate of the graphene-added materials was faster than the unadded materials, the material which the proportion of graphene was 0.1% had the best performance in the test. In summary, the composite can be a potential candidate for thermal storage applications due to the good thermal properties and heat transfer performance.
Keywords: Energy Storage, Graphene, Phase Change Material, Thermal Analysis.

1. INTRODUCTION

The thermal energy storage is considered as a promising technology in many fields. But there are still many problems and shortcomings in its application (Bhagat et al., 2018; Park et al., 2019). For example, the widely used organic phase change materials(short for PCMs) have poor thermal conductivity and high deformation degree during the phase transition(Sun et al., 2013). These deficiencies restrict the application of PCMs in energy storage.

The nanomaterials, such as graphene, have excellent thermal physical properties (Huang et al., 2015). The thermal conductivity of PCMs can be improved by adding nanomaterials. Li et al. (2017) synthesized a composite PCMs with montmorillonite (OMMT)/paraffin/grafted multi-walled nanotube (MWNT). The thermal properties of the materials were measured and the microstructure was characterized. The thermal conductivity of the OMMT/paraffin/grafted MWNT composites was 65% higher than paraffin wax. Low mass fraction of graphene oxide and paraffin wax composite were prepared in order to improve thermo-physical properties (Dsilva Winfred Rufuss et al., 2017). The results showed that the thermal conductivity stability of lower mass fraction P-GONP was higher than pure paraffin wax. The phase transition temperature was similar to pure paraffin wax but the latent heat of the composite decreased. In addition to carbon-based nanomaterials, some nano-metallic materials can also be used for thermal conductivity enhancement of PCMs. The Nickel foam and copper foam were both used as the composite in PCMs for comparison (Huang et al., 2017). The result showed that the latent heat of the composite PCMs for the melting process decreased by 3-29%. And the metal foam composites have an improved thermal conductivity. Mishra et al. (2018) used Al_2O_3, SiO_2, and TiO_2 as an addition to organic PCM, and the study showed that the nano-inclusion assisted thermal conductivity enhancement in a phenol-water system.

Besides the poor thermal conductivity, many solid-liquid PCMs also have leakage problem(Liu et al., 2014). One of the solutions is to prepare the form-stabled PCMs and therefore the application range of PCMs can be expanded. A cellulose gelling or thickening agent was introduced so that the PCMs became form-stable and the nano-graphene platelets were doped to enhance the thermal

properties(Saeed et al., 2018). Ramakrishnan et al. (2019) fabricated paraffin/EPO based form-stable PCMs with various carbon additives. The results showed that all additives have a significant enhancement in thermal conductivity and the graphene nanoplatelets lead to highest performance. From the present researches, The graphene nanomaterials have a high thermal conductivity, which can be mixed with the form-stable PCMs as additives (Mortazavi et al., 2017; Xiang et al., 2018). While the studies mentioned above were mainly focused on the physical properties and thermal conductivity, the thermal storage performance wasn't covered. In this study, physically stripped graphene was added into the paraffin/EVA composite. And the material characteristics and thermal properties were studied and the thermal storage test was conducted.

2. EXPERIMENTAL

2.1. Materials

Paraffin was used as the PCM in the composite materials. The paraffin's phase-transition temperature was about 60°C (supplied by Suixin chemical co., Ltd, see A1). A physically stripped graphene was used as the thermal enhancement material (supplied by Turing Evolutionary Technology Co.Ltd.).The EVA's melting temperature was 80°C (supplied by Yousuo chemical co.Ltd).

2.2. Preparation of Materials

The solid paraffin wax was melted at 80°C for 4 hours in an Electric Oven. And then a certain amount of liquid paraffin was taken into a flask. A certain amount of CTAB and graphene were added into the liquid paraffin. Afterward, this paraffin-graphene mixture (short for PG) was stirred in a magnetic stirring. The PG was dispersed by an ultrasonic disperser at 80°C for an hour. Then the EVA was added gradually into the PG and was stirred by the electric booster agitator at 120°C for three hours. Ultrasonic dispersion was carried out again on the paraffin/EVA/ graphene (short for GrPrE) mixture at 100°C for one hour. Finally, the mixture was molded in a mold. In this paper, four pieces of GrPrE material were prepared by the above method, the mass fractions of graphene in which were 0.05 %, 0.1 %, 0.25%, and 0.5%.

2.3. Test and Characterization

The materials' surface morphology was observed by a scanning electron microscopy (SEM, Scios. FEI Co., Ltd), which was conducted with an accelerating voltage of 5kV. The material fracture surface was prepared after being immersed in the liquid nitrogen and then treated by spray-gold. The phase transition temperature and the latent heat of the composite material were measured by the DSC method with heat flux DSC (DSC3, Mettler Toledo). The scanning temperature was range from 20℃ to 150°C in a nitrogen atmosphere. And the scanning rate of heating and cooling was 5°C/min. The thermal conductivity of the composites was measured by the Hot-Disk (TPS2500s, Hot Disk) (Fig. 1), and the test ambient temperature was 40°C. The material will be tested from different directions to reduce deviations. The thermal response curve was measured in a constant temperature water bath (Fig. 2) and the temperature data was collected by a data accumulator (Agilent 34972A, Keysight). The material temperature distribution during the heat storage process was tested by the self-made instrument (Fig. 3). The measure points were located with different distance to the heat source: 1cm, 2cm, 3cm and 4cm.



Figure 1: Thermal conductivity tester (Hot Disk)

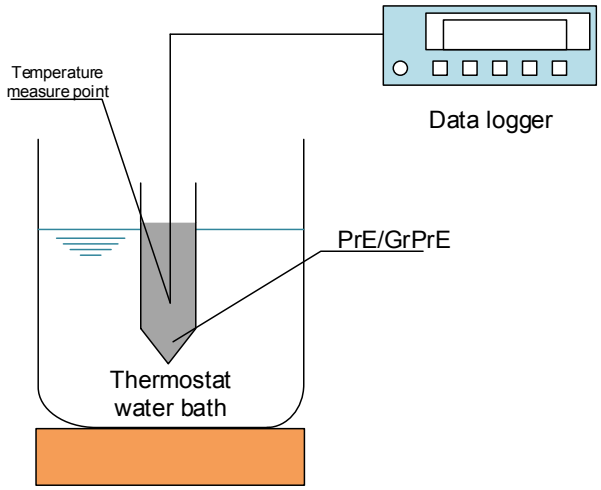

Figure 2: Schematic diagram of thermal response tester

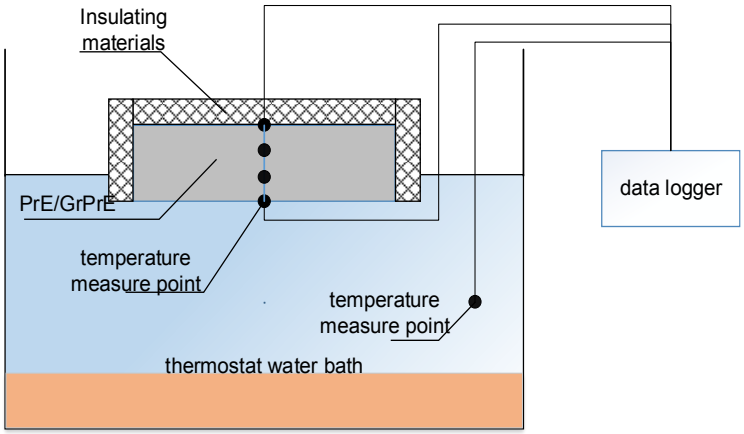

Figure 3: Schematic diagram of temperature field tester

3. RESULTS AND DISCUSSIONS

3.1. Leak Rate of Different Ratio

The samples were wrapped in filter paper and sulfate paper and placed in a constant temperature dryer for 3 hours. The filter and sulfate paper were used to absorb the leaked paraffin. The leakage rates of different composite ratio were obtained by weighting the materials before and after heating.

The results are shown in Table 1.

Table 1. The leakage rate of different composite ratios

Paraffin/EVA ratio	60% /40%	70% /30%	80% /20%
Leakage rate	0.08%	0.17%	1.2%

The results showed that the leakage rate increased with the increasing of paraffin ratio, which was unfavorable to the stability of the composite. On the contrary, the higher the paraffin ratio was, the more heat could be stored and released during the phase transition. When the ratio was 70%/30%, the composite had a respectable paraffin content and a lower leakage rate. Therefore, this ratio was chosen as the base proportion of further material synthesis.

3.2. Surface Topography

Fig. 4 shows the SEM surface topography of PrE and 0.1% GrPrE. It can be figured out from the SEM pictures that the separation surface of the section contains more concave and convex in the non-graphene composite. The paraffin was leaking at some places. The graphene-added composite had less concave and convex, and better isotropy. It can also be seen from the results of the characterization that graphene was uniformly dispersed in the composites.

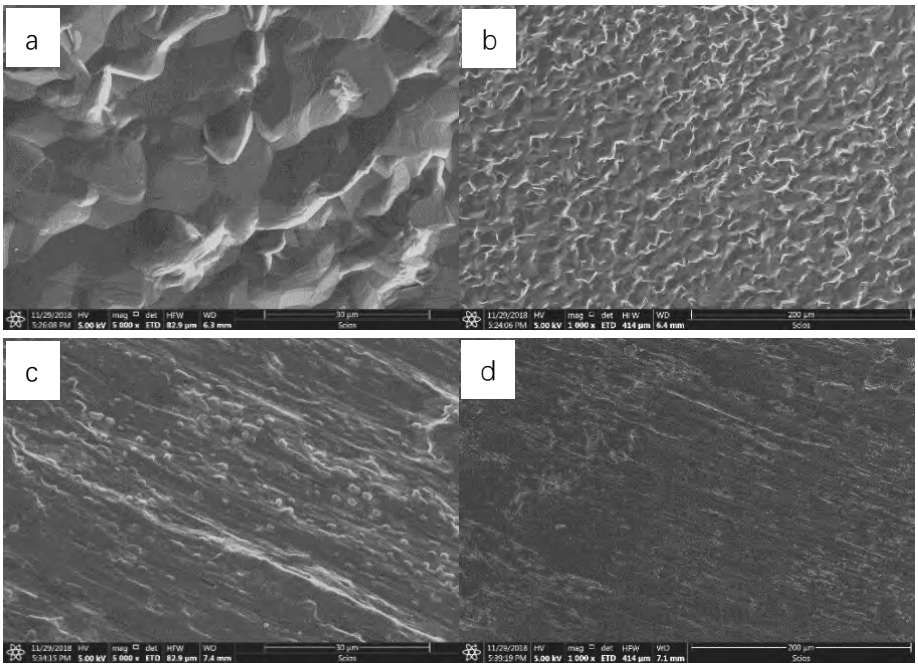

Figure 4：SEM fracture surface topography of composite materials (a) PrE in 30 μm, (b) PrE in 200 μm, (c) 0.1% GrPrE in 30 μm, (d) 0.1% GrPrE in 200 μm

3.3. Phase Transition Characteristics

The DSC curve in Fig. 5 indicates that the phase change absorption peak of paraffin wax was about 60°C during the heating process. The phase change temperature of the composites had no significant change after being added with graphene. And the latent heat of phase transition was also slightly lower than that of the composites without graphene. From the result, it could also be seen that the phase transition occurred at about 60°C and 75°C during the heating process while occurred at about 52°C and 62°C in the cooling process, which indicated that the graphene could not reduce the supercooling degree of the GrPrE. The heat absorption curve of the graphene-added composite flattened out in the heating process.

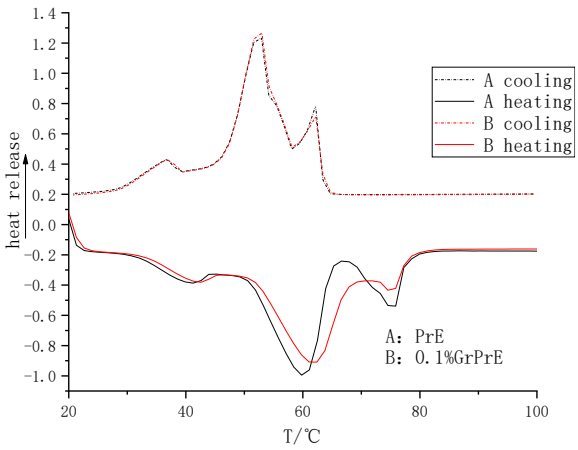

Figure 5: DSC curves of the composite materials

3.4. Thermal Conductivity

The curve in Fig. 6 shows that the thermal conductivity of the composites improved with the increasing of graphene content. When the percentage of graphene reached 0.25%, the thermal conductivity could be 0.28W/m·K. However, the thermal conductivity's improvement gradually decreased when the graphene content increased continuously. The possible reason may be the uneven dispersion of graphene with a high mass fraction.

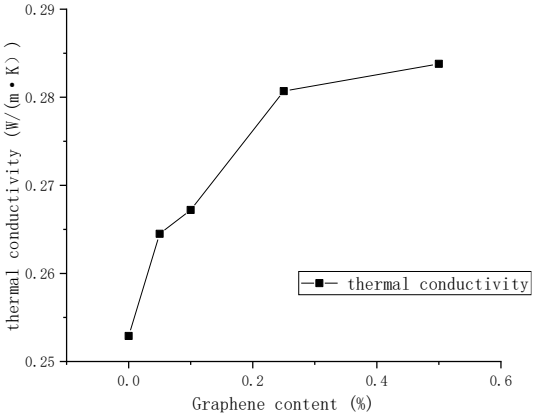

Figure 6: Thermal conductivity of composites with different graphene content

3.5. Thermal Response Test

After the test device was built, the heating surface of the material was placed in a thermostatic water bath, and the internal temperature was measured by the T-type thermocouple. The test steps were as below:

1. Connected the test instruments and heated the water bath to the set value.
2. The sample was heated in the water bath after the water temperature was stabilized. During the heating process, the sample's temperature variation was recorded by the data logger, and the process ended after the sample's temperature reached the set point.
3. The sample was cooled in a low-temperature thermostatic water bath, and the cooling process was finished when the sample's temperature reached the set point.

The temperature response curve in Fig. 7 shows that compared with composites without graphene, the temperature raising rate of the composites with graphene was improved greatly. Compared with the PrE, the reduction amount of the heating duration of 0.05% GrPrE, 0.1% GrPrE and 0.25% GrPrE were 570s, 1570s, and 1280s, respectively. It could be seen from the cooling process that the temperature dropping rate of the graphene-added composites was much faster than non-graphene composites. The reduction amount of the cooling duration of 0.05% GrPrE, 0.1% GrPrE and 0.25% GrPrE were 1320s,1295s and 820s, respectively. Summarized from the whole process, the 0.1% GrPrE had the shortest thermal response time.

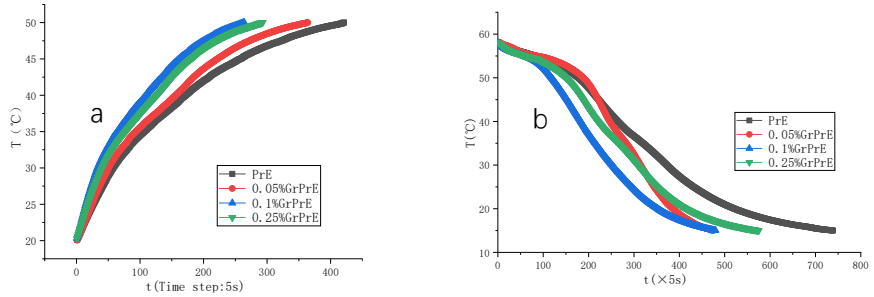

Figure 7: The curve of thermal response process (a) heating process (b) cooling process

3.6. Temperature Distribution in Thermal Storage Process

Fig. 8 shows that 0.25% GrPrE had the highest temperature in every measure point after heat storage process was conducted for 10mins. The temperature of 0.1% GrPrE at 1cm was approaching to the value of 0.25% GrPrE at 30mins and was higher at 1cm, 3cm, 4cm points after 60mins, which suggested that the 0.1% GrPrE had a faster thermal storage rate compared to higher mass fraction graphene samples. Besides, the temperature of the 0.05% GrPrE at 1cm was exceeded by the PrE from 60mins, which indicated the low mass fraction graphene had no obvious enhancement on the thermal storage.

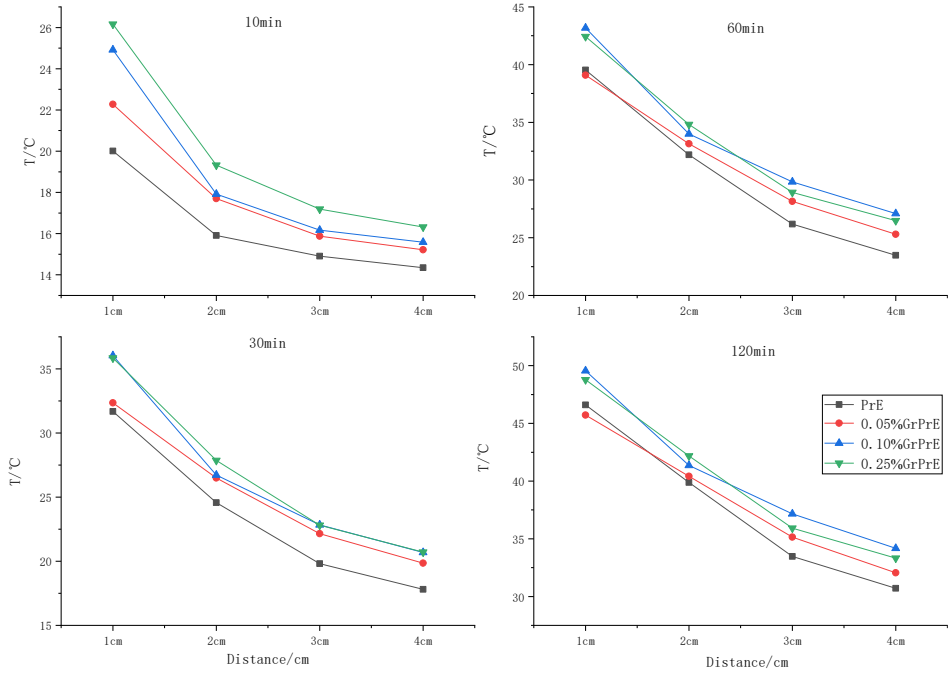

Figure 8：The changes of temperature field in the process of thermal storage

4. CONCLUSIONS

Graphene modified paraffin/EVA PCMs were successfully prepared by melting, blending and ultrasonic dispersion. The characterization results showed that the graphene was mixed uniformly in the composite and had no significant effect on the thermal properties of phase transition. The thermal

conductivity of graphene-added composites was significantly higher than non-graphene composite. In the thermal response and storage test, the heat response and thermal storage rate of the graphene-added materials were faster than that of the unadded materials, the 0.1% GrPrE had the best performance in the test. In summary, the graphene-added composite can be a potential candidate for thermal storage applications due to its good thermal properties and heat transfer performance.

ACKNOWLEDGEMENTS

This research work was supported by the international (regional) cooperation and exchange projects of the National Natural Science Foundation of China (Projects No. 51520105009) and the Basic Research Programs of Science and Technology Foundation of Shenzhen (Projects No. JCYJ20170817164951117).

REFERENCES

Bhagat, K., Prabhakar, M., Saha, S.K., 2018. Estimation of thermal performance and design optimization of finned multitube latent heat thermal energy storage. Journal of Energy Storage 19, 135-144.

Dsilva Winfred Rufuss, D., Iniyan, S., Suganthi, L., Davies, P.A., 2017. Low mass fraction impregnation with graphene oxide (GO) enhances thermo-physical properties of paraffin for heat storage applications. Thermochimica Acta 655, 226-233.

Huang, X., Lin, Y., Alva, G., Fang, G., 2017. Thermal properties and thermal conductivity enhancement of composite phase change materials using myristyl alcohol/metal foam for solar thermal storage. Solar Energy Materials and Solar Cells 170, 68-76.

Huang, Y.-R., Chuang, P.-H., Chen, C.-L., 2015. Molecular-dynamics calculation of the thermal conduction in phase change materials of graphene paraffin nanocomposites. International Journal of Heat and Mass Transfer 91, 45-51.

Li, M., Guo, Q., Nutt, S., 2017. Carbon nanotube/paraffin/montmorillonite composite phase change material for thermal energy storage. Sol Energy 146, 1-7.

Liu, C., Yuan, Y., Zhang, N., Cao, X., Yang, X., 2014. A novel PCM of lauric–myristic–stearic acid/expanded graphite composite for thermal energy storage. Materials Letters 120, 43-46.

Mishra, A.K., Lahiri, B.B., Philip, J., 2018. Thermal conductivity enhancement in organic phase change material (phenol-water system) upon addition of Al2O3, SiO2 and TiO2 nano-inclusions. Journal of Molecular Liquids 269, 47-63.

Mortazavi, B., Yang, H., Mohebbi, F., Cuniberti, G., Rabczuk, T., 2017. Graphene or h-BN paraffin composite structures for the thermal management of Li-ion batteries: A multiscale investigation. Applied Energy 202, 323-334.

Park, J., Shin, D.H., Lee, S.J., Shin, Y., Karng, S.W., 2019. Effective latent heat thermal energy storage system using thin flexible pouches. Sustainable Cities and Society 45, 143-150.

Ramakrishnan, S., Wang, X., Sanjayan, J., 2019. Effects of various carbon additives on the thermal storage performance of form-stable PCM integrated cementitious composites. Applied Thermal Engineering 148, 491-501.

Saeed, R.M., Schlegel, J.P., Castano, C., Sawafta, R., 2018. Preparation and enhanced thermal performance of novel (solid to gel) form-stable eutectic PCM modified by nano-graphene platelets. Journal of Energy Storage 15, 91-102.

Sun, D., Wang, L., Li, C., 2013. Preparation and thermal properties of paraffin/expanded perlite composite as

form-stable phase change material. Materials Letters 108, 247-249.
Xiang, N., Yuan, Y., Sun, L., Cao, X., Zhao, J., 2018. Simultaneous decrease in supercooling and enhancement of thermal conductivity of paraffin emulsion in medium temperature range with graphene as additive. Thermochimica Acta 664, 16-25.

Appendix

A1. Performance parameters of paraffin wax

Analysis project	Quality index	Test method
Melting point, °C	58-60	GB/T2539
Oil content, % (m/m)	0.5	GB/T3554
Color	+28	GB/T3555
Needle penetration (25°C)	18	GB/T4985
Impurities	None	

Manuscript ID: 1430
DOI: 10.18462/iir.icr.2019.1430

Options for low–global-warming-potential and natural refrigerants- Performance for heat pump application and analysis of systemic irreversibilities

Kashif NAWAZ [(a)], Moonis R. ALLY [(a)], Vishaldeep SHARMA [(a)]

[(a)]Oak Ridge National Laboratory
Oak Ridge, TN 37831-6070, USA, nawazk@ornl.gov

ABSTRACT

There is growing interest in substituting existing refrigerants with low global warming potential (GWP) refrigerants, including naturally occurring fluids, to reduce the impact of human activities on climate change. In this study we have evaluated prospective low-GWP refrigerants in four distinct heat pump cycles using the First and Second laws of thermodynamics. The essence of the study is to establish the performance of the low-GWP refrigerants when deployed in a heat pump system. Exergy analysis provides a true measure of lost work, or systemic inefficiencies, vividly quantifying areas of improvement and identifying the preferred cycle for a refrigerant. The combined knowledge of the properties of the phase boundary on either side of the critical point (DOI:10.1.18462/iir.icr.2019.442), and exergy analysis of prospective cycles is necessary for a better perspective on discriminating among refrigerants as hydrochlorofluorocarbons are phased out and replacement refrigerants must be found.

Keynotes: Propane, Refrigerants, Irreversibility, Energy Efficiency.

1. INTRODUCTION

In the context of reducing greenhouse gas emissions (GHGs) and increasing use of natural refrigerants, evaluation of low GWP fluids based on characteristics of the saturation phase boundary (Morrison 1994) is instructive and revealing. The path that a refrigerant takes within the heat pump cycle crosses the phase boundary, and its ultimate effect on the cycle performance and machinery depends on the shape of the temperature–entropy (T-S) phase boundary. Skewness in the T-S curve may cause the formation of a liquid in the compressor, resulting in inferior performance or failure of the component. The phase boundary by itself provides useful but partial information on the expected performance of refrigerants. Although phase boundary shape is helpful in screening and understanding fundamental characteristics of classes of refrigerants (detailed in paper ID 442), it is also necessary to evaluate their expected performance in typical heat pump cycles. This paper presents a detailed exergy analysis of refrigerants used or proposed for use in HVAC&R systems.

To displace existing HCFCs, HFC, and HFOs future refrigerants must preferably have zero ODP and zero or near-zero GWP. A summary of the progress of refrigerants toward these goals is given in Table 1. Notwithstanding their adverse flammability characteristics (A3 classification), the select HCs have zero ODP and GWP, possess good miscibility with mineral oil, and are compatible with a variety of existing compressors.

Why some refrigerants perform better than others remains an interesting research question. Although several researchers have conducted experimental studies and have developed models, these models are often too complex to accurately predict the impact of working fluid (Pitarch et al., 2017; Nanxi et al., 2005; Comakli et al., 2009; Nawaz et al., 2017a, 2017b; Sun et al., 2016; Wang et al., 2013). This paper evaluates heat pump cycles for low-GWP refrigerants under the same operating conditions. The First and Second law analysis provide a comprehensive paradigm to evaluate expected heat pump performance.

Table 1. ODP and GWP of various refrigerants (US Department of Health and Human Services)

Refrigerant group	Refrigerant example	ODP	GWP_{100}	Atmospheric lifetime (years)	Flammability
CFCs	R-11, R-12, R-115	0.6–1	4750–14400	45–1700	Nonflammable
HCFCs	R-22, R-141b, R-124	0.02–0.11	400–1800	5–20	Nonflammable
HFCs	R-407C, R-32, R-134a, R-152a	0	140–11700	0.6–300	Nonflammable or mildly flammable
HFOs	R-1234yf, R-1234ze(E), R-1234yz	0	0–12	-	Mildly flammable
Natural refrigerants	CO_2(R-744), NH_3(R-717), HC (Propane (R-290), n-Butane(R-600), iso-Butane (R-600a))	0	Less than 3.	Few days	HCs: Highly flammable R717: Flammable R744: Nonflammable

2. MODEL AND METHOD

The theoretical basis of our analysis is couched in the First and Second Laws of Thermodynamics, leading to the equations of energy conservation, Eq. Eq. (1), and entropy generation, Eq. (2):

$$\sum \dot{Q}_{cv} + \dot{W}_{cv} + \sum_{in} \dot{m}\left(h + \frac{v^2}{2} + gz\right) - \sum_{out} \dot{m}\left(h + \frac{v^2}{2} + gz\right) = \frac{dE_{cv}}{dt} = \frac{d}{dt}\left[m\left(u + \frac{v^2}{2} + gz\right)\right] . \quad \text{Eq. (1)}$$

$$\frac{dS_{cv}}{dt} + \sum_{out} \dot{m} \times s - \sum_{in} \dot{m} \times s = \sum \frac{\dot{Q}_{cv}}{T} + \dot{\sigma}_{cv} . \quad \text{Eq. (2)}$$

Since the First Law contains a work term but no entropy terms, and the Second Law contains entropy terms, but no work term, they are combined through their common thermal energy term, $\dot{Q}_{cv}$, to yield:

$$\dot{W}_{cv} = \sum_{out} \dot{m}\left(h - T_o s + \frac{v^2}{2} + gz\right) - \sum_{in} \dot{m}\left(h - T_o s + \frac{v^2}{2} + gz\right) - \sum_j \dot{Q}_j \left(1 - \frac{T_o}{T_j}\right) + \frac{dE_{cv}}{dt} - T_o \left[\frac{dS_{cv}}{dt} - \dot{\sigma}_{cv}\right] \quad \text{Eq. (3)}$$

where T_o is the reference temperature, taken to be 273.15 K; $\dot{Q}_j$ is the rate of thermal energy transfer at the control surface to or from thermal reservoirs at T_o or T_j ; S_{cv} is the entropy within the control volume, (cv); and $\dot{\sigma}_{cv}$ is the rate of entropy generation. Under steady-state uniform-flow, uniform-state conditions, Eq. Eq. (1) reduces to:

$$\sum \dot{Q}_{cv} + \dot{W}_{cv} + \sum_{in} \dot{m}\left(h + \frac{v^2}{2} + gz\right) - \sum_{out} \dot{m}\left(h + \frac{v^2}{2} + gz\right) = 0 . \quad \text{Eq. (4)}$$

Under steady-state, no-flow conditions, Eq. (2) and Eq. (3) reduce to Eq. Eq. (5) and Eq. Eq. (6) respectively:

$$\dot{\sigma}_{cv} = -\sum_j \frac{\dot{Q}_j}{T_j} \quad , \quad \text{Eq. (5)}$$

$$\dot{W}_{cv,actual} = -\sum_j \dot{Q}_j \left(1 - \frac{T_o}{T_j}\right) + T_o \dot{\sigma}_{cv} . \quad \text{Eq. (6)}$$

The last term on the right side of Eq. Eq. (6) is the irreversibility, or "lost work," within the control volume, defined as $\dot{I}_{cv} = T_o \dot{\sigma}_{cv}$.

The minimum steady-state, no-flow work is when $\dot{I}_{cv} = 0$, reducing Eq. Eq. (6) to,

$$\dot{W}_{cv,min} = -\sum_j \dot{Q}_j \left(1 - \frac{T_o}{T_j}\right) . \quad \text{Eq. (7)}$$

The cooling COP, $COP_c = \frac{Q_o}{W_{comp.}}$, in which both the numerator and denominator are in units of $\mathrm{kJ} \cdot \mathrm{kg}^{-1}$, is readily converted to units of kW by using the tabulated mass flow rates in succeeding tables. The actual compressor work is the sum of the Carnot work and the total cyclic irreversibility, given as Eqs. (8) and (9):

$$W_{actual} = W_{Carnot} + I_{Total} , \quad \text{Eq. (8)}$$

$$COP_{Carnot} = \frac{T_e}{(T_c - T_e)} , \quad \text{Eq. (9)}$$

and I_{Total} is the total cyclic irreversibility obtained from summing the respective $\dot{I}_{cv}$ (previously defined) applied to all the components in the cycle and converted via the mass flow rate to units of $\mathrm{kJ} \cdot \mathrm{kg}^{-1}$.

Besides COP, the volumetric capacity, $Q_{vol.}$, measured in $\mathrm{MJ} \cdot \mathrm{m}^{-3}$, defined as the cooling capacity per unit of volume of refrigerant vapor entering the compressor, quantifies the equipment size. Larger values of $Q_{vol.}$ signify greater compactness, and vice versa. McLinden et al. (2017) point out that both COP and $Q_{vol.}$ are related to the critical temperature, $T_{crit.}$, with higher values of $T_{crit.}$ resulting in high COP but low $Q_{vol.}$, and vice-versa.

Four discrete heat pump configurations are considered in this study as shown in

Figure 1. (a) a simple vapor compression cycle modified to transfer a portion of the condenser heat to the suction line; (b) a variation of configuration (a) in which the vapor–liquid mixture exiting the evaporator is routed through the condenser to attain saturation before entering the compressor suction port; (c) a standard vapor compression heat pump that serves as a benchmark; and (d) a heat pump cycle with a flash tank installed between two expansion valves, throttling pressure from the high-side condenser to the low-side evaporator. The flashed vapor is at a value that equalizes the discharge and suction pressures of two compressors between the evaporator and the condenser. Configurations (a) and (b) are two variations of the liquid line-suction line heat exchanger (LL/SL-HX) concept, and configuration (d) is a two-stage economizer cycle investigated for low-GWP refrigerants (McLinden et al.,2017). This paper emphasizes how exergy analysis clarifies the systemic inefficiencies of the four configurations to aid in understanding their disparate performance behavior for 12 of the refrigerants listed in *Table 1*

3. RESULTS AND DISCUSSION

3.1 Assumptions

For the cycle analysis and screening of refrigerants, representative evaporator (0°C) and condenser (60°C) temperatures for heat pumps and air conditioning were fixed. Pressure drops in the piping and equipment were neglected. The compressor efficiency is assumed to be 100%. These assumptions are justified for a preliminary analysis to avoid incurring unwanted complications of manufacturer's specifications, compressor types, and compressor maps.

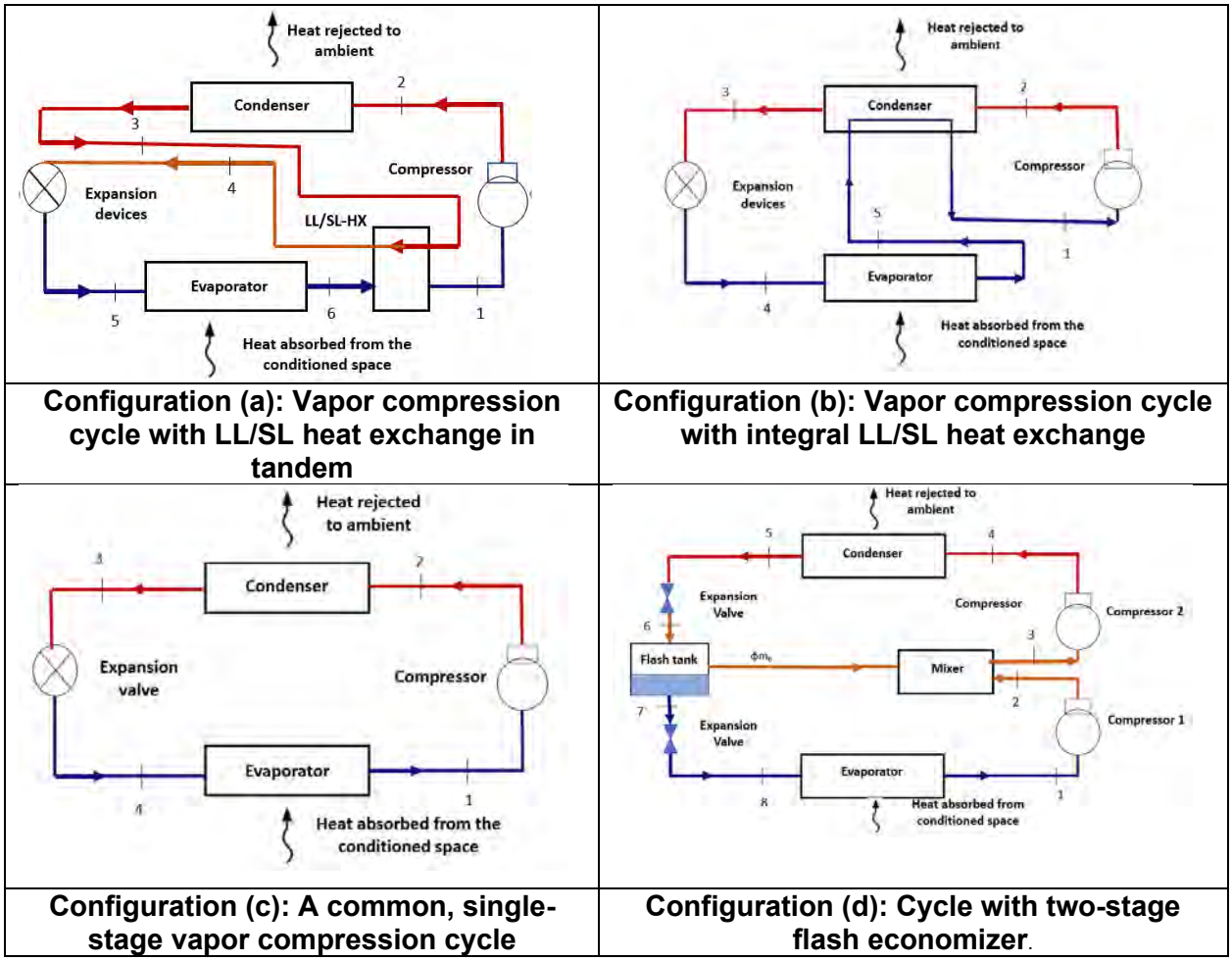

Configuration (a): Vapor compression cycle with LL/SL heat exchange in tandem

Configuration (b): Vapor compression cycle with integral LL/SL heat exchange

Configuration (c): A common, single-stage vapor compression cycle

Configuration (d): Cycle with two-stage flash economizer.

Figure 1: Cycle configuration considered in the analysis

For heat pump configurations (b) and (c) involving the LL/SL-HX concept, the vapor quality at the evaporator exit was fixed at 0.9, implying that heat is required before vapor enters the compressor as saturated vapor. In configuration (d), the compression ratio between the two compressors was fixed exclusively by the high and low pressures corresponding to the condensing and evaporating temperatures, respectively, of the given refrigerant; and the intermediate pressure at the mixer was given as the geometric mean of these two pressures. Cycle simulations were performed using Engineering Equation Solver (EES) model V10.259-3D (Klein, 2015).

3.1.1. Configuration (a): vapor compression cycle with LL/SL-heat exchanger in tandem

The cycle for configuration (a) is depicted in

Figure 1a**.** Applying Eqs. Eq. (4) – Eq. (9) yielded the energy balance, component-wise and total irreversibility, Carnot work, and actual work ($W_{actual.}$) which, through exergy analysis, must be and is in agreement with the work ($W_{Comp.}$) calculated from the First Law.

The amount of thermal energy to be recovered by LL/SL-HX is arguable. Too much recovery would increase the compressor suction temperature (state point 1), perhaps making the compressor exit temperature (state point 2) exceed its design capacity. In the limit, recovery of the entire condenser load by the LL/SH-HX would violate the Kelvin-Plank statement: It is impossible for a heat engine operating in a cyclic manner to exchange heat with only one reservoir. Considering these limitations, the quality of the vapor at state point 6 was held at 0.95 and the quality of the vapor entering the compressor at state point 1 at 1.0 to limit the heat recovery by the LL/SL-HX to a reasonable value. In future studies, it will be instructive to examine the influence of quality on cyclic performance.

While total irreversibility is the quantifiable measure of the lost opportunity to produce useful work, the component-wise irreversibility shows areas where improvement is most beneficial. For ammonia, the condenser is the most irreversible component, with lost work of 162.93 $\mathrm{kJ \cdot kg^{-1} \cdot K^{-1}}$ because of its high condenser thermal load. The next-largest condenser irreversibility is 34.61 $\mathrm{kJ \cdot kg^{-1} \cdot K^{-1}}$ is exhibited by R-600. A comparison of total cyclic irreversibility is illustrated in Figure 2. From the total cyclic irreversibility standpoint, ammonia ranks second.
The volumetric capacity based on the same set of state points and state variables. Ammonia represents the highest COP and the second highest volumetric efficiency, and its relative strength as a viable refrigerant is shown in Figure 3.

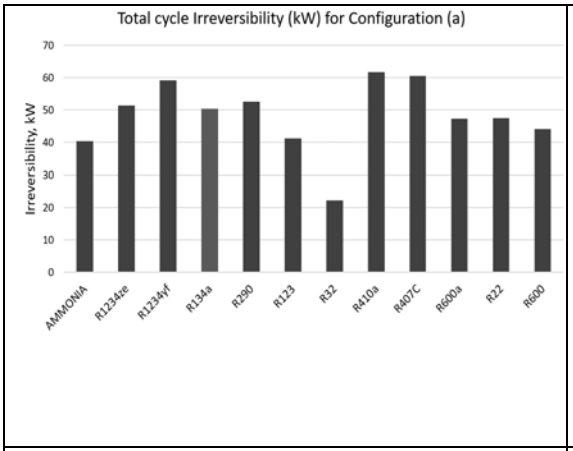

Figure 2: Relative magnitude of total cycle irreversibility of configuration (a) for various refrigerants

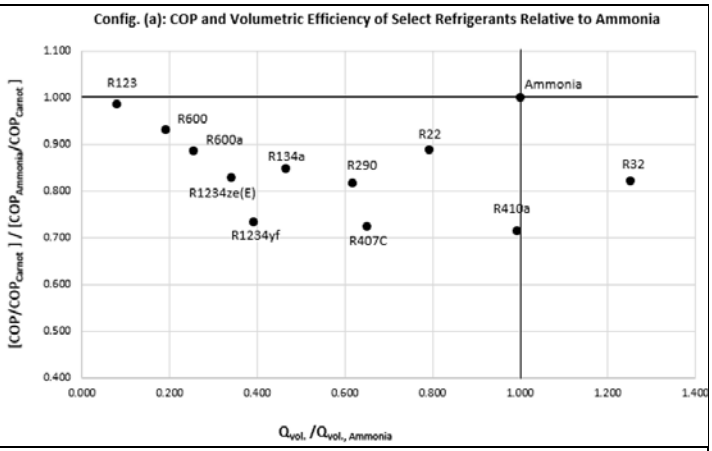

Figure 3: COP and volumetric efficiency of various refrigerants relative to ammonia for configuration (a). Higher relative volumes represent more compact system

3.1.2. Configuration (b): vapor compression cycle with integral LL/SL-heat exchanger

A variation of the LL/SL-HX is where partial heat recovery is achieved within the condenser, as shown in

Figure ***1***. The vapor quality at state points 5 and 1 are 0.95 and 1.0, respectively, for the same reasons discussed earlier for configuration (a).
Consistent with configuration (a), the quality of the vapor exiting the evaporator (state point 5,

Figure ***1***b) is held at 0.95 and the quality of the vapor entering the compressor at state point 1 is 1.0, to limit the heat recovery by the LL/SL-HX to a reasonable value (see discussion for configuration a). The component-wise and total irreversibility show that although the condenser with ammonia has the highest irreversibility, the total cyclic irreversibility of ammonia is the lowest, making the lost work the smallest among all 12 refrigerants simulated. This finding is due to the low mass flow rate ($0.19\ \mathrm{kg \cdot s^{-1}}$) of ammonia because of its high heat of vaporization compared with the other refrigerants. Based on the stated assumptions, the compressor irreversibility is zero (100% efficient compressor). R32 is a close competitor to ammonia in terms of total irreversibility, but R32 is unsuitable because of its high GWP (see Table 1). A vivid comparison of the total cyclic irreversibility of the single-stage vapor compression cycle in configuration (b) is shown in Figure 4***.*** Ammonia represents the highest COP and the second highest volumetric efficiency, with its relative strength among the refrigerant shown in Figure 5.

3.1.3. Configuration (c): single-stage vapor compression cycle

A simple, single-stage vapor compression cycle is presented in

Figure 1c with state points (1–4) corresponding to the state variables. The highest efficiency relative to the Carnot COP is shown by ammonia, followed by R123. As in configurations (a) and (b), the ammonia flow rate is the lowest for the cycle of

Figure 1c because of its high latent heat of vaporization.
The component-wise and total irreversibility data shows that although the condenser with ammonia has the highest irreversibility, the total cyclic irreversibility of ammonia is the lowest, making the lost work the smallest of all 12 refrigerants simulated.
This is due to the low mass flow rate ($0.19\ \mathrm{kg \cdot s^{-1}}$) because of its high heat of vaporization compared to the other refrigerants. R-32 is a close competitor to ammonia in terms of total irreversibility but has a higher GWP (677 vs. 0).The component-wise and total irreversibility data show a similar pattern for ammonia as for configurations (a) and (b): the ammonia condenser has the highest irreversibility, whereas the total cyclic irreversibility with ammonia is once again the lowest, making the lost work ($36.94\ \mathrm{kW}$) the smallest among all 12 refrigerants simulated. A comparison of the total cyclic irreversibility of the single-stage vapor compression cycle is shown in Figure 6. For the single-stage cycle of configuration (c), hydrocarbons (R-290, R-600, and R-600a) and ammonia are acceptable options among zero-GWP refrigerants. A choice among them would be based on balancing the flammability and toxicity risks and the materials of construction for the given application. Comparing the refrigerants in terms of volumetric capacity (Figure 7), ammonia shows the overall best efficiency and volumetric capacity; only two refrigerants, R-410A and R-32, show higher relative volumetric efficiency than ammonia, but they have lower cycle efficiency.

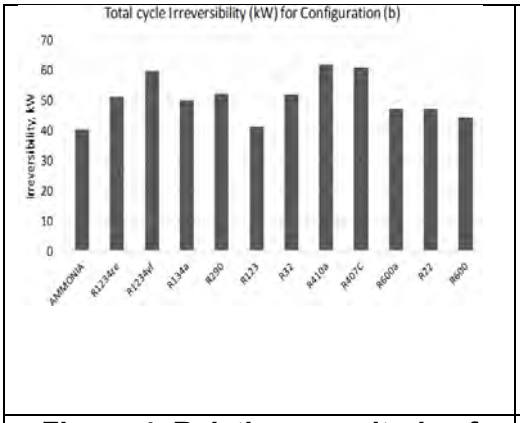

Figure 4: Relative magnitude of total cycle irreversibility of configuration (b) for various refrigerants

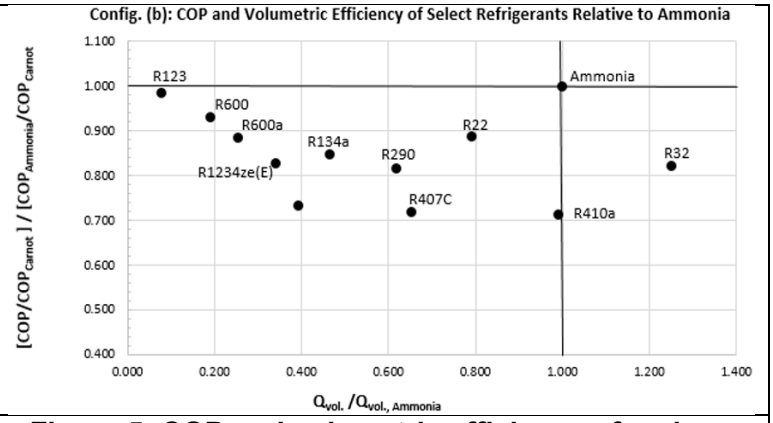

Figure 5: COP and volumetric efficiency of various refrigerants relative to ammonia for configuration (b). Higher relative volumes represent more compact system

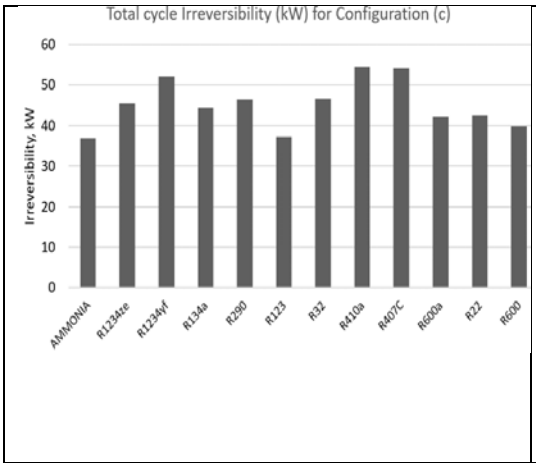

Figure 6: Relative magnitudes of total cycle irreversibility of configuration (c) for various refrigerants

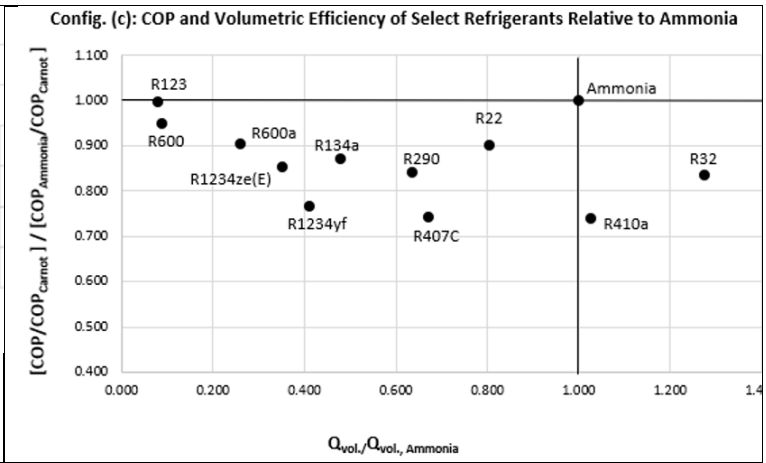

Figure 7: COP and volumetric efficiency of various refrigerants relative to ammonia for configuration (c). Higher relative volumes represent a more compact system

3.1.4. Configuration (d): Vapor compression cycle with a flash economizer

A two-stage vapor compression cycle with a flash economizer

Figure 1d is a way of improving the cycle efficiency by 4–16% (depending on flash tank pressure) relative to the single-stage cycle of configuration (c). The cycle with an economizer is shown in

Figure 1d*,* with the mixer equilibrating the inter-stage pressure between the two compressors. The inter-stage pressure varies with the refrigerant but is maintained at the geometric mean of the pressure between the evaporator and the condenser. The extent of flashing, denoted by $0 \leq \varphi = 1 - \frac{\dot{m}_8}{\dot{m}_6} \leq 1$ varies for each refrigerant. The cycle of

Figure *1*d could be modeled for all refrigerants, except R-410A and R-407C; the temperature glides of the latter precluded proper convergence, most likely because of blend fractionation. Plausibly, since R-410A and R-407C are zeotropic blends, the convergence issues could not be overcome. Therefore, these two refrigerants were excluded from further consideration in configuration (d). The highest efficiency relative to the Carnot COP is shown by ammonia, followed by R-32. As in configurations (a)–(c), the ammonia flow rate is the lowest for the cycle presented in

Figure 1d because of its high latent heat of vaporization. Unlike in the previous three configurations, ammonia has comparable total irreversibility with the HCs, whereas the remaining refrigerants have similar and lower total irreversibility. Irreversibilities of the evaporator, mixer, compressors, and flash tank are low for all refrigerants. The distinction is between the irreversibility of the condenser and those of the expansion valves, which remain high for ammonia, R-290, R-600, and R-600a. As for other cycles, a comparative view of total irreversibility among the various refrigerants is shown in Figure 8. Ammonia has the highest evaporator load per unit of mass (1136 kJ·kg^{-1}), almost three times greater than that for the HCs and almost an order of magnitude greater than those of R-1234ze(E), R-123, and R-1234yf. On a relative basis, except for R-32, the rest of the refrigerants show lower volumetric efficiency compared with ammonia. The COP of R-32 is only 72.6% that of ammonia. Comparative relative COP and volumetric ratios are shown in Figure 9. Among the zero-GWP refrigerants, ammonia has the best overall performance in terms of efficiency and compactness.

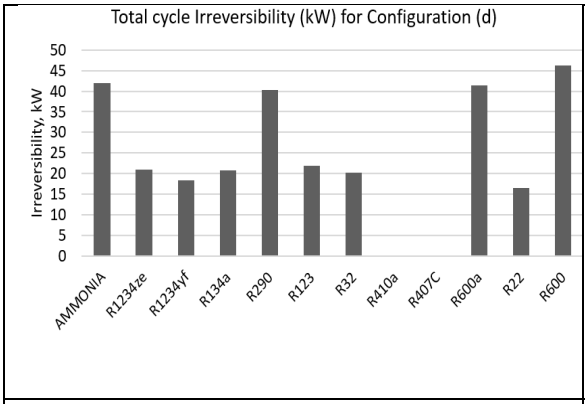

Figure 8: Relative magnitudes of total cycle irreversibility of configuration (d) for various refrigerants

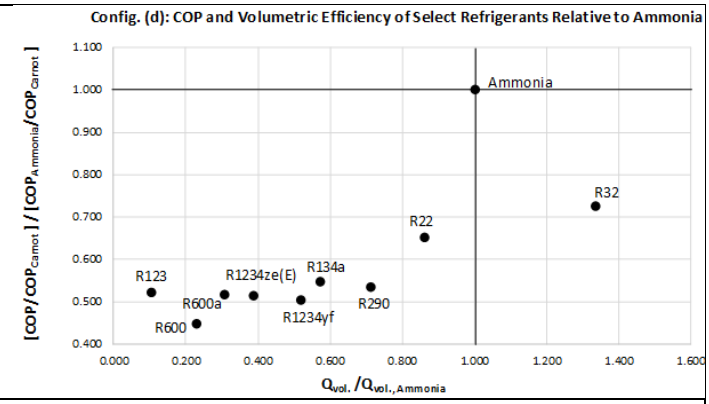

Figure 9: COP and volumetric efficiency of various refrigerants relative to ammonia for configuration (d). Higher relative volumes represent more compact systems

4. CONCLUSIONS

Exergy analysis is an indispensable tool to identify sources of systemic inefficiency where the opportunity to do useful work is lost to the surroundings. In this paper, we find that ammonia

outperforms several classes of refrigerants in terms of COP and volumetric capacity, a finding of enormous importance to future work on natural, zero-GWP working fluids for heat pump applications. The cycle of configuration (c) is the preferred choice for natural refrigerants because of its simplicity.

ACKNOWLEDGEMENTS

We are grateful to the U.S Department of Energy, Building Technologies Office, for supporting this work. Particularly the support provided by BTO program manager Antonio Bouza is acknowledged.

NOMENCLATURE

C specific heat, kJ·mol^{-1}·K^{-1} or kJ·kg^{-1}·K^{-1}
CFC chlorofluorocarbons
COP coefficient of performance
E Energy, kJ
EXV expansion valve
g gravitational acceleration, 9.8 m·s^{-2}
GHG Greenhouse gas
GWP Global warming potential
h specific enthalpy, kJ·mol^{-1}, or kJ·kg^{-1}
HCFC hydrochlorofluorocarbon
HFC hydro fluorocarbon
HFO hydrofluoro-olefins
$\dot{I}$ rate of irreversibility, kW
LL/SL-HXLiquid line suction line heat exchanger
$\dot{m}$ mass flow rate, kg·s^{-1}
ODP Ozone depletion potential
Q Capacity or thermal energy, kJ
$\dot{Q}$ rate of heat flow, kW or W
s specific entropy, kJ·mol^{-1}·K^{-1}
S total entropy, kJ·K^{-1}
T temperature, °C or K
t time, s
u specific internal energy, kJ·mol^{-1}·K^{-1}
V volume, m^3
$\dot{W}$ rate of work, kW

Greek symbols
Δ change of a property, variable or function
$\dot{\sigma}$ rate of change of entropy or entropy production, kW·K^{-1}
∂ partial derivative

Subscripts
b boiling point
c condenser; c is used for “cooling”
crit. critical point
cv control volume
e, evap. evaporator
j jth variable or component
molar per mole, mol^{-1}
o thermodynamic dead state, or ambient
P constant pressure
sat. saturated state or condition
V constant volume

REFERENCES

Comakli, K., Simsek, F., Comakli, O., Sahin, B., 2009. Determination of optimum working conditions R22 and R404A refrigerant mixtures in heat-pumps using Taguchi method, Applied Energy 86 2451–2458

Klein, S., 2015. EES-Engineering Equation Solver, V10.259-3D (2017-06-07), F-chart Software, Madison, WI 53744, www.fchart.com

McLinden, M. O., Brown, J. S., Brignoli, R., Kazakov, A. F., Domanski, P. A. (2017). Limited options for low-global-warming-potential refrigerants, Nature Communications 8, Article Number 14476, doi:10.1038/ncomms14476, https://www.nature.com/articles/ncomms14476

Morrison, G. 1994. The shape of the temperature-entropy saturation boundary, *International Journal of Refrigeration*. Vol. 17, Issue 7, 494-504. https://orproxy.lib.utk.edu:2113/10.1016/0140-7007(94)90011-6

Nanxi, L., Shi, L., Lizhong, H., Mingshan, Z., 2005. Moderately high temperature water source heat-pumps using a near-azeotropic refrigerant mixture, Applied Energy 80, 435–447

Nawaz, K., Shen, B., Elatar, A., Baxter, V., Abdelaziz, O., Performance Optimization of CO_2 HPWH System", International Journal of Refrigeration, 2018, 85, 213-228.

Nawaz, K., Shen, B., Elatar, A., Baxter, V., Abdelaziz, O., 2017. R-1234yf and R-1234ze(E) as Low GWP Refrigerants for Residential Heat Pump Water Heaters, International Journal of Refrigeration, 82, 348-365.

Nawaz, K., Shen, B., Elatar, A., Baxter, V., Abdelaziz, O., 2017. R-290 and R-600a as Natural Refrigerants for Residential Heat Pump Water Heaters", *Applied Thermal Engineering*, 127, 870-883.

Pitarch, M., Peris, E. N., Maciá, J. G., Corberán, J. M., 2017. Evaluation of different heat pump systems for sanitary hot water production using natural refrigerants, Applied Energy 190, 911–919

Sun, Z., Liang, Y., Liu, S., Ji, W., Zang, R., Liang, R., Guo, Z., 2016. Comparative analysis of thermodynamic performance of a cascade refrigeration system for refrigerant couples R41/R404A and R23/R404A, Applied Energy 184, 19–25

Manuscript ID: 1433
DOI: 10.18462/iir.icr.2019.1433

A practical heat and mass transfer model between air and ionic liquid solution in an internally cooled dehumidifier with partial wetting

Richard Jayson VARELA[(a)], Niccolo GIANNETTI[(b)], Hifni Ariyadi[(c)], Seiichi YAMAGUCHI[(c)], Kiyoshi SAITO[(c)], Xin-Ming WANG[(d)], Hiroshi NAKAYAMA[(e)]

[(a)] Research Organization for Open Innovation Strategy, Waseda University, 3-4-1 Okubo, Shinjuku-ku, Tokyo, 169-8555, Japan, rjvarela@aoni.waseda.jp
[(b)] Waseda Institute for Advanced Study, Waseda University, 1-6-1 Nishiwaseda, Shinjuku-ku, Tokyo 169-8050, Japan, niccolo@aoni.waseda.jp
[(c)] Department of Applied Mechanics and Aerospace Engineering, Waseda University, 3-4-1 Okubo, Shinjuku-ku,Tokyo, 169-8555, Japan, hifni.ariyadi@aoni.waseda.jp, sei_yamaguchi@aoni.waseda.jp, saito@aoni.waseda.jp
[(d)] Evonik Japan Co., Ltd., 2-3-1 Nishi-Shinjuku, Shinjuku-ku, Tokyo, 163-0938, Japan, xinming.wang@evonik.com
[(e)] Energy Applications R&D Center, Chubu Electric Power Co., Inc., 20-1 Midori-ku, Nagoya-shi, Aichi, 459-8522, Japan, nakayama.hiroshi2@chuden.co.jp

ABSTRACT

In falling film heat and mass transfer models, complete wetting of the substrate is usually assumed. In this paper, a practical model for the simultaneous heat and mass transfer processes in an internally cooled dehumidifier paired with a newly developed ionic liquid desiccant from Evonik Industries is presented. The heat and mass transferred were estimated using heat and mass transfer coefficient analogies from the literature incorporating variable film thickness and partial wetting model; therefore, accounting for the change in the film thickness and wetted area in each control volume, respectively.
Comparison between the predicted results from the partial and complete wetting models with the experimental data showed a better agreement for the former. Absolute deviations for the air outlet humidity ratio were within 15 and 35% for the partial and complete wetting models, respectively. The model with partial wetting is suggested for preliminary design and optimization of internally cooled contactors.
Keywords: Heat and Mass Transfer, Partial Wetting, Variable Film Thickness, Ionic Liquid, Internally Cooled Dehumidifier, Modeling.

1. INTRODUCTION

Liquid desiccant air conditioning systems are being recommended as possible alternative and solution to conventional vapor compression systems (VCS) due to their capability to address performance issues faced by VCS such as large energy consumption (Yamaguchi et al., 2011). In liquid desiccant air conditioning systems, the two general classifications of gas-liquid contactors are adiabatic and diabatic or more commonly known as internally cooled/heated contactors as shown in Fig. 1. The applications of these systems have favored the internally cooled/heated contactors over adiabatic packed bed contactors because of their capability to maintain the mass transfer potential of the desiccant solution by using a third cooling/heating medium (Sato et al., 2014).
Most of the models for internally cooled contactors assume constant film thickness (Rahamah et al., 1998; Ali et al., 2004) and complete wetting of the contactor (Park et al., 1994), which can result to the underestimation (Mesquita et al., 2006) and overestimation (Park et al., 1994) of the dehumidification capacity, respectively. Though constant film thickness has already been addressed in the studies of Mesquita et al. (2006) and Hueffed et al. (2009), complete wetting remains to be a problem due to the lack of conclusive research and models for the partial wetting

in internally cooled contactors. Earlier studies of the wetting fraction of a falling film on a vertical surface were conducted by Qi et al. (2013, 2013, 2014). The solution distributor thickness, plate surface temperature, and contact angle were found to have a significant influence on the wetted area. Their results mainly point out that by decreasing the film thickness, which can be done by reducing the distributor thickness or by increasing the plate surface temperature, the width of the film can be increased; thereby, decreasing the contact angle and increasing the solution spreading and the wetted area. However, these studies focused on selected parameters and the underlying fundamental principles of film breakage and dry spots formation were not explained. The recent experimental investigation of Varela et al. (2018) and theoretical studies of Giannetti et al. (2016, 2018) on the partial wetting in internally cooled contactors are promising methods to the qualitative prediction of the wetting ratio, which can be a key to a more accurate design and prediction of the heat and mass transfer performance of internally cooled contactors. These studies explore the basic principles of film stability and minimum wetting rates, and theoretically predicts the wetting ratio based on the principle of minimum energy, which weighs the conflicting effects of kinetic energy and surface tension.

In this study, a practical model for the heat and mass transfer in an internally cooled contactor paired with a newly developed ionic liquid (IL) desiccant is developed by applying variable film thickness of the solution and using the newly improved correlation for the wetting fraction by Giannetti et al. (2019). The model is validated by the experimental data and comparison between the predicted results of the models with the partial wetting and complete wetting assumption is conducted.

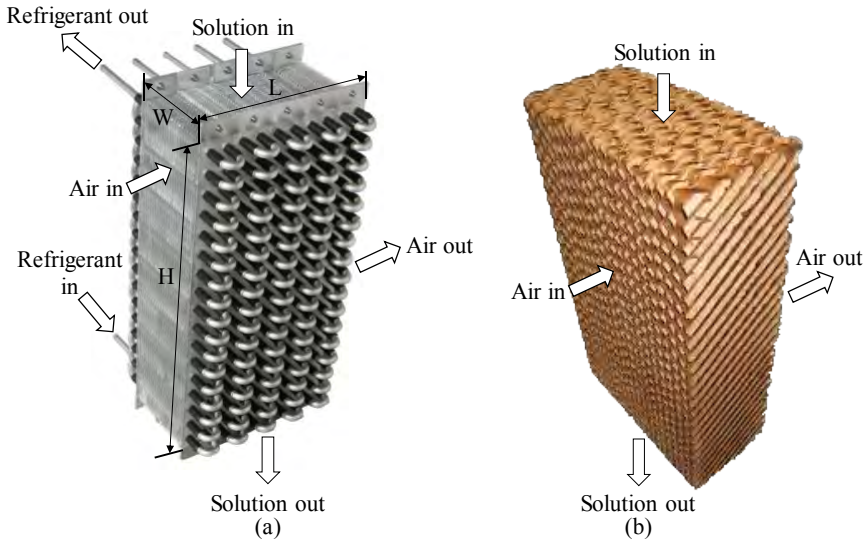

Figure 1: (a) Internally cooled fin-tube contactor and (b) adiabatic packed bed contactor

2. EXPERIMENTAL APPARATUS AND METHODS

2.1. Gas-Liquid Contactor and Working Fluid

The internally cooled contactor utilized in this study is a fin-tube type as designated in Fig. 1(a). Aluminum was chosen as the material for the fin and tube primarily because it is compatible with ionic liquid (IL) in terms of material corrosion, which is the liquid desiccant employed in this study. Aside from the compatibility, the aluminum contactor has also high thermal conductivity and is inexpensive. The dimensions and details of the internally cooled fin-tube contactor are given by Table 1 and Fig. 2, respectively. On the other hand, ILs are generally known for having high thermal and chemical stability, low volatility, excellent solubility, and are non-flammable (Butt et al., 2013), making them an excellent choice for absorption processes.

The air is blown horizontally through the length of the contactor by a blower and the solution flows vertically along the height of the contactor through the influence of gravity depicting a crossflow configuration between the two directly contacting fluids. This type of flow configuration between the air and solution not only benefits from low air pumping head but also the possibility of solution particle carryover is low in crossflow compared with counterflow configuration, which is of significant interest in liquid desiccant air conditioning systems. There are five channels of cooling

water with the inlet at the bottom and outlet at the top of the contactor. Higher effectiveness and energy recovery can be realized by making the cooling water and desiccant solution enter on opposite sides or counterflow instead of parallel flow; and since the two working media are not in direct contact with each other, solution carryover by the cooling water is not possible.

Table 1. Dimensions of the internally cooled fin-tube contactor

Parameter	Symbol	Unit	Dimension
Length (air flow direction)	L	m	200×10^{-3}
Height (solution flow direction)	H	m	400×10^{-3}
Width (refrigerant flow direction)	W	m	100×10^{-3}
Fin thickness	t_f	m	0.1×10^{-3}
Fin pitch	P_f	m	4.42×10^{-3}
Number of fins	N_f	-	23
Tube outer diameter	$D_{t,o}$	m	7.38×10^{-3}
Tube wall thickness	t_{tw}	m	1×10^{-3}
Tube columns (horizontal array)	N_{tc}	-	10
Tube rows (vertical array)	N_{tr}	-	17
Tube horizontal pitch	$P_{t,h}$	m	20×10^{-3}
Tube vertical pitch	$P_{t,v}$	m	20×10^{-3}

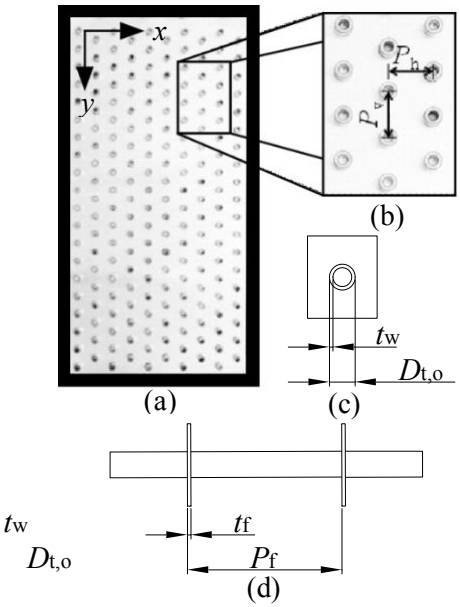

Figure 2: (a) Front view, (b) close-up view, (c) tube details, (d) fin details

2.2. System Description

Fig. 3 illustrates the schematic diagram of the internally cooled liquid desiccant air conditioning system. The experimental apparatus is divided into three parts: the process side, the solution control unit, and the regeneration side. The inlet air of both the process and regeneration sides, which are represented by the large arrows in light blue and orange colors, is supplied by a separate air handling unit connected to the experimental apparatus through ducts.

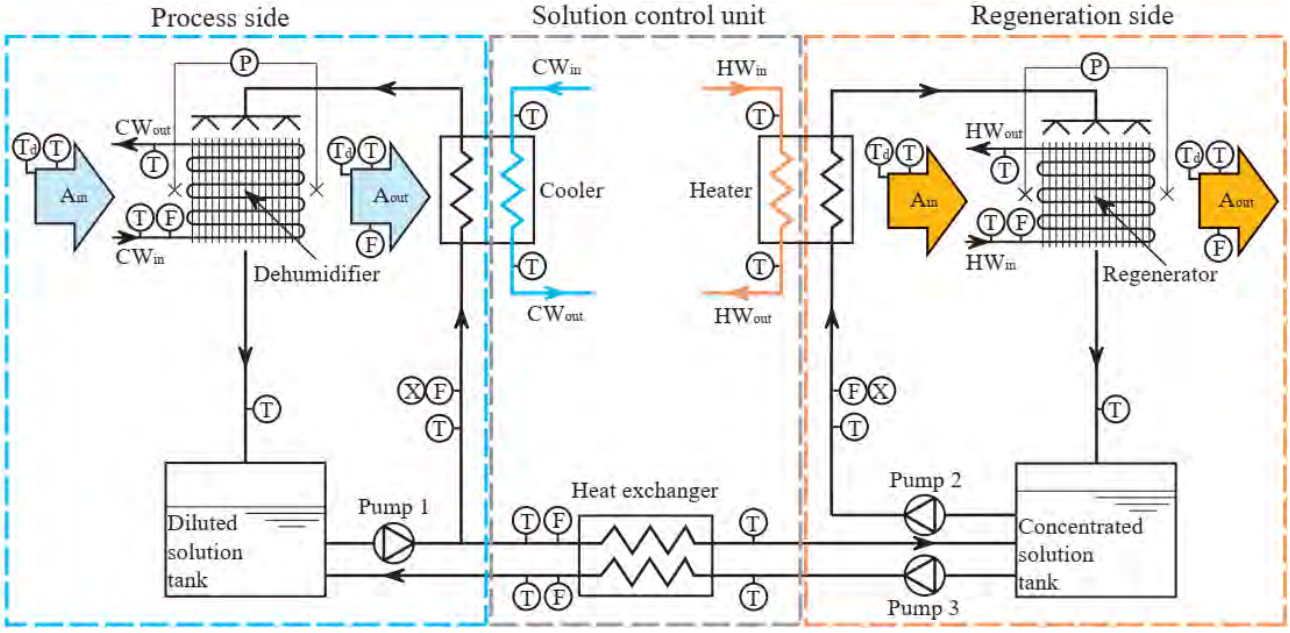

Figure 3: Schematic diagram of the internally cooled/heated liquid desiccant air conditioning system

In the process side, the solution is drawn from the Diluted solution tank by Pump 1 and is delivered to the solution Cooler to be adjusted to the required inlet temperature. Then, it is dispensed to the internally cooled Dehumidifier by the atomizing spray nozzles. In the Dehumidifier, the air makes direct contact and undergoes simultaneous heat and mass transfer with the solution, releasing

heat of condensation on the process. Part of this latent heat together with the sensible heat in the solution is absorbed and carried away by the cooling water passing through the dehumidifier, conserving the solution's low equilibrium vapor pressure and mass transfer capacity. The outlet air exits the Dehumidifier at a comfortable quality. On the other hand, the weak outlet solution enters the Diluted solution tank through the influence of gravity and mixes with the strong solution coming from the Concentrated solution tank through Pump 3. A fraction of the solution in the Diluted solution tank is pumped to the Concentrated solution tank for regeneration. Before entering the Concentrated solution tank, the weak solution, which is at a lower temperature compared with the strong solution, passes first through the solution-to-solution heat exchanger for heat recovery.
In the regeneration side, the solution is pumped from the Concentrated solution tank to the solution Heater where it is heated to the required inlet temperature and is, then, distributed by the spray nozzles to the internally heated regenerator. The solution is re-concentrated in the regenerator by making direct contact with the inlet air, which is at a lower temperature and vapor pressure compared to the solution. The process involves the release of the heat of vaporization, which is absorbed by the air; thereby, reducing the temperature and vapor pressure of the solution. To avoid this, the heating water keeps the temperature of the solution high, maintaining its regeneration capacity. Finally, the strong outlet solution enters the Concentrated solution tank ready to be circulated to the process side again.
To save writing space for more important discussions later, the readers are advised to refer to the work of Sato et al. (2018) for the measuring instruments and experimental conditions.

3. HEAT AND MASS TRANSFER MODEL

The internally cooled contactor shown in Fig. 1 is divided into control volumes according to the number of fins, tube column, and tube rows. Overall, the fin-tube contactor is comprised of 3,910 differential control volumes as illustrated in Fig. 4.

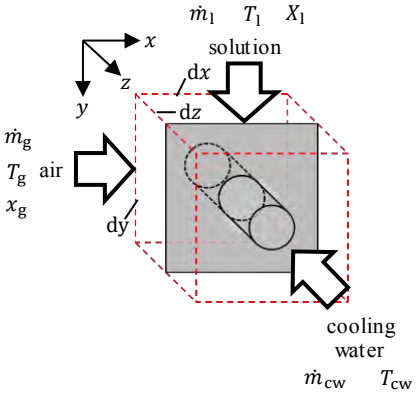

Figure 4: Differential control volume

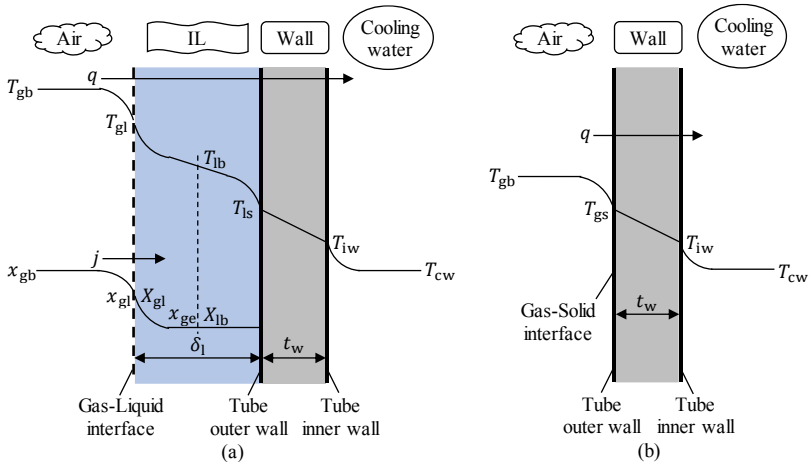

Figure 5: Schematic diagram of the heat and mass transfer flow: (a) wetted wall, (b) dry wall

3.1. Assumptions

The following assumptions were applied to simplify the mathematical analysis:
(a) The flow of the air is laminar, and the temperature and velocity profiles are fully developed.
(b) The properties in each control volume are constant.
(c) There is no pressure gradient across the flow direction.
(d) The Dufour and Soret effects are neglected.
(e) The flow of the solution is laminar and non-wavy.
(f) Thermodynamic equilibrium exists in the gas-liquid interface and no shear force is acting on it.
(g) Diffusion effect on the flow direction is neglected.
(h) There is no chemical reaction and viscous dissipation.
(i) Tube wall friction and thermal resistance are not considered.
(j) Steady-state one-dimensional transfer flow for all fluids.

3.2. Governing Equations

Following the assumptions listed above, the directions of the working fluids in Fig. 4, and the heat and mass transfer flow in Fig. 5, the governing mass, energy, and momentum equations are derived as follows:

To calculate the water mass fraction in the gas phase of the next control, the mass absorbed by the solution in the current control volume is subtracted

$$\dot{m}_{\mathrm{gb}} \frac{\partial x_{\mathrm{gb}}}{\partial x} + h_{\mathrm{m,gb-gl}} \rho_{\mathrm{gb}} A_{\mathrm{gl}} \left(x_{\mathrm{gb}} - x_{\mathrm{gl}}\right) = 0 \qquad \text{Eq. (1)}$$

In the case of partial wetting, the enthalpy of the gas in the next control volume is calculated by subtracting the heat conducted to the gas-liquid and gas-solid interfaces, and the latent heat of condensation. In the case of a completely wet or completely dry surface, the gas-solid or gas-liquid term cancels out, respectively:

$$\dot{m}_{\mathrm{gb}} \frac{\partial h_{\mathrm{gb}}}{\partial x} + A_{\mathrm{gl}} \left[h_{\mathrm{h,gb-gl}} \left(T_{\mathrm{gb}} - T_{\mathrm{gl}}\right) + h_{\mathrm{m,gb-gl}} \rho_{\mathrm{gb}} A_{\mathrm{gl}} h_{\mathrm{c}} \left(x_{\mathrm{gb}} - x_{\mathrm{gl}}\right) \right] + h_{\mathrm{h,gb-gs}} A_{\mathrm{gs}} \left(T_{\mathrm{gb}} - T_{\mathrm{gs}}\right) = 0 \qquad \text{Eq. (2)}$$

With water mass fraction and the enthalpy, the temperature of the gas can be calculated; subsequently, other properties of the air can be calculated as a function of either or both the mass fraction and temperature.

Considering the mass absorbed at the gas-liquid interface, the mass conservation of the solution is expressed as:

$$\frac{\partial \dot{m}_{\mathrm{lb}}}{\partial y} - h_{\mathrm{m,gb-gl}} \rho_{\mathrm{gb}} A_{\mathrm{gl}} \left(x_{\mathrm{gb}} - x_{\mathrm{gl}}\right) = 0 \qquad \text{Eq. (3)}$$

A non-isothermal absorption (Yuksel and Schlunder, 1987) of water vapor into the solution is employed in this model. In this method, the heat of absorption is solely damped at the gas-liquid interface and that heat is transferred from the gas-liquid interface to the bulk solution and to the wall purely by conduction; contrary to isothermal absorption where the interface and bulk temperatures are assumed equal. With this, the respective energy balance at the gas-liquid interface and the bulk solution can be expressed by Eq. (4) and Eq. (5):

$$\frac{\partial \left(\dot{m}_{\mathrm{gl}} h_{\mathrm{gl}}\right)}{\partial y} - A_{\mathrm{gl}} \left[h_{\mathrm{h,gb-gl}} \left(T_{\mathrm{gb}} - T_{\mathrm{gl}}\right) + h_{\mathrm{m,gb-gl}} \rho_{\mathrm{gb}} A_{\mathrm{gl}} h_{\mathrm{c}} \left(x_{\mathrm{gb}} - x_{\mathrm{gl}}\right) - h_{\mathrm{h,gl-ls}} \left(T_{\mathrm{gl}} - T_{\mathrm{lb}}\right) \right] = 0 \qquad \text{Eq. (4)}$$

$$\frac{\partial \left(\dot{m}_{\mathrm{lb}} h_{\mathrm{lb}}\right)}{\partial y} - h_{\mathrm{h,gl-ls}} A_{\mathrm{gl}} \left(T_{\mathrm{gl}} - T_{\mathrm{lb}}\right) + h_{\mathrm{h,gl-ls}} A_{\mathrm{gl}} \left(T_{\mathrm{lb}} - T_{\mathrm{ls}}\right) = 0 \qquad \text{Eq. (5)}$$

For the cooling water, the mass and energy conservations are written as follows:

$$\frac{\partial \dot{m}_{\mathrm{cw}}}{\partial z} = 0 \qquad \text{Eq. (6)}$$

$$\frac{\partial \left(\dot{m}_{\mathrm{cw}} h_{\mathrm{cw}}\right)}{\partial z} + h_{\mathrm{h,w}} \left[A_{\mathrm{ls}} \left(T_{\mathrm{ls}} - T_{\mathrm{iw}}\right) + A_{\mathrm{gs}} \left(T_{\mathrm{gs}} - T_{\mathrm{iw}}\right) \right] = 0 \qquad \text{Eq. (7)}$$

The velocity profile of the falling film is derived by integrating twice its momentum equation. This gives the maximum velocity at the gas-liquid interface and subsequently the average film velocity. Integrating the continuity across the film thickness per unit length of the contactor results to the equation of the film thickness

$$\delta_{\mathrm{l}} = \left(\frac{3 \mu_{\mathrm{l}} \Gamma_{\mathrm{l}}}{\rho_{\mathrm{l}}^2 g} \right)^{1/3} \qquad \text{Eq. (8)}$$

3.3. Heat and Mass Transfer Coefficients

The heat transfer coefficient of the air (Eq. (9)) is calculated from the Nusselt number correlation for laminar flow in rectangular ducts, assuming a constant tube wall temperature (Kays and Crawford, 1993). The mass transfer coefficient is then estimated using the Chilton-Colburn analogy (Eq. (10)):

$$\mathrm{Nu}_{\mathrm{gb}} = \frac{h_{\mathrm{h,gb-gl}} d_{\mathrm{h}}}{\lambda_{\mathrm{gb}}} = 7.54 \qquad \text{Eq. (9)}$$

$$\frac{h_{\mathrm{h,gb-gl}}}{h_{\mathrm{m,gb-gl}}} = \rho_{\mathrm{gb}} c_{\mathrm{p,gb}} \left(\frac{\alpha_{\mathrm{gb}}}{D_{\mathrm{gb}}}\right)^{2/3} \quad \text{Eq. (10)}$$

In the liquid-side, the heat transfer coefficient (Eq. (11)) is determined from the Nusselt number correlation of Karami et al. (2009), assuming viscous sublayers near the gas-liquid and liquid-solid interfaces. The description of the liquid-side mass transfer coefficient (Eq. (12)) is based on the penetration theory suggested by Higbie, which assumes a thick semi-infinite film with unequal interface and bulk solute concentrations. The overall mass transfer coefficient is calculated as the sum of both the air-side and liquid-side mass transfer coefficients and is used to determine the overall mass transfer by multiplying it to the difference of the air humidity ratio and the equivalent humidity ratio of the solution side. This approach is contrary to previous models (Mesquita et al., 2006; Hueffed et al., 2009), which assume only the air side neglecting the mass transfer resistance on the liquid side. From the overall mass transfer, the water mass fraction on the gas-liquid interface can then be estimated from the air-side equation of mass transfer with the air-side properties.

$$\mathrm{Nu}_{\mathrm{lb}} = \frac{h_{\mathrm{h,gl-ls}} \delta_{\mathrm{l}}}{\lambda_{\mathrm{lb}}} = 0.4764 \mathrm{Re}_{\mathrm{lb}}^{0.0477} \mathrm{Pr}_{\mathrm{lb}}^{0.334} \quad \text{Eq. (11)}$$

$$h_{\mathrm{m,gl-lb}} = 2\sqrt{\frac{u_{\mathrm{l,max}} D_{\mathrm{gl}}}{\pi P_{\mathrm{t,v}}}} \quad \text{Eq. (12)}$$

The wall heat transfer coefficient is calculated using the thermal conductivity of the aluminum wall, which equal to 0.236 kW·m^{-1}·K^{-1}. For the cooling water, the heat transfer coefficient is obtained from the Nusselt number provided by Gnielinski (Incropera et al., 2011):

$$\mathrm{Nu}_{\mathrm{cw}} = \frac{\left(f/8\right)(\mathrm{Re}_{\mathrm{cw}} - 1000)\mathrm{Pr}}{1 + 12.7\left(f/8\right)^{1/2}\left(\mathrm{Pr}^{2/3} - 1\right)} \quad \text{Eq. (13)}$$

3.4. Partial Wetting Model

The partial wetting model is given by Eq. (14). For the detailed derivation of the correlation, please refer to Giannetti et al. (2019).

$$WR = 0.83\theta_0^{-0.90}\left(\frac{\mathrm{Re_l}}{\mathrm{We_l}^3}\right)^{0.07} \quad \text{Eq. (14)}$$

4. RESULTS AND DISCUSSIONS

Fig. 6a presents the variation of the air humidity ratio with the IL solution mass flux. The predicted outlet air humidity ratios from the partial wetting model are higher than the experimental results at solution mass flux below 1 kg·m^{-2}·s^{-1}; equivalent at 1 kg·m^{-2}·s^{-1}, and lower at G_{l} greater than one. A possible explanation for the larger predicted air humidity ratios could be that at G_{l} values less than one, the wetting ratios are underestimated by the wetting model, which shows opposite

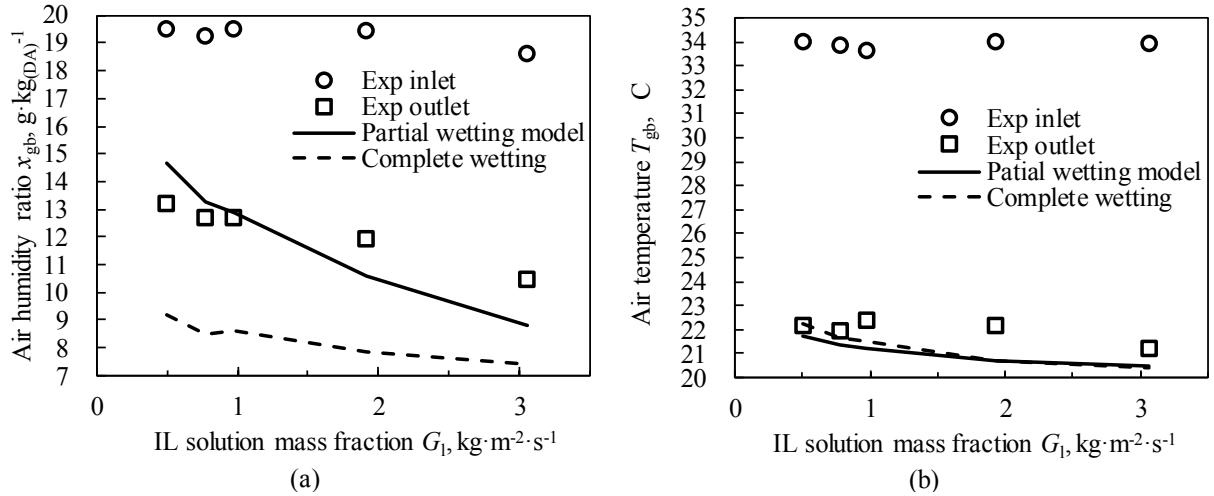

Figure 6: Variation of the (a) air humidity ratio and (b) air temperature with the IL solution mass flux

behavior at higher flow rates.
Absolute deviations between the predicted and experimental results are within 15% for the partial wetting model and 35% for the complete wetting model. The mean absolute error is 8.81 and 31.83% for the partial and complete wetting models, respectively.
Fig. 6b shows the variations of the air temperature with the solution mass flux. It can be observed that the heat transfer performance of the internally cooled contactor is not significantly affected by the wetting ratio as heat transfer can be conducted in either wetted or dry parts of the contactor. The predicted results for the air outlet temperature of both models agree within less than 10%. The mean absolute error is 4.05 and 3.17%, respectively, for the partial and complete wetting models. Based on the above comparison, it is desirable to achieve complete wetting to yield better dehumidification performance. This is achieved by satisfying the minimum wetting rate (minimum Reynolds number) that can assure complete wetting of the substrate (Giannetti et al, 2018, 2019; Varela et al., 2018). However, a proper selection of the solution mass flux should be made depending on the required dehumidification capacity of the system as higher flow rates require higher pumping power and can also increase the air pressure drop due to the reduction of the air flow area. Nonetheless, the internally cooled liquid desiccant air conditioning system can reach lower outlet air humidity ratio and temperature at equal solution mass flux compared to the adiabatic liquid desiccant air conditioning system as experimentally investigated by Sato et al. (2018).

5. CONCLUSIONS

Numerical models were developed for simultaneous heat and mass transfer in an internally cooled contactor with ionic liquid as a desiccant. Models with partial wetting and complete wetting as well as variable film thickness were developed to clarify the effect of the wetting ratio on the heat and mass transfer performance. The predicted results for both models were compared with the dehumidification experimental data. The predicted results for the air temperature from both models agree well with the experimental data. For the air humidity ratio, the partial wetting model underpredicted the experimental outlet results at low solution mass flux but for solution mass flux greater than 1 kg·m^{-2}·s^{-1}, the predicted results were overestimated. In spite of this, all results are within a mean absolute error of 10% with the experimental data. On the other hand, the complete wetting model overpredicted all the experimental data to within an average error of 35%.
Additional experimental data can be taken to further realize the potential of the partial wetting model in predicting the mass transfer performance of internally cooled contactors.

NOMENCLATURE

α	thermal diffusivity (m^2·s^{-1})	ρ	density (kg·m^{-3})
A	transfer area (m^2)	T	temperature (°C)
c_p	specific heat at constant pressure (J·kg^{-1}·K^{-1})	θ_0	film contact angle (°)
δ	film thickness (m)	We	Weber number
d_h	hydraulic diameter (m)	WR	wetting ratio
D	mass diffusivity (m^2·s^{-1})	x	water mass fraction, humidity ratio (kg·kg(DA)$^{-1}$), horizontal direction
Γ	solution mass flow rate per unit length of contactor (kg·m^{-1}·s^{-1})	y	vertical direction
h_c	heat of condensation (kJ·kg^{-1})	z	depth direction
h_h	heat transfer coefficient (kW·m^{-2}·K^{-1})		
h_m	mass transfer coefficient (m·s^{-1})		**Subscripts**
λ	thermal conductivity (kW·m^{-1}·K^{-1})	cw	cooling water
j	diffusion mass flux (kg·m^{-2}·s^{-1})	iw	inner wall
$\dot{m}$	mass flow rate (kg·s^{-1})	gb	gas bulk
μ	dynamic viscosity (Pa·s)	ge	gas equilibrium
Nu	Nusselt number	gl	gas-liquid
Pr	Prandtl number	gs	gas-solid
q	heat flux (kW·m^{-2})	lb	liquid bulk
Re	Reynolds number	ls	liquid-solid

REFERENCES

Ali, A., Vafai, K., Khaled, A.R.A., 2004. Analysis of heat and mass transfer between air and falling film in a cross flow configuration. Int. J. Heat Mass Transf. 47, 743–755.

Butt, H.J., Graf, K., Kappl, M., 2013. Physics and Chemistry of Interfaces. Wiley-VCH, Germany.

Giannetti, N., Varela, R.J., Ariyadi, H., Yamaguchi, S., Saito, K., Wang, X.-M., Nakayama, H., 2018. Semitheoretical prediction of the wetting characteristics of aqueous ionic liquid solution on an aluminum finned-tube desiccant contactor. J. Fluids Eng. 140, 121109.

Giannetti, N., Varela, R.J., Ariyadi, H., Yamaguchi, S., Saito, K., Wang, X.-M., Nakayama, H., 2019. Semitheoretical model of the wetting characteristics of aqueous ionic liquid on an aluminum finned-tube desiccant contactor. Proceedings of the 25th IIR International Congress of Refrigeration, Québec, Canada. IIF/IIR, 1059.

Giannetti, N., Yamaguchi, S., Saito, K., 2016. Wetting behavior of a liquid film on an internally-cooled desiccant contactor. Int. J. Heat Mass Transf. 101, 958–969.

Hueffed, A.K., Chamra, L.M., Mago, P.J., 2009. A simplified model of heat and mass transfer between air and falling-film desiccant in a parallel-plate dehumidifier. J. Heat Transfer 131, 052001.

Incropera, F.P., Bergman, T.L., Lavine, A.S., DeWitt, D.P., 2011. Fundamentals of Heat and Mass Transfer, USA.

Karami, S., Farhanieh, B., 2009. A numerical study on the absorption of water vapor into a film of aqueous LiBr falling along a vertical plate. Heat Mass Transf. 46, 197–207.

Kays, W.M., Crawford, M.E., 1980. Convective Heat and Mass Transfer, McGraw-Hill, USA.

Mesquita, L.C.S., Harrison, S.J., Thomey, D., 2006. Modeling of heat and mass transfer in parallel plate liquid-desiccant dehumidifiers. Sol. Energy 80, 1475–1482.

Park, M.S., Howell, J.R., Vliet, G.C., Peterson, J., 1994. Numerical and experimental results for coupled heat and mass transfer between a desiccant film and air in cross-flow. Int. J. Heat Mass Transf. 37, 395–402.

Qi, R., Lu, L., Yang, H., 2013a. Development of simplified prediction model for internally cooled/heated liquid desiccant dehumidification system. Energy Build. 59, 133–142.

Qi, R., Lu, L., Yang, H., Qin, F., 2013b. Investigation on wetted area and film thickness for falling film liquid desiccant regeneration system. Appl. Energy 112, 93–101.

Qi, R., Lu, L., Qin, F., 2014. Model development for the wetted area of falling film liquid desiccant air-conditioning system. Int. J. Heat Mass Transf. 74, 206–209.

Rahamah, A., Elsayed, M.M., Al-Najem, N.M., 1998. A numerical solution for cooling and dehumidification of air by a falling desiccant film in parallel flow. Renew. Energy. 13(3) 305–322.

Sato, T., Varela, R.J., Yamaguchi, S., Saito, K., Nakayama, H., Wang, X.M., 2018. Experimental study on a finned-tube internally cooled contactor for liquid desiccant air-conditioning systems with ionic liquid. Proceedings of the 17th International Refrigeration and Air Conditioning Conference, Indiana, USA, IIF/IIR, 2561.

Varela, R.J., Giannetti, N., Yamaguchi, S., Saito, K., Wang, X.M., Nakayama, H., 2018. Experimental investigation of the wetting characteristics of an aqueous ionic liquid solution on an aluminum fin-tube substrate. Int. J. Refrig. 88, 472–482.

Yamaguchi, S., Jeong, J., Saito, K., Miyauchi, H., Harada, M., 2011. Hybrid liquid desiccant air – conditioning system: Experiments and simulations. Appl. Therm. Eng. 31(17–18), 3741–3747.

Yüksel, M.L., Schlünder, E.U., 1987. Heat and mass transfer in non-isothermal absorption of gases in falling liquid films. Part I: Experimental determination of heat and mass transfer coefficients. Chem. Eng. Process. 22, 193–202.

Manuscript ID: 1465
DOI: 10.18462/iir.icr.2019.1465

Current Status of a New Fundamental Equation of State for trans-1-Chloro-3,3,3-trifluoro-1-propene [R-1233zd(E)]

Ryo AKASAKA[(a)] and Eric W. LEMMON[(b)]

[(a)] Research Center for Next Generation Refrigerant Properties, International Institute for Carbon-Neutral Energy Research (I2CNER), Kyushu University,
744 Motooka, Nishi-ku, Fukuoka, 8190395, Japan,
e-mail: ryo-a@ip.kyusan-u.ac.jp
[(b)] Applied Chemicals and Materials Division, National Institute of Standards and Technology,
325 Broadway, Boulder, Colorado, 80305, USA,
e-mail: eric.lemmon@nist.gov

ABSTRACT

The current status of a new fundamental equation of state for trans-1-chloro-3,3,3-trifluoro-1-propene [R-1233zd(E)] is given. Due to its non-flammability and preferable thermophysical properties, this refrigerant is considered as one possible alternative for 1,1,1,3,3-pentafluoropropane (R-245fa). The new equation is valid for temperatures from 215 K to 444 K and pressures up to 35 MPa. Expected uncertainties in calculated properties in this range are 0.01 % in liquid densities, 0.03 % in vapor densities, 0.05 % in vapor pressures, and 0.1 % in vapor- and liquid-phase sound speeds. Improvements from the currently available equation are that the upper limit of pressure is extended to 35 MPa and that liquid-phase sound speeds are represented more accurately. The equation shows quite reasonable extrapolation behavior at extremely low and high temperatures, and at high pressures. The ISO/TC86/SC8 committee will recommend the final form of this equation as an international standard formulation for R-1233zd(E).

1. INTRODUCTION

The fundamental equation of state developed by Mondejar et al. (2015) (referred to as the “first equation” in this paper) is currently the only available property formulation for R-1233zd(E) and has often been applied to the performance analysis of refrigeration cycles that use this refrigerant as a working fluid. The first equation is based on experimental data for density, vapor pressure, and vapor-phase sound speed covering temperatures from 215 K to 444 K and pressures up to 24 MPa. Although in most cases the experimental data are accurately represented with the first equation, some data show larger deviations than their uncertainties, probably due to sample degradation at high temperatures. In addition, as shown later, the first equation shows systematic and considerably large deviations from sound speed data in the liquid phase recently measured by McLinden and Perkins (2019).

A new fundamental equation of state is now being formulated under the collaboration between Kyushu University and National Institute of Standards and Technology. The new equation is designed so that it represents all experimental data within their experimental uncertainties. This paper shows the improvements in the new equation and gives the details on the future work to obtain a final equation of state. The final equation will be recommended by ISO/TC86/SC8/WG7 (Refrigerant properties) as an international standard formulation for this refrigerant in 2019.

Table 1: Critical parameters of R-1233zd(E)

Property	Symbol	First EOS	New EOS
Molar mass ($g\,mol^{-1}$)	M	134.04794	134.04794
Critical temperature (K)	T_c	439.6	438.75
Critical density ($mol\,dm^{-3}$)	ρ_c	3.68	3.658
Critical pressure (MPa)	p_c	3.624	3.574

2. EQUATION OF STATE

In a similar fashion to the development of the first equation, the new equation of state is formulated with the Helmholtz energy as the fundamental property with independent variables of temperature and density. The form of the equation is

$$\frac{a(T,\rho)}{RT} = \alpha(\tau,\delta) = \alpha^{\circ}(\tau,\delta) + \alpha^{r}(\tau,\delta), \qquad \text{Eq. (1)}$$

where $R = 8.3144598$ J mol^{-1} K^{-1} is the universal gas constant (Mohr et al., 2016), a is the molar Helmholtz energy, α is the dimensionless Helmholtz energy, $\tau = T_c/T$ is the inverse reduced temperature, and $\delta = \rho/\rho_c$ is the reduced density. The critical temperature and density used in the new equation are given in Table 1, as well as those used in the first equation. These values are tentative. In order to obtain better agreement with experimental data, ρ_c and T_c will be further adjusted during future fitting, and therefore these values may change in the final equation.

The dimensionless Helmholtz energy α is split into an ideal-gas part α° representing ideal-gas properties and a residual part α^{r} corresponding to the influence of intermolecular forces. The dimensionless ideal-gas Helmholtz energy α° is analytically calculated from an equation for the isobaric heat capacity of the ideal gas, c_p°, as follows:

$$\alpha^{\circ}(\tau,\delta) = h_0^{\circ} + \int_{T_0}^{T} c_p^{\circ}\,\mathrm{d}T - RT - T\left[s_0^{\circ} + \int_{T_0}^{T} \frac{c_p^{\circ}}{T}\,\mathrm{d}T - R\ln\left(\frac{\rho T}{\rho_0 T_0}\right)\right], \qquad \text{Eq. (2)}$$

where T_0 is the temperature at a reference state, p_0 is a reference pressure for the ideal-gas properties, and ρ_0 is the ideal-gas density at (T_0, p_0). The Planck-Einstein form is used in this work to formulate a c_p° equation. The equation has the form

$$\frac{c_p^{\circ}}{R} = n_0^{\circ} + \sum_{i=1}^{3} n_i^{\circ}\left(\frac{m_i^{\circ}}{T}\right)^2 \frac{\exp(m_i^{\circ}/T)}{[\exp(m_i^{\circ}/T)-1]^2}\,. \qquad \text{Eq. (3)}$$

The coefficients m_i° and n_i° are initially determined by fitting to experimental c_p° data, and they are further adjusted while fitting sound speed data in the development of the equation of state. For nonlinear polyatomic molecules, the value of n_0° is fixed to four to account for all but the vibrational contributions in the molecule. In addition, for R-1233zd(E) the value of c_p°/R should be 25 at extremely high temperatures, because the molecules of R-1233zd(E) (consisting of nine atoms) have 21 vibrational modes and the contribution of each mode attains the value of R at extremely high temperatures.

In recent developments of accurate equations of state, the residual Helmholtz energy is expressed with a functional form consisting of polynomial terms, simple exponential terms, and Gaussian bell-shaped terms. The number of terms, coefficients, and exponents are determined by fitting to selected experimental data. A tentative form of the new equation has a total of 19 terms (five polynomial, five exponential, and nine Gaussian bell-shaped terms), which is four more than that of the first equation. The form is expressed as

$$\alpha^{r}(\tau,\delta) = \sum_{i=1}^{5} N_i \tau^{t_i}\delta^{d_i} + \sum_{i=6}^{10} N_i \tau^{t_i}\delta^{d_i}\exp(-\delta^{l_i}) + \sum_{i=11}^{19} N_i \tau^{t_i}\delta^{d_i}\exp\left[-\eta_i(\delta-\varepsilon_i)^2 - \beta_i(\tau-\gamma_i)^2\right]. \qquad \text{Eq. (4)}$$

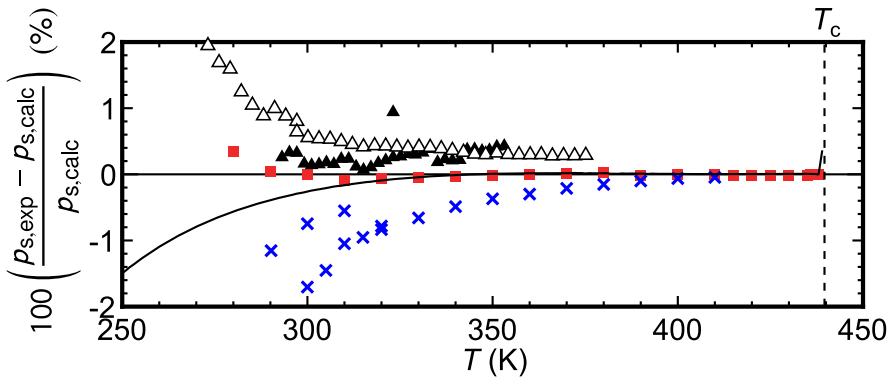

Figure 1: Deviations in experimental vapor pressures from calculated values with the new equation of state: (■) Mondejar et al. (2015), (▲) DiNicola et al. (2017)(ITC-CNR), (△) DiNicola et al. (2017)(UNIV-PM), (×) Higashi (2018), (——) Mondejar et al. (2015) (First equation)

The coefficients and exponents are optimized with a nonlinear fitting algorithm developed by Lemmon and Jacobsen (2005) and Lemmon et al. (2009). While fitting, various thermodynamic constraints are also applied to ensure that the equation of state is well behaved in the vicinity of the critical point and that it reliably extrapolates beyond the range of the experimental data. These constraints have been discussed in the literature, e.g., Span and Wagner (1997), Lemmon and Jacobsen (2005), Lemmon et al. (2009), and Akasaka and Lemmon (2019). Most coefficients and exponents are fixed within certain ranges. For example, temperature exponents t_i of the polynomial and exponential terms should be in the range from 0.3 to 2.5, and γ_i of the Gaussian bell-shaped terms are normally kept between 1.2 and 2.0.

3. COMPARISONS TO EXPERIMENTAL DATA

3.1 Vapor Pressure

Deviations in experimental vapor pressures from calculated values with the new equation of state are shown in Fig. 1. The new equation is fitted to vapor pressure data of Mondejar et al. (2015), and the data are generally represented within 0.1 % at temperatures between 290 K and the critical temperature. However, recent experimental data (DiNicola et al., 2017; Higashi, 2018) show different trends at temperatures below 370 K. Additional data are needed to determine which data are more reliable.

3.2 Density

Fig. 2 shows deviations in experimental densities from the new equation. The new equation is strongly fitted to the liquid and vapor densities of Mondejar et al. (2015), and the data are accurately represented; typical deviations in calculated values are 0.01 % for the liquid densities and 0.03 % for the vapor densities, except in the critical region where deviations over 0.05 % are sometimes observed due to larger experimental uncertainties. Recent measurements by Romeo et al. (2017) and by Fedele et al. (2018) are fitted with smaller weighting factors. These data agree with the new equation within their experimental uncertainties. The first equation shows similar trends and deviations in the vapor pressure and density, but with the use of the data of Fedele et al. (2018) the upper bound of validity in pressure is extended up to 35 MPa in the new equation, which was limited to 24 MPa in the first equation.

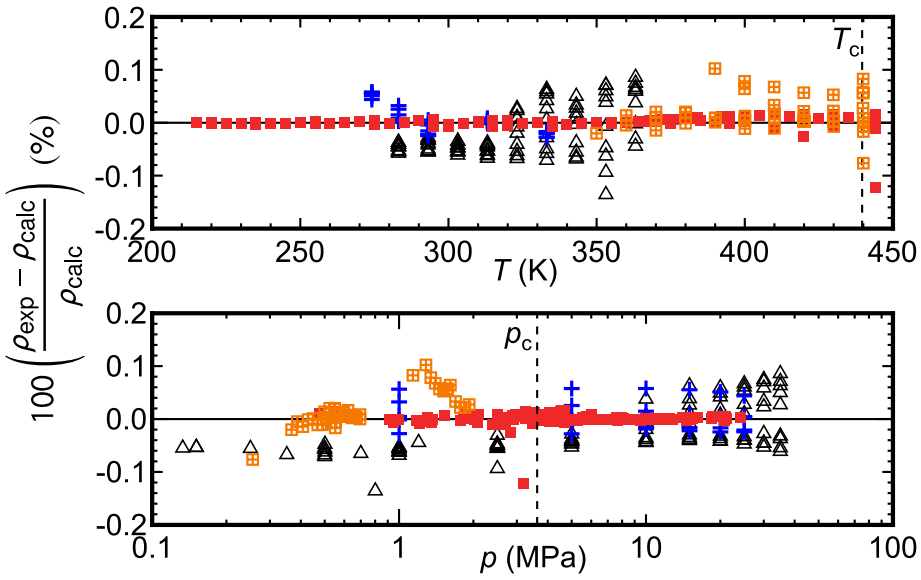

Figure 2: Deviations in experimental densities from calculated values with the new equation of state: (■) Mondejar et al. (2015) (Liquid), (⊞) Mondejar et al. (2015) (Vapor), (+) Romeo et al. (2017), (△) Fedele et al. (2018)

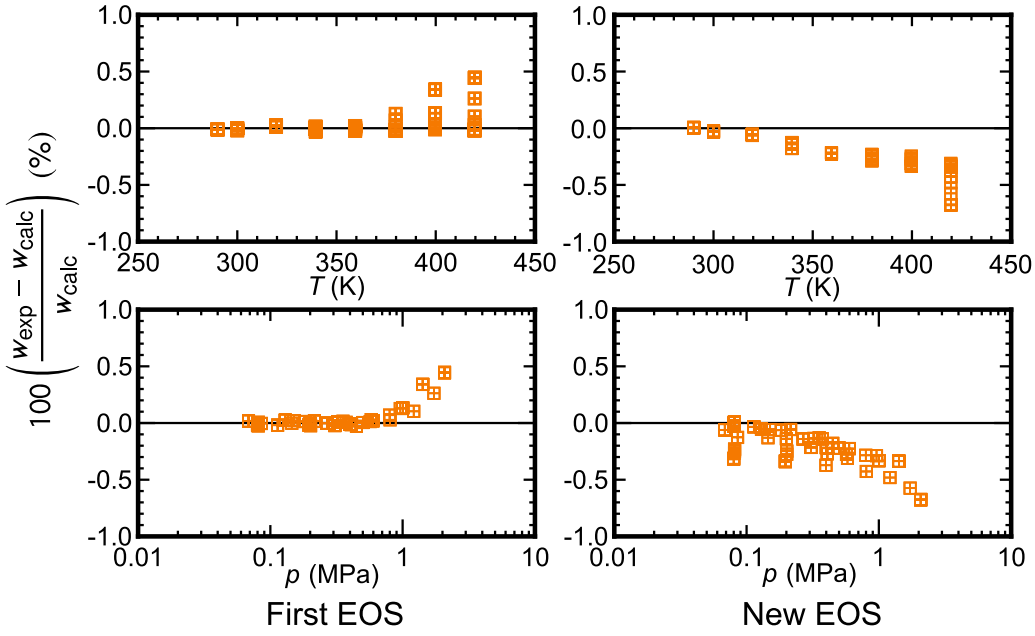

Figure 3: Deviations in experimental vapor-phase sound speeds from calculated values with the equations of state: (⊞) Mondejar et al. (2015)

3.3 Sound Speed

Fig. 3 shows deviations in experimental data for speed of sound in the vapor phase from the first and new equations. The first equation represents the data of Mondejar et al. (2015) within their uncertainties at temperatures below 350 K and pressures up to 0.6 MPa, but at higher temperatures and pressures deviations become positive up to 0.45 %. On the other hand, deviations from the new equation are always negative and more scattered and become larger as temperature and pressure increase. The deviations at the highest pressure are much greater than the experimental uncertainties; whether this is due to an experimental problem or is an artifact of the equation of state is still under investigation (see additional information in the conclusions).

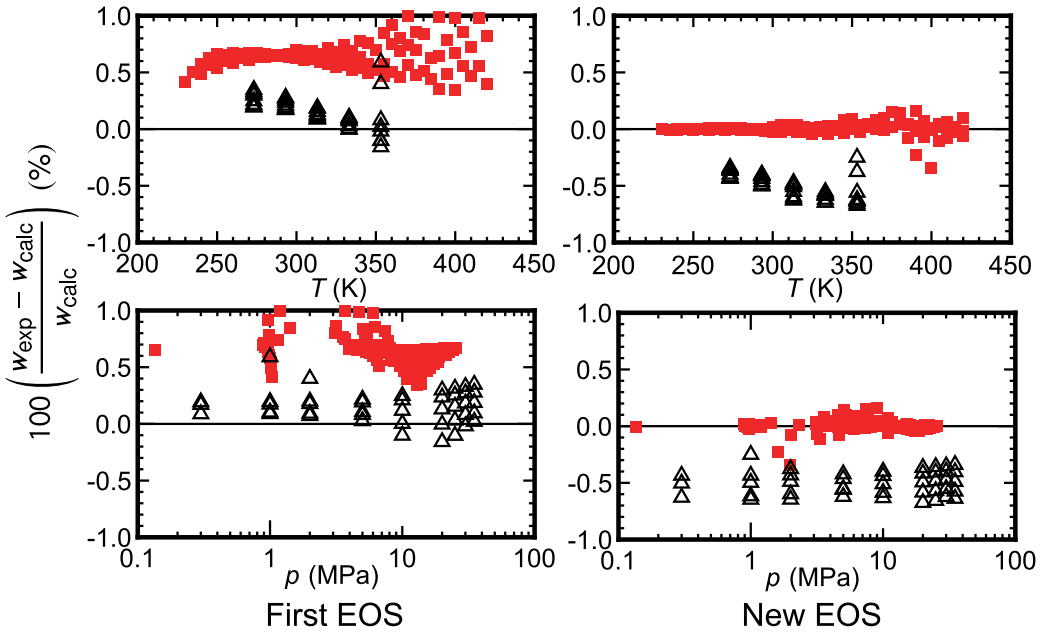

Figure 4: Deviations in experimental liquid-phase sound speeds from calculated values with the equations of state: (△) Lago et al. (2018), (■) McLinden and Perkins (2019)

Deviations in liquid-phase sound speeds from the first and new equations are shown in Fig. 4. The first equation always shows systematic positive deviations up to 1.8 % for the data of McLinden and Perkins (2019) because it was developed without liquid-phase sound speed data. The data of Lago et al. (2018) agree more with the first equation, but its averaged deviation (0.17 %) exceeds their experimental uncertainties. The new equation is fitted to the data of McLinden and Perkins (2019), and they are represented almost within their uncertainties. Conversely the data of Lago et al. (2018) show systematic negative deviations; the maximum deviation is about −0.7 %.

4. EXTRAPOLATION BEHAVIOR OF THE NEW EQUATION OF STATE

In order to verify the behavior of equations of state in regions away from the available experimental data, several plots are useful that depict constant property lines on various thermodynamic coordinates. Two symbolic examples of such plots are given here.

Fig. 5 shows plots of the second, third, and fourth virial coefficients (B, C, and D) calculated from the new equation of state. B and C should go to negative infinity at zero temperature, pass though zero at a moderate temperature, increase to a maximum, and then approach zero at extremely high temperatures. The theoretical trend in D is slightly different from those of B and C at temperatures higher than the first maximum. There should be a second maximum that is smaller in magnitude than the first maximum, and D should decrease to zero at very high temperatures.

Fig. 6 shows a plot of the phase identification parameters (PIP) defined by Venkatarathnam and Oellrich (2011) versus temperature. The PIP is given by the equation

$$\mathrm{PIP} = 2 - \rho \left[\frac{\dfrac{\partial^2 p}{\partial \rho \partial T}}{\left(\dfrac{\partial p}{\partial T}\right)_\rho} - \frac{\left(\dfrac{\partial^2 p}{\partial \rho^2}\right)_T}{\left(\dfrac{\partial p}{\partial \rho}\right)_T} \right]. \qquad \text{Eq. (5)}$$

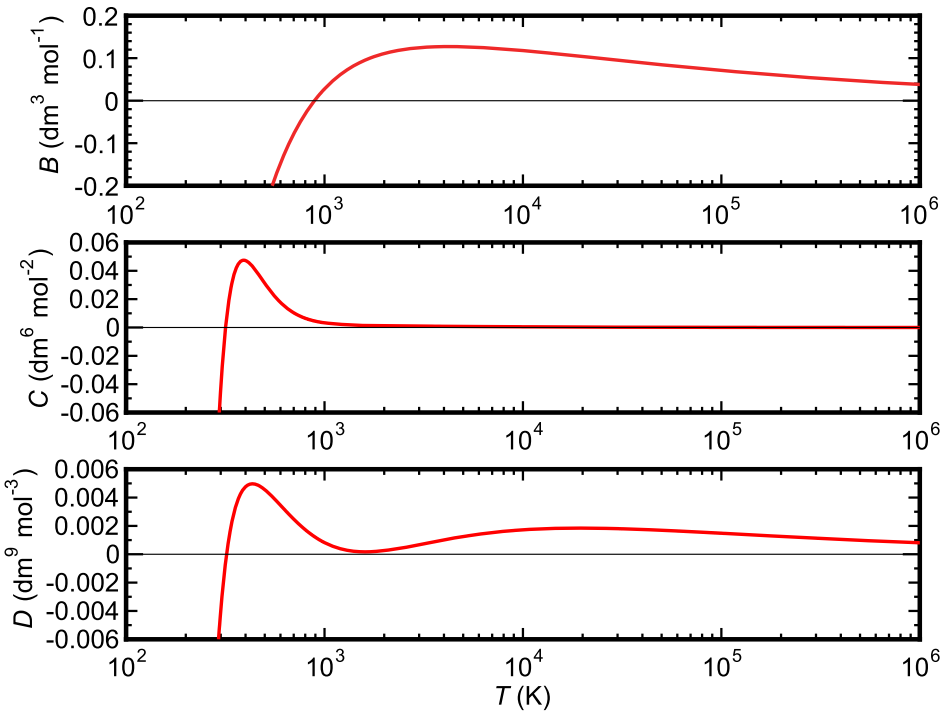

Figure 5: Second, third, and fourth virial coefficients (*B*, *C*, and *D*) calculated from the new equation of state.

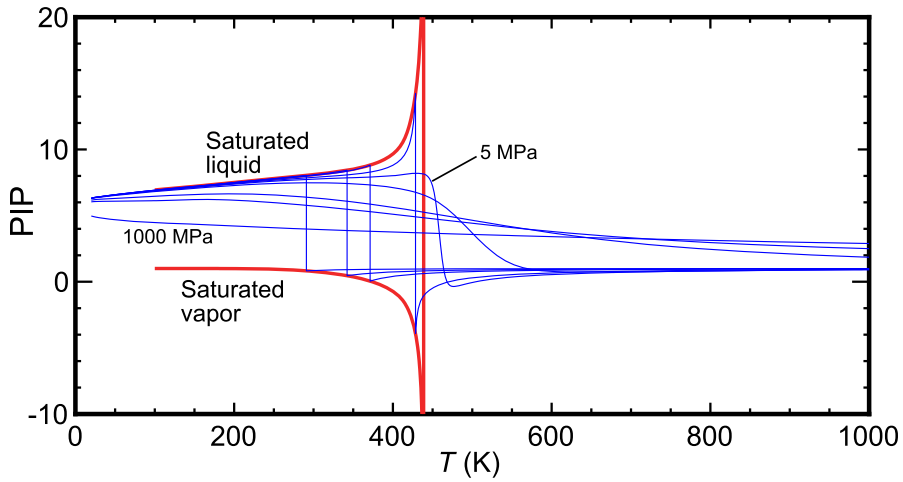

Figure 6: Phase identification parameter versus temperature along the saturation lines and isobars at 0.1, 0.5, 1, 3, 5, 10, 50, 100, and 1000 MPa.

This parameter is often used to inspect the behavior of equations of state. Lemmon et al. (2019) presents requirements for a physically correct PIP outside the valid range of an equation of state. The saturation lines and isobars in Fig. 6 mostly meet the requirements.

5. CONCLUSIONS

The new equation of state is mainly fitted to the experimental data for vapor pressures, densities, and vapor-phase sound speeds of Mondejar et al. (2015) and those for liquid-phase sound speeds of McLinden and Perkins (2019). For the vapor pressures and densities, typical deviations in calculated values with the new equation are similar to those with the first equation; however, deviations in the liquid-phase sound speeds from the new equation are considerably smaller than those from the first equation. For the vapor-phase sound speeds, systematic negative deviations

up to 0.7 % are observed in calculated values from the new equation, whereas deviations from the first equation show systematic positive deviations up to 0.45 %. These deviations become larger as temperature and pressure increase.

The data for vapor-phase sound speed of Mondejar et al. (2015) may include some data points inconsistent with other experimental data, particularly with the vapor pressures. Vapor-phase sound speeds are directly related to heat capacities, and very high accuracies in calculated values are required to obtain reliable values for energy (i.e., enthalpy differences in the superheated vapor region). We plan to make additional measurements of vapor pressures and vapor-phase sound speeds before obtaining the final equation of state.

ACKNOWLEDGEMENTS

The authors thank the suggestions by the ISO/TC86/SC8/WG7 members for the assessment of experimental data.

NOMENCLATURE

a	molar Helmholtz energy (J mol^{-1})	B	second virial coefficient (dm^3 mol^{-1})
C	third virial coefficient (dm^6 mol^{-2})	c_p°	ideal-gas isobaric heat capacity (J mol^{-1} K^{-1})
D	fourth virial coefficient (dm^9 mol^{-3})	M	molar mass (g mol^{-1})
PIP	phase identification parameter	p	pressure (MPa)
p_0	reference pressure (MPa)	p_c	critical pressure (MPa)
R	universal gas constant (8.3144598 J mol^{-1} K^{-1})	T	temperature (K)
T_0	reference temperature (K)	T_c	critical temperature (K)
w	sound speed (m s^{-1})	α	dimensionless Helmholtz energy
α°	ideal-gas part of α	α^r	residual part of α
δ	reduced density	ρ	density (mol dm^{-3})
ρ_0	ideal-gas density at (T_0, p_0)	ρ_c	critical density (mol dm^{-3})
τ	inverse reduced temperature		

REFERENCES

Akasaka, R., Lemmon, E. W. 2019. New Fundamental Equations of State for cis-1,3,3,3-Tetrafluoropropene [R-1234ze(Z)] and 3,3,3-Trifluoropropene (R-1243zf), to be published in J. Chem. Eng. Data.

Di Nicola, G., Fedele, L., Brown, J. S., Bobbo, S., Coccia, G. 2017. Saturated Pressure Measurements of trans-1-Chloro-3,3,3-trifluoroprop-1-ene (R1233zd(E)), J. Chem. Eng. Data, 62(9), 2496–2500.

Fedele, L., Pierantozzi, M., Di Nicola, G., Brown, J. S., Bobbo, S., 2018. Compressed Liquid Density and Vapor Phase PvT Measurements of trans-1-Chloro-3,3,3-trifluoroprop-1-ene [R1233zd(E)], J. Chem. Eng. Data, 63(1), 225–232.

Higashi, Y. 2018. unpublished data.

Lago, S., Giuliano Albo, P. A., Brown, J. S., Bertinetti, M., 2018. High Pressure Speed of Sound Measurements of trans-1-Chloro-3,3,3-triuoropropene(R1233zd(E)) in the Subcooled Liquid Region for Temperature from (273.15 to 353.15) K, J. Chem. Eng. Data, 63(11), 4039–4045.

Lemmon, E. W., Jacobsen, R. T. 2005, A New Functional Form and New Fitting Techniques for Equations of State with Application to Pentafluoroethane (HFC-125), J. Phys. Chem. Ref. Data, 34(1), 69–108.

Lemmon, E. W., McLinden, M. O., Wagner, W. 2009, Thermodynamic Properties of Propane. III. A Reference Equation of State for Temperatures from the Melting Line to 650 K and Pressures up to 1000 MPa, J. Chem. Eng. Data, 54(12), 3141–3180.

Lemmon, E.W., McLinden, M.O., Overhoff, U., Wagner, W., 2019. A Reference Equation of State for Propylene for Temperatures from the Melting Line to 575 K and Pressures up to 1000 MPa, to be submitted to J. Phys. Chem. Ref. Data.

McLinden, M. O., Perkins, R. A., 2019. A Dual-Path Pulse-Echo Instrument for Speed of Sound of Liquids and Dense Gases and Measurements on Four Halogenated-Olefin Refrigerants [HFO-1234yf, HFO-1234ze(E), HCFO-1233zd(E), and HFO-1336mzz(Z)], to be submitted to J. Chem. Thermodyn.

Mohr, P. J., Newell, D. B., Taylor, B. N., 2016. CODATA Recommended Values of the Fundamental Physical Constants: 2014, J. Phys. Chem. Ref. Data, 45, 043102.

Mondejar, M. E., McLinden, M. O., Lemmon, E. W., 2015. Thermodynamic Properties of trans-1-Chloro-3,3,3-trifluoropropene (R1233zd(E)): Vapor Pressure, (p, rho, T) Behavior, and Speed of Sound Measurements, and Equation of State, J. Chem. Eng. Data, 60(8), 2477–2489.

Romeo, R., Giuliano Albo, P. A., Lago, S., Brown, J. S., 2017. Experimental Liquid Densities of cis-1,3,3,3-Tetrafluoroprop-1-ene (R1234ze(Z)) and trans-1-Chloro-3,3,3-trifluoropropene (R1233zd(E)), Int. J. Refrig., 79, 176–182.

Span, R., Wagner, W. 1997, On the Extrapolation Behavior of Empirical Equations of State, Int. J. Thermophys., 18(6), 1515–1443.

Venkatarathnam, G., Oellrich, L. R. 2011, Identification of the Phase of a Fluid Using Partial Derivatives of Pressure, Volume, and Temperature Without Reference to Saturation Properties: Applications in Phase Equilibria Calculations, Fluid Phase Equilib., 301, 225–233.

Manuscript ID: 1503
DOI: 10.18462/iir.icr.2019.1503

Performance analysis of different ternary NH_3-H_2O-salt absorption heat pump cycle combined with electrodialysis technique

Mengkai XU, Shuhong LI，Kai DU

School of energy and environment, Southeast University
Nanjing, 210096, China, xumengkai@seu.edu.cn

ABSTRACT

LiBr, $LiNO_3$ and NaOH are three widely used additions that can significantly improve the performance of ammonia absorption heat pump cycle. To compare the enhancements of using different additions, Aspen plus process monitor is applied to simulate the performance of ternary NH_3-H_2O-salt absorption heat pump. The results indicate LiBr heighten the performance most, 16.52% higher than ternary cycle. However, the existence of additions has an adverse effect on absorption process because it decreases the absorption capacity of the ternary working fluid. To avoid the negative effect, electrodialysis technique is employed to separate additions from absorber to generator. The new models of NH_3-H_2O-salt absorption heat pump combined with electrodialysis device are established and simulated in Aspen plus process monitor. The results show that, LiBr can increase the COP of new absorption heat pump cycle up to 12.36%, highest in the three additions compared with traditional cycle.
Keywords: Ammonia Absorption Heat Pump, Ternary Working Fluid, Electrodialysis, Aspen Plus Process Monitor.

1. INTRODUCTION

With the rapid increase of energy consumptions and environment pollution problems appearance under the social development, it's a key issue that exploiting low-grade heat such as industrial waste heat in heat pump field efficiently. Absorption heat pump, with its unique advantages that can use low-grade heat source and apply nature refrigerants rather artificially manufactured CFCs, which have less negative effects on ozone layer and meet the environment protection needs, is coming into more people's vision (Abed et al., 2017). It's vital to investigate how to promote the COP of absorption heat pump cycle and expend its scope of applications.

Ammonia-water, as one main working pair in absorption chilling, cooling, heating, dehumidification fields, has its advantages and disadvantages. Ammonia can evaporate under freezing point, however, the high working pressure, distillation heat requirement and huge device volume limit the performance of ammonia-water absorption heat pump and popularize to utilization (Zheng et al., 2014). Researchers have done plenty of work on overcoming these disadvantages, it is a convenient way that adding the third substance in NH_3-H_2O solution to decrease the rectification heat demand and equipment volume (Wu et al., 2011). Åhlby et al. (1993) theoretically calculated the COP of NH_3-H_2O-LiBr compression/absorption refrigeration cycle at 60% mass fraction of LiBr and the results indicate the COP of ternary solution cycle was promoted at most 10%. Hernández-Magallanes et al., (2014) applied NH_3-H_2O-$LiNO_3$ ternary solution in a 3kW single-stage absorption cooling experiments, the results show that the COP varies between 0.45 to 0.7 when the generating temperature changes from 85°C to 105°C and obtaining 1.1°C to 12.5°C cold water. Steiu et al., (2009) studied the effect of alkaline hydroxides on the performance of ammonia absorption chiller, and the results propose that the COP increases by 28% for the 12% mass fraction of NaOH in solution.

However, all of these additions will prevent weak solution absorbing ammonia molecules which has contrary influence on the performance of absorption cycle (Wu et al., 2006). To take advantages of the ability of the additions that shift the chemical equilibrium toward effective separation of ammonia from aqueous solution, Balamuru et al., (2000) and Bruno et al(2005) used reverse osmosis

membrane as the separation device between generator and absorber to depart NaOH in absorber. Electrodialysis technique is a common method in seawater desalination industry, and Liang et al., (2017) put forward a new ternary solution absorption chiller cycle which combined electrodialysis device with traditional cycle to separate LiBr from weak solution stream to strong stream after heat exchange process.
The aim of this paper is to compare the performance increase ability by using three different additions respectively in traditional ammonia-water absorption heat pump. Moreover, the new absorption heat pump cycle model combined with electrodialysis device is proposed so as to clarify whether the separation device has opponent effect on performance and the increase ability of the new cycle, besides, the optimal addition in three alternatives is selected by the model.

2. MODELING AND ANALYSIS OF TERNARY SOLUTION ABSORPTION HEAT PUMP CYCLE

In this section, a traditional ammonia-water absorption heat pump cycle is established in Aspen plus process monitor and a validation of the model is carried out. The performance evaluation of the traditional absorption heat pump cycle is presented and the simulation results of the performance increase applied three different additions in working fluid are showed and compared.

2.1. Simulation of the Traditional Absorption Heat Pump Cycle

The performance of traditional NH_3-H_2O-salt absorption heat pump system is simulated by Aspen plus, a commercial process monitor used in chemical industry and absorption refrigeration/heat pump simulation fields. The COP of the traditional cycles with four working pairs (NH_3-H_2O, NH_3-H_2O-LiBr, NH_3-H_2O-$LiNO_3$, NH_3-H_2O-NaOH) are compared with each other. Table 1 gives the main simulation working condition parameters and Table 2 gives the blocks besides the parameters set used in Aspen plus modules. Fig.1 illustrates the traditional absorption heat pump cycle.

Table 1. Main design parameters of absorption heat pump cycle

Parameter	value
Generation temperature	393.15K
Generation pressure	1.5Mpa
Evaporation temperature	263.15K
NH_3 concentration at the outlet of absorber	50%/55%/60%
Addition concentration	5%/10%/15%/20%/25%/30%
Condensation temperature	298.15K
Heat exchange efficiency	0.85
Pump efficiency	0.7
heat and electrical energy transform efficiency	0.4

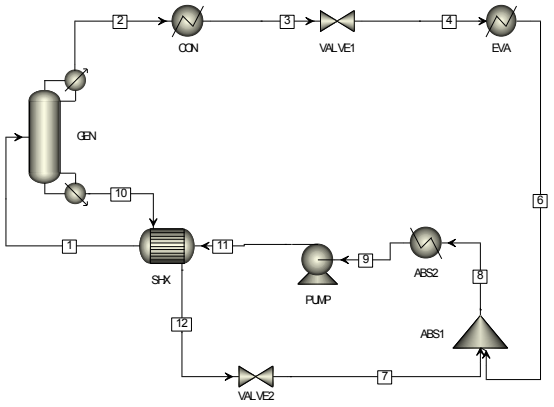

Figure 1: Traditional NH_3-H2O-salt absorption heat pump cycle (cycle 1)

Table 2. Main monitors used with input parameters in Aspen plus

Module Name	Monitor Type	Input Parameters
GEN	Radfrac-FRACT2	Input solution flow rate Reflux mass ratio Distillation mass ratio
CON	Heat exchanger-Heater	Outlet tempture Vapor fraction
EVA	Heat exchanger-Heater	Outlet tempture Vapor fraction
ABS	Heat exchanger-Heater	Outlet tempture Vapor fraction
PUMP	PUMP	Discharge pressure
SHX	HeatX	Exchange area U valve
VALVE1/2	VALVE2	Outlet pressure

To test and verify the accuracy of the NH_3-H_2O-salt absorption refrigeration cycle, a NH_3-H_2O-NaOH traditional absorption cycle is established to compare with the simulation results from Steiu et al., (2011). The comparison results are showed in table 3, and the results indicate that the errors are less than 2% under the same working conditions, therefore, the model is credible to absorption cycle simulation. The COPs of the absorption refrigeration cycle are calculated by Eq. (1) ：

$$COP = \frac{Q_{eva}}{Q_{gen} + Q_{pump}} \quad \text{Eq. (1)}$$

Table 3. Model verification results between this paper and ref

Mass fraction of NaOH	0	5%	10%	15%
COP of this paper	0.4818	0.5534	0.5822	0.6184
COP of Steiu et al	0.4860	0.5554	0.5934	0.6103
error	0.872%	0.367%	1.92%	1.31%

2.2. Performance Analysis

The initial mass fractions of NH_3, LiBr, $LiNO_3$ and NaOH are the mass fraction in binary or ternary solutions that come from the outlet stream of absorber. It is defined as follows (Wu et al., 2011):

$$w_{NH_3} = \frac{m_{NH_3}}{m_{NH_3} + m_{H_2O}} \quad \text{Eq. (2)}$$

$$w_{add} = \frac{m_{add}}{m_{add} + m_{H_2O}} \quad \text{Eq. (3)}$$

Because of the different NH_3 concentration in outlet of absorption under the same working temperature and pressure, the solution flow at the outlet of generator and the pure ammonia flow are different, which lead to different refrigerating capacities and heat duty. To evaluate the heat pump cycle impartially, COP is selected to be the index for performance comparison. The COP of the binary/ ternary absorption heat pump cycle is defined as Eq. (4) and Eq. (5):

$$COP = \frac{Q_{abs} + Q_{con}}{Q_{gen} + Q_{pump}} \quad \text{Eq. (4)}$$

$$Q_{pump} = \frac{P_{pump}}{\xi} \cdot t \qquad \text{Eq. (5)}$$

2.3. Simulation Results of the COP vs Different Working Fluids

The simulation results of the COP vs different working fluid for traditional absorption heat pump cycle are list in Table 4. In this part of simulation, the mass fractions of additions are set from 0 to 30% because it has been proved that the addition of salts or alkali can increase the performances of the absorption refrigeration/heat pump cycle.

Table 4. COP comparison of traditional cycle with different additions (NH_3 concentration is 50%)

Mass fraction of addition(%)	0	5	10	15	20	25	30
LiBr	1.458	1.498	1.548	1.595	1.634	1.673	1.699
Increase of COP(%)	\	2.713	6.154	9.410	12.081	14.720	16.523
$LiNO_3$	1.458	1.489	1.502	1.516	1.523	1.511	1.506
Increase of COP(%)	\	2.090	2.969	3.955	4.450	3.641	3.255
NaOH	1.458	1.504	1.533	1.554	1.570	1.559	1.557
Increase of COP(%)	\	3.147	5.159	6.601	7.677	6.918	6.770

Table 5. COP comparison of traditional cycle with different additions (NH_3 concentration is 55%)

Mass fraction of addition(%)	0	5	10	15	20	25	30
LiBr	1.492	1.518	1.547	1.599	1.637	1.676	1.709
Increase of COP(%)	\	1.723	3.660	7.060	9.653	12.305	14.482
$LiNO_3$	1.492	1.512	1.519	1.526	1.531	1.527	1.526
Increase of COP(%)	\	1.314	1.794	2.270	2.608	2.283	2.226
NaOH	1.492	1.524	1.543	1.556	1.565	1.571	1.574
Increase of COP(%)	\	2.125	3.365	4.273	4.864	5.249	5.457

Table 6. COP comparison of traditional cycle with different additions (NH_3 concentration is 60%)

Mass fraction of addition(%)	0	5	10	15	20	25	30
LiBr	1.541	1.562	1.592	1.625	1.673	1.708	1.736
Increase of COP(%)	\	1.383	3.294	5.447	8.559	10.824	12.685
$LiNO_3$	1.541	1.489	1.502	1.516	1.523	1.511	1.506
Increase of COP(%)	\	1.058	1.492	1.740	1.853	1.894	1.854
NaOH	1.541	1.504	1.533	1.554	1.570	1.559	1.557
Increase of COP(%)	\	1.769	2.727	3.421	3.919	4.212	4.780

When the mass fraction of NH_3 is 50%, the maximum increases of LiBr, $LiNO_3$, NaOH are 16.523%, 4.450% and 7.677% respectively. When the concentration is 5%, NaOH promotes COP most which is 3.147% higher than binary cycle. LiBr is more efficient to improve COP when the mass fraction exceeds 5% and the maximum COP is 16.523 and the mass fraction of LiBr is 30% at this time. $LiNO_3$ can promote the COP up to 1.523 when the mass fraction is 20% and the COP decreases when keep raising the concentration. NaOH can increase the performance better than $LiNO_3$ but worse than LiBr.

When the mass fraction of NH_3 is 55%, the maximum increase of LiBr, $LiNO_3$, NaOH is 14.482%, 2.608% and 5.457% respectively. When the concentration is 5%, NaOH promotes COP most which is 2.125% higher than binary cycle. LiBr is more valid to improve COP when the mass fraction exceeds 5% and the maximum COP is 1.709 and the mass fraction of LiBr is 30% at this time. $LiNO_3$

can promote the COP up to 1.531 when the mass fraction is 20% and the COP decreases when keep raising the concentration over 20%.
When the mass fraction of NH_3 is 60%, the maximum increase of LiBr, $LiNO_3$, NaOH is 12.685%, 1.894% and 4.780% respectively. When the concentration is 5%, NaOH promotes COP most which is 1.769% higher than binary cycle. LiBr is more valid to improve COP when the mass fraction exceeds 5%. $LiNO_3$ can promote the COP up to 1.523 when the mass fraction is 20%.
Generally speaking, the results indicate that all of these three additions can promote the performance of absorption heat pump cycle. NaOH has more effect on performance of absorption heat pump cycle at low addition concentration. However, with the raising of addition mass fraction, LiBr can increase the COP more than $LiNO_3$ and NaOH under the same working condition. Moreover, compare the performance between high and low concentration of ammonia, additions can affect COP more at lower ammonia mass fraction. LiBr, $LiNO_3$ and NaOH as the third addition of working fluid have positive effect on absorption heat pump system, however, the choose of additions depends on the working condition, especially the addition mass friction.

3. MODELING AND ANALYSIS OF TERNARY SOLUTION ABSORPTION HEAT PUMP CYCLE COMBINED WITH ELECTRODIALYSIS TECHNIQUE

In this section, a new ternary working fluid absorption heat pump cycle with electrodiaysis technique is established in Aspen plus process monitor. The electrodialysis energy consumption calculation method is introduced and the performance evaluation of the new absorption heat pump cycle is showed. The simulation results of the performance increase applied three different addition in working fluid are showed and compared.

3.1 Simulation of the Absorption Heat Pump Cycle with Electrodialysis Device

As the presence of the additions prevents the solution absorbing NH_3 in absorber, which has disadvantage on the COP of the absorption, separating additions in weak solution from absorber to generator before additions flow into the absorber is one effective method to promote the COP of the ternary absorption heat pump cycle further. Electrodialysis technology is put forward to achieve this separation process, which is widely researched and applied in brackish water desalination and water treatment fields (Mohammadi and Kaviani, 2003). The electrodialysis technique is composed of a pair of positive and negative electrodes, pairs of cation and anion exchange membranes (Fig. 2) (Liang et al., 2017). The pairs of ion exchanges membranes placed alternately to divide the equipment into several solution rooms, the weak and strong solutions are sent in two adjacent rooms waiting to achieve ion exchange.

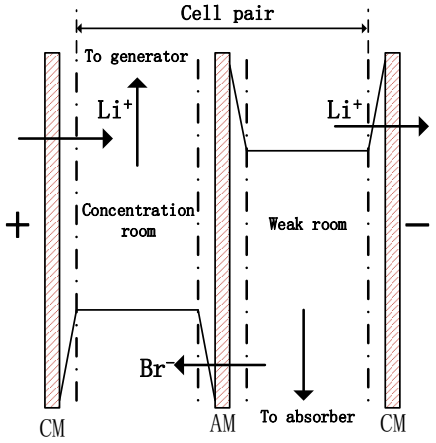

Figure 2: Structure of electrodialysis device

The model of the new ternary absorption heat pump cycle with electrodialysis device is shown in Fig. 3, which is established based on the conventional cycle (cycle 1) and the new cycle includes the electrodialysis device and all other components in cycle 1. The design parameters of the working conditions in the new cycle are same as the traditional cycle. Due to the results from part 2, the promotions of the performance by adding the third components rise up during the mass fraction from 0 to 20%, the ranges of the addition concentrations are set to 0 to 20%.The module applied for

electrodialysis device is the sep2 and the input data is the separation rate is set at 99% according to the paper from (Yue et al., 2018). The other modules are same with cycle 1.

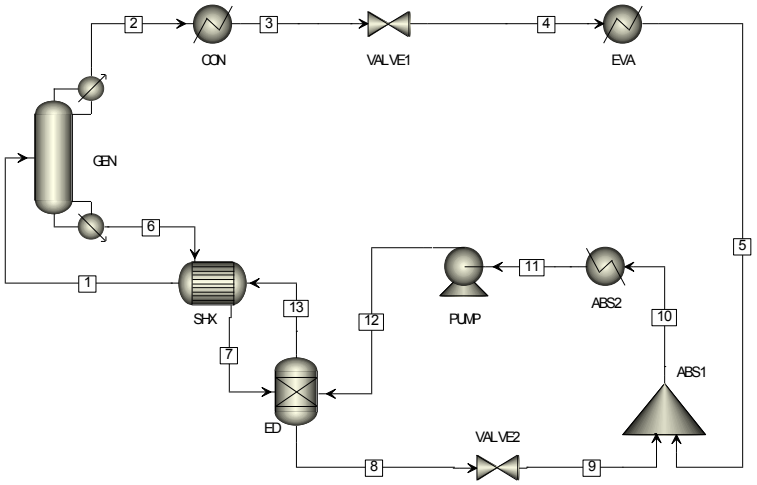

Figure 3: New ternary absorption refrigeration cycle combined with electrodialysis device (cycle 2)

3.2 Performance Analysis

Eqs. (2) and (3) are used to calculate the mass friction of NH_3 and LiBr in new cycle as well. The COP of the new NH_3-H_2O-LiBr ternary absorption refrigeration cycle is defined as Eqs. (5) (6) and (7):

$$COP = \frac{Q_{abs} + Q_{con}}{Q_{gen} + Q_{pump} + Q_{ed}} \quad \text{Eq. (6)}$$

$$Q_{ed} = \frac{P_{ed}}{\xi} \cdot t \quad \text{Eq. (7)}$$

The same electrodialysis device applied in the separation of addition in ternary solution, the power of the electrodialysis is calculated in limit current density model (Xiao-yang et al., 2018), the Eqs. are (8) to (10):

$$I_{\lim} = 0.0055979 C_{di} v^{0.66} \quad \text{Eq. (8)}$$

$$U_p = 0.065 C_{di}^{\ 0.1589} v^{0.67} \quad \text{Eq. (9)}$$

$$v = \frac{10^6 q}{3600 N t W} \quad \text{Eq. (10)}$$

3.3 Simulation Results of COP Applying New Cycle

The simulation results of the COP applied new cycle are listed in Table 5, and the comparisons between different additions are presented as well.

From the chart, the electrodialysis device can improve the COP of absorption heat pump cycle further in each concentration of NH_3 and additions. With the increase of additions mass frictions in the working fluid, the COPs of new absorption heat pump cycles are higher than the conventional cycle and the improvement. LiBr can lift the COP up to 1.639, 12.363% higher than traditional cycle when the mass fraction of NH_3 is 50% and LiBr is 20%. Compare Table 4 and Table 5, electrolysis is beneficial to all three kinds of additions especially to $LiNO_3$. Although the electrodialysis device consumes power, the proceeds by save energy in generator and absorber are more significant for the absorption heat pump cycle.

Table 7. COP comparison of new cycle with different additions(NH_3 concentration is 50%)

Mass fraction of addition(%)	0	5	10	15	20
LiBr	1.458	1.551	1.578	1.609	1.639
Increase of COP(%)	\	6.382	8.179	10.360	12.363
$LiNO_3$	1.458	1.542	1.560	1.569	1.566
Increase of COP(%)	\	5.762	6.985	7.588	7.407
NaOH	1.458	1.555	1.573	1.591	1.604
Increase of COP(%)	\	6.650	7.869	9.086	10.025

Table 8. COP comparison of new cycle with different additions (NH_3 concentration is 55%)

Mass fraction of addition(%)	0	5	10	15	20
LiBr	1.493	1.608	1.632	1.656	1.675
Increase of COP(%)	\	7.746	9.326	10.970	12.209
$LiNO_3$	1.493	1.592	1.588	1.591	1.588
Increase of COP(%)	\	6.693	6.421	6.596	6.413
NaOH	1.493	1.592	1.608	1.630	1.632
Increase of COP(%)	\	6.650	7.712	9.186	9.372

Table 9. COP comparison of new cycle with different additions (NH_3 concentration is 60%)

Mass fraction of addition(%)	0	5	10	15	20
LiBr	1.541	1.626	1.642	1.658	1.673
Increase of COP(%)	\	5.535	6.593	7.635	8.618
$LiNO_3$	1.541	1.625	1.641	1.608	1.621
Increase of COP(%)	\	5.432	6.493	4.334	5.219
NaOH	1.541	1.626	1.640	1.651	1.655
Increase of COP(%)	\	5.498	6.408	7.172	7.415

4. CONCLUSIONS

Adding LiBr, $LiNO_3$ and NaOH to NH_3-H_2O working solution promotes the performance of absorption heat pump cycle, because of their benefits to generation process. But the presence of additions has negative influence on ammonia absorption process. In the traditional cycle, LiBr has better results on COP increase compared with $LiNO_3$ and NaOH at 50% to 60% mass fraction of ammonia and 0 to 30% mass fraction of additions. Electrodialysis technique is useful to ease even eliminate the negative effect of additions on absorption process, so that the new ternary solution absorption heat pump cycle with electrodialysis has better performance than binary cycle and traditional ternary working fluid absorption cycle.

ACKNOWLEDGEMENTS

The authors gratefully acknowledge the financial support of the National Nature Science Foundation of China (No.51876033)

NOMENCLATURE

C	Salt mass fraction in solution (g/L)	I	Current (A)
m	Mass flow (kg/h)	N	Number of membranes
p	Pressure (mPa)	P	Power (kW)
q	solution flow (m^3/h)	Q	Heat (kJ)
U	Voltage (V)	T	temperature (K)
t	Thickness of partition (cm)	v	Solution velocity (cm/s)
W	Width of partition (cm)	ξ	Efficiency of thermal energy transforming to electrical energy
ABS	Absorber	COP	Coefficient of performance
CON	Condenser	EVA	Evaporator
GEN	Generator	PUMP	Solution pump
SHX	Solution heat exchanger	VALVE	Valve
ED	Electrodialysis device	lim	Limitation
di	Electrodialysis device inlet solution	add	Addition

REFERENCES

Abed, A.M., Alghoul, M.A., Sopian, K., Majdi, H.S., Al-Shamani, A.N., Muftah, A.F., 2017. Enhancement aspects of single stage absorption cooling cycle: A detailed review. Renewable and Sustainable Energy Reviews 77, 1010–1045.

Åhlby, L., Hodgett, D., Radermacher, R., 1993. NH3/H2OLiBr as working fluid for the compression/absorption cycle. International Journal of Refrigeration.

Balamuru, V.G., Ibrahim, O.M., Barnett, S.M., 2000. Simulation of ternary ammonia-water-salt absorption refrigeration cyclesSimulation des cycles frigorifiques à absorption à ammoniac / eau / sel. International Journal of Refrigeration 23, 31–42.

Hernández-Magallanes, J.A., Domínguez-Inzunza, L.A., Gutiérrez-Urueta, G., Soto, P., Jiménez, C., Rivera, W., 2014. Experimental assessment of an absorption cooling system operating with the ammonia/lithium nitrate mixture. Energy 78, 685–692.

Liang, Y., Li, S., Yue, X., Zhang, X., 2017. Analysis of NH3-H2O-LiBr absorption refrigeration integrated with an electrodialysis device. Applied Thermal Engineering 115, 134–140.

Mohammadi, T., Kaviani, a., 2003. Water shortage and seawater desalination by electrodialysis*1. Desalination 158, 267–270.

Steiu, S., Martínez-Maradiaga, D., Salavera, D., Bruno, J.C., Coronas, A., 2011. Effect of alkaline hydroxides on the vapor-liquid equilibrium of ammonia/water and the performance of absorption chillers. Industrial and Engineering Chemistry Research. 50, 13037–13044.

Steiu, S., Salavera, D., Bruno, J.C., Coronas, A., 2009. A basis for the development of new ammonia-water-sodium hydroxide absorption chillers. International Journal of Refrigeration. 32, 577–587.

Wu, T., Wu, Y., Yu, Z., Zhao, H., Wu, H., 2011. Experimental investigation on an ammonia-water-lithium bromide absorption refrigeration system without solution pump. Energy Conversion and Management. 52, 2314–2319.

Wu, Y., Chen, Y., Wu, T., 2006. Experimental researches on characteristics of vapor-liquid equilibrium of NH3-H2O-LiBr system. International Journal of Refrigeration. 29, 328–335.

Xiao-yang, Y., Shu-hong, L., Meng-kai, X., Yan-jun, L., Kai, D., Liu, Y., 2018. Experimental study of ternary NH3-H2O-LiBr absorption cycle combined with membrane separation technique. Sustainable Cities and Society. 40, 728–734.

Zheng, D., Dong, L., Huang, W., Wu, X., Nie, N., 2014. A review of imidazolium ionic liquids research and development towards working pair of absorption cycle. Renewable and Sustainable Energy Reviews. 37, 47–68.

Manuscript ID: 1508
DOI: 10.18462/iir.icr.2019.1508

Analysis of the arrangement and effects of air layer in external thermal insulation walls in hot summer and cold winter zone in China

Chengcheng XU[(a)], Shuhong LI[(a)], Kaikai ZOU[(a)], Kai DU[(a)]

[(a)] School of Energy and Environment, Southeast University
Nanjing, 210096, China, 230169329@seu.edu.cn

ABSTRACT

With the rapid development of economy and urbanization, human beings are facing a great challen ge of environmental pollution and energy shortage. To reduce energy consumption of HVAC in buil dings, thermal insulation and air layers are often utilized to reduce heat transfer through the buildin g envelope in Hot Summer and Cold Winter (HSCW) zone in China. To investigate heat transfer ch aracteristics of external thermal insulation walls with air layers, a coupled heat and moisture transfe r model of one-dimension wall was established. The relative humidity and temperature distribution of four types of envelope structures with air layers at three different interfaces or without air layers was simulated. The condensation and heat transfer characteristics were analysed, and the results show that the best arrangement configuration is provided by creating an air layer inside of the wall (Interface 3). The condensation and heat transfer characteristics of the wall are related. The more s erious the condensation phenomenon is, the greater the heat transfer of the wall will be.
Keywords: Air layer, Condensation Characteristics, Heat Transfer, Application Effects.

1. INTRODUCTION

In recent years, architects are facing the crucial task of reducing energy consumption in buildings. The energy consumption of buildings accounts for more than 30% of total energy consumption all o ver the world (Berardi, 2017). Furthermore, the energy consumption associated with the envelope i s an important factor with respect to the energy consumption of buildings (Liu et al, 2015). Therefor e, improving the performance of the envelope is vital to realize the energy conservation (Cho et al, 2017).

In recent years, air layers have often been installed to envelop the structures of existing buildings f or building optimization in China (Wang and Yan, 2004). The application of the air layer not only re duces the energy consumption of HVAC systems (Chowdhury, 2008), but also creates a comfortab le indoor environment for people (AM., 2007). At present, the thermal insulation layer and air layer arrangement system in North China is also used in South China (You et al, 2017). The difference o nly lies in the reduction of the thermal insulation layer thickness, with no great difference in technol ogy (Zhao et al, 2001). This direct application does not consider the local climate in South China, w hich may affect usage effect. Therefore, it is important to develop appropriate techniques that can a chieve the best applying effects of air layer (Li et al, 2017).

Up to now, many scholars have carried out a lot of research on the air layers (Saadatian et al, 2012), but these studies are carried out from the perspective of heat transfer only (Krueger E. et al, 201 3). However, the distribution of relative humidity will significantly affect the heat transfer of the wall (Zamora B and Kaiser AS, 2009). When considering the moisture effect inside walls, building energ y consumption will be 4.4% higher (Moon H J et al, 2014). Mendes's (2003) investigation shows tha t ignoring the influence of moisture transfer may underestimate the yearly integrated heat flux up to 59%. Therefore, to improve the accuracy of this research, both the moisture and heat transfer char acteristics of different types of envelope structures with air layers at three different interfaces or wit hout air layers are analysed and compared in this paper. A coupled heat and moisture transfer mod el of a one-dimensional wall with temperature and relative humidity (*RH*) as the driving potential is

established and verified. 4 types of external thermal insulation (ETI) walls with air layers at three dif ferent interfaces or without air layers are simulated and compared.

2. THE COUPLED HEAT AND MOISTURE TRANSFER MODEL

2.1. Construction of the Model

2.1.1. Moisture transfer equation

According to the law of conservation of mass, the moisture transfer equation is expressed as Eq(1)

$$\frac{\partial(\rho u)}{\partial t} = -\nabla(J_v + J_l) \quad \text{Eq. (1)}$$

u is determined by the isothermal absorption and desorption curve of the material (Zhou et al, 2008). The balanced moisture content of the material is $u = f(\varphi)$(Gao et al, 2012), and the following rela tion can be obtained:

$$\frac{\partial(\rho u)}{\partial t} = \rho\frac{\partial u}{\partial t} = \rho\frac{\partial u}{\partial \varphi}\frac{\partial \varphi}{\partial t} = \rho\xi\frac{\partial \varphi}{\partial t} \quad \text{Eq. (2)}$$

According to Fick's law and Darcy's law, the diffusion flux of vapour and liquid water are as follows:

$$J_v = -D_v\frac{\partial P_v}{\partial x} \quad \text{Eq. (3)}$$

$$J_l = -D_l\frac{\partial P_l}{\partial x} \quad \text{Eq. (4)}$$

The gradient of the partial pressure of water vapour can be transformed as follows:

$$\frac{\partial P_v}{\partial x} = \frac{\partial(\varphi P_{v,s})}{\partial x} = P_{v,s}\frac{\partial \varphi}{\partial x} + \varphi\frac{\partial P_{v,s}}{\partial T}\frac{\partial T}{\partial x} \quad \text{Eq. (5)}$$

The partial pressure of saturated vapour is a uniform function of temperature:

$$P_{v,s} = f(T) \quad \text{Eq. (6)}$$

The capillary pressure P_l of liquid water is as follows:

$$P_l = \rho_l R_v T\ln(\varphi) \quad \text{Eq. (7)}$$

According to above, the moisture transfer equation can be obtained as follows:

$$\rho\xi\frac{\partial \varphi}{\partial t} = \frac{\partial}{\partial x}\left[\left(D_v P_{v,s} + D_l\rho_l R_v\frac{T}{\varphi}\right)\frac{\partial \varphi}{\partial x} + \left(D_v\varphi\frac{\partial P_{v,s}}{\partial T} + D_l\rho_l R_v\ln(\varphi)\right)\frac{\partial T}{\partial x}\right] \quad \text{Eq. (8)}$$

2.1.2. Heat transfer equation

According to Fourier's law, the following heat transfer equation can be obtained.

$$\rho c\frac{\partial T}{\partial t} = \frac{\partial}{\partial x}\left(\lambda\frac{\partial T}{\partial x}\right) + s \quad \text{Eq. (9)}$$

During heat and moisture transfer in the wall, the heat source is mainly the phase change heat.

$$s = -L\frac{\partial J_v}{\partial x} \quad \text{Eq. (10)}$$

According to Eqs. 3, 5, 6, 9, and 10,

$$\rho c\frac{\partial T}{\partial t} = \frac{\partial}{\partial x}\left[\left(\lambda + LD_v\varphi\frac{\partial P_{v,s}}{\partial T}\right)\frac{\partial T}{\partial x}\right] + \frac{\partial}{\partial x}\left(LD_v P_{v,s}\frac{\partial \varphi}{\partial x}\right) \quad \text{Eq. (11)}$$

2.1.3. Coupled heat and moisture transfer equation

The heat and moisture transfer is influenced by the relative humidity and the temperature gradient. In conjunction with the two equations, the coupled heat and moisture transfer equation is obtained.

$$\begin{cases} a_\varphi(\varphi,T)\dfrac{\partial \varphi}{\partial t} = \dfrac{\partial}{\partial x}\left[D_{\varphi\varphi}(\varphi,T)\dfrac{\partial \varphi}{\partial x}\right] + \dfrac{\partial}{\partial x}\left[D_{\varphi T}(\varphi,T)\dfrac{\partial T}{\partial x}\right] \\ a_T(T,\varphi)\dfrac{\partial T}{\partial t} = \dfrac{\partial}{\partial x}\left[D_{TT}(T,\varphi)\dfrac{\partial T}{\partial x}\right] + \dfrac{\partial}{\partial x}\left[D_{T\varphi}(T,\varphi)\dfrac{\partial \varphi}{\partial x}\right] \end{cases} \quad \text{Eq. (12)}$$

The empirical formula for the partial pressure $P_{v,s}$ of saturated water vapour is as follows (Mendes N. et al, 2002):

$$P_{v,s} = 610.5\exp\left(\frac{17.268t}{237.3+t}\right) = 610.5\exp\left(\frac{17.268(T-273.15)}{T-35.85}\right) \quad \text{Eq. (13)}$$

The formula for calculating the gasification latent heat of water vapour is as follows (Zhao et al, 2009):

$$L = (2500 - 2.35t) \times 10^3 = (1858.9025 - 2.35T) \times 10^3 (\mathrm{J/kg}) \quad \text{Eq. (14)}$$

According to the BET equation (Richards R F et al, 2014), *u* can be calculated.

$$u = \frac{a\varphi}{(1+b\varphi)(1-c\varphi)}(kg/kg) \quad \text{Eq. (15)}$$

u reflects the moisture capacity of materials. Physically, this moisture content refers to the quality of water and water vapour contained in a material of unit mass. D_v embodies the rate of diffusion of water vapour in a wall (Fanney H. et al, 1991). According to Li et al. (2009), D_v is as follows:

$$D_v = d + e \cdot \varphi^f \quad \text{Eq. (16)}$$

2.2. Validation of the Model

Python language and the finite volume method was used for programming. To verify the accuracy of the model, the experimental data from Talukdar et al. (2007a) (2007b) are compared with numerical results.

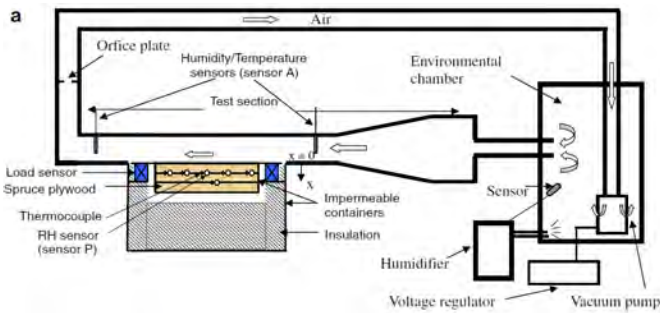

Figure 1: Experimental device

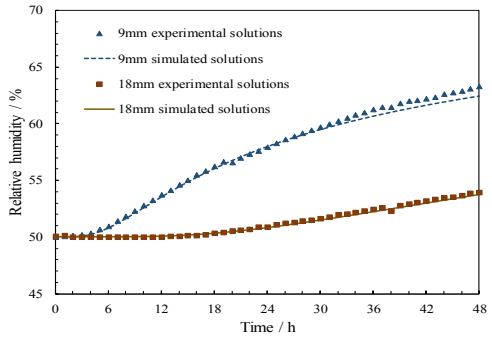

Figure 2: Simulated and experimental result

Fig. 1 is a diagram of the device designed for the experiment using spruce plywood. The spruce plywood had dimensions of 600×280×27 mm (Length × Width × Thickness). The initial temperature was 23 °C, and the initial *RH* was 50%. The upper side boundary conditions of the spruce plywood were kept at 23.1 °C and the *RH* at 85%. The lower side boundary of the spruce plywood was the approximate insulation interface.

The program was run according to the above mentioned physical parameters, initial conditions and boundary conditions, and the relative humidity distribution at each interface over 48 hours was obtained. The relative humidity simulation results were compared with experimental results at thicknesses of 9 mm and 18 mm; the results are shown in Fig. 2. The comparison between the experimental and simulated data further proved the accuracy of the model and the program.

3. METHODOLOGY

3.1. Outdoor and Indoor Boundary Conditions

Climatic divisions for building design divide China into the following five zones. In this paper, Nanjing is taken as the representative city of the HSCW zone. Its annual mean temperature is 15.4 °C, the mean temperature of the hottest month in a year is 27.8 °C, and the mean temperature of the coldest month is 2.4 °C.

Spring is from March 24th to May 25th; summer is from May 26th to September 18th; autumn is from September 19th to November 20th; and winter is from November 20th to March 23rd. The subsequent seasonal analysis in this paper is based on such a seasonal division standard.

Meteorological data for a typical meteorological year in Nanjing, including temperature, *RH* and solar radiation, are shown in Fig. 3, which are used as the outdoor boundary conditions. A wall has four orientations; thus, the hourly value of solar radiation is converted to magnitudes along four directions. Fig. 3 (b) shows the daily total solar radiation in Nanjing. For many occasions, indoor environments with constant temperature and *RH* must be maintained, such as in a laboratory, precision instrument production workshop, and hospital ward. In this paper, constant temperature and *RH* were

adopted as indoor boundary conditions. The temperature was held at 22 °C, and *RH* was held at 60%.

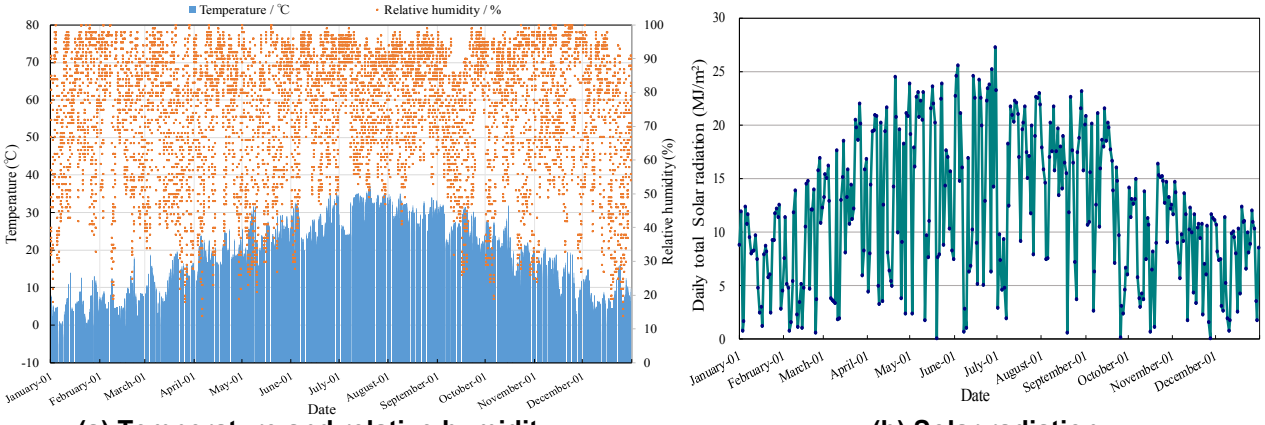

(a) Temperature and relative humidity **(b) Solar radiation**

Figure 3: Typical meteorological data of Nanjing

3.2. Numerical Simulations

All building materials considered in this paper are commonly used in Nanjing. EPS is taken as an example of the thermal insulation layer material. The base materials are clay brick and concrete. Cement mortar is used on both sides of the wall. The wall model in this paper is shown in Fig. 4.

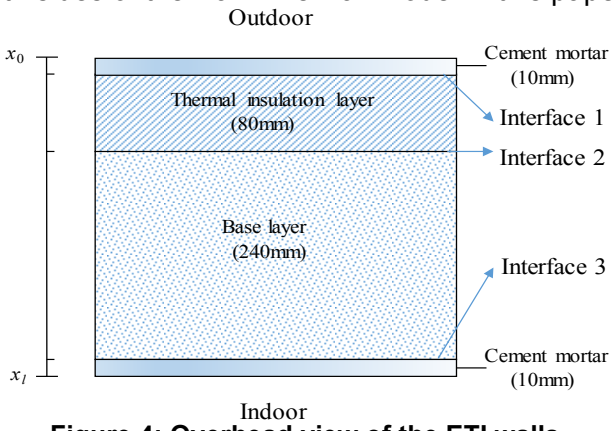

Figure 4: Overhead view of the ETI walls

The thicknesses of the base layer, insulation layer, cement mortar and air layer are 240 mm, 80 mm, 10 mm, 15 mm, respectively. It is assumed that the interface of different materials is thin such that there is no contact thermal resistance or moisture resistance.

The three interfaces in Fig. 5 are the locations of the air layer. Generally, the locations of the air layer are usually divided into the outer side of the wall (Interface 1), the interior side of the wall (Interface 3) and the interface between the base layer and the thermal insulation layer (Interface 2).

To explore the effect of air layers at different interfaces, 4 types of envelope structures with air layers at 3 different interfaces or without an air layer were simulated for a period of 5 years.

4. RESULTS AND ANALYSIS

4.1. Condensation Characteristics

According to numerical simulations, the *RH* distribution of ETI walls with different air layer arrangements can be generated. Fig. 5 is the result of ETI walls without an air layer considering or not considering solar radiation. Figs. 6, 7 and 8 are the results of insulation walls with air layer at Interface 3, 2 and 1, respectively. The transverse coordinate is the time axis, from left to right, which represent the time scale of 5 years; the longitudinal coordinate is the spatial axis, from up to down, which represents the distance from the external surface of the wall. The three dotted lines in each figure represent the interface between different layers. Figs. 9, 10 and 11 show the distribution of average r

elative humidity in the insulation wall with an air layer at three interfaces during the four seasons of the whole year.

It can be seen from Fig. 5 that in summer, there is a serious moisture accumulation phenomenon a t Interfaces 1 and 2, which leads to the high humidity environment and even the phenomenon of de w in the insulation layer. Under this condition, the relative humidity of the thermal insulation layer is much higher than that of the base layer. While the *RH* of the base layer varies slightly, and it is basi cally in the initial state. In winter, there will be a slight moisture accumulation phenomenon at Interf ace 3, and the relative humidity at Interface 3 is higher than that in other places.

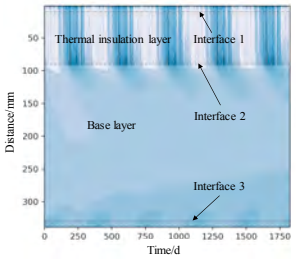

(a) With solar radiation

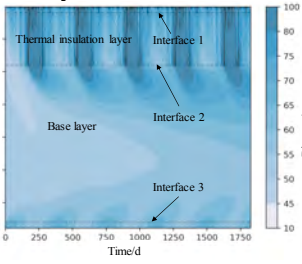

(b) Without solar radiation

Figure 5: Insulation walls without air layer

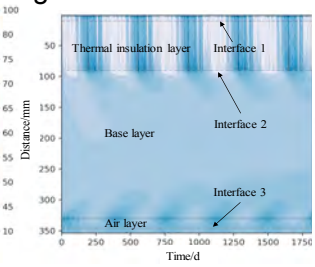

(a) With solar radiation

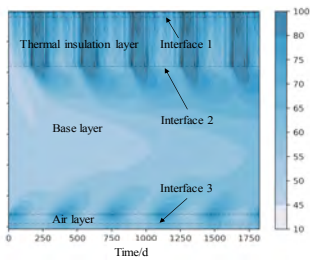

(b) Without solar radiation

Figure 6: Insulation walls with air layer at Interface 3

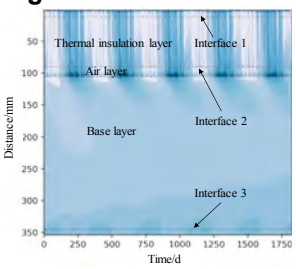

(a) With solar radiation

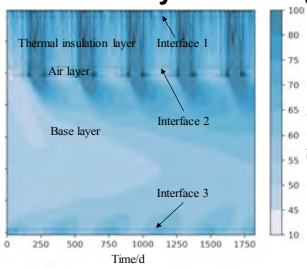

(b) Without solar radiation

Figure 7: Insulation walls with air layer at Interface 2

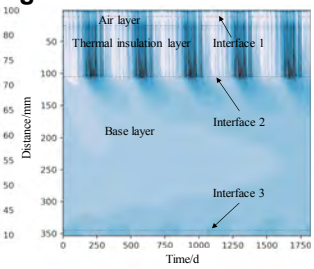

(a) With solar radiation

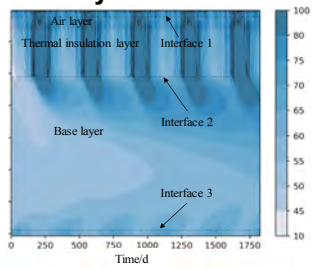

(b) Without solar radiation

Figure 8: Insulation walls with air layer at Interfa ce 1

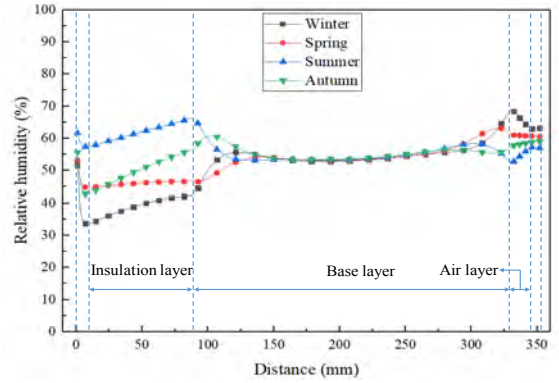

Figure 9: *RH* distribution (air layer at Interface 3)

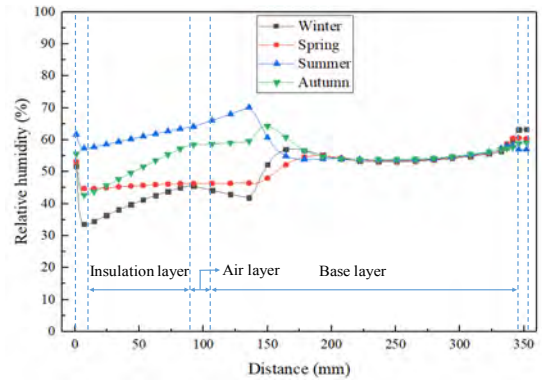

Figure 10: *RH* distribution (air layer at Interface 2)

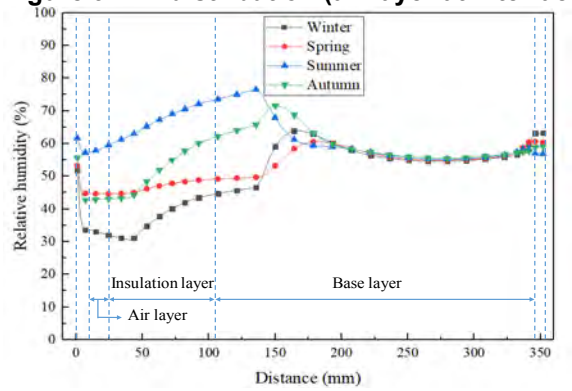

Figure 11: *RH* distribution (air layer at Interface 1)

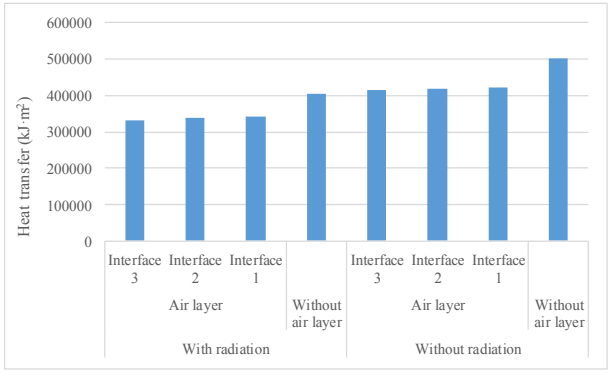

Figure 12: Heat transfer of the unit area in five years

According to Fig. 5, there is a serious moisture accumulation phenomenon at Interfaces 1 and 2 in summer, which leads to the high humidity environment and even the phenomenon of dew in the ins ulation layer. Under this condition, the relative humidity of the thermal insulation layer is much high er than that of the base layer. While the relative humidity of the base layer varies slightly, and it is b

asically in the initial state. In winter, there will be a slight moisture accumulation phenomenon at Int erface 3, and the relative humidity at Interface 3 is higher than that in other places.
Comparing with Figs. 5, 6, 7 and 8, it can be found that only the condensation phenomenon in Fig. 6 has almost no change compared with that in Fig. 5. The condensation of the insulation layers in F igs. 7 and 8 is more serious than that in Fig. 5. This shows that from the point of view of condensati on and moisture transfer, setting the air layer at Interface 3 is the best. This can also be found by c omparing Figs. 9, 10 and 11.
According to Figs. 9, 10 and 11, the relative humidity of insulation layer is the highest in summer, fo llowed by autumn, followed by spring and the lowest in winter. While the situation of the indoor side of the insulation wall (Interface 3) is completely opposite. For the majority of the base layer, the dis tribution of relative humidity keeps stable and unchangeable in the four seasons. The most serious condensation condition is to set the air layer at Interface 1 according to Figs.8 and 11, followed by setting the air layer at Interface 2 (Figs. 7 and 10), and the least serious is to set the air layer at Inte rface 3 (Figs. 6 and 9).
Above all, from the point of view of relative humidity distribution, it is the best to set an air layer at I nterface 3 of the external thermal insulation wall, and the average relative humidity is the lowest.

4.2. Heat Transfer Characteristics

According to the simulated hourly temperature distribution of the wall, the hourly quantity of the hea t transfer between the interior and the internal wall surface can be calculated using Eq. 17.

$$q_{in} = h_{in}\left(T_{surf,in} - T_{\infty,in}\right) + LJ_{v,in} \qquad \text{Eq. (17)}$$

Accumulating the hourly quantity of the heat transfer between the interior and internal wall surface of the unit area in five years, the results can be obtained as shown in Fig.12. It is obvious that when solar radiation is considered, the heat transfer of the wall is smaller than that without solar radiatio n. This is because solar radiation relieves the condensation phenomenon of the ETI walls. Accordin g to the results of heat transfer calculation, the heat transfer load of the envelope is the smallest wh en the air layer is set at Interface 3.

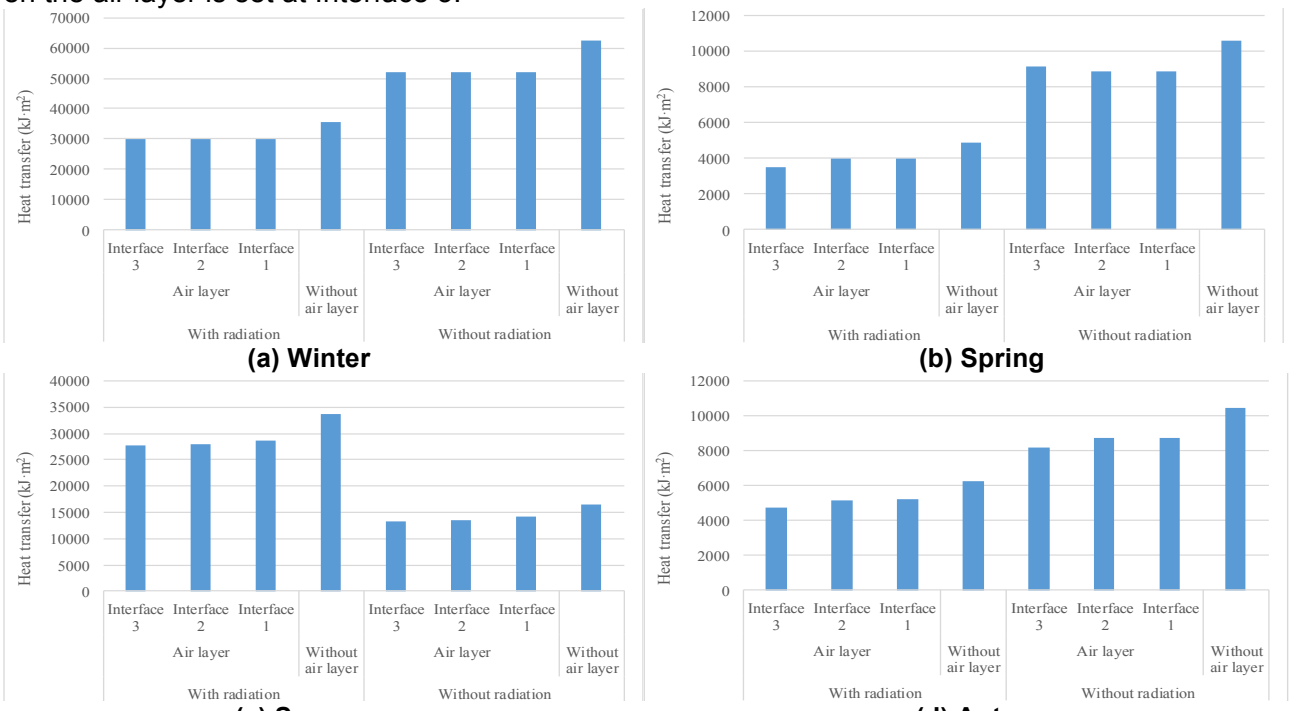

Figure 13: Heat transfer in the four seasons in the fifth year

In order to further analyze the heat transfer characteristics of the ETI wall, the results of the four se asons in the fifth year are summarized in Fig. 13. From Fig. 13, in addition to summer, when the sol ar radiation is not considered, the heat transfer of the wall is greater than that with solar radiation, w hich indicates that in summer, the solar radiation is not conducive to weakening the heat transfer th rough the wall and reducing the cooling load of the building. Therefore, building shading measures are needed in summer. In other seasons, building shading measures can be considered to be remo

ved. As can be seen from Table. 1, when the solar radiation is considered, the heat transfer per uni t area of the wall will decrease by 18.17% annually when the air layer is set at Interface 3. Interface 2 decreased by 16.72% while Interface 1 decreased by 15.69%. When solar radiation is not consid ered, it is the same trend.

Table. 1 Heat transfer in the fifth year

Conditions	Envelope arrangement	The quantity of heat transfer $kJ \cdot m^{-2}$
With solar radiation	Air layer (Interface 3)	65844.81
	Air layer (Interface 2)	67014.69
	Air layer (Interface 1)	67843.66
	Without an air layer	80466.83
Without solar radiation	Air layer (Interface 3)	82744.17
	Air layer (Interface 2)	83126.94
	Air layer (Interface 1)	83775.57
	Without an air layer	99850.14

Therefore, setting the air layer at Interface 3 can reduce the heat transfer load of the envelope mos t. The second is at Interface 2, and the least is at Interface 1, which corresponds to the condensatio n characteristics. The more serious the condensation is, the greater the heat transfer will be.

5. CONCLUSIONS

This paper focuses on the condensation and heat transfer load of building envelopes that contain in sulation layers and air layers. According to numerical simulations and analysis, the condensation a nd heat transfer characteristics of ETI walls are closely related and show a consistent conclusion.
(1) The condensation characteristics of the wall are related to its structural characteristics. The con densation characteristics of walls with different insulation arrangement configurations are different. When the air layer is set at Interface 3, the condensation is the least. It is the best to set an air laye r at Interface 3 of the ETI wall in Nanjing, and the average relative humidity is the lowest.
(2) From the perspective of the heat transfer considering the moisture transfer, setting the air layer at Interface 3 can reduce the heat transfer load the most. The second is at Interface 2, and the leas t is at Interface 1, which corresponds to the condensation characteristics of them. The more serious the condensation is, the greater the heat transfer will be. Therefore, it is recommended to set the a ir layer on the interior side of the wall (Interface 3) in Nanjing.
(3) From the perspective of the transmission load through the envelope of buildings, it is necessary to adopt shading measures in Nanjing in summer, but shading measures will increase the air-cond itioning load in spring, autumn and winter, which is not conducive to building energy saving.

ACKNOWLEDGEMENTS

The authors would like to acknowledge the 13th Five-Year National Science and Technology Supp ort Key Project of China (No. 2017YFC0702501-3) and the 12th Five-Year National Science and T echnology Support Key Project of China (NO. 2014BAJ01B05-2) for their financial support.

NOMENCLATURE

ρ	Density of materials ($kg \cdot m^{-3}$)	D_v	Penetration coefficient of water vapour ($kg \cdot Pa^{-1} \cdot m^{-1} \cdot s^{-1}$)
u	Balanced moisture content of materials ($kg \cdot kg^{-1}$)	D_l	Penetration coefficient of liquid water ($kg \cdot Pa^{-1} \cdot m^{-1} \cdot s^{-1}$)
J_v	Diffusion flux of water vapour ($kg \cdot m^{-2} \cdot s^{-1}$)	P_l	Capillary pressure of liquid water (Pa)
J_l	Diffusion flux of liquid water ($kg \cdot m^{-2} \cdot s^{-1}$)	$P_{v,s}$	Partial pressure of saturated vapour (Pa)
ξ	Slope of moisture absorption and liberation curve of materials	R_v	Gas constant of water vapour ($J \cdot kg^{-1} \cdot K^{-1}$)
φ	Relative humidity (%)	c	Specific heat capacity of materials ($J \cdot kg^{-1} \cdot K^{-1}$)

λ	Thermal conductivity of materials ($W \cdot m^{-1} \cdot K^{-1}$)	h	Heat transfer coefficient of wall surface ($W \cdot m^{-2} \cdot K^{-1}$)
s	Heat source term ($J \cdot m^{-2} \cdot s^{-1}$)	h_m	Mass transfer coefficient of water vapour ($m \cdot s^{-1}$)
L	Latent heat of water vapour ($J \cdot kg^{-1}$)	EPS	Expanded polystyrene

REFERENCES

Umberto B., 2017. A cross-country comparison of the building energy consumptions and their trend s. Resour. Conserv. Recycl. 123, 230-241.

Liu X., Chen Y., et al, 2015. Determination of optimum insulation thickness for building walls with m oisture transfer in hot summer and cold winter zone of China. Energy Build. 109(4), 361-368.

Cho B., Park D., Kim J., et al, 2017. Study on the heat-moisture transfer in concrete under real envi ronment. Construction & Building Materials 132, 124-129.

Wang J., Yan P., 2004. Influence of external thermal insulation compound system on the indoor te mperature and humidity. Low Temper Arch Technol 2, 80-81.

Chowdhury A., et al, 2008. Thermal-comfort analysis and simulation for various low-energy cooling -technologies applied to an office building in a subtropical climate. Appl Energy 85(6), 449-62 .

Kazim AM., 2007. Assessments of primary energy consumption and its environmental consequenc es in the United Arab Emirates. Renew Sustain Energy Rev 11(3), 426-46.

You S., Li W., Ye T., et al, 2017. Study on moisture condensation on the interior surface of building s in high humidity climate. Build. Environ. 125, 39-48.

Lihua Z., Zhongcheng D., et al, 2001. Study on moisture transfer of external thermal insulation wall. Journal of Harbin University of civil engineering and architecture 34(6), 78-81.

Yilin Li, Jo Darkwa, Georgios Kokogiannakis, 2017. Heat transfer analysis of an integrated double s kin façade and phase change material blind system. Build. Environ. 125, 111-121.

Saadatian O., Sopian K., Lim CH., et al, 2012. Trombe walls: a review of opportunities and challen ges in research and development. Renew Sustain Energy Rev. 16(8), 6340–51.

Krueger E., Suzuki E., Matoski A., 2013. Evaluation of a Trombe wall system in a subtropical locati on. Energy Build. 66(6), 364-72.

Zamora B., Kaiser AS., 2009. Thermal and dynamic optimization of the convective flow in Trombe Wall shaped channels by numerical investigation. Heat Mass Transf. 45(11), 1393-407.

Moon H. J., Ryu S. H., Kim J. T., 2014. The effect of moisture transportation on energy efficiency a nd IAQ in residential buildings. Energy Build. 75(2), 439–446.

Mendes N., F.C. Winkelmann, R. Lamberts, P.C. Philippi, 2003. Moisture effects on conduction loa ds. Energy Build. 35, 631–644.

J. Zhou, G. Zhang, Y. Lin, Y. Li, 2008. Coupling of thermal mass and natural ventilation in buildings . Energy Build. 40, 979-986.

W.Z. Gao, J.H. Liu, Y.P. Cheng, et al, 2012. Experimental investigation on the heat and mass trans fer between air and liquid desiccant in a cross-flow dehumidifier. Renew. Energy 37, 117-123 .

Mendes N., Philippi P., et al, 2002. A new mathematical method to solve highly coupled equations of heat and mass transfer in porous media. Int. Journal of Heat & Mass Transfer 45(3), 509-5 18.

Zhao R., Fan C., Xue D., et al, 2009. Air conditioning. China Construction Industry Press, Beijing.

Richards R. F., Burch D. M., Thomas W. C., 2014. Water vapor sorption measurements of common building materials. ASHRAE Transactions.

Fanney A. H., Thomas W. C., Burch D. M., et al, 1991. Measurements of Moisture Diffusion in Building Materials. ASHRAE Transactions 97(2), 99-113.

Li Kuishan, Zhang Xu, Han Xing, et al, 2009. Experimental study on water vapor permeability coefficient of building materials. Journal of Building Materials 12(3), 288-291.

Talukdar P, Olutmayin S O, et al, 2007. An experimental data set for benchmarking 1-D, transient heat and moisture transfer models of hygroscopic building materials. Part I: Experimental facility and material property data. Int. Journal of Heat & Mass Transfer 50(23), 4527-4539.

Prabal Talukdar, Olalekan F. et al, 2007. An experimental data set for benchmarking 1-D, transient heat and moisture transfer models of hygroscopic building materials. Part II: Experimental, numerical and analytical data. International Journal of Heat and Mass Transfer 50(23), 4915-4926.

PAPER ID: 1532
DOI: 10.18462/iir.icr.2019.1532

N_2O/CO_2-Mixtures as Refrigerants for Temperatures below -50 °C

Michael KAUFFELD, Timo MAURATH

Karlsruhe University of Applied Sciences
Karlsruhe, 76133, Germany, michael.kauffeld@hs-karlsruhe.de

ABSTRACT

The EU F-Gas Regulation grants exceptions from the GWP-related placing on the market prohibition for stationary refrigeration equipment for applications below -50 °C. Nonetheless, non-flammable refrigerants which can be used for that temperature range become increasingly expensive and rare inside the EU due to the phase down of HFCs under the regulation. Flammable alternatives based on Methane and Ethane are available, but are not viable for all applications due to their flammability. Carbon Dioxide cannot be used for applications below -50 °C due to CO_2's triple point at -56 °C. Nitrous Oxide with a triple point at -92 °C seems to be an alternative. But possible exothermal decomposition of N_2O calls for additional measures to be able to operate such systems safely.

A freeze dryer has been developed, built and successfully operated at evaporation temperatures down to -80 °C with mixtures of N_2O and CO_2 and different lubricants. The unit achieved similar energy efficiency as the standard HFC-equipment. Possible decomposition of N_2O could successfully be supressed by various measures.

CAUTION: Pure N_2O as well as mixtures of N_2O and CO_2 with hydrocarbon based lubricants can result in serious decomposition reactions increasing the pressure inside a refrigeration system approximately eightfold.

Keywords: Carbon Dioxide, Freeze-Dryer, low temperature, Nitrous Oxide, safety measures

1. INTRODUCTION

Climate change and the decarbonisation of the energy sector through the substitution of fossil fuels with renewable energy sources continues to be a central issue for mankind. The expansion of technologies for the use and storage of renewable energies is another aspect. In addition, however, the efficiency of all conversion chains from primary to useful energy must be increased. In the area of refrigeration and air conditioning, the substitution of potent greenhouse gas refrigerants with low-GWP or natural refrigerants can also reduce the global warming impact of RAC systems and consequently is also being promoted. Within the F-Gas Regulation (EU 517/2014), the European Union defines the reduction scheme of available refrigerant quantities in relation to their global warming potential (GWP), also known as "HFC phase-down". By the year 2030, the phase-down should result in savings of 79 % in greenhouse gas emissions from refrigerants.

Most low-GWP refrigerants are flammable (e.g. propane, R290) or toxic (e.g. ammonia, R717). These refrigerants are therefore subject to special requirements for operation. Cost-driving safety devices (explosion-protected components) must be installed and systems subjected to intensive monitoring and testing depending on the refrigerant charge.

The intended field of application in this project is cryogenic refrigeration at temperatures below -50 °C. Currently, the fluorinated refrigerants R23, R116 and the azeotrope of both (R508) as well as R14 are used for such applications. These chlorine-free, fluorinated refrigerants have a high direct contribution to the greenhouse effect, mainly due to their long average atmospheric lifetime. In addition to the direct greenhouse potential caused by leaks and disposal, it is also essential to consider the indirect effects in operation (efficiency, electricity consumption) and operational safety.

Efficient operation can only be achieved by refrigerants with comparably good thermodynamic properties, which include high volumetric cooling capacity, suitable vapour pressure curve and large evaporation enthalpy.

The material properties of various refrigerants prevent them from being used at low temperatures. Ammonia (R717) evaporates at atmospheric pressure (p = 1.013 bar) already at -33 °C. A lower evaporation or application temperature leads to a reduction in the working pressure, such that the plant is operated below atmospheric pressure. On the one hand, this is difficult or impossible to implement in terms of process technology and, on the other hand, there is an acute risk of air and moisture entering the system. As a result, the efficiency of the system decreases considerably and additional measures for periodic air/water discharge are required. In addition, the triple point temperature of -77.9 °C of Ammonia sets a limit for its use in low temperature applications.

Natural refrigerants can be used with evaporation temperatures below -50 °C, e. g. the flammable substances ethane (R170) and Ethene (R1150) with a normal boiling point temperature of -89 °C and -103.72 °C, respectively. Carbon dioxide, which is already widely used as a refrigerant in stationary applications, is almost climate-neutral and has a very good volumetric refrigerating capacity, so that the system components can be dimensioned small. However, the limitation here is given by its relatively high triple point of -56.6 °C. Nitrous oxide (N_2O), also known as laughing gas, is an alternative that has received little attention to date.

2. N_2O/CO_2-MIXTURES AND INFLUENCE OF LUBRICATING OIL

2.1. N_2O – Nitrous Oxide

The refrigerant designation for N_2O is R744A, as it has a molecular weight of 44 g mol^{-1}, which happens to be the same molecular weight as CO_2 (R744). The normal boiling point of R744A is -88.5 °C and the triple point is reached at a pressure of 0.8784 bar at -90.8 °C, which is why evaporation temperatures of -88 °C can be achieved permanently. Table 1 gives an overview of the extent of the greenhouse potential over a period of 100 years (GWP_{CO2} = 1).

Table 1. GWP of various low temperature refrigerants

	R14	R23	R116	R508	R744A
GWP_{100}	5 700	14 800	12 200	12 300	298

It can be seen that nitrous oxide (R744A) has a clear savings potential. In contrast to the conventionally used Trifluoromethane (R23), the GWP can be reduced by 98 %.

It has to be mentioned though that N_2O has a slight ozone depletion potential of currently approximately 0.017. The vast majority of human related N_2O emissions stems from farming and there are countless natural N_2O-emission sources as well. Similar to the early discussions on reviving CO_2 as refrigerant, where one of the arguments was that CO_2 is the greenhouse gas number one, additional emissions from low temperature systems will be negligible. First of all because there are relatively few such systems and secondly because those systems are very tight. Continued use of R23 and the other fluorinated refrigerants shown in Table 1 will not work in the EU due to the HFC phase down. R23 prices are already now more than twenty times higher than prior to the 63 % reduction scheme of the EU F-Gas regulation phase down.

N_2O has a suitable pressure curve similar to CO_2 (Fig. 1). Previous investigations have shown that N_2O also has similar values to the common refrigerant R23 in terms of efficiency and coefficient of performance. However, these results have so far only been based on theoretical findings and basic investigations. A statement on the practical application under static as well as dynamic loads was still pending. Experimental tests and the construction of a first test carrier on the scale of an industrial freeze drying plant are the first steps towards introduction into the refrigerant market.

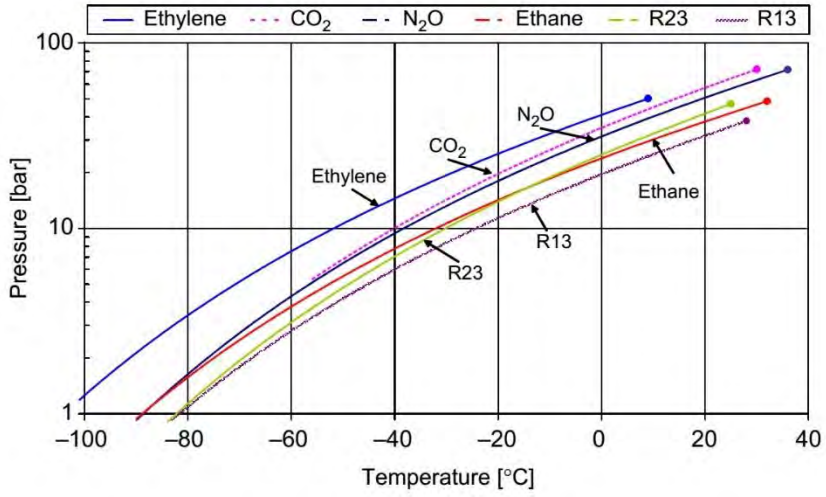

Figure 1: Vapour Pressure curve of various refrigerants for low temperature applications (Kruse and Rüssmann, 2006).

Looking at the safety data sheet for N_2O (Linde, 2011), it can be seen that N_2O is neither toxic nor flammable under normal conditions, but acts as an oxidiser and hence “May cause or intensify fire”. It should also be noted that N_2O decomposes irreversibly and exothermically into nitrogen and oxygen at atmospheric pressure at a temperature of 575 °C (Linde, 2011). Under pressure N_2O can decompose at temperatures above 300 °C (Linde, 2011). The decomposition is promoted by catalysts such as nickel, gold or platinum (Linde, 2011). Also warnings are given against possible violent reactions with reducing agents and combustible materials (Linde, 2011). This information in itself does not yet prevent the use of N_2O as a refrigerant, as the temperatures and materials mentioned above do not actually occur in a refrigeration system or contact of the refrigerant with organic substances can be avoided.

However, in-depth research into the decomposability of N_2O showed that the use of pure N_2O in a refrigeration system is not easily possible from a safety point of view. Investigations in various ignition autoclaves of the Federal Institute for Materials Research and Testing (BAM) showed that N_2O decomposes exothermically even at low temperatures of 50 °C and a pressure of 15 bar after ignition by a wire igniter with an ignition energy of 55 J and can lead to a pressure rise to more than 10 times the initial pressure, Fig. 2 (Gula, 2010).

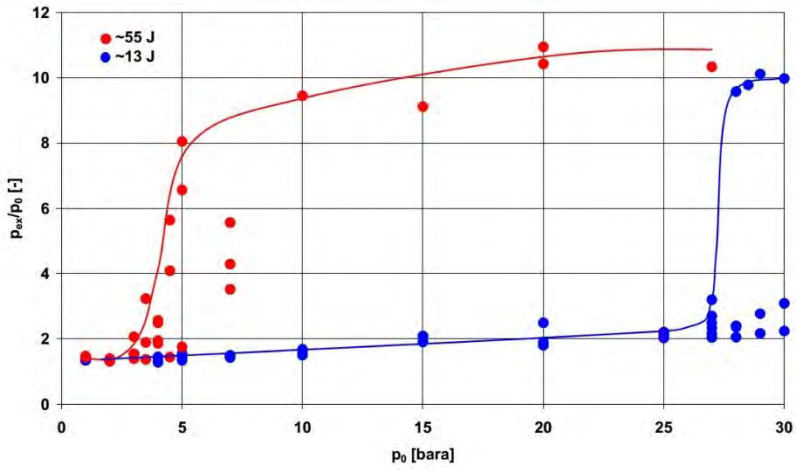

Figure 2: Explosion pressure ratio for N_2O decay as a function of the initial pressure for different ignition energies. 6.5 l autoclave, fuse in the middle, t_0 = 50 °C (Gula, 2010).

EIGA (European Industrial Gases Association), (2013) also describes the danger and provides instructions for safe handling of N_2O. Therefore, the use of **pure** N_2O as refrigerant is not recommended as a consequence of these results and the associated safety requirements.

2.2. N_2O/CO_2 Mixtures

Further investigations by BAM suggest that decomposition can be phlegmatized by adding other gases. In addition to nitrogen, oxygen and air, explosive decomposition can also be prevented by adding CO_2. Since CO_2 itself is established as a refrigerant and has a vapour pressure curve almost identical to N_2O (see Fig. 1), it can be used as an admixture. Due to its higher specific heat capacity, CO_2 is also the more suitable inert gas than, for example, nitrogen. Gula (2010) investigated the stability limit pressures of N_2O/CO_2 mixtures for vessel and hence gas temperatures of 25 °C and 200 °C (Fig. 3). It can be concluded from the diagram that the N_2O/CO_2 mixture remains stable even at a temperature of 200 °C if the CO_2 concentration is higher than 20 mol-% - even at a pressure of over 30 bar.

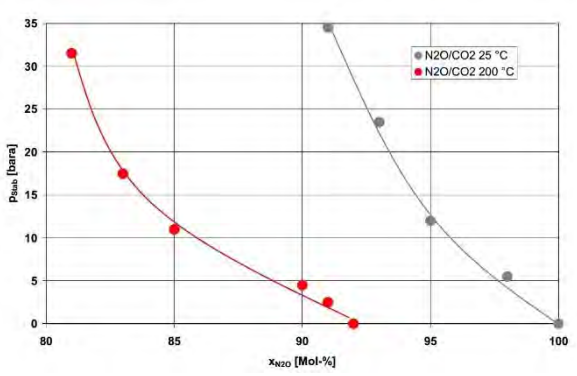

Figure 3: Stability limit pressure of N_2O/CO_2 mixtures as a function of the initial pressure at 25 °C or 200 °C vessel temperature, respectively, in 6.5 l autoclave, ignition source ~13 J (Gula, 2010).

However, the addition of CO_2 has an influence on the triple point. Pure N_2O has a normal boiling point of -88.5 °C and solidifies at -90.81 °C (Linde, 2011). Freeze drying, the topic of the research project connected with the investigations outlaid in this paper, is one of many applications where temperatures in the range of -80 °C are required and for which there is currently no safe alternative to HFC refrigerants. The addition of CO_2 reduces the triple (Fig. 4) and normal boiling point of the mixture and thus has a direct influence on the lowest possible evaporation temperature. At CO_2 concentrations of about 30 mol-%, the melting point of the N_2O/CO_2 mixture is about -78 °C, which was experimentally proven in the work of Di Nicola et. al. (2010). For the operation of the pilot plant described below, this means a maximum possible evaporation temperature of -75 °C, which is just sufficient for the freeze-drying process, Fig. 4.

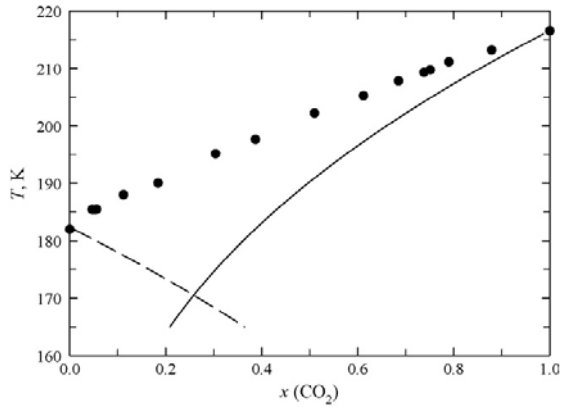

Figure 4: Solid–liquid equilibrium for a CO_2/N_2O mixture. Dots denote the experimental points while the lines refer to calculations using Raoult's law with the solute's activity coefficient set to 1 (Di Nicola et al., 2007).

2.3. Influence of Lubricating Oil on Exothermal Decomposition

In addition to the refrigerant or the refrigerant mixture, there is also lubricating oil in the circuit of a vapour compression refrigeration system, which is absolutely necessary for the lubrication of the compressor. In the tests at Karlsruhe University of Applied Sciences, initially a polyolester-based refrigeration machine oil was used for this purpose, as this is still sufficiently viscous at very low temperatures. Polyolesters are esterified alcohols with several hydroxyl groups and thus on an organic basis. As a rule, the refrigerating machine oil remains in the compressor or is transported back to the compressor by a suitable oil return system. As already mentioned above, organic substances promote the decomposition ability of N_2O (Linde, 2011). This gives rise to the justified suspicion that the presence of the polyolester oil used can have a negative effect on the decomposition behaviour of N_2O. Studies on the influence of oil on decomposition of N_2O/CO_2 mixtures cannot be found in the relevant literature. Experiments at BAM (Bundesanstalt für Materialforschung und –prüfung) in the scope of our project with the addition of propane, also an organic substance based on hydrocarbons, have shown that even small proportions in the order of 2-3 % propane lead to a significant reduction of the stability limit and exothermic decomposition is much more severe than without the addition of propane.

The polyolester-based oil is present in the refrigeration system as a pure liquid and is very well miscible with the N_2O/CO_2 mixture, as investigations at our industrial lubricant partner revealed. The centrifugal lubrication in the compressor distributes the refrigerating machine oil into very fine droplets, which can then contribute to possible decomposition. For this reason, BAM was commissioned to carry out appropriate ignition tests in which the refrigeration oil used was sprayed into an N_2O/CO_2 mixture with a pre-pressure of 15 bar to 50 bar using a commercially available fuel oil burner nozzle and an attempt was made to ignite the N_2O/CO_2/oil mixture at initial pressures of 1 bar, 10 bar and 25 bar with a fusible wire. The setup of this test facility is shown in Fig. 5.

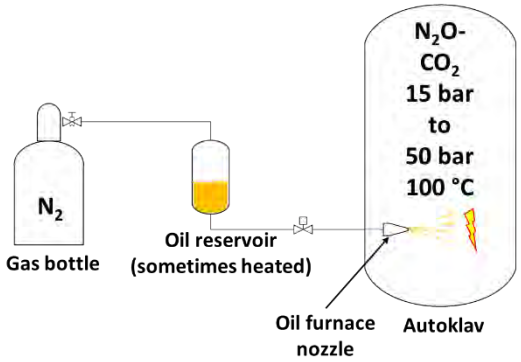

Figure 5: Test setup for N_2O/CO_2/oil mixture decomposition testing at BAM with starting pressures of 15 to 50 bar and initial temperatures of the N_2O vessel of 100 °C.

In the gas mixture of 70 mol-% nitrous oxide and 30 mol-% carbon dioxide, no explosion was observed in any of the ignition tests with oil mist. Only when the N_2O content was increased to 85 mol-% was ignition observed with a slight increase in pressure. Furthermore, explosions with lower explosion pressure ratios could also be observed without oil mist, if the ignition energy was increased far above the standard ignition energy of 10 J to 20 J.

It should be noted that the explosiveness of gas mixtures in the presence of fog depends very much on the type of fogging, especially on the droplet size and droplet size distribution. These parameters could not be specifically varied in these experiments. Therefore, it cannot be excluded that mixtures of 70 mol-% nitrous oxide and 30 mol-% carbon dioxide are explosive in the presence of an oil mist with a different type of misting. Polyolester oils are hydrocarbons and therefore can increase the reactivity of exothermal decomposition of N_2O.

Parallel investigations on the material compatibility, stability and miscibility of the Polyolester refrigerant-oil mixture were carried out by Fuchs Schmierstoffe GmbH, also a project partner in the

research project presented here. Various components such as bearing shells, part of the cylinder head and sealing materials used in the refrigeration system or in the refrigerant compressor were brought into contact with the refrigerant for 14 days at 120 °C and then analysed for possible material incompatibilities. As can be concluded from the data given in Fig. 6, no significant reaction between the refrigerant-oil mixture and the system components investigated can be detected under the tested conditions.

Test Parameters:

Temperature:	120°C
Time:	14 days
Refrigeration Oil:	~100 g Reniso Triton SEZ 32 water content: 59 ppm
Refrigerant:	~100g N2O
Compressor Parts:	valve plate
	bearing bushing
	tarnish ring and
	cylinder head



No loss of mass – no color change

Oil / Samples	TAN [mg KOH/g]:	Liquid	Material Samples
Before test:	0,01		
After test:	0,03	clear / unchanged / no deposits	unchanged

Weight of samples [g]	Valve plate	bearing bushing	tarnish ring and	cylinder head
Before test:	36,467	1,781	23,389	108,767
After test:	36,471	1,788	23,399	108,772
Change [%]	0,01	0,39	0,04	0,00

Figure 6: Sealed-tube-test Polyolester oil and compressor parts in N_2O atmosphere.

3. TEST PLANT

On the basis of the described knowledge, a safety assessment was carried out by the project partners involved and the pilot plant was set up by one of the partners (Martin Christ Gefriertrocknungsanlagen GmbH, Osterode, Germany). For photo of the plant see Fig. 7. In order to avoid too high standstill pressures, a 160-litre expansion vessel is connected to the suction side of the compressor, which provides the necessary volume, such that the refrigerant mixture is only present in the gaseous state during standstill. Due to the low evaporation temperature of down to -80 °C, the refrigeration system is designed as a cascade. A standard R404A system was used as upper stage of the cascade system. Corresponding lower GWP replacement refrigerants now being available on the market, R404A is planned to be replaced in future systems to be built commercially.

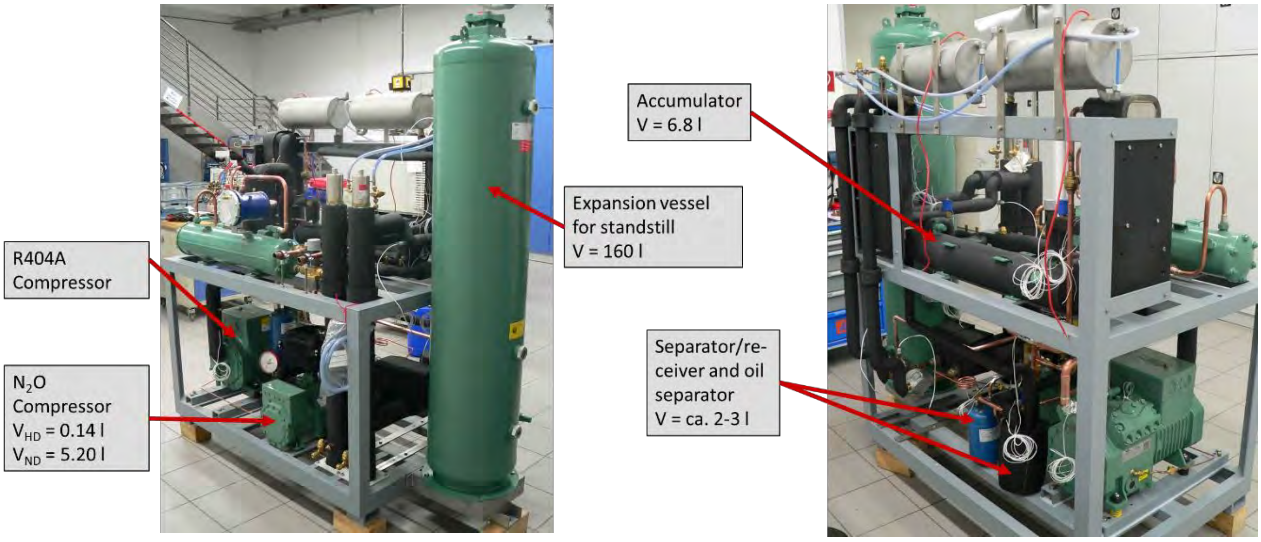

Figure 7: Test freeze drying test plant.

The lower stage plant, i.e. N_2O/CO_2 system, is equipped with two electronic expansion valves, which enable to set the ice condenser temperature and the shelf temperature independently of each other. As in commercial systems, the evaporating refrigerant cools two silicone oil circuits to the target temperature via one plate heat exchanger each. Different from commercial systems, no products were dried in the test series carried out, but the heat load was brought in by two independently adjustable heating elements.

In the test series, the evaporation temperature at the ice condenser was kept constant at -75 °C and the shelf temperature was slowly increased from -50 °C to 20 °C, which corresponds to the normal freeze-drying process. The system ran for over 550 operating hours without failure. After approx. 150 operating hours, the refrigerating machine oil (polyolester) and the gas composition were analysed and no signs of decomposition of N_2O could be detected.

4. TEST RESULTS

In summary, the tests were carried out under the following conditions:

- N_2O/CO_2 refrigerant mixture with 70 wt.-% N_2O and 30 wt.% CO_2[1]
- over 550 operating hours with refrigerating machine oil on polyolester oil
- experiments in stationary condition
- variation of product shelf temperature from -50 °C to +20 °C
- constant thermal load
- ice condenser temperature of -60 °C
- evaporation temperature of -75 °C

Fig. 8 shows the evaporation temperatures which were calculated using Refprop 9.0 from pressure measurements in the plate heat exchanger of the silicon circuit for the ice condenser (red Δ, T_0-IC) and the evaporation temperatures (calculated from pressure measurements) in the plate heat exchanger cooling the silicon oil of the shelfs (blue x, T_0-Sh) over the silicon oil temperature of the shelf temperature. The diagram also shows the temperature of the silicone oil circuit of the ice condenser (green ◇, IC T23).

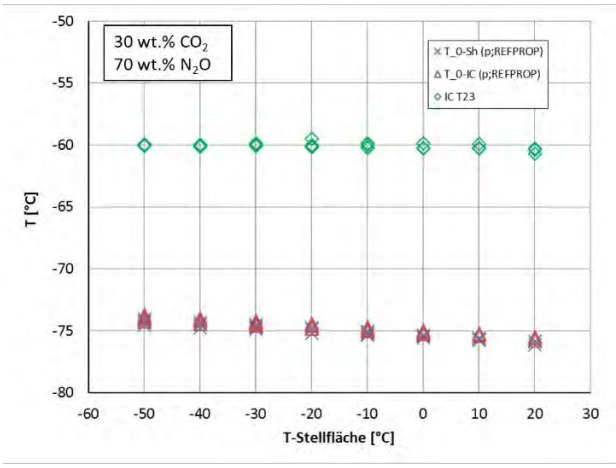

Figure 8: Temperatures measured during test runs. Explanation see text above.

The measuring points displayed in Fig. 8 are mean values from several measurement series. The actual controlled variable is the surface temperature, which is plotted on the x-axis. The deviation

[1] Due to the fact that N_2O and CO_2 have the same molecular mass (44.01 g/mol), wt.% and mol.% are identical.

between set point and actual value was less than 0.05 K for all tests. In addition, the reproducibility of the results was very good. The mean values from 5 measurement series are plotted in Fig. 8.. Since all tests gave the same results, it was concluded that no change in refrigerant composition occurred over the 550 operating hours. This was also confirmed by an oil and refrigerant analysis after the 550 operating hours.

5. CONCLUSIONS

In summary, the following results could be achieved so far:

- the thermodynamic suitability of a N_2O/CO_2 refrigerant mixture has been demonstrated
- no negative influence on materials in the refrigeration circuit was observed so far
- the influence of polyolester refrigerating machine oil on possible decomposition ability of N_2O and the phlegmatizing effect of CO_2 could be demonstrated by the tests at BAM
- for higher evaporation temperatures, the CO_2 content can be increased, which in turn leads to lower GWP and ODP as well as increased protection against exothermal decomposition.

Based on these positive results, it appears that a non-flammable and non-toxic alternative to the HFC substances used so far could be found. Following the publicly funded research project, further long-term measurements are planned including the investigation of a new class of lubricating oils on the base of Perfluoroethers, which are used already for the lubrication of oxygen compressors and are expected to further lower the possibility of exothermal decomposition.

CAUTION: Pure N_2O as well as mixtures of N_2O and CO_2 with hydrocarbon based lubricants can result in serious decomposition reactions increasing the pressure inside a refrigeration system approximately eightfold.

ACKNOWLEDGEMENTS

The research was funded by the Federal Ministry of Economic Affairs and Energy under the Central Innovation Programme SME (ZF4093102 RE5) and was carried out together with Martin Christ Gefriertrocknungsanlagen GmbH, BITZER Kühlmaschinenbau GmbH and Fuchs Schmierstoffe GmbH. The excellent project cooperation and mutual support is highly appreciated.

NOMENCLATURE

p	pressure (kPa)	t	temperature (°C)
T	temperature (K)	V	Volume (m^3)

REFERENCES

Di Nicola, G., Giuliani, G., Polonara, F., Stryjek, R. (2007). Solid-liquid equilibria for the CO_2 + N_2O, CO_2 + R32, and N_2O + R32 systems. Fluid Phase Equilibria, 256 (1-2), 86–92

EIGA (2013). Safe Practices for Storage and Handling of Nitrous Oxide. Doc 176/16 of EIGA (European Industrial Gases Association)

Gula, M.: Explosionstechnische Charakterisierung chemisch instabiler Gase. Berlin 2010

Kruse, H.; Rüssmann, H.: The natural fluid nitrous oxide – an option as substitute for low temperature synthetic refrigerants. International Journal of Refrigeration, Vol. 29, Issue 5, August 2006, Pages 799-806

Linde (2011). Safety data sheet Nitrous oxide. SDS No. 8330, Version 2.0, Creation Date 27.01.2005, rev. 05.01.2011

Manuscript ID: 1535
DOI: 10.18462/iir.icr.2019.1535

Experimental study of R454B drop-in performance in a R410A liquid-to-water heat pump

Ignacio ORTEGA[(a)], Jaime SIERES[(a)], Fernando CERDEIRA[(a)], Estrella ÁLVAREZ[(b)], J. Alberto DOPAZO[(a)]

[(a)] Área de Máquinas y Motores Térmicos, Escuela de Ingeniería Industrial, University of Vigo, Campus Lagoas-Marcosende 9, 36310 Vigo, Spain, iortega@uvigo.es, jsieres@uvigo.es, nano@uvigo.es, jdopazo@uvigo.es

[(b)] Chemical Engineering Department, Escuela de Ingeniería Industrial, University of Vigo Campus Lagoas-Marcosende 9, 36310 Vigo, Spain, ealvarez@uvigo.es

ABSTRACT

R410A is a widely used refrigerant in residential heat pumps. The Global Warming Potential (GWP) of refrigerant R410A is 1924 so lower GWP alternatives are being studied in the last years as potential replacements of R410A. One potential alternative is refrigerant R454B with a GWP equal to 466.
This paper presents an experimental study of the R454B drop-in performance in a R410A liquid-to-water heat pump. The main components of the heat pump are a scroll type compressor, two brazed plate heat exchangers (condenser and evaporator) and an electronic expansion valve.
Experimental results for typical operating conditions of liquid-to-water heat pumps (EN 14511-2, 2013) are presented and discussed. From the experimental measurements, parameters such as the COP, heating power or compressor electric power consumption are obtained and compared between the two refrigerants. Results show that R454B might be an adequate drop-in refrigerant for R410A as it closely matches its performance.
Keywords: Heat Pump, R410A, R454B, Low-GWP Refrigerants, Experimental Results.

1. INTRODUCTION

Nowadays, a number of companies manufacture liquid-to-water heat pumps for geothermal applications based on the scroll compressor technology and brazed plate heat exchanges. The two main refrigerants used for these applications are R407C and R410A.
Over the last several years, great research efforts have been focused on the development and application of low Global Warming Potential (GWP) refrigerants. For example, the Europe's EU regulation N°517/2014 prohibits the use of fluorinated gases with a GWP above 150 in domestic refrigerators and freezers by January 1 2015 and in new types of mobile air-conditioning systems by January 1, 2017.
In the particular case of refrigerant R410A, different manufactures have proposed lower GWP refrigerants such as R452B or R454B, which have GWP values of 675 and 466, respectively (Myhre et al., 2013). These two refrigerants have similar properties to R410A and were designed as drop-in or near drop-in replacements for R410A in residential heat pumps applications. On the other hand, other synthetic and natural refrigerant alternatives are also proposed, such as R32 or propane (R290); though, their properties are quite different to R410A so they should be considered as R410A alternatives to apply in new equipment.
Pham and Rajendran (2012) presented theoretical analyses and test results from various drop-in tests comparing R32 and HFO blends versus R410A. They showed that the HFO blends provide around 2% higher EER but 5% lower capacity than R410A. The refrigerants analysed were R1234yf or R1234ze blended with R32, with GWP values of around 500. Piao et al. (2012) performed drop-in tests to compare the performance of R1234yf, R32 and R1234yf/R32 mixtures with R410A. They found that R32 was the most balanced solution for residential and small commercial unitary applications. In et al. (2014) compared R410A versus R32 and L41b (a binary mixture of R32 and R1234ze(E)) in a residential heat pump and found a 5% higher and 9% lower

capacity for R32 and L41b, respectively, when compared with R410A. Alabdulkarem et al. (2015) presented drop-in tests of the three R410A low-GWP alternative refrigerants R32, D2Y60 (a binary mixture of R23 and R1234yf) and L41a (a ternary mixture of R32, R1234yf and R1234ze(E)) in a split heat pump unit. The test results showed that R32 was superior to R410A in terms of cooling and heating capacities, while L41a was superior in terms of compressor discharge temperature and D2Y60 in terms of COP.
The Air-Conditioning, Heating, and Refrigeration Institute (AHRI) launched an industry-wide cooperative research program to identify and evaluate alternative refrigerants that have low GWP values (Hickman et al., 2013). During the program drop-in tests were performed of different low-GWP alternative refrigerants for R407C and R410A in heat pumps. Though the results concerning cooling/heating capacities and COP depend on the tested conditions, in many tests R32 and the blend R32/R152a (95/5) showed higher capacities and similar COPs compared to R410A. Blends based on R32 and HFO refrigerants (such as DR5, L41b, ARM70a…) showed similar performance to R410A, but for many cases slightly higher COP but lower capacity values.
From Table 1 it can be seen that R454B has similar thermodynamic properties to R410A, but a much lower GWP value. As a result, R454B might be a good low-GWP alternative refrigerant to R410A; however, more experimental evaluation is required. In this paper experimental results for typical operating conditions of liquid-to-water heat pumps (EN 14511-2, 2013) are presented and discussed. From the experimental measurements the COP, the heating and the compressor powers, as well as suction and discharge temperatures and pressures are obtained for both refrigerants under different operating conditions.

Table 1. R410A and R454B properties

Property	R410A	R454B
Composition (wt%)	R32/R125 (50/50%)	R32/R1234yf (68.9/31.1%)
Molecular weight	72.6 kg/kmol	62.6 kg/kmol
Boiling point @ 1 atm	-51.4°C	-50.5°C
Critical temperature	71.3°C	78.1°C
Ozone Depletion Potential	0	0
GWP(AR4)	1924	466
ASHRAE Safety Classification	A1	A2L
Heat of vaporization @ 1 atm	19818 kJ/kmol	19799 kJ/kmol

2. DESCRIPTION OF THE EXPERIMENTAL SET-UP

The main component of the experimental set-up is a liquid to water heat pump for space heating and domestic hot water (DHW) production in a desuperheater. The original refrigerant used in the heat pump is R410A.
Fig.1 shows a schematic representation of the heat pump under consideration, where the main components are represented. The heat pump has a variable speed scroll type compressor and an electronic expansion valve. The compressor's drive has a cold plate heat exchanger in order to avoid high internal temperatures. As shown in the figure, water is used for cooling the drive and for the condensation process, so a fraction of the water flow rate is diverted to the drive heat exchanger and the remainder flows through the condenser. Brazed plate heat exchangers of stainless steel are used for the desuperheater, condenser and evaporator. The number of plates for the desuperheater, condenser and evaporator are 18, 24 and 26, respectively. As shown in Fig. 1, the heat pump does not contain a refrigerant tank, so the refrigerant charge is distributed throughout the heat pump components and lines. Different amounts of refrigerant charge are expected to give different values of the degree of subcooling at the condenser outlet, which will affect the heat pump performance.
A 15% (mass basis) propylene-glycol water mixture (PGW) is pumped through the evaporator from a 750 L PGW tank. Similarly, water is pumped from a 280 L tank to the condenser. Variable speed pumps were used in order to control the PGW and water flow rates through the evaporator and condenser, respectively. The supply temperature to each heat exchanger was controlled by adjusting the temperature levels of the corresponding tanks using an additional water circuit and an

air-to-water heat pump (not shown in Fig. 1). For the DHW tests, water is pumped from a 300 L tank to the desuperheater at the desired temperature. However, for this work, DHW tests were not considered.

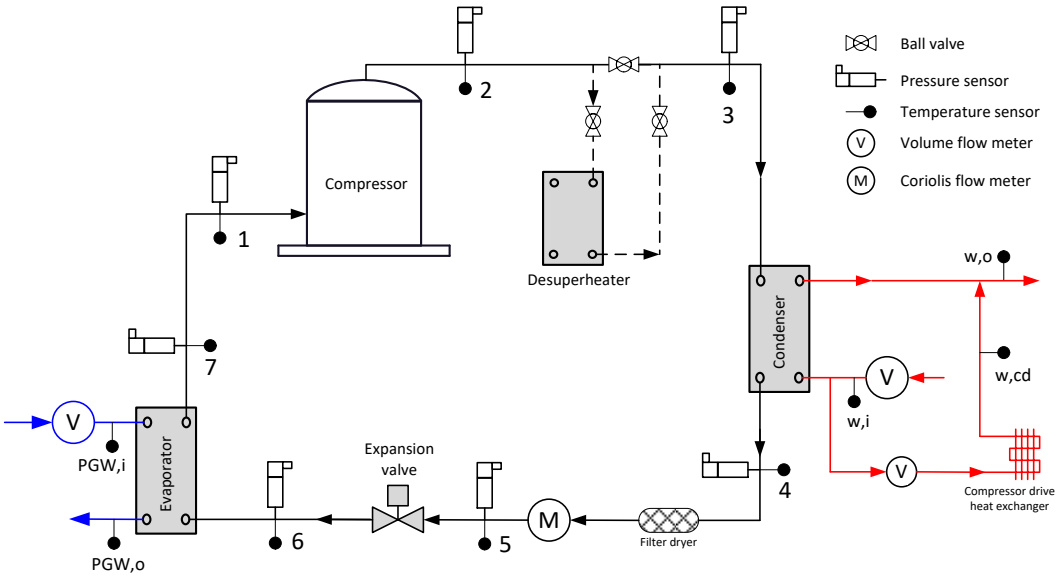

Figure 1: Schematic representation of the heat pump

The experimental facility has been equipped with proper instrumentation. Pressure transmitters were installed to measure the refrigerant pressure at different points of the system, as shown in Figure 1. Refrigerant temperatures were estimated by means of Pt100 probes clamped around the refrigerant pipes using an aluminium foil; afterwards, the probes and pipes were properly insulated. The refrigerant mass flow rate was measured with a Coriolis flow meter and electromagnetic flow meters were used to measure the PGW volumetric flow rate in the evaporator and the water volumetric flow rate in the condenser. The compressor's electric power is measured with a power transducer. Table 2 summarizes the main characteristics of the instrumentation used in the experimental set up.

Table 2. Types of sensors and accuracies

Variable	Instrumentation	Accuracy
Water and PGW volumetric flow rate	Electromagnetic flow meter	±0.2% reading
Water volumetric flow rate (compressor's drive heat exchanger)	Paddle-wheel flow meter	±(0.1 L×min^{-1}+2.5% reading)
Water and PGW temperatures	PT 100 Class B 1/10	±0.06 K
Refrigerant temperatures	PT 100 Class A	±0.4 K
Refrigerant pressures (gauge): points 2-5	Pressure transmitter	±0.04 bar
Refrigerant pressures (gauge): points 6, 7 and 1	Pressure transmitter	±0.02 bar
Refrigerant mass flow rate	Coriolis flow meter	±0.1% reading
Atmospheric pressure	Digital barometer	±0.003 bar
Compressor's electrical power	Power transducer	±0.5% reading

3. TEST CONDITIONS

Experiments were performed with R410A for constant inlet/outlet temperature values of the PGW mixture at the evaporator of 0/-3°C and two different water temperature values at the inlet/ outlet of the condenser of 30/35°C and 40/45°C. These are typical operating conditions of liquid-to-water heat pumps in the heating mode of operation for low and medium temperature applications (EN 14511-2, 2013). For each temperature level in the condenser, experiments were performed with compressor speed set points of 100% and 70% of the maximum compressor speed. The

experiments were performed setting a superheating degree value at the evaporator outlet equal to 10 K.
The amount of R410A in the system was adjusted in order to maximize the COP at the 30/35°C and 100% compressor speed operating conditions. Once the experiments with R410A were performed, the system was evacuated and charged with refrigerant R454B. The same group of experiments were repeated with R454B. Some small adjustments in the expansion valve were required in order to maintain the 10 K superheat value. As before, the amount of R454B charge in the system was optimized for the 30/35°C and 100% compressor speed operating conditions.
All sensors were scanned within a time interval of 3 s. During each experiment, steady state conditions were confirmed by visualizing the measured variables in the supervisory data acquisition system. In general, steady state operation was reached within a period of 1-2 hours. Thereafter, data recording during the next 40-60 minutes was performed for all the measured variables.

4. DATA REDUCTION

During the experiments, the temperature and absolute pressure of the refrigerant and the temperatures of the water and the PGW mixture at the inlet/outlet of the different components were measured. With these data, the corresponding thermodynamic states could be determined. All refrigerant and water properties were calculated using the REFPROP Database (Lemmon et al., 2010). The PGW properties were obtained using technical data from the propylene-glycol supplier.
For the thermal analysis of the heat pump, the following assumptions were considered:

- Steady state operation
- Heat gains/losses and pressure drops in the connecting pipes are negligible; i.e. pipes are of short length and well insulated.
- Kinematic and potential energy variations at the inlet/outlet of the different components are negligible.
- Heat transfer with the surroundings in the heat exchangers and in the electronic expansion valve are negligible

By virtue of the preceding assumptions, the process in the expansion valve can be considered to be isenthalpic. As a result, the enthalpy at the evaporator inlet (point 6 in Fig. 1) was considered to be equal to the enthalpy at the expansion valve inlet (point 5 in Fig. 1), rather than being calculated from the pressure and temperature measurements at the evaporator inlet.
From the water flow rate measurement through the condenser and the compressor's drive heat exchanger, and the temperature values before entering and after leaving both components, the following value of the heat power can be determined:

$$\dot{Q}_{cond+cd,w} = \dot{V}_w \cdot \rho_w \cdot c_{p,w} \cdot \left(T_{w_o} - T_{w_i}\right) \quad \text{Eq. (1)}$$

where the heat dissipated in the drive is given by:

$$\dot{Q}_{cd,w} = \dot{V}_{w,cd} \cdot \rho_w \cdot c_{p,w} \cdot \left(T_{w_{cd}} - T_{w_i}\right) \quad \text{Eq. (2)}$$

Then, the heat transfer rate in the condenser can be determined as:

$$\dot{Q}_{cond,w} = \dot{Q}_{cond+cd,w} - \dot{Q}_{cd,w} \quad \text{Eq. (3)}$$

In the previous equations the density is evaluated at the water inlet temperature and the specific heat is evaluated at the water average temperature through the corresponding devices.
For the evaporator:

$$\dot{Q}_{evap,PGW} = \dot{V}_{PGW} \cdot \rho_{PGW} \cdot c_{p,PGW} \cdot \left(T_{PGW_i} - T_{PGW_o}\right) \quad \text{Eq. (4)}$$

where the density is evaluated at the PGW inlet temperature and the specific heat is evaluated at the PGW average temperature.
The previous quantities may also be calculated from the refrigerant mass flow rate measured with the Coriolis flow meter and the enthalpy variation through the condenser and evaporator:

$$\dot{Q}_{cond,ref} = \dot{m}_{ref} \cdot (h_3 - h_4) \quad \text{Eq. (5)}$$

$$\dot{Q}_{evap,ref} = \dot{m}_{ref} \cdot (h_7 - h_6) \qquad \text{Eq. (6)}$$

In order to check the accuracy of the experimental measurements and the validity of the previous thermal assumptions, the calculated values of the heat transfer rates in the condenser and evaporator in the external fluid side and refrigerant side are compared in Fig. 2. In the figure, uncertainty bands (with a coverage factor of k = 3) are also shown for the estimated parameters. These uncertainties were obtained following the guidelines given in JCGM (2008). It can be seen that the calculated values are within ±4% bands and, in general, within the uncertainty of the estimated parameters.

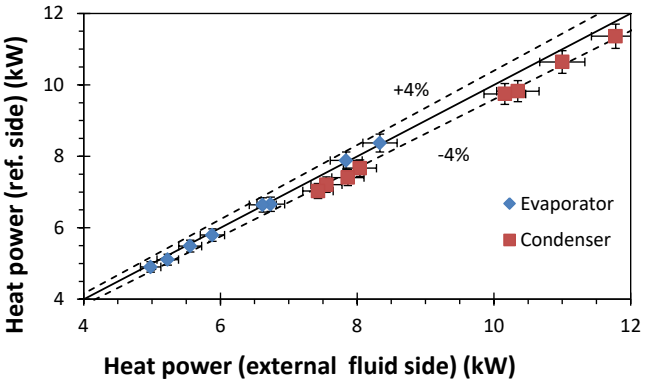

Figure 2: Deviation between heat transfer rate values in the refrigerant side and external fluid side

Finally, the coefficient of performance (COP) of the heat pump was calculated from the heating power in the condenser and the compressor's electric power (including the drive power consumption):

$$COP = \dot{Q}_{cond+cd,w} / \dot{W}_{elec} \qquad \text{Eq. (7)}$$

The heat gained in the drive's heat exchanger was introduced in the numerator of the previous equation. This might not be the case in other works. Anyway, the heat power dissipated in the drive's heat exchanger was always lower than 100 W and has a very small effect on the COP.

5. RESULTS AND DISCUSSION

A set of 8 experiments were performed for the operating conditions described in the previous sections, four with each refrigerant (R410A and R454B). Fig. 3 shows the heating power, the compressor's electric power and the COP with refrigerants R410A and R454B, for two different water inlet/outlet temperature values in the condenser (30/35 and 40/45°C) and two different compressor speed values (maximum and 70%). For the two refrigerants, it can be seen that if the water temperature level in the condenser increases then the heating power decreases, the compressor power increases and, consequently, the COP decreases. When the compressor speed decreases from the maximum speed to a 70% value, both the heating power and the compressor power decrease, whereas the COP increases slightly.

Fig. 3 also shows that for the 30/35°C and full speed operating conditions, the heating power with R454B is lower than with R410A (6.6% lower). However, the compressor electric power is also lower (7.1%) which finally results in a slightly higher COP value (0.6%). For the 30/35°C and 70% speed operating conditions, the experimental results show a similar trend, though the differences between the two refrigerants are reduced. For the 40/45°C and 70% compressor speed operating conditions, R454B shows better performance in terms of compressor power (5.9% lower), COP (0.3% higher) but a slightly lower (5.5%) heating power.

Regarding the 40/45°C and 100% set point conditions, it should be clarified that the 100% maximum compressor speed was not attained, since the compressor speed was reduced by the compressor's drive overcurrent protection control system. The horizontal axis of Fig. 3 indicates that the maximum compressor speeds at the 40/45°C temperature level were 90% and 94% for refrigerants R410A and R454B, respectively. As shown before, for the same operating conditions (temperature level and compressor speed), the compressor's electric power with R454B was lower than with R410A. As a result, the compressor's drive overcurrent protection allowed a higher speed

with R454B than with R410A. This explains the higher speeds attained with R454B. Fig. 3b also shows that the compressor powers are almost the same for the two refrigerants at the 40/45°C and maximum speed operating conditions, since these are limited by the compressor's drive overcurrent protection system. Finally, it can be seen that the heating power and COP values for R454B are similar to those with R410A (1.8% and 0.5% lower for the heating power and COP, respectively) at the 40/45°C and maximum speed operating conditions.

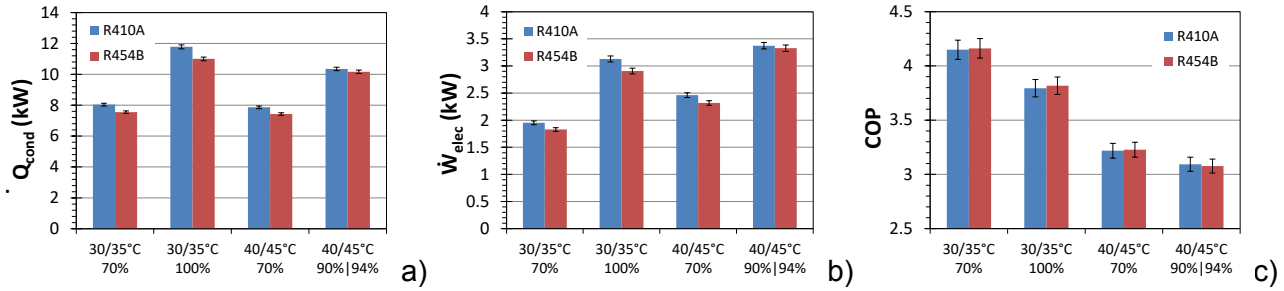

Figure 3: a) Heating power, b) compressor's electric power and c) COP, with R410A and R454B

Fig. 4 shows the suction pressure, discharge pressure and pressure ratio (discharge to suction pressure ratio) for the same operating conditions considered in Figure 3. As expected, the discharge pressure increases with the temperature level in the condenser (30/35°C or 40/45°C) and also it increases with the compressor speed. Figure 4a) shows that the suction pressure decreased slightly when the compressor speed was increased, but P_1 increased slightly when the water temperature level in the condenser was increased. Since the discharge pressure variations were more pronounced that the suction pressure variations, the pressure ratio followed a similar behaviour to the discharge pressure, as confirmed in Fig. 4c. For all the experiments, refrigerant R454B always showed lower suction and discharge pressures but slightly higher pressure ratio values than refrigerant R410A.

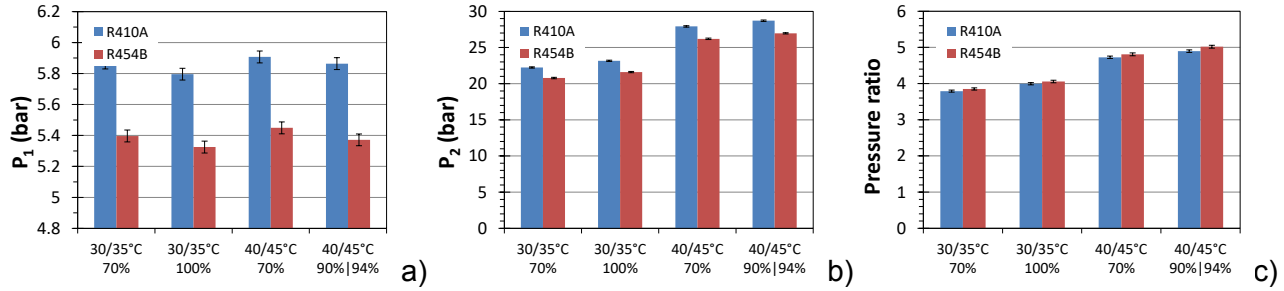

Figure 4: a) Suction pressure, b) discharge pressure and c) pressure ratio, with R410A and R454B

Fig. 5 shows the compressor volumetric and isentropic efficiencies for the same operating conditions considered in Figs. 3 and 4. It can be seen that both efficiencies decrease with the temperature level in the condenser (i.e. with the pressure ratio). When increasing the compressor speed, the volumetric efficiency increases but the isentropic efficiency decreases slightly. Experimental results also show that the efficiency differences between the two refrigerants are small and always within the uncertainty of the measured values.

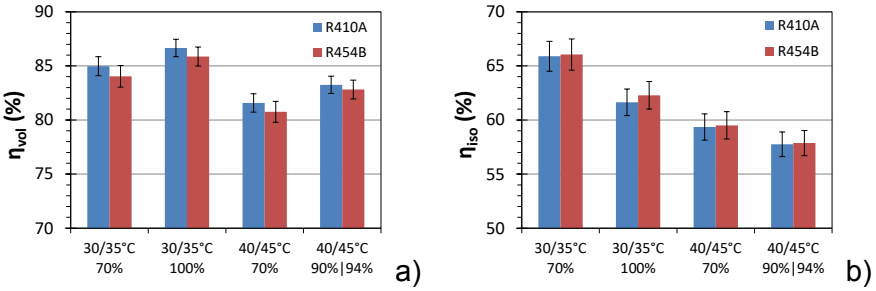

Figure 5: a) Compressor volumetric efficiency and b) compressor isentropic efficiency, with R410A and R454B

Fig. 6 shows the degree of subcooling at the condenser outlet and the suction and discharge temperatures. As explained previously, the refrigerant charge was adjusted in order to maximize

the COP at the 30/35°C and 100% compressor speed operating condition. At this operating condition, the degree of subcooling at the condenser outlet was merely the same (6.7 or 6.8 K) for the two refrigerants. Experimental results show that the degree of subcooling increased with the temperature level in the condenser and also with the compressor speed. However, it should be clarified that a clear comparison cannot be performed between the 30/35°C and 40/45°C maximum speed operating conditions since for the former the compressor speed was higher (100%) than for the latter (90% for R410A and 94% for R454B). Regarding the suction temperatures, the experimental results confirm that this variable was somehow constant with small variations that followed the same trend observed for the suction pressure of the corresponding refrigerant. Finally, it can be clearly seen in Fig. 6c that the discharge temperature increased with the temperature level in the condenser and with the compressor speed. Also, the discharge temperature with refrigerant R454B was always 8-10 K higher than with R410A.

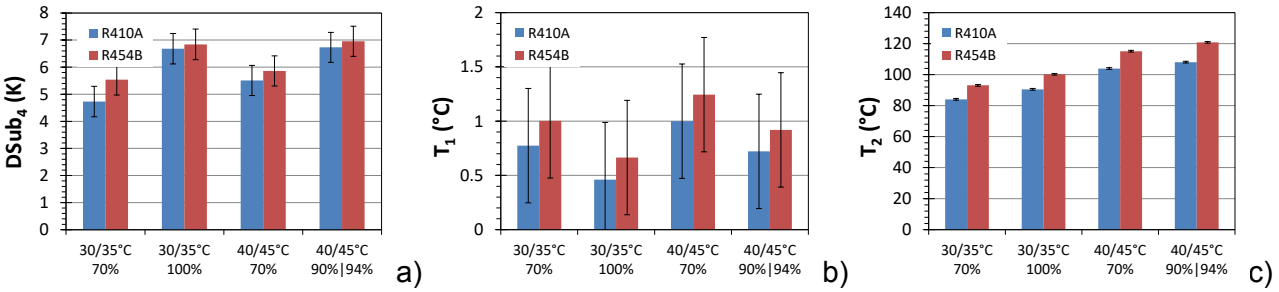

Figure 6: a) Degree of subcooling at condenser outlet, b) suction temperature and c) discharge temperature, with R410A and R454B

6. CONCLUSIONS

This paper presented an experimental study of the R454B drop-in performance in a R410A liquid-to-water heat pump. Experiments were performed at constant inlet/outlet temperature values of the PGW mixture at the evaporator of 0/-3°C, two different water temperature values at the inlet/outlet of the condenser of 30/35°C and 40/45°C, two compressor speed set points of 100% and 70% of the maximum compressor speed, and a superheating degree value at the evaporator outlet equal to 10 K. The amount of R410A and R454B refrigerant was adjusted in order to maximize the COP at the 30/35°C, 100% compressor speed and 10 K superheat operating conditions. From the analysis of the experimental results, the following conclusions are obtained:

- Increasing the water temperature level in the condenser (from 30/35°C to 40/45°C) led to lower heating powers in the condenser, higher compressor's electric powers and lower COP values.
- Increasing the compressor speed led to higher heating powers, higher compressor's electric powers and lower COP values.
- For the same operating conditions, R454B always showed lower suction and discharge pressure values than R410A; however, the pressure ratio values with R454B were always slightly higher than with R410A.
- For the same operating conditions, experimental results showed better performance of R454B in terms of compressor's electric power and slightly better in terms of COP (though the differences were within the uncertainty of the estimated values).
- R454B showed lower heating capacities than R410A. Depending on the tested conditions, the heating capacity with R454B varied from -6.6% to -1.8% of that obtained with R410A.
- For the same operating conditions, the discharge temperature with refrigerant R454B was always higher than with R410A, with differences from 8 to 10 K.

ACKNOWLEDGEMENTS

The authors would like to acknowledge the financial support from the Spanish "Ministerio de Economía y Competitividad" and FEDER (EU) through the research grant ENE2016-79771-R.

NOMENCLATURE

COP	coefficient of performance (-)	c_p	specific heat at constant pressure ($J \times kg^{-1} \times K^{-1}$)
DHW	domestic hot water	DSub	degree of subcooling (K)
h	specific enthalpy ($J \times kg^{-1}$)	$\dot{m}$	mass flow rate ($kg \times s^{-1}$)
P	pressure (bar)	PGW	propylene-glycol water mixture
$\dot{Q}$	heat power (kW)	T	temperature (°C, K)
$\dot{V}$	volume flow rate ($m^3 \times s^{-1}$)	$\dot{W}_{elec}$	electric power (kW)

Greek symbols

ρ	density ($kg \times m^{-3}$)

Subscripts

evap	evaporator	cd	compressor's drive
cond	condenser	i	inlet
o	outlet	PGW	propylene-glycol water mixture
ref	refrigerant	w	water

REFERENCES

Alabdulkarem, A., Eldeeb, R., Hwang, Y., Aute, V., Radermacher, R., 2015. Testing, simulation and soft-optimization of R410A low-GWP alternatives in heat pump system. Int. J. Refrigeration 60, 106-117.

European Committee for Standardization. Air conditioners, liquid chilling packages and heat pumps with electrically driven compressors for space heating and cooling - Part 2: Test conditions. EN 14511-2 -2013.

European Parliament and the Council, 2014. No 517/2014 of the European Parliament and of the Council of 16 April 2014 on fluorinated greenhouse gases and repealing regulation (EC) No 842/2006 text with EEA relevance. Off. J. Eur. Union L 150, 195–230.

Hickman, K. 2013. Reference list for low GWP refrigerants testing. Air-Conditioning, Heating, and Refrigeration Institute (AHRI) low-GWP alternative refrigerants evaluation program.

In, S., Cho, K., Lim, B., Kim, H., Youn, B., 2014. Performance test of residential heat pump after partial optimization using low GWP refrigerants. App. Therm. Eng. 72, 315-322.

JCGM, 2008. Evaluation of measurement data –Guide to the expression of uncertainty in measurement JCGM 10 0:20 08 (GUM 1995 with minor corrections). BIPM Joint Committee for Guides in Metrology, Paris.

Lemmon, E.W., Huber, M.L., McLinden, M.O., 2010. NIST Standard Reference Database 23: Reference Fluid Thermodynamic and Transport Properties - REFPROP v 9.0. National Institute of Standards and Technology (NIST), Standard Reference Data Program, Gaithersburg, MD.

Myhre, G., Shindell, D., Bréon, F.-M., Collins, W. Fuglestvedt, J., Huang, J., Koch, D., Lamarque, J.-F., Lee, D., Mendoza, B., Nakajima, T., Robock, A., Stephens, G., Takemura, T., Zhang, H., 2013. Anthropogenic and Natural Radiative Forcing. In: Stocker, T.F., Qin, D., Plattner, G.-K., Tignor, M., Allen, S.K., Boschung, J., Nauels, A., Xia, Y., Bex, V., Midgley, P.M. (eds.), Climate Change 2013: The Physical Science Basis. Contribution of Working Group I to the Fifth Assessment Report of the Intergovernmental Panel on Climate Change. Cambridge University Press, Cambridge, United Kingdom and New York, NY, USA.

Pham, H., Rajendran, R., 2012. R32 and HFOs as low-GWP refrigerants for air conditioning, International Refrigeration and Air Conditioning Conference at Purdue, July 16-19, Paper 2262.

Piao, C., Taira, S., Moriwaki, M.M., Tanimoto, K., Mochizuki, K., Nakai, A., 2012. Alternatives to high GWP HFC refrigerants: residential and small commercial unitary equipment. ASHRAE/NIST Refrigerants Conference.

Manuscript ID: 1541
DOI: 10.18462/iir.icr.2019.1541

Development of a new optical method to quantify local air-side heat transfer coefficient

Min CHE[(a)], Stefan ELBEL[(a) (b)]

[(a)] Air Conditioning and Refrigeration Center,
Department of Mechanical Science and Engineering,
University of Illinois at Urbana-Champaign,
1206 West Green Street, Urbana, IL 61801, USA, minche2@illinois.edu
[(b)] Creative Thermal Solutions, Inc.,
2209 North Willow Road, Urbana, IL 61802, USA, elbel@illinois.edu

ABSTRACT

Low air-side heat transfer coefficient (HTC) limits the performance of many heat exchangers. A new method is developed to obtain local air-side HTC of real heat exchangers without the use of complex experimental tools. The method relies on measuring mass transfer and applying the analogy between heat and mass transfer to determine heat transfer. A thin film coating is applied to the heat transfer surface which is exposed to a suitable trace gas, in this case, a 50 ppm ammonia-air mixture. The coating absorbs the ammonia and changes color.
A detailed description of the new measurement technique is given, including the application of the fundamental heat and mass transfer correlations, evaluation of suitable coating formulations, determination of surface morphologies, and discussion of the optical principle to quantify color change. For laminar flow across flat plates, the new method results in experimental HTC that are within 17% of the Blasius solution.
Keywords: Local Air-Side Heat Transfer, Convection Mass Transfer, Heat and Mass Transfer Analogy, Coating, Tracer Gas, Color Change.

1. INTRODUCTION

Heat transfer between liquid-to-gas is widely used in aerospace, transportation, electronics cooling, industrial processes, refrigeration, and air-conditioning areas. Therefore, liquid-to-gas heat exchangers are intensively investigated for energy saving considerations. Joardar and Jacobi (2005) have claimed that air-side convective resistance to be the most significant contributor, which accounts for 75% or more of the total heat transfer resistance in refrigerant-to-air heat exchangers. However, the existing experimental methods are difficult to be applied on complicated surfaces to obtain local air-side HTC's.
Therefore, a visualization method is developed to quantify local mass transfer by color change observation. This method is based on the analogy between heat and mass transfer. Since the method employs a coating material in combination with a tracer gas to achieve a local color change, this method will be abbreviated as CTC (coating, tracer gas and color change) in this paper.

2. THE PROPOSED CTC METHOD

2.1 Principle of the Proposed Method

A new visualization method which employs the analogy of heat and mass transfer is developed. A color change coating and tracer gas combination is developed; the chemical interaction between the coating material and a tracer gas is the driving force of mass transfer. As shown in Fig. 1, a color change acidic coating material is attached to the heat transfer surface of interest. A dye is mixed with the coating material, which changes color at a certain pH level from yellow to blue. A tracer gas (dilute ammonia at ppm level) and air flow are well mixed prior to passing across the coated sample. As the coating material absorbs tracer gas and is neutralized, the color change can be observed on

the surface. Therefore, convective mass transfer takes place as the tracer gas is transferred from the free stream flow to the coated surface. If the color change can be correlated with local mass flux and mass transfer coefficient, by applying the analogy, local HTC can be quantified. Since the coated surface is dry and some amount of water vapor is necessary for the chemical reaction to take place, humidity ratio of the air flow must be controlled. For the consistency of the experiment, 26 ºC, 60 % relative humidity, 50 ppm volumetric concentration of ammonia and air mixture, and 1 $m \cdot s^{-1}$ flow velocity are set as the baseline condition for the mass transfer experiment.

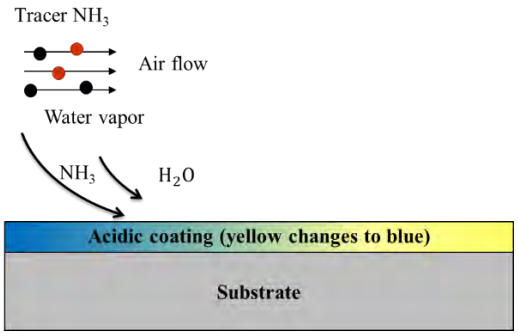

Figure 1: Principle of the proposed visualization method

2.2 Boundary Layer Assumptions and the Analogy Theory

A schematic of the convection boundary layer for laminar flow over a flat plate with infinite spanwise length is shown in Fig. 2. Isothermal mass transfer is assumed. In the boundary layer, it is assumed that the streamwise velocity profile and tracer concentration profile have a similar shape. The tracer concentration difference is caused by the chemical reaction between the coating material and the tracer gas. The chemical potential between the coating material and the tracer gas is strong enough that the tracer concentration at the wall is close to zero. The thin film coating is on top of the substrate represents the interactive wall. Ideally, the coated surface should be dry, thin and smooth. The incompressible fluid, no-slip, and impermeable wall assumptions are well accepted for laminar flow over a solid plate. For the plate covered by the thin film coating, these assumptions are still valid, because the bulk flow cannot penetrate through the wall. Although the tracer gas is absorbed by the coating material, the permeability is still negligible, because 50 ppm ammonia is negligible compared to the bulk flow (Bejan,1995).

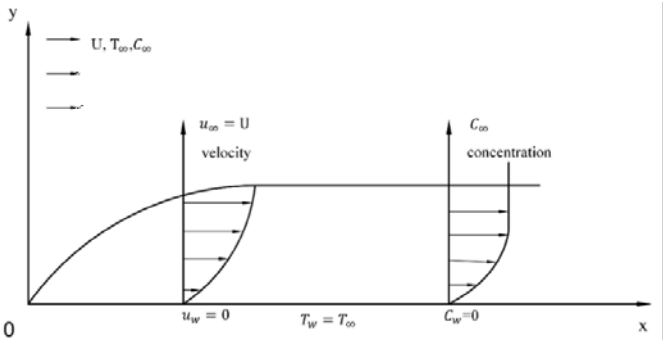

Figure 2: Laminar momentum and mass transfer boundary conditions over a flat plate

As shown in Fig. 2, the tracer concentration in the bulk flow is 50 ppm. Meanwhile, the tracer concentration at the wall is approximate 0 ppm. This constant concentration difference Eq. (2) is analogous to the constant temperature difference in the heat transfer Eq. (1).

$$u\frac{\partial T}{\partial x} + v\frac{\partial T}{\partial y} = \alpha\left(\frac{\partial^2 T}{\partial y^2}\right) \qquad \text{Eq. (1)}$$

$$u\frac{\partial C}{\partial x} + v\frac{\partial C}{\partial y} = D\left(\frac{\partial^2 C}{\partial y^2}\right) \quad \text{Eq. (2)}$$

It can be seen that the format of heat transfer equations and mass transfer equations are similar. The heat transfer Nusselt number is a function of Reynolds number and Prandtl number as shown in Eq. (3). The mass transfer Sherwood number is a function of Reynolds number and Schmidt number as shown in Eq. (4). Pr is the ratio of viscous diffusivity and thermal diffusivity, while Sc is the ratio of viscous diffusion and mass diffusion. Pr and Sc are known properties of fluids at known temperature and pressure. As a result, the ratio of Nu and Sh can be calculated (Eq. (5)), which is approximately equal to 1 when dilute ammonia is used as the tracer gas. The analogy theory is also explained by Kottke et al. (1977) and Ahrend et al. (2010), who employed the ammonia absorption method.

$$Nu_{loc} = 0.332 \cdot Pr^{1/3} {Re_{loc}}^{1/2} \text{ (Pr >0.5)} \quad \text{Eq. (3)}$$

$$Sh_{loc} = 0.332 \cdot Sc^{1/3} {Re_{loc}}^{1/2} \text{ (Sc ≥0.5)} \quad \text{Eq. (4)}$$

$$\frac{Sh_{loc}}{Nu_{loc}} = \left(\frac{Sc}{Pr}\right)^{1/3} = (Le)^{1/3} = \left(\frac{0.7478}{0.7421}\right)^{1/3} \approx 1 \quad \text{Eq. (5)}$$

3. EXPERIMENTAL APPARATUS AND PROCEDURES

3.1 Wind Tunnel

A suction type open-loop wind tunnel is designed and built for the mass transfer experiments as shown in Fig. 3. The design followed the principles described in ASHRAE STANDARD 41.2-1987 (RA 92) (1992). The size of the test section is W120 mm x H100 mm x L400 mm which is sufficient to test small samples such as flat plates, single fins, and fin arrays. The flow velocity across the test section can be adjusted from 0 to 3.5 m·s^{-1}. Water vapor and anhydrous ammonia tracer gas are injected and mixed. The test section is made of transparent polycarbonate sheets for color observation and image taking. A webcam is installed in close vicinity of the test section for image capturing. An electrochemical gas sensor (0-100 ppm) is connected to the test section to obtain real-time volumetric ammonia concentration measurements.

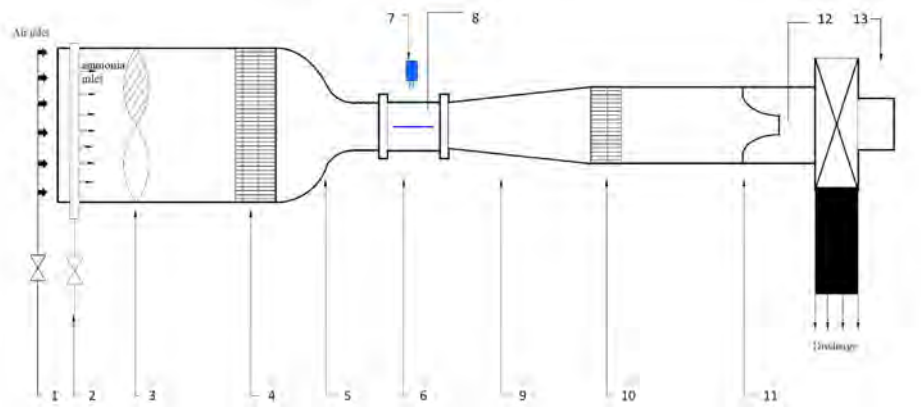

Figure 3: Schematic diagram of the wind tunnel

3.2 Ammonia Concentration Control

As ammonia gas is mixed with air flow to acquire a desired concentration of 50 ppm, a system to achieve precise ammonia flow control is designed. A 0.038 mm micro-orifice is used, and by adjusting the orifice inlet gas pressure, the ammonia mass flow rate can be controlled. A cylinder which contains anhydrous ammonia is immersed into a thermal bath. By controlling the temperature of the thermal bath, the ammonia vapor pressure is controlled. Ammonia concentration is measured

by an electrochemical sensor that the concentration of ammonia can be controlled. The accuracy of ammonia concentration measurement is within ±10%.

3.3 Image Processing and Local Mass Transfer Quantification Procedure

The procedure to quantify local HTC is developed and shown in Fig. 4. The first step is to prepare the coating solution which is diluted with ethanol by mass at the ratio of 1:3. Afterwards, the samples are coated with the coating solution according to the developed coating procedure. By conducting a titration experiment, the number of hydrogen protons (H^+) can be determined. For the baseline condition experiment, the maximum mass of ammonia gas absorption M_{max} is obtained which corresponds to 0.745 mg on the samples. Then the sample is exposed to the tracer gas in the wind tunnel for the mass transfer experiments. The wind tunnel is prepared to have constant temperature, pressure, humidity ratio, tracer concentration, and flow velocity. During the mass transfer experiment, the coated surface changes color from yellow to blue, while the tracer gas is reacting with the coating material. At the same time, the images of color change are recorded by a webcam, which is connected to a computer. The image acquisition toolbox of MATLAB R2018a is used to configure camera parameters to eliminate the variations caused by camera settings. The camera starts to record video as soon as the sample is located and stops image acquisition when the color of the entire surface has changed from yellow to blue. The duration of color change is 7 to 9 minutes at the baseline condition.

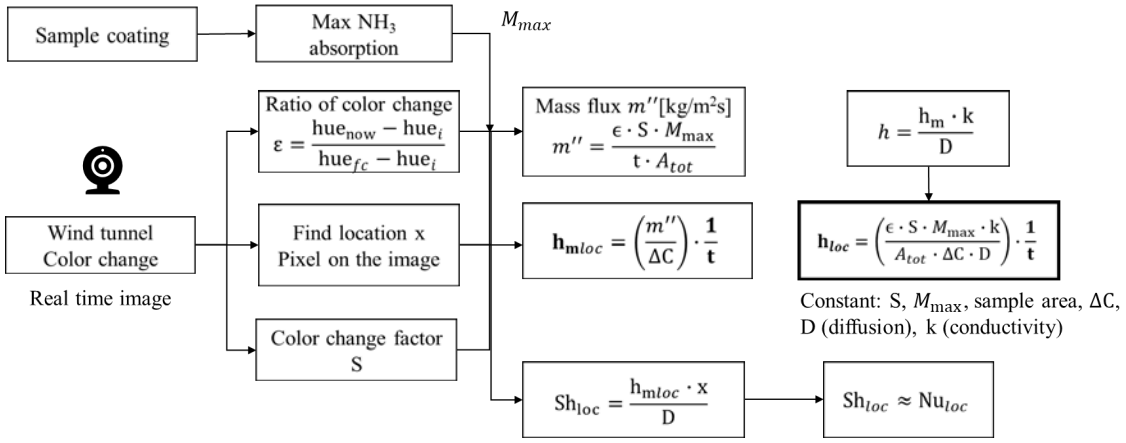

Figure 4: Procedure for acquiring local HTC

According to Camci et al. (1991), hue is directly related to color (wavelength). While saturation and intensity have some influence on hue, their influence can be controlled by the light source and the camera settings. Therefore, hue is sufficient to be used to quantify the change of color. The ratio of color change (ϵ) can be calculated by Eq. (6):

$$\epsilon = \frac{hue_{now} - hue_i}{hue_{fc} - hue_i} \qquad \text{Eq. (6)}$$

MATLAB R2018a is employed for image processing to quantify the ratio of color change (ϵ) at each pixel at a particular time (t). The streamwise location x of color change (50 x 50 mm square plate is equivalent to 300 x 300 pixels in the image) can be read from the image directly. The color change factor S is related to the experimental conditions and the characteristics of the dye which can be determined through calibration. At the baseline condition, S is 0.3 which means that when 30% of the coating reacts with ammonia gas, the color changes from yellow to blue. Thus, by multiplying the maximum mass transfer weight, S, and ϵ, the local mass transfer distribution at time t on the coated surface is obtained.

Local ammonia mass flux m'' at time t perpendicular to the coated surface can be calculated through Eq. (7). The local mass transfer coefficient can be acquired from Eq. (8). Due to the analogy of heat and mass transfer, the local HTCs are acquired by Eq. (9) and Eq. (10). Thermal conductivity and diffusion coefficient D for ammonia in the air can be treated as constants and known properties.

Therefore, the expression in the parenthesis can be treated as constants and the local mass transfer coefficient becomes a function of time only. Therefore, local HTC distribution on the surface is acquired.

$$m'' = \frac{\epsilon \cdot S \cdot M_{max}}{t \cdot A_{tot}} \quad \text{Eq. (7)}$$

$$h_{mloc} = \left(\frac{m''}{\Delta C}\right) \cdot \frac{1}{t} \quad \text{Eq. (8)}$$

$$h_{loc} = \frac{h_{mloc} \cdot k}{D} \quad \text{Eq. (9)}$$

$$h_{loc} = \left(\frac{\epsilon \cdot S \cdot M_{max} \cdot k}{A_{tot} \cdot \Delta C \cdot D}\right) \cdot \frac{1}{\mathrm{t}} \quad \text{Eq. (10)}$$

4. EXPERIMENTAL RESULTS

4.1 Coating Evaluations

Different coating solutions are developed and evaluated on aluminum alloy Al 1100. The criterion include solution stability, metal corrosion, coating quality, and color change characteristics. Finally, AMS 67 is the most preferred solution and 25% mass concentration is used for mass transfer measurements. The coating can be applied without any issues to most materials (Al 1100/3003/5005/5052/6061, Cu 110/260, stainless 304, polycarbonate, and acrylic) which means this method is can be used for many different types of heat transfer surfaces. Moreover, the aging influence is investigated by exposing the samples to environments which have different relative humidity. The reaction between the coating material and metal base happens in highly humid (RH>70%) environments in 1 to 2 hours. On the contrary, the coated samples are stable after 45 days which are stored in a relatively dry (RH<40%) environment.

4.2 Coating Thickness Quantification

Drop coating method is employed for the flat plate samples. The 0.5 g solution with 25% mass concentration is dropped on the sample and dried at 100 ºC. As the solution is a mixture of polymer, dye, acid, water and ethanol, more than 90% of the solution is liquid which will evaporate completely when heated (about 0.01 g solid in 0.5 g solution). The weight difference of the coated sample only represents the mass of the solid of the coating. By weight measurement, the average coating thickness is 4.8 μm.

The thickness determined by weight measurement represents the average thickness, not taking into account effects caused by non-uniform surface heights and surface roughness. A 3D surface profiler is employed to evaluate the uniformity of the coated surface. For the most part of the sample, the coating is uniform, and the mean thickness is 5.8 μm. However, the coating height close to the edges of the sample are thicker than at the inner locations due to the surface tension of the solution. The coating thickness at the edge location of a drop coated sample is shown in Fig. 5. It is shown that the variation of coating thickness is about 5 to 20 μm. Therefore, the measured HTC at the edges is smaller due to the thicker coating.

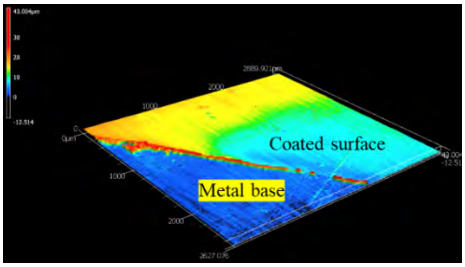

Figure 5: Surface topography of drop coated sample at an edge location

The roughness is also measured by the optical 3D profiler. The base metal to which coating was applied is Al 3003 with a mean surface roughness of 0.3 to 0.5 μm. The mean roughness of the coated surface was measured to be 0.6 to 2.1 μm. According to Goldstein and Cho (1993), the sublimation depth of naphthalene can be as much as 200 μm which also relies on the analogy between heat and mass transfer. The measured naphthalene sublimation depth by DeJong and Jacobi (1997) ranged from 25 to 120 μm. In conclusion, it appears that the coating layer is sufficiently thin and smooth compared to the well-applied naphthalene sublimation method and will therefore not influence the air flow characteristics across the test section. This is an important assumption that has to be made for the boundary layer in order to apply the analogy between heat and mass transfer.

4.3 Mass transfer and color change observation

A coated metal sheet is located at the center of the test section. The mass transfer experiment is conducted at the baseline condition. The webcam is installed at the top of the sample to record color change. The webcam parameters are set with MATLAB R2018a image acquisition toolbox to make sure the settings are consistent during the mass transfer process. A 25W LED white panel light is used to have stable illumination. The color change starts from the leading edge of the sample and spreads to the inner locations in the streamwise direction. The duration of color change is seven minutes. The images at different times are shown in Fig. 6.

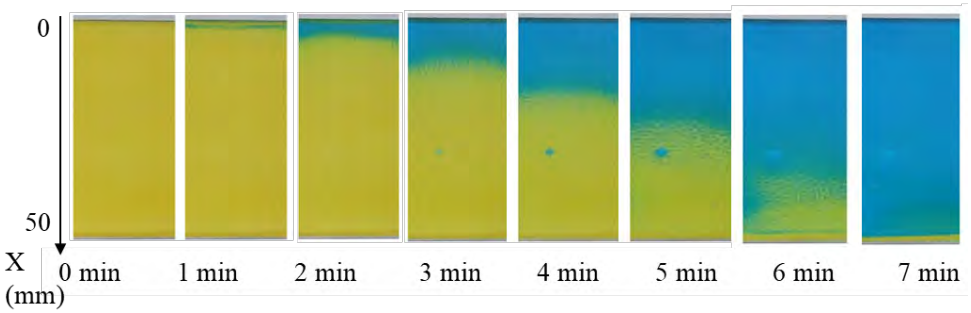

Figure 6: Mass transfer and color change at different times

4.4 Image Processing and Local Nusselt Number

The sample shown in Fig. 6 is analyzed according to the developed procedure explained in 3.3 and Fig. 4. The data shown in Fig. 7a is based on experimental measurements, while the graph shown in Fig. 7b is obtained by plotting the Blasius solution for flow across a flat plate.

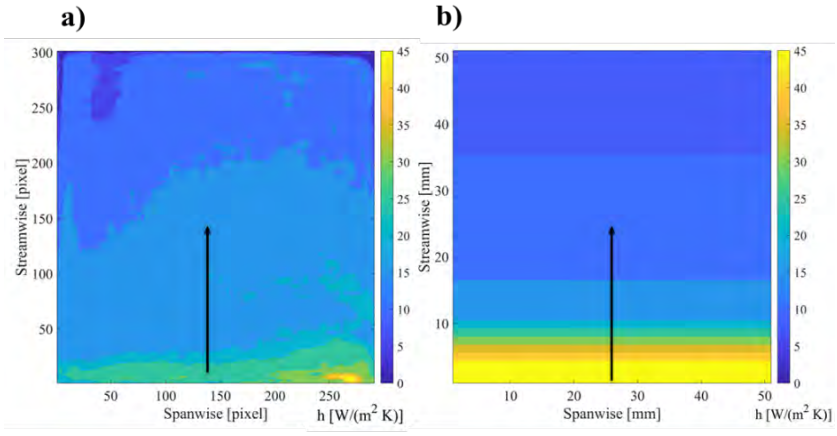

Figure 7: Two-dimensional distribution of HTC (Re=2950 at x=50 mm) a) Measured local HTC; b) HTC from Blasius solution

4.5 Uncertainty Analysis

The uncertainty analysis is conducted according to the methodology suggested by Moffat (1988). For the tested sample, the total uncertainty for each h_{loc} is calculated to be 17% by Eq. (11).

$$AE_{tot} = \left\{ \sum_i \left(\frac{\partial AE_i}{\partial X_i} \right)^2 \cdot {EA_{X_i}}^2 \right\}^{1/2} \quad \text{Eq. (11)}$$

In Fig. 8, the green curve represents the well-known Blasius solution, while the blue markers represent the experimental data points. Similar to the results shown in Fig. 7a, the span-averaged local HTC shown in Fig. 8 at edges is lower compared to the theoretical results because the coating is thicker at the edges. The thicker coating leads to slower color change by observation. Although the leading-edge results have higher error compared to the inner locations, the results obtained from the proposed method agree very well with Blasius solution.

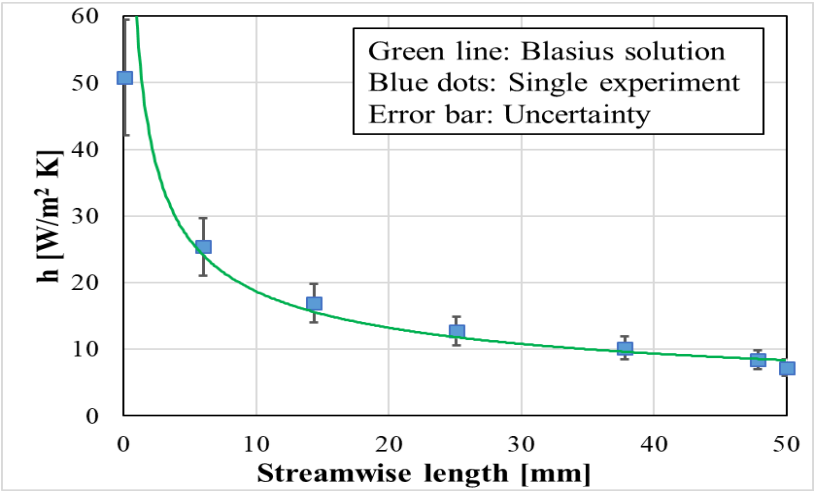

Figure 8: Results of a single measurement at baseline condition

5. CONCLUSIONS

A new method to quantify local air-side heat transfer coefficients has been developed, and this paper describes preliminary results for air flow across a flat plate at laminar flow conditions. While it has been demonstrated that the new method is capable of quantifying local air-side HTCs for simple flat plate geometries, it is believed to apply to more complex heat transfer surfaces as well. Compared to other existing experimental methods, this new method has several advantages: the coating material is not expensive; a simple coating method is suitable to be used for different geometries and materials. This thin film dry coating is superior to other mass transfer methods with respect to the influence on the boundary layer. Moreover, a generic wind tunnel can be used for the mass transfer experiments; a simple digital camera such as a webcam can be employed for color observation. The image processing method is simple, robust and is based on a widely accepted MATLAB toolbox. The most important is that the result for the flat plate sample shows good accuracy. Therefore, this method has the potential to be further developed to analyze more involved heat transfer problems.

ACKNOWLEDGMENTS

The authors would like to thank the member companies of the Air Conditioning and Refrigeration Center at the University of Illinois at Urbana-Champaign for their finical support, Creative Thermal Solutions, Inc. (CTS) for providing technical support and equipment. The coating solutions are made by Serionix, Inc. located in Champaign, IL, USA.

NOMENCLATURE

A	area of the surface (m^2)	*U*	bulk flow velocity ($m \cdot s^{-1}$)
AE	absolute uncertainty (-)	*u*	streamwise flow velocity ($m \cdot s^{-1}$)
C	concentration ($kg \cdot m^{-3}$)	*v*	flow velocity normal to the plate ($m \cdot s^{-1}$)
D	diffusion coefficient ($m^2 \cdot s^{-1}$)	*x*	streamwise dimension (m)
h	convection heat transfer coefficient ($W \cdot m^{-2} K^{-1}$)	y	coordinate direction normal to the plate (m)
h_m	convection mass transfer coefficient ($m \cdot s^{-1}$)	z	spanwise dimension (m)
H	hue: color property (-)	α	thermal diffusivity ($m^2 \cdot s^{-1}$)
m''	mass flux ($kg \cdot m^{-2} s^{-1}$)	k	fluid thermal conductivity ($W \cdot m^{-1} \cdot K^{-1}$)
$\dot{m}$	mass flow rate ($g \cdot s^{-1}$)	ν	kinematic viscosity ($m^2 \cdot s^{-1}$)
M	mass of ammonia absorption (g)	ϵ	ratio of color change (-)
Nu	Nusselt number (-)	Δ	difference (-)
Pr	Prandtl number (-)	*b*	blue (-)
q''	heat flux ($W \cdot m^{-2}$)	*fc*	final color (-)
Ra	surface roughness (μm)	*i*	a single variable (-)
Re	Reynolds number (-)	*ic*	initial color (-)
S	color change factor (-)	*loc*	local (-)
Sc	Schmidt number (-)	*max*	Maximum (-)
Sh	Sherwood number (-)	*now*	at current moment (-)
Le	Lewis number (= Sc/Pr) (-)	*tot*	Total (-)
t	time (s)	*w*	at the wall (-)
T	temperature (ºC)	∞	free stream flow (-)

REFERENCES

Joardar, A., Jacobi, A., 2005. Impact of leading edge delta-wing vortex generators on the thermal performance of a flat tube, louvered-fin compact heat exchanger. Int. J. Heat Mass Transf. 48(8) 1480-1493.

Kottke, V., Blenke, H., Schmidt, K. G.,1977. A remission photometry method for the determination of local mass transfer coefficients in the case of forced convection in air. Int. J. Heat Mass Transf. 10(1), 9-21.

Ahrend, U., Hartmann, A., Koehler, J., 2010. Measurements of local heat transfer coefficients in heat exchangers with inclined flat tubes by means of the ammonia absorption method. In 2010 14th International Heat Transfer Conference, American Society of Mechanical Engineers, 731-740.

Bejan, A., 1995. Convection Heat Transfer, second ed., Wiley, New York, 515-537.

ASHRAE Standard, 41.2, 1992. Standard methods for laboratory air-flow measurement, An American National Standard. 1987 (RA92)

Camci, C., Kim, K., Hippensteele, S.A., 1991. A new hue capturing technique for the quantitative interpretation of liquid crystal images used in convective heat transfer studies, In ASME 1991 International Gas Turbine and Aeroengine Congress and Exposition, American Society of Mechanical Engineers, V004T09A009-V004T09A009.

Goldstein, R., Cho, H., 1993. Review of mass (heat) transfer measurements using naphthalene sublimation. EXP THERM FLUID SCI 10(4), 416-434.

Dejong, N., Jacobi, 1997. A., An experimental study of flow and heat transfer in parallel-plate arrays: local, row-by-row and surface average behavior. Int. J. Heat Mass Transf. 40 (6) 1365-1378.

Moffat, R.J., 1988. Describing the uncertainties in experimental results, EXP THERM FLUID SCI 1(1), 3-17.

Manuscript ID: 1543
DOI: 10.18462/iir.icr.2019.1543

Application of a new method to quantify local air-side heat transfer coefficient on fundamental geometries

Min CHE[(a)], Stefan ELBEL[(a,b)]

[(a)] Air Conditioning and Refrigeration Center,
Department of Mechanical Science and Engineering,
University of Illinois at Urbana-Champaign,
1206 West Green Street, Urbana, IL 61801, USA, minche2@illinois.edu
[(b)] Creative Thermal Solutions, Inc.,
2209 North Willow Road, Urbana, IL 61802, USA, elbel@illinois.edu

ABSTRACT

A new optical method based on the analogy between heat and mass transfer is developed to obtain local air-side heat transfer coefficient (HTC). It uses thin-film coatings applied to the heat transfer surface in combination with a tracer gas. Experiments with fundamental geometries were conducted to calibrate the process and evaluate its accuracy. The local air-side HTCs results for laminar flow over a flat plate are within 20% compared to the Blasius solution except for the leading and trailing edges. The mass transfer experiments are conducted in a wind tunnel. Calibration for the flat plate experiments takes into account flow velocity, light source, relative humidity of air, tracer gas concentration, and sample aging effects. Correlations for these parameters have been established. The measurements of the basic geometries such as inclined plates, wedges, and cylinders agree with the experimental results of literatures which employed different methods. These promising validation experiments justify the exploration of more complex geometries and entire heat exchangers using this technique.
Keywords: Local HTC, Mass Transfer, Laminar Flow, Coating, Tracer Gas, Heat and Mass Transfer Analogy.

1. INTRODUCTION

Experimental techniques have been intensively studied in the past decades to quantify air-side HTC in order to seek opportunities to improve the efficiency of the fluid-to-gas heat exchangers. However, due to the complexity of air-side geometries, empirical correlations from experimental studies are usually used to predict heat transfer performance, and they are normally based on averaged HTC. Although several techniques are available to measure local air-side HTC, it is challenging to quantify local air-side HTC on complex geometries and entire heat exchangers.

Therefore, a new experimental method called coating, tracer gas, and color change (CTC) was proposed and explained by Che and Elbel (2018). The method is based on the analogy between heat and mass transfer. The CTC method shows a good accuracy within 20% (except for the leading and trailing edges of the sample) compared to the Blasius solution on flat plates. This paper is to further explore the potential applications of this method. Different flow velocity, light source, relative humidity of air, tracer gas concentration, and sample aging effects on the flat plates are tested. Other fundamental geometries such as inclined plates, wedges and cylinders are also measured and evaluated. It was confirmed that the method is robust and ready to be used to measure local HTCs for more complex geometries and heat exchangers found in HVAC&R applications.

2. METHODOLOGY

The CTC method employs an acidic coating material on the surface of interest. The coating changes color from yellow to blue at a certain pH level when it reacts with the tracer gas. Since the color change can be correlated with the local mass transfer coefficient, the local HTC can be quantified by applying the analogy theory. The CTC method applies a similar principle based on the well-established naphthalene sublimation method. Goldstein and Cho (1993) have reviewed and explained the naphthalene sublimation method in detail. The laminar flow boundary layer condition over a flat plate is shown in Fig 1.

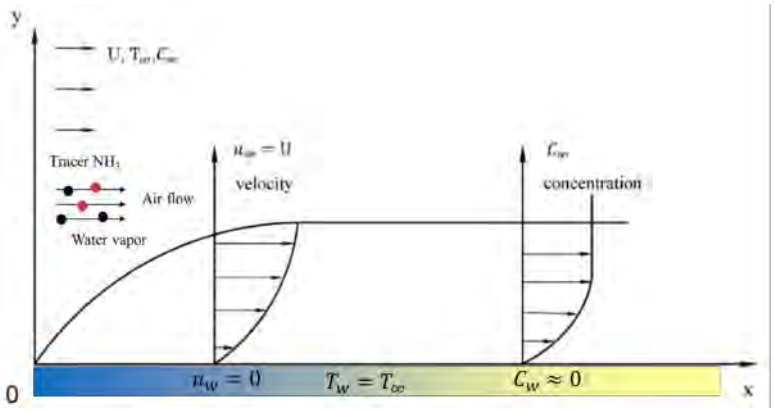

Figure 1: The principle and boundary layer assumptions of the CTC method

According to the analogy between convective heat and mass transfer, the format of heat transfer Eq. (1) and mass transfer Eq. (2) is the same.

$$u\frac{\partial T}{\partial x}+v\frac{\partial T}{\partial y}=\alpha\left(\frac{\partial^2 T}{\partial y^2}\right) \quad \text{Eq. (1)}$$

$$u\frac{\partial C}{\partial x}+v\frac{\partial C}{\partial y}=D\left(\frac{\partial^2 C}{\partial y^2}\right) \quad \text{Eq. (2)}$$

The analytical Blasius solution for heat transfer of laminar flow across a flat plate with an infinite spanwise length is shown in Eq. (3). The corresponding mass transfer solution is shown in Eq. (4). In this new method, Pr of air and Sc of ammonia are applied to Eq. (5) to obtain the correlation of the analogy which is equal to 1. Therefore, local heat transfer Nu number can be quantified by measuring local mass transfer.

$$\mathrm{Nu_{loc}}=0.332\cdot\mathrm{Pr}^{1/3}{\mathrm{Re_{loc}}}^{1/2}\ (\mathrm{Pr}>0.5) \quad \text{Eq. (3)}$$

$$\mathrm{Sh_{loc}}=0.332\cdot\mathrm{Sc}^{1/3}{\mathrm{Re_{loc}}}^{1/2}\ (\mathrm{Sc}\geq 0.5) \quad \text{Eq. (4)}$$

$$\frac{\mathrm{Sh_{loc}}}{\mathrm{Nu_{loc}}}=\left(\frac{\mathrm{Sc}}{\mathrm{Pr}}\right)^{1/3}=(\mathrm{Le})^{1/3}=\left(\frac{0.75}{0.74}\right)^{1/3}=1.00 \quad \text{Eq. (5)}$$

3. EXPERIMENTAL APPARATUS AND PROCEDURES

3.1 Experimental Apparatus

A suction type, open-loop wind tunnel is designed and built for the mass transfer experiments as shown in Fig. 2. The design followed the principles described by Barlow et al. (1999) and ASHRAE Standard 41.2-1987 (RA 92) (1992). The size of the test section is W120 mm x H100 mm x L400 mm to test small samples. The flow velocity across the test section can be adjusted from 0 to 3.5 $m{\cdot}s^{-1}$. Water vapor and anhydrous ammonia are injected and mixed with air flow at the entrance.

The test section is made of transparent polycarbonate sheets for color change observation. An electrochemical gas sensor is connected to the test section to obtain real-time volumetric ammonia concentration measurements. The images of color change are recorded by a webcam, which is connected to a computer. The image acquisition toolbox of MATLAB R2018a is employed to configure camera parameters and process the images. A 25W LED white panel is used as the light source to maintain a good image quality.

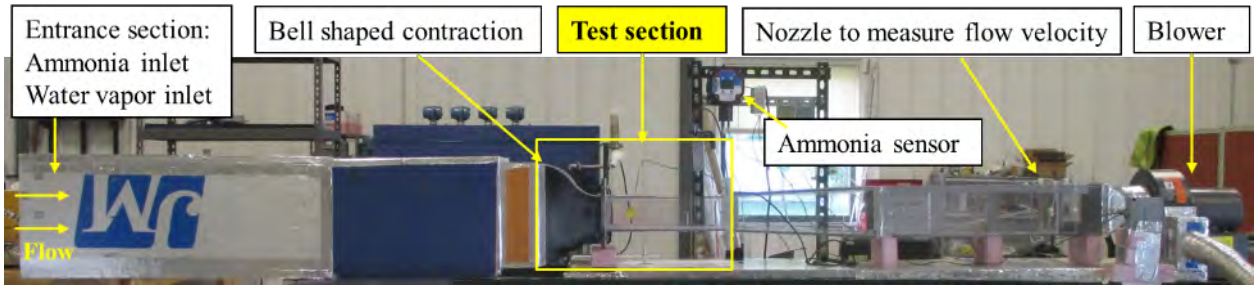

Figure 2: The wind tunnel for mass transfer experiments

3.2 Experiment Procedure to Quantify Local HTC

As shown in Fig. 3, a coupon with the original yellow coating is changing to a blue color in the wind tunnel. When the flow strikes the coated surface, the tracer gas is captured by the coating material, and a chemical reaction happens. The chemical reaction changes the pH level of the coating material and makes it change color from yellow to blue. If the color change and the mass transfer can be correlated, the mass transfer is quantified. The webcam starts recording as soon as the mass transfer starts and stops when the color of the entire surface has turned to blue.

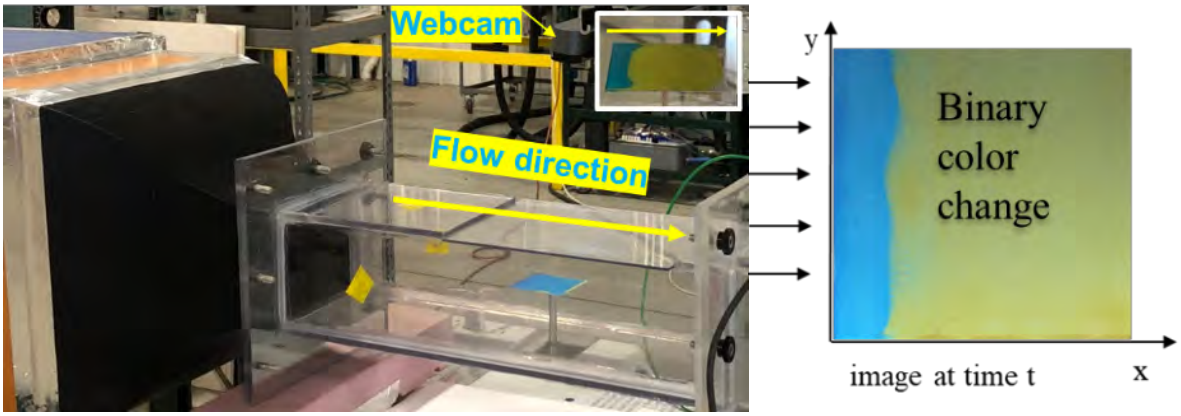

Figure 3: Mass transfer experiment on the flat plate

According to Ellinger (1963), hue is dependent on the wavelength of light being reflected or produced. Cantrell et al. (2010) explain the mechanism between hue and color wavelength. The equation to calculate hue value from the RGB image is embedded in the MATLAB R2018a toolbox. Therefore, the CTC method has been employed hue to quantify the color change.

Local HTC is calculated by Eq. (6) to Eq. (11). Eq. (6) shows how the ratio of color change (ϵ) is obtained at a specific time (t) for a single pixel of an image. As binary color change (yellow and blue) is observed, ϵ is either 0 or 1 for each pixel. Eq. (7) shows how mass flux (m'') is correlated to the color change. M_{max} represents the maximum mass of ammonia gas absorption which is determined from the chemical relations between the coating material and ammonia gas. The color change factor S is related to the experimental conditions and the characteristics of the dye. It has been confirmed by calibration tests that S can be approximated by a constant. The local mass transfer coefficient (h_{mloc}) is defined as the ratio of mass flux and concentration difference as shown in Eq. (8). As the analogy correlation of the method is explained in Eq. (5), the local HTC is related to the local mass transfer coefficient and shown in Eq. (9).

$$\epsilon = \frac{\text{hue}_{\text{now}} - \text{hue}_i}{\text{hue}_{fc} - \text{hue}_i} \quad \text{Eq. (6)}$$

$$m'' = \frac{\epsilon \cdot S \cdot M_{max}}{t \cdot A_{tot}} \quad \text{Eq. (7)}$$

$$h_{mloc} = \frac{m''}{\Delta C};\ Sh_{loc} = \frac{h_{mloc} x}{D} \quad \text{Eq. (8)}$$

$$h_{loc} = \frac{h_{mloc} \cdot k}{D} \quad \text{Eq. (9)}$$

4. EXPERIMENTAL RESULTS

4.1 Span-averaged HTC on Flat Plates

The flat plates are exposed to the tracer gas in the wind tunnel which is set at a baseline condition. The local HTCs are compared with the Blasius solution at various flow velocities within the range of the laminar flow. In Fig. 4, flow velocities from 0.6 m·s^{-1} to 3 m·s^{-1} are tested considering typical air-conditioning applications. When taking the total length (50 mm) as the characteristic length, the range of Re_L is 1934 to 10743. The data variation is within 20% except for the leading and trailing edges of the sample. A baseline condition is set which includes the following parameters: i) the flow with 25±1 ºC and 60±5 % relative humidity; ii) the tracer gas is 50±5 ppm volumetric concentration of ammonia iii) sample size is W50 mm x L50 mm x T0.3 mm; iv) 0.5 g coating solution with 25 % mass concentration is used to cover one side of the aluminum plate.

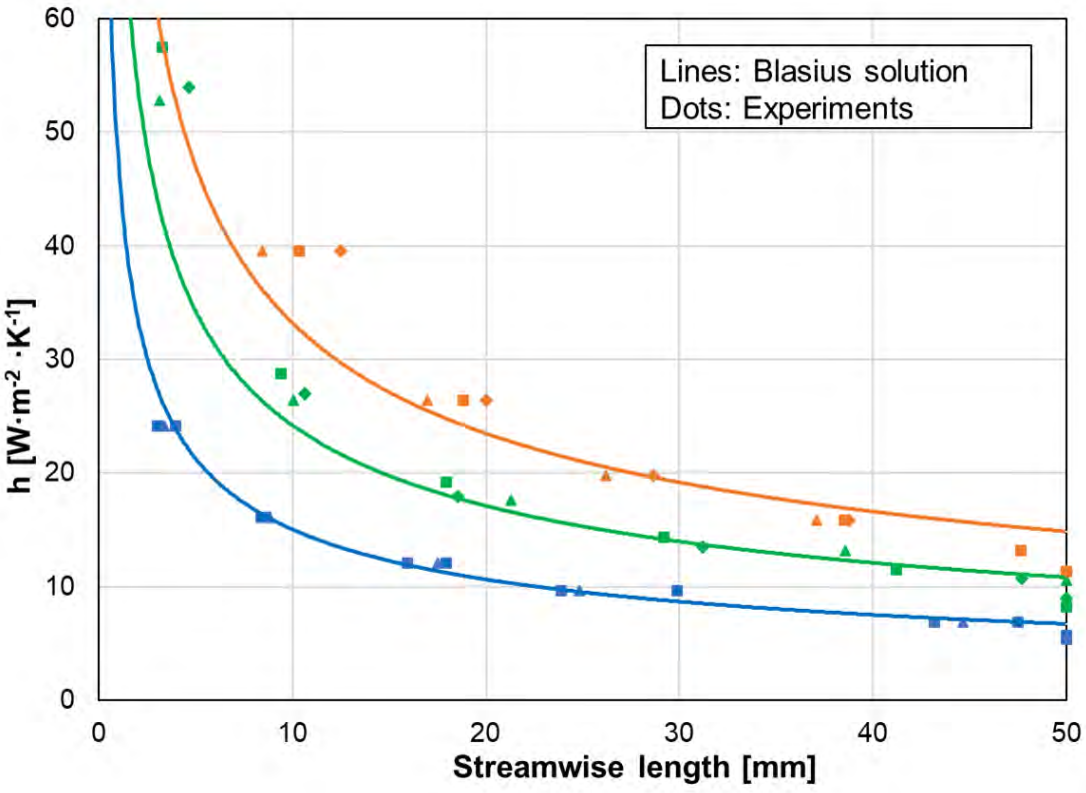

Figure 4: Local HTC at different flow velocities - flat plates

4.2 Local HTC of Wedges and Inclined Flat Surfaces

Wedges have been tested and compared with the tabulated analytical results of Eckert (1942). Wedges are tested with the CTC method to obtain local HTCs as shown in Fig. 5 and Fig. 6. Fig. 5 shows the span-averaged HTCs of a 90° wedge. Fig. 6 shows the surface color change at different time steps of a 180° wedge (impinging flow), and local HTC distribution is shown. The results have been compared with experimental results of different literature sources, namely, Ramirez et al. (2002) and Sparrow et al. (1979), who both employed the naphthalene sublimation method. However, Sparrow et al. (1979) only show the visualization of the flow pattern. Ramirez et al. (2002) have developed an optical measurement method which has a large scatter of data. The data cannot be used for the quantitative comparison.

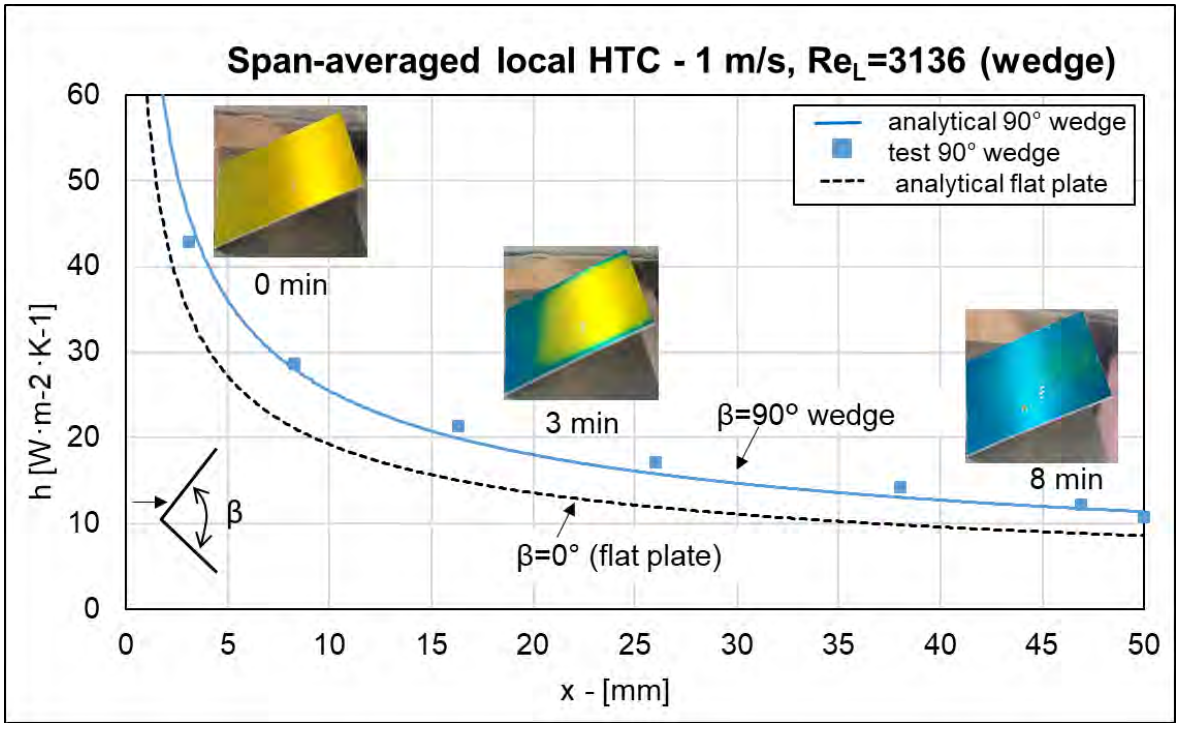

Figure 5: Span-averaged local HTCs of a 90° wedge

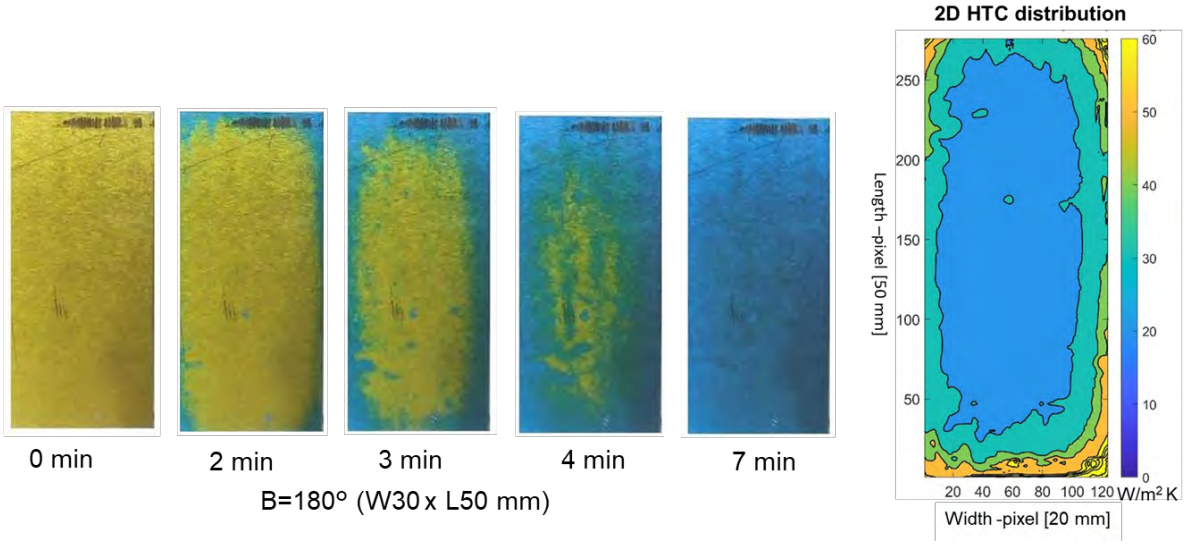

Figure 6: Color change and local HTC distribution of a 180° wedge (impinging flow)

4.3 Local HTC of Cylinders

Fig. 7 shows local HTCs of cylinders which are measured by the CTC method and compared with Krall and Eckert (1973) and Hong and Song (2007).

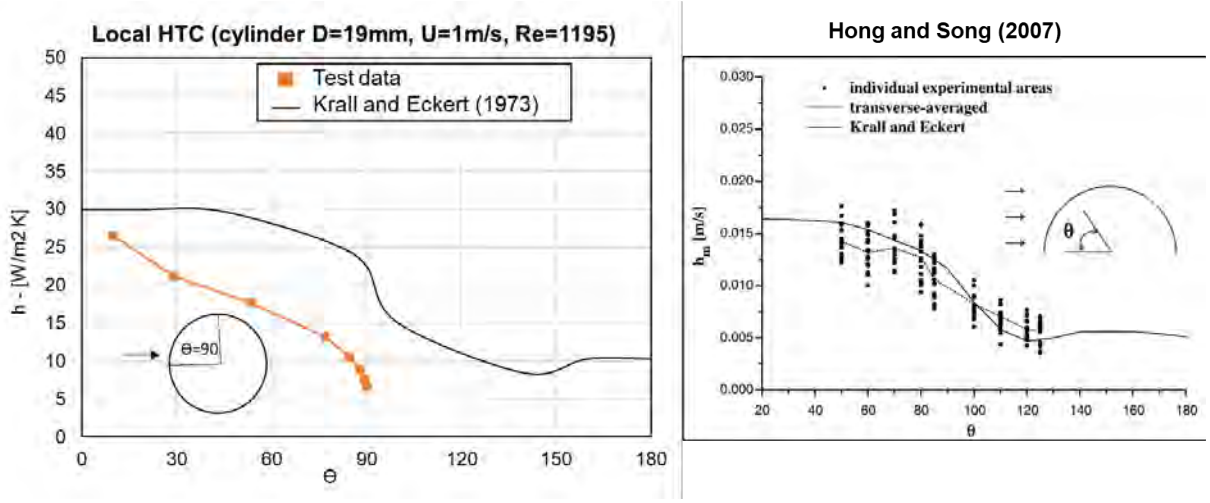

Figure 7: Local HTCs of cylinders

The HTC at the stagnation point is within 10% compared with the analytical results. All those experimental results show a similar curve shape. However, Krall and Eckert (1973) who have employed the temperature measurement method did not see local HTC difference from 0° to 50°. Hong and Song (2007) who have used the naphthalene sublimation method got a large scatter of data. Their measurement starts from 50°. The current measurements show a decrease of local HTCs from 0° to 50°. However, the cylinder size and flow velocities are different between these methods. Therefore, the quantitative comparison of the absolute HTC values is not necessarily possible in this case.

4.4 Light Source Influence

As color change is correlated to the mass transfer coefficient, the influence of the light source needs to be considered. At the baseline condition, a 25 W LED panel light and a yellow light bulb are used for comparison. As shown in Fig. 8, although absolute hue values are different, the maximum hue differences are consistent. ΔH of LED light is 0.3905 ($\mathrm{hue}_{fc} - \mathrm{hue}_i$), while ΔH of the yellow light bulb is 0.3896. The quantification of color change only requires a stable light source during the mass transfer experiment. Besides, the camera settings such as focus, brightness, saturation, etc. are also checked that once these parameters are fixed during the experiment, the color change results will not be influenced.



25 W LED initial hue=0.1664 | 25 W LED final hue=0.5569 | yellow light bulb initial hue=0.1189 | yellow light bulb final hue=0.5085

Figure 8: Initial and final color of the coated plates under different light sources

4.5 Method Robustness Evaluation

As the baseline condition is precisely controlled, the robustness of the method is checked under various conditions. Table 1 shows the range of test conditions that have been evaluated including flow temperature and relative humidity, ammonia concentration, and sample aging. The results show

that the color change factor is always 0.3 to obtain an accurate local HTC measurement. It means that the chemical reaction and color change are stable within these test conditions. It was also found that the color change will take 1 to 2 hours when relative humidity is lower than 50%. It is slightly slower compared to 7 to 9 minutes at 60% or higher relative humidity values. If the relative humidity is lower than 40%, no color change is observed. As the coating is sensitive to water vapor, it is proposed to put the sample is a dry environment for storage. For the ammonia, higher concentrations are not tested, because the sensor range is limited to 0-100 ppm.

Table 1: Mass transfer test at different conditions on flat plates

Variables	Range	S	$Nu_{loc} = Sh_{loc}$
Temperature (°C)	21-31	0.30	yes
Relative humidity (%)	50-85	0.30	yes
NH_3 [ppm]	35-85	0.30	yes
Sample aging [day]	0-45	0.30	yes

7. CONCLUSIONS

A new method to quantify local air-side heat transfer coefficients has been developed. The analogy between heat and mass transfer of this method has been verified with basic geometries. A good accuracy (within 20% except for the leading and trailing edges) is obtained compared to the Blasius solution. Moreover, this method shows a good repeatability within the tested experimental ranges which are commonly applied in typical HVAC&R applications. This paper shows that the developed procedure to quantify local HTCs can be applied at different flow velocity, light source, flow relative humidity, tracer gas concentration, and sample aging. As it has been demonstrated that the new method is capable of quantifying local air-side HTCs for simple flat plate geometries, it is believed to be applicable to more complex heat transfer surfaces. Therefore, this method has the potential to be further developed to analyze more involved heat transfer problems.

ACKNOWLEDGMENTS

The authors would like to thank the member companies of the Air Conditioning and Refrigeration Center at the University of Illinois at Urbana-Champaign for their finical support, Creative Thermal Solutions, Inc. (CTS) for providing technical support and equipment. The coating solutions are made by Serionix, Inc. located in Champaign, IL, USA.

NOMENCLATURE

A	area of the surface (m^2)	U	bulk flow velocity ($m \cdot s^{-1}$)
C	concentration ($kg \cdot m^{-3}$)	u	streamwise flow velocity ($m \cdot s^{-1}$)
D	diffusion coefficient ($m^2 \cdot s^{-1}$)	v	flow velocity normal to the plate ($m \cdot s^{-1}$)
h	convection heat transfer coefficient ($W \cdot m^{-2} K^{-1}$)	x	streamwise dimension (m)
h_m	convection mass transfer coefficient ($m \cdot s^{-1}$)	y	coordinate direction normal to the plate (m)
H	hue: color property (-)	z	spanwise dimension (m)
m''	mass flux ($kg \cdot m^{-2} s^{-1}$)	α	thermal diffusivity ($m^2 \cdot s^{-1}$)
$\dot{m}$	mass flow rate ($g \cdot s^{-1}$)	k	fluid thermal conductivity ($W \cdot m^{-1} \cdot K^{-1}$)
M	mass of ammonia absorption (g)	ν	kinematic viscosity ($m^2 \cdot s^{-1}$)
Nu	Nusselt number (-)	ϵ	ratio of color change (-)
Pr	Prandtl number (-)	Δ	difference (-)

q''	heat flux ($W \cdot m^{-2}$)	*b*	blue (-)
Re	Reynolds number (-)	*fc*	final color (-)
S	color change factor (-)	*i*	a single variable (-)
Sc	Schmidt number (-)	*ic*	initial color (-)
Sh	Sherwood number (-)	*loc*	local (-)
Le	Lewis number (= Sc/Pr) (-)	*max*	maximum (-)
t	time (s)	*now*	at current time (-)
T	temperature (ºC)	*tot*	total (-)
		w	at the wall (-)
		∞	free stream flow (-)

REFERENCES

Che, M., Elbel, S., 2018. Novel Visualization Method to Quantify Local Air-side Heat Transfer Coefficient, 24th International Compressor Engineering Conference at Purdue, July 9-12, 2018

Goldstein, R., Cho, H., 1993. Review of mass (heat) transfer measurements using naphthalene sublimation. EXP THERM FLUID SCI 10(4), 416-434.

Barlow, J. B., Rae, W. H., Pope, A., 1999. Low-speed Wind Tunnel Testing. John Wiley.

ASHRAE. Standard, 41.2, 1992. Standard methods for laboratory air-flow measurement. An American National Standard. 1987 (RA92)

Ellinger, R. G., 1963. Color Structure and Design. International Textbook Company.

Cantrell, K., Erenas, M.M., Orbe-Payá I. D., Capitán-Vallvey L. F., 2010. Use of the Hue Parameter of the Hue, Saturation, Value Color Space as a Quantitative Analytical Parameter for Bitonal Optical Sensors. Analytical Chemistry. 82(2), 531-542.

Eckert, E. R. G., 1942. Die Berechnung des Wärmeüberganges in der laminaren Grenzschicht umströmter Körper. VDI Forschungsheft 416: 1-24.

Ramirez, C., Murray, D. B., Fitzpatrick, J. A., 2002. Convective heat transfer of an inclined rectangular plate. Experimental Heat Transfer. 15(1), 1-18.

Sparrow, E. M., 1979. Effect of Finite Width on Heat Transfer and Fluid Flow about an Inclined Rectangular Plate. Journal of Heat Transfer, 101:199.

Krall, K. M, E. R. G. Eckert, 1973. Local heat transfer around a cylinder at low Reynolds number. Journal of Heat Transfer 95(2), 273-275.

Hong, K., Song, T.H., 2007. Development of optical naphthalene sublimation method. International journal of heat and mass transfer. *50*(19-20), 3890-3898.

Manuscript ID: 1547
DOI: 10.18462/iir.icr.2019.1547

An Experimental Study of Evaporative Coolers Using Elliptic Tubes

Jian-Cheng FANG, Liang-Han CHIEN , and De-Cian CHEN

Department of Energy and Refrigerating Air-Conditioning Engineering,
National Taipei University of Technology, Taipei, Taiwan, lhchien@ntut.edu.tw

ABSTRACT

This paper reports on the investigation of the heat/mass transfer and pressure drop performance characteristics of an evaporative cooler using elliptic or circular tubes. From the experimental results, correlations of the water film heat transfer coefficient and air-water mass transfer coefficient are developed. The experimental results show that the smaller contraction ratio of circular tube bundle results in higher air velocity between the tubes, and increases the fluid film waviness with water spraying outside the tubes. Consequently, the heat and mass transfer performance of the circular tube bundle is better than that of the elliptic one at the same air flow rate. However, the elliptic tube bundle yields only 1/3 pressure drop as compared with the circular one. Both the water film heat transfer coefficient and air-water mass transfer coefficient of elliptic and circular tube bundles increase with increasing air Reynolds number.
Keywords: Elliptic Tube, Evaporative Cooler, Pressure Drop, Heat and Mass Transfer.

1. INTRODUCTION

The structure design of different types of heat exchangers, including tube bundle arrangement and shape of tube has significant influence on the heat transfer performance of heat exchangers. For evaporative coolers, the heat transfer and pressure drop on the air side of the tubes are the main factors affecting the performance of heat exchangers. Therefore, the shape of the tube has great influence on evaporative coolers. As shown in Figure 1, due to the streamline shape of elliptic tube, less vortex generates behind the tube on the air side as compared with the circular tube, and hence can provide lower pressure drop, and improve the efficiency of heat exchangers.
In recent years, manufacturers have introduced elliptic tubes in evaporative coolers. The patent (Bugler et al., 2007) using elliptical connectors at both ends of the tube rows can make the tube bundle more closely arranged, as shown in Figure 2. The present study investigates the heat and mass transfer and pressure drop performance characteristics of an evaporative cooler using elliptic tubes, and compare with circular tubes at various air flow rate and spray water flow rate.

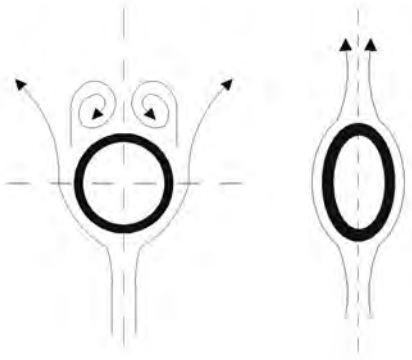

Figure 1: Steam line of circular tube and elliptic tube

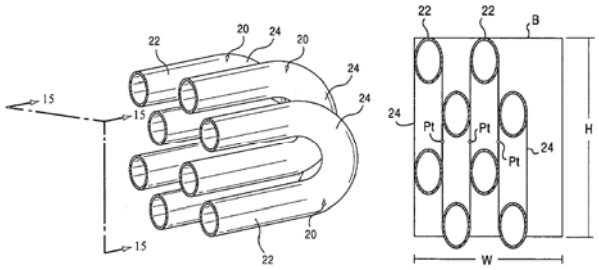

Figure 2: Elliptic tube patent of EVAPCO, Inc. (Parker and Treybal, 1961)

2. LITERATURE REVIEW

2.1. Research of Evaporative Cooling

Many researchers have investigated the evaporative coolers experimentally. Parker and Treybal (1961) were the first researchers to make the detailed analysis of counter-flow evaporative coolers in different modes of operation. They set up a staggered-tube evaporative cooler had an outside diameter of 19mm arranged in a 38mm triangular pattern, and made the empirical correlations. Mizushina et al. (1967) also set up an evaporative cooling experiment and determined the empirical correlations of film heat transfer coefficient and mass transfer coefficient. The outer diameter of the tube is 12.7mm, 19.05mm, and 40mm, and the tube pitch is twice outer diameter of the tube. Niitsu et al. (1969) tested evaporative coolers of plain and finned tubes, and developed empirical correlations of film heat transfer coefficient, mass transfer coefficient and pressure drop. The outer diameter of plain tube is 16mm, and using staggered arrangement. From the result of the experiment, the airside pressure drop affected by both air and spray water flow rate at the same time; however, the effect of spray water flow rate was relatively smaller than air flow rate. When spray water $\Gamma / d_o > 0.7$ kg m^{-2}s^{-1}, the mass transfer coefficient will be independent of spray water flow rate. In order to make the distribution of spray water and the wetting effect of the tubes better, the should higher than 0.8 kg m^{-2}s^{-1}.

Hasan et al. (2002) applied the cooling system consisted of a closed wet cooling tower (CWCT) to the ceiling of the building to reduce the indoor heat load. The prototype tower consists of 19 tubes of 10mm o.d. arranged in 12 rows in a staggered arrangement.

Heyns and Kröger (2010) tested an evaporative cooler consisting of 15 tube rows with 38.1 mm outer diameter arranged in a 76.2 mm triangular pattern. From the experimental tests show that, a deluge water mass velocity of 1.7 kg m^{-2}s^{-1} is required to ensure uniform wetting all the tubes. When the air mass velocity is higher than 3.5 kg m^{-2}s^{-1}, the deluge water partially held up on the tubes.

2.2. Research of Elliptic Tube Evaporative Cooler

Zheng et al. (2012) conducted the thermal performance characteristics of an oval tube CWCT. The tube bundle consists of 8 rows of externally galvanized steel oval tubes. The major axis of the tube is 31.8 mm, and minor axis is 21.6 mm with tube wall thickness 1.5 mm. The oval tubes are 1.2 m long and arranged in a stagger pattern at a transversal pitch of 44 mm and at a longitudinal pitch of 64 mm. There are 37 oval tubes per tube row. From the experimental results, the water-film heat transfer coefficient is a function of deluge-water temperature, deluge-water mass velocity and air mass velocity. The air-water mass transfer coefficient is a function of air mass velocity.

Hasan and Sirén (2004) investigated two kinds of evaporative coolers under similar operation conditions, one has plain circular tubes while the other one has plain oval tubes. The outer diameter of circular tube is 10 mm, and the oval tube (axis ratio 3.085) is formed from an 18 mm o.d. circular tube whose perimeter is preserved after forming. It is concluded that the average mass transfer Colburn factor j_m of the oval tube is 89% of the circular tube one, while the average friction factor f of the oval tube is 46% of the circular tube one. The ratio j_m / f of oval tube is 1.93-1.96 times of the circular tube one.

Although there are fewer literature about the evaporative cooler using elliptic tubes in practical application, the elliptic tube has been applied to the heat exchangers and improved the efficiency. According to the research by Hasan and Sirén (2004), the performance of elliptic tube applied to the evaporative cooler has more advantage than the circular one..

3. EXPERIMENTAL WORK

3.1. Test Apparatus

There are three part of the experimental system, including the process fluid flows (hot water) inside the tubes, the spray water on the tubes surface, and the air flows through the bank of tubes, as shown in Figure 3. The test has been set up in the environmental control room to control the outside air condition.

In order to make the air flow outside the tube bundle uniform, the test fan is placed at the end of the wind tunnel, drawing air over the tube bundle. The air flow enters from the both sides of wind tunnel below the tube bundle, and the air-guiding design is added to ensure uniform flow of air through the

tube bundle. A frequency changer is applied to allow the fan output to be varied. The average air velocity is determined by the pitot tubes inside the wind tunnel, and the dry bulb temperature and relative humidity of air inlet and outlet were measured by temperature/relative humidity transmitter.
To control the condition of hot water side, the temperature of the hot water is controlled by a constant temperature water tank, and the water flow rate is controlled by a pump and valve. The spray water is sprayed over the tube bundles surface through the spray nozzle, and then is pumped up to a circuit.
The water flow rate, inlet and outlet temperature on the both side of hot water and spray water are measured by turbine flowmeter and RTD. Figure 4 is the photograph of teat apparatus.

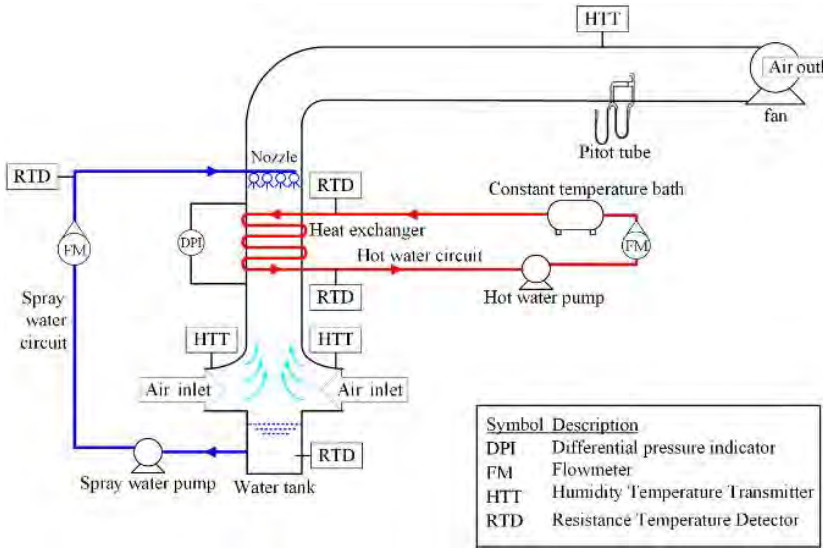

Figure 3: Schematic layout of experimental system



Figure 4: Experimental apparatus

3.2. Tube Bundle Geometry

Both the elliptic tube and circular tube bundles were tested. The heat exchanger test cross section is 600 mm by 266 mm, having a height of 350 mm. The outer diameter of circular tube is 15.88 mm, and the tube thickness is 0.41 mm. The elliptic tube (axis ratio= 2) is formed from a circular tube whose perimeter remains the same after forming. The elliptic tube has a major axis of 20.65 mm, and a minor axis of 10.2 mm. There are 8 tubes per each row, and 8 row in the tube bundles, arranged in a stagger pattern with transversal pitch of 31.2 mm and longitudinal pitch of 34.76 mm. On the left and right side of the tube bundles, transparent acrylic plates are installed for observation. Figure 5 shows the distribution of the circular tube and elliptic tube bundle geometries.

3.3. Scope of Tests

The tests were conducted under various operation conditions for the circular tube and elliptic tube bundles. The air inlet velocity ranges from 0.9 to 3.7 m s^{-1}. Three spray water flow rates were tested, which were 15, 20, and 25 L.$Min.^{-1}$(Liter per Minute). The hot water flow rate of the tube side was constant during the test and equal to 23.7 L.$Min.^{-1}$, and the inlet hot water temperature was 45℃.

3.4. Data Reduction

The hot water inside the tube of evaporative cooler transfer heat to the water film on tube surface through the wall of tube. The water film absorbs the heat and transfer to the air by the latent heat of evaporation and the sensible heat of temperature difference between water film and air as shown in Figure 6. The analysis assume a constant spray water temperature $\overline{t_s}$ equal to the inlet spray water temperature $t_{s,1}$, and make a $\mathrm{d}A_o$ as an element on the surface of the tube. Therefore, the heat transfer dq from the hot water to the spray water film can be expressed as Eq. (1):

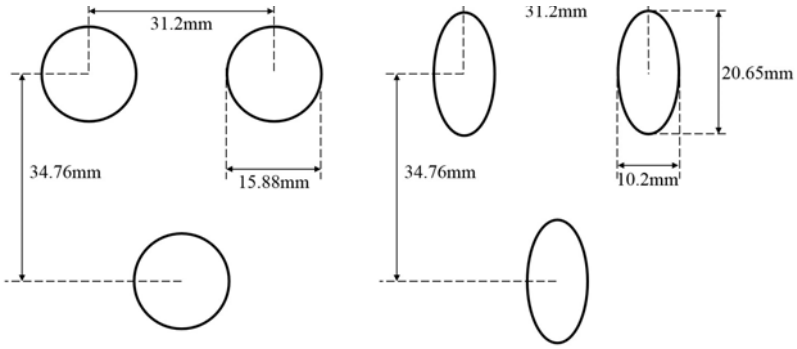

Figure 5: Tube bundle dimensions

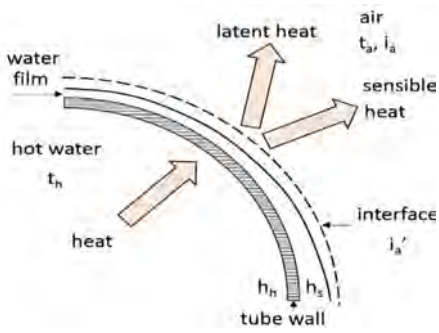

Figure 6: Heat transfer from the hot water to airside

$$dq = \dot{m}_h C_p dt_h = U_o\left(t_h - \overline{t_s}\right)dA_o \qquad \text{Eq. (1)}$$

Integrating the temperature of hot water from inlet to outlet, the overall heat transfer coefficient is given by Eq. (2):

$$U_o = \frac{\dot{m}_h C_p}{A_o}\ln\left(\frac{t_{h,1} - \overline{t_s}}{t_{h,2} - \overline{t_s}}\right) \qquad \text{Eq. (2)}$$

The total thermal resistance from the inside of the tube to the outer spray water film on tube surface can be express as Eq. (3), where h_s is the convective heat transfer coefficient between the tube and the spray water film, and h_h is the convective heat transfer coefficient between the hot water inside the tube:

$$\frac{1}{U_o} = \frac{1}{h_s} + \frac{d_o \ln\left(d_o/d_i\right)}{2k_t} + \frac{d_o}{d_i h_h} \qquad \text{Eq. (3)}$$

The convective heat transfer coefficient h_h is calculated by Gnielinski correlation. The water film heat transfer coefficient h_s is given by Eq. (4):

$$h_s = \left[\frac{1}{U_o} - \frac{d_o \ln\left(d_o/d_i\right)}{2k_t} - \frac{d_o}{d_i h_h}\right]^{-1} \qquad \text{Eq. (4)}$$

According to the Merkel equation, Jaber and Webb (1989) calculated the heat of mass transfer between wet surface and air as Eq. (5):

$$dq = \dot{m}_a di_a = K_m\left[i_a'\left(\overline{t_s}\right) - i_a\right]dA \qquad \text{Eq. (5)}$$

where $i_a'(\overline{t_s})$ is the saturated air enthalpy at the spray water temperature. Integrating the enthalpy of air from inlet to outlet, the mass transfer coefficient is given by Eq. (6):

$$K_m = \frac{\dot{m}_a}{A_o}\ln\left[\frac{i_a'\left(\overline{t_s}\right) - i_{a,1}}{i_a'\left(\overline{t_s}\right) - i_{a,2}}\right] \qquad \text{Eq. (6)}$$

The air side Reynolds number is defined by Eq. (7), where μ_w is the viscosity of air and the u_{max} is the maximum velocity calculated based on the minimum cross section area of air flow. The L_c in Eq. (7) is the characteristic length, which is the tube diameter of circular tube or the tube width of the narrow side of the oval tube. The film Reynolds number of spray water is given by Eq. (8), where Γ is the mass flow rate per unit length, μ_w is the viscosity of water.

$$Re_a = {\rho u_{max} L_c}/{\mu_a} \quad \text{Eq. (7)}$$

$$Re_w = {\Gamma}/{\mu_w} \quad \text{Eq. (8)}$$

The total energy balance between inlet and outlet of the experimental system is given by Eq. (9):

$$\dot{m}_h C_p \left(t_{h,1} - t_{h,2}\right) = \dot{m}_a \left(i_{a,2} - i_{a,1}\right) \quad \text{Eq. (9)}$$

4. RESULTS AND DISCUSSION

4.1. Air-Side Pressure Drop

The elliptic tube is expected to have a smaller pressure drop because of its streamline shape. Figure 7 shows the comparison of no spray water and various spray water flow rate for elliptic and circular tube bundles. When the water spraying on the tube bundles, the pressure drop was much higher than that without spraying water, and the pressure drop rises as the air Reynolds number increases. Due to the unstable sprayed water distribution in the air flow, the curves of pressure drop at different spray water flow rate are more irregular than that without spray water. The overall pressure drop increases with the increasing air flow Reynolds number for both cases.
The lower contraction ratio of circular tube bundle results in higher air velocity between the bundle. When the inlet air velocity of circular tube bundles is about 2.7 m s^{-1} (air Reynolds number 4000), the pressure drop with spraying water increases sharply. The observation through the side windows shows that excess water holds up on among the tubes, and increases the fluid film waviness with water spraying outside the tubes, which also causes the increase of pressure drop.

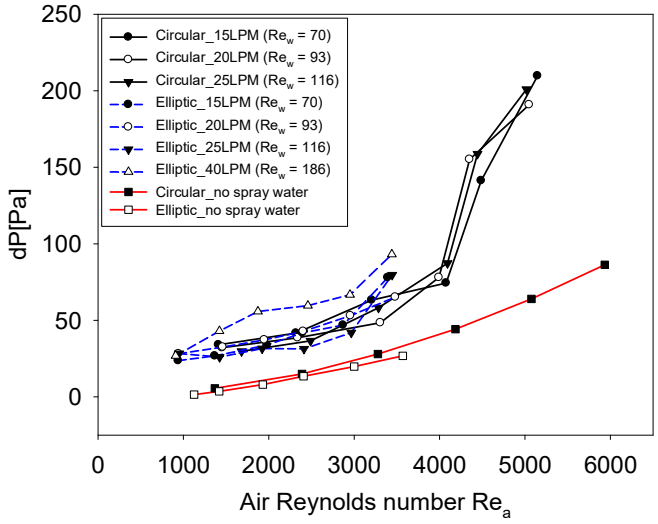

Figure 7: The dP-Re$_a$ of circular and elliptic tube

4.2. Water Film Heat Transfer Coefficient

The water film heat transfer coefficient of the elliptic and circular tube bundles at various spray water flow rate is shown in Figure 8. Note that the air Reynolds number of the elliptic tube bundle is smaller than that of the circular one at the same fan frequency (or fixed fan power consumption rate) because the air flow velocity and pressure drop of the elliptic tube bundle is smaller. For example, for the maximum fan power, the *Re$_a$* of elliptic tube is about 3500, yet the circular tube is about 5000. At the same fan frequency, the water film heat transfer coefficient of elliptic tube is smaller than that of circular one at the same spray water flow rate of 40 L.Min.$^{-1}$. The lowest water film heat transfer coefficient occurs at the spray water flow rate of 10 L.Min.$^{-1}$ because the distribution of spray water

at low flow rate is non-uniform. The water film heat transfer coefficient of the elliptic tube at various spray water flow rate is about 18~20% lower than that of the circular one.

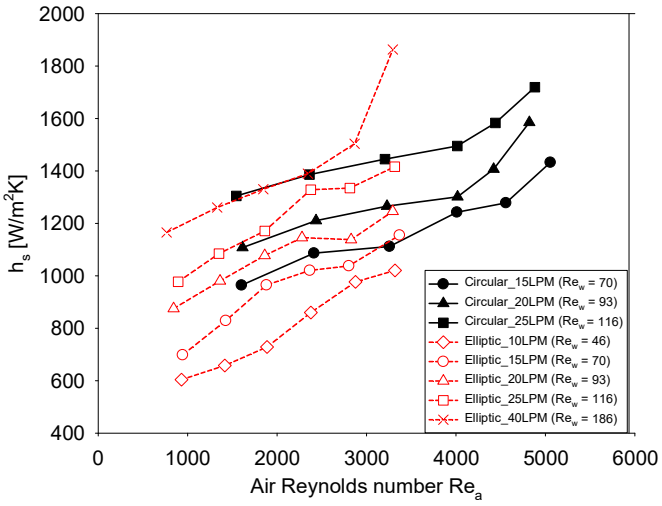

Figure 8: The h_s-Re_a of circular and elliptic tube

4.3. Mass Transfer Coefficient

The mass transfer coefficient of the elliptic and circular tube bundles at various spray water flow rate is shown in Figure 9. At the same fan frequency, the mass transfer coefficient increases as the spray water flow rate increases. However, comparing the effect of airflow and spray water on mass transfer coefficient, the increase of the mass transfer coefficient is mainly affected by the air flow. Similar to the trend of the pressure drop curves, when the air Reynolds number of circular tube bundles is about 4000, the mass transfer coefficient increases sharply. As a result, the mass transfer performance of the circular tube is better than that of the elliptic one in a higher air velocity condition.

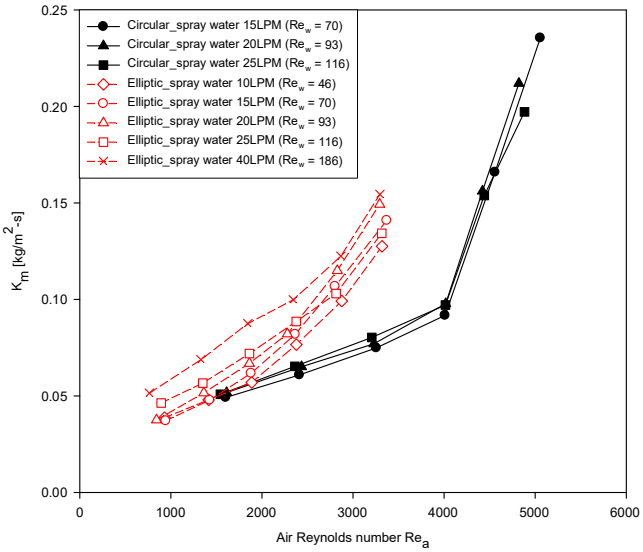

Figure 9: The K_m-Re_a of circular and elliptic tube

4.4. Correlations of h_s & K_m

From the experimental results, correlations for the water film heat transfer coefficient and mass transfer coefficient of both elliptic tube and circular tube are developed. It is found that when the fan frequency is greater than 25 Hz ($Re_a \approx 900$ for elliptic and $Re_a \approx 1600$ for circular), significant amount of spray water hold up on the surface of circular tube bundles and affects the heat and mass transfer. Therefore, the mass transfer coefficient of circular tube bundles is divided into two part according to the range of air Reynolds number.

The correlations of water film heat transfer coefficient developed by Parker and Treybal (1961) and Heyns and Kröger (2010) for circular tube bundles and the elliptic tube bundles by Zheng et al. (2012) considered the effect of spray water temperature. The correlation of water film heat transfer coefficient for both circular tube and elliptic tube in this study is a function of air Reynolds number Re_a, spray water Reynolds number Re_w and average spray water temperature T_w, and the inlet spray water temperature $t_{s,1}$ is regarded as the average spray water temperature as given by Eq. (10), valid for $765 < Re_a < 5056$，$45 < Re_w < 194$，$28 < T_w < 36$ ℃.

$$h_s = 0.3618\,\mathrm{Re}_a^{0.4263}\,\mathrm{Re}_w^{0.4165}\,T_w^{0.8176} \qquad \text{Eq. (10)}$$

The correlations of mass transfer coefficient developed by Mizushina et al. (1967) and Heyns and Kröger (2010), in addition to the effect of air flow rate, they also considered the effect of spray water floe rate. The correlation of mass transfer coefficients in this study including air Reynolds number Re_a and spray water Reynolds number Re_w. The correlations of mass transfer coefficient for elliptic tube as given by Eq. (11), for $1350 < Re_a < 3370$，$45 < Re_w < 187$).

$$K_m = 8.617\times10^{-6}\,\mathrm{Re}_a^{1.195}\,\mathrm{Re}_w^{0.169} \qquad \text{Eq. (11)}$$

The correlations of mass transfer coefficient for circular tube as given by Eq. (12) for ($1544 < Re_a < 4018$，$69 < Re_w < 122$), and Eq. (13) based on different range of air Reynolds number ($4010 < Re_a < 5056$，$66 < Re_w < 115$).

$$K_m = 0.0003\,\mathrm{Re}_a^{0.7113}\,\mathrm{Re}_w^{0.1336} \qquad \text{Eq. (12)}$$

$$K_m = 9.6267\times10^{-15}\,\mathrm{Re}_a^{3.7154}\,\mathrm{Re}_w^{-0.0134} \qquad \text{Eq. (13)}$$

Figure 10 compares the predictions of the correlations for water film heat transfer coefficient. The correlation of Zheng et al. (2012) at air Re_a of 3000 has the similar trend as the prediction of Eq. (10) at Re_a of 1000. The reason is due to the difference in the size of tube array, including the diameter of tube and tube pitch. Figure 11 shows the comparison of the mass transfer coefficient correlations. The studies of Zheng et al. (2012) and Hasan and Sirén (2004) does not account for the effect of spray water flow rate on the mass transfer coefficient. Since the tube pitch in this study is similar to the experimental size of Hasan and Sirén (2004), the predictions of these correlations are in good agreement. However, the tube pitch of Zheng et al. (2012) experiment is much larger than that in this study, which results in a significant different mass transfer coefficient. From these comparison, we found that the size of heat exchanger, diameter of tube, contraction ratio of tubes and type of spray nozzle may have a significant impact on heat and mass transfer performance in using these correlations.

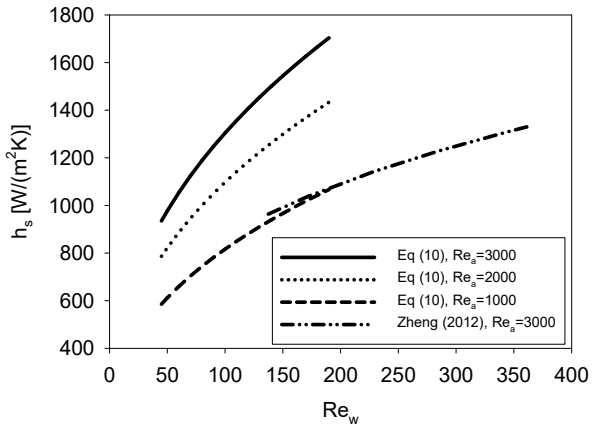

Figure 10: The water film heat transfer coefficient correlation of elliptic tubes

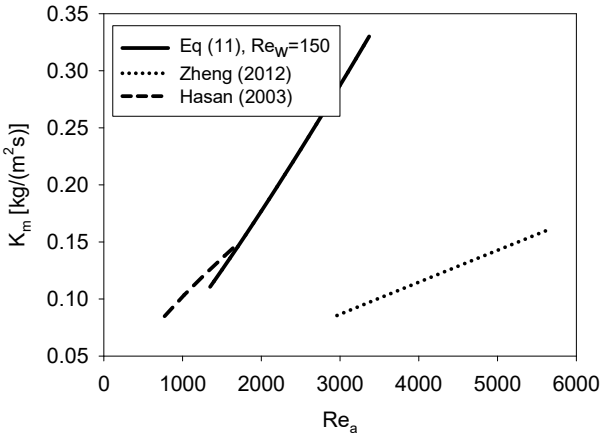

Figure 11: The mass transfer coefficient correlation of elliptic tubes

5. CONCLUSIONS

The performance of circular tube and elliptic tube evaporative coolers were investigated experimentally under various air flow rate and spray water flow rate, and analysis the pressure drop and heat-mass transfer performance. It is concluded that

(1) The pressure drop of elliptic tube is lower than the circular one at various spray water flow rates, and the main reason affecting the pressure drop is the air flow rate.

(2) When the inlet air velocity of circular tube bundles is about 2.7 m s^{-1}, the pressure drop with spraying water will increase sharply. The lower contraction ratio of circular tube bundle results in higher air velocity between the bundle, and increases the fluid film waviness with water spraying outside the tubes. Consequently, it also affects the heat and mass transfer performance.

(3) Both the water film heat transfer coefficient and air-water mass transfer coefficient of elliptic tube and circular tube increase with increasing air Reynolds number. The heat and mass transfer performance of the circular tube bundle is better than the elliptic one.

(4) Comparing the thermal-hydraulic performance of elliptical tube with circular tube, the heat and mass transfer performance of elliptic tube is slightly smaller than the circular one. However, the elliptic tube yields only 1/3 pressure drop as compared with circular tube.

(5) From the comparison of literatures, although the air flow rate and spray water flow rate are at the same condition, the size of heat exchanger, diameter of tube, contraction ratio of tubes and type of spray nozzle may have a significant impact on heat and mass transfer performance.

ACKNOWLEDGEMENTS

We are thankful for the financial support of Ministry of Science and Technology, Taiwan. Project no.: MOST-107-3113-E-027-001-CC2

REFERENCES

Bugler, T., Shriver, G. and Merrill, R., 2007. Heat exchanger apparatus incorporating elliptically- shaped serpentine tube bodies. US Patent 7,296,620 B2.

Parker, R., Treybal, R., 1961. Heat, mass transfer characteristics of evaporative coolers. *AIChE Chemical Engineering Progress Symposium Series* 57(32), 138–149.

Mizushina, T., Ito, R., Miyasita, H., 1967. Experimental study of an evaporative cooler., *International Chemical Engineering* 7 (4), 727–732.

Niitsu, Y., Naito, K., Anzai, T., 1969. Studies on characteristics and design procedure of evaporative coolers. *Journal of SHASE* 43.

Hasan, A., Sirén, K., 2002. Theoretical and computational analysis of closed wet cooling towers and its applications in cooling of buildings. *Energy and Buildings* 34 (5), 477–486.

Heyns, J., Kröger, D., 2010. Experimental investigation into the thermal-flow performance characteristics of an evaporative cooler. *Applied Thermal Engineering* 30, 492–498.

Zheng, W., Zhu, D., Song, J., Zeng, L., and Zhou, J., 2012. Experimental and computational analysis of thermal performance of the oval tube closed wet cooling tower. *Applied Thermal Engineering* 35, 233–239.

Hasan, A., Sirén, K., 2004. Performance investigation of plain circular and oval tube evaporatively cooled heat exchangers. *Applied Thermal Engineering* 24, 777-790.

Jaber, H., Webb, R.L., 1989, Design of cooling towers by the effectiveness-NTU method, *Journal of Heat Transfer*, 111 (4), 837-843.

Manuscript ID: 1563
DOI: 10.18462/iir.icr.2019.1563

Experimental assessment of a detachable plate falling film heat and mass exchanger couple using lithium bromide and water as working fluids

Tianle HU[(a)], Yuhao YI[(a)], Xiaoyun XIE[(a)], Yi JIANG[(a)]

[(a)] Building Energy Research Center, Tsinghua University
Beijing, 100084, People's Republic of China, hutl15@mails.tsinghua.edu.cn

ABSTRACT

Massiveness and cost have impeded the promotion of absorption heat pump (AHP) system for a long time. An improved detachable plate falling film heat and mass exchanger (HMX) couple using lithium bromide (LiBr) and water as working fluids is proposed and a resulting prototype is experimentally assessed. The HMX couple can work as either a generator-condenser couple, or an absorber-evaporator couple in an AHP using LiBr and water as working fluid. In generator-condenser condition, overall heat and mass transfer coefficients of the generator were 0.607~1.008 $kW \times m^{-2} \times K^{-1}$ and $4.4 \times 10^{-5} \sim 18.4 \times 10^{-5}$ $m \times s^{-1}$ respectively, and overall heat transfer coefficient of the condenser varies from 0.372 to 1.466 $kW \times m^{-2} \times K^{-1}$; in absorber-evaporator condition, overall heat and mass transfer coefficients of the generator were 0.235~0.422 $kW \times m^{-2} \times K^{-1}$ and $0.7 \times 10^{-5} \sim 1.5 \times 10^{-5}$ $m \times s^{-1}$ respectively, and overall heat transfer coefficient of the condenser varies from 0.785 to 1.173 $kW \times m^{-2} \times K^{-1}$. The experimental results of the HMX couple prototype show feasibility to scale down the size of AHP, and promote application of absorption technology accordingly.

Keywords: Absorption System, Falling Film, Heat Transfer Coefficient, Mass Transfer Coefficient, Plate Exchanger.

1. INTRODUCTION

Massiveness and cost have been long-standing problems of absorption heat pump (AHP) systems, which have impeded the promotion of this technology. Many researchers attempted to scale down the size of AHP using ammonia as refrigerant through adopting some compact heat exchanger configurations like plate heat exchanger(Boudéhenn et al., 2012; Zacarías et al., 2010), and micro-channel heat exchanger(Determan and Garimella, 2012). However, there are scarce researches focused on compact AHP systems using water as refrigerant. Mortazavi et al. (2015) introduced an absorber design suitable for the plate-and-frame absorber configuration. The design utilizes a fin structure installed on a vertical flat plate to produce a uniform solution film and minimize the film thickness, and to interrupt the boundary layer continuously. Similar structure has also been applied and tested in a generator (Mortazavi et al., 2017). Michel et al. (2017) developed a vertical grooved falling film absorber using a new plate-type falling film absorber design. A 1-D stationary model of water vapor absorption in a laminar vertical falling film was introduced and validated. In our previous study (Hu et al., 2017a), a plate falling film generator, which includes a directly connected overflow solution distributor, was presented. This more compact novel structure, with ensured stable falling-film flow(Hu et al., 2017b), provides better feasibility to regulate capacity by plate assembly compared with conventional falling film distributors. Based on the directly connected liquid distributor, a novel plate falling film heat and mass exchanger(HMX) couple was presented and experimentally tested when applied as a generator and condenser couple(Hu et al., 2019). However, the wetting behavior in the prior HMX is still to be improved to enhance the overall performance.

In this paper, a detachable plate falling film HMX couple with improved distributor when applied as both generator-condenser couple, and absorber-evaporator couple is experimentally assessed and analyzed.

2. DESIGN CONCEPT

A detachable plate falling film HMX couple was firstly developed in our previous study(Hu et al., 2019). As shown in Figure 1 b-d, a stream of working liquid (solution or refrigerant water) flows into liquid inlet chambers (1), and is then divided and introduced to each liquid storage zone (5).With the liquid level increasing in the liquid storage zone, it overflows the overflow weir (4) and flows into the working fluids channel (6) in the form of a falling film adhering to the plate surface. Liquids after experiencing a heat and mass transfer process (absorption, generation, evaporation, or condensation) in different working fluids channels of a module (11 or 12) are streamed into a liquid outlet chamber (8). Vapor generated (introduced) flows out of (in) a working fluids channel though an injected vapor channel (3), and the vapor channel also functions as a liquid baffle. The vapor is collected or divided in a vapor chamber (2). One module (11 or 12) can include multiple (although each module consists only two units in Fig.1) projecting heat and mass transfer units. Working fluids of the multiple units of each module are collected or divided in the chambers (1, 2, and 8) respectively. Especially, all the chambers of a unit are settled on the same side. Therefore, the solution distributor is asymmetric because the inlet solution enters into the distributor from only one side of it rather than both sides in our previous study mentioned above. Two modules are entwined together and accordingly heat medium channels (7) are developed within the spaces between the two entwined modules. Chambers used to collect or divide the working fluids are placed on the same side of each module, on the opposite side of the two entwined modules. The HMX presented above, which consists of two entwined modules, is detachable since its heat medium channels can be exposed by extracting the two entwined modules from the opposite direction. As show in Figure 1 (a), the attaching and detaching processes are similar to the entwining and loosing of fingers. Two HMXs are coupled to reduce vacuum connection components. HMX couple is realized by connecting two corresponding vapor chambers with two vapor pipes on the same side of two modules from different HMX. The two pipe-connected modules can be extracted as a whole in a detaching process. The HMX couple can be functioned as both a generator and condenser couple, and an absorber and evaporator couple in an AHP that uses water as refrigerant.

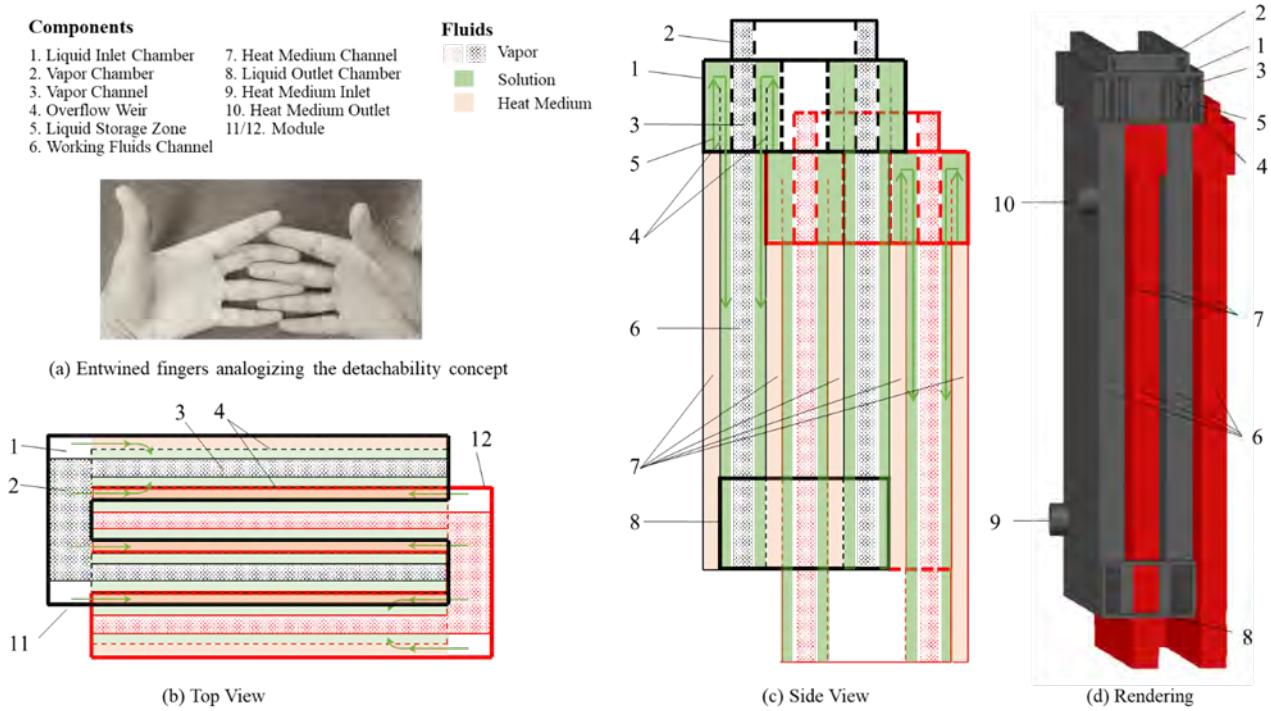

Figure 1: Conceptual sketch of a detachable heat and mass exchanger

In this paper, some modifications were made to liquid distribution zones based on the HMX couple prototype prior reported, in order to improve the wetting behavior and hence get a better performance. Heat transfer area of each HMX is 1.86 m^2.

3. EXPERIMENTAL ASSESSMENT AND DISCUSSION

3.1. Experiment Description

Two experiment conditions need to be conducted: generator-condenser condition and absorber-evaporator condition in order to experimentally assess the improved HMX couple comprehensively, and two different experimental setups are necessary accordingly. The experimental methodology for the generator-condenser condition has been presented in detail in our previous study(Hu et al., 2019), only a description for absorber-evaporator experiment is presented here.

As shown in Figure 2, the absorber-evaporator experimental setup consists of three flow lines: the working pair line (shown in blue), the heating water line (shown in red), and the cooling water line (shown in green). The heat sink of the absorber is a stream of circulating cooling water produced by an air-cooled chiller. A PID controller is used to ensure that temperature of the inlet cooling water fluctuates within ±1℃. The heat source of the evaporator is a stream of circulating hot water heated by electrical heaters. The strong solution is pumped from a solution tank into a pre-heater and then into the absorber. The refrigerant water is pumped from a refrigerant water tank into the evaporator. The electrical heaters for the heating water circuit and the solution circuit are controlled by changing the number of working heaters, and input heat capacity of the generator is then accordingly controlled.

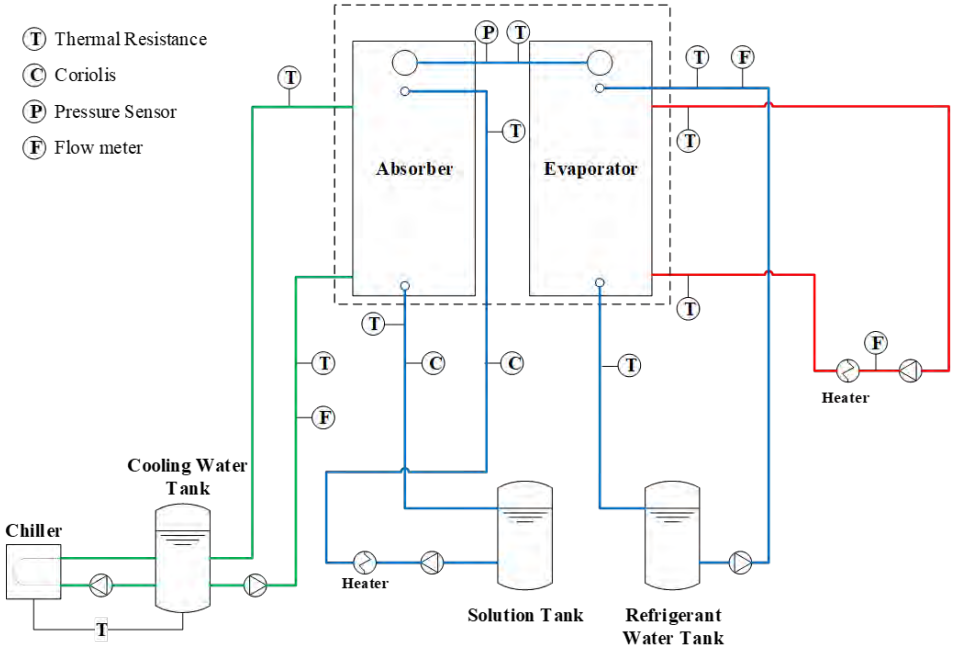

Figure 2: Piping and instrumentation diagram of the experiment apparatus for absorber-evaporator condition

The solution densities $\rho_{s,in}$ and $\rho_{s,out}$ are measured by corresponding Coriolis sensors. The temperatures of the working pairs and heat mediums $t_{s,in}$, $t_{s,out}$, $t_{ht,w,in}$, $t_{ht,w,out}$, $t_{cl,w,in}$, $t_{cl,w,out}$, and t_v are measured by T type thermocouples. The inlet solution mass flow rate $m_{s,in}$ is measured by a local Coriolis sensor. The flow rate of the cooling water $m_{cl,w}$ is measured by a magnetic flow meter. A pressure sensor was used to measure the working pressure P, and the thermal load of the generator Q_g or the evaporator Q_e is obtained through directly measuring the electrical heating rate in the heating water circuit. All the parameters, including pressure, are measured after they were stabilized. Under the experimental conditions, the working pressure fluctuates as the inlet temperature of cooling water fluctuates around the set temperature of the cooling water tank (the amplitude is usually within 20 Pa) and so are the other parameters influenced by the condensing pressure. The mean average values within 10 minutes after all the parameters reached stable state are taken as outcomes. Table 1 shows all the instruments mentioned above and their accuracies.

Table 1. Instruments and accuracy

Instruments	Accuracy
Coriolis flow/density meter	±0.2%
T type thermocouple	±0.3℃
Pressure sensor(Setra)	±0.5%
Magnetic flow meter	±0.5%
Wattmeter (Hioki 3169-20 Clamp On Power Hitester)	±0.5%

The range and uncertainty of the key operating conditions used in this parametric study namely solution and refrigerant flow rates, pressures, concentrations, and temperatures are summarized in Table 2.

Table 2. Range and uncertainty of parameters

Parameter		Range in G-C condition	Range in A-E condition	Uncertainty
Inlet solution mass flow rate per perimeter	$kg\times m^{-1}\times min^{-1}$	1.8-5.8	2.7-7.4	±0.2%
Heating water mass flow rate	$kg\times s^{-1}$	0.6-1.2	1.2	±0.5%
Cooling water mass flow rate	$kg\times s^{-1}$	1.0	1.1	±0.5%
Heat flux in generator or evaporator	$kW\times m^{-2}$	2.4-9.3	2.0-4.2	±0.5 %
Inlet temperature of cooling water	℃	20.8	25.5	±1.44%
Solute mass fraction of inlet solution	wt.%	48.0-54.5	47.4-52.1	±0.42%
Pressure	kPa	2.4-5.5	2.2-4.4	±0.5%

3.2. Data Reduction

During the data reduction process, the following assumptions were made to simplify the calculation:

1) Steady-state condition.
2) The interfacial mass transfer resistance is neglected and the interface is in an equilibrium state.
3) The pressure and temperature of vapor is assumed to be constant in the entire generator and condenser coupling.
4) Condensed refrigerant water at the outlet of the condenser is saturated.
5) Gas leakage is neglected and non-condensable gas is not existed in the HMXs.
6) Perfect heat insulation is assumed.

The thermodynamic properties of the water and lithium bromide mixtures were obtained using the computational formulations from Patek and Klomfar (2006). Through the computational formulations, $x_{s,in}$ and $x_{s,out}$ can be obtained based on $\rho_{s,in}$ and $t_{s,in}$, and $\rho_{s,out}$ and $t_{s,out}$ respectively. Equilibrium concentrations of solution $x_{eq,in}$ and $x_{eq,out}$ can be obtained based on $t_{s,in}$ and $t_{s,out}$ for a given(measured) working pressure P respectively. The enthalpy of solution was obtained based on solution temperature measured and solution concentration calculated, and the enthalpy of water was obtained through local temperature and generation pressure P. Programs were coded using EES (V10.113) (Klein and Alvarado, 2009).

Thermal load of the condenser is calculated as follows:

$$Q_c = c_{p,w} m_{cl,w} \left(t_{cl,w,out} - t_{cl,w,in} \right) \quad \text{Eq. (1)}$$

The logarithmic mean temperature difference in the condenser is calculated as follows:

$$\Delta t_{lm,c} = \frac{\left(t_r - t_{cl,w,in} \right) - \left(t_r - t_{cl,w,out} \right)}{\ln\left(\frac{t_r - t_{cl,w,in}}{t_r - t_{cl,w,out}} \right)} \quad \text{Eq. (2)}$$

The calculated thermal load of the condenser and the logarithmic temperature difference can be used to calculate the overall heat transfer coefficient in the condenser:

$$K_{h,c} = \frac{Q_c}{A_c \times \Delta t_{lm.c}} \quad \text{Eq. (3)}$$

The logarithmic mean temperature difference in the evaporator is calculated as follows:

$$\Delta t_{lm,e} = \frac{\left(t_r - t_{ht,w,in}\right) - \left(t_r - t_{ht,w,out}\right)}{\ln\left(\frac{t_r - t_{ht,w,in}}{t_r - t_{ht,w,out}}\right)} \quad \text{Eq. (4)}$$

The measured thermal load of the evaporator Q_e and the logarithmic temperature difference can be used to calculate the overall heat transfer coefficient in the evaporator:

$$K_{h,e} = \frac{Q_e}{A_e \times \Delta t_{lm.e}} \quad \text{Eq. (5)}$$

In a falling film generation or absorption process, energy conservation equation of heating water is as follows:

$$c_{p,w} m_w dt_w = K_h (t_w - t_s) dA \quad \text{Eq. (6)}$$

Assuming the equilibrium film exists at the interface between the gas phase and the liquid phase, thus the mass transfer equation between solution and vapor is as follows:

$$dm_s = K_m \rho_s (x_{eq} - x) dA \quad \text{Eq. (7)}$$

Energy conservation equation of solution is as follows:

$$d(m_s h_s) + h_{evap} dm_s = c_{p,w} m_w dt_w \quad \text{Eq. (8)}$$

Conservation equation of solute mass is as follows:

$$d(m_s x) = 0 \quad \text{Eq. (9)}$$

With the measured parameters $\rho_{s,in}$, $t_{s,in}$, $t_{s,out}$, $t_{w,in}$, $t_{w,out}$, and Q_g or Q_a as boundary conditions, $K_{h,g}$ and $K_{m,g}$ or $K_{h,a}$ and $K_{m,a}$ of each experiment condition can be attained by solving above differential Eq. (6)~(9) using finite-difference method.

Outlet solution mass flow rate of the generator or absorber can be calculated through the solute mass conservation equation. Accordingly, the generation rate is calculated as follows:

$$\Delta m_g = \left(m_{s,in} - m_{s,out}\right) \cdot 1000 \quad \text{Eq. (10)}$$

Similarly, the absorption rate is calculated as follows:

$$\Delta m_a = \left(m_{s,out} - m_{s,in}\right) \cdot 1000 \quad \text{Eq. (11)}$$

3.3. Generator-Condenser Condition

3.3.1. Generator

Figure 3 presents the effect of solution mass flow rate on heat and mass transfer performance of the generator, with heating flux being kept at 8.0 kW×m^{-2}. When solution mass flow rate increases from 1.8 kg×m^{-1}×min^{-1} to 5.8 kg×m^{-1}×min^{-1}, overall heat transfer coefficients increase from 0.607 kW×m^{-2}×K^{-1} to 1.008 kW×m^{-2}×K^{-1}, and mass transfer coefficients increase from 4.4×10^{-5} m×s^{-1} to 18.4×10^{-5} m×s^{-1}. Compared with our previous experimental results of the primitive prototype(Hu et al., 2019)

, the improved prototype in this paper shows obvious enhancement in mass transfer performance, and the mass transfer coefficients are in the comparable level with a conventional horizontal-tube absorber. However, the overall heat transfer coefficients are comparatively slow due to small water velocity in water channels(Hu et al., 2019).

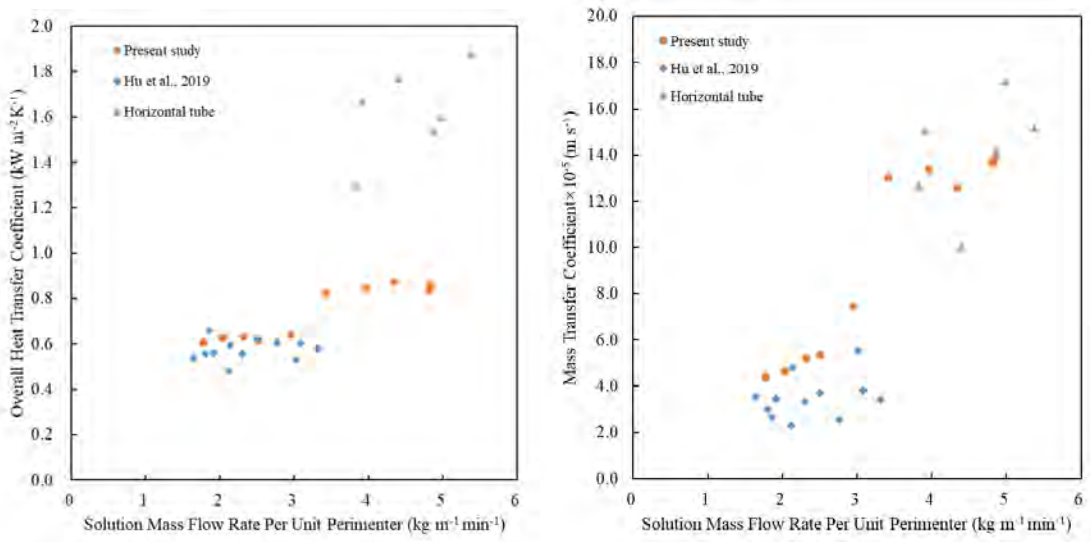

(a) (b)

Figure 3: Comparison of heat and mass transfer performance in different solution mass flow rates

3.3.2. Condenser

Figure 4 shows the experiment results of the condenser, taking heat transfer coefficients as functions of the evaporation rate, with cooling water mass flow and inlet cooling water temperature being kept at 1.0 kg×s^{-1} and 20.8 ℃ respectively. In the generation rate range of 1.32 g×s^{-1}-6.08 g×s^{-1}, heat transfer coefficients of the evaporator fluctuates randomly from 0.372 kW×m^{-2}×K^{-1} to 1.466 kW×m^{-2}×K^{-1}.

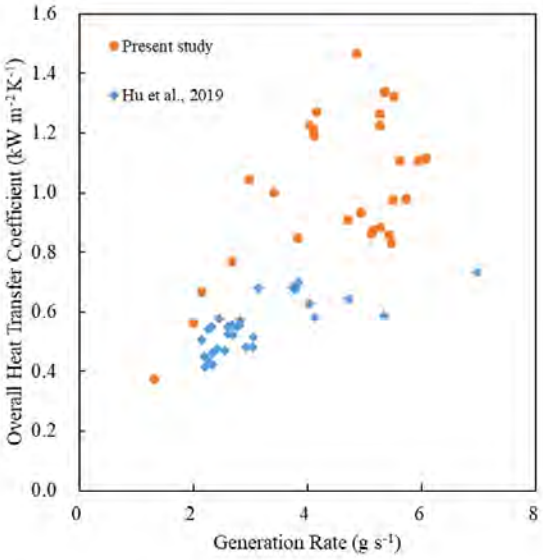

Figure 4: Effect of generation rate on the overall heat transfer coefficient in the condenser

3.4. Absorber-Evaporator Condition

3.4.1. Absorber

Figure 5 presents the effect of solution mass flow rate on heat and mass transfer performance of the absorber. When solution mass flow rate increases from 2.7 kg×m^{-1}×min^{-1} to 7.4 kg×m^{-1}×min^{-1}, overall heat transfer coefficients increase from 0.235 kW×m^{-2}×K^{-1} to 0.422 kW×m^{-2}×K^{-1}, and mass transfer coefficients increase from 0.7×10^{-5} m×s^{-1} to 1.5×10^{-5} m×s^{-1}. Both heat and mass transfer coefficients linearly increase with the solution mass flow rate.

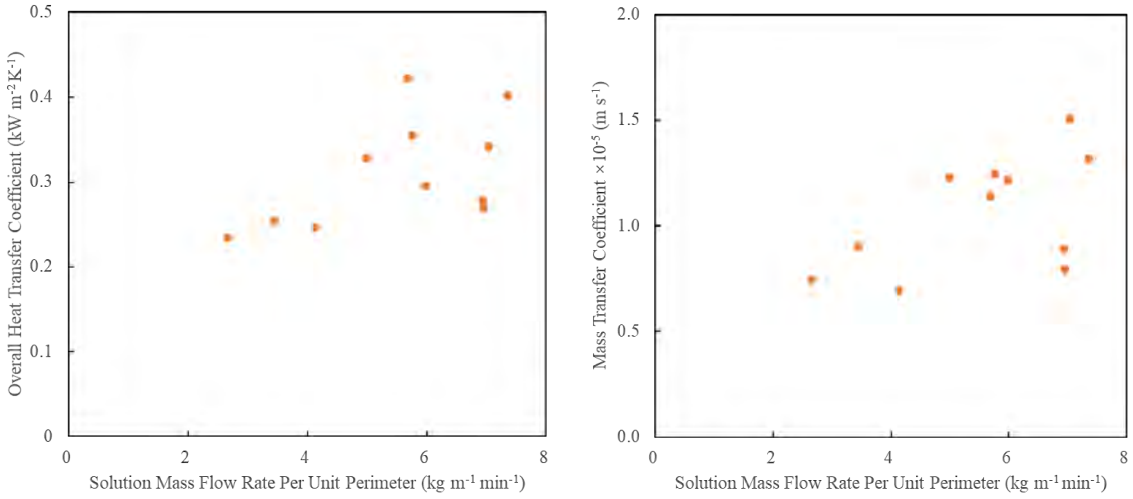

(a) (b)

Figure 5: Heat and mass transfer performance with different solution mass flow

In detail, the driving force for the absorption process is the difference between the water vapor pressure in the LiBr solution ($P_{s,w}$) and the absorber vapor phase pressure (P_v). Any change in temperature and concentration of the solution phase results in changes in the pressure potential and hence the mass flux of vapor absorbed. The solution water vapor pressure ($P_{s,w}$) is the average of the solution water vapor pressure (calculated using the corresponding solution temperature and concentration) at the absorber inlet and outlet. The water vapor pressure in the vapor phase (P_v) is the measured vapor pressure. Figure 6 presents variations of the absorption rate as a function of pressure potential for the present study as well as a membrane based absorber with heat and mass transfer areas larger than 1 m^2(Ali, 2010).Mass flux of vapor absorbed increases from 0.0007 $kg \times m^{-2} \times s^{-1}$ to 0.0018 $kg \times m^{-2} \times s^{-1}$, with water vapor pressure potential increased from 0.7 kPa to 1.8 kPa. The Mass flux of vapor absorbed achieved in this study is at the same level with that of the prior study.

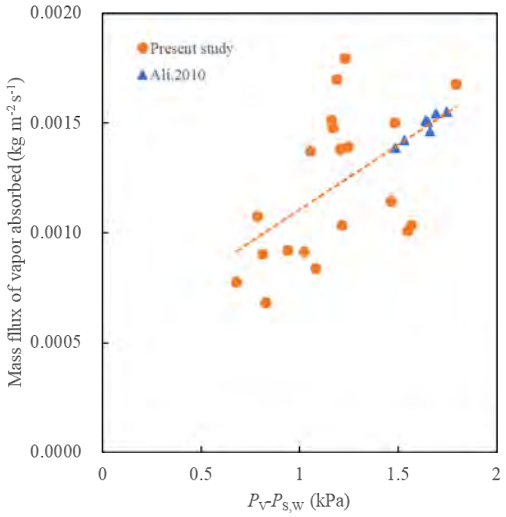

Figure 6 Variation of mass flux of vapor absorbed as a function of water vapor pressure potential

3.4.2. Evaporator

Figure 7 shows the experiment results of the evaporator, taking overall heat transfer coefficients as functions of the heat flux, with heating water mass flow being kept at 1.2 $kg \times s^{-1}$. Within the experimental heat flux range, the overall heat transfer coefficients are linearly increase with heat flux. The overall heat transfer coefficient of the evaporator increases by 49% from 0.785 $kW \times m^{-2} \times K^{-1}$ to 1.173 $kW \times m^{-2} \times K^{-1}$, when the heat flux increase from 2.0 $kW \times m^{-2}$ to 4.2 $kW \times m^{-2}$.

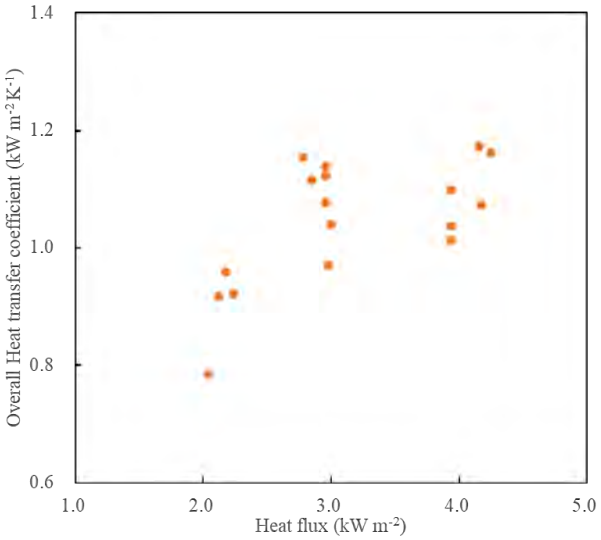

Figure 7: Effect of heat flux on overall heat transfer coefficient in the evaporator

4. CONCLUSIONS

A detachable plate falling film HMX couple, which is capable of functioning as either a generator-condenser couple, or an absorber-evaporator couple in an AHP using water as refrigerant, is proposed and experimentally assessed in this paper. Some conclusions can be made as follows:

1) The proposed improved HMX coupling yields higher mass transfer coefficients in the generator and higher overall heat transfer coefficients in the condenser;
2) The mass fluxes of vapor absorbed in the absorber achieved in this study are at a comparable level with that of the prior study with membraned structure;
3) In the experiment heat flux range of 2.0 kW×m^{-2} to 4.2 kW×m^{-2}, the overall heat transfer coefficient of the evaporator linearly increases by 49% from 0.785 kW×m^{-2}×K^{-1} to 1.173 kW×m^{-2}×K^{-1}.

ACKNOWLEDGEMENTS

The authors gratefully acknowledge the support from the National Natural Science Foundation of China (grant numbers 51306098, 51138005), the innovative Research Groups of National Natural Science Foundation of China (grant number 51521005), and Tsinghua University Initiative Scientific Research Program (No. 20151080470).

NOMENCLATURE

A	area (m^2)	*Subscripts*	
C_p	specific heat at constant pressure (kJ×kg^{-1}×K^{-1})	c	condenser
K_h	heat transfer coefficient (kW×m^{-2}×K^{-1})	g	generator
K_m	mass transfer coefficient (m×s^{-1})	e	evaporator
Q	heat rate (kW)	a	absorber
h	specific enthalpy (J×kg^{-1})	r	refrigerant water
m	mass flow rate (kg×s^{-1})	s	solution
P	pressure (kPa)	*v*	refrigerant vapor
t	temperature (℃)	w	water
x	solution mass fraction (%)	in	inlet of a component
		out	outlet of a component
Greek symbols		eq	equilibrium
Δt_{lm}	logarithmic mean temperature difference (℃)	ht	heating
Δm	mass transfer rate, g/s	cl	cooling
ρ	density		

REFERENCES

Ali, A. H. H. 2010. Design of a compact absorber with a hydrophobic membrane contactor at the liquid–vapor interface for lithium bromide–water absorption chillers. Appl. Energy, 87(4): 1112-1121.

Boudéhenn, F., Demasles, H., Wyttenbach, J., Jobard, X., Chèze, D., & Papillon, P. 2012. Development of a 5 kW Cooling Capacity Ammonia-water Absorption Chiller for Solar Cooling Applications. Energy Procedia, 30: 35-43.

Determan, M. D., & Garimella, S. 2012. Design, fabrication, and experimental demonstration of a microscale monolithic modular absorption heat pump. Appl. Therm. Eng., 47: 119-125.

Hu, T., Xie, X., & Jiang, Y. 2017a. Design and experimental study of a plate-type falling-film generator for a LiBr/H_2O absorption heat pump. Int. J. of Refrigeration, 74: 304-312.

Hu, T., Xie, X., & Jiang, Y. 2017b. Numerical Research on Flow Characteristics in a Plate-type Falling Film Heat Exchanger for a LiBr/H 2 O Absorption Heat Pump. Procedia Engineering, 205: 485-491.

Hu, T., Xie, X., & Jiang, Y. 2019. A detachable plate falling film generator and condenser coupling using lithium bromide and water as working fluids. Int. J. of Refrigeration, 98: 120-128.

Klein, S., & Alvarado, F. 2009. Engineering Equation Solver, F-Chart Software, Middleton, WI.

Michel, B., Le Pierrès, N., & Stutz, B. 2017. Performances of grooved plates falling film absorber. Energy, 138: 103-117.

Mortazavi, M., Isfahani, R. N., Bigham, S., & Moghaddam, S. 2015. Absorption characteristics of falling film LiBr (lithium bromide) solution over a finned structure. Energy, 87: 270-278.

Mortazavi, M., Schmid, M., & Moghaddam, S. 2017. Compact and efficient generator for low grade solar and waste heat driven absorption systems. Appl. Energy, 198: 173-179.

Pátek, J., & Klomfar, J. 2006. A computationally effective formulation of the thermodynamic properties of LiBr–H2O solutions from 273 to 500K over full composition range. Int. J. of Refrigeration, 29(4): 566-578.

Zacarías, A., Ventas, R., Venegas, M., & Lecuona, A. 2010. Boiling heat transfer and pressure drop of ammonia-lithium nitrate solution in a plate generator. Int. J. of Heat and Mass Transfer, 53(21-22): 4768-4779.

Manuscript ID: 1586
DOI: 10.18462/iir.icr.2019.1586

Experimental research and numerical simulation of the periodic frost melting process

Zheng REN[(a)], Xingqun ZHANG[(a)], Xiaojun DONG[(a)], Beile ZHANG[(b)], Xiaozhuan CHEN[(b)], Yu HOU[(a)], Tianwei LAI[(a)]

[(a)] State Key Laboratory of Multiphase Flow in Power Engineering, Xi'an Jiaotong University
Xi'an, 710049, China, laitianwei@mail.xjtu.edu.cn
[(b)] Institute of Mechanical and Power Engineering, Henan Polytechnic University
Jiaozuo, 454000, China, 211705010029@home.hpu.edu.cn

ABSTRACT

In order to study the frosting characteristics of the circular pipe below -60℃, a test rig for frosting visualization on a double-pipe heat exchanger has been built based on a cascade refrigeration system. In a series of experimental studies, the periodic melting phenomenon was observed during the frost development and maturity period, in which the thickness of the frost layer increases and decreases in a periodic way. The periodic frosting process in experiments is systematically summarized. For further investigation on the frosting characteristics, a frost melting criterion is added to the transient mathematical model of unsteady frosting on the circular pipe. The simulated results have the same trend as the experimental results, which show, that the model can accurately predict the melting process. The results show that the higher the humid air temperature or wall temperature is, the earlier the melting node appears. When the first melting phenomenon occurs, the interval of the periodic melting phenomenon becomes longer.
Keywords: Frost, Circular Pipe, Growth Rate, Periodic Melting, Low Temperature.

1. INTRODUCTION

Frosting is a common phenomenon in the field of refrigeration and cryogenic engineering, which often occurs on cold surfaces exposed to moist air. With the growth of the frost layer, the heat transfer efficiency of the heat exchanger decreases gradually. Therefore, it is important to investigate the frosting process on the surface of the different heat exchangers.

Most numerical simulation of frost research focuses on predicting frost characteristic parameters such as thickness, density and thermal conductivity (Kandula, 2012) and expanding its application range (Kim et al., 2015). Some others have studied frost growth under natural convection and forced convection (Lee et al., 1997) and its influencing parameters experimentally. In recent years, some scholars have used cryogenic heat exchangers in dehumidification. In rocket launching, the frosting also appears on the surface of cryogenic fuel tanks. These studies extend the temperature range of frosting characteristics. Zendehboudi et al. (2017) analysed 711 data points using artificial intelligence technology and then established a numerical model for estimating frost thickness in the vertical direction of a low temperature surface. Kim et al. (2009) numerically studied the heat transfer characteristics and frost formation on the surface of a low temperature oxidizer tank for a liquid propellant rocket, where a frost layer could be a significant factor in maintaining oxidizer temperature within a required range. Liu et al. (2016) established an experimental system of frosting on a low temperature surface under natural convection conditions, and carried out a series of frosting experiments under different conditions. It is found that under very low surface temperature and natural convection conditions, the frost layer thickness declines as the surface temperature drops. This is completely different from the phenomenon observed on ordinary cold surfaces.

In order to investigate the frost characteristic below -60℃, an experimental platform for visual frosting of a double-pipe heat exchanger is built. The frosting characteristics of a circular wall in confined space are studied. Then the transient frosting model on the surface of the circular tube is established to predict the frost parameters such as density, thermal conductivity and so on.

2. EXPERIMENTAL RESEARCH ON THE FROST PERIODIC MELTING PROCESS

2.1 Introduction and Error Analysis of the Test Rig

The test rig for frosting visualization on a double-pipe heat exchanger is shown in Fig. 1. The test rig is composed of three systems: the cascade refrigeration system, the visualization channel for frosting and data acquisition system. The two-stage cascade refrigeration system is designed to provide a constant low temperature through the refrigerant evaporation process in the pipe. The frost visualization channel is divided into three sections. The inlet and outlet of the frost visualization channel are the moist air parameters adjusting sections. The middle of the channel is the frosting observation section. In addition, the data acquisition system consists of temperature and humidity sensor, air velocity sensor, microscope, data recorder and computer.

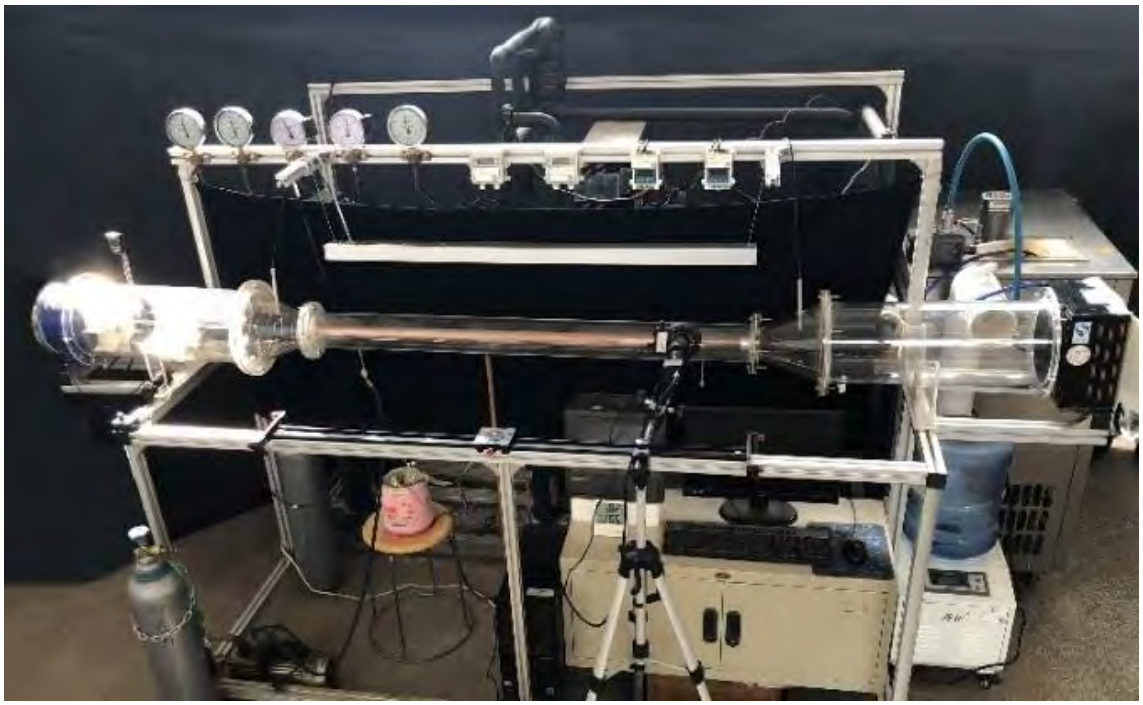

(a) Photograph of the test rig

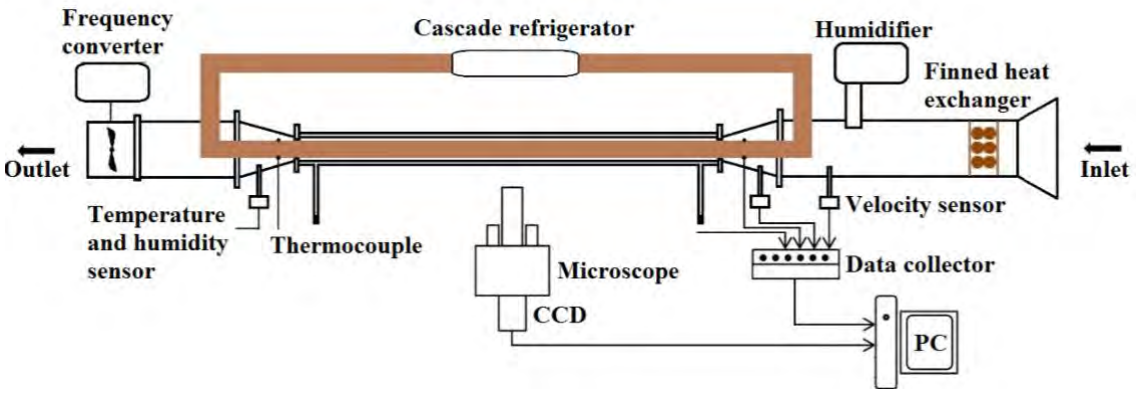

(b) Schematic diagram

Fig 1: The test rig for frosting visualization on the double-pipe heat exchanger

The detailed configuration of the double-pipe heat exchanger is shown in Fig. 2. The inner tube is a thin-walled copper tube, in which evaporative R23 refrigerant is used to provide constant low wall temperature. The frost accumulates at the outside of the copper pipe. The middle pipe is plexiglass in which moist air circulates. The outer vacuum layer is designed to eliminate the influence of ambient temperature on the frosting process. During the experiment, the frost formation is observed and frost images are collected by stereomicroscope.

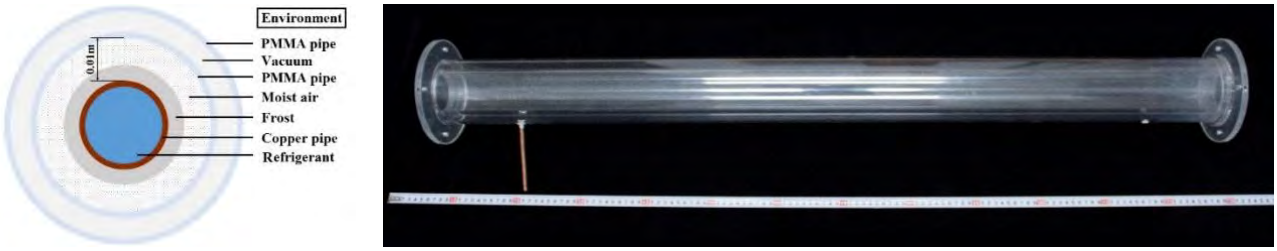

(a) Axial sketch (b) Polymethyl methacrylate(PMMA) channel

Fig 2: Frost visualization channel

As is known, the frosting process is affected by many parameters, such as wall temperature (T_w), air temperature (T_a), flow rate (v), air relative humidity (RH), and frosting wall characteristics (O'Neal et al., 1985). The precision of instrumentation used in this experiment is shown in Table 1.

Table 1. The precision of instrumentation

Equipment	Temperature and humidity sensor		Speed sensor	Thermocouple	Microscope
Precision	±0.3℃	±2%	±0.1m/s	±0.5℃	1080*1920

In order to ensure the reliability of the experiment, it is required that the experiment exclude the influence of irrelevant factors, such as compressor vibration, heat transfer between environment and frosting channel, radiation heat from light source, refraction of plexiglass tube, etc. The stability of working conditions and the accuracy of data acquisition have a great impact on the frost experiment. The repetitive experiment of the frost layer thickness growth is shown in Fig. 3. The air temperature and humidity in one of the experiments is shown in (a). It can be seen that the curves are stable, which indicates high accuracy of the test conditions. Two groups of experiments under the same working conditions (T_w=-60℃, T_a=35℃, v=3m/s, RH=51%) are shown in (b). The maximum difference of thickness between the two groups is 3.2×10^{-4}m, which is less than 6%. Thus, high repeatability and reliability of the experiment results are guaranteed.

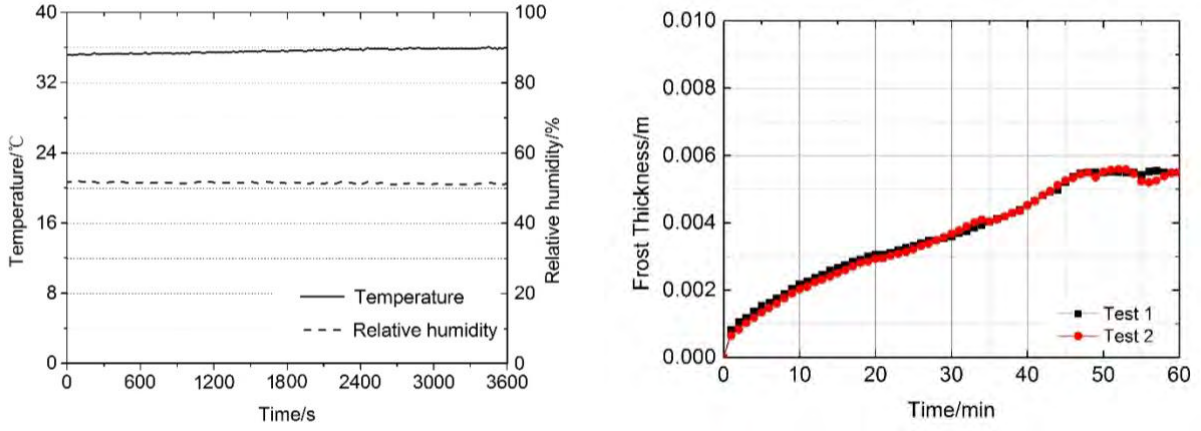

(a) Test conditions (b) Repeated experiments

Fig 3: Test repeatability verification

2.2 Experimental Results and Analysis

The frost thicknesses at T_w=-60℃, v=6m/s and RH=80% with different T_a(10℃, 15℃ and 20℃) are shown in Fig. 4. When T_a is 10℃, the thickness increases rapidly in the early frost stage, and then slows down gradually in the mature stage. During the whole process, the frost rises almost monotonously, and no obvious melting phenomenon occurs. When T_a is 15℃, the frost layer thickness declines at 49 min and increases again after a few minutes. When T_a is 20℃, the frost layer thickness drops at 21 min, 39 min and 58 min, showing a periodic melting-refrosting trend. For the three air temperatures, 10℃, 15℃ and 20℃, the first melting time is 60+ min (because there is no melting in the first 60 minutes of the blue curve), 49 min and 21 min respectively. It is because the frost surface temperature is higher with hotter air temperature under the same frost condition (frost thickness, frost density, etc.). The frost melting conditions is met earlier with higher

air temperature. In addition, its frost thickness is higher in the initial 20 minutes. This can be attributed to the larger moisture content with hotter air temperature at the same relative humidity. Therefore, the frosting rate is elevated with larger vapour concentration difference between air and frost layer (Leoni et al., 2017).

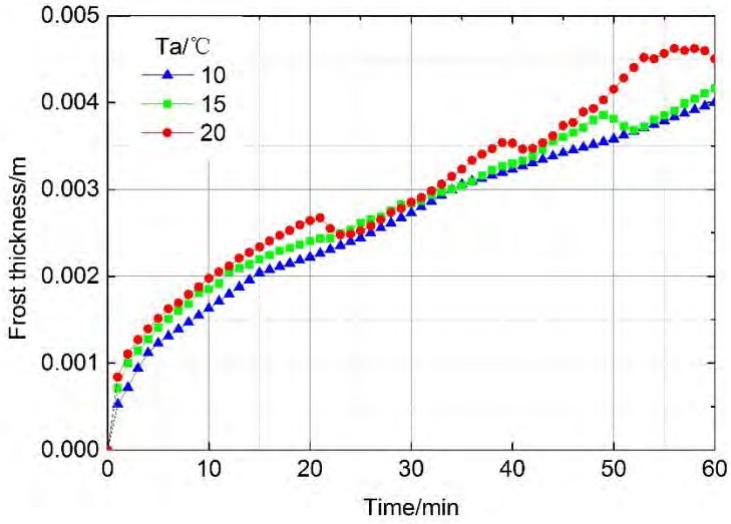

Fig 4: Experimental curves of the frost periodic melting process

The frost thickness is calculated from the original photo image. The frosting morphology with 15℃ air temperature is shown in Fig. 5. It drops at about 50min with obvious melted water droplets existing on the frost surface. Then the droplets freeze and disappear, and the frost thickness resumes to grow again at 53min. It implies that the melting of frost crystals on the frost surface is the direct reason for the decrease of frost thickness. In the initial frosting process, the frost layer rises gradually during the frost maturation and development period, which leads to the increase of frost thermal resistance. The frost surface temperature continues to rise until the water droplets temperature reaches the triple point. Afterwards, the frost crystals begin to melt and the melted droplets infiltrate into the frost pores. When the heat resistance is reduced to decrease the frost surface temperature, frost refreeze happens. On the one hand, frost melting reduces the frost layer thickness. On the other, it increases the frost density and reduces its thermal resistance. Therefore, the surface temperature and frost thickness of the frost layer behaves in a periodic way.

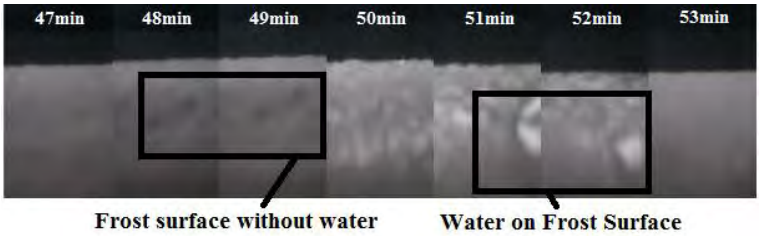

Fig 5: Frost surface image

3. NUMERICAL SIMULATION OF THE FROST PERIODIC MELTING PROCESS

In order to predict the frost parameters such as density, thermal conductivity conveniently, a transient frosting model on the circular tube is established. In the model, the melting criteria is added to the frosting model.

3.1 Frosting and Melting Models

Frosting is a very complex unsteady process with phase change, heat and mass transfer and moving boundary. There are two renowned frost growth models based on computational fluid dynamics and numerical heat transfer. One is O'Neal's porous medium diffusion model (ÓNeal et al., 1984), the other is the semi-empirical quasi-steady frost formation model (Padki et al., 1989). This paper mainly studies the characteristics of the melting process instead of the micro-

mechanism of frosting in frosting maturity and development period (Hayashi et al., 1977). Therefore, the semi-empirical quasi-steady frosting characteristic model is adopted to calculate the heat transfer coefficient according to the correlation formula. The Lewis analogy theory is introduced to calculate the corresponding mass transfer coefficients. Then the total amount of frost and the average thickness of the frost layer at different times can be obtained according to the experimental correlation of frost layer density (Jone and Parker, 1976). In the frosting process, the melting criterion and the re-frosting criterion are added to the transient frosting and melting model.
According to the characteristics of convective mass transfer, the mass transfer in frosting process is shown in Eq. (1).

$$\dot{m} = 0.018 h_m \left(C_a - C_s \right) \quad \text{Eq. (1)}$$

where, $\dot{m}$ is the mass transfer rate in kg·m^{-2}·s^{-1}, h_m is the mass transfer coefficient in m·s^{-1}, C_a is the vapour concentration of the air in mol·m^{-3}, C_s is the vapour concentration of the frost in mol·m^{-3}.
According to the analogy theory, the mass transfer coefficient can be calculated from the heat transfer coefficient (as shown in Eq.(2)).

$$\frac{h_m}{h} = \frac{\mathrm{Le}^{-\frac{2}{3}}}{\rho c_p} = \frac{\left(a / D \right)^{-\frac{2}{3}}}{\rho c_p} \quad \text{Eq. (2)}$$

where, h is the heat transfer coefficient in W·m^{-2}·K^{-1}, Le is the Lewis number, ρ is the density in kg·m^{-3}, c_p is the specific heat capacity in J·kg^{-1}·K^{-1}, a is the thermal diffusivity coefficient in m^2·s^{-1}, D is the coefficient of diffusion in m^2·s^{-1}.
According to the Eq. (1) and Eq. (2), neglecting the vapour in the frost, we can get Eq. (3).

$$\dot{m} = 0.018 h \frac{\left(a / D \right)^{-\frac{2}{3}}}{\rho c_p} \frac{p}{8.314 T_a} \quad \text{Eq. (3)}$$

where, p is the pressure in Pa, T_a is the temperature in K.
The heat exchange between moist air and frost layer consists of two parts: sensible and latent heat. Diffusion heat transfer coefficient is introduced to calculate latent heat flow. Therefore, the total heat transfer is shown in Eq. (4).

$$q = h \left(T_a - T_{fr} \right) + \dot{m}_{fr} \gamma_{fr} = \left(h + h_s \right) \left(T_a - T_{fr} \right) \quad \text{Eq. (4)}$$

where, q is the heat exchange in W, T_{fr} is the frost surface temperature in K, γ_{fr} is the desublimation latent heat of water vapour in J·kg^{-1}, h_s is the diffusion heat transfer coefficient in W·m^{-2}·K^{-1}.

3.2 Comparisons Between Simulation and Experimental Results

The experimental and simulated results of frost thickness at different T_a(10℃,15℃ and 20℃) is shown in Fig. 6. The “Sim” stands for the simulated result and the “Exp” stands for the experimental result. For T_a=10℃, as shown in (a), the two curves fit very well in the initial 15 minutes. After 15 min, the experimental results are slightly lower than the simulated results. The maximum discrepancy is 11.9% at 25min. There is no frost thickness undulation in both curves. For T_a=15℃, as shown in (b), the simulated curve drops at 40min, while the experimental curve drops at 49min. The results show that the thickness growth rate of the experimental curve is slightly lower than that of the simulated results between 15min and 49min. On the premise of the same vapour condensation quality, the experimental results have smaller thickness, larger density, smaller thermal resistance and lower surface temperature. Therefore, the experimental results reach the melting condition later. For T_a=10℃, as shown in (c), both the thickness of the frost layer and the melting time have high similarity between the simulation and the experimental result, which implies that the simulated results can predict the transient periodic frosting process.

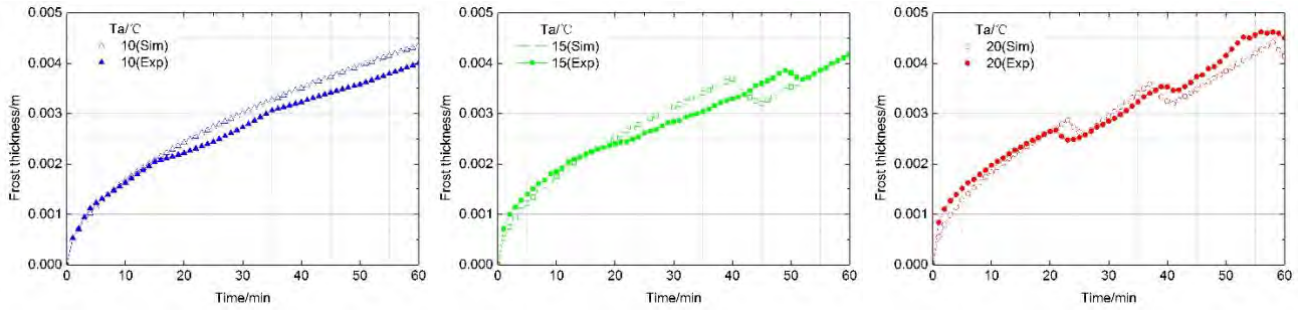

（a）T_a=10℃　　（b）T_a=15℃　　（c）T_a=20℃

Fig 6: Comparison of simulated and experimental results of frost growth curve at different T_a

3.3 Analysis of the Frosting Process at Different T_a and T_w

The simulated results of the frost thickness growth curve under different T_a are compared in Fig. 7. Before occurrence of frost melting, the frost growth rate is higher with hotter air temperature. The reason is that improved heat transfer can be obtained with larger temperature difference between the air and the wall. More water vapour condenses into frost according to Lewis analogy theory. In addition, earlier melting phenomena appear with higher air temperature. For instance, when T_a=20℃, the occurrence of the melting phenomenon in the simulation is 23 min, 37 min and 58 min. After the first melting phenomenon, the interval of the next melting phenomenon becomes longer. This is because the growth rate of the frost layer thickness gradually slows down during the frosting process in the curve of 10℃. Therefore, the deterioration rate of the frost thermal conductivity becomes slower (as shown in the curve of 10℃ in (b)), so the interval between the next melting phenomenon becomes longer.

The simulated results of the frost thickness growth curve under different T_w is shown in Fig. 8. All three curves show multiple periodic melting processes, the same as the red carve shown in Fig. 7. Earlier melting phenomena appear with higher wall temperature and frost surface. Moreover, after the first melting phenomenon, the interval of the melting phenomenon becomes longer.

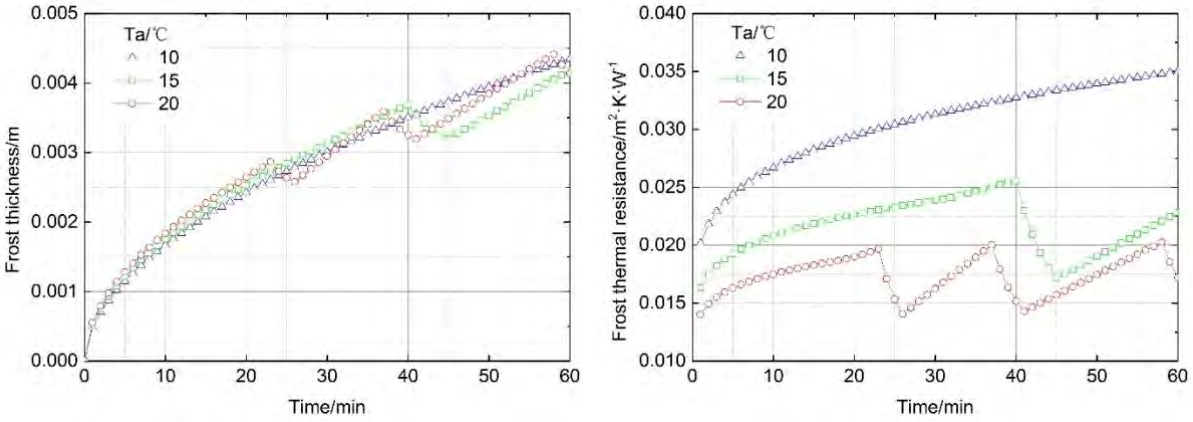

(a) Thickness　　(b) Thermal resistance

Fig 7: Simulated results of the frost periodic melting process at different T_a

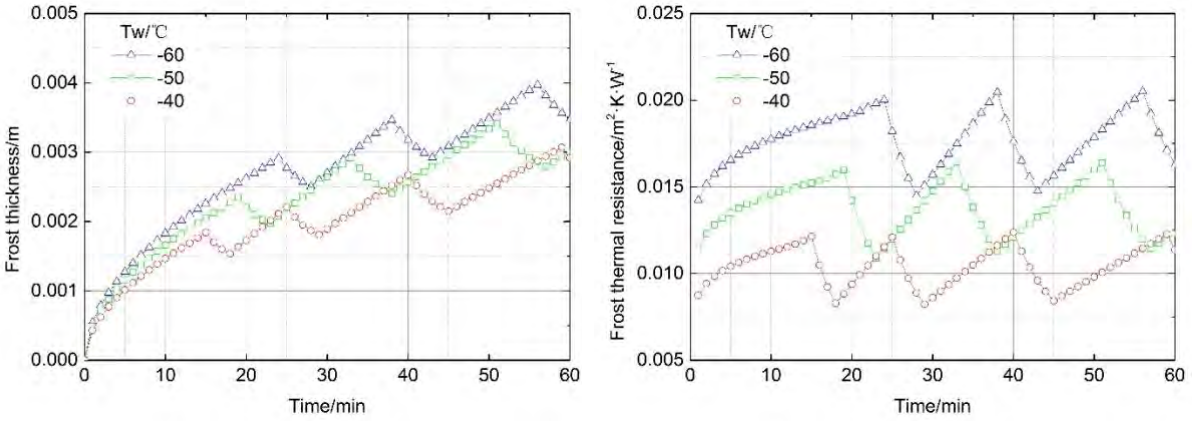

(a) Thickness (b) Thermal resistance

Fig 8: Simulated results of the frost periodic melting process at different T_w

4. CONCLUSIONS

The frost periodic melting process is observed in the frosting experiment of wall-temperature at -60 ℃. First, the experimental phenomena of the frost periodic process are systematically summarized. Then, the melting criterion is added to the transient mathematical model of frosting. The simulated results have the same trend as the experimental results, which shows that the model can accurately predict the melting process. Comparing the results of experiments and simulations, the following conclusions are drawn:

1) Frost thickness undulations and a clear periodic trend were observed as the air temperature rises. Water droplets on the frost surface were captured and it is assumed that the frost thickness reduction is caused by frost crystals melting.

2) The melting criterion is added to the transient mathematical model of unsteady frosting on the surface of a circular pipe. With experimental results validated, the transient model can be used to predict the periodic melting process.

3) The frost layer melts earlier with higher air temperature or wall temperature. Besides, after the first melting phenomenon, the interval of the periodic melting phenomenon becomes longer.

ACKNOWLEDGEMENTS

This project was supported by the Fundamental Research Funds for the Central Universities and Open Research Project of Key Laboratory of Cryogenics, TIPC, CAS (CRYO201806).

NOMENCLATURE

$\dot{m}$	mass transfer rate ($kg \cdot m^{-2} \cdot s^{-1}$)	a	thermal diffusivity coefficient ($m^2 \cdot s^{-1}$)
h_m	mass transfer coefficient ($m \cdot s^{-1}$	D	coefficient of diffusion ($m^2 \cdot s^{-1}$)
C_a	vapour concentration of the air ($mol \cdot m^{-3}$)	P	pressure (Pa)
C_s	vapour concentration of the air ($mol \cdot m^{-3}$)	T_a	temperature (K)
v	flow rate ($m \cdot s^{-1}$)	T_w	wall temperature (K)
h	heat transfer coefficient ($W \cdot m^{-2} \cdot K^{-1}$)	T_{fr}	frost surface temperature (K)
h_s	diffusion heat transfer coefficient ($W \cdot m^{-2} \cdot K^{-1}$)	ρ	density ($kg \cdot m^{-3}$)
γ_{fr}	latent heat of desublimation ($J \cdot kg^{-1}$)	q	heat exchange (W)
c_p	specific heat capacity ($J \cdot kg^{-1} \cdot K^{-1}$)	Le	Lewis number
RH	relative humidity(%)		

REFERENCES

Kandula, M., 2012. Frost growth and densification on a flat surface in laminar flow with variable humidity. Int. Commun. Heat Mass Transfer 39(8), 1030-1034.

Kim, D., Kim, C., Lee, KS., 2015. Frosting model for predicting macroscopic and local frost behaviors on a cold plate. Int. J. Heat Mass Transf. 82, 135-142.

Lee, K., Lee, T., Kim, W., 1997. A one-dimensional model for frost formation on a cold flat surface. Int. J. Heat Mass Transf. 40(18), 4359-4365.

Zendehboudi, A., Wang, B., Li, X., 2017. Application of smart models for prediction of the frost layer thickness on vertical cryogenic surfaces under natural convection. Appl. Therm. Eng. 115, 128-1136.

Kim, K. H., Ko, H. J., Kim, K., Kim, Y. W., Cho, K. J., 2009. Analysis of heat transfer and frost layer formation on a cryogenic tank wall exposed to the humid atmospheric air. Appl. Therm. Eng. 29, 2072–2079.

Liu, Z., Dong, Y., Li, Y., 2016. An experimental study of frost formation on cryogenic surfaces under natural convection conditions. Int. J. Heat Mass Transf. 97, 569-577.

O'Neal, D. L., Tree, D. R., 1985. A review of frost formation in simple geometries. ASHRAE Transactions 91(2), 267-281.

Leoni, A., Mondot, M., Durier, F., Revellin, R., Haberschill, P., 2017. Frost formation and development on flat plate: Experimental investigation and comparison to predictive methods. Exp. Therm. Fluid Sci. 88, 220-233.

ÓNeal, D. L., Tree, D. R., 1984. Measurement of frost growth and density in a parallel plate geometry[J]. ASHRAE Transactions 90(2), 278-290.

Padki, M., Sherif, S., Nelson, R., 1989. A simple method for modeling the frost formation phenomenon in different geometries. ASHRAE Transaction 95(2), 1127-1137.

Hayashi, Y., Aoki, A., Adachi, S., Hori, K., 1977. Study of Frost Properties Correlating With Frost Formation Types. J. Heat Transfer 99(2), 239-245.

Jone, B. W., Parker, J. D., 1976. Frost formation with varying environmental parameters. J. Heat Transfer 97(2), 167-178.

Manuscript ID: 1598
DOI: 10.18462/iir.icr.2019.1598

Increasing the efficiency of a carbon dioxide refrigeration system using a pressure exchanger

Brian A. FRICKE[(a)], Kashif NAWAZ[(a)], Ahmed ELATAR[(a)], Vishaldeep SHARMA[(a)]

[(a)] Oak Ridge National Laboratory[1]
Oak Ridge, TN, 37831, USA, frickeba@ornl.gov

ABSTRACT

Natural refrigerants such as carbon dioxide (R744) are gaining increased interest as industry searches for alternatives with minimal environmental impacts. However, R744-based systems have lower operating efficiencies as compared to hydrofluorocarbon-based systems, particularly in hot climates. Implementing pressure exchanger (PX) technology may enable R744 systems to operate over a broader range of operating temperatures. A PX consists of narrow longitudinal channels positioned radially around a rotating cylinder. High- and low-pressure fluids flow into the PX and exchange pressure, creating an intermediate-pressure flow. In this paper, the design of the PX will be discussed, and a model of the PX will be developed. Refrigeration system designs implementing the PX will be presented. It will be shown that the PX has the potential to boost the coefficient of performance (COP) of R744 systems by over 25% compared to standard transcritical R744 booster systems.
Keywords: Carbon Dioxide (Refrigerant), Commercial Refrigerator, Energy Efficiency, Pressure.

1. INTRODUCTION

The irreversibility associated with compression and expansion processes represents a significant portion of the total irreversibility in vapor compression refrigeration cycles. Throttling and compression losses can be reduced by taking advantage of the flow work which is otherwise lost when refrigerant is expanded from high pressure to low pressure. This is particularly attractive for carbon dioxide (CO_2) refrigeration systems since a high mean pressure exists and a significant amount of work can be produced in the liquid phase.

One solution for reducing throttling losses is to directly recover expansion work by using a work recovery expander. However, the work produced by the expander must be used immediately, for example, to drive a system compressor. Alternatively, the energy produced by the expander can be converted to electrical energy and stored in a battery; however, energy losses are associated with the conversion and storage processes. Cycle efficiencies may increase by up to 17% with expanders (Groll and Kim, 2007). Another solution to recover expansion losses is to use an ejector expansion device. In an ejector, the high-pressure stream exiting the gas cooler expands through a nozzle, partially compressing the vapor refrigerant exiting the evaporator. The cycle efficiency is increased because the compressor operates at a reduced pressure ratio as compared to a cycle without an ejector. Analysis shows that the simple CO_2 refrigeration system cycle efficiency may increase by up to 16% with an ejector expansion device (Groll and Kim, 2007). However, system control is challenging since a combination of liquid and vapor expanders is required.

In this project, it is proposed to use a pressure exchanger to reduce the expansion losses in refrigeration systems. A pressure exchanger consists of a cylindrical rotor with an array of channels arranged around the axis of the rotor. The rotor spins between two stationary end plates, each of

[1] Notice: This manuscript has been authored by UT-Battelle, LLC, under Contract No. DE-AC05-00OR22725 with the U.S. Department of Energy. The United States Government retains and the publisher, by accepting the article for publication, acknowledges that the United States Government retains a non-exclusive, paid-up, irrevocable, world-wide license to publish or reproduce the published form of this manuscript, or allow others to do so, for United States Government purposes.

which contains ports for controlling fluid flow into and out of the rotor channels. Through rotation, the channel ends are periodically exposed to differing port pressures, initiating compression and expansion within the rotor channels. Thus, the pressure of a high-pressure stream can be transferred to a low-pressure stream, thereby raising the pressure of the low-pressure stream and reducing the pressure of the high-pressure stream. A cut-away view of a pressure exchanger as well as the rotor are shown in Fig. 1 (Energy Recovery, 2017).

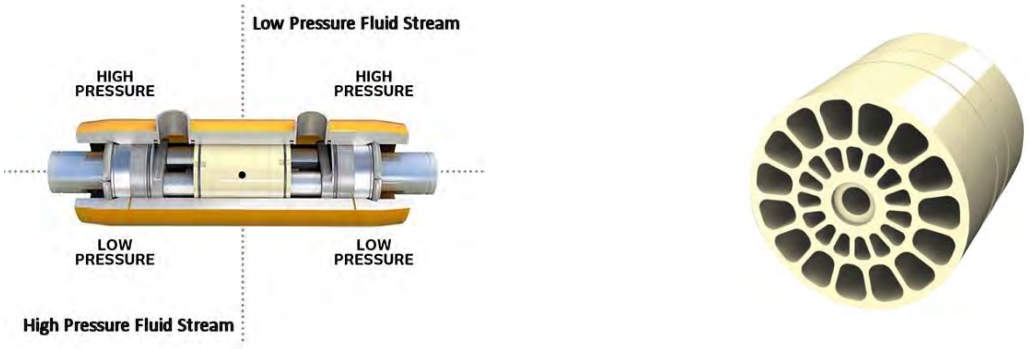

(a) (b)

Figure 1: Pressure exchanger: (a) cut-away view of pressure exchanger, showing rotor (center) and inlets and outlets for low-pressure and high-pressure flows, and (b) detail of rotor (Energy Recovery, 2017)

2. POTENTIAL APPLICATION AND APPROACH

An attractive application of the pressure exchanger is to increase the efficiency of transcritical CO_2 refrigeration cycles (Fig. 2a). It is proposed to pass the high-pressure refrigerant stream from the gas cooler into the pressure exchanger in order to increase the pressure of the flash gas exiting the flash tank (Fig. 2b). A significant flow of flash gas exists, particularly when the ambient temperature is high, and this flash gas does not produce any useful refrigerating effect. Rather than using the medium-temperature compressors to compress this flash gas, a pressure exchanger can be used to increase the pressure of the flash gas stream, thereby reducing the power consumption of the medium-temperature compressors. An alternative configuration consists of passing the medium-temperature suction flow through the pressure exchanger prior to entering the medium-temperature compressors (Fig. 2c).

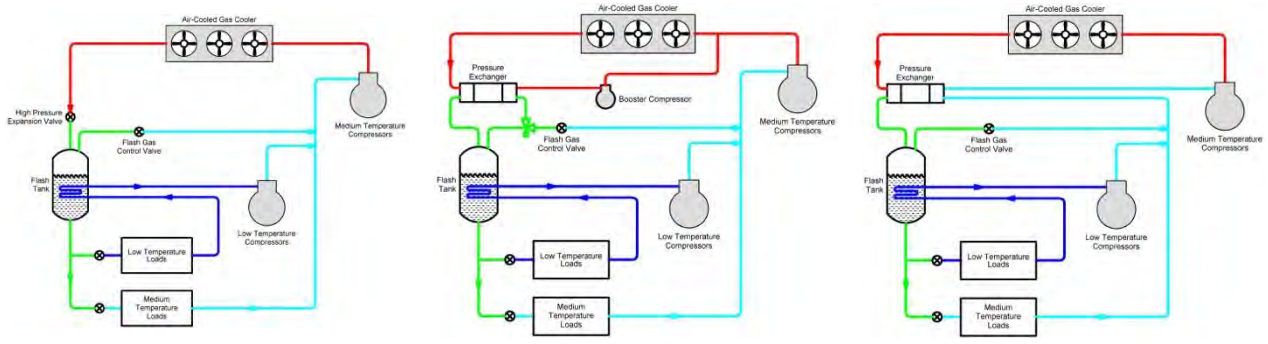

(a) (b) (c)

Figure 2: Transcritical CO_2 booster refrigeration system configurations: (a) Basic cycle without pressure exchanger, (b) Cycle with pressure exchanger on flash gas bypass, and (c) Cycle with pressure exchanger on medium-temperature compressor suction

In order to determine the potential enhancement in efficiency that a pressure exchanger could provide to refrigeration systems, an analytical model of the pressure exchanger will be developed to determine the pressure exchanger effectiveness under a variety of operating conditions, such as liquid-to-liquid, gas-to-gas, or gas-to-two-phase pressure exchange. In addition, computational fluid dynamics (CFD) simulations of the pressure exchanger will be performed to determine the details of

the fluid flow through the pressure exchanger. Such simulations will provide insight into the parameters which affect pressure exchanger design and allow for optimization of the device.

3. ANALYTICAL MODEL

The proposed pressure exchanger technology has fundamental resemblance to a heat exchanger. While a heat exchanger mainly transfers "heat" energy between two fluids streams, a pressure exchanger functions to transfer "work" energy between two streams. Table 1 summarizes the similarities and differences between heat and pressure exchangers.

Table 1. Similarities and differences between heat and pressure exchangers

Heat exchanger	Pressure exchanger
Transfer heat energy	Transfer work energy
Involves heat losses	Involves pressure losses
Fluids can be in liquid/gas or 2-phase state	Fluids can be in liquid/gas or 2-phase state
Phase change process can occur during the transport process	Phase change process can occur during the transport process
Geometry established the effectiveness	Geometry established the effectiveness

Regardless of the fundamentals and functions, the pressure exchanger belongs to the class of turbo-machines and it is important to establish the basic characterization parameters of the device. However, before going to the details of momentum transfer, it is advisable to develop the "effectiveness" of a pressure exchanger based on similarities between a heat exchanger and a pressure exchanger. Table 2 presents some important analysis in this regard where the effectiveness correlation for a pressure exchanger is developed on the same foundations as the effectiveness of a heat exchanger.

Table 2. Effectiveness of a pressure exchanger vs. a heat exchanger

Heat exchanger	Pressure exchanger
$q_{max} = C_{min}\left(T_{h,i} - T_{c,i}\right)$	$W_{max} = v_{min}\left(P_{h,i} - P_{l,i}\right)$
$\varepsilon = \frac{q}{q_{max}}$	$\varepsilon = \frac{W}{W_{max}}$
$\varepsilon = \frac{C_c\left(T_{c,o} - T_{c,i}\right)}{C_{min}\left(T_{h,i} - T_{c,i}\right)}$	$\varepsilon = \frac{v_l\left(P_{l,o} - P_{l,i}\right)}{v_{min}\left(P_{h,i} - P_{l,i}\right)}$
$q = \varepsilon C_{min}\left(T_{h,i} - T_{c,i}\right)$	$W = \varepsilon v_{min}\left(P_{h,i} - P_{l,i}\right)$
$\varepsilon = f\left(NTU, \frac{C_{min}}{C_{max}}\right)$	$\varepsilon = f\left(NTU, \frac{v_{min}}{v_{max}}\right)$
$NTU \equiv \frac{UA}{C_{min}}$	$NTU \equiv \frac{x}{v_{min}.\Delta P_{min}}$

It is important to note the numerator for last parameter (x) must be a pressure conductance term (reverse of resistance for work transfer), which is analogous to the overall heat transfer conductance for a heat exchanger.

Considering the pressure exchanger to be a class of turbo-machinery (Fig. 3), using the Euler's equation for a rotor running at an angular velocity of Ω, the rate at which the rotor does work on the fluid is given by the following equation:

$$\tau_A \Omega = \dot{m}\left(U_2 c_{\theta_2} - U_1 c_{\theta_1}\right) \quad \text{Eq. (1)}$$

From the above correlation, we can develop the following correlations for the two fluids streams of the pressure exchanger (Fig. 4). For the lower pressure stream, the work is defined as follows:

$$\Delta W_{LP} = \frac{\dot{W}_{LP}}{\dot{m}_{LP}} = \frac{\tau_A \Omega}{\dot{m}_{LP}} = \dot{m}_{LP}\left(U_2 c_{\theta_2} - U_1 c_{\theta_1}\right) > 0 \quad \text{Eq. (2)}$$

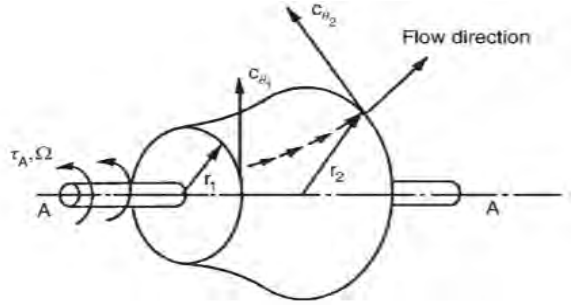

Figure 3: The schematic for turbomachinery

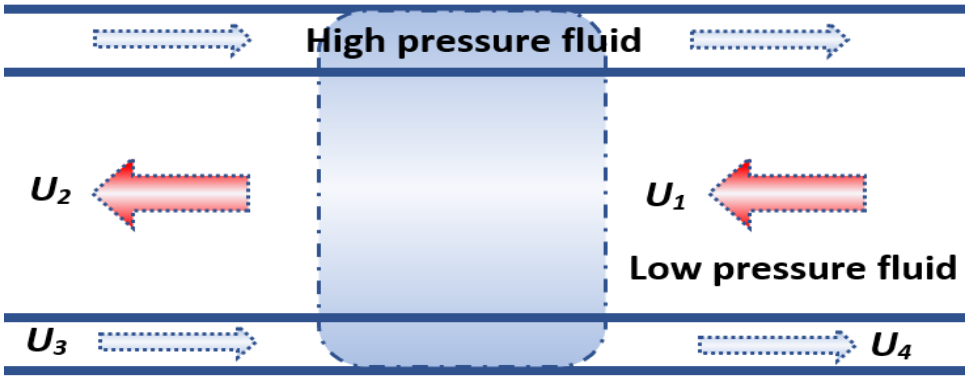

Figure 4: Pressure exchanger between high-pressure (HP) and low-pressure (LP) fluid streams

Similarly, for the fluid stream at higher pressure, the work is defined as follows:

$$\Delta W_{HP} = \frac{\dot{W}_{HP}}{\dot{m}_{HP}} = \frac{\tau_A \Omega}{\dot{m}_{HP}} = \dot{m}_{HP}\left(U_4 c_{\theta_4} - U_3 c_{\theta_3}\right) < 0 \qquad \text{Eq. (3)}$$

As such, we can define the efficiency of the pressure exchanger as the ratio of the work transfer to the low-pressure fluid from the high-pressure fluid:

$$\eta_{PX} = \frac{\Delta W_{LP}}{\Delta W_{HP}} \qquad \text{Eq. (4)}$$

By defining stagnation enthalpy as $h_0 = h + \frac{1}{2}c^2$, we can define a term commonly known as rothalpy, *R*, where $R = h + \frac{1}{2}c^2 - Uc_\theta$. Considering rothalpy, another characterization parameter is work lost due to the inefficiency of the pressure exchanger as follows:

$$R_{lost,PX} = \Delta R_{HP} - \Delta R_{LP} \qquad \text{Eq. (5)}$$

4. NUMERICAL MODEL

4.1. Numerical Model Development

The performance of the pressure exchanger was modelled and simulated using the computational fluid dynamics (CFD) software package ANSYS Workbench™. For the CFD modelling, a computer-aided design (CAD) model of the pressure exchanger was generated, as illustrated in Fig. 5. In the CAD model, the high-pressure fluid flows into and out of the pressure exchanger are designated as the “primary” flows while the low-pressure fluid flows into and out of the pressure exchanger are designated as the “secondary” flows. Two primary and two secondary inlet ports as well as two primary and two secondary outlet ports were modelled. The CAD model of the pressure exchanger has the following dimensions:

- Duct length = 0.19 m
- Duct diameter = 0.02 m
- Rotor outside diameter = 0.18 m
- Inlet/outlet port depth = 0.05 m.

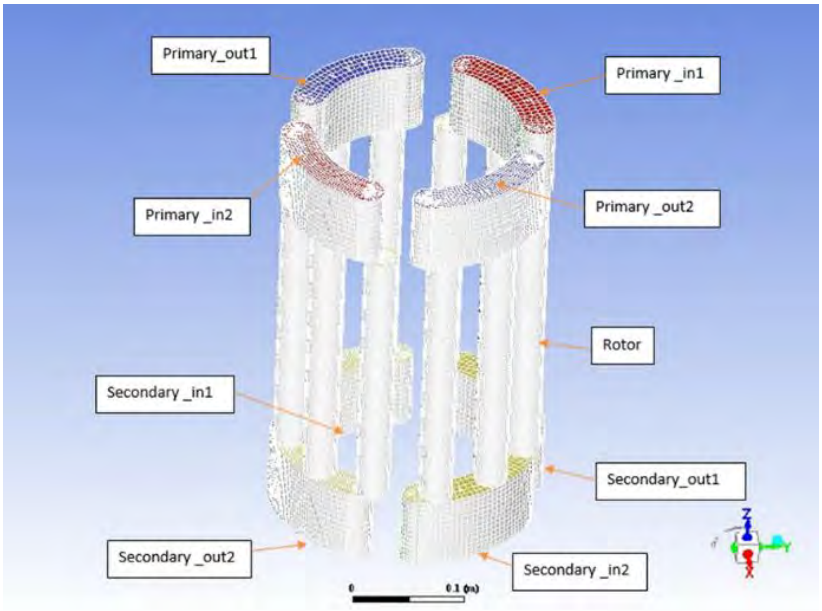

Figure 5: Pressure exchanger CAD model and generated mesh

A structured mesh for the pressure exchanger was created and the mesh was refined at the fluid inlets and outlets. The mesh consisted of a total of 316000 cells. A pressure-based transient model was used for the simulation. The velocity-pressure coupling selected for the simulation was Pressure-Implicit with Splitting of Operators Pressure (PISO) with second order spatial discretization for an accurate solution. The flow through the pressure exchanger was considered to be turbulent and the realizable k-ε algorithm was selected as the turbulence model. A fixed time step of 0.001 seconds was used, and convergence of the solution was satisfied by reaching iteration residuals below 10^{-4} for the mass and momentum equations and 10^{-6} for the energy equation. The thermodynamic properties of the fluid (R744) were generated using a user-defined function (UDF) consisting of the Redlich-Kwong equation-of-state to model the real gas properties. The rotational speed of the pressure exchanger rotor was set to 1000 RPM and a total simulation time of 0.75 seconds was achieved.

The inlet ports of the pressure exchanger were treated as velocity inlet boundary conditions and the outlet ports were considered to be pressure outlet boundary conditions. The inlet and outlet boundary conditions are summarized in Table 3. Note that the values in bold in the table are calculated by the software. The remaining boundaries were assumed to be adiabatic wall boundary conditions.

Table 3. Boundary conditions for the CFD model

	Primary inlet	Primary outlet	Secondary inlet	Secondary outlet
Boundary condition type	Velocity inlet	Pressure outlet	Velocity inlet	Pressure outlet
Temperature (K)	320	307	320	331
Pressure (MPa)	**6.96**	5.5	**5.7**	6.75
Velocity ($m \cdot s^{-1}$)	6	**7.63**	6	**7.88**

4.2. Numerical Model Results

The CFD model was stable and the convergence criteria was satisfied for each time step. Table 3 illustrates the change of the temperature, pressure and velocity of the fluid between the primary and secondary flow inlet and outlet ports. For the primary flow, the pressure and temperature of the fluid decrease from the inlet to the outlet while the velocity increases. However, for the secondary flow,

all of the fluid properties increase from the inlet to the outlet. The values shown in Table 3 represent an average over time. Furthermore, the CFD results show that the pressure of the fluid at the inlets and outlets oscillates with a frequency of around 18 Hz due to the rotor rotational speed of 1000 RPM. The amplitude of the pressure oscillation is below 5% of the mean pressure. Note that the secondary losses due to friction, heat transfer, eddies and leakage were not considered in this CFD simulation for simplicity. The simulated model has shown the ability of a pressure exchanger to be utilized for energy recovery in a transcritical CO_2 refrigeration system.
The magnitudes of the velocities at the primary and secondary flow inlets/outlets at time = 0.6 seconds are shown in Figs. 6a and 6b. The flow in general exhibits a uniform velocity at the inlet and outlet ports, except for one side of all the outlet ports where the flow accelerates. This is due to the relative motion between the rotor and the stationary outlet ports.

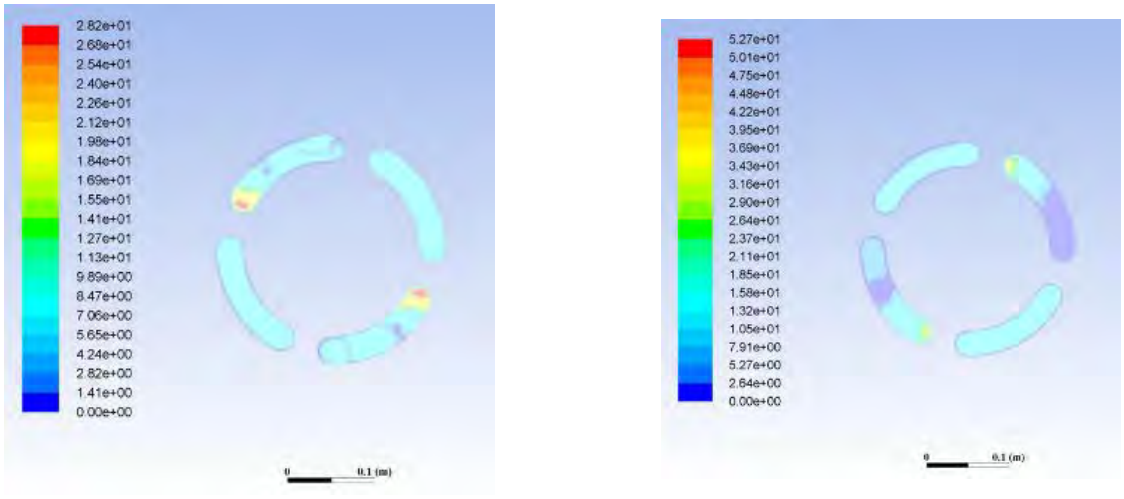

(a) (b)

Figure 6: Contour plot of velocity magnitude at 0.6 seconds at (a) the primary flow side, and (b) at the secondary flow side.

5. CONCLUSIONS

The pressure exchanger is a potential work recovery device which can lead to significant energy savings in commercial refrigeration system; particularly, CO_2 based trans-critical refrigeration systems operating at elevated pressures. To fully explore the potential of the device; first first-hand principles are used to compare the working principle to a heat exchanger. Based on analysis, a couple of performance parameters have been defined which can be used to characterize the operation of the device. Following that, a CFD model was generated for simulation of energy recovery of R744 fluid streams. The simulations have shown the validity of the device to recover energy between supercritical and superheated flow. At the outlets, a uniform outlet velocity magnitude has been observed except for local areas on one side of the outlet ports. As a next step, the both the analytical and CFD models will be expanded and experiments will be conducted to explore the full-potential of the technology.

ACKNOWLEDGEMENTS

This material is based upon work supported by the U.S. Department of Energy's Office of Energy Efficiency and Renewable Energy (EERE), Building Technologies Office (BTO). The authors wish to acknowledge Antonio Bouza, program manager, for funding and facilitating the project.

NOMENCLATURE

q	Heat transfer (W	W	Work (W)
C	Heat capacitance (W/K)	NTU	Number of transfer units
UA	Overall heat transfer coefficient (W/K)	v	Volumetric flow rate (m^3/s)
P	Pressure (Pa)	x	Non-dimensional parameter
c_Θ	Tangential velocity	U	Velocity
m	Mass flow rate	R	Rothalpy
ε	Effectiveness	Ω	Rotational velocity

Subscripts

min	Minimum	max	Maximum
h	Hot	c	cold
i	Inlet	o	Outlet
HP	High Pressure	LP	Low Pressure

REFERENCES

Groll, E., Kim, J.-H., 2007. Review Article: Review of recent advances toward transcritical CO_2 cycle technology. HVAC&R Research 13(3), 499-520.

Energy Recovery. 2017. http://www.energyrecovery.com Energy Recovery, Inc., San Leandro, California. (accessed July 2017).

Manuscript ID: 1608
DOI: 10.18462/iir.icr.2019.1608

Thermodynamic properties of binary mixtures of Trifluoroethene (HFO1123) + 2,3,3,3-Tetrafluoroprop-1-ene (HFO1234yf)

Naoya SAKODA[(a), (b)], Jiang SHIHENG[(a)], Masaya NAKAZAKI[(a)], Yasuyuki TAKATA[(a), (b)], Yukihiro HIGASHI[(b)]

[(a)] Department of Mechanical Engineering, Kyushu University, Fukuoka, 819-0395, Japan, sakoda@mech.kyushu-u.ac.jp
[(b)] Research Center for Next Generation Refrigerant Properties (NEXT-RP), International Institute for Carbon-Neutral Energy Research (WPI-I2CNER), Kyushu University, Fukuoka, 819-0395, Japan

ABSTRACT

PvTx properties of a binary mixture of 50 mass% HFO1123 (trifluoroethene) + 50 mass% HFO1234yf (2,3,3,3-tetrafluoroprop-1-ene) were measured in the temperature range from 294 to 410 K, in the density range between 83 kg·m^{-3} and 905 kg·m^{-3}, and at pressures up to 8.1 MPa by an isochoric method, and the obtained data are compared with an equation of state (EOS) compiled in REFPROP 10.0. In addition, the critical parameters and saturated densities of the mixture were measured. Vapor-liquid equilibrium of HFO1123 + HFO1234yf was also measured at temperatures from 273 to 313 K by a recirculation method, and the binary interaction parameter of a cubic EOS was determined.
Keywords: *PvTx* Property, Saturated Density, Critical Parameter, VLE, HFO1123, HFO1234yf

1. INTRODUCTION

Global warming is a very serious issue, and hydrofluorocarbon (HFC) refrigerants currently used in air conditioners, refrigerators, and heat pump systems are essential to be replaced to alternatives with lower GWPs (Global Warming Potentials) in the near future. Hydrofluoroorefins (HFOs) with carbon-carbon double bonds have low GWPs, and great attention has been taken to HFOs. HFO1123 (trifluoroethene, CF_2=CHF) is has a lower normal boiling temperature of 200 K compared with other HFOs and has a low GWP less than unity. Therefore, it is considered to be a one of the attractive refrigerants for air conditioners and refrigerators. Thermodynamic properties of HFO1123 were recently measured by the authors (Higashi and Akasaka,2016; Higashi et al.,2018) and by Fukushima et al. (2016), and then, an accurate equation of state (EOS) with Helmholtz free energy was formulated by Akasaka et al. (2016) based on the experimental data. However, pure HFO1123 is concerned with disproportionation reaction, and is expected to be used as mixtures with HFC32 (difluoromethane, CH_2F_2) and HFO1234yf (2,3,3,3-tetrafluoroprop-1-ene, CF_3CF=CH_2). Hence, thermodynamic properties of those mixtures are highly required, but there are no available experimental data of HFO1123 + HFO1234yf as of now. In this study, *PvTx* properties of a binary mixture of 50 mass% HFO1123 + 50 mass% HFO1234yf were measured in the temperature range from 294 to 410 K, in the density range between 83 kg·m^{-3} and 905 kg·m^{-3}, and at pressures up to 8.1 MPa by an isochoric method, and the critical parameters and saturated densities were measured. In addition, vapor-liquid equilibrium (VLE) of HFO1123 + HFO1234yf was also measured at temperatures from 273 to 313 K by a recirculation method.

2. EXPERIMENTAL

2.1. Samples

The samples of HFO1123 and HFO1234yf were furnished by AGC, Inc., Japan, and the sample purities of them are more than 0.999 in volume fraction. These samples were used without further purification.

2.2. *PvTx* Properties

PvTx properties were measured by an isochoric method, and details of the apparatus are described in previous papers (Kobayashi et al.,2011; Higashi,2016)). The vapor pressure of HFO1123 was also measured with this apparatus (Higashi et al.,2018). A pressure vessel of the apparatus, which is made of stainless steel, was installed in a silicone-oil thermostated bath, and temperature fluctuation of the silicone-oil in the bath was kept within 3 mK. The temperature was measured with a 25 Ω standard platinum resistance thermometer calibrated against ITS-90 with an AC thermometer bridge. The uncertainty in temperature measurements was estimated less than 5 mK. Pressure was measured with a pressure transducer connected to the pressure vessel directly, and the uncertainty in pressure measurements was estimated less than 1.0 kPa. The density was determined from the sample mass and the inner volume of the vessel with tubing and valves. The volume of the vessel was calibrated using HFC134a and HFC32 as reference fluids. The uncertainty in density measurements was estimated to be within 0.15 %.

2.3. Critical Parameters and Saturated Densities

The critical parameters and saturated densities of 50 mass% HFO1123 + 50 mass% HFO1234yf were measured by the visual observation of meniscus disappearance (Okazaki et al.,1983; Higashi,1994). The apparatus consists of three pressure vessels; optical cell, expansion cell, and supplying cell, the inner volumes of which are 11.638 ± 0.008 cm^3, 8.949 ± 0.003 cm^3 and 77.575 ± 0.016 cm^3, respectively. The optical cell is a barrel-type cylindrical vessel and has two Pyrex glass windows for observing the meniscus disappearance and the intensity of critical opalescence of sample. The apparatus was installed in a silicone-oil bath. The temperature was measured with a 25 Ω standard platinum resistance thermometer calibrated against ITS-90 with an AC thermometer bridge. The uncertainty in temperature measurements was estimated to be within 10 mK.

2.4. Vapor-Liquid Equilibrium

Vapor-liquid equilibrium of HFO1123 + HFO1234yf was measured by a recirculation method, and details of the apparatus are given in a previous paper (Sakoda et al.,2017). An equilibrium cell with an inner volume of 265 cm^3 has optical windows to observe the meniscus of sample at the vapor-liquid interface. In the recirculation method, the saturated vapor is extracted from the top of the cell and supplied to the liquid phase from the bottom of cell by a magnetic circulation pump. The saturated liquid is also extracted from the bottom of the cell and supplied to the vapor phase from the top of the cell. The samples of saturated vapor and liquid are extracted under steady state condition by hexagon valves, and the concentrations of the extracted samples were measured by a gas chromatograph. The cell was installed in a silicone-oil thermostated bath. The pressure of the sample was measured with the pressure transducer connected to the cell and installed in the bath. The uncertainties in temperature and pressure measurements were estimated to be within 10 mK and 2 kPa, respectively.

3. EXPERIMENTAL RESULTS

3.1. *PvTx* Properties

The distributions of the obtained *PvTx* properties of 50 mass% HFO1123 + 50 mass% HFO1234yf along seven isochores between 83 $kg \cdot m^{-3}$ and 905 $kg \cdot m^{-3}$, in the temperature range from 294 to 410 K and at pressures up to 8.1 MPa are shown on the temperature-pressure plane in Fig. 1. The data in Fig. 1 include those in the vapor-liquid two phase region, which are useful to confirm consistency among the obtained data. The isochore of 501 $kg \cdot m^{-3}$ is close to the critical density. There is not an accurate EOS for the binary system of HFO1123 + HFO1234yf although accurate EOSs for the pure components of HFO1123 (Akasaka et al.,2016) and HFO1234yf (Richter et al.,2011) have been already formulated, which are compiled in a NIST thermophysical properties database of REFPROP 10.0 (Lemmon et al.,2018). In REFPROP, an EOS for the binary system of HFO1123 + HFO1234yf are available using the pure EOSs for HFO1123 and HFO1234yf by Akasaka et al. (2016) and Richter et al. (2011), respectively, with mixing parameters estimated from a similar substance as a

default setting. For HFO1123 + HFO1234yf, the mixing parameters are estimated from the binary system of HFO1234yf + HFO1234ze(E). However it should be noted that the mixing parameters are not optimized using experimental data of HFO1123 + HFO1234yf because of no available data of this system. The present data are compared with the EOS of this system by REFPROP with the default mixing parameters. The density deviations of the present data in the only single phase from the EOS are shown in Fig. 2. The EOS represents the isochore of 83 kg·m^{-3} well within 0.5 %, but shows large deviations around the isochore of 510 kg·m^{-3}.

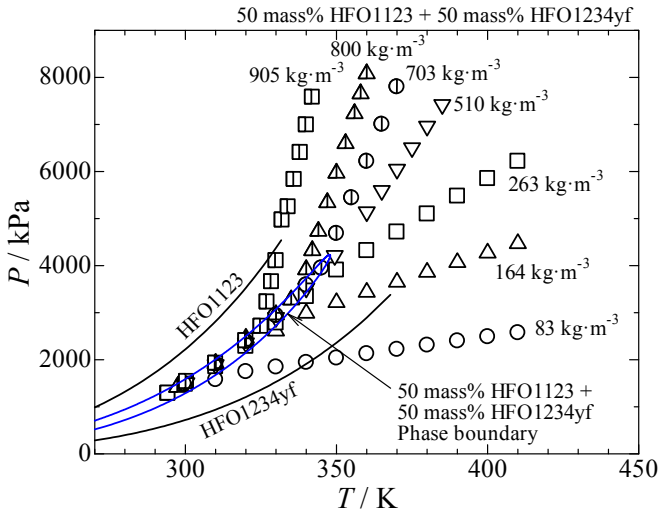

Figure 1: Experimental results of *PvTx* properties of 50 mass% HFO1123 + 50 mass% HFO1234yf on the temperature-pressure plane

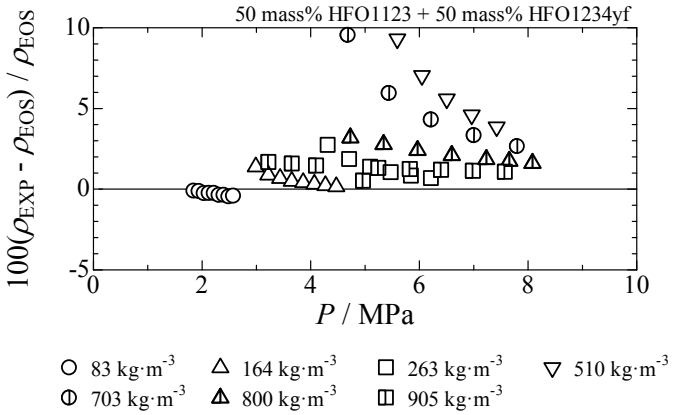

Figure 2: Density deviations of *PvTx* properties of 50 mass% HFO1123 + 50 mass% HFO1234yf in the single phase from the EOS by REFPROP with the estimated default mixing parameters

3.2. Critical Parameters and Saturated Densities

The saturated vapor and liquid densities of 50 mass% HFO1123 + 50 mass% HFO1234yf were determined by the visual observation of meniscus disappearance in the temperature range between 327.05 and 350.59 K. In addition, the saturated densities were also determined by the obtained *PvTx* property data in the temperature range from 313.15 to 347.89 K. The results are shown in Fig. 3 on the temperature-density plane. On the basis of the meniscus observation in the critical region, the critical temperature and critical density were determined in consideration of the meniscus disappearing level as well as the intensity of critical opalescence. The critical opalescence was observed at four densities between 348.9 kg·m^{-3} and 449.4 kg·m^{-3} in Fig. 3, and by the level of the disappearing and appealing of meniscus, the critical temperature and density are finally determined as:

T_c = 349.40 ± 0.02 K Eq. (1)

And:

ρ_c = 510 ± 3 kg·m^{-3} Eq. (2)

Moreover, the critical pressure was determined as:

P_c = 4212 ± 2 kPa Eq. (3)

from the *PvTx* property measurement of the isochore of 510 kg·m^{-3} at the critical temperature. The estimated critical temperature, density, and pressure by REFPROP 10.0 are 347.80 K, 478 kg·m^{-3}, and 4227 kPa, respectively. The saturated densities calculated from REFPROP are systematically lower than the experimental data as shown in Fig. 3. The experimental critical point of the mixture are useful to modify the EOS behavior by optimizing the mixing parameters to the critical point, and then, the calculated saturated densities will agree with the experimental data.

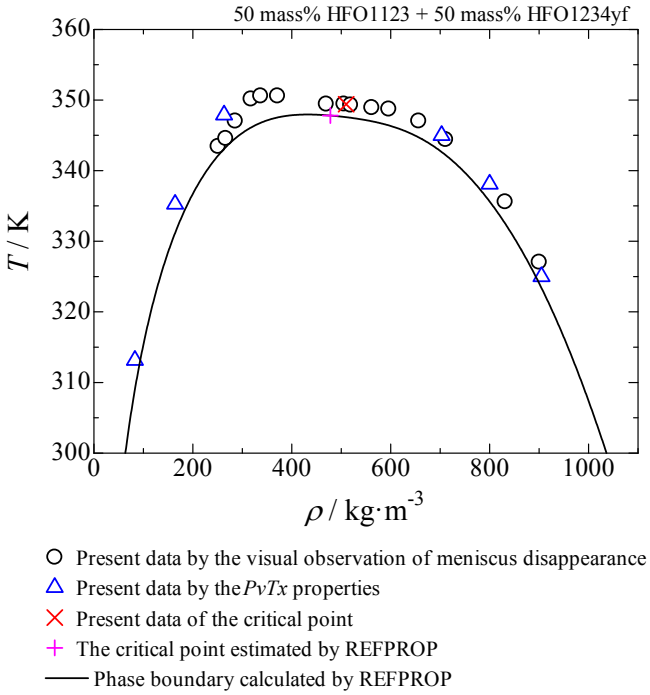

Figure 3: Saturated densities of 50 mass% HFO1123 + 50 mass% HFO1234yf by the visual observation of meniscus disappearance and *PvTx* properties with the critical point

3.3. Vapor-Liquid Equilibrium

The obtained VLE data at five isotherms from 273 to 313 K are shown in Fig. 4 on (a) the pressure-concentration plane and (b) vapor concentration-liquid concentration plane. In this work, a cubic Peng-Robinson (PR) EOS is adopted for comparisons, and the interaction parameter of k_{ij} was determined based on the experimental data as k_{ij} = 0.0102. The experimental data are compared with the PR EOS and the EOS by REFPROP with the estimated default mixing parameters as well as the comparisons of *PvTx* properties. The shapes of the VLE calculated by the PR EOS and the REFPROP EOS are very similar. Smaller pressure deviations from the REFPROP EOS are observed in Fig. 5 at (a) the dew points than the PR EOS, but on the other hand, the deviations at (b) the bubble points are larger. The two EOSs are slightly different from each other systematically, and the degree of agreement with the experimental data is almost the same.

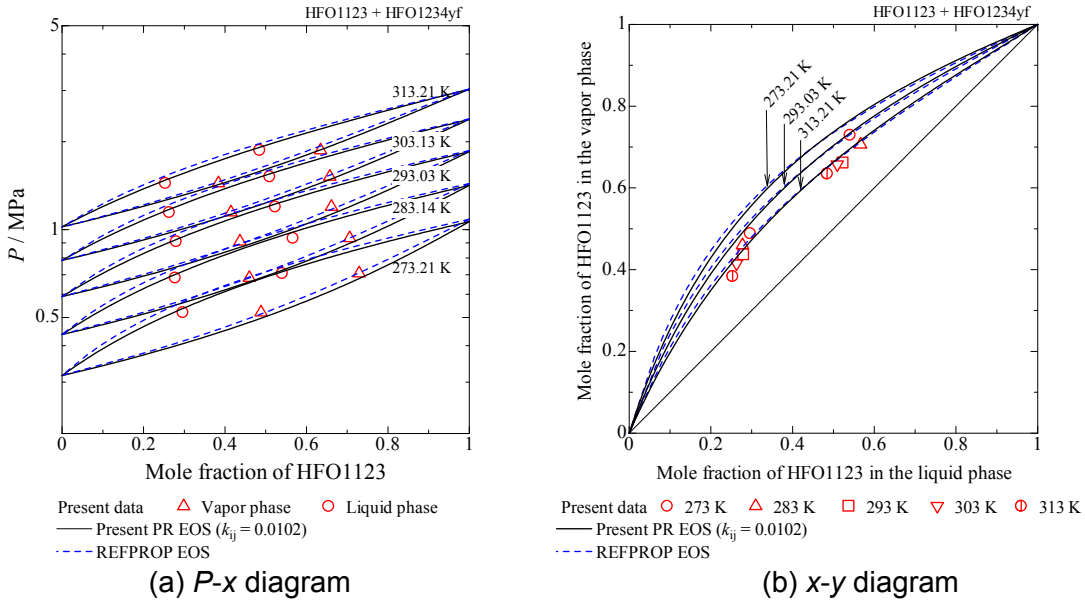

Figure 4: Experimental results of VLE for HFO1123 + HFO1234yf. (a) *P-x* diagram, (b) *x-y* diagram

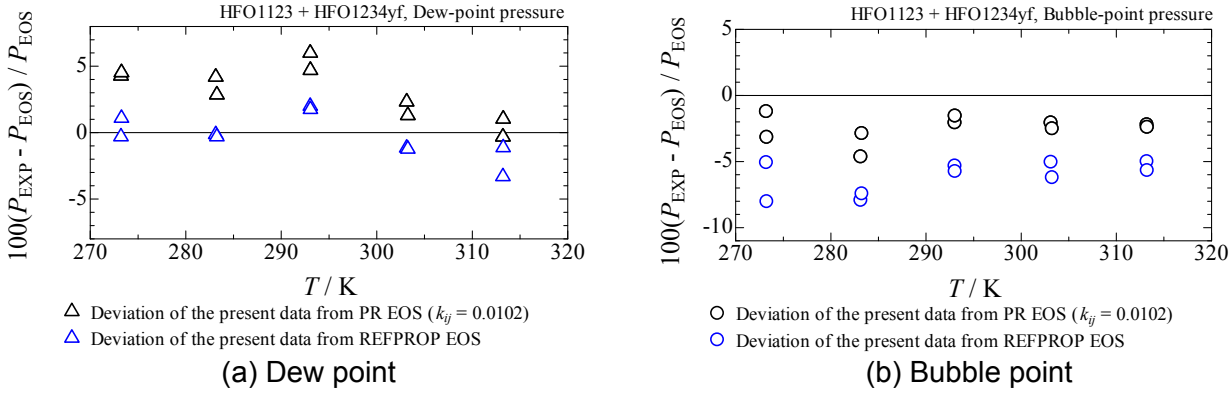

Figure 5: Pressure deviations of VLE for HFO1123 + HFO1234yf. (a) Dew point, (b) Bubble point

4. CONCLUSIONS

The *PvTx* properties of 50 mass% HFO1123 + 50 mass% HFO1234yf were measured by the isochoric method. The saturated densities of the mixture were measured by the visual observation and the obtained *PvTx* properties, and the critical parameters are determined. In addition, the VLE data of HFO1123 + HFO1234yf were measured by the recirculation method. The mixing parameter of PR EOS was determined based on the experimental VLE data. The present data are compared with the EOS by REFPROP, are useful to optimize the mixing parameters for the formulation of a more accurate EOS.

ACKNOWLEDGMENTS

This research has been conducted as part of a research for chemical safety founded by Ministry of Economy, Trade and Industry (METI), Japan. The authors greatly thank AGC, Inc., Japan, for providing the high purity samples of HFO1123 and HFO1234yf.

REFERENCES

Akasaka, R., Fukushima, M., Lemmon, E.W., 2016. A Helmholtz energy equation of state for trifluoroethylene (R-1123). International Refrigeration and Air Conditioning Conference at Purdue, West Lafayette, IN, USA, Paper No. 2297.

Fukushima, M., Hayamizu, H., Hashimoto, M., 2015. Thermodynamic properties of low-GWP alternative refrigerants. Proceedings of the 24th IIR International Congress of Refrigeration, Yokohama, Japan, Paper No. 443.

Higashi, Y., 1994. Critical parameters for HFC134a, HFC32 and HFC125. Int. J. Refrig. 17, 524−531.

Higashi, Y., 2016. Measurements of thermodynamic properties for the 50mass% R1234yf + 50mass% R1234ze(E). Sci. Technol. Built Environment 22, 1185−1190.

Higashi, Y., Akasaka, R. 2016. Measurements of thermodynamic properties for R1123 and R1123+R32 mixture. Proceedings of the 15th International Refrigeration and Air Conditioning Conference at Purdue, West Lafayette, IN, USA, Paper No. 2283.

Higashi, Y., Sakoda, N., Islam, Md. A., Takata,Y., Koyama, S., Akasaka R., 2018. Measurements of Saturation Pressures for Trifluoroethene (R1123) and 3,3,3-Trifluoropropene (R1243zf). J. Chem. Eng. Data 63, 417-421.

Kobayashi, K., Tanaka, K., Higashi, Y., 2011. $P\rho Tx$ property measurements of binary HFO-1234ze(E) + HFC-32 refrigerant mixtures. Trans. JSRAE 28, 415−426.

Lemmon, E. W., Bell, I. H., Huber, M. L., McLinden, M. O., 2018. NIST Standard Reference Database 23, NIST Reference Fluid Thermodynamic and Transport Properties Database (REFPROP), Version 10.0; Standard Reference Data; National Institute of Standards and Technology: Gaithersburg, MD.

Okazaki, S., Higashi, Y., Takaishi, Y., Uematsu, M., Watanabe, K., 1983. Procedures for determining the critical parameters of fluids, Rev. Sci. Instrum. 54, 21−25.

Richter, M., McLinden, M. O., Lemmon, E. W., 2011. Thermodynamic properties of 2,3,3,3-tetrafluoroprop-1-ene (R1234yf): vapor pressure and p-ρ-T measurements and an equation of state. J. Chem. Eng. Data 56, 3254-3264.

Sakoda, N., Shiheng, J., Kohno, M., Takata, Y., Higashi Y., 2017. Vapor-liquid equilibrium measurements of HFO refrigerant mixtures. Proceedings of the 5th IIR International Conference on Thermophysical Properties and Transfer Processes of Refrigerants, Seoul, Korea, Paper ID 108.

Manuscript ID: 1633
DOI: 10.18462/iir.icr.2019.1633

Sorption materials for the safe use of flammable refrigerants in cooling/heating cycles

Christian SONNER[(a)], Sebastian-Johannes ERNST[(a)], Lena SCHNABEL[(a)]

[(a)] Fraunhofer Institut für Solare Energiesysteme
Freiburg, 79110, Germany, christian.sonner@ise.fraunhofer.de

ABSTRACT

The F-Gas regulation and the resulting phasedown of fluorinated hydrocarbons (HFOs) as safe refrigerants (e.g R407C and R410A) effects an increase in research and development activities for alternative low GWP refrigerants. Besides new synthetic refrigerants, there is a focus on natural refrigerants like hydrocarbons, ammonia and carbon dioxide (Europäisches Parlament 2014).
The relevant alternative refrigerants are characterized by a low GWP and good thermodynamic properties. However, they are dangerous to humans (e.g., through a high flammability) and nature by different degrees in case of leakage. Thus, the development of safety concepts has become of central importance in the R&D of heat pumps and chillers with a strong focus on indoor units.
In this work, a safety element adsorbing the refrigerant in the event of an occuring leakage will be presented. The adsorption process is coupled to the refrigerant system in order to reduce the refrigerant release in huge amount. The main focus of this presentation is set on the evaluation and the choice of the adsorption material for the uptake of a flammable refrigerant. Therefore, the material characteristics of certain adsorptive materials were characterized with respect to the specific surface (BET surface), pore geometry and the adsorption equilibrium and enthalpy at different temperatures and pressures.

Keywords: Heat Pumps, Leakage, Safety, Natural Refrigerant, Sorption.

1. INTRODUCTION

Due to F-gas regulations and the resulting phase down of high GWP (global warmth potential) refrigerants like R207C and R410A, rising effort is spent in academic and industrial research and development towards the use of refrigerants with low GWP. Especially, natural refrigerants like hydrocarbons and carbon dioxide are of interest. Unfortunately, these are often dangerous to humans and nature by different degrees in case of leakage and their use demands a safety mechanism.
To reduce the mass of refrigerant released when a leak occurs, sorption materials can adsorb the refrigerant and keep it closed by the adsorption potential. Therefore, a safety element including sorption material like activated carbon, zeolite or metal organic framework (MOF) is adapted to the cooling cycle, (shown in Fig. 1). While there is no leakage detected, the sorption element can be evacuated or stay at ambient pressure flooded/flushed with nitrogen. This starting condition has an impact of the sorption capacity.
After detecting a leakage, the safety valve opens and the refrigerant can be adsorbed by the safety element. The safety element can be adapted to each point at the refrigerant cycle respected to the thermodynamically state of the refrigerant like pressure, aggregation state or temperature, which has also an impact on the adsorption.
To have an effective and volume optimized safety element it is very important to evaluate the sorption materials.

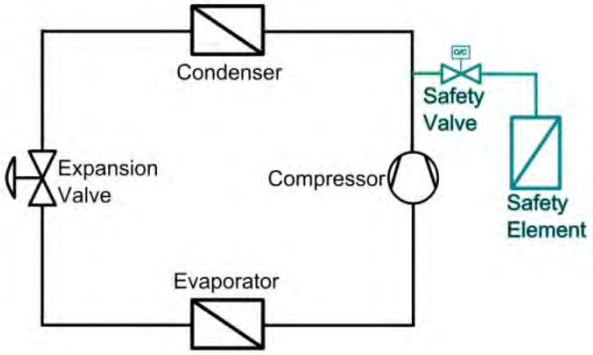

Figure 1: Refrigerant cycle with safety element

2. ADSORPTION

Adsorption is the adhesion of atoms, ions or molecules from a gas or liquid to a surface. The basic principle is shown in Fig. 2 (D. Bathen 2001). The adsorptive reaches the adsorbent by natural convection and diffusion or by a forced flow. The adsorption can be divided in chemisorption and physisorption, in the case of the propane adsorption on activated carbon a physisorption can be supposed. The quantitative description of the adsorption is based on a relationship between the loading X and the state variables pressure p and temperature T. This relationship can be described by several models like Langmuir-, Freundlich-, Toth- or BET-isotherms shown in Fig. 3. The resulting equations are listed in the Table 1 (W. Kast 1988; J. Toth 1971).

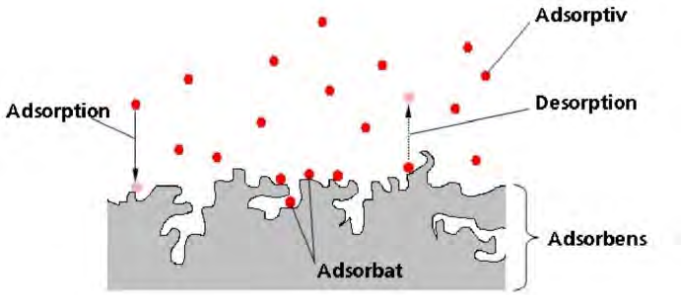

Figure 2: Principe of the sorption process (D. Bathen 2001)

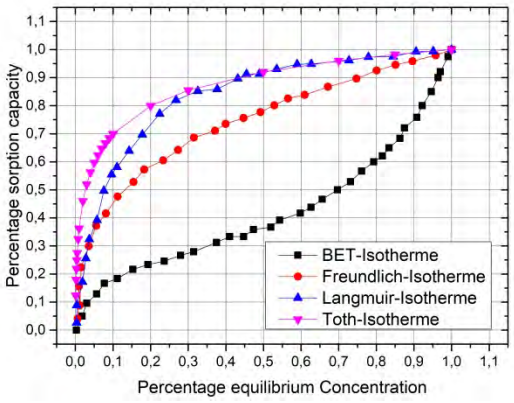

Figure 3: Principle behaviour of the BET-, Freundlich- and Langmuir-Isotherme

Table 1. Overview of the sorption parameters

Modell	Equation		Remarks
Freundlich isotherm	$X = kP^{1/n}$	Eq. (1)	X = Amount of adsorbate adsorbed per unit mass of adsorbent p = Pressure of adsorbate k, n = Temperature dependent constants attributed to the capacity and adsorption
Langmuir isotherm	$\theta = \frac{Kp}{1 + Kp}$	Eq. (2)	θ = Percentage coverage of the surface p = Gas pressure K = Equilibrium constant for adsorption and desorption depending on the temperature
BET isotherm	$\frac{p/p_s}{X(1 - p/p_s)} = \frac{1}{X_{mon}c} + \frac{(c-1)}{X_{mon}c}\frac{p}{p_s}$	Eq. (3)	X = Amount of adsorbate adsorbed per unit mass of adsorbent Xmon = Amount of adsorbate required to form a monolayer per unit mass of the adsorbent C = BET constant p = Equilibrium pressure of the adsorbate ps = Saturation pressure of the adsorbate
Toth isotherm	$\theta = \frac{K_t C_e}{(1 + (K_t C_e)^t)^{1/t}}$	Eq. (4)	θ = Percentage coverage of the surface Kt = Toth model isotherm constant 1/t = Toth model exponent

Freundlich described an isotherm valid for gaseous adsorbate. This isotherm equation is empirical and nonlinear in pressure. The function is not adequate for very high pressures because in reality X has an asymptotic maximum as pressure increases without bound (H. Freundlich 1907). As the temperature increases, the constants k and n change to reflect the empirical observation that the quantity adsorbed rises more slowly and higher pressures are required to saturate the surface.
(Langmuir 1918) published a new isotherm for gases adsorbed on solids. His isotherms are based on the following hypothesis - the surface of adsorbent is uniform i.e. all the adsorption sites are equal, the adsorbed molecules do not interact, all adsorption occurs through same mechanism and only one adsorbed molecular layer (monolayer) is formed, also shown in (G. Munz 2006).
The concept of BET theory is an extension of Langmuir theory, which is only valid for monolayer adsorption. However, molecules do form multilayers, which mean that adsorption takes place on the already adsorbed molecules. (Brunauer, Emmett, Teller 1938) have developed an isotherm which takes into account the multilayer adsorption. The BET theory has the following hypothesis - gas molecules physically adsorbed on a solid in layers infinitely, no interaction among adsorption layers, Langmuir theory can be applied to each layer.
The Toth isotherm is another isotherm that has three parameters Qt, Kt and 1/t, and useful in describing heterogeneous adsorption system, which satisfying both low and high-end boundary of the concentration (J. Toth 1971; Nimibofa Ayawei 2017).

3. EXPERIMENTS AND CHARACTERIZATION

3.1. Methods and Parameters for the Characterisation

For the characterization of porous adsorption materials

- the specific surface,
- the sorption capacity,
- the sorption enthalpy,

are of interest. The porosity has an influence on the adsorption isotherms. It represents the ratio between void volume and total volume of a substance or a mixture of substances. In order to determine these properties of porous materials, special analytical methods are required.

3.1.1. Bulk density

The bulk density of the sorption material is determinate by measuring the mass of the sorption materials at an accuracy volume. The bulk density is an indicator to calculate the needed volume of the safety element according to the refrigerant mass in the cooling cycle.

3.1.2. BET-surface

The BET-surface represents the size of the surfaces, in particular for porous solids. The BET-surface was determinate with gas adsorption from nitrogen using the analyser Quadrasorb (Quantachrome 2017). This method was developed by (Brunauer, Emmett, Teller 1938).

3.1.3. Sorption capacity

The sorption capacity was measured by Quantachrome V-Star (Quantachrome Instruments 2017). This analyser is a volumetric sorption system for several components like hydrocarbons or water. The working conditions are at subatmospehric pressure and different representative temperatures resulting in the adsorption isotherms.

3.1.4. Sorption enthalpy

The sorption enthalpy describes the thermodynamic interaction between adsorptive and adsorbent and can be derivate by the adsorption isotherms. Therefore, the adsorption enthalpy can by determinate with the Van't Hoff'schen (Chemgapedia), shown Eq. (1).

$$\frac{d\left(ln(p)\right)}{d\left(\frac{1}{T}\right)} = -\frac{\Delta h_{Ads}}{R} \quad \text{Eq. (5)}$$

After conversion of Eq. (1) to Eq. (2), the gradient curve correlates directly to the differential adsorption enthalpy

$$\Delta h_{Ads} = -\frac{d\left(ln(p)\right)}{d\left(\frac{1}{T}\right)} * R \qquad \text{Eq. (6)}$$

3.2. Results of the Characterization

The used fluid was propane for the adsorption analyses and nitrogen for the pore analyses. About 40 samples were analysed, which consisted zeolites, MOFs and activated carbon (AC). The forms are powder, granulate, form bodies and balls with several diameters. The presented results are focused on activated carbon. This is caused of a preselection by the presented parameters in section 3.1. The form, bulk density, BET-surface and the max. uptake of propane are shown in the following table 2.

Table 2. Overview of the sorption parameters

ID	Typ	Supplyer	Form	Bulk density [g cm^{-3}]	BET-surface [m^2 g^{-1}]	Max. Uptake [mg g^{-1}]
1	AC	Chemviron	Granulate	0,50	1045	221
2	AC	Chemviron	Granulate	0,36	1209	197
3	AC	Norit	Granulate	0,42	1161	221
4	AC	CarboTech	Granulate	0,33	1414	263
5	AC	CarboTech	Granulate	0,38	1288	229
6	AC	Blücher	mm-ball	0,67	1159	194
7	AC	Blücher	mm-ball	0,51	1549	280
8	AC	Chemviron	Granulate	0,49	1078	164
9	AC	CarboTech	Granulate	0,36	1350	235
10	AC	CarboTech	Split	0,40	1491	281
11	AC	Norit	Granulate	0,33	1729	242
12	AC	Norit	Granulate	0,40	623	183
13	AC	Norit	Granulate	0,38	2123	305

The bulk density has a variation from 0,33 g*cm^{-3} to 0,67 g*cm^{-3} and the maximum is two times higher than the minimum. This range belongs to the several forms of the activated carbon, like diameter of granulate, ranged from 1,5 mm up to 4mm and also to the percentage of ash depending on the manufacturing process. The same behaviour of the value range shows the propane uptake from 163,79 mg*m^{-3} at sample 8 to 305.44 mg*m^{-3} at sample 13. The uptake was measured at a propane concentration of 100vol% and system pressure of circa 103 kPa.
Therefore, by derivation of a specific uptake [mg*cm^{-3}] the sample 6 and 7 have the highest value in the range of 130 mg*cm^{-3} to 143 mg*cm^{-3}, followed by the sample 13 with a specific uptake of 116 mg*cm^{-3}. The sample 7 will results in the lowest volume of the safety element.
For time saving at sorption material characterisation and identification a correlation between BET-surface and the uptake was done. The interpolation of the measured propane uptake and the comparison between predicted and measured uptake are presented in the following Figs. 4 and 5.

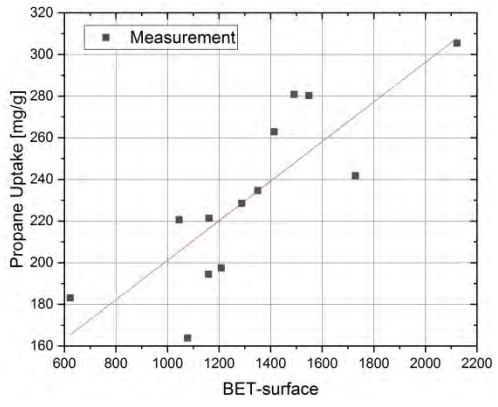

Figure 4: uptake over BET-surface with the corresponding correlation (R^2=68)

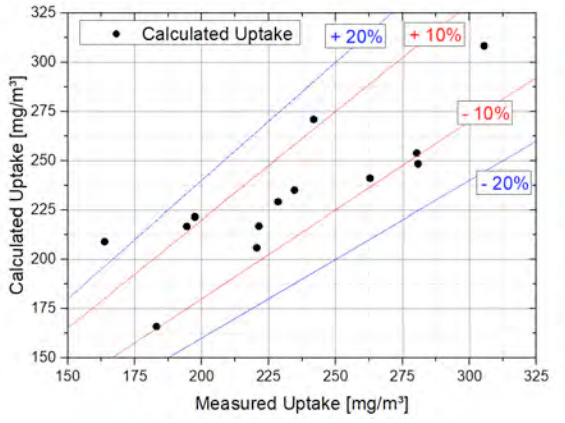

Figure 5: Comparisson of the predictaed and the measured uptake

On the left side, the Fig. 5 shows the propane uptake over the BET-surface and the corresponding correlation. By increasing the BET-surface an increasing of the propane uptake can be observed with a mean standard derivation of less than <15%. On the ride side, the ratio between calculated and measured uptake is presented. The figure shows a good correlation at an uptake from (220-235) mg*cm^{-3}. Over the whole range the standard derivation is less than ±20% expect on measured uptake at 164mg*cm^{-3}. Therefore, the correlation can be used for a preselection for sorption activated carbon material with a standard derivation about 12%. But a detailed analysis is recommended for BET-surfaces higher than 1400.
The adsorption process of propane at activated carbon is an exothermal reaction and the resulting heat increases the surface temperature of the sorption material. By increasing the surface temperature, the capacity will be decrease and the sorption kinetics will be reduced. The sorption enthalpies of the samples were measured by 100vol% of propane at atmospheric pressure, shown in the following Fig. 6. The measured sorption capacity depending on the temperature (283K and 308K) and the correlation of Toth are shown in Fig. 7.

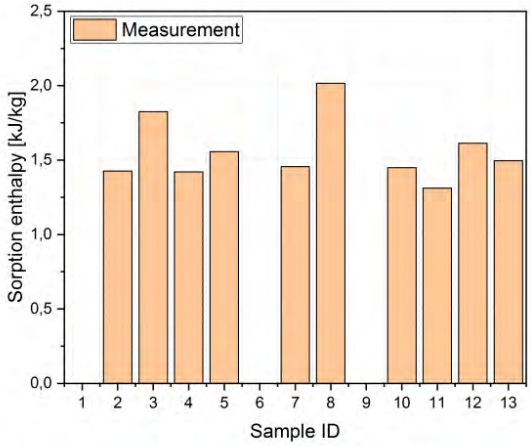

Figure 6: Sorption enthalpy of the samples

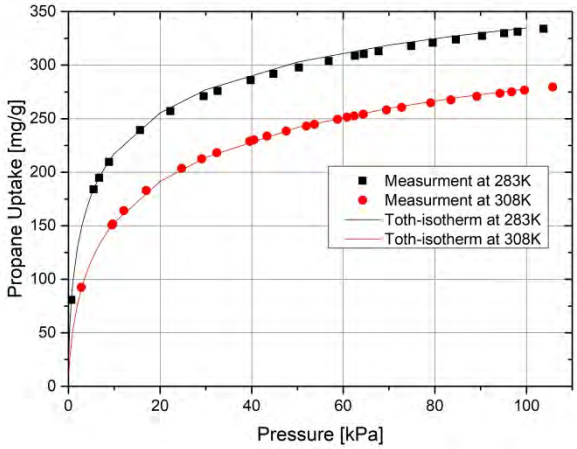

Figure 7: Sorption isotherm calculated via the model of Toth and the corresponding measurements

For the samples 1, 6 and 9 no results are available. The sample 11 shows the lowest adsorption enthalpy by a value of 1,3 kJ*kg^{-1} and the sample 8 shows the highest value of 2.0 kJ*kg^{-1}. Therefore, at the same process condition, like housing of the sorption material or the flow regime, the surface temperature of sample 11 will heat up more than the other samples. This temperature increase will reduce the propane uptake, shown in Fig. 7. The propane uptake decrease by increasing the pressure and the increase in temperature from 283 K to 308 K results in an uptake reduced by from 50% to 17%. Therefore, it is important to control the heat flux to optimise the sorption kinetics, the sorption uptake and also to get a handle volume of the safety element.

4. PROOF OF CONCEPT, SAFETY ELEMENT ADAPTED ON A HEAT PUMP

The safety element was adapted to the heat pump like shown in Fig. 1, with a pipe connection to the liquid line. The heat pump has an electric consumption from 3.6 kW, a heat capacity at the condenser of 12 kW and a refrigerant mass of 1,2kg of propane. The tested activated carbon has a BET-surface 1100 m², a bulk density of 0.5 g*cm^{-3}, particle size between 3-5 mm and was made of coal. By supposing a final pressure of 1kPa in the heat pump piping an uptake of 133 mg*g^{-1} is predicted and the resulting volume is 29 L. This assumption is an absolute unfavourable scenario - by resulting pressure of 100kPa in the piping to get a pressure equilibrium of the inside of the piping at atmosphere, the safety element volume will be 10 L.
For the experiment an amount of activated carbon of 12 kg was used. Temperature sensors and pressure sensors were adapted in the safety element, shown in Fig. 8. Also the weight of the safety element was measured.

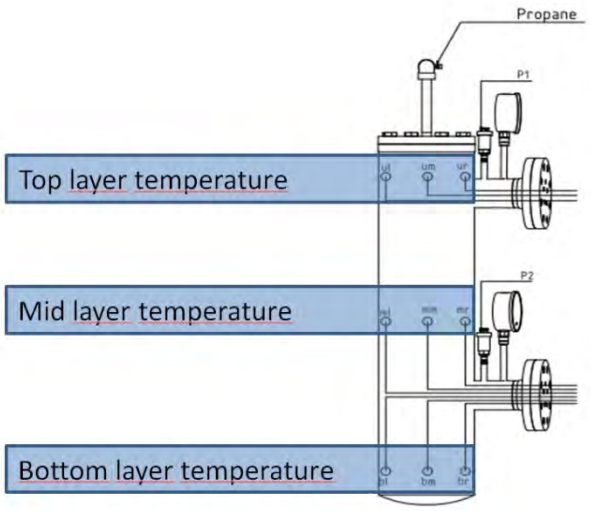

Figure 8: Temperature and pressure sensors in the safety element sorption

4.1. Experimental Procedure

The experimental procedure is described in the following steps:

1. Weighted amount of the activated carbon put into the safety element.
2. The safety element was evacuated again as it was necessary to reach a pressure below atmospheric pressure for the experiment.
3. Heat pump was turned on. The values for sub-cooler and super heater were set to 10 K and 5 K. The pump was kept on running until it attained the steady state condition.
4. Once the heat pump achieved the set values, it was turned off and at the same time safety valve was opened.
5. Propane flows into the safety element abruptly because of the adsorption potential.
6. After pressure and temperature stabilized the safety valve was shut off.
7. The vessel was detached from the system and weighed. The difference in weight between the adsorbed and loaded adsorbent can be used to calculate the uptake.

4.2. Results of the Proof of Concept – Safety Element

The following Figs. 9, 10 and 11 present the temperature behavior in the safety element during adsorption. The temperatures are divided in three sections - top layer, middle layer and bottom layer.

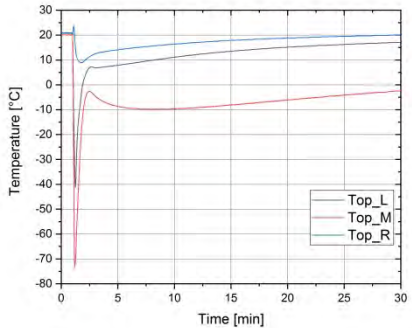

Figure 9: Temperature profile of the top layer in the safety element (L=left, M=middle, R= right)

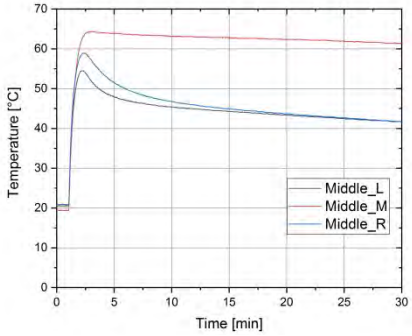

Figure 10: Temperature profile of the middle layer in the safety element (L=left, M=middle, R= right)

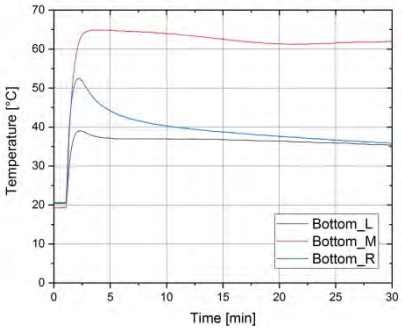

Figure 11: Temperature profile of the bottom layer in the safety element (L=left, M=middle, R= right)

After the inlet of the safety element, the propane pressure decreased rapidly from steady state condition $p_{heat\ pump}$ = 800 kPa to $p_{safety\ element}$ =<120 kPa, shown in Fig. 13. Caused by the liquid state of the propane a fast expansion occurred and the temperature reached -70°C in peak. Also the temperature sensors on the ride and left side of the safety element in the top layer showed a decrease to 10°C and -40°C. This effect is shown in figure 9 represented the top layer of the safety element and is an indicator for a failure in the flow distribution on the right side. Figs. 10 and 11 show the typical increase of temperature while adsorption in the middle and the bottom layer.
On each layer (middle and bottom) the highest temperature can be observed in the middle of the safety element and the temperature sensors of the right and the left side is decreased after circa 2.5 minutes. This effect is caused by the flow regime of the propane and the heat transfer to the wall. The main flow is in the middle of the safety element and therefore, the adsorption will be placed there. Additionally the heat transfer from inside the vessel to the wall is slower than for the left and the right side caused by the distance and the resulting heat resistant.

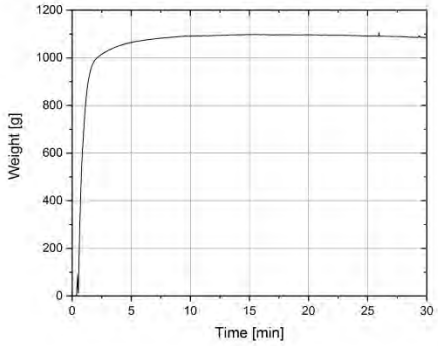

Figure 12: Weight profile of the top layer in the safety element (L=left, M=middle, R= right)

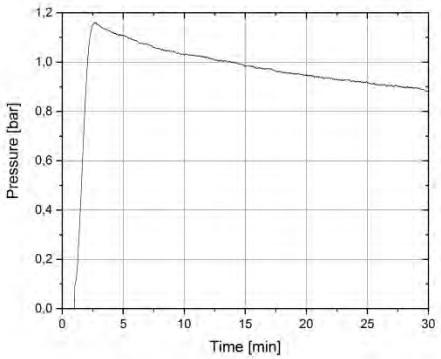

Figure 13: Pressure profile of the top layer in the safety element (L=left, M=middle, R= right)

Fig. 12 shows the weight increase of the propane entering the safety element. After the safety valve opened, the mass increased rapidly up to circa 1100 g. More than 90% of the propane mass in the heat pump was adsorbed in less than 2 min. The rest of the propane mass (<10% or <150 g) remains in the heat pump.

5. CONCLUSIONS

The paper presents the characterisation of 13 sorption materials by geometrical analysis and propane uptake. A correlation of BET-surface with the propane uptake shows a first indicator for the sorption material selection by an average variance of <15%. Furthermore, the model of Toth was adapted to the results of the propane uptake measurements with error amount of < 3 $mg*g^{-1}$ in the temperature range of -5°C to 35°C.
The experimental proof of concept shows the adsorption of 1,2 kg propane from the heat pump in less than 2min.

ACKNOWLEDGEMENTS

The financial support by the German Federal Ministry for Economic Affairs and Energy under grant no. 03ET1353 A is gratefully acknowledged.

NOMENCLATURE

p	pressure (kPa)	R	molar gas constant (8.314472 $J\times mol^{-1}\times K^{-1}$)
T	temperature (K)	V	molar volume (m^3*mol^{-1})
X	absolut sorption capacity ($mg*g^{-1}$)	C,K,n	Sorption model parameter (-)
Θ	percentage sorption capacity (%-weight)	ps	Saturation pressure of the adsorbate (kPa)

REFERENCES

Brunauer, Emmett, Teller (1938): Adsorption of Gases in multimolecular Layers. In: *Journal of the American Chemical Society* (vol. 60), S. 309.

Chemgapedia: Adsorption an Festkörperoberflächen- Stärke der Adsorption: Adsorptionsenthalpie. Online verfügbar unter http://www.chemgapedia.de/vsengine/vlu/vsc/de/ch/1/pc/pc_10/pc_10_01/pc_10_01_03.vlu/Page/vsc/de/ch/1/pc/pc_10/pc_10_01/pc_10_01_15.vscml.html, zuletzt geprüft am 01.08.2017.

D. Bathen, M. Breitenbach (2001): Adsorptionstechnik. Berlin Heidelberg: Springer Verlag.

Europäisches Parlament (2014): Verordnung (EU) Nr. 517/2014 über fluorierte Treibhausgase und zur Aufhebung der Verordnung (EG) Nr. 842/2006 (L 150/195).

G. Munz (2006): Experimentelle und Theoretische Untersuchungen zur Thermodynamik Experimentelle und Kinetik der Wasseradsorption in mikroporösen Schichtverbundsystemen, Regensburg. Experimentelle und Angewandte Physik.

H. Freundlich (1907): Über die Adsorption in Lösungen. In: *Zeitschrift für Physikalsiche Chemie* (Band 57U, Heft 1), S. 385–470. Online verfügbar unter DOI: https://doi.org/10.1515/zpch-1907-5723.

J. Toth (1971): State equation of the solid gas interface layer,. In: *Acta Chimica (Academiae Scientiarum) Hungaricae* (vol. 69), S. 311–317.

Langmuir (1918): The adsorption of gases on plane Surfaces of Glass, Mica and Platinum. In: *Journal of the American Chemical Society* (vol. 40).

Nimibofa Ayawei (2017): Modelling and Interpretation of Adsorption Isotherms. In: *Journal of Chemistry* (Article ID 3039817, 11 pages). Online verfügbar unter https://doi.org/10.1155/2017/3039817.

Quantachrome (2017): QUADRASORB evo und QUADRASORB evo MP. Online verfügbar unter http://www.quantachrome.de/analysegeraete/quadrasorb/.

Quantachrome Instruments (2017): V-Star Vapor Soprtion Analyzer Operating Manual.

W. Kast (1988): Adsorption aus der Gasphase: VCH.

Manuscript ID: 1643
DOI: 10.18462/iir.icr.2019.1643

A new analytical model for concrete sensible thermal energy storages simulation

Luca DORETTI [(a)], Francesca MARTELLETTO [(a)], Simone MANCIN [(b)]

[(a)] Dept. of Civil, Environmental and Architectural Engineering, University of Padova, Via Venezia, 1, Padova 35131, Italy, luca.doretti@unipd.it, francesca.martelletto@studenti.unipd.it.
[(b)] Dept. of Management and Engineering, University of Padova, Stradella S. Nicola, 3, Vicenza 36100, Italy, simone.mancin@unipd.it.

ABSTRACT

A simple lumped capacitance based computing model was developed and here presented. The code permits the thermal and energetic analysis of concrete thermal energy storages (TESs) during time. The simulated system consists of a parallelepiped concrete module that can be heated (charging phase) and cooled (discharging phase) by a single-phase working fluid flowing in a tube embedded in the concrete. The new simulation code was validated against the experimental data carried out by ENEA with two different concrete mixtures, during both the heating and cooling processes using mineral oil as working fluid. This simple and easy-to-use model allows for a drastic reduction of the computational time needed to simulate the TES and it can be easily integrated, in various arrangements, to any concentrated solar power plant (CSP) and associated energy conversion plant simulation models to have a quick evaluation of the system performance.
Keywords: Heat Storage; Sensible heat; Concrete Module; CSP Plant; Model.

1. INTRODUCTION

Electrical power generation by using concentrated solar thermal energy is one of the most promising renewable energy technologies. It is widely accepted that a great improvement in CSP plants can be accomplished by adding a thermal storage system (TES). It would permit to meet the peak demand through a rational optimization of the energy production by the CSP plant, especially during night time or cloudy weather. During energy storage process, commonly called charging or heating stage, the heat transfer fluid (HTF), heated by the solar field, warms up the TES, flowing through the modules and stores a certain amount of energy by increasing the TES temperature. Conversely, during the energy discharge process, commonly called discharging or cooling stage, the cold fluid is pumped through the TES to extract heat to be released to the power plant. The HTF flows in pipes that are commonly embedded in the thermal storage materials, which can be molten salts, concrete, soil, sand, or rocks, etc.
The technology for sensible thermal energy storage (STES) for CSP plants is well known and it has been widely investigated; in the last decades, various solar plants with different fluids and storage systems, have been built in USA, Spain, Germany, and Italy, as reported in Gil et al. (2010) and Medrano et al. (2010). Concrete is widely used for the construction of TES because it offers low cost, good, and stable thermal properties, appropriate structural conditions, long durability, and simple industrial production, as clearly reported in Salomoni et al. (2014) and Laing et al. (2006). Besides, the HTF is basically an energy-carrying medium, so the heat transfer process between TES material and the HTF is of crucial importance in order to properly study the charge and discharge processes. In the open literature, many different models to simulate various types of TES systems have been proposed and published. The models are generally subdivided into three main categories: analytical, finite element method (FEM), and simplified models. This classification could be debatable because various analytical models due to their assumptions could also be considered simplified models. Even if the concrete TES systems have already been studied, their application is still a matter of research; in particular, there is a strong need of practical prediction tools to enable simple and fast simulations of TES embedded in power plants.
From this standpoint, this work aimed at developing a new computational tool able to predict the behavior of the concrete storage modules. In particular, the attention was focused on a modular and flexible tool that, under the necessary assumptions, allows for the real-time simulation of the

general TES module's parameters during the operation of the entire system. The model was implemented in Fortran 90. As it clearly appears from this brief overview, the models reviewed have many limitations, which can be summarized as:

- high computational efforts and low flexibility (CFD/FEM models)
- high complexity (analytical models)
- adiabatic external boundary conditions (CFD/FEM and analytical models)
- no models consider the presence of insulating layers
- necessity of semi-empirical constants or parameters derived from FEM simulations.

Hence, those models are not suitable for on-field analysis, because in that situation it is essential to know the results in real time. The present code allows for basically instantaneous calculations, in fact, it is an executable tool which gets the results within a few seconds for 4-6 hours process. The main parameter describing the TES is the ability of each element (or module) to store (during heating stage) or to release (during cooling stage) the thermal energy from or to the HTF; in the case of concrete TESs and in general for STESs, this parameter is the mean temperature of the concrete TES. The developed model was meant to compute the stored or the transferable energy over time, and the related HTF temperature at the outlet of the module.

2. EXPERIMENTAL SETUP

In order to validate the developed model, a suitable set of experimental tests was selected. The experimental campaign investigated the effects of the concrete composition by testing two different mixtures during both heating and cooling phases. For the sake of clarity, in what follows, a brief description of the concrete prototypes and of the experimental procedure is given; more details can be found in Giannuzzi et al. (2014).

Two concrete modules were built, using two different concrete mixtures: Cestaro srl (called type A) and Italcementi Spa (called type B). The thermal-mechanics characteristics of the two concrete mixtures are described in Girardi et al. (2014) and Mazzucco et al. (2014); the Biot number is equal to 123 and 152 for the two concrete mixtures. The two modules presented the same sizes and piping layout; the SS tube was embedded into the concrete matrix in a 4-passages configuration. The concrete TES modules were tested in a dedicated experimental setup, built by ENEA. Paratherm™ NF mineral oil was chosen as HTF. Each concrete module was a square cross-section parallelepiped, with a total weight of around 290 kg. The concrete module was instrumented with many thermocouples which were installed during the manufacturing. The oil temperatures at the inlet and outlet of the module, the oil mass flow rate, and the room temperature were also measured and recorded. The main system properties and geometric parameters are reported in Table 1. Numerical simulation of the concrete TES allowed for the estimation of the volume weighted temperature over time on the entire TES where the experimental temperature was recorded. These results were then compared against the average value calculated from the temperature readings collected by the thermocouples: the deviation was always less than 3 °C. For these reasons, the mean concrete module temperature can be assumed as the main parameter which describes the entire module thermal behavior.

Table 1. TES properties.

TES length, L_{TES} (m)	3
TES side length, $L_{side,TES}$ (m)	0.2
TES equivalent diameter, $D_{eq,TES}$ (m)	0.226
Basic element side length, $L_{side,el}$ (m)	0.1
Basic element equiv. diameter, $D_{eq,el}$ (m)	0.113
Total tube length, L_t (m)	12
Tube inner diameter, $D_{t,int}$ (m)	0.014
Tube external diameter, $D_{t,ext}$ (m)	0.016
Tube thermal conductivity, λ_t (W m^{-1} K^{-1})	16
Insulating layer 1 thickness, s_{ins1} (m)	0.05
Insulating layer 2 thickness, s_{ins2} (m)	0.1
Ins. layer 1 therm. cond., λ_{ins1} (W m^{-1} K^{-1})	0.06
Ins. layer 2 therm. cond., λ_{ins2} (W m^{-1} K^{-1})	0.035
Insulating material density, ρ_{ins} (kg m^{-3})	80
Ins. material specific heat, c_{ins} (J kg^{-1}K^{-1})	1030
Environment coefficient, h_{env} (W m^{-2} K^{-1})	15
Concrete specific heat capacity (J kg^{-1}K^{-1})	820-930
Concrete density (kg m^{-3})	2483-1837
Concrete thermal conductivity (W m^{-1} K^{-1})	2.21-1.80

3. MODEL DESCRIPTION

The first problem to face up was to reduce the complexity of the geometry of the TES module, in which cylindrical tubes were embedded in a concrete parallelepiped, which then was covered by

multiple insulating layers. The entire concrete module was schematized to be a cylinder with an equivalent diameter based on volume defined as:

$$D_{eq,TES} = \sqrt{\frac{4L_{side,TES}^2}{\pi}} \qquad \text{Eq. (1)}$$

Similarly, the two external insulating layers were approximated with two equivalent annular volumes with diameters calculated keeping constant their actual heat transfer areas, as:

$$D_{eq,ins1} = \frac{A_{ins1,ext}}{\pi L_{TES}} \qquad D_{eq,ins2} = \frac{A_{ins2,ext}}{\pi L_{TES}} \qquad \text{Eqs. (2,3)}$$

The embedded steel tube presented a 4-passage configuration; thus, by neglecting the three curves that have no effect on the global system performance, the storage module can be considered of being constituted by 4 sub-units, called basic elements, arranged in series. A similar schematization was also used by different authors such as Sragovich (1989), and Salomoni et al. (2014). In this way, the basic element assumes the well-known geometry, often described as "washer", in which the tube is placed in the cylinder center; in the specific case, each of 4 elements has 2 adiabatic sides (towards the adjacent elements), and 2 diabatic sides (towards the external insulating layers). Also, in the case of the concrete sub-system, an equivalent diameter based on volume (to keep constant the mass) can be defined as:

$$D_{eq,cnc} = \sqrt{\frac{4L_{side,el}^2}{\pi}} \qquad \text{Eq. (4)}$$

All the simplified simulation models are based on the well-known lumped capacitance method, a good review of this method can be found in Xu et al. (2012), in which the former analysis of Schumann (1929) is reported and commented. In the lumped capacitance method, which cannot be applied for high values of Biot numbers, the basic assumption is that the concrete temperature must be constant along the cylinder radius. The model here proposed assumes the fundamental lumped capacitance hypotheses, but it also introduces a set of new assumptions.

- The heat exchange processes are described by means of suitable thermal resistances.
- The entire module is assumed to be characterized by the mean concrete temperature, being constant on both radial and axial directions; this temperature is assumed to be the temperature of the two symmetry planes which divide the entire module into 4 sub-units.
- The energy dissipation of the TES module towards the surroundings is estimated.
- The time-dependent mean temperature of each insulating layer is estimated and the internal energy variation is obtained at each time step.
- The temperatures of concrete, oil, and insulating layers are estimated by two energy balance equations (for charging and discharging phase), by discretizing the time variable in time steps ($\Delta\tau$). The balance equations of the heat fluxes and the consequent temperatures are solved with a simple numerical iterative procedure.

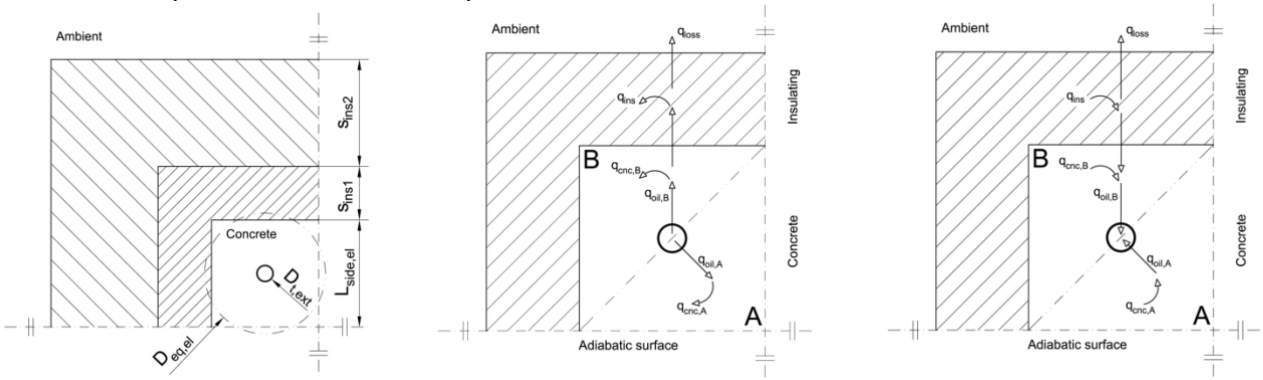

Figure 1: Geometry and heat fluxes schemes for heating (left) and cooling (right) test.

Governing equations

When combining the internal (A) and external (B) section calculations (Figure 1), and taking into account the 4 basic elements arranged in series that constitute the entire TES system, the heat flux balance for the entire TES element for the heating and cooling phase can be written.

Heating/charging phase energy balance (Fig. 1, left-hand side schematic):

$$q_{cnc,A}=q_{oil,A} \qquad q_{cnc,B}=q_{oil,B}-q_{ins}-q_{loss} \qquad \text{Eqs. (5,6)}$$

$$q_{cnc}=q_{cnc,A}+q_{cnc,B}=q_{oil,A}+q_{oil,B}-q_{ins}-q_{loss} \qquad \text{Eq. (7)}$$

Cooling/discharging phase energy balance (Fig. 1, right-hand side schematic):

$$q_{cnc,A}=q_{oil,A} \qquad q_{cnc,B}=q_{oil,B}-q_{ins}+q_{loss} \qquad \text{Eqs. (8,9)}$$

$$q_{cnc}=q_{cnc,A}+q_{cnc,B}=q_{oil,A}+q_{oil,B}-q_{ins}+q_{loss} \qquad \text{Eq. (10)}$$

In this way, after an iterative procedure on heat fluxes and temperatures, the internal energy variation of concrete TES and, consequently, the new value of TES element temperature can be obtained at each time-step:

$$\Delta t_{cnc}=\frac{q_{cnc}}{m_{cnc}c_{cnc}}\cdot\Delta\tau=\left|t_{cnc,\tau+\Delta\tau}-t_{cnc,\tau}\right| \qquad \text{Eqs. (11,12)}$$

$$t_{cnc,\tau+\Delta\tau}=t_{cnc,\tau}\pm\Delta t_{cnc} \qquad \text{Eq. (13)}$$

with the sign (+) for heating (the concrete temperature is increasing) and sign (-) for cooling (the concrete temperature is decreasing). After the concrete and oil heat fluxes calculation, the outlet oil temperature can be estimated and compared against the experimental results. The calculation of the heat fluxes in the governing equations is fully described in the following paragraphs (equations from 14 to 41). The detailed model description can be started from the definition of the thermal conductive resistances of the system and, in particular, from the insulating layer.
The total insulating cover area can be divided into the side surface of the equivalent hollow cylinder (Eqs. (2) and (3)) and the plane one of the two cylinder bases (the "heads" of the module) of the equivalent cylinder. The thermal resistances of side surfaces for each insulating layer can be evaluated as:

$$R_{ins1,c}=\frac{1}{2\pi\lambda_{ins1}L_{TES}}\ln\left(\frac{D_{eq,ins1}}{D_{eq,TES}}\right) \qquad R_{ins2,c}=\frac{1}{2\pi\lambda_{ins2}L_{TES}}\ln\left(\frac{D_{eq,ins2}}{D_{eq,ins1}}\right) \qquad \text{Eqs. (14,15)}$$

Being in series, the total thermal resistance for the side surface can be calculated as:

$$R_{ins,c}=R_{ins1,c}+R_{ins2,c} \qquad \text{Eq. (16)}$$

The thermal conductive resistances for each insulating layer, computing the "heads" surface as a plane wall, can be calculated as:

$$R_{ins1,h}=\frac{s_{ins1}}{\lambda_{ins1}2A_{ins1,h,m}} \qquad R_{ins2,h}=\frac{s_{ins2}}{\lambda_{ins2}2A_{ins2,h,m}} \qquad \text{Eqs. (17,18)}$$

Again, being in series, the total thermal resistance for the "heads" surface can be calculated as:

$$R_{ins,h}=R_{ins1,h}+R_{ins2,h} \qquad \text{Eq. (19)}$$

The overall thermal resistance of the insulating layers which cover the TES can be calculated considering that the thermal resistance of the side cylinder and the heads are arranged in parallel and subjected to the same temperature difference:

$$R_{ins}=\left(\frac{1}{R_{ins,c}}+\frac{1}{R_{ins,h}}\right)^{-1} \qquad \text{Eq. (20)}$$

The ambient thermal resistance, which combines convective and radiation effects, can be calculated as:

$$R_{amb}=\frac{1}{h_{amb}A_{ins2,ext}} \qquad \text{Eq. (21)}$$

Thus, the overall thermal resistance between concrete and environment is given by:

$$R_{ext}=R_{ins}+R_{amb} \quad \text{Eq. (22)}$$

The forced convective heat transfer coefficient h_{oil} is estimated by means of the well-known Dittus-Boelter semi-empirical correlation, thus the associated oil convective thermal resistance can be computed (every iteration cycle) as:

$$R_{oil}=\frac{1}{h_{oil}A_{t,int}}=\frac{1}{h_{oil}\pi D_{t,int}L_t} \quad \text{Eq. (23)}$$

The steel tube conductive thermal resistance is given by:

$$R_t=\frac{1}{2\pi\lambda_t L_t}\ln\left(\frac{D_{t,ext}}{D_{t,int}}\right) \quad \text{Eq. (24)}$$

The concrete elementary system conductive thermal resistance, between external tube surface and elementary sub-system external boundary, can be calculated as:

$$R_{cnc}=\frac{1}{2\pi\lambda_{cnc}(4L_{el})}\ln\left(\frac{D_{eq,cnc}}{D_{t,ext}}\right) \quad \text{Eq. (25)}$$

Finally, the overall thermal resistance between oil and concrete is given by:

$$R_{int}=R_{oil}+R_t+R_{cnc} \quad \text{Eq. (26)}$$

It has to be pointed out that the heat flux equations (with the exception of loss heat flux) are here reported for the two different processes: thus, referring to heating/charging process in which the oil heats the concrete TES (Fig. 1, left-hand side), and in the case of cooling/discharging (in which the concrete heats the oil mass flux) in which the absolute value has to be used (Figure 1, right-hand side).

As described in Figure 1, once the thermal resistances are defined, it is possible to present the heat flux between oil and concrete for the internal section (called "A", from the oil to the TES core), considering the complete TES system (the sum of the 4 sub-units), as:

$$q_{oil,A}=\left|\frac{t_{oil,m}-t_{cnc}}{2R_{int}}\right| \quad \text{Eq. (27)}$$

section A is geometrically equal to the B one, each section has half of the entire area, so the overall thermal resistance is multiplied by a factor 2.

The heat flux between oil and concrete for the external section (called "B", from the oil to the TES boundaries), considering the complete TES system (the sum of the 4 sub-units), is given by:

$$q_{oil,B}=\left|\frac{t_{oil,m}-t_{cnc,ext}}{2R_{int}}\right| \quad \text{Eq. (28)}$$

While the heat flux between concrete and environment is:

$$q_{loss}=\frac{t_{cnc,ext}-t_{env}}{R_{ext}} \quad \text{Eq. (29)}$$

The concrete external temperature can be estimated as:

$$t_{cnc,ext}=t_{oil,m}\pm\frac{q_{oil}}{R_{int}}=t_{oil,m}\pm\frac{q_{oil,A}+q_{oil,B}}{R_{int}} \quad \text{Eq. (30)}$$

with the sign (-) for heating, and sign (+) for cooling processes. Thus:

$$t_{ins1,int}=t_{cnc,ext} \qquad t_{ins1,ext}=t_{ins1,int}-\frac{q_{loss}}{R_{ins1}} \quad \text{Eqs. (31,32)}$$

$$t_{ins2,int}=t_{ins1,ext} \qquad t_{ins2,ext}=t_{ins1,int}-\frac{q_{loss}}{R_{ins}} \quad \text{Eqs. (33,34)}$$

The temperature along the radius in the insulating layer is supposed to follow a logarithmic profile, and a mean temperature by volume for each insulating layer can be calculated as:

$$t_{ins,m}=\frac{\int_{int}^{ext} t(r)2\pi r dr}{\pi(r_{ext}^2-r_{int}^2)} \qquad t(r)=t_{ins,int}+\frac{t_{ins,ext}-t_{ins,int}}{\ln\left(\frac{r_{ext}}{r_{int}}\right)}\cdot\ln\left(\frac{r}{r_{int}}\right) \qquad \text{Eq. (35)}$$

$$t_{ins,m}=t_{ins,int}-\frac{t_{ins,ext}-t_{ins,int}}{\ln\left(\frac{r_{ext}}{r_{int}}\right)}\cdot\ln(r_{int})+\frac{t_{ins,ext}-t_{ins,int}}{\ln\left(\frac{r_{ext}}{r_{int}}\right)}\cdot\frac{r_{ext}^2\left(\ln(r_{ext})-\frac{1}{2}\right)-r_{int}^2\left(\ln(r_{int})-\frac{1}{2}\right)}{(r_{ext}^2-r_{int}^2)} \qquad \text{Eq. (36)}$$

Finally, the temperatures variations of insulating layers to take into account the internal energy variation can be calculated as:

$$\Delta t_{ins1}=\left|t_{iso1,m,\tau+\Delta\tau}-t_{iso1,m,\tau}\right| \qquad \Delta t_{ins2}=\left|t_{iso2,m,\tau+\Delta\tau}-t_{iso2,m,\tau}\right| \qquad \text{Eqs. (37,38)}$$

where $\Delta\tau$ is the defined time step.
The internal energy stored in insulating layers due to their mean temperature variations is given by:

$$q_{ins1}=\frac{m_{ins1}c_{ins1}\Delta t_{ins1}}{\Delta\tau} \qquad q_{ins2}=\frac{m_{ins2}c_{ins2}\Delta t_{ins2}}{\Delta\tau} \qquad \text{Eqs. (39,40)}$$

$$q_{ins}=q_{ins1}+q_{ins2} \qquad t_{oil,out}=t_{oil,in}\pm\frac{q_{oil}}{\dot{m}_{oil}\cdot c_{oil}} \qquad \text{Eqs. (41,42)}$$

with (-) for charging (outlet oil temperature is lower than the inlet one) and (+) for discharging phase (outlet oil temperature is higher than the inlet one).

4. COMPARISON WITH EXPERIMENTAL DATA

The comparisons between experimental and model-calculated oil and concrete temperature profiles of the two concrete mixtures are reported in Figs. from 2 to 4, during both the charging and discharging processes.

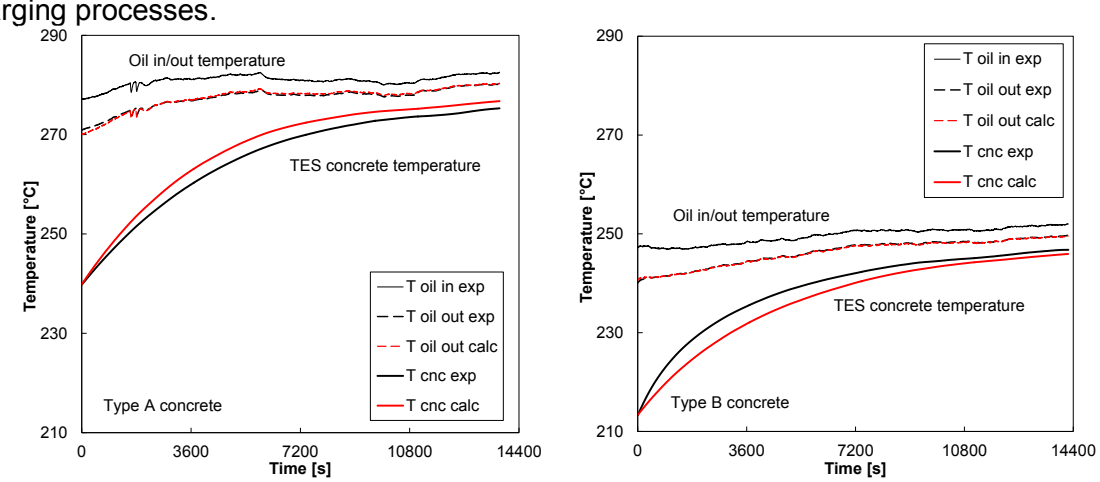

Figure 2. Experimental vs. calculated temperatures for the heating test (DEV=+4.08 and -2.49%).

In general, a good agreement between the calculated and the experimental results is found. However, the two concrete mixtures presented different behaviors. In the case of type A concrete, the numerical model slightly overestimates the heating profile while the final concrete temperature is correctly estimated (Fig. 2). Similarly, during the cooling phases (Fig. 3), the model slightly overestimates; the heat released by the concrete and the calculated final concrete temperature are lower than that measured values.
Differently, in the case of type B mixture, the code slightly underestimates the concrete's temperature compared to the experimental one, both during heating (Fig. 2) and cooling stages (Fig. 3). In fact, the calculated concrete temperature is lower than the real one during heating, but it is higher than the experimental one during cooling. Hence, with type B, the model slightly underestimates the stored or released thermal energy, again within the experimental uncertainty. It is also worth to underline that the calculated outlet oil temperature follows faithfully the experimental one, also when the inlet oil temperature shows contrary peaks compared to the general increasing or reducing trend. However, the first aim of the model was to predict the

concrete temperature during the two stages. The charts show that the calculated temperature is in fine agreement with the experimental one, both as instant values and global trend.
The model also allows for the calculation of the heat fluxes exchanged during the simulated process. Two examples are reported in Fig. 4. The two main heat fluxes are those related to oil and concrete, which are higher at the beginning of the test and then progressively decrease with time because the temperature difference between oil and concrete becomes accordingly lower. In Fig. 4 (right), which shows a cooling stage, the oil heat flux becomes even negative near to the end of the test, it means that the experiment has lasted enough time to allow the concrete to achieve a temperature lower than the oil one, so the oil heat flux becomes negative due to that temperature crossing. The insulating layer and loss heat fluxes are also plotted.

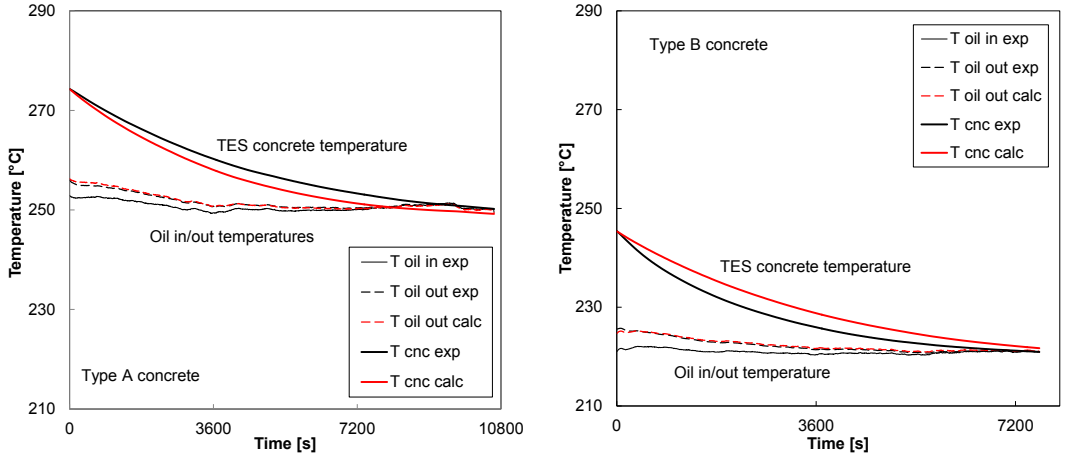

Figure 3. Experimental vs. calculated temperatures for cooling test (DEV=+4.15 and -3.07%).

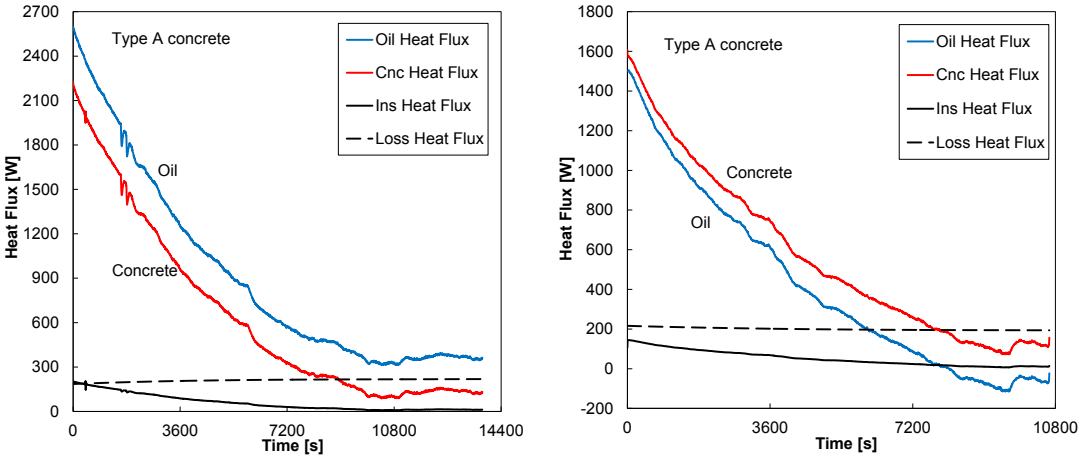

Figure 4. Calculated heat fluxes for heating and cooling.

5. CONCLUSIONS

A simplified lumped capacitance model, useful to predict the behavior of a concrete thermal storage module, was developed, validated, and proposed. These characteristics make this model suitable for the implementation in more complex solar thermal simulation tools and software, allowing for a fair estimation of the energy storable in concrete TES as well as its transient behavior during charging and discharging processes as a function of the main operating conditions. In fact, the model permits the thermal and energetic analyses of the concrete storage module during the time, both for charging and discharging phases. The developed calculation procedure can be considered a modular, flexible and quick tool that allows the computation of the module's parameters almost immediately. A unique reference concrete temperature was considered to describe the whole system; obviously, it involves a few simplifying assumptions, but the model computed accurate values with a computational effort drastically less than that of a CFD/FEM model. The model was compared against the data of experimental campaign on two concrete mixtures, during heating and cooling stages. The exchanged concrete energy deviation is very low for each test and always less than the experimental uncertainty. The experimental and calculated results achieve a very fine agreement, both as actual values and global trend.

NOMENCLATURE

Parameter			Subscript	
A	area	(m^2)	amb	ambient
c	specific heat capacity	($J\ kg^{-1}\ K^{-1}$)	c	cylinder
D	diameter	(m)	calc	calculated
Dev	deviation	(-)	cnc	concrete
h	convective HTC	($W\ m^{-2}\ K^{-1}$)	e	end
L	length	(m)	el	element
l_v	specific latent heat	($J\ kg^{-1}$)	eq	equivalent
$\dot{m}$	mass flow rate	($kg\ s^{-1}$)	ext	external
m	mass	(kg)	h	head
q	heat flow rate	(W)	in	inlet
Q	heat, energy	(J)	ins	insulat. layer
r	radius	(m)	int	internal
R	thermal resistance	($K\ W^{-1}$)	lat	latent
s	thickness	(m)	loss	dissipated
t	temperature	(°C)	m	mean value
			oil	oil
Greek symbols			out	outlet
Δ	difference	(-)	s	start
λ	thermal conductivity	($W\ m^{-1}\ K^{-1}$)	side	side
ρ	density	($kg\ m^{-3}$)	t	tube
τ	time	(s)	w	water

REFERENCES

Giannuzzi G.M., Giovannini E., Liberatore R., Mazzei D., Mele D., Crescenzi T., 2014. Analisi sperimentale e numerica del comportamento termodinamico di sistemi di accumulo a calore sensibile in materiali cementizi. ENEA Report RdS/PAR2014/118.

Gil A., Medrano M., Martorell I., Làzaro A., Dolado P., Zalba B., Cabeza L.F., 2010, State of the art on high temperature thermal energy storage for power generation. Part 1 - Concepts, materials and modellization. Renewable and Sustainable Energy Reviews 14, 31-55.

Girardi F., Di Maggio R., 2014, Realizzazione e caratterizzazione di un modulo di accumulo basata su mescola sviluppata da UNITN. ENEA Report RdS/PAR2014/119.

Laing D., Steinmann W.D., Tamme R., Richter C., 2006, Solid media thermal storage for parabolic trough power plants. Solar Energy 80, 1283-1289.

Mazzucco G., Xotta G., Majorana C.E., 2014, Progettazione termomeccanica, realizzazione e caratterizzazione di un modulo di accumulo in materiale cementizio. Simulazioni ed analisi dei dati sperimentali. ENEA Report RdS/PAR2014/120.

Medrano M., Gil A., Martorell I., Potau X., Cabeza L.F., 2010, State of the art on high-temperature thermal energy storage for power generation. Part 2 - Case studies. Renewable and Sustainable Energy Reviews 14,56-72.

Salomoni V.A., Majorana C.E., Giannuzzi G.M., Miliozzi A., Di Maggio R., Girardi F., Mele D., Lucentini M., 2014, Thermal storage of sensible heat using concrete modules in solar power plants. Solar Energy 103, 303-315.

Schumann T.E.W., 1929, Heat transfer: a liquid flowing through a porous prism. J. Franklin Inst. 208(3), 405-416.

Sragovich D., 1989, Transient analysis for designing and predicting operational performance of a high temperature sensible thermal energy storage system. Solar Energy 49, 7-16.

Xu B., Li P.W., Chan C.L., 2012, Extending the validity of lumped capacitance method for large Biot number in thermal storage application. Solar Energy 86, 1709-1724.

Manuscript ID: 1654
DOI: 10.18462/iir.icr.2019.1654

Optimized 3D periodic structures for advanced latent thermal energy storages ((LTESs) via additive manufacturing

Giulia RIGHETTI[(a)], Gianpaolo SAVIO[(b)], Roberto MENEGHELLO[(a)], Luca DORETTI[(b)], Simone MANCIN[(a)]

(a) Department of Management and Engineering, University of Padova, 36100, Italy

(b) Department of Civil, Environmental and Architectural Engineering, University of Padova, 35100, Italy

giulia.righetti@unipd.it, gianpaolo.savio@unipd.it, roberto.meneghello@unipd.it, luca.doretti@unipd.it, simone.mancin@unipd.it

ABSTRACT

The use of a Latent Thermal Energy Storage (LTES) system using suitable Phase Change Materials (PCMs) is an effective way of storing energy because of its high-energy storage density and isothermal nature of the storage processes. Unfortunately, PCMs present a few unfavorable thermophysical properties, among those the low thermal conductivity, which are limiting the development of efficient, reliable and convenient LTESs. However, LTES represents a promising technology, which can unlock unprecedented opportunities for multiple-sources energy integration, waste heat recovery, and efficient energy management. This paper aims at investigating new 3D periodic structures obtained via metallic additive manufacturing developed to enhance the phase change process during both loading and unloading processes of different paraffin waxes and sugar alcohols. The tests were run by imposing 20 W during the loading process and the monitoring the temperature distribution within the PCM.

Keywords: PCM, Thermal energy storage; phase change; additive manufacturing; renewable energy

1. INTRODUCTION

As described in several comprehensive papers (Kalapala and Devanuri 2018; Lin et al. 2018), phase change materials (PCMs) have been widely proposed for thermal energy storage applications due to their capability of storing and releasing large amounts of energy with a small volume and a relatively low temperature variation. Amongst the available kinds of PCMs, paraffin waxes have been found to exhibit many desirable characteristics, such as high latent heat, low vapor pressure in the melt, chemical inertia and stability, and non-toxicity. However, they also have a very low thermal conductivity and a high volume change during the melting process. Thus, one great interest of the scientific community is finding out efficient and cost effective heat transfer intensification techniques for the future implementation of PCMs inside LTES systems (Al-Maghalseh and Mahkamov 2018; Qureshi et al. 2018).

Among all these methods analyzed in the open literature, this paper wants to focus on the use of high thermal conductivity inserts to increase the available heat transfer surface. Mahmoud et al. (2013) tested six different heat sink designs one with single cavity, two with parallel fin arrangement, two with cross fin arrangement, and one with honeycomb insert inside the single cavity. They concluded that increasing the number of fins can enhance heat transfer and that the use of honeycomb insert to replace machined fin structures leads to comparable thermal performance with the advantage of light weight and reduced costs. Hosseinizadeh at al. (2015) investigated the effects of various parameters such as power levels, number of fins, fin height and fin thickness. The results showed that the increasing of fin number and fin height resulted in an appreciable overall thermal performance enhancement, whereas the increasing of the fin thickness only gave a slight improvement. The authors found an optimum fin thickness, above which the heat sink performance

showed no further improvement. Accordingly, also Kalbasi et al. (2019) after running some numerical optimization of a PCM-based heat sink for electronic cooling concluded that the horizontal spacing between vertical fins affects the melted PCM convection and heat distribution inside the heat sink. In case of small fin spacing, the viscous forces dominate the buoyancy forces limiting the liquid natural convection. Differently, in case of large fin spacing, the regions far from the fins do not properly contribute to the heat storage process. Hence, an optimal spacing can be considered for each heat sink, to optimize the heat transfer.
This paper aims at investigating new cellular structure materials with open 3D periodic cells based on a pyramidal shape obtained via metallic additive manufacturing developed to enhance the phase change process during both loading and unloading processes of PCMs. Three 3D structures having the same porosity equal to 95% but different base size of the pores are studied and their heat transfer behavior are compared by monitoring the temperature distribution within the PCM. Tests are run by imposing a constant electrical heat flow rate of 20 W during the loading process, while the unloading one is run into ambient air to reproduce the cooling characteristics of electronic devices.

2. TEST SAMPLES AND EXPERIMENTAL SET UP

In this study, four different test modules, represented in Fig. 1a, are investigated. They are 42x42x60 mm boxes obtained via metallic additive manufacturing from AlSi10Mg-0403 powder. AlSi10Mg-0403 alloy comprises aluminum alloyed with silicon of mass fraction up to 10%, small quantities of magnesium and iron, along with other minor elements. The presence of silicon makes the alloy both harder and stronger than pure aluminum due to the formation of Mg_2Si precipitate but it also limited its thermal properties. The thermal conductivity λ was calculated from the experimental value of the thermal diffusivity measured by means of a Hot Disk apparatus. The thermal diffusivity was equal to 41.57 $mm^2\ s^{-1}$, so that the thermal conductivity is 96 $W\ m^{-1}\ K^{-1}$.
One module is an empty box and works as reference sample, while the other three are filled with three different cellular structure materials. These structures, visible in Fig. 1a, are open 3D periodic cells based on a pyramidal shape with different base size of the pores, equal to 10, 20, and 40 mm, respectively. They all have the same porosity, equal to 95%, that means that the fiber thickness increases when increasing the pore size.

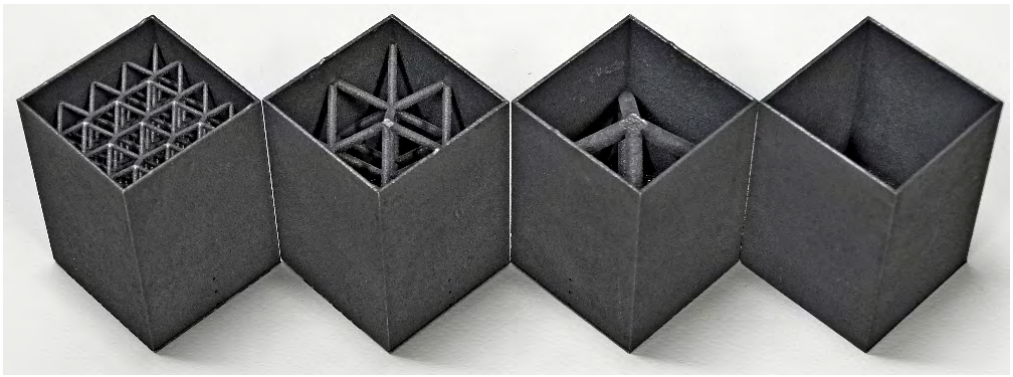

(a)

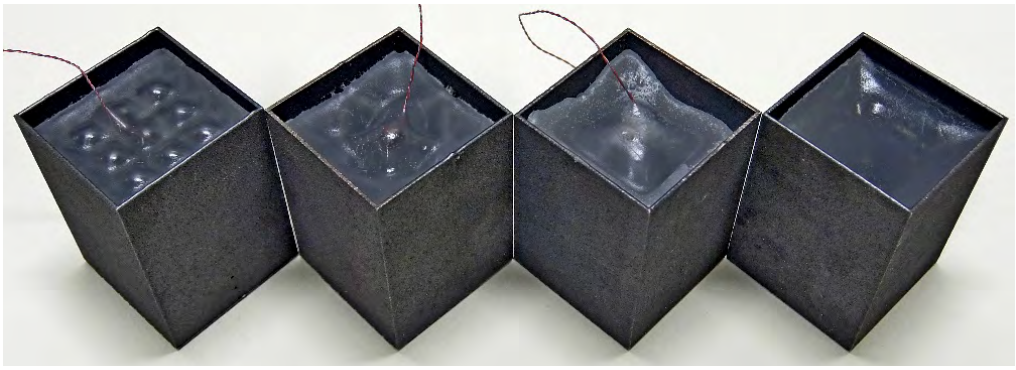

(b)

Figure 1: Four test modules

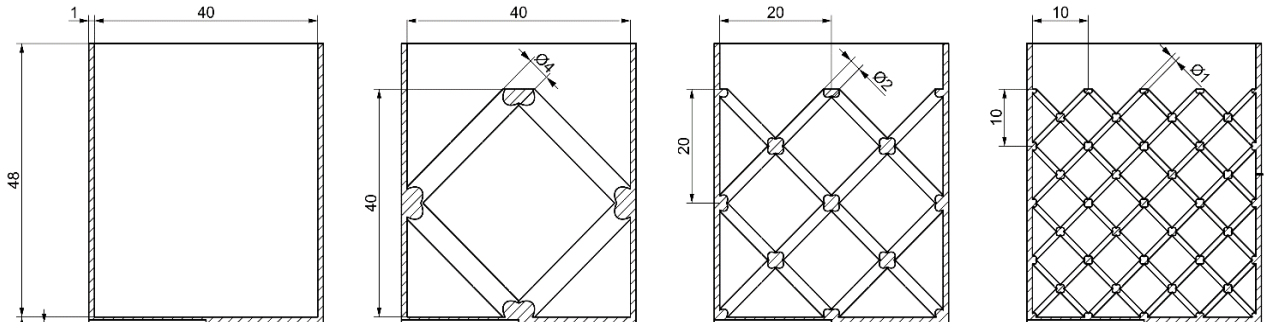

Figure 2: Schematic of the 3D aluminum structures with the main dimensions

They have been designed and realized in order to investigate the influence of the metallic cellular structure on the heat transfer performance of the PCM based system. Furthermore, since all the structures have the same porosity, it is possible to investigate the cell size effects on the two-phase heat transfer. Fig. 2 reports the main geometrical characteristics of the tested samples.
The experimental setup depicted in Fig. 3 consists of three main components: the test module on the top, the heater connected to the test module, and the data acquisition system. Furthermore, as can be seen in Fig. 3, five T-type thermocouples, named from P1 to P5, are located inside each sample to monitor the PCM temperatures in as many different locations. Another T-type thermocouple (named A1) is placed on the external wall and properly insulated to measure the wall temperature. Another T-type thermocouple (named A2) is glued on the central top aluminum fiber and insulated to evaluate the effectiveness of the aluminum 3D structure. Finally, J1 measures the junction temperature, which is very relevant in case of electronic cooling.

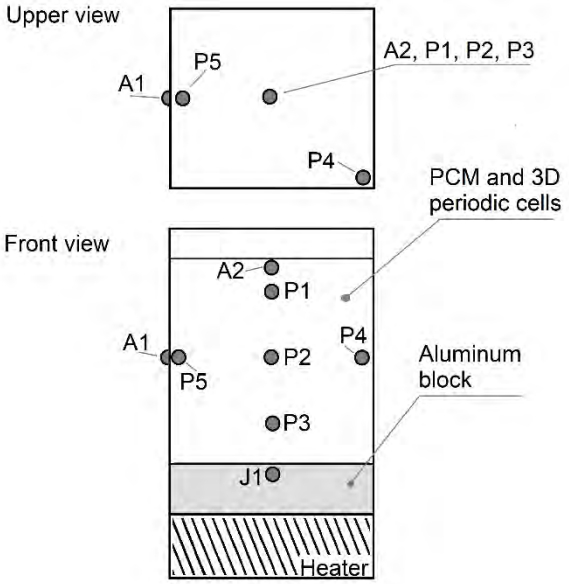

Figure 3: Schematic of the test rig and thermocouples' position

Table 1. RUBITHERM® RT55 declared thermo-physical properties

Melting area	51-57	°C
Congealing area	56-57	°C
Heat storage capacity ±7.5% (temp. range: 48 - 63 °C)	170	kJ kg^{-1}
Specific heat capacity	2	kJ kg^{-1} K^{-1}
Solid density	880	kg m^{-3}
Liquid density	770	kg m^{-3}
Heat conductivity (both phases)	0.2	W m^{-1} K^{-1}
Volume expansion	14	%
Flash point (PCM)	>200	°C
Max. operation temperature	90	°C

The heater is a 42x42x20 mm aluminum block containing an electric cartridge heater (200 W/240 V) controlled by a Variac. This block is located under the test module and connected to it by means of heat conducting paste.
The selected PCM is a RUBITHERM® RT55 paraffin. Table 1 lists the main thermo-physical properties of this paraffin wax which is not toxic nor flammable. Each module is filled with 51±0.1 g of RUBITHERM® RT55, as shown in Fig. 2b.

3. EXPERIMENTAL RESULTS

The tests involve both the melting and solidification processes. The melting process test procedure was run keeping constant the heat flow rate (20 W) supplied by the electric cartridge, while the solidification process by monitoring the temperature distribution within the PCM when the electric heater was switched off and the heat transfer occurred only with the ambient air. The loading (i.e. melting) process is considered completed once all the thermocouples located inside the PCM reach values higher than 65 °C (i.e. 10 °C more than the declared melting temperature); consequently, the unloading (i.e. solidification) process is considered concluded when all those temperature readings become close to that of the ambient air (i.e. 25 °C). In order to compare the unloading process, a normalized temperature can be defined as the ratio between the actual temperature difference between the paraffin and the ambient temperature and the maximum temperature difference between the load (i.e. 65°C) and unload conditions (i.e. 25°C). This value can vary from 1 (fully loaded) to 0 (fully unloaded).
The selected heat load of 20 W refers for example to those encountered in the lighting industry in particular light-emitting diodes (LEDs); see for instance (www.cree.com). In this work, the effects of the cell dimension of the 3D cellular structure materials is investigated.
Table 2 lists the loading and unloading total times and maximum junction temperatures (J1) measured for the four different test modules filled with the same amount (i.e., 51 g) of RT55 paraffin wax, with and without the 3D aluminum structures. From the analysis of the data listed in Table 2, it appears that the use of these 3D periodic structures slightly reduces the melting (loading) time, while notably reduces the solidification (unloading) time as compared to the case of the empty module. In particular, the melting process is speeded up of about 10-15%. While the solidification time was reduced up to -40% when the periodic structures were used. Since each module is filled with the same amount of paraffin wax, different considerations can be highlighted when considering the effect of the cell dimension on the phase change process. It appears that the melting time slightly decreases as the cell size decreases, passing from 26' at 40 mm, to 24' at 10 mm and 20 mm.
As reported in Table 2, the 3D period structures have also a great effect on the maximum junction temperature achieved at the end of the melting process. As expected, the junction temperature of the empty module reached more than 90 °C, while the 10 mm sample showed the lowest value around 67 °C. It is interesting to point out that the 20 mm and 40 mm exhibited almost the same maximum value, around 80 °C. By comparing the melting and solidification times and the maximum junction temperatures, it can be stated that the 10 mm sample appears to be the most effective, and when increasing the pore size, the heat transfer process is slightly penalized. Furthermore, the use of the 3D structured materials permitted to limit the presence of any void volume after the solidification process, contrarily to the reference "empty" test module, as can be seen in Fig.1b.

Table 2. Loading (melting) and unloading (solidification) times for RT55 at 20 W

Case	Time		Maximum Junction temperature (J1)
	Loading process (20 W)	Unloading (natural convection)	
Empty module	28 min	168 min	90.7 °C
3D periodic structures			
40 mm	26 min	153 min	80.9 °C
20 mm	24 min	139 min	80.2 °C
10 mm	24 min	118 min	67.2 °C

Different considerations can be drawn looking at the temperatures' distribution inside the PCM core. Fig. 4 reports the temperature profiles recorded during the loading process by the thermocouple

located at the centre of each sample (P2 in Fig. 3). It interesting to note that in the 10 mm cell sample, the temperature in the center of the PCM increases rapidly as compared to the other samples, even if all the 3D structures showed similar total melting times. A different behavior is observable in the case of the reference empty module, a solid PCM volume persisted inside the sample for longer since the heat came only from the bottom side. When all the paraffin around this solid core was melted and superheated, the core quickly melted, and the temperature increased accordingly.

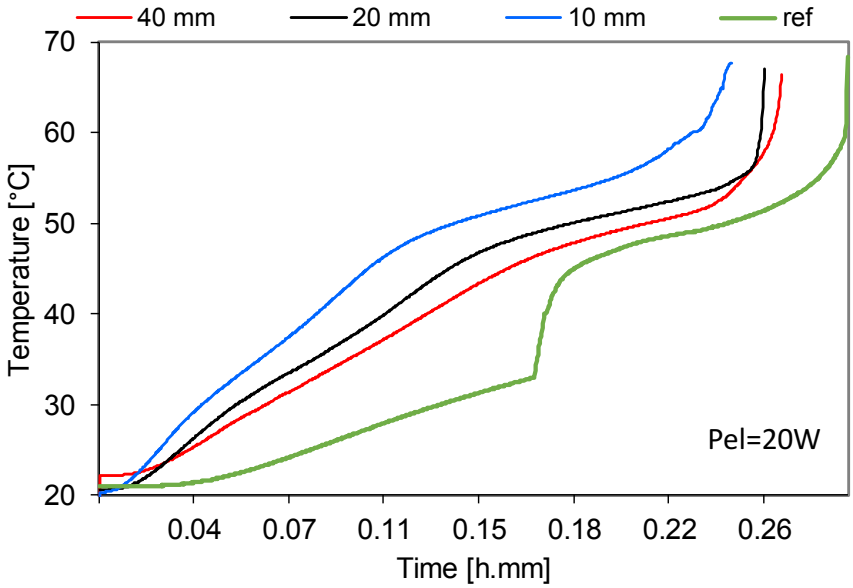

Figure 4: Temperature in the PCM core, measured by P2 thermocouple, for the different modules during the loading phase

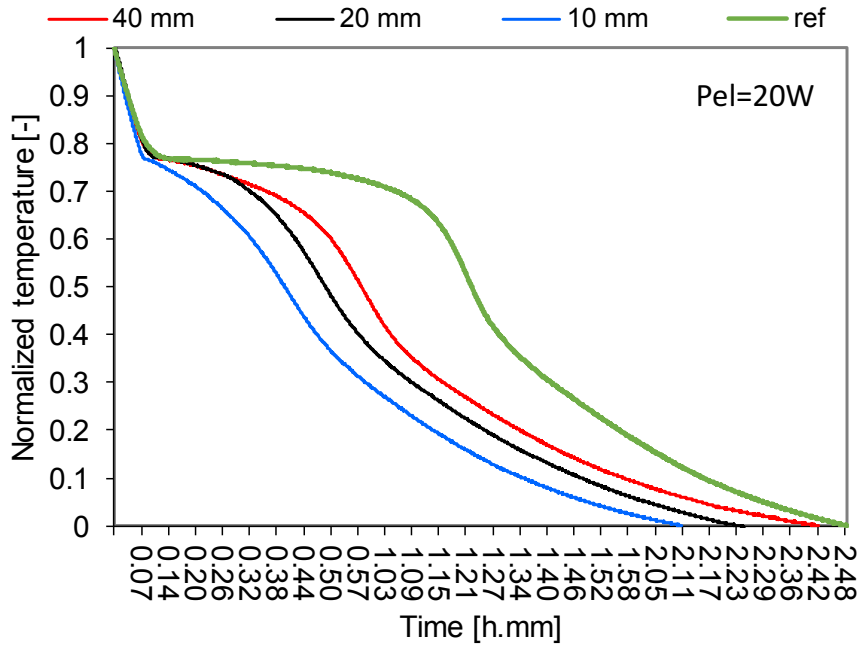

Figure 5: Temperature in the PCM core, measured by P2 thermocouple, for the different modules during the unloading phase

Fig. 5 compares the temperatures recorded by the central P2 thermocouples during the unloading process. After a similar de-superheating phase, the PCM quickly solidified in the 10 mm cell sample, because the 3D structure promoted an efficient heat transfer to the ambient air. On the other hand, the paraffin core in the empty box remained hot for more time. For example, a huge difference is notable considering the time needed to reach a normalized temperature of around 0.6 (i.e., approximately 40 °C). The 10 mm one required about 40 min, while the reference one took 80 min,

about was times more. This means that, in the analyzed range of cell dimensions and heat flux, the lower the pore size, the higher the heat transfer. This result differs from what found by Mancin et al. (2015) and by Lazzarin et al. (2018) where all the investigated foams with different pore values (PPI) resulted in similar heat transfer performance. This probably means that all the investigated PPI values by Mancin et al. (2015) and Lazzarin et al. (2018) were so high that a further increment in PPI was not noticeable in the final results.
Finally, the temperature distribution inside a single module is analyzed. For space constrains, only the reference module and the 10 mm cell module are taken into account. In the 10 mm cell sample all the PCM thermocouples measured similar values, so the temperature inside all the module increased with a similar trend, since the aluminum 3D structures effectively distributed the heat through the PCM. As expected, the junction temperature (J1) was the highest one; also the lateral wall temperature was higher than the paraffin one. It interesting to note that the temperature in the central top aluminum structure (A2, see Fig 3) is higher than the PCM temperature in the same area (P3), so that the addition of the metal net can improve the heating of the paraffin located in the upper zone.

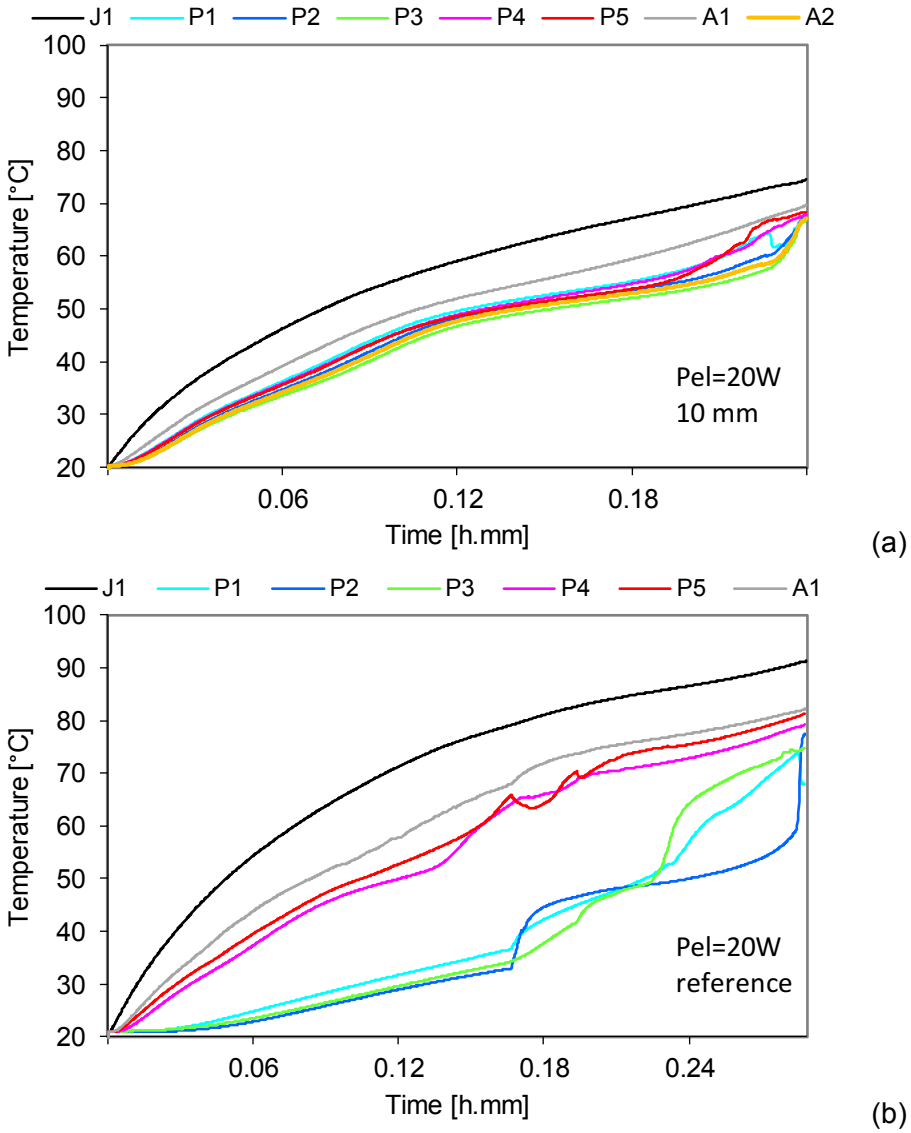

Figure 5: Temperature distribution in the PCM (P1 to P5), in the aluminum parts (A1 and A2) and in the heater block for the 10 mm cell sample (a) and the reference one (b)

On the other hand, in the reference module the temperatures' distribution inside the PCM is pretty scattered. The paraffin temperature close to the walls (P4 and P5) was close to the wall temperature (A1), while the temperature in the core remained low for a longer period of time. This is because no heat was transferred by the aluminum structures directly toward the central area. As expected, the last paraffin part to melt was in the center of the module (P2).

4. CONCLUSIONS

This paper experimentally investigates the possible use of different cellular structured materials to improve the solid-liquid phase change process of PCMs. A new test rig was designed and built to simulate a latent thermal energy storage (LTES). A paraffin wax with a nominal melting temperature of 55 °C (Rubitherm RT55) was studied during both the melting (loading) and solidification (unloading) processes. Four different 42x42x60 mm modules were filled with 51 g of paraffin wax: one was kept empty and used as reference, while three of them contained a new AlSi10Mg-0403 aluminum alloy cellular structure material with open 3D periodic cells based on a pyramidal shape obtained via metallic additive manufacturing developed to enhance the phase change process during both loading and unloading processes of PCMs. These structures had the same porosity, equal to 95%, different base size of the cells, equal to 10, 20, and 40 mm respectively. So, it was possible to investigate the cell dimension influence on the heat transfer.
The results highlighted that:
- the melting time slightly decreases as the cell size decreases, passing from 26' at 40 mm, to 24' at 20 mm and 10 mm;
- the maximum junction temperature is remarkably decreased by the presence of the 3D structure;
- In the unloading process, after a similar de-superheating phase, the PCM quickly solidifies in the 10 mm cell sample because the 3D structure promotes an efficient heat transfer to the ambient air. On the other hand, the paraffin core in the empty box remains hot for more time.
-The great difference between the investigated samples is related to the temperature field inside the paraffin: in the 10 mm cell sample, the temperature in the center of the PCM increases rapidly, following a similar trend as compared to the heater. On the other hand, in the reference empty module, a solid PCM volume persists inside the sample for longer since the heat comes only from the bottom side. When all the paraffin around this solid core is melted and superheated, the core quickly melts, and the temperature increases accordingly.

These preliminary results highlight the effects of the 3D structure on the melting and solidification processes of PCMs; they also confirm that there might be an optimum cell size, which maximize the heat transfer through the PCM. Additional tests to study the effects of the operating conditions (e.g heat flow rate) and 3D structure properties (e.g. cell size, porosity) are surely needed to better understand how it is possible to design efficient LTES.

ACKNOWLEDGEMENTS

This research project was partially funded by: CariVerona Foundation, Verona, Italy, Ricerca Scientifica e Tecnologica 2016-2019: "Sostenibilità e autenticazione nutrizionale di filiere lattiero-casearie a tutela del consumatore".

NOMENCLATURE

A	heat transfer area (m^2)	t	temperature (°C)
k	coverage factor (-)	x	position (m)
HT	heat flux, (W m^{-2})	ε	porosity (-)
Q	heat flow rate (W)	λ	thermal conductivity (W m^{-1} K^{-1})

REFERENCES

Al-Maghalseh M., Mahkamov K., 2018. Methods of heat transfer intensification in PCM thermal storage systems: Review paper, Renewable and Sustainable Energy Reviews 92, 62–94.

Hosseinizadeh S.F., Tan F.L., Moosania S.M, 2011. Experimental and numerical studies on performance of PCM-based heat sink with different configurations of internal fins, Applied Thermal Engineering 31, 3827-3838.

Kalapala L., Devanur J. K., 2018. Influence of operational and design parameters on the performance of a PCM based heat exchanger for thermal energy storage, Journal of Energy Storage 20, 497–519.

Kalbasi R., Afrand M., Alsarraf J., Tran M.D., 2019. Studies on optimum fins number in PCM-based heat sinks, Energy, In press, doi: 10.1016/j.energy.

Lazzarin R., Mancin S., Noro M., Righetti G., 2018. Porous media for advanced hybrid thermal energy storages. In Proceedings of the 12th IIR Conference on Phase-Change Materials and Slurries for Refrigeration and Air Conditioning (PCM 2018) Orford (Québec), Canada, May 21-23, 2018.

Lin Y., Alva G., Fang G., 2018. Review on thermal performances and applications of thermal energy storage systems with inorganic phase change materials, Energy 165, 685-708.

Mahmoud, S., Tang A., Toh C., AL-Dadah R., Soo S.L., 2013. Experimental investigation of inserts configurations and PCM type on the thermal performance of PCM based heat sinks, Applied Energy 112 ,1349–1356.

Mancin S., Diani A., Doretti L., Hooman K., L. Rossetto, 2015. Experimental analysis of phase change phenomenon of paraffin waxes embedded in copper foams, International Journal of Thermal Sciences 90, 79-89.

Qureshi Z. A., Ali H.M., Khushnood S., 2018. Recent advances on thermal conductivity enhancement of phase change materials for energy storage system: a review, International Journal of Heat and Mass Transfer 127, 838–856.

Manuscript ID: 1686
DOI: 10.18462/iir.icr.2019.1686

Performance evaluation on heat pump water heater with drop-in refrigerant R1234yf and condenser size modification

Ce SHI[(a)], Pega HRNJAK[(a)(b)]

[(a)] Department of Mechanical Science and Engineering,
University of Illinois at Urbana-Champaign
1206 West Green Street, Urbana, IL 61801, United States
Phone: (217) 721-1755, Email: ces3@illinois.edu
[(b)] Creative Thermal Solutions, Inc., 2209 N Willow Rd, Urbana, IL, 61802, United States
Phone: (217) 721-1755, Email: pega@illinois.edu

ABSTRACT

Refrigerant and heat exchanger design are significant factors of interest in Heat Pump Water Heater (HPWH) system. This paper presents the experimental study about R1234yf as a low global warming potential (GWP) drop-in substitute of R134a. Then condenser configuration analysis is conducted to explore the effects of condenser circuit number using the baseline R134a. It is experimentally demonstrated that the cooling capacity and COP obtained with R1234yf in a HPWH system is slightly lower than that obtained with R134a. It has been shown that R1234yf can be a desirable alternative for R134a with comparable performance but it is noted that extensive modifications should be considered if the same system performance need to be obtained. By closing the valves at the inlet and outlet of one condenser circuit, a one-circuit condenser system could be achieved. It is shown that a system operating with one-circuit condenser only brings the COP down within 5.5%.
Keywords: Condenser, Drop-In, Heat Pump Water Heater, Low GWP, Performance, R1234yf, R134a.

1. INTRODUCTION

A significant parameter is the refrigerant used in the vapor compression cycle. With the increasing concern with respect to its high GWP, R134a has been discouraged in the use of HPWH applications. Therefore, finding promising low-GWP alternative refrigerants for HPWHs becomes important. R1234yf has been universally considered as a possible drop-in replacement for R134a in HPWH applications due to its zero Ozone depletion potential (ODP) and similar thermodynamic properties and heat transfer coefficient as R134a. Lee and Jung (2012) compared the performance of R134a and R1234yf, and concluded that there were only tiny differences in capacities while the compressor discharge temperature reduced by 6°F. Zilio et al. (2011) investigated the experimental research using R1234yf as the drop-in to compare with a R134a baseline mobile air conditioning (MAC) system. Mota-Babiloni et al. (2014) and Navarro-Esbrí et al. (2013) compared with energy performance of vapor compression systems with R134a and R1234yf. By controlling the condensing and evaporating temperature, it is shown that the cooling capacity and COP of the R1234yf system decreased by 9% and 13%, respectively, while the volumetric efficiency was approximately 5% lower than that of R134a. It can be concluded from these researches that the COP and capacity of R1234yf are close to those of R134a.

In order to decrease the product expense, the system components need to be explored. Some

hardware modifications can be done regarding the tube size and tube length of the heat exchangers, which results in a change of the refrigerant charge quantity.

2. EXPERIMENTAL BENCH AND PROCEDURE

2.1 Experimental Facility

The system tested is an R134a based Heat Pump Water Heater system, and three systems were tested:

(a) the baseline R134a HPWH system with two-circuit condenser
(b) the same system as (a), operating with an optimal charge of R1234yf with the baseline rotary compressor and EEV setting
(c) the baseline R134a HPWH system with one-circuit condenser

Fig.1 illustrates a schematic drawing of the HPWH system and the experimental setup, which contains a fin and tube evaporator, a rotary compressor, a low-pressure side accumulator, an electronic expansion valve, a wrap-around coil condenser and a water tank. Since the superheat degree is supposed to be maintained by regulating the steps of the EEV but it cannot be always guaranteed, accumulator is placed at the inlet of compressor to avoid impact of refrigerant.

To implement a one-circuit condenser, 4 manually operated ball valves are installed in two refrigerant loops at the inlet and outlet. Therefore, by closing two of the ball valves of inlet and outlet from the same circuit, condenser circuit can be bypassed and only one circuit is connected to the system.

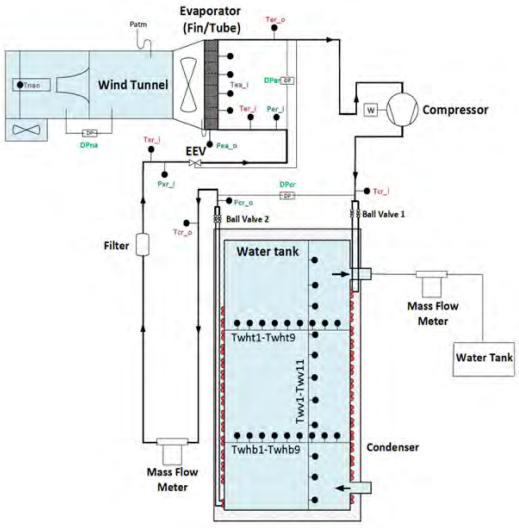

Figure 1: Schematic drawing of experimental facility

2.2 Experiment Procedure

For the purpose to obtain and compare the performance of two refrigerants and condenser circuits, a fair test condition should be carried out. Therefore, all four tests are performed with the fixed external heat transfer fluids (water and air) temperature, the evaporation and condensation saturation temperatures have been remained the same for each test. The operation contains a fully warm-up period to heat the water from 25℃ to 50℃.

Firstly, tests are conducted for R134a with the original two-circuit condenser, then comes with the subsequent tests conducted with the same system component design as well as external conditions for the drop-in refrigerant R1234yf. After that, R134a with one-circuit condenser is performed under the same operation condition.

2.3 Performance Evaluation Method

The performance and behavior of the HPWH system are calculated with the experimentally measured data. Evaporating and condensing temperatures are obtained by calculating the saturated conditions with the pressures at the evaporator inlet and condenser outlet. Condenser subcooling and evaporator superheat are calculated through Eq. (1) and (2), respectively:

$$T_{SC} = T_{cr,sat} - T_{cr,o} \quad \text{Eq. (1)}$$

$$T_{SH} = T_{er,o} - T_{er,sat} \quad \text{Eq. (2)}$$

Condenser capacity and cooling capacity is calculated with Eq. (3) and (4), the expansion process is assumed to be isentropic:

$$\dot{Q}_{cr} = \dot{m}_r * \Delta h_{cr} = \dot{m}_r * (h_{cr,o} - h_{cr,i}) \quad \text{Eq. (3)}$$

$$\dot{Q}_{er} = \dot{m}_r * \Delta h_{er} = \dot{m}_r * (h_{er,o} - h_{er,i}) \quad \text{Eq. (4)}$$

Where, $\dot{Q}_{cr}$ and $\dot{Q}_{er}$ are the heating and cooling capacity, $\dot{m}_r$ is the measured refrigerant mass flow rate, $h_{cr,i}$ and $h_{cr,o}$ are the refrigerant specific enthalpy at the condenser inlet and outlet, $h_{er,i}$ and $h_{er,o}$ are the refrigerant specific enthalpy at the evaporator inlet and outlet.
Air side capacity can be calculated based on Eq. (5):

$$\dot{Q}_{ea} = \dot{m}_{air} * (h_{ea,i} - h_{na,o}) \quad \text{Eq. (5)}$$

Where, $h_{ea,i}$ and $h_{na,o}$ are the enthalpy before and after passing through the evaporator. Air stream temperature are measured before and after passing through the evaporator to obtain the air enthalpy. $\dot{m}_{air}$ is the air flow rate that obtained and calculated by the differential pressure transducer in the nozzle.
COP can be used as a criteria to evaluate the performance of the HPWH. Eq. (6) defines the COP during the warm-up operation, as the ratio of condenser capacity to the compressor consumption. It is the quotient between specific heating and specific compressor consumption:

$$\mathrm{COP} = \frac{Q_{cond}}{W_{comp}} \quad \text{Eq. (6)}$$

Besides, the refrigerant mass flow rate, compressor discharge temperature, compressor power consumption are measured directly from the transducers that installed in the HPWH system.

3. RESULTS

3.1 Drop-in Refrigerant R1234yf

Table 1 lists the drop-in test results for R134a and R1234yf. Tests are conducted at least two times for the accuracy.

Table 1. Average COP, cooling capacity, compressor discharge temperature, charge and heating-up time for R134a and R1234yf

Refrigerant	COP	Diff. COP (%)	Q_e(kW)	Diff. Q_e (%)	T_{dis} (℃)	Diff. T_{dis} (%)	Charge (g)	Operation time (min)
R134a	4.42	-8.2	1.45	-11	59.5	-6.8	825	208
R1234yf	4.03		1.29		55.4		785	225

The average COP and cooling capacity for R1234yf is approximately 8.2% and 11 % lower than baseline R134a, respectively. While the measured compressor discharge temperature for R1234yf is 6.8℃ lower than those of R134a. Finally, the amount of refrigerant charge for R1234yf is 5% lower than those obtained for R134a due to the density decrease of R1234yf. The operation time using R1234yf is 8% higher than that of R134a to warm up the water from 25℃ to 50℃.
Fig. 2 presents the power and COP using both refrigerants at same working conditions.
Fig. 3 shows the refrigerant side temperature for both refrigerants. The temperatures at the

condenser inlet and outlet for R1234yf are up to 10% lower than using R134a, and the slope for R1234yf is sharper so that the temperature difference between two refrigerants becomes smaller with time. Furthermore, since the compressor discharge temperature is slightly lower for R1234yf than R134a, a similar compressor configuration and current compressor lubricant can be feasible to use for the drop-in refrigerant.

It is noted that the compressor power consumption increases with the increase of condensation temperature, which can be explained by the rise of compression ratio. The slope of the compressor power obtained by R134a is sharper than that of R1234yf.

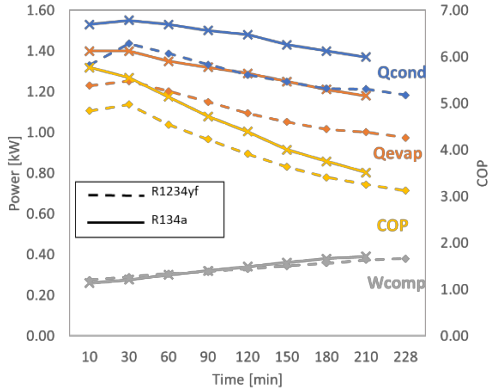

Figure 2: lower capacity, COP for R1234yf

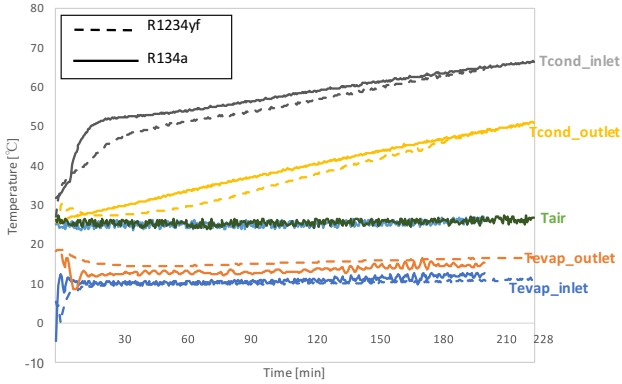

Figure 3: Compressor discharge temperature is up to 10% lower for R1234yf than R134a

The heat rejection rate for R1234yf is approximately 10% lower, with 1.5-2 ℃ lower liquid subcooling and higher condenser inlet pressure. Meanwhile, the pressure drop and the saturation temperature drop through the condenser for R1234yf remains almost the same with R134a, which clearly indicates that R1234yf could be used in the same condenser design as a drop-in refrigerant, and it may benefit more from an improved design.

On the evaporator side, the larger R1234yf saturation temperature drop (2.5 ℃ greater) at almost same superheat degree (0.8℃ higher), the R1234yf could benefit from a redesigned evaporator.

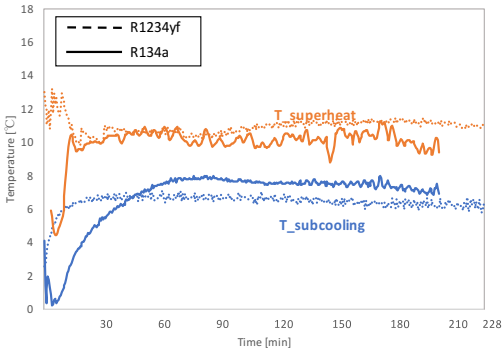

Figure 4: 0.8℃ higher superheat in evaporator and 2℃ lower subcooling in condenser

The refrigerant mass flow rate measured directly by the Coriolis mass flow meter, and it is a function of several variables in accordance with Eq. (7):

$$\dot{m}_{ref} = \frac{\eta_v \cdot V_{comp} \cdot N}{v_{comp,in} \cdot 60} \qquad \text{Eq. (7)}$$

Where, η_v is the compressor volumetric efficiency, V_{comp} is the geometrical volume that only relies on the compressor geometrical dimensions. N is the compressor rotation speed, $v_{comp,in}$ is the specific volume at compressor inlet. For a fixed compressor, the mass flow rate that measured in the experiments only relies on the volumetric efficiency and specific volume at compressor inlet.

Fig. 5 indicates the effect of compression ratio on the compressor volumetric efficiency when using R134a and R1234yf. The volumetric efficiencies of two refrigerants are relatively close (with difference ranging between 0.4% and 5%), with lower compression ratio, the volumetric efficiency for R1234yf is slightly higher than that of R134a, and is up to 5% lower compared with R134a when compression ratio is over than 3.5. Furthermore, the points' dispersion for R1234yf is larger than that obtained for R134a, which indicates higher pressure drops when using R1234yf would cause a larger influence of compressor speed on volumetric efficiency.

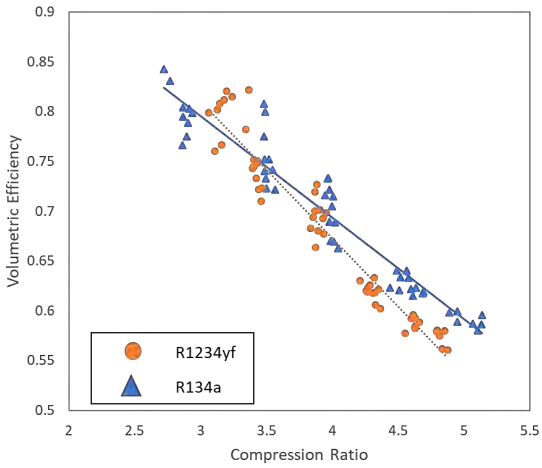

Figure 5: Volumetric efficiency versus compression ratio using R134a and R1234yf

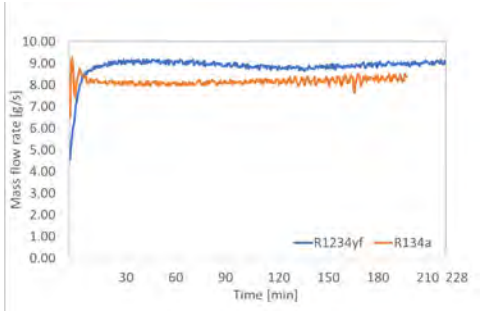

Figure 6: Refrigerant mass flow rate for R1234yf is up to 15% higher than that of R134a

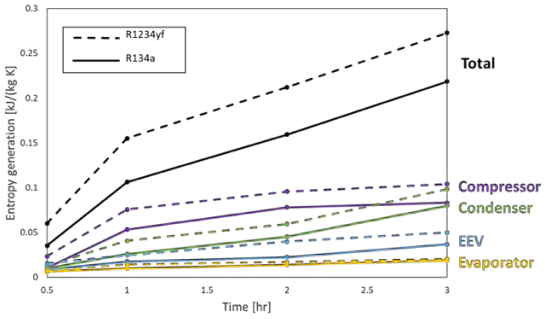

Figure 7: System using R1234yf generates 31% more entropy than R134a in total

The refrigerant mass flow rate driven by the compressor with R1234yf is higher (by up to 15%) than R134a, since R1234yf does not introduce a significant volumetric efficiency difference, and it obtains higher suction density as well as lower specific volume, higher mass flow rate is driven by the compressor. Entropy generation for each component can be specified from below:

$$\delta S_{evap} = \dot{m}\left(s_{er,o} - s_{er,i}\right) - \frac{\dot{Q}_e}{T_e} \quad \text{Eq. (8)}$$

$$\delta S_{cond} = \dot{m}\left(s_{cr,o} - s_{cr,i}\right) - \frac{\dot{Q}_c}{T_c} \quad \text{Eq. (9)}$$

$$\delta S_{comp} = \dot{m}\left(s_{cr,i} - s_{er,o}\right) \quad \text{Eq. (10)}$$

$$\delta S_{eev} = \dot{m}\left(s_{er,i} - s_{cr,o}\right) \quad \text{Eq. (11)}$$

The entropy generation of total HPWH system equals to the sum of all the entropy generations above:

$$\sum \delta S_{total} = \delta S_{evap} + \delta S_{cond} + \delta S_{comp} + \delta S_{eev} \quad \text{Eq. (12)}$$

Compressor has the highest amount of entropy generation in both cycles so that about 50% of the total entropy production is accumulated to the compressor.

The entropy generates more when the heat loss in the condenser increases, which indicates a lower condenser inlet temperature. The entropy generation obtained with R1234yf is 25% higher than that of R134a, this is because as the compressor discharge temperature decreases with R1234yf, the heat loss from the condenser increases.

Since entropy generation for individual components is higher when using R1234yf, therefore the

total entropy generation of 1234yf is 31% more than that of 134a.
The results indicates that entropy analyses can be used as a proper method to determine the occurrence point of the maximum loss and system irreversibility.

3.2 Effect of Condenser Circuit Number

Table 2. Average COP, cooling capacity, compressor discharge temperature, charge and heating-up time for one-circuit and two-circuit condenser using R134a

Condenser circuit	COP	Diff. COP (%)	Q_e(kW)	Diff. Q_e (%)	T_{dis} (℃)	Diff. T_{dis} (%)	Charge (g)	Operation time (min)
Two-circuit	4.26	-3.7	1.44	-0.7	56.6	1.2	625	218
One-circuit	4.42		1.45		55.4		830	208

Table 2 illustrates the performance results on one-circuit and two-circuit condenser with R134a. The average COP for one-circuit condenser decreases 3.7%, while cooling capacity decreases only 0.7%. The compressor temperature is 1.2℃ higher than that of two-circuit, and the charge for one-circuit condenser system is 24.6% lower than that of two-circuit, it takes 4.6% shorter operation time for the one-circuit system to heat up the water from 25 ℃ to 50 ℃.

Fig. 8 indicates the power and COP for two condenser designs during the operation. In the first 30 minutes, there is up to 4% increase for the one-circuit compressor work, 7.3% and 12.2% decrease in condenser capacity and COP, respectively. In the middle period of the operation, there is no obvious difference between two condenser designs, and in the last 60 minutes, the condenser capacity, cooling capacity for one-circuit condenser system decrease up to 4% and 7% respectively, while compressor work increases up to 4%, these cause the COP drops up to 7.4% compared with the original two-circuit condenser system.

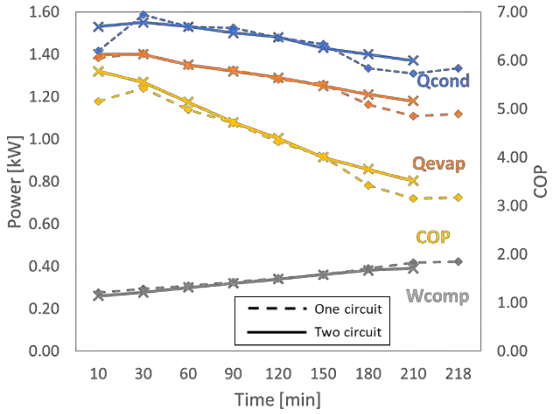

Figure 8: Power and COP for one-circuit is lower than that of two-circuit in the first and last hour of heating operation

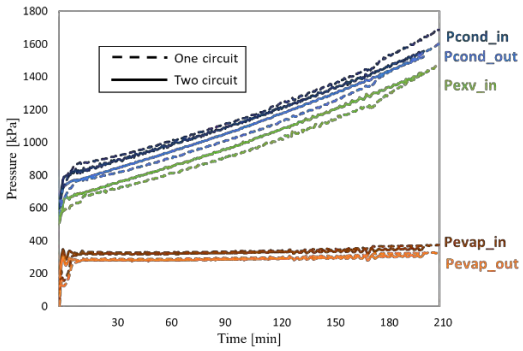

Figure 9: Higher pressure drop in condenser and liquid line for one-circuit condenser system

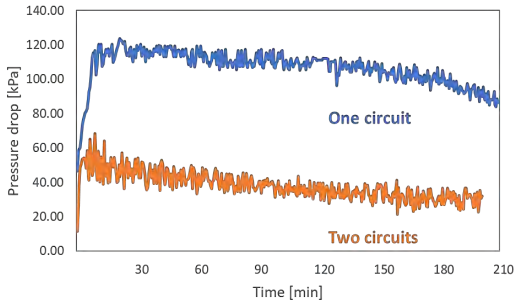

Figure 10: Pressure drop in the one-circuit condenser is two times of two-circuit condenser

Figs. 9 and 10 illustrate the pressure at each component and the pressure drop during the heating process. The difference of the pressure between one-circuit and two-circuit at evaporator inlet and

outlet are within 2%, while the pressure at EEV inlet for one-circuit is 6% lower than that of two-circuit, which indicates the pressure drop at liquid line is higher when using one-circuit condenser. The two-circuit design helps to minimize the pressure drop in the condenser, one-circuit condenser causes a large pressure drop since it decreases the condenser tube size, which in turn results in lower saturation temperature and hence drops the performance.

The condenser obtains a higher inlet pressure and lower outlet pressure compared with the original two-circuit design, the pressure drop in the condenser for one-circuit increases 157%.

Figure 11 shows the void fraction with quality in condenser. In general, the quality and void fraction decrease continuously along the condenser tubes, the mass flux *g* and void fraction α are obtained by Eqs. (13) and (14)

$$g = \frac{\dot{m}_r}{A} = \frac{\dot{m}_r}{\pi d^2/4} \quad \text{Eq. (13)}$$

$$\alpha = \frac{1}{1+\frac{1-x}{x}\frac{\rho_g}{\rho_v}S} \quad \text{Eq. (14)}$$

Where, $\dot{m}_r$ is the refrigerant mass flow rate, *A* is the cross-sectional area of the condenser tube, x represents the flow quality and S is the slip ratio.

Here, 1 represents the superficial quality which indicates the moment when liquid shows up at inner wall of the condenser. Since the mass flux depends on refrigerant mass flow rate and the cross-sectional area of the condenser tube, it is obvious that two-circuit condenser obtains lower refrigerant mass flux than that of one-circuit due to the increase of cross-sectional area, which indicates a higher refrigerant charge for two-circuit system. Fig. 12 experimentally proves that pressure drop across condenser section rises with the increase of the refrigerant mass flux. Larger cross-sectional area is occupied by the vapor phase for one-circuit condenser. P-h diagram of the warm-up period for two condenser configurations are given in Fig. 12. Condensation pressure and temperature increases with time due to the heating up process on the water side. The degree of liquid subcooling also generates more with condensation pressure, this can be explained by the sharper liquid phase curve of R134a. For both condenser configurations, only slightly increase on evaporation temperature and pressure during heating up process, due to constraint ambient temperature and condition. Relatively constant vapor superheat is obtained for both systems due to the control of EEV.

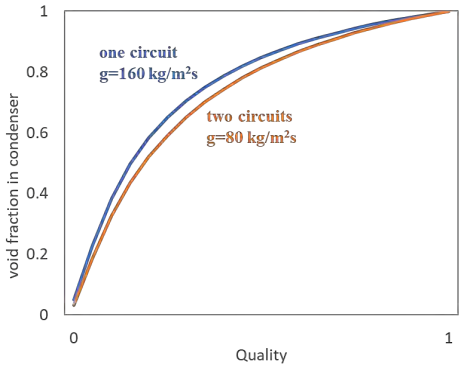

Figure 11: Higher void fraction in condenser for one-circuit condenser system

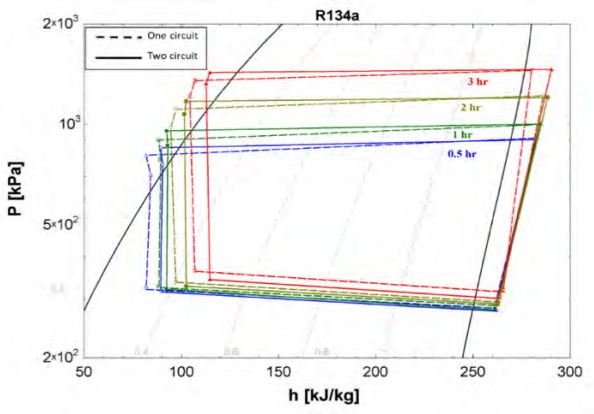

Figure 12: lower condensation temperature and higher evaporation temperature for one-circuit condenser system

Comparing the P-h diagram of one-circuit condenser system with the two-circuit, same constant vapor superheat value is obtained, the liquid subcooling for one-circuit condenser is higher. Furthermore, one-circuit condenser system gains a higher evaporation temperature and lower

condensation temperature compared to the original two-circuit design.

Fig. 13 shows the T-h diagram for two condenser configurations that undergo same condensation temperature. One-circuit condenser achieves higher temperature difference that it has lower evaporation temperature and higher air temperature, therefore a higher LMTD is obtained by one-circuit condenser compared to the two-circuit baseline system. This is reasonable since the cooling capacity for one-circuit condenser system is about tied with the baseline two-circuit, and contact area is 50% of the two-circuit.

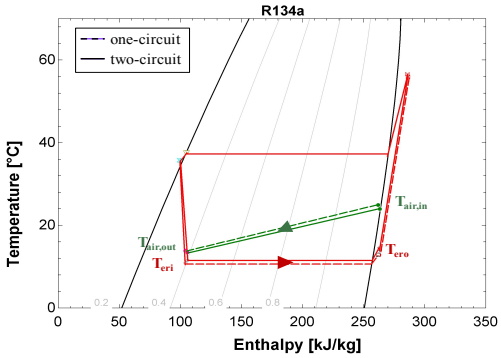

Figure 13: Higher LMTD for one-circuit system.

4. CONCLUSION

A drop-in analysis of R1234yf is carried out to compare the system performance with R134a on the same experimental facility at same working condition. According to Table 1, R1234yf obtains lower performance in an acceptable range (within 10%) comparing with baseline R134a. This indicates that R1234yf can be a desirable alternative for R134a with comparable performance but it needs be noted that extensive modifications should be considered if the same system performance need to be obtained.

(a) R1234yf introduces COP decreases ranging between 5.8% and 9.7%.
(b) The power consumption of R1234yf is 1.3% higher than that of R134a.
(c) The heating capacity of R1234yf is up to 10% lower than that of R134a.
(d) Refrigerant charge amount of R1234yf is 5% lower than that of R134a.

This paper also experimentally examines the effect of condenser circuit on system performance simply by closing the valves of one condenser circuit to achieve the modification.

(a) Compared with the system with two-circuit original condenser, COP of the system with one-circuit condenser obtains a reduction of 3.7%.
(b) Cooling capacity for the system with one-circuit condenser decreases by 0.2%-4.1%.
(c) Heating capacity for the system with one-circuit condenser decreases by 0.1%-4.3%.
(d) The charge amount of the system with one-circuit condenser decreases 25%.

REFERENCES

Lee, Y., Jung, D., 2012. A brief performance comparison of R1234yf and R134a in a bench tester for automobile applications. Applied Thermal Engineering 35, 240-242.

Zilio, C., Brown, J.S., Schiochet, G., Cavallini, A., 2011. The refrigerant R1234yf in air conditioning systems. Energy 36, 6110-6120.

Mota-Babiloni A., Navarro-Esbrí, J., Barragán, Á., Molés, F., Peris, B., 2014. Drop-in energy performance evaluation of R1234yf and R1234ze(E) in a vapor compression system as R134a replacements. Applied Thermal Engineering, 71, 259–265.

Navarro-Esbrí, J., Molés, F., Barragán-Cervera, Á., 2013. Experimental analysis of the internal heat exchanger influence on a vapour compression system performance working with R1234yf as a drop-in replacement for R134a. Applied Thermal Engineering 59, 153–161.

Manuscript ID: 1726
DOI: 10.18462/iir.icr.2019.1726

Experimental analysis of the hydrofluidisation freezing system for small fruits and vegetables

Michal PALACZ[(a)], Edyta PIECHNIK[(a)], Wojciech ADAMCZYK[(a)], Michal STEBEL[(a)], Jacek SMOLKA[(a)]

[(a)] Institute of Thermal Technology, Silesian University of Technology
Gliwice, 44-100, Poland,
michal.palacz@polsl.pl

ABSTRACT

In this work, an experimental analysis of the hydrofluidisation freezing system for small fruits or vegetables is presented. The analysis was focused on the fluid flow measurements around the spherical samples inside the hydrofluidisation chamber as well as the thermal measurements of the process. The measurements were performed on the experimental rig designed at the Institute of Thermal Technology, Gliwice, Poland. That test stand is equipped with the precise mass flow meters, thermocouples and pressure sensors. The walls of the hydrofluidisation chamber are transparent to visualise the fluid flow around the investigated sample. To capture the fluid flow, the PIV system was used. The experiments were conducted for various configurations of the orifice and sample positions. The gathered results were used for the evaluation of the heat transfer coefficient and the freezing time analysis as well as the developed CFD model validation. Finally, the recommendations for the HF system performance improvement were formulated.
Keywords: Hydrofluidisation, Food Freezing, PIV, Experimental Investigation.

1. INTRODUCTION

Freezing is one of the most efficient method to extend the shelf life of the food products. In particular, fresh fruits and vegetables (James et al. (2014)). In addition, the customers demand the high quality of the frozen products. Therefore, the applied freezing method should guarantee the proper food appearance, texture, flavour and aroma. The high nutritious values of the considered products after the freezing are also required. According to recent work Li et al. (2018), the selection of the food freezing technique affects the cell structure after the freezing. Namely, the size and distribution of the ice crystals created inside the processed product is strongly related to the freezing time. Therefore, the freezing technologies that offer short freezing time are highly recommended. One of the freezing method that guarantee the rapid freezing of the small fruits and vegetables is Hydrofluidisation Freezing (HF) introduced by Fikiin (1992). However, that freezing method is still relatively new. Consequently, the number of the research papers focused on HF investigation is fairly limited.

The hydrofluidisation freezing method combines the advantages of the immersion freezing and the impingement freezing. Namely, the processed product is immersed inside the tank filled with coolant which is pumped inside the tank through the orifices or nozzles. Moreover, the coolants used in HF systems are usually environment-friendly fluids. The two most common coolants used in HF-based freezers are aqueous solutions of sodium chloride or ethanol. Fikiin (1998) underlined that HF guarantees the very high heat transfer coefficient (HTC) and short freezing time. According to the results presented by Fikiin et al. (2003), the HTC values for the HF freezing exceeds 1000 $W \cdot m^{-2} \cdot K^{-1}$ which is significantly higher than for e.g. immersion freezing. Similar findings were reported by Verboven et al. (2003). The authors of that paper experimentally investigated the heat transfer coefficient in the laboratory scale HF system with ethanol and glucose aqueous solution. The results presented by the mentioned authors showed that HTC for the analysed system ranged from 154 to 1548 $W \cdot m^{-2} \cdot K^{-1}$.

More detailed investigation of the HF freezing method was performed by Peralta et al. (2009). In that study, the dedicated experimental rig was developed to analyse the HF method. Peralta et al. (2009) conducted numerous experiments including various coolant temperature, various Reynolds numbers

of the fluid and finally for various distance between the sample and the orifice. As a result of that investigation, Peralta et al. (2009) formulated the Nusselt number correlations for the HF system with the NaCl solution as a coolant. The same group of the authors developed the CFD model of the HF system (Peralta et al. (2010)). The initial model was formulated for the HF system similar to that presented in the paper by Peralta et al. (2009). The numerical approach presented in Peralta et al. (2010) was validated by comparison of the computational results with the literature data. Nevertheless, that comparison was performed only for the global and average process parameters, e.g. the average HTC values. In order to achieve the higher accuracy of the mathematical model and improve HF systems, more detailed experimental analysis of the process is highly desired. Hence, the scope of this paper is devote to the flow field and heat transfer measurements in laboratory scale HF system.

All the experiments presented in this study were conducted on the dedicated experimental rig designed and manufactured at the Institute of Thermal Technology (ITT), Gliwice, Poland. The general design of that stand was based on the work of Peralta et al. (2009). However, a number of modifications were introduced to an original concept of the mentioned authors. Namely, the HF chamber was equipped in the step motors for the sample movement simulation, the walls of the chamber were thermally insulated and partially made of transparent elements in order to enable flow field measurements by means of particle image velocimetry (PIV). The numerous measuring instruments were installed in the experimental stand such as T-type thermocouples, pressure sensors and precise Coriolis type mass flow meters.

As it was already mentioned, the experimental campaign presented in this study was dedicated to coolant flow field and heat transfer measurements. All the experiments were conducted for a single spherical sample mounted inside the HF chamber. Moreover, during the experiments, the orifice diameter, distance between the sample and the orifice outlet, coolant temperature and mass flow rate varied. Therefore, the experiments were conducted for various Reynolds and Prandtl numbers. Moreover, due to the variation of the distance between the sphere and the orifice, the influence of the distance between the sample and the orifice (H) to orifice diameter (d) ratio (H/d) was analysed.

2. EXPERIMENTAL RIG

The experimental rig designed for the HF investigation consists of two main parts such as coolant preparation loop and HF chamber. The coolant loop consists of a coolant tank with a spiral pipe connected to the refrigeration unit and piping connected to the HF tank. That loop is equipped with two motor valves in order to operate in coolant preparation mode or HF mode. The coolant preparation loop is used to stabilise the coolant temperature and mass flow rate before the fluid is pumped into the HF chamber. Therefore, the two Coriolis mass flow meters, five thermocouples and two pressure sensors are installed in that loop. The schema of that loop is presented in Fig. 1.

In addition, the position of thermocouples (T), pressure sensors (P), mass flow meters (MFM), pump and valves are depicted in that figure. The coolant tank and the HF chamber as well as the piping were made of the ASI 316L stainless steel. All the mentioned elements of the experimental rig were

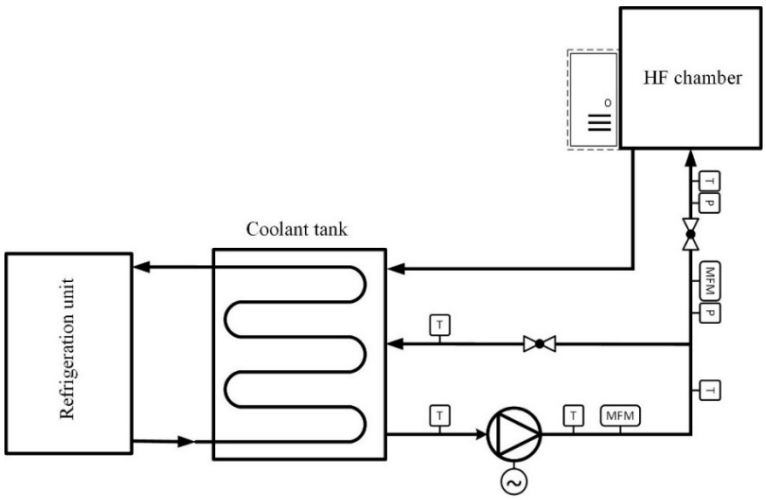

Figure 1: The layout of the experimental loop

thermally insulated to limit the heat transfer between the coolant and the environment. Moreover, the front and the side walls of the HF chamber were equipped with the double glass inspection windows. The HF chamber scheme is presented in Fig. 2. As it can be seen in that figure, the two step motor were used to position or simulate the sample movement. One of the most important components of the HF chamber is the HF tank presented in Fig. 2. The sample is immersed inside that tank during the HF process. The HF tank was fully made of transparent plexiglass. The bottom of the tank consists of the stainless steel plate with the orifices or nozzles. That plate can be easily removed or replaced in order to investigate various configurations of orifices or nozzles. In order to homogenise the coolant flow, the bottom chamber with the deflector was manufactured under the HF tank. Inside the HF chamber, the number of the thermocouples and pressure sensor are installed. The mentioned pressure sensor is mounted in the bottom chamber wall right under the plate with the orifices. The array of thermocouples is attached to sample mounting system and it is positioned behind the sample. The whole system is controlled with the WAGO 750 series PLC controller. The

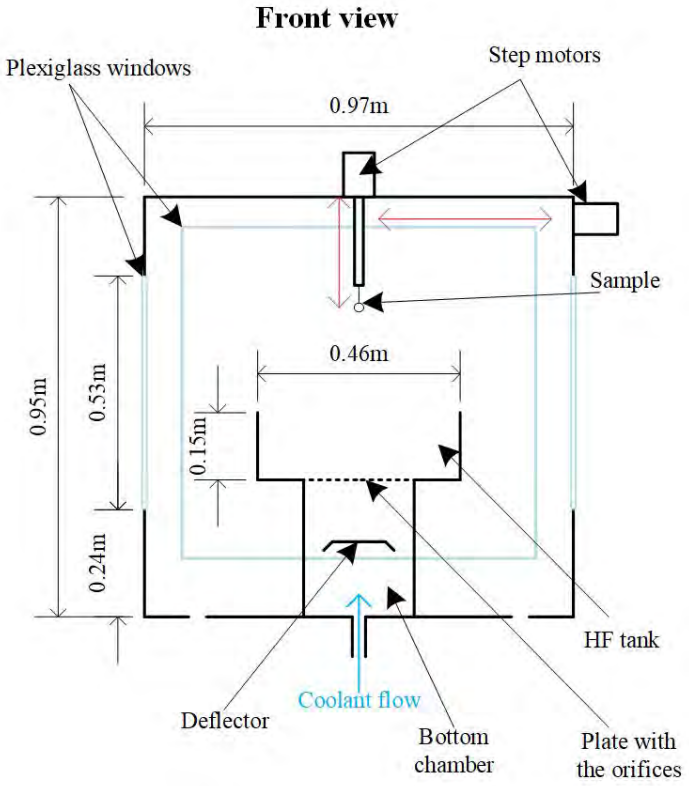

Figure 2: The scheme of the hydrofluidisation chamber

more detailed description of the measuring instruments installed inside the HF chamber as well as the description of the PIV system used for the flow field measurements are presented later in this paper.

2.1. Temperature and Pressure Measurements

The experimental rig was equipped with 53 T-type thermocouples. Most of them (48) are installed inside the HF chamber. These thermocouples are distributed around the sample to measure the temperature field near the processed product. The accuracy of the thermocouples for the temperature range from -40 °C to 375°C was rated as ± 0.5 °C. In order to measure the heat transfer inside the sample and heat transfer coefficient, two additional thermocouples were used. One of them was attached to the sphere wall and the second one was installed in the sphere centre. The laser flash analysis (LFA) was used to assess the thermal conductivity of the sample. As it was already mentioned, the remaining five thermocouples were installed in the coolant preparation loop. In addition to the thermocouples, the WIKA S-10 pressure sensors were used for the pressure measurements. The accuracy of these sensors was equal to ≤ 5% of the measuring range of the sensor.

2.2. Mass Flow Rate Measurements

Two Coriolis type mass flow rate meters were used for the mass flow rate measurements. The distribution of the mass flow meters is presented in Fig. 1 denoted as MFM. Both mass flow rate meters were manufactured by Endress+Hauser model Promass E 300. These devices were calibrated for the mass flow rate ranged from 50 $kg \cdot h^{-1}$ to 3600 $kg \cdot h^{-1}$. The accuracy of the mass flow rate measurements for that range was rated as ±0.1% of the reading. The maximum error of the applied mass flow meters for the mass flow rates lower than 50 $kg \cdot h^{-1}$ was equal to ±2% of the reading.

2.3. Circulation Pump

The EBARA multistage vertical pump model EVMSL 5 of 0.37 kW @50Hz was used to pump the fluid inside the HF chamber. The maximum operating pressure rate for that pump is 16 bar. The pump was made of ANSI 316L stainless steel. Moreover, the fluoroelastomer (FPM) insulation suitable for the temperatures ranged from -30°C to 80°C. Therefore, the possibility of the coolant leakage even for the relatively low temperatures was limited. The pump mass flow rate was controlled by TECO L510s inverter.

2.4. Data acquisition System

The experimental rig is equipped with the WAGO 750 PLC controller. That device is combined with the WAGO modules dedicated to the temperature measurements and current or voltage measurements. The frequency of data acquisition was set to 2 Hz. Then all the recorded data are saved in the CSV file.

2.5. PIV System and Analysis

The most important element of the measuring stand was the PIV system used for the flow field measurements. The PIV system used in this study consists of high-resolution Dantec Dynamics Flow Sense 4M MK4 II. That camera has 2048x2048 CCD sensor. The maximum frame rate of that camera is 16 frames per second (fps) in full resolution. The investigated region is illuminated by

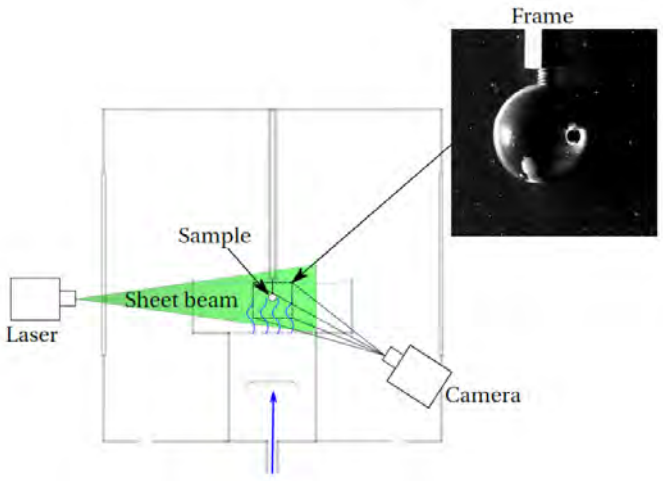

Figure 3: The PIV system set up

double-pulse Quantel Twin BSL 200 laser. The maximum energy output for that unit is 200 mJ for 523 nm wave length. The Dantec Dynamics Synchroniser was used to synchronise the laser and camera signal. The recordings and the post-processing of the gathered frames were conducted within Dantec DynamicStudio 3.41 software. The position of the camera and the laser is presented in Fig. 3. All the flow field measurements were conducted for the steady state flow conditions. The captured frames were processed with the Average Correlation method. Then the obtained velocity vector field was validated within the Peak Validation, Range Validation and Moving average methods.

3. RESULTS

The flow visualisation experiments were conducted for two orifice diameters (3 mm and 5 mm) and various distance between the sample and the orifice (ranged from 5 cm to 7 cm). In consequence, H/d for this study ranged from 10.0 to 23.3. The aqueous solution of the ethanol (5% mass) was used as the coolant. All the experimental runs were conducted for the Reynolds number (Re) equal to approximately 85 000. Therefore, the mass flow rate of the coolant was individually adjusted for each run. The Reynolds number was defined as follows:

$$Re = \frac{v_0 D}{\nu} \qquad \text{Eq. (1)}$$

where v_0 stands for velocity of the fluid at the orifice outlet, D is the sample diameter and ν is the kinematic viscosity for the coolant inlet temperature. A full list of the operating conditions for the investigated cases is presented in Table 1. At this stage of the study, the heat transfer was neglected. Hence, the PIV measurements were performed for the coolant at ambient temperature. Moreover, the flow field analysis was performed for steady state conditions in terms of the coolant mass flow rate.

Table 1. The operating conditions

Case no.	Orifice diameter, [mm]	Mass flow rate, [kg·h^{-1}]	Coolant temperature, [^{o}C]	~Re, -	H/d, -
1	5	411.75	16.7	85 000	10.0
2	5	407.57	16.7	85 000	12.0
3	5	404.06	16.7	85 000	14.0
4	3	146.83	17.4	85 000	16.7
5	3	146.35	17.6	85 000	20.0
6	3	145.55	17.6	85 000	23.3

3.1. Velocity Flow Fields

The PIV technique was used to analyse the 2D flow fields under and near the processed sample. The results of such analysis were used to create the velocity magnitude flow fields for the considered cases. The results of that analysis for cases 1-3 are presented in Fig. 4. As it can be seen in that

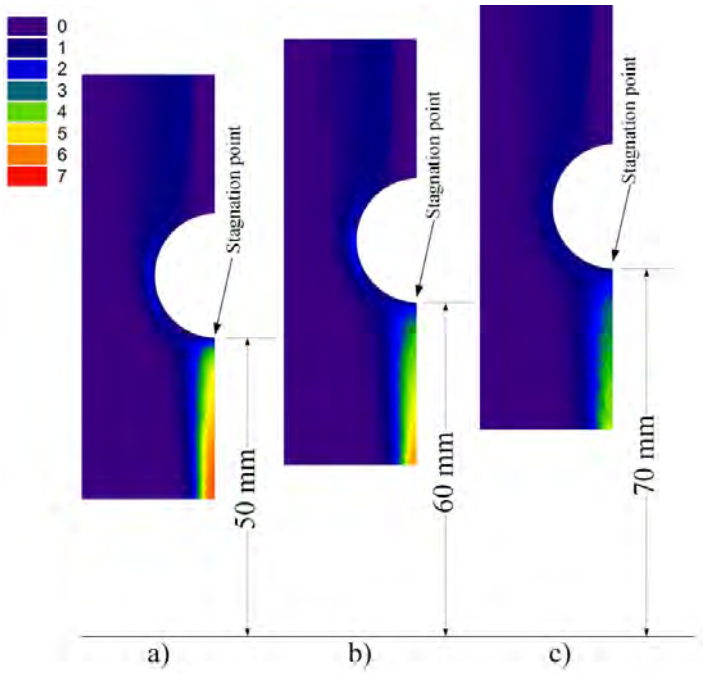

Figure 4: The velocity magnitude (m·s^{-1}) fields for cases a) 1, b) 2, c) 3

figure, the jet velocity decreases with the increase of the distance between the orifice and the sample stagnation point. On the other hand, the velocity magnitude near the sample walls was approximately the same for all three cases. Therefore, the influence of the H/d on the potential heat transfer coefficient for cases presented in Fig. 4 was negligible.
The velocity magnitude along the jet axis for cases listed in Table 1 is presented in Fig. 5. The decrease of the coolant velocity for H/d ranged from 10.0 to 14.0 can be considered as steady. Nevertheless, the variation of the jet velocity for the H/d ranged from 10.0 to 14.0 is significantly higher comparing to cases 4-6. The difference of the maximum jet velocity for case 1 and case 3 was equal to approximately 2 $m \cdot s^{-1}$. On the other hand, that difference for smaller orifice diameter (cases 4-6) was equal to approximately 0.4 $m \cdot s^{-1}$. It should be pointed out that the jet velocity for orifice diameter equal to 5 mm (cases 1-3) was significantly higher comparing for the orifice diameter equal to 3 mm (cases 4-6). It can be noticed that for the similar distance between the orifice outlet and the stagnation point the velocity of the fluid was approximately two times higher for orifice diameter equal to 5 mm comparing to the orifice diameter equal to 3 mm.

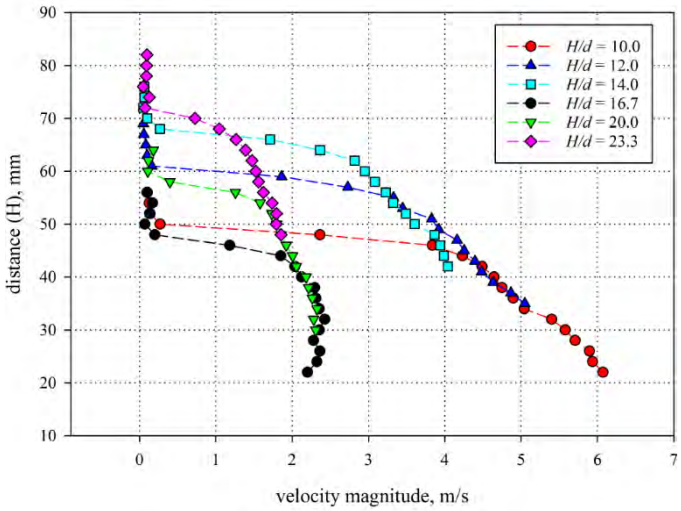

Figure 5: The velocity magnitude along the jet axis for various *H/d*

In order to investigate the relation between the distance to orifice diameter ratio (H/d) on the velocity of the fluid near the sample walls, the horizontal velocity profiles at the stagnation point level and at the sample centre level were created. These profiles as well as their location are presented in Fig. 6. According to the results presented in that figure, the H/d ratio had the minor effect on the velocity of the fluid close the processed sample walls. That shows a good agreement with the trends

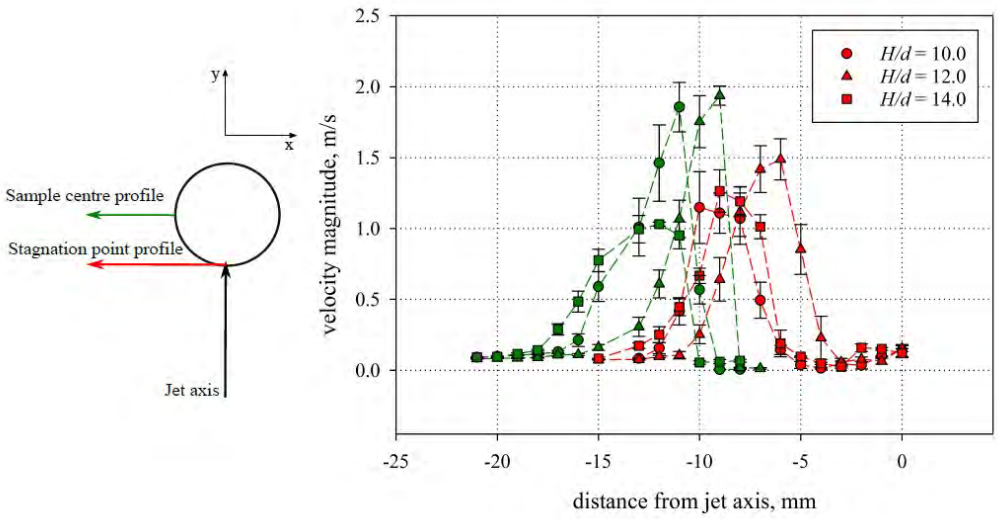

Figure 6: The horizontal velocity magnitude profiles

presented in Fig. 4. Moreover, it can be noticed that the difference between the velocity of the fluid at the stagnation point level and the sample centre level can be considered as relatively small.

4. CONCLUSIONS

A relatively novel experimental rig dedicated for the HF freezing was presented in this paper. That test rig was equipped in numerous precise measurement instruments such as mass flow meters, thermocouples and pressure sensors. The experimental rig can operate in two modes, namely the coolant preparation mode and the HF mode. The step motors and the mounting system were installed in the experimental rig in order to simulate the sample movement or position the sample. Moreover, the test stand was equipped with the transparent elements in order to run the PIV measurements.

The experiments conducted at this stage of the study focused mostly on the flow visualisation inside the HF chamber. In order to capture the fluid behaviour near the processed sample the high-resolution PIV system was used. The PIV measurements were performed for various orifice diameters and various distance between the orifice outlet and the sample stagnation point. In particular, the H/d ratio considered in this study ranged from 10.0 to 23.3.

The gathered results showed that the jet velocity rapidly decreased for H/d ratio higher than 14.0. Moreover, the velocity of the coolant jet was notably higher for the orifice diameter equal to 5 mm. On the other hand, the detailed analysis of the flow fields and velocity profiles showed that the variation of the velocity near the sample walls was negligible. Consequently, the variation of the heat transfer coefficient for the considered range of H/d was rather small.

It should be pointed out that the results presented in this paper are part of the on-going project. The next stage of the project is devoted to the heat transfer coefficient measurements together with the PIV measurements. That investigation will be performed for various mass flow rates of the coolant, various H/d ratio and finally for various coolant temperature. The results of the heat transfer coefficient analysis will be presented during the 25th ICR presentation. Moreover, the gathered results will be used for the validation of the CFD model of HF system which is developed as the part of the mentioned project.

ACKNOWLEDGEMENTS

Financial assistance was provided by grant no. DEC-2016/22/E/ST8/00517 funded by the National Science Centre, Poland and is here acknowledged. The work of MP was also supported by Silesian University of Technology through project No. BKM-533/RIE6/2018.

NOMENCLATURE

D	sample diameter (m)	v	velocity magnitude ($m \cdot s^{-1}$)
d	orifice diameter (m)	ν	kinematic viscosity ($m^2 \cdot s^{-1}$)
H	distance between orifice and sample (m)		
p	pressure (Pa)		
Re	Reynolds number (-)		

REFERENCES

Fikiin, A., 1992. New method and fluidized water system for intensive chilling and freezing of fish. Food Control 3 (3), 153 – 160.

Fikiin, K., Fikiin, A., 09 1998. Individual quick freezing of foods by hydrofluidisation and pumpable ice slurries. IIR Proceedings References, Series Refrigeration Science and Technology 319–326.

Fikiin, K., Tsvetkov, O., Laptev, Y., Fikiin, A., Kolodyaznaya, V., 01 2003. Thermophysical and engineering issues of the immersion freezing of fruits in ice slurries based on sugar-ethanol aqueous solutions. Eco Librium - Journal of AIRAH: Australian Institute of Refrigeration, Air Conditioning and Heating (Melbourne) 2, 10–15.I

James, C., Purnell, G., James, S. J., May 2014. A critical review of dehydrofreezing of fruits and vegetables. Food and Bioprocess Technology 7 (5), 1219–1234.

Li, D., Zhu, Z., Sun, D.-W., 2018. Effects of freezing on cell structure of fresh cellular food materials: A review. Trends in Food Science & Technology 75, 46 – 55.

Peralta, J. M., Rubiolo, A. C., Zorrilla, S. E., 2009. Design and construction of a hydrofluidization system. Study of the heat transfer on a stationary sphere. Journal of Food Engineering 90 (3), 358 – 364.

Peralta, J. M., Rubiolo, A. C., Zorrilla, S. E., 2010. Mathematical modeling of the heat transfer and flow field of liquid refrigerants in a hydrofluidization system with a stationary sphere. Journal of Food Engineering 99 (3), 303 – 313.

Verboven, P., Scheerlinck, N., Nikolai, B. M., 2003. Surface heat transfer coefficients to stationary spherical particles in an experimental unit for hydrofluidisation freezing of individual foods. International Journal of Refrigeration 26 (3), 328 – 336.

Manuscript ID: 1768
DOI: 10.18462/iir.icr.2019.1768

Numerical investigation of cooling properties of $La_{0.6}Ca_{0.4}MnO_3$ in an active magnetic regenerator system

A. El Boukili[(a,b,*)], H. Ez-Zahraouy[(a)], M. Hamedoun[(b)], A. Benyoussef[(a,b,c)], M. Balli[(d,e)], O. Mounkachi[(a)]

[(a)]LaMCScI Laboratory, B.P. 1014, Faculty of science-Mohammed V University, Rabat, Morocco.
[(b)] Materials and Nanomaterials Center, MAScIR Foundation, B.P. 10100-Rabat, Morocco.
[(c)] Hassan II Academy of Science and Technology, Rabat, Morocco.
[(d)]LERMA, ECINE, International University of Rabat, Parc Technopolis, Rocade de Rabat-Salé, 11100, Morocco.
[(e)]Institut Quantique & Département de Physique, Université de Sherbrooke, 2500 Boulevard de l'Université, J1K 2R1, Québec, Canada.

ABSTRACT

In this work, we report a numerical analysis and performance parameters of $La_{0.6}Ca_{0.4}MnO_3$ perovskite manganite as active magnetocaloric material (MCM) in an active magnetic refrigeration cycle (AMR). This material displays a second-order phase transition at 260 K. The needed magnetocaloric parameters for the AMR model such the adiabatic temperature (ΔT_{ad}) change and the heat capacity (Cp) of the solid material were taken from previous studies, while the thermodynamic performance are calculated according to the one-dimensional (1D) AMR model and, investigated as a function of frequencies and fluid flow rates. The implementation of $La_{0.6}Ca_{0.4}MnO_3$ material as a refrigerant in a 1T-AMR device would enable to generate a maximum no-load temperature span of about 11 K, a maximum cooling power of 62 W and a coefficient of performance of 0.5 at 10 K temperature span for a low operating frequency of 0.5 Hz.
Keywords: Magnetic Refrigeration, Cooling properties, Heat Transfer, AMR Cycle, COP, Magnetocaloric Material.

1. INTRODUCTION

Refrigeration is vital in a wide variety of applications such as building, transportation and food preservation. However, until today the traditional cooling technologies that are based on the compression-relaxation of some synthetic refrigerants remain as one of the biggest sources of greenhouse gases (GHG) emissions. On the other hand, the conventional refrigeration markedly enhances the electric energy consumption on account of its lower thermodynamic efficiency, being indirectly responsible for atmospheric pollutants emissions. In contrast, the magnetic refrigeration which is based on the magnetocaloric effect (MCE) seems to be an interesting alternative because of its potential high efficiency as well as the absence of the harmful CFCs and HFCs gases usually present in conventional refrigerators (Balli et al., 2017). The magnetic materials (ferromagnets and paramagnets) heat up in the presence of magnetic field and cool down when the magnetic field is removed. Usually the MCE presents its maximum in the magnetic phase transition region and can be amplified in functional devices by using the AMR thermodynamic cycles (Kitanovski et al., 2015).

Since the experimental discovery of the MCE in a sample of Ni by (Weiss and Picard, 1917), several experimental and theoretical research works were devoted to the investigation of magnetocaloric materials and understanding the mechanisms behind their magnetic and thermal features. For example, (Tishin, 1990, 2003) used the molecular field theory (MFT) to quantify the crucial thermo-physical properties such as specific heat (Cp) adiabatic temperature change (ΔT_{ad}) and entropy change (ΔS) of several rare earth and transition metal elements (Gd, Tb, Dy, Ho, Er, Tm, Fe, Ni, Co). It should be noted that the gadolinium metal which is a reference for magnetocaloric materials is widely used in magnetic refrigeration because of its excellent magnetocaloric properties at room-temperature. It exhibits an adiabatic temperature change of about 3 and 9 K under 1 and 5 T, respectively (Tishin, 2003 and Sari et al., 2009). However, the Gd is extremely expensive with a poor resistance against oxidation and corrosion phenomena. Aiming to find an alternative to Gd,

worldwide research activities were stimulated in the past leading to the discovery of more practical magnetocaloric materials (Balli et al., 2017) and (Pecharsky, 1997).
In this work, $La_{0.6}Ca_{0.4}MnO_3$ perovskite has been chosen as the solid refrigerant in the magnetic regenerator device, we are interested in the cooling performances of this compound because of its significant magnetocaloric effect, its low manufacturing cost and its good chemical stability. (Bohigas et al., 2000) have reported the magnetocaloric and magneto-transport properties of this compound. It exhibits a second order phase transition with an ordering (Tc) around 260 K, a heat capacity of about 640 J/KgK at 260 K, a maximum adiabatic temperature change (ΔT_{ad}) and a maximum magnetic entropy change (ΔS_{mag}) of about 1.1 K and 1.75 J/KgK respectively at 1T applied magnetic field. The obtained results in term of temperature span, the cooling power and the coefficient of performance are discussed and the possibility of using this is evaluated at sub-room temperature (250-300) K.

2. MODELING THE ACTIVE MAGNETIC REGENERATOR

The thermo-physical characteristics of $La_{0.6}Ca_{0.4}MnO_3$ around its curie temperature (260 K) and water are assumed to be constants and were taken from previous works (Bohigas et al., 2000). They are given in table 1. The mentioned MCE value (1.1 K) of $La_{0.6}Ca_{0.4}MnO_3$ in Table 1 corresponds to a magnetic field of 1 T that is easily accessible via permanent magnets.

Table 1: Geometrical and thermo-physical parameters of water and $La_{0.6}Ca_{0.4}MnO_3$ used in simulations. The thermal and physical properties were taken from (Bohigas et al., 2000).

Symbol	Parameter (Unit)	Value	
		Water	$La_{0.6}Ca_{0.4}MnO_3$
δ	Thickness (mm)	0.1	1
L	Length of the bed regenerator (mm)	50	50
l_{eq}	Equivalent cell width of the regenerator (mm)	525	525
λ	Thermal conductivity (w/m.K)	0.59	-
ρ	Volume density (kg/m^3)	1000	5940
C_p	Specific heat (J/Kg.K)	4185	640
μ	Dynamic viscosity (Kg/m.s)	0.001	-
MCE	Magnetocaloric effect (K)	-	1.1
$\dot{m}(t)$	Flow rate (ml/s)	3	-

2.1 Description of the Regenerator and the Working Cycle

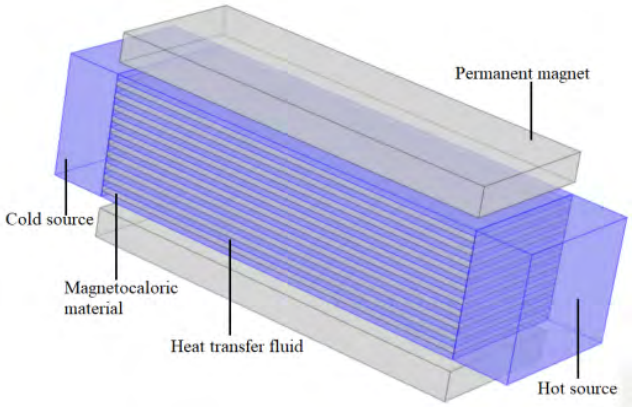

Figure 1: Parallel plates of MCM stacked in the regenerator. The MCM is in gray and the fluid channels in blue

The considered regenerator in this study is shown in Figure 1. It is constituted of 18 parallel plates of the magnetocaloric material $La_{0.6}Ca_{0.4}MnO_3$ with 1 mm thickness, 50 mm length and 25 mm width each. The plates are equidistant with an inter-space of about 0.1 mm while the water is used as a

heat transfer fluid. The regenerator experiences several AMR cycles where each cycle breaks up into four steps:

1- Isentropic magnetization of the magnetocaloric material.
2- Heat evacuation under constant applied magnetic field: heat transfer fluid flows from the cold side to the hot side of the regenerator.
3- Isentropic demagnetization of the magnetocaloric material.
4- Fridges recuperation under zero magnetic field: heat transfer fluid flows from the hot side to the cold side of the regenerator.

As the adiabatic temperature change of magnetocaloric materials (MCMs) is not enough to achieve refrigeration, it is necessary that the regenerator experience several AMR cycles. Thus, the temperature span between the hot and cold sources of the regenerator is continuously increased, to finally reach a steady state in which:

$$|\mathrm{Tc_k} - \mathrm{Tc_{k-1}}| < \varepsilon\varepsilon = 0.00005\ \mathrm{K}$$

$\mathrm{Tc_k} - \mathrm{Tc_{k-1}}$ represents the difference between the reached cold temperature ($\mathrm{Tc_k}$) and the previous cold temperature ($\mathrm{Tc_{k-1}}$).

2.2. Governing Equations

Based on the law of energy conservation, the main equations describing the heat transfer between a solid material and a carrier fluid in 1D model are given by the following partial differential equations (PDE):

$$\rho_s c_s \frac{\partial T_s}{\partial t} = \frac{\partial}{\partial x}\left(\lambda_s \frac{\partial T_s}{\partial x}\right) + \dot{Q}_{MCE} + \dot{Q}_{loss} + \dot{Q}_{HT} \qquad \text{Eq. (1)}$$

$$\rho_f c_f \left(\frac{\partial T_f}{\partial t} + u_x \frac{\partial T_f}{\partial x}\right) = \frac{\partial}{\partial x}\left(\lambda_f \frac{\partial T_f}{\partial x}\right) + \dot{Q}_{loss} - \dot{Q}_{HT} \qquad \text{Eq. (2)}$$

where s and f subscripts are referred to the solid (MCM) and the fluid, respectively. t is time; x is a spatial coordinate (0<x<L); $Tf = T_f(x,t)$ denotes the fluid temperature; $Ts = T_s(x,t)$ is the regenerator solid temperature; $\rho_s$is the mass density of the solid and $\rho_f$is the mass density of the fluid. The heat capacity of the solid and the fluid are denoted by $c_s and c_f$, respectively. λ_s is the thermal conductivity of the solid and $\lambda_f$is the fluid thermal conductivity; $u_x$is the velocity of the fluid; $\dot{Q}_{MCE}$ is the internal heat generation term; $\dot{Q}_{loss}$ represents the thermal losses; $\dot{Q}_{HT}$ denotes the heat transfer flux between the solid and the fluid in the bed regenerator.

The term $\dot{Q}_{MCE}$ in the Eq. (1) represent the internal heat flux generated during the interaction between the magnetic field and the magnetocaloric material can be calculated by using the Eq. (3):

$$\dot{Q}_{MCE} = \rho_s c_{p,s}(H,T)\frac{\Delta T_{ad}(H,T)}{dt} \qquad \text{Eq. (3)}$$

Where $c_{p,s}(H,T)$ and $\Delta T_{ad}(H,T)$ represents the specific heat and the adiabatic temperature change of the solid material, which depend on the applied magnetic field and temperature. These values can be measured experimentally or calculated by using the mean field theory, (Balli et al., 2007) or by using Monte carlo simulations as reported in (A. El Boukili et al., 2019). In this study the $\dot{Q}_{MCE}$ term is implemented in the model by applying directly the adiabatic temperature change to the solid during the processes of magnetization and demagnetization.

The term $\dot{Q}_{HT}$ in the Eq. (1) and Eq. (2) represents the heat exchanges by convection between a fluid in motion on a plate and this latter. It can be expressed by a convective heat transfer coefficient h. The heat transfer rate $\dot{Q}_{HT}$ can be expressed as:

$$\dot{Q}_{HT} = h\, A_{HT}(T_s - T_f) \qquad \text{Eq. (4)}$$

where A_{HT} is the wetted area per unit cell of the solid material. The convective heat transfer coefficient is calculated according to the empirical Nusselt-Reynolds correlations corresponding to a laminar flow.

3. RESULTS AND DISCUSSION

The $La_{0.6}Ca_{0.4}MnO_3$material is used as refrigerant while the heat transfer is carried out by using water. A magnetic field of 1 T that can be produced by simply using permanent magnets is considered in the calculations.
According to the results published in (Bohigas et al., 2000), the value of the specific heat for $La_{0.6}Ca_{0.4}MnO_3$ compound at 260 K is equal to 640 J/Kg K, and the density is equal to 5940 kg/m^3. These parameters for this magnetocaloric material have been implemented in 1D AMR-model, in addition of others described in computational details section.
At the beginning the solid material plates and water are at (260 K), then the temperature of the hot source increases while the temperature of the cold source decreases after each cycle to reach their steady state after about 80 AMR cycles. It can be seen in Fig.2 that the maximum temperature span ($\Delta T_{span} = T_{Hot} - T_{Cold}$) obtained by numerical simulations after 80 cycles is 11°C for $La_{0.6}Ca_{0.4}MnO_3$ for a 1 T-AMR operating frequency of 0.5 Hz.
The temperature span shown in (Fig. 2) between the cold and hot sources, the cooling capacity (Fig. 4) and the coefficient of performance (Fig. 5) are crucial parameters for a thermodynamic evaluation of magnetic refrigerators. (Fig. 3) shows several no-load temperature gradients that are induced in the $La_{0.6}Ca_{0.4}MnO_3$plates along the direction of the carrier fluid flow. It can be observed that initially the solid is at the temperature (T_i = 260 K), then the thermal gradient increases gradually to reach 11 °C at the steady state after 80 cycles, for a Reynolds number Re equal to 8600.

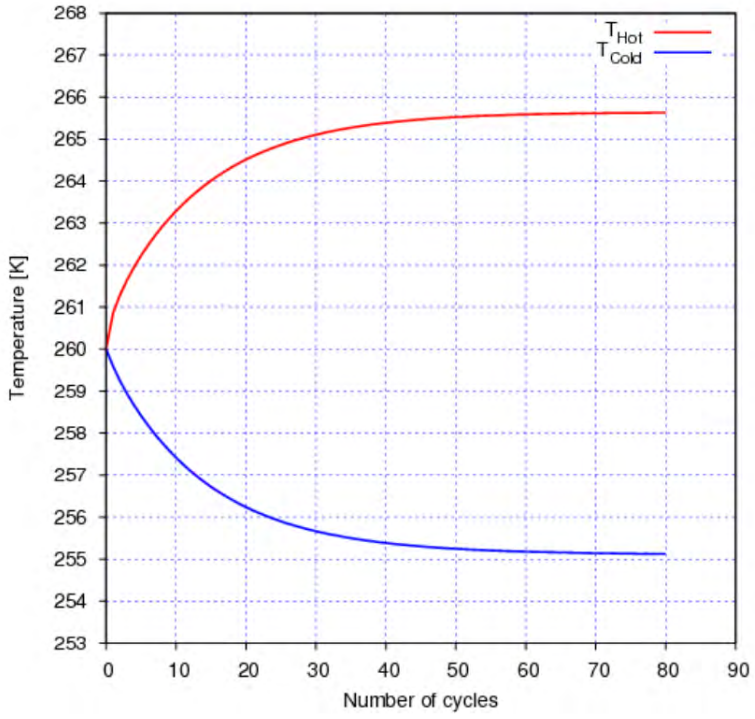

Figure 2: Temperature span between hot and cold sides of the regenerator

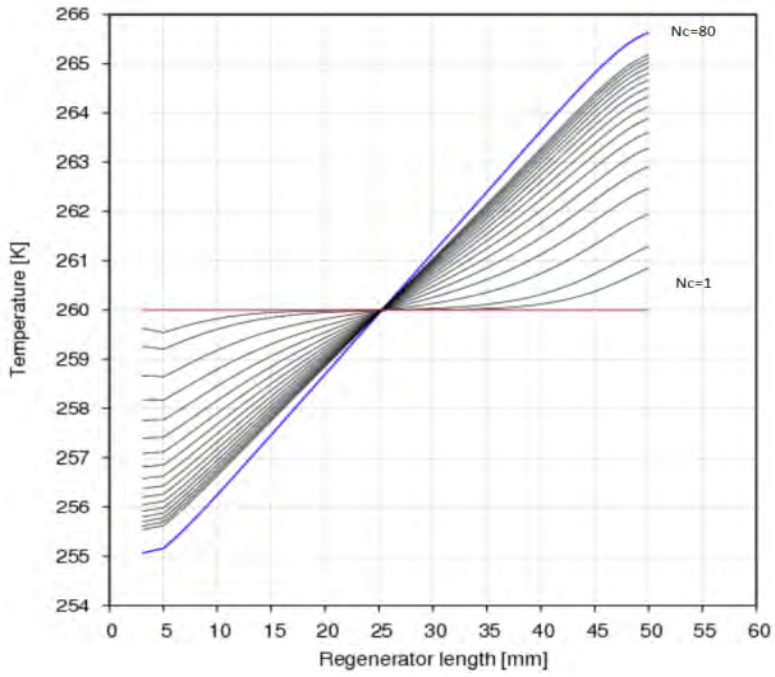

Figure 3: Temperature span between hot and cold sides of the regenerator

The cooling capacity$\dot{Q}_c$, is one of the cooling performance parameters of magnetocaloric devices, defined as the quantity of heat transferred per unit of time from the cold side to the hot side, given by the following Eq. (5).

$$\mathrm{Q_c} = \frac{1}{\tau}\int_0^{\tau} \dot{\mathrm{m}}(\mathrm{t})\mathrm{C_f}(\mathrm{T_c} - \mathrm{T}(\mathrm{x}=\mathrm{L},\mathrm{t}))\mathrm{dt} \qquad \text{Eq. (5)}$$

The coefficient of performance is calculated according to Eq. (6):

$$\mathrm{COP} = \frac{\mathrm{Q_c}}{(\mathrm{Q_h} - \mathrm{Q_c}) + \mathrm{w_{pump}}} \qquad \text{Eq. (6)}$$

Where,Q_H is the rejected heat calculated by:

$$\mathrm{Q_h} = \frac{1}{\tau}\int_0^{\tau} \dot{m}(t)C_f(T(x=0,t) - T_H)dt \qquad \text{Eq. (7)}$$

$$\mathrm{W_{pump}} = \frac{\mathrm{m}(\dot{\mathrm{t}})\Delta\mathrm{p}}{\rho_\mathrm{f}\zeta} \qquad \text{Eq. (8)}$$

Where,

$$\Delta_\mathrm{p} = \frac{96}{\mathrm{Re}}\rho_\mathrm{f}\frac{\mathrm{L_f}}{\mathrm{D_H}}\frac{\mathrm{u}^2}{2} \qquad \text{Eq. (9)}$$

In the above equations, τ is the cycle time, W_{pump} is the pumping power calculated using the pressure drop and the mass flow rate, u is the velocity of the fluid.

Fig. 4 shows the temperature span ΔT_{span} dependence of the cooling capacity evolution $(\dot{Q}_c)$ for the $La_{0.6}Ca_{0.4}MnO_3$ regenerator. The considered operating frequency is equal to 0.5 Hz, while the thermal load applied in the cold source is T_c=255 K. High cooling power $\dot{Q}_c$ results in low temperature spans. The maximum cooling power $\dot{Q}_c$ reached is 62 W for $\Delta T_{span} = 0$ K, while the device operating at a $\Delta T_{span,max}$ will not be able to support a heat load, the best performance was found for a fluid flow of 3 ml/s and low operating frequency of 0.5 Hz. As shown in (Fig. 5) the (COP) coefficient of performance obtained was around 0.5 at 10 K temperature span.

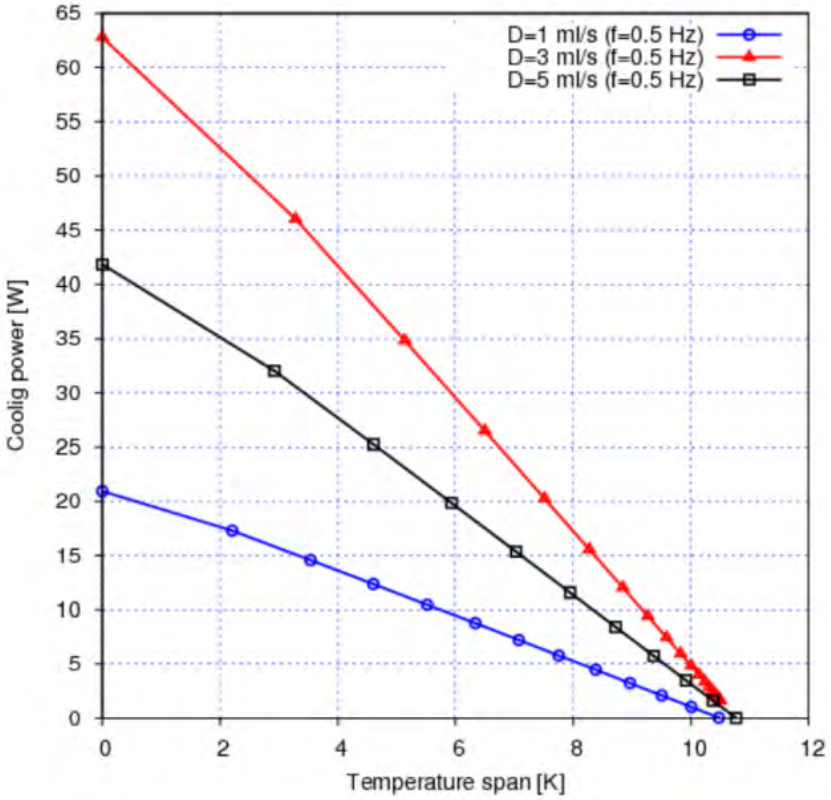

Figure 4: Cooling power vs. temperature span

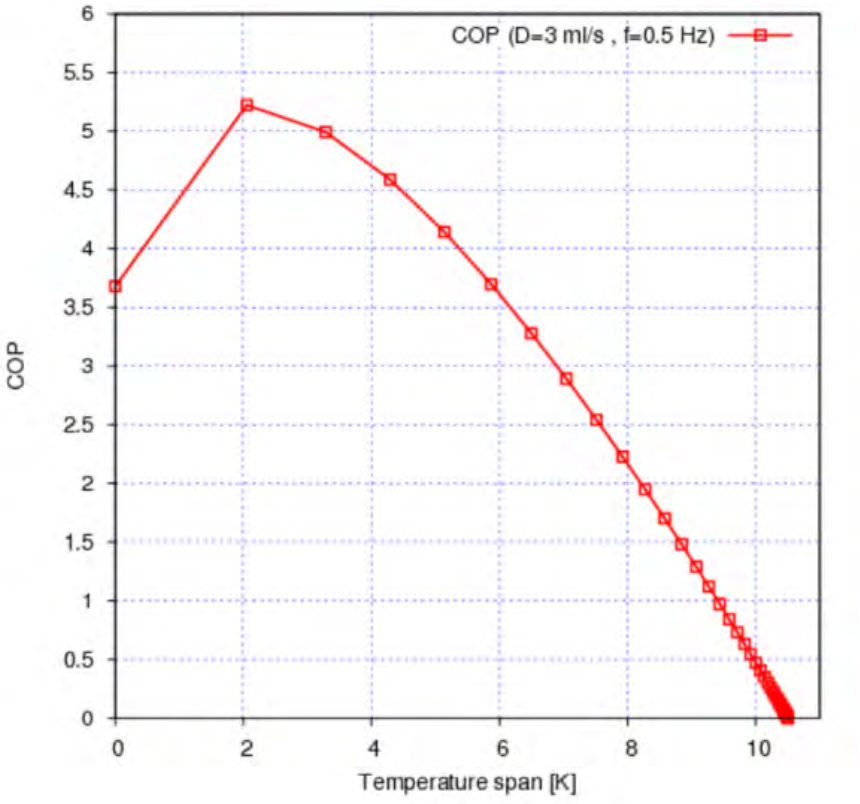

Figure 5: COP vs. temperature span

4. CONCLUSIONS

In this paper, we have reported preliminary numerical simulations that discuss the thermodynamic performance of a reciprocating magnetic cooling machine using $La_{0.6}Ca_{0.4}MnO_3$ as the solid refrigerant. We particularly found that the no load temperature span between the hot and cold ends of the magnetocaloric devices is about 11°C for 0.1 mm thickness because it strongly depends on the gap between the magnetocaloric material plates, the cooling capacity obtained is about 62 W, and a coefficient of performance (COP) of about 0.5 at 10 K temperature span. What remains now is to experimentally validate these obtained results. For this purpose, the development of a magnetic cooling prototype is in progress and its experimental performance will be communicated in the future. And to overcome the low value of MCE of these materials and achieve better performances, it is necessary to combine different magnetocaloric materials with different values of Tc in the regenerator in order to obtain a temperature span as large as possible.

ACKNOWLEDGEMENTS

The authorsthank the MESRSFC (ministere del'enseignement supérieur de la recherche scientifique et de la formation des cadres.) and MAScIR Fondation for financial support in the framework of the national program PPR undercontract no. PPR/2015/57.

NOMENCLATURE

MR	Magnetic refrigeration	F	Fluid
AMR	Active magnetic regenerator	S	Solid (MCM)
AMRR	Active magnetic regenerative refrigeration	T	Time steps
MCE	Magnetocaloric effect	X	Special nodes
ΔT_{ad}	Adiabatic temperature (MCE) (K)	PDE	partial differential equations
MCMs	Magnetocaloric materials	I	Special grid index
ΔS	Entropy change (J/Kg.K)	C	Cold source
ΔT_{ad}	Adiabatic temperature change (K)	H	Hot source
L, W, H	Regenerator / Lengh(m), width(m), high(m)	ε	Porosity
δ	Canal or plate thickness(m)	T	Time (s)
F	AMR cycle Frequency (Hz)	$\dot{m}$(t)	Mass flow rate (kg/s)
ρ	Density (kg/m^3)	Re	Reynolds number
ϑ	Velocity (m/s)	Nu	Nusselt number
μ	Dynamic viscosity (Kg/m.s])	H	Heat transfer coefficient (W/K.m^2)
λ	Thermal conductivity (W/m.K)	Dh	Hydraulic diameter
Cp	Specific heat capacity (J/kg.K)	Pr	Prandtl number

REFERENCES

D.M. Rowe, 1995. CRC Handbook of Thermoelectrics, New York. 16, 1251–1256. doi:10.1016/S0960-1481(98)00512-6.

S. L. Garrett and T. J. Hofler, 1991. “Thermoacoustic refrigeration,” Physics Department - Code PH/GxNaval Postgraduate School Monterey, CA 93943.

A. Allouhi, T. Kousksou, A. Jamil, and Y. Zeraouli, Oct. 2014. “Modeling of a thermal adsorber powered by solar energy for refrigeration applications,” *Energy*, vol. 75, pp. 589–596.

A. Kitanovski, J. Tušek, U. Tomc, U. Plaznik, M. Ožbolt, and A. Poredoš, 2015. Magnetocaloric energy conversion: From theory to applications, Springer International Publishing, Switzerland.

M. Balli, S. Jandl, P. Fournier, and A. Kedous-Lebouc, Jun. 2017. “Advanced materials for magnetic cooling: Fundamentals and practical aspects,” *Applied Physics Reviews*, vol. 4, no. 2, p. 021305.

P. Weiss and A. Piccard,1917.“Le phénomène magnétocalorique,” *J. Phys. Theor. Appl.*, vol. 7, no.

1, pp. 103–109.

A. M. Tishin and Yu. I. Spichkin, 2003. The Magnetocaloric Effect and Its Applications (IOP Publication, Bristol, UK).

A. M. Tishin, 1990. “Magnetocaloric effect in strong magnetic fields,” *Cryogenics*, vol. 30, no. 2, pp. 127–136.

O. Sari, M. Balli, G. Trottet, Ph. Bonhote, P.W. Egolf, C. Muller, J.C. Heitzler, S. Bour, 2009. “Initial results of a test-bed magnetic refrigeration machine with practical running conditions,” in 3d International Conference on Magnetic refrigeration at room temperature.

Pecharsky V.K., and Gschneidner K.A., 1997. Giant magnetocaloric effect in Gd5Si2Ge2, Phys. Rev. Lett., 78: 4494-4497.

J. Tušek, A. Kitanovski, I. Prebil, and A. Poredoš, Sep. 2011. “Dynamic operation of an active magnetic regenerator (AMR): Numerical optimization of a packed-bed AMR,” *International Journal of Refrigeration*, vol. 34, no. 6, pp. 1507–1517.

M. Balli,2007. “Etude structurale et magnétique en vue de la mise en oeuvre de nouveaux matériaux à effet magnétocalorique géant,”. Thèse de doctorat, Université Joseph-Fourier-Grenoble I.

A. El Boukili N. Tahiri, E. Salmani, H. Ez-Zahraouy, M. Hamedoun, A. Benyoussef, M. Balli, O. Mounkachi, Jan. 2019. “Magnetocaloric and cooling properties of the intermetallic compound AlFe2B2 in an AMR cycle system,” Intermetallics, vol. 104, pp. 84–89.

X. Bohigas, J. Tejada, and M. L. Mar, 2000. “Magnetic and calorimetric measurements on the magnetocaloric e!ect in $La_{0.6}Ca_{0.4}MnO_3$,” *Journal of Magnetism and Magnetic Materials*, p. 8.

Manuscript ID: 1849
DOI: 10.18462/iir.icr.2019.1849

L' économie d'énergie dans les machines de réfrigération sur la base de l'utilisation de technologies des mini-canaux

Malyshev A. ALEXANDROVICH[(a)], Kouadio K. FABRICE[(b)]

[(a)] Saint-Petersburg National Research University of Information Technologies, Mechanics and Optics
Saint-Petersburg, Lomonosova street 9, of. 2229, 191002, Russia, malyshev46@list.ru
[(b)] Sanit-Petersburg National Research University of Information Technologies, Mechanics and Optics
Saint-Petersburg, Belorusskaya street 6, 195298, Russia, fabrice-kouadio@mail.ru

ABSTRACT

L'économie d'énergie, comme principale tendance des procédés scientifiques et techniques du temps moderne, conduit à la création de nouveaux types d'équipements dans le domaine énergétique. Les échangeurs de chaleur avec des mini-canaux sont les plus prometteurs pour le domaine énergétique et la réfrigération grâce à leurs multiples avantages suivants: un coefficient de transfert de chaleur élevé, une haute résistance à la corrosion, un faible volume de réfrigérant, de petites dimensions et masses des échangeurs.
Cet article est consacré au développement d'une méthode intégrée de calcul des caractéristiques thermo-hydrodynamiques des flux diphasiques prenant en compte la spécificité du flux. L'approche proposée est basée sur la méthodologie de calcul de la teneur réelle volumétrique en vapeur et de prévision des modes de flux diphasiques des réfrigérants. L'article présente des données expérimentales sur la teneur réelle volumétrique en vapeur et une carte modifiée des modes de flux des réfrigérants.
Mots-clés: Mini-Canaux, Fux Diphasiques, Thermo-Hydrodinamique Caractérisques, Réelle Teneur Volumétrique en Vapeur, Modes de Flux, Carte du Mode de Flux.

1. INTRODUCTION

Selon les données de l'Institut International du Froid (IIF), la consommation totale énergétique des équipements à basse température en 2016 représentait plus de 15% de la production mondiale. D'ici 2025, il est prévu d'augmenter cette consommation énergétique à 25% quand bien même l'économie de l'énergie demeure l'une des principales orientations du développement des technologies modernes. D'où la nécessité de la création d'une nouvelle génération d'échangeurs de chaleur pour les centrales énergétiques et les systèmes de réfrigération pour la résolution du problème d'économie d'énergie et de la sécurité environnementale.
Aujourd'hui il est clairement établi que les tranferts de chaleur et les pertes de pression lors de l'ébullition des réfrégérants ou des combustibles dans les échangeurs de chaleur, dépendent du mode du flux des réfrégérants.
Il est nécésseraire de noter qu'actuellement, d'une manière générale, les technologies des mini-canaux sont les plus prometteuses dans l'ingénierie des appareils à échange de chaleur. En particulier, Shamirzaev (2007a), Shustov (2015a), Khovalyg et Baranenko (2015), Hrnjak et al. (2002) et Kozuline et al. (2011) dans leurs recherchers ont mentioné que les échangeurs de chaleur avec des mini-canaux commencent à être largement utilisés dans les nouveaux types de chaudières à vapeur et de pompes à chaleur, dans les technologies de l'énergie hydrogène et chimique, dans les équipements cryogéniques et de réfrigération, dans les systèmes informatiques.
Malyshev et al. (2017a) ont écrit que le coefficient de transfert de chaleur dans les d'échangeurs de chaleur avec des mini-canaux est 2 à 3 fois supérieur qu'à celui des appareils avec des canaux ordinaires, et le volume du combustible utilisé est de 3 à 4 fois inférieur.

Cependant, Khovalyg (2013a) a souligné que le calcul des caractéristiques thermo-hydrodynamiques des échangeurs de chaleur lors de l'ébullition du combustible dans les mini-canaux pose un problème ouvert en physique thermique.
Le procédé le plus fiable dans l'élaboration d'une méthodologie de calcul des paramètres des processus thermo-hydrodynamiques pour un canal restreint (y compris les mini-canaux) consiste à établir la connexion entre ces processus et les modes du flux diphasiques en utilisant les réels paramètres des phases.
Le but de notre travail consiste donc à élaborer un diagramme des modes des flux diphasiques stationnaires dans les mini-canaux avec l'utilisation des réels paramètres des phases.

2. LE CONTENU

Shamirzaev (2007b), Malyshev and Azarkov (1982a), Khovalyg (2013b), Kuznetsov (2010) et Malysevh et al. (2015a) ont proposé des méthodes pour le calcul des caractéristiques thermo-hydrodynamiques des canaux restreints, les tubes ordinaires, y compris les rainures.
Sur la base de l'analyse des approches appliquées par ces auteurs durant leurs travaux sur les processus thermo-hydrodynamiques, nous estimons que la classification suivante des canaux peut être utilisée: les mini-canaux sont des conduites de diamètre équivalent $D_e \leq 1{,}6$ mm; les canaux en forme de fente - $D_e = 1{,}6$ à 4 mm; les tubes ordinaires ou macro - $D_e > 4$ mm.
Les méthodes de calcul du transfert de chaleur et des pertes de pression dans les mini-canaux sont décrites dans plusieurs ouvrages. En particulier Khovalyg (2013c) a proposé des équations pour calculer les coefficients de transfert de chaleur et les pertes de pression pour deux modes d'ébullition des fluides frigorigènes dans un mini-canal ayant un diamètre équivalent $D_e = 0{,}56$ mm à des températures superieures à zéro, c'est à dire des températures positives, pour un intervalle de teneur massique en vapeur: $0 \leq X \leq 0{,}9$.
En règle générale, pour toutes les équations des sources ci-dessus, il convient de noter:
- l'utilisation des dépendances calculées est principalement limitée par les conditions des expériences;
- il n'existe pas de méthodologie suffisamment fiable et physiquement solide pour prévoir les modes de flux diphasiques comme Malyshev et al (2016a) l'ont signifié.
Afin de développer davantage la théorie hydrodynamique des flux diphasiques dans les conduites et les tuyaux, les auteurs de cet article ont proposé une approche intégrée, qui a été décrite pour la première fois par Malyshev (1982a). Ensuite, la méthodologie de l' approche intégrée a été développée et complétée par Malyshev et al (2015b), Malyshev et al (2016b) et Malyshev et al. (2017b).
Cette méthode repose sur l'utilisation de la teneur réelle volumétrique ($\boldsymbol{\varphi}$) en vapeur et des vitesses massiques (G) réelles des phases dans le calcul du transfert de chaleur locale pour divers modes de flux, et dans l'élaboration d'une carte de modes de flux.
Malyshev et al. (2017c) ont établi une dépendance pour le calcul de la teneur réelle volumétrique en vapeur en tenant compte des données expérimentales de divers auteurs. La méthode de calcul était basée sur la méthode utilisée par Malyshev (1982b) et Shustov (2015b) pour le traitement des données lors de l'ébullition des réfrigérants dans des tubes horizontaux, aussi sur les résultats des expériences concernant l'eau et la combinaison eau-air, dans des mini-canaux avec $D_e = 1{,}6$ mm.
Compte tenu des dispositions de similarité de la théorie de la thermodynamique, la méthode proposée peut être utilisée dans les calculs pour le méthane et le propane.
Malyshev et Azarkov (1982b) dans leurs travaux ont tenu compte de la spécificité de l'ébullition dans les mini-canaux à travers le critère de Fried Weber, qui inclut les forces de tension superficielle, contrairement à l'ébullition dans les tubes ordinaires dans lequel les forces d'inertie déterminent le glissement de phase.

$$\mathrm{w_e} = \frac{\rho \cdot D_e \cdot \omega^2}{\sigma} \qquad \text{Eq. (1)}$$

Où $\mathrm{w_e}$ – critère de Fied Weber, ρ - la masse volumique du fluide en $kg \cdot m^{-3}$, $\mathrm{D_e}$ - diamètre équivalent du canal en m, $_{\mathrm{cm}}$ – la vitesse du fluide en $m \cdot s^{-1}$, σ – les forces de tension surpeficielle en $N \cdot m^{-1}$.

En conséquence, la forme générale de la dépendance des paramètres sans dimension a acquis la forme suivante, comme le soutiennent Malyshev et al. (2017d):

$$\varphi = \beta - 0{,}06 \cdot \beta \cdot (1-\beta)^{0{,}5} \cdot \left(\frac{\frac{\sigma \cdot w_e}{g \cdot D_e^2 \cdot \rho}}{Re}\right)^{-0{,}23} \cdot \left(\frac{P_0}{P}\right)^{-0{,}15} \qquad \text{Eq. (2)}$$

où:, P_o la pression d'ébullition en Pa; P_{kp} - la pression critique d'ébullition en Pa, Re_{cm}- Nombre de Reynolds, g - vitesse de la chute libre m·s^{-1}, β - la teneur volumétrique en vapeur,$\boldsymbol{\varphi}$ la teneur réelle volumétrique en vapeur

Les résultats de calculs à l'aide l'Eq. (2) donnent un accord satisfaisant avec les données expérimentales sur les mini-canaux de D_e = 1 à 1,6 mm.

Pour des modes de flux dans des mini-canaux d'un diamètre équivalent D_e < 1 mm, une étude expérimentale supplémentaire est nécéssaire.

En utilisant l'Eq. (2), un diagramme modifié de mode de flux (-Fr_{cm} (Critère Fruda)) a été élaboré.

Le diagramme est avec une précision satisfaisante et aussi prend en compte les données d'ébullition de plusieurs réfrigérants, en particulier R134A et NH3 dans les tubes avec un diamètre D_e > 5 mm, ainsi que les données de Khovalyg (2013d). Concernant le réfrigérant R134A, sachant que dans un futur proche ou lointain son utilisation et sa production seront interdites, il est important de noter que nous l'avions ulitisé juste pour nos premières expéricences car c'est la première fois au monde d'une manière pratique grâce aux premiers résultats de nos travaux, nous obtenons des données sur son ébullition avec une température en-desous de 0 ^{o}C dans canal avec un diamètre équivalent D_e < 1 mm et une vitesse massique G ≥ 400 kg·s^{-1}·m^{-2}. Dans la suite de nos travaux nous nous focaliserons sur les réfrigérants NH_3 et le propane.

Notons que, selon les résultas des travaux de Khovalyg (2013e) un flux constant dans les mini-canaux a lieu s'il se produit avec une vitesse massique G ≥ 160 kg·s^{-1}·m^{-2}, mais lorsque les valeurs de la vitesse massique sont inférieures (G ≤ 160 kg·s^{-1}·m^{-2}), on observe l'invers du flux du fluide, des pulsations et des instabilités hydrodynamiques.

D'où la pertinence de l'élaboration d'une nouvelle méthodologie intégrée d'analyse thermo-hydrodinamique des flux diphasiques des combustible pour les mini-canaux.

Les résultats des études expérimentales utilisés dans cet article ont été obtenus sur un stand de laboratoire dont le schéma été présenté dans Malyshev et al. (2017).

Le bloc expérimental à été constitué avec un mini-canal vertical de diamètre équivalent D_e = 0,5 mm, et d'une plaque est en acier, et une autre plaque en verre, ce qui permet de réaliser des observations visuelles et d'identifier les modes du flux du réfrigérant. À l'entrée et à la sortie du bloc expérimental, sont installées des électro-vannes avec une grande vitesse de réaction permettant de controler le débit du flux du réfrigérant.

Nos études expérimentales ont été éffectuées dans les conditions suivantes:

- ✓ flux adiabatiques;
- ✓ température de saturation: t_{st} = -10 à +20 ° C;
- ✓ vitesse massique G = 100 ÷ 500 kg·s^{-1}·m^{-2}
- ✓ teneur massique en vapeur X = 0,1 à 0,9;

Au cours de nos études expérimentales, nous avions mesuré le débit du fluide, la vitesse du flux à l'entrée du bloc expérimental, la quantité de vapeur condensée (vapeur qui a été générée dans le générateur de vapeur et tranférée dans le bloc expérimental), la puissance du générateur de vapeur, les pertes de pression lors du passage du flux diphasique dans le bloc expérimental, la teneur réelle volumétrique (à l'aide de la méthode de coupure de débit).

Les résultats de nos études expérimentales sur la teneur réelle volumétrique en vapeur sont présentés sur les Figs. 1 et 2. Sur Les mêmes figures nous avons aussi les résultats des calculs l'aide de l'Eq. (2).

Les données présentées indiquent un accord satisfaisant entre les données expérimentales et celles calculées avec l'Eq. (2), ce qui signifie qu'on recommande l' utilisation de l'Eq. (2) pour éffectuer les calculs des paramètres réels des fluides lors de leurs ébullitions dans les mini-canaux.

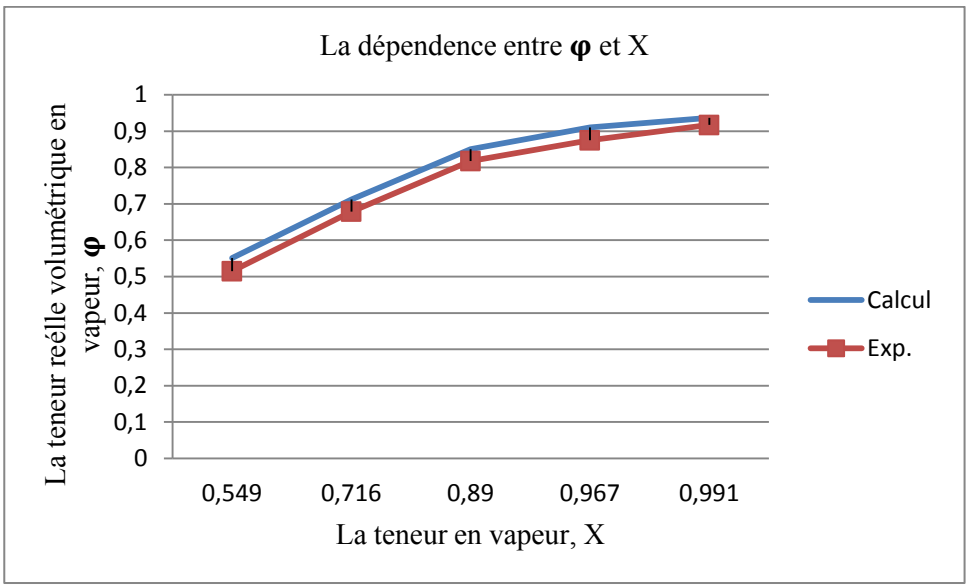

Figure 1 : Comparaison des données expérimentales (D_e = 0,5 mm, R134A et NH_3, t = –8 ° C, G = 450 kg·s^{-1}·m^{-2} = const.), à celles calculées à l'aide de l'Eq. (2)

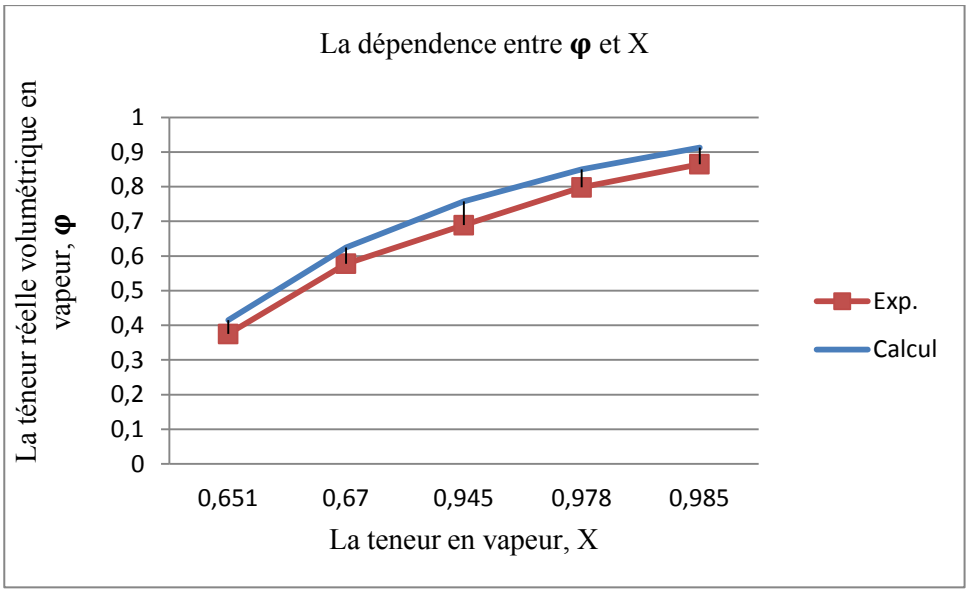

Figure 2: Comparaison des données expérimentales (D_e = 0,5 mm, R134A et NH_3, t = +10 ° C, G = 120 kg·s^{-1}·m^{-2} = const.), à celles calculées à l'aide de l'Eq. (2)

L'identification des modes du flux diphasiques a été réalisée sur la base d'observations visuelles et de photographies comme le montre la Fig. 3.
La caractéristique des modes observés est en accord qualitatif avec les résultats de Shamirzaev (2007c) et Khovalyg (2013f).

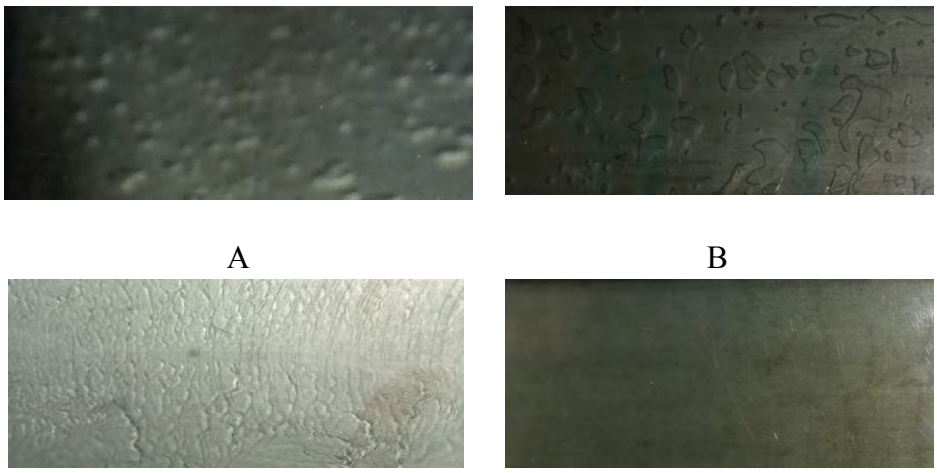

A- mode pétillant, B-mode de limace, C- mode transitif, D- mode circulaire

Figure 3 : Photograhpies des modes de flux lors de l'ébullition des réfrigérants R134A et NH_3 dans un mini-canal

Pour développer une méthode permettant de prédire les modes de flux des réfrigérants en ébullition dans les mini-canaux, le diagramme modifié des modes de flux des résultats des travaux de Malyshev et al (2016c) a été pris comme base.

Ce diagramme, est obtenu à l'aide des coordonnées φ-Fr_{cm}, les données expérimentales sur l'ébullition de différents réfrigérants dans des tubes de diamètre D_e = 6 à 10 mm, ainsi que dans des mini-canaux avec *De* = 0,56 à 1,6 mm, avec des vitesses massiques $G \leq$ kg·s^{-1}·m^{-2}. Ainsi au cours de nos travaux, le diagramme de modes de flux de Malyshev et al (2016d) a été complété par les résultats des nos études expérimentales obtenus avec des vitesses massiques comprises: $200 \leq G \leq 500$ kg·s^{-1}·m^{-2}. Contre le montre la Fig.4.

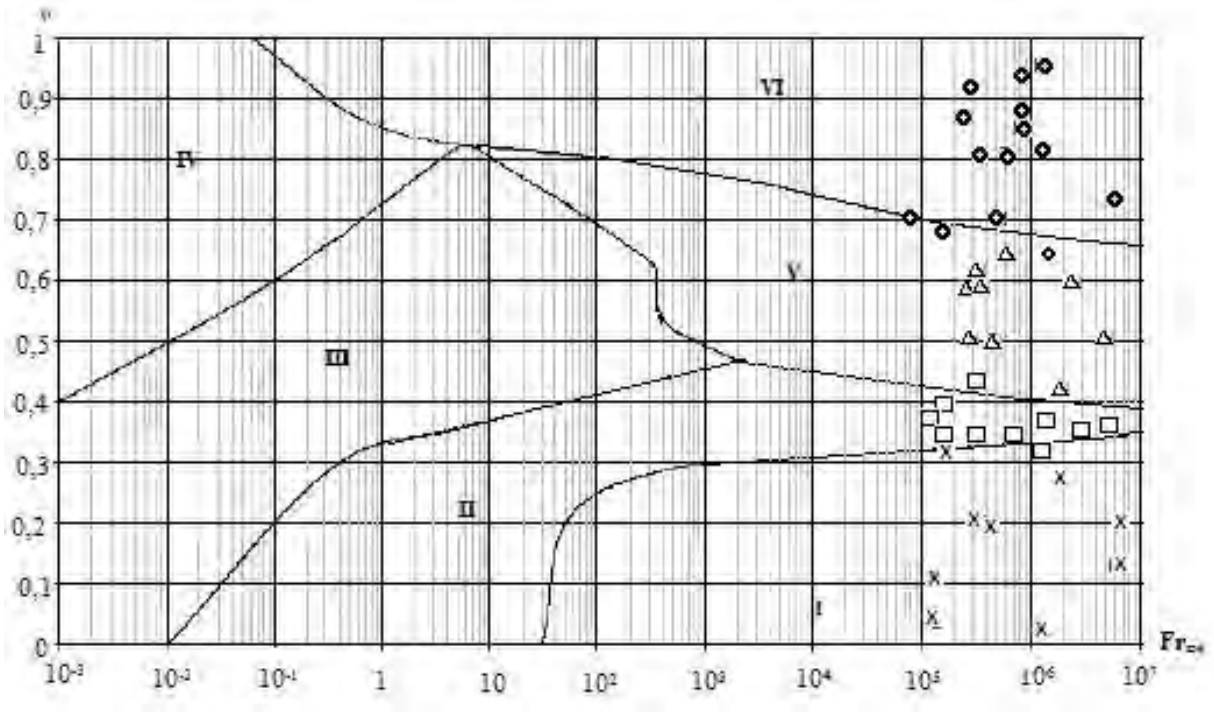

I- mode de bulles, II-mode de limace, III- mode de vagues, IV- mode stratifié, V- mode transitif, VI- mode circulaire

Figure 4 : Carte modifiée des modes de flux d'ébullition des réfrigérants (R134A et NH3) avec canal de D_e = 0,5 ÷ 1,6 mm et G = 200 ÷ 500 kg·s^{-1}·m^{-2}

Dans le diagramme présenté, en comparaison avec le diagramme bien connu de Malyshev et al (2016e) l'intervalle des valeurs du critère Fruda (Fr_{cm}) est étendu de 10^4 à 10^7, ce qui est plus typique pour les flux stables dans les mini-canaux. Le nouveau diagramme modifié élaboré décrit de manière satisfaisante les résultats de nos études expérimentales.

3. CONCLUSION

1) Aujourd'hui à l'aide de nos résultats obtenus, nous avons pu développer un modèle général de flux des fluides pendant leurs ébullitions dans un canal restreint.
2) Les résultats de nos études expérimentales obtenus sur la teneur réelle volumétrique en vapeur et les modes de flux diphasiques des réfrigérants pendant leurs ébullitions dans les mini-canaux, permettront l'utilisation de la méthode intégrée précédemment développée pour les calculs des paramètres des processus thermo-hydrodynamiques pour des conduites restreintes et aussi pour la modélisation des processus similaires à ceux dans les mini-canaux.

REFERENCES

Chinnov E., Kabov O., 2006. Flux diphasiques dans les tuyaux et les canaux capillaries. TVT. Vol 22. №5. p. 777–795.

Khovalig D., 2013. Les régularités de la dynamique des flux diphasiques et du transfert de chaleur lors de l'ébullition du réfrigérant R134A dans des microcanaux. Résumé de thèse de Candidat des sciences techniques. Saint-Pétersbourg.

Khovalyg D., Baranenko A., 2015. Two-phase flow dynamics during boiling of R134A refrigerant in minichannels. // Technical Physics. Vol. 85. № 3. p. 34-41.

Kozuline I., et autres, 2011. Modes de flux et de transfert de chaleur lors de l'ébullition des réfrigérants dans des microcanaux de différentes orientations. Int. Expo. GeoSibir № 2, vol. 5

Kuznetsov V, Shamirzaev A., 2007. Modes de flux et d'échange de chaleur lors de l'ébullition du réfrigérant R318C en circulation dans un mini-canal. Physique thermique et Aéromécanique, Vol.14, №1 p. 57-66.

Kuznetsov V., 2010. Heat and Mass Transfer with Phase Change and Chemical Reactions in Microscale // Proc. 14 Int. Heat Transfer Conf. Washington: ASME. – Keynote 22570.

Malyshev A., 1982. Caractéristiques locales thermiques et hydrodynamiques des flux diphasiques dans les canaux horizontaux. Résumé de thèse de Candidat des sciences techniques.

Malyshev A., Azarskov V., 1982. Étude des caractéristiques locales thermo-hydrodynamiques d'un flux diphasique horizontal du réfrigérant R12 // Résumé du rapport de la Conférence sur la Physique thermique et l'hydrodynamique des processus d'ébullition et de condensation. Riga. p.114-116.

Malyshev A., Kisser K., and Zaitsev A., 2017. Les réels paramètres des fluides frigorigènes lors de leurs ébullitions dans les tuyaux et les canaux. //J. de l'Académie internationale du froid. №2.

Malyshev A., Kisser K. et Kouadio F., 2017. Études expérimentales intégrées des processus thermohydrodynamiques des fluides frigorigènes en ébullition dans des mini-(micro) canaux. Revue Scientifique NRU ITMO. Série Réfrigération et Climatisation. №2, p.12-17.

Malyshev A., Kouadio F. et Kisser K. 2015, Local Heat Transfer by simmering into the tube». //Travaux VII Int. conferences des sciences techniques sur les technologies à basse température et alimentaires au XXIe siècle. Saint-Pétersbourg.

Malyshev.A., Kisser K., et Filatov A., 2016. Nouvelles méthodes de prévision des modes de flux des réfrigérants lors de l' ébullition dans les macro et mini-canaux // J. de l'Académie internationale du froid. № 2 . p. 67-70.

Niño V., Hrnjak P., and Newell T., 2002. Characterization of Two-Phase flow in microchannels // ACRC TR-202.

Shamirzaev A., 2007. Modes de flux et d'échange de chaleur lors de l'ébullition des réfrigérants en mouvement dans des mini-canaux. Résumé de thèse pour le diplôme de candidat des sciences physiques et mathématiques. Institut de physique thermique Kutateladze Novosibirsk.

Shustov M., 2015. L'étude de l'ébullition des réfrigérants dans un microcanal avec recouverture de nanoparticules. Résumé de thèse pour le diplôme de candidat des sciences techniques.

Sinitsyna K., Zaitsev A., et Baranenko A., 2016. Modèle analytique de condensation dans les mini-canaux // J. de l'Académie internationale du froid. №1. p. 66–72.

Manuscript ID: 1860
DOI: 10.18462/iir.icr.2019.1860

Study of heat exchange process in heat exchangers of refrigerating systems using electric hydraulic aerosols

Boris S. BABAKIN[(a)], Mikhail I. VORONIN[(a)], Anton G. BELOZEROV[(b)], Sergey B. BABAKIN[(b)], Georgy A. BELOZEROV[(c)]

[(a)]Moscow State University of Food Factories, FGBOU VO "MGUPP"
Moscow, 125080, Russian Federation, holod@mgupp.ru
[(b)]Federal Scientific Center of Food Systems
Moscow, 109316, Russian Federation, pr@vniimp.ru
[(c)]VNIKHI – Branch of V.M. Gorbatov Research Center of Food Systems, RAS
Moscow, 127422, Russian Federation, mail@vnihi

ABSTRACT

The current methods of heat exchange enhancement applying spraying dispersed liquids on the heat exchange surface are characterized by low scattering on developed surfaces, on complex geometry surfaces, and large size of liquid drops. The authors developed the method that allowed obtaining electric hydraulic aerosols by means of electric hydraulic sprayers and intensifying heat exchange in heat exchangers of refrigerating systems. It provides a regulated heat removal in a wide range of heat flows rates.
Keywords: Heat Exchange Intensification, Heat Exchange Apparatuses, Hydraulic Aerosol, Electric Hydraulic Aerosol, Electric Fields.

1. INTRODUCTION

Improving the technology of intensive refrigeration of different foodstuffs and semi-finished products of vegetable and animal origin as well as perfection of industrial heat exchange equipment is of great importance. For example, refrigeration of sausages by cooled water sprayed after cooking used in domestic and foreign practice. Electric power loss in electricity network is estimated about 10% of world consumption. The share of energy lost in heat exchangers apparatuses, in refrigeration equipment are undoubtedly higher considering that the part of heat exchange apparatuses in the total mass of a refrigerating machine is 70-80%. Power consumption during a refrigerating machine operating to a considerable degree depends on the process efficiency in heat exchange apparatuses. Efficiency enhancement of heat exchange apparatuses supposes reducing dimensions provided that their thermal characteristics improve. The heat transfer coefficient is the main parameter of heat exchanger efficiency. The coefficient consists of the heat conductivity coefficient and the coefficients of heat emission of sides exchanging by ambient heat. If the coefficient of heat conductivity depends on material of which a heat exchanger is made, the coefficient of heat transfer depends on many factors and represents the main part of thermal resistance of a heat exchanger. The increase of a cooling agent rate in a heat exchanger allows increasing the heat transfer coefficient of a cooling agent and the heat transfer coefficient of the apparatus. However, this increases losses due to increased pressure and power to the pump drive, which increases energy consumption. It is evident that the problem is to enhance the heat transfer by means of the least expenditure of energy.

All of the above is true not only for heat exchangers, but also for the cooling processes of food, where the more necessary to focus on increasing the heat transfer coefficient, since in this case we can not affect the thermal conductivity coefficient. Hydraulic aerosol evaporative refrigeration is an effective method to enhance the heat transfer coefficient. On the one hand, the rate of refrigeration increases as compared with air refrigeration at the expense of sprayed moisture evaporation due to periodical spraying of the product by water. On the other hand, the product does not absorb water thanks to air blow-off. In addition, the potable water consumption is considerably lower than when only water is used for refrigeration.

The method offered has an essential feature. The heat transfer coefficient varies considerably during heat removal process. It is obvious that to increase the cooling rate it is necessary to put the maximum amount of water on the surface to be cooled and at the same time to prevent the flow of moisture from it, as well as to distribute the moisture evenly, which is provided by the appropriate dispersion parameters. Currently such a method is applied at industrial enterprises. But it is difficult to provide an even distribution of moisture using sprayers along all surface of the product. The authors offer to form hydraulic electric aerosol media using electric fields and different forms of electrical discharges that are used when developing aseptic refrigerators and other devices in the frame work of the Project of the use of electrophysical methods in refrigeration engineering and technology (Rogov et al., 1996).

2. HEAT TRANSFER IN HEAT EXCHANGERS OF REFRIGERATING SYSTEMS USING ELECTRIC HYDRAULIC AEROSOLS

To investigate the process of application of hydraulic aerosols and hydraulic electric aerosols for intensification of the heat exchange a test bench was developed. At the test bench electric hydraulic aerosol media were obtained using specially adopted sprayers. Different additional devices and controlling and measuring apparatuses to study dispersion processes and hydraulic electric aerosols charging were developed too. The bloc diagram is given in Fig. 1.

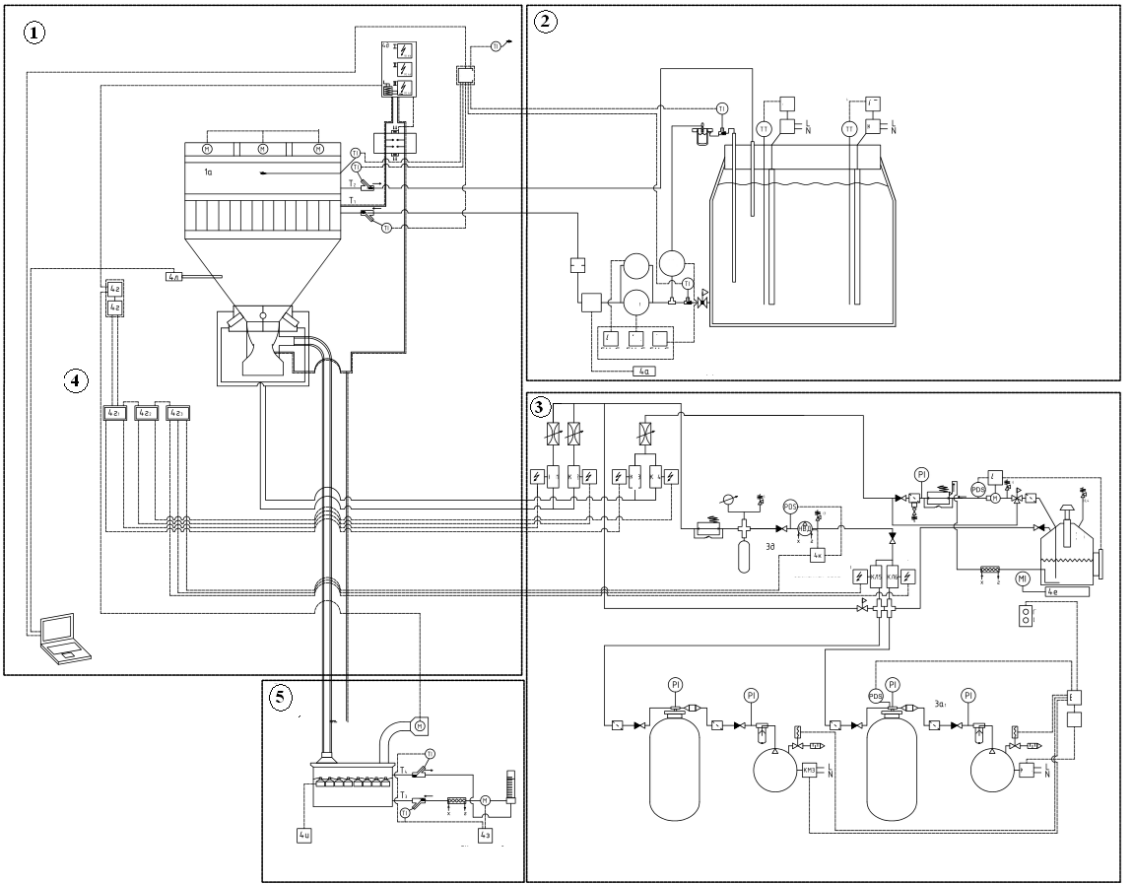

Figure 1: Block diagram of the plant to study heat exchange intensification. 1 – test block; 2 – block to maintain temperature and to supply coolant; 3- block of preparation and supply water-air mixture; 4 – controlling and measuring regulation block; 5 – lighting and stroboscopying control block

The test bench operates as follows: the refrigerant (coolant) at given temperature goes to the block of water-air mixtures supply; here a hydraulic aerosol is formed by the sprayers; the aerosol drop size depends on the operating regime of compressors and liquid rate. When a given structure of a jet is obtained a high-voltage power pack is switched on; it consists of a generator generating impulses in a large range of duration of amplitude and pulse ratio. The hydraulic aerosol is supplied to the surface of the heat exchange apparatus and the block of measurements reflects the

changes of thermal characteristics of the system. Fig. 2 illustrates the module of the movable carriages of the test bench with dispensers that distribute hydraulic electric aerosols along the heat exchanger surface. The liquid rate and the value of drop dispersion are controlled by the block of preparation and supply of water-air mixture.

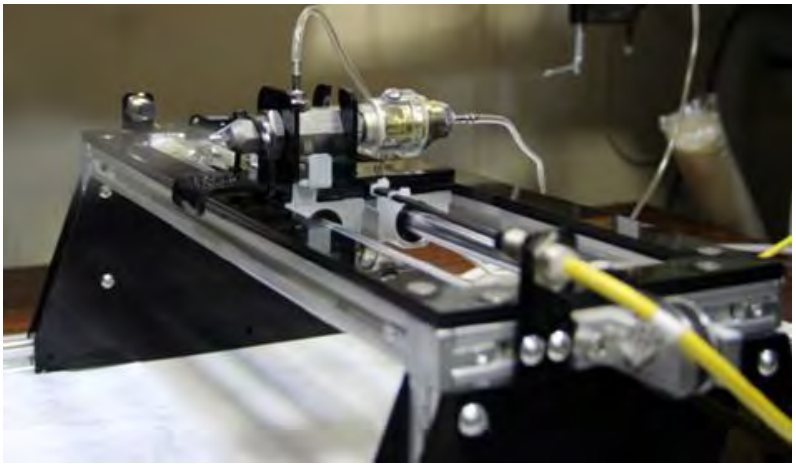

Figure 2: Module of movable carriages of the test bench with dispensers

Below the experimental variants of stable jets of dispersed liquid are presented. The next characteristics of aerosols distribution in working volume were obtained depending on regimes of liquid supply into the treatment zone. Fig. 3 shows the jet at maximal drop distribution on the average dispersed medium about **7** μm.



Figure 3: Working jet at7 μm drop dispersion

Fig. 4 shows more detailed distribution of dispersed drops.

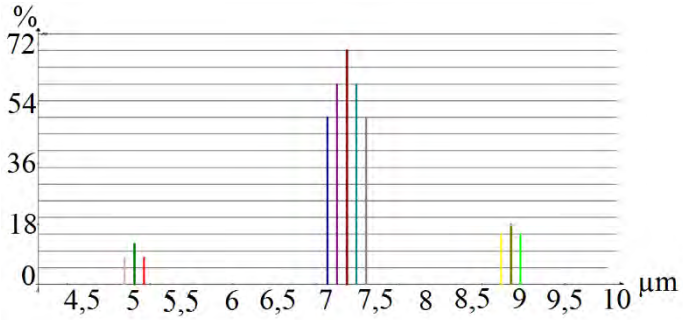

Figure 4: Liquid drop distribution in an average dispersed medium

A stable jet in a high dispersed electric medium at maximal distribution of 2 μm is presented in Fig. 5. This dispersed medium is well distributed over the surface of the cooling devices; it is worth noting that a significant part of it penetrates deep into the space between the lamellae.



Figure 5: Working jet at 2 μm drop dispersion

The drop distribution in a high dispersed medium is presented in Fig. 6.

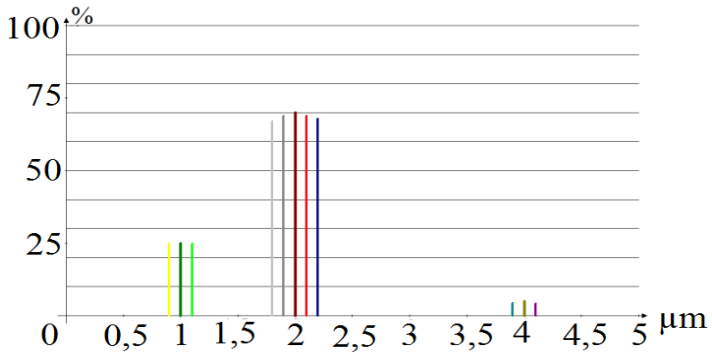

Figure 6: Liquid drops distribution in a high dispersed electric medium

The use of highly dispersed media made it possible to obtain cooling regimes of the surface of heat exchangers when the aerosol put on the surface by means of the movable carriage evaporates immediately after the passing through the cooling zone. Such a regime provides a maximal heat removal.

3. CONCLUSIONS

The test bench developed by the authors gave the possibility to realize the method of obtaining high dispersed hydraulic electric aerosols that provided a high-performance regulated heat removal in a large range of heat flows rates. Hydraulic electric aerosols with particles less than 1 μm were obtained using electric hydraulic sprayers. As compared with well-known methods the use of dispersed media increases the external heat transfer coefficient of heat exchangers by 20-50%. The time of evaporation of the hydraulic electric aerosol from the surface of the heat exchange apparatus decreases 2-3 times depending on working parameters of treatment. The water discharge decreases by 30-50%. Heat removal increases 1.5-2 times.

REFERENCES

Rogov, I.A., Babakin, B.S., Vygodin, V.A., 1996. Electrophysical methods in refrigeration engineering and technology. Kolos publishers, Moscow, 336 p.

Manuscript ID: 1874
DOI: 10.18462/iir.icr.2019.1874

Why and which insulation materials for refrigerators!

Sankarshan VERMA, Harjit SINGH

Institute of Energy Futures, College of Engineering, Design and Physical Sciences, Brunel University London
Uxbridge, UB8 3PH, UK, harjit.singh@brunel.ac.uk

ABSTRACT

Transmission is the major contributor (> 50%) to the total cooling load for typical domestic refrigerators. Understandably, insulation in refrigerator walls plays an important role in reducing it. In the present work, a system level computer model of domestic refrigerator has been developed and the effect of different insulation materials, with varying thickness, on the energy consumption, weight, inner-volume and payback periods investigated. The insulation materials studied include polyurethane (PU) foam and vacuum insulation panels (VIPs) made with fumed silica, glass fibre and alternative core materials.
A fumed silica VIP insulated refrigerator is predicted to consume around 20% lesser energy over its lifetime, yield 148 litres extra storage volume and offer a payback period of 3.2 years relative to PU foam insulated refrigerator. Glass fibre VIP insulated refrigerator was found to have no payback because of their increased thermal conductivity due to ageing.
Keywords: Vacuum Insulation Panels, Energy Efficiency, Insulation Comparison.

1. INTRODUCTION

Refrigeration consumes about 6% of the total energy generated in the world and accounts for about 14% of the total household energy consumption (Melo & Silva, 2010). More than 50% of the thermal load in a refrigerator is caused by heat gain from the walls (ASHRAE, 2006). Insulation, thus have a significant effect in reduction of overall energy consumption of a refrigerator. Due to its low thermal conductivity, low cost and light weight, polyurethane foam (thermal conductivity = 21-25 $mW \cdot m^{-1} \cdot K^{-1}$) has been widely used as the insulation material for refrigerators since 1960s and till date it's the most popular insulation. Does that mean there isn't much scope of improvement in insulation materials?
Vacuum insulation panels (VIPs) can achieve a thermal conductivity as low as 3 $mW \cdot m^{-1} \cdot K^{-1}$(7 times lower than PU foam) (Alam et al., 2011). VIPs are three phase systems comprising of an evacuated core, mixed with additives such as getters and opacifiers, sealed in an envelope. The thermal conductivity of a VIP depends upon a range of factors including materials, operating temperature, sealing pressure etc.
VIPs are being identified as the potential next generation thermal insulation for various cold chain equipment including refrigerators, freezers, vaccine boxes, reefer trucks etc. Thiessen et al. (2016) reported a 21% reduction in energy consumption when 56% of the refrigerator area was covered with glass fibre VIPs. Hammond et al. (2014) calculated a payback period of 9.7 years when it was insulated with VIPs with thermal conductivity of 4 $mW \cdot m^{-1} \cdot K^{-1}$. Tao et al. (2004) reported an 11.1% reduction in energy consumption by installing VIPs in side walls of a display case refrigerator. None of the above study analysed the effect of ageing on thermal conductivity, which can significantly change results.
In the present study, transmission load was calculated for refrigerators with various insulation materials. A parametric analysis was performed to find the optimum thickness of fridge and freezer insulation material with an objective to reduce the overall cost incurred during the lifetime of the refrigerator. The different materials with optimum thickness were then compared on the bases of life time energy consumption, insulation weight, inner volume and payback periods.
The rise in demand of VIPs have led the way to innovations in manufacturing. As of now, VIPs of sizes as large as 1.2m x 1.8m and of various geometrical shapes, including cylindrical shapes are available. In this study, it has been assumed that VIPs of any required size and shape to be fitted in the walls of refrigerator are available.

2. METHODOLOGY

2.1. Geometry

A 450-litre bottom-freezer refrigerator geometry with dimensions 2150mm x 762mm x 610mm (H x W x D) was modelled in COMSOL Multiphysics (Fig. 1). Rate of heat gain in the refrigerator was numerically solved for using the heat transfer module. Convection boundary conditions (inside and outside the refrigerator) were used as prescribed by ASHRAE guidelines (Table 1) (ASHRAE, 2006) and the temperatures were in accordance with the study conducted by Biglia et al., (2018). The geometry was meshed using custom mesh (element size: 172 mm to 8.6 mm) made of free tetrahedral elements. Total number of mesh elements solved for was 1039660.
The refrigerator compartment was modelled as a three phase system consisting of an outer metal shell, (0.5 mm thick), an inner plastic lining made of PVC (2 mm thick) and an insulation material (variable thickness) sandwiched between the metal sheet and the plastic liner (Fig. 1(b)). Different insulation materials (Table 2) were employed and their effects analysed based on energy and physical change.

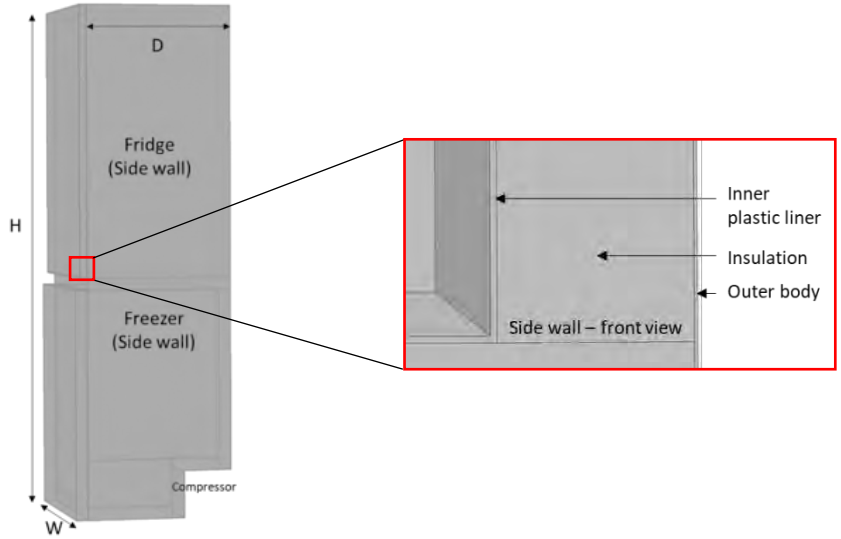

Figure 1: Refrigerator geometry a) full (semi-transparent) b) enlarged view of side wall without the door

Table 1: Boundary conditions used in the computer model

	Overall heat transfer coefficient ($W \cdot m^{-2} \cdot K^{-1}$)	Temperature (°C)
Inner walls – fridge	1.3	5
Inner walls – freezer	1.3	-20
Outer walls (excluding compressor)	1.3	25
Compressor walls	6	30
Evaporator wall	(Constant temperature)	-20

2.2. Materials

Four different insulation materials were studied for their effect on refrigerator performance (Table 2). Rigid polyurethane foam (PU foam) is the most common insulation material for cold chain equipment. Cyclo-pentane filled PU foam was used for this study. Vacuum insulation panels with cores made of fumed silica and glass fibre are commonly available. Glass fibre VIPs offer low cost and excellent initial thermal conductivity which rises rapidly with time; a major shortcoming that has hindered its reliable market acceptability. On the other hand, fumed silica VIPs have lower density and a low thermal conductivity, with a gradual increase over time. Due to cost and strength considerations, fumed silica VIPs haven't yet found much wide acceptability either. A large portion (around 60%) of the total VIP cost is the material cost and thus it is safe to assume that volumetric cost of VIPs is constant. A lot of research is focused on development of composite core materials to lower the overall VIP cost and improve VIP strength (Singh et al., 2015), (Alam et al., 2014). An example is a

composite core material formed with expanded perlite and polyester fibres developed by Alam et al. (Alam et al., 2014) which resulted in a cost reduction of 20% of the core.

Table 2: Materials employed in the research

Insulation material	Identifier	Initial thermal conductivity ($W \cdot m^{-1} \cdot K^{-1}$)	Density ($kg \cdot m^{-3}$)	Cost (£$\cdot m^{-3}$)
PU Foam	M1	0.0215	80	950
Fumed silica VIP	M2	0.0037	200	2390
Glass fibre VIP	M3	0.0029	250	1800
Alternate core VIP	M4	0.0076	220	2000

2.3. Thickness of insulation materials

The rise in insulation thickness lowers the energy consumption due to decreased U-value but results in higher initial equipment cost due to increased volume of insulation material being used. In order to determine the optimum thickness of insulation materials, which offers both low energy consumption and low initial cost, a parametric study was performed. The thickness of insulation material in the fridge and freezer was independently varied in the range of 10 mm to 50 mm, keeping the outer dimensions of the refrigerator constant and thermal transmission load with time was evaluated at each step. The transmission load was converted to cumulative energy consumption over the life time of 13 years and total cost of electricity (for 13 years) was calculated assuming a constant rate of 0.125 £$\cdot kWh^{-1}$ i.e. the present rate (UK Power, 2019). The energy consumption was then converted to equivalent CO_2 emissions for UK, considering an emission factor of 0.3072 $kgCO_2e \cdot kWh^{-1}$, including generation and transmission of electricity.
The data obtained was plotted in the form of 3D surfaces with the insulation thickness of fridge on x-axis, insulation thickness of freezer on y-axis and a cost function for resulting geometry on the z-axis. Cost function was defined as the sum of total electricity cost over the lifetime of refrigerator and the initial insulation material cost. Cost of various insulation materials employed in the study are given in Table 2. The point of minimum cost function was considered the optimum thickness of insulation.

$$CF = EC + IC \qquad \text{Eq. (1)}$$

where CF is cost function in £, EC is total electricity cost over the lifetime of refrigerator in £, and IC is initial insulation material cost in £.

2.4. Thermal Conductivity of Insulation Materials

Thermal conductivity of cyclo-pentane filled rigid polyurethane foam is reported to be 0.0215 $W \cdot m^{-1} \cdot K^{-1}$. Present blowing agents like cyclo-pentane (k = 12.8 $W \cdot m^{-1} \cdot K^{-1}$) and CO_2 (k = 16.6 $W \cdot m^{-1} \cdot K^{-1}$) have higher diffusion rates, as compared to CFCs (k = 8.2 $W \cdot m^{-1} \cdot K^{-1}$), due to which they escape out of the foam pores and are replaced by air (k = 0.027 $W \cdot m^{-1} \cdot K^{-1}$) (Macchi-Tejeda et al., 2007). Researchers at Oak Ridge National Laboratory claimed that the thermal conductivity of cyclo-pentane filled PU foam increases from 0.0215$W \cdot m^{-1} \cdot K^{-1}$ to 0.027$W \cdot m^{-1} \cdot K^{-1}$ in first year and to 0.028$W \cdot m^{-1} \cdot K^{-1}$ gradually (Fig. 2) (Wilkes et al., 2002).

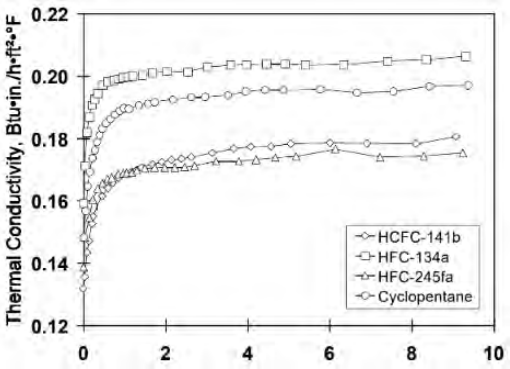

Figure 2: Aged thermal conductivity of PU foam for simulated refrigerator wall. (Wilkes, et al., 2002)

The effect of ageing on the thermal conductivity of Vacuum Insulation Panels is equally significant. It is well known that the overall thermal conductivity follows an S-curve when plotted with pressure on x-axis in log scale (Fig. 3). The transmission of air and water vapour inside the VIP core through envelope leads to rise in VIP pressure and thus a rise in overall thermal conductivity. The transmission of these components depend on the pressure inside VIP, the quality of the envelope and the area of VIP. In this study, an initial VIP pressure of 0.1 mbar has been considered which rises in step of 1.5 mbars each year for all the VIPs and the variation of thermal conductivity has been taken from Simmler et al. (2005) and Alam et al. (2014).

2.5. Payback Period

The per-unit cost of VIPs is more than two times the cost of PU foam. This gives a clear indication that the initial cost of VIP insulated refrigerator will be higher than present PU foam ones. On the other hand, the VIP insulated refrigerators are expected to save on cost of electricity due to lower energy consumption. Based on this information and the data obtained from heat transfer simulations, a payback period was defined as the number of years it requires to break-even the cost if one buys a VIP insulated refrigerator instead of PU foam one. The payback period is identified as the point

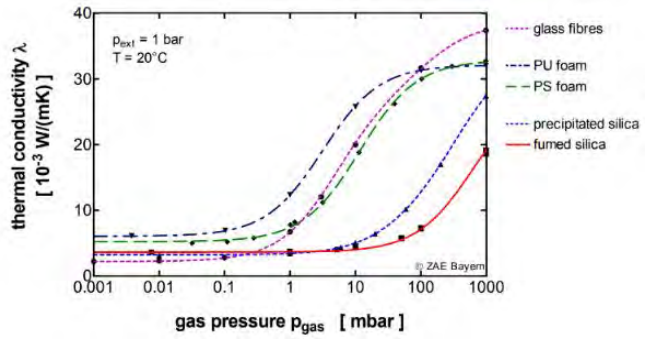

Figure 3: Variation of thermal conductivity of various core materials with pressure (Simmler, et al., 2005)

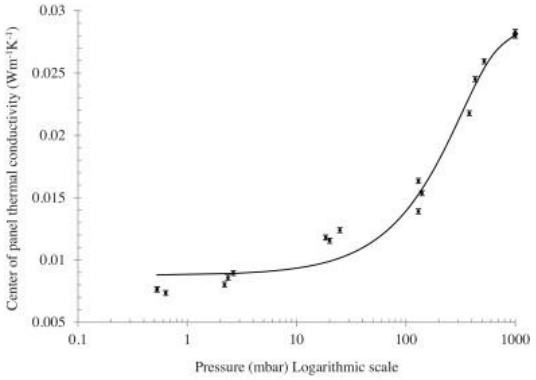

Figure 4: Variation of thermal conductivity of alternative core material with pressure. (Alam, et al., 2014)

where the cumulative electricity cost difference line (delta EC) intersects the increased cost line (delta IC).

3. RESULTS AND DISCUSSIONS

The parametric study for thickness optimisation resulted in set of values plotted as 3D surfaces (Figs. 5a-5d). The x and y-coordinate was the fridge and freezer thickness respectively and the z-coordinate was the cost function (Eq. 1). The minima on the surface was chosen as the optimum value for fridge and freezer thickness (see Table 3). It can be observed that optimum thickness for VIPs is lower than PU foam insulation which is due to low thermal performance and lower cost of PU foam. Also, the optimum thickness of freezer insulation is always higher than the fridge insulation because more heat is transferred to freezer due to large temperature difference between freezer and ambient temperature (around 45°C).

An analysis was then performed on the insulation with optimised thicknesses (Table 3). It was observed that fumed silica VIP offered the minimum energy consumption over lifetime (19.6% lesser than PU foam insulated refrigerator), results in the least value for cost function (£ 626.32) and the highest inner volume (598 litres; 148 litres more than PU foam insulated), because of its lowest optimum thicknesses. A weight gain of 2.48 kg from PU foam refrigerator was observed due to higher density of fumed silica VIP (2.5 times PU foam). Glass fibre, being the densest (250 kg·m^{-3}), resulted

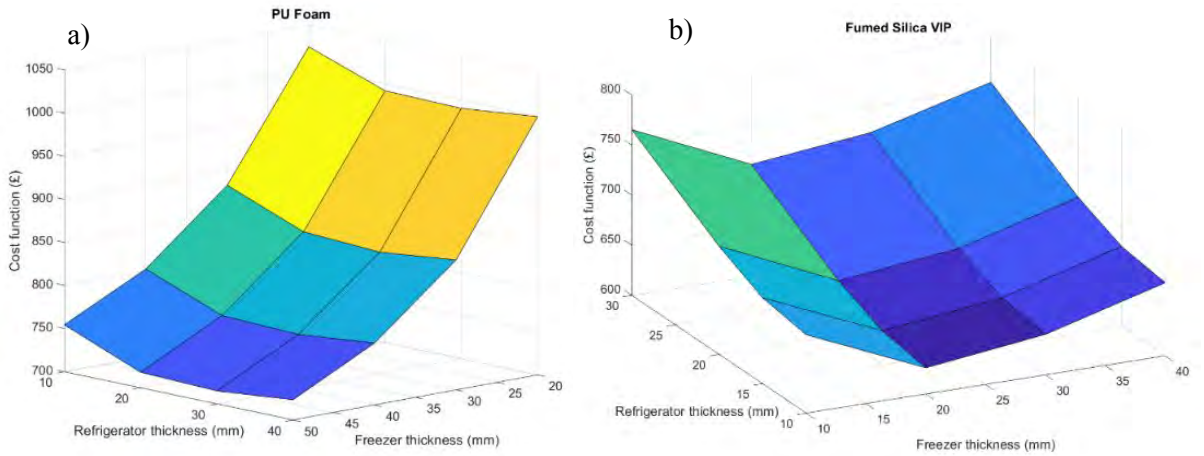

a weight increase of 19.56 kg. Also, due to its ageing characteristics, its energy consumption increases, leading to higher value of cost function.

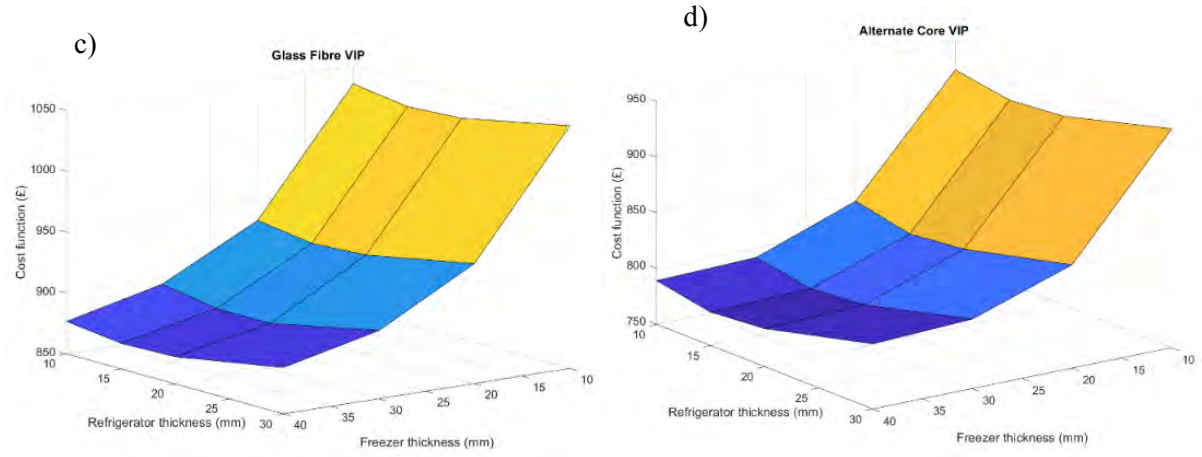

Figure 5: Parametric thickness optimisation surface for a) PU foam; b) fumed silica VIP; c) glass fibre VIP; d) alternate core VIP

Table 3: Optimised thickness of insulation materials and its relative effects

	Fridge insulation thickness (t_{fridge})	Freezer insulation thickness ($t_{freezer}$)	Lifetime energy consumption {% change} (kWh)	Cost function (£)	CO_2e emissions (kg)	Weight of insulation (kg)	Inner volume (l)
M1	30	50	3802.72 {0}	715.14	1168.2	24.72	450
M2	10	20	3057.62 {19.6}	626.32	939.3	27.2	598
M3	15	40	4418.38 {-16.2}	871.14	1357.3	44.28	527
M4	15	40	3405.41 {10.4}	779.94	1046.1	38.96	527

The transmission load for fridge and freezer at the end of each year of its lifetime is shown in Fig. 6 and 7. Surprisingly, at the optimised thickness, the energy consumption of fridge is minimum when it is insulated with PU foam, whereas the effect is fully reversed in freezers. This indicates that the marginal rate of return on insulating a freezer with a VIP is more than insulating a fridge.
The effect of ageing can be well observed in all the materials. Out of all materials, glass fibre VIPs are worst hit by ageing. The freezer transmission load for glass fibre VIP loses its VIP characteristics (low transmission load) just after 2 years and even surpasses PU foam in 8 years.

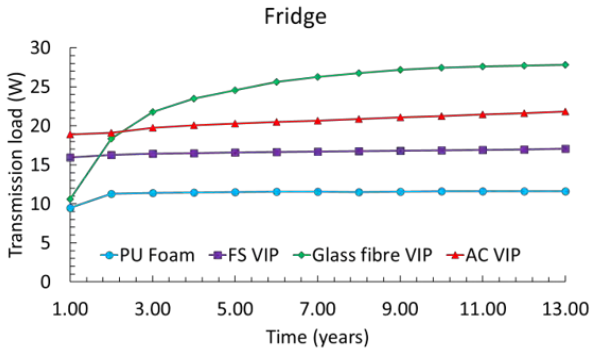

Figure 6: Yearly transmission load from a fridge

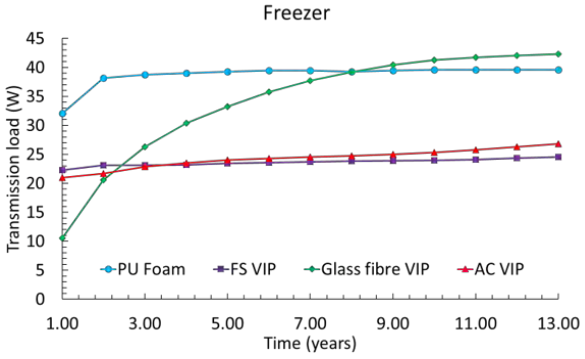

Figure 7: Yearly transmission load from a freezer

The payback period was calculated as the abscissa of the intersection point of increase in insulation material cost (delta IC) with respect to PU foam insulation and the cumulative gain because of reduced electricity bills (delta EC). The fumed silica VIP broke even in 3.2 years, because of excellent thermal and ageing properties of fumed silica (Fig. 8). A significantly higher payback period of 8-9 years is reported in literature (Hammond & Evans, 2014), the discrepancy being the underlying assumptions. In this study, the authors believe that VIPs of any size and shape could be manufactured in near future, which lowers the heat leakage from areas without VIPs. Also, the

consideration of effect of ageing of foam plays its role in terms of increased energy cost over the life time of refrigerator and decreased payback.

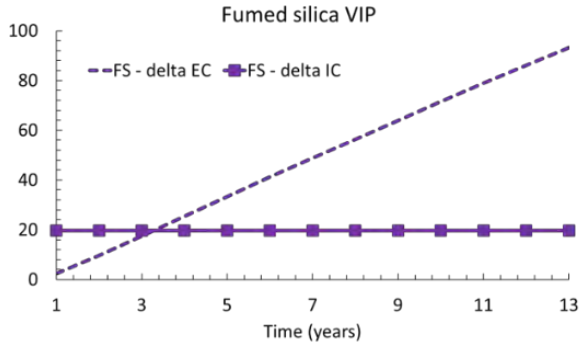

Figure 8: Payback period calculation for fumed silica VIP

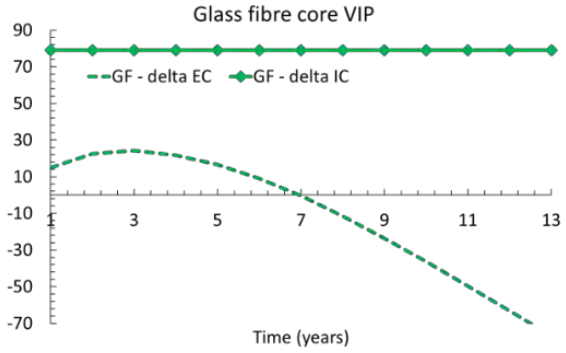

Figure 9: Payback period calculation for glass fibre VIP

The VIP with glass fibre core performed very well in the first year but its performance deteriorated as it aged (Fig. 9). This is because the thermal conductivity of glass fibre is very low initially (0.002 $W \cdot m^{-1} \cdot K^{-1}$) but rises rapidly as the pressure inside the VIP increases and eventually becomes higher than that of PU foam. The alternate core VIP doesn't break even either, even after reduced initial cost (Fig. 10). The reduced cost is achieved by addition of components which increase the overall thermal conductivity of VIP cores. This leads to two outcomes: i) usage of higher thickness of VIPs for insulation which leads to increased initial cost and ii) higher overall aged thermal conductivity.

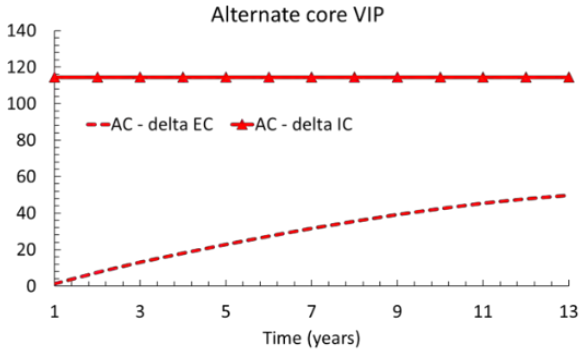

Figure 10: Payback period calculation for alternate core VIP

4. CONCLUSIONS AND FUTURE WORKS

Four different insulation materials were compared for their thermal, physical and economic performance by computer modelling, starting with identification of their optimum thicknesses independently for fridge and freezer to reduce the initial and operational costs through a parametric study. The results were analysed to compare three different VIP and PU foam on the basis of their transmission gain, carbon footprint over the lifetime and the payback period. Results indicated that a fridge insulated with 10mm thick and the freezer with 20mm thick fumed silica VIP reduced the energy consumption by 19.6% while increasing the inner volume by 148 litres and weight by 2.48 kg when compared with PU foam insulated refrigerator.

This study serves as a motivation for VIP manufacturers to make VIPs in various shapes and sizes to be fitted in refrigerators. Research is needed into new alternative materials for cores which could lower the VIP cost by 50%; into heat transfer phenomena through VIPs and the various material properties affecting it and into low permeating and low conducting envelopes so that glass fibre cores can be fully exploited. Both, policy makers and industry should promote research in this field.

REFERENCES

Alam, M., Singh, H., Brunner, S., Naziris, C., 2014. Experimental characterisation and evaluation of the thermo-physical properties of expanded perlite—fumed silica composite for effective vacuum insulation panel (VIP) core. Energy and Buildings, 442-450.

Alam, M., Singh, H., Limbachiya, M., 2011. Vacuum Insulation Panels (VIPs) for building construction industry–A review of the contemporary developments and future directions. Applied energy, 88(11), 3592-3602.

ASHRAE, 2006. 2006 ASHRAE Handbook - Refrigeration. Atlanta: American Society of Heating, Refrigerating and Air-Conditioning Engineers, Inc.

Biglia, A., Gemmell, A. J., Foster, H. J., Evans, J. A., 2018. Temperature and energy performance of domestic cold appliances in households in England. International Journal of Refrigeration, 87, 172-184.

Hammond, E., Evans, J., 2014. Application of Vacuum Insulation Panels in the cold chain–Analysis of viability. International Journal of Refrigeration, 47, 58-65.

Macchi-Tejeda, H., Opatovà, H., Guilpart, J., 2007. Contribution to the gas chromatographic analysis for both refrigerants composition and cell gas in insulating foams–Part II: Aging of insulating foams. International journal of refrigeration, 30(2), 338-344.

Melo, C., Silva, L.W., 2010. A perspective on energy savings in household refrigerators. In Sustainable refrigeration and heat pump technology conference, 1, 1-14.

Simmler, H., Brunner, S., Heinemann, U., Schwab, H., Kumaran, K., Mukhopadhyaya, P., Quénard, D., Sallée, H., Noller, K., Kükükpinar-Niarchos, E., Stramm, C., 2005. Vacuum Insulation Panels. Study on VIP-components and panels for service life prediction of VIP in building applications (Subtask A). FHBB Switzerland: Systems and Applications.

Singh, H., Geisler, M., Menzel., F., 2015. Experimental investigations into thermal transport phenomena in vacuum insulation panels (VIPs) using fumed silica cores. Energy and Buildings, 107, 76-83.

Tao, W., Huang, C., Hsu, C., Lin, J., 2004. Performance study of an energy-efficient display case refrigerator. Chemical Engineering Communications, 550-565.

Thiessen, S., Knabben, F., Melo, C., 2016. An Experimental Study on the Use of Vaccum Insulation Panels in Household Refrigerators. In International Refrigeration and Air Conditioning Conference, West Lafayette, IN, United States

UK Power, 2019. Gas & Electricity Tariff Prices per kWh. [Online] Available at: https://www.ukpower.co.uk/home_energy/tariffs-per-unit-kwh [Accessed 2019].

Wilkes, K. E., Yarbrough, D. W., Gabbard, W. A., Nelson, G. E., Booth, J. R., 2002. Aging of polyurethane foam insulation in simulated refrigerator panels–three-year results with third-generation blowing agents. Journal of cellular plastics 38(4), 317-339.

Manuscript ID: 1875
DOI: 10.18462/iir.icr.2019.1875

Experimental investigation of evaporation of propane (R-290) in small pipes

Ehsan ALLYMEHR[(a)], Trygve Magne EIKEVIK[(a)], Armin HAFNER[(a)]

[(a)] Norwegian University of Science and Technology, NTNU
Trondheim, Norway, ehsan.allymehr@ntnu.com

ABSTRACT

Two-phase flow boiling of propane has been characterized utilizing an experimental test facility. The effect of heat flux, mass flux and saturation temperature were studied on the heat transfer coefficient and pressure drop. Test conditions were mass flux from 250 to 525 $kg.m^{-2}.s^{-1}$, saturation temperature from -0.5°C to 9.5°C, heat flux from 16 to 61 $kW.m^{-2}$. A smooth copper tube with internal diameter of 4.1 mm and test section length of 0.5 m was used. Experimental results show an increase of heat transfer coefficient and pressured drop with mass flux, heat flux and vapor quality before dryout. Correlations were able to predict pressure drop accurately while heat transfer coefficient was under predicted.
Keywords: Propane, R-290, Hydrocarbon, Flow Boiling, Heat Transfer, Pressure Drop.

1. INTRODUCTION

Recent awareness of the global warming and introduction of new regulations have fueled a search for a new generation of working fluids, with a goal of an environmentally friendly fluid enjoying zero ozone depletion potential (ODP) and low global warming potential (GWP), all while improving efficiency of the system.
Propane has long been considered as an alternative refrigerant, since it has a favorable saturation curve suitable for different applications. Moreover, its physical properties are close to those of R-22 making it a suitable candidate for a charge switch without significant variation in the performance (Granryd, 2001). This combines with a modest environmental impact, as ODP is zero and GWP is smaller than 3 over 100 years; for comparison GWP for R-134a is 1300 (Bolaji and Huan, 2013). However, the major concern with the use of hydrocarbons as refrigerants remains to be flammability, in particular as the lower flammability limit (LFL) is very low (Granryd, 2001). Therefore, charge minimization is a major design objective for widespread usage of hydrocarbons as refrigerants. Theoretically the charge for propane can be half compared to R-134a (latent heat of vaporization is almost double) Nonetheless, the heat transfer performance has to be carefully investigated, especially in the case of small diameter pipes, since the literature is relatively lacking general predicting approaches.
(Thome et al., 2008) reviewed the available data for the flow boiling of ammonia and hydrocarbons, noting that the results between different studies show noticeable discrepancies and further work is needed for the small diameter tubes. (Lee et al., 2005) compared the characteristics of evaporation of different hydrocarbons and compared them to R-22 in 9.52 and 12.70 mm internal diameter smooth tubes, they found that hydrocarbons have a higher heat transfer coefficient and pressure drop compared to R-22, furthermore, (Kandlikar, 1990) best predicted the heat transfer coefficient data. (Wang et al., 2014) studied the evaporation of propane with low mass fluxes (from 62 to 104 $kg.m^{-2}.s^{-1}$) in a 6.0 mm internal diameter pipe. comparing the results with correlation they found that correlation of (Liu and Winterton, 1991) best predicted the heat transfer coefficient while (Müller-Steinhagen and Heck 1986) best predicted the pressure drop. (Shin et al., 1997) performed tests with propane, butane and different mixtures of them and compared them to R-22, R-32, R-134a in a 7.7 mm inner diameter test tube. The authors observed that their data on heat transfer coefficients were over-predicted by the correlation of (Gungor and Winterton, 1986).
While the majority of the studies seem to focus on tube diameter sizes larger than the one studied in this paper, there has been several studies in recent years dealing with characteristics of hydrocarbons flowing in smaller diameter. (Pamitran et al., 2010) examined the heat transfer coefficient of propane in stainless steel tubes of 1.5 and 3.0 mm inner diameter, based on the results

a correlation was developed for prediction of heat transfer coefficient. (Wen and Ho, 2005) conducted experiments with propane, butane and a mixture of them in a 2.6 mm internal diameter test tube, the results showed that the heat transfer was significantly higher compared to R-134a, furthermore, while test conditions were similar to (Shin et al., 1997) with the only major difference being the tube diameter, the results were noticeably dissimilar. More recently (Lillo et al., 2018) studied the flow boiling of propane in 6 mm internal diameter tube at high saturation temperatures, they noted that the main heat transfer mechanism seems to be nucleation, correlations of (Bertsch et al., 2009) and (Friedel, 1979) best predicted heat transfer coefficient and pressure drop. (Longo et al., 2017) compared evaporation of R-290 and R-1270 with R-404a in small diameter tube showing R-404a and R-1270 exhibit the highest heat transfer coefficient and lowest pressure drop while R-290 suffers from a particularly low dryout quality which is in disagreement with the results from (Lillo et al., 2018) In spite of relative abundance of studies and experiments, the results seem to be conflicting and the available data do not cover the full range of operating conditions for HVAC and process industry. This is the motivation of this work, where flow boiling of propane was experimentally studied. Test conditions were: mass flux from 250 to 525 $kg.m^{-2}.s^{-1}$, saturation temperature from -0.5 to 9.5°C, heat flux from 15.66 to 61.12 $kW.m^{-2}$. The test tube is made of smooth copper with an internal diameter of 4.1 mm and test section length was 0.5 m.

2. EXPERIMENTAL SETUP

An experimental test rig, shown in Fig. 1, was used to determine the pressure drop and heat transfer coefficient in different conditions. The test rig was rebuilt based on an existing setup and modified to achieve the accuracy required and to improve the operating range. A data logger system is installed on the set-up and connected to a personal computer for system control and data acquisition.

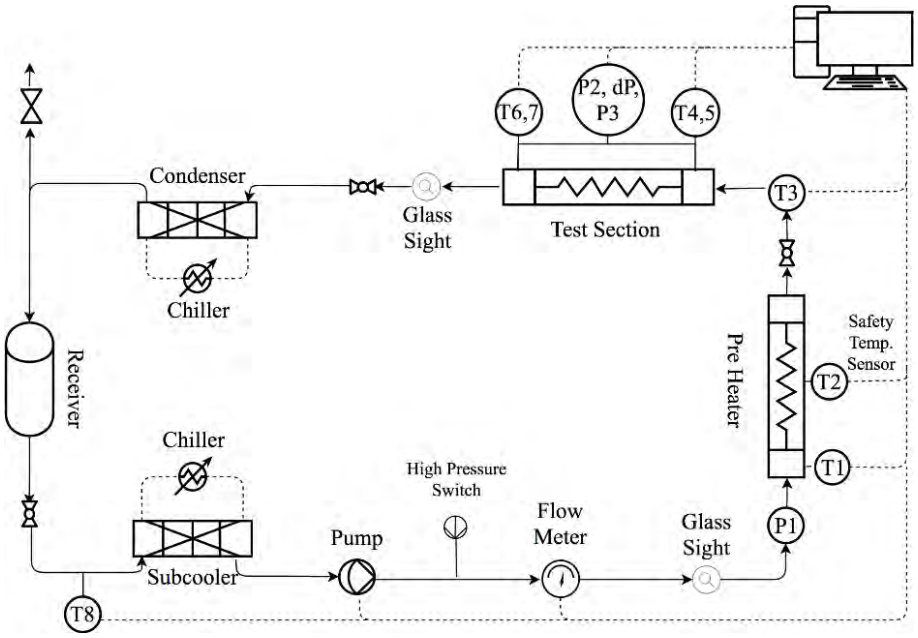

Figure 1: Test rig schematic

Propane flows in a closed cycle by a pump controlled with an inverter. The mass flow is measured with a Coriolis type mass flow meter placed after the pump. A sight glass is placed downstream of the flow meter enabling visual confirmation of single phase liquid flow. Then, the propane flows through the preheater, where the desired vapor quality is set with electrical heating. After an adiabatic section to ensure fully developed conditions, propane flows through the test section, where electrical heating provides the desired vapor quality variation. Electrical heat input is controlled with a thyristor and the resistor is wound around a copper block to distribute the heat evenly along the test section. Pressure drop values are read directly from the differential pressure transducer connected to inlet and outlet of the test section, while the wall temperature was measured with two pairs of Type T thermocouples soldered to the tube wall, each inserted 10 cm in the inlet and outlet of the test section, shown T4, T5, T6 and T7 in Fig. 1. At the outlet of the test section, a sight glass

enables visualizing the flow regime. Finally, propane flows through the condenser, and returns to the receiver.
Heat transfer coefficients were calculated using Eq. (1) for the inlet and outlet separately and averaged.

$$h = \frac{Q_{test}}{s\,(T_w - T_{sat})} \quad \text{Eq. (1)}$$

Where T_w is the wall temperature, Q_{test} is the heat input to the test section and s is the surface area for heat transfer. Saturation temperature are obtained indirectly from pressure sensors installed before and after the test section (P2 and P3 in Fig. 1), while thermodynamic properties of the fluid are acquired from REFPROP V9.1, developed by NIST.
The values of the heat transfer coefficient and pressure drop are reported for an average value of vapor quality calculated using the Eq. 2:

$$\mathrm{x} = \mathrm{x}_{\mathrm{inlet}} + \frac{\Delta \mathrm{x}}{2} = \frac{Q_{pre} - \mathrm{C_{p,l}}.m(T_1 - T_{sat,l})}{m.\mathrm{i_{lg@P1}}} + \frac{Q_{test}}{2.m.(\mathrm{i_{sat,g@P3}} - \mathrm{i_{sat,l@P2}})} \quad \text{Eq. (2)}$$

Where Q_{pre} is the heat input to the preheating section of the test rig.

2.1. Uncertainty Analysis

The method elaborated in (ISO, 1993) was used to obtain the uncertainty of measurements with a confidence level of 95%. Uncertainties of measurement equipment reported by the manufacturer is shown in Table 1.

Table 1. List of instruments and their uncertainties

Displayed text	Range	Uncertainty
Flow meter	0.038-5 kg/min	±0.1% (Of reading)
$P_{1,2,3}$	0-10 Bar	±0.25% (Of full scale)
dP	0-0.5 Bar	±0.15% (Of full scale)
Thermocouples		±0.05 K
$Q_{pre\ heater}$	3450 W	±3% (Of reading)
$Q_{test\ section}$	620 W	±3% (Of reading)

The maximum total uncertainty (random and systematic) was in average 3.9% and 8.4% for pressure drop and heat transfer coefficient, respectively. It should be noted that because of fluctuations in data uncertainties were significantly higher near dry out region, reaching values up to 6.9% and 23.7%, for pressure drop and heat transfer coefficient, respectively. To validate the test facility, the preheater was set to provide enough heat for complete flow vaporization and multiple test were run. Furthermore, the test section was disconnected from the rest of test rig and water was used as a single phase liquid flow. The data obtained for pressure drop and heat transfer coefficient in both cases were compared against Darcy Weisbach formula and correlation of (Gnielinski, 1975), showing an average deviation of 2.3% and 3.5% for pressure drop and heat transfer coefficient respectively.

3. RESULTS AND DISCUSSION

3.1. Pressure Drop

Total pressure drop (accelerational and frictional pressure drop) and the effect of heat flux on it is shown in Fig. 2. The pressure drop increases with increasing heat flux for all the range of vapor qualities. This can be explained by the increased vaporization, causing a higher void fraction and a higher gas velocity. Higher vaporization can also change flow pattern, creating bubbles and leading to a slug flow, further increasing the pressure drop. It is also worth noting that the results seems to show that dryout quality happens at rather high vapor quality which is in disagreement with (Longo et al., 2017).

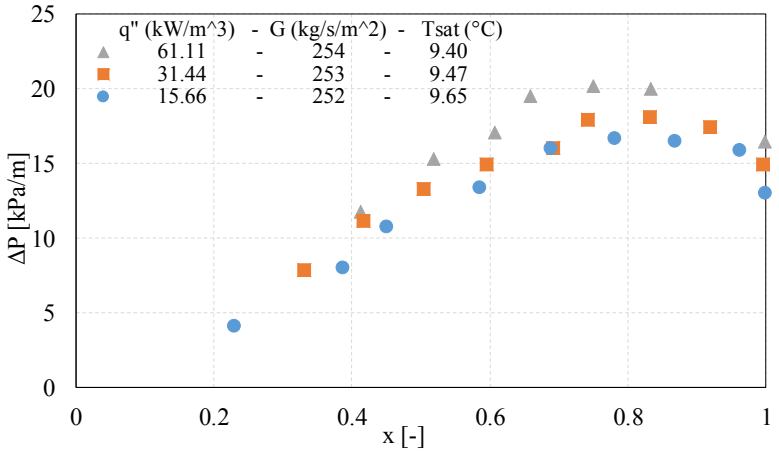

Figure 2: Effect of heat flux on total pressure drop, at constant mass flux and saturation temperature

Fig. 3 shows the effect of saturation temperature on pressure drop, there is a noticeable increase in the pressure drop with lowering temperatures as pressure drop for saturation temperature of -0.44°C is about 1.25 times greater than at saturation temperature of 9.59 °C.
The effect of mass flux on total pressure drop is shown in Fig. 4. As expected the total pressure drop is strongly dependent on mass flux.

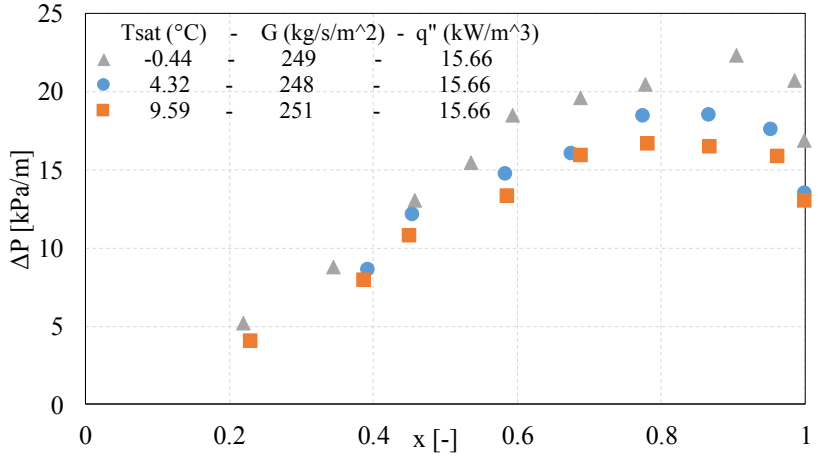

Figure 3: Effect of saturation temperature on total pressure drop, at constant mass flux and heat flux.

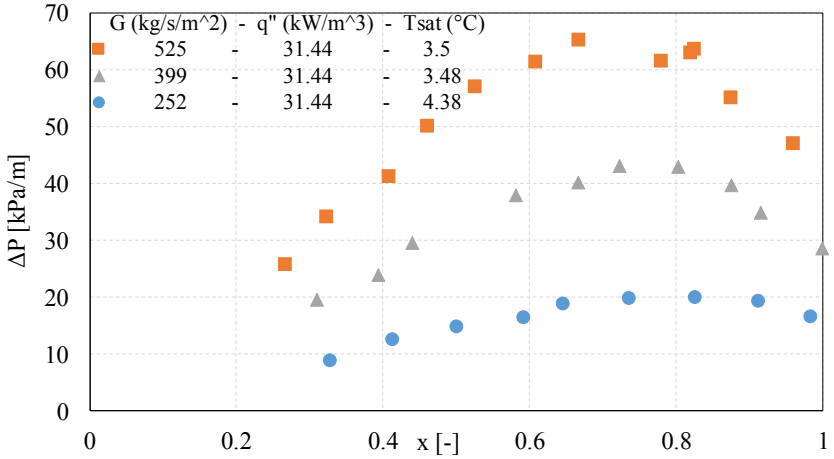

Figure 4: Effect of mass flux on total pressure drop, at constant mass flux.

3.2. Heat Transfer Coefficients

Fig. 5 shows the effect of mass flux on heat transfer coefficients. The dryout quality seems weakly dependent on mass flux, with a tendency to increase as the mass flux lowers. The heat transfer coefficient increases significantly in higher vapor qualities before dryout specially in higher mass fluxes, this implies the importance of convection as mechanism of heat transfer which is in contrast to findings of (Lillo et al., 2018) and (Longo et al., 2017).

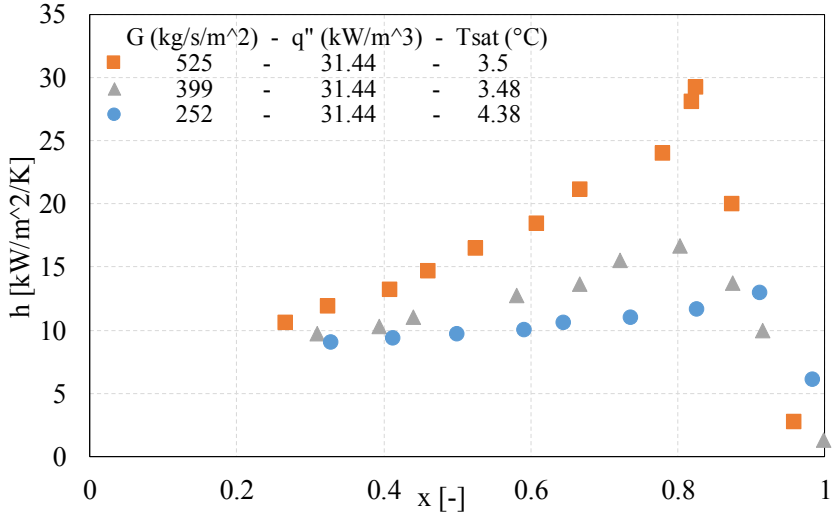

Figure 5: Effect of mass flux on pressure drop, at constant heat flux

Fig. 6 shows the effect of heat flux on the heat transfer coefficient. Heat transfer coefficient rises with the increase of the heat flux in the low vapor quality region. This can be explained by the fact that low vapor quality region is boiling dominant, hence the heat transfer coefficient is essentially related to the heat flux. Furthermore, at higher heat fluxes dryout is initiated at lower qualities.

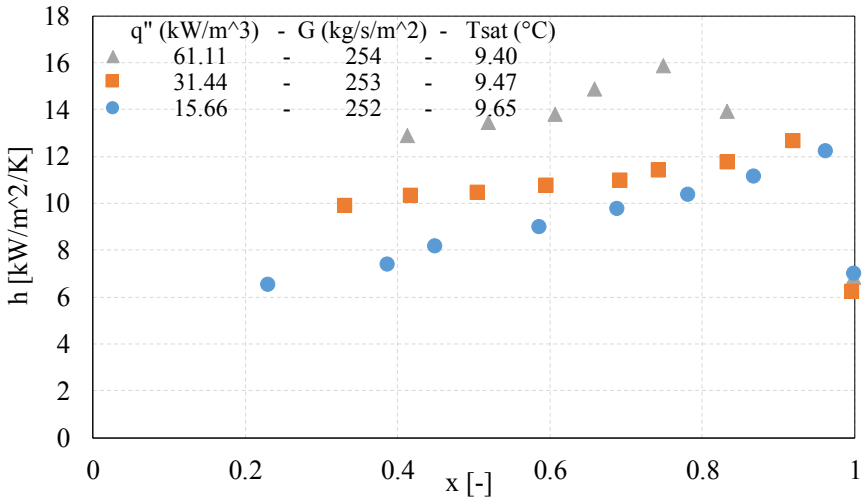

Figure 6: Effect of heat flux on heat transfer coefficient, at constant mass flux and saturation temperature.

Results show that for increasing saturation temperatures the heat transfer coefficient increases, but very often this difference lies within the uncertainty of the heat transfer coefficient measurement, eventually, a clear effect of the saturation temperature has not been put in evidence.

3.3. Prediction Methods

To evaluate the discrepancy between experimental data and correlations, three different statistical parameters were considered: MARD (Mean Absolute Relative Deviation), MRD (Mean Relative Deviation), and λ30%. They are defined as:

$$MRD = \frac{\frac{\Sigma(e-E)}{E}}{n} * 100 \quad \text{Eq.(3)}$$

$$MARD = \frac{\frac{\Sigma|(e-E)|}{E}}{n} * 100 \quad \text{Eq.(4)}$$

$$\lambda 30\% = \frac{number\ of\ predicted\ values\ with\ MRD<30\%}{total\ number\ of\ predicted\ values} * 100 \quad \text{Eq.(5)}$$

Where *E* is the experimental results and *e* is the predicted value. The experimental results for pressure drop were compared with correlations of (Friedel, 1979; Müller-Steinhagen and Heck, 1986; Tran et al., 2000; Cavallini et al., 2002; Sun and Mishima, 2008; Pamitran et al., 2010; Xu and Fang, 2012). The results show that the correlation of (Xu and Fang, 2012) has the best agreement with the experimental data with an MRD of 2.6%, while the MARD was 6.1% and the correlation was able to predict 96% of data points with less than 20% error.

Heat transfer coefficients calculated in this study were compared against correlations of (Shah, 1982; Gungor and Winterton, 1986; Kandlikar, 1990; Liu and Winterton, 1991; Tran et al., 1996; Choi et al., 2007; Bertsch et al., 2009; Li and Wu, 2010; Kim and Mudawar, 2014). The conclusion from this comparison is that the correlations by (Gungor and Winterton, 1986; Kandlikar, 1990; Liu and Winterton, 1991) conform best with the experimental results. However, most of this discrepancy between experimental results and correlations comes from the post dryout data points. If these data points were not to be considered (10 points), MARD values would improve significantly. The results of the comparison are summarized in
Table 2.

Table 2. Deviation between the experimental heat transfer coefficients and correlations

	All data points				Pre-Dryout		
-	(Liu and Winterton, 1991)	(Kandlikar, 1990)	(Gungor and Winterton, 1986)		(Liu and Winterton, 1991)	(Kandlikar, 1990)	(Gungor and Winterton, 1986)
MRD	-6.52	-13.87	-11.64	MRD	-22.52	-22.58	-17.47
MARD	40.69	36.43	32.11	MARD	22.70	22.70	20.15
λ30%	61.04	58.44	63.64	λ30%	83.08	75.38	75.38

This comparison shows that the correlations tend to under predict the experimental data of this study in pre dryout range, this is in agreement with the results of (Lillo et al., 2018). It can be concluded that the correlations available in literature provide a good prediction for pressure drop in evaporating flow assuming that proper attention is given to the defining characteristics of test. However, while there are many different correlations available for prediction of heat transfer coefficients, the results from these correlations seem to be wildly different and this should be noted carefully in design of any system.

4. CONCLUSIONS

Two-phase pressure drop and heat transfer characteristics during flow boiling of propane in different experimental conditions were studied. Test conditions were mass flux from 250 to 525 kg.m^{-2}.s^{-1}, saturation temperature from -0.5 to 9.5 °C, heat flux from 16 to 61 kW.m^{-2} corresponding to vapor quality variation Δx =0.1-0.4. A smooth copper test tube with an internal diameter of 4.1 mm was used and test section length was equal to 0.5 m. Mean vapor quality was between 0.2 and 1.0. From the analysis of the experimental data, the following conclusions can be drawn:

- An increase in heat flux and mass flux causes an increase of the heat transfer coefficient. The influence of the heat flux is more prominent at low vapor quality where the heat transfer regime is boiling dominated, while the effect of the mass flux is more significant at high vapor quality where the heat transfer regime is mainly convection dominated.
- Both mass flux and heat flux increase the pressure drop in the whole range of tested vapor quality. However, the effect of heat flux is relatively minor compared to the influence of mass flux.

- Saturation temperature has a tangible effect on the pressure drop. The decrease of saturation temperature causes an increase in the pressure drop; the effect of saturation temperature on heat transfer coefficient seems to be marginal.
- Correlation of (Xu and Fang, 2012) is the most accurate for prediction of frictional pressure drop with the ability of predicting more than 96 percent of data points with less than 20% error.
- Correlation of (Gungor and Winterton, 1986) is the most accurate in prediction of heat transfer coefficient, even though it tends to under predict the experimental results much like other heat transfer coefficient correlations.

ACKNOWLEDGEMENTS

This publication has been funded by HighEFF - Centre for an Energy Efficient and Competitive Industry for the Future, an 8-years' Research Centre under the FME-scheme (Centre for Environment-friendly Energy Research, 257632). The authors gratefully acknowledge the financial support from the Research Council of Norway and user partners of HighEFF.

NOMENCLATURE

p	Pressure (kPa)	i_{lg}	Enthalpy of evaporation (kJ.kg^{-1})
T	Temperature (°C)	T_w	Temperature of wall (°C)
G	Mass flux (kg.m^{-2}.s^{-1})	q''	Heat flux (kW.m^{-2})
m	Mass flow (kg.s^{-1})	x	Average vapor quality (-)
Q	Heat Input (kW)	s	Surface of the heated test section (m^2)
	Subscripts:		
Sat	Saturated flow	l	Liquid phase
g	Gas phase		

REFERENCES

Bertsch, S.S., Groll, E.A., Garimella, S. V., 2009. A composite heat transfer correlation for saturated flow boiling in small channels. International Journal of Heat and Mass Transfer 52, 2110–2118.

Bolaji, B.O., Huan, Z., 2013. Ozone depletion and global warming: Case for the use of natural refrigerant – a review. Renewable and Sustainable Energy Reviews 18, 49–54.

Cavallini, A., Censi, G., Col, D. Del, Doretti, L., Longo, G., Rossetto, L., 2002. Condensation of Halogenated Refrigerants Inside Smooth Tubes. HVAC&R Research 8, 429–451.

Choi, K.-I., Pamitran, A.S., Oh, C.-Y., Oh, J.-T., 2007. Boiling heat transfer of R-22, R-134a, and CO2 in horizontal smooth minichannels. International Journal of Refrigeration 30, 1336–1346.

Friedel, L., 1979. Improved friction pressure drop correlation for horizontal and vertical two-phase pipe flow, in: European Two-Phase Flow Group Meeting. Ispra, pp. 485–492.

Gnielinski V., 1975. New equations for heat and mass transfer in the turbulent flow in pipes and channels. Forschung im Ingenieurwesen 41, 8–16.

Granryd, E., 2001. Hydrocarbons as refrigerants — an overview. International Journal of Refrigeration 24, 15–24.

Gungor, K.E., Winterton, R.H.S., 1986. A general correlation for flow boiling in tubes and annuli. International Journal of Heat and Mass Transfer 29, 351–358.

ISO, 1993. Guide to Expression of Uncertainty in Measurement.

Kandlikar, S.G., 1990. A General Correlation for Saturated Two-Phase Flow Boiling Heat Transfer Inside Horizontal and Vertical Tubes. Journal of Heat Transfer 112, 219.

Kim, S.-M., Mudawar, I., 2014. Review of databases and predictive methods for heat transfer in

condensing and boiling mini/micro-channel flows. International Journal of Heat and Mass Transfer 77, 627–652.

Lee, H.S., Yoon, J.I., Kim, J.D., Bansal, P., 2005. Evaporating heat transfer and pressure drop of hydrocarbon refrigerants in 9.52 and 12.70mm smooth tube. International Journal of Heat and Mass Transfer 48, 2351–2359.

Li, W., Wu, Z., 2010. A general criterion for evaporative heat transfer in micro/mini-channels. International Journal of Heat and Mass Transfer 53, 1967–1976.

Lillo, G., Mastrullo, R., Mauro, A.W., Viscito, L., 2018. Flow boiling heat transfer, dry-out vapor quality and pressure drop of propane (R290): Experiments and assessment of predictive methods. International Journal of Heat and Mass Transfer 126, 1236–1252.

Liu, Z., Winterton, R.H.S., 1991. A general correlation for saturated and subcooled flow boiling in tubes and annuli, based on a nucleate pool boiling equation. International Journal of Heat and Mass Transfer 34, 2759–2766.

Longo, G.A., Mancin, S., Righetti, G., Zilio, C., 2017. Hydrocarbon refrigerants HC290 (Propane) and HC1270 (Propylene) low GWP long-term substitutes for HFC404A: A comparative analysis in vaporisation inside a small-diameter horizontal smooth tube. Applied Thermal Engineering 124, 707–715.

Müller-Steinhagen, H., Heck, K., 1986. A simple friction pressure drop correlation for two-phase flow in pipes. Chemical Engineering and Processing: Process Intensification 20, 297–308.

Pamitran, A.S., Choi, K.-I., Oh, J.-T., Hrnjak, P., 2010. Characteristics of two-phase flow pattern transitions and pressure drop of five refrigerants in horizontal circular small tubes. International Journal of Refrigeration 33, 578–588.

Shah, M.M., 1982. Chart correlation for saturation boiling heat transfer: Equation and further study. ASHREA Transactions 88.

Shin, J.Y., Kim, M.S., Ro, S.T., 1997. Experimental study on forced convective boiling heat transfer of pure refrigerants and refrigerant mixtures in a horizontal tube. International Journal of Refrigeration 20, 267–275.

Sun, L., Mishima, K., 2008. Evaluation analysis of prediction methods for two-phase flow pressure drop in mini-channels. International Journal of Multiphase Flow 35, 47–54.

Thome, J.R., Cheng, L., Ribatski, G., Vales, L.F., 2008. Flow boiling of ammonia and hydrocarbons: A state-of-the-art review. International Journal of Refrigeration 31, 603–620.

Tran, T.., Chyu, M.-C., Wambsganss, M.., France, D.., 2000. Two-phase pressure drop of refrigerants during flow boiling in small channels: an experimental investigation and correlation development. International Journal of Multiphase Flow 26, 1739–1754.

Tran, T.N., Wambsganss, M.W., France, D.M., 1996. Small circular- and rectangular-channel boiling with two refrigerants. International Journal of Multiphase Flow 22, 485–498.

Wang, S., Gong, M.Q., Chen, G.F., Sun, Z.H., Wu, J.F., 2014. Two-phase heat transfer and pressure drop of propane during saturated flow boiling inside a horizontal tube. International Journal of Refrigeration 41, 200–209.

Wen, M.-Y., Ho, C.-Y., 2005. Evaporation heat transfer and pressure drop characteristics of R-290 (propane), R-600 (butane), and a mixture of R-290/R-600 in the three-lines serpentine small-tube bank. Applied Thermal Engineering 25, 2921–2936.

Xu, Y., Fang, X., 2012. A new correlation of two-phase frictional pressure drop for evaporating flow in pipes. International Journal of Refrigeration 5, 2039–2050.

Manuscript ID: 61
DOI: 10.18462/iir.icr.2019.0061

Gas Supersonic Ejector Performance with Droplet Injection: a combined CFD and Thermodynamic modelling approach

Sergio CROQUER[(a)], Sébastien PONCET[(a)], Zine AIDOUN[(b)]
[(a)] Université de Sherbrooke, Faculté de génie, Département de génie mécanique,
2500 Boulevard de l'Université, Sherbrooke (QC), J1K 2R1, Canada
Sergio.Croquer@USherbrooke.ca
[(b)] CETC-Varennes, Natural Resources Canada,
P.O. Box 4800, 1615 Boulevard Lionel Boulet, Varennes (QC), J3X 1S6, Canada

ABSTRACT

The variations in limiting pressure and efficiency of supersonic ejectors when droplets are injected in the vapour core before the diffuser were assessed numerically. Results of a CFD and a thermodynamic model were used for a combined global and local perspective. In comparison with experimental data of a R134a ejector under typical refrigeration conditions, the CFD model predicts the double-choke entrainment ratio with an accuracy of 5% and the thermodynamic model has a deviation of about 18% (Resp. 2.5%) in terms of double-choke entrainment ratio (Resp. limiting pressure). Both models are in excellent agreement in terms of pressure, Mach number and temperature internal profiles. Results show that, for an injection fraction of 10%, the peak pressure in the shock train is reduced by 31%. Nonetheless, the net effect is a reduction of the exergy contained in the main gas as other factors (e.g.: lower main gas temperature) are introduced.
Keyword: Refrigeration, Supersonic Ejector, Exergy, Energy Efficiency, CFD.

1. INTRODUCTION

Ejector based refrigeration systems have risen a lot of interest in recent years, given their potential for a higher COP and lower environmental footprint over the standard cycles (Besagni et al., 2016). The central component in these systems is the supersonic ejector, which uses the thermal energy of a primary flow to entrain and compress a secondary flow. The mixture usually occurs at supersonic conditions and, after a series of shocks, is compressed in a diffuser to the outlet pressure. They are known for their simple operation, low operational costs and maintenance requirements, as well as the capacity to work in single- and two-phase conditions (Chunnanond and Aphornratana, 2004). In most ejector based refrigeration systems, this device is used to substitute the compressor or recover the exergy usually lost across the throttling stage (Lawrence and Elbel, 2015). Thus, the cycle performance is linked to that of the supersonic ejector, usually represented by the entrainment and compression ratios, respectively, the ratios of secondary to primary mass flow rates and outlet to secondary inlet static pressures. Many studies have been carried out in the last decade, with the objective of improving the ejector performance. The reader is referred for example to the review of Besagni et al. (2016). Hence, there is a general understanding of the behaviour of ejectors and the influence of the geometry and operating conditions on its performance. With objective of making ejector based cycles more competitive, attention now has focused on specific issues, one of which is the injection of droplets in gas supersonic ejectors. Al-Ansary and Jeter (2004) proposed that droplets injected with the primary flow may reduce the velocity mismatch in the mixing region. They tested this assumption on an air ejector and did not find any noticeable changes in the double-choke region, i.e. when both inlet flows are sonic throughout and the mass flow rates are independent of the outlet conditions. In single-choke, the secondary mass flow rate increased up to 98% for inlet air humidity between 4.3% and 11.2%. The same behaviour was observed on a similar installation when the primary inlet air humidity was 1% (Hemidi et al., 2009). It should be noted that in both cases the ejector was installed as an independent unit and the air-water fluid pair is uncommon for refrigeration systems. Little and Garimella (2016) applied a similar approach on an R134a ejector and observed

a reduction of 8% in entrainment ratio with the increase of motive inlet vapor fraction. An alternative location for droplet injection is the constant area section (CAS). In this position, the objective is to reduce the intensity of the shock train occurring at the start of the diffuser, which has been pointed out (identified?) as a major source of exergy losses (Banasiak et al., 2014). At the contact with a shock wave, droplets deform and break up, cooling the carrier gas and reducing its velocity, thus mitigating the passing shock wave (Jourdan et al., 2010). A recent thermodynamic model by Croquer et al., 2017 studied this phenomenon in the context of an R134a ejector for droplet injection fractions of up to 10%. Although the pressure jump across the shock was reduced by 8%, the limiting double-choke pressure (the maximum compression ratio in double-choke regime) and the exergy efficiency were reduced by, respectively, 5% and 15%. Nonetheless, given the global character of the model, no reasons are given for this behaviour. This study presents a RANS model using the Eulerian-Lagrangian approach to provide further insight on the changes in the ejector main flow structure as droplets are injected in the CAS.

2. NUMERICAL MODELING

2.1. Baseline Conditions

Four cases are compared in this study, the baseline case (no droplet injection) and three injected mass fractions of 1%, 5% and 10% relative to the primary mass flow rate. The baseline case data are extracted from the experimental work of García del Valle et al. (2014), who analyzed the global performance of three R134a ejector designs at typical refrigeration conditions. The study provides great detail about the geometry and uses operating conditions which ensure single-phase gas flow throughout the device. Case A, with a straight mixing section design, was chosen in this study. A schematic view of the ejector geometry and its dimensions are given in Figure 1 and Table 1, respectively. Across all cases, the ejector operating conditions were as shown in Table 2.

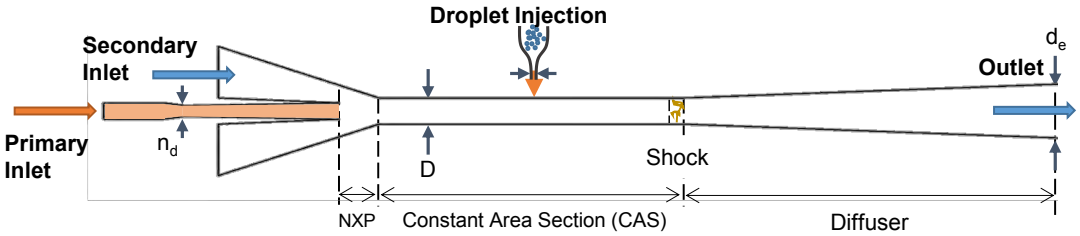

Figure 1: Schematic geometry of the ejector.

Table 1: Ejector main dimensions

Parameter	Value
Primary Nozzle Throat Diameter, n_d (mm)	2.00
Primary Nozzle Exit Diameter, d (mm)	3.00
Nozzle Exit Position, NXP (mm)	-5.38
Mixing Chamber Diameter, D (mm)	4.80
Constant Area Section Length, L_{CAS} (mm)	41.39
Diffuser Exit Diameter, d_e (mm)	20.00

Table 2: Ejector Operating Conditions.

Parameter	Value
Primary inlet total pressure (kPa)	2888.83
Primary inlet total temperature (ºC)	94.39
Secondary inlet total pressure (kPa)	414.61
Secondary inlet total temperature (ºC)	20.00
Outlet static pressure (kPa)	826.57
Experimental double-choke entrainment ratio (-)	0.398
Experimental maximal compression ratio (-)	1.994

Droplet effects are numerically assessed by considering their injection at halfway through the CAS. This ensures that they are inserted before the start of the shock train (as observed in the baseline case) while minimizing disruptions to the mixing shear layer. Droplets are injected in a direction normal to the ejector axis, with an injection diameter of 0.5mm and a temperature of -13ºC. The injection temperature was chosen to avoid vapor phase at the average pressure observed in the CAS in the baseline case.

2.2. Numerical Model

The local effects of droplet injection into the ejector flow field were studied using an Eulerian-Lagrangian approach. The continuous phase (main gas flow) was modeled as a 2D axisymmetric and compressible flow, with the numerical setup based on a previous RANS benchmark study (Croquer et al., 2016). The droplets, which conform the discrete phase, are considered as spherical particles with two-way momentum and thermal energy coupling.

2.2.1 Main gas (continuous phase)

The main gas flow is computed using an Eulerian approach, wherein the flow variables are determined by numerically solving the conservation equations for mass, momentum and total energy over the computational domain, which comprehends (covers?) half of the ejector geometry shown in Figure 1, with a symmetry condition imposed along the axial centerline. For spatial discretization, a mesh conformed by 645000 tetrahedral elements was used, with local size refining in the shear layer, near walls and shock train regions. In particular, a logarithmic grow function was imposed on the first 20 wall adjacent layers in order to accurately capture the boundary layer profiles. The average dimensionless wall coordinate is 0.79. For all cases, total pressure and total temperature were prescribed at the inlets, static pressure was imposed at the outlet and walls were considered as non-slip and adiabatic. The operating pressure and temperature conditions are summarized in

Table 2**.** The fluid properties were determined using the REFPROP 7.0 equation database which, for R134a, uses a formulation based on the Helmholtz free energy equation of state and accurately determines the real gas behaviour in the range 170 K to 455 K and up to 70 MPa (Baher and Tillner-Roth, 1994). Turbulent effects were accounted for using the k-ω SST turbulence model of Menter (1994) in its low Reynolds formulation, which adds additional damping to the k and ω transport equations in the wall adjacent region. The combination of the REFPROP 7.0 equation database and the k- ω SST low Reynolds turbulence model was shown to better capture the internal ejector flow structure and determine the entrainment ratio with an accuracy of about 5% relative to experimental values (Croquer et al., 2016).

2.2.2 Droplet injection (discrete phase)

Droplets were modeled as spherical particles of variable diameter having two-way momentum and energy coupling with the main flow. Their effects on the main flow were determined using a Lagrangian approach, i.e., their trajectories and temperature are calculated by integrating force and energy balances for each particle, from their origin at injection until their end by either breakage or leaving the domain. In this study, only total drag and convection heat transfer are considered as acting mechanisms on the particles. The drag coefficient is determined as a parametric function of the particle Reynolds number using the correlation of Morsi and Alexander (1972). The local convection heat transfer coefficient is calculated using the correlation of Ranz and Marshall (1952). At each discrete phase time step, momentum and thermal energy changes for each particle entering and leaving a computational cell are computed and the results added as source terms to the conservation equations for the continuous phase. These correlations are indirectly dependent on the droplet diameter (via the exchange surface area), which varies with breakage. Droplet breakage is modelled using the WAVE approach of Reitz (1987), which uses stability analysis to determine the break up conditions for a given droplet. This approach is suitable for Weber numbers > 100. Based on the injection and main flow gas conditions, the Weber number in this study is well over 1000. After breakage, daughter droplets inherit the thermodynamic properties and velocity from their mother droplet.

2.3. Flow Solver

The system of governing equations for the Eulerian phase was resolved using the commercial software ANSYS FLUENT v.15 via the finite volume technique. The advective terms were discretized using a second-order upwind scheme, except for the pressure equation where the PRESTO! scheme was used. A 2nd order central difference scheme was used for the diffusive terms. High-order term relaxation was applied to all equations to improve smoothness. The algebraic system was resolved with a pressure-based algorithm and full pressure-velocity coupling, which has been applied successfully in previous RANS studies of single- and two-phase supersonic ejectors (Li and Li, 2011; Yazdani et al., 2012; Zhu and Jiang, 2014). Simulations were initialized with a perfect gas solution on the same mesh as the final calculation and without any droplet injection. The fully developed gas flow solution without any injection was used as initialization for the cases comprising droplets. The ordinary differential equations describing droplets trajectory and temperature are integrated every 10 main-flow iterations using a semi-implicit trapezoidal method. At each discrete phase time step, momentum and thermal energy changes for each particle entering and leaving a computational cell are computed and the results added as source terms to the conservation equations for the continuous phase. The initial condition for the particle clusters (velocity, temperature and diameter) is introduced using a point-injection approach on the domain boundary as shown in Figure 1. Convergence was defined as RMS residuals under $1x10^{-4}$ for all equations plus stable values of mass flow and temperature across all boundaries. Calculations were carried out using a personal workstation with 32GB of RAM and a 4 core 3.40 GHz CPU. In average, each computation took about 180 minutes.

3. RESULTS AND DISCUSSION

3.1. Comparison between the RANS and Thermodynamic models

The capacity of the presented RANS model in determining the continuous phase characteristics has been validated against the experimental data of García del Valle et al., 2014. The results, which can be found in Croquer et al. (2016), show a very good agreement, with a deviation of 5% and 1.3% respectively for the double-choke entrainment ratio and limiting compression ratio. Concerning droplet injection, to the best of the authors' knowledge there is no available experimental data for cross-flow injection of liquid in a similar configuration to the assessed ejector. Figure 2 depicts a comparison of centreline profiles obtained using the RANS model with cross sectional values of pressure, temperature and Mach number, as determined with the thermodynamic model of Croquer et al., 2017 for the case with 10% injection fraction. The thermodynamic model determines the ejector performance for given geometry and operating conditions and different injection fractions. It showed an 18% deviation versus experimental entrainment ratio data for single- and two-phase conditions. In general, both models predict essentially the same flow behavior, particularly the pressure profiles. Two important differences are observed. The first one on the Mach number at position L6, where the thermodynamic model assumes subsonic flow while the RANS model captures the shock train extending into the diffuser. The second one concerns the temperature at position L7, the RANS higher exit temperature probably stems from neglecting vaporization effects, which are indirectly accounted for in the thermodynamic model.

3.2. Changes in CAS flow structure with droplet injection

Fig. 3 depicts the pressure field through the ejector CAS together with black iso-lines denoting Ma=1 for the four assessed cases. The train shock structure is clearly visible. No noticeable changes are observed for the lowest injection fraction (1%) in relation to the baseline case. At 5%, small disturbances are observed near the walls, right after the injection position. These are marked by a small bump in the iso-lines, as well as the generation of oblique waves earlier in the CAS. Nonetheless, at this condition the main flow momentum is capable of maintaining the structure and the shock onset position is similar to that for the baseline and 1% cases. At 10%, the increased injection triggers boundary layer detachment, as revealed by the changes in the near wall iso-lines.

This in turns provokes an earlier shock train onset. Moreover, the first cell peak values of the pressure are 1175.8 kPa, 1250.1 kPa, 1494.7 kPa and 810.75 kPa, respectively for the baseline, 1%, 5% and 10% injection fractions. Thus, at injected fractions of 1% and 5% the peak pressure is intensified. Although this seems to contradict the thermodynamic model results, it must be noted that the latter reports averaged results before and after the shock. At the 10%, the pressure peak is reduced by 31%. This suggests that the associated reduction in shock intensity is related with the earlier start of the shock train. A further remark is that in the RANS model setup the outlet pressure is prescribed, which could restrain the shock onset position as well as the overall pressure profile.

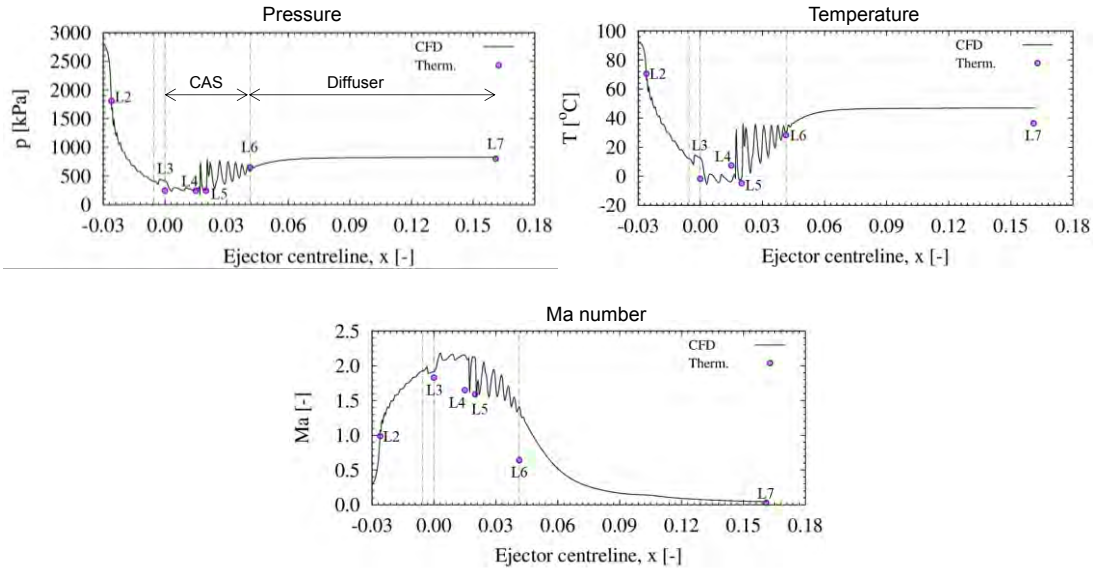

Figure 2: Comparison of pressure, temperature and Mach profiles at centreline obtained with the RANS model versus the results of the thermodynamic model of Croquer et al. 2017. Results for an injected fraction of 10%.

3.3. Changes in exergy profiles with droplet injection

Figure 4 shows exergy profiles along the centreline of the ejector for all assessed conditions. These are identical, up to the point of injection where a sudden exergy drop is observed with increasing injection fraction. This destruction is transported by the flow such that the outlet exergy is lower. A global accounting of these effects shows that, in these conditions, exergy efficiency reduces up to 15% with 10% droplet injection fraction. Furthermore, local exergy destruction also implies an entropy increase with injection, which supports the observations made in Croquer et al. (2017) about the lower limiting compression ratio when droplets are injected: this parameter is limited by the second law imposition that the outlet entropy rate must be higher than the inlet entropy rate (Galanis and Sorin, 2016). Thus, as droplets are injected, the minimum outlet entropy and the associated outlet pressure also increase.

With the objective of determining the reasons behind the exergy destruction, the entropy generation term was determined following the definition given by Lamberts et al. (2017):

$$Local\ Entropy\ Generation = \tau_{ij}^{t} \frac{\partial u_i}{\partial x_j} - q_j^{t} \frac{\partial T}{\partial x_j} \qquad \text{(Eq. 1)}$$

where $\boldsymbol{\tau_{ij}^{t}}$ and $\boldsymbol{q_j^{t}}$ are, respectively, the total (viscous + turbulent) stress tensor and heat flux vector. The comparison between the baseline and 10% injection cases is shown in Figure 5. Across both fields there is a series of cells corresponding to the shock train which, in the case with injection has an earlier start. For this case an important source of losses is observed at the point where the main flow first meets the droplets. However, since the shock intensity is mitigated, the associated losses through the shock train are less important in comparison with the baseline case. In fact, after integration over the surface shown in Figure 5, the total entropy generation in the case with 10% droplet injection is 7% lower than the baseline case. Thus a different mechanism might be in place

to reduce exergy. A possibility is the gas cooling down because of the low droplet temperature. To verify this, Figure 6 shows the temperature field after injection for the baseline and 10% cases, the main flow average temperature at the diffuser inlet reduces from 40ºC in the baseline case to 34ºC at 10% injection. This implies a lower useful energy potential for the outlet gas and hence a lower outlet exergy.

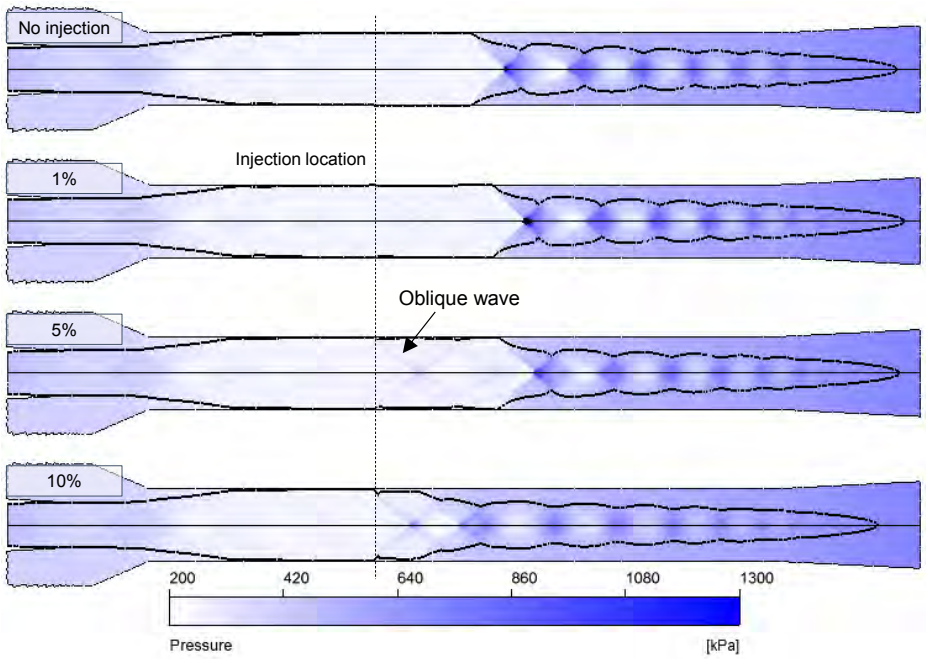

Figure 3: Static pressure field and Ma=1 iso-lines through the CAS of the ejector for different injection fractions.

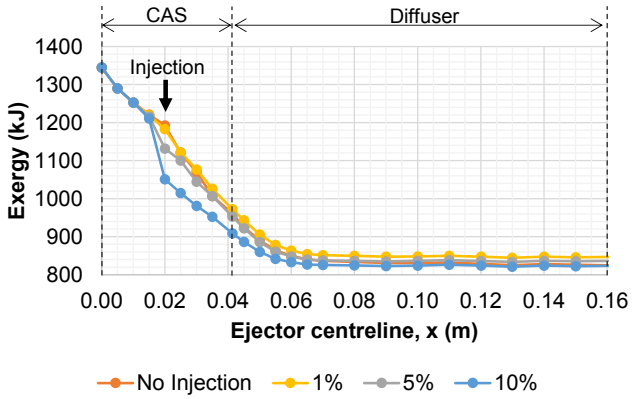

Figure 4: Exergy profiles through the ejector. Averaged values obtained at various flow cross sections.

4. CONCLUSIONS

The effect of droplet injection in the CAS of a gaseous R134a supersonic ejector has been assessed by implementing an Eulerian-Lagrangian approach in a RANS model. The results provide further insight on the reasons behind the performance detriment with the droplet injection reported in a previous thermodynamic model (Croquer et al., 2017). In particular, it is observed that for lower injection fractions (1% and 5%), there are no noticeable changes in the shock onset position but the peak pressure is almost doubled. At the highest fraction (10%), the peak pressure is diminished by 31% and the shock train starts earlier in the CAS. Furthermore, exergy profiles show a reduction in this quantity with droplet injection. Losses and temperature contours suggest that this drop is mainly associated with a reduction in the main gas temperature.

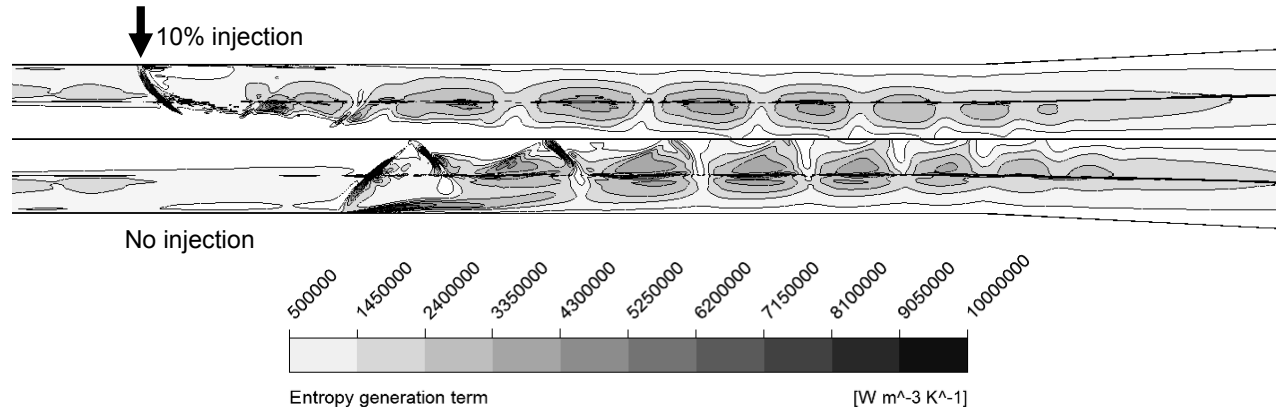

Figure 5: Contours of exergy losses source terms after droplet injection. Comparison between the baseline and 10% injection cases.

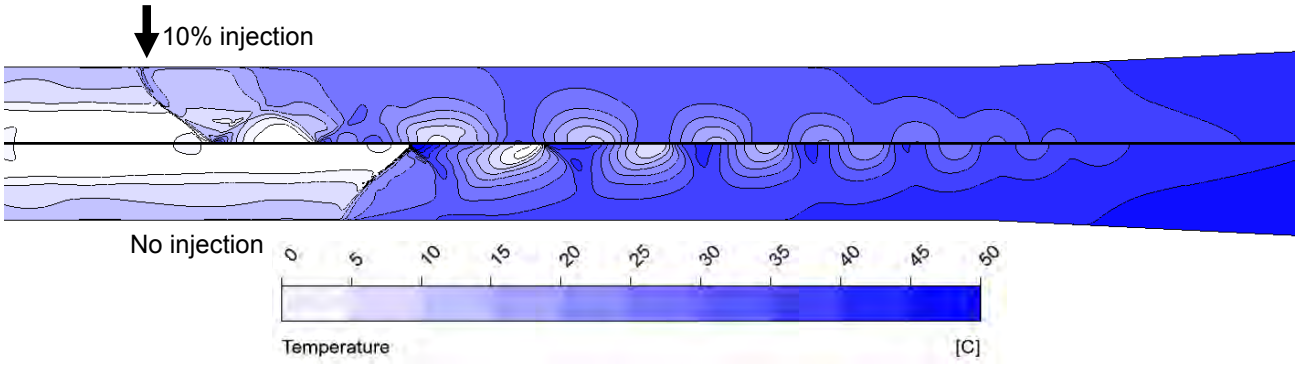

Figure 6: Contours of temperature after droplet injection. Comparison between the baseline and 10% injection cases.

ACKNOWLEDGEMENTS

This project is part of the research program of the Industrial NSERC Chair on Industrial Energy Efficiency, established at Université de Sherbrooke in 2014, with the support of Hydro-Québec, Canmet-Energie, Rio Tinto Alcan and the Natural Sciences and Engineering Research Council of Canada.

NOMENCLATURE

CAS	Constant area section	NXP	Nozzle exit position (mm)
COP	Coefficient of performance	p	Static pressure (kPa)
d	Primary nozzle exit diameter (mm)	q_j^t	Total heat flux in the j-direction (W.m^2)
D	Constant area section diameter (mm)	T	Temperature (^{o}C)
d_e	Diffuser exit diameter (mm)	u_i	Velocity in the i-direction (m.s^{-1})
k	Turbulence kinetic energy (m^2.s^{-2})	x	Axial coordinate (m)
L_{CAS}	Constant area section length (mm)	τ_{ij}^t	Total stress tensor component (Pa)
Ma	Mach number (-)	ω	Turbulent specific dissipation rate (s^{-1})
n_d	Primary nozzle throat diameter (mm)		

REFERENCES

Al-Ansary, H., Jeter, S., 2004. Numerical and Experimental Analysis of Single-Phase and Two-Phase Flow in Ejectors. HVAC&R Res. 10, 521–538.

Baher, H.D., Tillner-Roth, R., 1994. An international Standard Formulation for the Thermodynamic Properties of 1,1,1,2-tetrafluoroethane (HFC-134a) for Temperatures From 170K to 455K and Pressures up to 70MPa. J. Phys. Chem. Ref. Data 23, 657–729.

Banasiak, K., Palacz, M., Hafner, A., Buliński, Z., Smołka, J., Nowak, A.J., Fic, A., 2014. A CFD-based investigation of the energy performance of two-phase R744 ejectors to recover the expansion work in refrigeration systems: An irreversibility analysis. Int. J. Refrig. 40, 328–337.

Besagni, G., Mereu, R., Inzoli, F., 2016. Ejector refrigeration: A comprehensive review. Renew. Sustain. Energy Rev. 53, 373–407.

Chunnanond, K., Aphornratana, S., 2004. Ejectors: applications in refrigeration technology. Renew. Sustain. Energy Rev. 8, 129–155.

Croquer, S., Poncet, S., Aidoun, Z., 2016. Turbulence modeling of a single-phase R134a supersonic ejector. Part 1: Numerical benchmark. Int. J. Refrig. 61, 140–152.

Croquer, S., Poncet, S., Aidoun, Z., 2017. Thermodynamic modelling of supersonic gas ejector with droplets. Entropy 19, 1–21.

Galanis, N., Sorin, M., 2016. Ejector design and performance prediction. Int. J. Therm. Sci. 104, 315–329.

García del Valle, J., Sáiz Jabardo, J.M., Castro Ruiz, F., San José Alonso, J., 2014. An experimental investigation of a R-134a ejector refrigeration system. Int. J. Refrig. 46, 105–113.

Hemidi, A., Henry, F., Leclaire, S., Seynhaeve, J.-M., Bartosiewicz, Y., 2009. CFD analysis of a supersonic air ejector. Part I: Experimental validation of single-phase and two-phase operation. Appl. Therm. Eng. 29, 1523–1531.

Jourdan, G., Biamino, L., Mariani, C., Blanchot, C., Daniel, E., Massoni, J., Houas, L., Tosello, R., Praguine, D., 2010. Attenuation of a shock wave passing through a cloud of water droplets. Shock Waves 20, 285–296.

Lamberts, O., Chatelain, P., Bartosiewicz, Y., 2017. New methods for analyzing transport phenomena in supersonic ejectors. Int. J. Heat Fluid Flow 64, 23–40.

Lawrence, N., Elbel, S., 2015. Analysis of two-phase ejector performance metrics and comparison of R134a and CO_2 ejector performance. Sci. Technol. Built Environ. 21, 515–525.

Li, C., Li, Y.Z., 2011. Investigation of entrainment behavior and characteristics of gas–liquid ejectors based on CFD simulation. Chem. Eng. Sci. 66, 405–416.

Little, A.B., Garimella, S., 2016. Shadowgraph visualization of condensing R134a flow through ejectors. Int. J. Refrig. 68, 118–129.

Menter, F.R., 1994. Two-equation eddy-viscosity turbulence models for engineering applications. AIAA J. 32, 1598–1605.

Morsi, S.A., Alexander, A.J., 1972. An Investigation of Particle Trajectories in Two-Phase Flow Systems. J. Fluid Mech. 55, 193–208.

Ranz, W.E., Marshall, W.R., 1952. Evaporation from Drops. Chem. Eng. Prog. 48, 141–146.

Reitz, R.D., 1987. Modeling Atomization Processes in High-Pressure Vaporizing Sprays. At. Sprays Technol. 3, 309–337.

Yazdani, M., Alahyari, A. a., Radcliff, T.D., 2012. Numerical modeling of two-phase supersonic ejectors for work-recovery applications. Int. J. Heat Mass Transf. 55, 5744–5753.

Zhu, Y., Jiang, P., 2014. Experimental and analytical studies on the shock wave length in convergent and convergent–divergent nozzle ejectors. Energy Convers. Manag. 88, 907–914.

Manuscript ID: 76
DOI: 10.18462/iir.icr.2019.0076

Quasi-steady-state simulation of the on-off behaviour of household refrigerators: A self-tuning approach

Guilherme Z. SANTOS[(a)], Adriano F. RONZONI[(b)], Christian J.L. HERMES[(a)]

[(a)] POLO Labs, Department of Mechanical Engineering, Federal University of Santa Catarina
88040900 Florianópolis, SC, Brazil, hermes@polo.ufsc.br
[(b)] Embraco Compressors
89219901 Joinville, SC, Brazil

ABSTRACT

A self-tuning semi-empirical model for the transient simulation of domestic refrigerators is presented in this paper. The model is based on a quasi-steady approach, where the time variations associated with the thermal inertia of the refrigerated compartments and heat exchangers (condenser and evaporator) are considered, whereas the refrigeration loop is modelled assuming steady-state conditions. The model was coded in *Modelica* language and validated against experimental data obtained for two different refrigerator platforms namely, natural-draft all-refrigerator and fan-and-damper top-mount (Combi) refrigerator. Additionally, a self-tuning method was put forward to identify the values of the model closing parameters, such as thermal conductances and capacities. When compared with experimental data obtained in-house, an agreement between model predictions and experimental counterparts within ±10% error bands for the power consumption, and within ±1°C thresholds for the compartment air temperatures can be observed. Taking as reference an Intel® Core™ i5 7th generation processor, it is possible to simulate 3 h of cycling operation in 15 s of CPU.

Keywords: Transient simulation, Quasi-steady modelling, Semi-empirical, Self-tuning, On-Off

1. INTRODUCTION

According to the International Institute of Refrigeration, nearly 17% of the electric energy produced worldwide is consumed by refrigeration systems, being 45% of which due to the residential sector, so that household refrigerators and freezers respond for fairly 8% of the global electric energy consumption (Coulomb *et al.*, 2015). As a consequence, governments around the globe have adopted stringent labelling policies, leading manufactures towards highly efficient appliances achieved by means of super-insulated cabinets (e.g., vacuum insulating panels), nonconventional cycle architectures (e.g., multiple evaporators) and intelligent control strategies (e.g., variable-speed compressors).

Regardless of the refrigerator complexity, it has been advocated that system simulation can be a handy tool for decision making in the design of less costly, energy-efficient refrigerators, additionally reducing the number of prototypes and experiments needed. Essentially, two modelling approaches can be adopted for the system simulation namely, steady-state and transient. The former is usually adopted for component matching (Gonçalves *et al.*, 2009), and also to tackle with competing effects such as component-level heat versus friction, and system-level energy versus cost trade-offs (Negrão and Hermes, 2011). Transient simulation models, on the other hand, are crucial for assessing off-design conditions, such as start-up and shut-down pressure peaks (Hermes *et al.*, 2008), developing control strategies for capacity control (Schurt *et al.*, 2009) and defrosting operations (Borges *et al.*, 2015), and evaluating complex cycle architectures, such as those with multiple evaporators. In such cases, the model is called fully transient.

Despite their high mathematical complexity, which bears high computational cost, fully transient models can handle both mass migration inside the refrigeration loop (fast transients) and refrigerated compartment temperature evolution (slow transients). In the cases where the time constant of the refrigeration cycle is much lower than that of the refrigerated compartments, the former can be treated as steady-state while the latter is still modelled as transient (Borges *et al.*, 2011). In spite of

neglecting the mass migration effects, quasi-steady models can properly simulate the refrigerator behaviour in on-off regime demanding a much lower computational effort than a transient model.

A drawback lies in identifying the closing parameters, such as conductances and thermal capacities, which must be fed to the model. This work addresses this issue by introducing a self-tuning method to gather automatically the closing parameters from experimental data. In this paper, two different refrigerators have been investigated, a natural-draft all-refrigerator and a forced-convection top-mount refrigerator, both designed for the Brazilian market and, therefore, running with R134a. In both cases, the refrigerant loop follows an Evans-Perkins cycle with an internal heat exchanger, as depicted in Fig. 1, using a wire-and-tube condenser at the rear wall.

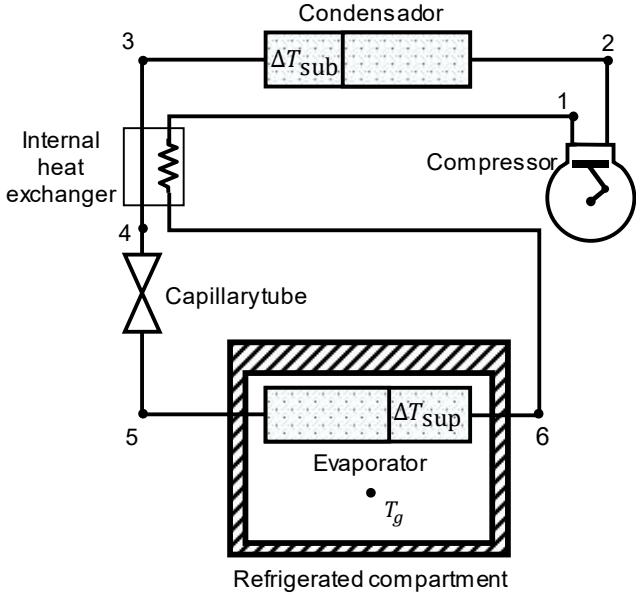

Figure 1: Schematic of the refrigeration loop

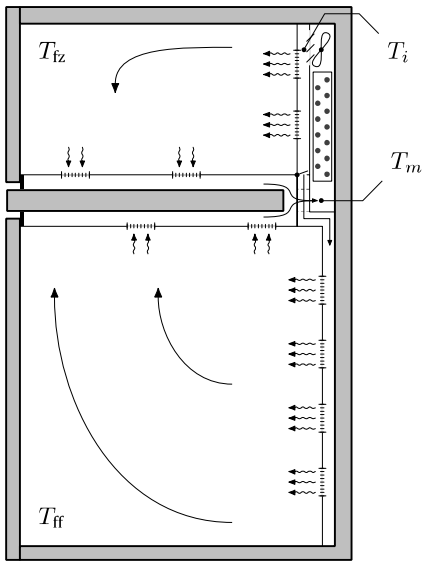

Figure 2: Schematic of the Combi refrigerator

2. MATHEMATICAL MODELLING

2.1. Refrigeration loop

According to Borges *et al.* (2011), the quasi-steady approach relies on the assumption that the time constant of the refrigeration system is much smaller than that of the cabinet, so that the first can be modelled in steady-state, meaning that the mass flow rate of refrigerant is uniform along the refrigeration loop at a given time (see Fig. 1). In addition, noting that mass inventory and refrigerant flow through the capillary tube tend to introduce strong non-linearities into the model, generating instabilities in the computation of the working pressures, Gonçalves *et al.* (2009) proposed to replace those equations by prescribing the superheating, ΔT_{sup}, and subcooling, ΔT_{sub}, degrees respectively at the evaporator and condenser outlets, so that their respective enthalpies are as follows:

$$h_3 = h(p_c, T_c - \Delta T_{\mathrm{sub}}) \quad \text{Eq. (1)}$$

$$h_6 = h\left(p_e, T_e + \Delta T_{\mathrm{sup}}\right) \quad \text{Eq. (2)}$$

By neglecting the energy accumulation in the refrigerant flow, the energy balances in the evaporator and condenser respectively yield,

$$UA_{\mathrm{int,e}}\left(T_{\mathrm{w,e}} - T_e\right) = \dot{m}(h_6 - h_5) \quad \text{Eq. (3)}$$

$$UA_{\mathrm{int,c}}\left(T_c - T_{\mathrm{w,c}}\right) = \dot{m}(h_2 - h_3) \quad \text{Eq. (4)}$$

where the sub-index ‘e’ refers to the evaporator and ‘c’ to the condenser walls, respectively. Applying the same reasoning to the compressor, an energy balance yields

$$h_2 = h_1 + \left(\dot{W}_k - \dot{Q}_k\right)/\dot{m} \quad \text{Eq. (5)}$$

The mass flow rate displaced by the compressor and the compression power are obtained from the following semi-empirical model (Santos *et al.*, 2019):

$$\dot{W}_k = \dot{m}\{a_0 T_1[(p_c/p_e)^{a_1} - 1] + a_2\} \quad \text{Eq. (6)}$$

$$\dot{m} = N p_e\{b_0 - b_1[(p_c/p_e)^{b_2} - 1]\}T_1 \quad \text{Eq. (7)}$$

where N is the operating frequency of the compressor and the coefficients $a_{0..2}$ and $b_{0..2}$ are fitted using calorimeter data. It is worth of note that the heat released by the compressor, $\dot{Q}_k$, is embedded in a_2, such that $\dot{Q}_k = \dot{m}a_2$.The heat exchange between the suction line and the capillary tube is solved by means of the heat exchanger effectiveness, ε_x, defined as follows:

$$\varepsilon_x = (T_1 - T_6)/(T_3 - T_1) \quad \text{Eq. (8)}$$

The enthalpy at the evaporator inlet is obtained from an energy balance in the heat exchanger:

$$h_1 - h_3 = h_6 - h_5 \quad \text{Eq. (9)}$$

Despite of the negligible energy accumulation in the refrigerant-side, the condenser and evaporator walls, on the other hand, have non-negligible thermal inertia due to their metallic masses. Thus, an energy balance in the heat exchangers walls provides the following evolving equation:

$$C_{\mathrm{w}} \frac{dT_{\mathrm{w}}}{dt} = UA_{\mathrm{ext,w}}(T_a - T_{\mathrm{w}}) + UA_{\mathrm{int,w}}(T_{\mathrm{ref}} - T_{\mathrm{w}}) \quad \text{Eq. (10)}$$

where C_{w} is the thermal capacity, T_a is the temperature of the surrounding air, T_{ref} the refrigerant temperature, and T_{w} is the average temperature of the heat exchanger wall ('e' for evaporator and 'c for condenser). Since the refrigerant flow in both the evaporator and condenser takes place with phase change, the internal conductance of the exchanger is much greater than the external one, the following approximation $UA_{\mathrm{int,w}} \approx 100UA_{\mathrm{ext,w}}$ was adopted in the present work.

2.2. Refrigerated compartment

2.2.1. All refrigerator

A 230-litre all-refrigerator comprised of a natural-draft plate-type roll-bond evaporator on the backwall was firstly assessed. This refrigerator is controlled by a thermostat placed inside the refrigerated compartment, which turns the compressor on and off keeping the compartment temperature in the desired range. To close the equation set, an evolving equation for the compartment air temperature is still needed, which can be obtained from the following energy balance

$$C_g \frac{dT_g}{dt} = UA_g\left(T_{\mathrm{amb}} - T_g\right) - UA_{\mathrm{ext,e}}\left(T_{\mathrm{w,e}} - T_g\right) + \dot{W}_g \quad \text{Eq. (11)}$$

where C_g is the thermal capacity of the air and $\dot{W}_g$ is the power dissipated inside the refrigerated compartment ($\dot{W}_g \approx 0$ in the present study). At all, the model has 7 closing parameters: $C_g, C_e, UA_e, C_c, UA_c, UA_g$ and ε to be obtained from experimental tests.

2.2.2. Combi refrigerator

A 440-litre frost-free top-mount fan-and-damper refrigerator was also assessed in the present work. A thermostat-driven damper is used to control the air flow rate to each of the two compartments, as shown in Fig. 2, whereas a second thermostat, located in the frozen-food compartment, turns the compressor on and off. The relationship between the thermostat temperature, the damper position and the airflow to fresh- and frozen-food compartments must be devised in order determine both compartment temperatures, which are obtained from the following evolving equations obtained from energy balances in the refrigerated compartments,

$$C_{\mathrm{fz}} \frac{dT_{\mathrm{fz}}}{dt} = UA_{\mathrm{fz}}(T_{\mathrm{amb}} - T_{\mathrm{fz}}) + \rho c_p \dot{V}\phi(T_i - T_{\mathrm{fz}}) + UA_m(T_{\mathrm{ff}} - T_{\mathrm{fz}}) + \dot{W}_{d,\mathrm{fz}} \quad \text{Eq. (12)}$$

$$C_{\mathrm{ff}} \frac{dT_{\mathrm{ff}}}{dt} = UA_{\mathrm{ff}}(T_{\mathrm{amb}} - T_{\mathrm{ff}}) + \rho c_p \dot{V}(1-\phi)(T_i - T_{\mathrm{ff}}) + UA_m(T_{\mathrm{fz}} - T_{\mathrm{ff}}) + \dot{W}_{d,\mathrm{ff}} \quad \text{Eq. (13)}$$

where ϕ and $\dot{V}$ are the freezer airflow fraction and total airflow rate supplied by the fan, respectively, obtained from the damper, ρ and c_p are the air density and specific heat of air, respectively, UA_m is the conductance of the mullion. The insufflation temperature, T_i, can be calculated through an energy balance in the evaporator,

$$\left[1-\exp\left(-UA_{\text{ext,e}}/\rho c_p\dot{V}\right)\right]\left[\phi T_{\text{fz}}+(1-\phi)T_{\text{ff}}-T_{\text{w,e}}\right]+\dot{W}_{\text{fan}}/\rho\dot{V}c_p=\left[\phi T_{\text{fz}}+(1-\phi)T_{\text{ff}}-T_i\right] \quad \text{Eq. (14)}$$

where $\dot{W}_{\text{fan}}$ is the power dissipated by the fan (7 W). At all, the model has 9 closing parameters: $C_{\text{ff}}, C_{\text{fz}}, C_e, C_c, UA_e, UA_c, UA_{\text{ff}}, UA_{\text{fz}}$ and ε to be obtained from experimental tests.

3. NUMERICAL SCHEME

3.1. Self-identification

Due to the non-linear nature of the refrigeration system, each of the closing parameters P_i has influence on one or more of the problem variables x_i. Thus, in a reverse manner, if the variables x_i are known, it is possible to achieve the set P that leads to the solution. Therefore, one could select which variables should be measured in the experiment so that the P parameters can be reduced. However, choosing variables that are not affected by the closing parameters would render the self-identification impossible as the sets of x and P are product-dependent.

The procedure for self-identification, illustrated in Fig. 3, consists of a Newton-Raphson procedure applied to minimize the errors between the model predictions and the experimental counterparts:

$$[P]=[P^*]-\alpha[J]^{-1}\left([x]-\left[x_{\text{exp}}\right]\right) \quad \text{Eq. (15)}$$

where P^* denotes the value of the previous iteration, $[J]^{-1}$ is the inverse of the Jacobian, and α is the under-relaxation factor. Due to the severe non-linearities of the equations, under-relaxation was needed with α never higher than 0.1. The experimental test should be performed in a climate-controlled room with the refrigerator running under cycling conditions. The test is recorded until the run time ratio no longer varies.

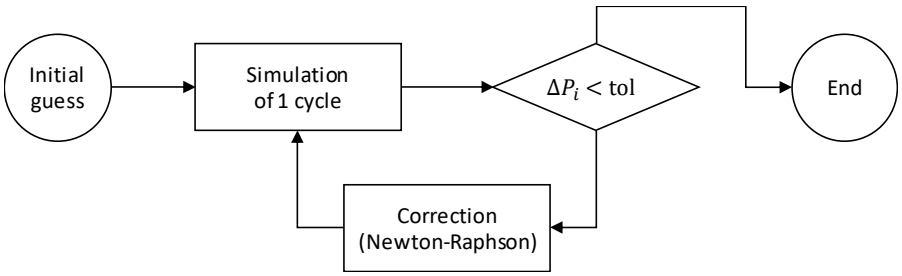

Figure 3: Self-identification procedure

3.2. Solution algorithm

The proposed model was implemented in *Dymola* (Dynasim, 2006), a modelling and simulation platform that relies on non-linear solvers and high-performance integrators, such as DASSL (Petzold, 1982), developed for EDA systems (differential-algebraic equations). *Dymola* uses the open and object-oriented programming language *Modelica*, an equation-based language that allows component and system models to be defined in a general way, without considering the causality of a specific problem. Due to the object orientation structure, the component models may be separated into blocks. The integration of the components to form the system model is then done graphically, coupling the blocks as shown in Figs. 4 and 9.

4. RESULTS AND DISCUSSION

4.1. All refrigerator

The experimental data used for model identification was obtained from Hermes *et al.* (2008b). The present work proposes a self-identification method where a single experiment returns up to 5 out the

7 closing parameters. The values adopted in the self-identification routine were: t_{on}=1026 s, t_{off}=920 s, T_e=-22.5 C, T_c=48.4°C, T_1=37.7°C. The fitting was carried out for the following parameters: C_g, UA_e, UA_c, UA_g and ε, whereas the values of C_c (900 J·K^{-1}) and C_e (1073 J·K^{-1}) were calculated from the heat exchangers masses and specific heats. The degrees of superheating and subcooling were considered null. The results from the self-identification routine are summarized in Table 1.

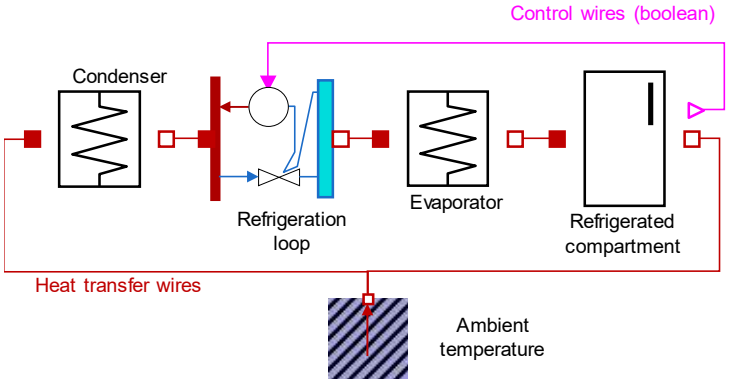

Figure 4: Block diagram of the all-refrigerator

Table 1: All-refrigerator parameters

Parameter	Value
C_g (kJ·kg^{-1})	13620
ε_x (-)	0.804
UA_e (W·K^{-1})	3.55
UA_c (W·K^{-1})	9.92
UA_g (W·K^{-1})	2.32

Fig. 5(a) shows the time evolution of the evaporation and condensation temperatures, as well as the average temperature in the cabinet. It is noted from Fig. 5 that the model is able to predict the on-off behaviour of the refrigerator quite well. The experimental trends are followed closely by the model, although a slight peak in the condensation pressure during the start of the compressor is observed, which is not observed experimentally. Fig. 6 shows the power consumed by the compressor over time, where good agreement between the experimental trends and model predictions can be observed, with an offset of 10 W (15%) after the initial peaks, which is due to the errors embedded in the compressor model (see eq. 6).

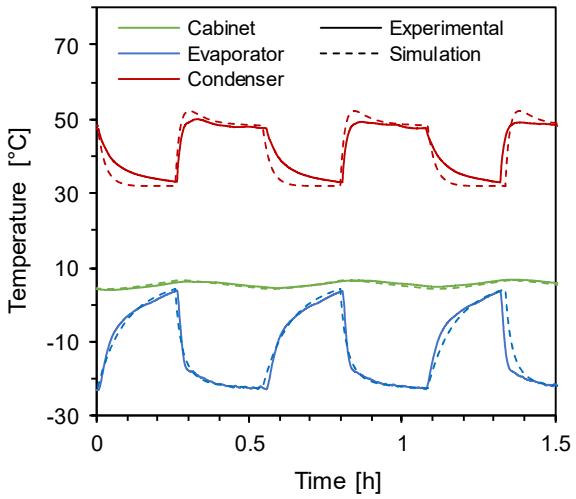

Figure 5: Simulation results for the all-refrigerator temperatures

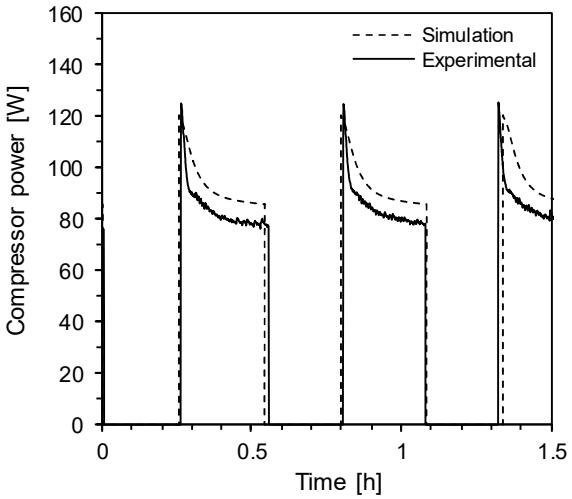

Figure 6: Simulation results for the all-refrigerator power consumption

To further explore the model capabilities, a sensitivity analysis was carried out. Fig. 7 shows the impact of the evaporator and condenser conductance over the energy consumption and run time ratio (RTR), where one can notice that improving the condenser conductance in up to 20% results in about 7% of energy savings. When same is done for the evaporator, no more than 1% is observed. Fig. 8 in turn reveals a linear relationship between energy consumption and cabinet thermal conductance (and therefore the thermal loads), as all energy entering the cabinet must be removed by the refrigeration system.

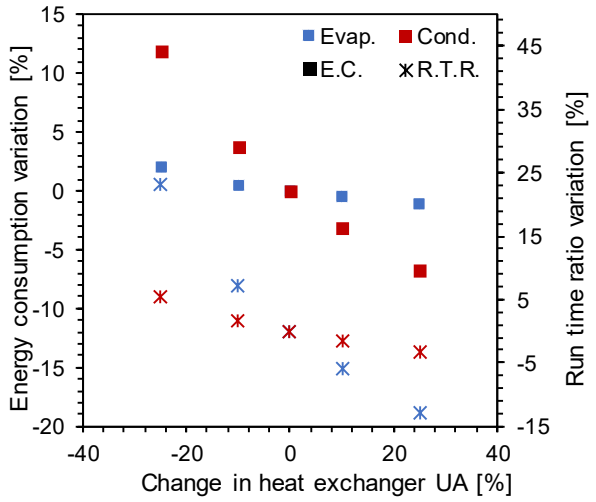

Figure 7: All-refrigerator sensitivity to the heat exchangers conductances

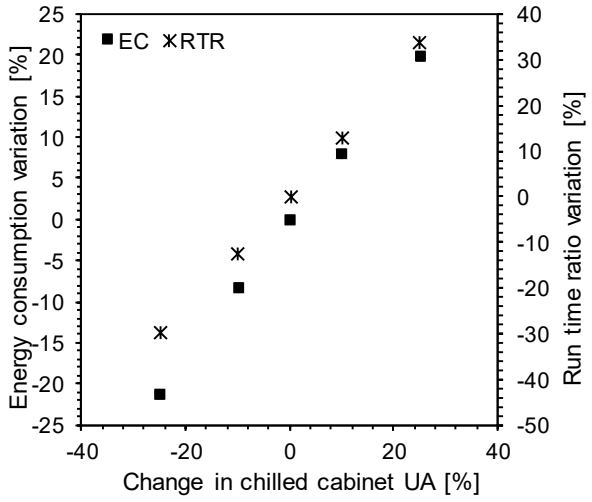

Figure 8: All-refrigerator sensitivity to the cabinet conductance

4.2. Combi refrigerator

The experimental data used for model identification was obtained from Hermes *et al.* (2008a). Since there are two compartments, 2 more parameters must be added to the self-identification routine, C_{fz} and UA_{fz}. In order to minimize the parameters to be fitted, the compartment capacities were determined from the refrigerator data, C_{ff}^{0} (7460 J·K^{-1}) and C_{fz}^{0} (2300 J·K^{-1}), and a factor, C^{*}, was introduced so that $C_{\mathrm{ff,fz}} = C^{*}C_{\mathrm{ff,fz}}^{0}$. The variables and their respective values used in the self-identification routine were: t_{on}=1600 s, t_{off}=2120 s, T_{e}=−29.4°C, T_{c}=51.3°C, T_{1}=36.5°C and ΔT_{ff}=6°C (fresh-food temperature swing). The fitting was carried out for the following parameters: $C^{*}, UA_{e}, UA_{c}, UA_{\mathrm{ff}}, UA_{\mathrm{fz}}$ and ε. The value of C_{c} (1100 J·K^{-1}) and C_{e} (465 J·K^{-1}) were calculated from the heat exchangers masses and specific heats. Once again, the degrees of superheating and subcooling were considered null. The results are summarized in Table 2.

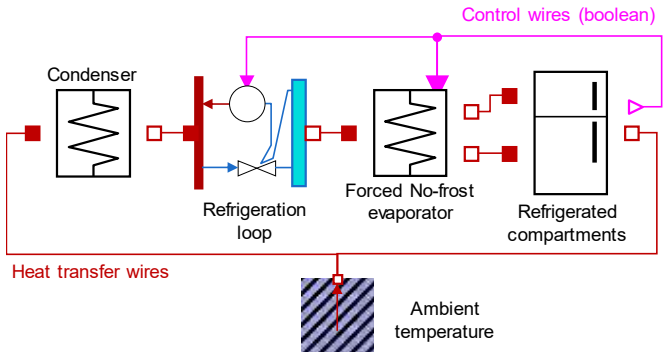

Figure 9: Block diagram of the Combi refrigerator

Table 2: Combi refrigerator parameters

Parameter	Value
C^{*} (-)	1.6
$\varepsilon_{\mathrm{TC\text{-}LS}}$ (-)	0.772
UA_{e} (W·K^{-1})	27.83
UA_{c} (W·K^{-1})	13.61
UA_{ff} (W·K^{-1})	4.05
UA_{fz} (W·K^{-1})	0.788

Fig. 10 illustrates the condensing and evaporating temperatures as well as the fresh- and frozen-food compartment temperatures over time, where one can see that the model is able to predict all temperatures with maximum error of 2.3°C. Fig. 11 depicts the compressor power over time, where errors of approximately 5% can be observed for the whole simulation.

A sensitivity analysis of the compartment conductances and compressor speed was also carried out. Fig. 12 explores the variation of energy consumption in response to changes in the conductance of the fresh- and frozen food compartments, where very expressive results were achieved, with a linear relationship of the energy consumption with the freezer conductance, a behaviour similar to that observed for the all refrigerator. The same is not observed for the fresh-food conductance because of the damper. Fig. 13 shows that the energy consumption increases with the compressor speed, which reduced the compressor on time. Thus, a speed decrease of 15% leads to 1.4% of energy savings, while a speed increase of 15% leads to 4.5% more energy consumption.

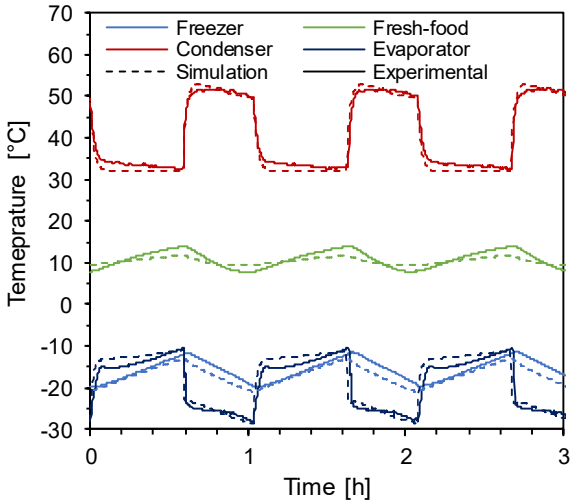

Figure 10: Simulation results for the Combi refrigerator temperatures

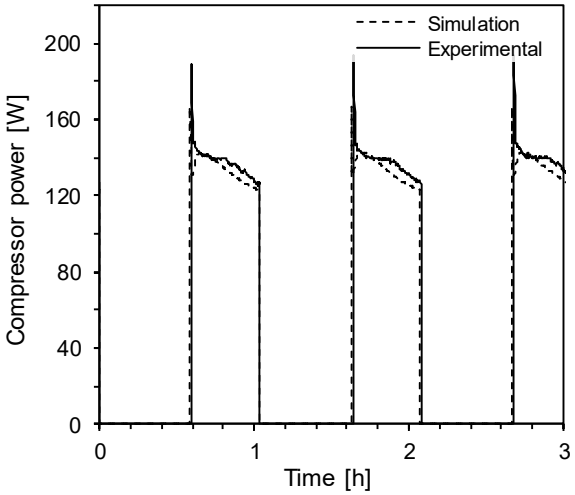

Figure 11: Simulation results for the Combi refrigerator power consumption

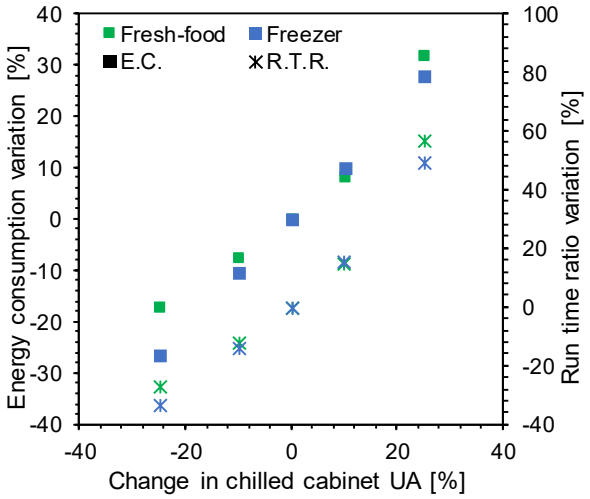

Figure 12: Combi refrigerator sensitivity to the cabinet conductance

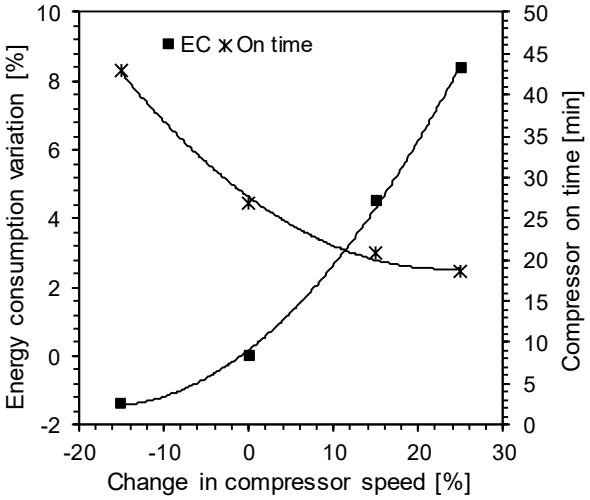

Figure 13: Combi refrigerator sensitivity to the compressor speed

5. CLOSING REMARKS

A quasi-steady-state model for simulating the on-off pattern for household refrigerators was put forward. A self-identification module for fitting the closing parameters based on a single experimental test containing on-off patterns was additionally advanced. Two different refrigerators have been used so far to validate the approach, an all-refrigerator and a Combi top-mount refrigerator. After the self-tuning procedure, a maximum deviation of ±1ºC was observed when comparing the model predictions for the cabinet air and heat exchanger wall temperatures with experimental data for the all-refrigerator and 2.3°C for the top-mount. The compression model, on the other hand, overestimated power consumption by 10% in the case of the all-refrigerator and underestimated by 7% in the case of the Combi refrigerator. For a 7th generation Intel® Core™ i5 7400 2.8 GHz, the code simulated 3 h of cycling operation in 15 s of CPU time when using the DASSL solver. Of course, in addition to being not suitable for simulating the pull-down operation, the model cannot predict refrigerant migration effects such as evaporator activation and pressure equalization.

ACKNOWLEDGEMENTS

This work was performed under the auspices of the Brazilian Government funding agencies CAPES, CNPq and EMBRAPII. The authors duly acknowledge the continuous support from EMBRACO.

REFERENCES

Borges, B. N., Hermes, C. J. L., Gonçalves, J. M., Melo, C., 2011. Transient simulation of a two-door frost-free refrigerator subjected to periodic door opening and evaporator frosting. Applied Energy 88, 748–754.

Borges, B. N., Melo, C., Hermes, C. J. L., 2015. Transient simulation of a two-door frost-free refrigerator subjected to periodic door opening and evaporator frosting. Applied Energy 147, 386–395.

Coulomb, D., Dupont, J.-L., Pichard, A., 2015. 29th Informatory Note on Refrigeration Technologies. The Role of Refrigeration in the Global Economy. Tech. rep. Paris, FR, 16.

Dynasim AB, 2006. Dynamic Modeling Laboratory. www.dynasim.se.

Gonçalves, J. M., Melo, C., Hermes, C. J. L., 2009. A semi-empirical model for steady-state simulation of household refrigerators. Applied Thermal Engineering 29(8–9), 1622–1630.

Hermes, C. J. L., Melo, C., 2008. A first-principles simulation model for the start-up and cycling transients of household refrigerators. International Journal of Refrigeration 31, 1622–1630.

Hermes, C. J. L., Melo, C., Negrão, C. O. R., 2008. A numerical simulation model for plate-type, roll-bond evaporators. International Journal of Refrigeration 31, 335–347.

Mitishita, R. S., Barreira, E. M., Negrão, C. O. R., Hermes, C. J. L., 2013. Thermoeconomic design and optimization of frost-free refrigerators. Applied Thermal Engineering 50(1), 1376–1385.

Negrão, C. O. R., Erthal, R. H., Andrade, D. E. V., Silva, L. W. da, 2011. A semi-empirical model for the unsteady-state simulation of reciprocating compressors for household refrigeration applications. Applied Thermal Engineering 31(6), 1114–1124.

Petzold, L. R., 1982. A description of DASSL: A differential/algebraic system solver. Proceeding of the 10th IMACS World Congress. Montreal, 65–68.

Santos, G. Z. dos, Ronzoni, A. F., Hermes, C. J. L., 2019. Semi-empirical modeling of variable-capacity crankshaft and linear compressors for household refrigeration applications. International Journal of Refrigeration. To be submitted.

Schurt, L. C., Hermes, C. J. L., Neto, A. T., 2009. A model-driven multivariable controller for vapor compression refrigeration systems. International Journal of refrigeration 32(7), 1672–1682.

Manuscript ID: 139
DOI: 10.18462/iir.icr.2019.0139

Design of a cold thermal energy storage unit for industrial applications using CO_2 as refrigerant

Håkon SELVNES[(a)], Armin HAFNER[(a)], Hanne KAUKO[(b)]

[(a)] Norwegian University of Science and Technology (NTNU), Department of Energy and Process Engineering
Trondheim, NO-7034, Norway, hakon.selvnes@ntnu.no
[(b)] SINTEF Energy Research
Trondheim, NO-7034, Norway, hanne.kauko@sintef.no

ABSTRACT

Natural refrigerants such as ammonia, hydrocarbons and CO_2 are becoming increasingly popular due to favorable thermo-physical properties, low environmental impact and low cost. Industrial refrigeration systems are often installed in applications where the difference in peak and average cooling load is substantial. Cold thermal energy storage (CTES) integrated into the system enables shifting of the load from peak hours to off-peak hours, which enables design of the system capacity closer to the average load rather than the peak load. This paper describes the design and development of a CTES unit and associated experimental test rig. The CTES unit consists of a stack of heat exchanger plates contained in a steel tank, initially filled with water as the phase change material (PCM). CO_2 circulates within the plates to freeze and melt the water during charge and discharge cycles, respectively.
Keywords: Refrigeration, Carbon Dioxide, Cold thermal energy storage, Energy Efficiency.

1. INTRODUCTION

CTES technology has over the years gained more attention as a measure to cope with high peaks in refrigeration demands in various applications, reducing the required installed capacity of equipment and offering a backup in case of system failure. Special attention is being paid to investigating latent CTES using phase change materials (PCMs) (Oró et al., 2012) (Li et al., 2013). Extensive literature reviews on CTES technology and PCMs applied in different sectors have been published, including domestic refrigeration (Joybari et al., 2015), integration in building applications (Cabeza et al, 2011) and domestic heat pump/air-conditioning systems (Moreno et al., 2014). These studies cover both short-term and long-term storages. Published research on large-scale cold thermal energy storages is scarcer, especially systems designed for short-term storage. Systems designed for seasonal storage are most commonly studied.
In many process industries, where large refrigeration systems are installed, there is a substantial difference in peak and average cooling load. In Norway, one of the largest sectors within industrial refrigeration is the food-processing industry. The peaks in refrigeration demand occur due to the throughput of product in the plant during processing, while the cold storage of products is the main contributor to off-peak demand. The change in refrigeration demand from off-peak to peak can be more than a multiplication of ten. Identifying this demand structure is one of the most important prerequisites to make a successful CTES implementation in a refrigeration system (Dincer and Rosen, 2002). The evaporation temperature level where the energy is required in these types of systems are in the range of -10°C to 0°C for chilling purposes and between -40°C and -50°C for freezing processes. To avoid using compressor power during peak hours for satisfying the thermal requirement, the thermal demand must be satisfied at these temperature levels. PCMs with fitting phase change temperature for this temperature range are salt-hydrates/water mixtures or organic paraffin PCMs.
Apart from identifying a suitable system where energy storage can offer beneficial features, reliable CTES units that are easily integrated directly into the refrigeration systems must be developed. Earlier studies have been focusing on units that are incorporated in the secondary circuits of the refrigeration systems, typically using ice water or glycol as brines. Typical examples in this category are tube-in-tank systems (Torregrosa-Jaime et al., 2013) and ice bank systems with brine circulation through pipes or vertical plates (Ismail et al., 1999). These systems have the additional heat transfer

loss by heat exchanging heat between the refrigerant and secondary circuit before being able to store the energy in the CTES system. The challenge when moving to large-scale systems requiring low temperature is to extract the energy stored in the CTES system fast enough during the period that the peak occurs. This varies from system to system, but the peak usually lasts from one up to a few hours. Large-scale systems with freezing and cooling demands in the megawatt range require high heat transfer from the CTES system in order to cut the demand peaks. There are in essence two approaches to enhancing the heat transfer in a latent CTES system. The designer can either act on the PCM by enhancing the thermal properties or act on the storage system itself. Enhancement strategies for PCMs have been studied intensively over the past years and thorough reviews are available (Fan and Khodadadi, 2011) (Milian et al., 2017). The focus of this study is to design a CTES unit by acting on the system, ensuring adequate heat transfer area to get high refrigeration duty during discharging.

The proposed design of a CTES unit in this paper is based on a type of heat exchanger (HX) plates called pillow plates. Pillow plates have the ability to withstand the relatively high operating pressures in CO_2 refrigeration systems, thus the refrigerant can be evaporated/condensed directly in the CTES and exchange heat with the PCM without additional secondary fluid circuit in between.

The published work on heat transfer in pillow plates is limited. Geometric description of the wavy surface is difficult due to the complex shape created by the applied hydraulic pressure during inflation. Piper et al. (2015) made an important contribution to this topic. The study focused on establishing methods for determining the geometric design parameters for pillow plates using forming simulations. The simulations could accurately represent the wavy surface of the plates, and equations for heat transfer area, hydraulic diameter and cross-sectional area were established based on the results. These expressions are important for further developing correlations for heat transfer and pressure drop in pillow plates.

Most studies of pillow plates deal with single-phase flow, only a few cover condensation and evaporation. To the authors' knowledge, the published research on condensation and evaporation in pillow plates covers only applications in the process and chemical industry. Mitrovic and Peterson (2007) published one of the first papers dealing with experimental investigation of condensation on pillow plates, where the HX was applied as a top condenser in a distillation column. In this study, the condensation process of isopropanol was on the outside surface of the pillow plate with cooling water on the inside. Later work by Mitrovic and Maletic (2011) concerned a numerical investigation of the flow and heat transfer characteristics of cooling water inside of a pillow plate.

Over the last four years, the number of publications treating numerical and experimental studies of single-phase flow pillow plates has increased. Piper et al. (2016) carried out a numerical investigation of the heat transfer characteristics of a small periodic element of the pillow plate. The study showed that two distinct zones, the meandering core and the recirculation zone, characterize the flow inside the plate. In single-phase turbulent flow, the core flow dominates the heat transfer. The highest efficiency was observed for the lowest Reynolds numbers and the highest inflation height, and an efficiency increase by up to 37% was predicted for oval shaped welding spots compared to circular. This work was followed up by establishing heat transfer correlations for forced turbulent convection based on the CFD results (Piper et. al., 2017). A recent study has investigated the effect of geometric variations of the flow channel and spot welds on the heat transfer in thermoplates, a variation of the pillow-plate with a single row of spot welds in the flow direction (Khalil et al., 2018). This study considered incompressible laminar flow with water as the fluid. Results from the study show improvement in heat transfer for large cross-sectional flow area, larger spot-weld spacing and smaller spot-weld diameter. The results from the numerical study were validated with experimental data.

Ice bank systems based on pillow plates have recently become commercially available, serving as a thermal storage for cold water systems with temperature set point of 0.5°C to 2°C. These follow the same operational regime as the traditional ice banks with tubes. This involves immersing the pillow plate HX in a water tank, where the circulation of cold coolant/refrigerant on the inside of the plates freezes an ice layer on the plate surface during charging. During discharging, warm return water from ice water system pumped into the tank and circulated on the outside of the ice layer to melt it and cool the water. This can be referred to as an internal freeze/external melt system. In this paper, the proposed design is a pillow-plate CTES unit based on the internal freeze/internal melt principle. The details of the CTES unit, operation and associated test rig will be presented in the following sections, as well as the proposed method of integration in a refrigeration system.

2. DEVELOPMENT AND DESIGN OF A CTES UNIT

2.1. CTES unit

The prototype CTES unit is shown in Fig. 1 below. The unit consists of a welded case in stainless steel supported by a frame of steel square tube, as well as a lid with handles to cover the unit to prevent evaporation of the PCM. The frame is required for structural support once the unit is filled with PCM. The prototype has two windows of thick acrylic plexiglass on each side for visually observing the melting/freezing process when the experiments are running. LED lights can be installed at one side of the case, and a camera at the other side to clearly see the solid PCM layer between each pillow plate. The case should be insulated when experiments are running, and the windows fitted with removable pieces of insulation. In case of service or need to empty the tank, there is a tube for draining the PCM at the bottom of each sidewall.



Figure 1: The designed prototype CTES unit (shown ten plates)

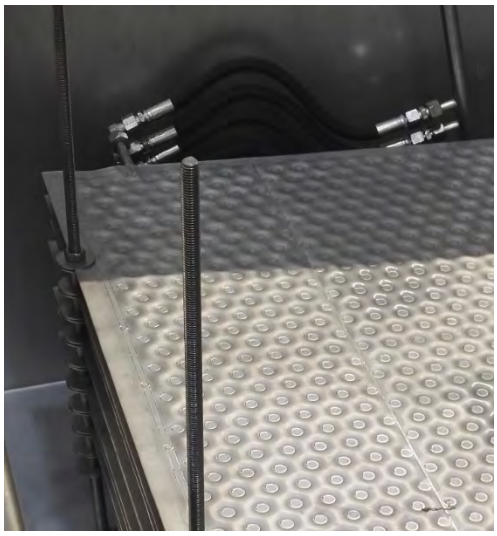

Figure 2: Detailed view of the plate stack in the unit

A stack of pillow-plates provides the heat exchange with the PCM in the unit. These plates consist of two thin metal sheets that are spot-welded together in a laser-welding machine. The diameter of the spot welds and the distance between them can be varied according to what type of refrigerant is used in the system. Higher operating pressures involves more spot welds per plate area. CO_2 requires relatively frequent spot welds due to the high pressure compared to other refrigerants. The spot welds are created in a certain repeating pattern. The pattern chosen in this unit has 50 mm longitudinal spot weld distance and 30 mm transversal spot weld distance. Other patterns are available. The plate pair is then seam welded along the edges to seal it completely, except for the inlet and outlet pipe. To create the flow channels for the refrigerant inside the plate, one of the pipes is blocked off and high pressure is applied on the inside of the plate with water. The plate is inflated and the channels are formed around the spot welds in between the two metal plates. This process gives the plates the characteristic wavy surface. The channel geometry promotes mixing of the flow and good distribution of refrigerant within the plate, which enhances heat transfer. In addition, longitudinal seam welds are made on each plate. This directs the refrigerant flow from the inlet pipe to the outlet via three passes over the plate. The longitudinal seam weld creating first refrigerant pass can be seen in Fig 2. Due to the width of the channel, the refrigerant velocities are relatively low, giving sufficient time for the refrigerant to evaporate/condense and exchange heat with the PCM on the outside.

The plate stack in the prototype is built to be flexible. Cylindrical spacers mounted in between the plates on the supporting rods set the distance between each plate. These can be changed with a set of different length to change the distance. The distance between the plates is an important parameter for the performance of the unit and the selection is depending on the thermal properties of the PCM, the time limit for charging/discharging and storage capacity requirements. As an example, lower thermal conductivity and high viscosity PCMs generally require shorter distance to activate all of the material in the tank. First tests are to be carried out with water as the PCM, and a distance of 50 mm between each plate is chosen. The first set of spacers are of unequal length, creating a tilt of the

plate stack from the inlet to the outlet pipe. This design feature allows for efficient draining of the condensate during discharging of the system. The flow direction is reversed during charging so that the refrigerant evaporates and flows upwards to the outlet. The unit is intended to work with pump-circulated oil-free CO_2 refrigerant, but if lubrication oil is used, the tilting of the plate can help avoid an accumulation of oil in the unit. The pipes at each end of the stack are connected to a common manifold by a high-pressure flexible hose, which distributes the refrigerant to each plate in the stack from the common inlet pipe. The plates are free to move up and down the rods, to avoid mechanical stresses resulting from the expansion of the PCM during solidification. Main geometric parameters of the CTES prototype unit are summarized in Table 1 below.

Table 1: Geometric parameters of the prototype CTES unit

Parameter	Value	Unit
Longitudinal spot weld pitch	50	mm
Transversal spot weld pitch	30	mm
Pillow plate length	1500	mm
Pillow plate width	750	mm
Distance between each plate	50	mm
Number of plates in the stack	20	-
Total heat transfer area (assuming flat plate)	45	m^2

2.2. CTES test rig

To test the performance of the newly developed prototype CTES unit, a test rig needs to be developed and constructed. Special focus is to make the rig as flexible as possible, with the ability to test the CTES unit with numerous PCMs of different composition, properties and phase change temperatures. A simplified process and instrumentation diagram (PID) of the test rig is shown in Fig 3. The two main functions of the rig are to add and remove heat from the refrigerant circuit during the discharging and charging process, respectively. Heat to the circuit is provided by a closed-loop glycol system, with 30% glycol concentration as heat transfer fluid. The heating circuit consists of 2 x 9 kW electric immersion heaters with thermostatic control (0°C to 50°C), a circulation pump and an expansion vessel with microbubble air separator and safety valve. The heat transfer to the CO_2 circuit is done in a CO_2/glycol plate HX from Alfa Laval, functioning as an evaporator. A differential pressure sensor measures the pressure drop over the evaporator on the refrigerant side. Flow data is collected by a Coriolis mass flow meter, while resistance temperature detectors (RTD) pt100 sensors measure the inlet and outlet glycol temperature to the evaporator. The probes of the temperature sensors are installed directly in the glycol flow. The heating circuit is completed with 28 mm copper tube with press fittings.

Heat is removed from the CO_2 circuit by connecting the test rig to the centralized CO_2 unit in the refrigeration laboratory. The centralized unit has three evaporation levels, -53°C, -25°C and -10°C, which can be chosen by operating a valve station. This gives the possibility to remove heat at a large temperature range, meaning PCMs with phase change temperatures from approximately 0°C to -45°C can be tested in the unit. The heat from the test rig CO_2 circuit is transferred to the centralized CO_2 unit by a plate HX from Alfa Laval. The HX serves as a condenser on the test rig side and as an evaporator for the centralized unit. A differential pressure sensor measures the pressure drop on the test rig side of the condenser. A Danfoss CCMT-2 electronic expansion valve controls the refrigerant flow and superheat of the suction gas to the centralized CO_2 unit. When the facility is not running, the pressure and temperature of the liquid CO_2 in the receiver are kept low by a subcooler HX (see Fig. 3). The HX consists of a 6 mm copper tube that is coiled around the liquid receiver, with a total length of 15 meters. This prevents the temperature of the liquid CO_2 in the system reaching room temperature and excessive pressures during standstill. A Danfoss AKVH electronic expansion valve controls the refrigerant flow and superheat of the subcooler.

A high-pressure hermetic refrigerant pump from HERMETIC-Pumpen GmbH equipped with a frequency converter provides circulation of CO_2 in the refrigerant circuit of the test rig. Liquid CO_2 is supplied to the pump from the refrigerant receiver. To avoid cavitation problems and provide the required suction head for the pump, it is placed in the basement while the rest of the rig is located at the ground floor. In addition, the suction pipe has an increased pipe diameter compared to the rest of the rig to obtain sufficiently low refrigerant velocities at the pump inlet. The test rig refrigerant circuit is constructed with K65 high-pressure copper tube and fittings that are brazed together. The

tubes are of 3/4" size, except for the suction tube of the pump, which is of 1.5/8” size. A recirculation line back to the receiver with a minimum flow orifice is fitted to the system to ensure the minimum flow requirement of the pump is maintained at all times.

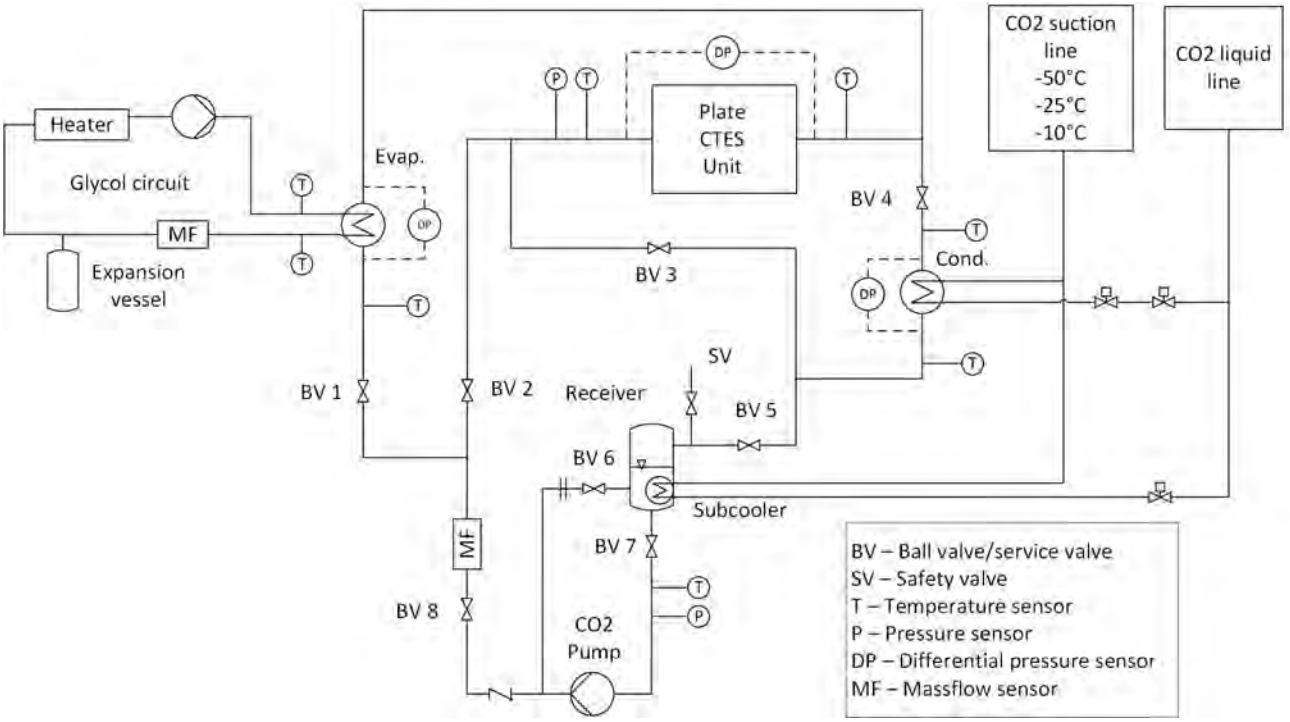

Figure 3: Simplified process and instrumentation diagram of the CTES test rig

The test rig can operate in two modes, charging or discharging of the CTES unit. When the system is running in charging mode, ball valve 1 and 3 are closed. The remaining valves are open. The refrigerant is pumped from the liquid receiver, through a Coriolis mass flow meter before entering the CTES unit. The liquid refrigerant evaporates in the unit as it exchanges heat with the PCM in the pillow plates, solidifying the PCM. The gas is then condensed in the CO_2/CO_2 condenser before it is drained to the receiver. The evaporated CO_2 from the centralized unit is transported back to the rack by operating the appropriate compressor suction level. During discharging of the CTES unit, ball valve 2 and 4 are closed. The rest of the valves are in the open position. Liquid CO_2 is pumped from the receiver through the Coriolis mass flow meter, and then to the evaporator. The heaters and the pump in the glycol circuit are activated, and warm glycol is circulated through the plate HX to evaporate the CO_2. The refrigerant gas then flows through the CTES unit and condenses as it exchanges heat and melts the PCM. The liquid CO_2 is drained back to the receiver by gravity.

The plates in the CTES unit are stacked horizontally. This choice was made to take advantage of the buoyancy effect on the solid PCM during the discharging/melting process. Since CO_2 is condensing in the plates, the PCM will melt close to the plate surface first. When the PCM between a pair of plates is melted from the top and bottom, it is free to move in the liquid PCM. Due to density differences between the solid and liquid PCM, the solid bulk will rise and make contact with the upper plate. This will create a situation called close-contact melting (CCM), providing high heat transfer between the solid PCM and the condensing refrigerant on the other side of the plate wall.

The test rig is installed with a differential pressure sensor over the CTES unit, evaporator and condenser. In addition, there are absolute pressure sensors fitted at the receiver outlet and in front of the CTES unit. 3 mm diameter closed-end tubes are fitted into the refrigerant flow in order to mount RTD pt100 temperature sensors. They are installed at the receiver outlet, before the evaporator, after the condenser and before/after the CTES unit. Up to 32 thermocouples can be fitted on the pillow plate surface in the CTES unit to observe the temperature distribution. Three plates in the stack (upper, middle and lower part of the stack) are fitted with thermocouples. All data from the test rig is transmitted by a central data acquisition system from National Instruments and logged by a program in the computer software LabVIEW. An overview of the measurement equipment and the indication of the accuracy are shown in Table 2.

With the latent heat of water as PCM (333.55 kJ kg^{-1}), the described geometry and by considering only the volume of PCM between the plates as the active PCM, the expected storage capacity of the

prototype CTES unit is about 104.1 kWh. The peak condensing duty for the unit with saturated CO_2 gas entering at 5°C (39.67 bar) is about 26 kW, slowly decreasing as the melting process continues.

Table 2: Measurement equipment

Component	Type/Producer	Indicated accuracy
Pressure sensor	Cerabar S PMP71 / Endress+Hauser	± 0.075 % of set span
Differential pressure sensor	Deltabar S PMD75 / Endress+Hauser	± 0.05 % of set span
Temperature sensor flow	Class B RTD Pt100 / RS PRO	± 0.12 % of resistance
Temperature sensor PCM	K-type thermocouples / RS PRO	± 0.75 % of range
Mass flow meter glycol	RHM 15 Coriolis meter/ Rheonik	± 0.2 % of rate
Mass flow meter CO_2	RHM 06 Coriolis meter / Rheonik	± 0.2 % of rate

2.3. Integration in a refrigeration system

The unit is designed to be integrated and operated as a CTES system in a pumped CO_2 secondary refrigeration circuit. A case example showing how to integrate and operate the CTES unit in an NH_3/CO_2 cascade refrigeration system for a food processing plant now follows. The design of the cascade system is taken from a poultry processing plant under construction in central Norway. NH_3/CO_2 cascade systems are gaining popularity for large refrigeration systems, and they show advantages over pure NH_3 systems for evaporation temperatures at -40°C and lower (Bingming et al., 2009) (Dopazo et al., 2011). Using CO_2 in the lower stage as a pump-circulated secondary refrigerant offers operating benefits compared to traditional brines, especially for long piping distances. Reduced pipe diameter, low pumping costs, no toxicity or flammability concerns, as well as high heat transfer in process equipment by direct evaporation are some of the favorable features of using CO_2 as a secondary fluid. CTES implemented in these types of systems can offer compressor power peak load shifting when they are installed in the low-temperature stages (Selvnes et al., 2018). The CTES unit proposed in this paper is intended to work as an alternative to the traditional sensible thermal storages, such as ice water tanks often used as peak shaving devices in the food industry. A simplified flowsheet of the bottom cycle of the cascade refrigeration system with integration of the CTES unit is shown in Fig. 4 below.

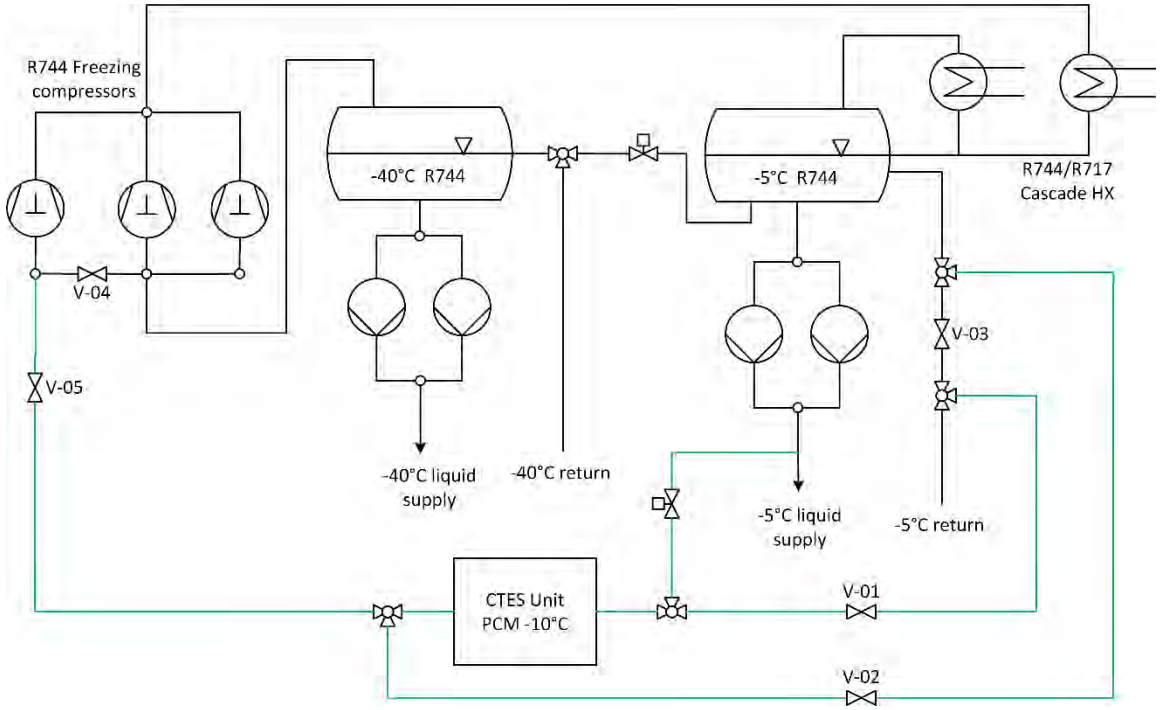

Figure 4: Example on how to integrate the CTES unit in a secondary refrigeration circuit

The bottom cycle consists of a -5°C and -40°C temperature level for cooling and freezing applications, respectively. The refrigerant is pump-circulated and distributed from the two liquid receivers with a typical circulating rate of 3, referring to the ratio of evaporated refrigerant to the

total amount of refrigerant pumped to the evaporators. The evaporated refrigerant at -40°C returning from the process equipment in the plant is compressed to -5°C saturation pressure (30.47 bar) and then condensed in the cascade HX. The return line from the -5°C distribution pipe is directed back to the liquid separator, and the gas is condensed in the cascade HX by natural circulation. The additional piping required for integration of the CTES system is displayed with green color in Fig. 4. In the example shown here, the CTES system works as a peak shaving device at the -5°C temperature level in the plant. The focus of the integration is to use the equipment already required for conventional operation to charge and discharge the CTES system. During the hours without production, (night) the load on the refrigeration system is only to maintain the set-point temperature in the cold storages. Consequently, there is compressor capacity available to charge the CTES system. During charging valve V-01, V-02 and V-04 are closed, while V-03 and V-05 are open. CO_2 liquid from the -5°C liquid separator is throttled to -20°C saturation temperature (19.72 bar), and evaporated in the CTES unit while exchanging heat with the PCM. An appropriate phase change temperature for the PCM for this temperature level is -10°C, giving a 5 K temperature difference between the refrigerant and the solid PCM. Possible candidates to use as PCM are based on paraffin or salt-hydrate/water mixture. The evaporated CO_2 is compressed and delivered to the cascade HX by one of the machines in the compressor rack.
During peak hours of production, the system can be discharged to unload the R717 compressors in the upper part of the cascade. Valve V-01, V-02 and V-04 are now open, while V-03 and V-05 are closed. The two-phase mixture in the -5°C return line from the plant is directed to the CTES unit where the gas is condensed before returned to the liquid separator. If the storage does not have the capacity to condense the returning refrigerant completely, the remaining gas is condensed in the cascade HX. The CTES system can be extended to the required storage capacity and condensing duty by connecting more units in parallel.

3. CONCLUSIONS

This paper presents the design of a novel CTES unit that is suitable for installing in industrial refrigeration systems using CO_2 as refrigerant. An example of how to integrate and operate the CTES unit in an NH_3/CO_2 cascade refrigeration system is shown in section 2.3. The design of the unit is based on a type of HX plates called pillow plates. The flexible design of the prototype allows for variation of important geometric parameters during the experimental campaign, such as the plate welding pattern, the distance between plates in the stack and the total number of plates. The arrangement enables optimizing the unit geometry to fit PCMs with different thermal properties.
An associated test rig using oil-free CO_2 as refrigerant was developed to investigate the performance of the prototype CTES unit. It is designed to handle experimental studies involving PCMs with phase change temperature in the range from 0°C to -45°C, which is adapted to the required temperature levels in the food processing industry. The working fluid in the test facility is pump-circulated. The test facility is able to operate both in charging and in discharging mode. During discharging, an electrically heated closed-loop glycol circuit provides heat input to the oil-free CO_2. The CO_2 condenses in the CTES unit while melting the PCM. In charging mode, liquid refrigerant is pumped through the CTES unit. The refrigerant evaporates while it solidifies the PCM. The refrigerant gas is condensed in an HX connected to a centralized CO_2 refrigeration unit in the laboratory. The centralized unit can provide refrigeration from -5°C down to -53°C. This enables tests of low-temperature PCMs, too. These investigations will be performed after the tests with water as PCM.

ACKNOWLEDGEMENTS

The work is part of HighEFF - Centre for an Energy Efficient and Competitive Industry for the Future, an 8-year Research Centre under the FME-scheme (Centre for Environment-friendly Energy Research, 257632). The first author gratefully acknowledges the financial support from the Research Council of Norway and user partners of HighEFF. The first author would also like to acknowledge the financial and technical support from Skala Fabrikk AS, HERMETIC Pumpen and HB Products.

REFERENCES

Bingming, W., Huagen, W., Jianfeng, L. and Ziwen, X., 2009. Experimental investigation on the performance of NH3/CO2 cascade refrigeration system with twin-screw compressor. International Journal of Refrigeration, 32(6), 1358-1365.

Cabeza, L.F., Castell, A., Barreneche, C.D., De Gracia, A. and Fernández, A.I., 2011. Materials used as PCM in thermal energy storage in buildings: a review. Renewable and Sustainable Energy Reviews, 15(3), 1675-1695.

Dincer, I., Rosen, M., 2002. Thermal energy storage: systems and applications. John Wiley & Sons, 599 p.

Dopazo, J.A. and Fernández-Seara, J., 2011. Experimental evaluation of a cascade refrigeration system prototype with CO2 and NH3 for freezing process applications. International Journal of Refrigeration, 34(1), 257-267.

Fan, L., Khodadadi, J.M., 2011. Thermal conductivity enhancement of phase change materials for thermal energy storage: a review. Renewable and sustainable energy reviews, 15(1), 24-46.

Ismail, K.A.R., Quispe, O.C. and Henrıquez, J.R., 1999. A numerical and experimental study on a parallel plate ice bank. Applied Thermal Engineering, 19(2), 163-193.

Joybari, M.M., Haghighat, F., Moffat, J. and Sra, P., 2015. Heat and cold storage using phase change materials in domestic refrigeration systems: The state-of-the-art review. Energy and Buildings, 106, 111-124.

Khalil, I., Hayes, R., Pratt, Q., Spitler, C. and Codd, D., 2018. Experimental and numerical modeling of heat transfer in directed thermoplates. International Journal of Heat and Mass Transfer, 123, 89-96.

Li, G., Hwang, Y., Radermacher, R. and Chun, H.H., 2013. Review of cold storage materials for subzero applications. Energy, 51, 1-17.

Moreno, P., Solé, C., Castell, A. and Cabeza, L.F., 2014. The use of phase change materials in domestic heat pump and air-conditioning systems for short term storage: A review. Renewable and Sustainable Energy Reviews, 39, 1-13.

Milian, Y.E., Gutierrez, A., Grageda, M. and Ushak, S., 2017. A review on encapsulation techniques for inorganic phase change materials and the influence on their thermophysical properties. Renewable and Sustainable Energy Reviews, 73, 983-999.

Mitrovic, J., Peterson, R., 2007. Vapor condensation heat transfer in a thermoplate heat exchanger. Chemical Engineering & Technology: Industrial Chemistry-Plant Equipment-Process Engineering-Biotechnology, 30(7), 907-919.

Mitrovic, J., Maletic, B., 2011. Numerical simulation of fluid flow and heat transfer in thermoplates. Chemical Engineering & Technology, 34(9), 1439-1448.

Oró, E., De Gracia, A., Castell, A., Farid, M.M. and Cabeza, L.F., 2012. Review on phase change materials (PCMs) for cold thermal energy storage applications. Applied Energy, 99, 513-533.

Piper, M., Olenberg, A., Tran, J.M. and Kenig, E.Y., 2015. Determination of the geometric design parameters of pillow-plate heat exchangers. Applied Thermal Engineering, 91, 1168-1175.

Piper, M., Zibart, A. and Kenig, E.Y., 2017. New design equations for turbulent forced convection heat transfer and pressure loss in pillow-plate channels. International Journal of Thermal Sciences, 120, 459-468.

Piper, M., Zibart, A., Tran, J.M. and Kenig, E.Y., 2016. Numerical investigation of turbulent forced convection heat transfer in pillow plates. International Journal of Heat and Mass Transfer, 94, 516-527.

Selvnes, H., Hafner, A., Kauko, H., 2018. Cold thermal energy storage integration in a large industrial refrigeration system. Proceedings of the 13th IIR Gustav Lorentzen Conference on Natural Refrigerants, Valencia, Spain.

Torregrosa-Jaime, B., López-Navarro, A., Corberán, J.M., Esteban-Matías, J.C., Klinkner, L. and Payá, J., 2013. Experimental analysis of a paraffin-based cold storage tank. International Journal of Refrigeration, 36(6), 1632-1640.

Manuscript ID: 141
DOI: 10.18462/iir.icr.2019.0141

Control optimization for cold-room (walk-in) refrigeration units

Pere MORENO[(a)], Xavier ALBETS-CHICO[(a)], Gabriel ZSEMBINSZKI[(b)], Alvaro DE GRACIA[(b,c)], Jose Miguel MALDONADO[(b)], Luisa F. CABEZA[(b)]

[(a)] AKO Group
Sant Pere de Ribes, 08800, Spain, xalbets@ako.com
[(b)] GREiA Research Group
INSPIRES Research Centre, University of Lleida
Lleida, 25501, Spain, lcabeza@diei.udl.cat
[(c)] CIRIAF – Interuniversity Research Centre, University of Perugia
Perugia, 06125, Italy, alvaro.degracia@udl.cat

ABSTRACT

Cold-rooms are widely used in food retail and food service industry. The objective of this work is to present an optimized control strategy to enhance the performance of the cold-rooms, with special emphasis on energy savings through defrost optimization. A novel cold-room control algorithm was developed to predict the frost level accumulated on the evaporator so the controller is able to launch defrosts only when necessary, skipping unnecessary defrosts, which negatively affects energy consumption. The control is also able to manage the evaporator fans according to the frost level, providing free-cooling when the frost level is suitable to cool down the cold-room without using the compressor. The new algorithm was tested in four cold-rooms working under different conditions and satisfactory results were obtained. All cold-rooms drastically decreased their number of defrosts (reaching up to 90% reduction) and obtained important energy savings, from 15.9% to 39.3%.
Keywords: Cold-room, Control (automatic), Cooling, Defrosting, Energy saving

1. INTRODUCTION

Refrigeration is an important energy consumer of the food preservation market (cold chain), for example supermarkets spend from 40% to 60% of their total energy requirements on refrigeration, to ensure the effectivity of the cold chain (Howell et al., 1999, and Axell and Fahlen, 2002).
One of the main problems of cold-rooms is the frost that builds-up on evaporators, decreasing heat transfer efficiency and, in the worst scenario, causing the blockage of the evaporator coil, impeding the cold-room temperature to reach the set-point. In order to avoid this issue defrosts are periodically launched to avoid frost accumulation. However, this process consumes an important amount of energy, especially if electric heaters are used. In this case defrost consumption can be around 25% of the total energy demand of a refrigerator (Kazachi, 2001). Therefore, decreasing the number of defrosts can produce important energy savings.
Many researchers carried out studies to accurately control defrost cycles, because they are commonly launched at pre-set times, resulting in unnecessary defrost processes and/or possible evaporator blockage situations. Allard and Heinzen (1988) designed a loop system for launching the defrost based on the defrost time. Also, Mastrullo et al. (2014) developed a transient model, which can be used as a tool for setting the parameters for defrost processes. However, the most extended frost detecting method is the ΔT method, patented by Kinoshita and Sasaki (1983), which quantifies the frost level on the evaporator by the difference between the indoor air and evaporator temperature.
This study presents a novel algorithm which is able to predict the frost level accumulated on the evaporator so defrost is launched only when necessary. The algorithm is also able to efficiently manage the evaporator fans by their activation according to the frost level, taking advantage of the cold stored in the frost, hence using it as free-cooling for the cold-room. The performance of this algorithm under real conditions is presented as the last part of this work, showing an important reduction of defrosts and high energy savings for all tested cases.

2. METHODOLOGY

The cold-room control optimization is achieved by a new algorithm integrated in the controller (patented under reference WO/2018/178465 (Albets et al., 2018)), which is able to optimize defrost launching and evaporator fan management. These features and some case studies are presented below.

2.1. Algorithm technical bases

2.1.1. Frost level calculations: Thermal Variation Easiness (*TVE*)

The algorithm is able to predict the frost level on the evaporator by calculating a parameter called Thermal Variation Easiness (TVE). This parameter is calculated using only two temperature sensors, which are commonly used in commercial refrigeration applications like cold rooms or refrigerated displays, so no additional sensors are required by the installation.

The TVE quantifies both the thermal inertia of the evaporator and the effectivity of the heat flux through the evaporator coil. This parameter decreases while the frost builds up on the evaporator due to the thermal inertia of the frost and its low conductivity, it is therefore necessary to first knowing the TVE value when the evaporator is free of frost, as a reference. When frost is building up on the evaporator, the TVE calculation can be compared to the reference value. As further detailed, if the parameter noticeably differs from reference, a defrost is needed and consequently launched.

The parameter TVE is calculated according to Eq. (1). Once the liquid solenoid valve is closed after the cold room air temperature reaches the set point, the evaporator temperature starts rising while the fans are kept on, thus the heating slope drawn by the evaporator temperature is measured. The data collection ends when either the solenoid valve opens again or when the evaporator temperature reaches 0ºC, whichever comes first.

$$TVE = \left(T_{evap,f} - T_{evap,o}\right)\left[t \cdot \sum_0^n \left(\left|T_{cold-room} - T_{evap}\right|\right)\right]^{-1} \qquad \text{Eq. (1)}$$

where $T_{evap,f}$ is the evaporator temperature at the end of the register, $T_{evap,o}$ is the evaporator temperature at the beginning of the register, t is the monitoring time step, and $T_{cold\text{-}room}$ and T_{evap} are the cold-room and evaporator temperature, respectively.

According to the TVE formula (Eq.1) a minimum temperature difference between the cold room and the evaporator is required, sensitive differences are recommended to ensure a consistent TVE calculation. Based on this, a key point for the new algorithm is the installation of the evaporator temperature sensor, responsible for measuring the evaporation temperature. Additionally, the evaporator temperature sensor must be placed where evaporator finishes defrost (evaporator area where frost remains the longest), ensuring that the evaporator is frost-free after defrost. Ideally, the temperature sensor should be placed at the entrance of the evaporator between two fins on a coil pipe right after the expansion valve.

2.1.2. Fan management based on *TVE*

An advanced fan management is included in the presented algorithm (as published by Maldonado et al. (2018)). Three modes of fan control were compared to evaluate optimal fan management regarding energy consumption. The results showed that switching fans and compressor activations simultaneously (*Refrigeration Mode*) when frost levels are low, together with activating fans for certain amount of frost on the evaporator without compressor activation (*Free-cooling Mode*) provide optimal energy savings to the system. A final last mode when fans are active regardless of the compressor status (*Evaluation Mode*) is applied for computing the frost level, as further detailed.

The *Free-cooling Mode* is used only when the algorithm detects enough frost level, in order to take advantage of the cooling power stored in the frost (as per thermal inertia). As seen in Fig.4 (detailed further down) when the walk-in temperature is within the regulation range and the compressor is OFF (CMP in Fig.4) the fans are switched ON, venting air on subcooled frost, which is able to cool down the room without making use of compressor energy. Sometimes this practice is able to reach set-point again. Energy savings can be achieved, since the compressor is not activated during this time. These energy savings are additional to the ones obtained from the

advanced defrost strategy. Therefore, the TVE parameter is used to calculate the frost level providing the optimization of both defrosts calls and evaporator fans management.

2.1.3. Algorithm general control loop

The two features described in this chapter were embedded in a global adaptive algorithm of the cold-room controller so that the controller is able to manage all the cold-room required functionalities.

The algorithm initially calculates the reference value TVE_{dry} , as previsouly explained, as a reference. TVE values are afterwards calculated at a certain frequency during normal refrigeration cycles (named TVE_{frost}) so they can be compared to TVE_{dry} to obtain the frost level. When TVE_{frost} is noticeably lower than TVE_{dry} frost presence is detected, due to an evaporator heat transfer reduction and increased thermal inertia. The TVE variation is named f_c and is calculated by dividing TVE_{frost} by TVE_{dry}. Hence, f_c=1 indicates a frost-free evaporator, while f_c<1 indicates some frost level. Since f_c indicates the evaporator frost level, a defrost is launched when f_s level is reached, being f_s the maximum frost level accepted. The coefficient f_s is initialized at the beginning of the process and modified by the algorithm based on the desired/expected defrosting time (t_{max}) as parametrized. The algorithm changes the fans running mode according to the frost level (f_c) so free-cooling techniques can be applied when the frost level is sufficient.

An algorithm flux diagram is shown in Fig.1. The first step (1) is the initialization of both parameters f_s (frost limit) and t_{max} (desired/expected defrosting time). In step (2) a defrost is launched in order to ensure there is no frost on the evaporator for the calculation of the reference TVE_{dry}. The cold-room is then cooled down to setpoint and kept within the desired temperature for a certain time while the fan is running in *Refrigeration Mode* (step 3). Afterwards fans are changed to *Evaluation Mode* to calculate the TVE parameter (step 4), which is performed by step 5, when TVE_{dry} is obtained. Fans are then changed to *Refrigeration Mode* again (step 6) and later the frost level is calculated as TVE_{frost} (step 7). Comparing TVE_{frost} to TVE_{dry} provides the frost level f_c (step 8). If the frost level is considered low the fans keep running in *Refrigeration Mode* (step 9), otherwise (sufficient frost is present) they are switched to *Free-cooling Mode* (step 10). The frost level is checked at a frequency depending on the frost level, thus lower evaluation frequencies are applied for low frost levels, while higher frequencies are used when high frost levels are computed. When the algorithm detects excessive frost level ($f_c \leq f_s$) a defrost is launched in order to melt all the ice and entirely clean the evaporator (step 11). Finally, the last step (12) calculates the time that was needed to melt the frost and compared to t_{max} (desired/expected defrosting time) such that f_s is corrected (increased or decreased) depending on the result; i.e. f_s is increased if the actual defrosting time was higher than desired, and decreased in the opposite scenario.

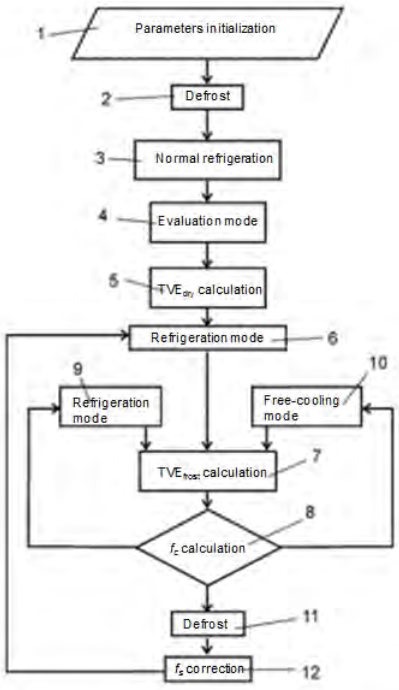

Figure 1: Algorithm control flux diagram (Albets et al., 2018)

2.2. Tests for algorithm evaluation: case studies

The new algorithm was tested under real conditions in different scenarios in order to evaluate the control performance when working in different cold-room temperature conditions and defrost systems (electric, air, etc.). Tests were performed in walk-ins used by restaurants and catering companies with remote condensing units. Among the tests cases, 2 freezers (using electric defrost) and 2 refrigerated cold rooms (using forced air as defrosting system) are detailed in next section.

3. RESULTS AND DISCUSSION

3.1. Test cases

The characteristics of the four tested walk-ins are listed in Table 1.

Table 1. Testing cold room characteristics

	Refrigerated cold room 1	Refrigerated cold room 2	Freezing cold room 1	Freezing cold room 2
Volume (m^3)	10	10	5	70
Setpoint (ºC)	1.5	1.5	-18	-19
Defrost type	Forced air	Forced air	Electric	Electric
Refrigerant type	R449A	R449A	R404A	R404A

Tests were carried out in order to evaluate the control performance under different ambient external conditions, during summer and winter for the refrigerated cold-rooms and during winter for the freezing cold-rooms. An initial monitoring of the cold-room (when controlled by a previous standard electronic controller) was performed for all tests cases, including electric energy consumption. For all test cases, defrosts were launched 4 times per day, lasting 20 minutes each; and fans were running 24h. Afterwards, the cold-room control was switched to the new presented algorithm, for evaluation and comparison of the control strategy. Monitoring with the standard control lasted at least one week, while the monitoring for the new control lasted at least 2 weeks. The previous control was not modified before the test, which means it worked as usual in each installation: defrost was finished by time in *Refrigerated cold room 1* and *Refrigerated cold room 2*. However, there were temperature sensors used to finish the defrost in *Freezing cold room 1* and *Freezing cold room 2* when they reached 15ºC and 8ºC, respectively.

3.2. Discussion

Results are presented and compared with the previous electronic controller evaluating the energy consumption, the number of defrosts and the time the cold-room temperature is within the regulation range (setpoint and setpoint+deadband).

Fig.2 shows a comparison of the number of defrost for *Freezing cold room 2*, first days in red are previous controller defrost, while data in green is related to the results for the new algorithm, colour-code applying throughout this work. The new algorithm calculates the frost level on the evaporator in order to launch defrosts only when necessary, so as it can be clearly seen there is an important reduction of the number of launched defrosts. The previous controller was programmed as a standard control to defrost four times per day, however the number of defrost drastically decreased working with the new algorithm. For several days defrost was not even necessary. These results demonstrate a good performance of the new algorithm and, at the same time, show how standard practices are related to excessive defrosts, which is currently the common defrost management in commercial and industrial refrigeration. It is also important to mention that there were several consecutive days (up to four) when no defrosts were needed. Also, these results demonstrate that freezing cold-rooms with refrigerated pre-chambers (as *Freezing cold room 1* and *Freezing cold room 2* in this study) do not generally need four daily defrosts.

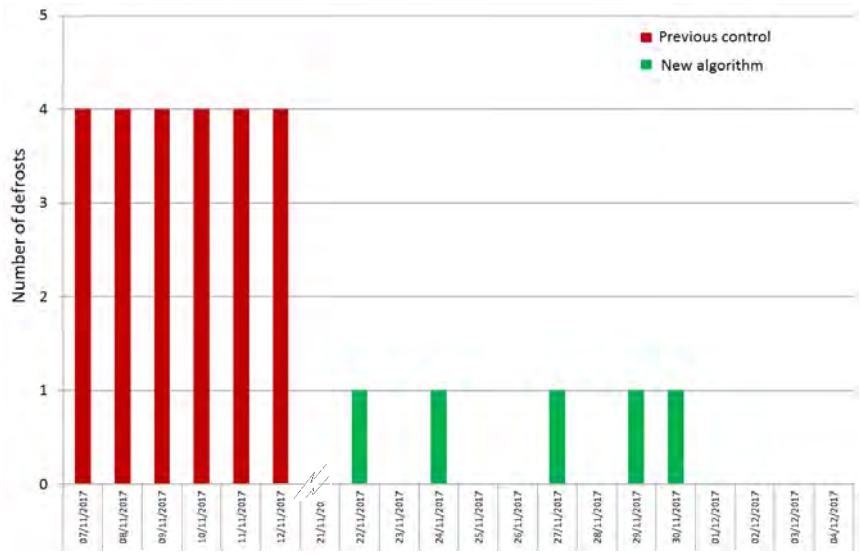

Figure 2: Freezing cold room 2 - Number of defrosts with both controls

Fig.3 shows an energy usage comparison for *Freezing cold room 2*, with standard control and optimized control (the presented new algorithm). A remarkable energy consumption reduction is obtained when the new algorithm is controlling the cold room. The consumption varies every day as it does the cold room activity (number of doors open, material inside the cold room, etc.), however, both controls follow the same trend according to the week day. The new algorithm shows energy savings up to 45% being an average of 39.3% for all the testing days.

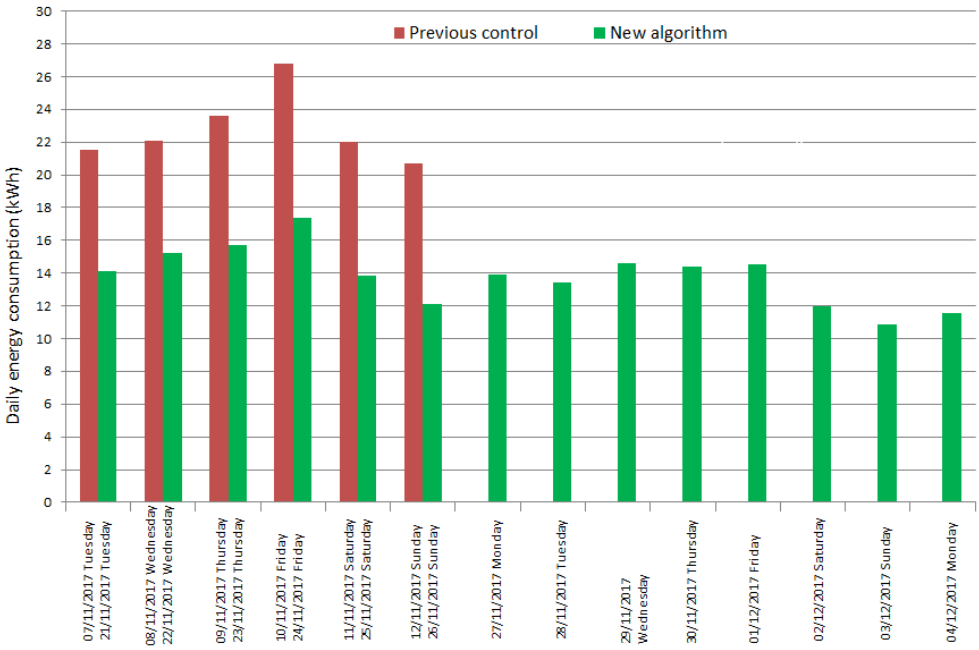

Figure 3: Freezing cold room 2 - Energy consumption comparison

Energy savings, as previously explained, are produced thanks to the reduction of defrost time (electric heaters) and the reduction of compressor running time. Since there are less defrosts, less heat from the defrost heaters is incorporated into the cold-room, hence requiring less refrigeration power. Additionally, the new algorithm allows the use of the frost accumulated on the evaporator as free-cooling, so the cycling time is extended and less compressor energy is needed. Moreover, when comparing to control strategies where fans are kept running 24h, the fans energy consumption is also lower as less fan time is used by the new algorithm. Fig.4 shows how the new algorithm is able to decrease the cold room temperature by switching on the evaporator fans instead of running the compressor (defined as *Free-cooling Mode*, as previously explained). As shown in the graph the cold room temperature is able to reach the set-point again (-19ºC) only by

using the fan, extending the refrigeration cycle. In this example free-cooling is running 9 minutes out of 37 minutes, an additional 33.3% of free-cooling time.

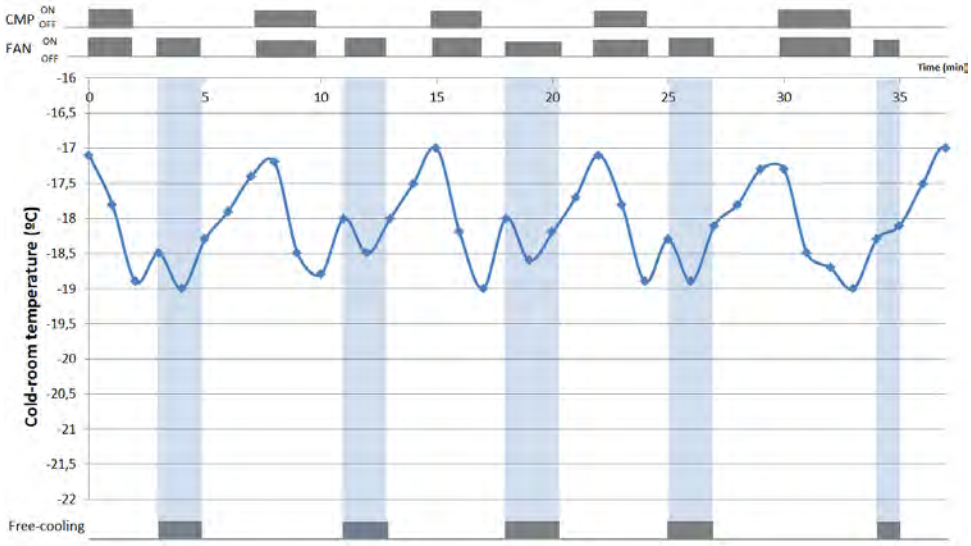

Figure 4: Free-cooling achieved by the fan management in Freezing cold room 2

A summary of the results for all the cold-rooms is shown in Tables 2 and 3. *Freezing cold room 1* obtains high energy savings as the new controller decreases energy consumption from 8.11 kWh to 5.43 kWh as a daily average (33%). Also, the average defrost calls is less than a defrost per day (0.6 defrost/day), which compared to 4 defrost/day represents 85% reduction. Similarly, *Freezing cold room 2* presents important energy savings as well, reducing from 22.78 kWh to 13.82 kWh per day, meaning 39.33% less energy than the needed with the previous control. The average number of defrosts is also less than one per day (0.4 defrosts/day). This important defrost reduction could be achieved thanks to the existence of refrigerated pre-chambers for both freezers, helping to keep low the humidity inside the cold-room, consequently building-up less frost on the evaporator. Nevertheless, previous controller was launching four defrosts per day, clearly showing how this amount of defrost was excessive. Finally, it can be observed that *Freezing cold room 2* reached an increase of 8.3% of time in temperature range.

The *Refrigerated cold room 1* shows a consumption decrease between 20.81% and 25.49% for summer and winter, respectively. The new algorithm launches 3.25 defrosts per day instead of 4, as commonly applied by standard controllers, and increases the time within the desired temperature range by 1.29% in summer. The *Refrigerated cold room 2* also presents energy consumption savings when the controller uses the new algorithm, decreasing between 15.97% and 23.24%. Also, defrosts are decreased from 4 to 2.79 and 2.35 in summer and winter, respectively. The time in temperature range was increased by 0.92% in summer, although no variation was found in winter, mostly because cold-room temperature is affected by the cold-room traffic.

Table 2. Freezing cold-rooms results

Test	Period test	Type of control	Daily average energy consumption (kWh/day)	Energy savings achieved (%)	Average defrosts per day	Time temperature within control range (%)
Freezing cold room 1	Winter	Previous control	8.11	-	4	*N/A*
		New algorithm	5.43	33	0.6	
Freezing cold room 2	Winter	Previous control	22.78	-	4	85
		New algorithm	13.82	39.33	0.4	93.3

Table 3. Refrigerated cold-rooms results

Test	Period test	Type of control	Daily average energy consumption (kWh/day)	Energy savings achieved (%)	Average defrosts per day	Time temperature within control range (%)
Refrigerated cold room 1	Summer	Previous control	11.29	-	4	95.8
		New algorithm	8.94	20.81	3.25	97.09
	Winter	Previous control	5.64	-	4	98.45
		New algorithm	4.20	25.49	2.45	98.44
Refrigerated cold room 2	Summer	Previous control	16.28	-	4	87.42
		New algorithm	13.68	15.97	2.79	88.34
	Winter	Previous control	8.39	-	4	96.5
		New algorithm	6.44	23.24	2.35	96.82
Freezing cold room 1	Winter	Previous control	8.11	-	4	*N/A*
		New algorithm	5.43	33	0.6	*N/A*
Freezing cold room 2	Winter	Previous control	22.78	-	4	85
		New algorithm	13.82	39.33	0.4	93.3

4. CONCLUSIONS

The new control algorithm presented in this paper is based on the TVE parameter. The new algorithm is able to estimate the frost level using two temperature sensors, using this information to launch defrosts only when necessary. The algorithm is also able to use the frost level information to optimally manage the evaporator fans, so that free-cooling is applied to cool down the cold room, providing remarkable energy savings, with respect to standard practices. Several case studies are also presented. The algorithm was embedded in a cold-room controller (Albets et al., 2018) to be tested under real conditions, evaluating its performance regarding defrosts calls, energy usage and time within temperature desired range. All four test cases presented high energy savings, ranging from 15.97% to 39.33%, especially for the cold-rooms that used electric heaters for defrosting. These energy savings are also attributed to the advanced fan management, which made use of free-cooling techniques. All cases also presented a drastic defrost call reduction. This fact demonstrates how standard controlling techniques generally perform unnecessary defrosts. For instance, current test cases presented a reduction from 4 defrosts per day (with previous controller) to 0.4-3.25 defrosts per day. Remarkably, *Freezing cold room 2* did not need more than a defrost in 4 days. Finally, the new algorithm allowed the cold-room temperature to be within the desired temperature range for longer periods of time, especially in summer, supporting the food conservation quality.

ACKNOWLEDGEMENTS

This work is part a project funded by CDTI, the public Spanish institution in charge of management and development policies from the Economy and Competitiveness Ministry. This work was partially funded by the Spanish government through CDTI project with reference code IDI-20160143. José Miguel Maldonado would like to thank the Spanish Government for his research fellowship (BES-2016-076554). The project also has received funding from the European Union's Horizon 2020

research and innovation programme under the Marie Sklodowska-Curie grant agreement No 712949 (TECNIOspring PLUS) and from the Agency for Business Competitiveness of the Government of Catalonia. Pere Moreno would like to thank Ministerio de Economía y Competitividad de España for Grant Torres Quevedo, PTQ-15-08025. GREiA is certified agent TECNIO in the category of technology developers from the Government of Catalonia. The authors would like to thank the Catalan Government for the quality accreditation given to their research group (2017 SGR 1537).

REFERENCES

Albets, X., Moreno, P., González, M.A., Cabeza, L.F., Maldonado, J.M., Zsembinszki, G., de Gracia, A., 2018. Adaptive control method for refrigeration systems. Ref. WO/2018/178465.

Allard, J., Heinzen, R., 1988. Adaptive defrost. IEEE Transactions on Industry Applications, 39–42.

Axell, M., Fahlen, P., 2002. Climatic influence on display cabinet performance. Proceedings of the IIR International Conference New Technologies in Commercial Refrigeration, Urbana, USA, 181-190.

Howell, R.H., Rosario, L., Riiska, D., Bondoc, M., 1999. Potentials savings in display case energy with reduced supermarket relative humidity. Proceedings of the 20th International Congress of Refrigeration. Sydney, Australia, IIR/IIF p. 113.

Kazachi, G., 2001. Project progress meeting in discussion of display case warm liquid defrosting test at EPA. Raleigh.

Kinoshita, M., Sasaki Y., 1983. Frost detector for refrigerating apparatus - U.S. Patent 4400949. 352,874.

Maldonado, J.M., Zsembinszki, G., de Gracia, A., Moreno, P., Albets, X., González, M.A., Cabeza L.F., 2018. Control strategies for Defrost and evaporator fans operation in walk-in freezers. Int. J. Refrigeration (91),101-110.

Mastrullo, R., Mauro, A.W., Menna, L., Palma, A., Vanoli, G.P., 2014. Transient model of a vertical freezer with door openings and defrost effects. Appl Energy (121), 38-50.

Manuscript ID: 142
DOI: 10.18462/iir.icr.2019.0142

Experimental comparison of the use of R134a and R1234ze(E) in a semi-hermetic reciprocating compressor

Luca MOLINAROLI[(a)], Andrea LUCCHINI[(a)], Luigi Pietro Maria COLOMBO[(a)]

[(a)] Dipartimento di Energia, Politecnico di Milano
Milano, 20156, Italy
luca.molinaroli@polimi.it, andrea.lucchini@polimi.it, luigi.colombo@polimi.it

ABSTRACT

An experimental comparison of the use of R134a and R1234ze(E) in a semi-hermetic reciprocating compressor is presented in this paper. The comparison deals with the mass flow rate at compressor suction, the compressor power consumption and refrigerant temperature at compressor discharge. These parameters are measured using a dedicated experimental set-up. Twenty-five experimental working conditions that cover a large part of the compressor envelope are considered and a fitting procedure as per international standards is carried out for a deeper comparison. The results show that the use of the refrigerant R1234ze(E) leads to an average reduction of the sucked mass flow rate equal to 19.4%, to an average reduction of the compressor power consumption equal to 24.4% and to an average reduction of refrigerant temperature at compressor discharge equal to 9.2 °C.
Keywords: Compressor; Experimentation; R1234ze(E); R134a

1. INTRODUCTION

In the last years, the EU 517/2014 regulation (European Union, 2014) together with the Kigali amendment (United Nations, 2016) have introduced more and more restriction on the use of refrigerants with high Global Warning Potential (GWP): As a consequence, new substances are continuously appearing on the market to respond to the need of the air conditioning and refrigeration industry. Both new synthetic refrigerants and old natural substances are considered, analysed and tested in vapour compression systems but, to date, no final substitutes are found.
Among the different alternatives (Domanski *et al.*, 2017), R1234ze(E) gained attention (Mota-Babiloni *et al.*, 2016) in the last years since it seems to be less flammable than R1234yf (Kondo et al., 2012) and it is suitable for high temperature heat pump (Fukuda et al., 2014).
Mota-Babiloni *et al.* (2014) carried out an experimental analysis of the use of R134a, R1234yf and R1234ze(E) in a drop-in application. They found that the volumetric efficiency of the compressor working with R1234ze(E) is from 5% to 6% lower than that of the R134a. Moreover, an average cooling capacity reduction equal to 30% and a COP reduction between 2% and 8% when using the HFO refrigerant was found.
Sethi *et al.* (2016) compared the performance of R1234yf and R1234ze(E) versus R134a in a vending machine system. They found that, in a drop-in application, the use of R1234ze(E) leads to about 25% capacity reduction with similar COP. Conversely, when a larger compressor was used to match the capacity of R134a, a lower efficiency was obtained due to higher pressure drop in the system.
Nawaz *et al.* (2017) theoretically analysed the use of R1234yf and R1234ze(E) on a residential heat pump water heater. A model of the system was first tuned on R134a experimental results and then used to carry out a series of parametric analyses. They found that R1234ze(E) exhibits a lower heating capacity, hence the need of a larger compressor, and slightly lower compressor discharge temperature, allowing for the use of the same lubricant.
Mota-Babiloni *et al.* (2017) experimentally compared the performance of a water-to-water system using R134a and R1234ze(E) with the aim of achieving the same cooling capacity. They found that an increase of compressor swept volume and the use of an internal heat exchanger compulsory for the HFO based system to perform similarly to the R134a one. Otherwise, a reduction of the

refrigerant mass flow rate between 18% and 29% and a subsequent reduction of the cooling capacity reduction, between 22% and 34%, might arise.
Aprea *et al.* (2018) carried out a comparative analysis of the use of R134a and of R1234ze(E) in a domestic refrigerator. They optimized the refrigerant charge in a pull-down test finding that the optimal charge of R1234ze(E) is 35% greater than the R134a. During 1-day tests, the R1234ze(E) system showed a reduction of the compressor power consumption that led to a 9% energy saving.
All the aforementioned papers provide valuable information about the use of R1234ze(E) in vapour compression systems. However, even if some information is provided, the literature analysis shows that the great majority of the studies are focused more on the system than on the compressor that works with R1234ze(E). Therefore, the goal of the present paper is to analyse only the performance of a semi-hermetic reciprocating compressor working with R1234ze(E). An experimental activity on R134a is carried out too in order to establish a baseline for performance comparison.

2. EXPERIMENTAL SET-UP

The layout of the experimental set-up used to assess the refrigerant performance is shown in Figure 1. The test rig mimics a water-to-water system and consists of three different loops: the refrigerant loop, the water-ethylene glycol cold loop and the hot water loop. The refrigerant loop is used to reach the desired superheating at compressor inlet acting on the expansion valve set-point whereas the two other loops are used to set the water mass flow rates and the temperatures at the outlets of their heat exchangers. This, in turn, leads to different evaporating and condensing pressure and, therefore, to different compressor operating conditions. More details about the experimental set-up are found in Molinaroli *et al.* (2018).
The compressor used in the experimental campaign is a semi-hermetic reciprocating compressor with nominal swept volume equal to 13.15 $m^3 \cdot h^{-1}$ at 50 Hz and ISO32 POE oil.

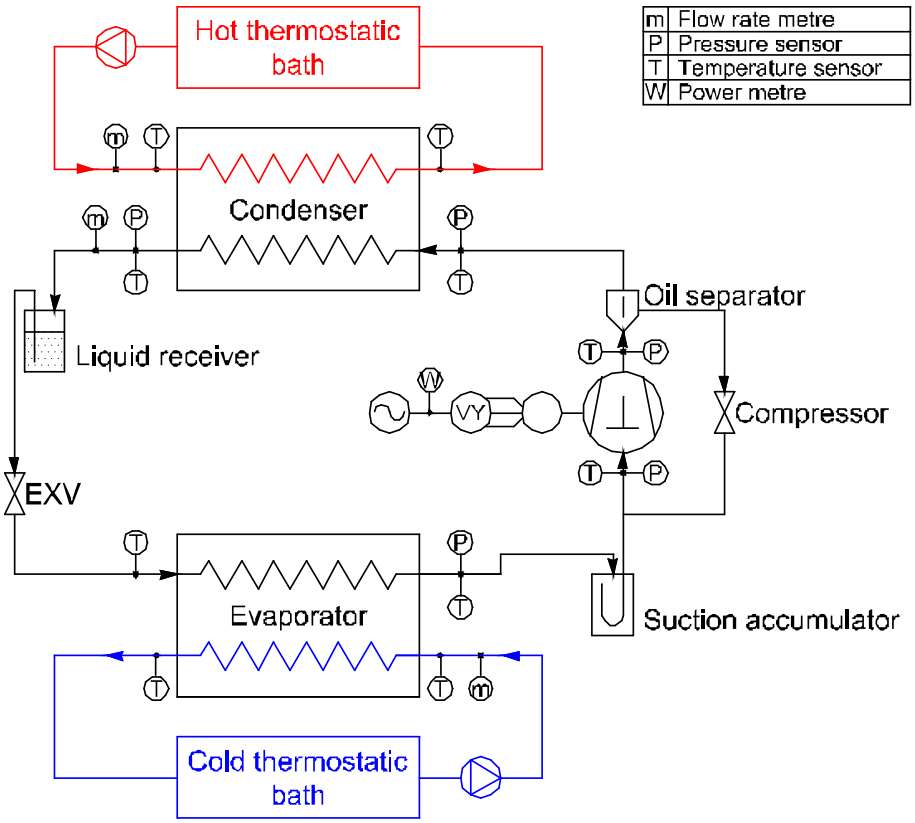

Figure 1. Layout of the experimental set-up.

The test rig was equipped with instrumentations that allow for the data acquisition of the main parameters such as pressures, temperatures, flow rates and power. The positions of all the measurement devices are shown in Figure 1 while the main characteristics of the instrumentation relevant to compressor analysis are collected in Table 1.

Table 1. Measurement instrumentation and accuracy.

Parameter	Instrument	Range	Accuracy
Refrigerant mass flow rate	Coriolis mass flow metre	0 kg·h^{-1} - 300 kg·h^{-1}	±0.15% r.v.
Refrigerant suction pressure	Pressure transducer	0 kPa - 600 kPa	±0.3% f.s.
Refrigerant discharge pressure	Pressure transducer	0 kPa - 4000 kPa	±0.3% f.s.
Refrigerant temperature	RTD Pt100	243.15 K - 343.15 K	±0.1 K
Electric power	Power transducer	0 W - 4000 W	±0.2% f.s.

Finally, the experimental procedure used to carry out each test of the experimental campaign is the following:

1. The temperatures of the cold and hot thermostatic baths are set to the desired value.
2. The pumps of the cold and hot loop are switched on and the RPM are set to values needed by the test.
3. The compressor and the electronic expansion valve are switched on. The oil level on the compressor glass is checked.
4. Once the pressures and the temperatures at compressor inlet and outlet has reached the value required by the test, the data acquisition starts with a sample rate equal to 1 s. For each of the measured datum, the simple moving average is calculated considering the last 900 samples. The oil level on the compressor glass is checked again for stability purpose.
5. If the deviation of each measured pressure and temperature lies within ± 10 kPa and ± 0.2 K respectively, the test is considered in steady-state condition and further 900 samples are recorded for data analysis.

3. RESULTS

The experimental campaign is organized in 5 groups of 5 tests each that are repeated for R134a and for R1234ze(E). The tests condition are reported in Table 2.

Table 2. Test conditions.

Group	f [Hz]	ΔT_{SUP} [°C]	$T_{G,OUT,EVAP}$ [°C]	$T_{W,OUT,COND}$ [°C]
1	50	8	-5	35,45,55,65,75
2	50	8	0	35,45,55,65,75
3	50	8	5	35,45,55,65,75
4	50	8	10	35,45,55,65,75
5	50	8	15	35,45,55,65,75

Overall, 25 working conditions are available for each refrigerant.
The experimental campaign is carried out setting a constant temperature at evaporator and condenser outlet instead of constant evaporating and condensing temperatures. This may lead to an improper comparison of the compressor performance between the R134a and R1234ze(E). Therefore, in order to overcome this issue, the performance data are interpolated using a third degree polynomial formula as per EN 12900 standard. The general form of the polynomial equation is the following:

$$X = a_0 + a_1 SST + a_2 SDT + a_3 SST^2 + a_4 SST \cdot SDT + a_5 SDT^2 + a_6 SST^3 + a_7 SST^2 \cdot SDT + \\ + a_8 SST \cdot SDT^2 + a_9 SDT^3 \quad \text{Eq. (1)}$$

Where X stands for the refrigerant mass flow rate at compressor suction ($\dot{m}_{SUC}$) or the compressor electric power consumption ($\dot{W}_{EL}$) or the refrigerant temperature at compressor discharge (T_{DIS}) whereas SST and SDT are the saturation suction and saturation discharge temperatures respectively, i.e. the evaporating and condensing dew point temperatures at the suction and discharge pressures respectively. The 10 coefficients of the polynomial are reported in Table 3.

Table 3. Coefficients of the polynomial representation of the compressor performance.

Coefficient	R134a			R1234ze(E)		
	$\dot{m}_{SUC}$	$\dot{W}_{EL}$	T_{DIS}	$\dot{m}_{SUC}$	$\dot{W}_{EL}$	T_{DIS}
a_0	$1.77 \cdot 10^{2}$	$7.56 \cdot 10^{2}$	$1.78 \cdot 10^{1}$	$1.76 \cdot 10^{2}$	$7.64 \cdot 10^{2}$	$2.67 \cdot 10^{1}$
a_1	$6.47 \cdot 10^{0}$	$-1.85 \cdot 10^{1}$	$-4.11 \cdot 10^{-1}$	$5.03 \cdot 10^{0}$	$-1.97 \cdot 10^{1}$	$-6.88 \cdot 10^{-1}$
a_2	$-2.33 \cdot 10^{-1}$	$3.57 \cdot 10^{1}$	$1.29 \cdot 10^{0}$	$-2.02 \cdot 10^{0}$	$2.08 \cdot 10^{1}$	$6.60 \cdot 10^{-1}$
a_3	$1.62 \cdot 10^{-1}$	$-9.21 \cdot 10^{-1}$	$1.65 \cdot 10^{-2}$	$1.18 \cdot 10^{-1}$	$-6.45 \cdot 10^{-1}$	$2.32 \cdot 10^{-2}$
a_4	$5.23 \cdot 10^{-3}$	$8.21 \cdot 10^{-1}$	$-1.12 \cdot 10^{-2}$	$-5.33 \cdot 10^{-3}$	$8.35 \cdot 10^{-1}$	$1.10 \cdot 10^{-2}$
a_5	$-1.01 \cdot 10^{-2}$	$-7.51 \cdot 10^{-2}$	$-8.18 \cdot 10^{-2}$	$2.30 \cdot 10^{-2}$	$1.57 \cdot 10^{-2}$	$6.30 \cdot 10^{-3}$
a_6	$-3.25 \cdot 10^{-4}$	$-8.62 \cdot 10^{-3}$	$-4.98 \cdot 10^{-4}$	$2.17 \cdot 10^{-4}$	$1.06 \cdot 10^{-2}$	$-1.68 \cdot 10^{-3}$
a_7	$-1.78 \cdot 10^{-3}$	$1.05 \cdot 10^{-2}$	$-9.90 \cdot 10^{-5}$	$-1.08 \cdot 10^{-3}$	$3.37 \cdot 10^{-3}$	$2.74 \cdot 10^{-4}$
a_8	$-2.70 \cdot 10^{-4}$	$4.16 \cdot 10^{-3}$	$1.30 \cdot 10^{-5}$	$1.33 \cdot 10^{-4}$	$1.27 \cdot 10^{-3}$	$-1.33 \cdot 10^{-4}$
a_9	$3.82 \cdot 10^{-5}$	$-1.01 \cdot 10^{-3}$	$5.18 \cdot 10^{-6}$	$-1.42 \cdot 10^{-4}$	$-1.19 \cdot 10^{-3}$	$-3.28 \cdot 10^{-5}$

The polynomial representation is valid for SST within the range from -10 °C to 12.5 °C and for SDT within the range from 30 °C to 80 °C.

The trend of the mass flow rate at compressor suction in the range of considered evaporating and condensing temperatures is depicted in Figure 2 for R134a and in Figure 3 for R1234ze(E). The results indicate the mass flow rate sucked by the compressor strongly reduces when R1234ze(E) is used as refrigerant since an average reduction equal to 19.4% is found. This is mainly due to the lower density of R1234ze(E) since its density at compressor suction is about 18.5% lower than that of R134a in the range of the evaporating temperatures used in this study. The reduction reaches its minimum value, 8.8%, in the top-right corner of the envelope, i.e. highest evaporating and condensing temperature, and gets lower as the evaporating or the condensing temperature reduce.

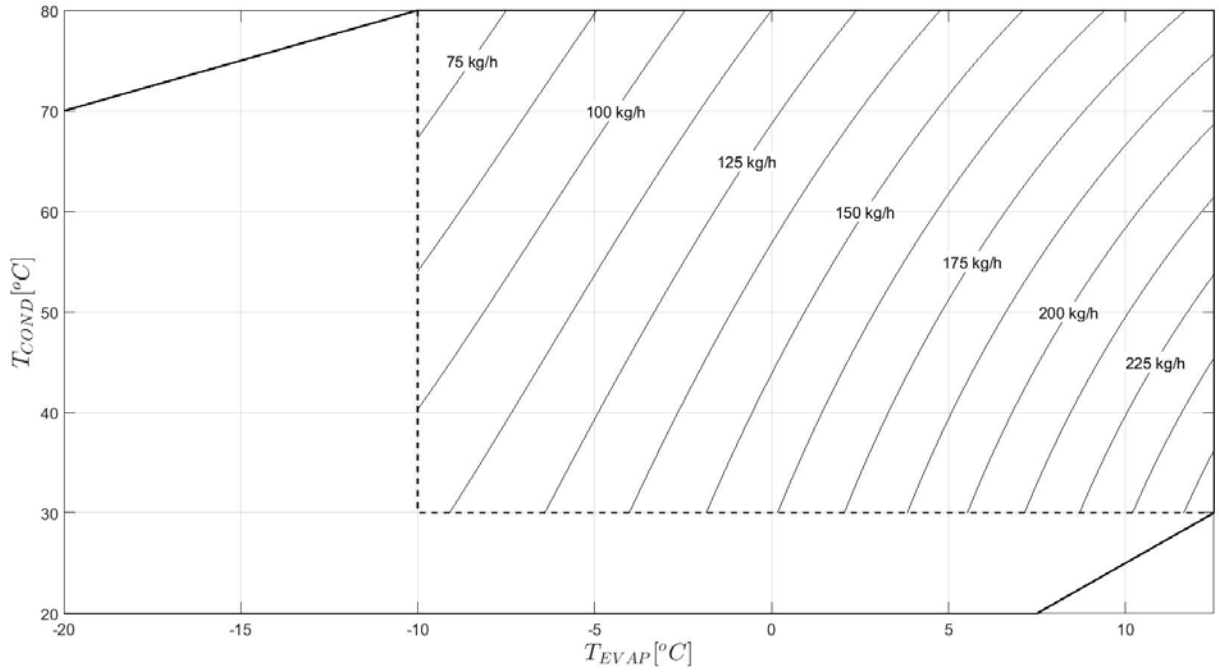

Figure 2. R134a mass flow rate at compressor suction.

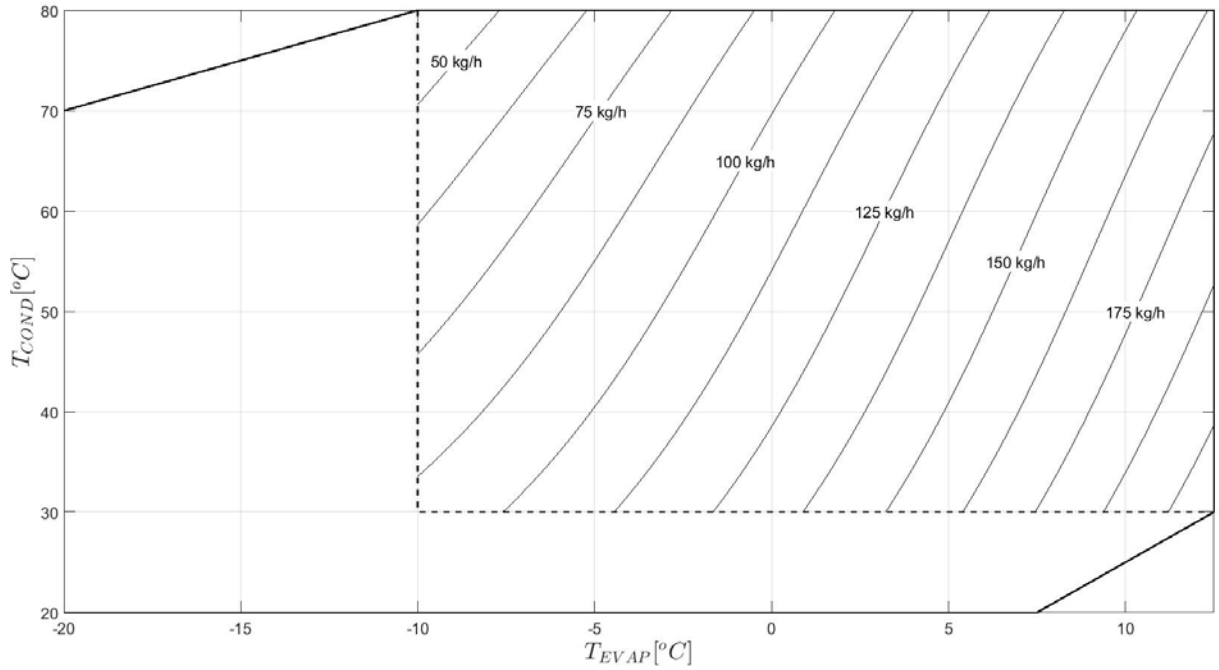

Figure 3. R1234ze(E) a mass flow rate at compressor suction.

The compressor electric power consumption as a function of evaporating and condensing temperatures is depicted in Figure 4 and in Figure 5 for R134a and for R1234ze(E) respectively. The results indicate the compressor power consumption is considerably lower when R1234ze(E) is used as refrigerant since an average reduction equal to 24.4% is found. This is mainly due to the just stated reduction of refrigerant mass flow rate. The reduction reaches its maximum value, 29.5%, in the top-left corner of the envelope, i.e. lowest evaporating temperature and highest condensing temperature, and gets lower as the evaporating or the condensing temperature increase.

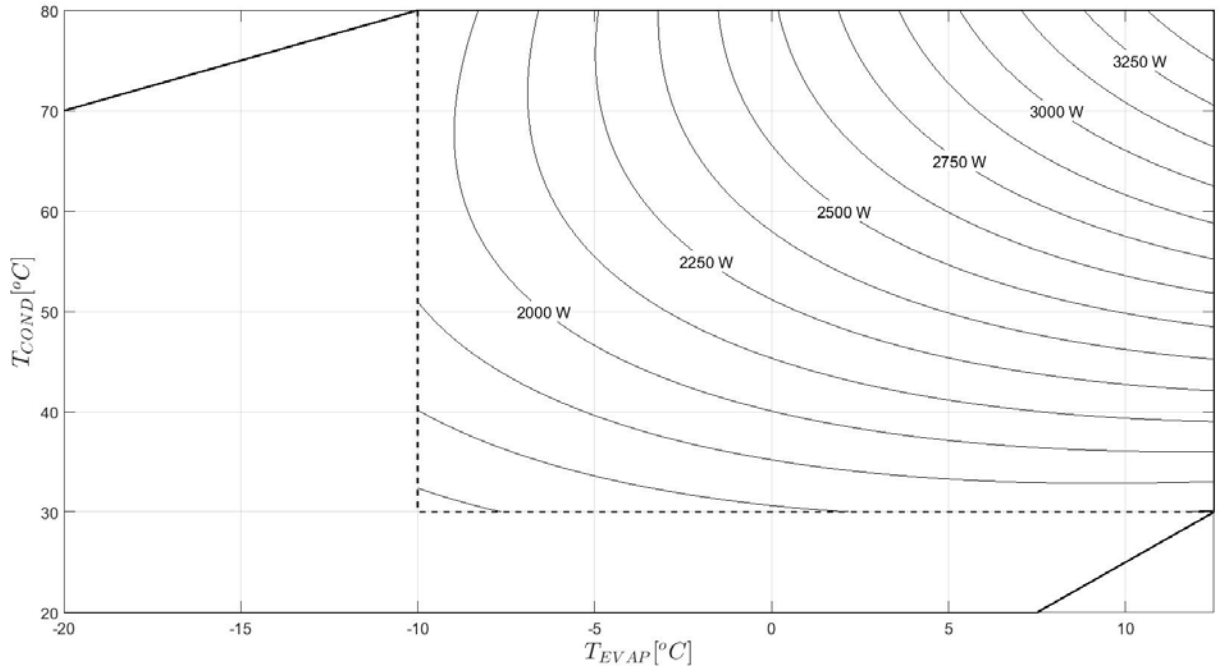

Figure 4. Electric power consumption for the compressor working with R134a.

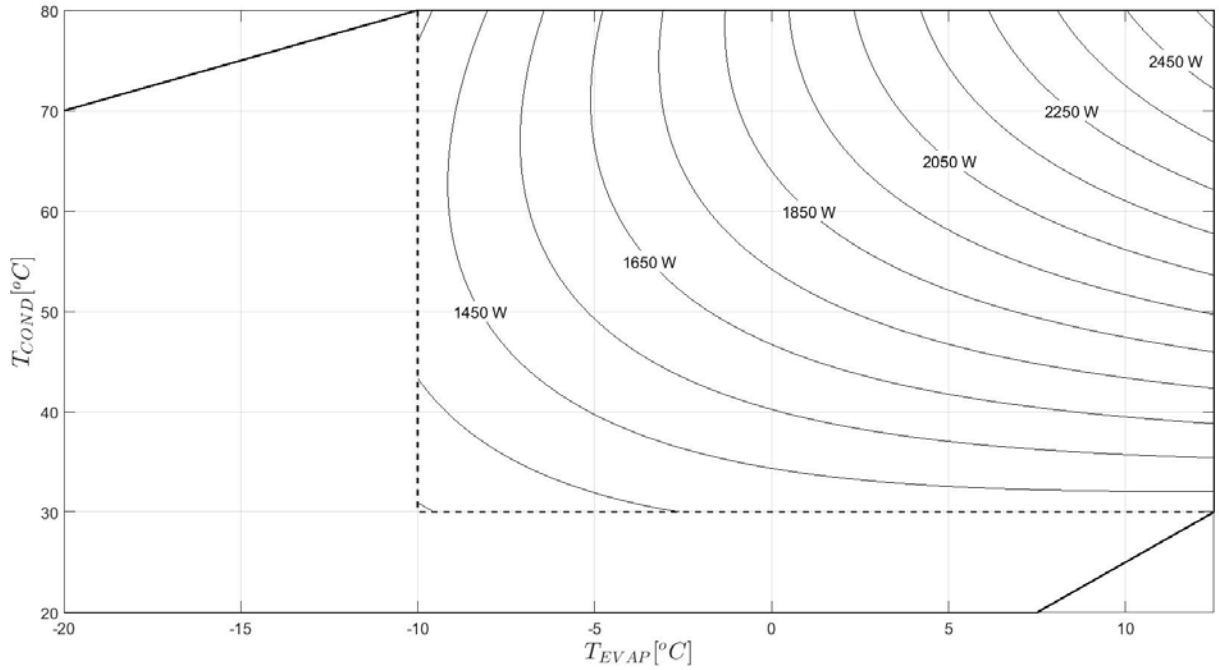

Figure 5. Electric power consumption for the compressor working with R1234ze(E).

Finally, Figure 6 and Figure 7 report the refrigerant temperature at compressor discharge for R134a and R1234ze(E) respectively. Overall, the results show that the temperatures at compressor discharge achieved with R1234ze(E) are lower than those achieved with R134a. The average difference is equal to 9.2 °C and is for sure beneficial for compressor operation. This can be explained considering that, at the same evaporating and condensing temperatures, the pressure ration of the two refrigerants is very similar but the molar mass is different. Indeed, the molar mass of R1234ze(E), 114 g·mol^{-1}, is higher than the molar mass of R134a, 102 g·mol^{-1}. Under the same pressure ratio, the higher the molar mass, the lower the temperature increase in an isentropic, and hence in a real, compression process. The discharge temperature reduction reaches its minimum value, 2.2 °C, in the bottom-right corner of the envelope, i.e. highest evaporating and lowest condensing temperature, and increases as the evaporating temperature reduces or the condensing temperature increases.

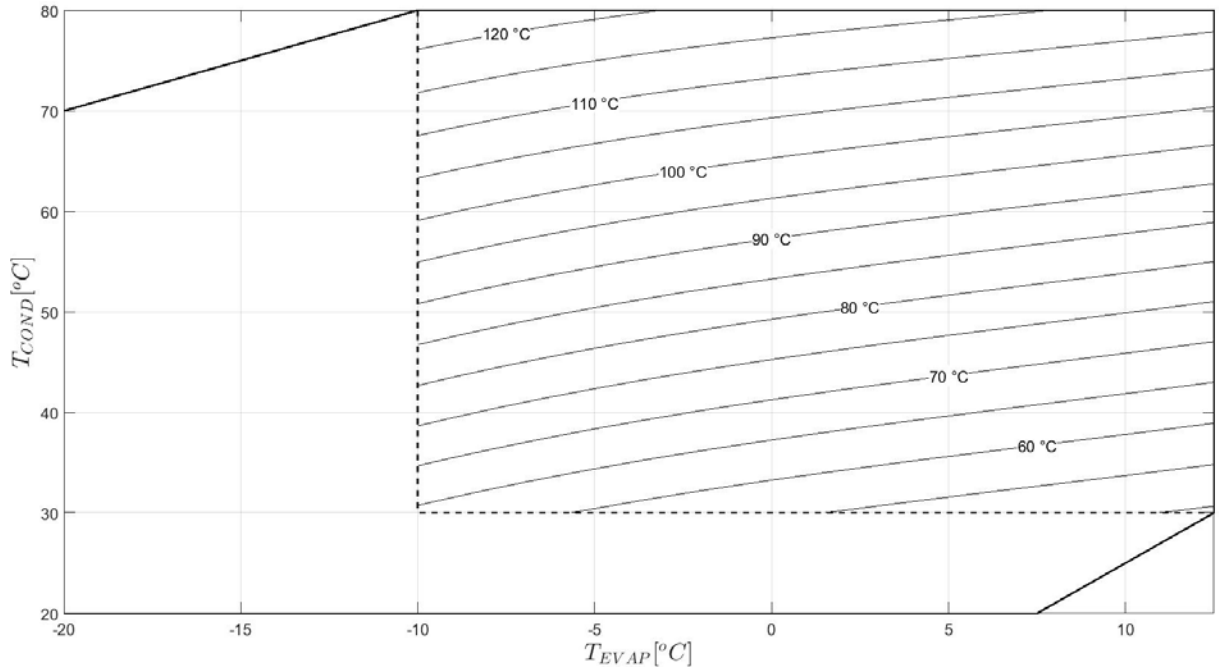

Figure 6. R134a temperature at compressor discharge.

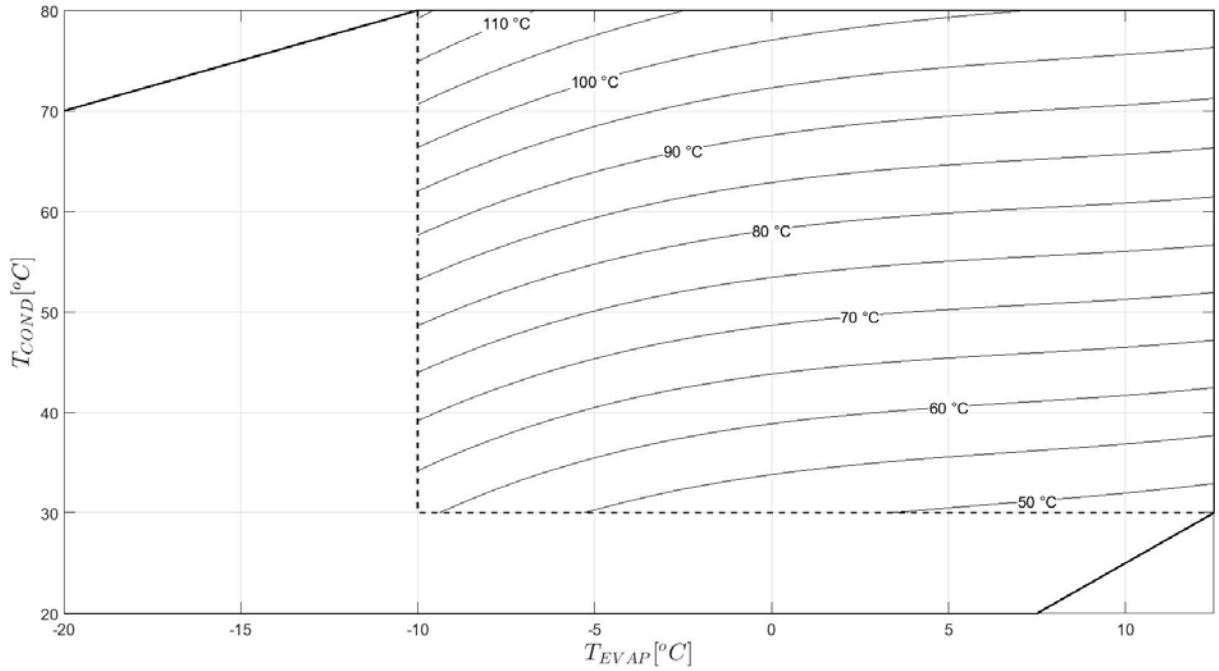

Figure 7. R1234ze(E) temperature at compressor discharge.

4. CONCLUSIONS

In the present paper, an experimental comparison of the use of R134a and R1234ze(E) in a semi-hermetic reciprocating compressor is carried out. The analysis considers the mass flow rate at compressor suction, the compressor power consumption and refrigerant temperature at compressor discharge. These parameters are first measured on 25 experimental test conditions that cover a large part of the compressor envelope and are then fitted using ten coefficients polynomials for a deeper comparison. The results show that when the refrigerant R1234ze(E), a general reduction of the sucked mass flow rate, of the compressor power consumption and of the refrigerant temperature at compressor discharge are achieved. More in detail, compared to R134a, the reduction of the refrigerant mass flow rate at compressor ranges from 8.8% to 38.9%, the reduction of power consumption ranges from 20.4% to 29.5% and, finally, the reduction of refrigerant temperature at compressor discharge ranges from 2.2 °C to 15.6 °C.

ACKNOWLEDGEMENTS

The financial support of the Italian Ministry of Education, University and research (MIUR) through the program PRIN 2015 (Grant Number 2015M8S2PA) is greatly acknowledged. Frascold company is acknowledged for providing the compressor used in the experimental campaign.

NOMENCLATURE

f	frequency (Hz)	T_{EVAP}	evaporating temperature (°C)
$\dot{m}_{SUC}$	mass flow rate at compressor suction (kg·h^{-1})	$T_{G,OUT,EVAP}$	temperature of the water-ethylene glycol at evaporator outlet (°C)
SST	Saturation Suction Temperature (°C)	$T_{W,OUT,COND}$	temperature of the water at condenser outlet (°C)
SDT	Saturation Discharge Temperature (°C)	$\dot{W}_{EL}$	electric power (W)
T_{COND}	condensing temperature (°C)		
T_{DIS}	temperature at compressor discharge (°C)	ΔT_{SUP}	superheating at compressor suction (°C)

REFERENCES

Aprea, C., Greco, A., Maiorino, A., Masselli, C., 2018. The drop-in of HFC134a with HFO1234ze in a household refrigerator. Int. J. Therm. Sci. 127, 117-125.

Domanski P.A., Brignoli, R., Brown, J.S., Kazakov, A.F., McLinden, M.O., 2017. Low-GWP refrigerants for medium and high-pressure applications. Int. J. Refrigeration 84, 198-209.

European Standard EN 12900, 2013 Refrigerant compressors - Rating conditions, tolerances and presentation of manufacturer's performance data.

European Union, 2014 Regulation (EU) No 517/2014 of the European Parliament and the Council of 16 April 2014 on fluorinated greenhouse gases and repealing Regulation (EC) No 842/2006. Off. J. Eur. Union 150, 195-230.

Fukuda, S., Kondou, C., Takata, N., Koyama, S., 2014. Low GWP refrigerants R1234ze(E) and R1234ze(Z) for high temperature heat pumps. Int. J. Refrigeration 40, 161-173.

Kondo, S., Takizawa, K., Tokuhashi, K., 2012. Effects of temperature and humidity on the flammability limits of several 2L refrigerants, J. Fluorine Chem. 144, 130-136.

Molinaroli, L., Lucchini, A., Colombo, L.P.M., 2018. Design and commissioning of an experimental facility for performance evaluation of pure and mixed refrigerants. Proocedings of the 36th UIT Heat Transfer Conference, Catania, Italy, 1-8.

Mota-Babiloni, A., Navarro-Esbrí, J., Barragán-Cervera, Á., Molés, F., Peris, B., 2014. Drop-in energy performance evaluation of R1234yf and R1234ze(E) in a vapor compression system as R134a replacements, Appl. Therm. Eng. 71, 259-265.

Mota-Babiloni, A., Navarro-Esbrí, J., Mendoza-Miranda, J.M., Peris, B., 2017. Experimental evaluation of system modifications to increase R1234ze(E) cooling capacity, Appl. Therm. Eng. 111, 786-792.

Mota-Babiloni, A., Navarro-Esbrí, J., Molés, F., Barragán-Cervera, Á., Peris, B., Verdú, G., 2016. A review of refrigerant R1234ze(E) recent investigations, Appl. Therm. Eng. 95, 211-222.

Nawaz, K., Shen, B., Elatar, A., Baxter, V., Abdelaziz, O., 2017. R1234yf and R1234ze(E) as low-GWP refrigerants for residential heat pump water heaters. Int. J. Refrigeration, 348-365.

Sethi, A., Becerra, E.V., Motta, S.Y., 2016. Low GWP R134a replacements for small refrigeration (plug-in) applications, Int. J. Refrigeration 66, 64–72.

United Nations Environment Programme, 2016 Further Amendment of the Montreal Protocol.

Manuscript ID: 143
DOI: 10.18462/iir.icr.2019.0143

A smart early detection system for gas leaks in refrigeration applications

X. ALBETS-CHICO[(a)], P. MORENO[(a)], X. PALOMINO[(a)], R. ROVIRA[(a)], M.A. GONZÁLEZ[(a)],

[(a)] AKO Group
St. Pere de Ribes, 08812, Spain, xalbets@ako.com

ABSTRACT

The current HFC refrigerant market scenario represents one of the biggest challenges that stakeholders of commercial & industrial refrigeration and HVAC systems have faced during the last years. Precisely, regulatory restrictions are nowadays causing acute inflation and limited availability for several HFC refrigerants in Europe. Refrigerant leaks are the main root of this situation and their reduction must be part of the final solution. With the ultimate goal of reducing refrigerant leakage in refrigeration systems, a novel smart early detection system for refrigerants, based on highly sensitive, selective and accurate HFC-gas transmitters, is presented. Thanks to a connected network of transmitters, the system provides information about the time, leak location and severity (economical, operative and environmental impact) of the refrigerant leaks, making use of computed smart leak indicators. The system is built on two main assets: (i) an early detection ability and (ii) a correct categorization and localization (in space and time) of the leak by the computing platform.
Keywords: Containment, F-Gas (Fluorinated Gas), Leakage, Maintenance.

1. INTRODUCTION

The European Union (EU), led by the F-Gas regulation, is nowadays under a strict HFC phase-down quota-production system which is inflicting a high inflation on HFC refrigerants (some of them becoming unavailable) (Putting into Use Replacement Refrigerants, 2018). Such scenario depicts how international refrigerant markets will evolve, since the Kigali amendment will impose a HFC phase-down worldwide (United Nations Environment Programme, 2016). Indeed refrigeration stakeholders are now facing in Europe a HFC refrigerant market shrinkage without clear technological alternatives, becoming an unprecedented challenge for the sector, as the widely used HFC refrigerants are becoming extremely expensive or even unavailable. More concretely, refrigeration end-users, owners of several thousands of HFC-based commercial and industrial refrigeration installations with high or very high leak rates -between 15% and 35% of total charge per year (Barrault et al., 2017) - depend upon big amounts of fresh refrigerant to replace the leaked quantities. This fresh refrigerant is therefore critical, as it is needed to maintain both refrigeration systems and business models operational. This is especially troubling for refrigeration installations that were designed and commissioned during the last 10 years (not fully amortized) that are fully operational and efficient, despite their leakages and their dependency upon big amounts of refrigerant. The sector is now timidly facing the problem in two different ways, a) retrofitting the refrigeration systems (usually without sufficient good practices) with lower-Global Warming Potential (GWP) HFC blends, despite decreasing the system efficiency and, sometimes, safety; and b) dismantling the HFC-based systems to shift towards new refrigeration apparatus based on natural refrigerants (especially CO_2 and centralised transcritical CO_2) or mildly flammable HFO refrigerants (EU commission, 2017). Unfortunately, both approaches are not either definite or, at present moment, general. On the one hand, retrofits are still based on HFC-blends, which will keep becoming more expensive and hardly available as HFC phase-down goes ahead in the next years. On the other hand, a complete conversion of all refrigeration installations towards natural/mildly flammable refrigerants could be possible in a time frame not shorter than 10-15 years from now, as per technical reasons (for instance, there is still a general current lack of know-how among small

and medium-sized contractors concerning new refrigerants) and – most importantly- due to financial aspects; remarkably for those refrigeration systems still not fully paid / amortized.
Refrigeration end-users are, therefore, facing a challenging scenario where decisions are difficult to make. Precisely, the goal of this paper is to present an additional low-cost alternative: a system to detect and localize refrigerant leaks at very early stages (under patent Albets-Chico et al., 2019). The system can, consequently, prevent refrigerant leakage in sensitive amounts without the need of constant, expensive and, sometimes, unfruitful maintenance leak inspections. Moreover, proper leak categorization through the computing power (on an internet-server or cloud) relating concentration readings (particles per million: *ppm*) with leak intensity (kg/year), allows to optimally manage the leak information, prioritising inspection and repair resources based on the severity of the leak. A proper use of the system will help to maintain the refrigerants inside the cooling system with only few selective and precise interventions on the refrigeration facility.
The paper is organized as follows: Section 2 presents the smart early detection system components and system performance. Section 3 briefly describes refrigerant leak modelling. Section 4 describes the computational method for the generation of smart leak indicators, based on the models. Section 5 shows some real-case early leak detection cases and comparison to the presented model. Finally, Section 6 summarizes the concluding remarks of this work.

2. COMPONENTS OF THE SMART EARLY DETECTION SYSTEM

The smart early detection system for gas leaks in refrigeration applications is composed by three main components: *i*) on-site early detection by means of sensitive sensors/transmitters, *ii*) a connectivity method to communicate the on-site information to a third component: *iii*) a computing platform where the information is registered, analysed and leak indicators are computed. The three components are briefly described in the next sub-sections.

2.1. Refrigerant sensor & transmitter network

There are several technologies for detection of refrigerants in general and HFC in particular. The refrigeration sector has historically and widely used the semi-conductor or Metal Oxide Semiconductor (MOS) technology for refrigerant detection. This technology is limited by several drawbacks and it cannot be used by an early detection system, as namely selectivity, sensitivity, precision and accuracy are slightly poor and detection below 50 particles per million (hereafter *ppm*) is not possible and/or related to many false alarms due to the limited selectivity of the target gas by MOS technology. As further discussed, refrigerant early detection systems require sensitivity thresholds below sometimes even 20 *ppm*, therefore requiring technologies such as NDIR (Non Dispersive Infrared) or PIR (Photoacoustic Infra Red), where sensitivity is below 10 *ppm* and both selectivity and accuracy are generally very high. For brevity, further discussions about the *pro* and *cons* related to gas detection technologies are here dismissed. The system here presented make use of a distributed network of NDIR sensors with accuracy/precision below 2% error, high selectivity and sensitivity below 5 *ppm*. The sensors are integrated into an on-site robust filtering device (transmitter) that reads the sensor information such that it can be communicated via different means, as discussed in section 2.2.

2.2. Connectivity

As said, the connectivity between the on-site sensing devices/transmitters and the computing platform (described in next section) is essential in terms of system performance and it is also related to system robustness and, obviously, acquisition cost. The connectivity is a critical accessory of the smart early detection system. The system here in consideration is able to connect the network of on-site transmitters and the computing platform in two different ways: through a wired RS-485 communication bus using MODBUS protocols, which centralizes the information in a local gateway which in its turn sends the information to an internet-based computing platform; or alternatively, through *IoT* (Internet of Things) cellular telecommunication modules embedded directly in the on-site transmitters. Such communication modules are based on Narrow Band technology and they allow to directly send the on-site read sensors/transmitters information to the

server-based computing platform, without going through wiring and on-site internet access facilities, factors that are always related to longer and more complex commissioning processes.

2.3. Computing Platform

Finally, the computing platform represents the core of the smart early detection system, as it is the component in charge of translating data (concentration readings, time, etc.) into leak information and the consequent notifications and alarms. Thanks to the alarming/reporting, the refrigeration end-user or contractor will prompt an early stage localization and repair of the refrigerant leak before important refrigerant losses are vented to the atmosphere. Beyond the computation of the leak indicators (which represent the core of this paper) the computational platform is also responsible for assessing the correct status of the refrigerant transmitters, registering the raw data, managing the notifications and alarms per transmitter, registering leak information and auditing leak actions: namely time of detection, time of repair and details about the leak repair that might become meaningful for maintenance processes, such personnel involved, cause of the leak and actions that were taken.

2.4. System performance

The principle of operation is as follows: a network of NDIR transmitters is deployed around the refrigeration apparatus, placing transmitters in the volumes with higher probability of leakage: compressor rooms, cold-rooms and/or above cold-rooms ceilings, refrigerated cabinets, liquid lines (usually in reduced volume ceilings) and condensing units (EPA Report 430-B-11-001, 2011). A good compromise between leak probability detection and acquisition cost might be between 10 and 25 sensing points for a standard supermarket, for instance. When a leak takes place, a change of concentration is detected by the closest transmitter and/or transmitters, which sends the information to the computing platform. When the leak is confirmed by the computing platform an alarm or notification is sent, together with the respective leak indicators: severity (by modelling the leak intensity), localization (by triangulation when possible, as further detailed) and probable leak time, in the case the leak presents some time pattern related to specific refrigeration processes. As seen, all three indicators provide meaningful information for the early repair: where, when and how severe is the leak (weight).

3. REFRIGERANT LEAK MODELLING

3.1. Gas concentration modelling for industrial applications

When a refrigerant leak takes place, refrigerant molecules expand around the refrigeration apparatus such that a refrigerant concentration distribution (in space and time) is present in the surrounding volume. How the concentration (hereafter c) of refrigerant evolves in space and time in such control volume is defined by a classic convection-diffusion equation (Patankar, 1980), i.e. Eq. (1):

$$\frac{\partial c}{\partial t} = \nabla \cdot (D \nabla c) - \nabla \cdot (\vec{v} c) + L \qquad \text{Eq. (1)}$$

Where t is time, D is the diffusivity of the refrigerant concentration, $vector\ v$ is the velocity field and L is the source of refrigerant concentration (i.e leak). For example, numerical simulations using CFD techniques are able to solve this transport equation (together with coupled mass and momentum conservation) and therefore predict the refrigerant concentration within the volume once leak and boundary conditions for the computational domain are known (Patankar, 1980). Obviously, numerical simulations are not a practical nor feasible approach for the current industrial problem in consideration, as computing power and especially modelling of the boundary conditions are not applicable in a general way. However, from the fundamental equation it is indeed possible to observe that the evolution of the concentration in time (left hand side of the Eq. 1) depends on the equilibrium of the diffusion part, the convective part and the source term, which is the refrigerant

leak when analysing the transport of refrigerant species. Then, for a steady state, an equilibrium between the source, the diffusive and the convective part is reached for any given control volume. Then, one could derive a much simpler equation by applying the conservation of mass and the definition of concentration *c* as the volume occupied by the refrigerant over the entire volume (occupied generally by air) where the concentration is sensed, as stated by Eq. (2):

$$c(T) = 10^6 \int_0^T \frac{L(t) - A(c) - B(t,c)}{\rho V} dt \qquad \text{Eq. (2)}$$

Being c the concentration in *ppm* (assuming it is homogenous within all the control volume V), T the filtering/integration time, L the leak (in grams of refrigerant per hour: g/h) function of time, A the diffused mass of refrigerant through seals of the volume (in g/h) depending on concentration, B the out-vented mass of refrigerant through openings and velocity fields of the volume (traffic, in g/h) function of time and concentration, ρ the density of the refrigerant (in g/m^3) and, as said, V the analysis volume (in m^3). This much simpler equation retains the essence of the convection-diffusion equation (Eq.1) and allows to work with leak intensity in mass/time units. Precisely, the mass of leaked refrigerant per hour in the volume V, can be obtained if terms A & B are modelled. Both terms depend on the concentration (the diffusive and convective fluxes are bigger for higher concentrations) and on the time (as term B might not be constant due to traffic in the volume, ventilation processes, etc.). As it will be described in next section, a way to statistically correlate concentration and leak intensity is to model terms A & B for different reference concentrations c and volumes V (c_{ref} and V_{ref}). Hence, when a statistical steady-state concentration c is reached for a volume V, the leak can be approximately estimated from the diffusion-convection modelled terms A & B, with corrections when needed, as further detailed.

4. COMPUTATIONAL MODEL FOR LEAK INDICATORS

As previously explained, the early detection of the refrigerant leak captured by the on-site transmitters require leak indicators for an efficient management, quick localization and repair. The calculations of the leak indicators are performed at the computing platform, as computing power and some system considerations are needed. This section will present the technical basis for the *TGCI* (Time-Gas Concentration Index) as a leak time indicator, the *LPI* (Leak Potential Index) and the *LCI* (Leak Charge Index) as leak severity indicators and, finally, the coordinates *LX*, *LY* and *LZ*, i.e. leak coordinates or leak predominant coordinate, when applicable.

4.1. *TGCI*: Leak Time indicator

Experience shows that several refrigerant leaks take place at precise moments of the refrigeration process, for example activation of Hot-Gas valves in defrost systems. In such cases, the refrigerant concentration reaches a non-trivial steady-state for some short hours during the day, as after the leaking process is finished, concentration tends to decrease again, as per Eq. (2) (being L=0). The leak final localization (and repair) must be done when the specific leaking process is taking place, sometimes at unusual or unavailable maintenance time. The *TGCI* is an indicator performed on hourly averages during several days (calendar on demand), indicating the concentration average per hour, hence showing the most probable hour for the leak to take place, should the leak not be constant in time. The *TGCI* is displayed as a histogram for 0-24h, as depicted in Fig. 1(a), indicating when the leak inspection, final localization and repair should be planned.

4.2. *LPI* & *LCI*: Leak Severity Indicators

After the leak concentration model described in section 3, the computing platform is able to estimate leak severity when terms A & B are modelled and the approximate volume of the application V is specified. It is therefore first needed to define the corresponding volume of detection for each on-site transmitter during commissioning. As said, the computing platform reads and registers the refrigerant concentration at a defined monitoring frequency. Once a statistical

averaged concentration c is reached (as filtered by the platform), the transient term of Eq. (1) vanishes, therefore obtaining the following relationship for the leak, Eq. (3):

$$\overline{L(T)} = \frac{1}{T}\int_0^T A(c) + B(t,c)dt \qquad \text{Eq. (3)}$$

Where T, as previously explained, is a finite filtering/averaging time such that average concentration c is approximately constant in the period of time T, as assessed by the platform. As the reader may guess, such approach would need a modelled database of the terms A & B for any (infinite) volumes V and concentration c, as these two application values can be *a priori* any real number and the terms A & B (modelled in terms of mass/time) are indeed different for all combinations of volumes and concentrations. In order to produce a manageable computational system, several terms for A & B pairs can be modelled at different (definite) volumes and concentrations V_{ref} and c_{ref}; the system correcting the final leak indicator L with the closest values of reference (V_{ref}, c_{ref}) with respect the real application values (V, c) after Eq. (4):

$$\overline{L(T)} = \frac{c}{c_{ref}}\frac{V}{V_{ref}}\frac{1}{T}\int_0^T A(c_{ref}) + B(t,c_{ref})dt \qquad \text{Eq. (4)}$$

This linear correction allows to extrapolate the modelled values of A & B defined for concentration c_{ref} when the on-site reading concentration c is of the same order of magnitude; the same reasoning applying for the volume V. Modelling of A & B pairs can be done both numerically and experimentally for multiple standard volumes in commercial and industrial refrigeration systems (ranging from few litters in refrigerated cabinets to thousands of m^3 for industrial cold rooms) and at different concentration levels. For brevity, the modelling of parameters A & B is not detailed in this work.

Once the averaged refrigerant leak L is computed (in g/h), the Leak Potential Index (*LPI*) is computed as the estimation of leaked mass of refrigerant (kg) per year or, alternatively, tons of CO_2 per year, making use of the GWP of the refrigerant of the system (if parameterized at the computing platform) assuming that the computed leak will remain unattended and constant throughout the year. This indicator allows to assess the severity of the leak, if left unattended, from both economic and environmental points of view and, therefore, manage its priority in terms of on-site inspection and repair. Additionally, a second severity indicator, the so-called Leak Charge Index (*LCI*), is computed at the platform. This index is obtained by dividing the yearly estimated leak (*LPI* in kg/year) by the total charge of refrigerant of the installation (kg), hence stating the % of refrigerant system loss that will be produced by the detected refrigerant leak, if left unattended. The *LPI* and the *LCI* indicators are displayed as a number by the system, as depicted in Fig. 1(b). It is important to mention that computing the severity of the leak from the concentration reading is essential for the industry, as the relationship between the severity of the leak and the concentration is clearly not linear and, therefore, the concentration reading is not a good indicator –sometimes even misleading- to acknowledge the severity of the refrigerant leak.



(a)

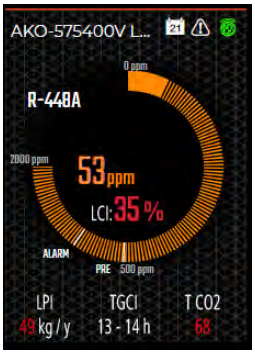

(b)

Figure 1: (a) Visual display for the *TGCI* indicator, showing the most probable leak time at 13h;

(b) Visual display for leak severity indicators LPI and LCI.

4.3. *LX*, *LY* and *LZ*: Leak coordinates

An important refrigerant leak early detection support indicator is the triangulation of the leak coordinates based on several concentration readings from different transmitters. As the reader may infer, when only one transmitter is placed in a volume V, such triangulation process is not possible, being the spatial coordinates of the on-site transmitter the best guess for the leak coordinates. On the other hand, when several transmitters share a generally extended volume (for instance, an industrial cold room or a suspended ceiling), the different time-concentration behaviour of the transmitters can be used to estimate the leak position, making use of the transient term of the leak modelling defined in section 3, since the detection time will be generally shorter at shorter distances of the leak.

Therefore, the computing platform requires the spatial coordinates (x, y, z) for all system transmitters (coordinates that can be defined either by Indoor Positioning Systems IPS or by a manual entry, together with the definition of a reference for the coordinates at the commissioning of the system). Additionally, the computing platform requires to relate the neighbour transmitters (those that share a volume V) in sets. The neighbour tagging is also performed during commissioning.

With this information, right after any of the neighbour transmitters detects a refrigerant concentration change, the computing platform assigns a count-down decreasing time t_{leak} to all neighbourhood set of transmitters. The leak time-stabilisation concentration for each transmitter (n), is computed as shown in Eq. (5):

$$TC^n = \left(t_{leak} c\right)^n = t_{leak}^n \cdot \overline{c^n} \qquad \text{Eq. (5)}$$

Being n an index defining each transmitter (ranging from 1 to N) and t_{leak} the count-down time for the neighbour set of transmitters. Once a steady-state concentration c is reached for each transmitter of the set, the respective time t^n_{leak} (count-down time required for the concentration to reach steady-state by transmitter n) is used to compute the leak time-stabilisation concentration TC for each transmitter, as explained by Eq. (5). Hence, the last transmitter of the set to reach a stable concentration will present a smaller leak-time than those closer to the leak (as leak-time is a decreasing but positive number). High leak time-concentration values will be associated to closer positions to the refrigerant leak (higher concentration and faster leak-time), while low leak time-concentration values are typical of further positions with respect to the leak (lower concentrations and slower leak-time).

When all leak time-concentration values have been obtained for the set of transmitters, the system correlates such values with the respective x, y and z transmitter coordinates. A polynomial regression model is then applied using the method of least squares, although similar techniques such splines could be used. For instance, for the leak-x-dependence modelling, a polynomial $TC^{fit}(x)$ is fitted to the points composed by the actual time-concentration values TC and their respective x-coordinate per set (generally from $x(1)$ to $x(N)$, N being the transmitters of the neighbour set, transmitters that share a volume V), as described by Eq. (6):

$$TC^{fit}(x) = \beta_0 + \beta_1 \cdot x + \ldots \beta_n \cdot x^n \qquad \text{Eq. (6)}$$

The regression model provides the polynomial $TC^{fit}(x)$ that produces the minimum least squares with respect the actual values of $TC(x)$. Depending on the number N of available correlation points, different polynomials can be obtained (linear, cubic, etc.). If an acceptable correlation is obtained (coefficient of determination R^2 >0.6) for any of the three polynomial fittings performed ($TC^{fit}(x)$, $TC^{fit}(y)$, $TC^{fit}(z)$) a maximum analysis of each fitted polynomial –per coordinate- can be carried out, as shown by Eq. (7) for the x-coordinate:

$$LX = leak(x) = MAX\left[TC^{fit}(x)\right]_{x(1)}^{x(N)} \quad \text{Eq. (7)}$$

If a maximum of the function is within the physical transmitters coordinates (in Eq. (7): $x(1)…x(N)$), the leak coordinates (LX, LY, LZ) are obtained as coordinates for maximum TC. It is important to mention that if the function does not present a maximum within the physical coordinates (as for example if a linear polynomial is obtained for TC with N=2) a leak preferred orientation can be derived from the analysis, i.e. increasing or decreasing x with respect to transmitter n.

5. ILLUSTRATIVE RESULTS

In order to illustrate the performance of the system, the *LPI* and *LCI* indicators obtained by the commercial realization of this smart early detection system are presented. The concentration reading displayed in Fig. 2 was obtained in a 30 m^3 cold room of a supermarket in Madrid (Spain) between 9th and 14th May 2018. This supermarket presented high leak rates for the last years (above 90% of the nominal refrigerant charge was refilled every year) and the deployment of the smart early detection system consisted in monitoring compressor room, 4 different cold-rooms, 7 refrigerated displays and the condenser unit.

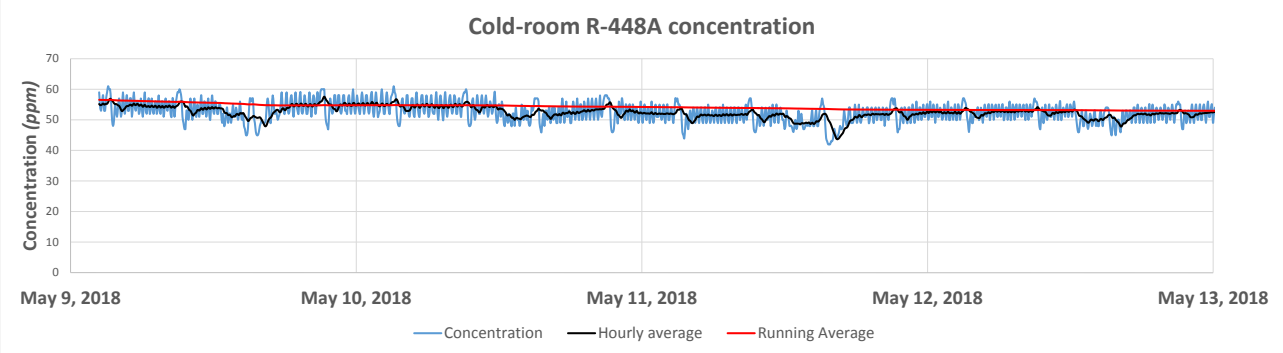

Figure 2: R448A concentration inside a supermarket cold-room between 9th and 14th May 2018.

As seen in Fig. 2, refrigerant concentration oscillates (as per the refrigeration cycles inside the evaporator of the cold room) but shows a clear stable behaviour around 53 *ppm*. The smart early detection system immediately identified the leak after commissioning (as the leak existed before the deployment of the detection system). Leak severity indicators were delivered after the initial two hours, as modelling values for the mean time integral of terms $A + B$ ($1/T\int A + B\,dt$) were available from experimental tests, as shown in Table 1.

Table 1. Modelling and computing values for leak severity indicators [Eq. (4)]

Model Data				*Application data*		*Leak Severity Indicators*	
V_{ref} (m^3)	C_{ref} (*ppm*)	$1/T\int Adt$ (g/h)	$1/T\int Bdt$ (g/h)	$V_{cold\ room}$ (m^3)	$C_{cold\ room}$ (*ppm*)	*LPI* (kg/year)	*LCI* (%) (140 kg nominal charge)
7	67	1.45	0.21	30	53	49.29	35.2

Hence, after Eq. (4), linearly correcting both concentration and volume, the leak is computed as 5.62 g/h, being the *LPI* (Leak Potential Index) 49.29 kg/year and the *LCI* (Leak Charge Index) 35.2%, as the system accounted for 140 kg nominal refrigerant charge. This is to say, the leak detected in the cold room, if left unattended, would cost around 50 kg of refrigerant per year, causing the loss of approximately one third of the total refrigerant charge annually. The supermarket owner, once obtained such information, had no doubts to replace the perforated evaporator in the following 10 days after detection, despite the very low value of refrigerant concentration: 53 *ppm*.

The model displayed by Eq. (3) can also reproduce the cold-room concentration in time, once the leak intensity, the diffusion and convection parts for the cold-room are known. For that, it is

necessary to include time-dependency to the terms B and L, such they mimic the refrigeration cycle, defrosting and cold-room traffic. Then, when the model applies the estimated leak (as said, with time average value of 5.62 g/h), a quasi-steady-state cold-room concentration pattern is obtained, displayed by Fig. 3. As seen, both model and real data remarkably agree, fact that demonstrates model consistency.

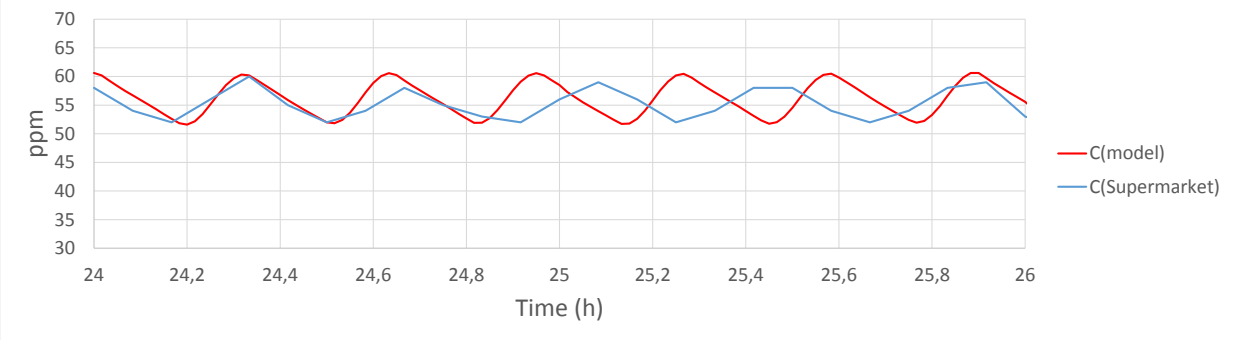

Figure 3: Comparison between model and real data for the supermarket cold-room (from 24th hour to 26th hour)

6. CONCLUSIONS

A smart early detection system for gas leaks in refrigeration applications has been presented. The system (under patent Albets-Chico et al., 2019) aims to support refrigeration stakeholders to detect and prevent important refrigerant leakages, nowadays especially relevant due to the current instable refrigeration HFC market. The system represents a tool to locate (in space and time) and to estimate the severity of the leak, all three factors essential to manage and optimize maintenance resources to address the potential refrigerant leaks. Indeed, the system provides information that, until now, was not available to owners and maintenance teams of refrigeration facilities, making of leak prevention, detection and repair an extremely difficult task due to the nature of the refrigerant leaks, generally of few grams per hour and distributed along extended multi-component refrigeration systems. These facts required the investment of massive leak inspection time to minimize refrigerant leakage, practice generally not carried-out by the sector.

REFERENCES

Putting into Use Replacement Refrigerants (PURR), 2018. Report of British Refrigeration Association Action Group. 2nd Edition.

United Nations Environment Programme UNEP/OzL.Pro.28/CRP/10, 2016. Twenty-Eighth Meeting of the Parties to the Montreal Protocol on Substances that Deplete the Ozone Layer, Kigali, 10th–14th October 2016.

Barrault, S., Fayolle, F., Pinel, K., Nemer, M., Clodic, D., 2017. Détection de fuite. Etude sur les moyens de détection de fuite des installations de refrigeration et de climatisation. Technical report for ADEME.

EU Commission Report, 2017. REPORT FROM THE EU COMMISSION of 4.8.2017. Assessing the 2022 requirement to avoid highly global warming Hydrofluorocarbons in some commercial refrigeration systems.

Albets-Chico, X. et al., 2019. A smart early detection system for gas leaks in refrigeration applications. UNDER PATENTING PROCESS WO/2019/XXXXXX.

EPA Report 430-B-11-001, 2011. Greenchill Best Practices Guideline. Commercial Refrigeration Leak Prevention & Repairs.

Patankar, S.V., 1980. Numerical heat transfer and fluid flow. Hemisphere Publishing Corporation, Washington, 197.

Manuscript ID: 160
DOI: 10.18462/iir.icr.2019.0160

Numerical and experimental study of the heat transfer for the ammonia condensers

Liviu Geo DRUGHEAN[(a)], Alina GIRIP[(a)], Anica ILIE[(a)], Rodica DUMITRESCU[(a)]

[(a)]Technical University of Civil Engineering,122-124, Lacul Tei, Bucharest 2, Zip code: 020396, Romania, anica_59@yahoo.com

ABSTRACT

The research included in this paper was performed in the Thermodynamics Laboratory, part of the Technical University of Civil Engineering, Bucharest. The research refers to ammonia condensation in a brazed plate heat exchangers. The authors present a comparative theoretical modeling of convective heat transfer coefficient on ammonia side, by calculating it using different correlations currently available in open literature.

At the same time the authors present the experimental set-up, procedures used and measured values recorded by the data acquisition system. A graphically illustrated comparison is shown between the experimental and theoretical data, aiming to confirm the correlation's validity for both geometry and given operating conditions of the ammonia condenser.

Ammonia use in PHE complies the curent trend of no ozone depleting potential and low global warming impact refrigerants.

Keywords: Refrigerating systems, ammonia condenser, plate heat exchanger.

1. INTRODUCTION

Plate heat exchangers are used in both condensation and evaporation processes in refrigeration systems. Plate heat exchangers (PHEs) of chevron type are currently widely used for a broad range of applications, such as refrigeration and heat pumps cycles, for both single and two-phase flow duties. Plate heat exchangers are known for their advantages, such as compactness, expressed in small size and high area to volume ratio, flexibility for desired load, by easily adding or removing plates, high thermal effectiveness, low operational and maintenance costs, easy operation and relatively low energy usage. Brazed plate heat exchangers are additionaly fit for condensation and vaporization of high pressure refrigerant fluids. Condensation performance is affected by many factors, such as: fluid property, vapor quality, mass flow, plate geometry and working conditions. There are only few ammonia correlations currently available in the open literature.

The experimental research has been developed in the Thermodynamics Laboratory of the Technical University of Civil Engineering in Bucharest.

Over the years, many studies have been done on the heat transfer and flow characteristics during condensation of refrigerants in plate heat exchangers. In the present study, main concern is to extend the existing heat transfer coefficient database of ammonia during condensation inside a brazed plate heat exchanger.

2. EXPERIMENTAL SET-UP

The experimental set-up is schematically shown in Fig. 1, Photo 1 and Photo 2. It consists of an ammonia loop, and a water/ethylene glycol solution loop, instrumentation and a data acquisition system. The ammonia loop is a single stage vapor mechanical compression refrigeration system, consisting of: semi-hermetic screw compressor of 60 kW refrigerating capacity; oil separator; water cooled plate heat exchanger condenser; horizontal ammonia receiver; liquid ammonia subcooler; vertical plate heat exchanger evaporator; horizontal liquid separator (surge drum); variable speed centrifugal pumps (Ilie et al., 2007).

Ammonia is condensed to saturated liquid in the condenser. Liquid ammonia from the condenser is stored in the horizontal receiver. The single stage vapor mechanical compression refrigeration

system using ammonia as a refrigerant is fully automated, so the condensing capacity may be adjusted depending on the cooling medium temperature. In addition, the experimental refrigerating plant is equipped with a centralized data acquisition system allowing remote control or adjusting of the working parameters in real time.
The water/ethylene glycol 30vol % solution (brine) loop rejects the thermal load of the PHE type condenser. This loop consists of a 2000 L capacity well insulated water/ethylene glycol solution tank provided with a circulation pump and connected to dry coller.

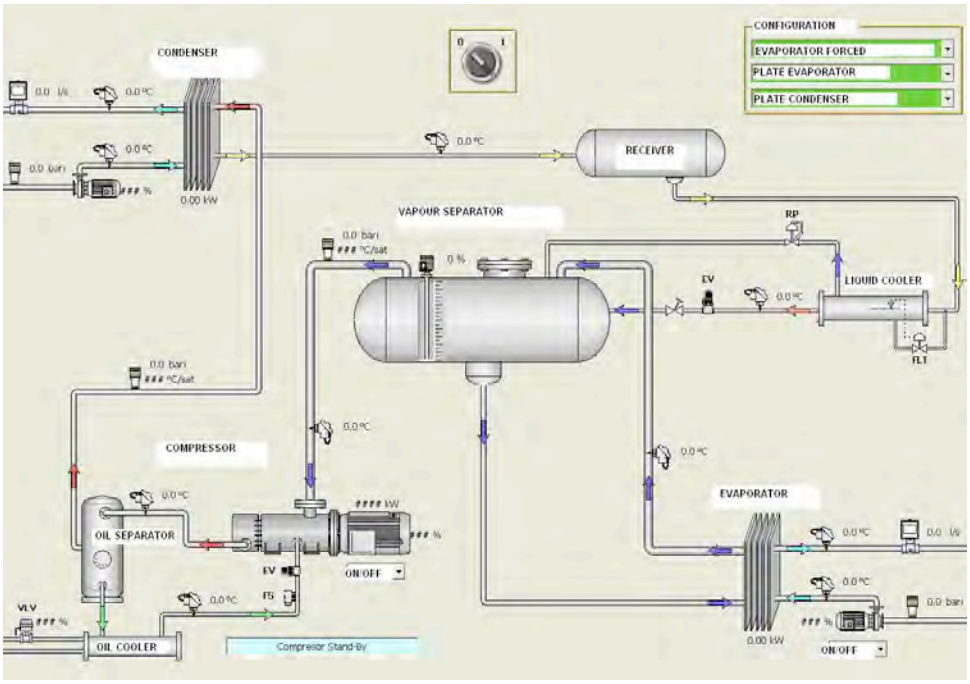

Figure 1: Schematic view of the experimental test rig



Photo 1. Experimental set up



Photo 2. Vertical industrial PHE

The PHE used in the present study is an industrial vertical brazed one (Photo 2), with counter flow setup (water/ethylene glycol solution flowing upwards on one side in the plates and the refrigerant flowing downwards on the other). It has 31 symmetric 60º chevron plates made of stainless steel. The most important geometric characteristics of chevron plates are given in Table 1.
The PHE was well insulated to ensure negligible heat loss. Hence, the heat transfer from the hot side (condensing ammonia) is assumed to be equal to the heat transfer to cold side (brine).

Table 1. Geometrical characteristics of the condenser

Chevron angle, β	60°
Corrugation depth, b	6 mm

Corrugation pitch, Pc	16 mm
Plate thickness, t	0.4mm
Heat transfer area	6.2 m^2
Total plate length, L_V	0.618m
Total plate width, L_W	0.191m
Port length, L_p	0.519m
Port width, L_h	0.092m
Diameter port	60 mm
Number of plates	30
Number of plates effective in heat transfer	28
Number of channel on refrigerant side	14
Number of channel on water side	15
Condenser heat transfer surface	6.2 m^2

3. METHODOLOGY

The research aimed to develop a comparative analysis of the convective heat transfer coefficients, at condensation of the ammonia flow, in brazed PHE determined both experimentally and theoretically (based on currently available correlations in open literature.

Thermal capacity of the experimental condenser has been determined based on measured parameters under the operating conditions shown in section 4, on both ammonia and brine side.

Thermal capacity on the brine side has been calculated by:

$$\dot{Q}_{c\,exp}^{b} = \dot{m}_b \cdot c_{pb} \cdot (t_b^{out} - t_b^{in})\,[W] \qquad \text{Eq. (1)}$$

Thermal capacity on the ammonia side has been calculated by:

$$\dot{Q}_{c\,exp}^{NH_3} = \dot{m}_0 \cdot \Delta h\,[W] \qquad \text{Eq. (2)}$$

The experimental values of $\dot{Q}_{c\,exp}^{b}$ and $\dot{Q}_{c\,exp}^{NH_3}$ have been considered reliable, if they satisfied the energy balance with a deviation of less than 5%.

The overall experimental heat transfer coefficient has been determined by:

$$k_{exp} = \frac{\overline{\dot{Q}}_c}{S_c \cdot \Delta T_m}\,[W/(m^2 \cdot K)] \qquad \text{Eq. (3)}$$

where: $\overline{\dot{Q}}_c$ - experimental heat transfer rate, [kW] was calculated based on the relation $\overline{\dot{Q}}_c = \frac{\dot{Q}_{c\,exp}^{b} + \dot{Q}_{c\,exp}^{NH_3}}{2}$; ΔT_m is the logaritmic mean temperature difference computed with reference to average saturation temperature without take into account any subcooling or super-heating (Bell and Muller, 1984).

The experimental convective heat transfer coefficient on the ammonia side of the condenser is derived from the global heat transfer coefficient assuming no fouling resistances (Longo, A. G., 2008):

$$\alpha_c^{exp} = \left(\frac{1}{k_{exp}} - \frac{\delta}{\lambda} - \frac{1}{\alpha_b}\right)^{-1}\,[W/(m^2 \cdot K)] \qquad \text{Eq. (4)}$$

where α_b is the brine single-phase heat transfer coefficient [W/(m^2·K)], calculated with correlations mentioned in open literature. The selected correlations are presented in Table 2.

The theoretical study on ammonia condensing heat transfer coefficient, α_c^{th}, was calculated with correlations indicated in Table 3.

Table 2. Corelations for brine side heat transfer coefficient

Investigator	Corelation

Longo and Gasparella (2007) $5 < Pr_b < 10; 200 < Re_b < 1200$	$\alpha_b = 0.277 \cdot \frac{\lambda_b}{d_{ech}} \cdot Re_b^{0.766} \cdot Pr_b^{0.33}$
Yi-Ye-Yan (1999)	$\alpha_b = 0.212 \cdot \frac{\lambda_b}{d_{ech}} \cdot Re_b^{0.778} \cdot Pr_b^{0.33}$
Mulek and Manglik (1999) $Re \geq 10^3;\ 30 \leq \beta \leq 60; 1 \leq \varphi \leq 1.5$	$\alpha_b = 0.46 \cdot \frac{\lambda_b}{d_{ech}} \cdot Re_b^{0.66} \cdot Pr_b^{0.333}$

Table 3. Corelations for ammonia side heat transfer coefficient

Investigator	Corelation
Yan et al (1999) R134a, Chevron plate $500 < Re < 1000$ $60 < G < 120$ $\beta = 60,\ 0.1 \leq x_m \leq 0.9$	$\alpha = 0.4118 \cdot \frac{\lambda_l}{d_{ech}} \cdot Re_{ech}^{0.4} \cdot Pr_l^{0.33}$ $Re_{ech} = \frac{G_{ech} \cdot d_{ech}}{\mu_l};\ G_{ech} = \left[(1 - x_m)\right] + x_m \cdot \left(\frac{\rho_l}{\rho_v}\right)^{1/2}$
Hausen (1998) $0.0001 < G_Z < 10$ $Re < 2300$	$\alpha = 3.66 + \frac{0.0668 \cdot G_Z}{1 + 0.04 \cdot (G_Z)^{2/3}} \cdot \frac{\lambda}{d_{ech}};\ G_Z = Re \cdot Pr \cdot \frac{d_{ech}}{H}$
Park et al (1999)	$\alpha = 3.223 \cdot \frac{\lambda_l}{d_{ech}} \cdot Re_{ech}^{0.4916} \cdot Pr_l^{0.33}$
McAdams (1954)	$\alpha = 0.0077 \cdot \left(\frac{\rho_l \cdot (\rho_l - \rho_v) \cdot g \cdot \lambda_l^3}{\mu_l^2}\right)^{1/3} \cdot Re^{0.4}$
Webb (1998)	$\alpha = \alpha_{sat} + F_{Webb} \cdot \alpha_v + \frac{c_{pv} \cdot \Delta h}{r_c};\ \alpha_{sat} = \varphi \cdot \alpha_{Akers}$ $\alpha_v = 0.2267 \cdot \frac{\lambda_v}{d_{ech}} \cdot Re_v^{0.631} \cdot Pr_v^{0.33};\ F_{Webb} = \frac{T_{sup} - T_{sat}}{T_{sat} - T_{wall}}$
Hays and Jokar (2009) $\beta = 60°$	$\alpha = 0.37 \cdot \left(\frac{G^2}{\rho_l^2 \cdot c_{pl} \cdot \Delta T}\right)^{1.07} \cdot \left(\frac{\rho_l^2 \cdot r_c}{G^2}\right)^{0.91} \cdot \left(\frac{\rho_l \cdot \sigma_l}{\mu_l \cdot G}\right)^{0.032} \cdot \left(\frac{\rho_l}{\rho_l - \rho_v}\right)^{1.18} \cdot Re_l^{0.706} \cdot Pr_l^{0.35}$
Han et al (2003) R410A, R22 $\beta = 45°, 55°$ and $70°$, Corrugation piches 7, 5.2 and 4.9 mm	$\alpha = G_{e1} \cdot \frac{\lambda_l}{d_{ech}} \cdot Re_{ech}^{G_{e2}} \cdot Pr_l^{0.33};$ $G_{e1} = 11.22 \cdot \left(\frac{p_c}{d_{ech}}\right)^{-2.83} \cdot \left(\frac{\pi \cdot \beta}{180}\right)^{-4.5};\ G_{e2} = 0.35 \cdot \left(\frac{p_c}{d_{ech}}\right)^{0.23} \cdot \left(\frac{\pi \cdot \beta}{180}\right)^{1.48}$
Akers et al (1979) Herringbone plate $20 < G < 240$ $\beta = 65°$	$\alpha = 5.03 \cdot \frac{\lambda_l}{d_{ech}} \cdot Re_{ech}^{0.78} \cdot Pr_l^{0.33}$

The measured parameters are:

- on the brine side: inlet and outlet temperature and mass flow rate: t_b^{out}, t_b^{in}, $\dot{m}_b$;
- on the ammonia side: evaporating and condensing pressure and temperatures (p_0, t_0), (p_c, t_c),compressor suction and discharge temperatures, liquid ammonia mass flow rate ($\dot{m}_0$) and the electrical power consumed by the compressor (P_k).

The measuring devices used are: for temperature:type K thermocouples of± 0.25°C accuracy; for brine flow rates: Danfoss electronic flow-meters with ±3% accuracy, for ammonia flow rate: Corriolis flow-meters with ±2% accuracy.
The measured parameters which were taken into consideration correspond to a quasi-steady state operating regime of the system. It was considered as such the regime characterised by maximum ±5% variation of the measured parameters, along 10 consecutive readings, at 10 minutes apart.

4. RESULTS AND DISCUSSION

4.1. Experimental results

Throughout the experiments, the brine mass flow rate varied between 2.85÷3.85 kg/s; the mean brine temperature at the condenser varied between 20÷21.5°C.
The condensing temperature was maintained quasi - constant, around the value of 25°C and the evaporating temperature varied between 3÷5°C. The overall increase in ammonia mass flow rate ranged between 21 g/s up to 34 g/s (a 39% increase); consequently the condensing capacity increased from 28 kW to 43 kW. The energy balance concerning heat transfer between the brine and ammonia side plays an important part in system analysis. Therefore, energy balance was looked at for each test conducted on the condenser side, to ensure that ammonia and brine side match within 5% of each other.

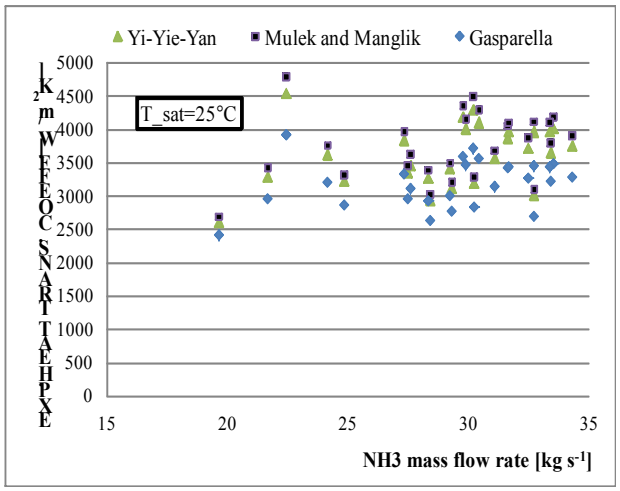

Figure 3: Experimental ammonia condentation heat transfer coefficient with all three brine side correlations

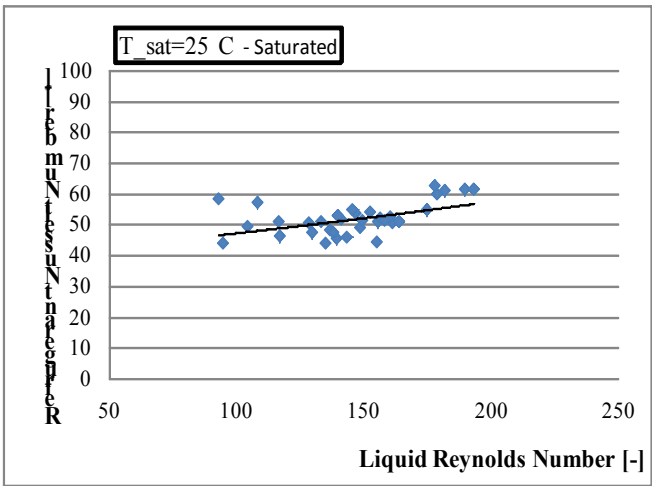

Figure 4: Experimental ammonia Nusselt Number vs liquid Reynolds Number

In Fig. 3 are shown experimental heat transfer coefficient on ammonia side using the brine side correlations from Table 2. The experimental heat transfer coefficients on ammonia side vs ammonia mass flow rate ilustrated in Fig. 3 shows the same trend for all three corelatins used. Therefore all three correlations may be further in this study.
Experimental ammonia condensig heat transfer coefficient range between 2838.4 and 3282.3W/(m^2·K) for the same value of the ammonia flow rate. The maximum values are obtained with Mulek and Manglick (1999) correlation, meann values are obtained with Yi Ye Yan (1999) and minmum values are obtained with Gasparella correlation (2007).
In Fig. 4 plots data on non-dimensional co-ordinates showing the average Nusselt Number on the ammonia side vs the liquid Reynolds Number, based on each of the three brine corelations considered (Table 2). Experimental rezults show that the liquid Reynolds Number ranges between 100 to 200, corresponding to laminar to transition flow regime in PHEs (Shah and Focke, 1988).

4.2. Theoretical results

The experimental ammonia condensing heat transfer coefficient was compareded with theoretical ammonia condensing heat transfer coefficient derived from the eight correlations listed in Table 3. In Fig. 5, 6 and 7 are plotted theoretical vs experimental results.

The Hays and Jokar correlation adapted for brazed PHE shows the larger influence than all the other corelations of the ammonia mass flow rate on ammonia condensing heat transfer coefficient, namely from 1991 W/(m^2·K) to 4093W/(m^2·K).
The Hausen (1998) correlation provides the lowest values for the heat transfer coefficient, leading to unacceptably large deviation compared to the experimental values, under the specified conditions related to the heat exchanger geometry and the system operating conditions.

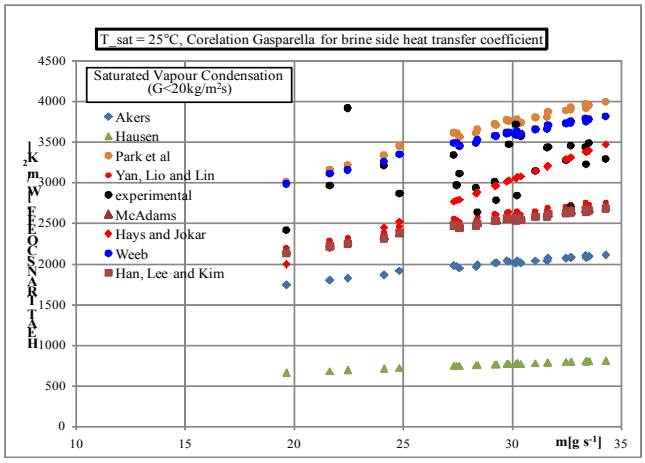

Figure 5: Experimental and theoretical ammonia condentation heat transfer coefficient with Gasparella correlation

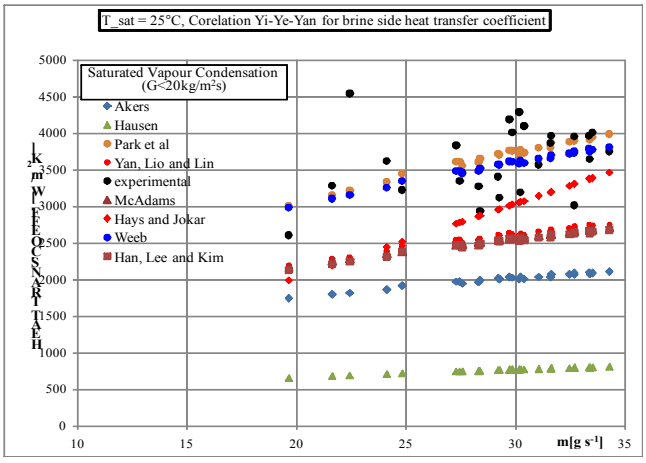

Figure 6: Experimental and theoretical ammonia condentation heat transfer coefficient with Yi-Ye-Yan correlation

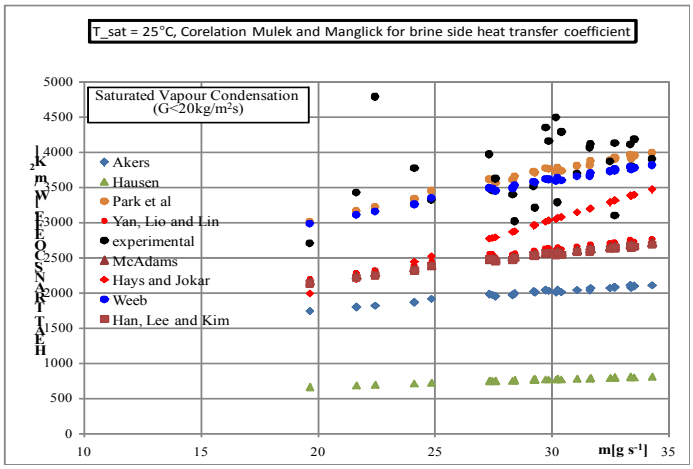

Figure 7: Experimental and theoretical ammonia condentation heat transfer coefficient with Mulek and Manglick correlation

The same increasing trend of ammonia condensing heat transfer coefficient with ammonia mass flow rate is observed according to correlations by: Han, Lee and Kim (2003), Mc Adams (1954), Weeb (1998), Yan, Lio and Lin (1999) and Hausen (1998). The increase in α_c^{th} values ranges from 30 to 36%, for ammonia mass flow rate ranging between 20-40g/s.
A diferent trend is observed with correlations by Park et al. (1999) and Akers (1979) where the increase in α_c^{th} is larger, namely 44% and 27%, respectivelly, for the same range of the mass flow rate.
The accuracy of prediction between experimental and theoretical ammonia condensing heat transfer coefficient was computed usin the mean absolute percentage error (MAPE) Eq (5):

$$MAPE = \frac{1}{n} \cdot \sum_{1}^{n} \frac{\left| \alpha_c^{th} - \alpha_c^{exp} \right|}{\alpha_c^{exp}} \cdot 100[\%] \qquad \text{Eq. (5)}$$

MAPE values range between 15% and 30% with correlations by Park et al. (1999), Webb (1999), Yan et al (1999), McAdams (1954), Han, Lee and Kim (2003) and Hays and Jokar (2009) and Gasparella (2007) corelation on brine side (Table 4).
The same range of MAPE results either by using Yi-Yie-Yan (1999) on brine side instead Gasparella (2007), but only with some of the ammonia correlation, namely: Park et al. (1999), Webb (1999) and Hays and Jokar (2009) or using Mulek and Manglick (1999) with Park et al. (1999), Webb (1999), Hays and Jokar (2009) and McAdams (1954).

Table 4. Mean absolute percentage error between predicted and experimental ammonia condensing heat transfer coefficient

Prediction method (35 runs)	Mean absolute percentage error, [%] MAPE		
	Gasparella (2007)	Yi-Yie-Yan (1999)	Mulek and Manglick (1999)
Park et al	19.06	15.21	15.88
Yan, Lio and Lin	24.33	34.17	36.49
Weeb	16.79	15.71	16.93
Hays and Jokar	15.30	24.34	26.88
Hausen	77.76	80.66	81.35
Akers	41.59	49.20	51.00
McAdams	25.74	35.44	26.02
Han, Lee and Kim	15.49	36.04	38,3

Fig. 5, 6, 7 and Table 4 also indicate that experimental results are in best agreement with theoretical results for Park et al. (1999) and Webb (1999) correlations used on ammonia side, coupled with any of the three correlations on the brine side.

5. CONCLUSIONS

This comparative study on ammonia condensation heat transfer coefficient has been performed under following working conditions: ammonia mass flow rate ranging between (20...40g/s); ammonia condensing mean saturation temperature of 25°C; ammonia liquid Reynolds Number ranging between 100 to 200.
The comparative analysis was developed between experimental ammonia condensation heat transfer coefficient, computed with three corelations on brine side (Gasparella (2007), Yi-Yie-Yan (1999) and Mulek and Manglick (1999)) and theoretical values computed with eight correletions on ammonia side (Park et al. (1999), Webb (1999), Yan et al (1999), McAdams (1954), Han, Lee and Kim (2003), Hays and Jokar (2009) Hausen (1998) and Akers (1979)). As a conclusion, this study showed that out of the eight correlations used to predict theoretical heat transfer coefficient, only two, namely Park et al. (1999), Webb (1999), valided the experimental values, within minimum MAPE range of 15.21% to 19.06%, irrespective of the brine side correlation used.

ACKNOWLEDGEMENTS

The experimental stand was financed by the National Authority of Scientific Research, within the National Program PNII, CAPACITATI, contract no. 14/2007.

NOMENCLATURE

S heat transfer area (m^2);
b corrugation depth (m)
c_p specific heat (J/(kg K))
pc corrugation pitch (m)
d equivalent diameter (m), $d_{ech} = 2 \cdot b$
g gravitational acceleration (m/s^2)
G mass flux ($kg/(m^2 s)$)
h enthalpy (kJ/(kg K))
k overall heat transfer coefficient ($W/(m^2 K)$)
h specific enthalpy (J/kg)
λ thermal conductivity (W/(m K))
L length of the plate (m)
$\dot{m}$ mass flow rate (kg/s)
Nu Nusselt number (-)
p pressure (Pa)
Pr Prandtl number (-)
$\dot{Q}$ heat transfer rate (W)
Re Reynolds number (-)
t plate thickness (m)
T temperature (K)
W - width of the plate (m)

x– quality vapor

Greek symbols

α heat transfer coefficient(W/(m^2 K))

β chevron angle (°)

φ enlargement factor (-), φ = 1.17

μ dynamic viscosity (kg/(m s))

ρ density (kg/m^3)

v specific volume, m^3/kg

Subscripts

b brine *(*water+Eg 30%)

c condenser

ech equivalent

exp experimental

g gravitational

h port width

in inlet

k compressor

l liquid

m mean

out outlet

p port length

ref refrigerant

sat saturation state

tot total

v vapor

w width

wall wall

0 evaporation

REFERENCES

ASHRAE Handbook - Fundamentals, 2017, CH. 5 Two-Phase Flow, pp. 5.11-5.14

Bell, K.J., Mueller, A.C., 1984. Condensing Heat Transfer, Volverine Heat Transfer Data Book. Volverine, pp. 163-165

Shah, R.K., Focke, W.W., 1988. Plate Heat Exchangers and their design theory, heat transfer equipment design. Hemisphere, Washington, pp. 227-254

Longo, A. G., 2008. Refrigerant R134a condensation heat transfer and pressure drop inside a small brazed plate heat exchanger. Elsevier, Int. J. of Refrigeration, pp. 780-789

Webb, R. L. 1998, Convective condensation of superheated vapor, ASME J. Heat Transfer 120, pp 418-421

Longo, G.A., Gasparella. A, 2007 Refrigerant R134a vaporisation heat transfer and pressure drop inside small brazed plate heat exchanger, Int. J. Refrigeration 30, pp 821-830

Muley, A., Manglik, R.M., 1999 Experimental study of turbulent flow heat transfer and pressure drop in a plate heat exchanger with chevron plates. ASME J. Heat Transfer 121, pp 110-121.

Kuo, W.S., Lie, Y.M., Hsiieh, Y.Y., Lin, T.F. 2005 Condensation heat transfer and pressure drop of refrigerant R410A flow in vertical plate heat exchanger. Int. J. Heat Mass Transfer 48, pp 5205-5220

Akers, W.W., Deans, H.A., Crosser, O.K. 1959. Condensing heat vtransfer ithin horizontal tubes. Chem. Eng.Prog.Symp. Ser. 55, pp 171-176

Y.Y. Yan,H.C. Lio,T.F. Lin,Condensation heat transfer and pressure drop of refrigerant R-134a in a plate heat exchanger, Int. J. of Heat and Mass Transfer 42 (1999) 993–1006

Mancin, S., Del Col, D., Rossetto, L., 2012, Condensation of Superheated Vapour of R410A and R407C Inside Plate Heat Exchangers: Experimental Results and Simulation Procedure, Int. J. Refrigeration*,* vol.35: p. 2003-2013

Yi-Yie Yan, Hsiang-Chao Lio, Tsing-Fa Lin: ”Condensation Heat transfer and Pressure Drop of Refrigerant R-134a in a Plate Heat Exchanger” Int. J. of Heat and Mass Transfer Vol. 42 (1999) pp 993- 1006

H. Hausen , ”New equation for heat transfer at free or forced fluid flow , Allgemeine Wurmetechik vol 9, no.45, pp. 75-79, 1959

N. Hayes, A. Jokar, Z.H. Ayub, Study of carbon dioxide condensation in chevron plate exchangers; pressure drop analysis, Int. J. Heat Mass Trans. 55 (2012) 2916-2925

Ilie A., Drughean L., Hera D., 2011, Plate Heat Exchanger Used As Evaporators*,*23rd IIR International Congress of Refrigeraton – Praga 2011

Hera D., 2009, Refrigerating Plants Vol.III, Refrigerating Equipments, Matrix Rom

Ilie, A., Dumitrescu, R., Chiriac, F. et al. 2007, Experimental stand for research on thermo-hydraulic processes and equipment for refrigeration systems, air-conditioning systems and heat pumps, Project Romanian National University Research Council, 2007 – 2009

Chiriac, F. Ilie, A., Dumitrescu, R., 2006. Complemente de transfer de caldura si masa, AGIR Publishing House, Bucharest, 2006

Manuscript ID: 170
DOI: 10.18462/iir.icr.2019.0170

Thermodynamic and numerical analysis of the ejector performance at off-design operation modes

Guangming CHEN, Oleksii VOLOVYK, Volodymyr IERIN, Kostyantyn SHESTOPALOV

Ningbo Institute of Technology, Zhejiang University
Ningbo City, Zhejiang Province, 315100, China, gmchen@zju.edu.cn

ABSTRACT

The study provides the results of the numerical and thermodynamic analysis of the ejector performance at off-design operation modes.
The CFD modeling is used to reveal the phenomena of the mixing process at different parts of the ejector and to study the effect of operating conditions on its performance. A thermodynamic method for the determination of the optimal adjustment range of three operating parameters is described.
The results show that the changing in even one operating parameter negatively affects the ejector efficiency. The back pressure affects the ejector performance more than the generator pressure and the evaporator pressure.
From the analysis it follows that the ejector has a lot of double-choking modes of operation with its maximum efficiency, but not only one mode as usually is stated in literature. It is found that double-choking condition for the constant geometry ejector depends on the combination of the operating parameters of the flows.
Keywords: Ejector, 1-D Model, CFD, Off-Design Mode, Double-Choking, Performance, Ejector Geometry, Entrainment Ratio.

1. INTRODUCTION

Ejector cooling cycle can be used for a wide range of purposes and has a great potential in the energy conservation and environmental protection (Milazzo and Mazzelli, 2017). The supersonic ejector is the key component of the ejector cooling cycle which is used for suction, compression and discharge of the secondary vapor by force of the primary vapor. The ejector efficiency affects the overall system performance and strongly depends and very sensitive to the operating conditions. There are three operating modes of the ejector according to the back pressure which are usually singled out: double-choking (critical) mode, single-choking (subcritical) mode and back-flow (malfunction) mode (Huang et al., 1999).
At the same time the influence of operating parameters of the primary and secondary flows on the ejector performance is usually not considered in details. The prediction of the ejector performance at off-design modes is very important especially at design stage because the ejector structure cannot be changed during operation.
This research aims to carry out a numerical study of the ejector performance at off-design modes. The CFD model of the ejector is used for analysis of the mixing process and for investigation the influence of changes in the operating conditions on the ejector performance. Also, the connection between design and off-design modes is shown based on the thermodynamic analysis of the ejector performance in wide range of operating conditions.

2. DESCRIPTION AND NUMERICAL ANALISYS OF THE EJECTOR

Fig. 1 shows the structure of the supersonic ejector. The ejector can be divided into four main parts: a nozzle, a suction chamber, a mixing chamber, and a diffuser.
The operating conditions of the ejector are specified by operating pressures P_S, P_M, and P_P, the expansion pressure ratio, $E = P_P/P_S$, and the compression pressure ratio, $C = P_M/P_S$. The ejector geometry is characterized by configuration of the nozzle (A_t – the primary nozzle throat area; A_1 – the primary nozzle exit area) and the cross-section areas of the other parts of the ejector (A_2 – the

entrance area of the mixing chamber; A_3 – the area of the cylindrical section of the mixing chamber). The primary nozzle design is determined by the area ratio $\phi = A_1/ A_t$, and the design of an ejector flow profile is defined by the area ratio $\alpha = A_3/ A_t$ (Shestopalov et al., 2015a).

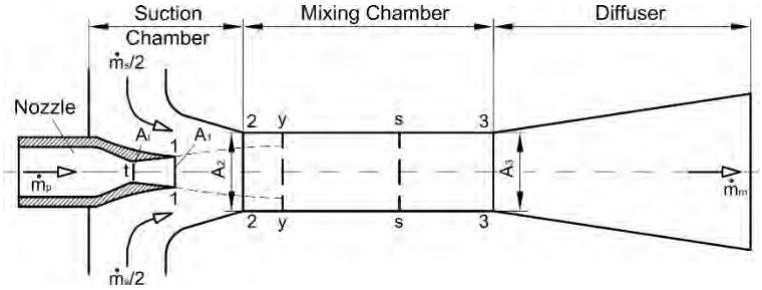

Figure 1: Structure of the supersonic ejector.

It is noted that in order to obtain the maximum performance, the ejector needs to be operated at critical (design) mode (Boumaraf and Lallemand, 2009; Dennis and Garzoli, 2011; Huang et al., 1999). But the real working conditions of the ejector and ejector cooling cycle are usually different from the design operating mode which is optimal. It results in changing both the ejector entrainment ratio and the efficiency of the ejector cooling cycle.
The relationship between the entrainment ratio and parameters of the primary, secondary and mixed flows for the ejector with fixed geometry is determined by the ejector characteristic. The ejector characteristic shows how the ejector entrainment ratio is changed when ejector operates at off-design conditions, and the additional losses are appeared in it.
The ejector characteristic consists of two branches – subcritical and supercritical, which are converged in one point. This point for the ejector with constant geometry is the design point. In this point ejector works at critical mode called "the second limiting regime" (Shestopalov et al., 2015a). This regime is characterized by reaching the critical value of the velocity of the secondary flow at cross-section of the mixing chamber y-y (see Fig. 1).
The CFD ejector model is used for detailed analysis of the mixing process and for investigation the influence of changes in the operating conditions on the ejector performance in the present study. CFD technique consists of two main parts: creating the physical model and solving the complex of mathematical equations. The ANSYS Workbench 19.0 environment is used as an intuitive up-front finite element analysis tool in the present study.

2.1. Physical Model

The numerical analysis of the ejector performance is based on the experimental results provided by Huang et al. (1999) in the present study. The ejector combination with nozzle A and mixing chamber D with area ratios $\phi = 2.91$ and $\alpha = 9.41$ is selected from 11 available combinations for the analysis (Huang and Chang, 1999). Fig. 2 shows the geometrical configuration of the investigated ejector model.
The ejector is modeled as a two-dimensional axial symmetric approach. The computational mesh with about 46500 quadrilateral elements was generated for a half of the ejector model based on X axle as a symmetric line for this investigation.

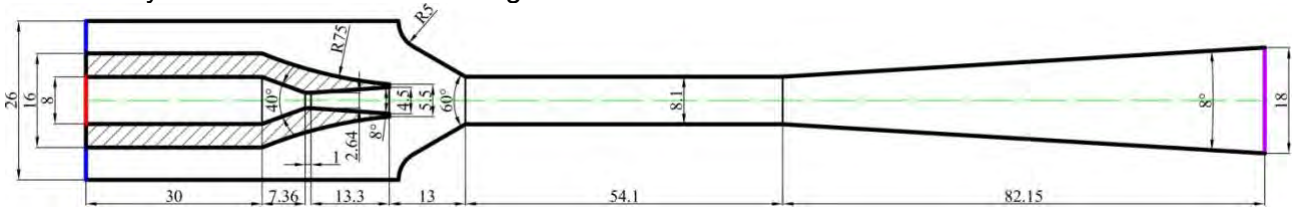

Figure 2: Ejector model considered in the present study.

2.2. Modeling Approach

The CFD software Fluent was used for steady-state simulation of fluid flow in the ejector. The density-based explicit solver was selected to solve the governing equations, and the second-order

upwind scheme was used to discretize the convective terms to improve the solution accuracy. The Realizable k-ε model was employed, which is widely used for the flow simulation inside the ejector, and which was described by Besagni et al. (2015) in details. The Standard Wall Function was used to simulate and provide reasonably accurate results for the turbulent flow near the walls. The ejector walls were considered to be adiabatic during the simulation, the no-slip conditions and smooth walls were also considered.
The ideal gas relationship was used to obtain the density of the refrigerant R141b. The other necessary thermodynamic properties of the fluid such as specific heat, thermal conductivity, viscosity, and molecular weight were taken from REFPROP software (Lemmon et al., 2007). The inlet boundary conditions for both the primary and the secondary flow were set as the "pressure inlet" corresponding to the saturation pressure of the fluid at the generator and evaporator desired temperatures, while the "pressure outlet" is set for the ejector outlet with the saturation pressure at the condenser temperature. The convergence of each simulation was considered at reaching the residuals for all equations the values 10^{-6}.

3. RESULTS AND DISCUSSIONS

3.1. Numerical Analysis of the Ejector at Off-Design Modes

The ejector simulation at off-design modes was made by sequential changing in one of the flows temperature T_C, T_G or T_E relatively the design value, while the other two temperatures remained at the design value.
The maximum compression ratio C as well as the critical condenser temperature T_C^* for the ejector at design generator and evaporator temperatures should be determined in the beginning of comparison the experimental results with CFD ones. Fig. 3 presents the ejector characteristic at ranging the condenser temperature T_C and fixed generator and evaporator temperatures T_G = 90ºC and T_E = 8ºC, respectively, according to design conditions. Fig. 4 represents the static pressure distribution of the secondary flow along the ejector walls, and Fig. 5 shows the behavior of the supersonic flow inside the ejector based on CFD simulation as the contour of Mach numbers.
From Fig. 3 it is seen that the CFD results are in good agreement with the corresponding experimental results within experimental error. The CFD ejector characteristic curve $\omega = f(T_C)$ has a knee at the condenser temperature $T_C = T_C^* = 31.2$ºC, as well as experimental characteristic curve has the same one at $T_C = T_C^* = 31.5$ ºC. At these values of T_C the ejector has the maximum entrainment ratios $\omega = 0.459$ and $\omega = 0.445$, respectively, and it works at critical mode, which is characterized by the filling of the whole cross-section of the mixing chamber by the supercritical flow (see Fig. 5c). For operation of the ejector at supercritical mode, when $T_C < T_C^*$, the entrainment ratio is not changed because the cross-section area of the mixing chamber is constant and it is still filled by the supersonic flow (see Fig. 5a and 5b). It is not allowed more secondary fluid to be entrained. From the other hand, when the ejector works at subcritical mode at $T_C > T_C^*$, the entrainment ratio is sharply reduced with increasing the condenser temperature T_C. In this mode the compression ratio C and the compression work are increased at the invariable expansion ratio E and the expansion work, and it leads to decrease the amount of the entrained secondary flow. In this case the cross-section area of the mixing chamber is not filled by the supersonic flow (see Fig. 5d and 5e).
From Figs. 4 and 5 it can be seen that the cross-section of the mixing chamber y-y, where the limiting regime is appeared, is located at the distance of about 11.5 mm from the enter cross-section of the mixing chamber 2-2, and its position does not depend on the condenser temperature. At the same time, the position of the cross-section of the mixing chamber s-s where the second choking is appeared depends on the condenser temperature, and it is moved down from the enter cross-section of the mixing chamber 2-2 at condenser temperature decreasing.
As can be seen from Fig. 6, the ejector characteristic curve $\omega = f(T_G)$ also has a knee at generator temperature T_G = 90ºC at which the ejector works at critical mode. At the generator temperature decreasing, the ejector operates at subcritical mode. The mass flow rate of the primary flow decreases in this mode, the supersonic nozzle is over-expanded and works in off-design condition (see Fig. 8d and 8e). It leads to decrease both the secondary mass flow rate and the entrainment ratio significantly due to decreasing the expansion ratio E and the expansion work of the primary flow at the invariable of compression ratio C.

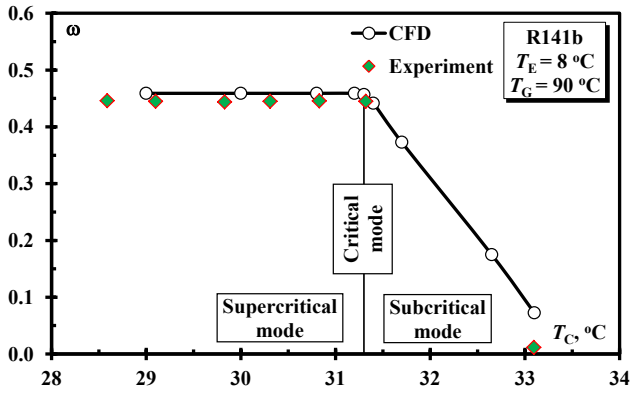

Figure 3: Ejector characteristic $\omega = f(T_C)$.

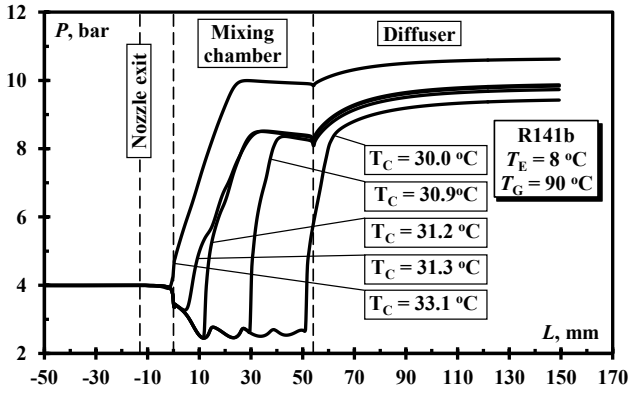

Figure 4: Static pressure at different T_C.

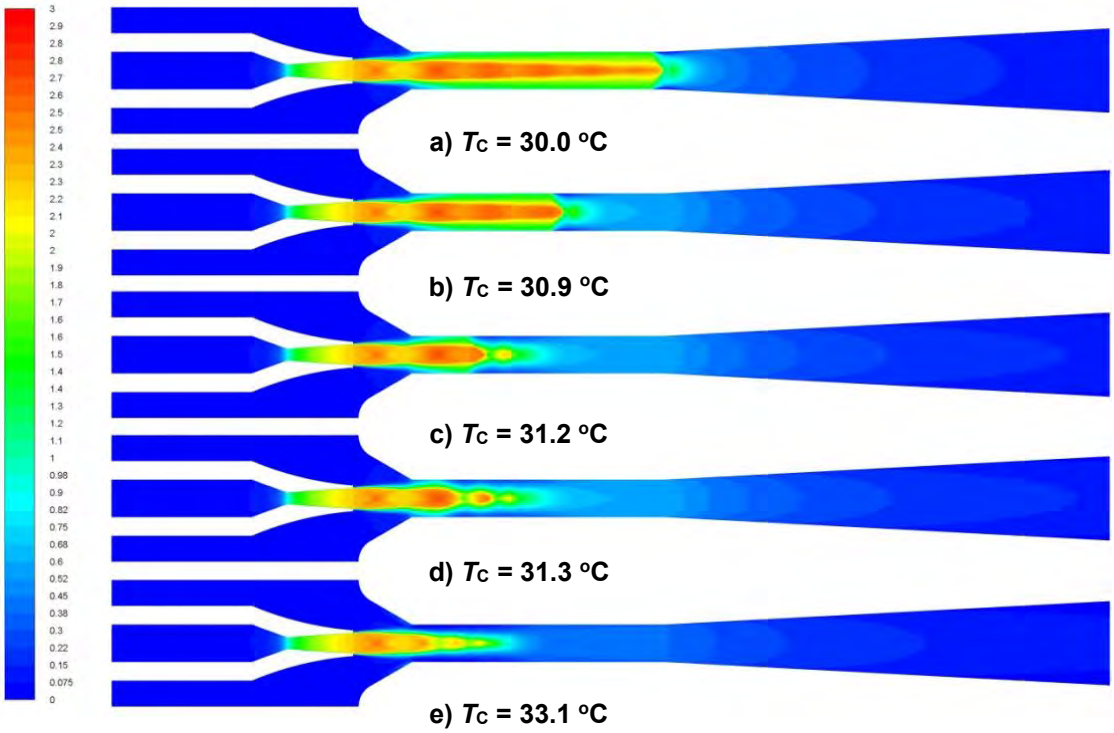

Figure 5: Contour of Mach numbers inside the ejector at different T_C.

From Fig. 6 it follows that the increasing in the generator temperature relatively the design one also leads to decrease in the entrainment ratio in spite of increasing the expansion ratio *E*, the expansion work and the mass flow rate of the primary flow. The ejector operates at supercritical mode and the nozzle is under-expanded for these conditions (see Figs. 8a and 8b). It leads to increase the cross-section area of the primary flow exiting from the nozzle, which results decreasing the cross-section area of the secondary flow and its mass flow rate at the invariable cross-section area of the mixing chamber 2-2.

From Figs. 7 and 8 it follows that the increasing in generator temperature leads to the appearing of the choking effect at the end of the mixing chamber, and even at the beginning of the diffuser section 3-3 (see Figs. 8d and 8e). At the same time the position of the cross-section y-y changes insignificantly.

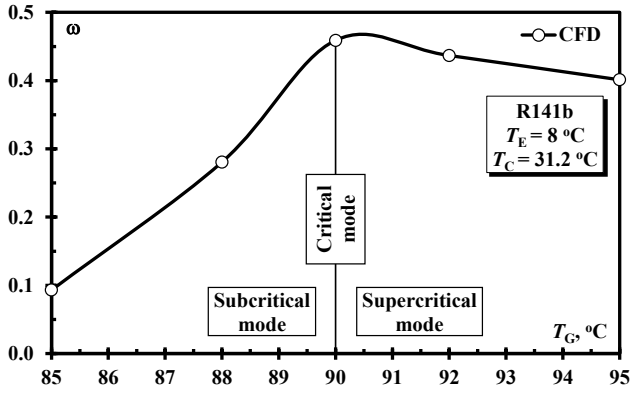

Figure 6: Ejector characteristic $\omega = f(T_G)$.

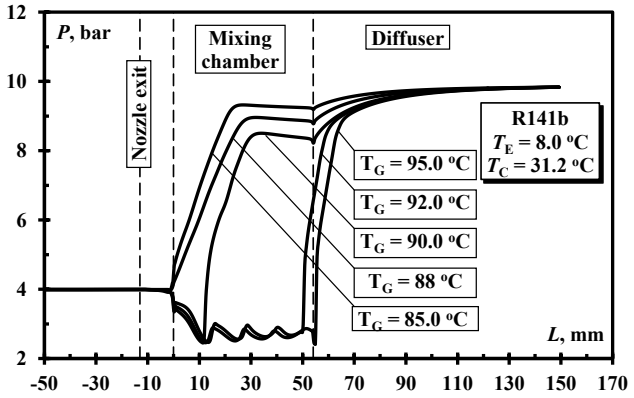

Figure 7: Static pressure at different T_G.

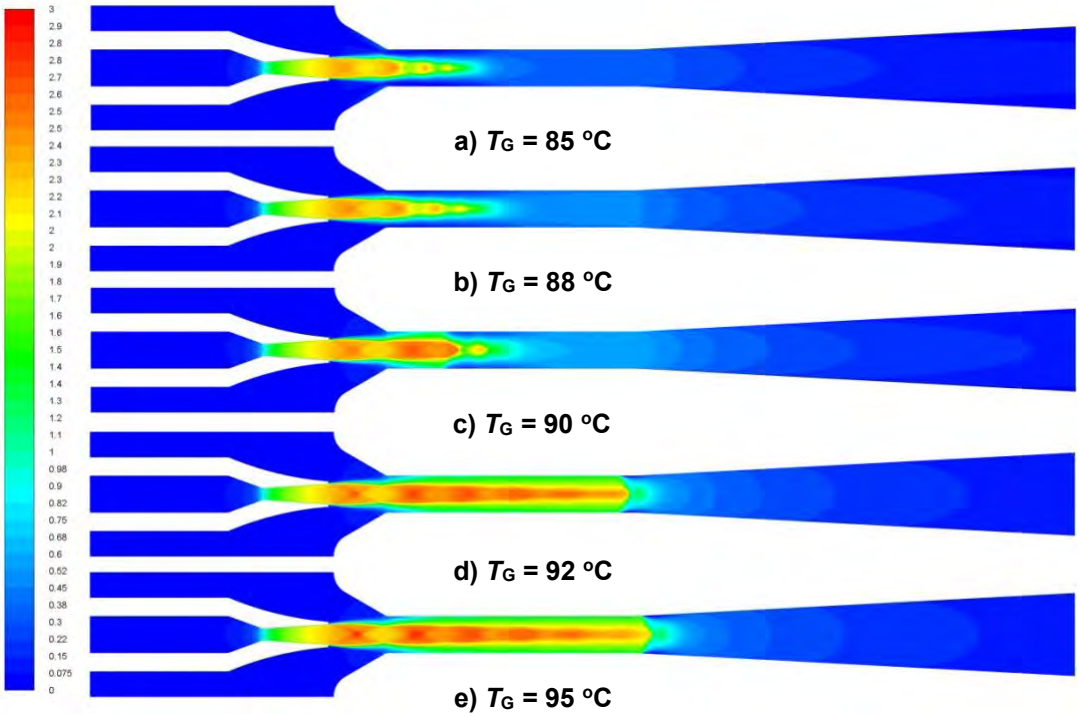

Figure 8: Contour of Mach numbers inside the ejector at different T_G.

Analysis of the ejector characteristic curve $\omega = f(T_E)$ shows that the entrainment ratio increases with increasing in evaporating temperature (see Fig. 9). It can be explained by simultaneous decreasing the compression ratio *C* and the expansion ratio *E* and approaching its working conditions to the design ones. From Figs. 11a and 11b it follows that the supersonic nozzle is significantly under-expanded at subcritical mode that leads to decrease the cross-section area for the secondary stream at section 2-2 of the mixing chamber, and results in decrease the secondary mass flow rate. At T_E = 8°C the ejector reaches the design conditions and it works at critical mode (see Fig. 11c). Further increasing in the evaporator temperature results in increasing the entrainment ratio, but its growth rate decreases as evidenced by the knee on the characteristic curve $\omega = f(T_E)$ (see Fig. 9). The ejector works at supercritical mode and the primary nozzle is over-expanded (see Figs. 11d and 11e). The cross-section area of the secondary flow at section 2-2 is increasing and it leads to increase the amount of the entrained secondary flow.

From Fig. 10 it follows that the mixing process pressure increases at the evaporator temperature increasing. At the same time the choking effect appears closer to the entrance section of the diffuser 3-3.

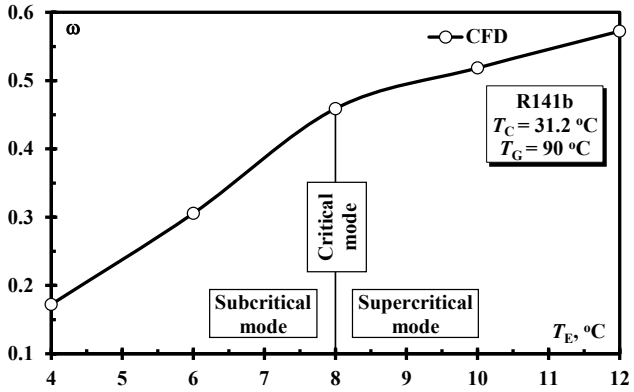

Figure 9: Ejector characteristic $\omega = f(T_E)$.

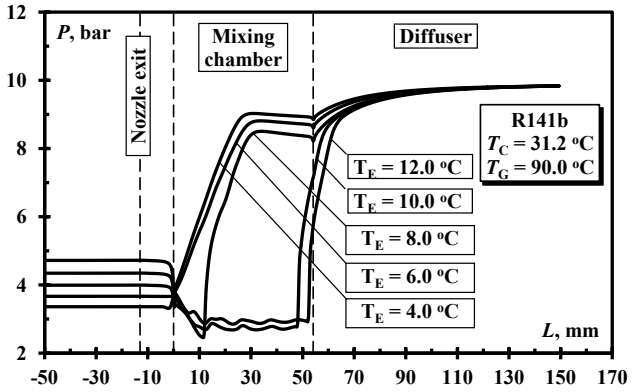

Figure 10: Static pressure at different T_E.

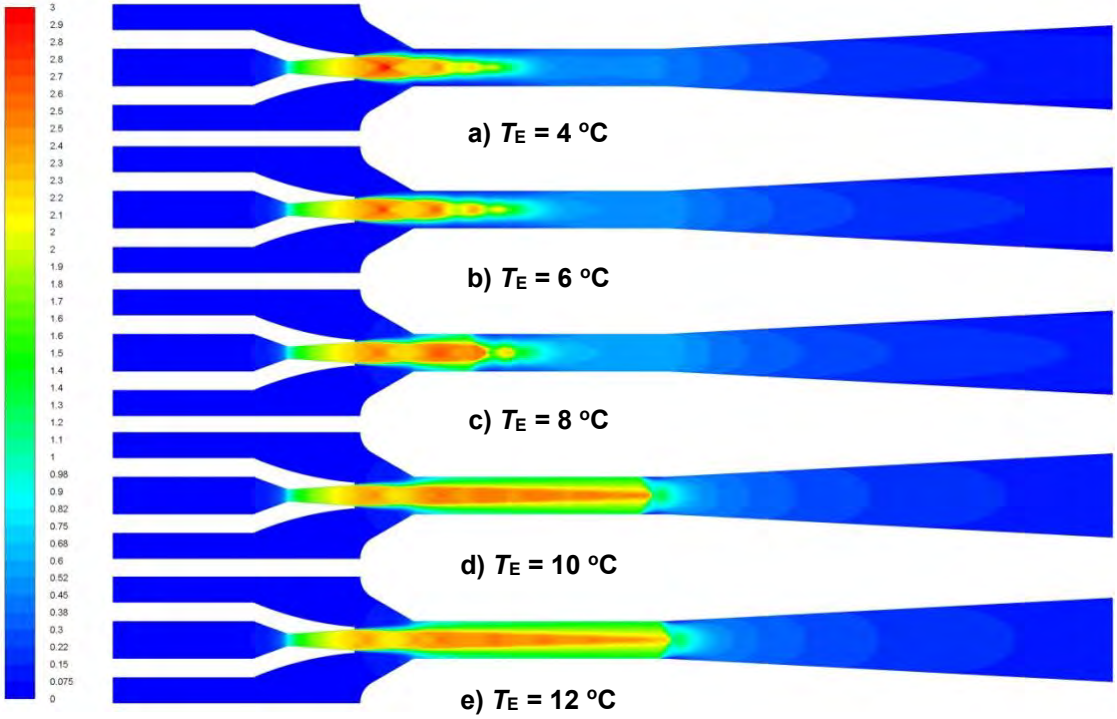

Figure 11: Contour of Mach numbers inside the ejector at different T_E.

3.2. Thermodynamic Analysis of the Ejector at Off-Design Modes

From the numerical analysis it follows, that variation in one flow parameter significantly influences the ejector performance. Especial negative effect is observed at increasing the condenser temperature, at decreasing the evaporator temperature, and at changing the generator temperature. Shestopalov et al. (2015b) obtained the experimental data for the ejector performance in wide range of operating conditions and noted that the ejector performance maps can be useful assistance for the development of an automatic control system with the aim to provide the ejector operation at critical mode with its maximum efficiency. For realization of that method, the optimal adjustment range of three independent operating parameters T_E, T_C and T_G should be determined. To find this range, the graphical layouts presented in Figs. 12, 13, 14 and 15 can be used and analyzed.

Fig. 12 shows the theoretical curves $\phi = f(T_G)$ for different evaporator temperatures which were determined by 1-D ejector model proposed by Shestopalov et al. (2015a). The horizontal line $\phi = 2.91$ corresponds to nozzle area ratio of the considered ejector. Fig. 12 illustrates the way to determine the generator temperatures for the supersonic nozzle for different evaporator temperatures with the aim to ensure the nozzle operation in design mode. To do this, the perpendiculars should be dropped on the abscissa axis from the intersection points between curves $\phi = f(T_G)$ and the line $\phi = 2.91$. In Fig. 13 theoretical curves $\alpha = f(T_C)$ for the generator

temperatures determined from Fig. 12 as well as a horizontal line α = 9.41 corresponded to geometrical parameter for the considered ejector are presented. In turn, Fig. 13 shows the way to determine the critical condenser temperatures at which the designed ejector works at critical modes. By analogy with Fig. 12, to determine T_C^* the perpendiculars should be dropped on the abscissa axis from the intersection points between curves α = f(T_C) and the line α = 9.41.
Fig. 14 shows the theoretical curves ω = f(T_C) for the generator temperatures determined from Fig. 12. From this figure the critical entrainment ratio for the considered ejector can be determined. To do this it is needed to draw vertical lines correspond to values of T_C^* obtained from Fig. 13 to intersection with curves ω = f(T_C). The values of critical parameters T_C^* and ω^* for the other evaporator temperatures are determined in a similar way. Based on the obtained data the diagram of the ejector critical modes presented in Fig. 15 can be built. From Fig. 15 it follows that at given adjustment range of T_E which varied from 6 to 10ºC, in order to achieve the maximum of the ejector performance with a variation of T_C in the range 28.8-33.6ºC, the temperature T_G should be also adjusted in the range 86.4-93.6ºC. The values of the entrainment ratio determined by numerical analysis at the same operation conditions are very close to the theoretical one.

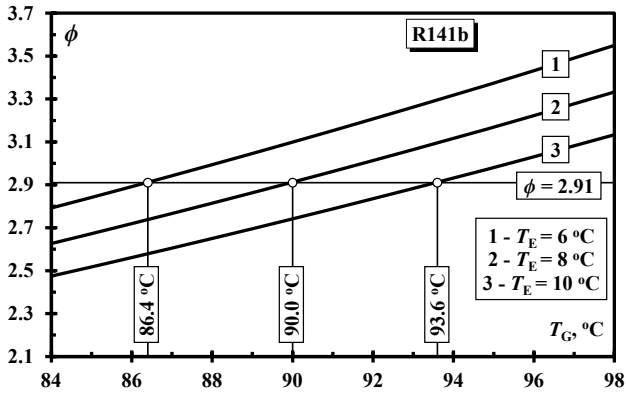

Figure 12: Ejector area ratio ϕ = f(T_G).

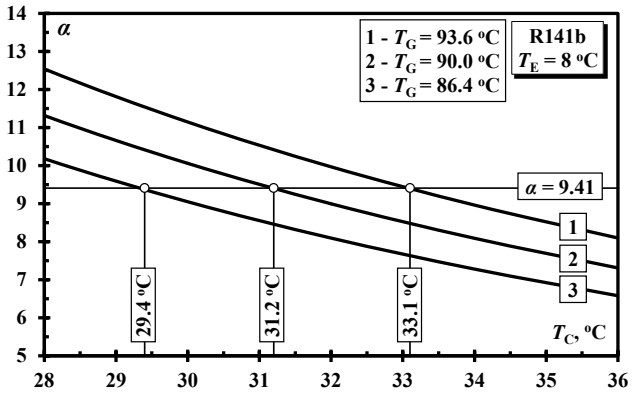

Figure 13: Ejector area ratio α = f(T_C).

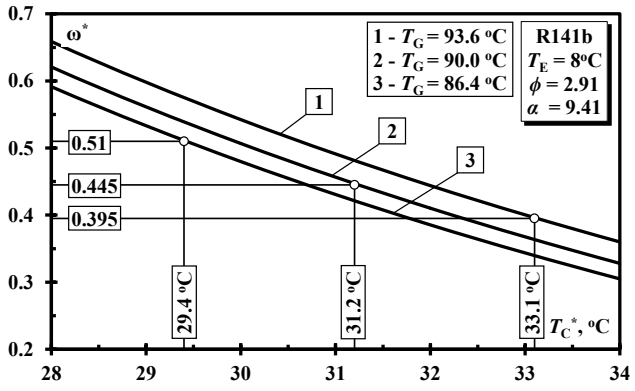

Figure 14: Ejector entrainment ratio ω^* = f(T_C^*).

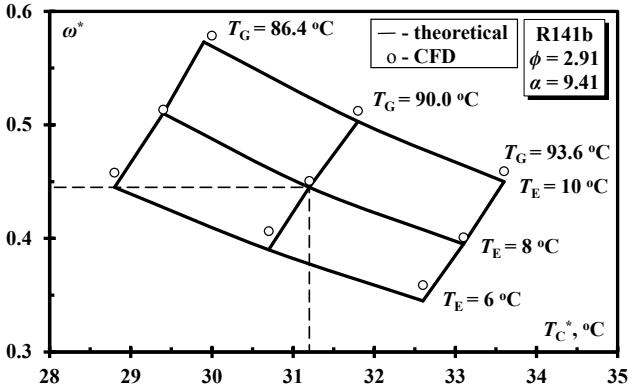

Figure 15: Ejector map of critical modes.

4. CONCLUSIONS

In this paper the operation of the ejector at off-design modes is investigated. According to the results of numerical and thermodynamic study, the most important findings are as follows:
1. The ejector can work at three typical operational modes – subcritical, critical and supercritical, depending on the combination of the operating parameters of the flows.
2. The ejector performance significantly depends on the variation of flows parameters. The increasing in condenser temperature, the decreasing in evaporator temperature and the changing in generator temperature are the most negative effects on the ejector entrainment ratio.
3. The critical ejector mode ensures the maximum of its efficiency and it is a preferable mode for the ejector operation. The analysis shows that the ejector has a lot of critical modes, but not only

one as usually is stated in literature. Each critical mode can be achieved by work at appropriate combination of the flows parameters.
4. The thermodynamic method for the determination of the optimal adjustment range of three independent operating parameters T_E, T_C and T_G is described. The theoretical diagram of the ejector critical modes obtained by this method can be used at design stage of the ejector cooling cycle to determine the maximum values of the heat exchanger capacities needed for the automatically maintaining the ejector operation at critical modes with a slight deviation from the designed efficiency.

ACKNOWLEDGEMENTS

The paper was financially supported in part by the Natural Science Foundation of China (Projects No. 51776187), by Zhejiang Province Natural Science Foundation of China (Project No. LY16E060004), and by Ningbo Science and Technology Bureau from the International Cooperation (Project No. 2017D10006).

NOMENCLATURE

A	area (m^2)	T	temperature (°C)
C, E	ejector pressure ratios	ϕ, α	ejector area ratios
P	pressure (bar)	ω	entrainment ratio

REFERENCES

Besagni, G., Mereu, R., Chiesa, P., Inzoli, F., 2015. An Integrated Lumped Parameter-CFD approach for off-design ejector performance evaluation. Energy Convers. Manag. 105, 697-715.

Boumaraf, L., Lallemand, A., 2009. Modeling of an ejector refrigerating system operating in dimensioning and off-dimensioning conditions with the working fluids R142b and R600a. Appl. Therm. Eng. 29, 265-274.

Dennis, M., Garzoli, K., 2011. Use of variable geometry ejector with cold store to achieve high solar fraction for solar cooling. Int. J. Refrigeration 34, 1626-1632.

Huang, B.J., Chang, J.M., Wang, C.P., Petrenko, V.O., 1999. A 1-D analysis of ejector performance. Int. J. Refrigeration 22, 354-364.

Huang, B.J., Chang, J.M., 1999. Empirical correlation for ejector design. Int. J. Refrigeration 22, 379-388.

Lemmon, E.W., Huber, M.L., McLinden, M.O., 2007. Reference Fluid Thermodynamic and Transport Properties Database (REFPROP). National Institute of Standarts and Technology, Standard Reference Data Program, Gaithersburg, Maryland, USA. Version 8.0.

Milazzo, A., Mazzelli, F., 2017. Future perspectives in ejector refrigeration. Appl. Therm. Eng. 121, 344-350.

Shestopalov, K.O., Huang, B.J., Petrenko, V.O., Volovyk, O.S., 2015a. Investigation of an experimental ejector refrigeration machine operating with refrigerant R245fa at design and off-design working conditions. Part 1. Theoretical analysis. Int. J. Refrigeration 55, 201-211.

Shestopalov, K.O., Huang, B.J., Petrenko, V.O., Volovyk, O.S., 2015b. Investigation of an experimental ejector refrigeration machine operating with refrigerant R245fa at design and off-design working conditions. Part 2. Theoretical and experimental results. Int. J. Refrigeration 55, 212-223.

Manuscript ID: 184
DOI: 10.18462/iir.icr.2019.0184

A correlation for the air-side heat transfer coefficient of natural-draft wire-on-tube condensers

Rodolfo S. ESPÍNDOLA, Cláudio MELO

POLO Labs, Department of Mechanical Engineering, Federal University of Santa Catarina
Florianópolis, 88040-970, Brazil, melo@polo.ufsc.br

ABSTRACT

In order to improve performance, manufacturers of household refrigerators are constantly updating the design of natural-draft wire-on-tube condensers. As a consequence, the geometrical application range of the current correlations became outdated. In this context, the aim of this work was to extend the limits of the existing mathematical models by proposing a new and updated correlation to predict the air-side heat transfer coefficient. To this end, a test bench was designed and built to circulate hot brine through the condenser tubes, controlling the inlet temperature and the mass flow rate. Fifty-four condenser samples with distinct design parameters, such as height, tube and wire diameters and pitches were manufactured and tested. The experimental results showed that the condenser height, and the wire and tube pitches had the strongest impact on the heat transfer rate. Finally, a semi-empirical correlation was put forward, where 90% of the experimental data were predicted within a ±10% error band.
Keywords: Wire-on-tube Condenser, Household Refrigeration, Semi-empirical Correlation

1. INTRODUCTION

When it comes to household refrigeration, cost and energy efficiency are the driving forces of most research works. Sometimes cost reduction is even more important than energy savings. That is the case for appliances mounted with natural-draft wire-on-tube condensers. Such heat exchangers are made of carbon-steel and consist of a single-pass coil with several wires spot-welded in an in-line or staggered arrangement on both sides. The combination of material and manufacturing process makes the wire-on-tube condenser perhaps the cheapest heat exchanger on the market and the preferred choice of most engineers. However, despite the widespread use of wire-on-tube condensers, the literature is still scarce on the topic.

Among the available works stand the pioneer studies of Witzell and Fontaine (1957), Witzell et al. (1959), Cyphers et al. (1959) and Collicott et al. (1963). Witzell and Fontaine (1957) assembled the first experimental apparatus to measure the heat transfer rate based on the circulation of hot water through the coil. The condensers were tested in a horizontal position and only the number and diameter of the wires were varied. Cyphers *et al*. (1959) adopted a similar test bench and analysed the impact of both inclination and confinement. Semi-empirical correlations based on the Grashof number were proposed to predict the convection heat transfer coefficients for both tubes and wires. Later, Witzell et al. (1959) improved the test section used by Witzell and Fontaine (1957) by placing the condensers in a black wood box with openings at the bottom and top parts. Tests varying the inclination of the condenser and the wires pitch were conducted. The number of tubes was kept constant. In addition, a single correlation for the convection heat transfer was put forward based on an equivalent diameter. All previous studies, however, assumed a unitary shape factor and neglected its effect on the radiation heat transfer calculation. In order to address this issue, Collicott et al. (1963) calculated the effective shape factor of 12 samples with the same tube diameter but with different wire pitches. The authors performed all tests in an evacuated chamber seeking to quantify the radiative contribution. Decades later, Tagliafico and Tanda (1997) revisited the subject by carrying out tests with 42 samples. Geometric parameters such as condenser height, tubes and wires pitch and tube diameter were varied. The effect of confinement was not evaluated. Temperature differences between air and tubes of almost 50°C were observed in some cases. A correlation based on the Rayleigh number and geometry was proposed and validated within a ±6% error band.

Years later, Arsego (2003) tested 24 samples with in-line wires under several operating conditions by pumping water into the tubes. An experimental apparatus capable of reproducing the condenser behavior as if it was mounted on a real appliance was assembled. Parameters such as number, diameter and pitch of tubes and wires were investigated. The condensers height and width, however, were kept constant. The convection and radiation heat transfer shares were calculated and the latter took the tubes and wires shape factors into account. Melo *et al*. (2004) used the same test bench of Arsego (2003) to study the effect of the gap between the refrigerator back wall and the surroundings on the heat transfer. To this end, a 19-tube rows and 130 wires condenser was tested at an ambient temperature of 32°C. Also, the temperature difference between the condenser inlet and outlet was maintained between 43 and 44°C. It was shown that the gap between the rear wall and the refrigerator plays an important role and that when the condenser is positioned at the middle of the gap the heat transfer rate is maximized.

Recently, Melo and Hermes (2009) used the experimental database of Arsego (2003) to devise an easy-to-use π-type correlation based on geometric parameters and the temperature difference between air and tube wall. The wires fin-efficiency was incorporated in the air-side heat transfer coefficient and the surface shape factor was neglected. Even though, 90% of the experiments were predicted within a 10% error band. A comparison with the correlations proposed by Cyphers et al. (1959), Witzell et al. (1959) and Tagliafico and Tanda (1997) was reported and it was found that all produced larger errors.

In order to reduce cost and maintain reasonable energy consumption levels, wire-on-tube condensers are constantly being redesigned with the aid of the currently available correlations. However, such equations are restricted to specific geometric ranges and have proven to be unable of predicting well the heat transfer rate of the new condenser designs, especially those with different heights and staggered and smaller wires. In this context, the present work aimed to fill this gap by proposing a new semi-empirical model. Fifty-four samples covering a wide range of geometric parameters were tested in a water-loop calorimeter to leverage the correlation.

2. EXPERIMENTAL WORK

Fifty-four condensers were designed and manufactured specifically for this work where the following parameters were varied: height (H = 480, 900 and 1400 mm), tube pitch (s_t = 25, 40 and 60 mm), tube outer diameter (d_t = 4.76 and 4.00 mm), wire pitch (s_w = 4, 10 and 20 mm) and wire diameter (d_w = 1.25 and 1.35 mm). An illustrative sketch of the condensers is shown in Fig. 1. All samples were fabricated in carbon steel, with staggered wires and a constant width (W) of 440 mm.

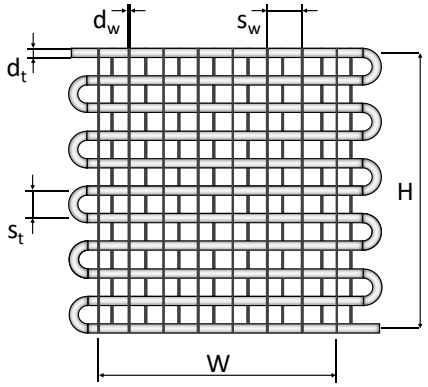

Figure 1: Wire-on-tube condenser sketch

2.1. Experimental Apparatus

The experimental apparatus is comprised by three main facilities: the test bench, the test section and the test chamber, as schematically shown in Fig. 2. The test bench is responsible for circulating a hot brine composed by water and glycol (80/20% in mass) inside the carbon steel tubes. It is basically comprised by a thermostatic bath, a rotary vane pump, valves and filters. An electric heating wire was placed around the tubes to fine-adjust the fluid inlet temperature.

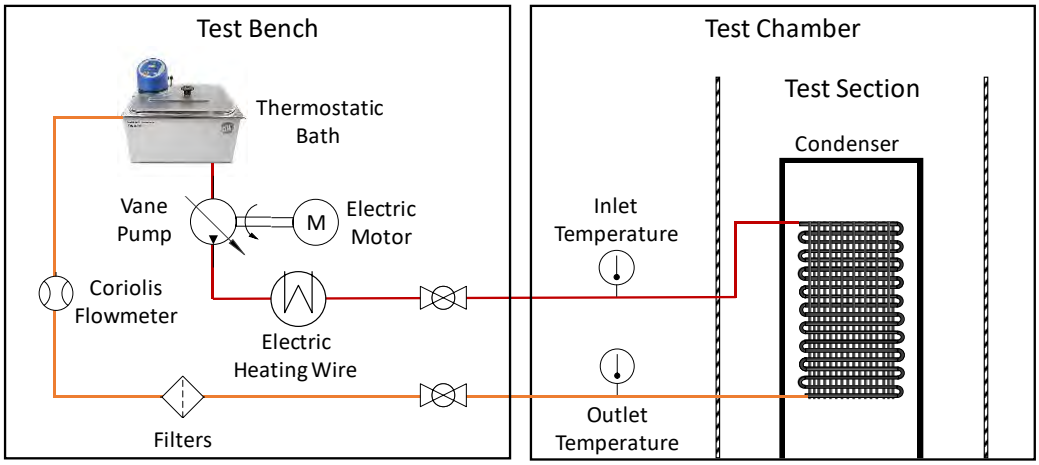

Figure 2: Experimental apparatus

The test section was built in order to mimic a domestic refrigerator (Fig. 3). The section height could be varied in such a way that the condenser distance from the ground and from test section top was always 300 mm, regardless of the height of the condenser. The distance from the test section side walls and the surrounding walls was also kept at 300 mm. The test section and surroundings walls were made of dull black wood in accordance the recommendations of ISO 15502 (2005). Finally, the gap from the test section rear wall and the test chamber was 100 mm, and the condensers were always placed in the middle of this gap, at 50 mm from the test section rear wall.

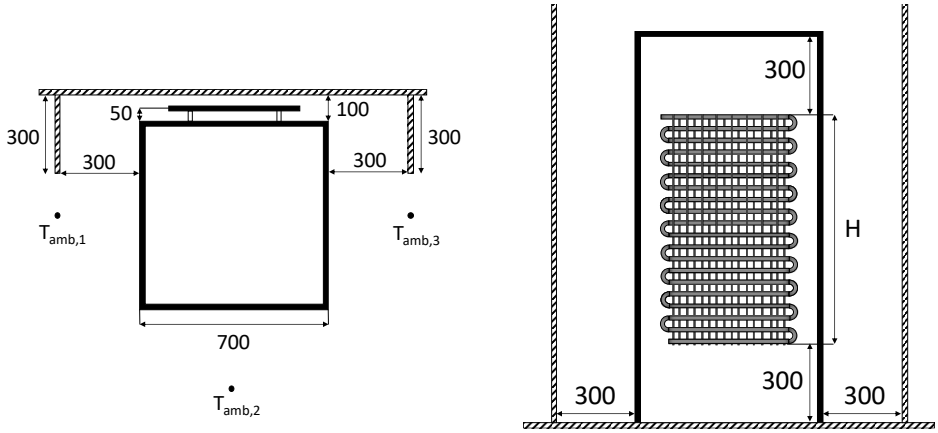

Figure 3: Test section top and back view

The tests were performed in a climate-controlled chamber also built in accordance to the ISO 15502 (2005) recommendations. The ambient temperature was measured by three T-type thermocouples, as shown in Fig. 3. The fluid mass flow rate was measured by a Coriolis-type flow meter and the temperature difference by two T-type immersion thermocouples placed in the condenser inlet and outlet (see Fig. 2).

The condensers were tested at ambient temperatures of 32 and 16°C. The brine temperature difference from the inlet and outlet of the condenser was always kept at 3°C, in order to provide an almost uniform temperature in the condenser tubes. The tests were performed with brine average temperatures (T_{br}) of 8, 13 and 20°C higher than the ambient temperature. In total, 228 experiments were performed and used to leverage an air-side heat transfer correlation.

3. DATA REGRESSION

The total heat transfer rate ($\dot{Q}$) was calculated through an energy balance on the brine side, considering the brine mass flow rate ($\dot{m}$) and the inlet and outlet temperature difference:

$$\dot{Q} = \dot{m} c_p \left(T_{br,i} - T_{br,o}\right) \qquad \text{Eq. (1)}$$

where c_p was obtained at the brine inlet ($T_{br,i}$) and outlet ($T_{br,o}$) average temperature.
The condenser overall thermal conductance (UA) was derived from the relation between the heat released rate and the temperature difference between the brine and surroundings:

$$UA = \dot{Q}(T_{br} - T_{amb})^{-1} \quad \text{Eq. (2)}$$

where T_{br} and T_{amb} are respectively the brine and ambient average temperatures.
Generally, when the fluid temperature difference is high, it is appropriate to use log-mean difference temperature or the ε-NUT method. However, as in the present study the brine temperature difference was as low as 3°C, this simplification is of reasonable use. The air-side heat transfer coefficient, h_0, was then calculated by subtracting the internal convection resistance from the overall thermal resistance:

$$\eta_0 h_0 = A_0^{-1}[UA^{-1} - (h_i A_i)^{-1}]^{-1} \quad \text{Eq. (3)}$$

where η_0 is the overall outer surface efficiency, h_i is the internal heat transfer coefficient and A_i and A_0 are respectively the internal and external total heat transfer areas. The conduction through the tube walls and fouling resistances on both sides were neglected. The internal side heat transfer coefficient was estimated by Gnielinski's (1976) correlation when $\mathrm{Re} > 3000$. Laminar fully developed flow with uniform wall temperature ($Nu = 3.66$) was considered when $Re < 2300$. The transition between Gnielinski and laminar flow ($2300 < Re < 3000$) was obtained through the method of the asymptotes.
Assuming that the heat transfer coefficient is constant along the wires and tubes, a simplified approach was employed to evaluate the overall surface efficiency, which was given by:

$$\eta_0 = 1 - A_w A_0^{-1}(1 - \eta_w) \quad \text{Eq. (4)}$$

where η_w is the wire rectangular pin fin efficiency with adiabatic tip defined as (Incropera *et al.*, 2002):

$$\eta_w = \tanh\left(m\frac{s_t}{2}\right)\left(m\frac{s_t}{2}\right)^{-1} \quad \text{Eq. (5)}$$

$$m = [4h_0(k_w d_w)^{-1}]^{1/2} \quad \text{Eq. (6)}$$

The total rate of heat rejection to the environment of the wire-on-tube condenser is a result of convective and radiative phenomena. Thus, the total air-side heat transfer coefficient is comprised by the sum of both coefficients, $h_0 = h_c + h_r$. The radiation heat transfer coefficient is derived from the well-known Stefan-Boltzmann law:

$$h_r = \varepsilon_{app}\sigma(T_c + T_{amb})\left(T_c^2 + T_{amb}^2\right) \quad \text{Eq. (7)}$$

where T_c is the condenser surface average temperature calculated through an energy balance:

$$T_c = T_{amb} + \dot{Q}(\eta_0 h_0 A_0)^{-1} \quad \text{Eq. (8)}$$

σ is the Stefan-Boltzmann constant and ε_{app} is the apparent emissivity defined by the product of surface emissivity, ε, and condenser to environment shape factor, F. The condenser surface emissivity was measured through thermography techniques and an average value of 0.95 was found. The condenser to environment shape factor was analytically calculated as follows (Siegel and Howell, 1972):

$$F = \frac{A_t F_{t\to\infty} + A_w F_{w\to\infty}}{A_t + A_w} \quad \text{Eq. (9)}$$

where $F_{t\to\infty}$ and $F_{w\to\infty}$ are the tubes and wires to the surroundings shape factors, respectively. The condenser shape factor ranged from 0.58 to 0.85 for all samples.
Accounting for all instrument errors and propagated uncertainties, the maximum uncertainty levels corresponding to the temperature, mass flow rate and heat transfer rate were respectively ±0.2°C, ±0.02 kg/h, and ±5%.

4. RESULTS

4.1. Experimental Results

Fig. 4 summarizes the relative contribution of the radiation and convection to the combined air-side heat transfer coefficient. It is known that both are strongly dependent on the wire pitch. As the wire pitch reduces, the confinement reduces both the condenser shape factor and the buoyancy effect, reducing respectively the radiative and convective phenomena, and therefore the combined air-side heat transfer coefficient. Nonetheless, it can be noted that the radiative relative contribution (which ranged from 22% to 57%) increases with a decreasing h_0, indicating that the confinement has a stronger effect in the convection counterpart. Similar results were obtained by Melo and Hermes (2009), except by the overestimation of the radiative contribution due to the shape factor negligence.

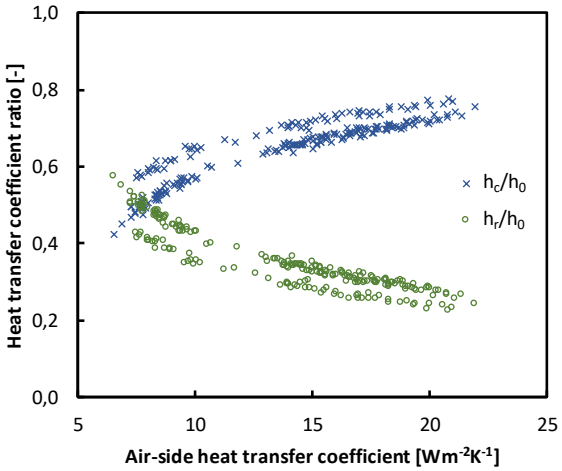

Figure 4: Convective and radiative contributions to the air-side heat transfer coefficient

Fig. 5 summarizes the condenser heat transfer rate results as a function of the condenser height, wire pitch and tube pitch. The total heat transfer rate ranged from 35 W to 175 W, as a combination of the selected geometric parameters and operational conditions. As expected, the higher the condenser, the higher the total heat transfer rate. The wire pitch is another parameter that strongly affected the heat transfer rate, especially because the total heat transfer area increases as the wire pitch decreases. A similar trend was observed for the tube pitch. In this case, it can be noted that, the higher the condenser the stronger the variations in heat transfer rate, due to the stronger buoyancy effect. The influence of tubes and wires diameters on total heat transfer rate were not significant, with variations lower than 4%.
One important issue of the industry nowadays is evaluating the cost-benefit relationship in the refrigeration components. In this context, Fig. 6 shows the relation between the ratio of heat transfer rate per the condenser steel mass to the same geometric parameters analysed previously. Such ratio is directly proportional to the manufacturing cost. Note that the condenser height barely affects the cost-benefit relationship, so it is just a matter of capacity designing. On the other hand, a clear trend was observed regarding the wire pitch. The larger the wire pitch, the better the cost-benefit, due to the confinement effect provoked by short pitches. It can also be seen that there is an optimum tube pitch that maximizes the benefit-cost relation. Such results might be related to the physics of natural convection in in-line tubes. As the condenser tubes are heated up, a thermal plume is formed around the tube, driving the air upwards and dissipating heat to the surroundings. This means that, if the condenser tubes are very close to each other, the upper tubes are affected by the thermal plume, hindering the condenser performance. On the other hand, if the tubes are too far from each

other, the thermal plume is dissipated far from the upper tube, meaning that space could be optimized. This analysis shows a clear trade-off relationship, leading to an optimum point that, for this specific work, seems to be close to the 40 mm tube pitch.

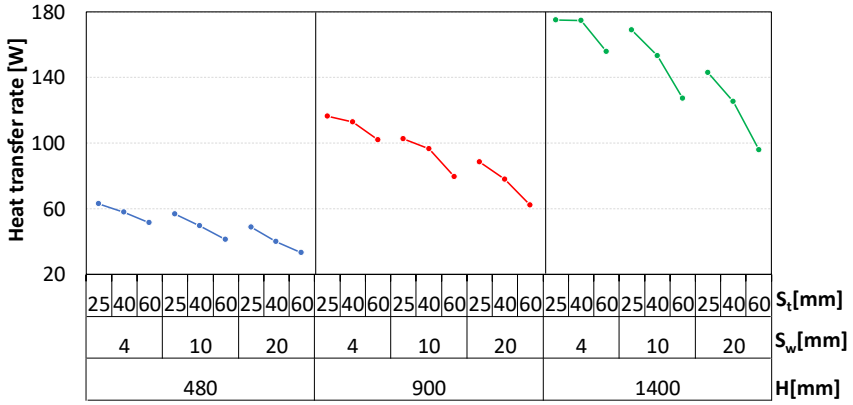

Figure 5: Heat transfer rate vs. height, wire pitch and tube pitch

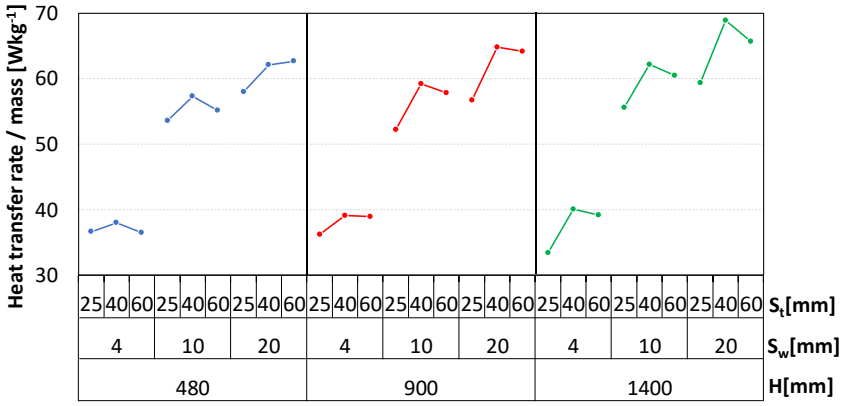

Figure 6: Heat transfer rate per unit of mass vs. height, wire pitch and tube pitch

4.2. Proposed correlation

A semi-empirical correlation was proposed to predict the air-side heat transfer coefficient considering the geometric range of the condenser samples. The combined coefficient was calculated by adding the convective and radiative counterparts ($h_0 = h_c + h_r$). The radiation contribution is obtained through Eq. 7, and a correlation was proposed for the convection heat transfer coefficient. The equation takes into account the buoyancy effect and geometric parameters, as follows:

$$Nu_{L_c} = \frac{h_c k_a}{L_c} = 6.2 {Ra_{L_c}}^{1/5} Z^{3/5} \qquad \text{Eq. (10)}$$

The Rayleigh number is defined by:

$$Ra_{L_c} = \frac{g\beta(T_{br} - T_{amb})L_c^3}{\nu_a \alpha_a} \qquad \text{Eq. (11)}$$

where the air properties must be evaluated in the film temperature, the characteristic length is defined as the ratio between the outer heat transfer area and the condenser height, $\mathrm{L_c} = \mathrm{A_0}/H$, and the dimensionless parameter (Z) is defined by:

$$Z = \frac{\text{Void area}}{\text{Available area}} = \frac{WH - N_t d_t W - N_w d_w H + N_t N_w d_t d_w}{WH} \qquad \text{Eq. (11)}$$

The parameter Z is the ratio of the void area and the available area in a perpendicular point of view. That is, the larger the void area, the larger the tube and wire pitches, increasing Z and h_c. The validation results are shown in Fig. 7, where 99% and 90% of the predicted data fell within ±15% and ±10% error bands, respectively.

Finally, the correlations available in the literature were implemented to predict the air-side heat transfer coefficient, as shown in Fig. 8. It can be noted that much larger errors were found, especially because of the design parameters range of the actual wire-on-tube condenser samples. Since most of the correlations are empirical, they are not suitable for extrapolations. Cyphers *et al*. (1959) correlation substantially overestimated the heat transfer coefficient, with errors up to +200%. The correlation of Tanda and Tagliafico (1997), which is far more complex than that proposed herein, underpredicted most of the data and large deviations were observed. On the other hand, the empirical π-type correlation of Melo and Hermes (2009), which is reasonably recent, overestimated most of the experimental data.

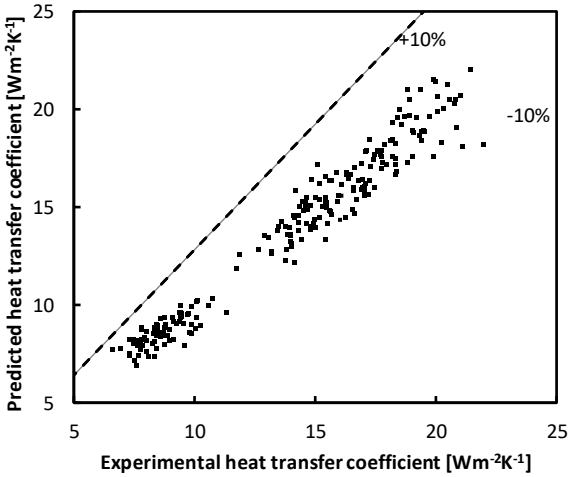

Figure 7: Validation of the proposed semi-empirical correlation

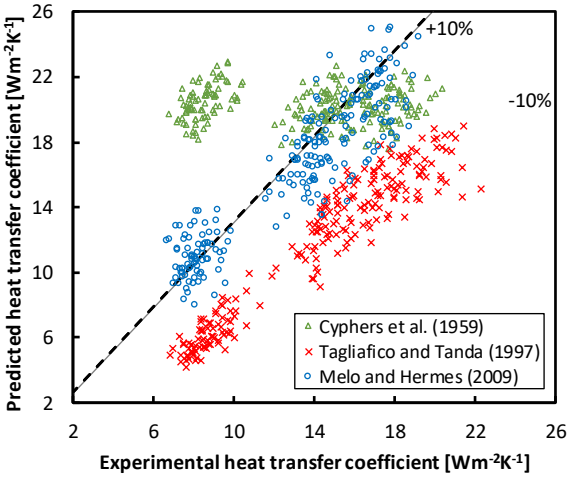

Figure 8: Comparison of the experimental data to the correlations available in the literature

5. CONCLUSIONS

This paper addressed an theoretical and experimental work on natural-draft wire-on-tube condensers. Fifty-four condenser samples were manufactured varying the following design parameters: height (480, 900 and 1400 mm), tube diameters (4.00 and 4.76 mm), wire diameters (1.25 and 1.35 mm), tube pitches (25, 40 and 60 mm) and wire pitches (4, 10 and 20 mm). The condensers were tested on an experimental apparatus built specifically for this activity. The experimental results showed that the tube and wire diameters impacted less than 4% the condenser heat transfer rate. Furthermore, the wire and tube pitches were the most significant parameters on a cost-benefit analysis. Finally, a semi-empirical correlation was proposed for the air-side heat transfer coefficient, where 90% of the experimental data were predicted with deviations lower than ±10%. The condenser shape factor was calculated to account the radiative contribution, which was responsible for an average of 35% of the total heat transfer rate. The convective contribution was much stronger specially due to the free convection buoyancy effect.

ACKNOWLEDGEMENTS

This study was made possible through the financial investment from the EMBRAPII Program (POLO/UFSC EMBRAPII Unit - Emerging Technologies in Cooling and Thermophysics). Whirlpool and Bundy are also duly acknowledged for their financial and technical support. The authors also thank Cesar A. Pacheco, Flávia L. de Araujo and Niklas Assfalg for their help with experiments.

NOMENCLATURE

A_0	external area (m^2)	A_i	tubes internal area (m^2)
A_t	tubes external area (m^2)	A_w	wires area (m^2)
α_a	air thermal diffusivity (m^2s^{-1})	β	air vol. coef. of thermal expansion (K^{-1})
c_p	specific heat ($Jkg^{-1}K^{-1}$)	d_t	tube external diameter (m)
d_w	wire diameter (m)	ε	surface emissivity (-)
ε_{app}	surface apparent emissivity (-)	η_0	overall fin efficiency (-)
η_w	fin efficiency (-)	g	gravity (ms^{-2})
F	surface shape factor (-)	H	condenser height (m)
h_0	air-side heat transfer coefficient ($Wm^{-2}K^{-1}$)	h_c	convective heat transfer coef. ($Wm^{-2}K^{-1}$)
h_i	internal heat transfer coef. ($Wm^{-2}K^{-1}$)	h_r	radiative heat transfer coef. ($Wm^{-2}K^{-1}$)
k_a	air thermal conductivity ($Wm^{-1}K^{-1}$)	k_w	wire thermal conductivity ($Wm^{-1}K^{-1}$)
L_c	characteristic length (m)	$\dot{m}$	brine mass flow rate (kgs^{-1})
N_t	number of tubes (-)	N_w	number of wires (-)
Nu	Nusselt number (-)	ν_a	air kinematic viscosity (m^2s^{-1})
$\dot{Q}$	heat transfer rate (W)	Ra	Rayleigh number (-)
Re	Reynolds number (-)	σ	Stefan-Boltzmann constant ($kgs^{-3}K^{-4}$)
s_t	tube spacing (m)	s_w	wire spacing (m)
T_{amb}	ambient temperature (K)	T_{br}	brine average temperature (K)
$T_{br,i}$	brine inlet temperature (K)	$T_{br,o}$	brine outlet temperature (K)
T_c	surface average temperature (K)	UA	overall thermal conductance (WK^{-1})
W	condenser width (m)		

REFERENCES

Arsego, C., 2003. Experimental evaluation of wire-and-tube condensers performance, MSc thesis, Federal University of Santa Catarina, Florianopolis, SC, Brazil (in Portuguese).

Collicott, H.E., Fontaine, W.E., Witzell, O.W., 1963. Radiation and free convection heat transfer from wire and tube heat exchangers. ASHRAE J. 5 (12), 79–83.

Cyphers, J.A., Cess, R.D., Somers, E.V., 1959. Heat transfer character of wire and tube heat exchangers. ASHRAE J. 1 (5), 86–110.

Gnielinski, V., 1978. New equations for heat and mass transfer in turbulent pipe and channel flow. Int. J. of Chem. Eng. 16 (2), 359–387.

Holman, J.P., 1994. Experimental Methods for Engineers. McGraw-Hill, New York City, 640 p.

Incropera, F.P., DeWitt, D.P., Bergman, T.L., Lavine, A., 2002. Fundamentals of Heat and Mass Transfer. John Wiley & Sons, Hoboken, 1050 p.

ISO 15502, 2005. Household Frost-free Refrigerating Appliances – Characteristics and Test Methods. International Organization for Standardization, Geneva, 85 p.

Melo, C., Arsego, C., Maykot, R., 2004. Experimental evaluation of wire-and-tube condensers: confining walls effect. Proceedings of the 10th International Refrigeration and Air Conditioning Conference at Purdue, West Lafeyette, Illinois, United States.

Melo, C., Hermes, C.J.L, 2009. A heat transfer correlation for natural draft wire-and-tube condensers. Int. J. Refrig. 32, 546–555.

Siegel, R., Howell, J.R., 1972. Thermal Radiation Heat Transfer. McGraw-Hill Kogakusha, Tokyo, 814 p.

Tagliafico, L., Tanda, D.W., 1997. Radiation and natural convection heat transfer from wire-and-tube heat exchangers in refrigeration appliances. Int. J. Refrig. 20 (7), 461–469.

Witzell, O.W., Fontaine, W.E, Papanek, W.J., 1959. Convective films evaluated for wire and tube heat exchangers. ASHRAE J. 1 (6), 35-37.

Witzell, O.W., Fontaine, W.E., 1957. What are the heat transfer characteristics of wire and tube condensers. Refrigerating Engineering 65 (3), 33-37.

Manuscript ID: 187
DOI: 10.18462/iir.icr.2019.0187

An Experimental Analysis of HC-600a Flow Through Electronic Expansion Valves

Fernando T. KNABBEN, Cláudio MELO

POLO – Research Laboratories for Emerging Technologies in Cooling and Thermophysics
Florianópolis, SC, Brazil, melo@polo.ufsc.br

ABSTRACT

The present work analyzed the isobutane flow through electronic valves with hydraulic diameters smaller than 0.19mm. Three valves were firstly tested with nitrogen in order to obtain the equivalent capillary tubes. The most promising valves were then tested with isobutane under domestic refrigeration conditions. To this end, a test bench capable of operating with condensation and evaporation temperatures respectively between 25 and 45°C and -28 and -10°C was constructed. In order to check for choked flow occurrence, complete mass flow curves were additionally obtained for several opening ratios. It was found that the valves are nearly insensible to the sub-cooling degree and that the flow is choked under all practical conditions. Finally, a semi-empirical mathematical model based on a correlation for the flow coefficient was proposed and fitted with a reduced number of points. A reasonable agreement was observed with approximately 94% of the 138 points within a 15% error band.
Keywords: Electronic valves, isobutane, domestic refrigeration, experimental work

1. INTRODUCTION

Capillary tubes are certainly the most common expansion device in household refrigeration. They are nothing but a long tube with a very small internal diameter that reduce pressure mainly by friction effects. The major drawback of such device is that its geometry is fixed. Thus, once sized, the capillary tube may not respond to operating conditions other than the designed ones. Therefore, the refrigerator coefficient of performance may decrease and the overall energy consumption increase. In order to comply with labelling programs and government policies manufacturers are constantly being pushed to improve their products. In Brazil, for instance, the most efficient refrigerator is called ‘class A’. In European countries, there are classes A+, A++ and A+++. Also, a new version of the energy consumption global standard, IEC 62552 (2015), is about to take place and tests at 16 °C will be mandatory. It is expected that systems mounted with capillary tubes and on-off single speed compressors may not perform satisfactorily at lower condensation temperatures. Lazzarin and Noro (2008), for instance, pointed that the performance of a refrigeration system can be strongly affected by low ambient and evaporating temperatures, which would motivate the use of variable action expansion devices. Hence, the use of variable action devices such as electronic expansion valves (EEVs), which are capable of modulating the restriction, could be an alternative. However, although typical in commercial and industrial refrigeration systems, valves are barely seen in domestic appliances. Possible reasons are skepticism, cost and, for sure, the small range of mass flow rate involved. As a consequence, the literature concerning EEVs for domestic refrigeration is extremely scarce, especially when it comes to studies focused on the current dominant fluid, HC-600a (isobutane). Ronzoni et al. (2013), for example, tested a PWM-driven valve originally designed for light commercial appliances in series with a capillary tube (Thiessen and Klein, 2007) in order to obtain suitable mass flow rates for small refrigerators, but used HFC-134a as the refrigerant fluid.

A meticulous literature review shows that there are several works focused on the refrigerant flow through expansion valves. However, most of them aimed at commercial and industrial applications with refrigerants such as R22, R407C and R410A (Shanwei et al., 2005, Park et al., 2007 and Li, 2013) and pressure and mass flow rates much higher than those observed in small refrigerators. Among the rare works focused on domestic appliances, stand out those of Marcinichen and Melo (2006), Björk and Palm (2006) and Boeng and Melo (2012), who did not analyze the expansion device itself but checked its effect on the refrigerator performance. Björk and Palm (2006) and Boeng and Melo (2012), however, carried experiments at only one compressor speed and without

controlling the superheating degree at the evaporator. Marcinichen and Melo (2006), on the other hand, conducted energy consumption and pull-down tests with the superheating control activated and at several compressor speeds, but didn't use an appropriate control logic and adopted a valve with an oversized orifice which, according to the authors, may have masked performance gains.
In this context, the main goal of this work is to characterize the thermodynamic behavior of three EEVs of the same design but with different orifices and check their applicability in household refrigerators. To this end, the following steps were planned. First, to carry out tests with dry nitrogen to obtain a preliminary envelope of the valves operating range and to check if they can provide mass flow rates similar to those of typical capillary tubes. After, to design and construct a test bench to measure the HC-600a mass flow through the two most promising valves by varying condensation and evaporation temperatures, sub-cooling degree and orifice opening ratio. Finally, to develop a semi-empirical model to predict the valves flow coefficient and to propose a methodology to reduce the number of tests required to characterize a valve.

2. EXPERIMENTAL WORK

The valves analyzed in this work are based on the MEMS (Micro Electrical Mechanical Systems) technology and are as small as a finger nail. Their body is formed by three superimposed silicon layers and they work through what the manufacturer calls the electrothermal principle. The top layer acts as a cover for the intermediate layer, which contains the thermal actuator. The thermal actuator contains filaments that dilate or contract depending on the intensity of the electrical current applied to them. The filaments work then as a sliding plate that can move over the orifice controlling its opening proportionally. The orifices are rectangular and with a constant width. The opening is regulated through the variation of the length covered by the sliding plate. The orifice dimensions of each valve and the equivalent maximum hydraulic diameter are presented in Tab. 1.

Table 1. EEV orifice dimensions [mm]

Valve	Width	Maximum length	Maximum hydraulic diameter
Smallest	0.22	0.120	0.155
Intermediate	0.26	0.135	0.178
Largest	0.32	0.135	0.190

In a preliminary attempt to check the valves applicability in domestic refrigerators, they were submitted to nitrogen flow with the aid of a specific test bench (see Fig. 1). The apparatus was assembled according to the recommendations of the ASHRAE 28 (1996) standard and was used to measure the volumetric flow rate through the valves as a function of the inlet pressure and orifice opening ratio. The measurement procedure is the following: (i) define the opening ratio, (ii) open the shut-off valve and release nitrogen from the cylinder, (iii) set the inlet pressure with the micrometric valve and (iv) wait for steady conditions and measure the flow rate with the Coriolis meter.
Based on the volumetric flow rates, typical tube lengths can be applied in the well-known Kipp and Schmidt (1961) equation in order to obtain the inner diameters of the capillary tubes that would provide the same flow rates of the EEVs for each opening ratio at each inlet pressure.

$$D = \left(\frac{V L^{a_2}}{a_1 \sqrt{P^2 - 1}} \right)^{1/a_3} \qquad \text{Eq. (1)}$$

Where the constants a_1, a_2 and a_3 are respectively 2.369, 0.465 and 2.574 (Montibeller et al., 2016), V is the volumetric flow rate, P is the inlet pressure, and D and L are respectively the inner diameter and length of the tube.
The full characterization of expansion devices still requires, however, tests with refrigerant fluid since physical phenomenon such as phase change are not captured by nitrogen tests. To fill this gap, another test bench was specifically constructed to operate with HC-600a. Details of the refrigeration circuit are presented below.

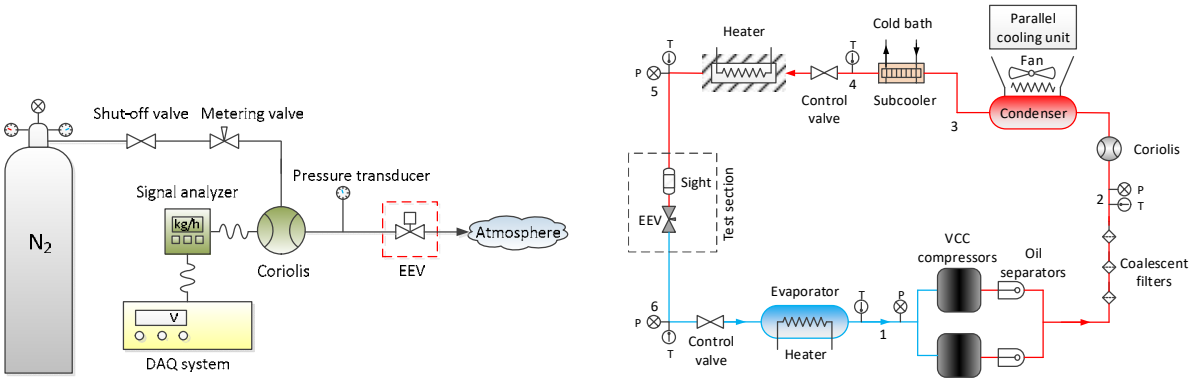

Figure 1: Test benches: nitrogen (left) and isobutane (right)

The isobutane test bench was especially built in order to measure the mass flow rate as a function of the downstream and upstream pressures, and the sub-cooling at the valve inlet. As shown in Fig. 1, the apparatus was designed with two parallel variable speed compressors which were also used to control the evaporating pressure. To this end, a PI (proportional integrative) controller based on the pressure signal from a transducer installed at the EEV outlet was used to modulate the compressors speed. An additional control valve installed after the EEV was also used to increase the evaporating pressure when needed. In order to avoid the presence of oil and impurities at the EEV inlet, oil separators and coalescent filters were installed after the compressors. The mass flow rate was measured with a Coriolis meter of the same model adopted in the nitrogen test bench with an uncertainty of ±0.1% of the readings. The condensation pressure, was controlled by means of another PI controller that modulated the power of a heater installed at the air inlet of a tube-and-fin condenser. The arrangement also counts with a centrifugal fan and a parallel cooling unit which was used to reach lower condensation pressures. After the condenser (3), a brazed-plate heat exchanger (sub-cooler) in counter-flow with cold water was used to decrease the refrigerant temperature (4). The fine tuning of the sub-cooling degree was then promoted by a PI-driven heater attached to a coil after the sub-cooler (5). Finally, the refrigerant expands at the EEV (6) and flows through the evaporator, which in this work is nothing but a long tube in contact with an electrical heater. This heater is responsible for vaporizing the refrigerant from the evaporator and keeping the compressors suction temperatures constant. The pressures at the EEV inlet and outlet were both measured by strain-gauge transducers with an uncertainty of ±0.1% of the readings. The temperature at the EEV inlet, on the other hand, was registered by a T-type thermocouple with an uncertainty of ±0.2°C immersed at the refrigerant flow.

In total 37 tests were carried out with the intermediate valve and 101 were conducted with the largest valve. As will be explained later, the smallest valve was considered inappropriate for domestic refrigeration and was not submitted to HC-600a flow. For the largest valve, four opening ratios were evaluated: 25, 50, 75 and 95%. For each one, three condensation temperatures (25, 35 and 45°C), three sub-cooling degrees (5, 10 and 15°C) and two evaporation temperatures (-28 and -10°C) were analyzed. For the intermediate valve, the same conditions were evaluated, except of the sub-cooling. To simplify the test matrix, sub-cooling degrees of 10°C were not tested. Also, due to limitations of the test bench sub-cooling degrees of 15°C were evaluated only for some cases. The choice of the condensation and evaporation temperatures was based on the air temperatures typically observed in the internal and external environments of the refrigerator: 16 to 32°C for the ambient and -18 to 4°C for the compartments (IEC 62552, 2015). Additional tests were also performed for evaporation temperatures higher than -10°C in order to check for choked flow occurrence.

3. RESULTS

3.1. Experimental Analysis

The nitrogen tests were conducted with inlet pressures from 4 to 15bar and orifice opening ratios from 2 to 95%. Fig. 2 shows the volumetric flow rate as a function of the opening ratio and inlet pressure for the largest orifice valve. It can be seen that such valve presents a continuous behavior throughout its opening range. Although not presented here, the results and that it covers almost entirely the volumetric flow rate range of the intermediate orifice valve.

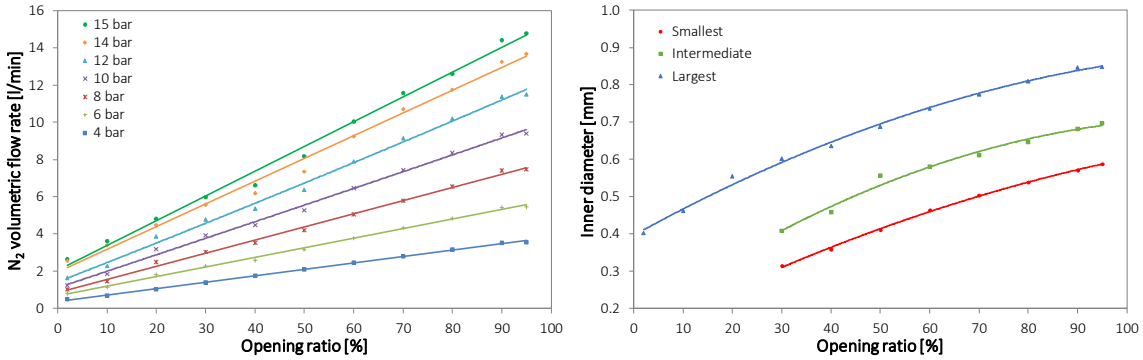

Figure 2: N_2 volumetric flow rate vs. opening ratio: intermediate valve (left) and largest valve (right)

The inner diameter of the equivalent capillary tubes was then estimated by Eq. (1) considering lengths of 1, 2 and 3m. A comparison between the EEVs for a length of 3m and an inlet pressure of 6 bar is presented in Fig. 2. Note that the behavior of the intermediate valve is closer to that of the smallest valve. This valve, however, corresponds to capillary tubes with diameters way too restrictive for domestic appliances, being perhaps more indicated to meso-scale cooling systems (Lara et al., 2016). The largest orifice valve, in turn, is equivalent to capillary tubes up to 0.9mm in diameter, depending on the operating conditions. For example, for a 90% opening ratio, the smallest and intermediate valves respectively produce a mass flow equivalent to that of 0.57 and 0.66-mm capillary tubes, while the largest valve provides flow rates equal to those of capillary tubes with 0.85 mm inner diameter. Hence, one can affirm, at least preliminarily, that the intermediate and the largest valves have potential to be applied in domestic refrigerators, and that the largest orifice valve is the most promising one since it covers the range of the intermediate valve and the range of capillary tubes found matches the geometries observed in practice (Melo et al., 2002).

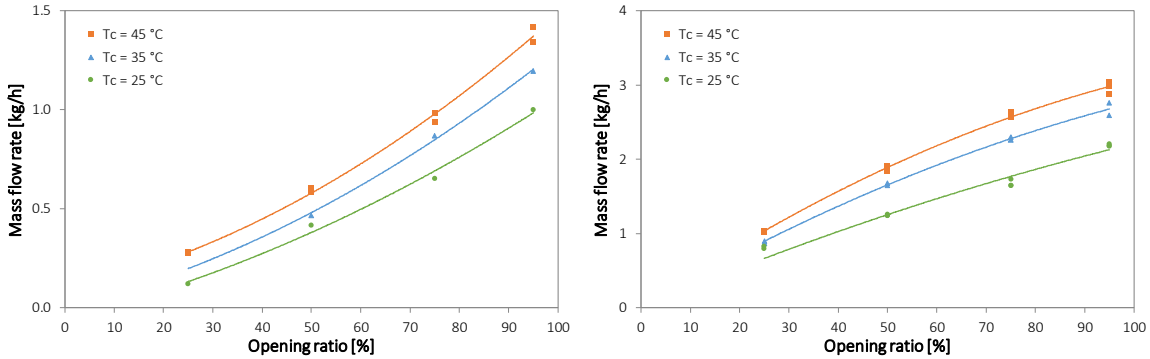

Figure 3: HC-600a mass flow vs opening ratio: intermediate valve (left) and largest valve (right)

Based on the previous analysis, tests with refrigerant were conducted with the intermediate and the largest orifice valves. Fig. 3 presents the HC-600a mass flow rate as a function of the opening ratio and the condensation temperature for a constant evaporation temperature of -28°C for the largest and intermediate valves. By tracing a vertical line along a given opening ratio the points corresponding to distinct sub-cooling degrees (5, 10 and 15°C) can be identified. A closer look reveals that such points are almost coincident, indicating that the valves are barely affected by the sub-cooling degree at the inlet. This is associated to the weak dependence of the mass flow rate on the fluid density (as suggests the orifice equation) and by the small variation of density for the temperature range studied herein. It should be mentioned that the points for the evaporation temperature of -10°C were not shown because the mass flow values were very similar to those of -28°C, since the flow was choked. Fig. 5 shows such behavior for an opening ratio of 50%, a condensing temperature of 45°C and a sub-cooling of 10°C. It is observed that the mass flow rate remained practically constant with the variation of the evaporating temperature between -10°C and -35°C. It should be mentioned that due to experimental instabilities the points for condensation of 35°C and opening ratio of 25% were not recorded for the intermediate orifice valve.

3.2. Mathematical Model

In view of the difficulty in quantifying the physical phenomena mentioned earlier, many authors choose to model the behavior of valves based on the well-known orifice equation, which includes the effect of the fluid partial vaporization on the empirical flow coefficient, C_v. Nevertheless, some authors such as Roming et al. (1966), Davies and Daniels (1973) and Li (2013) argue that the incorporation of the compressibility effects on the C_v may lead to inaccurate mass flow rate values under some conditions. Thus, considering the recommendations of these authors and those of the ANSI/ISA-75.01 (2007) standard, the following modified version of the orifice equation was used:

$$\dot{m} = A_o C_v Y \sqrt{2 \rho_1 P_1 X} \qquad \text{Eq. (2)}$$

Where P_1 and P_2 are respectively the upstream and downstream pressures, X is the pressure ratio, $(P_1-P_2)/P_1$, and Y is the so-called expansion factor, given by $Y = 1 - X/3X_t$, being X_t the pressure ratio from which the flow becomes choked. It is defined that the value of Y can vary from 0.667 to 1, where 0.667 corresponds to the choked flow conditions.

Note that X_t is unknown and must be obtained from experimental data. As mentioned in item 3.1, the experiments showed that flow was choked for several conditions. Additional tests, where the evaporation temperature was varied and both condensation temperature and sub-cooling were kept constant, were then carried out to check the choking pressure and also to characterize the mass flow rate under non-choking conditions.

Fig. 4 shows the mass flow rate of the largest orifice valve as a function of the evaporating temperature for a constant sub-cooling of 10°C, a condensing temperature of 45°C and opening ratio of 50%. It is observed that initially, for temperatures higher than that of saturation, there is liquid at the valve outlet and the mass flow rate responds approximately linearly to the square root of the pressure ratio. However, as the evaporation increases the flow experiences a transition region where the mass flow dependence of the square root of the pressure ratio is smaller. In this region, the valve capacity of converting pressure drop into flow rate is reduced due to the change in the fluid density as it crosses the *vena contracta*. The mass flow rate becomes then proportional to the product expansion factor-square root of pressure ratio. From evaporations lower than -10°C, however, further increments in the pressure ratio produce no effect on the mass flow rate. The flow then reaches sonic speed and becomes choked.

Table 2 shows the X_t values for opening ratios of 50, 75 and 95% considering different condensing temperatures. Assuming that X_t depends mostly on the opening ratio, i.e. its dependency on the condensing temperatures is negligible (Monsen, 2015), an almost linear correlation can be observed. Thus, in order to verify this assumption, extra tests were carried for different condensation temperatures (25, 35 and 45°C) but keeping the same opening ratio (95%) and sub-cooling (10°C). The results presented in Fig. 5 show that the choking pressure changes with the condensation temperature, but X_t remains approximately constant at 0.69, which validates the previous hypothesis. Finally, a linear curve fit based on Tab. 2 can be performed for the largest EEV providing $X_t = 0.003246 * OR - 1$, where OR is the opening ratio. Note that the intercept of the curve is 1, meaning that for very low opening ratios X_t goes to 1. In order words, as the OR tends to zero so does the pressure at the EEV outlet, which results in a unitary pressure ratio. Assuming that this holds for every valve, only one mass flow curve is actually necessary to fit the slope of the linear equation. Therefore, for the intermediate valve, only one mass flow curve was obtained for an opening ratio of 95%, resulting in X_t = 0.748.

Table 2. Choking pressure ratio for the largest orifice EEV

Opening ratio [%]	Condensation [°C]	X_t [-]
50	45	0.82
75	35	0.77
95	25	0.69

To close the model the following π-type correlation was proposed to predict the flow coefficient. The dimensionless parameters, π_1 to π_4, are described in Tab. 3.

$$C_v = c_0 \pi_1^{c_1} \pi_2^{c_2} \pi_3^{c_3} \pi_4^{c_4} \qquad \text{Eq. (3)}$$

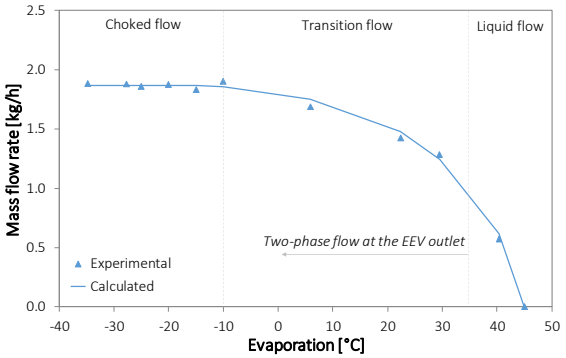

Figure 4: Mass flow vs. evaporation (largest EEV, opening ratio = 50%)

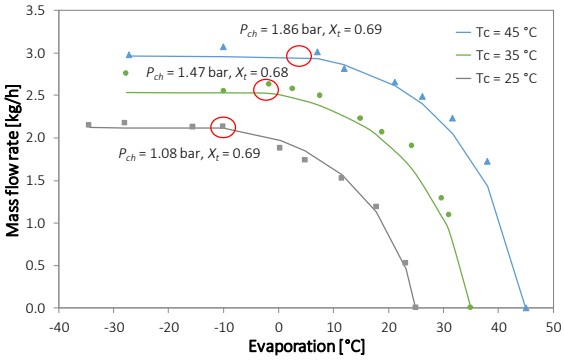

Figure 5: Mass flow vs. evaporation (largest EEV, opening ratio = 95%)

Table 3. Dimensionless parameters

Parameter	Definition	Description
π_1	X	Pressure ratio
π_2	A/A_o	Orifice opening ratio
π_3	$1+(h_l-h_{in})/h_{crit}$	Sub-cooling effect
π_4	$\mu_l^2/(\rho_l\sigma_l D_h)$	Friction and bubble growth

where ρ_l, σ_l, μ_l and h_l are respectively the density, surface tension, viscosity and enthalpy of the of the saturated liquid at P_{in}. A is the orifice free-flow area, D_h is the maximum orifice hydraulic diameter, h_{in} is the enthalpy at the valve inlet and h_{crit} is the critical enthalpy. For the largest orifice valve the coefficients c_0 to c_4 are respectively 0.00155, 0.235, 0.938, 0.362 and -0.634. For the intermediate orifice valve c_0 = 8.06e-6, c_1 = 0.323, c_2 = 1.5, c_3 = 0.184 and c_4 = -1.0772.

A π-type correlation was chosen since polynomial equations may provide inconsistent values in interpolations or extrapolations (Jähnig et al., 2000). In addition, enthalpy was used instead of temperature in the sub-cooling dimensionless parameter to minimize possible problems with two-phase flow at the inlet of the valve, which would impair the use of the correlation in refrigerators simulation models. Also, note that in Eq. (2) it was assumed that A_o is the maximum orifice area so that the effect of the opening ratio was incorporated in the flow coefficient.

Fig. 6 shows the validation against experimental data. A reasonable agreement between measured and calculated values was observed, being 94.2% of the points within a ±15% error band and 89.1% within ±10%. It should be pointed that the agreement would have been better if it weren't for the larger errors verified for some points of opening ratios of 25% for the intermediate valve, caused mainly by the very low mass flow rates involved (lower than 0.5kg/h). The error was also a bit higher for some points concerning very low pressure ratios. For such conditions, small variations on the evaporation temperature lead to large variations on the mass flow rate. The proposed model, however, captured correctly the experimental trends, including those representing non-choked flow.

It should be noted that only 20 out of 101 points were used to fit the coefficients for the largest valve. After an extensive analysis, it was found that if the following steps were taken when selecting the 20 points, the quality of the fitting would be as good as that obtained with all points:

1. Define the highest and lowest condensing temperatures (25 and 45°C).
2. For each condensing temperature, choose three distinct opening ratios (25, 50 and 95%).
3. For each opening ratio, select two points: one for the highest and the other for the lowest sub-cooling degree (5 and 15°C).
4. Select 8 additional points that illustrate the transition from choked to non-choked flow (as shown in Fig. 4), for a given condensation, sub-cooling and opening ratio (respectively 25°C, 10°C and 95%), so that X_t can also be obtained.

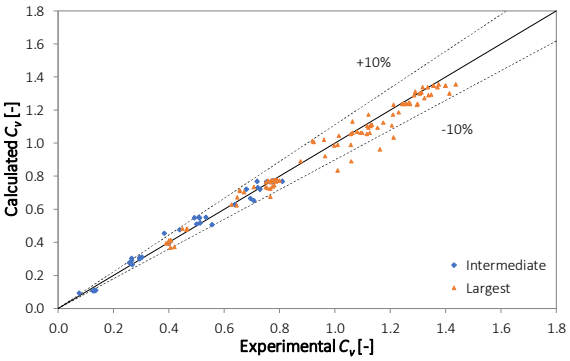

Figure 6: Mathematical model validation

4. CONCLUSIONS

The literature review showed that there are very few studies with focus on variable expansion devices specifically manufactured for household refrigerators. To fill this gap, this work focused on an experimental analysis of three electronic valves with hydraulic diameters smaller than 0.19mm that were firstly tested with dry nitrogen. With the obtained volumetric flow rate and the Kipp and Schmidt equation the equivalent capillary tube geometries were defined and it was found that the range of inner diameters matched that observed in practice. To provide a more realistic analysis a test bench able to reach condensation temperatures as low as 25°C was specifically built to characterize the HC-600a flow through the most promising valves. Results showed that the intermediate and the largest orifice EEVs were capable of supplying the pressure differences typically found in real appliances, without a capillary tube in series. Also, it was found that they were almost insensible to sub-cooling variations and that the flow was choked under several practical conditions. Additional tests were conducted to obtain the complete mass flow curves of the largest orifice valve, which included choked and non-choked conditions. It was observed that the choking pressure ratio depends basically on the valve opening and that it is not affected by the inlet pressure. A mathematical model based on the orifice equation was put forward and an empirical correlation for the valves flow coefficient was proposed. A reasonable agreement between experimental and calculated results was observed with approximately 94% of the points within a 15% error band. Finally, a methodology to reduce the number of tests was proposed where it was found that only 20 points were necessary to fit the correlation.

ACKNOWLEDGEMENTS

This study was made possible through the financial investment from the EMBRAPII Program (POLO/UFSC EMBRAPII Unit - Emerging Technologies in Cooling and Thermophysics). The authors thank Mr. Jean R. Backer, Mr. Matheus C. Machado and Ms. Débora T. Kohara for the support in the experiments and Embraco for financial support.

REFERENCES

ANSI/ISA-75.01, 2007. Flow Equations for Sizing Control Valves. NC, USA.

ASHRAE 28, 1996. Method of Testing Flow Capacity of Refrigerant Capillary Tubes. American Society of Heating, Refrigeration and Air Conditioning Engineers. Atlanta, GA, USA.

Björk, E., Palm, B., 2006. Performance of a domestic refrigerator under influence of varied expansion device capacity, refrigerant charge and ambient temperature. Int. J. Refrig. 29(5), 789–798.

Boeng, J., 2012. Uma metodologia para a seleção do par tubo capilar - carga de refrigerante que maximiza o desempenho de refrigeradores domésticos. *Master Thesis*, Department of Mechanical Engineering, Federal University of Santa Catarina, Florianópolis, Brazil (in Portuguese).

Boeng, J., Melo, C., 2012. A capillary tube-refrigerant charge design methodology for household refrigerators-Part II: Equivalent diameter and test procedure. Proceedings of the 14th International Refrigeration and Air Conditioning Conference at Purdue, West Lafayette, IN, USA.

Davies, A., Daniels, T. C., 1973. Single and two-phase flow of dichlorodifluoromethane, R12, through sharp-edged orifices. ASHRAE Trans. 79, 109–123.

IEC 62552, 2015. Household refrigerating appliances – Characteristics and test methods. Geneva, Switzerland.

Jähnig, D. I., Reindl, D. T., Klein, S. A., 2000. A semi-empirical method for representing domestic refrigerator/freezer compressor calorimeter test data. ASHRAE Trans. 106(2), 122–130.

Kipp, E., Schmidt, H., 1961. Bemessung von Kapillarrohren als Drosselorgan für Kaltesatze, Kaltetechnik, 13 Jahrgang, Heft 2.

Lara, J. F. P., Melo, C., Boeng, J., 2016. Theoretical and experimental analysis of expansion devices for meso-scale cooling systems. Proceedings of the 16th International Refrigeration and Air Conditioning Conference at Purdue, West Lafayette, IN, USA.

Lazzarin, R., Noro, M., 2008. Experimental comparison of electronic and thermostatic expansion valves performances in an air conditioning plant. Int. J. Refrig. 31*(*1), 113–118.

Li, W., 2013. Simplified modeling analysis of mass flow characteristics in electronic expansion valve. Appl. Therm. Eng. 53(1), 8–12.

Liu, J., Chen, J., Chen, Z., 2008. Choking phenomenon and pressure drop mechanism in electronic expansion valves. Energy. Convers. Manage. 49(6), 1321–1330.

Marcinichen, J. B., Melo, C., 2006. Comparative analysis between a capillary tube and an electronic expansion valve in a household refrigerator. Proceedings of the 11th International Refrigeration and Air Conditioning Conference at Purdue, West Lafayette, IN, USA.

Melo, C., Vieira, L. A. T., Pereira, R. H., 2002. Non-adiabatic capillary tube flow with isobutane. Appl. Therm. Eng. 22(14), 1661–1672.

Monsen, J., 2014. Control Valve Application Technology Book – Techniques and considerations for properly selecting the right control valve. Valin Corporation, 137 p.

Montibeller, A. L., Knabben, F. T., Melo, C., 2016. A methodology to forecast the performance of electronic expansion valves focused in household refrigeration. Proceedings of the 9th National Congress of Mechanical Engineering, Fortaleza, CE, Brazil.

Park, C., Cho, H., Lee, Y., Kim, Y., 2007. Mass flow characteristics and empirical modeling of R22 and R410A flowing through electronic expansion valves. Int. J. Refrig. 30(8), 1401–1407.

Roming, R. P., Rothfus, R. R., Kermode, R. I., 1966. Partial vaporization in orifices and valves. Ind. Eng. Chem. P. Design and Develop. 5(3), 342–350.

Ronzoni, A. F., Hermes, C. J. L., Melo, C., 2013. Assessment of pulse-width modulated flow through serial expansion valve/capillary tube arrangements. Int. J. Refrig. 36(1), 258–269.

Shanwei, M., Chuan, Z., Jaingpin, C., Zhiujiu., C., 2005. Experimental research on refrigerant mass flow coefficient of electronic expansion valve. Appl. Therm. Eng. 25(14-15), 2351–2366.

Thiessen M. R. & Klein F. H., 2007. Flow rate control system in refrigeration circuits, method for controlling a refrigeration system. World Intellectual Property Organization, Patent WO 2007/118293 A2.

Manuscript ID: 202
DOI: 10.18462/iir.icr.2019.0202

Experimental analysis of the use of R290 in a small ice maker

Luca MOLINAROLI[(a)], Guido ROMAGNOLI[(b)], Tommaso VANIA[(b)], Sergio ZANZOTTERA[(b)]

[(a)] Dipartimento di Energia, Politecnico di Milano
Milano, 20156, Italy, luca.molinaroli@polimi.it
[(b)] Scotsman Ice
Pogliano Milanese, 20100, Italy, guido.romagnoli@scotsman.it, tommaso.vania@scotsman.it, sergio.zanzottera@scotsman.it,

ABSTRACT

In the present paper, an experimental study of the use of R290 in an ice maker is presented. The analysis deals with a vapour compression system that originally works with R404A and produces 85 kg per day of ice with water inlet temperature equal to 10 °C and air temperature equal to 10 °C. A redesign of the system is carried out to reduce internal volume, allowing the system to be charged with less than 150 g of R290 as per international standards. The experimental results show that, in the range of the testing conditions, the ice production reduces a little, from 0.30% to 5.45% whereas the specific electric consumption significantly reduces, with measured value from 14.46% to 21.23% lower than those of R404A system. Therefore, R290 is a good candidate for refrigerant substitution in this kind of systems.
Keywords: Energy Efficiency, Ice Maker, Propane, Refrigerant Charge.

1. INTRODUCTION

In the last years, more and more severe limits on Global Warning Potential (GWP) of refrigerants have arisen as a consequence of the EU 517/2014 regulation (European Union, 2014) and the Kigali amendment (United Nations, 2016). As an example, in the field of ice-making systems, the aforementioned EU 517/2014 regulation bans all the refrigerants with GWP equal or greater than 2500 starting from January, 1st 2020. Therefore, the air conditioning and refrigeration industry has to face the challenge of finding suitable refrigerants and new synthetic substances or old natural refrigerants are considered, analysed and tested in vapour compression systems.
Among the possible alternatives candidates, hydrocarbon are seen as one of the viable solution. Palm (2008) reviewed the use of propane (R290), isobutene (R600a) and propylene (R1270) in small heat pump and refrigeration systems concluding that their performance are similar, or even better, than those of HFC based systems. However, safety issues are the main concern and therefore actions like the charge reduction together with precautions such as hydrocarbon sensors, alarms and forced ventilation may be considered to reduce the risks under normal operation.
He *et al.* (2014) carried out an experimental analysis aimed at investigating the substitution of R134a in a large capacity chest freezer with pure R290 and a mixture of R290 and R600a. They found that the power consumption of the R290 freezer is lower by 26.7% with respect to the R134a freezer while a reduction equal to 27.5% is achieved when the mixture R290-R600a is used at the optimal ratio 93.75%-6.25% on a mass basis.
Mastrullo *et al.* (2014) experimentally analysed the performance of two prototypes of a professional freezer for light commercial refrigeration charged with R290. A redesign of the heat exchanger allowed to reduce the internal volume by 40% which, in turn, led to a charge reduction from 120 g to 80 g in the optimum conditions. Compared to the baseline R404A system, the R290 prototypes showed a reduction of the energy consumptions up to 34%.
Padilla Fuentes *et al.* (2015) carried out a theoretical analysis to identify the components that trap most of the refrigerant charge during the operation of two bottle coolers. They found that the compressors, with the refrigerant dissolved in the oil, could hold up to 25% of refrigerant that does not contribute to the refrigerating effect. Therefore, a strong redesign of the condenser and the liquid line and the removal of the liquid receiver were mandatory to reduce the R290 charge below the maximum allowed value of 150 g. Two prototypes were then assembled to analyse their

performance finding that they properly worked and concluding that highly efficient bottle coolers could be designed with R290 refrigerant charge lower than 150 g.
Antunes and Filho (2016) carried out an experimental analysis of the use of several refrigerants in a water-to-water system in a drop-in application. The best evaporator cooling capacities and COPs were achieved with hydrocarbons, namely R290 and R1270, whereas the worst performance was achieved with R404A. A TEWI analysis showed the same trend.
Finally, Sánchez *et al.* (2017) experimentally compared several refrigerants in a water-to-water system in a drop-in application. Compared to all the refrigerants tested, R290 obtained the best results in terms of cooling capacity and COP, leading to an increase in the range 40.5%–67.4% and 22.4%-2.8% respectively. However, it requires a redesign of the system component, especially the compressor, in order to cope with different thermophysical properties.
All the previous papers provide useful information about the use of R290 in vapour compression system as potential substitute refrigerants traditionally used in the refrigeration application, namely R134a and R404A. The goal of the present paper is to contribute to the on-going discussion presenting the results of the use of propane in a small ice-making machine originally designed to work with R404A.

2. PROTOTYPE DESCRIPTION AND EXPERIMENTAL SET-UP

2.1. Prototype description

The ice maker considered in this study is a simple vapour compression system that produces ice cubes with a batch process. The system mainly consists of a reciprocating compressor, a fin-and-tube condenser, a capillary tube and an evaporator specifically designed for this application. For the sake of charge reduction, the liquid receiver is not considered in the R290 prototype while a molecular sieve filter is installed at condenser outlet for safety system operation. At evaporator outlet, a suction accumulator is installed in order to handle two-phase refrigerant during transient operation and, besides, the capillary tube is wrapped to it in order to increase the liquid subcooling and, hence, system performance. Finally, a hot gas by-pass line is added to allow for proper system operation as detailed below. The layout of the considered prototype is shown in Fig. 1.

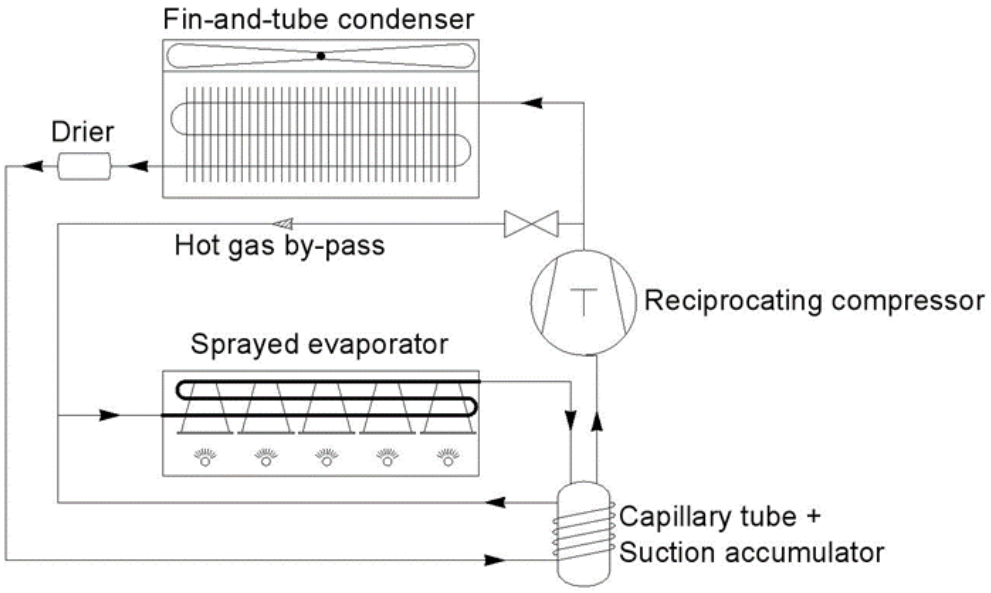

Figure 1. Schematic of the R290 ice-maker prototype.

The most peculiar component of the prototype is the evaporator. It consists of a series of small, upside down cups where the inner surface, i.e. the hollow part, faces a water nozzles array while the refrigerant tubes are soldered on the cups outer surface. Fig. 2 reports a detail of the evaporator; it is worth specifying that the number of cups shown in the figure is arbitrary.

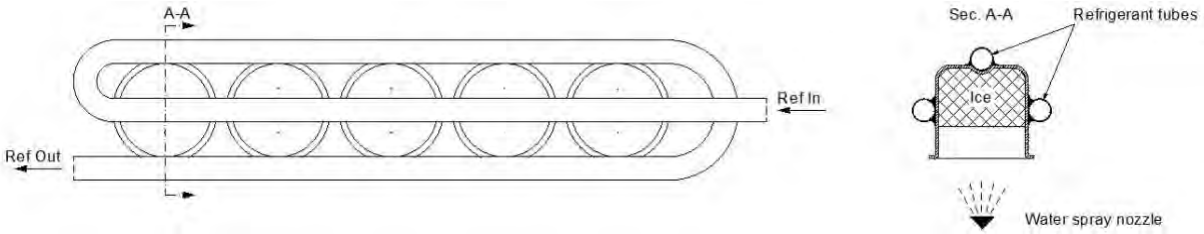

Figure 2. Detail of the evaporator of the ice maker.

The ice maker system works with a batch process as follows:

1. Ice-making cycle. The ice-making cycle begins with completely empty cups. Water is sprayed on the inner surface of the cups while the refrigerant is evaporating inside the tubes soldered on the outer surface. Water droplets hit the cold cups surface and freeze. As the process continues, more water is sprayed and more ice forms inside the cup filling it. During the whole cycle, the hot gas by-pass valve is closed.
2. De-icing cycle. Once the cups are full of ice, i.e. after a predefined amount of time, the water spray system is switched off and the hot gas by-pass valve is simultaneously opened. In this way, the high pressure, high temperature refrigerant at compressor outlet flows inside the evaporator tubes and condenses. This leads to the melting of a thin layer of ice near the cups inner surface which, in turn, causes their downfall into the bottom receiving bin. Once all the cups are emptied, the hot gas by-pass is closed, the water spray system is switched on and a new ice-making cycle begins.

The R290 prototype has the same evaporator used in the R404A system whereas all the other components are chosen/sized according to the refrigerant specific properties. More in detail:

1. Compressor. At the same (dew) saturation temperature, the propane vapour density is largely lower than that of R404A. This leads to a reduced volumetric cooling capacity, although the liquid-to-vapour enthalpy difference is higher for R290. As a result, the compressor used in the propane system is larger than the compressor used in the R404A system.
2. Condenser. The amount of heat that has to be rejected at the condenser is different in the two systems. Moreover, it is of fundamental importance, in the propane system, to reduce the condenser internal volume in order to reduce the refrigerant charge. As a result, the R290 condenser is designed with reduced diameter tubes which, in turn, allow for higher mass flux and higher heat transfer coefficient. In order to deal with potentially too high pressure drop, the number of refrigerant circuit is increased. Headers size is reduced as much as possible. Finally, as previously stated, the liquid receiver is removed in the propane prototype.
3. Capillary tube. The length of the capillary tube is modified according to the different mass flow rate that has to flow through it and to the different working conditions, namely pressure and temperature at its inlet.
4. Molecular sieve filter. With the aim of reducing the refrigerant charge, a low volume molecular sieve filter is installed in the R290 prototype.

The main features of the just mentioned components are reported in Table 1 for the R290 prototype. For the sake of clarity, the characteristics of the original R404A system are reported as well.

Table 1. Main features of the compressor, the condenser and the molecular sieve.

Component	Feature	R404A	R290
Compressor	Swept volume	10.33 cm^3	12.11 cm^3
	Amount of oil	280 dm^3	350 dm^3
	Cooling Capacity[1]	758 W	770 W

[1] Condensing temperature 45 °C, evaporating temperature -15 °C, suction temperature 32 °C.

Condenser	Tube outer diameter	7.52 mm	5 mm
	Transversal pitch	21.0 mm	17.3 mm
	Longitudinal pitch	24.5 mm	20 mm
	Number of tubes	36	38
	Number of rows	4	3
	Number of circuits	1	2
	Fin thickness	0.1 mm	0.1 mm
	Fin pitch	3.0 mm	2.5 mm
Molecular sieve filter	Volume	46 cm^3	10 cm^3

Overall, the condenser internal volume reduces from 0.43 dm^3 to 0.195 dm^3, i.e. 55% reduction, when moving from the R404A system to the R290 prototype. Additional 0.036 dm^3 reduction is achieved through the molecular sieve filter replacement. Finally, the R290 prototype is charged with 100 g of propane, while the charge of the original R404A system is equal to 340 g.

2.2. Experimental set-up

The performance of the R404A and R290 ice makers are evaluated installing each prototype in a climatic room, i.e. a room where the air temperature and relative humidity together with the water sprayed temperature are monitored and set by a control system. The layout of the experimental set-up and the position of the measurement devices are shown in Figure 3.

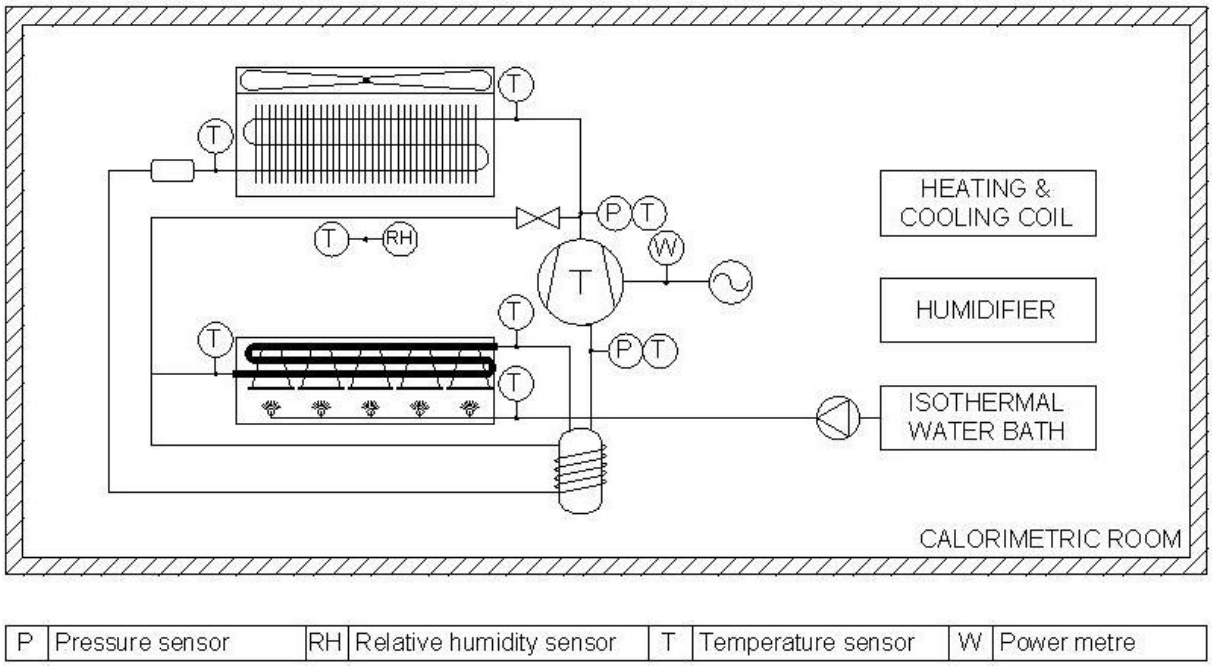

Figure 3. Layout of the experimental set-up.

The main characteristics of the instrumentation are collected in Table 2.

Table 2. Measurement instrumentation and accuracy.

Parameter	Instrument	Range	Accuracy
Refrigerant pressure	Pressure transducer	0 kPa - 4000 kPa	±1% r.v.
Refrigerant temperature	T thermocouples	-50 °C - 160 °C	± 0.5 °C
Water pressure	Pressure transducer	0 kPa - 1000 kPa	±0.15% r.v.
Water temperature	RTD Pt 100	-10 °C - 90 °C	± 0.1 °C
Air dry bulb temperature	RTD Pt 100	-10 °C - 90 °C	± 0.1 °C

Air relative humidity	R.H. transducer	0 % - 100 % R.H.	± 2 % R.H.
Power	Power transducer	0 W - 5500 W	±0.2% r.v.

3. RESULTS

The test conditions used in the experimental campaign to analyse the performance of the R290 ice-maker are shown in Table 3.

Table 3. Test conditions.

Run	Air dry bulb temperature	Relative humidity	Water inlet temperature	Water inlet pressure
1	10 °C	80%	10 °C	200 kPa
2	21 °C	65%	15 °C	200 kPa
3	32 °C	55%	21 °C	200 kPa
4	38 °C	50%	32 °C	200 kPa
5	43 °C	35%	32 °C	200 kPa

Due to the batch working cycle, each run consists of a series of 3 test in controlled working conditions so as to check test validity and repeatability.
An example of the two systems operation during the ice-making cycle is shown in Figs. 4 and 5. In the former, the refrigerant temperatures at evaporator inlet and outlet as a function of time for the R404A and the R290 system are reported while in the latter the refrigerant saturation temperature at compressor suction and at compressor discharge, calculated starting from the measured suction and discharge pressures, for both systems are depicted.

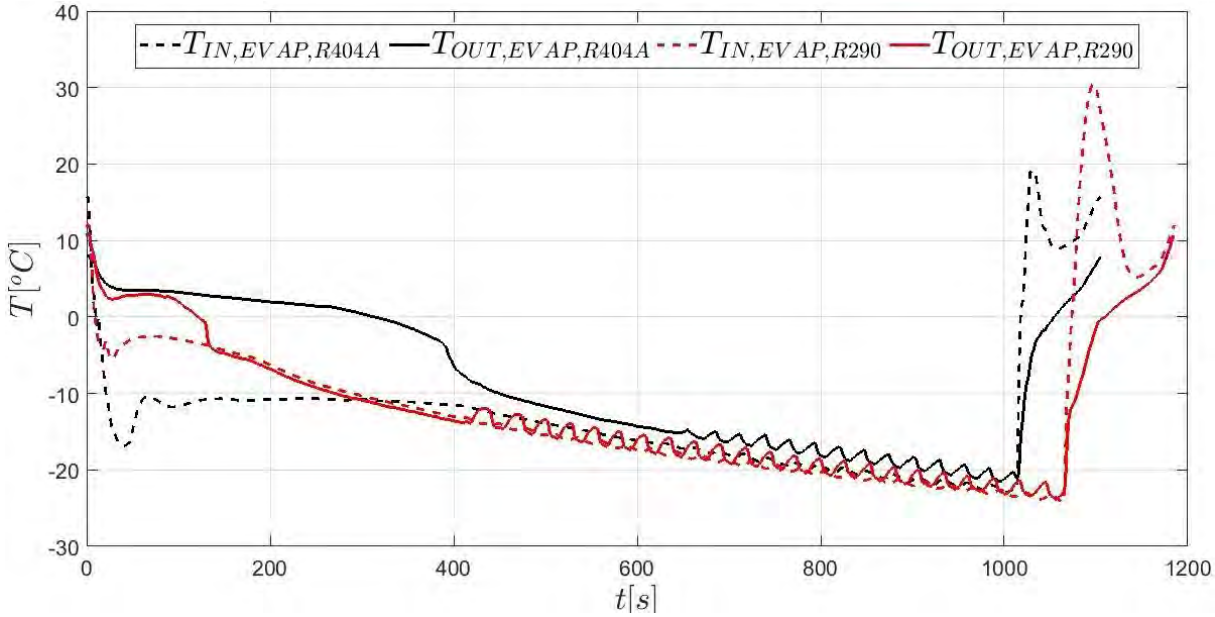

Figure 4. Refrigerant temperature at evaporator inlet and outlet for the R404A and R290 ice-makers at Run 2 conditions.

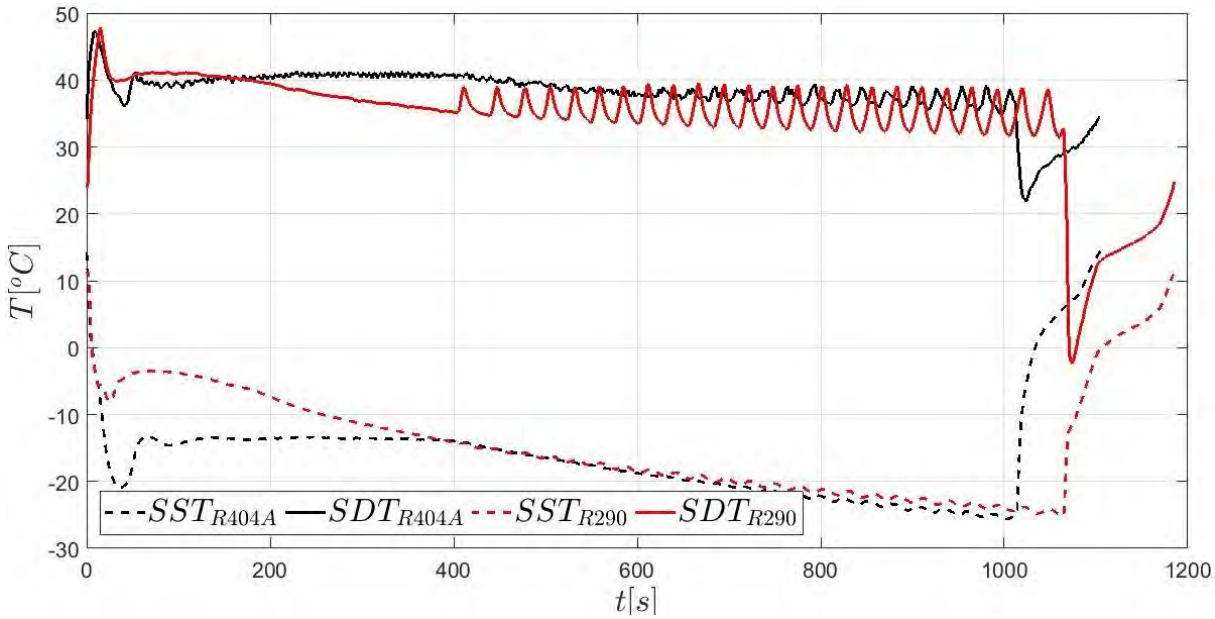

Figure 5. Saturation suction temperature (SST) and saturation discharge temperature (SDT) as a function of time for the R404A and R290 ice-makers at Run 2 conditions.

From the analysis of the two figures, it is possible to conclude that the two systems operate is a very similar way. Indeed, the refrigerant temperatures at evaporator inlet and outlet reduces with time since the ice cube size increases and the thermal resistance increases too (Fig. 4). Analogously, the trends of the saturation suction and discharge temperatures are very similar, with a slightly lower temperature lift for the R290 system (Fig. 5). The duration of the ice-making cycle is about 5% higher for the propane system because of the lower system capacity (see further in the text). Finally, both systems exhibit a cyclic trend of the refrigerant temperature at evaporator outlet and of the saturation discharge temperature which is typical of vapour compression systems equipped with capillary tubes.

The overall comparison of the two ice-makers is carried out considering two key performance indexes: the produced ice mass and the system energy consumption. The ice mass is measured at the end of the de-icing cycle whereas the system energy consumption is calculated integrating the measured electrical power over the ice-making and de-icing cycles. The performance of each ice-maker is finally assessed evaluating the amount of ice produced in 24h of continuous operation and the amount of energy consumed to produce 100 kg of ice.

The experimental results of the ice mass production are shown in Fig. 6.

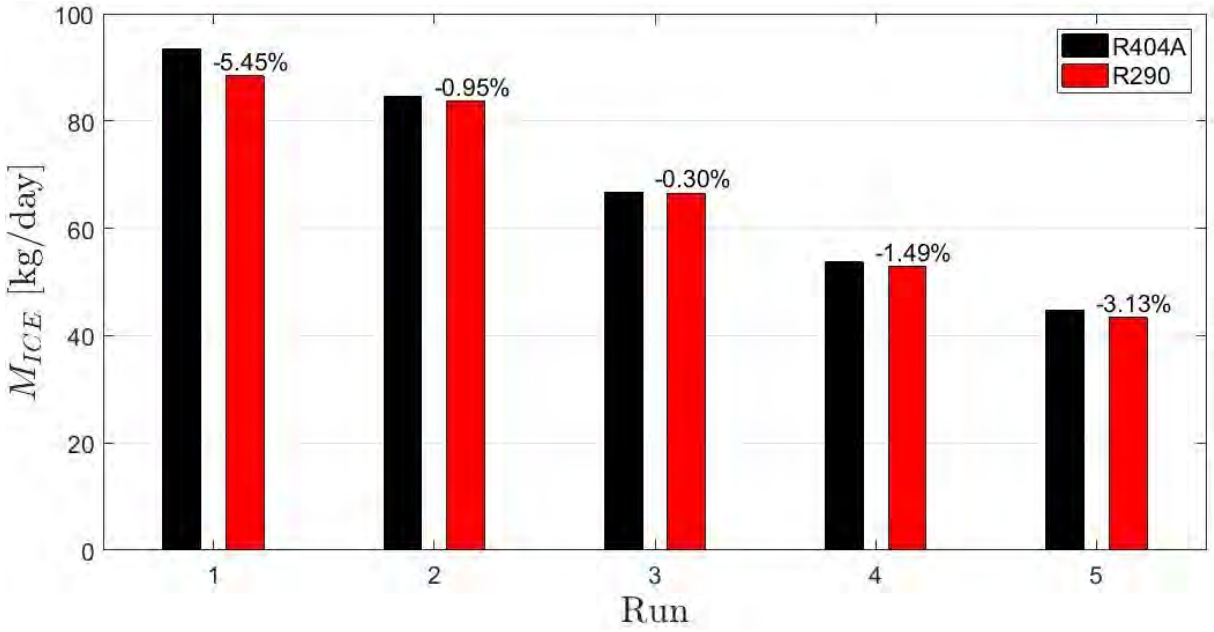

Figure 6. Daily production for the R404A and R290 ice-makers.

The specific energy consumptions are shown in Fig. 7.

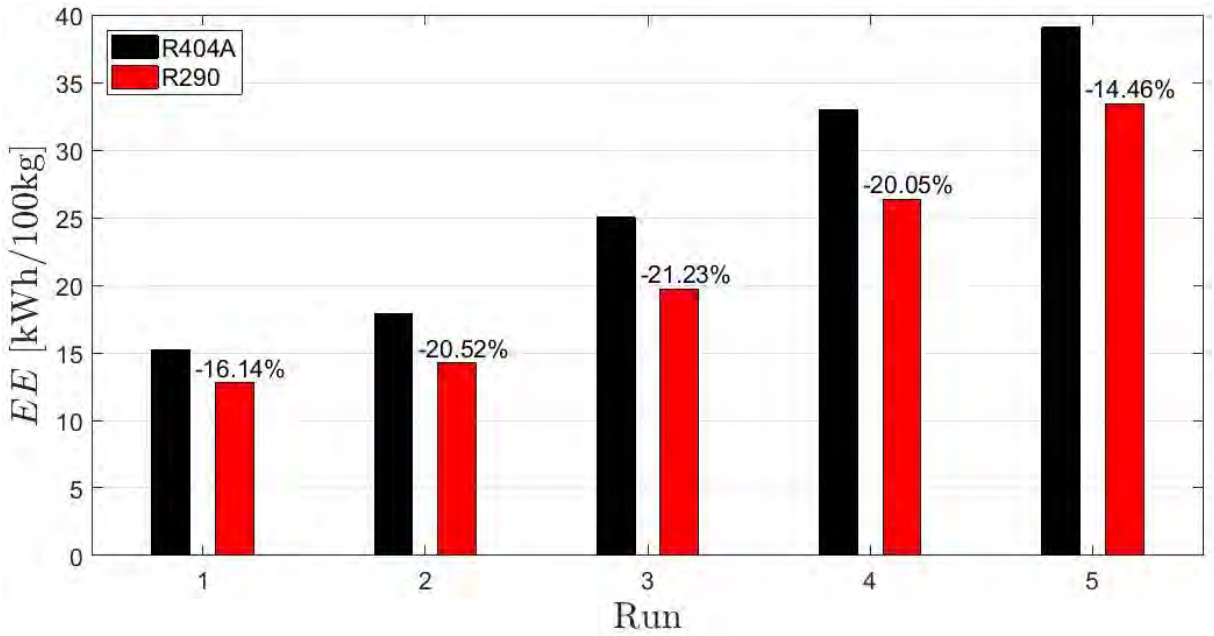

Figure 7. Specific energy consumption for the R404A and R290 ice-makers.

From the experimental results it is evident that the daily ice mass productions of the R290 system undergo a slightly reduction, with values from 0.30% to 5.45% lower than those found with R404A. This is a direct consequence of the lower refrigerating capacity of the R290 system related to propane thermophysical properties. Indeed, although the propane enthalpy difference across the evaporator is higher (roughly twice) than that of R404A, the R290 density at compressor suction is lower (roughly one third) than that of the R404A, leading to a lower refrigerant mass flow rate even if the compressor swept volume of the propane system is higher than that of the R404A system. Overall, the reduced density effect prevails over the increased enthalpy difference effect and the final refrigerating capacity slightly reduces.

On the other side, the specific energy consumptions of the R290 system are significantly lower than those of the R404A system, with reductions that span the range from 14.46% to 21.23%.Again, this is related to the thermophysical properties of R290 that are more favourable with respect to those of the R404A. More in detail, the propane critical temperature is higher than

the R404A critical temperature which is strongly beneficial for system COP (Domanski *et al.*, 2014).

4. CONCLUSIONS

An experimental analysis aimed at assessing the use of R290 in an ice maker is discussed in the present paper. A prototype of a propane ice-making system as substitute of the R404A unit is built with the aim of producing 85 kg per day of ice with water inlet temperature is equal to 10 °C and air temperature equal to 10 °C. The prototype is designed with low internal volume to reduce the R290 to 100 g which is 33% lower that the international standards allowed value of 150 g. In the range of experimental testing conditions, the experimental results show a slight reduction of the daily ice production, from 0.30% to 5.45% but a significant reduction of the specific electric consumption significantly, from 14.46% to 21.23%. Therefore, it is possible to conclude that in the ice-making application R290 is a good candidate for conventional refrigerant substitution.

NOMENCLATURE

EE	Specific energy consumption (kWh·kg^{-1})	*SST*	Saturation Suction Temperature (°C)
M_{ICE}	Mass of ice produced daily (kg·day^{-1})	*t*	Time (s)
SDT	Saturation Discharge Temperature (°C)	*T*	Temperature (°C)

REFERENCES

Antunes, A.H.P., Filho, E.P.B., 2016. Experimental investigation on the performance and global environmental impact of a refrigeration system retrofitted with alternative refrigerants. Int. J. Refrigeration 70, 119-127.

Domanski, P.A., Brown, J.S., Heo, J., Wojtusiak, J., McLinden, M.O., 2014. A thermodynamic analysis of refrigerants: Performance limits of the vapor compression cycle. Int. J. Refrigeration 38, 71-79.

European Union, 2014 Regulation (EU) No 517/2014 of the European Parliament and the Council of 16 April 2014 on fluorinated greenhouse gases and repealing Regulation (EC) No 842/2006. Off. J. Eur. Union 150, 195-230.

He, M.-G., song, X.-Z., Liu, H., Zhang, Y., 2014. Application of natural refrigerant propane and propane/isobutene in large capacity chest freezer. Appl. Therm. Eng. 70, 732-736.

Mastrullo, R., Mauro, A.W., Menna, L., Vanoli, G.P., 2014. Replacement of R404A with propane in a light commercial vertical freezer: A parametric study of performances or different system architectures. Energy Convers. Manage. 82, 54-60.

Padilla Fuentes, Y., Hrnjak, P., Elbel, S., 2015. Low-charge propane refrigeration system technology for single and multi-door bottle coolers. Proceedings of The 24th IIR International Congress of Refrigeration, Yokohama, Japan, Paper 303.

Palm, B., 2008, Hydrocarbons as refrigerants in small heat pump and refrigeration systems – A review. Int. J. Refrigeration 31, 552-563.

Sánchez, D., Cabello, R., Llopis, R., Arauzo, I., Catalán-Gil, J., Torrella, E., 2017. Energy performance evaluation of R1234yf, R1234ze(E), R600a, R290 and R152a as low-GWP R134a alternatives. Int. J. Refrigeration 74, 269-282.

United Nations Environment Programme, 2016 Further Amendment of the Montreal Protocol.

Manuscript ID: 213
DOI: 10.18462/iir.icr.2019.0213

Investigation of heat exchange of ice slurry flow in a coil

Georgy A. BELOZEROV, Natalia MEDNIKOVA, Victor P. PYTCHENKO
VNIKHI - Branch of V.M. Gorbatov Research Center of Food Systems, RAS
Moscow, 127422, Russian Federation, mail@ vnihi.ru

ABSTRACT

The paper presents the results of investigations of heat exchange in a plate single-raw vertical coil of 6 horizontal tubes at coolant flowing in tubes. The coolant used was ice slurry or single-phase propylene glycol solution. Ice slurry is formed of propylene glycol water solution at mass concentration of 14 ± 2 %. The heat transfer coefficients dependences on density of heat flow of tubes were defined as well as on ice slurry rate through the coil and on concentration of water ice crystals in ice slurry. Ice slurry at ice concentration to 15% was investigated. It was defined that the heat transfer coefficient increased by 15-20% with increasing ice crystals concentration as compared with a single-phase coolant, but when concentration is higher than 5 the coefficients didn't differ much at the same heat load. The increase of the heat flow density from 2 to 10 kW/m^2 led to the heat transfer coefficients increasing by 25-30% on the average. To a considerable degree the heat transfer coefficients depend on the flow speed.
Keywords: Coil, Ice Slurry, Propylene-Glycol, Heat Transfer Coefficients, Water Ice Crystals Concentration, Heat Flow Density.

1. INTRODUCTION

Many technological processes in chemical and food industries are of non-stationary character and new approaches to their intensification are needed. Ice slurry is of great practical interest to be used for this purpose. It represents the mixture of water solution of substances (salt, alcohol, organic acids) with small particles of water ice. When using ice slurry refrigeration technologies high-rate refrigeration of objects is reached, stable temperatures at thermostating, cold accumulation are provided. The industrial and environment safety is increased as well. Kawaji and Egolf (2005) cite the data of temperatures and processes when it makes sense to use ice slurry. Recently some works were published on investigation results of heat exchange and hydraulic resistance in single tubes and different type air coolers operating on ice slurry (Belozerov et al., 2017; Grozdek et al., 2009; Egolf et al., 2005). But the heat exchange processes in technological apparatuses such as air coolers on ice slurry are not enough studied (Illán andViedma, 2009; Fernández-Seara et al., 2010; Shire et al., 2009); in particular, the dependences of heat transfer coefficients on key parameters. The current study deals with investigation of heat exchange when ice slurry flows in a coil fabricated as a model of an industrial heat exchange apparatus of cold chambers of food factories.

2. SUBJECTS AND METHODS OF INVESTIGATION

2.1. Subjects of inquiry

The subjects of inquiry are as follows: plate single-raw vertical coil consisting of 6 horizontal tubes at 19 mm inner diameter and 1mm wall thickness. The tubes are connected by bends under 180^0 at 38 mm radius. The total length of the coil is 9920 mm, the length of rectilinear sectors is 1500 mm, that of a heated tube sector is 1040 mm. The tube is made of steel 20.

2.2. Methods of investigation

The process of heat transfer depending on the heat flow density on the coil inner surface, on ice slurry rate in tubes as well as on water ice crystals concentration in ice slurry was studied. To compare some tests were carried out with a single-phase water solution. To obtain ice slurry a water solution of propylene glycol at 14 ± 2% concentration was prepared. Modeling a heat flow was performed by electric heaters at equal electric resistance placed on each tube. The heaters were connected in parallel. A total resistance of coil heaters was R_{coil} = 9.507 ohm, the heat flow density was provided up to12 kW/m^2. The thermal convertors - platinum (Pt100) thermometers of resistance with the limits of reduced basic error ± 0.25% and the multichannel technological recorder with the limits of reduced basic error ± 0.2% were used to measure the temperatures of

ice slurry t_{is} , single-phase solution t_{ss} and coil tube walls t_{coil}. The temperature of ice slurry and single-phase solution was measured by thermal convertors placed in the thermometer pocket at inlet and outlet of coolants from the coil. The temperature of the coil tube wall was measured in 9 points using the thermal convertors placed on the tubes surface. To measure the size of water ice crystals in ice slurry the optical microscope at 1 μm resolution with a photocamera incorporated and a thermocryotable were used. Ice slurry and a single-phase solution consumed were weighed in the following way: the ice slurry or solution went to the measuring reservoir and the filling time was defined. The laboratory balance with the limits of acceptable error ± 3 g was used. The filling time was determined by the seconds counter with the limits of measurement 0-30 s and 0.1 s division value.The test bench for study (as shown in Fig. 1) included ice slurry generator, tank with an agitator to accumulate ice slurry at generator operation, tank for discharging the solution warmed in the coil, circulating pumps supplying ice slurry into the test coil, control and inspection devices. Ice slurry and a single-phase solution were supplied to the coil from the bottom.

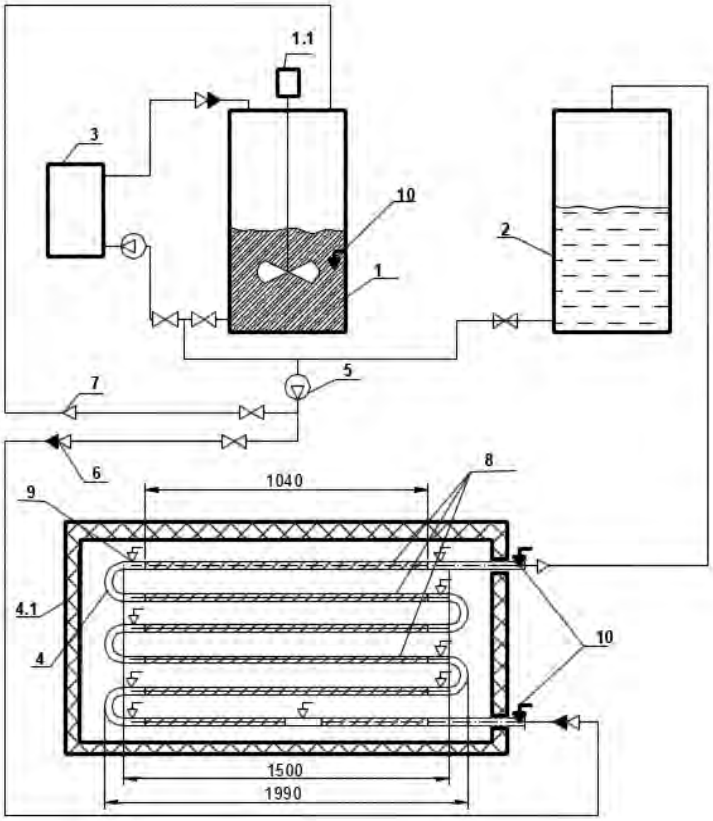

1. Ice slurry accumulation tank
1.1 Agitator
2. Tank for solution picking up after coil
3. Ice slurry generation (with pump)
4. Test coil
4.1 Heat-insulated casing
5. Circulating pump
6. Ice slurry
7. Single-phase solution
8. Coil tube with electric heater
9. Tube surface temperature probe
10. Coolant temperature probe

Figure 1: Test bench schematic circuit

When the needed concentration of water ice crystals in ice slurry in the accumulation tank was achieved, the generator was switched off and the agitator acted to obtain a homogeneous mass. After that the pump was switched on and a given ice slurry quantity was supplied through the coil using a regulating valve. The needed heating power was provided by electric load on the heaters of the coil. The heat load was regulated by the voltage regulator. The tests were carried out at once after the crystallizer switching off that provided crystals of 20- 50 μm size on the average. The wall temperature of each tube was accepted as an arithmetical mean of two values measured in this section. The coil temperature was an arithmetical mean of temperatures as illustrated by Fig. 1. The water ice crystals concentration was estimated by calorimetry. The ice slurry and single-phase propylene glycol water solution of fixed volumes (propylene glycol was at positive temperature) were mixed up in the calorimeter. The initial mass and temperature of the mixture were measured, also the final temperature of the solution resulted from the media mixture and the phase transition into ice slurry was measured. The water ice crystals mass in ice slurry was defined based on the heat balance.

The concentration in the tank ξ_{tank} taking into account the heat received by ice slurry in the pump was accepted as ξ_{in} concentration at inlet into the coil. The difference between ξ_{in} and ξ_{tank} doesn't exceed 2-3%.The error of definition of the heat transfer coefficient α was estimated by the

sum of errors: measurement of temperature difference of tubes wall and ice slurry; measurement of heat load applied to inner face of tubes. The maximal error of α determination was noted in tests with a minimal value $\Delta t = t_{coil} - t_{is}$ and q_{coil} didn't exceed 20%. The maximal error of water ice crystals concentration and ice slurry rate doesn't exceed 5%.

2.3. Results of experimental studies

Initial concentration ξ_{in} of ice crystals at the coil inlet was 12-15% in all tests. Along the coil length it decreased from 8 to 1.4% due to heat supply. On the basis of experimental data the dependence of the coil heat transfer coefficient on the heat flow density of the inner face of tubes was defined as demonstrated by Fig. 2.

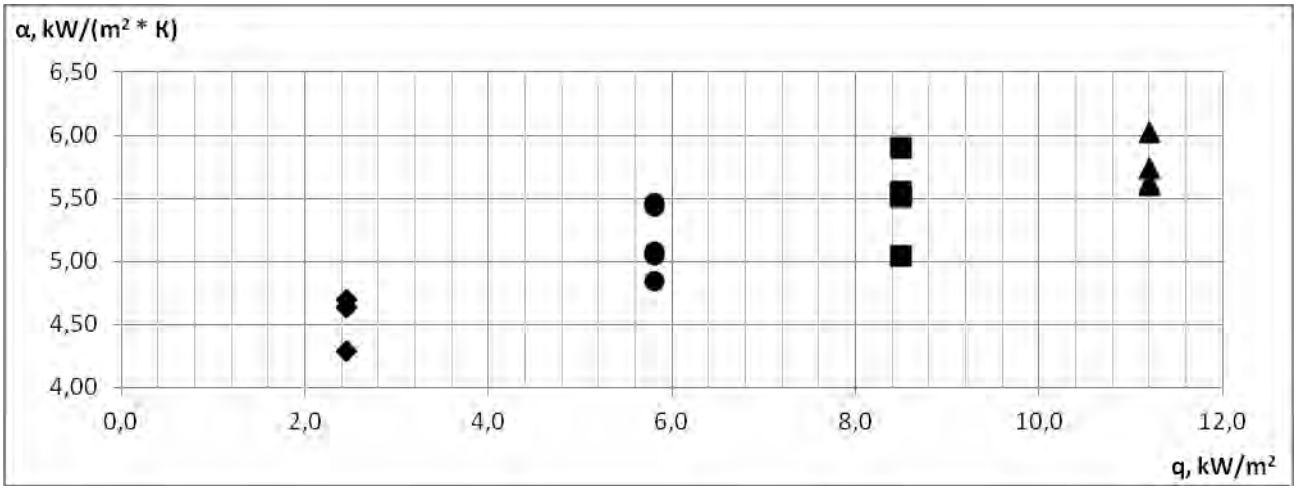

Figure 2: Dependence of the coil heat transfer coefficient on the heat flow density. Ice slurry rate G =0.31-0.34kg/s; ice crystals concentration: ◆ ξ = 9…1.5%, ● ξ = 12.5….1.5%, ■ ξ =11…1.5%, ▲ ξ=12…3%

It was established that the heat flow increase from 2 to 11 kW/m^2 led to the increase of heat transfer coefficients by 25-30% when ice slurry flowed through the coil, at this the values of heat transfer coefficients along the coil length decreased from 9.0 – 7.0 kW/(m^{2}K) to 4.0 -2.6 kW/(m^{2}K) depending on the initial concentration of ice crystals and ice slurry rate through the tube.

Fig. 3 shows the dependence of the coil heat transfer coefficient α_{coil} on concentration of water ice crystals in ice slurry.

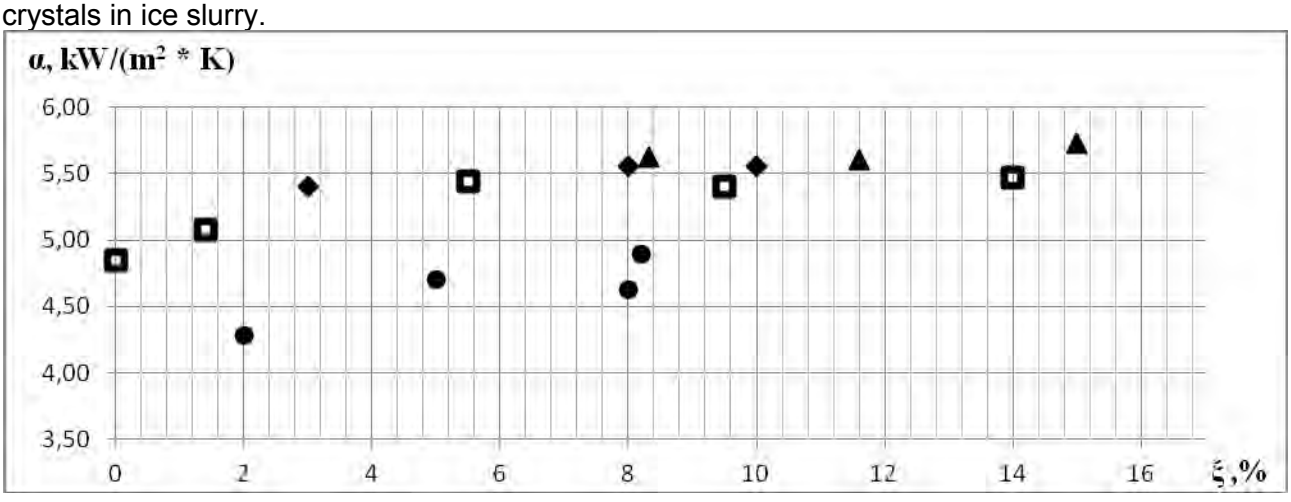

Figure 3: Dependence of the coil heat transfer coefficient on the concentration of ice crystals in ice slurry. Rate G = 0.31- 0.34kg/s; heat load:

● q=2,45 kW/m^2, ◘ q= 5,80 kW/m^2, ◆ q=8,50 kW/m^2, ▲ q=11,20 kW/m^2

It was defined that with increase of ice crystals concentration the heat transfer coefficient increased by 15-20% as compared with a single-phase coolant, but the coefficients didn't depend on concentration when it was higher 5% at the same value of heat load. These data are correlated with the research results (Egolf et al., 2005).
Fig. 4 demonstrates the dependence of the coil heat transfer coefficient on ice slurry rate. To a large degree the heat transfer coefficients depend on flow rate.

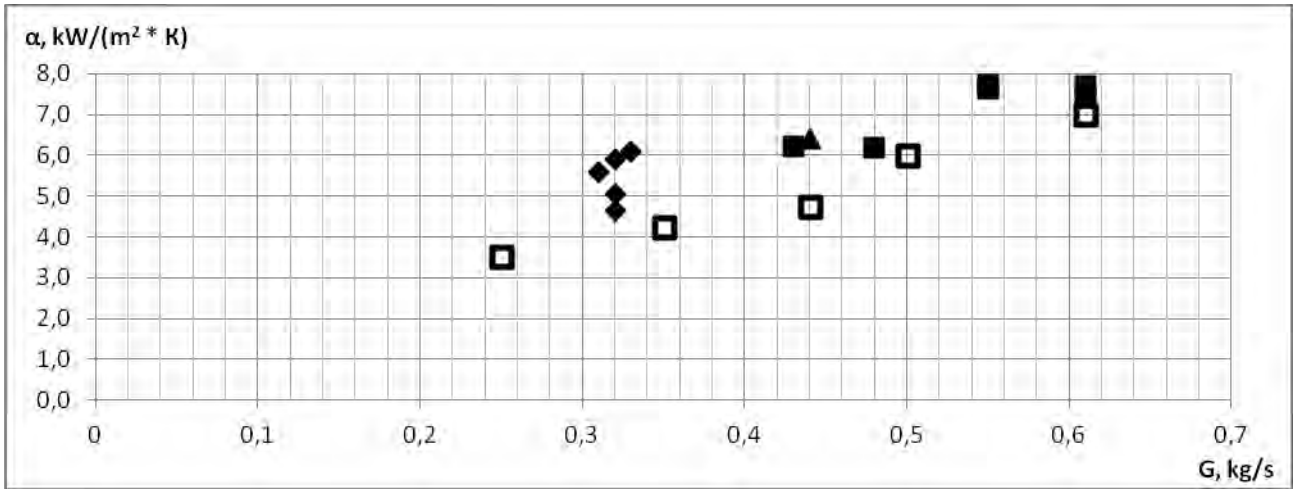

Figure 4: Dependence of the coil heat transfer on the ice slurry rate (at concentration ξ = 9-11%) and single-phase solution, at heat loads
◆ q=6.18 kW/m², ▲ q=7.44 kW/m², ◘ q=7.60 kW/m²; single-phase solution ■ q=5.31 kW/m²

The change of the rate through the coil from 0.25 kg/s to 0.6 kg/s leads to the increase of the heat transfer coefficient more than 2 times. The values of α_{is} are correlated according to recommendations (Snoek and Bellamy, 1997) with the values calculated for turbulent flow of single-phase solution by equation of Dittus and Boelter (Egolf et al., 2005; Snoek and Bellamy, 1997). Meanwhile the thermal properties of ice slurry were calculated using equations by (Thomas, 1965) and (Jeffrey, 1973). Calculations by Dittus and Boelter equation with dynamical viscosity and ice slurry effective heat conductivity corrections showed that the values of the heat transfer coefficient α_{is} for the coil were 2 times higher than calculated using the equation. So, the Dittus and Boelter equation offered by C.W. Snoek and J.Bellamy for generalizing ice slurry heat transfer coefficients can't be applied for description of heat transfer in the coil in toto.

3. CONCLUSIONS

The studies of heat exchange process in the plate single-raw vertical coil consisted of 6 horizontal tubes with coolants (ice slurry and single-phase solution) supplied from the bottom were carried out. It was defined that with increase of water ice crystals concentration the heat transfer coefficient increased by 15-20% in comparison with a single-phase coolant, but the coefficients didn't differ much at the same heat load at concentration higher 5%.
The increase of the heat flow density from 2 to 11 kW/m^2 leads to the increase of the heat transfer coefficients by 25-30% on the average, at this the values of heat transfer coefficients along the coil length decrease from 9.0-7.0 kW/(m²·K) at inlet to 4.0-2.6 kW/(m²·K) at outlet depending on the initial concentration of ice crystals and the ice slurry rate when flowing through the tube.
To a large degree the heat transfer coefficients when ice slurry flows through the tube depend on the rate. The change of the rate in the tube from 0.25 to 0.6 kg/s leads to the increase of the heat transfer coefficient more than 2 times.

NOMENCLATURE

ξ_{tank}	concentration of water ice crystals in the tank (%)	t_{is}	the temperature of ice slurry (^{0}C)
ξ_{in}	concentration of water ice crystals at the coil inlet (%)	t_{coil}	an arithmetical mean of 9 temperatures measuring the coil tube wall (^{0}C)
		t_{ss}	the temperature of single-phase solution (^{0}C)

REFERENCES

Kawaji, M., Egolf P.W., 2005. Handbook on Ice Slurries. Fundamentals and Engineering. International Institute of Refrigeration, Paris. 245 p.

Belozerov, G.A., Mednikova, N.M., Pytchenko, V.P. 2017. Investigation of heat exchange of ice slurry of propylene glycol water solution in a horizontal tube. Chemical and Petrolium Engineering, 4, 36-39.

Grozdek, M., Khodabandeh, R., Lundqvist P., Palm, B., Melinder, Å., 2009. Experimental investigation of ice slurry heat transfer in horizontal tube. Int. J. Refrigeration 32, 1310 – 1322.

Egolf, P.W. Kitanovski, A., Derrick, A-C., Stamatiou, E., Kawaji, M., et al., 2005. Thermodynamics and heat transfer of ice slurries. Int. J. Refrigeration 28 (1), 51 – 59.

Illán, F., Viedma, A., 2009. Experimental study of ice slurry performance in a standard fan coil. Int. J. Refrigeration 32 (6), 1808 – 1814.

Fernández-Seara, J., Diz, R., Uhia, F.J., Dopazo, J. A., 2010. Experimental analysis on pressure drop and heat transfer of a terminal fan-coil unit with ice slurry as cooling medium. Int. J. Refrigeration 33 (5), 1095 – 1104.

Shire, G.S.G., Quarini, G.L., Evans, T.S., 2009. Pressure drop of flowing ice slurries in industrial heat exchangers. Appl. Thermal Eng. 29, 1500 – 1506.

Snoek, C.W., Bellamy, J., 1997. Heat transfer measurements of ice slurry in tube flow. Experimental Heat Transfer, Fluid Mechanics, and Thermodynamics, 1993-1997.

Thomas, D.G., 1965. Transport characteristics of suspension. Journal of colloid science 20, 267-277.

Jeffrey D.J., 1973. Conduction through a random suspension of spheres. Proceedings of R. Soc. Lond. A335, 355-367.

Manuscript ID: 229
DOI: 10.18462/iir.icr.2019.0229

Energetic and exergetic analyses of ejector cooling cycle with feed pump driven by expander

Guangming CHEN, Volodymyr IERIN, Oleksii VOLOVYK, Kostyantyn SHESTOPALOV

Ningbo Institute of Technology, Zhejiang University
Ningbo City, Zhejiang Province, 315100, China, gmchen@zju.edu.cn

ABSTRACT

The paper presents the results of the energy and exergy analysis of the ejector cooling cycle with feed pump driven by expander. In the proposed ejector cooling cycle the working fluid is supplied to the generator by a feed pump at the expense of work obtained from expansion of liquid refrigerant in the expander. A mathematical model is proposed to determinate the energy and exergy characteristics of the pumping device and the ejector cooling system as a whole. Refrigerant R245ca is selected as the environmentally friendly low-boiling working fluid of ejector cooling cycle in the present study. The results of the calculations show that there are operating modes of the ejector cooling cycle when its operation is unfeasible. The optimal operating conditions of the ejector cooling cycle with feed pump driven by expander are determined. In addition, the effect of the proposed pumping device on the energy and exergy losses of the cycle is investigated.
Keywords: Ejector, Ejector cooling cycle, Expander, Feed pump, Performance.

1. INTRODUCTION

An ejector cooling machine (ECM) refers to the class of vapor heat-driven cooling machines and it is an installation in which the Rankine (power) cycle and the vapor mechanical compression cooling cycle are combined and performed (Chen et al., 2016). At the same time, the ejector performs the functions of a turbine and a compressor, but it has no moving elements, and it is structurally significantly simpler than the latter (Chunnanond and Aphornratana, 2004).

It is necessary to use a feed pump to supply liquid refrigerant from the condenser to the vapor generator for power cycle realization. For this purpose the electrically driven feed pumps are usually used in the ECMs. The use of feed pump that consumes heat for its operation is one of the means for improving the operational reliability, technical and economic characteristics of ECM and the expansion of application area. This can make the ECMs independent from the electric power supply source (Petrenko et al., 2010).

At the present time, there are many proposals for the design of ECMs with various heat-driven pumping devices, both periodical and continuous principle of operation. However, none of the proposed technical solutions has been brought to the level of a reliable operating device so far (Besagni et al., 2016).

The analysis of the ejector cooling cycles with heat-driven feed pumps showed that using of additional energy from an external source to supply the working fluid to the vapor generator leads to a decrease in the ejector cycle efficiency. At the same time, in the ejector cooling cycle it is possible to obtain the work for feed pump operation by using the expansion work of the refrigerant obtained in the expander. This solution allows avoiding the supply of additional energy to the ejector cooling cycle from external sources and losses during throttling, thereby increasing cycle efficiency.

The research aims of the study are to determine the possibility of using the expansion work of the refrigerant obtained in the expander to drive the feed pump that supplies the working fluid to the vapor generator, as well as the optimal operating conditions of the ejector cooling cycle with the feed pump driven by expander. The paper presents the analysis of the proposed ejector cooling cycle and investigation the effect of the proposed pumping device on the energy and exergy losses

of the cycle. Refrigerant R245ca is selected as the environmentally friendly low-boiling working fluid of ejector cooling cycle (Shestopalov et al., 2015).

2. EJECTOR COOLING SISTEM DESCRIPTION

The schematic diagram of the ECM with feed pump driven by expander is shown in Figure 1. In the proposed cycle the expansion work of the refrigerant obtained in the expander is directly used to increase the pressure of the working fluid supplied to the vapor generator. In this case, the expander and the feed pump are connected by a transmission gear, which ensures the transfer of mechanical energy between the devices. The thermodynamic cycles of the proposed and conventional (with expansion valve) ejector cooling systems in T-s diagram is shown in Figure 2.

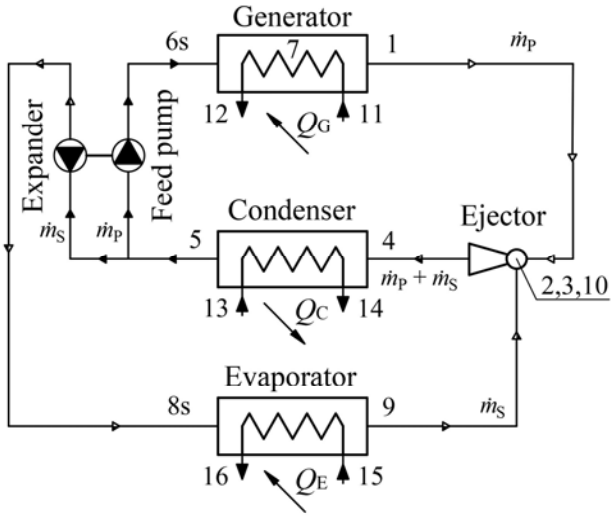

Figure 1: Diagram of the ejector cooling system with feed pump driven by expander

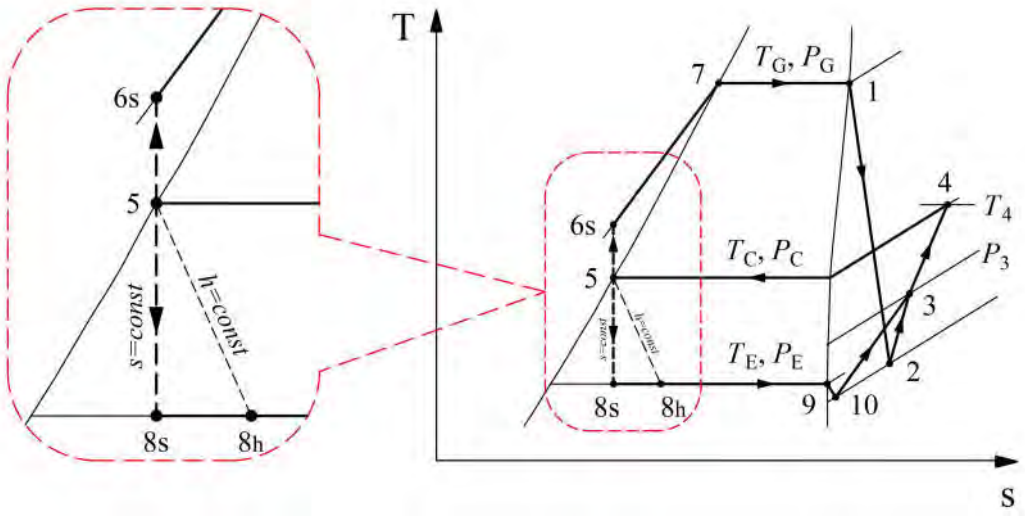

Figure 2: Ejector cooling cycles in T-s diagram

The operating principle of ejector cooling cycle is as follows. The refrigerant is boiled at relatively high pressure P_G and temperature T_G in the vapor generator by heat Q_G supplied from the external heat source. Then the primary vapor with a mass flow rate of $\dot{m}_P$ enters the primary nozzle of the ejector where it is accelerated to supersonic speed at the nozzle outlet with a significant reduction in pressure. This supersonic flow creates a very low pressure in the mixing chamber and it ensures a suctioning effect of secondary flow with a mass flow rate of $\dot{m}_S$ from the evaporator at low pressure P_E. Then the mixture of primary and secondary vapors enters the diffuser where its

pressure is increased. After that the compressed mixture flows to the condenser. This compressed mixture is condensed to a liquid state at condensing pressure P_C and temperature T_C due to heat Q_C rejected to the environment. After condenser the obtained liquid refrigerant is divided into two parts. One part of the refrigerant is expanded in an expander to the low-pressure state P_E producing work $\dot{W}_{EXP}$. Then this refrigerant enters the evaporator, where it is evaporated at low temperature T_E consuming heat Q_E supplied from a cooled medium. This vapor is entrained by the ejector. The other part of liquid refrigerant is pumped back to the vapor generator by the feed pump with consumption of the work $\dot{W}_{FP} = \dot{W}_{EXP}$. The liquid is finally entered the vapor generator, thus completing the ejector cooling cycle.

The expander and the feed pump should be made as a single unit to reduce irreversible losses in the transfer of work between these elements. The transfer of mechanical energy in such unit is carried out by means of a shaft on which the expander impeller and the operating element of the feed pump (impeller, gear, etc.) are located.

In the present study, an ejector with a conical-cylindrical mixing chamber is considered (Figure 3). When analyzing the proposed ECM the real gas-dynamic processes are taken into account. This approach will allow evaluating the operational integrity of the proposed solution in a real ejector cooling cycle. In this case, the entrainment ratio ω as characteristic of the ejector performance is defined by the method proposed by Shestopalov et al. (2015). According to this method the irreversible losses of the refrigerant flowing through the nozzle, mixing chamber, diffuser, and entrance part of the mixing chamber are taken into account by the velocity coefficients φ_1, φ_2, φ_3 and φ_4, respectively. The values of these coefficients are determined experimentally and they are assumed to be $\varphi_1 = 0.95$, $\varphi_2 = 0.975$, $\varphi_3 = 0.9$ and $\varphi_4 = 0.925$ in this study.

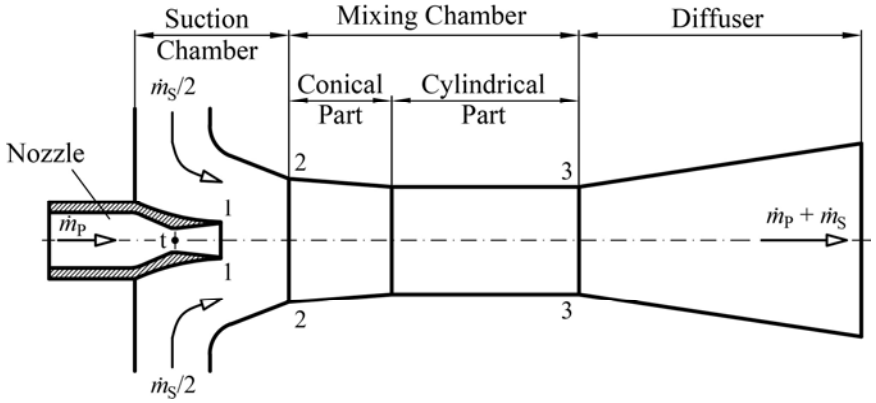

Figure 3: Design of supersonic ejector with conical-cylindrical mixing chamber

3. ANALYSIS OF THE EJECTOR COOLING CYCLE

For simplicity, the analysis of the ejector cooling cycle with feed pump driven by expander is carried out taking into account the following assumptions:

1. The refrigerant in the cycle is at steady state.
2. Heat transfer processes in the heat exchangers of the ejector cooling system occur without hydraulic and thermal losses.
3. Only physical exergies are used for proposed refrigerant. Chemical exergy is neglected because chemical reactions are rare and have negligible impact when compared to the physical exergy of organic substances.
4. The potential and kinetic exergy of materials is also neglected, since the proposed system and its components are at rest relative to the environment.
5. The rate of exergy loss is neglected, because all outer surface of the system is at constant reference temperature.

3.1. Energy analysis

In the proposed ejector cooling cycle, the obtained in the expander expansion work of the refrigerant must be fully spent on increasing the pressure of the liquid working fluid supplied to the

generator. The deficiency of the expansion work leads to the impossibility of driving the feed pump. At the same time, the excess of the expansion work results in the need to divert excess work from the cycle. Taking into account the irreversibility of the processes in the devices, the balance of mechanical work for the expander and the feed pump can be expressed with Eq. (1).

$$\dot{W}_{\mathrm{EXP,S}} \cdot \eta_{\mathrm{EXP}} = \frac{\dot{W}_{\mathrm{FP,S}}}{\eta_{\mathrm{FP}}} \quad \text{Eq. (1)}$$

where η_{EXP} and η_{FP} are the efficiency of the expander and feed pump, respectively; $\dot{W}_{EXP,S}$ and $\dot{W}_{FP,S}$ are the adiabatic work of the expander and the feed pump, respectively, which can be determined by Eq. (2) and Eq. (3):

$$\dot{W}_{\mathrm{EXP,S}} = \dot{m}_{\mathrm{E}} \cdot \dot{w}_{\mathrm{FP}} = \dot{m}_{\mathrm{E}} \cdot \left(h_5 - h_{8\mathrm{S}}\right) = \dot{m}_{\mathrm{E}} \cdot \upsilon_5 \cdot \left(P_{\mathrm{C}} - P_{\mathrm{E}}\right) \quad \text{Eq. (2)}$$

$$\dot{W}_{\mathrm{FP,S}} = \dot{m}_{\mathrm{P}} \cdot \dot{w}_{\mathrm{FP}} = \dot{m}_{\mathrm{P}} \cdot \left(h_{8\mathrm{S}} - h_5\right) = \dot{m}_{\mathrm{P}} \cdot \upsilon_5 \cdot \left(P_G - P_C\right) \quad \text{Eq. (3)}$$

After the conversion, Eq. (1) can be represented in the following form Eq. (4):

$$\dot{W}_{\mathrm{FP,S}} = \dot{W}_{\mathrm{EXP,S}} \cdot \eta_{\mathrm{O}} \quad \text{Eq. (4)}$$

where η_O is the overall efficiency of the unit, which includes the expander and the feed pump

$$\eta_{\mathrm{O}} = \eta_{\mathrm{EXP}} \cdot \eta_{\mathrm{FP}} \quad \text{Eq. (5)}$$

Taking into account Eq. (2) and Eq. (3), the overall efficiency of the unit, including the expander and the feed pump can be expressed from Eq. (4) in Eq. (6):

$$\eta_{\mathrm{O}} = \frac{\dot{m}_{\mathrm{P}} \cdot \upsilon_5 \cdot \left(P_{\mathrm{G}} - P_{\mathrm{C}}\right)}{\dot{m}_{\mathrm{E}} \cdot \left(h_5 - h_{8\mathrm{S}}\right)} \quad \text{Eq. (6)}$$

Considering that the entrainment ratio ω is defined as the ratio of the secondary and primary flow rates

$$\omega = \frac{\dot{m}_{\mathrm{S}}}{\dot{m}_{\mathrm{P}}} \quad \text{Eq. (7)}$$

then Eq. (6) can be represented in Eq. (8)

$$\eta_{\mathrm{O}} = \frac{\upsilon_5 \cdot \left(P_{\mathrm{G}} - P_{\mathrm{C}}\right)}{\omega \cdot \left(h_5 - h_{8\mathrm{S}}\right)} \quad \text{Eq. (8)}$$

The thermal coefficient of performance for the proposed ejector cooling cycle is determined by the Eq. (9):

$$\mathrm{COP}_{\mathrm{THERM}} = \frac{Q_{\mathrm{E}}}{Q_{\mathrm{G}}} = \frac{\dot{m}_{\mathrm{S}} \cdot \left(h_9 - h_{8\mathrm{S}}\right)}{\dot{m}_{\mathrm{P}} \cdot \left(h_1 - h_{6\mathrm{S}}\right)} \quad \text{Eq. (9)}$$

3.2. Exergy analysis

An evaluation of the energy usage efficiency in the ejector cooling cycle with feed pump driven by expander is carried out on the basis of the method proposed by Bejan et al. (1996).
The exergy of each state point can be calculated with Eq. (10):

$$\dot{E}_{\mathrm{i}} = \dot{m}_{\mathrm{i}} \cdot e_{\mathrm{i}} = \dot{m}_{\mathrm{i}} \cdot \left[h_{\mathrm{i}} - h_0 - T_0 \cdot \left(s_{\mathrm{i}} - s_0\right)\right] \quad (10)$$

The exergy balance for the system's i-th component can be expressed in Eq. (11) by using proper definitions for the exergy of fuel $\dot{E}_{F,i}$, exergy of product $\dot{E}_{P,i}$, and exergy destruction $\dot{E}_{D,i}$:

$$\dot{E}_{\mathrm{F,i}} = \dot{E}_{\mathrm{P,i}} + \dot{E}_{\mathrm{D,i}} \quad (11)$$

Equations for each component of the proposed and conventional (with electric feed pump and expansion valve) ejector cooling systems are given in Table 1.

Table 1. Equations for exergy analysis of the ejector cooling systems

Proposed ejector cooling system			
Component	Exergy of product $\dot{E}_{P,i}$	Exergy of fuel $\dot{E}_{F,i}$	Exergy destruction $\dot{E}_{D,i}$
Evaporator	$\dot{E}_{P,E} = \dot{E}_{16} - \dot{E}_{15}$	$\dot{E}_{F,E} = \dot{E}_{8S} - \dot{E}_{9}$	$\dot{E}_{D,E} = \dot{E}_{F,E} - \dot{E}_{P,E}$
Generator	$\dot{E}_{P,G} = \dot{E}_{1} - \dot{E}_{6S}$	$\dot{E}_{F,G} = \dot{E}_{11} - \dot{E}_{12}$	$\dot{E}_{D,G} = \dot{E}_{F,G} - \dot{E}_{P,G}$
Ejector	$\dot{E}_{P,EJ} = \dot{E}_{4}$	$\dot{E}_{F,EJ} = \dot{E}_{1} + \dot{E}_{9}$	$\dot{E}_{D,EJ} = \dot{E}_{F,EJ} - \dot{E}_{P,EJ}$
Condenser	$\dot{E}_{P,C} = \dot{E}_{14} - \dot{E}_{13}$	$\dot{E}_{F,C} = \dot{E}_{4} - \dot{E}_{5}$	$\dot{E}_{D,C} = \dot{E}_{F,C} - \dot{E}_{P,C}$
Expander	$\dot{E}_{F,EXP} = \dot{W}_{EXP}$	$\dot{E}_{P,EXP} = \dot{E}_{5} - \dot{E}_{8S}$	$\dot{E}_{D,EXP} = \dot{E}_{F,EXP} - \dot{E}_{P,EXP}$
Feed pump	$\dot{E}_{P,FP} = \dot{E}_{6S} - \dot{E}_{5}$	$\dot{E}_{F,FP} = \dot{W}_{FP}$	$\dot{E}_{D,FP} = \dot{E}_{F,FP} - \dot{E}_{P,FP}$
System total	$\dot{E}_{P,TOT} = \dot{E}_{P,E} + \dot{E}_{F,EXP} - \dot{E}_{P,FP}$	$\dot{E}_{F,TOT} = \dot{E}_{F,G}$	$\dot{E}_{D,TOT} = \sum_{i=1}^{n} \dot{E}_{D,i}$
Conventional ejector cooling system			
Component	Exergy of product $\dot{E}_{P,i}$	Exergy of fuel $\dot{E}_{F,i}$,	Exergy destruction $\dot{E}_{D,i}$
Evaporator	$\dot{E}_{P,E} = \dot{E}_{16} - \dot{E}_{15}$	$\dot{E}_{F,E} = \dot{E}_{8h} - \dot{E}_{9}$	$\dot{E}_{D,E} = \dot{E}_{F,E} - \dot{E}_{P,E}$
Generator	$\dot{E}_{P,G} = \dot{E}_{1} - \dot{E}_{6S}$	$\dot{E}_{F,G} = \dot{E}_{11} - \dot{E}_{12}$	$\dot{E}_{D,G} = \dot{E}_{F,G} - \dot{E}_{P,G}$
Ejector	$\dot{E}_{P,EJ} = \dot{E}_{4}$	$\dot{E}_{F,EJ} = \dot{E}_{1} + \dot{E}_{9}$	$\dot{E}_{D,EJ} = \dot{E}_{F,EJ} - \dot{E}_{P,EJ}$
Condenser	$\dot{E}_{P,C} = \dot{E}_{14} - \dot{E}_{13}$	$\dot{E}_{F,C} = \dot{E}_{4} - \dot{E}_{5}$	$\dot{E}_{D,C} = \dot{E}_{F,C} - \dot{E}_{P,C}$
Expansion valve	$\dot{E}_{P,EV} = \dot{m}_{S} \cdot e_{8h}^{T}$	$\dot{E}_{F,EV} = \dot{m}_{S}\left(e_{5}^{M} + e_{5}^{T} - e_{8h}^{M}\right)$	$\dot{E}_{D,EV} = \dot{E}_{F,EV} - \dot{E}_{P,EV}$
Feed pump	$\dot{E}_{P,FP} = \dot{E}_{6S} - \dot{E}_{5}$	$\dot{E}_{F,FP} = \dot{W}_{FP}$	$\dot{E}_{D,FP} = \dot{E}_{F,FP} - \dot{E}_{P,FP}$
System total	$\dot{E}_{P,TOT} = \dot{E}_{P,E}$	$\dot{E}_{F,TOT} = \dot{E}_{F,G} + \dot{E}_{F,FP}$	$\dot{E}_{D,TOT} = \sum_{i=1}^{n} \dot{E}_{D,i}$

The following indicators are used for the system's performance evaluation.
The exergetic efficiency for i-th component $\eta_{EX,i}$ is defined as the ratio between the exergy of product for the i-th component and the exergy for the i-th component, as shown in Eq. (12):

$$\eta_{EX,i} = \frac{\dot{E}_{P,i}}{\dot{E}_{F,i}} \tag{12}$$

The total exergy efficiency of the system $\eta_{EX,TOT}$ is determined in Eq. (13):

$$\eta_{EX,TOT} = \frac{\dot{E}_{P,TOT}}{\dot{E}_{F,TOT}} \tag{13}$$

where $\dot{E}_{P,TOT}$ and $\dot{E}_{F,TOT}$ are the total exergy of product and the total exergy of fuel, respectively.
The exergy destruction ratio for i-th component y_i, percentage of exergy destruction with i-th component $y_{D,i}$ in the overall exergy destruction and ratio y_{TOT} are defined in Eq. (14), Eq. (15), and Eq. (16), respectively:

$$y_i = \frac{\dot{E}_{D,i}}{\dot{E}_{F,TOT}} \tag{14}$$

$$y_{D,i} = \frac{\dot{E}_{D,i}}{\dot{E}_{D,TOT}} \tag{15}$$

$$y_{TOT} = \frac{\dot{E}_{D,TOT}}{\dot{E}_{F,TOT}} \tag{16}$$

4. RESULTS AND DISCUSSION

The proposed ejector cooling cycle has been investigated for air-conditioning application with fixed cooling capacity Q_E = 1 kW, and fixed evaporating temperature T_E = 8 °C. The condensing temperatures T_C and generating temperatures T_G used in the parametric study are taken in the range from 30 to 40 °C and from 70 to 100 °C, respectively. The results of the theoretical study are presented in Figures 4–6.

Figure 4a and Figure 4b show that ω and COP_{THERM} are increasing with decreasing T_C and increasing T_G. This is explained by the increasing in the expansion pressure ratio $E = P_G/P_E$, and the decreasing in the pressure lift ratio $C = P_C/P_E$. As it is seen from Figure 4a, the value of ω is the same for the proposed and conventional ejector cooling cycles. At the same time, the COP_{THERM} values are slightly higher for the ejector cooling cycle with feed pump driven by expander. It is caused by increasing the specific cooling capacity q_E in the proposed cycle due to reducing of irreversible losses during expansion of the refrigerant in the expander. The relative reduction in COP_{THERM} for the proposed system compared to conventional system for T_C = 30–40 °C and T_G = 70–100 °C is from 0.63 to 1.41%.

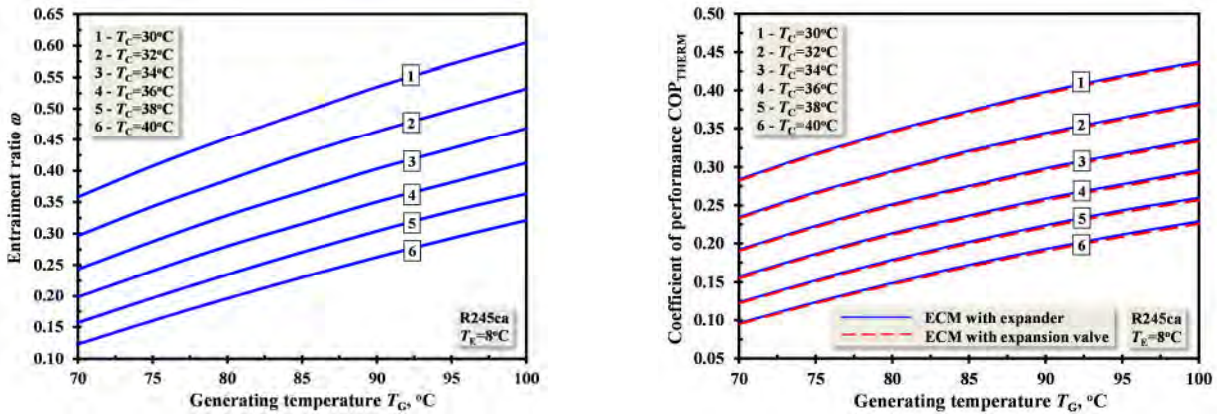

a) b)

Figure 4: Variation of ω (a) and COP_{THERM} (b) with T_G for R245ca at T_E = 8 °C and different T_C

Figure 5a illustrates the effect of temperatures T_C and T_G on the overall efficiency η_O of the proposed ejector cooling cycle. As evident in Figure 5a, the variation of η_O with T_G has minimal values that shift towards lower temperatures T_G with decreasing T_C. For the considered operating modes, the minimum values of η_O are 0.558–0.581 at T_C = 30–36 °C and T_G = 70 °C, 0.609 at T_C = 38°C and T_G = 75 °C, and 0.635 at T_C = 40°C and T_G = 80 °C. Thus, from Figure 5a, it follows that the operation of a real pumping device is mostly appropriate at low T_C and T_G. In addition, the η_O values in a given mode for a real pumping device must be higher than the values shown in Figure 5a. In this case, the irreversible losses for expanding of the refrigerant in the expander and increasing the pressure of the working fluid in the feed pump can be considered.

In the proposed ejector cooling system, the exergy of fuel is provided by only the heat of the hot water supplied to the generator, because the feed pump obtains the work from expander. The exergy of product is a cooling effect provided by the evaporator. The system's total exergy destruction includes the exergy destruction of each system component, while the system's exergy losses are rejected into the environment through the condenser. The exergy analysis shows that using of the feed pump driven by expander results in reduction the total exergy destruction. As shown in Figure 5b, the $\dot{E}_{D,TOT}$ values increase when T_C increases. At the same time, the $\dot{E}_{D,TOT}$ values decrease when T_G increases in the range of T_C = 30–36 °C and have minimum values in the range of T_C = 38–40 °C. The relative reduction in $\dot{E}_{D,TOT}$ for the proposed system in compared to conventional system for T_C = 30–40 °C is from 1.92 to 2.66% at T_G = 70 °C, and from 1.99 to 3.32% at T_G = 100 °C.

The using of the feed pump driven by expander leads to increasing the exergetic efficiency of the proposed system. The function $\eta_{EX,TOT} = f(T_G)$ has maximum values that shift toward higher temperatures T_G with increasing T_C (see Figure 6a). The maximum values of $\eta_{EX,TOT}$ are 3.82–

7.01% for the proposed system and 3.36–6.55% for the conventional system when T_C varies from 40 to 30 °C. Thus, the relative increase in $\eta_{EX,TOT}$ for condensing temperatures T_C = 30–40 °C is 7.02–13.69%.

Low energy efficiency of the ejector cooling cycle leads to significant losses in the exergy of fuel. As it can be seen from Figure 6b, the y_{TOT} values increase with decreasing temperature T_C and reach maximum values at T_C = 30 °C. At the same time, the effect of generating temperature T_G on the value of y_{TOT} at low condensing temperatures T_C becomes insignificant. In general, for the considered operating modes of the ECM, the y_{TOT} values are 73.78–92.47% and 74.29–92.45% for the proposed and conventional ejector cooling cycles, respectively.

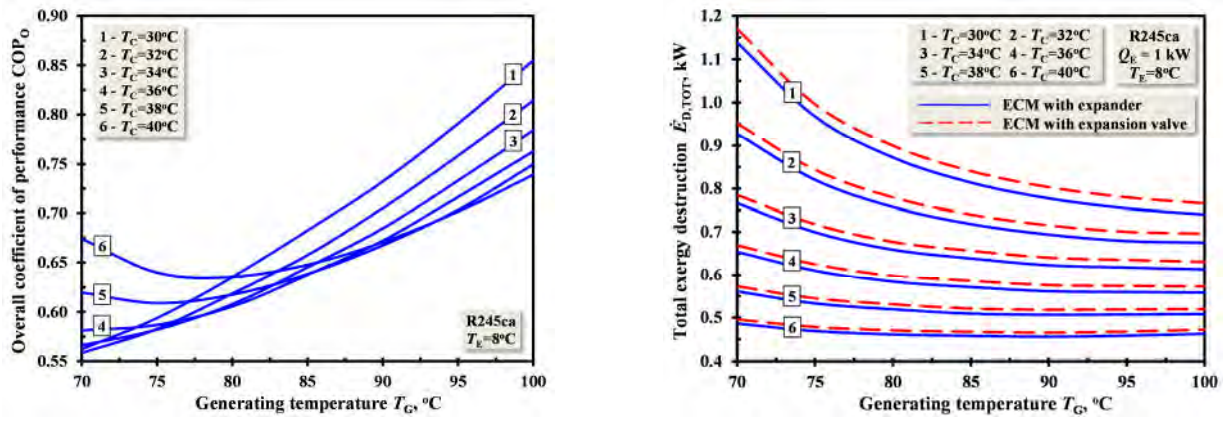

a) b)

Figure 5: Variation of COP_O (a) and $\dot{E}_{D,TOT}$ (b) with T_G for R245ca at T_E = 8 °C and different T_C

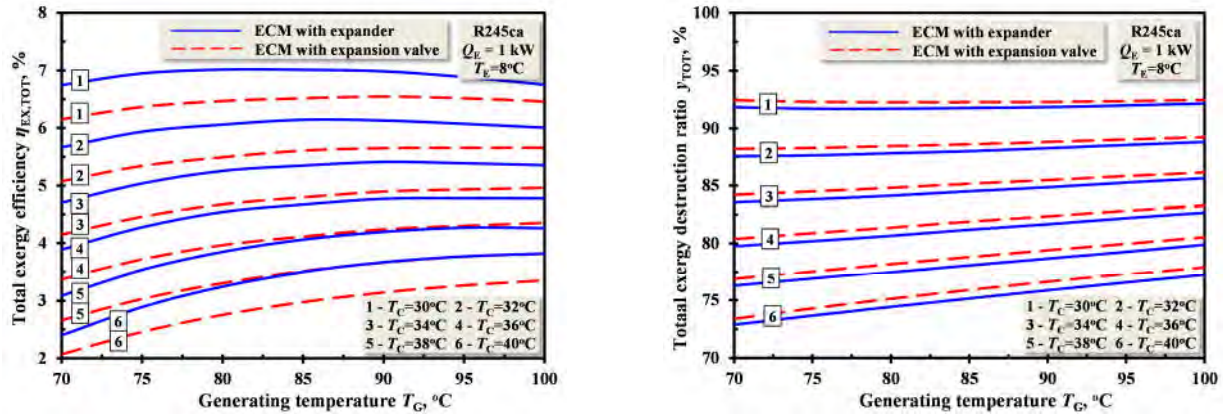

a) b)

Figure 6: Variation of $\eta_{EX,TOT}$ (a) and y_{TOT} (b) with T_G for R245ca at T_E = 8 °C and different T_C

5. CONCLUSIONS

In this paper, an ejector cooling cycle with feed pump driven by expander was proposed. Thermodynamic analysis of this ejector cooling cycle with evaporating temperature T_E = 8 °C, condensing temperatures T_C = 30–40 °C and generating temperatures T_G = 70–100 °C was conducted. Refrigerant R245ca was investigated as working fluid.

According to theoretical study for the design of proposed ejector cooling cycle, the most important findings are as follows.

1. The using of the expansion work obtained in the expander for driving the feed pump is possible only at low condensing temperatures T_C and generating temperatures T_G. The operation of the ECM at high temperatures T_C and T_G will require the creation of a pumping device with an efficiency η_O close to 1. This leads to significant limitations in the possibility of using such device in actual operating conditions.

2. The need to take into account irreversibility when expanding the refrigerant in the expander and increasing the pressure of the working fluids in the feed pump increases the required values of η_O for the pumping device operation in comparison with those values obtained in this study. Creating such pumping device with minimal losses in structural elements is very difficult, and the pumping device will have a high cost. In addition, higher η_O values will further narrow the allowable operation modes of the ECM.
3. Replacing the expansion valve into the expander and using of the expansion work for driving the feed pump leads to increasing the energy and exergy efficiency of the proposed system. However, this increase in efficiency is not significant. Thus, the relative increase in the COP_{THERM} value for the proposed system compared to the conventional ejector cooling cycles for condensing temperatures T_C = 30–40 °C and generation temperatures T_G = 70–100 °C is 0.63–1.41%, and the relative increase in $\eta_{EX,TOT}$ is 7.02–13.69%.
In view of the above, it should be noted that the using of the expansion work obtained in the expander for driving the feed pump in the ejector cooling cycle is possible, but the area of application is limited.

ACKNOWLEDGEMENTS

The paper was financially supported in part by the Natural Science Foundation of China (Projects No. 51776187), Zhejiang Province Natural Science Foundation of China (Project No. LY16E060004), and by Ningbo Science and Technology Bureau from the International Cooperation Project No. 2017D10006.

NOMENCLATURE

COP	coefficient of performance	e	specific exergy (kJ kg^{-1})
$\dot{E}$	exergy (kW)	h	specific enthalpy (kJ kg^{-1})
$\dot{m}$	mass flow rate (kg s^{-1})	P	pressure (kPa)
q	specific heat (kJ kg^{-1})	Q	heat transfer (kW)
s	entropy (kJ $kg^{-1}·K^{-1}$)	T	temperature (°C or K)
υ	specific volume (m^3 kg^{-1})	$\dot{w}$	specific work (kJ kg-1)
$\dot{W}$	work (kW)	y	exergy destruction ratio
η	coefficient of efficiency	ω	entrainment ratio

REFERENCES

Chen, G., Volovyk, O., Ierin, V., Shestopalov, K., 2016. Thermodynamic study of a mechanical analog of the heat-driven ejector refrigeration cycle. Proceedings of the Heat Powered Cycle Conference, Nottingham, Great Britain, 29-30.

Chunnanond, K., Aphornratana, S., 2004. Ejectors: applications in refrigeration technology. Renew. Sustain. Energy Rev. 8, 129-155.

Petrenko, V.O., Shestopalov, K.O., Volovyk, O.S., Ierin, V.O., Huang, B.J., 2010. Design and modeling of innovative solar ejector air conditioners and chillers operating with low-boiling working fluids. Proceedings of the International Conference on Solar Heating, Cooling and Buildings (EuroSun 2010), Graz, Austria.

Besagni, G., Mereu, R., Inzoli, F., 2016. Ejector refrigeration: A comprehensive review. Renew. Sustain. Energy Rev. 53, 373-407.

Shestopalov, K.O, Huang, B.J, Petrenko, V.O, Volovyk, O.S., 2015. Investigation of an experimental ejector refrigeration machine operating with refrigerant R245fa at design and off-design working conditions. Part 1. Theoretical analysis. Int. J. Refrigeration 55, 201-211.

Bejan A, Tsatsaronis G, Moran M. Thermal design and optimization. New York, USA: John Wiley; 1996.

Manuscript ID: 235
DOI: 10.18462/iir.icr.2019.0235

Synthesis and characterization of nano-PCM in water for phase-change secondary refrigerants applications

David CABALEIRO[(a,b)], Filippo AGRESTI[(c)], Simona BARISON[(c)], Stefano ROSSI[(a)], Sergio BOBBO[(a)], Laura FEDELE[(a)]

(a) Construction Technologies Institute, National Research Council (ITC-CNR), Padova, I-35127, Italy.
(b) Departamento de Física Aplicada, Universidade de Vigo, Vigo, E-36310, Spain.
(c) Institute of Condensed Matter Chemistry and Technologies for Energy, National Research Council (ICMATE-CNR), Padova, I-35127, Italy.

laura.fedele@itc.cnr.it

ABSTRACT

Phase Change Materials have been largely studied in the last decades, due to their capability to store (and release) thermal energy, with a consequent energy savings in several applications.
They are applied in buildings industry, food storage, smart textiles, medicine, space, automotive, and solar application.
PCMs are employed in encapsulated forms or immersed in different matrix. In the last years, nanoparticles of PCMs dispersed in a base fluid have been studied to understand their possible capability as heat transfer fluids, especially in solar or HVAC applications, where the latent heat of fusion of these materials can be exploited as additional heat capacity.
This study focuses on the development and characterization of phase change materials emulsions, in order to understand their possible use as secondary fluids. Stability, density, thermal conductivity, heat capacity and latent heat were measured and reported.

Keywords: Phase Change Material Emulsion (PCME), Water, Paraffin, Latent Heat, Thermal Conductivity, Density.

1. INTRODUCTION

Over last decades, phase change materials (PCMs) have been largely studied due to their capability to store thermal energy available or produced during off-peak hours, with consequent energy savings in several applications (Mehling and Cabeza, 2008). From a technological point of view, solid-liquid and solid-solid transitions are particularly attractive, since associated volume modifications are considerably lower than in other phase changes. However, bulk PCMs in solid state cannot be pumped and thus the utilization of solid-liquid and solid-solid latent heat is usually restricted to systems involving conventional storage components that contain the PCM (Fischer et al., 2017). A possibility to face this limitation is to employ two-phase fluids in which PCMs are suitably mixed/dispersed in conventional carrier fluids. Resulting materials, usually known as phase changing slurries (PCS), can be used as media to both transport and store thermal energy, avoiding heat losses due to intermediate heat exchangers. Potential interest in PCS is evidenced by the relatively extensive research developed in that field during just over a decade (Delgado *et al.*, 2012; Youssef *et al.*, 2013), as well as the fluids patented and/or commercialized by several companies and international research centers (BASF; Fraunhofer; Rajagopalan and Prieto, 2018). Among different technologies to produce PCSs, phase change material emulsions (PCMEs) are especially attractive as, in this case, PCMs are not encapsulated, but directly dispersed in the carrier fluid by means of an appropriately selected surfactant (mixture). Thus, PCM and carrier fluid must exchange stored energy simply through a surfactant protective layer with almost negligible thermal resistance (Shao et al., 2016). In addition,

since shell material and coating process are avoided, PCMEs can be formulated in a cost-effective manner (Zhang and Zhao, 2017).

PCMEs can combine the latent capacity provided by the PCM used as dispersed phase and the good transport properties of the carrier fluid employed as continuous matrix. However, a proper design is also key issue to balance the main disadvantages of resulting emulsions. Thus, small PCM drops are usually preferred to avoid large increases in dynamic viscosity and to ensure long-term thermal stabilities. However, a great number of PCMs exhibit differences in temperature between melting and solidification processes and this effect worsens as the fraction of material undergoing the phase change reduces in size. Thus, size reduction can lead to large sub-cooling. Sub-cooling or over-cooling is an undesirable phenomenon due to which a material remains liquid below its melting temperature. Solidification temperatures up to 15ºC lower than melting point were observed by Huang et al. (2010), when they experimentally studied the phase change transition of different paraffin-in-water emulsions. This behavior has been attributed in the literature (Günther et al., 2011) to isolation of nucleation sites, which requires that every single droplet has to be nucleated separately. A common strategy to reduce the sub-cooling of PCMEs is to introduce additional seeds that act as impurities and trigger heterogeneous solidification. Nanoparticles or PCMs with a higher melting point than the dispersed phase were utilized as nucleating agents (NA) in the literature (Huang et al., 2010; Wang et al., 2017). However, since nucleating agents do not participate in the storage of thermal energy (while contribute to viscosity increase and destabilizing process), the content of NAs in the PCMEs must be minimized as much as possible.

Aqueous emulsions or slurries of paraffin have been investigated as possible energy storage and heat transfer media in heating, ventilation and air conditioning (HVAC) systems or thermal facilities based on solar technologies, among others (Shao et al., 2015; Zhang et al., 2016). In these applications, the latent heat absorbed/released by PCM drops can be exploited as additional energy to enhance the storage capacity of the facility or for temperature regulation. This last option can be particularly interesting in cooling applications. Zhang and Niu (2010) experimentally studied the performance of a slurry of microencapsulated n-hexadecane (melting temperature around 18ºC) in a storage tank cyclically heated and cooled between 5 and 25ºC. Although PCS was found potentially interesting for building temperature regulation, the large sub-cooling (with a melting temperature below 7-8ºC) did not allow exploiting the full potential of the emulsions. Shao et al. (2016) produced water-based emulsions of RT10 at 30 wt.% paraffin concentration with almost negligible sub-cooling and nearly double storage heat capacity compared to water. However, the large average droplet size (~3 μm) and high paraffin content resulted in huge dynamic viscosity increases and thermal conductivity reductions of up to 30%. Thus, more research on the design and characterization of phase change material emulsions is necessary to better understand their behavior during phase change and better evaluate their potential as secondary fluids.

In this work, new water-based PCMEs of pure n-heptadecane or commercial RT21HC paraffin with nanometric drops are formulated. Sample stability was evaluated over time and after submitting emulsions to freeze-thaw cycles and mechanical shearing. Phase change transitions were characterized in terms of latent heat and temperature and this information was used to evaluate the enhancement in heat storage capacity provided by PCM drops. Finally, thermal conductivities and densities are also reported.

2. EXPERIMENTAL SECTION

2.1. Materials and nanoemulsion design

Phase change material nanoemulsions with PCM concentrations of 2 wt.%, 4 wt.% and 10 wt.% were prepared by using a hexane-assisted emulsification method proposed in Agresti *et al.* (2019). Deionized water (18.2 MΩ·cm at 25ºC), utilized as base fluid, was produced by a Millipore system (Billerica MA, USA). *n*-heptadecane, (C17, mass purity >99%, Alfa Aesar) and a technical grade RT21HC paraffin (Rubitherm Technologies GmbH, Germany) were used as dispersed phases, while RT55 and RT70HC paraffin waxes (Rubitherm

Technologies GmbH, Germany) were tested as nucleating agents. Sodium dodecyl sulfate, SDS, (98%, Sigma Aldrich) was utilized as surfactant.

Zeta potential and hydrodynamic droplet size measurements were performed by a Zetasizer Nano ZS (Malvern Instruments Ltd, United Kingdom) based on Dynamic Light Scattering (DLS) technique. Experiments were carried out at 25ºC with a scattered angle of 173° by using a 4 mW He-Ne laser (wavelength of 633 nm). Studied representative samples exhibit negative Zeta potentials larger than -71 mV. These results (in absolute value) are considerably higher than the threshold of 30 mV usually assumed as indication of good stability in aqueous suspensions. Nano-PCMEs formulated with 2 wt.% and 4 wt.% paraffin contents exhibit average droplet diameters ~90-110 nm, while this value is ~130-150 nm for the samples formulated with 10 wt.%. No destabilization evidences or significant variations in average diameter were observed when nano-emulsions were kept in static conditions along a month (Fig. 1a) or when samples were subjected to several freeze-thaw cycles in the temperature range between 3ºC and 30ºC (Fig. 1b). The good stability was also verified when RT21HC/W emulsion prepared with 10 wt.% was mechanically sheared for 6 hours at temperatures of 10ºC (solid paraffin droplets) or 30ºC (liquid paraffin droplets).

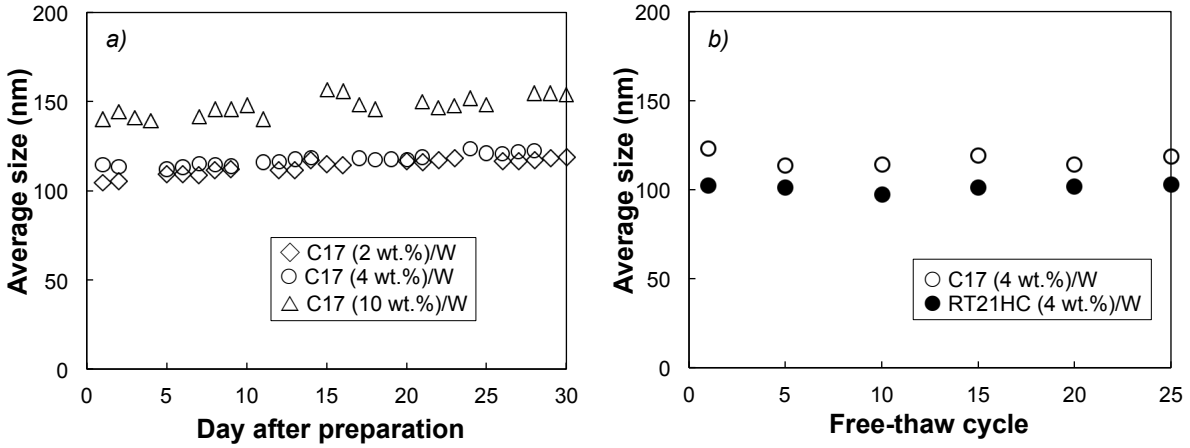

Figure 1. (a) Droplet average diameter vs. time for C17/Water nano-PCMEs and (b) average size evolution with freeze-thaw cycling for nanoemulsions with 4 wt.% paraffin contents

2.2. Thermophysical characterization

Solid-liquid and solid-solid phase change transitions were analyzed in the temperature range from ~0ºC to 60ºC by means of a differential scanning calorimeter, DSC, Q2000 (TA Instruments, New Castle, USA) refrigerated with a cooling system RSC90. Samples sizes of ~2 mg (in the case bulk paraffin) and ~10 mg (for nanoemulsions) were inserted and hermetically crimped in aluminum pans. DSC cells were weighted before and after the tests in order to check that no change in mass had occurred during experiments. Analyses were carried out with scanning rates from 1 to 5 ºC/min, in nitrogen (molar purity higher than 0.99999) atmosphere by following a three-run method (IEA SHC, 2011). Experimental uncertainties in enthalpy and temperature measurements with this device are 1.2 J/g (repeatability of 0.7 J/g) and 0.3 ºC (repeatability of 0.1 ºC), respectively (Cabaleiro *et al.*, 2014).

Thermal conductivities in the temperature interval between 2ºC and 60ºC were obtained using a hot disk thermal constants analyzer model TPS 2500 (Hot Disk AB, Sweden). This instrument ensures accurate measurements of liquids, solids and powders over a thermal conductivity range from 0.005 to 500 W/(m·ºC). In this study a TPS sensor consisting of a double spiral with a radius of 2 mm, made of nickel wire and covered with Kapton was selected for experiments. Although instrument uncertainty declared by manufacturer is 5%, previous tests performed on stainless steel and deionized water show percentage absolute average deviations lower than 2% (Colla *et al.*, 2017; Fedele *et al.*, 2012). A further description of instrument and experimental method can be found in (Colla *et al.*, 2017; Fedele *et al.*, 2012).

Density measurements were carried out at temperatures from 15ºC to 30ºC by means of a DMA 500 densimeter (Anton Paar, Austria). Experimental device was calibrated with water and toluene as reference materials and an uncertainty better than 0.1% was estimated (Żyła *et al.*, 2018).

3. RESULTS AND DISCUSSION

3.1. Phase Change Characteristics

DSC curves obtained for some representative PCMEs are presented in Fig. 2. The two characteristic endothermic transitions of *n*-heptadecane (Acree and Chickos, 2017) can be observed in the three heating thermograms of C17-nanoemulsions prepared without any nucleating agent (Fig. 2b). The peak at lower temperature (~8-10ºC depending on the nanoemulsion and 10.5ºC for pure *n*-heptadecane) corresponds to a solid-solid transition in which *n*-heptadecane passes from an orthorhombic crystalline structure to a disordered phase, while the peak at higher temperature (~19-20ºC for PCMEs and 21.3ºC for pure C17) is the melting transition.

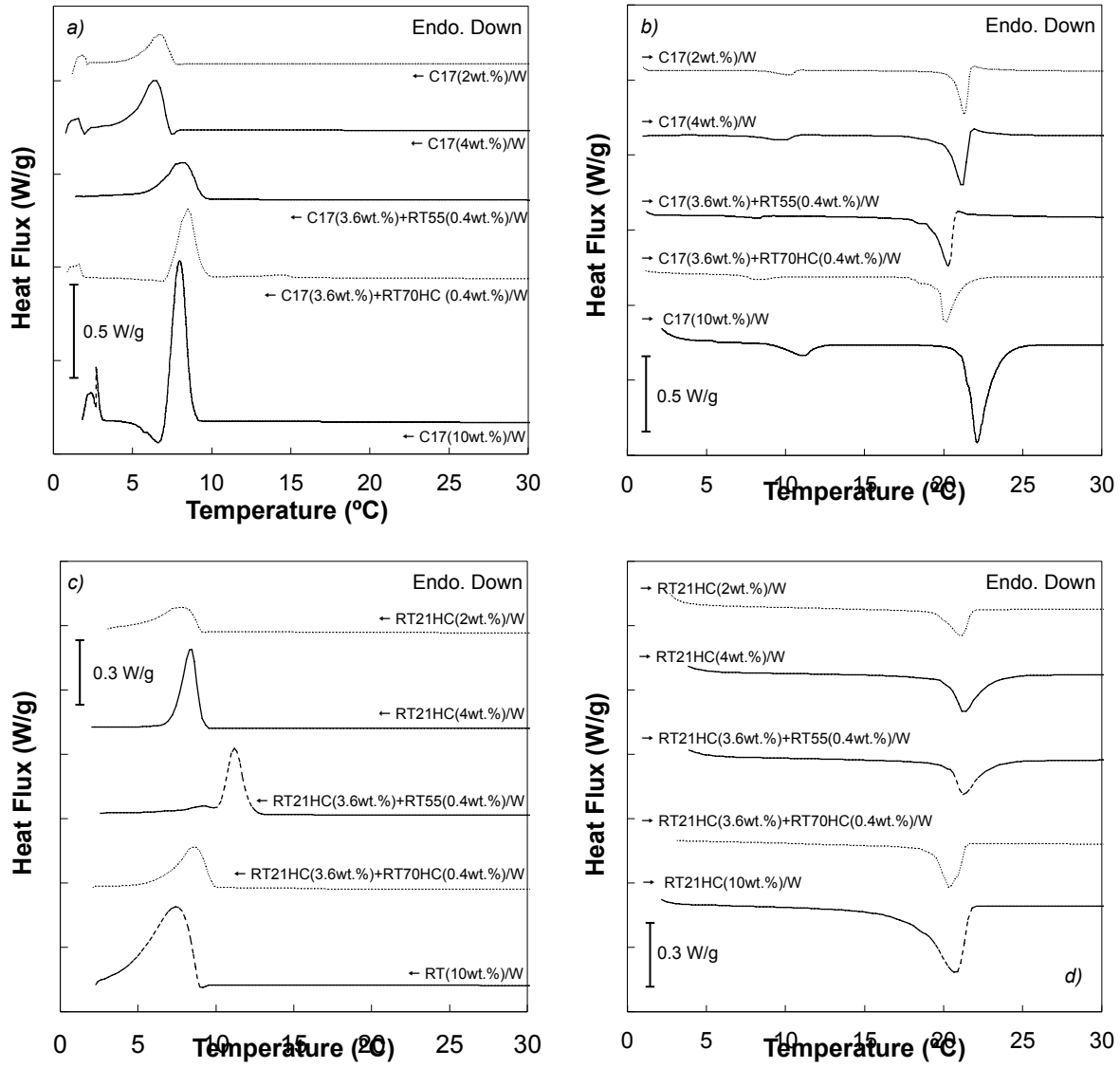

Figure 2. (a,c) Cooling and (b,d) heating DSC thermograms of some representative nanoemulsions formulated using (a,b) C17 and (c,d) RT21 paraffins as dispersed phase. Scanning rate: 5 ºC/min

Shifts towards lower temperatures were previously reported in the literature (Puupponen et al., 2015) for melting transitions of nano-PCMEs. This behavior was attributed to the larger free energy of PCM droplets as a consequence of a higher surface to volume ratio (Puupponen *et al.*, 2015). Likewise, cooling DSC curves of C17/Water samples without nucleating agent (Fig. 2a) also present two exothermal events. However, while the sub-cooling (difference between onset temperatures of melting and solidification transitions) of the bulk-C17 is ~1ºC only, this difference reaches 13ºC for some studied nanoemulsions. Regarding commercial RT21HC paraffin (Fig. 2c and 2d), similar behaviors were observed. In this case, the main differences are that DSC curves present only one peak (as also occurs to bulk-RT21HC in the analyzed temperature range) and maximum sub-cooling is 11.1ºC.

In order to try to reduce sub-cooling effect, two different commercial waxes (RT55 and RT70HC) with higher transition temperatures than the dispersed phase were considered (55 and 70°C, respectively). In all cases, the NA:C17 or NA:RT21HC mass ratio was fixed at 10%:90%. The addition of tested nucleating agents decreases the difference between melting and solidification temperatures. However, obtained reductions in sub-cooling (up to 3.2ºC with RT55 and 2.3ºC with RT70HC) are far from our initial expectations.

Enthalpies variations associated to these transitions increase with the concentration of the dispersed phase. However, these values are about 12-35% lower than the values expected according to the following mass relation:

$$\Delta h_{lat,PCME} = \varphi_{PCM} \cdot \Delta h_{lat,PCM} \qquad \text{Eq. (1)}$$

Experimental latent heats up to 20% lower than Eq.(1) were also found by Zhang *et al.* (2016) when studied aqueous emulsions of *n*-octacosane. These differences may be due to the existence of a paraffin layer anchored to the surfactant that does not participate in the phase transition (Agresti *et al.*, 2019).

Given the additional latent heat absorbed/released by paraffinic droplets during their melting/solidification, PCM-emulsions are expected to exhibit larger heat storage capacities than those of water (in which thermal energy is simply stored as sensible heat). Fig. 3a shows the improvement in heat storage capacity of nanoemulsions formulated without any nucleating agent as a function of the temperature range covered by the thermal fluid (only thermal energy related to melting transitions was considered for C17/W samples).

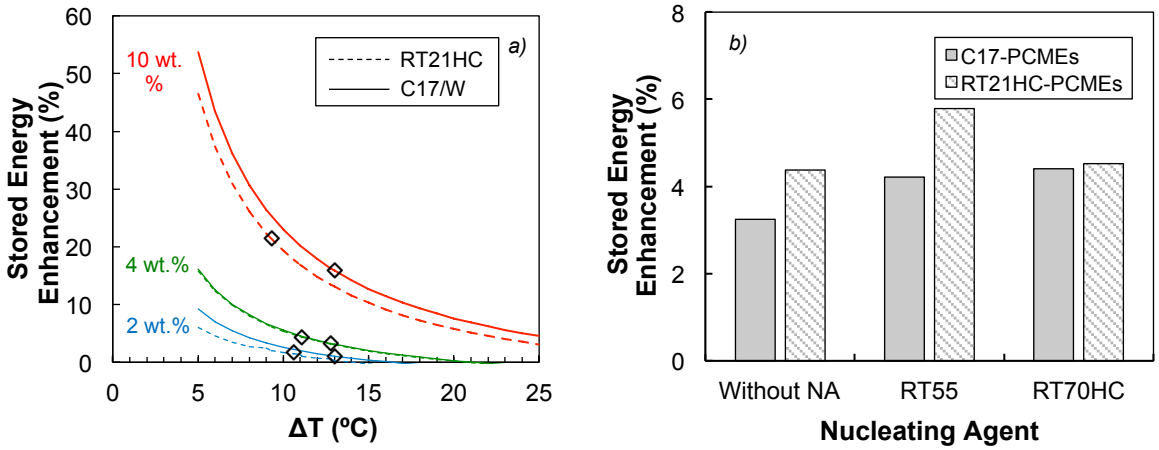

Figure 3. (a) Heat storage capacity enhancements vs. temperature interval covered by the PCME, *ΔT*.
(◇) Enhancements obtained for an ideal Δ*T*= sub-cooling. (b) Improvements in heat storage capacity for PCMEs prepared at 4 wt.% with and without nucleating agent

Considering a temperature difference equal to the sub-cooling (minimum ideal interval to be covered by emulsions so that PCM drops reversely undergo solid-liquid phase change), maximum improvements in storage capacity reach 16% and 21% for the C17 (10 wt.%)/W and RT21 (10 wt.%)/W samples. A comparison between the results obtained for

nanoemulsions prepared with 4 wt.% of total dispersed phase with and without nucleating agents (Fig. 3 b) shows that, despite the lower latent heat provided for the samples with NA, the reductions in sub-cooling lead to larger heat storage capacities in most of the cases. This fact highlights the need to continue reducing sub-cooling effect in these PCM nanoemulsions.

Finally, emulsion thermal reliability was also assessed through an analysis in which several samples were subjected to 100 cooling-heating cycles. Results do not show any appreciable difference between first and last solidification or melting transitions.

3.2. Thermal Conductivity

Experimental thermal conductivities of *n*-heptadecane and RT21HC aqueous emulsions are plotted together with the values obtained for water and bulk-paraffins in Fig. 4.

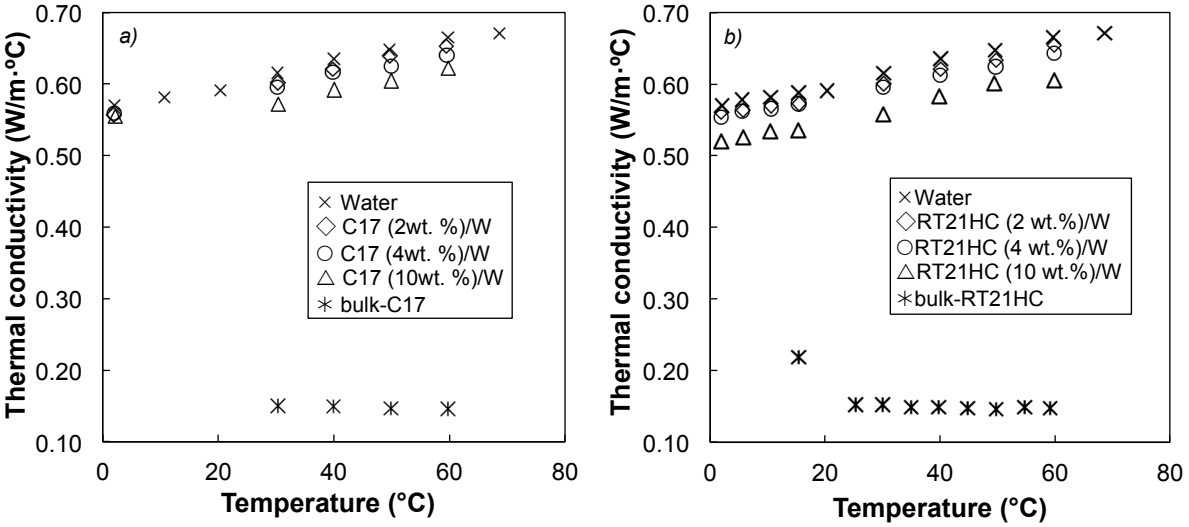

Figure 4. Thermal conductivity of (a) C17 and (b) RT21HC systems

As expected, considering the lower thermal conductivity of bulk-C17 (0.149 W/m·ºC at 30ºC) and bulk-RT21HC (0.153 W/m·ºC at 30ºC) in comparison with water, thermal conductivity reduces with the increasing PCM concentration present in the emulsion. Reductions in this property reach 9% at the highest concentration of dispersed phase (10 wt.%). In this case, no significant differences were observed when a 10% of paraffinic nucleating agent was incorporated to the dispersed phase.

3.3. Density

Density temperature dependence obtained for the nano-PCMEs prepared at 4 wt.% and 10 wt.% paraffin concentrations is presented in Fig. 5.

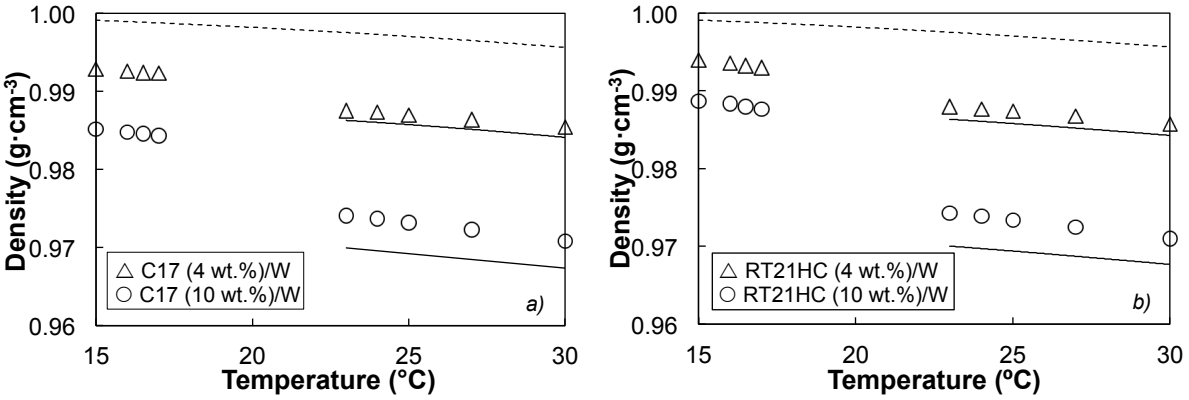

Figure 5. Density temperature dependence for (a) C17 and (b) RT21H aqueous nanoemulsions prepared at paraffin concentrations of 4 wt.% and 10 wt.%. (- -) Water densities reported by Refprop 9.0 (Lemmon *et al.*, 2010) and (—) values predicted by Eq. (2)

Density reduces as increases the paraffinic content in the emulsion increases. In this case, reductions reach 1.4% at 15ºC (when PCM drops are solid state) and 2.5% at 30ºC (liquid PCM drops) for the C17(10wt.%)/W sample. Changes in density around melting transition are consequence of the volumetric expansion of PCM drops when paraffin undergoes the solid-liquid transition. Experimental results were also compared with the values calculated by means of the following equation based on mixing theory:

$$\frac{1}{\rho_{PCME}} = \frac{\varphi_{PCM}}{\rho_{PCM}} + \frac{\varphi_{SDS}}{\rho_{SDS}} + \frac{1-\varphi_{PCM}-\varphi_{SDS}}{\rho_{W}} \qquad \text{Eq. (2)}$$

Maximum deviations of 0.35% were found between theoretical and experimental values when the PCM drops were liquid.

4. CONCLUSIONS

A solvent-assisted method was used to produce PCM-in-water emulsions with nanometric paraffin drops. Samples proved stability (no evidences of phase separation or significant growth in droplet size) through storage, after freeze-thaw cycling or under mechanical shearing. Two different commercial paraffin waxes with higher melting point than *n*-heptadecane and RT21HC were considered as nucleating agents to try to decrease the strong sub-cooling effect (up to 13ºC) of considered PCMs. However, only partial reductions (≤3.2ºC) in this undesirable phenomenon were obtained. Latent heat capacity of nanoemulsions reduces when a nucleating agent is incorporated to the dispersed phase. However, the lower sub-cooling of those last samples allows better profiting stored heat. As expected, thermal conductivity and density decrease with increasing paraffin concentration: maximum reductions reach 9% and 3%, respectively. Further research is necessary to control the sub-cooling effect and comprehensively evaluate the potential of these materials as possible secondary fluids. The characterization of other transport properties such as dynamic viscosity is part of the ongoing investigation of the authors.

ACKNOWLEDGEMENTS

Authors greatly appreciate the valuable contribution of M.A. Marcos with DSC measurements. D.C. was recipient of a postdoctoral fellowship from Xunta de Galicia (Spain).

NOMENCLATURE

c_p	Isobaric specific heat capacity [J/g·ºC]	PCS	Phase changing slurry
C17	n-heptadecane	PCME	Phase change material emulsion
DSC	Differential scanning calorimeter	ρ	Density [g/cm^3]
Δh	Enthalpy [J/g]	RT21HC	Rubitherm RT21 paraffin
φ	Mass fraction	RT55	Rubitherm RT55 paraffin wax
k	Thermal conductivity [W/m·ºC]	RT70HC	Rubitherm RT70HC paraffin wax
lat.	Latent	SDS	Sodium dodecyl sulfate
NA	Nucleating agent	T	Temperature [ºC]
PCM	Phase change material	W	Water

REFERENCES

Acree, W., Chickos, J.S., 2017. Phase transition enthalpy measurements of organic and organometallic compounds and ionic liquids. sublimation, vaporization, and fusion enthalpies from 1880 to 2015. Part 2. C11-C192. J. Phys. Chem. Ref. Data 46.

Agresti, F., Fedele, L., Rossi, S., Cabaleiro, D., Bobbo, S., Ischia, G., Barison, S., 2019. Nano-encapsulated PCM emulsions prepared by a solvent-assisted method for solar applications. Sol. Energy Mater. Sol. Cells Submitted.

BASF, Micronal® PCM http://www.construction.basf.com/p05/industry/en/content/building_green/energy_efficiency/micronal [last access December 2018].

Cabaleiro, D., Gracia-Fernández, C., Lugo, L., 2014. (Solid + liquid) phase equilibria and heat capacity of (diphenyl ether + biphenyl) mixtures used as thermal energy storage materials. J. Chem. Thermodyn. 74, 43-50.

Colla, L., Fedele, L., Mancin, S., Danza, L., Manca, O., 2017. Nano-PCMs for enhanced energy storage and passive cooling applications. Appl. Therm. Eng. 110, 584-589.

Delgado, M., Lázaro, A., Mazo, J., Zalba, B., 2012. Review on phase change material emulsions and microencapsulated phase change material slurries: materials, heat transfer studies and applications. Renew. Sust. Energy. Rev. 16, 253-273.

Fedele, L., Colla, L., Bobbo, S., 2012. Viscosity and thermal conductivity measurements of water-based nanofluids containing titanium oxide nanoparticles. Int. J. Refrig. 35, 1359-1366.

Fischer, L.J., von Arx, S., Wechsler, U., Züst, S., Worlitschek, J., 2017. Phase change dispersion properties, modeling apparent heat capacity. Int. J. Refrig. 74, 238-251.

Fraunhofer, ISE-MIKOPUK https://www.ise.fraunhofer.de/en/research-projects/mikopuk.html [last access December 2018].

Günther, E., Huang, L., Mehling, H., Dötsch, C., 2011. Subcooling in PCM emulsions-Part 2: Interpretation in terms of nucleation theory. Thermochim. Acta 522, 199-204.

Huang, L., Günther, E., Doetsch, C., Mehling, H., 2010. Subcooling in PCM emulsions-Part 1: Experimental. Thermochim. Acta 509, 93-99.

IEA SHC, 2011, Task 42/ECES Annex 24. Compact thermal energy storage. http://task42.iea-shc.org/ [Last Access December 2018].

Lemmon, E.W., Huber, M.L., McLinden, M.O., 2010. NIST Standard Reference Database 23: Reference Fluid Thermodynamic and Transport Properties (REFPROP), Version 9.0. . Phys. Chem. Prop.

Mehling, H., Cabeza, L.F., 2008, Heat and cold storage with PCM, an up to date introduction into basics and applications, Springer, Berlin.

Puupponen, S., Seppälä, A., Vartia, O., Saari, K., Ala-Nissilä, T., 2015. Preparation of paraffin and fatty acid phase changing nanoemulsions for heat transfer. Thermochim. Acta 601, 33-38.

Rajagopalan, S., Prieto, G.A.F., 2018, Nanostructured phase change materials for solid state thermal management. US Patent 9,963,627.

Shao, J., Darkwa, J., Kokogiannakis, G., 2015. Review of phase change emulsions (PCMEs) and their applications in HVAC systems. Energy Build. 94, 200-217.

Shao, J., Darkwa, J., Kokogiannakis, G., 2016. Development of a novel phase change material emulsion for cooling systems. Renew. Energ. 87, 509-516.

Wang, F., Zhang, C., Liu, J., Fang, X., Zhang, Z., 2017. Highly stable graphite nanoparticle-dispersed phase change emulsions with little supercooling and high thermal conductivity for cold energy storage. Appl. Energy 188, 97-106.

Youssef, Z., Delahaye, A., Huang, L., Trinquet, F., Fournaison, L., Pollerberg, C., Doetsch, C., 2013. State of the art on phase change material slurries. Energy Convers. Manage. 65, 120-132.

Zhang, G.H., Zhao, C.Y., 2017. Synthesis and characterization of a narrow size distribution nano phase change material emulsion for thermal energy storage. Sol. Energy 147, 406-413.

Zhang, S., Niu, J., 2010. Experimental investigation of effects of supercooling on microencapsulated phase-change material (MPCM) slurry thermal storage capacities. Sol. Energy Mater. Sol. Cells 94, 1038-1048.

Zhang, X., Wu, J.Y., Niu, J., 2016. PCM-in-water emulsion for solar thermal applications: The effects of emulsifiers and emulsification conditions on thermal performance, stability and rheology characteristics. Sol. Energy Mater. Sol. Cells 147, 211-224.

Żyła, G., Vallejo, J.P., Fal, J., Lugo, L., 2018. Nanodiamonds – Ethylene Glycol nanofluids: Experimental investigation of fundamental physical properties. Int. J. Heat Mass Transf. 121, 1201-1213.

Manuscript ID: 255
DOI: 10.18462/iir.icr.2019.0255

Dynamic model of heat and mass transfer in a ventilated and refrigerated display cabinet loaded with products

Sébastien BUSSONNIERE(a), Valérie SARTRE(a)*, Jocelyn BONJOUR(a)

[(a)] Univ Lyon, CNRS, INSA-LYON, CETHIL UMR5008
Villeurbanne, 69621, France, valerie.sartre@insa-lyon.fr

ABSTRACT

This paper presents simulation results concerning the temperature distribution in a ventilated and refrigerated display cabinet loaded with products. Using the nodal method, a numerical model of the dynamic thermal behaviour of a ventilated display cabinet was developed. A CFD simulation study of the entire cabinet was made to determine the airflow distribution between the shelves as well as the heat transfer coefficient along the evaporator plate. The dynamic behaviour of the cabinet with a temperature control of the refrigerating system was simulated. Such numerical results are useful to discuss the dynamic thermal behaviour of the cabinet and the phenomenon of thermal stratification.
Keywords: Closed Cabinet, Heat Transfer, Household Refrigerator, Model, Temperature Variation, Unsteady State

1. INTRODUCTION

Domestic and commercial refrigeration represent an important part of the global energy consumption. For example, in 2015 in France, domestic refrigerator consumption reached about 30% of the residential electricity consumption by end-users (Belman-Flores et al., 2015) (without including the electrical heating consumption). In addition to a huge electricity consumption, it has been observed that at the scale of France, 40% of perishable products located in a domestic refrigerator are not being kept at the best preservation temperature (Cemagref and ANIA, 2004), while it is recognized that temperature is the first parameter which certifies the preservation quality, even though others could be considered.
The temperature field of domestic refrigerators has been studied for many years by CFD simulations (Belman-Flores and Gallegos-Muñoz, 2016; Laguerre et al., 2007; Alfaro-Ayala et al., 2017).
Owing to CFD, Ding et al. (2004) discussed the uniformity of the temperature field and highlighted how it is improved when the system is ventilated. Indeed, when the compartment is ventilated, the heat is transferred by mixed convection, or forced convection may even dominate (Gupta et al., 2007). In order to reduce the calculation time, some studies explored other ways: Laguerre and Flick (2004) developed a simple dynamic model of an unventilated refrigerator taking into account heat transfer by natural convection, conduction and radiation. This model was found to be in good agreement with experiments. Using a nodal method to reduce the calculation time, Laguerre et al. (2012) proposed a nodal heat transfer model to predict the load temperature in an open vertical display cabinet depending on various parameters (ambient temperature, radiation temperature, …).
CFD is a powerful simulation tool, but its use is limited by the calculation time (e.g. more than 1 million cells for a loaded cabinet, which can result in several days of calculation (Bayer et al., 2013)). The aim of the present communication is to report on the development of a dynamic nodal model for a ventilated, refrigerated cabinet loaded with products. The model provides predictions of the time evolution of the temperature field in the cabinet as a function of various parameters such as ambient temperature, airflow distribution, material properties, mass airflow, etc., that all contribute to condition the quality of preservation of the products. The reliability of the model is tested and simulations are made for various external to internal temperature differences (T_{ext}-T_{int}).

2. DESCRIPTION OF THE MODEL

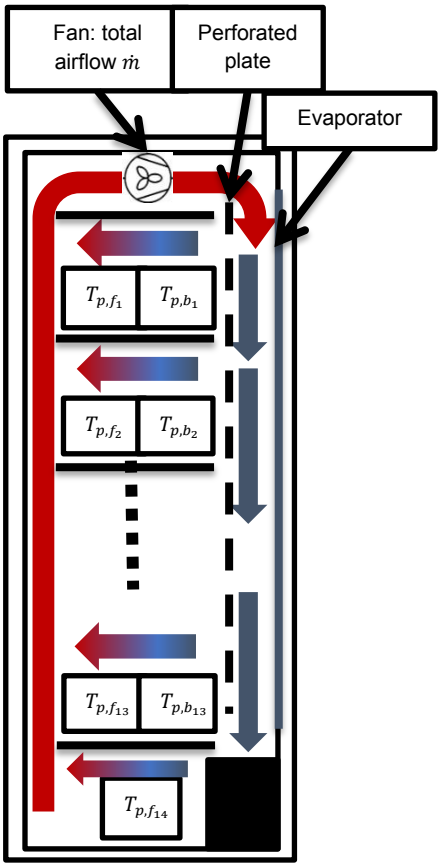

Figure 1 : Schematic view of a closed, ventilated and refrigerated display cabinet with product location (of temperature T_p) and air flow directions

Figure 1 is a schematic view of a closed cabinet with cabinet walls, airflows, product positions on shelves (one charge at the front and one at the back for each shelf except for the bottom of cabinet where only one charge is present at the front). Two vertical airflows (one ascending at the front and one descending at the back) as well as several horizontal airflows (from back to front) are created in the closed refrigerated cabinet using a fan. The refrigerated cabinet is closed, considered as perfectly hermetic (no mass exchange with the environment). The external air is supposed to be at a uniform and constant temperature that is higher than the internal temperature. Radiation heat transfer is neglected as compared to convection heat transfer. Conduction is neglected in the perforated back plate whose purpose is to ensure the distribution of the airflow. All the properties of materials (including air) such as density, heat capacity, thermal conductivity and kinematic viscosity are considered as constant in the small temperature range of interest.

The simulation of the thermal cabinet behaviour is based on a model of heat and mass transfer in the enclosure. It is described in the next section for one shelf and it must be duplicated for each shelf.

2.1. Model of a single shelf

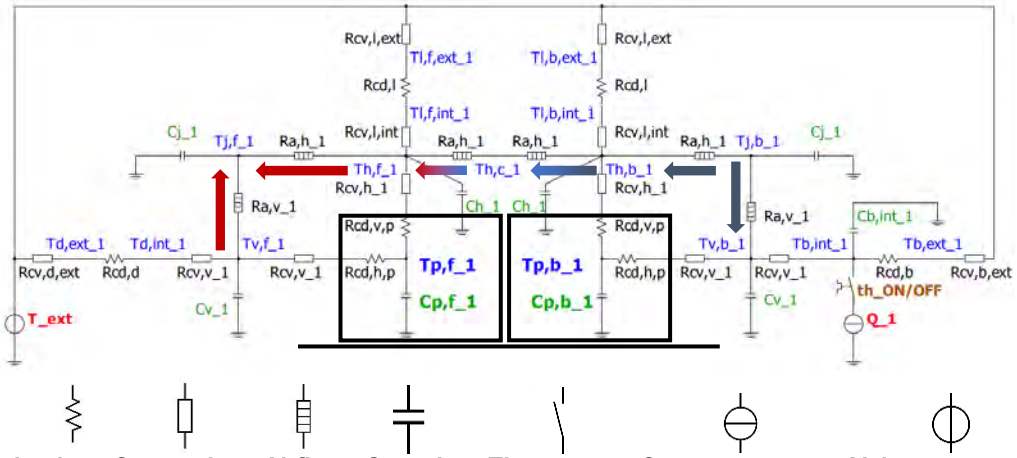

Figure 2 : Thermal-electrical analogy of one shelf inside a closed, ventilated and refrigerated cabinet (conduction (cd); convection (cv); airflow (a); thermal inertia (C))

Figure 2 shows the nodal network used to represent the shelf located at the top (*1* is relative to the first shelf) with resistors for vertical and horizontal airflow transport (*a*), convection (*cv*), conduction (*cd*). The subscript *v* (resp. *h*) is related to the conductive heat transfer in the vertical (resp. horizontal) direction or to the convective heat transfer with the vertical (resp. horizontal) airflow. This scheme does not include heat and mass transfer with the top area and shelf n°2. On Figure 2, *Tp,f_1* is the temperature of the product located at the front on the shelf n°1. *Tj,f_1* is the air temperature at the junction of the horizontal and front vertical airflow on the shelf n°1. *Td, Tl*, *Tb*

T_ext are respectively the door, side (lateral) panel, back panel and ambient temperatures. Thermal inertias are represented by capacitors with the following descriptors: *p* for product, *v* and *h* for vertical and horizontal airflows, resp., *j* for junction airflows.
The evaporator, modelled as a heat source whose value is an input data, is located at the contact of the internal back panel of temperature *Tb,int_1*. The cooling capacity is controlled by the thermostat (th_ON/OFF): it is an ON/OFF controller to simulate the ON/OFF cycles of the cooling system. When the thermostat is set ON (closed contact), the cooling capacity is injected into the circuit: the temperatures decrease and the products are being cooled down. On the contrary, when the thermostat is set OFF (open contact), the temperatures increase as the system tend to an equilibrium with the external air (temperature T_{ext}). The thermostat controls the mean value of *Tp* with a differential of ±0.5 K.

2.1.1. Thermal resistances associated to convection heat transfer

Convection is a major heat transfer mode for ventilated systems (see Figure 2). It is related to the airflows present in the cabinet. The thermal resistance is expressed as:

$$R_{cv} = \frac{1}{hS} \quad \text{Eq. (1)}$$

$$h = Nu\frac{\lambda_a}{L_c} \quad \text{Eq. (2)}$$

With *h* the convective heat transfer coefficient, *S* the heat exchange surface area, *Nu* the Nusselt number, λ_a the thermal conductivity of air, L_c the characteristic length. The top, back, bottom, side external panel areas are respectively 0.3, 0.8, 0.3, 0.8 m^2 and the door area is 0.9 m^2.
Heat transfer between the external panels and the outside is governed by natural convection. For the sake of simplicity and as this is not the limiting side for the heat transfer, all the heat transfer coefficients *h* for natural convection around the enclosure were set to 5 $W \times m^{-2} \times K^{-1}$.
Regarding the internal side of the panels, forced or mixed convection is present and the heat transfer coefficient is to be determined owing to CFD simulation (section 3.2). Indeed, the vertical airflows are not classical configurations because, contrary to most studies on forced convection heat transfer, the mass flow rate along the channel boundaries is not constant. It decreases along the rear wall (descending flow, with a part of the flow diverted in the successive channels formed by the shelves), while it increases along the front door (ascending flow, with an added flow coming from each channel). Leung et al. (1999) proposed a model for forced convection in a rectangular duct having one wall perforated, but the geometry was too different from the cabinet one.
Finally, horizontal airflows between the shelves can be viewed as flows in rectangular narrow channels formed by infinite parallel plates, an adiabatic one (shelf above the airflow) and one at uniform temperature (products below the airflow). Because of the low velocities involved (cf. section 3.1), the flow is always laminar ($Re = UL_c/\nu < 2200$). The classical solution for fully-developed laminar flow between parallel plates was used: $Nu = 4.86$ (Rohsenow et al., 1998), by assuming that the temperature gradients along the products, which are lower than 2 K/m, would not change drastically the value of the Nusselt number.

2.1.2. Thermal resistances associated to conduction heat transfer

The cabinet is composed of several different materials. Each panel and door is considered as a multi-layered material, which thermal conductivity is lumped together with the thickness *w* of the materials to form the overall thermal resistance, with the parameters given in Table 1:

$$R_{cd} = \frac{w}{\lambda A} \quad \text{Eq.(3)}$$

Table 1 : Conduction resistance parameters of different materials of the cabinet

Material	λ ($W \times m^{-1} \times K^{-1}$)	w (m)
Cabinet panels	0.0237	0.06
Door	0.0237	0.032
Product, vertical direction	0.6	0.1
Product, horizontal direction	0.6	0.04

The conductive cross-sectional surface areas *A* are identical to convective heat exchange surface areas *S* for cabinet walls and door. For the products, the conductive cross-sectional surface areas in vertical and horizontal directions are 0.15 and 0.03 m^2, respectively.

2.1.3. Thermal resistances associated to heat transport

The transport resistance is linked to the mass flow rate $\dot{m}$ and to the specific heat of the fluid *Cp*:

$$R_a = \frac{1}{\dot{m}Cp} \quad \text{Eq. (4)}$$

The horizontal mass flow distribution is related to the distribution of the vertical flow through the perforated plate. Simple CFD simulations and experimental data were used to quantify this complex flow distribution.

2.1.4. Thermal inertia

Thermal inertia *C* represents the thermal energy that the material can accumulate:

$$C = m\,Cp \quad \text{Eq. (5)}$$

The masses *m* of the air volumes represented by the horizontal node, by the vertical node, air junction node, of the internal back panel node and of the product are 0.005, 0.01, 0.004, 0.16 and 7 kg, respectively. The specific heats of air, of the internal back panel and of the product are 1005, 890 and 4100 $J \times kg^{-1} \times K^{-1}$, respectively.

2.2. Entire model

The model presented in Figure 2 was duplicated for each of the 13 shelves, and heat transfer through the top and bottom panels were added. The lowest shelf (analogous to the vegetable box on a domestic refrigerator) was also added to obtain the entire model.

3. IDENTIFICATION OF PARAMETERS

Two parameters are required in order to close the problem: the horizontal airflow distribution and the convective heat transfer coefficient associated to the vertical airflows of non-homogeneous mass flow rate. As explained previously (cf. end of section 2.1.1), these parameters were determined from simple CFD simulations and experimental data.

3.1. Horizontal airflow distribution

The airflow distribution was obtained by a CFD simulation that was compared against experimental data to evaluate the possibility to generalise light (2D) computational approaches in future systematic analyses of parametric influences.

3.1.1. Horizontal airflow distribution by CFD simulation

The CFD model developed to determine the distribution of the airflow between the shelves is 2D, with the boundary conditions summarized in Table 2. The mesh comprises more than 1.9 million cells.

Table 2 : Boundary conditions for the refrigerated cabinet airflow model

Boundary	Thermal specification	Mass flow rate	Pressure
Fan inlet			101325 Pa
Fan outlet	$T_{out} = T_{in}$	$\dot{m}$ = 0.014 $kg \times s^{-1}$	ΔP_{out-in} =0.5 Pa
Top Wall	4.5 W		
Evaporator	-34.5 W		
Bottom Wall	5 W		
Door	25 W		

For a temperature difference between the outside and inside of the cabinet equal to 13 K (T_{ext}-T_{int} = 13 K), conduction heat gains through the walls were calculated and found to be equal to 34.5 W, which was thus the cooling power that was imposed at the evaporator to simulate a steady-state behaviour; as a matter of fact, the thermal time constants are far larger than the air flow time constant, so that the air flow can be analysed in steady-state conditions. The heat gains

can be distributed over three areas (door, top and bottom walls, cf. Table 2) according to their respective conductive resistances. The fan is simulated as a zone of mass flow inlet (into the computational domain) at its outlet, and as a pressure outlet (of the computational domain) at its inlet. The values of these inlet and outlet conditions were set at the operating conditions according to the fan supplier datasheet.

The velocity field predicted by the CFD simulation is presented in Figure 3. A zoom on the fan area exhibits the inlet and outlet of the fan as well as the velocity magnitude on the right. On the left, a symmetry plane cross-sectional view of the whole cabinet shows the flow direction at each inter-shelves channel. The velocity is found to be maximum at channel n°2 and the minimum velocity is observed at the bottom channel (n°14). Moreover, the air velocity decreases rapidly toward the lower inter-shelves channels (increasing index number) so that to a certain extent, if these predicted velocity fields are correct, one can consider that only the first channels are well ventilated.

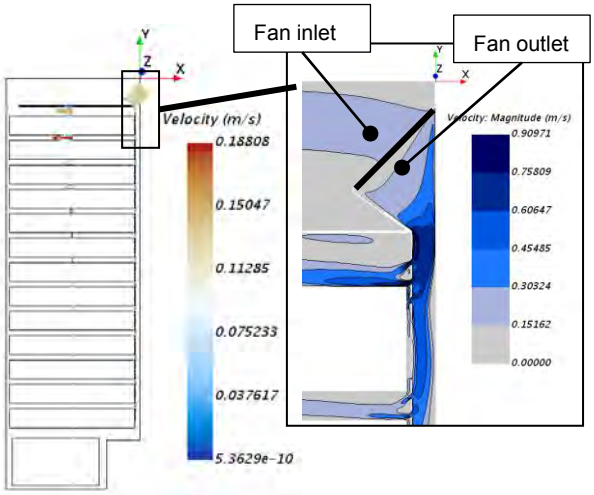

Figure 3 : Predicted velocity field on the vertical symmetry plane of the cabinet loaded with products

3.1.2. CFD simulation vs. experimental results

To confirm the airflow distribution obtained by CFD simulation, experimental measurements were carried out in a closed, ventilated and refrigerated cabinet: a hot-wire anemometer was used to register velocities at different positions along the Z- axis (5 measurement locations) and the X-axis at each inter-shelves channel. Instead of reasoning in terms of velocity, it may be more convenient to use mass flow rates that can be calculated as:

$$\dot{m} = UA\rho \qquad \text{Eq. (6)}$$

Where ρ = 1.24 kg×m^{-3} (density of air) and A = 0.014 m² (cross-sectional area of the airflow between the shelves).

Horizontal mass flow distributions obtained from CFD and experimental measurements are compared in Figure 4: the percentage of the total mass flow is given for all channels (1 to 14). The CFD simulation results overestimate the mass flow rate on the first channels and underestimate others. This overestimation is so large that according to the CFD results, the two first shelves should be crossed by more than 50% of the total fan mass flow rate, while it is of about 20% only. Besides, the experimental mass flow rate distribution appears to be symmetrical and centred at the inter-shelves channel n°7: the mass flow rate is large at the top and at the bottom of the cabinet, and low at mid-height.

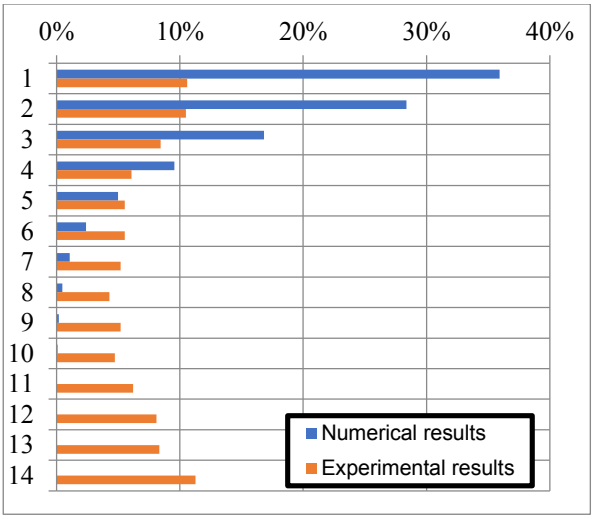

Figure 4 : Percentage of horizontal mass flow rate distribution through the perforated back plate at each inter-shelves channel

The discrepancies between the numerical and experimental results are probably mainly due to the oversimplified 2D description of the geometry, while the actual flow must exhibit non-negligible 3D local effects. The tiny geometrical details of the perforated back plate that is present to help the flow to be distributed homogeneously may also be invoked, as it could not be modelled precisely without drastically increasing the mesh size and computational memory requirements. For the nodal model, the experimental horizontal mass flow rate distribution was used to set the transport resistances. Furthermore, it has been shown experimentally that the temperature difference between the outside and inside of the cabinet has no influence on this distribution.

3.2. Convective heat transfer at vertical airflow

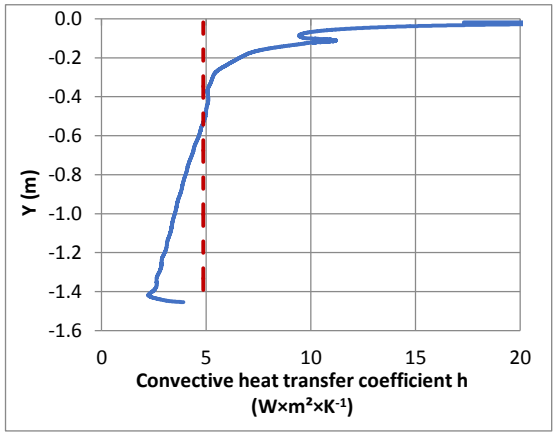

Figure 5 : Convective heat transfer coefficient at the evaporator/back vertical airflow boundary along the Y-axis (local values in blue, mean value in red) obtained by CFD simulation with experimental horizontal airflow distribution.

A huge amount of engineering tools (correlations, models) are available to determine the convective heat transfer coefficient of a fluid flow at a constant mass flow rate along a duct. However, such tools are not applicable when the mass flow rate is not constant, which is the case of the vertical airflows: at the front door, the mass flow rate increases along the upward direction because of the air input from each channel formed by the shelves. At the back plate, the mass flow rate decreases along the downward direction (output of air to each horizontal channel formed by the shelves). To evaluate the effect of non-constant airflow distribution on the local heat transfer coefficient, the CFD simulation was run for the same conditions as previously (cf. Table 2) but by imposing the experimental airflow distribution as the mass flow rate has a major impact on the convective heat transfer coefficient. The computed vertical profile of convective heat transfer coefficient along the vertical back plate is plotted on Figure 5. The heat transfer coefficient is higher at the top than at the bottom of the evaporator because of the higher mass flow rate. The mean value of the convective heat transfer coefficient at the vertical airflow/evaporator boundary is h = 4.8 W×m^{-2}×K^{-1} (Figure 5). Finally, for the sake of simplicity and as the variations are not extremely strong except at the entrance region (i.e. over about only 10 cm while the total height is 1.5 m, cf. Fig. 5), it was decided that this mean value would be taken to describe the convection at the vertical airflow boundary.

4. RESULTS

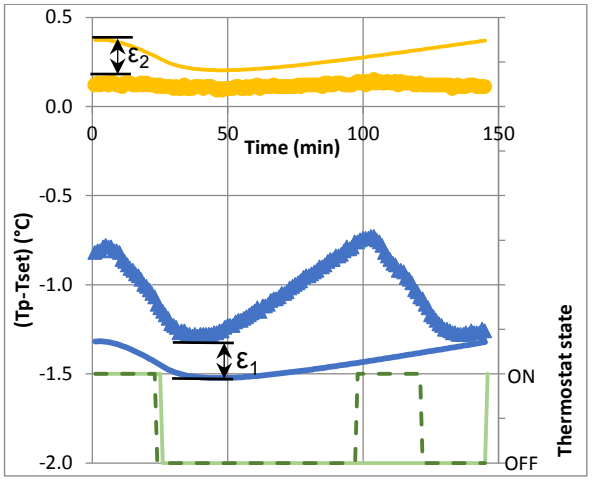

Figure 6: Dynamic temperature differences between product and the set value in reaction to the refrigeration system state for the coldest and the warmest products - Comparison of experimental/numerical values for (T_{ext}-T_{int}) = 13 K
Legend: *Tp,min* numerical; *Tp,max* numerical; *Tp,min* experimental; *Tp,max* experimental; Num. thermostat state; Exp. thermostat state

With all the resistances and thermal inertias defined previously, and taking into account the value of the installed cooling capacity (Q = 150 W), the time evolution of the temperatures can be computed. The cooling capacity is set to Q when the thermostat is ON (contact closed) and to zero when it is OFF (contact open). Figure 6 shows the dynamics of experimental and numerical temperature variations for (T_{ext}-T_{int}) = 13 K, for the coldest and warmest products. The absolute error between the numerical and experimental data at the time when the coldest product reaches the minimum temperature value is ε_1 = 0.23 K. The maximum error for the warmest product is of ε_2 = 0.22 K (Figure 6). Interestingly, there is always a delay (of a few minutes) between the instant when the state of thermostat changes (from ON to OFF or from OFF to ON) and the moment when the temperature of the air starts to increase or decrease, respectively. This is due to the thermal inertia of the internal back panel in contact with the evaporator itself that absorbs (or releases, respectively) heat to the circulating air. This is also a clue to justify that the air flow analysis can be done in steady-state (cf. section 3.1): the thermal

time constants are much larger than the air flow time constants.
The predicted and measured values are in reasonably good agreement with respect to the experimental uncertainties and to the necessary simplifications of the nodal model. Figure 7 shows the differences between the set point temperature and the time-averaged product temperature for different outside to inside temperature differences (13, 18, 23 and 28 K). Whatever the outside to inside temperature difference, products located at the front (left side) are warmer than those located at the back (right side). The coldest product is always located at the level of the 9th or 10th shelf, whatever the outside to inside temperature difference. When the temperature difference increases, the location of the warmest product shifts from the top to the middle shelf. It can be observed on Figure 7d that the maximal and minimal product temperatures are located in the same zone (shelves n° 8-9), where the temperature difference between the front product and the back product is the highest: this must be related to the lower shelf ventilation that was observed at this location (Figure 4).

a)

0.70	0.52
0.68	0.22
0.67	-0.04
0.67	-0.26
0.62	-0.49
0.56	-0.70
0.54	-0.84
0.54	-0.93
0.41	-1.06
0.35	-1.08
0.26	-1.07
0.17	-1.00
0.20	-0.74
0.22	

b)

0.78	0.54
0.80	0.17
0.82	-0.15
0.85	-0.41
0.81	-0.70
0.76	-0.94
0.76	-1.11
0.79	-1.19
0.64	-1.35
0.58	-1.36
0.47	-1.33
0.38	-1.21
0.43	-0.84
0.47	

c)

0.86	0.56
0.90	0.12
0.96	-0.26
1.02	-0.57
0.99	-0.90
0.95	-1.19
0.98	-1.38
1.03	-1.46
0.86	-1.64
0.81	-1.64
0.69	-1.58
0.58	-1.42
0.66	-0.94
0.73	

d)

0.93	0.57
1.01	0.06
1.09	-0.37
1.19	-0.72
1.17	-1.11
1.14	-1.44
1.19	-1.64
1.27	-1.72
1.08	-1.92
1.03	-1.90
0.90	-1.83
0.78	-1.62
0.88	-1.03
0.99	

Figure 7 : Comparison of differences between mean product and set point temperatures (($Tp - T_{int}$), expressed in K) depending on the outside to inside temperature difference: a) ($T_{ext} - T_{int}$) = 13 K, b) ($T_{ext} - T_{int}$) = 18 K, c) ($T_{ext} - T_{int}$) = 23 K, d) ($T_{ext} - T_{int}$) = 28 K

5. CONCLUSION

Refrigerated cabinets can be the source of significant energy consumption while the homogeneity of the temperature field conditions the quality of the preservation of the perishable products it contains. This is why efforts to improve the efficiency of refrigerated cabinets are always desirable. Numerical simulation can be a useful tool to test the influence of various operating parameters. The main objective of the present communication was to report on the development of a nodal model to simulate the dynamic behaviour of a refrigerated cabinet containing food products. While some parameters can be calculated from classical tools for thermal analysis, some others (essentially the main features of thermohydraulics in the enclosure, i.e. mass flow rate distribution and local heat transfer coefficients) were expected to be based on a simple 2D CFD simulation. It was however shown that this oversimplified model was not sufficient, and that experiments concerning the air velocity were needed to better represent the thermohydraulics in the ventilated cabinet.
The numerical results obtained by the nodal model were compared to experimental data. The absolute error for local, maximum and minimum product temperatures (resulting from the ON/OFF control) is less than 0.23 K, which is within the experimental uncertainty. The product temperature distribution, that exhibits a certain stratification, was determined numerically for different outside to inside temperature differences. The results highlighted that the inhomogeneity of the temperature distribution increases with the outside to inside temperature difference.
For perspectives, the thermal nodal model could be coupled to a model of the refrigerating unit to analyse the parameters influencing the energy consumption of the cabinet. In such an overall model, humidity could also be taken into account as latent heat load may be the origin of a significant part of the energy consumption.

NOMENCLATURE

A	Area (m^2)
C	Thermal inertia ($J \times K^{-1}$)
Cp	Specific heat ($J \times kg^{-1} \times K^{-1}$)
h	Convective heat transfer coefficient ($W \times m^{-2} \times K^{-1}$)
L_c	Characteristic length (m)
m	Mass (kg)
$\dot{m}$	Mass flow ($kg \times s^{-1}$)
Nu	Nusselt number
Q	Heat Power (W)
R	Thermal resistance ($K \times W^{-1}$)
Re	Reynolds number
S	Heat exchange surface area
T	Temperature (K)
U	Velocity ($m \times s^{-1}$)
w	Thickness (m)

Greek letters

λ	Thermal conductivity ($W \times m^{-1} \times K^{-1}$)
ρ	Density ($kg \times m^{-3}$)
ν	Kinematic viscosity ($m^2 \times s^{-1}$)

Subscripts

a	Transport by airflow
b	Back
c	Central
cd	Conduction
cv	Convection
d	Door
ext	External
f	Front
h	In horizontal direction or with horizontal airflow
in	Inlet
int	Internal
j	Airflow junction
l	Lateral (side) panel
out	Outlet
p	Product
v	In vertical direction or with vertical airflow

REFERENCES

Alfaro-Ayala, J. A., Uribe-Ramírez, A. R., Minchaca-Mojica, J. Isaac, J. I., Ramírez-Minguela, J., Alvarado-Alcalá, B. U., López-Núñez, O. A., 2017. Numerical prediction of the unsteady temperature in a cooling cabinet. International Journal of Refrigeration(73), 235-245.

Bayer, O., Oskay, R., Paksoy, A., Aradag, S., 2013. CFD simulations and reduced order modeling of a refrigerator compartment including radiation effects. Energy Conversion and Management(69), 68-76.

Belman-Flores, J. M., Gallegos-Muñoz, A., 2016. Analysis of the flow and temperature distribution inside the compartment of a small refrigerator. Applied Thermal Engineering(106), 743-752.

Belman-Flores, J. M., Barroso-Maldonado, J. M., Rodríguez-Muñoz, A. P., Camacho-Vázquez, G., 2015. Enhancements in domestic refrigeration, approaching sustainable refrigerator - A review. Renewable and Sustainable Energy Reviews(51), 955-968.

Cemagref and ANIA. (2004). La chaîne du froid du fabricant au consommateur: Résultats de l'audit. Revue Générale du Froid (1042), 29-36.

Ding, G.-L., Qiao, H.-T., Lu, Z.-L., 2004. Ways to improve thermal uniformity inside a refrigerator. Applied Thermal Engineering(24), 1827-1840.

Gupta, J. K., Ram Gopal, M., Chakraborty, S., 2007. Modeling of a domestic frost-free refrigerator. International Journal of Refrigeration(30), 311-322.

Laguerre, O., Flick, D., 2004. Heat transfer by natural convection in domestic refrigerators. Journal of Food Engineering(62), 79-88.

Laguerre, O., Ben Amara, S., Moureh, J., Flick, D., 2007. Numerical simulationof air flow and heat transfer in domestic refrigerators. Journal of Food Engineering(81), 144-156.

Laguerre, O., Hoang, M. H., Flick, D., 2012. Heat transfer modelling in a refrigerated display cabinet: The influence of operating conditions. Journal of Food Engineering(108), 353-364.

Leung, C. W., Chan, T. L., Probert, S. D., Kang, H. J., 1999. Forced convection from a horizontal ribbed rectangular bas-plate penetrated by arrays of holes. Applied Energy(62), 81-95.

Rohsenow, W. M., Hartnett, J. P., Cho, Y. I., 1998. Handbook of heat transfer. McGraw-Hill.

Manuscript ID: 273
DOI: 10.18462/iir.icr.2019.0273

Energy Performance of Industrial Cold Storage Facilities

Andy PEARSON

Star Refrigeration Ltd, Thornliebank Industrial Estate
Glasgow, G46 8JW, United Kingdom, apearson@star-ref.co.uk

ABSTRACT

The objective of this paper is to facilitate improvements in energy efficiency of cold stores.

Over the last twenty five years several studies of energy performance have shown that the operation of a low temperature cold store of an industrial size typically requires about 30kWh per m^3 per year but in each study a very large variation in performance is noted, ranging from less than half of the nominal figure to more than five times higher.

This paper reviews the previous literature and adds performance data from a number of stores utilising a range of energy saving techniques. Opportunities for improvement in existing facilities are discussed and design guidance for new facilities is provided.

The paper concludes with a review of the ways in which store operators can track their energy performance, including methods of justifying additional expenditure on energy saving opportunities.

Keywords: Refrigeration, Cold Stores, COP, Evaporators, Energy Efficiency.

1. INTRODUCTION

The increasing cost of energy worldwide, coupled with national and international pressures to reduce carbon emissions have created an unprecedented demand for energy efficiency in the cold chain. This is matched by a variety of new monitoring and control technologies which offer the means to manage electrical usage but to date these measures do not seem to have been effective in the main. There appear to be several reasons for this lack of uptake.

2. FACTORS AFFECTING COLD STORE EFFICIENCY

There is not a universally recognised definition of cold store efficiency – sometimes the term is used in a very specific manner to relate to the condition of the fabric or the operating effectiveness of the equipment but in other cases it is generally used to indicate business performance. It can be difficult to relate this back to equipment operation. The general definition used in this paper is operating output divided by required input. When looking specifically at equipment, such as compressor performance, this might be cooling capacity divided by electrical input, for the building as a whole it could be product throughput divided by cost of operation. The general principle is that efficiency is benefit divided by cost; where it is not obvious from the context the measure of efficiency will be stated each time.

2.1. Building Utilisation

It is obvious that the resource input to building operation is a factor of how busy it is but this measure is not often used in analysis of possible performance improvements. Business managers need to know the cost of operation in order to ensure that their service charges are sufficient and to know where their break-even point lies. However, operators and maintenance teams often do not see this type of information and may have no way of accounting for it in their assessment of system performance. This is unfortunate because it can lead to a fatalistic attitude about performance improvement or can mask the effects of improvement initiatives. A suitable metric in

this case is product movement per kWh or per energy cost. A useful surrogate would be to count the number and duration of door openings by monitoring their drive mechanisms and to track openings per kWh.

2.2. Weather

Another factor which can often be viewed fatalistically is the effect of weather on system performance. Hot weather makes the compressor discharge pressure higher and also increases the cooling load through solar gain and air ingress. Since the air carries moisture with it this is a double blow – the additional heat load imposed by the moisture is far greater than the sensible heat of the dry air, and since the moisture has to be removed by a defrost process the energy penalty is doubled again. Consider the following table of enthalpies, for a dry bulb temperature of 25°C.

Table 1. Enthalpy of moist air

Dry bulb (°C)	25	25	25	25	25	25	25	25	25
Wet bulb (°C)	20	15	10	5	0	-5	-10	-15	-20
Enthalpy (kJ $kg^{-1}K^{-1}$)	57.22	41.75	29.04	18.44	12.55	4.89	-1.65	-7.42	-12.65
Latent portion	92.3%	90.3%	87.7%	84.2%	81.2%	75.1%	65.4%	47.3%	0.0%

The figure of "latent portion" in Table 1 is the proportion of the total cooling load attributable to the moisture content when cooling the air to -20°C. The enthalpy of saturated air at -20°C is -18.48 kJ $kg^{-1}K^{-1}$ so when there is no latent portion to the heat load the cooling requirement to bring air from 25°C is 5.83 kJ $kg^{-1}K^{-1}$. Despite the very heavy burden placed on refrigeration systems by moisture leaking into the cold room through open doors or badly fitting seals many systems operate with significant moisture ingress and consequent high energy use. It should be noted that the wet bulb temperature is usually within 5 degrees of the dry bulb, so the latent portion is typically more than 93% of the total heat load due to moist air ingress.

The cold store owner can take action against the weather. Heat reflective surfaces can reduce the solar gain, as shown in Fig. 1, which is taken from the Institute of Refrigeration's Cold Store Code.

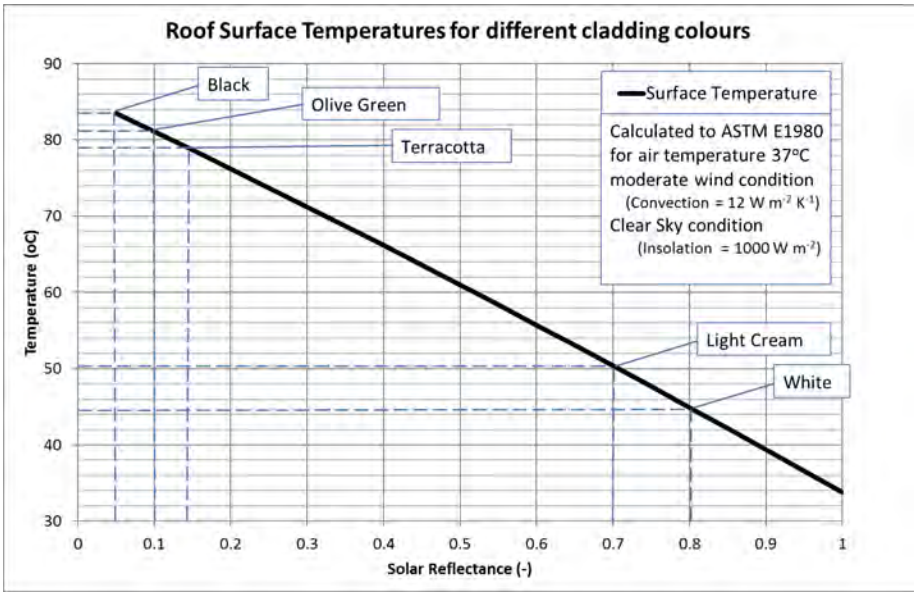

Figure 1: The effect of surface colour on roof surface temperature (IOR, 2016)

If moisture ingress through open doors cannot be prevented, for example due to the very high utilisation of the building, then there is some merit in dehumidifying the loading docks in order to minimise the impact of the imposed heat load on the plant. It is not necessary to cool the air after dehumidification provided the dew point is low enough. If the air coming into the store is very dry but at 30°C or higher, the heat load will still be substantially less than that from the moist air. The

energy required to run the dehumidification will also be far less than that required to freeze the moisture and then defrost it again.

2.3. Building fabric condition

The problem of moisture ingress is greatly exacerbated if the doors do not fit to the frame, the trucks are not sealed to the dock or the door mechanism is broken and fails to close properly. These failures allow ambient air, carrying moisture, to flow into the refrigerated space. It is rare to find gaps in the seams of an insulated box allowing air and moisture to pass through because the gap usually blocks quickly with ice, but if water gets into an insulated panel it destroys the mechanical integrity of the unit and also reduces the insulating properties significantly. The thermal conductivity of ice (2.4 W $m^{-1}K^{-1}$) is about one hundred times higher than that of typical polyisocyanurate insulation panels (0.025 W $m^{-1}K^{-1}$) so will greatly increase the heat load on a refrigeration system. Although a store operator cannot control the weather, they have total control of the condition of their building and the way in which it is used.

2.4. Building and process management

When a cold store is handling large amounts of chilled or frozen product the temperature of the incoming goods can impose a substantial additional load, up to 50% of the total heat load. Ideally the product load should be zero because the produce should already be down to temperature before arriving in the store. In a short term store where the produce is only held for a day or two the effect of warm incoming product may be less because it does not stay in storage long enough to come down in temperature, particularly if the pallets are tightly stacked. In this case the pallets when despatched from the store will still be warmer than the required temperature. For longer term storage, where the product is held for more than a week, the additional load on the plant is more significant because the product has time to cool down to store temperature.

Control of door operation is also key to minimising load, as described above. The length of door opening is significant because it takes between 10 and 15 seconds for full airflow to be established. It is not usually feasible to have a door opening time of less than 20 seconds, but every effort should be made to keep the opening time as short as possible. Airlocks, fast acting double doors and dehumidified vestibules can be used to reduce air and moisture ingress. Air curtains tend to be very much less effective even when set up correctly, particularly in a cross-dock application. The slightest variation in pressure across the building is enough to destroy the effect of the air curtain.

2.5. Refrigeration plant condition

If the factors above are properly taken into consideration then the external load on the system will be reduced to the minimum feasible, but if the refrigeration system is not kept in good condition then the building efficiency (product throughput divided by cost of operation) will still be low. Worn and damaged compressors will be less effective than their as-new condition. They require the same power input to run as when new, but produce less refrigerating effect so the length of time in operation increases. Another major cause of inefficient operation is internal heat leakage within the system. This could either be the direct leakage of high pressure gas to the low pressure side of the system, for example during defrost or through a faulty hot gas bypass or defrost valve, or it could be indirect; the transfer of heat from warm side to cold side without gas leakage, for example if a suction/liquid heat exchanger is oversized or is controlled incorrectly. A special case of direct internal heat leakage is when the liquid seal at the expansion device is lost and high pressure gas passes through the valve with the liquid. Non-optimal defrost timing (too frequent or not enough) is another case of internal heat leakage and dirty evaporators have the same effect as insufficient defrosting. One of the biggest causes of wasteful operation of cold store plant is the way in which it is controlled, either because inappropriate set points are used or because the control system design was not good from day one.

2.6. Compensating Factors

Even if the plant is not in the best condition and the loads are not minimised, a store operator can invest in infrastructure to improve performance. The addition of photovoltaic solar panels to the roof of a cold store has the double advantage of shading the roof from direct sunlight and

generating some power when the sun shines. The effect can be enhanced by linking the solar panel output to the store set point, lowering the temperature when the output is high and raising it if the output drops. Until recently this would not have been economic but the lower cost of solar panels and increasing electricity cost has made it more attractive and government incentives may also be available locally.

2.7. Cost avoidance measures

Several technical systems to link cold store energy use to grid supply have been introduced in recent years. These tend to track either the cost of electricity on a variable tariff, or the grid load factor, by detecting very small changes in supply frequency. If the grid load increases beyond the generation capacity then the mains frequency reduces and this can be used to trigger the same type of offset action described in 2.6, or it can be used to shut down the refrigeration plant completely. Since the frequency response system requires a very rapid response and a significant step reduction, the complete shutdown of the plant is preferred. This is of course subject to the store temperature being within an acceptable band. An innovative control system implemented on a national basis in the Netherlands (Van der Sluis, 2014) sought to compensate for the intermittency of wind-generated electricity by loading and unloading large cold stores across the country in order to create a better match between instantaneous demand for power and available generating capacity. In a simple version of this system the matching was achieved simply by using the spot price for electricity to drive the store temperature control.

3. REVIEW OF PREVIOUS INFORMATION

In the mid 1990s several studies reported on what was perceived to be “best practice” in the energy performance of industrial refrigerated storage. The Energy Technology Support Unit in the United Kingdom identified a best practice benchmark of 30 kWh m^{-3} yr^{-1} for large stores (above 100,000 m^3) with higher specific consumption in smaller stores (ETSU, 1994). A similar study in the Netherlands (Bosma, 1995) indicated consumption in the range 34 to 120 kWh m^{-3} yr^{-1}.and this figure was confirmed by a study conducted on behalf of the International Institute of Refrigeration in 2002 (Duivan and Binard). More recently a pan-European review project called “Improving Cold-store Equipment in Europe” (ICE-E) surveyed over 300 stores and considered information from a further 500 sites (Evans et al, 2013). Although these studies present different metrics it is useful to compare them all using the method originally adopted by ETSU in their 1994 survey, reporting the energy in kWh of electrical input to the site per annum divided by the cubic volume of the refrigerated space. This is known as the “specific energy consumption” (SEC). Several of the studies are unclear about whether the energy figure reported is for the whole site or only for the refrigeration system but it is generally acknowledged that the refrigeration plant will be responsible for about 70% of the total site energy use, so with the wide range of values reported it can be seen that to a large extent the location of the electrical meter (whether it is only recording usage for the refrigeration plant or for the whole building) is somewhat irrelevant as the difference is less than the variation from site to site.

A common shortcoming of all of the previous studies mentioned above is that they did not make any assessment of how effective the systems were at achieving their primary goal, which is to maintain the space at a desired temperature. It is assumed that all the buildings are doing sufficiently well in this respect but practical experience of conducting energy audits on site suggests that this is often not the case. It is important to understand this key point because one of the best ways to reduce energy requirements for a store is to raise the temperature setpoint. This is only feasible if the store temperature setpoint is being achieved. Sometimes the temperature target is set lower than necessary in order to provide a perceived buffer against unreliable operation. The first step in improving energy performance in this situation is to give the store operator confidence in the resilience of the operation. Only then can the comfort factor of lower temperature be reduced or removed.

The European study reported by Evans et al (2013) provides equations for the average of energy performance per year for cold stores, chill stores and mixed use stores. These equations are

For chill stores $E = 64.535V - 148235$ Eq. (1)

For cold stores $E = 374.93V^{0.8173}$ Eq. (2)

For mixed stores $E = 480.28V^{0.7846}$ Eq. (3)

where E is the energy used per year in kWh and V is the store volume in m^3. The form of these equations suggests that for chill stores the specific energy use is not affected by volume (when the researchers used a non-linear curve fit it did not improve the curve fit regression) but that for cold and mixed stores larger volumes require less specific energy use.

The effect of the power law in the best fit curves from Eq (2) and Eq. (3) means that these curves follow the general shape of the ETSU curve. However, the chill store curve requires further investigation. The curve proposed by Evans et al as the average energy use for chill stores is linear, of the form y = mx+c, where in the case of Eq. (1) the constant, c, is a negative number. This is the best fit to the data collected, but it does not make sense when applied to very small stores as it suggests that there is a certain size of room for which the energy use is zero and for smaller rooms the energy "use" would be negative. This is clearly not physically possible, so the true best fit curve
would likely have a positive constant and a slightly shallower gradient. Similar consideration of Eq. (2) and Eq. (3) suggests that they also should have a positive constant. For the purposes of this analysis a positive baseload of 100,000 kWh per year is applied to all three equations, using the same indices as in the Evans et al paper. Fig. 2 shows the benchmark guidance published by ETSU and the three curves for the ICE-E averages with the modified baseload. The ICE-E study was extended and updated by Evans et al in 2015, with 44% more data. The 2015 update did not fundamentally change the observations although it showed that geographical location was not a particular factor in the average or range of SEC indicated.

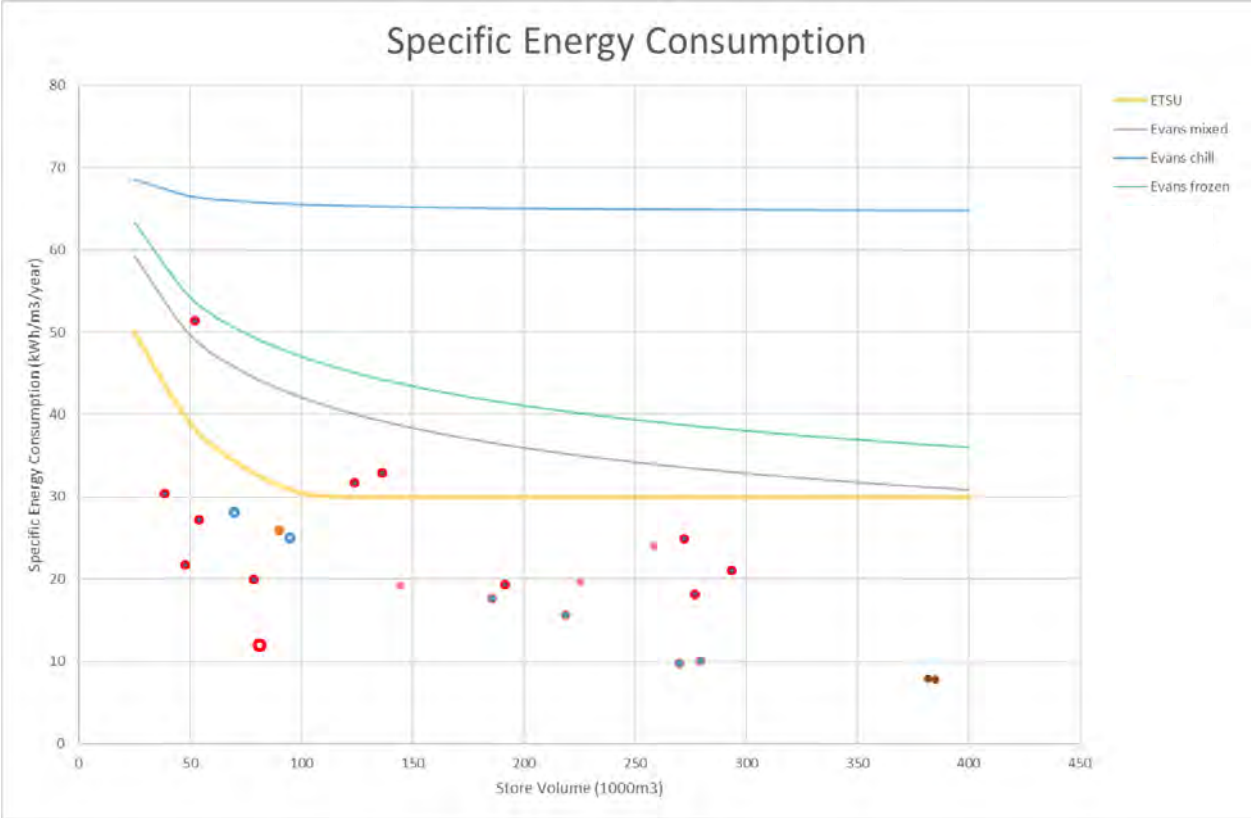

Figure 2: Specific Energy Consumption under various scenarios and for a number of sites

4. ANALYSIS OF RECENT ENERGY MONITORING

It must be remembered that the ETSU line in Fig. 2 represented what was perceived to be "best practice" back in 1994 and the three ICE-E lines represent the averages from about 300 sites across Europe fifteen years later. The points plotted in Fig. 2 represent actual electrical usage on

21 sites in the UK, most of which are managed under a common maintenance regime with a strong focus on energy performance and continuous improvement. The data presented as solid dots is for 2017 with energy use recorded on a daily basis and aggregated for the year. In all cases the figure reported is only for the refrigeration system including ancillary loads such as evaporator and condenser fans, glycol pumps and electric heaters. The energy use was metered at the individual refrigeration units, not for the site as a whole. Some specific observations on some of the sites are noted below.

4.1. Pumped ammonia systems

The two stores on the right of the graph with volumes of approximately 380,000 m^3 were built about five years ago for a UK based supermarket. They are distribution centres with a high daily throughput of chilled product and short term storage of frozen goods. These are the type of operation described in the ICE-E project as "mixed". Great care was taken in the design of the system to minimise the possibility of wasteful operation. For example the expansion valve control enables the discharge pressure to be as low as the ambient temperature will permit and the defrost system (hot gas) eliminates the possibility of heat leakage. Dock doors to the cold store are dehumidified and there is a detailed review of energy performance on a monthly basis. These stores are achieving a specific energy consumption of less than 8 kWh m^{-3} yr^{-1} based on 2017 data, excluding non-refrigeration uses such as office lighting, vehicle washing and fork truck charging.

4.2. Ammonia/Carbon dioxide cascade systems

The two stores to the right of centre on the graph with volumes of approximately 275,000 m^3 use an ammonia/carbon dioxide cascade system and were built about ten years ago. They have a SEC of about 10 kWh m^{-3} yr^{-1} based on 2017 data, excluding non-refrigeration energy use. These plants use hot gas defrosting of the CO_2 evaporators with screw compressors on the carbon dioxide circuit for the cold store, pumped CO_2 fed to chill evaporators and a low charge ammonia system with screw compressors and evaporative condensers rejecting heat to ambient.

4.3. Low charge Ammonia systems

The result of recent developments in low charge systems can be seen in the graph. The two data points represented as blue circles on the left of the graph represent data collected in 1995 for comparison with the ETSU guide (Pearson, 1996). These stores were considered at that time to be "better than the best" of the sites surveyed for ETSU but this design has been subsequently improved. The 1995 figures can be compared with a smaller store, installed in 2018 with a volume of 81,000 m^3 and an initial estimated SEC of 12 kWh m^{-3} yr^{-1}. This new store is represented in Fig. 2 as a red circle. The main developments of these low charge systems between 1995 and now have been in evaporator design and compressor control but it is also notable that the newer systems use air-cooled condensers and allow the compressor discharge pressure to drop low in cold weather. This makes the air-cooled system cheaper to operate on an annualised basis than an evaporative condenser as reported by Clark and Gillies (2014).

4.4. Secondary refrigerant systems

Some of the stores displayed use glycol as a secondary refrigerant for the chill store part of the distribution centre and direct ammonia for the cold stores. The energy penalty paid is that the glycol pumps run all the time to provide cooling and can sometimes use more energy in aggregate than the compressors which cycle on and off from time to time. Two stores of this type are shown with volume of 145,000 m^3 and 225,000 m^3, both with SEC of about 19.5 kWh m^{-3} yr^{-1}. This is about the same as the old low charge system although the smaller store with the secondary system is about half the size. Much lower SEC can be achieved with extensive use of variable speed drives on pumps and fans and by using waste heat for defrost instead of electric heaters (Gillies, 2014)

4.5. Discussion of the various systems

The large pumped ammonia systems described in 4.1 are considered to be as good an example of efficient operation as can at present be achieved with this type of system. They embody many of

the load reduction techniques mentioned in sections 2.1 to 2.4 and the building fabric is well maintained. The cascade systems described in 4.2 achieve comparable performance but the glycol system in 4.4 is less efficient because of the effect of the glycol pump power and the defrost system. Taking the scope for improvement in some of the older, smaller systems covered by this survey a revised estimate of what could be considered “best practice” in 2019 was created. This was done by fitting a curve to estimated energy figures for a range of sizes and then calculating SEC for the model results. This curve is not as flat as the ETSU best practice curve from 1994, showing some economy of scale for larger stores. It is believed that the sites surveyed in 1994 were not as large as some of the modern stores included in the present survey as the largest site referenced in the 1994 study was just under 250,000 m^3. This may mean that the 1994 guidance was inaccurate for larger stores.

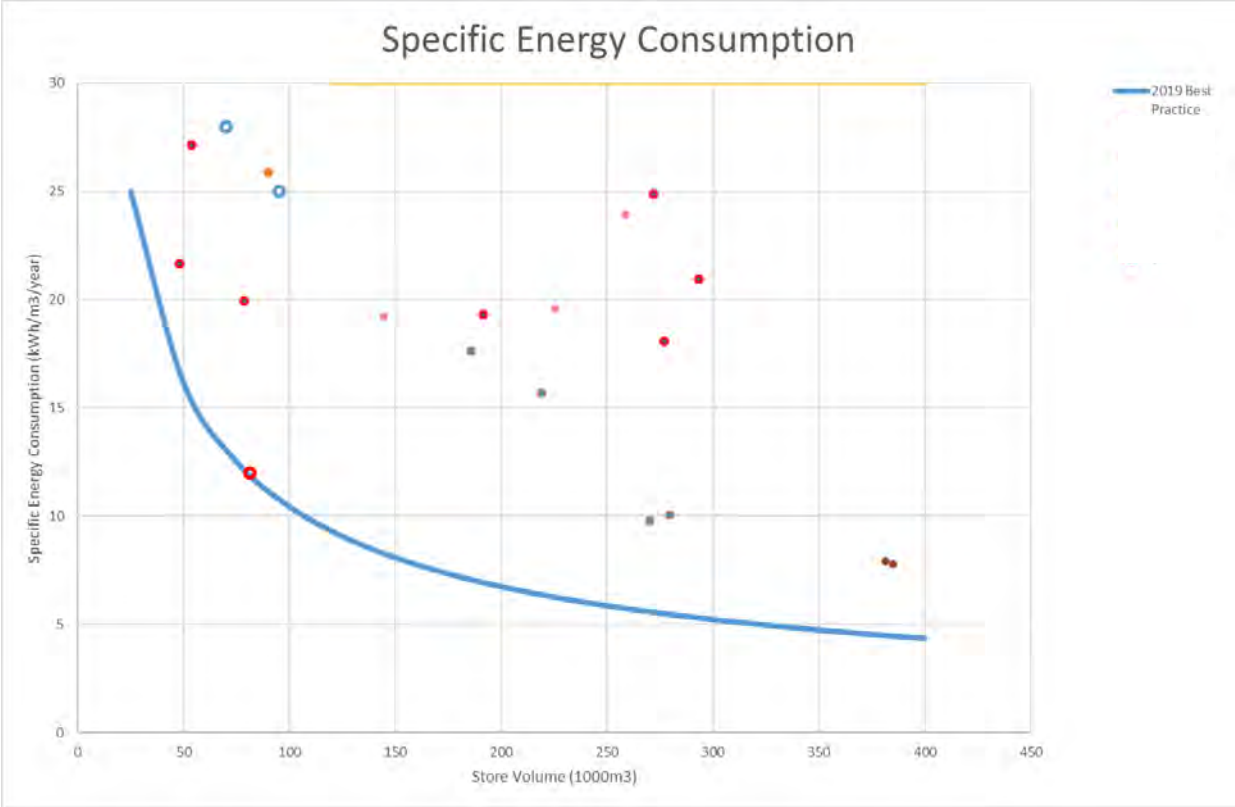

Figure 3: Proposed Best Practice Curve for modern cold and chill stores

The curve fitted to the kWh per year consumption graph has a power form, given by

$$E = 15500V^{0.37} \qquad \text{Eq. (4)}$$

When the resultant figures for annual energy use are plotted as specific energy consumption the curve in Fig. 3 is obtained. The SEC curve is given by equation (4) divided by the volume, V, so

$$SEC = E/V = 15500V^{-0.63} \qquad \text{Eq. (5)}$$

5. CONCLUSIONS

Analysis of some recent installations indicates that the reported levels of energy efficiency for cold and chill storage can be significantly improved. A new curve for best practice performance is proposed which aims at an energy use level in large facilities which is about 15% to 30% of the generally accepted figure from 25 years ago. This level of performance cannot be achieved by retrofitting bolt on equipment to an existing system which was not designed to target this level of efficiency. Many of the techniques required to achieve the new benchmark, such as the method of defrost, the type of condenser and the control of compressor operation need to be designed into

the plant from the start. It is also evident from the study that energy use is adversely affected if the system is too small for the duty imposed. The result is that the compressors run continually and the target temperature is not reached. The solution in this case may be to take much tighter control of the operation of the business to ensure that product load is minimised, ancillary loads are eliminated wherever possible and product movement is more tightly controlled, including the temperature of goods entering the store. There is scope for further investigation to determine separate best practice curves for chill and cold storage operations. Other electrical loads on site also require a more detailed analysis to confirm what proportion of the total electricity bill is attributable to refrigeration.

Cold store operators are encouraged to include the volume of their store in their measurement of energy consumption, using the SEC metric at all times, otherwise it is impossible to say whether the figure is good, bad or indifferent. For a 50,000 m^3 cold store an SEC of about 16 kWh m^{-3} yr^{-1}can be considered to be best practice. For a 500,000 m^3 store the SEC could be less than 5 kWh m^{-3} yr^{-1}. The refrigeration system should be fitted with individual power meters for each self-contained module of plant and the electrical usage aggregated on a daily basis to provide an ongoing measurement of performance. This will enable an understanding of energy use, including performance degradation over time and the effect of improvement initiatives on the annualised figures. Where a company has several facilities within their estate the figures should be compared between sites to establish an understanding of relative performance and to highlight the areas of greatest potential for efficiency improvement and cost reduction across the estate.

ACKNOWLEDGEMENTS

The author would like to thank the directors of Star Refrigeration Ltd for their support of this study and permission to publish the results, and all the colleagues who assisted with the collection and analysis of the data.

REFERENCES

Bosma, J. 1995. Inventory study of the energy conservation potential in cold storage installations in the Netherlands. Proc. 19th International Congress of Refrigeration, The Hague vol II, IIF/IIR

Clark, J. and Gillies, A. 2014. Comparison of evaporative and air cooled condensers in industrial applications, Proc. Inst Ref 2014-15, London

Duiven, J. E and Binard, P. 2002. Refrigerated storage: new developments. IIR Bulletin – 2002-2.

ETSU, 1994. Energy Consumption Guide 37: Cold Storage Sector. Energy Efficiency Office, Department of the Environment, Harwell, United Kingdom

Evans, J.A. Huet, J-M. Reinholdt, L. Fikiin, K. Zilio, C. Houska, M. Landfeld, A. Bond, C. Scheurs, M. and van Sambeeck, T.W.M., 2013. Cold Store Energy Performance, Proceedings of the 2nd IIR Conference on the Cold Chain and Sustainability, Paris, IIF/IIR

Evans, J.A. Foster, A. Huet, J-M. Reinholdt, L. Fikiin, K. Zilio, C. Houska, M. Landfeld, A. Bond, C. Scheurs, M. and van Sambeeck, T.W.M., 2015. Specific Energy Consumption Values for Various Refrigerated Food Cold Stores, Proceedings of the 24th IIR Congress, Yokohama, IIF/IIR

Gillies, A. 2014. Efficient Control of Modern Industrial Refrigeration Plant, Proceedings of the 3rd IIR Conference on the Cold Chain and Sustainability, London, IIF/IIR

IIR, 2008. Saving Energy in Refrigeration, Air-Conditioning and Heat-Pump Technology, International Institute of Refrigeration, Paris

IOR, 2016. Cold Store Code of Practice, Institute of Refrigeration, London, part 2 p9

Pearson, S.F. 1996. Ammonia Low Pressure Receivers, Proc. Inst Ref 1995-96, London

Van der Sluis, S.M., Hoogendoorn, E., de Geus, A.C., 2014. "Night Wind" Energy Storage Concept Develops Into A Product: A Cold Store Time Of Use (Tou) Controller, Proceedings of the 3rd IIR Conference on the Cold Chain and Sustainability, London, IIF/IIR

Manuscript ID 275
DOI: 10.18462/iir.icr.2019.0275

Continuous Monitoring of Energy Performance in Industrial Systems

Andy PEARSON

Star Refrigeration Ltd, Thornliebank Industrial Estate
Glasgow, G46 8JW, United Kingdom, apearson@star-ref.co.uk

ABSTRACT

The objective of this paper is to demonstrate improved methods of performance assessment.

Despite recent improvements in computing capability built into refrigeration systems and chillers, coupled with low cost sensor technology, energy performance monitoring of industrial systems remains very basic, limited in many cases to an ammeter on the compressor supply with no trend recording or analysis of whether the measured figure is good or bad. It is even less common to find the energy use integrated over time to give a true picture of the life cycle energy performance of the plant.

This paper identifies and discusses the main barriers which prevent operators from collecting meaningful data on energy performance.

A review of previous efforts is provided, with a summary of their shortcomings, particularly when applied to large industrial systems. Guidelines for cost-effective ways to make better use of energy data are presented.

Keywords: Refrigeration, Energy, Analysis, Fourier Transform, Cold Store

1. INTRODUCTION

The technology for the detailed analysis of refrigeration system operation has been readily available for over forty years but there is a lack of appetite for anything more than the most superficial overview. It is reported that savings of up to 40% of energy use can be achieved on most systems (Evans *et al*, 2013a) and an international overview of a very large number of cold and chill stores indicated that the energy use of the highest consumers could be up to twice that of the lowest, ignoring the top and bottom 10% "outliers" (Evans *et al*, 2013b). Such a large discrepancy cannot be explained by operating constraints alone. The examples in this paper are based on a low temperature cold store but much of the learning could equally well apply to chill stores, food processing plants such as freezers and water or glycol chillers.

2. OVERVIEW OF COMMON SYSTEM FAULTS

There are several common errors which appear time and time again. Some of them are obvious but others are less evident. They are listed here but for the sake of brevity readers are referred to other sources such as the IIR publication "Saving Energy in Refrigeration, Air-Conditioning and Heat-Pump Technology" (IIR, 2008) for more complete analysis of the various faults.

2.1 Failure to minimise the heat load – this could be the result of poor control of doors on the system, poor maintenance of the building fabric or poor control of incoming product temperature.

2.2 Poor compressor control – if the system has several compressors they will usually operate more efficiently when fully loaded. The drive motors will also be more efficient under these conditions. When a plant operates with several fixed speed compressors on low load it will be less then optimally efficient.

2.3 Too low suction pressure – this could be due to incorrect setting of controls, poor evaporator performance or blockages in the suction of the compressors.
2.4 Too high discharge pressure – this could be internal to the system, caused for example by a build up of non-condensibles or it could be external, caused for example by scale build up on condenser tubes. It could also be the result of inappropriate head pressure control on the compressors or poor system design which requires a high head pressure to be maintained at all times.
2.5 Internal heat leakage – this could either be the direct leakage of high pressure gas to the low pressure side of the system, for example during defrost or through a faulty hot gas bypass or defrost valve, or it could be indirect; the transfer of heat from warm side to cold side without gas leakage, for example if a suction/liquid heat exchanger is oversized or is controlled incorrectly. A special case of direct internal heat leakage is when the liquid seal at the expansion device is lost and high pressure gas passes through the valve with the liquid. Another special case is excessive wear and tear on compressors causing an increase of leakage from the discharge side back to suction. This could be caused by tip seal wear in a screw compressor or it could be piston ring wear or discharge valve damage in a piston compressor. Non-optimal defrost timing (too frequent or not enough) is another case.
2.6 Excessive auxiliary power consumption – the most common auxiliary consumers are fans and pumps, which are sometimes run on full power when the plant is lightly loaded or even switched off. Some auxiliary power is essential for trouble free running, for example drain line heaters in a cold store or pumps for an underfloor heater mat. They need to be on all the time but should not be oversized as the excess heat needs to be removed by the refrigeration system. Condenser fan control often gives scope for improvement.

Some faults result in a combination of these root causes. For example if a thermostatically controlled DX system is undercharged then the suction pressure will be low because the evaporator is not receiving sufficient liquid. This will cause the expansion valve to open wider, attempting to reduce the suction gas superheat, but this will cause a loss of liquid seal at the expansion valve, giving the classic symptom of bubbles in the liquid line sight glass upstream of the expansion valve.

3. OVERVIEW OF COMMON EFFICIENCY MEASURES

The ways in which cold store efficiency is assessed vary widely from site to site and must be one of the key reasons for the large variance in energy use.

3.1 Many operators do not have separate power metering for the refrigeration system. It is very difficult to assess the effect of energy saving measures.
3.2 Some systems measure compressor motor current but these readings are not recorded and are generally only useful for diagnosing compressor faults and repair effectiveness.
3.3 Some systems measure kWh energy input and display an instantaneous value
3.4 Some systems aggregate the instantaneous kWh figure to give a daily total which can usefully be displayed as “kWh yesterday” and can be recorded for longer term trend analysis
3.5 Some systems monitor the power factor to ensure that the phase angle between voltage and current is not too large. This may be used in conjunction with power factor correction

It is very uncommon to find any measure of system coefficient of performance as this is notoriously difficult to calculate due to the difficulty of assessing the refrigeration load on the plant. In any event it is a rather unhelpful measurement since a cold store with good door discipline with compressors which run for 12 hours a day and maintains its set temperature will have a lower coefficient of performance (due to the lower operating temperature) than one which has very poor door discipline (suffers from common system fault 2.1 described above), runs for 24 hours per day and fails to achieve the desired temperature. If the only measure of plant performance was compressor CoP then the latter system would appear to be better than the former.

It is also very uncommon to find daily, weekly or annual energy use correlated with business activity although this is relatively easy to do. A business metric relating energy use to production output may be used in management accounts but it is not normal to see it relayed back to the operators and maintenance staff of the refrigeration system to give guidance on what to look for in making improvements. For a cold store the level of activity has a direct effect on energy use. This can either be correlated manually by analysing pallet movements against energy, or it could be approximated by logging the number and duration of door openings and using that as a proxy for pallet movements. Since the doors are controlled electrically it would only require a digital input from each door controller to the refrigeration plant control system to enable this metric, but this is almost never done.

4. PROPOSED METHOD OF DATA ANALYSIS

With modern control systems and sensor technology it is feasible to record key efficiency parameters and store them at relatively high frequency enabling a range of investigations to be conducted. The key is to spot patterns in energy use and then drill down to the root cause of deviations from the expected benchmark performance for the site. In most cases the root cause will be one of the faults listed in 2.1 to 2.6 above. Plant performance is clearly related to weather and product throughput so some method of smoothing the data to account for these is desirable. If weather data is not recorded for the plant it can usually be downloaded from a national climate service, but to account for local effects such as air recirculation it is always better to have the values recorded locally. Measuring wet bulb temperature for evaporative cooling equipment is difficult (although modern sensors are cheaper and more reliable than ever before) so a useful compromise can be to install an ambient temperature sensor close to the condenser, a second ambient temperature sensor in open space away from any external influence and then correlate these two against each other to check for the effects of recirculation and against a national climate service to get a rough indication of the wet bulb depression. An example of climate service data over a three year period is shown in Fig. 1 for a site used in subsequent analysis.

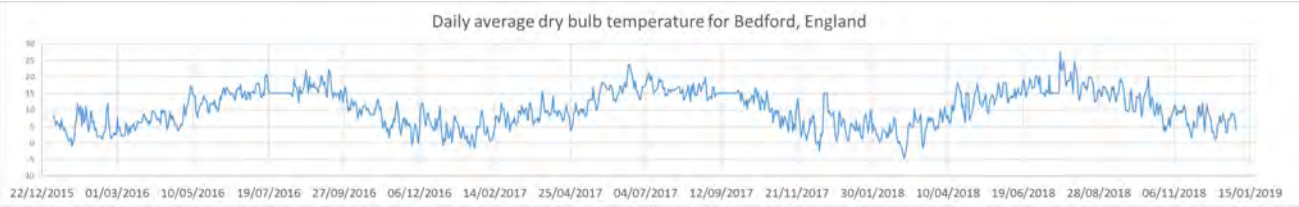

Figure 1: Ambient Temperature Recording

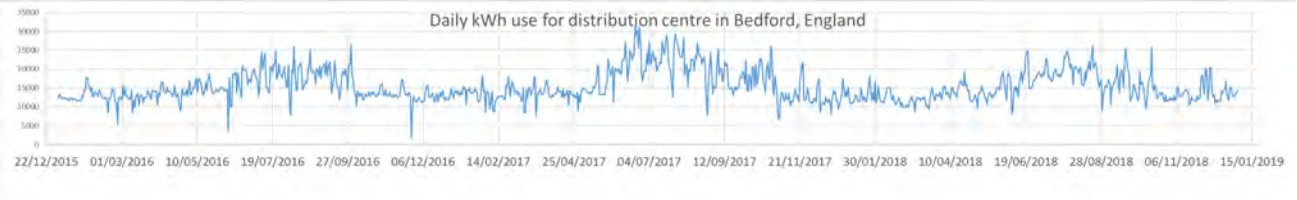

Figure 2: Daily energy use

Comparison of Fig. 1 and Fig. 2 shows that there is some correlation between ambient temperature and kWh use, so these can be correlated in order to calculate a regression as shown in Fig. 3.

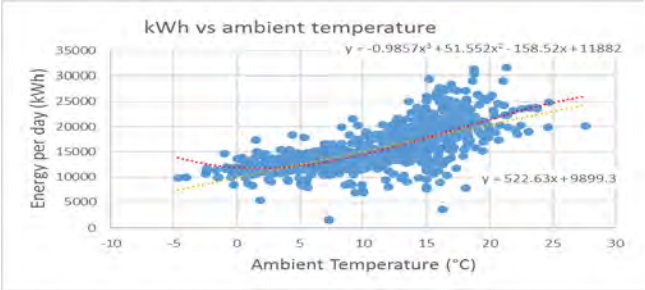

Figure 3: Temperature-Energy correlation

The regression lines in Fig. 3 show that a simple linear regression (the orange line) is sufficient to account for variation in performance due to the weather. The cubic curve fit (the red line) improved the regression slightly but only reduced the standard deviation for this data set from 3096 to 3041. A standard energy per day for a given temperature can be calculated from this equation and subtracted from the actual figure to give a graph of energy discrepancy as shown in Fig. 4.



Figure 4: Daily Energy discrepancy

This is still a great deal of information with many small factors overlaid on each other. For example, one remedial action that was identified from close analysis of the compressor performance in April 2018 was that the volume ratio of the screw compressor had been incorrectly set at some point in the past. An adjustment was made on 27 April and the effect on compressor motor power was very obvious as shown in Fig. 5. The compressor performance is also shown in Figs. 6a, 6b and 6c, giving the performance over a two week period in October 2017, April 2018 (when the adjustment was made) and December 2018. The improvement is evident in Fig. 6b and seems to have been sustained, but this is not obvious from the overall site performance, even allowing for weather conditions as shown in Fig. 4.

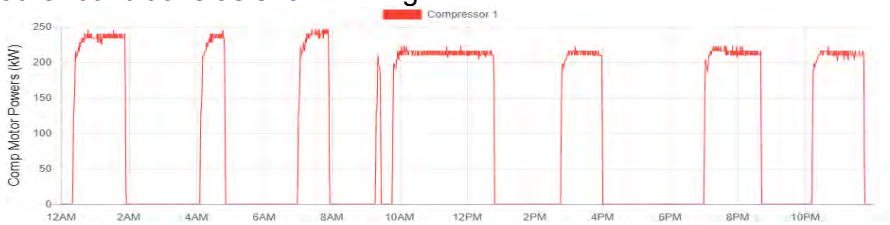

Figure 5: Motor Power showing the effect of Vi adjustment

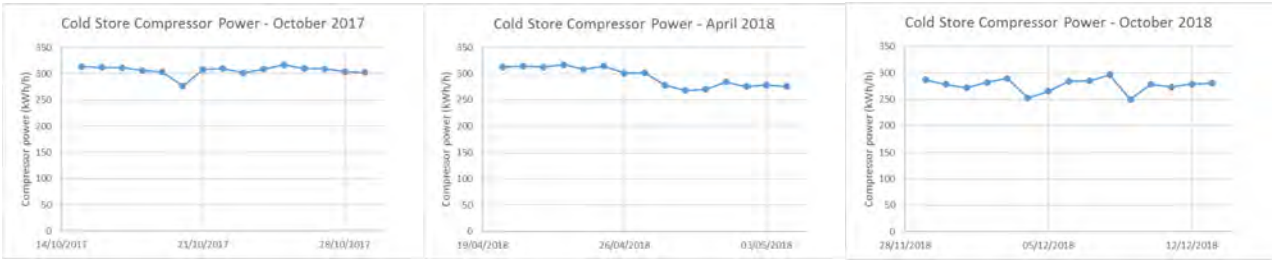

Figure 6a:Power in October 2017 **6b: April 2018** **6c: December 2018**

The graphs in Fig. 6 suggest that this improvement has been sustained since the adjustment was made, but this is not evident when the individual compressor power is aggregated into the overall site consumption. This demonstrates the need for data to be sufficiently detailed to be meaningful.

5. FOURIER ANALYSIS

A further method of analysis is suggested by Spyrou *et al* (2015). Their study took compressor run signal data and applied a Fourier transform to identify whether there was any periodic behaviour that could be an indication of inefficient operation. This type of analysis has been made relatively simple with the introduction of spreadsheets with advanced mathematical functions. A useful description of how to perform a discrete Fourier transform on a dataset is given in Kerr (2009). Following Kerr's description a series of tests of large data sets was performed in order to assess the usefulness of this technique for analysing large data archives.

Fourier transformation is the conversion of a set of data into a series of trigonometric functions, the sum of which gives the original function. This is normally found in mechanical systems as the method of displaying noise and vibration measurements as a spectrum since it is very useful to know which frequencies are present in the overall signal. When applied to a dataset such as kWh yesterday readings or compressor run signals, the discrete Fourier transform can identify actions which are repeated on a regular basis. Performing a Discrete Fourier Transform on a set of data in a spreadsheet requires the number of datapoints to be a power of 2 (eg 32, 64, 128 etc up to a maximum of 4096). The more data points that are processed the more accurate the transform will be but the longer it will take to perform.

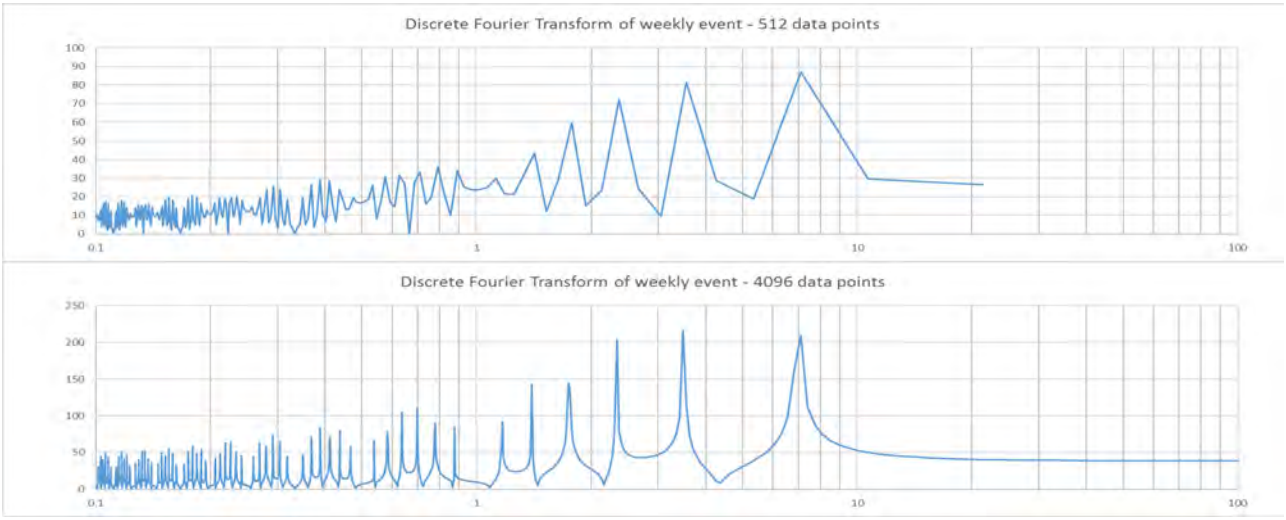

Figure 7a and b: Discrete Fourier Transforms with different amounts of data

The graphs in Fig. 7 show the benefit of using a higher number of data points – the curves are smoother and more accurately defined. However the data processing takes longer – in this case it took 35 seconds to produce the first graph and 377s for the second. The data analysed was a set of values representing hourly readings which were 100 for 24 readings and 1 for the following 144 readings, repeating on a 168 period for 4,700 readings. This simulates an event which occurs one day in seven over a period of 28 weeks. In the graphs the x-axis is shown on a logarithmic scale marked in days.

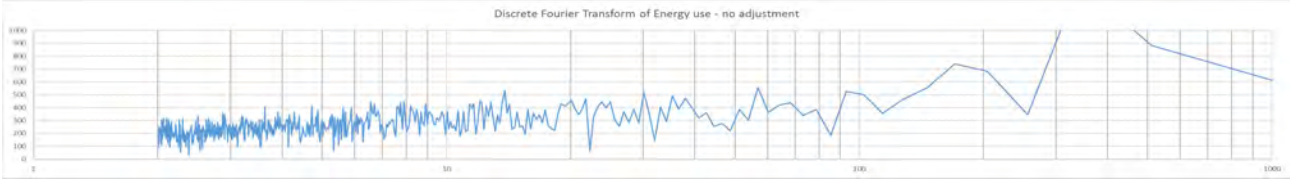

Figure 8: DFT for a distribution centre power consumption over a three year period

The right hand peak is recorded at 7 days in both cases but in both cases harmonic multiples of the real frequency are created by the transform process at 2x, 3x, 4x and so on – the source of the response is the lowest frequency peak, ie that with the highest period of repetition, which in this case is 7 days. Applying this technique to live data can be a useful way to determine whether, in among everything else that is happening, there is a periodic repetition which should either be

investigated or discounted. To investigate this possibility the set of data shown in Fig. 2 was transformed, as shown in Fig. 8 and then modified to introduce a weekly variance in the numbers. The readings are taken once per day (kWh yesterday) so an increase of 20% was applied to the reading for every Saturday, with the other readings unchanged. The revised dataset was transformed and is plotted in Fig. 9. A peak with a period of 7 days is clearly evident, confirmed by the accompanying harmonics at 3.5 days and 2.33 days (2x and 3x frequency).

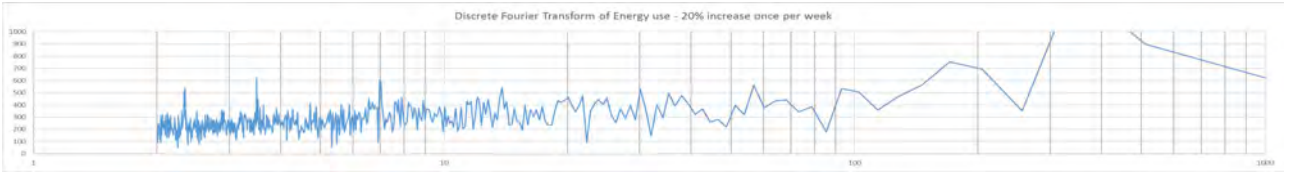

Figure 9: DFT for a distribution centre power consumption with a 20% weekly spike

This exercise was then repeated, but with the 20% increase on Saturdays replaced with a 30% reduction. The resultant transform is plotted in Fig. 10. The shows the same peaks at 7 days, 3.5 days and 2.33 days as was observed in Fig. 9.

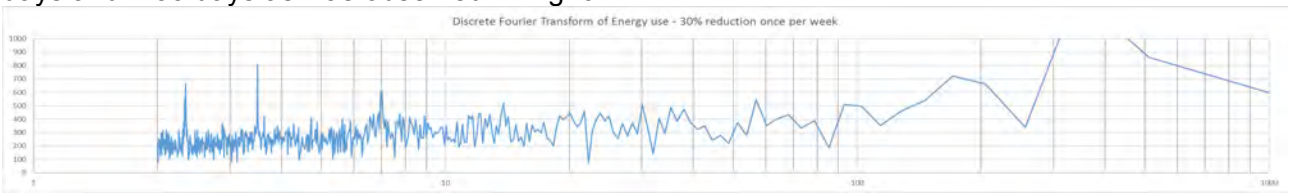

Figure 10: DFT for a distribution centre power consumption with a 30% weekly dip

Comparison of Figs. 8, 9 and 10 shows that the rest of the transform is not affected by these adjustments to the data set. Detection of a periodic increase in this way is useful for identifying recurring events which result in excessive power use such as leakage of hot gas through defrost valve stations or high power consumption under different operating regimes, for example different shift patterns. These would be worthy of further investigation to reduce the energy requirements. If the plant works a weekly production pattern, for example a bakery producing for 140 hours per week and then being offline this will also be identified by the transform analysis as shown in Figure 10 but it should be noted that two independent events, both with a 7 day period will only produce a single set of harmonics on the transform so care is needed to correctly interpret the result. All three of the transforms show a high peak (off the scale of the graph) between 300 and 500 days. The curve is very granular at this point due to the relatively small sample size of 1024 readings, but this peak is the effect of weather data on the transform. There are no accompanying harmonics at lower periods because the change in weather is approximately a sine curve as shown in Figs. 1 and 2, so the effect of weather is transformed more or less to a single peak on the spectrum. To illustrate this point a transform was applied to the discrepancy data in Fig. 4. The result is shown in Fig. 11. Although the absolute value of the transform still rises as the period increases the major peak at about 360 days has been eliminated. This effect is discussed in more detail in the next section.

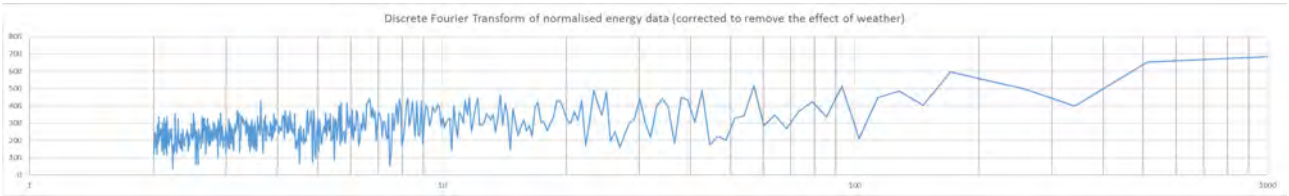

Figure 11: DFT for a distribution centre power consumption adjusted for weather effects

6. LIMITATIONS OF FOURIER ANALYSIS

Several constraints can be observed in the transform graphs. When data is captured on a daily basis (a sampling rate of once per day) the minimum period effect that can be observed is two days. This is why only the second and third harmonics of the 7 day period are shown in Figs. 9

and 10. However the maximum period that can be analysed is dependent on the number of data points captured so although a peak is evident in Figs. 8, 9 and 10 somewhere between 300 and 500 days it can't be placed more accurately than this because there are only 1024 data points (33.7 months of data) which produces 512 spectral lines in the transform. The spectral lines at this part of the transform are at 256 days and 512 days.

The DFT process in the spreadsheet requires the number of data points to be a power of 2. Therefore to process more than 33.7 months of data would require double the amount of information – over five and a half years of readings. It would seem attractive then to take hourly readings rather than daily, but the second limitation then comes into effect as seen in Fig. 7. The maximum number of data points that can be processed is 4096, giving 2048 spectral lines but when taking one reading per hour this only equals 170 days of data – less than half a year. This is sufficient for investigating events that happen on a weekly basis, but it does not allow whole year effects to be addressed. To give full flexibility it would be necessary to record much more frequently but then apply some kind of aggregating before the transform if longer term effects were of interest. This is of course subject to data storage constraints. A 16-bit analogue signal recorded every second requires about 170kB to store just one day of readings. Therefore storing 5 years of meaningful data from a large system, say 50 channels of data, would require 15GB. It becomes difficult to manipulate such large spreadsheets and the files are typically much too big to send by email.

In addition to pre-processing to match the processing capability of the spreadsheet, all the data must be checked for spurious readings, lost signals and other errors. These can be patched with typical values but if the missing data includes any of the periodic information under investigation it may adversely affect the result. In the example shown in Fig. 7 one week's data was removed. The transform with 512 data points failed to pick up the period (but it is only just over three weeks of data) but with 2048 data points (12 weeks) the pattern was still clearly detected. The process of cleaning the data could be very labour intensive for a large site, so it is better to build a sense check into the initial data storage to ensure that the transform can proceed correctly.

The harmonics created by the discrete Fourier transform process for a single point disturbance seem at first sight to be a disadvantage. They are simply the true result of transforming a square wave, which would be converted to an infinite series of sine waves at the harmonic frequencies and of diminishing amplitude. For periodic disturbances it is actually useful to have the harmonics, which help to identify the peak in amongst the background noise created by the variation of the base signal. If a peak is suspected of indicating an issue it would be accompanied by signals at half the period, one third of the period, one quarter of the period and so on. This can easily be misinterpreted – it does not indicate that there is also something happening every three and a half days, every two and a third days and so on. It is indicative of the abrupt nature of the change event that is happening every seven days.

A further limitation of the technique is that it does require a detailed knowledge of the operation of the plant and the general business patterns in order to draw conclusions. For example consider a cold store with a hot gas defrost system with ten evaporators which each defrost once per day where the main hot gas header is pressurised all the time and one of the hot gas solenoid valves is leaking. The system energy use will show a higher than normal kWh figure all the time that the faulty valve station is leaking and the consumption will drop to a lower level when that evaporator is defrosting because the leak path for the hot gas to get to the compressor suction is temporarily shut off by the suction valve. If two of the valve stations are leaking there will still be a daily pattern but it may be harder to spot because there will always be at least one valve leaking. It is preferable to design a hot gas system that only puts gas into the header when a defrost is required. If each defrost takes 30 minutes then that is 5 hours per day for this plant, not 24 hours per day. It is more difficult to design a hot gas system on this basis, but it is worth it to avoid the risk of internal heat leakage as described in section 2.5.

It should also be noted that the x-axis of the Fourier transform plots shows the period between events. This is the reciprocal of the frequency as it is more useful to talk about the period of time between events rather than the number of times they occur. The y-axis of the plots is the square root of the magnitude of the transform, which is a complex number. The period is calculated by dividing the number of data points by the sampling frequency, so for example if samples are recorded every hour and there are 1024 data points the period represented by each spectral line in the transform will be 1024/24 divided by the line number. Hence the largest period that can be displayed in this case is 42.7 days but in practice anything above 10 days will be a rough approximation. With more data points the maximum period is increased, for example with 4096 data points the maximum period is 170 days and the curve becomes sufficiently accurate if the period is less than 40 days.

8. CONCLUSIONS

Several methods for the analysis of large data sets related to industrial refrigeration facilities have been demonstrated. Electrical consumption of refrigeration systems should be sub-metered at a suitable level to enable meaningful diagnosis. A single meter on the distribution board feeding the refrigeration plant room is not sufficient. The electrical usage should be recorded electronically, including power factor information where appropriate, and the readings should be sufficiently frequent – at least one reading per hour is recommended and preferably per minute. These figures can then be aggregated to a “kWh yesterday” figure for further analysis. System operators should always seek to correlate their energy use in refrigeration to business activity and this should be done automatically where possible, for example by counting door openings in a cold store. In production plants the best measure is product throughput, but this may be more difficult to capture automatically.

The most significant factor affecting energy use is the ambient temperature so for meaningful comparisons a simple correlation should be used to remove the effect of ambient temperature from the analysis. It is important to ensure wherever possible that the ambient temperature used is that which actually affects the plant performance, including the effects of air recirculation at the condensers.

Fourier analysis can be used to identify periodic events, either to account for increased energy use or to discount periods of low use that happen on a regular basis. Data collection should be on as frequent a basis as possible, but recognising the limits on data storage and manipulation.

ACKNOWLEDGEMENTS

The author gratefully acknowledges Star Refrigeration Ltd for their support and permission to publish this paper.

REFERENCES

Evans, J.A., Hammond, E. C., Gigiel, A. J., Reinholdt, L., Fikiin, K., and Zilio, C., 2013a. Improving the Energy Performance of Cold Stores, Proceedings of the 2nd IIR Conference on the Cold Chain and Sustainability, Paris, IIF/IIR

Evans, J.A. Huet, J-M. Reinholdt, L. Fikiin, K. Zilio, C. Houska, M. Landfeld, A. Bond, C. Scheurs, M. and van Sambeeck, T.W.M., 2013b. Cold Store Energy Performance, Proceedings of the 2nd IIR Conference on the Cold Chain and Sustainability, Paris, IIF/IIR

IIR, 2008. Saving Energy in Refrigeration, Air-Conditioning and Heat-Pump Technology, International Institute of Refrigeration, Paris

Kerr, D., 2009, The Fourier Analysis Tool in Microsoft Excel, published on www.dougkerr.net, last accessed on 5 January 2019

Spyrou, M., Cook, M., Mardaljevic, J., McMullen, A., Lee, R and Pitcher, J, 2015, The operational efficiency of commercial food refrigeration systems: a data mining approach, ASHRAE Winter Conference, Chicago

Manuscript ID: 290
DOI: 10.18462/iir.icr.2019.0290

Heat transfer characteristics of R-134a inside an inclined helical coiled tube-in-shell type condenser

Anand K. SOLANKI, Ravi KUMAR

Department of Mechanical and Industrial Engineering
Indian Institute of Technology Roorkee, Roorkee, 247667, India
asolanki@me.iitr.ac.in, ravikfme@iitr.ac.in

ABSTRACT

An experimental investigation has been carried out to investigate the two-phase flow heat transfer characteristics of R-134a inside an inclined helical coiled tube-in-shell condenser. The helix axis of helical coiled tube makes an inclination angle of 0°, +45° and +90° from the horizontal. The test runs were performed at a fixed saturatioin temperaure of 35°C with a different refrigerant mass fluxes of 115, 156 and 191 kg $m^{-2}s^{-1}$. During the experiments, the effects of vapor quality, mass flux and inclination angle of helical coiled tube on average heat transfer coefficient of refrigearnt have been analyzed. It is found that the average heat transfer coefficient for all inclination angle of helical coiled tube rised with an increase of vapor quality and mass flux. The results also showed that the maximum and minimum heat transfer coefficient were obtained at +45° and +90° inclination angles, respectively.

Keywords: Condensation, Condenser, Heat Transfer Coefficient, Helical Tube, Refrigerant, Two-Phase Flow.

1. INTRODUCTION

The condenser is an essential part of any refrigeration and air conditioning unit where vapor is condensed to liquid state by removing the latent heat. Nowadays, the effective design of the condenser is quite important for refrigeration industries to obtain maximum heat transfer with minimum pressure drop in the heat exchanger. As such, helical coiled tubes have been widely used in the condensers to enhance the heat transfer by producing centrifugal effect on the flow inside the tube (Reay, 1991).

A number of research investigations have been performed on the heat transfer and pressure drop characteristics inside a helical coiled tube. Kang et al. (2000) carried out the experimental study of heat transfers and pressure drops data of R-134a inside a long helical coil tube. The results revealed that the overall heat transfer coefficient raised with increase of the water mass flux. The heat transfer and the pressure drop decreased with increase of tube wall temperature from 12°C and 22°C. Yu et al. (2003) conducted an experimental investigation of heat transfer of R-134a during condensation inside horizontal, inclined and vertical helical tube at refrigerant mass flux from 100 to 400 kg $m^{-2}s^{-1}$, cooling water Reynolds number between 1500 and 10000. They investigated that the helical tube orientation had significant influence on the overall heat transfer coefficients. The highest and the lowest heat transfer coefficient was observed at inclined position and vertical position, respectively. Han et al. (2005) reported the experimental results of condensation heat transfer and pressure drop of R-134a inside helical tube with mass flux vary from 100 to 420 kg $m^{-2}s^{-1}$ at a different condensation saturation temperature 35, 40 and 46°C. Wongwises and Polsongkram (2006) presented experimental studies on two-phase flow condensation heat transfer and pressure drop of R-134a inside concentric helical coil tube in tube condenser. The results showed that the heat transfer coefficient of the helical coiled tube were about 33–53% higher than that of smooth round tube while pressure drop were about 29–46% higher. They also proposed the correlation for predicting the heat transfer coefficient and pressure drop. Shao et al. (2007) compared the condensation heat transfer coefficient for the helical tube with straight tube at different saturation temperature 35, 40 and 45°C, mass flux varies from 100 to 400 kg $m^{-2}s^{-1}$. The heat transfer coefficients of helical tube were found

to 4-13.8% higher than that of straight tube. Hajeri et al. (2007) examined the performance of heat transfers and pressure drops of R-134a inside annular helical tubes at different saturation temperature of 36, 42 and 48°C with the mass flux varying from 50 to 680 kg $m^{-2}s^{-1}$. The results showed that the heat transfer coefficients of the refrigerant-side rise with increase of the refrigerant mass flux and decline with increase of the saturation temperature of refrigerant. Mosaad et al. (2009) investigated the effect of refrigerant mass flux and condensation temperature difference on the heat transfer coefficients and pressure drops of R-134a inside coiled double tube. They found that, with increase of refrigerant mass flux and decrease of condensation temperature difference, the overall heat transfer coefficient increased. Similarly, pressure drop of refrigerant increases with rise of the refrigerant mass flux. Murai et al. (2006) used a high-speed video system to take photographs of interfacial structure of gas-liquid flow inside the helical coiled tube. They observed that the flow transition from bubbly to plug flow for helical coiled tube compared to straight tube was obtained earlier duo to the centrifugal acceleration generating by curvature of the tube. Genić et al. (2013) also investigated experimentally the shell-side fouling factors of eight heat exchangers with parallel helical coils. The fouling resistances were slightly lesser than usual values for shell-and-tube heat exchangers with straight pipes. Gupta et al. (2014) determined the effect of mass flux, vapor quality and saturation temperature on the heat transfer coefficients and pressure drop of R-134a inside horizontal helical coiled tube-in-shell type heat exchanger. The heat transfer coefficient and pressure drop of refrigerant increase with rise of mass flux and vapor quality and decrease with increase of the saturation temperature. Salimpour et al. (2017). Both curvature radii and coil pitch of helical coil tube had significant influence on the heat transfer coefficient. They also found that, the effect of coil pitch on heat transfer coefficient was more pronounced at low vapor qualities. Mozafari et al. (2015) conducted the experimental studies of heat transfer and pressure drop of R600a inside helical tube-in-tube heat exchanger at different inclination angles of zero, +30°, +60° and +90° with different mass flux ranging from 155 to 265.5 kg $m^{-2}s^{-1}$. The results showed that the heat transfer coefficients were remarkably influenced by inclination angle but pressure drop were slightly affected.

Although, a number of investigations have been carried out on single phase and two-phase flow of refrigerants inside a helical coiled tube but a few investigations have been reported on two phase flow inside the helical coiled tube at inclined position. Only single work has been reported by Mozafari et al. (2015) which investigated the effect of inclination position of helical coiled tube in tube type heat exchanger on condensation heat transfer and pressure drop of R-600a. In this study, the condensation heat transfer coefficient of R134a for different inclination position of the helical coiled tube in shell has been examined. In addition, the effect of inclination angle,vapor quality and mass flux on average heat transfer coefficient have also been investigated.

2. EXPERIMENTAL APPARATUS AND PROCEDURES

The schematic diagram of the experimental set-up has been depicted in Fig. 1. The main components of experimental set-up were composed of a pre-heater, test-condenser, post-condenser, three refrigerant magnetic gear pumps, Coriolis mass flow meter and data acquisition system. The test-section was a counter flow type heat exchanger. The test-section was connected to post condenser, where two phase quality of refrigerant coming from test-section was sub-cooled to a liquid state by extracting heat to cold water circulated from the condensing unit. The municipal water was employed for cooling purpose which was circulated inside the shell of the test-section. The temperature of water inside the test-section was controlled by variac of 2 kW capacity. A slight glass after the post-condenser was placed to ensure the continuous liquidity of refrigerant before entering the three magnetic gear pump connected side by side. The flow rate of refrigerant was monitored by operating the speed of the magnetic gear pump through frequency inverter. The Coriolis mass flow meter followed by magnetic gear pump was accommodated to measure the refrigerant flow rate. In order to control the vapor quality at the inlet of the test-condenser, an appropriate pre-heater was designed from a 6 m long U-bend stainless steel tube. By supplying high current and low voltage through step down auto transformer, liquid refrigerant was evaporated by heating the tube. A standard filter-drier was incorporated following the pre-heater to remove any foreign particles and moisture in refrigerant loop. A number of hand shut-off valves were facilitated to provide facile installation of a component in the apparatus.

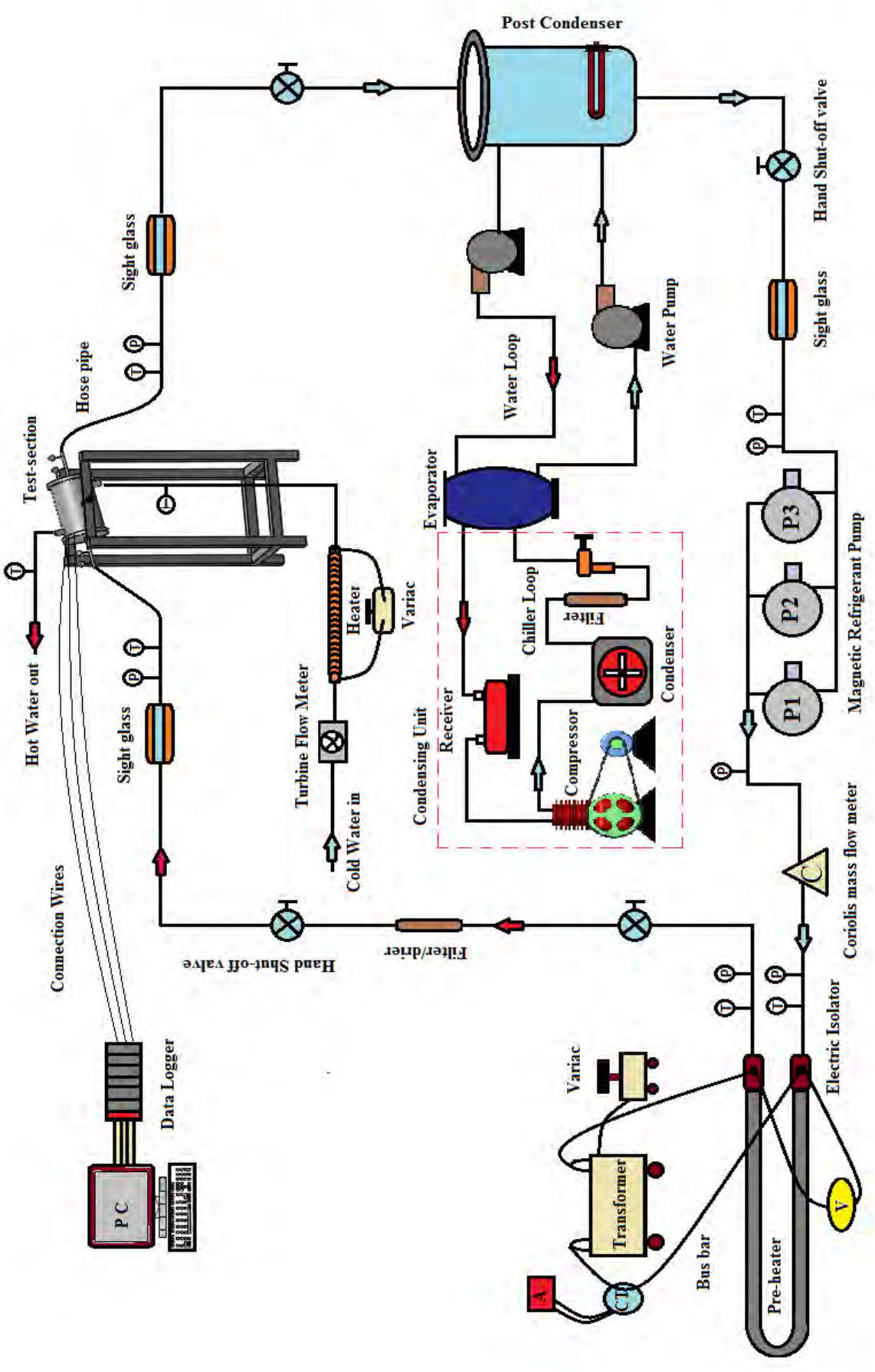

Figure 1: Schematic diagram of experimental set-up

Fig. 2 depicts a schematic diagram of the test-section. The test-section was a counter flow helical coiled tube in shell type heat exchanger in which the refrigerant flowing inside the inner tube extracts the heat to the cooling water flowing the opposite direction to refrigerant flow inside the shell. The inner helical coiled tube, which was made by turning the straight tube over the wooden block. Details of the test tube are given in Table1. It can be seen from the Fig. 2 that a mild steel frame was constructed to support the test-section by means of two rod. One end of the rods is welded on the test-section, while, another end is threaded which was used to fix the test section at the particular inclination position by mean of bolts. The T-type thermocouples were fixed to measure the refrigerant temperature at the inlet of the pre-heater, inlet and outlet of the test-section. The outer wall temperature of the helical coiled tube was also measured with T-type thermocouple at six positions. In each position, four thermocouples were placed 90° apart over the top, bottom and two sides. A special glue was used to fix thermocouples on the wall to avoid water resistance. The accuracy of thermocouples was ±0.1°C of full scale. The pressure Transducers with accuracy 0.25% were utilized to measure the refrigerant pressure at the inlet and outlet of the test-section and at the entrance of the pre-heater. Also Pressure drop between the test-section was measured by a differential pressure drop transducer. The saturation temperature of refrigerant was taken at an average pressure of the inlet and outlet pressure of the test-section. The Coriolis flow meter with an accuracy of 0.1% was employed to measure the refrigerant mass flow rate. The water flow rate in annulus tube was measured by a turbine flow meter. The turbine flow meter has an accuracy of 1% of the full scale. All thermocouple and pressure transducer signal was transferred to the multichannel data acquisition system with PXI controller. The steady state condition was assumed when reading of temperatures, pressure and mass flow rate remain constant for at least 20 min. The details of the experimental condition are shown in Table 2.

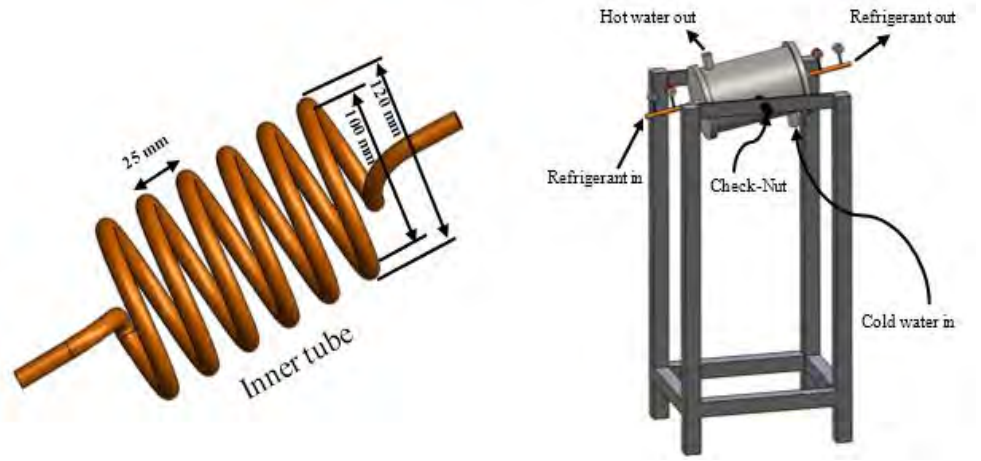

Figure 2: Sketch of Inner tube and test-section

Table 1. Test-section specifications

Parameter	Dimensions (in mm)
Inner diameter of tube	8.33
Outer diameter of the tube	9.52
Coil mean diameter	110
Number of turns	6
Length of copper tube	2200
Pitch of the coil	25
Inner diameter of the shell	140
Outer diameter of the shell	160
Length of the shell	200

Table 2. Experimental conditions

Parameter	Range
Refrigerant	R-134a
Average saturation temperature (°C)	35
Mass flux (kg $m^{-2}s^{-1}$)	115,156,191
Heat flux (kW m^{-2})	1.5-10.4
Vapor quality	0.1- 0.83

3. DATA REDUCTION

The data reduction analysis is employed to evaluate the average heat transfer coefficient and the average frictional gradient during an experiment at steady state conditions. The thermo-physical properties of R-134a have been determined by using REFPROF-9. The average heat transfer coefficient (h_{avg}) is obtained by the following equation:

$$h_{avg} = \frac{Q_w}{A_i(T_{sat} - T_{wi})} \quad \text{Eq. (1)}$$

Where, Q_w, T_{sat}, A_i and T_{wi} are the heat transfer rate inside the test-section from tube to flowing water, saturation temperature of refrigerant corresponding to the average pressure of the test section at the inlet and outlet, inner surface area on tube and average inner wall surface temperature of the tube, respectively.

The average vapor quality of the refrigerant is calculated by taking the arithmetic mean of vapor quality at inlet and outlet of the test section which can be defined as following equation:

$$x_{avg,ts} = \left(\frac{x_{in,ts} + x_{out,ts}}{2}\right) \quad \text{Eq. (2)}$$

Where, inlet vapor quality (x_{in}) of the test-section is evaluated by applying energy balance equation at the preheater as follows:

$$x_{in} = \frac{1}{h_{fg,ts,in}} \left(h_{in,ph} + \frac{Q_{ph}}{m_R} - h_{f,in,ts}\right) \quad \text{Eq. (3)}$$

Where, Q_{ph} is the electrical power supplied to the pre-heater. The $h_{in,ph}$ is the enthalpy at the inlet of the preheater which is calculated by measuring the temperature and pressure of sub-cooled liquid refrigerant. It is assumed that energy loss between the preheater outlet and test section inlet is neglected. Hence, the enthalpy at the test section inlet is equal to the enthalpy at the outlet of pre-heater. The enthalpy of saturated liquid ($h_{f,in,ts}$) and enthalpy of vaporization ($h_{fg,ts,in}$) are determined based on the temperature at the inlet of the test-section.

The outlet vapor quality of the test section is given by:

$$x_{out} = \left(\frac{h_{out,ts} - h_{f,out,ts}}{h_{fg,out,ts}}\right) \quad \text{Eq. (4)}$$

Where, $h_{f,out,ts}$ and $h_{fg,out,ts}$ are the enthalpy of the saturated liquid and vaporization at the outlet of the test section, respectively, which are calculated by outlet temperature of the test section. The $h_{out,ts}$ is the enthalpy of the refrigerant at the outlet of the test section which is determined by energy balance equation on the test section as follows:

$$h_{out,ts} = (h_{in,ts} - \frac{Q_w}{m_R}) \quad \text{Eq. (5)}$$

Where, $h_{in,ts}$ and m_r are the enthalpy of refrigerant at the inlet of the test section and mass flow rate of the refrigerant, respectively.

4. RESULTS AND DISCCUSION

In this study, the effect of vapor quality, mass flux (115, 156 and 191 kg $m^{-2}s^{-1}$) and inclination angle of the helical coiled tube on average heat transfer coefficient have been discussed. First of all, the Fig. 3 shows the comparison of the experimental Nusselt number of horizontal helical coiled tube with renowned correlations which was proposed by Wongwises and Polsongkram (2006) and Gupta et al. (2014). The results showed that these correlations predicted accurately the experimental data for horizontal helical coiled tube. Moreover, it is revealed that Wongwises and Polsongkram correlation (2006) overestimated the most of experimental results, while Gupta et al. (2014) correlation underestimated the experimental data. However, the data predicted by those correlations exists within an error band of ±30%. Hence, this is confirmed that the experimental results determined by using the test facility were found to be reliable.

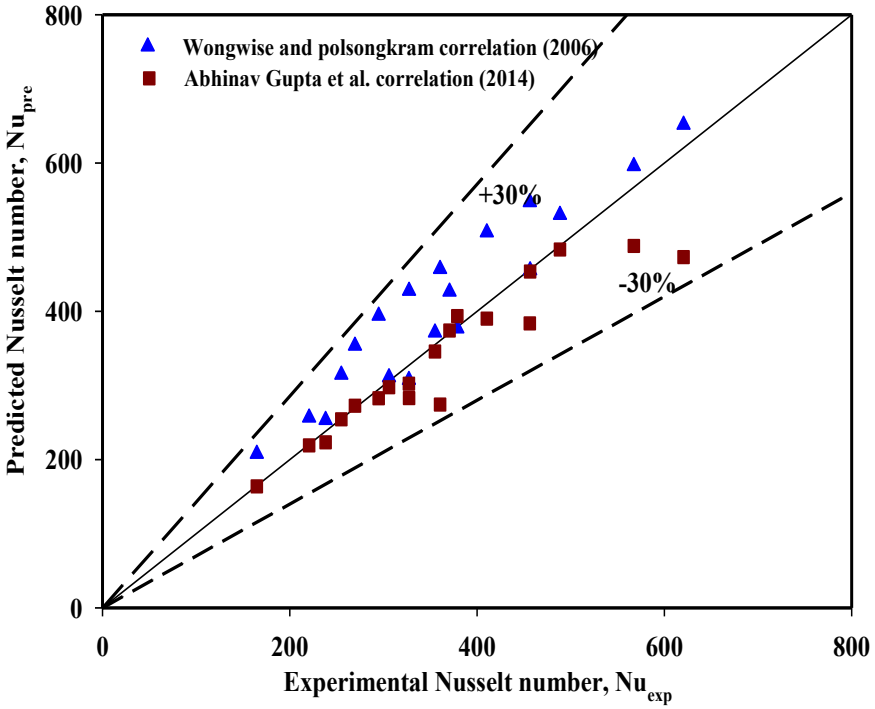

Figure 3: Comparison of experimental Nusselt number of horizontal helical coiled tube with existing correlations

In Fig. 4, the heat transfer coefficient for different inclination position of helical coiled tube data have been shown. This figure has been drawn taking average vapour quality as abscissa and average heat transfer coefficient as ordinate. The effect of the vapor quality and mass flux of refrigerant on average heat transfer coefficient for several inclination position of helical coiled tube were investigated. It is apparent from the Fig. 4, the heat transfer coefficient of R-134a increases for the mass flux rise from 115 to 191 $kgm^{-2}s^{-1}$, at any given vapor quality. The experimental results indicate that there is higher heat transfer coefficients at high vapor quality for any flow rate of refrigerant in the range of 115 to 191 $kgm^{-2}s^{-1}$. This is attributed duo the fact that during the condensation process inside the tube, the high vapor velocity is attained as vapor quality increased and then it produced the higher shear stress between the vapor- liquid interfaces, resulting more waves formed on the surface of condensate film which in turn increased the heat transfer surface area. Therefore, the heat transfer coefficient of R-134a has been increased. Besides this, the increase in the mass flux also enhances the heat transfer coefficient. This is because, velocity of the vapor and liquid film

raises, as mass flux of refrigerant increases and, thereby, more turbulence exists in flow field. At high velocity of vapor-liquid mixture, secondary flow turns out to be stronger, causing high shear stress on the condensate film form inside the tube. Which results in a thin liquid film thickness because of the high deposition of liquid droplets in the vapor phase of refrigerant. Consequently, the heat transfer coefficient is enhanced with the rise in mass flux of refrigerant. For instance, the mass flux increases from 115 to 191 kg $m^{-2}s^{-1}$, the heat transfer coefficient increased nearly 70-98% for horizontal position (0°), 72-99% for upward 45 degree (+45°) and 76-95% for upward 90 degree (+90°) in the all range of the vapor quality.

Fig. 5 shows the effects of inclination position of helical coiled tube on the average heat transfer coefficient for the refrigerant mass flux of 115 and 191 kg $m^{-2}s^{-1}$. It can be observed in the Fig. 5 that the inclination position of helical coiled tube has notable effect on heat transfer coefficient. The different trend is found for the different inclination position of helical coiled tube. This possibly will be clarified by inconsistency of heat transfer during the phase variation which causes different flow pattern inside the helical coiled tube for different inclination position of helical coiled tube. The similar investigation is reported in past study e.g. M. Mozafari et al. (2015) on a condensation of R-600a on helical tube in tube type heat exchanger and Azer et al. (1976) on the smooth tubes. Moreover, it has been observed in Fig. 5 that the maximum and minimum heat transfer coefficients have been found at +45 degree and +90 degree inclination angle of the helical axis from the horizontal position, (in the upward direction), respectively. In addition, the heat transfer coefficient for zero degree inclination angle was found to be slightly less than that of inclination angle of +45 degree and considerably higher than that of that of +90 degree. For instance, the heat transfer coefficient for +45 degree angle of helical coiled tube is almost 2-11% higher than that of zero degree angle and about 17-40% higher than that of +90 degree angle. This is because, at high mass flux and high vapor quality, the gravitational force is insignificant, while the effects of interfacial shear stress are noticeable. On the contrary, at low vapor quality and low mass flux, gravitational force has a prominent effect on the heat transfer

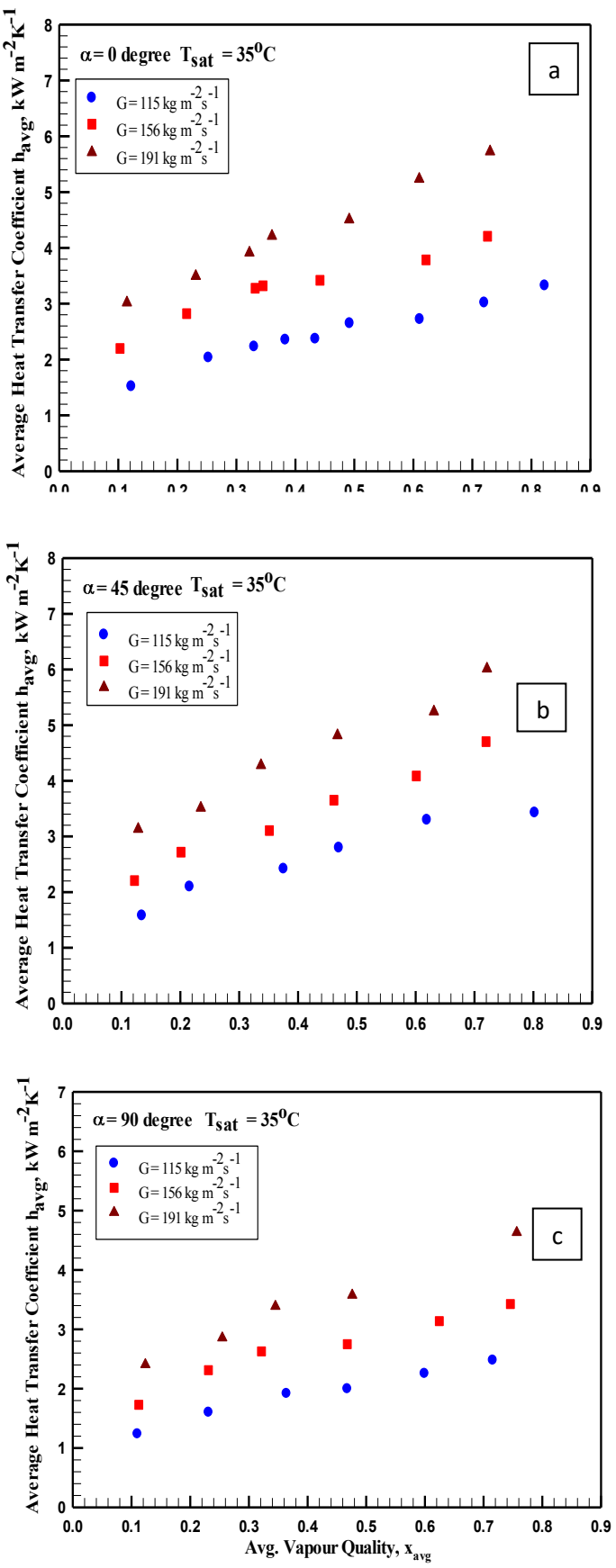

Figure 4: Effect of mass flux and vapor quality on the average heat transfer coefficient for different inclination position (a) 0° (b) +45° (c) +90°

coefficient. Consequently, the heat transfer coefficient at low vapor quality and low mass flux is different for different inclination angle.

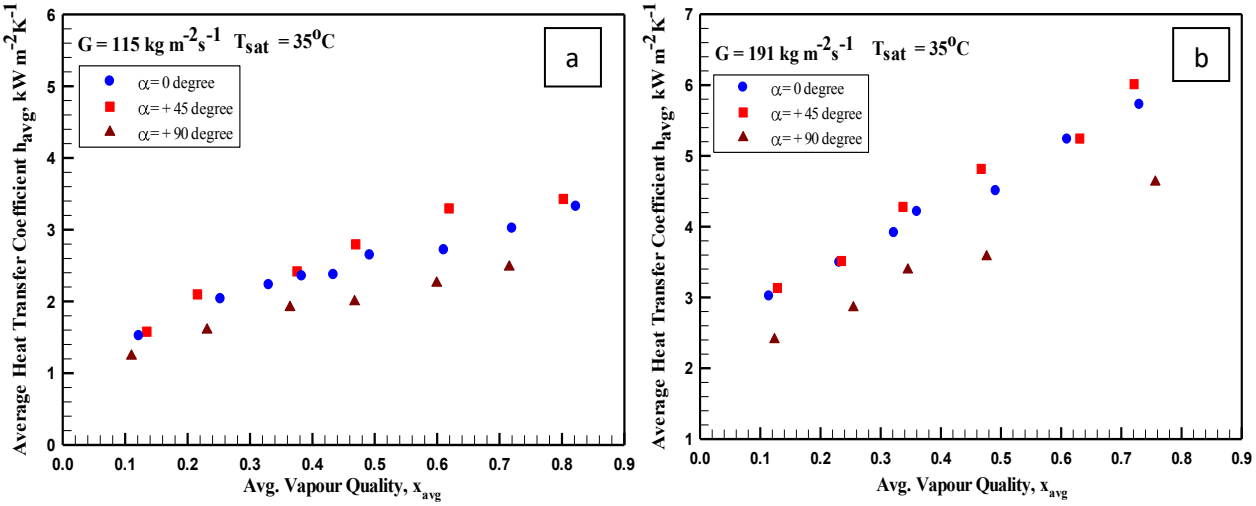

Figure 5: Effect of inclination position of helical coiled tube on average heat transfer coefficient (a) 115 kg $m^{-2}s^{-1}$ (b) 191 kg $m^{-2}s^{-1}$

5. CONCLUSIONS

In this study, the effect of vapor quality, mass flux and inclination angle of the helical coiled tube on average heat transfer coefficient have been discussed. The following conclusions can be drawn:

1. The average heat transfer coefficient for smooth inclined helical coiled tube increases when vapor quality or mass flux increases.
2. Inclination angle of helical coiled tube has significant effect on heat transfer coefficient. The highest heat transfer coefficient is for the inclination angle of 45° at the refrigerant mass flow rate of 115 $kgm^{-2}s^{-1}$ and 191 $kgm^{-2}s^{-1}$ as well.
3. The heat transfer coefficient for +45 degree angle is almost 2-11% higher than that of zero degree angle and about 17-40% higher than that of +90 degree angle.
4. For the mass flux increases from 115 to 191 kg $m^{-2}s^{-1}$, the heat transfer coefficient increases 70-98% for horizontal position, 72-99% for upward 45 degree and 76-95% for upward 90 degree in the all range of the vapor quality.

NOMENCLATURE

A	test-section tube area (m^2)
C_p	Specific heat at constant pressure (J kg^{-1} K^{-1})
d	Tube diameter (mm)
D	Coil mean diameter (mm)
G	Mass flux (kg $m^{-2}s^{-1}$)
h_{avg}	average heat transfer coefficient (kW m^{-2} K^{-1})
h	Enthalpy (kJ kg^{-1})
k	Thermal conductivity (W $k^{-1}m^{-1}$)
l	Length (m)
Nu	Nusselt number
Q	heat transfer rate (W)
T	Saturation temperature (°C)
x	Vapor quality
ph	Preheater
α	inclination angle, (°)

subscripts

f	fluid
fg	latent heat of vaporization
i	inner
in	inlet
out	outlet
o	outer
R	Refrigerant
sat	saturation
ts	test-section
w	wall
wi	inside wall
W	water

REFERENCES

Al-Hajeri, M.H., Koluib, A.M., Mosaad, M., Al-Kulaib, S., 2007. Heat transfer performance during condensation of R-134a inside helicoidal tubes. Energy Conversion and Management 48(8), 2309–2315.

Azer, N.Z., Fan, L.T., Lin, S.T., 1976. Augmentation of Condensation Heat Transfer With In-Line Static Mixers. Proceedings of the 25th Heat Transfer and Fluid Mechanics Institute, pp. 512-526.

El-Sayed Mosaad, M., Al-Hajeri, M., Al-Ajmi, R., Koliub, A.M., 2009. Heat transfer and pressure drop of R-134a condensation in a coiled, double tube. Heat and Mass Transfer/Waerme- und Stoffuebertragung. 45(8), 1107–1115.

Genić, S.B., Jaćimović, B.M., Jarić, M.S., Budimir, N.J., 2013. Analysis of fouling factor in district heating heat exchangers with parallel helical tube coils. Int J. of Heat and Mass Transfer. 57(1), 9–15.

Gupta, A., Kumar, R., Gupta, A., 2014. Condensation of R-134a inside a helically coiled tube-in-shell heat exchange. Exp. The. and Fluid Sci. 54, 279–289.

Han, J.T., Lin, C.X., Ebadian, M.A., 2005. Condensation heat transfer and pressure drop characteristics of R-134a in an annular helical pipe, Int. Comm. in Heat and Mass Trans., 32(10), 1307–1316.

Kang, H.J, Lin, C.X., Ebadian, M.A., 2000. Condensation of R134a flowing inside helicoidal pipe. Int. J. of Heat and Mass Trans. 43(14), 2553–2564.

Mozafari, M., Akhavan-Behabadi, M.A., Qobadi-Arfaee, H., Fakoor-Pakdaman, M., 2015. Condensation and pressure drop characteristics of R600a in a helical tube-in-tube heat exchanger at different inclination angles. App. Ther. Eng. 90, 571–578.

Murai, Y., Yoshikawa, S., Toda, S.I., Ishikawa, M.A., Yamamoto, F., 2006. Structure of air-water two-phase flow in helically coiled tubes, Nuclear Engineering and Design, Vol. 236(1), 94–106.

Reay, D.A., 1991. Heat transfer enhancement-a review of techniques and their possible impact on energy efficiency in the U.K. Heat Recovery Systems and CHP. 11(1), 1–40.

Salimpour, M.R., Shahmoradi, A., Khoeini, D., 2017 Experimental study of condensation heat transfer of R-404A in helically coiled tubes, Int. J. of Refrig. 74, 584–591.

Shao, L., Han, J. Tian, Su, G. Ping, Pan, J. Hong., 2007. Condensation Heat Transfer of R-134A in Horizontal Straight and Helically Coiled Tube-in-Tube Heat Exchangers. J. of Hydrodynamics. 19(6), 677–682.

Wongwises, S. and Polsongkram, M., 2006. Condensation heat transfer and pressure drop of HFC-134a in a helically coiled concentric tube-in-tube heat exchanger, Int. J. of Heat and Mass Trans. 49(23–24), 4386–4398.

Yu, B., Han, J.T., Kang, H.J., Lin, C.X., Awwad, A., Ebadian, M.A., 2003. Condensation heat transfer of R-134A flow inside helical pipes at different orientations', Int. Comm. in Heat and Mass Trans. 30(6), 745–754.

Manuscript ID: 313
DOI: 10.18462/iir.icr.2019.0313

Sensor-less position detection of oil-free linear compressor for refrigeration

Hanying JIANG[(a)], Kun LIANG[(a)], Zhaohua Li[(a)]

[(a)] University of Sussex
Brighton, BN1 9QT, UK, information@sussex.ac.uk

ABSTRACT

Linear compressors can be used for refrigeration systems due to higher efficiency, oil-free operation and compactness. One major challenge for linear compressor is the sensing of piston position. This paper presented a novel method to detect the piston position at resonance without a piston position sensor. Inductive coil was wounded around the middle core and the end core. The peak-to-peak flux linkage at two zero crossing points of measured current was calculated for various strokes for resonance operation. The results show that both the peak-to-peak flux linkage of end core and middle core vary linearly with the stroke. A linear function was fitted for peak-to-peak flux linkage at various strokes. The maximum error between calculated peak-to-peak flux linkage with measured current and linear fitting result is about 6%. When linear compressor is operated off resonance, the flux linkage difference is smaller than that at resonance. It can be concluded that inductive coil can be used to detect the compressor stroke thus to modulate the cooling capacity of the refrigeration system.

Keywords: Refrigeration, Linear Compressors, Control, Resonance, Sensor-less, Inductive Coil.

1. INTRODUCTION

Linear compressors driven directly by linear motors have been used for refrigeration systems. Compared with conventional rotary induction motors, linear motors can achieve a higher efficiency when a linear motion is required, as the absence of crank mechanism reduces the friction loss. Linear compressors are more efficient and simple with the cooling capacity modulation (Bansal et al., 2011), and the linear compressor could operate more efficiently over a wider range of dead volumes than the crank-drive compressor (Bradshaw et al., 2012).

Three types of linear motors are distinguished by the structure: moving coil, moving magnet and moving iron. Liang (2017) summarized the pros and cons of each type. For moving coil motors, it is easier to design and control the stroke, but low power density and high cost restrict their application in household refrigerators. With the development of moving magnet topologies, high-energy permanent magnet material such as NdFeB (Neodymium-Ferro-Boron), and soft magnetic composites for core, high force capacity and energy-saving effect have made moving magnet motors suitable choices for linear compressors.

One of the most practical approach to control the piston stroke is to modulate the voltage applied to the motor coils. In most cases, a piston displacement sensor is used to detect the piston stroke and the coil voltage will be adjusted accordingly in the next operation cycle. Using piston displacement sensor to sense piston position increases cost and require certain room for the instrumentation of the piston sensor, which also makes it difficult to install the piston sensor in a small size linear compressor. Liang et al (2016) wounded a search coil around a main coil and the peak-to-peak flux linkage was calculated with measured current and voltage of search coil. The proposed method requires an accurate value of mutual inductance between main coil and search coil.

In this work, an inductive coil was wounded around end core and middle core to detect the piston position at resonance. The peak-to-peak flux linkage at two zero crossing points of current for various strokes was calculated when linear compressor was operated at resonance. The configuration and specification of the linear compressor are shown in Fig. 1 (Liang, 2013). The linear compressor consists of a moving magnet linear motor, flexure spring and virtual radial clearance of about 10 mm. The linear motor is composed of four laminated cores wounded by coils and three moving magnets. The slotting of cores forms an air gap where magnets are placed. When an alternating current is supplied to the cores, an alternating axial force will be induced in the moving magnet assembly, which drives the piston reciprocating at the same frequency.

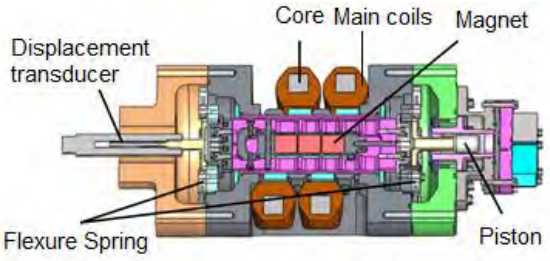

Figure 1: Design of the linear compressor (Liang, 2014)

2. INSTRUMENTATION & POSITION SENSING METHOD

2.1. Experimental Apparatus

Fig. 2 shows the schematic of the refrigeration system using the linear compressors and instrumentation apparatus. A throttling/expansion valve was used for pressure ratio regulation. Except for the main flow loop introduced above, a bleed flow loop which connects the compressor body side to the suction line of the main flow loop was also included in the test loop. Two PID controllers were employed. One was used for stroke control, and the other was for piston offset adjustment. In the stroke control, the amplitude of sinusoidal waveform excitation voltage was determined according to measured piston displacement and set point of stroke. A PWM (Pulse Width Modulation) signal was generated to drive the solenoid valve. The duty cycle of the digital pulse signal determined the fraction of time that solenoid valve was open. The resonant frequency was calculated automatically with linearized gas spring stiffness and mechanical spring stiffness in LabVIEW (Liang et al., 2013). The operating frequency can be adjusted manually during operation.

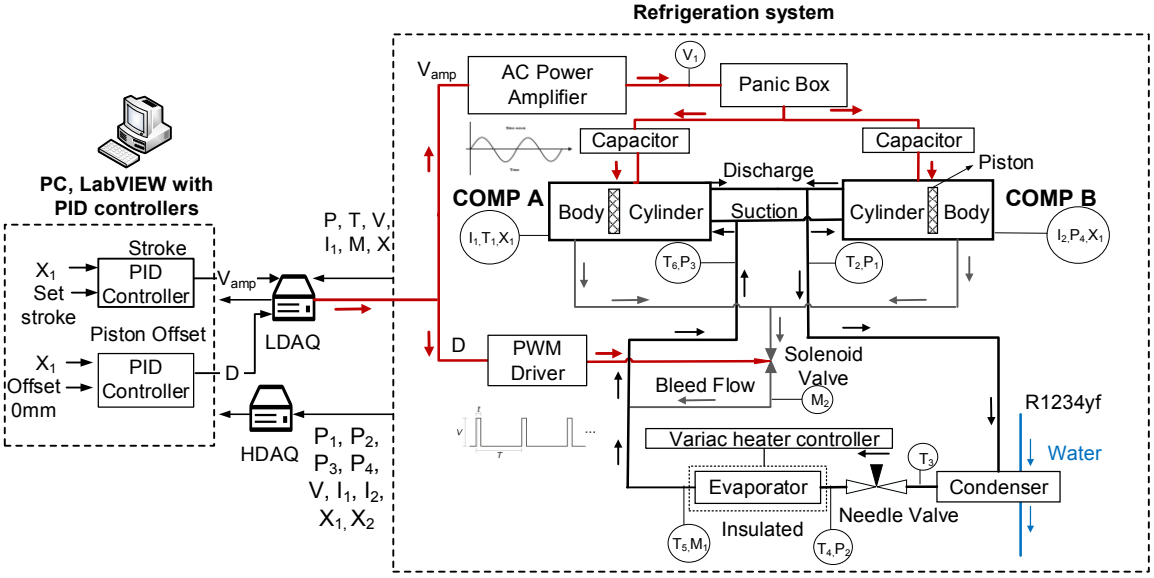

Figure 2: Schematic of the control of the linear compressor in the refrigeration system and instrumentation (P: pressure transducer, T: thermocouple, M: mass flow meter, V: voltage sensor, I: current transducer, X: linear variable differential transducer, D: duty cycle)

Table 1. Test conditions for the linear compressor and refrigeration system

Refrigerant	R1234yf
Charge (g)	250
Pressure ratio	2.5, 3.0, 3.5
Compressor stroke (mm)	11, 11.5, 12, 12.5, 13
Condenser temperature (°C)	45
Operating frequency (Hz)	32-38
Suction temperature (°C)	20-30
Ambient temperature (°C)	22

2.2. Piston Position Sensing Method

The inductive coil wound around the main coil is used to detect the piston stroke by calculating the variation of flux linkage. Fig. 3 shows a search with 10 turns wounded around a main coil with a magnet placed in the air gap. During operation, one inductive coil was wound around the middle core and one inductive coil was wound around the end core.

When linear compressor is operated at resonance, the phase difference between displacement and current should be 90º (shown in Fig. 4). At maximum and minimum piston displacements, the current is zero and flux linkage induced by current equals to zero. By calculating the flux linkage difference between two zero crossing points of current, the peak-to-peak flux linkage versus stroke can be concluded.

The peak-to-peak flux linkage $\Delta\varphi$ can be calculated by

$$\Delta\varphi = \varphi_{\max} - \varphi_{\min} \quad \text{Eq. (1)}$$

$$\varphi = \int V_s \, dt \quad \text{Eq. (2)}$$

where V_s is the voltage of inductive coil, φ is flux linkage, $\varphi_{\max}$ is the flux linkage at maximum piston displacement, $\varphi_{\min}$ is the flux linkage at minimum piston displacement.

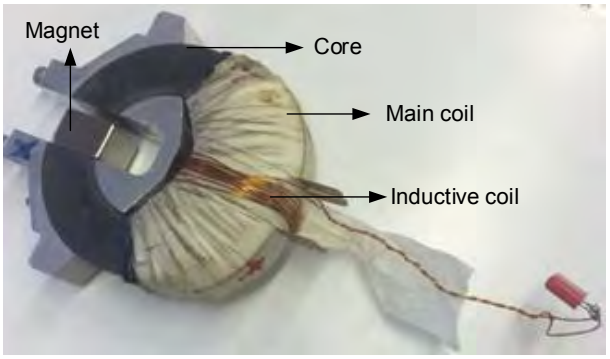

Figure 3: Core with main coil and inductive coil wound around

3. RESULTS and DISCUSSION

3.1. Current, Displacement and Flux Linkage

Fig. 4 shows the measured current and displacement at resonance with a stroke of 8 mm. The amplitude of current is 1.7 A, and the operating frequency is 34 Hz. Both the current and displacement signal are not in perfect sinusoidal waveform, the harmonic components cannot be neglected. When current is zero, the piston displacement is close to maximum or minimum displacement. As the operating frequency was adjusted manually according to the calculated resonant frequency, the maximum and minimum displacement occur slightly earlier than the zero crossing point of current as shown in Figure 4. At zero crossing point of current, the flux linkage calculated by the integration of the voltage of inductive coil is induced by the permanent magnets.

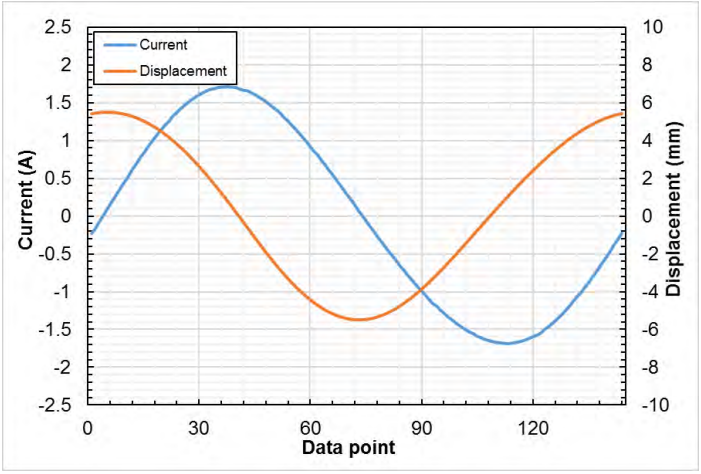

Figure 4: Measured current and displacement at resonance with a stroke of 11 mm and operating frequency of 35 Hz

Fig. 5 shows the measured voltage of the end inductive coil and calculated peak-to-peak flux linkage of the end core with a stroke of 8 mm and frequency of 35 Hz for resonance operation. The amplitude of voltage of the end inductive coil is 0.62 V, the amplitude of flux linkage calculated by the integration of the voltage across the end inductive coil is 0.53 mWb. As shown in Fig. 5, the calculated peak-to-peak flux linkage at resonance is 0.23 mWb.

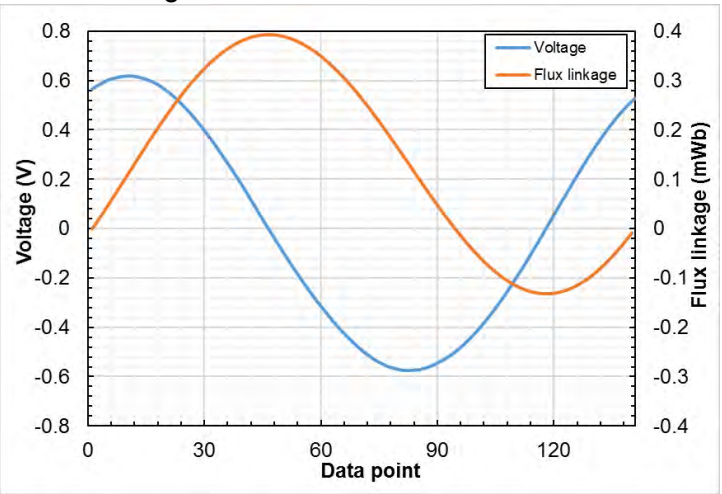

Figure 5: Measured voltage of the end inductive coil and calculated peak-to-peak flux linkage of the end core with a stroke of 8 mm and operating frequency of 35 Hz for resonance operation

3.2. Peak-to-peak Flux Linkage at Resonance

For different piston positions, the flux linkage induced by magnets in one core is different as the magnetic resistance of air gap between magnets and core vary with armature position. The peak-to-peak flux linkage at resonance between two zero crossing points of current in a cycle is because magnets move from one side to the other. With measured current and methods introduced in section 2.2, the peak-to-peak flux linkage at resonance can be calculated. Fig. 6 (a) and (b) show the peak-to-peak flux linkage for end core and middle core respectively. Both the peak-to-peak flux linkage of end core and middle core increase linearly with stroke. The slope for the end core is smaller than that of the end core. When stroke increase from 8 mm to 13 mm, peak-to-peak flux linkage of end core and middle core increase from 0.18 mWb to 0.26 mWb, 0.29 mWb to 0.46 mWb respectively. The maximum error between calculated peak-to-peak flux linkage with measured current and linear fitting result is about 6%.

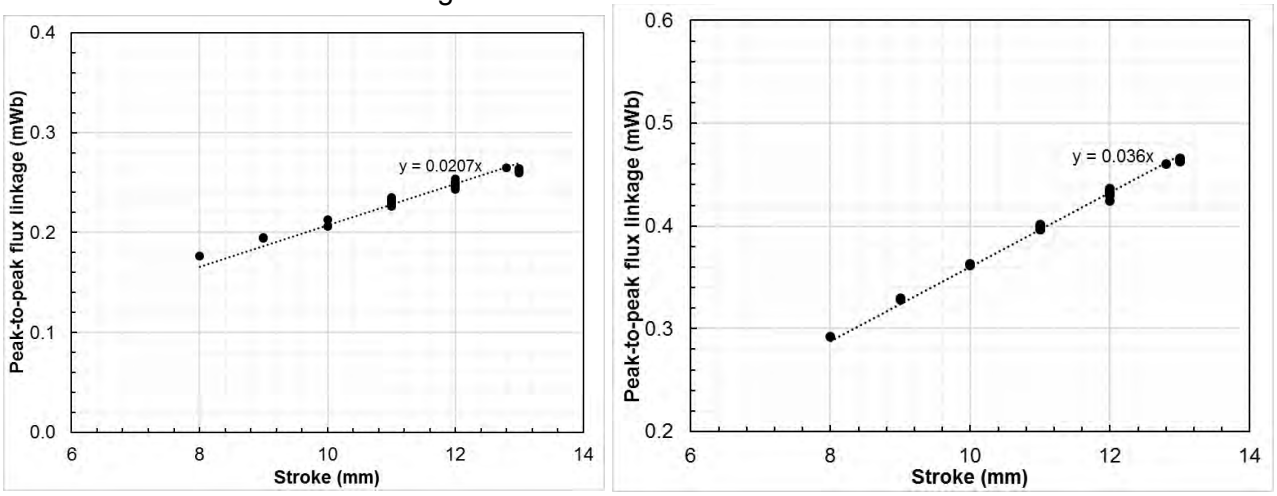

(a) (b)

Figure 6: Peak-to-peak flux linkage versus stroke at resonance (a) end core (b) middle core

3.4. Flux Linkage Difference for Off Resonance Operation

When linear compressor is operated off resonance, the piston displacement at zero crossing point of current is not maximum or minimum. The integration of the voltage of inductive coil between two zero crossing points in one cycle will be smaller than the peak-to-peak flux linkage at resonance. Fig. 6 shows the flux linkage difference between two zero crossing points of current in one cycle with operating frequency with a stroke of 11 mm. Fig. 7 (a) and (b) show the results for end core and middle core respectively. Both the flux linkage difference for end core and middle core increase to a maximum value with the increase of operating frequency from 32 Hz to 39 Hz, and both of

them decrease when operating frequency increases from 37 Hz to 39 Hz. The flux linkage difference at operating frequency of 37 Hz is closest to the linear fitting result for a stroke of 11 mm as introduced in section 3.1, which indicates that the resonant frequency approaches 37 Hz. The closer the operating frequency approaches resonance, the larger the flux linkage difference is. When the difference between operating frequency is ±2 Hz, the error for end core and middle core is 7.5% and 8.5% respectively. This means that the inductive coil can still give reasonable accuracy of compressor stroke though the compressor is off-resonance by 2 Hz.

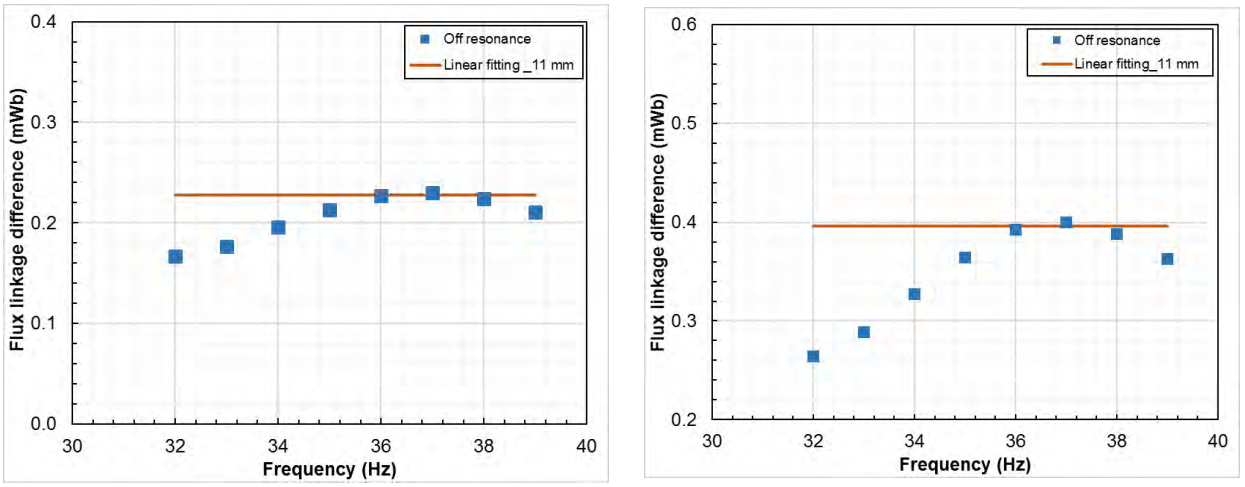

(a) (b)

Figure 7: Flux linkage difference at two zero crossing points of current versus operating frequency for a stroke of 11 mm (a) end core (b) middle core

3.4. Cooling Capacity

Cooling capacity of the refrigeration system can be modulated by adjusting stroke of the piston that is a linear function of flux linkage. Fig. 8 shows the cooling capacity with fitted peak-to-peak flux linkage of end core for a pressure ratio of 2.5 using R1234yf for resonance operation. With the increase of fitted peak-to-peak flux linkage of middle core from 0.4 mWb to 0.47 mWb, which corresponds to stroke from 11 mm to 13 mm, cooling capacity increases almost linearly from 158 W to 270 W. It can be seen that the modulation of the cooling capacity of linear compressor can be simply implemented by adjusting the drive voltage/current with compressor stroke being detected by inductive coil. Displacement transducer will not be needed for low-cost control system.

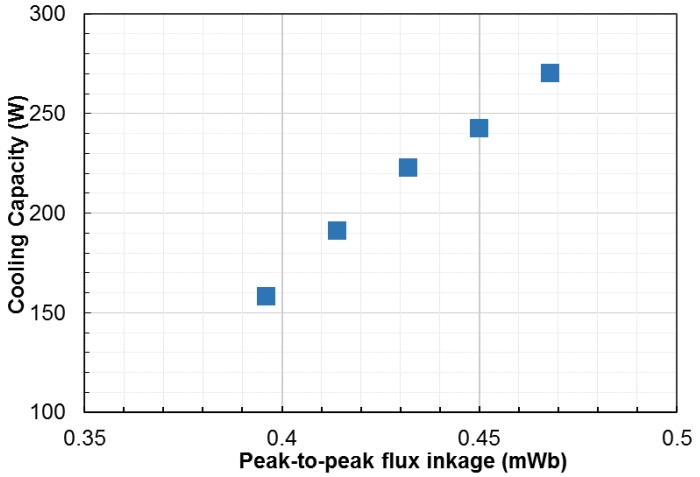

Figure 8: Cooling capacity versus peak-to-peak flux linkage of end core for a pressure ratio of 2.5 using R1234yf for resonance operation

4. CONCLUSIONS

In this work, an inductive coil was wounded around end coil and middle coil to detect piston position of a linear compressor. The peak-to-peak flux linkage at resonance was calculated with measured current. Main conclusions are listed below:

1. When linear compressor is operated at resonance and current is zero, the piston is at its maximum or minimum displacement in one cycle.

2. Both the peak-to-peak flux linkage at resonance of end core and middle core increase linearly with stroke. The slope for end core is about 0.0207 mWb/mm and the slope is about 0.036 mWb/mm for end core.

3. When linear compressor is operated off resonance, the flux linkage difference at two zero crossing points of current is smaller than resonant result.

ACKNOWLEDGEMENTS

The Research Development Fund from the University of Sussex (UA016-05) for supporting the instrumentation of the VCR system is acknowledged. The authors are also grateful to Prof Richard Stone, Dr Mike Dadd and Paul Bailey at the University of Oxford for the prototype oil-free linear compressor. The authors are grateful to Andy White and Barry Johnson at the University of Sussex for the lab support, and to the School of Engineering and Informatics for the PhD Studentship.

NOMENCLATURE

φ	flux linkage (Wb)	max	maximum displacement
V	voltage (V)	min	minimum displacement
s	inductive coil		

REFERENCES

Bansal, P., Vineyard, E., Abdelaziz, O., 2011. Advances in household appliances – a review. Appl. Therm. Eng. 31, 3748–3760.

Bradshaw, C.R., Groll, E.A., Garimella, S.V., 2012. Linear compressors for electronics cooling: energy recovery and the useful benefits. Int. J. Refrigeration 36(7), 2007-2013.

Liang, K., 2017. A review of linear compressor for refrigeration. Int. J. Refrigeration 84, 253–273.

Liang, K., Stone, R., Davies G., Dadd, M., Bailey, P., 2014. Modelling and measurement of a moving magnet linear compressor performance. Energy 66, 487-495.

Liang, K., Stone R., Dadd, M., Bailey, P., 2016. Piston position sensing and control in a linear compressor using a search coil. Int. J. Refrigeration 66, 32-40.

Liang, K., Stone R., Dadd, M., Bailey, P., 2013. A novel linear electromagnetic-drive oil-free refrigeration compressor using R134a. Int. J. Refrigeration 40, 450-459.

Manuscript ID:320

DOI: 10.18462/iir.icr.2019.0320

Condensation Characteristics of R-134a and R-404A in Horizontal Micro Finned Tubes

Rajeev KUKREJA[a], Sanjeev SINGH[b]

[a] Dr. B. R. Ambedkar National Institute of Technology
Jalandhar-144011,India. kukrejar@nitj.ac.in
[b] Dr. B. R. Ambedkar National Institute of Technology
Jalandhar-144011,India. snrn_1976@rediffmail.com

ABSTRACT

Internally Micro finned (MF) tubes are being used presently in the Condensers and Evaporators of Unitary air conditioning systems. In the present study, condensation characteristics of HFC refrigerants, R-134a and R-404A have been investigated experimentally inside horizontal smooth and MF tubes (OD 9.52mm) of 15° and 18° helix angle respectively, in mass flux range of 200-600 kg/m^{2}s with vapour quality varying between 0.1-0.9 at condensation saturation temperatures of 35°C and 40°C. The calculated quasi-local condensation HTCs for R-134a and R-404A inside MF tubes are 1.21-1.82 and 1.18-1.54 times higher and corresponding frictional PD are 1.97-2.56 and 1.71-2.22 times higher compared to that obtained for ST. The HTCs and frictional PDs for refrigerant R-134a are higher compared to refrigerant R-404A. A new heat transfer correlation has been proposed. The overall uncertainty in the heat transfer coefficient varied between 5% to 15%.

Keywords: Heat transfer coefficient, Frictional pressure drop, Micro-fin tube, Condensation, HFC refrigerants

1. INTRODUCTION

The presence of micro-fins (MF) enhances the HT rate inside horizontal tubes of condensers and evaporators of refrigerators and air conditioners in1980s. For decreasing size of condensers and evaporators in air conditioning systems, manufacturers of heat exchangers have been focusing on designing micro-fined tubes. Micro-fins are extensively used in copper tube of condensers and evaporators of industrial chillers and heating ventilation and air conditioning units.
Condensations in micro-fin horizontal tubes have shown the improvement in terms of heat transfer, when compared by identical smooth horizontal tubes working under similar circumstances. The plausible reasons for this phenomenon are increase in the useful surface area, decrease in liquid film thickness and secondary swirl flow generation with internal micro-fins. From the various research studies, condensation of refrigerants through horizontal tubes is well known. The review of various research studies of flow condensation of various refrigerants using micro-fin tubes has been presented here. Cavallini et al. (2009) developed a correlation for HTC for refrigerants R-134a, R-22, R-410A, R-123 and CO_2 for micro-fin tube. This revised model describes physical properties for refrigerants, geometrical characteristics of tubes and flow patterns inside horizontal MF tubes. Nozu et al. (1998) proposed a correlation for horizontal ST and MF tubes using R-11. Han and Lee (2005) suggested correlation for condensation in MF tubes with refrigerants R-22, R-134a and R-410A. Liebenberg et al. (2005) suggested spectral density distributions for flow pattern recognition throughout condensation in both ST and MF tubes with refrigerants R-134a, R-22 and R-407C. Cavallini et al. (2009) predicted the new model for HTC applied to pure and blends of refrigerants during condensation. This updated model obtains real properties and flow patterns of

two phase flow for refrigerant. Sapali and Patil (2010) and Vu et al. (2015) suggested the experimental average HTC raises by raise in vapour quality, mass fluxes and heat fluxes but reduces by inner diameter and raising condensing temperature for ST and MF tubes for R-134a and R-404A.
The performance of a MF tube during condensation of HFC (R-134a and R-404A) has been studied experimentally in this work. Also a correlation of heat transfer coefficient has been proposed with mass fluxes from 200-600kg/m^2s inside MF tubes.

2. EXPERIMENTAL TEST RIG AND TEST CONDITIONS

The experimental test rig is schematically presented in the Fig. 1. The test facility has refrigerant loop in which refrigerant flows through the evaporator coil and changes into the superheated vapour with the help of hot water in the tank. After that it goes to the pre-condenser where it is partly condensed by cold water flowing in the annulus. The pre-condenser is counter flow heat exchanger (HE) where the quality of vapour changes by increasing or decreasing the length of pre condenser, mass flow rate of cold water in annulus and temperature of cold water. Test condenser is also a tube in tube counter flow heat exchanger in which refrigerant flows through the copper tube at required vapour quality and mass flux. T-type (copper-constantan) thermocouples have been installed on the upper wall of copper tube by brazing in such a manner that thermocouples make cross shape in the circumference and located at six positions as shown in schematic diagram of test section (Fig 2). The liquid and vapour phase refrigerant from the test condenser enters into the post condenser. The post condenser is single shell and two tubes pass type HE in which refrigerant flows in shell side and cold water in copper tubes, where it fully condensed. This fully condensed liquid refrigerant flows to the evaporator through needle type valve by open type reciprocating compressor. This open type reciprocating compressor is compatible with refrigerants R-134a and R-404A. The refrigerant flow can be controlled by needle type expansion valve. The temperature and pressure of refrigerant at test condenser, post condenser, evaporator and pre-condenser are measured by using thermocouple wires and pressure sensors inserted into the refrigerant flow in tube wall and the pressure difference at test condenser inlet and outlet are measured by differential pressure transmitter (DPT). The mass flow rate of refrigerant displayed by coriolis mass flow meter installed between post condenser and evaporator. A data acquisition system of Make: Agilent, with three armature multiplexer cards has been attached to computer to achieve the experimental raw data. Thermo-physical properties of the refrigerants used in this study are calculated by REFPROP 7 (2002).
In hot water loop, evaporator is tube coil and tank type heat exchanger. In tube coil refrigerant is vaporized by surrounding hot water which is heated by resistance heater immersed inside the tank. Hot water flow rates have been measured by acrylic rotameter and temperature by resistance temperature detector (RTD).
ST and MF tubes geometrical parameters are tabulated in Table 1. In the cooling water loop, temperature of cold water in pre-condenser and test condenser is regulated with the help of dimmer stat they regulating the electrical power supply to the resistance heater.
The resistance heater and chiller are used for increasing and decreasing the temperature of water. Cold water flow rates are measured by using acrylic rotameter and temperature by resistance temperature detector (RTD). The uncertainty analysis for heat transfer coefficients has been performed by using method proposed by Moffat (1988). The uncertainties of different parameters are tabulated in Table 2.

Table 1. Geometrical features of horizontal smooth and micro-fin tube

Parameters	Smooth tube	Micro-fin tube (MF-1)	Micro-fin tube (MF-2)
Outer diameter, OD (mm)	9.52	9.52	9.52
Bottom wall thickness(BWT), (mm)	-	0.30	0.28
Fins height (F.H.) (mm),e_h	-	0.17	0.15
Fins angle (α)		25	30
Helix angle (β)		18	15
No. of fins, N		70	70

Length of tube, (m)	2.32	2.32	2.32
Cross sectional area, mm^2	48.97	62.45	63.02

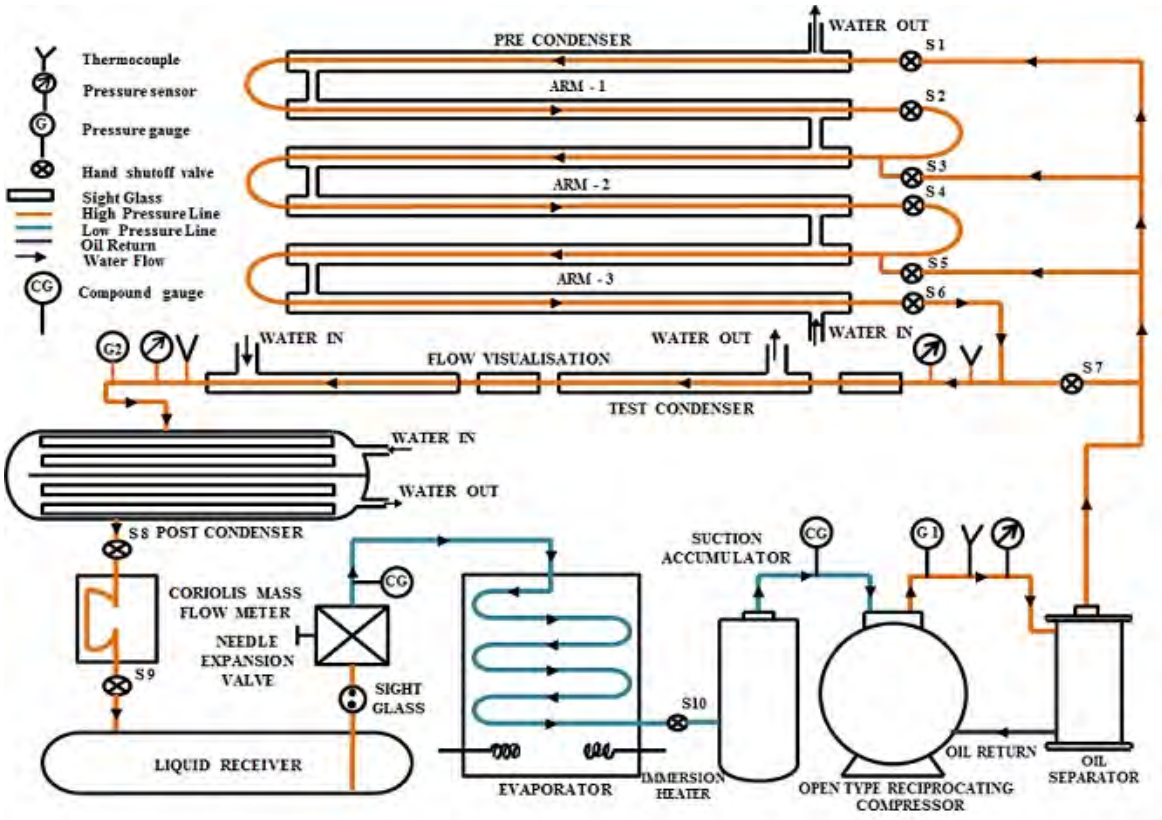

Figure 1: Schematic diagram of Experimental test rig

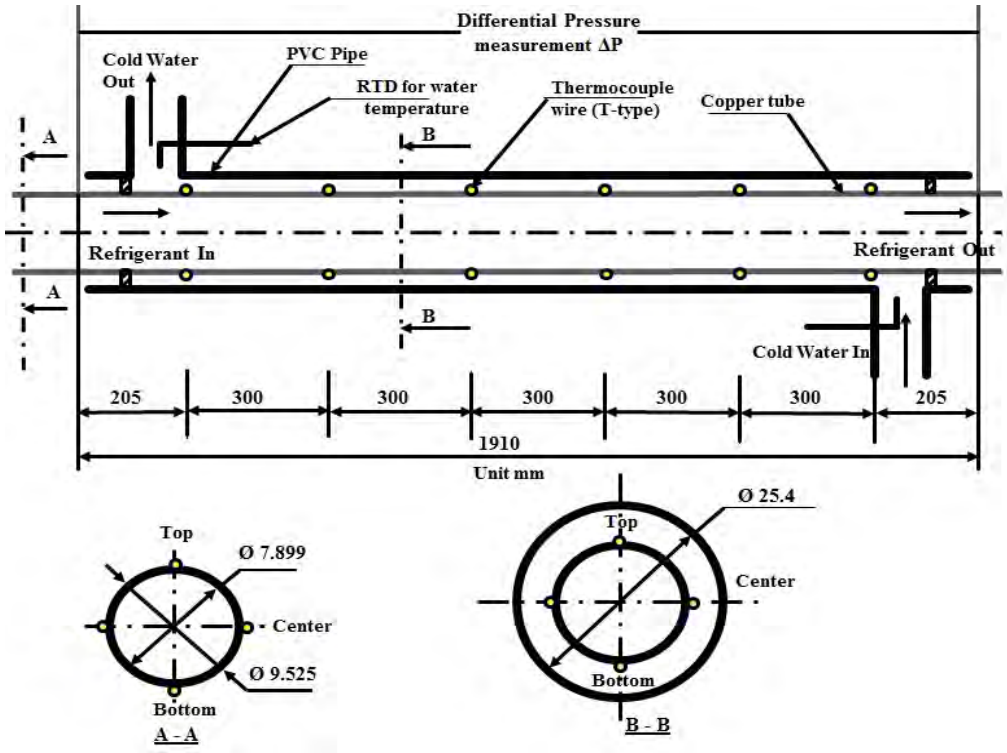

Figure 2: Schematic diagram of test section

Table 2. Measured uncertainties

Items	Accuracy
Refrigerant temperature	±0.1°C
Cooling water temperature	±0.5°C
Differential pressure	±0.05% of span
Refrigerant flow rate	±0.2% of span
Water flow rate	±5%
Average heat transfer coefficient	±6.18%

3. DATA REDUCTION

3.1. Local heat transfer coefficient (HTC)

The condensation local HTC inside horizontal tubes for two phase flow is obtained as:

$$h = \frac{Q}{A(T_{sat} - T_{wi})}$$

Eq.(1)

The heat absorbed by the cooling water Q in test condenser is calculated as

$$Q = m_w C_{pw} \Delta T_{tc}$$ Eq. (2)

Vapour quality at inlet and outlet of test condenser has been calculated from enthalpy balance of Precondenser and Test condenser. Therefor, mean vapour quality in test condenser is determined by average of vapour quality at test condenser inlet and outlet.

3.2. Pressure drop (PD)

The total PD inside the horizontal tubes in two phase flow is the sum of momentum, frictional and gravity component,

$$\Delta P_{total} = \Delta P_{mom} + \Delta P_{fric} + \Delta P_{gravity}$$ Eq. (3)

The flow is horizontal, then, $\Delta P_{gravity} = 0$, so that the frictional PD is calculated by subtracting the momentum or acceleration PD from the total measured PD. This total PD at test condenser is measured by using DPT.

$$\Delta P_{fric} = \Delta P_{total} - \Delta P_{mom}$$ Eq. (4)

The momentum PD is calculated by the equation given below as

$$\Delta P_{mom} = G^2 \left[\left\{ \frac{(1-x)^2}{\rho_l (1-\varepsilon)} + \frac{x^2}{\rho_g \varepsilon} \right\}_{out} - \left\{ \frac{(1-x)^2}{\rho_l (1-\varepsilon)} + \frac{x^2}{\rho_g \varepsilon} \right\}_{in} \right]$$

Eq.(5)

The void fraction ε is calculated by Smith correlation (1971)

$$\varepsilon = \left[1 + \frac{(1-x)\rho_g}{x\rho_l} \left\{ 0.4 + 0.6 \sqrt{\frac{\frac{x\rho_l}{\rho_g} + 0.4(1-x)}{x + 0.4(1-x)}} \right\} \right]^{-1}$$ Eq.(6)

4. RESULTS AND DISCUSSION

HTC during the condensation inside ST and two MF tubes (referred as MF-1, helix angle 18° and MF-2, helix angle 15°) are experimentally obtained with R-134a and R-404A at condensation temperature 35°C and 40°C. During whole experiments on test sections of smooth and micro-fins 420 points are recorded.

4.1. Condensation heat transfer coefficient

Experimental HTCs for pure R-134a and blended refrigerant R-404A inside ST and MF tubes are presented as shown in Fig. 3.

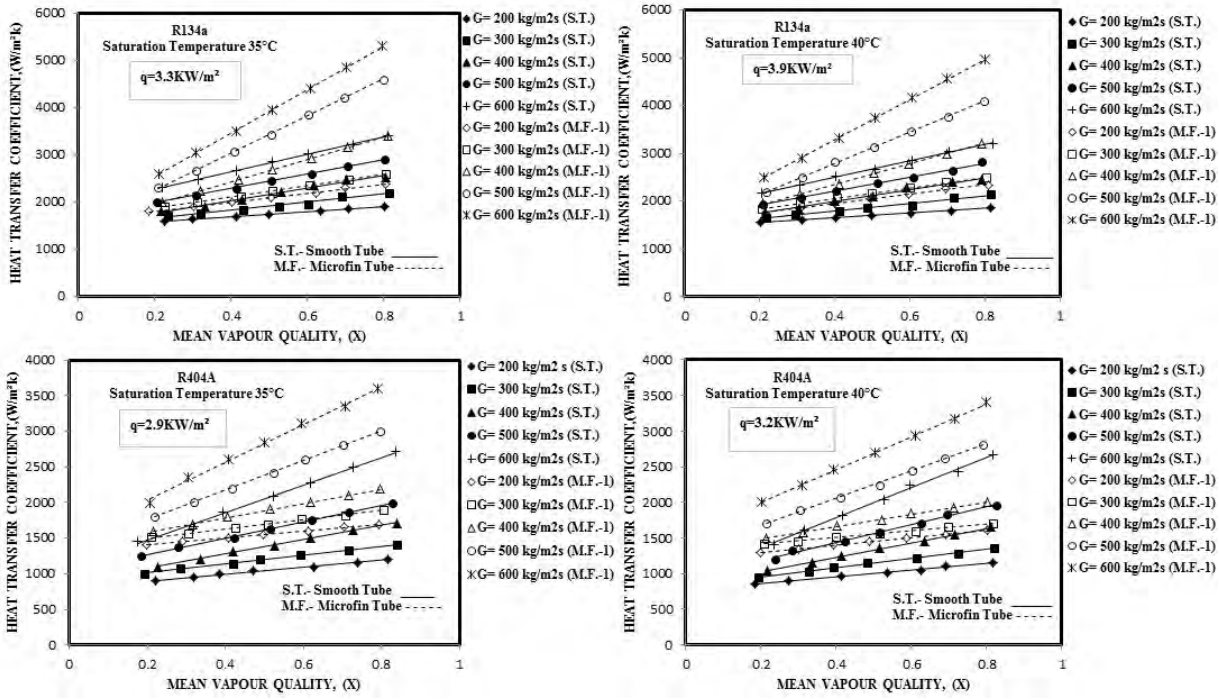

Figure 3: Comparison of heat transfer coefficient of R-134a and R-404A in a smooth and micro-fin tube (helix angle 18°) at saturation temperature of 35°C and 40°C

When the mass flux and vapour quality increases then the HTC at low vapour quality and mass flux increases gradually and after that at high values it increases rapidly. Also the HTC depends on condensation temperature, its value increases with decrease of condensation temperature. The trend line of experimental data is sort of linear at stable mass flux and condensation temperature versus vapour quality.

The experimental HTCs obtained from MF tubes are larger than STs at steady mass flux and condensation temperatures because spiral shape inside the micro-fin tubes stretching the film of liquid phase as results film thickness decreases by this thermal resistance decreases. The experimental values of HTC inside MF tubes were 1.21- 1.82 times and 1.18-1.54 times greater than those of smooth tubes at saturation temperature 35°C, 40°C and mass flux from 200 to 600kg/m^{2}s with R-134a and R-404A because the liquid phase density of R-134a is greater than R-404A (1.17 times). Due to higher liquid density of R-134a thickness of liquid film decreases at fin tip resulting in HTC increases. The HTCs obtained inside MF tube (MF-1) greater than that of MF tube (MF-2) due to greater helix angle and fin height. Higher values of helix angle and fin height improves turbulence and surface area for HT in MF tubes and develop large Nusselt number and friction factors. A higher helix angle forms fins more inclined to the incoming axial flow so that stronger interactions developed between the fins and fluid flow which arise higher heat transfer. High fin height increases the surface area of heat transfer also increases heat transfer rapidly when the helix angle is greater than 20° because it increases the interactions between incoming fluid flow and fin tip.

4.2. Predicted heat transfer coefficient correlation for micro-fin tubes

Equation 7 shows the new developed correlation by multiple linear regression technique, Chapra and Raymond (1990) for computation HTCs inside horizontal MF tubes. The coefficient of correlation determined for micro-fin tubes is 0.94274, mean absolute deviation is 7.92% and standard deviation is 9.33%. In new correlation equivalent Reynold number is taken as a significant measure of kinematic and dynamic similarities in forced convection heat transfer whereas Prandtl number strongly influences the relative growth of mass velocity and thermal boundary layers. The involvement of reduced pressure or pressure ratio forms the developed correlation more convenient for large range of saturation temperatures. The product of Froude and Bond number gets the influence by inertia, surface tension and gravitational forces.

$$Nu = 0.637 \,.\, Re_{Eq}^{0.5798} \,.\, Pr_l^{-0.789} \,.\, \left(\frac{P}{P_{cr}}\right)^{-0.3} \,.\, R_x^{0.5097} \,.\, (Fr \,.\, Bo)^{-0.0144} \qquad \text{Eq.(7)}$$

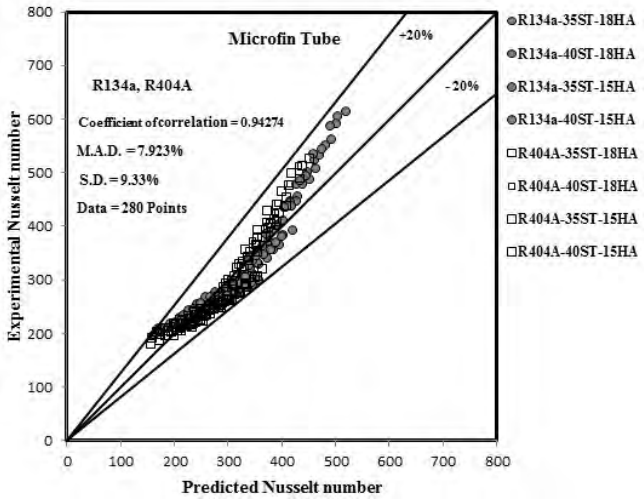

Figure 4. Comparison of experimental heat transfer coefficient with new correlation in micro-fin tube

The main controlling parameter than the dimensionless numbers for MF tubes is HT area enhancement factor (R_x). Fig. 4 shows the comparison between experimental and predicted HTC determined by new developed correlation inside the horizontal micro-fin tubes.

4.3. Pressure drop

The frictional pressure drops are calculated in 1.91m length of horizontal ST and MF tube test sections. Total PD is measured by DPT connected at test condenser inlet and outlet.

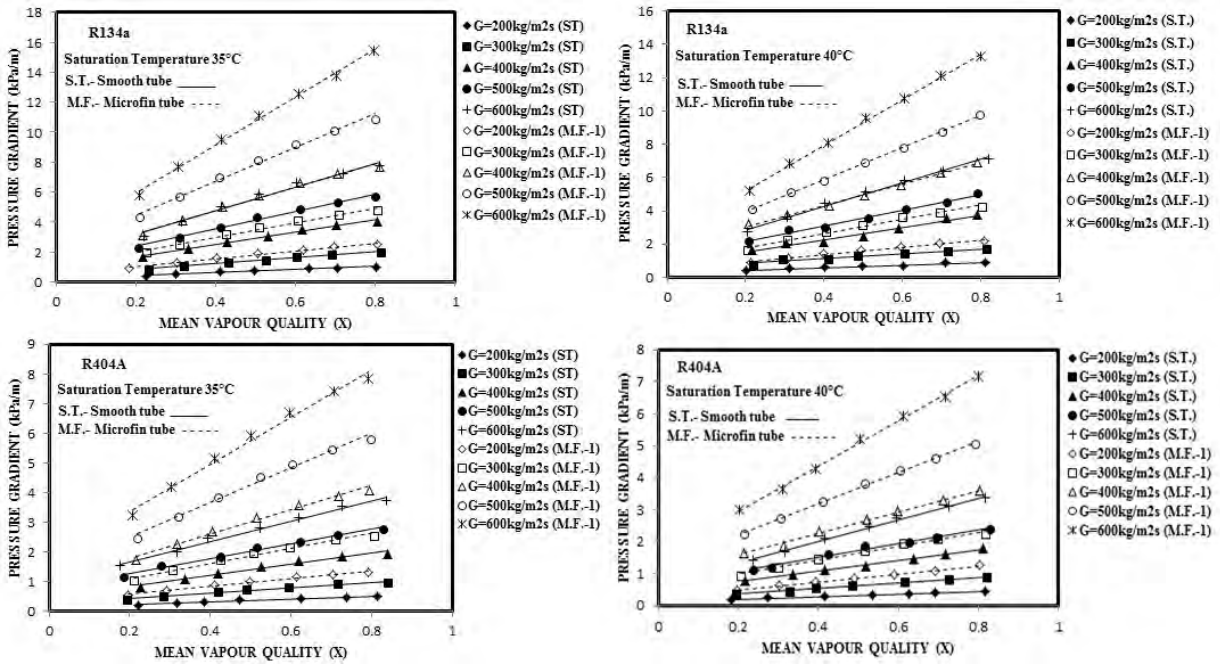

Figure 5. Comparison of Pressure drop of R134a and R-404A in a smooth and micro-fin tube (helix angle 18°) at saturation temperature 35°C and 40°

The experimental frictional PD can be calculated by subtracting the momentum PD from the total measured PD. The frictional PG inside ST and MF tubes at condensation temperature 35°C and 40°C with R-134a and R-404A are as presented in Fig. 5. The frictional pressure gradient inside micro-fin tubes has been compared to similar diameter smooth tube working under similar conditions as presented in Fig. 5. The pressure drop of friction throughout the condensation process inside micro-fin tubes with R-134a and R-404A is nearly 1.97 to 2.56 and 1.71 to 2.22 times greater than those of smooth tubes due to large value of liquid phase density of R-134a than R-404A.

5. CONCLUSIONS

The conclusions from the current investigation have been given as below:

[1] The experimental HTC and frictional PG throughout the condensation of refrigerants namely R-134a and R-404A are calculated inside horizontal ST and two different MF tubes MF-1 and MF-2 of helix angle 18°and 15° in the mass flux range of 200 to 600kg/m^{2}s at condensing saturation temperatures 35°C and 40°C.

[2] During experiments it has been found that the condensation HTC and frictional PD increase with increase in vapour quality and mass flux and decrease in condensation saturation temperature in ST and MF tubes.

[3] The HTC and frictional pressure drop inside two tubes (MF-1 and MF-2) has been compared to the equivalent inner diameter smooth tube working in similar conditions to present the benefits of MF tubes over STs. The obtained condensation local heat transfer coefficients inside tubes MF-1 and MF-2 were 1.21 to 1.82 and 1.18 to 1.54 times greater and pressure drop of friction 1.97 to 2.56 and 1.71 to 2.22 times larger than smooth tubes with condensation of R-134a and R-404A.

[4] A new correlation for calculation of heat transfer coefficients (280 data points) inside micro-fin tubes has been developed by the use of multiple linear regression technique. A good agreement with experimental results having coefficient of correlation is found 0.9427.

ACKNOWLEDGEMENT

This whole research was supported and financed by National Institute of Technology, Jalandhar, India, SERB/ DST. The microfin tubes were provided by M/s Spirotech Heat Exchangers (P) Ltd., Bhiwadi, Rajasthan (India)

NOMENCLATURE

A	Heat transfer surface area (m^2)
Bo	Bond number (-)
c_p	Specific heat capacity at constant pressure, (kJ/kg-K)
D	Tube inner diameter (m)
Fr	Froude number (-)
G	Mass flux (kg/m^2-s)
h	Heat transfer coefficient (W/m^2-K)
m	Mass flow rate (kg/s)
Nu	Nusselt number (-)
p	Pressure (bar)
Pr	Prandtl number (-)
Q	Heat transfer rate (W)
q	Heat flux (kW/m^2)
Re_{Eq}	Equivalent Reynold number, $\left(Re_l + \left(\frac{\mu_v}{\mu_l}\right)\left(\frac{\rho_l}{\rho_v}\right)^{0.5} . Re_v\right)$
Re_l	Reynold number of liquid phase, $\left(\frac{G(1-x)D}{\mu_l}\right)$
Re_v	Reynold number of vapour phase, $\left(\frac{GDx}{\mu_v}\right)$
Re	Reynolds number (-)
T_{sat}	Saturation temperature of refrigerant (k)
T_{wi}	Inside tube wall temperature (k)
x	Mean vapor quality

Greek symbols

α	Fin angle (^{o})
β	Spiral or helix angle (^{o})
ε	Void fraction (-)
μ	Dynamic viscosity (Ns/m^2)
ρ	Density (kg/m^3)

Subscripts

BWT	Bottom wall thickness
exp	Experimental
FH	Fin height
g	Gas phase
HT	Heat transfer
HE	Heat exchanger
i	Inlet
l	Liquid phase
MF	Micro-fin
o	Outlet
sat	Saturation

REFERENCES

Cavallini, A., Del Col, D., Mancin, S., Rossetto, L., 2009. Condensation of pure and near-azeotropic refrigerants in micro-fin tubes: a new computational procedure. Int. J. Refrigeration 32(1), 162-174.

Chapra, S.C., and Raymond, C.P., 1990. Numerical methods for engineers, *McGraw-Hill International Editions*, Chapter 17 (Least-Squares Regression), 330-360.

Han, D., Lee, K.J., 2005. Experimental study on condensation heat transfer enhancement and pressure drop penalty factors in four micro-fin tubes. Int J Heat Mass Transf 48(18), 3804-3816.

Liebenberg, L., Thome, J.R., Meyer, J.P., 2005. Flow visualization and flow pattern identification with spectral density distributions of pressure traces during refrigerant condensation in smooth and micro-fin tubes. J. Heat Transfer 127(3), 209-220.

Moffat, R.J., 1988. Describing the uncertainties in experimental results. Exp. Therm. Fluid Sci. 1(1), 3-17.

NIST, NIST Standard Reference Database 23: NIST Thermodynamic properties of Refrigerants and Refrigerant Mixtures (REFPROP), version7.0, National Institute of Standards and Technology (NIST), Gaithersburg (2002) MD.

Nozu, S., Katayama, H., Nakata, H., Honda, H., 1998. Condensation of a refrigerant CFC11 in horizontal micro-fin tubes (proposal of a correlation equation for frictional pressure gradient). Exp. Therm. Fluid Sci. 18, 82-96.

Sapali, S.N., Patil, P.A., 2010. Heat transfer during condensation of HFC-134a and R-404A inside of a horizontal smooth and micro-fin tubes. Exp. Therm. Fluid Sci. 34, 1133–1141.

Smith, S.L., 1971. Void fraction in two-phase flow: a correlation base on equal velocity head model. Heat and Fluid Flow 1, 22-39.

Vu, P.Q., I, C.K., Taek, O.J., Honggi, C., Taehum, K., Jungho, K., Jaeyoung, C., 2015. An experimental investigation of condensation heat transfer coefficient using R-410A in horizontal circular tubes. International Conference on Applied Energy 75, 3113–3118.

Manuscript ID: 326
DOI: 10.18462/iir.icr.2019.0326

High efficiency air cooled heat exchangers for CO2 applications

Stefano FILIPPINI[(a)], Umberto MERLO[(a)], Giovanni MARIANI[(a)], Livio PERROTTA[(a)],

[(a)] LU-VE GROUP, Uboldo, 21040, Italy, stefano.filippini@luvegroup.com

ABSTRACT

CO2 is often proposed as a radical solution to eliminate the greenhouse effect caused by halogenated hydrocarbons belonging to the HFC category. Even though the direct contribution of CO2 is practically zero, the indirect effect would be increased if the CO2 refrigeration cycles were less efficient than traditional ones (lower COP), due to larger electricity consumption bringing about larger emissions of CO2 and of other pollutants from power stations. The appropriate choice of heat exchanger technology is a fundamental condition for obtaining COP values form CO2 cycles allowing for a real reduction of the greenhouse effect. However, CO2 is significantly different from all the other halogenated and non-halogenated fluids and it poses peculiar opportunities to heat exchanger designers: their discussion is the subject of this paper, underlining in particular innovative solutions and test laboratory to enhance the heat exchange efficiency and to improve the overall performance of the refrigeration plant.

Keywords: CO2, unit coolers, gas coolers, heat exchangers, COP, high efficiency

1. INTRODUCTION

In several refrigeration applications, CO2 is an excellent and environmentally-friendly solution; LU-VE has designed very efficient heat exchangers for CO2 applications and has been able to make important developments thanks to the use of its modern test ring. This plant can test the performance of CO2 finned heat exchangers, both air cooled unit coolers and gas coolers. The new testing plant enabled the launch of a specific project for a CO2 fin-and-tube heat exchanger, with the primary aim of improving knowledge of heat exchange phenomena in evaporation, condensation and during trans-critical gas cooling. The influence of oil on internal heat exchange coefficient also enters into the scope of the research. The paper describes the testing activity, the calibration made on software that calculates product performance, and potential improvements to products. In particular, it was possible to calibrate a specific method able to take into account the behaviour of the fluid during trans-critical cooling, properly considering all the parameters affecting real performance.

2. TEST PLANT

The CO2 plant (Fig. 1) was designed to be able to test condensers, gas coolers and unit coolers. The maximum operating pressure is 120 bar, while the maximum temperature is 120°C. The capacities of the plant in the standard conditions specified below are:

- Unit Coolers (SC2): 15 kW
- Gas Coolers e Condensers (100bar, 120°C, DTmin=3°C) e (25/40/65°C): 40 kW.

A dedicated software programme was developed in-house using LabView to monitor and acquire data. The tests were conducted making a thermal balance between the test unit and a contrast group in order to guarantee the reliability of the experimental data. This required a great deal of time for the calibration of the measurement instrumentation and in particular for the definition of dispersion inside the climatic test chamber.

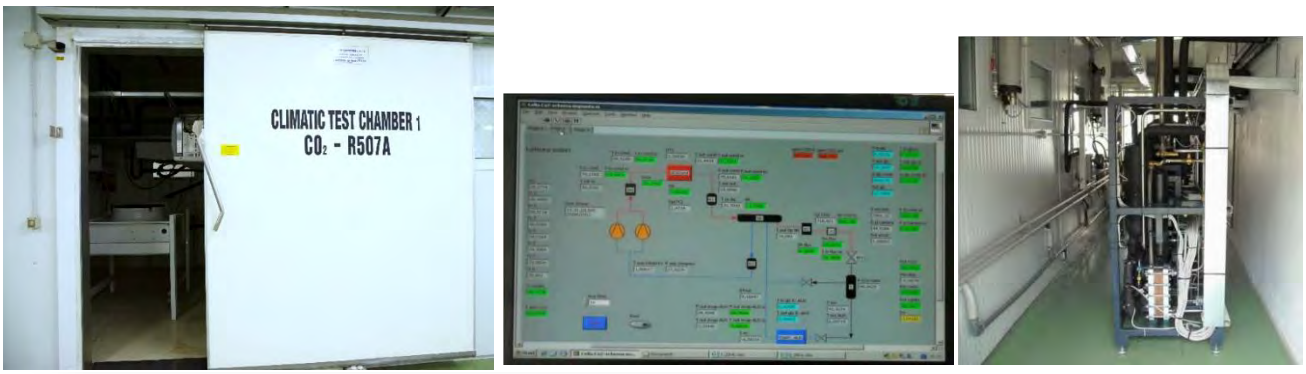

Figure 1: Image of data acquisition codes and view of the plant

3. CO2 HEAT EXCHANGERS

In refrigeration plants using CO_2 as the working fluid, two types of heat exchangers are used:

- Evaporators, which are included in every proposed plant configuration: in direct CO_2 cycles, in binary cycles (using a low temperature CO_2 cycle and an higher temperature cycle, operated by another fluid and rejecting heat towards the ambient) and in other systems using CO_2 as the cold energy carrier, condensed by a refrigerating machine and evaporated by the users device. Evaporators, working at low temperature, do not require elevated operating pressure and therefore are not substantially different from models for halogenated fluids.
- Gas-coolers, which are included in direct cycles only to reject heat towards the ambient. They perform the same duty of conventional fluid condensers, but rather than condensation (implying a two-phase equilibrium) a simple transition from the expanded gas phase to the liquid state takes place. As a matter of fact, as CO_2 has a very low critical temperature of 31°C, a supercritical operating pressure is necessary to maintain a temperature higher than the one of ambient receiving heat from the cycle. The critical pressure being 73.8 bar, operating pressures much larger than those of conventional cycles will be adopted.
- The typical shape of supercritical cycles is shown in Fig. 2. Compared to conventional cycle rejecting most of their thermal capacity at a constant temperature, supercritical cycle performance is not only influenced by the minimum and maximum pressure, but their COP is strongly affected by the gas cooler outlet temperature, i.e. the temperature of the liquid at the expansion device entrance[1]. This is very important to obtain acceptable COP: as a matter of fact, CO_2 cycles perform very well with low coolant temperatures (e.g. water-heating heat pumps, low ambient temperatures in cool regions). For a given ambient temperature, the gas cooler exit temperature is imposed by the design characteristics of the gas cooler, therefore assuming a fundamental role as far as the cycle performance are concerned.

[1] Liquid temperature also affects the performance of conventional cycles, provided that a specific heat transfer section is devoted to sub-cooling, but at a much lower extent.

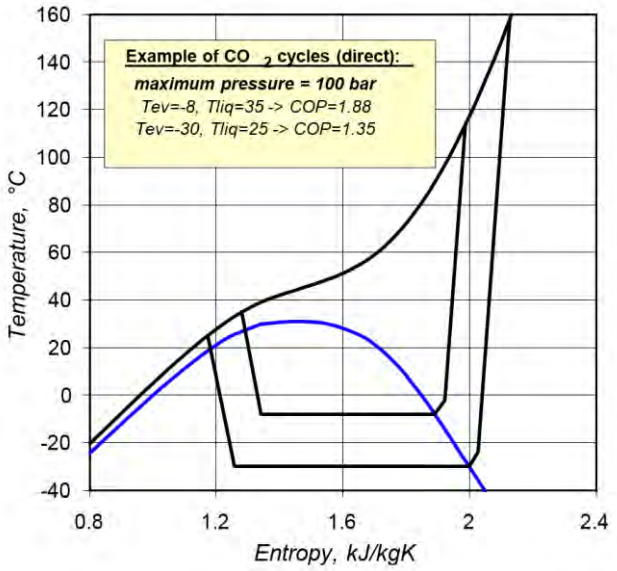

Figure 2: Examples of inverse CO_2 supercritical cycles.

4. EVAPORATORS

A CO_2 evaporator for refrigeration applications does not have to undergo especially high working pressures (Table 1). However it is necessary to prevent overpressures caused by prolonged standstill of the equipment or by defrosting, when the temperature can rise well over that of the cooling room. Rather than oversizing the evaporator and the refrigerant lines, it is preferable to adopt expedients which can limit the project pressure to 60 bar or even less (safety valves, pump-down to remove liquid from the evaporator). Such pressure values are just a little above those normally used in refrigeration (all LU-VE evaporators are available up to 85 bar) and do not impose any special design, even if larger thickness of coil tubes and headers are usually adopted.

Table 1: Relationship between temperature [°C] and pressure [bar] for CO_2.

T	-40	-35	-30	-25	-20	-15	-10	-5	0	5	10	15	20	25	30
p	10.04	12.02	14.26	16.81	19.67	22.88	26.45	30.42	34.81	39.65	44.97	50.81	57.22	64.25	72.05

On the other hand, it is interesting to determine if an evaporator designed for conventional refrigerants can operate correctly for CO_2, with no or limited modifications, and, if so, to estimate the variations of thermal power. It should be stated in advance that the thermophysical properties of CO_2 are favourable to obtaining elevated heat transfer performance. Compared to R404A, CO_2 has higher specific heat, higher thermal conductivity and lower viscosity. This last fact, along with the greater vapour density, allows fewer pressure drops at the same mass velocity. Considering that (at equal capacity) the larger heat of evaporation brings about a lower throughflow, pressure drop reductions at the same power turn out to be very significant indeed. Table 2 shows the results of a theoretical prediction of a LU-VE unit cooler running on CO_2 (in terms relative to R404A) at two different evaporation temperatures, in the following hypotheses;

- Unchanged specifications: a slight increase in power at -8°C, becoming more consistent at low temperatures (from 3.5 to 11%); fluid velocity and pressure drops are very low.
- Reducing the number of feeds: in-tube velocity return to optimal values and 6-7% capacity improvement is shown compared to the previous case; reducing the number of feedings reduces the cost of the gas header and distributor.
- Reducing the number of inlets and using smooth tubes instead of microfin tubes (helically grooved microfins such as those normally used in LU-VE unit coolers): microfin tubes are particularly useful with poor refrigerant heat transfer coefficient: their convenience is very reduced at high evaporation temperature, but remains significant at low temperature with a low density fluid (-30°C).

Table 2: Comparative performance of unit coolers for R404A and CO_2. The ratios are valid for some representative models but are not applicable in general.

fluid	R404A	CO_2		
type of tube	microfin			smooth
no. of parallel inlets	N	N	N/2	N/3
rating (rel. to R404A), Tev= –8°C, ΔT_1= 8K	100.0	103.5	110.6	108.2
rating (rel. to R404A), Tev= –30°C, ΔT_1= 6K	100.0	111.1	117.7	112.0

The last two solutions permit a modest improvement of the specific cost (€/kW) of the equipment, as long as the pressures of the design do not exceed 40-60 bar. LU-VE has already supplied various clients with CO_2 unit coolers up to now no visible indications have arisen of the slightest power deficit nor of any operating problems.

5. CO2 HEAT EXCHANGERS

The gas cooler design is notably more complex, also due to the larger operating pressure (up to 150 bar), and poses some relevant peculiarities. The fundamental aspect for the thermodynamic design is that, as a consequence of the high average temperature along the upper isobar (responsible for the modest COP values), with CO_2 it is possible to bring the cooling air to much higher temperatures than those occurring with a refrigerant having a condensation phase at constant temperature. Fig. 3 shows this situation very clearly: it is evident that with CO_2 an air ΔT 2-3 times greater can be obtained. Consequently it is possible to use an airflow reduced by the same proportion at equal thermal capacity. The large reduction in the airflow gives notable advantages in terms of reduced front area of the fin pack, of electric power required for ventilation and of the initial cost of the fans and their regulators.
To quantify these statements, a calculation method was developed capable of accounting for the particular distribution of the ΔTs between CO_2 and air (as in Fig. 3), provided that flows are arranged to run countercurrent[2].

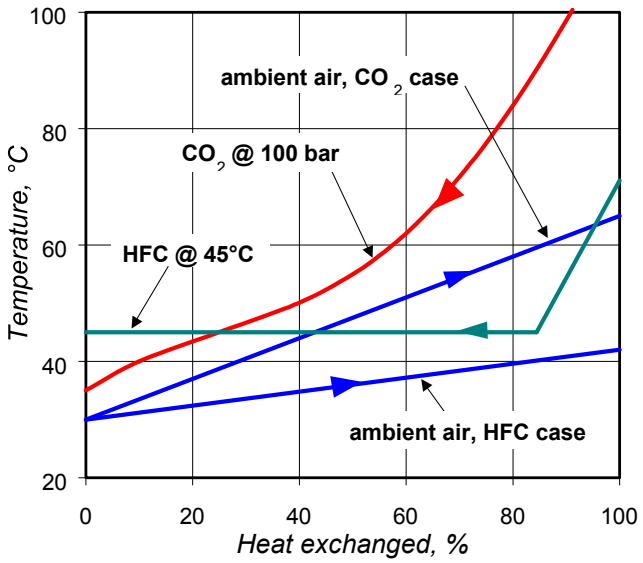

Figure 3: Heat transfer diagram for a CO_2 gas cooler and for a condenser using a conventional refrigerant.

[2] In plate-fin coils with 3-4 rows (or more) it is usually possible to arrange the circuiting in order to obtain a fluid path very close to counterflow, with negligible influence on the predicted performance.

The exchanger is subdivided into 20 computational sections: for each one an independent evaluation is done of the average logarithmic ΔT and of the in-tube heat transfer coefficient, with the Gnielinski correlation for single phase flows. Fig. 4 shows an example of how some important parameters vary in the computational sections. It can be noticed that: (i) the heat transfer coefficient presents a maximum close to the critical point , (ii) the required surface area increases significantly in the cold end, due to the reduced ΔT between the two fluids and to the low liquid velocity.

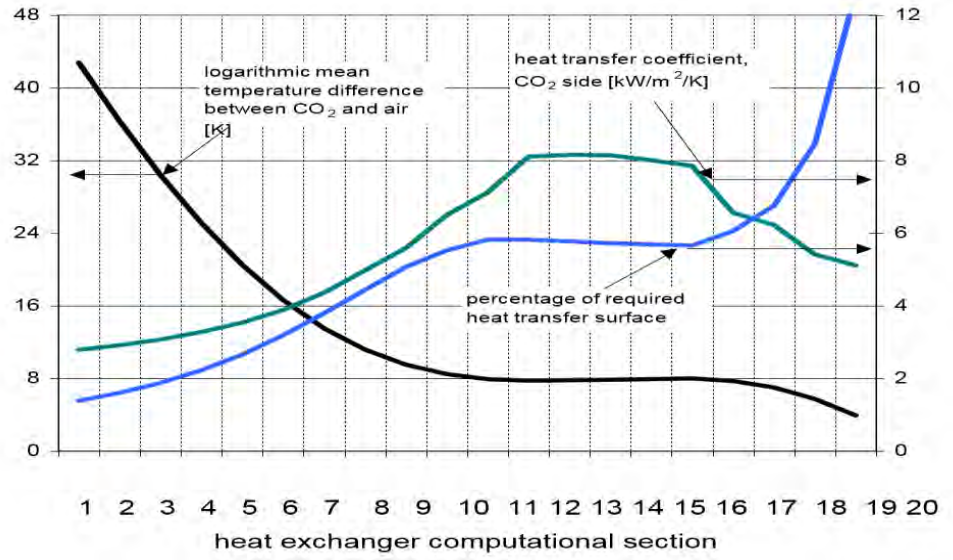

Figure 4:Variations of some parameters in the computational sections of a CO_2. gas cooler

Table 3 shows a comparison between a R404A condenser (capacity of about 170kW with initial ΔT of 15K) and CO_2 gas coolers of the same power range. Since the CO_2 outlet temperature plays a preponderant role, the comparison was carried out in two ways: (i) at equal power, varying the final temperature, and (ii) at a final ΔT of 5 K, varying the power. The number of parallel feedings is optimised in all cases. The following solutions are proposed in table 3**:**

- The first solution is the R404A reference (in normal production).
- The second solution presents the same fin dimensions (frontal area and rows) and the same ventilation. The rating is exuberant (last line) or, as an alternative, a very reduced ΔT can be obtained (the 0.3 value is, however, only valid for perfect counterflow) all of which is caused by the very large ΔT between CO_2 and air (at equal air flow). The above mentioned possibility of reducing the airflow was not exploited in this solution
- The third solution thoroughly exploits this possibility, using only one fan instead of three.
- The exchanger surface is redistributed to best adapt to a reduced airflow: the number of rows is doubled and the front section was halved, with a heat transfer surface practically the same as the original. The thermal rating at final ΔT of 3K is slightly less than the reference (-4%) in the presence of major reductions in the dimensions (50%), in the ventilation power (66%) and in the noise level (4.8dB). It should be pointed out that in these cases the outlet air temperature is in the range of 60°C: it is therefore convenient to place the fans at the coil inlet (forced draft) to avoid thermal stress to the motor and to increases the mass air flow, compared to the usual solution of induced draft (fan at coil outlet).

Table 3: Comparative performances of air cooled condensers with R404A and CO_2 under the following conditions: air temperature 25°C, condensation R404A 40°C, CO_2 pressure 100 bar.

fluid	R404A	CO2	CO_2
number of fans	3	3	1
front coil area, m^2	5.28	5.28	2.56
number of rows	3	3	6
number of inlets	66 (std)	22	21
fan positioning	induced-draft	induced-draft	forced-draft
cooler outlet temperature, at equal power (air at 25°C)	40°C (condensation)	25.3°C (ΔT=0.3)	28.8°C (ΔT=3.8)
or: (relative) thermal rating cooler outlet temp. =30°C	100 (ΔT=15K)	158 (ΔT=3K)	96.0 (ΔT=3K)

In general, the optimum solutions may vary depending on the design survey and on the requirements imposed by the compatibility with existing models, for industrial reasons. However, one can conclude that the use of CO_2 could bring about significant reductions in the size of the equipment (in relation to the reduced ventilation) compared to equipment with similar ratings for conventional refrigerants, even with small final ΔT values (for example, 3K as in table 3).
LU-VE has over 13 years of experience in CO2 ventilated heat exchangers and it participated in the construction of the first trans-critical supermarket in Europe (2004), providing gas coolers with adiabatic spray system in trans-critical operation.
The CO_2 gas cooler product can therefore be considered “proven technology” in the refrigeration field. This achievement was made possible because of the design strategy adopted by LUVE, consisting of the utilization of high performance heat transfer surfaces and of miniaturized geometries (small diameter tubes) even for large heat exchangers.



Figure 5: COOP WETTINGEN - Zurig - Switzerland Gas cooler CO2.SHVDT 696 CO2 (2004)

6. EMERITUS

EMERITUS® is the latest innovation developed for the range of condensers, dry coolers and gas coolers manufactured by LU-VE Exchangers. This new technological advance (patent pending) brings together the benefits of spray systems and adiabatic pre-cooling. A sophisticated control system maximizes the effects of these combined systems.
The specific features of this product make it especially suitable for use in air conditioning and refrigeration. When EMERITUS® is applied to CO2 gas coolers, high system COP can be reached even during the hottest hours of the year. This means that the “CO2 equator” can be redrawn, extending the geographical area where trans-critical systems can be cost-effectively constructed.

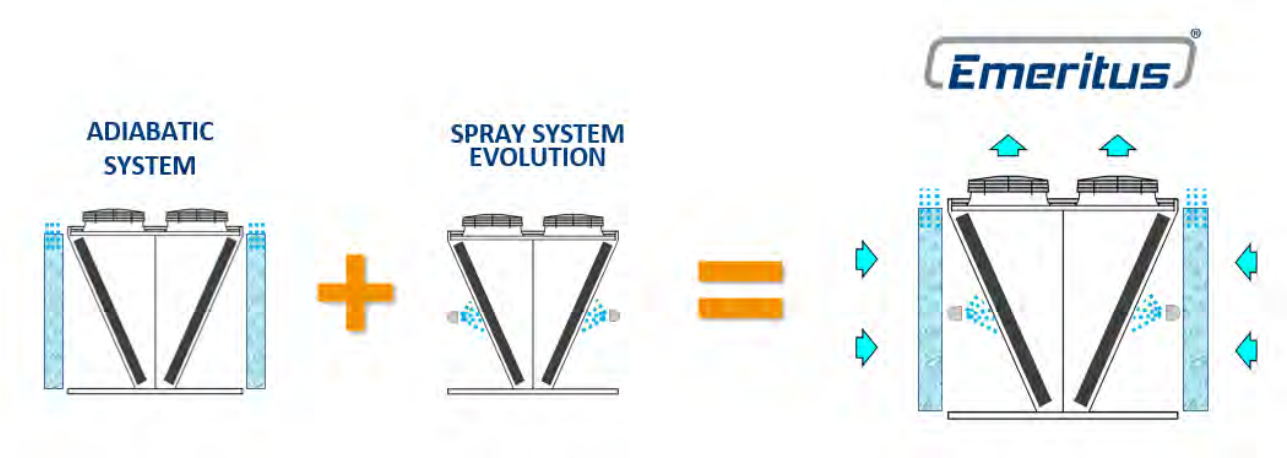

Figure 6: Emeritus® technology

The ability to use just the adiabatic system in the absence of a water treatment plant is a further example of its versatility. The graph shows the performance levels of a gas cooler with Adiabatic Panel technology compared with a traditional dry system. The technology with adiabatic system shows clearly superior performance. At equal capacity, it is possible to bring the CO2 outlet temperature down from 40°C to 30°C. A reduction of 10 K of the CO2 has a positive consequent impact on the COP of the system. In a comparison made at equal conditions (the same capacity, the same evaporation temperature, etc.), a COP increase of 69%* was obtained (*hypothesis of a simple cycle with evaporation temperature of -8°C. The COP goes from 1.31 (temp. Tout CO2 gas at 40°C) to 2.21 (T.out CO2 gas at 30°C)).

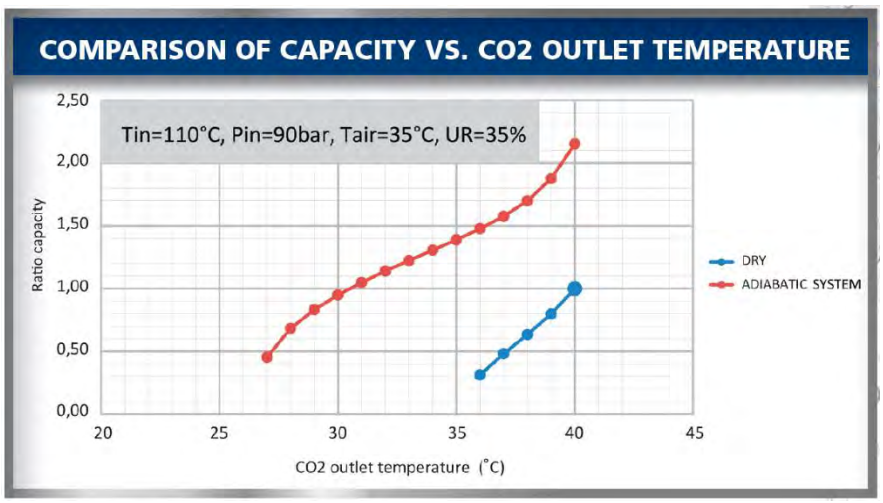

Figure 6: Comparison of gas cooler capacity ADIABATIC SYSTEM vs DRY



Figure 7: EMERITUS® 2017 - France – Gas cooler with adiabatic system

7. CONCLUSIONS

The applications of CO_2 in the refrigeration industry could shortly become an important reality. From the heat exchanger point of view, the utilization of CO_2 poses some problems (greater operating pressures) but also offers notable opportunities, especially in the most difficult design case of the gas coolers. We have seen that reductions of the airflow and of the coil front area can be achieved, at equal capacity and with very small final ΔT values (this last being an essential parameter for obtaining a good COP of the cycle). It brings about lower fan consumption, smaller size and some production cost savings, counterbalanced by the increased use of copper resulting from the thicker tube walls and headers. The fin-and-tube geometries used for conventional fluids are perfectly adequate to CO_2 application, in the case of LU-VE production which has for many years concentrated on small diameter tubes even for large units.

Manuscript ID: 337
DOI: 10.18462/iir.icr.2019.0337

STUDY ON METHOD ENSURING SAFETY OF BUILT-IN REFRIGERATED DISPLAY CABINET USING R290

Koji YAMASHITA[(a)], Yoshihisa SAKAMOTO[(a)], Toshimasa KATO[(a)], Shigeki ISHIHARA[(a)], Akira KOBAYASHI[(a)], Hidekazu KAINUMA[(a)], Makoto SATO[(a)], Katsuyuki OSAWA[(a)], Hiroshi NAGAI[(a)], Masahiko NAKAGAWA[(a)]

[(a)] The Japan Refrigeration and Air Conditioning Industry Association
3-5-8, Shibakoen, Minato-ku,Tokyo, 105-0011, Japan
Yamashita.Koji@aj.MitsubishiElectric.co.jp

ABSTRACT

In Japan, from 2011 to 2016, risk assessment of each type of equipment using A2L refrigerant was carried out and JRAIA standard which prescribed safe operating method was created, resulting in the relaxation of law was realized. In order to respond to demand in recent years to further lower GWP, risk assessment of built-in refrigerated display cabinet using R290 was carried out. CFD analyses on refrigerant leakage from inside or outside the refrigerated space of each type of refrigerated display cabinet was carried out, flammable volume was calculated, potential ignition sources were investigated, and ignition probability was calculated. Risk assessments were carried out at each stage of transportation, storage, installation, usage, service, and disposal. In this paper, the contents of the study and the safety operation method created as a result are summarized.
Keywords: CFD, Display Cabinet, Flammability, R290

1. INTRODUCTION

The use of A2L refrigerants for HVAC&R products was investigated in Japan from 2011 to 2016. Risk assessments of the products have been carried out, e.g. Yajima et al. (2016), to establish methods for ensuring the safe use of the products using A2L refrigerants, resulting in the relaxation of relevant regulation and followed by product launches in Japanese market. However, further reduction of GWP are expected in response to the Kigali Amendment to the Montreal Protocol. In view of the development, the Japan Refrigeration and Air Conditioning Industry Association (JRAIA) has been carrying out the risk assessment for built-in refrigerated display cabinets using R290 by using CFD analysis on refrigerant leakage from inside or outside the cabinet's refrigerated space.
CFD analysis results on refrigerant leakage from inside the refrigerated space of the reach-in refrigerated display cabinet was examined in the previous paper by Yamashita et al. (2018). In this paper, the duration of flammable region and the mean flammable volume obtained by CFD analysis for each refrigerated display cabinet were formulated. The investigative findings on the characteristic ignition sources in the stages of usage and working are shown, and the methods for ensuring safe operation are explained.

2. RISK ASSESSMENT

Ignition probability is calculated by multiplying the temporal encounter probability representing the time rate of contacting between the ignition source and the flammable region, spatial encounter probability representing the spatial distribution of the flammable region and the refrigerant leakage probability. Flammable region is the area where refrigerant concentration is between the lower flammability limit (LFL) and the upper flammability limit (UFL). Flammable volume is the volume of the flammable region. Time when flammable region exists is the duration of the flammable region. Temporal encounter probability is calculated by using the duration of the flammable region, the duration of the ignition source and the frequency of the ignition source. Spatial encounter probability is calculated by dividing

the mean flammable volume by the volume of the target space. The duration of flammable region and the mean flammable volume are determined by CFD analysis. The ignition probability is obtained by calculating the weighted average of the ignition probabilities for the two cases of fan operation and of fan stoppage (e.g. due to system failure) by operating rate.

3. CFD ANALYSIS OF REFRIGERANT LEAKAGE

CFD analysis was carried out with STAR CCM+ using the Realizable k-ε model. The subject refrigerant is R290, and the values at 25 °C in atmospheric pressure calculated by REFPROP Ver. 8.0 are used as its physical properties. The value 1.12×10^{-5} (m^2/s) is used as the diffusion coefficient of R290, 2.1 (vol%) and 9.5 (vol%) are used as LFL and UFL values, respectively. Leakage analysis was carried out for reach-in, horizontal and vertical open refrigerated display cabinets. Analysis models and calculation results of the reach-in refrigerated display cabinet and the horizontal refrigerated display cabinet are shown below. Validity of the results of CFD analysis has been verified by comparison of measuring and simulation of R32 leak from an air conditioner indoor unit.

3.1. Analysis of Reach-in Refrigerated Display Cabinet at the time of Refrigerant Leakage

3.1.1. Analysis Model for Refrigerant Leakage

Because flammable region in the shop becomes the largest when the door is fully opened rapidly after refrigerant leakage inside the refrigerated space of the reach-in refrigerated display cabinet, CFD analyses were carried out for this case. The CFD model of the reach-in refrigerated display cabinet is shown in Fig. 1. The display cabinet has 1.08 m^3 of refrigerated volume, and its external dimensions are 2.0 m in height, 1.542 m in width, 0.7 m in depth. The condensing unit consists of a compressor, a condenser and a fan installed in the lower part of the display cabinet. Air inlet of the condensing unit is located on the bottom-front, from which air passes through the rear side and is exhausted from the top of the display cabinet. Area of the air inlet opening is set to 8.3×10^{-2} m^2, and the air flow rate is varied from 0 to 0.249 m^3/s, which corresponds to air velocity of 0 to 3 m/s. The display cabinet is assumed to be installed at the center of a wall of a shop with square-shaped floor. Both without and with the down flow air curtain from the top-front of the refrigerated space have been considered in this study. CFD analysis assumed that the front doors are opened rapidly after the refrigerated space was filled with leaked refrigerant. Calculation was started from the state in which the refrigerant is distributed uniformly in refrigerated space, followed by refrigerant leakage from the front of the display cabinet assuming that there is no door. The air velocity of the air curtain is set to 2.08 m/s and the air flow rate is 0.137 m^3/s. CFD analyses were carried out for cases with the floor area of 17.14 m^2, 24.01 m^2, 36.00 m^2, 64.00 m^2 and 100.00 m^2 while the refrigerant amount was varied from 0.358 kg to 0.500 kg. The dimensions of the shop were set to 4.14 m×4.14 m, 4.9 m×4.9 m, 6.0 m×6.0 m, 8.0 m×8.0 m and 10.0 m×10.0 m, respectively. The ceiling height of the shop was set to 2.2 m.

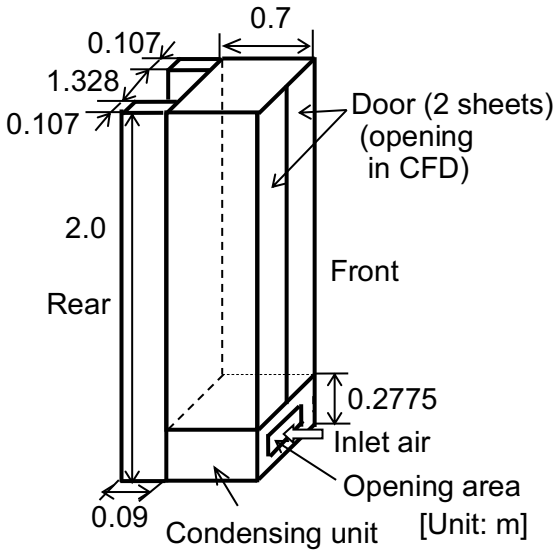

Figure 1: CFD model of reach-in refrigerated display cabinet

3.1.2. Calculation Results of at the time of Refrigerant Leakage from Inside of Refrigerated Space

Since there are several types of reach-in refrigerated display cabinet with different air flow pattern in refrigerated space, e.g. top-face-forward discharge and bottom-front suction type refrigerated cabinet (air curtain type system), and top-rear discharge and upper-front suction type refrigerated cabinet, risk assessment by JRAIA is based on the worst-case scenario of having no air curtain, and the values with and without the condensing unit fan are used as values representing cabinet operation and stoppage, respectively. Fig. 2 and Fig. 3 show the results of analysis of the duration of the flammable region and the mean flammable volume without air curtain. The figures show the case without air curtain, and with the air flow rates of 0 m^3/s and 0.208 m^3/s, respectively. In the figures, the horizontal axis shows the value obtained by dividing the refrigerant amount by the floor area

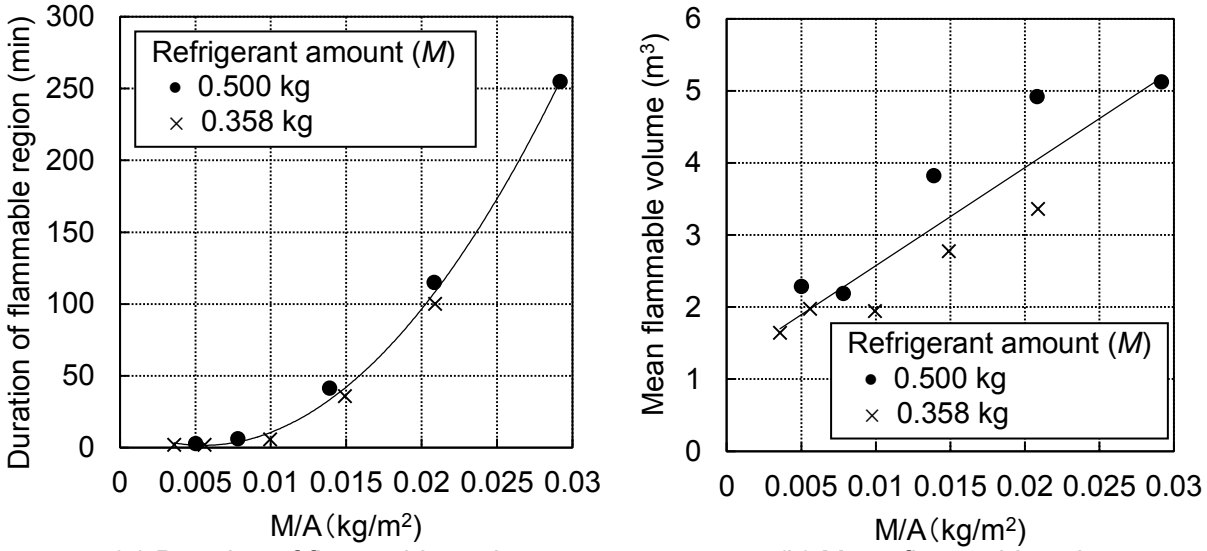

(a) Duration of flammable region (b) Mean flammable volume

Figure 2: Calculation results for a reach-in refrigerated display cabinet without air curtain at air flow rate of 0 m^3/s

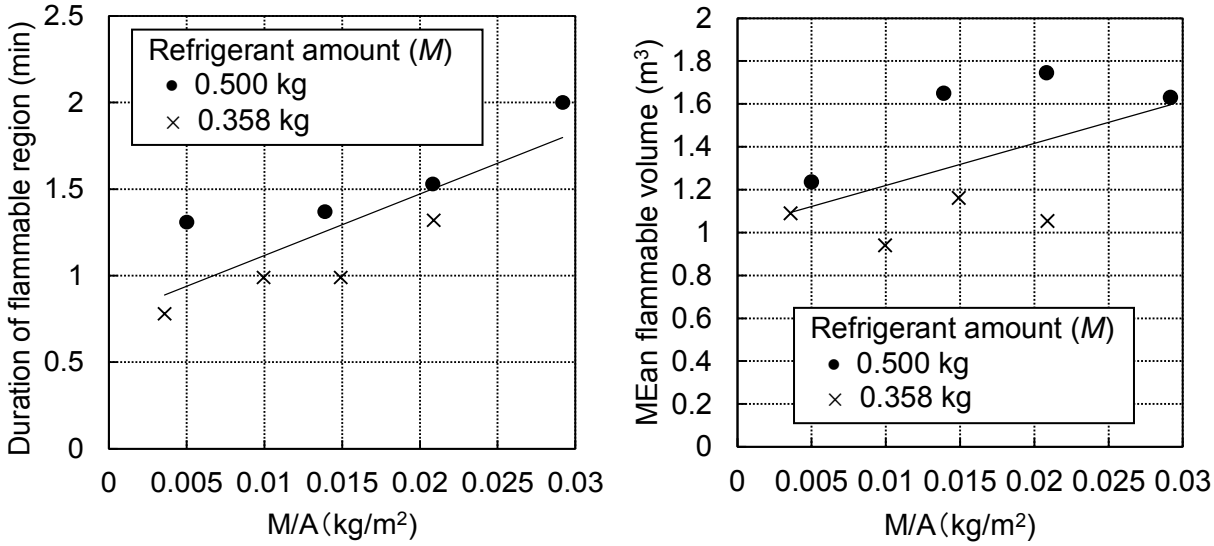

(a) Duration of flammable region (b) Mean flammable volume

Figure 3: Calculation results for a reach-in refrigerated display cabinet without air curtain at air flow rate of 0.208 m^3/s

inside the shop. Both the duration of flammable region and the mean flammable volume can be expressed as a function of the value M/A obtained by dividing the refrigerant amount by the floor area inside the shop. The obtained least squares approximate equations are expressed by Eq. (1) to Eq. (4) and shown as solid lines in Fig. 2 and Fig. 3, respectively. In the case of leakage inside a reach-in refrigerated display cabinet, the flammable region outside of refrigerated space did not disappear even when the air flow rate of condensing unit was increased.

$T_v = 4.53\times10^5\times(M/A)^2 - 5.01\times10^3\times(M/A) + 1.54\times10^1$ (air flow rate ; 0 m^3/s) Eq. (1)

$V_v = 1.36\times10^2\times(M/A) + 1.21$ (air flow rate ; 0 m^3/s) Eq. (2)

$T_v = 3.56\times10^1\times(M/A) + 7.61\times10^{-1}$ (air flow rate ; 0.208 m^3/s) Eq. (3)

$V_v = 1.96\times10^1\times(M/A) + 1.02$ (air flow rate ; 0.208 m^3/s) Eq. (4)

3.1.3. Refrigerant Leakage from Condensing Unit

As a result of CFD analysis of refrigerant leakage from a condensing unit at the bottom of reach-in refrigerated display cabinet, the duration of the flammable region was almost the same in value as the horizontal refrigerated display cabinet described later and mean flammable volume was about half of the value of horizontal refrigerated display cabinet, when the air flow rate of condensing unit was 0 m^3/s. CFD analysis showed clearly that the influence of the difference in the leak rate on the generation of flammable region is small when condensing unit is at the bottom of the refrigerated display cabinet.

Since the area of lower opening of a reach-in refrigerated display cabinet where refrigerant leakage occurred was half of that of the horizontal refrigerated display cabinet, the mean flammable volume was likewise halved. If the airflow rate of the condensing unit was increased, the flammable region was not generated outside of the refrigerated display cabinet in the case of refrigerant leakage from outside of the refrigerated space.

3.2. Analysis of Refrigerant Leakage in the Open Refrigerated Display Cabinet

3.2.1. Analysis Model for Refrigerant Leakage from the Condensing Unit of a Horizontal Refrigerated Display Cabinet

CFD analyses were carried out for refrigerant leakage from the condensing unit at the bottom of a horizontal refrigerated display cabinet. The CFD model for the horizontal refrigerated display cabinet is shown in Fig. 4. The external dimensions of the display cabinet are 0.81 m in height, 1.8 m in width and 1.09 m in depth. The condensing unit consists of a compressor, a condenser and a fan installed in the lower part of the display cabinet. Air is sucked from one side of the condensing unit and exhausted from another side. Area for both air inlet and outlet openings is set to 6.89×10^{-2} m^2 (0.733 m×0.094 m), and the air flow rate was varied from 0 to 0.207 m^3/s, which corresponds to air velocity of 0 to 3 m/s. The display cabinet is assumed to be installed at the center of a square-shaped shop floor. The refrigerant concentration at the opening of the condensing unit was changed as 100%, 70% and 30% when the air flow rate is 0 m^3/s, and the concentration is set as calculation value when the air flow rate was over 0 m^3/s. When the air flow rate is 0 m^3/s, the refrigerant was leaked evenly from both air inlet opening and air outlet opening. The refrigerant was leaked from the air outlet opening when the air flow rate was over 0 m^3/s. The leak rate was set to the value at which the total refrigerant amount was leaked in 4 minutes. CFD analyses were carried out for the cases with the floor area of 15.21 m^2, 24.01 m^2, 36.00 m^2, 64.00 m^2 and 100.00 m^2 while refrigerant amount is 0.500 kg. The dimensions of the shop were set to 3.9 m×3.9 m, 4.9 m×4.9 m, 6.0 m×6.0 m, 8.0 m×8.0 m and 10.0 m×10.0 m, respectively. The ceiling height of the shop is set to 2.2 m.

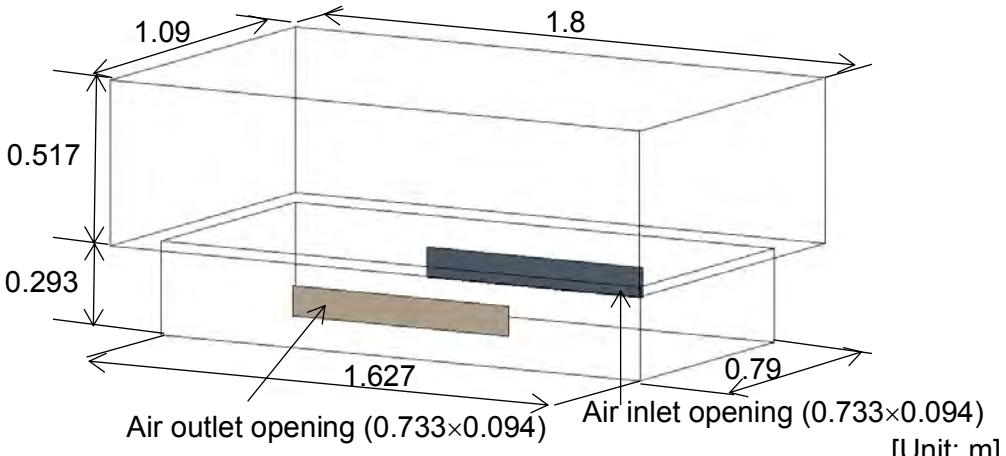

Figure 4: CFD model of horizontal refrigerated display cabinet

3.2.2. Calculation Results for Refrigerant Leakage from the Condensing Unit of a Horizontal Refrigerated Display Cabinet

Fig. 5 shows the results of analysis of the duration of flammable region and the mean flammable volume when air flow rate of the condensing unit of a horizontal refrigerated display cabinet is 0 m^3/s. Its horizontal axis shows the value obtained by dividing the refrigerant amount by the area inside the shop. Both the duration of flammable region and the mean flammable volume can be expressed as a function of the value M/A obtained by dividing the refrigerant amount by the area inside the shop. The obtained least squares approximate equations are expressed in Eq. (5) and Eq. (6) and as solid lines in Fig. 4 and Fig. 5, respectively. If the airflow rate of the condensing unit was increased, flammable region was not generated outside of the refrigerated display cabinet at the time of refrigerant leakage from outside of the refrigerated space.

$$T_v = 4.41\times10^5\times(M/A)^2 - 1.42\times10^3\times(M/A) + 3.94 \quad \text{(air flow rate ; 0 m}^3\text{/s)} \qquad \text{Eq. (5)}$$

$$V_v = 8.90\times10^1\times(M/A) + 2.58 \quad \text{(air flow rate ; 0 m}^3\text{/s)} \qquad \text{Eq. (6)}$$

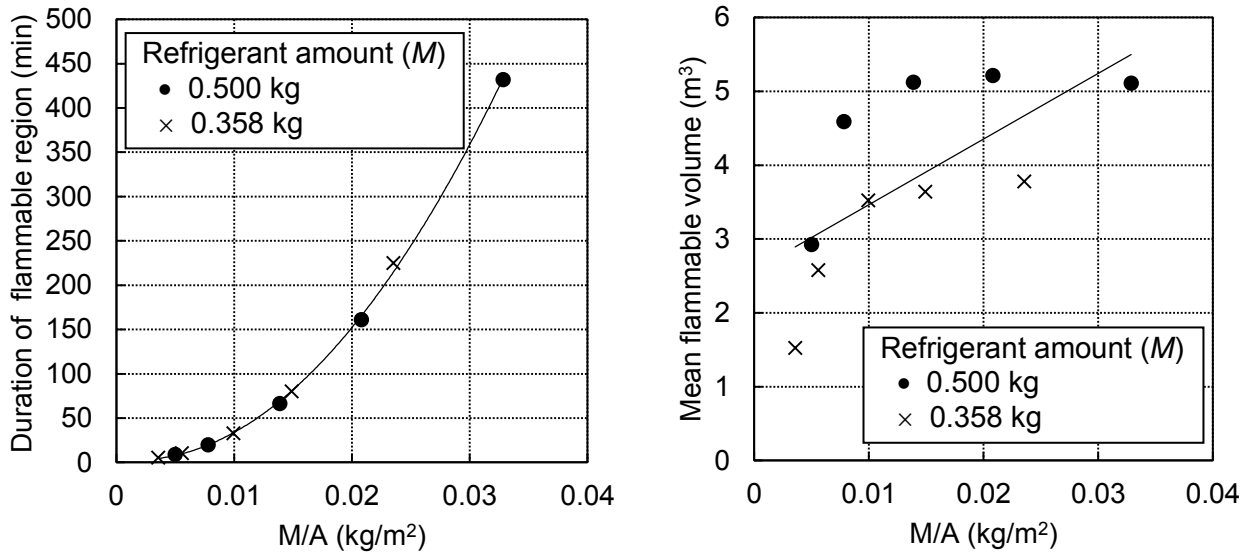

(a) Duration of flammable region (b) Mean flammable volume

Figure 5: Calculation results for a horizontal refrigerated display cabinet at air flow rate of 0 m^3/s

3.2.3. Refrigerant Leakage from Inside the Refrigerated Space of an Open Refrigerated Display Cabinet

Since air curtain is formed in the upper opening of a horizontal refrigerated display cabinet and built-in refrigerated display cabinet has a small refrigerant amount, almost of the refrigerant leaked inside of refrigerated space does not leak out of the refrigerated space.

As a result of CFD analysis for refrigerant leakage from inside of a vertical refrigerated display cabinet, a slight flammable region was generated outside the refrigerated display cabinet when there was no airflow outside the refrigerated display cabinet. However, there was nearly no formation of a flammable region outside the refrigerated display cabinet, even with little airflow, when there was a condensing unit at the bottom.

3.2.4. Refrigerant Leakage from the Condensing Unit of a Vertical Refrigerated Display Cabinet

Behaviour at the time of refrigerant leakage from condensing unit at the bottom of a vertical refrigerated display cabinet is the same as in the condensing unit of a reach-in refrigerated display cabinet.

4. CALCULATION OF THE IGNITION PROBABILITY AND SAFETY MEASURES

4.1. Equations for calculating Ignition Probability

Temporal encounter probability representing the time rate of contacting between the ignition source and the flammable region is calculated by using Eq. (7), based on the theory of geometric probability, Okabe (2010), using the total time of the target stage, the duration of the flammable region, the duration of the ignition source and the frequency of the ignition source. The coefficient k is a coefficient representing the abundance ratio of the ignition source, dissemination rate of the electric equipment, or the degree of concentration when operation of the ignition source concentrates in a certain time zone. Spatial encounter probability is calculated with Eq. (8), using mean flammable volume and volume of target space. Ignition probability is calculated with Eq. (9) by using the temporal encounter probability, the spatial encounter probability and the refrigerant leak probability.

$$P_t = k\times[1-\{1-(T_i+T_v)/T_a\}^n] \quad \text{Eq. (7)}$$

$$P_s = V_v/V_a \quad \text{Eq. (8)}$$

$$P = P_t\times P_s\times P_R \quad \text{Eq. (9)}$$

Assuming the allowable level of ignition probability is on the level of a serious accident occurring once every 100 years, the allowable level was set to 5.26×10^{-9} by using 1.9 million units which is the number in operation in the market. Also, since the work is carried out by experts, the allowable level at the time of work was set to 5.26×10^{-8} which is 10 times the value for usage.

4.2. Calculation of Ignition Probability at the Usage Stage and Safety Measures

Ignition probability for convenience stores was investigated. Table 1 shows the main ignition sources assumed at the usage stage. Occurrence probability of static electricity was set to 18.2 %, with attention to change in humidity through the year. It is assumed that ignition does not occur if air is flowing around the brush motor at velocity exceeding the burning velocity of the refrigerant. Additionally, ignition accidents involving electrical equipment were also taken into consideration, based on survey data of the National Institute of Technology and Evaluation (NITE). The air flow rate of the condensing unit of refrigerated display cabinet was assumed to be set at the air flow rate at which flammable region does not generate. Regarding leakage outside the refrigerated space, it is assumed that no flammable region is generated during operation, but flammable region is generated during stoppage, for defrosting or due to system failure. The duration of the flammable region and the mean flammable volume were calculated with Eq. (5) and Eq. (6), respectively. As for the refrigerant leakage from inside refrigerated space of a reach-in refrigerated display cabinet, Eq. (3) and Eq. (4) were used to calculate the duration of the flammable region and the mean flammable volume at operation, and Eq. (1) and Eq. (2) were used for cases of stoppage. The area inside the shop and refrigerant amount of each refrigerated display cabinet are set to 84.7 m^2 and 0.5 kg, respectively. M/A is set to 0.0059 in Eq. (1) through Eq. (6). It is assumed that no flammable region is generated outside the refrigerated space at the time of refrigerant leakage from inside of the refrigerated space. Calculation of refrigerant leakage probability in usage was based on the survey results of refrigerant leak accidents in the market involving built-in refrigerated display cabinets manufactured by JRAIA member companies. The refrigerant leak probability was set for the burst leak to 5.26×10^{-7}, for the rapid leak to 1.89×10^{-5}, for the slow leak to 9.82×10^{-4}, and for the total refrigerant leak to 1.00×10^{-3}.
As a result, the ignition probability exceeded the allowable value, and fell the allowable value or less by taking the safety measures shown in Table 2.

Table 1. Ignition sources assumed at the usage stage

Name	Type	T_i (sec)	n	Note
Coffee machine	Electric spark	5×10^{-3}	186	Relay operates when selling
Switch of deep frying machine	Electric spark	5×10^{-3}	10	Cooking every 4 hours in a span of 20 hours
Chinese-style buns steamer	Electric spark	5×10^{-3}	10	Cooking every 4 hours in a span of 20 hours
Heating appliance for “Oden”	Electric spark	5×10^{-3}	10	Cooking every 4 hours in a span of 20 hours
Power outlet	Electric spark	5×10^{-3}	4	Plugging/unplugging twice a day for cleaning
Light switch	Electric spark	5×10^{-3}	4	Switch on/off twice a day
Static electricity (door of reach-in refrigerated display cabinet)	Electrostatic spark	1×10^{-6}	44	Taking out iced coffee
Static electricity (exterior of open refrigerated display cabinet)	Electrostatic spark	1×10^{-6}	22	Shoppers touch metallic parts
Static electricity (other doors)	Electrostatic spark	1×10^{-6}	22	Assumed to share the same value as above
Brush motors of other equipment	Electric spark	5×10^{-3}	144	Turn on 6 times in a hour
Electronic lighter	Open flame	5	5	Five people trying ignition in a day
Combustion type boiler	Open flame	3.6×10^{4}	1	Use 10 h in a day. Dissemination rate of 0.01%

Table 2. Safety measures for usage stage

Stage	Safety measures
Usage	The fan of the condensing unit is operating even while defrosting.
	The air flow rate of the condensing unit is set to a specified value or higher
	Equipped with the function of detecting refrigerant leakage into the refrigerated space of reach-in refrigerated display cabinet, function of triggering warning not to open the door or function of shutting off the refrigerant leakage into the refrigerated space in case of refrigerant leakage.

4.3. Calculation of Ignition Probability at Various Working Stage and Safety Measures

In the various working stages, such as transportation, storage, installation, repair and disposal, ignition sources were assumed and the ignition probabilities were calculated. Table 3 shows the main ignition sources assumed at each stage. Transportation on a minivan with an internal volume of 3 m^3 was assumed as the transportation stage. Storage was assumed to be in a medium-sized warehouse of 1000 m^2 or a small-sized warehouse of 15 m^2 in storage stage. For installation, repair and disposal, ignition sources described in Table 1 were considered in addition to the ignition source at the time of work since such work is carried out while using the equipment in the shop. The probability of static electricity occurrence was set to 18.2 %, considering the changes in humidity through the year. As for the refrigerant leakage probability, the value was calculated for each stage by using the value of human error or similar. The duration of the flammable region and the mean flammable volume were calculated with Eq. (3) and Eq. (4) for the value at the time of leakage inside the refrigerated space, and Eq. (5) and Eq. (6) for the value at the time of leakage outside the refrigerated space.

Table 3. Ignition sources assumed at each working stage

Name	Type	T_i (s)	n	Note
Common; Smoking by workers	Open flame	4.5×10^{1}	1 per 1 hour	Cigarette smoked: 1 stick/person/h; ignition time with lighter: 5 sec; duration of high cigarette temperature: 40 sec; smoking rate: 28.2%
Transportation (minivan)				2 hrs, 2 workers
Static electricity when opening / closing door	Electrostatic spark	1.0×10^{-6}	2	Opening and closing: 2 times
Static electricity when undressing	Electrostatic spark	1.0×10^{-6}	1 per 1 person	Acrylic sweater: 1 time per person; usage ratio 25%
Storage (small-sized warehouse)				2 h, 2 workers, 15 m^2
Static electricity	Electrostatic spark	1.0×10^{-6}	1 per 1 person	Contact with worker (reuse, without cover)
Oil heater	Open flame	7.2×10^{2}	1	Usage of 120 days per year; usage rate of oil heater 25%
Install, repair or disposal				1 to 4 hrs, 1 to 2 workers
Ignition source in usage	-	-	-	See Table 1
Power outlet	Electric spark	5.0×10^{-3}	2	Plugging/unplugging; Occurrence rate 25%
Electric screwdriver	Brush motor	3.0	10	Opening/closing screws; occurrence rate 50%
Static electricity	Electrostatic spark	1.0×10^{-6}	10	Contact with display cabinet, occurrence rate 33.3%
Burner for brazing	Open flame	1.2×10^{2}	4	2 min × 2 places

Table 4. Safety measures for working stage

Stage	Safety measures
Transportation (for minivan transportation only)	Caution regarding opening windows or turning air conditioner to external air pulling mode before smoking
	Using a portable leak detector and ventilating after detection of leakage
Storage	Use of work gloves to prevent electrostatic discharge
	Caution regarding the existence of ignition sources around the product
Installation	Use of work gloves to prevent electrostatic discharge
	Caution regarding the existence of ignition sources during working
Repair	Use of work gloves to prevent electrostatic discharge
	Using a portable leak detector and diffusing refrigerant to the surroundings at the time of leakage (e.g. electric fan, paper fan)
Disposal	Use of work gloves to prevent electrostatic discharge
	Caution not to unplug the power line from the outlet before turning off the breaker

As a result, the ignition probability exceeded the allowable value at all stages, and fell the allowable value or less by taking the safety measures for each stage shown in Table 4.

5. CONCLUSIONS

For built-in refrigerated display cabinet using R290, CFD analysis of refrigerant leakage from inside or outside of refrigerated space of each display cabinet were carried out, and risk assessments at the stages of usage and working were carried out by using the CFD results. This led to the clarification of methods to ensure safe operation of the equipment.

(1) Flammable region was generated outside of the refrigerated space when the door was opened suddenly after all refrigerant leaked in the reach-in refrigerated display cabinet. Equations were introduced to calculate the duration of the flammable region and the mean flammable volume without air curtain and with or without air flow of the condensing unit.

(2) Equations were introduced to calculate the duration of the flammable region and the mean flammable volume with or without air flow of the condensing unit in case of refrigerant leakage from the condensing unit of the horizontal refrigerated display cabinet.

(3) Flammable region was not generated when the air flow rate was set to a specified value or higher at the time of refrigerant leakage from condensing unit.

(4) Risk assessments were carried out by identifying the ignition sources at the stages of usage and working for a convenience stores. The ignition probability at the usage stage did not exceed the allowable value by taking safety measures, such as the product function enabling the fan of the condensing unit to keep operating even while defrosting, the function of detecting refrigerant leakage into the refrigerated space of reach-in refrigerated display cabinet and the function of triggering warning not to open the door or the function of shutting off the refrigerant leakage into the refrigerated space at the time of refrigerant leakage. The safety measures at each stage of working were also clarified.

ACKNOWLEDGEMENTS

This study was carried out by member companies of JRAIA, Mitsubishi Electric and its affiliate, Sanden Retail Systems, Okamura, Toshiba Carrier, Nakano Refrigerators, Panasonic, Fukushima Industries, Fuji Electric, and Hoshizaki. Observers from each company are Hiroichi Yamaguchi, Makoto Handa, Takeshi Shinmyou, Masahiro Onoguchi, and Akio Oki, who cooperated with this study. The authors would like to deeply appreciate these members support.

NOMENCLATURE

A	shop area (m^2)	k	coefficient
M	refrigerant amount (kg)	n	frequency of ignition source
P	ignition probability	P_R	refrigerant leak probability
P_s	spatial encounter probability	P_t	temporal encounter probability
T_a	total time of target stage (s)	T_i	duration of ignition source (s)
T_v	duration of flammable region (s)	V_a	volume of target space (m^3)
V_v	mean flammable volume (m^3)		

REFERENCES

Okabe, Y., 2010. Probability and Statistics. Asakura Publishing, Tokyo, 131-133. (in Japanese)

Yajima, R., Kiguchi, Y., Sekine, T., Sasaki, S., Ito, S., Yamashita. K., Kannon, T., 2016. Risk Assessment for VRF System with Mildly Flammable Refrigerants. Trans. JSRAE 33(1), 23-39. (in Japanese)

Yamashita, K., Sakamoto, Y., Kato, T., Ishihara, S., Kobayashi, A., Kainuma, H, Sato, M., Osawa, K., Nagai, H., Anzai. Y., 2018. Study on CFD Analysis of Refrigerant Leakage and Ignition Source about Built-In Refrigerated Display Cabinet using R290. Proc. 13th IIR-Gustav Lorentzen Conference on Natural Refrigerants, 1255.

Manuscript ID: 347
DOI: 10.18462/iir.icr.2019.0347

Performance of a non-uniform width rotating discharge valve in the revolving vane (RV) compressor

Kim Rui HENG[(a)], Kim Tiow OOI[(a)], Weng Kong CHAN[(a)]

[(a)] Nanyang Technological University, School of Mechanical and Aerospace Engineering
50 Nanyang Ave, Block N3, Nanyang Ave, S639798, Singapore, HENG0179@e.ntu.edu.sg

ABSTRACT

The Revolving Vane (RV) compressor achieves improved mechanical efficiency over existing compressor designs through the use of a rotating cylinder that helps reduce relative rubbing velocity with the rotor. As a result, the discharge valve rotates due to the rotation of the cylinder, since the valve is mounted on the cylinder. This paper presents a theoretical investigation on the dynamic behaviour of a non-uniform width reed-type discharge valve undergoing rotary motion. Finite element modelling of the valve reed vibration will be shown and the transient response of the valve under centrifugal and pressure forces is analysed. Results show that the valves' performance and reliability depend significantly on the rotational speed.
Keywords: Modelling, Discharge valve, Rotary compressor, Revolving vane, Design.

1. ROTATING DISCHARGE VALVE OF REVOLVING VANE (RV) COMPRESSOR

The revolving vane (RV) compressor design was first introduced by Teh and Ooi (2009) as a more mechanically efficient compressor alternative to the rolling-piston compressor. In its basic form, the RV compressor is made up of a rotor, a vane and a cylinder, as shown in Fig. 1. The vane is attached to the cylinder via a pin-joint and is allowed to slide within the vane slot in the rotor. The vane divides the working chamber into the suction and compression chambers. The rotor and cylinder are both supported individually and concentrically on two journal bearings, where they rotate about their respective axis while keeping a virtual line of contact between the rotor and the cylinder. This simultaneous rotation of both the cylinder and rotor in RV compressor helps reduce relative endface rubbing between both components, by reducing their relative rubbing velocity. During the operation, the cylinder rotates the vane which in turns rotates the rotor. This rotational motion causes the volumes bounded by the vane, cylinder wall and rotor to vary; resulting in suction, compression and discharge of the working fluid.

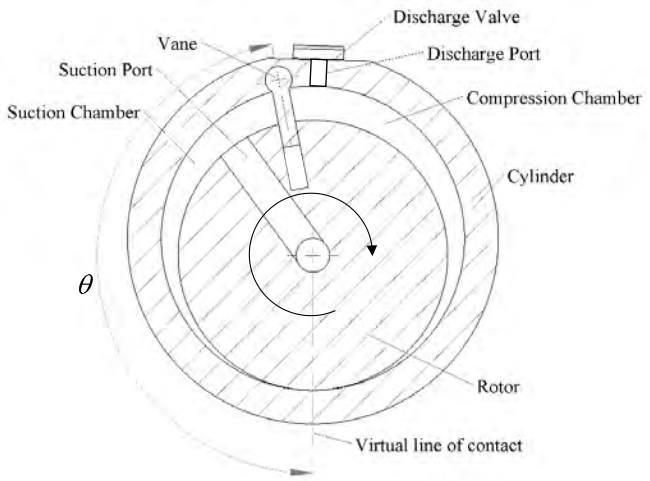

Figure 1: Schematic diagram of RV compressor.

The discharge process of the RV compressor is regulated by a discharge valve reed. However, as the discharge valve reed is mounted on the outer surface of the rotating cylinder (Fig. 2a), the valve rotates together with the cylinder during operation. Consequently, the valve is subjected not only to

the net pressure loading from both sides of the valve but also centrifugal and Coriolis forces. As the dynamic response of the reed dictates the discharge process, which in turn, affects the efficiency of the compressor, it is thus important to investigate the effects of rotation which influences the operation of the reed valve, on the overall performance of the compressor.

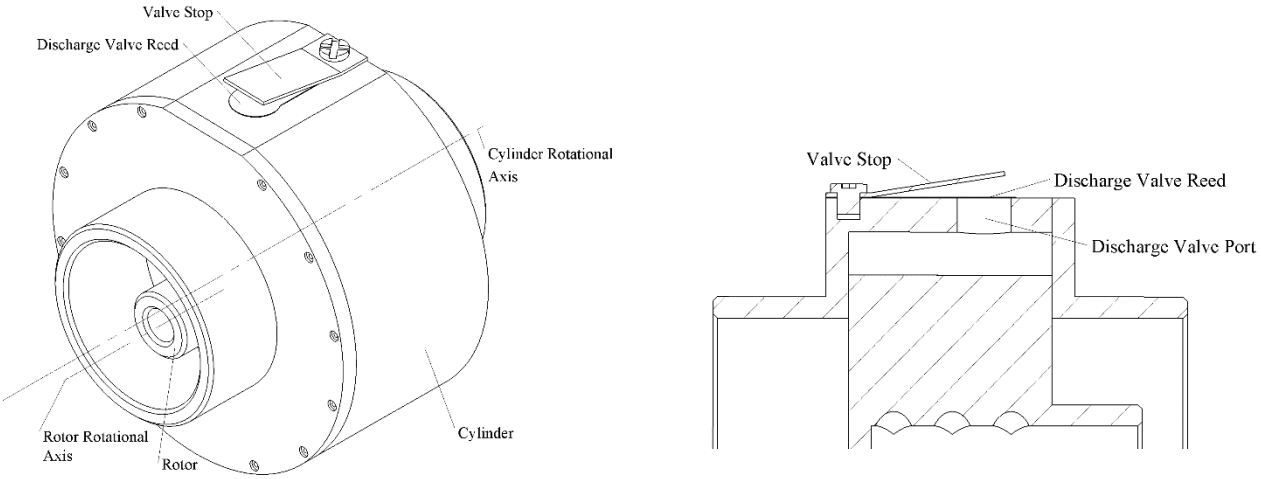

Figure 2: (a) Position and orientation of discharge valve on the radial surface of the cylinder; (b) sectional view of the discharge valve.

To date, a study on the dynamic response of the valve reed subjected to forced excitation with additional dynamic effects due to rotational motion has been carried out by Teh et al. (2009). However, the study was performed on a uniform cross-section rectangular valve reed which only focuses on the effect of the rotational velocity on the valve's response. Since the reed with a non-uniform width is often employed in practice, in this paper, a non-uniform width valve reed is studied. Effects of various parameters on the valve's performance will be presented, assessed and discussed.

2. THEORETICAL MODEL

Fig. 2a shows the valve orientation relative to the rotating cylinder. In this orientation, the Coriolis force affects the flexural and torsional vibrations. However, based on the results from Teh et al. (2009), the effect of Coriolis force on valve deflection is found to be negligible as the flexural rigidity at its lateral axis is much smaller than its flexural rigidity at the vertical axis and, is also smaller than its torsional stiffness at the longitudinal axis (Fig. 3) and thus, the deflection of the valve is dominated by the flexural deformation at the lateral axis.

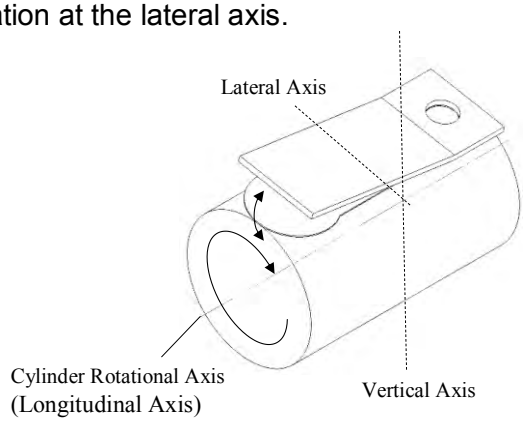

Figure 3: Different possible deformation axes of a rotating valve reed.

The free body diagram of a valve element of an arbitrarily shaped valve plate is presented in Fig. 4 and is modelled as a clamped-free cantilever beam. With Coriolis force neglected, the general governing force balanced equation of transverse vibration of an arbitrarily shaped valve is given as:

$$-\frac{\partial^2}{\partial x^2}\left(EI(x)\frac{\partial^2 y}{\partial x^2}\right)-c\frac{\partial y}{\partial t}+P(x,t)w=\rho A(x)\frac{\partial^2 y}{\partial t^2}-\rho A(x)\omega^2\left(R+y\right) \quad \text{Eq. (1)}$$

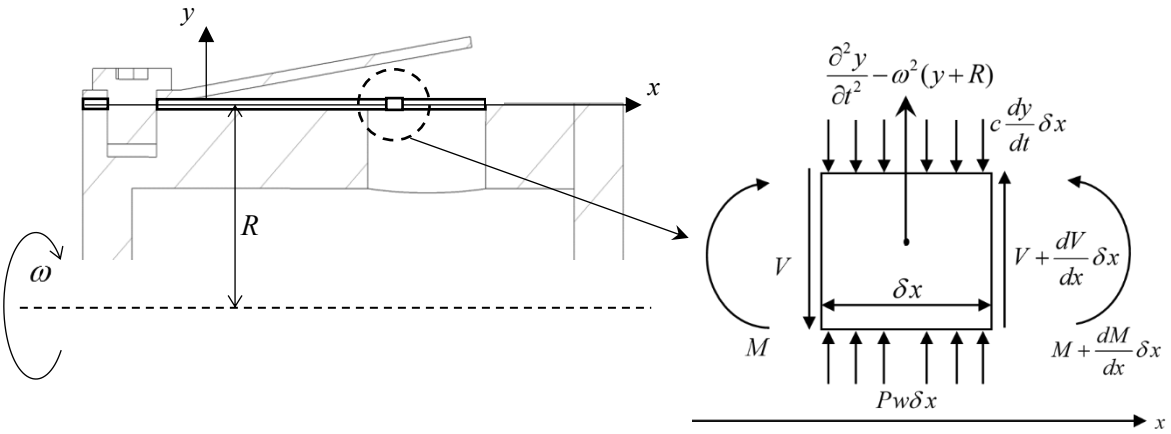

Figure 4: Free body diagram of infinitesimal element along the valve.

in which the first to third term on the left-hand side of Eq. (1) represent the internal shear force, gas damping force and external pressure force respectively while the first and second term on the right-hand side of Eq. (1) represent the linear and centripetal acceleration respectively. Considering principle of superposition for transverse vibration, the valve deflection is assumed to take on the form of series of separable variable shape functions (Meirovitch, 2001):

$$y(x,t)=\sum_{n=1}^{\infty}Y_n(x)\bullet\tau_n(t) \quad \text{Eq. (2)}$$

As the mode shapes are invariant under free or forced vibrations, the homogeneous part of Eq. (1) is first to be addressed which yields Eq. (3) via method of separation of variables:

$$\frac{1}{\rho A(x)Y_n(x)}\frac{d^2}{dx^2}\left(EI(x)\frac{d^2Y_n(x)}{dx^2}\right)=\omega^2-\frac{1}{\tau_n(t)}\frac{d^2\tau_n(t)}{dt^2}-\frac{c}{\rho A(x)\tau_n(t)}\frac{d\tau_n(t)}{dt}=\lambda_n^2 \quad \text{Eq. (3)}$$

By rearranging the left-hand side of Eq. (3) to yield Eq. (4),

$$\frac{d^2}{dx^2}\left(EI(x)\frac{d^2Y_n(x)}{dx^2}\right)=\lambda_n^2\rho A(x)Y_n(x)$$

$$\text{During valve lift-off (clamped-free): at } x=0, Y_n=0, \frac{dY_n}{dx}=0 \text{ \& at } x=L, \frac{d^2Y_n}{dx^2}=0, \frac{d^3Y_n}{dx^3}=0$$

$$\text{Hitting stop plate (clamped-pinned): at } x=0, Y_n=0, \frac{dY_n}{dx}=0 \text{ \& at } x=L, Y_n=0, \frac{d^2Y_n}{dx^2}=0 \quad \text{Eq. (4)}$$

It can be observed that the mode shapes, Y_n, are orthogonal in nature, considering the clamped-free or clamped-pinned boundary conditions during valve lift-off and valve hitting of stop plate scenarios respectively:

$$\int_0^L \rho A(x)Y_nY_m dx=\begin{cases}0, & \text{if } m\neq n\\ 1, & \text{if } m=n\end{cases} \quad \text{Eq. (5)}$$

However, Eq. (4) is a non-linear fourth-order partial differential equation since the cross-sectional area and second moment of area of the valve reed are both non-uniformly distributed parameters, making closed-formed exact solution to Eq. (4) impossible. The approximated mode shapes, Y_n, are obtained using Finite Element Method.

2.1. Finite Element Method

The Finite Element Method is an approximation method where the stiffness and mass properties of all individual elemental parts of a structure which is the valve reed here, are assembled to form the

overall stiffness matrix, K and mass matrix, M. The array of individual elements' displacement of free vibration or nodal displacements vector, $\mathbf{a}$, is obtained by solving an eigenvalue problem from Rayleigh's quotient:

$$K\,\mathbf{a} = \lambda^2 M\,\mathbf{a} \qquad \text{Eq. (6)}$$

With the nodal displacements obtained, the mode shapes function, Y_n are approximated by polynomial functions of fourth-order or higher using multiple linear regression method. The approximated eigenvalues of Eq. (6) are the natural frequencies, λ_n, but due to the nature of excitation of the valve, only the first mode shape corresponding to the lowest natural frequency or eigenvectors associated to λ_1 are considered in this paper.

Different boundary conditions when the valve departs from the valve seat and when it hits and departs from the valve back plate, are considered to obtain different valve mode shapes. When the valve reed was first in clamped and free conditions during initial valve lift, the first and last individual element matrices expressed in Eq. (7) are imposed when solving the eigenvalue problem Eq. (6), assuming constant EI over each individual element:

$$K_1 = \frac{EI_1 k^3}{L^3}\begin{bmatrix} 12 & -6 \\ -6 & 4 \end{bmatrix} \qquad M_1 = \frac{m_1 L}{420k}\begin{bmatrix} 156 & -22 \\ -22 & 4 \end{bmatrix}$$

$$K_k = \frac{EI_k k^3}{L^3}\begin{bmatrix} 12 & 6 & -12 & 6 \\ 6 & 4 & -6 & 2 \\ -12 & -6 & 12 & -6 \\ 6 & 2 & -6 & 4 \end{bmatrix} \qquad M_k = \frac{m_k L}{420k}\begin{bmatrix} 156 & 22 & 54 & -13 \\ 22 & 4 & 13 & -3 \\ 54 & 13 & 156 & -22 \\ -13 & -3 & -22 & 4 \end{bmatrix} \qquad \text{Eq. (7)}$$

During the impact with the valve stop, the valve reed was in the clamped and pinned conditions and the first and last individual element matrices are expressed in Eq. (8), assuming constant EI over each individual element:

$$K_1 = \frac{EI_1 k^3}{L^3}\begin{bmatrix} 12 & -6 \\ -6 & 4 \end{bmatrix} \qquad M_1 = \frac{m_1 L}{420k}\begin{bmatrix} 156 & -22 \\ -22 & 4 \end{bmatrix}$$

$$K_k = \frac{EI_k k^3}{L^3}\begin{bmatrix} 12 & 6 & 6 \\ 6 & 4 & 2 \\ 6 & 2 & 4 \end{bmatrix} \qquad M_k = \frac{m_k L}{420k}\begin{bmatrix} 156 & 22 & -13 \\ 22 & 4 & -3 \\ -13 & -3 & 4 \end{bmatrix} \qquad \text{Eq. (8)}$$

2.2. Numerical Iteration of Mode Participation Factor

To solve for the time-variant factor or mode participation factor that is dependent on external excitations, fourth-order Runge-Kutta numerical iterative method (RK4) has to be applied on Eq. (9). Eq. (9) is obtained by multiplying Y_n throughout Eq. (1), integrating the equation over the length of valve and applying orthogonality of Y_n (Eq. (5)):

$$\frac{d^2\tau_n}{dt^2} = \int_0^L P(x,t) w Y_n dx + \omega^2 R \int_0^L \rho A(x) Y_n dx - c\frac{d\tau_n}{dt}\int_0^L {Y_n}^2 dx + (\omega^2 - {\lambda_n}^2)\tau_n \qquad \text{Eq. (9)}$$

Eq. (9) is solved simultaneously with the thermodynamic relations (Ooi, 2004) via RK4 iteration as the external pressure force that affects the valve's dynamic response is dependent on the pressure variation of the compression chamber of the RV compressor.

3. RESULTS AND DISCUSSION

3.1. Effect of rotational motion on valve response

Before conducting parametric studies on the effects of dimensions and shapes of the valve reed, it is necessary to first examine the dynamic response of the valve reed under the influence of the

centrifugal effect, as the valve rotates together with the cylinder. All the cases studied are based on properties prescribed in Table 1. To investigate the effect of centrifugal force on the response of the valve caused by the rotational motion of the compressor, a comparison is made between the deflections of a rotating and a non-rotating valve reed. A thin metal plate having the dimensions prescribed in Table 2 is employed as the reed for the discharge valve.

Fig. 5 shows the dynamic responses of the reed when the compressor operates at 3000 rpm for both rotating and non-rotating reed conditions. It can be observed that the magnitude and number of oscillations of the rotating reed is smaller than that of the non-rotating one. The higher occurrence of fluttering of the non-rotating reed results in higher pressure oscillations when the rotational angle is between 260° to 360°. In addition, the rotating valve opens earlier during the discharge process, hence resulting in noticeably lower over-compression losses.

The earlier opening of the rotating reed is attributed to the centrifugal force which is an additional force that pulls the reed radially outwards, away from its seat. Similarly, when the reed tends to close, the centrifugal force acts as a force to counter the tendency to close under the valve's own stiffness, and hence reduces the chance of the valve reed to fully close during the entire discharge process, therefore reducing the magnitude and frequency of the valve and pressure oscillations. As a result of the centrifugal force, it is also observed that the rotating valve is unable to close completely at the end of the discharge process. This effect is more pronounced when the rotational speed of the compressor increases, causing the centrifugal force on the valve reed to increase. This incomplete valve closure at the end of the discharge process will result in reversed flow and lower the volumetric efficiency of the compressor. Although the centrifugal force reduces over-compression losses, it may lower the volumetric efficiency. This calls for an appropriate design of the rotating valve to take advantage of its centrifugal effects while at the same time reduces its negative impact on compressor performance.

Table 1. Operating conditions of RV compressor and material properties of valve reed.

Radial distance from rotational axis, R	55 mm
Working Fluid of RV compressor	R32
Discharge Port Diameter	12 mm
Height of Valve Stop	5 mm
Discharge Pressure, P_{disc} (abs)	3472.66 kPa
Density of valve plate	7800 kg m^{-3}
Elastic modulus, E	210 Gpa

Table 2. Geometry and dimensions of valve reed.

Length, L (From tip to end)	27 mm
Thickness	0.405 mm
Number of elements defined, k	100
Length of interval between nodes	0.27 mm
Width of node 1st *to* node 50th	12 mm
Width of node 51st *to* node 100th	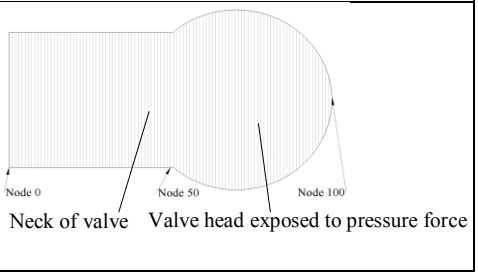
12.11,12.55,12.96,13.34,13.68,13.99,14.28, 14.54,14.63,14.99,15.18,15.35,15.50,15.63, 15.73,15.82,15.90,15.95,15.98,16.00,16.00, 15.98,15.94,15.88,15.80,15.71,15.59,15.46, 15.31,15.13,14.93,14.72,14.47,14.21,13.91, 13.59,13.24,12.86,12.44,11.98,11.48,10.94, 10.33,9.65,8.89,8.03,7.02,5.78,4.12,0.00 [mm]	

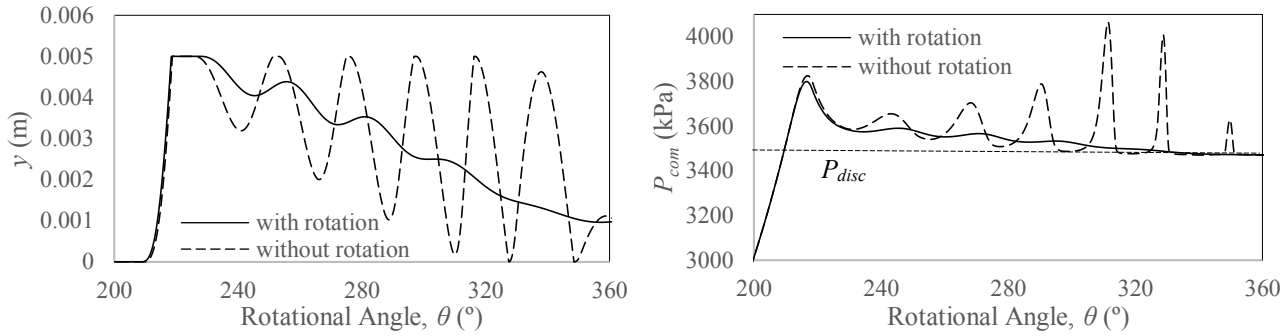

Figure 5: Comparison of valve deflections under rotating and non-rotating conditions. Solid line, rotating valve; dashed line, non-rotating valve.

3.2. Effect of geometry and dimensions of valve plate on valve response

In this section, parametric studies on the effect of valve dimension and shape on the vibrational response are presented. From Eq. (9), it is observed that both damping force acting on the valve and flexural rigidity of the valve reed (third and fourth terms of the right-hand side of Eq. 9) help to counteract the effect of centrifugal force which prevents the valve from fully closing. It is expected that by increasing the thickness and neck width of the reed and decreasing its length, it will be stiffened to resist the outward pull from the centrifugal force and fully close the discharge port when discharge process ends. Fig. 6 shows the comparison of the valve deflections of rotating reeds with increased thickness, wider neck width and shorter length to that of Table 2's reed. It has clearly showed that with increased thickness and shortened length, the stiffened reed is able to close the discharge port completely but with a compromise in increased discharge losses due to greater pressure oscillations and over-compression. The valve with a wider neck width is observed to have greater dampened oscillations with increased over-compression but it is unable to close the port completely. This suggests that width of a reed affects the intensity of damping but does not significantly affects its stiffness. A wider width will contribute to greater damping of oscillations but a moderate increase in the reed stiffness. Overall, all the valves shown in Fig. 6 require a greater over-compression for initial valve lift-off for discharge process to occur due to increased stiffness. An improved rotating reed should be sufficiently thickened and shortened such that it is stiffened to overcome the centrifugal force while designed to have a wider neck to dampen the oscillations. A bigger valve head should also be designed to increase the pressure force so as to reduce the over-compression during the initial valve lift-off.

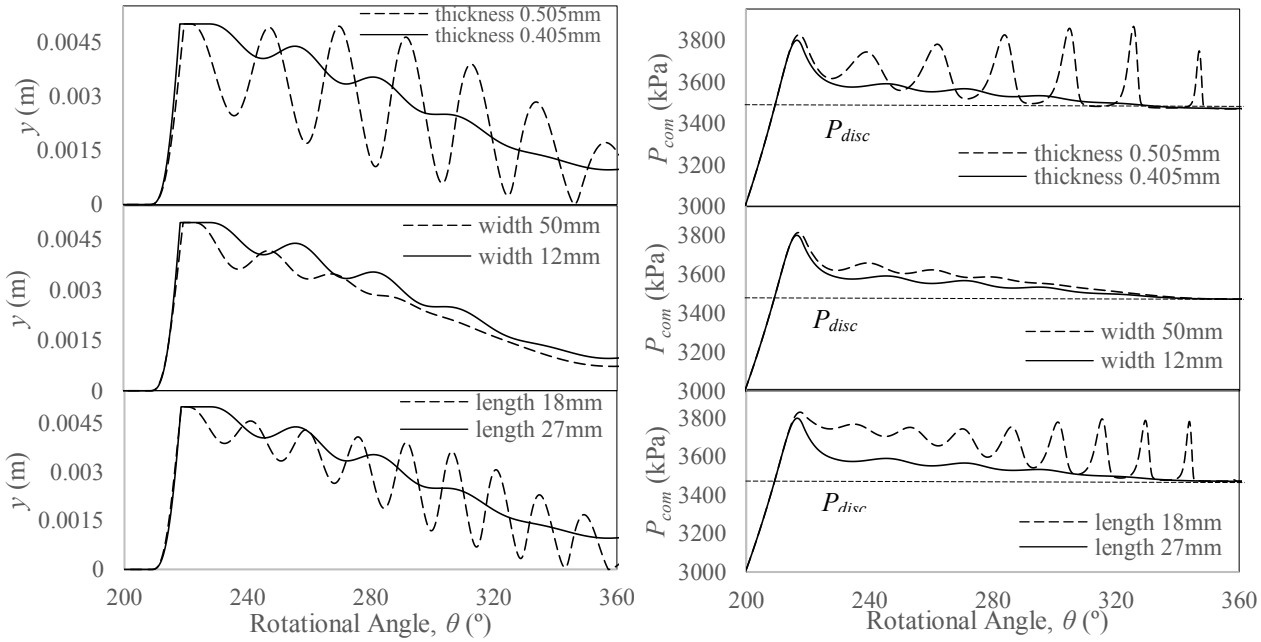

Figure 6: Comparison of valve reed deflections of rotating reeds with different dimensions to that of Table 2's reed.

Fig. 7 shows the dynamic response of an improved rotating valve reed having the dimensions prescribed in Table 3. It is thickened and shortened with a wider neck and a bigger head. Although the number and magnitude of valve fluttering has increased as compared to that of the valve reed from Table 2, the valve reed does not require a greater pressure build-up for lift-off due to a larger exposed area which leads to a stronger pressure force. Furthermore, it is sufficiently stiffened to close the discharge port completely at the end of discharge process. Overall, the discharge loss of Table 3's valve due to over-compression is also similar to that of Table 2's valve. However, it should be noted that the dimension of the valve is designed to operate at a rotational speed of about 3000 rpm. Above 3000 rpm, it is predicted that the valve will be unable to close completely due to centrifugal overloading and under-compression losses will dramatically increase. Below 3000 rpm, valve fluttering will be severe due to the stiffer reed and weaker centrifugal force. To verify the predictions, simulations are conducted at different operating speed as shown in Fig. 8. At 2000 rpm, the number and magnitude of valve fluttering increase significantly. At 4000 rpm, the valve reed is unable to close the discharge port completely.

Table 3. Geometry and dimensions of improved non-uniform valve reed.

Length, *L* (From tip to end)	25 mm
Thickness	0.48 mm
Number of elements defined, *k*	100
Length of interval between nodes	0.25 mm
Width of node 1st to node 100th	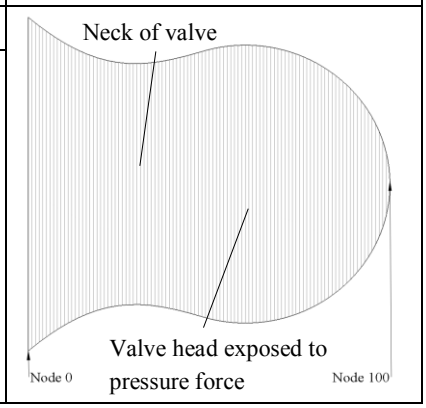
24,23.58,23.16,22.76,22.37,21.99,21.63,21.28,20.94,20.61, 20.30,20,19.72,19.46,19.20,18.97,18.75,18.54,18.36,18.18, 18.03,17.89,17.76,17.65,17.56,17.49,17.43,17.38,17.35, 17.33,17.33,17.34,17.37,17.41,17.46,17.52,17.59,17.68, 17.77,17.87,17.98,18.10,18.22,18.35,18.49,18.63,18.77, 18.92,19.08,19.23,19.36,19.49,19.60,19.69,19.77,19.84, 19.90,19.94,19.97,19.99,20,19.99,19.97,19.94,19.90,19.84, 19.77,19.69,19.60,19.49,19.36,19.23,19.08,18.91,18.73, 18.54,18.33,18.10,17.86,17.60,17.32,17.02,16.70,16.36,16, 15.61,15.20,14.76,14.28,13.77,13.23,12.64,12,11.30,10.54, 9.68,8.72,7.60,6.24,4.44,0.00 [mm]	

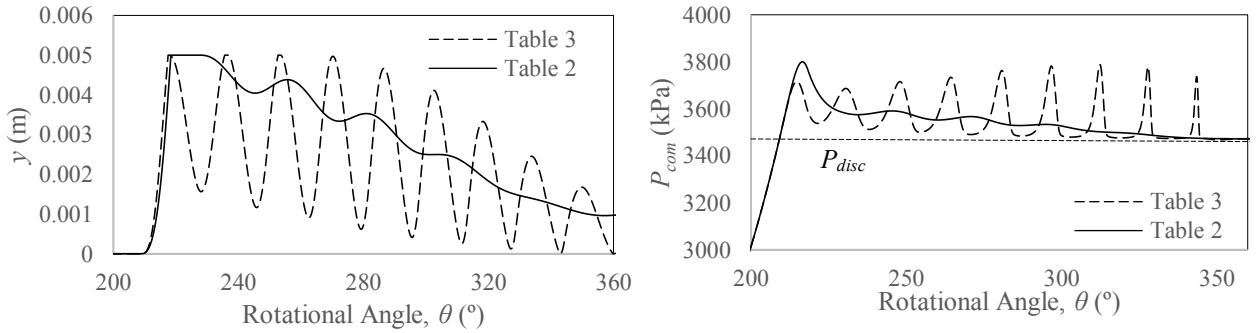

Figure 7: Comparison of valve deflections of valves from Table 3 and 2.

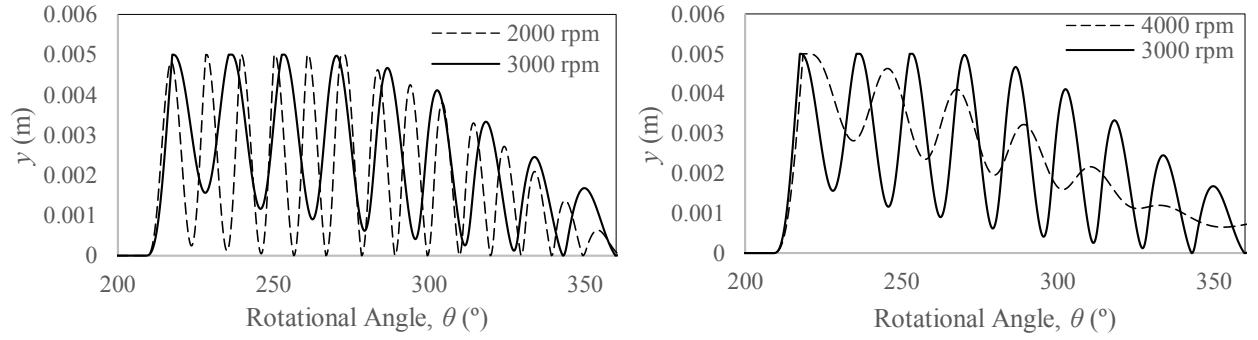

Figure 8: Comparison of valve deflections at different operating speed using reed from Table 3.

4. CONCLUSION

In this paper, the effect of rotational motion on the performance of a rotating valve reed has been investigated. A parametric study on the effect of valve's dimensions on the vibrational response has also been conducted. Finite Element modelling of the modal shape of a non-uniform width valve reed is presented and a mathematical model for the time-variant response of the rotating reed under centrifugal and pressure forces is also formulated. Simulation comparisons between rotating and non-rotating reeds have revealed that the centrifugal force from rotational motion has a 'dampening' effect of reducing valve fluttering and has helped reduce over-compression. However, if the rotating valve is not sufficiently stiffened, the valve will not close the discharge port completely when discharge process has ended as the centrifugal force constantly pulls the reed radially outwards away from its seat. The parametric study done has shown that well-chosen dimensions of a rotating reed can help reduce over-compression and sufficiently stiffened the reed to overcome the centrifugal force in closing the discharge port completely. Overall, it can be concluded that the rotational motion allows the usage of a stiffer and stronger valve reed in a compressor and can enhance the performance as well as the durability of the valve reed if it is carefully designed for a designated rotational speed. Beyond the designated rotational speed, the reed is unable to close the port and its dimension must be re-designed. Below the designated rotational speed, severe over-compression will result.

ACKNOWLEDGEMENTS

The authors wish to thank Mr Pradeep Shakya, Mr Lim Yeu De and Mr Cheng Kai Xian for providing valuable time and help during the study.

NOMENCLATURE

$\mathbf{a}$	vector of nodal displacements (-)	t	time (s)
A	cross-sectional area of valve reed (m^2)	V	shear force (N)
c	coefficient of viscous damping (N s m^{-2})	w	width of valve (m)
E	elastic modulus of valve material (Pa)	x	distance along valve length (m)
I	second moment of area A (m^4)	y	valve deflection height (m)
k	total number of finite elements defined (-)	Y	mode shape/ valve displacement (m)
K	stiffness matrix (-)	λ	natural frequency of valve reed (rad s^{-1})
L	length of valve reed (m)	θ	rotational angle of RV compressor (Deg)
m	mass per unit length (kg m^{-1})	ρ	density of valve material (kg m^{-3})
M	bending moment/mass matrix/ (Nm/-)	τ	mode participation factor (-)
n	vibration mode (-)	ω	rotational velocity of compressor (rad s^{-1})
P	pressure (Pa)		***Subscripts***
R	radial distance from cylinder axis to valve position (m)	com	compression
		$disc$	discharge

REFERENCES

Teh, Y. L., Ooi, K. T., 2009. Theoretical Study of a novel refrigeration compressor - Part I: Design of the revolving vane (RV) compressor and its frictional losses. Int. J. Refrigeration vol. 32, 1092-1102.

Teh, Y. L., Ooi, K. T., Wibowo Djamari, D., 2009. Theoretical Study of a novel refrigeration compressor - Part II: Performance of a rotating discharge valve in the revolving vane (RV) compressor. Int. J. Refrigeration vol. 32, 1103-1111.

Meirovitch, L., 2001. Fundamentals of Vibrations. McGraw-Hill, an imprint of The McGraw-Hill Companies, Inc. 1221 Avenue of the Americas, New York, NY, 10020. 789 pages.

Ooi, K.T., 2004. Simulation of a Piezo-Compressor. Applied Thermal Engineering 24, 549–562.

Manuscript ID: 365
DOI: 10.18462/iir.2019.0365

Experimental Study on Frost Suppression Performance of Super-hydrophobic Surface

Yaxiu GU, Xinglong WANG, Zexiang GONG, Qinglong MENG, Wentao WANG

Department of Building Environment and Energy Engineering, Chang'an University
Xi'an, 710061, China, guyaxiu@foxmail.com

ABSTRACT

There is an inevitable frost phenomenon on the surface of evaporator when the air source heat pump (ASHP) is operating for heating in cities which have cold and wet winter. And the frost formation will decrease the Coefficient of Performance (COP) of ASHP. The used common defrosting modes for ASHP consume the indoor energy, and make a negative effect on the indoor thermal comfort. The super-hydrophobic technology on fabrication of super-hydrophobic surface is improved in this paper. The super-hydrophobic aluminum-based surface with an average contact angle of 154.6° was prepared by chemical etching and fluoroalkylsilane modification. An experimental system for frost suppression was set up. The frosting and defrosting properties of super-hydrophobic aluminum surface and conventional aluminum surface at temperatures ranging from 0 °C to –15 °C and wind speeds ranging from 1 m/s to 3 m/s were studied. It is concluded that the super-hydrophobic surface can effectively inhibit the formation of condensate droplets and frost layer, and has good drainage property, and wind speed has little effect on the formation of frost layer. Results show that the frost suppression performance of super-hydrophobic surface is obviously better than that of bare aluminum surface. And the super-hydrophobic aluminum surface is more suitable for restraining frost formation because of its preferable performance of retarding frost formation and drainage characteristics.
Keywords: Air source heat pump, Super-hydrophobic surface, Frosting, Defrosting

1. INTRODUCTION

Most areas in the south of China are cold and humid in winter. Air source heat pump (ASHP) has become the main heating mode for users in hot summer and cold winter areas because of its high efficiency, energy saving, and without cooling water system, which can meet the demands of both summer cooling and winter heating. There is an inevitable frost phenomenon on the surface of evaporator when the ASHP is operating for heating in cold and wet winter. And the frost formation will decrease the Coefficient of Performance (COP) of ASHP. The used common defrosting modes for ASHP consume the indoor energy, and make a negative effect on the indoor thermal comfort. However, when the ambient temperature is between –12.8 °C and 5.8 °C, and the relative humidity is more than 67%, the frosting phenomenon of the outdoor evaporator of air source heat pump will occur in varying degrees (Jing Shang and Fan, 1986). The existence of frost layer reduces the heat transfer coefficient of heat exchanger surface. Moreover, with the increase of frost layer, the effective spacing between fins becomes narrower and the air flow through heat exchanger decreases, which seriously affects the operation of heat pump units and reduces the COP of units (Barrow, 1985; Stoecker, 1957; Yao, et al., 2004). Therefore, some measures should be taken to defrost the outdoor units of heat pump units to ensure the normal operation of the units. If we can find a fundamental way to suppress frost, which will not affect the operation of heat pump system, but also delays or inhibits the formation of frost, then the performance of air source heat pump will be greatly improved, and the scope of application will be promoted (Di, 2017). In this paper, the surface of fins was modified by super-hydrophobic treatment, and the frost suppression and defrosting characteristics were studied by experimental methods.

2. EXPERIMENTAL SETUP AND RESULTS ANALYSIS

The aluminum sheets used in the experiment were all 20 mm×20 mm×2 mm. In this paper, the aluminum sheets were roughened with 800#~1500# sandpaper until there were no obvious scratches on the surface of the aluminum sheets. Ultrasonic cleaning of aluminum sheet was carried out with acetone, methanol and deionized water. Then, the prepared 3.0 mol/L hydrofluoric acid and 4.0 mol/L hydrochloric acid were used to etch the aluminum sheet for 15 min and 10 min respectively. After etching, ultrasonic cleaning and drying were carried out on the aluminum sheet. Modified with 1 wt% fluoroalkylsilane ethanol solution for 40 min, a super-hydrophobic surface with an average contact angle of 154.6° was prepared (Li, et al., 2008). From Figure 1, it can be seen that there are some nano-scale small convex platforms on the large convex platforms of micron scale in the scanning electron microscopy of super-hydrophobic aluminum-based surface. The small convex platforms overlap layer by layer to form a step-like distribution, which indicates that the super-hydrophobic aluminum surface prepared by the experiment has formed a micro-nano dual structure.

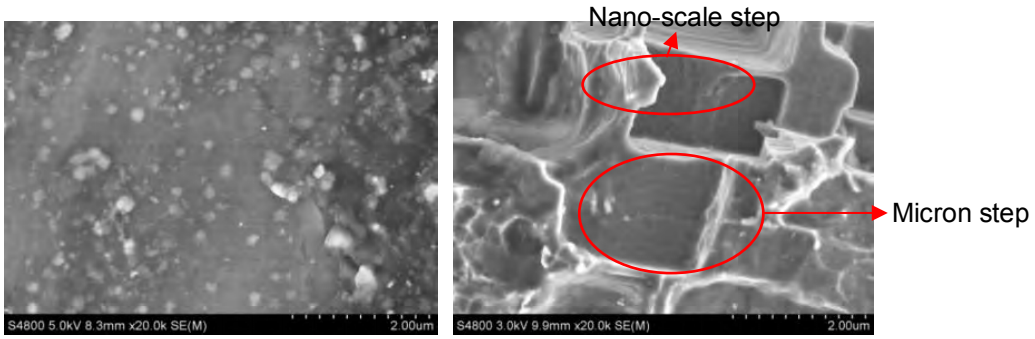

(a) Conventional aluminum (b) Super-hydrophobic aluminum
(Magnify 20 thousand times)

Figure 1: Scanning electron microscopy of different aluminum-based surfaces

As shown in Figure 2, the whole frost suppression test system can be divided into two parts, the thermo-electric cooler water cooling system (left part of red dotted line) and the variable air velocity air supply system (right part of dotted line). The water cooling system of thermo-electric cooler is composed of copper plate, semiconductor refrigerating sheet, water cooling head, temperature control switch, circulating water pump and cooling water tank. The variable speed air supply system is composed of centrifugal fan, acrylic duct, rectifier grid, fan speed controller and humidifying device. The fan speed controller is used to control the air supply speed of the centrifugal fan. The rectifier grille and yarn mesh homogenize the air speed at the cross section of the acrylic air duct. The humidifying device is used to regulate the air supply humidity.

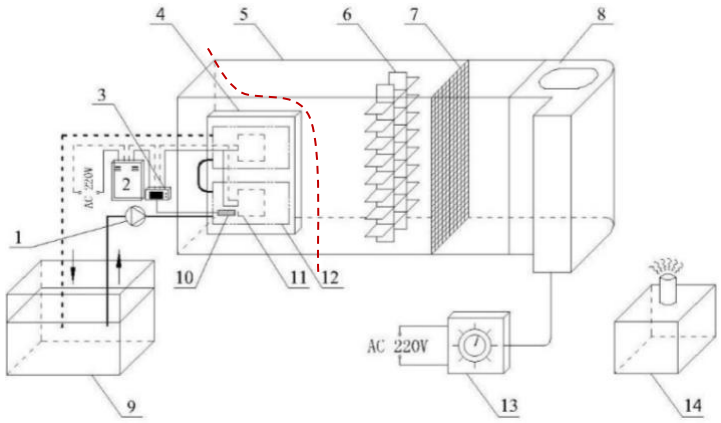

1 Circulating water pump 2 DC power supply 3 Temperature control switch 4 Copper plate
5 Acrylic duct 6 Rectifier gate 7 Yarn mesh 8 Centrifugal fan 9 Cooling water tank
10 Temperature sensor 11 Semiconductor refrigerator 12 Water-cooled head
13 Fan speed controller 14 Humidifier

Figure 2: Principle of frost suppression test system

Through field measurement, it is found that the wind speed at the fin air inlet of the outdoor air source heat pump in winter is between 1 m/s and 3 m/s. By adjusting the fan speed controller, the air supply speed is set to 1 m/s, 2 m/s and 3 m/s respectively. After setting the wind speed, the copper plate sticking to the aluminum sample and the thin film temperature sensor to be measured is placed vertically at the central axis of the Acrylic wind pipe. By adjusting the temperature control switch, the surface temperature of the copper plate is set to 0 °C. After that, the experimental temperature of each group is lowered by 1 °C until it drops to –15 °C. The frosting process on the surface of the aluminum base is recorded with a camera. During the experiment, the indoor ambient temperature was 5 °C and the relative humidity was controlled at about 70%.

2.1 The frosting experiment on the surface of aluminum substrate with a wind speed of 2 m/s

When the temperature of aluminum base is 0 °C, –1 °C and –2 °C respectively, only the condensation of water vapor occurs on the surface of aluminum base, and the time it takes for the first condensation droplets to form on the surface of super-hydrophobic aluminum base is obviously longer than that of conventional aluminum base. As shown in Figure 3(a), with the decrease of temperature, condensate droplets appear earlier and earlier. Compared with conventional aluminum, the time when the first condensate droplets appear on the surface of super-hydrophobic aluminum is about 180 seconds later. As shown in Figure 3(b), the amount and volume of condensate droplets on conventional aluminum based surfaces are large, while the size of condensate droplets on super-hydrophobic aluminum based surfaces is small, and some areas are even invisible to the naked eye.

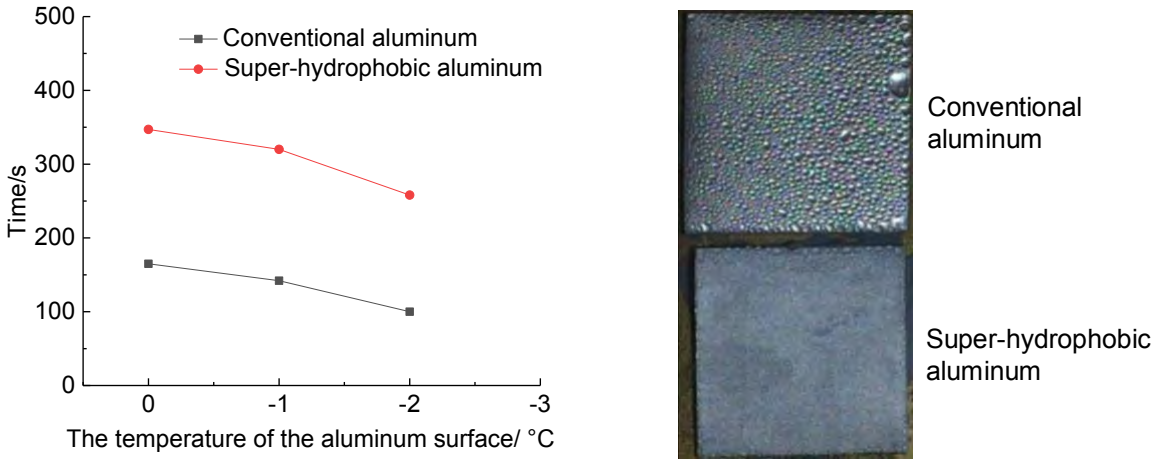

(a)Time contrast **(b) Effect contrast**

Figure 3: Comparison of time and effect of condensate droplets on two aluminum surfaces

When the surface temperature of aluminum is −3 °C to −4 °C, the condensation water droplets first appeared on the surface of aluminum, and then the condensation water droplets were frozen into ice droplets. However, these two phenomena occur on the surface of superhydrophobic aluminum substrates later than those on conventional aluminum substrates. The distribution of ice beads on the surface of the two aluminum bases is similar to that of condensed water beads: the number and volume of ice beads on the surface of conventional aluminum are more than those on the surface of super-hydrophobic aluminum, as shown in Figure 4.

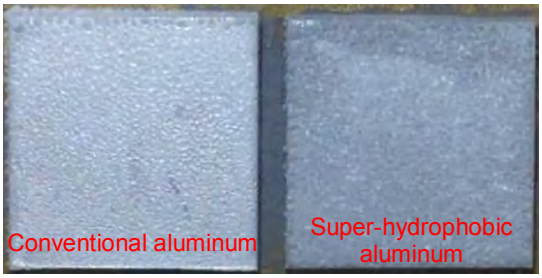

Figure 4: Comparison of frozen ice beads on two kinds of aluminum surfaces

When the aluminum surface temperature is –5 °C, a layer of aluminum surface come first observable small water droplets to the naked eye film, and then covered by needle-like frost.
When the temperature of the aluminum surface is lower than –5 °C, the two kinds of aluminum surface directly generate needle-like frost layer. It can be inferred from Figure 5(a) that the appearance of needle-like frost layer on the surface of super-hydrophobic aluminum base is later than that of conventional aluminum base, which has an obvious effect of delaying frosting. Fig. 5(b) is two kinds of frosting phenomena on the surface of aluminum base. It is found by electronic balance weighing that the weight of frost layer on the surface of superhydrophobic aluminum base at the same time is less than that on the surface of conventional aluminum base, and the frost suppression performance is good.

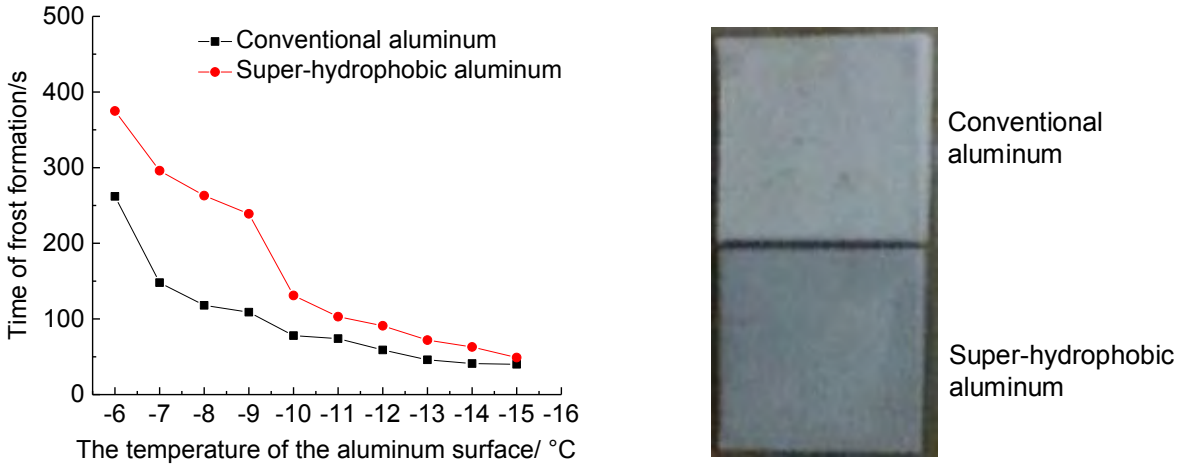

(a) Time contrast **(b) Effect contrast**

Figure 5: Comparison of the time and effect of needle like frost on two kinds of aluminum substrates

2.2 Effect of wind speed on the surface of aluminum base frosting process

In this section, the time of needle frost on the surface of two kinds of aluminum is compared when the temperature is below –5 °C and the wind speed is 1 m/s, 2 m/s and 3 m/s, as shown in Figure 6.

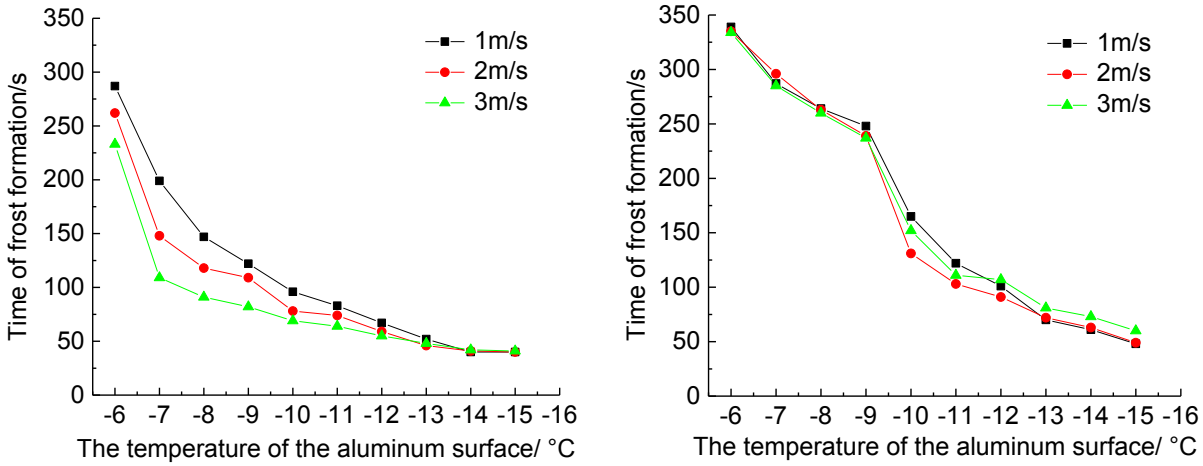

(a) Conventional aluminum **(b) Super-hydrophobic aluminum**

Figure 6: The relationship between the time of frost formation and wind speed on two kinds of aluminum substrates

In Figure 6(a) conventional aluminum base, when the temperature is high, the higher the wind speed is, the earlier the frost layer appears on the surface of aluminum base. The reason is that with the increase of wind speed, the heat transfer rate of aluminum base and nearby air increases, which accelerates the condensation of water vapor in air and accelerates the formation of frost layer. As the temperature decreases, the effect of wind speed on frost layer decreases gradually. The reason

is that the lower the surface temperature of aluminum base, the faster the frosting rate of water vapor in air, the less the influence of wind speed. In Figure 6(b) for super-hydrophobic aluminum base, it can be seen from the figure that the time of frost layer on the surface of super hydrophobic aluminum base does not change much at different wind speeds. The reason is that when the wind speed increases, the convective heat transfer speed increases. Due the frost layer formed is lighter, it will be blown away by air, and the larger the wind speed, the more obvious this phenomenon is.

2.3 Experimental results and analysis of defrosting process

When the surface temperature of aluminum base is –15 °C and the wind speed is 2 m/s, the frosting performance of conventional aluminum base and super-hydrophobic aluminum base is tested for 20 minutes, then the water cooling system is turned off and the natural melting process of frost layer on two kinds of aluminum base surfaces is recorded by camera, as shown in Figure 7. It can be seen from the figure that at 130 s, the obvious melting area can be seen on the surface of conventional aluminum base. By 140 s, the frost layer has all melted into water droplets. The volume of water droplets is larger and the adhesion time on the surface of aluminum base is longer. The frost layer on super-hydrophobic aluminum base begins to melt a little later, but the volume of water droplets after surface melting is small, the number of water droplets is small, and some of them evaporate rapidly at 140 s. More than half of the area has become dry. The reason is that the contact angle of super-hydrophobic aluminum base surface is large, the contact area between water droplets and aluminum base is small, and the contact area with air is large, so it is easier to absorb heat evaporation of air. Overall, the super-hydrophobic aluminum surface can evaporate the water droplets that melt on its surface in a shorter time, and effectively suppress the secondary freezing of the melted water on the fin surface when defrosting mode is turned off in the air source heat pump.

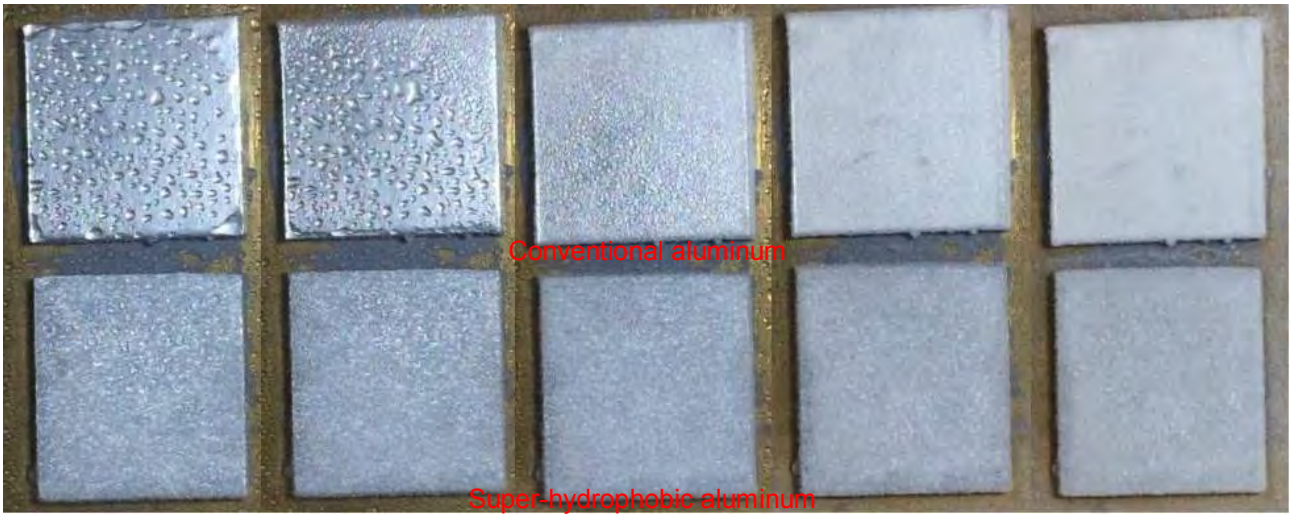

115 s 125 s 130 s 135 s 140 s

Figure 7: Melting phenomena of frost on two kinds of aluminum substrates

In the process of defrosting experiment, the temperature of the experimental environment is controlled at about 10 °C. Since the temperature of the aluminum base surface is gradually increased from –15 °C to 10 °C when the frosting experiment is stopped, the frost layer melts from the surface to the bottom. The frost layer formed on the surface of conventional aluminum base can be divided into dense layer at the bottom and sparse cloud floc layer on the surface. Therefore, the frost melting phenomenon first appeared on the surface of conventional aluminum base at the beginning of defrosting experiment. In the study of Wang et al., (2016) of Southeast University, the defrosting experiment of super-hydrophobic surface was carried out by placing the aluminum base with frost layer on the hot surface at 40 °C. Because the bottom of the frost layer is heated in this experiment, the surface of super-hydrophobic aluminum base defrosts first and the defrosting time is shorter than that of conventional aluminum base, which is contrary to the experimental results in this paper. In practical application, the defrosting effect of two kinds of aluminum surfaces is affected by defrosting methods, and the specific situation needs to be further studied.

3. CONCLUSIONS

1) Condensation droplets will appear on the surface of aluminum base at temperatures ranging from 0 °C to –2 °C. With the decrease of temperature, condensation droplets will appear earlier and earlier. The time of condensation droplets on the surface of super-hydrophobic aluminum base is obviously delayed compared with that of conventional aluminum base. When the temperature ranges from –3 °C to –4 °C, the condensate droplets first appear on the surfaces of the two kinds of aluminum substrates, and then freeze into ice droplets. The ice beads on the surface of super-hydrophobic aluminum base are small in size and small in number, while those on the surface of conventional aluminum base are large in volume and large in number. When the temperature is below –5 °C, acicular frost layer appears directly on the surface of the two kinds of aluminum base, and with the decrease of temperature, the time of frost layer appears earlier and earlier. At the same time, the thickness of frost layer appearing on the surface of super-hydrophobic aluminum base is smaller.
2) The change of wind speed has a great influence on the formation of frost layer on the surface of conventional aluminum base. When the wind speed increases, the formation of frost layer will be accelerated. For super-hydrophobic aluminum base, the increase of wind speed will aggravate the phase change of water vapor in the air around the aluminum base. It will disperse the light frost layer which has been formed, so it has little effect on the formation time of frost layer.
3) The frost layer on the surface of conventional aluminum base shows signs of melting, but the volume of the melted water droplets is huge, the adhesion is strong, and it is difficult to evaporate. On the contrary, the melting time of super-hydrophobic aluminum base surface is slightly later, but the small droplets formed by melting are easy to evaporate, resulting in a large area of drying area on the aluminum base surface.

ACKNOWLEDGEMENTS

This project was supported by Natural Science Basic Research Plan in Shaanxi Province of China (Grant No. 2018JM5084), Shaanxi Provincial Key Program of Science and Technology Innovative Research Groups under the contract No.2016KCT-22, and the Special Fund for High-tech cultivation project of Central Universities.

REFERENCES

Barrow H. 1985. A note on frosting of heat pump evaporator surfaces. Heat Recovery System 5(3): 195-201.

Wang F, Liang C.H, Zhang X.S, 2016. Frost suppression mechanism and defrosting characteristics of super-hydrophobic surfaces. Journal of Engineering Thermophysics 37(5): 1066-1070.

Di H. 2017. Experimental study on frost suppression performance of aluminium-based super-hydrophobic surface in air source heat pump evaporator. Chang'an University.

Jing Shang Y.S, Fan C.Y, 1986. Air conditioning manual. China Construction Industry Press, Beijing.

Stoecker W.F. 1957. How frost formation on coils affects refrigeration systems. Refrigeration Engineering 65(2): 42-46.

Li Y.F, Yu Z.J, Yu F.Y, Huo S.B, Song S.P, 2008. Preparation of super-hydrophobic surface on aluminium alloy substrate. Journal of Chemical Engineering in Colleges and Universities 22(1): 624-627.

Yao Y, Jiang Y.Q, Deng S.M, Ma Z.L, 2004. A study on the performance on the air-side heat exchanger under frosting in air-source heat pump water heater/chiller unit. International Journal of Heat and Mass Transfer 47(17-18): 3745-3756.

Manuscript ID: 367
DOI: 10.18462/iir.icr.2019.0367

Simulation Studies and In-situ Measurement Analysis of a New Evaporative Condenser

Yaxiu GU[(a)], Yang ZOU[(a)], Song PAN[(b)], Junwei WANG[(a)], Guangdong LIU[(a)]

[(a)] Department of Building Environment and Energy Engineering, Chang'an University
Xi'an, 710061, China, guyaxiu@foxmail.com
[(b)] College of Architecture and Civil Engineering, Beijing University of Technology
Beijing 100124, China, pansong@bjut.edu.cn

ABSTRACT

In this paper, a new evaporative condenser with an annular elliptic finned tube heat exchanger was introduced and some of its main performance parameters were simulated. For comparison, the actual operating parameters of the round finned tube evaporative condensation air conditioning system using in a subway station were also measured and simulated. This paper provides a reference for related researches on the actual operation of subway stations. Meanwhile, the heat transfer performance of the annular elliptic finned tube heat exchanger was compared with the round finned tube heat exchanger by numerical simulation. The results showed that the annular elliptic finned tube heat exchanger had a smaller air resistance and a larger heat transfer coefficient. Besides, the new annular elliptic finned tube proposed in this paper could increase the COP of the air conditioning system by roughly 5% to 17%, and the energy consumption is reduced by about 8% to 22%.
Keywords: Evaporative condenser, Theoretical analysis, Annular elliptic finned tube, Practical measurement.

1. INTRODUCTION

The evaporative condenser is a combination of air-cooled and water-cooled condenser. It is researched that the condensing temperature of the air-cooled condenser is greatly affected by the environment and is about 5-10 °C higher than it of the evaporative condenser (Thu et al., 2013). Water-cooled condenser has lower condensing temperature than evaporative condenser, but it needs more cooling water, as a result, the water pump consumes more energy (Sreejith et al., 2014, Chen et al., 2008). Many studies showed that evaporative condensation air conditioning system could save energy by 11%~70% compared to air-cooled or water-cooled air-conditioning units (Hajidavalloo, 2007).

The heat transfer enhancement and energy saving of evaporative condenser is widely investigated in recent years. Yu and Chan (2006) studied the performance of a residential evaporative condensation air conditioner with various strategies for staging evaporative condenser fans under different operating conditions. Hao et al. (2013) changed the cooling-pad's thickness of an evaporative air-cooled condenser to research its heat transfer enhancement and energy saving. Salah et al. (2009, 2013) investigated a new rotating disk evaporative condenser under a wide range of option parameters, and they found that the ability to reject heat of this evaporative condenser is 13 times higher than the air-cooled one. Vrachopoulos et al. (2007) presented an incorporated evaporative condenser with basin of water condensates and system of water-drop cloud, and the results showed that it could save roughly 58% energy. Hwang et al. (2001) put forward a new evaporative condenser with tube immersing in a water tub. Yang et al. (2012) developed a mater mist evaporative condenser in a subtropical climate. It is found that the COP could be improved by around 18.6%.

Many researchers have carried out experiments and numerical simulation studies of evaporative-cooling system (Ertunc et al., 2006, Islam et al., 2015), however, the investigation of evaporative condenser composed with new tubes is scarcely reported. This paper introduced a evaporative condenser with new oval annular tube-fin heat exchanger, built up the 2D and 3D models for numerical simulation and compared it with the traditional evaporative condenser with round finned

tube heat exchanger, for the sake of verifying the accuracy of the result, the simulated result was compared with the measured data testing in a practical evaporative condensing air-conditioning systems in a subway station.

2. METHODS

2.1. Actual system synopsis

The air conditioning system measured in this paper is located in a subway station in Beijing, China. This subway station is an underground two-story island station, and its total length is 249.6 m, standard section width is 21.3 m and main building area is 19,184 m^2. This station has part A and part B, which are jointly responsible for the indoor loads of this station. Part A offers the cooling capacity for the large system (including the station hall and the platform), and bears the small system's loads of the station office area and the equipment room at the same time. The large system and the small system operate independently. The measured data used in this paper is mainly derived from the operating test results of the refrigeration system at the part A.

The system consists of several single decentralized systems comprising a surface cooler (evaporator), an evaporative condenser (condenser) and a compressor unit. The surface cooler (evaporator) was placed in the air supply channel, and the evaporative condenser was placed in the air exhaust channel. The design value of the cooling capacity of the evaporative condenser is 1150 kW, and the cooling air is mainly from the exhaust air in the subway station. When the air volume is insufficient, it will be assisted by fresh air.

2.2. Actual measurement methods and contents

This paper selected one week per year with the highest temperature in Beijing from July to August in 2016-2018 to measure the air conditioning system. The test contents mainly included the relevant environmental parameters of the station hall and the platform of this subway station. Besides, this paper also tested the main operating parameters of the air conditioning system such as the air speed, air temperature, air relative humidity, the compressor power, the pump power, the fan power, and so on. This test used the automatic recording instruments to continuously monitor the above parameters of the air conditioning system.

When testing the air speed of the evaporative condenser, 25 survey points were uniformly distributed in the cross section of the wind channel, and the average value of the testing data was taken as a standard operating value.

3. MODELING

In the actual tested evaporative condensation air conditioning system, the heat exchanger used in the evaporative condenser is the round finned tube heat exchanger. The schematic diagram of the round finned tube flow cross-sectional structure was shown in Figure 1(a). The length of the round tube is l_1 = 1.42 m and the diameter is d_r=10 mm, the tube is arranged in a row, and the distance between two adjacent tube center is 30 mm. The new annular elliptic finned tube heat exchanger was shown in Figure 1(b). The heat exchanger is constituted by two tubes: the inner tube and the outer tube. The outer tube is an elliptical tube, and the inner tube is a round tube. Because the refrigerant is flowing in the annular space between the two tubes, in order to keep the same cross-section areas as the round finned tube heat exchanger, the size of the new heat exchanger was computed as follow: length l_2=1.42 m, inner round tube diameter d_e=8 mm. As for the outer elliptic tube, its long axis length is 2a =16 mm, and its short axis length is 2b=12 mm. And the distance between two adjacent centers of the annular elliptic tube is 35 mm, and the cross-section schematic diagram of the annular elliptic finned tube heat exchanger was shown in Figure 1(b).

In this paper, the heat transfer and flow conditions inside and outside the tubes were separately modeled and calculated. This paper took a single complete heat exchange tube as the calculation unit, in order to avoid the interference of the inlet effect and export effect. The length of the model was 1.42 m the same with the real tube. This paper took the cross section of the tube to establish the 2D model. Fig. 2(a) and 2(b) showed the 2D model of the round finned tube heat exchanger and the new annular elliptic finned tube heat exchanger.

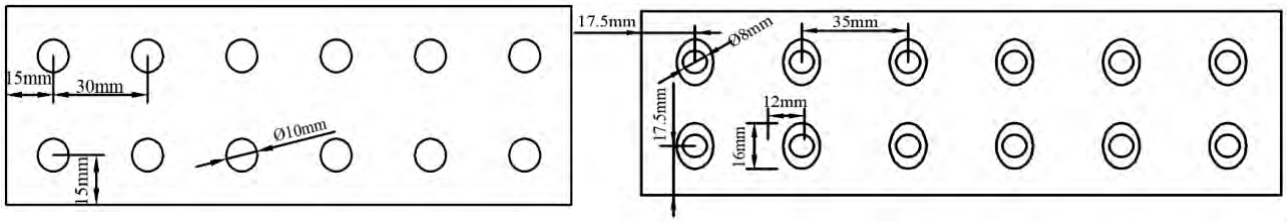

(a) round finned tube (b) annular elliptic finned tube

Figure 1: The cross-section schematic diagram

In the calculation 2D model of the round tube shown in Figure 2(a), the left boundary was the refrigerant-liquid inlet, the right boundary was the refrigerant-vapor outlet, the upper boundary was the wall boundary, and the lower boundary was the symmetry axis. In the 2D model of the annular elliptic finned tube heat exchanger shown in Figure 2(b), the upper left boundary was the refrigerant-liquid inlet, the lower left boundary was the cooling-water outlet; the upper right boundary was the refrigerant-vapor outlet, the lower right boundary was the cooling-water inlet, the upper boundary was the outer-tube wall, the middle boundary was the inner-tube wall, and the lower boundary was the symmetry axis.

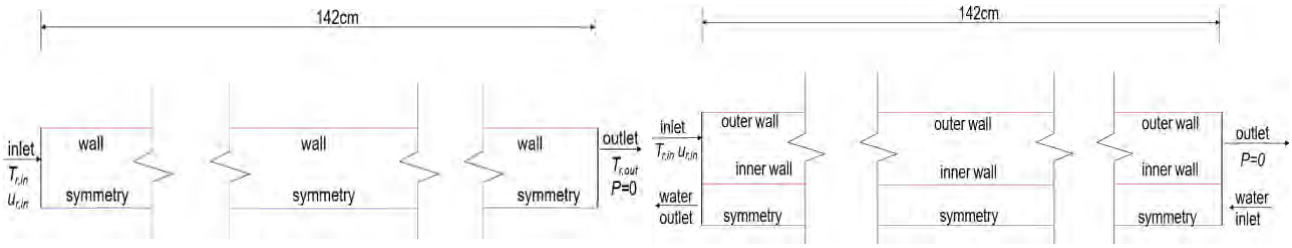

(a) round finned tube (b) annular elliptic finned tube

Figure 2: The 2D model of the heat exchangers

Fig. 3(a) and 3(b) are the 3D models of the traditional round finned tube heat exchanger and the new annular elliptic finned tube heat exchanger respectively, which were used to simulate the flow and heat exchange of the air and spray water outside the tube. In the actual system, the fin pitch of the round finned tube heat exchanger is 6 mm. In this paper, the geometric model used for numerical simulation chose a 6 mm long tube section with one fin as the calculation unit.

As shown in Figure 3(a), according to the actual flow process, the cooling air and the cooling water entered from the inlet shown in the figure, flowed into the heat exchange unit along the negative direction of the y-axis which was perpendicular to the pipe length direction, and then flow out from the outlet after heat exchanging. The up and down face of the model were both symmetrical planes, and the two sides of the model were both periodic surfaces. As shown in Figure 3(b), the cooling air and cooling water flowed into the heat exchange unit in the negative direction of the x-axis which was perpendicular to the length of the tube, and then flowed out from the outlet. The up and down sides of the model were symmetrical planes, and the two sides of the model were periodic surfaces.

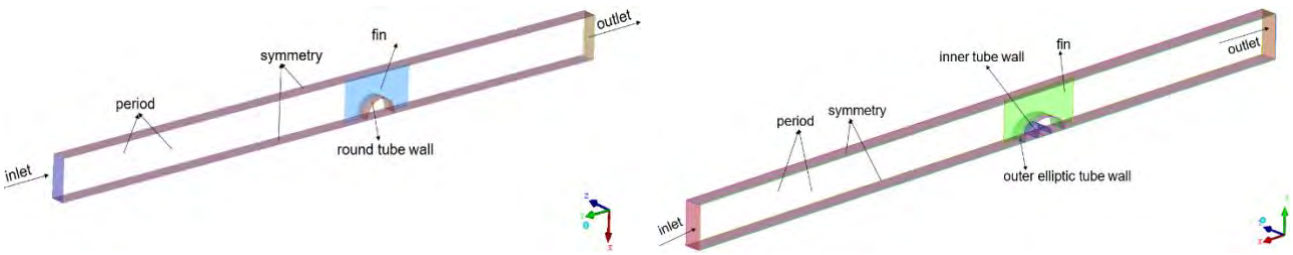

(a) round finned tube (b) annular elliptic finned tube

Figure 3: The 3D model of round finned tube

4. EQUATIONS AND PARAMETERS SETTING

In this paper, the vaporization condensation model in the mixed multiphase flow model of FLUENT software was used to simulate the phase transition between vapour and liquid phases. The principle of the model is to apply the Lee model for calculating the phase transition. The governing equation for mass transfer (evaporation condensation) between liquid and vapour is:

$$\frac{\partial}{\partial t}(\alpha_v \rho_v) + \nabla(\alpha_v \rho_v \vec{V}_v) = \dot{m}_{lv} - \dot{m}_{vl} \quad \text{Eq. (1)}$$

Where α_v is vapour volume fraction, ρ_v is vapour density in kg×m^{-3}, V_v is vapor speed in m/s, $\dot{m}$ is quality flow in kg×s^{-1}×m^{-3}, and the lower angle label '*lv*' is from liquid to vapor, '*vl*' is from vapor to liquid.

The mass transfer of evaporative condensation is determined by the equation (2)-(3), which is mainly determined by the relationship between the vapour and liquid phase's temperature and the saturation temperature. The specific calculation process is as follows:

When the liquid phase temperature is higher than the saturation temperature, the mass transfer direction is from the liquid phase to the vapour phase, which is the evaporation process:

$$\dot{m}_{lv} = \xi_{coef} * \alpha_l \rho_l \left(\frac{T_l - T_{sat}}{T_{sat}}\right) \quad \text{Eq. (2)}$$

When the vapour phase temperature is higher than the saturation temperature, the mass transfer direction is from the vapour phase to the liquid phase, which is the condensation process:

$$\dot{m}_{vl} = \xi_{coef} * \alpha_v \rho_v \left(\frac{T_{sat} - T_v}{T_{sat}}\right) \quad \text{Eq. (3)}$$

According to the kinetic theory of vapour phase condensate flux given by Hertz Knudsen's formula (Tanasawa, 1991), the evaporation coefficient and condensation coefficient in the mass transfer process in equation (2) and (3) can be finally calculated and determined:

$$\xi_{coef} = \frac{6}{d_{buble}} \beta \sqrt{\frac{M}{2\pi\pi R_{sat}}} L \left(\frac{\alpha_v \rho_v}{\rho_L - \rho_v}\right) \quad \text{Eq. (4)}$$

Where ξ_{coef} is evaporation and condensation coefficient in s^{-1}, d_{buble} is bubble diameter in m, β is constant, T is temperature in K.

5. DISCUSSION

In order to study the heat transfer and flow performance of the annular elliptic finned tube heat exchanger, this paper simulated the annular elliptic finned tube and the traditional round finned tube heat exchangers on the basis of the measured data. The measured values would be compared with the simulated values under the same conditions, such as the refrigerant outlet temperature, condensing temperature, heat transfer coefficient, heat dissipation, and external pressure of the heat exchanger. In this paper, 2268 sets of continuously recorded data were arranged in order of refrigerant inlet temperature, and 1 °C were taken as a calculation node to divide all data into groups, for example, when the refrigerant inlet temperature ranged from 39.5 to 40.5 °C, the eligible data would be counted as a group, and the average value of this group would be the valid data for the simulation calculation.

5.1. **Analysis of refrigerant temperature**

As shown in Figure 4, this paper used FLUENT simulation software to calculate the condensing temperature value of the refrigerant in the condensing tube of the annular elliptic finned tube heat exchanger and the round finned tube heat exchanger under the same conditions. In order to ensure the accuracy of the simulation value, the measured value and simulation value of the condensing temperature were compared and analysed. The Fluent simulation results and the measured value of the condensing temperature of the round finned tube heat exchanger are between 0.9% and 1.2%, and the error was less than 10%. So it could be concluded that the simulation results were basically consistent with the actual situation.

Besides, according to the simulation results, under the same conditions, the condensing temperature of the refrigerant in the annular elliptic finned tube heat exchanger was obviously lower than that of

the round tube, and with the temperature of the spray water increasing gradually, the advantage became more obvious. This was because that the annular elliptic finned tube heat exchanger had cooling water circulating inside and outside the heat exchanger, as a result, the refrigerant flowing in the annular space could exchange heat with more cooling waters than the round tube. Therefore, under the condition that the cross-sectional area of the refrigerant was the same, the heat exchange area of the annular elliptic finned tube heat exchanger was significantly higher than that of the round one.

According to the calculation, the heat transfer area of the annular elliptic finned tube heat exchanger was 52.797% higher than that of the traditional round one of the same size. The simulation results showed that under the spray temperature varying from 27.21 °C to 33.24 °C, the condensing temperature of the annular elliptic finned tube heat exchanger was 2.71~4.32 lower than that of the conventional round finned tube heat exchanger. Studies showed that for every 1 °C reduction in condensing temperature, the energy consumption of the refrigeration system will be reduced by 3% to 5%, and the COP of the air conditioning system will increase by 2% to 4% (Chow et al., 2002). Based on this analysis, the new annular oval tube proposed in this paper can increase the COP of the air conditioning system by roughly 5% to 17%, and the energy consumption is reduced by about 8% to 22%.

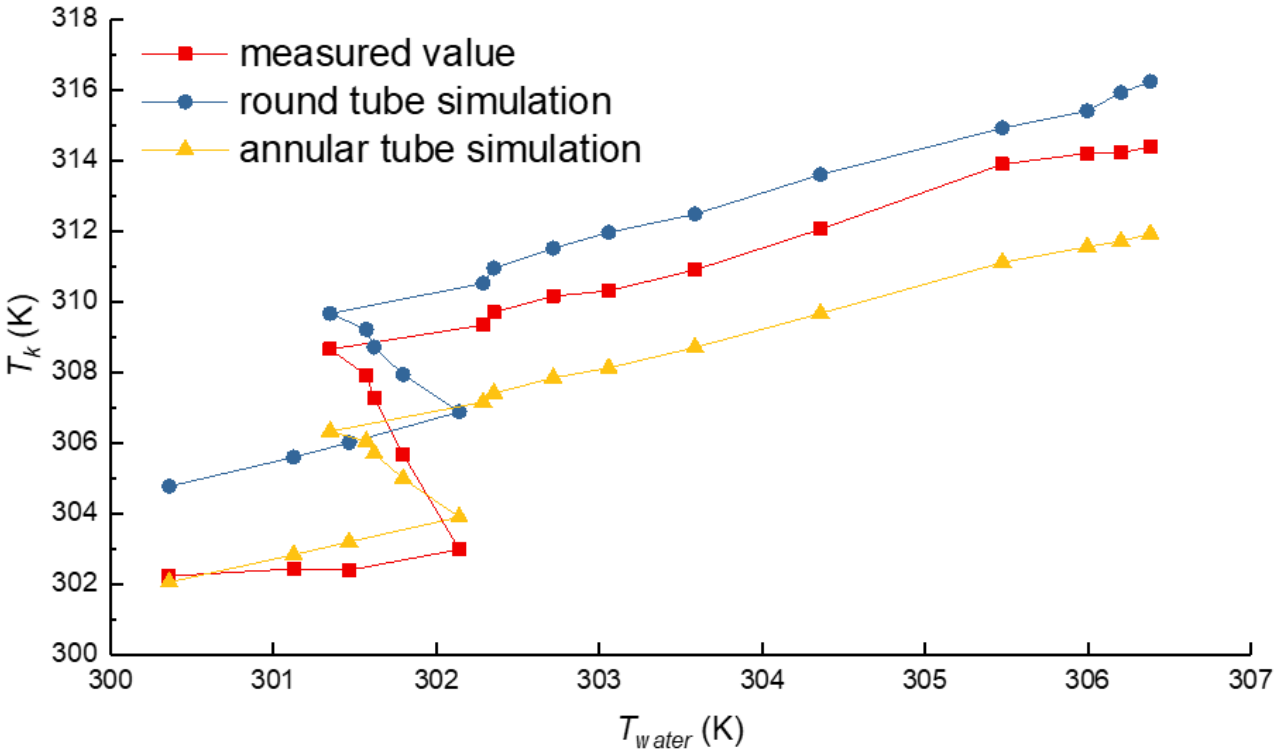

Figure 4: Comparison of T_k under the same water temperature of the two types of tubes

5.2. Analysis of heat transfer capacity and air resistance

In this paper, the influence of inlet air velocity on the heat transfer capacity of the evaporative condenser was studied, as shown in Figure 5(a), it could be known that when the inlet air velocity was less than 1.52 m/s, the evaporation heat exchanger would decrease with the increasing of the air velocity. Due to the increasing of the inlet air velocity, the contact time between cooling air and the liquid film would decrease, so the heat transfer capacity at the gas-liquid interface would be insufficient. When the inlet air velocity was higher than 1.52 m/s, the increase of the air velocity would promote the heat transfer capacity of the evaporative condenser. When the air velocity was higher than 2.88 m/s, with the air velocity increasing the increasing speed of the heat transfer capacity would gradually slow down.

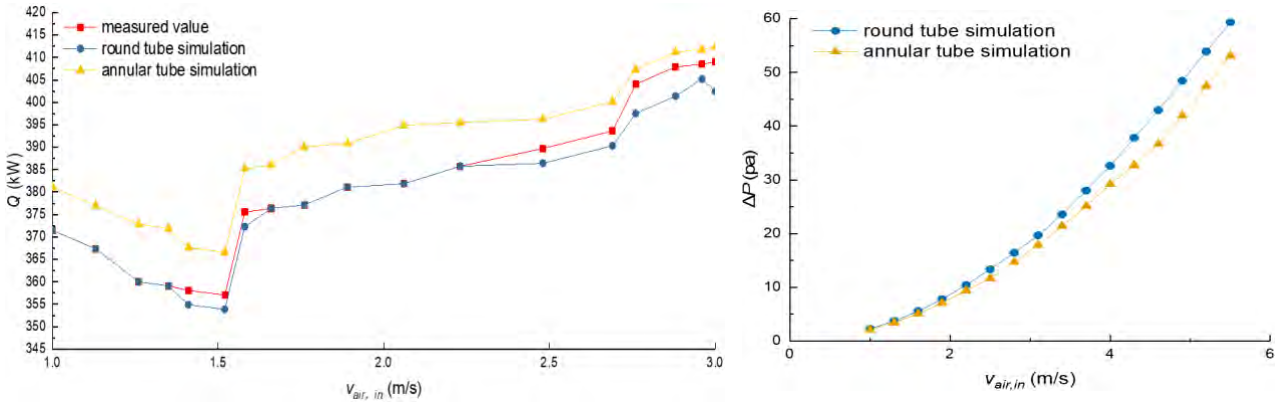

(a) effect on heat transfer capacity (b) effect on pressure drop

Figure 5: Effect on heat transfer and pressure drop

According to other research results (Chow et al., 2002, Anica et al., 2017), when the air velocity exceeded 5 m/s, the continually increasing of the air velocity would cause heat transfer capacity reducing again. This is because the larger the inlet air velocity become, the larger the amount of cooling air would flow through the heat exchanger per unit time, as a result, the more latent heat exchange of vaporization would be carried out by the air. When the flowing direction of the air was the same as the spray direction of the spray water, the liquid film on the surface of the heat exchanger would be thinner with the a larger the air velocity. Within a certain range, the heat transfer resistance would be reduced and the heat transfer coefficient would be increased. But when the air velocity was too large, the liquid film formed by the spray water would be blown off and form the dry spots on the surface of the heat exchanger at the same time, this would not benefit the heat exchange.

This paper also compared the air resistance of the round finned tube and the annular elliptic finned tube heat exchanger under the same air velocity, and the air pressure drop between the entrance and the exit of the heat exchanger would be taken as the judgement criteria of the air resistance. As shown in Figure 5(b), the new annular elliptic finned tube heat exchanger proposed in this paper had a larger cross-section area, so the air pressure drop was lower than that of the round finned tube at the same air velocity. With the inlet air velocity becoming larger, this advantage would be more obvious. It showed that when the inlet air velocity was between 1.0~5.5 m/s, the average pressure drop of the annular elliptic finned tube heat exchanger was about 11.74% lower than that of the round finned tube heat exchanger.

6. CONCLUSIONS

This paper firstly conducted the measurement of the actual evaporative condensation air conditioning system, got the working condition of the traditional round finned tube evaporative condenser in actual engineering. Then based on the measured data, the models of the traditional round finned tube heat exchanger and the new annular elliptic finned tube heat exchanger were established for simulation calculation. Through the actual measurement combined with simulation, the new annular elliptic finned tube heat exchanger and the traditional one were analysed from the aspects of condensing temperature, refrigerant inlet and outlet temperature difference etc. After the above analysis, the results can be concluded as follows:

(1) Under the same spray water temperature, the condensing temperature of the new annular elliptic finned tube heat exchanger was 2.71 °C ~4.32 °C lower than that of the traditional round finned tube heat exchanger. And the lower spray water temperature decrease, the more obvious the advantages of annular elliptic finned tube heat exchanger would be.

(2) When the inlet air flow rate was between 1.0~5.5 m/s, the air resistance of the annular elliptic finned tube heat exchanger was smaller than the round finned tube heat exchanger. The calculation results showed that the pressure drop was about 11.74% lower than that of the round tube.

ACKNOWLEDGEMENTS

The project is supported by Natural Science Basic Research Plan in Shanxi Province of China (Number 2018JM5084), Shaanxi Provincial Key Program of Science and Technology Innovative Research Groups (Number 2016KCT-22) and the Fundamental Research Funds for the Central Universities, CHD300102289203.

NOMENCLATURE

p	pressure (kPa)	$\dot{m}$	quality flow ($kg \times s^{-1} \times m^{-3}$)
T	temperature (K)	$\vec{V}_v$	vapor speed ($m \times s^{-1}$)
ρ_v	vapour density ($kg \times m^{-3}$)		

REFERENCES

Anica I., et al., 2017. Experimental investigation of heat and mass transfer in evaporative condenser. Energy Procedia 112, 150-157.

Chow T.T., et al., 2002. Placement of condensing units of split-type air conditioners at low-rise residences. Applied Thermal Engineering 22(13), 1431-1444.

Chen H., et al. 2008. Applying water-cooled air conditioners in residential buildings in Hong Kong. Energy Convers Management 49(6), 1416-1423.

Ertunc H.M., Hosoz M., 2006. Artificial neural network analysis of a refrigeration system with an evaporative condenser, Applied Thermal Engineering 26(5-6), 627-635.

Hwang Y., et al., 2001. An experimental evaluation of a residential-sized evaporatively cooled condenser. International Journal of Refrigeration 24(3), 238-249.

Hajidavalloo E., 2007. Application of evaporative cooling on the condenser of window air conditioner. Applied Thermal Engineering 27(11-12), 1937-1943.

Hao X.L., et al., 2013. Optimizing the pad thickness of evaporative air-cooled chiller for maximum energy saving. Energy and Buildings 61, 146-152.

Islam M.R., et al., 2015. Experimental and numerical study of an evaporatively-cooled condenser of air-conditioning systems. Energy 87(1), 390-399.

Michalis G.V., et al, 2007. Incorporated evaporative condenser. Applied Thermal Engineering. 27, 823-829.

Nasr M.M., Salah M.H., 2009. Experimental and theoretical investigation of an innovative evaporative condenser for residential refrigerator. Renewable Energy 34(11), 2447-2454.

Salah H., Youssef M.A., 2013. Theoretical model for a rotating disk evaporative condenser used in a split air conditioner. Journal of Engineering &Technology (32), 1-20.

Sreejith K., et al., 2014. Experimental investigation of a household refrigerator using air-cooled and water-cooled condenser. International Journal of Engineering and Science 4(6), 13-17.

Tanasawa I., 1991. Advances in Condensation Heat Transfer. Advances in Heat Transfer. 21, 55-139.

Thu H.T.M., Sato H., 2013. Proposal of an eco-friendly high-performance air-conditioning system Part 1. Possibility of improving existing air-conditioning system by an evapo-transpiration condenser. International Journal of Refrigeration 36(6), 1589-1595.

Thu H.T.M., Sato H., 2013. Proposal of an eco-friendly high-performance air-conditioning system part 2. Application of evapo-transpiration condenser to residential air-conditioning system. International Journal of Refrigeration 36(6), 1596-1601.

Vrachopoulos M.G., et al., 2007. Incorporated evaporative condenser. Applied Thermal Engineering 27(5-6), 823-828.

Yu F.W., Chan K.T., 2006. Improved condenser design and condenser-fan operation for air-cooled chillers. Applied Energy 83(6), 628-648.

Yang J., et al., 2012. Performance enhancement of air-cooled chillers with water mist: experimental and analytical investigation. Applied Thermal Engineering 40, 114-120.

Manuscript ID: 373
DOI: 10.18462/iir.icr.2019.0373

A novel marine ejector-refrigeration rotary-desiccant air-conditioning system and its working fluid analysis

Chaoyu Zheng[(a)], Chenxu Zhao[(a)], Wu Chen*[(a)]

[(a)]School of marine engineering, Jimei University
Xiamen, 361021, China, chenwu73@jmu.edu.cn

ABSTRACT

Ships have abundant waste heat which can be recovered to act as the driving heat source for the ejector refrigeration and desiccant air-conditioning (A/C) systems. In this paper a novel marine ejector-refrigeration rotary-desiccant A/C system is proposed and its configuration and working principle are introduced in detail. The novel A/C system driven totally by ship's waste heat is composed of an ejector-refrigeration unit and a rotary-desiccant A/C sub-system. The A/C system has some excellent advantages to apply on ship such as the independent temperature and humidity control and energy saving. Taking into account the thermal quality of ship's waste heat, the special ambient environment including the cooling sea water readily available overboard, and the specific working conditions for the A/C system proposed, some environment-friendly working fluids or refrigerants are compared and analyzed for the system's ejector refrigeration unit. It can be concluded that water should be the most suitable working fluid for the A/C system proposed.
Keywords: Marine A/C System, Ejector Refrigeration, Rotary Desiccant, Working Fluid.

1. INTRODUCTION

With the continuous growth of global trade, the scale of shipping industry is becoming bigger and bigger, which has greatly promoted the social and economic development of both sides of the trade. However, at the same time, it also brought some problems, for example, the increasing carbon emissions. According to the statistics from the report of the Marine Environment Protection Committee (MEPC) on its fifty-ninth session, the carbon emission of shipping industry accounted about 3.3% of total global carbon emission in 2007(Marine Environment Protection Committee, 2009). In order to avoid the deterioration of the situation, the MPEC of International Maritime Organization (IMO) has developed some indices including Energy Efficiency Design Index (EEDI), Ship Energy Efficiency Management Plan (SEEMP), Energy Efficiency Operation Index (EEOI) and so on to reduce carbon emission and enhance energy efficiency of both newly-designed ships and ships in service. In addition, the IMO has put forward a series of measures for energy conservation and emission reduction, among them, the utilization of waste heat has been strongly recommended. In modern ships, the efficiency of main diesel engine is only about 50%, which means abundant waste heat can be obtained on the ships.

Air-conditioning was one of the most important auxiliary equipment of modern ship, which creates a relatively comfortable working and living environment for the crew. However, traditional vapor-compression refrigeration unit for air-conditioning consumed about 15%-20% of electric power generated on board. On the other hand, there is abundant waste heat on ships. Therefore, waste heat-driven refrigeration technologies are considered for the application on ships. Chen W. and his research group proposed a one-rotor two-dehumidification rotary-desiccant A/C system for the application in marine air-conditioning(Chen et al., 2011; Zheng et al., 2012; Zhu et al., 2014; Zhu et al., 2015). However, since the designed cooling sea water temperature reaches 32℃, the requirements of supply air cannot be met by the sea water cooling alone. Therefore it needs an auxiliary refrigeration unit to further lower the temperature of supply air. As a potential alternative technology, ejector refrigeration can be driven by waste heat and the green refrigerants such as water can be used as its working fluid. Moreover the ejector refrigeration unit has few moving parts, which is very advantageous to the maintenance and management on ship. In this paper, a novel marine ejector refrigeration rotary desiccant (ERRD) A/C system which consists of an ejector-refrigeration unit and a rotary-desiccant A/C subsystem will be introduced and its working fluid will be analyzed.

2. CONFIGURATION OF MARINE ERRD A/C SYSTEM AND ITS ADVANTAGES

2.1. Configuration of Marine ERRD A/C System

The configuration of marine ERRD A/C system was showed in Fig. 1. The system can be seen as the combination of two subsystems, i.e., the ejector refrigeration subsystem and rotary desiccant subsystem.

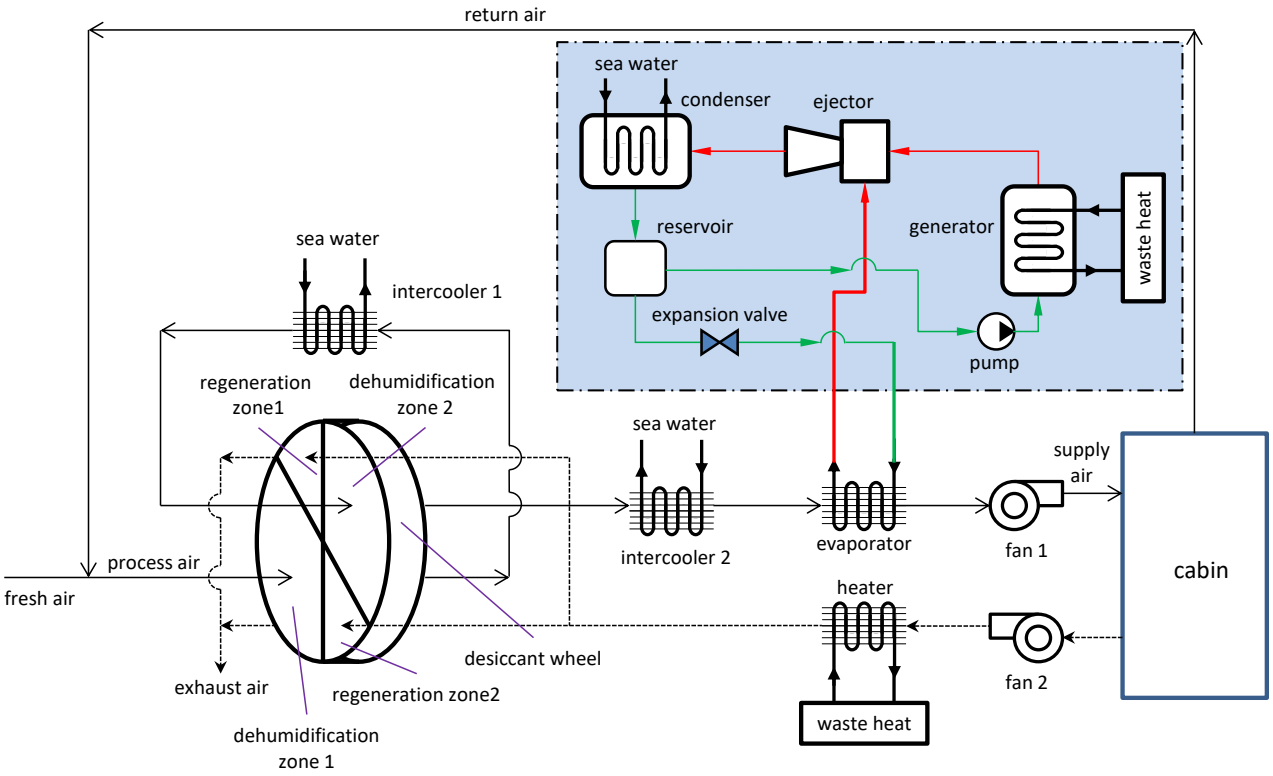

Figure 1: Configuration of marine ERRD A/C system

In the rotary desiccant subsystem, a desiccant wheel having two dehumidification zones and two regeneration zones is used to deal with the latent load of processing air. On the one hand, the processing air which is composed of the outdoor fresh air mixing with indoor return air as per fresh air ratio flows through the dehumidification zone 1. Part of the latent load of processing air is converted into sensible load, leading to the temperature increase of processing air. Meanwhile the processing air is firstly cooled by the sea water and then by the intercooler 1. After that, processing air continues to flow through the dehumidification zone 2 to further remove moisture and then is cooled again by the intercooler 2. Finally, the processing air is cooled by evaporator to meet the requirement of supply air temperature. On the other hand, the regeneration air from indoor exhaust air is heated to the regeneration temperature and then is sent to and flow through the wheel's regeneration zone 1 and 2 to recover the dehumidification capacity of the desiccant wheel.

In the ejector refrigeration subsystem, the main components include the ejector, generator, condenser, evaporator and expansion device. Among these main components, the ejector is the key one which consists of the nozzle, suction chamber, mixing chamber and diffuser. The liquid working fluid in the reservoir is divided into two streams, one entering the evaporator through an expansion device to absorb heat load, the other entering the generator through a circulating pump. The primary fluid stream is heated to the high pressure and high temperature state in the generator driven by waste heat, and then flows through the nozzle of ejector and entrains the secondary fluid stream from evaporator into the suction chamber. After that, the two streams mix together in the mixing chamber. Finally, the mixing fluid is pressurized in the diffuser and then flows out to the condenser for condensation.

2.2. The Advantages of Marine ERRD A/C System

The combination of ejector refrigeration and rotary desiccant technologies in the marine A/C system can bring the following advantages.
(1) Both ejector refrigeration and rotary desiccant can be driven by waste heat. When rotary desiccant technology is used alone in the marine A/C system, it is impossible to meet the requirements of supply air state and usually the auxiliary vapour-compression refrigeration unit is needed.
(2) Since the latent load and sensible load can be handled by the rotary desiccant subsystem and ejector refrigeration subsystem respectively, the independent control of temperature and humidity of A/C system can be achieved to some extent, which improves the comfort and health of ship cabin air.
(3) Because the system's latent load is nearly all deal with by the rotary desiccant subsystem, the ejector refrigeration subsystem need not undertake the dehumidification load. Hence, the evaporation temperature can be increased great. For example, when the supply air temperature is 17℃, the evaporation temperature can be raised to 10℃ and above. In an ejector refrigeration A/C system, the evaporation temperature is required to be about 5℃ due to the requirement of dehumidification. Under the same condensation temperature, the pressure ratio can be reduced by 28.95%. The decreased pressure ratio can help improve the working condition of the ejector.
(4) Compared with the conventional vapour-compression refrigeration system, EERD A/C system has the possibility of using more environment-friendly refrigerants.
(5) Except for the auxiliary pumps, both subsystems have not moving parts. Hence the maintenance and management requirements can be reduced, which is very advantageous for ship.
(6) Through a reasonable selection and matching of desiccant and refrigerant, it is possible that the waste heat required in two subsystems has different energy levels. Consequently, the utilization efficiency of waste heat can be improved.

3. WORKING FLUID ANALYSIS

The selection of working fluid should consider its safety, environmental acceptability, device applicability and economic performance. In this paper, some pure refrigerants including R718, R134a, R245fa, R1234yf and R1234ze(E) were selected as the potential working fluid for the ejector refrigeration subsystem. Water (R718) is the most environment-friendly working fluid and easy to obtain. R134a is the most popular refrigerant today used in marine A/C system. R1234yf and R1234ze(E) is the next generation refrigerants most likely to replace R134a. As an environment-friendly refrigerant with fast market share growth, R245fa is also selected for analyzing. Another widely-used refrigerant, ammonia (R717) is introduced here just for comparison analysis due to its good environmental and thermodynamic performance.
The important properties of the selected refrigerants are as shown in Table 1 including critical temperature, critical pressure, normal boiling point, molecular weight, safety group of ANSI/ASHRAE, ODP, GWP and atmospheric lifetime. The properties of the selected refrigerants are obtained from the professional software Refprop 9.1, ANSI/ASHRAE Standard 34-2016 (ANSI/ASHRAE, 2016) and 2017 ASHRAE Handbook Fundamentals (ASHRAE, 2017).

Table 1. Properties of the selected refrigerants

Property	R134a	R245fa	R717	R718	R1234yf	R1234ze(E)
Critical temperature(°C)	101.06	154.01	132.25	373.95	94.70	109.36
Critical pressure (MPa)	4.0593	3.651	11.333	22.064	3.3822	3.6349
Normal boiling point (°C)	-26.07	15.14	-33.33	99.974	-29.45	-18.97
Molecular weight (g/mol)	102.03	134.05	17.03	18.015	114.04	114.04
Safety group (ANSI/ASHRAE)	A1	B1	B2L	A1	A2L	A2L
ODP	0	0	0	0	0	0
GWP	1300	858	-	-	<1	<1
Atmospheric lifetime (years)	13.4	7.7	-	-	0.029	0.045

Note: Symbol '-' means no influence.

3.1. Safety and Environmental Acceptability

Safety is the most important issue on the ship. Therefore, toxicity and flammability are the primary considerations and surely the non-toxic and non-flammable working fluids are preferable. As for environment acceptability, with the increasing attention to global warming the refrigerants not only require zero ODP, but also require GWP to be as small as possible and atmospheric lifetime as short as possible.

As shown in Table 1, from the safety point of view, R134a and R718 have the optimal safety group A1 which means low toxicity and non-flammable. R1234yf and R1234ze(E) have the safety group A2L that means low toxicity and low combustibility. R245fa and R717 have the safety group B1 and B2L respectively, which means both refrigerants are high toxicity, although one is non-flammable and the other low combustible. As for environmental acceptability, natural refrigerants R717 and R718 have the best environmental protection performance. R1234yf and R1234ze(E) also have very good environmental protection performance with zero ODP, low GWP(<1) and low atmospheric lifetime(0.029 and 0.045 years respectively). R134a and R245fa have relatively poor environmental protection performance with zero ODP, high GWP (1300 and 858 respectively) and relatively long atmospheric life time (13.4 and 7.7 years respectively). In general, in terms of safety and environmental acceptability, R718 has the best advantages, and R1234yf and R1234ze(E) are also good choices.

3.2. Device Applicability and Economic Performance

As for the device applicability and economic performance, there are many aspects to be considered. However, due to no need of moving parts in ejector refrigeration system there is almost not any lubrication problems. Therefore the main considerations are thermal parameters and cycle efficiency. Good device applicability and economic performance require that the system has good performance under standard condition and can adapt to a wide range of working conditions. The economic performance of refrigerant requires that refrigerants should be cheap and easy to be obtained.

3.2.1. Working Condition and Performance Index

In order to analyze the device applicability and economic performance of different refrigerants, the analysis were carried out under the following working conditions as shown in Table 2. Although the designed cooling temperature of sea water can be as high as 32℃, the actual seawater temperature is changing during voyage. In order to investigate the system performance under variable working conditions, the range of condensation temperature was extended from 32 to 42℃. In order to make full use of the refrigerants and avoid supercritical state, the generation temperature of each selected refrigerant except for R718 is all about 10℃ below its critical temperature. Taking account of the thermal quality of waste heat on ships, the refrigerant R718 with relatively high critical temperature is analyzed at the generation temperature from 110℃to170℃ ,which most marine exhaust gas boiler can reach.

Table 2. Working conditions of ejector refrigeration subsystem

Refrigerants	Evaporation temperature, ℃	Condensation temperature, ℃	Generation temperature, ℃
R134a	10	32~42	91
R245fa	10	32~42	144
R717	10	32~42	122
R718	10	32~42	110~170
R1234yf	10	32~42	84
R1234ze(E)	10	32~42	99

In order to evaluate the performance of the ejector refrigeration subsystem, some performance indices including entrainment ratio and COP defined by Eq. (1) and (2) were used. Because very small energy is consumed by circulating pump, the COP can be expressed as Eq. (3). The model of ejector developed by Eames I.W. et al. (1995) with constant mixing pressure was used in this paper to calculate maximum entrainment ratio under the given operating condition. In addition, in order to evaluate the economic performance of refrigerant the total mass flow rate of the ejector was defined as Eq. (4) and introduced under the assumption that each refrigerant has the same circulating times in the system.

$$\omega = \frac{m_s}{m_p} \quad \text{Eq. (1)}$$

where ω is entrainment ratio, m_s mass flow rate of secondary fluid in kg/h, m_p mass flow rate of primary fluid in kg/h.

$$COP = \frac{Q_{cool}}{Q_{heat} + W_{pump}} \quad \text{Eq. (2)}$$

where COP is coefficient of performance, Q_{cool} cooling capacity of evaporator in kW, Q_{heat} heat input of generator in kW, W_{pump} power consumption of circulating pump in kW.

$$COP = \frac{Q_{cool}}{Q_{heat}} = \omega \cdot \frac{h_e - h_c}{h_p - h_c} \quad \text{Eq. (3)}$$

where h_e is enthalpy of secondary fluid at evaporator outlet in kJ/kg, h_c enthalpy of working fluid at condenser outlet in kJ/kg, h_p enthalpy of primary fluid at generator outlet in kJ/kg.

$$m_{total} = m_p + m_s \quad \text{Eq. (4)}$$

where m_{total} is total mass flow rate of ejector in kg/h.

3.2.2. Entrainment Ratio and COP under Variable Working Condition

Under the working conditions in Table 1, entrainment ratio and COP of different refrigerants in ejector refrigeration subsystem were calculated using the models developed by Eames I.W. et al. (1995) with constant mixing pressure. The results were shown in Fig.2 and Fig.3.

From Fig.2, it can be seen that entrainment ratio of all refrigerants decreased with the increase of condensation temperature. The entrainment ratios of R245fa and R717 were far larger than that of other refrigerants. The entrainment ratios of R1234ze(E) were similar to that of water at 170℃. The entrainment ratios of R134a were similar to that of water at 150℃. The entrainment ratios of R1234yf were similar but lightly larger than that of water at 130℃.

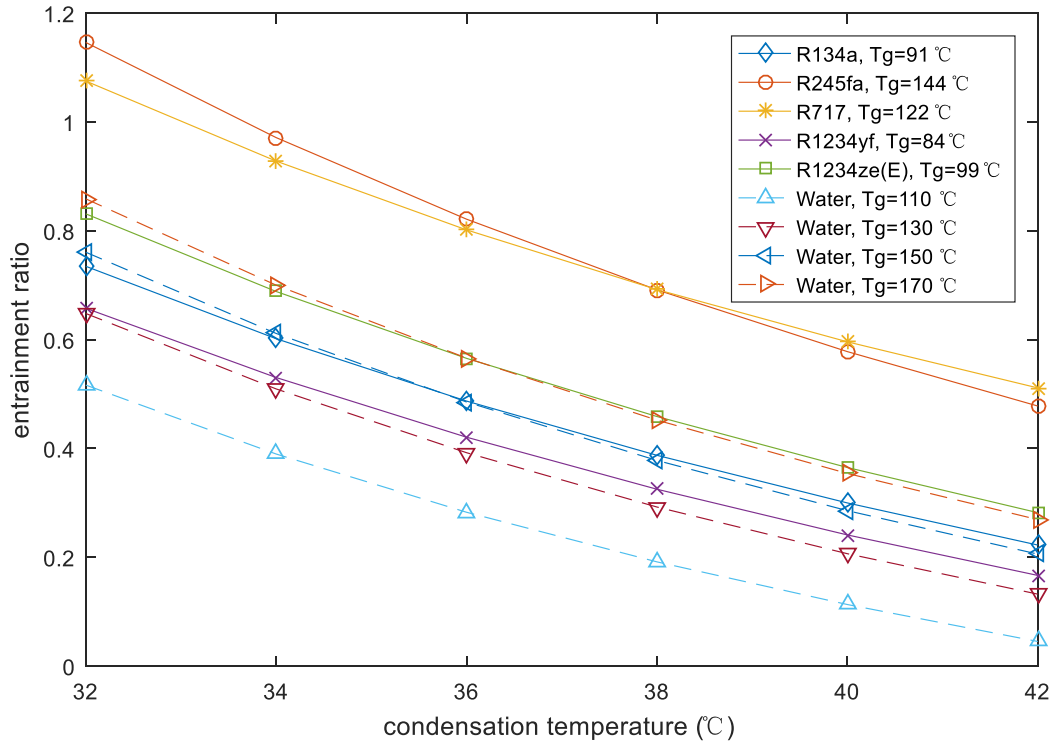

Note: Tg is generation temperature of primary fluid.

Figure 2: Entrainment ratio of different refrigerants under different condensation temperature and 10 ℃ evaporation temperature

From Fig. 3 it can be seen that COP of all refrigerants decreased with the increase of condensation temperature. Except for water, the COP of all refrigerants ranged from large to small as R717, R245fa, R1234ze(E), R134a and R1234yf. However, the COPs of R717 were far greater than other refrigerants. The COPs of R1234ze(E) were just slightly greater than that of R134a. The COPs of water at 170℃ were located between R245fa and R1234ze(E). The COPs of water at 150℃were similar to that of R1234ze(E) and R134a. The COPs of water at 130℃ were similar to that of R1234yf.

Figure 3: COP of different refrigerants under different condensation temperature and 10℃

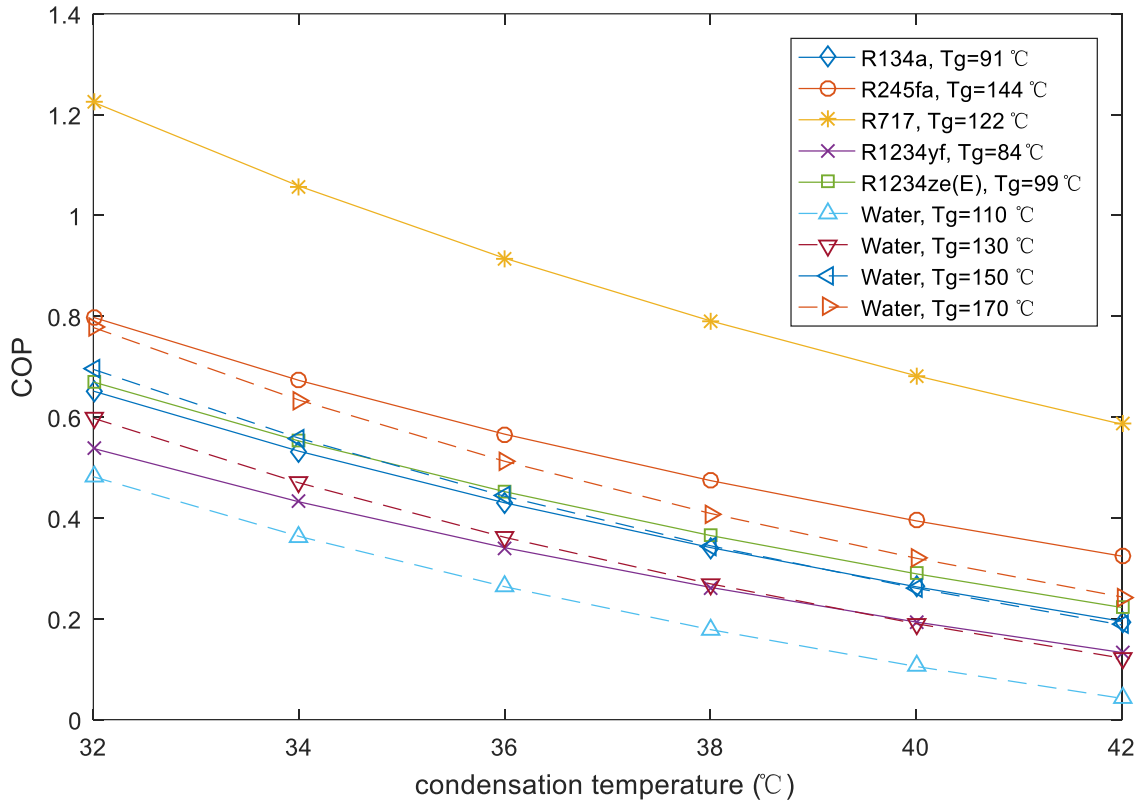

evaporation temperature

3.2.3. Evaluation the Charge Amount of Different Refrigerants

From Fig. 4, it was clear that the total mass flow rate of all refrigerants ranged from large to small as R1234yf, R134a, R1234ze(E), R245fa and R717. However, total mass flow rate of R717 and water were much smaller than other refrigerants. More details will be analyzed in the next section.

3.3. Further Analysis of Calculation Results

The average value of three performance indices were shown in Table 3. The smaller total mass flow rate, the less charge amount of refrigerant. Therefore the sorting method from small to large is adopted in this paper. For the convenience of analysis, the maximum entrainment ratio, the maximum COP and minimum total mass flow rate were selected as benchmarks. Four refrigerants with the best comprehensive performance were chosen to analyze, including R717, R245fa, W170 and R1234ze(E). It can be found from Table 2 that the R717 had maximum COP, secondary-ranged entrainment ratio and the fourth-ranged total mass flow rate. R245fa had maximum entrainment ratio, secondary-ranged COP and the sixth-ranged total mass flow rate. However, the COP of R245fa was only 61.44% of that of R717, and the total mass flow rate 6.17 times of that of R717. W170(water with 170℃ generation temperature) had minimum total mass flow rate, the third-ranged entrainment ratio(68.29% of the benchmark) and the third-ranged COP(55.10% of benchmark). R1234ze(E) had the fourth-ranged entrainment ratio(68.08% of the benchmark) and the fourth-ranged COP(48.53% of the benchmark), but the total mass flow rate was 13.7853 times the benchmark.

Another important aspect was that the comprehensive performance of R1234ze(E), R134a and R1234yf were very similar to that of W170, W150 and W130 respectively, if the effect of refrigerant charge amount was not taken into consideration. It means that water can match the best performance of different refrigerants by increasing generation temperature due to its high critical temperature and the high thermal quality of waste heat on ship. The advantages of water acting as working fluid in marine ERRD A/C system were further proven.
On the whole, although R717 and R245fa have excellent performance, the strict requirements of safety and environmental acceptability would limit their application on ships. W170 and R1234ze(E) are preferable refrigerants for ejector refrigeration subsystems. And the performance of the W170 was better and should be the best choice.

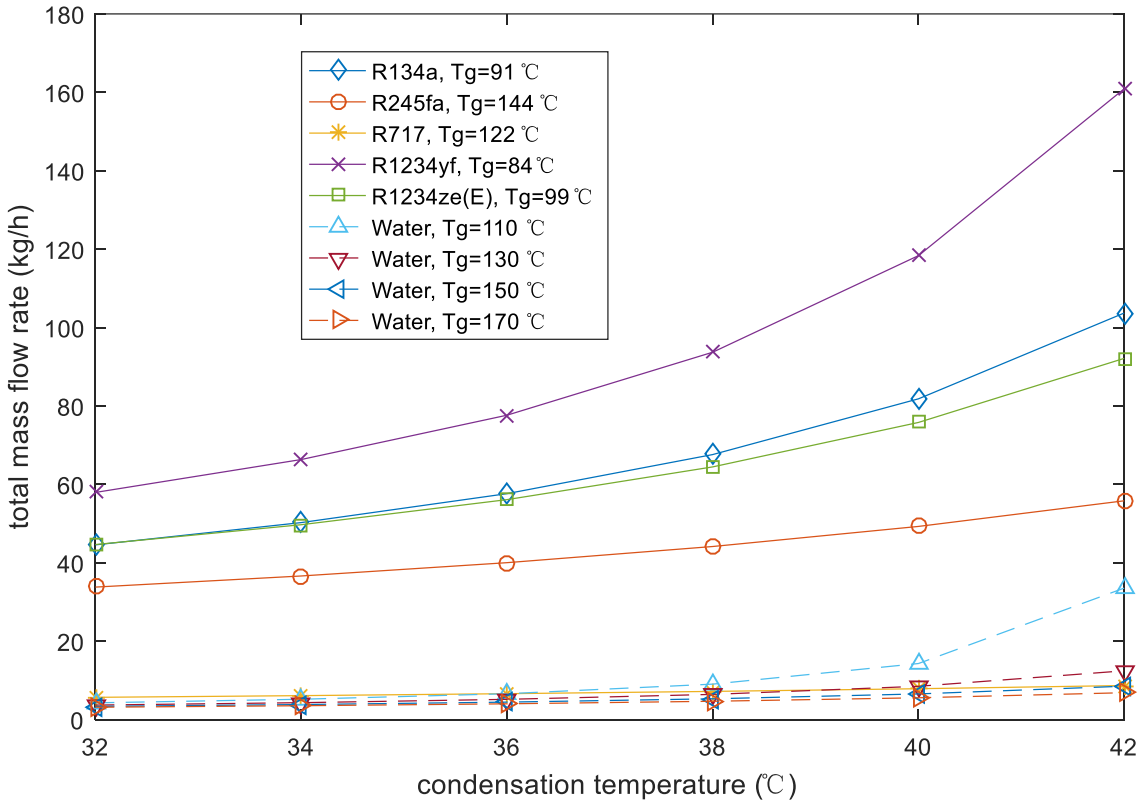

Figure 4: Total mass flow rate of different refrigerants corresponding to 1kW cooling capacity under different condensation temperature and 10℃ evaporation temperature

Table 3. Average value of different performance indicators

Refrigerant	Entrainment ratio		COP		Total mass flow rate(kg/h)	
	average	order	average	order	average	order
R134a	0.4556	5(58.33%)	0.4023	6(45.92%)	67.5869	8(14.6033)
R245fa	**0.7811**	**1(100.0%)**	0.5383	2(61.44%)	43.2732	6(9.3499)
R717	0.7674	2(98.25%)	**0.8761**	**1(100.0%)**	7.0174	4(1.5162)
R1234yf	0.3903	7(49.97%)	0.3167	8(36.15%)	95.8048	9(20.7002)
R1234ze(E)	0.5318	4(68.08%)	0.4252	4(48.53%)	63.8012	7(13.7853)
W110	0.2565	9(32.84%)	0.2392	9(27.30%)	12.1507	5(2.6254)
W130	0.3635	8(46.54%)	0.3351	7(38.25%)	6.7515	3(1.4588)
W150	0.4545	6(58.19%)	0.4149	5(47.36%)	5.3317	2(1.1520)
W170	0.5334	3(68.29%)	0.4827	3(55.10%)	**4.6282**	**1(100.0%)**

Notes: W110, W130, W150 and W170 indicate that the generation temperature of water are 110℃, 130℃, 150℃ and 170℃ respectively.

4. CONCLUSIONS

The novel marine ejector-refrigeration rotary-desiccant air-conditioning system is composed of an ejector refrigeration unit or subsystem and a rotary desiccant wheel, which can be fully driven by the abundant high thermal quality of waste heat on ships so as to realize ship's energy saving and emission reduction. Meanwhile the comfort of ship cabins can be improved due to the independent control of temperature and humidity which can be realized by the ERRD A/C system. Moreover, the working conditions of ejector refrigeration subsystem can be improved and the system COP can be increased, which further provide the flexibility of the selection of green refrigerant.

Taking into account of the refrigerant's safety and environmental acceptability, device applicability and economic performance, from the analysis results of theoretical calculation it can be found that water has good applicability and should be the best choice of refrigerant for marine ERRD A/C system because the abundant high quality waste heat are readily available on ship and therefore the relatively high generation temperature can be easily obtained.

ACKNOWLEDGEMENTS

This research was supported by National Natural Science Foundation of China (No.51679107) and Natural Science Foundation of Fujian Province, China (No.2017J01705) and the High-level Technical Talent Training Project for Transportation Industry in China.

NOMENCLATURE

h	enthalpy (kJ/kg)	m	Mass flow rate (kg/h)
p	pressure (Pa)	Q	heat or cooling capacity (kW)
T	temperature (℃)	W	power consumption (kW)
ω	Entrainment ratio		

REFERENCES

ANSI/ASHRAE, 2016. Designation and Safety Classification of Refrigerants, ANSI/ASHRAE Standard 34-2016, ANSI/ASHRAE, Atlanta, 6-12.

ASHRAE, 2017. Chapter 29: Refrigerants, 2017 ASHRAE HANDBOOK FUNDMENTALS. ASHRAE, Atlanta, 2-7.

Eames I.W., Aphornratana S., and Haider H., 1995. A theoretical and experimental study of a small-scale steam jet refrigerator. Int. J. Refrigeration 18(6), 378-386.

Chen, W., Yang, G.H., 2011. Study on the application of rotary desiccant air-conditioning system on ships. Adv. Sci. Lett. 4, 1410-1415.

Marine Environment Protection Committee, 2009. Report of the Marine Environment Protection Committee on Its Fifth-ninth session. IMO, London, 1-3.

Zheng, G.J., Zheng, C.Y., Yang, G.H. & Chen, W., 2012. Development of a new marine rotary desiccant air-conditioning system and its energy consumption analysis. Energy Procedia, 16(part B), 1095-1101.

Zhu, J., Chen, W., 2014. Energy and exergy performance analysis of a marine rotary desiccant air conditioning system based on orthogonal experiment. Energy, 77, 953-962

Zhu, J., Chen, W., 2015. A novel multivariate linear prediction model for the marine rotary desiccant air-conditioning by adding a dynamic correction factor. Appl. Therm. Eng. 78, 101-109.

Manuscript ID : 374
DOI : 10.18462/iir.icr.2019.0374

Smart control of screw compressors in industrial conditions

J. GUILPART[(a,b,c)],

[(a)] IIR president of section C and French delegate to the IIR
[(b)] Associate professor, Laboratoire du Froid, des Systèmes Energétiques et Thermiques (LaFSET), Cnam, HESAM Université, 292 rue Saint-Martin 75003 Paris, France
jacques.guilpart@lecnam.net
[(c)] MF Conseil executive manager
MF Conseil, 21 avenue de la Baltique, F91140 Villebon sur Yvette, France
j.guilpart@mfconseil.fr

ABSTRACT

The compressors of a machinery room in food industries are often designed on the maximum refrigeration capacity required for the process, even if it is well known that this maximum requirement is effective a very scarce time fraction. Therefore, the compressors often run at partial charge. This situation lead to poor energy efficiency of compressors, and especially of screw compressors controlled with slide valves.
To partially solve the problem, the use of variable speed devices are recommended, guessing important energy savings.
This paper compares different control strategies of screw compressors in a machinery room of a dairy industry requiring 1 MW refrigeration and composed of 1 to 3 screw compressors of different size and models. It will demonstrate that a smart management of cascade and slide valve control delivers interesting results with a reduced investment cost. The interest of adding variable speed device on a selected compressor will be highlighted.
Keywords: industrial application, screw compressor, capacity reduction, slide valve, variable speed, control.

1. INTRODUCTION

The adjustment between cold production and needs is a key point when designing a refrigeration installation. Indeed, it is accepted that the design has to be based on the maximum reasonable need, knowing that the installation will work very few time at its maximum capacity.
Answering this question needs on one hand to have a good knowledge of the refrigeration needs (chronogram, histogram), and on the other hand, to dispose of actuators allowing to adjust the cold production. In industrial conditions, the use of screw compressors with slide valve is often proposed. In addition, variable speed devices are sometime proposed, expecting energy savings.
The drawing of the chronogram of refrigeration needs and the modeling of the performances of screw compressors controlled with slide valves and variable speed devices is therefore necessary to assess the performance of different control strategies.

2. DESCRIPTION OF THE INSTALLATION

2.1. Refrigeration needs

The studied installation is connected to a dairy process (sterilized milk, yoghurts and other flavored milk dessert). The process is based on the utilization of different equipments (pasteurizers, sterilizers, plate heat exchangers, blast coolers, …) fed with iced water. This iced water is produced with a MPG loop (-11°C / -6°C) in a plate heat exchanger with an adequate system preventing the exchanger's freezing. MPG is produced with an ammonia facility with a low pressure receiver feeding a plate heat exchanger (thermosiphon, cycle temperature : -15°C / +35°C). The MPG is also directly used in air coil heat exchangers located in storage facilities and in workshops. The refrigeration needs have been studied in detail with the production service and led to the following chronogram:

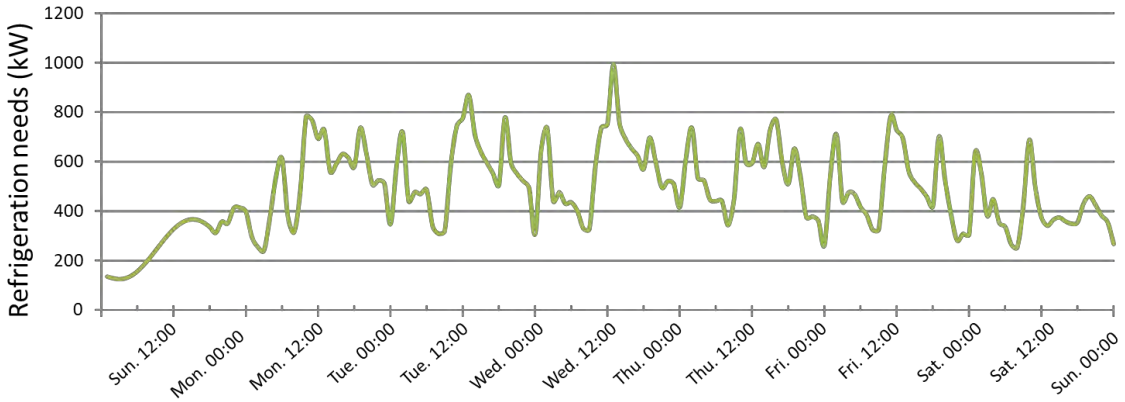

Figure 1 : Chronogram of refrigeration needs for a typical production week

This chronogram indicates following statistics:

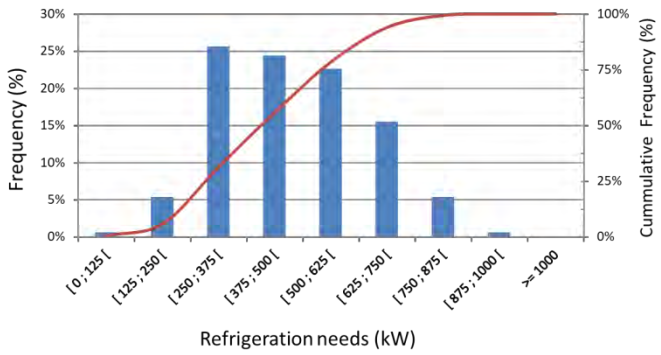

Figure 2 : histogram of refrigeration needs

Table 1. Statistics on refrigeration needs

Capacity (kW)	Frequency	Cumm.
[0 ; 125 [	1%	1%
[125 ; 250 [	5%	6%
[250 ; 375 [	26%	32%
[375 ; 500 [	24%	56%
[500 ; 625 [	23%	79%
[625 ; 750 [	15%	94%
[750 ; 875 [	5%	99%
[875 ; 1000 [	1%	100%
>= 1000	0%	100%
Max :	992	kW

The reading this data indicates that:

- the maximum need of 992 kW is only called for a short time on Wednesday afternoon
- most of the time, the refrigeration need is between 250 and 750 kW

Therefore, the choice of the number of installed compressor and of their control mode is of great importance.

2.2. Retained compressors models

For different reasons (including end-user requirements and habits), the use of GEA screw compressors is proposed. From this, different possibilities are studied:

- use of one big compressor (≈ 1 MW) fulfilling all the requirements and adjusting its refrigeration capacity with a slide valve
- use of two medium size compressors (2 x 500 kW)
- use of three compressors (250 kW + 350 kW + 500 kW)

Following table summarizes the main characteristics of these compressors (cycle temperature: -15°C / +35°C):

Table 2. Main characteristics of the selected GEA screw compressors

Model	Ref. capacity (kW)	Elec. Capacity (kW)	COP
LR-L2655S-28	282.4	90.4	3.12
MR-M2655S-28	371.2	116.4	3.19
RR-R2240S-28	562.8	162.2	3.47
WR-W2240S-28	1078.5	317.7	3.39

2.3. Studied control strategies

In order to adjust the production to the needs, different control strategies are studied and compared:

Strategy 1 : only one big compressor (1MW) in use, with capacity control with slide valve to adjust the production to the needs.

Strategy 2 : two medium compressors (2 x 500 kW)

Strategy 2.1 : 1st compressors with slide valve until 100%, then 1st compressor 100% + 2nd compressors with slide valve to adjust the production to the needs

Strategy 2.2 : 1st compressors with slide valve until 100%, then 1st + 2nd compressors at the same slide valve position

Strategy 3 : three compressors (250 + 350 + 500 kW))

Strategy 3.1 : small compressor with slide valve until 100%, then small compressor 100% + medium compressors with slide valve to adjust the production to the needs, then small and medium compressors at 100% and big compressor with slide valve to adjust the production to the needs

Strategy 3.2 : small compressors with slide valve until 100%, then small + medium compressors at the same slide valve position, then all compressors to the same slide valve positon.

These strategies are completed with the use of variable speed devices, this device being installed on the biggest compressor for the strategy 3.

The comparison of the performances of these different strategies requires the modeling of the performances of each compressor working with slide valves and variable speed devices.

3. MODELING THE PERFORMANCES OF COMPRESSORS

3.1. COP vs slide valves position

Due to international recirculation of sucked gases (Moseman, 1999), the slide valve position has a direct and important impact on the coefficient of performance as shown Fig. 3.

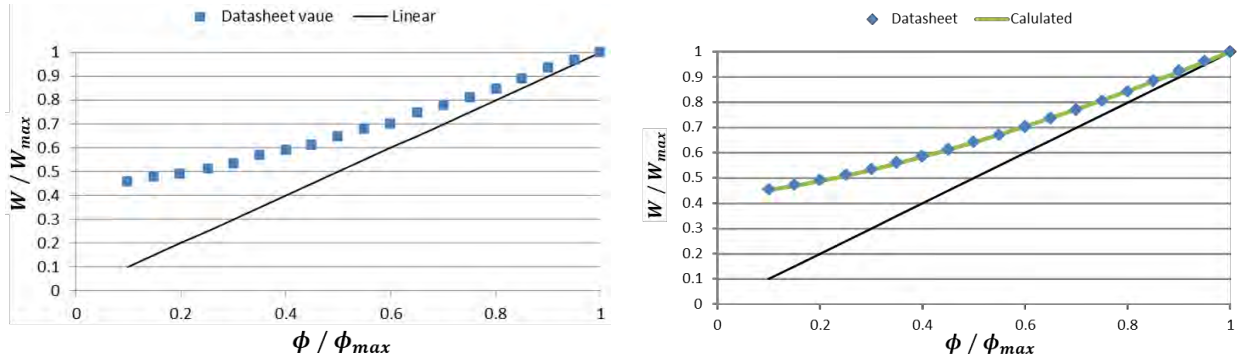

Figure 3 : Impact of the slide valve position on a screw compressor performance

These figures come from the data selection sheets of the compressor provider. It indicates that when the slide valve is in “low” position (corresponding to low refrigerating capacity), the performances or compressor decreases dramatically. As the relation between the slide valve positon and the reduction capacity is quite complex to establish (Widell 2010, Chen 2011), we will directly adopt the reduction capacity (ϕ / ϕ_{max}) as an input to our approach.

We propose to model this decrease by a power law inspired by pressure drop laws as followed :

$$\frac{W}{W_{max}} = \alpha \left(\frac{\phi}{\phi_{max}}\right)^{n} + \beta \qquad \text{Eq. (1)}$$

where :

W is the electric power input of the compressor (kW),
ϕ is the refrigeration capacity (kW)
α and β are calculated by forcing the function through two points :

- one point coming from datasheet, for instance the ratio $\frac{W}{W_{max}}$ indicated on compressor’s datasheet for $\left(\frac{\phi}{\phi_{max}}\right) = 0.1$
- the second point coming from the limit $\left(\frac{\phi}{\phi_{max}}\right) = 1$, where $\frac{W}{W_{max}} = 1$, leading to $\beta = 1 - \alpha$

The exponent *n* is adjusted to minimize the sum of the squared differences between the datasheet values and the calculated values.
Table 3 indicates the values of α and *n* obtained for the selected compressors. Fig. 4 shows the quality of the fitting, all coefficient of correlation being greater than 0.999.

Table 3. α and *n* coefficients used in Eq. (1) for selected compressors

Model	α	n
LR-L2655S-28	0.566	1.424
MR-M2655S-28	0.564	1.432
RR-R2240S-28	0.578	1.404
WR-W2240S-28	0.568	1.437

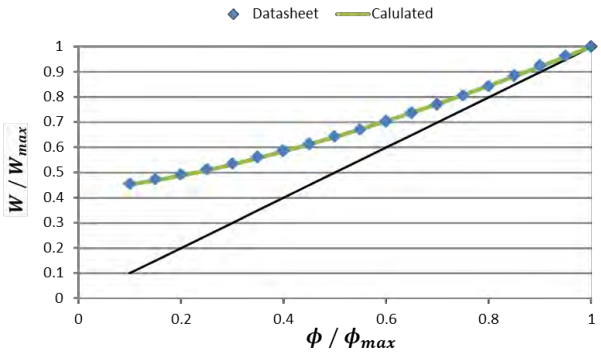

Figure 4 : example of fitting for compressor WR-W2240S-28

3.2. Introducing a variable speed device

In order to better adjust the refrigeration capacity to the refrigeration needs, the implementation of variable speed device on compressor is often recommended. It is well known that these VSD allow energy savings. It is also well known that the efficiency of the electric motor somewhat decreases with the adopted frequency, and that a low limit of frequency has to be fixed in order to prevent lubrication concerns and motor warming-up.

VSD can be implemented in complement of slide valve action :

- While VSD low limit is not reached, VSD is actioned in proportion of the needs
- Below this limit, VSD is fixed to the minimum possible value, and the refrigeration production is adjusted to the need by acting the slide valve.

As a first approach, we propose to model the consequence of both actions on the performances of compressors by moving the base line (linear behavior between 0 and 1) to a affine straight line defined as: $y = A\ x + (1 - A)$ where $A = \left(\frac{1-\eta_{min}}{1-x_{min}}\right)$, $x = \frac{Freq.}{50}$, $Freq$= applied frequency (Hz) and η_{min} =motor efficiency at $Freq_{min}$.

Fig. 5 illustrate the assessed performance of compressor WR-W2240S-28 with la limit of VSD fixed at 25 Hz (that is ϕ / ϕ_{max} = 50%) and with η_{min} =90% at $Freq_{min}$= 10 Hz.

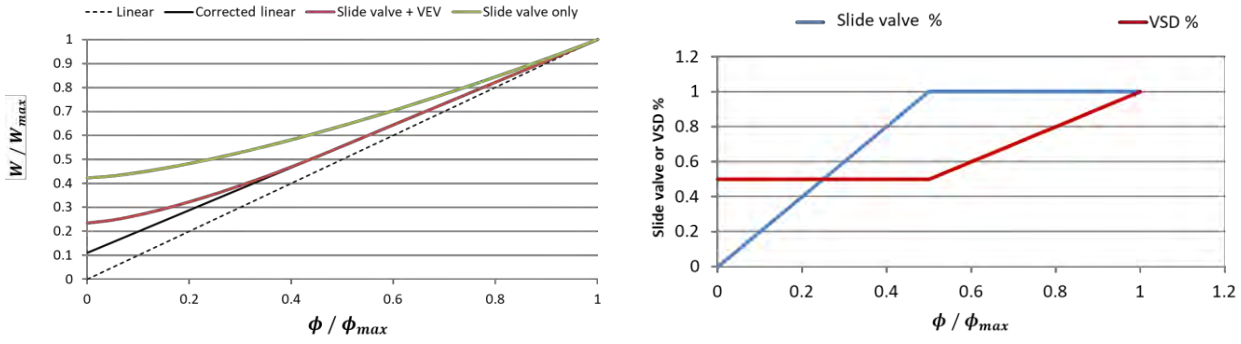

a- performances of the compressor

b- Position of actuators

Figure 5 : Performance of a screw compressor associating slide valve and VSD

For some compressors, the low limit of acceptable frequency could be lower, especially if a lubricant pump and an additional cooling system of the motor are installed. The maximum $Freq$ could also be geater than 50 Hz. These two points would further improve the benefits of VSD.

4. EVALUATION OF DIFFERENT CONTROL STAGTEGIES

The approach presented above allows the assessment of the performances of compressors when their refrigeration capacity is adjusted by using slide valve and/or variable speed device.
The different control strategies introduced in paragraph 2.3 are compared in Fig. 6.

4.1. Evaluation of Coefficient of performances

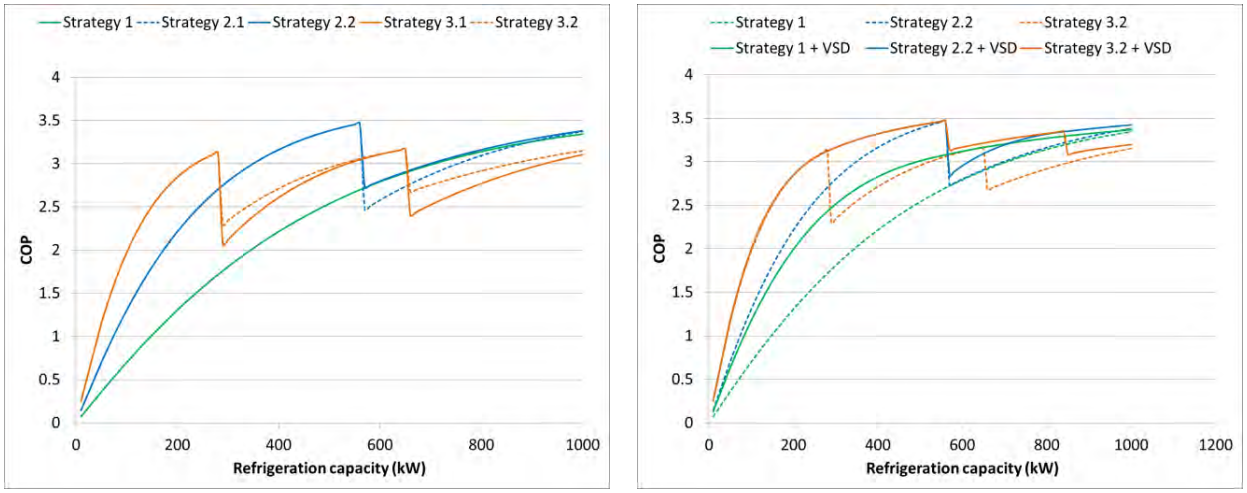

a- without VSD b- With VSD on the biggest compressor

Figure 6 : COP of the different control strategies vs refrigeration capacity

The observation of Fig. 6 indicates that :

- The use of only one big compressor (strategy 1) delivers lowers COP, even if VSD is used in complement of slide valves
- The use of two compressors (strategy 2) delivers better COPs, especially at low charge when using VSD
- The use of 3 compressors delivers the best COPS on a wide range of refrigerating capacities, and especially at low charge.

It also appears that the global energy consumption of the installation depends on the histogram of refrigeration needs.

4.2. Evaluation of energy consumption

In order to assess the best strategy to be retained for the studied case, these results are applied to the chronogram presented paragraph 2.1.
Results are presented in the table 4

Table 4. Weekly electric consumption of the different studied strategies

	MWh / week
Strategy 1	33.0
Strategy 1 + VEV	27.5
Strategy 2.1	27.4
Strategy 2.2	26.7
Strategy 2.2 + VEV	25.2
Strategy 3.1	29.6
Strategy 3.2	28.5
Strategy 3.2 + VEV	24.8

5. CONCLUSION

For the chronogram corresponding to the studied application, it is confirmed that:

- the fractionation of the refrigerating capacity led to lower energy consumptions : for the studied case, installing 2 or 3 compressors instead of a big one allows to reduce the energy consumption of 15 to 20%.
- the use of variable speed devices (on the biggest compressor) led to substantial energy savings : for the studied case, it allows to reduce the energy consumption in between 5 and 15% depending on the number of installed compressors.

For the studied case, the installation of 3 compressors with VSD on the biggest of them led to the lowest energy consumption. For instance, and compared to the lowest investment cost (only one big compressor without VSD), savings of 8.2 MWh / week – it is 410 MWh / year can give precious information on the payback time necessary to balance the incremental investment cost.

It is important to mention that a different histogram of refrigeration needs would lead to somewhat different result. For instance, a histogram centered around high refrigeration needs would privilege the functioning at high charge, and therefore would disadvantage the use of small compressor – generally presenting poorest COP at high charge than bigger compressors.

Nevertheless, the approach presented in this paper would benefit to be used for many industrial configurations.

REFERENCES

Mosemann D., 1999, Refrigeration screw compressor with part load ctrol and VI adjustment, Proceedings of the 20th International Congress of refrigeration, IIF/IIR, Sydney 1999 – Volume III (paper 585).

Widell K. L., Eikevik T., 2010, Reducing power consumption in multi-compressor refrigeration systems. Int. J. Refrigeration 33 (2010) 88 – 94.

Chen W., Xing Z. Tang H. Wu H., 2011, Theoretical and experimental investigation on the performance of screw refrigeration compressor under part-load condition. Int. J. Refrigeration 34 (2011) 1141 – 1150.

PAPER ID: 379
DOI: 10.18462/iir.icr.2019.0379

Design parametric study of a lateral configured diabatic straight capillary tube with R-134a

Santhosh K. DUBBA, Ravi KUMAR

Department of Mechanical and Industrial Engineering
Indian Institute of Technology, Roorkee, 247667, India
Email: santhosh.nita@gmail.com, ravikfme@iitr.ac.in

ABSTRACT

An experimental investigation was conducted to observe the effect of sub-cooling degree on the mass flow rate of R-134a through a diabatic laterally configured straight capillary tube. The variation of mass flow rate of refrigerant through the capillary with the sub-cooling degree is observed to be independent of capillary tube geometry and the inlet pressure. When the diameter of the capillary tube decreased from 1.52 mm to 1.27 mm, the mass flow rate through the capillary tube also decreased by 16 percent. Also The mass flow rate of refrigerant was observed to increase by 12 to 17 percentage in all the tested capillary tubes with an increase of sub-cooling from 6°C to 9°C.
Keywords: Capillary tube, Expansion, Pressure, Refrigerant, Sub-cooling, Two-phase Flow.

1. INTRODUCTION

The capillary tube with usual dimensions of diameter from 0.5 mm to 2.0 mm and length from 1.0 m to 6.0 m is used in the low capacity refrigerating systems like domestic refrigerators and window air conditioners. With the simplicity, low cost, zero maintenance and low torque requirement to the compressor, capillary tubes are widely used in vapor compression system. The dependence of mass flow rate of R-12 and R-22 on inlet sub-cooling degree was experimentally investigated by Bolstad and Jordan (1948) and Cooper et al. (1957), a linear variation has been observed. Lathrop (1948) and Prosek (1953) showed that mass flow rate had proportional dependence on inlet sub-cooling degree. Jabaraj et al. (2006) investigated the effect of refrigeration sub-cooling on the mass flow rate of HCFC22 and HFC407C/HC600a/HC290 through the capillaries. The mass flow rate through an adiabatic capillary with diameter 1.397 mm, increases with the increase of sub-cooling for a given condensing temperature.

The metastable flow of pure refrigerants R-134a and R-600a and refrigerant-oil mixtures through capillary tubes was studied by Silva Huerta et al. (2007). The influence of inlet sub-cooling, internal diameter and inlet pressure on the underpressure of vaporization has been investigated. An increase of metastable liquid region retarding the flashing flow inception of mixture was occurred in case of mixture due to oil presence as compared to pure R-134a. The above was verified at low sub-cooling degree where a little liquid superheating is required to begin the nucleation. Khan et al. (2008) demonstrated the effect of various geometric parameters on mass flow rate of R-134a through an adiabatic spirally coiled and a straight capillary tube for different inlet sub-cooling degrees. The mass flow rate through the coiled capillary is reduced by 5-15% as compared to straight capillary tube for similar operating conditions and is due the coiling of the capillary tube. As fact that, the variation of mass flow rate of R-134a with inlet sub-cooling is follows same trend as the R-407C discussed in further sections. In the present study a total of nine capillary tubes (combination of diameter and length) were tested with different operating conditions viz., varying capillary tube inlet pressure and inlet sub-cooling degree. The effect of inlet operating conditions and the geometry of the capillary tube were examined.

2. EXPERIMENTAL SET-UP AND PROCEDURE

An experimental set-up is a simple vapor compression system provided with expansion device of capillary tube in which the high pressure refrigerant expanded to a low pressure. A schematic sketch of an experimental setup is shown in Fig.1. The low pressure refrigerant enters the evaporator (coil-

in-shell type heat exchanger) where the load was given by an electric heater. The heat load can be varied by using variac through which the power supply given to heater. An agitator is provided in the evaporator to maintain the uniform bulk mean temperature. The vapor refrigerant coming out from evaporator coil enters the compressor through an accumulator which avoids the liquid refrigerant to enter the compressor. An open type compressor run by three phase motor with belt and pulley system has been used in the set-up. The high pressure vapor emerged from compressor enters the condenser through an oil separator which separates the oil particles from refrigerant. The superheated vapor condensed to the saturated liquid in water cooled condenser. The saturated liquid is collected in a receiver to ensure the continuous supply of refrigerant to the capillary tube. A drier-cum-filter was used to remove any moisture or foreign particle present in the refrigerant. A hand operated expansion valve was fitted between the condenser and evaporator to bypass the excess refrigerant into the evaporator to avoid the accumulation of refrigerant at the inlet of the capillary tube and to control the evaporator pressure. A Coriolis flow meter was fitted to measure the mass flow rate of high pressure liquid refrigerant.

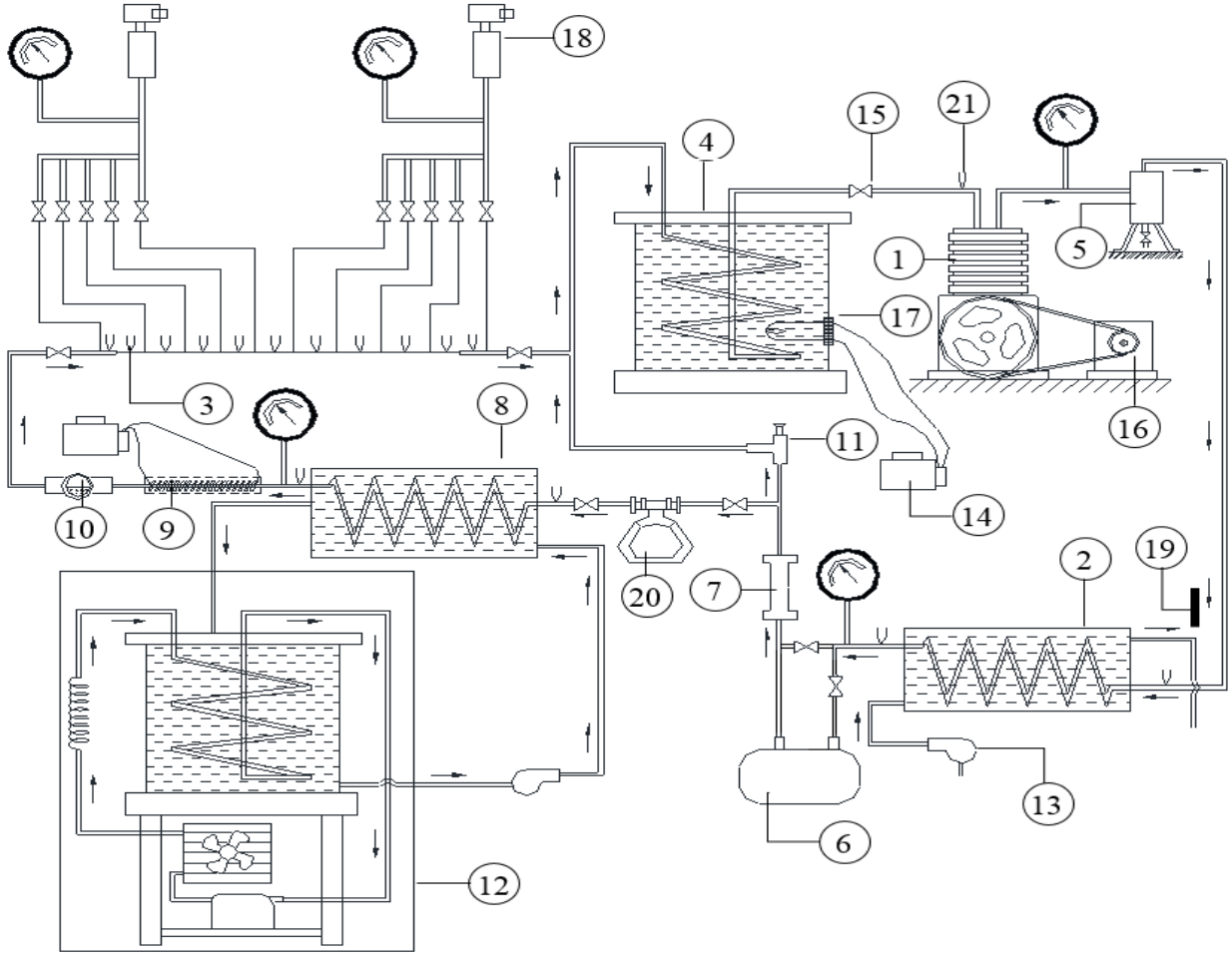

Major components: 1.Compressor 2.Condenser 3.Expansion Device/Test section 4.Evaporator
Auxiliary components: 5.Oil separator 6.Receiver 7.Drier-Filter 8.Sub-cooler 9.Preheater 10.View glass 11.Hand operated expansion valve 12.Chiller unit 13.Centrifugal pump 14.variac 15.Shutoff valve 16.Electric motor 17.Electric heater
Measuring devices: 18.Pressure transducer 19.Thermometer 20.Coriolis flow meter 21.Thermocouple

Figure 1: Schematic diagram of experimental set-up

A sub-cooler is provided with chiller unit connected to it which supplies the chilled water to sub-cool the refrigerant. The chilled water circulates in sub-cooler by means of centrifugal pump. A preheater is arranged after sub-cooler, to vary the sub-cooling degree and which was controlled by variac. A needle valve is provided at the inlet of capillary tube, to regulate the pressure of refrigerant entering the capillary tube. A sight glass was also fitted to visualize the state of refrigerant entering the

capillary tube. To read the temperature along the capillary tube length T-type thermocouples with an accuracy of ±0.2% were fitted. The pressure transducers having an accuracy of ±0.25% FS (2000kPa) were used to measure the refrigerant pressure.

2.1. Instrumentation

A simple thermometer was fitted to condenser to measure exit temperature of cooling water. The pressure taps as shown in Fig. 2(a) were provided at critical locations viz., condenser line, capillary inlet, suction line and capillary exit. The pressure transducers having an accuracy of ±0.25% FS (2 MPa) were used to measure the refrigerant pressure. A total of eight T-type thermocouples (21) with an accuracy of ±2% are fitted along the length and two of the same were fitted at entry and exit of a capillary tube. These thermocouples attached directly on to the tube surface as shown in Fig. 2(b). Hand shut-off valves (15) were fitted before and after to every major component for ease of repairs, if any.

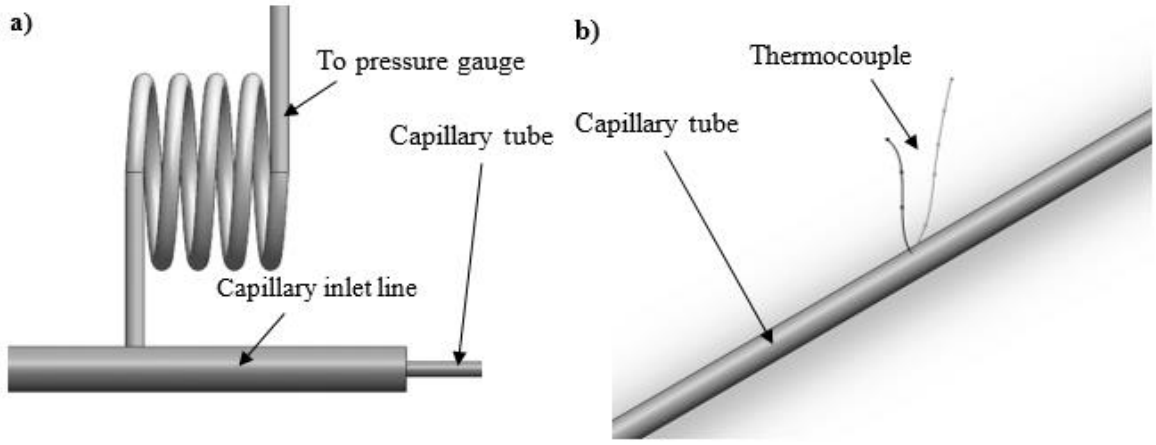

Figure 2: Provision of measuring instruments (a) Pressure tap (b) T-type thermocouple

3. RESULTS AND DISCUSSION

The diabatic capillary tubes of different combinations of length and diameter were tested to study the flow characteristics of a refrigerant. The parametric study of the capillary tube helps to design a capillary tube i.e. deciding the dimensions of a capillary tube. The effect of inlet sub-cooling degree on the mass flow rate of refrigerant, has also been examined. The inlet sub-cooling degree was varied from 3-12°C. All the capillary tubes were tested under three different inlet pressures. Thus, the effect of capillary inlet pressure on the mass flow rate has been revealed.

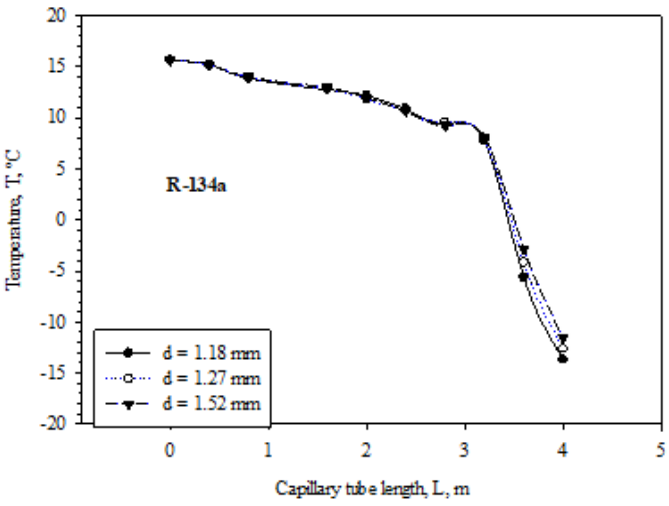

Figure 3: Temperature profiles showing the performance of capillary tube

3.1. Performance of a Capillary Tube

The performance of refrigeration system can be estimated with the drop in temperature of refrigerant while flowing through an expansion device. The temperature of refrigerant entering the evaporator is defined by the pressure difference across the expansion device. In the present study the capillary tube fulfils the function of expansion device and designed to drop the pressure of refrigerant as well as to regulate the flow of refrigerant to the evaporator.

The Fig. 3 Shows the temperature profiles along the length of the capillary tube. Fig. 3 plotted for the temperature as an ordinate and capillary tube length as an abscissa. From the Fig. 3, it is noted that the temperature reduces significantly with the increase of capillary tube length. The variation of temperature drop with respect to capillary tube diameter was noticed to be insignificant. The drop in temperature at the end portion of the capillary tube is predominant. This is due to the fact that; the pressure drop is high in case of two phase flow. During the liquid length of the capillary tube the drop in pressure is less as compared to two phase length.

3.2. Effect of inlet operating conditions on mass flow rate

The variation of mass flow rate with capillary inlet sub-cooling for the different lengths, diameters and capillary inlet pressures was shown in Fig. 4. The mass flow rate for all the diameters and lengths is observed to be increase with the raise of inlet sub-cooling degree.

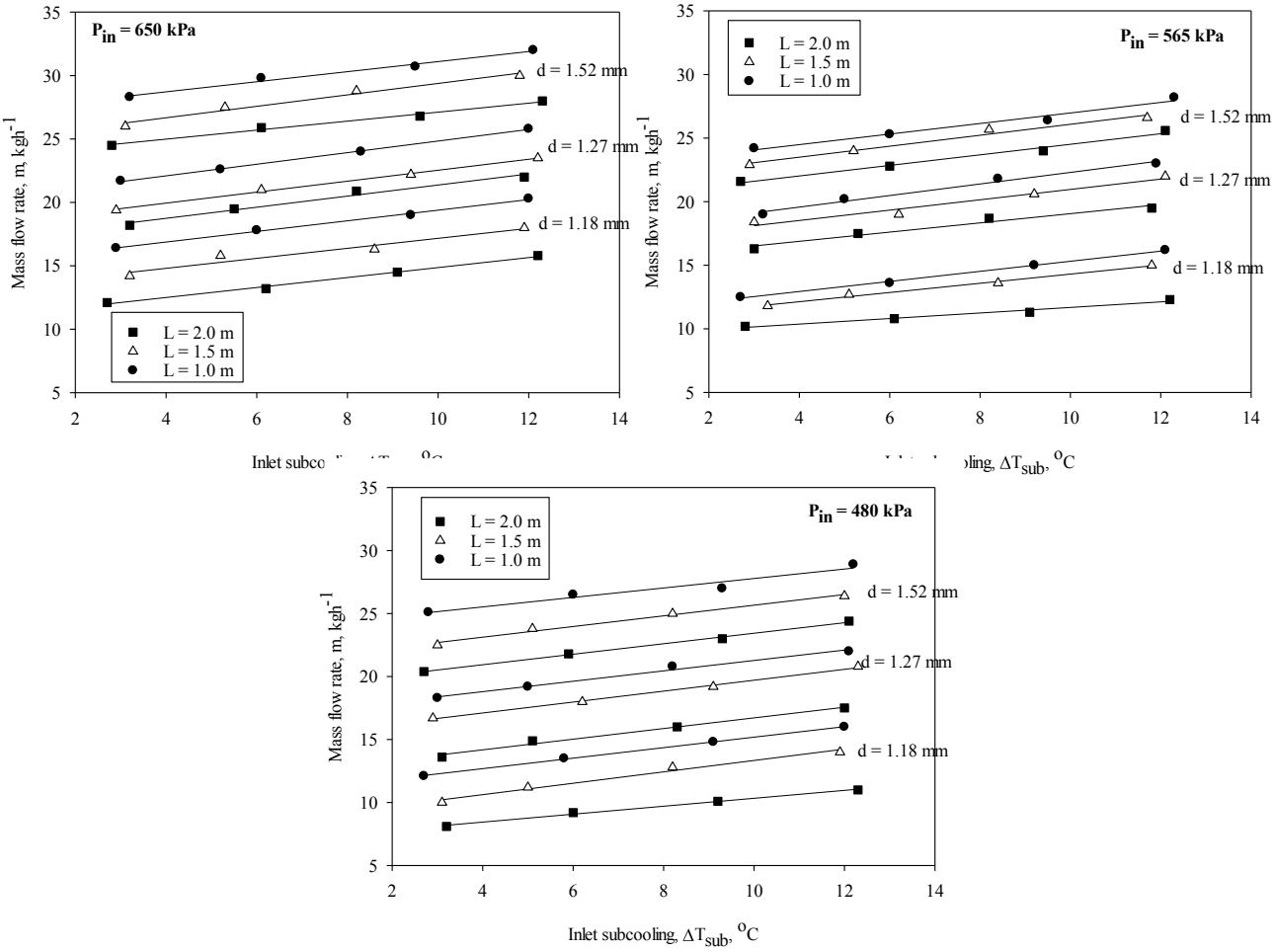

Figure 4: Variation of mass flow rate of R-134a with inlet sub-cooling degree for different length, diameter and inlet pressure of a diabatic straight capillary tube

As an example, in the capillary tube (d = 1.27 mm & L = 1.5 m), the raise of sub-cooling degree from 6°C to 9°C resulting the mass flow rate to increase by 14 percent. The capillary tube flow can be divided into two regions of liquid at the entrance and two-phase mixture at the exit of the capillary tube. The flash point shifted away from the capillary inlet with increased sub-cooling degree and resulting longer liquid length of refrigerant flow inside the capillary tube. The quality at the exit of capillary tube was reduced with increase of sub-cooling degree due to longer liquid length. This phenomenon leads to high mass flow rates inside the capillary tube to overfeed the evaporator. The above observed less in case of smaller diameter due to high flow resistance, resulting in smaller liquid lengths. The temperature along the capillary tube length from the inlet to exit is observed to be reduced while the quality of refrigerant increasing.

A significant effect of capillary tube inlet pressure on the mass flow rate of refrigerant was also noticed. The mass flow rate data scattered up with the raise of capillary inlet pressure. This may be

due to the more driving force at the entrance of the capillary tube. For the 9°C inlet sub-cooling, as the capillary inlet pressure increased from 480 kPa to 565 kPa, the average rise in refrigerant mass flow rate is 9.3%, 8.8% and 7% for the capillary tube diameters of 1.52 mm, 1.27 mm and 1.18 mm respectively. However, as compared to the inlet sub-cooling degree the effect of pressure on the mass flow rate of the refrigerant was significantly low.

3.3. Effect of geometry on mass flow rate

The geometry of the capillary tube also showed significant effect on the refrigerant flow. The longer tube and reduced diameter of the capillary tube leads to low mass flow rate inside the capillary tube. As an example, when the diameter of the capillary tube decreases from 1.52 mm to 1.27 mm, the mass flow rate through the capillary tube is decreased by 16 percent. Fig. 5 shows the variation of mass flow rate of re

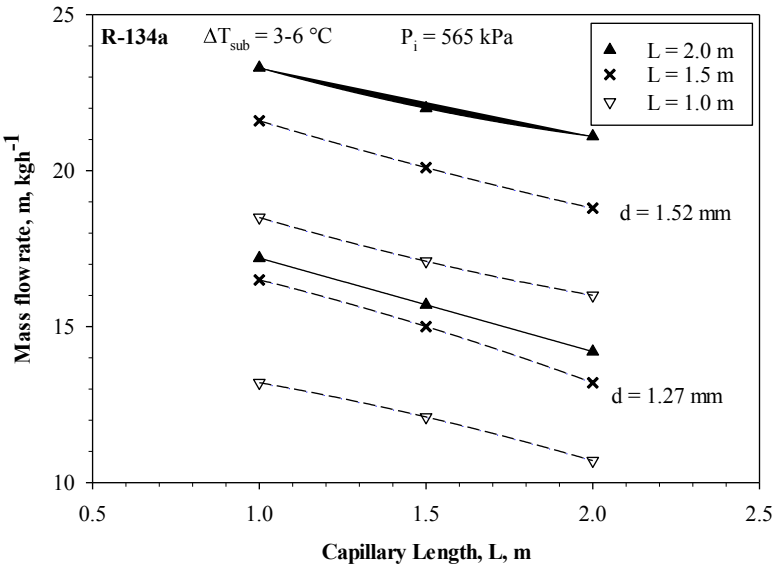

Figure 5: Variation of mass flow rate of R-134a with respect to capillary length

3.4. Non-dimensional correlation to predict the mass flow rate data

The mass flow rate of refrigerant through a capillary tube is observed to be influenced by the geometry of the capillary tube, inlet operating conditions. The Buckingham-π model has been developed to evaluate the parametric change in mass flow rate with respect to the geometry, inlet operating conditions and thermo-physical properties. The Eq.1 shows mathematical representation of mass flow rate as a function of influencing variables.

$$\dot{m} = f\left\{d, L_{cap}, P_{in,c}, \rho_f, \mu_f, C_{pf}, \Delta T_{sub}\right\} \quad \text{Eq.(1)}$$

Eq.1 can also be written in the form of π-groups as follows.

$$\pi_1 = f\left\{\pi_2, \pi_3, \pi_4\right\} \quad \text{Eq.(2)}$$

Table 1. Description of non-dimensional parameters

$\boldsymbol{\pi}$-Group	Mathematical formula	Consideration	Description
$\boldsymbol{\pi_1}$	$\dot{m}/d_c\mu_f$	Mass flow rate	Reynolds effect
$\boldsymbol{\pi_2}$	$P_{in,cap}\rho d_c^2/\mu_f{}^2$	Capillary tube inlet pressure	Condenser pressure
$\boldsymbol{\pi_3}$	L_{cap}/d_c	Full length of capillary tube	Geometry effect
$\boldsymbol{\pi_4}$	$\Delta T_{sub} C_p \rho^2 L^2/\mu_f{}^2$	Capillary tube inlet sub-cooling	Degree of sub-cooling

The non-dimensional π-groups were derived by eliminating the primary dimensions of mass, length and time (Khan et al., 2008; Melo et al., 1999). The non-dimensional π-groups were intend to

describe (refer Table 1) the operating parameters and geometry. The Eq.2 further simplified to form a non-linear equation as follows.

$$\pi_1 = K.\pi_2^a.\pi_3^b.\ \pi_4^c \qquad \text{Eq.(3)}$$

A multiple variable regression method was applied to set of experimental data to evaluate the above constants. The Eq.3 solved for the minimum error from measured data and which is reduced to the following generalized semi empirical correlation as Eq.4. The proposed correlation predict the measured mass flow rate within the error band of ±20 percentage.

$$\pi_1 = 0.431.\pi_2^{0.296}.\pi_3^{-0.176}.\pi_4^{0.721} \qquad \text{Eq.(4)}$$

The above correlation is valid for 3°C ≤ ΔT_{sub} ≤ 12°C; 470 kPa ≤ p_{in} ≤ 650 kPa; 1.18 mm ≤ d ≤ 1.52 mm; 1.0 mm ≤ L ≤ 2.0 mm;

4. CONCLUSIONS

The following conclusions are drawn from the above investigation on the diabatic flow of R-134a:

1. The mass flow of refrigerant is increased by 12-21 percentage, with the increase of sub-cooling degree of R-134a.
2. Small diameters lead to high pressure drop and thereby low temperatures are achieved at the exit of the capillary tube.
3. The effect of sub-cooling and geometry is found to be independent. The geometry of capillary tube shows predominant effect on the mass flow rate of refrigerant.

NOMENCLATURE

p_{in}	Inlet pressure (kPa)
T	temperature (°C)

REFERENCES

Bolstad, M.M., & Jordan, R.C., 1948. Theory and use of the capillary tube expansion device. Refrigerating Engineering, 56, 577–583.

Cooper, L., Chu, C.K., & Brisken, W. R., 1957. Simple selection method for capillaries derived from physical flow conditions. Refrigerating Engineering, 65(7), 37–41.

Jabaraj, D.B., Vettri Kathirvel, A., & Mohan Lal, D., 2006. Flow characteristics of HFC407C/HC600a/HC290 refrigerant mixture in adiabatic capillary tubes. Applied Thermal Engineering, 26(14–15), 1621–1628.

Khan, M.K., Kumar, R., & Sahoo, P.K., 2008. An experimental study of the flow of R-134a inside an adiabatic spirally coiled capillary tube. International Journal of Refrigeration, 31(6), 970–978.

Lathrop, H.F., 1948. Application and characteristics of capillary tubes. Refrigerating Engineering, 56(2), 129–133.

Melo, C., Ferreira, R.T.S., Neto, C.B., Gonalves, J.M., & Mezavila, M.M., 1999. Experimental analysis of adiabatic capillary tubes. Applied Thermal Engineering, 19(6), 669–684. https://doi.org/10.1016/S1359-4311(98)00062-3

Prosek, J., 1953. Practical method of selecting capillary tubes. Refrigerating Engineering, 61(6), 644–647.

Silva Huerta, A.A., Sanzovo Fiorelli, F.A., & de Mattos Silvares, O., 2007. Metastable flow in capillary tubes: An experimental evaluation. Experimental Thermal and Fluid Science, 31(8), 957–966.

Manuscript ID: 405
DOI: 10.18462/iir.icr.2019.0405

Thermodynamics analysis of CO_2 refrigeration cycles working with mechanical subcooling systems

Laura NEBOT-ANDRÉS[(a)], Rodrigo LLOPIS[(a)], Jesús CATALÁN-GIL[(a)], Daniel SÁNCHEZ[(a)], Daniel CALLEJA-ANTA[(a)], Ramón CABELLO[(a)]

(a) Thermal Engineering Research Group. Department of Mechanical Engineering & Construction, Jaume I University, Castellón, E12071, Spain, lnebot@uji.es

ABSTRACT

In the last years, CO_2 is acquiring a lot of weight in refrigeration due to the reduction of the use of HFCs, but its energy performance in some working conditions decreases significantly.
The energetic parameters of the cycle can be improved by subcooling the gas at the exit of the gas-cooler, especially at high hot sink temperatures, as presented in recent studies. The purpose of this work is to do a thermodynamic study of subcooling systems in order to quantify these improvements.
The analyzed subcooling systems are the dedicated mechanical subcooling and the integrated mechanical subcooling. Using simplified models of the systems, the optimum working conditions are evaluated and discussed, obtaining the increments in COP and cooling capacity compared to the base cycle.
The systems are evaluated in a theoretical way for different environmental and evaporating conditions, in order to determine the overall energy performance improvement obtained thanks to the subcooling systems.
Key-words: CO_2, mechanical subcooling, integrated, dedicated, COP, Cooling capacity

1. INTRODUCTION

Refrigeration and air conditioning account for 17% of the total electricity consumption in the world according to the IIR (International Institute of Refrigeration, 2015). In addition, 2% of the total emissions of greenhouse gases in the world are caused by emissions to the atmosphere of refrigerants used in these systems (IPCC, 2014), the also called F-Gas, collected in the Kyoto Protocol (United Nations, 1997) and recently in the Montreal Protocol through the Kigali agreement. Considering the predominance of vapor compression systems in the refrigeration sector in the last 20 years (International Institute of Refrigeration, 2007), the industrialized countries must develop more efficient and environmentally responsible equipment.
The recent restrictions approved in Europe to reduce emissions of fluorinated refrigerants significantly condition the current commercial refrigeration market. The European F-Gas Regulation (European Commission, 2014) limits the use of these gases in order to reduce the environmental impact they generate, aiming to reduce the amount of HFCs with high global warming potential (GWP) present in the market, up to 79% by 2030. This framework has given way to the use of refrigerants with low GWP, such as natural refrigerants or HFOs. The use of these fluids reduces the direct impact of refrigeration (emissions to the atmosphere) but, due to their lower performance, the direct impact of their use increases: the electrical consumption of the installations increases.
For centralized commercial refrigeration systems, CO_2 is seen as the generalized option in the colder countries of Europe in recent years, since it has a GWP = 1, is non-toxic, non-flammable,has good heat transfer characteristics and operates with a good level of energy efficiency. But its use in warm countries is not so widespread since at high ambient temperatures the energy efficiency reached by the CO_2 cycles is much lower than that of the HFC-based

facilities. It is therefore necessary to search for solutions to achieve new competitive CO_2 equipment in regions whose annual average temperature exceeds 15ºC, thus reducing emissions and always adapting to regulations.

In last years, some alternatives based on subcooling CO_2 gas have been studied in order to improve their performance, either thanks to the intermediate heat exchanger (IHX), or, more recently, in combination with a dedicated mechanical subcooling cycle. Both alternatives present improvements in the performance of the cycles. On the one hand, the IHX allows the increase of the COP and the cooling capacity of the system but modifies the suction conditions of the compressor, thus increasing the compression work and significantly increases the discharge temperature, which is detrimental to its operation (Llopis et al., 2015). More recently, the dedicated mechanical subcooling cycle has been studied, which allows not only to increase the refrigeration production of the plant but also to reduce the optimum working pressure of this cycle. Llopis et al. (2015) applied this system from a theoretical perspective to a transcritical CO_2 cycle, determining that the increase in efficiency that this system can provide is around 23% at high hot sink transfer temperatures, thus guaranteeing energy efficiency in zones of warm weather. Later, Llopis et al. (2016) presented the experimental validation of these theoretical results, where it was observed that the limits of energy improvement are superior to those established by the conservative theoretical simulations. Finally, and less studied, we find the integrated mechanical subcooling cycle, which is a cycle that provides subcooling using a CO_2 compressor. The effect of this subcooling system is similar to the rest: the specific cooling capacity is increased but the electrical consumption also increases, as in the case of the dedicated cycle, since an additional compressor is needed. The effect of this cycle has not been studied either theoretically or experimentally so far and therefore it is necessary to know in detail its behavior to determine its effect and interest.

Therefore, this work aims to study solutions that improve the performance of CO_2 cycles, responding to environmental and technological needs. Specifically, it focuses on the two cycles of mechanical subcooling: the dedicated and the integrated, in order to contribute to the implementation of CO_2 systems in warm areas, defining which of them is most suitable for implementation.

2. MODEL DESCRIPTION OF THE SUBCOOLING SYSTEMS

In order to compare both subcooling cycles, each of them has been modeled to study them theoretically under different conditions. In this section the cycles and the calculations models are descripted.

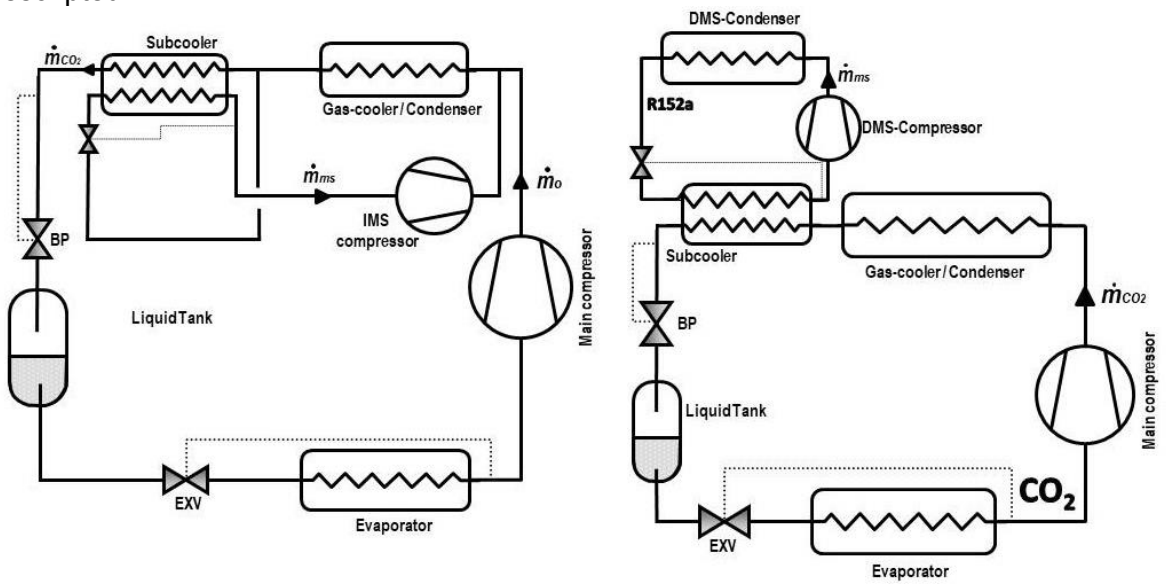

Figure 1. Esquema of the cycle with IMS (left) and with DMS (right)

2.1. Integrated mechanical subcooling

The CO_2 cycle with integrated mechanical subcooling (Fig.1 left) has a single working fluid: carbon dioxide. Part of the CO_2 is extracted from the exit of the gas-cooler ($\dot{m}_{ims}$) and expanded in order

to use it to subcool the rest of the gas going through the subcooler. Then, the extracted rate is recompressed and returned to the main cycle. The rest of flow ($\dot{m}_o$) is expanded and arrives to the evaporator and the main compressor, while the back-pressure valve regulates the discharge pressure. Before the gas-cooler entrance, both flows are re-mixed ($\dot{m}_{CO_2}$).

The benefits provided by the subcooling are an increase of the specific cooling capacity, a reduction of the optimum gas-cooler pressure (compression ratio decreases) and a decrease of the specific compression work, which increase the capacity and the COP of the overall system. The calculations are carried out considering that the temperature at the exit of the gas-cooler is:

$$T_{gc,o} = T_{env} + approach \quad \text{Eq. (1)}$$

The subcooling degree defines the temperature at the exit of the subcooler:

$$T_{SUB} = T_{gc,o} - SUB \quad \text{Eq. (2)}$$

The evaporation level in the subcooler is defined by a pinch temperature referring to the temperature at the exit of the subcooler, being the pinch 2K when working in transcritical and 5K in subcritical conditions.

$$T_{o,ims} = T_{SUB} - pinch \quad \text{Eq. (3)}$$

The RU considered is 10K in the evaporator and 5K in the IMS evaporator/subcooler. The behavior of the compressors is defined by its volumetric and global performance curves, defined as shown in Eq. (4) and Table 1, obtained from the manufacturer data.

$$\eta_V = \eta_G = a_0 + a_1 \cdot P_{suc} + a_2 \cdot P_{dis} + a_3 \cdot \left(\frac{P_{dis}}{P_{suc}}\right) + a_4 \cdot v_{suc} \quad \text{Eq. (4)}$$

Table 1. Coefficients for volumetric and global performance curves of main and IMS compressors

	Transcritical		Subcritical	
	η_v	η_g	η_v	η_g
a_0	1.04732360	0.76339328	1.03502109	0.48684658
a_1	0.00310608	-0.00209763	0.00187469	-0.00860962
a_2	-0.00299916	0.00134440	-0.00173232	0.01152106
a_3	0.00121579	-0.05713840	-0.05880831	-0.26866360
a_4	-11.12818829	0.54246804	-3.61739020	20.84319985

The mass flow rates $\dot{m}_o$ and the nominal for the IMS compressor ($\dot{m}_{ims,nom}$) are obtained from volumetric efficiencies of each compressor as shown in Eq. (5).

$$\dot{m}_o = \eta_v \cdot \frac{\dot{V}_g}{v_{suc}} \; ; \qquad \dot{m}_{ims,nom} = \eta_v \cdot \frac{\dot{V}_{g,ims}}{v_{suc,ims}} \quad \text{Eq. (5)}$$

The real mass flow rate in the IMS is defined by the optimum subcooling degree, as shown in Eq.(6):

$$\dot{m}_{ims} = \dot{m}_o \cdot \frac{(h_{gc,o} - h_{sub})}{(h_{suc,ims} - h_{gc,o})} \quad \text{Eq. (6)}$$

And the main mas flow rate is:

$$\dot{m}_{CO_2} = \dot{m}_o + \dot{m}_{ims} \quad \text{Eq. (7)}$$

The relation between the needed mas flow rate and the nominal one will determine the compressor's rotational speed and consequently the power consumption:

$$N = 1450 \cdot \frac{\dot{m}_{ims}}{\dot{m}_{ims,nom}} \quad \text{Eq. (8)}$$

$$P_{c,ims} = P_{c,ims,nom} \cdot \frac{N}{1450} \quad \text{Eq. (9)}$$

The capacity and COP of the cycle are evaluated as follows:

$$\dot{Q}_o = \dot{m}_o \cdot (h_{suc} - h_{\mathrm{sub}}) \quad \text{Eq. (10)}$$

$$COP = \frac{\dot{Q}_o}{P_c + P_{c,ims}} \quad \text{Eq. (11)}$$

2.2. Dedicated mechanical subcooling

The aim of the dedicated mechanical subcooling (Fig.1 right) is the same as the IMS: subcool the gas at the exit of the gas-cooler in order to enhance COP and capacity. In this case, the DMS is an external cycle coupled thermally with the CO_2 main cycle through the subcooler. The DMS cycle works with R152a. The main effects of the subcooling are the same: reduction of the gas-cooler pressure, reduction of the specific compression work and increment of the specific cooling capacity.

Temperatures at the exit of the gas-cooler and at the exit of the subcooler are evaluated as in the IMS. To obtain DMS condenser outlet temperature ($T_{k,dms}$) an approach temperature to the environment of 10K is chosen, Eq. (12).

$$T_{k,dms} = T_{env} + 10K \quad \text{Eq. (12)}$$

The evaporation level of the DMS is obtained considering an efficiency of 60% for the heat exchanger, obtained experimentally. The parameters of the main cycle are obtained from the main compressor curves that are the same as in the IMS (Eq. 4 and Table 1). The DMS compressor behavior is defined by Eq. 4 and coefficients from Table 2.

Table 2. Coefficients for volumetric and global performance curves of DMS compressor

	Transcritical & Subcritical	
	η_v	**η_g**
a_0	0.99260315	0.9691981
a_1	0.09931207	-0.1177961
a_2	0.02478241	0.02630836
a_3	0.07862542	-0.04952195
a_4	0.76829186	-0.60421472

The CO_2 mass flow rate is obtained as shown in Eq. 5 as well as the DMS nominal mass flow rate, while the real mass flow rate in the DMS is defined by the heat balance in the subcooler, and depends on the optimum subcooling degree:

$$\dot{m}_{dms} = \dot{m}_o \cdot \frac{(h_{gc,o} - h_{sub})}{(h_{suc,dms} - h_{exp,dms})} \quad \text{Eq. (13)}$$

As it happens in the IMS, in this system the DMS mass flow rate determines the compressor's rotational speed and the power consumption:

$$N = 1450 \cdot \frac{\dot{m}_{dms}}{\dot{m}_{dms,nom}} \quad \text{Eq. (14)}$$

$$P_{c,dms} = P_{c,dms,nom} \cdot \frac{N}{1450} \quad \text{Eq. (15)}$$

The capacity and COP of the cycle are evaluated as follows:

$$\dot{Q}_o = \dot{m}_{CO_2} \cdot (h_{suc} - h_{\mathrm{sub}}) \quad \text{Eq. (16)}$$

$$COP = \frac{\dot{Q}_o}{P_c + P_{c,dms}} \quad \text{Eq. (17)}$$

All the thermodynamic properties have been calculated with the REFPROP software (Lemmon et al., 2013). This simulation allows to study the cycles in transcritical and subcritical mode, varying the working pressure (in transcritical) for different ambient temperatures and evaporation levels. In the simulation of this model the modifiable parameters are the working pressure and the degree of subcooling, thus allowing to obtain the optimum points of operation: maximum COP.

3. RESULTS

Different levels of evaporation in the CO_2 evaporator are simulated: from -15ºC to +5ºC covering a wide range of ambient temperatures that varies between 15ºC and 40ºC. The transcritical mode is simulated when for the same ambient temperature; the COP in transcritical mode is higher than in subcritical mode, being the transition zone always between 22ºC and 25ºC of hot sink. In transcritical regime gas-cooler pressures are simulated between 74bar and 120bar until finding the optimal point, while the degree of subcooling is optimized at the same time. The results are compared to the base cycle with internal heat exchanger (IHX), considered with an efficiency of 40%.

Fig. 2 displays the main points of each cycle for an evaporation level of 0ºC and ambient temperature of 35ºC. It can be seen that the three cycles experiment an increase of the specific cooling capacity due to the subcooling made by the additional heat exchanger (the IHX or the subcooler). This enhancement produces also a reduction in the vapor quality, which improves the heat exchange in the evaporator. As it can be seen, the IMS and the DMS prevent the overheating in the compressor suction temperature, getting lower discharge temperatures. The subcooling also reduces the optimum gas-cooler pressure, being the lowest one the discharge pressure of the IMS.

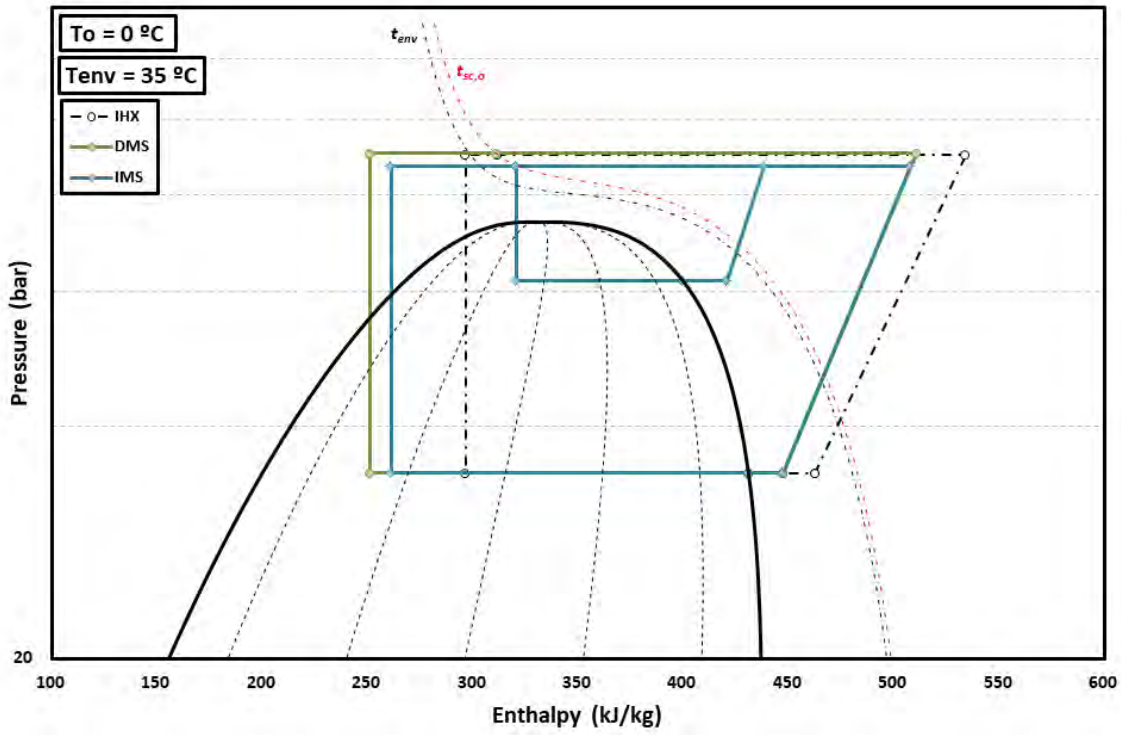

Figure 2. Ph diagram of the cycles: base with IHX (black), with IMS (blue) and with DMS (green)

In order to quantify the positive effects of both sistems, the COP and cooling capacity are studied along the range of environmental temperatures.

3.1. COP

The COP obtained in the simulations corresponds to the maximum possible COP of each working condition, without physic limits of the cycle components, therefore, in some working points, the compression rate of the IMS compressor is less than 1.5. According to the manufacturer, this low compressor ratio would be out of the recommended application range, but data has also been considered.

In Fig. 3 (left) we can observe the evolution of each cycle's COP for the range of environment temperatures. For all the cycles, the trend is to go to lower values of COP when higher is the temperature, but both the DMS and the IMS represent an important increment in terms of COP with respect to the cycle with IHX. Between the DMS and IMS the difference is very light, being the

IMS a bit greater in the zone of temperatures between 23ºC and 33ºC. Fig. 3 (right) shows the compression rate (τ) of the auxiliary compressor, of the DMS in green and in blue for the IMS. It can be notice that for the IMS the τ is smaller, being near the manufacturer's limit of 1.5; even sometimes below it, so the simulation of the cycle must be fixed to this limit to well adapt to the compressor operating region, so it will not be working on the optimal conditions.

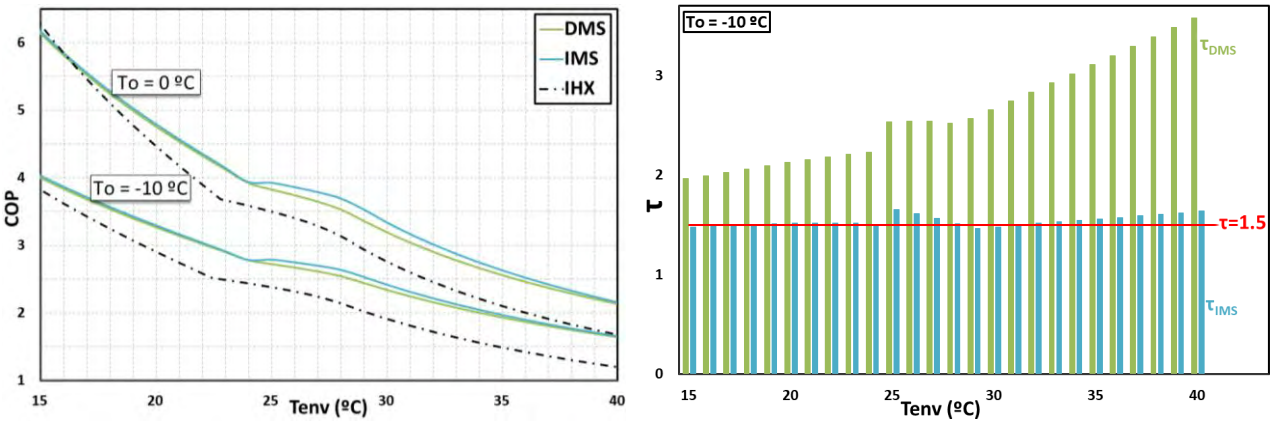

Figure 3. Evolution of COP vs environement temperature and compression rates of auxiliary compressors

Fig. 4 shows the increments of COP obtained with the MS with respect to the base cycle (Eq. 18), limiting the compression rate to 1.5 or more. This has an effect in some of the IMS points (blue) that are no more the highest ones, and now in some points, the increment obtained by the DMS (green) is greater.

$$\Delta COP\ (\%) = \frac{COP_{MS} - COP_{IHX}}{COP_{IHX}} \times 100 \qquad \text{Eq. (18)}$$

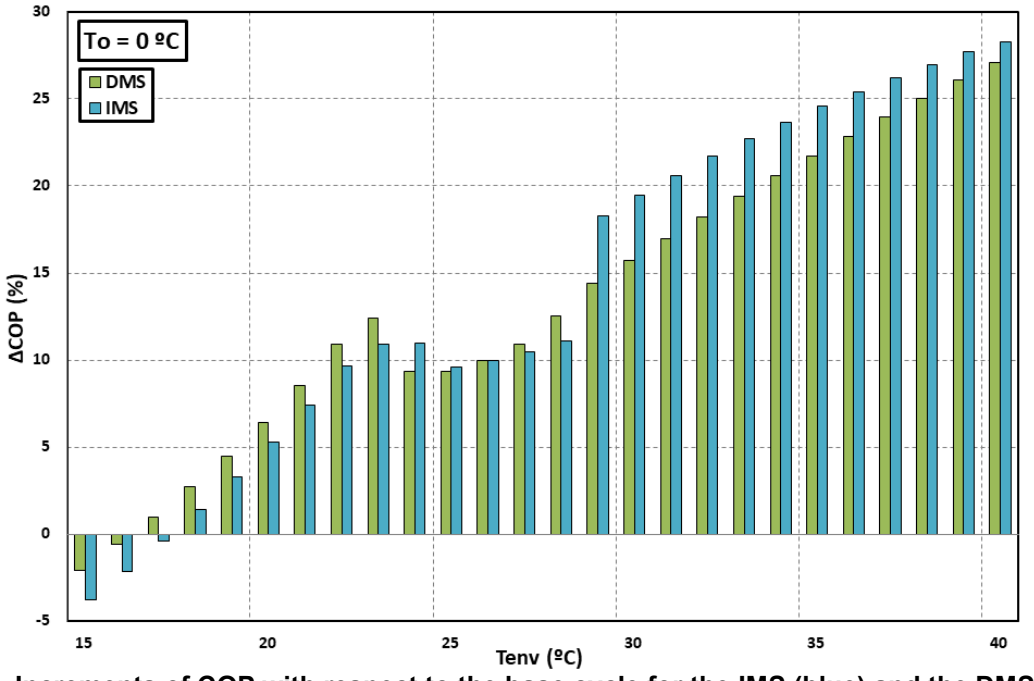

Figure 4. Increments of COP with respect to the base cycle for the IMS (blue) and the DMS (green)

3.2. Cooling Capacity

The increments on cooling capacity (Eq. 19) can be shown in Fig. 5 for an evaporation level of 0ºC and -10ºC.

$$\Delta Q_O\ (\%) = \frac{Q_{O_{MS}} - Q_{O_{IHX}}}{Q_{O_{IHX}}} \times 100 \qquad \text{Eq. (19)}$$

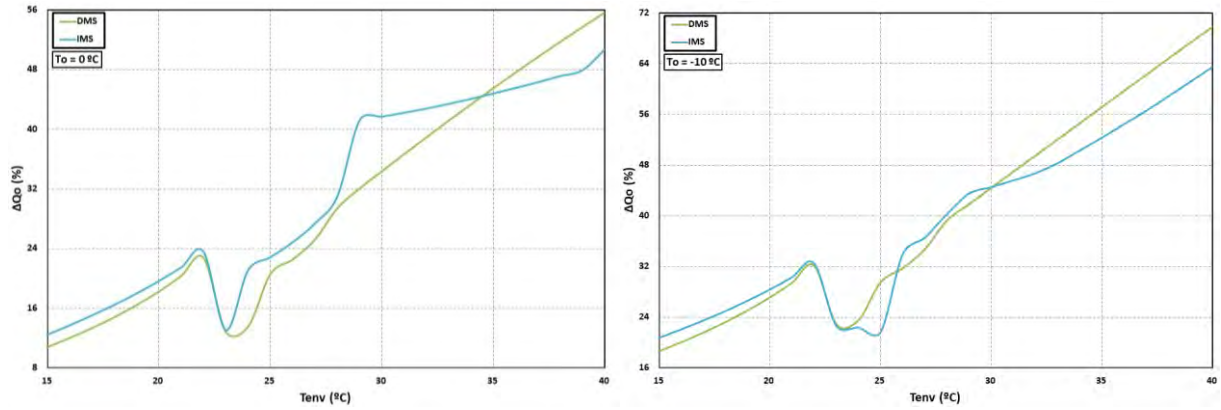

Figure 5. Increments of Qo with respect to the base cycle for the IMS (blue) and the DMS (green)

For low temperatures, the IMS gets a higher increment and it is larger when higher is the environment temperature. But when the exit of the gas-cooler is in the critical region, the increments are a bit reduced being this trend modified due to the physical restrictions of the components. At the highest temperatures, the DMS cycle is the one that reaches a higher enhancement, being it the most significant for the lowest evaporation level.

4. CONCLUSIONS

The current state of the refrigeration has forced to develop new solutions that allow reducing his impact, obtaining refrigeration plants with better performance and reducing the use of high GWP gases. In this work, two modifications of simple CO_2 systems have been theoretically evaluated as an alternative to the classic cycles, with the aim of making this natural refrigerant competitive in hot climates where until today they were not viable due to their low performance. The cycles studied, the dedicated mechanical subcooling and the integrated mechanical subcooling, provide numerous benefits to the classical system, such as a considerable increase in the COP and also in the cooling capacity of the system. The increases achieved, both in COP and power, are very important, reaching high levels above all for very high temperatures, where simple CO_2 systems drastically reduce their performance. For each range of temperature, there is one cycle that fits better: for warm and medium temperatures the IMS has better conditions while for very high ambient temperatures, the DMS gets higher enhancements. While both cycles have shown a very similar effect, it is necessary to do an experimental study of these systems to define more accurately their behavior, in order to optimize these systems for each climate.

ACKNOWLEDGEMENTS

The authors thank the Ministry of Economy and Competitiveness - Spain (project ENE2014-53760-R.7), the Ministry of Education, Culture and Sports - Spain (grant FPU16/00151) and the Jaume I University (project UJI-B2017-06) for financing this research work.

NOMENCLATURE

COP	coefficient of performance	***Subscripts***	
GWP	global warming potential	dis	compressor discharge
h	enthalpy, kJ·kg^{-1}	dms	dedicated mechanical subcooling
IHX	internal heat exchanger	env	environment
$\dot{m}$	mass flow rate,kg·s^{-1}	exp	expansion
N	compressor speed, rpm	g	global
p	Absolute pressure, bar	gc	gas-cooler

Pc	Power consumption, kW	ihx	internal heat exchanger
Q	Cooling capacity, kW	ims	integrated mechanical subcooling
RU	degree of superheat, K	in	inlet
s	entropy, $kJ \cdot kg^{-1} \cdot K^{-1}$	k	condensing level
SUB	degree of subcooling, K	nom	nominal
T	Temperature, ºC	o	evaporating level
$\dot{V}_g$	compressor displacement, $m^3 \cdot s^{-1}$	out	outlet
Greek symbols		sub	subcooled
Δ	increment	suc	compressor suction
η	performance	v	volumetric
τ	compression ratio		
ν	specific volume,$m^3 \cdot kg^{-1}$		

REFERENCES

European Commission, 2014. Regulation (EU) No 517/2014 of the European Parliament and of the Council of 16 April 2014 on fluorinated greenhouse gases and repealing Regulation (EC) No 842/2006.

International Institute of Refrigeration, 2007. Refrigeration drives sustainable development. State of the Art - Report Card. . IIR/IIF–UNEP.

International Institute of Refrigeration, 2015. 29th Informatory Note on Refrigeration Technologies. The Role of Refrigeration in the Global Economy. IIR, France.

IPCC, 2014. Climate Change 2014: Synthesis Report. Contribution of Working Groups I, II and III to the Fifth Assessment Report of the Intergovernmental Panel on Climate Change [Core Writing Team, R.K. Pachauri and L.A. Meyer (eds.)]. IPCC, Geneva, Switzerland, 151 pp.

Lemmon, E.W., Huber, M.L., McLinden, M.O., 2013. REFPROP, NIST Standard Reference Database 23, v.9.1. National Institute of Standards, Gaithersburg, MD, U.S.A.

Llopis, R., Cabello, R., Sánchez, D., Torrella, E., 2015a. Energy improvements of CO2 transcritical refrigeration cycles using dedicated mechanical subcooling. International Journal of Refrigeration 55, 129-141.

Llopis, R., Nebot-Andrés, L., Cabello, R., Sánchez, D., Catalán-Gil, J., 2016. Experimental evaluation of a CO2 transcritical refrigeration plant with dedicated mechanical subcooling. International Journal of Refrigeration 69, 361-368.

Llopis, R., Sanz-Kock, C., Cabello, R., Sánchez, D., Torrella, E., 2015b. Experimental evaluation of an internal heat exchanger in a CO2 subcritical refrigeration cycle with gas-cooler. Applied Thermal Engineering 80, 31-41.

United Nations, 1997. The Kyoto Protocol to the Framework Convention on Climate Change. 1997. Available at: <http://unfccc.int/essential_background/kyoto_protocol/background/items/1351.php>.

Manuscript ID: 407
DOI: 10.18462/iir.icr.2019.0407

Performance Analysis of Vapor Compression Refrigeration Systems with Oil-free Linear Compressor Vapor Injection and Regeneration

Xinye ZHANG[1], Davide ZIVIANI[2], James E. BRAUN[3], Eckhard A. GROLL[4]

Center for High Performance Buildings, Purdue University, Ray W. Herrick Laboratories
West Lafayette, IN 47907, USA
[1]xinye@purdue.edu, [2]dziviani@purdue.edu, [3]jbraun@purdue.edu, [4]groll@purdue.edu

ABSTRACT

Previous studies showed that compressor vapor injection combined with economizing increases the efficiency of vapor compression cycles by decreasing compressor specific work and increasing cooling capacity. However, most of the previous studies focused on injection for scroll/screw compressors with oil or vapor gas, which limits the refrigerant compatibility and compressor designs. Recently, linear compressors have drawn much attention due to their high efficiencies and oil-free operation. The unique design of linear compressors allows the integration of cooling paths into the piston-cylinder assembly to cool the compressor by an economizing refrigerant. This paper proposes an oil-free linear compressor piston-cylinder cooling design and assesses its potential for approaching a quasi-isothermal compression process through utilization of refrigerant economizing and regeneration technology. A system simulation model was developed and used to analyze the system performance. Performance comparisons between the proposed system and a conventional system are presented along with an assessment of the improvement of system efficiencies.

Keywords: Linear Compressors, Vapor Injection, Regeneration, Oil-free, Energy Efficiency.

1. INTRODUCTION

Compressor performance is often referenced to one of three ideal reference processes: adiabatic, polytropic, and isothermal. These different reference processes have been extensively investigated and compared (Heidari et al., 2014). It is well known that an adiabatic and reversible (isentropic) compression process requires more work input than an isothermal and reversible compression process for the same suction conditions and discharge pressure. However, in order to establish an isothermal process, the heat generated during the compression process must be removed from the system at the same rate that it is added by the mechanical work of compression. Isothermal compression processes are extremely difficult to achieve due to the fact that two opposing effects need to be balanced. On the one hand, the isothermal compression process needs to occur in small confined volumes at very high speeds in order to achieve high efficiencies. On the other hand, the heat transfer process needs to take place over large surfaces at very slow velocities to achieve high effectiveness. As a consequence, isothermal compression has not been approached in a real application.

In the literature, different approaches have been investigated to approach an isothermal compression process. For instance, the use of multi-stage compression with inter-cooling could be used to remove the compression heat. However, this approach results in complex systems with high manufacturing costs. Heidari et al. (2017) designed, manufactured, and analyzed a finned piston compressor and an equivalent electric analogy was used to simulate the transient heat transfer process inside the compressor. The results showed that the temperature rise during compression decreased by 33% in the proposed design compared to a conventional process. Penazzo (2018) proposed an aqueous foam liquid compressor. In particular, a large heat transfer area as well as a high heat transfer coefficient were achieved with such design. It was reported that the proposed design reduced the discharged temperature approximately by 15 oC and improved the compressor

efficiency by 4 to 8%. The challenging part of the aforementioned novel compressor designs are the high manufacturing and maintenance costs. In addition, the selection of the working fluids and the scale of application are also limited.

Other popular techniques to achieve a quasi-isothermal compression process are fluid injection during the compression process and liquid-flooded compression. The injected fluid can be superheated, two-phase, or subcooled refrigerant. The most common fluid to flood the compression process is a lubrication oil. A detailed comparison of four different vapor compression cycle (VCC) performances using refrigerant injection was conducted by Heo et al. (2011) by utilizing the combination of a sub-cooler and flash tank. It was experimentally observed that the cycle configuration slightly improved the system capacity, but the system COP did not change significantly. Shuxue and Guoyuan, (2011) characterized the performance of a heat pump coupled with economized vapor injection. In this study, the optimal injection location and the injection ratio were discussed in-depth, and the system performance was improved by approximately 4%. Bell et al. (2010) investigated the feasibility of achieving a quasi-isothermal compression by employing oil-flooding. The proposed cycle configuration included an internal regenerator. The theoretical and experimental analyses resulted in cycle efficiency improvements between 5% and 20% depending on the operating conditions.

By surveying the literature, it is apparent that most of the researchers focused on scroll and screw-type compressors due to their favorable designs that allow an easier integration of the injection ports and their suitability for flooded compression. However, limited work was found related to vapor injected linear compressors.

In this paper, a novel cylinder cooling design in a linear compressor and its evaluation when integrated within a VCC are presented. A thermodynamic system model was developed in order to conduct parametric studies, which were further used to identify the key parameters and compare the designed system with a conventional VCC.

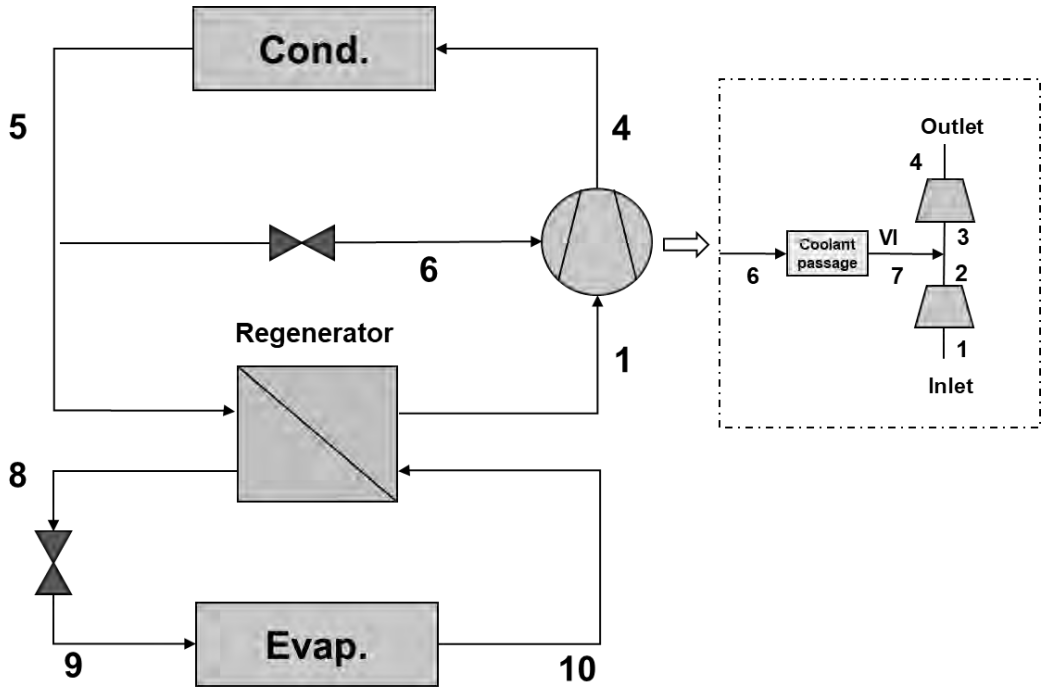

Figure 1: Schematic of an integrated vapor injection and piston-cylinder cooling system.

2. VAPOR INJECTION CYCLE WITH PISTON COOLING

Linear compressor technology is characterized by the absence of a crank mechanism, which has gained increasing attention for application to vapor compression systems due to its compactness and lower friction losses in comparison with conventional reciprocating compressors. Furthermore,

the absence of a crank mechanisms allows for oil-free operation. The absence of oil eliminates refrigerant compatibility issues and opens up more options for environmentally-friendly working fluids. Furthermore, the appropriate working fluids can be selected to operate at higher temperatures and pressures. Lastly, oil-free design significantly reduces the costs associated with filter replacement and oil condensate treatment. Due to its compactness and scalability, the linear compressor is an appealing technology for domestic and miniature-scale refrigeration systems, which have space constraints. The reduction of space occupied by the compressor enables of the use of additional components in alternative system configurations that can improve overall efficiency for space-constrained systems.

The schematic of the proposed system architecture is shown in Fig. 1. Two distinct system features can be noted: (1) a regenerator transfers heat from the liquid refrigerant exiting the condenser to the compressor suction line to ensure high superheat at the compressor inlet; (2) two-phase refrigerant at an intermediate pressure is injected into compressor cooling paths to enable a quasi-isothermal compression process (Domanski, 1995; Domanski et al.,1994). In this configuration, the sub-cooled refrigerant, exiting the condenser at state point 7 is divided into two flow paths, i.e., injection line and evaporation line. The flow in the injection line is throttled to an intermediate pressure at state point 8 and passes through piston cylinder cooling paths absorbing the heat from the compression chamber to a superheated injected vapor at state point 10, also shown in Fig. 2. The injected flow and the compressed vapor, already inside the compression chamber at state point 2, are mixed and compressed together from state point 3 to state point 4. On the other hand, the liquid to evaporator line enters the regenerator and exchanges heat with the refrigerant vapor exiting from the evaporator. Then, the liquid refrigerant with higher subcooling at state point 11 is throttled and passes through the evaporator to state point 14.

Fig. 2 shows the cylinder-piston assembly that includes cooling paths and cylinder injection. The coolant inlet is the two-phase refrigerant that has been throttled from the liquid line to an intermediate pressure between condensing and evaporating pressures (state 8 in Fig. 1). The coolant passes through cooling paths around the compressor chamber to absorb the heat from compression process, as shown in Fig. 2(a), and is evaporated to a superheated vapor at the exit. The coolant flow can be controlled to maintain a desired exit superheat by a thermal expansion valve within the cycle.

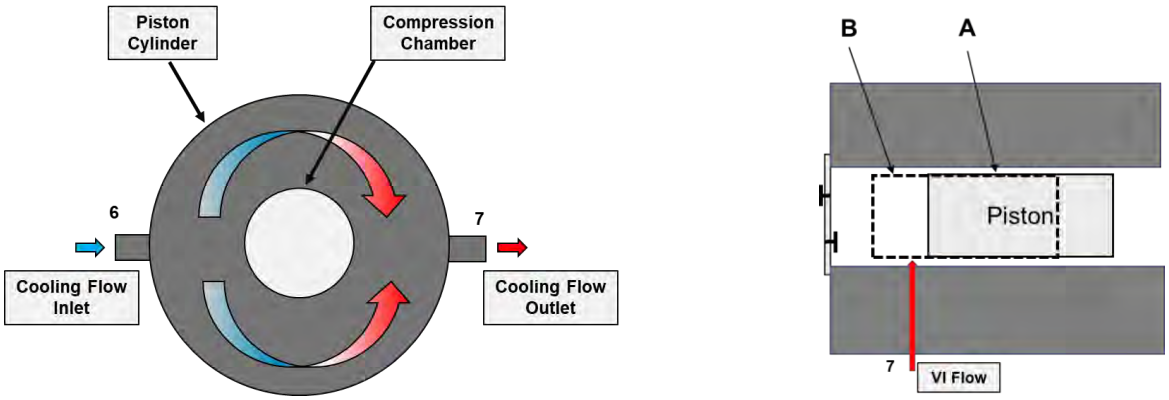

(a) (b)

Figure 2: Proposed piston-cylinder cooling assembly; (a) top view of the piston cylinder integrated with cooling paths; (b) side view of the piston with vapor injection port.

With the help of the connecting pipe (not shown in the schematic), the superheated vapor at state point 10 is injected into the compression chamber through the cylinder wall, as indicated in Fig. 2(b). The timing of the vapor injection process is determined by the location of the reciprocating piston. For example, when the piston is at location A in Fig. 2(b), the chamber pressure is below the intermediate injection pressure and the injection flow will be pushed into the compressor chamber. However, if the piston moves over the injection port, e.g., location B, the injection port will be blocked by the piston wall and there is no further vapor injection until the next cycle. However, some back-flow from compression chamber to the injection line could occur due to the differential pressure, and

it may result in a small amount of internal leakage in the compressor. Therefore, the location of the vapor injection port should be chosen wisely.

The state points of the aforementioned thermodynamic cycle are shown in P-h and T-s diagrams in Fig. 3. In particular, different solid line colors indicate different flow paths, and the dash black lines represent the thermodynamic process of a conventional VCC having the same compressor efficiency. It can be seen in Fig. 3(b) that the compressor inlet temperature in the new design (point 1) is significantly higher than that of the conventional cycle, which is due to the use of the regenerator to achieve high superheat. The injection flow at the intermediate pressure is mixed with compressed gas from state point 2 and then compressed together to state point 4 with lower discharge temperature compared to the conventional cycle.

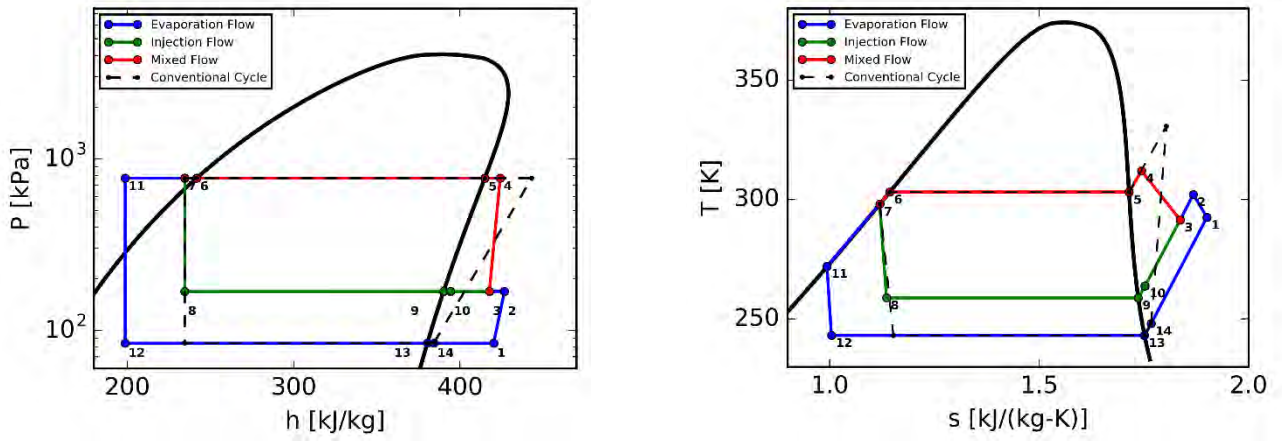

Figure 3: Vapor injection cycle system with cylinder cooling design: (a) P-h diagram; (b) T-s diagram.

3. CYCLE MODELING AND RESULTS

A thermodynamic cycle model has been developed and was used to analyze the proposed system and predict its performance in comparison to the baseline system. As previously outlined, the primary differences between the baseline and proposed system are the vapor injection line, the regenerator, and the cylinder cooling design. A simplified regenerator model with a constant effectiveness is used to model the heat exchange between the compressor suction line and liquid line after the condenser. Moreover, the cylinder cooling effects are considered in a new linear compressor simulation model with constant cylinder wall temperature, which is intimately linked to the cylinder wall temperature and heat transfer surface area. The mixing process between the injected flow and compressed flow is modeled by imposing a mixture energy balance and calculating the resulting mixture temperature.

For the baseline system, the compressor was modeled with a specific isentropic efficiency. The cooled compressor in the proposed system was modeled using polytropic efficiency to account for the significant heat transfer during the compression process. It is also worth pointing out that a cylinder cooling efficiency is used to represent the heat transfer ratio between heat rejection from the compression chamber and heat absorption to the two-phase flow inside the coolant passage. The in-cylinder compression process is modeled as a two-stage compression process with intercooling due to the injection process at the intermediate pressure. The cylinder wall temperature and therefore, the in-cylinder heat transfer during the cooling process is significantly affected by the intermediate pressure (and the corresponding intermediate temperature). The simulation system model described above was employed to investigate the system performance. The inputs to the model are listed in Table 1.

Table 1. Inputs used for the system simulation model

Description	Parameter	Proposed Sys.	Baseline Sys.	Unit
Working Fluid	-	R134a	R134a	-
Evaporating Temperature	T_{evap}	-30	-30	°C
Condensing Temperature	T_{cond}	30	30	°C
Superheat Temperature	ΔT_{sup}	5	5	°C
Subcooling Temperature	ΔT_{sub}	5	5	°C
Compressor Efficiency	η_{com}	0.8	0.8	-
Cylinder Cooling Efficiency	η_{cyl}	0.85	-	-
Regenerator Efficiency	ε_{re}	0.8	-	-
Intermediate Pressure Ratio	PR_{int}	2.5	-	-

Fig. 4 and Fig. 5 depict different injection processes at different intermediate pressures ratios. It can be seen that a smaller intermediate pressure ratio results in lower cylinder wall temperatures, which results in more heat removal from the compression chamber as a larger temperature difference exists for the in-cylinder heat transfer. In addition, larger cooling capacities can be obtained at lower intermediate pressures for the cylinder cooling, which is determined by the enthalpy change between state points 10 and 8. Therefore, with the decrease of the intermediate pressure ratio from 4.5 to 1.5, the compressor discharge temperatures decrease accordingly (state points 4c, 4b, 4a), which makes the overall two-stage compression process (1 to 4) closer to a quasi-isothermal process (also see Fig. 6). For that reason, the polytropic index n approaches unity (isothermal process), which leads to a decrease in reversible polytropic and actual specific work. However, a lower intermediate pressure also leads higher bypass flow to the compressor and reduced refrigerant flow through the evaporator. Thus, there is an optimum intermediate pressure.

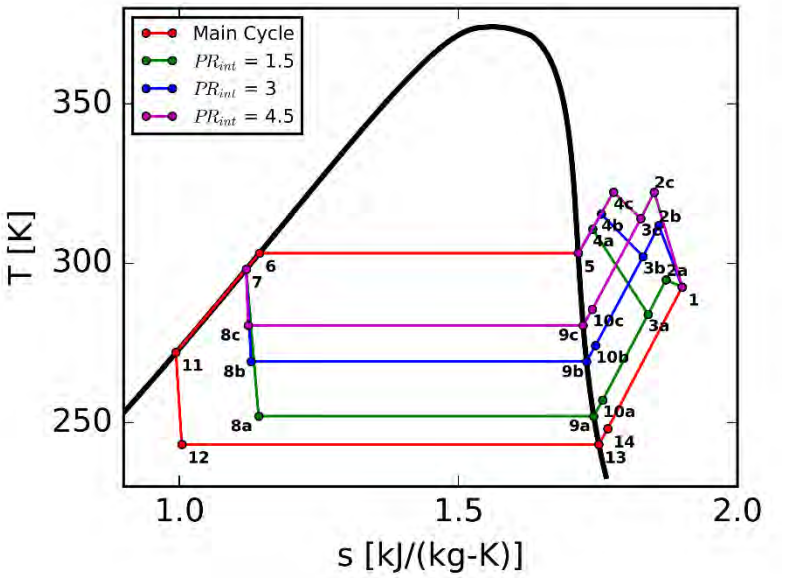

Figure 4: T-s diagram of vapor injection cylinder cooling system with different intermediate pressures.

Fig. 6 depicts the variation of the compressor temperature rise as a function of different intermediate pressure ratios for three different values of the regenerator efficiency. As previously discussed, decreasing intermediate pressure leads to a reduced temperature rise due to a lower coolant temperature. Moreover, it is also observed that a higher regenerator efficiency leads to a lower temperature rise since a higher inlet temperature allows for larger temperature difference for in-cylinder heat transfer.

However, the refrigerant flow to the evaporator decreases with increasing flow to the compressor as the intermediate pressure is reduced. This leads to a reduction in system cooling capacity which counters the positive effect of reduced compressor specific work. Therefore, there is an optimal intermediate pressure for the best system performance, which is very similar to a standard multiple-

stage compression process. Fig. 7 shows system COP as a function of intermediate pressure ratio for different regenerator efficiencies. The optimum intermediate pressure ratio is between about 5 and 6 for this case. COP increases with regenerator efficiency, but it has an insignificant effect on the optimum intermediate pressure that maximizes COP.

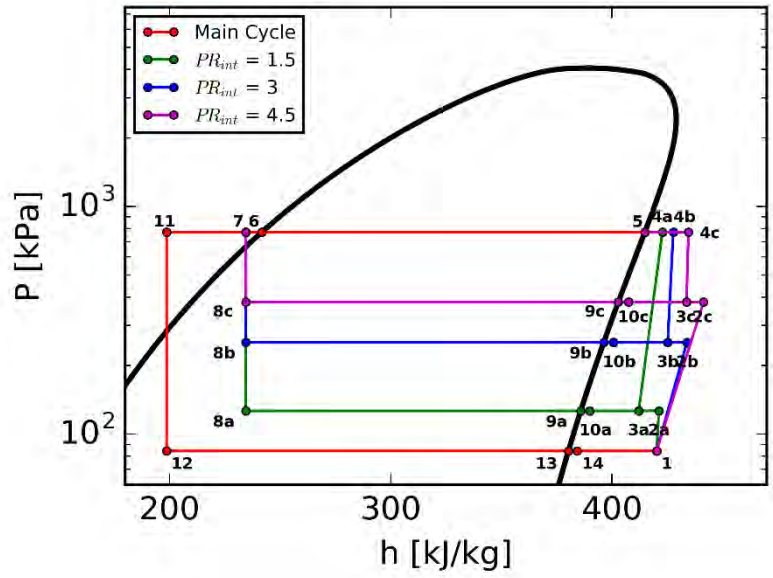

Figure 5: P-h diagram of vapor injection cylinder cooling system with different intermediate pressures.

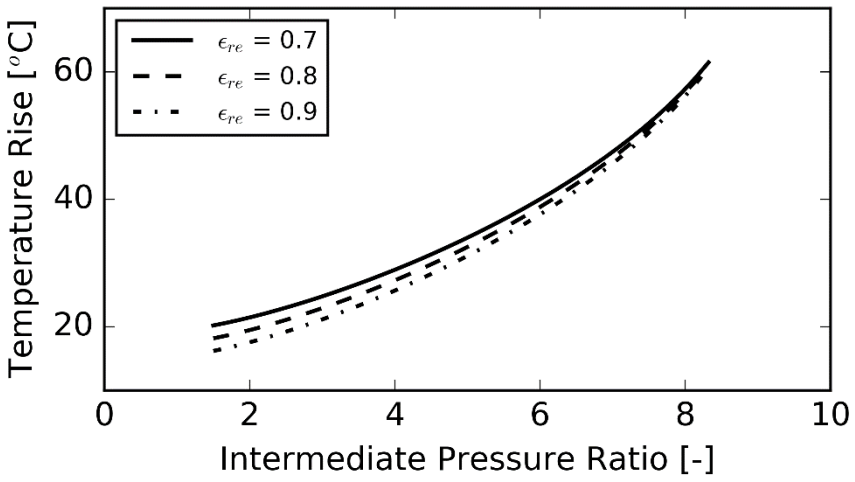

Figure 6: Compressor temperature rise versus intermediate pressure ratio for different regenerator efficiencies.

To further investigate the benefits of the designed cylinder cooling and vapor injection system with respect to the conventional vapor compression system, the simulation model is exercised to account for different operating conditions. To ensure a consistent comparison, all selected operating conditions are imposed to both cycle architectures, and the COP improvements from the conventional cycle is used as the parameter to identify the differences. Additionally, some of the common working fluids are selected to quantify the effect of working fluid selection on the system performance. It is shown in Figure 8 that the designed system has higher COPs than that of the conventional vapor compression system for all four selected refrigerants. In particular, an improvement can be found with the use of refrigerant R1234yf operating at lower evaporating temperatures because the proposed system can reduce the desuperheating loss, which is a predominant loss in the conventional vapor compression system when the evaporating temperature drops for a constant condenser temperature.

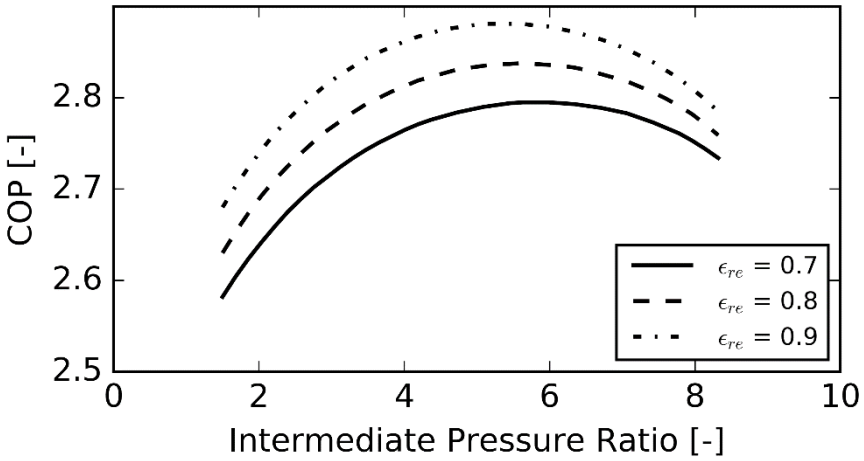

Figure 7: System COP versus intermediate pressure for different regenerator efficiencies.

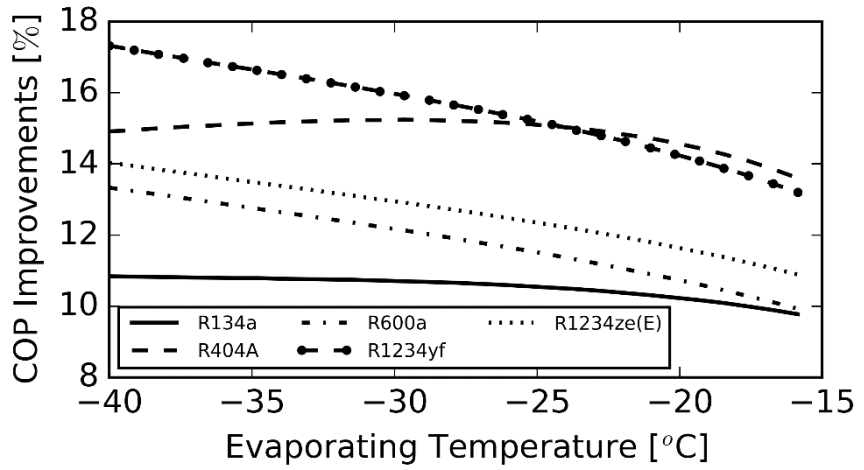

Figure 8: System COP improvements from a conventional VCRC versus evaporating temperature for different working fluids.

4. CONCLUSIONS AND FUTURE WORK

This paper presents a new concept of an oil-free linear compressor with piston/cylinder cooling, vapor injection, and regeneration. The performance of this technology was assessed for a number of different refrigerants and operating conditions using a system simulation model. Several conclusions can be drawn from the results as follows:

- The proposed system design can significantly reduce the compressor temperature rise compared to a conventional system, but the temperature rise depends on the intermediate pressure.
- There is an optimum intermediate pressure for cylinder cooling and vapor injection in terms of achieving the best overall system COP.
- Although overall system performance is strongly dependent on the regenerator effectiveness, the optimum intermediate pressure is relatively insensitive to the regenerator effectiveness.
- The proposed system showed between 10% and 18% improvements in performance compared to the conventional system. The greatest improvements occurred with R1234yf as the working fluid, especially at larger temperature lifts.

Future work will involve development of an improved piston-cylinder design with enhanced heat transfer surfaces. Once the designs are finalized, the core elements will be 3-D metal printed. The printed elements will be assembled into linear compressor prototypes, which will be used for performance characterization and model validation.

ACKNOWLEDGEMENTS

The authors would like to thank the Center of High Performance Building (CHPB) for sponsoring this project.

NOMENCLATURE

p	pressure (kPa)	*PR*	pressure ratio (-)
T	temperature (°C)	*η*	efficiency (-)
ε	regenerator efficiency (-)	*VI*	vapor injection

Subscripts

cond	condensing	*evap*	evaporating
com	Compressor	*cyl*	cylinder
Hx	Heat exchanger	*re*	regenerator
Int	Intermediate	*sub*	subcooling
sup	superheat		

REFERENCES

Bell, I. H., Groll, E. A., & Braun, J. E., 2011. Performance of vapor compression systems with compressor oil flooding and regeneration. Int. J. Refrigeration, 34(1), 225–233.

Domanski, P. A., Didion, D. A., & Doyle, J., 1994. Evaluation of suction-line/liquid-line heat exchange in the refrigeration cycle. Int. J. Refrigeration, 17(7), 487–493.

Domanski, P. A., 1995. Theoretical evaluation of the vapor compression cycle with a liquid- line/suction-line heat exchanger, economizer, and ejector. National Institute of Standards and Technology Gaithersburg, USA.

Heidari, M., Lemofouet, S., & Rufer, A., 2014. On the strategies towards isothermal gas compression and expansion. International Compressor Engineering Conference, Paper 2285.

Heidari, M., Mortazavi, M., & Rufer, A., 2017. Design, modeling and experimental validation of a novel finned reciprocating compressor for isothermal compressed air energy storage applications. Energy, 140, 1252–1266.

Heo, J., Jeong, M. W., Baek, C., & Kim, Y., 2011, Comparison of the heating performance of air-source heat pumps using various types of refrigerant injection. Int. J. Refrigeration, 34(2), 444–453.

Penazzo, S., 2018. Experimental investigation of aqueous foam based heat transfer in liquid piston compressor for improvement in compression efficiency. International Compressor Engineering Conference, Paper 1628.

Shuxue, X., & Guoyuan, M., 2011. Research on air-source heat pump coupled with economized vapor injection scroll compressor and ejector. Int. J. Refrigeration, 34(7), 1587–1595.

Zhang, X., Ziviani, D., Braun, J. E., & Groll, E. A., 2018, Modeling the dynamic characteristics and performance of linear compressors. In Proceedings: International Compressor Engineering Conference at Purdue. Paper 1667.

Manuscript ID: 413
DOI: 10.18462/iir.icr.2019.0413

Water vaporization inside a smooth plate-type heat exchanger at subatmospheric pressure: impact of the channel thickness

Florine GIRAUD[(a)], Lisa FLURO[(a)], Brice TREMEAC[(a)]

[(a)] Laboratoire du Froid, des Systèmes Energétiques et Thermiques (LaFSET), Cnam, HESAM Université, 292 rue Saint-Martin 75003 Paris, France, florine.giraud@lecnam.net

ABSTRACT

Using water as refrigerant requires to work at operating condition close to its triple point. At these low pressures, knowledge on heat transfer phenomena is insufficient. Thus, in order to increase experimental data available in this range of pressure, the impact of the channel thickness on the performance of a low pressure smooth plate-type evaporator is studied. Performances obtained with a channel thickness of 2 mm, 4 mm and 6 mm are compared. It is shown that although the performances might slightly increase with the increase of the channel thickness, for some operating conditions the trend is reversed. In all the experimental domain covered, the highest cooling capacity is obtained for a thickness of the channel of 2 mm.
Keywords: Subatmospheric pressure, Water, Narrow spaces, Plate heat exchangers, Evaporators.

1. INTRODUCTION

Due to a change of several mechanisms, like the flattened of bubbles which foster site-seeding or an increase of the velocity of the feeding fluid at the channel entrance, heat transfer could be enhanced in confined space. At low heat fluxes, this enhancement could be all the more significant as the thickness of the narrow channel decreases. However, according to several authors, this trend is observed only at low heat fluxes and for a thickness of the narrow channel lower than a given thickness (Katto and Yokoya, 1966, Bonjour, 1996, Ait Ameur, 2006). This given thickness is commonly accepted to be given by the capillary length ($\sqrt{\frac{\sigma}{g(\rho_l - \rho_v)}}$). If the thickness of the narrow space is higher than the capillary length, bubbles are not affected by the confinement. However, heat transfer is degraded as the confined plate prevents both the formation of convective cells above the heated surface and the rise of vapor masses created (Stutz et *al.,* 2009). If the thickness of the narrow space is lower than the capillary length, bubbles are flattened and the enlarged microlayer fosters the evaporation at low heat fluxes. According to Ait-Ameur (2006), the best performance would then be obtained for a thickness given at 0.25 time the capillary length. Indeed, several authors observed that, when a very narrow space is given, the heat transfer is degraded whichever the given heat flux (Katto and Yokoya, 1966, Bonjour, 1996, Ait Ameur, 2006). This is due, according to Ait Ameur (2006), to the viscous effects limiting the increase of the velocity for very small channels thicknesses.

When boiling water at subatmospheric pressure, bubbles of centimeter size are observed (Van Stralen *et al*., 1975). The capillary length in this range of pressure is, however, of a few millimeters (e.g. 2.7 mm at 2 kPa). Thus, transition given by the literature and mentioned previously may be

different at subatmospheric pressure. Indeed, there is a factor 100 between the capillary length and the bubbles departure diameter observed by Van Stralen *et al.* (1975). The effect of the confined space should then be observed even for channel thicknesses higher than the capillary length. It might be also possible that the given thickness of the channel is very narrow compare to the size of the bubble. A degraded heat transfers may be observed whichever the confined space and the heat flux given. Yet, to optimize evaporators used in this range of pressure (for example in chillers using water as refrigerant), is fundamental to apprehend these phenomena. Thus, experiments were conducted in a smooth plate-type heat exchanger in which the spacing of the working fluid could be set at 2, 4 or 6 mm (i.e. for channel thicknesses lower and higher than the capillary length). After a short presentation of the experimental set-up, experimental and theoretical results based on a mathematical model obtained following the design of experiments methodology are shown. Results obtained with a high-speed camera (3000 fpr, resolution 1024 x 800) are then discussed before concluding the paper.

2. EXPERIMENTAL SET-UP

The experimental set-up is the same as used in Giraud *et al.* (2016). It is a pump-assisted closed-loop thermosiphon which allow to set operating conditions that might occur in chillers working with water as refrigerant (R-718). It is constituted by a condenser, a smooth stainless steel plate evaporator, a liquid supply line and a vapor exhaust line (Fig. 1). The saturation temperatures are set by means of two heating/cooling devices (B1 and B2). A third heating device (B3) is used to set the fluid temperature at the expander inlet so that it corresponds to the temperature of the refrigerant at the condenser outlet in a chiller.

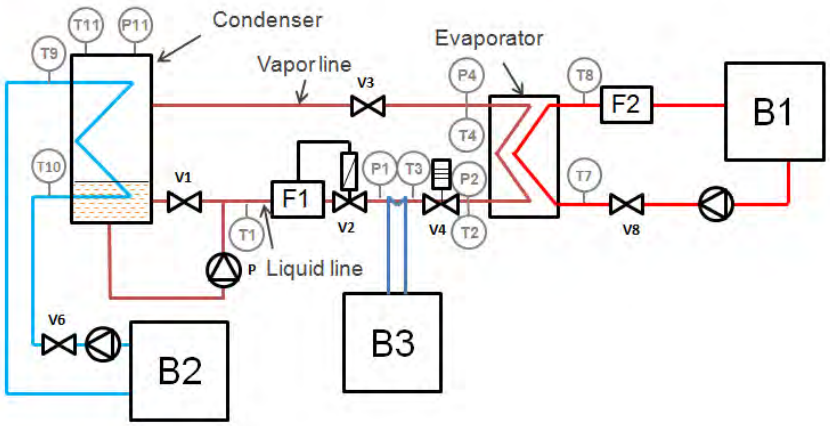

Figure 1: Drawing of the experimental test setup

In the liquid line, the water is fed into the evaporator by three tubes of 2 mm inner diameter. Once the refrigerant is vaporized, the fluid flows back to the condenser through the vapor line. The condenser is a stainless steel vessel of 300 mm inner diameter and 720 mm height. An oversized copper-tube coil heat exchanger is located inside the container in order to condense the vapor along the outer surface of the tube and in order to store the refrigerant at liquid state. The evaporator (Fig. 2) is made up of two stainless steel plates and one transparent PMMA (polymethyl methacrylate) plate of 500 mm height and 200 mm width. The transparent PMMA plate is used as the external plate on the refrigerant side in order to observe boiling phenomena by means of a high-speed camera. The central plate of the evaporator is made of 6 mm stainless steel in order to allow the insertion of 44 thermocouples (22 homogeneously distributed for each side of the central plate) and avoid any buckling without disturbing the flow. Three different spacing can be chosen between the PMMA plate and the central plate (refrigerant side): 2 mm, 4 mm and 6 mm.

The spacing between the two stainless steel plates (secondary fluid side) is set at a given value of 1 mm.

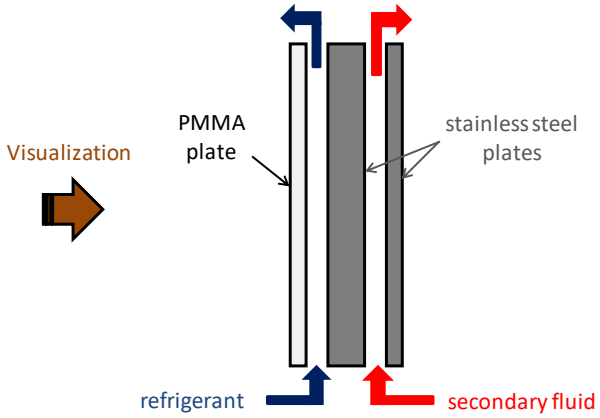

Figure 2: Schematic of the evaporator

K-type thermocouples are inserted at different points of the test facility. They allow to measure the temperatures with an accuracy of ± 0.1 K at the inlet and outlet of each component for the two fluids (primary and secondary). Five pressure transducers measure the absolute pressure at different points of the test rig with an accuracy of ± 0.075% of the reading.
In order to promote nucleate boiling, the parallel flow configuration was chosen in agreement with the results obtained by Clause *et al.* (2011) for a heat exchanger of similar size. The coolant mass flow rate is adjustable by manipulating the valve noted V8 on Fig. 1 and its flow rate is measured using an electromagnetic flow meter (F2) in a range of 1-2 $dm^3.min^{-1}$ and with an accuracy of ± 0.5% of the measured flow rate.

3.THERMAL BEHAVIOR

The experimental domain covered during these studies is given in Table 1. Experimental data are homogeneously distributed in this experimental domain (i.e. if one considers a chart of four dimensions, each set of operating conditions given are located at equal distance of each other).

Table 1. Domain covered by the experimental test

Parameters	Field
Filling ratio (H_l)	[5 – 25] cm
Temperature set point at the condenser (bath B2 - T_{sf})	[2 – 15] °C
Temperature set point at the thermostatic bath B3	[30 – 45] °C
Temperature set point at the evaporator (bath B1 – $T_{sf,in}$)	[0 – 25] °C
Channel thickness (refrigerant side - e)	2 mm, 4 mm, 6 mm

3.1 Experimental results

Time-averaged data obtained during this experimental campaign are shown on Fig. 3. They are calculated as the mean value of data obtained every one second during at least 20 minutes once steady state is set on. In the Fig. 3a, results obtained for a channel thickness of 2 and 6 mm are compared to data obtained for 4 mm (diagonal of the graph). The Fig. 3b introduced the characteristics of the exchangers (a modified overall heat transfer coefficient and the mean logarithm temperature difference) for all the data. The modified overall heat transfer coefficient (K*) is calculated by considering the entire heat exchanger surface (liquid area + vaporization area

+ vapor area) and the logarithmic mean temperature difference in the vaporization area (called falling film area in Giraud et al., 2016):

$$K^* = \frac{\dot{Q}_{cool}}{S\Delta T_{LM}} \quad \text{Eq. (1)}$$

With:

$$\Delta T_{LM} = \frac{T_{fs,in} - T_{fs,out}}{ln\left(\frac{T_{fs,in} - T_{sat}}{T_{fs,in} - T_{sat}}\right)} \quad \text{Eq. (2)}$$

Where T_{sat} is the saturation temperature of the fluid at the free interface (Giraud et al., 2017). Although this coefficient has no physical meaning, it could be seen as an apparent overall heat transfer coefficient taking into account that the liquid area is essential to the generation of a large bubble and to the projection of liquid up to a certain height, but that the effective variation of temperature is only due to the phase-change in the falling film area. Its underestimates the effective overall heat transfer coefficient due to the evaporation of the film.

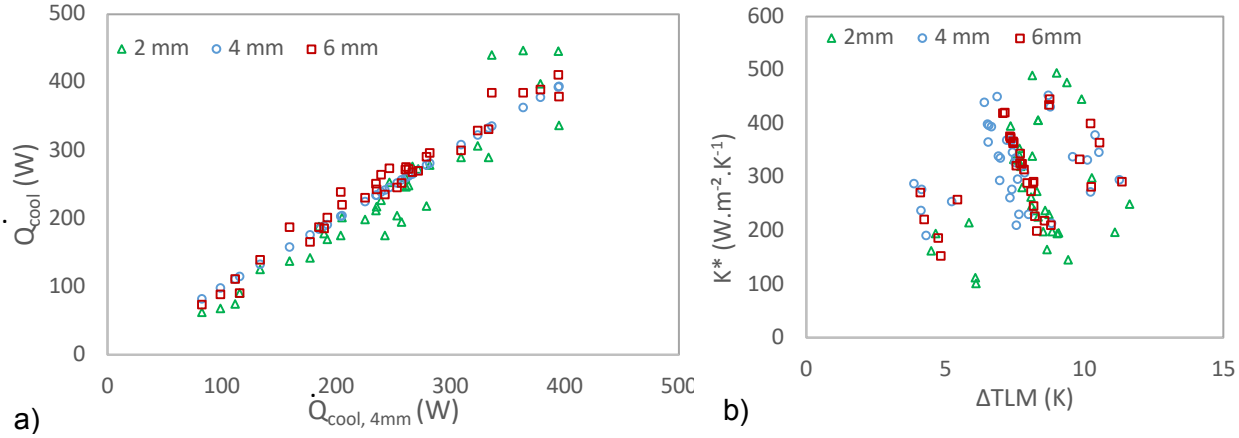

Figure 3: time-averaged a) cooling capacities and b) global heat transfer coefficient for a thickness of the channel of 2, 4 and 6 mm

During operating conditions leading to cooling capacities from 0 to 350 W, one might see on Fig. 3a that performances obtained slightly increase with the increase of the channel thickness. Then, for higher cooling capacities, performances are better with a narrow channel of 2 mm thick. However, this trend is not significant and the experimental uncertainties must be taken into account. These uncertainties, calculated from the logarithm method (which overestimate the uncertainties), vary from 6 to 20 %, which correspond to a variation of around +/- 20 W for each data. Nevertheless, one can clearly see that, even with an overestimation of the uncertainties, a given narrow channel of a thickness of 2 mm leads to the best but also to the worst performances in the experimental domain covered. Time-averaged cooling capacities obtained for e = 4 mm and e = 6 mm are instead quite similar. The difference observed between in one hand a channel thickness of 2 mm and in other hand channel thicknesses of 4 and 6 mm may be due to the significance of the capillary forces. Indeed, a channel thickness of 2 mm is lower than the capillary length whereas thicknesses of 4 and 6 mm are higher than this one (whichever operating conditions set in this paper). As for phenomena linked to the flattened of bubble, bubbles are probably large enough with respect to the channel thicknesses to do not significantly change phenomena occurring inside the channel.

3.2 Mathematical model (DOE Methodology)

Mathematical models were developed for each thicknesses tested following a Design Of Experiments methodology of Doelhert type (Goupy, 2000). In order to validate these models, twenty-four set of operating conditions were chosen arbitrarily in the entire experimental domain. Set of operating conditions leading theoretically to the best performances for each thicknesses were also given. Models developed allow to predict the mean experimental cooling capacities for each of these set of operating conditions and each thicknesses at +/- 15 % (Fig. 4).

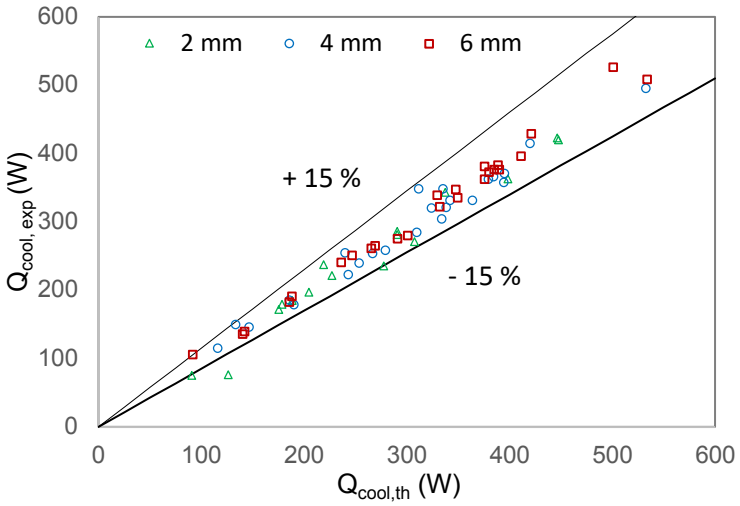

Figure 4: Validation of models obtained by a DOE methodology

According to these models, the thickness which leads to the best performances depends on running conditions (Fig. 5).

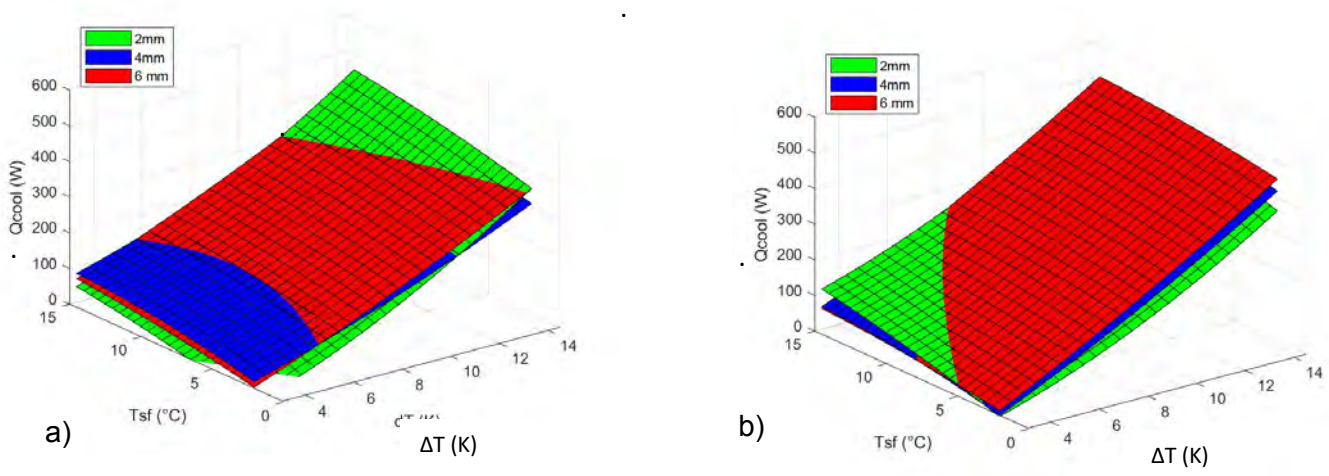

Figure 5: Theoretical response areas for a) H_l = 10 cm; b) H_l = 20 cm (TB_3=37.5 °C)

According to Fig. 5, as the working pressure increases (increase of T_{sf}), the performances obtain with a channel thickness of 2 mm increase. For a filling ratio of 20 cm, it shows the best performance at low superheat (ΔT) and relatively high pressure (T_{sf} of 5 °C corresponds to a working pressure of around 9 mbar). At low filling ratio (10 cm), the best performances with e = 2 mm will be obtained for high superheat whatever the working pressure. Still according to

these models, in the experimental domain covered, the best performance will be obtained for a thickness of 2 mm (compared to 4 and 6 mm). Indeed, models predicts an optimal performance of 508 +/- 22 W for 6 mm; 500 +/- 20 W for 4 mm and 553 +/- 24 for 2 mm. The best performance was however experimentally found for 6 mm (533 +/- 2 W versus 503 +/- 30 W for 2 mm and 531 +/- 14 W for 4 mm). However, the experimental data obtained for e = 2 mm may not be relevant for this point since a lot of refrigerant were evacuated off the evaporator by the vapour flow and the filling ratio couldn't be hold with the current experimental set-up. Moreover, the model may not be valid since there is thus a change in the vaporisation mechanisms. In any case, this situation should be avoided since a refrigerant evacuated without being evaporated could damage the compressor if a mechanical compressor is used or lead to a drastic decrease of the performance of the system if a thermal compressor is used.

4. VISUALIZATION

Results obtained with the high speed camera show that the vaporization mechanism is relatively similar for a channel thickness of 4 mm and 6 mm: the liquid is splashed on the wall, a downward liquid flow is observed and evaporation immediately takes places. Example of this vaporization phenomenon is shown on Fig. 6. On contrary, for a thickness of the channel of 2 mm, for several set of operating conditions, the liquid is splashed on the wall but an upward flow is observed and droplets are dragged by the vapor flow or trapped between the two surfaces disturbing the flow. Areas of fluid recirculation were observed around the droplets trapped between the two walls. Dry spots are also observed. Thus, the area of the liquid film is increase thanks to the vapour flow but its follow a preferential path which lead to a thicker film and dry patch and thus to the decrease of heat transfer mechanism. An illustration of this vaporisation phenomena is shown on Fig. 7. The difference of performances obtained for e = 2mm may be also explained by the way the bubble breaks. Indeed, a defragmentation of the bubble is observed for almost all the set of operating conditions tested when the bubble is growing. An example of this phenomenon is given in Fig. 8. Contrary to what happen for 4 and 6 mm, droplets are thus not projected homogeneously into the wall above the free interface but following the "arms" formed by the bubble when breaking.

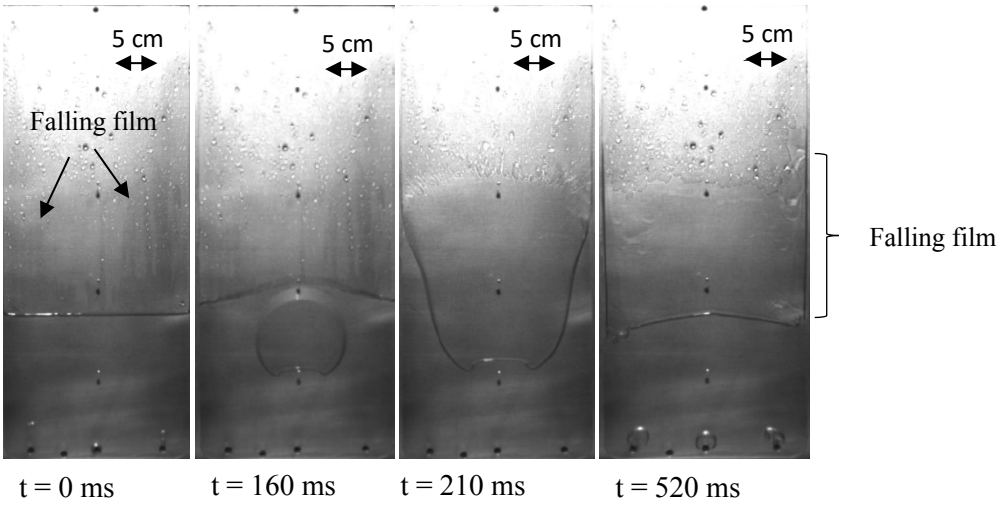

Figure 6: Video sequence of phenomena observed inside the channel of the evaporator for e = 4 mm (H_l = 15 cm, T_{sf} = 8.5 °C, $T_{fs,in}$ = 17.5 °C) (Giraud *et al.*, 2016)

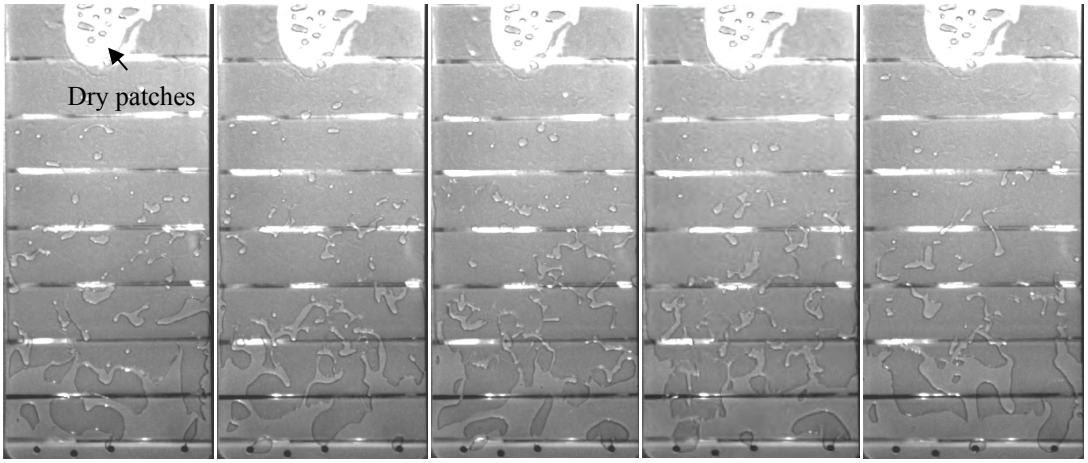

Figure 7: Video sequence of phenomena observed inside the channel of the evaporator for e = 2 mm (H_l = 25 cm, T_{sf}= 14 °C, $Tf_{s,in}$= 28 °C)

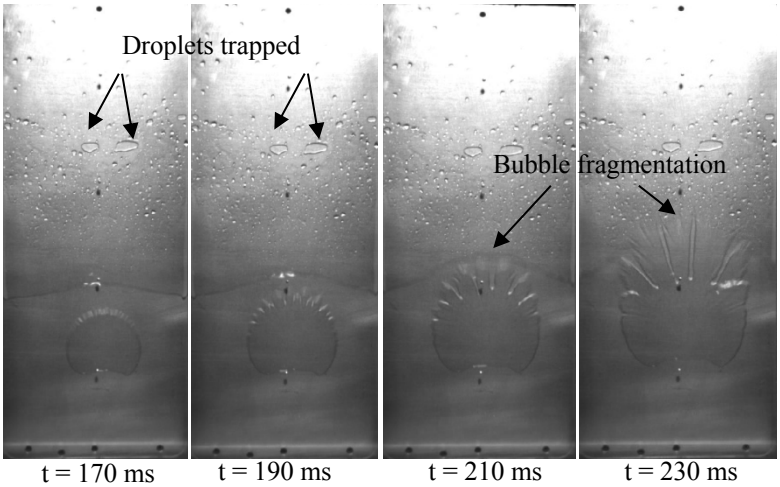

Figure 8: Bubble fragmentation observed for e = 2 mm (H_l = 15 cm, T_{sf} = 10 °C, $Tf_{s,in}$= 19 °C)

Others phenomena could explain the difference between performances obtained for 4 or 6 mm and performances obtained for 2 mm such as the presence or not of heat transferred by convection and the size of the bubbles. Indeed, visualization shows that the free interface is always moving for a thickness of 4 mm and 6 mm. On the contrary, for e = 2 mm, the movement of the free interface rapidly vanishes after the growth and the breaking of large bubbles. Moreover, for e = 2 mm, the apparent bubbles size (recalculated from the area observed on pictures and the channel thickness set) are smaller than bubbles observed for a thickness of 4 mm and 6 mm. Thus, the heat transferred by convection after the rupture of the membrane is probably lower. Another phenomenon to consider is the bubbles frequency. The mean wall temperature is higher at 2 mm than at 4 mm and the bubbles frequency is higher. Thus, the liquid film is more often regenerated, the mean thickness of the falling film is thus thicker which leads to lower mean heat transfer coefficient.

5. CONCLUSION

According to results obtained from visualization and from transducers (thermocouples and pressure transducers), there is a change in vaporization mechanisms between in one hand, 2 mm, and in other hand, 4 and 6 mm. Since a thickness of 2 mm is lower than the capillary length and 4 and 6 mm are higher than this one (whichever operating conditions set in this paper), these

results are probably mainly due to the significance of the capillary forces. As bubbles observed are much larger than the channel thickness set, phenomena due to the flattened of the bubble cannot be observed with this experimental campaign.
In order to further observe the influence of the channel thickness on phenomena observed, experimental campaigns must be conducted with several channel thickness thicker and narrower than the capillary length. Some tests should be also conducted with a channel thickness larger than the bubble size. Then, efforts must be done to increase the accuracy of results obtained.

NOMENCLATURE

e	channel thickness (m)
H_l	filling ratio (m)
K^*	overall heat transfer coefficient ($W.m^{-2}.K^{-1}$)
$\dot{Q}_{cool}$	Cooling capacity (W)
T	temperature (K)
t	time (s)
subscrits	
in,fs	inlet secondary fluid
visu	visualization
sf	cold sink

REFERENCES

Ait Ameur M., 2006. Etude experimentale de l'ébulltion naturelle confinée: analyse des instabilités et des transferts thermiques. Ph.D. Thesis, Insa de Lyon. France.

Bonjour J., 1996. Amélioration des transferts thermiques en ébullition naturelle convective par effet de confinement. Ph.D. Thesis, Insa de Lyon. France.

Clausse M., Leprieur J., Meunier F., 2011. Experimental test of plate evaporator for sorption refrigeration systems. ISHPC 11, Padua Italy, paper I-86.

Giraud F., Rullière R., Toublanc C., Bonjour J., Clausse M., 2016. Experimental study of water vaporization occurring inside a channel of a smooth plate-type heat exchanger at subatmospheric pressure. Applied Thermal Engineering. (106) 180–191.

Giraud F., Toublanc C., Rullière R., Bonjour J., Clausse M., 2015. Establisment of an experimental design in the context of water vaporization occuring on a plate cross section. ICR2015, Yokohama, Japan, paper 0542.

Giraud F., Vallon P., Tremeac B, 2017. Experimental study of water vaporization occurring inside the channel of a smooth-plate type heat exchanger connected to an adsorber and comparison with trends observed in absorption configuration. Int. Journal of Refrigeration. (77) 60-74.

Goupy J., 2000. Modélisation par les plans d'expériences. Technique de l'ingénieur R 275.

Katto Y., Yokoya S., 1966. Experimental study of nucleate pool boiling in case of making interference-plate approach to the heating surface. 3rd International Heat Transfer Conference, Chicago. (33) 219-227.

Stutz B., Lallemand M., Raimbault F., Passos J., 2009. Nucleate and transition boiling in narrow horizontal spaces. Heat Mass Transfer. (45) 929–935.

Van Stralen S. J. D., Cole R., Sluyter W. M., Sohal M. S., 1975. Bubble growth rates in nucleate boiling of water at subatmospheric pressures. International Journal of Heat and Mass Transfer. (18) 655-669.

Manuscript ID: 417
DOI: 10.18462/iir.icr.2019.0417

Wet Compression with NH_3-CO_2-H_2O in Twin Screw Compressors

Dionne GRUIJTHUIJSEN [(a)], Vilborg GUDJONSDOTTIR[(a)], Carlos INFANTE FERREIRA [(a)]

[(a)] Delft University of Technology,
Delft, 2628 CB, Netherlands, v.gudjonsdottir@tudelft.nl

ABSTRACT

Industrial waste streams can be upgraded efficiently with heat pumps. However, heat pumps are rarely used in industry. One of the main problems is long payback periods. Compression-resorption heat pumps (CRHPs) have potentially a better performance than traditional technologies for industrial applications when there is a temperature glide of the heat sink or source. CRHPs normally use ammonia-water as working fluid. Alternative working fluids have the potential to increase the performance even further. NH_3-CO_2-H_2O has been identified as a potential candidate and heat exchanger experiments confirmed that the heat transfer rate increases compared to ammonia-water. In this study the effects of this mixture on the compressor of CRHPs are investigated. The preliminary results indicate that adding similar amounts of CO_2 as in the heat exchanger experiments has a positive effect on the isentropic efficiency of the compressor so that a significant performance increase can be expected for the CRHP system.

Keywords: CRHP, wet compression, twin screw compressor, NH_3-CO_2-H_2O, NH_3-H_2O

1. INTRODUCTION

It is a well-known fact that we need to act quickly if we want to reduce the effects of global warming. We need to start using renewable energy sources to a larger extent, and we also need to become more energy efficient. Industry is a large consumer of energy, in Europe it is responsible for approximately a quarter of the final energy consumption (European Council, 2014). Heat pumps can efficiently upgrade industrial waste streams and in that way make industrial processes more efficient. However, heat pumps are barely implemented and one of the main reasons according to the International Energy Agency (IEA) is its large payback periods (IEA, 2014).
Compression-resorption heat pumps (CRHPs) utilizing wet compression have the potential to have a better performance than traditional technologies to upgrade industrial waste streams where there is a temperature glide of the heat source and/or heat sink. The working fluid in CRHPs is a mixture that is typically ammonia-water. However, alternative mixtures can have even better performance. Gudjonsdottir et al. (2017) studied NH_3-CO_2-H_2O as a possible candidate. Their study suggested that, in some cases, the mixture can increase the coefficient of performance (COP) with approximately 5 % compared to only operating with ammonia-water. In this study the compressor efficiency was assumed to be constant. Shi et al. (2017) experimentally studied the performance of that mixture in a mini-channel heat exchanger. Those experiments did indeed indicate an increase in the heat flow rate when CO_2 was added to an ammonia water mixture. In this study the compressor performance is studied as well as the entire heat pump cycle with and without added CO_2. The results suggest that the isentropic efficiency slightly increases by adding CO_2 to ammonia water and as well the delivered heat. This indicates that there might be even a larger gain than previously expected on the performance of CRHPs with added CO_2.

2. THEORETICAL MODEL OF WET COMPRESSION WITH NH_3-CO_2-H_2O

To study the compressor performance with NH_3-CO_2-H_2O a compressor model is needed as well as thermodynamic properties such as enthalpy and specific volume of the mixture. For this purpose a model developed by Gudmundsdottir (2018) is used. This model is a simple and fast twin screw compressor model. The model was developed in Matlab operating with ammonia water

as a working fluid. Ammonia-water is a widely used mixture and its thermodynamic properties can be found in thermodynamic libraries such as REFPROP (Lemmon et al., 2013). The properties of NH_3-CO_2-H_2O are not as widely investigated and section 2.2 discusses possible implementations.

2.1. The twin screw compressor model

Various twin screw compressor models have recently been developed (see for example Cao et al. (2011), Chamoun et al. (2013), Jianfeng et al. (2009), and Tian et al. (2017)) and they normally consist of a geometry part and a thermodynamic part. A common problem is that the detailed geometry of a compressor is not readily available. Therefore, Gudmundsdottir (2018) constructed generic geometry profiles using the available profiles from Tang (1995) and Zaytsev (2003). The main geometrical characteristics of the compressor that is used for further analysis in this study are listed in table 1.

Table 1. Main geometrical characteristic of the compressor used in this study

Maximum volume per cavity, m^3	$6.04 \cdot 10^{-5}$
Length of the compressor rotors, mm	$337 \cdot 10^{-3}$
Rotational speed, rpm	10,000
Number of lobes on male rotor	5
Number of lobes on female rotor	6
Clearances, μm	50
Discharge opens at, º	690
Stop angle, º	760
Mechanical efficiency, %	90

In the thermodynamic model the conservation equations for mass and energy developed by Zaytsev (2003) are solved. The mass conservation is defined as:

$$\frac{dp}{d\varphi} = \frac{1}{\left(\frac{\partial v}{\partial p}\right)_{T,x}} \left[\frac{v}{m} \left(\sum_{k=1}^{n} \left(\frac{dm_{out}}{d\varphi} \right)_k - \sum_{k=1}^{n} \left(\frac{dm_{in}}{d\varphi} \right)_k \right) + \frac{1}{m} \frac{dV}{d\varphi} - \left(\frac{\partial v}{\partial T} \right)_{P,x} \frac{dT}{d\varphi} \right] \quad \text{Eq. (1)}$$

The energy conservation equation as

$$\frac{dT}{d\varphi} = \frac{T \left(\frac{\partial v}{\partial T} \right)_{P,x} \left[\frac{v}{m} \left(\sum_{k=1}^{n} \left(\frac{dm_{out}}{d\varphi} \right)_k - \sum_{k=1}^{l} \left(\frac{dm_{in}}{d\varphi} \right)_k \right) + \frac{1}{m} \frac{dV}{d\varphi} \right]}{\left(\frac{\partial v}{\partial p} \right)_{T,x} \left(\frac{\partial h}{dT} \right)_{p,x} + T \left(\frac{\partial v}{\partial T} \right)^2_{P,x}} + \frac{\frac{\partial Q}{d\varphi} + \sum_{k=1}^{l} \left(h_{in,k} - h \right) \left(\frac{dm_{in}}{d\varphi} \right)_k}{m \left(\frac{\partial h}{dT} \right)_{p,x} + \frac{mT}{\left(\frac{\partial v}{\partial p} \right)_{T,x}} \left(\frac{\partial v}{\partial T} \right)^2_{P,x}} \quad \text{Eq. (2)}$$

The equations are solved with a simplified iteration scheme similar to that of Chamoun et al. (2013) where the compression cycle (suction, compression and discharge) are divided into small finite control volumes. Initially, the compression process is solved without any leakages and then including the main leakages encountered in a twin screw compressor. That is through the contact line between the two rotors, the sealing line between the tip of the rotors and the housing, the cusp blowhole at the high pressure side, the compression start blowholes at the suction side and through the discharge end clearances. The iteration goes on until the pressure during the compression process, at 530 º, converges to a value of less than 1 Pa. A schematic of the model is shown in Fig. 1. The only part of the model that has to be modified when changing the working fluid is the Thermodynamic property model.

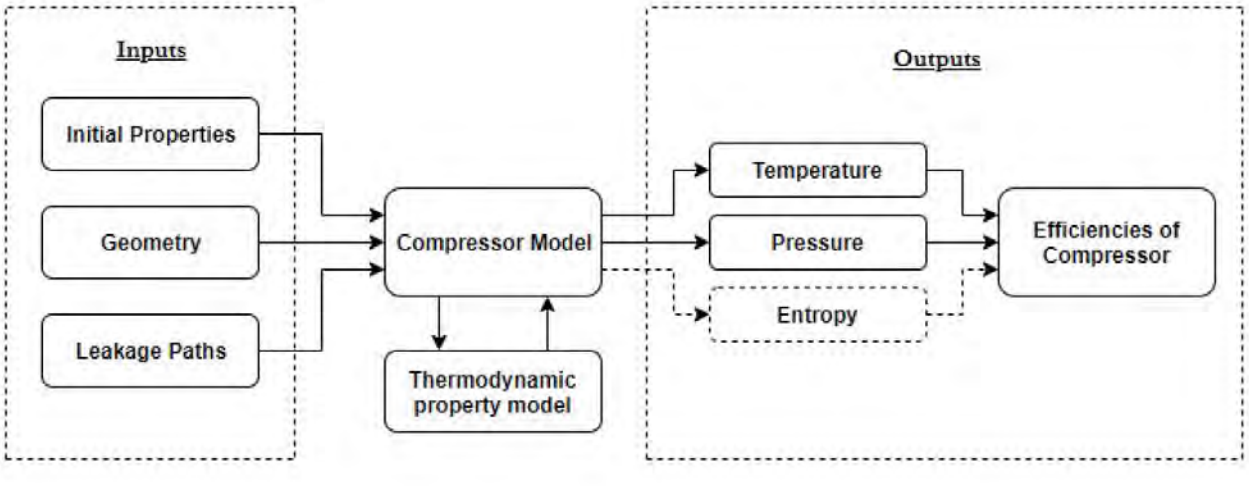

Figure 1: Schematic structure of the compressor model. (Gudmundsdottir, 2018)

2.2. Thermodynamic properties of NH_3-CO_2-H_2O

Gudjonsdottir et al. (2017) studied the thermodynamic properties of NH_3-CO_2-H_2O and developed a version in Aspen Plus suitable for heat pump applications. There are several ways of implementing this model in Matlab including:

1. Implementing the physical properties of the ternary mixture as a Matlab executable function (MEX).
2. Creating a direct connection between Matlab and Aspen.
3. Generating tables using the thermodynamic model available in Aspen.
4. Developing equations as a function of the pressure and temperature using the Aspen model.

The first option is eliminated for being too time consuming. The second option as well since the computational time is significantly longer than for the last two options. The last option was initially the preferred option since it does save significant memory compared to the third option, however, fitting for example the enthalpy to the pressure and temperature (see equation 3) resulted in too large deviations compared to the Aspen model, of up to 20 %

$$h(p,T) = a(p) \cdot e^{b(p)T} + c(p) \cdot e^{d(p)T} \qquad \text{Eq. (3)}$$

Only fitting to the temperature at fixed pressure resulted in acceptable results (less than 1% deviation), but then the results need to be interpolated between different pressure levels. This will always result in larger inaccuracies than using directly the Aspen data in table form. Therefore, for the desired conditions, tables have been generated from the Aspen model and implemented in the compressor model.

3. RESULTS

3.1. The compressor model

There are various parameters that affect the compressor performance, for example, compressor clearances, rotational speed and operational parameters such as the ammonia concentration, vapor quality and the pressure ratio. To make a fair comparison of added CO_2 these parameters are kept constant. In order to keep the vapor quality constant, the suction pressure and temperature are slightly varied for each case. During the calculation, the specific volume at the inlet is kept constant as well. This is done because the specific volume has influence on the mass flow displaced by the compressor. In case the specific volume is larger, the compressor needs to be larger to displace the same mass flow, and the capital cost becomes higher. In that case, the addition of CO_2 can still be disadvantageous and thus the size of the compressor is kept constant as well. An overview of the properties used in the comparison are listed in table 2.

Table 2. Properties used for comparing the performance of a compressor operating with 0, 2.5, 5 and 10 wt% CO_2 addition to ammonia water.

CO_2 concentration, wt%	0	2.5	5	10
NH_3 concentration, wt%	20	20	20	20
H_2O concentration, wt%	80	77.5	75	70
Specific volume at the suction, kg m^{-3}	1.064	1.068	1.068	1.067
Pressure ratio	5	5	5	5
Suction pressure, bar	1.0	0.965	0.952	0.917
Discharge pressure, bar	5.0	4.825	4.76	4.585
Suction temperature, °C	90.0	88.3	87.3	84.8
Vapor quality at suction, -	0.63	0.63	0.63	0.63

Fig. 2 shows the results from the compressor model and table 3 lists the resulting isentropic efficiencies. From the table it is seen that by adding small amounts of CO_2 a slight increase is observed in the efficiency up to a certain limit where it starts to decrease again. However, it is also clear from Fig. 2 that the operating temperatures are slightly different to maintain more or less the same conditions as discussed above. In practice a certain heat sink and source are available and needed at certain temperature levels. Therefore, the following section looks at the effects that added CO_2 will have on the entire heat pump cycle.

Table 3. Isentropic efficiencies, with and without mechanical losses, for different concentrations of CO_2.

CO_2 concentration, wt%	0	2.5	5	10
η_{is},%	77.25	79.95	80.77	80.33
η_{tot},%	69.53	71.96	72.69	72.30

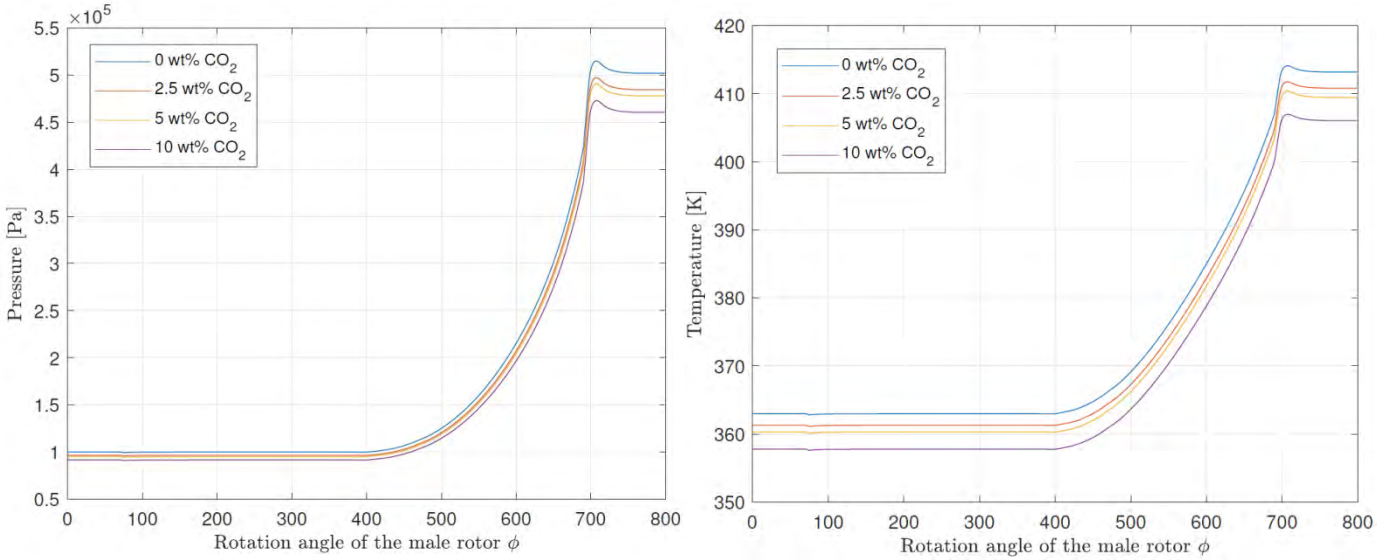

Figure 2: Pressure (left) and temperature (right) during the compression process for 0, 2.5, 5 and 10 wt% added CO_2.

3.2. The complete heat pump cycle

To evaluate the performance two applications are analysed. The first one where a waste stream of 60 °C is upgraded to 105 °C and the second where a waste stream of 95 °C is upgraded to 140 °C. The first application was already discussed by Gudjonsdottir et al. (2017), however, during the calculations of the COP a fixed value of the compressor efficiency was used. Using a fixed isentropic efficiency resulted in approximately 5 % increase in the COP with 15 wt% CO_2. The

second application was chosen since there has been an increased interest in high temperature heat pumps as pointed out by Arpagaus et al. (2016). CRHPs utilizing wet compression are ideal for high temperature applications since the superheating region, which limits operation for conventional technologies, is completely eliminated. An overview of the first case is shown in Fig. 3, the second one is similar except at different temperature levels.

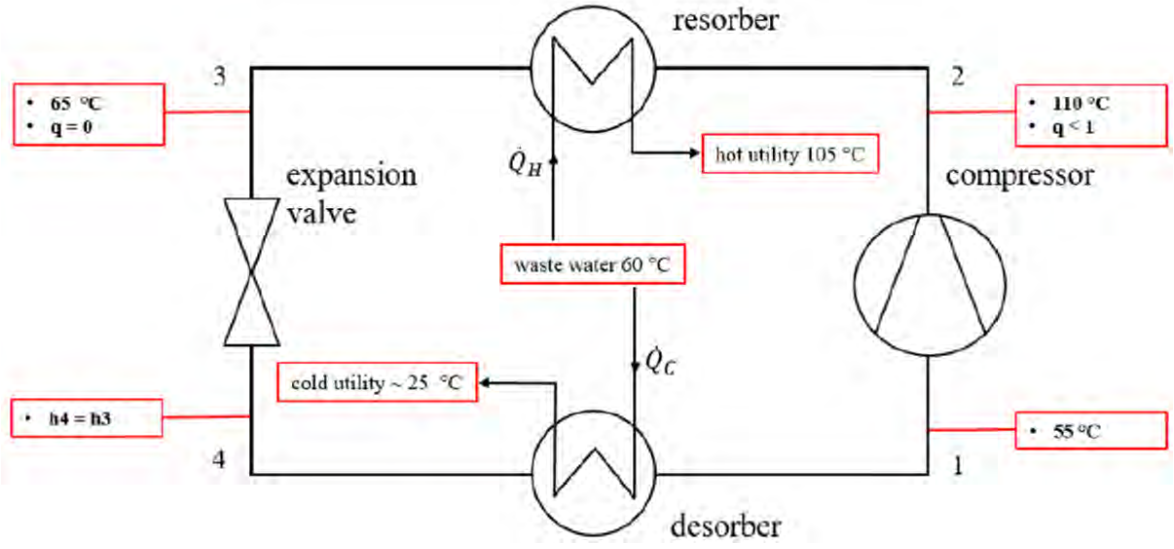

Figure 3: Constraints and fixed values for the application of heating a waste stream from 60 °C to 105 °C.

In Fig. 3 some of the assumptions that are used for the cycle calculations are shown. That is that the minimum temperature approach in the heat exchangers is kept as 5 K and isenthalpic expansion is assumed. An initial isentropic efficiency of 0.7 is used for the first cycle calculation. Then from the operating condition the efficiency is calculated with the compressor model. This is done until the change in efficiency is less than 0.1 % (see Fig. 4). Additionally, no pressure drop is assumed in the heat exchangers. The COP is then calculated as

$$COP = \frac{h_2 - h_3}{h_2 - h_1} \qquad \text{Eq. (4)}$$

Where the state points are the same as in Fig. 3. For calculations with only ammonia water the REFPROP database is used (Lemmon et al., 2013).

The main results for both cases with 0, 5 and 10 wt% CO_2 are listed in tables 4 and 5, respectively. Since the operating conditions differ for each case the specific volume at the compressor inlet also differs. Therefore, with a fixed compressor each case will deliver various amounts of heat which can be calculated as:

$$\dot{Q} = \dot{m}(h_3 - h_2) \qquad \text{Eq. (5)}$$

For both cases a significant increase in the COP is observed as well as an increase in the delivered heat with the addition of CO_2. With 5 wt% CO_2 the COP increase for the first case is approximately 4.4 % and 4.1 % for the second case compared to only operating with ammonia water. When operating with 10 wt% CO_2 the COP increase is 6.77 % and 5.4 %, respectively, for each case. The increase in the delivered heat is even more significant: 8.4 % and 10 % for 5 wt% CO_2, and 17.5 % and 25 % for 10 wt% CO_2. This increase for the same compressor size means that a smaller compressor can be used to deliver the same heat load with the added CO_2 which can bring significant costs reduction.

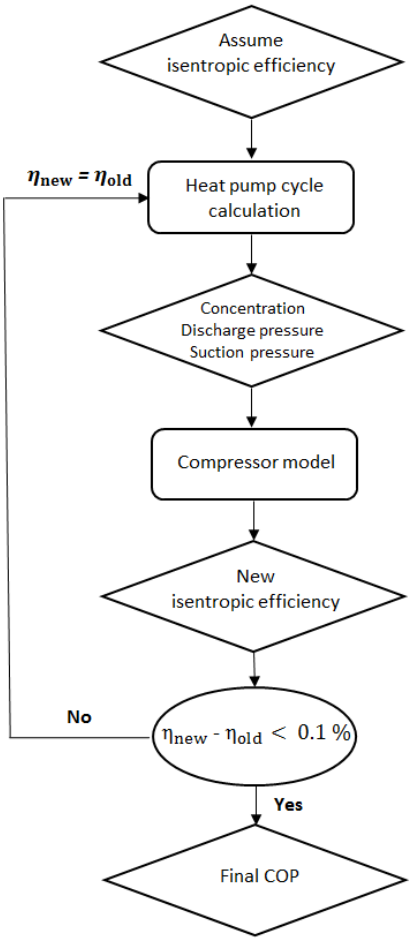

Figure 4: Schematic representation of the iteration process between the cycle calculations and the compressor model.

Table 4. Mixture composition, pressure, heat delivered and COP for the CRHP cycle for heating a waste stream from 60 °C to 105 °C.

Property model	Wt%			P_{low}	P_{high}	$\dot{Q}$ (kW)	COP
	NH_3	H_2O	CO_2				
REFPROP	19.1	80.9	0	0.202	1.76	15.4	5.02
Aspen Plus New fit (Gudjonsdottir et al. 2017)	18.5	76.5	5	0.21	1.83	16.7	5.24
Aspen Plus New fit (Gudjonsdottir et al. 2017)	20.4	69.6	10	0.226	1.95	18.1	5.36

Table 5. Mixture composition, pressure, heat delivered and COP for the CRHP cycle for heating a waste stream from 95 °C to 140 °C.

Property model	Wt%			P_{low}	P_{high}	$\dot{Q}$ (kW)	COP
	NH_3	H_2O	CO_2				
REFPROP	19.1	80.9	0	1.0	5.7	62.7	5.92
Aspen Plus New fit (Gudjonsdottir et al. 2017)	20.9	74.1	5	1.06	6.01	68.9	6.16
Aspen Plus New fit (Gudjonsdottir et al. 2017)	23.3	66.7	10	1.19	6.69	78.4	6.24

4. CONCLUSIONS

The results indicate that a small amount of CO_2 results in an increased isentropic efficiency of the compressor at fixed operating conditions. Additionally, for a compressor of fixed size, adding CO_2 increases the amount of delivered heat. For a heat pump cycle this means that even larger benefits are observed than was previously expected operating an CRHP with NH_3-CO_2-H_2O mixture compared to only ammonia water. The next step is to confirm the compressor performance when operated under wet conditions with experiments.

ACKNOWLEDGEMENTS

This is an ISPT (Institute for Sustainable Process Technology) project.

NOMENCLATURE

h	Specific enthalpy, J kg^{-1}		*Sub- and superscripts*
$\dot{m}$	Mass flow, kg s^{-1}	*C*	Heat source
m	Mass, kg	*H*	Heat sink
p	Pressure, Pa	*high*	Higher pressure level
$\dot{Q}$	Heat transfer rate, W	*in*	Inlet
Q	Heat, J	*is*	Isentropic
q	Vapor quality, kg kg^{-1}	*low*	Lower pressure level
T	Temperature, K	*out*	Outlet
v	Specific volume, m^3 kg^{-1}	*tot*	*Total*
V	Volume, m^3		*Abbreviations*
x	Ammonia concentration, kg kg^{-1}	COP	Coefficient of Performance
	Greek	CRHP	Compression-resorption heat pump
η	Efficiency	IEA	International Energy Agency
φ	Male rotor turning angle		

REFERENCES

Arpagaus, C., Bless, F., Schiffmann, J., Bertsch, S. S., 2016. Multi-temperature heat pumps: A literature review. Int. J. Refrigeration 69, 437–465.

Cao, F., Gao, T., Li, S., Xing, Z., Shu, P., 2011. Experimental analysis of pressure distribution in a twin screw compressor for multiphase duties. Expe. Therm Fluid Sci. 35(1), 219–225.

Chamoun, M., Rulliere, R., Haberschill, P., Peureux, J., 2013. Modelica-based modelling and simulation of a twin screw compressor for heat pump applications. Appl Therm Eng. 58, 479–489.

European Council, 2014. Climate and energy policy framework.

Gudjonsdottir, V., Infante Ferreira, C. A., Rexwinkel, G., Kiss, A. A., 2017. Enhanced performance of wet compression-resorption heat pumps by using NH_3-CO_2-H_2O as working fluid. Energy 124, 531–542.

Gudmundsdottir, K., 2018. Theoretical and experimental investigation of a wet compression process operating with ammonia-water in the application of a CRHP. Master thesis, Delft University of Technology.

IEA. 2014. Application of industrial heat pumps. Technical report: https://www.energiteknologi.dk/sites/energiteknologi.dk/files/slutrapporter/annex_xiii_part_a.pdf

Jianfeng, L., Huagen, W., Bingming, W., Ziwen, X., Pengcheng, S., 2009. Research on the performance of water-injection twin screw compressor. Appl. Therm. Eng., 29(16), 3401–3408.

Lemmon, E. W., Huber, M. L., McLinden, M. O., 2013. NIST Standard Reference Database 23: Reference Fluid Thermodynamic and Transport Properties-REFPROP, Version 9.1, National Institute of Standards and Technology, Standard Reference Data Program, Gaithersburg.

Shi, L., Gudjonsdottir, V., Infante Ferreira, C. A., Rexwinkel, G., Kiss, A. A., 2017. Absorption of CO_2-NH_3-H_2O mixture in mini-channel heat exchangers. Proceedings of the 12th IEA Heat Pump Conference, Rotterdam, the Netherlands, paper 189, pp 1-12.

Tang, Y., 1995.Computer aided design of twin screw compressors. PhD thesis, University of Strathclyde.

Tian, Y., Shen, J., Wang, C., Xing, Z., Wang, X., 2017. Modeling and performance study of a Water-injected Twin-screw Water Vapor Compressor. Int. J. of Refrigeration, 83, 75-87

Zaytsev, D., 2003. Development of wet compressor for application in compression-resorption heat pumps. PhD thesis, Delft University of Technology.

Manuscript ID: 449
DOI: 10.18462/iir.icr.2019.0449

Effect of punching holes on the thermofluids characteristics of wavy fin-and-tube heat exchangers

Ali SADEGHIANJAHROMI[(a)], Chi-Chuan WANG[(b)]

[(a)] Malek-Ashtar University of Technology
Shahin-shahr, P.O. Box 83145/115, Iran, asadeghi63@yahoo.com
[(b)] National Chiao Tung University
EE474, University Rd., Hsinchu 300, Taiwan, ccwang@mail.nctu.edu.tw

ABSTRACT

In this study, improvements upon the airside performance of wavy fin-and-tube heat exchangers are made by punching holes on top of leeward wavy fin surfaces. Detailed parametric studies concerning location, width and length of holes are performed by 3D numerical simulations. It is found that punching holes on top of wavy fin surfaces can result in 7% decrease in thermal resistance while punching holes on top of leeward parts and bottom of windward parts of wavy fins will only increase pumping power without any heat transfer enhancement. Increasing width of holes imposes negligible effect on heat transfer characteristics. Conversely, increasing length of holes is comparatively effective. Punching holes with width of 1 mm and length of 12 mm can result in a decrease in thermal resistance up to 10%.
Keywords: Air, Air-Cooled Exchanger, Corrugated Surface, Fin, Heat Exchanger, Heat Transfer, Heat Transfer Coefficient, Pressure Drop.

1. INTRODUCTION

Air-cooled heat exchangers are widely used in air conditioning systems, refrigeration, power generation, automobiles, process industry, and other applications. In these heat exchangers, air acts as the cold fluid and flows outside the tubes while hot fluid is flowing inside the tubes. Since heat transfer coefficient of air is extremely low, extended surfaces (fins) are usually needed outside the tubes in order to increase airside heat transfer performance. In addition to adding more fin surface, surface morphology can also help to reduce the airside resistance, and wavy fin is one of the most common ways for further augmentation of the airside. The use of wavy fins not only increases heat transfer surface area but also lengthens the flow path and provides effective corrugations for vortical motions and mixing of cooling air, thereby resulting in higher heat transfer performance. Despite the heat transfer of wavy fins are inferior to interrupted surfaces like louver or slit fins, its continuous fin configuration offers reliable operation to resist unfavorable ambient conditions. Yet, it is also superior to the other continuous flat fin geometries. Wavy fins are mostly used in air-conditioning condensers and contain some unique features to resist potential fouling or clogging problems from particulates, freezing moisture, etc. (Shah and Sekulic, 2003).
Many experimental and numerical researches have been performed on wavy fins. Sparrow and Comb (1983) performed the pioneer researches on corrugated wall duct in two fin pitches with the Reynolds numbers ranging from 2000 to 27000. Wang (1999) developed correlation for a specific wavy fin configuration which can describe 93.02% of Colburn factors and 91.8% of friction factors within 10%. The effect of fin pitch and the number of tube rows on the airside performance of herringbone wavy fin-and-tube heat exchangers were reported by Wongwises and Chokeman (2005). Dong et al. (2007) developed correlations for heat transfer and pressure drop of the wavy finned tube heat exchangers (flat tube) with the Reynolds numbers ranging from 800 to 6500. Cheng et al. (2007) carried out 3D periodically developed flow in the triangular wavy fin-and-tube heat exchanger. Tian et al. (2009) performed a numerical study on the air-side performance of wavy fin-and-tube heat

exchanger having punched delta winglets in association with staggered or in-line arrangements. Gong et al. (2013) investigated the air-side performance of wavy fin-and-tube heat exchanger punched with combined rectangular winglet pairs (CRWPs). Du et al. (2013) performed experimental and numerical study on heat transfer enhancement of wavy fin-and-flat tube heat exchangers with longitudinal vortex generators (six delta winglet pairs). Bhuiyan et al. (2015) investigated geometrical parameters such as fin pitch, wavy angle and longitudinal and transversal tube pitches for wavy fin-and-tube heat exchangers in turbulent flow regime. Lotfi et al. (2016) performed a 3D numerical investigation on the airside performance of the smooth wavy fin-and-tube heat exchangers having elliptical tube configuration by utilizing some new type vortex generators. Darvish Damavandi et al. (2017) performed multi-objective optimization of a wavy-fin-and-elliptical-tube heat exchanger using GMDH type Artificial Neural Network and NSGA-II optimization algorithm. The frosting process on wavy fin-and-tube heat exchanger surfaces is numerically simulated by Ma et al. (2017). Zhang et al. (2017) improved heat transfer characteristics for a heat exchanger (duct) by using a new humped wavy fin. Three fin configurations including plain, wavy, and rectangular grooved fins attached to three by three arrays of flat tube banks were examined by Moorthy et al. (2018). Xue et al. (2018) proposed three kinds of wavy plate fins, namely perforated wavy fin, staggered wavy fin and discontinuous wavy fin. Li et al. (2018) conducted a comparative study of fin-and-tube heat exchangers having wavy fin and a plain fin with radiantly arranged winglets.

As clearly seen in literature review, most of the studies were associated with performing parametric studies or developing correlations for wavy fin geometry, but very few researches have concerned with further improvements of wavy fins except punching vortex generators. Hence, it is the objective of this study to propose the novel design of punching holes on peak of wavy fin-and-tube heat exchanger and it will be shown subsequently that considerable improvements can be achieved subject to the same pumping power constraints.

2. NUMERICAL ANALYSIS

Physical model and computational domain of the simulated wavy fin-and-tube heat exchanger are illustrated in Fig. 1(a) and Fig. 1(b), respectively. Basic parameters of the simulated geometries for two cases of validation and reference wavy fin for improvement study are tabulated in Table 1. The computational domain is extended to 10 times distance of the fin pitch at the inlet and is 30 times distance of the fin pitch at the outlet to ensure uniform velocity and to avoid the influence of recirculation, respectively.

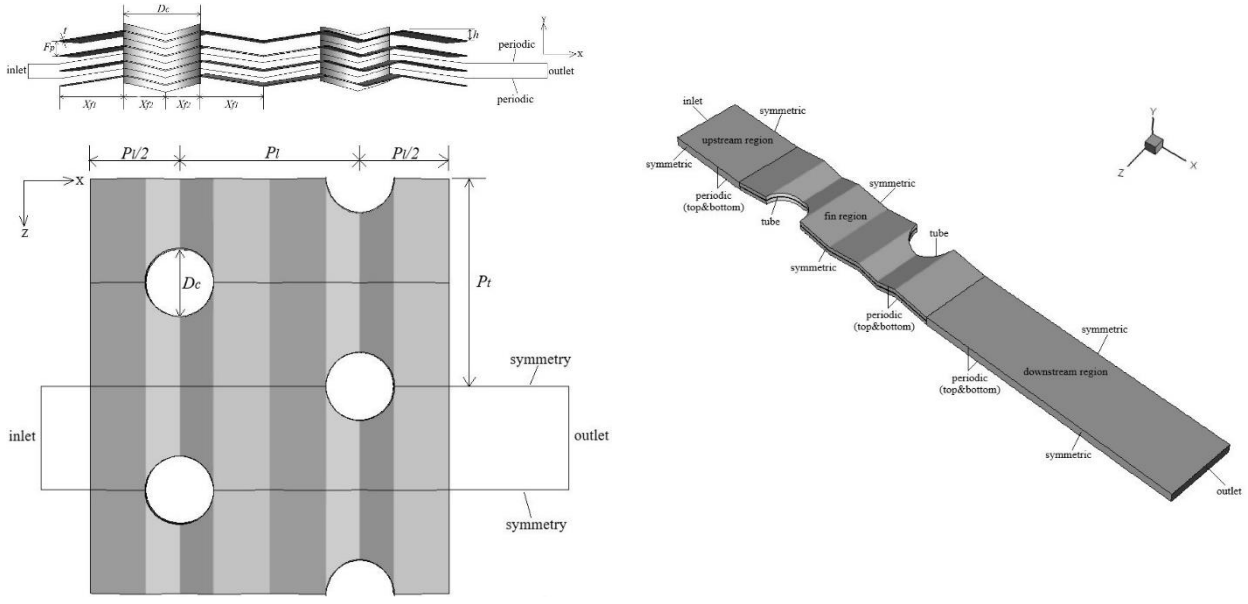

(a) Physical model and geometrical parameters (b) Computational domain

Figure 1: Physical model, geometrical parameters and computational domain of simulated wavy fin

Table 1. Geometrical parameters of simulated wavy fins

Parameters	Values for validation	Values for reference wavy fin
Tube collar outside diameter (D_c) (mm)	10.38	7.2
Number of tube rows (N)	1	2
Fin thickness (t) (mm)	0.12	0.105
Fin pitch (F_p) (mm)	1.62	1.4
Longitudinal tube pitch (P_l) (mm)	19.05	19.05
Transversal tube pitch (P_t) (mm)	25.4	22
Waffle height (h) (mm)	1.18	0.95
Projected wavy length (1st part) (X_{f1}) (mm)	4.7625	5.975
Projected wavy length (2nd part) (X_{f2}) (mm)	4.7625	3.55

2.1. Governing Equations and Boundary Conditions

The flow is assumed to be three dimensional, incompressible, steady and turbulent. Natural convection and radiation are ignored. Working fluid is air with constant properties and tube walls have constant temperatures.

Governing equations include continuity equation, momentum (RANS) equation, and energy equation (Sadeghianjahromi et al., 2018). RNG k-ε is selected for turbulence model (Gong et al., 2013). Detail description of RNG theory has been presented by Orszag et al. (1993). Enhanced wall function is used near the wall zones ($Y^+ < 5$).

Computational domain with boundary conditions is illustrated in Fig. 1(b). Air enters the computational domain with uniform velocities u_{in} ranging from 0.5 to 4 $m \cdot s^{-1}$ at a constant inlet temperature of T_{in} = 308 K. The pressure is atmospheric pressure at the air outlet. Side boundaries are symmetric planes on which normal gradients are zero. For solid surfaces, coupled ($T_{solid} = T_{fluid}$) and non-slip condition are assigned. Constant tube temperature of T_s = 318 K and non-slip condition are imposed on the tube surfaces. Periodic boundary conditions are assumed for top and bottom planes. Symmetric and periodic boundary conditions are applied to the side boundaries and top and bottom boundaries of upstream and downstream extended regions, respectively.

2.2. Numerical Method

Discretization of the governing equations is done by finite volume method. Fluent software is used for solving equations and boundary conditions. SIMPLE algorithm is applied for pressure and momentum coupling and second order upwind is used in order to achieve a higher calculation accuracy. The coupled equations are solved until values of residuals for continuity, velocities, kinetic energy and dissipation rate are less than 10^{-6} and residual for energy is less than 10^{-8} which are considered as the convergence criteria. Unstructured fine grids are applied for the fin region and structured coarse grids are used for upstream and downstream extended regions. Grid study is performed in the maximum air inlet velocity and 1373000 cells is selected for balancing accuracy and simulation time. Also, for keeping $Y^+<5$, some adoptions for cells near wall surfaces are made.

2.3. Definition of Parameters

Pumping power (P_p) is calculated as follows.

$$P_p = \frac{\dot{m}}{\rho}(\Delta P) \qquad \text{Eq. (1)}$$

Thermal resistance (R_{th}) can also be obtained from the following formula.

$$R_{th} = \frac{1}{\eta_o h_o A_o} = \frac{LMTD}{\dot{Q}} \qquad \text{Eq. (2)}$$

LMTD is air log-mean temperature difference which can be determined from the following formula.

$$LMTD = \frac{(T_s - T_{in}) - (T_s - T_{out})}{\ln\left[(T_s - T_{in})/(T_s - T_{out})\right]} \qquad \text{Eq. (3)}$$

3. VALIDATION OF NUMERICAL SIMULATIONS

Validation of numerical simulations is carried out by comparison with the experimental data of a 1-row wavy fin-and-tube heat exchanger from Wang et al. (1999). Geometrical parameters for validation are tabulated in Table 1. The air inlet temperature is 291 K and air inlet velocity is changed from 0.5 m·s^{-1} to 4.6 m·s^{-1}. Fig. 2 illustrates the calculated thermal resistance vs. pumping power for comparison between numerical simulations and experimental results. Mean deviations for thermal resistance vs. pumping power is 12%. The results substantiate the applicability of the present numerical simulation.

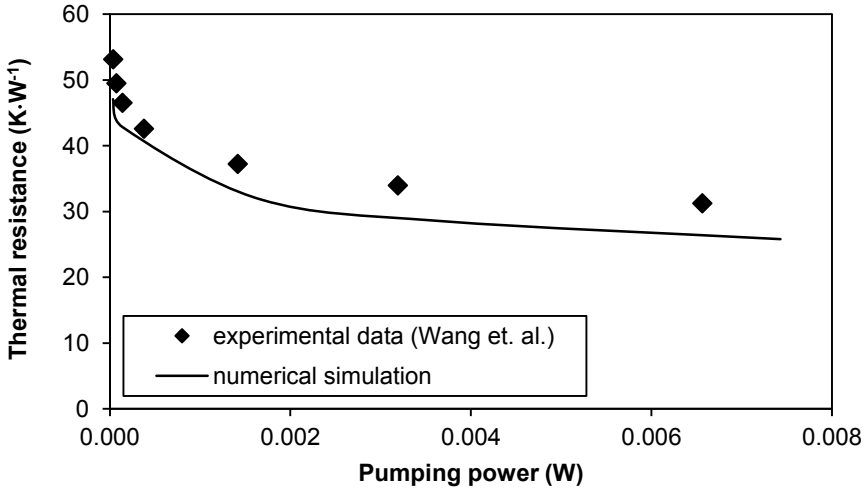

Figure 2: Thermal resistance vs. pumping power for comparison of numerical simulation with experimental data from Wang et al. (1999)

4. PUNCHING HOLES ON WAVY FINS

Fig. 3(a) shows velocity vectors in the convex part of the reference wavy fin at an air inlet velocity of 2 m·s^{-1}. It is obvious that the airflow sustains a very low velocity under the convex part of wavy fin due to flow redirection. This phenomenon will result in a lower heat transfer rate and a higher pressure drop. Hence, it would be beneficial to punch some holes on the crest (top) and valley (bottom) to eliminate the re-circulation region. As illustrated in Fig. 3(b), with the presence of hole on top, flow is directed through the hole. This not only eliminates the re-circulation area but also provides some extra mixing between adjacent wavy channels. As a consequence, considerable enhancement can be achieved.

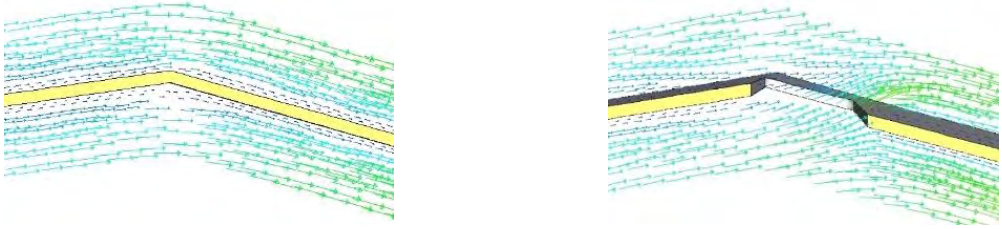

(a) Wavy fin without holes (b) Wavy fin with holes on top

Figure 3: Velocity vectors in wavy fins with and without holes on top part

The punched holes with W = 1 mm and L = 8 mm are made on top of the leeward wavy fins and bottom of the windward wavy fins as shown in Fig. 4. W and L are width and length of holes,

respectively. Air inlet velocity is changed from 0.5 m·s^{-1} to 4 m·s^{-1} and other parameters remain unchanged as specified in Table 1. Two cases are examined about the influence of punching holes, including holes on the top and holes on both top and bottom.

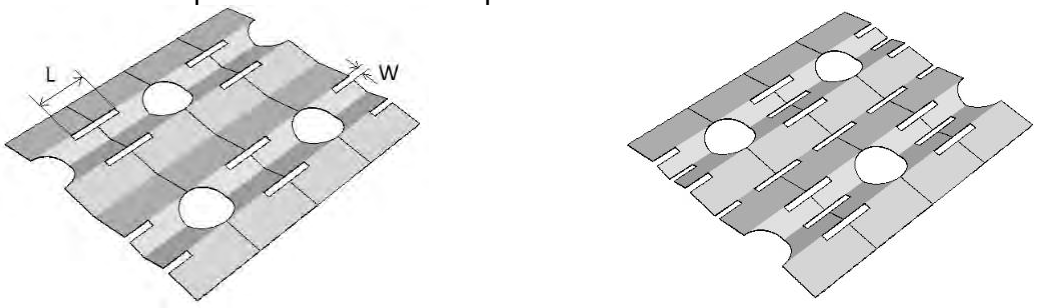

(a) Holes on top of wavy fins (b) Holes on top and bottom of wavy fins

Figure 4: Schematics of the punching holes on the wavy fin-and-tube heat exchangers

Fig. 5 shows thermal resistance vs. pumping power for these two cases and their comparisons with the referenced wavy fin. There is no considerable difference between punching the holes on top and both top and bottom. This is somewhat expected for hole on the top side locates at the leeward side of the fin while it is the windward side of the flip side. Hence, making holes only on top of wavy fins may be more preferable to maintain the rigidness of the wavy fin. By adding the punching holes on the top of the wavy fins, thermal resistances will decrease 7% and 6% subject to pumping powers of 0.001 W and 0.005 W, respectively.

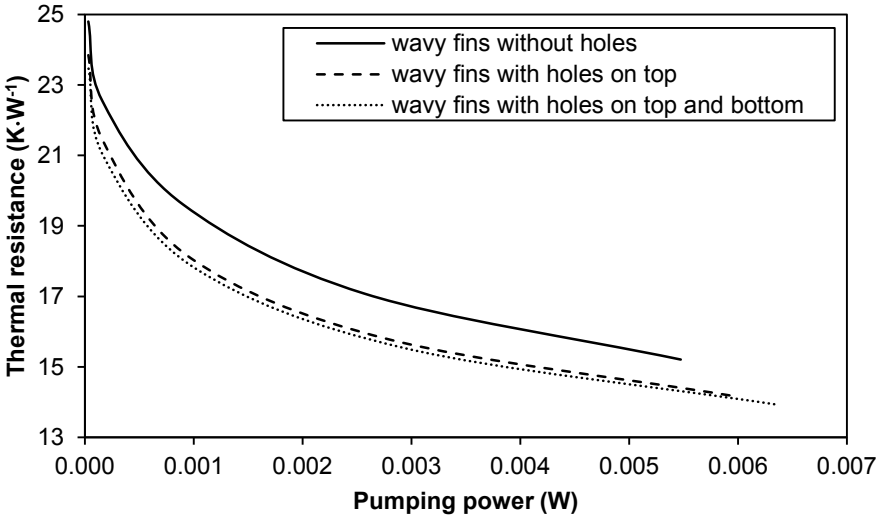

Figure 5: Thermal resistance vs. pumping power for wavy fin-and-tube heat exchangers with and without holes (*W* = 1 mm, *L* = 8 mm)

The effects of length (*L*) and width (*W*) of holes on top of wavy fins are further studied. Firstly, the length of holes is fixed at 8 mm and the width is changing from 0.5 mm to 2 mm. The simulations are then followed by fixing a hole width of 1 mm while changing the length from 4 mm to 12 mm. Analogously, the rest of geometrical parameters remain the same as Table 1 and air inlet velocity is changed from 0.5 m·s^{-1} to 4 m·s^{-1}. Thermal resistance vs. pumping power curves for different widths and lengths of holes are shown in Fig. 6. It can be seen from Fig. 6(a) that changing width of holes has no significant effect on the thermal resistance. The hole having a width of 1 mm imposes marginal improvement. This is because the re-circulation is already eliminated and no further mixing of airflow is observed. On the other hand, a larger length of hole depicts a smaller thermal resistance subject to the same pumping power as shown in Fig. 6(b). This is associated with effective removal of span-wise re-circulation.

Detailed improvements about the reduction of thermal resistances for different hole lengths (*W* = 1 mm) for pumping powers 0.001 W and 0.005 W are tabulated in Table 2. Based on the tabulated results, the holes with *W* = 1 mm and *L* = 12 mm show the most superior improvements (10%) at

pumping power of 0.001 W.

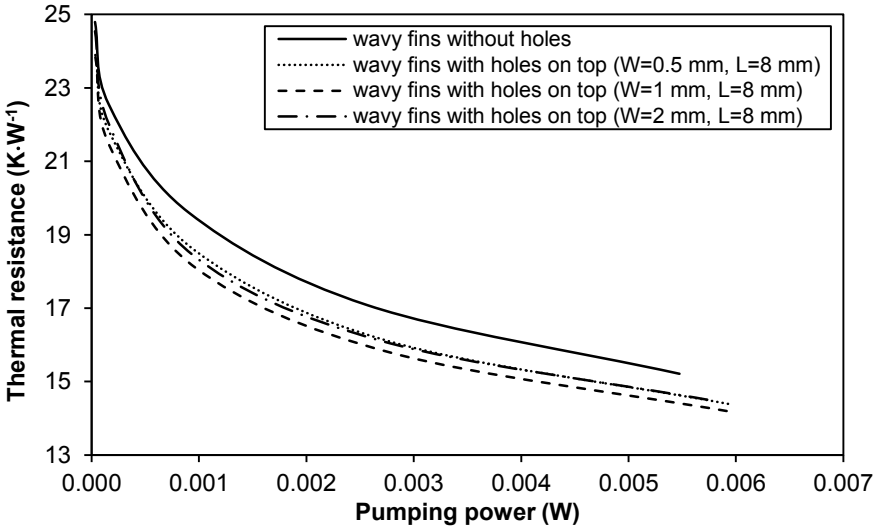

(a) Effect of width of holes on the thermal resistance (L = 8 mm)

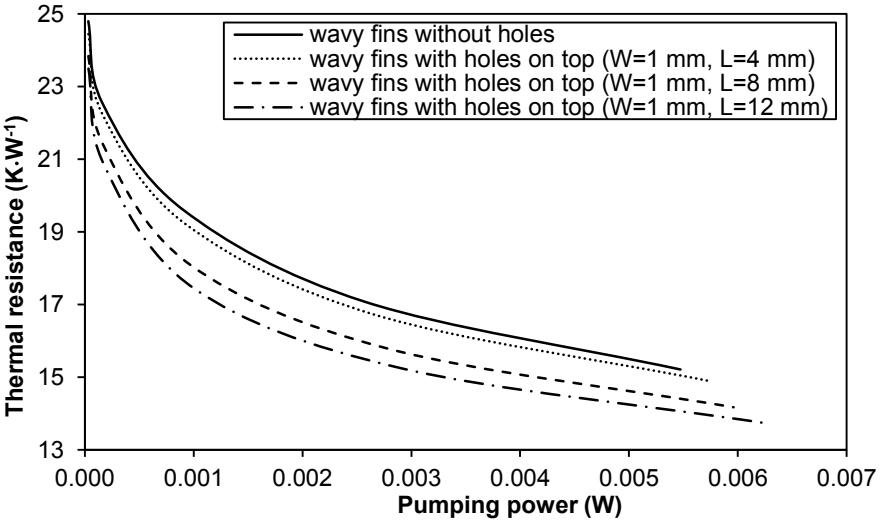

(b) Effect of length of holes on the thermal resistance (W = 1 mm)

Figure 6: Thermal resistance vs. pumping power for different widths and lengths of holes on top of wavy fin-and-tube heat exchangers

Table 2. Reduction values of thermal resistances for different sizes of holes

Hole length	Reduction in R_{th} for P_p = 0.001 W	Reduction in R_{th} for P_p = 0.005 W
L = 4 mm	2%	1%
L = 8 mm	7%	6%
L = 12 mm	10%	8%

Contours of air temperatures in the middle of fin pitch for wavy fins with and without holes on top (W = 1 mm and L = 12 mm) at an inlet velocity of 2 m·s^{-1} are shown in Fig. 7. It can be seen that the air temperatures increase substantially for the wavy fins with holes on top, indicating a comparatively better mixing of airflow. In fact, a notable portion of airflow flowing between the tubes of the wavy fins with holes on top (Fig. 7(b)) has a much higher temperature than the reference case (Fig. 7(a)).

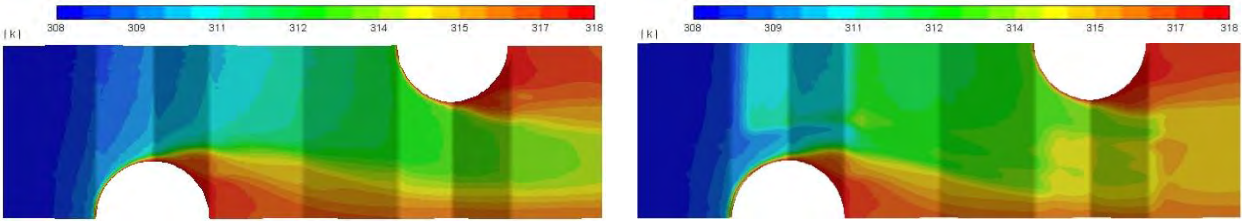

(a) Wavy fins without holes on top (b) Wavy fins with holes on top

Figure 7: Air temperature contours in the middle of fin pitch at an air inlet velocity of 2 m·s^{-1} for comparison between wavy fins with and without holes on top (*W* = 1 mm, *L* = 12 mm)

5. CONCLUSIONS

The present study conducts a numerical examination upon improvements of the airside performance for wavy fin-and-tube heat exchangers. The nominal tube diameter is 7.2 mm while the longitudinal and transversal tube pitches are 19.05 mm and 22 mm, respectively. The corresponding waffle height is 0.95 mm. The model is first validated with experimental data from literature. Subsequently, the improvements are made by punching holes on top of leeward wavy fin surfaces. The effects of holes on wavy fins on thermal resistance of wavy fin-and-tube heat exchangers are investigated by performing 3D turbulent flow numerical simulations. Punching holes on top of leeward parts can improve heat transfer characteristics of wavy fins. Holes with width of 1 mm and length of 8 mm can decrease thermal resistance 7% to 6% for pumping powers of 0.001 W and 0.005 W, respectively. Punching holes on top of leeward and bottom of windward parts of wavy fins has no improvement in comparison with just punching holes on top of leeward parts of wavy fins. Increasing the width of holes imposes negligible effect on heat transfer characteristics. Conversely, increasing length of holes will be much more effective. It is found that holes with a width of 1 mm and a length of 12 mm can decrease thermal resistance by 10% and 8% for pumping powers of 0.001 W and 0.005 W, respectively.

ACKNOWLEDGEMENTS

The authors would like to thank for the support from the Ministry of Science and Technology of Taiwan, under contract 107-2622-E-009-002-CC2 and 107-2221-E-009-142.

NOMENCLATURE

A_o	total surface area (m^2)	D_c	tube collar outside diameter (m)
F_p	fin pitch (m)	h	waffle height (m)
h_o	heat transfer coefficient of air (W·m^{-2}·K^{-1})	k	turbulent kinetic energy (J·kg^{-1})
L	length of hole on top of wavy fin (m)	$LMTD$	air log-mean temperature difference (K)
$\dot{m}$	air mass flow rate (kg·s^{-1})	N	number of tube rows
P_l	longitudinal tube pitch (m)	P_p	pumping power (W)
P_t	transversal tube pitch (m)	$\dot{Q}$	total heat transfer rate to the fluid (W)
R_{th}	thermal resistance (K·W^{-1})	T_s	surface temperature (K)
T_{in}	inlet temperature (K)	T_{out}	outlet temperature (K)
t	fin thickness (m)	u	velocity (m·s^{-1})
W	width of hole on top of wavy fin (m)	X_{f1}	projected wavy length (1st part) (m)
X_{f2}	projected wavy length (2nd part) (m)	Y^+	Y plus
α	wavy angle (°)	ΔP	pressure drop (Pa)
ε	dissipation rate (m^2·s^{-3})	η_o	surface efficiency
ρ	density (kg·m^{-3})		

REFERENCES

Bhuiyan, A. A., Amin, M. R., Naser, J.,Islam, A., 2015. Effects of geometric parameters for wavy finned-tube heat exchanger in turbulent flow: a CFD modeling. Frontiers in Heat and Mass Transfer (FHMT), 6, (1).

Cheng, Y., Lee, T.,Low, H., 2007. Numerical analysis of periodically developed fluid flow and heat transfer characteristics in the triangular wavy fin-and-tube heat exchanger based on field synergy principle. Numerical Heat Transfer, Part A: Applications, 53, (8), 821-842.

Darvish Damavandi, M., Forouzanmehr, M.,Safikhani, H., 2017. Modeling and Pareto based multi-objective optimization of wavy fin-and-elliptical tube heat exchangers using CFD and NSGA-II algorithm. Applied Thermal Engineering, 111, 325-339.

Dong, J., Chen, J., Chen, Z., Zhang, W.,Zhou, Y., 2007. Heat transfer and pressure drop correlations for the multi-louvered fin compact heat exchangers. Energy Conversion and Management, 48, (5), 1506-1515.

Du, X., Feng, L., Yang, Y.,Yang, L., 2013. Experimental study on heat transfer enhancement of wavy finned flat tube with longitudinal vortex generators. Applied Thermal Engineering, 50, (1), 55-62.

Gong, J., Min, C., Qi, C., Wang, E.,Tian, L., 2013. Numerical simulation of flow and heat transfer characteristics in wavy fin-and-tube heat exchanger with combined longitudinal vortex generators. International Communications in Heat and Mass Transfer, 43, 53-56.

Li, M. J., Zhang, H., Zhang, J., Mu, Y. T., Tian, E., Dan, D., Zhang, X. D.,Tao, W. Q., 2018. Experimental and numerical study and comparison of performance for wavy fin and a plain fin with radiantly arranged winglets around each tube in fin-and-tube heat exchangers. Applied Thermal Engineering, 133, 298-307.

Lotfi, B., Sundén, B.,Wang, Q., 2016. An investigation of the thermo-hydraulic performance of the smooth wavy fin-and-elliptical tube heat exchangers utilizing new type vortex generators. Applied Energy, 162, 1282-1302.

Ma, Q., Wu, X., Chu, F.,Zhu, B., 2017. Numerical simulation of frosting on wavy fin-and-tube heat exchanger surfaces. Journal of Physics: Conference Series, IOP Publishing, 012052.

Moorthy, P., Oumer, A.,Ishak, M., 2018. Experimental investigation on effect of fin shape on the thermal-hydraulic performance of compact fin-and-tube heat exchangers. IOP Conference Series: Materials Science and Engineering, IOP Publishing, 012070.

Orszag, S. A., Yakhot, V., Flannery, W. S., Boysan, F., Choudhury, D., Maruzewski, J.,Patel, B., 1993. Renormalization group modeling and turbulence simulations. International Conference on Near-Wall Turbulent Flows.

Sadeghianjahromi, A., Kheradmand, S.,Nemati, H., 2018. Developed correlations for heat transfer and flow friction characteristics of louvered finned tube heat exchangers. International Journal of Thermal Sciences, 129, 135-144.

Shah, R. K.,Sekulic, D. P., 2003. Fundamentals of heat exchanger design. John Wiley & Sons.

Sparrow, E. M.,Comb, J. W., 1983. Effect of interwall spacing and fluid flow inlet conditions on a corrugated-wall heat exchanger. International Journal of Heat and Mass Transfer, 26, (7), 993-1005.

Tian, L., He, Y., Tao, Y.,Tao, W., 2009. A comparative study on the air-side performance of wavy fin-and-tube heat exchanger with punched delta winglets in staggered and in-line arrangements. International Journal of Thermal Sciences, 48, (9), 1765-1776.

Wang, C. C., 1999. Investigation of wavy fin-and-tube heat exchangers: a contribution to databank. Experimental Heat Transfer, 12, (1), 73-89.

Wang, C. C., Jang, J. Y.,Chiou, N. F., 1999. A heat transfer and friction correlation for wavy fin-and-tube heat exchangers. International Journal of Heat and Mass Transfer, 42, (10), 1919-1924.

Wongwises, S.,Chokeman, Y., 2005. Effect of fin pitch and number of tube rows on the air side performance of herringbone wavy fin and tube heat exchangers. Energy Conversion and Management, 46, (13), 2216-2231.

Xue, Y., Ge, Z., Du, X.,Yang, L., 2018. On the heat transfer enhancement of plate fin heat exchanger. Energies, 11, (6), 1-18.

Zhang, X., Wang, Y., Li, M., Wang, S.,Li, X., 2017. Improved flow and heat transfer characteristics for heat exchanger by using a new humped wavy fin. Applied Thermal Engineering, 124, 510-520.

Manuscript ID: 459
DOI: 10.18462/iir.icr.2019.0459

A detailed dynamic modeling of the split air conditioner

Yang Y.[a], Ren C.Q.[a.*], Yu L.[a], Wan Y.D.[a], Wang Z.[a]

[a] State Key Laboratory of Advanced Design and Manufacturing for Vehicle Body, College of Mechanical and Vehicle Engineering, Hunan University, Changsha 410082, China
renchengqin@163.com

ABSTRACT

For the distributed parameter model for vapor compression cycle systems (VCCs), there are several assumptions compromising the simulation accuracy. Such as the refrigerant-side pressure drop is neglected, the accumulator, connecting pipe and compressor lubricant are not considered sometimes and so on. In this paper, a detailed dynamic model of split-type air conditioner was developed based on SIMULINK. This system model contains multiple sub-models including the evaporator, the condenser, the compressor, the electronic expansion valve, the accumulator, and the pipe. The evaporator and condenser were modeled using the distributed-parameter method with the estimated refrigerant-side pressure drop. The accumulator with lubricant and connecting pipe adopted the single-node lumped parameter model. Thereafter, the model was verified via experimental data. The results showed that the system dynamic was captured accurately.
Keywords: vapor compression cycle, split-type air conditioner, distributed parameter model, simulation accuracy.

1. INTRODUCTION

The vapor compression cycle systems are the well-known form for the HVAC-R system, and its model study plays an important role in the reduction of energy consumption. The mathematical model of VCCs can be mainly divided into single-node model (Qi and Deng, 2008; Qi and Deng, 2009; Yang and Ordonez, 2018), moving-boundary(MB) model (Li and Alleyne, 2010; Cecchinato and Mancini, 2012; Bonilla et al., 2015; Qiao et al., 2016; Shang et al., 2016) and distributed parameter model (Macarthur and Grald, 1989; DembaNdiaye and MichelBernier, 2010; Koury et al., 2013; Zhang et al., 2014, Bastos et al., 2018). Although the MB model has the characteristics of fast simulation speed and acceptable accuracy, the advantages of the distributed parameter model are equally significant due to its high flexibility since it is extremely suitable for heat exchangers with different physical structures (Pangborn et al., 2015). In order to describe in detail the dynamic behavior and distribution of internal parameters for two-phase heat exchangers.The distributed parameter model of the heat exchanger is an extremely suitable choice. Several assumptions can be summarized from the above-mentioned work. They involved: (1) the pressure drop in heat exchange coils is neglected frequently; (2) the accumulator and connecting pipe are not considered sometimes, and (3) the impact of compressor lubricants on system simulation is always neglected. For the assumption (1), Zhang et al. (2009) found that the results with transient and steady-state momentum equation are pretty close in the dynamic simulation of both component level and system level. In addition, for controller design, it is appropriate for the model to not consider the pressure

drop. However, the related comparison work about the other assumptions is rare. Therefore, in order to better understand the influence of these assumptions on the system, and to develop a simulation model with higher accuracy, it is necessary to carry out the comparison work of the model under different assumptions. In this paper, a detailed dynamic model was established for the most common split-type air conditioners using finite volume method. Thereafter, the model was verified via experimental data. Finally, the comparative study of the system with different assumptions was carried out.

2. MATHEMATICAL MODEL

The VCCs consists of 10 components. The refrigerant vapor flows from the compressor and goes through the pipe 2, the condenser, the pipe 3, the electronic expansion valve (EEV), the pipe 4, the evaporator, the pipe 0, the accumulator and pipe 1 in turn. Finally, the refrigerant returns back to the compressor and proceeds to the next cycle.

In this paper, one-dimensional (1-D) distributed parameter model is used for the heat exchangers (Macarthur and Grald,1989). The detailed heat exchanger models are involved some key correlations: heat transfer of single-phase refrigerant (Dittus and Boelter,1985), heat transfer of refrigerant boiling flow (Gungor and Winterton, 1987), heat transfer of refrigerant condensation flow (Shah, 1979), void fraction (Chisholm, 1973; Xu and Fang, 2013), pressure drop of refrigerant side (Fang et al., 2012) and heat transfer and pressure drop of air side (Wang and Chi, 2000; Wang et al., 2000). A semi-empirical model of the compressor and EEV are established by the literatures (Yang et al., 2006) and (Li, 2013) respectively.

A single-node lumped parameter dynamic model of the accumulator is established. Before the analysis of the mass and energy conservation of the accumulator, some assumptions need to be made: (1) the pressure drop caused by the accumulator is ignored(Macarthur and Grald, 1989); (2) the mass of the lubricant in accumulator is not changed ($\frac{dM_{oil}}{dt} = 0$); (3) the volume of refrigerant vapor in accumulator is constant. The differential equation of conservation of accumulator's mass and energy is as follows:

$$\frac{dM_{acc}}{dt} = m_{acc.in} - m_{acc.out} \quad \text{Eq. (1)}$$

$$\frac{dH_{acc}}{dt} = m_{acc.in}h_{acc.in} - m_{acc.out}h_{acc.out} + Q_{acc} \quad \text{Eq. (2)}$$

In accumulator, due to the influence of lubricating oil on the physical properties for liquid refrigerant, the solubility equation of R410A/POE-VG68 mixture needs to be introduced.

$$r = \frac{M_{acc.f}}{M_{acc.f} + M_{acc.oil}} \quad \text{Eq. (3)}$$

$$P_{acc} = S_o P_{set}(T_{acc}) \quad \text{Eq. (4)}$$

Where, the coefficient S_o is a function of temperature (T_{acc}) and the ratio of liquid-phase refrigerant mass (r), unchanging approximately over the temperature range of 10-40°C. The S_o is evaluated via the experimental data (Wei et al., 2007) under a specific temperature (30°C). The parameter $P_{set}(T_{acc})$ means saturated pressure of pure refrigerant under the changed accumulator temperature T_{acc}.

In order to describe the refrigerant mass distribution characteristics of the refrigeration system comprehensively, a lumped-parameter model is used for the connected pipes. The differential equation for the mass and energy conservation of pipes can be expressed as follows:

$$\frac{dM_{pipe}}{dt} = m_{pipe.in} - m_{pipe.out} \quad \text{Eq. (5)}$$

$$\frac{dM_{pipe}h_{pipe}}{dt} = m_{pipe.in}h_{pipe.in} - m_{pipe.out}h_{pipe.out} + Q_{pipe} \quad \text{Eq. (6)}$$

3. SOLUTION PROCEDURES

A variable time step is adopted here calculated by the following equation.

$$\Delta t = \Delta\tau(0.05 \times j_{time} + 1), \Delta t \in [0.1,1] \quad \text{Eq. (7)}$$

Where, fixed time step $\Delta\tau = 0.1s$, the number for time-level iterations j_{time}.

Fig. 1(a) shows the iterative solution procedures of system-level. The iterated parameters $X_{iter.sys}$ in Fig. 1(a) are the input of compressor and EEV model. In addition, the mass flow of compressor is used as a criterion for time-level iterative convergence and its accuracy requirement is set to 0.00001 kg/s. Fig. 1(b) shows the information flow diagram of the low-pressure-side solution algorithm taken as an example for illustration. The absolute difference between the mass flow rates for pipe1's outlet and compressor ($|m_{com} - m_{pipe1.out}|$) as the criterion for the convergence, and its accuracy requirement is set to 0.00001 kg/s as well. It is noteworthy that the pressure drop is estimated using the state of the previous moment ${X_{LowP}}^{n}$.

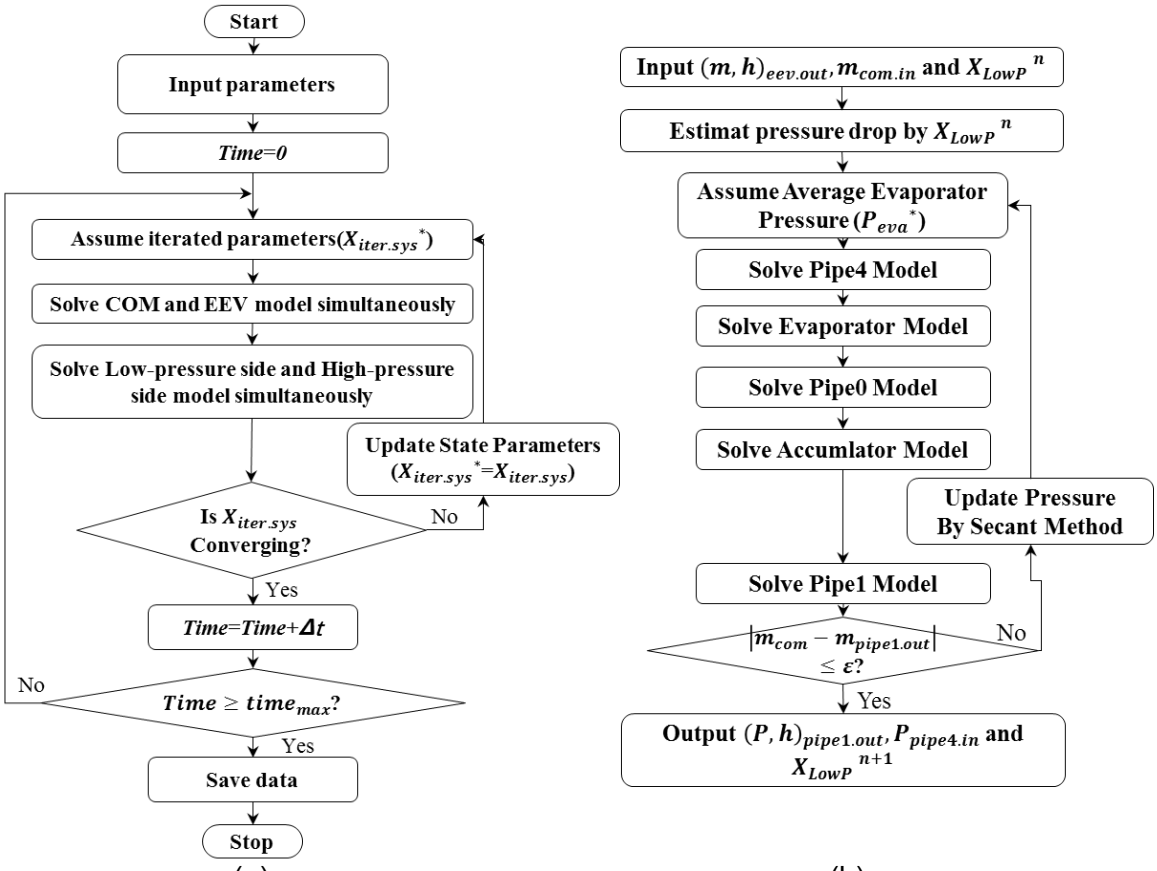

Figure. 1: Information flow diagram of solution algorithm
(a) time-level model. (b) low-pressure-side model

4. VERIFICATIONS AND DISCUSSIONS

Table 1 lists the structural parameters and operating parameters of the main components of the

system, and the basic structural parameters of the heat exchanger are based on the literature (Kim and Bullard, 2001),the detailed structural parameters are listed in Table 2. In addition, the dry and wet bulb temperatures for the indoor and outdoor are 27/19.5℃ and 35/24℃, respectively. For the initial condition for the system, the refrigerant state in the evaporator and condenser are two-phase and superheated respectively. The initial pressure of the system is the saturation pressure for the refrigerant in evaporator.

Table 1.Structural and operating parameters for the main components

Items	Specification	Value of operating parameters
Evaporator	Φ7.0mm,2-row 12tubes	Frontal velocity f_{eva} =1.2m×s^{-1}
Condenser	Φ9.52mm,1-row 28tubes	Frontal velocity f_{con} =2.5 m×s^{-1}
Compressor	Piston type, d_{com} =24mm, L_{com} =80mm	Speed N =1700 r×min^{-1}
Expansion valve	EEV,F_{eev} = 2.3mm^2	Opening degree A_{eev} =54.6%

Table 2. Specifications of the components for simulation

Components	Structural parameters	
Piston type compressor	Cylinder diameter 24mm	Compressed stroke 80mm
EEV	Full open flow area 2.3mm^2	
Evaporator	Length 17m	Inside/Outside tube diameter 7/7.7mm
	Row 2	Flow trip 3
	Transverse tube pitch 12.7mm	Longitudinal tube pitch 16mm
	Fin pitch 1.3mm	Fin thickness 0.105mm
Condenser	Length 19.5m	Inside/Outside tube diameter 9.52/10.22mm
	Row 1	Flow trip 3
	Transverse tube pitch 15mm	Longitudinal tube pitch 21mm
	Fin pitch 1.3mm	Fin thickness 0.105mm
Accumulator	Volume 1000cm^3	
Pipe	Inside/Outside tube diameter 10/11mm	Pipe0 length 3m
	Pipe1 length 0.4m	Pipe2 length 0.4m
	Pipe3 length 0.4m	Pipe4 length 3m

Table 3. Several cases of the air conditioner model with different assumptions

Case number	Contents
Case 1	Complete system model
Case 2	Model without lubricating oil in accumulator
Case 3	Model without lubricating oil in accumulator and pipes
Case 4	Model without lubricating oil in accumulator, pipes and accumulator

In order to simulate the start-up process of the air conditioner accurately and stably, a zero-order delay model (Ding, 2006) of the compressor is used here. Four cases of the air conditioner model with different assumptions listed in the Table 3 are represented on the same diagram against time. They simulation results are shown in Fig 2. Fig. 2(a) illustrates the comparison of the results of four cases and experimental data. The pressure dynamic behavior for case 4 has the largest discrepancy at 60s, so that the accumulator model is indispensable for the system model. The behavior of case 1, 2 and 3 are relatively close. However, when the refrigerant in accumulator is superheated, the

dynamic curves of case 2 and case 3 are not smooth enough. The reasons are that the single-node assumption for the accumulator and the calculation error for the physical property parameters under the varying refrigerant phase. Owing to lubricating oil in accumulator for case 1, the liquid-phase refrigerant in the accumulator does not fully evaporate. Therefore, the pressure curve is smooth continuously, being closest to the experimental data. The temperature responses of the condenser outlet for case 4 are displayed in Fig. 2(b) changing drastically during the first 10 s in the start-up process due to the rapid rise for the condensing pressure. In addition, the evaporator inlet temperature of case 3 varies greatly, reaching 310K, but only 302K in case 2 since the connecting pipes between the evaporator and condenser have the buffering effect on the change of the evaporator inlet temperature. The steady-state discrepancy between the refrigerant temperature and the test data of tube wall is within 3K, mainly due to the existence of heat transfer temperature difference.

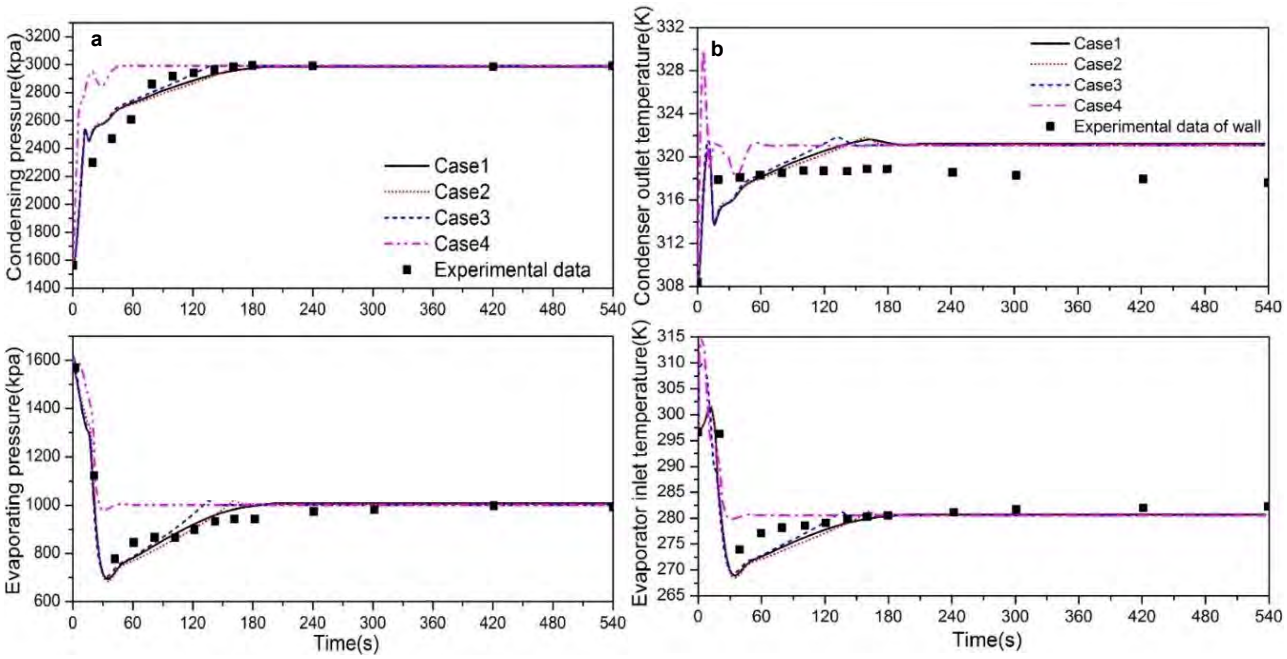

Figure.2: Validation of performance parameter at start-up

(a) Pressures. (b) Temperatures

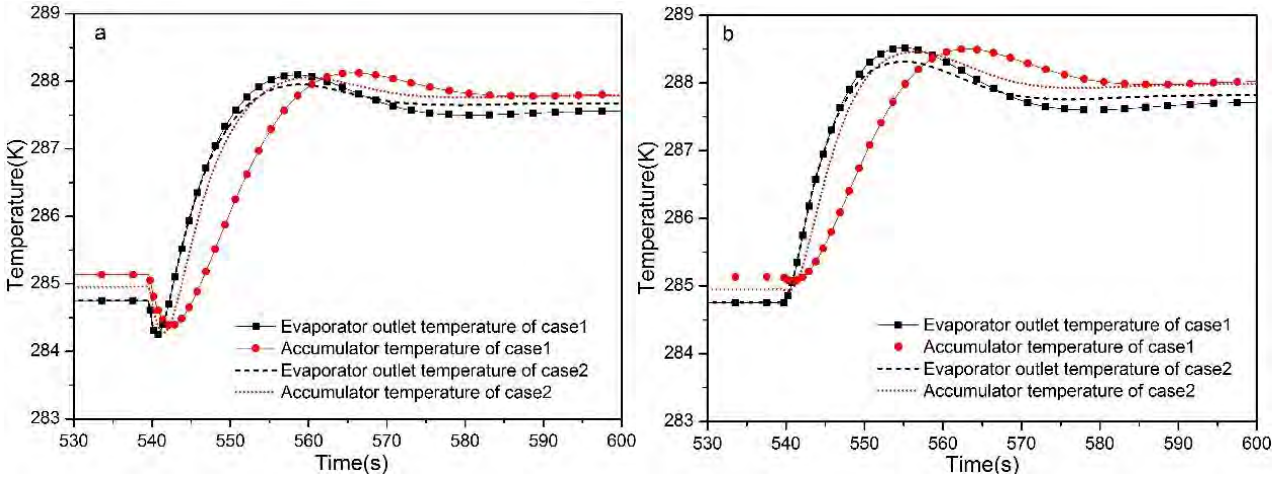

Figure.3: The temperature validation for a step change of operating parameter

(a) Compressor speed (+250r/min). (b) Valve opening (-2%)

It is observed from Fig. 2(b) that the dynamic curve of case 1 and case 2 are very close. In order to

further analyze the influence of the lubricating oil on the dynamic behavior of the system in the accumulator, the parameter-changed transient investigations of case 1 and case 2 are carried out. The transient behavior of the evaporator outlet and accumulator temperature is observed by the step change of the compressor speed (Fig. 3(a)) and the electronic expansion valve opening (Fig.3(b)) .Fig. 3 shows that the transient behavior of evaporator outlet temperature in case 1 and case 2 is identical nearly. In addition, the hysteresis effect of the accumulator temperature of the case 1 is reflected well, while the performance in case 2 is not obvious. Therefore, case 1 can better describe the transient behavior for the actual system.

5. CONCLUSIONS

In this paper, a detailed dynamic simulation model was established for the most common split-type air conditioners, in which the heat exchangers were modeled by the distributed parameter method. The steady-state lumped parameter model with semi-empirical equations for the EEV and the compressor were given. A single-node dynamic model of the accumulator with lubricating oil and connecting pipe was established. In addition, there were also three cases of the system model which were obtained by modifying the complete model under different assumptions. The system simulation model was then built based on MATLAB/SIMULINK. Thereafter, the models with different assumptions were verified by experimental data and then the transient comparison work of case 1 and case 2 was carried out. The results shown that case 1 had the best start-up transient performance. In addition, several conclusions were obtained as follows: (1) the accumulator model was indispensable for the system model; (2) the connecting pipes had a buffering effect on the change of the heat exchanger inlet temperature; (3) the lubricating oil in accumulator could smooth the start-up dynamic curve of pressure and temperature even though it had a limited impact on the start-up dynamic; (4)the accumulator model with lubricating oil could reflect the hysteresis effect of the system under changed parameter well.

Nomenclature

A	Cross-sectional or surface Area (m^2)	*Greek symbols*	
C_p	Specific heat ($J \times kg^{-1} \times K^{-1}$)	ρ	Density ($kg \times m^{-3}$)
d	Diameter (m)	γ	Void fraction
f	Frontal velocity($m \times s^{-1}$)	*Subscripts*	
G	Refrigerant mass flow flux ($kg \times m^{-2} \times s^{-1}$)	a	Air
h	Enthalpy ($J \times kg^{-1}$)	r	Refrigerant
M	Mass (kg)	w	Tube wall
m	Mass flow rate ($kg \times s^{-1}$)	o	Lubricating oil
P	Pressure (kpa)	f	Liquid-phase refrigerant
Q	Heat transfer (J)	*Superscripts*	
q	Heat flux ($W \times m^{-2}$)	n	Previous time step
T	Temperature (K)	*	Assumed value
U	Heat transfer coefficient ($W \times m^{-2} \times K^{-1}$)		
V	Volume (m^3)		

REFERENCES

Bastos, H. M. C., Torres,P. J. G., Álvarez,C. E. C. 2018. Numerical simulation and experimental validation

of a solar-assisted heat pump system for heating residential water. International Journal of Refrigeration 86,28-39.

Bonilla, J., Dormido,S., Cellier,F. E. 2015. Switching moving boundary models for two-phase flow evaporators and condensers. Communications in Nonlinear Science and Numerical Simulation 20(3), 743-768.

Cecchinato, L., Mancini,F. 2012. An intrinsically mass conservative switched evaporator model adopting the moving-boundary method. International Journal of Refrigeration 35(2), 349-364.

Chisholm, D. 1973. Pressure gradients due to friction during the flow of evaporating two-phase mixtures in smooth tubes and channels. International Journal of Heat & Mass Transfer 16(2), 347-358.

Demba,N.,Michel,B., 2010. Transient Modeling of Refrigerant-to-AirFin-and-Tube Heat Exchangers. Hvac & R Research 16(3), 355-381.

Ding, G.L., 2006. Simulation technology for refrigeration and air conditioning appliances. Chinese Science Bulletin **51**(16), 1913-1928.

Dittus, F. W., L. M. K. Boelter , 1985. Heat transfer in automobile radiator of the tubular type. International Communications in Heat & Mass Transfer **12** (1), 3-22.

Fang, X., Zhang,H., Xu,Y., Su,X. 2012. Evaluation of using two-phase frictional pressure drop correlations for normal gravity to microgravity and reduced gravity. Advances in Space Research 49(2), 351-364.

Gungor, K. E., Winterton,R. H. S. 1987. Simplified general correlation for saturated flow boiling and comparison with data. Chemical Engineering Research & Design 65(2), 148-156.

Kim, M. H. , Bullard,C. W. 2001. Dynamic characteristics of a R-410A split air-conditioning system. International Journal of Refrigeration 24(7), 652-659.

Koury,R.N.N., Faria,R. N., Nunes,R. O., Ismail,K. A. R., Machado,L. 2013. Dynamic model and experimental study of an air–water heat pump for residential use. International Journal of Refrigeration 36(3),674-688.

Li, B. , Alleyne,A. G. 2010. A dynamic model of a vapor compression cycle with shut-down and start-up operations. International Journal of Refrigeration 33(3),538-552.

Li, W. 2013. Simplified modeling analysis of mass flow characteristics in electronic expansion valve. Applied Thermal Engineering 53(1),8-12.

Macarthur, J. W. , Grald,E. W. 1989. Unsteady compressible two-phase flow model for predicting cyclic heat pump performance and a comparison with experimental data. International Journal of Refrigeration 12(1), 29-41.

Pangborn, H., Alleyne,A. G. , Wu,N. 2015. A comparison between finite volume and switched moving boundary approaches for dynamic vapor compression system modeling. International Journal of Refrigeration 53,101-114.

Qi,Q.,Deng,S. 2008. Multivariable control-oriented modeling of a direct expansion (DX) air conditioning (A/C) system. International Journal of Refrigeration 31(5),841-849.

Qi,Q., Deng,S. 2009. Multivariable control of indoor air temperature and humidity in a direct expansion (DX) air conditioning (A/C) system. Building and Environment 44(8),1659-1667.

Qiao, H., Laughman,C. R., Aute,V. , Radermacher,R. 2016. An advanced switching moving boundary heat exchanger model with pressure drop. International Journal of Refrigeration 65,154-171.

Shah, M. M. ,1979. A general correlation for heat transfer during film condensation inside pipes. International Journal of Heat & Mass Transfer **22**(4), 547-556.

Shang, Y., Wu,A., Fang,X. , You, Y. 2016. Dynamic simulation of electronic expansion valve controlled refrigeration system under different heat transfer conditions. International Journal of Refrigeration

72, 41-52.
Wang, C. C. ,Chi K.Y. 2000a. Heat transfer and friction characteristics of plain fin-and-tube heat exchangers, part I: new experimental data. International Journal of Heat & Mass Transfer 43(15), 2681-2691.
Wang, C. C., Chi,K. Y. , Chang,C. J. 2000b. Heat transfer and friction characteristics of plain fin-and-tube heat exchangers, part II: Correlation. International Journal of Heat & Mass Transfer 43(15), 2693-2700.
Wei,W.J., Ding,G.L.,Hu,H.T.,Wang,K.J.,2007. Models of thermodynamic and transport properties of POE VG68 and R410A POE VG68 mixture. Journal of Refrigeration 28(1),37-44(in Chinese).
Xu, Y. , Fang, X. 2013. Correlations of void fraction for two-phase refrigerant flow in pipes. Applied Thermal Engineering 64(1–2),242-251.
Yang,S.,Ordonez,J.C.2018.Integrative thermodynamic optimization of a vapor compression refrigeration system based on dynamic system responses. Applied Thermal Engineering 135,493-503.
Yang,T., Chen,J.P., Chen,J,Z., 2006. Dynamic simulation and experimental validation of a transcritical CO2 automobile air conditioning system. Journal of Shanghai Jiaotong University. 40(8),1365-1368(in Chinese).
Zhang, D., Wu,Q. B., Li,J. P., Kong,X. Q. 2014. Effects of refrigerant charge and structural parameters on the performance of a direct-expansion solar-assisted heat pump system. Applied Thermal Engineering 73(1),522-528.
Zhang, W.J., Zhang, C.L., Ding, G.L., 2009. On three forms of momentum equation in transient modeling of residential refrigeration systems. International Journal of Refrigeration 32(5), 938-944.

Manuscript ID: 474
DOI: 10.18462/iir.icr.2019.0474

The potential of water as a refrigerant - past, present and future approaches

Florian HANSLIK[(a*)], Juergen SUESS[(a)], Juergen KOEHLER[(b)]

[(a)]Efficient Energy GmbH
Feldkirchen, 85622, Germany, florian.hanslik@efficient-energy.de
[(b)]Technische Universität Braunschweig, Institut für Thermodynamik
Braunschweig, 38106, Germany, juergen.koehler@tu-bs.de
[(*)]Corresponding author

ABSTRACT

The paper starts with an overview of past options where water (R718) was used as a refrigerant and introduces various applications focusing on ad- and absorption technologies but mainly on compression systems.
In the second part of the paper a low capacity centrifugal compressor system based on using water as refrigerant is introduced. The working principle of the machine with a number of various energy efficient operational modes gets explained and the machines performance under these conditions is discussed.
Finally, favorable applications get specified resulting in energy savings up to 80% compared to state of the art technologies. These findings are confirmed by long term field test data, as machines are already in operation in various sites since many years.
Finally, an outlook is given, where water as a refrigerant can expect a promising future contributing to reduce the global warming impact of the refrigeration industry.
Keywords: Refrigeration, Water, Vapor Compression, Chiller, Energy Efficiency

1. INTRODUCTION

Water (R718) as a refrigerant is one of the oldest fluids being used for refrigeration applications down to about the freezing point. When water is mixed with protective solutions to prevent freezing (i.e. propylene or ethylene glycol), it can also be used well below water's normal freezing point in applications such as ice slurries. Water is easily available and has excellent thermodynamics and chemical properties. Fig. 1 shows on the left side the vapor pressure curves and on the right side the pressure ratio for a 30 K temperature lift of various refrigerants. In the case of R718, it is noticeable that the pressures in the temperature range for a typical cooling application are between 10 and 100 mbar and the pressure ratio ranges between 7 down to 5.
The curves of the respective refrigerants are shown in Fig. 1 and were calculated using REFPROP (Lemmon et al., 2013).

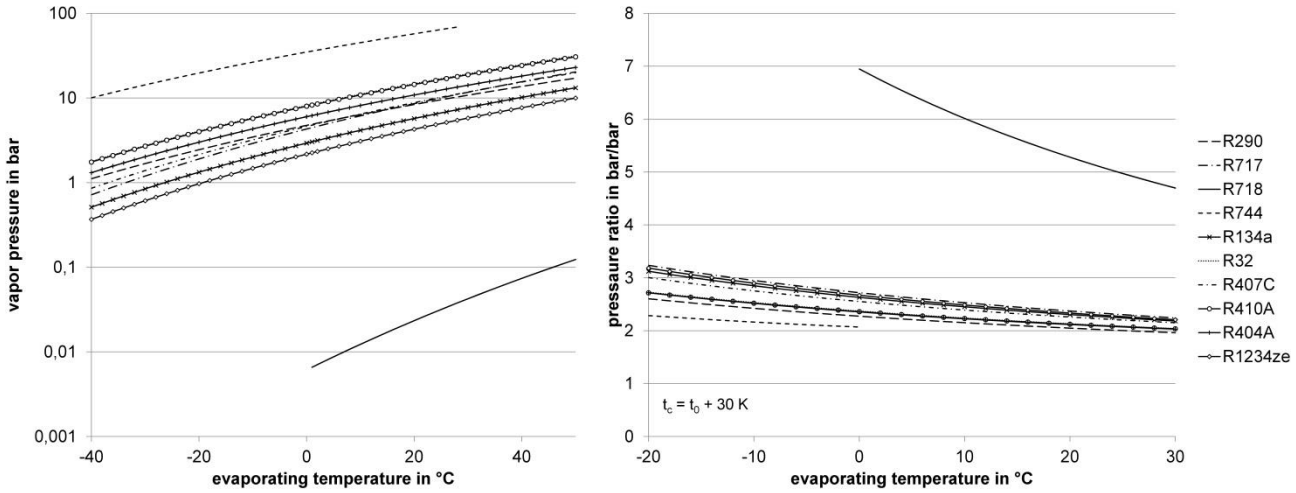

Figure 1: properties of selected refrigerants

On the one hand, the use of positive displacement machines would make sense because of the high pressure ratio required. On the other hand, due to the low vapor pressure and the concomitant low density of the water vapor, a large volume flow is required to deliver sufficient mass. For this reason, when using R718 in compression refrigeration machines it makes sense to use multistage turbomachines as compressors. Taking into account the increase of the vapor pressure and the reduction of the pressure ratio with increasing evaporation temperatures, the application range for R718 shown in Fig. 2 can be derived. The color gradient from black (conditionally good application area) to light gray (very good application area) shows the field of application. The limitation to a hot gas temperature of 200 °C is related to the material compatibility of the compressor components.

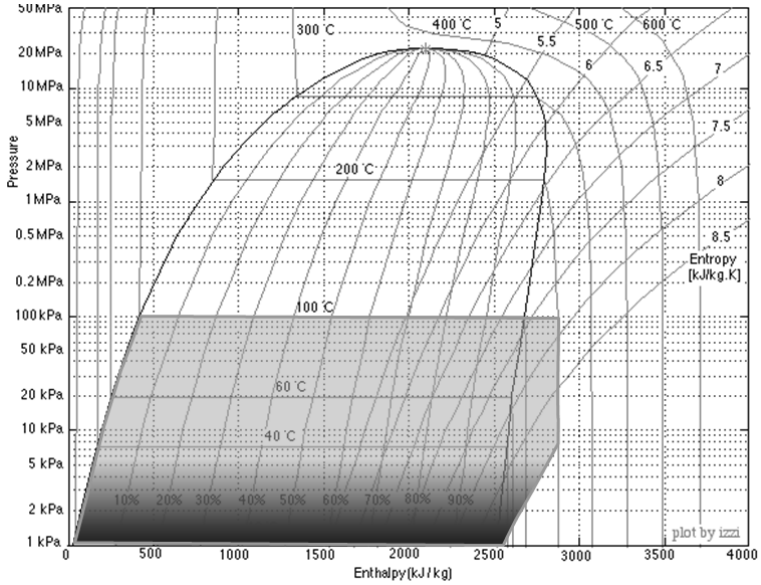

Figure 2: log p, h-diagram of R718 including the optimal application range

2. THE USE OF WATER AS REFRIGERANT

As shown in the previous section, the use of water as refrigerant, in addition to some challenges, also has some advantages. It has no negative effects on the environment and, under certain conditions, also allows for a significant increase in efficiency compared to common refrigerants.
Absorption refrigeration systems are often operated with water as a refrigerant. The process, developed by the Carré brothers in the middle of the 19th century, works in almost all installed systems with a combination of water with lithium bromide. In another variant of the thermally driven systems, the adsorption, water is used because of its large evaporation enthalpy as a working fluid.

In the chemical industry there are applications with steam ejector systems with water as refrigerant.
Another application of water as a refrigerant are high-temperature heat pumps (Bantle et al., 2014), (Chamoun et al., 2012) and (Ponweiser and Schlögl, 2015). However, in this application, absolute pressures above 1 bar occur, and the benefit of the system is the generation of heat and not of cooling.
Compression refrigeration systems with water as a refrigerant are not yet very relevant on the refrigeration market. On the one hand, this is due to the already mentioned challenges that this process entails and, on the other hand, to the projects that have been implemented so far in this area. The following passage presents the most important projects in this area.
Water as a refrigerant in compression refrigeration systems has been used in various projects since the mid-1980s. Fig. 3 gives an overview of the various manufacturers, the approximate cooling capacity and the approximate time commitment in this area. The most relevant projects of the manufacturers are listed in Table 1. The cooling capacity of the machines is typically over 500 kW and, with the exception of the chiller described from Sasakura (2014), all machines use centrifugal compressors.

Table 1. Centrifugal chiller projects using R718 as refrigerant, (Süß, 2016)

Year	Location	Project group	Application	Cooling Capacity	Literature source
1990	Denmark	IDE/Sabroe	sea water heat pump	1,3 MW	Ophir, 2008
1995	Denmark	IDE/Sabroe/TI	plastic molding cooling	2 MW	Ophir, 2008
1995	RSA	IDE/Integral	gold mine cooling	6x3 MW	Ophir, 2008
1999	Germany	ILK/GHS Essen	chilled water	1 MW	Albring, 2009
1999	Germany	ILK/VW	chilled water	1 MW	Albring, 2011
2000	Germany	ILK/Daimler	chilled water	1 MW	Albring, 2009
2002	Japan	IDE/Sanken	vacuum ice	350 kW	Ophir, 2008
2007	Japan	IDE/Nissan	vacuum ice	1,5 MW	Ophir, 2008
2008	RSA	IDE	gold mine cooling	3x3 MW	Ophir, 2008
2008	Switzerland	IDE	artificial snow	1,4 MW	Ophir, 2008
2008	Austria	IDE	artificial snow	1,4 MW	Ophir, 2008
2011	USA	MSU	chilled water	-	Li et al., 2011
2012	Denmark	Rotrex/Topsøe	heat pump	350 kW	Borup and Jensen, 2008
2013	Japan	Kawasaki HI	chilled water	350 kW	Murayama, 2014
2012	Germany	ILK/Engie	chilled water	800 kW	Honke et al., 2015
2014	Japan	Sasakura	chilled water	17,5 kW	Sasakura, 2014
2015	Denmark	TI/JCI	chilled water	800 kW	Madsbøll, 2013
2015	Germany	ILK	vacuum ice	50 kW	Honke et al., 2015
2015	Germany	efficient energy	chilled water	35 kW	Süß, 2014

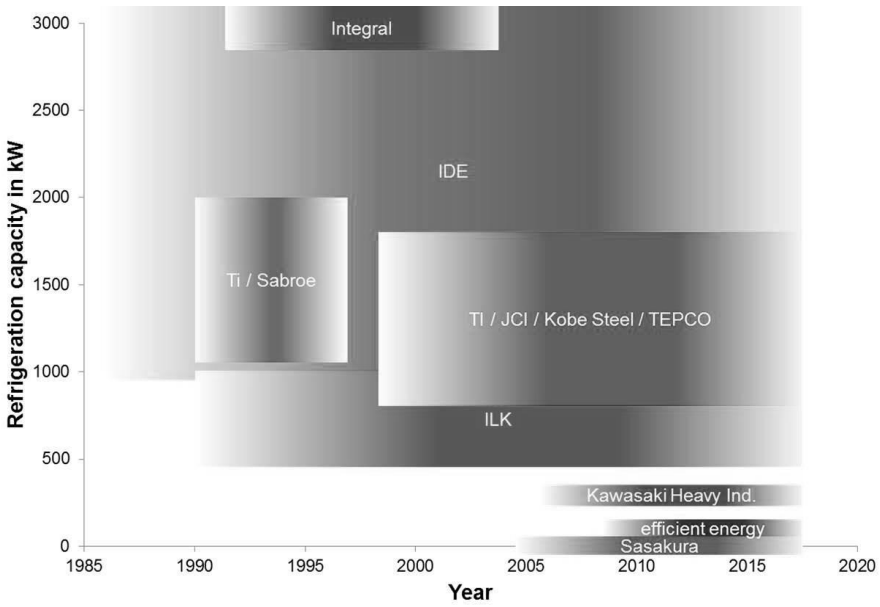

Figure 3: Projects with water as refrigerant, (Kauffeld and Süß, 2016)

2. LOW CAPACITY CENTRIFUGAL COMPRESSOR SYSTEM

2.1 The Principle

The construction of a compression refrigeration system for R718 consists of the same functional assemblies - evaporator, compressor, condenser and expansion device - as with systems for all refrigerants.

As compressors mostly turbomachines are used with oil-free bearings. Examples include water-bearing systems, lifetime-lubricated hybrid ball bearings or magnetic bearing systems. The evaporator or condenser can be designed in two systems: with internal or external heat exchanger. Both systems are operated in vacuum due to the properties of water, assuming that the evaporation as the condensing temperatures are below 100 °C. The pressure difference between condenser and evaporator is in the absolute range of 50 mbar to 70 mbar. This makes it possible to dispense with a fixed expansion valve and to use for a simple overflow with corresponding water column of 500 mm to 700 mm. Owing to the operating conditions in a vacuum and the usually non-hermetic design of the systems, external gas extraction is required to keep the system free of inert gases. Air entering from outside is fed into the system, which has a negative influence on the evaporation and condensation. This results in a higher energy consumption of the compressor. In generally pressure losses should be kept as small as possible.

In systems with external heat exchangers (Fig. 4a), the entire system is evacuated between the chilled and the cooling water heat exchangers. The pressure in the respective areas depends on the respective prevailing temperature. The heat transfer between the refrigerant and the chilled water, as well as the cooling water, take place in each of the plate heat exchangers. The phase change of the refrigerant occurs within a module containing the evaporator and condenser area, the compressor and the expansion device. The evaporation takes place between the liquid and vapor phases in the lower region of the module due to pressure reduction. For liquefaction, the gaseous refrigerant is passed together with liquid refrigerant through a packed bed. In this case, the gaseous refrigerant condenses to the liquid refrigerant. The packed bed serves to increase the surface area of the liquid refrigerant. The described system can be carried out alternatively to the plate heat exchangers with air registers on the cold water, as well as on the cooling water side. In cool air applications, this can save a heat transfer loss and an additional secondary circuit. The integration of an air register on the cooling water side allows the operation as an air-cooled machine with outdoor installation, provided that the system is secured frost-free.

In systems with internal heat exchangers (Fig. 4b), the heat exchangers are inside the evacuated module, which contains the same areas as the system described above. The heat transfer

between cold water and the refrigerant takes place in a classic finned tube evaporator. Likewise, the liquefaction of the refrigerant is carried out on a finned tube in the vacuum container heat exchanger, which is flowed through inside the cooling water.

2.2 Description of a Compact R718 Chiller

The majority of the projects shown in 1 are in the cooling capacity range >500 kW and at chilled water temperatures below 10 °C. Exceptions to the cooling capacities are Kawasaki, Sasakura and Efficient Energy GmbH. In addition to the cooling capacity, the latter also differ in the temperature range of the produced chilled water from the remaining manufacturers, as they have specialized in cold water temperatures >16 °C. This has made it possible to develop a compact system that bridges the gap between classic cold water production and cooling tower applications. Furthermore, the manufacturer has succeeded in developing a mass produced chiller with water as the refrigerant. It is therefore to be expected that the relevance of R718 in the area of compression refrigeration systems will continue to rise and establish itself as a serious refrigerant in this area. For the reasons mentioned above, we take a closer look at the technology of Efficient Energy GmbH below.

The currently available chiller consists of two modules, two plate heat exchangers, two hydraulic switches and the necessary hydraulic connecting pipes (Fig. 5). The two modules in the system operate according to the principle illustrated in Fig. 4 with external heat exchangers, with the inlet of the evaporator of the second module connected to the outlet of the condenser of the first module and thus connected downstream as a cascade of the first stage. As already described, the two plate heat exchangers represent the delimitation of the vacuum system and the interface to the secondary side. With the two switches integrated into the hydraulic connecting lines, it is possible to switch between different operating states. This is done automatically depending on the cooling water temperature in relation to the required chilled water temperature and ranges from pure free cooling operation over single-stage operation up to two-stage operation at highest cooling water temperatures.

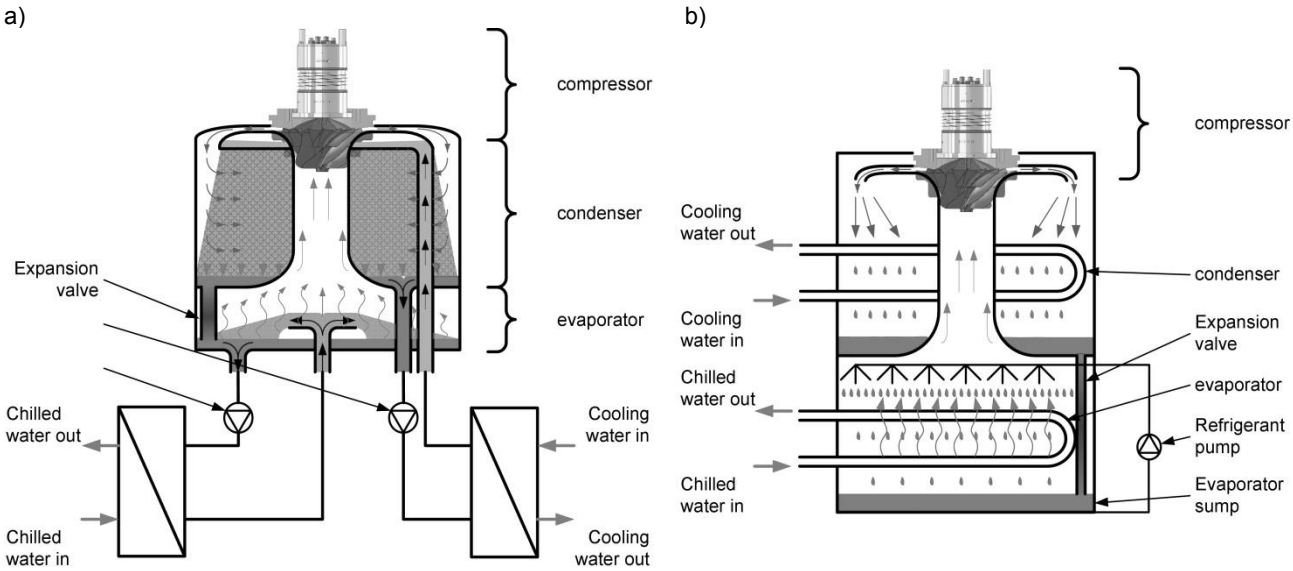

Figure 4: single stage R718 process with a) external and b) internal heat exchangers

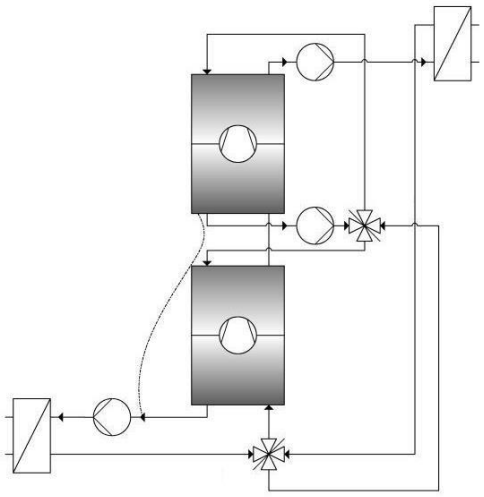

Figure 5: Schematic of the Efficient Energy R718 chiller

3. APPLICATIONS

This section presents application examples that successfully use water as a refrigerant in compression refrigeration systems.
Cooling of small data centers / server rooms

The task is to cool a highly efficient data center with a maximum cold air temperature of 25 °C. The special feature of this application was the slowly growing demand for cooling due to the gradual expansion of the servers. The challenge was the initially low cooling capacity of around 8 kW to 10 kW, which corresponds to approximately 10 % to 15 % of the installed cooling capacity. As a solution, the racks in the server room were set up in a warm aisle containment. The cooling air is supplied to the servers via Sidecooler.
After commissioning in the summer of 2016, it quickly became clear that operation was highly efficient even at this low part load. This is due to the continuously variable speed centrifugal compressors in conjunction with the integrated free cooling.
Over a period of 18 months, this measurement has been used to establish a work data based on a measured annual energy efficiency >18.

Air conditioning
In this example, two alternative systems were combined, a chiller with the refrigerant R718 and a PV system for the necessary energy supply.
Water as a refrigerant has the advantage that no extra machine room is needed for the installation and thus the chiller could be placed in an adjoining room of the staircase. To compensate for fluctuations in power generation, a power storage of 28 kWh was installed, which can cover a complete daily cycle in the summer. The combination of electrical and thermal storage (cold water hydraulics) in conjunction with the part-load-efficient centrifugal compressor ensures that the cooling is covered by the daily cycle, including pre- and post-cooling of the building structure. At favorable outdoor temperatures, a partial or complete free cooling is used at night, which significantly prolongs the service life of the battery storage.
By selecting the appropriate ceiling cassettes, the cold water inlet temperature of 16 °C could be confirmed. In summer there is a cooling load of 25 kW. The use of office space initially led to an occupancy rate of only 40 % - 60 %. By exploiting the pre- and post-cooling of the building structure, an annual work figure (averaged EER) for the refrigeration system of more than 12 is aimed for. This is unique in connection with a mechanical office cooling with the possibility of unlimited indoor installation of refrigeration.
Sustainable validation of the targeted efficiency can only be achieved after at least 12 months. However, previous experience on days with high outside temperatures already exceeded all expectations.

Process cooling

As an example of the process cooling, the cooling of an extruder for the production of an endless product is presented. Due to the processing of different product recipes and resulting changes in the heat load and the temperature control, the extruder is not connected to the central cold water supply.

The required temperature range of the generated cold water is between 16 °C and 20 °C and the cooling capacity at about 30 kW. Further criteria were the installation as close as possible to the extruder, integrated free cooling to reduce energy costs and the use of an environmentally friendly and sustainable refrigerant.

Since commissioning in July 2017, the chiller has been in continuous operation. The operator on site confirms the ease of use when changing the product and thus changing flow temperatures between 16 °C and 18 °C depending on the dimension. After one year of operation, the eChiller Monitoring has determined an annual energy efficiency of over 16 refrigeration.

4. OUTLOOK

Due to the freezing point of water at 0 °C, this refrigerant can't be used for low-temperature refrigeration without admixture of other substances. This is only possible by combining water as a high-temperature stage with other natural refrigerants in the low-temperature stage in a cascade. The refrigerants CO_2 (R744) and propane (R290) are also proposed for the use of such cascade systems in the small power range.

The possible interconnections can be divided into partial and full cascades as well as direct and indirect constructions. Fig. 6 on the left shows an indirect full cascade with secondary circuit between condenser of the R290 stage and evaporator of the R718 stage. In the middle you see a direct full cascade, which makes the liquefaction of the CO_2 stage directly in the evaporator of the R718 stage. On the right side a partial cascade is shown. In this setup, the supercritical CO_2 gas after the gas cooler is further subcooled by means of the water stage.

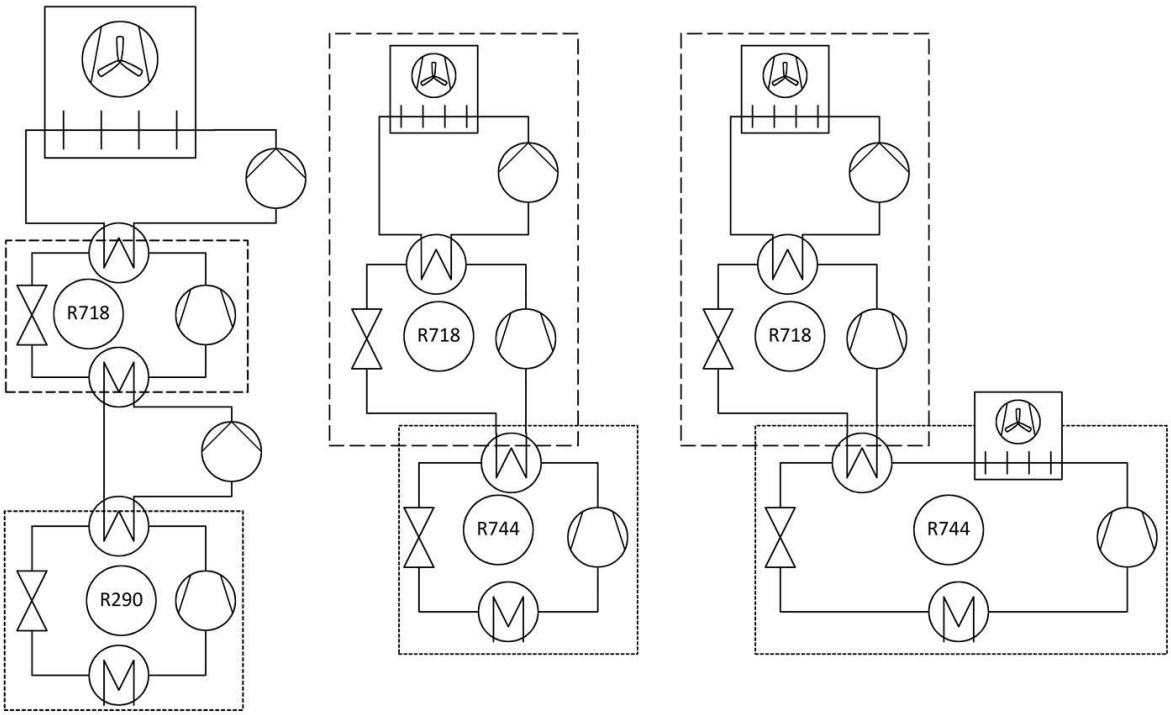

Figure 6: cascade systems

5. CONCLUSION

Due to the currently applicable F-Gas Regulation, the Ecodesign Directive and the strong increase in environmental awareness among users, the trend in refrigeration with compression refrigeration machines is moving towards natural refrigerants. Water (R718) occupies a special position not only in this group, as it is neither flammable nor toxic and has an ODP and GWP value of zero. In addition to the future-proof availability is not foreseeable that the use is prohibited neither nationally nor internationally.
Applied with these requirements and in the right temperature and cooling range, water, as the oldest known refrigerant, is a forward-looking solution for ensuring the supply of refrigeration safely, efficiently and in an environmentally friendly manner.

REFERENCES

Albring, P., 2009. Kältetechnik mit Wasser als Kältemittel, Netzwerk Kältetechnik.

Albring, P.; Honke, M., 2011. Ice-Making and Ice Storage, with Water as Refrigerant. Proceedings of the 23rd IIR International Congress of Refrigeration, Prague, Czech, IIF/IIR.

Bantle, M., Tolstorebrov, I., Hafner, A., 2014. Energierückgewinnung mittels Brüden-Kompression in Trocknungssystemen mit überhitztem Dampf, DKV-Tagung (2014), Düsseldorf

Borup, J; Jensen, J., 2012. Udvikling af Rotrex turbokompressor til vanddamp compression, Nr. 344-009, PSO Program 2012

Chamoun, M., Rulliere, R., Haberschill, P., Peureux, J-L, 2012. Experimental Investigation of a New High Temperature Heat Pump Using Water as Refrigerant for Industrial Heat Recovery, International Refrigeration and Air Conditioning Conference, Purdue

Honke, M.; Safarik, M.; Herzog, R., 2015. R718 turbo chillers and vacuum ice generation - Two applications of a new generation of high speed, high capacity R718 centrifugal compressors. Proceedings of the 24th IIR International Congress of Refrigeration, Yokohama, Japan, IIF/IIR.

Ponweiser, K., Schlögl, T., 2015. Wärmepumpen mit Wasser als Arbeitsmedium – Perspektiven und Grenzen, VDI-Forum 2015, Universität Linz

Kauffeld, M., Süß, J., 2016. Kaltdampfkompressionskältemaschinen mit Wasser als Kältemittel – Vor- und Nachteile dieser Technologie. KI Kälte Luft Klimatechnik 11, 44-48

Lemmon, Eric W; Huber, Marcia L; McLinden, M O, 2013. NIST Reference Fluid Thermodynamic and Transport Properties Database (REFPROP), Version 9.1

Li, Q.; Piechna, J.; Müller, N., 2011. Thermodynamic potential of using a counter rotating novel axial impeller to compress water vapor as refrigerant. International Journal of Refrigeration 34(5), 1286-1295.

Madsbøll, H., 2013. Competitive chiller concept with water as refrigerant, Danske Køledage 2013

Murayama, S., 2014. Report 2014 Kawasaki Heavy Industries, Ltd. Kawasaki Heavy Industries, Ltd. Tokyo Office, 14-5 Kaigan 1-chrome, Minato-ku, Tokyo 105-8315, Japan.

Ophir, A., 2008. Mechanical Heat Pumps Using Water as Refrigerant for Ice Production and Air Conditioning. In: IDEA 99th Annual Converence & Trade Show, Orlando, Florida.

Sasakura, T., 2014. Report 2014 Sasakura Engineering Co., Ltd. Sasakura Engineering Co., Ltd. 7-32 Takejima 4-chome, Nishiyodogawa-ku, Osaka 555-0011, Japan

Süß, J., 2014. Eine kompakte Kälteanlage mit Wasser als Kältemittel. Deutsche Kälte- und Klimatagung

Süß, J., 2016. A centrifugal compressor cooling system using water as working fluid. Proceedings of the 12th IIR-Gustav Lorentzen Natural Working Fluids Conference, 1178-1184

Manuscript ID: 482
DOI: 10.18462/iir.icr.2019.0482

Dynamic simulation of a triple-effect absorption chiller with a reverse-parallel solution flow

Sangmoo HAN [(a)], Hojin SEO[(a)], Sungmin WOO[(b)], Siyoung JEONG[(c)]

[(a)] Graduate School of Sogang University, Department of Mechanical Engineering
Seoul, 04107, Korea, laman32@naver.com
[(b)] R&D Center, Samjungtech Co.
Changwon, 51430, Korea, sungm.woo@samjungtech.com
[(c)] Department of Mechanical Engineering, Sogang University
Seoul, 04107, Korea, syjeong@sogang.ac.kr

ABSTRACT

A LiBr-H_2O triple-effect absorption chiller is currently under development in Korea. The chiller has three generators and a newly developed reverse-parallel solution flow was applied. Since the triple-effect absorption chiller has more system components and the flow of the solution is complicated, the control of the system is much more difficult than a conventional double-effect absorption chiller. Therefore, dynamic simulation is required to understand the characteristics due to the change of operation conditions. In this study, a dynamic simulation model has been developed for a reverse-parallel flow triple-effect absorption chiller, and the transient behaviours due to the change of operation conditions have been studied. The effects of the variation of the gas input, the cooling water temperature, and the chilled water temperature have been investigated. The simulation results will be compared with the experiments. It is expected that this study will be able to supply important information in developing an optimal control method of the triple-effect absorption chiller.
Keywords: Triple-effect Absorption Chiller, LiBr-H_2O, Dynamic Simulation.

1. INTRODUCTION

Double-effect absorption chillers which have two generators are commonly used to reduce the electric peak caused by the cooling load. However, there are increasing needs for the research and development of triple-effect absorption chillers which have much higher COP than double-effect ones. Compared with a double-effect absorption chiller, a triple-effect absorption chiller cycle becomes more complicated by adding one more generator. Various solution flows are possible depending on the way to connect the absorber and the generators. Seo and Jeong (2017) investigated the characteristics of the triple-effect absorption chiller cycles with 4 different solution flow types, and suggested that a reverse-parallel solution flow is most suitable because it has a relatively high COP and requires a low maximum pressure in the high temperature generator.

Dynamic simulations are required to control the system effectively in various situations such as the start and stop of the system. Several studies have been conducted on the dynamic simulation for absorption systems. Jeong *et al*. (1998) suggested a dynamic simulation model and carried out a simulation on an absorption heat transformer using waste heat. Matsushima *et al.* (2010) carried out a dynamic simulation to investigate transient behaviour of double-effect and triple-effect absorption chiller. However, the effect of the change of operating conditions which affect the performance of the system have not been investigated. In this study, a dynamic simulation model has been developed for a reverse-parallel flow triple-effect absorption chiller, and the transient behaviours due to the change of operation conditions have been studied. The effects of the variation of the gas input, the cooling water temperature, and the chilled water temperature have been investigated. The simulation results have not been verified yet, however, it is expected that this study will be able to supply important information in developing an optimal control method of the currently developed triple-effect absorption chiller.

2. TRIPLE-EFFECT ABSORPTION CHILLER WITH REVERSE-PARALLEL SOLUTION FLOW

Seo and Jeong (2017) suggested an advanced triple-effect absorption chiller cycle with a reverse-parallel solution flow as shown Fig. 1 (left side). The system has three generators (LTG, MTG, HTG), two-stage evaporators (EVA 1&2), two-stage absorbers (ABS 1&2), a condenser (CON), three solution heat exchangers (HSX,MSX,LSX), and auxiliary heat exchangers. Auxiliary heat exchangers (ESX, RSX) were applied to further increase the COP. In case of reverse-parallel solution flow the solution from ABS1 flows to LTG, then it is divided parallelly into MTG and HTG. Since the solution flow is a combination of a reverse and parallel flow, the new cycle was named as a 'reverse-parallel' flow. It is expected that the COP of 1.74 could be obtained.

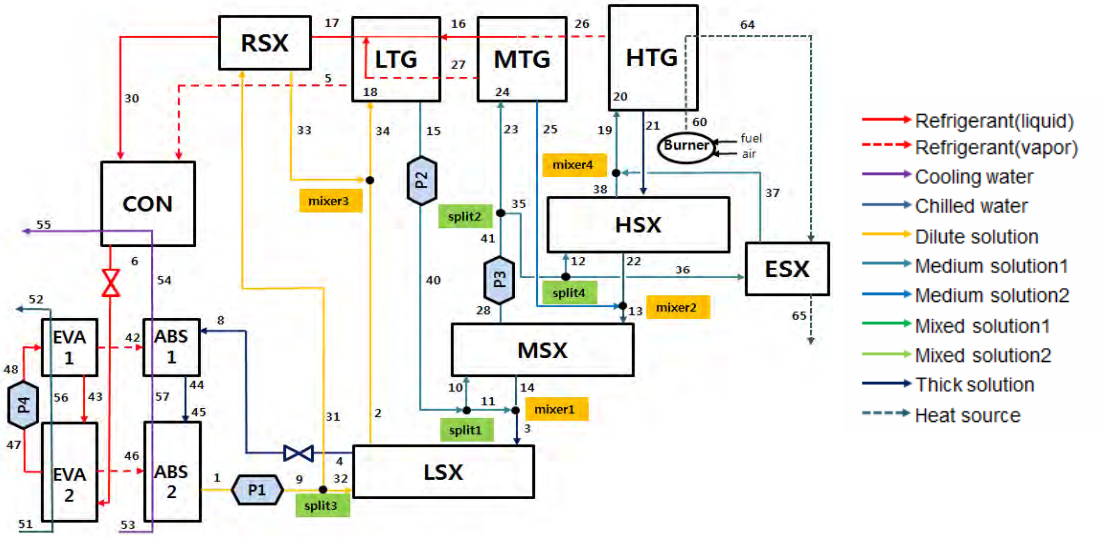

Figure 1: Flow diagram of triple-effect absorption chiller with reverse-parallel solution flow.

3. DYNAMIC SIMULATION PROGRAM

A dynamic simulation program has been developed to investigate the unsteady characteristics of the triple-effect absorption chiller described above. Important features of the program are summarized as follows.

(a) Main heat exchangers (EVA1&2, ABS1&2, LTG, MTG, HTG, and CON) are described as lumped system with the mass flow and heat transfer.
(b) The mass and the thermal capacity are neglected for solution heat exchangers (LSX, MSX, HSX) and auxiliary heat exchangers (RSX, ESX) because they have much smaller masses compared with main components.
(c) The working fluid is lithium bromide aqueous solution, and it is in a saturated state.
(d) It is assumed that the LNG fuel is burned with 20% excess air.
(e) Because the mass of vapour in a main heat exchanger is negligible, only the liquid phase of the solution or refrigerant is considered as a control volume.

3.1. Mathematical Modelling

The balance equations for mass, concentration, and energy are applied to the control volume.

(Mass balance)

$$\frac{dM}{dt} = \sum_i \dot{m}_i - \sum_e \dot{m}_e \qquad \text{Eq. (1)}$$

(LiBr mass balance)
For the absorber and generators, concentration balance equation is given as below.

$$M\frac{d\xi}{dt} + \xi\frac{dM}{dt} = \sum_i \dot{m}_i\xi_i - \sum_e \dot{m}_e\xi_e \qquad \text{Eq. (2)}$$

(Energy balance)
For the evaporators and condenser, the energy balance is given as follows.

$$\left[M\frac{\partial h}{\partial T}\right)_{sat} + M_c C_p \left] \frac{dT}{dt} + h\frac{dM}{dt} = \dot{Q} + \sum_i \dot{m}_i h_i - \sum_e \dot{m}_e h_e \qquad \text{Eq. (3)}$$

For the absorbers and generators, the energy balance equation is given as follows.

$$\left[M\frac{\partial h}{\partial T}\right)_{\xi} + M_c C_p \left] \frac{dT}{dt} + M\frac{\partial h}{\partial \xi}\right)_T \frac{d\xi}{dt} + h\frac{dM}{dt} = \dot{Q} + \sum_i \dot{m}_i h_i - \sum_e \dot{m}_e h_e \qquad \text{Eq. (4)}$$

The mass flow rate of vapour from the evaporator and the generator is described as follows.

$$\dot{m}_v = C\sqrt{\Delta P} \qquad \text{Eq. (5)}$$

If C is large enough, ΔP becomes very small and the pressure of the evaporator and the absorber becomes almost the same, which represents the condition of the actual system.
The mass flow rate of solution from the generator is assumed to be controlled by the solution level. It is described using the ratio of the instantaneous volume to the reference volume.

$$\dot{m}_s = \dot{m}_{s,ref}\sqrt{V_s \cdot V^{-1}_{s,ref}} \qquad \text{Eq. (6)}$$

Heat transfer is described using the UA-value and the log mean temperature difference (LMTD) in each heat exchanger. This is expressed by Eq. (7) as below.

$$\dot{Q} = UA \cdot LMTD \qquad \text{Eq. (7)}$$

3.2. Input Conditions

The design values of the first prototype of 100RT triple-effect absorption chiller were used to carry out the simulation. Some of the design conditions such as the overall heat transfer coefficient multiplied by heat transfer area (UA-value) are given in Table 1. The initial temperature and concentration which had been obtained from the steady-state simulation were used for the dynamic simulation as shown in Table 1.

Table 1. Initial condition and the UA-value of each component

Component	EVA1	EVA2	ABS1	ABS2	CON	LTG	MTG	HTG
UA-value [kW·K^{-1}]	75	75	51.8	51.8	46.5	23.4	18.4	0.45
$T_{initial}$ [°C]	5.4	8.5	36.2	34.2	38.5	74.8	127.8	200.4
$\xi_{initial}$	-	-	0.561	0.534	-	0.551	0.584	0.622
Component	LSX	MSX	HSX	ESX	RSX	-	-	-
UA-value [kW·K^{-1}]	11.4	13	5.6	1	0.08	-	-	-

4. RESULTS AND DISCUSSION

Since the absorption chiller does not always in a steady state, dynamic simulation was carried out to investigate the operation characteristics due to the change of operating conditions. In this study, three operation parameters were considered that mainly influence the system performance; the mass flow rate of fuel, the inlet temperature of the chilled water, and that of the cooling water.
At the initial state, the mass flow rate of fuel is 0.0039[kg·s^{-1}], the chilled water temperature is 12℃ and the cooling water temperature is 32℃. The simulation was carried out for an operation cycle of 14,400 seconds or 4 hours. A cycle is composed of 5 stages; ① a steady process at the design condition for 600 seconds, ② a linear change process for 600 seconds, ③ a steady process at the changed condition for 6,600 seconds, ④ a linear change process to the design condition for 600 seconds, and finally ⑤ a steady process at the design condition for 6,000 seconds.

4.1. Effect of mass flow rate of fuel

Fig. 2(a) shows the periodical change of mass flow rate of fuel as described above. The mass flow rate is reduced linearly by 60% for 600 sec, and the operating condition is maintained for 6,600 seconds until the system almost reached the new steady state. After the design condition is restored, the system is stabilized in the same way. Fig. 2(b) and (c) represent the effect on the cooling capacity and the COP with the change of mass flow rate of the fuel. The cooling capacity gradually decreases as shown in Fig. 2(b) with decreasing mass flow rate of fuel. As the mass flow rate of the fuel decreases, the heat input to the HTG is reduced, which in turn reduces the vapor generation. As shown in Fig. 2(c), the COP increases rapidly at the second stage when the fuel mass flow rate decreases. At the third stage, it gradually decreases as the cooling capacity decreases.

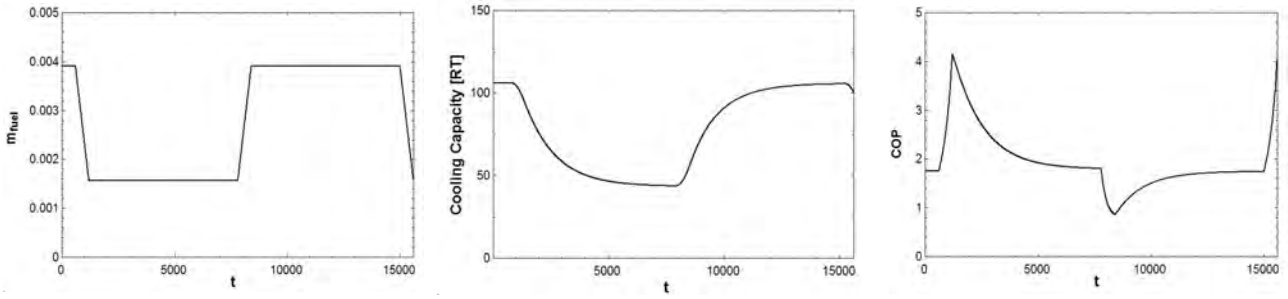

Figure 2: Characteristics for change of mass flow rate of fuel
(a) mass flow rate of fuel; (b) cooling capacity; (c) COP

4.2. Effect of inlet temperature of chilled water

Fig. 3(a) shows the periodical change of the inlet temperature of the chilled water. The temperature is increased linearly up to 14℃ for 600 sec. Fig. 3(b) and (c) represent the effect on the cooling capacity and the COP with the change of the inlet temperature of chilled water. The cooling capacity is directly affected by the chilled water temperature because the chilled water exchanges heat with the refrigerant in the evaporator. Therefore, the cooling capacity rapidly increases with increasing inlet temperature of the chilled water as shown in Fig. 3(b). However, at the second stage, the cooling capacity decreases gradually. As shown in Fig. 3(c), the COP shows the same tendency as the cooling capacity since the heat input to HTG does not change for the whole cycle.

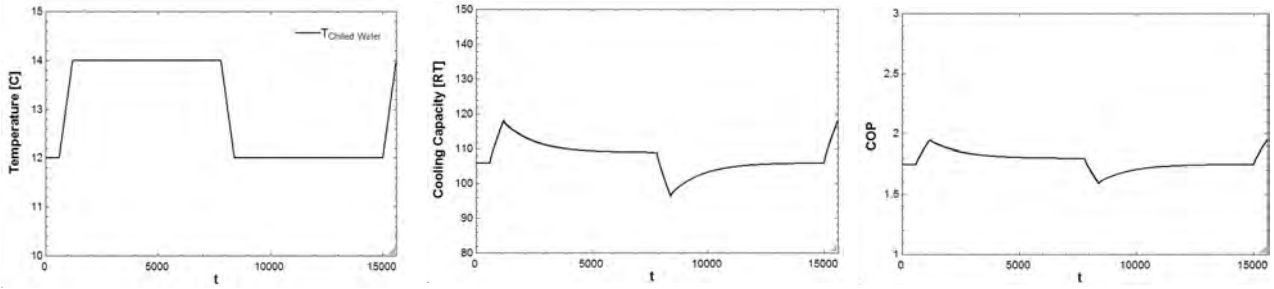

Figure 3: Characteristics for change of chilled water inlet temperature
(a) chilled water inlet temperature; (b) cooling capacity; (c) COP

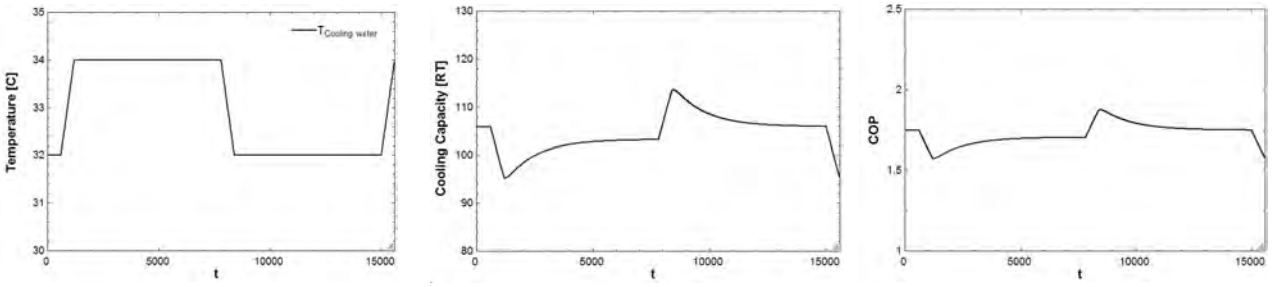

Figure 4: Characteristics for change of cooling water inlet temperature
(a) cooling water inlet temperature; (b) cooling capacity; (c) COP

4.3. Effect of inlet temperature of cooling water

As shown in Fig. 4(a), the temperature increases linearly by 2 K at the second stage. Fig. 4(b) and (c) show the results of the change of the cooling water temperature. Due to the increase of the cooling water temperature, the temperature and pressure of the absorber increase. Therefore, the pressure difference between the evaporator and the absorber is decreased, and in turn the evaporation is reduced. Also, the condensation of the refrigerant is decreased with decreasing cooling water temperature. Therefore, the cooling capacity is seriously reduced if the cooling water temperature is increased as shown in Fig. 4(b). As shown in Fig. 4(c), the COP is changed similarly to the cooling capacity, because the heat input to the HTG remains constant during the cycle.

5. CONCLUSIONS

In this study, a dynamic simulation program for a triple-effect absorption chiller with a reverse-parallel solution flow has been developed and the operation characteristics at transient state were investigated with the change of three operation parameters; the mass flow rate of fuel, the inlet temperature of the chilled water, and that of the cooling water. The simulation was carried out for an operation cycle of 14,400 seconds or 4 hours. It is found that the cooling capacity and the COP change as expected. The change of the operating parameters influences the system with a time delay because of the thermal capacity of the system components. It is expected that the simulation program can describe the system response properly at a transient process. The simulation results in this study can be usefully applied for the optimal control of the triple-effect chiller. The verification of the simulation program will be carried out using the experimental results.

ACKNOWLEDGEMENTS

This work was supported by the Korea Institute of Energy Technology Evaluation and Planning (KETEP) and the Ministry of Trade, Industry & Energy (MOTIE) of the Republic of Korea (No. 10060218).

NOMENCLATURE

M	Mass of working fluid in container (kg)	t	Time (s)
M_c	Mass of container (kg)	$\dot{Q}$	Heat transfer rate (kW)
C_p	Specific heat capacity ($kJ \cdot K^{-1} \cdot kg^{-1}$)	$\dot{m}$	Mass flow rate ($kg \cdot s^{-1}$)
h	Specific enthalpy ($kJ \cdot kg^{-1}$)	ξ	Concentration (%)
H	Enthalpy (kJ)	U	Heat transfer coefficient ($kW \cdot K^{-1} \cdot m^{-2}$)
P	Pressure (kPa)	A	Heat transfer area (m^2)
T	Temperature (K)		
EVA	Evaporator	ABS	Absorber
CON	Condenser	LTG	Low temperature generator
MTG	Middle temperature generator	HTG	High temperature generator
LSX	Low solution heat exchanger	MSX	Middle solution heat exchanger
HSX	High solution heat exchanger	RSX	Refrigerant solution heat exchanger
ESX	Exhaust gas solution heat exchanger		

REFERENCES

Seo, H., Park, J., Jeong, S., 2017. A new cycle for LiBr-H_2O Triple-effect absorption chillers; Reverse-parallel flow cycle. International Sorption Heat Pump Conference, 222(paper number).

Jeong, S., Kang, B.H., Karng, S.W., 1998. Dynamic simulation of an absorption heat pump for recovering low grade waste heat. Applied Thermal Engineering 18(1-2), 1-12.

Mastsushima, H., Fujii, T., Komatsub, T., Nishiguchic, A., 2010. Dynamic simulation program with object-oriented formulation for absorption chillers (modelling, verification, and application to triple-effect absorption chiller). Int. J. Refrigeration 33(2), 259-268.

Manuscript ID: 483
DOI: 10.18462/iir.icr.2019.0483

A table-top demonstration unit for CO_2-sublimation cycles

Yixia XU, Thomas TANNERT, Ullrich HESSE

Technical University Dresden, Institute of Power Engineering,
Bitzer Chair of Refrigeration, Cryogenics and Compressor Technology,
01062 Dresden, Germany, yixia.xu@tu-dresden.de

ABSTRACT

A small-scale cascade refrigeration system using CO_2-sublimation is introduced in this study. The upper stage is provided with a condensing unit and operates with R-452A. The lower stage is equipped with a rolling piston compressor, a capillary tube as throttling device and the sublimation unit including a visualization section. An operation point below the triple point of CO_2 is achieved in a laboratory test. Clogging effects in the system were observed and are discussed. Design improvements are considered in order to reduce and omit the risk of clogging. It is shown that the CO_2-sublimation cycle can be realized by the presented demonstration unit. Further work should focus on long term reliability tests and the improvement of the system performance.
Keywords: Carbon Dioxide, Sublimation, Cascade

1. INTRODUCTION

Carbon dioxide (CO_2), as a natural refrigerant, is widely used in many refrigeration and heat pump applications covering a large temperature range. The lower temperature limit for common CO_2 vapor compression cycles is usually considered to be the triple point of CO_2 (-56 °C and 0.52 MPa). Below that the occurrence of solid CO_2 could cause blockage in the components and pipe lines, which is generally avoided.

Recent studies, however, have shown the possibility of extending the application range of CO_2 beneath its triple point in a refrigeration cycle, or in other words, a sublimation cycle. Yamaguchi and Zhang (2009) established for the first time a working cycle of CO_2-sublimation on a laboratory scale. The blockage issues were further investigated under specific operation conditions (Yamaguchi et al., 2011) and design improvements were made (Iwamoto et al., 2015). This kind of system using pure CO_2 sublimation is considered as “dry sublimation” (Langebach et al., 2016), which means exclusively solid and gaseous CO_2 exist in the sublimation heat exchanger or “sublimator” without an extra carrier fluid. A basic CO_2 dry sublimation cycle is presented in Fig. 1.

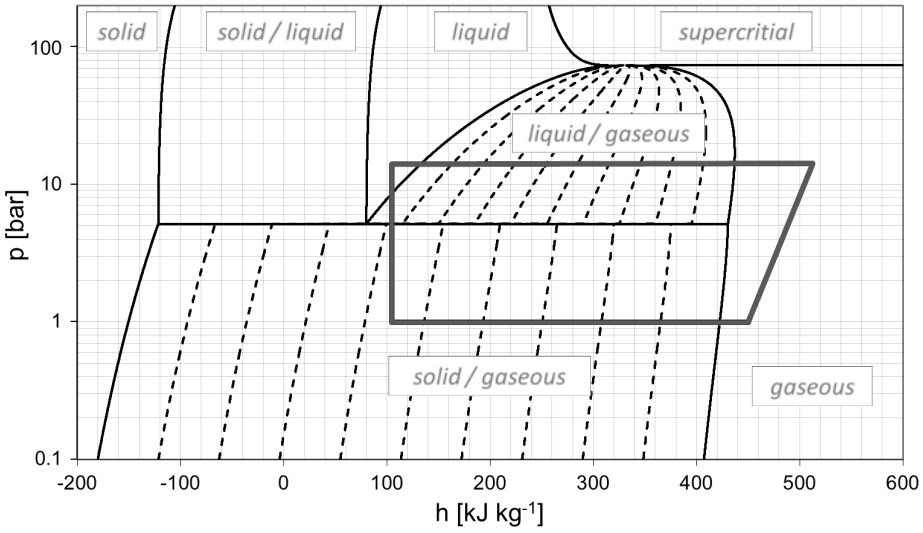

Figure 1: A basic sublimation cycle in log (p)-h-diagram

The main theoretical basis behind it is, that within a homogeneous solid-gaseous two-phase flow of CO_2 the volume fraction of solid is normally considerably small due to the large density difference between the solid and gaseous phase. Taking the cycle in Fig. 1 as an example, the vapor quality is approximately 0.4 after an isenthalpic expansion and the equivalent volume fraction of the solid CO_2 is less than 0.3 %. However the assumed ideal homogeneous flow conditions cannot always be achieved. Previous experiments of several expansion devices in the open cycle have shown that flow behavior is strongly depending on the inlet condition of the expansion (Xu et al., 2018). The tube wall in the downstream of expansion could greatly influence particle agglomeration (Liu et al., 2010 and 2012) which could eventually influence the homogeneity of the flow and reduce the heat transfer as well (Yamasaki et al., 2017). Further investigations are still required in order to fully understand the CO_2 solid-gaseous sublimation flow in a refrigeration cycle, so that it could be brought into practical applications.
If the technical challenges could be overcome, CO_2, especially regarding the non-flammability, would be a reasonable replacement for R-23[1] in certain refrigeration applications such as environmental simulation and freeze drying process at temperatures of down to -80 °C (Langebach et al., 2016).
In this study, a small scale demonstration unit featuring a visualization section is designed also based on the principle of “dry sublimation”. First experimental results on this system are presented.

2. SYSTEM SETUP

In this section the design of the demonstration unit and its main components are introduced. The cycle and dimensions of the machine can be seen in Fig. 2.

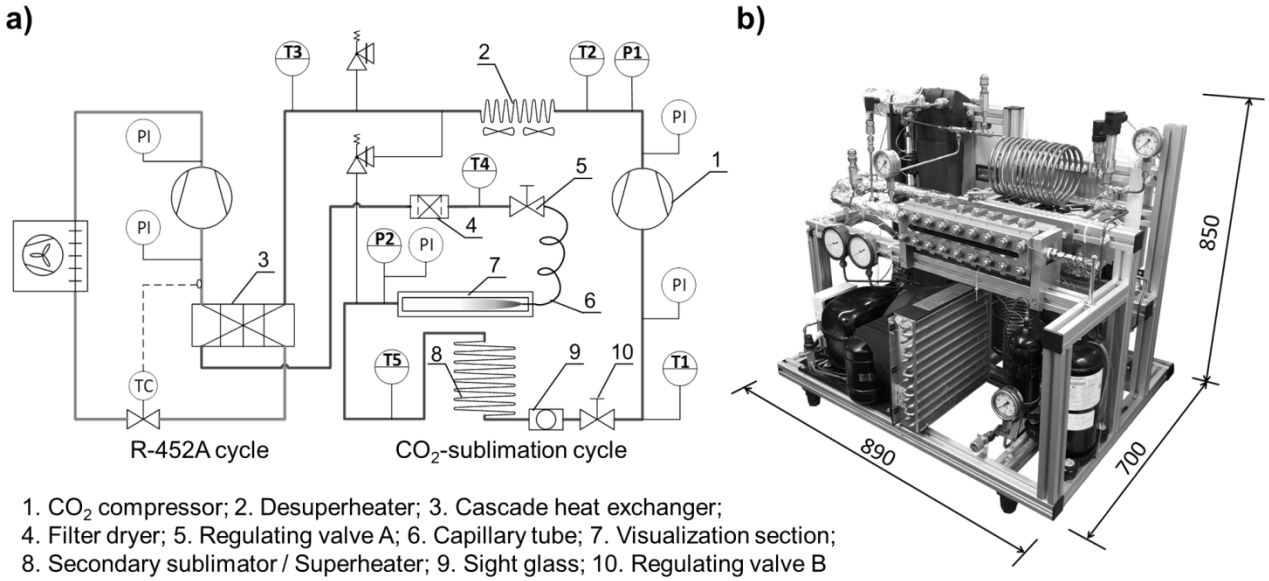

1. CO_2 compressor; 2. Desuperheater; 3. Cascade heat exchanger;
4. Filter dryer; 5. Regulating valve A; 6. Capillary tube; 7. Visualization section;
8. Secondary sublimator / Superheater; 9. Sight glass; 10. Regulating valve B

Figure 2: The demonstration unit: a) schematic diagram; b) photo

The upper stage of the cascade is a conventional refrigeration cycle consisting of a condensing unit, a plate heat exchanger as well as a thermostatic expansion valve and is operated with the refrigerant R-452A.
The lower stage is equipped with a standard hermetic rolling piston compressor for CO_2 with a displacement of 5 cm³. The rotation speed can be varied between 2700 and 6000 rpm by means of a frequency converter. PAG PZ100S is used as Lubricant oil. There is no oil separator in the system. Since the discharge temperature of CO_2 is expected to be very high, a simple desuperheater is built in between the compressor and the cascade heat exchanger. It consists of a horizontally installed copper-helix with a length of approximately 5 m and two DC fans utilized as air supply.
The main throttling device of the lower stage is a capillary tube with a length of 1 m and inner diameter of 0.7 mm. In addition there are two regulating valves in the system. Valve A is located at the inlet of the capillary tube while valve B is installed in the suction line of the compressor. The

[1] Trifluoromethane: normal boiling point -82.1°C; Global Warming Potential GWP_{100}=14800.

interplay of these two valves should enable to adjust the evaporation / sublimation pressure within a certain range.
The sublimation section is the most important part in this system and it has two main tasks. Firstly the solid CO_2 should be able to go through the whole section with less clogging and get fully sublimated. Secondly the flow and sublimation process should be preferably visible.
The first design with 3 standard round sight glasses in series is failed. On the one hand, the repeating change in cross-section area between the sight glasses and connection pipes increase the chance of blockage, and on the other hand the observed flow is not fully developed and can hardly represent the condition of a typical pipe flow. A glass tube could be a better option for the visualization in this case. However the high system pressure of CO_2 is problematic, especially considering the potential blockage in operation. Concerning safety issues, a robust long sight glass is finally chosen. It has a square flow channel with an area of 18 mm × 30 mm and the visible length is 298 mm. The detailed view and geometry of the sight glass is illustrated in Fig. 3 and Fig. 4.

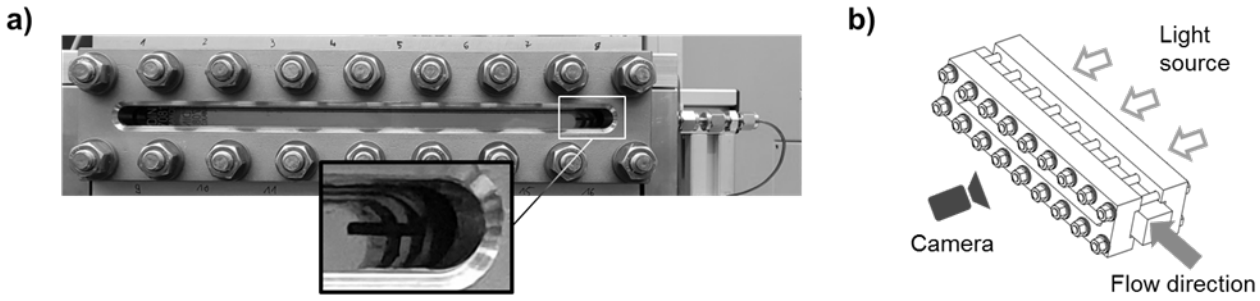

Figure 3: The visualization section: a) photo in detailed view; b) setup for the visualization

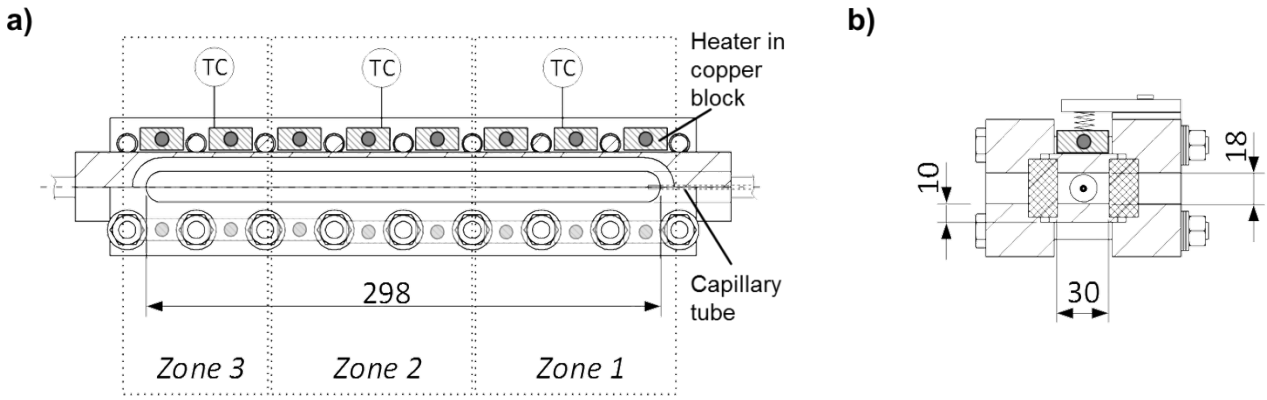

Figure 4: Geometry of the sight glass with electrical heating: a) frontal view; b) cross-section view

The sight glass is equipped with electrical heaters. The heating area is divided into 3 zones. Overall 16 cartridge heaters are used. The single heater is firstly installed in the center of a copper block and then the block is pressed onto the outer surface of the flow channel in the area between two screws. For each zone, a thermocouple measures the upper surface temperature of the sight glass wall and is connected to a temperature controller, so that the heating temperature of each zone can be set separately. The first two heating zones are equipped with 6 heaters and the last with 4 heaters. Each heater has a nominal heating power of 30 W. Thus the maximal heating power for the whole section is 480 W. However, due to the limitation of the geometry as well as lack of the way to install proper thermal isolation, an accurate heat balancing is very difficult and thus is renounced in this study.
As secondary sublimator/superheater, a copper-helix is vertically installed in downstream of the visualization section. An additional sight glass at the end of the entire sublimation section enables to observe if all solid CO_2 has been fully sublimated.
Besides the temperature measurements of the sight glass, there are 5 temperature and 2 pressure measuring points for the lower stage, which are shown in Fig. 2a. Pressures are measured with pressure transmitter with an uncertainty of ±0.25 %. The CO_2 sublimation pressure is obtained directly after the outlet of the visualization section. Temperatures are measured by clamp-on thermocouples of type T. The measuring data are sampled every 0.5 s. For the upper stage, two

manometers indicate the evaporation and condensing pressure and there are no direct temperature measurements. The environment temperature during the experiments is 18±2 °C.

3. RESULTS AND DISCUSSIONS

3.1 Pressure and Temperature Measurements

All experiments shown in this paper were carried out with the same compressor speed of 45 rps, corresponding to a theoretical suction volume of 0.81 $m^3 \cdot h^{-1}$. Valve B was set to full open. Two settings of valve A were used: one for sublimation operation and the other for conventional evaporation operation (set to full open).

During first tests the lower stage of the machine is filled with 500 g CO_2. The temperature and pressure developments after a start-up of the machine for the sublimation operation are shown in Fig. 5. The operation with sight glass heating on (Fig. 5a) is compared with the one without extra heating (Fig. 5b), where all heat intakes comes from the ambient and the supporting frame. The sublimation temperature is calculated based on the measured pressure values using fluid property software TREND 3.0 (Span et al., 2016). They are presented together with the surface temperatures of the sight glass in Fig. 6. The timelines of the diagrams are marked with 6 timestamps (TS) in total.

The first impression of the pressure curves is, that the CO_2 charge is too high. It can be seen from Fig. 5a that the condensing pressure of CO_2 reaches 60 bar, equivalent to a condensing temperature of 22°C. In this case, the machine is operated without much benefit of the upper stage. However, in other aspects, this specific operation condition reveals quite interesting results.

From Fig. 5a, shortly after the machine starts up, the sublimation pressure reduces below the triple point of CO_2 down to 3.2 bar at TS1 and remains nearly constant for about 3 min until TS2. Then temporary clogging periodically occurs and the pressure starts to fluctuate. At TS3 the pressure reaches the triple pressure within 2 s. Liquid CO_2 comes out of the capillary tube and the previous blockage is fast melted. This kind of self-cleaning mechanism by pressure fluctuations is very close to the findings by Huang et al. (2007). From Fig. 5b, where there is no extra heating, the sublimation pressure curve is similar at the beginning until TS4. After that the pressure decreases gradually. Most part of sight glass is blocked with CO_2 and the flow channel becomes increasingly smaller. The drop of condensing pressure also indicates that at this moment most of the CO_2 in the system becomes solid and accumulated in the sight glass instead of the condenser. The whole visualization section is fully blocked at TS5. However, the compressor continues running and eventually the suction pressure drops below the ambient pressure. At TS6 the compressor is stopped manually. Further visual observations related to the timeline are discussed in next subsection.

It has been found out that the heat transfer directly after the outlet of the capillary tube is much better than that in the downstream areas. As can be seen from the diagram, the installed heating power is not sufficient to maintain the surface temperature of the heating zone 1 at the preset temperature of 20°C. When heating is turned off, the surface temperature of zone 1 also drops much faster than that of other two zones.

In addition, temperature diagrams shows that T5, which is measured at the outlet of the visualization section, is 20 – 30 K higher than the sublimation temperature. It tells that the CO_2 after the visualization section is already superheated. However, at the same time solid CO_2 can still be seen in the sight glass within close proximity to the outlet. Although the clamp-on thermocouple does not measure the fluid temperature directly, it should not be the main cause of such large temperature deviation. It is believed that the solid and gaseous two phases are in non-equilibrium states. Considering the low heat transfer between the solid and gas, it is more difficult for a solid-gaseous two-phase system to reach its equilibrium than a liquid-gaseous system. In comparison, the occurrence of liquid CO_2 at TS3 makes a fast temperature equalization, which causes a sudden decrease of T5. Similar results can also be found at a time around 23 min in Fig. 5a and 21 min in Fig. 5b. At the outlet of the secondary sublimator, where the temperature is close to the ambient temperature (T1), no solid CO_2 particles have been observed. Thus, an extra superheating or rather long particle residence time should be considered when making sublimation heat exchanger designs, in order to prevent solid particles from entering the compressor.

In the following experiments CO_2 charge is reduced to 400 g. The new pressure and temperature curve for the operation without heating are presented in Fig. 7.

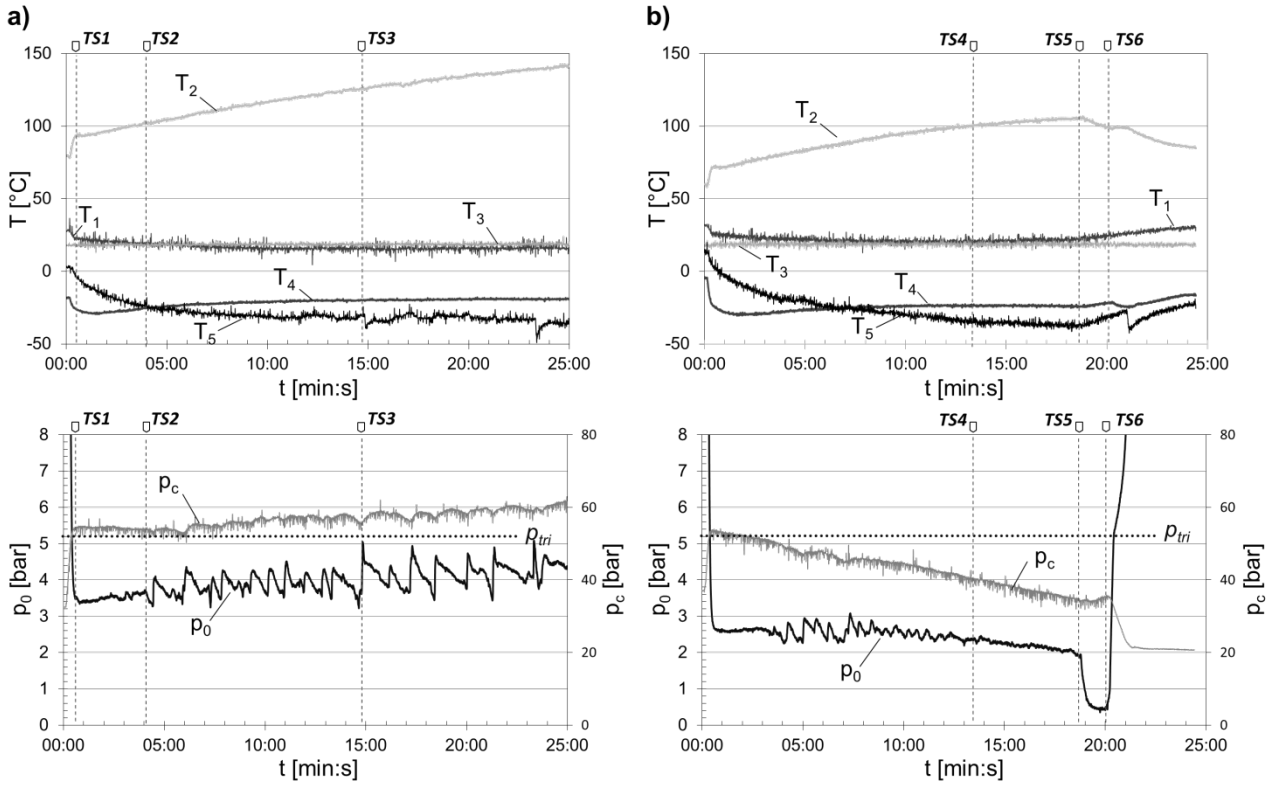

Figure 5: Development of temperatures and pressures for unstable sublimation operations. CO_2 charge 500 g: a) heating on at 20°C; b) heating off.

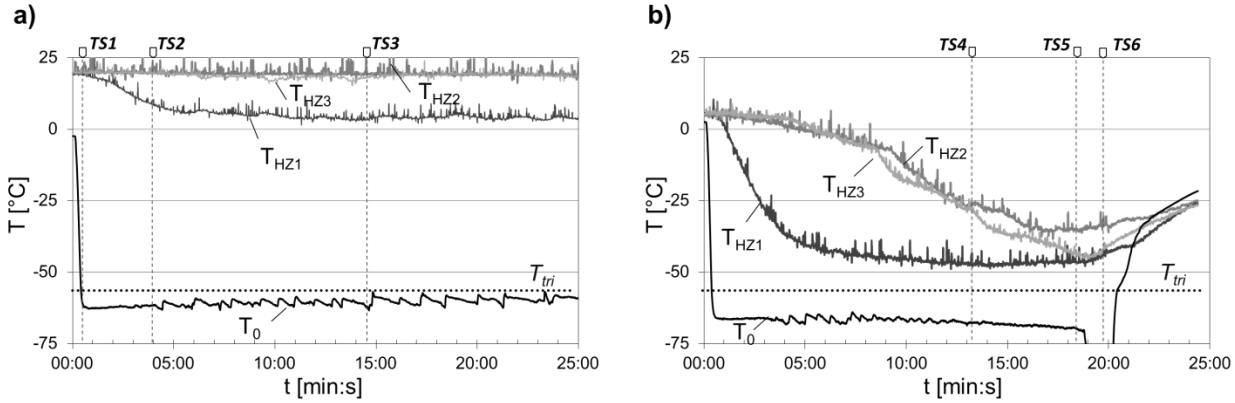

Figure 6: Surface temperature development for different heating zones (HZ) and calculated saturated sublimation temperature using TREND 3.0 (Span et al., 2016): a) heating on at 20°C; b) heating off.

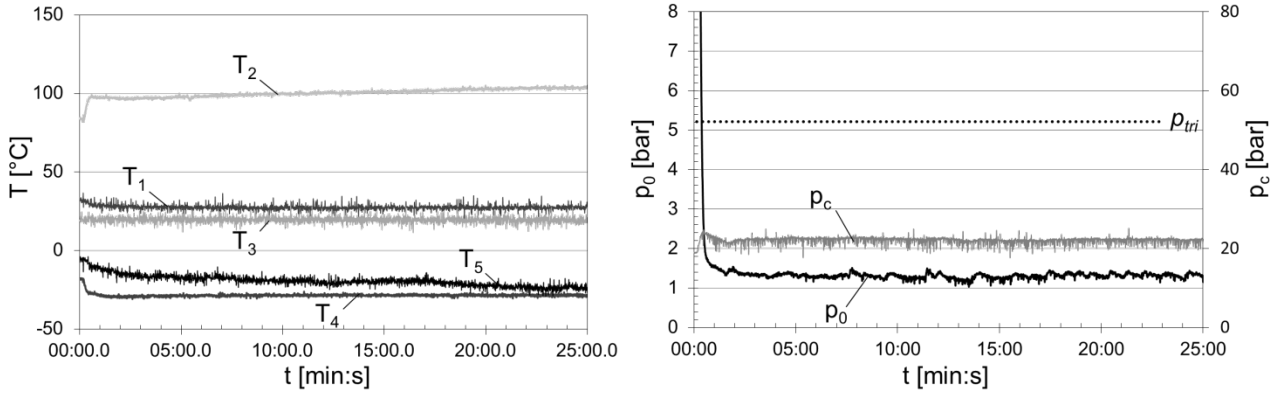

Figure 7: Development of temperatures and pressures for a stable sublimation operation. CO_2 charge 400 g.

Compared to Fig. 5b, there is a significant decrease in the condensing pressure and discharge temperature. The sublimation pressure is lower and with less fluctuation, though the overall cooling capacity should also be lower. It shows that a stable CO_2 sublimation cycle can be realized under the prescribed operating conditions, however, by no means an optimized one. For other operating conditions, for example at higher compressor speeds or higher opening degrees of the valve, large pressure fluctuation and blockage could still happen. It requires further investigations.

3.2 Observation of the Flow Patterns

Different flow patterns observed during the experiments are shown in Fig. 8.

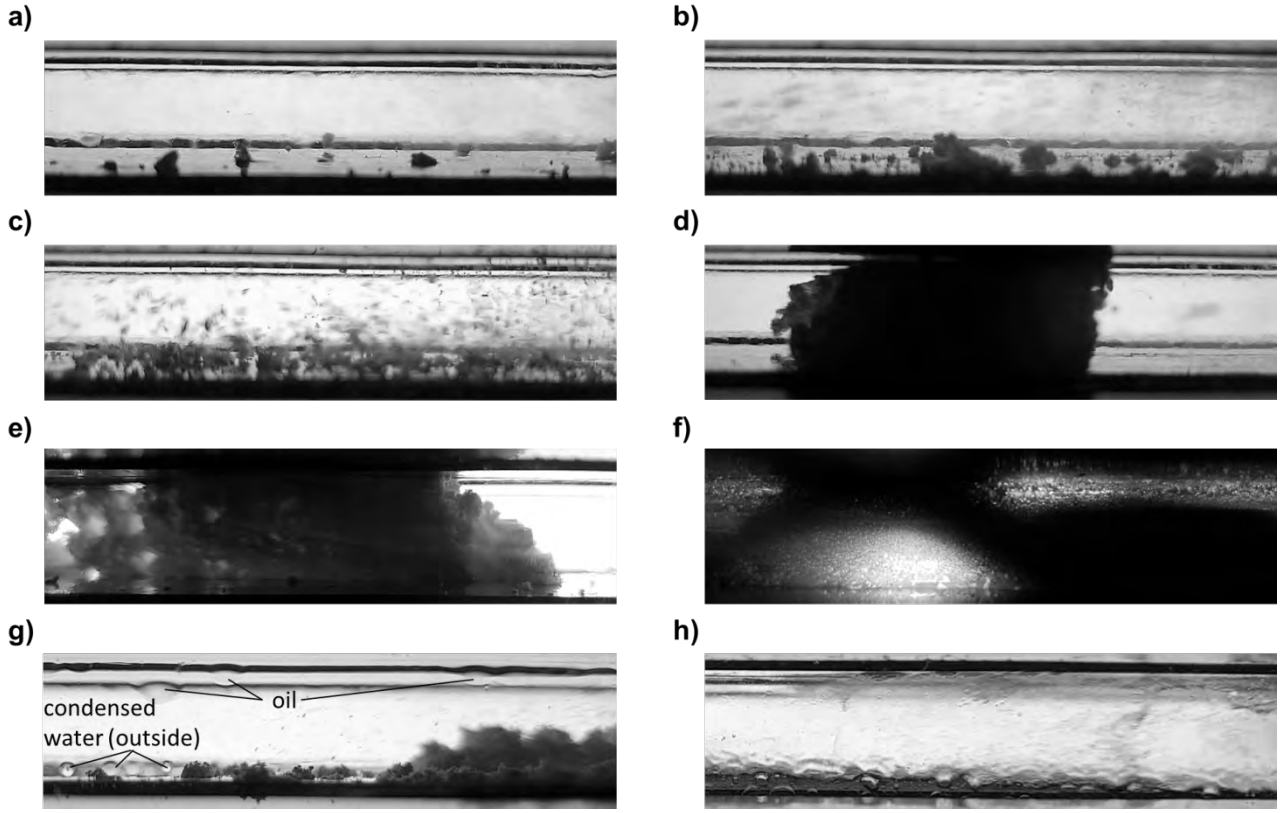

Figure 8: The two phase flow pattern: a) homogeneous S-G (solid-gaseous) flow; b - e) unstable S-G flow with temporary blockage; f) full blockage; g) stable S-G flow (stratified); h) liquid-gaseous (L-G) flow (stratified / annular).

A homogeneous solid-gaseous (Fig. 8a) flow can be seen shortly after the machine starts up at a time between TS1 and TS2 (compare Fig. 5). The solid CO_2 in the main stream are mostly primary particles and their sizes are in range of several microns (Xu et al. 2018), so it is hardly resolvable by the camera. When the primary particles contact the hot surface, it gets immediately sublimated. Only few solid CO_2 particles remain on the surface. As more and more CO_2 particles are deposited on the surface (Fig. 8b), they serve as an isolation layer and reduce the rate of sublimation. At the same time some deposited CO_2 get entrained into the main stream (Fig. 8c) and forms larger agglomerated particles in size of several millimeters (Liu et al., 2010 and 2012). At this stage, if no new balance for sublimation, deposition and re-entrainment can be achieved, the flow will become unstable and turn into two new forms (Fig. 8d and 8e). They both look like the plug flow with solid CO_2. The difference between these two is that the “plug” in Fig. 8d is pushed by the pressure difference and moves in the downstream direction, while in Fig. 8e the “plug” is stationary. With the porous structure it does not fully block the flow channel and can still be fast sublimated. After the release of the “plug” the flow pattern changes back to its starting form (Figs. 8b and 8c).This process repeats periodically and causes the pressure fluctuation (starting from TS2 on the timeline). If the sublimation speed is even slower (for example without extra heating), the porous CO_2 plug will gradually turn into a large dense block (Fig. 8f) between TS4 and TS5 on the timeline (compare Fig. 5b). The flow channel will become increasingly smaller and eventually a full clogging takes place.

The discovered stable solid-gaseous flow is stratified (Fig. 8g). It should be achieved when the rate

of sublimation, deposition and re-entrainment reach a balance. Unlike the stratified liquid-gaseous two-phase flow (Fig. 8h), however, there is no regular phase boundary for the solid-gaseous flow.
It should be mentioned, that the observed flow pattern is influenced by the lubricant oil to some degree. Sometimes, a thin oil layer or droplets can be found near the upper and lower surface of the sight glass wall, as can be seen in Fig. 8g. It is distinguished from the condensed water on the outer surface of the sight glass. However in most cases, it is not clear, how the oil flows together with the solid-gaseous CO_2. It is believed that there is no oil return problem during the experiments, since oil can be constantly seen in the sight glass at the compressor suction line. However, it should be noted that the wall temperature of an actual sublimator under practical operating conditions is much lower than the experimental conditions in this study, which could cause oil return problems. Therefore, further investigations on oil management for the sublimation cycle are required. The effect of oil in the sublimation heat exchanger is complicated. On the one hand, it could potentially reduce the heat transfer, while on the other hand it could serve as lubricant for the solid particles and lower the chance of blockage as well.

4. CONCLUSIONS

A novel small scale demonstration unit for CO_2-sublimation cycles featuring a visualization section is introduced, which enables for the first time observations of solid-gaseous two-phase flow in a closed refrigeration cycle. A basic study of the flow patterns is made. The development in flow patterns is compared with the temperature and pressure changes simultaneously. A stable operation of the CO_2 cycle below the triple point has been achieved under particular operating conditions, in which the rate of sublimation, deposition and re-entrainment reach a balance. It can be inferred that refrigerant charge, valve opening degrees and compressor speed all have influences on the stability of the process. Further investigations will be focused on the system performance under different operating conditions and oil management.

ACKNOWLEDGEMENTS

We gratefully acknowledge financial support provided by the Federal Ministry of Education and Research, Germany (grant No. 03VP01860)

NOMENCLATURE

GWP_{100}	global warming potential over 100 years (-)	HZ	heating zone (-)
p	pressure (kPa)	T	temperature (K)
t	time (s)	TS	timestamps (-)

Subscript

0	evaporation / sublimation	c	condensation
tri	triple point		

REFERENCES

Huang, D., Quack, H., & liang Ding, G., 2007. Experimental study of throttling of carbon dioxide refrigerant to atmospheric pressure . Applied Thermal Engineering , 27(11–12), 1911-1922.

Iwamoto, Y., Yamasaki, H., & Niu X., D., 2015. Experimental study on system performance of ultra-low temperature cascade refrigeration system using carbon dioxide with tapered evaporator/sublimator. Proceedings of the 24th IIR International Congress of Refrigeration Yokohama, Japan. IIF-IIR

Langebach, R., Hesse, U., & Xu, Y., 2016. CO_2 as an Alternative Refrigerant for Applications Below -50°C. 2016 Purdue Conferences. 16th International Refrigeration and Air Conditioning Conference at Purdue, West Lafayette, United States.

Liu, Y.-H., Calvert, G., Hare, C., Ghadiri, M., & Matsusaka, S., 2012. Size measurement of dry ice particles produced from liquid carbon dioxide. Journal of Aerosol Science, 48(Supplement C), 1-9.

Liu, Y.-H., Maruyama, H., & Matsusaka, S., 2010. Agglomeration process of dry ice particles produced by expanding liquid carbon dioxide. Advanced Powder Technology, 21(6), 652-657.

Span, R., Eckermann, T. H., Hielscher, S., Jäger, A., & Thol, M., 2016. TREND. Thermodynamic Reference and Engineering Data 3.0, Lehrstuhl fuer Thermodynamik, Ruhr-Universitaet Bochum.

Xu, Y., Langebach, R., Alvear, R. S., & Hesse, U., 2018. Investigation on flow pattern, particle size and clogging during the expansion of CO_2 into the solid-gaseous region below the triple point. Proceedings of the 13th IIR Gustav Lorentzen Conference on Natural Refrigerants, Valencia, Spain.

Yamaguchi, H., & Zhang, X.-R., 2009. A novel CO_2 refrigeration system achieved by CO_2 solid–gas two-phase fluid and its basic study on system performance. International Journal of Refrigeration , 32(7), 1683-1693.

Yamaguchi, H., Niu, X.-D., Sekimoto, K., & Neksa, P., 2011. Investigation of dry ice blockage in an ultra-low temperature cascade refrigeration system using CO_2 as a working fluid. International Journal of Refrigeration, 34(2), 466-475.

Yamasaki, H., Yamaguchi, H., Hattori, K., & Neksa, P., 2017. Experimental Observation of CO_2 Dry-ice Behavior in an Evaporator/Sublimator. Energy Procedia, 143, 375-380.

Manuscript ID: 486
DOI: 10.18462/iir.icr.2019.0486

Experimental analysis on the thermal performance of a R290 air source heat pump water heater

Dehua CAI[(a)], Lijuan Niu[(a)], Guogeng HE[(a)], Xiao Liang[(a)]

[(a)] School of Energy and Power Engineering, Huazhong University of Science and Technology Wuhan, 430074, China, 490316551@qq.com

ABSTRACT

In this paper, an experimental apparatus of air source heat pump water heater (ASHPWH) using R290 as working fluids was established in a climatic chamber to evaluate its performance and application feasibility. The air source heat pump water heater increased the water temperature up to 70℃ at working conditions of 0℃, to 65 ℃ and 55 ℃ at working conditions of -7℃ and -15℃, respectively, without coefficient of performance (COP) decreasing compared to the typical range of ASHPWH. Among all the testing conditions, the maximum discharge pressure of the compressor is 3.11MPa, the maximum discharge temperature is 98.8℃, and the maximum pressure ratio is 8.1, which are in the valid operating range of the compressor. The influence of refrigerant charge and capillary tube length on the system performance were also investigated, results show that the suitable charge not only increases COP, but also reduces pressure ratio and discharge temperature.
Keywords: R290, air source heat pump water heater, experimental analysis, high water temperature, performance analysis

1. INTRODUCTION

Refrigerants used in the heat pump system may cause environmental problems such as ozone layer depletion and the greenhouse effect. The studies of alternative environmentally friendly refrigerants can be divided into four sectors: pure hydrofluorocarbons (HFCs) with low-GWP, natural refrigerants, hydrofluoroolefins (HFOs) and blends of the above mentioned refrigerants (Calm, 2008).

R290, as a hydrocarbon, is a natural existing substance which causes almost no damage to the environment with zero ODP and very low GWP and has been considered as a potential substitute. R290 is also a by-product in the refinery process and is therefore inexpensive. Its thermodynamic properties are very similar to R22 and it has good compatibility with naphthenic mineral oils, thus it can be used in the original system without major modification. D. Sánchez et al. (Sánchez et al., 2017) evaluated the performance of R1234yf, R1234ze(E), R600a, R290 and R152a as R134a alternatives and found that R290 obtained the best results: cooling capacity and COP increased by 40.5% to 67.4% and 2.8% to 22.4% respectively, with a increment in power consumption up to 44.8% compared to R134a. Ki-Jung Park et al. (Park and Jung, 2007) measured the thermodynamic performance of two pure hydrocarbons and seven mixtures to replace R22 in a heat pump/air-conditioner at the evaporation and condensation temperatures of 7 ℃and 45 ℃ ,respectively. The COP of R290 is 1.8% higher than that of R22 and evaporation capacity decreased by 11.5%. The discharge temperature was reduced by 17.3 ℃ and the refrigerant charge was 44.4% of R22. Other researchers got the similar conclusion. Yunho Hwang (Hwang et al., 2007) found the COP of R290 is 11-12% and 4-9% higher than that of R404A and R410A respectively under the condensing temperature of 35℃ and evaporating temperature of -23.3 ℃ and 1.7 ℃.

The main drawback of R290 is its flammability. In fact, many studies have been done to deal with this problem, including reducing the refrigerant charge by optimizing the heat exchanger, capillary tube length or system control, and studying refrigerant distribution regularities in various components (Blanco Castro et al., 2005; Fernando et al., 2004; Ghoubali et al., 2017; Saravanan et al., 2016; Tang et al., 2017; Thonon, 2008). In addition, for an ASHPWH system, the units containing refrigerant can be positioned outside of the house and has hardly any danger of explosion, there are

no severe limitations for the use of hydrocarbon refrigerants in most countries (Granryd, 2001). Therefore, it's quite possible to achieve the safe use of R290 in small capacity heat pump water heaters with precautions. However, there are limited studies about R290 heat pump water heaters. Redouane Ghoubali et al. (Ghoubali et al., 2017) researched a R290 ASHPWH system at the environmental temperature of 7 ℃ and raised the water temperature up to 53.3 ℃, mainly to reduce the refrigerant charge by testing three types of condensers. P. Fernando et al (Fernando et al., 2007) established a water-to-water heat pump using R290 to simulate the ground source heat pump and the heat source fluid are varied from -10 ℃ to 10 ℃ with the constant condensing temperature up to 60 ℃. Studied the relation between refrigerant charge and evaporating/condensing temperature. Other studies on the heat pump water heater involved R290 are mainly about the mixture refrigerant of R290 and other HFCs (Lv et al., 2015; Yu et al., 2010). On the other hand, Chinese standard provides that the outlet temperature of the heat pump water heater is 55 ℃. But the hot water of 40-55 ℃ have health risks, because it is suitable for the propagation of legionella, which can cause atypical pneumonia of a high mortality rate and usually spread by air conditioning system and the living hot water system (Puckorius, 1995). In order to ensure the safety of water supply, this paper try to raise up the water temperature up to 70 ℃.

No researcher has tried to raise the water temperature up to 70 ℃ in ASHPWH using pure refrigerant R290 or extend the working condition down to -15 ℃. As well known, it is difficult for air source heat pump water heater to heat water at low ambient temperature conditions or raise the water temperature up above 60 ℃ under nominal conditions because the low evaporating temperature and high condensing temperature will make the discharge temperature and pressure ratio exceed the operating range the compressor can endure. Taking advantage of R290's low saturation pressure at the high temperature range, this paper tried to raise the hot water temperature up to 70 ℃ in a heat pump water heater bench tester under different temperature conditions, and measured the performance mainly about the discharge temperature, pressure ratio and water heating rate, to validate its feasibility.

2. EXPERIMENTAL FACILITY AND PROCEDURE

2.1. Comparison of discharging temperature with different refrigerant

The performance of R290 ASHPWH producing 70 ℃ hot water was compared with other refrigerants under various conditions. The thermal calculation was carried out and the condensing temperature was set to 75 ℃, while the evaporating temperature was set to 7.2 ℃, 1 ℃, -5 ℃, -12 ℃ and -20 ℃ respectively. The superheat degree is 10 ℃ and the subcooling degree is 8.3 ℃. The isentropic efficiency of compressor is assumed to be 0.72. R410A and R404A are not involved because of their relatively low critical temperature (<75 ℃).

The theoretical calculation of discharge temperature for the assumed isentropic efficiency are shown in Figs.1. Under the same conditions, the discharge temperature of R290, R417A and R134a are approximately the same which is considerably lower than that of R32, R22 and R407C, while the pressure ratio of R134a and R417A are the highest which exceed 10 when the evaporating temperature is below -5 ℃. Generally, the highest discharge temperature and pressure ratio that an ordinary compressor can endure are 130 ℃ and 10, respectively. Therefore R290 with low discharge temperature and pressure ratio has obvious advantages in producing high temperature hot water especially at low temperature conditions. For a R290 ASHPWH, when the condensing temperature is 75 ℃ and the evaporating temperature is -12 ℃, the discharge temperature and pressure ratio are 108 ℃ and 8.823 respectively. When the condensing temperature is 65 ℃ and the evaporating temperature is -20 ℃, the discharge temperature and pressure ratio are 101 ℃ and 9.58 respectively. So, it is feasible for a R290 ASHPWH to produce hot water of 70 ℃ when the evaporating temperature is above -12 ℃ and obtain 60 ℃ hot water when the evaporation temperature is -20 ℃ through the above thermal calculation.

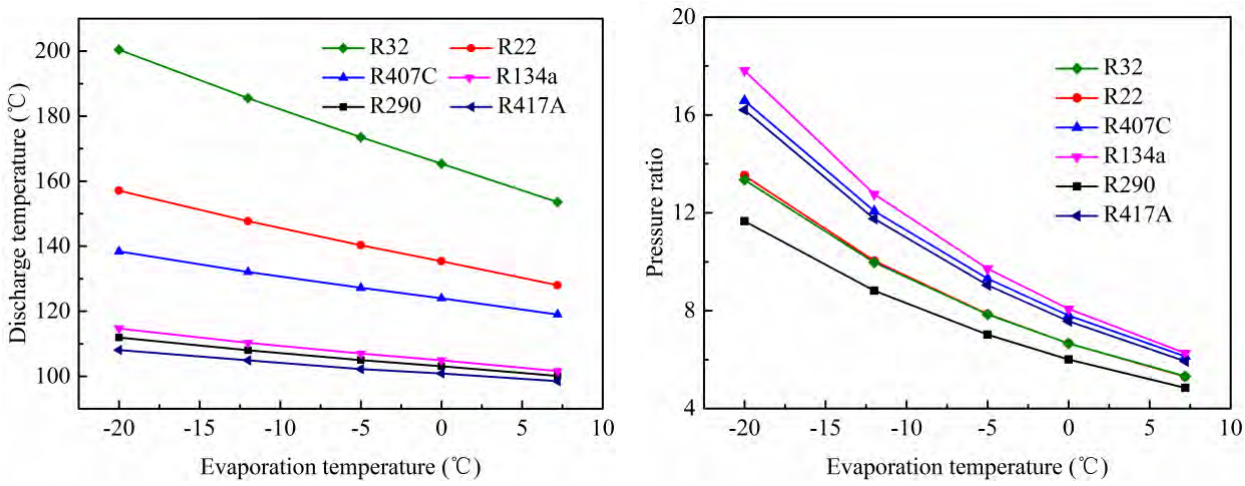

Figure 1. Evolution of discharge temperature and compression rate with the evaporation temperature for six refrigerants

2.2. Description of the experimental facility

As shown in Fig.2, the testing ASHPWH system consists of a R290 specific rotary compressor (629 W) for HPWH, the external machine of a heat pump air conditioner (833 W) as evaporator, a double-pipe heat exchanger as condenser, capillary, a water pump and a water tank (20 L). The whole testing system was placed in a climatic chamber designed for the performance measurement of a 5 kW ASHPWH, in which the temperature and humidity can be controlled at a constant value independently. The climatic chamber can create the constant temperature from -25 ℃ to 40 ℃. The connection line of water and refrigerant were wrapped by thermal insulation cotton with a thickness of 5 cm.

The ASHPWH works all the year round and is influenced by the annual temperature variation severely, especially when working at low temperature. In order to evaluate the influence, the experiment was performed under five different working conditions, as shown in table 1. Before the HPWH system starts, the climatic chamber needs to reach the set temperature and maintain stability, which is controlled by PID controllers.

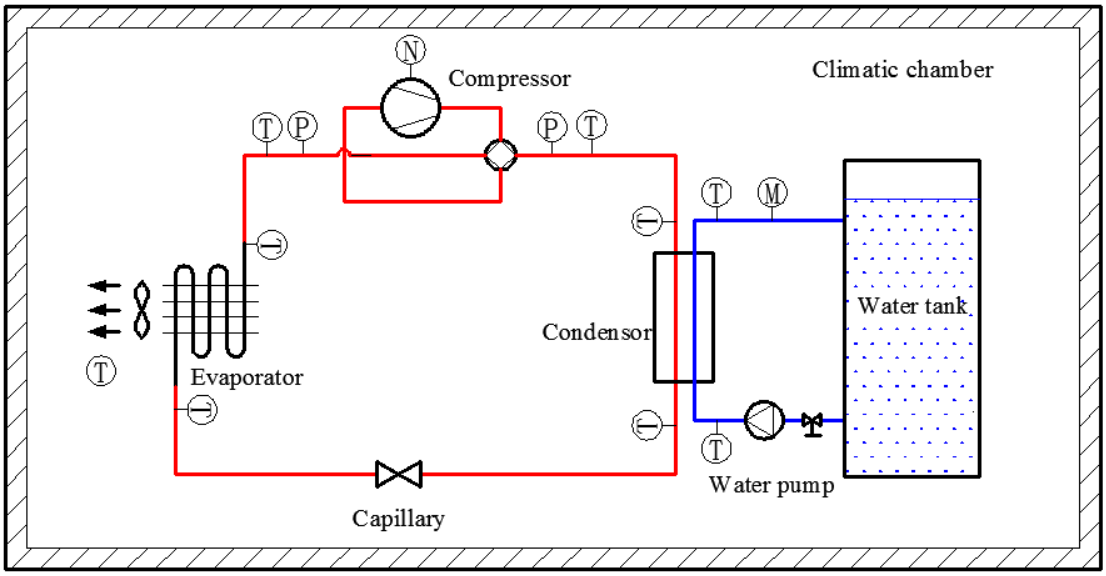

Figure 2 Schematic diagram of the ASHPWH system.

Table 1. Testing condition

	A	B	C	D	E
Dry-bulb temperature/℃	20	7	0	-7	-15
Wet-bulb temperature/℃	15	6	-1	-8	-15

2.3. Data reduction and experimental uncertainties

Many measurement points were arranged to evaluate the performance of system in real time. The wet bulb temperature and wet bulb temperature of the climatic chamber were acquired by temperature and humidity sensors equipped in the chamber. The mass flow rate of the circulating water was measured by a electromagnetic flowmeter, which was adjusted to 0.85m3/h according to heat transfer coefficient. The water temperature at the inlet and outlet of the condenser were measured by two PT_100 sensors and the other temperature parameters such as refrigerant temperature at inlet and outlet of condenser, evaporator and compressor were also precisely acquired by thermocouples. All the RTD sensors and thermocouples have been calibrated by ice water mixture and boiling water. The suction and discharge pressure were measured by two pressure transmitters. And transient electric input power was acquired by an electrical parameters meter. All the data were stored in a PC automatically through an advanced data acquisition unit (Agilent model 34970A), the time step was set to 5 seconds. In this paper the inlet water temperature of the condenser is used to evaluate the performance change. The average COP is calculated by Eq.1 Eq.2 and Eq.3 in a certain time interval, which depends on the choice of t1 and t2.

$$Q = C_P * V * \rho * (T_2 - T_1) \quad \text{Eq. (1)}$$

$$P = (t_2 - t_1) * \frac{1}{n} * \Sigma_{T_1}^{T_2} \quad \text{Eq. (2)}$$

$$COP = \frac{Q}{P} \quad \text{Eq. (3)}$$

Table 2. Specifications of instrumentation

Instrument	Type	Range	Uncertainty
Thermocouple	Type T		±0.5 ℃
Thermo-resistance	RTD PT-100	-50~200 ℃	±0.1 ℃
Pressure transmitters	MPM4730 JUMO 401010/000	-0.1~3.5 MPa 0~1 MPa	±0.25%
Electrical parameters meter			±0.5%
Electromagnetic flowmeter	MFE600-8-102-2.5H00-0000	0.09~0.9 m3/h	±0.5%

3. RESULTS AND DISCUSSION

3.1. Water heating performance

Fig.3 shows the evolution of water temperature and transient COP with the time under five different working conditions. When the environmental temperature was above 0 ℃, the water temperature rose to 70 ℃, while under conditions of -7 ℃ and -15 ℃, the water temperature went to 65 ℃ and 55 ℃, respectively. The final water temperature was chosen depending on the heating rate and transient COP. It is meaningless to continue heating up when the instantaneous COP is below 1.The water heating rate decreases as the environmental temperature decreases and the water temperature rises, the water temperature curve also becomes gentle. To raise water from initial temperature to 55 ℃, it takes 49min, 35 min, 25 min, 23 min and 19 min for conditions of -15 ℃,

-7 ℃, 0 ℃, 7 ℃and 20 ℃. While it takes 43 min, 36 min and 29 min to get 70 ℃ under conditions of 0 ℃, 7 ℃, and 20 ℃, the highest hot water productivity is 40.5L/h. There are three reasons for the decrease of heating rate as the environmental temperature decreases and the water temperature rises: first, the volumetric heating capacity decreases; second, the refrigerant mass flow rate decreases due to low compressor volumetric efficiency and low specific volume of the refrigerant at the compressor suction inlet; third, the water side heat transfer coefficient also decreases with the increase of water temperature.

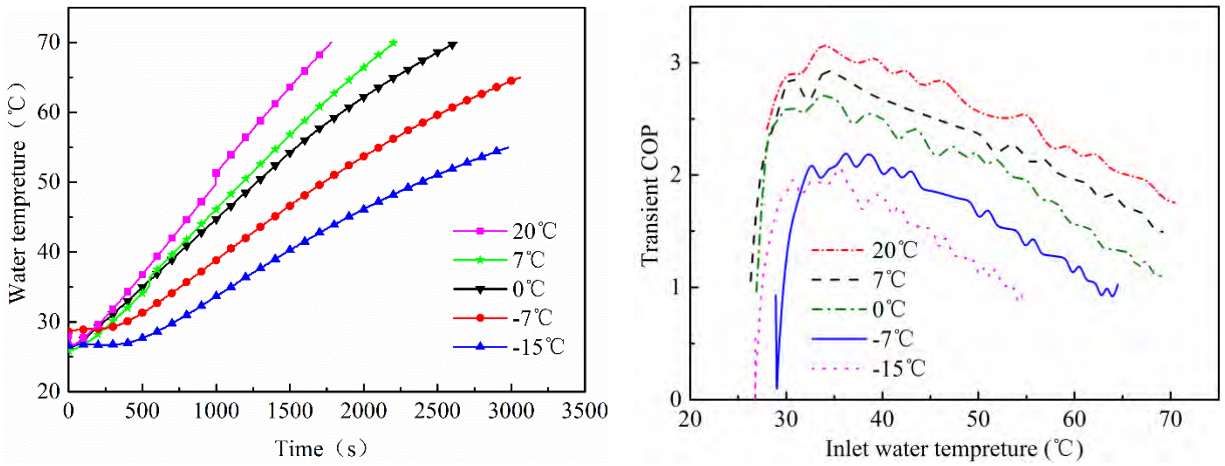

Figure 3. Evolution of water temperature and transient COP with the time under different working conditions

The transient COP is the average COP during 1min. As shown in Fig.3, with a higher environmental temperature, the transient COP increases apparently. At each environmental temperature, the transient COP increases at first and then decreases with a peak at the water temperature of 35 ℃. The peak values are above 2 for all of the conditions and above 3 at conditions of 20 ℃.The average COP is 1.9, 2.3 and 2.5 at conditions of 0 ℃, 7 ℃ and 20 ℃, when raising water temperature up to 70 ℃. Many studies about HPWH show that the typical range of COP is between 1.8 to 2.5 (Willem et al., 2017) and the COP is below 2 when the ambient temperature is between 4.4℃ and 15.6 ℃ (Shapiro and Puttagunta, 2013), which is corresponding with the test data but without hot water temperature up to 70 ℃. The further research about this test bench can perform from these aspects to improve COP: reduce the initial water temperature to 15 ℃, increase the volume of water tank (20 L) (Kim et al., 2004) and avoid the heat leakage by moving the condenser and water circulation system out of the climatic chamber

3.2. Discharge temperature and pressure

As well known, the discharge temperature, discharge pressure and pressure ratio of the compressor are three essential parameters for a high temperature ASHPWH. In this study, suction/discharge pressure and discharge temperature had been precisely acquired in real time through an advanced data acquisition unit, and the pressure ratio had been calculated, as shown in Fig.4. In Figs.4 (a) and (b), it can be seen that for a given environmental temperature, the suction pressure and the discharge pressure increase with the increase of the water temperature, but the discharge pressure increases at a higher rate based on the increase of pressure ratio in Fig.4 (c). For the same inlet water temperature, the higher environmental temperature means the higher suction pressure and discharge pressure, but the change of the discharge pressure is less obvious for that the pressure ratio decreases as the environmental temperature increases. The maximum of suction pressure is 0.603 MPa with a corresponding evaporating temperature of 8.1 ℃. The maximum of discharge pressure is 3.109 MPa with a corresponding condensing temperature of 79.6 ℃.

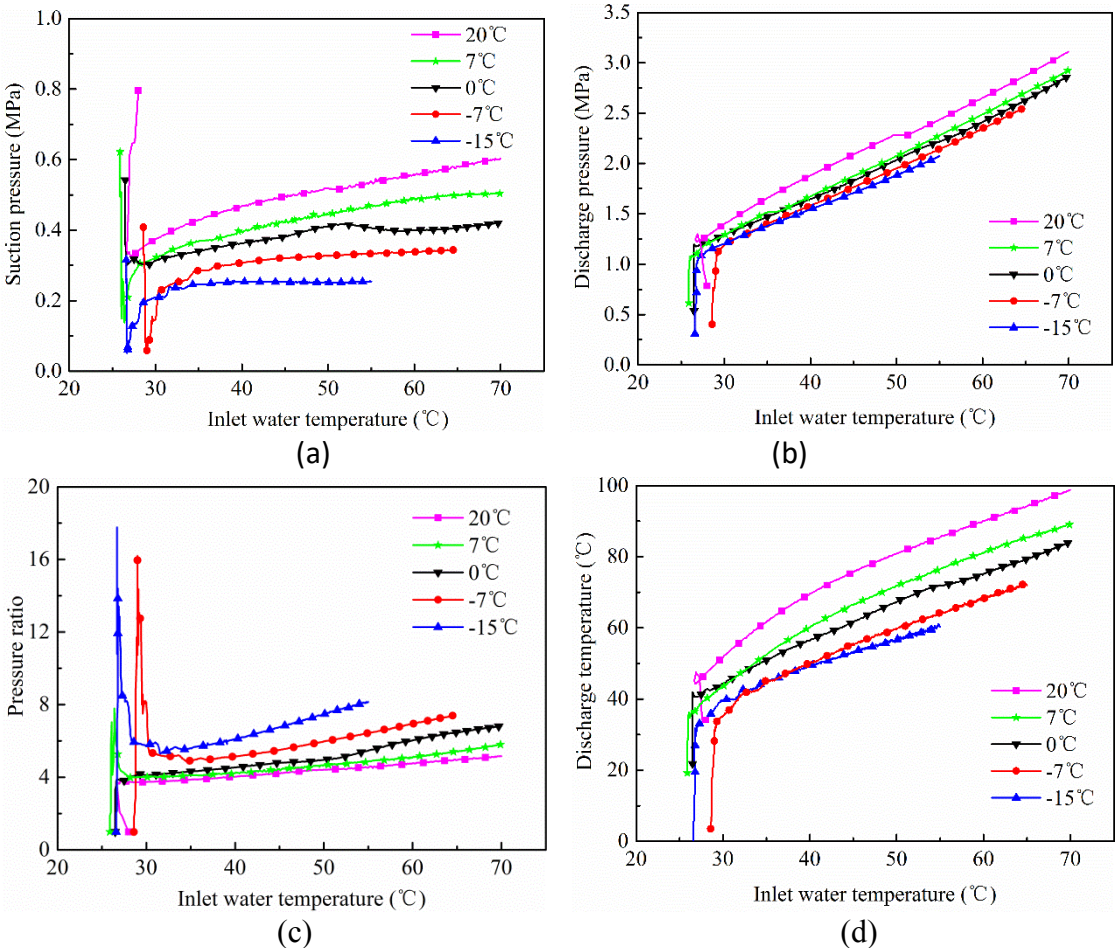

Figure 4. Evolution of suction pressure(a), discharge pressure(b), compression rate(c), discharge temperature(d) with the water temperature under five conditions

According to the Fig.4 (c), among the working conditions, when the environmental temperature is -15 ℃ and the inlet water temperature is 55 ℃, the pressure ratio has the maximum value of 8.1, which is still in the valid operating range of the compressor. When the environmental temperature is 20 ℃, 7 ℃ and 0 ℃, the pressure ratios is 5.2, 5.8 and 6.8 respectively for the certain inlet water temperature of 70 ℃.

According to the Fig.4 (d), the discharge temperature increases with the increase of environmental temperature. The discharge temperature reaches maximum value at the environmental temperature of 20 ℃ and the inlet water temperature of 70 ℃, which is 98.8 ℃ and very close to the thermal calculation of 100 ℃. For the other conditions of 7 ℃,0 ℃,-7 ℃and -15 ℃, the discharge temperature are 88.9 ℃, 84.3 ℃, 72.3 ℃ and 60.3 ℃ at the end of the heating cycle.

3.3. The influence of capillary tube length

Three types of capillary lengths are selected respectively to study the influence of capillary lengths on COP under five working conditions, as shown in table 3. The capillary lengths are 30 mm, 50 mm and 80 mm with the uniform diameter of 1mm. The average COP is 2.57 with the optimal capillary length of 30 cm at 20 ℃, and 2.07 with the optimal capillary length of 50 cm at 7 ℃. When the environmental temperature is below 0 ℃, the capillary length of 80 cm is more suitable. The pressure ratio increases with the increase of capillary lengths It can be seen that when the environmental temperature is below 0 ℃, the effect of capillary length on the pressure ratio is small, which is more obvious with the environmental temperature of 0 ℃ and above , especially the suction pressure.

Table 3. Performance of different capillary length under five conditions

Environmental temp./℃	Capillary length/ cm	Initial water temp./ ℃	Final water temp. /℃	reaching the final water temperature				
				Suction pressure/ MPa	Discharge pressure/ MPa	Pressure radio	Pressure change rate/%	COP
-15	50	26.3	55	0.264	2.155	8.16	1.1	1.30
	80	26.9	55	0.261	2.152	8.25		1.45
-7	50	27.5	65	0.348	2.634	7.57	2.5	1.34
	80	26.8	65	0.346	2.684	7.76		1.47
0	50	23.1	70	0.433	2.983	6.89	2.5	1.64
	80	27.2	70	0.428	3.02	7.06		1.76
7	30	25.6	70	0.523	2.867	5.48	10	1.90
	50	25.4	70	0.51	3.073	6.03	5	2.07
	80	26.5	70	0.495	3.135	6.33		1.92
20	30	25.4	70	0.62	2.961	4.78	8.8	2.57
	50	24.4	70	0.644	3.315	5.15		2.41
	80	27.1	70	0.578	3.233	5.59	7.5	2.35

4. CONCLUSIONS

The natural refrigerant R290 has been proposed as a promising substitute to the small heat pump system because of its similar thermodynamic properties with R22, the advantages of low saturation pressure, low GWP and zero ODP. This paper made calculations and experiments to confirm the feasibility of R290 heat pump water working under low temperature and heating high temperature water. The experiment was performed using an ASHPWH (629 W, 20 L) in a climatic chamber. The performance can be concluded as follows:

(1) Results show that the R290 ASHPWH can heat the water up to 55℃ at environmental temperature of -15℃, to 65℃ at environmental temperature of -7℃ and to 70℃ at the environmental temperature above 0℃, which improves the outlet water temperature up to 15℃ and has great significance for sanitary water use.

(2) The heating rate decreases with the increase of water temperature and the decrease of environmental temperature. For five conditions, the transient COP reaches peak value at water temperature of 33-36 ℃, and the peak value is above 2 for all conditions.

(3) The suction pressure, discharge pressure and discharge temperature increases with the increase of water temperature and environmental temperature. While the pressure ratio decreases with environmental temperature for the same water temperature. Among the testing conditions, the maximum discharge pressure is 3.109MPa, the maximum discharge temperature is 98.8℃, and the maximum pressure ratio is 8.1.

(4) For different environmental temperature and hot water temperature, the optimal capillary length is different. A short capillary is suitable for high environmental temperature and a long one is better for low environmental temperature.

ACKNOWLEDGEMENTS

This present study was supported by the National Natural Science Foundation of China (No. 51706077).

NOMENCLATURE

Cp	specific heat capacity (kJ/kg℃)	V	Volume flow rate(m^3/s)
ρ	Density (kg/m^3)	Q	cooling or heating power (kJ/s)
T	temperature (℃ or K)	P	Power consumption (kW)
t	Time (second)	COP	Coefficient of performance

REFERENCES

Blanco Castro, J., Urchueguía, J.F., Corberán, J.M., Gonzálvez, J., 2005. Optimized design of a heat exchanger for an air-to-water reversible heat pump working with propane (R290) as refrigerant: Modelling analysis and experimental observations. Applied Thermal Engineering 25, 2450-2462.

Calm, J.M., 2008. The next generation of refrigerants – Historical review, considerations, and outlook. International Journal of Refrigeration 31, 1123-1133.

Fernando, P., Palm, B., Lundqvist, P., Granryd, E., 2004. Propane heat pump with low refrigerant charge: design and laboratory tests. International Journal of Refrigeration 27, 761-773.

Fernando, P., Palm, B., Lundqvist, P., Granryd, E., 2007. Performance of a Single-Family Heat Pump at Different Working Conditions Using Small Quantity of Propane as Refrigerant. Experimental Heat Transfer 20, 57-71.

Ghoubali, R., Byrne, P., Bazantay, F., 2017. Refrigerant charge optimisation for propane heat pump water heaters. International Journal of Refrigeration 76, 230-244.

Granryd, E., 2001. Hydrocarbons as refrigerants— an overview. International Journal of Refrigeration 24, 15-24.

Hwang, Y., Jin, D.-H., Radermacher, R., 2007. Comparison of R-290 and two HFC blends for walk-in refrigeration systems. International Journal of Refrigeration 30, 633-641.

Kim, M., Kim, M.S., Chung, J.D., 2004. Transient thermal behavior of a water heater system driven by a heat pump. International Journal of Refrigeration 27, 415-421.

Lv, X., Yan, G., Yu, J., 2015. Solar-assisted auto-cascade heat pump cycle with zeotropic mixture R32/R290 for small water heaters. Renewable Energy 76, 167-172.

Park, K.-J., Jung, D., 2007. Thermodynamic performance of HCFC22 alternative refrigerants for residential air-conditioning applications. Energy and Buildings 39, 675-680.

Puckorius, P., 1995. Why Evaporative Coolers Have Not Caused Legionnaires' Disease. Ashrae Journal 37, 29-33.

Sánchez, D., Cabello, R., Llopis, R., Arauzo, I., Catalán-Gil, J., Torrella, E., 2017. Energy performance evaluation of R1234yf, R1234ze(E), R600a, R290 and R152a as low-GWP R134a alternatives. International Journal of Refrigeration 74, 269-282.

Saravanan, A.L., Murugan, R.S., Lal, D.M., 2016. Investigations on charge reduction strategies to use R290 as an alternative to R22 in a split air conditioner. Experimental Heat Transfer 30, 126-138.

Shapiro, C., Puttagunta, S., 2013. Field Performance of Heat Pump Water Heaters in the Northeast. Office of Scientific & Technical Information Technical Reports.

Tang, W., He, G., Cai, D., Zhu, Y., Zhang, A., Tian, Q., 2017. The experimental investigation of refrigerant distribution and leaking characteristics of R290 in split type household air conditioner. Applied Thermal Engineering 115, 72-80.

Thonon, B., 2008. A review of hydrocarbon two-phase heat transfer in compact heat exchangers and enhanced geometries. International Journal of Refrigeration 31, 633-642.

Willem, H., Lin, Y., Lekov, A., 2017. Review of energy efficiency and system performance of residential heat pump water heaters. Energy and Buildings 143, 191-201.

Yu, J., Xu, Z., Tian, G., 2010. A thermodynamic analysis of a transcritical cycle with refrigerant mixture R32/R290 for a small heat pump water heater. Energy and Buildings 42, 2431-2436.

Manuscript ID: 488
DOI: 10.18462/iir.icr.2019.0488

Refrigerant-distribution characteristics of a horizontal header with branch holes of 0.3 mm in diameter

Kazuhiro ENDOH

Hitachi, Ltd., Research & Development Group
832-2, Horiguchi, Hitachinaka, Ibaraki, 312-0034, Japan, kazuhiro.endo.un@hitachi.com

ABSTRACT

To improve heat-exchange performance, heat exchangers with channels with inner diameter of less than 0.5 mm have been studied. However, there is no knowledge about the distribution of vapor-liquid two-phase refrigerant. Therefore, the effect of inflow configuration of a horizontal header (channel cross-section: 0.7 x 0.7 mm^2) with branch holes (inner diameter: 0.3 mm; number of holes: 10) arranged vertically downward was experimentally evaluated. The results of the evaluation demonstrate that dimensionless standard deviation of refrigerant distributed in the present header with a one-side inflow configuration is 10%. The effect of mass flux at the header inlet on the distribution for the one-side inflow configuration is small but that for the both-side inflow configuration is large. Moreover, the dimensionless standard deviation for the present header (10%) is much smaller than that for a conventional header (65%) with 13-times-bigger hydraulic diameter.

Keywords: Refrigerant distribution, Vapor-liquid two-phase flow, Header, Small-diameter tube, Microchannel, Heat exchanger.

1. INTRODUCTION

To decrease air-side pressure loss and increase heat-transfer performance, heat exchangers with small-diameter tubes (i.e., inner diameter less than 0.5 mm) have been studied by Shikazono et al. (2006) and Endoh (2016). Endoh's experimental results show that the air-side pressure loss of the proposed heat exchanger (named a "tube-in-fin" heat exchanger, with tubes of 0.4-mm outer diameter) is 62% of that of a conventional fin-and-tube heat exchanger (with tubes of 5-mm outer diameter) for the same heat-transfer performance.

As for the evaporation heat-transfer coefficient of the refrigerant inside small-diameter tubes, correlations for an inner diameter greater than 0.5 mm were proposed by Miyata et al. (2011) and Enoki et al. (2015). Endoh (2018) reported the measurement results for an inner diameter of 0.3 mm. When the two correlations are extrapolated below an inner diameter less than 0.5 mm, Endoh's data exist between the two extrapolated correlations.

On the other hand, a header that distributes a vapor-liquid two-phase fluid to small-diameter channels with hydraulic diameter less than 0.5 mm has not been reported. Although differing in size, the horizontal headers studied by Koyama et al. (2004, 2006) and Kim et al. (2006, 2008, 2011, 2012) distribute fluids vertically downward. Koyama et al. (2006) used a header with an inner diameter of 9 mm (13 times that used in the present study) and six branches of multiport flat tubes, and Kim et al. (2011) used a header with an inner diameter of 17 mm (24 times) and ten branches of multiport flat tubes. They tested the distribution characteristics of the header without an internal protrusion of tubes in the case of one-side inflow of refrigerant R134a. The experimental results from both studies are twofold: as a branch becomes farther from the inlet of the header, the liquid phase ratio decreases; and as the quality of the refrigerant at the inlet increases, distribution performance worsens.

To understand the characteristics of the refrigerant distribution to small-diameter channels, in this study, the effect of inflow configuration of a horizontal header with ten branch holes (0.3 mm in diameter) distributing fluid vertically downward was investigated. The results of that investigation were then compared with those for conventional large-size headers.

2. EXPERIMENTAL SETUP AND TEST PROCEDURE

The header is horizontal, and the refrigerant flows into the end(s) and out of the bottom of the header. The specifications of the header used for an element experiment are listed in Table 1. The header has ten branch holes with diameter 0.3 mm. The inner cross-sectional shape of the header is square, and its dimensions were determined as follows. Under the assumption that a heat exchanger has a capacity of 100 W and 111 branches of tubes with an inner diameter of 0.3 mm, and refrigerant R134a is used, refrigerant flow rate is 0.022 kgh^{-1} per branch, the flow rate for the experimental header is 0.22 kgh^{-1}, which is ten times that for a branch. To be able to compare the experimental results with those of Koyama et al. (2004) and Kim et al. (2011), mass flux of refrigerant at the header inlet was set to 124 $kgm^{-2}s^{-1}$, which is close to the values used in those studies. This assumption leads to the cross-sectional dimensions of header of 0.7 x 0.7 mm^2. A hole pitch was set to 1.38 mm, whose value had been used for the tube-in-fin heat exchanger proposed by Endoh (2016). Two inflow configurations were used: “one side” and “both sides.” To create the both-side inflow, a T-shaped branch was set horizontally upstream of the header.

A system diagram of the experimental setup is shown in Fig. 1. The experimental setup has a vapor cycle that consists of a compressor (1), a heat exchanger (2), and an expansion valve (8). A small amount of high-pressure vapor is bypassed from the vapor cycle to a condenser (3), where the vapor becomes subcooled refrigerant. The refrigerant is then depressurized through an expansion (5) and is delivered to a preheater (6), where its quality is adjusted. The refrigerant is then sent to a test section of the header and a measuring part of refrigerant distribution.

The test section and the measuring part are shown in Fig. 2, and cross-sectional diagrams of one-side and both-side inflow configurations are shown in Fig. 3. Parts of the test section are bolted, and a sight glass is set on the top of the header for visualizing the fluid flow inside the header.

The branch holes of the test section are connected with small-diameter tubes (ϕ0.6 x ϕ0.3 x 300 mm^3) of the measuring part of refrigerant distribution, which are heated via heat-conducting plates by electric heaters. The refrigerant flowing into each branch hole is heated by an electric heater. The power of the heater for each branch is controlled in such a way that the temperature of heat-conducting plate at the outlet of each heated part is set at a superheated value of 6°C. A power value is obtained on the basis of a voltage between both ends of the heater and a current calculated from the value of a precision resistance and the voltage between both ends of the resistance. The refrigerant flowing through each tube merges in a junction part. Each part of experimental setup was insulated.

Since a liquid-phase refrigerant that has evaporative latent heat contributes to cooling in an evaporator, the distribution ratio of the liquid phase is important. However, the refrigerant flow rate for this experiment is so small that the flow rate of the liquid-phase refrigerant for each branch cannot be measured directly. Therefore, the distribution performance is evaluated on the basis of the electric-power ratio for each branch instead of the distribution ratio of the liquid phase, where electric power ratio $R_{We,i}$ for the i th branch is given as

$$R_{W_{e,i}} = W_{e,i}/W_e \qquad \text{Eq. (1)}$$

$$W_e = \sum_{i=1}^{n} W_{e,i} \qquad \text{Eq. (2)}$$

where $W_{e,i}$ is electric power of the heater for the i th branch, W_e is total electric power of heater, and n is number of branches.

The dimensionless standard deviation related to electric power (σ) is used as an index for the distribution performance and is given as

$$\sigma = \frac{1}{\overline{W_e}} \sqrt{\frac{1}{n} \sum_{i=1}^{n} (W_{e,i} - \overline{W_e})^2} \qquad \text{Eq. (3)}$$

$$\overline{W_e} = \frac{1}{n}\sum_{i=1}^{n} W_{e,i} \qquad \text{Eq. (4)}$$

where $\overline{W_e}$ is the arithmetic mean of electric power. Hereafter, the liquid-phase flow rate used in the experiments of Koyama et al. and Kim et al. is substituted by the electric power of the heater.

The test conditions at the header inlet are listed in Table 2. Refrigerant R134a was used, and the saturated temperature was 15°C. For evaluating the effect of mass flux, *G* was set to 62 and 124 kgm^{-2}s^{-1} for the one-side inflow. For the both-side inflow, the actual mass fluxes were half of those values. Qualities of refrigerant *x* were set to 0.2 and 0.4 for evaluating the effect of quality.

To reduce the heat exchange with the surroundings, the experimental setup was installed in a temperature-controlled room, where surrounding temperature was set close to the evaporation temperature of the refrigerant. The difference between the total amount of refrigerant-side heat exchange and the total electric power of the heaters was within 5% at *G*=124 kgm^{-2}s^{-1} and 10% at *G*=62 kgm^{-2}s^{-1}.

The test conditions were set by adjusting compressor speed, temperature of the cooling water for the condenser, openings of the two expansion valves, and the amount of refrigerant charged. REFPROP was used for the thermodynamic properties of R134a. Fluid flow in the header was observed by taking pictures at a capture rate of 2,000 fps with a high-speed camera through the sight glass.

Table 1. Specifications of header

Header	Inner shape	-	Square
	Width	mm	0.7
	Height	mm	0.7
	Hole pitch	mm	1.38
	Number of branches	-	10
Branch hole	Shape	-	Circle
	Inner diameter	mm	0.3
Inflow configuration		-	One side or both sides

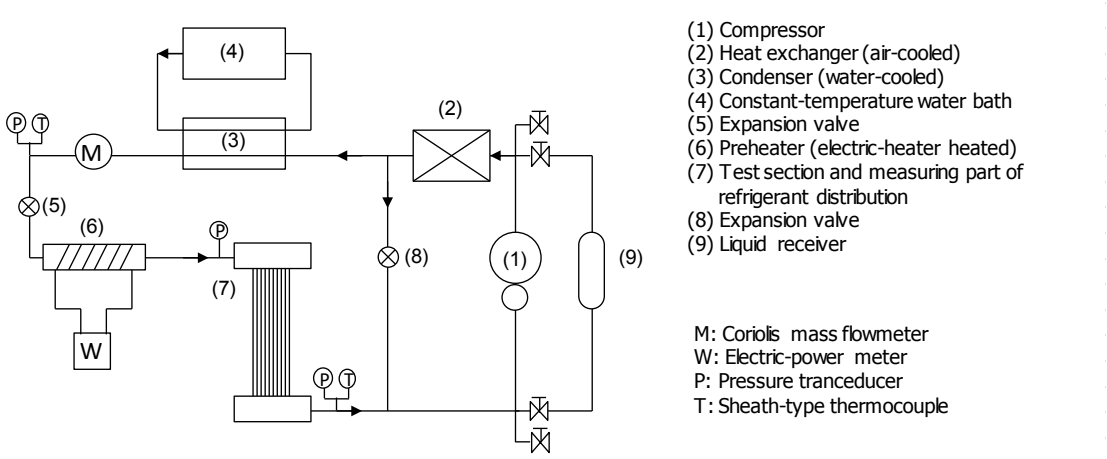

Figure 1. System diagram of experimental setup

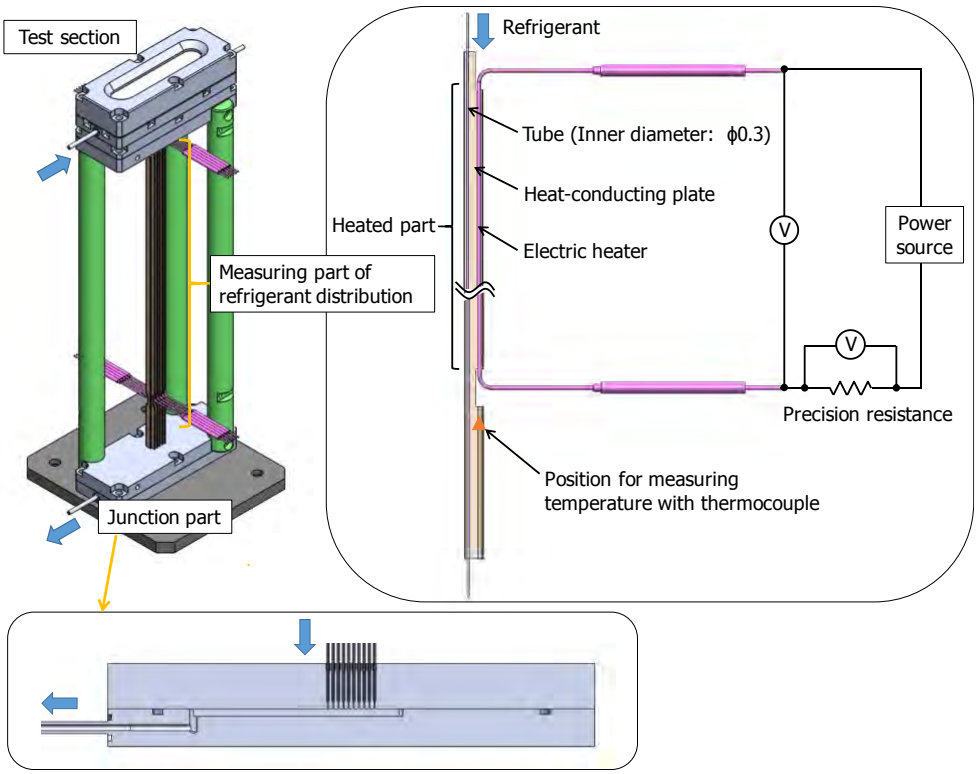

Figure 2. Test section of header and measuring part of refrigerant distribution

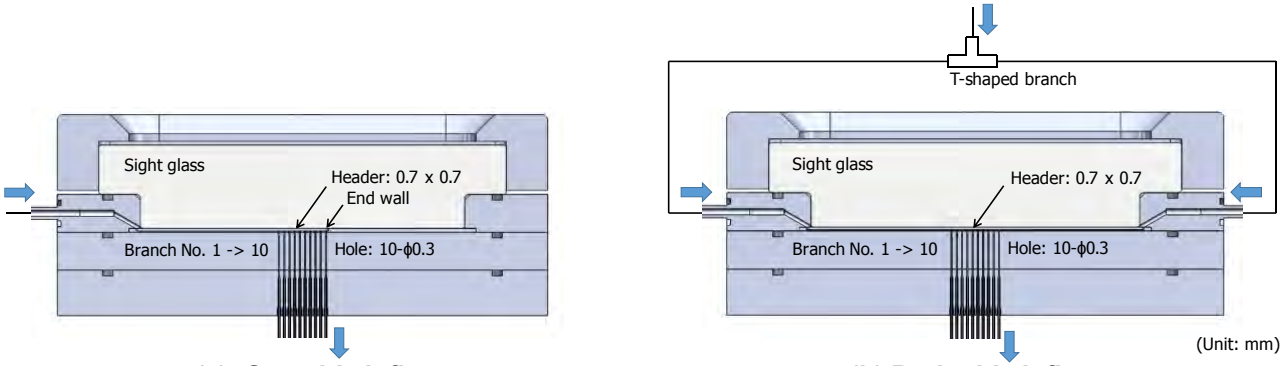

(a) One-side inflow **(b) Both-side inflow**

Figure 3. Cross-sectional diagrams of test section

Table 2. Test conditions at header inlet

Refrigerant	-	R134a
Pressure	MPa	0.488
Saturated temperature	°C	15
Mass flux for one-side inflow *G*	$Kgm^{-2}s^{-1}$	62, 124
Quality *x*	-	0.2, 0.4

3. EXPERIMENTAL RESULTS AND DISCUSSION

3.1. One-Side Inflow Configuration

Measured distribution ratios $R_{We,i}$ for the one-side inflow configuration at G=124 kgm^{-2}s^{-1} and at qualities x=0.2 and 0.4 are shown in Fig. 4. Dimensionless standard deviation σ is also indicated in the graph. The branches are numbered 1-10 from the inlet side of the header. $R_{We,i}$ for the equal distribution is 0.1. The distribution of refrigerant forms a convex-downward profile. As quality increases from 0.2 to 0.4, depth of the convex profile increases. Although a photograph is not presented here, observation with the high-speed camera from the top of the header shows that the liquid-phase refrigerant inflowing from the inlet reaches the opposite wall of the inlet, hits the wall, and returns. This finding implies that although the liquid-phase inflow rate into a branch is lower, as the branch is farther from the inlet, the increases in the distribution ratios for the branches in the downstream of the central part of the header are caused by the liquid-phase refrigerant that returned from the opposite wall of the inlet.

Both experimental results of Koyama et al. (2004) for the header with an inner diameter of 9 mm and of Kim et al. (2011) for the header with an inner diameter of 17 mm show that as a branch becomes farther from the inlet of the header, the liquid phase ratio decreases. Their observations indicate that the liquid-phase refrigerant does not reach the opposite wall of the inlet. The present results differ from theirs.

Measured heater-power distributions at the qualities of 0.2 and 0.4 are shown in Fig. 5. The electric power $W_{e,i}$ is assumed to be proportional to the liquid-phase flow rate. The declination of liquid-phase flow rate with increasing branch number from 1 to 6 at x=0.4 is larger than that at x=0.2. This finding means that as the quality increases, it is more difficult for the liquid phase to enter the branch downstream. This trend is probably related to the fact that as the quality increases, total of liquid-phase flow rate decreases.

Dimensionless standard deviation σ at G=124 kgm^{-2}s^{-1} and x=0.2 is 10%. σ for the header of Koyama et al., whose inner diameter is 13 times that used in this study, is 65%, and σ for the header of Kim et al., whose inner diameter is 24 times, is 99%. In other words, σ of this study is much better than those values. This result is probably because the branch pitch of this study is much shorter than those of the studies by Koyama et al. and Kim et al. As quality x increases from 0.2 to 0.4, σ of the present experiment increases from 10% to 19%: namely, it is nearly doubled.

The total pressure drop of the test section and the measuring part at G=124 kgm^{-2}s^{-1} and x=0.2 is 7 kPa, and the difference between the corresponding saturated temperatures is 0.4°C. This small pressure drop indicates that the pressure drop of this small-sized header has a small effect on the refrigeration system performance.

Measured distribution ratios $R_{We,i}$ at G=62 kgm^{-2}s^{-1}and at x=0.2 and 0.4 are shown in Fig. 6. Comparing Figs. 4 and 6 reveals that the profiles at x=0.2, and at G=124 kgm^{-2}s^{-1} and 62 kgm^{-2}s^{-1} are quite similar. σ at G=62 kgm^{-2}s^{-1} is slightly larger than that at G=124 kgm^{-2}s^{-1}. According to the observation from the side of the header by Koyama et al. and Kim et al., as the liquid level becomes higher, distribution ratio of the liquid phase tends to increase. In this experiment, although the state of fluid flow seen from the side of the header is unknown, since the profiles of the liquid-phase distribution at G=124 kgm^{-2}s^{-1} and 62 kgm^{-2}s^{-1} are quite similar, the distributions of liquid level also seems to be similar.

For quality x=0.4, as G decreases from 124 kgm^{-2}s^{-1} to 62 kgm^{-2}s^{-1}, the profile changes a little, and σ increases slightly. The effect of G on the distribution characteristics at x=0.4 is like that at x=0.2.

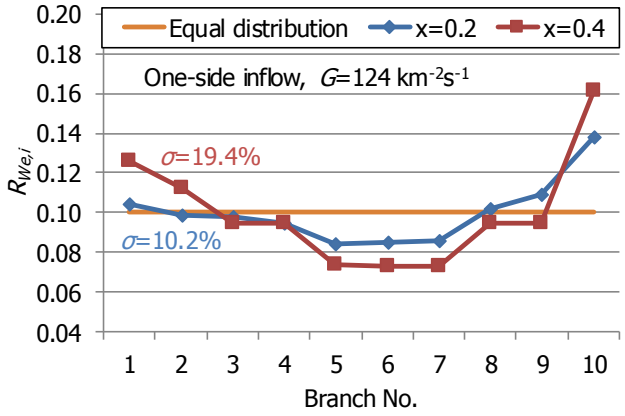

Figure 4. Measured distribution ratios for one-side inflow at G=124 kgm^{-2}s^{-1}

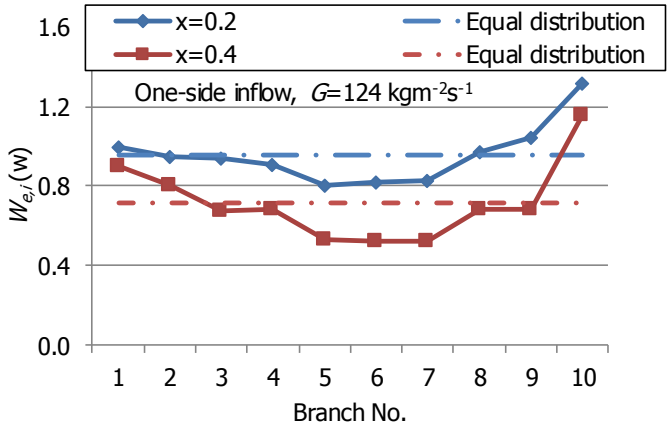

Figure 5. Measured heater power distribution for one-side inflow at G=124 kgm^{-2}s^{-1}

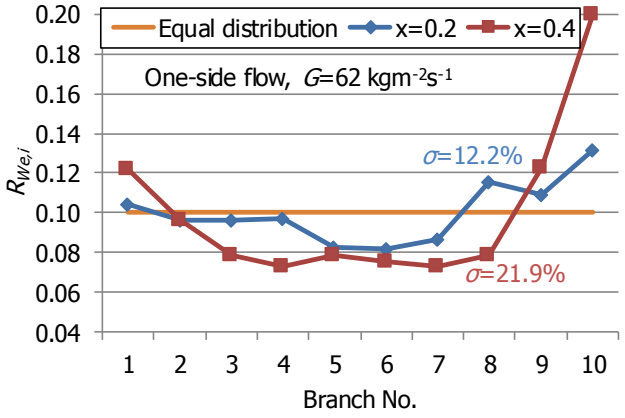

Figure 6. Measured distribution ratios for one-side inflow at G=62 kgm^{-2}s^{-1}

3.2. Both-Side Inflow Configuration

Measured distribution ratios $R_{We,i}$ for the both-side inflow configuration at G=124 kgm^{-2}s^{-1} and 62 kgm^{-2}s^{-1} and at x=0.2 and 0.4 are shown in Fig. 7. For G=124 kgm^{-2}s^{-1} and x=0.2, except for branch No. 9 and 10, the distributions are relatively equal. This asymmetric distribution is probably caused by the bias of liquid-phase distribution in the T-shaped branch, which is set up upstream of the header.

For G=124 kgm^{-2}s^{-1} and x=0.4, the distribution ratios on the side of branch No. 1 are small, and those on the side of branch No. 10 are large. Under the assumption that the distribution ratio of the liquid phase is related to the liquid level in the header, as a branch becomes nearer to branch No. 10, the liquid level increases. As quality x increases from 0.2 to 0.4, σ for both-side inflow is nearly doubled similarly to that for one-side inflow.
When G decreases from 124 kgm^{-2}s^{-1} to 62 kgm^{-2}s^{-1} at quality x of 0.2, σ is doubled. As described before, for one-side inflow, σ at G=124 kgm^{-2}s^{-1} and 62 kgm^{-2}s^{-1} varies a little. The reason for the considerable effect of G on σ for both-side inflow is given as follows. The T-shaped branch, where the refrigerant hits the inside wall vertically, distributes the refrigerant in two directions. As refrigerant velocity decreases, the refrigerant tends to be more sensitive to gravity. In this experiment, a little misalignment of the setting angle of the T-shaped branch may cause the maldistribution of the vapor-liquid refrigerant.
When G decreases from 124 kgm^{-2}s^{-1} to 62 kgm^{-2}s^{-1} at quality x of 0.4, the distribution performance becomes worse, resulting in the twofold increase in σ. This phenomenon is also probably due to the misalignment of setting angle of the T-shaped branch.
As described before, the effect of the mass flux at the header inlet on the distribution for the one-side inflow is small; on the other hand, that for the both-side inflow is large.

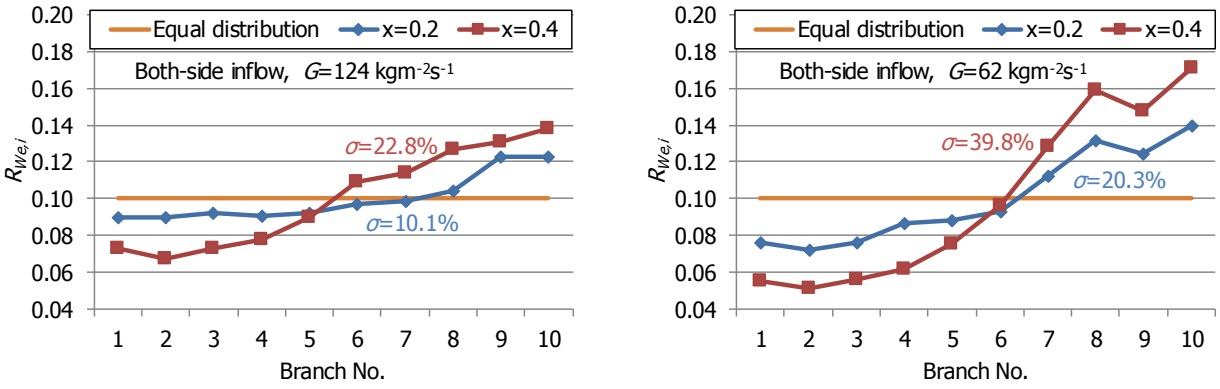

Figure 7. Measured distribution ratios for both-side inflow

4. CONCLUSIONS

The conclusions drawn from above discussion on refrigerant-distribution characteristics of the horizontal header with 0.3-mm diameter holes are given as follows.

- The dimensionless standard deviation of refrigerant distributed in the present header with the one-side inflow configuration is 10%. The effect of mass flux at the header inlet on the distribution for the one-side inflow configuration is small but that for the both-side inflow configuration is large.
- The dimensionless standard deviation for the present header (10%) is much smaller than that for a conventional header (65%) with 13-times bigger hydraulic diameter.

NOMENCLATURE

G	mass flux (kgm^{-2}s^{-1})	R_{We}	distribution ratio of liquid phase (-)
W_e	electric power of heater (W)	x	quality (-)
σ	dimensionless standard deviation (-)		

Subscript

i	branch number (-)	n	number of branch (-)

REFERENCES

Endoh, K., Study on tube-in-fin heat exchanger, 2016, Proceedings of 2016 JSRAE annual conference, Kobe, Japan, JSRAE, A312.

Endoh, K., 2018, Effect of inlet quality on flow pattern inside tube with inner diameter of 0.3mm, Proceedings of 2016 JSRAE annual conference, Koriyama, Japan, JSRAE, A321.

Enoki, K., Miyata, K., Mori, H., 2015, Modification of the prediction correlation for flow boiling heat transfer in small diameter tubes, Trans. of the JSRAE, 32(3), 275-283.

Kim, N.H., Sin, T.R., 2006, Two-phase flow distribution of air–water annular flow in a parallel flow heat exchanger, Int. J. Multiphase Flow, 32(12), 1340-1353.

Kim, N.H., Han, S.P., 2008, Distribution of air–water annular flow in a header of a parallel flow heat exchanger, Int. J. Heat Mass Trans., 51, 977–992.

Kim, N.H., Kim, D.Y., Byun, H.W., 2011, Effect of inlet configuration on the refrigerant distribution in a parallel flow minichannel heat exchanger, Int. J. Refrig., 34, 1209–1221.

Kim, N.H., Lee, E.J., Byun, H.W., 2012, Two-phase distribution in a parallel flow minichannel heat exchanger having horizontal headers, Int. J. Heat Mass Trans., 55, 7747–7759.

Koyama, S., Kuwabara, K., Miyazaki, H., Wijayanta, A.T., Ikuta, S., 2004, Experimental study on refrigerant flow characteristics inside an evaporator header, 2004 JSRAE annual conference, Hamamatsu, Japan, JSRAE, A313.

Koyama, S., Wijayanta, A.T., Kuwabara, K., Ikuta, S., 2006, Developing two-phase flow distribution in horizontal headers with downward microchannel-branches, Proc. 11th Int. Refrigeration and Air Conditioning Conference at Purdue, USA, Purdue University, R142.

Lemmon, E. W., Huber, M. L., McLinden, M. O., 2013, NIST Standard Reference Database 23: Reference Fluid Thermodynamic and Transport Properties-REFPROP, Version 9.1, National Institute of Standards and Technology, Standard Reference Data Program, Gaithersburg.

Miyata, K., Mori, H., Hamamoto, Y., 2011, Correlation for the prediction of flow boiling heat transfer in small diameter tubes, Trans. of the JSRAE, 28(2), 137-148.

Shikazono, N., Okawa, D., Kobayashi, M., Kasagi, N., 2006, Proposal and assessment of high performance finless heat exchanger composed of micro tubes, Trans. JSME, B, 72(717), 1295-1302.

Manuscript ID: 492
DOI: 10.18462/iir.icr.2019.0492

Improving the heating performance of a residential air conditioner by using a vapor-bypassed evaporator

Chaochao FAN, Gang YAN, Jianlin YU

Department of Refrigeration & Cryogenic Engineering, School of Energy and Power Engineering, Xi'an Jiaotong University, Xi'an 710049, China,1406833851@qq.com

ABSTRACT

This paper presents an experimental investigation on the heating performance of a residential air conditioner with a vapor-bypassed evaporator. The vapor-bypassed evaporator, in which a phase separator is set in the middle of the refrigerant circuit to bypass vapor refrigerant, can reduce the refrigerant pressure drop and enhance the heat transfer coefficient at refrigerant side. The tested system contains two operation modes, i.e., vapor-bypassed (VB) mode and conventional heat pump (CH) mode. It is indicated that as the heating capacity ranges 1,800~4,800 W, the COP of VB mode is improved 3.2%~11% over CH mode under conventional heating condition. Under low-temperature heating condition (frosting condition), the system at VB mode yields 16.1% higher average integral heating capacity and 5% higher COP over CH mode at a fixed compressor frequency of 100 Hz. In conclusion, using the vapor-bypassed evaporator is a promising way for enhancing the heating performance of an air conditioner.

Keywords: Air Conditioner, Heating Performance, Vapor-Bypassed Evaporator.

1. INTRODUCTION

Heat pump air conditioners (HPACs) are widely used to provide thermal comfort for residential and commercial applications due to their high energy efficiency. In recent years, due to the large-scale applications, HPACs have consumed much more electricity in cold winter (Wu et al., 2016). Therefore, the performance improvement of HPAC systems is of great significant to contribute energy savings. Actually, for a residential HPAC, the condenser and evaporator are two major components, whose performance is critical to the system performance. Thus, the interest in improving heat exchanger performance has grown continuously in recent years.

Generally, the heat transfer process of an air-refrigerant finned-tube heat exchanger consists of out-tube and in-tube heat transfer processes. The out-tube heat transfer performance can be improved by optimizing fin spacing, fin type, tube spacing (Zhou, 2018; Joardar and Jacobi, 2008). Besides, several methods have been proposed to enhance the performance of in-tube heat transfer, for example, using specific surfaces (rough surface or extended surface) in the flow channel (Liebenberg and P.Meyer, 2007; Liu and Sakr, 2013). In addition to these above approaches, using phase-separation heat exchangers is also a very promising way for enhancing the in-tube heat transfer coefficient and reducing the refrigerant pressure drop (Chen et al., 2018; Chen et al., 2013). It is indicated that using the liquid separation condenser in an air conditioner can significantly improve the cooling capacity and energy efficiency under cooling mode (Chen et al., 2015; Li and Hrnjak, 2017; Chen et al., 2012). However, the main performance restriction of a heat pump system is that the heating capacity can not meet the heating demand at low ambient temperature especially at frosting condition, which is due to the lower compressor suction pressure. It is found that reducing the evaporator refrigerant pressure drop can increase the compressor suction pressure and partiality solve this problem, which can be achieved by using a phase-separation evaporator. As mentioned above, applying a phase-separation evaporator may be a significant approach for improving the performance of a HPAC.

Flash gas bypass (FGB) is a method to achieve the phase-separation in evaporator, which separates the flash vapor after the expansion valve and sends it back to compressor suction, while only liquid refrigerant is set into the evaporator (Tuo and Hrnjak, 2013; Tuo and Hrnjak, 2014). Tuo and Hrnjak (2012) obtained 13~18% higher cooling capacity and 4~7% higher COP with FGB over direct

expansion baseline for a mobile air conditioning system using R134a. Then, when adjusting the compressor frequency to match capacity with the baseline, the COP of FGB system is increased 37-58%. Elbel and Hrnjak (2004) illustrated that applying FGB can increase cooling capacity by 9% while improving COP by 7% at the same time for a R744 air conditioner. However, for a FGB system, the mass flow rate of the bypassed flash vapor would be lower with the higher subcooling degree at condenser outlet, and in this condition, the refrigerant pressure drop decreasing value of the evaporator would be reduced, which restricts the performance improvement of FGB. In fact, setting the phase separator in the middle of the refrigerant circuit to bypass evaporated vapor can solve this problem. Besides, it is found that the research on using phase-separation evaporator in heat pump air conditioner systems is still lacking. Therefore, the objective of this paper is to present an experimental investigation on the heating performance of a residential air conditioner with a vapor-bypassed evaporator.

In this study, the vapor-bypassed evaporator, in which a phase separator is set in the middle of the refrigerant circuit to bypass vapor refrigerant, can reduce the refrigerant pressure drop and enhance the heat transfer coefficient at refrigerant side. The tested system contains two operation modes, i.e., vapor bypassed (VB) mode and conventional heat pump (CH) mode. The heating performance of the VB mode are investigated and then compared with CH mode under two operation conditions (conventional heating condition (without frosting) and low-temperature heating condition (frosting)). Moreover, the system performance parameters including compressor suction pressure, input work and evaporator refrigerant pressure drop are investigated in detail.

2. EXPERIMENTAL SETUP

2.1. System Description

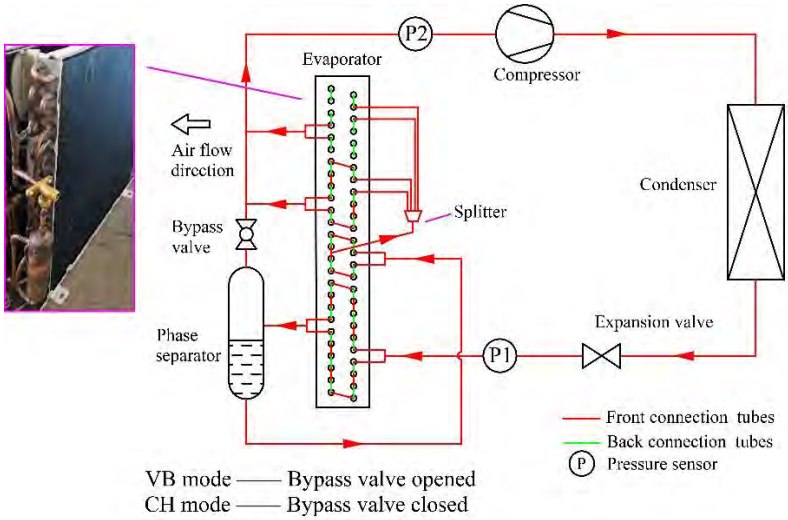

Figure 1: Schematic diagram of the vapor-bypassed system

The vapor-bypassed evaporator was developed on the basis of a conventional finned-tube evaporator. Fig. 1 displays the schematic diagram of the vapor-bypassed system. This system contains two operation modes, i.e., VB mode and CH mode. These two operation modes can be switched by controlling the bypass valve. When opening the bypass valve, the VB mode is conducted in the following manner. The compressed vapor is condensed and subcooled by passing through the condenser. Then, the subcooled refrigerant is expanded to two-phase fluid by the expansion valve. This two-phase fluid is partially evaporated in the first part of the evaporator and then split into two streams (vapor and liquid) in the separator. The liquid refrigerant is completely evaporated in the second part of the evaporator and then mixed with the vapor refrigerant leaving the separator. At last, this mixed vapor refrigerant is compressed by the compressor. Moreover, the CH mode is operated by closing the bypass valve. The performances of the two modes are discussed and compared in this study. It is noted that in the defrosting process, the bypass valve is closed and the reverse cycle defrosting approach is applied. Besides, two pressure sensors were set at the evaporator inlet and outlet to measure the compressor suction pressure and evaporator refrigerant pressure drop.

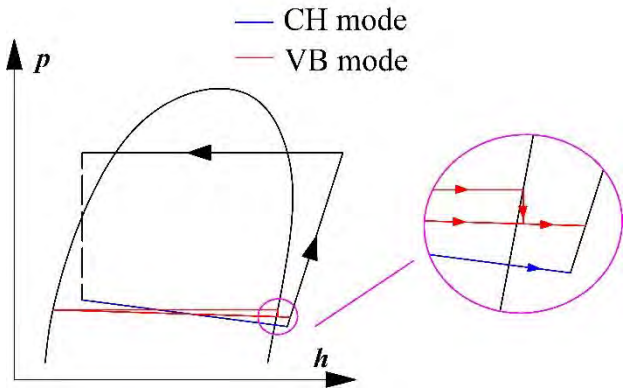

Figure 2: Pressure-enthalpy diagram for the two operation modes

Actually, applying the vapor-bypassed evaporator can reduce the refrigerant pressure drop and enhance the heat transfer coefficient at refrigerant side. Fig. 2 shows the pressure-enthalpy diagram of both operation modes. It is observed that due to the decreased evaporator refrigerant pressure drop, the compressor suction pressure of VB mode is higher than that of CH mode. On one hand, as the suction pressure increases, the refrigerant specific volume at compressor inlet is decreased, which can increase the refrigerant mass flow rate at a fixed compressor speed. This means that the heating capacity of VB mode would be much higher when fixing the compressor speed. On the other hand, increasing the suction pressure can reduce the compression ratio, which is beneficial to the compressor efficiency improvement. As mentioned above, applying the vapor-bypassed evaporator is a promising way for enhancing the performance of a heat pump system.

2.2. Experimental Device Description

Table 1 Specifications of compressor and heat exchangers

Component	Specifications	
Compressor	Type: rotary DC inverter compressor Displacement volume: 9.8 cm^3	
Condenser	Number of depth rows: 2 Number of tubes per row: 18 Horizontal tube spacing: 16.5 mm Vertical tube spacing: 20 mm Tube length: 720 mm Tube outside diameter: 7 mm	Tube inside diameter: 6.5 mm Tube internal surface: Smooth Tube arrangement: Stagger Fin thickness: 0.1 mm Fin space: 1.35 mm Airflow rate: 510 $m^3 \cdot h^{-1}$
Condenser	Number of depth rows: 2 Number of tubes per row: 26 Horizontal tube spacing: 18.5 mm Vertical tube spacing: 21.4 mm Tube length: 770 mm Tube outside diameter: 7 mm	Tube inside diameter: 6.5 mm Tube internal surface: Smooth Tube arrangement: Stagger Fin thickness: 0.1 mm Fin space: 1.35 mm Airflow rate: 2100 $m^3 \cdot h^{-1}$
Refrigerant	R410A (1050 g)	

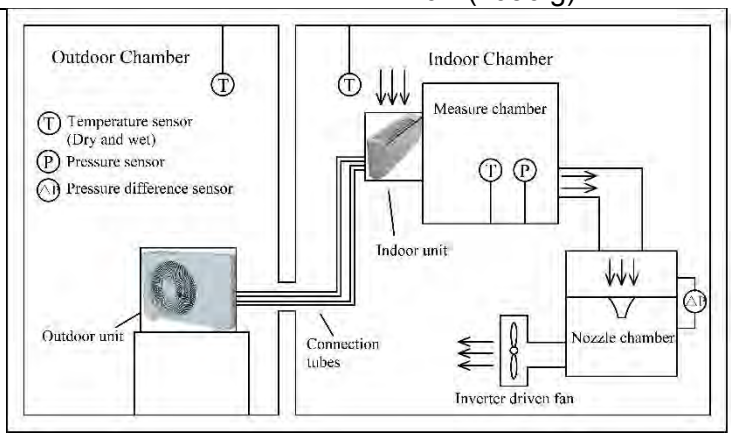

Figure 3: Schematic diagram of experimental device

A heat pump inverter air conditioner with a rated heating capacity of 3800W was selected as the experimental installation, and the specifications of heat exchangers and compressor are listed in Table1. As shown in Fig. 3, the experiments were performed in two environmental chambers. In the indoor chamber, the air enthalpy difference between condenser outlet and inlet is measured out by the temperature sensors. The air volume flow rate is measured in the nozzle chamber. Therefore, the heating capacity can be calculated by the product between the enthalpy difference and air mass flow rate. And COP is defined as the ratio between the heating capacity and system input work. According to the ISO 5151 standard, the heating performance of the air conditioner were tested under both conventional and low-temperature heating conditions, which are listed in Table 2. Moreover, the measure instruments and corresponding uncertainties are shown in Table 3.

Table 2. The testing conditions

Conditions	Conventional (without frosting)	Low-temperature (frosting)
Outdoor chamber	dry bulb temperatures:7℃ wet bulb temperatures:6℃	dry bulb temperatures:2℃ wet bulb temperatures:1℃
Indoor chamber	dry bulb temperatures:20℃ wet bulb temperatures:15℃	

Table 3. The measure instruments and corresponding uncertainties

Parameters	Measurement	Uncertainty
Pressure	Pressure sensor (0-4 MPa)	0.01%
Heating capacity (W)	Data acquisition	0.5%
Input work (W)	Dynamometer (0-3.5 kW)	0.5%
COP (-)	Data acquisition	1%

3. RESULTS AND DISCUSSION

3.1. System Heating Performance Under Conventional Heating Condition

Table 4. The heating performance comparison between two modes when operated at same compressor frequencies

f(Hz)		30	40	50	60	70	80	90
Q(W)	CH	1825	2408	2881	3414	3899	4416	4834
	VB	1863	2534	3069	3616	4198	4769	5230
Improvement		**2.1%**	**5.2%**	**6.5%**	**5.9%**	**7.7%**	**8.0%**	**8.2%**
COP(-)	CH	4.44	4.32	3.87	3.46	3.1	2.79	2.49
	VB	4.54	4.42	3.99	3.57	3.21	2.9	2.59
Improvement		**2.3%**	**2.3%**	**3.1%**	**3.2%**	**3.8%**	**3.9%**	**4.0%**
p_s(kPa)	CH	919	876	865	835	812	776	755
	VB	926	894	885	861	845	828	830
Increment (kPa)		**7**	**18**	**20**	**26**	**33**	**52**	**75**
Δp_e(kPa)	CH	47	68	97	137	177	214	265.
	VB	26	41	59	86	111	145	195
Decrement		**44.7%**	**39.7%**	**39.2%**	**37.2%**	**37.3%**	**32.2%**	**26.4%**

As Table 4 displays, the heating capacity of VB mode is higher than that of CH mode. The main reason is that the evaporator refrigerant pressure drop of VB mode is decreased by bypassing the vapor refrigerant, which can increase the compressor suction pressure. The increased compressor suction pressure leads to the increasing refrigerant mass flow rate, thus, the heating capacity of VB mode is improved. As the compressor frequency ranges from 30Hz to 90Hz, the corresponding heating capacity improvement of VB mode varies from 2.1% to 8.2% compared with CH mode. Meanwhile, the COP of VB mode yields about 3% improvement over CH mode. It is seen that the corresponding heating capacity improvement of VB mode shows an increasing trend when compressor frequency rises. As compressor frequency increases, the refrigerant mass flow rate is increased, which increases the evaporator refrigerant pressure drop, thus, when operated at high

compressor frequency conditions, applying VB mode have a much higher potential for reducing the evaporator refrigerant pressure drop and improving the system performance. It is also observed from Table 4 that when compressor frequency ranges 30~90Hz, the VB mode yields 7~75kPa higher compressor suction pressure and 44.7~26.4% lower evaporator refrigerant pressure drop compared with CH mode. Actually, according to ISO 5151 standard, when testing the COP of an inverter air conditioner, the compressor frequency should be adjusted to maintain the same heating capacity with the baseline, and the COP comparison would be much more reasonable. The heating performance comparison between the two modes that operated at same heating capacities is investigated as follows.

Table 5. The heating performance comparison between two modes that operated at same heating capacities

Q(W)		1800	2400	2900	3400	3900	4400	4800
COP(-)	CH	4.44	4.32	3.87	3.46	3.10	2.79	2.49
	VB	4.58	4.54	4.15	3.78	3.44	3.07	2.78
Improvement		**3.2%**	**5.0%**	**7.3%**	**9.4%**	**11.0%**	**10.1%**	**11.8%**
p_s(kPa)	CH	919	876	865	835	812	776	755
	VB	928	908	881	859	839	847	843
Increment (kPa)		**9**	**32**	**16**	**24**	**27**	**71**	**88**
Δp_e(kPa)	CH	47	68	97	137	177	214	265
	VB	24	37	53	74	94	125	143
Decrement		**48.6%**	**45.3%**	**45.4%**	**45.9%**	**46.6%**	**41.4%**	**46.1%**

As shown in Table 5, when operated at same heating capacities, the COP of VB mode is higher than that of CH mode especially under high heating capacity conditions. It is seen that the evaporator refrigerant pressure drop of VB mode is decreased about 45% in comparison with CH mode, which results in the higher compressor suction pressure and lower compression ratio of VB mode. Hence, the compressor efficiency of VB mode would be higher compared with CH mode. This results in the lower input work of VB mode, thus, the COP of VB mode is significantly improved. As the heating capacity ranges 1800~3400W, the corresponding COP improvement of VB mode varies 3.2~9.4% compared with CH mode, and when the heating capacity ranges 3900~4800W, this improvement is about 11%. As mentioned above, applying VB mode can significantly enhance the system performance including heating capacity and COP under conventional heating condition. In next section, the heating performance of both modes under low-temperature heating condition is investigated in detail.

3.2. System Heating Performance Under Low-Temperature Heating Condition

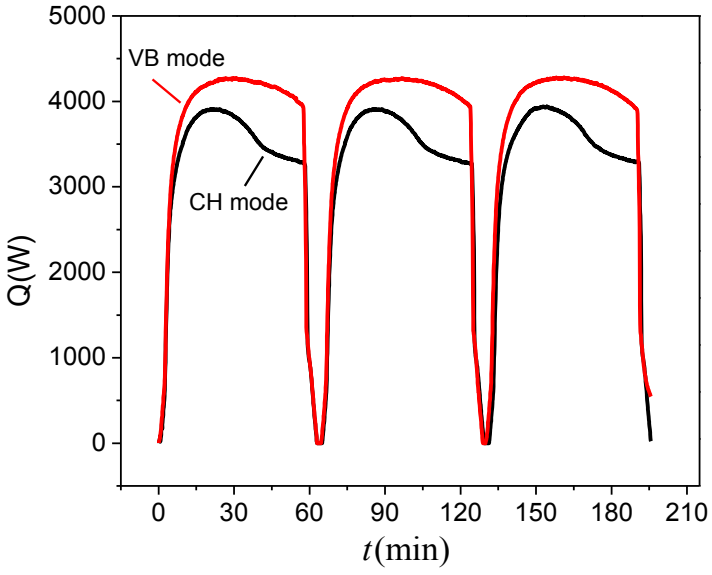

(a)

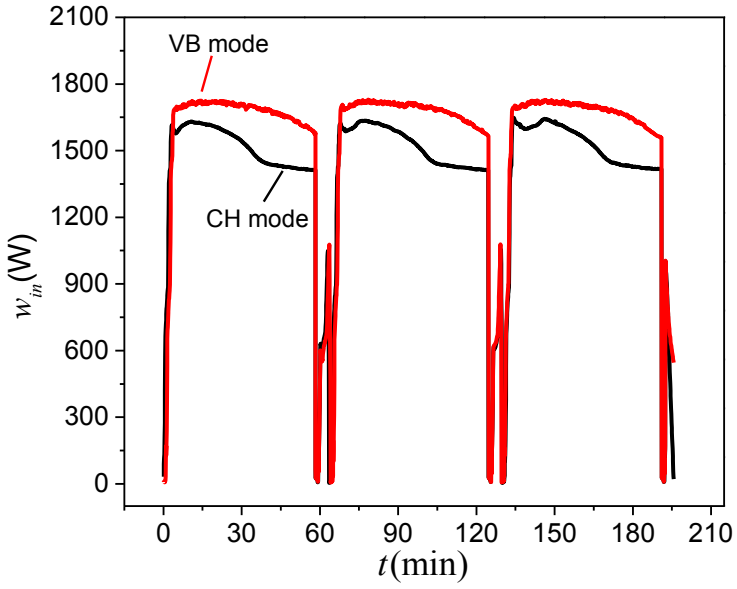

(b)

Figure 4: The heating capacity and input work variations of both modes under low-temperature heating condition. (a) heating capacity; (b) input work

It should be noted that when the system was operated at lower-temperature heating condition, the heating period and defrosting period were set as 60 min and 7 min, respectively, and the compressor frequency was set as 100 Hz. Fig. 4 displays the heating capacity and input work variations of both modes under low-temperature heating condition. As Fig. 4 shows, in the heating period, the heating capacity and input work of VB mode are higher than those of CH mode, and their attenuation rates of VB mode are much lower. There are two main reasons for this phenomenon. On one hand, when bypassing the vapor refrigerant, the evaporator pressure drop is decreased, which could increase the temperature uniformity at evaporator fin surface by reducing the refrigerant temperature drop. Hence, the frosting uniformity of the evaporator is improved, and the heating capacity attenuation rate of VB mode is reduced. On the other hand, when the system is operated at VB mode, the refrigerant soakage ratio in the evaporator is increased by bypassing the vapor refrigerant, which is beneficial to the heat transfer coefficient improvement at refrigerant side, thus, the average heat transfer temperature between refrigerant and air is decreased. Therefore, the frosting rate of VB mode is lower, which reduce the heating capacity and refrigerant mass flow attenuation rates. To further illustrate this aspect, the compressor suction pressure and evaporator refrigerant pressure drop variations are studied, which are shown in Fig. 5.

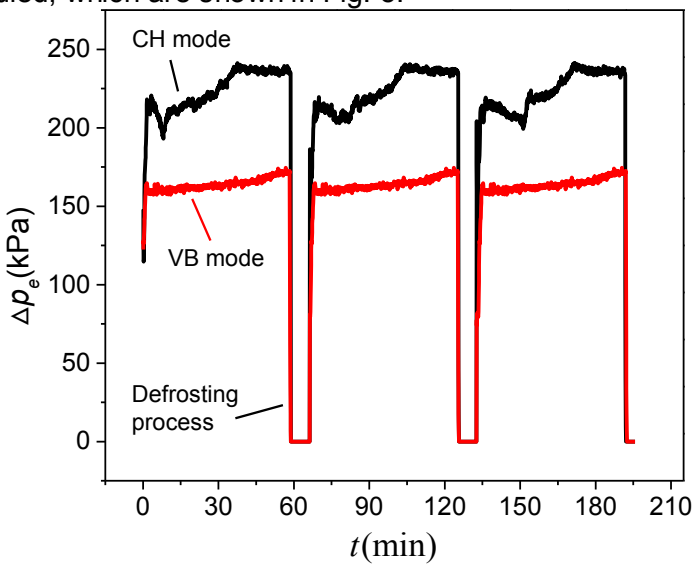

(a)

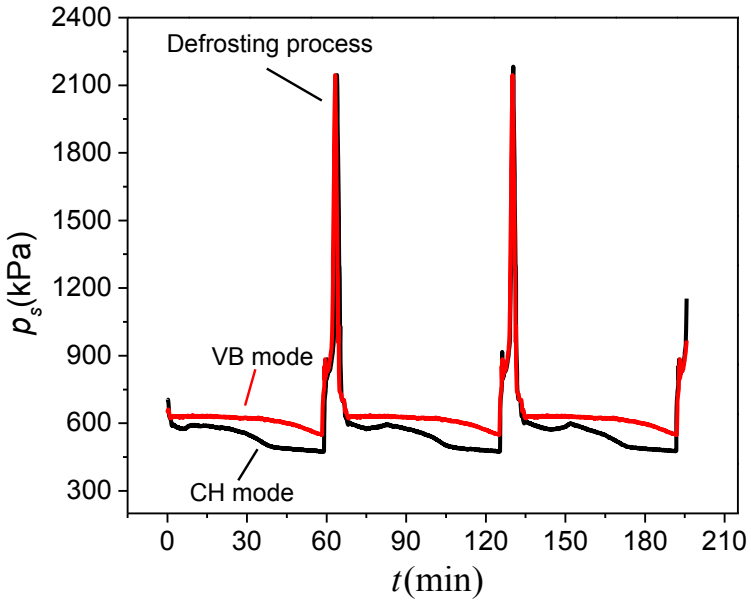

(b)

Figure 5: (a) The evaporator refrigerant pressure drop variations of both modes; (b) The compressor suction pressure variations of both modes

As shown in Fig. 5(a), the evaporator refrigerant pressure drop of VB mode is lower than that of CH mode, which results in the higher compressor suction pressure. For VB mode, the higher suction pressure leads to the lower specific volume at compressor inlet, which could increase the refrigerant mass flow rate and heating capacity of VB mode. As Fig. 5(b) displays, in the heating period, the suction pressure decreasing rate of VB mode is lower compared with CH mode, which is due to the higher frosting uniformity and lower frosting rate mentioned above. Actually, the lower suction pressure decreasing rate results in the lower refrigerant mass flow attenuation rate. Hence, the heating capacity attenuation rate of VB mode is lower and the corresponding average heating capacity would be higher. The average integral heating capacities, input works and COPs of both modes under low-temperature heating condition are listed in Table 6. It is observed that the VB mode yields 16.1% higher average integral heating capacity and 5% higher COP compared with CH mode. In conclusion, applying VB mode is a promising way for enhancing the heating performance of an air conditioner under low-temperature heating condition.

Table 6. The heating performance of both modes under low-temperature heating condition

Modes	Q(W)	w_{in}(W)	COP(-)
CH	3086	1377	2.241
VB	3584	1523	2.353
Improvement	16.1%	—	5%

4. CONCLUSIONS

This paper presents an experimental study on the residential air conditioner with a vapor-bypassed evaporator under heating conditions. The vapor-bypassed evaporator can significantly reduce the refrigerant pressure drop and enhance the heat transfer coefficient at refrigerant side. Thus, the performances of a vapor-bypassed system including heating capacity and the COP could be significantly improved. The tested system contains two operation modes, i.e., VB mode and CH mode. Two testing conditions are operated, which are the conventional heating condition (indoor temperature: 20/15℃; outdoor temperature:7/6℃) and low-temperature heating condition (indoor temperature: 20/15℃; outdoor temperature:2/1℃; frosting condition). The experimental results show that compared with CH mode, the VB mode yields 2.1~8.2% higher heating capacity when operated at the same compressor frequency ranging 30~90Hz under the conventional heating condition. Moreover, when the compressor frequency is adjusted to maintain the same heating capacity ranging from 1,800 to 4,800 W, the COP of VB mode is improved by 3.2%~11% compared with the CH mode. When operated at the low-temperature condition (frosting condition), the system at VB

mode yields 16.1% higher average integral heating capacity and 5% higher COP at a fixed compressor frequency of 100 Hz in comparison with CH mode. In conclusion, using the vapor-bypassed evaporator can significantly improve the heating performance of an air conditioner.

NOMENCLATURE

COP	coefficient of performance (-)
Q	heating capacity (W)
w	work (W)
p	pressure (kPa)
f	compressor frequency (Hz)
VB	vapor-bypassed
CH	conventional heat pump

Greek symbols

Δ	difference

Subscripts

in	input
s	suction
e	evaporator

REFERENCES

Chen, Y., Hua, N., Deng, L., 2012. Performances of a split-type air conditioner employing a condenser with liquid–vapor separation baffles. Int. J. Refrig. 35(2), 278-289.

Chen, X., Chen, Y., Deng, L., Mo, S., Zhang, H., 2013. Experimental verification of a condenser with liquid-vapor separation in an air conditioning system. Appl. Therm. Eng. 51(1-2), 48-54.

Chen, Y., Deng, L., Mo, S., Luo, X., 2015. Energy and exergy analysis on a parallel-flow condenser with liquid-vapor separators in an R22 residential air-conditioning system. Heat Transfer Eng. 36(1),102-112.

Chen, J., Li, Y., Ding, R., Lin, X., Chen, Y., Luo, X., Yang, Z., 2018. Comparative performance of air-conditioning systems with different refrigerant circuitries in liquid-separation condenser. Int. J. Refrig. 92, 154-164.

Elbel, S., Hrnjak, P., 2004. Flash gas bypass for improving the performance of transcritical R744 systems that use microchannel evaporators. Int. J. Refrig. 27(7), 724-735.

Joardar, A., Jacobi, A.M., 2008. Heat transfer enhancement by winglet-type vortex generator arrays in compact plain-fin-and-tube heat exchangers. Int. J. Refrig. 31(1):87-97.

Liebenberg, L., P.Meyer, Josua., 2007. In-tube passive heat transfer enhancement in the process industry. Appl. Therm. Eng. 27(16), 2713-2726.

Liu, S., Sakr, M., 2013. A comprehensive review on passive heat transfer enhancements in pipe exchangers. Renewable Sustainable Energy Rev. 19, 64-81.

Li, J., Hrnjak, P., 2017. Improvement of condenser performance by phase separation confirmed experimentally and by modeling. Int. J. Refrig. 78, 60-69.

Tuo, H., Hrnjak, P., 2012. Flash gas bypass in mobile air conditioning system with R134a. Int. J. Refrig. 35(7), 1869-1877.

Tuo, H., Hrnjak, P., 2013. New approach to improve performance by venting periodic reverse vapor flow in microchannel evaporator. Int. J. Refrig. 36(8), 2187-2195.

Tuo, H., Hrnjak, P., 2014. Enhancement of vapor-liquid separation in vertical impact T-junctions for vapor compression systems with flash gas bypass. Int. J. Refrig. 40, 43-50.

Wu, J., Liu, C., Li, H., Ouyang, D., Cheng, J., Wang, Y., You, S., 2016. Residential air-conditioner usage in China and efficiency standardization. Energy 119, 1036-1046.

Zhou, Y., 2018. Study on Heat Transfer Performance of ASHP Heat Exchanger with Variable Fin Spacing. Contamination Control & Air-Conditioning Technology 1, 26-28.

Manuscript ID: 541
DOI: 10.18462/iir.icr.2019.0541

Experimental evaluation of low-GWP replacements of R-404A in a stand-alone commercial cabinet for fresh product

Daniel CALLEJA-ANTA[(a)], Laura NEBOT-ANDRÉS[(a)], Jesús CATALÁN-GIL[(a)], Rodrigo LLOPIS[(a)], Daniel SÁNCHEZ[(a)], Ramón CABELLO[(a)]

[(a)]Thermal Engineering Research Group. Department of Mechanical Engineering & Construction, Jaume I University, Castellón, E12071, Spain, e-mail: lnebot@uji.es

ABSTRACT

Commercial stand-alone refrigeration appliances (32 million units worldwide) are responsible of 2.6% world electric energy consumption. Most commercial refrigeration systems still rely on HFC refrigerants, such as R-134a and R-404A. However, the European F-Gas Regulation (EU 517/2014) has established a GWP refrigerant limit of 150 from 1/1/2022 on for this equipment.
Small systems were converted to R-290 cycles, however, medium to large ones are restricted by the 150g charge limit in Europe (IEC 60335-2-24) and must discover new alternatives.
Using a stand-alone commercial cabinet for fresh product originally designed for R-404A, this work presents the performance and energy evaluation of the refrigeration system using low-GWP refrigerant substitutes, all of them with a GWP below 150. The work establishes the optimum refrigerant charge and the overall environmental impact of the cabinet using the newly developed refrigerants R-454C, R-455A, R-457A, and R-459B.
Keywords: Stand-alone commercial refrigeration, R-404A, low GWP, experimental evaluation

1. INTRODUCTION

Commercial refrigeration sector includes hermetic stand-alone, condensing unit and multipack refrigeration systems, accounting for approximately 32% of world HFC consumption. Hermetic stand-alone appliances reached 32 million units plus 20.5 million vending machines in 2011, and they usually rely on R-22, R-134a, R-404A and R-507A or in small new equipment on R-290, however, the most used refrigerant for commercial plug-in display cases for all temperature levels is still R-404A (UNEP, 2015). Although plug-in display cases are supposed to present a low annual leakage rate, of 2% according to Defra (2012), Europe has fixed a GWP limit of 2500 from 01/01/2020 on and of 150 from 01/01/2022 on to the refrigerant used in refrigerators and freezers for commercial used hermetically sealed, which results in the end of use of R-404A and other high GWP refrigerants (European Commission, 2014).
Current low-GWP (<150) alternatives to R-404A (R-454C, R-455A, R-457A and R-459B) belong to an A2L Ashrae classification, thus in addition to be competitive in terms of energy efficiency, they must be able to operate with reduced refrigerant charges. At the moment, the maximum allowed refrigerant charge for stand-alone commercial refrigeration systems is of 150g, however, the standard IEC 60335-2-89 is being revised. It seems to be that the future allowed refrigerant charge for A2L fluids would be of 1200g (Kopchick and Scancarello, 2017).
In relation to alternative fluids to R-404A or R-507Asince their behaviour is similar (Llopis et al., 2010) with GWP below 150, R-454C and R-455A were tested experimentally by Mota-Babiloni et al. (2018) and Bella et al. (2018), who measured reductions in capacity and similar COP in steady-state operations. However, no experimental works with R-457A and R-459B have been found by the authors.
Accordingly, this communication aims to complete the R-404A substitution process by summarizing the energy optimization procedure made with an open-fronted vertical commercial cabinet designed to operate with R-404A for fresh product at 5ºC. The optimization, conducted as

established by ISO 23953-2:2015 (2015) in 24-hour tests, evaluates the optimum refrigerant charge and energy consumption of the refrigerants R-454C, R-455A, R457A and R-459B.

2. THERMODYNAMIC APPROACH

Properties of R-404A substitutes are detailed in Table 1. Main components are HFC-32 and HFO-1234yf, with small proportions of CO_2 (R-455A), HFC-152a (R-457A) or HFO-1234ze(E) (R-459B). They all present a GWP below 150 and had an A2L Ashrae security classification. Pressure-enthalpy diagrams are presented in Figure 1, where it can be observed that the blends in relation to R-404A present a similar bubble saturation line, higher critical pressure/temperature, larger latent heat of phase change (between 27.8 to 38.4% at t=40ºC and 17.8 to 24.9% at t=-7ºC) and higher specific suction volume (between 24.4 to 56.1%, saturation at t=-7ºC). In addition, one common characteristic is that the blends present a large glide due to the association of components with very different NBP, it varying between 6.1 to 9.9 K at t=40ºC and between 7.0 to 12.15 K at t=-7ºC. The large glide could have influence in the thermal performance of evaporator and condenser.

Table 1. Physical, environmental and safety characteristics of low-GWP drop-ins of R-404A

	R-404A	**R-454C**	**R-455A**	**R-457A**	**R-459B**
Composition (% wt)	R-125 (4.0%) R-143a(52.0%) R-134a (4.0%)	R-32(21.5%) R-1234yf (78.5%)	R-744(3.0%) R-32(21.5%) R-1234yf (75.5%)	R-32(18.0%) R-1234yf (70.0%) R-152a (12.0%)	R-32 (21.0%) R-1234yf (69.0%) R-1234ze(E) (10.0%)
M (g·mol^{-1})	97.6	90.8	87.5	87.6	91.2
NBP (ºC)	-46.2	-45.6	-52.0	-42.6	-45.0
t_C (ºC)	72	85.7	85.6	91.3	87.5
p_C (bar)	37.2	43.2	46.5	43.4	43.6
Glide at 40ºC (K)	0.34	6.82	9.86	6.14	7.04
Glide a -7ºC (K)	0.54	7.82	12.15	7.01	8.13
λ (40°C) (kJ · kg^{-1})	120.5	154.0	160.0	166.8	156.2
λ (-7°C) (kJ · kg^{-1})	172.31	202.73	211.83	215.18	204.17
v (-7°C) (m^3 · kg^{-1})	0.041	0.054	0.051	0.064	0.056
GWP 100year	3943	146	146	139	143
Ashr. 34 safety group	A1	A2L	A2L	A2L	A2L

A thermodynamic analysis based on an ideal refrigeration cycle indicates that the substitutes, at t_O=-7ºC, t_K=40ºC, RU=10K and SUB=2K, offer theoretically and in relation to R-404A, COP increments of 5.3% R-454C, 5.8% R-459B, 7.4% R-457A and 5.8% R-455A, but different behaviour in terms of VCC, -8.4% R-454C, -10.5% R-457A, -15.4% R-457A and +0.9% R-455A. All the mixtures present a large glide in condenser (from 6.1K R-457A to 9.9K R-455A) and in evaporator (from 4.5K of R-457A to 7.2K of R-455A), but they present lower vapour quality at the inlet of the evaporator (0.29 to 0.30) in relation to R-404A one (0.39).

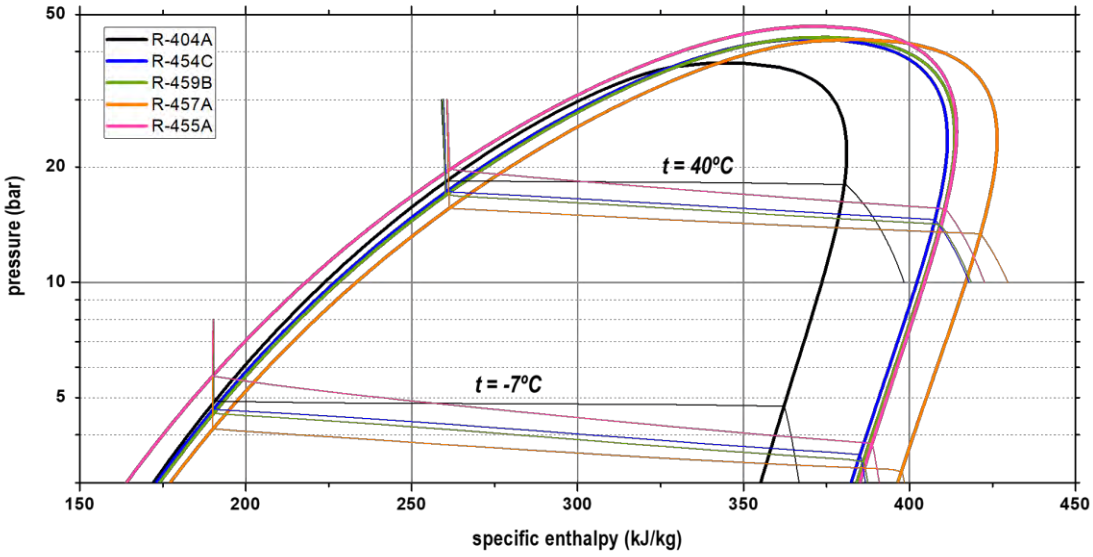

Figure 1: Pressure-enthalpy diagram of low-GWP alternative refrigerants

3. EXPERIMENTAL SET-UP AND PROCEDURE

The evaluation used an open-fronted vertical display cabinet with a frontal air curtain for refrigerated food, using a single-stage vapour compression system to maintain product temperature, being its schematic diagram represented in Figure 2. The system is driven by a hermetic compressor (22.37cm^3) for R-404A. Condensation uses a minichannel air condenser and at the exit of the condenser is placed the liquid receiver. For the purpose of this work, the system has the possibility to operate with and without the liquid receiver using manual sectioning valves. Then, liquid refrigerant pipe enters into the refrigerated section of the cabinet in contact to the vapour pipe, thus there is a small heat transfer between the liquid and vapour lines. The refrigerant is expanded using an EEV that controls the degree of superheat at the evaporator exit. The driver of the EEV can be customized for any kind of refrigerant mixture by programming bubble and dew point curves. Next, refrigerant is evaporated in a finned tube evaporator that uses three high-efficient fans. Air is suctioned by the fans at the front part of the cabinet, then passes through the evaporator and it is driven through the rear part of the cabinet. The air current is propelled from the top of the cabinet, creating the air current that isolates the refrigerated space from the surroundings.

Cabinet is instrumented to measure the product, air and refrigerant temperatures, pressures, humidity and power consumption, as presented in Figure 2. Product temperature is evaluated as average of temperature of 6 M-test packages according to ISO 25953-2:2015.

In this work the refrigerants in the cabinet were evaluated using 24-hour energy consumption tests according to ISO 25953-2:2015. First, the charge of the refrigeration cycle was optimized (steps of 100g) in terms of energy consumption operating without liquid receiver, which was isolated using manual sectioning valves. Then, the system was evaluated with the liquid receiver with the minimum charge that ensured in all the test liquid at the exit of the receiver.

Tests were done in a climatic chamber that maintained a constant temperature of 25.5 ºC (±0.8K) and 50% of relative humidity (±7%). Compressor was operated using ON/OFF control activated by air return temperature to the evaporator. The set point was adjusted (0.7 to 1.1ºC) to obtain the required product temperature (5ºC) and the hysteresis of the regulator was set to 2K. The fixed set point in the EEV was of 10K. Also, a defrosting each six hours was set, it done with electrical resistors (540W). It ended when air return temperature to the evaporator was of 14.5ºC. Also, in the defrosting period compressor and EEV were not in operation.

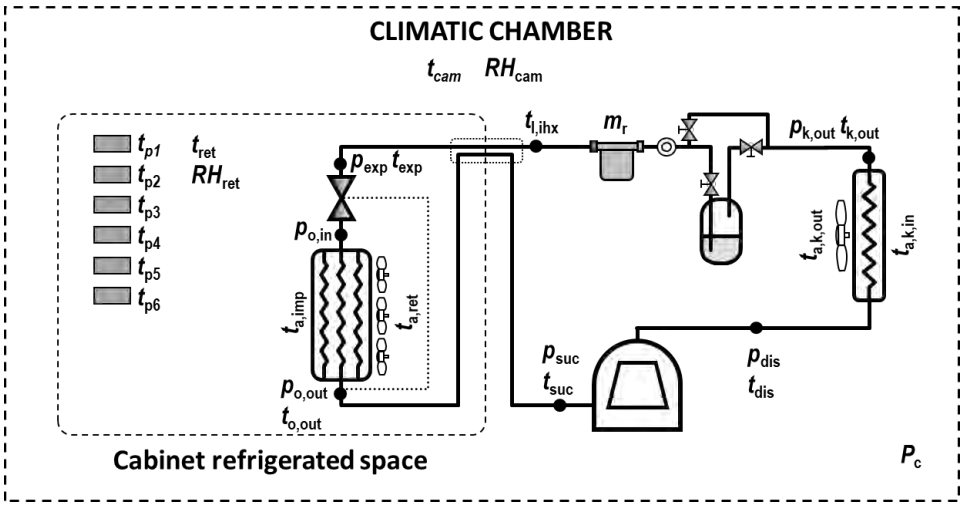

Figure 2: Schematic diagram of the refrigeration cycle of the display cabinet

4. RESULTS

Cabinet was subjected to a subsequent charge optimization process working without liquid receiver with step charges of 100g, being the balance measurement error of 2g. Optimization was referred to the energy consumption during the 24-hours, it evaluated using Eq. Eq. (**1**), where P_C is the power consumption of the cabinet and '*j*' each sampled data. The sampling step was of 5 seconds.

$$E_i = \frac{1}{36 \cdot 10^5} \cdot \int_0^{24h} P_C(t) \cdot dt = \frac{1}{36 \cdot 10^5} \cdot \sum_{j=1}^{24h} \left\{ \left[\frac{P_C(j) + P_C(j-1)}{2} \right] \cdot [t(j) - t(j-1)] \right\} \quad \text{Eq. (1)}$$

Energy consumption in the optimization process is presented in Figure 3. As it can be observed, when working without receiver the energy consumption is reduced for increased refrigerant charge until reaching a minimum, then it increases, as observed in similar systems (Maiorino et al., 2018). The optimization process revealed that the optimum refrigerant charges for the substitute were: 1100g R-454C, 1460g R-459B, 1500g R-457A and 1600g R-455A. All mixtures, with optimized refrigerant charge, were able to reduce energy consumption in relation to the R-404A configuration. Also, denoted with 'R' the energy consumption of the cabinet with liquid receiver is presented, where it can also be observed that all refrigerants improve energy performance in relation to the reference.

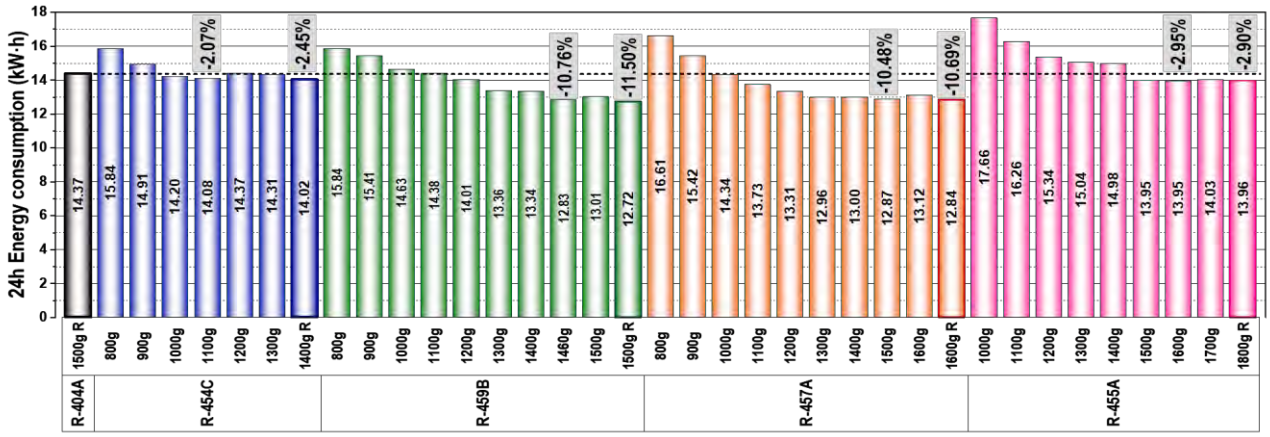

Figure 3: Refrigerant charge optimization

For the optimized configurations and for the operation with liquid receiver, Figure 4 summarises the phase-change temperatures of the system. Evaporating temperature, Eq. Eq. (**2**), was evaluated

during the 24h (evaporator fans always in operation) with the outlet pressure measurement in the evaporator and the average enthalpy in the evaporator. Condensing pressure, Eq. Eq. (**3**), was calculated with discharge pressure and vapour title of 50%.

$$t_O = f\left(p_{O,out}; h = \frac{h_{O,in} + h_{v,p_{O,out}}}{2}\right) \quad \text{Eq. (2)}$$

$$t_K = f(p_{dis}, x_v = 50\%) \quad \text{Eq. (3)}$$

A significant increment in the average evaporating temperature was measured for all the substitutes in relation to R-404A: 3.5 to 3.7K for R-454C, 4.6 to 4.8K for R-459B, 3.9 to 4.9K for R-457A and 5.7 to 6.5K for R-455A (Figure 4). That indicates that evaporator's thermal performance improved with the mixtures, thus the negative effects of the glide are compensated by lower vapour quality at the inlet of the evaporator.

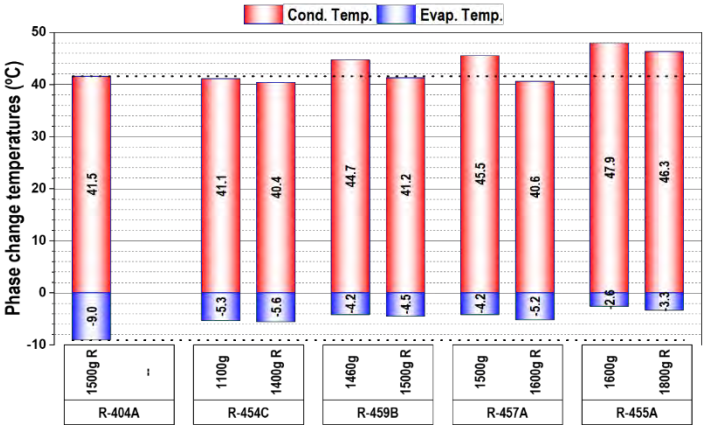

Figure 4: Average phase-change temperatures during 24h (t_K when compressor ON)

Figure 5 presents the maximum discharge temperature and pressure during the 24-hour test in relation to R-404A results. It can be observed that maximum working pressure with optimized refrigerant charge and liquid receiver for R-454C, R-459B and R-457A are below the reference. Similar maximum dicharge temperatures were observed for the same refrigerants. However, R-455A, with a 3% of CO_2 in its composition, presents a significant increment in the maximum operating pressure and temperature which must be considered. In fact, it does not bring operating problems for the considered plant because the duty cycle of the compressor is around 50%, but for refrigeration systems with longer duty cycle, the increment of the discharge temperature could be higher (not cooling of compressor during OFF periods) and must be taken into account.

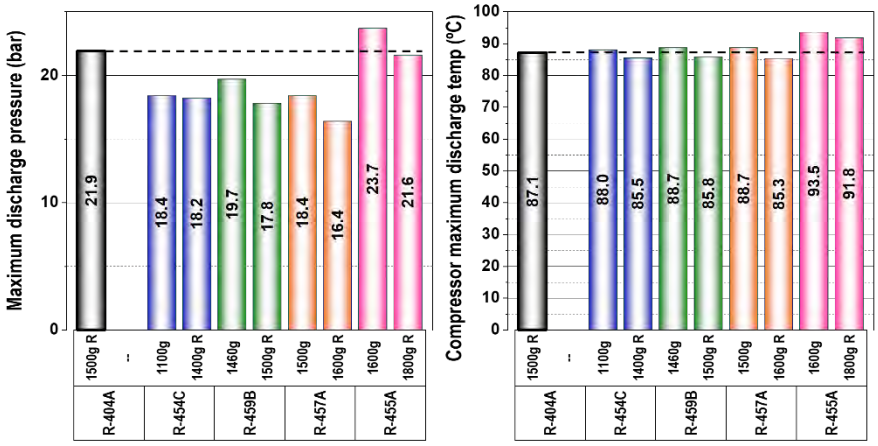

Figure 5: Maximum discharge pressure and temperature during 24h

Finally, Figure 6 presents the disaggregated energy consumption during the 24-hour test for the charge optimized and receiver configurations, which details the energy consumption of the fans,

lighting and electronics (in green), the energy consumption during the defrosting period (in red) and that of the compressor (in blue).
R-454C, in relation to R-404A, presents compressor's consumption. In addition, defrosting period average time of R-454C [19.3min, 16.0min (R)] was similar to that of R-404A [19.3 min (R)].
For R-459B, compressor power consumption is also reduced, resulting in lowest energy consumption in relation to R-404A. Shortest defrosting periods were measured for R-459B [13.5min, 12.1min (R)] in relation to R-404A, which reduces the thermal load of the cabinet. This reduction in time is caused by the increased evaporating temperature (Figure 4).
R-457A presented reduced compressor power consumption in relation to R-404A. Again, the similar duty cycle among them is related to the shortest defrosting period [13.3min, 12.6min (R)].
Finally, R-455A obtained similar energy consumption in relation to R-404A. In terms of average defrosting time, with this mixture the shortest periods were measured [10.2min, 11.3min (R)]. Those shortest periods are also related to the highest evaporating level (Figure 4).

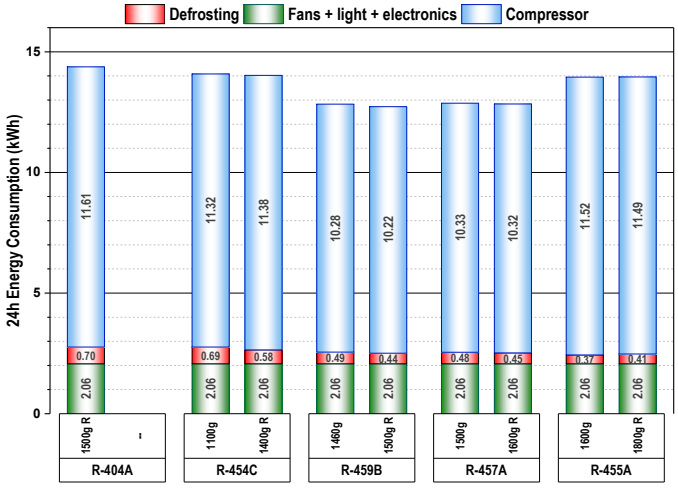

Figure 6. Disaggregated energy consumption during 24h

5. CONCLUSIONS

Experimental and theoretical substitution process of R-404A by the low-GWP alternatives R-454C, R459-B, R-457A and R-455A has been addressed with an open-fronted vertical cabinet for fresh product (-5ºC) according to energy consumption tests based on ISO 25953-2.Thermodynamic approach indicates that the substitutes offer similar VCC and a slight increase in COP for the operation at t_O=-7ºC and t_K=40ºC. A relevant reduction of the inlet vapour quality to the evaporator is predicted, which will compensate the large glide of the mixtures.
For the cabinet without receiver, optimized refrigerant charges offered energy consumption reductions in relation to R-404A: 2.07% for 1100g of R-454C, 10.76% for 1460g of R-459B, 10.48% for 1500g of R-457A and 2.95% for 1600g of R-455A. Those improvements were slightly larger when working with receiver: 2.45% for 1400g of R-454C, 11.55% for 1500g of R-459B, 10.69% for 1600g of R-457A and 2.9% for 1800g of R-455A.
For both system configurations, an increase in the evaporating level was measured for all the mixtures, indicating an improvement of the evaporator's thermal performance, which is not much affected by the large glide of the mixtures. The increased evaporating level resulted in general in shortest defrosting periods, which reduced the thermal load to the cabinet. Compressor discharge temperatures and pressures were similar to R-404A ones; thus, no difficulties are expected in the substitution process.
From the experimentation, it is concluded that it is possible to substitute R-404A by the new low-GWP refrigerant mixtures in stand-alone systems, with reduced refrigerant charges and with reduced energy consumption.

ACKNOWLEDGEMENTS

Authors gratefully acknowledge Conselleria d'Educació, Investigació, Cultura i Esport de la Generalitat Valenciana for financing this research work (project AICO/2018/058) and to Frost-Trol S.A. (www.frost-trol.com) for supplying the original cabinet.

NOMENCLATURE

COP	coefficient of performance
E	energy consumption, kWh
EEV	electronic expansion valve
Glide	temperature difference in a constant pressure phase-change, K
GWP	100 global warming potential
h	enthalpy, $kJ \cdot kg^{-1}$
M	molecular mass, $g \cdot mol^{-1}$
m	refrigerant mass flow rate, $kg \cdot s^{-1}$
NBP	normal boiling point, ºC
p	absolute pressure, bar
P_C	power consumption, kW
RH	relative humidity, %
RU	degree of superheat, K
s	entropy, $kJ \cdot kg^{-1} \cdot K^{-1}$
SUB	degree of subcooling, K
t	temperature, ºC and time, s
VCC	volumetric cooling capacity, $kJ \cdot m^{-3}$
x_v	vapour title

Greek symbols

Δ	increment
v	specific volume, $m^3 \cdot kg^{-1}$
λ	latent heat of phase change, $kJ \cdot kg^{-1}$

Subscripts

a	air
c	critical point
cam	climatic chamber
dis	compressor discharge
exp	expansion valve
ihx	internal heat exchanger
imp	impulsion
in	inlet
K	condensing level
O	evaporating level
out	outlet
p	product
R, ref	reference test. R-404A with 1500g and liquid receiver.
ret	return
s	isentropic process
suc	compressor suction

REFERENCES

Bella, B., Pham, H., Rajendran, R., 2018. Sustainable refrigerants for comfort and refrigeration, 1st IIR International conference on the application of HFO refrigerants, Birmingham, UK. Int. Inst. Refrigeration,, Birmingham, UK.

Defra, 2012. 2012 Guidelines to Defra / DECC's GHG conversion factors for company reporting: methodology paper for emission factors. Department for Environment, Food and Rural Affairs, London, UK.

European Commission, 2014. Regulation (EU) No 517/2014 of the European Parliament and of the Council of 16 April 2014 on fluorinated greenhouse gases and repealing Regulation (EC) No 842/2006.

ISO 23953-2:2015, 2015. Refrigerated display cabinets - Part 2: Classification, requirements and test conditions.

Kopchick, S., Scancarello, M., 2017. New refrigerants designation and safety classifications, E360 Forum, Chicago, IL, USA. (https://climate.emerson.com/documents/chicago-%E2%80%93-new-refrigerants-designation-safety-classifications-en-us-3663334.pdf) (last acces: november 2018).

Llopis, R., Torrella, E., Cabello, R., Sánchez, D., 2010. Performance evaluation of R404A and R507A refrigerant mixtures in an experimental double-stage vapour compression plant. Applied Energy 87, 1546-1553.

Maiorino, A., Aprea, C., Del Duca, M.G., Llopis, R., Sánchez, D., Cabello, R., 2018. R-152a as an alternative refrigerant to R-134a in domestic refrigerators: An experimental analysis. International Journal of Refrigeration 96, 106-116.
Mota-Babiloni, A., Haro-Ortuño, J., Navarro-Esbrí, J., Barragán-Cervera, Á., 2018. Experimental drop-in replacement of R404A for warm countries using the low GWP mixtures R454C and R455A. International Journal of Refrigeration 91, 136-145.
UNEP, 2015. 2014 Report of the refrigeration air conditioning and heat pumps technical options committee. 2014 Assessment., Kenya.

Manuscript ID: 558
DOI: 10.18462/iir.icr.2019.0558

Modeling the heat transfer and the pressure loss in flat fin-and-tube compact heat exchangers

Martim AGUIAR [(a, b)], Pedro D. GASPAR[(a, b)], Pedro D. SILVA[(a, b)]

[(a)] University of Beira Interior, Rua Marquês d'Ávila e Bolama, 6201-001, Covilhã, Portugal
[(b)] C-MAST - Centre for Mechanical and Aerospace Science and Technologies, Covilhã, Portugal

ABSTRACT

Fin-and-tube heat exchangers (HX) have wide application in the industry. The study of HXs with reduced tube diameter has allowed the development of more compact and equally efficient equipment. Most of the HXs of this type are composed of flat fins, not only due to the ease of construction but also to their reliability in long-term operation and reduced friction characteristics. The formulation of mathematical equations that predict the effect of the geometric characteristics on the heat transfer and friction factors of the HXs lead many researchers to try to establish correlations that approximate the experimental results. In this paper is developed a computational tool based on literature correlations is used to evaluate the Colburn and friction factors for flat fin-and-tube compact HXs. The results of predictions show the Colburn and friction factors behavior for different geometrical parameters (fin pitch, tube diameter, tube number) and typical Reynolds number.
Keywords: Refrigeration, Heat exchangers, Compact, Computational simulation, Evaporators, Energy Efficiency.

1. INTRODUCTION

Fin-and-tube heat exchangers are widely used in engineering applications such as air-conditioning systems, gas heaters and refrigeration systems. This type of exchanger is usually composed of mechanically or hydraulically expanded round tubes in continuous and parallelly arranged fin blocks. The fins associated with the exchangers can take several forms, the most common of which are the flat type. Although the wavy, louver and slit fins significantly improve the heat transfer coefficient compared to the flat fins, they do not guarantee as much reliability in long-term operation, as they have characteristics regarding higher friction. Many researches have been developed in the field of heat transfer and friction characteristics in flat-geometry fin plate changers, and the most influential works in this area are synthesized by Wang et al. (2000). These collected tests differ essentially in the geometric characteristics of the exchangers, such as the number of rows of tubes, the diameter of the tubes, the thickness of the tube wall, the transverse distance between tubes, the longitudinal distance between tubes, the space between the fins and the thickness of the fins.

Tests on this subject have been based on smaller diameters of the exchanger tubes, lower than 9.0mm, due to the increasing use in domestic applications. This geometry enhances the development of more compact heat exchangers, with high heat transfer coefficients and low load losses, as well as using smaller amounts of refrigerant (Wang and Chi, 2000; Wang et al., 1997; Seshimo and Fujii, 1991).

The experimental tests conducted by researchers in this area are usually governed by recommendations from ASHRAE (1993) and ASHRAE Standard 41.2 (1987), thus allowing uniformity among the various measured values.

The main objective of the data collection is to try to establish mathematical correlations, with minimal error, in order to predict the values of the performance parameters of the exchanger for different geometric dimensions. This will enable, without experimental testing, to predict the best geometry of the exchanger in order to optimize it.

Experimentally, obtaining the coefficient of heat transfer and the loss of load are what allows the study of heat exchangers. These are generally obtained by applying the ε-NTU method to determine

the product of UA. This situation then allows to know the overall transfer coefficient of the exchanger between the fluid circulating inside the exchanger and the surrounding circulating air.
Considering the ε-NTU method and the global thermal transfer resistance, which is given by:

$$\frac{1}{UA} = \frac{1}{\eta_o h_o A_o} + \frac{1}{2}\log_e\left(\frac{D_o}{D_i}\right)\frac{D_o}{k_w A_w} + \frac{1}{h_i A_i} \quad \text{Eq. (1)}$$

whose coefficients are obtained from other studies (Gnielinski, 1976; Schmidt, 1949), according to Wang et al. (1996, 2000a) the heat transfer characteristics are presented in terms of the factor Colburn by:

$$j = \frac{Nu}{Re_{D_c} Pr^{1/3}} = \frac{h_o}{\rho V_{max} c_{p_a}} Pr^{2/3} \quad \text{Eq. (2)}$$

The friction factor is calculated from the equation of pressure drop described by Kays and London (1984), being expressed by:

$$f = \frac{A_c}{A_o}\frac{\rho_m}{\rho_1}\left[\frac{2\Delta P \rho_1}{G_c^2} - (1+\sigma^2)\left(\frac{\rho_1}{\rho_2} - 1\right)\right] \quad \text{Eq. (3)}$$

2. CORRELATION

Result of the 74 samples collected by Wang et al. (2000), a database was created that allowed to obtain the performance of the passage of the air by the exchanger based on the Colburn factor (j) and the friction factor (f). The increase of the database induces better correlations, increasing their reliability. Many attempts have been made to correlate the results of the experiments, and the basic forms of correlations are:

$$j = C_1 Re_{D_c}^{C_2} \quad \text{Eq. (4)}$$

$$f = C_3 Re_{D_c}^{C_4} \quad \text{Eq. (5)}$$

Where the parameters C_1, C_2, C_3, and C_4 are dependent on the physical dimensions of the heat exchanger. From the detailed evaluation of this database, Wang *et al.* (2000) indicates that the final expressions for heat transfer performance are given by:
For N = 1

$$j = 0.108 Re_{D_c}^{-0.29}\left(\frac{P_t}{P_l}\right)^{P1}\left(\frac{F_p}{D_c}\right)^{-1.084}\left(\frac{F_p}{D_h}\right)^{-0.786}\left(\frac{F_p}{P_t}\right)^{P2} \quad \text{Eq. (6)}$$

Where

$$P1 = 1.9 - 0.23\log_e\left(Re_{D_c}\right) \quad \text{Eq. (7)}$$

$$P2 = -0.236 + 0.126\log_e\left(Re_{D_c}\right) \quad \text{Eq. (8)}$$

For N ≥ 2

$$j = 0.086 Re_{D_c}^{P3} N^{P4}\left(\frac{F_p}{D_c}\right)^{P5}\left(\frac{F_p}{D_h}\right)^{P6}\left(\frac{F_p}{P_t}\right)^{-0.93} \quad \text{Eq. (9)}$$

Where

$$P3 = -0.361 - \frac{0.042N}{\log_e(Re_{D_c})} + 0.158\log_e\left(N\left(\frac{F_p}{D_c}\right)^{0.41}\right) \quad \text{Eq. (10)}$$

$$P4 = -1.224 - \frac{0.076\left(\frac{P_l}{D_h}\right)^{1.42}}{\log_e(Re_{D_c})} \quad \text{Eq. (11)}$$

$$P5 = -0.083 + \frac{0.058N}{\log_e(Re_{D_c})} \quad \text{Eq. (12)}$$

$$P6 = -5.735 + 1.21\log_e\left(\frac{Re_{D_c}}{N}\right) \quad \text{Eq. (13)}$$

The friction factor is given by:

$$f = 0.0267Re_{D_c}^{F1}\left(\frac{P_t}{P_l}\right)^{F2}\left(\frac{F_p}{D_c}\right)^{F3} \quad \text{Eq. (14)}$$

Where

$$F1 = -0.764 + 0.739\frac{P_t}{P_l} + 0.177\frac{F_p}{D_c} - \frac{0.00758}{N} \quad \text{Eq. (15)}$$

$$F2 = -15.689 + \frac{64.021}{\log_e(Re_{D_c})} \quad \text{Eq. (16)}$$

$$F3 = 1.696 + \frac{15.695}{\log_e(Re_{D_c})} \quad \text{Eq. (17)}$$

These correlations, however, should only be applied to exchangers with the characteristics described below, since only these ranges were taken into account when obtaining them:

- Type of fin – flat
- N - between 1 and 6
- D_O - between 6.35 and 12.7 mm
- F_p - between 1.19 and 8.7 mm
- P_t - between 17.7 and 31.75 mm
- P_l - between 12.4 and 27.5 mm

Other correlations have been established by several researchers, however they are focused on the tests carried out by each researcher and are not assigned to a large database.

3. SIMULATION OF CORRELATIONS

From the correlations established by Wang et al. (2000), a simulation of the same was done using the MATLAB program, providing the study of the effect of the various geometric parameters on the thermal transfer characteristics.

Table 1 shows the geometric dimensions assumed in the computational simulations. The choice of these dimensions was based on the experimental tests performed by Wang et al. (2000) for small

diameters of the exchanger tubes. In order to carry out the study, different air velocity values were assumed, implying different Reynolds numbers.

Table 1. Geometric dimensions of heat exchangers

No	D_0 (mm)	F_p (mm)	P_t (mm)	P_l (mm)	δ_t (mm)	N
1	7	1.22	21	12.7	0.115	2
2	7	1.78	21	12.7	0.115	2
3	7	1.22	21	12.7	0.115	4
4	7	1.78	21	12.7	0.115	4
5	9.52	1.23	25.4	19.05	0.115	1
6	9.52	2.23	25.4	19.05	0.115	1
7	9.52	1.23	25.4	19.05	0.115	2
8	9.52	2.23	25.4	19.05	0.115	2
9	9.52	1.23	25.4	19.05	0.115	4
10	9.52	2.31	25.4	19.05	0.115	4

4. ANALYSIS OF RESULTS AND DISCUSSION

Figs. 1 and 2 illustrate the resulting values of the simulations performed from the above-described correlations. These are relatively close to the experimental values published by Wang *et al.* (2000). As Wang *et al.* (2000) described, the proposed correlation for heat transfer can describe 88.6% of the Colburn (*j*) factors with ±15% deviation, while the correlation of the friction factor correlates 85.1% of the factors by ±15%.

Figs. 3 and 4 show the effect of the space between the fins (F_p) on the heat transfer and the friction factor, respectively, on heat exchangers with 4 rows of tubes. As can be seen in Fig. 3, the Colburn factor for heat transfer is practically independent of the spacing between the fins in any of the configurations. The same was concluded in the works developed by Rich (1973) and Wang *et al.* (1996), who reported that although the space between fins was not the same, the coefficient of heat transfer is independent.

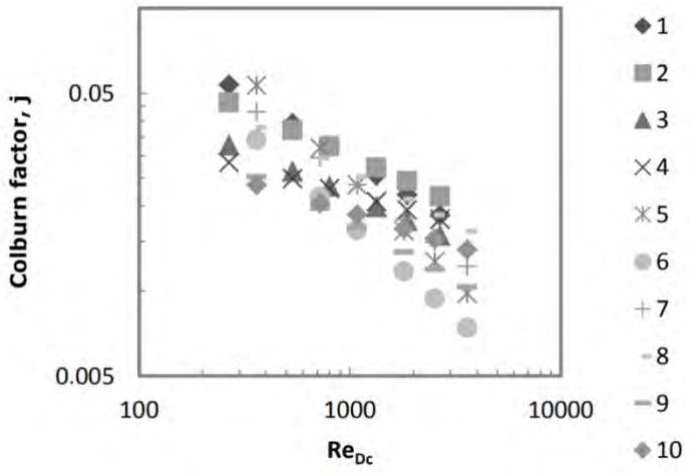

Figure 1: Simulation of the Colburn factor correlation for different Reynolds numbers and for the different geometric dimensions of the heat exchangers.

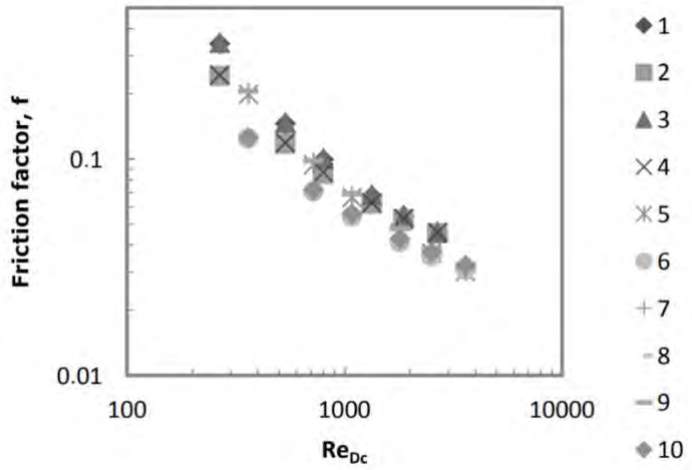

Figure 2: Simulation of the correlation of the friction factor (f) for different Reynolds numbers and for the different geometric dimensions of the heat exchangers.

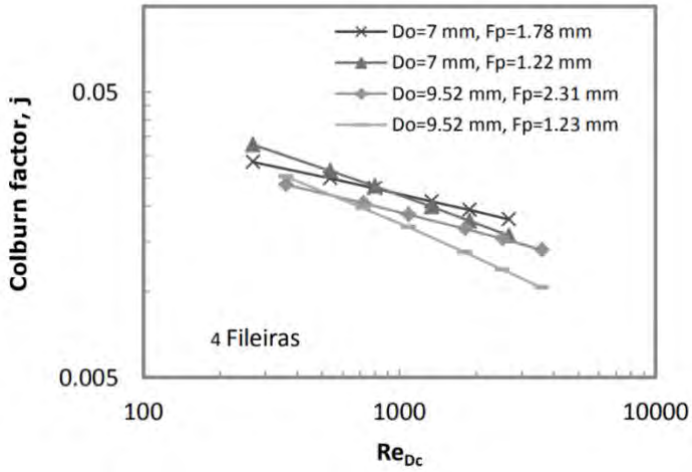

Figure 3: Effect of the space between fins on the Colburn factor for N = 4.

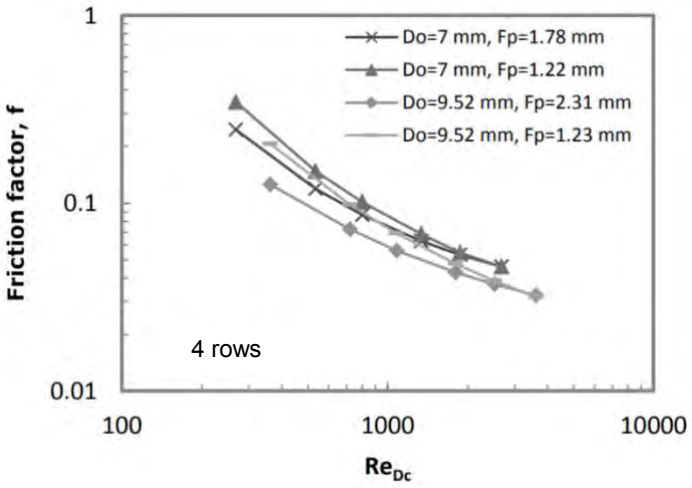

Figure 4: Effect of the space between fins on the friction factor for N = 4.

The effect of the spacing between fins is also shown in Fig. 5 and 6 for heat transfer and coefficient of friction, respectively, but now for one and two rows of tubes. Contrary to the previous situation, here we see that there is a relation between the space between fins with the Colburn factor and the coefficient of friction. Regardless of the Reynolds number, for N = 1 it is observed that the heat

transfer factor increases with the decrease of the spacing between the fins. For N = 2, the same situation exists, but only for $Re_{D_c} < 1200$, once when $Re_{D_c} > 1200$ this situation is reversed.

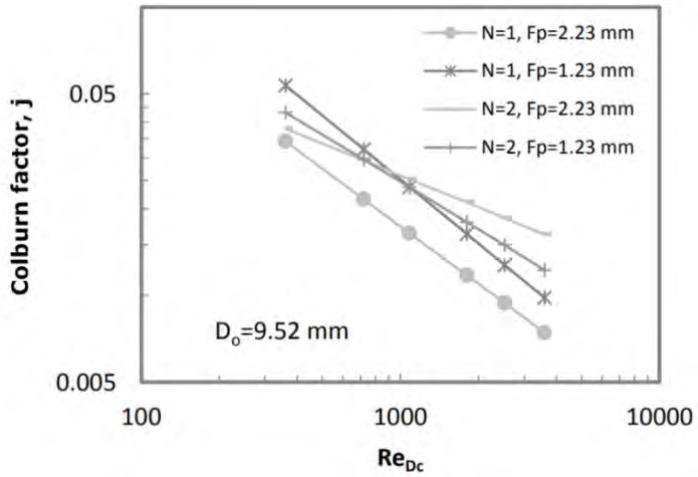

Figure 5: Effect of the space between fins on the Colburn factor for N = 1 and N = 2.

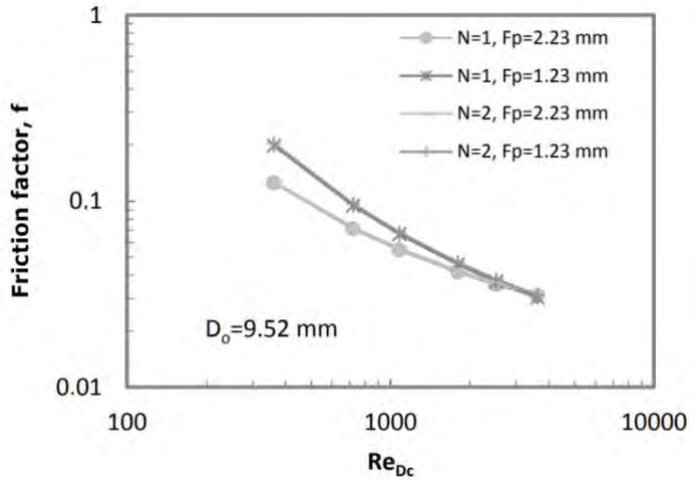

Figure 6: Effect of the space between fins on the friction factor for N = 1 and N = 2.

Similarly, it is also observed that the friction factor increases with the reduction of the spacing between fins, independently of the number of rows of tubes, a situation which is also verified experimentally by Wang et al. (2000).

Figs. 7 and 8 illustrate the effect of the number of rows of tubes on heat transfer and the coefficient of friction. As can be seen, for values of $Re_{D_c} < 1200$ the Colburn factor decreases with increasing number of rows of tubes. However, this effect tends to attenuate with the increase of Reynolds number. This same situation is identified by Wang et al. (1996) and Rich (1975), although for higher Reynolds numbers. The friction factor is independent of the number of rows of tubes, also confirmed experimentally by Wang et al. (2000)

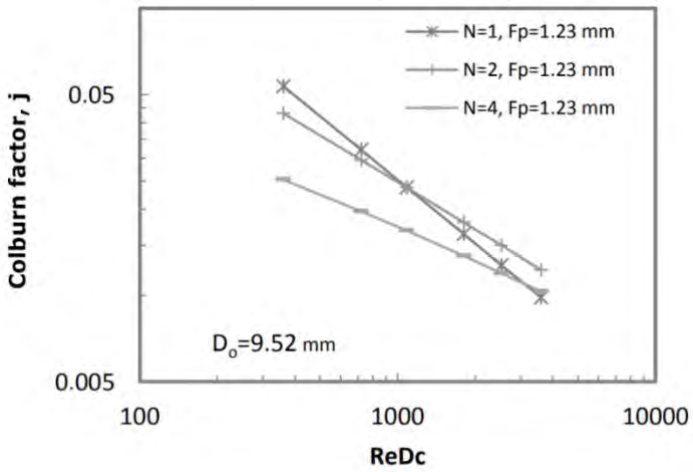

Figure 7: Effect of the number of rows of tubes in the heat transfer (Fp = 1.23mm).

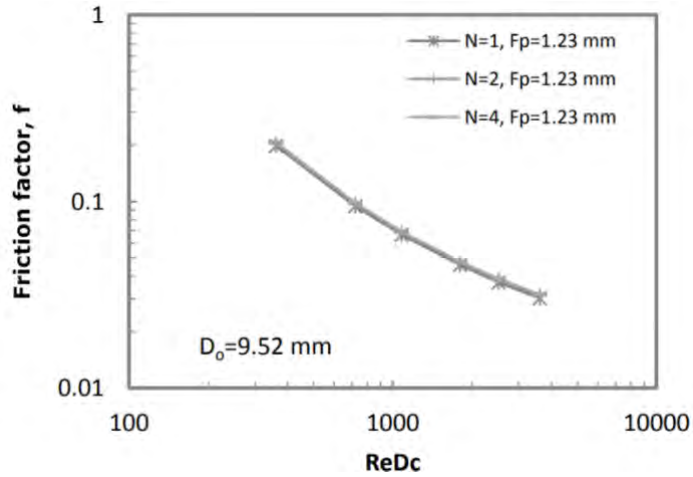

Figure 8: Effect of the number of rows of tubes on the coefficient of friction (Fp = 1.23mm).

5. CONCLUSIONS

The attempt to establish mathematical correlations with the minimum of errors in relation to the experimental results has shown to be very relevant for the most different test conditions, with mean deviations of less than 7.51% and 8.31% being obtained for the correlations of the coefficient of heat transfer and the friction coefficient, respectively (Wang *et al.*, 2000). Among the many correlations that have been published, we highlight the correlation presented here, not only because of the average deviations of the values being reduced, but also because of the large data base that supported the formulation. Although some simulations of correlations do not accurately rewrite the assays, as has been found, they are a good approximation to the assays. In this way, although in a general way, this situation allows to conjecture the influence of the geometric characteristics on the coefficients of transference of heat and friction. In short, we can therefore state that the correlations described above are presented as a good solution to the experimental tests.

ACKNOWLEDGEMENTS

This work has been supported by the project Centro-01-0145-FEDER-000017 - EMaDeS - Energy, Materials and Sustainable Development, co-financed by the Portugal 2020 Program (PT 2020), within the Regional Operational Program of the Center (CENTRO 2020) and the European Union through the European Regional Development Fund (ERDF). The authors wish to thank the opportunity and financial support that permitted to carry on this project.

REFERENCES

ASHRAE, 1993, Handbook Fundamental, SI-Edition, American Society of Heating, Refrigerating and Air-Conditioning Engineers, Atlanta, pp.14-15.

ASHRAE, 1987, Standard 41.2, Standard Methods for Laboratory Air-flow Measurement, American Society of Heating, Refrigerating and Air-Conditioning Engineers.

Gniclinsk, V, 1976, New equation for heat and mass transfer in turbulent pipe and channel flow, Int. Chem. Eng. 16, 359-368.

Rich, D.G., 1973, The effect of the fin spacing on the heat transfer and friction performance of multirow, smooth plate fin-and-tube heat exchangers, ASHRAE Transactions 79, 135-145.

Rich, D.G., 1975, The effect of the number of tubes rows on heat transfer performance of smooth plate fin-and-tube heat exchangers, ASHRAE Transactions 81, 307-317.

Schmidt, 1949, Th.E.. Heat transfer calculations for extended surfaces, Refrigerating Engineering, pp. 351-357.

Seshimo, Y., M. Fujii, 1991, An experimental study of the performance of plate fin and tube hea exchangers at low Reynolds number. Proceeding of the 3rd ASME/JSME Thermal Engineering Joint Conference 4, 449-454.

Wang, C.C. e K.-Y. Chi, 2000, Heat transfer and friction characteristics of plain fin-and-tube heat exchangers, part I: New experimental data, Int. J. Heat Mass Transfer 43, 2681-2691.

Wang, C.C. e K.-Y. Chi, 2000, Heat transfer and friction characteristics of plain fin-and-tube heat exchangers, part I: Correlation, Int. J. Heat Mass Transfer 43, 2693-2700.

Wang, C.C., Y.C. Hsish, Y.J. Chang, Y.T. Lin, 1996, Sensible heat and friction characteristics of plate fin-and-tube heat exchangers having plane fins, Int. J. Refrig. 19, 223-230.

Wang, C.C., W.S. Lee, C.T. Chang, 1997, Sensible heat transfer characteristics of plate fin-and-tube exchangers having 7-mm tubes, AIChe Symposium Series 93, 211-216.

Manuscript ID: 562
DOI: 10.18462/iir.icr.2019.0562

Further development and experimental testing of a resistive sensor for monitoring frost formation in refrigeration systems

Martim AGUIAR [(a, b)], Pedro D. GASPAR[(a, b)], Pedro D. SILVA[(a, b)]

[(a)] University of Beira Interior, Rua Marquês d'Ávila e Bolama, 6201-001, Covilhã, Portugal
[(b)] C-MAST - Centre for Mechanical and Aerospace Science and Technologies, Covilhã, Portugal

ABSTRACT

Refrigeration systems are widely accepted as a mean to prevent food degradation. These systems usually rely on fin-and-tube heat exchangers to lower the air temperature. Due to long operation times and surface temperatures below dew point, frost may form and accumulate on the evaporators fin surface. This frost accumulation reduces and may clog the airflow, decreasing the system efficiency. Usually, most systems use a time-controlled system (stopping the compressor with or without powering a heating resistor inserted among fins to heat) to melt the ice. This method does not measure or predict the amount of frost formed, thus it is not reliable. Ice sensors that are cheap, reliable and easy to implement in commercial systems are studied. A resistive sensor is purposed, that measures the voltage between two electrodes with the water phase change (condensation and solidification -freezing-), as these states have different resistive values. Different electrode materials, morphologies and configurations are studied in order to obtain the best design.
Keywords: Refrigeration Systems, Frost, Monitoring, Testing.

1. INTRODUCTION

The issue of frost formation in air conditioning and refrigeration systems, more specifically on the fin-and-tube evaporators has been studied for several years, and yet it is the main cause of inefficiency (Popovac, et al., 2015), (Guo, et al., 2008).These fin-and-tube evaporators have a large area-to-volume ratio because they are used in light commercial systems. The demand for subfreezing operating temperatures causes the formation of a frost layer on the fin surface (Melo, et al., 2011), (Hermes, et al., 2009) as shown on Fig. 1.

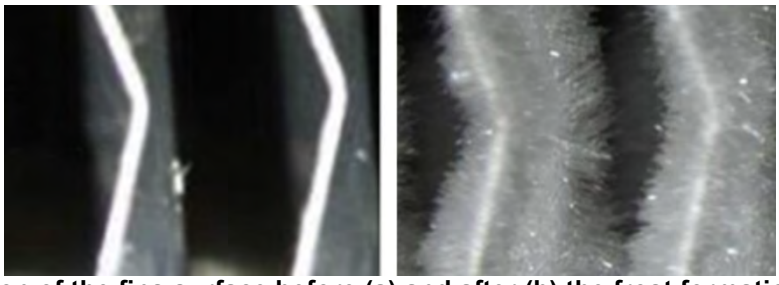

Figure 1: Visualization of the fins surface before (a) and after (b) the frost formation process (adapted from (Melo et al., 2011)

A frost layer is a porous medium comprised of ice crystals and pores filled with moist air. The frost buildup on the evaporators fin surface increases its air-side thermal resistance, decreasing the overall efficiency of the system. The efficiency keeps decreasing if the frost is allowed to continue growing due to not only the increment of the heat transfer resistance, but also to the blockage of the air passage between the fins. Full blockage of the evaporator can occur if no defrost method is applied (Melo et al., 2017). Several parameters can influence frost growth, but those with most influence are air relative humidity, velocity and supercooling degree (difference between inlet air

dew point and fin surface temperature) (Hermes et al., 2009), but may also be influenced by other parameters such as fin shape and spacing (Melo et al., 2011), type of flow (laminar or turbulent) (Yang et al., 2006), or air cleanliness (Wang et al., 2011). The lower system efficiency caused by the frost layer on fin surfaces result in a higher energy demand, and in extreme cases, system damage, besides threaten food safety. Defrost methods are used to reduce the problem, although additional energy is usually also consumed for them to operate (Wang et al., 2017). These defrost methods can be classified as seen in Fig. 2.

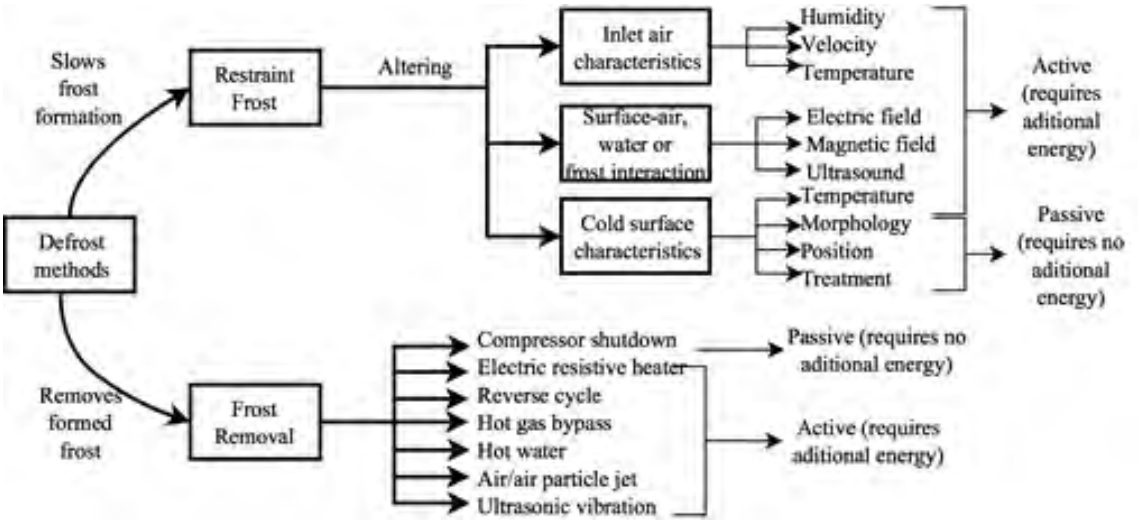

Figure 2: Classification of available defrost methods (Aguiar et al., 2018)

Time controlled with on-off defrosting and electric resistive heater or reverse cycle are the most used defrost methods. Apart from these, none of the abovementioned methods has gained significant acceptance from the refrigeration industry, due to complex, expensive and unreliable sensing and prediction methods (Xiao et al. 2010; Jiang, et al. 2013). This can cause a huge impact on energy consumption, as the timed defrost operations have to be timed for the worst-case scenario (warm and high air relative humidity) and thus, as these properties vary during the year, the amount of defrosting cycles could vary as well. Tassou et al. (2001) studied frost formation and defrost control parameters for vertical open refrigerated display cabinets (VORDC) and concluded that the ideal time between defrosts varies greatly with air temperature and humidity. As shown in Fig. 3, the ideal operation time between defrosts on VORDC can range from 4 hours to around 9.5 hours during different times of the year. A time-controlled defrosting must have in consideration the worst-case scenario on time between defrosting operations.

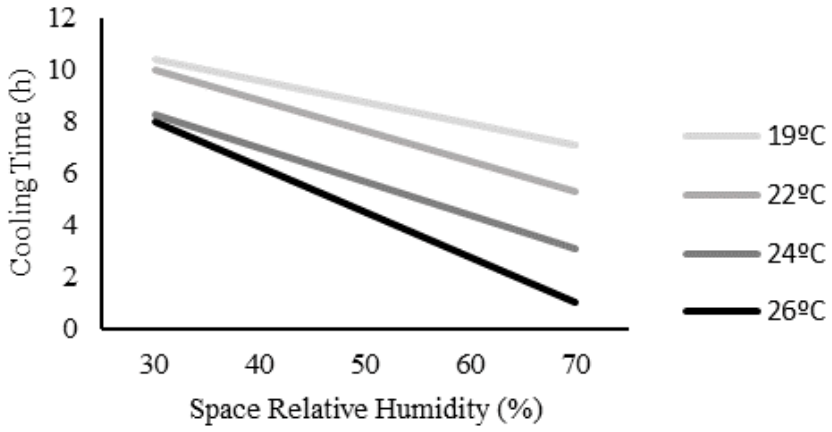

Figure 3: Optimum time between defrosts in relation to air temperature and humidity (adapted from (Tassou et al., 2001)

Demand defrost tries to solve this problem by predicting frost formation. This prediction can be done by computing the measured factors that influence frost formation (such as surface temperature, and inlet air characteristics: relative humidity, temperature and velocity) (Cui et al., 2011), computing the measurable system changes caused by the frost accumulation on the evaporator (temperature difference between the air and evaporator surface (Buick et al., 1978), pressure drop (Jarrett, 1972), degree of refrigerant superheat (Lawrence and Parker, 1998), fan power sensing (Muller, 1975) or both (Datta et al., 1997), using methods such as artificial intelligence (Kalogirou, 2000) and other algorithms (Cao et al., 2013; Bagyaveereswaran et al., 2017). Alternatively, demand defrost cycles can be controlled by directly measuring frost on the evaporator coils. In this scenario no prediction is necessary, as sensors positioned on the evaporator directly evaluate the state of the frost accumulation and their data is processed so that the defrost operation occurs when best suited. The resistance of a given sample varies with its form and material. Air, ice and water have quite different electrical resistance values, meaning that if two electrodes are positioned in the evaporator (but close enough for a voltage drop to be measured on a highly resistive material such as ice) and a voltage is applied on the terminals, a characteristic voltage drop will be measured as water forms, and this voltage drop will decrease as this water freezes, giving accurate measures of the ice formation. A device based on this characteristic was developed by Gaspar et al. (2016) and Caetano et al. (2018), as shown in Fig. 4.

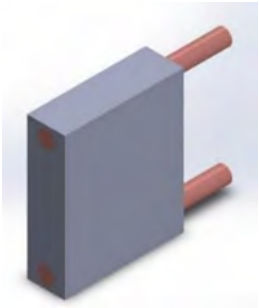

Figure 4: Apparatus for water and ice detection using a resistive sensor (Caetano et al., 2018)

In the present paper, more materials and distances between the electrodes were tested in order to optimize the sensor operation by trying to find the optimal configuration for ice detection on the evaporator. The tested parameters are based on Eq. (1):

$$R = \frac{\rho L}{A} \qquad \text{Eq. (1)}$$

Where R is the measured resistance, ρ the resistivity of the material between the electrodes which is the variable that indicates if there is water, ice or air between the electrodes, L the length of this material (directly related with the distance between the electrodes), and A the section area of this material. In order to increase the sensibility of the sensor, R must as low as possible when there is water, and high when there is air in between the electrodes. Therefore, L is decreased and A is increase. The section A automatically increases with the decrease of L as the droplets of water that form upon the water condensation on the evaporator. Ultimately, a bridge between the electrodes is formed, and this happens easier if the gap between these electrodes is smaller as seen on Figure 5. This condensed water will result in a decrease of the resistance of the sensor and consequent higher voltage drop.

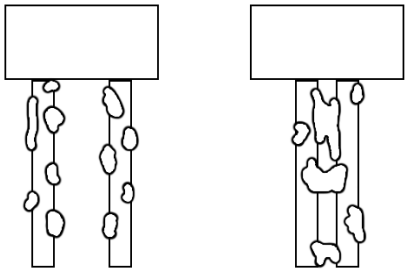

Figure 5: Formation of water droplets on the electrodes of the sensor (left) and bridges of water formed during condensation on a sensor with the electrodes closer (right)

2. EXPERIMENTAL SETUP

An analog-to-digital converter (ADC) uses a voltage divider to measure the voltage drop between the electrodes as shown in Fig. 6. The ADC returns a value between 0 and 1023, that represents lower and higher resistances respectively. Ice and air should be expected to give values near 1023, as they have high resistive values, and water should have a lower value.

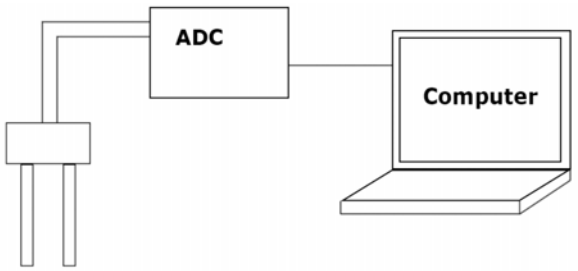

Figure 6: Experimental setup scheme

Sixteen sensor configurations are tested: eight with copper electrodes and eight with zinc plated electrodes. Both copper and zinc sensors have electrode distances of 3.0, 3.5, 4.0, 4.5, 5.0, 6.0, 7.0 and 8.0 mm.

3. RESULTS

Ten measurements were made for each set of electrodes distance, material and substance between the electrodes due to measurement fluctuations. The average results of ADC conversion is shown on Table 1.

Table 1. Values of ADC conversions obtained for the different electrode distances and materials

Electrodes distance (mm)	Air		Water		Ice	
	Copper	Zinc plated	Copper	Zinc plated	Copper	Zinc plated
3.0	1023	1023	461.2	435.6	1010	1009
3.5	1023	1023	812	750.9	1014	1010
4.0	1023	1023	902.3	844.7	1017	1013
4.5	1023	1023	932.7	910.3	1020	1019
5.0	1023	1023	1004.3	984.6	1021	1019
6.0	1023	1023	1023	1023	1023	1023
7.0	1023	1023	1023	1023	1023	1023
8.0	1023	1023	1023	1023	1023	1023

4. ANALYSIS OF RESULTS AND DISCUSSION

Fig. 7 shows the comparison between copper and zinc plated. No significant difference is observed between the curves, as the values for each distance are close. Although, the zinc plated electrode usually has a slightly lower value.

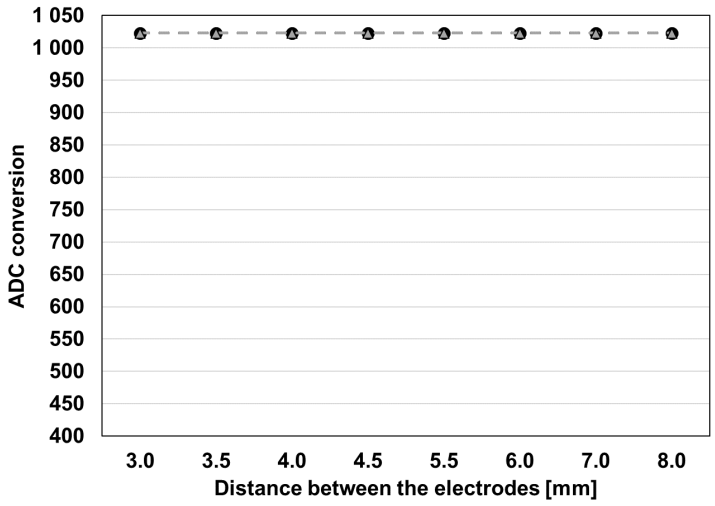

(a) Air.

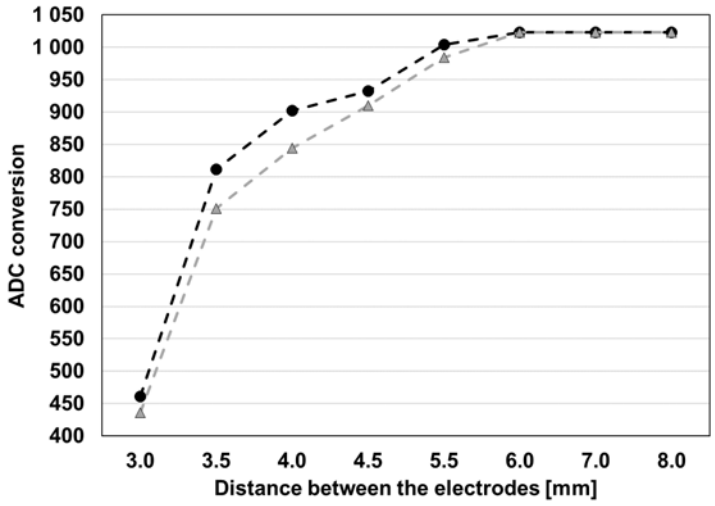

(b) Water.

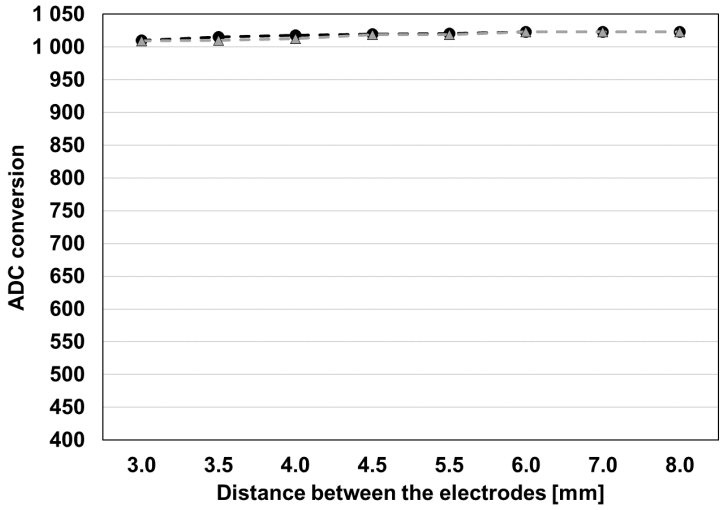

(c) Ice.

Figure 7: ADC conversion value vs. distance between electrodes for values for copper and zinc plated electrodes (cooper: ●; zinc plated: ▲)

Fig. 8 shows the comparison between air, water and ice for zinc plated and copper electrodes. Because of the high resistivity of ice, it is hard to distinguish between ice and air. The water is the medium with the most variation with the electrode distances, as the water droplets easily form water bridges between the electrodes that are closer to each other, and as these distances increase it becomes harder to establish a water connection between the electrodes.

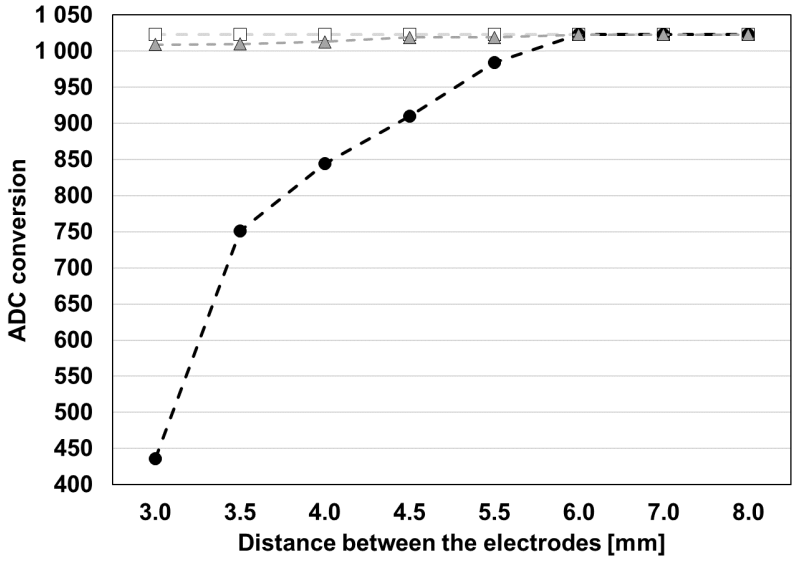

(a) Zinc plated electrodes.

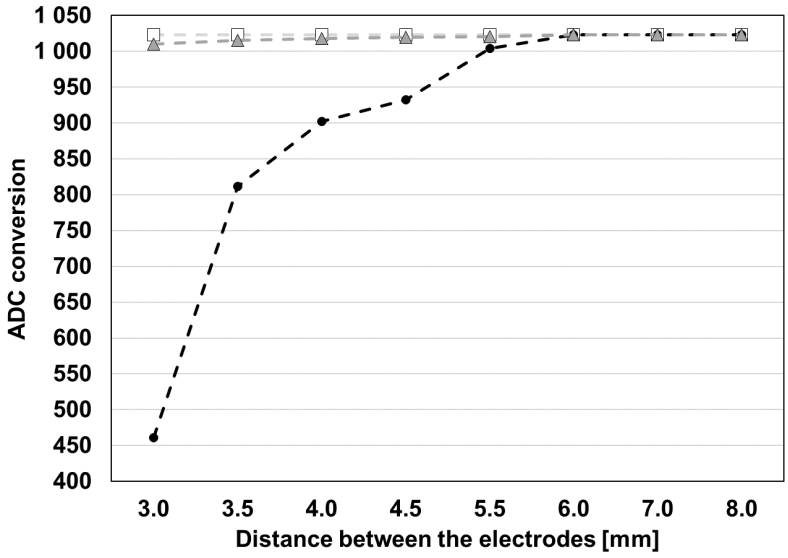

(b) Cooper electrodes.

Figure 8: Values obtained for air, water and ice for the zinc plated electrodes (Air: □; - Water: ●; Ice: ▲)

5. CONCLUSIONS

As expected, the closer the electrodes are, the easier it is to distinguish between ice, water and air, which is the main objective of implementing these sensors in evaporators. The difference between copper and zinc plated electrodes is not significant, so it is recommended to use the most corrosion resistant material, or even test more corrosion resistant materials such as stainless steel, to evaluate if the difference in measurements amongst electrode materials is still not relevant. This can be important as the materials that can form oxide layers might have different resistances and therefore different readings and lower durability.

Further research should be made on the subject, regarding other morphologies (smaller and larger electrode diameters, flat electrodes, non-parallel electrodes, etc).

Although it can be difficult to distinguish ice from air, the fact that one doesn't form right after the other might help with misreading. Water forms before ice, and when frozen, ice melts into water before the electrodes dry. This causes a significant drop in the resistance of the sensor that can help to know if a defrosting operation is due, or if a defrosting operation has been successful and can be terminated.

This paper further proves the concept of a resistive sensor being used for demand defrosting. Nonetheless, further studies should be done to increase the precision of ice detection, and reduce the sensor size to make it more practical for implementation.

ACKNOWLEDGEMENTS

This work has been supported by the project Centro-01-0145-FEDER-000017 - EMaDeS - Energy, Materials and Sustainable Development, co-financed by the Portugal 2020 Program (PT 2020), within the Regional Operational Program of the Center (CENTRO 2020) and the European Union through the European Regional Development Fund (ERDF). The authors wish to thank the opportunity and financial support that permitted to carry on this project.

REFERENCES

Aguiar, M. L., Gaspar, P. D. & Silva, P. D., 2018. Frost Measurement Methods for Demand Defrost Control Systems: A Review. London, IAENG.

Bagyaveereswaran, V., Subramanian, S. S. & Anitha, R., 2017. Smart Defrost Control for Refrigeration System. International Journal of Applied Engineering Research, 12(22), pp. 12202-12207.

Buick, T. R., McMullan, J. T., Morgan, R. & Murray, R. B., 1978. Ice detection in heat pumps and coolers. Energy Research, Volume 2, pp. 85-98.

Caetano, D., Gaspar, P. D. & da Silva, P. D., 2018. Experimental testing of a resistive sensor for monitoring frost formation in refrigeration systems. Valencia, s.n.

Cao, Z.-K., Zhang, C.-X. & Gu, B., 2013. Application of a support vector machine algorithm for improving effects of defrosting of commercial refrigerated display cabinets in supermarkets. HVAC&R Research, 19(3), pp. 230-241.

Cui, J., Li, W. Z., Liu, Y. & Jiang, Z. Y., 2011. A new time- and space-dependent model for predicting frost formation. Applied Thermal Engineering, Volume 31, pp. 447-457.

Datta, D., Tassou, S. A. & Marriott, D., 1997. Frost prediction on evaporator coils of supermarket display cabinets using artificial neural networks. Brussels, s.n.

Gaspar, P. D., Silva, P. D., Nunes, J. & Andrade, L. P., 2016. Monitoring device of ice formation in evaporator surface of refrigeration systems. Coimbra - Portugal, s.n.

Guo, X.-M., Chen, Y.-G., Wang, W.-H. & Chen, C.-Z., 2008. Experimental study on frost growth and dynamic performance of air source heat pump system. Applied Thermal Engineering , Volume 28, p. 2267–2278.

Hermes, C. J. L., Piucco, R. O., Barbosa Jr., J. R. & Melo, C., 2009. A study of frost growth and densification on flat surfaces. Experimental Thermal and Fluid Science, Volume 33, pp. 371-379.

Jarrett, J. H., 1972. A New Demand Defrost Control for Domestic Forced Draft Refrigerator Freezers and Freezers. IEEE Transactions on Industry Applications, IA-8(3), pp. 356-364.

Jiang, Y. et al., 2013. A novel defrosting control method based on the degree of refrigerant superheat for air source heat pumps. International journal of refrigeration, Volume 36, pp. 2278-2288.

Kalogirou, S. A., 2000. Applications of artificial neural-networks for energy systems. Applied Energy, Volume 67, pp. 17-35.

Lawrence, J. M. W. & Parker, B. C., 1998. Defrost control method and apparatus. United States of America, Patente Nº 5,813,242.

Melo, C., Hermes, C. J. & Silva, D. L., 2011. Experimental study of frost accumulation on fan-supplied tube-fin evaporators. Applied Thermal Engineering, Volume 31, pp. 1013-1020.

Melo, C., Hermes, C. J. & Silva, D. L., 2017. Effect of frost morphology on the thermal-hydraulic performance of fan-supplied tube-fin evaporators. Applied Thermal Engineering, pp. 1060-1068.

Muller, E. D., 1975. A new concept for defrosting refrigeration plants. Kalte, 28(2), pp. 52-54.

Popovac, M., Seichter, S. & Benovsky, P., 2015. Numerical analysis of the frosting performance of the air-side of a heat pump. Yokohama, Japan, s.n.

Tassou, S. A., Datta, D. & Marriott, D., 2001. Frost formation and defrost control parameters for open multideck refrigerated food display cabinets. Proceedings of the Institution of Mechanical Engineers - Part A - Power & Energy, pp. 213-222.

Wang, F., Liang, C. & Zhang, X., 2017. Research of anti-frosting technology in refrigeration and air conditioning fields: A review. Renewable and Sustainable Energy Reviews, Volume 81, pp. 707-722.

Wang, W. et al., 2011. Field test investigation of the characteristics for the air source heat pump under two typical mal-defrost phenomena. Applied Energy, Volume 88, p. 4470–4480.

Xiao, J., Wang, W., Guo, Q. C. & Zhao, Y. H., 2010. An experimental study of the correlation for predicting the frost height in applying the photoelectric technology. International Journal of Refrigeration, Volume 33, pp. 1006-1014.

Yang, D.-K., Lee, K.-s. & Cha, D.-J., 2006. Frost formation on a cold surface under turbulent flow. International Journal of Refrigeration, Volume 29, pp. 164-169.

Manuscript ID:564
DOI: 10.18462/iir.icr.2019.0564

Steady-state performance of electrochemical ammonia compression

Joe BAKER[(a)], Yunho HWANG[(a*)], Longsheng CAO[(b)], Chunsheng WANG[(b)]

[(a)] Center for Environmental Energy Engineering
Department of Mechanical Engineering, University of Maryland,
4164 Glenn Martin Hall Bldg., College Park, MD 20742, United States
*Corresponding author: email: yhhwang@umd.edu

[(b)] Department of Chemical and Biomolecular Engineering, University of Maryland,
1223A Chemical and Nuclear Engineering Bldg., College Park, MD 20742, United States

ABSTRACT

An electrochemical compressor is a solid-state compression device. For decades, researchers have been studying the electrochemical compressor for applications in energy storage. This paper introduces the working principle of eletrochemical ammonia compression process and the test facility constructed, and examines the performance data of an electrochemical ammonia compressor and the electrical power input requirements. The minimum required electrical energy input is defined for isothermal and isentropic conditions. The real steady-state electrical power input is compared to ideal conditions.
Keywords: Electrochemical, Compressor, Ammonia, Energy Storage.

1. INTRODUCTION

The electrochemical compressor (EC) is a solid-state compression device that uses an electrochemical reaction to incite mass transport of a given working fluid across a solid membrane. Research groups around the world have verified the electrochemical compression process for hydrogen (Rohland et al., 1998; Strobel et al., 2002; Grigoriev et al., 2011). However, recent experiments have demonstrated that electrochemical compression is possible with a variety of working fluids, including ammonia (Tao et al., 2017). Following the verification of ammonia electrochemical compression on a small scale, the current project work aims to scale up the operation to achieve more compression work and also to improve the efficiency of the compression process. While the compression efficiency in the previous experiments was low, we hope to increase the cell efficiency by improving the distribution of gases inside the cell and by reducing the cell's electrical impedance. Ammonia is a commonly used refrigerant and may also be used for power generation, either in ammonia fuel cells (Ganley, 2008) or in internal combustion engines (Reiter and Kong, 2010). These power generation applications require high pressure storage of ammonia; therefore, an efficient ammonia compressor becomes necessary for both refrigeration and energy storage applications.

2. WORKING PRINCIPLES

The EC may be a useful component in ammonia energy storage, as it may be able to compress ammonia gas with higher efficiency than a conventional mechanical compressor. The EC device consists of three main components: the gas distribution channels, the electrodes, and the membrane. The gas distribution channels, shown in Fig. 1(a), supply the working fluid to the electrodes, which are made of a porous, electrically conductive material. Within the electrodes, two separate half-reactions occur. In the first half-reaction, the working fluid reacts to form an ammonium ion that is permeable through the membrane. The ion then passes through the membrane, after

which the second half-reaction occurs in the opposite electrode. In the second half-reaction, an ammonium ion reacts to reform the ammonia and hydrogen gases at an elevated pressure. A second gas distribution channel receives the high-pressure fluid from the electrode. Fig. 1 illustrates the process.

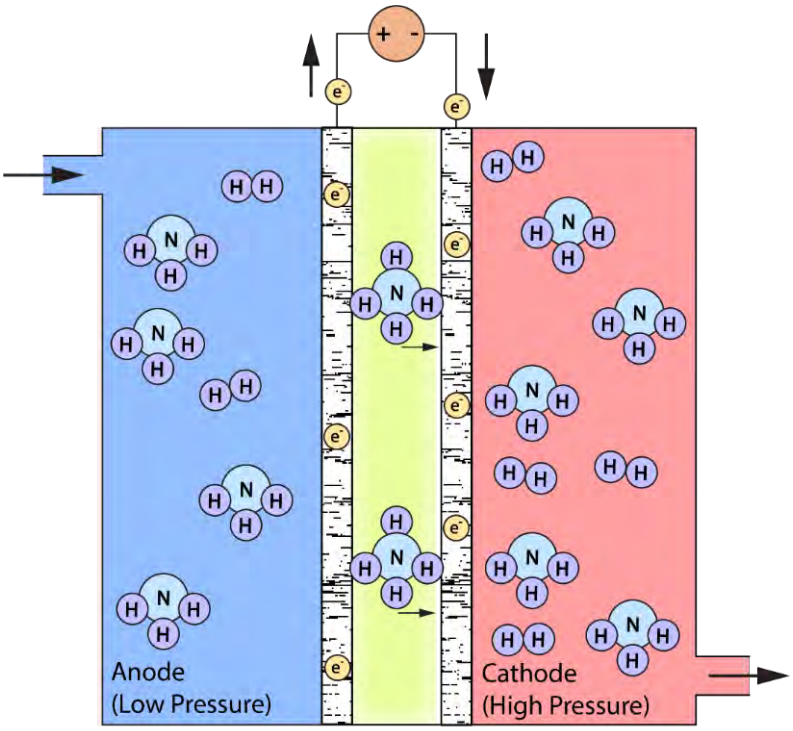

Figure 1: Diagram of NH_3 EC cell

The following analysis considers an ammonia compression process. Eq. (1) governs the oxidation reaction on the anode side, while Eq. (2) governs the reduction reaction on the cathode side.

$$2NH_3 + H_2 \rightarrow 2NH_4^+ + 2e^- \quad \text{Eq. (1)}$$

$$2NH_4^+ + 2e^- \rightarrow 2NH_3 + H_2 \quad \text{Eq. (2)}$$

From the reaction, mass transport is caused by the movement of electrons. Thus, to generate mass flow, current must be supplied to the cell, which requires an electrical potential. The total cell potential can be expressed by

$$U_{tot} = U_N + \eta_{Ohm} + \eta_{act} + \eta_{conc} \quad \text{Eq. (3)}$$

where U_{tot} represents the total electrical potential in the cell, U_N is the Nernst voltage, η_{ohm} is the Ohmic polarization loss, and η_{conc} is the concentration polarization loss. For now, we assume the concentration loss is negligible.

The Nernst potential is the cell potential required to maintain a given concentration difference across the membrane. The value is given by Eq. (4) in terms of absolute suction pressure P_{in} and absolute discharge pressure P_{out} and is valid for constant temperature reactions and assumes ideal gas behavior.

$$U_N = \frac{3RT}{2F} \ln\left(\frac{P_{out}}{P_{in}}\right) \quad \text{Eq. (4)}$$

where R is the universal gas constant, F is Faraday's constant, and T is the absolute temperature.

The Ohmic loss term may be given by

$$\eta_{ohm} = i * r \quad \text{Eq. (5)}$$

where i is the current density and r is the area-specific resistance, a property of the membrane.

The current density requirement can be deduced from the required mass flow of ammonia gas using Faraday's law of electrolysis, assuming no drag of additional ammonia molecules occurs.

$$i = \frac{\dot{m}_{NH3}}{M_{NH3}} * \frac{zF}{A} \qquad \text{Eq. (6)}$$

where $\dot{m}_{NH3}$ is the mass flow rate of ammonia gas, M_{NH3} is the molar mass of ammonia, z is the number of electrons displaced per molecule of ammonia transported (equal to 1 for this reaction), and A is the total membrane area.

3. EXPERIMENTAL SETUP

Fig. 2 shows a schematic diagram of the EC test facility. We supplied NH_3 and H_2 to the EC in known quantities via two mass flow controllers, labeled MFC on the diagram. The hydrogen line was then passed through a humidifier to introduce moisture into the fluid mixture. The inlet pressure was measured with an absolute pressure transducer. The EC was heated to a desired temperature. A constant stream of gas was flowed through the suction side to ensure there were enough reactants for the electrochemical reaction. The suction side pressure was then regulated by a capillary expansion device. On discharge side, a second absolute pressure transducer measured the discharge pressure. Gases left the EC through a back-pressure regulator, which maintained constant pressure in the cell.

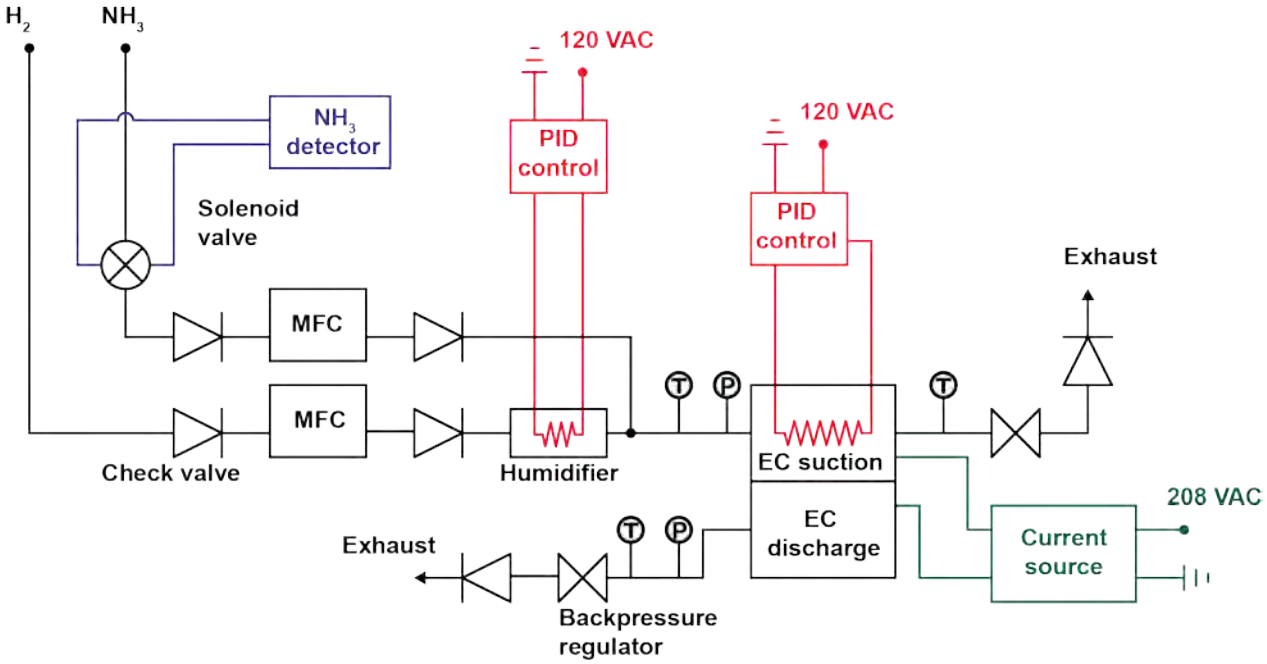

Figure 2: Schematic of experimental setup

The compressor consisted of two cells in parallel, as illustrated by Fig. 3. Gas was introduced to each membrane via graphite bipolar plates with embedded parallel flow channels. We used preassembled membrane electrode assemblies, consisting of Nafion 115 membranes and carbon cloth gas diffusion layers. Each electrode was coated with 0.5 mg/cm² of Pt supported carbon catalyst. The experiments were carried out under galvanostatic conditions, with a constant current of 1.5 A for all experiments. Additionally, inlet flow rates of 200 sccm of NH_3 and 100 sccm of H_2 were used for each experiment. In each test, we observed the increase in pressure of the discharge side and adjusted the back-pressure regulator to the desired outlet pressure. We ran the tests until steady states were achieved for both pressure and cell voltage.

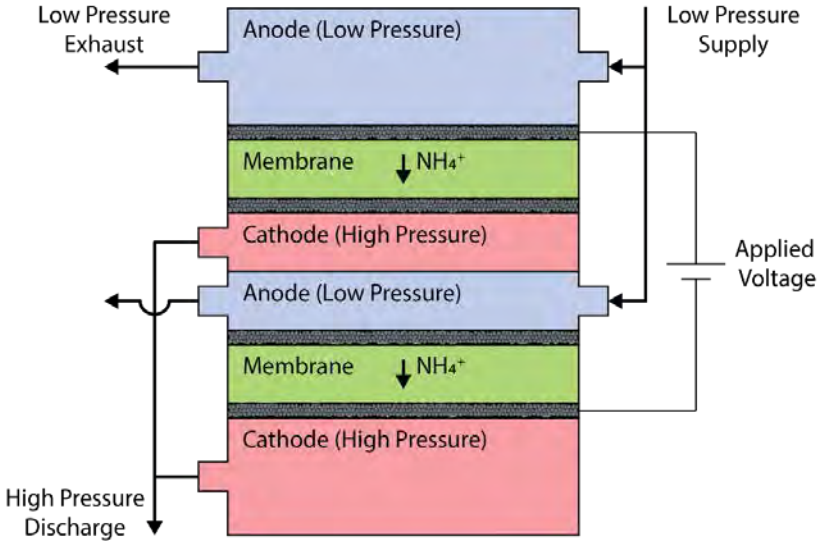

Figure 3: Diagram of EC stack

4. RESULTS

Table 1 details both the set parameters for each test, including total current, stack temperature, and inlet humidity as well as the measured variables, suction pressure, discharge pressure, and total voltage. The Nernst voltage is a calculated variable based on temperature and pressure.

Table 1. Steady state experimental data

Test	Current (A)	Temp. (°C)	Cell RH (%)	Suction Pressure (bar_a)	Discharge Pressure (bar_a)	Total Voltage (mV)	Nernst Voltage (mV)	ir Loss (mV)
1	1.5	27.7	28	1.77	9.88	354	133	220
2	1.5	51.7	41	1.73	9.92	295	147	149
3	1.5	25	33	3.70	12.28	219	92	126

Fig. 4 shows the cell pressurization process for Test 1. The pressure-time curve shows the gradual pressurization of the discharge side. At around 800 seconds, the pressure in the discharge side reached the setpoint of the back-pressure regulator, at which point gas began flowing out of the discharge line at a steady pressure. From the voltage-time curve, we see that the stack voltage strongly correlates to the pressure. The real voltage increases until the pressure reaches its steady condition and the decreases. We noted that the voltage decreased significantly after the high-side pressure stabilized. However, the increase was likely due changes in the low-side pressure. As the test ran on, the suction side pressure increased slightly even after the discharge pressure stabilized. The increase in suction pressure decreased the pressure ratio which was a likely reason why the total voltage decreased after the discharge pressure stabilized. Fig. 5 shows the pressurization curves for Test 3, in which we maintained the suction-side at 4 bar_a. The pressure-time curve again shows the pressure increasing to a steady condition. The jump in pressure near the 4,000 second mark resulted from adjustments made to the back-pressure regulator to get to our desired discharge pressure of 12 bar_a. The voltage curve again shows the dependence of the stack voltage on the pressure ratio, noting that, after the high-side pressure stabilized, the low-side pressure increased, decreasing the overall pressure ratio, which brought down the stack voltage.

In both Figures, we notice the difference between the Nernst voltage and the real voltage is nearly constant, which implies the electrical do not change significantly over the course of the experiment, implying there were not major electrochemical losses due to the differential pressure. Additionally, the ir loss in Test 1 is significantly larger than that of Test 3, despite the similar operating conditions. Further experimentation will examine whether the increased ir loss is due to the elevated pressure or whether the increased loss was due to membrane properties, such as insufficient membrane hydration.

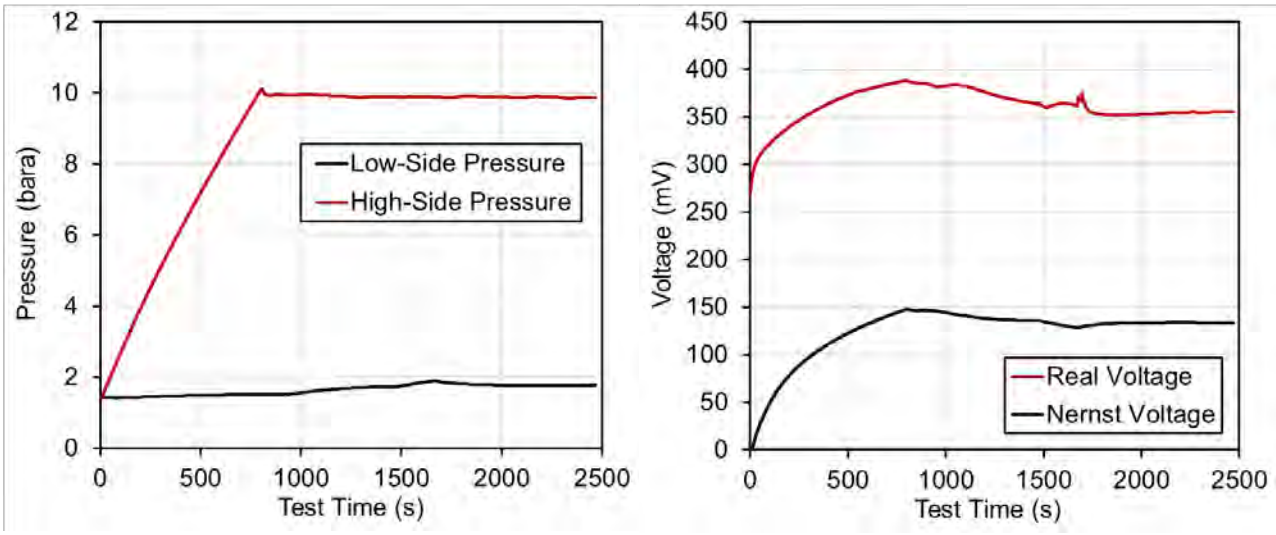

Figure 4: EC pressurization from 2 bar_a to 10 bar_a

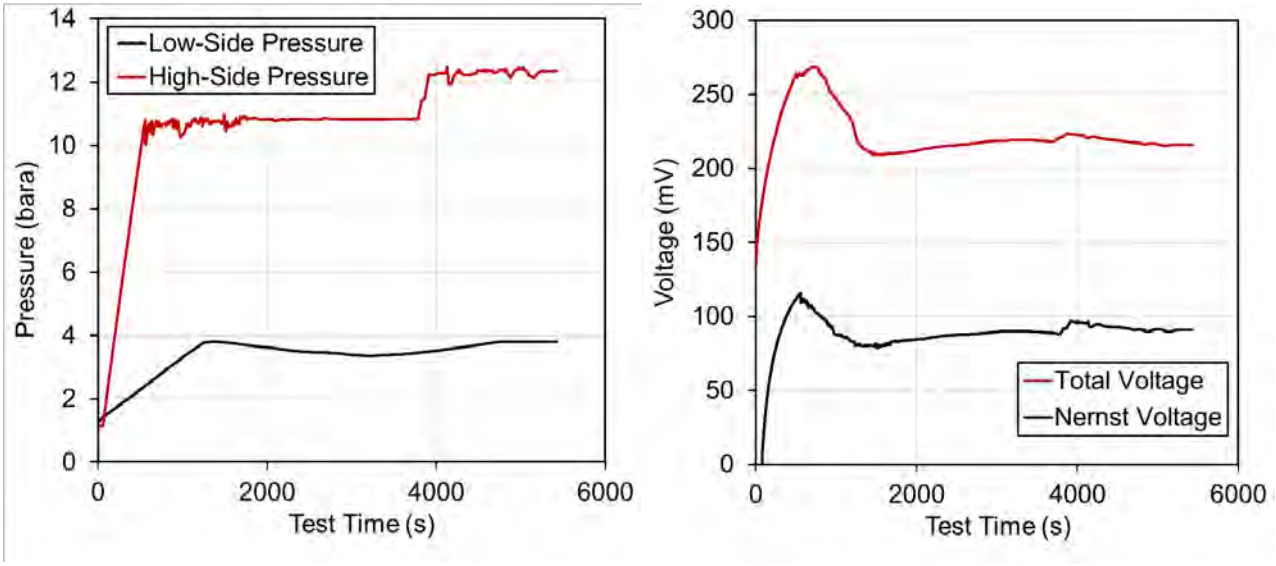

Figure 5: EC pressurization from 4 bar_a to 12 bar_a

5. ANALYSIS

In this work, as well as many previous experimental investigations into electrochemical compression, electrochemical cells are heated to a constant, elevated temperature. Consequently, the suction and discharge sides are maintained at the same temperature. Because the Nernst Eq., Eq. (4), is valid for constant-temperature electrochemical processes, researchers often expect isothermal compression behavior. Suermann et al. (2017) considered isothermal processes in their hydrogen compression experimentation, reporting very high efficiencies. Onda et al. (2006) demonstrated steady-state compression of hydrogen at constant temperature, reporting reasonable power consumption. Shen at al. (2018) report both values of isothermal and isentropic efficiency in their study to characterize a prototype electrochemical compressor stack. While the cell temperature may not change perceptibly, the compression process may not be thought of as isothermal. Any isothermal compression requires heat removal. In this analysis, we evaluate the minimum electrical power input required for both the isothermal and isentropic cases.

First, we define the properties of the ammonia/hydrogen gas mixture. For the ammonia compressor, we may define the fluid properties for a stoichiometric ratio of ammonia and hydrogen. Thus, for the

2/3 ammonia, 1/3 hydrogen fluid, the molar mass, *M*, becomes 12 g/mol. The total mass flow rate of the gas may be defined as

$$\dot{m} = \frac{3IM}{2F}. \quad \text{Eq. (7)}$$

When we multiply the Nernst voltage by the current density, we obtain the following,

$$W_{isothermal} = I\frac{3RT}{2F}\ln\left(\frac{P_{out}}{P_{in}}\right). \quad \text{Eq. (8)}$$

Substituting current density for mass flow rate based on Eq. (7) we find

$$W_{isothermal} = \frac{\dot{m}RT}{M}\ln\left(\frac{P_{out}}{P_{in}}\right) \quad \text{Eq. (9)}$$

which is an expression of power required for an isothermal compression process.

Losses in electrochemical efficiency stem from the overpotential terms were introduced in Eq. (3). Thus, neglecting activation and concentration overpotential, the total electrical power input is

$$W_{isothermal\,EC} = \frac{\dot{m}}{M}\left[RT\ln\left(\frac{P_{out}}{P_{in}}\right) + \frac{2irF}{3}\right]. \quad \text{Eq. (10)}$$

In much of the reported electrochemical compression experimentation, the compression cells were temperature controlled. However, for any isothermal compression process, the entropy of the working fluid after compression must be less than the fluid entropy prior to compression. The second law of thermodynamics requires that heat be removed from the system in order to decrease its entropy.

Thus, if we do not spend energy to maintain the cell at constant temperature, we must conclude that the Nernst voltage is not the minimum voltage needed to maintain compression. This seems reasonable, as the Nernst Eq. is only valid for constant temperature processes. In this case, the second law of thermodynamics tells us that an adiabatic and reversible process is the lowest energy compression without active thermal management. In this case, we may be able to determine the minimum voltage required for the electrochemical reaction based on the power required for an isentropic process. The power requirement for an isentropic process for a given ideal gas with constant specific heat, is defined as

$$W_{isentropic} = \frac{k}{k-1}\frac{\dot{m}RT_1}{M}\left[\left(\frac{P_2}{P_1}\right)^{\frac{k-1}{k}} - 1\right] \quad \text{Eq. (11)}$$

where *k* is the ratio of the fluids specific heat for constant pressure to the specific heat for constant volume. If we define the specific heats of the fluid mixture as $c_p = x_{H_2}c_{p,H_2} + x_{NH_3}c_{p,NH_3}$ and similarly for c_v, then we can define the *k* value for the fluid mixture as well.

Without any other energy flows into or out of the cell, the minimum electrical consumed by the compressor must be equal to the isentropic power. Using the mass flow relation from Eq. (5*)*, we establish a value for the minimum cell potential, U_{rev}, needed to satisfy the thermodynamic requirements

$$U_{rev} = \frac{3kRT_1}{2(k-1)F}\left[\left(\frac{P_2}{P_1}\right)^{\frac{k-1}{k}} - 1\right]. \quad \text{Eq. (12)}$$

This cell potential represents an adiabatic case. If the cell experienced heat loss to the surrounding environment, as would occur as the cell heats up and rejects heat to the environment, the minimum voltage required to sustain the reaction may decrease. Therefore, U_{rev} represents an upper limit on the voltage required to maintain the pressure differential.

Considering the EC ir loss, we get the following expression for the maximum cell power consumption

$$W_{isentropic\ EC} = \frac{\dot{m}}{M}\left[\frac{kRT_1}{(k-1)}\left(\left(\frac{P_2}{P_1}\right)^{\frac{k-1}{k}} - 1\right) + \frac{2irF}{3}\right]. \qquad \text{Eq. (13)}$$

In Fig. 6 we compare the power requirement per gram per second of gas for the different cases using experimentally obtained ir values. We consider the ir loss from Test 3. We expect that the real EC power consumption will lie between the isentropic EC and the isothermal EC conditions, depending on how much heat is rejected by the compressor. However, this also depends on the cell resistance, which may change with different operating conditions. In this simplified model, the cell resistance is fixed, but, as seen in Table 1, the ir loss changed significantly. These two cases are plotted with the ideal isentropic and isothermal work, which do not consider ir loss. Further investigation is required to develop a model for cell resistance as well as to evaluate the power consumption at higher pressure ratios.

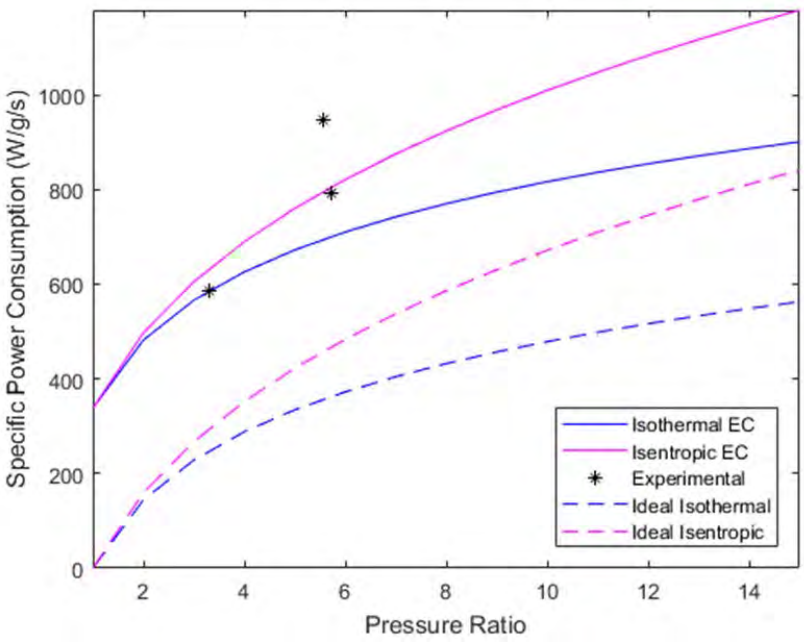

Figure 6: EC specific power consumption versus pressure ratio

6. CONCLUSIONS

In this work, we examined the steady-state performance of an electrochemical ammonia compressor for different pressure ratios under different operating conditions. We noticed the real EC power consumption was significantly higher than that of the ideal cases, due to electrical losses inherent to the membrane. We noticed that the ir losses in the EC stack were not constant and seemed to fluctuate significantly. Further investigation is required to determine the relationship between cell operating conditions and electrochemical losses. Additionally, we investigated the minimum power requirements for the EC. From first law analysis, we noted that the Nernst voltage could not be the minimum voltage required to maintain steady-state compression. We proposed a new minimum voltage requirement for an isentropic case that reflected the heat produced by the compression process. For a totally reversible non-adiabatic process, we theorized that the minimum voltage required would lie somewhere between these two cases, as the compressor would reject some heat to the environment at its temperature increased. Considering the real ir loss from the steady-state experiments, we compared the power requirements for the different cases to our real compressor data. From this comparison, we observed that, assuming the cell resistance remains fixed, the compressor work may approach that of the ideal case for very high-pressure ratios. We also found that the observed variation in the measured ir loss made predicting the real compressor work rather difficult. Further experimentation is required to develop a more refined model.

ACKNOWLEDGEMENTS

We gratefully acknowledge the support from the Advanced Research Projects Agency-Energy (Grant no. DEAR0000962) and the Center for Environmental Energy Engineering (CEEE) at the University of Maryland.

NOMENCLATURE

A	membrane area (cm^2)	EC	Electrochemical compressor
F	Faraday's constant (96,500 mol C^{-1})	I	current (A)
i	current density (A cm^{-2})	k	specific heat ratio
$\dot{m}$	mass flow rate (g s^{-1})	M	molar mass (g mol^{-1})
P	absolute pressure (bar_a)	R	universal gas constant (8.314 J mol^{-1} K^{-1})
r	area specific resistant (Ω cm)	T	temperature (K)
U	electric potential (V)	W	electrical power (W)
z	number of electrons transferred		

REFERENCES

Ganley, J. C., 2008. An intermediate-temperature direct ammonia fuel cell with a molten alkaline hydroxide electrolyte. *Journal of Power Sources, 1*, 44-47.

Grigoriev, S., Shtatniy, I., Millet, P., Porembsky, V., and Fateev, V., 2011. Description and characterization of an electrochemical hydrogen compressor/concentrator based on solid polymer electrolyte technology. *International Journal of Hydrogen Energy, 36*, 4148-4155.

Onda, K., Ichihara, K., Nagahama, M., Minamoto, Y., and Araki, T., 2007. Separation and compression characteristics of hydrogen by use of proton exchange membrane. *Journal of Power Sources, 164*, 1-8.

Reiter, A. J. and Kong, S.C., 2010. Combustion and emissions characteristics of compression-ignition engine using dual ammonia-diesel fuel. *Fuel, 90*, 87-97.

Rohland, B., Eberle, K., Strobel, R., Scholta, J., and Garche, J., 1998. Electrochemical hydrogen compressor. *Electrochimica Acta, 43*, 3841-3846.

Shen, B., Bahar, B., and Fackler, S., 2018. Experimental Study to Characterize Performance of a Prototype Electrochemical Compressor. *17th International Refrigeration and Air Conditioning Conference at Purdue.* West Lafayette, IN.

Strobel, R., Oszcipok, M., M. Fasil, B. R., and Garche, J., 2002. The compression of hydrogen in an electrochemical cell based on a PE fuel cell design. *Journal of Power Sources, 105*, 208-215.

Suermann, M., Kiupel, T., Schmidt, T. J., and Buchi, F. N., 2017. Electrochemical Hydrogen Compression: Efficient Pressurization Concept Derived from an Energetic Evaluation. *Journal of The Electrochemical Society, 164*, F1187-F1195.

Tao, Y., Gibbons, W., Hwang, Y., Radermacher, R., and Wang, C., 2017. Electrochemical Ammonia Compression. *Chem. Commun., 53*, 5637-5640.

Manuscript ID: 570
DOI: 10.18462/iir.icr.2019.0570

Integration of Supermarket's CO_2 Refrigeration System and Geothermal Storage

Mazyar KARAMPOUR[(a)], Carlos MATEU-ROYO[(b)], Jörgen ROGSTAM[(c)], Samer SAWALHA[(a)]

[(a)] Royal Institute of Technology (KTH), Energy Technology Department
Brinellvägen 68, SE-100 44, Stockholm, Sweden, mazyar.karampour@energy.kth.se

[(b)] ISTENER Research Group, Department of Mechanical Engineering and Construction, Universitat Jaume I, Campus de Riu Sec s/n, E12071 Castelló de la Plana, Spain

[(c)] Energi & Kylanalys AB, Varuvägen 9, Älvsjö 125 30, Sweden

ABSTRACT

This paper investigates the energy efficiency of geothermal storage integration into the state-of-the-art CO_2 trans-critical booster systems. Three scenarios of integration are studied including stand-alone and integrated supermarket building systems.

The results show that for a stand-alone supermarket, heat recovery from the CO_2 system should be prioritized over extracting heat from the ground, which this heat extraction can be done either by an extra evaporator in the CO_2 system or by a separate ground source heat pump. In the case of supermarket integration with a nearby district heating consumer, geothermal storage integration with extra evaporator in the CO_2 refrigeration system can reduce the total annual running cost of the two buildings by 19-31% and with a payback time of less than three years.

This integration is beneficial if the full efficient heat recovery capacity of the CO_2 system is not sufficient to provide the entire demands.

Keywords: state-of-the-art CO2 trans-critical booster system, Supermarket, Geothermal storage.

INTRODUCTION

While CO_2 refrigeration systems have become standard system solution for supermarkets in some relatively cold climate countries, other "integrated thermal functions" of these systems, and their performance in warmer climates have been subject to research and optimization. Various modifications to increase the energy efficiency of CO_2 systems have been evaluated in a previous study by the authors (Karampour and Sawalha, 2018). Based on their results, the definition of the state-of-the-art (SotA) CO_2 system has been introduced. This system is presented in section 2.

A potential improvement, which was not covered in the authors' previous research and is minimally covered in the literature, is the integration of geothermal storage into the CO_2 SotA system. The potential advantage of this integration is that the ground can be used as a heat sink to provide sub-cooling for the CO_2 system in summer and as a heat source in the winter for the heat pumping function of the CO_2 refrigeration system or via a separate Ground Source Heat Pump (GSHP). As the number of CO_2 systems with integrated geothermal storage are increasing in Scandinavian supermarkets, it is necessary to discuss the advantages and limitations of this integration in more details. Using computer simulations, this paper evaluates the integration of geothermal storage into supermarket CO_2 trans-critical booster systems. This paper is a summary of a journal paper submitted to International Journal of Refrigeration, special issue "SI: R744 Technology Status".

SYSTEMS DESCRIPTION

The reference system in this study is a state-of-the-art (SotA) CO_2 trans-critical booster system, which is represented by the black lines in Fig. 1a. The features of this system have been discussed in detail by the authors in previous research (Karampour and Sawalha, 2018). The CO_2 SotA system takes advantage of flooded evaporation to run at high evaporation temperatures and uses parallel compression to compress the flash gas vapour. It has been shown that these features decrease the refrigeration annual energy use (AEU) of the standard CO_2 booster system by 15%.

The integrated geothermal storage system (represented by green lines) is also shown in Fig. 1a. Early modelling evaluation of this systems was done by Mateu-Royo (2017). The geothermal sub-cooler is located after the gas cooler and provides sub-cooling in summer. Heat is stored in the ground during this season and an extra evaporator (Geothermal Heat Extractor in Fig. 1a) is used to extract the heat from the ground during winter. The extracted heat is then "pumped" by the compressors to provide heat in the heat recovery de-superheater.

The extracted heat can be added at either the P_{MT} level and compressed by high stage compressors or at P_{rec} level and processed by parallel compressors. In the case of heat extraction at P_{rec} level, the expansion valve before the geothermal heat extractor is fully open and the exit line is connected to the receiver. Both methods have been applied in field installations in Sweden and are evaluated in this paper. Another option to extract and use the stored heat from the ground in winter is by running the CO_2 system in floating condensing mode with minimum condensing temperature of 10°C, i.e. lowest pressure possible, and use a separate ground source heat pump (GSHP) to provide the supermarket's heating demand. A schematic of this system, designated as "hybrid" in this paper, is shown in Fig. 1b.

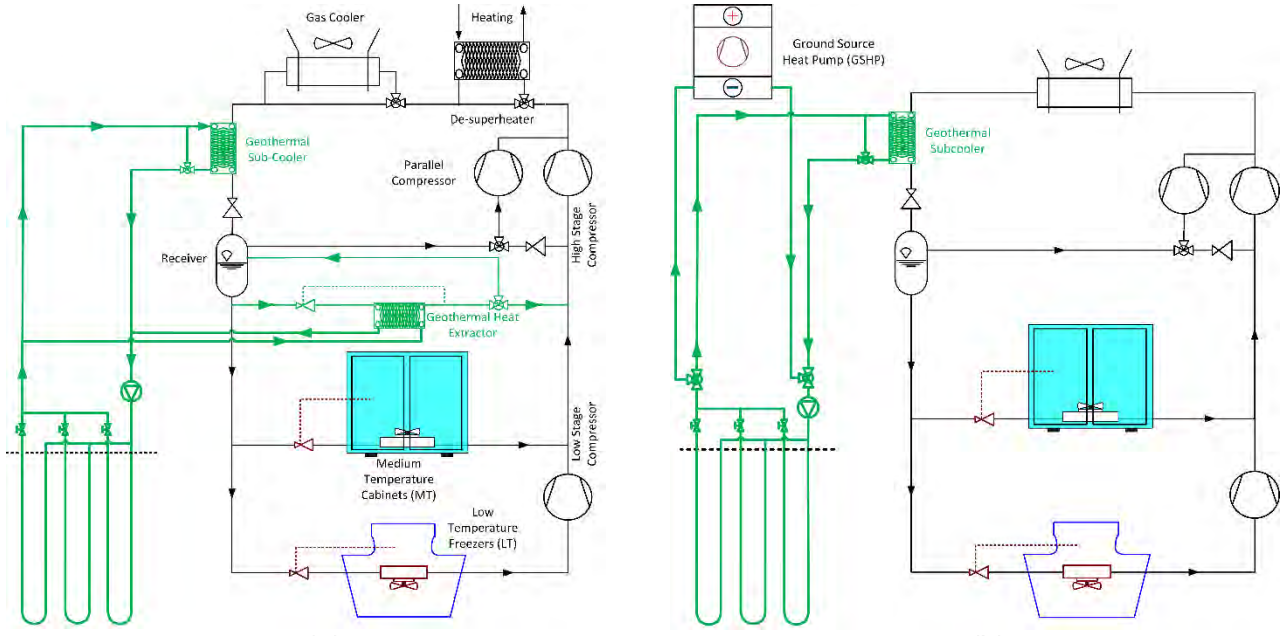

(a) (b)

Figure 1: (a) SotA CO_2 booster system (black) and integrated geothermal storage (green) and (b) Hybrid: refrigeration system sub-cooling in summer, heat source for GSHP in winter

RESEARCH SCENARIOS

The integration of geothermal storage into a CO_2 system is evaluated for three integration scenarios:
S1 (S is short for Scenario): In this scenario, the AEU of the CO_2 systems with full heat recovery and without geothermal storage (referred to as S1a) and with geothermal storage (S1b) are compared. S1a and S1b are visualized in Fig. 2, where all the integration scenarios are also visualized.

S2: The first case in this scenario (S2a) is the reference without coupling, it consists of two separate energy systems of a supermarket that recover all its heating needs and a neighboring facility that buys its heating needs from district heating network. The second case (S2b) couples the supermarket and neighbor energy systems by integrating the geothermal storage, and providing the entire heating demands of the two buildings by heat recovery from the refrigeration system.
S3: In the third scenario of geothermal integration (S3), the ground is used for summer sub-cooling of the refrigeration system and a separate ground source heat pump (GSHP) is used in winter to extract the stored heat and provide the supermarket heating demand.

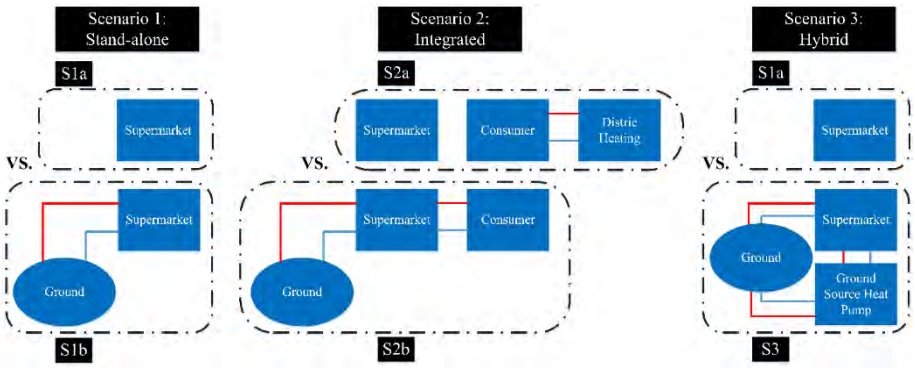

Figure 2: The three research scenarios

SYSTEM MODELLING

4.1 Boundary Conditions and Assumptions

The cooling demands and refrigeration boundary conditions are based on field measurements of five Swedish supermarkets using CO_2 as the refrigerant (Sawalha et al., 2015). Some parameters are updated according to a previous research study on the characteristics of the SotA CO_2 systems (Karampour and Sawalha, 2018).
Medium temperature cooling demand in an average size supermarket is assumed to be 200 kW at 35°C and decreases linearly to 100 kW at 10°C, below which the demand remains constant. Low temperature cooling demand is assumed to be 35 kW. Medium and low stage evaporation temperatures of the CO_2 SotA are -4°C and -29°C, respectively.
The main heating demand in supermarkets is space heating, which starts at the ambient-temperature set-point of 10°C. The heating demand is estimated to be 40 kW at 10°C ambient temperature and increases linearly to 190 kW at -20°C ambient temperature. Water return temperature from the heating system is assumed to be 30°C. 5K approach temperature is assumed between the water return temperature and the refrigerant in the condenser of the separate GSHP, or the de-superheater in the case of heat recovery from the refrigeration system. The heating demand and temperature requirements of the neighbouring building are assumed to be the same as the supermarket.
The system runs in the floating condensing mode in the summer. The optimum pressure for trans-critical operation $P_{opt,gc}$ [bar] is a function of the gas cooler exit temperature $T_{gc,exit}$ [°C], as follows (Sawalha, 2008):

$$P_{opt,gc} = 2.7 \cdot T_{gc,exit} - 6 \qquad \text{Eq. (1)}$$

The heat recovery control strategy in winter follows the recommendations presented by Sawalha (2013) and Madsen and Bjerg (2016), and heat recovery max optimum pressure follows Eq(1) but de-superheater exit temperature is used.

4.2 Geothermal Storage and GSHP Hybrid Solution

Simulations for the ground heat exchanger have been performed for Stockholm conditions; therefore, the ground properties used for the borehole design are rock thermal conductivity = 3.1 $W.m^{-1}.K^{-1}$., volumetric heat capacity = 2.16 $MJ.m^{-3}\cdot K^{-1}$, and ground surface temperature = 6.6 ºC (Acuña, 2013).
An aqueous ethanol solution of 24% weight concentration is used as the heat-carrier fluid for the geothermal loops. The operating temperature of this fluid T_f is restricted to the range of -5°C to +20°C. The flow rate is 0.5 l/s per borehole, which is constant during the entire operation. The boreholes uses single U-tube heat exchangers and their depth varies in the 150-200m range. The GSHP uses R407C as the working fluid, with a heating capacity of 200 kW. The evaporator has a capacity of 150 kW.

4.3 Energy Efficiency Calculations

A computer model developed in EES (Engineering Equation Solver) software (Klein, 2015) is used to analyze the performance of the CO_2 SotA and GSHP systems. The calculations for the geothermal storage and its borehole field design are performed using Earth Energy Designer (EED) software (Blomberg et al., 2017) (Hellström and Sanner, 1994). EED evaluates the secondary fluid temperature evolution in a specific borehole arrangement based on imposed heating and cooling loads.
The compressor electricity use $\dot{E}_{comp}$ [kW] is calculated using Eq. (2):

$$\dot{E}_{comp} = (\dot{m}_{ref}.\Delta h_{is})/\eta_{tot} \quad \text{Eq. (2)}$$

where η_{tot} is the overall efficiency of the compressors, and Δh_{is} [$kJ.kg^{-1}$] is the isentropic enthalpy difference over each compressor unit. Compressor commercial datasheets are used to obtain the total efficiency of the compressors as a function of pressure ratios (BITZER, 2017). Refrigerant mass flow rate $\dot{m}_{ref}$ [$kg.s^{-1}$] is calculated based on the cooling loads in the evaporators.
The total electricity use $\dot{E}_{tot}$ [kW] of the system is calculated based on Eq. (3):

$$\dot{E}_{tot} = \dot{E}_{MT} + \dot{E}_{LT} + \dot{E}_{PC} + \dot{E}_{fan} + \dot{E}_{geo,pump} \quad \text{Eq. (3)}$$

where $\dot{E}_{MT}$, $\dot{E}_{LT}$, and $\dot{E}_{PC}$ [kW] are the electricity use of the three MT, LT and parallel compressor units. $\dot{E}_{fan}$ [kW] is the electricity use of the gas cooler fans, estimated to be 3% of the heat rejected in the gas cooler. $\dot{E}_{geo,pump}$ is the pump electricity used to circulate the secondary fluid, which is estimated to be approximately 5% of the extra evaporator capacity in winter or geo sub-cooler capacity in summer.
Heat recovery COP (COP_{HR}) of the CO_2 SotA system is defined as:

$$COP_{HR} = \frac{\dot{Q}_{HR}}{(\dot{E}_{tot} - \dot{E}_{tot,fc})} \quad \text{Eq. (4)}$$

$\dot{Q}_{HR}$ [kW] is the amount of recovered heat, $\dot{E}_{tot}$ [kW] is the total electricity use calculated from Eq. (3), and $\dot{E}_{tot,fc}$ [kW] is the amount of electricity use if the system is not controlled for heat recovery and is operated in floating condensing mode with minimum condensing pressure in winter.
Annual energy use AEU [MWh] is calculated using the following equation:

$$AEU = \sum_{i=1}^{n} (\dot{E}_{tot,i}.f_i) \quad \text{Eq. (5)}$$

where $\dot{E}_{tot}$ [kW] is the total electricity use calculated from Eq. (5), n is the number of temperature-bin hours, and f is the frequency, i.e. number of hours, of each temperature bin.

RESULTS AND DISCUSSION

5.1 S1-Stand-alone Supermarket

The first research scenario compares a CO_2 refrigeration system without (S1a) and with (S1b) geothermal storage in a stand-alone supermarket. The performance of eight system arrangements, or designs, have been calculated in this research scenario.

- S1a (reference): the system has no geothermal storage and heat recovery through its de-superheater is used to provide the space heating demand in the supermarket building.
- Sub-cooling in the summer (SC summer): The system is similar to the reference case in winter (i.e. no heat extraction from the ground) but uses geothermal sub-cooling in summer. This case is shown as "S1b: SC summer" in Fig. 3.

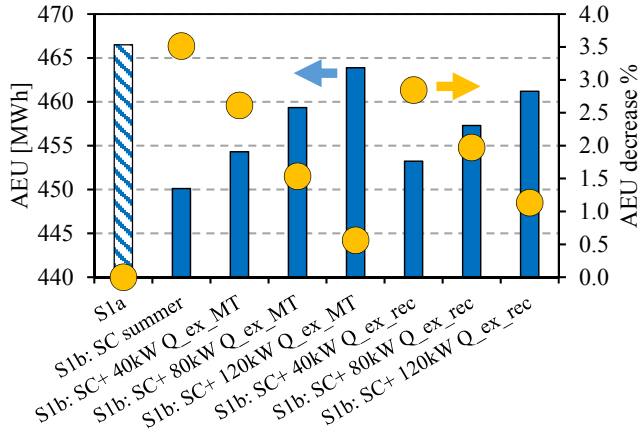

Figure 3: Annual energy use and savings compared to the reference case for S1 cases

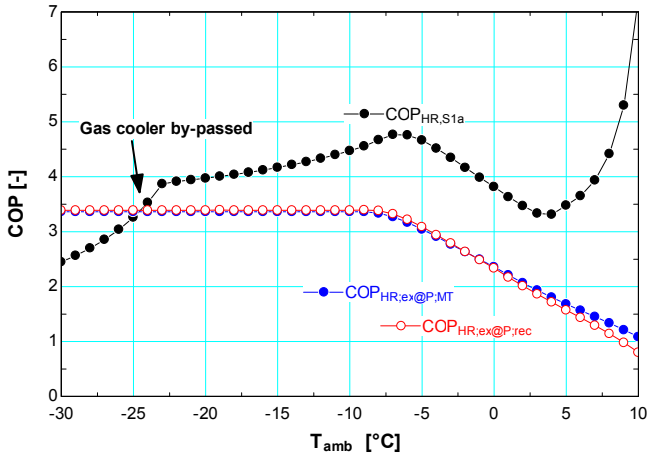

Figure 4: Annual energy use and savings compared to the reference case for S1 cases

- Sub-cooling in summer and heat extraction from the ground in winter (SC summer + winter $\dot{Q}_{ex}$, as presented in Fig.1a): six cases are studied; three cases of heat extraction at P_{MT} level, and three at P_{rec} level. System performance is examined for three levels of extra evaporator capacity ($\dot{Q}_{ex}$): 40, 80, and 120 kW. These values are based on the reasonable capacity that could be provided by the installed compressors; no additional compressors are needed. This is because the compressors typically run in the summer time to extract vapor from the receiver but are switched off during the winter. The control strategy to extract the heat from the ground is explained later in this section. Summer sub-cooling is also studied for a reasonable range up to 15K sub-cooling; this results in a sub-cooling design capacity of about 60 kW at warmest summer outdoor temperature. System performance in terms of AEU [MWh] (presented as bars) and AEU decrease [%] (presented as dots) for the eight arrangements is presented in Fig. 3.

As shown in Fig. 3, geothermal sub-cooling in summer can provide about 3.5% AEU saving compared to the reference system. However, if the number of boreholes is not sufficient, the ground will not be cold enough after few summers to be used as an efficient heat sink. For instance, the results of modelling in EED shows that 12 boreholes each 165m deep are required to keep the secondary fluid temperature lower than 15°C during a 15-year lifetime of the system.

To study the heat extraction effect on AEU saving in the latter six cases, various heat extraction starting points have been studied by computer simulations; i.e. the ambient temperature at which the heat extraction from the ground should be started. The results indicate that only at cold ambient temperatures below 0°C is it beneficial to extract heat from the ground. "Beneficial" is a compromise between energy efficiency and ground thermal energy balance in summer-winter. In scenario S1, the ground heat extraction is set to be activated for ambient temperatures lower than -5°C.

The savings for these six cases that employ geothermal storage the entire year are less than 3%, as shown in Fig. 3. Compared to the "SC summer" case (3.5%), this implies that heat recovery in the geothermally integrated CO_2 systems has negative impact on energy saving; i.e. not as efficient as heat recovery in the stand-alone CO_2 system, referred to as S1a in this paper. The reason that these six cases are more efficient than S1a is the sub-cooling in summertime.

To understand why heat recovery in the integrated solution is not as efficient as the stand-alone CO_2 system S1a, COP_{HR} of the CO_2 refrigeration system without geothermal connection ($COP_{HR,S1a}$) is compared to the heating COP of the geothermal heat extraction only ($COP_{HR,GEO}$) system. In $COP_{HR,S1a}$ there is no geothermal connection and the only heat source is the refrigeration load. In $COP_{HR,GEO}$ the extracted heat is added to the refrigeration load while the system control is the same as in S1a; thus, the sole effect of the geothermal heat extraction is calculated. In this way the system is seen as a heat pump extracting heat from the ground and supplying heat via the de-superheater. $COP_{HR,S1a}$ is calculated using Eq. (4). Heat recovery COP from the extra evaporator $COP_{HR,GEO}$ is defined as the ratio of the amount of recovered heat $\dot{Q}_{HR,ex}$ [kW] (by the addition of the extra heat source) to the amount of extra electricity use in compressors, pumps, and gas cooler fans $\dot{E}_{tot,ex}$ $[kW]$.

$$COP_{HR,GEO} = \frac{\dot{Q}_{HR,ex}}{\dot{E}_{tot,ex}} \quad (6)$$

The result of the comparison is shown in Fig. 4. It is indicated that $COP_{HR,S1a}$ is greater than $COP_{HR,GEO}$ for most of the ambient temperature range. $COP_{HR,GEO}$ only exceeds $COP_{HR,S1a}$ when the gas cooler is fully bypassed at very low ambient temperatures. This is the point where further increase in the discharge pressure beyond the maximum value for high efficiency results in a sharp decrease in COP_{HR}. If the supermarket is larger with higher heating demands, the gas cooler is fully bypassed at higher ambient temperatures.

5.2 S2-Integrated Supermarket

A comparison of “separate supermarket and district heating (DH) consumer” systems (S2a) with “integrated supermarket, geothermal system and district heating consumer” (S2b) is considered in the second research scenario. This case is quite common, for example, when the supermarket is located inside a larger shopping mall. The consumer is assumed to have the same heating demand profile as the supermarket. Since the heat and electric energies are of different types, separate and integrated solutions are compared based on the annual cost for purchasing the two types of energies to cover the refrigeration and heating demands. Two scenarios for energy prices are compared: 1) relatively high electricity price and low district heating price, and 2) low electricity price and high district heating price. Price values are based on the Swedish market.

A comparison of the annual running cost for the four different scenarios is shown in Fig. 5. Depending on energy prices, the integrated solution produces an annual running cost savings of 19-31%. The integrated solution offers lower heating cost for the consumer and provides some profits to the supermarket due to the winter time heating sale and summer time sub-cooling. Considering the present energy prices and heating COP of the CO_2 system, there is a good margin of savings where the supermarket can charge the neighbouring building for heat and still be profitable for both supermarket and the neighbouring building.

The number of boreholes to have reseoanble ground energy balance is caluclated in EED software to be 12, in a 3*4 rectangular arrangement, with 10m spacing, and an approximate depth of 159m. The total cost of borehole drilling and the U-tube heat exchanger is approximately 25 €/m in Sweden. Thus, the total cost for the desired borehole heat exchanger is 47.700 €. Comparing with the annual energy savings presented in Fig. 5 and the present energy prices in Sweden, it is found that this integration solution has a payback time of less than three years.

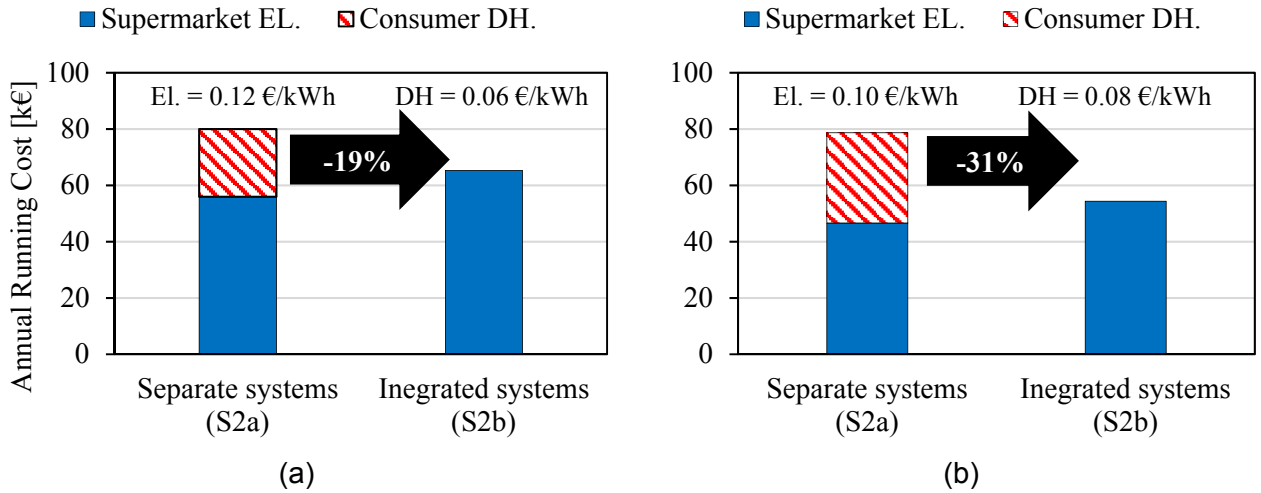

Figure 5: Separate (S2a) and integrated (S2b) systems annual running cost [k€]. (a) Electricity Price = 0.12 €/kWh, DH Price = 0.06 €/kWh and (b) Electricity Price = 0.10 €/kWh, DH Price = 0.08 €/kWh

5.3 S3-Hybrid Solution

The third research question compares stand-alone CO_2 (S1a) and "hybrid CO_2 + GSHP" (S3) systems. As mentioned earlier, the entire supermarket heating demand is provided by heat recovery from the CO_2 system in a stand-alone supermarket. However, the heat demand in the supermarket with the hybrid solution is provided by the GSHP. The ground is the heat source for the GSHP in winter while the refrigeration system runs at floating condensing mode (i.e. no heat recovery), the ground is also the heat sink for the CO_2 sub-cooler in summer. Performance comparisons of the two systems in terms of AEU on a seasonal and annual basis are shown in Fig. 6. The hybrid system consumes about 8% less electricity than the stand-alone CO_2 system in summer, thanks to the geothermal sub-cooling. On the other hand, the winter energy use of the stand-alone system is approximately 5% less than the hybrid system. These seasonal energy use effects counterbalance, and the hybrid system is only 2% more efficient than the stand-alone CO_2 system annually. However, EED calculations show 24 boreholes of 160m deep are required for this case, which results in payback time of more than 7-8 years.

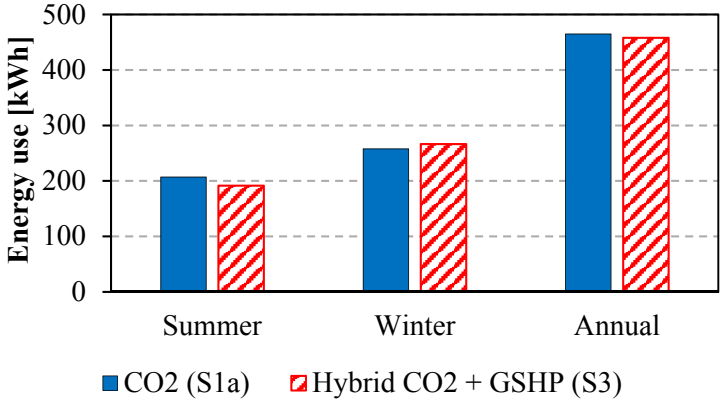

Figure 6: Energy use of stand-alone CO2 (S1a) vs hybrid system (S3) solutions

CONCLUSIONS

The results show that heat recovery from a stand-alone CO_2 SotA system, S1a, is more efficient than providing part of the heating demand from the ground at medium or receiver pressure level, S1b. The analysis of the second scenario, S2, indicates that annual running cost of a separate supermarket and district heating consumer (S2a) can be decreased by 19-31% if the systems are coupled, geothermal

storage is applied, and the supermarket provides heating for the consumer (S2b). The investigation of the hybrid solution, S3, which couples a CO_2 system, geothermal storage, and a separate GSHP, shows that approximately 2% of the AEU can be saved compared to a stand-alone CO_2 system.

In summary, geothermal storage integration into a CO_2 supermarket refrigeration system does not have a significant impact on energy use in the case of a stand-alone average size supermarket. For a supermarket combined with a neighboring building/facility, geothermal storage integration can contribute to significant running cost savings compared to separate systems running costs. The application of a separate GSHP is also not recommended as heat recovery from the CO_2 system is more efficient than this system. The CO_2 SotA is an efficient heat pump, with built in large heat source, i.e. refrigeration load. This load is the primary heat source and if more heat is required the ground storage can be used as the secondary heat source for the CO_2 SotA as a heat pump.

REFERENCES

Acuña, J., 2013. Distributed Thermal Response Tests: New Insights on U-pipe and Coaxial Heat Exchangers in Groundwater-filled Borehole (Doctoral Thesis). Royal institute of technology (KTH), Stockholm, Sweden.

Arias, J., 2005. Energy usage in supermarkets-modelling and field measurements (Doctoral Thesis). Royal institute of technology (KTH), Stockholm, Sweden.

BITZER, 2017. Bitzer semi-hermetic reciprocating compressors, Selection software, Retrieved 2017.04.15 from https://www.bitzer.de/websoftware/.

Blomberg, T., Claesson, J., Eskilson, P., Hellström, G., Sanner, B., 2017. Earth Energy Designer: EED.

Hellström, G., Sanner, B., 1994. Earth Energy Designer: software for dimensioning of deep bore holes for heat extraction., in: Calorstock. Presented at the 6th International Conference on Thermal Energy Storage, Espoo, Finland, pp. 195–202.

Ignatowicz, M., Melinder, Å., Palm, B., 2017. Properties of different ethyl alcohol based secondary fluids used for GSHP in Europe and USA. Presented at the IGSHPA Technical/Research Conference and Expo, Denver, USA.

Karampour, M., Sawalha, S., 2018. State-of-the-art integrated CO2 refrigeration system for supermarkets: A comparative analysis. International Journal of Refrigeration 86, 239–257. https://doi.org/10.1016/j.ijrefrig.2017.11.006

Kavanaugh, S., Kavanaugh, J., 2012. Long-Term Commercial GSHP Performance. Part 2: Ground Loops, Pumps, Ventilation Air and Controls. ASHRAE Journal, July 2012 54, No 7, 26–34.

Klein, S.A., 2015. Engineering Equation Solver (EES) V9, F-chart software, Madison, USA, www.fchart.com.

Madsen, K.B., Bjerg, P., 2016. Transcritical CO2 refrigeration with heat reclaim, Retrieved 2017.04.15 from http://refrigerationandairconditioning.danfoss.com/technicalarticles/rc/transcritical-co2-refrigeration-with-heat-reclaim/?ref=17179926134.

Mateu-Royo, C., 2017. Field Measurements and Modelling Analysis of CO2 Refrigeration Systems with Integrated Geothermal Storage (Master Thesis). Royal institute of technology (KTH), Stockholm, Sweden.

Sawalha, S., 2013. Investigation of heat recovery in CO2 trans-critical solution for supermarket refrigeration. International Journal of Refrigeration 36, 145–156. https://doi.org/10.1016/j.ijrefrig.2012.10.020

Sawalha, S., 2008. Carbon dioxide in supermarket refrigeration (Doctoral Thesis). Royal institute of technology (KTH), Stockholm, Sweden.

Sawalha, S., Karampour, M., Rogstam, J., 2015. Field measurements of supermarket refrigeration systems. Part I: Analysis of CO2 trans-critical refrigeration systems. Applied Thermal Engineering 87, 633–647. https://doi.org/10.1016/j.applthermaleng.2015.05.052

Manuscript ID: 571
DOI: 10.18462/iir.icr.2019.0571

Design optimization of an air-cooled bifurcated tube heat exchanger

Zhiwei HUANG[(a)], Jiazhen LING[(b)], Vikrant AUTE[(b)], Yunho HWANG[(b)], Reinhard RADERMACHER[(b)]

[(a)] Johnson Controls, Inc.
Moore, 73069, USA, joy.huang@jci.com
[(b)] University of Maryland
College Park, 20742, USA, yhhwang@umd.edu

ABSTRACT

Air-cooled heat exchangers are a major research topic due to their significance in air-conditioning and heat pump systems. Such heat exchangers, mainly fin-and-tube and minichannel types, use fins to augment the air-side heat transfer area. Whereas, researchers found heat exchangers using small diameter (< 2 mm) bare tubes can achieve two times higher airside heat transfer coefficient than conventional ones with finned tubes. In this study, a novel finless air-cooled heat exchanger consisting of two-level bifurcated bare tubes is proposed and optimized using approximation assisted optimization methodology. Optimization objectives are minimization of total pumping power and heat exchanger envelope volume. Optimization results show that this heat exchanger has 38% less pumping power and 83% smaller volume compared with baseline heat exchanger (louvered fin mini-channel) having same frontal area under same operating conditions. The key feature of current design is the addition of bifurcation, which enhances both air- and water-side heat transfer by boundary layer interruption and redevelopment. Although several manufacturing issues need to be further addressed, this heat exchanger is a promising next generation heat exchanger design.
Keywords: Finless, bifurcated, heat exchanger, boundary layer.

1. INTRODUCTION

Significant effort is devoted to improving performance of air-to-refrigerant heat exchangers through innovative and advanced geometries. Researchers have studied heat transfer enhancement for decades. The traditional way to maximize the overall HX conductance (hA) is to increase surface area by employing extended surfaces (for instance fins) to air-side to reduce air-side thermal resistance, which is responsible for 75~90% of total thermal resistance. However, fin surfaces have lower heat transfer coefficients than primary heat transfer surfaces (tube surface) due to the boundary layer development. Moreover, additional fins inevitably result in more material consumption and complicate the end-of-life disposal. Thus, conventional fin-and-tube heat exchanger designs have intrinsic limitation of further improving heat transfer performance for given certain amount of volume and material volume. Recently, a few researchers proposed and investigated small diameter (< 2 mm) finless heat exchangers. Bacellar et al., (2016, 2017) investigated bare tube heat exchangers and plain fin-and-tube heat exchangers with diameter of 2 ~ 5 mm and developed heat transfer correlations based on CFD simulation results. Heat exchanger prototypes have been optimized (Huang et al., 2016), manufactured (Shabtay et al., 2016) and tested. Paitoonsurikarn et al. (2000) found that the bare tube heat exchanger can achieve a much higher air-side heat transfer coefficient (300 W/m^{2}K) within the air velocity range of 1 ~ 6 m/s by reducing tube diameter to 0.3 ~ 0.5 mm. Thus, finless designs using bare tubes with hydraulic diameter less than 1 mm can exceed the air-side heat transfer performance of conventional heat exchangers. As inspired by fractal geometry in nature (Huang et al., 2017a). Huang et al. (2017b) invented a bifurcated bare tube heat exchanger (bBTHX). Numerical air-side parametric study shows bifurcated bare tube heat exchanger has 15% higher air-side heat transfer coefficient and 4%~12% lower air-side pressure drop than those of baseline bare tube heat exchanger with the same outer diameter (0.8 mm), frontal area, volume, and air velocity (3.5~5 m/s). The key feature is the addition

of bifurcation that enhances air-side flow mixing. In this paper, the authors further optimized the heat exchanger by using multi-scaled approximation assisted optimization methodology.

2. BIFURCATED HEAT EXCHANGER

This novel heat exchanger consists of two levels of tubes, the main tubes and the branch tubes. Main tubes are all vertical tubes in Figure 1 of which outer diameters are symbolled as D1 while branch tubes are symbolled as D2. Longitudinal tube pitch (Pl) is defined as the centre distance of two adjacent main tubes. The transversal tube pitch (Pt) is then defined as the centre distance of two adjacent layers, as shown in Figure 2. Bifurcation angle (θ) is the angle between brunching tube and the centre line.

Both air- and water-side thermal and hydraulic performances are simulated using ANSYS® Workbench™ 18.0. Figure 3 shows water-side simulation domain. Mesh element is tetrahedral and the boundary layer mesh is refined at tube walls. Simulation used two-equation k-ε realizable (RKE) model (Shih and Zhu, 1994) because it has improved performance for problems involving boundary layers under strong adverse pressure gradients or separation, rotation, recirculation and strong streamline curvature. Assumptions and boundary conditions include: constant and homogeneous velocity distribution at inlet; constant pressure at outlet (0.0 Pa gauge); periodic boundaries at longitudinal section; tubes as walls; tube wall temperature fixed at 350 K; water inlet temperature fixed at 360 K. The Grid Convergence Index (GCI) method (Roache et al., 1993, ASME, 2009) was used to evaluate the grid convergence. The numerical uncertainties of heat transfer coefficient and pressure drop are 4.0% and 3.6% for finer mesh, and 4.9% and 5.6% for coarse mesh, respectively. Thus, intermediate mesh was selected as the final mesh.

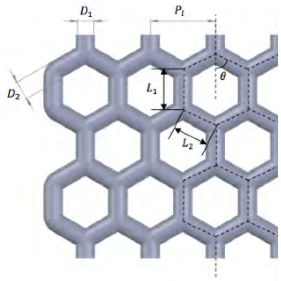

Figure 1: Bifurcated tube structure

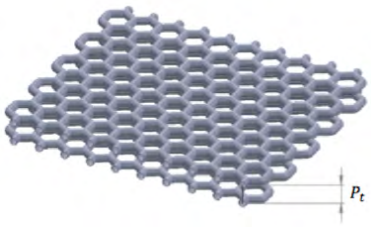

Figure 2 : BTHX staggered pattern

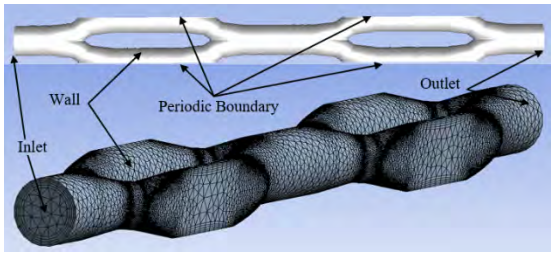

Figure 3: Water-side computational domain

Detailed air-side simulation and analysis could be found in Huang et al., 2017b. Airside CFD model was validated against experimental data measured from a 3D printed sample, as shown in Figure 4. Due to leakage issue, this sample was only tested to validate the air side pressure drop for now and a new leak tight prototype is on the way to validate heat transfer. Experimental validation shows a good agreement of less than 3% after applying a correction factor of 0.51, as shown in Figure 5. The potential reasons for deviation include but are not limited to experimental uncertainties, model uncertainties and manufacturing uncertainties.

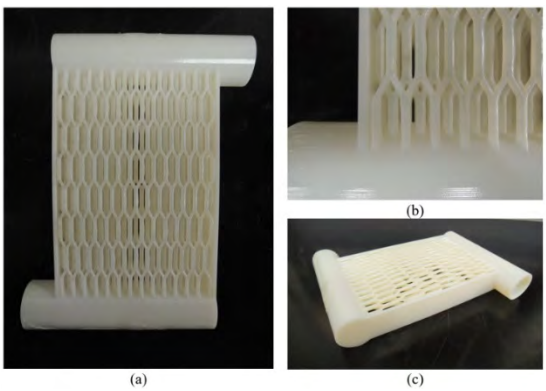

Figure 4: bBTHX sample

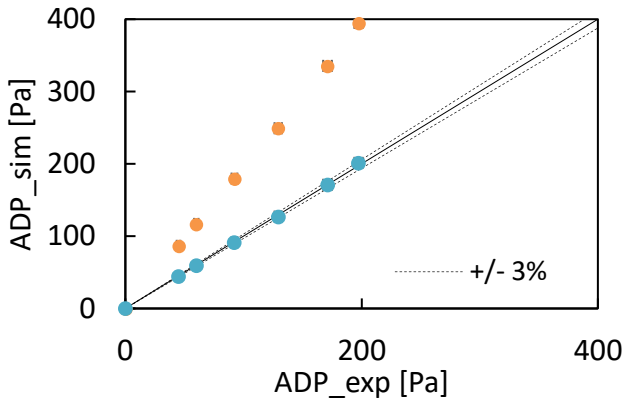

Figure 5: Experimental validation for bBTHX air side pressure drop

3. BIFURCATED HEAT EXCHANGER

3.1. Methodology

Multi-scale approximation assisted optimization is a methodology for innovative heat exchanger design optimization. It enables efficient integration of the enhanced HX segment performance prediction using CFD simulations with overall HX performance prediction using segmented ε-NTU method, which provides significant computational savings. Detailed steps are presented in Huang, 2017. Main steps are: (1) parameterize the new geometry; (2) run parallel parameterized CFD (an automatic approach to CFD simulations) for Design of Experiment (DoE) space; (3) generate meta-model for selected parameters, such as j and f factors (these meta-model functions as heat transfer and pressure drop correlations); (4) solve heat exchanger performance using ε-NTU method; and (5) optimize design using multi-objective optimization algorithm. The accuracy of meta-models was evaluated using the Metamodel Acceptability Score (MAS) (Hamad, 2006). Table 1 summarizes the specifications of air- and water-side models.

3.2. Optimization Problem and Baseline Heat Exchanger

In current study, a single-phase air-to-water heat exchanger was optimized using the innovative geometry. This new heat exchanger was optimized to deliver the same capacity (835W) for such application. A louvered fin mini-channel heat exchanger (MCHX) was manufactured, as shown in Figure 4. This MCHX is a single slab heat exchanger with 11 tubes and 2 ports per tube. The air-side hydraulic diameter is 1.94 mm. Table 2 summarized other dimensions. This MCHX has been tested under dry condition using air and water, and design condition used here is one of the testing conditions. The MCHX's experimental data has been compared to predictions using correlations from literature. The maximum deviation for capacity and pressure drop are ± 6 and ± 10% respectively. MCHX was chosen as the baseline heat exchanger mainly because it is more compact compared with fin-and-round tube heat exchangers. The flat tube shape of MCHX makes it possible to squeak in more fin area in between tubes which is an advantage over round tube heat exchanger.

Table 1. Summary of air- and water-side meta-models

	Air-side		Water-side	
Input parameters	N_r, D_1, P_l / D_1, P_t / D_1, LR, θ, V_a		D_1, P_l / D_1, LR, θ, V_w	
Output parameters	j, f		Nu, WDP	
Meta-model Samples	783		258	
Random points for verification	50		25	
Metamodel Acceptability Score	j	f	Nu	WDP
	100% within 15%	100% within 15%	100% within 8%	98% within 10%



Figure 6: Baseline mini channel louvered fin heat exchanger

The design problem here is described as below. Two objectives are minimization of total power and heat exchanger volume. The constraints include (1) total heat exchanger capacity should be similar or larger than baseline; (2) frontal area should be less than baseline; (3) total power is 30% less than baseline; (4) total heat exchanger volume is 80% less than baseline; and (5) aspect ratio (AR) is similar to baseline. The last three constraints are dismissed for the real calculation because these will cause the calculation time to be much longer.

$$\text{Optimization:}$$
$$\min Power$$
$$\min V_{HX}$$
$$s.t.$$
$$\dot{Q}_{baseline} \leq \dot{Q} \leq 1.1 \cdot \dot{Q}_{baseline}$$
$$A_{fr} \leq A_{fr\_baseline}$$

3.3. Results and discussion

Figure 7 shows the Pareto front points, which have 30% lower total power and 80% smaller volume than those of baseline MCHX with smaller frontal area. Pareto front points without the last three constraints are plotted on the graph as well. Along the Pareto front line (from left to right), the volume increases while power decreases. The outer diameter of the tube increase is the main reason of volume increase. Transverse pitch (Pt/OD) reaches the minimum limit (1.5). P_l/OD has a negative relationship with LR: as P_l/OD increases, LR tends to decrease. This is because larger P_l/OD results in lower air-side heat transfer coefficient, thus LR needs to be smaller to increase the heat transfer coefficient, and vice versa.

Table 2 compares one selected optimal design with baseline MCHX. It shows bBTHX design has higher air-side heat transfer coefficient, lower air-side pressure drop, higher water-side heat transfer coefficient, lower water-side pressure drop, lower total pumping power, and smaller envelope volume and material volume. The summary and reasons causing the differences in each parameter are:

- Higher air-side heat transfer coefficient: bBTHX has 134% higher air-side heat transfer coefficient than baseline. Mechanisms of enhancing heat transfer include larger mass flux, branch tube with smaller diameter and 3D flow caused by the addition of bifurcation (details are in Huang et al., 2017b). Another reason is the air frontal velocity of bBTHX (2.2 m/s) is slightly higher than that of MCHX (2.02 m/s).
- Lower air-side pressure drop: The addition of bifurcation causes flow bypass and lower flow rate at bare tube region (details are in Huang et al., 2017b). However, the most important reason for a lower pressure drop is the reduction in depth. bBTHX's depth is 75% smaller than that of MCHX. The ADP/Depth value of bBTHX is higher than MCHX.
- Higher water-side heat transfer coefficient: bBTHX has five times higher water-side heat transfer coefficient than baseline. The reasons are smaller OD branch tube, boundary layer redevelopment and flow separation at the bifurcation.
- Lower water-side pressure drop: Water-side pressure drop of bBTHX is 25% lower than baseline. The reason is that it has smaller water flow path. Tube length of bBTHX is 11.24 mm while that of MCHX is 23 mm. bBTHX has larger WDP/Length value.
- Lower total pumping power: bBTHX has 38% lower total pumping power, which is mainly due to the reduction on airside pressure drop.
- Smaller volume and material volume: bBTHX has about 83% smaller volume and 87% smaller material volume than baseline.

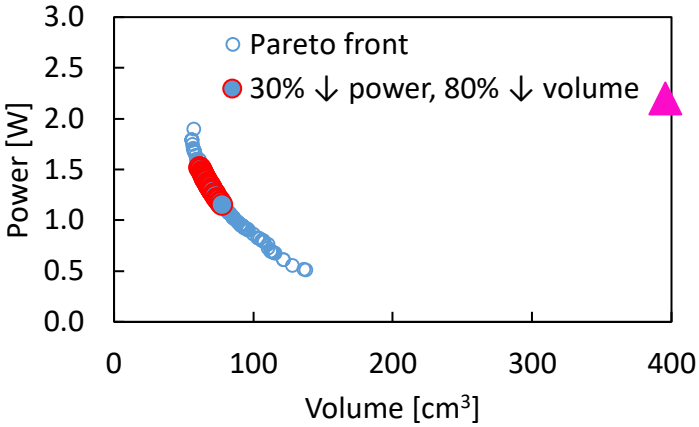

Figure 7: Pareto front

Table 2 Comparison of selected optimal design and baseline MCHX

Metric	Unit	MCHX (experimental data)	bBTHX (simulation data)	%diff
Material		Aluminum	Aluminum	
Air flow rate	m^3/s	0.05	0.05	
Air inlet temperature	K	308.15	308.15	
Water flow rate	g/s	50	50	
Water inlet temperature	K	333.15	333.15	
Heat load	W	835	845.9	1.3%
Air pressure drop	Pa	32.8	18.8	-42.7%
Water pressure drop	kPa	11.0	8.3	-24.5%
Air heat transfer coefficient	$W/m^2 \cdot K$	158	370	134.2%
Air-side heat transfer area	m^2	0.5525	0.1639	-70.3%
Water heat transfer coefficient	$W/m^2 \cdot K$	2007.4	13665	580.7%
Water-side heat transfer area	m^2	0.0735	0.13115	78.4%
Total pumping power (air+water)	W	2.2	1.36	-38.2%
Volume	cm^3	395	67.71	-82.9%
Material volume	cm^3	59.5	7.96	-86.6%
Length	m	0.23	0.2022	-12.1%
Height	m	0.1175	0.1124	-4.3%
Depth	m	0.016	0.004	-75.0%
Airside frontal area	m^2	0.0247	0.022744	-7.9%
Number of banks	-	1	4	
Tube per bank	-	11	200	
Fin per inch (FPI)	-	20	-	
P_l /OD	-	-	1.8739	
P_t /OD	-	-	1.506	
LR	-	-	6.609	
θ	°	-	62.79	

4. CONCLUSIONS

A novel heat exchanger consisting of two levels of bifurcated bare tubes was proposed, simulated and optimized using approximation assisted optimization. The key feature is the addition of bifurcation, which enhances air-side heat transfer by creating 3D flow and improves water-side heat transfer by boundary layer interruption and redevelopment. Optimization results show that the novel design achieves 38% reduction in pumping power, 83% reduction in heat exchanger envelope volume and 87% reduction in material volume as compared to a baseline MCHX having the same frontal area under same operating conditions. These performance metrics are based on simulation and the next step of the research is to fabricate the prototype and experimentally validate the performance of this novel heat exchanger. Potential manufacturing methods include additive manufacturing, laser-sintering and industrial 3D printing should also be investigated in future.

ACKNOWLEDGEMENTS

This work was supported by the Center for Environmental Energy Engineering at the University of Maryland.

NOMENCLATURE

A_{fr}	frontal area (m^2)	V_{HX}	heat exchanger volume (m^3)
$A_{fr\_baseline}$	baseline heat exchanger frontal area (–)	V_a	air velocity ($m \times s^{-1}$)
AR	aspect ratio (–)	V_w	water velocity ($m \times s^{-1}$)
$AR_{basline}$	baseline heat exchanger aspect ratio (–)	f	Chilton and Colburn f factor (–)
D_1	main tube diameter (mm)	j	Chilton and Colburn j factor (–)
D_2	branch tube diameter (mm)	OD	outer diameter (mm)
L_2	branch tube length (mm)	WDP	water-side pressure drop (Pa)
N_r	row number (–)	Nu	Nusselt number (mm)
P_l	longitudinal tube pitch (mm)	u	maximum velocity ($m \times s^{-1}$)
P_t	transversal tube pitch (mm)	θ	bifurcation angle (deg)
$\dot{Q}$	heat exchanger capacity (W)	v	kinetic viscosity ($m^2 \times s^{-1}$)
$\dot{Q}_{baseline}$	baseline heat exchanger capacity (W)		

REFERENCES

Bacellar, D., Aute. V., Huang, Z., Radermacher, R., 2016. Airside Friction and Heat Transfer Characteristics for Staggered Tube Bundle in Crossflow Configuration with Diameters from 0.5 mm to 2.0 mm. International Journal of Heat and Mass Transfer. 98: 448-454, ISSN 0017-9310.

Bacellar, D., Aute, V., Huang, Z., Radermacher, R., 2017. Design Optimization and Validation of High Performance Heat Exchangers using Multi-Scale Approximation Assisted Optimization and Additive Manufacturing. Science and Technology for the Built Environment.

Huang, Z., Li, Z., Hwang, Y. and Radermacher, R., 2016. Application of Entransy Dissipation Based Thermal Resistance to Design Optimization of a Novel Finless Evaporator. Sci China Tech Sci. 59: 1486. doi:10.1007/s11431-016-0312-3

Shabtay, Y., Huang, Z., Aute, V., Sharma, V., Radermacher, R., 2016. Manufacturing & Testing of Air-to-refrigerant Heat Exchangers Based on 0.8mm Diameter Tubes. International Refrigeration and Air Conditioning Conference. Paper 1694

Paitoonsurikarn, S., Kasagi, N., Suzuki, Y., 2000. Optimal Design of Micro Bare-Tube Heat Exchanger. Proceedings of the Symposium on Energy Engineering (SEE2000), vol. 3, pp. 972-979.

Huang, Z., DEVELOPMENT OF A COMPACT HEAT EXCHANGER WITH BIFURCATED BARE TUBES, PhD diss, University of Maryland, College Park, 2017. https://doi.org/10.13016/M2P26Q52Q

Huang, Z., Hwang, Y., Radermacher, R., 2017a. Review of Nature-inspired Heat Exchanger Technology. International Journal of Refrigeration, 78: 1-17, ISSN 0140-7007, https://doi.org/10.1016/j.ijrefrig.2017.03.006.

Huang, Z., Ling, J., Hwang, Y., Aute, V., Radermacher, R., 2017b. Design and Numerical Parametric Study of Fractal Heat Exchanger. Science and Technology for the Built Environment, 23:6, 970-982, DOI: 10.1080/23744731.2017.1335164

Shih., T. and Zhu, J., 1994. A new Reynolds Stress Algebraic Equation Model. NASA Lewis Research Center, Cleveland, OH.

Roache, P. J., 1993. A Method for Uniform Reporting of Grid Refinement Studies. Proceedings of Quantification of Uncertainty in Computation Fluid Dynamics, Edited by Celik, et al., ASME Fluids Engineering Division Spring Meeting, Washington, D.C., June 23–24, ASME Publ. No. FED-Vol. 158.

ASME, 2009. Standard for verification and validation in Computational Fluid Dynamics and heat transfer - ASME V&V 20-2009, New York: ASME.

Hamad, H., 2006. A new metric for measuring metamodels quality-of-fit for deterministic simulations. Proceedings of the 38th conference on Winter simulation, Monterey, California, Winter Simulation Conference.

Manuscript ID: 638
DOI: 10.18462/iir.icr.2019.0638

A Study on Novel High Efficiency Vane Compressor

Yusheng HU[(a)(b)], Huijun WEI[(a)(b)] ,Jia XU[(a)(b)], Pengkai WAN[(a)(b)], Fei WU[(b)], Fayou LUO[(b)], Liping REN[(a)(b)]

[(a)] State Key Laboratory of Air-conditioning Equipment and System Energy Conservation China, Zhuhai, 519070, China

[(b)] Gree Electric Appliances, Inc.
Zhuhai, 519070, China, wpk_1219@163.com

ABSTRACT

Aiming at reducing the excessive friction loss of conventional vane compressor between vane tip and cylinder wall, this paper proposed a novel vane compressor. By using rolling bearing instead of cylinder, the vane tip only contacted the bearing inner ring, and the inner ring rotated with vane. Thus the sliding friction between vane tip and cylinder was converted into rolling friction of the bearing, which could significantly reduce the mechanical power consumption. The structure and characteristics of the novel vane compressor were introduced, then the mechanical power consumption of the two kinds of compressors were theoretically calculated. The calculation results indicated that, under the design condition, vane tip power consumption of the novel vane compressor was reduced by 86.5% comparing with that of the conventional one. The experimental results showed that total power consumption of the novel vane compressor was reduced by 5.53% comparing with that of the conventional one.
Keywords: Friction, Performance, Structure, Vane Compressor.

1. INTRODUCTION

With the advantages of simple structure, easy processing, self-balance of rotor, low noise, less vibration, little torque ripple, low cost of manufacturing, etc., vane compressor is widely used in the fields of air compressor, vacuum pump, small refrigeration and air conditioning equipment, and automotive air conditioning compressors.

The main disadvantage of conventional vane compressor (CVC) is that the mechanical friction between vane tip and cylinder is serious. Wu and Ma (2003) discussed the optimal back pressure of the vane and accordingly designed a segmented throttling back pressure chamber. Huang and Chang (1993) and Huang (1995) pointed out that the frictional power of rotary vane compressor can account for about 50% of the power required by the compressor. Ma and Li (2001), Fukuta (1993) and Fukuta (1994) analyzed the back pressure acting on the tail of vane, indicated that under the premise of ensuring the contact between the vane tip and the inner wall of cylinder, reduced the contact force could decrease the friction loss and thus improve the performance of compressor. Guo et al. (1998) set three back pressure states. By comparing those different influences on motion state and characteristics of the vane, it is shown that constant back pressure is more conducive to improve the motion characteristics, and then improve the performance of compressor. The above studies have focused on how to reduce the power consumption of vane tip. Therefore, the frictional power consumption and reliability between vane tip and cylinder are the biggest bottlenecks limiting the application of the vane compressor in a wider field.

This paper proposes a novel high efficiency vane compressor (HEVC). The cylinder of CVC is changed into a cylinder and two rolling bearing, with the vane tip contacting the inner ring of bearing, and keeping a certain clearance with the inner wall of cylinder. The inner ring of bearing rotates together with the vane under the action of friction, which reduces the relative speed of the vane tip and the inner wall of cylinder. Therefore, the frictional power consumption of the vane tip is reduced, and overcomes the defect of CVC to a certain extent, and then expanded its application range.

2. THE STRUCTURE AND CHARACTERISTICS

Fig. 1 shows the basic structure and the related friction pairs of CVC (The number ①~⑨ in Fig 1), including the main bearing, the cylinder, the sub bearing, the shaft and the vane. The shaft is supported and oriented by main bearing and sub bearing. The vane is pressed against the inner wall of cylinder under the action of back pressure, and then rotates with the shaft.

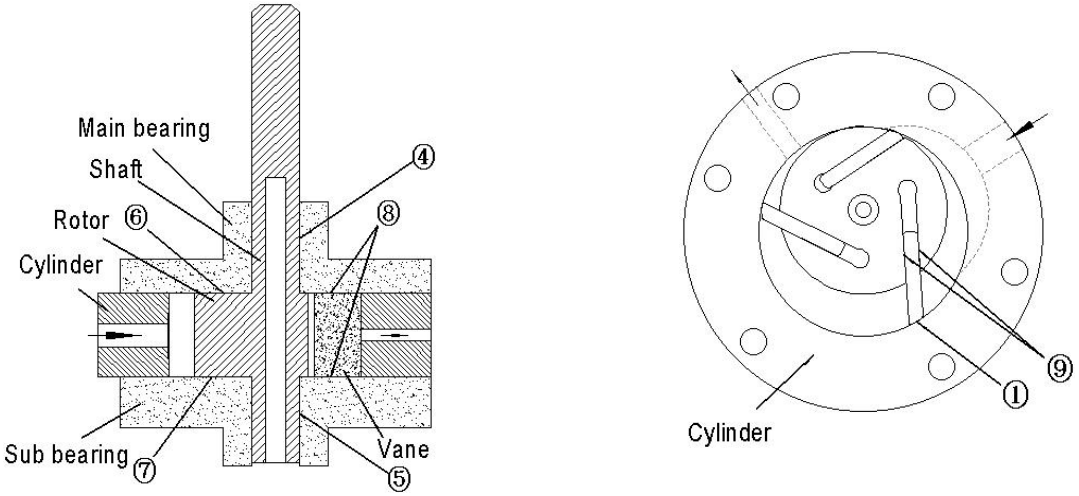

(a) Longitudinal section **(b) Horizontal section**

Figure 1: The structure of CVC

Fig. 2 shows the basic structure and the related friction pairs of HEVC (The number ①~⑨ in Fig 2). The difference is that the cylinder of CVC is divided into cylinder and rolling bearing structure. Then the sliding friction between vane and cylinder is transformed into rolling friction, which greatly reduces the friction power consumption.

The relative speed between the vane and cylinder inner wall is a key factor affecting the characteristic of HEVC. When the compressor runs, the vane is pressed against the inner ring wall of bearing by the high pressure oil from the back of vane. Because of the friction between the vane tip and the inner wall of bearing, the bearing inner ring rotates with a certain angular velocity, which reduces the relative speed between the vane tip and the inner ring of bearing.

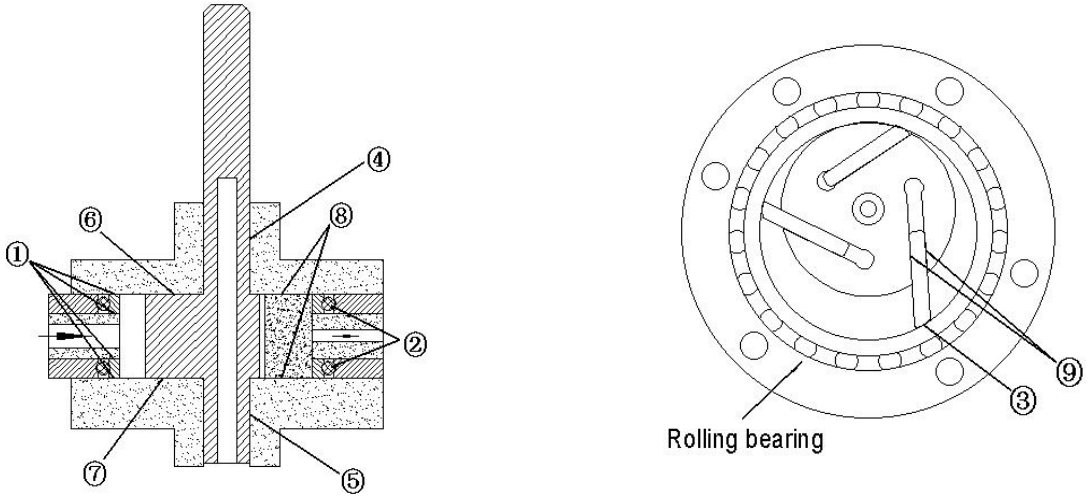

(a) Longitudinal section **(b) Horizontal section**

Figure 2: The structure of HEVC

Fig. 3 shows the assembly of vane tip with cylinder and rolling bearing. The cylinder and rolling bearing are misaligned. So the vane tip contacts with the inner ring of bearing, then forms a clearance δ_c with the inner wall of cylinder. The δ_c is the key control point for the design of HEVC. If the δ_c is too small, the poor assembly or deformation may lead to the produce of friction between the vane tip with the cylinder, and if the δ_c is too large, it will lead to the leakage of refrigerant, then reduce the cooling capacity of compressor.

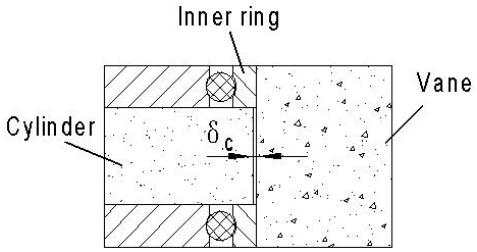

Figure 3: The assembly of vane tip with cylinder and rolling bearing

3. THE CALCULATION MODEL OF FRICTION

The locations of friction pair are shown in Fig. 1 and Fig. 2. Table 1 lists the calculation models and types of each friction pairs of HEVC.

Table 1. The calculation models and types of friction

NO.	Location of friction	The calculation model of friction		Friction type
		HEVC	CVC	
1	Inner Ring End	$W_1 = \frac{\pi\eta({R_w}^4 - R^4)\omega_n^2}{C_n}$	/	Fluid
2	Rolling Bearing	$W_2 = \frac{M \cdot n}{9550}$	/	Other
3	Vane Tip and Inner Ring(Cylinder) Wall	$W_3 = \mu_3 f_N v_t$	$W_3 = \mu_3 f_N v_t$	Boundary
4	Shaft and Main Bearing	$W_4 = \frac{2\pi\eta\omega_r^2 R_s^3 h_s}{C_s}$		Fluid
5	Shaft and Sub Bearing	$W_5 = \frac{2\pi\eta\omega_r^2 R_x^3 h_x}{C_x}$		Fluid
6	Rotor end and Main Bearing End	$W_6 = \frac{\pi\eta\omega_r^2 (R_z^2 + R_s^2)(R_z^2 - R_s^2)}{2C_g}$		Fluid
7	Rotor end and Sub Bearing End	$W_7 = \frac{2\mu_1\omega_r F({R_z}^3 - {R_x}^3)}{3({R_z}^2 - {R_x}^2)}$		Boundary
8	Vane end and Bearing End	$W_8 = \frac{2\eta b L v_h^2}{C_v}$		Fluid
9	Vane and Vane Groove	$W_9 = \mu_2 f_1 v_c + \mu_2 f_2 v_c$		Boundary

Friction pairs 1 and 2 are new friction pairs of HEVC. The inner ring face do not contact with the upper and lower thrust faces due to the limitation of the balls, and the clearance is filled with the lubricating oil, so the calculation model is derived based on the Reynolds equation (Wen and Huang, 2002), which is performed according to the fluid dynamic lubrication model. The calculation of rolling bearing power consumption of friction pair 2 is relatively complex. By referring to relevant data, this paper uses the calculation model from the SKF comprehensive catalogue (Guo, 1994) with a higher calculation accuracy. During the operation of compressor, the vane is tightly pressed against the inner ring wall of cylinder (bearing) under the action of the high pressure from its back, and the force in the rotation process is variable, so it is difficult to form the oil film. The friction pair 3 is calculated with the boundary friction. Friction pairs 4 and 5 are the coordination of shaft with main bearing and sub bearing, which belongs to a typical fluid dynamic lubrication model. The calculation model is also derived based on Reynolds equation. The resultant force direction of shaft is downward with the upper thrust face of shaft being not contact with the end face of main bearing, and there is lubricating oil in the clearance. Therefore, friction pair 6 is derived and calculated according to the model of fluid lubrication. The lower thrust face of shaft is subjected to the electromagnetic force of the motor and the gravity of roller, etc., and there

is physical contact with the end face of sub bearing, so the friction pair 7 is calculated according to the model of boundary friction theoretically. The two end faces of vane and the two sliding bearing are not contacts during the operation of the compressor, and the clearance is filled with lubricating oil. Therefore, the friction pair 8 is calculated according to the fluid lubrication.
In friction pair 9, the force on the vane and the vane groove is relatively complex, its size and direction are time-varying. It is difficult to form a good oil film, which is a typical boundary friction
The mechanical power consumption of most friction pairs in the calculation models shown in Table1 are determined by their structural dimensions. Table 2 lists the reference value of the compressor related parameters. Table 3 shows the common operating conditions of air conditioner.
It should be specially noted that F in Equation W_7 is the force of the lower thrust face, which is determined by the gravity of the rotor and the electromagnetic pulling force. f_1 and f_2 in Equation W_9 are the reaction forces between the vane and the vane groove, which are determined by the gas force difference on both sides of vane and the length of vane extension. f_N in Equation W_3 is the reaction force of the cylinder (bearing) inner wall to vane, which is determined by the difference between the high pressure from vane tail and the gas force from vane tip. v_t in Equation W_7 is the relative speed of the vane tip and the cylinder (bearing) inner wall, which is determined by the linear velocity of vane tip and the actual rotation speed of bearing inner ring.
For the HEVC, the inner ring of bearing is affected by combined actions of friction force of the vane tip to the inner ring, the viscous resistance of the lubricating oil acting on the inner ring end face, and the frictional resistance of bearing rollers. The friction of vane tip is the impetus force, and the other two forces are the obstructive force. Due to the linear speeds of the three vane tips are not synchronized, when the compressor is running stably, the rotation speed of bearing inner ring will fluctuate within a small range between the maximum linear velocity and the minimum linear velocity of the vane tip. In this paper, the value is $(v_{max}+v_{min})/2$.

Table 2. The relate parameters of compressor

The signification of symbol	Parameters	The signification of symbol	Parameters
The radius of cylinder R	60	The central radius of shaft R_z (mm)	24.8
The high of cylinder H (mm)	44	The width of vane b (mm)	4
The outer radius of inner ring	70	The high of vane L (mm)	43.97
The radius of long shaft R_s	10.504	The high of main bearing h_s (mm)	60
The radius of short shaft R_x	10.504	The high of sub bearing h_x (mm)	32
The coefficient of friction μ_1	0.1	The dynamic viscosity of oil η (MPa.s)	3.28×10^{-9}
The coefficient of friction μ_2	0.084	The coefficient of friction μ_3	0.1

Table 3. Working conditions and related parameters

Working condition	Related parameter
Refrigerant	R410A
Condensation Temperature(°C)	47.1
Evaporation Temperature(°C)	10
Displacement V (cc)	42.8
Rotation Speed n (r/min)	1800

According to the above structural parameters and compressor operating conditions, the models in Table 1 were calculated. And the specific results are listed in Table 4 and Fig. 4. The result indicates that the power consumption of the vane tip and the vane side are larger than other ones in CVC, accounting for 65% and 22% of the total power consumption, respectively. The vane tip power consumption of the HEVC decreased 168.33W (86.5%) compared with that of the CVC, and the total power of compressor decreased 138.52W (47.5%). This is a great improvement, which greatly enhances the competitive advantage of the vane compressor.

Table 4. The theoretical calculation values of power consumption of CVC and HEVC

NO.	The numerical value of theoretical calculations /(W)	
	HEVC	CVC
W_1	11.41	/
W_2	13.93	/
W_3	25.68	189.56
W_4	11.85	
W_5	6.50	
W_6	4.41	
W_7	14.24	
W_8	1.77	
W_9	63.27	
W	153.08	291.6

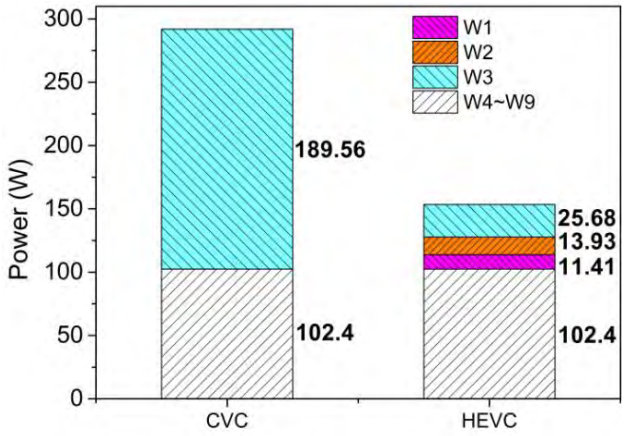

Figure 4: The power consumption comparison of those two compressor

4. PROTOTYPE VERIFICATION EXPERIMENT

The performance of CVC and HEVC were verified experimentally with the same structural parameters and working conditions to confirm the above conclusions.

Two kinds of vane compressors are designed according to the parameters in Table 2, and the difference of them is that the HEVC replaces the cylinder of CVC with the rolling bearing and cylinder. Fig. 5 indicates two schematic diagrams showing the structure of the cylinder and the rolling bearing after dissecting the two prototypes.



(a) HEVC **(b) CVC**

Figure 5: The schematic diagram of cylinder and rolling bearing after dissecting the two prototypes

After completing the production of the two prototypes, the performance tests of the two prototypes were carried out under the operating conditions of air conditioning shown in Table 3. The test results are as follows:

Table 5. The measured data of CVC and HEVC and their difference

Type	Cooling Capacity /(W)	Power /(W)	COP /(W/W)
CVC	8204.7	2257.1	3.64
HEVC	8389.1	2132.3	3.93
Difference	184.4	-124.8	0.29
Ratio	2.25%	-5.53%	8.23%

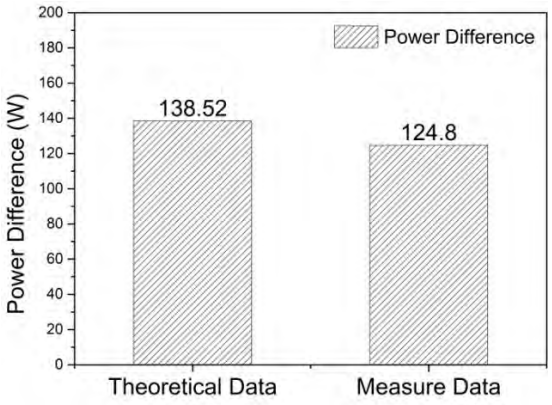

Figure 6: The theoretical and measured power difference of CVC and HEVC

Because the premise of the calculation is that the friction pair operates with an ideal condition, but in the actual test, the internal system of compressor is complicated, with the temperature, pressure and refrigerant state affecting each other. For example, the heat generated by the friction between the vane and the cylinder of CVC reduces the suction of the compressor, thereby affects the actual compression work, resulting the fluctuations of power consumption, etc.) Therefore, the theoretical calculation results and the actual test results have a tiny difference, which is also the reason why the cooling capacity of HEVC is slightly higher than that of the CVC in Table 5. However, the change trend is same, because the two compressors are compared under the same premise.

In order to further verify the performance difference of the two compressors, the performance tests under the same working conditions with the different frequencies and the same frequencies with the different working conditions were carried out, respectively.

4.1. Performance Tests of Compressors under Different Working Conditions

Compressor performance under four working conditions (1#, 2#, 3# and 4#) were tested, and the working condition degree from 1# to 4# shows more and more heavy. The change trend of cooling capacity, power consumption, and COP are shown in Fig. 7.

The tested results indicated that, the power consumption reduction of the HEVC is more obvious, with the working conditions be heavier under 30 Hz operating conditions. The main reason is that as the working condition is heavier, the pressure difference between tip and tail of vane increases, so the force and mechanical power consumption between vane tip and inner wall of cylinder increases. The greater the head power consumption, the greater the reduction.

However, the advantage of cooling capacity decreases with the increase of frequency, and the COP increment reduces firstly and then stabilize, but it still has advantages compared with CVC.

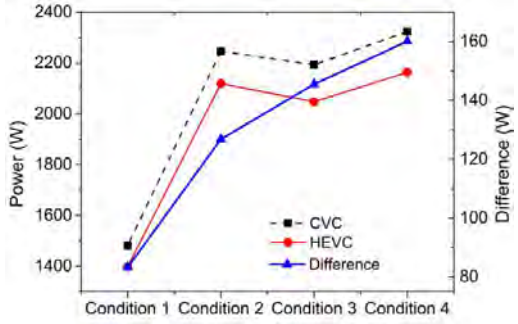

(a) The comparison of Power

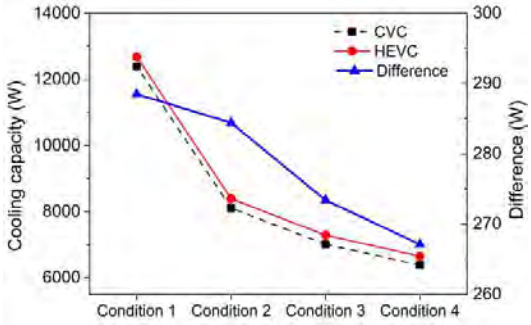

(b) The comparison of Cooling capacity

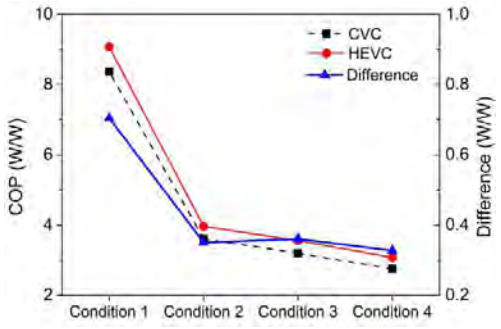

(c) The comparison of COP

Condition	Condensation Temperature(°C)	Evaporation Temperature(°C)
1	21	40
2	10	47.1
3	9	50
4	7.2	54.4

(d) The conditions

Figure 7: The comparison of compressors performance at different conditions

4.2. Performance Tests of Compressors at Different Frequencies

Under the same working conditions, the performance tests were performed at the frequencies of 20 Hz, 25 Hz, 30 Hz, 35 Hz, 40 Hz, 45 Hz, and the results are shown in Fig. 8. The tested results indicated that, the power consumption advantages of the HEVC increases first and then decreased compared with that of CVC under the same conditions. This is because that, with the increase of operating frequency, the power consumption of the bearing inner ring increases, although the power consumption of the vane tip is advantageous, so the entirety trend does not always increase, and there is an optimum frequency point.

The advantages of cooling capacity and COP decrease with increasing frequency, but they still have advantages compared with CVC.

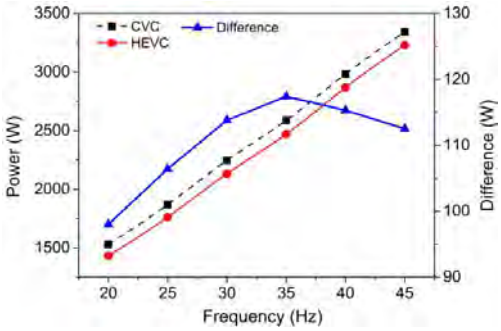

(a) The comparison of Power

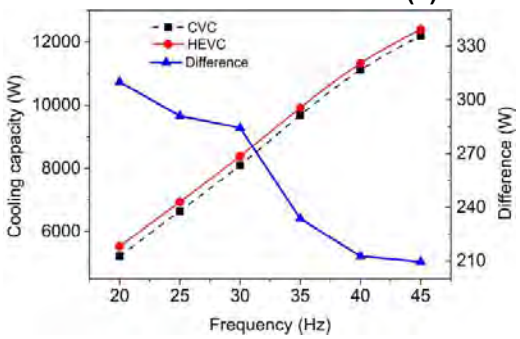

(b) The comparison of Cooling capacity

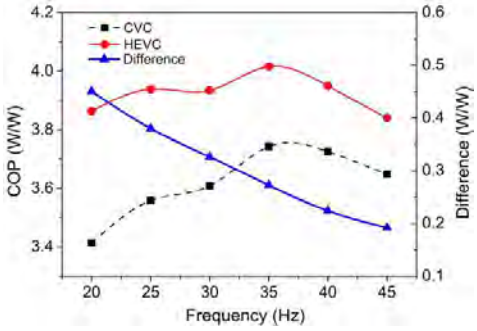

(c) The comparison of COP

Figure 8: The comparison of compressors performance at different frequencies

5. CONCLUSIONS

A HEVC is designed compared with the CVC, and the friction models are listed to calculate the mechanical power consumption. In addition, the prototype verification experiments are carried out to verify the calculated results. The main conclusions are drawn as follows.

In CVC, the mechanical power consumption of vane tip is large. Under the design condition, the vane tip power consumption accounts for 65% of that of the pump body.

Comparing with the CVC, the vane tip power consumption of HEVC reduced by 86.5% and the mechanical power consumption reduced by 47.5%.

Under the design working conditions, the power consumption of the HEVC reduced by 5.53% compared with that of the conventional one, and the COP increased by 8.23%.
Further experiments have been found that, at the same frequency, the heavier the working conditions, the more obvious the advantages of the HEVC, and under the same working condition, the advantages of the HEVC are less affected by the frequency.

NOMENCLATURE

η	oil viscosity (MPa·s)	ω_n	angular speed of inner ring (rad·s^{-1})
R_w	outer radius of inner ring (mm)	ω_r	angular speed of shaft (rad·s^{-1})
R	inner radius of inner ring (mm)	C_n	clearance of inner ring and bearing (mm)
R_s	radius of main bearing (mm)	C_g	clearance of rotor end and main bearing (mm)
R_x	radius of sub bearing (mm)	C_s	clearance of shaft and main bearing (mm)
R_z	radius of rotor end (mm)	C_x	clearance of shaft and sub bearing (mm)
h_s	height of main bearing (mm)	C_v	clearance of vane and bearing end (mm)
h_x	height of sub bearing (mm)	v_t	relative velocity of vane tip and cylinder wall (m·s^{-1})
f_N	support reaction of cylinder (N)	v_h	absolute velocity of vane tip (m·s^{-1})
b	width of vane (mm)	v_c	relative velocity of vane and vane groove (m·s^{-1})
μ_1	friction coefficient	L	length of vane (mm)
μ_2	friction coefficient	F	weight of motor and shaft (N)
μ_3	friction coefficient	f_1	support reaction of vane groove (N)
		f_2	support reaction of vane groove (N)

REFERENCES

Wu, L Z., Ma, G., 2003. Analyzing of Friction and Wear of Twin-piece Vane Compressors. Fluid Machinery 31(1), 13-16.

Huang, Y M., Chang, C H., 1993. Effect of Radial Blades and Port Location on the RCAC System. ASME. PVP 253, 185-191.

Huang, Y M., 1995. Analysis of the Rotor-Cooler Air Conditioning System. Int. J. Refrigeration 18(6), 367-372.

Ma, G Y., Li, H Q., 2001. Rotary Compressor, China Machine Press.

Fukuta, M., 1993. Vane Behavior in Vane Compressors under Start-up Operation (1st Report, Force Acting on Vane). Nippon Kikai Gakkai Ronbunshu. B Hen/Transaction of the Japan Society Mechanical Engineers, Part B, 58(567), 3487-3492.

Fukuta, M., 1994. Vane Behavior in Vane Compressors under Start-up Operation (2nd Report, Vane Behavior with Pressure Rise in Back Chamber). Nippon Kikai Gakkai Ronbunshu. B Hen/Transaction of the Japan Society Mechanical Engineers, Part B, 60(571), 879-884.

Guo, B., Hu, J H., Shu, P Z., 1998. Influence of Vane Slot Back Pressure on the Characteristic of Vane Motion in Rotary Vane Compressor. Chinese Journal of Applied Mechanics 15(1), 65-70.

Wen, S Z., Huang, P., 2002. The fundamentals of tribology (2nd edition). Tsinghua Publishing House.

Guo, H J., 1994. SKF rolling bearing general catalogue. The Science &Technology Press, part2, 89-101.

Manuscript ID: 644
DOI: 10.18462/iir.icr.2019.0644

Experimental investigations of two-phase ejector operating with isobutane

Kamil ŚMIERCIEW, Jerzy GAGAN, Dariusz Butrymowicz, Adam DUDAR

Bialystok University of Technology
Wiejska 45C, 15-351 Białystok,Poland, d.butrymowicz@pb.edu.pl

ABSTRACT

Application of a two-phase ejector in a vapour compression refrigeration system is a promising way to increase the system efficiency. Most of the investigations deal with the performance of the whole compression-refrigeration system. In contrary the paper deals with two-phase ejector only. Low GWP natural refrigerant R600a was used in the experiment. The velocity coefficients have been determined. Velocity coefficients φ for nozzles in range $0.4 < \varphi < 1.0$ and $\varphi < 0.4$ for suction and mixing chambers and diffuser were obtained. Basing on the experimental results correlations for velocity coefficient for components of the ejector have been proposed. Two physical parameters: quality of fluid, and the volumetric entrainment ratio, were selected as parameters describing relation of the velocity coefficient. The numerical results based on the proposed correlations fits with experimental data within 30%.
Keywords: two-phase, correlations, isobutane, ejector, velocity coefficients

1. INTRODUCTION

Application of an two-phase ejector in compression refrigeration systems is a promising way to increase the system efficiency. Depending on system configuration the ejector can operate as a second step-compressor or a throttling device (Bergander et al, 2010). In the first case ejector operates at high temperatures especially at suction chambers since ejector entrains vapour from compressor. The efficiency improvement results from the fact that less mechanical work is required to compress a liquid than to compress a vapour. Therefore increasing the efficiency of the standard single-stage vapour compression cycle is achieved by reduction of mechanical compression at the expense of harnessing kinetic energy of a vapour in the ejector device. For the second case the ejector operates at relatively low temperatures at suction chamber inlet since the ejector entrains vapour from the evaporator. In both cases the ejector is fed by liquid from the compressor. This configuration allows to reduce losses in the compression refrigeration and heat pump systems caused by the throttling process in the expansion valve by means of application of the liquid expansion instead of the isenthalpic throttling process.
Very simple theoretical model of the operation of the ejector in the system proposed in paper by Li and Groll (2005) require assumed values of the efficiencies of the main parts of the ejector without any specific consideration of the momentum transfer producing suction and compression effects. Butrymowicz et al (2009) have shown the effect of the motive nozzle diameter on performance of the two-phase ejector for the case of refrigerant R-123. The theoretical model for two-phase ejector as an expansion device has been presented by Elbel and Hrnjak (2008). In this model governing equations were formulated for all passages of the ejector based on the differential equations for mass, momentum, and energy balance as well as a differential representation for the equation of state. The model was completed by closing equations for mass, momentum and energy transfer between the primary and secondary flow. The model based on principles of Homogeneous Equilibrium Model (HEM) was presented by Banasiak et al (2014). The results of the numerical modelling of the two-phase ejector using CFD techniques were presented by Yazdani et al. (2012) where the pressure profile along the mixer and diffuser walls and the entrainment ratio were compared with test data. Deviation between the numerical and experimental results is 10%. The CFD techniques can be thought as a practical designing tool, however it requires integration of separate sub-models for e.g. two-phase sonic velocity with CFD code through user-defined

functions. The experimental works of the two-phase ejector for R-12 as a working fluid were carried out and presented by Disawas and Wongwises (2004). The experimental results of improvement of COP of the split air-conditioning system due to application of the two-phase ejector as a throttling device instead capillary tube have been presented by Sumeru et al. (2014). Mentioned above investigations in most cases deal with the performance of the whole compression-refrigeration system. There is a strong need for the further investigation in order to better understand the physical phenomena and the operation of the ejector, especially for other fluids than CO_2. All presented model for two-phase ejector require assumption for the efficiency of the ejectors components, i.e. motive nozzle, suction and mixing chambers and diffuser. In this paper the model of the two-phase ejector have been shown along with correlations for velocity coefficients for the components of the ejector. The correlations have been developed based on the experimental investigation of compression-ejection cycle operating with isobutane.

2. DESCRIPTION OF THE CYCLE WITH TWO-PHASE EJECTOR

The schematic diagram of vapour compression refrigeration device equipped with the two-phase ejector as a throttling device with the representation of the thermodynamic cycle in simple form is shown on Fig. 1.

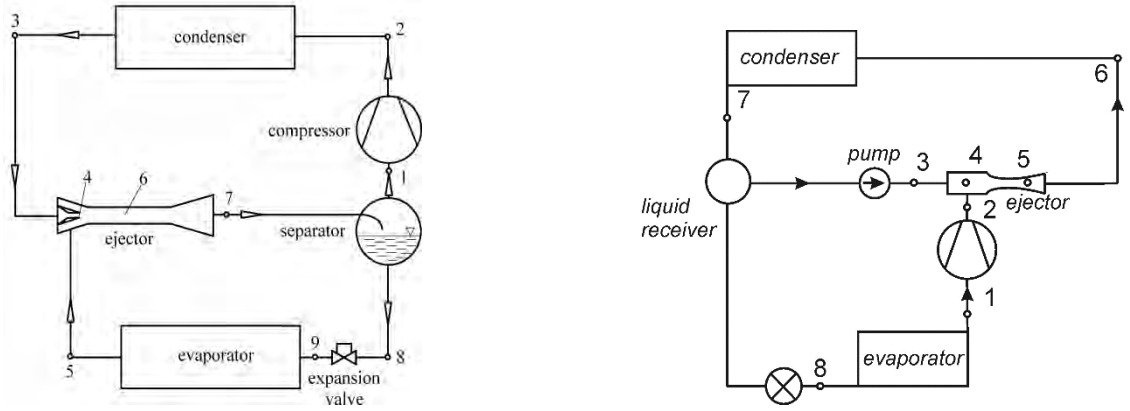

Figure 1. Schematic diagram of ejection-compression refrigeration device: a) operating as throttling device and b) operating as second-step compressor

In the system presented in Fig. 1a liquid refrigerant (3) as the motive fluid expands in the motive nozzle and partly evaporate. In isentropic nozzle the expansion takes place along isentropic line 3-4s (see Fig. 1), while with the throttling valve expansion is represented by line 3-4d. In real motive nozzle expansion is represented by line 3-4. Motive fluid of high velocity emanating from the nozzle (4) causes suction of vapour from the evaporator (5) and compression in the mixing chamber (6) due to the momentum transfer. The additional compression of two-phase mixture takes place in the diffuser producing the inter-stage pressure in the system (7). Compressed two-phase mixture is separated in the separator, so the compressor sucks the vapour (1) while the liquid (8) flows to the evaporator through the throttling valve. In the system presented in Fig. 1b liquid refrigerant (7) is compressed by mechanical pump in order to produce high motive pressure (3). The suction chamber is connected with mechanical compressor (2). The compressor operates between the evaporation pressure and the interstage pressure, while the ejector operate between the interstage pressure and the condensation pressure.

3. EXPERIMENTAL TEST BENCH

The test facilities were designed and built for the investigations of the ejection refrigeration system operating with natural working fluids. In this case isobutane was used as a refrigerant The schematic of the experimental stand equipped with the ejector is shown in Fig. 2, and the schematic of tested two-phase ejector is presented in Fig. 3. The ejector shown in Fig.3 was equipped with several types of nozzle geometries during experiments. Detail information about tested nozzles is given in Table 1.

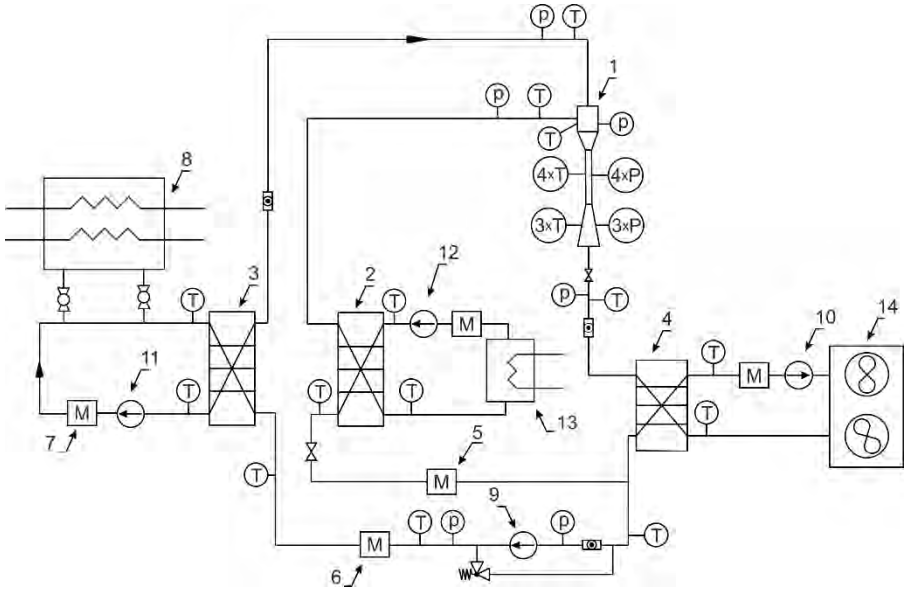

Figure 2. Schematic of the testing stand:
1 – tested two-phase ejector; 2 – evaporator; 3 – preheater/vapour generator; 4 – condenser; 5, 6, 7 – mass flow meters; 8,13 – electric heaters, 9,10,11,12 - circulation pumps; 14 –dry cooler

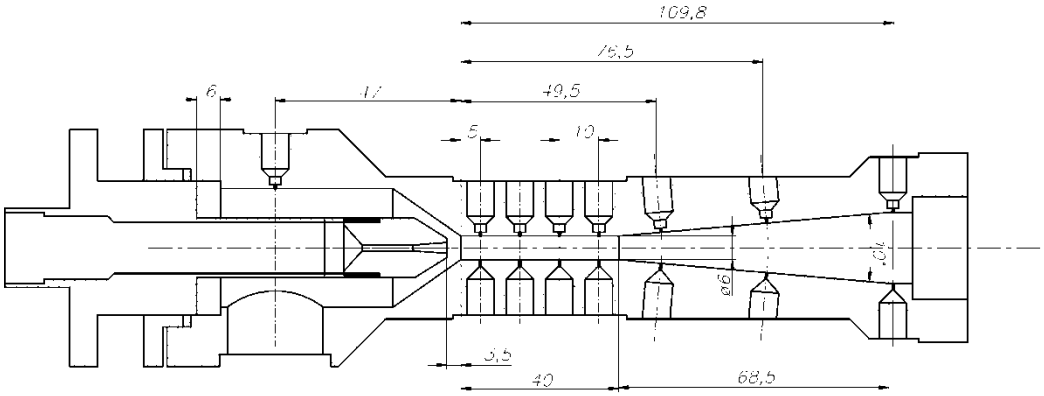

Figure 3. Schematic diagram of the tested two-phase ejector

Table 1. Diameters of the tested nozzles for two-phase ejector

nozzle	type	throat diameter D_n [mm]	outlet diameter D_{no}[mm]
1	de Laval	1.0	2.4
2	de Laval with an orifice plate at the nozzle inlet	1.0	2.4
3	de Laval	1.0	3.1
4	de Laval	1.4	4.1
5	de Laval with 13mm of cylindrical throat (shown in Fig. 3)	1.5	2.7
6	de Laval with 13mm of cylindrical throat and an orifice plate at the nozzle inlet	1.5	2.7
7	sharp edged	1.0	1.0
8	sharp edged	1.5	1.5

In the system presented in Fig. 1 the motive nozzle is feed by liquid with pressure p_{li} equal the condensation pressure. Pressure in suction chamber p_{vi} is equal to evaporation pressure. Depending on the thermodynamics properties of the fluid the pressure ratio p_{vi}/p_{li} can be lower than gas dynamic critical pressure ratio. In that case, using of the supercritical de Laval nozzle is well-founded. It is worth to note that in two-phase ejector the metastable flow can be observed. In this

case, the disturbing of the flow or initiation of the flashing vaporisation by means of orifice plate located at the nozzle inlet can be thought as a good practice. In presented experimental investigation the orifice plate of 1.0 mm and 1.5 mm were used along with de Laval nozzle, see Table 1.

In the ejection loop the liquid refrigerant flows through the reciprocal pump 9. The flow of refrigerant is splited; one part flows through the expansion valve to the evaporator while the other part flows to the heat exchanger 3. Compressed liquid is heated up to saturation condition. The motive nozzle of the ejector was feed by saturated liquid. The temperature of the motive liquid was in range between t_{li} = 40 ÷ 80 °C . During experiments the mass flow rate of the motive liquid was in range m_{li} = 50 ÷ 110 kg/h. This range of temperatures of the primary and secondary stream can be thought as appropriate for operation of the ejector as a throttling device as well as second step compressor. Temperature of evaporation was set in range 15 ÷ 35 °C. Temperature of condensation not exceed 40 °C during experiments. The testing rig was equipped with the temperature sensors and pressure transducers installed at the critical locations and other locations of interest. The pressure transducers accuracy of 0.25% the measuring range are used during the experiments. First-class K-type thermocouples were applied for the experiments. The thermocouples were calibrated with total accuracy of ±0.2 K. The Coriolis mass flow meters of the accuracy of 0.15% the measuring range were used. Sight-glasses were installed at various locations to observe the flow. The plat plate heat exchanger were used. The diaphragm pump in ejector refrigeration cycle was used.

The test rig was equipped with two additional loops: the first one for the thermal load for the evaporator and the second one for the condenser cooling. Centrifugal pumps were applied in the additional loops. These systems allow for adjusting of the refrigerant flow rates as well as for changing of the operation parameters in a wide range. The condenser cooling system was equipped with the automatically controlled dry cooler. The thermal load system was equipped with the automatically controlled electrical heater. The data acquisition system logs all main parameters and controls valves, pumps, electric heaters and safety system. During the experiments 100 readings at the steady-state conditions were taken and averaged to make one experimental run.

4. CORRELATION FOR VELOCITY COEFFICIENTS BASED ON EXPERIMENTAL INVESTIGATIONS

In most of the modelling approaches available in literature, the efficiencies of the ejector components are assumed as constant quantities. Although the dependence of the efficiency of the ejector components from the quality of its surface is undisputed, the efficiency still should depend on the flow structure, operating conditions, etc. Therefore, these quantities should not be treated as constant. Below, the correlation for the velocity coefficients of ejector components are proposed on the basis of own experimental data. The efficiency of the specific component of the ejector can be found from general relation $\eta = \varphi^2$.

4.1. Two-phase motive nozzle

Velocity coefficient is defined as a ratio of velocity at the nozzle outlet w_n to the velocity at the nozzle outlet in isentropic condition w_{ns}:

$$\varphi_n = \sqrt{\eta_n} = \frac{w_n}{w_{ns}} . \qquad \text{Eq. (1)}$$

Estimation of the velocity coefficient for nozzles operating in two-phase region may not be treated as a standard issue since the outlet fluid parameters are not known, especially the quality of the wet vapour x. Below, there is presented own approach in terms of estimation of the velocity coefficient for nozzle operating in two-phase region. For the given inlet parameters and outlet pressure the isentropic velocity is given by:

$$w_{ns} = \sqrt{2\left(h_{li} - h_{ns}\right)}, \qquad \text{Eq. (2)}$$

where h_{ns} is specific enthalpy of the fluid at isentropic nozzle outlet. Kinetic energy of the fluid at nozzle inlet was neglected. The theoretical mass flow rate is compared with measured mass flow rate given by:

$$\dot{m}_{li} = A_{no}\rho_n w_n , \qquad \text{Eq. (3)}$$

where A_{no} is area of the nozzle outlet. Ratio of the mass velocities:

$$\psi_n = \frac{\dot{G}}{\dot{G}_s} = \frac{\rho_n}{\rho_{ns}}\frac{w_n}{w_{ns}} . \qquad \text{Eq. (4)}$$

Using eq. (1) velocity coefficient can be written as

$$\varphi_n = \psi_n \frac{\rho_{ns}}{\rho_n} , \qquad \text{Eq. (5)}$$

where density of the wet vapour is given by:

$$\rho_n = \left[v'(p_n) + x_n h_{fg}(p_n) \right]^{-1} . \qquad \text{Eq. (6)}$$

In equation (6) the quality x_n is unknown parameter. However, the velocity coefficient can be written in form

$$\varphi_{nh} = \sqrt{\frac{h_{li} - h_n}{h_{li} - h_{ns}}} , \qquad \text{Eq. (7)}$$

where enthalpy of wet vapour can be found as:

$$h_n = h'(p_n) + x_n h_{fg}(p_n) . \qquad \text{Eq. (8)}$$

The quality of the wet vapour at the nozzle exit can be found with numerical solution of equation

$$\varphi_n(x_n) = \varphi_{nh}(x_n) . \qquad \text{Eq. (9)}$$

On the basis of the experimental results of the nozzles presented in Table 1 the relation between velocity coefficient φ_n and quality of the fluid at the nozzle outlet x_n can be found. This relation is presented in Fig. 5a.

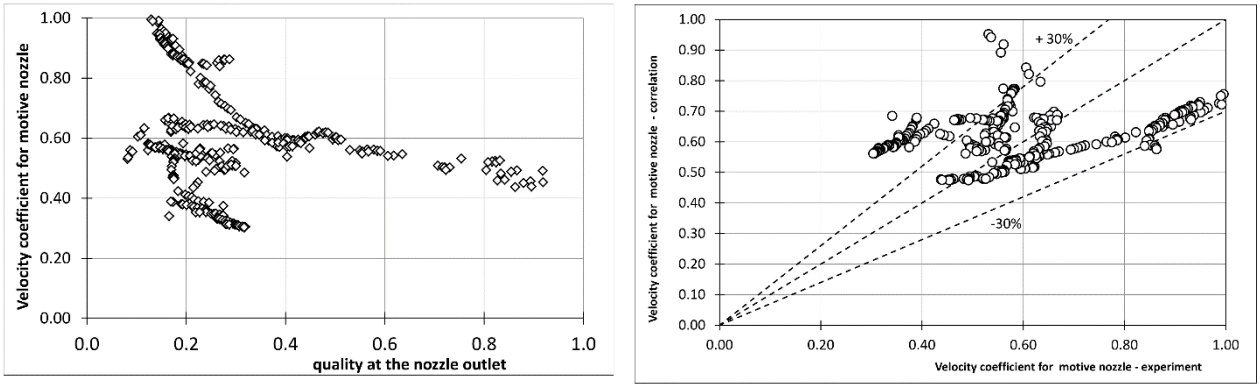

Figure 5. Velocity coefficient for motive nozzle vs. quality at the nozzle outlet (a); Calculated velocity coefficient vs. experimental velocity coefficient (b)

The experiments show that velocity coefficient for tested nozzle covers the range $0.3 < \varphi_n < 1.0$ in full range of quality. However, most of the experimental results shows that the quality of the fluid at the nozzle outlet was lower than 0.50. The proposed correlation for velocity coefficient has a form:

$$\varphi_n = C_{no} + C_{n1} x_{ns}^{C_{n2}} . \qquad \text{Eq. (10)}$$

Systematic experimental results of investigation of the nozzles with various geometry (Table 1) were used to determination of constants $C_{n0} = 0.4286$, $C_{n1} = 0.04177$ and $C_{n2} = -1.0085$. As it can be seen in Fig. 5b. numerical results obtain from correlation given by eq. (10) in most cases fits to experimental data. The discrepancy is ±30% and it result from the different operation of the nozzles due to application of the orifice plate.

4.2. Suction chamber

Velocity coefficient for suction chamber was numerically calculated for experimental data according to eq. (11) and eq. (12). Experimental data demonstrate that the velocity coefficient is correlated with volumetric entrainment ratio and distance between motive nozzle outlet and mixing chamber inlet, which is shown in Fig. 6

$$\frac{\dot{m}_{vi}}{A_{vi}\rho_v} = \varphi_s \sqrt{2\left(h_{vi} - h_{vs}\right)}\,. \qquad \text{Eq. (11)}$$

According to Fig.6a. relation between the velocity coefficient φ_s for suction chamber and volumetric entrainment ratio χ is linear. Therefore, the correlation in final form of correlation for velocity coefficient was obtain

$$\varphi_s = \left(0.06907 - 0.05149\ \Lambda\right)\chi\,. \qquad \text{Eq. (12)}$$

where $\Lambda = L_{no}/D_m$ and L_{no} is distance between nozzle outlet and mixing chamber inlet.
The results presented in Fig. 6a shows that the velocity coefficient for suction chamber is relatively small and not exceed φ_s = 0.35, which indicates low efficiency of the suction chamber. Velocity coefficient increases proportionally to the entrainment ratio. The volumetric entrainment ratio χ varies between 0 and 8.0. The relation of the velocity coefficient of the geometry module $\varphi_s = f(\Lambda)$ is inversely proportional, e.g. for the highest tested module Λ = 0.750 velocity coefficient varies between 0.10 – 0.13 for χ = 4.0 and for lowest tested module Λ = 0.417 velocity coefficient exceeds highest values and varies between 0.17 – 0.25 for the same value of volumetric entrainment ratio χ = 4.0.

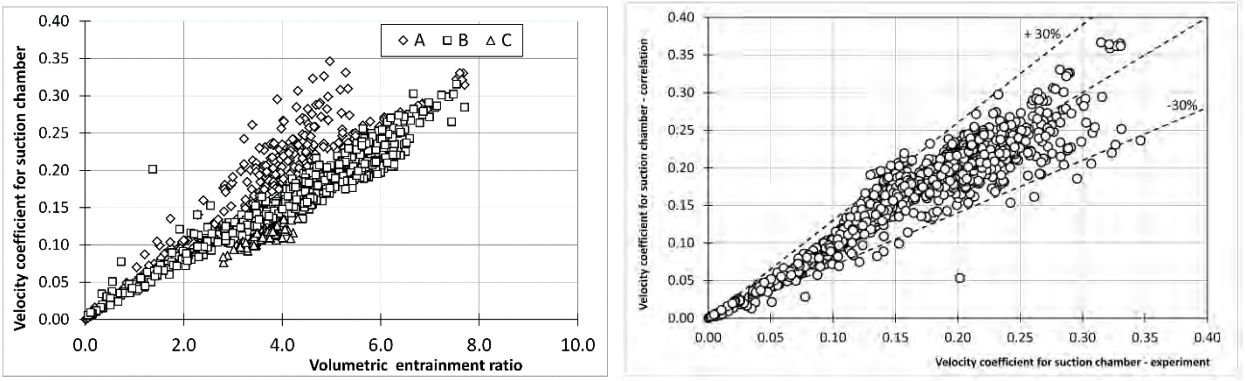

Figure 6. Velocity coefficient for suction chamber vs. volumetric entrainment ratio: A) Λ = 0.417; B) Λ = 0.583; C) Λ = 0.750 (a); Calculated velocity coefficient vs. experimental velocity coefficient (b).

Comparison of calculated velocity coefficient (eq. 12) with experimental velocity coefficient is shown in Fig. 6b. It can be seen that calculated velocity coefficient for suction chamber well agree with experimental results. Excluding individual cases, the discrepancy of the results is less than 30% for proposed correlation.

4.3. Mixing chamber

In presented investigations the location of the shock wave was not the object of our interest, also the shock wave was not identified. In that case, it was assumed that the mixing process is isobaric. Experimental data demonstrate that the velocity coefficient is correlated with volumetric entrainment ratio χ and module Ψ, which is shown in Fig 7. The correlation for mixing chamber velocity coefficient in the presented form was proposed:

$$\varphi_m = \left(0.03747 + 0.08462\,\Psi\right)\chi\,. \qquad \text{Eq. (13)}$$

Comparison of calculated velocity coefficient (eq. 13) with experimental velocity coefficient is shown in Fig. 7b. It can be seen that calculated velocity coefficient for mixing chamber well agree with experimental results. Again, excluding individual cases, the discrepancy of the results is less than 30% for proposed correlation

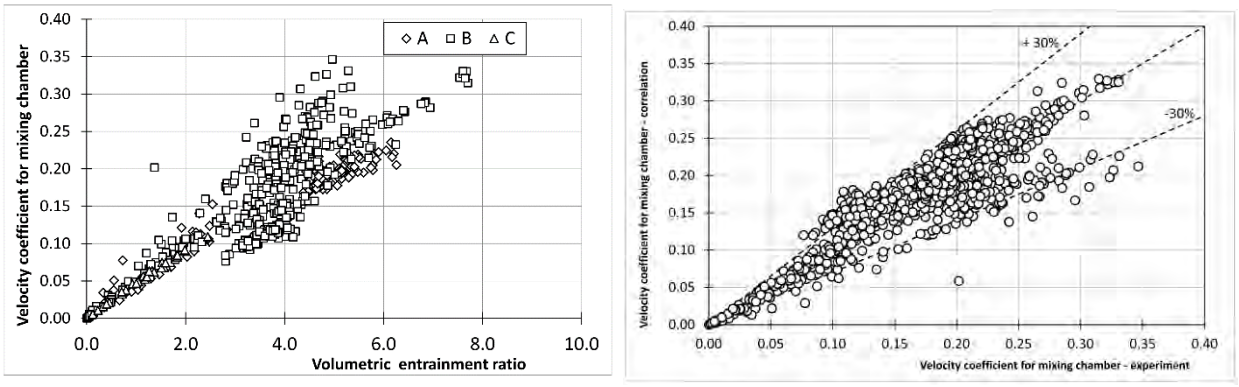

Figure 7. Velocity coefficient for mixing chamber vs. volumetric entrainment ratio: A) Ψ = 0.0278; B) Ψ = 0.0625; C) Ψ = 0.111, (a); Calculated velocity coefficient for mixing chamber vs. experimental velocity coefficient (b).

4.4. Diffuser

Taking the diffuser into consideration it is worth to note that the diffuser in two-phase ejector do not play the major role since the effect of compression is obtain due to shock wave in most cases. Again, taking into consideration geometrical module Ψ and operation parameters, i.e. volumetric entrainment ratio χ of the two-phase ejector the relation between those parameters and velocity coefficient for diffuser φ_{dk} is shown in Fig 8.

Keeping in mind the randomness of the operation of the diffuser, the results with largest discrepancy have been omitted. Therefore, the correlation for velocity coefficient in linear form has been proposed:

$$\varphi_d = \left(0.075 + 0.108\,\Psi\right)\chi\,. \qquad \text{Eq. (14)}$$

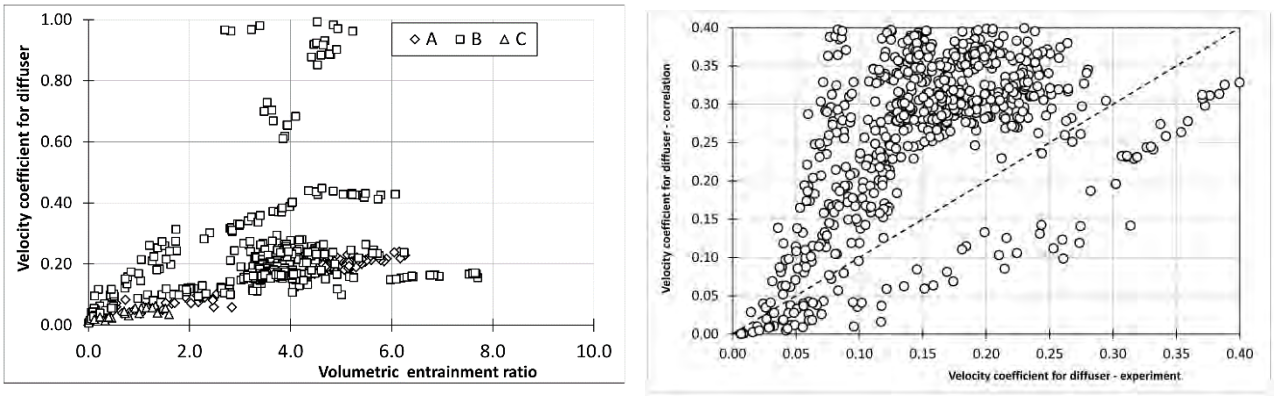

Figure 8. Velocity coefficient for diffuser vs. volumetric entrainment ratio: A) Ψ = 0.0278; B) Ψ = 0.0625; C) Ψ = 0.111, (a); Calculated velocity coefficient for diffuser vs. experimental velocity coefficient (b)

The experiment shows that for tested ejector with geometry described by module Ψ the velocity coefficient for diffuser are in general lower than $\varphi_d < 0.40$. Proportional relation between velocity coefficient and entrainment ratio can be observed. Despite the large discrepancy of the results it can be seen that for ejector with module Ψ = 0.0625 the efficiency of the diffuser is slightly better than with module Ψ = 0.0278. The lowest efficiency of diffuser is observed for the ejector with geometrical module Ψ = 0.111. For this case the velocity coefficient is lower than 10%, $\varphi_d < 0.10$. Comparison of calculated velocity coefficient (eq. 14) with experimental velocity coefficient was shown in Fig. 8b. It can be seen that the adjustment of calculated velocity coefficient and the experimental value can be considered as relatively good, however diffuser is the ejector's part with smallest efficiency, and the pressure increase in the diffuser is in many cases minor.

5. CONCLUSIONS

The presents the correlation for velocity coefficients of motive nozzle, suction and mixing chambers and diffuser of two phase liquid-vapour ejector. The correlations were developed on the basis of own experimental results of the ejector with various geometry, described by geometrical modules Λ and Ψ performed for isobutane as a working fluid. The quality of fluid x for the case of motive nozzle and the volumetric entrainment ratio χ for other ejectors components were chosen as a parameters describing relation of the velocity coefficient. For the components of the ejector the velocity coefficient lower than 0.4 were obtain for tested ejector and operation conditions. Except motive nozzle linear proportional relation between velocity coefficient and entrainment ratio have been found. The numerical results based on the proposed correlations fits with experimental data within 30%.

ACKNOWLEDGEMENTS

The research was carried out as part of research work no. S/WM/1/2018 at the Bialystok University of Technology and financed from a subsidy provided by the Minister of Science and Higher Education

REFERENCES

Bergander, M.J., Butrymowicz,D., Śmierciew, K., Karwacki, J. (2010). Refrigeration Cycle With Ejector for Second Step Compression. International Refrigeration and Air Conditioning Conference. Paper 1053. http://docs.lib.purdue.edu/iracc/1053

Li, D., Groll, E.A., (2005) Transcritical CO2 refrigeration cycle with ejector-expansion device, International Journal of Refrigeration 28, 766–773.

Butrymowicz, D., Śmierciew, K., Regulska, D., Karwacki, J., Trela, M., (2009). Experimental investigation of effect of motive nozzle diameter on performance of liquid-vapour ejector, International Seminar On Ejector/Jet-Pump Technology And Application, Louvain-La-Neuve, Paper No. 24.

Elbel, S., Hrnjak, P., (2008) Experimental validation of a prototype ejector designed to reduce throttling losses encountered in transcritical R744 system operation, International Journal of Refrigeration 31, 411-422

Banasiak, K., Palacz, M., Hafner, A., Bulinski, Z., Smołka, J., Nowak, A., Fic, A., (2014). A CFD-based investigation of the energy performance of two-phase R744 ejectors to recover the expansion work in refrigeration systems: An irreversibility analysis, International Journal of Refrigeration 40, 328-337

Yazdani, M., Alahyari, A.A., Radcliff, T.D., (2012) Numerical modeling of two-phase supersonic ejectors for work-recovery applications, International Journal of Heat and Mass Transfer 55, 5744–5753

Disawas, S., Wongwises,S., (2004) Experimental investigation on the performance of the refrigeration cycle using a two-phase ejector as an expansion device, International Journal of Refrigeration 27, 587–594

Sumeru, K., Sulaimon, S., Nasution, H., Ani, F.N. (2014) Numerical and experimental study of an ejector as an expansion device in split-type air conditioner for energy savings, Energy and Buildings 79 (2014), 98–105

Manuscript ID: 646
DOI: 10.18462/iir.icr.2019.0646

Thermodynamic analysis of zeotropy mixtures for ejection refrigeration cycle

Jerzy GAGAN[(a)], Pawel JAKONCZUK[(a)], Dariusz Butrymowicz[(a)], Kamil SMIERCIEW[(a)]

[(a)] Bialystok University of Technology, Wiejska 45C, 15-351 Bialystok, Poland
d.butrymowicz@pb.edu.pl

ABSTRACT

Ejection refrigeration cycles are driven by thermal energy. Application of low-grade heat as a motive source, e.g. district heating system requires sufficient mass flow rate of the heating water or large change of temperature of the water in order to provide required heat flux. The latter is more economically advantageous. In some cases, however, either requirements cannot be fulfilled. One of the reasons is isothermal evaporation of refrigerant in vapour generator. Because of this the refrigerant with temperature glide is highly recommended. The paper deals with thermodynamic analysis of low GWP refrigerant mixtures applied for ejection cycle. The results show that depending on the type and proportion of mixed refrigerants the temperature of the heating medium change from 5 to 25 K and more. As an effect the COP of the system vary between 5 to 25%.
Keywords: refrigerants, mixture, ejection cycle, temperature change, COP.

1. INTRODUCTION

Growing world energy consumption and environmental concerns increased interest in utilising alternative sources, like low and medium temperature heat sources. Another concern is low efficiency of combined heat and power (CHP) plants in warm months, when demand for heat is low.

Organic Rankine Cycle (ORC) technology is a popular solution. There are many commercial solutions available, but most of them are large plants, suitable for use with high temperature sources (200 - 300°C). This is economically justified, as smaller installations working with lower temperatures are less efficient. Another way of using low grade energy sources are ejector refrigeration cycles. They achieve lower COP than ammonia absorption chillers, but can work with lower motive temperatures, as low as 50 - 70°C. This makes possible to pair ejector cycles with district heating systems, thus increasing efficiency of the CHP plant in the summer and generating cooling power. Coupling a steam generator of an ejector refrigerator to cogeneration plant's turbine outlet would allow to achieve higher COP (Coefficient of Performance) due to higher motive temperature, as steam leaving the turbine in a CHP plant is usually about 100 °C.

Gagan et al., (2018) proved that it is possible to run ejector cycles with such low source temperatures. They investigated the performance of an ejector cycle with ecological HFO R-1234ze(Z) refrigerant. The system achieved COP=0.25 for evaporation temperature 0°C and COP=0.4 for 6 °C. The motive temperature was kept below 65°C.

Research on both heat and refrigeration cycles working with zeotropic blends were carried out. Kang et al. (2015) investigated the performance of zeotropic mixtures of HFC/HC and HFO/HC in ORC working with low-to-medium temperature heat source. The performance of R-245fa and R-600a (0.9/0.1) mixture was found to be the best.

Hakkaki-Fard et al. (2014) have developed a numerical model of an air-source heat pump to check how heat pumps work with zeotropic blends of several environmentally friendly refrigerants (CO2, propane, R-32) and R-125.

Yang and Zhao (2015) and Yang et al. (2015) looked at utilising zeotropic fluids in combined power and ejector cycle. Such systems are created by adding an expander between the steam generator and the ejector in a standard ejector refrigeration cycle.

Connecting the ejector cycles working e.g. as coolers in air conditioning systems to the heating network at substations is more practical, as the device would be closer to cooling power receivers and cold medium transmission over long distances would be unnecessary. This solution has a major drawback which is low temperature of water in the network, oscillating around 60 – 65 °C. Another problem arising in this configuration is low COP of the ejector refrigeration cycle, additionally reduced when it's working with low motive temperatures.
The largest obstacle in utilising this technology is a high drop in water temperature at the heat consumer's side required by heating networks, up to 30 °C, that would have to be achieved in ejector cycle steam generator. This requirement can be met by critical cycles, subcritical or cycles with zeotropic refrigerant. Devices with azeotropic fluids can't cool the heating water down enough due to isothermal phase change in the steam generator and require a higher flow rate of motive water, thus increasing operating and investment costs. There is a lack of research on ejector refrigeration cycles operating with high temperature glide working fluids employed to increase the match between the heat source and the cycle. This paper presents the results of theoretical analysis of an ejector cycle working with a high temperature glide blends of environmentally friendly, safe refrigerants.

2. SELECTION OF WORKING FLUIDS

Because of climate changes and legislation, the proposed system cannot contain any ozone depleting or high-GWP fluids. Additionally, Regulation of the European Parliament and the EU Council No. 517/2014, enacted on April 16th, 2014 forbids the use of commercial and domestic air conditioning units with more than 3 kg of refrigerant with GWP higher than 150 in EU countries. Hydrocarbons meet the environmental criteria and have been widely used in refrigerators and AC units for years. Extreme flammability of hydrocarbons is not a concern in small devices that contain several dozen grams of refrigerant. However, in case of large systems, comprising significant quantities of fluid, compliance with regulations and standards regarding operation in an explosive environment is required. Therefore, authors of this paper decided to only consider non-flammable or mildly flammable, low-toxicity fluids (ASHRAE A1 and A2L class).

2.1. Requirements

Suitable refrigerant should:
- have low critical parameters to avoid high pressures in the system and maximise the temperature drop of motive water in the steam generator due to operation of the steam generator in close proximity to the critical point and low heat of evaporation,
- provide as high COP as possible,
- have a positive or infinite saturated vapour slope (dry and isentropic fluids) in order to avoid additional losses in the ejector,
- be relatively inexpensive and easily available,
- have GWP lower than 150 in order to comply with strict EU regulations regarding substances with higher global warming potential,
- be safe, i.e. non-flammable and non-toxic.

Meeting all the criteria at the same time drastically narrows down the list of potentially suitable fluids. A lot of substances comply with some, or even most of the requirements, but don't provide a high enough drop in water temperature in steam generator (20°C - 30°C) or yield COP too low to consider them as economically feasible solution. Substances appropriate for critical cycle with heat source temperature as low as 60°C that would meet all the criteria were not found, and authors believe that the easiest solution to this problem is using a zeotropic refrigerant mixture instead of a pure fluid.
Non-isothermic phase change is usually undesirable, so commercially available zeotropic blends, e.g. R-410A have a low or even negligible temperature glide (several K). In the designed system the glide as high as 10 – 15 K is necessary, therefore a new mixture had to be developed.

2.2. Properties of selected refrigerants

Six different fluids were chosen: R-454c, R-455a, R-1234yf, R-1234ze(E), R-1234ze(Z) and Novec 649. Table 1 presents their properties. Many refrigerants were rejected just because of their high environmental impact even if they were thermodynamically suitable for proposed ejector cycle, e.g. R-125.

Table 1. Selected properties of analysed fluids

Fluid name	R-454c	R-455a	R-1234yf	R-1234ze(E)	R-1234ze(Z)	Novec 649
Group	HFO	HFO	HFO	HFO	HFO	N/A
GWP	148	146	<1	<1	<1	1
ODP	0	0	0	0	0	0
Replacement for	R-22 R-404A	R-404A R-507	R-134a	R-134a	R-134a	SF6 R-134a R-245fa
ASHRAE class	A2L	A2L	A2L	A2L	A2L	N/A
Critical temp.	82.4 °C	85.6 °C	94.7 °C	109.4 °C	150.1 °C	168.7 °C
Critical pressure	3.88 MPa	4.66 MPa	3.38 MPa	3.67 MPa	3.53 MPa	1,87 MPa

Five binary blends listed in Table 2. were selected for analysis, based on their thermodynamic properties and performance in ejector cycle working in set conditions. They were compared with R-454c, R-455a and pure R-1234ze(E). Properties of fluids were obtained in REFPROP 9.1.

Table 2. Analysed blends

Blend	Novec 649 /R-1234ze(E)	Novec 649 /R-1234ze(Z)	Novec 649 /R-1234ze(Z)	Novec 649 /R-1234yf
Composition	0.1/0.9	0.5/0.5	0.1/0.9	0.9/0.1
Critical temp.	115.3	159.4	152	161.2
Critical pressure	3.42	2.41	3.22	1.99

3. MATHEMATICAL MODEL OF THE CYCLE

The most important parameters of the proposed cycle, i.e. evaporation, condensation and motive steam temperature of the ejector are determined by application and temperature of the heat source. In this case, motive steam is generated by water from district heating system, condenser is air-cooled, and evaporator outlet temperature is set to 0°C so the system could be used for low-temperature air conditioning. As this is a theoretical study and geometry of the ejector were not taken into account, some simplifying assumptions were made, although their influence on the results is negligible. Pressure-enthalpy diagram of the cycle is presented in Figure 1. Assumed parameters are listed below:

- district heating water temperature: 65 °C,
- steam generator pinch point temperature: 5 °C,
- motive steam temperature: 60 °C,
- condenser outlet temperature: 30 °C,
- subcooling: 0 K,
- condenser inlet temperature: 35 °C,
- evaporator outlet temperature: 0 °C,
- superheating: 0 K,

- steam generator thermal power: 100 kW,
- isentropic expansion and compression in the ejector,
- ejector efficiency: 0.7.

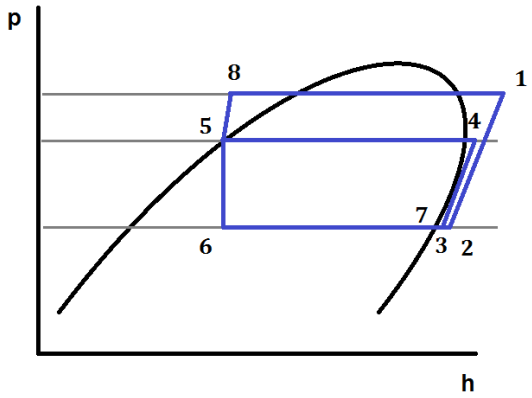

Figure 1: Diagram of the analysed cycle

State parameters in each point of the cycle were determined by using assumed values listed above and fluid properties obtained in REFPROP 9.1. Motive flow inlet temperature t1 was held constant at 60°C and saturated vapour temperature in the steam generator varied from 50°C to 59°C, meaning that superheating value was between 1°C and 9°C. A fragment of calculations are shown below.

$$t_1 = t_{wi} - t_{pp} = 60°C \quad \text{Eq. (1)}$$

$$p_1 = f(t_{gs}, x = 1) \quad \text{Eq. (2)}$$

$$s_1 = f(t_1, p_1) \quad \text{Eq. (3)}$$

$$h_1 = f(t_1, p_1) \quad \text{Eq. (4)}$$

$$s_1 = s_2 = s_4 \quad \text{Eq. (5)}$$

$$t_5 = 30°C \quad \text{Eq. (6)}$$

$$p_5 = f(t_5, x = 0) \quad \text{Eq. (7)}$$

$$h_8 = h_5 \quad \text{Eq. (8)}$$

Entrainment ratio formula is shown in Eq. (9).

$$U = k\left(\sqrt{\frac{h_1 - h_2}{h_4 - h_2}} - 1\right) \quad \text{Eq. (9)}$$

Compression ratio is defined by Eq. (10). It was assumed that in case of zeotropic mixtures pressure in every heat exchanger (steam generator, condenser, evaporator) is the arithmetic mean of pressures at the inlet and the outlet of the exchanger, calculated by using fluid properties and parameters of state calculated earlier, as shown in Eq. (1) – (8)

$$\prod = \frac{p_c - p_e}{p_g - p_e} \quad \text{Eq. (10)}$$

Coefficient of performance (Eq. (11)) was calculated by using specific evaporator and steam generator output. Power consumption of the liquid pump was not considered as negligible.

$$COP = U\frac{q_e}{q_g} \quad \text{Eq. (11)}$$

4. RESULTS AND DISCUSSION

Entrainment ratio, coefficient of performance, pressure ratio, cooling capacity and drop in motive water temperature in the steam generator were determined. The type of the working fluid and saturated vapour temperature in the steam generator (steam superheating value) are the variables. Condensation and evaporation temperatures are fairly strictly determined by the application of the proposed ejector cycle and were not changed.

Entrainment ratio of zeotropic mixtures rises with increase of vapour saturation temperature in the steam generator and decreases in case of pure R-1234ze(E). It is lower for fluids with temperature glide than for azeotropes. Only one zeotropic blend (Novec 649/R-1234ze(Z), 0.5/0.5) achieves higher entrainment than pure substance at low superheating values. Zeotropic mixtures have a much more inclined isentropes in superheated vapour area (Figure 1., points 1, 2, 3, 4) than azeotropic R-1234ze(E). This is the cause of increase of U for mixtures and decrease for pure fluid with increase in saturated vapour temperature in the steam generator. Because of this property enthalpy at the beginning and the end of vapour compression (Figure 1., point 2 and 4) is changed more with altering of vapour saturation temperature in the generator in case of pure fluid, hence the trends visible in the Figure 1. COP and cooling capacity are also influenced by this property, as they are calculated by using entrainment ratio.

Compression ratio highly depends on fluid properties. It varies from about 0.3, typical for standard single phase ejectors to up to 0.5. Trends are inverse to ones for entrainment ratio.

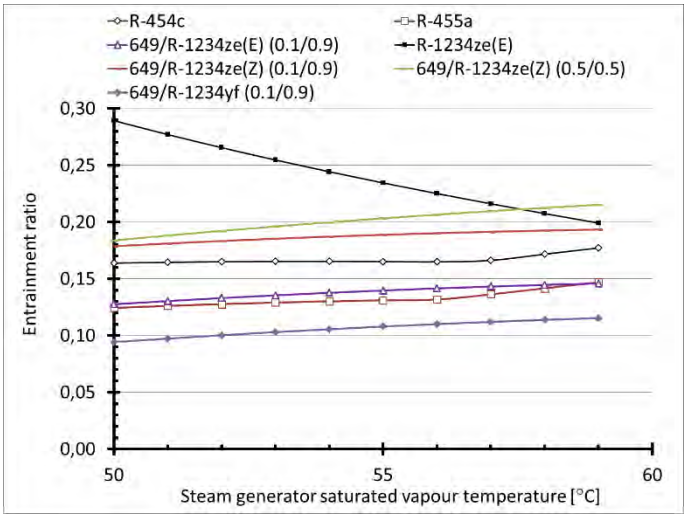

Figure 2: Entrainment ratio

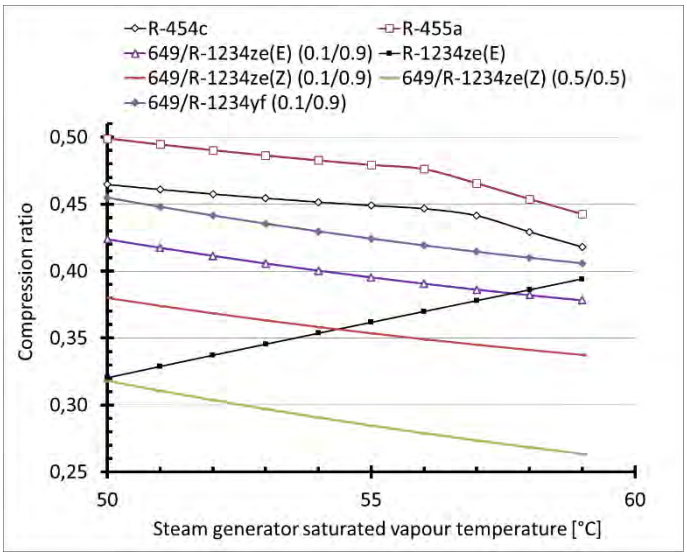

Figure 3: Compression ratio

Trends for COP (Figure 3) are the same as for entrainment ratio. For zeotropic mixtures values are fairly low, ranging from 0.05 to 0.15, and are lower than for pure fluids. COP doesn't change much with increase of vapour saturation temperature in the steam generator. At low superheating values he best mixtures have COP almost as high as pure R-1234 ze(E). Refrigeration capacity (Figure 5) can be easily calculated out of heat source capacity (100 kW) and COP. In case of zeotropic fluids it rises with increase in vapour saturation temperature in the generator.

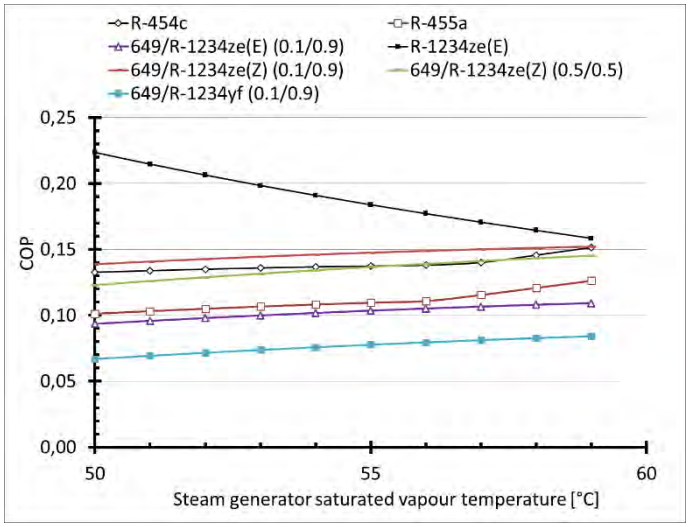

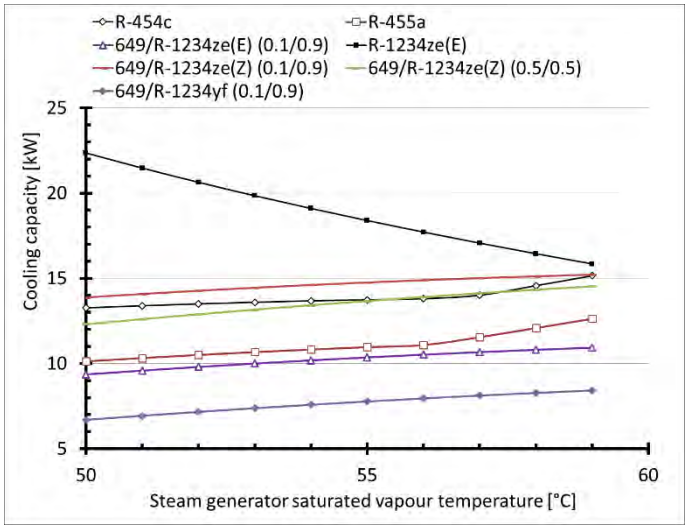

Figure 4: Coefficient of performance

Figure 5: Cooling capacity

Drop in motive water temperature is determined by temperature glide of refrigerant and its enthalpy of vaporization at steam generation pressure. Most heat is transferred to the working fluid during vaporisation, so unless the refrigerant is zeotropic, has very low enthalpy of vaporisation or the cycle is subcritical, motive fluid cannot be cooled down significantly and it is not used efficiently. In case of district heating, water returning to the system has to be cooled down by 20 – 30°C, hence the need of using zeotropic fluids.

Blend of Novec 649 and R-1234yf (0.1/0.9) provides the highest drop in motive water temperature due to high temperature glide. This mixture also yields very low COP (0.067 – 0.084) and high compression ratio (0.41 – 0.46). The best balance of efficiency and motive water temperature drop was achieved by a blend of Novec 649 and R-1234ze(Z) (0.1/0.9). At vapour saturation temperature in the steam generator of 50°C motive water is cooled down by 21.07°C and COP is 0.14.

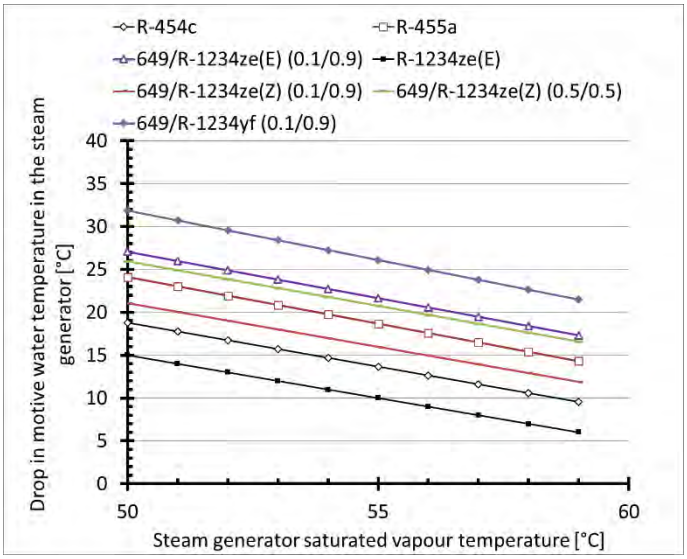

Figure 6: Decrease of motive water temperature in the steam generator

5. CONCLUSIONS

Ejector refrigeration system with zeotropic fluids for low-temperature air conditioning was theoretically analysed. Following conclusions can be drawn:

1. Regulation of the European Parliament and the EU Council No. 517/2014 was the basis for the selection of working fluids for investigation.
2. The use of zeotropic blends decreases coefficient of performance of an ejector refrigeration cycle in comparison to pure fluids. The lower vapour saturation temperature in the steam generator (i.e. higher superheating of the steam), the higher the drop in COP.
3. Compression ratio varies significantly for different blends and can range from about 0.3 to 0.5.
4. Ejector refrigeration cycles with zeotropic mixtures can significantly reduce the temperature of the motive fluid, thus using the heat source more efficiently than cycles with pure working fluid.
5. Analysis shows that Novec 649 and R-1234ze(Z) (0.1/0.9) blend can achieve the cooling capacity of 14 kW with low temperature motive heat source capacity of 100 kW while reducing the temperature of motive water by approx. 21°C.

ACKNOWLEDGEMENTS

The research was financed under the program of the Minister of Science and Higher Education under the name "Regional Initiative of Excellence" in 2019 - 2022 project number 011/RID/2018/19 amount of financing 12,000,000 PLN supported by Bialystok University of Technology research Project No. MB/WM/6/2018.

NOMENCLATURE

COP	coefficient of performance (-)	*s*	entrophy (kJ/kg×K)
h	enthalpy (kJ/kg)	*V*	molar volume ($m^3 \times mol^{-1}$)
k	ejector efficiency factor	*t*	temperature (Celsius)
p	pressure (MPa)	*U*	rntrainment ratio (-)
q	specific heat (kJ/kg)	*П*	compression ratio (-)

Subscripts:

1-8	characteristic points of the ejector cycle	*gs*	steam generator, saturation
c	condenser	*pp*	pinch point
e	evaporator	*wi*	motive source water inlet
g	vapour generator		

REFERENCES

Gagan, J., Śmierciew, K., Łukaszuk, M., Butrymowicz, D., 2018. Investigations of thermal performance of ejection refrigeration system driven by low grade heat. Appl. Therm. Eng. 130, 1121-1138.

Kang, Z., Zhu, J., Lu, X., Li, T., Wu, X., 2015. Parametric optimization and performance analysis of zeotropic mixtures for an organic Rankine cycle driven by low-medium temperature geothermal fluids. Appl. Therm. Eng. 89, 323-331.

Hakkaki-Fard, A., Aidoun, Z., Ouzzane, M., 2014. Applying refrigerant mixtures with thermal glide in cold climate air-source heat pumps. Appl. Therm. Eng. 62, 714-722.

Yang, X., Zhao, L., 2015. Thermodynamic analysis of a combined power and ejector refrigeration cycle using zeotropic mixtures. The 7th International Conference on Applied Energy – ICAE2015. Energy Procedia 75, 1033 – 1036.

Yang, X., Zhao, L., Li, H., Yu, Z., 2015. Theoretical analysis of a combined power and ejector refrigeration cycle using zeotropic mixture. Appl. Energy 160, 912-919.

Regulation (EU) No 517/2014 of the European Parliament and of the Council on fluorinated greenhouse gases and repealing Regulation (EC) No 842/2006.

Paliwoda, A., 1971. Ejection cooling devices. WNT, Warsaw (in Polish).

Manuscript ID: 657
DOI: 10.18462/iir.icr.2019.0657

Thermodynamic analysis of performance of two-phase injector

Andrzej PAWLUCZUK[(a)], Dariusz BUTRYMOWICZ[(a)], Kamil ŚMIERCIEW[(a)]

[(a)] Organization Bialystok Technical University, Wiejska 45C, Bialystok, 15-351, Poland, d.butrymowicz@pb.edu.pl

ABSTRACT

Energy required to drive a mechanical pump in thermally driven systems in most of the cases is a few percent of the overall energy balance of the system and in most cases is of the order of magnitude 1%. The most important problem is a special difficulty to select of a commercially available liquid pump for the thermal driven cycle. Mechanical liquid pump liquid is the only element of the refrigeration system that consume electric power. It is desirable that the whole system would be fully thermal driven one, without consumption of electric power to drive. Two-phase vapour-liquid ejectors may be thought as required alternative. They are using vapour that is generated already in the system; operates as pre-heater of liquid phase supplied to the vapour generator that additionally improve the system efficiency; and have no moving parts. Paper deals with thermodynamic analysis of operation of the system with two-phase vapour-liquid injector as a liquid pump in refrigeration systems. New perspective fluids were selected and tested as potential working fluids in the discussed system. Results of thermodynamic analysis were presented and discussed in the paper.

Keywords: Injector, compression efficiency, ORC, ejection refrigeration system, refrigerants, two-phase ejector

1. INTRODUCTION

Two-phase injector can be applied as a passive device operating without electricity because to compress and preheat a cold liquid a thermal energy of motive vapour is used. Such devices were used widely in the past for feeding water into boilers. Now, they are still operating in power station and this may be thought as the majority of their applications. Recently, the thermally driven devices become very popular in various systems of thermal power engineering including ORC systems, refrigeration and air conditioning systems (Liu and Groll 2013). This also applies to various possible applications of the two-phase injectors as a liquid pumping device.

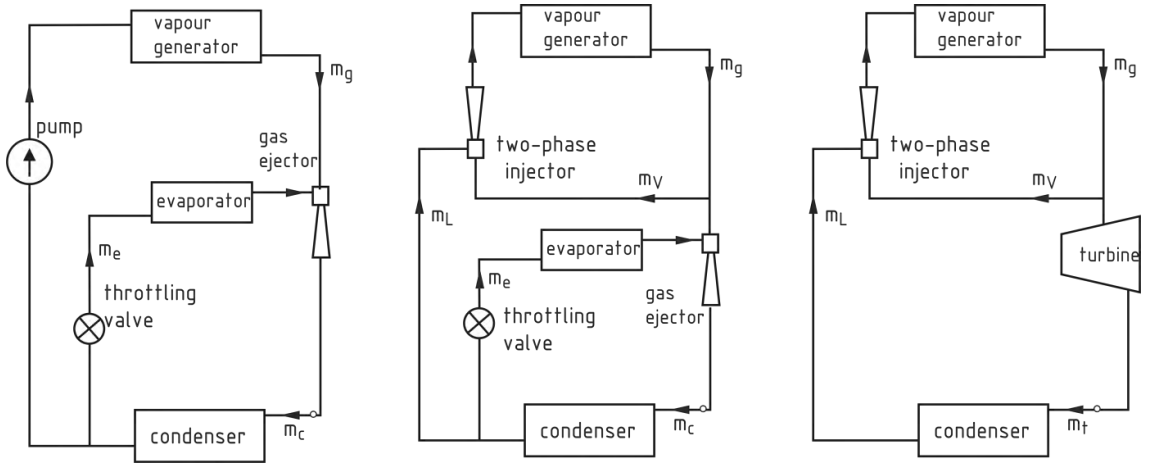

Figure 1. Heat driven systems: a) basic refrigeration ejection system with a mechanical pump; b) modified ejection refrigeration system fitted with the two-phase injector, c) ORC system fitted with two-phase injector instead of a mechanical pump

Two-phase vapour-liquid injector can be applied in ejection refrigeration system with vapour ejector operating as a compressor, see Fig. 1a,b. The other possible application is ORC system, see Fig. 1c. In both showed configurations the vapour-liquid injector operates as a liquid pump. Substitution

of the mechanical pump with a vapour-liquid injector may be thought as very attractive especially for small-scale systems. For example, in small ORC systems the liquid pumps usually have low efficiency (Meng et al., 2017) and consumes a large amount of electricity for various working fluids that deteriorate the overall efficiency of the system. In addition, the mechanical liquid pumps suitable for applications for most of working fluids are available for systems of large scale which are not suitable for low scale applications. Also, in the case of change of temperature level or heat flux in heat source or heat sink the pump operates beyond its nominal design operation conditions which deteriorate their internal efficiency. Fluids used in ORC systems and refrigeration heat driven systems generate cavitation problems due to operation under near saturation conditions. Increasing the cavitation margin has usually negative impact on thermal efficiency of the discussed systems. Also, the mechanical liquid pumps applied in the discussed systems should be hermetic devices suitable for operation with chemically aggressive working fluids. The above considered problems may be not applied to the two-phase injectors as a liquid pumping device.

Two-phase injector applied as a liquid pumping device may be thought as fully heat driven system. The temperatures and pressures in the system fitted with the two-phase injector are at the same level as for the basic system configuration with a mechanical pump. Because the vapour generator – two-phase injector loop is the additional sub-cycle then the application of the injector influences the overall system thermal efficiency. In addition, the efficiency of the compression process produced by the injector is limited since the condensation shock wave phenomenon that occur in the injector produces high irreversibility rate. Therefore, the application of the injector in heat driven systems requires careful analysis of the availability of compression of liquid phase up to required pressure level as well as availability to achieve compression efficiency suitable for the efficient operation of the system for selected working fluid.

The applications of two-phase injectors in refrigeration systems are very rare up to date. Only few reports that demonstrate the possibility of such application can be found in literature (Abdulateef et al., 2009) where performance of a vapour-liquid injector based on simple mathematical models were discussed. The possible application of such device in absorption systems with water as refrigerant was studied in Kumar and Kumar (2014). The performance of the vapour – liquid injector and the refrigeration cycle were studied using numerical modelling. Influence of various operation conditions, mostly motive temperature and condensation temperature for various refrigerants, e.g. R717, R718, R134a on performance of the vapour – liquid injector was studied (Abdulateef et al., 2009) and (Kumar and Kumar 2014). The results show that refrigerants properties as well as operation conditions are crucial for the performance of the system with the injector applied. The moderate deterioration of the cycle efficiency due to application of the two-phase injector as a liquid pump device was reported in these papers. In general, the entire system operation was studied without special attention on the injector design. The investigations of steam-water injectors are more popular among the researchers because such injector can be applied as a passive cooling system for the nuclear power plants (Miwa et al., 2016), (Takeya et al., 2015), Water-steam injector was also experimentally investigated by Miwa et al. (2016). In the previous authors papers the theoretical analysis of possible application of the two-phase injector as a liquid compression device for the case of isobutane along with the experimental tests focused on heat transfer investigations were shown (Śmierciew et al., 2015 and 2017).

Concerning the possible improvement of the ORC system efficiency, few approaches in pump elimination must be pointed out (Li et al., 2013), (Jiang et al., 2017). Chen et al. (2018) presented the theoretical model and showed results of operation of ORC cycle with liquid-vapour injector for three potential fluids: R123, R1233zd(E) and R1336mzz(Z). Authors have analysed several important parameters, namely: the entrainment ratio, the ejector area ratio, the condensation temperature, and the liquid subcooling at the condenser outlet. These authors found that the ORC systems with two-phase injector require much less pump work than basic ORC systems and regenerative ORC systems and offer the same expander output power as basic ORC and higher than that of regenerative ORC system. The temperature source assumed for calculation was higher than 95 °C. Calculations were based on the lumped parameter model developed based on using mass, momentum and energy balance equations. The results show that condensation temperature has severely influence on all tested parameters and the liquid subcooling has great impact on the injector pressure lift. However, the injector application produces a moderate influence on the system efficiency.

In this paper the thermodynamic analysis of the two-phase injector operation for low or moderate motive heat source temperature is presented. The results were obtained using model based on the dimensionless mass, momentum, and energy conservations equations that enables clear

analysis of the achievable operation parameters for the injector with consideration of the dimension quantities as well as thermal capacity of the discussed systems. Analysis of operation of the injector were performed for refrigerants already used in refrigeration and ORC technologies and new potential low GWP substances. Therefore, the following working fluids were selected for the analysis: R1234ze (E), R1234yf, R600a, R290, R717, R152a, R513A, R454A and R134a.

2. THEORETICAL BACKGROUND

Operation of the two-phase vapour-liquid injector depends on the working fluid as well as the geometry of its elements: motive nozzle, liquid nozzle (suction chamber), mixing chamber, and diffuser. This means that the geometry of the injector should be adapted for the specified operation conditions and selected working fluid. Therefore, the direct comparison of the operation of the injector as a liquid pumping device in thermal engineering for variety of operation parameters and working fluids may be thought as impossible. This is the motivation to provide the rigorously thermodynamic approach.

There are two general criteria of the operation of the two-phase injector that should be considered in the context of the working fluid selection, namely:

- the ability to produce the discharge pressure exceeding the motive vapour pressure;
- the achievable compression efficiency.

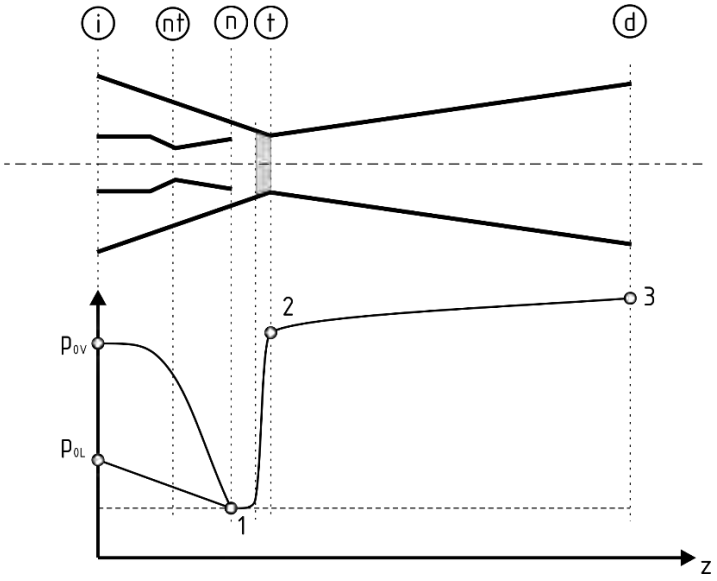

Figure 2. Vapour - liquid injector:

Both criteria will be studied for the two-phase injector on the basis of the assumed inlet operation conditions for the variety of the analysed working fluids without any consideration of the assumed injector dimensions nor flow rates.

The following assumptions were made:

- vapour phase is treated as perfect gas;
- liquid phase is treated as incompressible fluid of constant physical properties;
- the motive vapour nozzle operates under supersonic conditions;
- the velocities at the injector inlets and outlet are omitted so that only static thermodynamic parameters are taken into consideration;
- the injector along with the motive nozzle is treated as adiabatic device.

The injector is fed with the superheated vapour phase and the subcooled liquid phase. The vapour expands adiabatically in the motive nozzle up to the critical pressure in the nozzle throat that is denoted as '*nt*' and further adiabatically expands to the supersonic conditions at the outlet cross section 1. It is assumed that the nozzle outlet pressure is equal to the static pressure in the mixing chamber inlet denoted as p_1. The liquid phase expands in the suction chamber of the injector from inlet pressure p_{L1} up to the inlet pressure to the mixing chamber denoted as p_1. Inside the mixing chamber the momentum transfer process occurs between the two-phases that is conjugated with direct contact condensation heat transfer (Śmierciew et al., 2015 and 2017). During mixing process

of the two phases the momentum and heat transfer occur almost under constant pressure conditions due to convergent shape of the mixing chamber. Along with the phase change and phases mixing due to momentum transfer the two-phase flow pattern change from annular flow up to almost homogeneous bubbly flow. The phenomenon of two-phase condensation shock wave is observed in the injector. Contrary to the gas dynamic shock wave, the condensation shock wave thickness may not be treated as negligible and may be roughly assessed as comparable with the channel hydraulic diameter. The location of the condensation shock wave depends on the discharge pressure so that under conditions of low back-pressure this wave is located in the diffuser and with increase of the back-pressure at the injector outlet its location moves towards the throat of the mixing chamber and outlet part of the mixing chamber. Under back-pressure at the injector outlet the exceeds the certain maximum level the condensation shock wave rapidly moves towards the motive vapour nozzle that deteriorates the operation of the injector. This phenomenon is called as the stalling process. Therefore, the injector may operate under discharge pressure that is lower than the maximum pressure to avoid the stalling process. However, the prediction of the maximum discharge pressure for the two-phase vapour-liquid injector may be still thought as an open issue. Consequently, it is assumed in the developed model that the condensation shock wave is located at the throat of the mixing chamber so that static pressure after the shock wave is denoted as p_2. Inside the condensation shock wave the vapour phase condenses entirely so that only liquid one phase flow appears in the diffuser. Further slight static pressure increase occurs inside the diffuser up to pressure p_3 due to decrease of the liquid velocity.
A comparative analysis of the work evaluation of a two-phase injector for various working factors was made on the basis of model descriptions published in (Pawluczuk et al., 2017).

$$\Pi = \frac{p_3 - p_{L0}}{p_{V0} - p_{L0}} \qquad \text{Eq. (1)}$$

where: p_{L0} is the pressure of liquid sucked in by the injector, approximately equal to the condensing pressure; p_3 is the pressure at the outlet from the diffuser, and p_{V0} is the pressure of steam supplied from the steam generator. The influence of suction defined as the ratio of the mass stream of the sucked liquid to the mass stream of the driving steam is the main influence on the injector's work:

$$U = \frac{\dot{m}_L}{\dot{m}_v} \qquad \text{Eq. (2)}$$

3. ANALYSIS RESULTS FOR THE TWO-PHASE INJECTOR

The initial parameters of the system operation should be given during the calculations. Constant parameters taken for analysis were as follows:

- condensation temperature was assumed as T_c = 40 °C;
- two levels of saturation temperature in the vapour generator were analysed, i.e.: T_{V0s} = 70°C,
- superheating of vapour at the outlet of the vapour generator ΔT_V = 5 K.

Liquid refrigerant at the condenser outlet is equal to $T_{L0} = T_c - \Delta T_{L0}$, where ΔT_{L0} was assumed as varying quantity in the range of 5 – 20 K. Therefore, the temperature of the liquid phase at the injector liquid nozzle inlet is T_{L0}. Geometric modulus Mo and Ω are treated as free parameters. In presented analysis Mo = 0.9 and Ω =0.7 were assumed to analyse the effect produced by the thermodynamic parameters on the injector operation. The velocity coefficients for the vapour nozzle φ_{nV}, liquid nozzle φ_{nL}, the mixing chamber φ_m, and the diffuser φ_d were assumed as 1.0 in other to analyse the maximum achievable levels of the performance parameters describing the injector operation.
Two levels of the motive temperature were taken for the present analysis because of different of practical application of proposed injector. Lower level T_{V0s} = 70 °C can be proposed for low temperature heat driven ejection refrigeration system, while higher level T_{V0s} = 90 °C can be applied both for ORC systems and ejection refrigeration systems. Vapour generation temperatures higher than 100 °C are not considered in this paper due to limitation of the proposed model formulation based on the ideal gas approach that may be thought as less accurate for conditions close to the critical pressure of the some of the discussed working fluids.
At first, results for lower motive temperature T_{V0s} = 70 °C are presented. Influence of liquid subcooling ΔT_{L1} on mass entrainment ratio U is presented in Fig. 3. For all of the tested fluids the mass entrainment ratio decreases with increasing of the liquid subcooling. The reason for this

effect is that in order to condensate vapour inside the injector the required amount of entrained liquid is smaller when its temperature is lower, i.e. for higher level of liquid subcooling. Maximum mass entrainment ratios are required by ammonia (R717) and it change from $U_{maxR717}$ = 7.5 to $U_{minR717}$ = 5. Minimum mass entrainment ratios are required by R454A and it change from $U_{maxR454A}$ = 2.7 to $U_{minR454A}$ = 1.9. From application point of view lower levels of mass entrainment ratio may be thought as more favourable because of lower flow rates, and smaller diameters of tubes and charge with working fluid.

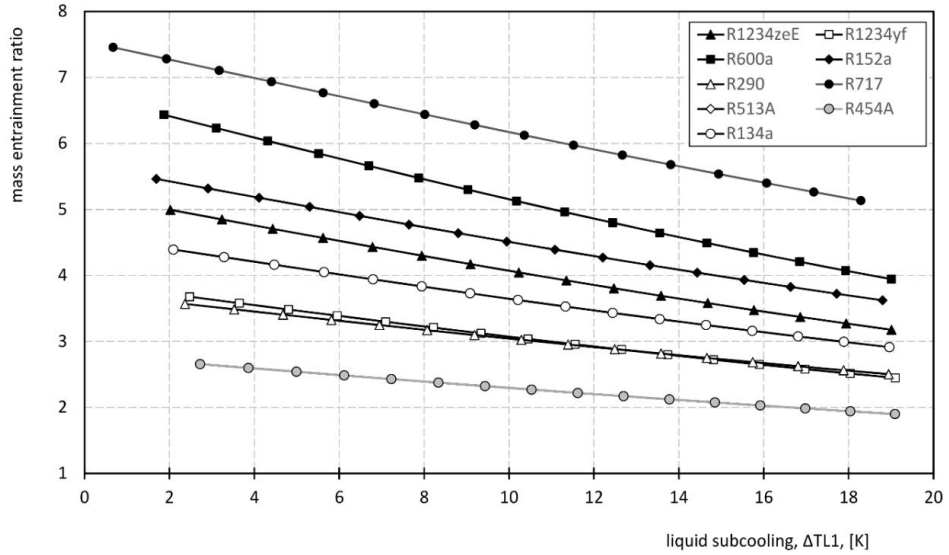

Figure. 3. Mass entrainment ratio vs. liquid subcooling ΔT_{L1}

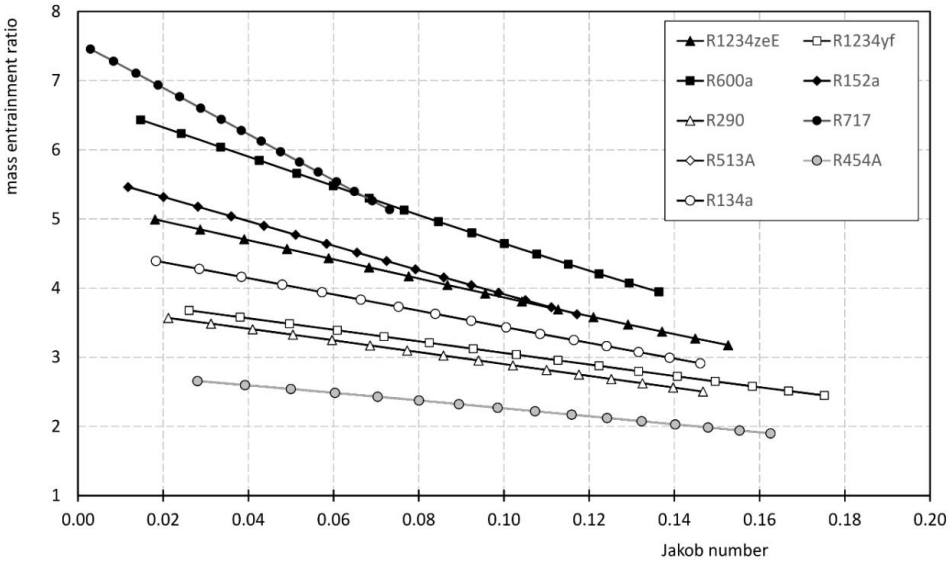

Figure 4. Mass entrainment ratio vs. Jakob number

In refrigeration systems and ORC systems the liquid subcooling depends on many variables (i.e. type of condenser, heat transfer surface area, cooling water temperature or cooling water mass flow rate, properties of refrigerant, and others) therefore, it is obvious that obtaining the specified liquid subcooling requires different operation conditions for different working fluids. For this reason, liquid subcooling can be presented in more convenient dimensionless form, as Jakob number:

$$Ja = \frac{c_{pL}\Delta T_L}{h_{fg}} \qquad \text{Eq. (3)}$$

Relation between mass entrainment ratio and Jakob number is presented in Fig. 4. As it is seen increasing of Jakob number (i.e,. dimensionless liquid subcooling) causes decrease of mass entrainment ratio. However, it may be observed significant effect of *Ja* number on achievable *U* for

natural working fluids (ammonia, isobutane) while for most of the synthetic fluids this effect may be thought as moderate.
From the thermodynamic point of view the theoretical maximum pressure of vapour which can be recovered in the injector is equal to the motive vapour pressure. This can be obtained when reversible, lossless processes are taken into consideration and outlet velocity is assumed to be zero. However, the aim of the injector operation is to produce the discharge pressure higher than the motive vapour pressure. This additional pressure above the motive pressure comes from the entrained liquid momentum. Therefore, contrary to the gas ejector, if the mass entrainment ratio of the injector increases, then the compression ratio also increases. This is shown in Fig. 5. Successful operation of the injector as a liquid pump in presented system is when compression ratio exceeds unity: $\Pi > 1$. In order to obtained compression ratio $\Pi > 1$ the liquid subcooling should be less than $\Delta T_{L1} < 10$ K for R600a and the subcooling $\Delta T_{L1} < 20$ K is required by R290, R717 and R454A. For the rest of the tested fluids the liquid subcooling should be in range 11-20 K. General conclusion that could be draw on the obtained results is: the lower level of liquid subcooling then the better performance of the injector.

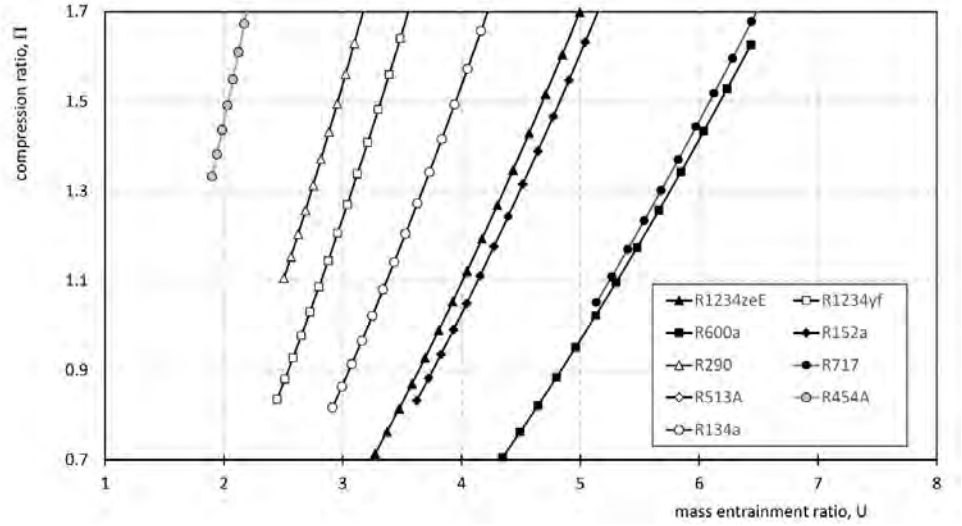

Figure 5. Relationship of compression ratio vs. mass entrainment ratio

It is required for the practical implementation of the injector, that the following criterion should be fulfilled:

$$\Pi \geq 1 \qquad \text{Eq. (4)}$$

The compression efficiency η_c may be defined as a ratio of power consumption for the isochoric compression of the liquid phase (since injector operates as a liquid pump) to the motive power consumption defined as thermal capacity of the vapour generator (since the injector is a heat driven device):

$$\eta_c = U \frac{p_3 - p_{L0}}{\rho_L \left(h_{V0} - h_{L0} \right)} \qquad \text{Eq. (5)}$$

Negative impact of increasing of liquid subcooling on the injector operation can be observed when relation efficiency vs. liquid subcooling $\eta = f(\Delta T_L)$ is plot. Figure 6 presents this relationship. For all of the tested fluids the injector efficiency does not exceed 10%. Note that this are the maximum levels since the isentropic processes are considered. Refrigerants R454A and R290 offers the greatest efficiencies and are able to effective operation at wider range of the liquid subcooling. The lowest values are reported for the case of isobutane R600a, and only slightly better is refrigerant R1234ze(E). For liquid subcooling $\Delta T_L > 8$ K the injector efficiency drops below 2%. This is an interesting phenomenon because R600a has great potential for application in ejection refrigeration systems [18,19] and it offers very promising performance operation in reference to other fluids, e.g. R134a, propane. Here, the trend is opposite. However, selection of the fluid for the systems operating with the injector is not limited to the injector efficiency, rather the several

parameters like *Π*, *U*, *S*, thermodynamic and thermokinetic properties as well as environmental safety, should be also taken into consideration.

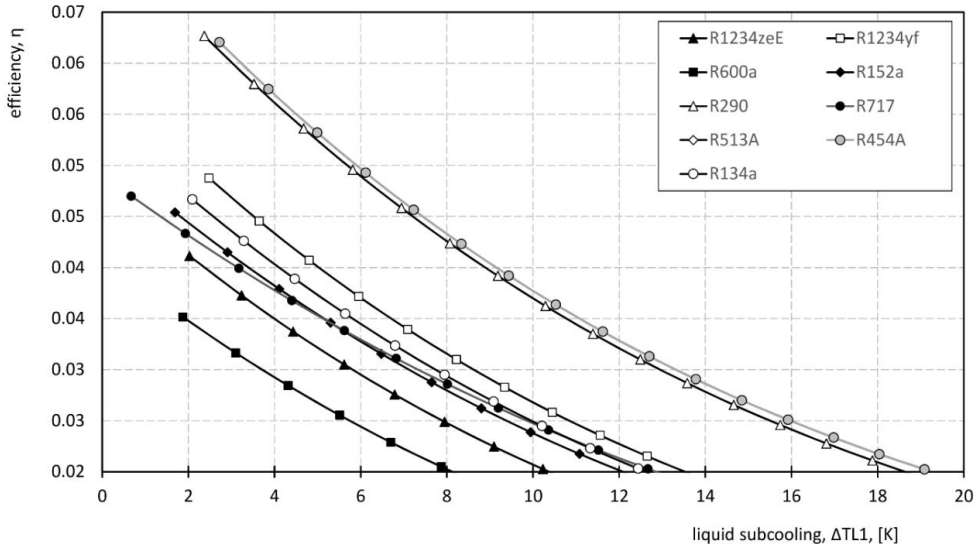

Figure 6. Injector efficiency vs. liquid subcooling

4. CONCLUSIONS

The paper presents the results of theoretical analysis of the operation of a two-phase vapour-liquid injector. Nine refrigerants were analysed, however proposed procedure is suitable for other fluids that were not taken into consideration in this paper.

Presented results demonstrated the usefulness of the proposed thermodynamic approach. This approach allows for selection of the working fluid for systems operating with the two-phase injector. Proposed approach is based on the thermodynamic relations only, uses dimensionless quantities and includes all physical phenomena related with operation of the injector. Proposed approach in authors opinion can be thought as valuable tool for application of the two-phase injectors in thermal engineering, both in power generation cycles and refrigeration cycles.

Results show that for assumed operating conditions may be thought as not suitable for all of the analysed fluids for the effective operation of the injector as a liquid pumping device. Depending on the operation conditions, minimum values of compression ratio were reported for natural working fluids: ammonia (R717) and isobutane (R600a). Propane (R290) and R454A offers the greatest efficiency.

However, for the working fluid selection not only the compression efficiency and compression ratio have to be taken into consideration. The other operation parameters such as mass flow rates and liquid subcooling should also be analysed to obtain the effective injector operation on the system. The proposed approach allows for comprehensive analysis of the influence of the crucial thermodynamic parameters on the injector performance under low and moderate motive heat source temperature conditions.

ACKNOWLEDGEMENTS

The research was carried out as part of research work no. S/WM/1/2018 and project MB/WM/11/2018 at the Bialystok University of Technology and financed from a subsidy provided by the Minister of Science and Higher Education. They are partially are supported by the National Science Centre, Contract No. 2017/01/X/ST8/01221

NOMENCLATURE

A	surface area (m^2)	p	pressure (MPa)
D	diameter (m)	S	liquid to vapour velocity slip ratio at the inlet to the mixing chamber
h	Specific enthalpy ($kJ \times kg^{-1}$)	T	temperature (K)
Ja	Jakob number eq. (3)	U	mass entrainment ratio
M	geometry modulus of the mixing chamber $M = A_t \times A_{nV}^{-1}$	z	coordinate of flow direction
$\dot{m}$	mass flow rate ($kg \times s^{-1}$)		

Greek symbols

δ	liquid nozzle throat thickness (m)	Ω	liquid nozzle throat thickness to outlet vapour nozzle diameter ratio, $\Omega = \delta \times D_{nV}^{-1}$
η	efficiency	ρ	density ($kg \times m^{-3}$)
Π	injector compression ratio, eq. (1)	φ	velocity coefficient

subscripts

c	compression	n	nozzle
d	diffuser	s	isentropic process
L	liquid	t	throat of the mixing chamber
m	mixing chamber	V	vapour
$0 - 3$	cross-sections of the injector		

REFERENCES

Abdulateef J.M., Sopian K., Alghoul M.A., Sulaiman M.Y., 2009, Review on solar-driven ejector refrigeration technologies, Renewable and Sustainable Energy Reviews, Vol. 13, pp. 1338–1349

Kumar A., Kumar R., 2014, Thermodynamic analysis of a novel compact power generation and waste heat operated absorption, ejector-jet pump refrigeration cycle, Journal of Mechanical Science and Technology 28, No. 9, pp. 3895-3902

Li J, Pei G, Li Y, Ji J. Analysis of a novel gravity driven organic Rankine cycle for small-scale cogeneration applications. Appl Energy 2013;108(8):34–44.

Liu F., Groll E.A., 2013, Study of ejector efficiencies in refrigeration cycles, Applied Thermal Engineering, 52, pp. 360-370.

Meng F, Zhang H, Yang F, Hou X, Lei B, Zhang L, et al. Study of efficiency of a multistage centrifugal pump used in engine waste heat recovery application. Appl Therm Eng 2017; 110:779–86.

Miwa S., Endo H., Moribe T., Sakashita H., Mori M., Hibiki T., 2016. Investigation of the thermal-hydraulic characteristics of supersonic steam injector, Applied Thermal Engineering 109, pp. 261-271.

Pawluczuk A., Butrymowicz D., Śmierciew K., Gagan J., 2017. Thermodynamic analysis of performance of liquid injector for ejection refrigeration system, IIR Conference on Compressors and Coolants, Slovak Republik, Paper No. 0249; DOI: 10.18462/iir.compr.2017.

Śmierciew, K., Butrymowicz, D., Kwidziński, R., Przybyliński, T., 2015. Analysis of application of two-phase injector in ejector refrigeration systems for isobutane, Applied Thermal Engineering 78, pp. 630–639

Śmierciew, K., Butrymowicz, D., Przybyliński, T., Pawluczuk A., 2017 Investigations of heat and momentum transfer in two-phase injector operating with isobutane, Applied Thermal Engineering 127 (2017) 1495–1505.

Takeya, Y., Miwa, S., Hibiki, T., Mori, M., 2015. Application of steam injector to improved safety of light water reactors, Progress in Nuclear Energy 78, pp. 80-100.

Manuscript ID: 665
DOI: 10.18462/iir.icr.2019.0665

Analysis of heat recovery system for air-conditioning application in motor yachts

Dariusz BUTRYMOWICZ[(b)], Mateusz KĘDZIERSKI[(a)], Kamil ŚMIERCIEW[(b)], , Jerzy GAGAN[(b)]

[(a)] Marine Projects Ltd.
Gdańsk, 80-605, Poland, m.kedzierski@marpro.pl
[(b)] Bialystok University of Technology
Bialystok, 15-351, Poland, d.butrymowicz@pb.edu.pl

ABSTRACT

Combustion engine is a primary source for electric energy consumed in all electrical devices in ships and yachts. Conversion of fuel energy into mechanical and electrical energy is related to creation of a significant amount of heat, which is irretrievably removed. Ejection system can be effectively driven by low-grade heat source such as waste heat from the engine. The paper presents analytical analysis of thermal-flow operating parameters of waste heat node used for small yachts air-conditioning systems. The results show that such solution can produce 15 kW of cold consuming 70 kW of heat at temperature of 120 ºC. Cooling capacity of 15 kW should satisfy cooling demand of small- and mid-size yachts.
Keywords: Air-conditioning, Marine, Heat Recovery, Yacht, Ejection Refrigeration System, Energy Efficiency, Desiccant Wheel.

1. INTRODUCTION

Production of cold on ships is used primarily for the needs of air handling units. The demand for it is related with place of sailing of the ship and conditions of climatic zones which it stays. Usually, ships are designed for sailing around the world. Therefore, especially on hot climate the outside weather conditions i.e. the air temperature and relative humidity are high.
To minimize the electricity consumption, the refrigeration system powered by heat can be used. There are known refrigeration devices powered by heat waste. However, these solutions for cooling systems powered by non-electric energy is no available on the market for yachts. This is because absorption systems have more components and as the heat and mass transfer of absorption equipment is poor, large heat transfer areas are required. Ezgi (2014) presented design and thermodynamic analysis of a water-lithium bromide absorption heat pump as an HVAC system for a naval surface ship application. Despite that absorption system can be used in naval ships, they are not suitable for small yachts due to its dimensions and weight.
Production of cold, which consumes significant amounts of electricity, is especially crucial for small vessels due to:

- significant load on the energy system of the vessel through electrically controlled air conditioning systems;
- particular importance of air conditioning systems on small vessels (e.g. yachts) due to the required comfort conditions in different climate zones.

Another aspect that should be taken into consideration is the availability of waste heat, including mainly heat exhausted from the internal combustion engine driving the vessel. Currently, it does not apply to the vessels of low or medium capacity recovery systems of waste heat. One of the key problems of refrigeration technology, especially on vessels, is the fulfillment of strict legal requirements regarding working fluids: currently, typical working fluids are being applied, which will be withdrawn under the EU Directive 517/2014 on fluorinated greenhouse gases from use. The developed proposed solution meets the rigors imposed by legal regulations, which will also facilitate servicing such a system around the world. One of the key problems of technologies specific to small vessels is the requirement of high compactness of devices and reliability of the refrigeration system. The ejector refrigerant system requires the smallest dimensions from other

refrigeration systems powered by heat, and therefore it seems to be the best solution for use on small yachts.

2. APPLICATION OF THE EJECTOR SYSTEM AND THE DESICCANT WHEEL

Ejector refrigeration system was shown in Fig. 1. it is possible to distinguish the refrigeration circuit and the drive circuit in this system.

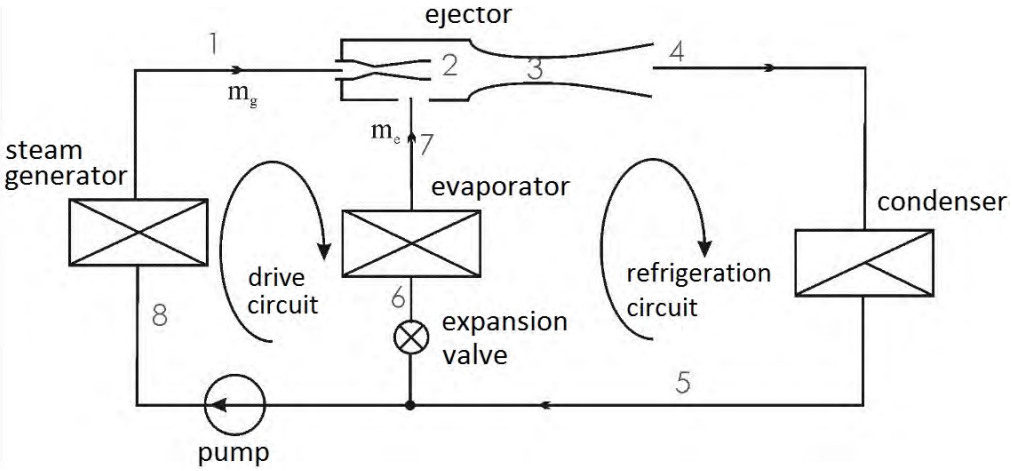

Figure 1 Schematic diagram of ejector refrigeration system

In an ideal system the motive vapour (state 1) expands isentropically in the motive nozzle to state 2. During this expansion vapour velocity increases as a result of the pressure drop. Usually, the motive vapour reaches the supersonic velocity at the outlet of the nozzle. Vapour of low pressure and high velocity (state 2) entrains vapour from the evaporator at state 7. Inside the ejector both streams are mixed. It is the result of the momentum transfer between both streams. The effect of this process is decrease of the motive vapour velocity and increase of velocity of the entrained vapour. The velocity decrease causes a simultaneous increase in pressure. Despite the velocity decrease, it can be assumed that after complete mixing (state 3) the velocity of the mixed streams is supercritical. The transition from supercritical to subcritical flow takes place in the mixing chamber. This results in a shock wave and a sharp rise in pressure. Depending on the design and operation conditions of the ejector- the shockwave can be created in the mixing chamber or in the diffuser. A further small increase of pressure occurs in the diffuser. The vapour mixture leaving the ejector (state 4) has pressure equal to the pressure in the condenser. After condensation (state 5) the flow is separated. Part of the liquid refrigerant is throttled in the expansion valve to the pressure p_e and then evaporates in the evaporator. The working fluid reaches the state 7 and is entrained again by the ejector. The rest part of liquid is pumped to the vapour generator. During pumping process, pressure of the working fluid rises from p_c (state 5) to p_g (state 8). The boiling in the vapour generator consumes the recovered waste heat and changes parameters of refrigerant from state 8 to state 1.

Authors of this paper have developed a solution for the ejector refrigerant system using a fully ecological working medium R-1234ze indicating a wide range of motive heat temperatures used for production of cold (Gagan et al., 2018a,b, Śmierciew et al., 2017). Authors demonstrated the significant influence of the evaporation temperature on the efficiency of the system. For operation conditions corresponded to high-temperature air-conditioning (16/19°C) in comparison with the standard chilled water parameters (6/12°C) the efficiency of the system was nearly doubled.

The conditions for the air conditioning systems on vessels are defined by:

- the ISO 7547: 2002: Ships and marine technology standard - Design conditions and basis of calculations
- ISO 31-4: 1992, Quantities and units - Part 4: Heat;
- ISO 3258: 1976, Air distribution and air diffusion.

The standards define design parameters for air processing for winter and summer, as well as the conditions of thermal comfort in all of the rooms on vessels. General guidelines for air parameters according to these standards are: outdoor air temperature +35 °C; relative humidity 70%; for indoor air: +27 °C on summer. The standards do not explicitly define conditions for relative humidity for the winter period. However, it is good practice to maintain a relative humidity in the room at the level of 40-60%. The amount of fresh air supplied to the room should be at least 40% of the entire supplied air.

Operation of A/C system on a vessel is associated with the need of much higher cooling capacity than is resulted exclusively from the sensible heat gains. Due to the very high relative humidity of the outdoor air - the cooling capacity needed to absorb latent heat gains is significant. This leads to high electric power consumption of the air-condition unit. However, taking into account the possible application of exhaust waste heat, it is possible to use the air conditioning system that ensures operation in the conditions required by the indicated standards with a significantly reduced electric power need to drive the refrigeration system. Usage of the air-conditioning system equipped with a desiccant wheel additionally enhances this opportunity.

Figure 2 shows the basic schematic of the desiccant wheel. It is a rotary heat and mass exchanger with a porous structure. The larger part of the wheel surface operates as an air dryer. The dried air is further processed in the A/C unit. The smaller share of the wheel operates as a regenerator of the porous coating. In the regeneration process, the wheel contacts with hot air which causes humidity absorption and wheel temperature increases. The wheel coating is drying during the regeneration process and then, during next rotation, it contacts with the intake air and absorbs its humidity. Due to the contact of the process air with the wheel, the air is simultaneously heated, so the dried air requires cooling to the required level in the cooling system. An important advantage of this wheel in application to marine vessels is the possibility of direct use of waste heat to dry humid air. In the standard A/C units air is dried by surface coolers far below the dew point. However, this process requires significant cooling capacity and resulting air temperature is far below required supply temperature and then must be heated. Application of the desiccant wheel technology allows for significant reduction of cooling capacity by utilisation of the engine exhaust waste heat. In addition, this process increases the effective use of fuel oil in vessels.

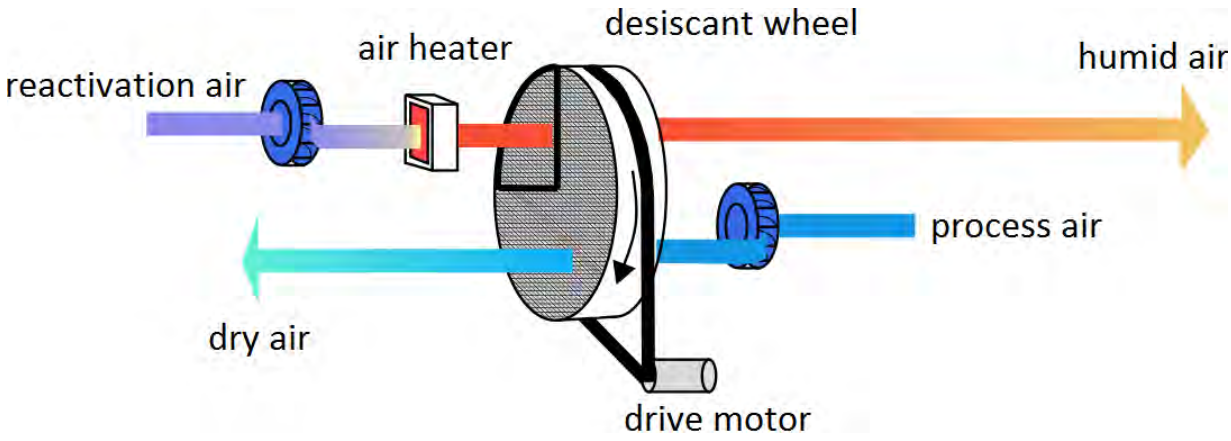

Figure 2 Schematic diagram of the operation of the desiccant wheel

Issues related with design and efficiency analysis of the desiccant wheel are the subject of numerous researches. Due to the fact that the heat transfer process takes place in conditions similar to the operation of rotary regenerative heat exchangers (Butrymowicz et al., 2016), it is not so clear how the channel geometry of the wheel influence on the heat and mass transfer efficiency (Camargo et al., 2005, Eicker et a., 2015, Kamar et al., 2016, O'Connor et al., 2016). Guojie et al. (2012) and Zheng et al. (2017) proposed system dedicated directly to the application in air conditioning systems on offshore units. A separate problem is the evaluation of the efficiency of the desiccant wheel operating in the air conditioning units (Bassuoni, 2014, Chung, 2017, Kara et al., 2017). Nevertheless, the proposed system is not yet a sufficiently widespread solution. There is a clear need to assess the possibilities of such a solution applied for A/C systems for vessels. The paper presents an analysis of the possibilities of reduction of cooling capacity by means of usage of the engine exhaust waste heat potential for the exemplary vessel case.

3. ANALYSIS OF AN EXEMPLARY CLASSIC AIR-CONDITION SYSTEM

The paper shows, the application of an air-conditioning system with a desiccant wheel used for the case of the exemplary vessel. For selected vessel, a detailed heat and humidity balance was performed for the summer period. The heating load covers:

- heat gains from people on the vessel: sensible heat 0.70 kW and latent heat 0.50 kW;
- heat gains from the vessel devices located in the wheelhouse 2.50 kW;
- heat gains from solar radiation and the technical equipment in the vessel 11.3 kW;
- latent heat gains associated with infiltration of humid air 7.20 kW.

The total heat gains are 22.2 kW, and the ratio Δi/Δx was calculated as 7234 kJ/kg. Required air flow is 4475 m^3/h, while the required fresh air is 1790 m^3/h.

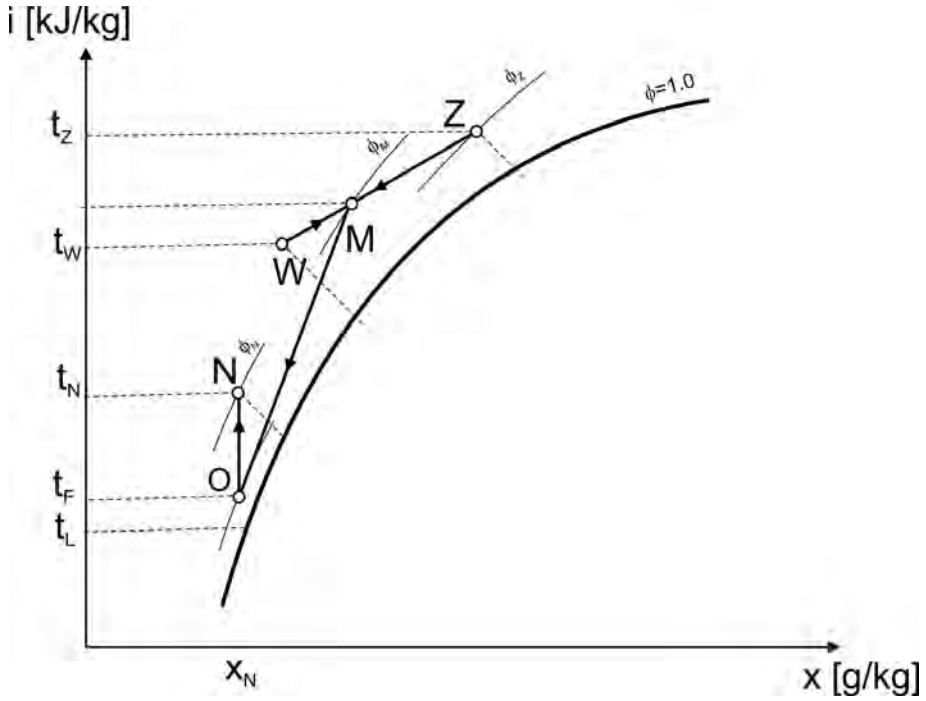

Figure 3 Schematic of the air processing in an air conditioning unit with the dehumidification of the air by a refrigeration device

At first, the classical approach with compression refrigeration device used to remove the moisture for air is considered. The processes of the air-treatment in standard approach are shown in Fig. 3. In standard air-conditioning unit the chilled water is produced by compression refrigeration system. The fresh air (Z) is mixed with the exhaust air removed from the room (W), assuming that the removed air has the same parameters as the internal air (W). The mixed air (M) goes to the evaporator that receives the total heat gain, so the "M" mixture must be cooled down to temperature (O) below the dew point so that the moisture can be condensed. The final moisture content at point O must be equal to the moisture content of the supply air $x_O = x_N$. Due to the fact that the air at the point (O) has a temperature lower than the supply air (N), a heater operating between the points O-N should be used. Usually it is an electric heater.

The calculation procedure of the analysed processes is based on the mass and energy balance formulated for each of the process which may be thought as conventional approach, see Ezgi and Girgin (2015), Zheng et al. (2015), Suono et al. (2011).

It is assumed that the system operates in standard conditions of chilled water, i.e. the supply temperature is 6 °C, while the return one is 12 °C. Schematic of air processing in the air conditioning unit with dehumidification of the air by a refrigeration device obtained from calculation software is shown in Fig. 4. In the analysed case the cooling load of the evaporator is 48.8 kW,

which is two times higher that total heat gains on the vessel, and the heat load of the air heater is 6.5 kW.

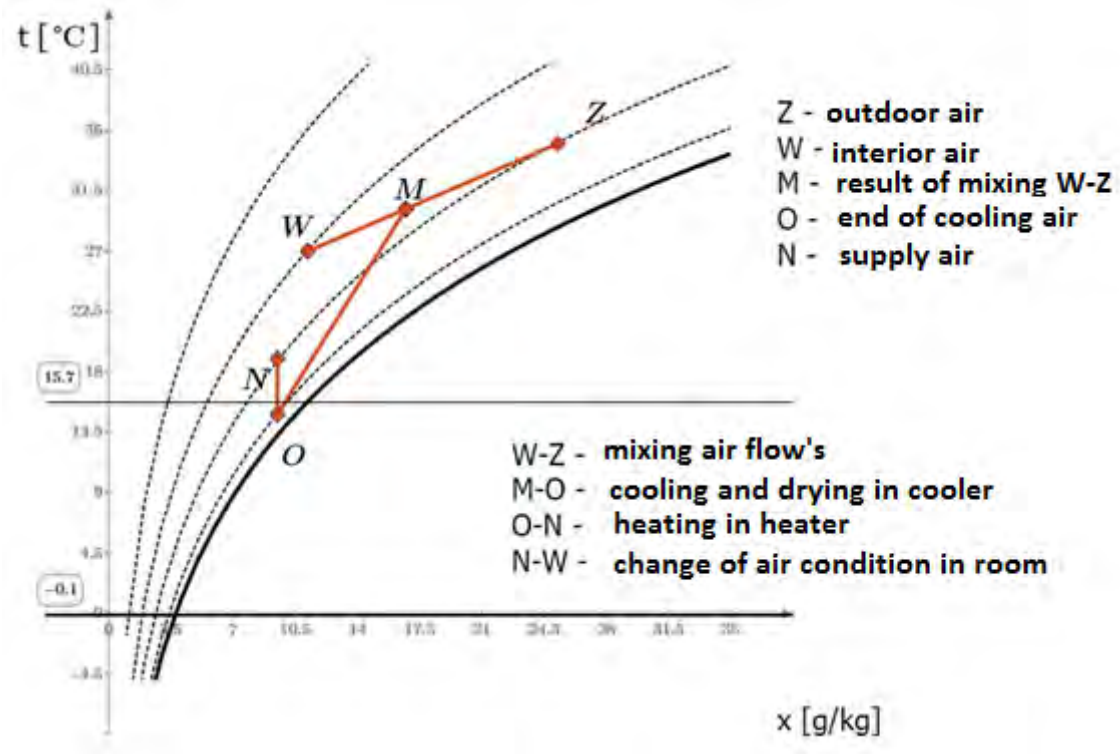

Figure 4: Schematic of the air processing in an air conditioning cycle with the dehumidification of the air by a refrigeration device obtained from calculation software

4. ANALYSIS OF CIRCUIT OF AIR CONDITIONING WITH A DESICCANT WHEEL

As it was indicated above, it is possible to use the ejector refrigeration system that is powered by the waste heat generated by the engine on the vessel. An alternative solution to the air-conditioning system that also uses the waste heat potential to dry the air is the desiccant wheel. The air conditioning system equipped with the desiccant wheel is schematically shown in Fig. 5. The expected temperature of the fluids at characteristic points are shown in the figure.

The air processes in the air-conditioning system using the desiccant wheel are shown in Fig. 6. This system is additionally equipped with intercooler allowing for pre-cooling of the air with sea water, which additionally reduces the demand for cooling power in the considered case.

In the proposed system, fresh air (Z) is mixed with the exhaust air removed from the room (W), assuming that the exhaust air has the same parameters as the internal air (W). The mixed air (M) is dried and heated in the desiccation wheel, obtaining the parameters of point (D). Pre-cooling takes place in the additional heat exchanger cooled by sea water (K). The evaporator in this case only receives the sensible heat gains cooling the air from point (K) to the point (N).

Schematic of the air processing in the air conditioning unit with application of the desiccant wheel obtained from calculation software is presented in Fig. 7. In the analysed case, the heat load of the evaporator is 23.6 kW which is almost the same as heat load of the vessel, heat load of the heater for the regeneration process is 29.1 kW, and the heat power of the pre-cooling is 17.8 kW. The ejector refrigeration system requires 49.2 kW motive heat.

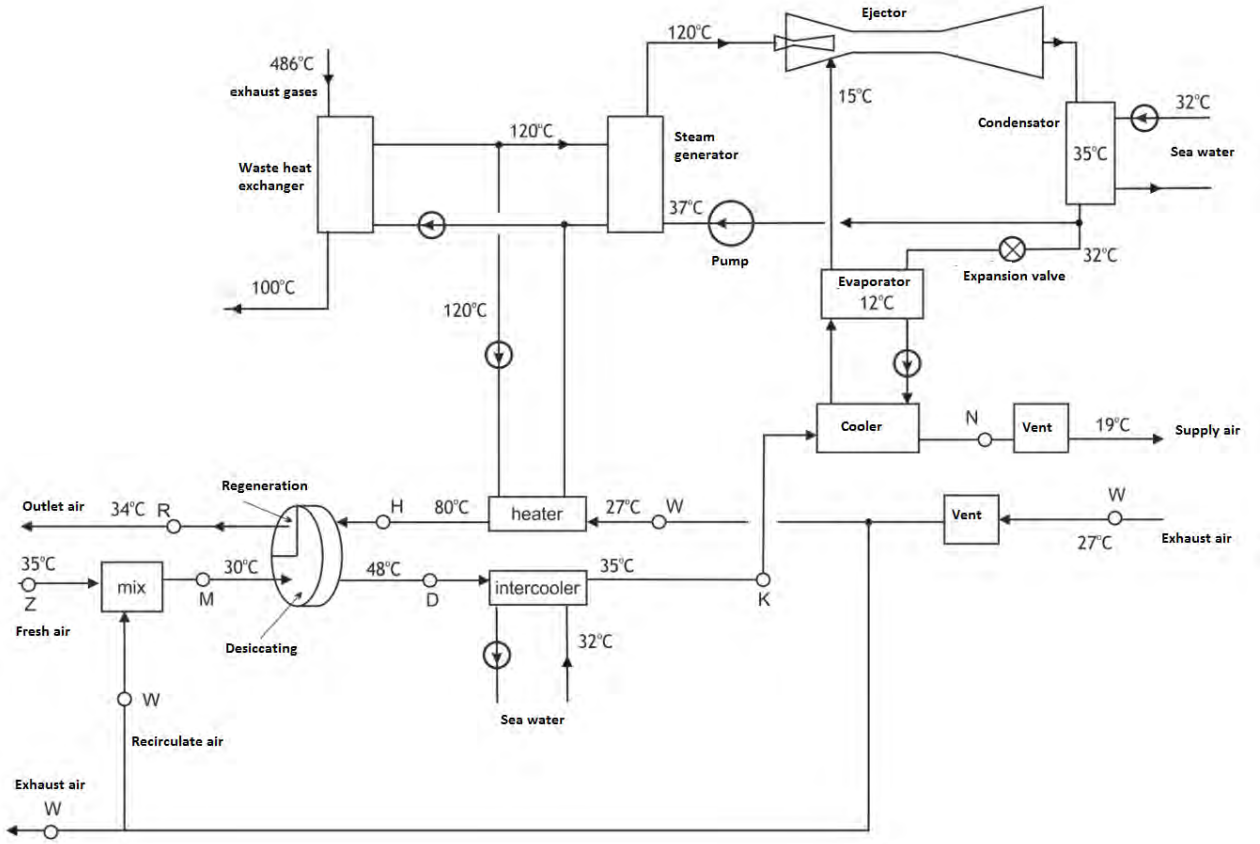

Figure 5 Schematic of high temperature air conditioning system using desiccant wheel and ejector refrigeration system powered by exhaust waste heat

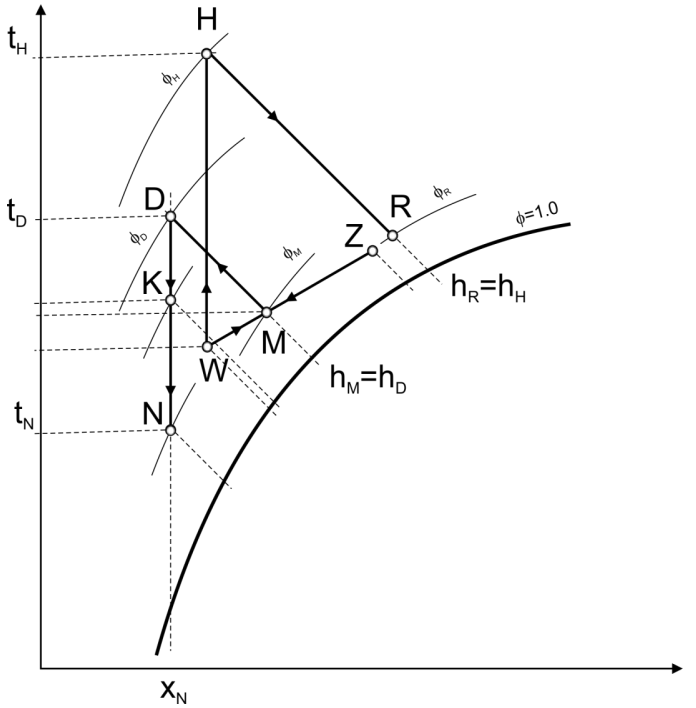

Figure 6 Air conditioning cycle with latent heat absorption in desiccant wheel

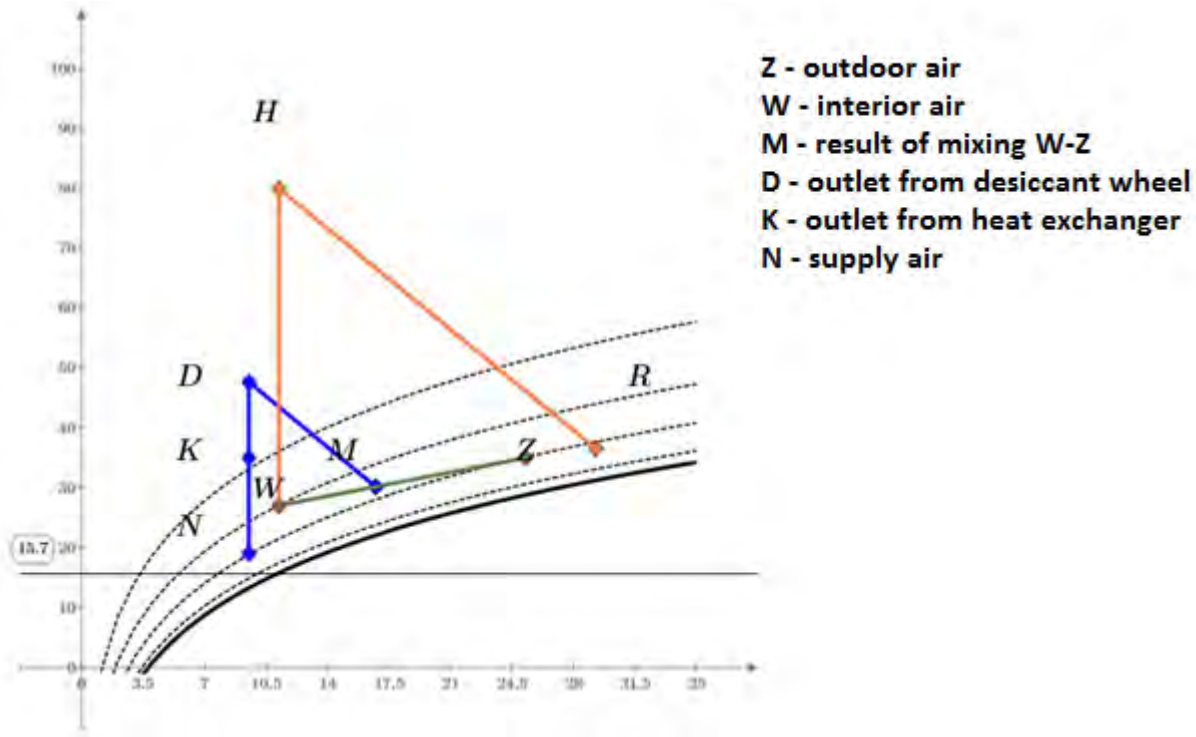

Figure 7 Air conditioning cycle with latent heat absorption in desiccant wheel for assumed operating parameters

5. CONCLUSIONS

The air-conditioning system for vessels equipped with a desiccant wheel and ejection refrigeration system was presented and briefly discussed. Both devices, i.e. desiccant wheel and ejection system use waste heat gained from exhaust gases from combustion engines.

Exemplary results of calculation have been presented. Results show that in the proposed air-conditioning system equipped with the desiccant wheel the cooling power is almost the same as total heat load of the vessel, while for conventional system with compression refrigeration system the cooling power is over two times higher than total heat load of the vessel. The use of the waste heat to drive the ejector refrigeration system allows for a significant reduction of an electric power consumption in the vessel.

The indicated solution is implemented by present shipyard in application to vessel of small and medium capacities. Due to the major innovative potential of the developed solution, further work is planned towards developing a configuration of the system ensuring high compactness and energy efficiency.

ACKNOWLEDGEMENTS

The research results presented in the paper were supported by the National Centre of Research and Development, Contract No. RPPM.01.01.01-22-0067/16

REFERENCES

Bassuoni A.A., 2014, Experimental performance study of a proposed desiccant based AC system, Cairo University Journal of Advanced Research, Vol. 5, 87–95.

Butrymowicz D., Karwacki J., Kwidziński R., Śmierciew K., Gagan J., Przybyliński T., Skiepko T., Łapin M., 2016, Methodology of heat transfer and flow resistance measurement for matrices of rotating regenerative heat exchangers, Chemical and Process Engineering, Vol. 37, No. 3, 341-358.

Camargo J.R., Godoy E., Ebinuma C.D., 2005, An Evaporative and Desiccant Cooling System for Air Conditioning in Humid Climates, J. of the Braz. Soc. of Mech. Sci. & Eng., Vol. 28, No. 3, 243-247.

Chung J.D., 2017, Modeling and Analysis of Desiccant Wheel, Chapter 2 in: Enteria N. et al. (eds.), Desiccant Heating, Ventilating, and Air-Conditioning Systems, Springer Nature Singapore Pte Ltd., 11-62.

Eicker U. Schürger U., Köhler M., Ge T., Dai Y., Li H., Wang R., 2012, Experimental investigations on desiccant wheels, Applied Thermal Engineering, Vol. 42, 71-80.

Ezgi, C., (2014). Design and thermodynamic analysis of an H2OeLiBr AHP system for naval surface ship application, International Journal of Refrigeration 48, 153-165.

Ezgi C, Girgin I. (2015) Design and Thermodynamic Analysis of a Steam Ejector Refrigeration/Heat Pump System for Naval Surface Ship Applications, Entropy, Vol. 17, 8152–8173

Gagan J., Śmierciew K., Łukaszuk M., Butrymowicz D., 2018a, Investigations of thermal performance of ejection refrigeration system driven by low grade heat, Applied Thermal Engineering, Vol. 130, 1121-1138.

Gagan J., Śmierciew K., Butrymowicz D., 2018b, Performance of ejection refrigeration system operating with R-1234ze(e) driven by ultra-low grade heat source, International Journal Of Refrigeration, Vol. 88, 458–471.

Guojie Z., Chaoyu Z., Guanghai Y., Wu C., 2012, Development of a New Marine Rotary Desiccant AC System, Energy Procedia, Vol. 16, 1095 – 1101.

Kamar H.M., Kamsah N., Alhamid M.I., Sumeru K., 2016, Effect of Regenaration Air Temperature on Desiccant Wheel Performance, International Journal of Technology, Vol. 2, 281-287.

Kara O., Hürdoğan E., Büyükalaca O., 2017, Analysis of dehumidification and humidity removal process of desiccant wheel, European Mechanical Science, Vol. 1, Issue 1, 9-14.

O'Connor D., Calautit J.K., Hughes B.R., 2016, A novel design of a desiccant rotary wheel for passive ventilation applications, Applied Energy, Vol. 179, 99-109.

Suyono, T., Mat, S., Yahya M., Ruslan M.H., Zaharim A. & Sopian K., 2011. Theoretical and Experimental Analysis of Desiccant Wheel Performance for Low Humidity Drying System, Proceeding ICOSSSE'11 Proceedings of the 10th WSEAS international conference on System science and simulation in engineering Pages 132-137

Śmierciew K., Gagan J., Butrymowicz D., Łukaszuk M., Kubiczek H. (2017) Experimental investigation of the first prototype ejector refrigeration system with HFO-1234ze(E), Applied Thermal Engineering, Vol. 110, 115-125.

Zheng C.Y., Zheng G.J., Yu W.S., Chen W., 2017, Study on the marine ejector refrigeration-rotary desiccant AC system, IOP Conference Series: Earth and Environmental Science, Vol. 81, Issue 1, No. 012184.

Manuscript ID: 670
DOI: 10.18462/iir.icr.2019.0670

Virtual-prototype-based development of household refrigerator-freezer appliances

Primož POREDOŠ[(a)], Andrej LJUBENSKO[b)], Andrej KITANOVSKI [(a)], Alojz POREDOŠ [(a)]

[(a)] University of Ljubljana, Faculty of mechanical engineering
Ljubljana, 10000, Slovenia, primoz.poredos@fs.uni-lj.si
[(b)] Gorenje, d.d.
Velenje, 3320, Slovenia

ABSTRACT

This paper presents the virtual-prototype-based development of household refrigerator-freezer appliances. The virtual prototype (VP) consists of five sub-models for the compressor, the diabatic capillary tube (DCT), the condenser, the refrigerator/freezer evaporators and the transient heat transfer inside the appliance envelope. The first two sub-models rely on semi-empirical modelling, the second two on the finite control volume, while the last one is based on finite-difference modelling. The VP was experimentally validated by performing temperature and refrigerant mass flow measurements for an actual appliance in a constant climate chamber at an ambient temperature of 25 °C. The average difference between the predicted and measured values was ±13%. The presented VP was used for a case-based development, in which different sizes of the DCT, the evaporators, the condenser and the compressor-displacement sizes were used in the simulations. The experiences of using the VP show that this tool has a great impact on reducing the experimental time and costs during the prototyping phase for new refrigerator and freezer appliances.
Keywords: Simulation, Refrigerant, Optimization, Household refrigerator, Development.

1. INTRODUCTION

Refrigeration and heating in buildings and the industry sector are nowadays responsible for about one-half of the EU's energy consumption, as stated by European Commission (2016). According to Isaac and Vuuren (2009), the energy demand for refrigeration will surpass the energy demand for heating in the coming decades. The International Energy Agency (2009) states that in the field of domestic refrigeration such appliances use up 10–30% of a household's overall electrical energy.
One of the most widespread cooling cycles according to the International Energy Agency (2018) is based on the vapor-compression cycle (VCC). Developers of VCC-based refrigeration, heat pump (HP), air-conditioning, etc. devices usually apply two basic principles: an experimental- and virtual-based system design/prototyping. Both terms represent different approaches in the system design: the experimental is mostly based on experiences that were gathered during decades of refrigeration/HP devices' assembly, testing, and experiences from the end-user. It is not based on an analytical approach, using a fundamental knowledge from the thermodynamic and fluid flow domains; rather it is based on a heuristic approach. From today's point of view, this prototyping method is rather obsolete, since it is based on a trial-and-error principle. The two very important downsides in such a case of dated prototyping are an excessive time and monetary investment.
An alternative to the experimental-based product development is virtual prototyping (VP). This is the process of creating and analyzing mathematical-based models that are built upon physical models (Hermes and Melo, 2008). The main idea behind VP is to predict the operation of a device/system by testing different components, refrigerants, system controllers, even under different operating conditions, like frost formation (Borges, 2015). Besides, the process itself does not require the production of a physical prototype in the first phase of development, which reduces the development costs and time.

In the field of designing VCC-based systems, computer-aided simulations gathered momentum in the 1990s, since those tools were extensively used for new refrigerant assessments (Ding, 2007). The term “virtual prototype/ing” has appeared recently in the scientific community in the field of refrigeration numerical modelling, for instance, in the paper by Garrido and Silveyra (2018). The main goal of such a virtual experimental system (Virtual Prototype) is to ensure a comprehensive, fully customable engineering analysis tool that gives a complete overview of the underlying physics. Such sophisticated VPs represent a powerful tool for low-cost virtual experiments. In addition, it has a wide variety of uses, for instance: performing sensitivity, thermo-economic, cost-benefit and performance analyses as well as predicting failures by helping to understand the physics of failure.
This paper presents a case-based development of household refrigerator-freezer appliances (HRFA) by using a VP that is based on a combination of 0D and 1D numerical models for the compressor, the diabatic capillary tube (DCT), the evaporator, the condenser and the transient heat transfer inside the HRFA envelope. During the development of HRFA, the prototype was used for several sensitivity analyses that employed different sizes of compressors, condensers, evaporators and DCT.

2. VIRTUAL PROTOTYPE

The VP of a HRFA has five sub-models for the following components: compressor, DCT, refrigerator and freezer evaporators, condenser and transient heat transfer inside HRFA compartments. All those sub-models were written in the Python (compressor, DCT, both evaporator, condenser) and C++ programming languages (heat transfer inside the HRFA compartments). The thermodynamic and thermophysical refrigerant properties within all the sub-models were calculated using the REFPROP and CoolProp libraries. The interaction between the user and the VP is provided by the Graphic User Interface (GUI), which connects all five sub-models. The GUI was developed in LabVIEW, since it exhibits a simple and intuitive way to create a GUI. The upper layer of the GUI, available to the user through the front panel, consists of buttons, indicators, controls, graphs and tabs, as shown in Figure 1 (left-hand side). The programming of the GUI is based on connecting the blocks, which is performed in the block diagram (lower layer), as shown in Figure 1 (right-hand side). In addition, this layer allows us to connect all the sub-models, as shown in Fig. 1 (right).

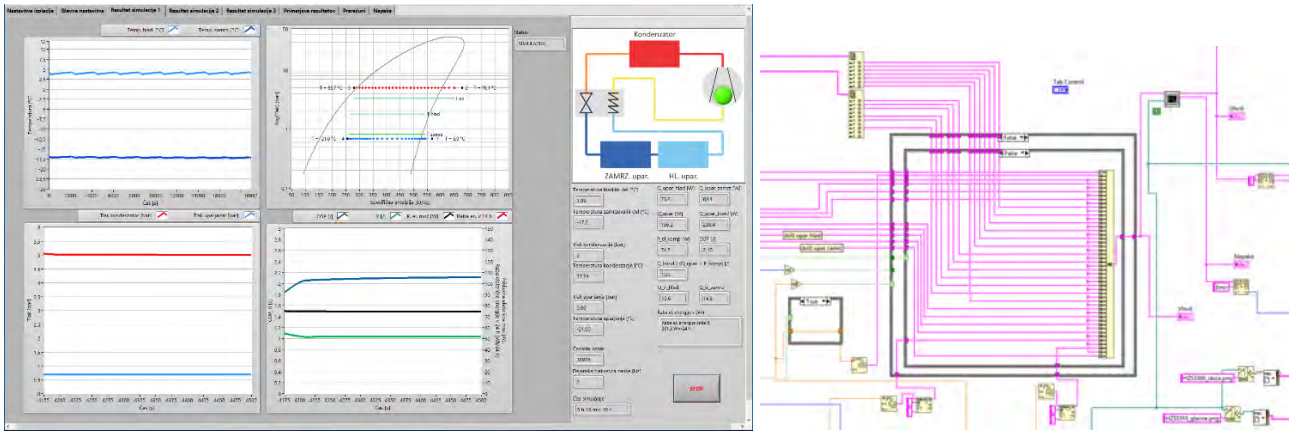

Fiugre 1: left: Front panel of the virtual prototype's GUI, which enables user interaction with the VP. Right: block diagram of a VP, within which all five sub-models are connected. Also, buttons, indicators, controls, graphs and tabs are connected to the input and outputs of all the sub-models

A schematic of the VCC-based HRFA VP is shown in Fig. 2. In addition to all the connections between all the sub-models, this figure also presents all the required inputs and outputs of a specific model.

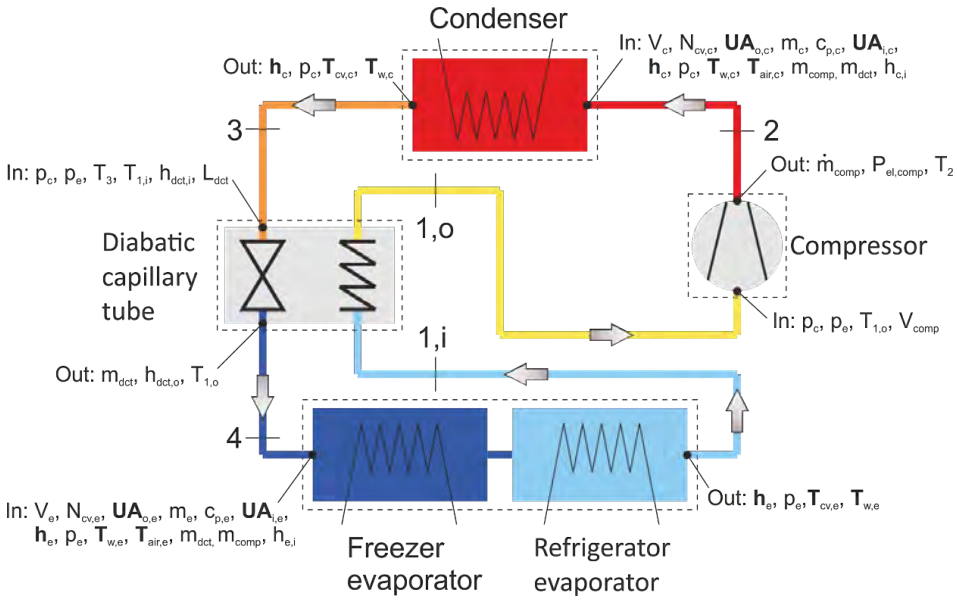

Figure 2: Schematic of a VCC-based HRFA VP sub-model, its connections, inputs and outputs to each specific simulation sub-model

2.1. Compressor Modelling

A compressor model is based on semi-empirical modelling, which has been proposed by many researchers in the household-refrigeration domain (e.g., Heimel et al., 2016; Borges et al., 2015). The compressor used in the VP is a hermetic, fixed-speed, piston compressor. The volume of the cylinder is 8.67 cm^3, with a rotational frequency of 50 Hz, while the refrigerant used in the HRFA is R-600a. All the outputs of this sub-model (see Figure 2) are calculated according to the work of Heimel et al. (2015). The compressor refrigerant mass flow, the electrical power and the temperature at point 2 are calculated with the following equations:

$$\dot{m}_{comp} = \lambda_v \frac{V_{comp} f_{comp}}{v_{1,o}};\ \lambda_v = a_5 + a_6 \left(\frac{p_c}{p_e}\right)^{\frac{1}{\kappa_{1,o}}} \qquad \text{(Eq. 1, 2)}$$

$$P_{el,comp} = \frac{\dot{m}_{comp} \frac{\kappa_{1,o}}{\kappa_{1,o}-1} p_e v_{1,o} \left[\left(\frac{p_c}{p_e}\right)^{\frac{\kappa_{1,o}-1}{\kappa_{1,o}}} - 1\right]}{\eta_{ov}} + \dot{Q}_{comp,loss};\ \eta_{ov} = \frac{1}{\frac{a_7}{p_e} + \frac{a_8}{p_c}} \qquad \text{(Eq. 3, 4)}$$

$$T_2 = T_{1,o}\left(a_9 + a_{10}\left(\frac{p_c}{p_e}\right)^{\frac{\kappa_{1,o}-1}{\kappa_{1,o}}}\right) \qquad \text{(Eq. 5)}$$

We must point out that the coefficients a_5 – a_{10} were calculated by multiple linear regression according to the compressor manufacturer's data and calorific measurements as well as to measurements of an actual appliance, performed by our industrial partner.

2.2. Diabatic Capillary Tube Modelling

Similar to compressor modelling, DCT modelling relies on semi-empirical modelling, which is based on the model established by Hermes et al. (2010). The capillary length was 3.26 m, while the inner and outer DCT diameters, and the outer suction pipe diameters were 0.72 and 1.85 mm, and 8 mm, respectively. The output variables of this model (see Fig. 2) were calculated using the following equations:

$$\dot{m}_{act} = \left\{ \frac{\pi^{2-d} 2^{2d-3}}{c} \frac{D_{i,dct}^{5-d}}{\eta_{f,l}^{d} L_{dct}} \left[\frac{p_c - p_f}{v_{f,l}} + \frac{p_f - p_e}{a} + \frac{b}{a^2} \right] \ln\left(\frac{a p_e + b}{a p_f + b} \right) \right\}^{1/(2-d)} \quad \text{(Eq. 6)}$$

$$\Lambda = \frac{\dot{m}_{dct}}{\dot{m}_{act}} = c_{11} \left(\frac{L_{sp,comp}}{L_{dct}} \right)^{c_{12}} \left(\frac{D_{o,sp,comp}}{D_{i,dct}} \right)^{c_{13}} \varepsilon_{dct}^{c_3} \left(\frac{v_{f,l} \eta_{f,l}}{v_{1,o} \eta_{1,o}} \right)^{c_{14}} \quad \text{(Eq. 7)}$$

$$h_{dct,o} = h_{dct,i} - \varepsilon_{dct} c_{p,1,o} (T_3 - T_{1,i}) \quad \text{(Eq. 8)}$$

$$T_{1,o} = T_{1,i} + \varepsilon_{dct} (T_3 - T_{1,i}) \quad \text{(Eq. 9)}$$

2.3. Heat Exchanger Modelling

Heat exchangers (evaporator, condenser) inside the VP were modelled by following the procedure proposed by (Braun and Bendapudi, 2002; Bendapudi, 2004; Rossi and Braun, 1999). The solution was created for first-order differential equations regarding the mass and energy conservation (left-hand sides of Eqs. (10) and (11)). The final differential equations by transforming the state variables are shown in the right-hand sides of Eqs. (10) and (11). The lengths of the freezer and refrigerator evaporator tubes were 15.65 and 6.135 m, respectively, while the length of the condenser evaporator tube was 17.11 m. The tubes' inner and outer diameters for the evaporator and condenser tubes were 6 and 8 mm and 3.35 and 4.75 mm, respectively. All the inputs and outputs for both evaporators and the condenser are shown in Fig. 2.

$$\frac{\partial \rho}{\partial t} + \frac{\partial (\rho w)}{\partial x} = 0 \rightarrow V_{cv} \left(\frac{\partial \rho}{\partial p} \right)_{cv} \frac{dp}{dt} + V_{cv} \left(\frac{\partial \rho}{\partial h} \right)_{cv} \frac{dh_{cv}}{dt} = \dot{m}_{cv-1} - \dot{m}_{cv} \quad \text{(Eq. 10)}$$

$$\frac{\partial (\rho h - p)}{\partial t} + \frac{\partial h}{\partial x} = \dot{Q} \rightarrow V_{cv} \left[h_{cv} \left(\frac{\partial \rho}{\partial p} \right)_{cv} - 1 \right] \frac{dp}{dt} + V_{cv} \left[h_{cv} \left(\frac{\partial \rho}{\partial h} \right)_{cv} + \rho_{cv} \right] \frac{dh_{cv}}{dt} = \dot{m}_{cv-1} h_{cv-1} - \dot{m}_{cv} h_{cv} - \dot{Q}_1 \quad \text{(Eq. 11)}$$

2.4. Transient Heat Transfer inside Compartments

The transient heat transfer modelling of the heat transfer inside the HRFA compartments is based on a 1-D heat equation (Eq. (15)), which was discretized by a finite-difference method using an implicit time-discretization scheme, as proposed by Poredoš et al. (2018). The output of the model was a temperature distribution of each wall and a calculated heat flow. The experimental model's validation was performed by steady-state and transient experiments. The average discrepancy for the former validation is 14.5%, while for the latter validation the average RMSD between the predicted and measured temperatures is 0.8 K.

$$\frac{\partial^2 T}{\partial x^2} = \frac{1}{\alpha} \frac{\partial T}{\partial t} \quad \text{(Eq. 12)}$$

3. VALIDATION OF THE VIRTUAL PROTOTYPE

The VP's validation was performed with temperature and refrigerant mass flow measurements of a typical HRFA in a constant climate chamber at 25 °C. The temperature measurements were performed with a T-type thermocouples having an expanded measurement uncertainty of 1 K. The refrigerant mass flow was measured with a Coriolis flow meter (Endress Houser Proline Promass F300) with a maximum measurement uncertainty of ±0.35% when measuring gases. The measurements of the combined refrigerator and freezer household appliance were carried out according to the standard IEC 62552 2013, which describes test methods for household refrigeration appliances. However, the standard states that in the freezing compartment the ISO packet should be present during the tests. That was not the case in our experiments, since the VP currently anticipates empty compartments. The experimental validation was performed at the end

of the cooling cycle. All the predicted and measured values are shown in Table 1. The average difference between the predicted and measured values was ±13%. We must point out that the comparison was made at the end of the cooling cycle, since the VP starts the cooling cycle with an already established pressure difference. Besides, since the current experimental measurements rely solely on the temperature measurements, the most representative evaporation and condensing temperatures were acquired by measuring the temperature on the outer surface area of the evaporator and the condenser tubes.

Table 1. Comparison of predicted (by VP) and measured values of several variables of a HRFA

-	$T_{ref,max}$ (°C)	$T_{ref,min}$ (°C)	$T_{fr,max}$ (°C)	$T_{fr,min}$ (°C)	T_e (°C)	T_c (°C)	$\dot{m}_{comp}$ (kg/h)	$\dot{Q}_e$ (W)	$\dot{Q}_c$ (W)	P_{comp} [W]	Energy consumption (Wh / 24 h)
Measured	4.6	3.9	-18.1	-21.2	-27.4	35.7	2.12	189	219	75	563
Predicted	4.6	3.9	-17.2	-19.2	-20.4	39.8	2.26	157	239	84	479
Difference [%]	0	0	5	10	25	12	6	17	9	13	15
Average	13%										

4. CASE-BASED DEVELOPMENT BASED ON VIRTUAL PROTOTYPING

In the following sections, a case-based development with the VP will be shown. All the components inside the VP are the same as in the HRFA, which is currently available on the market. Section 4.1. shows a sensitivity analysis in which the refrigerator's performance with different DCT lengths is analysed. In Sections 4.2, 4.3 and 4.4 three cases of evaporator, condenser length and compressor-displacement sizing analysis will be presented.

4.1. Capillary Tube Size

The operating performance when using five different DCT lengths (2.934, 3.097, 3.26 (a base case), 3.423 and 3.586 m) is shown in Fig. 3.

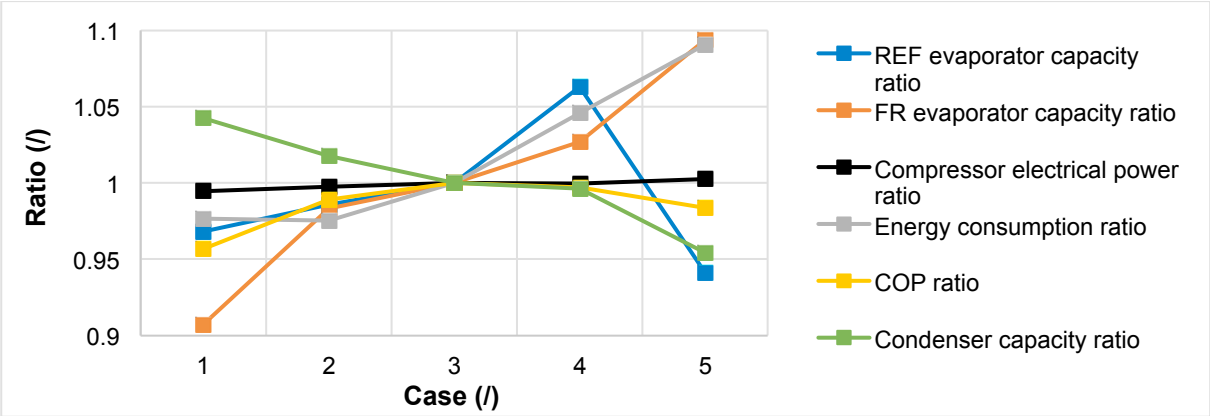

Figure 3: Sensitivity analysis of HRFA operational performance by changing the DCT size

By increasing the DCT tube length, the condenser's capacity and the compressor's power ratio are decreasing and increasing, respectively. The longer DCT manifests in higher pressure ratios, which in turn increases the compressor's electrical power consumption, decreases the refrigerant mass flow and consequently the condenser's capacity is decreased. The VP also predicts the increasing capacities of both evaporators (refrigerator and freezer) by increasing the DCT length. However, case 5 shows a point at which the refrigerator evaporator gains a significant loss in capacity, unlike the freezer's evaporator. Case 3 also shows that the base length of the DCT is optimal for this appliance if we consider the COP. This is also true from the energy consumption point of view, since case 1 shows only a 2.3% decrease, while case 5 shows a 9.1% increase in the energy consumption within 24 h of the refrigerator's operation.

4.2. Evaporator Sizing

Fig. 4 shows an analysis provided by the VP for five cases (the base case is 3) with different evaporator sizes. From case 1 it can be seen that when increasing the refrigerator's evaporator size by 21%, the freezer's evaporator should be increased by 47% in order to keep the temperature ratio 5/-18 °C (refrigeration/freezing compartment). On the other hand, this will cause an increase in the energy consumption by 19%. VP also predicts that by increasing and decreasing the evaporator sizes we cannot decrease the energy consumption of this particular appliance.

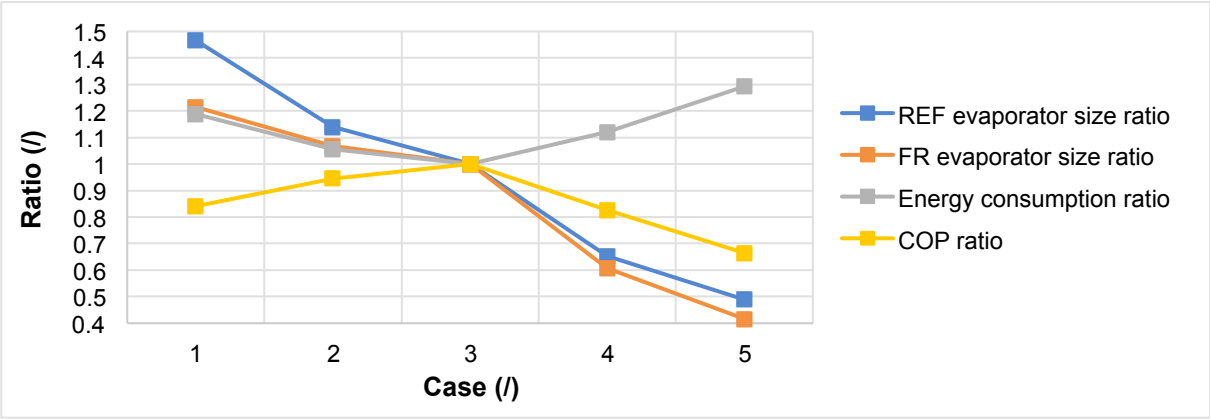

Figure 4: Sensitivity analysis of HRFA operational performance by changing the evaporator size

4.3. Condenser Sizing

When performing a condenser-sizing analysis, as shown in Fig. 5, case 5 shows that by increasing the refrigerator's condenser by 40 % the freezer's evaporator size should be decreased by 18 % in order to keep the temperature ratio 5/-18 °C (using the same refrigerator evaporator). This will cause a decrease in the energy consumption by 2 %. The VP also predicts that by increasing the condenser size we can have a small decrease in the energy consumption of the HRFA. However, existing sizes should be close to optimal, since the improvements are predicted to be insignificant.

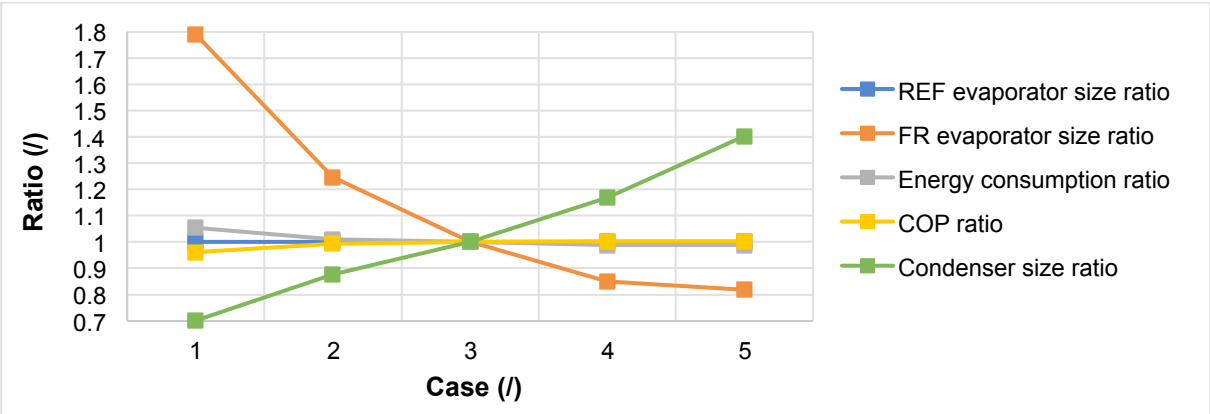

Figure 5: Sensitivity analysis of HRFA's operational performance by changing the condenser size

4.4. Compressor Sizing

If the compressor displacement is decreased by 19% (case 1), the freezer evaporator should be increased by 156% in order to keep the temperature ratio 5/-18 °C (using the same refrigerator evaporator), as shown in Fig. 6. This selection leads to an energy consumption decrease of 8%. On the other hand, the VP predicts that by increasing the compressor displacement a decrease in the energy consumption of the HRFA can be observed. However, the need for a larger increase in the freezer's evaporator should be further investigated.

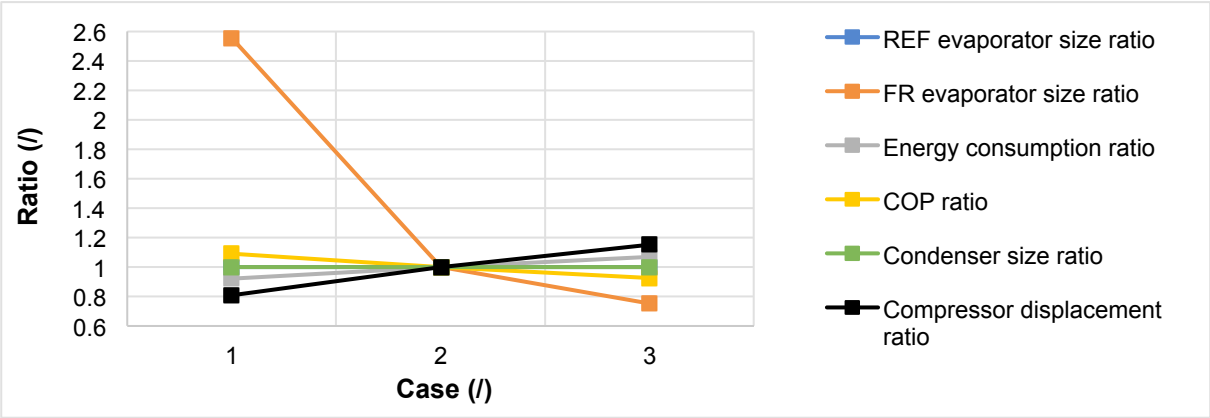

Figure 6: Sensitivity analysis of HRFA operational performance by changing the compressor-displacement ratio.

5. CONCLUSIONS

This paper presents a virtual-prototype-based development of household refrigerator-freezer appliances. The VP consists of five sub-models for the compressor, the DCT, the condenser, the refrigerator/freezer evaporators and the transient heat transfer inside the HRFA envelope. The VP has been experimentally validated by performing measurements for an actual appliance in a constant climate chamber at an ambient temperature of 25 °C. The average difference between the predicted and measured values is ±13%. Based on the constructed VP several sensitivity analyses were performed in which the different sizes of the DCT, the evaporators, the condenser and the compressor-displacement sizes were used in the simulations. This shows that the VP could serve as a powerful tool with a huge potential, since it is able to predict the impact of operational and geometric parameters on several output variables. By using the proposed tool, it is also possible to get an important insight into the underlying physics. So far, a great influence on reducing the experimental time and costs during the prototyping phase for new refrigerator and freezer household appliances was registered.

ACKNOWLEDGEMENTS

This research project is a result of an industrial project (contract number 2 2015/RKC HZA), which was a collaboration between the Faculty of Mechanical Engineering, University of Ljubljana and Gorenje gospodinjski aparati, d.d. The project has also been co-financed by the Republic of Slovenia and the European Union under the European Regional Development Fund, as the part of the IQ HOME program (contract number: C3330-16-529006).

NOMENCLATURE

A	surface area (m^2)	a	coefficient (/), variable (/)
b	variable (/)	c	constant (/), specific heat ($J \times kg^{-1} \times K^{-1}$)
D	tube diameter (m)	d	constant (/)
f	frequency (s^{-1})	h	specific enthalpy ($kJ \times kg^{-1}$)
L	length (m)	m	mass (kg)
$\dot{m}$	refrigerant mass flow ($kg \times s^{-1}$)	N	number of control volumes (/)
P	electric power (W)	p	pressure (bar)
$\dot{Q}$	heat flow rate (W)	T	temperature (K)
t	time (s)	U	overall heat transfer coefficient ($W \times m^{-2} \times K^{-1}$)
V	volume (m^3)	v	specific volume ($m^3 \times kg^{-1}$)
w	velocity ($m \times s^{-1}$)	x	coordinate (/)

Greek nomenclature

α	thermal diffusivity ($m^2 \times s^{-1}$)	ε	heat exchanger effectiveness (/)

η	compressor overall efficiency (/), dynamic viscosity (Pa×s)	κ	heat capacity ratio (/)
Λ	diabatic correction multiplier (/)	λ	volumetric efficiency (/)
π	pi constant (/)	ρ	density (kg×m^{-3})

Subscripts, superscripts

1,i	suction pipe inlet / evaporator outlet	*1,o*	suction pipe outlet / compressor inlet
1	interface control volume - wall	*2*	compressor outlet
3	capillary tube inlet	*4*	capillary tube outlet
act	adiabatic capillary tube	*c*	condenser
comp	compressor	*cv*	control volume
dct	diabatic capillary tube	*e*	evaporator
el	electrical	*f*	flash point
fr	freezing compartment	*i*	inlet, inner
l	liquid	*loss*	losses
max	maximum value	*min*	minimum value
o	outlet, outer	*p*	constant pressure
ref	refrigerated compartment	*sp*	suction pipe
v	volumetric		

REFERENCES

Bendapudi, S., 2004. Development and Evaluation of Modeling Approaches for Transients in Centrifugal Chillers. Dissertation.

Borges, B. N., Melo, C., Hermel, C. J. L, 2015. Transient simulation of a two-door frost-free refrigerator subjected to periodic door opening and evaporator frosting. Appl. Energ. 147, 386-395.

Braun, J., Bendapudi, S., 2002. Development and validation of a mechanistic, dynamic model for a vapor compression centrifugal liquid chiller. Deliverable for Research Project 1043-RP.

Ding, G.I., 2007. Recent developments in simulation techniques for vapour-compression refrigeration systems. Int. J. Refrig. 30(7), 1119-1133.

European Commission, 2016. Communication from the Commission to the European Parliament, the Council, the European Economic and Social Committee and the Committee of the Regions on an EU Strategy for Heating and Cooling. Luxembourg: Publications Office of the European Union.

Garrido, J. M. C., Silveyra, J. M, 2018. Virtual prototype of a low-cost vacuum baffle based on thermoelectric cooling. Vacuum 151, 156-162.

Heimel, M., Berger, E., Posch, S., Stupnik, A., Hopfgartner, J., Almbauer, R., 2016. Transient cycle simulation of domestic appliances and experimental validation. Int. J. Refrig. 69, 28-41.

Hermes, C. J. L., Melo, C., 2008. A first-principles simulation model for the start-up and cycling transients of household refrigerators. Int. J. Refrig. 31(8), 1341-1357.

Hermes, C. J. L., Melo, C., Knabber, F. T., 2010. Algebraic solution of capillary tube flows: Part I: Adiabatic capillary tubes. Appl. Therm. Eng. 30, 449-457.

Hermes, C. J. L., Melo, C., Knabber, F. T., 2010. Algebraic solution of capillary tube flows. Part II: Capillary tube suction line heat exchangers. Appl. Therm. Eng. 30, 770-775.

International Energy Agency, 2009. Gadgets and gigawatts – policies for energy efficient electronics.

International Energy Agency, 2018. The Future of Cooling Opportunities for energy efficient air conditioning.

Isaac, M., Vuuren, D. P., 2009. Modeling global residential sector energy demand for heating and air conditioning in the context of climate change. Energ Policy 37(2), 507–521.

Poredoš, P., Lorbek, L., Vidrih, B., Ljubenko, A., Kitanovski, A., Poredoš, A., 2018. Transient Heat Transfer Simulation of Fresh and Frozen Food Compartments in a Household Two-Door Refrigerator. Proceedings of the 31st International Conference on Efficiency, Cost, Optimization, Simulation and Environmental Impact of Energy Systems, Guimarães, Portugal.

Rossi, T., Braun, J. E., 1999. A real-time transient model for air conditioners. Proceedings of the 20th International Congress of Refrigeration, Sydney, Australia, IIF/IIR, 1–7.

Manuscript ID: 686
DOI: 10.18462/iir.icr.2019.0686

A performance analysis of absorption heat pump using R1234ze(E) and R1234ze(E) for PEMFC(Proton-Exchange Membrane Fuel Cells) vehicles

Gabyong Kim[(a)], Han Sol Jung[(b)], Hyun Jin Kim[(c)] YongTae Kang[(d*)]

(a) Graduate School of Mechanical Engineering, Korea University
Seoul, 02841, Republic of Korea, brothergab@korea.ac.kr
(b) Graduate School of Mechanical Engineering, Korea University
Seoul, 02841, Republic of Korea, razorleaf@korea.ac.kr
(c) School of Mechanical Engineering, Korea University
Seoul, 02841, Republic of Korea, eathj0625@korea.ac.kr
(d*) School of Mechanical Engineering, Korea University,
Seoul, 02841, Republic of Korea, ytkang@korea.ac.kr

ABSTRACT

Absorption heat pump system using R1234ze(E)/ionic fluid is developed for cooling and heating application in Proton-Exchange Membrane Fuel Cells (PEMFC) vehicles. Waste heat from the PEMFC is utilized as the heat source of the absorption heat pump system. A low global warming potential (GWP) refrigerant of (R1234ze(E)) and an ionic fluid of [hmim][Tf2N] are used as refrigerant and absorbent, respectively. Additionally, the heat pump system is assisted by a compressor placed between evaporator and absorber. Cooling and heating performance of the absorption heat pump is evaluated under various generator and absorber temperatures and concentrations. The results show that the coefficient of performance of refrigeration (COP_c) is up to 0.446 and the COP of heat pump(COP_H) is up to 1.423.
Keywords: Absorption system, Cooling, COP, Heat pump, Ionic liquid, R1234ze(E)

1. INTRODUCTION

Research and development on low GWP refrigerants have been actively proceeded. In addition, fossil fuels are the main cause of micro dust that directly affects respiratory diseases, and regulations on the use of internal combustion engines are being tightened. In the automobile industry, development and technical research on the next-generation automobiles are being carried out all over the world. One of the next generation of automobiles is a fuel cell automobile. The vehicle converts electricity into thermal energy inefficiently, thereby reducing the fuel efficiency. On the other hand, the amount of waste heat generated in the process of electricity generation in a fuel cell vehicle is about 50% with the temperature range of 70 to 80 degree Celsius and an additional cooling system is required to cool it (Fly and Thring, 2015).
Therefore, in this study, a sorption heat pump system that uses waste heat from the PEMFC as a driving heat source is proposed. The sorption heat pump system uses a low GWP refrigerant and ionic solution as absorbent, which can solve the problems mentioned above at the same time.
Regarding the development of absorption cycles, working fluid pairs (refrigerant/absorbent) are as important as all of the components of absorption cycles. H_2O/LiBr and NH_3/H_2O are most widely used at present. Despite the outstanding performance of the existing pairs, as shown in Table 1, these pairs have some critical disadvantages. To deal with this, the use of an ionic liquid and hydrofluorocarbon (HFC) as a working pair for the absorption refrigeration cycle has been proposed. As hydrofluoroolefins (HFO) stand out due to very low global warming potential (GWP) compared to HFCs, there are a few studies on the performance of absorption cycles using the HFOs and ionic liquid (IL) as the working fluid pair (Wu et al. 2018).

Table 1. Characteristics of representative refrigerants for absorption refrigeration system

-	NH_3/H2O	H_2O/LiBr
Absorbent	H_2O	LiBr
Refrigerant	NH_3	H_2O
Crystallization	N	Y
Toxicity	Y	N
Flammability	Y	N
Disadvantages	1. Flammable, Explosive, Toxic 2. Regulated by national regulations	1. Frozen/refrigeration system: Not applicable 2. Difficulty in air cooling due to high boiling point of refrigeration

In this study, a sorption heat pump cycle for fuel cell automobiles is developed using the ionic liquid and HFO as the working fluid pair, and the performances of summer and winter seasons are estimated according to the temperature and concentration variations.

2. SIMULATION METHODOLOGY

2.1. Description of Sorption Heat Pump in Automobile

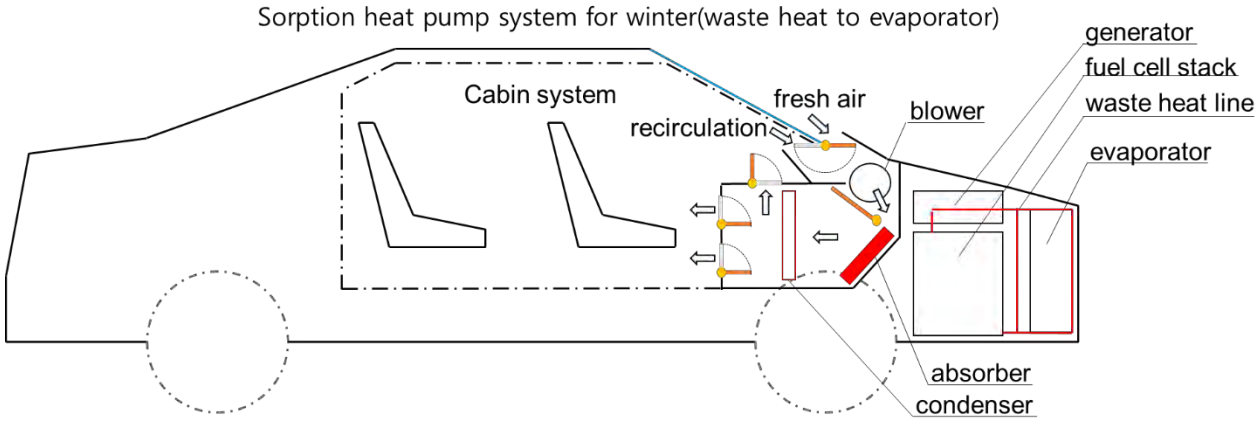

Figure 1: Arrangement of sorption heat pump system in automobile

Fig. 1 shows the interior layout of the sorption heat pump system for winter mode in fuel cell vehicles. In order to reduce the defrosting operation of the heat pump system in winter, the waste heat line and by-pass to the evaporator are constructed.
Fig. 2 and Fig. 3 show the cycle simulation model of the sorption heat pump proposed in this study for summer and winter modes, respectively. To extend the operating ranges of the heat pump system, an additional compressor is set to the basic components to increase the operating temperature and pressure ranges. Also, according to (Wu et al., 2018), it is confirmed that the coefficient of performance of the heat pump is significantly improved by adding the compressor.

2.2. Selection of Refrigerant and Absorbent Pair

After considering toxicity, safety, stability, flammability, corrosivity, GWP and ODP values, it is found that R1233zd(E), R1234ze(E), and R1234yf are suitable to replace ammonia as a refrigerant. Furthermore, by considering melting point (below -10℃), boiling point (over 150℃), heat capacity and saturation pressure, R1234ze(E) is finally selected. Due to the negligible vapor pressure, good thermal and chemical stability and solubility with many refrigerants, ILs (composed of one organic cation and one organic or inorganic anion) are considered as the promising absorbents for sorption cycles.

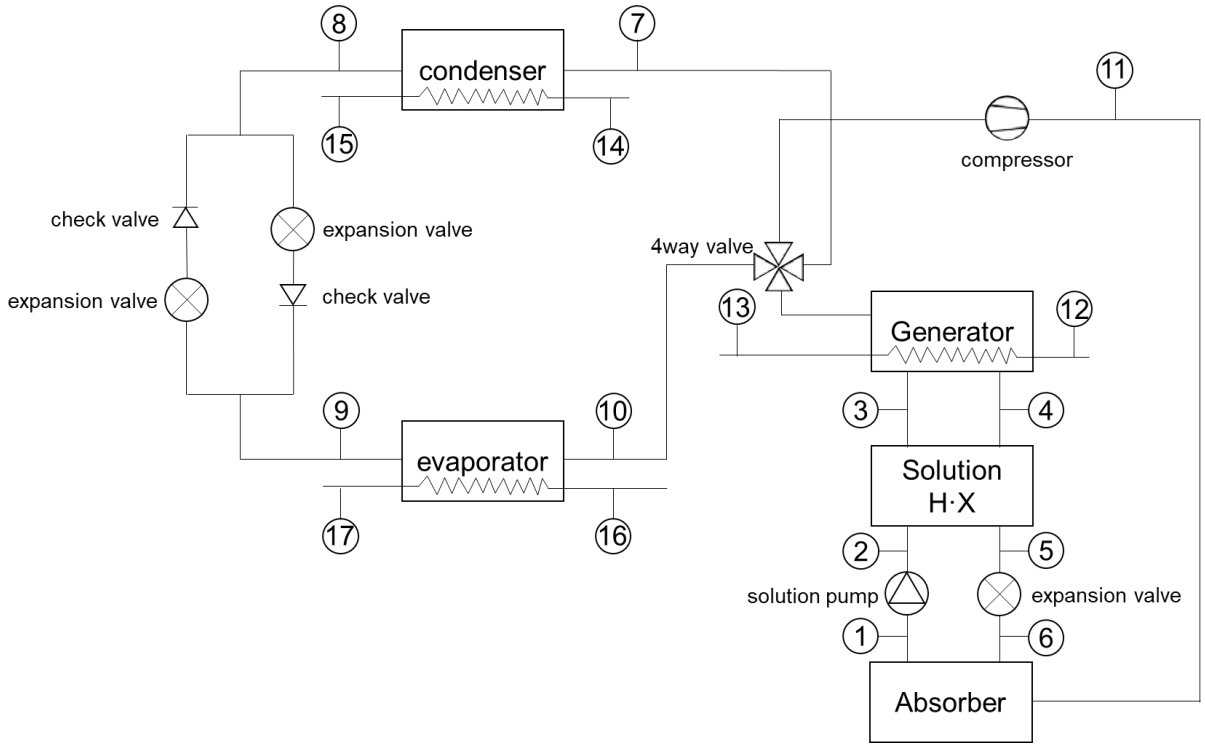

Figure 2: Schematic diagram of sorption heat pump cycle for summer mode

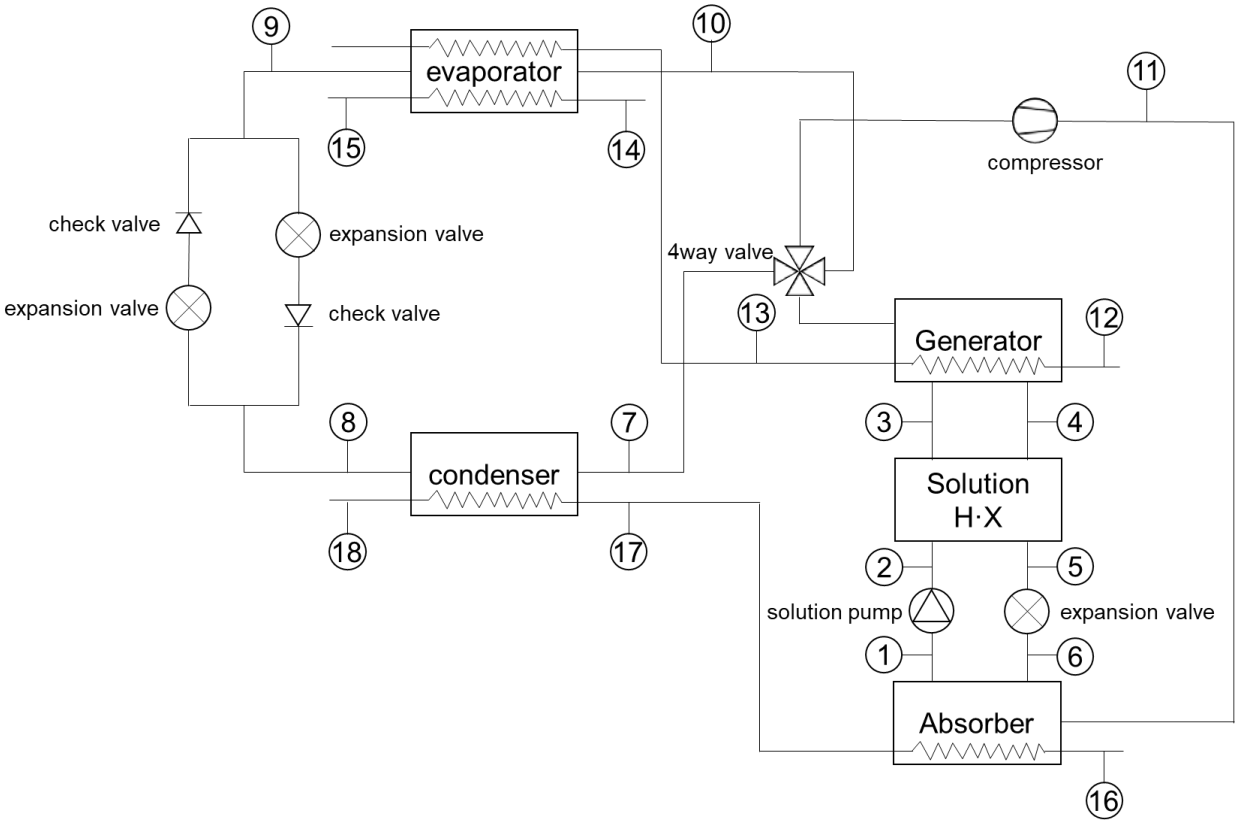

Figure 3: Schematic diagram of sorption heat pump cycle for winter mode

2.3. Property Estimation of HFO/IL

2.3.1. Pressure, Concentration and Temperature Relation

To analyze the system performance, pressure, concentration, and temperature equilibrium correlation of multi-components gas-liquid system is essentially acquired. These properties can be

derived from the experimental vapor-liquid equilibrium (VLE) data using the non-random two liquid (NRTL) activity coefficient property method. The VLE behavior of a multi-component system can be described by the following formulations (1)–(5)

$$Y_i p\Phi_i = X_i \gamma_i p_i^s (i = 1, \dots, N) \quad \text{Eq. (1)}$$

where X_i and Y_i are the mole fractions of the ith species in the liquid and vapour phases, respectively, γ_i is the activity coefficient of the ith species, p_i^s is the saturated vapour pressure of the ith species, and Φ_i is the correction factor for the ith species, which can be calculated as

$$\Phi_i = exp\left[\frac{(B_i - V_i^L)(p - p^s)}{RT}\right] \quad \text{Eq. (2)}$$

where B_i and V_i^L are the second virial coefficient and the saturated molar liquid volume for the ith species at temperature T, respectively. They can be calculated from the EES(Engineering Equation Solver) software. The NRTL equation is expressed as

$$ln\gamma_1 = X_2^2\left[\tau_{21}\left(\frac{G_{21}}{X_1 + X_2 G_{21}}\right)^2 + \frac{\tau_{12}G_{12}}{(X_2 + X_1 G_{21})^2}\right] \qquad ln\gamma_2 = X_1^2\left[\tau_{12}\left(\frac{G_{12}}{X_2 + X_1 G_{12}}\right)^2 + \frac{\tau_{21}G_{21}}{(X_1 + X_2 G_{21})^2}\right] \quad \text{Eq. (3)}$$

$$G_{12} = ex\,p(-\alpha\tau_{12}) \qquad G_{21} = ex\,p(-\alpha\tau_{21}) \quad \text{Eq. (4)}$$

$$\tau_{12} = \tau_{12}^0 + \frac{\tau_{12}^1}{T} \qquad \tau_{21} = \tau_{21}^0 + \frac{\tau_{21}^1}{T} \quad \text{Eq. (5)}$$

where $\alpha, \tau_{12}^0, \tau_{12}^1, \tau_{21}^0$ and τ_{21}^1 are adjustable parameters corresponding to [hmim][Tf_2N]/R1234ze(E). These parameters for the four working pairs are obtained based on the experimental data from the reference (Liu et al. 2016) and are listed in Table 2. The NRTL property model is implemented in the EES software.

Table 2. Adjustable parameters corresponding to [hmim][Tf2N]/R1234ze(E)

coefficients	α	τ_{12}^0	τ_{12}^1	τ_{21}^0	τ_{21}^1
value	-12.83	0.3359	-76.07	0.2888	80.25

2.3.2. Enthalpy of Binary Mixture

The enthalpy of the binary mixture is calculated by equations (6)-(9)

$$H = X_1 H_1 + X_2 H_2 + H^E \quad \text{Eq. (6)}$$

where H_1 and X_1 are the enthalpy and molar concentration of liquid phase R1234ze (E), respectively, and are calculated using EES. H_2 is the enthalpy of [hmim] [Tf_2N] and is calculated by

$$H_2 = \int_{T_0}^{T} C_{p,IL} dT + H_0 \quad \text{Eq. (7)}$$

where H_0 is the reference enthalpy at reference state, which is set as 200 kJ/kg when converted to mass-based enthalpy; T_0 is the reference temperature, which is set as 273.15 K here; $C_{p,IL}$ is the heat capacity of the IL, which can be calculated by

$$C_{p,IL} = C_0 + C_0 T \quad \text{Eq. (8)}$$

The experimental data for IL heat capacities are obtained from the reference(Liu et al. 2016) and the mole based coefficients of equation (9). For the R1234ze(E)/IL binary systems, the excess enthalpy can be calculated by

$$H^E = -RT^2\left[X_1\left(\frac{\partial ln\gamma_1}{\partial T}\right)_{p,X} + X_2\left(\frac{\partial ln\gamma_2}{\partial T}\right)_{p,X}\right] \quad \text{Eq. (9)}$$

where *R* is the universal gas constant, which is 8.314472 J mol^{-1} K^{-1}

2.4. Cycle Modelling of the Sorption Cycle

During the cycle simulation process, the following assumptions are used.

(1) Steady state operation.
(2) The pressure drop is small enough to be negligible.
(3) Condensation and evaporation occur completely in condenser and evaporator, respectively.
(4) The temperature of the generator is kept constant by controlling the inflow of heat source.
(5) The efficiency of pump and the compressor are assumed 0.85(Ally and Sharma. 2018) and 0.7(Wu et al., 2018), respectively.
(6) The efficiency of the solution heat exchanger is assumed 0.8. (Wu et al., 2018)
The entire simulation of the sorption heat pump is carried out using the Engineering Equation Solver (EES), and the thermal conditions for the cycle simulation are summarized in Table 2.

Table 2. Cycle simulation conditions

Modes	Ambient temperature(℃)	Absorber outlet mass flow rate (kg/s)	Air flow rate ($m^3.h^{-1}$)	
			Inflow	Outflow
Summer	35	0.1	500	3931
Winter	0			

2.4.1. Mass and Species Conservations

Principles of mass, species and energy conservations are applied to each component of the system as follows.
· Mass balance:

$$0 = \sum \dot{m}_i - \sum \dot{m}_o \quad \text{Eq. (10)}$$

$$0 = \sum \dot{m}_i x_i - \sum \dot{m}_o x_o \quad \text{Eq. (11)}$$

· Energy balance

$$0 = \sum \dot{m}_i h_i - \sum \dot{m}_o h_o + \sum \dot{Q}_i - \sum \dot{Q}_o + \dot{W} \quad \text{Eq. (12)}$$

2.4.2. COP and Work

Pump and compressor works are defined in Equations (13) and (14), respectively. The coefficients of performance (COP) for cooling (summer mode) and heating (winter mode) are calculated form of Equations (15) and (16), respectively.
· Solution pump and compressor:

$$\dot{W}_{pump} = \frac{\dot{m}_1(P_{gen} - P_{abs})}{\rho_1 \eta_p} \quad \text{Eq. (13)}$$

$$\dot{W}_{comp} = \frac{\dot{m}_1(h_{abs,in,ref} - P_{evap,out,aref})}{\eta_{comp}} \quad \text{Eq. (14)}$$

Coefficient of performance:

$$COP_C = \frac{Q_{evap}}{Q_{gen} + W_{pump} + W_{comp}} \quad \text{Eq. (15)}$$

$$COP_H = \frac{Q_{cond} + Q_{abs}}{Q_{gen} + W_{pump} + W_{comp}} \quad \text{Eq. (16)}$$

3. RESULTS AND DISCUSSION

3.1. Analysis Conditions

The concentration and temperature of the absorber are kept constant and the sensitivity analysis is conducted by changing the concentration and temperature of the generator. Table 3 shows the temperatures and concentrations of generator outlet and absorber outlet for summer and winter modes. As the generator temperature increases, the saturation pressure in the condenser of the superheated refrigerant from the generator becomes higher for a given concentration, confirming that the operating pressure range of this system becomes wider. As the absorber temperature

increases, the saturation pressure in the absorber outlet becomes higher for a given concentration, confirming that the operating pressure range of the generator becomes more restricted.

Table 3. Simulation condition of each component outlet

Modes	Generator (Absorber properties variable)		Absorber (Generator properties variable)	
	Temperature	Outlet concentration	Temperature	Outlet concentration
Summer	60 (℃)	11%	40 (℃)	23%
Winter	50 (℃)	12%	30 (℃)	28.5%

3.2. Effect of the Concentration Difference on the Cooling and Heating COP

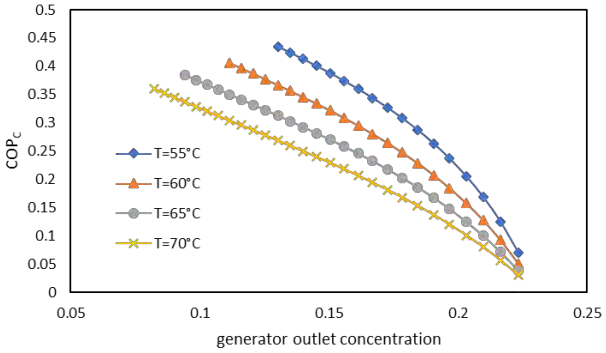

Figure 4: Effect of generator outlet concentration of different temperature on cooling COP

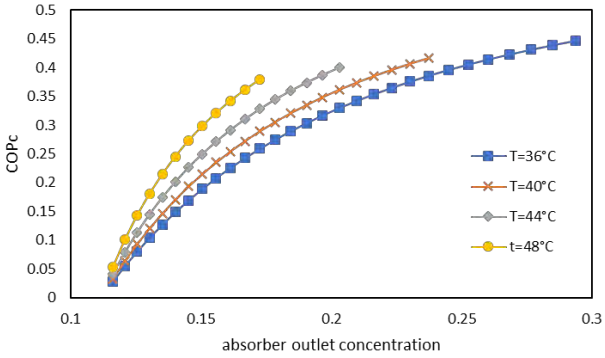

Figure 5: Effect of absorber outlet concentration of different temperature on cooling COP

Fig. 4 shows the cooling COP variation according to the generator outlet concentration for each generator temperature. The performance of the cycle is evaluated by varying the generator temperature from 55℃ to 70℃ with 5℃ intervals. As the generator outlet concentration increases, the flow rate of the generated refrigerant decreases, which reduces the cooling capacity and reduces the total COP. When the outlet temperature and concentration of the generator are 55℃ and 13%, respectively, the maximum cooling COP is 0.435. It is found that the COP is sensitive to the generator outlet concentration.

Fig. 5 shows the cooling COP variations according to the absorber outlet concentration. As the outlet concentration of absorber increases, the saturation pressure of the absorber increases and the compressor work also increases, but the flow rate of the refrigerant becomes relatively larger due to the concentration difference, which increases the cooling capacity of the evaporator leading to the increase total COP. When the outlet temperature and concentration of the absorber are 36℃ and 29.3%, respectively, the maximum cooling COP is 0.446. It is found that the COP is sensitive to the absorber outlet concentration.

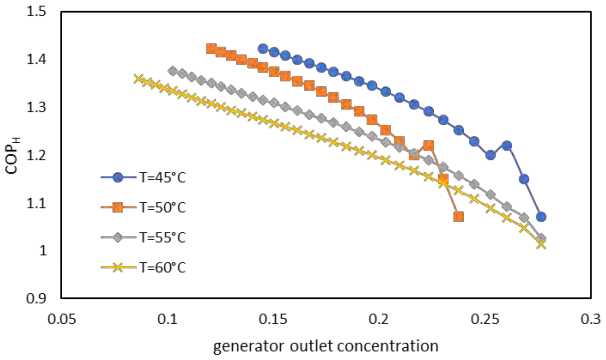

Figure 6: Effect of generator outlet concentration of different temperature on heating COP

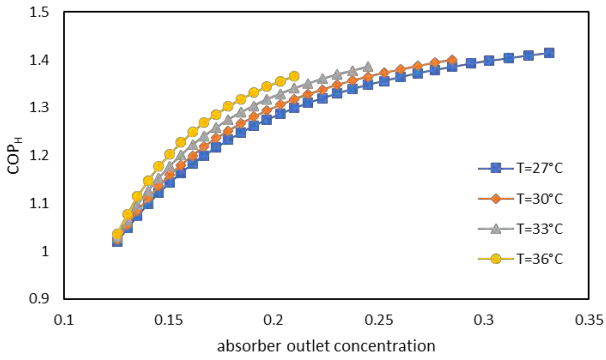

Figure 7: Effect of absorber outlet concentration of different temperature on heating COP

Fig. 6 shows the heating COP variations according to the generator outlet concentration. The performance of the cycle is evaluated by varying the generator temperature from 45℃ to 60℃ with 5(℃) intervals. As the outlet concentration increases, the refrigerant flow through the condenser decreases and the corresponding compressor work decreases. However, as the heat capacity in the condenser and the energy absorbed from the outside air in the evaporator become relatively much smaller, the total COP decreases. When the outlet temperature and concentration of the generator are 45℃ and 14.5%, respectively, the maximum heating COP is 1.423.
Fig. 7 shows the heating COP variations according to the absorber outlet concentration. As the outlet concentration increases, the flow rate of the refrigerant in the generator increases and the compressor work increases. However, the heat capacity also increases in the condenser and the energy absorbed from the outside air in the evaporator increases and the total COP increases. When the outlet temperature and concentration of the absorber are 27℃ and 33.1%, respectively, the maximum heating COP is 1.414.

3.3. Effect of Temperature on Performance of the System

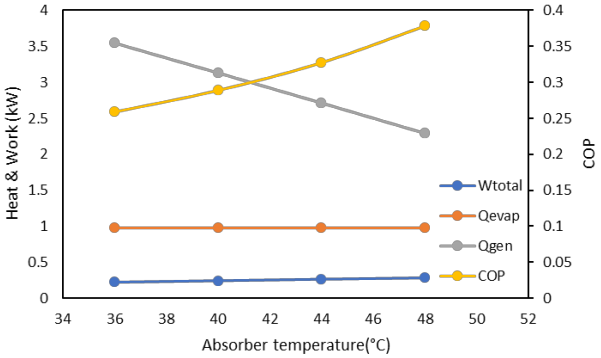

Figure 8: Effect of absorber temperature on cooling performance in summer

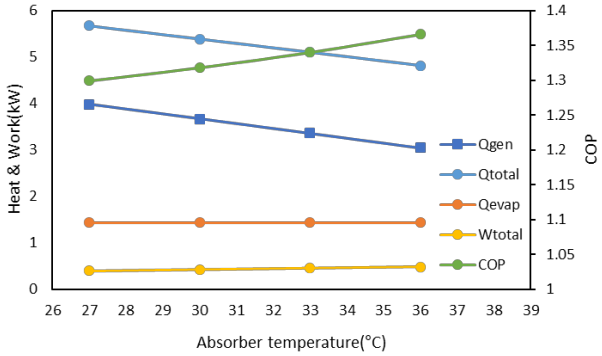

Figure 9: Effect of absorber temperature on heating performance in winter

Fig. 8 shows the performance of the system in summer. The concentrations of the absorber and generator are maintained at 17.2% and 11%, respectively, and the cycle performance is evaluated according to the temperature of the absorber. As the concentration difference between generator and absorber outlets is constant, the amount of boiling refrigerant keeps constant and the heat absorbed by the evaporator keeps constant. As the temperature of the absorber increases by 12℃, the amount of total work increases by 22.6%, and the heat input to the generator decreases by 35.3%. At this time, the COP is improved by 46%. As the temperature of the absorber increases, the higher the saturation pressure, the greater the work of the compressor to compensate for it, but the temperature difference between the generator and the solution decreases and the heat required to heat the solution decreases drastically. Therefore, the COP increases significantly as the amount of heat given to the generator is greatly reduced according to Equation (15)
Fig. 9 shows the performance of the system in winter. The concentrations of the absorber and generator in winter are kept constant at 20.9% and 12.5%, respectively, and the cycle performance is evaluated according to the temperature of the absorber. As the concentration difference between generator and absorber outlets is constant, the amount of boiling refrigerant and the heat absorbed by the evaporator are constant. In summer, as the temperature of the absorber increases by 9 ° C, the total amount of work increases by 26.0%, and the heat input to the generator decreases by 7.7%. At this time, the COP is improved by 5%. In the case of the heating system, the heat from the generator is recovered from the condenser and the absorber to the cabin system, and the energy of the outside air recovered from the evaporator is compressed as an auxiliary. Therefore, the overall system mainly depends on the heat supplied to the generator. However, as the temperature difference between the absorber and the generator decreases, the heat input to the generator decreases and the amount of heat recovered from the evaporator takes up more of the system element. Therefore, the COP increases as the absorber temperature increases, which reduces the amount of heat given to the generator according to Equation (16)

4. CONCLUSIONS

The performance of a sorption heat pump for fuel cell vehicle according to the change of absorber and generator outlet concentration and temperature is analysed. The working fluid pair is selected for the sorption heat pump using a low GWP refrigerant R1234ze (E) as refrigerant and ionic solution [hmim] [Tf2N] as absorbent. The following conclusions are drawn from the present study.

1. It is confirmed that the cooling COP decreases as the generator temperature increases for a given generator outlet concentration. The cooling COP increases as the generator outlet concentration decreases. it is found that the maximum cooling COP is 0.435 when the generator temperature is 55℃ at the outlet concentration of 13.0%. Also, it is confirmed that heating COP decreases as the generator outlet temperature increases for a given outlet concentration, and it is confirmed that the heating COP increases as the generator outlet concentration decreases. It is found that the maximum heating COP is 1.423 when the generator temperature is 45℃ at the outlet concentration of 14.5%.
2. It is confirmed that the cooling COP decreases as the absorber temperature increases for a given absorber outlet concentration. The cooling COP increases as the absorber outlet concentration increases. It is found that the maximum cooling COP is 0.446 when the absorber temperature is 36℃ at the outlet concentration of 29.3%. Also, it is confirmed that the heating COP decreases as the absorber temperature increases for a given outlet concentration, and it is also confirmed that the heating COP increases as the absorber outlet concentration increases. It is found that the heating COP has a maximum of 1.414 when the generator temperature is 27℃, at the outlet concentration of 33.1%,
3. Cooling COP changes sensitively according to the temperature change of the absorber when other conditions are constant. However, the heating COP is relatively small because the waste heat from the whole system is supplied to the cabin system as it is, and the ambient energy is recovered.

NOMENCLATURE

$\dot{m}$	mass flow rate, kg s^{-1}	$\dot{Q}$	heat transfer rate, kJ s^{-1}
T	temperature, K	p	pressure, kPa
COP	coefficient of performance	W	power rate, kW
x	concentration	h	mass based enthalpy, kJ kg^{-1}

5. REFERENCES

Ally, M. R., Sharma. V., 2018. Variability of absorption heat pump efficiency for domestic water heating and space heating based on time-weighted bin analysis. Applied Thermal Engineering 130, 515-527.

Fly, A., Thring, R. H., 2015. Temperature regulation in an evaporatively cooled proton exchange membrane fuel cell stack. Int. J. Hydrogen Energy 40, 11976-11982.

Liu, X., Bai, L., Liu, S., He, M., 2016. Vapor-liquid equilibrium of R1234yf/[HMIM][Tf2N] and R1234ze(E)/[HMIM][Tf2N] working pairs for the absorption refrigeration cycle. Journal of Chem. Eng. Data 61, 3952-3957.

Wu, W., You, T., Zhang, H., Li, X., 2018. Comparisons of different ionic liquids combined with trans-1,3,3,3-tetrafluoropropene(R1234ze(E)) as absorption working fluids. Int. J. Refrigeration 88, 45-47.

Manuscript ID: 717
DOI: 10.18462/iir.icr.2019.0717

Design of heat pipe heat sink used for cooling controller of inverter air conditioner

Guanghui XIA[(a)], Dawei ZHUANG[(a)], Guoliang DING[(a)]

[(a)] Institute of Refrigeration and Cryogenics, Shanghai Jiao Tong University
Shanghai 200240, China, glding@sjtu.edu.cn

ABSTRACT

The inverter controller produces large heat flux during the high-frequency operation of inverter air conditioners and the heat flux should be dissipated in time. The objective of this study is to propose a novel cooling method based on the heat pipe heat sink (HPHS) for the inverter controller. The heat flux of the chips in the controller is transferred to heat pipes by conduction and then dissipated to the ambience by the efficient heat convection between the dense fins and the air. Two types of HPHSs (i.e. vertical U-type and L-type) are designed, and their cooling performance are investigated and compared with the conventional plate-fin heat sink based on simulation. The application of HPHS cooling method in a real inverter air conditioner shows that, L-type HPHS and U-type HPHS can reduce the average temperatures of chips by 7.9 ºC and 5.2 ºC compared to the conventional plate-fin heat sink, respectively.
Keywords: Air Conditioner, Cooling, Heat Pipe, Heat Sink, Inverter.

1. INTRODUCTION

Inverter air-conditioners (ACs) have been widely used in the household appliances for the advantages of energy saving and good comfort comparing to the conventional constant frequency air conditioners (Yurtseven et al., 2014). The cooling/heating capacity of an inverter AC is regulated by the controller containing several chips (Li and Deng, 2007). The chips will generate large heat flux during the high-frequency operating of inverter air conditioners. The heat flux must be dissipated in time because the temperature rises of chips resulted from the heat flux may deteriorate the controller (Zhao et al., 2014).

The existing methods for the heat dissipation of the controller of ACs include the plate-fin heat sink method and the refrigerant cooling method, and their limitations are listed as follows. With the plate-fin heat sink, the heat flux is dissipated by the plate-fin heat sink sticking on the chips (Bar Cohen and Iyengar, 2002; Kim et al., 2010). The cooling performance of plate-fin heat sink is determined by the fin area and fin efficiency. However, the contradiction between the fin area and fin efficiency limits the cooling capability of plate-fin heat sink. If the fin area increases, the fin number will increase and the fin thickness decrease, resulting in low fin efficiency; if the fin efficiency increases, the fin thickness will increase and the fin number decreases, leading to small fin area.

With the refrigerant cooling method, a cold plate is sticking on the controller and a part of refrigerant in the outdoor heat exchanger is used to flow through the cold plate and cool the chips (Trutassanawin et al., 2006). Since the refrigerant temperature is commonly lower than the dew point temperature of outdoor air in winter (TenWolde, 2014), water vapor in the air may be condensed on the controller and damage the chips. Besides, the refrigerant cooling method may increase the thermal load of the outdoor heat exchanger and influence the COP of inverter ACs.

A heat pipe heat sink (HPHS) has the capability to dissipate heat with high efficiency, it may replace the plate-fin heat sink to efficiently cool the controller. The efficient cooling of HPHS is realized by the large heat dissipation area and the super high heat conductivity of heat pipes. The large heat dissipation area is achieved by increasing the fins numbers and reducing the fins thickness, and the decreased fin efficiency resulted from the small fin thickness will be improved by using heat pipes to connect the middle with the root of fins. The super high heat conductivity of heat pipes is achieved by the alternate evaporation and condensation of working fluid inside the heat pipe. The liquid working fluid at the evaporation part of heat pipe evaporates to vapor by absorbing the heat flux of the chips, and then flows to the condensation part; the vapor is condensed by the cooling of outdoor air, and consequently the heat flux of the chips can be transferred to the ambience through the HPHS.

HPHS has already been well used for cooling the electronic systems and saving energy of refrigeration systems. Relevant researches cover the following three aspects: 1) the effects of capillary structure and working fluid on the performance of HPHS (Cai and Bhunia, 2014; Jiao et al., 2008); 2) the effects of the operation conditions, such as the inclination of heat pipe (Yousefi et al., 2013); 3) the industrial applications of HPHS (Ye et al., 2014), such as the dehumidification enhancement for air conditioners (Nethaji and Mohideen, 2017). Until now, the HPHS has not been applied in the heat dissipation for controller of the inverter AC.

In order to apply a HPHS in the controller of inverter AC, the following two requirements have to be satisfied simultaneously. Firstly, the heat transfer performance of HPHS should be good enough to ensure the chip temperature in the controller is lower than that employing plate-fin heat sink. Secondly, the HPHS should be installed in the compact outdoor unit of ACs conveniently after replacing the plate-fin heat sink.

The purpose of this paper is to develop a HPHS cooling method based on the heat pipe for the controller of inverter AC and the cooling effectiveness of the HPHS cooling method is validated experimentally.

2. MECHANISM OF HEAT DISSIPATION BASED ON HPHS

Fig. 1 schematically shows the compressor cabin of the outdoor unit of a typical inverter AC. The controller is vertically located at the boundary of the compressor cabin as shown in Fig.1(a). The chips with large heat flux, including a compressor intelligent power module (IPM), a bridge, a diode and an insulated gate bipolar transistor (IGBT), are located at the back side of the controller, as shown in Fig. 1(b). The four chips generate various heat flux and the heat flux will increase as the frequency of the inverter AC increases. During the high-frequency operation of the inverter AC, the plate-fin heat sink cannot efficiently dissipate the heat flux of chips and some chip temperatures will exceed the limited values. The reason for the limited cooling capacity of plate-fin heat sink are the contradiction between the fin area and fin efficiency as well as the bad temperature uniformity.

The idea for realizing the efficient cooling of the chips in the controller is to employ a HPHS to replace the plate-fin heat sink. The HPHS includes several heat pipes, some fins and a cold plate. The root of fins contact with the cold plate and the heat pipes connect the middle part of fins with the cold plate. By applying the proposed HPHS, the heat flux of chips is firstly transferred from the cold plate to the fins through the heat pipes and the contact of fin root in the way of conductivity, and then dissipated to the outdoor ambience by the forced convection of the air flow from the outdoor fan.

The heat dissipation performance of the proposed HPHS depends on whether the structure of HPHS is well designed. Thus, the design of the HPHS method includes the design of the HPHS structure and the simulation analysis of the HPHS structure.

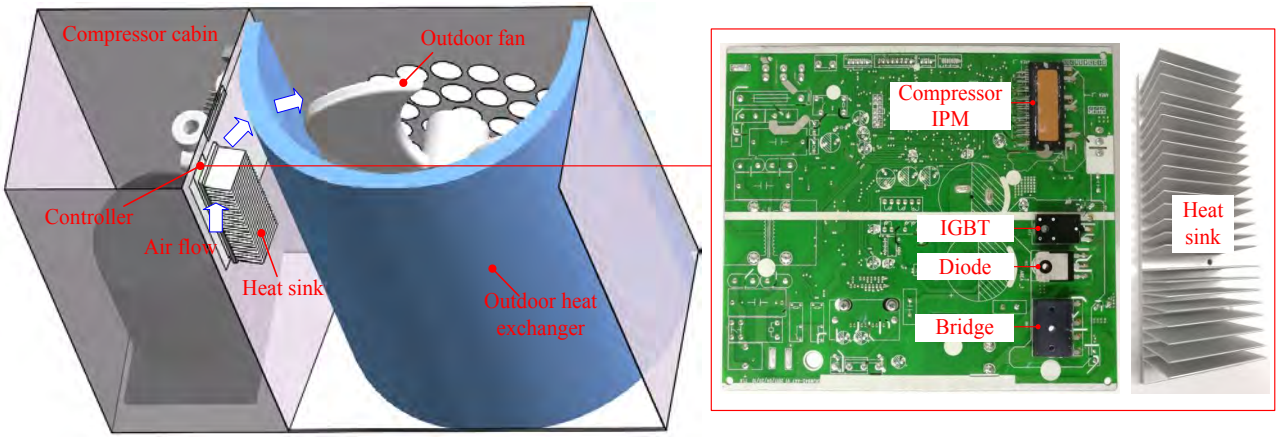

(a) Outdoor unit of inverter air conditioner (b) Chips in the back of controller

Figure 1: Structure schematic of controller in outdoor unit of typical inverter air conditioners

3. DESIGN METHOD OF HPHS FOR CONTROLLER

3.1. Design of the layout and the structure of HPHS

The design requirements of HPHS include that HPHS should be installed conveniently in the compact outdoor unit, and the heat dissipation performance of HPHS should be as good as possible. Thus, the design of HPHS includes: 1) the layout design of HPHS; 2) the structural design of HPHS.
1) Layout design of HPHS
The layout design of HPHS in the outdoor unit includes the locations of the cold plate, the fins and the heat pipes. The cold plate contacts with the chips in the controller and the contact interface is filled with the thermal silicone grease to enhance heat transfer. The fins are located at the windward side of the outdoor heat exchanger. And the heat pipes connect the cold plate and fins.
2) Structural design of HPHS.
The structural design of HPHS aims at achieving good heat transfer performance of HPHS. According to the distribution of chips in the controller, Two types of HPHS structures are proposed in this study, including: 1) the vertical U-type HPHS (VU-HPHS) and 2) L-type HPHS (L-HPHS), as shown in Fig. 2.
The structure of VU-HPHS is illustrated in Fig. 2(a). One end of the vertical U shaped heat pipes contacts with the cold plate and this end is treated as the evaporation part; the other end contacts with the fins and is treated as the condensation part. VU-HPHS has the advantage of high fin efficiency due to the middle position of heat pipes in the fins. The difficulty for applying VU-HPHS is that, gravity may hinder the condensed liquid to flow to the evaporation part of the heat pipes, resulting in little liquid and bad heat dissipation performance at the top of the evaporation part.
The structure of L-HPHS is illustrated in Fig. 2(b). In this type of structure, one end of L-shaped heat pipes is designed to be horizontal and is treated as the evaporation part; the other end is vertical and treated as the condensation part. The advantage of L-HPHS is that the gravity can promote the backflow of the condensed liquid and improve the heat transfer efficiency of heat pipes. The challenge for applying VU-HPHS is that the installation of L-HPHS requires the controller to be rotated 90 degrees clockwise so that the large-power chips can contact with the cold plate of L-HPHS.

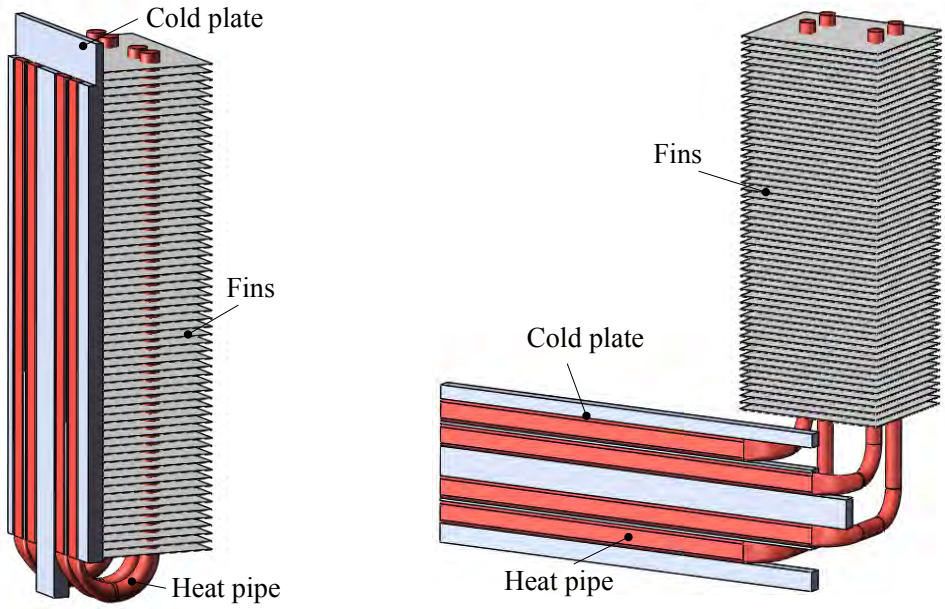

(a) Vertical U-type of HPHS (b) L type of HPHS

Figure 2: Structures of two types of heat pipe heat sinks

3.2. Simulation analysis and comparison of HPHSs

The proposed two types of HPHSs may have different cooling effects on the chips in controller, and the simulation analysis and comparison have been carried out to obtain the optimal HPHS structure. The temperature distribution of chips and HPHSs in the controller is simulated based on the CFD software (ANSYS Icepak 15.0). In the simulation, the heat pipes are simplified as solids with thermal conductivity of 10000 $W \times m^{-1} \times K^{-1}$ (Solomon et al., 2016); and the gravity and thermal radiation are considered in the air flow and the heat transfer calculation, respectively; the simulation is taken as

converged when the scaled residuals of the energy equation, the continuity equation, and the momentum equation are below 10^{-10}, 10^{-6} and 10^{-6}, respectively.
The simulation results of the chip temperatures under various HPHSs as well as the plate-fin heat sink are shown in Fig. 3. It can been seen that the VU-HPHS can obviously decrease the chip temperatures, and the maximum temperature reduction and average temperature reduction are 6.9 °C and 4.8 °C respectively. The L-HPHS may further decrease the chip temperatures, and the maximum temperature reduction and average temperature reduction are 7.7 °C and 5.8 °C respectively. Moreover, both VU-HPHS and L-HPHS can obviously improve the temperature uniformity of chips, and the max temperature difference among chips are reduced from 13.7 °C to 10.4 °C and 9.5 °C if the plate-fin heat sink is replaced by VU-HPHS and L-HPHS, respectively.
It can be concluded that the VU-HPHS and L-HPHS both have good cooling effectiveness for the chips in the controller of inverter AC and they will be further validated by experiments.

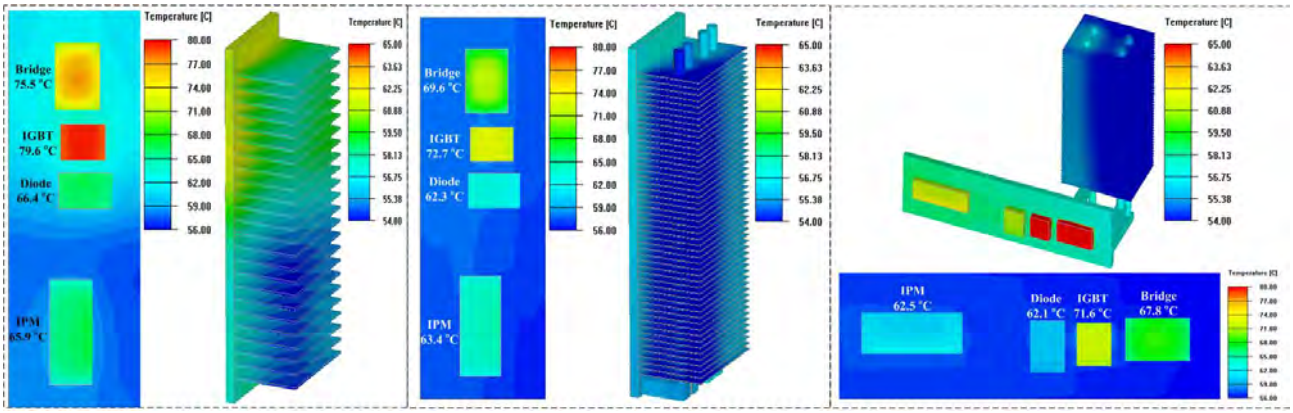

(a) Plate-fin heat sink (b) VU-HPHS (c) L-HPHS

Figure 3: Simulation results of temperature distribution for various cooling methods

4. APPLICATION EFFECT OF HPHS IN AN INVERTER AC

The proposed HPHS method in this study is applied in cooling the controller of a real inverter AC, and the effect is validated.

4.1. Prototypical controller and test samples

The structure of the prototype controller in the real inverter AC is shown in Fig. 7. In the prototype controller, the chips such as the compressor IPM, the bridge, the diode and the IGBT are located at the back side of the controller as shown in Figs. 4(a) and (c) and they produce a heat flow of approximate 63W in operation. The test samples of the HPHSs are manufactured based on the designed structures of HPHSs as shown in Fig. 4(b) and (d), and the detailed structures of the designed HPHSs are listed in Table 1. The manufacture processes of the HPHSs follow the two steps shown as below: 1) the evaporation parts of heat pipes are processed into flat shape and embedded in the cold plate for achieving a large contact area and a small thickness of the cold plate; 2) the contacts between the heat pipes, the cold plate and the fins are all welded for reducing contact thermal resistance.

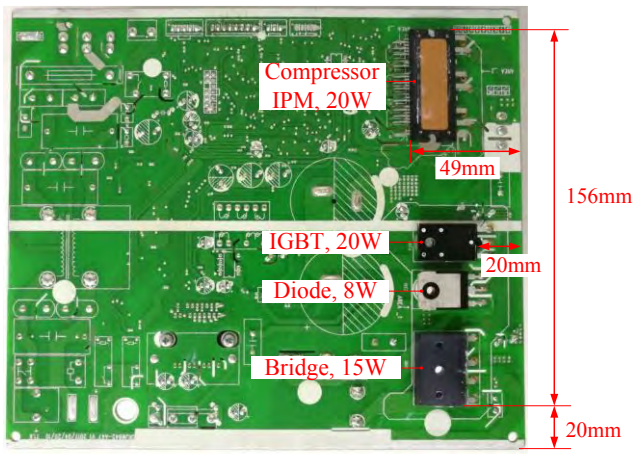

(a) Back side of controller



(b) Test sample of VU-HPHS

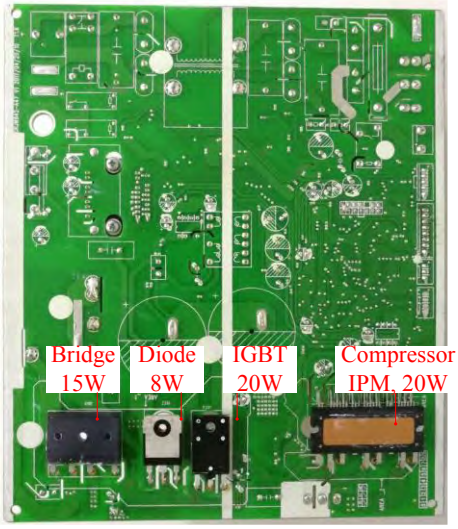

(c) Back side of controller rotated 90 degrees clockwise

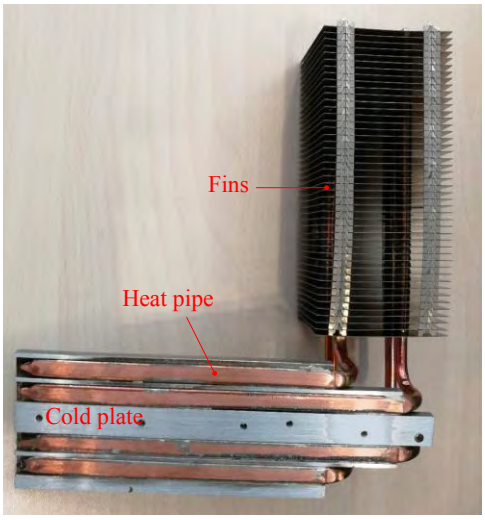

(d) Test sample of L-HPHS

Figure 4: The prototype controller and test samples of HPHSs in a real inverter AC

Table 1. Structure parameters of two types of HPHSs

HPHS types		VU-HPHS	L- HPHS
Heat pipe	Diameter / mm	6.0	6.0
	Number	4	4
	Evaporation / mm	150.0×4	133.0×2+163.0×2
	Condensation / mm	157.0×4	145.0×4
Cold plate	Length / mm	178.0	178.0
	Width / mm	59.0	59.0
	Thickness / mm	5.0	5.0
Fin	Length / mm	59.0	60.0
	Height / mm	37.0	48.0
	Number	52	48
	Fin pitch / mm	3.0	3.0
	Area / m^2	0.2270	0.2765
	Fin thickness / mm	0.3	0.3

4.2. Experimental method

The temperatures of chips are the key parameters to evaluate the heat dissipation performance of a cooling method for the controller. For verifying the effectiveness of the proposed HPHSs, the temperatures of chips in the controller with the proposed two types of HPHSs are measured and compared to those in the controller with plate-fin heat sink. The temperatures of chips are measured by thermocouples under the maximum operation condition of an inverter AC because the maximum operation condition enables each chip in the controller to achieve the highest temperature in operation.

The experiments are conducted in the real operation environment of the inverter AC, and the real operation environment is realized in the national standard enthalpy difference lab of China. The controller with various cooling methods are placed in the inverter AC and the temperatures of chips in the controller are measured by thermocouples. The thermocouples are located in the poor heat dissipation parts of chips, such as the chip surfaces that do not contact with HPHS. The measurement error of the calibrated thermocouple is within a range of ±0.2 °C. The experiment is carried out corresponding to the test standard "T1" of GB/T 7725-2004 (AQSIQ, 2004). The outdoor ambience varies from 43.0 °C to 50 °C. The inverter AC is operated at full thermal load with the input power of 1565W and the outdoor fan speed of 900 rpm. The controller with VU-HPHS and L-HPHS as well as the plate-fin heat sink are tested in the experiment comparatively.

4.3. Experimental results

Figure 5 shows the experimental results of the temperatures of chips in the controller with VU-HPHS and L-HPHS as well as the plate-fin heat sink.

From Fig. 5(a), it can be seen that the chip temperatures decrease significantly as the controller is employing the VU-HPHS. The maximum and average temperature reductions of chips are 6.8 °C and 5.2 °C, respectively. Moreover, VU-HPHS has little improvement for the temperature uniformity of chips. The possible explanation for this phenomenon is that the gravity affects the liquid flow inside the U-shaped heat pipe, resulting in the uneven heat dissipation performance at various positions of VU-HPHS.

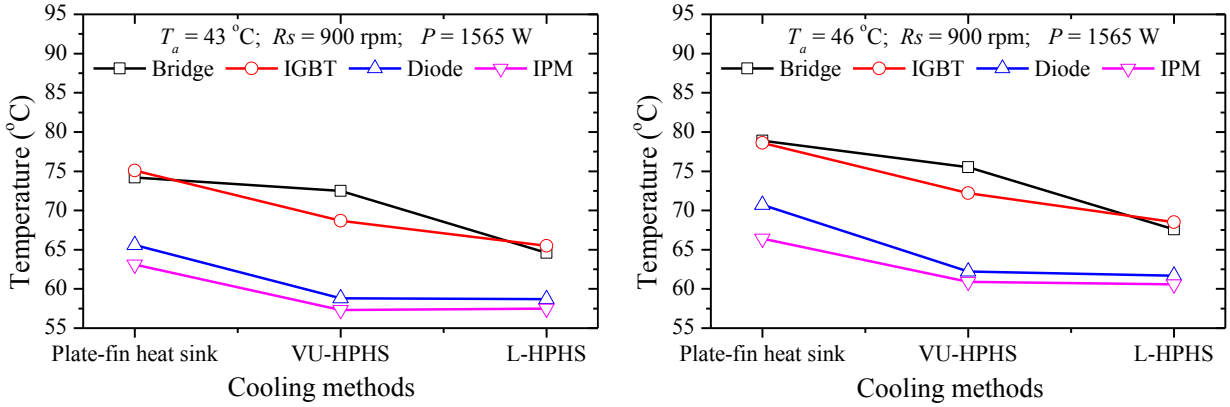

(a) Ambient temperature of 43 °C

(b) Ambient temperature of 46 °C

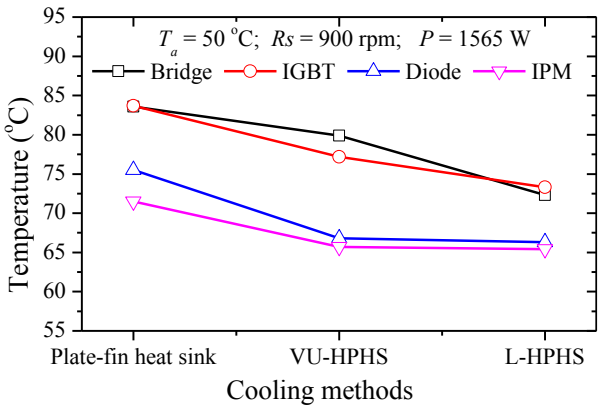

(c) Ambient temperature of 50 °C

Figure 5: Experimental results of various cooling methods under various ambient temperatures

The cooling performance of L-HPHS is better than that of VU-HPHS and plate-fin heat sink. After employing L-HPHS, the average temperature of chips are 7.9 °C and 2.7 °C lower than that employing plate-fin heat sink and VU-HPHS, respectively. Besides, L-HPHS can significantly improve the temperature uniformity of chips, making the maximum temperature difference among the chips less than 8.0 °C. The possible explanation for the efficient cooling performance of L-HPHS is that the gravity promotes the liquid flow inside the L-shaped heat pipes.
From Figs. 5(b) and 5(c), it can been seen that the chip temperatures increase with the increase of ambient temperature and the VU-HPHS and L_HPHS still have good cooling performance under high ambient temperature. The average temperatures of chips decrease by 6.0 °C and 9.1 °C respectively after employing VU-HPHS and L_HPHS under the ambient temperature of 46 °C, and the average temperature decreases are 6.2 °C and 9.3 °C respectively under the ambient temperature of 50 °C.

5. CONCLUSIONS

A HPHS cooling method is proposed and designed in this paper to realize the efficient heat dissipation of the controller during the high-frequency operation of an inverter AC. The heat dissipation performance of the proposed method is verified by measuring the temperatures of chips inside the controller and then compared with the plate-fin heat sink. The following conclusions are obtained from the designed and experimental results:
1) The application of the HPHS can efficiently dissipate the heat flux of chips in the controller to the outdoor ambience. Two types of HPHS, including U-type and L-type, are recommended to achieve the optimal cooling effectiveness of HPHS.
2) The heat dissipation performance of the proposed HPHS is better than that of plate-fin heat sink. The average temperature of chips decrease by 5.2 °C and 7.9 °C respectively after employing VU-HPHS and L-HPHS under the ambient temperature of 43 °C, and the temperature decreases are 6.2 °C and 9.3 °C respectively under the ambient temperature of 50 °C.

ACKNOWLEDGEMENTS

The authors gratefully acknowledge the supports from the National Nature Science Foundation of China (Grant No. 51606119), the Foundation for Innovative Research Groups of the National Science Foundation of China (Grant no. 51521004), the Program of Shanghai Academic Research Leader (Grant no. 16XD1401500), and the National Natural Science Foundation of China (Grant no. 51506117).

NOMENCLATURE

P	input power of air conditioner, W	HPHS	heat pipe heat sink
Rs	outdoor fan speed, rpm	IPM	intelligent power module
T_a	ambience temperature, K	IGBT	insulated gate bipolar transistor
Abbreviations		L-HPHS	L-type heat pipe heat sink
AC	air conditioner	VU-HPHS	vertical U-type heat pipe heat sink
CFD	computational fluid dynamics		

REFERENCES

AQSIQ (General Administration of Quality Supervision, Inspection and Quarantine of the People's Republic of China), 2004. GB/T 7725-2004: National Standard for Room Air Conditioners (in Chinese).

Bar-Cohen, A., Iyengar, M., 2002. Design and optimization of air-cooled heat sinks for sustainable development. IEEE Transactions on Components and Packaging Technologies 25(4), 584–591.

Cai, S.Q., Bhunia, A., 2014. Geometrical effects of wick structures on the maximum phase change capability. Int. J. Heat Mass Transfer 79, 981–988.

Jiao, B., Qiu, L.M., Zhang, X.B., Zhang, Y., 2008. Investigation on the effect of filling ratio on the steady-state heat transfer performance of a vertical two-phase closed thermosyphon. Appl. Therm. Eng. 28(11), 1417–1426.

Kim, D.K., Jung, J., Kim, S.J., 2010. Thermal optimization of plate-fin heat sinks with variable fin thickness. Int. J. Heat Mass Transfer 53(25), 5988–5995.

Li, Z., Deng, S., 2007. A DDC-based capacity controller of a direct expansion (DX) air conditioning (A/C) unit for simultaneous indoor air temperature and humidity control – Part I: Control algorithms and preliminary controllability tests. Int. J. Refrigeration 30(1), 113–123.

Nethaji, N., Mohideen, S. T., 2017. Energy conservation studies on a split air conditioner using loop heat pipes. Energy and Buildings 155, 215-224.

Solomon, A.B., Sekar, M., Yang, S.H., 2016. Analytical expression for thermal conductivity of heat pipe. Appl. Therm. Eng. 100, 462–467.

TenWolde, A., 2014. Ventilation, humidity, and condensation in manufactured houses during winter. ASHRAE Transactions 100(1), 103–115.

Trutassanawin, S., Groll, E.A., Garimella, S.V., Cremaschi, L., 2006. Experimental investigation of a miniature-scale refrigeration system for electronics cooling. IEEE Transactions on Components and Packaging Technologies 29(3), 678–687.

Ye, H., Li, B., Tang, H., Zhao, J., Yuan, C., Zhang, G., 2014. Design of vertical fin arrays with heat pipes used for high-power light-emitting diodes. Microelectron. Reliab. 54(11), 2448–2455.

Yousefi, T., Mousavi, S.A., Farahbakhsh, B., Saghir, M.Z., 2013. Experimental investigation on the performance of CPU coolers: Effect of heat pipe inclination angle and the use of nanofluids. Microelectron. Reliab. 53(12), 1954–1961.

Yurtseven, M.B., Erkin, E., Acuner, E., Mete, S., Onaygil, S., 2014. An experimental investigation of energy saving potentials for room type variable-speed air conditioners in public offices: A case study from Istanbul. Energy and Buildings 68, 165–171.

Zhao, X., Sun, J., Wang, C., Zhang, Z., 2014. Experimental and numerical study of electronic module-cooling heat sinks used in a variable frequency air-conditioner outdoor unit. Int. J. Refrigeration 38, 10–21.

Manuscript ID: 719
DOI: 10.18462/iir.icr.2019.0719

Research on heat transfer of the closed-loop thermosyphon system with microencapsulated phase change material suspension

Yixuan LI[(1)], Shugang WANG[(1)], Jihong WANG[(1)], Xunjia DENG[(1)]
Tengfei ZHANG[(1)] , Zhenjun MA[(2)]

[(1)] Dalian University of Technology
Dalian, 116024, People's Republic of China, sgwang@dlut.edu.cn
[(2)] University of Wollongong
Wollongong, NSW 2500, Australia, zhenjun@uow.edu.au

ABSTRACT

Heat generation of datacenters becomes larger and larger because of the improvement of operational performance of equipment and the expansion of datacenter scale. Two-phase closed-loop thermosyphon system as a new type of cooling system, which has a large cooling capacity, has gotten a widespread attention. This paper investigates experimentally heat transfer performance of a closed-loop thermosyphon system by testing under different mass concentrations, heating and cooling scenarios. The system, filled with microencapsulated phase change material suspension (MPCMS), contains heating, cooling and adiabatic sections. The result shows that the convective heat transfer coefficient at the heating section inlet with 0.5% MPCMS is twice as much as that of base fluid. Hence, a closed-loop thermosyphon system with MPCMS is an effective scheme to enhance the performance of the cooling system.
Keywords: Cooling Capacity, Phase-change Material, Thermosyphon, Two-Phase Flow.

1. INTRODUCTION

The large-scale and high-performance of electronic equipment lead to an increase in requirement for cooling capacity of air-conditioning cooling system. As a conventional cooling technology, Air cooling technology (Li and Kandlika, 2015) which has maximum heat dissipation capacity of 37 W/cm^2 (Saini and Webb, 2002) and water cooling technology (Khalaj and Halgamuge, 2017) which transfers heat only by sensible heat are slightly inadequate in heat dissipation when dealing with super-high heat flow. A new cooling system, incorporating thermosyphon into a traditional refrigeration system which has become a hot topic in HVAC (Heating, Ventilating and Air-Conditioning) recent years, can be switched to the optimal operation mode according to different outdoor working conditions and heat dissipation requirements of datacenters.

Phase-change material, absorbing or releasing a large amount of latent heat when phase change occurs, can have greater cooling capacity. The closed-loop thermosyphon system is mostly filled with gas-liquid phase-change material (Bodjona et al., 2017 and Lamaison et al., 2017), which has the complex boiling process. MPCMS (Microencapsulated Phase Change Material Suspension) as a solid-liquid phase-change medium can solve the poor thermal stability, the larger volume changes, the determination of the optimal filling rate and other problems which are caused by gas-liquid phase-change medium. However, the existing experimental investigations were mainly focus on heat transfer characteristics of MPCMS in straight tube sections, such as Chen, B., et al. (2008), Song et al. (2014), Roberts et al. (2017) and so on. The experimental results showed that the heat transfer capacity of MPCMS was better than that of single-phase fluid significantly. Also, there were a few investigations of closed-loop thermosiphon system with MPCMS. Ho et al. (2014) investigated experimentally the thermal performance of a rectangular circulation loop with a mini-channel heat sink and source, filled with different concentration of nanocapsule suspensions. There is another structural form for the heating section of the system. Lamoureux and Baliga (2013) carried out an experiment with a heating section that the copper tube is tightly wound around by heating wire, and validated the proposed mathematical models. They did not report a detailed parametric study on

closed-loop thermosyphons operated with MCPCM slurries, especially the effect of cold source temperature on performance of the system.
Hence, there are a few experimental data about the closed-loop thermosiphon system with solid-liquid phase-change material currently. This paper studies experimentally heat transfer performance of a closed-loop thermosyphon system which is filled with different mass fractions of MPCMS and conducted a test under different heating and cooling scenarios.

2. EXPERIMENT

2.1. Preparation and Properties of MPCMS

MPCMS is a solid-liquid multiphase heat transfer fluid, prepared by mixing microencapsulated phase change material (MPCM) particles with traditional single-phase fluid. The MPCM particles, which have been purchased from Changzhou Meisheng Biomaterials Co., Ltd, have a core of paraffin enclosed in a thin solid shell made of the melamine-formaldehyde resin. The MPCM particles, which the average volume particle diameter is about 5 μm, are used to formulate the MPCMS with the mixture of deionized water and anhydrous ethanol as the base fluid. The melting and freezing characteristics and the latent heat of fusion of the MPCM particles are determined by differential scanning calorimeter. DSC measurements are undertaken with a heating rate of 5 °C/min and temperature range of 0-50°C. The corrected melting point, heating peak, freezing point, cooling peak, heating enthalpy and cooling enthalpy are 29.9°C, 34.5°C, 23.4°C, 18.2°C, 125.4 J/g, and 112.6 J/g, respectively.
The mixture-based microfluids dispersed with various mass fractions of the MPCM particles ranging from 0.1 to 2.0 wt.% are prepared for the present study. The following steps are adopted to prepare the MPCMS: (1) weighing the required amount of the MPCM particles, and adding them to the mixed base fluid which is conducted with the base fluid of anhydrous ethanol mass fraction 46 wt.%. (2) stirring the mixture of MPCM and the base fluid at 600 r/min with a magnetic stirrer for more than 30 min at room temperature, and then, dispersing MPCM into the base fluid more homogeneously with ultrasonic cleaner at 53 Hz for 30 min below the melting temperature of the phase change material. MPCM in the finished samples can remain in suspension for longer than one month by static observation.

2.2. Experimental Apparatus

The natural circulation loop constructed and measuring point distribution are schematically illustrated in Fig. 1. The system contains heating, cooling and adiabatic sections. And the major equipments for the system operation are a diaphragm pump, a DC power supply, a constant temperature bath and a data acquisition system. Adiabatic sections of the circulation loop are made of stainless steel pipe with an inner diameter of 10 mm and a wall thickness of 2 mm. The heating section is formed that nichrome heating wire is tightly wound around the outer surface of the 30 mm copper tube. Electrical power input (from a DC power supply) to this nichrome wire coil is used to obtain an essentially uniform heat flux on the outer surface. The cooling section is fabricated with the 500 mm long double pipe heat exchanger. The inner tube of the heat exchanger has an inner diameter of 10 mm and a wall thickness of 2 mm. And its outer tube has an outer diameter of 32 mm and a wall thickness of 1.5 mm. For considering the thermal expansion effect of suspension, an expansion chamber is set at the top of the experimental system to ensure that the system is always full of slurry and does not spill over. To further minimize the heat loss to (or gains from) the ambient environment, the outer surface of the closed-loop thermosyphon is wrapped with the Armaflex insulation layer of 24 mm in thickness. The heating section is insulated with two layers of Armaflex insulation.
For analyzing thermal transport capacity of the closed-loop thermosyphon system under different working conditions, PT-100 temperature sensors are used to record the temperature changes of the system. Before experimental testing, temperature sensors have been calibrated by using constant temperature bath and high precision thermometer. The working fluid is mainly driven by density difference and volume expansion caused by temperature difference. Hence, velocity of the working fluid is very small. So as not to add the flow resistance of the pipeline, the calibrated PT-100 temperature sensors are placed in the grooves about 1 mm deep which are polished at the measuring point of stainless steel pipes. Eight PT-100 temperature sensors are fixed on the grooves by thermal conducted and electrical insulated silica gel. Four sensors of them are put at the inlet and outlet of the heating and cooling sections. For observe variations of the temperature along the way,

a measuring point which is marked as 4# is set at the adiabatic section. Another temperature sensor is set on the heating wire to monitor the maximum heating temperature of the system in real time. Two sensors are used to record the inlet and the outlet of the constant temperature bath. The ninth temperature sensor is put in the air for recording ambient temperature changes. The measurement error of the temperature sensors is less than 0.15°C.

The working fluid (distilled water or MPCM suspension) is pumped from beaker and flows through the loop. It is stopped when the working fluid reach the middle of the expansion chamber to ensure that the loop of the thermosyphon is always full of fluid. The working fluid is heated at a certain power when proceeding to the heating section where heating wires provide uniformly distributed heat flux. The heat flux provided to the heating section must guarantee complete phase change when the working fluid is MPCMS, so that the difference between the inlet and the outlet temperatures is noticeable and higher than the PT-100 uncertainty. Then, the heated fluid flow through the inside of the inner pipe of the double-pipe heat exchanger, and exchange heat with the cooling water supplied from the constant temperature bath which flow through the annulus. Thus, the working fluid which is driven by density and system height difference circulates in the closed-loop thermosyphon system.

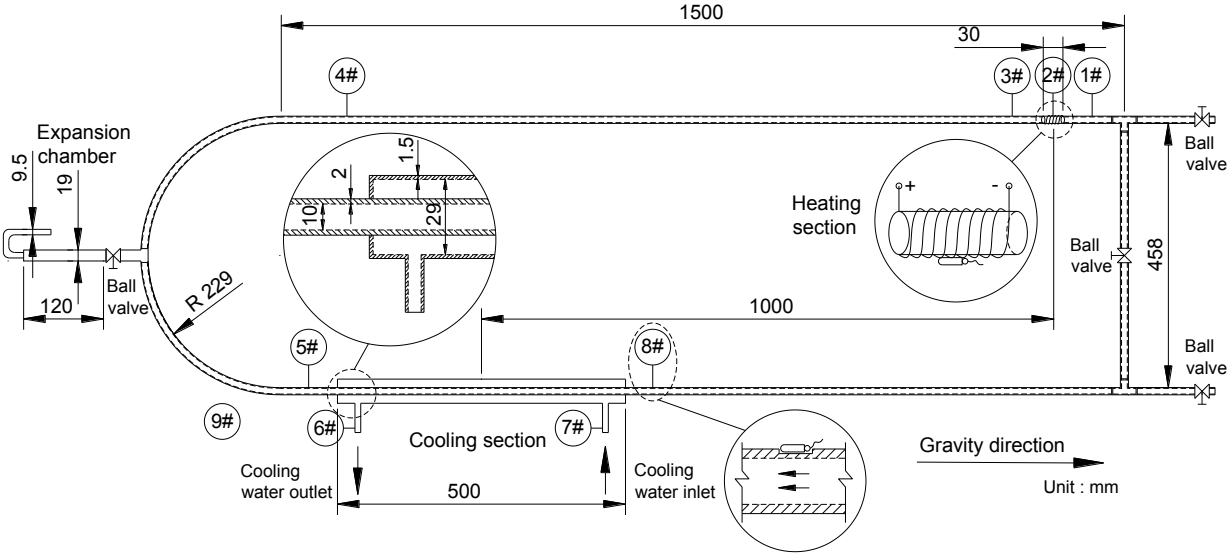

Figure 1: Schematic of the experimental setup and measuring point distribution

3. RESULTS AND DISCUSSION

Heat transfer characteristics of the closed-loop thermosyphon system are compared by changing the heating power of the heat source, the temperature of the cold source and the mass concentration of MPCMS. The heating powers are 10, 20 and 30 W. Temperatures of the cold source are 22, 24, 26, 28, and 30°C. As the working fluid, Base fluid and MPCMS are prepared through the above preparation steps. The mass fractions of the formulated MPCMS are 0%, 0.1%, 0.2%, 0.5%, 1.0% and 2.0%. The start-up characteristics of the system and axial distribution of the wall temperature are illustrated primarily. The heat transfer performance of the closed-loop thermosyphon system are analyzed by comparing the temperature of the heating wire T_h, the loop system thermal resistance R_{sys}, the heat-transfer thermal resistance of working fluid R_f and the convective heat transfer coefficient at the heating section inlet $H_{h,in}$ for different working conditions.

The start-up characteristics of the system are analyzed by observing temperature changes of each measuring point which is recorded by the data acquisition system. MPCMS with mass fraction of 0.5% is taken as an example to illustrate the start-up characteristics of the system. The trends of the wall temperature for various heating powers (10, 20 and 30 W) under a cold source temperature of 28°C, as shown in fig.2. Fig. 2(b) presents that the partial enlarged detail of temperatures varies with time when increasing heating power from 10 W to 20 W.

On the one hand, the temperature of the heating section outlet increases quickly when the DC power supply is switched on and the heating power is increased suddenly. The density difference of the MPCMS between heating and cooling sections increases with increasing in the temperature difference between them. Thereby, the driving force, generated by the density difference and the system height difference, makes the MPCMS start running in the system. On the other hand, the temperature of 3# rises first when MPCMS flow through the heating section with increasing in heating

power suddenly, as shown in Fig. 2(b). Subsequently, temperatures of 4# and 5# rise along the flow direction sequentially. Variations of temperature of the above three measuring points (3#, 4# and 5#) indicate that the system is started successfully. When the system is running stably, the temperature difference between the heating section inlet and the cooling section outlet is small. It proves that the insulation effect on the loop is better, and the heat loss is small from the loop to the ambient environment.

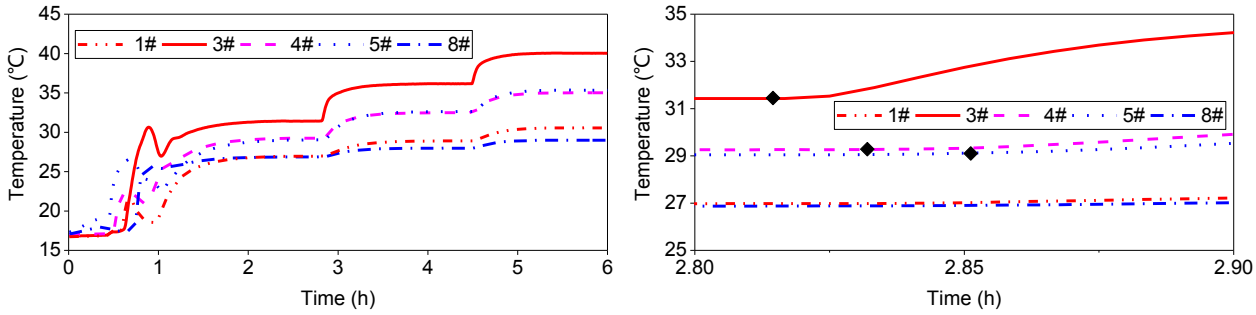

(a) the complete operation process of the system **(b) the partial enlarged detail**

Figure 2: The trends of the wall temperature for various heating powers (10, 20, 30 W) under a temperature of the cold source of 28°C and MPCMS of 0.5%

When the experimental system operates in stable state, the wall temperature distribution of the system loop is analysed for 0% and 0.5% suspensions under various heating powers (10 ,20, 30 W) and a temperature of the cold source of 22°C (Fig.3). The four dashed lines in the figure divide the loop into five sections along the flow direction. They are the adiabatic section, the heating section, the adiabatic section, the cooling section and the adiabatic section. The first adiabatic section begins at the lower-right corner of the system loop and is recorded as x_{loop}=0. x_{loop} values of the first adiabatic section before the heating section are 0-0.03212. x_{loop} values of the heating section are 0.03212-0.03926. x_{loop} values of the second adiabatic section between the heating section and the cooling section are 0.03926-0.55553. x_{loop} values of the cooling section are 0.55553-0.67450. x_{loop} values of the last adiabatic section after the cooling section are 0.67450-1.0000. An x_{loop} value of 1.0000 represents a return to the starting point of the loop.

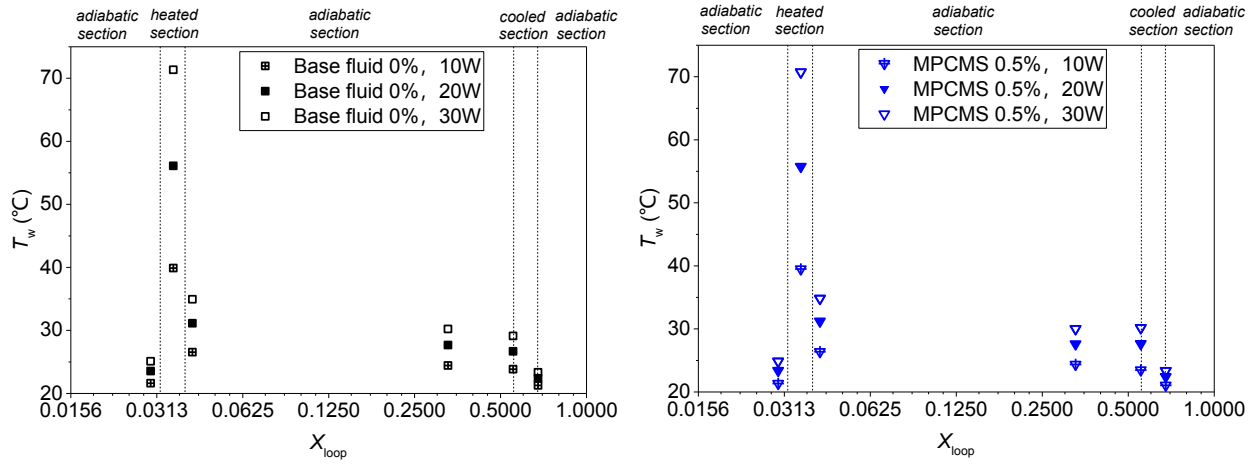

(a) the base fluid **(b) MPCMS of 0.5%**

Figure 3: Axial distribution of the wall temperature for 0% and 0.5% MPCMS under various heating powers (10, 20, 30 W) and a temperature of the cold source of 22°C

When the working fluid flows through the heating section, the wall temperature of the heating section outlet is higher than inlet. Temperature of measuring point 3#, 4#, 5# which are in the second adiabatic section decreased slightly, possibly due to a small amount of heat loss. When the working fluid flows through the cooling section, the wall temperature quickly decreased to the set temperature of the cold source. At last, the working fluid enters into the heating section circularly. The wall temperature of the heating section inlet in the first adiabatic section which is before the heating section is little higher than the cooling section outlet, due to axial heat conduction. It may because temperature sensor of the heating section inlet closes to the heating section. From Fig.3, it can also get the same law of the wall temperature changes for different working conditions.

Cooling effect of the closed-loop thermosyphon system with MPCMS can evaluated by the temperature of heating wire (T_h). The comparison of T_h for different MPCMS is shown in Fig. 4 when the system runs in the steady-state.

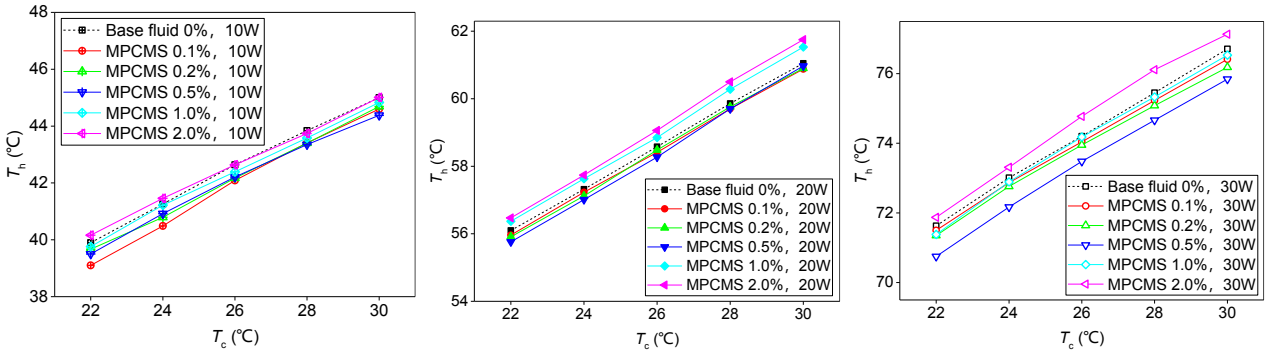

(a) heating power of 10 W **(b) heating power of 20 W** **(c) heating power of 30 W**

Figure 4: The measuring point temperature of the heating wire with various temperatures of the cold source (22, 24, 26, 28, 30°C) for various MPCMS (0%, 0.1%, 0.2%, 0.5%, 1.0%, 2.0%) and heating powers (10, 20, 30 W)

Fig.4(a) presents that T_h with 0.1%, 0.2%, 0.5% and 1.0% suspensions are lower than the base fluid under various temperatures of the cold source and heating power of 10 W. T_h with 0.1% suspension at 10 W are the lowest when the temperature of the cold source is less than 26°C. The experimental data show that the difference in T_h among 0.1% 0.2% and 0.5% MPCMS is very small at 10 W/26°C and 10 W/28°C (heating power/cold source temperature). When the temperature of the cold source grows to 30°C, T_h with 0.5% suspension is the lowest. In addition, T_h with 2% suspension at 10 W is lower slightly than that of base fluid when the temperature of the cold source is higher than 26°C. Fig. 4(b) indicates that T_h with 1.0% and 2.0% suspensions under various temperature of the cold source and heating power of 20 W are higher than the base fluid. It illustrates that heat transfer performance of 1.0% and 2.0% suspensions is not as good as that of the base fluid. T_h with 0.1%, 0.2% and 0.5% suspensions are lower than the base fluid. And T_h decreases with increasing in mass fraction of MPCMS from 0.1% to 0.5% under the temperature of the cold source of 22 and 24°C. T_h with 0.1%, 0.2% and 0.5% suspensions at 20 W/26°C, 20 W/28°C and 20 W/30°C do not exhibit large differences from each other. So, the best cooling effect is achieved when the working fluid is 0.5% suspension with heating power of 20 W. Fig.4(c) illustrates that T_h with 1.0% suspension is lower than the base fluid when heating power is increased from 20 W to 30 W. T_h with 0.1%, 0.2%, 0.5% and1.0% suspensions are lower than the base fluid. And T_h with 0.5% suspension is the lowest under different temperature of the cold source. T_h with 1.0% suspension is slightly lower than 0.2% suspension. In summary, the result here is accordant with Ho et al. (2014), that 0.5% MPCMS is most prominent in the hot wall temperature reduction considering the influence of the heating power and cold source temperature.

The loop system thermal resistance (R_{sys}) is shown in Eq. (1).

$$R_{sys} = \frac{T_h - T_c}{q_h} \qquad \text{Eq. (1)}$$

where q_h is the total heating power in W, T_h is the temperature of the heating wire in °C, and T_c is the cold source temperature in °C. Fig. 5 shows the loop system thermal resistance for different working conditions, which are calculated by Eq. (1).

Physical meaning of the R_{sys} is the strength of heat transfer capacity. When the system is at the same cooling conditions, the thermal resistance of the system R_{sys} increases with decreasing in the temperature of the heating source at the same heating power. It indicates that the heat-transfer capacity of the loop is stronger. Different mass fractions of MPCMS at 20 W/22°C are taken as an example to illustrate heat transfer characteristics of the system. It shows that the temperature of the heating wire T_h is the lowest with the 0.5% suspension and the loop system thermal resistance R_{sys} is the smallest, combined Fig. 4(b) with Fig. 5(b). Hence, under 20 W/22°C condition, the closed-loop thermosyphon system with 0.5% suspension has the stronger heat transfer capacity, compared with other suspensions (0%, 0.1%, 0.2%, 1.0% and 2.0%). The thermal resistance of the loop system R_{sys} decreases with increasing in the temperature of the cold source for the same MPCMS and

heating power. The resistances at 30 W are lower than those at 20 W for the same MPCMS and the temperature of the cold source. The heat-transfer capacity of the closed-loop thermosyphon system increases with decreasing in the thermal resistance of the loop system, and it has the best capacity with 0.5% MPCMS.

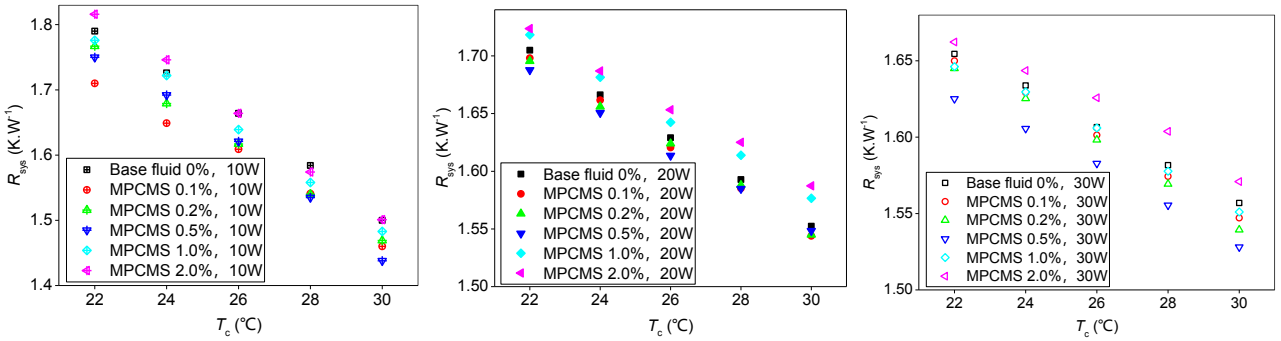

(a) heating power of 10 W **(b) heating power of 20 W** **(c) heating power of 30 W**

Figure 5: Variations of the loop system thermal resistance R_{sys} with various temperatures of the cold source (22, 24, 26, 28, 30°C) for various MPCMS (0%, 0.1%, 0.2%, 0.5%, 1.0%, 2.0%) and heating powers (10, 20, 30 W)

The heat-transfer thermal resistance of working fluid (R_f) is shown in Eq. (2).

$$R_f = \frac{T_{h,out} - T_{c,out}}{q_h} \quad \text{Eq. (2)}$$

where $T_{h,out}$ is the temperature of the heating section outlet in °C, and it represents the maximum temperature of the working fluid in the heat transfer process. $T_{c,out}$ is the temperature of the cooling section outlet in °C, and it represents the minimum temperature of the working fluid. Fig. 6 shows the heat-transfer thermal resistance of working fluid for different working conditions, which are calculated by Eq. (2).

Under the same temperature of the cold source, the heat-transfer thermal resistances of working fluid (R_f) for various MPCMS at 10 W are totally greater than R_f at 20 W which is completely greater than those at 30 W. R_f decreases with increasing in heating power for the same MPCMS and cooling conditions. And the resistances have a downward trend with increasing in the temperature of the cold source. It indicates that the heat-transfer capacity of the working fluid is stronger and the loop system has a better uniformity of temperature with the lower resistances.

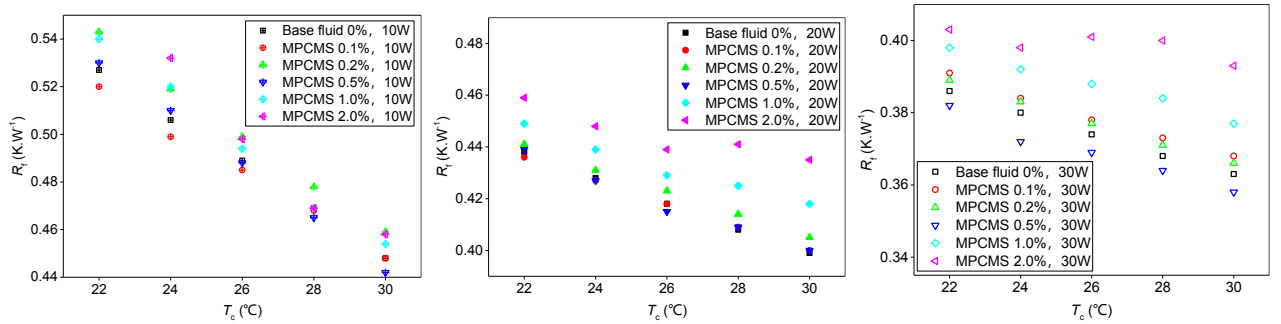

(a) heating power of 10 W **(b) heating power of 20 W** **(c) heating power of 30 W**

Figure 6: Variations of the heat-transfer thermal resistance of working fluid R_f with various temperatures of the cold source (22, 24, 26, 28, 30°C) for various MPCMS (0%, 0.1%, 0.2%, 0.5%, 1.0%, 2.0%) and heating powers (10, 20, 30 W)

The convective heat transfer coefficient at the heating section inlet ($H_{h,in}$) is shown in Eq. (3).

$$H_{h,in} = \frac{q_h}{A(T_h - T_{h,in})} \quad \text{Eq. (3)}$$

where $T_{h,in}$ is the temperature of the heating section inlet in °C. A is the inner surface area of circular tube. Fig. 7 shows the convective heat transfer coefficient at the heating section inlet for different working conditions, which are calculated by Eq. (3).

Under the same temperature of the cold source, the convective heat transfer coefficients at the heating section inlet ($H_{h,in}$) for various MPCMS at 30 W are totally greater than the coefficients at 20 W which is completely greater than those at 10 W. $H_{h,in}$ increases as the heating power increases. In addition, $H_{h,in}$ has an upward trend with increasing in the temperature of the cold source. $H_{h,in}$ with 0.5% MPCMS is twice as much as that of base fluid under different working conditions.

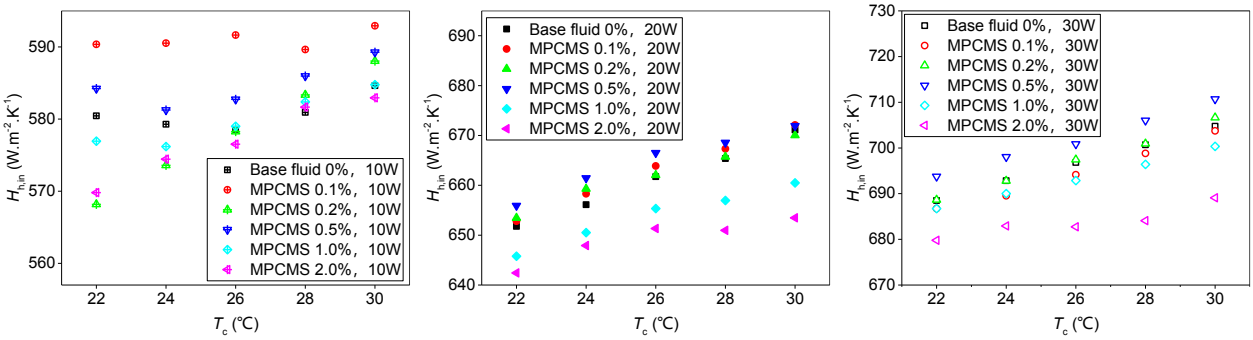

(a) heating power of 10 W **(b) heating power of 20 W** **(c) heating power of 30 W**

Figure 7: Variations of the convective heat transfer coefficient at the heating section inlet $H_{h,in}$ with various temperatures of the cold source (22, 24, 26, 28, 30°C) for various MPCMS (0%, 0.1%, 0.2%, 0.5%, 1.0%, 2.0 %) and heating powers (10, 20, 30 W)

The concentration of MPCMS is relatively low in the system test. The convective heat transfer of 0.5% MPCMS in the system has a better effect compared with other MPCMS. For a given heating power, 0.1%, 0.2% and 0.5% suspensions can reduce the hot-wall temperature, the loop system thermal resistance and the heat-transfer thermal resistance of working fluid, and increase the convective heat transfer coefficient at the heating section inlet. When mass fraction of the MPCM particles increases to 2.0%, the heat transfer performance of the system with the base fluid is better than that with 2.0% MPCMS. Viscosity of MPCMS increases with increasing in mass fraction of the MPCM particles. The lower thermal conductivity of MPCMS and the higher flow resistance which are caused by viscosity may influence heat transfer characteristics of the closed-loop thermosyphon system with high concentration of MPCMS.

4. CONCLUSIONS

The heat transfer characteristics of the closed-loop thermosyphon system with the base fluid and different MPCMS are experimentally investigated. The major findings can be summarized as follows:

(1) MPCMS can lower the wall temperature of the heating section and enhance the heat transfer performance of the system compared with the base fluid, except some cases with 2.0% MPCMS and with 1.0% MPCMS at 20 W.

(2) For a given heating power, the thermal resistance of the loop system decreases with an increase in the temperature of the cold source. The temperature of the cold source which is approaching phase-change temperature could make the system have a better heat transfer capacity with lower resistances.

(3) For a given the temperature of the cold source, the heat-transfer thermal resistance of working fluid decreases with increasing in heating power. For a given heating power, the resistances have a downward trend with increasing in the temperature of the cold source. The loop has a better uniformity of temperature with the lower resistance.

(4) For a given the temperature of the cold source, the convective heat transfer coefficient at the heating section inlet increases as the heating power increases. For a given heating power, the convective heat transfer coefficient at the heating section inlet has an upward trend with increasing in the temperature of the cold source.

ACKNOWLEDGEMENTS

This work was supported by National Natural Science Foundation of China (Grant NO. 51678102, 51508067).

NOMENCLATURE

T_c	the temperature of the cold source (°C)	q_h	heating power (W)
$T_{c,out}$	the temperature of the cooling section outlet (°C)	Subscripts	
T_h	the temperature of the heating wire (°C)	h	heating
$T_{h,in}$	The temperature of the heating section inlet (°C)	c	cooling
$T_{h,out}$	the temperature of the heating section outlet (°C)	in	heating or cooling section inlet
R_{sys}	the loop system thermal resistance ($K \times W^{-1}$)	out	heating or cooling section outlet
R_f	the heat-transfer thermal resistance of working fluid ($K \times W^{-1}$)	sys	loop system
$H_{h,in}$	the convective heat transfer coefficient at the heating section inlet ($W \times m^{-2} \times K^{-1}$)	f	working fluid

REFERENCES

Li, Z., Kandlikar, S. G., 2015. Current status and future trends in data-center cooling technologies. Heat Transfer Engineering 36(6), 523-538.

Saini, M., Webb, R. L., 2002. Heat rejection limits of air cooled plane fin heat sinks for computer cooling. IEEE Transactions on Components & Packaging Technologies 26(1), 71-79.

Khalaj, A. H., Halgamuge, S. K., 2017. A Review on efficient thermal management of air-and liquid-cooled data centers: From chip to the cooling system. Applied energy 205, 1165-1188.

Bodjona, S., Videcoq, E., Saurel, R., Chinnayya, A., Benselama, A. M., Bertin, Y., 2017. Transient simulation of a two-phase loop thermosyphon with a model out of thermodynamic equilibrium. International Journal of Heat and Mass Transfer 108, 2321-2332.

Lamaison, N., Ong, C. L., Marcinichen, J. B., Thome, J. R., 2017. Two-phase mini-thermosyphon electronics cooling: Dynamic modeling, experimental validation and application to 2U servers. Applied Thermal Engineering 110, 481-494.

Chen, B., Wang, X., Zeng, R., Zhang, Y., Wang, X., Niu, J., Di, H., 2008. An experimental study of convective heat transfer with microencapsulated phase change material suspension: laminar flow in a circular tube under constant heat flux. Experimental Thermal and Fluid Science 32(8), 1638-1646.

Song, S., Shen, W., Wang, J., Wang, S., Xu, J., 2014. Experimental study on laminar convective heat transfer of microencapsulated phase change material slurry using liquid metal with low melting point as carrying fluid. International Journal of Heat and Mass Transfer 73, 21-28.

Roberts, N. S., Al-Shannaq, R., Kurdi, J., Al-Muhtaseb, S. A., Farid, M. M., 2017. Efficacy of using slurry of metal-coated microencapsulated PCM for cooling in a micro-channel heat exchanger. Applied Thermal Engineering 122, 11-18.

Ho, C. J., Chen, Y. Z., Tu, F. J., Lai, C. M., 2014. Thermal performance of water-based suspensions of phase change nanocapsules in a natural circulation loop with a mini-channel heat sink and heat source. Applied Thermal Engineering 64(1-2), 376-384.

Lamoureux, A., Baliga, B. R., 2013. Experimental study of a closed-loop thermosyphon operating with slurries of a microencapsulated phase-change material. Proceedings of the ASME 2013 Heat Transfer Summer Conference, Minneapolis, MN, USA. HT2013-17547, 13 p.

Manuscript ID: 728
DOI: 10.18462/iir.icr.2019.0728

Electrical demand side flexibility from refrigeration systems with thermal energy storage based on a model predictive control strategy – influence of model uncertainties

Daniel PFEIFFER[(a)], Sebastian HAUSSER[(a)], Stefan HUDJETZ[(a)], Martin BECKER[(a)]

[(a)] University of Applied Sciences, Biberach
Biberach, 88400, Germany, pfeiffer@hochschule-bc.de

ABSTRACT

Motivated due to boosting shares of renewable energy resources and the associated need for demand side flexibility, electrical driven refrigeration systems can specifically supply capacities through adequate use of cold-water energy storage. Therefore, a model predictive control approach is presented, mainly focusing on a simplified model to estimate the useable amount of the storage capacity. Aim of this investigation is to identify the influence of the uncertainties by this estimation. Using a simulation model of a cold-water refrigeration system a sensitivity analysis is performed. Based on synthetic incentive signals, various load shifting scenarios are represented and the feasibility of the suggested cooling supply schedules is evaluated. The examination of necessary schedule corrections by a basic plant control as well as the utilization of the incentive signals show a distinct dependence on the model accuracy.
Keywords: Energy Storage, Simulation, modelling, Thermal Analysis, Control (Automatic), indirect system

1. INTRODUCTION

1.1. Background

The aim to incorporate highly distributed renewable energy resources into the electrical grid involves new requirements for the energy management in buildings.
With regard to building automation, concepts such as smart grids require a system approach that goes beyond the consideration of the appropriate interplay of room and plant controls, i. e., future buildings should be considered as embedded energy systems in a wider context. In addition to established objectives such as a high energy efficiency and a comfortable climate in buildings, a grid supportive building operation is expected to be a new but increasingly significant automation functionality. Such a functionality implies an optimized energy interaction with the electrical grid, dependent on the local electricity supply by means of load shaping measures, i. e., increasing electricity demand in times with a high supply and vice versa.
Motivated by utility control, Gellings (1985) early defined major measures for demand side management to adjust the electrical load shape, e. g., through peak clipping, valley filling, load shifting, strategic conservation, etc. Originally, the application of these methods was utility-driven and either dedicated for energy-intensive industrial processes or reserved for simple control measures combined with robust energy systems.
Due to the highly volatile energy supply of solar and wind power plants, the future demand for electrical flexible energy consumption will probably not only increase significantly, but is also expected to be much more dynamic and decentralized. The associated complexity cannot be handled by the utility alone, thus a certain shift of the control task to the demand side is necessary. Therefore, much more sophisticated optimization and communication methods are required on the demand side, as well as dynamic incentives to motivate changes in the consumer load profiles. For this purpose, Vardakas *et al.* (2015) define such much more dynamic programs as Demand Response and as a subset of the DSM.

1.2. Utilization of Thermal Energy Storage in Refrigeration Systems – State of the Art

Electrical driven refrigeration systems as those widely used for instance in air conditioning systems or in industrial cooling applications are a relevant electrical consumer type in non-residential buildings. Especially, due to their thermal capacity those systems offer noticeable flexibility potential for demand response programs. Many investigations concern the flexibility resource associated with the optimal operation of a thermal energy storage system (TES).
Arteconi *et al.* (2012) thoroughly distinguish between different types of TES, summarise their state of art and indicate their significance for DSM. Further, they refer to other literature that investigates proper thermal stratification of water based TES and its influence on storage efficiency. Particularly, the characteristic of the thermocline is of special interest in this type of investigations. For instance, Karim (2011) exposed the impact of diffuser design and layout on the thermocline shape of the thermal stratification through an experimental study with different flow rates for charging and discharging a TES. A sophisticated review on further methods to characterize thermal stratification is provided by Haller *et al.* (2009).
Due to the ability to consider predictions of important system inputs and the possibility to integrate system knowledge into an optimization model, model predictive control (MPC) is very well suited to optimally use the flexibility in a TES. There are numerous investigations in this context. However, many of them are focused on determining the economic potential of a suggested MPC approach, without addressing its model uncertainties and the integration into an existing automation system, e. g. Arteconi *et al.* (2017). Partly, the designed MPC approach is not applicable for implementation, because of the ambitious non-linear model formulation, for instance in Hovgaard *et al.*(2012).
In contrast, Ma *et al.* (2012) attached importance to making the proposed MPC approach as simple and robust as possible for implementation. In particular, the model of the TES is cleverly simplified by a four state formulation and shows good results compared to experimental studies.

1.3. Issue of this study

This study presents an MPC approach aimed at exploiting the given flexibility potential of a cold-water refrigeration system, in particular through the adequate use of a TES in the form of a cold-water storage tank. Compared to the cited literature, the influence of model uncertainties within the MPC algorithm is investigated by means of a simulative sensitivity analysis over a detailed one-day analysis period.

2. SYSTEM DESCRIPTION

2.1. Overview

This section shows the system structure considered in this study and gives an overview of the essential system components and their interactions. With regard to the automation structure, the system can be divided into low and high-level control hierarchies, whereby the high level hierarchy is also separated into a control (HLC) and scheduling (HLS) unit, see Fig. 1.
At the low-level hierarchy, the refrigeration system contains the thermodynamically interacting process components and the low-level controller, e. g. PID control. Low-level controllers are responsible for dedicated control tasks of individual components, e. g. for temperature control in the cold water circle by adjusting the mixing ratio in a three-way valve. The basic plant control unit arranged in the high-level hierarchy coordinates the switching sequences and continuously maintains significant system temperatures via a simple bang-bang control of the main cooling components, e. g. through actuation of the compressor, pumps and ventilator units.
The proposed Model Predictive Control unit (MPC) is implemented in the high-level hierarchy above the basic plant control, which forwards relevant system states, see Fig. 1. The purpose of the MPC is to provide optimal schedules for the capacity control of the refrigeration plant by using an incentive signal containing the information at which times it is favorable or unfavorable to consume electricity or, in the case of the compression chillers considered here, to supply cooling energy. Compared to the outputs of the High-Level Control (HLC), the predicted schedules (HLS) are not obligatory for safe plant operation. Rather, they are to be understood as a proposal, which in the best case, is completely adopted by the basic plant control. Schedule inaccuracies resulting from the forecast uncertainty of the MPC are absorbed by the basic plant control. This ensures that the cooling demand and the required system temperatures are maintained at all times.

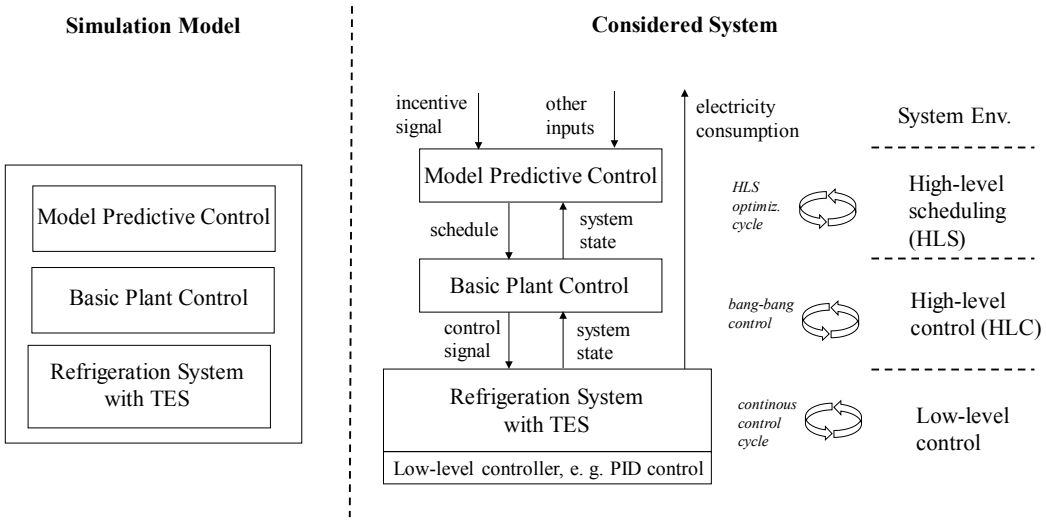

Figure 1: Comparison of the considered system and the depicted simulation model

Further information on the functionality and structure of the proposed MPC approach is given in section 2.2. A description of the depicted simulation model is given in section 2.3.

2.2. Model Predictive Control Approach

Based on the automation concept introduced by Pfeiffer and Becker (2018), the main system components of the proposed MPC are shown in Fig. 2 a).

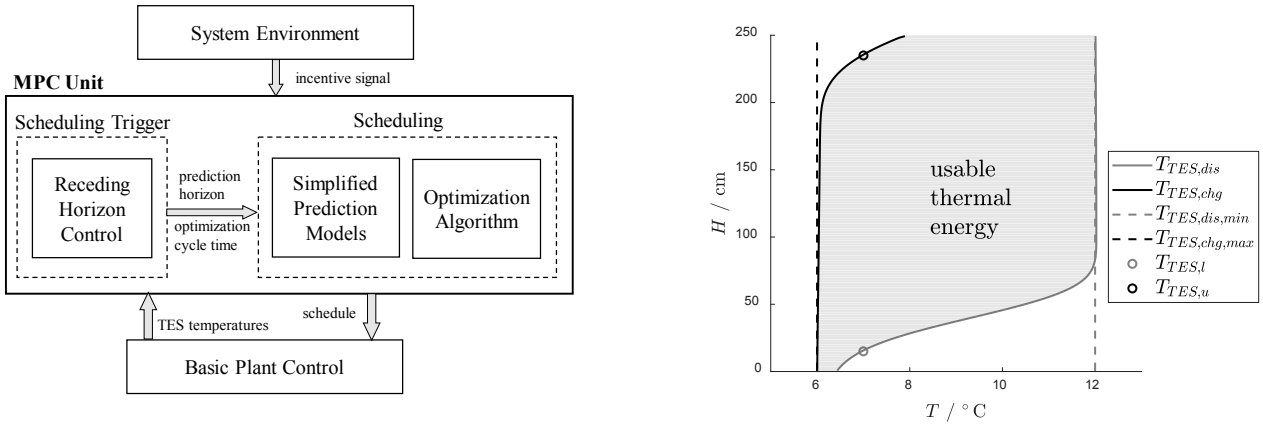

a) MPC system structure

b) TES temperatures (*T*) as function of tank height (*H*)

Figure 2: Essential elements of the proposed MPC approach

The basic concept contains a receding horizon control strategy which triggers the scheduling algorithm by a constant optimization cycle time to calculate an optimized schedule for a given prediction time horizon, e. g. for predicting 24 hours based on the start time of each optimization. The scheduling function mainly comprises simplified prediction models and an optimization algorithm. Essential for an optimized schedule are the prediction of the expected cooling load, the expected energy efficiency of the refrigeration plant and the estimated dynamics of the TES tank.
The optimization method used with the underlying MATLAB® algorithm and their relationships to the simplified models are discussed in further detail by Bachseitz *et al.* (2019).
Fig. 2 b) shows the simplified model of a TES as used in the proposed MPC. As it is shown, the assumed inlet temperatures into the storage tank at the top and bottom, here given as 6 and 12 °C, result in a maximum storage capacity proportional to the area between these constant temperature functions. In the following, it is assumed that this maximum area or capacity is reduced to a useable amount of energy under real operation criteria and through the resulting

temperature functions in a fully charged ($T_{TES,chg}$) and discharged ($T_{TES,dis}$) state. In this study the temperature profile $T_{TES,chg}$ is simply assumed to be constant, as depicted in Fig. 2 b). Additionally, the current state of charge (*SOC*) of the TES is estimated on the basis of the current temperature distribution $T_{TES,cur}$ and the correlation from Eq (1), before each schedule optimization.

$$SOC = 1 - \frac{Q_{TES,cur}}{Q_{TES,p}} = 1 - \frac{A_{TES}\,\rho_W\,c_{p,w}\int_{x=0}^{H_{TES}} T_{TES,cur}(H) - T_{TES,chg}(H)\,dH}{f_{ue,p}\,Q_{TES,max}} \quad \text{Eq. (1)}$$

Given by the ratio of the current thermal energy in the TES ($Q_{TES,cur}$) to the predicted useable thermal energy ($Q_{TES,p}$). While the predicted useable energy is assumed as a predicted constant fraction ($f_{ue,p}$) of the maximum capacity ($Q_{TES,max}$).
The expected cooling load and energy efficiency of the refrigeration plant are assumed to be given in this study.

2.3. Simulation model

The depicted simulation model contains a refrigeration plant, a cold-water circle including a thermal energy storage filled with cold water, a consumer unit, a basic plant control and the introduced MPC unit. Fig. 3 shows the structure of the model with its main components, their principle interaction and their assignment to the control hierarchies introduced in section 2.1.

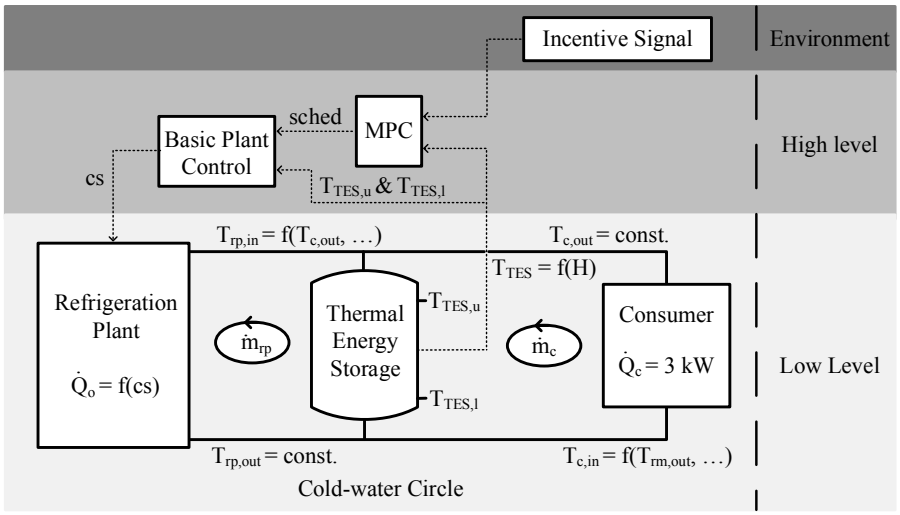

Figure 3: Structure of the simulation model

The physical phenomena of the considered refrigeration system components are modeled on various degrees of fidelity.
The TES is represented by a 200-layer model from the MATLAB® SIMULINK® toolbox extension CARNOT© and respects the essential thermodynamic effects by a numerical finite volume calculation, i. e. forced convection, conduction between adjacent storage layers and thermal heat gains (cold losses) by heat transmission over storage walls, according to the model developer Solar-Institute Jülich (2018). The observed dynamics of the TES model showed satisfactory agreement with measurement results provided by Karim (2011). Only minor deviations are found, which may be caused by differences between the experimental setup and the ideal simulation model.
In contrast to the sophisticated TES model, the cooling supply and consumer sides are considered in a simplified mathematical description, by one basic equation for the thermal heat flow and a predefined, i.e. ideally controlled, water outlet temperature for each component (refrigeration plant/consumer). This means 6 °C for $T_{rp,out}$ when refrigeration plant is active and 12 °C for $T_{c,out}$ when cooling load is present. The cooling load is considered constant at 3 kW. The electrical load and cooling capacity of the refrigeration plant is represented by a proportional correlation to the control signal (*cs*) and by a constant coefficient of performance (*COP*). The control signal (*cs*) which originates either by the basic plant control or by the schedule (*sched*) of the MPC has a value range between 0 and 100 %. This is expressed in a range for the cooling capacity of the refrigeration plant ($\dot{Q}_o$) between 0 and 6 kW. The water inlet temperature in the refrigeration plant

($T_{rp,in}$) and the consumer unit ($T_{c,in}$) are each calculated by the mass flow balances at the respective mixing nodes.
The MPC unit gets at each start of the schedule optimization the current temperature profile of the TES as function of the 200 depicted storage layers ($T_{TES} = f(H)$) and the assumed incentive signal. Based on this, the schedule (*sched*) for the refrigeration plant will be determined as described in section 2.2. The basic plant control receives the schedule trajectory (timeseries reaching up to the next optimization step) as well as the current upper and lower storage temperature measurements ($T_{TES,u}$ / $T_{TES,l}$) as input and decides whether the schedule is valid to the temperatures limits for the upper and lower measurement ($T_{TES,u}$ / $T_{TES,l}$). The limit temperatures are used as follows:
the refrigeration plant is activated when the lower temperature measurement ($T_{TES,l}$) exceeds the preset limit value ($T_{TES,l,thr}$) (TES is fully discharged) and is deactivated when the upper temperature measurement ($T_{TES,u}$) falls below the second limit value ($T_{TES,u,thr}$) (TES is fully charged). Fig. 2 b) shows the resulting temperature profiles for a fully charged and discharged TES defined by the threshold value 7 °C for each of both limits ($T_{TES,u,thr}$/$T_{TES,l,thr}$.).

3. RESULTS

3.1. Simulation Scenarios

Based on the description of the simulation model in section 2.3, each scenario defined below is represented by the parameter set in Table 1.

Table 1: Simulation parameters

$\dot{Q}_c$	$\dot{Q}_{o,max}$	COP	V_{TES}	$T_{rp,out}$	$T_{c,out}$	$T_{TES,l,thr}$	$T_{TES,u,thr}$
3 kW	6 kW	3.23	2.2 m³	6 °C	12 °C	7 °C	7 °C

Several sequential charging and discharging cycles of the TES, each with a constant thermal energy flow of 3 kW, have shown in a preliminary study that the value of the useable thermal energy of the TES changes only negligibly under these uniform conditions. Therefore, the determined value of 12.3 kWh can be considered as a reasonable baseline value. Translated to the theoretical potential for shifting the electrical refrigeration plant peak load, this corresponds to four hours of continuous charging or discharging the TES at 3 kW thermal heat flow.
However, only a suitable incentive signal invokes the motivation to use this given load shifting flexibility. This requirement is met by specifying an incentive signal with a recurrent sequence of two value levels, i. e. a high and low incentive, and a cycle time of eight hours (duration of a high and low value pair). This scenario Arteconi (2012) defines as full storage (*FS*) strategy, as the entire peak load can be shifted to off-peak hours (here equivalent to a high incentive). In the subsequent parameter analysis this scenario is named as “Quasi Perfect Design”, as the system design technically fits almost perfect to the introduced incentive signal.
In addition to this scenario, it is distinguished between two other incentive scenarios as input signal for the MPC, with the same two-level value characteristic but various cycle times. Examined are an incentive signal with a cycle time of four hours and another one with twelve hours. In relation to the given load shifting flexibility, these scenarios can be classified as an “Oversized TES” (in case the incentive cycle time is four hours) and an “Undersized TES” (in case the incentive cycle time is twelve hours) respectively. Each of the considered incentive signals start with a high incentive value. Further, the optimization cycle time of the proposed MPC is selected equivalent to half the cycle time of the assumed incentive signal of each scenario.
In the following section, the influence of the useable energy model of the TES within the MPC on the feasibility of the predicted schedule is investigated by means of varying the predicted value from the baseline value of 12.3 kWh.

3.2. Sensitivity analysis

Fig. 4 shows the results from three parameter variations for the predicted usable thermal energy of the TES ($Q_{TES,p}$), in the following shortly named estimated TES energy, for the Quasi Perfect TES Design scenario. Fig. 4 a) shows the time series of the thermal energy content in the TES (Q_{TES}), and the occurrence of interventions by the basic plant control (lower part of the figure). Fig. 4 b) shows the associated time series of the schedule (*sched*), represented as the suggested degree of

capacity modulation of the refrigeration plant and the time series of the state of charge (*SOC*), as it is interpreted by the MPC at each start of an optimization.

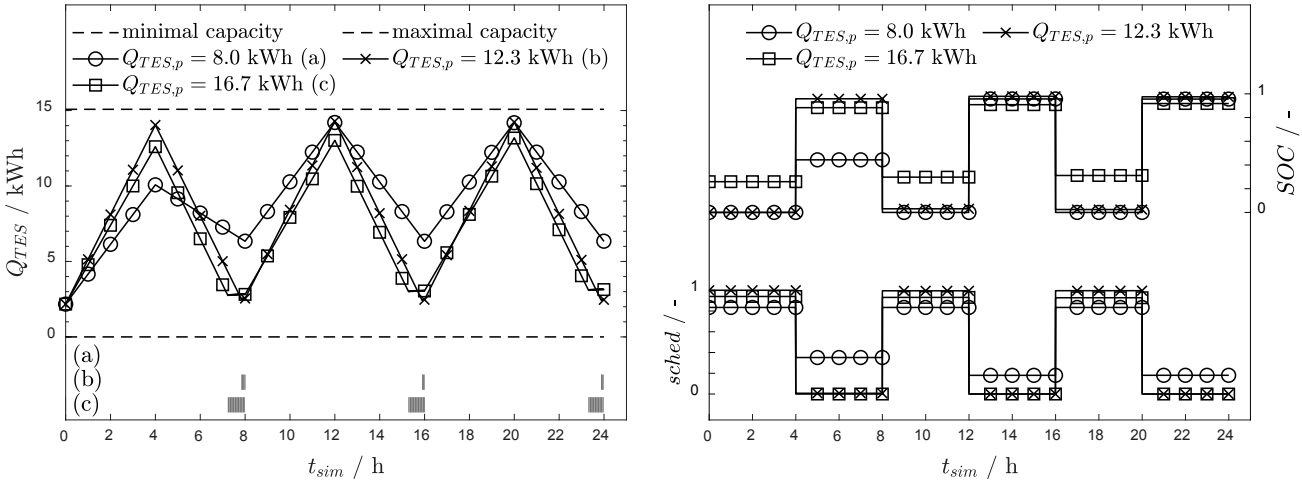

a) Energy content in TES (Q_{TES}) and indexing of interventions by the basic plant control

b) Interpreted state of charge (*SOC*) and resulted schedule (*sched*) of the MPC

Figure 4: Influence of simplified TES model on the system dynamics (Quasi Perfect TES Design)

In each of the three variants, a completely discharged TES is specified at the beginning of the simulation, i. e. fully discharged according to the criteria of the basic plant control (see section 2.3). This result in an offset at the beginning of the simulation of about 2 kWh in comparison to a TES discharged to homogenous 12 °C.
During the initial period of a constantly high incentive over four hours, it can be observed that the variant with the lowest value for the estimate of the TES energy ($Q_{TES,p}$ = 8.0 kWh) introduces the smallest amount of cooling energy into the TES. This is caused by the lowest degree of modulation of the suggested schedule (*sched*) by the MPC. The highest increase of internal cooling energy in the TES is achieved by the variant with an well estimated TES energy ($Q_{TES,p}$ = 12.3 kWh), caused by a maximum modulation degree of 100 %. The variant with the overestimated TES energy ($Q_{TES,p}$ = 16.7 kWh) lies between the two other variants in terms of the cooling energy growth in the TES and in terms of the level of the proposed schedule trajectory. This unexpected behavior can be explained by the fact that an incorrect estimation of the TES energy is always accompanied by an incorrect estimation of the current *SOC*, as can be observed at the beginning of the simulation. In the case of an overestimated TES energy, the *SOC* is assumed to be over 20 %, which reduces the overestimated TES energy in the schedule calculation by this amount. In the case of the underestimated TES energy, the exact opposite relationship can be observed in the first discharge interval. Due to this coupled misinterpretation, in the case of an underestimated TES energy, a course of the stored cooling energy in the TES results, which moves in the upper half of the maximum TES capacity. In the case of an overestimated TES energy, the proposed schedule at the end of each discharge interval violates the temperature criteria in the TES, leading to corrective interventions by the basic plant control. In the variant with a well-estimated TES energy, this also happens, but significantly less.

Fig. 5 summarizes the effects of different values for the estimation of the TES energy on the necessary intervention time of the basic plant control, see Fig. 5 a), and on the utilization of the available times with high incentive, see Fig. 5 b). A distinction is made here between the scenarios presented in section 3.1.
The summarized results confirm the behavior observed in the above detailed consideration for the other scenarios as well, that in case of an underestimated TES energy no corrective interventions by the basic plant control are necessary. Starting from an estimated value close to the baseline TES energy (12.3 kWh), the necessary intervention times increase with increasing values for the estimated TES energy.
When analyzing the utilization of the incentive signal in Fig. 5 b), it should first be mentioned that the maximum amount of cooling energy that can be supplied by the refrigeration plant during high

incentive periods is for all three scenarios 72 kWh. Only the scenario of an oversized TES achieves a maximum utilization of the high incentive times despite an underestimation of the useable TES energy. In all design scenarios shown, a break in the course of the supplied cooling energy for estimation values of the TES energy near to 12 kWh can be detected.
Further, can be seen the significantly lower level of supplied cooling energy in times of a high incentive in case of the “Undersized TES” scenario.

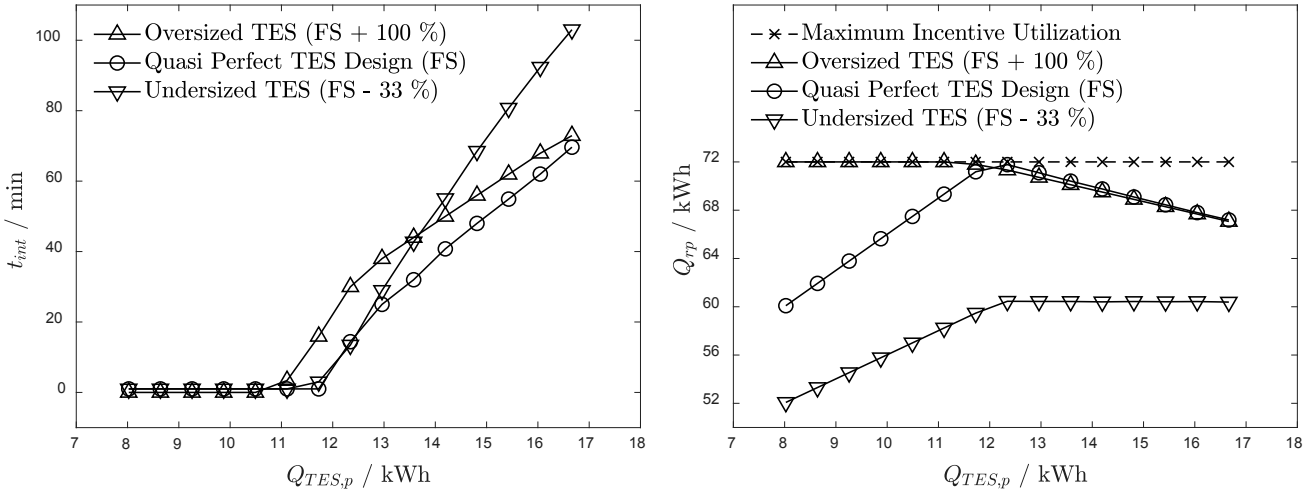

a) Cumulative intervention time (t_{int})

b) Supplied cooling energy (Q_{rp}) in times with a high incentive

Figure 5: Effect of the predicted useable energy of TES ($Q_{TES,p}$) on necessary corrective interventions by the basic plant control a) and on the utilization of the incentive signal b)

This can be explained by the fact that even with an ideal estimate of the TES energy, the physical TES volume is too small to fully shift the electrical load of the refrigeration plant over the underlying six-hour intervals.

4. CONCLUSION

Through the presented MPC approach for the predictive optimization of plant schedules in refrigeration systems, the influence of the estimate for the usable thermal energy of the TES on the feasibility of the suggested schedules could be demonstrated. By varying the prediction quality from a high underestimation to a high overestimation, a clear sensitivity could be determined with regard to the necessary corrective interventions of the basic plant control and the degree of utilization of the assumed incentive signals. In further work, the various control loops in a cold-water refrigeration system have to be included, to be able to evaluate the consequences of frequent schedule corrections and thus receive a better understanding which degree of fidelity for the used models in the MPC approach are adequate.

ACKNOWLEDGEMENTS

The authors thank the Federal Ministry of Education and Research for the support of the R&D project AutTherm within the framework of the funding program FHprofUnt - Forschung an Fachhochschulen mit Unternehmen. The project on which this report is based was funded by the Federal Ministry of Education and Research under the number 13FH047PX5. The authors are responsible for the content of this publication.





NOMENCLATURE

Q	thermal energy capacity (kWh)	*TES*	thermal energy storage
$\dot{Q}$	thermal capacity (kW)	*FS*	full storage
T	temperature (°C)	*SOC*	state of charge
V	volume (m^3)	*chg*	charged state
$\dot{m}$	mass flow (kgs^{-1})	*dis*	discharged state
c_p	specific thermal capacity ($Jkg^{-1}K^{-1}$)	*cur*	current state
ρ	density (kgm^{-3})	*max*	maximal value
A	area (m^2)	*min*	minimal value
t	time (h)	*l*	lower
H	height (cm)	*u*	upper
w	water	*sim*	simulation
MPC	model predictive control	*rp*	refrigeration plant
sched	schedule	*c*	consumer
p	predicted	*out*	outlet
cs	control signal	*in*	inlet
int	intervention of the basic plant control	*thr*	threshold
$f_{ue,p}$	predicted useable capacity factor		

REFERENCES

Arteconi, A., Hewitt, N.J., Polonara, F., 2012. State of the art of thermal storage for demand-side management. Applied Energy (93), 371-389

Arteconi, A., Ciarrocchi, E., Pan, Q., Carducci, F., Comodi, G., Polonara, F., Wang, R., 2017. Thermal energy storage coupled with PV panels for demand side management of industrial building cooling loads. Applied Energy (185), 1984-1993

Bachseitz, M., Pfeiffer, D., Koenigsdorff, R., Becker, M., 2019. Method for the predictive optimization of refrigeration plant operation for electrical demand side management. GI – Gebäudetechnik in Wissenschaft & Praxis (3), (to be published)

Gellings, C.W., 1985. The Concept of Demand-Side Management for Electric Utilities. Proceedings of the IEEE 73(10), 1468-1470

Haller, M.Y., Cruickshank, C.A., Streicher, W., Harrison, S.J., Andersen, E., Furbo, S., 2009. Methods to determine stratification efficiency of thermal energy storage process – Review and theoretical comparison. Solar Energy (83), 1847-1860

Hovgaard, T.G., Larsen, L.F.S., Edlund, K., Jørgensen, J.B., 2012. Model predictive control technologies for efficient and flexible power consumption in refrigeration systems. Energy (44), 105-116

Karim, M.A., 2011. Experimental investigation of a stratified chilled-water thermal storage system. Applied Th. Engineering (31), 1853-1860

Ma, Y., Borelli, F., Hencey, B., Coffey, B., Bengea, S., Haves, P., 2012. Model Predictive Control for the Operation of Building Cooling Systems. IEEE Transactions on Control Systems Technology 20(3), 796-803

Pfeiffer, D., Becker, M., 2018. Automatisierung von Kälteanlagen mit Einbindung in ein Demand Side Management. Einbindung von übergeordneten Algorithmen in neue Kommunikationskonzepte. Proceedings of the VDI Automation Congress 2018 (VDI-Berichte Nr. 2330), 933-946

Solar-Institute Jülich of the FH Aachen, Copyright 1998-2018, CARNOT Toolbox Version 6.3 released 10.2018

Vardakas, J.S., Zorba, N., Verikoukis, V., 2015. A Survey on Demand Response Programs in Smart Grids: Pricing Methods and Optimization Algorithms. IEEE Communications Surveys and Tutorials 17(1), 152-178

Manuscript ID: 781
DOI: 10.18462/iir.icr.2019.0781

A new design method of vortex tube based on unsteady processing vortex core and its experimental verification

Bo LIU, Xiangji GUO, Bo ZHANG

Key Laboratory of Complex Energy Conversion and Utilization of Liaoning Province;
School of Energy and Power, Dalian University of Technology
Liaoning, China, zhangbo@dlut.edu.cn

ABSCTRACT

Although the vortex tube had been invented over 80 years ago, its design method on the key structure parameters has not be achieved because of the complex swirl flow and its special energy separation phenomenon. In this paper, a new design method is proposed, based on the flow structure and the unsteady oscillation of the fluid flow. The energy separation phenomenon is modeled with the unsteady processing vortex core, which combined the flow field, the heat and mass transfer process in the vortex tube. And then, the optimization criteria for the main tube design can be achieved. The PIV/LDV is adopted to derived the steady and unsteady fluid field characteristics, to present the verification. Not only does the experimental performance of vortex tube based upon this method show exciting improvement, but also present better feasible and wider future for the vortex tube.
Keywords: Vortex Tube, PIV, Flow Structure, Energy Separation, Design.

1. INTRODUCTION

Since it was invented by Ranque in 1933 (Ranque, 1933), the unique energy separation phenomenon of the Ranque-Hilsch vortex tube (RHVT) has always been a mystery concealed by the violent turbulence. Without any moving part, the pressurized gas goes through the tangential inlet nozzles and generates a strong swirling flow within the main tube of the vortex tube. After both of the flow and energy separation, gas temperature drop can be gained at the cold exit near the inlet, meanwhile, temperature rise can be obtained at the hot exit away from the inlet, and a control valve is situated at the hot end to adjust the mass flow rate and energy separation performance at the two exits. The energy separation phenomenon has attracted the attention of physicists owing to the fantastic energy and mass transfer process, which can be related to the principle of Maxwell's demon (Liew et al., 2012) and the accretion disk (Kolmes et al., 2017). Besides, it is also used by engineers s as an energy and mass separator device for various industrial applications (Zhang and Guo, 2018), especially for the latest applications proposed in the gas industry (Ghezelbash et al., 2016, Zhidkova et al., 2015, Gutak, 2015) and in various thermodynamic systems (Kukis et al., 2015, Terekhin and Zolotykh, 2015, Mohiuddin and Elbel, 2014).
The energy separation phenomenon breeds within the gas flow field. To figure out the energy separation processes, studies on the flow field is necessary, and the studies were widely carried out since last 50s. However, both the observation and understanding of the flow field and energy separation are stuck by the complicated strong swirling flow, especially at the quantitative level. Although no agreement has been achieved in past studies on the specific mechanism of causing energy separation,

more and more attentions had attached on the investigations of the flow structure within the main tube of RHVT. In recent decades, evidence gradually appears that there exists specific flow structure within the strong swirling flow field of vortex tube, and more researchers considered that the energy separation was formed inside the flow structure. Besides, how the energy separation performance changes can be related to the variation of the flow structure. With observations and calculations on the flow fields, the discussions on flow structure had been increasingly fierce, such as the secondary flow proposed by Ahlborn (Ahlborn and Groves, 1997), while almost all the later researchers related the secondary flow to the deterioration of energy separation performance.
In this paper, the experimental investigation on the flow field with PIV to verify the existence of the unsteady flow structure is provided, and finally a mathematical model to compute the key parameters of the optimized vortex tube is discussed.

2 THE TIME-AVERAGE FLUID FLOW STRUCTURE INSIDE THE VORTEX TUBE AND ITS VERIFICATION

A strong swirling flow dominates the flow inside the vortex tube owing to the strong tangential injection of the compressed gas in the inlet nozzle(s). Unlike a chaotic turbulence, the remarkable characteristic of a strong swirling flow structure is the occurrence of a large-scale vortex structure comprising vortex breakdown and precessing vortex core, which are also observed in vortex tubes. When the vortex breakdown occurs, a central recirculation zone (CRZ) is formed in the core. The CRZ is unstable, precesses around the axis, and induces a large-scale flow structure that contains a three-dimensional time dependent instability, the PVC. The vortex breakdown and PVC are usually not only asymmetric but highly time dependent, and they may excite and/or couple with certain acoustic modes leading to velocity and pressure field oscillation. The vortex core deviates from the tube axis, rotating around the tube axis, and revolving on the axis of its own. However, there were few successful attempts to combine the vortex breakdown (or PVC) with the heat and mass transfer processes and subsequently study the flow structure and energy separation in vortex tubes.
From the computation results, the characteristics are derived (we neglected the CFD results here, please refer to our other published papers (Zhang et al., 2016a).
The optimum flow feature showing how vortex breakdown and PVC influence the flow structure in an RHVT is presented in Fig. 1, which is a combination of our previous works (Zhang et al., 2016b, Guo and Zhang, 2018).

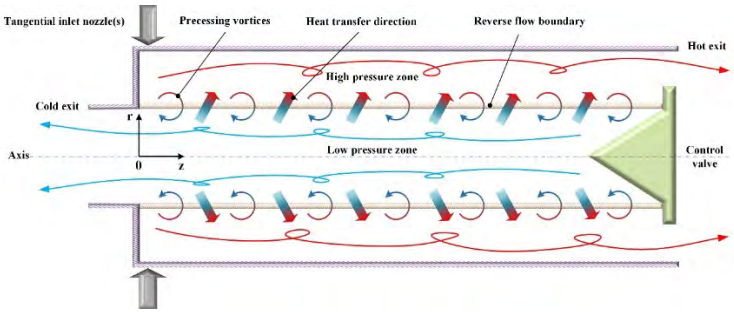

Figure 1: The common flow structure bears the best energy separation performance

In order to verify the computation results, a 2-D PIV experimental rig was built up to capture the velocity distribution in the vortex tube, as shown in Fig. 2.

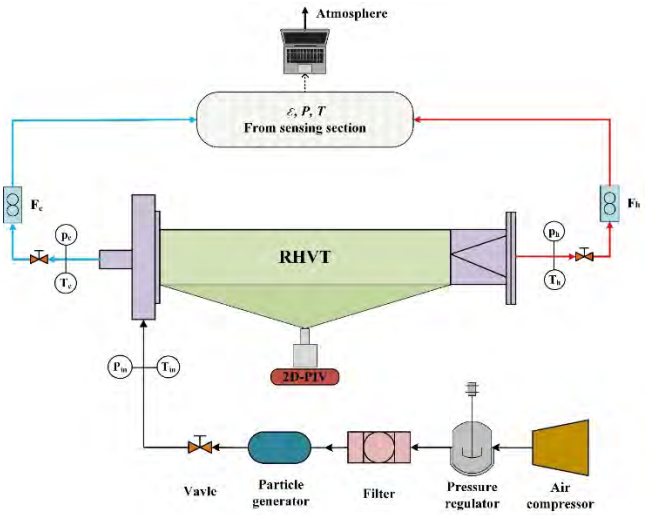

Figure 2: Schematic view of the 2-D PIV experimental rig

To realize PIV measurement and main tube visualization, transparent quartz tubes were used and other parts were made by steel with four rods to provide a flexible integration for different tube lengths. Four tangential nozzles with diameter of 3mm were made for the inlet. Originally, the vortex tube parameter with tube diameter of 9mm adopted in our previous numerical calculation was used to design the experimental vortex tube. However, the moment the gas flow with trace particles tangential goes into the vortex tube, the particles were pushed toward to the wall by the centrifugal force due to the overlarge curvature radius, leading to the particle information missing. Thus, the main tube diameter *D* of 30mm was used in our experiment with cold exit diameter of 15mm. Different tube lengths *L* of 360mm, 600mm, 750 and 900mm were used, and the length-diameter ratio *L*/*D*=12, 20, 25 and 30. Key parameters of these configurations were summarized in Table 1.

The experimental campaign was performed at a standard room temperature, with air as the working fluid supplied by the air compressor. After pressure regulating, the pressurized gas was passed through four Laskin nozzles in the particle generator to generate gas flow with uniform tracing particles. The adopted tracer is pure paraffin oil, and the liquid droplets diameter after atomization can be near $1\ \mu m$. After seed generating, the micron-sized liquid droplet is mixed up with air gas flow go to the vortex tube together and forms the strong swirling flow inside the RHVT. ILA GmbH 2D PIV system was adopted for the flow field measurement as presented in Fig.4, and the source of illumination for the PIV experiments was a 532nm Nd-YAG double-pulsed laser (Evergreen 145 laser, 145mJ, 15Hz), which was used to generate a 1~1.5 mm thick laser sheet. PIV images were recorded using a Pco. Edge 5.5 scientific CMOS camera, with a spatial resolution of 2560*2160 pixels; benefiting from the high-performance camera with 1.0 electronic low noise, 60% quantum efficiency and 10000 anti-blooming factor, most of the optical distortion was minimized to ensure the high quality of the particle images. The meridian plane in the main tube was lightening by the laser sheet, and the particle picture in the observation region was captured by the PIV camera. Other PIV device includes a seeder (aerosol generator PivPart45), a synchronizer and data acquisition system (with PIVView as the post-processing software to correct any remaining optical distortion). The PIV vectors were calculated using a 32 by 32-pixel interrogation window (IW) size with a 50% overlap. Due to the domination of the tangential velocity among the three velocity components, short pulse distance of $10\ \mu s$ was adopted in our experiment. Besides, because the camera cannot capture the view over the whole length of the main tubes, a monoaxial stepping slide (KTH12-L05-300-BC, stroke: 300mm, precision: 0.02mm) with vortex tube fixed on it was used for switching observation region. Fig. 5 gave the image integration strategy over the whole main tube on the meridian plane for different tube lengths. For each measurement part, 100 PIV image pairs were recorded. After recording, the slide

stepped forward 150mm length for the next part. Due to the wall reflection, some areas in the main tube had bad particle image quality, and the red parts (150mm*25mm, or 100mm*25mm) were available for flow field calculation.
Firstly, Six instantaneous axial velocity time series with interval of 10 μs was presented in Fig. 3 to reveal the unsteady characteristics of the strong swirling flow inside the vortex tube. From the axial velocity contours, there exists two flow direction, simultaneously: the positive axial velocity in the periphery toward to the hot end; the negative axial velocity in the core toward to the cold end. The streamline demonstrates the flow field are full of large-scale presscessing vortices, and these vortices responsible for the mass transfer processes between different layer, that is, turning the flow direction from hot stream to cold stream. Even the time interval is as short as 10 μs , the flow field shifts rapidly and intensely turbulent, which seems like irregular. Time averaged was performed for this operation condition and the image was compared to the instantaneous images as presented in the right in Fig. 3. Although the flow field becomes smoother and some small vortices were filtered out, there was no symmetry at all, and the large-scale vortices still exists. No matter in the steady or the time-averaged numerical simulations, the fluid fields inside the main all present nearly perfect axial symmetry, and there are not any vortices at all in the flow field, which is not match with the PIV results.

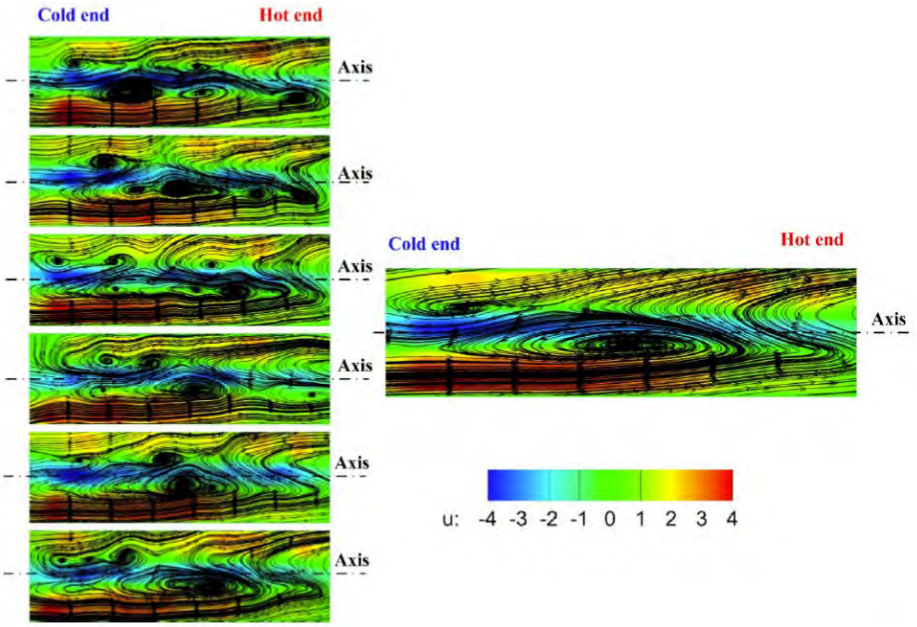

Figure 3: Streamline and axial velocity contours for 900-0.1-0.5-P4. Six instantaneous axial velocity time series with interval of 10 us (left); time averaged flow field for 100 shots (right)

Besides, to better depict the flow structure, the reverse flow boundary (iso-zero axial velocity surface) was draw in Figure 4, and the boundary separates the fluid field into hot stream in the periphery (the red region) and cold stream in the core (the blue region). From the radial coordinate ranges from -7.5 to 7.5mm indicates the diameter of cold exit, and the equivalent diameter of the reverse flow boundary is lower than the cold exit diameter. Both of the instantaneous flow field and the time-averaged flow field indicates the precessing vortex cores locate at the reverse flow boundary, and the gas particles in the vortices move back and forth to undertake the flow separation, even the energy separation.

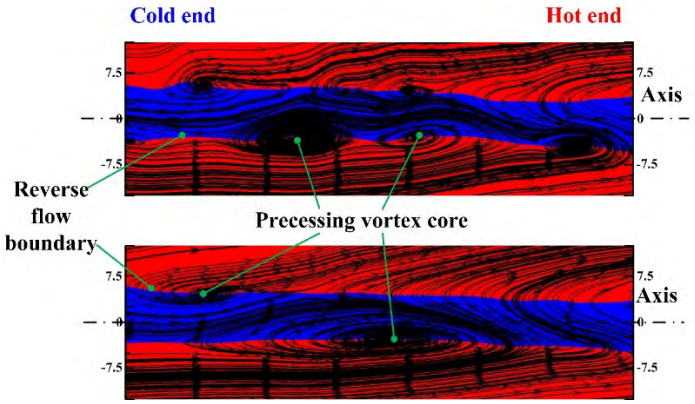

Figure 4: Streamline and reverse flow boundary demonstration for 900-0.1-0.5-P4. One instantaneous shot (top); time-averaged flow field for 100 shots (bottom)

The streamline and time-averaged axial velocity distribution in the main tube for all the four vortex tube under inlet pressure of 0.1bar and five cold mass fractions of 0.3 and every axial velocity distribution was marked by its legend below it, is shown in Figure 5. All the pictures appear litter regularity and no symmetry at the first impression, especially the streamlines for any part. The common feature of the flow structure at the inlet is the nearly zero axial velocity which has also been revealed in DLR's PIV experiment [23], which results from the dominating tangential velocity near the inlet in the tube. Besides, the maximum reverse flow velocity increases with larger cold mass fraction, and the reverse flow velocity accelerates when it towards to the cold end with the help of negative pressure gradient.

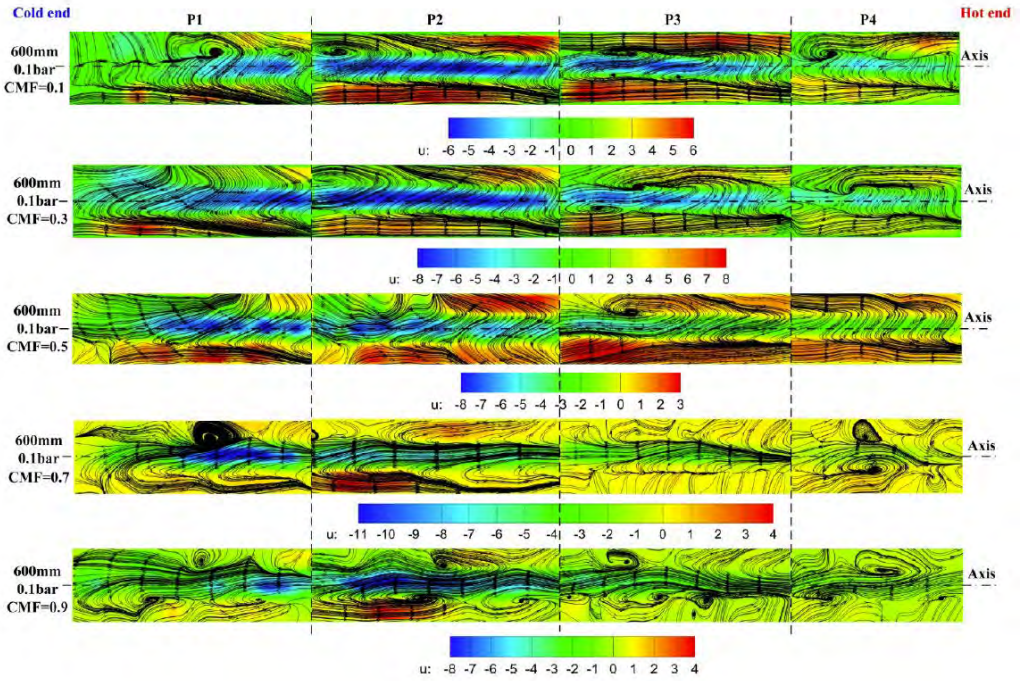

Figure 5: Streamline and axial velocity contour for 600mm tube

For better understanding of the effect on the flow structure with various operation conditions, the reverse flow boundary distribution in the main tube under inlet pressure of 0.1bar and five cold mass fractions of 0.1,0.3,0.5,0.7 and 0.9 are shown in Figure 6. The time-averaged boundaries show cylindrical or cone shapes to some degree. On the whole, the central recirculation zone (CRZ) becomes thinner as it moving toward to the hot end, especially for longer tube. Increasing the cold mass fraction, the CRZ gets thicker, which identifies the results presented by numerical calculation, and

verifies the vortex breakdown theoretical analysis by quasi-cylindrical approximation. Besides the energy separation performance gets better for the other three tubes with increasing cold mass fraction.

Although the reverse flow boundary did not present perfect in cylindrical or cone shape as expected, the reverse flow boundary behaves at the same trend as found by numerical simulations when the cold mass fraction increases. Combining with the behaviour change tendency of the boundary under different tube lengths proofs the proposed tube optimization criteria as shown in Fig. 1. Increasing the cold mass fraction, the size of the reverse flow boundary expands. In order to achieve the better performance, the length of the tube should be optimized, according to the operation conditions and the diameter of the tube. The swirl significantly decays in the over long tube, resulting to the axial retraction of the stagnation point.

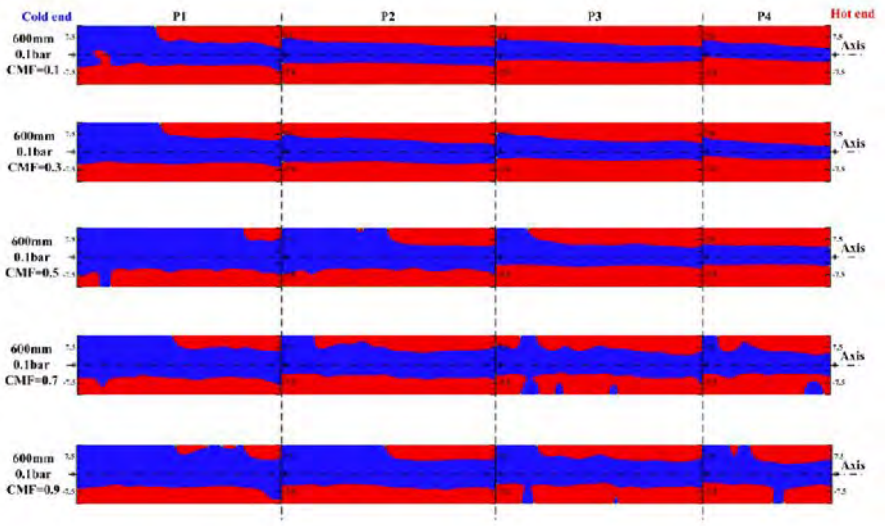

Figure 6: Variety of reverse flow boundary size under different cold mass fraction

3 THE MATHEMATICAL MODEL FOR THE VORTEX TUBE DESIGN

The vortex tube design includes some key parameters, such as diameter of the main tube *D*, tube length *l*, and diameter of the cold exit D_c, or the dimensionless parameters $l = L/D$, $d = D_c/D$, and $r = R_c/R$. The shape of the control valve proved not to play an important role on the energy separation performance, and thus it will not be included in this model.

As the flow structure in the vortex tube has been confirmed we can build the mathematical model accordingly to calculate the key parameters.

Three flow streams can be distinguished in the vortex tube: the hot stream in the periphery, $m_h = (1-\varepsilon)m_{in}$, the cold stream in the core, $m_c = \varepsilon m_{in}$, and the annular circulation region (CR) between periphery and core, as shown in Figure 1.

According to the Navier–Stokes equations for a steady axisymmetric swirling flow of an incompressible viscous fluid in cylindrical coordinate, the vortex structure can be derived as,

$$v_r \partial v_r/\partial r + v_z \partial v_r/\partial z - v_\phi^2/r + \partial p/\partial r = \mathrm{Re}^{-1}\left[r^{-1}\partial/\partial r(r\partial v_r/\partial r) - v_r/r^2 + \partial^2 v_r/\partial z^2\right] \quad \text{Eq. (1)}$$

$$v_r \partial v_z/\partial r + v_z \partial v_z/\partial z + \partial p/\partial r = \mathrm{Re}^{-1}\left[r^{-1}\partial/\partial r(r\partial v_z/\partial r) + \partial^2 v_z/\partial z^2\right] \quad \text{Eq. (2)}$$

$$v_r \partial v_\phi/\partial r + v_z v_\phi/\partial z + v_z \partial v_\phi/\partial z = \mathrm{Re}^{-1}\left[\partial^2 v_\phi/\partial r^2 + r^{-1}\partial v_\phi/\partial r - v_\phi/r^2 + \partial^2 v_\phi/\partial z^2\right] \quad \text{Eq. (3)}$$

$$\partial(rv_r)/\partial r + \partial(rv_z)/\partial z = 0 \qquad \text{Eq.(4)}$$

Here, v_r, v_ϕ, and v_z are the velocity components of the in cylindrical coordinates (r, ϕ, z); $\mathrm{Re} = v_{mr} R_{in} / \nu$ is the Reynolds number; $v_{mr} = m_{in} / (\rho \pi R_{in}^2)$ is the mass rate velocity, R_{in} is the length scale of main tube; and v is the kinematic viscosity.

$$v_\phi = F(r)exp(-\lambda z) + O(\lambda^2), \quad \psi_s = Q(r)exp(-\lambda z) + O(\lambda^2) \qquad \text{Eq. (5)}$$

An appropriate boundary stream function is

$$Q_L(r) = -(1-\varepsilon) \quad \text{for} \quad 0 < r < r_h \qquad \text{Eq. (6)}$$

$$Q_L(r) = \Psi_c(r, L) \quad \text{for} \quad r_h < r < 1 \qquad \text{Eq. (7)}$$

According to the optimization criteria, the tube geometric parameters should be calculated with an iterative procedure to gain the optimum flow structure. However, considering that several assumptions have been made to solve the N–S equation, further experiments still need to be performed to obtain the correction coefficients of the quantitative model.

Another meaningful aspect of the proposed optimum flow structure is that the corresponding energy separation model can be greatly simplified because the structure is the neatest flow structure and it avoids useless turbulence mixing. Besides, the past energy separation model seldom considered the effect of the tube geometric parameters, while with the optimum flow structure, for the analysis of energy separation, all the parameters are suited to the optimum flow structure. Therefore, there is reason to believe that a more convincing and brief energy separation quantitative model can be fulfilled in the near future.

REFERENCES

Ahlborn, B. and Groves, S. 1997. Secondary flow in a vortex tube. Fluid Dynamics Research, 21, 73-86.

Ghezelbash, R.Farzaneh-Gord, M. and Sadi, M. 2016. Performance assessment of vortex tube and vertical ground heat exchanger in reducing fuel consumption of conventional pressure drop stations. Applied Thermal Engineering, 102, 213-226.

Guo, X. and Zhang, B. 2018. Computational investigation of precessing vortex breakdown and energy separation in a Ranque–Hilsch vortex tube. International Journal of Refrigeration, 85, 42-57.

Gutak, A. D. 2015. Experimental investigation and industrial application of Ranque-Hilsch vortex tube. International Journal of Refrigeration, 49, 93-98.

Kolmes, E. J.Geyko, V. I. and Fisch, N. J. 2017. Heat pump model for Ranque–Hilsch vortex tubes. International Journal of Heat and Mass Transfer, 107, 771-777.

Kukis, V. S.Omelchenko, E. A. and Raznoshinskaia, A. V. 2015. Results of Vortex Tube Usage in Diesel Exhaust Gas Recirculation System. Procedia Engineering, 129, 151-155.

Liew, R., Zeegers, J. C., Kuerten, J. G. and Michalek, W. R. 2012. Maxwell's demon in the Ranque-Hilsch vortex tube. Physical Review Letters.

Mohiuddin, M. and Elbel, S. 2014. A Fresh Look at Vortex Tubes Used as Expansion Device in Vapor Compression Systems. 15th International Refrigeration and Air Conditioning Conference, Purdue University.

Ranque, G. J. 1933. Experiments on expansion in a vortex with simultaneous exhaust of hot air and cold air. J Phys Radium (Paris), 4, 112-4 S-115.

Terekhin, A. A. and Zolotykh, I. К. 2015. Evaporator System of Water Desalination Based on Ranque-Hilsch Vortex Effect. Procedia Engineering, 129, 337-343.

Zhang, B. and Guo, X. 2018. Prospective applications of Ranque–Hilsch vortex tubes to sustainable energy utilization and energy efficiency improvement with energy and mass separation. Renewable and Sustainable Energy Reviews, 89, 135-150.
Zhang, B.Guo, X. and Yang, Z. 2016a. Analysis on the fluid flow in vortex tube with vortex periodical oscillation characteristics. International Journal of Heat and Mass Transfer, 103, 1166-1175.
Zhang, B.Guo, X. and Yang, Z. 2016b. Analysis on the fluid flow in vortex tube with vortex periodical oscillation characteristics. International Journal of Heat and Mass Transfer, 103, 1166-1175.
Zhidkova, M. A., Devisilovb, V. A., Zhidkovb, D. A., Kirikovab, O. V. and Spiridonovb, V. S. 2015. Thermodynamics of the Ranque – Hilsch Effect in the Three Flow Vortex Tubes. Theoretical Foundations of Chemical Engineering, 49, 523-531.

Manuscript ID: 828
DOI: 10.18462/iir.icr.2019.0828

A study of ice slurry production process based on electric heating of heat transfer surface

Andrey KOLESNIKOV[(a)], Alexander KROTOV[(a)], Dmitry PRONIN[(a)], Anna EGOROVA[(a)], Yaroslav SAMOKHVALOV[(a)], Anatoly ZHERDEV[(a)]

[(a)] Bauman Moscow State Technical University
Moscow, 105005, Russia, kolesnikov.as@mail.ru

ABSTRACT

The active development of ice slurry technology began more than 25 years ago. Despite its many advantages, it is not widespread yet. One of the significant constraints is the imperfection of the most common scraper-type ice slurry crystallizers. The solution is to develop crystallizers that use other methods of separation the ice from the heat transfer surface instead of using mechanically moving parts. One of the promising ways is electric heating. An experimental study of the process of obtaining ice slurry by electric heating is carried out. The influence of the solution flow parameters and the electric heating parameters on the process of continuous formation of an ice sludge is studied. The results obtained are necessary for determining the mode of operation in the design of a new type of crystallizers.
Keywords: Crystallization, Heating, Induction, Ice Slurry.

1. INTRODUCTION

The use of ice slurry can be effective in many fields. The useful effect of ice slurry is often associated with such fundamental tasks of refrigeration as reducing energy consumption, improving food quality (Shinbayeva et al., 2015) or new medicine technologies (Burkov et al., 2018; Shakurov et al., 2017).
Despite the significant evolution of technology in recent decades, it is still not widespread. There are a number of reasons for this, including incomplete knowledge of the behavior of ice slurry in hydraulic systems and heat exchangers, the cost and insufficient development of ice storage systems, the difficulty of determining the mass concentration of ice and control systems in general. But one of the most important reasons is the imperfection of the existing ice generators – the basis of any system. Today the most common, affordable and suitable for most applications are scraper type crystallizers. Such crystallizers have a complex of moving elements: a shaft, scrapers, drive elements, as well as bearings and seals necessary for their operation (Stamatiou et al., 2004). These elements require periodic maintenance and replacement, which greatly complicates and increases the cost of using such crystallizers. In addition, the crystallizers require supercooling of the refrigerant with respect to the crystallization temperature of the ice at a value of about 9 ... 13K (Kolesnikov et al., 2015). This leads to a lower boiling point and an increase in energy consumption of compressors compared to systems using a liquid coolant. Finally, the crystallizers themselves are expensive, much more expensive than conventional heat exchangers for cooling liquid secondary coolant.
All this leads to the fact that the economic efficiency of ice slurry is not always obvious (Belozerov et al., 2015; Brom et al., 2016), and the risk of possible complications further scares customers. In turn, the lack of active demand slows down research and design work.
For the development of technology, it is important to create new, more efficient and cheaper ways to obtain ice, preferably not using moving parts. One of these promising ways is considered the method in which the separation of ice particles from the freezing surface instead of scrapers is carried out by its periodic heating with an electric current (Kauffeld and Gund, 2019). Two types of heating are possible. The first is resistive heating (Petrenko et al., 2011). In this case, the heat exchange surface itself, on which the ice is frozen, or the metal coating on its surface acts as a resistive element, which is periodically supplied with electric current. The surface is heated by

current and the ice due to reduced adhesion (Schaaf et al., 2015) or complete melting of the layer at the surface is separated from it. The second method is induction heating. In this case, the heat exchange surface is exposed to an alternating magnetic field, which induces eddy currents in the metal of the heat exchange surface. These currents lead to the heating of the metal and the separation of ice particles from it. At a high frequency of an alternating magnetic field, eddy currents are displaced to the surface of the metal and only a thin layer on its shell is exposed to heat (skin effect). It is assumed that this circumstance, along with others, will allow the separation of ice in a more efficient way than with resistive heating.
Schaaf and Kauffeld (2018) investigated the process of separating ice from an aluminum surface using induction heating. Using this method, a number of other problems have been solved (Schaaf, 2016; Kim et al., 2005).
The aim of this study is to carry out a continuous process of obtaining ice slurry in a tubular heat exchanger by induction heating without the use of additional means for the separation of ice and experimental study of this process.

2. EXPERIMENT

2.1. Process Scheme and Test Element

To obtain ice slurry, a “pipe in pipe” type heat exchanger is used. The inner tube is made of metal with ferromagnetic properties (steel), covered with a layer of enamel to reduce adhesion. The outer tube is made of non-metallic material with good magnetic permeability (Plexiglas). Outside the outer tube is wound an inductor to which a high-frequency AC source is connected. The coil is made of Litz wire - many thin wire strands, individually insulated and woven together. In the central part of the coil, three turns are made with an increased step to form a “window” for visual observation of the process. The process is carried out as follows (Fig. 1): a low temperature coolant (strong ethylene glycol solution) is continuously fed into the inner tube. A solution to obtain ice (a weak solution of ethylene glycol) is continuously fed into the annular space - step “a” in Fig.1. Ice crystals form on the outer surface of the inner tube, the ice layer begins to grow (step “b”). Further a current is applied to the inductor for a short time, as a result, the metal surface of the inner tube is heated and the ice at the surface melts (step “c”). The current supply is stopped. Next, the ice above the molten layer is separated from the pipe surface and is carried away by the solution flow to the ice storage (step “d”). The freezing of a new layer of ice begins and the process repeats.

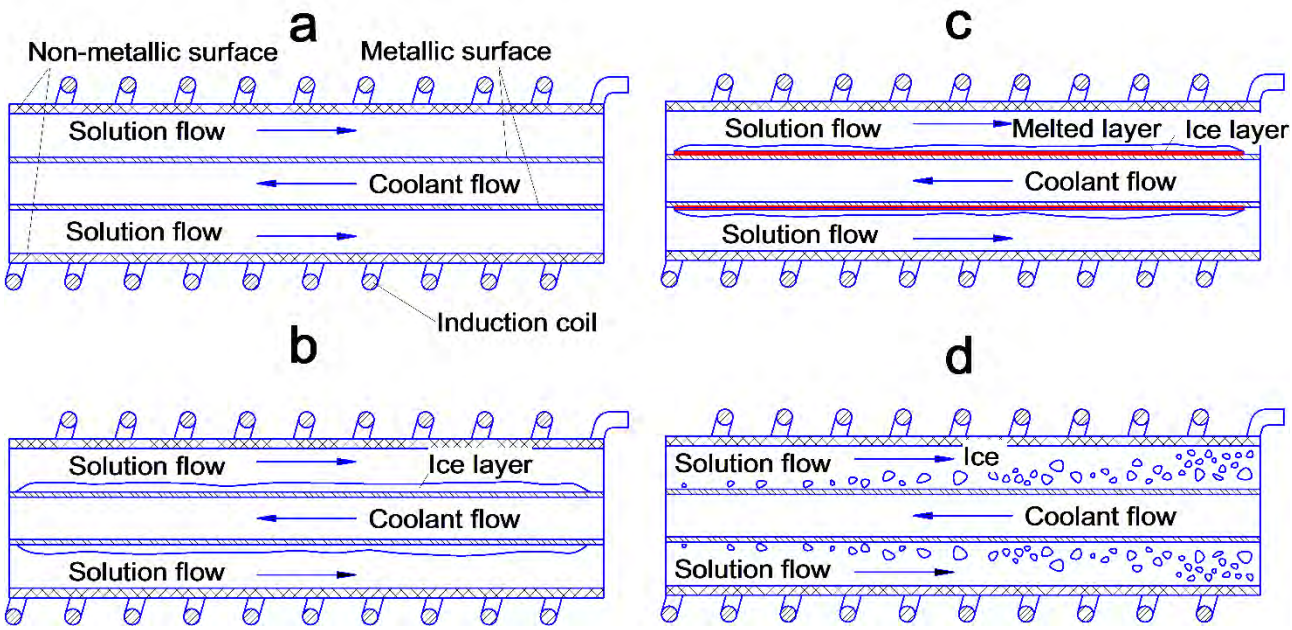

Figure 1: Ice slurry production process

To implement the described process, a test element was made (Fig. 2).

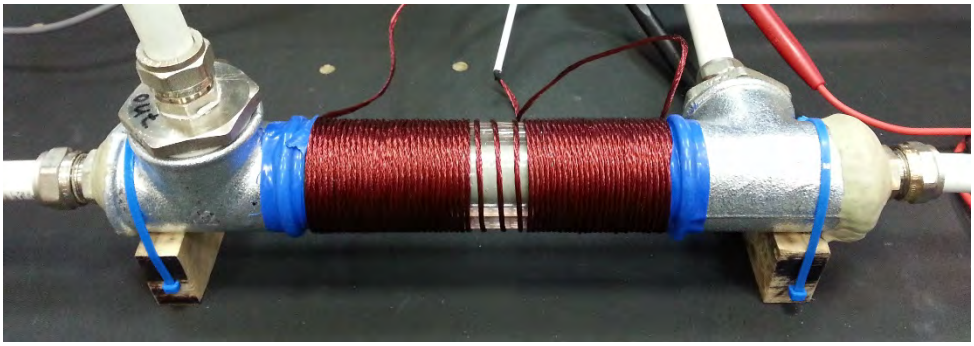

Figure 2: Test element

Characteristics of the test element are shown in table 1.

Table 1. Test element specifications

Outer tube material	Plexiglass
Inner diameter of outer tube	36 mm
Outer tube thickness	4 mm
Outer tube length	150 mm
Inner tube material	Steel
Inner diameter of inner tube	24.1 mm
Inner tube thickness	0.3 mm
Thickness of the enamel layer on the inner tube	0.1 mm
Inner tube length	180 mm
Inner diameter of the coil	44 mm
Total coil length	145 mm
Number of turns	58
Material of Litz wire	Copper
Characteristics wire Litz wire	d0.3 mm x 16
Fluid supplied to the inner tube	Ethylene glycol solution 45%
Fluid supplied to the annular space	Ethylene glycol solution 10%

2.2. Experimental Setup

To provide the process parameters, an experimental setup is used, a simplified diagram of which is shown in Fig. 3. The unit contains a coolant circuit and a solution circuit to produce ice slurry. The coolant circuit is used to keep temperature of the coolant, which is a cold source for the test element. The coolant circuit contains a pump for the coolant, an evaporator in which the coolant's heat is removed, and a control valve for regulating the flow rate of the coolant. The liquid in the evaporator is cooled by the vapor compression-type chiller. An ethylene glycol aqueous solution with a mass concentration of 45% is used as a coolant. The ice slurry circuit contains a pump for the solution, a heat-insulated container for ice accumulation and a control valve for regulating the flow rate of the solution. An ethylene glycol aqueous solution with a mass concentration of 10% is used for ice production (the crystallization start temperature is approximately minus 3.67°C). Resistance thermometers are used to measure flow temperatures in both circuits. An ultrasonic flow meter is used to measure the flow rate of the coolant. A rotameter is used to measure the flow rate of the solution. The electrical parameters of the induction coil are measured by appropriate meters.

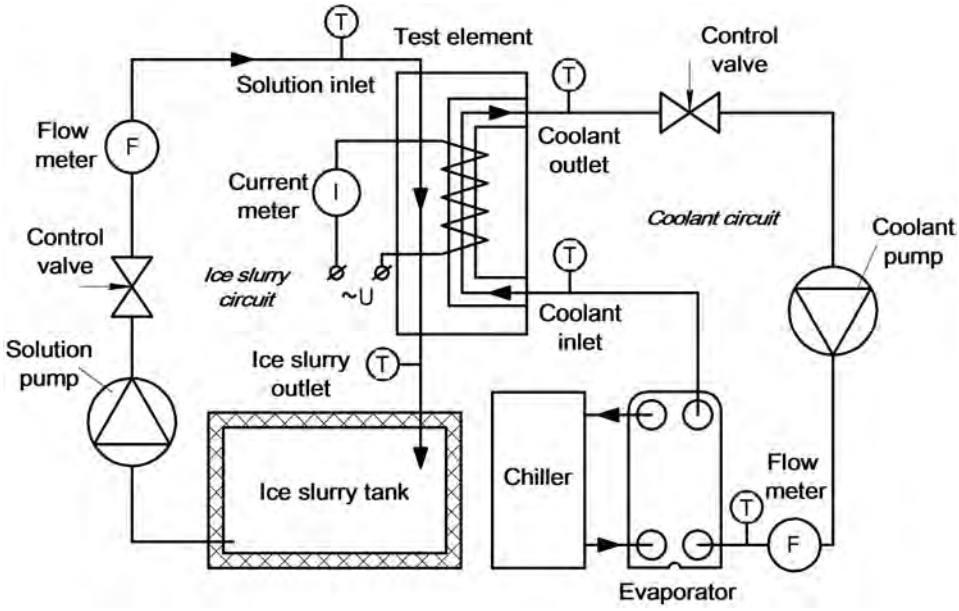

Figure 3: Experimental setup

2.3. Experimental Procedure and Results

As a result of the experiment, a mode of operation was obtained in which ice was formed on the walls of the inner tube of the test element and was separated under the action of heating by the forces of the fluid flow in the annular space in a continuous mode of operation (Fig. 4). The mode of operation was obtained at an average coolant temperature of about minus 19°C. The coolant flow rate was 0.93 l/s. The flow rate of the solution was in the range of 0.017-0.115 l/s. The temperature of the solution at the entrance to the test element was 1.5-2.5 ° C. The frequency of the alternating current applied to the coil was 38.1 kHz. Current: 1.9 A.

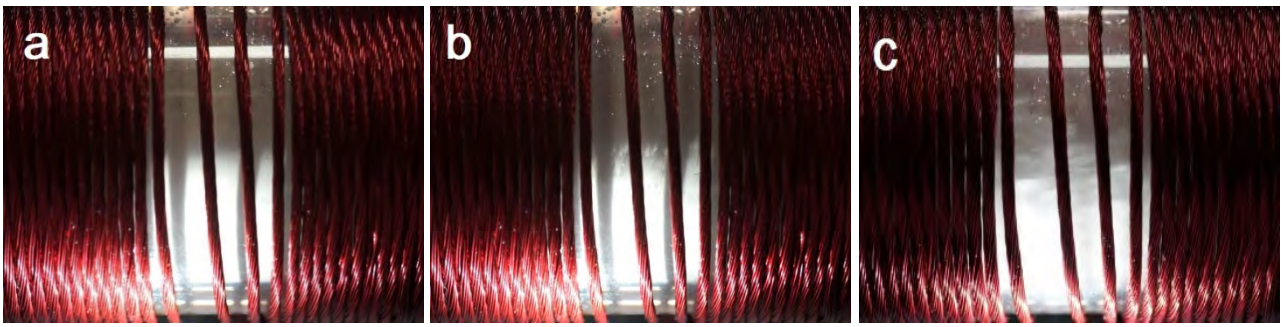

Figure 4: Ice slurry production process

(a) clean surface, (b) ice layer formation, (c) ice compartment

The process goes cyclically, and the periods of freezing lasted much longer than the cycles of thawing: 5-25 seconds freezing and 1-2 seconds thawing. It is also specific that the time between the separation of ice portions significantly exceeds the time interval between the passes of the scraper in the scraper crystallizers. In the process of ice formation, there was no significant heating of the coil, which can affect the Plexiglas.

The frequency of heating action and its duration varied. Figure 5 shows the obtained values of the specific mass flow rate of particles of ice formed, related to the cooling capacity, depending on the duration of freezing periods for different values of the solution flow rate. Heating duration in all cases is 1.5 seconds. The amount of ice is determined from the heat balance of the test element (Goncharova et al., 2015), taking into account the heat supplied through the induction coil. For periods of freezing less than 5 seconds, a decrease in ice formation is observed, since there is no enough time for ice to freeze on the surface. With increasing periods of freezing, on the contrary,

an increased layer of ice is observed, which acts as an additional thermal resistance. By reducing the flow rate of the solution, in other words, reducing the linear flow rate of the solution along the pipe, the separation of ice becomes difficult. This leads to the fact that with a small flow rate of the solution and long periods of freezing, the ice layer ceases to separate at all.

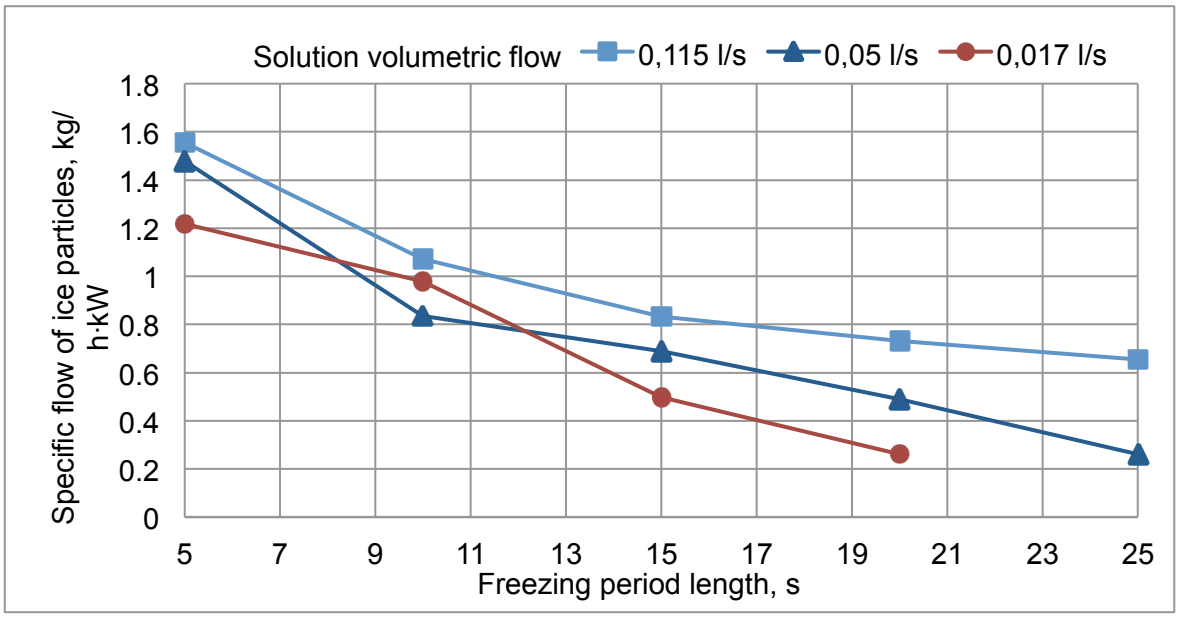

Figure 5: Specific flow of ice particles depending of freezing period length

Fig. 6 shows the obtained values of the specific mass flow rate of particles of ice formed, related to the cooling capacity, depending on the duration of heating periods for different values of freezing periods. The solution flow rate was 0.115 L/s.

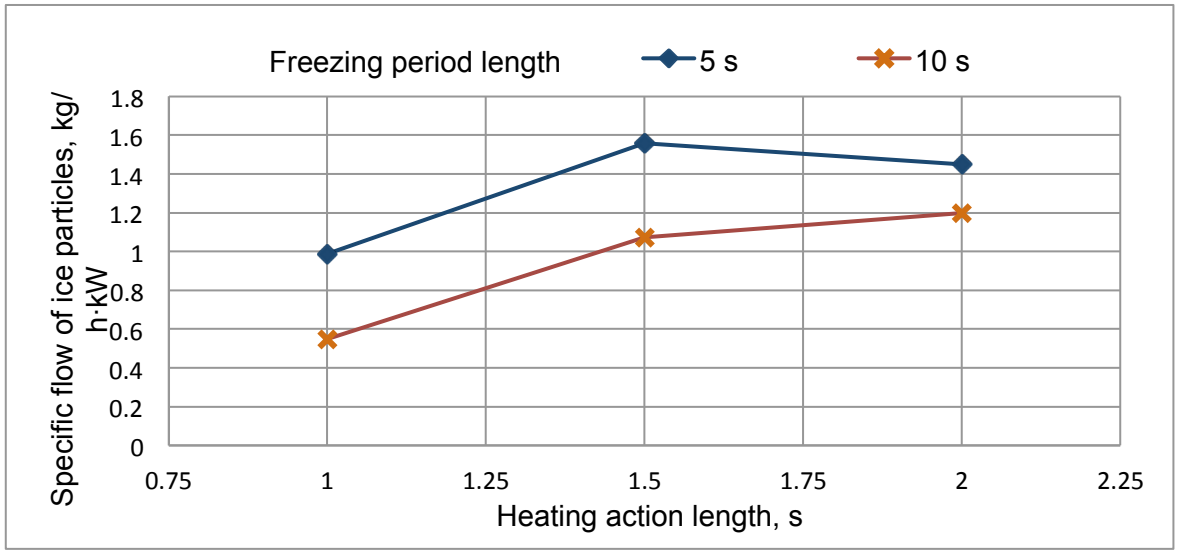

Figure 6: Specific flow of ice particles depending of heating action length

For the freezing period of 5 seconds, with an increase in the heating time of more than 1.5 seconds, the amount of ice produced begins to decrease, which can be explained by its excessive melting. While for a longer period of freezing, the growth of ice production with increasing heating continues, consequently, the optimal heating period has not yet been reached.

3. CONCLUSIONS

The continuous process of obtaining ice slurry in a tubular heat exchanger by induction heating without the use of additional means for ice separation has been successfully carried out. The

achieved efficiency of the method is still low, but it is clear that for the further development of the method and the creation of ice crystallizer samples on its basis, it is necessary to solve a complex optimization problem. Ice production with electric heating is based on a balance of versatile factors, each of them requires optimization. Among them:
- frequency and duration of heating action;
- current frequency and voltage;
- material of the cooling pipe and the surface roughness;
- gap between coil and heating element;
- degree of supercooling of the refrigerant or coolant.

REFERENCES

Belozerov, G., Mednikova, N., Pytchenko, V., Umanskiy, V., Kolesnikov, A., Krotov, A., Klyachko, L., 2015. Use of coolants at phase transition for foodstuffs refrigeration. Proceedings of 24th IIR international congress of refrigeration, Yokohama, Japan, IIF/IIR, 2248-2253.

Brom, A.E., Belova, O.V., Sissinio, A., 2016, Lifecycle Costs for Energy Equipment: FMECA & Lifecycle Costing Models as "decision Making" Tools for Cost Reduction during the Whole Equipment Life. Procedia Engineering, 152,173-176.

Burkov, I.A., Zherdev, A.A., Pushkarev, A.V., Tsiganov, D.I., Shakurov, A.V., 2018. Simulation of fluid hypothermia for robot-assisted prostatectomy. Journal of Enhanced Heat Transfer, 25 (2), 121-136.

Goncharova, G., Ustugova, T., Nikiforova, I., Razomasov, N., 2015. Experimental study of heat and mass transfer in modified ice structures resulted from diffusion of polymeric compounds used for sports ice objects. Refrigeration Science and Technology, 1099-1106.

Kauffeld, M., Gund, S., 2019, Ice slurry history, current technologies and future developments. Int. J. Refrigeration 99, 264-271.

Kim, K.S., Kim, Y.G., Kim, S.Y., Chun, C.H., Lee, Y.S., Lim H.K., 2004, Icemaker for refrigerator. European patent No EP 1 536 195 A2.

Kolesnikov, A., Buzukashvili, I., Krotov, A., Klyachko, L., Umanskiy, V., Makarov, B., 2015, A study of ice-slurry production process in scraped-surface type generator. Proceedings of 24th IIR international congress of refrigeration, Yokohama, Japan, IIF/IIR, 2075-2082.

Petrenko, V.F., Sullivan, C.R., Kozlyuk, V., Petrenko, F., Veerasamy, V., 2011, Pulse electro-thermal de-icer (PETD). Cold Reg. Sci Technol 65, 70–78.

Schaaf, J., Koffler, M., Kauffeld, M., 2015, Influence of a heat flux to ice adhesion force. Proceedings of 24th IIR international congress of refrigeration, Yokohama, Japan, IIF/IIR, 2171-2176.

Schaaf, J., 2016, Vorrichtung und Verfahren zur Erzeugung von Eisbrei. German patent No DE102012218349A1.

Schaaf, J., Kauffeld, M., 2018, Ice aluminum debonding with induction heating. Journal of Adhesion Science and Technology, 32 (19), 2111-2127.

Shakurov, A.V., Pushkarev, A.V., Pushkarev, V.A., Tsiganov, D.I., 2017, Prerequisites for developing new generation cryosurgical devices. Sovremennye Tehnologii v Medicine, 9 (2), 178-187.

Shinbayeva, A., Aldiyarov, A., Arkharov, I., Drobyshev, A., 2015, Investigations of the dynamics of meat freezing at various modes of cryotreatment. Refrigeration Science and Technology, 2634-2641.

Stamatiou, E., Meewisse, J.W., Kawaji, M., 2004, Ice slurry generation involving moving parts. Int. J. Refrigeration 28, 60–72.

Manuscript ID: 829
DOI: 10.18462/iir.icr.2019.0829

Future refrigerant mix estimates as a result of the European Union regulation on fluorinated gases

Pavel MAKHNATCH[(a)], Adrian MOTA-BABILONI[(b)], Rahmatollah KHODABANDEH[(a)]

[(a)] KTH Royal Institute of Technology, Department of Energy Technology, Division of Applied Thermodynamics and Refrigeration
Stockholm, 100 44, Sweden, pavelma@kth.se
[(b)] ISTENER Research Group, Department of Mechanical Engineering and Construction, Universitat Jaume I (UJI)
Castelló de la Plana, E-12071, Spain, mota@uji.es

ABSTRACT

The requirements of the European Union (EU) regulation on fluorinated greenhouse gases has created an incentive to reduce their amount that can be placed on the EU market (including many commonly used refrigerants) to 21% of the baseline level. This study attempts to develop a methodology to predict the future refrigerant mix in refrigeration, air conditioning, and heat pumps that will be available to the EU customers by 2021 and 2030 years. The work is based on the relevant current statistical data, refrigerant distribution, and future technology acceptance and trends in refrigerants. The study presents a refrigerant demand grow scenario and provides a basis for closer market follow up in order to facilitate decision making for refrigeration industry stakeholders. The results of the study indicate that by 2021 will be difficult to accomplish the fluorinated gas quota but by 2030 the transition is possible. By that time, the natural refrigerants will dominate the market, and a small share of lower GWP refrigerants will be necessary for specific applications.
Keywords: F-gas (fluorinated gas), global warming, HFC, HFO, low GWP, refrigerant.

1. INTRODUCTION

Global society is facing a severe environmental challenge to reduce its impact on climate. Refrigeration, air conditioning and heat pumps (RACHP) are well-known contributors to global warming and account for 7.8% of global CO_2-eq. emissions (IIR, 2017) with the projections of the growing impact (Peters, 2018). A significant contribution to reducing the impact is the global agreement that has been enforced from the 1st January 2019, i.e., Kigali Amendment to the Montreal Protocol (UN, 2016). The Agreement sets the distinct phase-down schedule to reduce the global production and consumption of hydrofluorocarbons (HFCs). Before the global agreement, legislation that includes a similar action (among others) has been implemented in the European Union, the regulation No 517/2014 of the European Parliament and of the Council on fluorinated greenhouse gases (F-gas regulation) (European Parliament, 2014).
Most importantly, the regulation sets a target fluorinated gases (F-gases) supply level that is gradually reduced till 2030 and prescribes control mechanisms to prevent the use of a greater amount of HFCs. Additionally, a number of prohibitions based on the global warming potential (GWP) values are included to guide the industry over the process. Thus, clear incentives have been established for the RACHP industry to reduce the supply of high GWP refrigerants by, for instance, replacing them with alternative refrigerants with lower GWP.
While the list of available low GWP refrigerants has been identified (McLinden et al., 2017), their use is currently limited due to their varying properties, e.g., flammability or toxicity characteristics. In such circumstances, several refrigerant mixtures have been proposed to satisfy different requirements (trade-off) (Bitzer, 2018).

Depending on the RACHP application, the characteristics required to the refrigerant vary, and hence their GWP. However, the maximum allowed quota is set for the entire EU market and not linked or separated based on application type. Given the uncertainty present in the RACHP working fluids market, this work aims to present an estimation for the future refrigerant mix that is plausible to establish when attending to the F-gas regulation quotas and GWP limitations.

2. METHODOLOGY

The results of this study are based on the allocation model of refrigerants that will be replacing the commonly used HFC refrigerants. It is based on current and historical data and assumptions of future refrigerant use and regulations development.

2.1 Approach

The methodology followed in this study is based on the current levels, and future predictions of high GWP refrigerants use as input data. The model is therefore based on the baseline supply levels of a set of high GWP refrigerants. Accounting to the historical data obtained from the recent report on F-gases (European Environment Agency, 2018), the baseline levels of selected HFC refrigerants that have been placed on the European market has been defined.
Further, the future refrigerant options have been identified considering the current technology and refrigerant development levels as well as on their future development projections. Two key periods have been selected, 2021 and 2030 years, which are the target years of the F-gas regulation for the two major coming quota reductions (European Parliament, 2014).
Finally, the future refrigerant mix has been identified under the assumption of a gradual reduction of the baseline amount of HFCs that can be placed on the European Union's (EU) market (placing on the market, POM, amount expressed in million tons CO_2 equivalent, $MTCO_2e$) according to the schedule stipulated by the F-gas regulation.

2.2 Data and Assumptions

The main data source is the historical data reported by companies on the production, import, export, and destruction of F-gases in the European Union available from the European Environment Agency (2018). This document provides statistic on F-gases use in the EU during 2007-2017 years. The current study has been focused on a limited set of HFC refrigerants that were representing the major share of refrigerant supplied during the referencing period. The historical data outside of the reference period has been explicitly neglected since it is not representative of the typical refrigerant supply profile due to the fluctuations caused by the F-gas regulation. The projections of future supply are instead based on the reasonable refrigerant market development under the requirements of the F-gas regulations that were assumed by the authors. These assumptions are further introduced in the respective parts of the paper.

2.3 Model Uncertainty

The results of the given study are subject to uncertainty due to the uncertainty of input parameters, identified data gaps, and the assumptions. The model also implies various assumptions helping to substitute data inputs for which the exact values cannot be obtained. The reliability of the model output will be benefited from additional efforts taken to improve the quality of the input data. This uncertainty can be incorporated into the model by integrating statistical methods. However, this is out of the scope of the current study and suggested for future studies. The modelling error of the presented evaluation is dependent on the input assumptions and not quantified in a given study.

3. REFRIGERANT INVENTORY ESTIMATION

3.1 Implications of the F-Gas Regulation

The F-gas regulation established a legal requirement for a 79% gradual reduction in the F-gases that can be placed on the EU market based on the average amount placed during the period 2009-

2012 as the baseline reference. The reduction started in 2015, but the first significant reduction took place in 2018, passing from 93% to 63% of fluorinated substances allowed. It is considered that this year the refrigeration and HVAC industry faced the first challenge. In the same way, its next great challenge to face is the year 2021, when 55% reduction is required.
The phase-down schedule established by the F-gas regulation can be translated into the amount of CO_2-equivalent allowed to be placed on the EU market, given the available historical data. Thus, the 100% quota is 183.1 $MTCO_2e$. It is based on the allowed quota value, set by the regulation, total CO_2-equivalent value of the baseline F-gases use (as listed in the F-gas regulation). The resulted values are compiled in Table 1.

Table 1. F-gas reduction quota translated into CO_2-eq. emissions

Year	15	16	17	18	19	20	21	22	23	24	25	26	27	28	29	30
Quota, %	100	93	93	63	63	63	45	45	45	31	31	31	24	24	24	21
POM, $MTCO_2e$	183.1	170.3	170.3	115.4	115.4	115.4	82.4	82.4	82.4	56.8	56.8	56.8	43.9	43.9	43.9	38.5

The allocated quotas are carefully monitored, and the statistics are regularly published presenting past use of the F-gases. According to the most recent statistics, the quotas have been met successfully during the 2015-2017 years.
Most of the F-gases have been used in the “Refrigeration, airconditioning and heating and other heat transfer fluids” category, followed by the “Foams, including pre-blended polyols” and “aerosols” sectors. The statistics present the supply data for different F-gases. In the refrigeration sector, these gases have been consumed in pure form (e.g., R134a and R32 refrigerants), as well as combined in mixtures with other F-gases (e.g., R134a as a component of R404A, R32 as a component of R410A). The quantitative data of the past refrigerant supply is however not presented in the report, neither available to the authors in any other form. Such data is therefore evaluated.

3.2 Identifying Baseline Refrigerant Inventory

Depending on the requirements of the specific refrigerating application, various F-gases are used in pure form, as well as components of a refrigerant mixture. The most widely used synthetic HFC refrigerants before the HFCs phase down are R134a, R404A, R407C, R410A, and R507. The composition of the HFC mixtures in mass percentage is presented in Table 2.

Table 2. Composition in mass percentage of commonly used HFC refrigerants

	R134a	R404A	R407C	R410A	R507
R134a	100	4	52	0	0
R125	0	44	25	50	50
R143a	0	52	0	0	50
R32	0	0	23	50	0

These refrigerants are used in different applications, for some of which the F-gas regulation establishes additional measures of regulation: products and equipment placing on the market prohibitions. Thus, a baseline refrigerant supply scenario for 2009-2012 average has been obtained from the historical F-gases supply amounts, composition of the conventional HFC refrigerants used, statistical data presented by the European Environment Agency (2018), and assuming the refrigerant inventory in the European Union to be similar to that of France, for which detailed data is available (Clodic et al., 2013). The results are presented on a mass basis in Figure 1a and on CO_2 equivalent basis on Figure 1b.

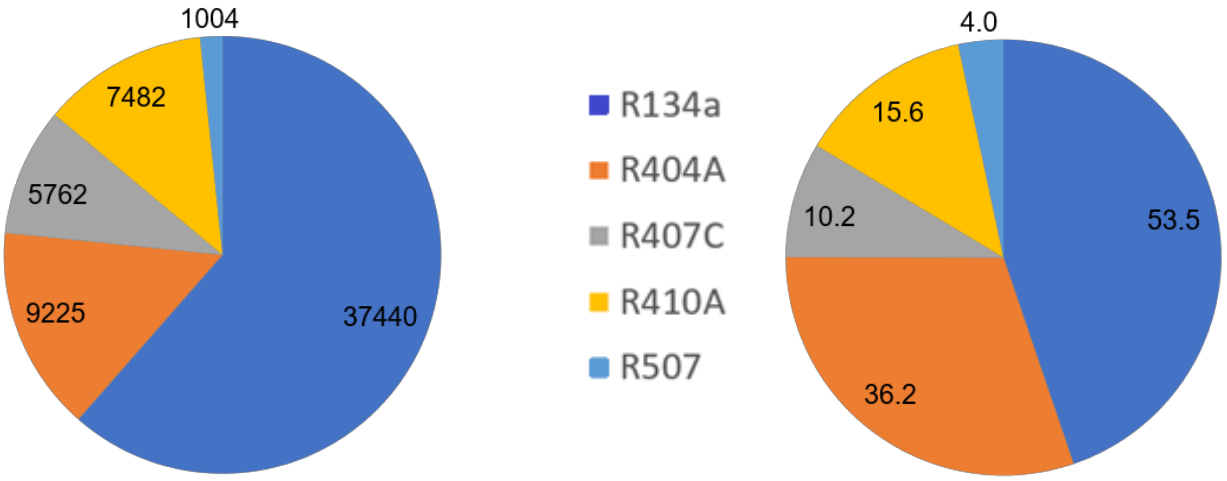

a) Mass basis (tonnes)

b) CO_2 equivalent basis ($MTCO_2e$)

Figure 1: Baseline refrigerant inventory, common HFC refrigerants only

3.3 Identifying Distribution of Refrigerants

The choice of the refrigerant that replaces a conventional one is dependent on the intended application. For instance, R404A that is used in commercial refrigeration can be replaced, depending on the application, by lower and low GWP refrigerant mixtures (Makhnatch et al., 2017), as well as naturally occurring substances (CO_2, propane). Several replacements for R134a have been developed for R134a and are suitable to replace it in different applications (Makhnatch et al., 2019). Similarly, a wide range of alternatives exists for other HFC refrigerants considered in the current analysis (Mota-Babiloni et al., 2017a). The choice of the alternative is dependent on a few factors, including the type of equipment, possibility, and viability to retrofit, as well as the availability of alternatives, given the projected timeframe. Therefore, the distribution of the refrigerants has been estimated, based on the values provided by Clodic et al. (2013).
The distribution of the refrigerants over the equipment type (Table 3) has been assessed by applying the data available for France at a similar period (Clodic et al., 2013) under the assumption that this data can be translated to the refrigerant supply inventory over the entire EU region at that time by extending the inventory of French refrigeration sector to the entire EU inventory. It can be seen that the dominating refrigerant is R134a given the different applications in which can be used, followed by R404A, because it is used in applications that require a large charge of refrigerant.

Table 3. Baseline supply inventory of the assessed high GWP refrigerants

Baseline scenario	R134a	R404A	R407C	R410A	R507
Domestic refrigeration. ton	2749.9				
Commercial refrigeration. ton	1150.9	4238.9	6.6	24.3	966.3
Road transport. ton	62.4	416.8		1.1	
Industries. ton	2902.6	3747.4	260.8	118.3	38.1
Air-conditioning. ton	308.7		2038.1	4474.1	
Chillers. ton	3313.1		2755.4	901.9	
Heat pumps	231.5		612.3	1963.0	
Mobile air conditioning	25419.4		88.4		
Sea transport	1301.9	11.6			
TOTAL, $MTCO_2e$	53,54	36,18	10,22	15,62	3,78
TOTAL, ton	37440	9225	5762	7482	1004

This calculation results in the development of the baseline refrigerant inventory for the initial period. It is worth to mention that this assumption should be re-evaluated in future studies.

4. FUTURE REFRIGERANT INVENTORY

4.1 Refrigerant Options

Many refrigerants mentioned in a baseline scenario have GWP values over the limits set by the F-gas regulation for some applications, or these GWP values are too high to comply with the reduced quotas. Therefore, they will be replaced in order to comply with the requirements of the current legislation. The transition to lower GWP refrigerants will happen gradually and will rely on the availability of the lower GWP refrigerants and equipment using thereof; availability of lower GWP refrigerants that can replace with no or low amount of modifications high GWP refrigerants already used in equipment (drop-in replacement), monetary and legislative incentives.
In this work, a scenario of the refrigerant supply development by the beginning of 2021 and 2030 is presented. This scenario is based on the expert opinion on future developments expressed elsewhere (IIR, 2016) (Danfoss, 2018), as well as the authors' personal opinion. The future possibly used alternatives can be briefly summarised in Table 4. It can be seen as by 2021, a wide variety of possibilities can be combined in several applications. However, by 2030, HFC/HFO mixtures and latest considered HFCs are going to disappear from that range of options and natural refrigerants are going to dominate the refrigerant market.

Table 4. Future refrigerants adaptation based on the category

Category	Refrigerant	By 2021	By 2030
Domestic refrigeration	R134a	HC	HC
Commercial refrigeration	R134a	HFC/HFO, HFO, CO_2/HC	Mostly CO_2/HC
	R404A/R507	HFC/HFO, CO_2/HC	Mostly CO_2/HC
	R410A/R407C	HFCs	HC
Road transport	R134a	HFCs, HFC/HFO	HFO
	R404A	HFC/HFO	HC/CO_2
	R410A	HFCs, HFC/HFO	HC, HFC
Industries	R134a	HFC/HFO, NH_3/CO_2	HFC/HFO, NH_3/CO_2
	R404A/R507	HFC/HFO, NH_3/CO_2	HFC/HFO, NH_3/CO_2
	R410A/R407C	NH_3/CO_2/HC	NH_3/CO_2/HC
Air-conditioning	R134a	HFC, HFC/HFO	HC
	R410A/R407C	HFC	HFC, HC
Chillers	R134a	HFC/HFO, HFO	HFO
	R410A/R407C	HFC, HFC/HFO	HFC, HFO/HFC
Heat pumps	R134a	HFC, HFC/HFO, HC	CO_2, HC
	R410A/R407C	HFC, HFC/HFO, HC	HFC, HFC/HFO, HC
Mobile air conditioning	R134a	HFO	HFO, CO_2
	R407C	HFC, HC	HC, HFC/HFO
Sea transport	R134a	HFC, HFC/HFO	HFO
	R404A	HFC/HFO, CO_2/NH_3	CO_2/NH_3

4.2 Modelling Future Scenarios under POM Limitations of F-Gas Schedule

Finally, the modelled use values for the future refrigerant quota have been obtained by projecting the future energy mix onto the possible future consumption patterns of the refrigerants in each sector. The quota use values represent the future refrigerants that are expected to be placed on the European market (POM) to satisfy the proposed refrigerants' demand.
The refrigerants that are POM are utilised in new equipment that is produced and imported to the European market, but also eventual top-up leakages from remaining RACHP equipment. Since the refrigerant top-up amount is dependent on the typical refrigerant lifetime (LT, adopted from Clodic et al. (2013)) and typical annual leakage rate (LR, adopted from the reported data (IIR, 2014)), the refrigerant amount (in tonnes) in new equipment at a baseline year is calculated as POM/(1+LT·LR). A detailed description of the scope of the POM metric that is relevant to compliance with the EU HFC phase-down can be obtained from the report by the European Environmental Agency (2018).

The modelled future POM of refrigerants accounted by the quota mechanism of the F-gas regulation are estimated for 3 cases: during 2021 and 2030 at no POM refrigerant growth (mass basis); during 2030 at the consideration of 3% annual growth (a.g.) of POM (mass basis) from 2021. The estimation relies on several parameters, most notably not accounting for possible refrigerant reclamation and recycling and neglecting HFCs exempted under Article 15.2 of the F-gas regulation. The future POM of refrigerants intended to be used in new equipment was assumed based on the considerations presented in Section 4.1. The share of the POM intended to be used to top-up leakages from remaining RACHP equipment was estimated based on the historical refrigerant mix, expected refrigerant mix in new equipment, as well as the removal of equipment from the market due to the end of life. The increase in refrigerant demand due to the potential retrofit of RACHP equipment is not taken into account here. The resulting values are summarised in Table 5.

Table 5. Modelled future POM of HFC refrigerants at the European market

	Refrigerant	Baseline (including imports)		by 2021	by 2030	by 2030. 3% a.g.
		Ton	$MTCO_2e$	$MTCO_2e$		
Domestic refrigeration	R134a	2749.9	3.932	0.00	0.00	0.00
Commercial refrigeration	R134a	1150.9	1.646	0.96	0.15	0.17
	R404A/R507	5205.2	20.476	8.64	4.40	4.98
	R410A/R407C	30.9	0.063	0.03	0.00	0.00
Road transport	R134a	62.4	0.089	0.08	0.05	0.06
	R404A	416.8	1.635	0.54	0.38	0.42
	R410A	1.1	0.002	0.00	0.00	0.00
Industries	R134a	2902.6	4.151	3.44	0.00	0.00
	R404A/R507	3785.5	14.849	4.07	0.00	0.00
	R410A/R407	379.1	0.710	0.68	0.11	0.11
Air-conditioning	R134a	308.7	0.441	0.26	0.06	0.07
	R410A/R407C	6512.2	12.958	11.32	2.22	2.51
Chillers	R134a	3313.1	4.738	3.20	0.00	0.00
	R410A/R407C	3657.3	6.771	6.68	3.18	3.39
Heat pumps	R134a	231.5	0.331	0.09	0.00	0.00
	R410A/R407C	2575.3	5.185	5.16	1.26	1.40
Mobile air conditioning	R134a	25419.4	36.350	13.50	0.00	0.00
	R407C	88.4	0.157	0.09	0.00	0.00
Sea transport	R134a	1301.9	1.862	0.70	0.11	0.12
	R404A	11.6	0.045	0.01	0.00	0.00
TOTAL				59.4	11.9	13.2
Quota POM			116.4	52.4	33.8	33.8

The results presented in Table 5 indicate that at a given rate of new refrigerants adoption, and taking into account anticipated consumer preference of new equipment with reduced GWP refrigerant, the amount of HFC refrigerants that is expected to be POM is 7.0 $MTCO_2e$ greater than that is necessary to meet the steep quota reduction set by the F-gas regulation for 2021. Such results are likely due to the delayed response of the European refrigeration and air conditioning stakeholders to the requirements of the F-gas regulation and the postponed implementation of the requirements of the Directive 2006/40/EC on mobile air conditioning.
The delay in the implementation of available low and lower GWP refrigerants caused that installed equipment that uses high GWP refrigerants represents a bank of high GWP refrigerants needed to be maintained (top-up to compensate for leakages). Additionally, such equipment retrofit is often limited to the non-flammable HFO/HFC mixtures, which GWP is still rather high (Makhnatch et al.. 2018b) (Makhnatch et al., 2018a). However, to use refrigerants with different safety classification, this equipment could have to be replaced due to safety concerns.

Regarding the modelled future CO_2e emissions from refrigerants to be POM in 2030, the result of the model is quite promising, since the emissions will be lower than the predicted limit. It is due to the availability of low GWP alternatives and under the assumption that all the stakeholders will move to options using the lowest GWP possible in each of the analysed sectors. Meanwhile, the limited lifetime of the refrigeration equipment allows older equipment designed to be used with high GWP refrigerants to eventually greatly phase-out by 2030.
The sectors with highest contribution to refrigerants POM by 2030 will be commercial and industrial refrigeration, produced by lower GWP HFC/HFO mixtures alternatives to R404A and R507 (e.g., R448A. R449A. R455A or R454C) (Mota-Babiloni et al., 2018), and in air conditioning, heat pumps and industries, in lower GWP HFC/HFO mixtures (e.g. R454B. R466A) and pure HFC alternatives (R32) to R410A and R407C (Mota-Babiloni et al.. 2017b).

5. CONCLUSIONS

The currently used high GWP HFC refrigerants are about to be phased down or phased out, and the reduction of their use will be dictated by the European F-gas Regulation and the Kigali Amendment to the Montreal Protocol. For the coming years, we must consider that low GWP refrigerants are going to dominate the market, but there is still a wide variety on them and a great uncertainty on how they are going to be distributed in the market. In this paper, we aimed to model and obtained the future refrigerant mix distribution in the European Union for two target years, 2021 and 2030, when the major reductions in F-gas quota will take place.
The applications here considered where those with higher HFC consumption, and their associated refrigerants, R134a, R404A, R507C, R410A, and R407C. Then, we assumed that the refrigerant distribution where similar to that of the French market and the main data source is retrieved from a report of the European Environment Agency.
For the future refrigerant distribution, the future share of the market and possibilities are based on on the expert opinion on future developments as well as authors personal opinion. The most likely scenario that considers growth in the refrigerant demand is also included in this work.
Results show that, under current assumptions, the POM by 2021 could not be satisfied since the sector is not prepared for the fast transition. In many sectors low GWP refrigerants are suitable for newly manufactured equipment, and their short term implementation is limited by a turn-over rate of the equipment and their applicability for retrofit. However, by 2030, the refrigerant industry will be able to adapt to the situation. In this year, the use of natural refrigerants such as CO_2, HCs, and NH_3, is likely to increase but still synthetic low and lower GWP refrigerants may take a share of the market in applications where R404A/R507 and R410A/R407C are being used.
The excess of POM of refrigerants observed in 2021 can explain the current illegal refrigerant trading in Europe, recognized and warned by several associations and nonprofit organizations. It is expected that the development of the technology, the necessity of renovation of equipment, and better and detailed training of engineers and technicians will reduce to the minimum the illegal acquisition of HFC refrigerants.
Moreover, it is worth to highlight that the conclusions depicted from this model can be extended to benefit the worldwide transition to low and lower GWP refrigerants since the Kigali Amendment is also incorporating an HFC phase-down mechanism. Lessons and experiences learned from the European transition can also be useful. Thus, relevant data should be collected from early stages of Kigali Amendment implementation to provide the industry with more transparency and knowledge, and eliminate uncertainty in decision making when choosing refrigerant and refrigeration equipment use. It is also important to act early since the significant share of current HFC demand is used to maintain previously instaled equipment.

ACKNOWLEDGEMENTS

Pavel Makhnatch and Rahmatollah Khodabandeh acknowledge the financial support of the Swedish Energy Agency within the Termo research program. Adrián Mota-Babiloni acknowledges the financial support of the Spanish Government under the grant FJCI-2016-28324.

NOMENCLATURE

a.g.	Annual growth	HC	Hydrocarbon
CO_2e	Carbon dioxide equivalent	HFC	Hydrofluorocarbon
EU	European Union	HFO	Hydrofluoroolefin
GWP	Global warming potential	LR	Leakage rate
F-gases	Fluorinated gases	LT	Lifetime
F-gas regulation	Regulation (EU) No 517/2014 of the European Parliament and of the Council of 16 April 2014 on fluorinated greenhouse gases	$MTCO_2e$	Million ton CO_2 equivalent
		POM	Placing on market
		RACHP	Refrigeration. air conditioning and heat pump
HC	Hydrocarbon		

REFERENCES

Bitzer, 2018. Refrigerant report 20.

Clodic, D., Pan, X., Devin, E., Michineau, T., Barrault, S., 2013. Alternatives to high GWP in refrigeration and air-conditioning applications. final report.

Danfoss, 2018. Refrigerant options now and in the future.

European Environment Agency, 2018. Fluorinated greenhouse gases 2018. Data reported by companies on the production, import, export and destruction of fluorinated greenhouse gases in the European Union, 2007-2017.

European Parliament, 2014. Regulation (EU) No 517/2014 of the European Parliament and of the Council of 16 April 2014 on fluorinated greenhouse gases and repealing Regulation (EC) No 842/2006 Text with EEA relevance, OJ L.

IIR, 2017. 35th Informatory note on refrigeration technologies. The impact of the refrigeration sector on climate change.

IIR, 2016. 31st Informatory note on refrigeration technologies. Current long-term alternative refrigerants and their possible applications.

IIR, 2014. Containment of refrigerants within refrigeration, air conditioning and heat pump systems (24th Informatory Note on Refrigeration Technologies).

Makhnatch, P., Mota-Babiloni, A., Khodabandeh, R., 2018a. Energy evaluation of drop-in replacements for R134a in cascade CO2/R134a refrigeration units.

Makhnatch, P., Mota-Babiloni, A., Khodabandeh, R., Haro-Ortuño, J., 2018b. Field measurements of a R404A low-temperature supermarket refrigeration system retrofitted with R449A. Refrig. Sci. Technol.

Makhnatch, P., Mota-Babiloni, A., López-Belchí, A., Khodabandeh, R., 2019. R450A and R513A as lower GWP mixtures for high ambient temperature countries: Experimental comparison with R134a. Energy 166, 223–235. https://doi.org/10.1016/j.energy.2018.09.001

Makhnatch, P., Mota-Babiloni, A., Rogstam, J., Khodabandeh, R., 2017. Retrofit of lower GWP alternative R449A into an existing R404A indirect supermarket refrigeration system. Int. J. Refrig. 76, 184–192. https://doi.org/10.1016/j.ijrefrig.2017.02.009

McLinden, M.O., Brown, J.S., Brignoli, R., Kazakov, A.F., Domanski, P.A., 2017. Limited options for low-global-warming-potential refrigerants. Nat. Commun. 8, 14476. https://doi.org/10.1038/ncomms14476

Mota-Babiloni, A., Haro-Ortuño, J., Navarro-Esbrí, J., Barragán-Cervera, Á., 2018. Experimental drop-in replacement of R404A for warm countries using the low GWP mixtures R454C and R455A. Int. J. Refrig. 91, 136–145. https://doi.org/10.1016/j.ijrefrig.2018.05.018

Mota-Babiloni, A., Makhnatch, P., Khodabandeh, R., 2017a. Recent investigations in HFCs substitution with lower GWP synthetic alternatives: Focus on energetic performance and environmental impact. Int. J. Refrig. 82, 288–301. https://doi.org/10.1016/j.ijrefrig.2017.06.026

Mota-Babiloni, A., Navarro-Esbrí, J., Makhnatch, P., Molés, F., 2017b. Refrigerant R32 as lower GWP working fluid in residential air conditioning systems in Europe and the USA. Renew. Sustain. Energy Rev. 80, 1031–1042. https://doi.org/10.1016/j.rser.2017.05.216

Peters, T., 2018. A cool world. Defining the energy conundrum of cooling for all. University of Birmingham.

UN, 2016. Amendment to the Montreal Protocol on substances that deplete the ozone layer. Kigali.

Manuscript ID: 835
DOI:10.18462/iir.icr.2019.0835

Performance analysis of finned-tube CO_2 gas cooler with advanced CFD modelling development and simulation

Xinyu ZHANG[(a)], Yunting GE[(a)], Jining SUN[(b)]

[(a)]Sustainable Environment Research Centre, Faculty of Computing, Engineering and Science, University of South Wales, Pontypridd, CF37 1DL, UK, e-mail xinyu.zhang@southwales.ac.uk; yunting.ge@southwales.ac.uk
[(b)]RCUK National Centre for sustainable Energy Use in Food Chains (CSEF), Institute of Energy Future, Brunel University London, Uxbridge, Middlesex, UB8 3PH, UK, e-mail jining.sun@brunel.ac.uk

ABSTRACT

A three-dimensional Computational Fluid Dynamics (CFD) modelling investigation in a finned-tube CO_2 gas cooler has been presented and compared with literatures in terms of airside heat transfer coefficient and refrigerant side temperature profile. For the heat exchanger air flow, the Reynolds number is varied in the range of 94.1-282.3 such that laminar flow and viscous model are selected in the CFD model. Simulation results were analyzed and compared at different operating parameters of both air and refrigerant sides including air inlet velocity, air inlet temperature, refrigerant inlet temperature, pressure and mass flow rate. The numerical results have been validated with the public literature results. The simulation results show that when the air inlet velocity varies from 1 m/s to 3 m/s, airside average heat transfer coefficient increases from 88.58 W/m^{2}k to 138.69 W/m^{2}k. In addition, it is found that the higher velocity leads to lower the approach temperature and thus improving the performance of the gas cooler. The research methods and outcomes can be used for further investigation and optimization in this area.
Keywords: CO_2 Finned-Tube Gas Cooler, Heat Transfer Coefficient, Refrigeration System, Computational Fluid Dynamics (CFD) Modelling.

1. INTRODUCTION

Global extensive energy consumption and resulted environmental issues in refrigeration sectors encourage researchers to develop high efficient refrigeration systems with environmental friendly working fluids. The utilization of CO_2 as a refrigerant in CO_2 refrigeration systems has been more attractive due to its superb thermophysical properties and negligible environmental impact. On the other hand, finned-tube CO_2 gas coolers have been widely used in CO_2 refrigeration systems owning to their simplicity and using ambient air as cooling medium. The CO_2 gas cooler also plays an important roles in the system efficiency and controls such that the further performance improvement and optimal design are desired for the heat exchanger.
Correspondingly, a great deal of researches have been carried out to investigate the heat transfer and hydraulic behaviours of the finned-tube CO_2 gas coolers with both theoretical and experimental analyses. Gnielinski (1976) and Pitla et al. (2002) proposed empirical equations for calculating refrigeration side heat transfer coefficient. Wang, Jang and Chiou (1999) generalized a correlation for evaluating airside heat transfer coefficient and friction factor of finned-tube heat exchangers with wavy fins. These heat transfer and hydraulic calculations are important to understand and investigate heat exchanger performance and modelling development. Several modelling methods could be applied to analyse the performance of CO_2 finned-tube gas coolers at different operating conditions including ε-NTU or LMTD i.e. lumped, tube-in-tube and distributed. However, the ε-NTU or LMTD method should be used carefully due to CO_2 thermophysical properties change rapidly with temperature during an isobaric gas cooling process (Kim et al., 2004). Ge and Cropper (2009) used a distributed method to calculate CO_2 temperature profile along CO_2 flow process with localised

working fluid heat transfer and hydraulic parameters. The simulation results showed that the larger heat exchanger circuit number could increase its heating capacity.
Although the empirical correlations of airside heat transfer coefficient and hydraulic calculations could be used to predict the performance CO_2 gas coolers, these correlations are not universal since the gas coolers with different geometrical structures have different heat transfer characteristics. To obtain accurate modelling of the CO_2 gas cooler with complicated structural and operational parameters, 3D CFD modelling strategy in CO_2 finned-tube gas coolers is therefore expected. Yaïci et al. (2016) proposed a CFD modelling to investigate the influence of inlet air flow mal-distribution on the performance of a plate-fin-tube water-air heat exchanger. Although some researches have been carried out for finned-tube heat exchanger, to the authors' acknowledge, there is no detailed CFD modelling on the CO_2 finned-tube gas cooler found in public literatures.
Due to the difficulty in obtaining local airside heat transfer coefficient and CO_2 refrigerant temperature profile along pipes, this study presents a new 3D CFD modelling method and modelling simulation to evaluate the heat transfer performance of the CO_2 gas cooler at different operating conditions. The characteristics of average airside heat transfer coefficient have been plotted at different air flow Reynolds numbers. The developed CFD model is also used to predict the refrigerant temperature profiles at different operating conditions. The results of this study are expected to be valuable for the development of CFD modelling strategies and performance evaluation on the CO2 finned-tube gas coolers.

2. NUMERICAL METHODOLOGY

A 3D CFD model has been developed to simulate the performance of a CO_2 finned-tube gas cooler at different operating conditions. The modelling routine firstly starts from airside, and then the simulation runs through each numbered pipe starting from refrigerant inlet to outlet. There are two models created in this study, which are two consecutive fins with air flow region model and model with ten consecutive fins. They are named as airside model and CO_2 side model respectively in this paper. Airside model is used to calculate airside heat transfer coefficient and the CO_2 side model is applied to predict refrigerant temperature profile along the pipe. The heat exchanger modelling depends on the calculations of conservation equations of mass, momentum and energy for both air and refrigerant sides. To simplify the modelling process and save computing time, the heat exchanger is divided evenly into 10 segments along the pipe direction and only one segment of the heat exchanger is modelled by CFD. In addition, for one coil segment, each pipe is further divided into a number of sections or small finite elements. As shown in Fig. 1, there are totally 54 pipes in the heat exchanger. Setting up conservation equations for each element will calculate the CO_2 temperature of each pipe segment and thus the whole pipe. The output temperature of each pipe is then used as the inlet temperature for the next numbered pipe. After iteration, the refrigerant outlet temperature of the final coil pipe can be calculated. Iteration should be carried on until conservation equations reach convergence. The modelling approach is summarized and listed as below:

- Symmetry condition is assumed on the mid plane between two consecutive fins in the heat exchanger.
- Due to the coil symmetry structure, the airside heat transfer coefficient of each passage between two consecutive fins is assumed the same. The model of two fins with air flow region is then used to obtain local airside heat transfer coefficient which is then exported into a txt type file. The User Defined Function (udf) from CFD and a code developed in Visual Studio 2017 are then applied to assign the heat transfer coefficient to the coil external surface.
- The gas cooler is divided into 10 segments along the pipe length direction. Since there are 375 fins in the coil, each segment contains about 37 fins. To simplify the simulation process, the entire gas cooler model is developed based on one segment model. Meanwhile, the transverse heat conduction is also considered in the model.
- The developed CFD model is then validated with the test results from public literature.

2.1. Physical Model

An identical CO_2 finned-tube gas cooler is selected for CFD modelling which was used by Ge and Cropper (2009) and is shown in Fig.1. Airflow passes from right to left and refrigerant flows into the

top tube numbered 0 and out from the bottom tube numbered 54. The specification of the modelled gas cooler is listed in Table 1.

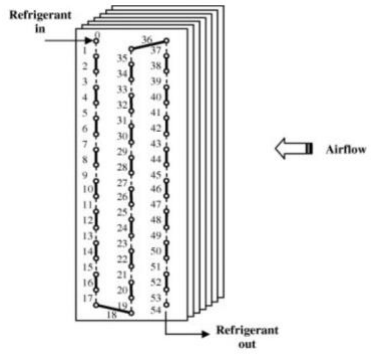

Figure 1: Modelled gas cooler of numbered tube pipes.

Table 1. Specification of the modelled gas cooler

Dimensions	
W × H × D (m)	0.61 × 0.46 × 0.05
Front area (m^2)	0.281
Fin shape	Raised lance
Fin pitch (mm)	1.5
Fin thickness (mm)	0.13
Number of tubes row	3
Tube outside diameter (mm)	7.9
Tube inside diameter (mm)	7.5
Tube shape	smooth

2.2. CFD Model

In this present work, the 3D CFD model of the plain finned-tube CO_2 gas cooler has been developed and demonstrated. The overall modelling process is composed of three parts. In the first part, the created geometry consists of fins and tubes having one refrigerant inlet (pipe '0') and one refrigerant outlet (pipe '54') while SOLID WORK software is applied to draw the geometry. Then the geometry of STEP format is imported to ANSYS ICEM CFD 18.2 while in ICEM each part of the geometry is named. The geometry is meshed using hexahedral type elements. Meshing is a significant step for pre-processing simulation since the model accuracy increases with larger cell numbers but is limited by computer memory. For the airside model, it consists of two consecutive fins and 54 tube pipes while the region between two fins is selected as the air domain. As for the CO_2 side model, it consists of 10 consecutive fins and 54 tube pipes. The meshing of geometries is depicted in Fig. 2 while the mesh details for both two models are described in Table 2. In the second part, the meshed gas cooler is imported to ANSYS Fluent 19.2 to solve mass, momentum and energy governing equations. After iteration, each equation achieves convergence with the maximum error of 10^{-6} and 10^{-15} for two models respectively. The final part of modelling is post-processing including the demonstrations of temperature, velocity and pressure contours as well as other key characteristics to evaluate the gas cooler performance.

Table 2. Mesh size

Case	Number of nodes	Number of faces	Number of cells
airside model	1263000	3393606	1060928
CO_2 side model	2220000	5113610	1427024

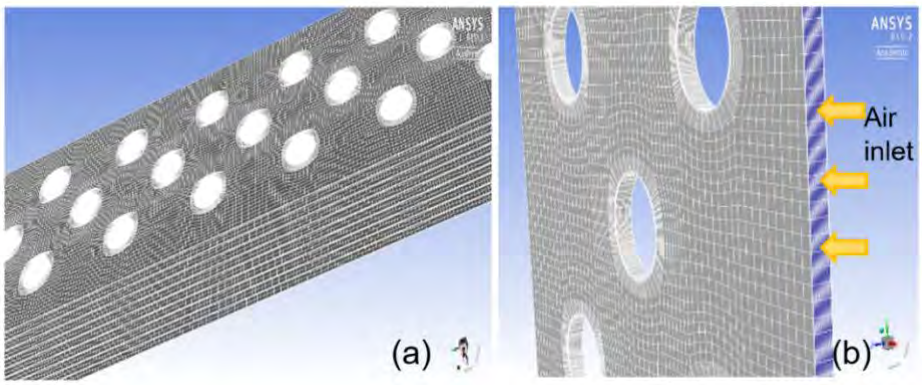

Figure 2: Meshing of geometry, (a) 10 fins gas cooler model, (b) 2 fins and air flow region model

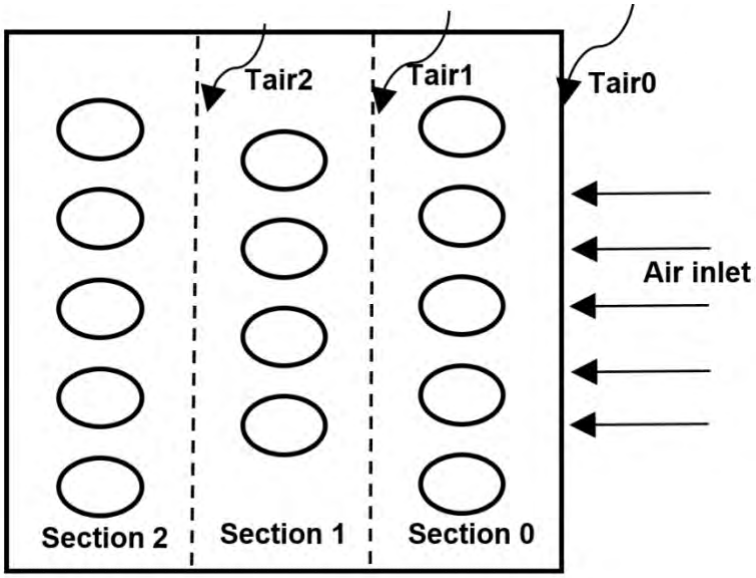

Figure 3: evaluation planes for average temperature Tair0, Tair1 and Tair2 used in CFD simulation

2.3. Airside Heat Transfer Coefficient

Heat transfer coefficient is an important parameter to calculate convective heat transfer between solid surface and fluid. The local airside heat transfer coefficient is determined for each individual surface of either fin or tube. However, it is difficult to obtain. If air inlet average temperature is used for the coil heat flux calculation, the heat transfer coefficient near the second and third rows could be inaccurate. The reason is primarily caused by lager air temperature changes when flowing through fins. The feasible method is to use air bulk temperatures in different sections to obtain heat transfer coefficient.

A modified method for obtaining local airside heat transfer coefficient using the results of CFD model contains two consecutive fins and an air domain. In this method, local air side heat transfer coefficient is determined by air temperature distribution in fluid domain. The total air temperature increase equals to the temperature increases over the first row, the second row and the third row. For improving the modelling results, air temperatures along the gas cooler are changed through three sections, which are section 0, section 1 and section 2. The evaluation planes between two consecutive fins are assumed to obtain the average air temperature of Tair1 and Tair2, as shown in Fig.3. The local heat transfer coefficient is determined by the temperature difference between surface and air bulk temperature of different sections. The performance of airside heat transfer coefficient in one passage between two consecutive fins will be used for the whole gas cooler model.

$$h_{a,i} = \frac{Q_i}{A_i(T_{w,i} - T_{air,bulk})} \quad \text{Eq. (1)}$$

2.4. Refrigerant Side Heat Transfer Coefficient

On the refrigerant side, Gnielinski correlation is used to calculate the respective heat transfer coefficient:

$$Nu = \frac{\xi/8(Re-1000)Pr}{12.7\sqrt{\frac{\xi}{8}}\left(Pr^{\frac{2}{3}}-1\right)+1.07} \quad \text{Eq. (2)}$$

Where, Filonenko's correlation is used to predict the friction coefficient:

$$\xi = (0.79\, ln(Re) - 1.64)^{-2} \quad \text{Eq. (3)}$$

While Reynolds number (Re), Nusselt number (Nu) and Prandtl number (Pr) are calculated respectively as below:

$$Re = \frac{\rho u d}{\mu} \quad \text{Eq. (4)}$$

$$Pr = \frac{\mu c_p}{k} \quad \text{Eq. (5)}$$

$$Nu = \frac{h_r k}{d} \quad \text{Eq. (6)}$$

Refrigerant side heat transfer coefficient can be determined by Eq. (7):

$$h_r = \frac{Nu}{d} k \quad \text{Eq. (7)}$$

The Gnielinski correlation has been widely applied and validated in the calculation of CO2 heat transfer coefficient at supercritical region(Ge and Cropper (2009)). Furthermore, the refrigerant outlet temperature is calculated from heat transfer rate. The CO_2 thermo-physical properties of density, viscosity, specific heat capacity and thermal conductivity are all functions of temperature and pressure, which are obtained from REFPROP software:

$$T_r = \frac{Q_r}{h_r A} + T_w \quad \text{Eq. (8)}$$

$$Q_r = \dot{m} c_p (\Delta T_r) \quad \text{Eq. (9)}$$

The fanning f-friction factor is defined as the ratio of sheer stress and flow kinetic energy density, relating to the pressure drop of refrigerant in tube pipe. It should not be confused with friction coefficient. The difference is that the value of friction coefficient is four times the value of fanning f-friction factor:

$$\mathrm{f} = \frac{\Delta P F p}{\frac{1}{2}\rho u_{in}^2 4L} \quad \text{Eq. (10)}$$

$$\xi = 4\mathrm{f} \quad \text{Eq. (11)}$$

The Colburn j-factor is expressed as:

$$\mathrm{j} = \frac{Nu}{RePr^{1/3}} \quad \text{Eq. (12)}$$

2.5. Boundary Conditions

In this numerical study, since the calculated Reynolds number of airflow based on fin space is less than 2000, laminar flow and viscous model are selected. The following boundary conditions have been used in airside model for investigating airside local heat transfer coefficient:

- The materials of fin and tube are aluminium and copper respectively.
- The outer side walls of fins are assigned as adiabatic wall.
- Airflow region between two consecutive fins is selected and studied.
- The air thermo-physical properties of density, viscosity, specific heat capacity and thermal conductivity are all functions of temperature and pressure, which are obtained from REFPROP software. Each property can be input into FLUENT 19.2 by means of piecewise-linear function.
- For each pipe section, tube inside wall temperature is set as constant.
- The air inlet is set as velocity inlet and outlet as pressure outlet.

Fin, tube outside and inside surfaces are set as convection boundary conditions. To acquire the refrigerant temperature and pressure changes, boundary conditions have been set up as below for CO_2 side model:

- Import local airside local heat transfer coefficient derived from airside model calculation and assign three different air bulk temperatures to fin and tube outer surface using User Defined Function(udf), of which a code has been developed in Visual Studio 2017 for this purpose.

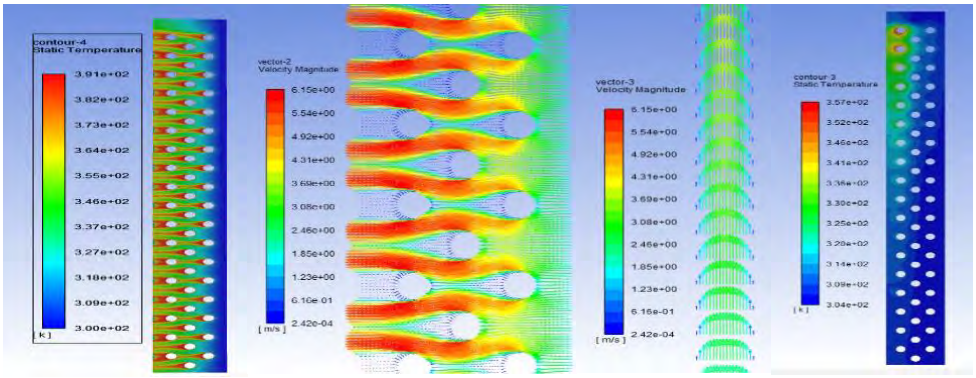

Figure4: Temperature and velocity contour (air inlet velocity = 2m/s): (a)temperature contour of middle plane in air flow region (2 fins model), (b)velocity contour of middle plane in air flow region (2fins model), (c) air inlet velocity contour between fins (2 fins model), (d) temperature contour of each fin surface (10 fins model)

The temperature and velocity distributions are showed in Fig. 4. Fig. 4a presents air temperature characteristic at the middle plane between two consecutive fins. Airflow temperature around the first-row pipe from the right has the lowest temperature compared to the other two rows. Fig. 4b indicates airflow velocity characteristics. The velocity distribution is nearly symmetric due to the highly geometric symmetry. The maximum velocity of airflow is thus occurred close to the transverse plane of boundary layers. When the air flows externally through tubular area, it separates into two side streams and then forms a stagnant area behind upstream of tubes. Fig. 4d presents the fin surface temperature profile of CO_2 side model. Fin surface near the third-row tube has higher temperature than the other part due to refrigerant flows into gas cooler from the top left corner. It can also be observed that tube row temperature can influence each other, which is caused by the transverse heat conduction and is also considered in the model.

3. MODEL VALIDATION

In this present CFD model, the air inlet Reynolds number is in the range of 90-300 based on the fin pitch while based on the tube collar diameter is in the range of 1400-4600. Fig. 5c presents airside

heat transfer coefficient increases with the higher air inlet velocity. When the air inlet velocity increases from 1 m/s to 3 m/s, average heat transfer coefficient varies from 88.58 $W \cdot m^{-2}K^{-1}$ to 138.69 $W \cdot m^{-2}K^{-1}$. Numerical research of Ge and Copper (2009) has been validated with experimental research of Wang et al. (2001) to determine the airside fanning f-friction and Colburn j-factor. Validation is performed with air inlet and refrigerant temperature set at 302.55 K and 391.25 K separately. The simulation performance of f-factor and j-factor corresponding to three different Reynolds numbers have been compared with the results calculated by Wang et al.'s correlations, as shown in Figs. 5a and 5b. The maximum deviation value of f-friction factor and j-factor are 35.6% and 33.7% respectively. Subsequently, reasonable agreement can be obtained between CFD results and the literature correlations.

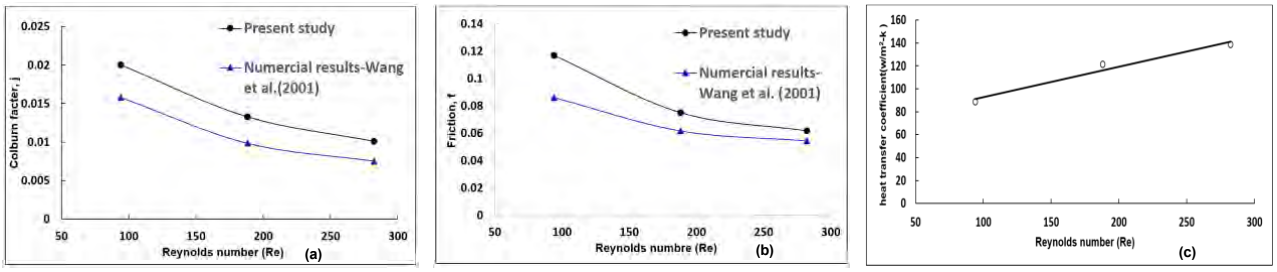

Figure 5: Comparison of performance parameters of varying Reynolds number. (a) Colburn j-factor, (b) Fanning f-friction factor, (c) airside average heat transfer coefficient

This model is used to predict refrigerant temperature of each pipe. Test conditions contain several measurements, including air inlet temperature, air velocity, refrigerant inlet temperature, refrigerant pressure as well as refrigerant mass flow rate as shown in Fig. 6. It can be seen from both simulation and experimental results that most of refrigerant temperature drop occurs in the first-row tube from numbered '0' to '18'. In the second row, refrigerant temperature changes slightly from pipe '19' to '26'. However, there is a step up when refrigerant flows from pipe '26' to '34'. It can be explained that although refrigerant temperature should be decreased gradually with the increasing pipe number, the influence of transverse heat conduction cannot be neglected in this model. Meanwhile, the second reason may be caused by the air wake behind upstream tube is trapped in the stagnant area for a long time, which could also heat up tube and fin surface temperature. According to the results, under the same test condition except air inlet velocity, refrigerant temperature of specified point is always lower for higher air inlet velocity. This is because, higher velocity can improve the heat transfer coefficient and thus heat transfer rate. In addition, when air inlet temperature is the only variable, the refrigerant temperature can be cooled more with lower inlet temperature as shown in Figs. 6a and 6e. This can be explained that air temperature can influence heat transfer coefficient. It is observed from Figs. 6c and 6d that refrigerant temperature drops more dramatically when refrigerant mas flow rate decreases. With increasing operating pressure, the temperature difference between different air inlet velocity for each specified point also increases as shown in Figs. 6e and 6f.

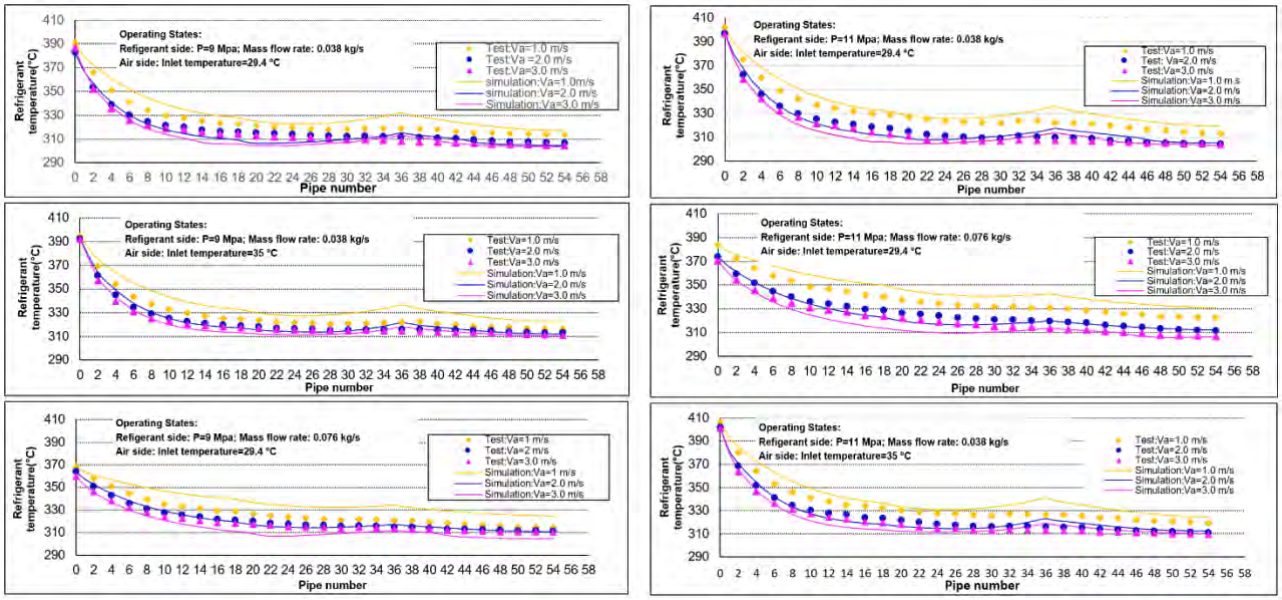

Figure 6: Comparison of simulation with test results of different test conditions

4. CONSLUSIONS

A three-dimensional CFD model method for fin-and-tube CO_2 gas cooler has been proposed in this paper, allows predicting airside local heat transfer coefficient and the effect of different operating conditions. Although some researches have carried out different modelling investigations on the heat transfer performance of finned-tube gas coolers, the modelling method utilized in this study is new. Comparisons of airside heat transfer coefficient and refrigerant outlet temperature for a variety of operating measurements were carried out. Fanning f-friction and Colburn j-factor were used to compare with empirical correlations and they show reasonable agreement. The validated model can be used to predict the performance of fin-and-tube gas cooler through evaluating approach temperature. Some conclusions are obtained:

- Airside heat transfer coefficient and heat transfer rate increase with higher air inlet velocity.
- Refrigerant temperature drops dramatically at the beginning of heat exchanger pipes.
- Lower air inlet temperature leads to lower refrigerant outlet temperature.
- The higher velocity leads to lower the approach temperature and thus improving the performance of gas cooler.

ACKNOWLEDGEMENTS

The authors would like to acknowledge the support received from GEA Searle and Research Councils UK (RCUK) for this project.

NOMENCLATURE

A	Area (m^2)	T	temperature (k)
C_p	specific heat at constant pressure (J kg^{-1} K^{-1})	u	velocity (m/s)
d	tube diameter (m)	va	air velocity(m/s)
D	Depth (m)	W	width (m)
f	fanning friction factor		
Fp	Fin pitch (m)	Greek symbols	
j	Colburn factor	Δ	difference
H	height (m)	ρ	density (kg m^{-3})
h	heat transfer coefficient (W m^{-2} K^{-1})	ξ	friction coefficient
k	thermal conductivity (W m^{-1} K^{-1})	μ	dynamic viscosity (Pa·s)
L	flow length (m)		

$\dot{m}$	mass flow rate (kg/s)	Subscripts	
Nu	Nusselt number	a	air
P	pressure (Pa)	i	ith grid
Pr	Prandtl number	r	refrigerant
Q	heat transfer (W)	w	wall
Re	Reynolds number based on fin spacing		

REFERENCES

Gnielinski, V., 1976. New equations for heat and mass transfer in turbulent pipe and channel flow. International Chemical Engineering 16(2), 359-368.

Ge, Y.T., Cropper, R., 2009. Simulation and performance evaluation of finned-tube CO2 gas coolers for refrigeration systems. Applied Thermal Engineering 29(5-6), 957-965.

Kim, M.H., Pettersen, J., Bullard, C.W., 2004. Fundamental process and system design issues in CO2 vapor compression systems. Progress in Energy and Combustion Science 30(2), 119-174.

Pitla, S., Groll, E., Ramadhyani, S., 2002. New correlation to predict the heat transfer coefficient during in-tube cooling of turbulent supercritical CO2. Int. J. Refrigeration 25(7), 887-895.

Wang, C., Jang, J., Chiou, N., 1999. Technical Note A heat transfer and friction correlation for wavy fin-and-tube heat exchangers. Int. J. Heat Mass Transfer 42(10), 1919-1924.

Wang, C.C., Lee, W.S., Sheu, W.J., 2001. A comparative study of compact enhanced fin-and-tube heat exchangers. Int. J. of Heat Mass Transfer 44(18), 3565-3573.

Yaïci, W., Ghorab, M., Entchev, E., 2016. 3D CFD study of the effect of inlet air flow maldistribution on plate-fin-tube heat exchanger design and thermal–hydraulic performance. Int. J. Heat Mass Transfer 101, 527-541.

Manuscript ID: 836
DOI: 10.18462/iir.icr.2019.0836

Numerical simulation of phase separation in the second header of microchannel condenser

Jun LI[(a)], Pega HRNJAK[(a,b)*]

[(a)] Air Conditioning and Refrigeration Center, University of Illinois at Urbana-Champaign, 1206 West Green Street, Urbana, IL 61801, USA
[(b)] Creative Thermal Solutions, 2209 Willow Rd., Urbana, IL, USA
[(*)] Corresponding author

ABSTRACT

Microchannel condensers with separation circuiting have been proved to increase condenser effectiveness. In the vertical second header, liquid separates from vapor mainly due to gravity, leaving vapor-rich flow with higher heat transfer coefficient to go upward into more microchannel tubes.
Separation is usually not perfect, expressed through the separation efficiency. This paper presents the numerical study of phase separation efficiency. The Eulerian multiphase model of Euler-Euler approach of Computational Fluid Dynamics (CFD) is used. The two-phase refrigerant R-134a for mobile air conditioning (MAC) application is simulated. The inlet mass fluxes to the second header are 166 $kg \cdot m^{-2} \cdot s^{-1}$, 207 $kg \cdot m^{-2} \cdot s^{-1}$ and 311 $kg \cdot m^{-2} \cdot s^{-1}$. The inlet quality is in the range of 0.16 – 0.21.Simulation agrees well with the experiments. The CFD results are also compared to a 1-D numerical model previously built by the authors and a good agreement has been found.
Conclusion can be drawn that liquid separation efficiency η_l decreases with increasing vapor separation efficiency η_v following a linear trend in the experimental range. Reversed flow can be seen in the cross section of the header.
Keywords: Microchannel Condenser, Second Header, CFD, Two-phase Flow, R134a.

1. INTRODUCTION

Li and Hrnjak (2017a; 2017b) proved that an automotive condenser with separation circuitry (separation condenser) improved the condenser flow rate by 7.4% (5.1% on capacity). The inlet of the multi-pass separation condenser is designed to be at the middle of the condenser height. Then in the vertical second header, vapor phase is expected to move upward owing to buoyancy based on the density difference between vapor phase and liquid phase, as shown in Fig. 1a. Meanwhile, liquid phase moves downward along the gravity direction. This separation between vapor and liquid is based purely on property differences, which does not incur too much additional cost.
A physical understanding needs to be acquired towards the extent of separation between the two phases in the second header of a microchannel condenser. Usually upward moving gas flow will drag liquid droplets/ligaments with it and liquid flow will be mixed with gas bubbles. Fig. 1b shows the nomenclature for the quantification of phase separation in the second header. Two separation efficiencies have been defined for liquid and for vapor. Liquid separation efficiency η_l is evaluated by Eq. (1). Vapor separation efficiency η_v is calculated by Eq. (2).

$$\eta_l = \frac{\dot{m}_{l,l}}{\dot{m}_{l,v} + \dot{m}_{l,l}} \quad \text{Eq. (1)}$$

$$\eta_v = \frac{\dot{m}_{v,v}}{\dot{m}_{v,v} + \dot{m}_{v,l}} \quad \text{Eq. (2)}$$

where $\dot{m}_{v,v}$ and $\dot{m}_{l,v}$ are the vapor mass flow rate and liquid mass flow rate, respectively, at the vapor exit; $\dot{m}_{v,l}$ and $\dot{m}_{l,l}$ are the vapor mass flow rate and liquid mass flow rate, respectively, at the liquid exit. $\eta_v = \eta_l = 1$ will be the ideal case of separation (complete phase separation). $0.5 < \eta_v < 1$ and $0.5 < \eta_l < 1$ will indicate partial phase separation.

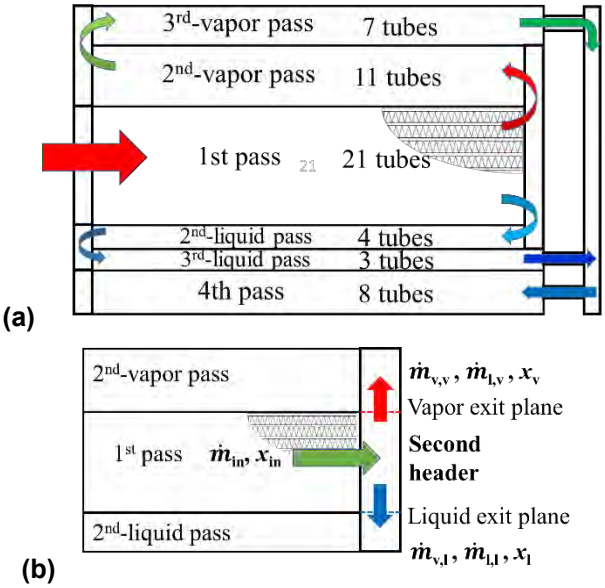

Figure 1: a) Condenser with separation circuiting; b) Variable to determine the separation efficiency

Representative work in the past two decades using computational fluid dynamics (CFD) to model the header flow included Fei and Hrnjak (2004), Li et al. (2005), Ha et al. (2006), Stevanovic et al. (2012), and Stevanovic and Hrnjak (2017). Different authors have been focusing on different types of headers or distributors, but not second headers that are of our interest. The generic characteristics of headers for uniform distribution need to be further studied. Also, no universal CFD model has been proved to work for all the cases

This paper provides the CFD modeling results for two-phase R134a refrigerant flow in the second header of the separation condenser represented by Fig. 1a. To the authors' best knowledge, it is the first time in literature to present CFD simulation for this type of header. Simulation results show fair agreement with experiment results. A 1-D numerical model was also built previously in Li and Hrnjak (2019) based on force analysis. It is also one goal of this paper to compare the CFD results with the results of the 1-D model.

2. MODEL DESCRIPTION

ANSYS-Fluent is employed to simulate the two-phase flow. The simulation of the vapor–liquid monodispersed flow is conducted using the Eulerian multiphase model based on the Euler–Euler approach (ANSYS, 2018), in which the vapor phase is regarded as continuum and liquid phase as dispersed phase. Refrigerant fluid properties are calculated from REFPROP 9.1 (Lemmon et al., 2013).

To simplify numerical simulation while still keeping the basic characteristics of the process, the following assumptions are made in the present simulations:

(1) The thermal properties of the fluids are constants. The continuous vapor phase is macroscopically regarded as continua, and the dispersed liquid phase is spherical in shape.
(2) For the 21 inlets to the second header, uniform flow rates are assumed for both the gas phase and the liquid phase. This is because the inlet to the 1st pass of the condenser is usually single-phase vapor which should be uniformly distributed with uniform air velocity over the whole face of the condenser.
(3) The two-phase flow processes are in steady state and the interfacial mass transfer is not considered.

For the interfacial forces, drag force (Schiller and Naumann, 1933, 1935) and lift force (Legendre and Magnaudet, 1998) are considered. Based on the definitions in ANSYS (2018), the wall lubrication force $\vec{F}_{\mathrm{wl,q}}$ (the forces that pushes the bubbles away from the walls for bubbly flows) and virtual mass force $\vec{F}_{\mathrm{vm,q}}$ (the inertia force of the vapor encountered by the accelerating liquid droplets) are relatively small and not considered in the study. The turbulence dispersion force $\vec{F}_{\mathrm{td,q}}$ is the instantaneous drag minus the mean drag $\vec{F}_{\mathrm{drag,q}}$ and normally denotes the turbulent diffusion in dispersed flow. Since Reynolds number is on the order of 10^3 in header, the turbulence dispersion force is also assumed to be small and negligible in the current calculation.

The governing mass and momentum conservation equations are discretized by the finite volume method; the convection term is discretized by 1st order scheme. The calculation is performed in double precision. The Phase Coupled SIMPLE (PC-SIMPLE) algorithm is used for the pressure-velocity coupling.

The 3-D computational domain of the CFD model is the inlet part of the second header as shown in Fig. 2. The upper part to the 2nd-vapor pass and the lower part to the 2nd-liquid pass are essentially two inlet headers that have been widely studied. Therefore, they are not of interest in this study. The computational domain is all fluid volume and is discretized into a number of nodes forming a hexahedral mesh. Two necessary modifications are done to the original domain:

(1) The domain is cut to be half due to symmetry;
(2) The vapor exit end and the liquid exit end are elongated by eight times of the diameter to prevent big amount of reversed flow at the two exits (almost half of the tube).

The elongated parts have simpler geometry that is only two half round tubes, so flow field should be less complex than that in the inlet part with intrusions. So, the axial length of one node is twice of that in the inlet part.

The grid independence test is carried out to ensure a grid-independent solution is obtained. The size of one node is kept small enough to have 2 nodes along the height of the microchannel tube slot. Three different grid systems with 972,871, 1,539,867 and 1,997,222 nodes are adopted for calculation of the whole computational domain. For the 972,871-node grid, the maximum cell size of the inlet part is 0.4 mm; for the 1,539,867-node grid, the maximum cross-sectional cell size is 0.3 mm and the maximum axial cell size of the inlet part is 0.4 mm; for the 1,997,222-node grid, the maximum cell size of the inlet part is 0.3 mm. Fig. 3 shows the cross-sectional view and the microchannel view of the mesh with 1,539,867 nodes. When the node number is 1,997,222, the difference of the liquid and vapor separation efficiencies is less than 2% compared to the 1,539,867-node system. Considering the computational time cost and precision, the 1,539,867-node system is taken for the computation.

The velocity boundary condition is adopted for the gas and liquid inlets. The average static pressure boundary conditions are used for the outlet.

An iterative solution process in Fluent is implemented by a steady-state solution process. The convergence criterion in the simulation is that the residuals for all the variables are lower than 1.0×10^{-2} and the mass flow imbalance between the outlet and inlet is less than 1%. When checking the mass flow balance between outlet and inlet, 6000 iteration steps are needed to reach the level of less than 1%.

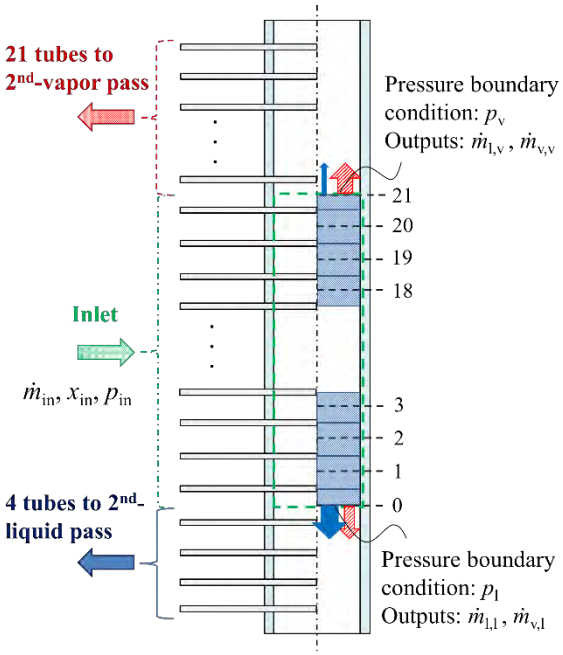

Figure 2: Computational domain of the 1-D model

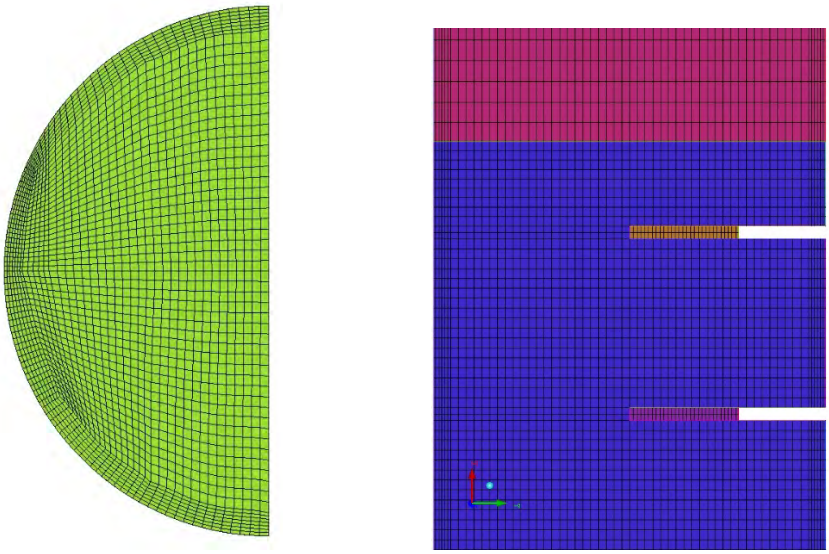

(a) (b)

Figure 3: The mesh with 1,539,867 nodes: (a) Cross-sectional view of the header; (b) Microchannel 2-D view

3. RESULTS AND DISCUSSION

A pump-powered closed loop for testing the separation efficiency in the second header was built. Its schematic is shown in Fig. 4. More details about the test facility can be referred in Li and Hrnjak (2018).

The tested second header was made to have the similar geometry to the header of a real condenser. It had 21 inlet tubes same as the tube number of the first pass of the real automotive condenser. The main pipe of the tested header was round in shape, with an inner diameter of 15.8 mm. The lateral tubes were flat microchannel tube with a dimension of 13.6 mm x 1.0 mm. Hydraulic diameter of the microchannel port was 0.54 mm. The tube pitch was 7.0 mm. The geometry model in CFD is built to be the same as the header in the experimental tests.

In the phase separation condenser, the upper vapor path and the lower liquid path finally mix in the integrated receiver/drier. Different flow resistances of the vapor path and the liquid path give different pressure drop, which will set the pressure boundary condition for flow field inside the second header,

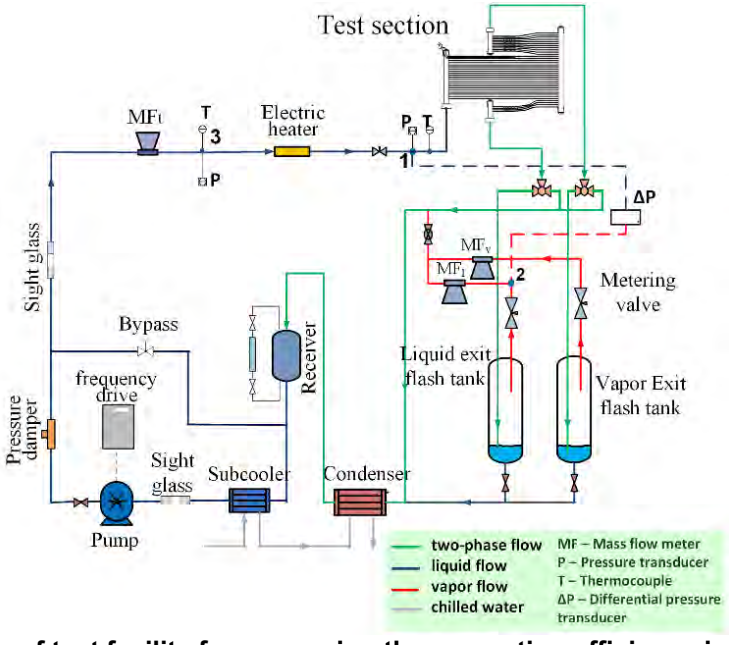

Figure 4: Schematic of test facility for measuring the separation efficiency in the second header prototype

thus altering the flow separation phenomenon. The real automotive condenser has less tubes in the liquid path than in the vapor path; flow resistance on the path of liquid exit is normally higher. Therefore, in experiments, to simulate the higher path resistance, the metering valve on the path of the liquid exit is gradually closed in Fig. 4. When closing the valve on the path of liquid exit, less and less flow goes through that path. This will cause η_v to increase and η_l to decrease. That is the general trend for all the inlet conditions.

The 18 cases studied in the numerical simulation are listed in Table 1. The working fluid is R-134a. Three pairs of mass flux and gas quality at the inlet are investigated: G_{in} = 166 kg·m^{-2}·s^{-1}, x_{in} = 0.21; G_{in} = 207 kg·m^{-2}·s^{-1}, x_{in} = 0.2; G_{in} = 311 kg·m^{-2}·s^{-1}, x_{in} = 0.16.

The CFD simulation results are compared here to the experimental data and the results of the 1-D mechanistic model presented in Li and Hrnjak (2019). Fig. 5 plots pairs of η_l and η_v from experiments as discrete points (EXP as the legend). The uncertainty of η_v is within 2.1% and the uncertainty of η_l within 1.6%. With the values of vapor separation efficiency η_v from Fig. 5 being the inputs of the mechanistic model, η_l will be calculated and the relationship is plotted as a continuous curve (MOD as the legend) for each inlet condition. With Eq. (1) and Eq. (2) in mind, Fig. 5 demonstrates more liquid ($\dot{m}_{l,v}$) moves upward when there is more upward-moving vapor ($\dot{m}_{v,v}$). In the range that the experimental conditions cover, the η_l decreases linearly with increasing η_v. That is the consequence of the fact that the portion of the liquid that gets “dragged” upward becomes bigger for several inlet tubes.

For the same inlet condition with the experiment, estimated pressure boundary condition is the input for each case of the CFD model and the results are shown as the discrete dots also in Fig. 5. It shows that the CFD simulation captures the changing trend of η_l as a function of η_v. More than 90% of the data points are predicted within +/- 5% deviation from the experimental results for both condensers. One of the reasons for the deviation of experiment data from the 1-D model result is

Table 1. Conditions for the cases in the CFD simulation

Case	G_{in} [kg/m^2-s]	x_{in} [-]	η_v [-]	Case	G_{in} [kg/m^2-s]	x_{in} [-]	η_v [-]
1	166	0.21	0.598	10	207	0.2	0.643
2			0.609	11			0.703
3			0.624	12			0.763
4			0.674	13	311	0.16	0.578
5			0.733	14			0.586
6			0.776	15			0.596
7	207	0.2	0.582	16			0.627
8			0.604	17			0.694
9			0.611	18			0.751

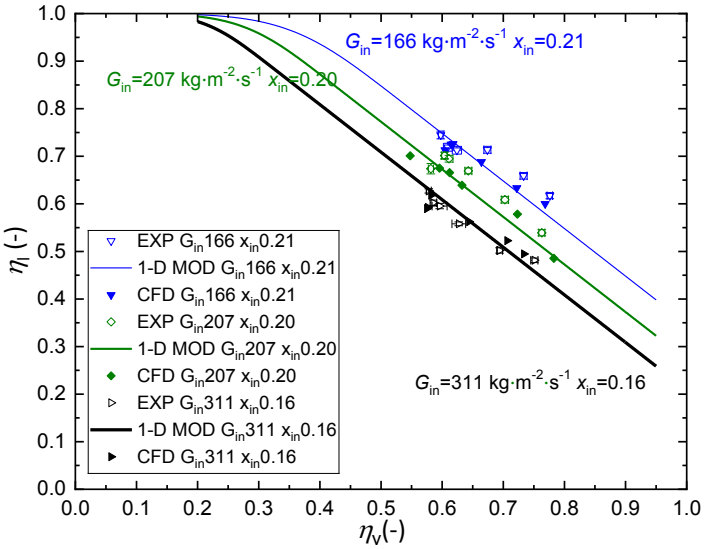

Figure 5: η_l changes as function of η_v for three simulated inlet conditions

due to small variance of inlet condition, because in experiment the inlet mass flux, quality and pressure cannot be controlled perfectly to be the constants inputted to the model. Inlet pressure in experiments is within ±15 kPa difference to an average for each inlet condition.

Fig. 6 demonstrates the comparison of the liquid location between CFD simulation results and snapshots of flow visualization videos for three cases. The CFD results show the vapor volume fraction, e.g. void fraction, on the wall of the header. It is confirmed through the CFD results that most of the liquid accumulates on the opposite side to the inlet tubes on the wall of the header. This is mainly due to the intrusion of the inlet tubes into the header.

Even though this kind of comparison is intuitive, it has two limitations: (1) the flow visualization video always shows the smallest void fraction because it captures the flow not only at the plane of focus but also at planes closer to or farther away from the camera; (2) the video of two-phase flow shows a period, while the CFD result only shows the result of a steady state solution. Even though measurements were taken at a steady state, the two-phase flow itself has instability in nature, so in the video there is fluctuation involved. One snapshot from a video may not represent the average position of the liquid. This may cause the difference between a snapshot of the video and the CFD result.

For the 18 cases, a general phenomenon exists that there are vortices between adjacent microchannel tubes. At steady state, these local vortices prevent most of the liquid coming to the intrusion side of the header and make liquid flow mostly along the opposite side. Fig. 7 indicates the vortices from the cross-sectional view. It shows the vapor velocity contours on the two exit planes. For both contours, the vapor velocity has opposite directions on the intrusion side of the header and on the other side. While flow velocity on the vapor exit plane is supposed to be positive and on the liquid exit plane negative, there are clearly reverse flow on the intrusion side of these two exit planes.

For the same case as in Fig. 7, Fig. 8 shows the local vapor and liquid superficial velocities together with the snapshot of flow visualization. Results generated by the 1-D model and the CFD simulation are compared. The velocity of each cross-sectional plane in the CFD results is calculated as the average velocity of that plane. In the 1-D model, the segment where a phase changes its direction is defined as the critical location for that phase. Above the liquid critical location $loc_{l.crit}$, there is upward churn flow based on the flow map by Taitel et al. (1980); below $loc_{l.crit}$ and the vapor critical location $loc_{v.crit}$, the directions of vapor velocity and liquid velocity are opposite, thus there is counter-current flow.

Fig. 8 demonstrates a good match between the 1-D model result and the CFD result. The vapor superficial velocity u_{vs} is offset by about 0.025 m/s because the estimated pressure inputs for CFD did not give exactly the same u_{vs}. But the deviation is small and the point is with the very close u_{vs}

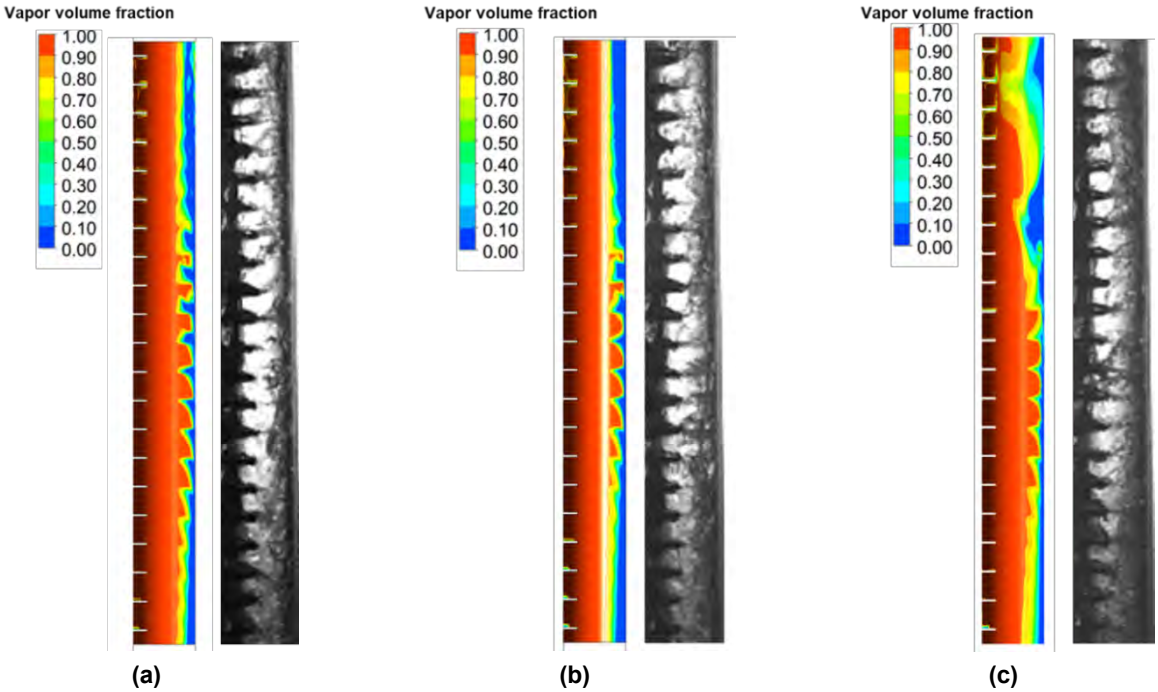

Figure 6: Comparison of liquid location between the CFD simulation and experimental flow visualization (dark region): (a) G_{in} = 166 kg/(m^2·s), x_{in} = 0.21, η_v = 0.60; (b) G_{in} = 207 kg/(m^2·s), x_{in} = 0.21, η_v = 0.58; (c) G_{in} = 311 kg/(m^2·s), x_{in} = 0.16, η_v = 0.58

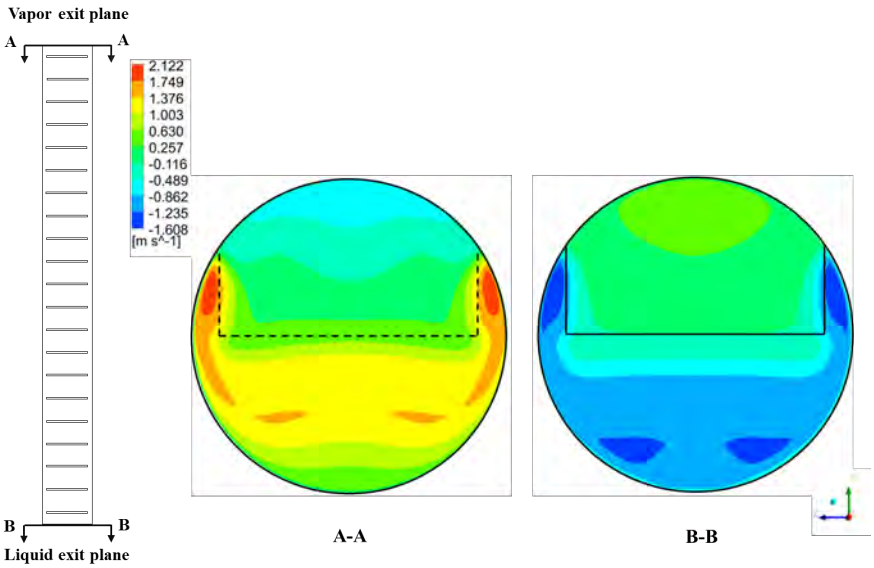

Figure 7: Vapor velocity at two exit planes. R134a, G_{in} = 207 kg/(m^2·s), x_{in} = 0.21, P_{in} = 511.4 kPa, η_v = 0.58

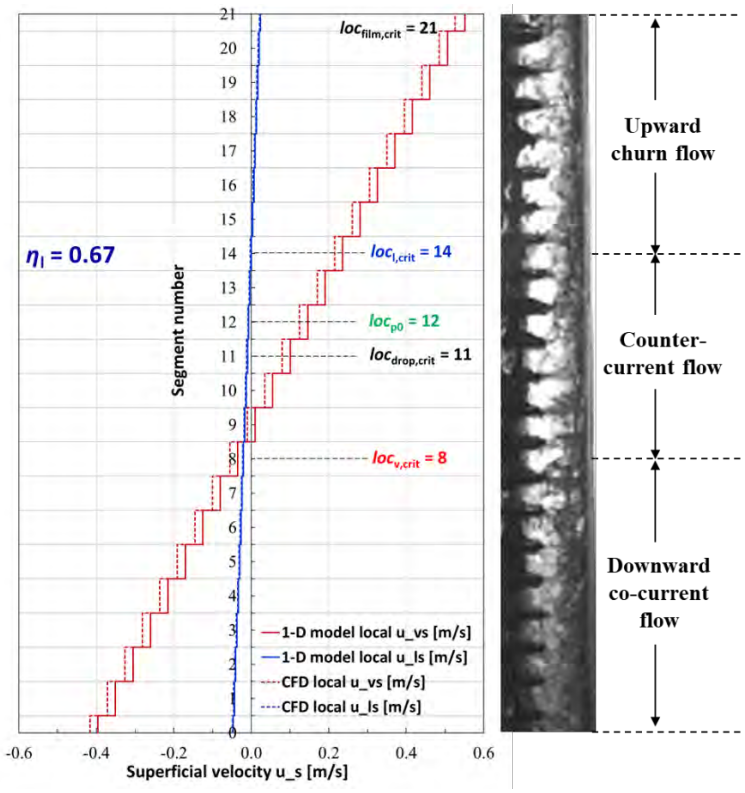

Figure 8: Velocity comparison between CFD and the quick 1-D model. Same operating condition with Figure 7

the liquid superficial velocity is matched well. More importantly, the agreed trend with CFD proves the assumption made about liquid velocity in the 1-D model is valid. Basically, a larger portion of the liquid from top inlet tubes will get dragged due to higher local vapor velocity compared with those from lower inlet tubes. With higher vapor velocity due to bigger η_v, the portion of liquid that gets dragged increase for all the inlet tubes above $loc_{v,crit}$.

4. CONCLUSION

Two-phase flow in a second header for separation condensers is numerically studied. The CFD model is validated against experiment data and a 1-D quick mechanistic model based on

experimental correlations. Conclusion can be drawn that liquid separation efficiency η_l decreases with increasing η_v following a linear trend.
The match on velocity profile between the CFD result and the 1-D model result provides supports for the assumption about liquid drag in the 1-D model: a higher portion of the liquid from top inlet tubes will get dragged due to higher local vapor velocity compared with those from lower inlet tubes. It is also found from the CFD results that there are vortices between adjacent MC tubes. These vortices keep most of the liquid flowing on the opposite side of the header to the side of intrusion. Reverse flow is strong on the exit planes to the 2nd passes of the condenser. Reverse flow happens on the intrusion side of the second header.

REFERENCES

ANSYS-Fluent, ANSYS-Fluent Solver Theory Guide, ANSYS, Inc, 2018.

Clift, R., Grace, J.R., Weber, M.E., (1978). Bubbles, Drops, and Particles, Academic Press New York.

Ha, M.Y., Kim, C.H., Jung, Y.W., Heo, S.G., 2006. Two-phase flow analysis in multi-channel, Journal of Mechanical Science Technology 20, 840–848.

Fei, P., Hrnjak, P.S., 2004. Adiabatic developing two-phase refrigerant flow in manifolds of heat exchangers. Technical Report TR-225, Air Conditioning and Refrigeration Center, Univ. Illinois at Urbana-Champaign, Urbana, IL, USA.

Legendre, D., Magnaudet, J., 1998. The Lift Force on a Spherical Bubble in a Viscous Linear Shear Flow, J. Fluid Mech. 368, 81–126.

Lemmon, E., Huber, M., McLinden, M., 2013. Reference Fluid Thermodynamic and Transport Properties Database – REFPROP, Version 9.1, National Institute of Standards and Technology, Colorado.

Li, G., Frankel, S., Braun, J.E., Groll, E.A., 2005. Application of CFD models to two-phase flow in refrigerant distributors, HVAC & R Research 11, 45–62.

Li, J, Hrnjak, P., 2017a. Separation in condensers as a way to improve efficiency. Int. J. Refrigeration 79, 1-9.

Li, J, Hrnjak, P., 2017b. Improvement of condenser performance by phase separation confirmed experimentally and by modeling. Int. J. Refrigeration 78, 60-69.

Li, J., Hrnjak, P., 2018. Visualization and quantification of separation of liquid-vapor two-phase flow in a vertical header at low inlet quality. International Journal of Refrigeration 85,144-156

Li, J., Hrnjak, P., 2019. Phase separation in vertical header of microchannel condensers – a mechanistic model. Journal of Fluids Engineering, FE-19-1128.

Schiller, L., Naumann, A., 1933. uber die grundlegenden Berechnungen bei der Schwerkraftaufbereitung, Ver. Deut. Ing. 77, 318.

Schiller, L., Naumann, Z., 1935. A drag coefficient correlation, Vdi Zeitung 77, 318–320.

Stevanovic, V., Cucuz, S., Carl-Meissner, W., Maslovaric, B., Prica, S., 2012. A numerical investigation of the refrigerant maldistribution from a header towards parallel channels in an evaporator of automotive air conditioning system, Int. J. Heat Mass Transf. 55, 3335–3343.

Stevanovic, V. D., Hrnjak, P., 2017. Numerical simulation of three dimensional two-phase flow and prediction of oil retention in an evaporator of the automotive air conditioning system. Applied Thermal Engineering 117, 468-480.

Taitel, Yehuda, Bornea, Dvora, and Dukler, A.E., 1980. Modelling flow pattern transitions for steady upward gas-liquid flow in vertical tubes. AIChE Journal 26(3), 345-354

Manuscript ID: 841
DOI: 10.18462/iir.icr.2019.0841

Optimization of a procedure for model calibration using a method based on scattered data interpolation

Sergio MORALES-RUIZ[(a)], Carles OLIET[(a)], Jesús CASTRO[(a)], Joaquim RIGOLA[(a)], Asensio OLIVA[(a)]

[(a)] Technical University of Catalonia-BarcelonaTech, CTTC
C/ Colom, 11, Terrassa, E-08222, Spain, +34 93 739 87 36, www.cttc.upc.edu

ABSTRACT

In order to develop advanced control strategies for complex thermal systems such as in the case of refrigeration and air-conditioning systems, calibrated models against experimental measurements are necessary to reproduce with accuracy the behavior of the real plant, under static and dynamic conditions. Even if accurate information (e.g.: look-up tables) for each component (e.g.: heat exchangers, compressors, etc.) is known, and incorporated to the model plant, the effect of integration of the components in the whole plant has to be taken into account. In a context of fast industrial development, a procedure of minimization of nº tests for the whole plant oriented to model plant calibration has been developed, suitable for Simulink or Modelica environments. This procedure is based on the optimized generation of the nº of tests to be done, according to the error against the available previous data. Once the experimental is doing the generated matrix of new data is used to calibrate the model, using scattered interpolation strategies.
Keywords: HVAC&R, Model Calibration, Interpolation Method.

1. INTRODUCTION

The numerical simulation is a powerful tool that allow predicts the thermal behaviour of devices used in refrigeration and air-conditioning systems. These tools are based on a mathematical model which describes the physical phenomena by means of a set of equations and/or previous empirical information. Many times this previous information is organized in an array or matrix of data, which is known as look-up table. Besides of the previous information, a model calibration against experimental measurement is required to develop and configure an accuracy numerical simulation tool.

The calibration methodology is based on identifying a general rule, which defines a phenomenon, and compare it with the numerical results obtained. Defining a general rule is not easy, because the rule is evaluated from a set of data that has been obtained in limited conditions and this rule has to be extended to other conditions in which the measurements were not obtained. Thus, the effort consist of finding a rule (function P_f) that fit very well with measurements and gives good fit in points outside of the measured range. A way to achieve this objective is using any kind of interpolation method (Fasshauer, 2007).

In this paper, a calibration methodology is proposed to recalibrate the numerical model of an air-conditioning system, which uses empirical information collected in form of look-up tables. The information of the look-up tables help to predict the thermal and dynamic behaviour of any kind of device (e.g.: compressor, heat exchangers, expansion valve, etc.) that make up the system. Besides of this, a pre-process tool to define the minimum number of experimental points required to recalibrate each one of the devices included into the model is described. The final results for each one of the components of the air-conditioning system are detailed.

2. CALIBRATION METHOD

2.1. Numerical Model

The numerical model is based on a set of mathematical equations, which generates an output that depends of the inputs. Sometimes the numerical model uses empirical information organized in form of a look-up table to give a solution of the problem. A schematic representation of a numerical model is shown in Fig. 1.

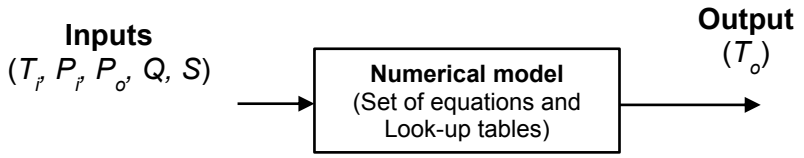

Figure 1: Schematic representation of a numerical model.

The numerical model of a compressor is used to present an optimization procedure for model calibration, in which the inputs are: the inlet temperature of the fluid, the inlet and outlet pressures, the mass flow, and the speed of the compressor. The output of the model is the temperature of the fluid at the outlet of the compressor. The mathematical expression used to evaluate the outlet temperature is:

$$T_o = T_i + \frac{T_i}{\varepsilon}\left(PR^{\frac{\gamma-1}{\gamma}} - 1\right) \quad \text{Eq. (1)}$$

Where the efficiency (ε) is obtained from a look-up table, which is function of the mass flow (*Q*) and the compressor speed (*S*).

2.2. Model Calibration

The strategy followed to calibrate a numerical model is the comparison between experimental data obtained from an experimental unit ($Y_{MEASURED}$) and the numerical results obtained from the model (Y_{MODEL}). Both values obtained using the same input (*I*). A corrector value ($E_{CORRECTOR}$) is obtained from the comparison, which will be a new input of the numerical model. This corrector value will modify the original numerical model results with the aim of finding an accuracy result, looking for a better representation of the real behaviour of the component or system simulated. A blocks diagram with the calibration method is shown in Fig. 2.

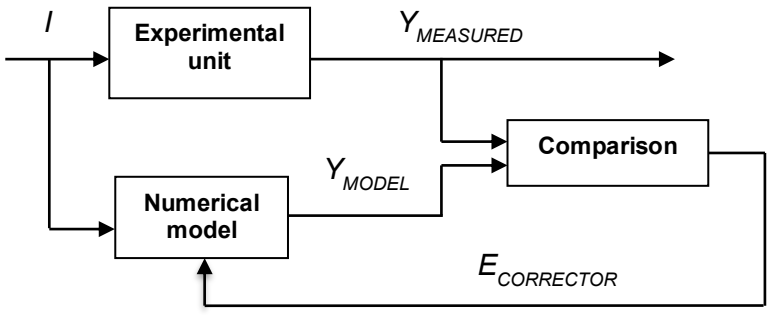

Figure 2: Block diagram of the calibration.

2.2. Calibration Strategy of Look-up Tables

The calibration method consists of modifying the original look-up table (previously known, which was obtained using an isolated bench of test) to a new look-up table that considers integration effects. To achieve this objective the next re-calibration strategy of the look-up table is proposed to be applied on the compressor efficiency value (ε):

- Generating a look-up-table with corrector values ($E_{CORRECTOR}$), which takes old efficiency and obtains a new efficiency, therefore acquiring all previous information as the baseline values:

$$\varepsilon_{new}(i,j) = \varepsilon_{old}(i,j) * E_{CORRECTOR}(i,j) \quad \text{Eq. (2)}$$

- Scattered values of this corrector will be obtained from experiments at certain values (*i,j*), for this specific case the mass flow (*Q*) and the compressor speed (*S*):

$$E_{CORRECTOR} = Integrated_{\varepsilon} / Isolated_{\varepsilon} \quad \text{Eq. (3)}$$

- Applying an interpolation-extrapolation method to obtain the $E_{CORRECTOR}$ for points without experimental information from the scattered values previously evaluated.

An important factor is defining the minimum number of experimental points required to apply the strategy presented, looking for an optimized process without loss accuracy in the results.

2.3. Interpolation Methods

Different interpolation/extrapolation methods can be used to obtain the $E_{CORRECTOR}$ value for all points with and without experimental information; some of them are shortly described:

- Scattered interpolant: This method is used when the location of measurement is not distributed in a regular grid (scattered data). This function returns a surface of the form V = F(x, y). This surface always passes through the sample values at the point locations. The surface can be evaluated at any query point, (xq,yq), to produce an interpolated value, vq.
- Grid data interpolation: This method fits a surface of the form V = F(x,y) to the scattered data in the vectors (x,y,v), in which v is the vector of sample values that correspond to the sample coordinates x, y (for 2D). Griddata interpolates the surface at the query points specified by (xq,yq) and returns the interpolated values, vq. The surface always passes through the data points defined by x and y. The griddata function is useful when you need to interpolate to find the values at a set of predefined grid-point locations. In practice, interpolation problems are often more general, and the scatteredInterpolant provides greater flexibility
- Fit: This method fits curve or surface to data. Different kind of fit type can be used in function of the model selected to fit, some of them are: i) Least squares: This model proves the parameter values that defining the best data fit. A model function F(x,B) is defined, where m parameters are held in the vector B. The result of the fitting process is an estimate of the model parameters, together with the sum of the squares of the residuals; and ii) Polynomial estimation: Returns the coefficients for a polynomial *p(x)* of degree n that is a best fit (in a least-squares sense) for the data in *y*. Others fit type can be used (MathWork, MATLAB, 2018).

3. APPLICATION OF THE CALIBRATION STRATEGY

Applying the calibration strategy proposed in previous section, the look-up table of the compressor efficiency has been analysed.

The original look-up table (previous known) and the modified look-up table of the compressor efficiency are depicted in Fig. 3. The comparison between both efficiency values (original and modified) is represented in function of the mass flows (Q) and the speed compressor (S); both variables are expressed in dimensionless way (which value is defined from 0 to 1). Some difference can be seen between both surfaces, the modified compressor efficiency gives a higher value than the original value from look-up table.

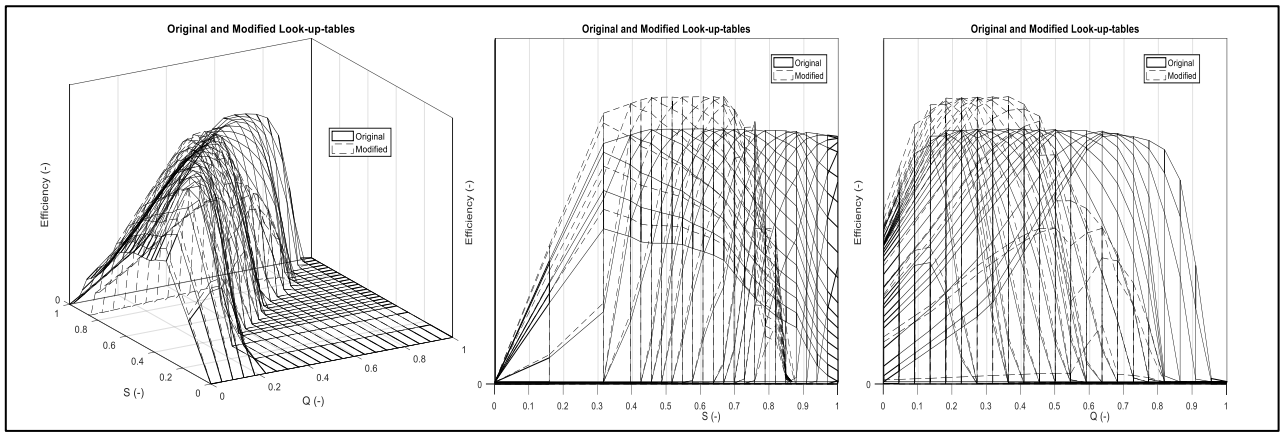

Figure 3: Original and modified Look-up table comparison (left); Efficiency vs. Speed (middle); and Efficiency vs. Mass Flow (right).

The scattered corrector values ($E_{CORRECTOR}$) are shown in Fig. 4, together with the surface generated from these and its projection on the Q vs S plane. The $E_{CORRECTOR}$ values will be used to done the correction of the original look-up tables. However, the corrector values cover a small area of the Q vs S plane giving as result that more experimental data are required to carry out a recalibration of the look-up table of compressor in its total operating range. Then, a strategy to define the perimeter operating range and the minimum number of points required to carry out an efficient and complete calibration of the compressor will be presented.

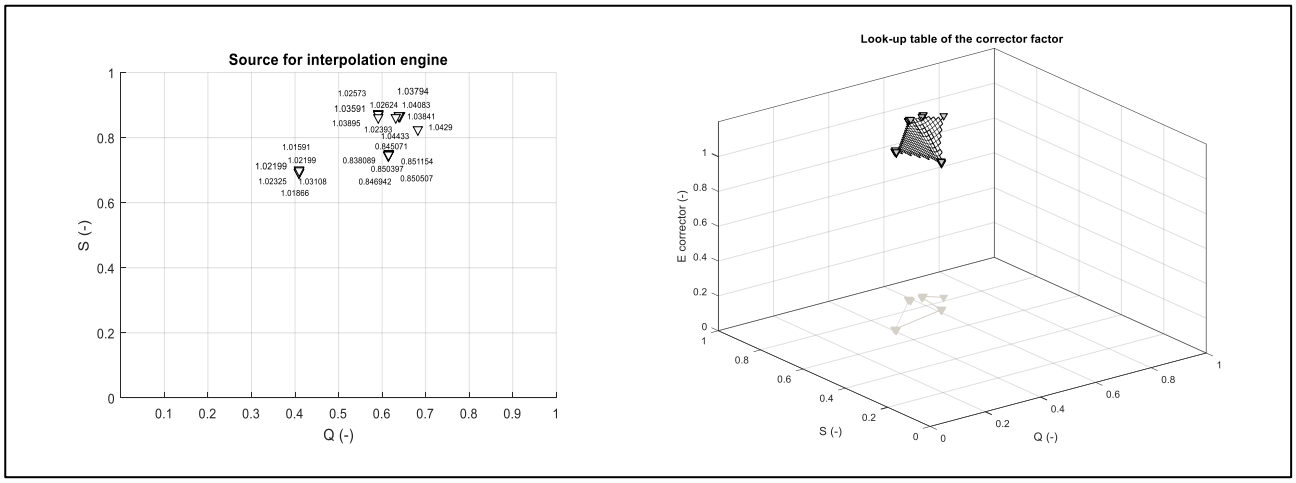

Figure 4: Scattered corrector values (left) and corrector value surface (right).

4. OPTIMIZATION FOR MODEL CALIBRATION

After finding that the available experimental data is not enough to apply correctly the recalibration strategy proposed, an optimization procedure based on defining the minimum number of point required to achieve the compressor calibration will be presented.

A group of working points should be defined, which will be into an operating range previously defined in function of the device analysed (the compressor) and the others devices that make up the whole system. Once the valid points are defined, the valid perimeter of the matrix of points and the minimum number of points will be evaluated.

4.1. Valid Points to be Tested

The first step is defining well the operating range of the device (compressor), therefore the main variables of the compressor: the speed compressor and the pressures ratio, and the fluid: mass flow and temperature should be taken into account to establish a zone in which the device can work without any problem. It is important not forget the restrictions imposed by the system at which is coupled the device.

Using a virtual tool (Plant Model including the control security rules) a matrix of possible points is generated. Taking into account some criteria, the valid points are defined in function of the operating range (safety working conditions of the component and the system). In this form the points are classified in two types: points with value equal to 1 mean a valid point to test, whilst points with value equal to 0 mean invalid points. The invalid points will be out of the test. The matrix point with valid and invalids points are depicted in Fig. 5, together with a second graphical representation that shows the final valid points.

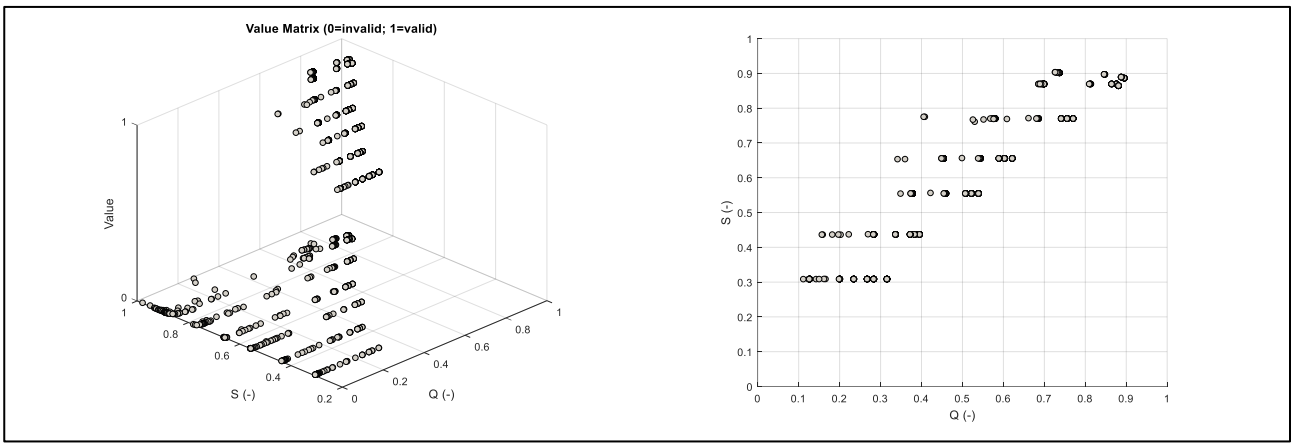

Figure 5: Matrix of points (left) and Matrix of point with valid points to be tested (right).

4.2. The Perimeter Operating Range

The group of points classified as valid helps to define a contour or perimeter, which can be evaluated from any set of scattered values (Mclain, 1974). This contour is defined as “perimeter operating range”.

The shape of the perimeter operating range for the compressor can be affected by some conditions, as an example the influence of the fluid temperature at the inlet of the compressor has been used to show the change of the perimeter shape, it is shown in Fig. 6. This occurs because variations in the fluid temperature value at the inlet (increasing it) affect the thermal behaviour of the compressor, which is conditioned by the control security rules of the system.

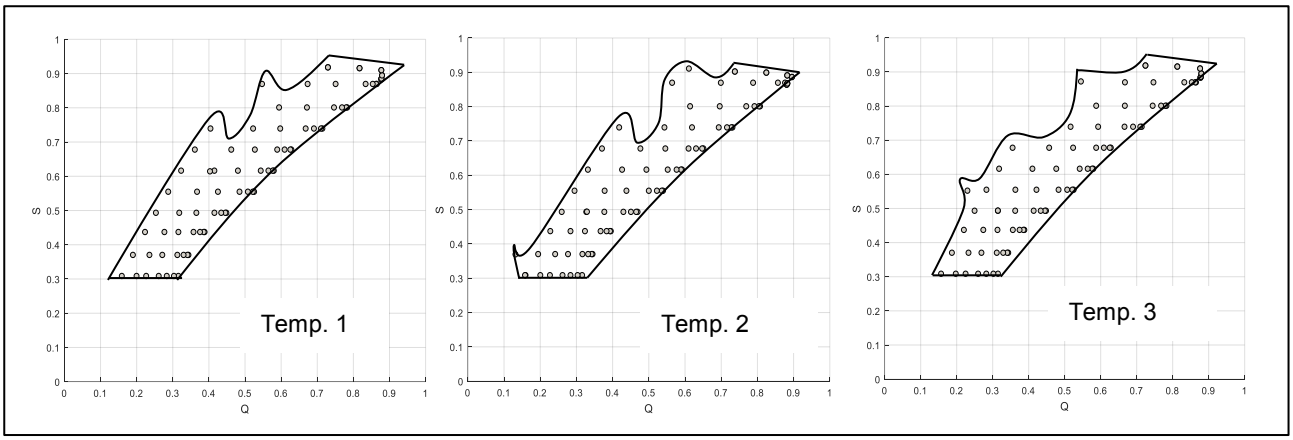

Figure 6: Perimeter shape in function of the fluid temperature at the inlet.

4.3 The Location of the Point into the Perimeter

Once the perimeter operating range has been defined, a number of points and the location of these points into the perimeter will be carried out. The proposal consists of using the variation of the variable defined by the look-up table in function of the dependent parameters to obtain the module gradient, i.e.: evaluating the variation of the Efficiency (ε) in function of the mass flow (Q) and the compressor speed (S) variation, $\frac{d\varepsilon}{dQ}$ and $\frac{d\varepsilon}{dS}$. The module gradient is depicted in Fig. 7.

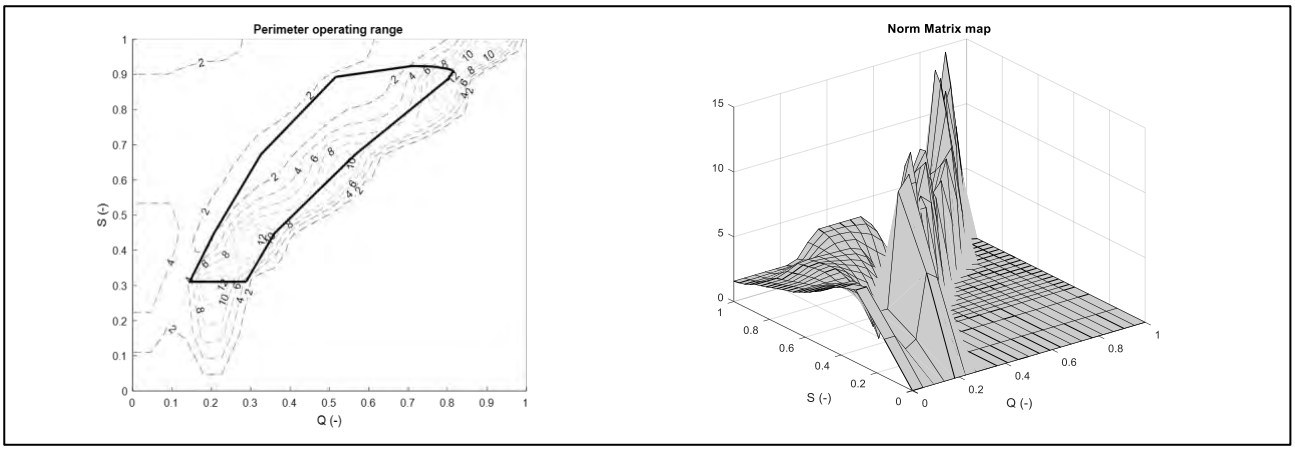

Figure 7: Perimeter and efficiency gradient map (left); and Module gradient of the efficiency (right).

Regarding to the distribution of points into the perimeter, two different ways could be used: a regular or a random distribution of points. A graphical representation of both alternatives is shown in Fig. 8.

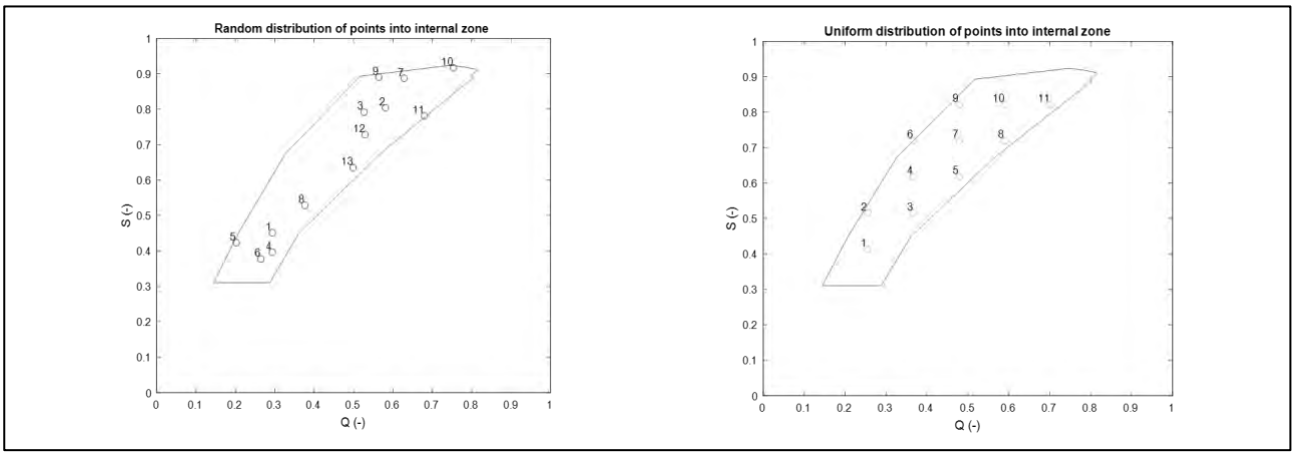

Figure 8: Distribution of the points into the perimeter operating range.

4.4 The Minimum Number of Points

The criterion followed to define the minimum number of points is the mean relative error evaluated between the original value ($\varepsilon_{original}$) and the new value ($\varepsilon_{interpolated}$). The original value is obtained from a look-up table (previously known), whilst the new value is obtained after applying an interpolation method on the scattered points proposed to be tested. The way to obtain the new value is: i) applying a linear interpolation method on the look-up table to find the value of the variable analysed in the position of the scattered points; ii) generating a surface that define the new values from the group of scattered new values by means of an interpolation function; and iii) using the same position than the original value, evaluate the new value from the surface generated. Once the new values are obtained these should be compared with original values to evaluate the error in each point of the look-up table and the mean error. If the group of points is not enough to find a good representation of the variable, the mean relative error will be high and the number of points will be increased.

$$Difference = \left|\varepsilon_{original} - \varepsilon_{interpolated}\right| \quad \text{Eq. (4)}$$

$$Error = \frac{\left|\varepsilon_{original} - \varepsilon_{interpolated}\right|}{\varepsilon_{original}} x100 \quad \text{Eq. (5)}$$

4.5 The Interpolation Influence

The influence of applying the scatteredInterpolant function, the griddata function and the fit function, all from MATLAB, in the value interpolated has been analysed.

Using the scatteredInterpolant and griddata function give as result a high value in the relative error of the variable studied (Compressor Efficiency) as consequence of the triangulation method used by these both interpolation functions (MathWork, MATLAB, 2018). Using the fit function is a way to avoid this problem, because this function does not apply any triangulation method to solve the interpolation. Applying the fit function gives better results than the others. The surfaces obtained by means of different interpolation functions, which define the compressor Efficiency value for a case of 48 points is shown in Fig. 9.

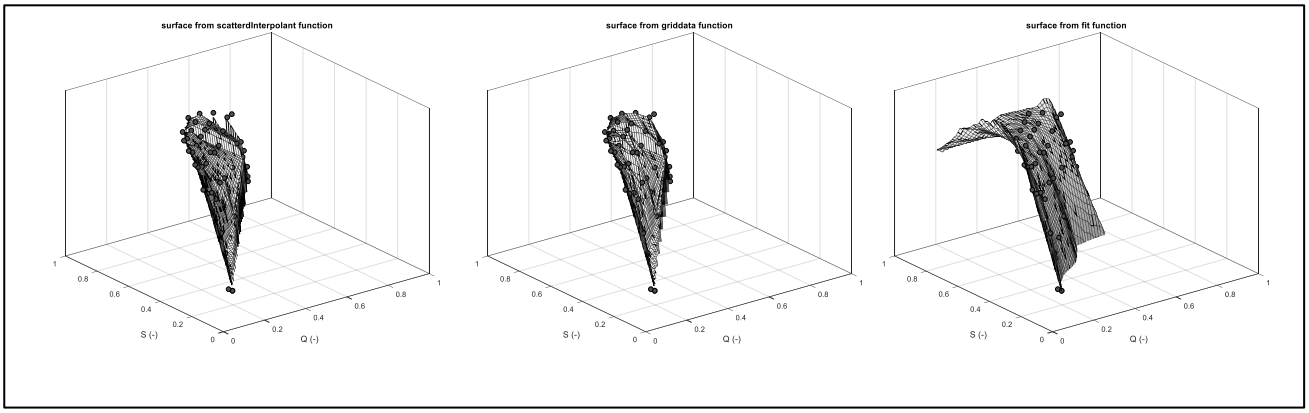

Figure 9: Efficiency surface obtained from different interpolation methods: scatteredInterpolant, griddata and fit function for a uniform distribution of points.

Using the fit function produces a surface that represents better the set of scattered points than the surface obtained with scatteredInterpolant or griddata function. The error of the compressor Efficiency value in function of the interpolation methods applied and the number of points (using the fit function) is detailed in Table 1.

Table 1. Errors in function of: the interpolation method (left); and number of points (right)

Interpolation method	Max error (%)	Mean error (%)	Number of points	Max error (%)	Mean error (%)
Scattered interpolant	34.39	12.01	25	77.74	10.50
Grid data	34.06	9.95	48	37.99	4.61
Fit (poly23)	89.10	7.68	86	39.68	3.03
Fit (loess)	37.99	4.61			

4.6. Final Results

The application of the optimization test points on the compressor gives as result that the minimum number of points to test is 48. The distribution of points into the operating range perimeter and the relative error for each one of the points are represented in Fig. 10.

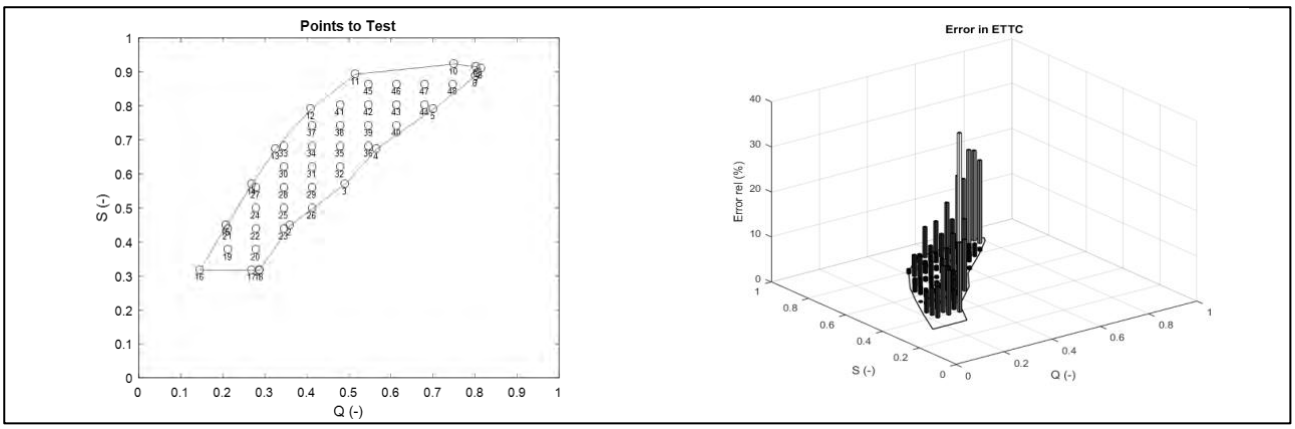

Figure 10: Points to be tested in the compressor and relative error.

Using 48 points, the maximum difference obtained between the original and the interpolated value is about 12.8% of the measurement range, achieving a mean error value of 4.61% when the fit function is applied on the compressor.
Applying the methodology proposed in this paper, the others devices that make up the air-conditioning system have been analysed. The minimum numbers of points for each one of the components or devices are detailed in Table 2, including the errors obtained.

Table 2. Results after applying the optimization method on others devices

Device	Number of points	Max error (%)	Mean error (%)
Dev. 1	44	8.14	2.60
Dev. 2	26	4.61	1.30
Dev. 3	36	13.21	1.81
Dev. 4	14	1.85	0.42
Dev. 5	14	0.65	0.21

Using the number of points obtained with the optimization method for each one of the components, a general test procedure process can be defined to obtain the experimental data of the whole system.

5. CONCLUSIONS

A calibration method for numerical simulation models has been presented. This proposal is based on a look-up table correction strategy, which requires an original look-up table (information previously known) and a set of experimental data (new information). An optimization procedure to obtain the set of data, which is based on the test number minimization according detailed error comparison against existing previous data, is described. The calibration and optimization methodology has been applied on a compressor, which is a component of an air-conditioning system. A tool has been also implemented to define the perimeter operating range, the location of the points into the contour and the minimum number of points required to find a good correction of the variable studied (e.g.: a compressor efficiency). The final result gives that 48 points are required to calibrate the compressor. The methodology explained has been followed to analyse the other devices of the air-conditioning system, obtaining the minimum number of points for each one.

ACKNOWLEDGEMENTS

This research has been financed and supported by Research project (H2020-CS2-CFP04-2016-02 CleanSky project), ref. 755517.

NOMENCLATURE

P	pressure (-)	*T*	temperature (-)
PR	pressure ratio (-)	ε	efficiency (-)
Q	mass flow (-)	γ	isentropic coef. (-)
S	speed (-)		

REFERENCES

Fasshauer, G. E., 2007. Meshfree Approximation Methods with MATLAB, Interdisciplinary Mathematical Sciences: Vol. 6, Illinois Institute of Technology, USA.

Mclain, D. H., 1974. Drawing contours from arbitrary data points, The Computer Journal 17, 318-324.

MathWork, MATLAB – Mathematics - user Guide, 2018.

Manuscript ID: 853
DOI: 10.18462/iir.icr.2019.0853

Design recommendations for plate heat exchangers in heat pumps using pure and mixed refrigerants

Roberta MANCINI [(a)], Benjamin ZÜHLSDORF [(a)], Wiebke BRIX MARKUSSEN[(a)], Brian ELMEGAARD[(a)]

[(a)] Section of Thermal Energy, Department of Mechanical Engineering, Technical University of Denmark (DTU), 2800 Kgs. Lyngby, Denmark, Tel: +45 45254161
Emails: robman@mek.dtu.dk*, bezuhls@mek.dtu.dk, wb@mek.dtu.dk, be@mek.dtu.dk

ABSTRACT

This paper aims at deriving design recommendations for plate heat exchanger (PHE) evaporators and condensers in heat pump (HP) systems using different refrigerants. A coupled HP - PHE simulation framework was used to carry out cycle and component design for a case study, with different combinations of PHE geometrical parameters, and propane, butane and propylene/butane (0.5/0.5) as refrigerants. An operating model subsequently evaluated the heat pump thermodynamic and economic performance with the different designed PHEs: the trade-off between heat transfer area and refrigerant pressure drops was therefore taken into account for both components. Only evaporator pressure drops affected the Coefficient of Performance (COP), and different refrigerants presented dissimilar slopes of degradation. Condenser design did not influence the COP, and the economic optimum corresponded to the lowest size. The evaporator design at minimum cost was instead found as a trade-off between heat transfer area and pressure drops for all the working fluids. Despite the different rates of COP drop, the three refrigerants resulted in the same optimal pressure drop at the evaporator, equal to around 5 kPa.

Keywords: Pressure drops, Zeotropic mixtures, Evaporators, Condensers, Economic analysis

1. INTRODUCTION

Optimal design of evaporators and condensers in heat pumps plays a key-role for overall system thermodynamic and economic optimization. Plate heat exchangers (PHEs) offer a compact design that is feasible for both pure fluids and zeotropic mixtures. Contrary to the most common configurations of micro-channel heat exchangers (HEXs), PHE allows counter-current flow arrangement, which is essential for temperature glide matching between mixed refrigerants and heat source/sink. Nonetheless, HEX design often relies on criteria based on heuristics, such as maximum allowable inlet velocities or maximum pressure drop, possibly leading to suboptimal solutions, depending on the working fluid (Mancini et al., 2018). Previous studies (Muralikrishna and Shenoy, 2000; Wang and Sundén, 2003) attempted at establishing trade-off criteria between pressure drops and investment in heat transfer area, yet mostly focusing on single-phase application or without considering the impact on the thermodynamic cycle performance. On the other hand, HEX design optimization (with or without system integration) was addressed by several works in literature, also focusing on PHEs (Walraven et al., 2014; Xu et al., 2015). However, a simultaneous component/system optimization may entail a high computational cost, especially during the preliminary system design phase and working fluid selection. For example, screening of multiple combinations of pure fluids at different compositions to evaluate the performance of mixed refrigerants (Zühlsdorf et al., 2019), may require too many evaluations of system performance.

In this context, the present work aims at: (i) comparing the relative impact of condenser and evaporator design on the heat pump thermodynamic and economic performance, by looking at both area investment and pressure drops. (ii) Estimating the differences between three working fluids (pure and mixed refrigerants), for a case study. (iii) Discussing similarities and differences considering fluids thermo-physical properties. (iv) Attempting at the definition of general design recommendations for PHE evaporator and condenser in HP systems to be used during the preliminary system design phase.

2. METHODS

This section describes the chosen case study, the overall procedure and the numerical modelling.

2.1. Case Study

A case study previously published in (Zühlsdorf et al., 2019) was chosen for the analysis. A heat pump (HP) was integrated in a data centre facility for waste heat recovery purposes, with the aim of supplying heat to the district heating (DH) network. Propane, butane and a mixture of propylene/butane at (0.5/0.5) mass composition were found among the best performing working fluids. The heat pump was sized by fixing the heat transfer rate at the evaporator, i.e. 500 kW to use as waste heat. Moreover, the heat source was considered to be water entering the evaporator at 50 °C and leaving at 25 °C, while the heat sink was considered to be water entering the condenser at 50 °C to be heated up to 75 °C, i.e. the temperature level required by the DH network.

Table 1. Heat pump design and operating parameters for the three considered refrigerants

Working fluid	$\dot{Q}_{\mathrm{cond}}$, kW	$\dot{Q}_{\mathrm{eva}}$, kW	p_{cond}, bar	p_{eva}, bar	COP, -	$\dot{V}_{\mathrm{out,eva}}$, $\mathrm{m^3/h}$
Propane	638	500	28.1	8.8	4.4	370
Butane	630	500	9.5	2.2	4.5	1100
Propylene/Butane	600	500	16.4	5.6	5.6	460

2.2. Coupled heat pump-plate heat exchanger simulation framework

The simulation framework structure is shown in Figure 1. The models were built in MATLAB (Mathworks, 2017), and fluid properties were estimated by REFPROP 10 (Lemmon et al., 2018). The reader is referred to (Mancini et al., 2018) for a detailed description of the PHE design models, and to (Mancini et al., 2019) for a comprehensive description of the heat pump design and operating models, with detailed PHE characterization.

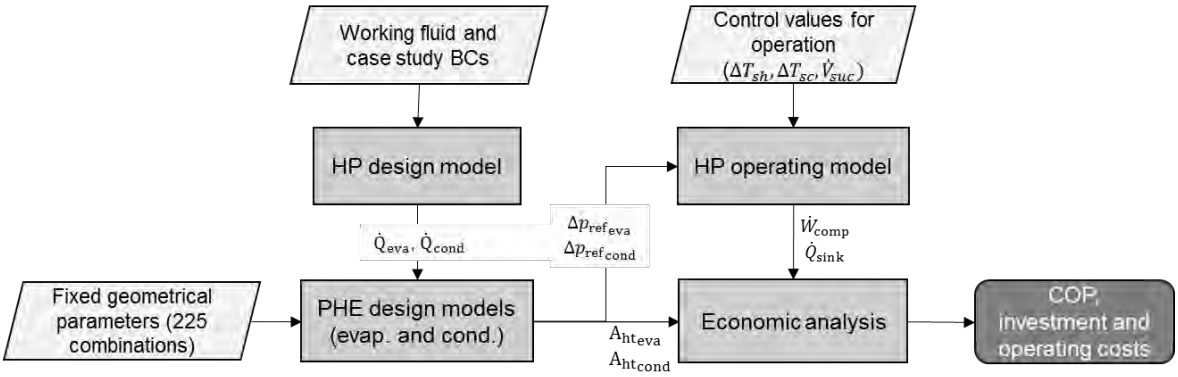

Figure 1: Workflow of the overall method

First, the working fluid and the case study boundary conditions (BCs) were defined and used in the HP design model. The PHE evaporator and condenser designs were subsequently carried out, for different combinations of geometrical parameters. The aim of the parametric analysis was to obtain PHE designs with different heat transfer areas and pressure drops. The resulting configurations were finally used in a HP operating model, which additionally received as input the control values chosen for the operation, namely a fixed superheat, subcooling and suction volume flow rate at the compressor inlet. The resulting HP operating conditions, affecting the compressor power requirement and the heat supply of the condenser, were used in an economic analysis to estimate the COP and operating costs.

2.2.1. Parametric Analysis on PHE geometry

A parametric study was conducted on the geometry of both evaporator and condenser. It was decided to fix the corrugation geometry of the PHEs and to carry out a sensitivity study on the plate size and count. The plate width W and number of channels N_{ch} were varied for both the components, while the plate length was estimated as an output of the design model. The values used in the parametric analysis are reported in Table 2.

Table 2: Plate width and number of channels values used in the parametric study

Parameter	Working fluid	Values	Unit
W_{eva}	All fluids	0.250 – 0.400 – 0.600	m
$N_{\mathrm{ch,eva}}$	Propane	50 – 100 – 150 – 200 – 250	-
	Butane	70 – 120 – 170 – 220 – 270	
	Propylene/butane	80 – 130 – 180 – 230 – 280	
W_{cond}	All fluids	0.200 – 0.400 – 0.600	m
$N_{\mathrm{ch,cond}}$	Propane	50 – 100 – 150 – 200 – 250	-
	Butane	70 – 120 – 170 – 220 – 270	
	Propylene/butane	50 – 100 – 150 – 200 – 250	

2.2.2. Evaluation of thermodynamic and economic performances

The thermodynamic and economic performance of the heat pump for different PHE geometries of both evaporator and condenser were assessed by means of performance indicators. The COP, estimated by Eq. (1), indicated the thermodynamic performance.

$$\mathrm{COP} = \frac{\dot{Q}_{\mathrm{sink}}}{\dot{W}_{\mathrm{comp}}} \qquad \text{Eq.(1)}$$

The specific cost of heat, calculated by means of Eq. (2) and expressed in €/MWh, was instead chosen to quantify the economic performance (Zühlsdorf et al., 2019). In Eq. (2), CF represents the fuel cost to run the compressor, TCI the total capital investment and CRF the capital recovery factor, estimated as function of an effective interest rate. OH represents the HP yearly operating hours.

$$\mathrm{c_h} = \frac{\mathrm{CF_{el}} + \mathrm{TCI} \cdot \mathrm{CRF}}{\dot{Q}_{\mathrm{sink}} \cdot \mathrm{OH}} \qquad \text{Eq.(2)}$$

The use of the specific cost of heat allows estimating the price at which the heat must be sold to the DH network in order to compensate for the investment and running cost of the HP. In this specific case study, the heat source was assumed as free waste heat from the data centre facility.

3. RESULTS

Section 3.1 deals with the impact of PHE designs on the heat pump COP, while Section 3.2 introduces the results of the economic analysis. Section 3.3 presents optimal designs obtained for the different refrigerants. Design recommendations are finally summarized in Section 3.4.

3.1. Impact of Evaporator and Condenser Design on Thermodynamic Performance

Figure 2 shows how the refrigerant pressure drops of the evaporator affected the heat pump COP. Each point corresponds to one combination of the design variables reported in Table 2, e.g. different evaporator and condenser geometries. The different marker styles and colours represent the working fluid. The COP value was reported by scaling it with respect to the design value. The thermodynamic performance degradation due to pressure drops for the different PHE evaporator designs was fitted linearly for each working fluid, and Figure 2 also reports the value of the slopes. For example, choosing a design with 30 kPa pressure drops entails around 4 % COP drop for butane, 3 % for propylene/butane, while it stays lower than 2 % for propane.

It must be noted that only few design points are visible in the figure compared to the 225 different combinations evaluated in the sensitivity study. This is due to the condenser design, which does not affect the COP, hence the points with the same evaporator geometry and different condenser designs overlap. Figure 3 (a) further illustrates this result, reporting the COP for the three working fluids vs. the total refrigerant pressure drops at the condenser. There is no dependency between the COP and the condenser design, and the colour scale – indicating different normalized evaporator pressure drops – shows that maximum COP was obtained for minimum evaporator pressure drops in all the cases. Note that Figure 3 (a) shows that the relative ranking of the working fluids in terms of COP was slightly affected by the PHE designs. Propylene/butane remained the refrigerant with the highest COP regardless of the evaporator and condenser configuration, while butane and propane were found to overlap depending on the evaporator design (pressure drops).

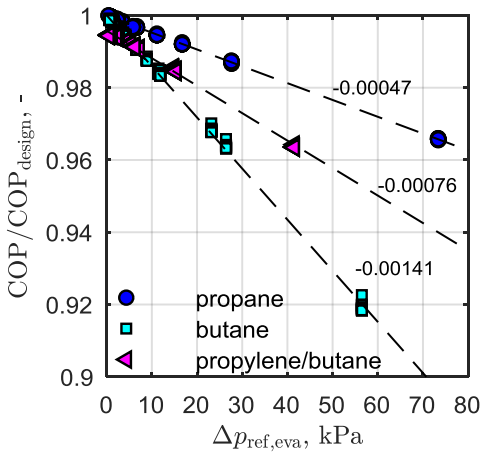

Figure 2: Normalized COP as a function of total refrigerant pressure drop in the evaporator

Table 3: Bubble and dew temperatures and thermo-physical properties at design pressure

Working fluid	p_{eva}, bar	ρ_V, kg/m^3	dT_{bubble}/dp K/kPa
Propane	8.8	19.1	0.044
Butane	2.2	5.7	0.140
Propylene/Butane	5.6	13.6	0.054

The stronger dependence of the COP to the evaporator pressure drops was related to a number of reasons. First, a higher value of pressure drops entailed a decrease in the heat output of the condenser. This was due to the impact of evaporator operation on the operating parameters of the cycle, i.e. refrigerant mass flow rate and pressures. The mass flow rate was in fact diminished at fixed superheat and subcooling, and the HP operated at a lower pressure ratio, i.e. a lower compressor power was required. However, the decrease in total heat flow rate of the condenser affected the COP negatively to a larger extent, as shown in Figure 3 (b): the condenser total heat flow rate – normalized by the design value – is plotted as a function of the evaporator pressure drops, with different colours representing different magnitudes of normalized condenser pressure drops. Similarly to the COP degradation reported in Figure 2, butane reports the steepest degradation, followed by propylene/butane and propane. The slopes of degradation were found to be similar to the COP drop plotted in Figure 2. Condenser pressure drops, represented by the different colour scale, were found not to affect the total heat flow rate at the condenser, and different condenser designs overlap in Figure 3 (b) similarly to Figure 2.

The higher drop of heat pump COP for butane compared to the other two fluids is due to another main reason: evaporator pressure drops also imply a saturation temperature drop, which increases the exergy destruction due to finite temperature differences in the evaporator component, thus contributing to the COP degradation. Depending on some relevant fluid thermo-physical properties, refrigerants can be more or less subject to this effect.

(Brignoli et al., 2017) identified the ones characterizing refrigerants sensitivity to pressure drops, namely vapour density and saturation temperature drop due to pressure drop. These are reported in Table 3 for the three working fluids at design conditions. Lower vapour density implies higher pressure drops for the same mass flux and PHE geometry. Therefore, a design that is feasible for propane and propylene/butane, possibly enhancing the heat transfer coefficient, might entail too large pressure drops for butane, with vapour density much lower than the other two refrigerants. This was one of the reasons why the bounds for plate width and number of channels variation in the sensitivity study (see Table 2) were chosen differently for the working fluids, i.e. to ensure feasible PHE designs with similar values of pressure drops.

The refrigerant vapour density is thus a property that must be carefully taken into account when choosing the working fluid and subsequently selecting the HEX design. Higher saturation temperature drop due to pressure drop, estimated by the Clapeyron relation (Moran, 2017), entails a larger drop of the saturation temperature due to pressure drop, thereby increasing the exergy losses due to the temperature difference between the refrigerant and the heat source side in the evaporator. Table 3 shows how the ranking between the working fluids in terms of vapour density and dT_{bubble}/dp respects the slopes of the COP degradation reported in Figure 2. Therefore, despite both propane and propylene/butane reported similar slopes for the degradation of condenser heat flow rate, the mixture was found to be more sensitive to saturation temperature drop due to pressure drop, resulting in a steeper COP drop.

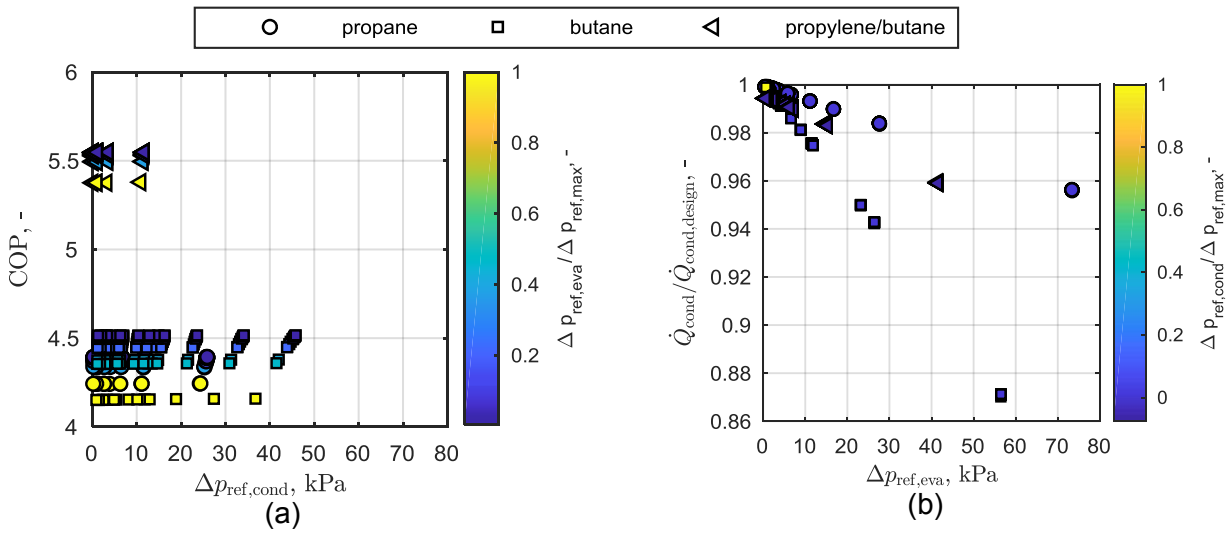

Figure 3: (a) COP as a function of total refrigerant pressure drop in the condenser; (b) Normalized condenser heat flow rate as function of total refrigerant pressure drop in the evaporator

3.2. Impact of Evaporator and Condenser Design on Economic Performance

The economic performance was evaluated by looking at the specific cost of heat, which is influenced by both condenser and evaporator design. The TCI is dependent on both HEX sizes (related to the heat transfer area), while the operating costs are strongly related to the heat pump COP. The economic performance indicator is reported in Figure 4 (a) for the three refrigerants as function of the pressure drop at the evaporator. The three working fluids present similar trends, with a trade-off and a minimum for a certain value of refrigerant pressure drops. Figure 4 (a) reports a close-up for the case of propane, where the colours represent different values of condenser heat transfer area. The results show that evaporator and condenser have different types of impact on the specific cost of heat. For a fixed condenser design – thus a fixed value of heat transfer area shown by the colours of Figure 4 (b) – the economic performance was a trade-off between heat transfer area and pressure drops of the evaporator. The minimum cost was determined by a certain value of evaporator pressure drops, which was similar for all the different condenser designs.

On the other hand, the condenser design influences the economic performance in a different manner: it was always desirable to employ condenser designs with minimum heat transfer area (shown by the darker blue colour in Figure 4 (b)). In fact, since the COP was not found to be affected by condenser pressure drops, the operating costs were not influenced by its design. The TCI was instead related to the heat transfer area, thereby suggesting a minimization of the condenser size. A relevant finding shown by Figure 4 is thus given by the fact that the evaporator and condenser geometry optimization, despite aimed at minimizing the cost of the overall system, could be considered as decoupled problems. The designer can choose to optimize the evaporator geometry and to find the design leading to the minimum cost, regardless of the condenser design (and the opposite holds). One additional relevant aspect highlighted by Figure 4 (a) is that all the refrigerants presented a minimum of specific cost of heat for similar values of refrigerant pressure drops. These values lie in the interval 5 – 10 kPa, which is relatively low, compared to usual manufacturer guidelines setting the limitation to around 50 kPa (SWEP International AB, 2015).

The results might therefore suggest that in this particular case study – regardless of the refrigerant chosen – an optimal value of pressure drops could be defined preliminarily to the refrigerant selection and HEX sizing. In this way, it is possible to define a guideline – based on optimal pressure drops – to design the PHE evaporators and condensers prior to the working fluid screening. This would enable the screening to avoid suboptimal solutions or the computational cost of optimizing the HEX design for all the working fluids, some of which the screening will in any case subsequently disregard. This result might seem contradictory if one thinks about the different slopes of COP degradation for the different fluids, previously shown in Figure 2. However, Figure 4 (a) reports an effective steeper increase of the specific cost of heat for butane rather than propane and propylene/butane. This increase started however after reaching the minimum specific cost of heat (after around 30 kPa), thus the different slopes of the working fluids for the COP degradation were not relevant to define the optimum. Moreover, since the optimal values of refrigerant pressure drops was found to be as

low as 5 kPa to 10 kPa, the COP degradation (shown in Figure 2) admissible for this case was found to be lower than 2 %.

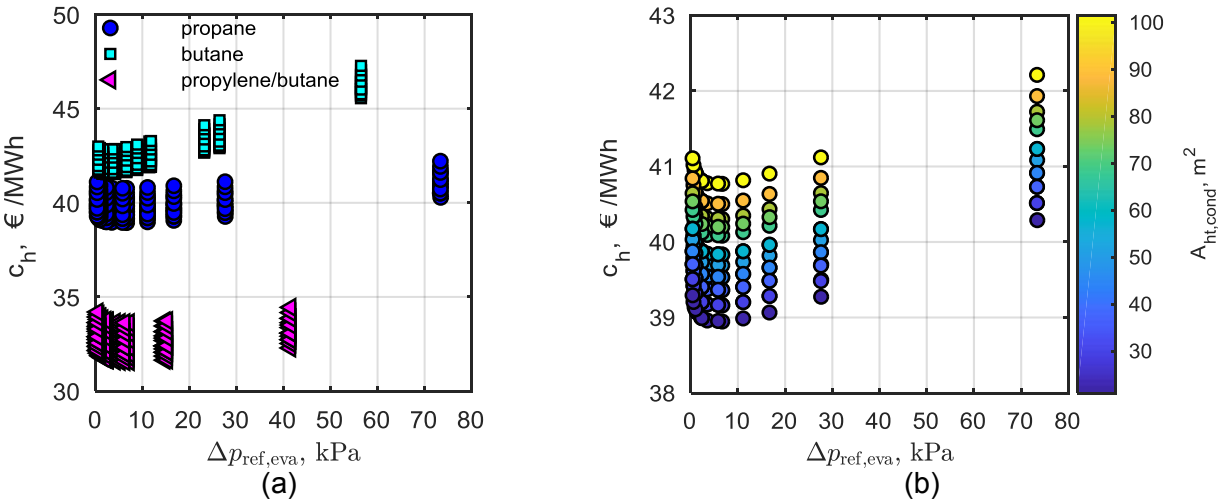

Figure 4: Specific cost of heat as function as a function of total refrigerant pressure drops in the evaporator for: (a) all fluids, (b) propane (close-up)

3.3. Economic Optimum: PHE Designs

Table 4 shows the geometrical specification of the PHE evaporator and condenser designs corresponding to the economic optimum shown in Figure 4. Moreover, heat transfer area, total refrigerant pressure drops and heat pump COP and specific cost of heat are reported. The designs minimizing the specific cost of heat are in agreements with the results presented above. The PHE evaporator design was limited to pressure drops from 4.2 kPa for butane and 7.2 kPa for propylene/butane. The optimal values are thus close for all the working fluids. Similar plate size was found for propane (P) and propylene/butane (P/B), while a plate with a lower aspect ratio (length-to-width ratio) was obtained for butane (B). Due to the lower vapour density, butane is in fact subject to higher pressure drops for the same velocity and channel geometry. The condenser design was instead found to be similar for propane and butane, e.g. high pressure drops over 100 kPa were allowed. With similar channel geometry, the condenser design for propylene/butane led instead to low pressure drops, e.g. 11.5 kPa. This was likely due to the lower dependency of the total heat flow rate at the condenser on the pressure drops, as previously explained in Section 3.1. Note that the condenser design corresponding to the economic optimum is an extreme design case of very high aspect ratio, due to the large bounds for variation of width and channels imposed in the sensitivity study. Such designs might be unrealistic compared to commercial plate size. The economic optimum would in any case correspond to the same evaporator design and more realistic plate size for the condenser could be easily obtained by choosing solutions with higher condenser heat transfer area (e.g. going up in the parallel curves reported in Figure 4).

Table 4: PHE designs corresponding to the economic optimum

	Evaporator design					Condenser design						
	W	L	N_{ch}	A_{ht}	Δp_{ref}	W	L	N_{ch}	A_{ht}	Δp_{ref}	COP	c_h
	m	m	-	m^2	kPa	m	m	-	m^2	kPa	-	€/MWh
P	0.250	0.460	150	20.5	6.7	0.200	1.768	50	21.1	113.3	4.4	38.9
B	0.400	0.447	170	36.0	4.2	0.200	1.472	80	28.1	140.2	4.5	41.5
P/B	0.250	0.655	180	35.1	7.1	0.200	1.774	100	42.3	11.5	5.5	31.6

3.4. Design Recommendations

The results presented so far led to the following findings, summarized as design recommendations for evaporator and condenser design in heat pump systems:

- Design criteria such as maximum allowable pressure drops and fixed velocities possibly lead to suboptimal solutions depending on the case study and the working fluid.
- Evaporator and condenser designs can be carried out as decoupled geometry optimization problems, e.g. the design of each component does not affect the other.
- Evaporator design influences the heat pump COP to a large extent, while the condenser design is not found to be relevant for the thermodynamic performance.
- Both components influence the economic performance: the minimum cost is found by defining optimal trade-offs between heat transfer area and pressure drop in the evaporator, while it is always desirable to minimize condenser heat transfer area.
- The economic optimum could be defined by a maximum allowable COP degradation, which theoretically corresponds to different allowable pressure drops for each refrigerant.
- The same optimal evaporator pressure drop was found for different refrigerants for this case study. This is not necessarily a general conclusion, given the very low allowable COP degradation and the dependence of the results from the economic boundary conditions.

4. DISCUSSION

The results presented in this paper were based on numerical modelling of PHE and HP, in both design and performance mode. The PHE models were based on a 1D discretization along the fluid-flow direction, thus neglecting the occurrence of channel-to-channel maldistribution effects. (Mancini et al., 2019) showed that refrigerant pressure drops have a major impact on the heat transfer degradation due to maldistribution effects, causing an additional COP degradation. This implies that the optimal value of refrigerant pressure drops found in this study could be even lower for those refrigerants (like butane) that are particularly sensitive to maldistribution effects. The results of economic analysis are strongly dependent on the boundary conditions assumed for the case study. The heat from the source was considered to come at no cost, and the COP degradation solely implied an increase of the compressor running cost. A COP decrease could also imply a reduction of the heat source utilization, which might partially counteract the cost increase in those cases where the heat source is not free (e.g. district heating applications). Last, the importance of tailoring design criteria depending on the working fluid and application is stressed: designers must be aware that limiting inlet velocities or imposing allowable pressure drops can lead to suboptimal solutions, since the slope of COP degradation has a strong dependence on refrigerant properties. For example, for the economic analysis of propane shown in Figure 4(b), choosing an evaporator design with pressure drops around 50 kPa would entail an increase of almost 1 €/MWh in the specific cost of heat.

5. CONCLUSIONS

This paper presented an approach to derive recommendations for PHE design in HP using pure and mixed refrigerants. A sensitivity study was carried out by simultaneously varying plate size and count for both evaporator and condenser, and PHE geometrical configurations with different trade-offs between heat transfer area and pressure drops were obtained. This study constitutes an attempt to derive design guidelines during a preliminary cycle design phase, where a full component optimization is computationally expensive, and adopting heuristics criteria might lead to suboptimal solutions. The results showed that only evaporator pressure drops affected the COP, and the different refrigerants were subject to different degradation slopes. Butane, with lowest vapour density and higher saturation temperature drop due to pressure drop, resulted in the steepest drop, with 30 kPa generating a 4 % COP drop. Condenser design solely influenced the economic performance, thus a minimization of the size was always preferable. The trade-off between evaporator size and pressure drops was found to be independent from the condenser design, and the analysed case study resulted in optimal COP degradation of maximum 2 % for all the working fluids, thereby defining optimal pressure drop values in a narrow range, around 5 kPa.

ACKNOWLEDGEMENTS

This research was funded by Innovations Fund Denmark with project title "THERMCYC".

NOMENCLATURE

A_{ht}	heat transfer area (m^2)	Abbreviations	
c_h	specific cost of heat (€×MWh^{-1})	BC	boundary conditions
$\mathrm{CF_{el}}$	annual cost of electricity (€)	HEX	heat exchanger
COP	coefficient of performance (-)	HP	heat pump
CRF	capital recovery factor (-)	PHE	plate heat exchanger
L	plate length (m)	Greek symbols	
N_{ch}	number of channels (-)	ρ	density (kg×m^{-3})
OH	operating hours (h)	Δ	Difference (-)
p	pressure (bar)	Subscripts	
$\dot{Q}$	heat flow rate (W)	comp	compressor
T	temperature (K)	cond	condenser
TCI	total capital investment (€)	eva	evaporator
W	plate width (m)	V	vapour

REFERENCES

Brignoli, R., Brown, J, Skye, H, Domanski, P.A., 2017.Refrigerant performance evaluation including effects of transport properties and optimized heat exchangers. Int. J. Refrig. 80, 52–65.

Lemmon, E.W., Bell, I.H., Huber, M., McLinden, M.O., 2018. NIST Standard Reference Database 23: Reference Fluid Thermodynamic and Transport Properties - REFPROP, version 10.0.

Mancini, R, Zühlsdorf, B, Jensen, J., Brix Markussen, W., Elmegaard, B., 2018. Deriving guidelines for the design of plate evaporators in heat pumps using zeotropic mixtures. Energy 156.

Mancini, R., Zühlsdorf, B, Aute, V, Markussen, W., Elmegaard, B., 2019. Performance of heat pumps using pure and mixed refrigerants with maldistribution effects in plate heat exchanger evaporators. Submitt. to Int. J. Refrig.

Mathworks, 2017. Matlab R2017b URL https://www.mathworks.com/products/new_products/latest_features.html (accessed 11.7.17).

Moran, M.J., 2017. Engineering thermodynamics: Fundamentals, in: CRC Handbook of Thermal Engineering, Second Edition. pp. 3–14. https://doi.org/10.4324/9781315119717

Muralikrishna, K., Shenoy, U.V., 2000. Heat Exchanger Design Targets for Minimum Area and Cost. Chem. Eng. Res. Des. 78, 161–167. https://doi.org/10.1205/026387600527185

SWEP International AB, 2015. SWEP Products URL https://www.swep.net/ (accessed 2.23.18).

Walraven, D, Laenen, B, D'Haeseleer, W, 2014. Comparison of shell-and-tube with plate heat exchangers for the use in low-temperature organic Rankine cycles. Energy Convers. Manag. 87, 227–237.

Wang, L., Sundén, B., 2003. Optimal design of plate heat exchangers with and without pressure drop specifications. Appl. Therm. Eng. 23, 295–311.

Xu, J., Luo, X., Chen, Y., Mo, S., 2015. Multi-criteria Design Optimization and Screening of Heat Exchangers for a Subcritical ORC. Energy Procedia 75, 1639–1645.

Zühlsdorf, B., Jensen, J.K., Elmegaard, B., 2019. Heat pump working fluid selection – Economic and thermodynamic comparison of criteria and boundary conditions. Int. J. Refrig. 98, 500–513.

Manuscript ID: 854
DOI: 10.18462/iir.icr.2019.0854

Optimization of copper-tube coils for energy-efficiency and charge reduction in heat pumps, air conditioners and refrigerators

Nigel COTTON[(a)], Hal STILLMAN[(b)], Dennis NASUTA[(c)], Yoram SHABTAY[(d)]

[(a)] European Copper Institute
Brussels, 1150, Belgium, nigel.cotton@copperalliance.eu
[(b)] International Copper Association, Ltd.
Washington, DC, 20001, United States, hal.stillman@copperalliance.org
[(c)] Optimized Thermal Systems, Inc.
Beltsville. Maryland, 20705, United States, nasuta@optimizedthermalsystems.com
[(d)] Heat Transfer Technologies LLC
Prospect Heights, Illinois, 60070, United States, yoram@heattransfertechnologies.com

ABSTRACT

Smaller-diameter copper tubes offer favorable thermal performance and material savings but may restrict air and refrigerant flow without proper design. Heat exchangers can be optimized using simulation tools and a multi-objective genetic algorithm (MOGA). The examples in this paper show how to realize performance objectives while meeting design constraints of actual applications. Replacing microchannel aluminum tubes with 5 mm copper tubes in a heat pump application reduced the material mass as much as 28 percent while maintaining equivalent capacity and airside pressure drop. Switching from 6.25 mm to 5 mm tubes in an R600a residential refrigerator reduced the internal tube volume by 41 percent while maintaining acceptable airside pressure drop. In a PTAC application, the target COP was reached while reducing the material cost by 50 percent. These and other applications demonstrate that charge reduction and efficiency gains can be achieved through the use smaller-diameter copper tubes.
Keywords: Copper, Heat Transfer Coefficient, Pressure Drop, Airside Pressure Drop, Heat Exchanger, Microfins, MicroGroove, CoilDesigner, Genetic Algorithm, MOGA.

1. INTRODUCTION

Smaller-diameter copper tubes offer many advantages for heat pumps, refrigeration equipment and air-conditioners, regardless of the type of refrigerant; hence, a steady progression from larger diameter tubes such as 9.52 mm to smaller diameter tubes such as 7 mm, 6.25 mm or 5 mm has taken place over the past twenty years as manufacturers have sought to realize design objectives.
Heat exchanger design is often facilitated by computer modelling, where thermal-hydraulic performance of airside and refrigerant-side surfaces is predicted by empirical correlations from experimental data. In recent years, new empirical tube-side correlations and computational fluid dynamics (CFD)-based airside correlations have been developed for smaller-diameter tube-fin heat exchangers. Implementation of these newer correlations in coil modelling software, such as CoilDesigner®, has allowed designers to weigh the benefits of smaller-diameter tubes.
Tube-side behaviour of refrigerants in smaller diameter copper tubes has been measured in laboratories around the world. For examples, Longo et al. (2018a) and Jige et al. (2018) researched flow boiling of low-GWP refrigerants and Longo et al. (2018b) investigated condensation in smaller diameter copper tubes. Also, the effects of various microfin geometries on smaller diameter copper tube performance were investigated by Inoue et al. (2018). Research underpinning the airside correlations is discussed by Nasuta et al. (2018) and Bacellar et al. (2015). Using laboratory measured correlations for smaller diameter copper tubes, including tubes with inner-grooves or microfins, ensures that computer modelling can predict system performance within a few percent.
The availability of comprehensive correlations for airside heat transfer and airside pressure drop of small-diameter tube-fin heat exchangers allows optimization with a multi-scale methodology

(Bacellar et al., 2016). Design of experiments is used to sample a wide design space of tube-fin geometries relevant to small-diameter tube-fin heat exchangers. CFD tools then are used to simulate and characterize thermal-hydraulic performance on a small scale and new airside correlations are developed from these simulations. These correlations are then implemented into heat exchanger simulation software (such as CoilDesigner) so the entire heat exchanger can be optimized in accordance with relevant operating conditions and constraints.

Typically there are multiple constraints and objectives in the design of heat exchangers and the design space to be explored through simulations is very large. A Multi-Objective Genetic Algorithm (MOGA) was used in sampling the design space for several of the case studies presented here. Genetic algorithms were originally developed by Holland (1975) and have been reviewed in textbooks by Goldberg (1989) and Engelbrecht (2007). Evolutionary algorithms and specifically genetic algorithms (GA) are widely used in many fields. These algorithms are based on ideas about natural selection and natural genetics as originally developed in the 1960s and 1970s by John H. Holland at the University of Michigan. Interest in this multidisciplinary subject has only increased in recent years as computer simulations have improved in accuracy.

MOGA is an especially powerful approach toward optimization of designs in which there are multiple constraints and objectives. A description of the use of MOGA in the optimization of heat exchangers was presented by Li et al. (2018). MOGA allows for a large space of design solutions to be searched in a computationally efficient manner. The system performance can be simulated for each candidate solution and if the performance improves then it can be the basis for further mutations, i.e., alterations of variables.

MOGA has ushered in a new era of design in many fields and especially in heat exchanger design as evidenced by the case studies presented in this paper. Optimized heat exchanger designs that would otherwise be missed can be identified through the combination of accurate simulations and MOGA. Five manufacturer-driven case studies in design optimization are presented here to illustrate the value of optimization as applied to a new generation of tube-fin heat exchangers made from MicroGroove™ smaller diameter copper tubes.

2. CASE STUDIES

Five different optimization studies were performed by Optimized Thermal Systems in collaboration with the International Copper Association and five different manufacturers. In each case, copper tubes with diameters of five millimetres or less were specified and MOGA was used to optimize the configurations of heat-exchanger-geometry parameters. The case studies included (1) heat-pump condensers to replace microchannel tubes with smaller diameter copper tubes; (2) a window air-conditioner condenser to improve system efficiency while reducing cost and refrigerant charge; (3) a refrigerator-freezer condenser to reduce hydrocarbon refrigerant charge; (4) the condenser of a packaged terminal AC system to minimize raw material costs and airside pressure drop while maintaining performance; and (5) an evaporator coil for a heat pump water heater to maximize capacity and minimize fan pumping power.

2.1. Heat-Pump Condenser

This optimization was for drop-in replacements of the existing microchannel heat exchanger (MCHX) condensers in a commercial heat-pump system. The manufacturer's objective was to develop a tube-fin heat exchanger with equivalent performance of its existing MCHX design. Geometric constraints included the coil height, width and depth; fin density, refrigerant pressure drop and refrigerant charge.

An initial study used currently available wavy and louvered fin patterns for 5 mm tubes. The replacement condensers showed a 15 to 38% increase in airside pressure drop for wavy fin patterns; and 29 to 42% increase for louvered fin patterns, while maintaining less than a four percent decrease in heating capacity compared to the baseline MCHX commercial condenser. The material mass was reduced by as much as 35%.

MOGA was then used to explore fin patterns not yet available in the market. The design space consisted of variable ranges consistent with current manufacturing capabilities. This optimization found 5 mm tube-fin designs competitive with the baseline microchannel condenser. The additional degrees of freedom allowed the optimizer to identify designs with airside pressure drops and capacities similar to the baseline. The best design demonstrated a reduction of 28 percent in material mass while maintaining the same airside pressure drop and capacity as the baseline.

Other designs were found with capacity increases of up to three percent and airside pressure drop decreases as great as 19 percent while maintaining other performance metrics within the constraints specified by the manufacturer. A smaller residential-sized condenser was also optimized as a drop-in replacement following a similar approach. Airside pressure drop decreases as great as 20 percent were realized while maintaining the drop-in replacement constraints.

2.2. Window AC Condenser

For another manufacturer, an exploratory study of small-diameter (5 mm) copper tubes was conducted on an existing 5.3 kW (1.5 ton) window air conditioning system. The objective was to improve system efficiency while reducing cost and refrigerant charge.
Tube-fin heat exchangers with 5 mm copper tubes and aluminium slit fins were initially modelled using available off-the-shelf configurations. The manufacturer provided baseline performance data for an existing unit, including fan curves. The initial study showed that 5 mm condenser designs using commercially-available slit fins could improve system coefficient of performance (COP) while maintaining capacity.

Table 1. Optimization Results for Drop in Replacement of Window Air Conditioner

Design	Tube Material (kg)	Fin Material (kg)	Percent Material Reduction Simulated	Percent Charge Reduction Simulated	COP Simulated (Measured)	Percent COP Improvement Simulated (Measured)
Baseline	1.8	2.5	—	—	2.60 (2.86)	—
Slit fin, 17 fpi	1.4	2.0	21	24	2.76 (2.97)	6.1 (3.8)
Louver Fin 15 fpi, 3 row	1.0	1.3	47	46	2.64	1.5
Louver Fin 13 fpi, 4 row	1.3	1.4	37	10	2.77	6.5

MOGA was then used to assess the performance of fin designs not yet available. Designs with as much as a 15% improvement in COP and more than a 60% reduction in material consumption were identified. The manufacturer constructed a prototype 5.86 kW (20,000 BTU·h^{-1}) system for testing, using one of the commercially available 5 mm slit fin heat exchangers.
Simulations predicted the new system would achieve a 6.1% higher COP and use 24% less refrigerant charge inside the condenser, while reducing total material mass by 21 percent. The manufacturer's experiments found that COP was increased by 3.8% while reducing the entire system's charge level by 10%. The manufacturer expressed that the new coil was about 40 percent less expensive than the original design.

2.3. Refrigerator-Freezer Condenser

For a third manufacturer, the condenser for a refrigerator and freezer was optimized for reduced refrigerant charge using smaller-diameter copper tubes. This condenser had three operation modes, including refrigerator circuit running, freezer circuit running and both circuits running,
The objective was to find small-diameter tube condensers that provide a reduction in internal volume to enable lower refrigerant charge while minimizing airside pressure drop. All designs used wavy-

herringbone fins with a reduced fin thickness compared to the baseline 6.25 mm copper tube design. Variables included tubes per bank, tube length, horizontal spacing, vertical spacing, fin density, and wavy fin pattern depth.
The baseline condenser coil uses copper tubing, flat plate fins and a low fin density. The condenser has two refrigerant circuits, with each circuit serving an independent vapor compression cycle for the refrigerator and freezer compartments. A CoilDesigner model of the condenser was developed and validated against experimental data.
Prior to evaluating potential small diameter replacements, a study was conducted to evaluate the effect of refrigerant circuitry on the existing coil performance. From this review, the best circuitry design was selected and used as the baseline reference for the optimization study. Significant reductions in internal tube volume were found over the baseline. The best 5 mm design provided a reduction in internal tube volume of 41 percent over the baseline, along with a 57 percent reduction in coil-volume (footprint) as shown in Fig. 1.

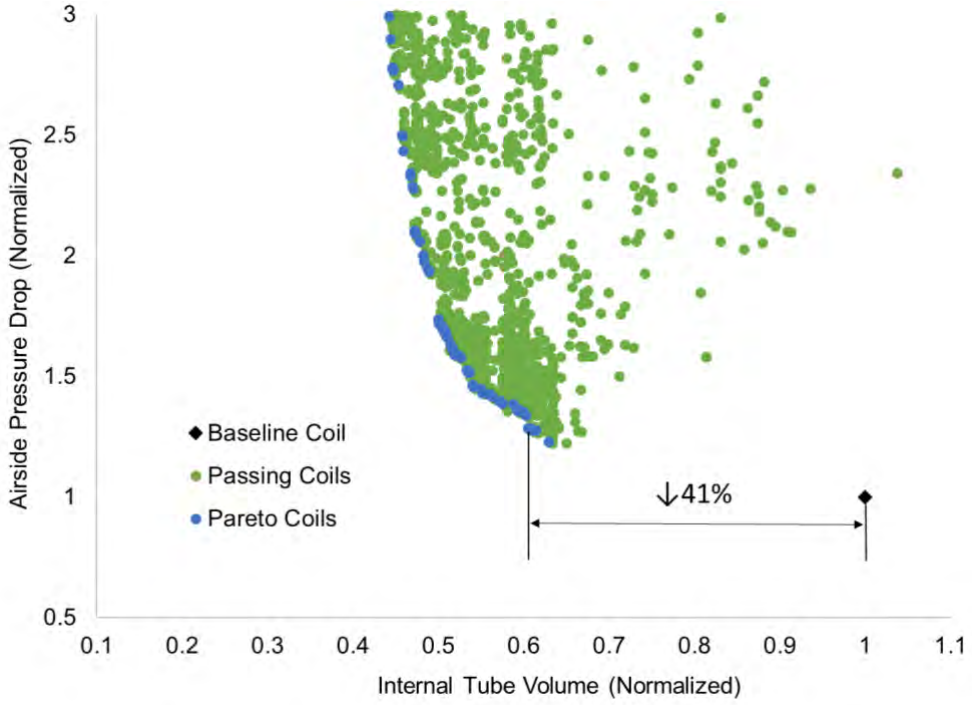

Figure 1: The best 5 mm design reduced internal tube volume by 41 percent

All optimized designs had a higher airside drop in pressure (ADP), i.e., the ratio of the ADP to the baseline ADP was greater than one. This increase is due to multiple factors, including the aggressive fin type, fin density and face area of the coils. The baseline system used flat fins while the optimized designs used wavy fins, which inherently create more pressure drop. The face areas of all coils were reduced to maintain the tube spacing ratio, which when using a fixed airflow volume results in increased air velocity. However, the increases in airside pressure drop for the designs identified are not a problem for this application. The fan motors used in this system can overcome the increased resistance without significant increase in power consumption.
In summary, several new condenser designs were identified with significant potential to reduce internal volume while maintaining performance, thereby reducing total system charge. The increased airside pressure drop of the designs can be accommodated by the existing fan motors. The reduced footprint of the coils allows for a smaller cassette and allows for regulations that would limit the charge of flammable refrigerant in the system.

2.4. PTAC Condenser

A fourth manufacturer sought to optimize a drop-in replacement for the condenser of an existing packaged terminal air conditioner (PTAC) product. The objectives were to minimize raw material costs and airside pressure drop while providing the same heat rejection. Geometric constraints included the coil height, width, and depth.

Fig. 2 highlights the optimization results. Using a commercially available slit-fin pattern (light blue triangles), one design reduced raw material costs by 47% and lowered the airside pressure drop by more than 15%, while reducing internal volume by 58% and maintaining acceptable refrigerant pressure drop. Further optimization studies, using fin geometries not yet available but consistent with current manufacturing capabilities, yielded as much as 50% savings in raw material costs while keeping pressure drops close to the baseline (green squares). The greatest reduction in internal volume of 62% used two tube banks in the airflow direction (dark blue dots). However, one existing slit-fin design showed a similar reduction in cost and air pressure drop as indicated by the single light blue triangle near the cluster of dark blue dots.
In summary, new condenser designs with significant potential to reduce costs while maintaining performance were identified. Reductions in airside pressure drop are favourable for noise reduction and material savings and make it possible to develop energy-efficient systems at a low cost. Furthermore, the study indicated that a currently-manufactured fin sheet provides excellent performance comparable to other optimized designs. This finding means that the manufacturer can achieve a high level of savings using an available fin die.

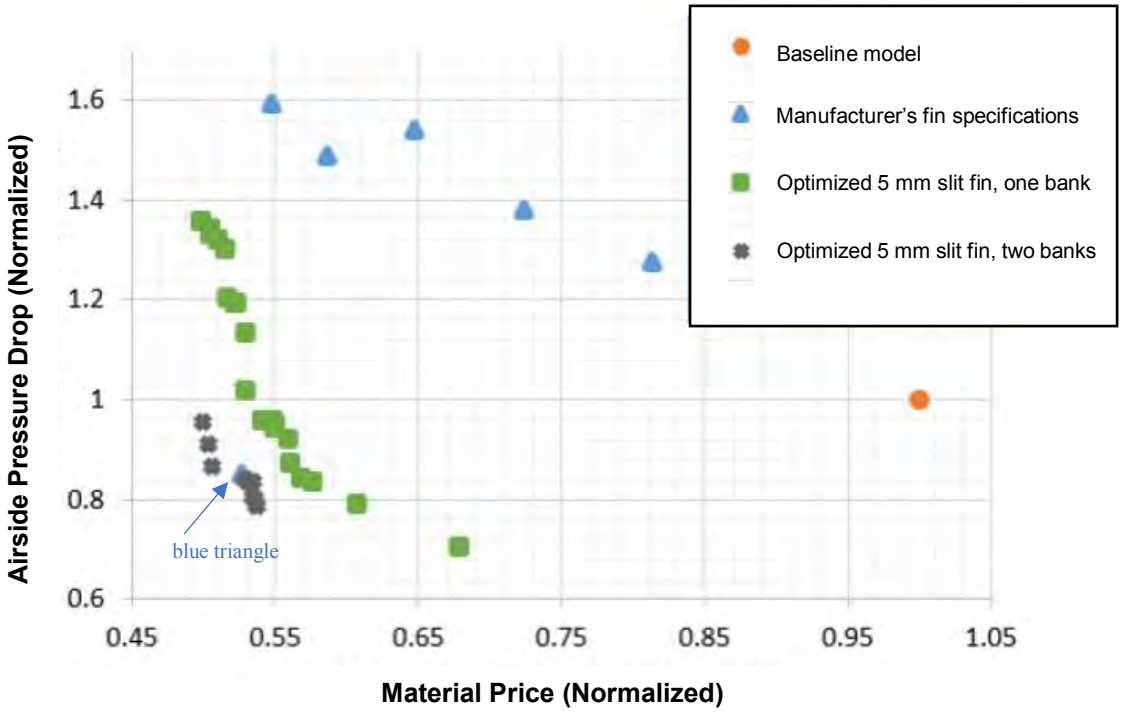

Figure 2: Low-cost PTAC condenser designs

2.5. Residential HPWH Evaporator

A fifth manufacturer sought to optimize the evaporator of a residential heat pump water heater (HPWH). Objectives were to maximize capacity and minimize fan pumping power, and the constraints were the existing size and operating conditions. In other words, capacity must exceed the baseline, outlet refrigerant pressure must match or exceed the baseline and superheat must equal or exceed the baseline. These objectives were achieved using CoilDesigner and MOGA.
An initial analysis was conducted with the goal of replacing the baseline evaporator with a higher-capacity coil using smaller diameter copper tubes within the size constraints. The baseline evaporator coil uses 7.94 mm (5/16 inch) copper tubing laced through louvered aluminium fins and R134a refrigerant flowing through two refrigerant circuits.
The baseline model predictions matched the experimental testing data. Cooling capacity was predicted within one percent without requiring correction factors. Correction factors were applied to match outlet superheat within one degree Celsius and refrigerant pressure drop within one percent. Air pressure drop was validated against a manufacturer prediction software to be within two percent. MOGA was used to select and simulate heat exchanger candidates until optimal configurations were identified. Optimization studies included designs throughout a wide range of geometry configurations

and then focused on commercially available heat exchanger geometries. The algorithm allowed the air flow rate, refrigerant flow rate, and fin and tube density to be varied, generating and simulating thousands of new heat exchanger designs. For each configuration, the non-dominated set of Pareto-optimal points are shown in Fig. 3. Using greater air and refrigerant flow rates, new 5 mm designs can more than double capacity compared to the baseline. As such, this study seeks to maximize capacity while minimizing fan pumping power.

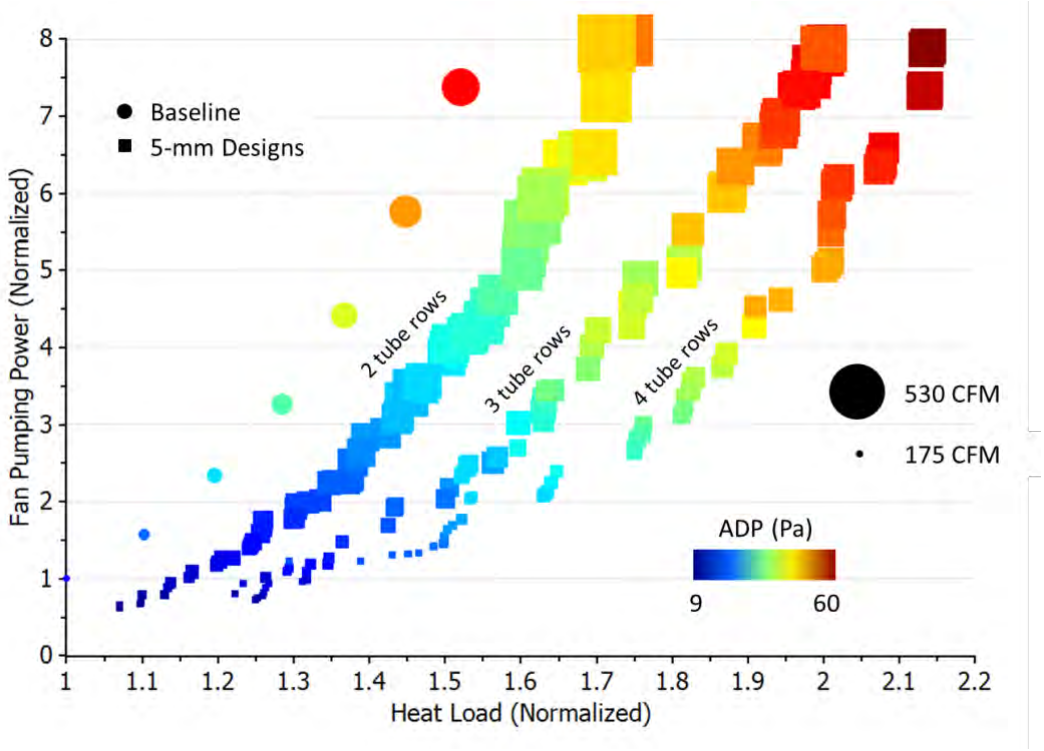

Figure 3: Performance of 5 mm designs normalized against the baseline 7.9 mm heat exchanger. Circles and squares of increasing area represent performance at higher flow rates.

Three designs were selected for further review. Design 1 maintains equivalent fan pumping power to the baseline model but increases capacity by 32%. Design 2 increases capacity by 50% when compared to the original baseline but requires a 104% increase in fan pumping power. Design 3 is capable of increasing capacity by 100 percent but requires a 401% increase in fan pumping power. Design 1 and 2 mainly differ in air flow rate. The manufacturer plans to build and test a prototype 5 mm coil similar to the Design 1 coil and further evaluate the trade-offs between flow rates and inlet conditions.

The baseline design does not compete with the new 5 mm designs on performance even at higher flow rates. When provided with an 86% higher air flow rate, the capacity of the baseline design increases by more than 35%; this requires 4.5 times more fan pumping power. A 5 mm design operating at the same fan power can reject nearly 90% more capacity than the original baseline. Throughout the design space, the best 5 mm designs deliver 30 to 40 percent more capacity at the same fan power as the 7.9 mm baseline.

In summary, new evaporator designs support a HPWH system with significantly greater capacity than the baseline system. The new systems can deliver greater quantities of hot water and/or recover the tank temperature more quickly after water draws, improving user comfort and satisfaction. In general, because they provide more heat transfer surface area within the allowable space, 5 mm heat exchangers deliver 30 to 40% more capacity than the baseline for the same fan power input. New evaporator designs can increase capacity by as much as 100% by increasing the fan power. In all scenarios presented here, for a given fan power, the 5 mm designs can always deliver more capacity than the 7.9 mm baseline heat exchanger.

3. CONCLUSIONS

Diverse case studies from five manufacturers clearly demonstrate the advantages of smaller copper tubes and the value of MOGA for design optimization. MicroGroove heat exchangers clearly outperform heat exchangers made from larger diameter copper tubes with performance comparable to microchannel heat exchangers. Results for specific applications are summarized as follows:

(1) Heat-pump condenser. The MOGA-optimized designs were similar to the baseline microchannel coil with regard to airside pressure drop and capacity.
(2) Window AC condenser. MOGA designs increased the efficiency of the heat exchanger while reducing materials usage and refrigerant charge. MOGA designs improved the COP by as much as 15% and reduced material usage by more than 60%.
(3) Refrigerator-freezer condenser. Hydrocarbon refrigerant charge was dramatically reduced in the 5 mm designs. MOGA designs reduced the internal tube volume up to 41 percent along with a 57% reduction in overall coil volume compared to the baseline 6.25 mm copper tube designs.
(4) PTAC condenser. Raw material costs and airside pressure drop were reduced while maintaining performance. MOGA designs provided as much as 50% savings in raw material costs while keeping the pressure drop close to the baseline. The best design reduced the overall internal volume by 62%.
(5) HPWH evaporator. MOGA was used to show that capacity could be doubled by increasing fan power; and that 5 mm designs delivered more capacity than the 7.9 mm baseline heat exchanger for a given fan power.

MOGA facilitates the optimization of heat exchanger performance using algorithms that mimic evolution in nature by carrying forward the traits of successful designs into future populations. MOGA has proven effective in the optimization of MicroGroove heat exchangers for commercial and residential air-conditioners as well as refrigerators, heat pumps and hot-water heat pumps.

ACKNOWLEDGEMENTS

Acknowledgement is made to the Copper Alliance for its financial support as well as the Center for Environmental Energy Engineering (CEEE) at the University of Maryland, JCI, Friedrich, Sub-Zero, GE Appliances and A.O. Smith for their participation.

NOMENCLATURE

ADP	airside drop in pressure	fpi	fins per inch
CFM	cubic feet per minute	HPWH	heat pump water heater
COP	coefficient of performance	MOGA	multi-objective genetic algorithm

REFERENCES

Bacellar, D., Aute, V., Huang, Z., Radermacher, R., 2016, Novel Airside Heat Transfer Surface Designs Using an Integrated Multi-Scale Analysis with Topology and Shape Optimization, 17th International Refrigeration and Air Conditioning Conference at Purdue, Paper 2117.

Bacellar, D., Aute, V., Radermacher, R., 2015. CFD-Based Correlation Development for Air Side Performance of Small Diameter Tube-Fin Heat Exchangers with Wavy Fins. 24th IIR International Conference of Refrigeration-ICR2015. Yokohama, Japan: IIR. Paper

Cotton, N., Rhoads, A., Bortoletto, A., Shabtay, Y., 2018. Optimization of MicroGroove Copper Tube Coil Designs for Flammable Refrigerants, 17th International Refrigeration and Air Conditioning Conference at Purdue, Paper 2532.

Engelbrecht, A.P., 2007. Computational Intelligence: An Introduction, 2nd Edition, Wiley, Chichester, West Sussex, UK. 628 pages. Chapter 9 Genetic Algorithms, 143-174

Goldberg, D. E., 1989. Genetic Algorithms in Search, Optimization and Machine Learning. Addison-Wesley Publishing Company, Reading, MA.

Holland, J.H., 1975. Adaptation in Natural and Artificial Systems: An Introductory Analysis with Applications to Biology, Control and Artificial Intelligence. MIT Press, Cambridge, MA, USA.

Inoue, N., Hirose, M., Jige, D., 2018. Effect of Fin Geometries on Condensation Heat Transfer and Pressure Drop inside Horizontal Small-Diameter 4 mm Microfin Tubes, 17th International Refrigeration and Air Conditioning Conference at Purdue, Paper 2511.

Li Z., Ling, J., Aute, V., 2018. Tube-Fin Heat Exchanger Circuitry Optimization Using Integer Permutation Based Genetic Algorithm, 17th International Refrigeration and Air Conditioning Conference at Purdue, Paper 2598.

Longo, G.A., Mancin, S., Righetti, G., Zilio, C., 2018a. R134a And Its Low GWP Substitutes R1234yf and R1234ze(E) Flow Boiling Inside a 4mm Horizontal Smooth Tube, 17th International Refrigeration and Air Conditioning Conference at Purdue, Paper 2204.

Longo, G.A., Mancin, S., Righetti, G., Zilio, C., 2018b. R134a and Its Low GWP Substitutes R1234yf and R1234ze(E) Condensation inside a 4 mm Horizontal Smooth Tube, 17th International Refrigeration and Air Conditioning Conference at Purdue, Paper 2205.

Jige, D., Iizuka, I., Inoue, N., 2018. Boiling Heat Transfer and Pressure Drop of R1234ze(E) inside a Small-Diameter 2.5 mm Microfin Tube, 17th International Refrigeration and Air Conditioning Conference at Purdue, Paper 2542.

Nasuta, D., Li. S. Hwang, Y. Martin, C., 2018. Experimental Validation of CFD-Based Correlations for 5 mm Louver- and Slit-Fin Heat Exchangers: Lessons Learned, 17th International Refrigeration and Air Conditioning Conference at Purdue, Paper 2582.

Manuscript ID: 889
DOI: 10.18462/iir.icr.2019.0889

Experiments on condensation heat transfer and tube bundles simulation with falling liquid film of R245fa / R134a outside enhanced tubes

Tomonobu MATSUNO [(a)], Hiroyuki TAKAHASHI [(b)], Norihiro INOUE [(c)]

[(a)] Kobelco & Materials Copper Tube, LTD. Hadano Plant, 65 Hirasawa, Hadano-city, Kanagawa, 257-0056, Japan, matsuno.tomonobu@gl.kmct.jp
[(b)] Kobelco & Materials Copper Tube, LTD. Hadano Plant, 65 Hirasawa, Hadano-city, Kanagawa, 257-0056, Japan, takahashi.hiroyuki@gl.kmct.jp
[(c)] Tokyo University of Marine Science and Technology, 2-1-6 Etchujima, Koto-ku, Tokyo, 135-8533, Japan, inoue@kaiyodai.ac.jp

ABSTRACT

From the viewpoint of global warming, there is an urgent need for refrigerants with lower Global Warming Potential (GWP) values. However, since they have different physical properties from conventional refrigerants, the performances of their heat transfer tubes are insufficient. The purpose of this study is to prepare predicted correlations of the outside condensation heat transfer coefficient corresponding to refrigerants with different physical properties. In this experiment, a smooth tube and four types of enhanced tubes, each with an outer diameter of approximately 19 mm, were used as test heat transfer tubes. The experiments were conducted using R245fa and R134a as the test refrigerants, at a condensation saturated temperature of 40 °C, and with a film Reynolds number range of 40 to 1500. The enhanced tubes displayed different tendencies from that of the smooth tube in the high film Reynolds number range. The experimental results of the smooth tube showed good correlation with the proposed predicted correlation.
Keywords: Film Condensation, Heat Transfer, R134a, R245fa, Single Tube, Tube Bundle.

1. INTRODUCTION

Most countries have set ambitious goals for reducing their greenhouse gas emissions, in an attempt to counteract global warming. Furthermore, due to the Kigali revision of the Montreal Protocol, it is necessary to switch to lower-GWP refrigerants or non-fluorocarbon refrigerants. In order to achieve these goals, it is necessary to further promote higher efficiency and lower GWP refrigerants in the fields of refrigeration and air conditioning.

Centrifugal chiller systems use large amounts of refrigerant, and have a long working life. For this reason, it is necessary to reduce their environmental risk by improving their efficiency, adopting lower-GWP refrigerants, and by reducing the amount of refrigerants used, due to the downsizing of equipment. In the centrifugal chiller condenser, enhanced tubes have been used to downsize equipment and improve efficiency. Further, hydro-fluorocarbon (HFC) refrigerants, such as R134a and R245fa, have been used to date, but there has been a recent shift to Hydro-fluroolefins (HFO) refrigerants. Against this backdrop, it is expected that a more high-performance enhanced tube, corresponding to various refrigerants, will emerge.

For equipment design, it is important to be able to predict the condensation heat transfer performance of an enhanced tube. Several experiments have been conducted into condensation heat transfer for tube bundles, using both smooth tubes and enhanced tubes. Kutateladze et al. (1985) conducted an experiment using R21 as a test refrigerant, and proposed a correlation to predict the experimental heat transfer coefficient of a smooth tube with an outer diameter lager than 10 mm. Fujii and Oda (1986) proposed a prediction correlation that takes into consideration the influence of innards, using previously established experimental values of R21 vapor and steam. Gstöhl and Thome (2006a, 2006b) conducted an experiment on a smooth tube using R134a, and modified the prediction correlation of Kutateladze et al. (1985) based on their

findings. However, there have been few detailed experiments that have used R245fa, for either single tubes or tube bundles.
In this study, we aim to determine the basic heat transfer characteristics of both smooth and enhanced tubes when using R245fa. Furthermore, we prepare predicted correlations for condensation heat transfer coefficients corresponding to refrigerants with different physical properties. These experiments were conducted using the smooth tube and four kinds of enhanced tubes, each with an outer diameter of 19 mm. The condensation heat transfer coefficients of R134a and R245fa were measured for both a horizontal single tube and tube bundles was simulated of inundation, and the basic heat transfer characteristics were clarified. In addition, by modifying previously made correlations, we obtained predicted correlations for smooth tubes applicable to R134a and R245fa.

2. EXPERIMENTAL APPARATUS AND PROCEDURE

2.1. Experiment on the Condensation Heat Transfer of the Single Tube

Fig. 1 shows a schematic diagram of the test equipment. The condenser is a stainless steel shell-and-tube type heat exchanger with an inner diameter of 333 mm. A test heat transfer tube with an effective heat transfer length of 974 mm is horizontally installed in the center of the condenser. Observation windows are provided on both side surfaces of the condenser so that the condensed flow state can be observed. The condenser and the evaporator are connected by vapor and liquid piping. The refrigerant vapor is generated by raising the temperature of the refrigerant liquid with the electric heater installed in the evaporator; this heater has a capacity of 10 kW. The generated vapor is supplied from the evaporator to the condenser through the vapor piping, and the liquid

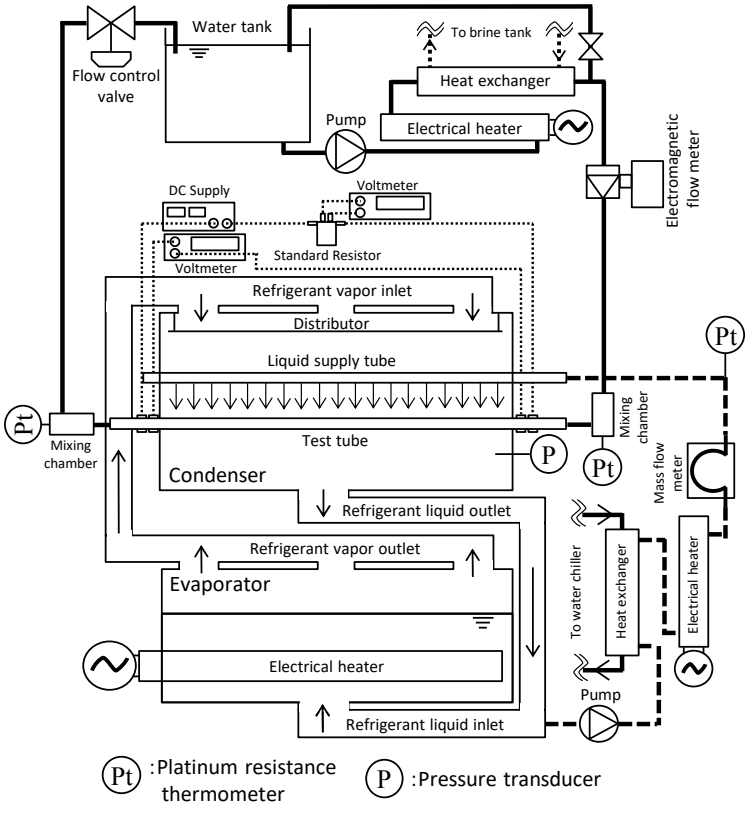

Figure 1: Schematic diagram of experimental apparatus

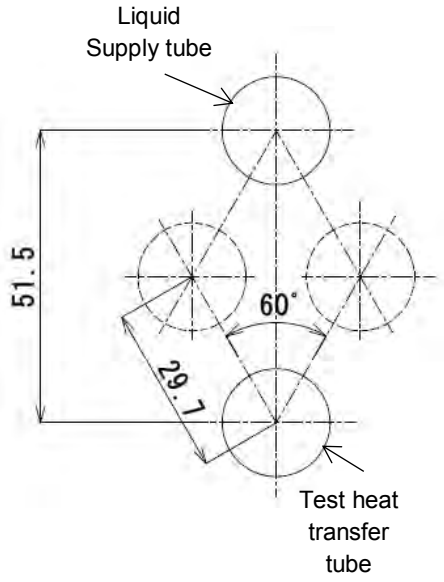

Figure 2: Tube arrangement

condensed
in the condenser is returned to the evaporator through the liquid piping. The cooling water temperature is kept constant by controlling the brine flow rate of the cooling heat exchanger, and the electric heater, with a controller. The flow rate of the cooling water is kept constant by controlling the automatic flow control valves with a controller. The temperature of the cooling water was measured using platinum resistance thermometers, installed in the mixing chamber at the test

section inlet and outlet. The cooling water flow rate was measured with an electromagnetic flow meter, and the refrigerant vapor pressure in the condenser was measured with an absolute pressure transducer. The wall temperature of each test heat transfer tube was calculated based on changes in the resistance of the tube wall, in accordance with changes in temperature.
The test conditions of the single tube experiment were set as follows: the cooling water flow rate was kept at a constant of 1.75 m/s, the cooling water inlet temperature was changed stepwise within a temperature range of 12 - 34 °C (8 - 26 °C for the smooth tube), and R134a and R245fa were used as test refrigerants. The vapor pressure inside the condenser was controlled at a refrigerant saturation temperature of 40 °C for each refrigerant. The physical properties of the refrigerant were calculated using Refprop ver. 10.0 (Lemmon et.al., 2018).
Details of the test heat transfer tube are shown in Table 1. The test heat transfer tubes are a smooth tube (SM tube), a two-dimensional low-finned tube (LF tube), and three kinds of three-dimensional microscopic-grooved tubes (MG tubes); all tubes have an outer diameter of 19 mm. The subscripts for each of the MG tubes (Table 1) represent the difference in the shape of the split in the circumferential direction of each fin. Fig. 3 shows cross-sectional photographs of these LF and MG tubes. From Figure 3b, it can be seen that the shape of the fin split in the circumferential directions of MG tubes are different.

2.2. The Inundation Simulation Experiment

In the inundation simulation experiment, a liquid supply tube is installed in the upper stage of the test heat transfer tube to simulate the influence of the inundation. Assuming that the tube arrangement is 60 ° for staggered tube bundles with a pitch of 29.7 mm (tube bundles), the tube pitch between the liquid supply tube and the test heat transfer tube (vertical direction) is therefore 51.5 mm. A smooth tube is used for the test heat transfer tube. Fig. 2 shows the

Table 1. Details of the test tubes

	SM	LF	MGv	MGs	MGu
Diameter at fin tip, D_o [mm]	19.1	19.2	18.8	18.7	18.7
Inside diameter, D_{in} [mm]	-	15.7	15.4	15.4	15.5
Fin height, h [mm]	-	0.84	0.90	0.86	0.83
Fin pitch, p [mm]	-	0.78	0.78	0.78	0.79

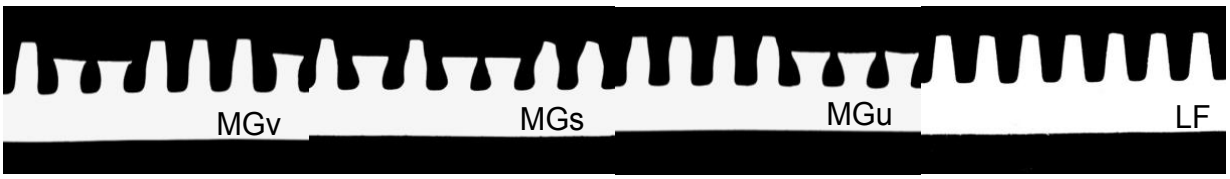

(a) Axis direction

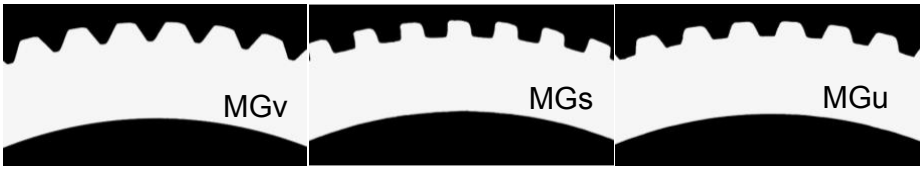

(b) Circumferential direction

Figure 3: Cross-section views of the low-finned and microscopic-grooved tubes

arrangement of

the liquid supply tube and test heat transfer tube. The liquid refrigerant for the liquid supply was transported from the evaporator to the liquid supply tube by a pump, using dedicated liquid refrigerant piping. The temperature of the liquid refrigerant for is cooled by a cold water heat exchanger, which is installed in the piping. Thereafter, the amount of heating of the electric heater is kept as a constant temperature with a controller.

The temperature of the liquid refrigerant is measured with a platinum resistance thermometer, installed on the inlet side of the liquid supply tube. The flow rate of the liquid refrigerant to be supplied is measured with a mass flow meter installed on the inlet side of the liquid supply tube. Other measurements of parameters such as cooling water temperature and vapor pressure, are carried out in the same manner as in the single tube experiment.
The inundation simulation experiment is conducted under cooling water inlet temperatures of 12 °C and 22 °C, with a liquid supply temperature of 39.5 °C. The feed flow rate changes stepwise within the range of 1.0–4.5 kg/s for R134a and 1.5–9.0 kg/s for R245fa.

3. DATA REDUCTION

The condensation heat transfer, α_o, is defined as follows:

$$\alpha_o = q_o/(T_r - T_{wall}) = Q_s/[\pi \cdot D_o \cdot L \cdot (T_r - T_{wall})] = [W_s \cdot Cp_s \cdot (T_{sout} - T_{sin})]/[\pi \cdot D_o \cdot L \cdot (T_r - T_{wall})] \quad \text{Eq. (1)}$$

where q_o is the heat flux standard, based on heat transfer area criteria outside tube, T_r is the refrigerant saturated vapor temperature, T_{wall} is the tube wall temperature, Q_s is the exchange heat transfer quantity between the condensed refrigerant outside the tube and the cooling water, D_o is the tube's outside diameter at the fin tip, W_s is the mass flow rate of the cooling water, Cp_s is the isobaric specific heat, and $T_{s,\,in}$ and $T_{s,\,out}$ are the cooling water temperatures at the test heat transfer tube's inlet and outlet, respectively. The outer surface area is calculated based on the assumption of a smooth surface, from the tube's outside diameter at the fin tip. The film Reynolds number, Re_f, is defined as follows:

$$Re_f = 2\left[W_{liq} + (Q_s / \Delta h_{LV})\right]/(L \cdot \mu_{liq}) \quad \text{Eq. (2)}$$

where Δh_{LV} is the latent heat of condensation of the refrigerant, μ_{liq} is the viscosity of the condensate film, Γ is the amount of refrigerant flowing on both sides of the tube per unit time, and W_{liq} is the amount of liquid refrigerant supplied from the top of the test heat transfer tube. The condensation number, Nu^*, is based on heat the transfer area criteria from outside of the tube, and is defined as follows:

$$Nu^* = \alpha_o \cdot \left(\nu_{liq}^2/g\right)^{1/3}/\lambda_{liq} \quad \text{Eq. (3)}$$

where, ν_{liq} and λ_{liq} are the kinematic viscosity and the thermal conductivity of the condensate film, respectively, and g is the gravitational acceleration.

4. RESULTS AND DISCUSSION

4.1. The Single Tube Experiment

Fig. 4a shows the heat transfer coefficient of the measured SM tube. The solid line in the figure is Nusselt's equation (Nusselt, 1916) for a horizontal smooth tube:

$$\alpha_o = 0.725\left(D_o/\lambda_{liq}\right)\left[\left(Ga_{liq} \cdot Pr_{liq}\right)/Ph_{liq}\right]^{0.25} \quad \text{Eq. (4)}$$

where, Ga_{liq}, Pr_{liq}, and Ph_{liq} are the Galileo number, Prandtl number, and phase change number of the condensate, respectively. The experimental values are 5 to 20%, higher than Nusselt's equation. This may be due to the fact that Nusselt's equation does not consider the influences of turbulence and convection of the liquid film.

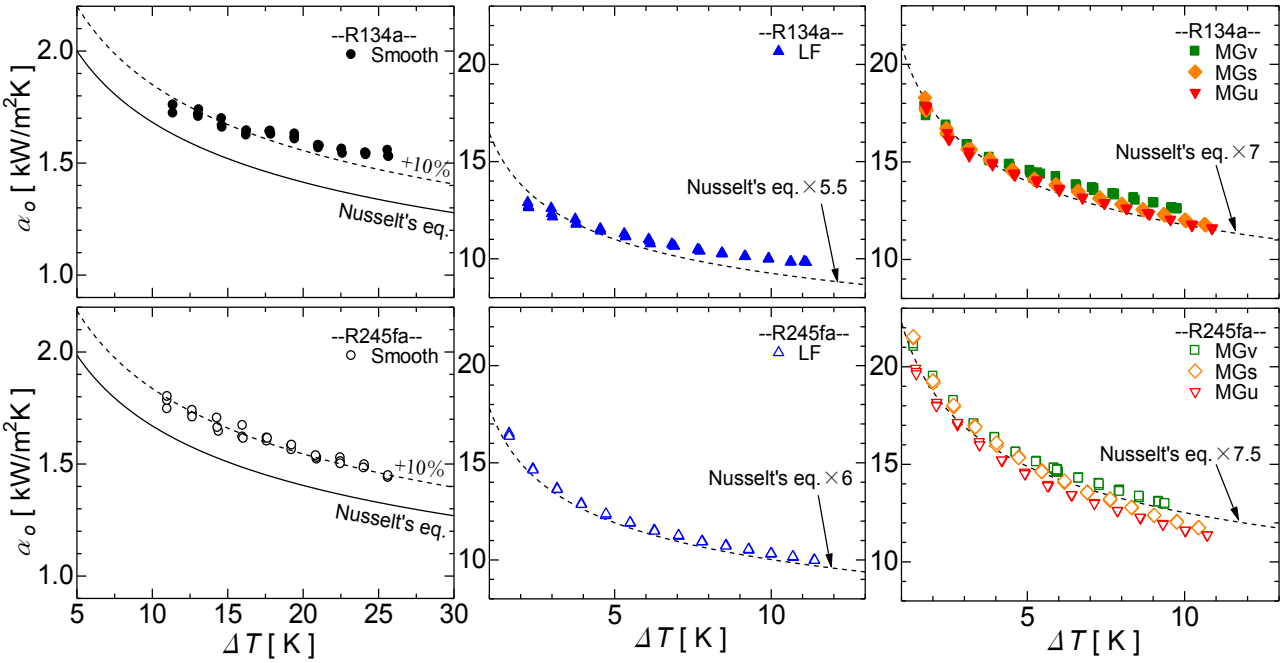

Figure 4: Condensation heat transfer coefficients of SM, LF, and MG tubes

Fig. 4b shows the heat transfer coefficient of the measured LF tube. The dashed lines in the figure are 5.5 times (R134a) and 6 times (R245fa) the value predicted by Nusselt's equation. Regardless of the difference in refrigerant, the LF tube displays the same tendency as predicted by Nusselt's equation. The rate of increase of α_o is higher in R245fa than in R134a. As R245fa has a stronger surface tension than R134a, this promotes the formation of a thin liquid film on the fin-side surface. Fig. 4c shows the heat transfer coefficients of the measured MG tubes. The dashed lines in the figure are 7 times (R134a) and 7.5 times (R245fa) the value predicted by Nusselt's equation. For R134a, in the region where $\Delta T \geq 2$ K, increasing ΔT results in high α_o values, in the order of MGu < MGs < MGv. This tendency becomes stronger when $\Delta T \geq 4$ K. When $\Delta T < 2$ K, however, α_o remains relatively constant. Furthermore, the above tendency is more conspicuous in R245fa than in R134a. MGu shows a lower α_o value than MGv and MGs in both cases. When $\Delta T \leq 3$ K, MGv and MGs show similar α_o values; with increasing ΔT, the α_o of MGs decreases below that of MGv. This is considered to be due to the following reasons. From the cross-sectional photograph shown in Figure 2 (b), the grooves of MGs are smaller than those of MGs and MGu, and are also sharper. In addition, the angle of each part of MGs is sharper than that of MGu. It appears, therefore, that the three tubes can be ranked in terms of their ability to draw condensation liquid into the tip of the fin in the order of MGu < MGs < MGv. Therefore, the thinning effect on the condensation liquid film on the side surface of the fin is also ranked in the order of MGu < MGs < MGv. This affects the heat transfer coefficient. Furthermore, since the surface tension of R245fa is stronger than that of R134a, this effect is more intense in R245fa.

4.2. The Inundation Simulation Experiment

Fig. 5 shows the heat transfer coefficient of the measured SM tube in the inundation simulation experiment. When liquid refrigerant is supplied to the SM tube, its α_o is lower than that of the single tube experiment at the same cooling water temperature, regardless of the difference in refrigerant. However, as Re_f increases with liquid supply, α_o increases again. The reason for this is that the convective diffusion of the liquid film is promoted by the influence of the liquid supply from the upper stage. The results of an experiment on R134a by Gstöhl and Thome (2006a) are also plotted in Figure 5 for comparison, showing that similar results were obtained in that paper. However, the tube pitch used by Gstöhl and Thome (2006a) is different from 51.5 mm in this study. Comparing the experimental value of the nearest tube pitch to this value (44.5 mm) with the experimental value of this study shows a similar tendency. However, tube pitches of 25.5

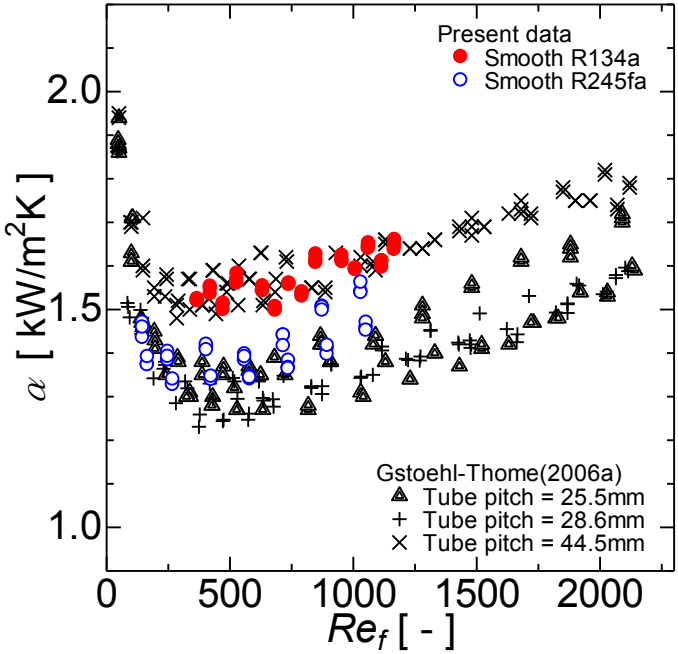

Figure 5: Condensation heat transfer coefficients of smooth tube in the Inundation simulation experiment

mm and 28.6 mm of Gstöhl and Thome (2006a) show lower heat transfer coefficients than in this study. For this reason, larger tube pitches increase the speed of the droplet, until it contacts the lower tube. Therefore, the influence of convection diffusion on the liquid film increases.

4.3. Comparison between Measured and Predicted Values for the Smooth Tube

4.3.1. Predicted correlation of Gstöhl and Thome

Gstöhl and Thome (2006a, 2006b) conducted an experiment with R134a single row tube bundles, and proposed the following correlation:

$$Nu^* = \left[\left(1.2 / Re_f^{0.3} \right)^4 + \left(0.04 Pr_{liq}^{1/3} \cdot Re_f^{0.2} \right)^4 \right]^{0.25} \qquad \text{Eq. (5)}$$

Fig. 6 (a) shows a comparison between the predicted correlation of Gstöhl and Thome (2006b) and the experimental values from this study. The experimental values of Gstöhl and Thome (2006a) are also plotted. Eq. (5) agrees with the experimental values within the range of -20% to +25%; the correlation coefficient is 0.78. In the absence of liquid supply, a good correlation is shown. However, there is a tendency to underestimate the experimental data where there is a liquid supply, especially for R245fa. This is likely due to an underestimation of the influence of *Pr* during turbulent heat transfer. In addition, since the difference in tube pitch is not taken into consideration, there is a tendency for overestimation for the experimental values where Gstöhl and Thome (2006a) have a narrow tube pitch. Conversely, there is a tendency for underestimation for the experimental values of this study with a wide tube pitch.

4.3.2. New predicted correlation

Using the results detailed in 4.3.1, a new correlation can be predicted, considering the influence of refrigerant properties and the tube pitch on condensation heat transfer for a smooth tube:

$$Nu^* = \left\{ \left(1.2 / Re_f^{0.3} \right)^4 + \left[0.04 \left(0.43 \cdot S / D_o \right)^{0.32} \cdot Pr_{liq}^{0.42} \cdot Re_f^{0.2} \right]^4 \right\}^{0.25} \qquad \text{Eq. (6)}$$

Figure 6 (b) shows a comparison between the new predicted correlation and the experimental heat transfer coefficient. The experimental values of Gstöhl and Thome (2006a) are also plotted for comparison. The new predicted correlation agrees with the experimental values within a range of -15% to +25%, with a correlation coefficient of 0.93. The new predicted correlation shows a good correlation irrespective of the presence or absence of a liquid supply. The differences in the refrigerant and tube pitch also show good correlation.

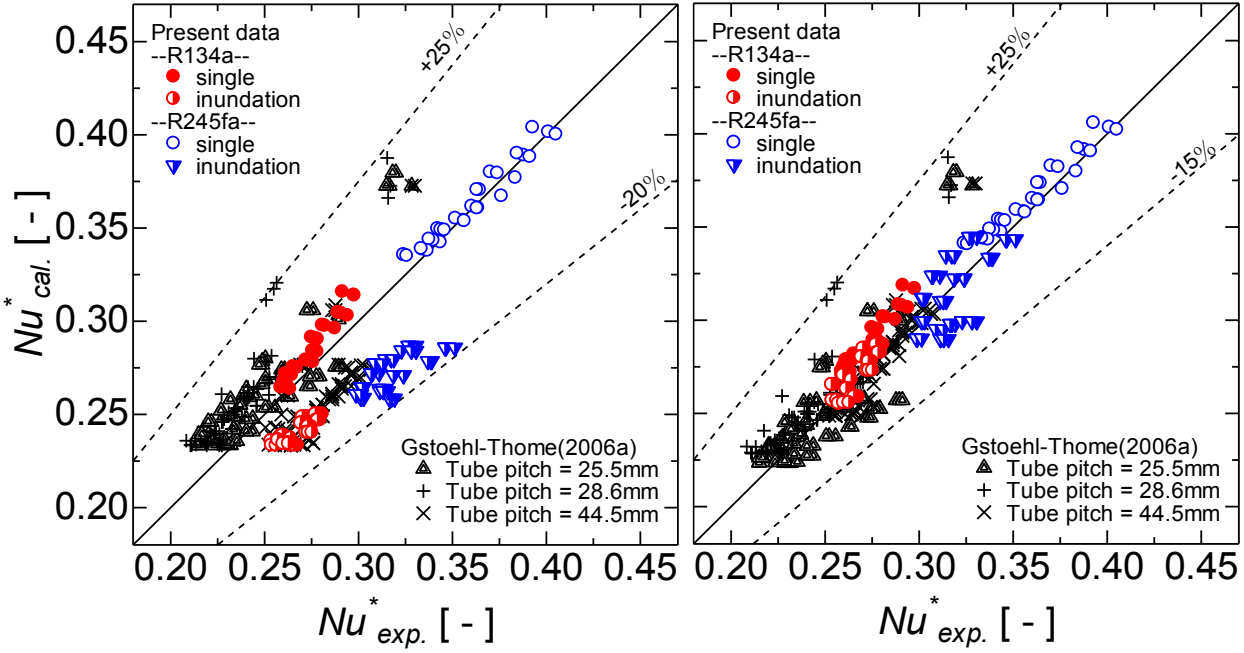

(a) Correlation of Gstöhl and Thome

(b) New predicted correlation

Figure 6: Comparison with predicted heat transfer coefficient for smooth tube

5. CONCLUSIONS

Here, we have reported on experiments on horizontal tubes used for outside condensation heat transfer, for an SM tube, an LF tube, and MG tubes, for both R134a and R245fa. In order to determine the influence of inundation by the tube bundles, we also performed an inundation simulation experiment using the SM tube. By using the obtained experimental values, we were able to modify a previously predicted correlation for a smooth tube, obtaining a good correlation. The main conclusions of our study are summarized below.

(1) Compared to Nusselt's equation, the α_o of the LF tube was 5.5 times higher for R134a and 6 times higher for R245fa. Further, α_o was higher in R245fa than in R134a. This was because the surface tension of R245fa was stronger than that of R134a, making the formation of a thin liquid film on the side surface of the fin easier.

(2) Compared to Nusselt's equation, the α_o of MG tubes was 7 times higher for R134a and 7.5 times higher for R245fa. Furthermore, when compared with each test heat transfer tube, it showed high α_o values in the order of MGu < MGs < MGv. This was due to differences in the shape of the fin split in the circumferential direction for each tube. In addition, since the surface tension of R245fa is stronger than that of R134fa, this effect was more pronounced.

(3) When an inundation simulation experiment was carried out with the SM tube, α_o was lower than for the single tube experiment. However, as Re_f increased with liquid supply, the convection diffusion of the liquid film was promoted by the influence of the liquid supply from the upper stage, so α_o increased again.

(4) The predicted correlation of Gstöhl and Thome (2006b) coincided with the experimental values within a range of -20% to +25%; the correlation coefficient was 0.78. However, their predicted correlation tended to underestimate the inundation simulation experiment values of R245fa. Experimental values with different tube pitches were predicted to be either too small or excessive.

(5) The predicted correlation of Gstöhl and Thome (2006b) was modified to take into consideration the influence of the *Pr* number on turbulent heat transfer and the influence of the tube pitch. Compared to the experimental values of this study and of Gstöhl and Thome (2006a), the new predicted equation coincided within a range of-15% to +25%, and had a high correlation coefficient of 0.93.

ACKNOWLEDGEMENTS

Mr. Norihiko Izumikawa assisted the authors with the experimental aspects of this study; we would like to express our gratitude for the support provided.

NOMENCLATURE

A	area (m)
Cp	isobaric specific heat ($kJ \cdot kg^{-1} \cdot K^{-1}$)
g	gravitational acceleration ($m \cdot s^{-2}$)
Ga	galilei number (-)
h	fin height (m)
Δh_{LV}	latent heat ($J \cdot kg^{-1}$)
L	length (m)
p	fin pitch (m)
Ph	phase change number (-)
Pr	Prandtl number (-)
Q	heat flow rate (kW)
q	heat flux ($kW \cdot m^{-2}$)
S	between the tubes distance (m)
Re	Reynolds number (-)
T	temperature (°C)
W	mass flow rate (kg·s-1)

Greek Symbols

α	heat transfer coefficient ($kW \cdot m^{-2} \cdot K^{-1}$)
Γ	film flow rate per unit length of one side ($kg \cdot s^{-1} \cdot m^{-1}$)
λ	thermal conductivity ($kW \cdot m^{-1} \cdot K^{-1}$)
μ	dynamic viscosity (Pa·s)
v	kinematic viscosity ($m \cdot s^{-1}$)

Subscripts

f	film
in	inside
L	saturated liquid
liq	liquid
o	outside
out	outlet
r	saturate
s	water
V	saturated vapor
wall	wall

REFERENCES

Fujii T., Oda K., 1986, Correlation equations of heat transfer for condensation inundation on horizontal tube bundles, Trans. Jpn. Soc. Mech. Eng., B, 52(474): 822-826. (in Japanese)

Gstöhl, D, and Thome, J.R., 2006a, Film condensation of R-134a on tube arrays with plain and enhanced surfaces: Part 1-Experimental heat transfer coefficients, ASME Journal of Heat Transfer, 128: 21-32.

Gstöhl, D. and Thome, J.R., 2006b, Film condensation of R-134a on tube arrays with plain and enhanced surfaces: Part 2-Empirical prediction of inundation effects, ASME Journal of Heat Transfer, 128: 33-43.

Kutateladze, S.S., Gegonin, I.I, and Sosunov,V.I., 1985, The influence of condensate flow rate on heat transfer in film condensation of stationary vapor on horizontal tube banks, International Journal of Heat and Mass Transfer, 28(3): 1011-1018.

Lemmon E. W., Bell I. H., Huber M. L., and McLinden M. O., 2018, Reference fluid thermodynamic and transport properties REFPROP ver.10.0, National Institute of Standards and Technology, Gaithersburg.

Nusselt, W, 1916, Die oberflächenkondensation des wasserdampfes, Zeitschrift des Verein Deutscher Ingenieure, 60(27): 541-546, 569-575. (in German)

Manuscript ID: 892
DOI: 10.18462/iir.icr.2019.0892

Analysis of rigid rotor of magnetic refrigeration compressor

Yusheng HU [(a),(b)], Bin CHEN[(a)], Fang ZHANG[(a)], Xiaobo ZHANG[(a)], Gao GONG[(a)], Xin LI[(a)]

[(a)] State Key Laboratory of Air-conditioning Equipment and System Energy Conservation

Zhuhai City, 519070, China, zhangfang1900@163.com

[(b)] Gree Electric Appliances. Inc. of Zhuhai

Zhuhai City, 519070, China

ABSTRACT

The application of magnetic bearings has significant advantages to centrifugal compressors, such as improving operating speed, ameliorating energy efficiency and reducing noise and vibration. Modal frequency and unbalance response of a maglev centrifugal compressor rotor-bearing system are important index parameters to ensure stable operation of the compressor. Thus, it is inevitable to optimize those parameters when designing compressor structure. In this paper, basing on the basic theories of rotor dynamics, ANSYS is used to analyze vibration mode and unbalance response of a compressor rotor-bearing system. Basic excitation sources caused by impellers in pneumatic section and magnetic bearings' stiffness parameters are considered when doing rotor dynamics modal simulation. Influences on critical speed of the rotor-bearing system caused by support stiffness of magnetic bearings and impellers aerodynamic force is analyzed during the simulation, by which the rotor modal frequency adjustment method is obtained. Besides, the unbalance response sensitivities of different unbalanced amount at different rotor parts are analyzed. Those simulation results have provided a reference to designing the rotor in long axis system of maglev high-speed centrifugal compressor.
Keywords: Refrigeration Compressors, Rigid rotor, Rotor Dynamic Analysis, Stiffness/damping Parameters, Vibration mode, Modal frequency, ANSYS, Long Axis System.

1. INTRODUCTION

The application of magnetic bearings has significant advantages to centrifugal compressors, such as improving operating speed, ameliorating energy efficiency and reducing noise and vibration (Wen et al., 2000 and Huang et al., 2016). A rigid rotor does not bend or deform, which is beneficial to detection and control, during operation process. The main purpose of dynamic design on maglev compressor rotor system is to ensure the rotor system having stable and reliable dynamic characteristics throughout whole operating speed range, so that the rotor system can maintain high accuracy and stability in operation process.

In this paper, basing on the basic theories of rotor dynamics, ANSYS is used to analyze modal shape and modal frequency of a rigid maglev compressor rotor-bearing system. Besides, due to unbalance of the rotor is the most important source of excitation for rotating machinery (Hu et al., 2006), unbalance response of the rotor is analyzed. Those results have provided a reference to design the rotor in long axis system of magnetic high-speed centrifugal compressor.

2. MATHMATICAL MODEL OF MAGLEV RIGID ROTOR

The Cartesian coordinate system is established with the centroid of the rotor as the origin, the axis of the rotor as the axis of *Oz*, the vertical direction as the axis of *Ox* and the horizontal direction as the axis of *Oy*, as shown in Fig. 1.

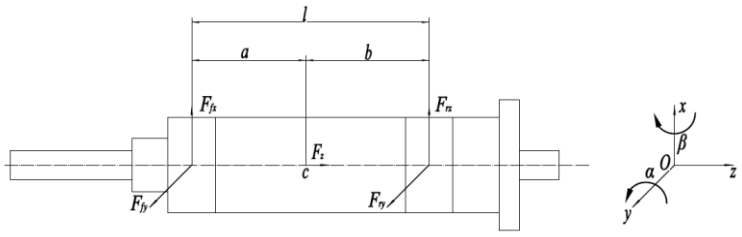

Figure 1: Five-degree-of-freedom maglev rotor system

The system consists of two radial magnetic bearings and one axial magnetic bearing. The front radial magnetic bearing controls two radial degrees of freedom x_f and y_f, and the rear radial magnetic bearing controls two radial degrees of freedom x_r and y_r, and the axial magnetic bearing controls the axial degree of freedom z.
The displacement of the centroid O_c of the rotor is shown in Eq. (1).

$$\begin{cases} x_c = \dfrac{bx_f + ax_r}{l} \\ y_c = \dfrac{by_f + ay_r}{l} \end{cases} \quad \text{Eq. (1)}$$

Where, x_c and y_c are the displacements of the centroid in m, a is the distance between the front radial magnetic bearing and the centroid in m, b is the distance between the rear radial magnetic bearing and the centroid in m, l is the distance between the two radial magnetic bearings in m.
Without considering the bending deformation of the rotor, the rotation angles of the rotor in the xz plane and in the yz plane are respectively α and β, as shown in Eq. (2).

$$\begin{cases} \alpha = \dfrac{x_r - x_f}{l} \\ \beta = \dfrac{y_r - y_f}{l} \end{cases} \quad \text{Eq. (2)}$$

Differential equations of motion for a five-degree-of-freedom maglev rotor system are as shown in Eq. (3).

$$\begin{cases} m\ddot{x}_c = F_{fx} + F_{rx} + F'_x \\ m\ddot{y}_c = F_{fy} + F_{ry} + F'_y \\ J_d\ddot{\alpha} = -aF_{fx} + bF_{rx} - \omega J_p\dot{\beta} \\ J_d\ddot{\beta} = -aF_{fy} + bF_{ry} - \omega J_p\dot{\alpha} \\ m\ddot{z} = F_z \end{cases} \quad \text{Eq. (3)}$$

Where, m is the mass of the rotor in kg, J_d and J_p are the cross-section and polar moment of inertia around the centroid in kg·m^2, ω is the angular velocity of the rotor in rad·s^{-1}, F_{fx} and F_{fy} are the electromagnetic forces of the front radial magnetic bearing in N, F_{rx} and F_{ry} are the electromagnetic forces of the rear radial magnetic bearing in N, F_z is the electromagnetic force acting on the axial magnetic bearing in N, F'_x and F'_y are the unbalanced forces or external disturbance forces in response in N.
The linear equations of the electromagnetic force of the maglev rotor are as shown in Eq. (4).

$$\begin{cases} F_{fx}\left(x_f, i_{fx}\right) = k_{xfx} x_f + k_{ifx} i_{fx} \\ F_{fy}\left(y_f, i_{fy}\right) = k_{yfy} y_f + k_{ify} i_{fy} \\ F_{rx}\left(x_r, i_{rx}\right) = k_{xrx} x_r + k_{irx} i_{rx} \\ F_{ry}\left(y_r, i_{ry}\right) = k_{yry} y_r + k_{iry} i_{ry} \end{cases} \quad \text{Eq. (4)}$$

Where, k_{xfx} and k_{yfy} are the stiffness of front radial magnetic bearing in $N \cdot m^{-1}$, k_{xrx} and k_{yry} are the stiffness of rear radial magnetic bearing in $N \cdot m^{-1}$, k_{ifx} and k_{ify} are the current coefficients of front radial magnetic bearing in NA^{-1}, k_{irx} and k_{iry} are the current coefficients of rear radial magnetic bearing in NA^{-1}, i_{fx} and i_{fy} are the currents of front radial magnetic bearing in A, i_{rx} and i_{ry} are the currents of rear radial magnetic bearing in A.

At present, the decentralized control modes of each degree of freedom are adopted, and there are no couplings between radial and axial direction. The mathematical model of maglev rigid rotor can be expressed as a four-degree-of-freedom rigid rotor model. The differential equations of motion of rigid rotor as shown in Eq. (5) can be obtained.

$$\begin{pmatrix} m\frac{b}{l} & m\frac{a}{l} & 0 & 0 \\ 0 & 0 & m\frac{b}{l} & m\frac{a}{l} \\ -\frac{J_d}{l} & \frac{J_d}{l} & 0 & 0 \\ 0 & 0 & -\frac{J_d}{l} & \frac{J_d}{l} \end{pmatrix} \begin{pmatrix} \ddot{x}_f \\ \ddot{x}_r \\ \ddot{y}_f \\ \ddot{y}_r \end{pmatrix} + \begin{pmatrix} 0 & 0 & 0 & 0 \\ 0 & 0 & 0 & 0 \\ 0 & 0 & \omega\frac{J_p}{l} & -\omega\frac{J_p}{l} \\ -\omega\frac{J_p}{l} & \omega\frac{J_p}{l} & 0 & 0 \end{pmatrix} \begin{pmatrix} \dot{x}_f \\ \dot{x}_r \\ \dot{y}_f \\ \dot{y}_r \end{pmatrix} + \quad \text{Eq. (5)}$$

$$\begin{pmatrix} k_{xfx} & k_{xrx} & 0 & 0 \\ 0 & 0 & k_{xfy} & k_{xry} \\ -ak_{xfx} & bk_{xrx} & 0 & 0 \\ 0 & 0 & -ak_{xfy} & bk_{xry} \end{pmatrix} \begin{pmatrix} x_f \\ x_r \\ y_f \\ y_r \end{pmatrix} + \begin{pmatrix} k_{ilx} & k_{irx} & 0 & 0 \\ 0 & 0 & k_{ily} & k_{iry} \\ -ak_{ilx} & bk_{irx} & 0 & 0 \\ 0 & 0 & -ak_{ily} & bk_{iry} \end{pmatrix} \begin{pmatrix} i_{fx} \\ i_{rx} \\ i_{fy} \\ i_{ry} \end{pmatrix} = \begin{pmatrix} F'_x \\ F'_y \\ 0 \\ 0 \end{pmatrix}$$

According to Eq. (5), the free vibration or forced vibration response of the system can be calculated. When F'_x and F'_y are equal to zero, the modal frequencies and modal modes of the system can be obtained.

3. MODAL ANALYSIS OF MAGLEV RIGID ROTOR

The shafting of maglev system includes radial magnetic bearing rotor parts, motor rotor parts (magnets, etc.), thrust bearing, and some pneumatic parts (impellers). According to the structural characteristics of the rotor of the maglev system, the processing of rotor position is the most important factor affecting the modeling accuracy in the model study. At the same time, the influence of the different Young's modulus of axial and radial caused by the laminated form of silicon steel sheets on the rotor modal can not be ignored. Therefore, simulation and verification should be emphasized in the modal study. In addition, the support stiffness also has a certain influence on the shafting mode. In the magnetic refrigeration compressor, not only the magnetic bearing will provide the support stiffness to the rotor, but the labyrinth seal will also provide a certain support stiffness to the rotor, and this part of the stiffness should also be emphasized.

3.1. Modal Analysis of Maglev Rotor

With the development of rotor dynamics, the application of finite element method (FEM) in modern calculation method is more and more in-depth. Its simulation accuracy is high and the simulation effect is good. In the design process, the dynamic simulation design of rotor modal is carried out by combining the finite element analysis software ANSYS. At the same time, compared the simulation results with the measured modes and modified the simulation parameters, so that the simulation results are basically the same as the measured results.

The laminated silicon steel sheets on maglev rotor has different radial and axial Young's modulus due to lamination and immersion paint. Adjusting the coefficient of Young's modulus of laminated silicon steel sheets can approximate the effect of the difference between the radial and axial states of laminated silicon steel sheets. Built the model of maglev rotor to analyse the modal simulation of the model by using finite element analysis software, and compared the consistency between the model and the measured modal of the rotor. The 2 and 9 measuring points in the measured model are located in the center of the front and rear bearing respectively.
The flexible modal frequency of the rotor of the maglev system obtained by simulation and measurement are shown in Table 1.

Table 1. Flexible frequency comparison table of simulation and measurement

	First-order Flexible Frequency	Second-order Flexible Frequency
Simulation	758Hz	1343Hz
Measurement	759Hz	1339Hz

The vibration mode of the first-order flexible frequency of the simulation is shown in Fig. 2, and the vibration mode of the first-order flexible frequency of the measurement is shown in Fig. 3. The positions of the nodes are basically the same.

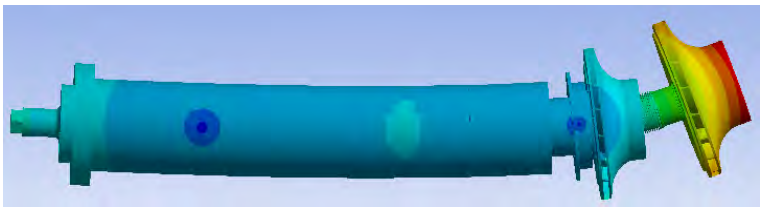

Figure 2: Finite element simulation result of the first-order flexible modal shape

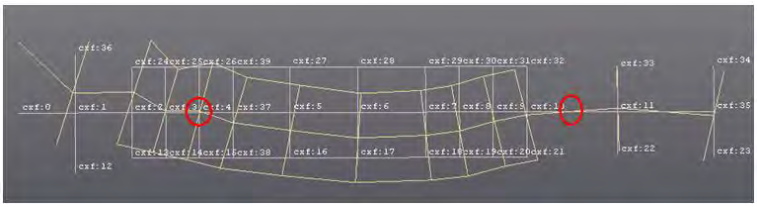

Figure 3: Measurement result of the first-order flexible modal shape

The flexible modal frequency and the positions of the nodes are almost the same with actual situation when doing ANSYS modal simulation if the coefficient of Young's modulus of silicon steel sheets were adjusted, which verifies the accuracy of the finite element simulation and the rationality of the Young's modulus of the laminated silicon steel sheets.
The first-order flexible frequency 758Hz is 1.5 times of the normal maximum operating speed frequency 500Hz. Therefore, the rotor can be considered as a rigid rotor.

3.2. The Influence of the Stiffness of the Magnetic Bearing on the Modal Frequency of the Rotor

Different bearing stiffness is given to the bearing rotor at the radial magnetic bearing in order to compare the influence of different support stiffness on the mode frequency of the rotor. The relationship curves are shown in Fig. 4.

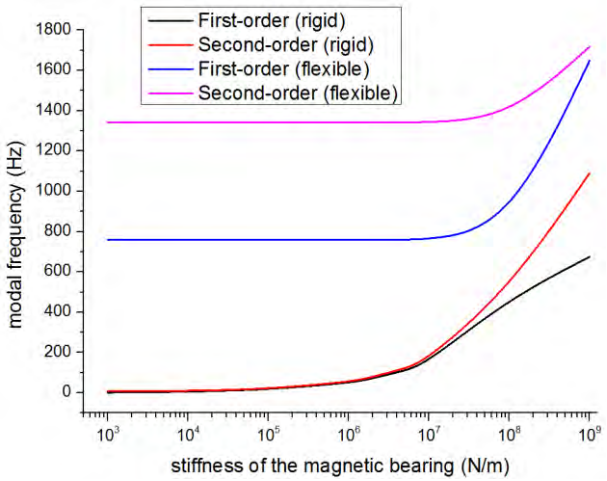

Figure 4: The influence of the stiffness of the magnetic bearing on the modal frequency

It can be found from Fig. 4 that the rotor modal frequency hardly changes with the support stiffness in the low stiffness interval. After the support stiffness reaches 1×10^6 N/m, the rigid modal frequency starts to increase significantly with the increase of the support stiffness. After the support stiffness reaches 1×10^7N/m, the rigid modal frequency and the flexible modal frequency will increase obviously with the increase of the support stiffness.

Normally, the stiffness of magnetic bearing has a great relationship with the control system due to the particularity of the maglev system. Therefore, the stiffness can be designed in the interval where the modal frequency changes significantly with the support stiffness. By adjusting the control parameters, the modal frequency of the rotor can be effectively adjusted, avoiding resonance interval.

The rotor will have a certain unbalanced quality in the actual situation, which leads to the critical speed become different due to the existence of the Coriolis Effect. Using the software ANSYS, the Campbell diagram of the rotor when the support stiffness of the radial magnetic bearing is 1×10^7 is shown in Fig. 5.

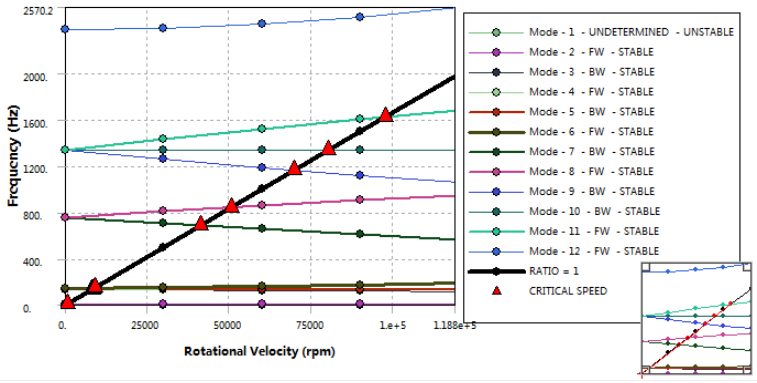

Figure 5: Campbell diagram of the rotor with bearing support stiffness of 1×10^7 N/m

Due to the Coriolis Effect of the rotor, the rotor may undergo forward eddy and reverse eddy. Forward eddy will increase the modal frequency of the rotor, and reverse eddy will reduce the modal frequency of the rotor. The intersections of the synchronous excitation line and each forward eddy mode frequency curves are the critical speed of the rotor. Therefore, due to the existence of the Coriolis Effect, the critical speed of the rotor can be further increased.

3.3. The Influence of the Stiffness of the Labyrinth Seal on the Modal Frequency of the Rotor

The rotor used in the magnetic refrigeration compressor is provided the support stiffness not only by the rotor, but also by the impellers in pneumatic section due to the small gap between the

impeller and the labyrinth seal at a high speed. Comparing the influence of different stiffness of the labyrinth seal on the rotor modal frequency, the relationship curves are shown in Fig. 6.

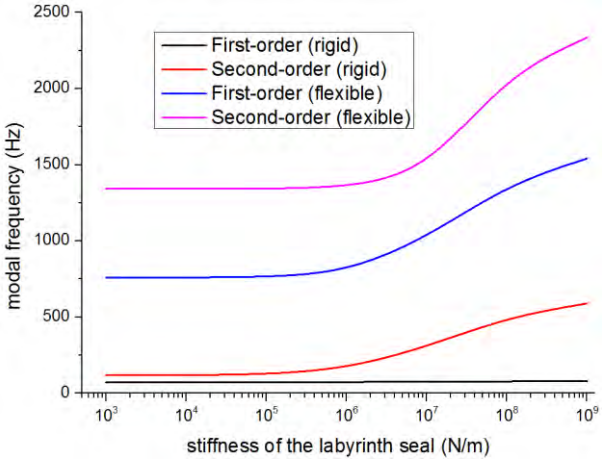

Figure 6: The influence of the stiffness of the labyrinth seal on the modal frequency of the rotor

It can be found from Fig. 5 that the rotor modal frequency hardly changes with the support stiffness in the low stiffness interval. After the support stiffness reaches 1×10^5 N/m, the support stiffness has a great influence on the rotor modal frequency.
Therefore, when performing the modal analysis of the rotor of the magnetic refrigeration compressor, the influence of the labyrinth seal on the rotor modal analysis can not be ignored if the support stiffness provided by the labyrinth seal is large enough.

4. UNBALANCE RESPONSE ANALYSIS OF MAGLEV RIGID ROTOR

It can be known from Eq. (5) that the unbalanced forces or external disturbance forces F'_x and F'_y will have an influence on the rotor response, so the existence of the unbalanced quantity will affect the running accuracy of the maglev system and the performance of the magnetic refrigeration compressor. The small disturbance force is used to simulate the influence of the unbalanced quantity of the parts on the rotor. The same 10N interference force is given to the mounting positions of the different parts on the rotor. The unbalance response of the simulated rotor is studied for the sensitivity of the rotor to unbalanced quantities at different locations and the influence on the modal of the rotor. The unbalance response simulation results are shown in Fig. 7 and Fig. 8 below.

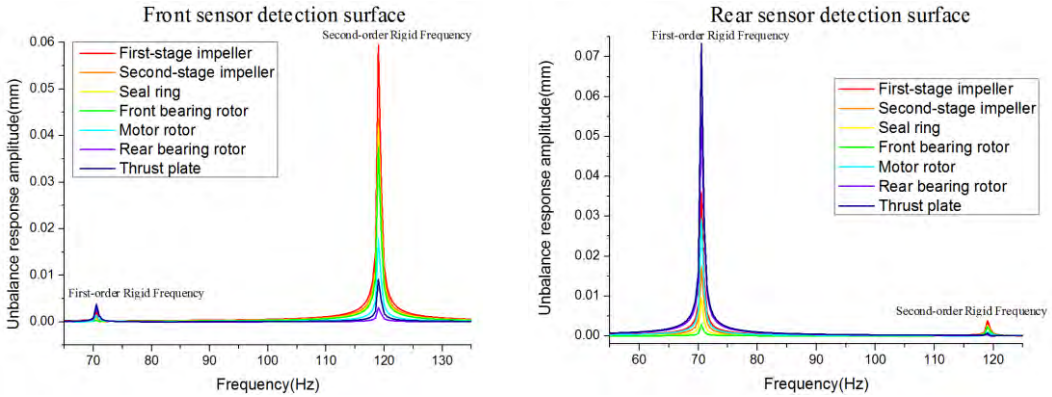

Figure 7: Unbalance response curve with interference force at different position

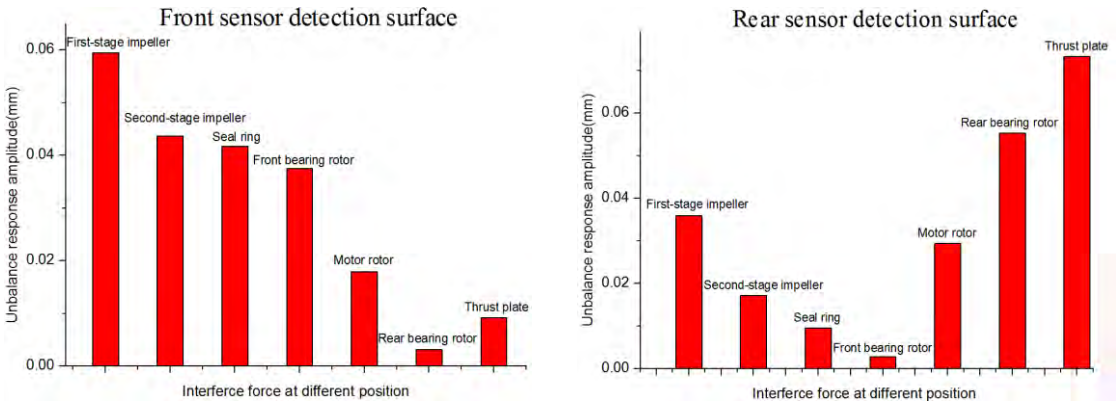

Figure 8: Unbalance response amplitude with interference force at different position

It can be seen from Fig. 7 that the unbalance response of the rear sensor detection surface is much larger than that of the front sensor detection surface when the frequency is close to the first-order rigid frequency, and the unbalance response of the front sensor detection surface is much larger than of the rear sensor detection surface when the frequency is close to the second-order rigid frequency.

It can be seen from Fig. 8 that the front sensor detection surface response is sensitive to the unbalanced amount at the first-stage impeller, the second-stage impeller and the seal ring, and the rear sensor detection surface response is sensitive to the unbalance amount at the thrust plate.

In general, the unbalanced amount at different positions have little effect on the modal frequency of the rotor, and the unbalanced amount far from the bearing causes larger amplitude of the unbalance response at detecting position. The sealing ring and the thrust plate are relatively regular ring parts, which can be processed to ensure a relatively small unbalance amount, but the impellers are relatively complicated, and the unbalanced amounts are difficult to ensure. Therefore, it is necessary to do dynamic balance check on first-stage and second-stage impeller separately before performing the overall assembly of the rotor to ensure stability of rotor operation to reduce the unbalance response of the shafting. The equipment for dynamic balance check is shown as Fig. 9.

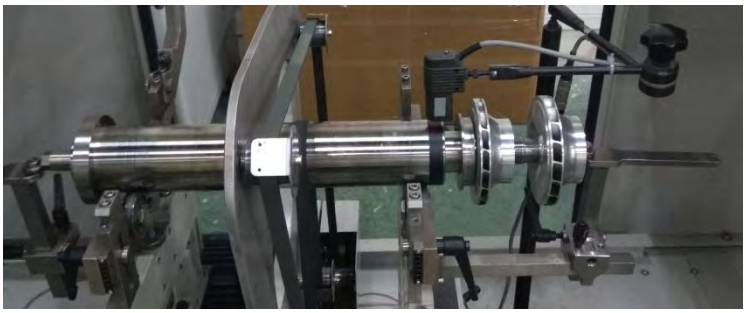

Figure 9: The equipment for dynamic balance check

5. CONCLUSIONS

1. It is almost the same with actual situation when doing ANSYS modal simulation if the coefficient of Young's modulus of silicon steel sheets were adjusted. Because the laminated silicon steel on maglev rotor has different radial and axial Young's modulus due to lamination and immersion paint, and appropriate coefficient is needed to modify the affection.
2. In appropriate stiffness interval, rotor modal frequency changes significantly with supporting stiffness. Since the supporting stiffness of the maglev system can be adjusted by control parameters, this interval can be used to reduce vibration around resonance frequency extent by adjusting control parameters.
3. The influence of labyrinth seal on maglev centrifugal compressor rotor modality cannot be ignored if the support stiffness provided by labyrinth seal were large enough.

4. Unbalanced amount at different positions have little effect on modal frequency of maglev compressor rotor. And the unbalanced amount far from bearing support position causes larger amplitude than nearby region on unbalanced response at detecting position. For the maglev compressor rotor, it is necessary to do dynamic balance check on first-stage and second-stage impeller separately to ensure stability of rotor operation.

ACKNOWLEDGEMENTS

The authors thank the State Key Laboratory of Air-conditioning Equipment and System Energy Conservation.

NOMENCLATURE

x_f	radial degree of freedom of the front radial magnetic bearing in the *x* direction (m)	x_r	radial degree of freedom of the rear radial magnetic bearing in the *x* direction (m)
y_f	radial degree of freedom of the front radial magnetic bearing in the *y* direction (m)	y_r	radial degree of freedom of the rear radial magnetic bearing in the *y* direction (m)
z	axial degree of freedom (m)	x_c	displacement of the centroid in *x* direction(m)
y_c	displacement of the centroid in *y* direction(m)	l	distance between the two radial magnetic bearings (m)
a	distance between the front radial magnetic bearing and the centroid (m)	b	distance between the rear radial magnetic bearing and the centroid (m)
α	rotation angle in the *xz* plane (rad)	β	rotation angle in the *yz* plane (rad)
F_{fx}	electromagnetic force of x_f (N)	F_{fy}	electromagnetic force of y_f (N)
F_{rx}	electromagnetic force of x_r (N)	F_{ry}	electromagnetic force of y_r (N)
m	the mass of the rotor (kg)	ω	angular velocity (rad·s^{-1})
J_d	cross-section moment of inertia (kg·m^2)	J_p	polar moment of inertia (kg·m^2)
F'_x	unbalanced force in the *x* direction (N)	F'_y	unbalanced force in the *y* direction (N)
k_{xfx}	stiffness of x_f (N·m^{-1})	k_{yfy}	stiffness of y_f (N·m^{-1})
k_{xrx}	stiffness of x_r (N·m^{-1})	k_{yry}	stiffness of y_r (N·m^{-1})
k_{ifx}	current coefficient of x_f (NA^{-1})	k_{ify}	current coefficient of y_f (NA^{-1})
k_{irx}	current coefficient of x_r (NA^{-1})	k_{iry}	current coefficient of y_r (NA^{-1})
i_{fx}	current of x_f (A)	i_{fy}	current of y_f (A)
i_{rx}	current of x_r (A)	i_{ry}	current of y_r (A)

REFERENCES

Hu, Y., Zhou, Z., Jiang, Z., 2006. Basic theory and application of magnetic bearings . Mechanical Industry Publishers, Beijing, 118 p

Huang, Z., Le, Y., Han, B., 2016. Design of AMBs and Rotordynamics for a 30kW, 60000rpm Permanent-magnet Machine. Proceedings of the 15th International Symposium on Magnetic Bearings, Kitakyushu, Japan, F1A3-10053

Wen, L., Gerald, B., Roger, N., Raymond, A., Joseph, E., 2000. Novel High-Speed Induction Motor for a Commerical Centrifugal Compressor. IEEE Transaction on Industry Applications 36(3), 706-712

Manuscript ID: 894
DOI: 10.18462/iir.icr.2019.0894

Multi-bank Microchannel Heat Exchanger Pass Optimization Using Integer Permutation Based Genetic Algorithm

Zhenning LI[(a)], Jiazhen LING[(a)], Vikrant AUTE[(a)*]
[(a)]Center for Environmental Energy Engineering
Department of Mechanical Engineering, University of Maryland,
College Park, MD 20742 USA,vikrant@umd.edu

ABSTRACT

Microchannel heat exchangers(MCHX) are increasingly applied in heat pump applications due to their compactness, high heat transfer effectiveness and reduced charge. Their performance is strongly influenced by the pass arrangement. For multi-bank MCHX, pass optimization is particularly challenging since the number of candidate designs is exponentially large. Neither the exhaustive search nor traditional optimization algorithms can effectively find optimal designs in this case. So far, very few studies on MCHX pass arrangements have appeared in the literature, and no study presents a systematic optimization approach to solve this problem. This paper presents a novel integer permutation based Genetic Algorithm(GA) for multi-bank MCHX pass optimization. Novel genetic operators are designed such that all individuals generated by GA can be decoded as feasible MCHX pass configurations. Case studies are presented to show that the proposed approach yields MCHX designs with 8.1-10.3% improved capacity than non-optimized pass configurations.
Key words: Microchannel Heat Exchanger, Pass Optimization, Integer Permutation, Genetic Algorithm

1. INTRODUCTION

Microchannel heat exchangers (MCHX) have been increasingly applied in air-conditioning and heat pumps because they offer greater compactness, significant charge reduction, lower refrigerant pressure drop and lower air-side fan power consumption compared to tube-fin heat exchangers (TFHXs). Typically, for the given envelope volume and operating condition, the system designer has the freedom to choose the suitable geometry for optimization of MCHX performance.

Optimization of MCHX is not a new topic. Heun and Dunn (1996) provided a systematic evaluation of the effect of port shape on microchannel tube performance. They carried out an analytical study to improve microchannel condenser design. They found that refrigerant side pass arrangement and port shape significantly impact their design. Kulkarni *et al.* (2001) optimized a sawtooth condenser for refrigerators. The optimal design was obtained when the added condenser area caused so much pressure drop that the air flow rate dropped to the point where the air and refrigerant temperatures pinched. Using a more powerful and efficient fan was recommended to achieve further increase in condenser performance. Martínez-Ballester *et al.* (2013) presented a numerical model for microchannel condensers. Fin cuts was studied as a function of the refrigerant pass arrangement. Huang *et al.* (2015) explored the effect of variable geometry (fin depth, fin density, port size etc.) on air cooled microchannel condensers using a novel variable geometry microchannel heat exchanger model. Capacity was plotted as a function of material mass for variable geometry and conventional geometry MCHX. It shows that optimization of variable geometry MCHX is an effective way to improve HX performance and reduce material cost. Li and Pega (2018) presented a parametric study on MCHX pass arrangement for condensers with separation circuiting based on their experimentally validated MCHX condenser model. The best pass arrangement among all 310 pass arrangements they enumerated offers 17.9% performance improvement compared to the baseline condenser. Since they only evaluated a small number of designs, their best pass arrangement is not necessarily the optimal.

Design engineers usually choose MCHX pass arrangement based on their experience or the benchmark result of a limited number of simulations for a few artificially designed pass arrangements. For instance, one of the most common pass arrangement for MCHX has multiple passes, which starts from the top and ends at the bottom. There is no guarantee that manually designed pass arrangements are optimal designs, especially for large HXs. The pass arrangement optimization for multi-bank MCHX is particularly challenging due to the extremely large design space whose size increases exponentially with the increase of tube numbers. To the authors' knowledge, there is no optimization algorithm which has appeared in the literature to optimize MCHX pass configurations.

In this paper, Genetic Algorithm is used to solve microchannel heat exchanger pass optimization problem. A finite volume heat exchanger model, CoilDesigner® (Jiang *et al.* (2006)) is used to simulate the performance of MCHX with different pass arrangements. The primary contribution of this paper is to present a new integer permutation-based GA algorithm. This new algorithm can generate valid pass arrangement designs without requiring extensive domain knowledge. Manufacturing constraints are incorporated in the newly developed GA operators.

2. INTEGER PERMUTATION BASED GENETIC ALGORITHM

2.1 Representation of MCHX Pass Configurations

A good individual representation (chromosome) can not only improve the efficiency of genetic algorithm by reducing the searching space, but it should be easy to interpret by simulating the nature of the problem (Deb, 2012)). It has been shown that a meaningful and appropriate chromosomal representation of the problem can speed up Genetic Algorithm to converge to a global optimal (Kargupta et al., 1992)). For microchannel heat exchanger pass optimization problem, the proposed approach represents tubes in one pass as an array of integers. The optimization technique is independent of the actual numbering of the tubes. For an integer permutation, each integer (i.e., tube number) appears exactly once, thus, any chromosome generated by the Genetic Algorithm can be mapped to a valid pass arrangement design and the size of the search space is dramatically reduced by the elimination of redundant designs.

Consider a 20-tube, 2-bank MCHX. as an example (shown in Figure 1a). There are 2 circuits (i.e. 2 refrigerant streams). One circuit has 4 passes and the other circuit has 3 passes. The 2 red arrows indicate the refrigerant inlets and the 2 blue arrows indicates the refrigerant outlets. The refrigerant streams flowing through the headers are represented by black arrows. A novel chromosome (Figure 1b) is developed to represent MCHX pass arrangement. It uses the concept of jagged arrays, each element of this array stores the pass arrangement in each circuit (i.e. refrigerant stream). Each circuit contains a sequence of integer arrays, and each of these arrays represents the tube numbers in each pass. By using this chromosome, number of circuits, number of passes in each circuit and number of tubes in each pass are all flexible and can be varied by the optimizer. Intuitively, the designed chromosome represents MCHX pass arrangement in a realistic manner because it "physically" separates different circuits and different passes from each other.

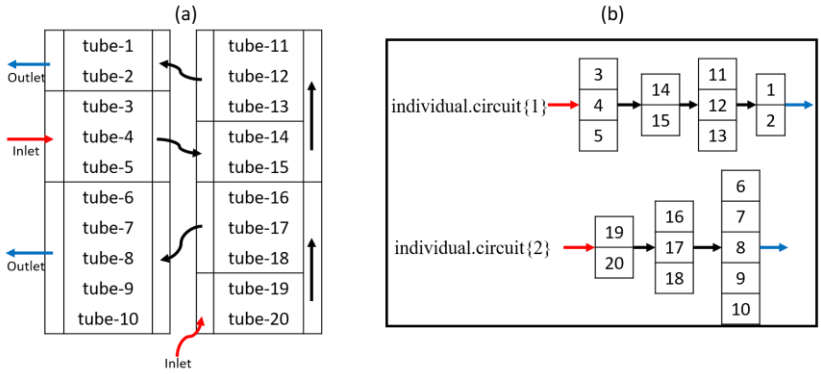

Figure 1: Pass Arrangement Representation: (a) 20-tube MCHX; (b) Chromosome

2.2 Selection Operator & Constraint handling

The selection operator selects superior individuals in a population and forms a mating pool. The common selection methods from Genetic Algorithm literature are tournament selection, proportionate selection (i.e. Roulette wheel selection) and ranking selection (Goldberg, 1989)). The essential idea is to pick the above-average individuals from the current population and insert duplicates of those elite individuals in the mating pool in a probabilistic manner. In this paper, a tournament selection operator with tournament size 2 is adopted to cooperate with an efficient constraint handling method (Deb (2000)). Li and Aute (2018) have shown that this selection operator and constraint handling technique can solve tube-fin heat exchanger circuitry optimization problem efficiently.

Coit and Smith (1996) has shown that constraint handling method such as penalty method cannot efficiently avoid the infeasible individual if Genetic Algorithm generates too many infeasible individuals than feasible ones and the optimization process will remain stagnant. According to Deb (2001), the most efficient constraint handling approach is to incorporate constraint inside the working principles of the GA operators, such that all generated designs are feasible designs. In this MCHX pass arrangement optimization problem, since there is usually an upper limit of refrigerant mass flux in individual tubes to avoid large pressure drop, design engineers have the demand to set 'minimum number of tubes per pass' as a manufacturability constraint. This necessitates specially designed genetic operators which can incorporate manufacturability constraints as their intrinsic working principles.

2.3 GA Operators

The creation of new individuals relies on the genetic operators. In this study, six novel genetic operators are developed. As shown in Figure 2a, 'circuit union' operator merges 2 randomly selected circuits into 1 circuit. 'Circuit split' operator (Figure 2b) split 1 circuit from a randomly selected location into 2 circuit. Because 'circuit union' and 'circuit split' can vary number of circuits, these two operators impose the most prominent change on MCHX design. 'Pass union' operator (Figure 2c) selects two adjacent passes in the same bank and merge them into 1 pass.

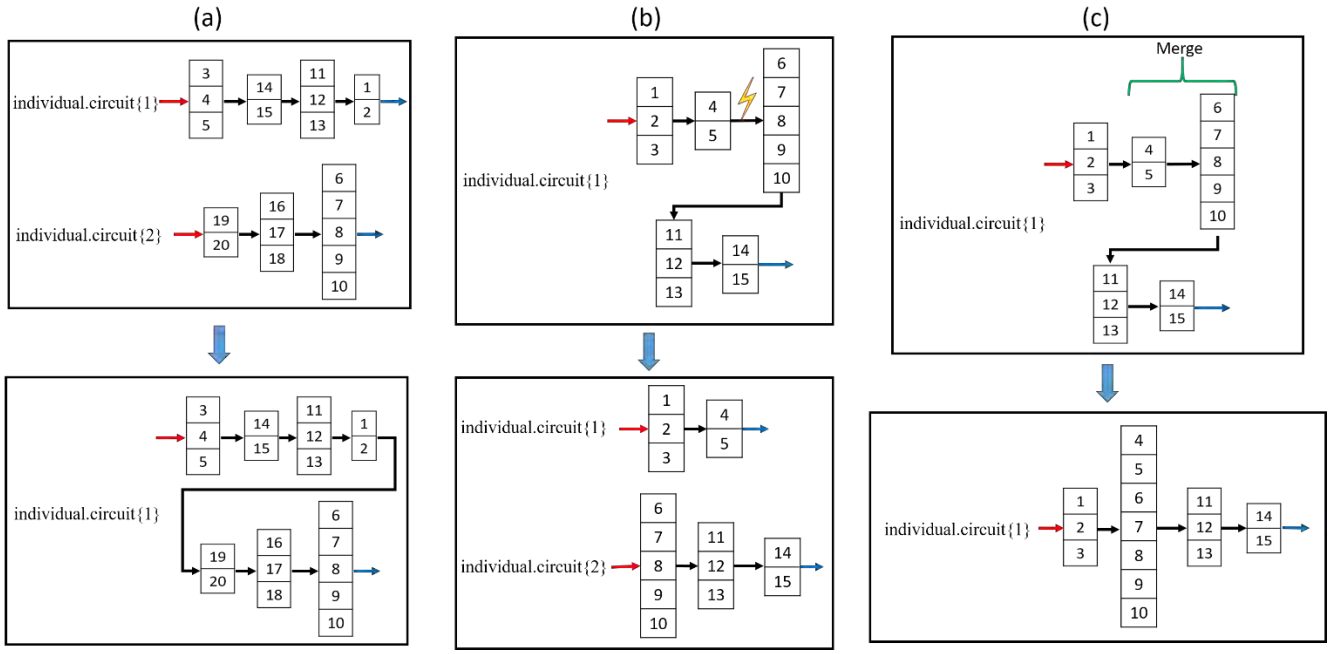

Figure 2: GA Operators: (a) Circuit union; (b) Circuit split; (c) Pass union

In addition, 'pass split' operator (Figure 3a) selects 1 pass and split it into 2 passes. It needs to be mentioned that 'pass split' operator will only select those passes whose total number of tubes are more than 2 times of 'minimum allowed number of tubes in each pass' to perform splitting operation. And the

splitting location, although randomly determined, can guarantee that each of 2 generated passes after splitting satisfies the 'minimum number of tubes in one pass' constraint. 'Pass sequence inversion' operator (Figure 3b) will randomly select one circuit and reverse its pass sequence (reverse the refrigerant flow direction). As shown in Figure 3c, 'tube redistribution operator' reallocates tubes into different passes while maintaining the total number of passes the same. It needs to be mentioned that when redistributing tubes, different tubes are only relocated to adjacent passes in the same bank. Despite the group of tubes which will be relocated are selected randomly, the algorithm is implemented in such a way that it will guarantee there are enough tubes left after the tubes removal. In this way, manufacturability constraint is implemented as the intrinsic working principle of the GA operators.

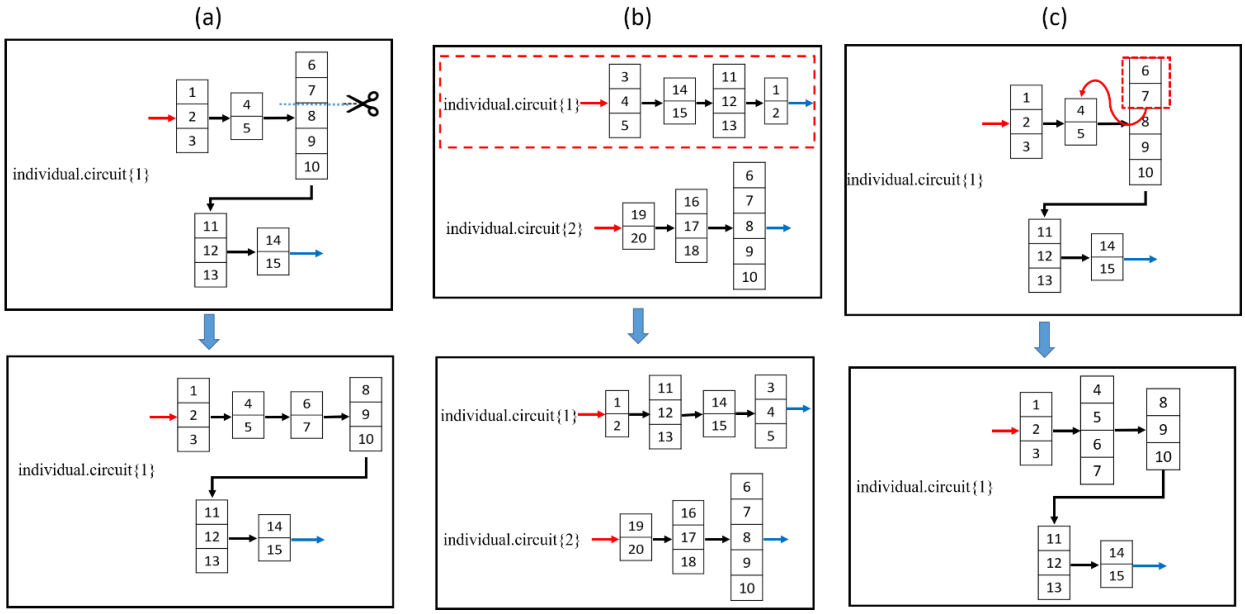

Figure 3: GA Operators: (a) Pass split; (b) Pass sequence inversion; (c) Tubes redistribution

3. CASE STUDY

3.1 Baseline Heat Exchanger

This section represents two case studies to demonstrate the efficacy of the proposed optimization framework. In order to compare the optimal design obtained from the proposed algorithm with the best design obtained from previous research (Mehendale et al., 2016). The 1st case study adopts a single-bank MCHX evaporator from Mehendale et al. (2016) as the baseline. It has 36 tubes and 12-12-12 pass arrangement from top to bottom. The 2nd case study uses a 2-bank MCHX evaporator to illustrate the capability of the proposed approach to handle multi-bank MCHX. Its tube and fin dimensions are similar to those MCHXs typically applied in commercial heat pump applications.

The air side operating conditions are adopted from AHRI (2008). In order to conduct a fair comparison with the finite search results obtained from Mehendale et al. (2016), the evaporator outlet superheat is fixed at 5°C and the evaporator inlet conditions as well as the R410A mass flow rate are iteratively solved by CoilDesigner® (Jiang et al., 2006). A finite volume heat exchanger model, CoilDesigner® (Jiang et al., 2006) is used to simulate the performance of MCHX with different pass arrangements. This model has been validated with multiple sets of measured data from different sources and the deviation of HX capacity between simulations and experiments is within 3% (Huang et al., 2014).

Table 1 summarizes the structural parameters of the two baseline MCHXs and the operating conditions under which all simulations are performed. In both case studies, the airflow distribution is assumed to be uniform. The empirical correlations used for local heat transfer and pressure drop calculations during the performance simulation of the MCHX evaporators can be found in Mehendale et al. (2016). A finite

volume heat exchanger model, CoilDesigner® (Jiang et al., 2006) is used to simulate the performance of MCHX with different pass arrangements. This model has been validated with multiple sets of measured data from different sources and the deviation of HX capacity between simulations and experiments is within 3% (Huang et al., 2014).

Table 1: Structural Parameters and Operating Conditions of Baseline MCHXs

Parameters	MCHX 1 (single bank)	MCHX 2 (multi-bank)
Total number of tubes	36	58
Number of banks	1	2
Number of tubes per bank	36	29
Number of passes	3	4
Pass arrangement	12-12-12	13-13-16-16
Tube Length (m)	0.562	0.252
Tube Height (m)	0.0018	0.0018
Tube Width (m)	0.0254	0.02
Tube Vertical Spacing (m)	0.01641	0.0078
Bank Horizontal Spacing (m)	0.01905	0.022
Port shape	circular	rectangular
Port size (m)	0.001 (diameter)	0.00091 (width) * 0.00132 (height)
Number of ports per tube	18	17
Fin density (fins per inch)	20	18
Air inlet dry bulb (°C)	8.33	
Air relative humidity	72.7%	
Average air face velocity (m/s)	2.0, uniform distribution	
R410A Inlet State	Keep the same enthalpy as R410A @ 40 °C saturation temperature, -5 °C subcooling (inlet state of expansion valve)	
Target outlet superheat (°C)	5	

3.2 Objectives and Constraints

As discussed in Huang et al. (2015), various performance metrics have been used as objectives and constraints in heat exchanger optimization formulations. For instance, in tube-fin heat exchanger circuitry optimization problem, three objectives were used by different investigators (Li and Aute (2018)):

1. Maximize HX capacity
2. Minimize the total material mass (material used to manufacture U-bends)
3. Maximize the ratio of heat capacity to refrigerant pressure drop

The proposed optimization framework supports various objective functions. In this case study, the MCHX capacity is maximized to demonstrate the capability of the proposed method. There are 3 constrains imposed on this problem. The 1st constraint limits the optimal design has equal or less refrigerant pressure drop than 1.2 times the refrigerant pressure drop of the baseline, where 1.2 is the relaxation parameter. The 2nd constraint limits the optimal design offers larger capacity than the baseline. The 3rd constraint is a manufacturability constraint. The required minimum number of tubes per pass is set as 3 in order to prevent large refrigerant pressure drop in single pass, by this change the validity of this constraint can be assessed by observing optimal designs. Eq. (1) is the problem formulation.

$$\begin{aligned} &\text{Objective: } \textit{Maximize}(Q) \\ &\text{Subject to:} \\ &\Delta P_{refrigerant} \le 1.2 \times \Delta P_{refrigerant,baseline} \\ &Q \ge Q_{baseline} \\ &\text{Minimum number of tubes per pass = 3} \end{aligned} \qquad \text{Eq. (1)}$$

3.3 Case Study I – Single-bank MCHX

The first optimization is performed on the single-bank 36 tube MCHX evaporator. The population size is 200 and the number of generations is 500. Figure 4a shows the GA progress. Figure 4(b) shows the optimal pass arrangement. From Figure 4a, the optimization yields an optimal design with a capacity increase from 4088 W to 4510 W by 10.3%. As expected, there is no pass which has less than 3 tubes in the optimal design. The pass arrangement of the baseline is 12-12-12, while the pass arrangement of the optimal design (Figure 4b) is 5-9-22. The advantage of 5-9-22 pass arrangement can be explained like this. In an evaporator the density of the refrigerant progressively decreases as it flows through the MCHX, thus, it necessitates successively larger inner volumes in the refrigerant flow direction considering the relationship between fluid velocity and refrigerant pressure drop.

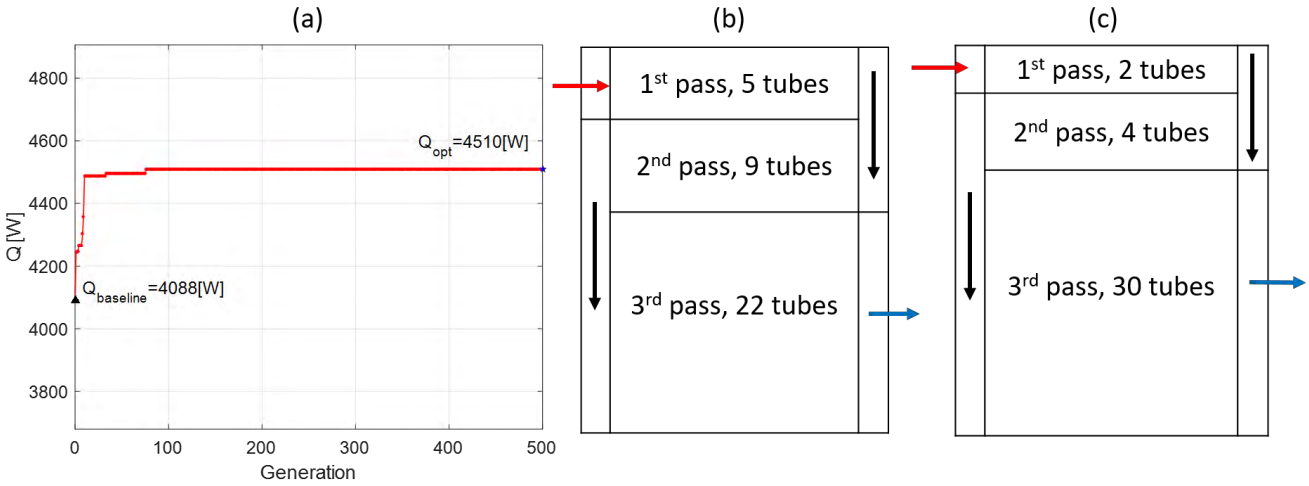

Figure 4: 1-bank MCHX (a) GA progress; (b) Optimal design; (c) Best design in Mehendale et al. (2016)

As a comparison, Mehendale et al. (2016) also investigated the influence of refrigerant pass arrangement for the same evaporator under the same operating condition. Their parametric study explored all possible two-, three-, and four-pass MCHX configurations. As a summary, 54 two-pass, 374 three-pass, and 1554 four-pass designs were simulated and the best performing design in terms of capacity has 2-4-30 pass arrangement (Figure 4c). Table 2 presents a detailed comparison of the baseline, the optimal design obtained from this proposed approach and best design found in Mehendale et al. (2016). It can be observed that although the best design from parametric study yields 12.7% capacity improvement, which is larger than 10.3% capacity improvement of the optimal design, however, its refrigerant pressure drop is 2.8 times to that of the baseline. This is due to the small number of tubes in the 1st and 2nd passes. Table 2 also lists the solved R410A inlet state and mass flow rates for each design since they are iteratively calculated to reach target outlet condition.

Table 2: Single Bank MCHX Optimization Results

Case	Baseline	Optimal Design	Best design (Mehendale et al., 2016)
Capacity (W)	4088	4510 (10.3%↑)	4607 (12.7%↑)
Ref. DP (kPa)	8.1	9.7 (19.8%↑)	22.7 (2.8x)
Pass arrangement	12-12-12	5-9-22	2-4-30
Outlet Superheat (°C)	4.98	5.01	4.97
Refrigerant mass flow rate (kg/s)	0.0249	0.0268	0.0276
R410A inlet Tsat (°C)	2.30	2.97	2.33
R410A inlet quality	0.240	0.237	0.240

3.4 Case Study II – Multi-bank MCHX

In order to assess the efficacy of the proposed framework to optimize multi-bank MCHX. A 2-bank, 58-tube MCHX evaporator describe in section 3.1 is used as the baseline. The population size is 200 and the number of generations is 500. The problem formulation is the same as Eq. (1). Figure 5(a) shows the GA iteration progress, Figure 5b and Figure 5c shows the pass arrangements of the baseline and the optimal design, respectively. It can be seen that the baseline has 4 passes, while the optimal design has 5 passes.

Table 3 shows that the optimal design yields a capacity increase of 8.1% (i.e., from 6005 W to 6493 W), while the pressure drop increases from 9.4 kPa to 11.2 kPa by 19.1%. This pressure drop increase is acceptable, given that the relaxation parameter is set as 1.2.

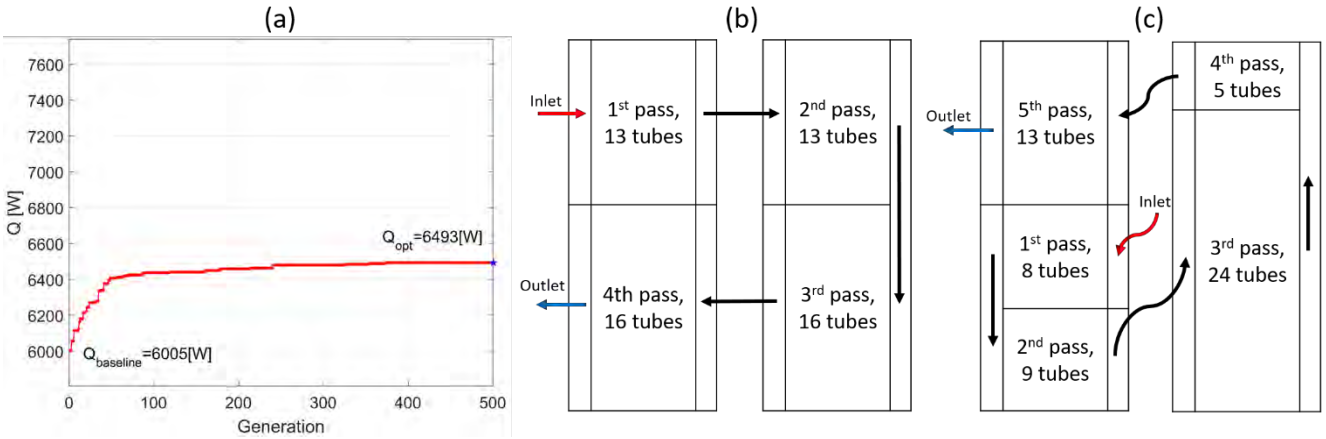

Figure 5: 2-bank MCHX (a) GA progress; (b) Baseline; (c) Optimal design

Table 3: Multi-bank MCHX Optimization Results

Case	Baseline	Optimal Design
Capacity (W)	6005	6493 (8.1%↑)
Ref. DP (kPa)	9.4	11.2 (19.1%↑)
Pass arrangement	13-13-16-16	8-9-24-5-13
Outlet Superheat (°C)	4.97	5.00
Refrigerant mass flow rate (kg/s)	0.035	0.038
R410A inlet Tsat (°C)	2.35	2.56
R410A inlet quality	0.240	0.238

4. CONCLUSIONS

A novel integer permutation-based GA algorithm is presented to solve the microchannel heat exchanger pass optimization problem. Six genetic operators are designed to generate pass arrangement with potentially better performance. The manufacturability constraint is handled inside the generic operators, such that all resulting pass arrangements generated by those operators are feasible. Two case studies on a single bank MCHX evaporator and a multi-bank MCHX evaporator show that the proposed optimization approach can generate pass arrangement designs with predicted capacities superior to pass arrangements designed manually, meanwhile guarantee good manufacturability, despite the actual improvement needs to be further validated by manufacturing and testing those optimal MCHXs in the future study. The proposed approach yields MCHX designs which have 8.1-10.3% improvement in heat exchanger capacity than non-optimized MCHX pass configurations.

REFERENCES

AHRI, A., 2008. Standard 210/240-2008. Performance Rating of Unitary Air Conditioning and Air-Source Heat Pump Equipment, AHRI, Ed.

Coit, D. W. and Smith, A. E., 1996. Penalty Guided Genetic Search for Reliability Design Optimization. Computers & industrial engineering 30(4): 895-904.

Deb, K., 2000. An Efficient Constraint Handling Method for Genetic Algorithms. Computer Methods in Applied Mechanics and Engineering 186(2): 311-338.

Deb, K., 2001. Multi-Objective Optimization Using Evolutionary Algorithms, John Wiley & Sons.

Deb, K., 2012. Optimization for Engineering Design: Algorithms and Examples, PHI Learning Pvt. Ltd.

Goldberg, D. E., 1989. Genetic Algorithms in Search, Optimization, and Machine Learning. New York, Addison-Wesley.

Heun, M. K. and Dunn, W. E., 1996. Principles of Refrigerant Circuiting with Application to Microchannel Condensers. Part 2: The Pressure-Drop Effect and the Cross-Flow Heat Exchanger Effect, American Society of Heating, Refrigerating and Air-Conditioning Engineers, Inc., Atlanta, GA (United States).

Huang, L., Aute, V. and Radermacher, R., 2014. A Model for Air-to-Refrigerant Microchannel Condensers with Variable Tube and Fin Geometries. International Journal of Refrigeration 40: 269-281.

Huang, L., Aute, V. and Radermacher, R., 2015. A Survey of Optimization Formulations and Techniques for the Design of Heat Exchangers Using Lower Gwp Refrigerants. ASHRAE Transactions 121(CH-15-C039).

Jiang, H., Aute, V. and Radermacher, R., 2006. Coildesigner: A General-Purpose Simulation and Design Tool for Air-to-Refrigerant Heat Exchangers. International Journal of Refrigeration 29(4): 601-610.

Kargupta, H., Deb, K. and Goldberg, D. E., Year. Ordering Genetic Algorithms and Deception. PPSN, Citeseer.

Kulkarni, T., Kim, M. and Bullard, C., 2001. Condensing Units for Household Refrigerator-Freezers, ACRC Report CR 38. Air Conditioning and Refrigeration Center. University of Illinois at Urbana-Champaign.

Li, J. and Pega, H., 2018. An Experimentally Validated Model for Microchannel Condensers with Separation Circuiting. 17th International Refrigeration and Air Conditioning Conference, Purdue University, USA.

Li, Z. and Aute, V., 2018. Optimization of Heat Exchanger Flow Paths Using a Novel Integer Permutation Based Genetic Algorithm. EngOpt 2018 Proceedings of the 6th International Conference on Engineering Optimization, Lisboa, Portugal.

Martínez-Ballester, S., Corberán, J.-M. and Gonzálvez-Maciá, J., 2013. Numerical Model for Microchannel Condensers and Gas Coolers: Part Ii–Simulation Studies and Model Comparison. International Journal of Refrigeration 36(1): 191-202.

Mehendale, S., Li, Z. and Aute, V., 2016. Refrigerant Circuit Optimization of Dual-Mode Single-Row Microchannel Heat Exchangers Used for R410a Heat Pumps. 16th International Refrigeration and Air Conditioning Conference Purdue, July 11-14, 2016.

Manuscript ID: 914
DOI: 10.18462/iir.icr.2019.0914

Combustion suppression effect of additives for lubricating oil during Diesel explosion at pump-down of air conditioner

Tomohiro HIGASHI[(a)], Chaobin DANG[(a)], Eiji HIHARA[(a)], Yuji SHITARA[(b)]

[(a)]The University of Tokyo
5-1-5, Kashiwanoha, Kashiwa, 277-8563, Japan, t.higashi@hee.k.u-tokyo.ac.jp
[(b)]JXTG Nippon Oil & Energy Corporation
8, Chidorichou, Chuuouku, Yokohama, 231-0815, Japan, shitara.yuji@jxtg.com

ABSTRACT

Lower global warming potential refrigerants tend to be highly flammable, and therefore, their safety evaluation is necessary. Pump-down is an operation used to collect the entire refrigerant in an air conditioner to its outdoor unit; however, some accidents have been reported where the compressor exploded owing to air contamination because of operational error. In this study, self-ignition of air, refrigerant, and lubricating oil were investigated experimentally. Additives to suppress combustion were mixed with oil and subsequently tested. Compared with the results of pure oil, the flammable range of the mixture became narrower for the oil mixed with the additives. It was revealed that the additives effectively suppressed the combustion at pump-down.
Keywords: Heat Pump, Pump-Down, Low GWP, Flammability, Safety.

1. INTRODUCTION

Environmental and safety characteristics are important for refrigerants used in air conditioners, as well as physical properties such as the cooling capacity and performance coefficient. To conserve the global environment, the refrigerants' ozone depleting potential (ODP) should be zero, and the global warming potential (GWP) should be low. The GWP of R410A, which is a conventional refrigerant for air conditioners, is extremely high that new low-GWP refrigerants such as R1234yf and R32 have been introduced. However, R32 still exhibits a high GWP, thereby causing hydrocarbon refrigerants such as R290 to attract increasing attention as a solution to global warming. Nevertheless, these refrigerants with lower GWPs are higher in flammability; therefore, safety investigations are required. Table 1 lists the ODP, GWP, and flammability of several refrigerants (Japan Society of Refrigerating and Air Conditioning Engineers, 2017).

Table 1. Properties of refrigerants

-	R290	R1234yf	R32	R410A	R22
Chemical formula	$CH_3CH_2CH_3$	$CH_2 = CFCF_3$	CH_2F_2	CH_2F_2 (50%) CHF_2CF_3 (50%)	$CHClF_2$
ODP	0	0	0	0	0.055
GWP	3	4	675	2090	1810
LFL* (vol, %)	2.02	6.7	13.5	No flame propagation	
UFL** (vol ,%)	9.81	12	28		
ASHRAE flammability classification	A3	A2L	A2L	A1	A1

* Lower flammable limit; ** Upper flammable limit

The authors focused on a compressor explosion accident at the pump-down of air conditioners. Pump-down is an operation used to gather an entire refrigerant into the outdoor unit of a split air conditioner. By closing the outlet valve of an outdoor unit and forcefully driving the air conditioner, the refrigerant is gathered into a condenser as a liquid. When the split air conditioner is relocated or discarded, a pump-down operation must be performed to prevent refrigerant leakage into the atmosphere. During the pump-down operation, the suction line of a compressor becomes vacuum. If the penetration of air into the refrigerant tube occurs because of an error during the operation of a three-way valve or damaged tubes, the pressure and temperature inside the compressor would increase. The authors have tested several lubricating oils with fluorocarbon refrigerants by reproducing the combustion from the mixture of air, refrigerant, and oil. It was revealed that the flammability was affected by not only the flammability of refrigerants but also that of the lubricating oil (Higashi, et al., 2017). In this research, additives exhibiting a combustion suppression effect were mixed to a lubricating oil, and the flammability of the gaseous mixture of air, refrigerant, and oil was investigated experimentally.

2. METHODS

2.1. Experimental Apparatus

An experimental apparatus was built to reproduce a diesel explosion at pump-down. Fig. 1 shows a schematic of the experimental apparatus. The apparatus primarily consists of a compressor, refrigerant supply system, temperature-control system, and lubricating oil supply system. For safety, a model engine (R155-4C, 4-stroke, stroke volume: 25.42 cc compression ratio: 16.0 made by ENYA) was used as a simulated compressor by driving its shaft with a motor. Fig. 2 shows the cut model of the engine. The air and refrigerant were supplied in their gaseous states, and the flow rate was controlled independently. They were mixed at a certain level of concentration and heated using a heater in front of the intake port of the engine. The lubricating oil was injected into the mixture by spraying. The quantity of oil per injection was changed using the injection time. A mixture of refrigerant, air, and lubricating oil was compressed by the engine. The pressure in the engine was measured using a pressure sensor (6045A, made by Kistler, linearity: ± 0.4% FSO). The pressure sensor was attached to a port for the spark plug instead of the plug itself. The exhaust gas of the engine was analyzed using a Fourier transform infrared spectrometer ([FT-IR], FT/IR-4700, made by Jasco, resolution: 0.5 cm-1, S/N: 35000:1). The database provided by the Pacific Northwest National Laboratory (PNNL) was referred to identify substances from the results of the measurements from the FT-IR (PNNL, 2018). The reference can be referred for further information on the experimental apparatus.

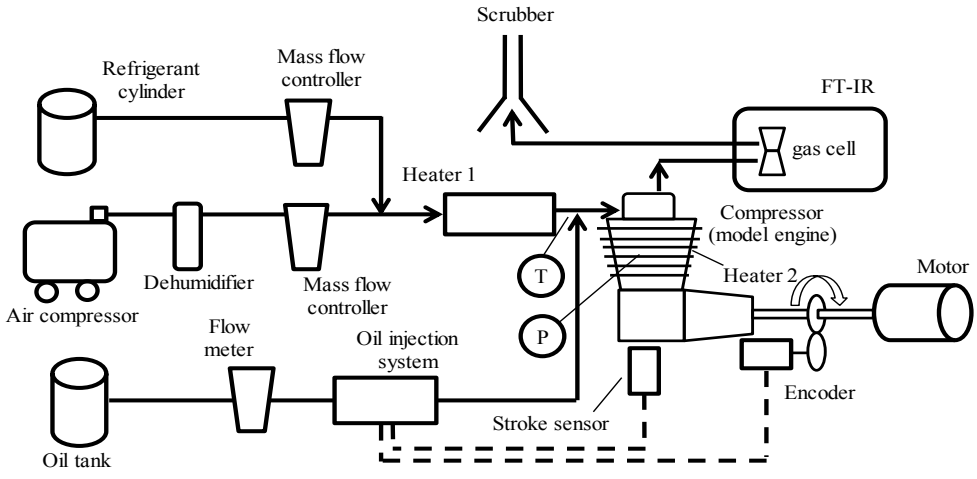

Figure 1: Schematic of experimental apparatus



Figure 2: Cut model of engine

2.2. Experimental Conditions

Table 2 lists the refrigerants, lubricating oil, and additives used in this research. R290 (propane, higher flammable hydrocarbon refrigerant), and R32 and R1234yf (mildly flammable refrigerants) were used. Polyolester (POE) oil is generally used as a lubricating oil for compressors.

Table 2. Refrigerants, lubricating oil, and additives

Refrigerant	R290, R32, R1234yf
Lubricating oil	Polyolester (POE) oil
Additive	A1, A2
Additive mix ratio	5 wt%

Additive A1 is a phenolic antioxidant. The phenyl group captures radicals that are generated by oil combustion. Additive A2 is an epoxy stabilizer. It captures hydrogen fluoride generated by refrigerant combustion. Both the additives are expected to demonstrate a combustion suppression effect. The additives were mixed with pure POE oil by 5 wt%.

Table 3 lists the experimental conditions. The flow rate of a gaseous mixture was calculated using the number of revolutions and the stroke volume of the engine. During actual accidents, the temperature of the compressor may increase because it compresses the gaseous mixture continuously; therefore, in this study, the mixture was heated to 260 °C such that burning occurs easily. The heater temperature was controlled such that refrigerant decomposition does not occur, as reported in a research on the thermal decomposition of refrigerants (Ito, et al., 2014). The oil flow ratio was calculated based on the standard oil flow rate, which will be discussed later. The oil flow rate was controlled by injection time, which was calibrated on each lubricating oil.

Table 3. Experimental conditions

Number of revolutions of engine (rpm)	1500
Gaseous mixture flow rate ($l.min^{-1}$)	18.75
Inlet gas temperature (°C)	260
Oil equivalence ratio (-)	0.0 (without oil), 0.7, 1.0, 1.3, 1.6

Table 4 lists the properties of the lubricating oil. The standard flow rate was calculated such that the oil flow rate would become the theoretical air fuel ratio.

Table 4. Properties of lubricating oil

CHO ratio (mass %)	70.1:10.8:19.1
Ignition point (°C)	408
Theoretical air fuel ratio ($kg.kg^{-1}$)	10.91
Standard flow rate ($l.min^{-1}$)	3.519×10^{-4}

3. RESULTS AND ANALYSIS

3.1. R290

Fig. 3 shows the typical pressure changes in an engine when the gaseous mixture of air and lubricating oil is compressed. The horizontal axis shows the crank angle of the engine, while the vertical axis shows the pressure. The oil equivalent ratio of the mixture was 1.0. The gaseous mixture was compressed in the compression stroke with the crank angle between 180° and 360°; therefore, the pressure was increased. The pressure was decreased in the expansion stroke with the crank angle between 360° and 540°, and subsequently the gas was exhausted.
Under this condition, the self-ignition of the lubricating oil occurred, and the pressure increased. The maximum pressure reached approximately 4 MPa. The pressure increased significantly, a loud noise was heard, and strong vibrations were observed; furthermore, carbon monoxide (CO) was detected in the exhaust gas.

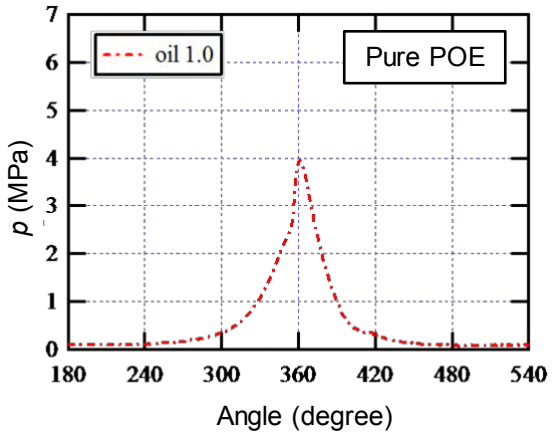

Figure 3: Change in pressure with pure POE oil

Fig. 4 shows the pressure changes in the engine when the gaseous mixture of air, R290, and lubricating oil was compressed. The R290 concentration was 0.6 vol%. An intense combustion was observed, and the pressure increased higher than the result obtained without R290 shown in Fig. 3. The maximum pressure exceeded 5 MPa. Fig. 5 shows the infrared adsorption spectrum of the exhaust gas under the same condition as measured by FT-IR. The horizontal axis shows the wavenumber of the infrared spectrum, and the vertical axis shows the adsorption ratio. The spectra of R290 was observed between the region from 3050 to 2800 cm^{-1}, and that for CO was observed between the region from 2250 to 2050 cm^{-1}. R290 underwent combustion, and the combustion contributed to an increased pressure.

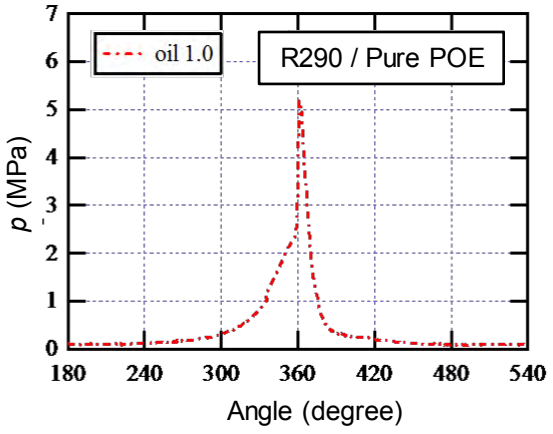

Figure 4: Change in pressure with R290 and pure POE oil

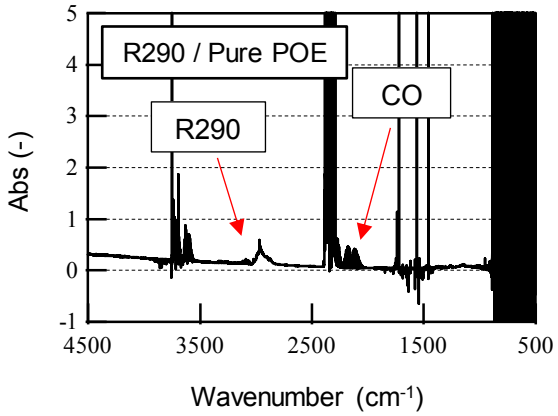

Figure 5: Infrared adsorption spectrum of exhaust gas

Fig. 6 shows the relationship between R290 concentration and the maximum pressure. The horizontal and vertical axes show the R290 concentration and maximum pressure, respectively. The maximum pressure p'_{max} was normalized to p_0; the pressure when the air was compressed is as shown in Eq. (1). The legends show the amount of oil; 0.0 represents the results without oil, and 1.0 shows the results when the oil equivalence ratio was 1.0. The theoretical value of the maximum pressure (p_{th}) was calculated by assuming the adiabatic compression of a gaseous mixture of the refrigerant, as shown in Eq. (2).

$$p'_{max} = \frac{p_{max}}{p_0} \qquad \text{Eq. (1)}$$

$$p_{th} = p_{atm} \times \varepsilon^{\kappa} \qquad \text{Eq. (2)}$$

In the results with pure POE oil shown in Fig. 6 (a), combustion did not occur when the refrigerant concentration was higher than 0.6 vol%. The maximum pressure was low, and any combustion production such as carbon monoxide (CO) were not detected by FT-IR. At the lower refrigerant concentration, a combustion was observed. The pressure increased significantly, and CO was observed in the exhaust gas. Figs. 6 (b) and (c) show the results with the additives. In both results, no combustion was observed with R290 mixed. Even when the combustion occurred only with air and the oil mixture, the maximum pressure during combustion was lower than that with pure POE oil. The results indicate that the additives could suppress the flammability of the gaseous mixture of air, refrigerant, and lubricating oil.

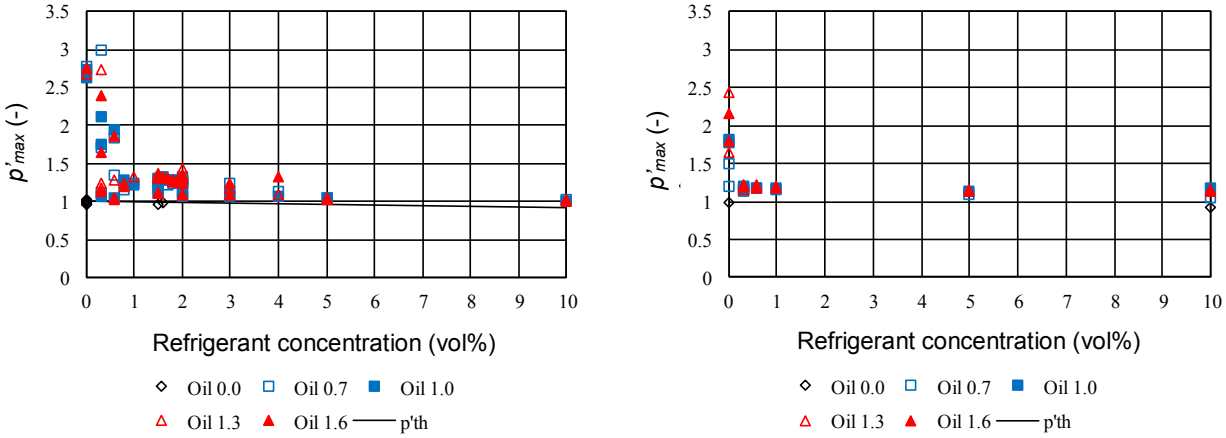

(a) with pure POE oil

(b) with POE oil + A1

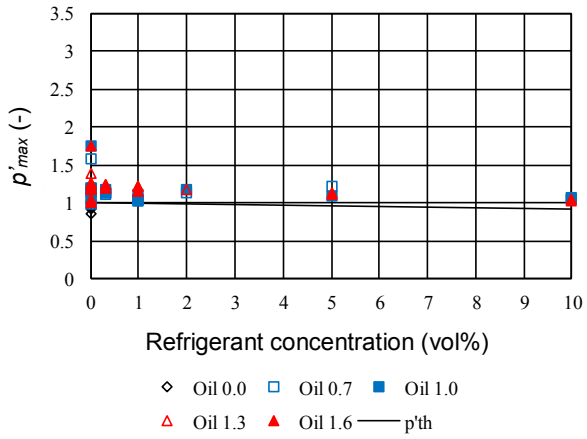

(c) with POE oil + A2

Figure 6: Results with R290

3.2. R32

Fig. 7 shows the results with R32. The flammable range with pure POE was lower than 20 vol%. When the additives were mixed, both results exhibited a narrower flammable range than that with pure POE oil, lower than 15 vol% for POE with A1, and lower than 10 vol% for POE with A2. Regarding the result with A1, the maximum pressure during combustion was lower than that with pure POE oil. The results indicate that the additives could narrow the flammable range, and the additive A1 could inhibit the intensity of combustion.

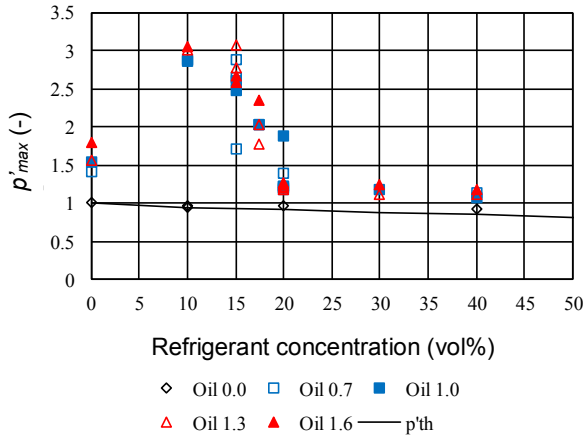

(a) with pure POE oil

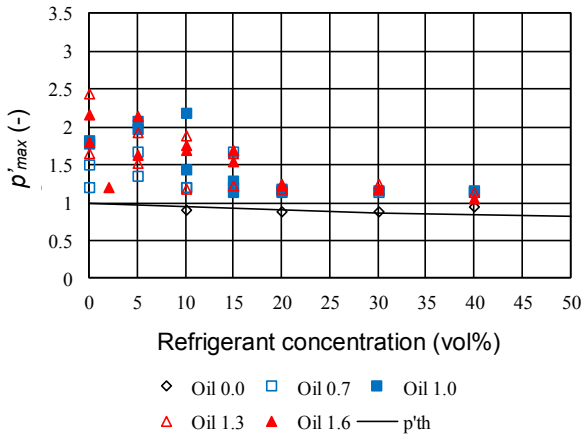

(b) with POE oil + A1

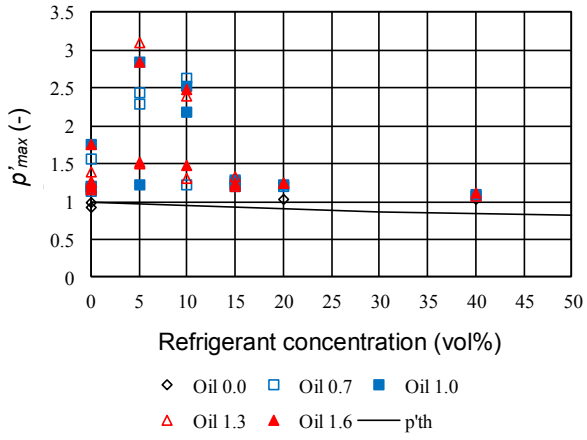

(c) with POE oil + A2

Figure 7: Results with R32

3.3. R1234yf

Fig. 8 show the results with R1234yf. The combustion was observed with a lower refrigerant concentration than 5 vol% with pure POE. The results with the additives indicated a narrower flammable range than that with pure POE, lower than 0.5 vol% for A1, and lower than 2 vol% for A2. The tendency of the additives in inhibiting a combustion was similar to the results with R32.

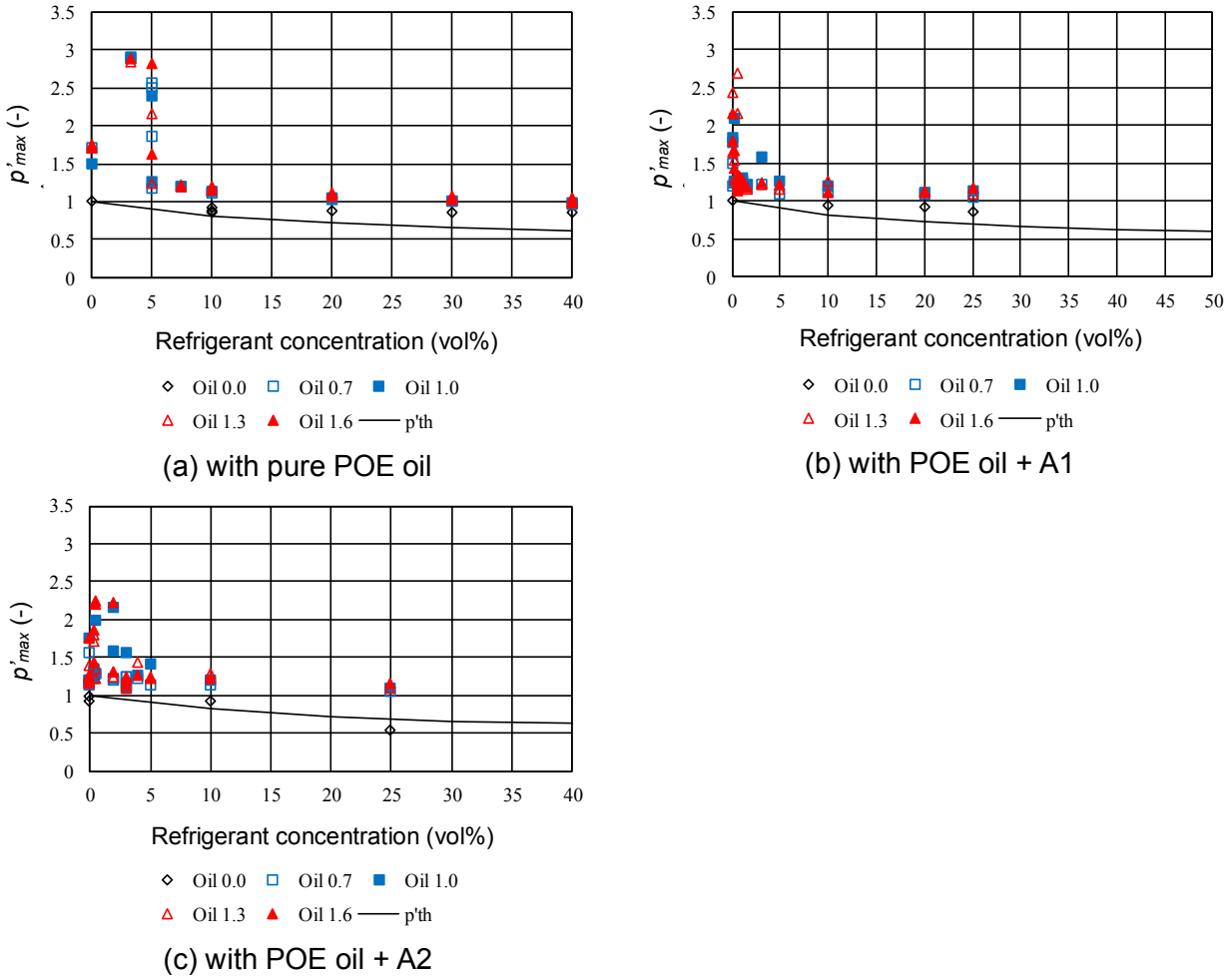

(a) with pure POE oil

(b) with POE oil + A1

(c) with POE oil + A2

Figure 8: Results with R1234yf

3.4. Effect of Additives

Tables 5 and 6 list the summary of the flammable range and normalized maximum pressure at each condition. The flammable range was narrowed by adding the additives to the lubricating oil. Previously, the authors have revealed that oil first becomes self-ignited, and subsequently the combustion propagates to the refrigerant. In this study, it is presumed that the additives suppress the first step, i.e., self-ignition of the oil, thereby resulting in a narrower flammable range. Even if combustion had occurred, the maximum pressure becomes lower especially with additive A1. The results suggest that additives for lubricating oils may decrease the potential of accidents at pump-down, even with a lower GWP but higher flammability refrigerants.

Table 5. Comparison of upper flammable limit

	pure POE	POE+A1	POE+A2
R290 (vol%)	0.6	(< 0.33)	(< 0.33)
R32 (vol%)	20	15	10
R1234yf (vol%)	5	0.5	2

Table 6. Comparison of normalized maximum pressure

	pure POE	POE + A1	POE + A2
R290	2.99	*(2.44)	*(1.76)
R32	3.07	*(2.44)	3.01
R1234yf	2.97	*(2.44)	2.22

4. CONCLUSIONS

Compressor distraction accident during pump-down was investigated experimentally. R290, R32, and R1234yf were used. Two types of additives; a phenolic antioxidant and an epoxy stabilizer; were mixed to a lubricating oil and its properties were compared when a gaseous mixture of air, refrigerant, and oil was compressed adiabatically. In the results with every refrigerant, the flammable range with the additives was narrower than that without the additives. The additives could suppress the pressure when the combustion of the mixture occurred. It was revealed that the additives for the lubricating oil could potentially decrease the possibility of accidents at pump-down.

NOMENCLATURE

p	pressure (MPa)
ε	compression ratio (-)
κ	specific heat ratio (-)
0	standard
atm	atmospheric
max	maximum
th	theoretical
‘	normalized

REFERENCES

The Japan Society of Refrigerating and Air Conditioning Engineers, 2017, Risk Assessment of Mildly Flammable Refrigerants Final Report 2016.

Higashi, T., Saitoh, S., Dang, C. and Hihara, E., 2017, Diesel combustion of oil and refrigerant mixture during pump-down of air conditioners. Int. J. of Refrigeration, 75, 300-310.

Pacific Northwest National Laboratory, Vapor phase infrared spectral library, available from https://secure2.pnl.gov/nsd/nsd.nsf/Welcome, (accessed on Jan. 24, 2019)

Ito, M, Dang, C. and Hihara, E., 2014, Thermal Decomposition of Lower-GWP Refrigerants, Int. Ref. and A.C. Conf., Indiana, U.S.A, IIF/IIR, 1538.

Manuscript ID: 946
DOI: 10.18462/iir.icr.2019.0946

Data-driven modelling of a R744 refrigeration system with parallel compression configuration

Glenn ANDREASEN[(a)], Jakob STOUSTRUP[(a)], Ángel Á. Pardiñas[(b)], Armin HAFNER[(b)], Roozbeh IZADI-ZAMANABADI[(c)]

(a) Faculty of Electrical Engineering, Automation and Control, Aalborg University Aalborg, 9220, Denmark, jakob, ga@es.aau.dk
(b) Department of Energy and Process Engineering, NTNU, Trondheim, 7491, Norway angel.a.pardinas, armin.hafner@ntnu.no
(c) Department of Intelligent Systems, Danfoss A/S, 6430, Nordborg, Denmark, Roozbeh@danfoss.com

ABSTRACT

The type and characteristics of the employed components, subsystems and refrigerant in a commercial refrigeration system varies significantly depending on required functionalities (e.g. MT (medium temperature), LT (low temperature), AC (air conditioning)) and external factors (e.g. ambient temperature). Thus, modeling for control-oriented objectives becomes a challenging task. As these systems provide a large amount of data, modelling for control-oriented objectives based on a data-driven method become an appealing option. This work focuses on obtaining a (control-oriented) data-driven MIMO (multiple input multiple output) model of a CO_2 booster refrigeration system, supported by parallel compression and ejectors, producing refrigeration for MT, LT, AC. Subspace identification is used for obtaining the data-driven MIMO model. The data-driven modelling approach is validated with data from a CO_2 system where negligible deviations are observed even with change in the main disturbances.

Keywords: Commercial refrigeration, Data-driven modelling, Subspace identification, Control-oriented modelling, R744 (CO_2), Ejector, Parallel compression

1. INTRODUCTION

Refrigeration systems are complex dynamic systems with many interacting subsystems, where the dynamic/static characteristics are dependent on the physical components (i.e. valves, compressors, etc.), operation conditions and configuration (existence of heat recovery, parallel compressors, etc.). Much of this essential information is not known prior to design of control-oriented applications (controller, optimization and process monitoring schemes). Hence control-oriented applications are often based on a first principle white box model of a general system and then later tuned for the specific system during commissioning phase. (Shafiei, 2015; Vinther, 2014)
A more appealing approach would be to base the control-oriented applications on a data-driven model which captures the underlying dynamics/static characteristics of the respective refrigeration system. Thus, this work focuses on utilization of data-driven modelling on a R744 (CO_2) refrigeration system specifically controlled variables for the gas cooler and receiver. This data-driven model is derived off-line using experimental data and is designed to capture the dynamics from the inputs (measured disturbances and actuators) to the outputs (controlled variables). The resulting model is linear and therefore applicable for controller-oriented methods.
Within the data-driven modelling domain several methods are proposed. Among these, the PEM (predictive error methods) are popular choices. PEM are well defined for SISO (single input single output) systems. However, PEM methods are based on iterative algorithms. Hence there is the risk of getting stuck in a local minimum when utilized on non-linear MIMO (multiple input multiple output), i.e. non-convex, systems (Ljung, 1999). Another method that does not suffer from this effect is subspace identification. Subspace identification is based on non-iterative and robust numerical algorithms, which makes it an appealing approach for data-driven modelling. (Katayama, 2005)

To data little research has been conducted on the application of subspace identification on refrigeration systems and even less on refrigeration systems utilizing the environmentally friendly coolant R744 which is receiving increased interest (Paride Gullo et al., 2018). In (Shafiei, 2015) subspace identification has been utilized for model predictive control, and in recent years received increased attention in process monitoring area (Ding, 2014).
In section 2 the considered refrigeration system is described. In section 3 a description of the methodology behind subspace identification is provided, followed by section 4 where the selection of the inputs for the system identification is derived. Then in section 5 validation of the derived model is performed and lastly in section 6 the concluding remarks are given.

2. R744 REFRIGERATION SYSTEM

The system utilized in this paper is a R744 refrigeration system located at NTNU/SINTEF in Trondheim, Norway. A detailed description of the system can be found in (Pardiñas, Hafner, & Banasiak, 2018) which includes components, sizing, possible configurations, etc. In the following, a brief overview of the selected configuration and relevant aspects are given.

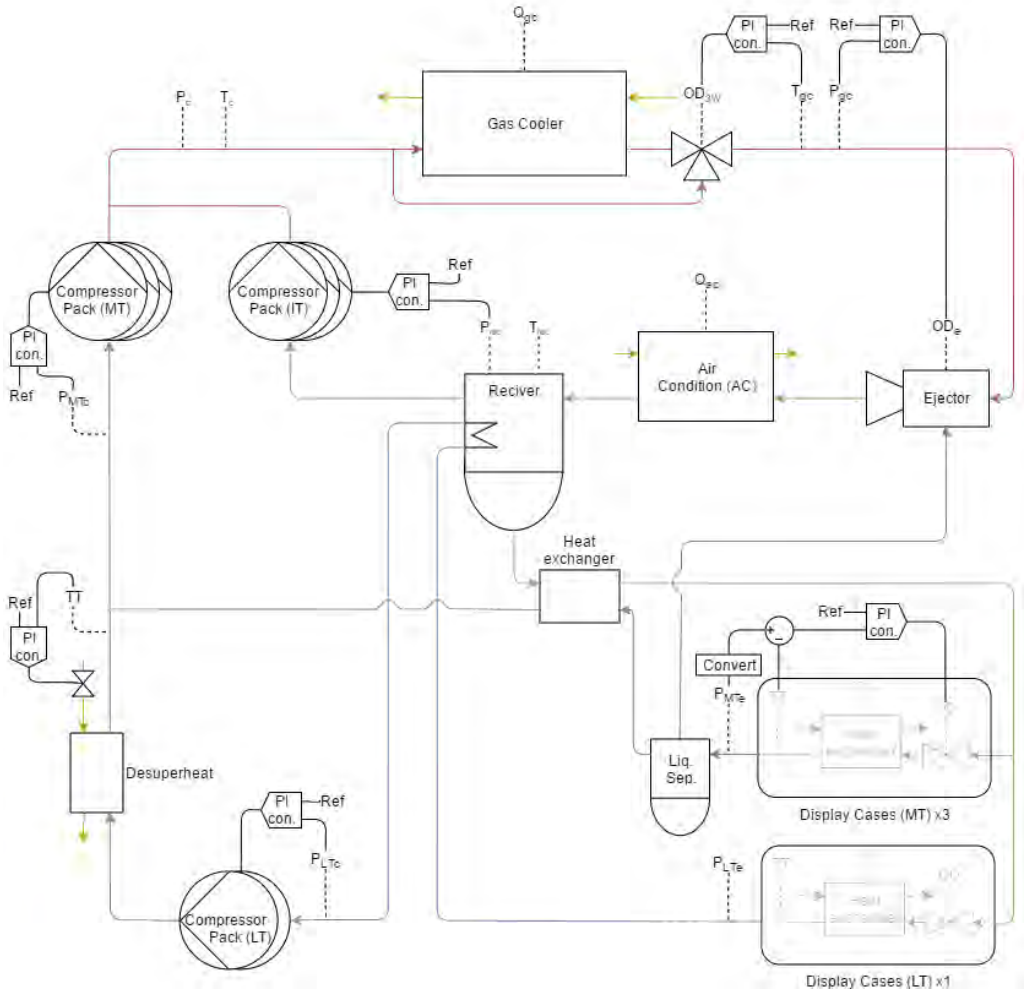

Figure 1: Schematic of the R744 refrigeration system in parallel configuration, with measured sensor and actuator indication

The selected system configuration is a booster supported by parallel compression and gas ejectors, liquid ejectors. The unit produces AC (air conditioning), cooling at MT (medium temperature) in three evaporators and freezing at LT (low temperature) in one evaporator. The maximum loads for AC, LT and MT are 45 kW, 20 kW and 60 kW, respectively. A simplified schematic of this configuration with relevant controllers, sensors and actuators is shown in Figure 1, where T, P, OD and Q represent temperature, pressure, opening degree and load measurements, respectively. It should be mentioned that the system has secondary loops to regulate the load and

outlet temperature (on the secondary side) of LT, MT, AC and de-superheater, thereby emulating consumer demand. The coolant on this loop is a mixture of glycol and water. This secondary loop also absorbs heat from the CO_2 at the GC (gas cooler).
The controlled variables on the R744 side of the refrigeration system are itemized in the following:

- Pressures before the LT and MT compressor packs are controlled according to desired temperature in the evaporators.
- Temperature and pressure downstream of the three-way valve and GC are controlled in order to reach a desired cooling point.
- The IT (intermediate temperature) or parallel compressor(s) are controlling the pressure in the receiver in order to reach a desired temperature for the air conditioning and reduce fluctuations in the flow to MT and LT evaporators.
- Superheat at the outlet of the LT and MT evaporator(s) is controlled to avoid liquid in the compressor packs.
- Temperature at the outlet of the desuperheater is controlled to reduce fluctuations in the suction temperature of the MT compressor pack.

Normally, the controller units for the LT and MT evaporators are distributed to the individual evaporator, as a result of the physical setup in e.g. a supermarket. The remaining controllers are running on the same (central) controller unit. Low bandwidth communication is available between the distributed controller units and the central controller unit. Data-driven modelling is very dependent on the available measurements (inputs and disturbances). Hence, control variables in focus in this paper are the receiver pressure and the GC temperature and pressure. The configurations, individual controller references, load of evaporators, etc. can be managed using a local PC, from where experimental data also can be extracted.

3. DATA-DRIVEN MODELING

For data-driven modelling, subspace identification method is utilized due to the robust numerical algorithms and it does not suffer from the risk of getting stuck in a local minimum (Katayama, 2005). Subspace identification aims to describe the system dynamics in a linear state space form by utilizing the given I/O (input/output) data. Consider the discrete-time LTI (linear time-invariant) system:

$$x_{t+1} = Ax_t + Bu_t + Ke_t, \qquad y_t = Cx_t + Du_t + e_t \qquad \text{Eq. (1)}$$

where $\mathrm{x} \in \mathbb{R}^{\mathrm{n}}$ are states, $\mathrm{u} \in \mathbb{R}^{\mathrm{m}}$ are inputs , $\mathrm{y} \in \mathbb{R}^{\mathrm{l}}$ are outputs, $\mathrm{e} \in \mathbb{R}^{\mathrm{l}}$ (innovation) white noise vector and $\mathrm{A} \in \mathbb{R}^{\mathrm{n}\times\mathrm{n}}$, $\mathrm{B} \in \mathbb{R}^{\mathrm{n}\times\mathrm{m}}$, $\mathrm{C} \in \mathbb{R}^{\mathrm{l}\times\mathrm{n}}$, $\mathrm{D} \in \mathbb{R}^{\mathrm{l}\times\mathrm{m}}$, $\mathrm{K} \in \mathbb{R}^{\mathrm{n}\times\mathrm{l}}$ are constant matrices. The subspace identification problem is now to identify the constant matrices and the order of the system (n) given the I/O data. To solve the problem a few assumptions are required; the number (N) of measurements is sufficiently large, u is persistently exciting. Furthermore, u and e are uncorrelated (open-loop conditions). It should be mentioned that there exist several subspace identification algorithms. The difference between the algorithms is how the algorithms are implemented and how the various parameters are selected. The following theory for subspace identification is based on the previous works, see (Katayama, 2005; Ljung, 1999).

3.1. Step one

The first step in subspace identification is to build block Hankel matrices which originates from the extended system. The extended system is obtained by recursive substitution of Eq. (1):

$$Y_p = \Gamma X_p + H^d U_p + H^s E_p, \qquad Y_f = \Gamma X_f + H^d U_f + H^s E_f \qquad \text{Eq. (2)}$$

where $\mathrm{H}^{\mathrm{d}} \in \mathbb{R}^{\mathrm{im}\times\mathrm{im}}$, $\mathrm{H}^{\mathrm{s}} \in \mathbb{R}^{\mathrm{im}\times\mathrm{il}}$ are lower triangular Toeplitz matrices with the superscripts (d, s) denoting deterministic and stochastic. Γ is the extended observability matrix. $\mathrm{E_f} \in \mathbb{R}^{\mathrm{il}\times\mathrm{N}}, \mathrm{E_p} \in \mathbb{R}^{\mathrm{il}\times\mathrm{N}}, \mathrm{U_p} \in \mathbb{R}^{\mathrm{im}\times\mathrm{N}}, \mathrm{U_f} \in \mathbb{R}^{\mathrm{im}\times\mathrm{N}}, \mathrm{Y_p} \in \mathbb{R}^{\mathrm{il}\times\mathrm{N}}, \mathrm{Y_f} \in \mathbb{R}^{\mathrm{il}\times\mathrm{N}}$ are block Hankel matrices, where the subscripts p, f denote "past" and "future" respectively. $\mathrm{X_p} \in \mathbb{R}^{\mathrm{n}\times\mathrm{N}}$ and $\mathrm{X_f} \in \mathbb{R}^{\mathrm{n}\times\mathrm{N}}$ are the extended past and future state sequences. Eq. (2) can be reformulated as:

$$Y = \Gamma X + H^d U + H^s E \qquad \text{Eq. (3)}$$

where the block Hankel matrices $\mathrm{Y}, \mathrm{U}, \mathrm{E}$ are built in a similar manner and have the structure as shown below for Y:

$$\mathrm{Y} = \begin{bmatrix} \mathrm{Y_p} \\ \\ \mathrm{Y_f} \end{bmatrix} = \begin{bmatrix} \mathrm{y_0} & \mathrm{y_1} & \cdots & \mathrm{y_{N-1}} \\ \mathrm{y_1} & \mathrm{y_2} & \cdots & \mathrm{y_N} \\ \vdots & \vdots & \ddots & \vdots \\ \mathrm{y_{i-1}} & \mathrm{y_i} & \cdots & \mathrm{y_{i+N-2}} \\ \\ \mathrm{y_i} & \mathrm{y_{i+1}} & \cdots & \mathrm{y_{i+N-1}} \\ \mathrm{y_{i+1}} & \mathrm{y_{i+2}} & \cdots & \mathrm{y_{i+N}} \\ \vdots & \vdots & \ddots & \vdots \\ \mathrm{y_{2i-1}} & \mathrm{y_{2i}} & \cdots & \mathrm{y_{2i+N-2}} \end{bmatrix}$$

with $\mathrm{i} > \mathrm{n}$ and N sufficiently large. It should be mentioned that the number of row blocks in the past and future Hankel matrices are for simplicity selected to have the same number of block rows although they could be selected different from one another, e.g. the past and future in block Hankel matrices could be selected as $\mathrm{Y_p} \in \mathbb{R}^{\mathrm{il} \times \mathrm{N}}, \mathrm{Y_f} \in \mathbb{R}^{\mathrm{hl} \times \mathrm{N}}$, where past is i block rows and future is h block rows. The extended state sequence X has the form $\mathrm{X} = [\mathrm{X_p} \quad \mathrm{X_f}]^T$.

3.2. Step two

The second step is to identify the extended observability matrix (Γ) based on Eq. (3) and then derive A and C from Γ. Thus, the U-term is removed by utilizing orthogonal projection and E-term is removed "correlated" away with another matrix (Ljung, 1999).The matrix utilized for removing the E-term is often selected to consist of the past inputs ($\mathrm{U_p}$) and outputs ($\mathrm{Y_p}$). Thus, Eq. (3) becomes:

$$\psi = \frac{1}{N} Y \Pi_{U^T}^{\perp} W_p^T \approx \Gamma X \qquad \text{Eq. (4)}$$

where $\Pi_{\mathrm{U^T}}^{\perp} = \mathrm{I} - \mathrm{U^T}\left(\mathrm{UU^T}\right)^{-1}\mathrm{U}$ and $\mathrm{W_p} = \left[\mathrm{U_p}\ \mathrm{Y_p}\right]^{\mathrm{T}}$. The extended observability matrix can be found by utilizing the left orthonormal vectors in the singular value decomposition (SVD) of Eq. (4) with some weights ($\mathrm{W_1}, \mathrm{W_2}$) pre- and post-multiplied. The SVD is:

$$W_1 \psi W_2 = [U_1 \quad U_2] \begin{bmatrix} \Sigma_1 & 0 \\ 0 & \Sigma_2 \end{bmatrix} \begin{bmatrix} V_1 \\ V_2 \end{bmatrix} \approx [U_1 \quad U_2] \begin{bmatrix} \Sigma_1 & 0 \\ 0 & 0 \end{bmatrix} \begin{bmatrix} V_1 \\ V_2 \end{bmatrix}$$

where $\Sigma_1 \in \mathbb{R}^{\mathrm{n} \times \mathrm{n}}$. Note that the order of the system can be estimated by inspecting Σ for the most significant singular values i.e. Σ_1. The weights ($\mathrm{W_1}, \mathrm{W_2}$) highly affect the result of the system identification (Ljung, 1999). The extended observability matrix is found as $\Gamma = \mathrm{W_1^{-1}U_1T}$, where T is an arbitrary matrix, which is often selected to be Σ_1, Σ_1^{-1} or I (the identity matrix). Finally, A and C can be found by solving the latter equations in a least squares sense (note $\mathrm{Matlab}^{®}$ notation for the indexes is used):

$$C = \Gamma(1\!:\!l, 1\!:\!n), \quad \Gamma(1\!:\!(i-1)l, 1\!:\!n)A = \Gamma(l+1\!:\!il, 1\!:\!n) \qquad \text{Eq. (5)}$$

3.3. Step three

With A and C estimated in Eq. (5), the remaining deterministic parts (B, D) can be estimated by solving the linear regression:

$$\arg\min_{B,D} \frac{1}{N} \sum_{t=1}^{N} \| y_t - C(zI - A)^{-1} B u_t - D u_t \|^2 \qquad \text{Eq. (6)}$$

Eq. (6) is often an overdetermined problem. Additionally, initial conditions could be included and estimated in Eq. (6). For estimation of the stochastic part in Eq. (1) as well as the covariance matrix for the innovation white noise (e_t) see (Ljung, 1999).
Refrigeration systems are open-loop unstable. Thus, the I/O data have to be collected when the loop is closed which is inconsistent with the assumption mentioned concerning the noise being uncorrelated with the input. Hence in this paper a direct approach is applied, meaning that the feedback is ignored. (Katayama, 2005)

4. SELECTION OF INPUTS

The purpose of this section is to give a brief overview of the dynamics of the gas cooler and the receiver along with formulation of the dynamic equations such that relevant measurements can be selected as inputs for the data-driven model of the controlled variables behavior (outputs). The aim is to obtain an accurate data-driven model with the least inputs. However, in general adding more relevant inputs increase in accuracy while adding more outputs decrease the accuracy of the data-driven model (Ljung, 1999). The data-driven model is derived as a MIMO system. Throughout this section the assumptions stated in (Lucas, Koehler, Schroeder, & Tischendorf, 2012) are applied.

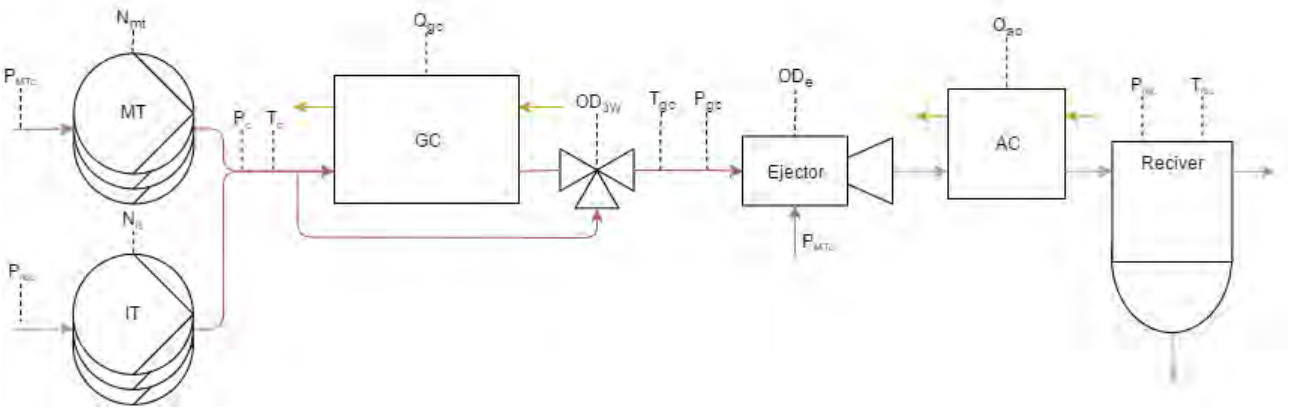

Figure 2: Schematic of the gas cooler and nearest measurements

4.1. Gas cooler

The simple energy balance for the gas cooler is based on observing the energy flow entering and the energy flow leaving the point where the temperature (T_{gc}) and pressure (P_{gc}) are measured. Then the terms in the energy balance is formulate such it can be described with the available measurements. A schematic of the gas cooler and nearest measurements is shown in Figure 2.
The (simple) energy balance is:

$$\frac{d\,M_{gc}h_{gc}}{dt} = \dot{m}_c h_c - OD_{3W}\dot{Q}_{gc} - \dot{m}_{gc}h_{gc} \qquad \text{Eq. (7)}$$

where $OD_{3W} \in [0,1]$ denotes the position of the three-way valve on the outlet of the gas cooler. The mass flow rate through the compressors ($\dot{m}_c$) can be estimated by utilizing the compressor speeds (N_{mt}, N_{it}) as (Zheng, Deng, He, & Jiang, 2015):

$$\dot{m}_c = \sum_{k=1}^{j_{mt}} \rho_{mt}\eta_{mt,k}V_{mt,k}\frac{N_{mt,k}}{60} + \sum_{k=1}^{j_{it}} \rho_{it}\eta_{it,k}V_{it,k}\frac{N_{it,k}}{60}$$

where j_{mt}, j_{it} is the number of MT and IT compressors respectively and ρ, η, V are density at the inlet of the compressor, compressor efficiency, compressor displacement volume and are assumed to be constant since the pressure before each compressor unit is controlled. The energy flow leaving the gas cooler point (i.e. $\dot{m}_{gc}h_{gc}$) is described using the energy flow entering the receiver (

$\dot{m}_{ej}h_r = \dot{m}_{gc}h_{gc} + \dot{m}_{mt}h_{mt} + \dot{Q}_{ac}$). The primary mass flow rate through the ejector ($\dot{m}_{gc}$), can be estimated with the total energy equation (Lucas et al., 2012):

$$\dot{m}_{ej} = \dot{m}_{gc} + \dot{m}_{mt} \Leftrightarrow \dot{m}_{ej} = \rho_{gc}A_{gc}\sqrt{2(h_{gc} - h_r)} + \rho_{mt}A_s\sqrt{2(h_r - h_{mt})}$$

where A_{gc} is determined by the ejector's opening degree (OD_{ej}). The specific enthalpy at the gas cooler (h_{gc}), after the compressor (h_c) and in the receiver (h_r) can be described using the temperature and pressure measurements at the respective points. The enthalpy at the secondary inlet of the ejector (h_{mt}) is calculated utilizing the pressure and assuming saturated gas, since the superheat is controlled (temperature ≈ constant) the assumption is reasonable. With the above information and through a linearization (not shown due to its size) the temperature (T_{gc}) and pressure (P_{gc}) at the gas cooler can be estimated as a function of several variables as shown below:

$$\begin{bmatrix} T_{gc} \\ P_{gc} \end{bmatrix} = f\left(N_{mt}, N_{it}, T_c, P_c, OD_{3W}, \dot{Q}_{gc}, T_r, P_r, P_{mt}, \dot{Q}_{ac}, OD_{ej}\right) + \bar{C}_{gc} \qquad \text{Eq. (8)}$$

where $\bar{C}$ is a constant and N_{mt}, N_{it} are vectors containing the individual compressor speed. Note that the dynamics are removed from the linearization as they are determined through the parameter n in the system identification.

4.2. Receiver

The selection of inputs to model the receiver pressure is based on the same procedure as of the gas cooler. The energy balance is described by:

$$\frac{d\,M_r h_r}{dt} = \dot{m}_{ej}h_r - \dot{m}_{it}h_r - \dot{m}_{evap}h_r$$

where the energy flow to the evaporators ($\dot{m}_{evap}h_r$) is assumed negligible as required measurements are not guaranteed to be available on commarginal refrigeration systems. The energy flow to the IT compressors can then be estimated with $\dot{m}_{it}h_r = \dot{m}_c h_c - \dot{m}_{mt}h_{mt}$. The receiver pressure can then be estimated as:

$$P_r = f\left(N_{mt}, N_{it}, T_c, P_c, T_r, P_{mt}, \dot{Q}_{ac}, OD_{ej}, T_{gc}, P_{gc}\right) + \bar{C}_r \qquad \text{Eq. (9)}$$

The three outputs in the MIMO system are thus estimated by utilizing subspace identification with the inputs and outputs described in Eq. (8) and Eq. (9).

5. EXPERIMENTAL VERIFICATION OF THE DATA-DRIVEN MODEL

The experimental data are derived from the test setup located at NTNU, Trondheim with the configurations mentioned in section 2 (Figure 1). The data are obtained with controllers active, where the references for the controllers are selected as shown in Table 1.

Table 1: The reference values for the controllers in R744 refrigeration systems

$R_{P_{gc}}$	$R_{T_{gc}}$	R_{P_r}	$R_{P_{mt}}$	$R_{P_{lt}}$	$R_{SH_{lt}}$, $R_{SH_{mt}}$
67 bar	23 C	41 bar	28 bar	14.5 bar	8 K

The gas cooler pressure reference is also adjusted by a secondary controller (not shown) for energy efficiency reasons. The load for the system is varied as shown in Figure 3. The algorithm described in section 3 is implemented in Matlab®'s system Identification toolbox, where (through turning) a third order model and MOESP weights are used. The first 400 minues of the data are utilized for training a MIMO model. The resulting output of the identified model is shown in Figure 4. The measured and the model output in the two plots of the pressure can be hard to distinguish from each other even when the system changes to transcritical operation point. Furthermore, the deviation in temperature becomes visible during the transient periods. A zoom-in on the three plots

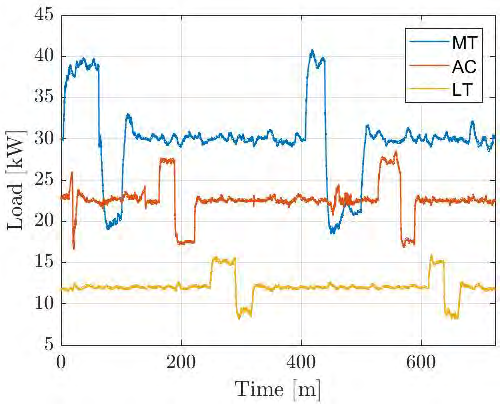

Figure 3: Shows the variation in load for MT, AC and LT with a blue, red and yellow line, respectively

is shown in Figure 5, where the fit of the two pressures and the (wourst case deviation in) temperature are illustrated. The temperature also shows a small off-set when the system changes to a transcritical operation points. The reason for the good fit of the gas cooler pressure is due to

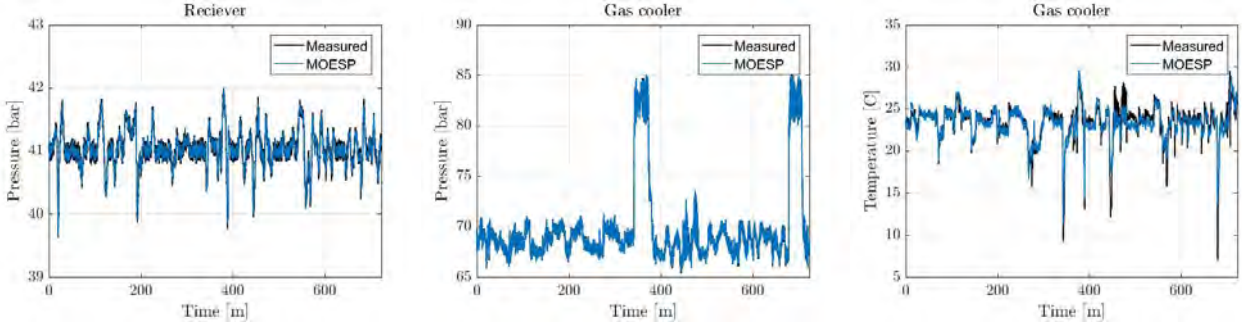

Figure 4: Validation of model outputs with the experimental data. The blue line in the three plots are the outputs from the identified third order MIMO model and the black line are the measurements for the experimental data. Left plot shows the pressure in the receiver (P_r), the middle plot shows the gas cooler pressure (P_{gc}) and the right plot shows the gas cooler temperature (T_{gc})

the strong correlation of the pressure at the discharge of the IT and MT compressors which is an input to the data-driven model. The good fit for receiver pressure is caursed by the temperature measurement in receiver, as the state of the refrigerant in the receiver is in the mixed phase. Hence the temperature and pressure in the reciever are directly correlated with one another. The gas cooler temperature does not yield as good a fit as it is not directly correlated with the available measurements and is additionally subject to the non-linearties of the refrigerant, ejector, densities, etc. Despite these challenges, the temperature fit is satisfactory even when the system changes to a transcritical operation point.

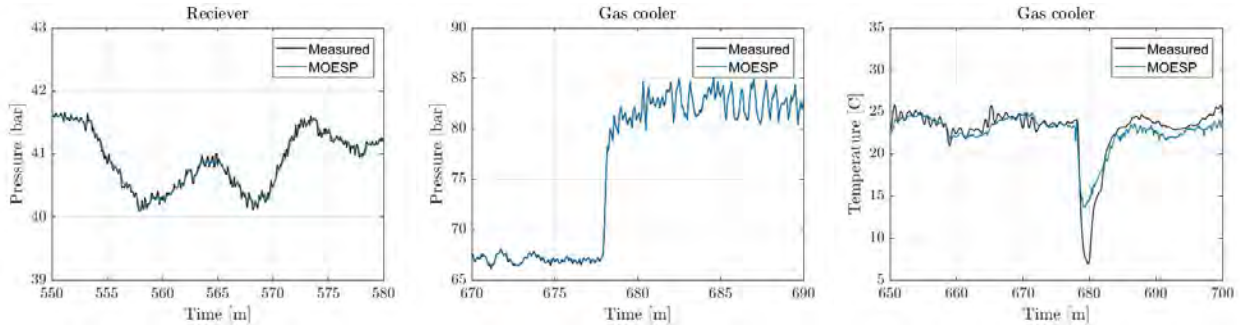

Figure 5: Zoom-in of Figure 4, where the fit of the pressures and the temperature is apparent

6. CONCLUSIONS

In this paper a third order data-driven MIMO model based on subspace identification is obtained where the selection of the inputs is conducted through utilization of the energy balance. The purpose of the data-driven model is to capture the dynamics of the control variables, i.e. temperature and pressure after the gas cooler and the pressure in the receiver. The resulting data-driven MIMO model shows a good fit for the two pressures even when exposed to substantial disturbances, which are caused by (among others) change in the operating conditions; from subcritical to transcritical. The precision of the data-driven model is achieved by exploiting the correlation between the inputs and outputs. The GC temperature is subject to many non-linearities, but still yields a satisfactory fit. This paper shows the application of data-driven modelling on an industrial refrigeration system and provides a sufficient estimation for essential control variables by utilizing the available measurements. The application of such a model is control-oriented problems as fault diagnosis, fault tolerant control and system optimization in regard to energy as well as controller performance.

ACKNOWLEDGEMENTS

This works is conducted with the support of the Innovationsfonden, 7038-00100B, Denmark.

NOMENCLATURE

M	mass (kg)	SUBSCRIPTS	
V	volume (m^3)	gc	gas cooler
P	pressure (kPa)	c	compressor
T	temperature (K)	3W	three-way valve
h	specific enthalpy (j×kg^{-1})	mt	medium temperature
ρ	density (kg×m^{-3})	it	intermediate temperature
η	Volumetric efficiency (-)	ac	air condition
$\dot{m}$	mass flow rate (kg×s^{-1})	r	receiver
ω	rotational speed (rad×min^{-1})	evap	evaporator
$\dot{Q}$	energy transfer (j×s^{-1})	ej	ejector
		SH	superheat

REFERENCES

Ding, S. X. (2014). *Data-driven Design of Fault Diagnosis and Fault-tolerant Control Systems*. (M. A. Grimble, Michael J.; Johnson, Ed.) (2014th ed.). Springer.

Katayama, T. (2005). *Subspace Methods for System Identification*. Springer.

Ljung, L. (1999). *System Identification: Theory for the User* (Second). Prentice-Hall.

Lucas, C., Koehler, J., Schroeder, A., & Tischendorf, C. (2012). Experimentally validated CO2 ejector operation characteristic used in a numerical investigation of ejector cycle. *International Journal of Refrigeration*, *36*(3), 881–891.

Pardiñas, Á. Á., Hafner, A., & Banasiak, K. (2018). Integrated R744 Ejector Supported Parallel Compression Racks for Supermarkets. Experimental Results. *IIR*.

Paride Gullo, Konstantinos M. Tsamos, Armin Hafner, Krzysztof Banasiak, Yunting T. Ge, & Savvas A. Tassou. (2018). Crossing CO2 equator with the aid of multi-ejector concept: A comprehensive energy and environmental comparative study. *Energy*, *164*, 236–263.

Shafiei, S. E. (2015). *Control Methods for Energy Management of Refrigeration Systems*. Aalborg University.

Vinther, K. (2014). *Data-Driven Control of Refrigeration Systems*. Aalborg University.

Zheng, L., Deng, J., He, Y., & Jiang, P. (2015). Dynamic model of a transcritical CO2 ejector

expansion refrigeration system. *International Journal of Refrigeration*, *60*, 247–260.

Manuscript ID: 947
DOI: 10.18462/iir.icr.2019.0947

Comparing energy consumption and life cycle cost of industrial size refrigeration systems

Thomas LUND[(a)], Morten Juel SKOVRUP[(a)], Mads HOLST[(a)]

[(a)] Danfoss A/S
6000 Kolding, Denmark

ABSTRACT

In this paper we present a comparison of the energy consumption of common industrial size systems, including the appropriate variations in system design, ambient conditions and life cycle costs.
The systems selected for comparison is:

1. Transcritical R744, DX
2. Transcritical R744, pumped
3. Two-stage R717, pumped
4. R744/R717 cascade, pumped
5. Two-stage R507, pumped

All systems have been investigated in 4 different sizes, in both a 'standard' and an optimized execution. Optimizations include parallel compression, hybrid coolers, ejectors and economizers where applicable. Calculations are performed for various climate conditions, ranging from cold to hot climates.
As the comparison results are depending on the inputs to the simulation software, the paper provides an overview of the impact of the choices made in the simulation software on the overall results. Finally, a total cost of ownership calculation, based on the supplier installation prices and the calculated power consumption, has been performed.
Keywords: Refrigeration, Carbon Dioxide, Ammonia, COP, Energy Efficiency.

1. INTRODUCTION

Much has been stated with regards to the differences between the types of refrigeration systems available today. The intention of this paper is to provide some key figures for this discussion, based on calculations of selected systems. While it is important to compare operating data from actual systems in operation, these data can easily be corrupted by several reasons that can make the conclusion less transparent or even faulty. The factors that might corrupt the comparison can be differences in operation, split between LT and MT loads, ambient conditions and not least how the system has been designed, constructed and maintained. The present paper aims to use as much factual data as possible, including real compressor efficiencies, real ambient data, complex condenser/gas cooler models and control strategies in simulation software (Pack Calculation Pro ver 4.20, by IPU) to compare system types in the same situations and under the same restrictions, while being fair to all types with regards to benefits and penalties of these.
Since the authors do not work for a contractor we were dependent on those to get information on installation prices and operating costs. Unfortunately, these data did not materialize and thus the economic comparison is reduced some generalized considerations.

2. CALCULATION PARAMETERS

Without a doubt the choices made with regards to calculation parameters can be discussed, but every effort was made to select 'fair' values. In any case, the values will be stated here with the reasoning and in some cases, calculations will be made to investigate the impact of changes.
5 different types of systems will be investigated:

- Transcritical R744, DX operation (R744 TC DX in tables)
- Transcritical R744, flooded operation (R744 TC FL in tables)

- Two-stage R717, flooded operation (R717 2ST in tables)
- R744/R717 cascade, flooded operation (R744/R717 in tables)
- Two-stage R507, flooded operation (R507 2ST in tables)

All systems are calculated in both a 'standard' configuration and an 'optimized' configuration. For the transcritical systems, a 'standard' system is a simple booster unit as this was the system quoted by the supplier, while the optimized systems involve hybrid (adiabatic) gas coolers, parallel compression (DX only) and gas ejectors. The remaining systems differ from standard to optimized only in the use of economizers and a reduced temperature difference in the cascade cooler. Some might think that 'optimizing' would entail smaller temperature differences in air coolers and condensers/gas coolers. However, as this optimization can be done equally for all system types with a minimal change in the relative result, it has been decided not to do this but rather size heat exchangers by using consistent rules.
Compressors for the transcritical systems were selected by a supplier, while the compressors for the remaining systems were selected by the authors. The R744 compressor performance correlations were supplied with the simulation software, although it originated from a supplier's software. The compressor performance data for the R717, R507 and R744 compressors in the cascade were extracted from supplier calculation programs and inserted into the simulation software.
Ambient conditions for the calculation have been chosen to represent a spread from relatively cold regions to relatively warm regions. The locations have been chosen to be Oslo, Norway, Frankfurt, Germany and Rome, Italy.

Table 1. Mean ambient temperatures for chosen locations

	Dry bulb temperature			Wet bulb temperature		
	Min	Max	average	Min	Max	Average
Rome	- 4.0°C	31.8°C	15.8°C	- 6.0°C	25.8°C	13.4°C
Frankfurt	- 8.9°C	33.6°C	10.1°C	- 9.3°C	22.4°C	7.7°C
Oslo	- 17.0°C	28.2°C	6.7°C	- 17.2°C	20.5°C	4.4°C

The common basis of all systems is that the duty to be delivered is the same. The duty has been split into a low temperature (LT) and a medium temperature (MT) load, defined as cooling loads to be delivered to air temperatures of -2°C and -25°C respectively. The MT cooling load is 3 times the LT cooling load in the bulk of the calculations, however the calculations of the reverse split, e.g. LT cooling load = 3 MT cooling loads, has been performed on a few of the cases to provide information on the significance of the LT/MT split. Although the simulation software enables variable cooling load simulations, the cooling load has generally been set to constant from the viewpoint that any functionality dependent on time and/or ambient temperatures will clutter the inherent behaviour of the refrigeration systems. Generally, two different mechanisms would be used to generate a variable load profile – ambient temperature changes and production cycles. Most production cycles would entail full production during the day and a reduced activity during the night. Thus, for both the ambient temperature driven and the production cycle driven load profile, the capacity is reduced during the colder part of the day/year. Keeping the capacity constant will have the refrigeration systems running relatively more during the colder periods which favours the transcritical R744 systems since the efficiency loss at high temperature is higher with the transcritical systems than the other systems.
Initially the system types are calculated in 4 different sizes, with LT/MT cooling loads at 50/150kW, 150/450kW, 300/900kW and 900/2700kW.
With the room air temperatures fixed at -2°C and -25°C for MT and LT respectively, the evaporating temperatures has been determined from the following assumptions:
- Flooded evaporator temperature difference to air inlet: 8K
- DX evaporator temperature difference to air inlet: 10K with 7K superheat
- Suction line pressure loss for R717 and R507: 1K
- Suction line pressure loss for R744: 0K

It can be noted that DX evaporators have a larger temperature difference to air inlet than flooded evaporator. This is due to the need to create superheat. The superheat has been set to 7K which, after discussions with the industry, has been decided is a good value for the lowest safe superheat. The additional 2K temperature difference is a rather moderate penalty for running DX.
Condensers/gas coolers were sized according to the following rules:

- Evaporative condensers: Temperature difference to wet bulb temperature is 7K at maximum design capacity and at maximum wet bulb temperature in the actual location.
- Dry gas coolers: In transcritical operation 2K temperature outlet temperature difference to dry bulb. In subcritical operation a temperature difference of 5K to dry bulb is used for condensing at 25°C.
- Hybrid gas coolers: Same temperature differences as for dry gas coolers, but a 75% adiabatic temperature efficiency is used.
- Cascade coolers are calculated with a temperature difference of 5K, while for the optimized systems this has been reduced to 3K.

The gas coolers have been designed with a relatively low temperature difference in subcritical operation since they are running at less than maximum load.
The compressors selected are commercially available types from major manufacturers. As mentioned, some were already included in the simulation software, while others were defined by the authors through output from the manufacturer's software.

Table 2. Selected compressor types

Load	R744 TC DX	R744 TC FL	R717 2ST	R744/R717	R507 2ST
50/150	Recip/Recip	Recip/Recip	Recip/Recip	Recip/Recip	Recip/Recip
150/450	Recip/Recip	Recip/Recip	Recip/Recip	Recip/Recip	Recip/Screw
300/900	Recip/Recip	Recip/Recip	Screw/Screw	Recip/Screw	Screw/Screw
900/2700	Recip/Recip	Recip/Recip	Screw/Screw	Recip/Screw	Screw/Screw

Finally, heat recovery has been excluded from the calculations. The simulation program focuses on controlling the system to deliver the desired cooling capacity and incorporating the heat recovery would result in situations where the refrigeration cycle could be at a less than optimal situation to allow for heat recovery for an overall better economy. However, as the constraints on the heat recovery systems, with respect to temperatures and required capacity, vary significantly from one host to another, then it would introduce a baffling number of variation that the authors felt would rather clutter the result than provide clarity.

3. STANDARD SYSTEM CALCULATIONS

Initial calculations were on all systems sizes, all types in all locations naturally resulting in a bewildering amount of numbers. The central figure is the amount of power used throughout a year, in MWh, stated here because it is the core result (table 3) along with the associated COP's (table 4)
First look at these COP reveal a few trends. For the transcritical systems the COP is basically constant across the sizes, if the 50/150kW size is ignored. The authors believe this is an unfortunate compressor type selection made by the supplier and thus regards the 3 larger sizes to be representative. For the remaining systems there is a slight increasing trend in COP with system size, although not a large increase. Because of this it is decided to focus only on the 300/900kW system in the subsequent calculations both to reduce the workload and increase the clarity.
Another observation is that in all situations, the 2 stage R717 system offers the best COP, but a few comments needs to be made to that result. The LT room temperature of -25°C results in evaporating temperatures of -33°C in the R744/R717 cascade system. This is only on the fringe of where a cascade system starts to become sensible compared to a two-stage R717 system. As the evaporating temperature drops, for instance with more heavy-duty freezing applications, the cascade eventually gains the lead in efficiency.
The R507 system is included mostly for reference, but it is not far off the two stage R717 and cascade system in efficiency, although always slightly behind.
However, as the main focus is energy efficiency it makes more sense to look at a year average COP, using the total delivered cooling effect from the individual system sizes:

Table 3. Yearly power consumption

-	Load (LT/MT in kW)	R744 TC DX (MWh)	R744 TC FL (MWh)	R717 2ST (MWh)	R744/R717 (MWh)	R507 2ST (MWh)
Rome	50/150	781	705	500	535	518
	150/450	2079	1948	1503	1650	1595
	300/900	4181	3926	2891	3150	3140
	900/2700	12608	11966	8542	9424	9400
Frankfurt	50/150	613	561	448	485	459
	150/450	1621	1494	1344	1490	1377
	300/900	3265	3046	2575	2820	2723
	900/2700	9833	9301	7597	8397	8169
Oslo	50/150	544	507	428	463	439
	150/450	1432	1313	1284	1431	1302
	300/900	2884	2674	2457	2699	2579
	900/2700	8691	8179	7243	8035	7242

Table 4. Yearly COP

COP	Load	R744 TC DX	R744 TC FL	R717 2ST	R744/R717	R507 2ST
Rome	50/150	2,24	2,49	3,50	3,28	3,38
	150/450	2,53	2,70	3,50	3,18	3,30
	300/900	2,51	2,68	3,64	3,34	3,35
	900/2700	2,50	2,64	3,69	3,35	3,35
Frankfurt	50/150	2,86	3,12	3,91	3,61	3,81
	150/450	3,24	3,52	3,91	3,53	3,82
	300/900	3,22	3,45	4,08	3,73	3,86
	900/2700	3,21	3,39	4,15	3,76	3,86
Oslo	50/150	3,22	3,46	4,09	3,78	3,99
	150/450	3,67	4,00	4,09	3,67	4,04
	300/900	3,64	3,93	4,28	3,90	4,08
	900/2700	3,63	3,86	4,35	3,92	4,35

Looking at the 300/900kW systems, in colder climates, e.g. Oslo, the transcritical systems approach the two stage R717 with the flooded version being some 9% higher in power consumption and the DX version being 17% higher. In a hot climate, e.g. Rome, the transcritical systems are 32% and 45% higher respectively. Relatively to the two stage R717 system, the power consumption is:

Table 5. Power consumption relative to two-stage R717

-	R744 TC DX	R744 TC FL	R717 2ST	R744/R717	R507 2ST
Rome	145%	132%	100%	109%	109%

Frankfurt	127%	118%	100%	110%	106%
Oslo	117%	109%	100%	110%	105%

Clearly the transcritical systems suffer with warmer climates, which is not surprising. Making the comparison with Oslo as the reference, the systems response to ambient temperature becomes apparent:

Table 6. Power consumption relative to Oslo

	R744 TC DX	R744 TC FL	R717 2ST	R744/R717	R507 2ST
Rome	145%	147%	118%	117%	122%
Frankfurt	113%	114%	105%	105%	106%
Oslo	100%	100%	100%	100%	100%

As mentioned, the load profile was constant in these calculations. To shed some light on how the load profile influence the result, a sample load profile was adopted in the simulation program. Load profiles can have a variety of forms, but in this sample the cooling load was set to vary from the capacity used above at maximum dry bulb temperature at the given location down to 35% of this at a temperature that equaled the room temperature. The variation was linear with temperature. The delivered cooling effect was constant across system types but varied with the location. Looking at the relative power consumption compared to two stage R717, which was again the most efficient, the result is:

Table 7. Power consumption relative to two-stage R717- varying load profile

-	R744 TC DX	R744 TC FL	R717 2ST	R744/R717	R507 2ST
Rome	150%	141%	100%	108%	109%
Frankfurt	135%	126%	100%	109%	106%
Oslo	126%	117%	100%	109%	105%

In general, the transcritical systems benefitted in the region of 5 to 10% from the constant load profile, although as mentioned it will depend on the actual setup of the load profile. The individual system types response to the climate, e.g. power consumption relative to Oslo data, was slightly better than with all Rome data being 4 to 5% lower than with the constant load profile.
Finally, the split between LT and MT load was examined with the original constant load profile. The recalculation of the 300/900kW system to 900/300kW gave the following power consumptions in MWh:

Table 8. Yearly power consumption - reverse LT / MT split

-	R744 TC DX	R744 TC FL	R717 2ST	R744/R717	R507 2ST
Rome	5616	5242	4182	4242	4446
Frankfurt	4610	4282	3835	3886	3989
Oslo	4193	3878	3705	3755	3831

In relative terms, again with two stage R717 as the reference, although the cascade system came close:

Table 9. Power consumption relative to two-stage R717 - reverse LT / MT split

-	R744 TC DX	R744 TC FL	R717 2ST	R744/R717	R507 2ST
Rome	134%	125%	100%	101%	106%
Frankfurt	120%	112%	100%	101%	104%
Oslo	113%	105%	100%	101%	105%

Although the transcritical system did a little better the picture is much the same. The gain for the transcritical systems is due to the LT compressors having a larger part of the total consumption and the better COP of the R744 compressors in LT operation is responsible for this shift.

4. OPTIMIZED CALCULATIONS

All calculations so far have been performed on ‘standard’ system, however several improvements can be made. Especially the transcritical systems has seen significant and innovative improvements in recent years. The changes from standard systems (only 300/900kW) are:

- Transcritical R744 DX systems: Added parallel compression, hybrid coolers and gas ejectors.
- Transcritical R744 flooded systems: Added hybrid coolers and gas ejectors.
- Two stage R717 systems: Economizers added to screw compressors.
- R744/R717 cascade systems: Economizers added to screw compressors, cascade temperature difference reduced from 5K to 3K
- Two stage R507 systems: Economizers added to screw compressors.

Parallel compression is a feature of the simulation software. Generally, the MT compressor types were used. Hybrid coolers is also a feature of the simulation software. Generally, the hybrid coolers were dimensioned as evaporative condensers, using an air temperature attained with 75% efficiency of the adiabatic process. Gas ejectors is not a feature of the simulation software. Discussions with the commercial refrigeration experts, the general rule of a 7% reduction of MT compressor power when the gas cooler outlet was above 22°C was deducted. Implementing this was done in Excel. The output of the calculation is an hour-by-hour tabulation of the operation of the system, and the data rows where the gas cooler outlet was above 22°C had the MT compressor power consumption reduced and a new yearly sum was created. Economizers are not a feature of the simulation software. The compressors in question was calculated at the actual running conditions and compared with and without open economizers. The resulting COP gain was used to reduce the compressor power. Finally, the cascade temperature difference, which is a parameter in the software, was changed. The resulting power consumption in MWh is as follows:

Table 10. Yearly power consumption. Optimized systems

-	R744 TC DX	R744 TC FL	R717 2ST	R744/R717	R507 2ST
Rome	3578	3675	2778	2915	2933
Frankfurt	2818	2772	2494	2578	2582
Oslo	2565	2482	2384	2456	2455

Again, in relative terms with two stage R717 as a reference

Table 11. Power consumption relative to two-stage R717. Optimized systems

-	R744 TC DX	R744 TC FL	R717 2ST	R744/R717	R507 2ST
Rome	129%	132%	100%	105%	106%
Frankfurt	113%	111%	100%	103%	104%
Oslo	108%	104%	100%	103%	103%

It can be observed that the transcritical systems gain more than the traditional systems, narrowing the field. Also, since the flooded R744 transcritical system is not able to run parallel compression, the DX version surpasses it in hot climates.

As a variation to this result, the transcritical systems were calculated without hybrid coolers, but all other optimization employed. This was due to two considerations: First of all, the operating costs of a hybrid cooler is much higher than a dry gas cooler, and second the lowering of condensing/gas cooler outlet temperature reduced the time where the ejector was active. Since the economic calculations fell through, the full benefit of not running with hybrid coolers is not directly apparent, but the result is presented anyway. The calculated power relative to the R717 two stage system is shown in the table and figure below:

Table 12. Power consumption relative to two-stage R717. Optimized systems - dry cooler

-	R744 TC DX	R744 TC FL	R717 2ST
Rome	132%	136%	100%
Frankfurt	120%	119%	100%
Oslo	113%	110%	100%

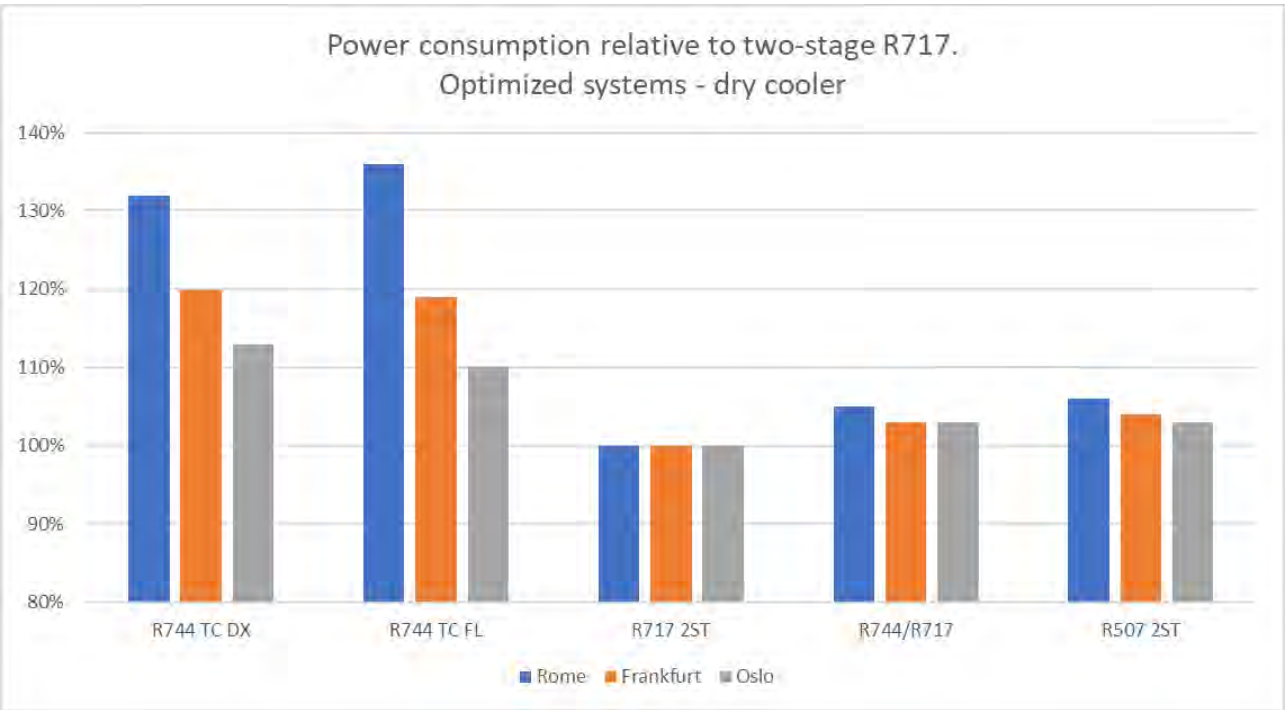

Figure 1: Power consumption relative to two-stage R717. Optimized systems - dry cooler

Clearly a little of the gains are lost, but as mentioned this might be offset by significantly lower operating cost of a dry gas cooler.

5. TOTAL COST OF OWNERSHIP

As mentioned the data regarding installation and operation of these systems failed to materialize, which is unfortunate. However, a few general comments can be made to the pricing and operating costs of these systems.

It is clear that the transcritical systems and the traditional systems come from two different 'cultures.' This is in no way meant to criticize any of these cultures nor having a bias towards any. It is entirely possible that both sides could benefit from a critical look at what is being offered by themselves and the 'other side' and compare that to what is expected by the costumers. A good example of this is a conversation we had recently with a supplier of transcritical systems. They had problems with dirt in the compressors and we inquired to suction filters where our experience base dictate they be installed with 'bags' that were removed after commissioning. The reply was that if they did that the bags would never be removed. This speaks volumes as to the extent of supervision and service that is expected to be offered to these systems.

On the other hand, many of the features offered in industrial systems could be perceived as overdoing the solution. For instance, a recent study shows that in many cases evaporative condensers are more expensive to operate and maintain than the benefit they offer through lower condensing pressure with resulting lower power consumption.

As the situation stands right now, the systems offered by the transcritical R744 segment have a much lower installation price. From this starting point, it is most likely very difficult for the traditional systems to overcome this difference within a time frame that is realistic. This is especially true in the colder climates where the R744 transcritical systems approach the R717 two stage system in efficiency, while in hotter climate the final balance is less clear without hard data on the actual costs.

However, if the above considerations regarding the different cultures are taken into account, then the installation costs would most likely approach each other, and the resulting total cost of ownership could show a completely different picture.

6. CONCLUSION

Throughout the efficiency calculations it is clear that no matter how much a transcritical R744 system is optimized, it cannot compete with a two stage R717 system, although it does come relatively close in colder climates. Generally, a transcritical R744 system has a 5 to 10% higher energy consumption in cold climates which increase to around 30% higher in (relatively) warm climates. A location significantly warmer than Rome could easily have been found, but the trend is clear.

The cascade system is generally 5% higher in energy consumption compared to the two stage R717, however it must be considered that the investigated temperature range does not favour a cascade. In systems with a lower evaporating temperature on the LT side, the cascade will eventually gain ground as the R717 efficiency drops rapidly.

The two stage R507, included mostly for comparison purposes, is generally above the two stage R717 in power consumption and in the best cases for the transcritical R744 it is basically on par.

The total cost of ownership calculation had to be abandoned due to the hoped-for data regarding the installation and operational costs of the different systems did not materialize. Thus, the conclusion on this question must be seen in the light of great uncertainties of actual prices as well as extents of the features installed. The transcritical R744 systems offered today are less expensive than the traditional systems and from that standpoint, it is estimated that, especially in colder climates, that the traditional system will have difficulties in compensating for with their higher efficiency. In hotter climates there is a substantial gap in power consumption that would most likely make the two stage R717 a viable solution.

The recent decade has seen significant improvements in the transcritical system efficiency, which is very impressive. At the same time the R717 camp has put a large focus on reduction of charge, as this is one of the areas where R717 is troubled. So, the scene is constantly changing, and it is hoped that this paper will provide some clarity on the current state of at least some aspects of this.

Manuscript ID: 963
DOI: 10.18462/iir.icr.2019.0963

Characteristics of heat transfer on a microchannel flat tube applied to air-to-refrigerant heat exchangers of air conditioners using R32

Chen ZHENG [(a)], Tomoki HIROKAWA [(b)], Ryuhei KAJI [(c)], Hirokazu FUJINO [(d)]

[(a)(b)(c)(d)] Daikin Industries, LTD, Osaka, 566-8585, Japan
[(a)] chen.zheng@daikin.co.jp
[(b)] tomoki.hirokawa@daikin.co.jp
[(c)] ryuuhei.kaji@daikin.co.jp
[(d)] hirokazu.fujino@daikin.co.jp

ABSTRACT

Recently, air-to-refrigerant micro-channel heat exchangers have been applied to air-conditioners for their high heat-transfer performance with low air-side pressure drop. Some papers have presented the experimental data on microchannel flat tube applied to such heat exchangers. Among these papers, however, uniform heat load is applied to the test tube unlike a real situation. In the real use, heat load becomes un-uniform along air flow direction as air temperature changes during heat exchange. In this paper, the effect of un-uniform heat load on heat transfer is experimentally investigated. Measurements were carried out by heating microchannel flat tube flowing R32 horizontally. Un-uniform heating is achieved by two each heating blocks with different temperature attached to the test tube from top and bottom. It is found that un-uniform heat load degrades heat transfer comparing to uniform load and it becomes clear that understanding detail phenomena are necessary to predict heat exchanger accurately.
Keywords: Air Conditioner, Heat Exchanger, Heat Transfer, Microchannel, R32.

1. INTRODUCTION

Recently, air-to-refrigerant micro-channel heat exchangers have been applied to air-conditioners for their high heat-transfer performance with low air-side pressure drop. As a refrigerant, R32 has been often used for its low Global Warming Potential (GWP) and its good cycle performance. Some papers have presented the experimental data on microchannel flat tubes applied to such heat exchangers. Li et al. (Li et al., 2012) have measured flow boiling heat transfer of HFO1234yf and R32 in a horizontal smooth round tube of 2 mm diameter and concluded that R32 refrigerant has a better performance due to its higher latent heat and thermal conductivity. Cavallini et al. (Cavallini et al., 2009) presented that R32 has lower pressure drop than R134a which agrees with the literature reported by Hossain et al. (Hossain et al., 2013). Li et al. (Li et al., 2010) proposed a new correlation with the combined non-dimensional number ($BoRe_l^{0.36}$) by considering surface tension, body force and viscosity, and they obtained good agreement with existing data. Shah (Shah, 2017) verified the correlation with wide range of data for horizontal channels.
However, in the real use as air-to-refrigerant heat exchangers, heat load becomes un-uniform along the air flow direction as air temperature changes during heat exchange. Among these papers, the effect of un-uniformity of heat load on heat transfer is not mentioned. In this paper, the effect of un-uniform heat load on heat transfer is experimentally investigated. Measurements were carried out by heating microchannel flat tube flowing R32 horizontally. Un-uniform heating is achieved by separating with four heating blocks attached to the test tube from top and bottom and setting different temperature in the width direction.

2. FACILITY AND DATA REDUCTION

2.1. Facility

2.1.1. Experiment facility

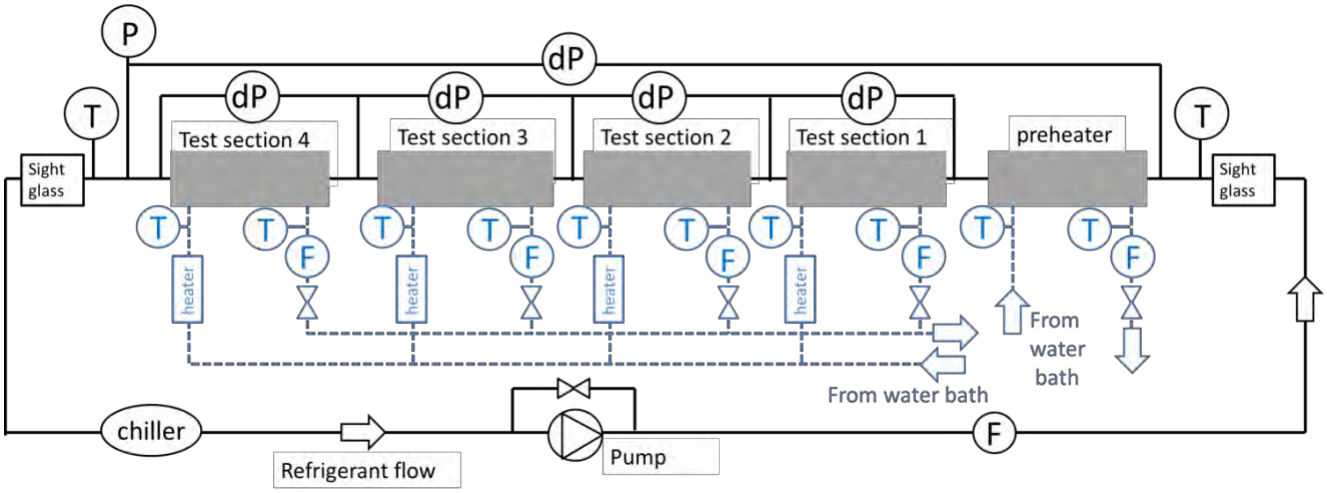

Figure 1: Schematic of the experiment facility

The experiment facility consists of a refrigerant loop (solid line) and two water loops (dotted line) as shown in Fig. 1. In the refrigerant loop, refrigerant is circulated by a pump and the flow rate is measured with a corliolis flow meter. Four test sections are horizontally set in series to investigate the local heat transfer coefficient and pressure drop simultaneously. The flow pattern is observed by two sight glasses located at inlet and outlet of test section. In order to remove uncertainty of quality distribution of two-phase flow into each channel of the flat tube at the inlet of the test section, a liquid-single phase state is set at the inlet. Then the inlet condition into the test section is adjusted by a preheater. After leaving four series of test sections, refrigerant is cooled down by a chiller and return to the pump. Heat sources to the preheater and the each test section are provided by water loops.

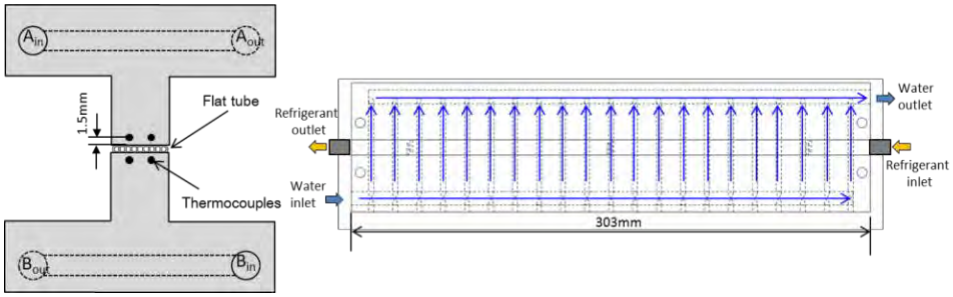

Figure 2: Uniform heat load test section

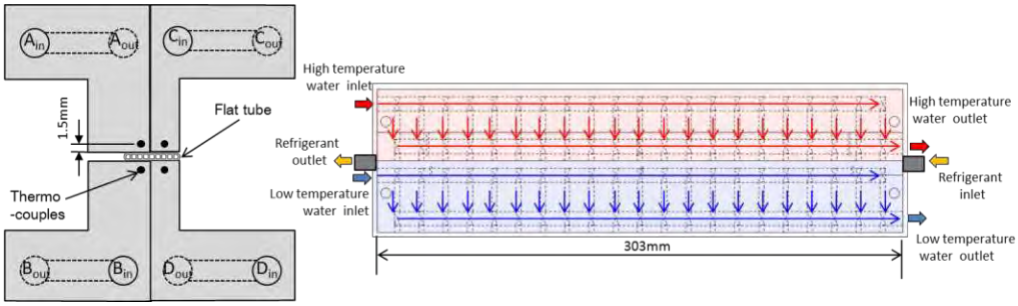

Figure 3: Un-uniform heat load test section

Fig. 2 shows details of the uniform heat load test section. Test section is designed into T shape to suppress temperature distribution in tube width direction. A flat tube, 400 mm in length, is sandwiched between two aluminium blocks of 303 mm in length. Water is provided from A_{in} and B_{in} and flows out to A_{out} and B_{out} illustrated in Fig. 2. Water flow of top and bottom side of the flat tube can be controlled to a desired condition by a heater and two control valves. Un-uniform heat load is applied to the flat tube by using a total of 4 blocks divided on the top and the bottom of the flat tube respectively as shown in Fig. 3. Each block is design into L shape. The width of higher heat load block is 17 mm and lower heat load block is 8 mm. Tube end is set by lower heat load side as shown in Fig. 3 to create gradual trend of un-uniform heat load. The ratio of high/low heat transfer surface is 4/5. Water for higher heat load is provided from A_{in} and B_{in} and outflows to A_{out} and B_{out}, while, for lower heat load is provided from C_{in} and D_{in} and flows out to C_{out} and D_{out}. Water temperature flows through higher and lower heat blocks can be controlled separately by two heaters. Water flowrate can be controlled separately by four control valves set for each block.

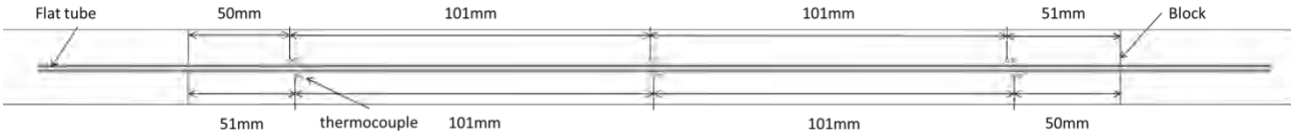

Figure 4: Locations of thermocouples

Between the block and the flat tube, in order to reduce the thermal resistance, it is in close contact with thermal grease. Heat flux is adjusted by a given inlet water temperature and water mass flow rate. The temperature difference between inlet water temperature and outlet temperature is set within 2 °C in order to keep the temperature to be as close as constant of the block near the tube in the flow direction. Twelve T-type thermocouples of 1 mm diameter, two located in width direction and three in flow direction, are inserted into blocks 1.5 mm close to the tube of each test section to measure the wall temperature. The properties of refrigerant are calculated by REFPROP Version 10.0.

2.1.2. Tube dimension

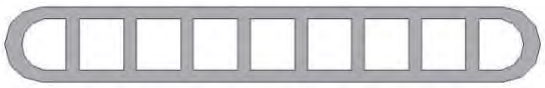

Figure 5: Tube configuration

Tube configuration is shown in Fig. 5 and the detailed dimensions are listed in Table 1. The effective heat transfer length of each test section is 303 mm.

Table 1. Tube dimension

Tube width (mm)	14.2
Tube height (mm)	2.0
Number of channels	9
Cross-sectional area (mm^2)	14.03
Hydraulic diameter (mm)	1.26
Wetted perimeter length (mm)	43.87
Tube length (mm)	400.0

2.2. Data Reduction

2.2.1. Analysis process

Local heat transfer coefficient h_{ref} is calculated from Eq. (1) ~ Eq. (3)

$$h_{ref} = \frac{q_i}{T_{wall} - Te} \quad \text{Eq. (1)}$$

$$q_i = \frac{Q_w}{A_i} \quad \text{Eq. (2)}$$

$$Q_w = \sum_i \left((T_{win,i} - T_{wout,i}) m_{w,i} Cp_{w,i} \right) \quad \text{Eq. (3)}$$

,where q_i is heat flux calculated from inner surface area in kW·m^{-2} T_{wall} is average local wall temperature and Te is saturated temperature determined by the local pressure in℃. A_i is the inner heat transfer area (the product of 9 channels' perimeters and effective heat transfer length) in m^2.Q_w is heat load in kW calculated by water side, in which T_{win} and T_{wout} are inlet and outlet water temperature in℃, m_w is water mass flow rate in kg/sec, Cp_w is water specific heat capacity in kJ·kg^{-1}K^{-1}. In this experiment, the ratio of heat capacities calculated from the water side and refrigerant side are over 98%.

T_{wall} is corrected to local wall temperature considered conductivity and contact resistance defined as follows:

$$T_{wall} = T_{ave} - q_o \left(\frac{d_1 + d_3}{\lambda_{Al}} + \frac{d_2}{\lambda_{gr}} \right) \quad \text{Eq. (4)}$$

,where T_{ave} is the average temperature of total twelve inserted thermocouples in ℃, d_1 is the distance from thermocouples to the edge in m, d_2 is the thickness of thermal grease in m, which is determined by an applicator with fixed thickness of 25 μm. d_3 is the top and bottom wall thickness of flat tube in m. λ_{AL} and λ_{gr} are thermal conductivities of aluminium and thermal grease. In this study, reported values 273 W·m^{-1}K^{-1} and 6.4 W·m^{-1}K^{-1} are used, respectively. q_o is the heat flux passing through the top and bottom surface of the flat tube.

2.2.2. Uncertainty propagation

The overall uncertainties of measuring instruments are listed in Table 2.

Table 2. Uncertainties of measuring instruments

$e(T_{win})$	0.06 ℃
$e(T_{wout})$	0.06 ℃
$e(m_w)$	0.167 kg·s^{-1}
$e(T_{wall})$	0.08 ℃

Variables for deriving relative error are expanded as Eqs. (5) ~ (9).

$$\frac{\partial h_{ref}}{\partial T_{win}} = \frac{m_w Cp_w}{A_i (T_{wall} - Te)} \quad \text{Eq. (5)}$$

$$\frac{\partial h_{ref}}{\partial T_{wout}} = -\frac{m_w Cp_w}{A_i (T_{wall} - Te)} \quad \text{Eq. (6)}$$

$$\frac{\partial h_{ref}}{\partial m_w} = \frac{(T_{win} - T_{wout}) Cp_w}{A_i (T_{wall} - Te)} \quad \text{Eq. (7)}$$

$$\frac{\partial h_{ref}}{\partial T_{wall}} = -\frac{(T_{win} - T_{wout}) m_w Cp_w}{A_i (T_{wall} - Te)^2} \quad \text{Eq. (8)}$$

$$e(h_{ref}) = \sqrt{\left(\frac{\partial h_{ref}}{\partial T_{win}}\right)^2 \left[e(T_{win})\right]^2 + \left(\frac{\partial h_{ref}}{\partial T_{wout}}\right)^2 \left[e(T_{wout})\right]^2 + \left(\frac{\partial h_{ref}}{\partial G_w}\right)^2 \left[e(m_w)\right]^2 + \left(\frac{\partial h_{ref}}{\partial T_{wall}}\right)^2 \left[e(T_{wall})\right]^2}$$

Eq. (9)

Relative error of heat transfer coefficient $er(h_{ref})$ is written as a percentage by Eq. (10).

$$er(h_{ref}) = \frac{e(h_{ref})}{h_{ref}} \times 100\%$$

Eq. (10)

In this experiment, uncertainties of heat transfer coefficient are mainly resulting from the measurement uncertainties of the wall surface temperature. Therefore, in the case of the low heat flux condition, the temperature difference between the tube wall and the refrigerant becomes small, and the relative error of the heat transfer coefficient becomes larger that is about 16.8% at the maximum.

3. RESULTS AND DISCUSSION

3.1. Evaporative Heat Transfer Coefficient

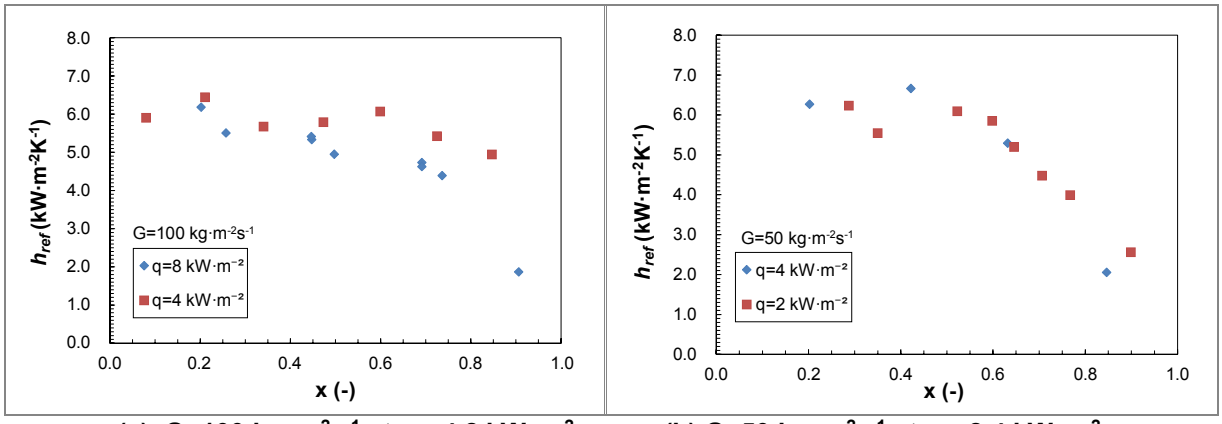

(a) G=100 kg·m^{-2}s^{-1} at q_i =4,8 kW·m^{-2} (b) G=50 kg·m^{-2}s^{-1} at q_i =2,4 kW·m^{-2}

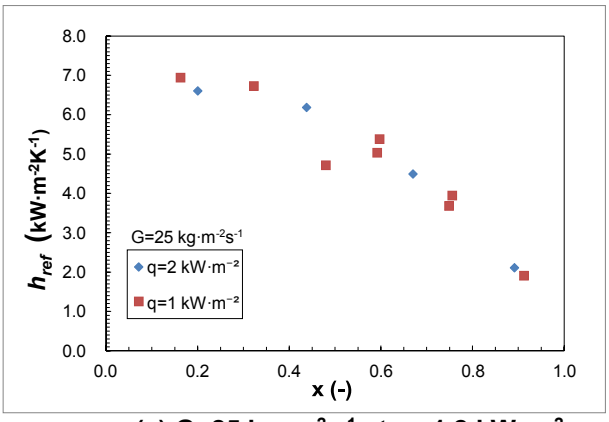

(c) G=25 kg·m^{-2}s^{-1} at q_i=1,2 kW·m^{-2}

Figure 6: Effect of heat transfer coefficient on quality at uniform heat load

Figs. 6a, 6b and 6c show experimental results of heat transfer coefficient under uniform heat load plotted against quality x while the mass flux G varies from 25 to 100 kg·m^{-2}s^{-1} and the heat flux q_i varies from 1 to 8 kW·m^{-2}. In each of Fig. 6, heat transfer coefficient is almost constant in low quality region and decreases at high quality region. The decrease in high quality region is thought to be dry out occurs. In low quality region, as the heat transfer coefficient is independent of mass flux and quality, it seems that the flow is dominated by nucleate boiling rather than forced convection boiling.

However, comparing the results of high and low heat flux, heat transfer coefficient is less sensitive and even worse in high heat flux specifically at 100 kg·m^{-2}s^{-1} in Fig. 6a. It is assumed that higher heat flux is also as a negative function in horizontal rectangular microchannel flat tube because, in such tubes, the flow tends to be slug flow and liquid film attaching to the top surface is prone to dry out, resulting in heat transfer deterioration.

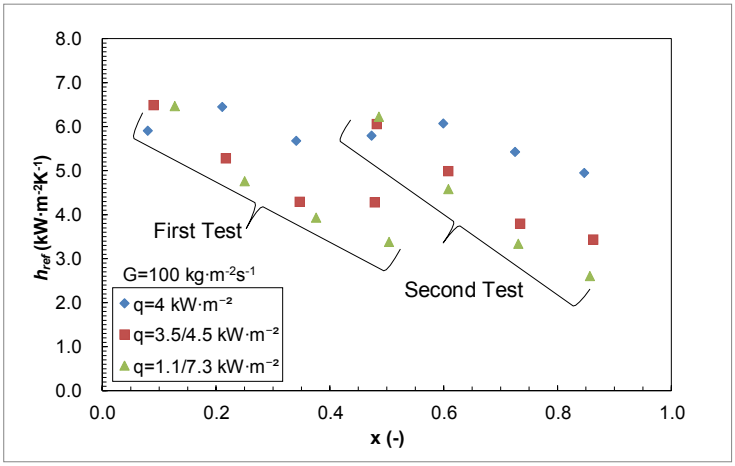

Figure 7: Heat transfer coefficient at uniform and un-uniform heat load

Fig. 7 shows experimental results of heat transfer coefficient at uniform and un-uniform head load plotted against quality x while the mass flux is at 100 kg·m^{-2}s^{-1} and the total average heat flux is 4 kW·m^{-2}. The equations used for obtaining the heat transfer coefficient is the same with those of uniform conditions, but applied to low and high heat flux individually; average 6 thermocouples for wall temperature and low/high side heat flux by separated aluminium blocks. Average of obtained data from low and high side heat flux is used here. The ratio of low/high heat flux varies from 0.15 to 0.78.

From Fig. 7, the heat transfer coefficient of uniform heat load is higher than un-uniform heat load through the whole quality. The difference is larger as increasing quality. The reason is that the quality of each channel of a flat tube for uniform heat load can be equally distributed while that for un-uniform heat load becomes uneven due to the difference of heat flux supplied each channel. Refrigerant flow in channel receiving high heat flux is encouraged to be vapour causing higher pressure drop. As this proceeds, flowrate of that channel becomes lower and that is further encouraged to be vapour causing much higher pressure drop. This flow mal-distribution results in occurring dryout in lower quality comparing to that in uniform heat load. Therefore, deterioration of heat transfer is observed.

Seeing the results of un-uniform heat load, within a series of experiment, the heat transfer coefficient decreases when the ratio of low/high heat flux increases as increasing quality. It is considered that the degree of flow mal-distribution resulting from un-uniform heat load becomes larger since the experiment is taken from low to high quality and un-uniform heat load at each measuring section promotes further mal-distribution for following test section.

There is a difference in heat transfer coefficient between the test series: the first test (quality 0.1 to 0.5) and the second test (quality 0.5 to 0.9) at the quality of 0.5. This difference occurs due to experimental procedure; the result at the first test was measured at the last of the test section, whereas one at the second test was measured at the first of the test section. Therefore the condition of refrigerant inlet to the flat tube is different. For the first test, at quality 0.5, the refrigerant has already been uneven due to the un-uniform heat load of the preceding test section, whereas the refrigerant enters equally to the test section for the second test.

3.2. Pressure Drop

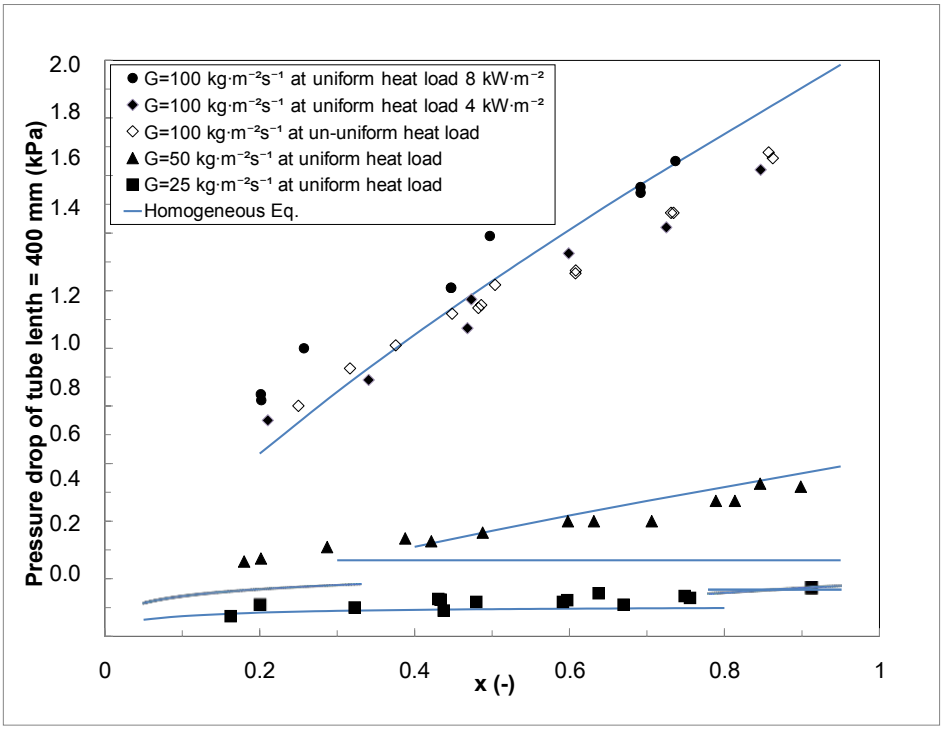

Figure 8: Effect of pressure drop on quality

Fig. 8 shows experimental results of pressure drop plotted against quality while the mass flux varies from 25 kg·m^{-2}s^{-1} to 100 kg·m^{-2}s^{-1} both at uniform and un-uniform heat load. From the Figure, at 100 kg·m^{-2}s^{-1}, there is slightly higher pressure drop for higher heat flux; however, compare to the effect by mass flux pressure drop is less sensitive to heat flux and uniformity of heat load. Lines in Fig. 8 illustrate the calculation results of homogeneous equation. Discontinuity of lines between low and high quality is transition between laminar and turbulent flow which is set Re= 2300. These lines give relatively good agreement with experimental results.

4. CONCLUSIONS

(1) In this experiment, the characteristics of heat transfer coefficient are measured at uniform and un-uniform heat load. Under the heat flux from 1 to 8 kW·m^{-2} and the mass flux from 25 to 100 kW·m^{-2}, it is clear that nucleate boiling in channels is more dominant than forced convection boiling for low quality region. It is considered that dry out at high quality region results in deterioration of heat transfer coefficient.

(2) The characteristics of heat transfer coefficient at uniform and un-uniform heat load conditions are compared when mass flux is 100 kg·m^{-2}s^{-1}. It is found that the heat transfer coefficient of un-uniform heat load is lower than uniform heat load. It is considered that dryout due to flow mal-distribution within the channel promotes deterioration of heat transfer under un-uniform heat load condition. The degree of un-uniformity of heat flux further decreases heat transfer coefficient as increasing quality.

(3) Pressure drop is less sensitive to heat flux. Homogeneous equation shows good agreement with the results obtained.

NOMENCLATURE

A	Area (m^2)	*Greek leters*	
Bo	Boiling number (-)	*e*	Uncertainty (-)
Cp	Specific heat capacity ($J \cdot K^{-1}$)	*er*	Relative error (-)
D	Diameter (m)	*Subscripts*	
d	Distance (m)	*ave*	Average
dP	Differential pressure (kPa)	*Al*	Aluminium
F	Flow meter ($kg \cdot s^{-1}$)	*gr*	Grease
G	Mass flux ($kg \cdot m^{-2}K^{-1}$)	*l*	Liquid
h	Heat transfer coefficient ($kW \cdot m^{-2}K^{1}$)	*i*	Inner
m	Mass flow rate ($kg \cdot s^{-1}$)	*o*	Outer
Q	Heat load (kW)	*ref*	Refrigerant
T	Temperature (°C)	*w*	Water
Te	Evaporation temperature(°C)	*wall*	Wall
Re	Reynolds number(-)	*win*	Water inlet
x	Vapor quality (-)	*wout*	Water outlet

REFERENCES

Li, M., Dang, C., Hihara E., 2012. Flow boiling heat transfer of HFO1234yf and R32 refrigerant mixtures in a smooth horizontal tube: Part I. Experimental investigation. Int. J. Heat Mass Transf 55, 3437–3446.

Cavallini, A., Del Col, D., Matkovic. M., Rossetto, L., 2009. Pressure drop during two- phase flow of R134a and R32 in a single minichannel. J. Heat Transfer 131, 033107.

Hossain, M.A., Onaka, Y., Afroz, H.M.M, Miyara, A., 2013. Heat transfer during evaporation of R1234ze(E), R32, R410A and a mixture of R1234ze(E) and R32 inside a horizontal smooth tube. Int. J. Refrig 36, 465-477.

Li, W., Wu, Z., 2010. A general criterion for evaporative heat transfer in micro/mini-channels[J]. International Journal of Heat and Mass Transfer 53, 1967-1976.

Shah, M.M., 2017. Unified correlation for heat transfer during boiling in plain mini/ micro and conventional channels. Int. J. Refrig 74 606–626.

Manuscript ID: 989
DOI: 10.18462/iir.icr.2019.0989

Experimental tests using deactivation of coolant fluid circulation to mitigate frost formation on the heat exchanger surface

Pedro PANOIAS[(a)], Pedro D. SILVA[(a,b)], Luís C. PIRES[(a)], Pedro D. GASPAR[(a,b)], José NUNES[(c)]

[(a)] University of Beira Interior, Rua Marquês d'Ávila e Bolama, 6201-001, Covilhã, Portugal, dinho@ubi.pt
[(b)] C-MAST - Centre for Mechanical and Aerospace Science and Technologies, Covilhã, Portugal, dinis@ubi.pt
[(c)] Agriculture School, Polytechnic Institute of Castelo Branco, Quinta da Senhora de Mercoles, 6001-909 Castelo Branco, Portugal, jnunes@ipcb.pt

ABSTRACT

The use of cold for conservation of food products requires large consumption of electricity. In order to obtain lower temperatures than those available in the same space, the evaporator coils, generally operate at temperatures lower than the freezing point of the water. The ice formed on the surface is detrimental both to the thermal and the energetic level of the refrigeration system. Thus, ice removal is critical to reestablish the desired operating conditions.
This paper presents a refrigeration apparatus setup composed by two heat exchangers connected in parallel. The coolant fluid circulation is deactivated during short periods of operation, and the ice formation on the coil surface is analyzed. The results show that this strategic deactivation of coolant fluid circulation proved to be a viable operating condition since allowed an extension of the refrigeration system operation with a stable cooling power and so better thermal efficiency.
Keywords: Ice Formation, Experimental Test, Refrigeration Systems, Ice Mitigation.

1. INTRODUCTION

The improvement of the energy efficiency in the refrigeration equipment is the main motivation for the accomplishment of this work. Cooling systems for comfort or food preservation are increasingly used today. With the massive use of cooling systems, it is increasingly urgent and necessary to study its most important element, the heat exchanger, since it is responsible for cooling the flowing fluid, because its surface with fins is revealed as the most effective way to transfer heat through convection (Amini et al., 2014). The wet air upon contact with the fins begins a process of deposition of droplets which, after a while, eventually solidify and form ice. The cooling process is becoming less efficient as time progresses, as the air passage becomes partially blocked (Seker et al., 2004).
Although there is a growing number of studies in this area, ice formation continues to be a problem that makes the use of these types of systems inefficient, since too many periods are devoted to defrosting, which causes the considerably oscillations in temperature of the space to be cooled. Thus, a greater need for energy consumption will occur to maintain the desired temperature value.
A non-stationary complex mechanism is defined during the process of ice formation on the outer surface of the heat exchanger coils, involving spatial and temporal variations of heat and mass transfer rates (Jiang et al., 2013). The formation of ice and the increase in size of the crystals lead to a loss of performance of the cooling system, since the joining of the ice crystals will have an insulating effect blocking the passage of air in the exchanger (Liu et al., 2005).
According to Al-Essa and Al-Zgoul (2012), in the food storage sector, deposition of ice occurs in the coils, since the coils operate at temperatures below 0ºC. In heat exchangers consisting of serpentines with fins, the ice deposited in the space between the fins block the passage of air. The deposition process will decrease the energy absorbed by the refrigerant which, according to Yang

(2010), will result in a decrease in cooling capacity between 30% and 57%. It is therefore relevant to find solutions that mitigate the formation of ice in heat exchangers. In this paper the effect of deactivating the operation of an evaporator at key moments during its operation in order to mitigate the formation of ice on its surface is studied.

2. MATERIAL AND METHODS

2.1 Experimental

The experimental prototype is shown in Fig. 1 and include a heat exchanger bank that consists in two finned-tube compact heat exchangers used in previous work (Carrilho *et al.,* 2017), each one with dimensions 110×216.8×205 mm^3, 16 tube (3/8 in) rows, 44 fins and heat exchange area of 572×10^3 mm^2. During the tests the first heat exchanger (upstream) is always working and the second one is momentary deactivated as soon as ice formation is visually detected in its surface.

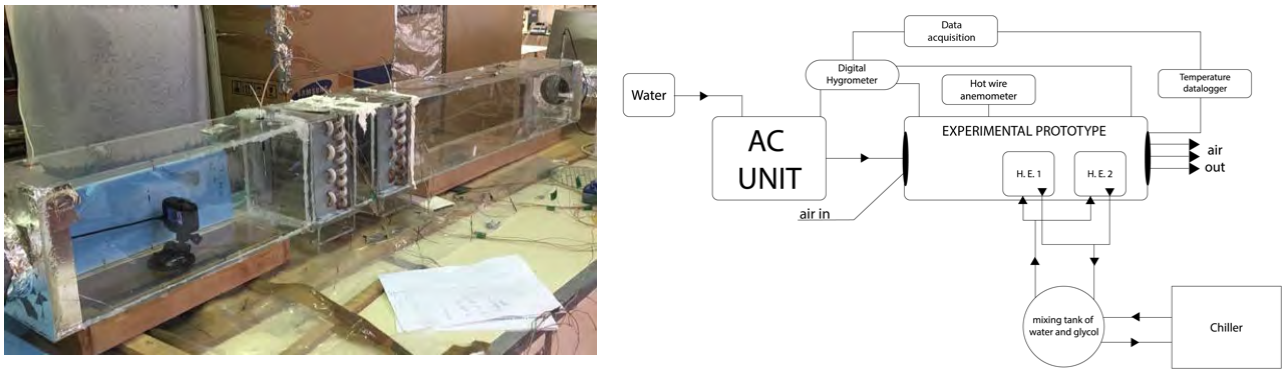

Figure 1: Experimental prototype and diagram of equipment connections

Additionally Fig. 1 shows the experimental prototype assembly. A cooling chiller (MTA, EVO031) is responsible for lowering the temperature of the water solution with glycol (60%-40%) to the desired values, and this is achieved by circulating the fluid between the tank where it is stored and the interior of the chiller. A submersible pump (Hydor, Seltz 40) was placed inside the tank to maintain the circulation of the water-glycol solution inside the tubes of the exchangers. An air conditioning unit (PA Hilton, A573) provides fresh air throughout the heat exchanger bank. Air temperature and relative humidity were measured both at the inlet and outlet of the heat exchanger bank using a digital hygrometer (Rotronic, HygroLog NT2). The temperatures on the heat exchanger surface as well at fluid entrance and exit of heat exchangers were measured with T-type thermocouples and a Temperature Datalogger (Pico, TC08). The airflow flow velocity was measured with a hot wire anemometer (Testo, 425). The collection of images of ice formation on the surface of the exchangers throughout the tests was performed with a video camera (GoPro, H5).

2.2 Mathematical Formulation

The evaluation of the heat exchanger cooling power is obtained throughout an energy balance to the air side. The set of equations that allows this evaluation is present in the following (ASHRAE, 2011). The saturation pressure of the vapor was initially calculated by the formula,

$$\ln(p_{ws}) = \frac{C_8}{T} + C_9 + C_{10}T + C_{11}T^2 + C_{12}T^3 + C_{13}\ln(T) \qquad \text{Eq. (1)}$$

Where C_8=-5800.22, C_9=1.391449, C_{10}=-0.04864, C_{11}=4.18E-05, C_{12}=-1.4E-08 and C_{13}=6.545967. Using the above result and the air relative humidity (ϕ), the partial pressure of the water vapor is given by Eq. (2).

$$\phi = \frac{p_w}{p_{ws}} \Leftrightarrow p_w = \phi \times p_{ws} \qquad \text{Eq. (2)}$$

With the previous result and total pressure value (p) it is possible to calculate the absolute humidity using Eq. (3):

$$\omega = 0.621945 \frac{p_w}{p - p_w} \quad \text{Eq. (3)}$$

The enthalpy of moist air is evaluated from:

$$h = h_{da} + \omega h_g \quad \text{Eq. (4)}$$

Where the enthalpy of dry air (h_{da}) is given by:

$$h_{da} \cong 1.006\mathrm{T} \quad \text{Eq. (5)}$$

In this equation T is the dry bulb temperature, in Celsius. The enthalpy of water vapor (h_g) is evaluated from:

$$h_g \cong 2501 + 1.86\ \mathrm{T} \quad \text{Eq. (6)}$$

In this way, the final equation is obtained, and the enthalpy of the moist air is calculated by:

$$h = 1.006\mathrm{T} + \omega(2501 + 1.86\mathrm{T}) \quad \text{Eq. (7)}$$

The cooling power, Q, is given by:

$$\mathrm{Q} = \dot{m}(h_1 - h_2) \quad \text{Eq. (8)}$$

With the enthalpy of the moist air evaluated before (h_1) and after (h_2) the heat exchanger bank. The air mass flow rate is given by:

$$\dot{m} = \dot{V} \times \frac{1}{v} \quad \text{Eq. (9)}$$

And the volumetric air flow rate is evaluated from:

$$\dot{V} = \mathrm{v} \times \frac{\pi \times d}{4} \quad \text{Eq. (10)}$$

Where d represents the hydraulic diameter of the channel and v the air velocity. The specific volume of the moist air is calculated from Eq. (11).

$$v = 0.287042(\mathrm{T} + 273.15) \frac{(1 + 1607858\omega)}{p} \quad \text{Eq. (11)}$$

3. RESULTS AND DISCUSSION

A preliminary reference test was carried out using the experimental setup. In this reference test both heat exchangers were working, meaning that both heat exchangers were feed, in parallel, by the water-glycol solution. Table 1 shows the parameters for the reference test. This reference test was performed to compare the behavior of the heat exchangers bank for two different operating conditions in which the first (upstream) heat exchanger is always operating but the second one suffers two different interruption cycles. The results are analyzed separately in the following sections.

Table 1. Reference test parameters

Test	HR (%)	T_{amb} (ºC)	P_{atm} (hPa)	Duration (min)
Reference	38.2%	25.9	1014.1	115

3.1 Performance Analysis for the First Operating Condition

In this first operating condition the second heat exchanger suffers an interruption of 3 minute every 15 minutes of operation. Additionally, two different air relative humidity values at inlet of the heat exchanger bank were used. Table 2 summarizes the parameters for this operating condition.

Table 2. Parameters for the test cycle 15-3

Test	HR (%)	T_{amb} (ºC)	P_{atm} (hPa)	Duration (min)
B1	30	23.8	1013.3	125
B2	50	23.3	1013.7	134

B1 and B2 test results for the air temperature at the heat exchanger bank outlet and the corresponding cooling power are shown in Fig. 2 together with reference test results. After the first interruption, it is possible to observe the stability of the system to the temperature recorded during the 15 minutes of activity period. As for the temperatures recorded during the 3-minute pause, it is observed that the higher the RH value of the test, the higher the temperature recorded in the area after the cooling section. There is a slight difference in the maximum temperature values recorded in the 3-minute pause. In the reference test the temperature decreases during the first 50 minutes, when the accumulated ice begins to disturb the air flow. From that moment the temperature increases until reaching values similar as those obtained during the interruption of the circulation of the fluid in tests B1 and B2. That means that the defrost method used ensures lower temperatures over time.

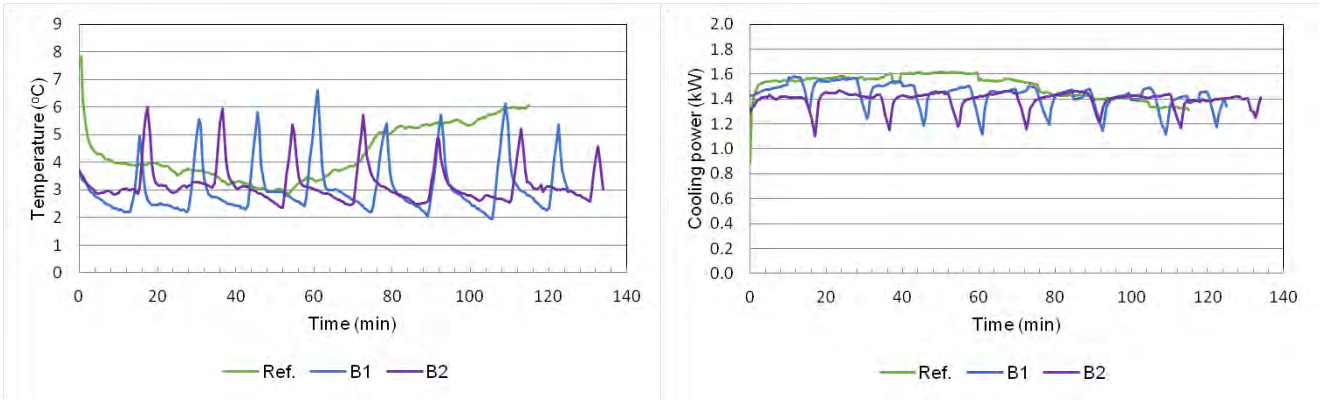

Figure 2: Air temperature outlet (left) and cooling power (right) of B1 and B2 tests

In Fig. 3 (left) and Fig. 4 (left), we can observe that there is a significant accumulation of ice at the final of the operation time, before the interruption.

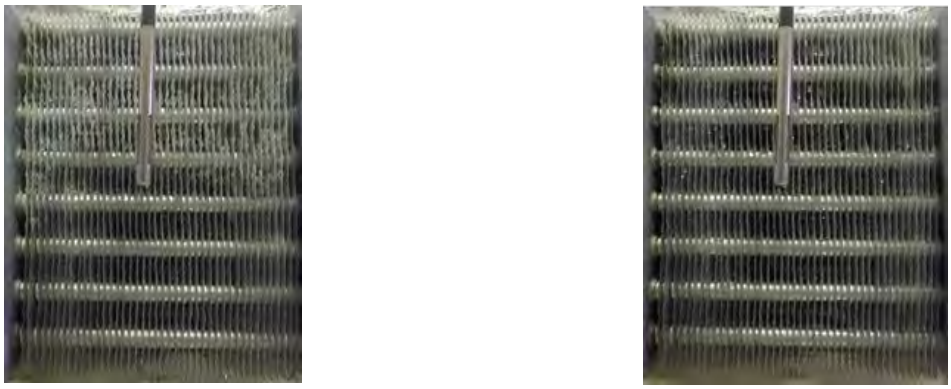

Figure 3: Ice accumulated in the exchanger at 105 min (left) / Ice accumulated after pause at 108 min (right) for test B1

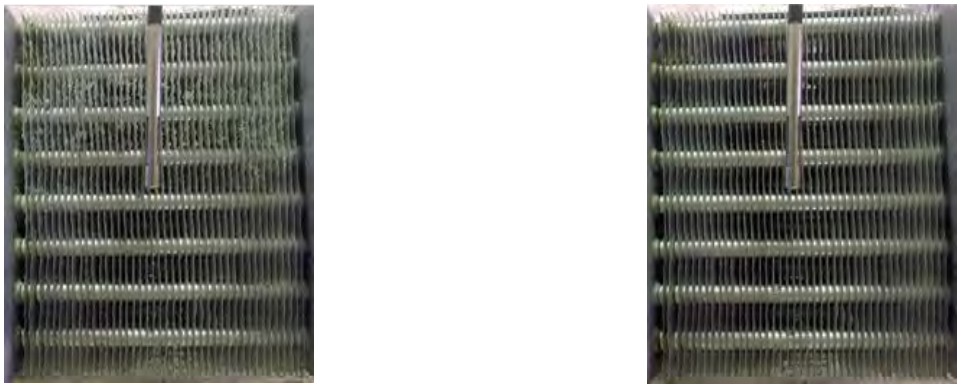

Figure 4: Ice accumulated in the exchanger at 112 min (left) / Ice accumulated after pause at 115 min (right) for test B2

However, after the interruption all the accumulated ice has been melted, Fig. 3 (right) and Fig. 4 (right), and the heat exchanger is again available for cooling as shown by the corresponding cooling power curve in Fig. 2 (right). In addition to the greater stability that can be verified, it is also verified that the system can keep the temperatures lower for longer, maintaining similar cooling power levels (see Fig. 2, right). This is due to the fact that the interruption time is enough to melt the formed ice and ensure good air flow conditions during the operation time of the refrigeration system.

3.2 Performance Analysis for the Second Operating Condition

Table 3 shows the parameters for the second operating condition. The second operating condition had as objective to verify how the increase of the circulation time of the fluid in the exchanger, maintaining the time of interruption, would affect the performance. So, the tests were performed for 30 minutes of operation of the second heat exchanger followed by 3 minute pause.

Table 3. Parameters for the test cycle 30-3

Test	HR (%)	T_{amb} (ºC)	P_{atm} (hPa)	Duration (min)
B3	50	23.2	1014.7	113

Fig. 5 shows the air temperature and cooling power recorded during the test together with the reference test values. As can be observed the recorded temperature reaches new minimums with the passage of time. It is possible to state that there is a certain tendency in the system to maintain the stability at the temperature which is recorded after the passage of air through the cooling zone. The cooling power presents a behavior better than that obtained to the reference test, and tends to maintain a quite similar value along the test.

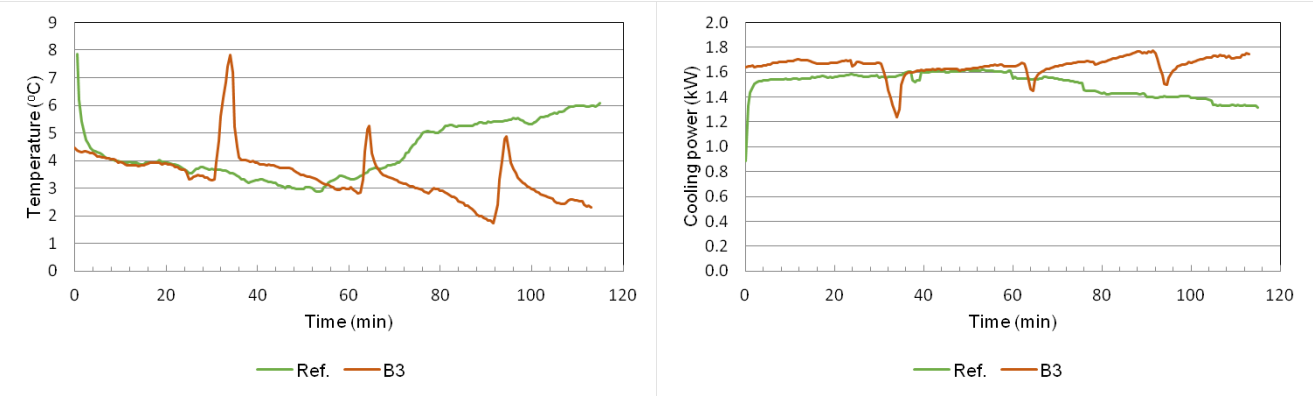

Figure 5: Air temperature outlet (left) and cooling power (right) of B3 test

In Fig. 6 it can be seen that the amount of ice formed is significant, but it is noteworthy that the time of interruption of circulation of the water-glycol solution for the B7 test was not sufficient to melt all the ice accumulated at 92 minutes. However the use of 30 minutes of operation of the exchanger bank with a programmed pause of 3 minutes, becomes a good defrost solution. It guarantees a longer period of operation avoiding changes of temperature and maintains the cooling power values quite similar to those obtained in the beginning of the reference test, still in the absence of the ice formation effect, in which the exchanger bank operates continuously without interruption.

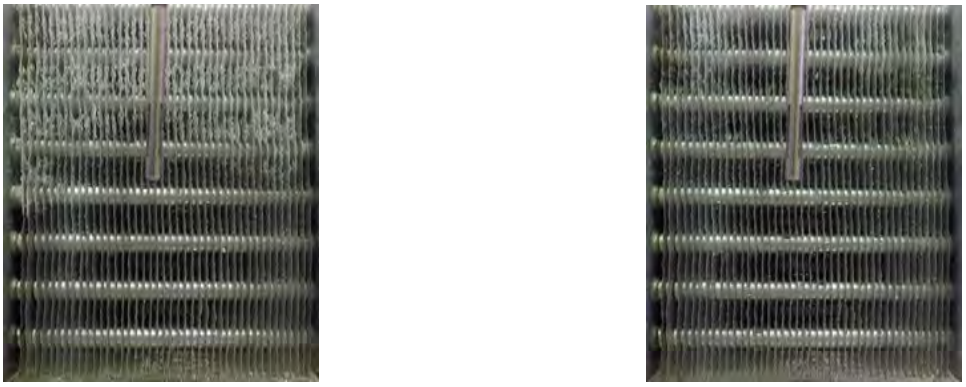

Figure 6: Ice accumulated in the exchanger at 92 min, before interruption (left) and ice accumulated at 95 min, after the interruption (right)

4. CONCLUSIONS

Refrigeration, in a domestic or industrial point of view, takes a very important role in society. Nowadays, a big portion of the refrigeration processes are taken into account in the food and drinks storage, and also in the cooling of closed spaces. The need to obtain lower temperatures implies that evaporator component operate at lower temperatures than the water freezing point, a fact which clearly favors the formation of ice on their surfaces. The ice formation is detrimental to the system at thermal and energy levels, reason why its mitigation or removal is essential to ensure the desired operating conditions. This paper proposes a strategy that consists in the deactivation, for short periods, of the circulation of coolant on the heat exchangers during the operation of the refrigeration system. The results of this experimental study showed that the strategic deactivation of the coolant fluid circulation proved to be a viable operating option since it allowed a prolongation of the effective operations of the refrigeration system. Additionally, the refrigeration cooling power was also maintained in an adequate range during the operating time.

ACKNOWLEDGEMENTS

This study is within the activities of Project “PrunusPós - Optimization of processes for the storage, cold conservation, active and/or intelligent packaging and food quality traceability in post-harvested fruit products”, project n.º PDR2020-101-031695, Partnership n.º 87, initiative n.º 175, promoted by PDR 2020 and co-funded by FEADER within Portugal 2020.

REFERENCES

Al-Essa, Al-Zgoul, B., 2012. Building up frost depending upon conditions of air cooler operation. Int. J. Mechanics and Applications 2 (2), 1-4.

Amer, M., Wang, C., 2017. Review of defrosting methods. Renewable and Sustainable Energy Reviews 73, 53-74.

Amini, M., Pishevar, A., Yaghoubi, M., 2014. Experimental study of frost formation on a fin- and-tube heat exchanger by natural convection. Int. J. Refrigeration 46, 37-49.

ASHRAE, 2011. HVAC Applications. In: ASHRAE Handbook Collection; American Society of Heating, Refrigerating and Air Conditioning Engineers, Atlanta.

Carrilho, D., Silva, P.D., Pires, L., Gaspar, P.D., Nunes, J., 2017. Quantification of the thermal resistance variation in evaporators surface due to ice formation. Energy Procedia 142, 4151-4156.

Jiang, Y., Dong, J., Qu, M., Deng, S., Yao, Y., 2013. A novel defrosting control method based on the degree of refrigerant superheat for air source heat pumps. Int. J. Refrigeration 36, 2278-2288.

Jiang, Y., Fu, H., Yao, Y., Yan, L., Gao, Q., 2013. Experimental study on concentration change of spray solution used for a novel non-frosting air source heat pump system. Energy and Buildings 68, 707-712.

Liu, Z., Wang, H., Zhang, X., Meng, S., Ma, C., 2005. An experimental study on minimizing frost deposition on a cold surface under natural convection conditions by use of a novel anti-frosting paint. Part I. Anti-frosting performance and comparison with the uncoated metallic surface. Int. J. Refrigeration 29, 229-236.

Seker, D., Karatas, H., Egrican, N., 2004. Frost formation on fin-and-tube heat exchangers. Part I - Modeling of frost formation on fin-and-tube heat exchangers. Int. J. Refrigeration 27, 367-374.

Manuscript ID: 997
DOI: 10.18462/iir.icr.2019.0997

A Study on flow boiling heat transfer in non-uniformly heated parallel mini-channels by numerical analysis

Kizuku KUROSE[(a)*], Takuya KAWASUSO[(a)], Kazushi MIYATA[(b)], Yoshinori HAMAMOTO[(b)], Hideo MORI[(b)]

(a) Graduate school of Mechanical Engineering, Kyushu University
Nishi-ku, Fukuoka, 819-0395, Japan, *kurose@therme.mech.kyushu-u.ac.jp
(b) Department of Mechanical Engineering, Kyushu University
Nishi-ku, Fukuoka, 819-0395, Japan

ABSTRACT

A novel heat exchanger using parallel refrigerant mini-channels has recently been developed to improve the performance of air conditioning systems. In the evaporator, due to unequal heat load among the parallel channels, boiling flow tends to be unevenly distributed. Since this phenomenon sometimes causes deterioration of heat exchange performance, it is important to clarify the characteristics of boiling heat transfer under the unequally heated condition. In the present study, a simulation model which predicts flow boiling heat transfer performance of a refrigerant heated unequally among parallel mini-channels has been developed, and simulation for two-parallel channels were carried out. Based on the calculation results, the effect of the inequality in wall temperatures between the channels on the heat transfer rate to the refrigerant was discussed. The channel mean heat transfer rate decreased with expanding the difference of wall temperatures between the channels and the deterioration rate became significant at a high mass flow velocity.
Keywords: Simulation, Boiling Heat Transfer, Parallel Mini-Channels, Flow Maldistribution.

1. INTRODUCTION

Recently, a novel high-performance refrigerant-air heat exchanger employing multiport extruded tubes which have parallel refrigerant mini-channels has been developed for air conditioning systems. In case that the heat exchanger is used as the evaporator, since the flow direction of refrigerant in the multiport tubes is perpendicular to that of heat source air, the heat transfer rate to the refrigerant channels on upstream side of air flow are larger than those on downstream side. Such an inequality in heat transfer rates, or evaporation rates, also causes inequalities in flow rate and heat transfer coefficient among the refrigerant channels. Furthermore, this phenomenon often induces the deterioration of boiling heat transfer of refrigerants. However, studies on this phenomenon are very limited (Onishi, 2017).
The authors have been conducted experiments on flow maldistribution and boiling heat transfer of a refrigerant heated unequally between two parallel mini-channels using a direct electrical heating, that is, heat flux of each channel is uniform in the refrigerant flow direction (Kurose, 2018). In addition, an unsteady simulation model which predicts flow boiling heat transfer performance in parallel channels heated unequally among the channels has been developed (Kawasuso, 2017), however, for the uniform heat flux in the flow direction. From these previous studies, it was found that the flow rate in the higher heat transfer rate channel was generally lower than the channel average value, and it led to expand the dryout region.
In the present study, the simulation code was improved to give a constant wall surface temperature for each channel as a boundary condition, which is more similar to the heat transfer form of actual evaporators. Then calculations of heat transfer performance in two parallel mini-channels heated unequally by giving unequal wall temperatures were carried out, changing the channel mean mass flow rate. Based on the calculation results, the effect of the unequal heat loads on the heat transfer

rate to the refrigerant was discussed.

2. CALCULATION METHOD

Fig. 1 shows a schematic diagram of the simulation model used in this study. Parallel channels are connected to a high pressure header and a low pressure header, and a fluid flows by differential pressure between the headers. In the present study, calculation was conducted for two horizontal circular parallel channels. The diameters of the channels were both 1.0 mm. Pressure in the low pressure header was kept at a constant value, and that in the high pressure header was controlled to keep the total inlet mass flow rate of the two channel constant at a target value. Entrance- and Exit-side non-heating sections and heating section are set in the flow direction in each channel.
Assumptions used in this model are as follows:
1. the flow is homogeneous
2. the two phases are in thermodynamic equilibrium.
3. the effect of pressure drop on fluid physical properties is neglected
4. subcooled boiling is neglected.
5. viscos dissipation, kinetic energy, potential energy and friction loss are neglected in the energy equation.
For these assumptions, the one dimensional conservation equations of mass and energy for an infinitesimal control volume moving with the fluid in the flow direction can be written as Eqs. (1) and (2), respectively

$$\frac{d}{dt}(\rho V) = 0 \qquad \text{Eq. (1)}$$

$$\frac{dh}{dt} = \frac{4q}{\rho D} \qquad \text{Eq. (2)}$$

where V is fluid volume in m^3, h is specific enthalpy in $J.kg^{-1}$, q is heat flux in $W.m^{-2}$, D is the channel diameter in m. ρ is fluid density in $kg.m^{-3}$, as defined by Eq. (3) for two-phase.

$$\frac{1}{\rho} = \frac{x}{\rho_G} + \frac{1-x}{\rho_L} \qquad \text{Eq. (3)}$$

where x is vapor quality, ρ_G and ρ_L are saturated vapor and liquid densities, respectively.
For discretization of Eqs. (1) and (2), the method of tracking a target fluid flowing in the flow direction, that is, Laglangian method was used and time step was set at 10^{-3} s. Fig. 2 shows the simple overview of the movement of control volumes. Mass preservation equation Eq. (1) shows that the refrigerant mass in a control volume is conserved. In the non-heating section, as enthalpy does not

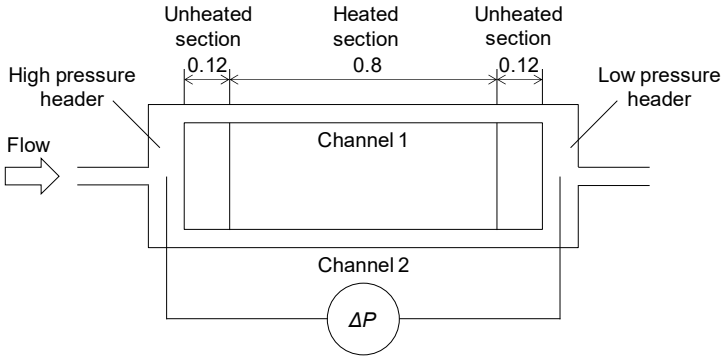

Figure 1: Schematic diagram of the simulation model

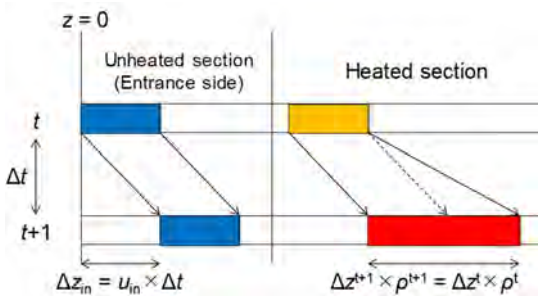

Figure 2: Simple overview of the control volume movement

change, density of the refrigerant in each control volume for the flow direction are constant, that is, the control volume length does not change. Whereas, in the heating section, since the refrigerant is heated and its enthalpy increases, if the refrigerant in two-phase region, density decreases and the length of the control volume increases. Energy preservation equation Eq. (2) shows the increment of enthalpy in the heating section.
The one dimensional conservation equation of momentum for an infinitesimal stationary control volume can be written as:

$$\frac{\partial}{\partial t}(\rho u)+\frac{\partial}{\partial z}\left(\rho u^2\right)=-\frac{\partial p_f}{\partial z}-\rho g\sin\theta-\frac{\partial p}{\partial z} \qquad \text{Eq. (4)}$$

where, u is fluid velocity in m.s^{-1}, g is the gravitational acceleration in m.s^{-2}, θ is the angle between the flow direction and the horizontal plane, p is pressure in Pa. $\partial p_f/\partial z$ is frictional pressure drop gradient in Pa.m^{-1}, which was estimated by a correlation equation developed based on measured two-phase pressure drop (Enoki, 2012) for two-phase. In this simulation, spatial distributions of velocity and enthalpy are obtained from Eqs. (1) and (2), then time change of velocity is obtained from Eq. (4).
In the present study, keeping wall surface temperature constant in the flow direction, the local heat flux q was evaluated by Eq. (5):

$$q=\alpha(T_w-T_b) \qquad \text{Eq. (5)}$$

where α is the heat transfer coefficient in W.m^{-2}.K^{-1}, T_w is the wall surface temperature in K, T_b is the bulk fluid temperature of the refrigerant in K. The heat transfer coefficient α was estimated by the Enoki et al. correlation (Enoki, 2015) for two-phase pre-dryout region and by the Dittus-Boelter correlation for superheated vapor single-phase region. The dryout inception quality x_{di} was obtained by a correlation equation which was made in this study based on the experimental results for mini-channel (Enoki, 2012), referring to the correlation by Yoshida et al (2000). For the two-phase post-dryout region, based on the experimental data trends (Enoki, 2012), the heat transfer coefficient was evaluated by linearly interpolating the heat transfer coefficients at the quality of x_{di} and 1.
Simulation conditions are listed in Table 1. Physical properties of R410A was used. The saturation temperature T_{sat} and inlet quality x_{in} were set at 10 °C and 0.2, respectively. The quality maldistribution from the inlet header to the respective channels was not taken into account. The channel mean inlet mass velocity G_{ave} was set at 50, 100 and 200 kg·m^{-2}·s^{-1}. The temperature difference between the wall surface temperature T_w and the saturation temperature T_{sat} in each channel ΔT_1 and ΔT_2 were given with keeping channel arithmetic mean temperature difference ΔT_{ave} (=(ΔT_1 +ΔT_2) / 2) constant. For each mass velocity condition, ΔT_{ave} was determined so that the quality increment was nearly 0.8 in the equally heating condition $\Delta T_2/\Delta T_1$ = 1.0. The physical properties of R410A was evaluated using REFPROP Ver. 9.1 (Lemon, 2013). Incidentally, noticeable flow oscillation did not occur in these conditions.
The validity of the model was confirmed by comparison with experimental results (Noboritate, 2018).

Table 1. Simulation conditions

Fluid	R410A		
Saturation Temperature T_{sat}, °C	10		
Channel inner diameter, mm	1		
Heated length, m	0.8		
Entrance- and exit-side unheated length, m	0.12, 0.12		
Inlet vapor quality x_{in}	0.2		
Channel mean inlet mass velocity G_{ave}, kg·m^{-2}·s^{-1}	50	100	200
Channel mean temperature difference between T_w and T_{sat}, ΔT_{ave}, K	0.65	1.50	1.95
The ratio of ΔT_2 to ΔT_1, $\Delta T_2/\Delta T_1$	0.2 ~ 1.0		

3. RESULTS AND DISCUSSION

As typical examples, Fig. 3a and Fig. 3b show the changes of predicted local quality x, local heat transfer coefficient α, and local heat flux q with the distance from inception of heating z, at the mean inlet mass velocity of 100 kg·m^{-2}·s^{-1} under equally heated condition $\Delta T_2/\Delta T_1$ = 1.0 and unequally heated condition $\Delta T_2/\Delta T_1$ = 0.4, respectively. In each figure, the dryout inception point $x = x_{di}$ is depicted by a black symbol. Also, the inlet mass velocity G_1, G_2 and the heat transfer rate to the refrigerant Q_1, Q_2 in each channel are denoted in the figures. The heat transfer rate to the refrigerant was obtained by Eq. (6).

$$Q_n = G_n A_c (x_{out,n} - x_{in}) \Delta h \qquad \text{Eq. (6)}$$

where suffix n is channel number, G is inlet mass velocity in kg.m^{-2}.s^{-1}, A_c is flow area of the channel in m^2, x_{out} is outlet quality, Δh is latent heat of evaporation in J.kg^{-1}.

As seen in Fig. 3 (a), for equally heated condition, the calculation results of respective channels are equal to each other. The quality increases from the inlet value in the flow direction and reaches the dryout inception quality x_{di} = 0.77 at z = 0.38 m. In the dryout region, the increasing gradient of quality becomes more gentle due to the reduction of the heat flux attributed to the intense decrement of the heat transfer coefficient. At the outlet of the heating section, the quality is 1.0 and the heat transfer coefficient is the value of vapor single phase. Then, the channel mean heat transfer rate to the refrigerant Q_{ave} (=(Q_1+Q_2)/2) is 0.0131 kW.

For the unequally heated condition, in Channel 1 with higher wall temperature, quality increases sharply and reaches the dryout quality at z = 0.17 m, which is more upstream than the equally heated

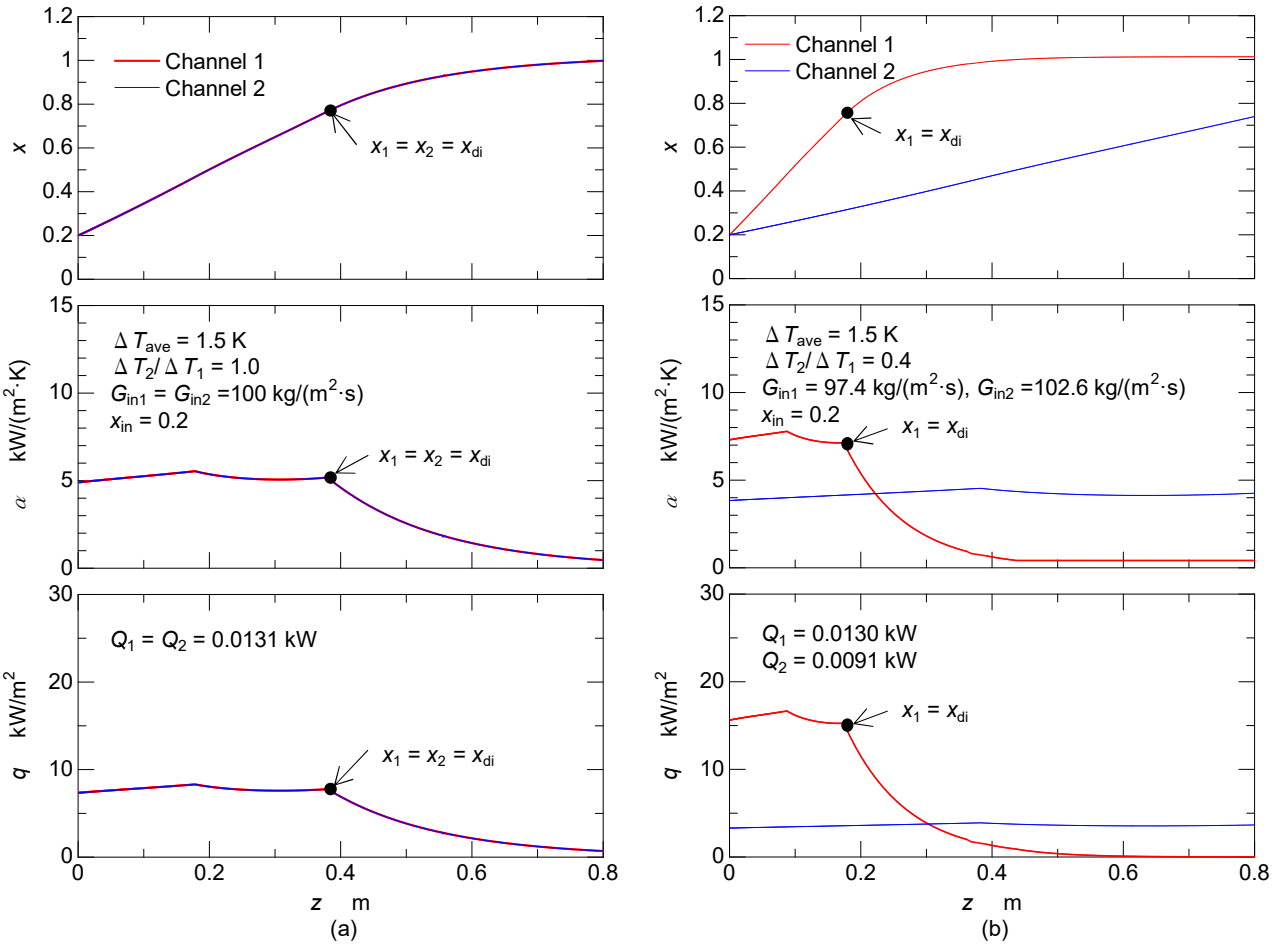

Figure 3: Changes of quality, heat transfer coefficient, and heat flux with the distance from inception of heating under equally and unequally heated conditions

case, and the dryout region expands. However, the heat transfer rate to the refrigerant Q_1 = 0.0130 kW is almost the same as the equally heated case, because the outlet quality and flow rate are also almost the same. Whereas, in Channel 2, the outlet quality is 0.74 and dryout does not occur. Consequently, the good heat transfer is kept in the whole heating section, however, the heat transfer rate Q_2 = 0.0091 kW is lower than the equally heated because of low evaporation rate. Therefore, the channel mean heat transfer rate Q_{ave} = 0.0111 kW is lower than that in the equally heated condition.

In Fig. 4 and Fig. 5, the changes of the channel inlet mass velocities G_1 and G_2 and the outlet qualities x_{out1} and x_{out2} are plotted against $\Delta T_2/\Delta T_1$, for different channel mean mass velocities G_{ave}. In general, as $\Delta T_2/\Delta T_1$ decreases, the inequality in mass velocity between the two channels expands, that is, G_1 decreases while G_2 increases. And the inequality at low $\Delta T_2/\Delta T_1$ becomes noticeable as the mean mass flow rate increases. The outlet quality of Channel 1 x_{out1} increases slightly while that of Channel 2 x_{out2} decreases markedly with decreasing $\Delta T_2/\Delta T_1$ for any mass velocity condition.

Fig. 6 shows an example of the changes of the length of pre-dryout and post-dryout regions in the heating section with $\Delta T_2/\Delta T_1$ at G_{ave} of 100 kg·m^{-2}·s^{-1}. The left and right diagrams denote the results in Channel 1 and Channel 2, respectively. In Channel 1 with high wall surface temperature, the post-dryout region broadens with decreasing $\Delta T_2/\Delta T_1$, and it accounts for 81 % of the heating section at $\Delta T_2/\Delta T_1$ of 0.2. In contrast, in Channel 2, as $\Delta T_2/\Delta T_1$ decreases, the post-dryout region contracts, and dryout does not occur when $\Delta T_2/\Delta T_1$ was 0.4 or less.

Fig. 7 shows the heat transfer rate Q_1 and Q_2 of different channel mean mass velocities. For any mass velocity condition, the heat transfer rate of Channel 1 Q_1 decreases gradually against the decrement of $\Delta T_2/\Delta T_1$ while that of Channel 2 Q_2 decreases sharply, and both decreasing of Q_1 and Q_2 becomes noticeable as the mean flow rate increases. As a result, the channel mean heat transfer rate Q_{ave} decreases with decreasing $\Delta T_2/\Delta T_1$. The deterioration degrees of Q_{ave} from equal heating

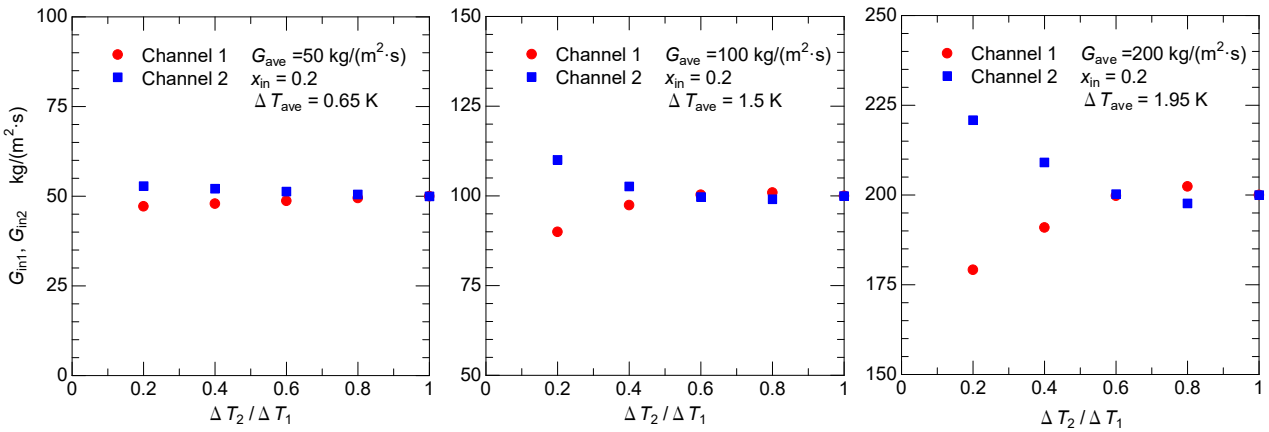

Figure 4: The relation between channel inlet mass velocities and $\Delta T_2/\Delta T_1$

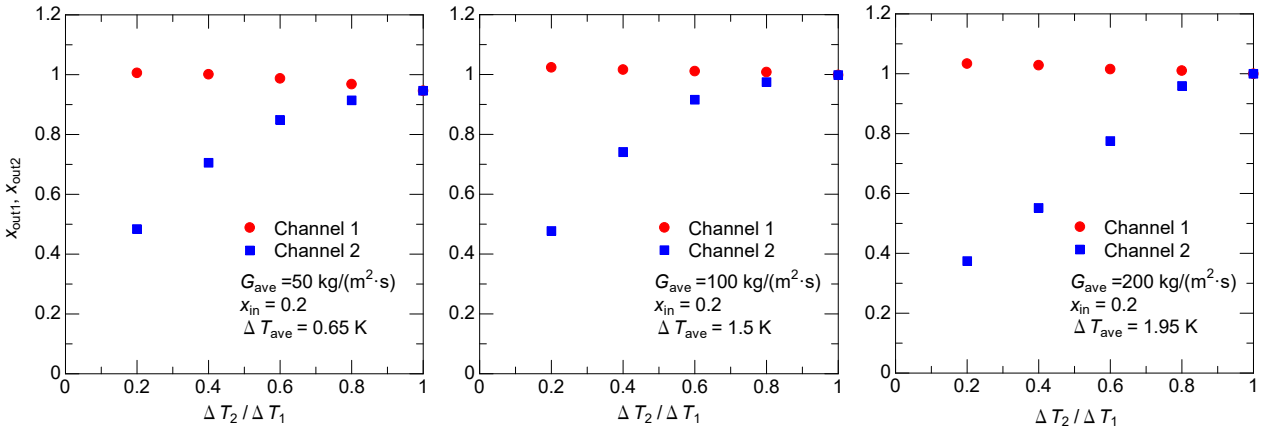

Figure 5: The relation between channel outlet qualities and $\Delta T_2/\Delta T_1$

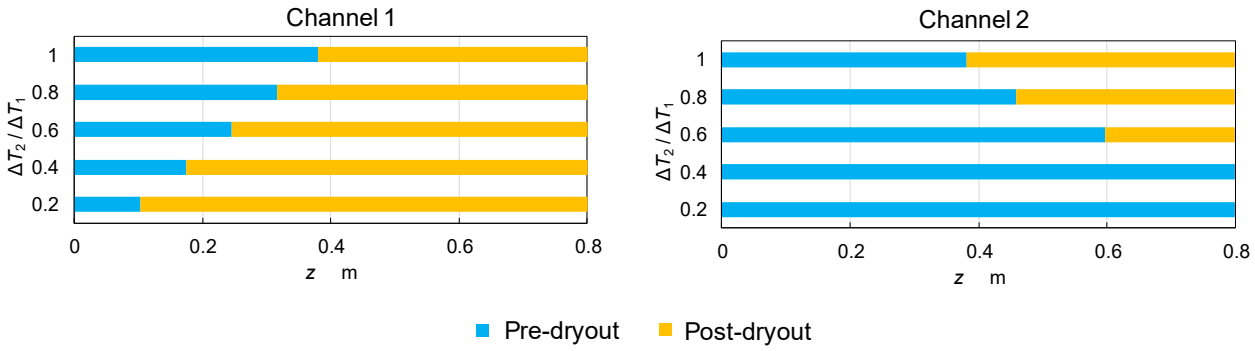

Figure 6: Changes the length of pre-dryout and post-dryout regions in the heating section

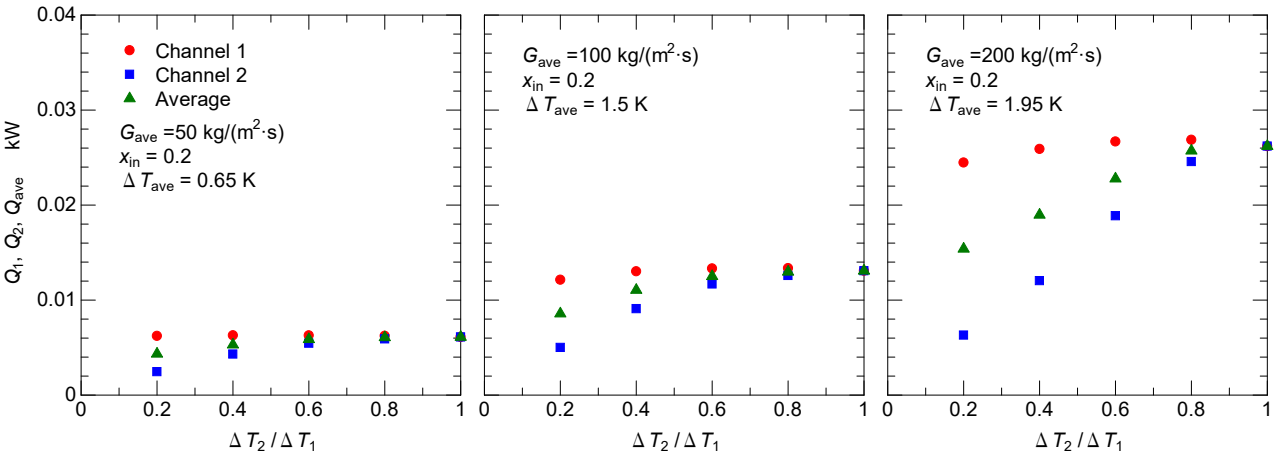

Figure 7: The relation between the heat transfer rates to the refrigerant and $\Delta T_2/\Delta T_1$

condition $\Delta T_2/\Delta T_1$ = 1.0 to unequal heating condition $\Delta T_2/\Delta T_1$ = 0.2 are 29% at G_{ave} of 50 kg·m^{-2}·s^{-1}, 34% at G_{ave} of 100 kg·m^{-2}·s^{-1}, and 41% at G_{ave} of 200 kg·m^{-2}·s^{-1}, that is, the inequality in wall surface temperatures has a large impact on the mean heat transfer rate at high flow rate.
Fig. 8 shows the changes of the ratio of channel averaged heat transfer coefficient to its value at equally heated condition with $\Delta T_2/\Delta T_1$ for the respective mean mass velocities. The channel averaged heat transfer coefficient was defined as the following equation:

$$\alpha_{ave} = \frac{Q_{ave}}{A\Delta T_{ave}} \qquad \text{Eq. (7)}$$

where A is the heat transfer area in m^2. Since ΔT_{ave} is constant in the present simulation, Q_{ave} is proportional to α_{ave}. Eq. (7) can be rewritten as Eq. (8) by using the area averaged heat transfer coefficients in the heating section in respective channels α_1, α_2.

$$\frac{1}{\alpha_{ave}} = \frac{Q_1}{Q_1+Q_2}\frac{1}{\alpha_1} + \frac{Q_2}{Q_1+Q_2}\frac{1}{\alpha_2} \qquad \text{Eq. (8)}$$

Therefore, the averaged heat transfer resistance of the two channels $1/\alpha_{ave}$ means the heat transfer rate weighted average of the heat transfer resistance of the respective channels $1/\alpha_1$, $1/\alpha_2$.
As seen in Fig. 8, The heat transfer coefficient ratio decreases with $\Delta T_2/\Delta T_1$ generally and it is found that the heat transfer coefficient ratio at G_{ave} of 200 kg·m^{-2}·s^{-1} decreases more significantly compared with those at 50 and 100 kg·m^{-2}·s^{-1}.

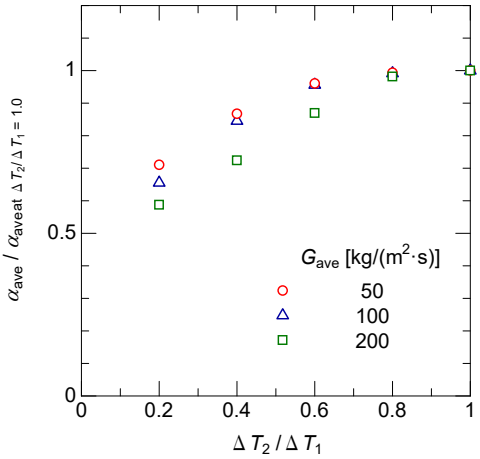

Figure 8: Changes of the ratio of the channel averaged heat transfer coefficient to its value at equally heated with $\Delta T_2/\Delta T_1$

4. CONCLUSION

The simulation of heat transfer performance of R410A heated unequally between two parallel mini-channels was conducted. The mean heat transfer rate of the parallel channels decreased with increasing the inequality in wall surface temperatures between the channels. The deterioration of mean heat transfer rate, or mean heat transfer coefficient, became significant at a high mass flow velocity of 200 kg·m^{-2}·s^{-1} compared with 50 and 100 kg·m^{-2}·s^{-1}.

NOMENCLATURE

α	Heat transfer coefficient (W×m^{-2}×K^{-1})	A	Heat transfer area (m^2)
ρ	Density (kg×m^{-3})	A_c	Flow area (m^2)
τ	Wall share stress (Pa)	D	Inner diameter (m)
g	Gravitational acceleration (m×s^{-2})	Q	Heat transfer rate (W)
h	Specific enthalpy (J×kg^{-1})	G	Mass velocity (kg×m^{-2}×s^{-1})
p	Pressure (Pa)	T_{sat}	Saturation temperature (K)
q	Heat flux (W×m^{-2})	T_{bulk}	Bulk fluid temperature (K)
u	Velocity (m×s^{-1})	T_{wall}	Wall surface temperature (K)
x	Quality	V	Volume (m^3)
		ΔT	The temperature difference between the wall surface temperature T_w and the saturation temperature T_{sat}

REFERENCES

Enoki, K., Miyata, K. and Mori, H., 2015. Modification of the Prediction Correlation for Flow Boiling Heat Transfer in Small Diameter Tubes. Trans. of the JSRAE 32(3), 275-283. (in Japanese)

Enoki, K., Mori, H., Miyata, K., Kariya, K. and Hamamoto, Y., 2012. Boiling Heat Transfer and Pressure Drop of a Refrigerant Flowing in Small Horizontal Tubes. Proc. of the 3rd Int. Forum on Heat Transfer, Nagasaki, Japan, HTSJ, IFHT2012-193.

Kurose, K., Miyata, K., Hamamoto, Y and Mori, H., 2018. Flow Boiling Heat Transfer and Flow Distribution in Non-uniformly Heated Parallel Mini-channels. Proc. of 3rd Thermal and Fluids Engineering Conference, Fort Lauderdale, USA, ASTFE, 1499-1502.

Kawasuso, T., Kurose, K., Miyata, K., Hamamoto, Y and Mori, H., 2017. A Simulation for the Flow

Distribution and Unsteady Behavior of Flow Boiling in Parallel Mini-Channels. Trans. of the JSRAE 34(4), 463-471. (in Japanese)

Lemon, E. W., Huber, M. L. and McLinden, M. O., 2013, Standard Reference Database 23 Version 9.1. NIST.

Noboritate, W., Kurose, K., Miyata, K. and Hamamoto, Y., 2019. An Experiment on Flow Boiling Heat Transfer of R410A Heated Non-uniformly between Two Parallel Mini-Channels. Proc. of the 5th International Conference on Polygeneration, Fukuoka, Japan, I^{2}CNER, ICP2019-032.

Onishi, H., Tokumoto, D., Haruki, M. and Tada, Y., 2017. Effect of inner diameter difference of parallel micro channels in airfoil-shaped tube on refrigerant distribution and evaporation characteristics, Proc. of NHTS54, Omiya, Japan, HTSJ, F244. (in Japanese)

Yoshida, S., Mori, H., Kakimoto, Y. and Ohishi, K., 2000. Dryout Quality for Refrigerants Flowing in Horizontal Evaporator Tubes. Trans. of the JSRAE 17(4), 511-520. (in Japanese)

Manuscript ID: 1010
DOI: 10.18462/iir.icr.2019.01

Investigation of magnetic field effect on frost formation on substrate

Yu MENG[(a)], Bin LIU[(a)], Rui ZHANG[(a)], Aiqiang CHEN[(a)], Georges EL ACHKAR[(a)], Rachid BENNACER[(a)]

[(a)]Tianjin Key Lab of Refrigeration Technology1, Tianjin University of Commerce, P.R.C, 300134, lbtjcu@tjcu.edu.cn

ABSTRACT

To reduce and avoid the frost on the cold fan surface is one of the most important way to improve the efficiency of the refrigeration system in the cold room. In the paper, the effect of different magnetic intensity on the condensing temperature and the freezing temperature of the wet air with a relative humidity of 45% and an initial temperature of 25°C were studied under the condition of a temperature decreasing rate of 5°C /min and the end temperature of -20°C. The results shown that frost formation process included five stage, such as the condensation, the combination and growth, shrink and taller, freezing and frost formation. As the magnetic field intensity increases gradually, the degree of undercooling gradually increases, the amount of frosting decreases, and the amount of frosting has a linear relationship with the intensity of the magnetic field.
key words: Magnetic Field, Condensation, Degree of Supercooling, Frost Quality.

1. INTRODUCTION

When wet air flows through the cold surface, if the cold surface temperature is lower than the air dew point temperature, the water vapor in the air will condense on the cold surface; if the cold surface temperature is also lower than the triple point temperature of the water, then the cold surface may occur frosting. Frosting problems are more widespread in the fields of refrigeration, air conditioning heat pumps, and refrigeration. Since the frost layer is a porous material composed of ice crystals and humid air, the effective thermal conductivity is small, so the frost layer increases the heat transfer resistance outside the evaporator and reduces the heat transfer coefficient; at the same time, the frost layer partially blocks the air side passage. Increase the flow resistance, thereby reducing the air flow, causing the heat exchange of the evaporator to decrease, and even causing system failure in severe cases. Therefore, the evaporator must be frosted regularly so that it consumes additional energy while it also causes instability in the operation of the system. The problem of frost on the surface of the evaporator has always been one of the most difficult problems in the field of refrigeration and air conditioning. Scholars at home and abroad have conducted a lot of experimental and theoretical research in recent decades. Although many academic achievements have been made, people have attached the understanding of the frosting process under the physical field is still not very clear.

Mok J.H. et al. (2014) researched the PEF strength of 1.78 V/cm with 0.5 duty ratio at various working frequencies were applied to 0.9% NaCl solution at -20 ºC to test the effects of PEF frequencies on ice crystallization. It is found that the phase transition time is shortened with the increase of electric field frequency, and the shortest phase transition time is 1443±2s. Under the action of PEF, the ice crystal pattern tends to the same roundness; the solution is presented under the magnetic field of the same pole and opposite pole. Obtain different ice crystal patterns, and the shortest phase change time is obtained under the condition of opposite poles; when PEF and SMF are used in superposition, the ice crystal is the smallest and the phase transition time is the shortest. Ding Zhenrui (2011) and others separately treated the tap water and the deionized water after boiling in a magnetic field of 2000 Gs to compare the changes in viscosity, surface tension and density after magnetization and magnetization. The experimental results show that under the action of the magnetic field, as the magnetization time changes periodically, there is no linear change, and multi-value changes occur, indicating that the effect of the magnetic field is not as large as possible, Wang and others believe that the thermal motion of charged atoms in water generates a Lorentz force. Because water

molecules are polar molecules, the positive charge center and the negative charge center are opposite.

2. EXPERIMENT

2.1. Experimental Device

Fig. 1 shows the experimental schematic diagram and some devices. The whole experimental system uses Linksys32 software to control the cooling rate of the liquid nitrogen cold stage. The temperature accuracy is 0.1°C. The Leica microscope is observed at 50X~200X without magnetic field, 20Gs, 25Gs, 30Gs. 35Gs, 40Gs, 45Gs, 50Gs, 55Gs, 60Gs, -20°C bare copper surface droplet crystallization process, using MX100 get temperature data, and electronic weigh with the bottom plate (Accuracy：0.01mg).

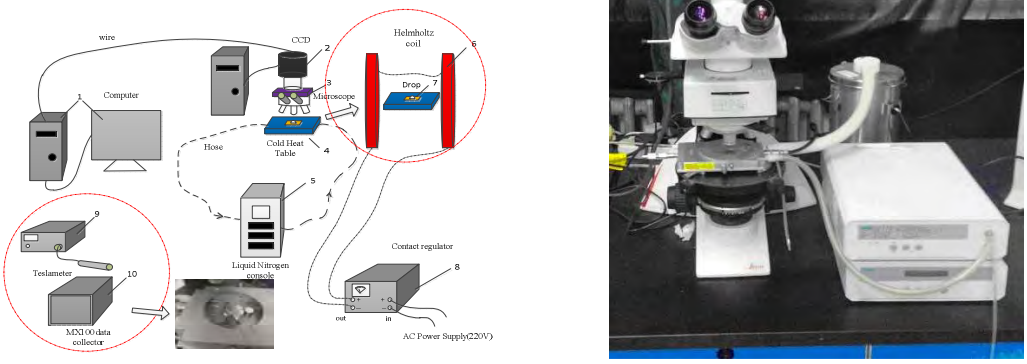

Figure 1: Experimental device schematic
1,2-Computer 3- Leica Microscope 4- Cold Heat Table 5-Liquid Nitrogen console 6- Helmholtz coil 7-Water drop 8-Contact regulator 9-Teslameter 10- Data acquisition instrument

In the experiment, select a common copper base with a size of 40mm × 40mm and a thickness of 1.5mm. The liquid is deionized water. Using the DSA100 of KRUSS, the droplets of 0.01ml are completely stabilized after the wetting on the bottom plate. The contact angle, ambient temperature control 25°C, relative humidity 49%, as shown in Fig.2, its contact angle is stable between 60 ° ~ 70 °.

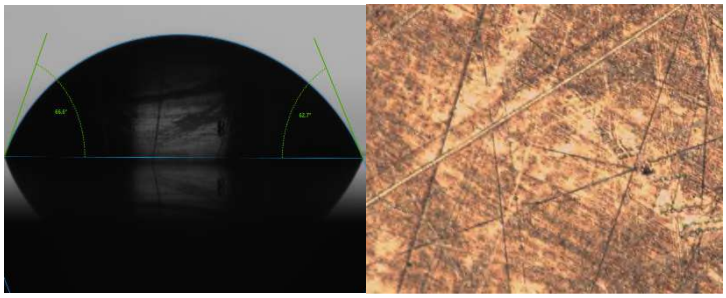

(a) **(b)**

(a) DSA100 Measure the contact Angle of droplets on bare copper surface (b) Surface of bare copper substrate under microscope
Figure 2: The contact Angle of the droplet under the bare copper base plate

2.2. Experimental Methods and Steps

(1) The droplets with a volume of 0.01 ml were dropped at the center of the bare copper substrate by hanging drop method. The humidity at a relative humidity of 49% and a temperature of 25°C was 5°C/min. The presser causes the center intensity of the alternating magnetic field to eventually bring the bottom plate temperature constant at -20°C.
(2) Connect to the 220V AC power supply, use the contact voltage regulator (TDGC2-3, 0V~250V) to adjust the output DC voltage. The Helmholtz coil center magnetic field meets the experimental requirements: 20Gs, 25Gs, 30Gs, 35Gs, 40Gs, 45Gs, 50Gs, 55Gs, 60Gs, magnetic field generator adjustment accuracy of 0.5Gs, Tesla meter measurement error range of ± 0.1Gs.

(3) The experiment used deionized water. The droplet is titrated on a cold stage by a pipette, and a small droplet is first dropped by the titration, and then the needle is inserted into the droplet, then slowly dripped, so that the shape of the droplet is a part of a circle, each time the titration volume of the droplet is 0.01 ml; two thermocouples are respectively connected to the center and surface of the droplet; the temperature and moisture content of the air are determined to be 25°C and 49%, respectively, and the outer lid is covered, and the inner cavity is in a Sealed state; add liquid nitrogen to liquid nitrogen dewar, connect the dewar tube to the cold stage, open the cold stage switch, connect the cold stage Linksys32 software, set the temperature rate to 5°C / min, set the final temperature to -20°C; open the real-time temperature observation record button. Open the software, Leica camera software, and click the Linksys32 cooldown button and the MX100 record button. During the cooling process, especially during the crystallization process, when the field of view light at the center of the droplet is observed to be dark, and the crystal is formed, the observation is stopped.

3. PHENOMENON AND ANALYSIS

3.1. Additional Degree of supercooling

It is found that under the action of DC magnetic field, the crystallization temperature of the droplets decreases, the degree of subcooling increases, and the degree of subcooling of the droplets is:

$$\Delta T = T_n - T_S \quad \text{Eq.(1)}$$

The degree of subcooling varies with the intensity of the magnetic field as shown in Fig.3. At a temperature of about -2°C, a sheet-like structure appears inside the droplet. When completely crystallized, the inside can see the clear crystal nucleation, and Internal bubbles after crystallization.

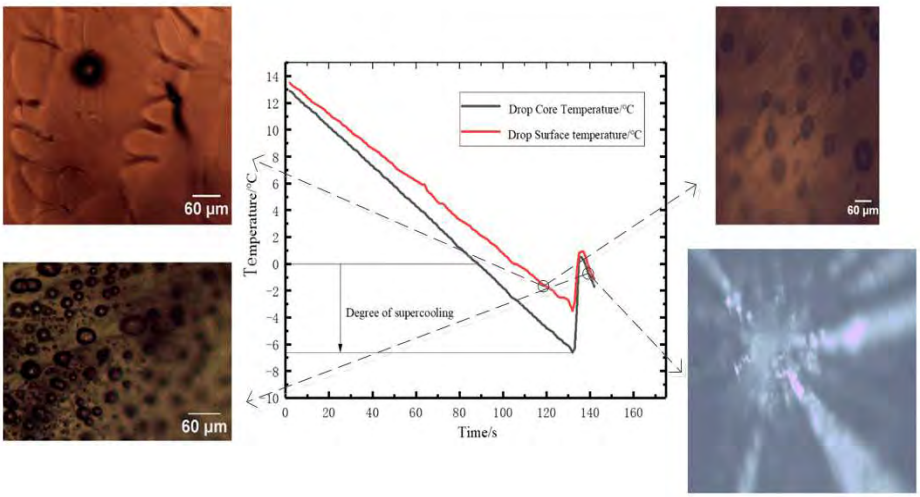

Figure 3: Change of droplet surface temperature and center temperature

By theoretically calculating the influence of different magnetic field intensities on the degree of subcooling, the magnetic field has an additional drive for the movement of water molecules. Under the action of the magnetic field, the additional subcooling under the action of the magnetic field changes is:

$$\Delta T_B = 2.03 \times 10^{-4} B^2 \quad \text{Eq. (2)}$$

For the center of the test plate, the magnetic field intensity is:

$$\mathrm{B} = \frac{\mu_0 NIR^2}{(\frac{5}{4}R^2)^{\frac{3}{2}}} \quad \text{Eq. (3)}$$

According to Eq.2, calculate the theoretical supercooling degree of 20Gs, 25Gs, 30Gs, 35Gs, 40Gs, 45Gs, 50Gs, 55Gs, 60Gs, and compare with the experimental supercooling degree to obtain Table1.

Table 1. Additional subcooling and theoretical values under magnetic field versus experimental values

Magnetic field intensity/Gs	Theoretical value/°C	Experiment value/°C	Deviation/°C
20	0.08	0.62	0.54
25	0.13	0.74	0.61
30	0.18	2.40	2.22
35	0.25	2.12	1.87
40	0.32	2.00	1.68
45	0.41	1.92	1.51
50	0.50	1.85	1.35
55	0.61	1.66	1.05
60	0.73	2.18	2.18

There are three reasons why the theoretical and experimental values are deviated and the degree of supercooling of the droplets does not change linearly with the magnetic field intensity under the action of the magnetic field: 1. The number of molecules of the crystal nucleus set by the theoretical formula is constant, with the intensity of the magnetic field. The number of molecules that change the nucleation will change. 2. The hydrogen bonds of water molecules are constantly breaking and combining. The equilibrium state of hydrogen bonds in water molecules changes under the action of magnetic field. 3. At the microscopic level, the magnetic field is added. After that, the electron cloud of the water molecule will change, and the interaction force between the water molecules will change. These three factors will cause the energy change of the droplet nucleation, and the subcooling of the droplet changes.

As shown in Fig. 4, when the electromagnetic field intensities are 0Gs, 20Gs, 25Gs, 30Gs, 35Gs, 40Gs, 45Gs, 50Gs, 55Gs, 60Gs, the subcooling degrees are: 5.83℃, 6.34°C, 6.56°C, 7.56°C, 8.34°C, 7.67°C, 6.78°C, 7.13°C, 7.42°C, 7.91°C.

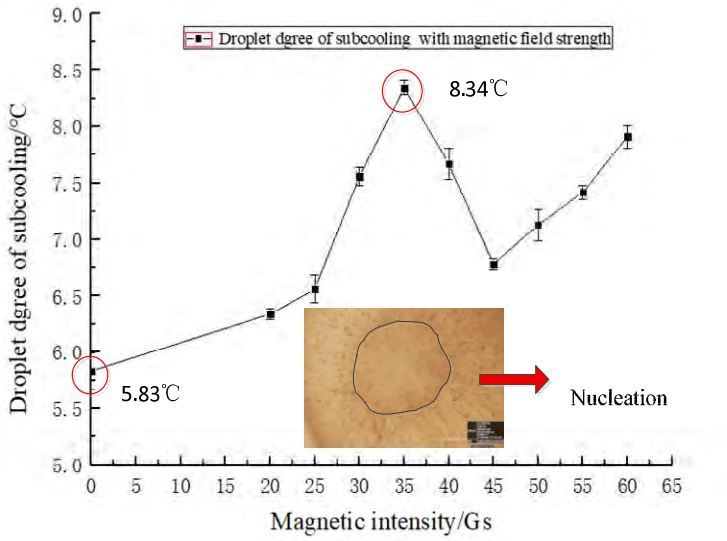

Figure 4: Droplet degree subcooling under different magnetic field intensities

Combined with the theoretical values of the additional subcooling under different magnetic field strengths and the experimental values, it is found that with the increase of the magnetic field intensity, the additional supercooling degree gradually increases, and the deviation is larger at 30Gs and 60Gs.The magnetic intensity changes the resonance of the molecules in the liquid, induces the electric dipole moment, changes or fission of the bonds inside the molecule, changes the configuration of the molecules to cause changes in the physical properties of the liquid; in addition, the effect of the magnetic field is beneficial to the atoms around the liquid. The two-electron layer structure is formed to be charged, so that the water molecule clusters have a large deviation in the supercooling degree under the two magnetic field intensities.

3.2. Magnetic Field Frosting Visualization

The experimental setup is the same as that of Fig.5 and Fig.6. The temperature in the closed chamber of the cold stage is controlled at 25°C, and keep the humidity at 49%. The liquid nitrogen is poured from the liquid nitrogen tank into the Dewar and connected to the cold stage. Adjust the contact voltage to a stable output voltage, so that the AC magnetic field is at 60Gs (the molecular crystallization drive is obvious under the magnetic field intensity), turn on the button of the cold stage device, open the Linksys32 software, connect the cold stage, set the temperature rate to 5°C /min, finally let the cold stage temperature reach -20°C, keep it constant.

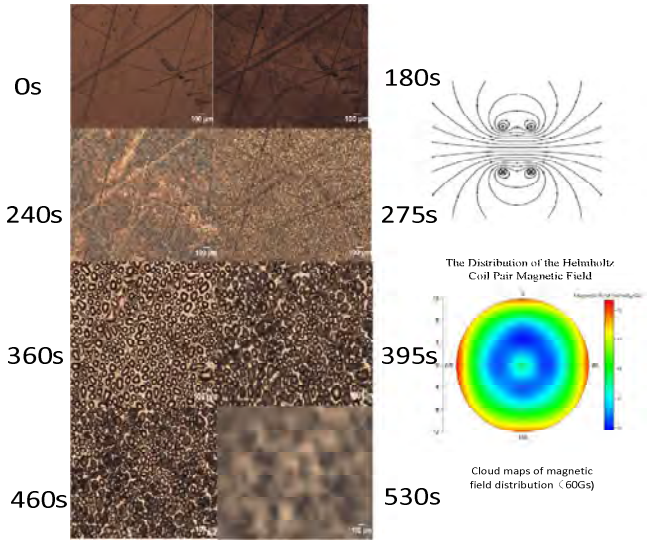

Figure 5: Magnetic field intensity under 60 Gs, the temperature is 25℃ relative humidity 49% bare copper surface frosting process

Under the action of the electromagnetic field, the frost crystals that have just begun to form are independent and are not connected together. The ice crystals formed by the droplets without the magnetic field are connected together to form a piece, and the frost crystal formed is more loose.
The water molecules in the liquid state do not exist as individual water molecules, but form a cluster under the action of hydrogen bonds. The hydrogen bond acts stronger than the interaction between molecules, and the hydrogen bonds of water molecules in the liquid water They are in a state of balance in constant synthesis and fracture. It is proved by spectroscopy that under the action of the magnetic field, the hydrogen bond angle between water molecules changes, and the bond angle of the water molecules after magnetization changes from 104.5°C to 103°C, which causes hydrogen bond rupture and the effective diameter of water molecules becomes shorter. Under the action of an electromagnetic field, the droplet size formed on the cold surface is small. Water molecules are polar molecules under the action of electromagnetic fields, and the droplets increase the probability of arrangement in the direction of the magnetic field, so the droplet distribution is more uniform under the action of the electromagnetic field.

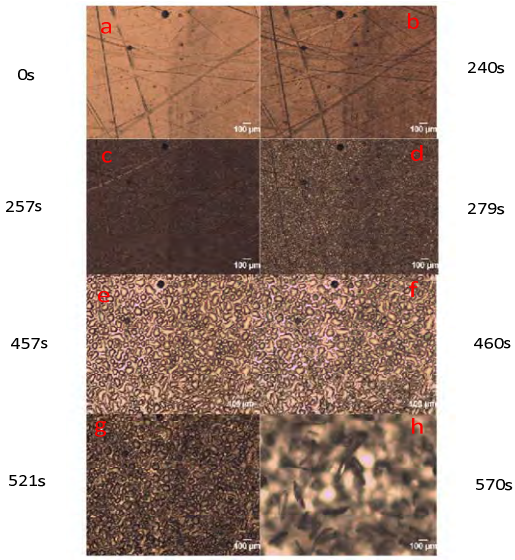

Figure 6: Without magnetic field, the temperature is 25℃, relative humidity 49% bare copper surface frosting process

In the course of the experiment, as shown in Fig.6, it can be observed that the initial stage of frost formation on the cold surface can be divided into the following processes: as the temperature decreases, the core is condensed on the cold surface to form a very small liquid. Dropping, under the microscope, it can be observed that dense black droplets on the surface of the cold table cover the entire cold stage, and blackening on the cold surface can be observed in the image. In a short period of time, small droplets will spread over the entire cold surface. Small droplets on the cold surface will slowly grow up around the small droplets. Due to the long assembly of the droplets, some places on the bottom plate are exposed. Come out, in these bare places will continue to condense nucleation to form small droplets, these small droplets will be swallowed by the large droplets around, the contact area of large droplets with the cold surface will increase. After that, the large droplets slowly shrink and then grow taller. The process of droplet growth then repeats the above process. As the temperature of the cold stage decreases, it rapidly crystallizes when the temperature of the droplet drops to a certain temperature. After crystallization, the tip will grow taller, and tiny crystals will form on the upper surface of the crystal, and then the frost crystal will grow slowly. After growing up, the frost crystals are mainly in the form of flakes, which is the initial stage of the frost growth. After the frost slowly grows up, the frost crystal slowly grows into leaves.
Compared with the frosting on the bare copper surface with magnetic field and no magnetic field, it is found that the nucleation particle size tends to be orderly and the shape is more regular under the action of magnetic field. In the total time of frosting, the addition of magnetic field to suppress the frosting process has no significant effect, only It is reflected in the increase of nucleation supercooling; but for the frost layer structure, the layered crystal structure is more obvious under the action of magnetic field, which is more conducive to defrosting.

3.3. The Relationship between Frosting Mass and Magnetic Field Intensity

When the frost crystal is not growing, use the electronic balance to weigh the total mass of the copper plate and the frost. The mass of the copper plate is known to be 473.00 mg. The change of the frosting mass and the magnetic field intensity is shown in Fig.7, and relevance about the magnetic field intensity and the frosting mass are given. The linear fit relationship of the frost amount is shown in Fig.7.

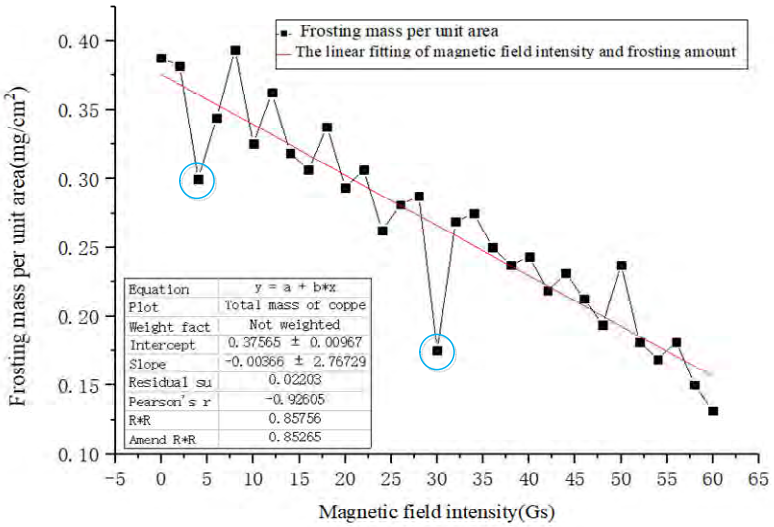

Figure 7: Linear fitting of frost amount per unit area and magnetic field intensity

As the intensity of the magnetic field increases, the per unit area of frosting gradually decreases. As shown in Fig.7, the assumption is made for the special point of the magnetic field intensity of 8Gs. At the initial stage of the magnetic field, the water clusters are not completely below 8Gs. Magnetization, the electrons easily transition from a simple state to a spin-three pure state under the action of a magnetic field, and the transition is hindered in turn, so the molecules in the liquid in the pure state of the spin cause the hydrogen bond to occur to a certain extent. Breaking, the molecular cluster breaks, changing the intermolecular forces, thereby changing some physical properties of the molecule. For the second special point before and after the magnetic field intensity is 30 Gs, as in the case of Table 1 above, the resonance phenomenon causes a sudden decrease in the frosting mass.

Table 2. Linear fit result

	Intercept		Slope		Statistics
	Value	Standard error	Value	Standard error	Amend R^2
The mass of frost per unit area	0.37565	0.00967	-0.00366	2.76729× 10^{-4}	0.85265

The fitting results in Fig.7 show that the goodness of fit R^2= 0.85265, according Table2, the results have a good fit, so the linear relationship between the magnetic field intensity and the total mass of the copper plate and frost is given as follows:

$$\mathrm{M} = -0.00366\mathrm{B} + 0.37565 \qquad \text{Eq.(4)}$$

4. CONCLUSION

when the intensity of the magnetic field increases, the degree of crystallization cold gradually increases, and the crystallization time is prolonged to some extent. The magnetic field intensities are 20Gs, 25Gs, 30Gs, 35Gs, 40Gs, 45Gs, 50Gs, 55Gs, 60Gs. The extra degree of subcooling degrees are 0.62°C, 0.74°C, 2.40°C, 2.12°C, 2.00°C, 1.92°C, 1.85°C, 1.66°C, 2.18°C, and the magnetic field intensity and crystallization under weak magnetic field (0~120Gs). The degree of subcooling changes periodically.

The magnetic field causes the liquid phase to change from disorder to order, from asymmetric structure to symmetrical structure, from mesh structure to layered structure. Using a high-magnification microscope, it can be observed that the initial frosting on the cold surface is divided into: the droplets condense on the cold surface - the droplets grow and devour the surrounding small droplets, the shrinkage grows high - the droplets freeze into ice crystals - the ice crystals are slow Growing up slowly.

The microscopic observation of the additional magnetic field on the exposed copper surface and the frosting without additional physical field revealed that the ice crystals frozen by the magnetic field

had smaller particle size and the crystal growth direction was more orderly, that is more benefits for the frost layer. As the magnetic field intensity increases, the per unit area of frosting mass and the magnetic field intensity have a good linear correlation under the weak field intensity, and the frosting amount has a smaller decreasing trend.

NOMENCKLATURE

B	Magnetic intensity(Gs)	T_n	Actual crystallization temperature(℃)
T_S	Liquid-solid-liquid coexistence temperature(℃)	μ_0	Magnetic permeability under vacuum($4\pi \times 10^{-7} H/m$)
T_B	Extra degree of supercooling (℃)	M	Experimental copper plate and total mass of frost(mg)

REFERENCES

Choi Y. S., Ku S. K., Jeong J. Y., 2015. Changes in Ultra-structure and Sensory Characteristics on Electro-magnetic and Air Blast Freezing of Beef during Frozen Storage. Korean Journal for Food Science of Animal Re-sources, 35(1):27-34.

Ding Zhenrui, Zhao Yajun, Chen Fengling, 2011. Study on the magnetization mechanism of magnetized water. Acta Physica Sinica, 60(6):432-439.

Guo, Z., Liu, W., Su, B.L., 2011. Superhydrophobic surfaces: from natural to biomimetic to functional, J. Colloid Interface Sci. 353 (2) 335–355.

Hao, Q., Pang, Y., Zhao, Y., Zhang, J., Feng, J., S. Yao, 2014. Mechanism of delayed frost growth on superhydrophobic surfaces with jumping condensates: more than interdrop freezing, Langmuir 30 (51) 15416–15422.

Hayashi, Y., Aoki, A., Adachi, S., 1977. Study of Frost Properties Correlating with Frost Formation Types. Transactions of the ASME, Journal of Heat Transfer, 99(2): 239-245.

Kawata, T., Kaku, M., Fujita, T., Ohtani, J., 2010.Water molecule movement by a magnetic field in freezing for tooth banking, Biomedical Research, (21): 351–354.

Kiani,H., Sun, D.W., 2011. Water crystallization and its importance to freezing of foods: A review.Trends in Food Science & Technology, 22(8):407-426.

Kim, C., Shin, J., Tikhonov, A.V.,2003. Experimental study on frost structure on surfaces with different hydrophilicity: density and thermal conductivity, J. Heat Transf. 125 (1) 84–94.

Kim, H., Kim, D., Jang, H., Kim, D.R., Lee, K.S., 2016. Microscopic observation of frost behaviors at the early stage of frost formation on hydrophobic surfaces, Int. J. Heat Mass Transf. 97:861–867.

Liangliang Shan, 2018.Visualization of frosting under weak DC magnetic field. Tianjin University of Commerce.(Chinese)

Mok, J. H., Choi, W. S., Park, H., 2014. Emerging pulsed electric field (PEF) and static magnetic field (SMF) combination technology for food freezing, International Journal of Refrigeration, 50:137-145.

Moallem, E., Cremaschi, L., Fisher, D.E., 2017. Effects of frost growth on louvered folded fins of microchannel heat exchangers on the time-dependent air side convective heat transfer coefficient, Exp. Therm. Fluid Sci. 88 326–335.

Onuki. A.,2002. Phase Transition Dynamics. Cambridge: Cambridge University Press.

Qian, B., Shen, Z.,2005. Fabrication of superhydrophobic surfaces by dislocationselective chemical etching on aluminum, copper, and zinc substrates, Langmuir 21 (20) 9007–9009.

Qin, H., Li, W., Dong, B., 2014. Experimental study of the characteristic of frosting on low-temperature air cooler, Exp. Therm. Fluid Sci. 55 106–114.

Rahman, M.A., Jacobi, A.M.,2012. Wetting behavior and drainage of water droplets on microgrooved brass surfaces, Langmuir 28 (37) 13441–13451.

Steele, A., Nayak, B.K., Davis, A., Gupta, M.C., Loth, E., 2013. Linear abrasion of a titanium superhydrophobic surface prepared by ultrafast laser micro-texturing, J. Micromech. Microeng. 23 (11) 115012.

Sahin. A. Z., 2000. Effective Thermal Conductive of Frost during the Crystal Growth Period. International Journal of Heat and Mass Transfer,43(4): 539~553.

Wang, C. C., Huang, R. T., Sheu. W. J., 2004. Some Observation of the Frost Formation in Free Convection with and without the Presence of Electric Field. International Journal of Heat and Mass Transfer, (47): 3491-3505.

Wang, F., Liang, C., Zhang, X., 2018. Research of anti-frosting technology in refrigeration and air conditioning fields: a review, Renew. Sustain. Energy Rev. 81: 707–722.

Wang, F., Liang, C.H., Yang, M.T., Zhang, X.S.,2015. Effects of surface characteristics on liquid behaviors on fin surfaces during frosting and defrosting processes, Exp. Therm. Fluid Sci. 61 113–120.

Zhongliang Liu, Lingyan Huang, Yujun Gou, Yaomin Liu, 2010. Research progress in frosting and frost suppression techniques. Journal of Refrigeration, 31(04):1-6+13. (Chinese)

Zhang, L., Hihara, E., Saikawa, M., 2012. Combination of air-source heat pumps with liquid desiccant dehumidification of air, Energy Convers. Manage. 57 107–116.

Zhang, X.J., Wu, P., Qiu, L.M., Zhang, X.B., Tian, X.J.,2010. Analysis of the nucleation of nanofluids in the ice formation process, Energy Convers. Manage. 51 (1) 130–134.

Manuscript ID: 1018
DOI: 10.18462/iir.icr.2019.1018

Thermal design of a vaporizer for cold recovery from LNG-regasification using CO_2 as heat transfer media

Antonio ATIENZA-MÁRQUEZ[(a)], Joan C. BRUNO[(a)], Atsushi AKISAWA[(b)], Alberto CORONAS[(a)]

[(a)] Universitat Rovira i Virgili, CREVER – Group of Applied Thermal Engineering
Tarragona, 43007, Spain, antonio.atienza@urv.cat
[(b)] Tokyo University of Agriculture and Technology, Engineering Systems Department
Tokyo, 184-8588, Japan, akisawa@cc.tuac.ac.jp

ABSTRACT

Liquefied Natural Gas (LNG) is a valuable exergy source because of its cryogenic temperature (-162ºC). However, LNG is usually regasified in Open Rack Vaporizers using seawater as heat source and without cold recovery.
Alternatively, double-bundle vaporizers are a promising technology for cold recovery from LNG-regasification. These vaporizers are like shell-and-tube heat exchangers with a thermal buffer fluid which vaporizes taking heat from a heat transfer media and condenses using LNG as heat sink. If the heat transfer media is properly selected, LNG will be regasified with cold recovery.
This paper deals with the thermal design of a double-bundle vaporizer using CO_2 as heat transfer media for LNG cold recovery and its subsequent use in refrigeration applications.
Since the thermal buffer fluid has a critical influence on the design, different candidates are considered. Among them, ethylene reports the lowest heat transfer area required for any tube lengths and diameters.
Keywords: Liquefied Natural Gas (LNG), Regasification, Exergy recovery, Double-Bundle Vaporizer, Carbon Dioxide, Thermal Buffer Fluid.

1. INTRODUCTION

The mitigation of climate change effects is one of the major challenges that today's society should face. In this sense, Natural Gas (NG) and, particularly, Liquefied Natural Gas (LNG) is forecasted to play a key role in the transition towards a decarbonized energetic model (International Energy Agency, 2018). Since the chemical composition of natural gas is mainly methane, natural gas is one of the most environmentally friendly fossil fuels with a lower carbon footprint than coal or oil and its combustion has near zero emissions of NO_X and SO_X gases. On the other hand, LNG entails a solution for the long-distance transport of natural gas and it is obtained by the liquefaction of the pre-treated natural gas, which is an intensive energy process (around 800 kWh per tonne of Natural Gas liquefied). Because of the liquefaction process, the temperature of LNG drops down to 111 K and this very low temperature makes LNG a "gold mine" from the exergetic point of view.
Previously to be supplied to costumers, LNG has to be regasified. Regasification is an opportunity to recover part of the energy consumed in the liquefaction process because the low-temperature cold has multiple industrial applications such as cryogenic power cycles, air separation processes, dry ice production, refrigeration applications in deep-freeze warehouses, etc. (Kanbur, 2018). However, the vast majority of LNG regasification facilities worldwide do not recover the LNG exergy. In fact, there are only a few LNG terminals worldwide with LNG cold recovery and most of them are located in Japan. The problem is that there are some hurdles blocking a widespread cold recovery from LNG-regasification. Some of these hurdles have non-technical nature, but others are technical (Atienza-Márquez et al., 2018a). For example, the lack of suitable heat transfer fluids and working fluids, and also the few specialised equipment commercially available. Regarding the equipment, vaporizer units (heat exchangers) play a key role in the challenge of cold recovery from LNG-regasification.
Fig. 1 shows a schematic diagram of the most common technologies of vaporizers utilized in LNG regasification (without LNG cold recovery). These vaporizers are the following:

- *Open Rack Vaporizers and super ORV* (Fig. 1 (A)): In these vaporizers LNG flows inside a set of tube-sheets and it is regasified by taking heat from seawater which flows downward and outside LNG tubes. However, the exergy content of LNG is wasted via seawater.
- *Submerged Combustion Vaporizers* (Figure 1 (B)): LNG stream flows inside a tube bundle submerged in a hot water bath which is heated by the combustion heat of a small fraction of the Natural Gas regasified. In these units, LNG exergy is wasted via the combustion gases.
- *Ambient Air Vaporizers* (Fig. 1 (C)): In these units LNG passes through a set of interconnected tubes which are exposed to the environment. The regasification heat is taken from the ambient air, but LNG exergy is wasted via this medium.
- *Intermediate Fluid Vaporizers* (Fig. 1 (D)): In these units, seawater is also used as heat source to regasify LNG but using an intermediate fluid as thermal buffer media.

According with the above descriptions, only Intermediate Fluid Vaporizers (IFVs) could be a promising alternative to regasify LNG and recover its cold simultaneously because of its structure and the utilization of a buffer fluid. The "conventional" IFV utilized in LNG facilities consist of a sort of shell-and-tube heat exchanger that has an intermediate fluid (e.g., propane) that vaporizes and condenses inside a tank (shell) where a condenser (LNG/NG side) and an evaporator (seawater side) are allocated. To adjust the supplying temperature of regasified NG, an additional heat exchanger integrated in the same unit (thermolator) is used. The company Osaka Gas Co., Ltd. developed originally this kind of vaporizer and Kobe Steel, Ltd. is authorized for its manufacturing. Some of the most remarkable advantages of IFV are: compact volume, environmentally friendly, the low quality required for the seawater and no ice formation (Pu et al., 2014). Another typology of vaporizer that could be a promising option for cold recovery from LNG-regasification are spiral-wound heat exchangers (Ding et al., 2017; La Rocca, 2010). However, the risk of crystallization of the heat transfer media in this type of vaporizer is much higher than for IFV because the heat transfer media is in direct contact with LNG.

But the conventional typology of IFV does not allow the cold recovery from LNG because it uses seawater as heating medium and cannot be used to distribute the cold. However, its structure and materials could be modified and adapted with the aim to use an alternative heat transfer media (instead of seawater) to distribute the cold. For instance, carbon dioxide could be an interesting option (low viscosity at low temperatures, prize, etc.). The objective of this paper is to study the thermal design of a vaporizer for the cold recovery from LNG regasification based on the structure of IFVs. Besides, a comparative assessment is performed between three different candidate intermediate fluids whose diligent selection is essential for a successful design of the vaporizer with LNG cold recovery.

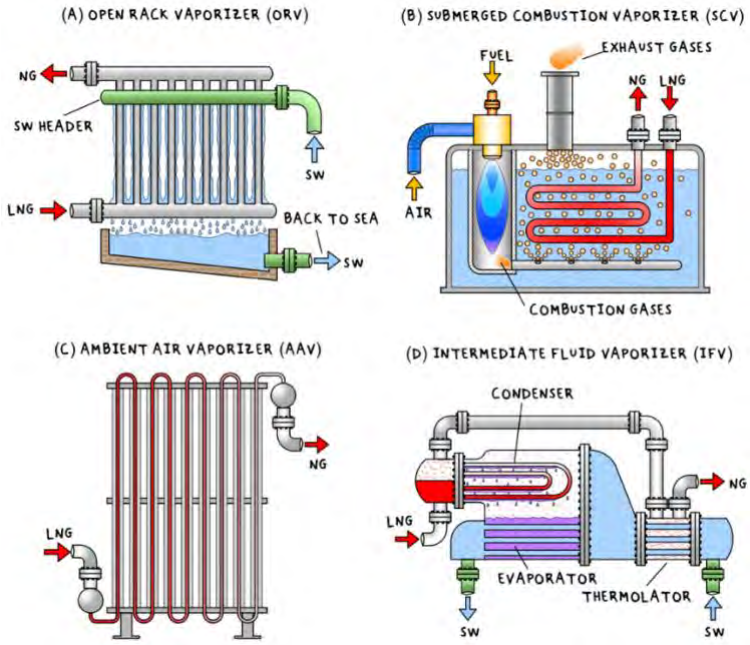

Figure 1: Common technologies of vaporizers utilized in LNG regasification facilities

2. DOUBLE-BUNDLE LNG VAPORIZER

2.1. Description of the vaporizer

Fig. 2 shows the schematic diagram of the proposed LNG vaporizer with cold recovery from LNG-regasification for off-site applications. Although this typology of vaporizer is commonly called "Intermediate Fluid Vaporizer", hereafter in this paper we will refer it as double-bundle vaporizer as in Hewitt (2002).

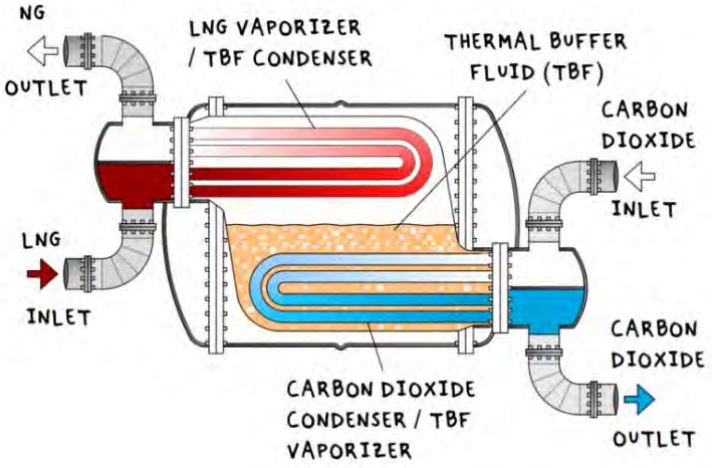

Figure 2: Double-bundle U-tube LNG vaporizer

The proposed vaporizer consists of a shell-and-tube type heat exchanger with two U-tube bundles both inside a single shell. The shell is filled with a fluid that floods the bottoming tube bundle. The LNG flows inside the upper tube bundle. On the other hand, carbon dioxide (CO_2), that flows inside the bottoming tube bundle, is not only used as heating medium to regasify LNG, but also it is used as heat transfer media to recover the cold from LNG. CO_2 enters the tubes at saturated vapour conditions and it leaves the tube bundle as saturated liquid. A similar vaporizer using ethylene as intermediate fluid was proposed in Pineda Quijano et al. (2017) (the vaporizer was called ethylene heat pump), although few details were given about the modelling, geometrical design parameters and the selection of the intermediate fluid. A benefit from using CO_2 instead seawater as heating medium is the mitigation of fouling phenomena that may leads into minor maintenance tasks. Regarding manufacturing materials, cost could be reduced because CO_2 is a non-corrosive fluid and expensive materials (e.g., titanium) are not required.

On the other hand, many authors have selected CO_2 as heat transfer media for long-distance transportation of the cold recovered from LNG-regasification plants to end-users with refrigeration demand (e.g., agro-food industry, commercial areas, etc.). Since liquid CO_2 has lower viscosities at very low temperatures and it requires lower flow rates than, e.g., water/glycol mixtures, the power consumption by pumping can be reduced (Eveloy and Ayou, 2019). Moreover, CO_2 is an environmentally-friendly substance, secure and cheap so that it is a suitable heat transfer media for a low-temperature District Cooling network. However, one of the main drawbacks of using CO_2 as heat transfer media is its relatively high freezing temperature (-55.6 ^{o}C) in comparison with the temperature of LNG at the inlet of the vaporizer (around -160 ^{o}C). Therefore, a special care is required to prevent the freezing of CO_2 inside the tubes. Regarding this issue, the intermediate fluid plays the key role of thermal buffer by "pumping" the heat from the heating medium (CO_2) to the LNG and avoiding the direct contact between CO_2 and LNG. Furthermore, the CO_2 tube bundle has to be fully submerged in the thermal buffer fluid (TBF) pool with the aim to avoid local surface temperatures of tubes below CO_2 freezing point.

The TBF filling the shell is at saturated conditions and it shifts continuously its phase between boiling and condensing. It condenses in the outside surface of the tubes of the upper tube bundle. The latent heat released from the TBF condensation is absorbed by the LNG stream, so that it is regasified. The condensate drops flows downward by the influence of gravity and they are accumulated in the bottoming part of the shell forming a pool that covers completely the CO_2 tube bundle. On the other hand, the TBF vaporizes by absorbing heat from the CO_2 stream in the bottoming tube bundle. Then, the vaporized fluid occupies the upper space of the shell where the LNG/NG tube bundle is located and the system remains working with a kind of closed-loop operation. Definitely, the TBF plays a key

role in this vaporizer and there are research works that deals with the selection of the most suitable TBF. For instance, Xu et al. (2015) discuss about the most suitable TBF as function of the required heat transfer area for a double-bundle vaporizer but using seawater as heat source and without recovering the cold from LNG-regasification.

2.2. Modelling

The model of the vaporizer is developed using the software Engineering Equation Solver (EES) (F-Chart, 2019). The modelling assumptions are:

- Simulation under steady state conditions.
- Thermal and pressure losses are not considered.
- The composition of LNG/NG is assumed as pure methane.
- Kinetic and gravitational energies are not considered.
- Stream of CO_2 is at saturated vapour state at the inlet of the bottoming tube bundle and at saturated liquid state at the outlet.
- The individual tubes of the upper and bottoming bundles have the same length and diameters.
- There are no leakages of any fluid to the environment.
- No flow misdistribution: Fluid flow rates are equally distributed in each individual tube of the tube bundles.
- Length differences between outer and inner U-tubes of the tube bundle are not considered.
- Fouling layers on heat transfer surfaces are not considered.
- The thermal resistance due to tube walls is not considered as it is much lower than the convective thermal resistance.

On the other hand, Table 2 shows the main settled parameters for studying the design of the double-bundle vaporizer presented in this paper. The regasification capacity of the vaporizer unit is chosen with the aim to recover around 15% of the low-temperature exergetic potential in a typical LNG terminal (e.g., the Barcelona LNG terminal in Spain). On the other hand, the velocity of CO_2 streams at vapour state at the entry of the tubes is limited (< 30 m s^{-1}) to avoid problems with erosion of the tube material and vibrations issues. Furthermore, the relatively low temperature of regasified NG at the exit of the vaporizer could allow its utilization for another application (e.g., electric power production in a cryogenic power cycle). In this way, a cascaded LNG exergy exploitation could be stablished to end up with a polygeneration system (Atienza-Márquez et al., 2018a, 2018b).

Table 2. Design parameters and constraints.

Parameter	Value
Regasification capacity of the vaporizer (Q)	5 MW
LNG temperature and pressure at the inlet ($T_{LNG,in}$)	-160 ºC, 4.6 MPa
Regasified natural gas design temperature ($T_{LNG,out}$)	-80 ºC
Inlet and outlet CO_2 temperature ($T_{CO2,in}$; $T_{CO2,out}$)	-50 ºC
Maximum straight length (L) allowed for LNG/NG and CO_2 U-tubes	< 20 m
CO_2 tubes inner wall temperature (average value, T_w)	-54 ºC

The heat transferred (Q) in the vaporizer is calculated from the energy balances in each tube bundle. Hence, the energy balances for the CO_2 tube bundle and the LNG/NG tube bundle are shown in Eq. (1) and Eq. (2), respectively:

$$Q = m_{CO2}\left(h_{CO_2,in} - h_{CO_2,out}\right) \quad \text{Eq. (1)}$$

$$Q = Q_{bc} + Q_{ac} = m_{LNG}\left[\left(h_{LNG,c} - h_{LNG,in}\right) + \left(h_{LNG,out} - h_{LNG,c}\right)\right] \quad \text{Eq. (2)}$$

Since the LNG pressure is above its critical value, it is necessary to divide the heat transfer in LNG/NG tubes into two parts depending on its temperature: heat transferred when the temperature is below the critical value (Q_{bc}); and heat transferred when temperature above the critical value (Q_{ac}). Alternatively, the heat transferred can be also determined from the overall heat transfer coefficient (U) and the heat transfer area (A) as follows:

$$Q = U_{btb}A_{o,btb}\left(\bar{T}_{CO_2} - T_w\right) = \left(\alpha_{o,btb}^{-1} + \alpha_{i,btb}^{-1}\, D_o D_i^{-1}\right)^{-1} A_{o,btb}\left(T_{CO_2} - T_{w,btb}\right) \quad \text{Eq. (3)}$$

$$Q_{bc} = U_{utb,bc}A_{o,utb,bc}LMTD_{subc} = \left(\alpha_{o,utb}^{-1} + \alpha_{i,utb}^{-1}\, D_o D_i^{-1}\right)^{-1} A_{o,utb,bc}LMTD_{bc} \quad \text{Eq. (4)}$$

$$Q_{ac} = U_{utb,ac}A_{o,utb,ac}LMTD_{ac} = \left(\alpha_{o,utb}^{-1} + \alpha_{i,utb}^{-1}\, D_o D_i^{-1}\right)^{-1} A_{o,utb,ac}LMTD_{ac} \quad \text{Eq. (5)}$$

Where the logarithmic mean temperature differences (*LMTD*) are defined as:

$$LMTD_{bc} = \left[\left(T_{TBF} - T_{LNG,in}\right) - \left(T_{TBF} - T_{LNG,c}\right)\right] \cdot \left\{ln\left[\left(T_{TBF} - T_{LNG,in}\right)/\left(T_{TBF} - T_{LNG,c}\right)\right]\right\}^{-1} \quad \text{Eq. (6)}$$

$$LMTD_{ac} = \left[\left(T_{TBF} - T_{LNG,c}\right) - \left(T_{TBF} - T_{LNG,out}\right)\right] \cdot \left\{ln\left[\left(T_{TBF} - T_{LNG,c}\right)/\left(T_{TBF} - T_{LNG,out}\right)\right]\right\}^{-1} \quad \text{Eq. (7)}$$

On the other hand, the heat transfer area based on the outer diameter of the tubes is calculated as a function of the length (*L*) of a single tube (total length of a straight U-tube) and the number of tubes:

$$A_o = (\pi D_o L) \times NT \quad \text{Eq. (8)}$$

Finally, since the wall tube temperature of the CO_2 is a fixed design parameter and the temperature of CO_2 during condensation remains constant, the temperature of the TBF is calculated as:

$$T_{TBF} = T_w - \left[\alpha_{i,btb}D_i \cdot \left(T_{CO2} - T_{w,btb}\right)\right]\left(\alpha_{o,btb}D_o\right)^{-1} \quad \text{Eq. (9)}$$

Notice the remarkably influence of convective heat transfer coefficients (HTCs) on an accurate calculation of the heat transfer areas. Despite there are many correlations published in the literature there is not any correlation generally satisfactory that will give accurate predictions over a wide flow range and valid for any fluid (Sinnott, 2000). In this paper, we have selected those HTCs recommended by specialized heat exchanger design handbooks and research papers dealing with the design of LNG vaporizers. The selected HTCs are the following: Correlation of Shah (2016) for the condensation of CO_2 inside the tubes; for TBF boiling, correlations of Mostinski (1963) or Jung et al. (2004) are used depending on the nature of the TBF; for the LNG boiling, the HTC correlation of Bae and Kim (2009) is used when the temperature of LNG is below its critical value, and the correlation of Liang et al. (1998) when the temperature of LNG is above its critical value.

2.3. Requirements of the Thermal Buffer Fluid (TBF)

The TBF candidate must fulfil the following features:

1. Freezing point lower than -162ºC to prevent crystallization of the fluid.
2. The normal boiling point must be lower than -50ºC, meaning that the saturation pressure must be higher than the ambient pressure at -50ºC. If the TBF operates at a vacuum pressure, air infiltrations can occur.
3. Critical temperature higher than LNG temperature to allow condensation of the TFB.

Therefore, there are only few fluids that can be considered as potential candidates: Ethane, Ethylene and PFC-14. Table 3 shows their main thermodynamic data, Global Warming Potential and safety group. Notice that the environmental impact of PFC-14 in terms of GWP is much higher than for ethane and ethylene. By the contrary, PFC-14 is a non-flammable substance while ethane and ethylene both have a high flammability risk. On the other hand, although propane is the most common TBF utilized in conventional double bundle vaporizers in which seawater is used as heat source, it is dismissed in this application due to its relatively high normal boiling point (-42.1ºC).
On the other hand, to predict the boiling heat transfer coefficient of the TBF, the correlation of Jung et al. (2004) which is suitable for flammable refrigerants (e.g., hydrocarbons) is used for ethane and ethylene; and the correlation given by Mostinski (1936) is used for PFC-14.

Table 3. Thermodynamic data of the candidate TFB

Fluid	Freezing point (ºC)	Normal boiling point (ºC)	Critical temperature (ºC)	Critical pressure (kPa)	Global Warming Potential (100 years)	Safety
PFC-14	- 183.6	- 128.1	- 45.6	3,750	7,340	A1
Ethane	- 182.8	- 88.6	32.2	4,872	5.5	A3
Ethylene	- 169.2	- 103.8	9.2	5,042	3.7	A3

3. RESULTS AND DISCUSSION

Table 4 and Table 5 show the results obtained when using each candidate TBF for two total straight U-tube lengths: 15 m and 19 m. In the case of Table 4, the results correspond to a tube diameter of 19/16.1 mm while those of Table 5 corresponds to diameters of 25.4/22.9 mm. The total heat transfer area (A_{tot}) based on the outer tube diameter is used to determine the size of the vaporizer. Also, the overall heat transfer coefficients are shown. The following observations can be withdrawn:

- The longer the tubes, the lower heat transfer area is required. If longer, the number of tubes needed to achieve the heat transfer area required are lower so that the velocity of fluid across tubes are higher. As a consequence, the heat transfer enhances because HTCs inside tubes increase with velocity. This statement is valid for both tube diameters evaluated, although the maximum length of the tubes might be limited by constructive constraints.
- The narrower the tube, the lower heat transfer area is required for all the candidates. Larger tube diameters lead into lower velocities of the CO_2 across them and, therefore, the heat transfer coefficient for the condensation inside the tubes decreases.
- Since the CO_2 temperature and the tube inner wall temperature are fixed design parameters, the heat transfer area of the CO_2 tube bundle does not depend on the thermal buffer fluid. As a result, the number of tubes and heat transfer area for the CO_2 tube bundle is the same for the three candidate TBFs.
- Regardless the length and the diameter of the tubes, ethylene is the candidate which reports the lowest heat transfer area. Since the features of ethane and ethylene are quite similar, the heat transfer area required by them is similar as well. However, major differences are observed for PFC-14. Because the critical temperature of PFC-14 is relatively low in comparison with the other candidates, the latent heat released along its condensation is the lowest, so a higher heat transfer area is required.

Table 4. Results obtained for each TBF (Tubes: D_o/D_i 19/16.1 mm)

L (m)	TBF	CO_2 tube bundle			LNG/NG tube bundle				T_{TBF} (ºC)	A_{tot} (m^2)
		Nt	A_o (m^2)	U_o (W m^{-2} K^{-1})	Nt	A_o (m^2)	$U_{o\,(T<Tc)}$ (W m^{-2} K^{-1})	$U_{o\,(T>Tc)}$ (W m^{-2} K^{-1})		
15	PFC-14	394	352.8	1990	255	228.3	442.6	575.7	-57.1	581.1
	Ethane	394	352.8	1559	120	107.4	974.2	1371	-59.1	460.2
	Ethylene	394	352.8	2097	111	99.4	991.8	1374	-56.8	452.2
19	PFC-14	151	171.3	3638	191	126.6	483.4	606.1	-58.0	387.9
	Ethane	151	171.3	2849	90	102.1	1070	1437	-60.2	273.4
	Ethylene	151	171.3	3832	83	94.1	1084	1432	-57.6	265.4

Table 5. Results obtained for each TBF (Tubes: D_o/D_i 25.4/22.9 mm)

L (m)	TBF	CO_2 tube bundle			LNG/NG tube bundle				T_{TBF} (ºC)	A_{tot} (m^2)
		Nt	A_o (m^2)	U_o (W m^{-2} K^{-1})	Nt	A_o (m^2)	$U_{o\,(T<Tc)}$ (W m^{-2} K^{-1})	$U_{o\,(T>Tc)}$ (W m^{-2} K^{-1})		
15	PFC-14	355	424.9	1697	239	286.1	344.2	490.8	-56.9	711.0
	Ethane	355	424.9	1332	117	140.0	721.6	1143	-58.8	564.9
	Ethylene	355	424.9	1790	107	128.1	746.2	1161	-56.6	553.0
19	PFC-14	242	366.9	1934	171	259.3	385.9	521.6	-57.0	626.2
	Ethane	242	366.9	1514	81	122.8	838.4	1241	-59.0	489.7
	Ethylene	242	366.9	2039	75	113.7	855.8	1244	-56.7	480.6

On the other hand, Fig. 3 shows the temperature profile in the vaporizer with ethylene as TBF and for tubes of 19 m-length and 19 mm-outer diameters. According to the results obtained, the temperature of LNG is below its critical point in a first part of the tubes and it is above it in the final part (-82.6ºC if natural gas is assumed as pure methane). On the other hand, since both CO_2 and

the TBF are pure substances and are in phase change conditions, their temperatures remains constant.
But the most valuable fact is that the TBF transfers the heat between CO_2 and LNG but avoiding the risk of CO_2 crystallization in the bottoming tube bundle. As shown in Fig. 3, this fact even more remarkably in the first part of the heat exchanger where the temperature difference between LNG and CO_2 is higher than 100ºC. Notice that the temperature of LNG/NG is lower than the freezing point of CO_2 along the whole heat exchanger. Therefore, the role of the TBF is crucial.

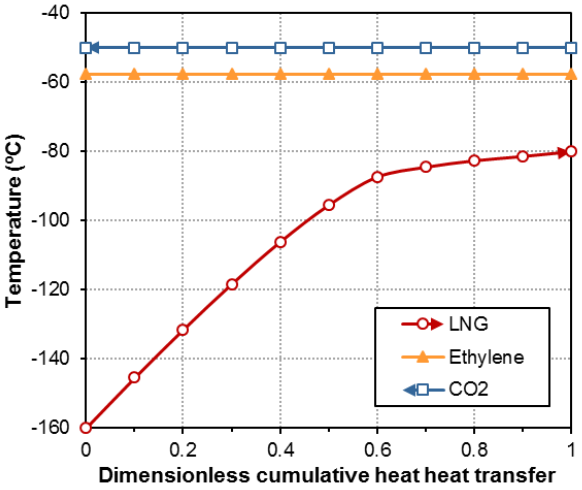

Figure 3: Temperature profile in the double-bundle LNG vaporizer

4. CONCLUSIONS

This paper deals with a double bundle vaporizer that allows the cold recovery from LNG-regasification for off-site applications (e.g., refrigeration in agro-food industry warehouses, commercial areas, etc.) and using CO_2 as heat transfer media. A thermodynamic and heat transfer model has been developed with the aim to study the thermal design of the vaporizer. Because the buffer fluid utilized in the vaporizer has a crucial influence on the design, we have selected the most suitable candidate based on the lower heat transfer area required. The main conclusions are:

1. Three candidate thermal buffer fluids have been compared: Ethylene, Ethane and PFC-14. All them fulfil the constrains regarding freezing point, critical temperature and normal boiling point. Among them, ethylene is the most suitable because it reports the lower heat transfer area required. This conclusion match with that of some references in the literature.
2. With the aim to reduce the heat transfer area required, long and narrow tubes are preferable for any of the candidate thermal buffer fluids compared. However, the selection of these geometrical parameters could be subjected to constructive limitations and other design constraints (e.g., velocities of streams inside tubes to avoid fouling or vibrations).
3. A diligent selection of convective heat transfer coefficients is crucial for an accurate calculation of the heat transfer area. If the heat transfer area is underestimated, the condensation of CO_2 inside the tubes might be only partial. By contrary, an overestimation of the area could cause an unduly CO_2 subcooling so that freezing problems could appear.

ACKNOWLEDGEMENTS

Antonio Atienza-Márquez acknowledges the Spanish Ministry of Science, Innovation and Universities the financial support of the predoctoral contract FPU15/04514.

NOMENCLATURE

A	Heat transfer area (m^2)	*Subscripts*	
α	Convective heat transfer coefficient (W m^{-2} K^{-1})	*ac*	Above critical point
D	Diameter (m)	*bc*	Below critical point
h	Enthalpy (kJ kg^{-1} K^{-1})	*btb*	Bottoming tube bundle

L	Total length of a straight U-tube (m)	*c*	Critical point
LMTD	Logarithmic mean temperature difference (K)	*in*	Inlet
m	Mass flow rate (kg s^{-1})	*o*	Based on outer diameter
Nt	Number of tubes	*out*	Outlet
Q	Heat flux (kW)	*tot*	Total (area)
T	Temperature (K)	*utb*	Upper tube bundle
U	Overall heat transfer coefficient (W m^{-2} K^{-1})	*w*	Tube's wall

REFERENCES

Atienza-Márquez, A., Bruno J.C., Coronas, A., 2018a. Cold recovery from LNG-regasification for polygeneration applications. Appl. Therm. Eng. (132), 463-478.

Atienza-Márquez, A., Bruno J.C., Akisawa, A., Coronas, A., 2018b. Selection of fluids for a polygeneration plant with cold recovery. Refrigeration Science and Technology, 2018-June, 1165-1172.

Bae, Y.Y., Kim, H.Y., 2009. Convective heat transfer to CO_2 at a supercritical pressure flowing vertically upward in tubes and an annular channel. Exp. Therm. Fluid Sci. 33, 329-339.

Ding, C., Hu, H., Ding, G., Chen, J., Mi, X., Yu, S., Li, J., 2017. Experimental investigation on downward flow boiling heat transfer characteristics of propane in shell side of LNG spiral wound heat exchanger. Int. J. Refrigeration 84, 13-25.

Eveloy, V., Ayou, D.S., 2019. Sustainable District Cooling systems: Status, challenges, and future opportunities, with emphasis on cooling-dominated regions. Energies, 12, 235.

F-Chart, 2019. Engineering Equation Solver (EES).

Hewitt, G.F., 2002. Heat Exchanger Design Handbook. Begal House, Inc. New York.

International Energy Agency (IEA), 2018. World Energy Outlook 2018.

Jung, D., Lee, H., Bae, D., Oho, S., 2004. Nucleate boiling heat transfer coefficients of flammable refrigerants. Int. J. Refrigeration 27, 409-414.

Kanbur, B.B., Xiang, L., Dubey, S., Choo, F.H., Duan, F., 2017. Cold utilization systems of LNG: A review. Renew. Sustain. Energy Rev. 79, 1171-1188.

La Rocca, V., 2010. Cold recovery during regasification of LNG part one: Cold utilization far from the regasification facility. Energy 35, 2049-2058.

Liang, K.M., Yang, B., Zhang, Z.L., 1998. Investigation of heat transfer and coking characteristics of hydrocarbon fuels. J. Propul. Power 14, 789-796.

Mostinski, I.K., 1963. Application of the rule of corresponding states for the calculation of heat transfer and critical heat flux. English Abstracts in Br. Chem. Eng. 8, 580.

Pineda-Quijano, D., Infante Ferreira, C., Duivenvoorden, W., Mieog, J., Noortgaete, T., Velpen, B., 2017. Tehcno-economic feasibility study of a system for the transfer of refrigeration capacity from LNG regasification plants to industrial assets. 12th IEA Heat Pump Conference 2017.

Pu, L., Qu, Z., Bai, Y., Qi, D., Song, K., Yi, P., 2014. Thermal performance analysis of intermediate fluid vaporizer for liquefied natural gas. Appl. Therm. Eng. 65, 564-574.

Shah, M.M., 2016. Comprehensive correlations for heat transfer during condensation in conventional and mini/micro channels in all orientations. Int. J. Refrigeration 67, 22-41.

Sinnott, R.K., 2005. Chemical Engineering Design. Coulson & Richardson's Chemical Engineering Series, Vol. 6, 4th Ed., Elsevier.

Xu, S., Cheng, Q., Zhuang, L., Tang, B., Ren, Q., Zhang, X., 2015. LNG vaporizers using various refrigerants as intermediate fluid: Comparison of the required heat transfer area. J. Nat. Gas Sci. Eng. 25, 1-9.

Manuscript ID: 1030
DOI: 10.18462/iir.icr.2019.1030

The advantages of natural working fluids

Armin HAFNER[(a)]

[(a)] Norwegian University of Science and Technology, NORWAY, armin.hafner@ntnu.no

ABSTRACT

The manufacturers of refrigeration equipment are facing challenges related to the legislative requirements forcing them to implement less conventional refrigerants with lower Global Warming Potential (GWP) in their new products.
Natural working fluids like Ammonia, Carbon Dioxide and Propane have demonstrated to be energy efficient and environmentally benign alternatives. Ammonia refrigeration systems have been successfully in the market for more than 140 years. Especially at high ambient temperature conditions, these units can outperform conventional HFC systems. The cost, availability and detection of the fluid are no issue on a global base. Hydrocarbon based AC split units, applying propane, are in focus and large-scale production lines are under preparation. The fluid- and thermosphysical properties of CO_2 are quite different from most other working fluids. Therefore, the refrigeration system design has to be carefully adapted to the properties of CO_2, thereby maximising the energy efficiency and minimising the total cost of ownership.
The article describes the challenges related to conventional refrigerants and examples of the latest system developments applying natural working fluids in industrial-, commercial and marine refrigeration will be described in the work.
Keywords: Natural Working Fluids, Ammonia, CO_2 Refrigeration Systems.

1. INTRODUCTION AND CURRENT STATUS

In his very last publication, Lorentzen (1995) outlined in a detailed way why it does not seem very logical to replace synthetic refrigerants having a significant environmental impact with another family of related halocarbons equally foreign to nature. By that time, it was the initial phase of the Montreal Protocol, i.e. the replacement of CFCs with HFCs, starting to protect the ozone layer of planet earth, but ignoring the possible impact to global warming. Lorentzen describes sustainable solution for the refrigeration sector focusing on systems applying natural working fluids. He concludes that three proposed refrigerants are sufficient for long-term solutions; these are ammonia, propane and carbon dioxide. Even if the forced change of refrigerants was seen as a costly problem, the perspective for the refrigeration industry applying natural working fluids were foreseen good. Especially with respect to the immense opportunities for engineers solving the technical issues and developing innovative system concepts, which end-users are able to implement and achieve cost saving.
As summarised by Ciconkov (2018), there is still a long way to go and lots of time has been used discussing endless phase down scenarios instead of focusing on a new approach: The phase in of natural refrigerants. On the other hand, despite the limited support, tremendous development steps within refrigeration systems applying natural working fluids happened during the past decades. As an example, the entire supermarket sector nowadays takes responsibility and introduces refrigeration equipment with natural working fluids globally, whenever local contractors are able to support them. Reputation and safety of customers is very important in this sectors as well as energy savings, leading to significant operational cost reductions. Within the heat pump market, hot water heat pumps, applying CO_2 as working fluid, are state of the art, too.
Due to the EU F-gas regulation and the Kigali amendment to the Montreal Protocol business as usual for decades within the refrigeration and heat pump sector is finally not possible any more.
Currently there are three main groups of refrigerant in the market place, the saturated hydrofluorocarbons, representing proposed substitutes from the chemical companies for CFC's and HCFC's under the umbrella of the Montreal Protocol. Their initial advantage was to protect the ozone layer, which was realised at a great success due to the Montreal Protocol. As the recovery of the Ozone layer has rapidly stopped during the past years as recently discovered by Montzka et al.

(2018), there are still issues for some countries to follow up international agreements and educating their industries avoiding such huge and unnecessary emission. However, due the high Global Warming Potential of the widely introduced HFCs, the churning of manmade refrigerants enters nowadays into a new era. The unsaturated hydrofluorocarbons are now the preferred solution provided by the chemical companies for all kind of applications. On the other hand, due to the intense effort from researchers and scientists, nowadays, natural working fluids became real alternatives for many application areas within the HVAC & refrigeration sector.

1.1. Saturated Hydrofluorocarbons

Saturated single component hydrofluorocarbons do have a relative long atmospheric lifetime and a corresponding high global warming potential. The mostly applied fluids were and are:
R-134a (CF_3CH_2F): This saturated HFC refrigerant is property wise comparable to R-22 and is widely used in medium temperature refrigeration systems. It has a $GWP_{100years}$ of 1430 $kg_{CO2}/kg_{R\text{-}134a}$ and it is possible to use it for some time under the EU F-gas directive if the GWP quota system certificates are in place for the supplier and end-user. It is non-flammable and classified in safety group A1.
R-152A (CHF_2CH_3): Property wise very similar to R-134a. It is mainly applied for blends, however, it is being used more now mostly due to the low GWP100years of 124 $kg_{CO2}/kg_{R\text{-}152A}$. It is flammable and classified in safety group A2.
R-32 (CH_2F_2): Property wise very similar to R134a. It is mainly applied for blends. Especially split AC units apply nowadays R-32, mostly due to the reduce $GWP_{100years}$ of 675 $kg_{CO2}/kg_{R\text{-}32}$. It is flammable and classified in the ASHRAE safety group: A2L.
Common hydrofluorocarbons blends, which are widely used:

- R-404A (CF_3CH_3 / CF_3CHF_2 / CF_3CH_2F; $GWP_{100years}$ = 3922 $kg_{CO2}/kg_{R\text{-}404A}$)
- R-507 (CF_3CH_3 / CF_3CHF_2; $GWP_{100years}$ = 3985 $kg_{CO2}/kg_{R\text{-}507}$)
- R-407C (CH_2F_2 / CF_3CHF_2 / CF_3CH_2F; $GWP_{100years}$ = 2107 $kg_{CO2}/kg_{R\text{-}407C}$)
- R-410A (CH_2F_2 / CF_3CHF_2; $GWP_{100years}$ = 2088 $kg_{CO2}/kg_{R\text{-}410A}$)

When converting traditional HCFC plants these HFC blends are substitutes to eliminate ozone depletion. However, all of them do have high GWP values, which limits their usage significantly in the future. This is already the case in Europe where they are taken from the market, as no emission quotas are reserved for such high GWP fluids anymore. The refrigerant suppliers forces the manufactures and contractors to apply unsaturated hydrofluorocarbons or their blends with lower GWP values.

1.2. Unsaturated Hydrofluorocarbons

Unsaturated hydrofluorocarbons represent another kind of HFCs, which are potential replacements for HCFCs and saturated HFCs. In general, unsaturated hydrofluorocarbons react more rapidly with OH radicals and their atmospheric lifetimes is much shorter, as described by Hurley et al. (2008). Due to their short lifetime, they do have lower global warming potentials than saturated hydrofluorocarbons. Mostly applied are:
R-1234yf ($CF_3CF{=}CH_2$; $GWP_{100years}$ = 4 $kg_{CO2}/kg_{R\text{-}1234yf}$): This unsaturated HFC refrigerant does have a chemical double bound and is a so-called hydro fluoro olefin (HFO). Its GWP value on a 100-year perspective is low since atmospheric lifetime is very short (~11 days) and the double bound is reacting with OH radicals present in the ambient. R-1234yf is defined as mildly flammable and classified in the newly developed safety group A2L. The auto-ignition temperature is 405 °C. $CF_3C(O)F$ is the major atmospheric oxidation product of R-1234yf. The atmospheric fate of $CF_3C(O)F$ is hydrolysis, which occurs on a time scale of approximately 10 days, ending up as $CF_3C(O)OH$ (trifluoroacetic acid = TFA) and HF (hydrogen fluoride)

- The acidity of TFA is approximately 34,000 times stronger than that of acetic acid. TFA is harmful when inhaled, causes severe skin burns and is toxic for water organisms even at low concentrations. TLV (Threshold Limit Value) = 5 ppm; IDLH (Immediately dangerous to life or health) = 30ppm.
- Upon contact with moisture, including tissue, HF immediately converts to hydrofluoric acid, which is highly corrosive and toxic, and requires immediate medical attention upon exposure. Breathing in hydrogen fluoride at high levels or in combination with skin contact

can cause death from an irregular heartbeat or from fluid build-up in the lungs. TLV = 3 ppm; IDLH = 30ppm.

The TLV, i.a. the maximum allowed concentration at a work place in Germany for R1234yf is 200 ppm.

R-1234ze(E) ($CF_3CH=CHF$; $GWP_{100years}$ = 7 $kg_{CO2}/kg_{R-1234ze}$) This unsaturated HFC refrigerant has also a chemical double bound. Exhibits flame limits at temperatures in excess of 28 °C. The auto-ignition temperature is 368 °C. When $CF_3CH=CHF$ is reacting with OH radicals present in the ambient, due to partly oxidation, both HC(O)F and CF_3CHO are formed

- HC(O)F (Formyl fluoride): decomposes autocatalytically near room temperature to carbon monoxide (CO) and hydrogen fluoride (HF)
- 2,2,2 –Trifluoroethanal: CF_3CHO → photolysis → $CF_3 + HCO$; $CF_3 + O_2 \rightarrow CF_3O_2 \rightarrow COF_2$

COF_2 -Carbonyl fluoride (Fluorophosgene) is extremely poisonous with a threshold limit value of 2 ppm for short-term exposure.

Example of blends:

R-513A ($CF_3CF=CH_2$/ CF_3CH_2F; $GWP_{100years}$ = 631 kg_{CO2}/kg_{R-513A}) & R-450A ($CF_3CH=CHF$/ CF_3CH_2F; $GWP_{100years}$ = 605 kg_{CO2}/kg_{R-450A}) are blends of the R-1234yf and R-1234ze(E) with R-134a. The refrigerants still exhibit non-flammable characteristics like R-134a and are classified in the safety group A1 as long as it is inside the system. However, decomposition of the fluids takes place as described for the single fluid when released into the ambient.

Decomposition takes also place when exposing these substances to hot surfaces, as experimentally investigated (JSRAE, 2017). The researchers show that independent of the absolute humidity the entire refrigerant concentration of 2.5 vol. % is decomposed on a hot surface of 600 °C and reaches HF concentration of 1.5 vol. % HF (1.5 vol % =15 000 ppm) for R-1234yf and around 1 vol. % HF (10 000 ppm) for R-32.

1.3. Natural Working Fluids

Natural working fluids do have favourable thermodynamic and fluid properties enabling energy efficient refrigeration system configurations. In addition, their environmental impact is well known and safety standards are established.

R-717 (ammonia, NH_3; $GWP_{100years}$ = 0): Ammonia has been used as a refrigerant during the last 140 years and is still widely used, especially for large industrial plants for food processing. It has neither a global warming potential and is not depleting the Ozone layer. R-717 will not be restricted under the F gas directive. Ammonia has very high latent heat and the refrigeration capacity per unit mass flow is the highest of all refrigerants used in traditional vapour compression systems. Because ammonia has low molar mass it can have much higher particle velocities than all other refrigerants and therefore allows for small pipe sizes. It is important to avoid copper components, because ammonia and water will corrode copper, zinc and their alloys. For example, ammonia and water will destroy the copper windings of the electrical motor in a hermetic compressor. It is flammable and toxic; therefore, it classifies for the safety group B2L and does require extra safety measures, similar to the HFCs with a short lifetime described above. TLV (Threshold Limit Value) = 50 ppm. IDLH (Immediately dangerous to life or health) = 300 ppm. It is necessary that the ammonia refrigeration system is located in a separate room, that personnel is well trained and has appropriate safety equipment available as for other flammable working fluids.

R-744 (carbon dioxide CO_2; $GWP_{100years}$ = 1 kg_{CO2}/kg_{R-744}): Carbon dioxide is a working fluid in refrigeration systems since the late 19th century. It disappeared from marine applications in the 1950's mainly due to technical difficulties and the introduction of synthetic working fluids, operating at lower working pressures. Engineers and researchers solved these technical difficulties nowadays and there is a wide range of applications where CO_2 is the preferred working fluid (freezing applications, commercial refrigeration, hot water heat pumps, mobile AC and heat pumping units, etc.) as described by Lorentzen (1995)..

R-744 is the only long-term non-flammable working fluid neither affecting the ozone layer nor contributing to global warming. During production, no environmentally unfriendly emissions occur, which is the reason for having the lowest direct environmental impact of all refrigerants. R-744 is the only non-flammable, low-GWP single working fluid classified as A1. It is non-toxic and will not be restricted under the F-gas directive. Independent on the concentration of oxygen in the air, the

human lung needs to reject CO_2 into the atmosphere; therefor the TLV is 5.000 ppm. The IDLH threshold for CO_2 is 40.000 ppm.
R-290 (propane, C_3H_8; $GWP_{100years}$ = 3 kg_{CO2}/kg_{R-290}): Propane is an example of another group of natural working fluids, the hydrocarbons. It has a very low GWP. Systems with R-290 are in operation globally since many years and is an energy efficient alternative to all HFCs. Currently it is widely used within compact systems with low charges such as light commercial refrigeration equipment. There are no charge limitations if these kinds of units applying hydrocarbons are located outdoors in restricted areas, sufficient refrigerant charge to achieve the required capacities is possible even if the equipment is located indoors when following existing standards and regulations. The major disadvantage is the high flammability; therefore, hydrocarbons are all classified in the safety group A3.

2. FAVOURABEL SYSTEM CONFIGURATIONS FOR NATURAL WORKING FLUIDS

This chapter highlights some examples of successful applications applying natural working fluids. Some of them have gained a significant market share while others have a significant growth.
Ammonia units:
Traditionally ammonia refrigeration units are characterised by high capacity and high refrigerant charges. The development focus in this sector is currently to enable low charge systems for a wide range of applications, to increase the market shares in chillers, cooling & freezing units, Lamb (2017). These so-called packaged systems reduce installation time, and enable smaller air-cooled units, located close to the point of cooling.
Cold store applications are favourable for ammonia refrigeration, enabling significant annual energy saving as described by Jensen et al. (2018)
In the northern part of Europe, marine installations, like refrigerated sea water coolers, are often utilised with ammonia refrigeration systems. Cascade units with CO_2 in the low stage, i.e. the freezing part, are nowadays state of the art. This configuration is also successfully applied in low temperature cold stores Hattori et al. (2019), it combines and strengthens the beneficial properties of these two natural working fluids by eliminating the challenge of low evaporation temperatures for ammonia and the high rejection temperatures for CO_2 units.
Hydrocarbon units:
After the fall of the Berlin wall Greenpeace (1992) encouraged a company in the Easter part of Germany to develop the first series of fridges, GreenFreez refrigerators, applying isobutene as working fluid. Decades later this has become a global standard. Beside the introduced household refrigeration devices like fridges and freezers, end-users of light commercial cabinets are also requesting more and more units equipped with propane as working fluid. When following the standards, there are no technical restrictions related to the required refrigerant charge for these units located in sales areas. This is ongoing and more and more companies are following this trend, as demonstrated by ‘Refrigerants, Naturally!’ the global, non-profit initiative of companies in the food and drink, food service and consumer goods sectors, with the non-profit
In 2018, the ‘All Easy Series R-290’ residential single-split air conditioner from Midea were certified by the German ecolabel "Blue Angel" for its ultra-low global warming potential (GWP), high energy efficiency, low noise, and stringent material safety control. These units and other similar units, e.g. developed by Godrej, will have a significant growth in the next years. End users will be aware of the local risk and environmental impact. As nowadays flammable synthetic refrigerants are dominating this market segment, there will be no restrictions to apply natural working fluids in the residential AC and heat pumping market. The households are familiar with gas fired cooking equipment and do have in many cases several natural gas cylinders in their storage places. Therefore, a RAC unit with a relative low charge of propane, compared to the equipment in the kitchen, will not represent an additional risk compared to flammable HFCs. When end user are aware of the additional risk of being exposed to decomposition products and the unknown total environmental impact of the newly introduce refrigerants, there will be a demand for alternative systems as developed by Midea, Godrej and others.
Carbon Dioxide units:
As mentioned above, CO_2 refrigeration applications are outperforming any other fluid in the temperature range below -35 °C and above -55 °C with respect to energy efficiency, compactness

and safety. Therefore, a tremendous increase in industrial refrigeration units are utilised within the food- and processing industry. Even if the total amount of these kind of systems are low compared to mass-produced units, their impact on food safety and quality is significant.
Commercial refrigeration systems with integrated AC are becoming a trend due to reduced maintenance cost and the trust of end-users to apply natural working fluids all over the supermarket building (Hafner 2014, 2016; Girotto, 2016). Fig. 1 shows the development of such an integrated MultiPACK unit, able to provide all the required cooling for the products inside the supermarket. The unit is equipped with a Multi Ejector and parallel compressors. In addition, the MultiPACK unit supplies heating and cooling to several indoor air handling units (IAHU). In case of heating demand inside the building, hot gas is supplied directly towards the IAHU's. The individually flow rates are controlled locally by feeding valves, located upstream of each IAHU. The cooled refrigerant enters the high side pressure part of the Multi Ejectors. If the building requests cooling, liquid CO_2 is supplied towards the IAHU's. The entire vapour of all IAHU's is sucked by the AC-Ejectors, discharging it towards the separator. The parallel / AC compressors maintain the pressure level of the separator, i.e. providing the cooling capacity for the building.
In many cases, when existing building infrastructure has to be taken into consideration during a refurbishment of a supermarket, AC needs to be integrated through a chilled water loop. Fig. 2 shows the development of such an integrated MultiPACK unit with a standard Multi Ejector and parallel compressors. Besides providing all the required cooling capacities for cabinets for chilled and frozen products inside the supermarket, the unit is equipped with the innovative chiller. The liquid receiver supplies liquid refrigerant towards the evaporators of the chiller producing cold process water. Two evaporators absorb the heat from the process water at different evaporation pressure levels, which reduces the exergy destruction of the process.

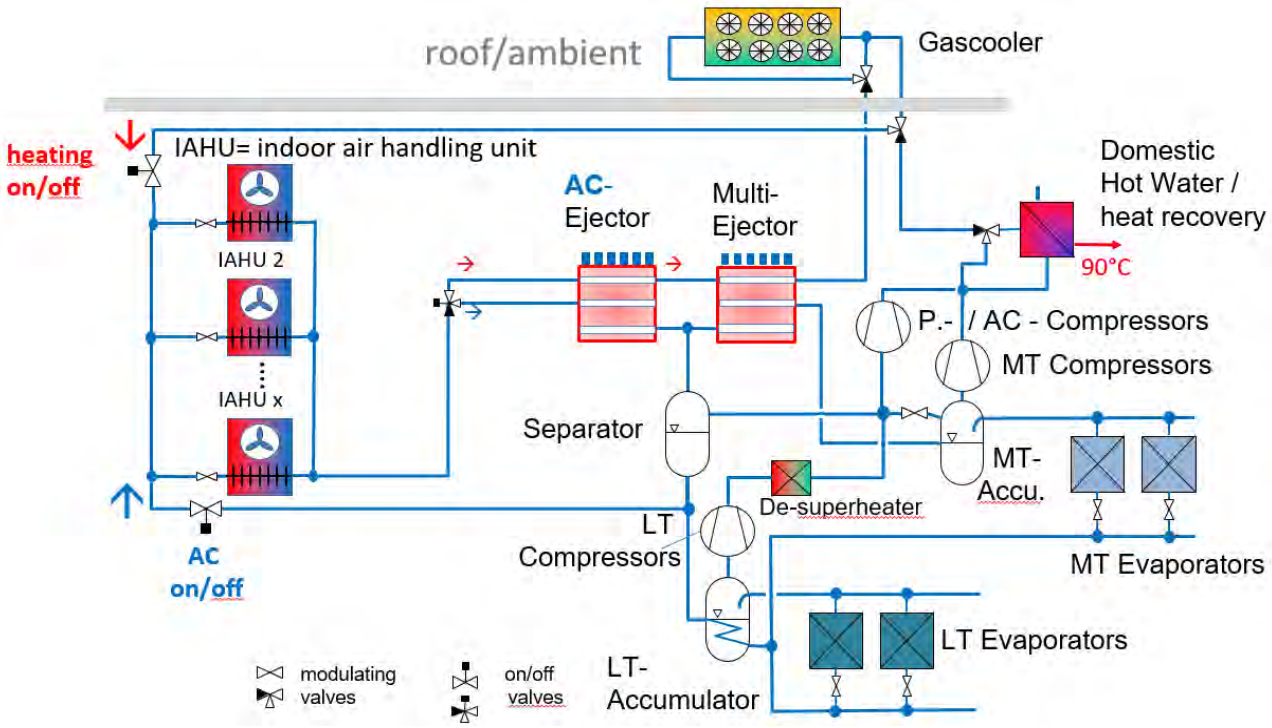

Figure 1: MultiPACK unit design with several individual indoor air handling units

The CO_2 chiller part shown in Fig. 2 represents an innovative approach to adapt water chillers to the properties of CO_2. This concept can also be applied in an AC chiller / heat pump application. The evaporators of the chiller part in combination with the Multi Ejectors allow an elevated suction pressure of the (parallel) compressors. The first chiller sections is connected to the liquid receiver tank at 42 bar ($t_o \approx +7$ °C). The liquid refrigerant is supplied by gravity and allows the pre-cooling of the process water at 12 °C. The second evaporator provides more cooling capacity, since it is able to further reduce the temperature of the process water to 7 °C. The suction pressure inside the second chiller evaporated is at 38 bar ($t_o \approx +3$ °C), due to the usage of the Multi Ejectors, which are

able to suck all the vapour out of the second evaporator and supply it back to the liquid receiver where the (parallel) compressors maintain the pressure level. The pressure level inside the separator can be adjusted to adapt the cooling capacity provided towards the building by the chilled water loop. In case of additional heating demand during the cold season, an outdoor heat exchanger is able to supply external heat via the second ejector, in this case acting as the Heat Pump (HP) ejector.

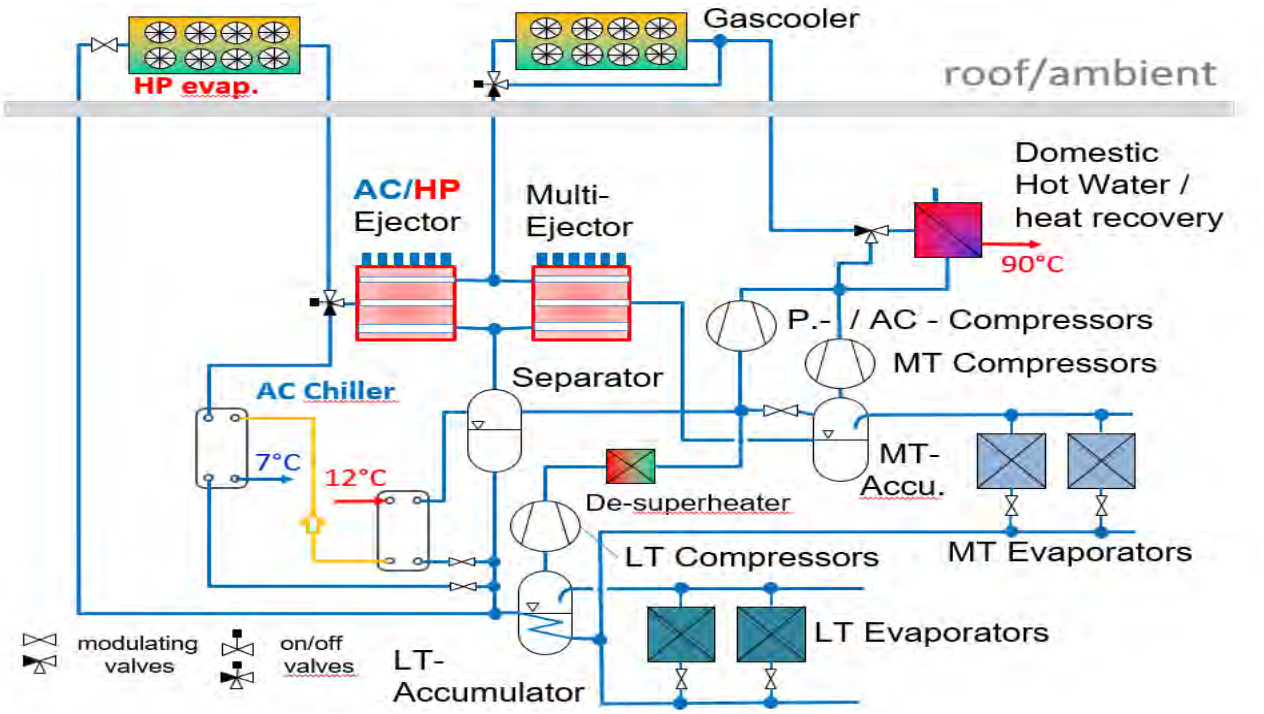

Figure 2: MultiPACK unit design with integrated AC chiller device and heat pump function

3. DISCUSSION

The preferred working fluid, when developing and introducing HVAC and refrigeration units should have:

- a long term prospective,
- a well-known and understood environmental impact,
- enable an energy efficient operation of the units,
- highest possible safety class

This means that the working fluid should not be restricted under the F-gas regulation. Therefore, none of the current HFC blends mentioned above are suitable choices. The safety classification is also of critical importance when the refrigeration systems are intended to be in the public domain, a part of mobile applications, e.g. marine vessels. Therefore, the use of R-152A, R-1234yf and R-1234zeE are unlikely and only possible when thorough risk analysis and mitigations have been made. The group of blends like R-513A and R-450A might have a potential short period in medium temperature applications due to the relatively low GWP and A1 safety classification. However, as indicated in the safety data sheet of the fluid suppliers, the *'hazardous decomposition products may include: Hydrogen fluoride, Carbon oxides Fluorinated hydrocarbons, Carbonyl fluoride'*. The question is if the end-user is willing to take the risk. Another problem is the complex chemical blend and composition, the global availability, and the higher GWP relative to R-744 that makes these non-natural working fluids less economical.

3.1. Recommendation to Estimate the Environmental Impact of the HVAC&R Units

Total Equivalent Warming Impact (TEWI) is an established method within the refrigeration sector. TEWI measures the global warming impact of a HVAC&R system by quantifying the amount of greenhouse gasses a unit emits. TEWI does not account for the energy embodied in product

materials, greenhouse gas emissions from chemical manufacturing and end of life disposal of the unit.
Therefore, a life cycle climate performance (LCCP) approach should be established for all refrigeration applications. LCCP is well established for commercial HVAC&R units and mobile air conditioning (MAC) units. This transparent method describing the environmental impact of systems allows an evaluation of alternative systems. LCCP can also account for minor emission sources that are not accounted for in TEWI such as transportation leakage, manufacturing leakage and refrigerant manufacturing emissions. LCCP is calculated as the sum of direct and indirect emissions generated over the lifetime of the refrigeration system. Direct emissions include all effects from the release of refrigerants into the atmosphere. This includes annual leakage and leakage during the disposal of the unit. The indirect emissions include emissions from the manufacturing process, energy consumption during operation and disposal of the system. LCCP allows to describe the environmental impact of the HVAC&R units based on transparent input parameters like system performance data at various load conditions and heat rejection temperatures. A single focus on GWP values doesn't inform the end-user about the real environmental impact of a working fluid and system configuration.

3.2. Natural Working Fluids

Ammonia (R-717) is an approved natural working fluid for industrial and maritime refrigeration system. The system architectures for ammonia units are understood, challenges with suction pressures below atmospheric pressure at low evaporation temperatures (> -33.5 °C) are known, while handling safety issues (classified as B2L) is standard.
Home appliances, like fridges and freezers and light commercial refrigeration equipment should only apply hydrocarbons as the working fluid. A fast market introduction of hydrocarbon based split AC and heat pumping units should be promoted, eliminating the dependency of local markets to import HFCs as most countries do have sources and the ability to handle hydrocarbons. This would significantly improve the energy efficiency within these sectors and eliminate any Fluor emission with all they unknown decomposition products.
Previously CO_2 refrigeration equipment was not available in the capacity range required for fishing vessels, however, the component manufactures do see the market potential and more large capacity equipment enters the market. For maritime refrigeration applications globally CO_2 should become the preferred choice, whenever ammonia units cannot be applied.

4. SUMMARY AND CONCLUSION

Safety of service people and end-users should have the highest priority, followed by the total environmental impact when evaluation alternative working fluids within the refrigeration and heat pumping sector. A low GWP values does not necessarily mean that fluids are superior and the best available choice. As Gustav Lorentzen said, it is not logical to replace a harmful substance with another substance which total environmental impact is still unknown. Therefore, the refrigeration society has to take responsibility and phase in natural working fluids whenever it is possible.
Ammonia is one option mainly for large industrial applications. In addition due to packaged designs, low charge systems are state of the art, enabling to apply these units as chillers and refrigeration units in many locations. In combination with CO_2, as the working fluid in the low temperature part of a cascade unit, such units are superior when storage or process temperatures below -45 °C are required in high ambient temperature regions.
Propane will play an important role, within the next years, replacing most of the HFCs applied in split AC and heat pumps units today.
A remarkable development of CO_2 refrigeration technology has taken place since the revival of the refrigerant in the late 1980s. The development has led to efficient CO_2 systems and their successful introduction into the market. Additionally, it inspired the development of other innovative technologies that focus on improving the energy efficiency and reducing the total cost of ownership.

The integration of expansion work recovery devices like ejectors allows today's CO_2 commercial refrigeration systems to outperform HFC units on annual energy consumption in any climate region. The integration of further functions like chilling of process water or direct evaporation for AC purpose into the centralised refrigeration unit is a key success factor for these sustainable vapour

compression systems replacing HCFC and HFC systems globally. CO_2 chillers can be applied where units with flammable refrigerants cannot be used.
The designers and engineers spreading CO_2 technology should remember when designing all of the integrated functions, that the fluid properties are an asset, not a hindrance. Therefore, all CO_2 evaporators should be operated without superheat, heat recovery should be employed whenever there is a heat demand and domestic hot water production should be a natural feature of the systems. The described innovations will further simplify CO_2 systems in the near future.
Training and knowledge transfer is the key for a successful and fast phase in of CO2 refrigeration units globally. Therefore, also World Bank and multi-lateral funds should support global education, training and certification as well as covering additional first costs with affordable loans (no interest rate), so the end-users can return the loan during the operational phase, since the new energy efficient system gives them a significant energy / cost saving.

ACKNOWLEDGEMENTS

The research leading to these results has received funding from the European Union under the programme H2020-EU.3.3.1. - Reducing energy consumption and carbon footprint by smart and sustainable use (Grant Agreement number: 723137).

REFERENCES

Banasiak, K., Hafner, A., Kriezi, E.E., Madsen, K.B., Birkelund, M., Fredslund, K., Olsson, R., 2015. Development and performance mapping of a multi-ejector expansion work recovery pack for R744 vapour compression units, International Journal of Refrigeration, Volume 57, 1 September 2015, pp. 265-276

Ciconkov, R., 2018. Refrigerants: There is still no vision for sustainable solutions. International Journal of M.D.Refrigeration, Volume 86, February 2018, Pages 441-448

Girotto, S., 2016. Direct space heating and cooling with refrigerant CO_2. ATMOsphere Europe, Barcelona. http://www.atmo.org/media.presentation.php?id=754.

Greenpeace, 1992. https://www.greenpeace.org/international/story/15323/how-greenpeace-changed-an-industry-25-years-of-greenfreeze-to-cool-the-planet/

Hafner, A., Claussen, I.C., Schmidt, F., Olsson, R., Fredslund, K., Eriksen, P.A., Madsen, K.B., 2014. Efficient and integrated energy systems for supermarkets. Proceedings of the 11th IIR Gustav Lorentzen Conference on Natural Refrigerants, Hangzhou, China.

Hafner, A., Banasiak, K., 2016. Full scale Supermarket Laboratory R744 Ejector supported & AC integrated parallel compression unit. Proceedings of the 12th IIR Gustav Lorentzen Natural Working Fluids Conference, Edinburgh, Scotland.

Hattori, K., Arimoto R., Terashima I., 2019. Development of a high efficient NH_3/CO_2 refrigeration system. Proceedings of the 8th IIR Conference: Ammonia and CO_2 Refrigeration Technologies, Ohrid, 2019

Hurley M.D., Wallington T.J., Javadi M.S., Nielsen O.J., 2008. Atmospheric chemistry of CF3CF=CH2: Products and mechanisms of Cl atom and OH radical initiated oxidation. Chemical Physics Letters, Volume 450, Issues 4–6, Pages 263-267

Jensen, S., Gerstenberger E., 2018. Einsatz von NH_3 DX Systemen für energieeffiziente und zukunftssichere Analgen. Proceedings of the DKV meeting 2019 in Aachen. JSRAE, 2017. Risk Assessment of Mildly Flammable Refrigerants, Report from The Japan Society of Refrigerating and Air Conditioning Engineers, March 2017

Lamb, R., 2017. Low Charge Packaged Ammonia Refrigeration Systems. Proceedings of the 7th IIR Conference: Ammonia and CO_2 Refrigeration Technologies, Ohrid, 2017

Lorentzen, G., Pettersen, J., 1992. New possibilities for non-CFC refrigeration. IIR Int. Symp. on Refrigeration, Energy and Environment, Trondheim, Norway, June 22-24, pp.147-163.

Lorentzen, G, 1995. The use of natural refrigerants: a complete solution to the CFC/HCFC predicament. Int. Journal of Refrigeration 9. Vol. 18, No. 3, pp. 190 197, 1995

Montzka S.A., Dutton G.S., Yu P., Ray E., Portmann R.W., Daniel J.S., Kuijpers L., Hall B.D., Mondeel D., Siso C., Nance J.D., Rigby M., Manning A.J., Hu L., Moore F., Miller B.R. & Elkins J.W., 2018. An unexpected and persistent increase in global emissions of ozone-depleting CFC-11. Nature, volume 557, pages 413–417.

Pardiñas, Á.Á., Hafner, A., Banasiak, K., Kvalsvik, K.H., Larsen, L., 2018. Strategy for the control of two groups of ejectors operating in parallel in integrated R744 refrigeration systems. Refrigeration Science and Technology, 2018-June, pp. 1069-1076.

Manuscript ID: 1032
DOI: 10.18462/iir.icr.2019.1032

Method of on-site determination of refrigerating machine efficiency

Yurii BAIDAK[(a)], Iryna VEREITINA[(a)]

[(a)] Odessa National Academy of Food Technologies
Odessa, 65082, Ukraine,e-mail kozak@admin@ukr.net

ABSTRACT

The refrigerating machine is considered as a system of closed pipelines of various diameters, which enables the excitation of thermodynamic processes in them by moving working body. The method of the on-site determination of the refrigerating machine efficiency based on the two temperature sensors data processing has been elaborated and the device for real time testing of refrigerating machine during one cycle of its operation has been created. Such assessment does not contradict the physical meaning of the concept of efficiency. The developed method and device can be used to indirect determination of the losses in the refrigerating machine as well as the type of refrigerant in the system without the need for refrigerating machine unsealing for extraction and laboratory analysis of the refrigerant, which is relevant during refrigerators routine servicing and vitally important for the environmental concerns solution.
Keywords: Refrigerating machine, Efficiency, Temperature, Heat, Mathematical model, Time constant, COP.

1. INTRODUCTION

The refrigerating machine (RM) is considered as a device providing the possibility of initiating in it a closed process of refrigerant aggregation state changing and refrigerant flowing in a sealed single-circuit piping system with tubes of various cross sections and volume. As a result we can observe decrease and increase in temperature in the individual sections of this piping system.
As the working fluid (refrigerant) in the RM serves the substance capable to alter its phase state (vapor - liquid) in dependence of pressure. In the considered single-circuit system of RM, the compressor increases the pressure of the refrigerant in the condenser and lowers it in the evaporator. The pressure difference ensures the movement of the refrigerant in the pipelines. The condenser realizes the phase transition of the refrigerant from the vapor to liquid state. The evaporator creates the condition for its boiling and stimulates the cooling process. The throttle - capillary tube - adjusts the amount of refrigerant (depending on its overheating) in the evaporator.
Basic principles for the evaluation of energy efficiency of complete refrigerating system have already been specified as well as coefficients for calculation of energy efficiency of its components (e.g. VDMA 24247-2; 24248). Electrical coefficient of performance is one of the power parameters of the RM capacity. It is equal to the ratio of heat transferred to the evaporator to the electric energy consumed by the compressor motor. The determination of the extracted heat is technically complex task, the solution of which is still relevant. Some other parameters of RM energy efficiency are also known (Arnemann, 2012). But for refrigerators of different types they give comparable results only under the same loads in cooling systems and at certain boiling points and condensation of the refrigerant. Based on the fact that the performance energy ratio or COP gives an integrated assessment of RM and does not allow evaluating the performance of its individual components, alternative relative parameters are being developed (Preuss, 2011). The integral assessment of the refrigerating machine energy efficiency implies a multiplicative convolution of relative parameters within the system between operating temperature and ambient one. Using of the differentiated approach in assessing of the RM energy efficiency is the most complex task.

2. METHOD OF INDIRECT DETERMINATION OF REFRIGERATOR COMPONENTS EFFICIENCY

The temperature of the evaporator (freezer compartment) is set by the vapor pressure of the refrigerant. At a constant rate of liquid refrigerant flow from the condenser to the evaporator the longer operation period of the compressor will decrease the vapor pressure. If it is not necessary to reduce the temperature in the evaporator to the lowest forced value θ_{forced}, the compressor is stopped when the desired cooling temperature is reached in the freezer compartment θ_{FR}. When the compressor is running, the vapors of the expanding refrigerant in the evaporator take away the heat $Q_2 = Q_{FR} + Q_{CAB}$ from the cooling objects in the freezer compartment. To perform the reverse Carnot cycle, electrical energy is supplied to the compressor from an external power source.

2.1. The Purpose and Method of Research

The aim of the work is to develop a method for indirect determination of the efficiency of RM components, using the example of its freezer compartment at a constant heat load, as the basis of a differentiated approach for an integrated indicator of the overall performance of refrigerator operation and one that is based on the results of temperature readings testing during one compressor operation steady state.
The heat load is considered as the ratio of the real heat gain into the evaporator to the maximum

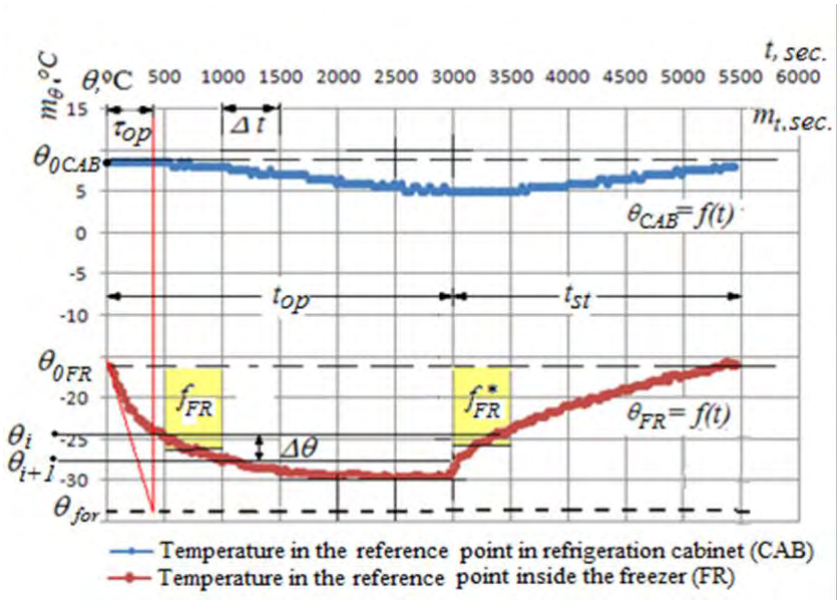

Figure 1: One cycle of temperature dependences in the refrigerating cabinet θ_{CAB} and freezer θ_{FR} compartments of the nominally loaded household refrigerator NORD-237 in the steady state operation mode

possible heat gain, to which the forced heat exchange process without shutting down the compressor corresponds. The subject of the research is the household refrigerator NORD-237 [6].
The experimentally obtained temperature dependences in the reference points inside the refrigeration cabinet θ_{CAB} and freezer θ_{FR} compartments of the NORD-237 refrigerator which display weighted averages of their values are given in Figure 1. The monitoring was carried out in a heat-insulated box at a temperature of 37 ºC according to the method and instruments described in Baydak (2011). Duration of one cycle of compressor operation is 90 minutes. Two TCN-75 sensors manufactured by Dallas Semiconductor with 0.25 ° C sensitivity were used.
Figure 1 shows that the heat supplied to the freezer compartment evaporator θ_{FR} and to the refrigerating cabinet θ_{CAB}, is proportional to the surface areas formed by the temperatures θ_{0FR}, θ_{0CAB} at the beginning of the compressor operation cycle and by their changing values during the cycle, i.e. by temperature dependencies $\theta_{FR} = f(t)$ и $\theta_{CAB} = f(t)$. The areas of these surfaces f_{FR} and f_{CAB}, that are equal to the product of temperature, time and scales $m_t, (s/mm)$, $m_\theta, (℃/mm)$ along the respective axes, can be written as $f_{FR} m_t m_\theta$ и $f_{CAB} m_t m_\theta$. For the general case, they are equal to a certain integral of temperature dependences.

An alternative to the method of indirect determination of the energy efficiency of the components of the RM, based on experimental dependences of temperature, can be a numerical method for constructing temperature dependences $\theta_{FR} = f(t)$ и $\theta_{CAB} = f(t)$ based on solving the heat balance equations.

2.2. Evaporator Heat Balance Equations

The system of equations of evaporator heat balance, on the example of the freezer compartment, for one compressor operation cycle in a steady state mode for the operation time Δt_{op} and non-operation time Δt_{st}, looks like:

$$\begin{cases} dQ_{op}^{'} - dQ_{op}^{''} = k_{op}F(\theta_{0FR} - \theta_{FR})dt - \begin{pmatrix} G_{met}c_{met} + \\ G_{LR}c_{LR} + \\ +G_{VR}c_{VR} \end{pmatrix} d\theta_{FR} = Q_0 dt, \\ dQ_{st}^{'} - dQ_{st}^{''} = k_{st}F(\theta_{0FR} - \theta_{FR})dt - \begin{pmatrix} G_{met}c_{met} + G_{LR}c_{LR} \\ +G_{VR}c_{VR} \end{pmatrix} d\theta_{FR} = 0, \end{cases} \quad \text{Eq. (1)}$$

To solve the equations, the following values must be known: k_{op}, k_{st} - coefficients of heat transfer to the evaporator and its heat exchange surface area F; the initial and current values of the temperature in the freezer compartment θ_{0FR}, $\theta_{FR} = f(t)$; weight G_{met} and specific heat capacity of the metal of the evaporator c_{met}; weight of the liquid refrigerant G_{LR} and its vapors G_{VR}, as well as their specific heat capacities c_{LR} и c_{VR}. Compressor performance can be represented by a linear approximation of the form $Q_0(\theta_{FR}) = A + B\theta_{FR}$.
To re-arrange heat balance equations to the form

$$\begin{cases} -(G_{met}c_{met} + G_{LR}c_{LR} + G_{VR}c_{VR})\frac{d\theta_{FR}}{dt} - k_{op}F\theta_{FR} = Q_0 dt - k_{op}F\theta_{0FR} \\ (G_{met}c_{met} + G_{LR}c_{LR} + G_{VR}c_{VR})\frac{d\theta_{FR}}{dt} + k_{st}F\theta_{FR} = k_{st}F\theta_{0FR} \end{cases} \quad \text{Eq. (2)}$$

the roots of the characteristic equations will be equal to:

$$p_{op} = \frac{-0{,}5[Q_0(\theta_{0FR}) + Q_0(\theta_{FR})] - k_{op}F}{G_{met}c_{met} + G_{LR}c_{LR} + G_{VR}c_{VR}} = \frac{-Q_{gen}^{p} - k_{op}F}{Gc},$$

$$p_{st} = \frac{-k_{st}F}{G_{met}c_{met} + G_{LR}c_{LR} + G_{VR}c_{VR}} = \frac{-k_{st}F}{Gc}.$$

Complete solutions of the heat balance equations with the compressor on and off will take the form

$$\theta_{FR} = \theta_{forced} - (\theta_{forced} - \theta_{0FR})e^{p_{op}t}, \quad \text{Eq. (3)}$$

$$\theta_{FR} = \theta_{0FR} - (\theta_{0FR} - \theta_{FR})e^{p_{st}t}. \quad \text{Eq. (4)}$$

To simplify the task, the addends in the roots of the characteristic equations are determined only through the mass and specific heat of the evaporator metal $Gc = G_{met}c_{met}$, as the most significant in their total amount. This simplification theoretically allows taking into account the heat gain in the evaporator during the time $\Delta t_{op} + \Delta t_{st}$ of one cycle of operation of the RM in the form:

$$Q_{op} = k_{op}F(\theta_{0FR} - \theta_{forced})\int_0^{t_{op}} dt - k_{op}F(\theta_{0FR} - \theta_{forced})\int_0^{t_{op}}(\theta_{0FR} - \theta_{FR})\,e^{p_{op}t}dt = k_{op}F(\theta_{0FR} - \theta_{forced})\left[t_{op} - \frac{1}{p_{op}}(\theta_{0FR} - \theta_{FR})(1 - e^{p_{op}t_{op}})\right], \quad \text{Eq. (5)}$$

$$Q_{st} = k_{st}F\int_0^{t_{st}}(\theta_{0MO} - \theta_{MO})e^{p_{st}t}dt = \frac{k_{st}F}{p_{st}}(\theta_{0MO} - \theta_{MO})(1 - e^{p_{st}t_{st}}). \quad \text{Eq. (6)}$$

Generally, heat is taken from the freezer compartment with refrigerant steam:

$$Q_{FR} = Q_{op} + Q_{st}. \quad \text{Eq. (7)}$$

The disadvantage of numerical analysis of heat transfer in case of determining the energy efficiency of components is the lack of information on the electrical energy *A*, required for heat removal.

2.3. Mathematical Model of Indirect Method of Determining Energy Efficiency from the Results of Temperature Testing

Right parts of Eq. (5) и Eq. (6) show that the heat gain into the evaporator over time t is equal to the product of thermal conductivity $k_{p,c}F$ and aperiodic thermal heads $\theta_{0FR} - \theta_{FR}$, $\theta_{0FR} - \theta_{forced}$. For a temperature dependence constructed according to the results of calculations, testing or monitoring, this product can be obtained by numerical calculation of the temperature dependence of the integrand surface area. In the time interval of 500 - 1000 seconds (Figure 2), the area is equal to $f_{FR}m_\theta m_t$, in the time interval of 3000 - 3500 seconds - $f^*_{FR}m_\theta m_t$. When monitoring or testing temperature with virtual, multimedia tools (Baydak, 2011), the results can be multiplied and summed up in time by a microprocessor device, in the form of

$$Q_{FR} = Q_{op} + Q_{st} = k_{op}F\sum_0^{t_{op}} f_{FR}m_\theta m_t + k_{st}F\sum_0^{t_{st}} f^*_{MO}m_\theta m_t. \quad \text{Eq. (8)}$$

To build the mathematical model and algorithm of indirect method for evaporator energy efficiency calculating based on the results of temperature testing and on Eq. (8) , it is necessary to know:
- time intervals Δt of temperature testing θ_{FR} at the reference point of the evaporator;
- forced temperature value θ_{forced} in the evaporator of freezer compartment (refrigerant boiling point);
- cooling time constants during operation $\tau_{op} = -\frac{1}{p_{op}}$ and non-operation $\tau_{st} = -\frac{1}{p_{st}}$ phases of the compressor;
- heat transfer coefficients in the evaporator during operation and non-operation phases $k_{op,st} = f(\theta_{FR})$ of the compressor;
- surface area of the evaporator F (catalog value).

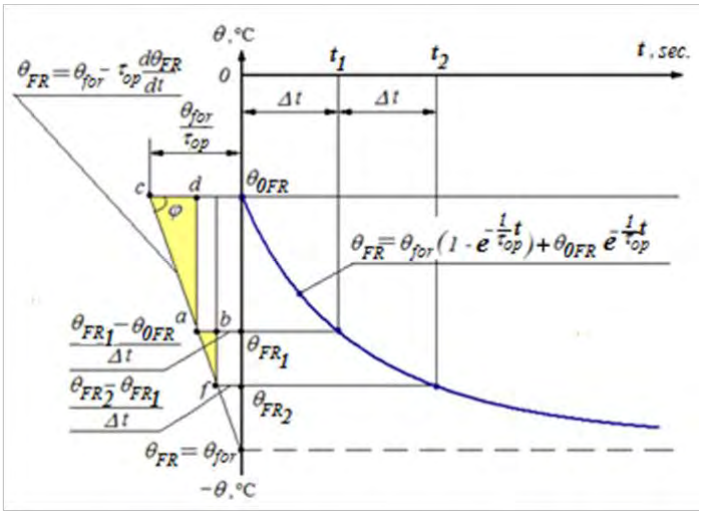

Figure 2: To the calculation of the cooling time constant and the forced temperature in the freezer compartment when the compressor is running

Theoretical dependence of the temperature of the freezer compartment at the beginning of the cooling cycle with a non-zero initial condition $\theta_{FR} = \theta_{0FR}$, determined by the thermostat is given in

Figure 2. Temperature $\theta_{forced} \le \theta_{FR} \le \theta_{0FR}$ over the entire change interval has an exponential dependence

$$\theta_{FR} = \theta_{forced}\left(1 - e^{-\frac{t}{\tau_{op}}}\right) + \theta_{0FR}e^{-\frac{t}{\tau_{op}}}. \quad \text{Eq. (9)}$$

Differentiating Eq. (9), we establish the dependence of the temperature change on the time of the transition process

$$\frac{d\theta_{FR}}{dt} = -\frac{1}{\tau_{op}}\left(\theta_{forced}e^{-\frac{t}{\tau_{op}}} - \theta_{0FR}e^{-\frac{t}{\tau_{op}}}\right). \quad \text{Eq. (10)}$$

From the same Eq. (9) we express the free component of the constrained temperature

$$\theta_{forced}e^{-\frac{t}{\tau_{op}}} = \theta_{forced} - \theta_{FR} - \theta_{0FR}e^{-\frac{t}{\tau_{op}}}. \quad \text{Eq. (11)}$$

After substitution of Eq. (11) in Eq. (10) we obtain an expression of the form

$$-\tau_{op}\frac{d\theta_{FR}}{dt} = \theta_{forced} - \theta_{FR} + \theta_{0FR}e^{-\frac{t}{\tau_{op}}} - \theta_{0FR}e^{-\frac{t}{\tau_p}} = \theta_{forced} - \theta_{FR},$$

from which the temperature of the freezer compartment in the function of its rate of change $\frac{d\theta_{FR}}{dt}$ takes the form of linear dependence

$$\theta_{FR} = \theta_{forced} - \tau_{op}\frac{d\theta_{FR}}{dt}. \quad \text{Eq. (12)}$$

Accordingly, the time constant of reducing the temperature of the freezer compartment in general will be

$$\tau_{op} = \frac{\theta_{forced} - \theta_{FR}}{\frac{d\theta_{FR}}{dt}}, \quad \text{Eq. (13)}$$

or numerically

$$\tau_p = \left(\theta_{forced} - \theta_{FR_i}\right)\frac{(t_i - t_{i-1})}{\left(\theta_{FR_i} - \theta_{FR_{i-1}}\right)}. \quad \text{Eq. (14)}$$

According to three temperature values $\theta_{0FR}, \theta_{FR_1}$ и θ_{FR_2}, obtained at equal intervals of time, in the Figure 2 the linear dependence of Eq. (12) has been built, the intersection points of which with the axes of coordinates graphically determine the forced temperature θ_{forced} and the cooling time constant τ_{op}. For their analytical definition, we use the triangle *abf*, formed by the linear dependence Eq. (12) with the time axis t, namely, we calculate:

1. The leg of the triangle corresponding to the weakening of the process of an exponential decrease in the rate of temperature change over a time interval $\Delta t = t_1 - t_0$ after the start of cooling

$$\overline{ab} = \frac{\theta_{FR_1} - \theta_{0FR}}{\Delta t} - \frac{\theta_{FR_2} - \theta_{FR_1}}{\Delta t} = \frac{2\theta_{FR_1} - \theta_{0FR} - \theta_{FR_2}}{\Delta t} \quad \text{Eq. (15)}$$

and the slope of the linear dependence Eq. (12)

$$\varphi = \tan^{-1}\frac{\theta_{FR_2} - \theta_{FR_1}}{\overline{ab}}; \quad \text{Eq. (16)}$$

2. The segment of reducing the rate of decrease in temperature after the first measurement

$$\overline{cd} = \frac{\theta_{FR_1} - \theta_{0FR}}{\tan\varphi} = \frac{(\theta_{FR} - \theta_{0FR})}{(\theta_{FR_2} - \theta_{FR_1})} \cdot \overline{ab}; \quad \text{Eq. (17)}$$

3. The ratio of a forced temperature in the freezer compartment for cooling time constant

$$\frac{\theta_{forced}}{\tau_{op}} = \overline{c0} = \frac{\theta_{FR_1} - \theta_{0FR}}{\Delta t} + \overline{cd}; \quad \text{Eq. (18)}$$

4. The slope of the linear dependence Eq. (12)

$$\tan\varphi = \frac{\theta_{forced} - \theta_{0FR}}{\frac{\theta_{forced}}{\tau_{op}}} \quad \text{Eq. (19)}$$

and the forced temperature in the freezer compartment (the boiling point of the refrigerant)

$$\theta_{forced} = \theta_{0FR} + \frac{\theta_{forced}}{\tau_{op}} \tan\varphi; \quad \text{Eq. (20)}$$

5. Cooling time constant by the Eq. (13)

$$\tau_{op} = \frac{\theta_{forced} - \theta_{FR}}{\frac{d\theta_{FR}}{dt}}. \quad \text{Eq. (21)}$$

and the coefficient of heat transfer to the evaporator

$$k_{op} = \frac{G_{met.} c_{met.}}{\tau_{op} F}. \quad \text{Eq. (22)}$$

Similarly is determined the coefficient of heat transfer to the evaporator during standstill of the compressor

$$k_{st} = \frac{G_{met.} c_{met.}}{\tau_{st} F}. \quad \text{Eq. (23)}$$

and heat gain to the evaporator by the expression Eq.(8)

$$Q_{FR} = Q_{op} + Q_{st} = k_{op,st} F \int_0^{t_{op}+t_{st}} (\theta_{FR} - \theta_{0FR})\, dt. \quad \text{Eq. (24)}$$

Based on the mathematical model of the method, as an indicator of the energy efficiency of the freezer compartment can be taken the ratio of the real heat gain to the evaporator $Q_{FR} = Q_{op} + Q_{st}$ to its maximum value $Q_{FR_{max}}$, to which corresponds fast temperature reduction up to the forced value $\theta_{FR} = f(t) = \theta_{forced}$ from the moment the compressor is turned on and during the operation time t_p it does not change. When the compressor stops, the forced temperature takes an initial nonzero value $\theta_{FR} = f(t) = \theta_{0FR}$ and does not change over the time t_{st}. Based on them, the maximum heat gain to the evaporator from the object of cooling during the compressor cycle time, at a sudden change in temperature in the freezer compartment to forced values, will be

$$Q_{FR_{max}} = k_{op} F \int_0^{t_{op}} (\theta_{forced} - \theta_{0FR})\, dt = k_{op} F (\theta_{forced} - \theta_{0FR}) t_{op}. \quad \text{Eq. (25)}$$

Using Eq.(24) and Eq.(25), the energy efficiency of the freezer compartment is estimated by the coefficient of efficiency

$$\eta = \frac{Q_{FR}}{Q_{FR_{max}}}. \quad \text{Eq. (26)}$$

2.4. Approbation of Method of Energy Efficiency Determination

The calculation of the energy efficiency index of the freezer compartment as well as any other component of the refrigerator begins when the compressor is turned on and is performed at regular intervals of time Δt by measuring temperature values at the beginning $\theta_{FR,i=1}$ and at the end $\theta_{FR,i+1}$, Figure 1. Based on the measured temperature values at each time interval $= 1, \dots (t_{op} + t_{st})/\Delta t$, the following values are calculated:
- the average temperature value, Figure 1

$$\Delta\theta_{FR.mid,i} = 0{,}5(\theta_{FR.i+1} + \theta_{FR.i}); \qquad \text{Eq. (27)}$$

- the area of the integrand surface of temperature dependence at its natural and forced change

$$f_{\frac{FR}{FR_{max}},i} m_t m_\theta = \frac{\Delta t}{3600} \sum_1^i (\theta_{\frac{FR}{FR_{max}}.mid,i} - \theta_{0FR}); \qquad \text{Eq. (28)}$$

- forced temperature value in the freezer compartment Eq. (15 ... 20) and the cooling time constant

$$\tau_{op,st} = \left(\theta_{forced} - \theta_{FRi}\right) \frac{\Delta t_i}{(\theta_{FR,i} - \theta_{FR,i-1})}; \qquad \text{Eq. (29)}$$

- heat transfer coefficients in the evaporator during operation and stoppage of the compressor

$$k_{op,st} = \frac{G_{met.} c_{met.}}{\tau_{op,st} F}, \qquad \text{Eq. (30)}$$

- heat gain to the evaporator, maximum heat gain and energy efficiency of the freezer compartment in terms of coefficient of efficiency are calculated by the expressions Eq. (8), Eq. (24) and Eq. (26). The closer the value of efficiency to 1, the more efficient the freezer compartment of the tested refrigerator works. The approbation of the indirect method of determining the energy efficiency in terms of the efficiency of a nominally loaded freezer compartment of the NORD-237 refrigerator was performed using an analyzer, the description of which is given in (Baydak, 2011)

Table 1. Performance indicators of the refrigerator freezer compartment operation

Δt, *sec*	$\Delta\theta_{FRmid}$, °C Eq. (27)	θ_{forced}, °C Eq. (20)	τ_{op}, *sec.* Eq. (21)	$k_{op,st}$, *W/(m² °C)* Eq. (22)	Q_{FR}, *W·h* Eq. (24)	Q_{FRmax}, *W·h* Eq. (25)	η, - Eq. (26)	*COP*, - Eq. (31)	COP_{max} - Eq. (31)
500	-20,5	-29,5	186,3	8,6	-49,87	-83,17	0,6	1,25	2,08

For shown in Figure 1 results of monitoring the temperatures in the freezer compartment of the refrigerator and at the selected time interval Δt = 500 sec, the indicators of the efficiency of its work are summarized in Table 1. Since, simultaneously with monitoring the temperature of the refrigerator freezer compartment, during one cycle of compressor operation, the active power of its engine and the consumed electrical energy $W = 40W \cdot h$ were recorded, the thermal load or the real and maximum possible electrical coefficient of performance can be calculated

$$COP = \frac{|Q_{FR}|}{W}, \qquad COP_{max} = \frac{|Q_{FR_{max}}|}{W}. \qquad \text{Eq. (31)}$$

3. CONCLUSIONS

The developed mathematical model and the algorithm of the indirect method for determining the energy efficiency of the freezer compartment are invariant for any component of refrigerating system (e.g. in domestic refrigerator) and complement the well-known methods of a differentiated approach to the integral assessment of the energy efficiency of the refrigerating system. The method allows adequate assessing the potential for improvement, reducing energy costs in refrigerators as well as conducting of an accurate comparative analysis and classification of the systems used in them. The forced temperature value is an exact characteristic of the properties of the used refrigerant (boiling

point) and may be used to determine its type indirectly. The coefficient of heat transfer to the evaporator, calculated taking into account the actual temperature change, significantly increases the adequacy of the proposed method compared to existing methods. The considered method and the testing and monitoring devices used do not require intervention in a hermetic refrigerating system, which makes them useful for servicing of any domestic refrigerators.

NOMENCLATURE

t	time	t_{op}, t_{st}	compressor running time, compressor stoppage time (sec.)
$dQ'_{op,st}$	heat gain to evaporator (W·sec)	$G_{met.}$	evaporator weight (kg)
$dQ''_{op,st}$	heat accumulated in the evaporator (W • s)	c_{met}	specific heat of evaporator metal
Q_{FR}	heat accumulated by the evaporator in a natural way (W • s)	θ_{forced}	forced temperature in the freezer (º C)
Q_{FRmax}	heat accumulated by the evaporator in a forced way (W • s)	θ_{0FR}	initial temperature in the freezer compartment (º C)

REFERENCES

Arnemann, M., 2012. Energy Efficiency of Refrigeration Systems. International Refrigeration and Air Conditioning Conference, Purdue University. 1–10.

Baydak, Y., 2011. Refrigerating unit energy efficiency analyzer. Proceedings of the 23rd IIR International Congress of Refrigeration. IIF/IIR,1745-1754.

Preuss, G., 2011. Energy demand for refrigeration in Germany: An estimation for all fields of application, VDMA (Publ.), (German language) Frankfurt am Main, 80 p.

VDMA 24247-2: Energy efficiency of refrigerating systems – Requirements for system design and components, published in the English language, 05-2011, 27 p.

VDMA 24248 Energy Efficiency of Electrically Powered Heat Pumps – Coefficients of Energy Efficiency and Their Definition

Manuscript ID: 1042
DOI: 10.18462/iir.icr.2019.1042

Effects of operating conditions on reciprocating room temperature magnetic refrigeration system

Georges EL ACHKAR[(a)], Bin LIU[(a)], Qi WANG[(a)], Rachid BENNACER[(a,b)]

[(a)]Tianjin Key Laboratory of Refrigeration Technology, Tianjin University of Commerce
Tianjin, 300134, P.R. China, georges.elachkar@tjcu.edu.cn
[(b)] LMT/ENS-Cachan/CNRS/Université Paris Saclay,
Cachan, 94235, France, rbennace@ens-cachan.fr

ABSTRACT

In this paper, the effect of the operating frequency on the cooling span of a reciprocating magnetic refrigeration system, with granular gadolinium (Gd) of particle size 0.3-0.5 mm used as magnetocaloric material, was investigated. The hot and cold end temperatures of an active magnetic regenerator (AMR) were measured over time for different operating frequencies (0.07 Hz, 0.12 Hz, 0.16 Hz, 0.19 Hz and 0.22 Hz) under a constant magnetic field of 1.5 T generated by a permanent magnet. The results showed that the temperature difference between the hot and cold ends increased with the operating frequency increase. Besides, the maximum refrigeration temperature of the system was 12.8 °C for an operating frequency of 0.22 Hz.
Keywords: Magnetic Refrigeration, Magnetocaloric Effect, Magnetocaloric Material, Gadolinium, Magnetic Field, Frequency, Room Temperature.

1. INTRODUCTION

The growing need for industrial refrigeration and air conditioning requires an increasing use of two-phase thermal systems with mechanical vapour compression. Nevertheless, these thermal systems have the disadvantage of operating with refrigerants, which often have a negative impact on the ozone layer and/or a significant contribution to the greenhouse effect. The quality of the new environmentally friendly refrigerants will probably be to the detriment of the energy performance or the stability of these thermal systems. It is therefore important to search for new cold production solutions ensuring high energy efficiency and low environmental impact. In this context, the magnetic refrigeration technology, based on the magnetocaloric effect (MCE) of magnetic materials, appears as a potentially viable solution (Russek and Zimm, 2006; Sari and Balli; 2014; Mezaal et al., 2017). Since the theoretical optimal coefficient of performance (COP) of magnetic refrigeration systems is of the same order as that of two-phase thermal systems with mechanical vapour compression and their operation occurs with solid materials coupled with water, the possibilities seem to fit with the current requirements. In addition, this new technology operates at low pressure and frequency (between 1 and 10 Hz instead of 50 Hz for conventional technology), which is positive for the security, the maintenance cost, the noise and the lifetime.

The MCE is a physical phenomenon that occurs in magnetic materials under the influence of a varying magnetic field (Warburg, 1881; Weiss and Picard, 1917; Smith, 2013; Zemansky, 1981). It is usually expressed as an adiabatic temperature change (ΔT_{ad}) or an isothermal total entropy change (ΔS_{tot}) of a magnetic material. In the absence of a magnetic field (H=0), the magnetic moments in the material are disordered (Fig. 1a). If a magnetic field is applied to the material (H>0), the magnetic moments will be forced to align in a higher order (Fig. 1b). As a consequence, the magnetic entropy (S_m) will decrease. In isentropic (i.e. adiabatic) conditions, the total entropy ($S_{tot}=S_m+S_l$) will remain constant. Therefore, the decrease of the magnetic entropy will manifest itself in an increase of the lattice entropy (S_l). The atoms in the material will start to vibrate more intensively, and as a consequence, the temperature of the material will increase. The opposite occurs when the magnetic field is removed. The magnetic entropy increases and the temperature decreases. This effect is maximal around the Curie temperature which marks the change between

the ferromagnetic state and the paramagnetic state of the magnetic material. This transition is the most frequently studied so far.

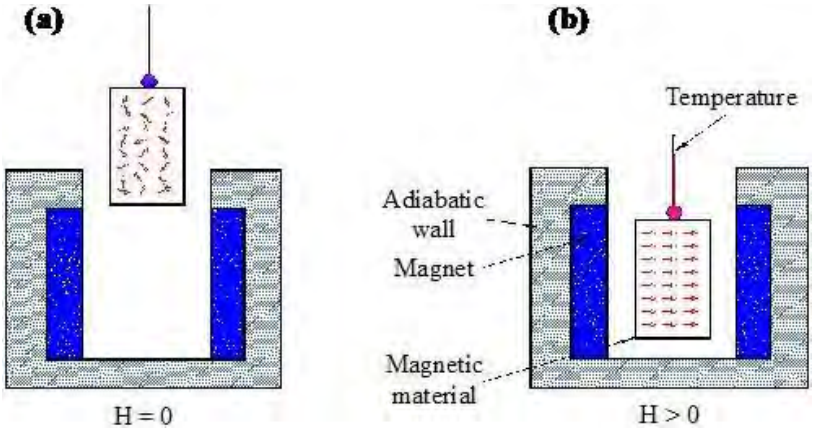

Figure 1: Schematic diagram of the magnetocaloric effect principle

On the basis of the magnetocaloric effect, it is thus possible to create energy conversion cycles by applying 4 thermodynamic processes: adiabatic magnetisation (phase 1), isomagnetic transfer of entropy (phase 2), adiabatic demagnetisation (phase 3) and isomagnetic transfer of entropy (phase 4).

2. EXPERIMENTS

2.1. Experimental Apparatus

In order to study the effects of the operating on the reciprocating room temperature magnetic refrigeration system, an experimental apparatus was designed and mounted (Fig. 2). This bench mainly consists of a condenser (A), a pump (B), a solenoid valve (C), a permanent magnet (D), (E) a test section, (F) a hot end 1, (G) a hot end 2 and (H) a cold end (Fig. 2a).

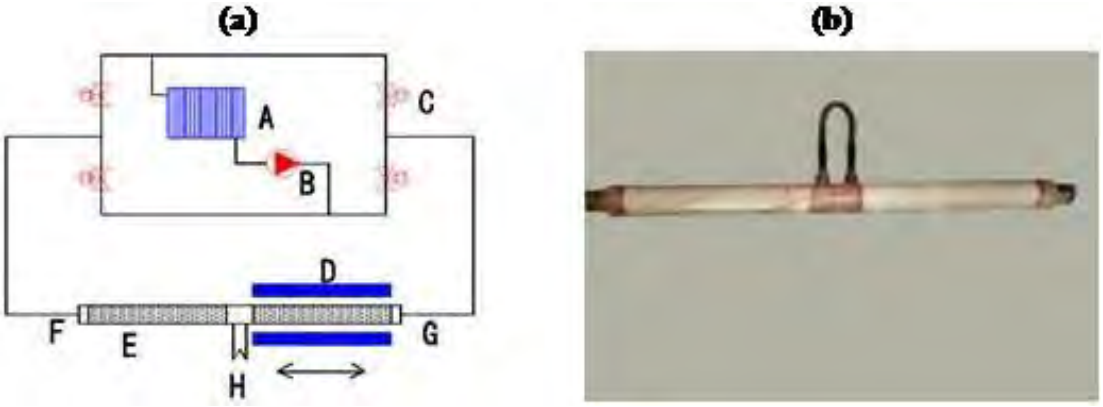

Figure 2: (a) Schematic diagram of the reciprocating magnetic refrigeration system; (b) Photography of the test section

The test section consists of two symmetrical cylindrical active magnetic regenerators, each filled with 900 g of Gd particles with a size of 0.3-0.5 mm (Fig. 2b). The permanent magnet alternatively moves towards the left and right AMRs, inducing thus alternative magnetisation and demagnetisation of these AMRs. When the permanent magnet covers the left AMR, the magnetised Gd heats up. The pump then runs and the water flow from the cold end (H) to the hot end 1 (F) recovers the heat. Similarly, when the right AMR is magnetised, the water flow is reversed, and the water flow from the cold end (H) to the hot end 2 (G) recovers the heat. After that, while one AMR is magnetised, along

with the demagnetisation at the other AMR, the temperature of the cold end gradually decreases, and the temperature of the hot end gradually increases.
The main function of the temperature acquisition module is the temperature of the acquisition system. The temperature acquisition module has four output ports, which can simultaneously collect four temperature changes. The temperature sensor used is PT100, and the accuracy level is 0.2 °C. The temperature measurement points are distributed at the cold end temperature (H), the hot end temperatures (F&G), and the room temperature measurement points of the suspended arrangement.

2.2. Experimental Procedure

The effects of different operating frequencies and room temperatures on the cooling temperature span were studied:
a) At a room temperature of 18 °C, by changing the magnetic moving speed corresponding to the different operating frequencies (Table 1), temperature measurement analysis of the cold end (H), hot ends (F&G) of the regenerator.
b) Using the system to test the magnetocaloric effect of the magnetocaloric material Gd (adiabatic temperature change ΔT_{ad} (Eq. 1) and compare it with the theoretical value.
c) In the different room temperature environments 14.5 °C, 15.9 °C, 16.7 °C, 18.1 °C, keep the operating frequency of 0.22 Hz unchanged, test the cold junction temperature of the regenerator, analyse the ambient temperature for the cooling temperature span for a limited time.

Table 1: Operating conditions of the magnetic refrigeration system

L (mm)	V ($mm.s^{-1}$)	t (s)	f=1/(L/V+t) (Hz)	H (T)
500	40	1.4	0.07	1.5
500	70	1.4	0.12	1.5
500	100	1.4	0.16	1.5
500	130	1.4	0.19	1.5
500	160	1.4	0.22	1.5

During the experiment, the temperature is cut for a period of time, and the temperature of the cold and hot ends of the magnetic working medium is measured. The adiabatic temperature change of the magnetic working medium during the magnetisation process can be cold and hot by the heat exchange fluid after the magnetic application. The difference in terminal temperatures is approximated to be expressed as in Eq. 1. The main reason is that in this experiment, the magnetic particle material is a small particle, the heat exchange fluid is directly in contact with the particle, and the fluid temperature is close to the magnetic particle temperature, so the fluid temperature change can represent the change of the magnetic particle temperature.

$$\Delta T_{ad} = T_H - T_C \qquad \text{Eq. (1)}$$

3. RESULTS AND DISCUSSION

In order to analyse the cooling effect of room temperature magnetic refrigerator under different working frequency conditions, the temperature difference between cold and hot end, the temperature difference between hot and cold end and the hot end and cold end temperature are analysed and compared at different working frequencies, as shown in Figs. 3-6.

3.1. Temperature Test at Different Operating Frequencies

At room temperature 18 °C, the temperature change of the cold and hot end of the active regenerator at room temperature magnetic refrigerator at different operating frequencies (see Table 1) was

tested. The temperature change of the hot and cold ends of the AMR for a magnet displacement frequency of 0.16 Hz was selected, as shown in Fig. 3.

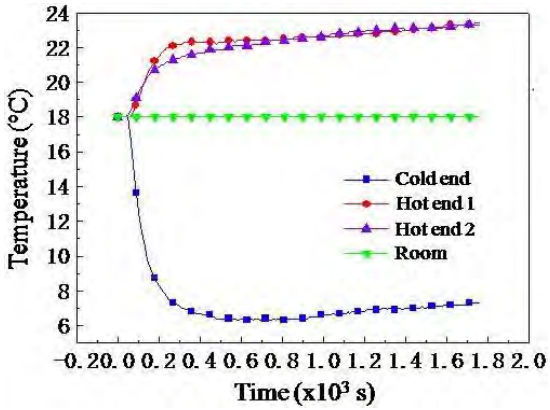

Figure 3: Evolution over time of the hot and cold ends temperature for a magnet displacement frequency of 0.16 Hz and a room temperature of 18 °C

When the room temperature is maintained at 18 °C, the operating frequency is 0.16 Hz, about 400 s, the temperature of the hot and cold end begins to change slowly, and gradually stabilises. And the temperature of the cold end is about twice that of the hot end 1 and the hot end 2, because the cold end of the active regenerator is the shared cold end of the two magnetic beds, and the cooling capacity is a superimposed amount. At the same time, the heat transfer time of magnetic heat conduction is about 1 s, and the temperature of the heat exchange fluid rises by about 1K. In the experiment, the rising temperature of the hot end is close in the process of adding magnetism, but there is a difference, because the test bench records every 10s, there is an error. The hot end temperature was maintained at 23.3 °C and 23.4 °C respectively. The cold junction temperature reached a minimum temperature of 6.3 °C, and the maximum cooling temperature span was 11.7 °C. At about 1000 s, the cold junction temperature began to rise. The reason may be that the cold end of the magnetic refrigerator has reached the minimum temperature under this condition, and part of the heat at the hot end is transmitted to the cold end with the flow, so that the cold end temperature shows a slight rebound.

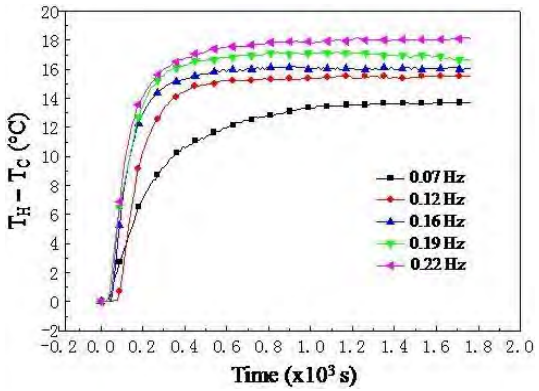

Figure 4: Evolution over time of the temperature difference between hot and cold ends for different magnet displacement frequencies and a room temperature of 18 °C

3.2. Hot and Cold Temperature Difference Between Different Working Frequencies

Fig. 4 shows the change of the temperature difference between cold and hot end with the running time when the room temperature is kept at 18 °C and the operating frequency is 0.07 Hz, 0.12 Hz, 0.16 Hz, 0.19 Hz and 0.22 Hz, respectively. About 400 s, the temperature difference between the cold and hot end except the working frequency of 0.07 Hz began to change slowly, and gradually became stable. The operating frequency was 0.16 Hz, 0.19 Hz, and the temperature difference between the hot and cold end of 0.22 Hz was 0.07 Hz. It is about doubled because the demagnetisation frequency increases with the addition of magnetism, that is, the exothermic heat and the heat absorption of the magnetic working fluid Gd increase in a limited time. With the increase

of the cooling capacity, the cooling rate of the cold end is correspondingly increased. Under the five different operating frequency conditions, the maximum temperature difference between the hot and cold ends of the room temperature magnetic refrigerator is 13.7 °C, 15.5 °C, 16.2 °C, 17.2 °C, 18.1 °C. And when the operating frequency is 0.22 Hz, the maximum temperature difference between the hot and cold ends can be 18.1 °C.

3.3. Hot End Temperature Difference Between Different Working Frequencies

As shown in Fig. 5, the trend of the cold junction temperature at different operating frequencies is consistent, and both rise sharply first. At about 500 s, the average temperature of the hot end corresponding to the five operating frequencies begins to change slowly. It can be found that as the operating frequency of the room temperature magnetic refrigerator increases, the temperature rise rate of the hot end before 500 s is larger, and the corresponding stable hot end temperature is higher.

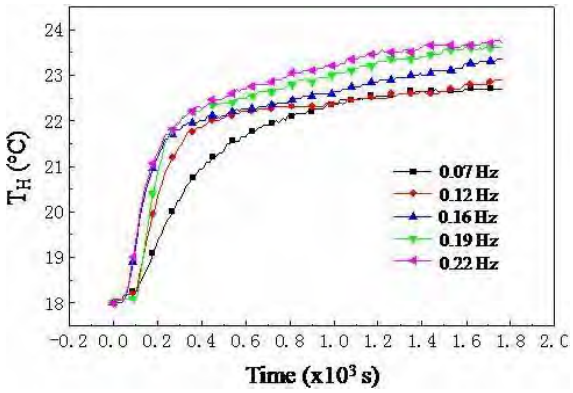

Figure 5: Evolution over time of the hot end temperature for different magnet displacement frequencies and a room temperature of 18 °C

3.4. Cold End Temperature Comparison of Different Working Frequencies

As shown in Fig. 6, the temperature trends of the cold junctions at different operating frequencies are consistent, and both drop sharply first. At about 500 s, the cold junction temperatures corresponding to the five operating frequencies gradually become stable. It can be found that as the operating frequency of the room temperature magnetic refrigerator increases, the rate of temperature drop of the cold end before 500 s is larger, and the corresponding stable cold end temperature is lower. From the left half of Fig. 6, it can be found that the cooling temperature spans are 9 °C, 11.1 °C, 11.7 °C, 12.3 °C, 12.8 °C under different operating frequencies of 0.07 Hz, 0.12 Hz, 0.16 Hz, 0.19 Hz and 0.22 Hz, respectively. Therefore, when the operating frequency increases, the cooling temperature span of the corresponding room temperature magnetic refrigerator increases, which plays a guiding role in improving the cooling effect of the room temperature magnetic refrigerator.

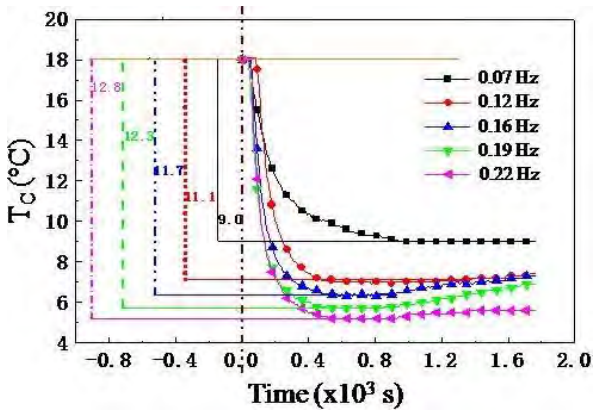

Figure 6: Evolution over time of the cold end temperature for different magnet displacement frequencies

4. CONCLUSIONS

By keeping the room temperature at 18 °C, when different operating frequencies are selected and the operating frequency is kept constant at 0.22 Hz, the experimental analysis of the reciprocating room temperature magnetic refrigerator cooling temperature span is obtained. The following conclusions are obtained:

- At different operating frequencies, the cold junction temperature of the active regenerator decreases sharply with time, then gradually stabilises, and as the operating frequency increases, the cold junction temperature decreases, when the operating frequency is 0.22 Hz. The cooling temperature span is at most 12.8 °C.
- In the process of magnetisation, the direct measurement of the adiabatic temperature change of the magnetocaloric material is close to the theoretical value of 4.2 °C, verifying thus the experimental feasibility of the system.

ACKNOWLEDGEMENTS

Financial support from the National Natural Science Foundation of China (No. 51706154) is gratefully acknowledged.

NOMENCLATURE

H	magnetic field (T)	t	duration (s)
f	magnet displacement frequency (Hz)	ΔT_{ad}	adiabatic temperature (s)
L	regenerator length (m)	T_C	cold end temperature (°C)
S_l	lattice entropy ($J.K^{-1}$)	T_H	hot end temperature (°C)
S_m	magnetic entropy($J.K^{-1}$)	V	magnet displacement velocity ($mm.s^{-1}$)
S_{tot}	total entropy($J.K^{-1}$)		

ACKNOWLEDGEMENTS

Financial support from the National Natural Science Foundation of China (No. 51706154) is gratefully acknowledged.

REFERENCES

Russek, S. L., Zimm, C. B., 2006. Potential for cost effective magnetocaloric air conditioning systems. Int. J. Refrigeration 29 (8), 1366-1373.

Sari, O., Balli, M., 2014. From conventional to magnetic refrigerator technology. Int. J. Refrigeration 37, 8-15.

Mezaal, N. A., Osintsev, K. V., Zhirgalova, T. B., 2017. Review of magnetic refrigeration system as alternative to conventional refrigeration system. IOP Conference Series: Earth and Environmental Science 87, 032024.

Warburg, E. G., 1881. Magnetische untersuchungen über einige wirkungen der coerzitivkraft. Annalen der Physik (Leipzig) 13, 141-164.

Weiss, P., Piccard, A., 1917. Le phénomène magnétocalorique. J. Physique Théorique et Appliquée 7 (1), 103-109.

Smith, A., 2013. Who discovered the magnetocaloric effect?. European Phys. J. H 38 (4), 507-517.

Zemansky, M. W., 1981. Temperatures very low and very high. Dover Publications.

Manuscript ID: 1057
DOI: 10.18462/iir.icr.2019.1057

Chiller Fault Diagnosis with the Technology of Imbalanced Data

Yuqiang Fan, Hua Han, Xiaoyu Cui, Hao Wu, Ling Xu, Hailong Lu, Hui Geng

Institute of Refrigeration and Cryogenics, School of Energy and Power Engineering, University of Shanghai for Science and Technology, 516 Jun Gong Road, Yang Pu, Shanghai 200093, PR China

happier_han@126.com xiaoyu_cui@usst.edu.cn

ABSTRACT

Data driven diagnostic model for refrigeration systems is often used exclusively to a dedicated object. When it comes to a different type of chiller, a new model must be trained with large among of normal and faulty data, which is both time-consuming and heavily data-depending, and accordingly, curbs its application. In this study, the technology for the tackling of imbalanced data was introduced to probe the possibility of extrapolating an old model trained for a centrifugal chiller to a new one that can diagnose the faults of a screw chiller, by just using small amount of new data. Synthetic Minority Oversampling Technique (SMOTE) is used to oversample the fault sample set with an unbalance ratio of 5% and support vector machine (SVM) is employed for fault diagnosis. By investigating oversampling ratios between 100% and 400%, it was found that the ratio of 100% was the best and the diagnostic accuracy reached 96.70% for the four types of faults of the screw chiller.
Keywords: Chiller, Imbalanced-learn, Fault detection and diagnosis (FDD), SMOTE, SVM.

1. INTRODUCTION

Commercial and residential buildings, which contribute to more than 40% of the total energy usage worldwide, primarily consume energy through heating, ventilation, and air-conditioning (HVAC) systems (Li D,2016). Therefore, the development of fault detection and diagnosis (FDD) techniques is critical in maintaining indoor environmental comfort, reducing equipment wear and tear, and saving energy (Li H, 2007). FDD techniques with high diagnostic accuracy and robustness that can present an early warning when slight faults occur are required.

In the last few decades, the FDD technology of chillers has been developed vigorously. In the HVAC field, FDD methods can be classified into two primary categories: model-based methods and data-driven methods (SrinivasKatipamula, 2005). In a model-based method, a priori knowledge of the chiller system is required to identify the differences between the actual measured values and the estimated ones obtained from the reference model (DAT Tran, 2016).Such methods have been developed by Wang Shengwei et al. (2005) and Zhao Xinzhi (2015). Wang established a model called the rule-based fault diagnosis method where when a fault occurs, it primarily uses the direction of the fault index changes, i.e., above or below a predefined threshold (Xiao F, 2011). A data-driven method is based on using a large amount of historical data of the real chiller system covering a wider range of operating conditions. It can overcome the limitations of model-based methods, where it may be difficult to give a precise description of the real chiller system operating at a wide range of operational conditions, especially at the off-design conditions (Li G, 2016). Therefore, the research on chiller fault detection and diagnosis based on data-driven methods has attracted wide attention in recent years. Data-driven methods, such as exponentially weighted moving average (Zhao Y, 2013), support vector machine (SVM) (Han H, 2011), and Bayesian networks (Wang Z, 2017) have been applied extensively to refrigeration systems. The advancement of an accurate and suitable reference model is critical in the efficiency of fault detection and diagnosis for chiller systems.

However, slight defects and deficiencies occur in the current FDD techniques. First, this prior knowledge is rarely considered in the current data-driven FDD literature. When the prior knowledge of centrifugal chillers is used, the training sample will contain centrifugal chiller fault samples (called

majority) and a small number of screw chiller fault samples (called minority). This study addresses a solution: the synthetic minority oversampling technique (SMOTE) for data classification, which balances datasets by resampling (Chen Y, 2009). This method is a heuristic oversampling technique proposed by Chawla et al. to solve the problem of data class imbalance. SMOTE has been used to solve imbalanced dataset problems in some medical areas, such as cardiotocography (Chawla N V, 2002), cancer diagnosis (Potharaju S P, 2018), enterprise credit evaluation (Wang K J, 2014), and fraud detection (Phua C, 2010). In this study, we used principal component analysis (PCA) to reduce the dimension of the characteristic parameters of the water chillers. After the data reconstruction of screw chillers using the SMOTE, a PCA–SOMTE–SVM fault detection and diagnosis method is established to solve the model generalization problem of the FDD technique when the dataset is imbalanced.

2. IMBALANCED DATA AND FIELD SENSORS

This section first introduces briefly the imbalanced data used from the ASHRAE project 1043 (majority data) and the variable-speed screw chiller system (minority data). Because of the imbalanced data, the solution to this problem will be proposed later. Next, the field sensors of the chiller parameters are used according to previous studies.

2.1. Majority data - centrifugal chiller system

The experimental data used were from the ASHRAE project 1043[24], where a 90-ton centrifugal chiller was installed indoors with a nearly constant ambient temperature of 72 °F (22.2 °C). Both the evaporator and condenser are the flooded-type, two-pass shell-and-tube heat exchangers, with water flowing in the tubes as the secondary coolant.
Seven faults (Table 1), chosen based on the results of the chiller fault survey, were introduced artificially and investigated in the laboratory with each of the four fault levels of severity. They were sequenced in the descending order according to the normalized occurring frequency (Comstock, M.C,1999).The screw water chiller only simulates three types of faults, i.e., reduced condenser water flow, refrigerant leakage/undercharge, and refrigerant overcharge.

Table 1. Seven typical faults.

Fault type	State description	Abbreviations
Local faults	Condenser fouling	ConFoul
	Reduced condenser water flow	ReduCF
	Non-condensable in the refrigerant	NonCon
	Reduced evaporator water flow	ReduEF
System faults	Refrigerant leak/undercharge	RefLeak
	Refrigerant overcharge	RefOver
	Excess oil	ExcsOil

2.2. Minority data - variable-speed screw chiller system

The experimental setup was employed to measure the performance of a 200-ton variable-speed screw chiller under three kinds of faults: reduced condenser water flow, refrigerant leak/undercharge, and refrigerant overcharge. Figure 1 shows a schematic of the experimental setup, which presents the major waterway and temperature sensors. The studied system is an R134a 368.9-kW variable-speed screw chiller system with the nominal charge of 180 kg.

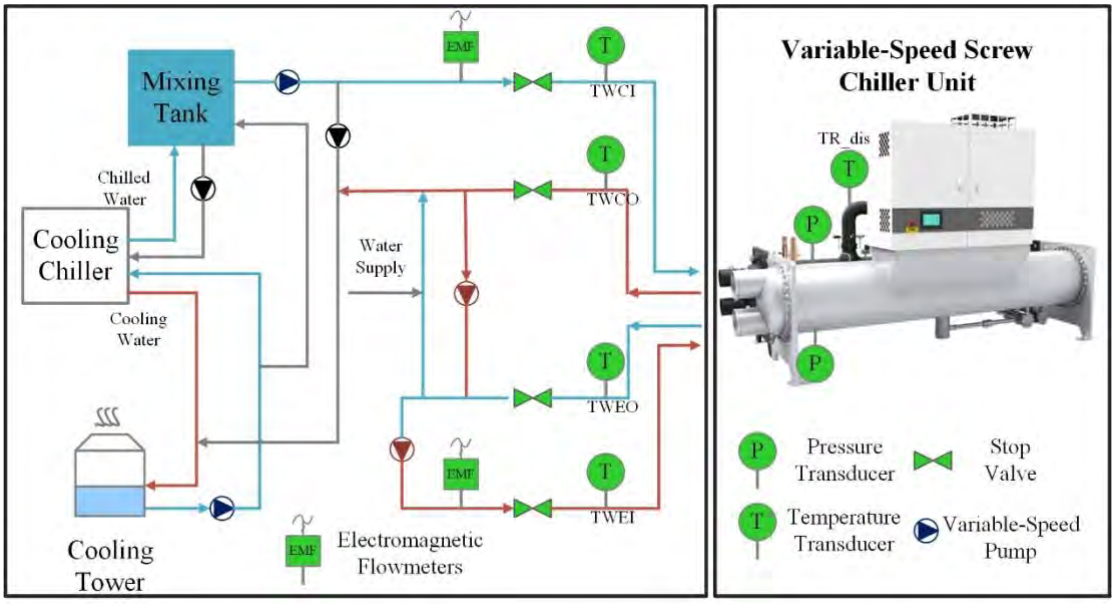

Figure 1: Schematics of the variable-speed screw chiller experimental system.

3. OVERSAMPLING TECHNOLOGY: PCA–SMOTE

In Section 2, the majority data and minority data are introduced. When the data is in an imbalanced state, the minority data are overwhelmed in the majority data and are difficult to diagnose. To solve the problem of imbalanced data, this section proposes the oversampling technology: PCA–SMOTE.

3.1. SMOTE Description

The SMOTE is a representative external method for balancing datasets by resampling (Chawla N V, 2002). The SMOTE algorithm implements an oversampling method to rebalance the original training set. The key idea of the SMOTE is to not apply a simple replication of minority class examples, but to introduce synthetic instances. This new data are created by the interpolation between several minority class instances that are within a defined neighborhood. Hence, the procedure is focused on the "feature space" rather than on the "data space." In other words, the algorithm is based on the values of the features and their relationships, instead of considering the data points as a whole. (Fernandez A, 2018) The minority class is oversampled by taking each minority class sample and introducing synthetic examples along the line segments joining any/all of the *k* minority class nearest neighbors. Depending upon the amount of oversampling required, neighbors from the *k* nearest neighbors are chosen randomly (Chawla N V, 2002). For example, if the required oversampling is 100% (the minority class was oversampled at 100%, 200%, 300%, and 400% of its original size (Chawla N V, 2002)), only one neighbor from the five nearest neighbors are selected and one sample is generated in each direction. The method of generating synthetic samples is as follows: Take the difference between the feature vectors (samples) and their nearest neighbors. The difference is multiplied by random numbers between 0 and 1 and added to the considered feature vectors. This leads to the selection of random points along the line segments between two specific features. This method effectively forces the minority decision areas to become more general.

3.2. PCA–SMOTE

The SMOTE improves the overfitting situation caused by a non-heuristic random oversampling method (Fang X, 2016). The core idea of the SMOTE is to insert randomly generated new samples between a small number of class samples and their neighbors to increase the number of minority class samples and improve the class imbalance distribution of the datasets. The primary steps of PCA–SMOTE technology are as follows:

1) First, the dimensionality of 17 selected feature parameters (Table 2) is reduced by PCA, and the

cumulative contribution ratio of the principal component is 99%, including three principal components. PCA is an effective multivariate statistical algorithm and has been used widely for dimension reduction and feature extraction (M.G. Jackson JE, 1979). It attempts to replace more variables with fewer comprehensive variables under the principle of minimizing the loss of data information, and the comprehensive variables are not related to each other.

2) The centrifugal chiller training sample is defined as S1, the screw chiller training sample is defined as S2 and S1 + S2 to form the training sample set Original. Table 3 shows the composition of the training samples. The S1 sample set has 1000 Normal and 7 types of fault samples, and the S2 sample set has 100 samples.

Table 3. Sample composition of original training set.

	Normal	RefLeak	ConFoul	ReduCF	NonCon	ReduEF	RefOver	ExcsOil	Total
S1	1000	1000	1000	1000	1000	1000	1000	1000	8000
S2	100	100	0	100	0	0	100	0	400
Original	1100	1100	1000	1100	1000	1000	1100	1000	8400

3) A new sample is synthesized for the reference formula of the screw chiller set (1).

$$S2OS_i = S2_i + rand(S2_{ij} - S_i) \quad \text{Eq. (1)}$$

Among them, $S2_i$ is the original sample set of screw chillers; $S2_{ij}$ represents the first *j* adjacent sample of $S2_i, j = 1, \cdots, N$; $S2OS_i$ represents the sample set of the screw chillers after oversampling; and *rand* represents a random number between 0 and 1. The new screw chiller fault samples are merged into the centrifugal chiller sample set to form a new balanced chiller training set.

First, the sample set is processed by PCA; subsequently, the screw chiller sample is processed by SMOTE oversampling and normalized by the MinMaxScaler. The formula for processing is shown in (2):

$$S_{std} = \frac{S_i - S_{min}}{S_{max} - S_{min}} \quad \text{Eq. (2)}$$

Among them, S_i is the original sample, S_{min} is the smallest sample, S_{max} is the largest sample, and S_{std} is the normalized sample.

The imbalance ratios of the centrifugal chiller sample set and screw chiller sample set are calculated to be 5% (8000:400), and the design oversampling ratios are 100%, 200%, 300%, and 400% (Table 4). *N* similar adjacent samples (*N* = 400, 800, 1200, and 1600) are found for the screw chiller sample set.

Table 4. Composition of samples under different oversampling ratios.

Model	Centrifugal chiller sample	Screw chiller sample	Imbalance ratio	Oversampling ratio
Original	8000	400	5%	0
PCA-SMOTE100%	8000	800	10%	100%
PCA-SMOTE200%	8000	1200	15%	200%
PCA-SMOTE300%	8000	1600	20%	300%
PCA-SMOTE400%	8000	2000	25%	400%

4. RESULTS AND DISCUSSIONS

The PCA–SMOTE–SVM model for the fault diagnosis of chillers after oversampling was used to handle the imbalanced training sets. The original model, PCA–SMOTE100%–SVM, PCA–SMOTE200%–SVM, PCA–SMOTE300%–SVM, and PCA–SMOTE400%–SVM were established according to oversampling of 100%, 200%, 300%, and 400% of the screw chiller sample set, and the results were analyzed.

4.2. Result Analysis

4.2.1. Overall performance of the PCA–SMOTE–SVM technology

Figure 2 shows the overall performance change diagram of the model under different sampling ratios. The training accuracy, test accuracy, G-means and MCC of the original SVM model were 93.62%, 95.90%, 91.90%, and 0.8505, respectively. The SVM diagnostic model after PCA–SMOTE oversampling technology has improved the diagnostic performance.

The accuracy of training increases with the increase in the oversampling ratio of the sample set of screw chillers. When the sample set of screw chillers reaches over 300%, the accuracy of training reaches the maximum value of 94.84%. However, when the sample was over 400%, the training accuracy decreased slightly. The accuracy of the test reached the highest when it was oversampled 100%, i.e., 96.70%. When the oversampling ratios are 200%, 300%, and 400%, the test accuracies decrease slightly, but remain above 96%. The SVM diagnosis model based on SMOTE oversampling technology exhibits higher robustness.

The G-mean value was improved significantly after using SMOTE oversampling technology. The maximum G-mean value increased when the oversampling was 100%, i.e., 1.57% higher than that of the SVM model. When the oversampling was increased to 200% and 300%, the G-mean value was higher and still superior to the SVM model. When oversampling was 400%, the G-mean value decreased again. The change trend of the MCC value was the same as that of the G-mean value. When the sample size was 100%, the MCC value reached the optimum value, and subsequently decreased with increased sample size. When the sample size was 400%, the MCC value increased again, but was better than that of the SVM model.

In conclusion, the SVM diagnostic model based on PCA–SMOTE oversampling technology still maintained a high performance in the fault diagnosis of two chillers, and the performance was improved based on the original SVM diagnostic model. The PCA–SMOTE100%–SVM model is the best diagnostic model with strong generalization ability and robustness, suitable for the fault diagnosis of chillers, can be extended to other chillers of similar or different type, and may facilitate in diagnosis strategies when involving imbalanced data.

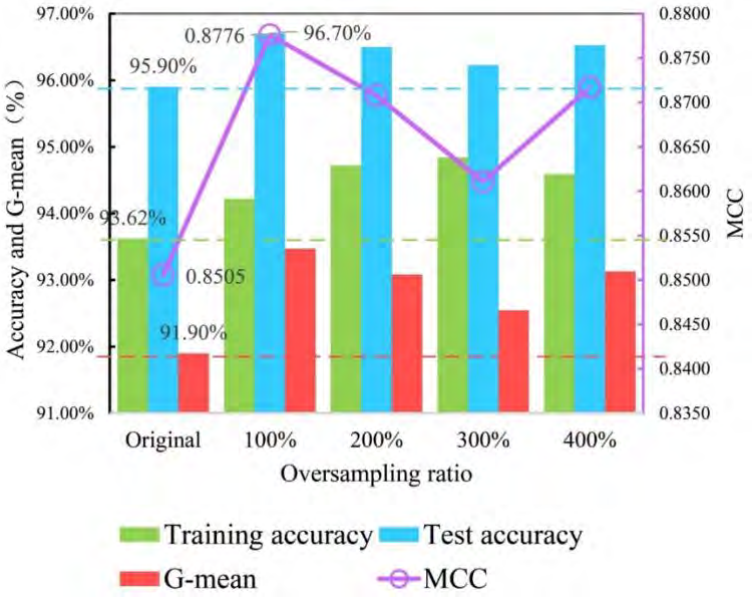

Figure 2: Overall diagnostic performance changes under different oversampling ratios.

4.2.2. Individual performance for each model

Figures 3 and 4 compare the performance of different faults under different oversampling ratios. From the figures, the PCA–SMOTE oversampling diagnosis model indicates superiority over the original SVM model in terms of the sensitivity rate and precision rate.

As shown in Figure 3, the Sensitivity–Normal increases first and subsequently decreases with the oversampling ratio, reaching a maximum of 95.30% at the oversampling ratio of 200%, i.e., 2.8% higher than that of the SVM model. The five models of Sensitivity–RefLeak and Sensitivity–ReduCF remain unchanged as the oversampling ratio increases. The best model of Sensitivity–RefOver is PCA–SMOTE100%–SVM, with a value of 96.20%, which is 1.3% higher than that of the original model. It decreases at the 200% oversampling ratio, and tends to be stable with the increase in oversampling ratio.

Figure 4 shows that the Precision value of RefLeak remains unchanged with the increase in the oversampling ratio; the PCA-SMOTE100%-SVM model performed better in Precision–Normal and Precision–ReduCF, especially Precision–ReduCF that was 2.34% higher than the SVM model. The best performance of Precision–RefOver was the PCA–SMOTE 200%–SVM model that increased

from 98.75% of the SVM model to 99.47%. The RefLeak fault of the five models exhibit the same performance.

In summary, PCA–SMOTE100%–SVM is the best among the five models, which can improve the Normal, ReduCF, and RefOver faults. When the imbalance ratio reaches 10%, the screw chiller still exhibits better diagnostic performance when the sample size is small. Therefore, the fault diagnosis method based on PCA–SMOTE–SVM is feasible. Although the primary part of the training set is the centrifugal chiller and the smaller part is the screw chiller, the PCA–SMOTE–SVM model still maintains a high diagnostic performance. It can be proven that the diagnosis model can be used for different types of chillers, and the generalization of the diagnosis model can be improved.

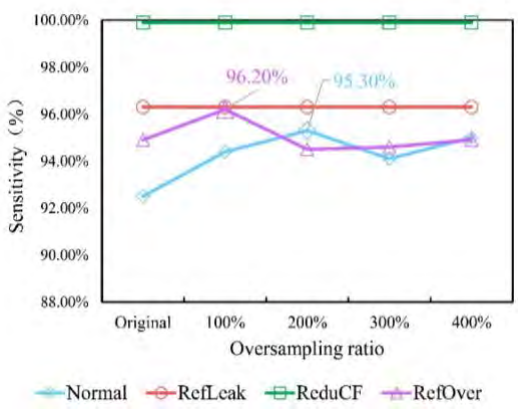

Figure 3: Different fault Sensitivity values under different oversampling ratios.

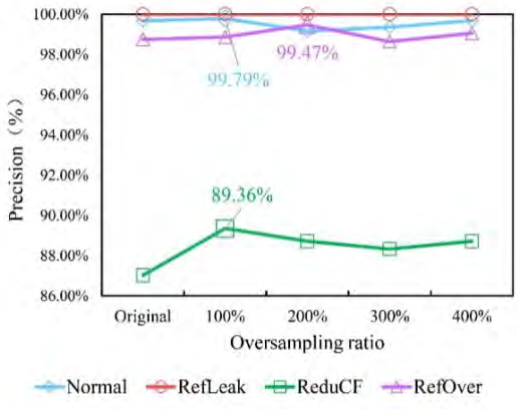

Figure 4: Different fault Precision values under different oversampling ratios.

From the analysis of the evaluation criteria of Sensitivity, Precision, and F-measure for different types of faults, it can be concluded that PCA–SMOTE100%–SVM performs well in all kinds of faults. It is the best diagnostic model for chillers, and the model achieves the best performance in the case of equivalence fiction.

5. CONCLUSION

The PCA–SMOTE–SVM fault diagnosis technology was proposed herein. It combined high accuracy, low computational effort, and numerical stability for variable-speed screw chiller systems. Mixing 400 screw chiller fault samples into a centrifugal chiller training set, PCA–SMOTE was used to oversample the Normal sample set, reduced condenser water flow, refrigerant leakage/undercharge, and refrigerant overcharge fault samples when the imbalance ratio of the training sample set was 5%. The oversampling ratio was 100%–400%, and a new training sample set after PCA–SMOTE processing was obtained. Subsequently, SVM was used to diagnose the fault of the new sample set, and Accuracy, G-mean, Precision, Sensitivity, and other evaluation criteria were used to evaluate the model under different oversampling ratios. The details are as follows:

(1) The PCA–SMOTE–SVM model established by oversampling processing performed better in the fault diagnosis of the chillers. Compared with the original SVM model, the PCA–SMOTE–SVM model improved the training accuracy by 1.22%, the test accuracy by 0.8%, and the G-mean value by 1.57%. All the performance indicators of the PCA–SMOTE–SVM models were superior to those of the original SVM model.

(2) The PCA–SMOTE100%–SVM chiller fault model was the best when the oversampling ratio was 100%, i.e., the equivalence fiction. The diagnostic accuracy was 96.70%, and the G-means value was 93.47%. The diagnostic model demonstrated strong generalization ability.

Generally, the PCA–SMOTE–SVM fault diagnosis technology employed in this study proved to be effective in improving FDD performance, reducing time, and reducing the initial cost on the simulation of fault experiments. It could be used as a practical application of chiller fault diagnosis technology.

ACKNOWLEDGEMENT

The current article was supported by the National Natural Science Foundation of China under Grant No. 51506125.

REFERENCES

Li D, Hu G, Spanos C J. A data-driven strategy for detection and diagnosis of building chiller faults using linear discriminant analysis [J]. Energy & Buildings, 2016, 128:519-529.

Li H. Economic Evaluation of Benefits Associated with Automated Fault Detection and Diagnosis in Rooftop Air Conditioners [J]. Ashrae Transactions, 2007(July).

SrinivasKatipamula, Brambley M. Review Article: Methods for Fault Detection, Diagnostics, and Prognostics for Building Systemsâ--A Review, Part I [J]. Hvac & R Research, 2005, 11(1):3-25.

DAT Tran,Y Chen,C Jiang. Comparative investigations on reference models for fault detection and diagnosis in centrifugal chiller systems [J]. Energy and Buildings, 2016, 133(2016)246–256.

Cui J, Wang S. A model-based online fault detection and diagnosis strategy for centrifugal chiller systems [J]. International Journal of Thermal Sciences, 2005, 44(10):986-999.

Zhao X. Lab test of three fault detection and diagnostic methods' capability of diagnosing multiple simultaneous faults in chillers [J]. Energy & Buildings, 2015, 94:43-51.

Li G, Hu Y, Chen H, et al. An Improved Fault Detection Method for Incipient Centrifugal Chiller Faults Using the PCA-R-SVDD Algorithm [J]. Energy & Buildings, 2016, 116:104-113.

Zhao Y, Wang S, Xiao F. A statistical fault detection and diagnosis method for centrifugal chillers based on exponentially-weighted moving average control charts and support vector regression [J]. Applied Thermal Engineering, 2013, 51(1-2):560-572.

Han H, Gu B, Hong Y, et al. Automated FDD of multiple-simultaneous faults (MSF) and the application to building chillers [J]. Energy & Buildings, 2011, 43(9):2524-2532.

Wang Z, Wang Z, He S, et al. Fault detection and diagnosis of chillers using Bayesian network merged distance rejection and multi-source non-sensor information [J]. Applied Energy, 2017, 188:200-214.

Comstock, M.C., Braun, J.E., 1999b. Experimental Data from Fault Detection and Diagnostic Studies on a Centrifugal Chiller. ASHRAE. HL 99e18, Report # 4036-1Research Project 1043.

Chawla N V, Bowyer K W, Hall L O, et al. SMOTE: synthetic minority over-sampling technique [J]. Journal of Artificial Intelligence Research, 2002, 16(1): 321-357.

Potharaju S P, Sreedevim M, Ande V K, et al. Data Mining Approach for Accelerating the Classification Accuracy of Cardiotocography[J]. Clinical Epidemiology & Global Health, 2018.

Wang K J, Makond B, Chen K H, et al. A hybrid classifier combining SMOTE with PSO to estimate 5-year survivability of breast cancer patients [J]. Applied Soft Computing Journal, 2014, 20(7):15-24.

Phua C, Lee V, Smith K, et al. A Comprehensive Survey of Data Mining-based Fraud Detection Research [J]. Artificial Intelligence Review, 2010, abs/1009.6119.

Comstock, M.C., Braun, J.E., 1999a. Development of Analysis Tools for the Evaluation of Fault Detection and Diagnostics for Chillers. HL 99e20, Report # 4036-3. ASHRAE. Research Project 1043.

Chawla N V, Bowyer K W, Hall L O, et al. SMOTE: synthetic minority over-sampling technique [J]. Journal of Artificial Intelligence Research, 2002, 16(1): 321-357.

Fernandez A, Garcia S, Herrera F, et al. SMOTE for Learning from Imbalanced Data: Progress and Challenges, Marking the 15-year Anniversary[J]. Journal of Artificial Intelligence Research, 2018, 61:863-905.

Chawla N V, Cieslak D A, Hall L O, et al. Automatically countering imbalance and its empirical relationship to cost[J]. Data Mining & Knowledge Discovery, 2008, 17(2):225-252.

Fang X, Liang C, Zhang H. Imbalanced Feature Selection with Random Forest for Ovarian Cancer Diagnosis and Survival Prediction [J]. Journal of Computational and Theoretical Nanoscience, vol. 13, issue 10, pp. 7303-7309, 2016, 13(10):7303-7309..

M.G. Jackson JE, Control procedures for residuals associated with principal component analysis, Technometrics 21 (3) (1979) 341–349.

Devi D, Biswas S K, Purkayastha B. Redundancy-driven modified Tomek-link based Undersampling: A Solution to Class Imbalance [J]. Pattern Recognition Letters, 2016.

Guo H, Liu H, Wu C, et al. Logistic discrimination based on G-mean and F-measure for imbalanced problem[J]. Journal of Intelligent & Fuzzy Systems, 2016, 31(3):1155-1166.

Wikipedia F. Matthews correlation coefficient [M]// Matthews Correlation Coefficient. Betascript Publishing, 2010.

Manuscript ID: 1081
DOI: 10.18462/iir.icr.2019.1081

Case study of the adsorption chiller driven by combined municipal heat and solar energy

Tomasz HALON[(a)] , Pawel LUKMIN[(a)], Malgorzata SZYC[(b)], Boguslaw BIALKO[(a)], Bartosz ZAJACZKOWSKI[(a)]

[(a)]Wroclaw University of Science and Technology, Wroclaw, Wybrzeze Wyspianskiego 27, 50-370, Poland, tomasz.halon@pwr.edu.pl, +48 71 320 35 05
[(b)] Fortum Power and Heat Polska, ul. Antoniego Slonimskiego 1A, 50-304 Wroclaw, Poland

ABSTRACT

One of the most important advantages of adsorption refrigeration systems is that they can be supplied with heat at a temperature as low as 60°C. Such heat can come from the district heating (DH) or solar collectors. Here, we test the pilot system connected to the DH in Wroclaw, Poland. We conducted experimental analysis of a silica gel-water adsorption chiller driven with DH heat (62-82°C). Chilled water inlet temperature was 16°C and cooling water temperature 27°C. We compared the system cooling capacity and Coefficient of Performance (COP) for different driving water temperatures. We confirmed that the COP rose with increasing the driving temperature (from around 0.4 at 65°C to 0.47 at 82°C and 27°C cooling water).
Keywords: Refrigerating Equipment; Absorption, Adsorption and Ejector Systems.

1. INTRODUCTION

Poland is a country with a temperate climate with relatively cold winters and warm summers. The maximal electrical power consumption in the winter is approx. 15.6 GWh gross electrical production. In the last decade, the total electrical power consumption in winter months increased by 7 – 15%, while in summer months during the same period it increased by 10 – 17%, as seen in Fig. 1 (Eurostat, 2018). This higher growth is summer seasons is caused by the rapid growth of compressor air-conditioning industry both in Poland and in the whole European Union. The final energy consumption for space cooling increased by more than 50% from the year 2000 to 2016 in the EU (Motherway et al., 2018).

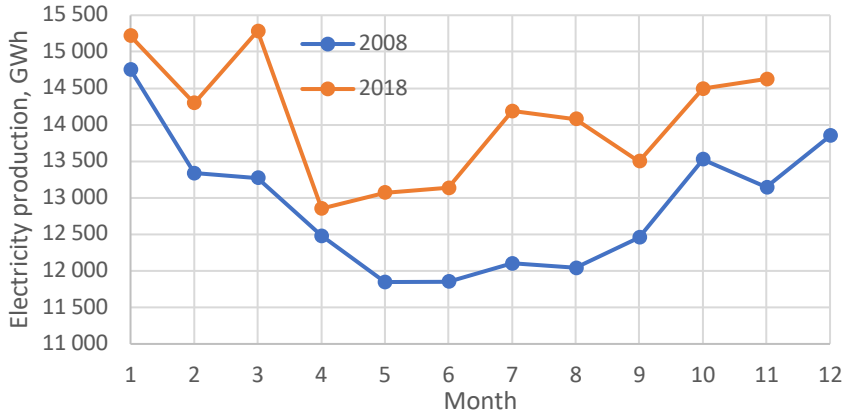

Figure 1: Gross electricity production in Poland in 2008 and 2018 (Eurostat, 2018)

This increased power consumption in summer months can be reduced by the introduction of heat driven sorption coolers, such as absorption or adsorption chillers. The first type requires the heat source to be at least 70°C, still it offers very low efficiency (0.6 – 0.7) at such driving temperature

(Noro and Lazzarin, 2014). The second type can work with the heat source at the temperature as low as 50°C, but its overall efficiency is even lower than that of an absorption devices (Chorowski and Pyrka, 2015). The cost of a solar driven sorption cooling system was calculated to be not competitive, primarily due to low COP values of temperature driven chillers and substantial cost of solar collector arrays (Bataineh and Taamneh, 2016).
Total amount of heat sold to the customers in Poland is approx. 400 PJ/year (Juroszek and Juroszek, 2018). The majority is distributed using municipal heating networks (DH, District Heating). The temperature of water in DH networks is different in different cities and varies during the year. For the city of Wroclaw (largest city in south-west Poland), it is approx. 65°C in summer months and 95-98°C in winter. The range of 60-70°C is too low for absorption units. Adsorption chillers are still capable to work at this temperature, although at substantialy reduced efficiency. One way to improve their performance is to rely on solar power and use solar collectors to increase the temperature of heating medium above the network's 65°C. During cloudy days and during nights, the adsorption chiller will work driven solely by district heating water, but during sunny days it will be supported by heat from solar collectors that would improve its thermal efficiency.
In this paper, we provide the experimental data concerning the cooling capacity of an adsorption chiller driven by water in temperature range 65 – 82°C. We also present the calculations of cooling capacity and total daily cooling effect for the system driven by the district heating with the support of solar collectors. For the simulation, the solar irradiation and collector array are modeled mathematically.

2. METHODOLOGY

The analyzed adsorption chiller is a hybrid type. It consists of a two-bed adsorption system and an R-407C vapor-compression system for peak hours. The adsorption system is an integrated type (patented and commercialized by Fahrenheit AG) with silica gel and water as the working pair. The integrated adsorption chiller has two vacuum tight compartments that contain an adsorption bed and heat exchanger, so it does not require any valves working in the vacuum conditions. In the experiments discussed in this paper, the chiller is running in adsorption-only mode, i.e. the vapor compression system is switched-off completely. The purpose is to determine cooling capabilities of the device that is only thermally powered, i.e. during peak hours it is supplied by additional heat from the solar collectors instead of electricity.
The outline of the system that is installed and tested in Wroclaw is presented in Fig. 2. The system is designed to provide cooling for the machinery room and for the canteen located in the neighbouring building. The 16 kW (nominal, estimated for hot water temperature 90°C, cooling water temperature 27°C and chilled water inlet temperature 19°C) adsorption chiller is driven with heat supplied from the district heating. The driving temperature depends on the actual operating conditions of the heating network, while the cooling load is determined by the consumer, however for the experimental purposes the load can be simulated.

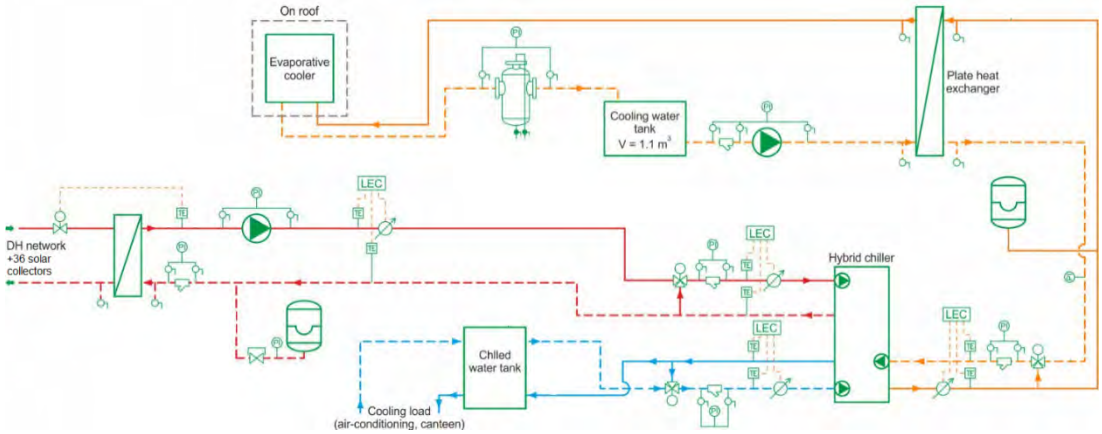

Figure 2: Test stand

The hot water for driving the adsorption chiller is supplied from the local district heating network. The intermediate heating medium can be routed by and heated up with 36 solar collectors mounted on a roof three floors above the machinery room. Solar collectors are flat plate, positioned to the south east on a 45° angle to the roof. The solar collector's absorber working area is 2.1 m^2. The length of the insulated pipeline on the roof is 100 m total (50 m before and 50 m after the collectors). The photographs of the installation are presented in Fig. 3.



Figure 3: Photographs of the system, starting from the left: hybrid chiller, system heat exchangers and pumps, solar collectors' array on the roof

Measurement data acquisition is done using the DL2 Datalogger with a time interval of 15 seconds. The data logger is integrated with the chiller. Inlet and outlet chilled and cooling water temperature, outlet hot water temperature and chilled water mass flow are measured from the device level. Hot water inlet temperature T_{hwin} is measured with a PT-500 sensor. All other temperatures are measured with PT-1000 sensors. The temperature measurement tolerance is equal to ±(0.15 + 0.002 [t])°C. The flow of cooling and hot water is measured with ULTRA- FLOW 54 ultrasonic flow meter. Its uncertainty is ~4%.

3. EXPERIMENTAL DATA

The data were conducted during multiple experiments that span over several seasons of the year. The behavior of the device was evaluated under multiple driving temperatures, ambient temperatures, etc. For this particular analysis, we have selected 8 distinct data points that result from averaged 6-hour data acquisition period (from more than 100 days of analyses). Selected days were characterized by stable operating conditions, similar and controlled cooling wated temperature and similar chilled water temperature at the inlet to the chiller.

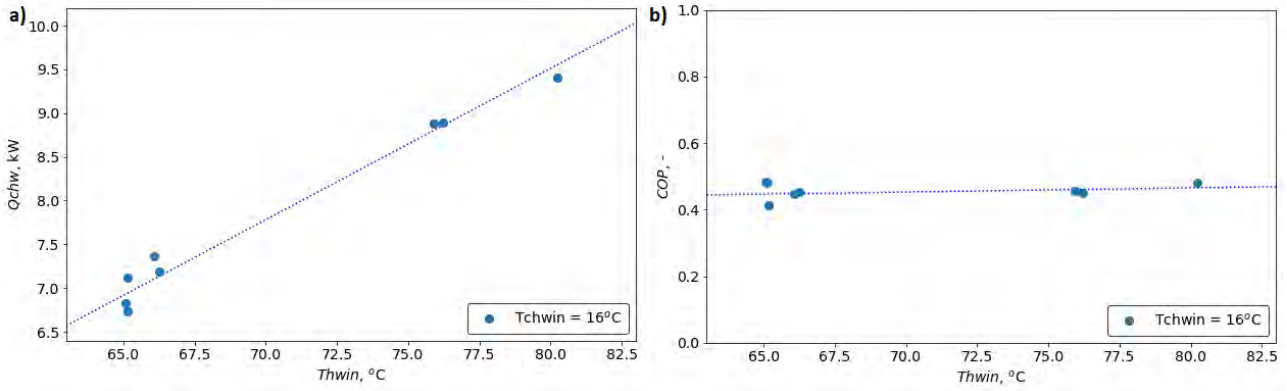

Figure 4: a) Cooling capacity and b) COP of the chiller as the function of driving water temperature

The increase of hot water inlet temperature increases the cooling capacity Q_{chw} of an adsorption chiller, as seen in Fig. 4a. At chilled water inlet temperature T_{chwin} = 16°C, the cooling capacity Q_{chw} is 36% smaller for the hot water temperature T_{hwin} = 65°C than for 82°C (7 and 9.4 kW respectively). This is due to the fact, that the increase of the regeneration temperature increases the sorption capacity of the bed, as seen in Fig. 5. Desorption that takes place at higher temperatures means that the silica gel gets drier. During adsorption the adsorber is able to take more refrigerant

vapor, and consequently more refrigerant evaporates in the evaporator. It means that the cooling capacity of an evaporator will be higher. Additionally the suction effect between the heat exchanger and the sorption bed increases.

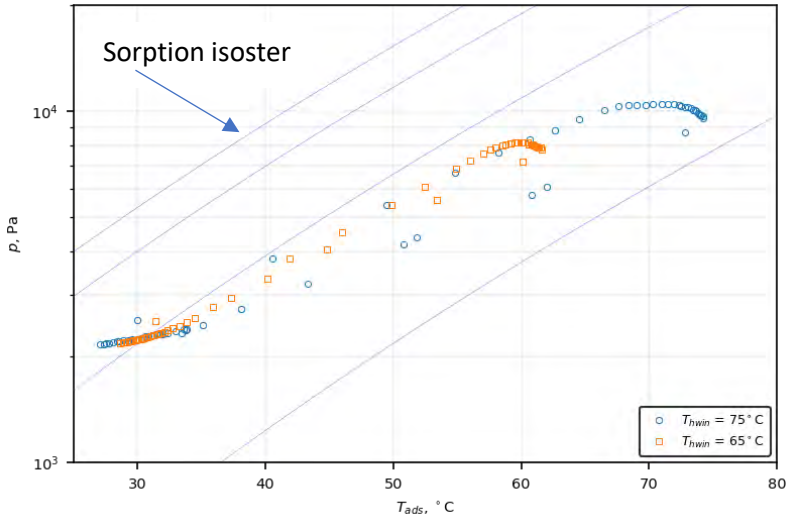

Figure 5: Duhring diagram for two different hot water temperatures

The increase of hot water temperature does not highly increase the COP for given pair of chilled/cooling water inlet temperatures (see in Fig. 4b). It is because increasing the temperature of regeneration also increases the needed heat for regeneration when the adsorption temperature is constant. It means that more heat is needed to increase the temperature of the sorption bed and to desorb more water from the sorbent at higher temperature. This increase is proportional to the cooling capacity gain in the case of adsorber construction used in the experiments.

For the compact adsorption chillers it is characteristic that there is no distinct isosteric phase. This is because both adsorption bed and heat exchanger are closed in one casing without any valves or pipes between them. For example the refrigerant after being desorbed from silica gel does not have to wait in the desorber until the valve between condenser and desorber opens due to equalization of pressure with the condenser. Instead it is instantly in the heat exchanger.

During the change of operating mode of the bed (from adsorption to desorption and vice versa), for the first seconds of the new mode the cooling capacity is lost to change the temperature of the heat exchanger. For example during the condensation, the heat exchangers plates temperature was near the condensation temperature. Then, after the switch from desorption to adsorption mode, the cooling water in the condenser is changed by the chilled water at lower temperature. Before any cooling effect is obtained, some time has to pass before the heat exchanger cools down.

Adsorption chillers are characterized by unsteady working cycles (Szyc and Nowak, 2014). The outlet chilled, cooling and hot water temperature is different at the beginning of each cycle than in the middle or at its end, as in Fig. 6.

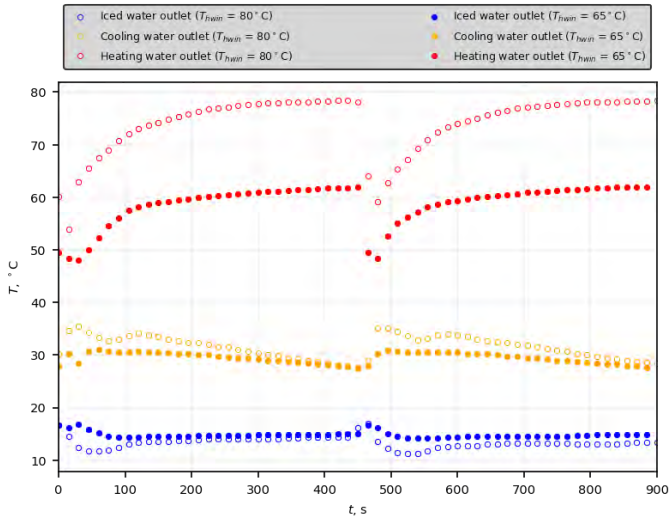

Figure 6: water temperature at the chiller outlet

Similarly, sorption beds can absorb or reject different heat values in different parts of the cycle. Because of that, the COP changes in time, as in Fig. 7. It can even be lower than 0 at some times, meaning there is a small heating effect instead of cooling. It is due to the cycle switch. In order to represent uniform data the points in Fig. 4 and Fig. 7 represent the average values for experimental runs.

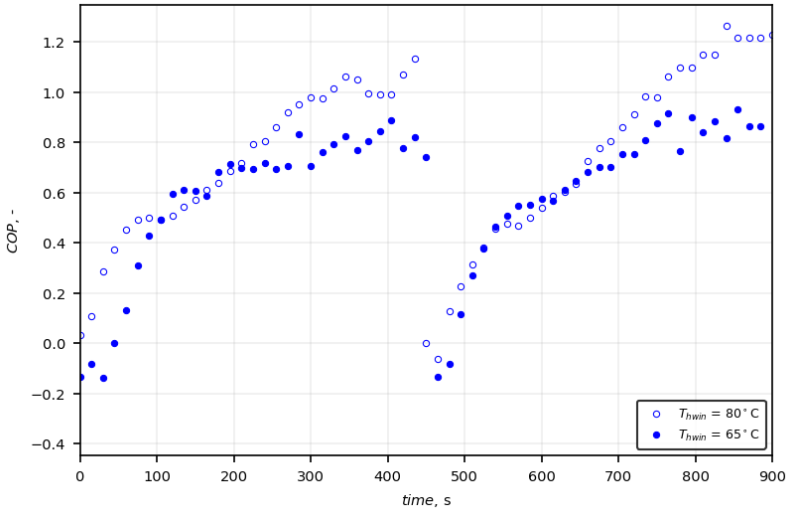

Figure 7: Instantaneous COP change during example cycles for driving water temperature T_{hwin} 65°C and 80°C

In solar adsorption systems it is crucial to know what is the outlet hot water temperature in order to know what will be the hot glycol temperature at the inlet to the solar collector. The outlet hot water temperature T_{hwout} as a function of the inlet hot water temperature T_{hwin} is presented in Fig. 8.

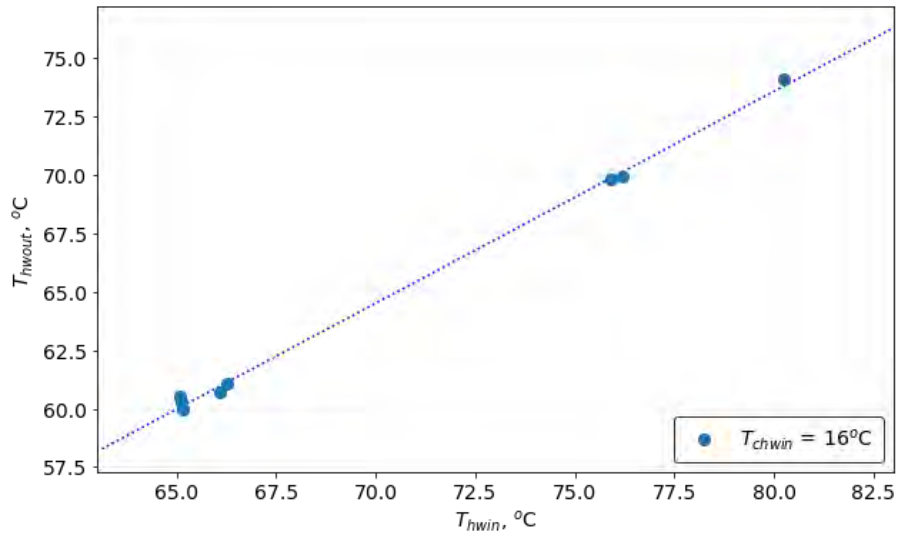

Figure 5: Hot water outlet temperature as a function of inlet hot water temperature

4. SOLAR SYSTEM MODELING AND RESULTS

The solar radiation was simulated using online software Solarsym 4 (Kasperski et al., 2006). The collectors were positioned to the south east on a 45° angle to the roof with no shading during the day. The simulation is performed with data adaptation for the meteorological data (incliuding ambient temperature) for the city of Wroclaw, Poland. The solar radiation and ambient temperature is simulated for the period from March 01 to August 31 every 10 minutes.

After the solar radiation and ambient temperature were calculated by the software, the glycol temperature at the collector's inlet is calculated. It is done on the basis of heat losses on the pipeline from the heat exchanger to the inlet of solar collectors (DN 32 PVC with 40 mm polyurethane foam insulation), assuming the district heating water temperature 65°C. Next, the solar collector efficiency was calculated. The outlet temperature from the solar collectors T_{out} was calculated from a heat balance, as in Eq. (1). Heat losses on the pipeline from the collectors and the temperature inlet to the adsorption chiller were calculated in the same way as on the first pipeline. All the above-mentioned calculations were also performed for the period March – August every 10 minutes.

$$T_{out} = T_{in} + \frac{\dot{Q_{solar}}\,\eta\,A_{sol}\,n}{\dot{m_{gl}}\,cp} \qquad \text{Eq. (1)}$$

When the driving temperature is known, the cooling capacity of the adsorption chiller was calculated on the basis of experimental work performed on the system. The COP was not calculated, because hot water temperature does not influence it highly.

There are two ways of operating the system with solar collectors coupled with DH. The first way is to maintain constant connection of adsorption chiller driving water to the District Heating and solar collectors. The second way is that when the day starts, the DH water is used for the initial heating of the glycol for solar collectors. This will ensure a fast way of increasing glycol temperature. After the initial heating of the glycol, the DH is not used until the next night. In both methods the chilled water produced at night from the DH only is stored in insulated tank or PCM storage vessel.

In the first method, the temperature of glycol going to the solar collectors is always close to the DH water temperature. The hot water outlet temperature from the adsorption chiller is usually higher than the DH water, so the heat is given away to the network. This situation is unwanted by both the District heating company, as the higher District Heating water temperature influences the CHP plant, and the user, as he loses the heat from his solar collectors. In the case of solar, decentralized or semi-decentralized District Heating it could be profitable depending on the heat prices.

The blue line Q_{chw} in Fig. 9 represents the cooling power of the chiller driven by district heating water heated by solar collectors in the abovementioned manner (Solar and DH). During the whole time, the medium daily cooling capacity changes from around 8.2 to 9.2 kW. For comparison, the cooling capacity obtained only by driving by district heating water is presented by orange line Q_{chw} (DH). It

is rather stable 6.6 – 6.9 kW, because the district heating water temperature during the chosen period is stable, with small fluctuations ranging from 63 to 65°C.
In the second method the medium daily cooling capacity for the chosen chiller is presented in Fig. 9 as dotted blue line Q_{chw} (Solar, DH at beginning). As the glycol temperature is higher at the solar collector inlet, the outlet temperature is also higher which leads to higher hot water temperature and thus higher cooling capacity.
At nights and early morning/late evening hours the driving water temperature would be cooled down in the solar collectors. The adsorption system can work during the night using the district heating water as a driving source and "producing" chilled water.

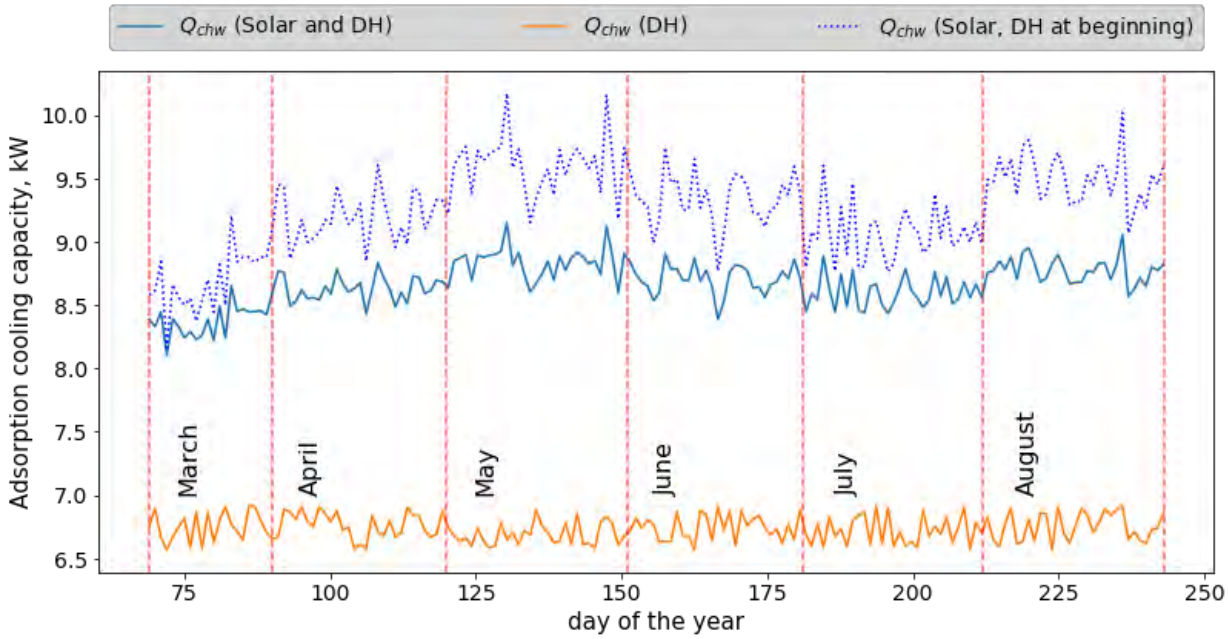

Figure 6: Adsorption chiller daily medium cooling capacity when driven by only District Heating (DH), by District Heating heated by solar collectors (Solar and DH) and by solar collectors that use the District Heating only for preheating glycol after the night

The cooling capacity of the chiller changes through the chosen days, but never reaches the nominal value for the used chiller. The nominal power of 16 kW was evaluated only at hot water inlet temperature T_{hwin} 90°C, cooling water inlet temperature T_{cwin} = 25°C and chilled water temperature at the inlet to the chiller T_{chwin} = 19°C. In our system, the chilled water inlet could not be higher than 16°C due to the temperature requirements of the canteen that was cooled by the chiller. The cooling water temperature T_{cwin} was around 27°C. The hot water temperature that drives the adsorption chiller, obtained by heating up the water by the glycol from solar collectors is never higher than 90°C on our system. The biggest problem in reaching more than 90°C is the solar collectors drop of efficiency at higher temperatures. On the other hand, the silica gel/water adsorption chiller cannot be driven by water temperature higher than 95°C, so usage of concentric or vacuum collectors is not advised.
The total cooling effect obtained for the whole day is shown in Fig. 10. It compares the total daily cooling effect for the chiller being driven only by the District Heating – Q_{tot} (DH), only by the solar collectors – Q_{tot} *(solar)*, by the solar collectors and DH (releasing the solar power to the DH) – Q_{tot} (solar and DH) and by solar collectors with DH only connected at night – Q_{tot} (solar, DH at beginning). The biggest advantage of driving the adsorption chiller by DH coupled with solar collectors is that it combines the advantages of both heat sources: The increase of cooling capacity due to the increase of driving temperature during the day and constant supply of heat when the sun is down or covered. The usage of district heating coupled with solar collectors enables to obtain doubled or even tripled total cooling effect during the day compared to driving by the heat from only solar collectors. The usage of solar collectors can increase the total cooling effect by 14 % on average, for the chosen time range, compared with the driving by district heating only.

Solar collectors system highly increases the initial investment costs. The price of 36 flat plate solar collectors in Poland is around 19 000 USD which is almost the price of the hybrid chiller. This price excludes the price of glycol, pump, control system, piping and the costs of construction. The glycol pump consumes electricity which increases the operating expenditures. The economic analysis has to be performed to check if the 14 % increase of the total daily cooling effect is worth the investment into solar system. Government subsidy and special tariff for the district heat could increase the economic profitability of this kind of system.

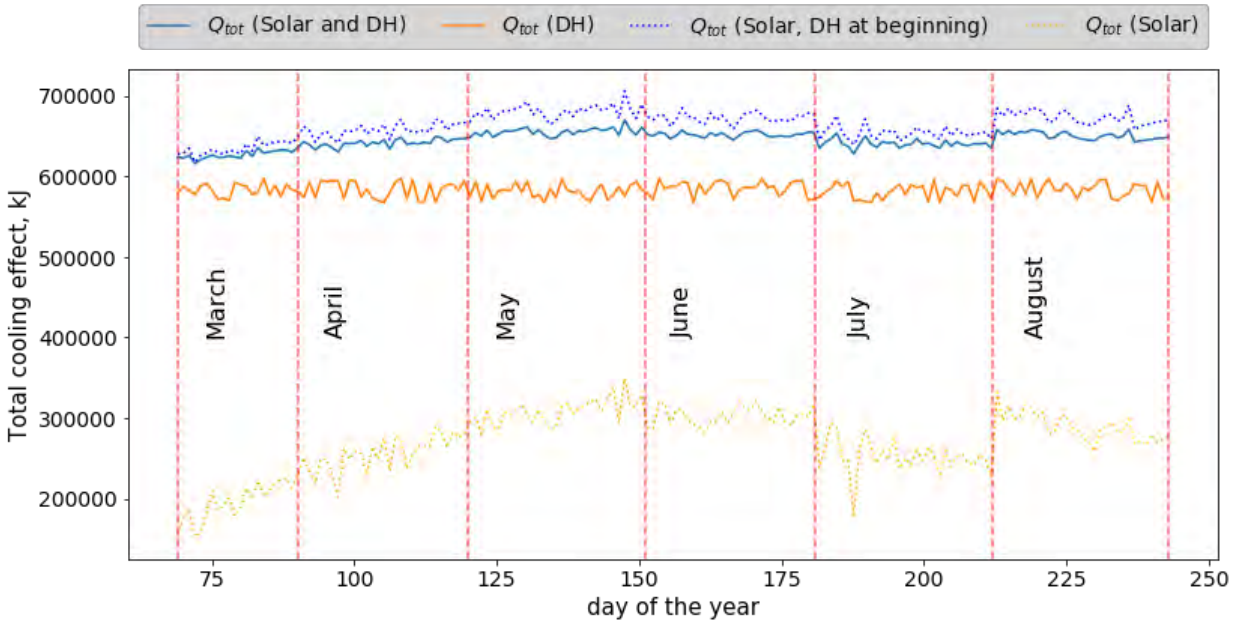

Figure 7: Total amount of cooling effect obtained during the whole day.

5. CONCLUSIONS

We presented an experimental analysis of a silica gel-water adsorption chiller working in Wroclaw, Poland. It was driven with DH heat (62-82°C). Chilled water inlet temperature was 16°C and cooling water temperature 27°C. We compared the system cooling capacity Q_{chwin} and Coefficient of Performance COP for different driving water temperatures.

The increase of hot water temperature does not highly increase the COP for a given pair of chilled/cooling water inlet temperatures. We confirmed that the COP rose with increasing the driving temperature (from around 0.4 at 65°C to 0.47 at 82°C and 27°C cooling water). At chilled water inlet temperature T_{chwin} = 16°C, the cooling capacity Q_{chw} is 36% smaller for the hot water temperature T_{hwin} = 65°C than for 82°C (7 and 9.4 kW respectively).

During the chosen time range, the cooling capacity of the chiller driven by the heat from solar collectors changes from around 9 to 10 kW during the day. For comparison, the cooling capacity obtained only by driving the chiller by district heating water is a rather stable 6.4 kW.

The usage of district heating coupled with solar collectors and chilled water storage enables to obtain tripled total cooling effect during the day compared to driving by the heat from only solar collectors. The usage of solar collectors can increase the total daily cooling effect by 14 % on average compared with the driving by District Heating only. The economic analysis has to be performed to check if the 14 % increase of total daily cooling effect is worth the investment into solar system.

ACKNOWLEDGEMENTS

This publication has been prepared in collaboration with Fortum Power and Heat Poland, which has financed research works necessary to prepare this publication under contract no. 01/08/2018 (U/0180/343/2018).

NOMENCLATURE

a Experimental coefficient (-)
A_{sol} – Solar collectors' absorber area (m^2)
b Experimental coefficient (-)
COP Coefficient Of Performance (-)
c_p Specific heat of glycol ($J \times kg^{-1} \times K^{-1}$)
$\dot{m}_{gl}$ Mass flow of glycol ($kg \times s^{-1}$)
n number of solar collectors (-)
T_{cwin} Cooling water inlet temperature (°C)
T_{chwin} Chilled water inlet temperature (°C)
T_{hwin}, T_{hwout} Chiller hot water (driving) inlet/outlet temperature (°C)
T_{in}, T_{out} Inlet/ outlet temperature for solar collector (°C)
Q_{chw} Cooling capacity (kW)
Q_{solar} Solar radiation on the absorber of solar collector ($W \times m^{-2}$)
η solar collector efficiency (-)

REFERENCES

Bataineh K., Taamneh Y., 2016. Review and recent improvements of solar sorption cooling systems. Energy and Buildings. 128, 22–37.

Chorowski M., Pyrka P., 2015. Modelling and experimental investigation of an adsorption chiller using low-temperature heat from cogeneration. Energy, 92, 221–229.

Eurostat, 2018. Supply electricity - short term monthly data [Datafile]. Retrived Jan. 15 2019 from: https://ec.europa.eu/eurostat/web/energy/data/database

Juroszek Z., Juroszek W., 2018. Attitudes of heat plant managers as one of the key obstacles to district heating decarbonization in Poland. Energy & Environment, 29, (7), 1116 – 1129.

Kasperski J., Drzeniecka-Osiadacz A., Lewkowicz M., Nems M., 2006. Solar radiation calculation program. Retrieved from htp://fluid.itcmp.pwr.wroc.pl/~kasper/solarsym4/

Motherway B., Dean B., Dulac J., Morgan T., Remme W., 2018. The Future of Cooling Opportunities for energy-efficient air conditioning. International Energy Agency, Online document, 92.

Noro M., Lazzarin R. M., 2014. Solar cooling between thermal and photovoltaic: An energy and economic comparative study in the Mediterranean conditions. Energy, 73, 453–464.

Szyc M., Nowak W., 2014. Operation of an adsorption chiller in different cycle time conditions. Chemical and Process Engineering - Inzynieria Chemiczna i Procesowa, 35, (1), 109–119.

Manuscript ID: 1086
DOI: 10.18462/iir.icr.2019.1086

Comparison of compressor control strategies for solar direct drive refrigerators

Jonas K. JENSEN[(a)], Hendrik MOELLER[(C)], Ivan KATIC[(b)], Per Henrik PEDERSEN[(b)], Wiebke B. MARKUSSEN[(b)]

[(a)] Department of Mechanical Engineering, Technical University of Denmark
Kgs Lyngby, 2800
[(b)] Danish Technological Institute,
Gregersensvej 2, DK-2630 Taastrup
[(c)] Nidec Global Appliance Germany GmbH,
Flensburg, 24939, Germany, europe@mail.nidec.com

ABSTRACT

The influence of the applied compressor control strategy on the performance of a solar direct drive refrigeration system was investigated using numerical modelling and simulations. Two compressor types and three compressor control strategies where investigated. Further, four configurations where included: a 360 W and a 180 W PV panel both with and without compressor start power delivered from the PV panel. Results showed that both the choice of compressor and the applied control strategy affected the systems ability to utilize the available power from the PV panel, especially under lower irradiance conditions and when the PV panel was downsized. However, results show that if the need for compressor start power delivered by the PV panel was alleviated the size of the PV panel can be halved without significant reductions in performance.
Keywords: Solar Direct Drive, PV Panel, Control Strategy, Compressor Speed Control, Ice Bank Storage.

1. INTRODUCTION

People in rural areas of many developing countries have non or unreliable access to electricity (IEA, 2012). In such areas correct storage of temperature sensitive products such as food or more importantly medical equipment such vaccines is a significant challenge. This may affect as many as 1.3 billion people worldwide (IEA, 2012), wherefore finding good solutions for off-grid refrigerators is an important task.

Different types of absorption refrigeration systems driven by combustibles such as kerosene or gas have been developed but have been found to be unreliable and require high maintenance (McCarney et al., 2013). Alternatively solar driven systems have been developed since the 1980s first utilizing batteries to store electricity to power the system during night time. Later battery free systems or solar direct drive system have been developed as presented by Pedersen et al. (2019). McCarney et al. (2013) state that battery free solar direct drive systems are the most promising solution for off-grid vaccine storage.

Myers et al. (2017) investigate the potential for harvesting excess energy from solar direct drive refrigerators applied as medical cold chain equipment and found that significant amounts of energy could be utilized to power secondary equipment without compromising the temperature of the stored goods. This is investigated with a traditional on/off compressor control. The potential to harvest excess energy may though be reduced if more advanced compressor control strategies are applied. The present work focused on analysing the operation of a direct drive solar powered refrigeration

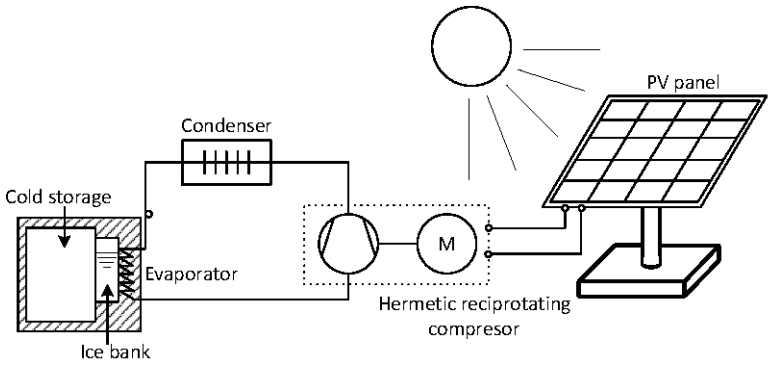

Figure 1: Principle sketch of the direct drive solar refrigeration system with ice bank storage

system with an ice bank storage under different compressor control strategies. A principle sketch of such a system may be seen in Fig. 1. As seen the refrigeration system consists of a hermetic reciprocating compressor, a finned tube condenser, a capillary tube and an evaporator placed in direct contact with an ice bank storage.

2. METHODS

In a configuration such as the one seen in Fig. 1 it is the control of the compressor speed that will ensure optimal utilization of the available power from the PV panel. Here it is important to realize that the operation of a PV panel is characterized by the voltage - current curves seen in Fig. 2 (right). Herethe solid black lines represent the voltage - current relation for a given solar irradiance. As seen for a given solar irradiance the current first shows a small decrease with increased voltage up to, in this case 25 V, where after it will experience a rapid decrease to a current of 0 A. Further, the greater the solar irradiance the higher the current will be for the same voltage.
Realizing that the power extracted from the PV panel is the product of the voltage and current results in the dashed blue lines. These naturally assume values of 0 W when either the voltage or current are 0. Further, it may be seen that for each solar irradiance there is a peak power point and that this point occurs at approximately the same voltage. Finally, it is seen that the higher the solar irradiance the higher the peak power.
If the system driven by the PV panel, in this case the compressor, tries to draw more power from the panel than the peak power at the given irradiance, the PV panel will experience was is called a collapse. A collapse results in no power being delivered and consequently that the system is turned off. If the compressor is run to fast there is thus a risk that it will collapse the PV panel and force a shut down of the system. However, if the compressor is run to slow, the refrigeration system will not be utilizing as much of the available power.
Therefore, it is relevant to find compressor control strategies that can ensure that the system will operate as close to the peak power point as possible at the varying solar irradiance the system will experience during a day or a year. In the present work is was assumed that the PV panel was south facing and located on the northern hemisphere somewhere close to the equator. On a location such as this the duration of which sunlight will reach the PV panel is roughly 8 hours per day with the peak irradiance in the middle of this period and a symmetrical increase and decrease around the peak.

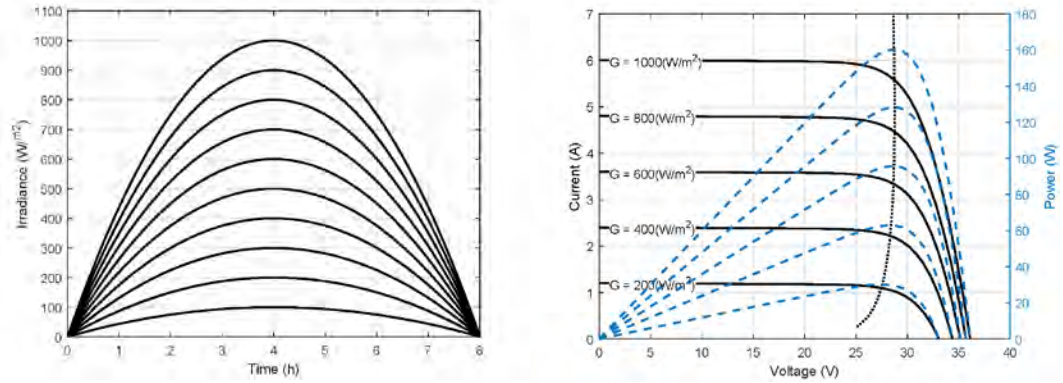

Figure 2: Daily solar profile and principle sketch of the operating characteristics of a PV panel

A sketch of the daily solar profile may be seen in Fig. 2 (left). As seen here the profile is sketched for peak irradiances from 100 Wm^{-1} to 1000 Wm^{-1}. These peak irradiance variations may resemble both seasonal variation but also cloud covers of different intensity. The present work will be limited to the smooth profiles seen in Fig. 2 and will thus not include spotted cloud covers and the rapid transients involved in these. The different compressors and compressor control strategies will be evaluated at the different range of solar profiles seen in Fig. 2. This, as it was relevant to investigate both the minimum peak irradiance needed for the system to deliver a cooling load but also the peak irradiance at which the available power from the solar panel cannot be fully utilized due to speed restriction of the compressor.
To perform this investigation numerical models where developed for both the PV panel and the refrigeration system. Further, the different control strategies where implement in these models.

2.1. Photovoltaic Modelling

The behavior of the PV-panel was modelled using a "one diode" model as described in Duffie and Beckmann (2013). The one diode model uses an equivalent circuit to describe the operation of a single solar cell. Assuming all cells to operate identically the one diode cell model can used to model a complete PV panel.
The values for the shunt and series resistances as well as the diode quality factor was determined based on standard test conditions (STC) data for a given 60 cell PV panel. The STC data may be seen in Table 1 where the assumed cell operating temperature is also stated.
As seen in Table 1 each PV panel has a STC max power output of 90 W. In order to supply sufficient power to the refrigeration systems several PV panels in parallel were applied. The present work investigated the application of both 2 and 4 PV panels in parallel, these two solutions will in the following be referred to as the 180 W and 360 W PV panels, respectively, in reference to the resulting STC maximum power output of the total installation. It should be noted that the actual maximum power of the PV panels, may be reduced as the assumed cell operating temperature of 35 °C was higher than the STC cell operating temperature.

2.2. Refrigeration System and Compressor

Table 1. Input data for the PV panel model of a single 60 cell array, operating conditions for the refrigeration system and data for the investigaed compressors

PV panel			Refrigeration system			Compressor			
Number of cells	60	-	T_{evap}	-10	°C		BD35K	BDS5.0K	
Temp. Coeff.	0.03	K^{-1}	T_{cond}	50	°C	Disp. Vol.	3	5	cm^3
STC Max Power	90	W	ΔT_{SH}	10	K	Min. Speed	2000	1000	RPM
STC Max Power Voltage	32	V	ΔT_{SC}	5	K	Max. Speed	3500	3000	RPM
STC Open Circuit Voltage	39.5	V							
STC Short Circuit Current	3	A							
Cell operating temp.	35	°C							

The modelled refrigeration system may be seen in Fig 1. Assuming a constant ambient temperature in the room where the refrigeration system was located and that the ice bank storage was kept at a constant temperature of 0 °C, it was assumed that the evaporation and condensation temperatures as well as the level of super-heating and sub-cooling would not change significantly during the operation of the system. Therefore, these values where assumed constant at the values stated in Table 1.
Two different compressors were investigated for the application in the refrigeration system, both compressors are built for R600a. The first was the BD35K which is a DC compressor produced by Nidec, the second compressor was the BDS5.0K, also produced by Nidec. The displacement volumes and speed ranges of the two compressors are stated in Table 2. As seen the BD35K has a lower displacement volume compared to the BDS5.0K and further the dynamic range of the BD35K is also significantly lower than that of the BDS5.0K.
The operational characteristics of the two compressors, i.e. isentropic and volumetric efficiencies, where modelled using speed specific compressor polynomials supplied by the manufacturer. The polynomials where supplied at four values of compressor speed ranging from the minimum to the

maximum speed. For operation at speeds in between the supplied polynomials the efficiencies where interpolated between the values of the nearest polynomials.
A part from the work derived from the application of the compressor polynomials, the initial start-up of the compressor requires additional power. This will in the following be referred to as the compressor start power. The compressor start power is associated with the initial positioning of the rotor. The start power for both compressors has been assumed to be 60 W. However, soft start procedures or the application of super capacitors may alleviate the need for the PV panel to supply the start power. Consequently, results were derived both with and without the 60 W compressor start power.

2.3. Compressor Speed Control Strategies

As the compressor in the suggested system was driven directly by the PV panel, the only manner by which sufficient utilization of the available power can be ensured was to impose a suitable compressor speed control strategy. In the present work three different speed control strategies have been investigated and compared based on their ability to utilize as much of the available power during a complete day.
To quantify to which extent the compressors utilize the available power a Utilization Factor was defined. The Utilization Factor was defined as the ratio of the integrated compressor work from sunrise to sundown over the integrated peak power over the same duration. The Utilization Factor thus indicates how well the compressor control strategy was at adapting the speed during the increasing and decreasing irradiance experienced during a day.
A part from the utilization factor the Accumulated Daily Cooling Load was also determine as the integrated cooling load delivered over the full day.
The first control strategy investigated was the PPT control. This control strategy requires the application of an external peak power tracker. The peak power tracker required the measurement of both solar irradiance and cell operating temperature which the peak power tracker then used to calculate the peak power point. This was then applied as a set point for the compressor speed regulation. Consequently, the PPT control ensured that when the compressor was on it ran at a speed at which the needed compressor power was equal to the PV panels peak power. However, the ability to run at the requested speed was limited by the minimum and maximum speeds of the compressors.
An alternative to the PPT control is CVC. As seen in Fig 2 the peak power points for increasing irradiance coincide at a close to constant voltage. Hence, it is possible to approximate the peak power point by measuring only the voltage over the PV panel. Supplying the speed control of the compressor with a set point for the PV panel voltage would thus allow the compressor to adjust the speed in order to attain a constant voltage and thus operate close to the peak power point. This control strategy alleviates the need for solar irradiance and cell temperature measurements and may thus be simpler to implement. The set point for the CVC was set to 22 V.
The final investigated control strategy was AEO. The AEO control strategy requires no additional measurements and was therefore implemented directly in the compressor, it may therefore be the most simple to implement. The principle of the AEO strategy was to continuously ramp up the compressor speed until the compressor would collapse the PV panel thus shutting the compressor off. The speed at which the collapse occurred was then stored in the controller. The compressor was then kept off for a short duration to allow pressure equalization between the condenser and

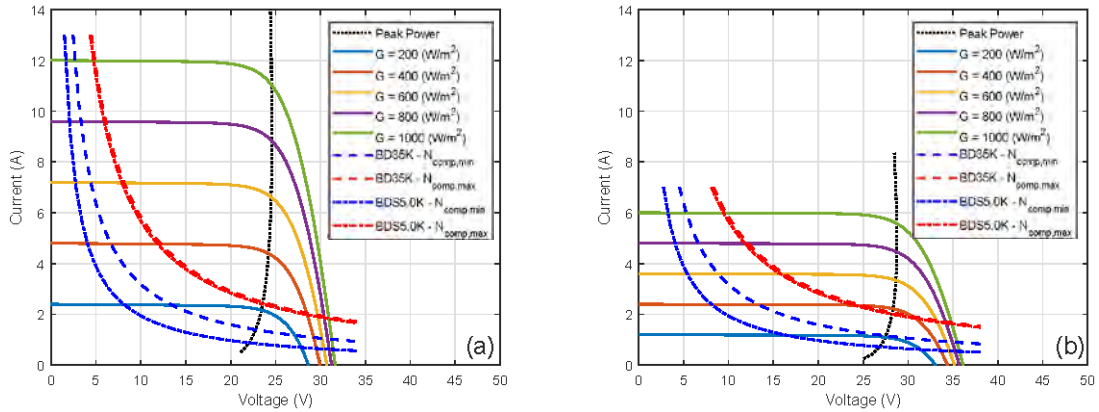

Figure 3: Current - voltage curves for the 360 W (a) and 180 W (b) PV panels, with the current - voltage curve for the two investigated compressors at their minimum and maximum compressors

evaporator in order to reduce the power consumption during start-up. It was assumed that three minutes would allow sufficient pressure equalization. After the short off-period the compressor was then turned on at a speed lower than the one at which the collapse occurred.
Two inputs are thus needed in order to run the AEO strategy, the compressor speed ramp-rate and the speed reduction when restarting the compressor. These where assumed to be constants during the operation of the system. The choice of these two constants both influence the utilization factor of the PV panel. It was found that a ramp rate of 2000 RPM $h^{-1}$and a speed reduction of 400 RPM was a good trade-off for all investigated combinations of PV panels size and compressor types.

3. RESULTS

Fig. 3 shows the voltage - current curves for the 360 W (a) and 180 W (b) PV panels, respectively. Further, the voltage - current curves for the two compressors are presented under the operating conditions shown in Table 1 and their respective minimum and maximum compressor speeds. The compressor voltage - current curves are thus iso-power lines corresponding the compressor power at minimum and maximum speeds. For a given solar irradiance the compressor must thus run between the intersections of the minimum and maximum compressor curve and the voltage - current curve at the given irradiance. If the curves do not intersect the compressor will collapse the PV panel at the minimum compressor speed and will thus not be able to run. If the PV panel voltage - current curve only intersects with the minimum speed compressor curve the compressor will be able to run at the peak power point for that irradiance and will thus be able to utilize all the available power. If the PV panel voltage - current curve intersects with both the minimum and maximum compressor speeds the compressor will not be able to run a the peak power point and will thus not be able to utilize all the available power.
This figure thus gives an indication of how well the compressor can utilize the available power from the PV panel. It may be seen that the maximum speed curves for the two compressors occurred at more or less the same point. However, the BDS5.0K could run at a lower power as the BDS5.0K had a lower minimum speed. The BDS5.0K would thus be able to run at lower levels of irradiance. Further, it may be seen that for the 360 W PV panel both compressors would not be able to run at the peak power point at irradiances much higher than 200 $Wm^{-2}$for the 180 W this was possible upto 400 Wm^{-2} However, the 180 W PV panel would require a higher irradiance before the compressor could run.

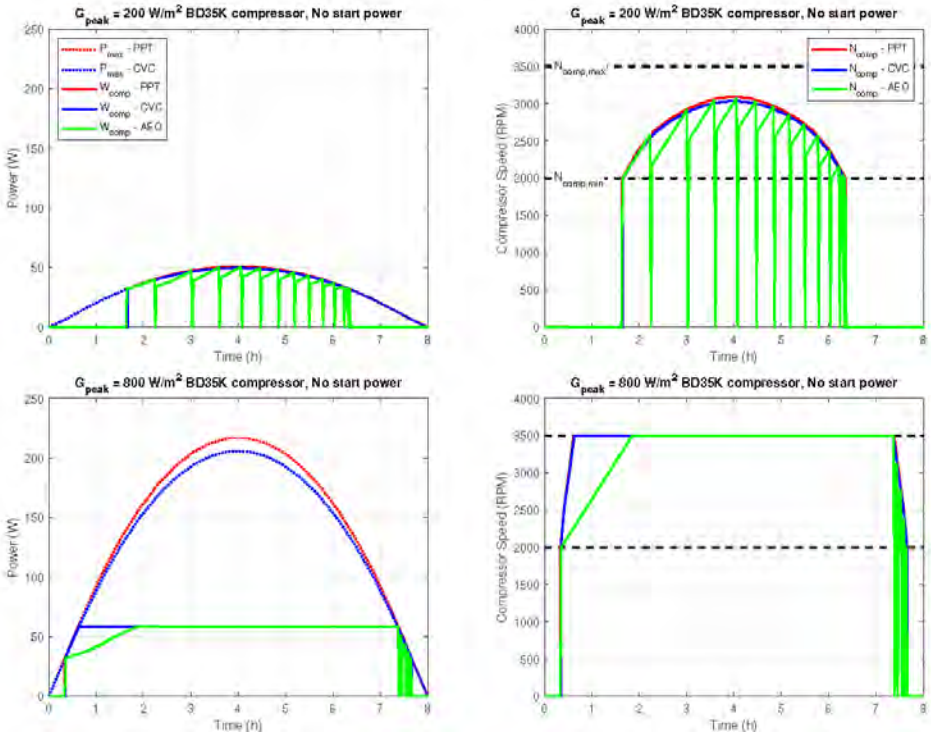

Figure 4: Compressor power and compressor speed for the PPT, CVC and AEO control strategies under two different irradiance profiles with 200 Wm^{-2} and 800 Wm^{-2} peak irradiance, respectively. Results are shown for the BD35K compressor without start power

It should be noted that the compressor start power was not included in the curves shown in Fig. 3. The need for compressor start power would shift the minimum speed curves upwards thus reducing the gap between the minimum and maximum curves.

Fig. 4 shows an example of how the different control strategies perform under two different daily profiles, with 200 $Wm^{-2}$and 800 Wm^{-2}peak irradiance, respectively. This was exemplified with the BD35K compressor without the inclusion of compressor start power and the 360 W PV panel. Fig. 4 presents both the available and utilized power and the compressor speed. As seen for both the low and the high peak irradiance profiles the three different control strategies turned the compressors on and off at more or less the same time. It may further be seen that for the 200 Wm^{-2} profile both the PPT and CVC ran at their respective maximum values while the compressors where on, further it should be noted that the difference between the PPT and CVC maximum power was insignificant. For the 200 Wm^{-2} profile the

AEO control resulted in 13 on/off cycles, however it may also been seen that the AEO actually kept the power consumption close the power consumption of the PPT and CVC control. For the 800 Wm^{-2} profile all three compressor controls strategies ran the compressors at maximum speed after 1.8 hours of sunlight, the PPT and CVC already after 0.4 hours. The compressors then ran at maximum speed until approximately 0.5 hour before sunset. The PPT and CVC subsequently reduced their speeds to the minimum before turning off 0.25 hours before sunset. In the same duration the AEO control ran 5 on/off cycles. It is clear that under the 800 Wm^{-2} peak irradiance profile non of the three control strategies would be able to utilize close the total available power.

Figs. 5 and 6 show the Utilization Factor and the Accumulated Daily Cooling Load as a function of the daily peak irradiance. This was presented for both compressors under the three compressor control strategies. Further, this was presented under four different system configuration: the 360 W PV panel and the 180 W PV panel, both with and without compressor start power.

As seen for the 360 W PV panel with 60 W of compressor start power, Figs. 5 (a) & 6 (a) the BDS5.0K compressor can deliver a cooling load as soon as the daily peak irradiance exceeds 300 Wm^{-2}, it may further be seen that the CVC control will require a slightly higher peak irradiance to run. For the BD35K the daily peak irradiance must exceed 350 Wm^{-2} to deliver a cooling load for the PPT or AEO, while the CVC again required a higher peak irradiance of about 360 Wm^{-2}.

As seen in Fig. 5 (a) the Utilization Factor increases rapidly after the minimum peak irradiance was attained and peaks shortly hereafter. Here the BDS5.0K attained the highest Utilization Factor with the PPT or CVC with a value of approximately 55 %. Here only 45 % was attained for the AEO. The

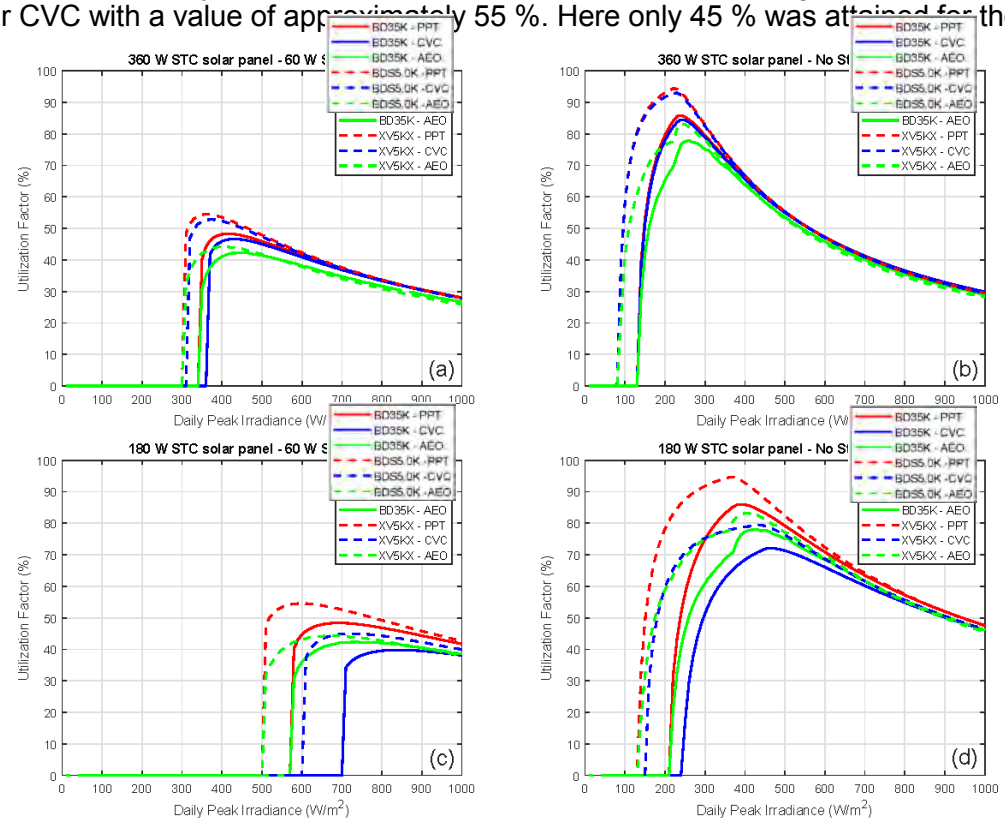

Figure 5 Compressor power and compressor speed for the PPT, CVC and AEO control strategies under two different irradiance profiles with 200 Wm^{-2} and 800 Wm^{-2} peak irradiance, respectively. Results are shown for the BD35K compressor without start power

BD35K utilized less of the available power, peaking at around 48 % for the PPT and CVC and around 42 % for the AEO. As the daily peak irradiance increases the differences between the Utilization Factor of the two compressors and the different control strategies diminished and at a daily peak irradiance of a 1000 Wm^{-2} the Utilization Factor was approximately 28 % for all six options.
As seen in Fig. 6 (a), then although there was only a minor difference between the Utilization Factor of the two compressors, the Accumulated Daily Cooling Load differs significantly. Here the BDS5.0K was capable of delivering more cooling load than the BD35K, as the BDS5.0K compressor was more efficient. Again it may be seen that the PPT and CVC attain comparable cooling loads while the AEO delivered slightly less.
Assuming that the need for compressor start power can be alleviated but keeping the PV panel size of 360 W results in the Utilization Factor and Accumulated Daily Cooling Loads seen in Figs. 5 (b) & 6 (b). As seen this allowed the compressors to run at significantly lower daily peak irradiances. Here the all three strategies delivered a cooling load already from a daily peak irradiances of 90 W for the BDS5.0K and 120 W for the BD35K. Again the Utilization Factors show a rapid increase as soon as the minimum irradiance was attained. Here the BDS5.0K with the PPT and CVC peaks at a Utilization Factor of 94 % while the AEO reached around 83 %. The BD35K again utilized less of the available power peaking at around 84 % for the PPT and CVC and 78 % for the AEO. Again the differences between the utilization Factors of the two compressors and the three control strategies diminishes with increasing peak irradiance reaching approximately 30 % with a peak irradiance of 1000 Wm^{-2}. As shown previously, the BDS5.0K delivers significantly more cooling load than the BD35K, see 6 (b). As was also shown earlier the AEO delivers less cooling load compared to the CVC and PPT, however when the need for start power was alleviated the AEO approaches the load delivered by the CVC and PPT.
When the PV panel size was reduced to 180 W while still supplying the 60 W of start power, the minimum peak irradiance increases significantly, see Figs. 5 (c) and 6 (c). As seen the BDS5.0K with either the PPT or AEO requires a peak irradiance in excess of 500 Wm^{-2}, while the CVC requires 600 Wm^{-2}.For the BD35K this was 590 Wm^{-2} for the PPT and AEO and 700 Wm^{-2} for the CVC. In light of these results, this configuration was deemed infeasible as it would result in the lack of cooling load for too many days.

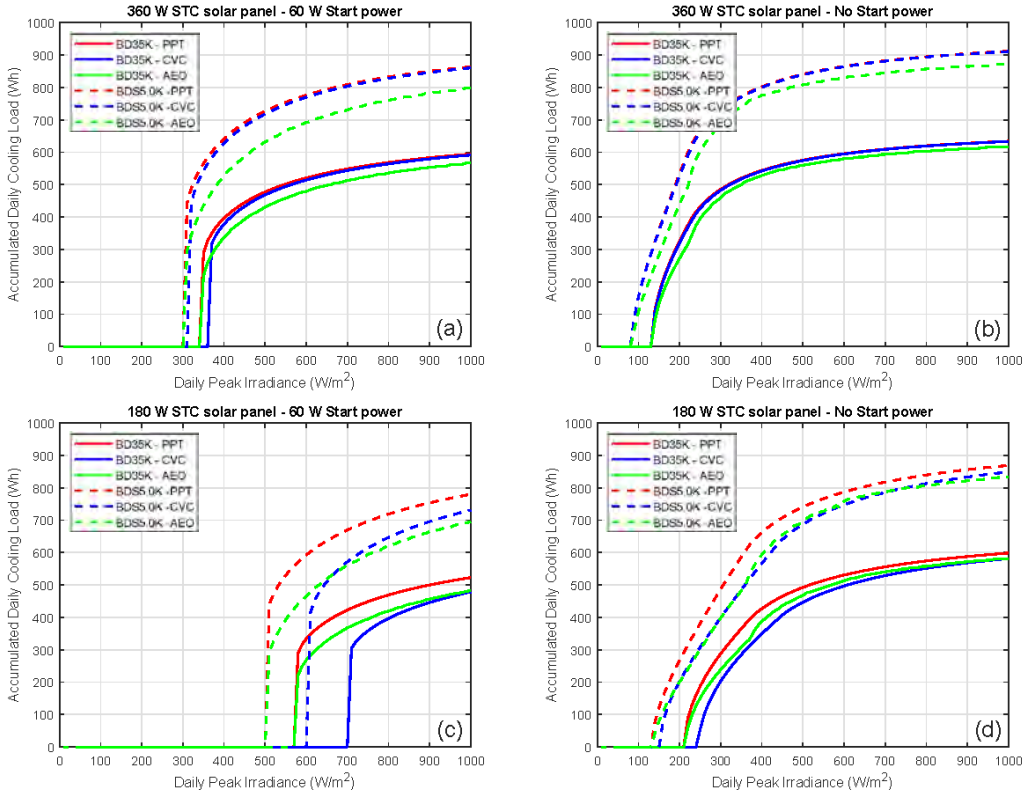

Figure 6: Daily accumulated cooling for the BD35K and BDS5.0K compressors under the PPT, CVC and AEO control strategies using both the 180 W and 360 W PV panels and with and without compressor start power delivered from the PV panel

However, if the need for compressor start power was alleviated for the 180 W panel the minimum peak irradiance was again significantly reduced, see Figs. 5 (d) and 6 (d). Here the BDS5.0K will be able to deliver a cooling load from around 120 Wm^{-2} while the BD35K would require slightly more than 200 Wm^{-2}. Generally, it may be seen that the Utilization Factor for this configuration was higher than the remaining configurations. Even at 1000 Wm^{-2} almost 50 % of the available power was utilized. As seen the Accumulated Daily Cooling Load was actually comparable to that of the 360 W with 60 W start power when both are running. As such it can be concluded that if the compressor start power can be alleviated the PV panel size can be halved without reducing the delivered cooling load, actually the cooling load can be delivered at lower irradiances with half the PV panels if start power was avoided. Finally, it may seen that for this configuration there was slightly higher difference between the applied control strategy.

4. CONCLUSIONS

The influence of compressor type and compressor control strategy on the performance of a solar direct drive refrigeration system was investigated using numerical modelling and simulations. The Utilization Factor and Accumulated Daily Cooling Load were determined for a full day under varying daily peak irradiances. Two compressor types, the BDS5.0K and BD35K and three compressor control strategies, PPT, CVC and AEO where investigated. Further, four configuration where included: a 360 W and a 180 W PV panel both with and without compressor start power delivered from the PV panel. Results showed that both the choice of compressor and the applied control strategy affected the systems ability to utilize the available power from the PV panel, especially under lower irradiance conditions and when the PV panel was downsized. Generally, the PPT strategy delivered the highest Utilization Factor and thus the highest cooling load. The CVC was comparable to the PPT for the 360 W PV panel, while performing worse than the PPT for the 180 W configurations. The AEO generally had a lower performance than the PPT and CVC. However, compared to the simplicity of this control strategy the AEO actually performed well compared to the more challenging PPT and CVC controls. The BDS5.0K performed better than the BD35K due to both the increased efficiency and the increased speed range. Finally, results show that if the need for compressor start power delivered by the PV panel was alleviated the size of the PV panel can be halved without a significant reduction in performance.

ACKNOWLEDGEMENTS

This research project is financially funded by EUDP (Energy Technology Development and Demonstration). Project title: "Second Generation Solar Direct Drive Refrigerators", project number: 64017-0556

REFERENCES

Duffie, J.A., Beckmann, W.A., 2013. Solar Engineering of Thermal Processes. John Wiley and Sons, New Jersey.

IEA, 2012. Measuring progress towards energy for all: power to the people? World energy outlook, Organisation for Economic Co-operation and Development, Paris, France.

McCarney, S., Robertson, J., Arnaud, J., Lorenson, K., Lloyd, J., 2013. Using solar-powered refrigeration for vaccine storage where other sources of reliable electricity are inadequate or costly. Vaccine 31, 6050–6057. doi:10.1016/j.vaccine.2013.07.076.

Myers, D., Diesburg, S., Lennon, P., McCarney, S., 2017. Energy harvesting controls for solar direct drive medical cold chain equipment. Ghtc 2017 - Ieee Global Humanitarian Technology Conference, Proceedings 2017-, 1–9. doi:10.1109/GHTC.2017.8239228.

Pedersen, P.H., Katic, I., Markussen, W.B., Jensen, J.K., Cording, C., Moeller, H., 2019. Direct drive solar coolers. The 25th IIR International Congress of Refrigeration, August 24-30, Montreal, Canada doi:10.18462/iir.icr.2019.

Manuscript ID: 1088
DOI: 10.18462/iir.icr.2019.1088

Demand side management of a commercial refrigeration system with cold thermal energy storage

Gianluca COCCIA[(a)], Alessia ARTECONI[(a)], Paola D'AGARO[(b)], Fabio POLONARA[(a,c)], Giovanni CORTELLA[(b)]

[(a)] Università Politecnica delle Marche, Dipartimento di Ingegneria Industriale e Scienze Matematiche Via Brecce Bianche 12, Ancona (AN), 60131, Italy, g.coccia@univpm.it, a.arteconi@univpm.it, f.polonara@univpm.it

[(b)] Università degli Studi di Udine, Dipartimento Politecnico di Ingegneria e Architettura Via delle Scienze 206, Udine (UD), 33100, Italy, paola.darago@uniud.it, giovanni.cortella@uniud.it

[(c)] Consiglio Nazionale delle Ricerche, Istituto per le Tecnologie della Costruzione Viale Lombardia 49, San Giuliano Milanese (MI), 20098, Italy

ABSTRACT

Accounting for about 17% of the overall electricity consumption worldwide, the refrigeration sector requires improvements in energy reduction and management. Demand side management (DSM) could be adopted to improve the overall system energy efficiency. In this work, a CO_2 commercial refrigeration system coupled with different cold thermal energy storages (CTES) is studied through a DSM approach. A fire prevention water tank of 950 m^3 and low-melting-point phase change materials are considered. Based on a demand response strategy, the CTES are used to change the timing of end-use consumption from high electricity cost periods to low-cost periods. During off-peak times, cold thermal energy can be generated by electricity, stored in the CTES and then used during peak-hours to flatten the utility load profile. Results show that a similar application can lead to economic savings if the system takes advantage of the different electricity prices during peak and off-peak hours.

Keywords: Demand Side Management, Demand Response, Thermal Energy Storage, Real-Time Pricing, National Electricity Price.

1. INTRODUCTION

The refrigeration sector accounts for about 17% of the overall electrical energy use worldwide (IIR, 2015). In supermarkets, display cabinets and cold rooms for food storage require 45% of the overall electricity demand, while household refrigerators and freezers are responsible of almost 4% of residential electrical energy use. Air conditioners consume around 5% of the global electricity consumption and the impact of heat pumps is increasing (800,000 units sold in European Union only), thus making the refrigeration sector an appropriate candidate for energy reduction and management initiatives (Arteconi and Polonara, 2017).

Among the solutions available to improve the energy flexibility of refrigeration systems, demand side management (DSM) consists of a set of policies that can be adopted to influence and modify the customer's energy demand (Lund et al., 2015). In particular, a DSM strategy referred to as demand response (DR) allows to change the electricity use by end customers in response to variations of the electricity price over time (Aazami et al., 2011).

In the last years, carbon dioxide has received growing attention as refrigerant, thanks to its favorable thermophysical properties, non-toxicity, non-flammability and very low global warming potential (Cavallini and Zilio, 2007). On the other hand, its low critical temperature and high operating pressure levels could negatively affect a refrigeration system efficiency, when compared with the adoption of traditional HFCs. This issue is particularly evident for cooling applications in mild and warm climates, where CO_2 systems could operate in transcritical conditions for long periods of time. A decisive

improvement of such systems can be accomplished performing subcooling of CO_2 exiting the gas cooler (Ge and Tassou, 2011).

In this work, a CO_2 transcritical/subcritical commercial refrigeration system was integrated with display cabinets and cold rooms of a supermarket. Subcooling of CO_2 is performed by means of a 950 m^3 cold sink consisting of a fire prevention water tank. The refrigeration system can be managed with a DSM program intervening either in the cycle or in the demand side. In the former case, it can be noted that the large fire prevention water tank acts as a cold thermal energy storage (CTES) whose recharging mode can be managed through a DSM strategy. On the demand side, instead, DSM can be accomplished by modifying the medium temperature (MT) and low temperature (LT) evaporators set-point temperatures.

The chosen DSM strategy is based on a DR program activated by a real-time pricing (RTP). As the proposed strategy was adopted for an existing system, electricity-price-based predictive rule based controls were considered (Fischer and Madani, 2017). Relevant advantages of predictive rule based controls include their inexpensiveness and no need of modifications of the setup under study. The analysis was conducted for the whole year 2018.

2. CASE STUDY

Figure 1 shows the schematic of the CO_2 plant under study. The considered refrigeration plant is installed in a supermarket and has a cooling capacity of 140 kW in the MT section and a capacity of 22 kW in the LT section. The supermarket includes 17 display cabinets and 10 cold rooms refrigerated through the MT section, and 4 frozen food display cases and 2 cold rooms refrigerated through the LT section.

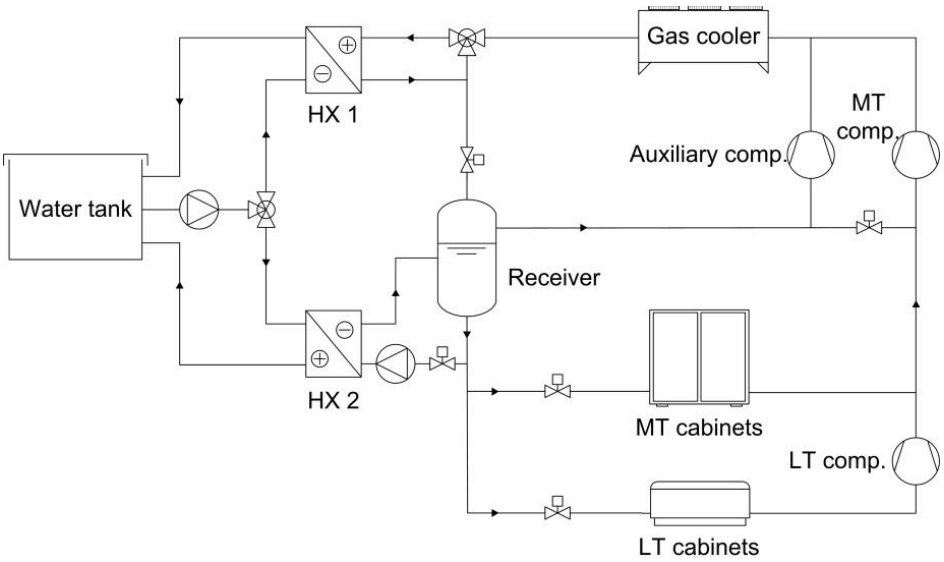

Figure 1: Schematic of the CO_2 refrigeration system

As can be seen in the scheme, the cycle includes a mid-pressure receiver where flash gas can be removed by the MT compressor rack or, if necessary, by an auxiliary compressor. The cycle operates both in subcritical and transcritical conditions depending on the external temperature. Two heat exchangers (HX1 and HX2) connect the refrigeration cycle to a 950 m^3 fire prevention water tank. HX1 allows the subcooling of the CO_2 exiting the gas cooler, while HX2 allows the recharge of the water tank by means of liquid CO_2. The most important design parameters of the refrigeration plant are reported in Table 1.

The supermarket is located in Genoa, Italy, a location characterized by mild climate conditions. The yearly profiles of the LT and MT cooling loads are depicted in Figure 2.

Table 1. Main design parameters

Parameter	Value
LT evaporating temperature (°C)	-35
MT evaporating temperature (°C)	-10
Superheating at evaporators (K)	5
ΔT approach of the gas cooler (K)	3
Liquid receiver temperature (°C)	3
ΔT approach of HX1 and HX2 (K)	3
Water tank volume (m^3)	950

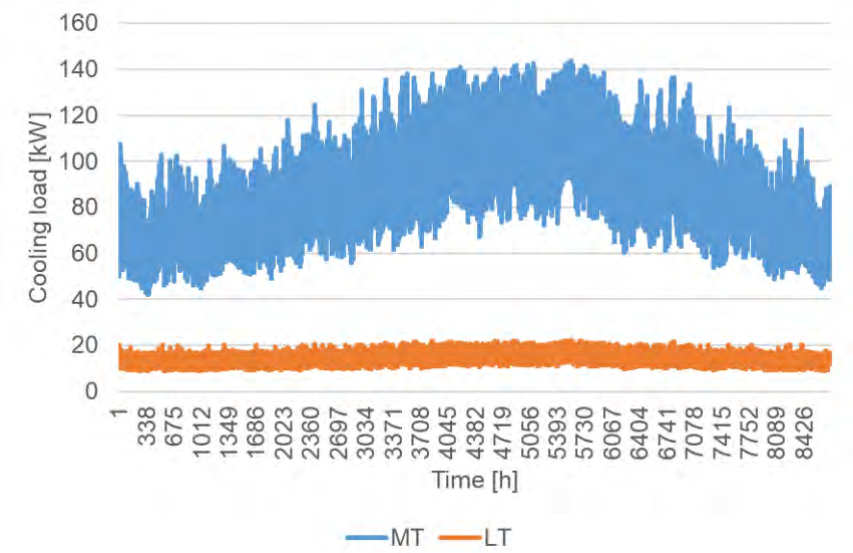

Figure 2: Yearly profiles of the MT and LT cooling loads

3. MODEL DESCRIPTION

The mathematical model of the entire refrigeration system, which includes the display cabinets, the cold rooms and the refrigerating unit was developed in TRNSYS (Klein et al., 2010). As concerns the refrigerating cycle, the thermodynamic and thermophysical properties of the refrigerant were calculated by linking our in-house routines to the CoolProp libraries (Bell et al., 2014). The expansion in all valves was considered isoenthalpic and the pressure drop in the suction lines was neglected. The isentropic efficiency of the compressor racks, as a function of the pressure ratio, was inferred by manufactured data. In subcritical operation the system runs in floating condensing mode; in transcritical and transitional operation the parallel compressor is activated and the high stage pressure is set according to the control rules described in Polzot et al. (2016).

The cooling load profiles from the refrigerated display cabinets (DC) and the cold rooms (CR) were determined according to the procedure reported in Polzot et al. (2016). Specifically, the cooling capacity of the display cabinets (q_{DC}) is equal to:

$$q_{DC} = q_{sen} + q_{lat} + q_{aux} \qquad \text{Eq. (1)}$$

where q_{sen} is the sensible load, q_{lat} is the latent load due to ambient air infiltration and q_{aux} is the sensible load from auxiliary devices (lighting, fans, defrost). The overall cooling capacity at rated conditions is adjusted taking into account the actual and time-dependent working conditions in the supermarket, such as the indoor air temperature and humidity or defrost schedule.

The fire prevention water tank is based on a TRNSYS type of stratified constant volume storage. It takes into account the heat transfer with the refrigeration system and the conductive losses to the ground, whose temperature was assumed to be dependent on the external temperature.

The heat exchangers HX1 and HX2 were modeled assuming appropriate approach temperatures (3 K). In HX2, the pressure in the liquid receiver was kept equal to 3.8 MPa (which corresponds to a saturation temperature of 3 °C) in order to avoid water freezing.

The climate conditions of the site were imported in TRNSYS through a Meteonorm typical meteorological year file (Remund et al., 2014) and the simulations were carried out using a time step of one hour.

4. DEMAND SIDE MANAGEMENT ANALYSIS

The DSM strategy applied to the refrigeration cycle under study aims to reduce the annual electricity cost by shifting the electricity demand from peak hours to off-peak hours. The strategy can be accomplished either by operating at cycle level, modifying the water tank recharging control strategy, or operating at demand level, by varying the evaporating set-point temperatures in the MT/LT sections. For these purposes, it is assumed that the supermarket could adhere to a RTP-based DR program.

Being the supermarket sited in Italy, the Italian PUN (Prezzo Unico Nazionale, National Single Price) referred to 2018 was considered as real-time price applied to the customer. The PUN has a resolution of one hour, is tax-free (it accounts for electrical energy generation only) and is based on a day-ahead market (the Italian Power Exchange).

4.1. Baseline Configuration

The baseline configuration of the refrigeration system includes the subcooling of CO_2 operated by HX1 and the auxiliary compression used to remove the surplus of flash gas in the receiver. The recharge of the fire prevention water tank operated by HX2 was not included in the baseline configuration because, as determined in Polzot et al. (2016), this solution does not seem to be convenient under the point of view of energy use. As shown in the following section, however, we will try to apply a DSM strategy to the recharge control, in order to verify if there is at least the possibility of economic savings.

As regards the subcooling, the baseline configuration operates according to the following control strategy:

$$\text{if } t_{\text{tank}} < t_{\text{GC,out}} - \Delta t_{\text{ap}} \text{ and daytime} \rightarrow \text{subcooling active} \qquad \text{Eq. (2)}$$

Subcooling is therefore allowed only during daytime, when the water temperature t_{tank} is lower than the CO_2 temperature at the exit of the gas cooler $t_{\text{GC,out}}$ (with an appropriate temperature approach Δt_{ap}). The MT and LT evaporators have set-point temperatures equal to -10 °C and -35 °C, respectively. The yearly electricity consumption of the baseline configuration is 303.02 MWh.

Non-household consumers, such as the one considered, usually adopt time of use or fixed price tariff schemes. Taking into account the data provided by Eurostat for non-household consumers, in 2018 the average electricity price in Italy, with the exclusion of taxes and levies, was equal to 89.20 EUR/MWh (Eurostat, 2019). Thus, considering a fixed tariff based on this price, subtracted by a conservative -10% amount that accounts for the supplier's markup, the electricity price would be equal to 80.28 EUR/MWh. With this price, the overall electricity cost of the baseline configuration in 2018 is 24,326 EUR.

4.2. DR Applied to the Recharging of the Fire Prevention Water Tank

In the work by Polzot et al. (2016), it was seen that the recharging of the fire prevention water tank does not provide a yearly energy saving respect to a plant configuration with subcooling only. The non-convenience in the adoption of the recharging system was due to small outdoor temperature excursions. In the original plant setup, the control strategy regulating the recharging was:

$$\text{if } t_{\text{tank}} > t_{\text{tank,set}} \text{ and nighttime} \rightarrow \text{recharging active} \qquad \text{Eq. (3)}$$

Recharging, therefore, could occur when the water temperature t_{tank} was higher than the tank set-point temperature $t_{tank,set}$ (that was fixed to 17 °C) but only at nighttime when the cooling load from DC and CR was lower and the refrigerating capacity available with the highest COP thanks to the lower outdoor temperature.

In order to verify a possible economic convenience of the recharging solution, in the present work we tried to combine the original recharging control strategy with a DR program based on real-time pricing. The strategy described by Equation (3) was then integrated with the following one:

$$\text{if } PUN_i > \overline{PUN} \rightarrow \text{recharging not active} \quad \text{Eq. (4)}$$

where PUN_i is the value of PUN in the ith hour of the year and $\overline{PUN}$ is the yearly mode of PUN in 2018, which is equal to 50 EUR/MWh. In this way, the recharging system is not allowed to operate when the PUN is too high.

4.3. DR Applied to the MT/LT Evaporators Set-Point Temperatures

A DR program can be applied to the MT and LT evaporators set-point temperatures to shift the electricity demand from peak hours to off-peak hours. In a similar fashion of the DR program applied to the recharging system, the following strategy was applied to the MT evaporators set-point temperatures:

$$\text{if } PUN_i > \overline{PUN} \text{ and } q_{MT} < 120 \text{ kW} \rightarrow t_{sp,MT} = -8 \text{ °C} \quad \text{Eq. (5)}$$

$$\text{if } PUN_i < \overline{PUN} \text{ and } q_{MT} < 120 \text{ kW} \rightarrow t_{sp,MT} = -12 \text{ °C} \quad \text{Eq. (6)}$$

According to this strategy, the MT evaporators are allowed to increase their set-point temperature $t_{sp,MT}$ when the hourly PUN is higher than its yearly mode, and to decrease their set-point temperature when the hourly PUN in lower than its yearly mode. The condition referred to the MT cooling capacity q_{MT} was included to avoid variations of the MT evaporators set-point temperatures when the cooling load is too high. In this last case, the MT set-point temperature is kept equal to -10 °C, as defined in the baseline configuration.

As concerns the LT evaporators, a similar strategy was defined:

$$\text{if } PUN_i > \overline{PUN} \rightarrow t_{sp,LT} = -30 \text{ °C} \quad \text{Eq. (7)}$$

$$\text{if } PUN_i < \overline{PUN} \rightarrow t_{sp,LT} = -40 \text{ °C} \quad \text{Eq. (8)}$$

In this case, no condition was added to the cooling capacity q_{LT}, as the load profile defined for the LT section is much lower than that defined for the MT section (see Figure 2) and the frozen food is less sensible to temperature variations.

5. RESULTS OF THE ANALYSIS

In this section, the DR strategies applied at the refrigeration cycle level (recharging system) and at the demand level (MT and LT evaporators set-point temperatures) will be analyzed and discussed separately.

5.1. Results of the Water Tank Recharging DR Strategy

Figure 3 depicts how the yearly electricity demand and cost vary among the following setups: baseline (i.e., without recharging system) with a fixed tariff (FT), original configuration with the recharging system able to operate at nighttime (REC with fixed tariff), and DR configuration including the recharging system able to operate in the same nighttime period (REC+DR with a PUN-based tariff).

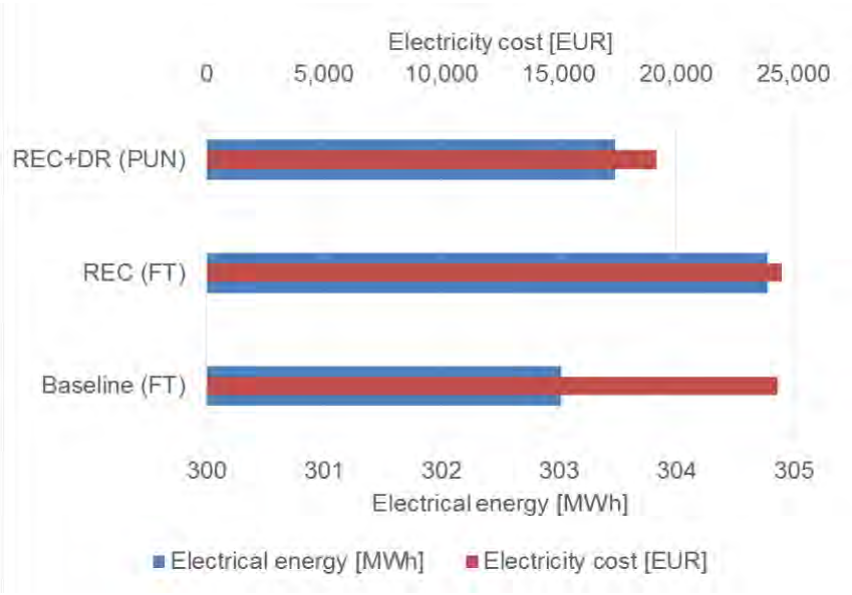

Figure 3: DR strategy applied to the water tank recharging (FT: fixed tariff)

As can be seen, there is an energy and cost convenience in adopting a DR strategy respect to the original configuration REC. However, the setup REC+DR is not able to perform better than the baseline configuration. In fact, even if the REC+DR configuration shows a lower yearly electricity cost respect to the baseline with a fixed tariff, this result depends only on the different tariff schemes adopted, and not on the DR strategy implemented. Considering a baseline with a variable tariff based on PUN, the REC+DR setup is not able to be more competitive than the first solution.

It can be therefore concluded that the plant setup including the recharge of the fire prevention water tank by heat exchange with liquid CO_2 does not provide any electricity energy/cost convenience, at least for the location under study.

5.2. Results of the MT/LT Evaporators DR Strategy

The DR strategies applied to the MT and the LT evaporators were studied separately at first. As shown in Figure 4, the DR strategy applied to the MT evaporators provides, respect to the baseline configuration, an energy saving of -2.15% and an electricity cost saving of -23.41%. Instead, when the DR strategy is applied to the LT evaporators, the electrical energy saved respect to the baseline is equal to -2.09%, while the electricity cost saving is -23.37%. When the MT and the LT strategies are applied together, the amount of energy saving is -4.25% and the electricity cost saving is -25.40%, corresponding to around 6178 EUR saved in a year respect to the baseline configuration.

It is worth noting that a variation in the evaporators set-point temperatures should be carried out carefully, as too wide intervals could influence the temperature of the stored food, leading to an undesired deterioration of the product. This is particularly true for the MT section, where chilled products should absolutely avoid freezing. For the considered case study, stabilization of the products' temperature could be guaranteed by providing the display cabinets and the cold rooms with appropriate cold thermal energy storages, e.g. phase change materials (PCMs). Properly sized PCMs, in fact, can be adopted for taking advantage of their high latent heat of fusion/solidification, allowing to keep the temperature of the stored products steady. PCMs based on eutectic water-salt solutions have melting temperatures lower than 0 °C and proved to be a good choice for use in refrigeration applications (Oro et al., 2012). In literature, many works depict the advantage of PCMs used in display cabinets and cold rooms, highlighting that the adoption of PCMs allows to maintain the same cooling power of the original cabinets and can lead to a temperature reduction of core food, an improvement of temperature distribution uniformity and a reduction in temperature rise during defrost period (Lu et al., 2010; Sevault et al., 2018; Beek and Jong, 2014; Alzuwaid et al., 2015; Fioretti et al., 2016). In this way, it is possible to raise/decrease the evaporation temperature

of few degrees for limited time while still maintain the required cooling conditions for the display cabinets and the cold rooms.

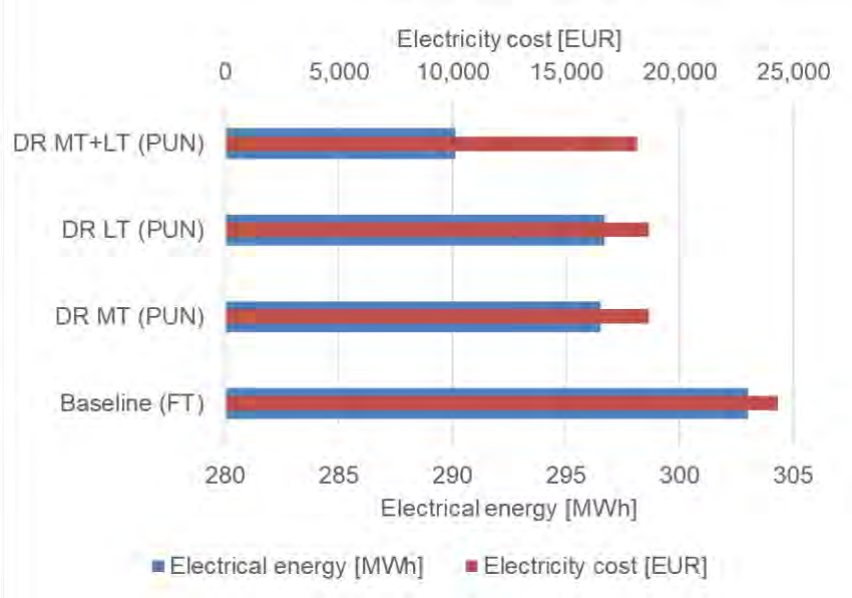

Figure 4: DR strategy applied to the MT/LT evaporators (FT: fixed tariff)

6. CONCLUSIONS

In this work, a demand side management (DSM) program based on a demand response (DR) strategy was applied to a CO_2 transcritical/subcritical commercial refrigeration system installed in a supermarket. The DR strategy was defined according to a real-time pricing (RTP) algorithm that takes into account the 2018 Italian National Price (PUN). The DR strategy was applied at both the refrigeration cycle level and the demand level. As regards the former, a DR algorithm was applied to the control strategy of the fire prevention water tank recharging system, which uses liquid CO_2 exiting the refrigeration system receiver. In this case, however, the simulation gave negative results: the DR-based configuration shows a yearly electricity cost lower than that of the original non-DR configuration, but the setup without recharging system still provides the lowest electricity cost. Two DR strategies were also applied at the demand level, specifically to the MT and LT evaporators set-point temperatures. It was found that the two strategies perform well, providing the best result when applied together. In this case, the yearly electrical energy saving is equal to -4.25% and the electricity cost saving corresponds to -25.40% respect to the non-DR baseline configuration.

ACKNOWLEDGEMENTS

This work was supported by the Italian Ministero dell'Istruzione, dell'Università e della Ricerca (MIUR) within the framework of PRIN2015 project "Clean Heating and Cooling Technologies for an Energy Efficient Smart Grid", Prot. 2015M8S2PA.

REFERENCES

Aazami, R., Aflaki, K., Haghifam, M. R., 2011. A demand response based solution for LMP management in power markets. Int. J. Elec. Power 33, 1125-1132.

Alzuwaid, F., Ge, Y. T., Tassou, S. A., Raeisi, A., Gowreesunker, L., 2015. The novel use of phase change materials in a refrigerated display cabinet: An experimental investigation. Appl. Therm. Eng. 75, 770-778.

Arteconi, A., Polonara, F., 2017. Demand side management in refrigeration applications. Int. J. Heat Tech. 35, S58–S63.

Beek, M. V., Jong, H. D., 2014. Reducing display bottle cooler energy consumption using PCM as active thermal storage. 15th International Refrigeration and Air Conditioning Conference, Purdue University, USA.

Bell, I. H., Wronski, J., Quoilin, S., Lemort, V., 2014. Pure and pseudo-pure fluid thermophysical property evaluation and the open-source thermophysical property library CoolProp. Ind. Eng. Chem. Res. 53, 2498-2508.

Cavallini, A., Zilio, C., 2007. Carbon dioxide as a natural refrigerant. Int. J. Low-Carbon Tech. 2(3), 225-249.

Eurostat, 2018. Electricity prices for non-household consumers. URL: https://ec.europa.eu/eurostat/web/energy/data/database

Fioretti, R., Principi, P., Copertaro, B., 2016. A refrigerated container envelope with a PCM (Phase Change Material) layer: Experimental and theoretical investigation in a representative town in Central Italy. Energ. Convers. Manage. 122, 131-141.

Fischer, D., Madani, H., 2017. On heat pumps in smart grids: A review. Renew. Sust. Energ. Rev. 70, 342-357.

Ge, Y. T., Tassou, S. A., 2011. Thermodynamic analysis of transcritical CO_2 booster refrigeration systems in supermarket. Energ. Convers. Manage. 52(4), 1868-1875.

International Institute of Refrigeration, 2015. The role of refrigeration industry in the global economy. 29th Inform, Note on Refrigeration Technology, Paris, France.

Klein, S., Beckman, W., Duffie, J. et al., 2010. TRNSYS 17: A Transient System Simulation Program. Mathematical reference. Solar Energy Laboratory, University of Wisconsin-Madison.

Lu, Y. L., Zhang, W. H., Yuan, P., Xue, M. D., Qu, Z. G., Tao, W. Q., 2010. Experimental study of heat transfer intensification by using a novel combined shelf in food refrigerated display cabinets (Experimental study of a novel cabinets). Appl. Therm. Eng. 30(2-3), 85-91.

Lund, P. D., Lindgren, J., Mikkola, J., Salpakari, J., 2015. Review of energy system flexibility measures to enable high levels of variable renewable electricity. Renew. Sust. Energ. Rev. 45, 785–807.

Oró, E., De Gracia, A., Castell, A., Farid, M. M., Cabeza, L. F., 2012. Review on phase change materials (PCMs) for cold thermal energy storage applications. Appl. Energ. 99, 513-533.

Polzot, A., D'Agaro, P., Gullo, P., Cortella, G., 2016. Modelling commercial refrigeration systems coupled with water storage to improve energy efficiency and perform heat recovery. Int. J. Refr. 69, 313-323.

Remund, J., Lang R., Kunz, S., 2014. Meteonorm. Meteotest, Bern (CH). URL: www.meteonorm.com

Sevault, A., Banasiak, K., Bakken, J., Hafner, A., 2018. A novel PCM accumulator for refrigerated display cabinet: design and CFD simulations. 12th IIR/IIF International Conference on Phase-Change Materials and Slurries for Refrigeration and Air Conditioning.

Manuscript ID: 1099
DOI: 10.18462/iir.icr.2019.1099

Modelling of a diphasic CO_2 ejector for cooling circuit

Pierre-Henri NATTES[(a)], Brice TREMEAC[(a)], Marie-France TERRIER[(a)], Pascal TOBALY(a)

[(a)] Laboratoire du Froid, des Systèmes Energétiques et Thermiques (LaFSET), Cnam, HESAM Université,
292 rue Saint-Martin 75003 Paris, France
pierre-henri.nattes@lecnam.net

ABSTRACT

Ejectors as alternative to expansion valves are used to increase efficiency of cooling circuits. To cope with different mass flows or inlet pressures, adaptable ejectors and multiple ejectors are utilized. A simplified model is needed to size an ejector in a circuit. It must be fast and accurate to be included in dynamic simulations of cooling circuits. This article proposes a 1D model to calculate the entrainment ratio and the pressure recovery of a supersonic ejector. It is based on data from literature and a CO_2 test bench with adaptable ejector not presented in this paper. The model uses few experimental points for calibration and the mixing process is modelled in a different way compared to previous articles. The entrainment ratio is calculated with a precision of 10%. The model is validated with CO_2 for high pressures ranging from 9.0 MPa to 12.0 MPa and low pressure from 2.3 MPa to 3.6 MPa.
Keywords: Refrigeration, Carbon Dioxide, Ejector, Modelling.

1. INTRODUCTION

To decrease the impact of the refrigeration on the climate change, new refrigerants and cycles are used. CO_2 is an interesting refrigerant with a low GWP (Global Warming Potential), is non-flammable and not-toxic (Kuikpers and Peixoto, 2014). However, the performances of the units are lower than for other refrigerants, especially when its cycle is transcritical. Ejectors are a solution to improve the performance by using the energy of expansion. They can be equipped with needles or multiple ejectors can be used to adapt it at the outlet conditions on the cycle (Llopis et al., 2018). One limit of the use of ejector is the absence of simplified models to test their impact on the cycle.
The principle of this study is to propose a simplified model allowing to predict the two characteristics of an ejector, the entrainment ratio (*e*) and the pressure recovery (*PR*) defined by Eq. (1) and Eq. (2). Entrainment ratio characterises the capacity to create a mass flow at the secondary inlet (*s*) with the pressure and mass flow of the primary fluid (*p*). Pressure recovery characterises the increase of pressure between the secondary inlet and the outlet of the ejector (*out*).

$$e = \frac{\dot{m}_s}{\dot{m}_p} \quad \text{Eq. (1)}$$

$$PR = \frac{P_{out}}{P_s} \quad \text{Eq. (2)}$$

One of the advantages of the model is to use few experimental points for calibration, in this case eleven. These data are provided by tests made at the laboratory on an industrial unit, modified to include sensors (not presented here). This unit is working with CO_2 and has a capacity of 12 kW at 0/30 °C. Mass flows, pressures and temperatures are measured at the inlets of the ejector.

2. EJECTOR MODEL

The model is similar to the models developed by Liu and Groll (2013) and Cardemil and Colle (2012). The idea is to describe the flow inside the ejector with a 0D model. Each transformation is simplified and characterised by an isentropic coefficient. These isentropic coefficients can be fixed or variable. Cardemil and Colle model was developed for vapour ejector, and later adapted for diphasic. Cardemil and Colle (2012) use their models on R-141b (vapour ejector) and water (diphasic ejector). An advantage of this kind of ejector model is to be compatible for system modelling. For example, Zheng et al., (2015) use this method on a dynamic model of a CO_2 system. A different approach will be used by Zhu and Jiang (2018) by taking directly into account the impact of the liquid mass fraction at the nozzle throat with a CO_2 ejector. Their work is for high pressure going from 7.98 MPa to 9.28 MPa, with the low pressure from 4.15 MPa to 4.36 MPa. These models have in common to redefine coefficients for each ejector and refrigerant. Recently a new approach has been proposed to predict the behaviour of ejector for off-design conditions. Off-design conditions are points where the two fluids aren't chocked in the case of a supersonic ejector. According to the inlet conditions Wang et al., (2019) are able to evaluate the entrainment ratio of a vapour ejector working with R-245fa with an error of 10% for the off-design mode. Taslimi Taleghani et al., (2018) are working on a CO_2 model able to work in all conditions, they use fixed polytropic coefficients to adapt the model. They are able to predict the primary mass flow with an error between 1% and 16% for a high pressure between 7.6 MPa and 8.9 MPa. A difficulty of this kind of model is that test benches are usually not able to work for off-design conditions, validation of these models are complicated. For this study, it was decided to work on increasing the range of validity of a diphasic model. The case study is a CO_2 supersonic ejector which was designed for refrigeration application with an inlet high pressure ranging from 9.0 MPa to 12.6 MPa and a low pressure from 2.3 MPa to 3.1 MPa.

2.1. Description of the Flow

Fig. 1 represents a supersonic ejector with constant mixing area and the profiles of pressure and velocity of the fluid inside it. This evolution was proposed by (Huang et al. 1999) from a model of (Munday & Bagster 1977) on vapour ejector. At the primary inlet, the fluid at high pressure enters the nozzle, with the decrease of area, speed increases while pressure decreases, until the primary flow becomes choked (t). With the increasing of section, the supersonic flow continues to accelerate while the pressure decreases (1). At the end of the nozzle, the pressure is lower than the pressure at the secondary inlet. Hence, the secondary flow is sucked. At the outlet of the nozzle, the primary flow is assumed to keep expanding without mixing with the secondary flow (1 to 1'). Secondary fluid is assumed to reach its maximal speed for its lowest cross section (1') formed by the primary core flow and the ejector wall. The secondary flow becomes supersonic. The mixing process happens after the secondary flow is supersonic. The two fluids mix achieving same speed and pressure (2). A shock wave happens before the diffuser (3), the flow becomes subsonic, then the pressure rises while the cross section increases and the velocity decreases (4 to 5).

The model is based on the three conservation laws. The diphasic flow that appears in the ejector is supposed homogeneous, impact of one phase on the other is neglected. The flow is supposed to be steady-state and one-dimensional; it is supposed at thermodynamic equilibrium. The ejector is modelled as adiabatic and kinetic energy at the inlets as negligible. The thermodynamic data is provided by CoolProp (Bell et al., 2014). The inputs of the model are for the primary fluid, temperature and mass flow, for the secondary fluid, pressure, and enthalpy. Contrary to usual approaches, the mass flow is taken as an input instead of the pressure, the aim is to have a model compatible with complete simulation of a refrigeration cycle. The outputs are the mass flow at the secondary inlet and the pressure at the outlet of the compressor. In the following paragraphs the subscripts correspond to Figure 1 with *p* for the primary flow and *s* for the secondary flow.

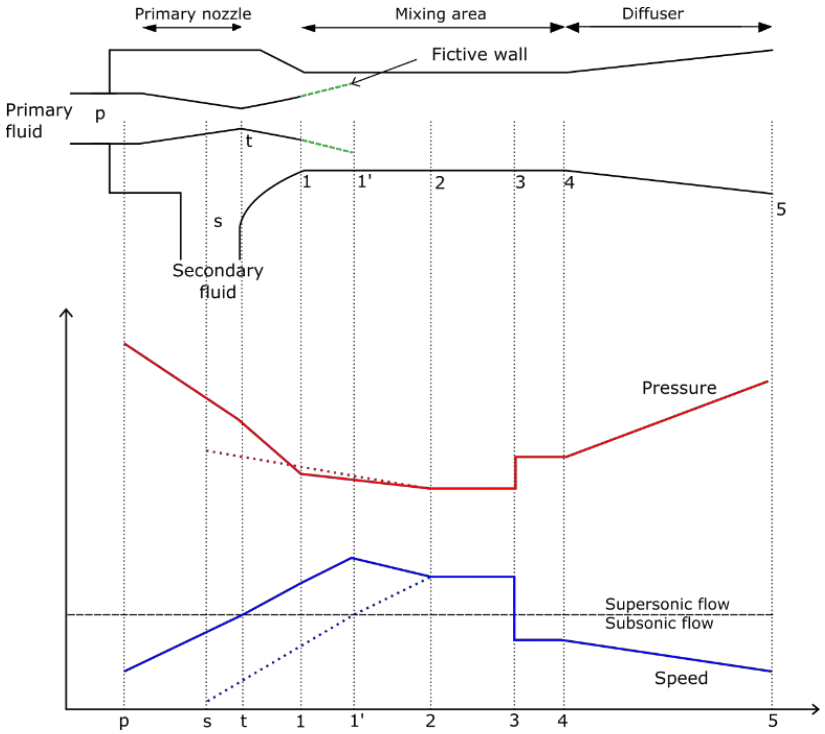

Figure 1: Representation of the flow inside the ejector

2.1.1. Nozzle

According to our previous assumptions, the expansion is not-isentropic. Fig. 2 shows the method to evaluate the conditions at the throat and the outlet of the divergent. The isentropic efficiency at the nozzle is defined as Eq. 3. The input data are the mass flow, the temperature and the area of the throat. The outputs at the throat are the pressure, enthalpy and velocity of the primary fluid. The pressure at the inlet is initialized, allowing to calculate the entropy. Then the pressure at the throat is initialized. The isentropic efficiency of the nozzle allows to calculate the enthalpy at the throat. With the first law of thermodynamics the speed is calculated. If this speed corresponds to the maximal mass velocity (G_p), the mass conservation is tested. If not, the inlet pressure is changed. If the velocity and density at the throat don't correspond to the maximal mass velocity, the pressure at the throat is changed. The characteristics of the fluid (pressure P, enthalpy h and density ρ) are calculated from CooProp ($f_{CoolProp}$).

$$\eta_t = \frac{h_p - h_t}{h_p - h_{tis}} \qquad \text{Eq. (3)}$$

Cardemil and Colle (2012) suppose the expansion of the fluid after the throat in the diverging section (t to 1, Figure 1) is isentropic due to the small angle. On Figure 2 this assumption is not used, an isentropic coefficient is associated to the expansion. At the end of the diverging part, the expansion through the fictive wall (1 to 1', Figure 1) is supposed not-isentropic due to the possibility of oblique shock wave and the friction with the secondary fluid. The state of the fluid in 1 is calculated with an iterative loop on the pressure and the mass conservation as in 1'. The expansion coefficient ϕ is calculated from the inlet data and determined by adjustment on experimental data points as the other coefficients (section 3). The area $A_{p1'}$ is calculated with Eq. 4.

$$\phi = \sqrt{\left(\frac{A_{p1}}{A_{p1}'}\right)} \qquad \text{Eq. (4)}$$

This expansion coefficient characterises the expansion of the primary fluid from the outlet of the diverging part until the section where the two fluids begin to mix. If the expansion ratio is close to 1, the primary flow doesn't expand, the cross area of the secondary fluid is important, the ejector has

a high entrainment ratio. If the primary fluid expands a lot, the expansion ratio is low, its pressure decreases a lot too and there is less area for the secondary flow, the ratio entrainment is low.

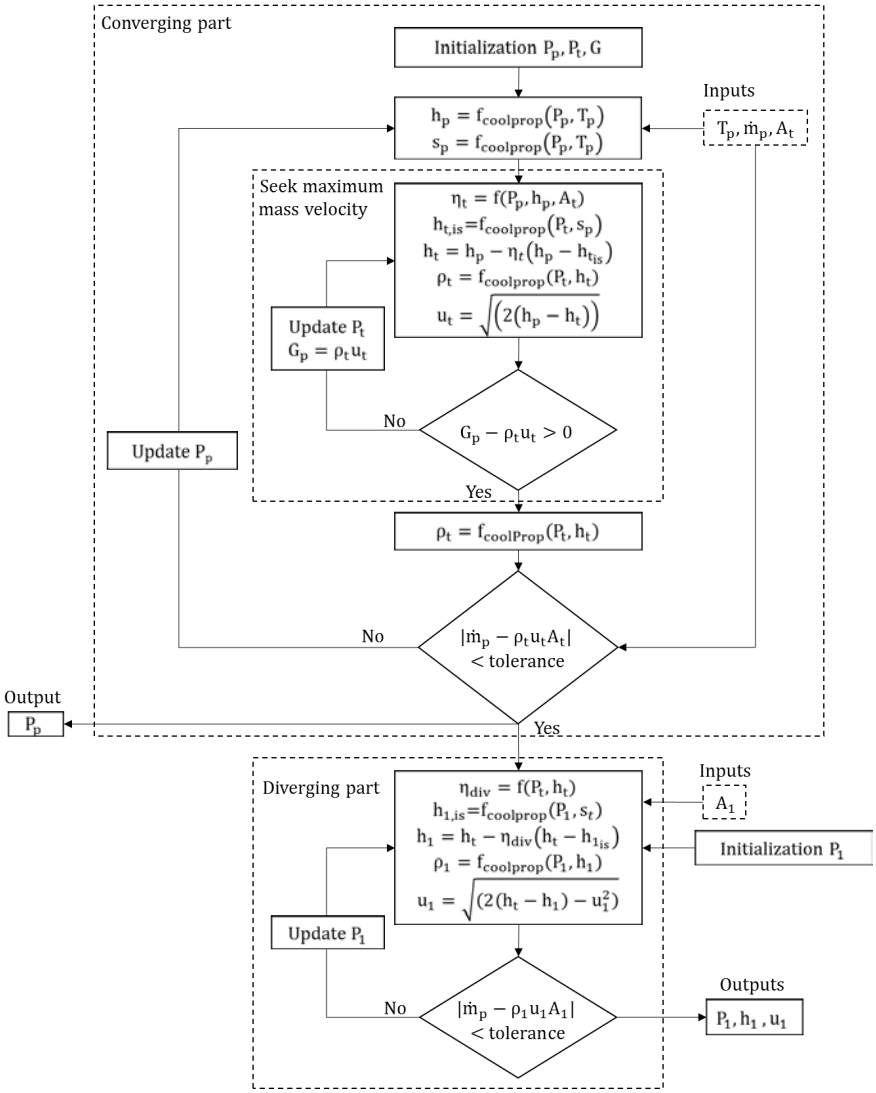

Figure 2: Flowchart of the model of the nozzle

2.1.2. Aspiration

Similarly, to the nozzle evolution, an isentropic coefficient is associated with the suction of the secondary fluid. The pressure and enthalpy from the secondary flow are used as input of the model. The flow is supposed choked at fictive throat. The enthalpy allowing to achieve maximal mass velocity in 1' is sought. With the isentropic coefficient and the first law of thermodynamics, the characteristics of the two flows in 1' are determined as shown in Fig. 3. The secondary mass flowrate is determined in this step and so the entrainment ratio.

2.1.3. Mixing

The energy conservation and momentum conservation are used to calculate the state of the fluid at the end of the mixing process. Unlike with other models, the mixing process is not assumed to take place at constant pressure. Also, no adjustable coefficient is used to characterise this evolution. Without the constraint to mix at the same pressure, it is possible to suppress one coefficient and the corresponding correlation. CFD analysis tends to agree with this observation (Banasiak et al. 2014).

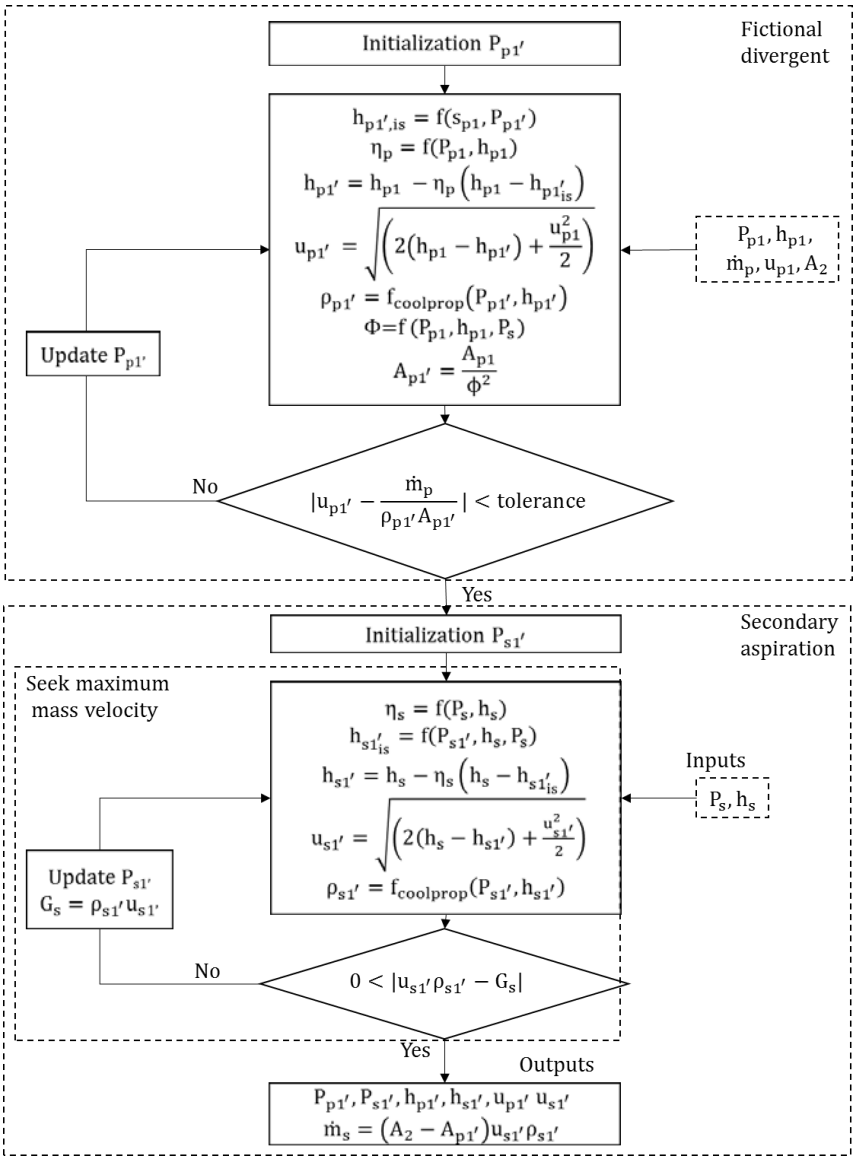

Figure 3: Flowchart of the model of the aspiration

2.1.4. Shock wave and diffuser

The supersonic flow is supposed to become subsonic before the diffuser. The Hugoniot equation (Anderson 2002) is written to solve the shock wave (Eq. 7) with the mass conservation.

$$\frac{P_4 - P_3}{\rho_4 - \rho_3} = u_3^2 \qquad \text{Eq. (7)}$$

The expansion of the subsonic flow inside the diffuser is characterised with an isentropic efficiency. The first law of thermodynamics and the mass conservation allow to determine the enthalpy, velocity and pressure at the outlet of the ejector. The pressure recovery is known.

2.1.5. Supersonic flow

The speed sound of the fluid is needed inside the models of the throat and suction. It is difficult to define the sonic speed of a diphasic flow; each phase has its own. We have decided to calculate it by considering the expansion of a monophasic fluid in a convergent and by seeking the maximal mass velocity at the minimal cross section. With an isentropic efficiency for the evolution, for each pressure at the throat, a mass velocity is calculated with the energy conservation. The pressure giving the maximal mass velocity corresponds to the pressure at the throat. This method was used by Copigneaux et al. (1984). In previous studies the correlations of Nguyen et al, (1981); Lund and

Flatten, (2010); Attou and Seynhaeve, (1999) were used. Such methods consider a difference between the sonic speed of liquid and vapour. In the present method, the fluid is considered homogeneous and a mean velocity for the diphasic fluid is considered.

2.2. Identification of the Coefficients

The efficiencies and expansion ratio used in the models are calculated from polynomial equations. The coefficients of the equations are deduced from measured data points. Eleven experimental points were used. The aim was to use few points to decrease the time of tests. An example is given with the Eq. 8 for the nozzle. Reduced pressure (P_{red}) and enthalpy (h_{red}) are defined by dividing the pressure or enthalpy by its value at the critical point.

$$\eta_n = aP_{red} + bh_{red} + cP_{red}^2 + dh_{red}^2 + eP_{red}h_{red} + fP_{red}h_{red}^2 + gP_{red}^2h_{red} + i \quad \text{Eq. (8)}$$

Each coefficient (at the nozzle, fictive throat, suction, expansion and diffuser) is calculated according to the same method. The efficiency ranges from 0.55 to 0.99 for the nozzle, from 0.30 to 0.60 for the fictive throat, from 0.41 to 0.62 for the suction, from 0.40 to 0.50 for the diffuser. Liu and Groll (2013), obtain similar values from 0.50 to 0.93 for the nozzle and from 0.37 to 0.90 for the suction. Values for the diffuser are quite low compared to other ejectors. An explanation could be the presence of liquid which is greater than for other ejectors. The expansion coefficient (ϕ) is between 0.45 and 0.50, which is lower than for Cardemil and Colle (2012) (around 0.87). An isentropic efficiency of 1 is used for the diverging part of the primary nozzle.

2.3. Validation of the Models

Nineteen points are used to validate the model, they are different from the points used for the calibration of the efficiencies. Entrainment ratio and pressure recovery are calculated and compared to experimental data. The primary pressure is between 9 MPa and 12.6 MPa, the secondary pressure is between 2.3 MPa and 3.0 MPa. To change the conditions at the inlet of the ejector, the speed of the compressor and the temperature at the inlet of the ejector are changed. The entrainment ratio is calculated with a relative deviation of 10% and represented on Fig. 4. HP stands for high pressure at the primary inlet of the ejector and LP for low pressure at the secondary inlet of the ejector. Entrainment ratio is between 0.4 and 0.6, which are values compatible with this ejector. Entrainment ratio was known with a relative error of 1.5% from our experimental data.

On Figure 4, three levels of temperature for the high pressure were used. We can draw the entrainment ratio as a function of the ratio between high pressure and low pressure for one temperature 301 K on Fig. 5. The decrease of the entrainment ratio can be correlated with the increase of the ratio of high pressure over low pressure.
The pressure recovery is calculated with a relative error of 10% and represented on Fig. 6. The values are between 1.02 and 1.17. The highest pressure rise is achieved for the highest primary pressure inlet.

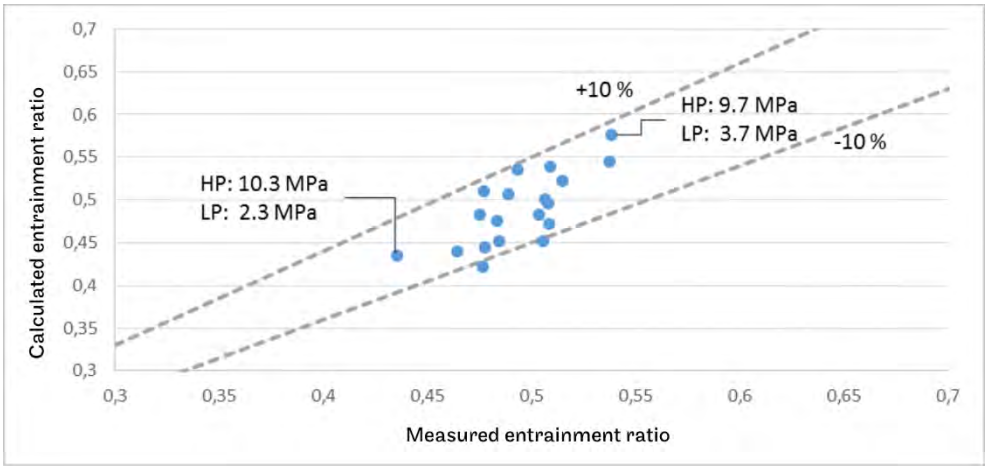

Figure 4: Comparison between the predicted and the measured entrainment ratio

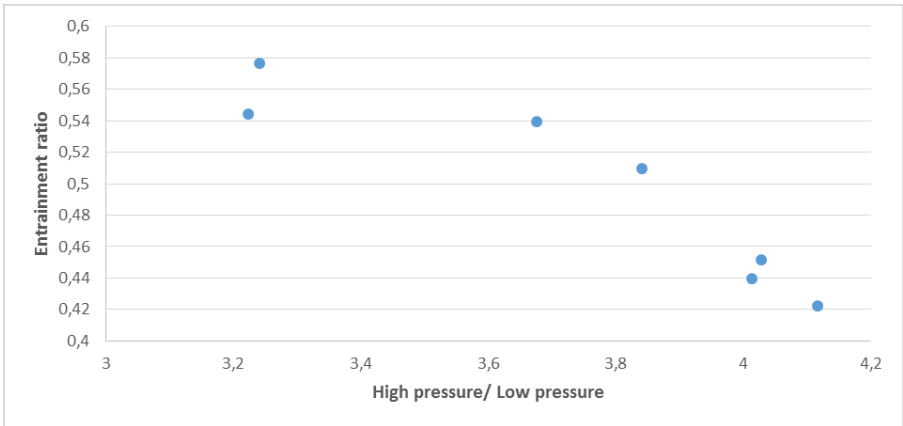

Figure 5: Evolution of the entrainment ratio according to the ratio High pressure/Low pressure (P_p/P_s)

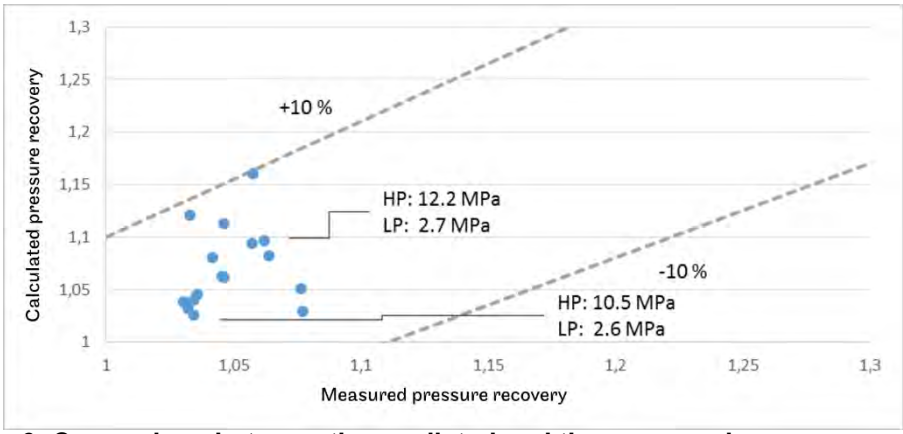

Figure 6: Comparison between the predicted and the measured pressure recovery

3. CONCLUSIONS

In this study a diphasic, supersonic, ejector model was developed and calibrated from eleven experimental points. Compared to previous models for CO_2 ejectors, the mixing process is not described as happening at a constant pressure. Compared to Cardemil and Colle (2012), the precision of the calculation of the entrainment ratio is lower, they achieve an error of +/-2.5% but on a narrower range 0.603 to 0.640 compared to 0.4 to 0.6 in the present study.
Some modifications were made compared to previous models. The advantages of the present model are to use few experimental points for calibration and to work on different range of conditions that previous models. A new method to evaluate the sonic speed was proposed. The choice to use few experimental points allows the model to be easily used for new ejectors and fluid. Upgrades on the calculations of efficiency can still be made to achieve new improvements on the circuit.

NOMENCLATURE

η	efficiency	h	enthalpy ($J.kg^{-1}$)
P	pressure (Pa)	u	speed ($m.s^{-1}$)
T	temperature (K)	e	entrainment ratio
ρ	density ($kg.m^{-3}$)	PR	pressure recovery
A	area (m^{-2})	G	mass velocity ($kg.m^{-2}.s^{-1}$)
crit	critical	ϕ	expansion coefficient
t	throat	$\dot{m}$	mass flow ($kg.s^{-1}$)
red	reduced	s	entropy ($J.kg^{-1}.K^{-1}$)
is	isentropic	*out*	outlet
in	inlet	*LP*	low pressure
coolprop	CoolProp	G	mass velocity ($kg.m^{-2}.s^{-1}$)
HP	high pressure	*1-5*	ejector cross section

REFERENCES

Anderson, J., 2002. *Modern Compressible Flow: With Historical Perspective*,

Attou, A. & Seynhaeve, J.M., 1999. Steady-state critical two-phase flashing flow with possible multiple choking phenomenon. *Journal of Loss Prevention in the Process Industries*, 12(5), pp.335–345.

Banasiak, K. et al., 2014. A CFD-based investigation of the energy performance of two-phase R744 ejectors to recover the expansion work in refrigeration systems: An irreversibility analysis. *International Journal of Refrigeration*, 40, pp.328–337.

Bell, I.H. et al., 2014. Pure and pseudo-pure fluid thermophysical property evaluation and the open-source thermophysical property library coolprop. *Industrial and Engineering Chemistry Research*, 53(6), pp.2498–2508.

Cardemil, J.M. & Colle, S., 2012. A general model for evaluation of vapor ejectors performance for application in refrigeration. *Energy Conversion and Management*, 64, pp.79–86.

Copigneaux, P., Tobaly, P. & Godin, M., 1984. Isentropic Expansion of a Saturated Dry Vapor. *Journal of Pressure Vessel Technology*, (17), pp.62–68.

Huang, B.J. et al., 1999. 1-D analysis of ejector performance. *International Journal of Refrigeration*, 22(5), pp.354–364.

Kuikpers, L. & Peixoto, R., 2014. *Report of the refrigeration, air conditioning and heat pumps*,

Liu, F. & Groll, E. a., 2013. Study of ejector efficiencies in refrigeration cycles. *Applied Thermal Engineering*, 52(2), pp.360–370.

Llopis, R. et al., 2018. Subcooling methods for CO_2 refrigeration cycles: A review. *International Journal of Refrigeration*, 93, pp.85–107.

Lund, H. & Flatten, T., 2010. Equilibrium conditions and sound velocities in two-phase flows. *Proceedings of the SIAM annual meeting*, 1(7465), pp.1–15.

Ma, Z., Bao, H. & Roskilly, A.P., 2017. Modélisation thermodynamique et détermination des paramètres de l'éjecteur pour des systèmes frigorifiques à éjection. *International Journal of Refrigeration*, 75, pp.117–128.

Munday, J.T. & Bagster, D.F., 1977. A New Ejector Theory Applied to Steam Jet Refrigeration. *Industrial & Engineering Chemistry Process Design and Development*, 16(4), pp.442–449.

Nguyen, D.L., Winter, E.R.F. & Greiner, M., 1981. Sonic velocity in two-phase systems. *International Journal of Multiphase Flow*, 7(3), pp.311–320.

Taslimi Taleghani, S., Sorin, M. & Poncet, S., 2018. Modeling of two-phase transcritical CO_2 ejectors for on-design and off-design conditions. *International Journal of Refrigeration*, 87, pp.91–105.

Wang, F. et al., 2019. Performance analysis of ejector at off-design condition with an unconstant-pressure mixing model. *International Journal of Refrigeration*, 99, pp.204–212.

Zheng, L. et al., 2015. Dynamic model of a transcritical CO_2 ejector expansion refrigeration system. *International Journal of Refrigeration*, 60, pp.247–260.

Zhu, Y. & Jiang, P., 2018. Theoretical model of transcritical CO_2 ejector with non-equilibrium phase change correlation. *International Journal of Refrigeration*, 86, pp.218–227.

Manuscript ID: 1105
DOI: 10.18462/iir.icr.2019.1105

Variable capacity operation of a vapor ejector equipped with an adjustable needle

Michel POIRIER[(a)], Christopher REDDICK[(b)], Hristo SAPOUNDJIEV[(a)]

[(a)] CanmetENERGY-Varennes, Natural Resources Canada
Varennes, J3X 1S6, Canada, michel.poirier@canada.ca
[(b)] Mechanical Engineering Department, University of Sherbrooke
Sherbrooke, J1K 2R1, Canada, j.christopher.reddick@usherbrooke.ca

ABSTRACT

Vapor ejector technology compresses gas using thermal rather than mechanical or electrical energy. For a given motive pressure, ejector capacity is constant; it is a direct function of the motive nozzle throat area. When the available thermal motive power is changed, an adjustable needle could move within the motive nozzle, varying the throat area. A steam activated vapor ejector test bench was used to investigate this design strategy. First, tests were completed with two constant area motive nozzles having throat areas of 12.8 mm^2 and 20.3 mm^2. Then, a needle-equipped motive nozzle, having a maximum throat area of 20.1 mm^2, was evaluated over approximately the same throat area range. Experimentally evaluated ejector performance was similar for both the needle-equipped and the constant area nozzles, for moderate throat area reduction. However, for throat area reductions greater than 24%, the needle-equipped ejector showed a performance penalty compared to the constant area ejector.

Keywords: Ejector, Steam, Needle, Entrainment Ratio.

1. INTRODUCTION

In many industrial processes, an amount of heat is rejected to the surroundings as waste. On the other hand, newer transformative technologies such as solar panels produce low grade thermal energy. Both waste heat and low grade thermal energy can be used successfully in refrigeration or heating systems to decrease their power demand. Ejectors that act as thermally activated compressors are one of the very promising technologies for reducing energy intensity in processes by upgrading low grade heat. They are also attractive due to their low cost and simple design (no moving parts), and can be manufactured with chemically resistant materials to survive harsh environments. Ejectors can not only be used for compression, but also for pumping, creating vacuum, or mixing. Successful ejector applications often make use of some combination of these functions, or the thermal effects associated with them.

In the past decades, the main ejector research has focused on improving air conditioning and refrigeration cycles (Little et Garimella, 2011, Chen et al., 2013, Besagni et al., 2016). Recently ejector applications have also been reported for some industrial processes such as carbon capture from flue gas (Reddick et al., 2014, 2016) where an ejector is used to increase the efficiency of the absorption process for post-combustion carbon capture in electric power plants. In other cases, ejectors provide thermal compression of low grade heat, or renewable sources, such as solar energy. Ashrafi et al. (2018)

demonstrated ejector integration in the Selexol gas purification process to reduce the energy demand as well as capital and operating costs for the process.

The main previous research efforts concentrated on the development of ejector models, ejector geometric optimization and selection of the proper working fluid and its influence on ejector operation. Important research subjects focus on ejector geometric optimization and operating conditions to improve ejector performance. An important key parameter is the non-dimensional area ratio (ψ), which is the ratio between the area of the ejector constant diameter duct (Figure 1) and the area of the motive nozzle throat. Most of the research work was dedicated to finding the optimum area ratio for specific operating conditions. For example Nahdi et al. (1993), using R-11, evaluated ejectors having area ratios from 4.00 to 13.44, by using seven different ejector motive nozzle diameters. They found an optimal area ratio value of 9.87, for a compression ratio of 2.2 and a fixed primary pressure. Yapici et al. (2008) performed experiments with R-123 as the working fluid and concluded that the optimum area ratio increases almost linearly with the generator temperature. Yan and Cai (2012) performed experiments with a R-134a, 2 kW cooling capacity ejector refrigeration system in which the area ratio was varied from 2.74 to 5.37 by using different ejector motive nozzle diameters. They observed that the optimum performance is obtained at higher area ratio when the outlet pressure is fixed and the primary pressure increases. Ruangtrakoon et al. (2001), and Reddick et al. (2018), both using experimental steam ejector systems, observed that the critical pressure decreased with the increase of the area ratio at fixed primary pressure. Poirier et al. (2018), using R-134 refrigerant, investigated ejectors having three different area ratios from 4.2 to 8.5. The results showed that when the area ratio decreases from 8.5 to 4.2 the maximum of the entrainment ratio moves to the higher ejector outlet pressure, for fixed primary pressure. The reason for this is that the larger throat diameter (area ratio of 4.2) delivers higher primary mass flow rate, which results in the ejector attaining optimum operation at higher ejector outlet pressure.

All these results show that a given ejector can only perform at optimal performance over very narrow operating conditions. A small change in the operating conditions can require a different ejector design, particularly when ejector performance targets must be satisfied. This can easily occur when the downstream process is sensitive to the ejector output. The main reason for this is the inability of supersonic ejectors to change the mass flow rate of the primary motive steam while maintaining the entrainment ratio and outlet pressure at constant values. To solve this problem, Varga et al. (2011) introduced a new ejector design that uses a variable motive nozzle, where the mass flow rate of the motive steam changes with the motive nozzle throat diameter. The experiment was performed with a 5 kW capacity steam ejector and the variable geometry was achieved by applying a movable needle at the motive nozzle inlet. Yen et al. (2013) studied a solar supply refrigeration system with variable throat ejector design, also obtained by the use of a needle. They concluded that the variable throat ejector can consistently achieve optimal and stable performance under varying solar heat supply. Li et al. (2014, 2016) also experimentally evaluated the influence of a variable area motive nozzle ejector on a multi-evaporator refrigeration system. They showed that energy efficiency with a variable area motive nozzle could be improved by 12%. Motive nozzle needle position also proved to have a great impact on system performance by lowering power consumption. Pereira et al. (2014) experimentally verified the advantages of using an ejector with variable area motive nozzle compared to a fixed ejector geometry by using R-600a refrigerant. It was also shown that the larger the difference between the actual and design condenser pressure, the larger the benefits of using an ejector with variable area motive nozzle. Similar results were obtained by Varga et al. (2017), showing that adequate selection of the needle position achieved thermal COP improvements as high as 35%.

The reported research with variable throat area ejectors shows a promising step forward in optimal and stable ejector operation under varying heat supply and operating conditions, but most of the research was limited to few experimental tests. There is thus a need to further investigate this technology. This paper presents an experimental comparison of the performance of a needle-equipped motive nozzle with the performance of two constant area motive nozzles when installed into the same ejector body.

First, tests were completed with two constant area motive nozzles having throat areas of 12.8 mm^2 and 20.3 mm^2. Then, a needle-equipped motive nozzle, having a maximum throat area of 20.1 mm^2, was evaluated over approximately the same throat area range. In addition, two needle designs were fabricated and tested.

2. METHODS

This section will present the test bench, the ejector, the needles, the test procedure, and the instrumentation.

2.1. Test bench

The test bench was constructed at CanmetENERGY, in Varennes, Canada. It is made up of five major components: boiler, superheater, ejector, flash tank and atmospheric condenser. A 75 kW electric boiler, with a maximum pressure of 600 kPa, provides the main source of energy input to the test bench as well as the ejector primary inlet steam flow. The steam leaving the boiler splits into two branches. The main branch, which constitutes the primary inlet flow, passes through a 3 kW superheater and continues to the primary inlet port of the ejector. This main branch provides the thermal motive power to the ejector. The secondary branch leaves the boiler and is routed to the flash tank, where it provides the energy input to the secondary inlet steam of the ejector. This secondary branch simulates the cooling load. A more detailed description of the test bench is found in Reddick et al. (2018).

2.2. Ejector and needles

The ejector used, which is shown in Figure 1, was custom designed and fabricated for CanmetENERGY. It includes a motive nozzle located in the convergent of the ejector main body (this region can also be identified as the "secondary nozzle") and allows the displacement of a needle (not shown in Figure 1) within the throat of the motive nozzle. The throat diameter is identified D_{2p} in Figure 1. Three different motive nozzles were used. One with a throat diameter of 5.06 mm (throat area of 20.1 mm^2) was fabricated to allow needle movement within the throat, identified "New nozzle". Its dimensions are reported in Table 1, as well as the dimensions of the ejector body. The two other motive nozzles were fabricated for the work of Reddick et al. (2018), and are identified "Reddick-2018". They have throat diameters of 4.03 mm and 5.09 mm corresponding to throat areas of 12.8 mm^2 and 20.3 mm^2, respectively.

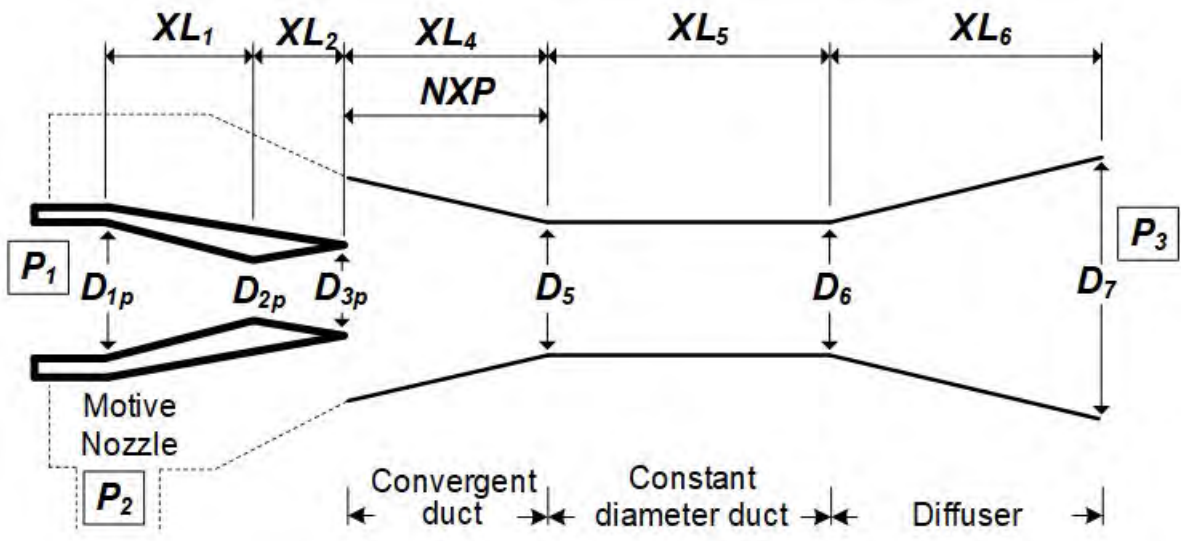

Figure 1: Ejector geometry

Table 1. Dimensions of the ejector

New nozzle		Ejector body	
Dimension	Value	Dimension	Value
XL_1 (mm)	65.94	*NXP* (mm)	30.00
XL_2 (mm)	16.61	XL_4 (mm)	30.00
D_{1p} (mm)	22.22	XL_5 (mm)	58.00
D_{2p} (mm)	5.06	XL_6 (mm)	139.24
D_{3p} (mm)	6.83	D_5, D_6 (mm)	9.50
conv. half-angle (°)	7.41	D_7 (mm)	28.97
div. half-angle (°)	3.00	conv. half-angle (°)	4.00
		diff. half-angle (°)	4.00

Two different needles were fabricated; they are identified as the Long-needle (shown in Figure 2a) and the Short-needle (shown in Figure 2b). They are moved by a screw mechanism and the position relative to the throat of the motive nozzle is measured with a caliper. The dimensions of the needles are reported in Table 2.

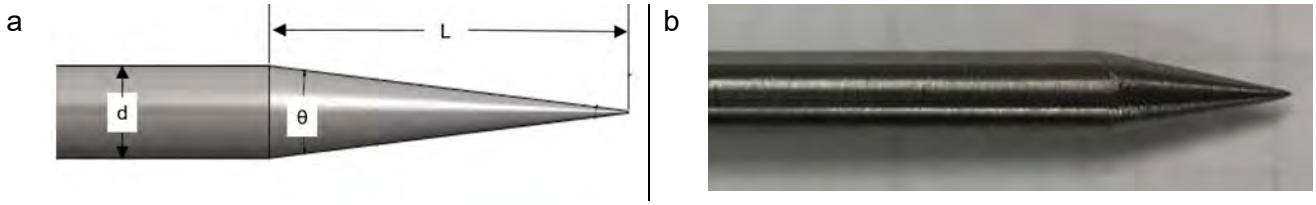

Figure 2: Needles (a: Long-needle, b: Short-needle)

Table 2: Dimensions of the needles

Dimension	Long-needle	Short-needle
d (mm)	6.35	3.95
L (mm)	33.88	9.34
θ (°)	10.5	22.0

An important ejector parameter is the area ratio (ψ). It is the area of the constant diameter duct portion of the ejector body (XL_5 in Figure 1) divided by the area of the motive nozzle throat ($\psi = A_{XL5}/A_t$), where $A_t = \pi \cdot (\varphi_{eq})^2/4$. When the needle is inside the throat of the motive nozzle, it blocks a fraction of the throat area. An equivalent throat diameter (φ_{eq}) can be calculated for the annular cross-section corresponding to the unobstructed throat area for fluid flow (that will in fact have the shape of a donut). Since the area of the constant diameter duct is fixed, ψ increases when the needle enters the throat of the motive nozzle. There is thus a correlation between φ_{eq} and ψ. The Reddick-2018 motive nozzles tested in this work, having φ_{eq} of 4.03 mm and 5.09 mm, equate to ψ of 5.6 and 3.5, respectively. The motive nozzle equipped with the needle was tested within this ψ range by varying the needle position.

2.3. Test procedure

All the tests that will be discussed in this paper were performed by increasing the ejector outlet pressure (P_3) stepwise, at fixed primary inlet pressure (P_1) and fixed secondary inlet pressure (P_2). The two important parameters extracted from the data are the entrainment ratio (ω), obtains from Equation 1, and the critical outlet pressure (P_{crit}) that corresponds to the outlet pressure (P_3) where ω starts to decrease (Chen et al., 2013). The entrainment ratio and critical pressure together characterize the ejector performance.

$$\omega = m_2/m_1 \qquad \text{Eq. (1)}$$

2.4. Instrumentation

The temperature, the pressure and the flow rate at the primary inlet, the secondary inlet and the outlet of the ejector are measured. The information on the instrumentation, including the accuracy, was provided by Reddick et al. (2018). A data acquisition system recorded the values of all instruments, at two second intervals. The data points presented in the figures in the next section are average values calculated over a one minute interval (the average of 30 consecutive measurements), taken during a period of steady state operation.

3. RESULTS AND DISCUSSION

The primary inlet flow rate (m_1) was measured for several positions of the Long-needle within the throat of the motive nozzle. During normal operation, the velocity at the throat is sonic and there is a possibility that the insertion of the needle into the throat region could lead to a disturbance of the flow stream that induces a decrease in the flow rate. Using the numbers in Table 2 and the position of the needle as determined by a caliper measurement, the percent free throat area and the equivalent diameter (φ_{eq}) were calculated. The results are reported in Figure 3, which show three sets of data. The curve identified "Theory" corresponds to the theoretical flow rate calculated at fixed inlet pressure and temperature with the method given by Poirier et al. (2018). The fixed inlet pressure and temperature (453 kPa/174°C in Figure 3a and 552 kPa/181°C in Figure 3b) correspond to the average values of the experimental points for the tests done with the motive nozzle equipped with the Long-needle. A discharge coefficient (C_d) of 0.98 was applied to these data (Poirier et al., 2018). The data identified "Reddick-2018" were obtained with the two motive nozzles used by Reddick et al. (2018), as described in section 2.2. Finally, the data identified "Long-needle" are the results obtained with the motive nozzle equipped with the Long-needle. Both Figures 3a and 3b show that the experimental and theoretical results are very close, which confirms that the measured positions of the needle are accurate and that the insertion of the Long-needle into the motive nozzle throat does not have a negative impact on the primary mass flow rate (m_1). Consequently, the insertion of a needle into the motive nozzle of an ejector system is an appropriate way to reduce the primary flow rate and thus reduce the thermal motive power input.

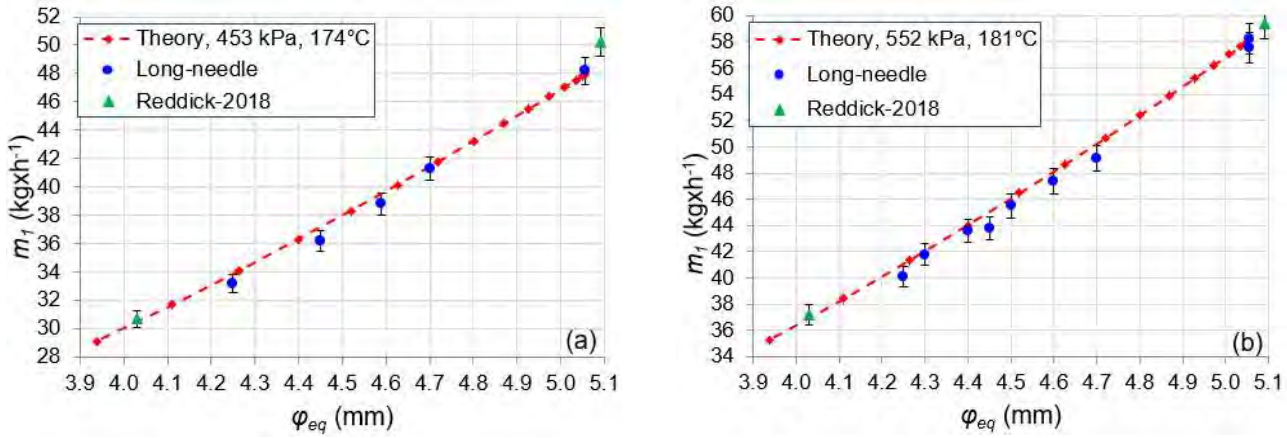

Figure 3: m_1 as a function of φ_{eq} (a: P_1 = 453 kPa, T_1 = 174°C, b: P_1 = 552 kPa, T_1 = 181°C)

Figure 4 shows ω as a function of P_3 for tests done with the three motive nozzles, for fixed P_1 and P_2. The results indicate a decrease in P_{crit} and an increase in ω when ψ increases, which is in agreement with previous works (e.g.: Poirier et al., 2018 and Reddick et al., 2018). This figure also shows that the new nozzle (Long-needle), which has ψ of 3.5 when the needle has not entered the throat of the motive nozzle, leads to ω and P_{crit} values comparable to the "Reddick-2018" nozzle of ψ of 3.5.

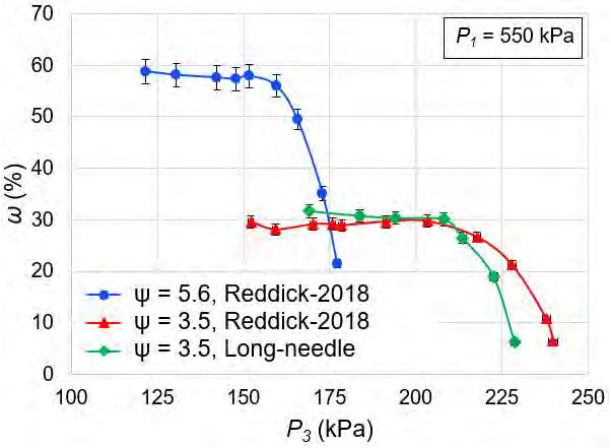

Figure 4: ω as a function of P_3 for three motive nozzles (P_2 is 92 kPa for blue curve and 98 kPa for red and green curves)

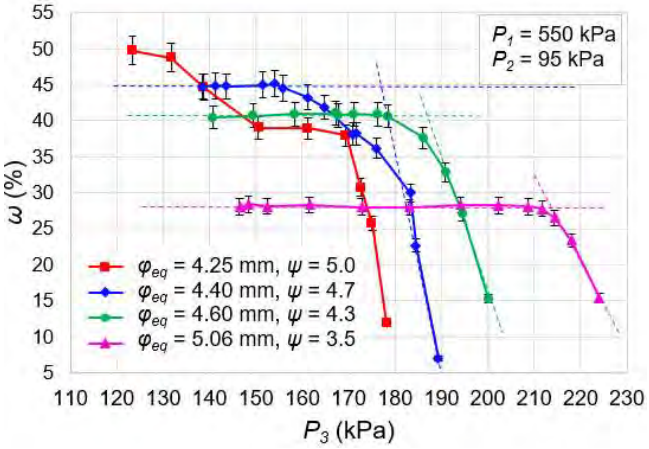

Figure 5: ω as a function of P_3 for different ψ obtained with the "New nozzle" equipped with the Long-needle (P_1 = 550 kPa, P_2 = 95 kPa)

Now, Figure 5 presents the results obtained with the progressive insertion of the long-needle into the throat of the motive nozzle, for fixed P_1 and P_2. As expected, ω increases and P_{crit} decreases with the decrease in φ_{eq}, and the associated increase in ψ. However, the results of Figure 5 show a detrimental effect of the needle for an important decrease of the effective throat area. Results observed when P_3 is increased stepwise at fixed P_1 and P_2 are a plateau of constant ω at low values of P_3 and a fast decrease of ω at $P_3 > P_{crit}$. In Figure 5, the results when the needle has not entered the throat of the motive nozzle (purple curve, φ_{eq} = 5.06 mm) are in agreement with the well documented results when testing an ejector. The two dotted lines, added to show both important trends in the course of the increase of P_3, meet at a P_3 value close to P_{crit}, which is the desired outcome. For φ_{eq} of 4.60 mm (83% free throat area), the results (green curve) are quite similar to those for φ_{eq} of 5.06 mm (100% free throat area); there is no detrimental effect of the needle at this point. Then, for φ_{eq} of 4.40 mm (76% free throat area), the results (blue curve) show a more fuzzy P_{crit}, and the P_3 value where the dotted lines meet is around 20 kPa higher than the P_3 value where ω starts to decrease. Finally, for φ_{eq} of 4.25 mm (71% free throat area), the results (red curve) show a two-plateau decrease of ω; the higher ω value being obtained at a much lower P_3, which constitutes a decrease in performance.

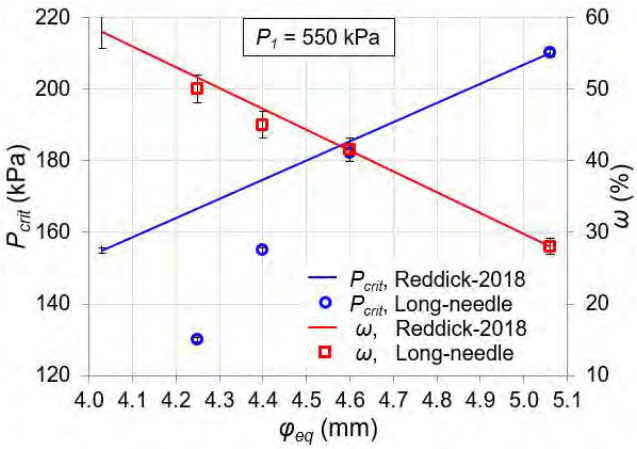

Figure 6: P_{crit} and ω versus φ_{eq} for Reddick-2018 nozzles and the New nozzle with the Long-needle

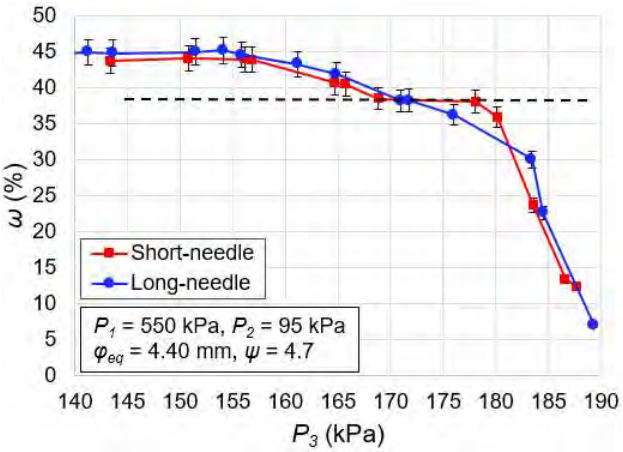

Figure 7: ω versus P_3 for the New nozzle with the Long- and the Short-needle at φ_{eq} = 4.40 mm

To better visualize the effect of the Long-needle, Figure 6 compares the evolution of ω and P_{crit} for motive nozzles of equal φ_{eq}, obtained without (Reddick-2018) and with (Long-needle) the use of the needle. There is roughly no difference for ω, but P_{crit} is lower for the case of the long-needle, and this

difference become quite significant when the distance of the needle inside the throat increases (i.e. for low φ_{eq}). Thus, this Long-needle allows the proper operation of the ejector for φ_{eq} between 5.06 mm and 4.60 mm. At that point, the long-needle is 11.80 mm inside the divergent of the motive nozzle, where the velocity is supersonic and increasing with the distance from the throat. The presence of the tip of the needle in the high supersonic location could be the reason of the detrimental effect observed at the lower φ_{eq} of 4.40 mm and 4.25 mm, for which the Long-needle distances inside the throat are 13.95 mm and 15.34 mm, respectively.

To investigate the impact of the presence of the needle inside the divergent of the motive nozzle, a second, shorter needle, was fabricated. The results of the first test done with this Short-needle are compared with the results obtained with the Long-needle at similar conditions, shown in Figure 7. The φ_{eq} and ψ are the same for both cases, but the distances inside the throat are 13.95 mm for the Long-needle and 5.93 mm for the Short-needle. Although the Short-needle also has a detrimental effect, there is an improvement of ω for P_3 of 178 kPa, which could be associated to a first critical pressure not seen in the test with the Long-needle. The tests with the Short-needle will be continued and the design of the needle will continue to be optimized.

4. CONCLUSIONS

The objective of this work was to investigate the performance impact using a needle inserted into the motive nozzle of an ejector for the control of the system capacity. The results showed that the insertion of a needle into the ejector motive nozzle is an appropriate design method for reducing the primary mass flow rate, and consequently for reducing the ejector motive power input. Experimentally evaluated ejector performance was similar for both the needle-equipped and the constant area nozzles, when the effective throat area was between 83% to 100% of the free throat area. However, when the effective throat area of the needle-equipped ejector was less than 76%, there was a decrease in the critical pressure compared to a constant throat area motive nozzle of equal area, which constitutes a loss in performance. A better design of the needle could decrease or eliminate this detrimental effect. This will be investigated in our future works.

ACKNOWLEDGEMENTS

The authors acknowledge Mr. Stéphane Günther and his colleagues of the Engineering and Technical Services Group at CanmetENERGY-Varennes for their invaluable contribution to the building of the test bench. The authors also acknowledge the support of the Office of Energy Research and Development (OERD), Natural Resources Canada.

NOMENCLATURE

A	area (mm^2)
D	diameter (mm), see Fig. 1
L	length of the conical needle tip (mm)
m	mass flow rate ($kg \times h^{-1}$)
NXP	Nozzle eXit Position
P	pressure (kPa)
T	temperature (°C)
XL	section length (mm), see Fig.1

Greek symbols

θ	angle of the needle (°)
φ	diameter (mm)
ψ	area ratio (-)
ω	Entrainment ratio (-)

Subscripts and superscripts

1	ejector primary inlet stream
2	ejector secondary inlet stream
3	ejector outlet stream
crit	critical
eq	equivalent
t	throat

REFERENCES

Ashrafi, O., Bashiri, H., Esmaeili, A., Sapoundjiev, H., Navarri P., 2018. Ejector integration for the cost effective design of the Selexol™ process. Energy 162, 380-392.

Besagni, G., Mereu, R., Inzoli, F., 2016. Ejector refrigeration: a comprehensive review. Renew. Sustain. Energy Rev. 53, 373-407.

Chen, X., Omer, S., Worall, M., Riffat, S., 2013. Recent developments in ejector refrigeration technologies. Renew. Sustain. Energy Rev. 19, 629-651.

Li, C., Li, Y., Cai, W., Hu, Y., Chen, H., Yan, J., 2014. Analysis on performance characteristics of ejector with variable area-ratio for multi-evaporator refrigeration system based on experimental data. Applied Thermal Engineering 68, 125-132.

Li, C., Yan, J., Li, Y., Cai, W., Lin, C., Chen, H., 2016. Experimental study on a multi-evaporator refrigeration system with variable area ratio ejector. Applied Thermal Engineering 102, 196–203.

Little, A.B., Garimella, S., 2011. A review of ejector technology for refrigeration applications. Int. J. Air Cond. Refrig. 19, 1-15.

Nahdi, E., Champoussin, J., Hostache, G., Chéron, J., 1993. Les paramètres géométriques optima d'un éjecto-compresseur frigorifique. Int. J. Refrigeration 16(1), 67-72.

Pereira P.R., Varga S., Soares J., Oliveira A.C., Lopes A.M., Almeida F.G., Carneiro J.F., 2014. Experimental results with a variable geometry ejector using R600a as working fluid. Int. J. Refrigeration 46, 77-85.

Poirier, M., Giguère, D., Sapoundjiev, H., 2018. Experimental parametric investigation of vapor ejector for refrigeration applications. Energy 162, 1287-1300.

Reddick, C., Sorin, M., Rheault, F., 2014. Energy savings in CO_2 (carbon dioxide) capture using ejectors for waste heat upgrading. Energy 65, 200–208.

Reddick, C., Sorin, M., Sapoundjiev, H., Aidoun, Z., 2016. Carbon capture simulation using ejectors for waste heat upgrading. Energy 100, 251–261.

Reddick, C., Sorin, M., Sapoundjiev, H., Aidoun, Z., 2018. Effect of a mixture of carbon dioxide and steam on ejector performance: an experimental parametric investigation. Exp. Therm. Fluid Sci. 92, 353-365.

Ruangtrakoon, N., Aphornratana, S., Sriveerakul, T., 2011. Experimental studies of a steam jet refrigeration cycle: effect of the primary nozzle geometries to system performance. Exp. Therm. Fluid Sci. 35, 676-683.

Varga, S., Oliveira, A.C., Ma, X., Omer, S.A., Zhang, W., Riffat, S.B., 2011. Experimental and numerical analysis of a variable area ratio steam ejector. Int. J. Refrigeration 34(7), 1668-1675.

Varga, S., Oliveira, A.C., Palmero-Marrero, A., Vrba, J., 2017. Preliminary experimental results with a solar driven ejector air conditioner in Portugal. Renewable Energy 109, 83-92.

Yan, J., Cai, W., 2012. Area ratio effects to the performance of air-cooled ejector refrigeration cycle with R-134a refrigerant. Energy Convers. Manag. 53, 240-246.

Yapici, R., Ersoy, H.K., Aktoprakoglu, A., Halkaci, H.S., Yigit, O., 2008. Experimental determination of the optimum performance of ejector refrigeration system depending on ejector area ratio. Int. J. Refrigeration 31(7), 1183-1189.

Yen, R.H., Huang, B.J., Chen, C.Y., Shiu, T.Y., Cheng, C.W., Chen, S.S., Shestopalov, K., 2013. Performance optimization for a variable throat ejector in a solar refrigeration system. Int. J. Refrigeration 36, 1512-1520.

Manuscript ID: 1123
DOI: 10.18462/iir.icr.2019.1123

Design optimization of high performance, reduced charge condensers with novel tube shapes

James TANCABEL[(a)], Vikrant AUTE*[(a)], Jiazhen LING[(a)], Reinhard RADERMACHER[(a)]

[(a)]Center for Environmental Energy Engineering
Department of Mechanical Engineering, University of Maryland
College Park, Maryland 20742 United States of America
*Corresponding Author: Email: vikrant@umd.edu; Tel: +1-301-405-8726

ABSTRACT

Air-to-refrigerant heat exchangers (HXs) are vital components of HVAC&R systems. Such HXs often use extended surfaces (fins) to overcome large airside thermal resistance despite fins' intrinsic increased pressure drop, material cost, and fouling potential. However, advancements in Computational Fluid Dynamics (CFD), Finite Element Analysis (FEA), and optimization algorithms have led to a paradigm shift to eliminate fins through primary heat transfer surface optimization. In this work, automated CFD and FEA simulations and approximation-assisted optimization are used to design novel condensers with shape-optimized tubes that are lighter, more compact, and outperform current state-of-the-art tube-fin condensers without compromising tube integrity. The optimal condensers deliver similar capacity with 20% reductions in airside pressure drop and envelope volume. The novel designs also feature more than 20% charge reduction which can enable lower-GWP A2L refrigerants.
Keywords: air-cooled exchanger, condenser, heat exchanger, optimization

1. INTRODUCTION

Air-to-refrigerant heat exchangers (HXs) serve as critical components of HVAC&R systems, and, as such, have been the topic of considerable research. Compact HXs, i.e., HXs with characteristic diameters smaller than 6.0 mm (Kays and London, 1984), are of particular interest since their large heat transfer area to volume ratio allow for significant size and packaging reductions. Conventional practice utilizes secondary surfaces (fins) to achieve high performance, compact HXs. This is especially the case for HXs featuring small characteristic diameter tubes, which by themselves do not have adequate primary heat transfer area to achieve the required thermal resistance.

However, fins are unattractive due to increased hydraulic penalties, fouling/frosting potential, and material consumption. Recent work by Bacellar et al. (2017a) argued that as tube diameter decreases, finless surfaces achieve higher heat transfer coefficients for lower hydraulic losses compared to finned surfaces. The use and potential performance improvements which can be realized by finless HXs with small diameter round tubes has been well-studied (Paitoonsurikarn et al., 2000; Saji et al., 2001; Kasagi et al., 2003; Chen et al., 2016).

More recently, Bacellar et al. (2017a, 2017b) argued that conventional HX design practices for improving performance should be renovated in line with modern computational and manufacturing capabilities. The authors presented a comprehensive multi-scale analysis and shape and topology optimization framework which explores the potential improvements which could be realized by HXs featuring novel finless tube shapes with small characteristic diameters. The authors experimentally validated an additively manufactured proof-of-concept optimal design, showing the viability of shape optimization and additive manufacturing.

In a related work, Radermacher et al. (2017) indicated that shape-optimized tubes do not possess the same level of structural integrity as conventional round tubes. Thus, detailed and computationally expensive structural analyses must be carried out for each candidate geometry to verify whether the tube shape meets pressure-holding requirements. Further, Tancabel et al. (2018) noted that no air-to-refrigerant HX shape and topology optimization studies in literature explicitly consider tube structural integrity, calling into question whether an optimal design is feasible from a pressure-holding standpoint.

This paper presents the development of a HX optimization framework featuring multi-scale and multi-physics analyses and tube-level shape and topology optimization. The methodology was applied to design a finless condenser which could serve as a drop-in replacement in a state-of-the-art 1.5TR air-conditioning system. Comprehensive numerical verifications were performed and are discussed in detail. The future outlook of this integrated optimization framework is also discussed.

2. METHODOLOGY

2.1 Design & Optimization Framework

Fig. 1 presents the numerical HX optimization framework, which consists of an Approximation-Assisted Optimization (AAO) involving automated CFD (Abdelaziz et al., 2010) and FEA simulations, Kriging metamodeling (Cressie, 1993), and optimization with Multi-Objective Genetic Algorithm (MOGA) (Deb, 2001).

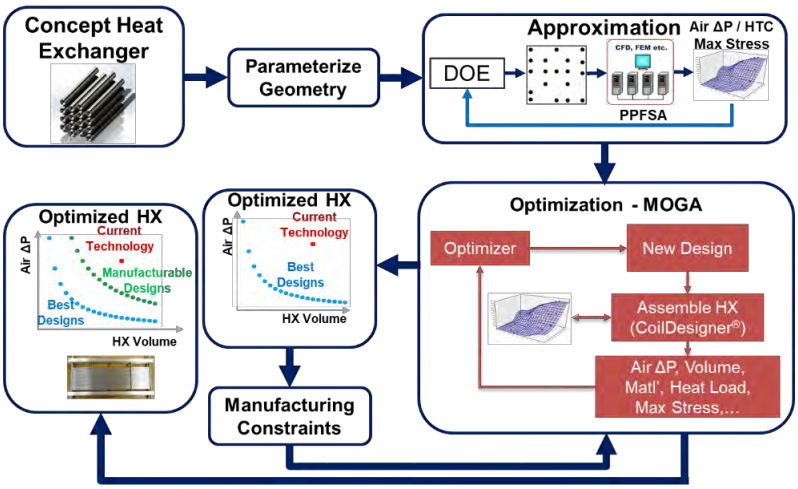

Figure 1: Optimization framework

2.2 Problem Description

This research considers air-to-refrigerant HXs in cross-flow configuration. All HXs models consider the following assumptions: (i) frontal air velocity is uniformly distributed and normal to the HX face area; (ii) fully-developed refrigerant-side flow without maldistribution. The airside thermal-hydraulic performance is simulated with CFD, while FEA simulations determine tube-level mechanical performance. The refrigerant-side thermal-hydraulic performance is evaluated with existing correlations for single- and two-phase flow in small channels. The optimization framework is applied to design of novel, finless air-to-R410A condenser which could serve as a drop-in replacement in a state-of-the-art 1.5TR air-conditioning system. Fig. 2 presents schematics of a generic finless HX with shape-optimized tubes and a generic multi-pass tube-fin condenser which is representative of the baseline condenser for this study.

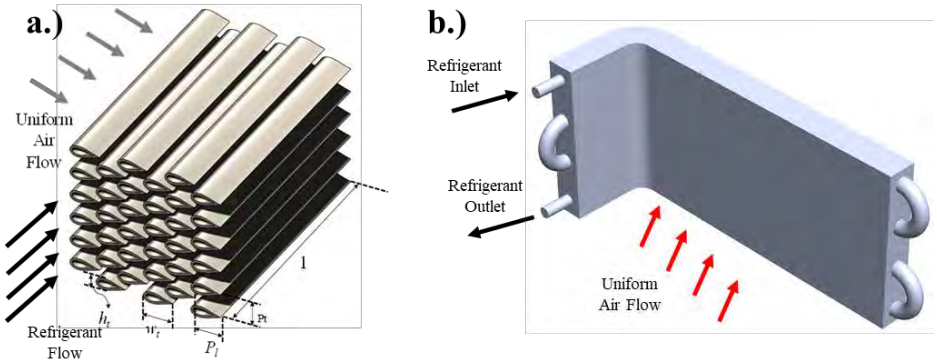

Figure 2: a.) Generic HX with shape optimized tubes; b.) Generic multi-pass tube-fin condenser

2.1.1 Tube Shape Parameterization

The variable tube shapes are represented by fourth-order Non-Uniform Rational B-Spline (NURBS) curves (Tiller, 1995) as shown in Fig. 3. The NURBS curve (C) is defined as given in Eq. (1). The control point coordinates ($\mathbf{x}_i$) are normalized between 0 and 1 with the leading edge (le) and trailing edge (te) points fixed at (0,0) and (1,0), respectively. The shape design variables (u_s) are defined as the location of the three middle control points. The control point x-coordinates are bounded to equally-spaced slices of the domain to prevent self-intersecting curves.

$$C(u_s) = \sum_{i=0}^{4} R_{i,4}(u_s)\mathbf{x_i}; \quad R_{i,4} = \text{Basis functions}; \quad \mathbf{x_i} = \text{Control Points}; \quad 0 \le u_s \le 1 \qquad \text{Eq. (1)}$$

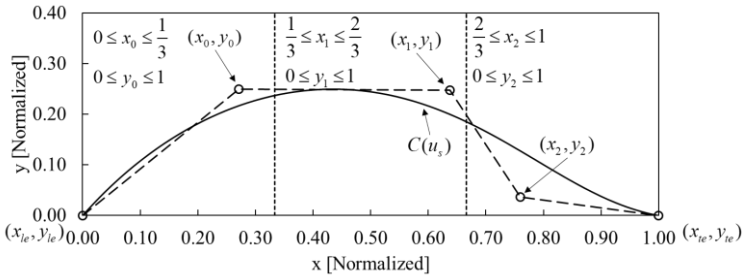

Figure 3: Tube shape parameterization using NURBS

2.3 Parallel Parameterized Fluid & Structural Analysis

Manually simulating a full Design of Experiments (DoE) in CFD and FEA is computationally expensive and impractical. To this end, Abdelaziz et al. (2010) presented a methodology termed Parallel Parameterized CFD (PPCFD) to automate CFD simulations. The framework allowed for shape and topology changes at runtime, which, compared to manual simulations, achieved over 90% engineering and computational time savings.
Following the same motivation, a new framework termed Parallel Parameterized Fluid & Structural Analysis (PPFSA) was developed. This framework combines PPCFD with automated static structural FEA simulations, allowing researchers to conduct multi-physics analyses on HXs with any tube shape. Input data is read by an external C# code, which generates batch and journal files for creating model geometries, running simulations, and exporting results. The C# code reads the output files and post-processes them into text files containing all CFD and FEA results. All geometry creation and simulation is completely automated.
All present analyses utilize ANSYS® 18.0. Specifically, the CFD models utilize Gambit® 2.4.6 for geometry and meshing and Fluent 18.0 for simulation. FEA models utilize Gambit® 2.4.6 for geometry creation and ANSYS® Mechanical 18.0 for meshing and simulation. Fig 4 presents a flowchart for the automated structural analysis simulations. The reader is referred to Abdelaziz et al. (2010) for additional information on PPCFD.

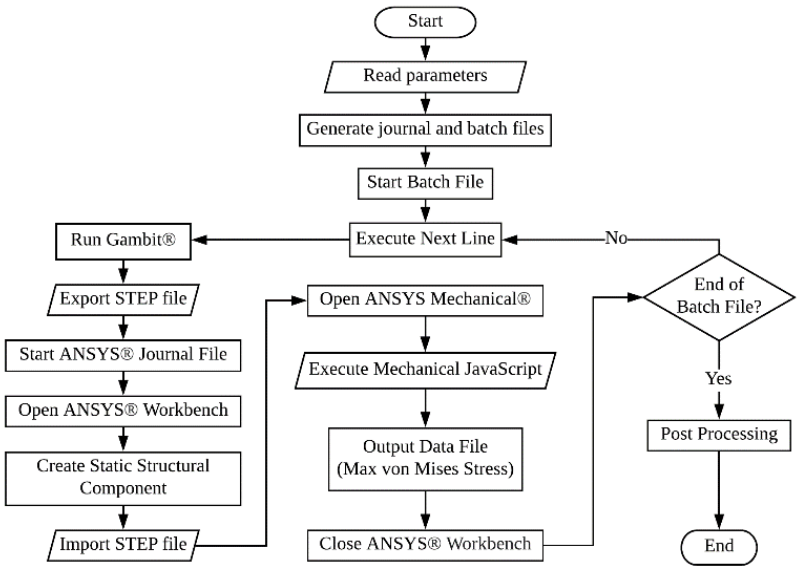

Figure 4: Automated structural analysis flowchart

2.3.1 CFD modeling

Fig. 5 presents a sample CFD computational domain, which is a 2D HX cross-section segment where all end effects are considered negligible. A fine map scheme mesh with growing layers (growth ratio = 1.2) is employed in the near-wall region to capture boundary layer physics. A pave mesh scheme with average element size equal to the last row of the boundary layer is utilized for the core of the computational domain.

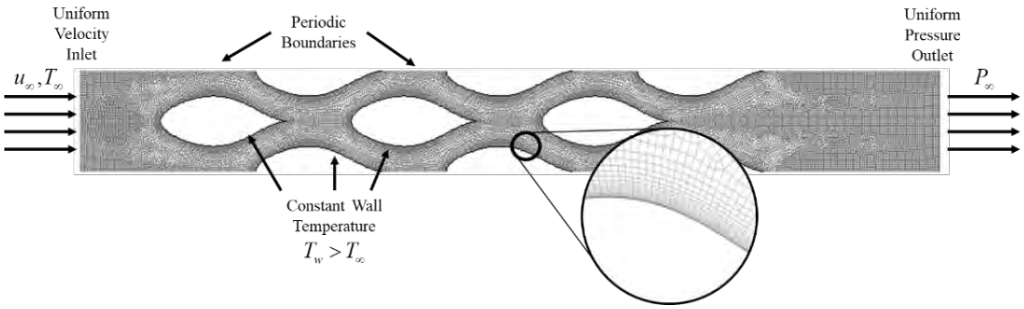

Figure 5: Sample CFD computational domain & boundary conditions

A uniform temperature (300 K) and velocity inlet is applied at the left boundary, and the right boundary is a constant atmospheric pressure outlet. The tube walls are kept at constant temperature (340 K). The upper and lower boundaries are periodic. The model assumes dry air properties where density is computed using the ideal gas model and all other thermophysical properties are polynomial curve fits of temperature. Turbulence is computed with the realizable k-ε (RKE) model (Shih et al., 1995). The convergence criteria are set to maximum residuals of 10^{-5} for continuity and momentum, 10^{-6} for energy, and 10^{-3} for turbulence. If the simulation stabilizes but does not converge as per the above criteria, the simulation is considered converged if the standard deviation of the final 100 iterations is less than 0.5% of the average of the same 100 iterations. The CFD simulations determine airside thermal-hydraulic performance. Thus, it is unnecessary to consider other thermal resistances (e.g., tube wall). To this end, the UA-Log Mean Temperature Difference (UA-LMTD) method is used for CFD data reduction. The reader is referred Bacellar et al. (2014) for more detailed analysis.

2.3.2 CFD modeling uncertainty analysis

The Grid Convergence Index (GCI) method (Roache, 1997, ASME, 2009; Oberkampf and Roy, 2010; Roy and Oberkampf, 2011) is a standard method for quantifying model uncertainty due to grid resolution for a minimum of three mesh sizes. We quantify CFD uncertainty for boundary designs for three grid sizes using a constant refinement ratio (r = 1.3). The GCI is computed as Eq. (2) based on its absolute relative difference between two grid sizes. The recommended factor of safety is 3.0 (Roach, 1997). To avoid unnecessary uncertainty estimations, Roy and Oberkampf (2011) recommended that the effective order of accuracy (p^{**}) be bounded by a minimum of 0.5 and the formal spatial order of accuracy (p) when the observed order of accuracy (p^{*}) deviates from the formal value by more than 10%. Fig. 6 presents the GCI analysis in this study.

$$GCI_\beta = \frac{F_s \cdot e_\beta^{21}}{r^{p^{**}} - 1}; \quad p^{**} = \min\left\{\max\left[p^{*}; 0.5\right]; p\right\}; \quad p = 2 \qquad \text{Eq. (2)}$$

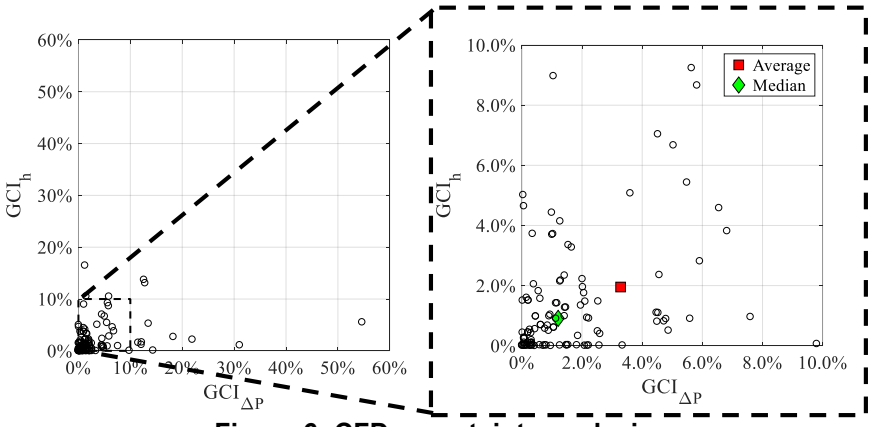

Figure 6: CFD uncertainty analysis

2.3.3 FEA modeling

Fig. 7a presents a sample FEA geometry, which is a 2D, plane strain cross-section of a single tube geometry with a structured quad mesh with constant element edge size. A uniform static pressure is applied along the internal channel edge and can be set to any pressure of interest. Previous experience with non-round tubes indicated that the tube critical point is typically the x-axis point with minimum membrane thickness. A fixed support is applied to the end with larger membrane thickness, while a free x-displacement, fixed y-

displacement support is applied at the end with smaller membrane thickness. These boundary conditions do not restrict the tube from failing at only the x-axis point with minimum membrane thickness.
The FEA simulations determine tube-level mechanical performance. Thus, the metric of interest is maximum von Mises stress, which can be utilized to select an appropriate material for the given application.

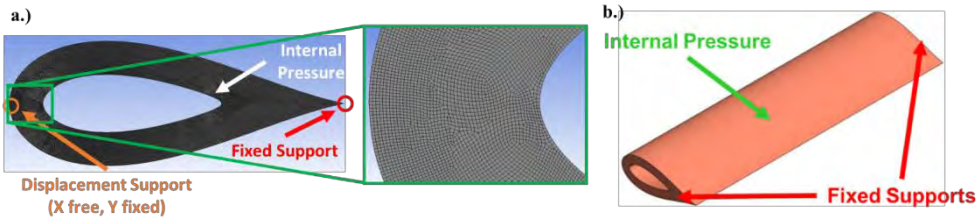

Figure 7: Sample FEA model & boundary conditions: a.) 2D model; b.) 3D model

2.3.4 FEA modeling verification

The plane strain assumption allows the use of simpler 2D FEA models rather than detailed, computationally expensive 3D FEA models. This assumption should hold since tube length is orders of magnitude larger than tube height and width. This assumption was verified by simulating 2D and 3D FEA models of four proprietary tube shapes (Private communications, 2018). Figs. 7a and 7b present descriptions of the 2D and 3D FEA models, respectively. Table 1 contains verification data and clearly shows that a 2D FEA model is appropriate.

Table 1. Plane strain verification

Geometry	Internal Pressure	Max σ_{VM} (2D)	Max σ_{VM} (3D)	Percent Diff.
-	MPa	MPa	MPa	[-]
NTHX1	6.00	310.20	310.0	+0.06%
NTHX1-1P-A		82.17	81.3	+1.08%
NTHX1-1P-C		65.20	65.0	+0.31%
NTHX1-2P-A		26.84	27.0	-0.60%

2.4 Metamodeling

To save computational time, CFD- and FEA-based metamodels were developed. A 5000-design Latin Hypercube Sampling (LHS) DoE (McKay et al., 1979) was generated and simulated using the PPFSA framework. Kriging metamodels (Cressie, 1993) of airside heat transfer coefficient, airside pressure drop, and maximum von Mises stress were developed using 2673 samples. Metamodel verification was conducted by comparing metamodel responses to the results of CFD and FEA simulations for 544 random samples. Metamodel accuracy was measured using the Metamodel Acceptance Score (MAS) (Hamad, 2006), which gives the percentage of predicted random responses ($\hat{y}_i$) whose absolute relative error (e_i) compared to the simulated response (y_i) is below an established threshold (e_{th} = 10%). The metamodel is considered acceptable if the following holds: $MAS_{th} \geq 1 - e_{th}$. Fig. 8 presents the metamodel verification results.

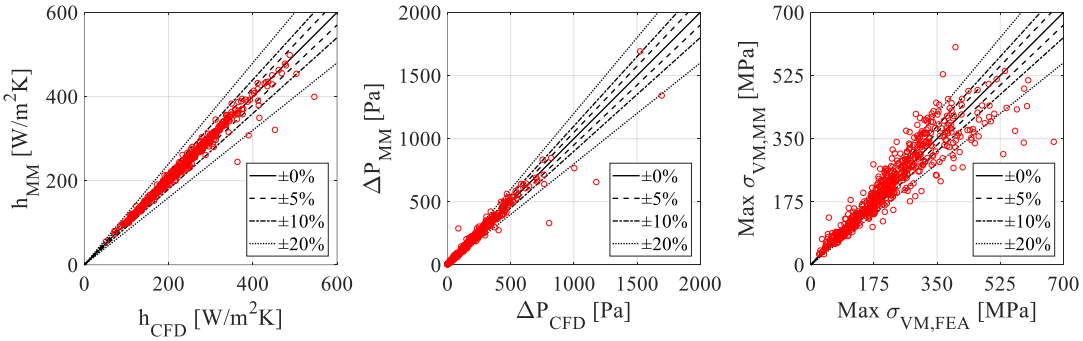

Figure 8: Metamodel verification

2.5 Multi-Objective Optimization

HX optimization studies have gained popularity due to recent improvements in computational tools such as CFD and FEA packages and optimization algorithms such as MOGA (used herein). This work combines the shape and topology optimization method of Bacellar et al. (2017a) with the new PPFSA framework to achieve novel HX designs. The optimizer models full HXs with CoilDesigner® (Jiang et al., 2006), an in-house code for

air-to-fluid HX modeling and simulation. Airside thermal-hydraulic performance is computed using the constructed metamodels, and refrigerant-side performance is modeled using empirical correlations and correction factors. Tube mechanical performance is computed using the von Mises stress metamodel. This allows the optimizer to model full-sized HXs with novel tube shapes that achieve a desired pressure-holding capability. The optimizer output includes two files: (i) one containing all simulated HX models and (ii) another containing all Pareto-optimal designs. Following the optimization, all optimal designs must be simulated in CFD and FEA to further verify the metamodel prediction accuracy.

3. OPTIMIZATION RESULTS

3.1 Optimization Problem Definition

A multi-objective optimization problem with two objectives, minimizing airside pressure drop and minimizing HX envelope volume, was considered. The goal was to design a finless condenser with novel tube shapes which could serve as a drop-in replacement in a state-of-the-art 1.5TR air-conditioning system. Two optimization problems were investigated as shown in Table 2. The tube thickness-to-height ratio was fixed for all optimizations, and all flow rates were kept the same as the baseline. The airside pressure drop was allowed to be at most double that of the baseline since the baseline pressure drop was quite restrictive. Further, the von Mises stress constraint includes a factor of safety on ultimate strength to allow the flexibility to consider many different pressure holding capabilities (Private communications, 2018). An Aluminum alloy was considered for analysis based on prior experience (Private communications, 2018).

Table 2. Optimization Problem Definition

Optimization	I	II
Objectives	$\min \Delta P_{air}; \min V_{HX}$	$\min \Delta P_{air}; \min V_{HX}$
Constraints	$\dot{Q}_{BL} \le \dot{Q} \le 1.1 \cdot \dot{Q}_{BL}; \quad 0.5 \le \frac{H_{HX}}{L_{HX}} \le 2.0$ $\Delta P_{air} \le 2.0 \cdot \Delta P_{air,BL}; \quad \Delta P_{Ref} \le \Delta P_{Ref,BL}$ $V_{HX} \le 0.8 \cdot V_{HX,BL}; \quad \sigma_{VM} \le \frac{S_{ult}}{F_s}$	$\dot{Q}_{BL} \le \dot{Q} \le 1.1 \cdot \dot{Q}_{BL}; \quad 0.5 \le \frac{H_{HX}}{L_{HX}} \le 2.0$ $\Delta P_{air} \le 2.0 \cdot \Delta P_{air,BL}; \quad \Delta P_{Ref} \le \Delta P_{Ref,BL}$ $V_{HX} \le 0.8 \cdot V_{HX,BL}; \quad \sigma_{VM} \le \frac{S_{ult}}{F_s}$ $FA \le FA_{BL}$

3.2 Optimization Results & Discussion

Fig. 9 presents the results of the optimization problem colored by face area and internal volume, respectively. The designs are normalized with respect to the baseline for all performance metrics. It is clear that the optimal designs can achieve 20% reductions in both airside pressure drop and envelope volume. Further, since the optimizer was allowed to probe designs with larger airside pressure drops than the baseline, some of the optimal could achieve envelope volume reductions of ~75% for the same baseline airside pressure drop. Additionally, all optimal designs achieve at least 30% internal volume reduction, which helps facilitate the use of A2L refrigerants. It must also be noted that the optimal designs can also achieve significant face area reductions, which benefits HX manufacturers in that smaller face areas result in smaller system footprints (Private communications, 2018).

Fig. 9 also include a sample optimal tube shape. Overall, the tube shapes tend to be more round to match the excellent pressure-holding capabilities of round tubes. It should be noted that not all optimal designs are manufacturable using today's technology.

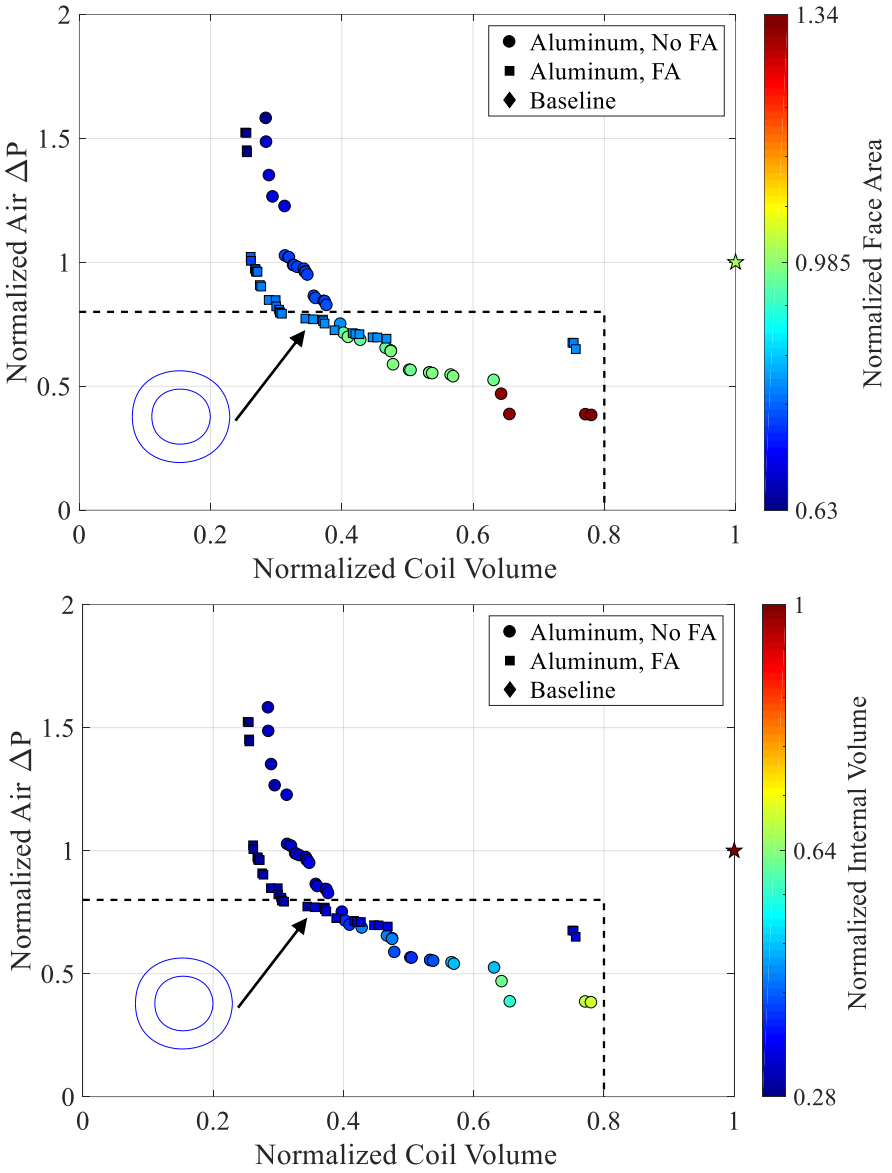

Figure 9: Optimization results colored by (top) face area; (bottom) internal volume

4. CONCLUSIONS

This paper presents the development and application of a novel multi-scale, multi-physics analysis and shape and topology optimization method for air-to-refrigerant HXs. Automated CFD and FEA simulations are utilized to develop metamodels which approximate the thermal-hydraulic and mechanical performance of tube shapes, and a MOGA uses the metamodels to generate optimal designs. The methodology was applied to design condensers for drop-in replacement in a 1.5TR air-conditioning system. The optimal designs indicated potential for more than 20% airside pressure drop reduction and 50% envelope volume reduction. Further, the optimal designs deliver over 40% reduction in internal volume, which helps facilitate the use of A2L refrigerants. The proposed methodology results in greater than 90% savings in engineering and computational time. Future work includes prototyping and performance validation of the novel heat exchanger designs.

ACKNOWLEDGEMENTS

This work was supported by the United States Department of Energy Grant Number DE-EE0008221 and the Modeling and Optimization Consortium at the University of Maryland.

NOMENCLATURE

e	Absolute relative error	(–)	T	Temperature	(K)
FA	Face area	(m^2)	u	Fluid velocity	(ms^{-1})

F_s	Factor of safety	(–)	V_{HX}	HX envelope volume	(m^3)
GCI	Grid convergence index	(–)	x_i , y_i,	Control point coordinates	(–)
h	Airside heat transfer coefficient	($W.m^{-2}.K^{-1}$)	ΔP_{air}	Airside pressure drop	(Pa)
H_{HX}	HX height	(m)	ΔP_{ref}	Refrigerant pressure drop	(Pa)
L_{HX}	HX length	(m)	*Greek Letters*		
P	Pressure	(Pa)			
$\dot{Q}$	Heat transfer rate	(W)	β	Metric of interest	(–)
S_{ult}	Ultimate strength	(MPa)	σ_{VM}	von Mises Stress	(MPa)

REFERENCES

Abdelaziz, O., Aute, V., Azarm, S., & Radermacher, R., 2010. Approximation-assisted optimization for novel compact heat exchanger designs. *HVAC&R Res.*, *16*(5), 707-728.

ASME, 2009. Standard for Verification and Validation in Computational Fluid Dynamics and Heat Transfer, *ASME V&V 20-2009,* American Society of Mechanical Engineers, New York, 89p.

Bacellar, D., Aute, V., and Radermacher, R, 2014. CFD-Based Correlation Development for Air Side Performance of Finned and Finless Tube Heat Exchangers with Small Diameter Tubes. *Proceedings of the 14th International Refrigeration and Air Conditioning Conference*, Purdue University, West Lafayette, Indiana, USA, Paper 1410.

Bacellar, D., Aute, V., Huang, Z., & Radermacher, R., 2017a. Design optimization and validation of high-performance heat exchangers using approximation assisted optimization and additive manufacturing. *Sci. Technol. Built En.*, *23*(6), 896-911.

Bacellar, D., Huang, Z., Tancabel, J., Aute, V., & Radermacher, R., 2017b. Mutli-scale analysis, shape optimization and experimental validation of novel air-to-refrigerant heat exchangers. *Proceedings of the 9th World Conference on Experimental Heat Transfer, Fluid Mechanics, and Thermodynamics*. Iguazu Falls, Brazil.

Chen, H.T., Lin, Y.S., Chen, P. C., & Chang, J.R., 2016. Numerical and experimental study of natural convection heat transfer characteristics for vertical plate fin and tube heat exchangers with various tube diameters. *Int. J. Heat Mass Tran.*, *100*, 320-331.

Cressie, N., 1993. *Statistics for spatial data*. John Wiley & Sons, New York, 900p.

Deb, K. 2001. *Multi-objective optimization using evolutionary algorithms*. John Wiley & Sons. New York, 515p.

Hamad, H., 2006. A New Metric for Measuring Metamodels Quality-of-Fit for Deterministic Simulations. *Proceedings of the 38th Conference on Winter Simulation*, Monterey, California, USA, 882-888.

Jiang, H., Aute, V., & Radermacher, R., 2006. CoilDesigner: A General Purpose Simulation and Design Tool for Air-to-Refrigerant Heat Exchangers. *Int. J. Heat Mass Tran.*, *29*(4), 601-610.

Kasagi, N., Suzuki, Y., Shikazono, N., & Oku, T., 2003. Optimal design and assessment of high performance micro bare-tube heat exchangers. *Proceedings of the 4th International Conference Compact Heat Exchangers and Enhancement Technologies for the Process Industries*, Crete, Greece, 241-246.

Kays, W. & London, A., 1984. *Compact Heat Exchangers*, McGraw-Hill, New York, 335p.

McKay, M.D., Beckman, R.J., & Conover, W.J., 1979. Comparison of Three Methods for Selecting Values of Input Variables in the Analysis of Output from a Computer Code. *Technometrics*, *21*(2), 239-245.

Oberkampf, W. & Roy, C., 2010. *Verification and Validation in Scientific Computing*, Cambridge University Press, Cambridge, 790p.

Private communications. 2018.

Radermacher, R., Bacellar, D., Aute, V., Huang, Z., Hwang, Y., Ling, J., Muehlbauer, J., Tancabel, J., Abdelaziz, O., & Zhang, M., 2017. *Miniaturized Air-to-Refrigerant Heat Exchangers*. United States Department of Energy Report DOE-UMD-EE-00006114. doi:10.2172/1358252.

Roache, P.J., 1997. Quantification of Uncertainty in Computational Fluid Dynamics. *Annu. Rev. Fluid Mech*, *29*(1), 123-160.

Roy, C. & Oberkampf, W., 2011. A Comprehensive Framework for Verification, Validation, and Uncertainty Quantification in Scientific Computing. *Comp. Meth. Appl. in Appl. Mech. and Eng.*, 200(25), 2131–2144.

Saji, N., Nagai, S., Tsuchiya, K., Asakura, H., & Obata, M., 2001. Development of a compact laminar flow heat exchanger with stainless steel micro-tubes. *Physica C*, *354*(1-4), 148-151.

Shih, T.H., Zhu, J. & Lumley, J.L., 1995. A new Reynolds stress algebraic equation model. *Comp. Meth. Appl. in Appl. Mech. and Eng.*, *125*(1-4), 287-302.

Tancabel, J., Aute, V., & Radermacher, R., 2018. Review of Shape and Topology Optimization for Design of Air-to-Refrigerant Heat Exchangers. *Proceedings of the 17th International Refrigeration and Air Conditioning Conference*, Purdue University, West Lafayette, Indiana, USA, Paper 1965.

Tiller, P. L., 1995. *The NURBS Book*. Springer, New York, 628p.

Manuscript ID: 1143
DOI: 10.18462/iir.icr.2019.1143

Steps toward standardized calculations of LCCP

Paul DE LARMINAT

Johnson Controls Industries,
Carquefou, 44473, France, paul.delarminat@jci.com

ABSTRACT

TEWI or LCCP indicators provide evaluations of total direct and indirect greenhouse gasses emissions from cooling or HP (heat pump) systems. Yet, the results are awkward to use due to the variety of systems by capacity, technology, and operating conditions. This paper proposes steps toward standardized TEWI calculations. Many cooling and HP systems are subject to global or regional standards, defining typical year-round operating conditions and rules for performance evaluation. Per the method proposed, input values for TEWI calculations are evaluated at standard operating conditions, with performance also evaluated per relevant standards. Results are presented as "specific TEWI", in reference to the standards. The end result is simply the number of kilos of CO_2 equivalent emitted over the life time, per kWh of cooling energy at standard operating conditions. Comparisons between systems are thereby made much easier, which should allow TEWI to become a more practical tool for decision making.
Keywords: TEWI, LCCP, Standards, Energy Efficiency.

1. INTRODUCTION

Due to concerns about global warming, there is increasing will to reduce the emissions of GHG's (Green House Gasses). RACHP (Refrigeration, Air Conditioning and Heat Pumps) systems use refrigerant fluids that may have a significant GWP (Global Warming Potential). For these systems, GHG emissions are of two kinds, "direct" and "indirect". The "direct" emissions are caused by leakage of refrigerant to atmosphere. But the operation of the systems also consumes energy. The energy consumption is a major concern on its own because of cost, energy independence of countries etc. But the energy consumed also causes emissions of CO_2, referred to as "indirect". Over the life time, the indirect emissions are much larger than the direct ones, and can account for up to 98% of the total emissions.

In a recent past, there has been a major focus on reducing the GWP of fluids, to tackle the "direct" part of GHG emissions, through International regulations such as the EU "F-gas" regulation, or the Kigali amendment to the Montreal protocol. But these GWP reductions must not result in higher energy consumptions that could end up increasing the total GHG emissions instead of reducing them, which would be counterproductive to the underlying intention.

The "TEWI" (Total Equivalent Warming Impact) methodology has long been known to aggregate the direct and indirect emissions into a single indicator. It is used to calculate the total CO_2 equivalent emissions of a system over its life time. Yet this indicator is still little used, because of its relative complexity, and also because the results are not easily compared between different systems. This paper is introducing a methodology that could enable a more "standardized" method to calculate a TEWI, by linking this calculation to existing energy efficiency standards. The results are presented as "specific TEWI", reflecting the equivalent CO_2 emissions per kWh of cooling capacity generated, ending up with a single figure allowing simple comparisons between systems.

2. PRINCIPLES OF ENERGY EFFICIENCY STANDARDS

In the past, manufacturers of RACHP equipment used to present the ratings of their products in very different formats. For instance, chiller ratings could be presented with a leaving chilled water temperature at 6°C by some manufacturers, and 7° by others, with also different temperatures or flow rate ratios at the condenser, etc. This made it very difficult for customers to make apple to apple

comparisons between different machines. Also, ratings were usually presented at full load although most systems operate most of the time at part load, off-design conditions. Having only the design point gave no indication about real life energy consumptions. To alleviate this, sate of the art Energy Efficiency ("EE") standards now require ratings at conditions intended to be representative of actual year-round operation. While there are many EE standards in various parts of the world, they now all tend to be structured in the same way, per principles described below.

2.1. The ambient outdoor conditions and building load profiles

The ambient outdoor conditions are needed to assess the operating conditions of a system for two reasons. First, the conditions at the condenser of the refrigerant circuit depend on these outdoor conditions. Various data bases are providing outdoor conditions at a wide number of locations; data are typically provided as "bin hours", giving the number of hours per year spent in a given temperature range (or "bin"), usually incremented by temperature steps of the order of 1K. In addition, the building load profile, especially for A/C applications also depends strongly on the outdoor temperature. To represent this, standards define typical load profiles depending on outdoor conditions. These load profiles can also depend on the application, such as comfort A/C for residential or commercial buildings. In EE standards, one or several sets of climate data are generally imposed to define "reference" outdoor conditions, but flexibility can be left for performance evaluation at different locations, with different climate conditions.

2.2. Reference rating conditions

EE standards define "reference" operating conditions intended to be representative of typical operating conditions at full and part load for the family of products considered. But as a given product can be installed in various locations and can be used for different purposes, standards also provide methods to provide a realistic and well defined assessment of performance while allowing this flexibility between different locations and applications. For instance for a water cooled chiller, full load design conditions are defined by the temperatures of water leaving from the evaporator and entering the condenser, and by the temperature differences (or flows) at both heat exchangers. For part load, reference points of operation are defined, typically three of them, around 75, 50 at 25% of full load capacity for comfort cooling. For each of these points, the temperatures and flow rates at the exchangers are also defined, and the input power is declared by the manufacturer. These data are used to evaluate the year round energy efficiency SEER per rules defined by the standards.

2.3. Useful ratios: "SEER" and "ACR"

From the above, two important ratios are derived: the first it the "SEER" (Seasonal Energy Efficiency Ratio), defined by Eq. (1):

$$SEER = Q_C \times E_{annual}^{-1} \qquad \text{Eq. (1)}$$

Where Q_C, is the total cooling energy generated (kWh/year), and E_{annual} is the total annual energy input. A second ratio is of interest to simplify TEWI calculations. It can be called the Annual Capacity Ratio *(ACR)*; it is the ratio between E_{annual}, and the cooling energy that would be generated if running the same system continuously (8760 h/year) at full load. With Q_0 being the design cooling capacity:

$$ACR = Q_C \times [\, Q_0 \times 8760 \,]^{-1} \qquad \text{Eq. (2)}$$

In the above, reference was made to cooling applications, but the same principle would apply to Heat Pumps, by using the heating energy instead of cooling. The names can vary depending on the applications, and on the regional regulations and standards. For instance, in European ecodesign, the name of SCOP (Seasonal Coefficient of Performance) is used for heat pumps, versus SEER for cooling. Likewise, the AHRI Standard 550/590 would designate the concept of SEER under the name of IPLV (Integrated Part Load Value). The units also can vary depending on regional units and standards. For instance, in imperial units, the IPLV is expressed in kW $\times$ ton_R^{-1}. Also, some recent EU ecodesign regulations include in the SEER a conversion factor for the generation of electricity from primary energy. For the sake of simplicity in the following, we will stick to the generic term of SEER, and assume it to be expressed in kWh/kWh. Conversion to other units is straightforward.

2.4. Energy performance regulations

One purpose of EE standards is to enable customers to make “apple to apple” performance comparisons between similar products from different suppliers. In addition, the general need to save energy and reduce GHG emissions is driving a tendency toward mandatory energy performance regulations aiming at gradually raising the overall energy efficiency of the products by stipulating Minimum Energy Performance Standards (“MEPS”). To avoid ambiguities, these regulations normally specify the MEPS in reference to existing EE standards. For instance in EU, many products are subject to “Ecodesign” regulations. A product cannot be placed on the market unless it reaches a minimum value of SEER. In addition appliances sold directly to customers are subject to “Energy labeling”: products are classified per their SEER in various categories of efficiency, ranging for instance from “A” to “E”, to provide information to customers.

3. TEWI CALCULATIONS

3.1. Basic methodology

The TEWI methodology is well known, and very precisely defined. Among other sources, it is described in the Annex B of the standard EN-378.1, by the following Eq. (3).

$$TEWI = GWP \times L \times n + [GWP \times m \times (1-\alpha_{recovery})] + n \times E_{annual} \times \beta \quad (\text{kg } CO_{2e}) \quad \text{Eq. (3)}$$

This formula gives the total GHG emissions of a system over its life time, in kg CO_{2e} (CO_2 equivalent). In Eq. (3), m is the refrigerant charge in kg. L is the leak rate in kg/year. The life time of the equipment is n (years); $\alpha_{recovery}$ is the rate of refrigerant recovery at EOL (End of Life). β is the carbon foot print of the electricity used to run the system (in kg of CO_2 / kWh). In Eq. (3), the last term $[n \times E_{annual} \times \beta]$ gives the indirect emissions from the energy consumption, while the first two terms give the direct emissions, respectively from continuous leakage and from the refrigerant not recovered at EOL.

3.2. Specific TEWI

Unfortunately, the TEWI expressed in kg CO_{2e} is a rather awkward metrics, as this figure is nearly impossible to use for simple comparisons between systems of different capacities, life times, operating conditions, technologies etc. To facilitate comparisons, it has been suggested, for instance in IIR, 2016, to use the concept of “specific TEWI” that evaluates the TEWI in kg CO_{2e} per kWh of cooling energy generated.

3.3. The Indirect part of emissions

Let us first focus on the indirect emissions. Combining Eq. (1) and (3) gives:

$$TEWI_{Indirect} = n \times Q_C \times \beta \times SEER^{-1}$$

Normalizing it to the cooling energy over the life time to make it “specific” gives:

$$Specific\ TEWI_{Indirect} = \beta \times SEER^{-1} \quad (\text{kg } CO_2 \times \text{kWh cooling}^{-1}) \quad \text{Eq. (4)}$$

Once the SEER of a system is known, calculating the indirect part of specific TEWI from Eq. (4) is therefore remarkably simple: it is simply β divided by the SEER. It does not require any detail of the system configuration, not even its cooling capacity or life time. Indeed, the SEER calculation is not straightforward, but it is part of the data that are now required from manufacturers for nearly any system placed on the market; it is also subject to minimum values (“MEPS”) wherever energy performances regulations are in force.

3.4. The direct emissions

From Eq. 3, the contribution of the direct emissions to the TEWI is:

$$TEWI_D = GWP \times L \times n + [GWP \times m \times (1-\alpha_{recovery})] \quad (\text{kg } CO_{2e} \text{ over life time}) \quad \text{Eq. (5)}$$

In Eq. (5), the refrigerant charge m appears directly. It is also “hidden” in the annual leakage L. It is common practice to evaluate L by the following Eq. (6):

$$L = m \times ALR \quad (\text{kg refrigerant per year}) \quad \text{Eq. (6)}$$

Wherein ALR is the percentage of Annual Leak Rate. Combining Eq. (5) and (6) gives:

$$TEWI_D = GWP \times m \times [\, ALR \times n + (1-\alpha_{recovery}) \,] \quad \text{Eq. (7)}$$

Like for the indirect emissions, it would be desirable to have access to approximate values allowing comparisons between different systems without knowing details of their configuration. This is feasible to a certain extent for the refrigerant charge of the systems, as shown in section 3.5 below.

3.5. The refrigerant charge of systems – Specific values

The refrigerant charge is a key input for the TEWI calculation. If a precise value is desired, using manufacturer's data is indeed the best solution; but even if it is not available, it is possible to have reasonable estimates by using the concept of "specific charge" *(C_{Sp})*, which is the ratio between the refrigerant charge of a system (in kg) and its design capacity Q_0. As shown by Poggi & al (2008), this ratio is relatively constant for a given family of products. For instance, for water cooled chillers using shell and tube heat exchanger with halogenated refrigerants, a typical value is of the order of 0,20 to 0,25 kg of refrigerant per kW of design cooling capacity. The precise value can vary slightly around these limits; but irrespective of such variations, the order of magnitude of C_{Sp} remains the same. Generic values can therefore be used by default unless more precise data are available. The charge is then be calculated as:

$$m = C_{Sp} \times Q_0 \qquad \text{Eq. (8)}$$

4. EXAMPLE: WATER COOLED CHILLERS IN EU

The methodology as defined in §-2 will now be illustrated in the example of electrically driven water cooled chillers with cooling towers, according to the EU standard and ecodesign regulation. The applicable EE standard is EN-14825-2013; and the applicable energy performance regulation is the ecodesign regulation (EU) 2016/2281 which will be further referred to as "ecodesign". Both the standard and "ecodesign" differentiate between chillers used for comfort cooling A/C, or for industrial processes, as detailed in §-4.4. In the following, the implementation will be first detailed for the A/C ("comfort") chillers.

4.1. Reference conditions (A/C chillers)

The standard and the regulation are aligned. The full and part load conditions are the same, in table 5 (page 24) of EN-14825, and in table 21 (page 38) of ecodesign. The reference parameters design point "A" and the three part load points B, C, D, with corresponding conditions at the heat exchangers. These values are given in table (1), together with similar values applicable to "process chillers" as will be explained in §-4.4.

Table 1. Reference points for comfort and HT process chillers

Ref. point	% of cooling capacity		Outdoor Temp. (°C)		Condenser inlet Temp. (°C)	
	A/C	Process	A/C	Process	A/C	Process
A	100		35		30	
B	74	93	30	25	26	23
C	47	87	25	15	22	16
D	21	80	30	5	18	9

4.2. Temperature conditions

For comfort A/C, 24 temperatures bins are defined, from 17 to 40°C. They are given in table 27, annex E of ecodesign, identical to table A1 in EN-14825. The table (2) below shows these temperature bins, emphasizing the four reference points in grey. The h_j values are the typical numbers of operating hours at each of the temperature bins, based on a typical average temperature profile in Europe, and on a typical building load profile. The lines 1, 2 and 4 are copied directly from the sources, while lines 3 and 5 are additional calculations as explained in §-4.3.

Table 2. Temperature bins for comfort cooling

Line					D					C			
1	j	1	2	3	4	5	6	7	8	9	10	11	12
2	T_j	17	18	19	20	21	22	23	24	25	26	27	28
3	%	21.0	21.0	21.0	21.0	26.2	31.4	36.6	41.8	47.0	52.4	57.8	63.2

4	h_j	205	227	225	225	216	215	218	197	178	158	137	109
5	$h_j \times \%$	43.1	47.7	47.3	47.3	56.6	67.5	79.8	82.3	83.7	82.8	79.2	68.9

		B					A						Sum
j	13	14	15	16	17	18	19	20	21	22	32	24	
T_j	29	30	31	32	33	34	35	36	37	38	39	40	
%	68.6	74.0	79.2	84.4	89.6	94.8	100	100	100	100	100	100	
h_j	88.0	63.0	39.0	31.0	24.0	17.0	13.0	9.0	4.0	3.0	1.0	0	2602
$H_j \times \%$	60.4	46.6	30.9	26.2	21.5	16.1	13.0	9.0	4.0	3.0	1.0	0	1018

4.3. SEER and "ACR" calculation

To calculate the annual cooling load and input energy, the capacity and input power are first evaluated at each of the reference points A to D. The percentage of the full load at the part load points B, C, D is imposed by the standard. The Energy Efficiency Ratio (EER) at any point is the ratio between the input power and the cooling capacity. Its values at the four reference points, not shown in Table (2), are calculated or measured by the manufacturer. From these, the performance (cooling capacity and EER or input power) is then evaluated at each of the temperature bins. For the reference points, the actual "declared" values are used. For temperatures higher than point A or lower than point D, the values are extrapolated, by keeping the same the capacity and EER as for points A and D respectively. For other bins in between, linear interpolations are made between the two neighboring reference points. Line 3 in table (2) shows the percentage of cooling capacity for each bin per these rules. Likewise, it would be straightforward to interpolate and extrapolate the EER values for each bin, from the EER's provided by the supplier at the reference points. It is also straightforward to convert these figures to cooling and input energies for each bin. Last, summing these values over the 24 bins gives the total annual cooling energy generated, and the input energy. The ratio between these two energies gives the SEER by using Eq. (1).

The calculation of "ACR" from these data is also straightforward, as all the data used in Eq. (2) are available. The ACR calculation uses the line 5 of table (2) giving the values of *"$h_j \times \%$"*. In this case, the sum of these values for all the bins is 1018. It is equivalent to the number of hours of operations at full capacity that would generate the same annual cooling energy. On the other hand, if the unit were operated year round at 100% capacity, this figure would be 8760 (= 365 × 24 × 100%), in hours of operation at full capacity. From Eq. (2), the value of ACR in this case is:

$$ACR = 1018 \times (8760)^{-1} = 0.116 \qquad \text{Eq. (9)}$$

A key take away is that ACR is directly derived from the standard, and does not require any information about the performance of the unit. It only depends on the standard applied. In other words in this case, it can be said that *ACR* = 0.116 for any water cooled chiller used for comfort cooling and evaluated at standard rating conditions per the standard EN-14825.

4.4. The case of HT process chillers

Besides their most frequent use for comfort cooling, chillers can also be used to cool industrial processes. When the needed chilled water temperature is close the 7°C, as typically needed for A/C, then exactly the same chillers can be used, but they are then referred to as "High Temperature (HT) process chillers", to differentiate this application from the use as brine chillers at lower temperature. The standard and the ecodesign differentiate the operating conditions between process and comfort cooling. The differences in reference points between the A/C and process chillers is shown above in Table (1). The full load point A is the same, but the part load points and the bin hours are drastically different. Also, per table 28 of ecodesign, there are 58 temperature bins from -19 to 38°C for process chillers, versus 24 bins from 17 to 40°C for A/C. The number of operating hours is also very different: a process chiller is running continuous (8760 hours per year); while a comfort chiller at reference European temperatures is operating only 2602 hours. As a consequence, the *ACR* values are very different: if a calculation similar to that of §-4.3 is done for a process chiller, then *ACR* = 0.846, i.e. 6.1 times larger than the value 0.116 for comfort chillers.

In addition, the standard and the ecodesign use a different name for the seasonal energy efficiency: it is called SEPR (Seasonal Energy Performance Ratio) to differentiate it from the "SEER" of comfort chillers, although the concept and calculation procedures are the same.

4.5. Conversion Coefficient CC and MEPS values

Energy performance regulations specify the mandatory MEPS as minimum values of the SEER per the standards, i.e. the ratio between Q_C and the input energy, equal to the electrical input energy in the case of an electrically driven unit. In addition, for comfort cooling, ecodesign stipulates to express this input energy in terms of primary energy used. To do this, a "Conversion Coefficient" *(CC)* is used. To reflect the estimated 40 % average EU generation efficiency, the reference value of *CC* is 2.5. Accordingly, instead of the usual formulation of a SEER, the ecodesign stipulates its MEPS as "seasonal space cooling energy efficiency" (η_{sc}), expressed in percent. This is done for comfort cooling only, not for process chillers.

$$\eta_{sc} = SEER \times 100 / CC$$

With CC = 2.5, this gives:

$$SEER = \eta_{sc} \times 0.025 \qquad \text{Eq. (10)}$$

The ecodesign regulation is setting two "tiers" for the MEPS. Table (3) is recalling the *ACR* values, and giving the MEPS for comfort or process cooling chillers with cooling capacity 400 to 1500 kW. For comfort chillers, the SEER's are calculated from the stipulated values of η_{sc} by using Eq. (10).

Table 3. MEPS per ecodesign. Tier values.

	ACR	MEPS			
		η_{sc}		SEER (SEPR)	
		Tier 1	Tier 2	Tier 1	Tier 2
Comfort	0.116	227	252	5.68	6.3
Process	0.846	N/A		7.5	8.0

5. SPECIFIC TEWI CALCULATIONS

From the above, we will now proceed to a specific TEWI calculation for chillers of capacity 1000 kW for both applications, assuming that their SEER just complies with ecodesign Tier 1. The calculation data and results are summarized in Table (4):

Table 4. Specific TEWI calculations

Common input data	β		0.454		$kgCO_2 \times kWh^{-1}$
	GWP		1300		
	Life time *n*		20		years
	$\alpha_{recovery}$		90		%
	Design cooling capacity		1000		kW
	Specific refrigerant charge		0.22		$kg \times kW^{-1}$
	ALR		2		$\% \times year^{-1}$
	Application		Comfort	Process	
	SEER (SEPR)		5.68	6.3	$kWh \times kWh^{-1}$
Calculation Indirect TEWI	Cooling energy	ACR	0.116	0.846	
		E_{life}	20323	148219	MWh
	Specific $TEWI_{SInd}$		79.9	72.1	$gCO_{2e} \times kWh^{-1}$
	Actual $TEWI_{Ind}$		1624425	10681193	ton CO_{2e}
Calculation Direct TEWI	Refrigerant charge *m*		220		kg
	Actual $TEWI_D$		143000		$kgCO_{2e}$
	Specific $TEWI_D$		7.04	0.96	
Total TEWI	Specific		87	73.0	$gCO_{2e} \times kWh^{-1}$
	Actual		1767425	10824193	ton CO_{2e}
Ratio	TEWI Direct / Total		8.1	1.3	%

5.1. Indirect emissions

As per §-3.3, the calculation is straightforward, but requires an assumption about the carbon foot print of electricity β. Per the Ecometrica study (2011), a value of β = 0.454 kg $CO_{2e} \times kWh^{-1}$ is taken. A simple application of Eq. (4) gives: $Specific\ TEWI_{Indirect}$ = 79.9 for comfort, or 72.1 for process, both in (g $CO_{2e} \times kWh^{-1}$)

5.2. Direct emissions

The direct emissions are calculated from Eq. (7) in §-3.4:

$$TEWI_D = GWP \times m \times [\ ALR \times n + (1-\alpha_{recovery})\ ] \qquad \text{Eq. (7)}$$

Assumptions are needed for the input parameters, as reflected in Table (4). The fluid is R-134a, with *GWP = 1300* ("AR-5" value). The charge is evaluated from the "specific charge" approach. From our experience as a chiller manufacturer, it is reasonable to assume C_{Sp} = 0.22 kg$\times$ kW^{-1}, the charge *m* is *220 kg*. The life time *(n)* is 20 years, with an annual leak rate *ALR* of 2% per year, and a rate of EOL refrigerant recovery $(\alpha_{recovery})$ of 90%, suitable for proper maintenance and EOL decommissioning. Then Eq. (7) gives the total life time direct emissions: $TEWI_D = 143000$ (kg CO_{2e}). In order to normalize it to specific TEWI, this value must now be divided by the cooling energy generated over the life time, according to Eq. (11):

$$E_{Life} = ACR \times Q_0 \times n \times 8760 \qquad \text{Eq. (11)}$$

5.3. Results

The results of the calculations per the above §-5.2 and 5.3 are summarized in table (4). It shows the specific TEWI for both applications, and the ratios between direct and indirect emissions. These results are commented in the following section.

6. COMMENTS

Some aspects of the above calculation are similar to "actual" TEWI calculations. Yet, some significant differences result from the simultaneous uses of the specific TEWI, and of the EE standards and ecodesign regulation.

6.1. Benefits from the specific TEWI

Unless the TEWI is normalized to make it "specific", the results of the "actual" TEWI vary by several orders of magnitude, from a few thousand tons CO_{2e} for small systems, to megatons for large ones; while if using the specific TEWI, the size of the system has very small impact. For a family of similar products with same SEER, the specific TEWI even turns out to be exactly the same irrespective of the size and capacity if the refrigerant charge is evaluated from the "specific charge", which is a reasonable assumption. The actual TEWI can also vary by nearly one order of magnitude depending on the application: per table (4), the actual TEWI is 6.1 times larger for the process chiller than for the same one used for A/C. There would also be large variations in actual TEWI even for a same comfort cooling machine, when applying it in different climate zones. On the opposite, the difference in specific TEWI between comfort and process remains in a much narrower range, with differences only 19%. Specific TEWI of different machines or applications can thus be compared much more easily, and a fine analysis of differences is facilitated.

6.2. Benefits from the link to the standards and regulations

Going back to table (4), other points are worth mentioning. A major input item is the evaluation of the life time energy consumption. The use of existing standards for this purpose is not new; it was mentioned for instance in (IIR, 2016) and various other sources. But using it to evaluate the contribution of the indirect emissions to the specific TEWI per Eq. 4, makes it outstandingly simple, especially as this indirect contribution is generally by far dominant in the emissions. At equivalent β, the indirect contribution depends only on the SEER when evaluated as "specific". As SEER values are now frequently regulated for various products, this makes it possible to make "generic" comparisons between various families of products, assuming that the SEERs are equal to the MEPS, as was done in this sample calculation. It would also allow assessing the impact on overall emissions of various policy scenarios about energy efficiency regulations.

It is also of great interest to use the "ACR" parameter, that is easily calculated from the standards, and depends on the application (e.g. process versus comfort) and on the climate zone. This

parameter has a major impact on the ratio between direct and indirect emissions, as seen in table (4). The contribution of direct emissions is 8.1 % for the comfort cooling application, versus only 1.3 % for process. It could be expected to be in between for A/C in warmer climate zones. This would provide an interesting tool to compare the relative impacts of using lower GWP fluids depending on the applications and locations.

7. CONCLUSIONS

Many more comments could be made about this methodology. A major conclusion is that it can substantially facilitate the TEWI calculations in reference to standards applicable to specific products, and thereby facilitate comparisons between various solutions. A good news is that the use of EE standards as proposed provides a robust, simple and consistent answer to the issue of the input power, and an easy way to normalize it to the cooling energy produced. The principle of using the single figure of specific TEWI in reference to a standard could be compared to what has become common practice in automobiles: car manufacturers publish the emissions in (kg CO_2 / km) according to a standardized driving cycle. Once customers are used to this metric, anyone can instantly benchmark the relative values of various models in terms of GHG emissions. With this method, the same could be done for various families of cooling products, for instance for chillers.
Of course, some controversies will still remain about some input parameters such as the carbon foot print of electricity or the leak rates. To minimize their detrimental impact on the acceptability of a more general use of TEWI, more research and discussion would be needed about such parameters. But even within the current ranges of uncertainty, when an analysis of the sensitivity to uncertain input parameters is made, unambiguous conclusions can still often (but not always) be derived. It is therefore hoped that this should enable a wider use of TEWI as a useful tool for decision making regarding trade-offs between various technical choices, in relation to existing standards.

NOMENCLATURE

ACR	Annual Capacity Ratio	*n*	system operating time (years)
ALR	percentage of Annual Leak	*m*	refrigerant charge (kg)
$\alpha_{recovery}$	recovery/recycling factor (0 to 1)	Q_0	design cooling capacity (kW)
β	carbon foot print of electricity ($kgCO_2 \times kWh^{-1}$)	Q_C	Total cooling energy ($kWh \times year^{-1}$)
C_{Sp}	specific charge of refrigerant ($kg \times kW^{-1}$)	$TEWI_D$	direct TEWI (kg CO_{2e})
E_{annual}	energy consumption ($kWh \times year^{-1}$)	$TEWI_{Ind}$	Indirect TEWI (kg CO_2)
L	leakage rate ($kg \times year^{-1}$)	$TEWI_{SD}$	Direct Specific TEWI ($gCO_{2e} \times kWh^{-1}$)
η_{sc}	seasonal space cooling energy efficiency	$TEWI_{SInd}$	Indirect Specific TEWI ($gCO_2 \times kWh^{-1}$)

REFERENCES

Ecometrica, 2011. Electricity-specific emission factors for grid electricity.

European standard EN-378.1, 2017. Refrigerating systems and heat pumps - Safety and environmental requirements - Part 1: Basic requirements, definitions, classification and selection criteria.

European standard EN-14825, 2013. Air conditioners, liquid chilling packages and heat pumps, with electrically driven compressors, for space heating and cooling - Testing and rating at part load conditions and calculation of seasonal performance.

EU Commission Regulation 2016/2281, 2016. Ecodesign requirements for energy-related products, with regard to ecodesign requirements for air heating products, cooling products, high temperature process chillers and fan coil units.

IIR Working Group, 2016. Guidelines for Life Cycle Climate Performance.

Poggi F., and al, 2008. Refrigerant charge in refrigerating systems and strategies of charge reduction, International Journal of Refrigeration, Vol. 31: 353-370.

Manuscript ID: 1145
DOI: 10.18462/iir.icr.2019.1145

Design of experiments methodology for the characterization of the performance map of refrigeration and heat pump units

José M. CORBERÁN, Javier MARCHANTE-AVELLANEDA, Emilio NAVARRO-PERIS, Belén LLOPIS

Instituto Universitario de Investigación de Ingeniería Energética (IUIIE)
Universitat Politècnica de València, Valencia, 46022, Spain
e-mail: corberan@ter.upv.es, web:http://www.iie.upv.es

ABSTRACT

A heat pump or refrigeration unit has minimum 2 independent input conditions to fix per side: source and sink. For instance, water inlet temperature and mass flow rate, or air temperature and flow rate. The compressor frequency is an additional independent input. Therefore, the domain for the characterization of a modern unit with variable flow rates and compressor speed is a space of 5 independent variables. A test campaign following a full factorial plan with 5 levels per input requires 3125 test points.
This paper presents first how the authors have studied the kind of multidimensional surface that could be characteristic of the performance of this kind of equipment. Then, the paper presents a methodology based on the Design Of Experiments theory to define the experimental test matrix which, with a low number of tests (around 30), provides the basis for an accurate characterization of the unit performance all over the entire domain by means of fitted polynomials.
Keywords: Refrigeration, Heat Pumps, Empirical Models, Design of Experiments.

1. INTRODUCTION

Nowadays, the use of empirical polynomial models of system components or entire systems is widely extended in industry and research. The objective of these simple models is to characterize, with enough accuracy, the behaviour of systems or their components under different operating conditions. These models allow the estimation of the corresponding equipment performance and therefore are very useful in assisting the systems design, analysis and control. In the field of refrigeration systems, the AHRI Standard 540(2015) for the characterization of compressor performance are a clear example. These polynomials are able to provide a very accurate prediction of the compressor performance across its entire working envelope by adjusting 10 coefficients.
An alternative approach is the development of more complex models, including the main physical processes that have an influence on the system. However, these models require a much higher computing time and a significant amount of detailed information about the components which is usually not available, and additionally the estimation of a large number of un-known, as for instance, heat transfer coefficients, friction factors, energy losses… which have a large uncertainty.
However, the empirical models must be based on reliable experimental data, and good experimentation is very time consuming and high costly. Therefore, it is very important to know how many experiments are the minimum required and at which operating conditions should be tested in order to reach a sufficient accuracy in the prediction of a system performance all across its operation envelope. A modern refrigeration/heat pump incorporates variable speed compressor, and variable pump or fan speed at both evaporator and condenser. This means minimum 2 independent input conditions to fix per side: source and sink. For instance, water inlet temperature and water mass flowrate, or dry air temperature and air flowrate. The compressor frequency or speed is an additional independent input. Therefore, the domain for the characterization of one unit is a space of minimum 5 independent input variables (air source could also need web bulb or humidity as an additional input variable). A test campaign following a full factorial plan with 5 levels per variable requires 3125 test points.
This paper presents first how the authors have studied the kind of multidimensional surface, which could be characteristic of this kind of equipment and then which Design Of Experiments methodology (DOE) results the most effective for its adjustment by regression.

According to this, the document is structured in two main parts. The first part describes the process to get the functional that characterizes the Response Surface (RS) of HP performance with a high accuracy. The parameters that define the HP performance are the condenser capacity (Qc), evaporator capacity (Qe) and the compressor power input (Wc).
The entire experimental database used in this work originates from the Geot€ch project (2015), a 4 years' research project funded by the European Union. The authors have developed in the framework of that project an innovative prototype of Dual Source Heat Pump (DSHP), which is able to produce either domestic hot water with a dedicated condenser, or heating or cooling water for the building depending on the season. This DSHP combines the aerothermal and geothermal technology in a single equipment allowing it to work in 7 different modes. The methodology presented in this paper have been applied to all the different operation modes with very good results. The paper will only deal with the mode (M5: Winter-Ground) GSHP because of the extension limit.
The second part of the paper deals with the analysis of which is the best DOE for the performance characterization of the heat pump.

2. TEST CAMPAIGN

A total of 227 test points were used as experimental database in this study. These experimental data were collected from the experimental campaign performed for the dual source heat pump mentioned above (Marchante et al., (2018)a). The dual heat pump unit had 7 different operating modes for supply of hot water, chilled water or domestic hot water, using two possible sink/source: ground or air. Further details of the DSHP design can be found in Marchante et al., (2018b).Table 1 shows a summary of the number of experimental data collected:

Table 1. DSHP experimental database

Test	M1 Summer Air	M2 Summer Ground	M3 DHW User	M4 Winter Air	M5 Winter Ground	M6 DHW Air	M7 DHW Ground
Number of tests (Total:227)	32	22	23	51	49	25	25

3. PERFORMANCE CHARACTERIZATION

The performance of a vapour compression heat pump/refrigeration unit is characterized by three results: condenser capacity Qc, evaporator capacity Qe and compressor or unit power input Wc. The performance of units with variable speed compressors is defined by the operating conditions at both sink and source and by the frequency of the compressor. The boundary conditions for the condenser or evaporator are characterised by only two independent variables, these variables can be any combination among the involved three variables: inlet and outlet temperatures and mass flow rate of the secondary fluid. The primary independent variables are the inlet temperature and the mass flowrate. However, inlet and outlet temperatures are usually always measured and monitored while mass flowrate is seldom measured. Given that the mass flowrate is for a given capacity directly related to the temperature difference, the authors have chosen to use either the inlet or outlet temperature, and the temperature difference across the heat exchanger as the independent variables.
Fig. 1 shows a schematic diagram of a GSHP and shows the selected independent variables: compressor frequency fc; condenser outlet temperature (hot water supply temperature to the building) Tco; temperature difference across the condenser dTc; evaporator inlet temperature Tei; and temperature difference across the evaporator dTe. Both dTc and dTe are defined positive, i.e. dTc=Tco-Tci and dTe=Tei-Teo.

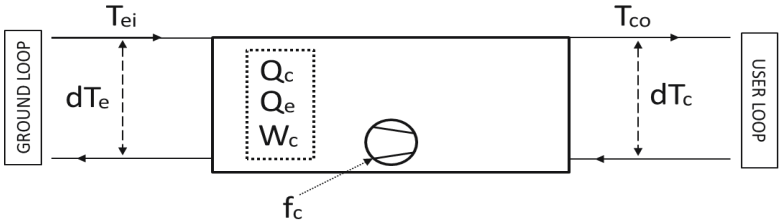

Figure 1: Selected independent variables for a GSHP

Once we have identified all the independent variables, the second step is to look for the functional that is able to predict the response surface of each performance (Qc, Qe, Wc) with the highest accuracy in the entire independent variable domain, which is 5D. The true response surface is of course unknown and perhaps complex. Fortunately, the unit performance surface is continuous with only smooth variations of the slope, therefore, polynomials are usually efficient functionals to describe them. Compressors, which are the basis for the unit performance, are very well studied and it is well known that AHRI polynomials are able to characterise their performance with very high accuracy. Compressor performance is characterized by the condensation and evaporation temperatures. These parameters cannot be employed for the unit characterization since they are unknown. However, evaporation and condensation temperatures are dependent on the boundary conditions at the evaporator and condenser sides. Therefore, polynomials based on the described independent variables should be able to characterize the unit performance as it has been found in this work, and it has been previously reported in the Literature.

Allen and Hamilton (1983) already presented the idea of employing second order degree polynomials with the evaporator and condenser outlet temperatures to predict the full load performance (evaporator capacity and consumption) of chillers. This same methodology is employed inside EnergyPlus energy building simulation software for the evaporator capacity, while for the consumption a polynomial for the Energy Input to cooling output Ratio (EIR) was employed instead the energy consumption. These models usually only took into account the variation of the inlet (or outlet) temperatures of the secondary fluid to the evaporator and the condenser. Therefore the space of the independent variables domain is only 2D. The usual procedure was to characterization the performance at full load and then apply a correction for part load operation. Jin and Spitler (2002) present a good review of these kind of equation fit models and thermodynamics based models.

However, new refrigeration/heat pump units are currently incorporating variable speed compressors and also variable speed fans and water pumps. Therefore, characterization of new and future equipment requires taking into account the whole 5D domain described. Unfortunately, the characterization of equipment with so many independent variables (5) cannot be done exhaustively by experimentation because of the huge amount of data required. The number of test points necessary to characterize a response surface with 5 independent variables following a full factorial test plan, depending on the number of levels one would like to consider for each variable, is:

- 3 levels for each variable → 3^5 = 243 test points
- 4 levels for each variable → 4^5 = 1024 test points
- 5 levels for each variable → 5^5 = 3125 test points

Taking into account that the performance variation with each independent variable is not linear but includes at least some curvature, the number of levels to be considered should be around 4 or 5. Therefore, between 1000 and 3000 test points would be necessary. Obviously, this is not possible and some Design Of Experiments methodology should be employed to reduce the necessary amount of tests to something feasible. However, which is the best DOE method to be employed? In order to answer this question, the authors have first adjusted a very detailed unit model (IMST-ART, http://www.imst-art.com/), which is able to take into account the majority of the complex processes taking place inside the heat pump, to a large set of experimental data, and then have used this model to investigate which is the shape of the unit performance in the 5D domain, and found adequate polynomials able to predict the unit performance with a high accuracy.

3.1. Compressor Submodel

The AHRI polynomials for the employed compressor were not available at the beginning of the development of the mentioned DSHP because it was designed to employ R32 as refrigerant. Only data with R410A was available, so the efficiencies with R410A were employed to assist the design of the unit. In any case, at the end of the development and testing campaign a total of 227 test points were acquired among the different operation modes. Those points were then employed to characterize the compressor performance. The independent variables in this case are 3: the evaporation Te, condensation temperatures Tc, and the compressor speed (frequency)

As described in Li et al. (2004), we can expect that the dependence of the compressor performance with the evaporation and condensation temperatures is almost independent of the compressor speed. Following Li et al. (2004) the compressor performance can be described by the following functionals:

$$W_c^* = b_1 T_c^2 + b_2 T_c + b_3 T_c T_e + b_4 T_e^2 + b_5 T_e + b_6 \qquad \text{Eq. (1)}$$

$$\frac{W_c}{W_c^*} = d_1(f - f^*)^2 + d_2(f - f^*) + d_3 \qquad \text{Eq. (2)}$$

Where W_c^* is the compressor consumption at the given condensation and evaporation temperatures at the nominal frequency f^*. The same functionals and strategy can be employed for the refrigerant flowrate. Fig. 2 shows the maximum error applying this approach for our 227 experimental points. We also adjusted Eq. (1) using the complete AHRI polynomial with 10 coefficients but we did not observe a significant improvement. As it can be observed in Fig. 2, the prediction of the compressor performance with the fitted polynomials is very good. The difference between the measured and calculated results of the refrigerant flow rate show a higher scattering because the experimental value of the mass flowrate does not come from a direct measurement but from the heat balance at the condenser side. It should also be pointed out that the compressor input is the total unit consumption including inverter and parasitic internal losses (electronics) but not including water circulation pumps or fan consumption.

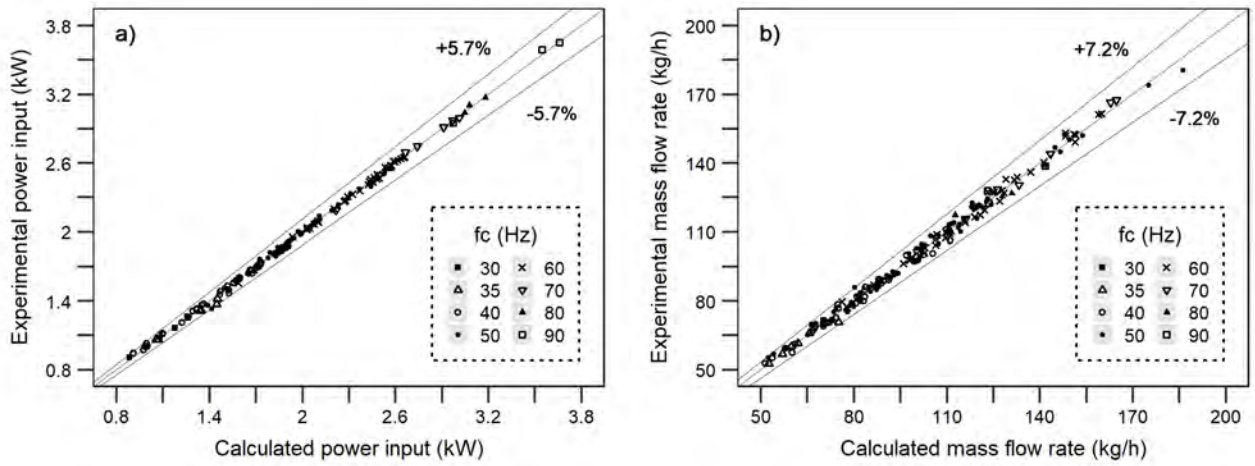

Figure 2: Calculated vs experimental compressor power input (a) and mass flow rate (b)

3.2. Heat Pump Performance Modelling

The compressor performance polynomials were implemented in IMST-ART in order to have an accurate physical model of the heat pump and then the model was employed to evaluate the unit performance for the complete full factorial of the 5 independent variables with 5 levels per variable, totalizing 3125 performance points. Table 2 reports the selected variable levels according to the HP working range. As it can be seen the temperature difference across the heat exchangers was varied from 2 to 9 K, 1K difference (which would make the test matrix symmetrical) was not considered because in practice it would require a huge flow rate. In this respect, it should be highlighted that a variation from 2 to 9 K implies a 4.5 times flow rate variation, which is already very high.

Table 2. Independent variables levels

Independent variables	Range values	Independent variables	Range values
fc	[30, 40, 50, 60, 70] Hz	Tei	[-5, 0, 5, 10, 15] ºC
Tco	[35, 40, 45, 50, 55] ºC	dTe	[2, 3, 5, 7, 9] K
dTc	[2, 3, 5, 7, 9] K		

With a large number of points (3125) and an efficient suite of regression tools, R Core Team (2018), we were able to study the better polynomials to describe the unit performance Qc, Qe and Wc. We limited the search to second-degree polynomials and carefully selected the terms with high significance (low p-value). In the following, the result of two different approaches for the unit consumption is described.

We worked first with the heat pump consumption because a priori it should follow a similar characterization as the one employed in the compressor model. Therefore, the first approach consisted in assuming that the influence of the source and sink temperatures on the unit consumption is independent of the frequency of the compressor. With this assumption, we first searched for the best polynomial describing the unit consumption with the compressor running at 50

Hz, with the described independent variables: Tco, dTc, Tei and dTe. The following polynomial was able to provide very good predictions (0.6% max. error):

$$W_c^* = k_0 + k_1 T_{co}^2 + k_2 T_{co} + k_3 T_{co} T_{eo} + k_4 T_{eo}^2 + k_5 T_{eo} + k_6 dT_c + k_7 dT_e + k_8 T_{co} dT_c + k_9 T_{eo} dT_e \quad \text{Eq. (3)}$$

The substitution of Tei by Teo (which is a mere linear combination of Tei and dTe) brought some improvement, probably because it is a better representation of the evaporation temperature in counter-current HXs. Then, we fitted Eq. (2) in order to characterize the performance at any other frequency. Therefore, the functional for the unit consumption had total 10 + 3 = 13 coefficients. The results of the prediction were very good and are shown in figure 3 a. However, it can be observed a certain remaining curvature that was not possible to eliminate and which was mainly due to the hypothesis of independence of the influence of temperatures and frequency on the unit consumption. In order to improve the results we decided to add the frequency to the polynomial and employed the total 3125 points. We found that the results did not improve. Alternatively, we found that it was good to divide the unit consumption by the compressor frequency before performing the fitting since there is a clear dependence between them. The result was a new response surface without the main dependence with fc. The best polynomial we found following this second approach is the following:

$$\frac{W_c}{f_c} = k_0 + k_1 T_{co}^2 + k_2 T_{co} + k_3 T_{co} T_{eo} + k_4 T_{eo}^2 + k_5 T_{eo} + k_6 dT_c + k_7 dT_e + k_8 T_{co} dT_c + k_9 f_c + k_{10} \frac{1}{f_c} + k_{11} f_c T_{eo} \quad \text{Eq. (4)}$$

Eq. (4) has almost the same terms as eq. (3) plus two additional terms with the compressor frequency. These terms take into account the second order effects of the frequency that the division by the frequency is not able to eliminate. In total, this polynomial has 12 coefficients, one less than the combination of eq. (3) and (2). Figure 3 b) show the results with eq. (4). As it can be observed, it provides an almost perfect explanation of all 3125 unit consumption points.

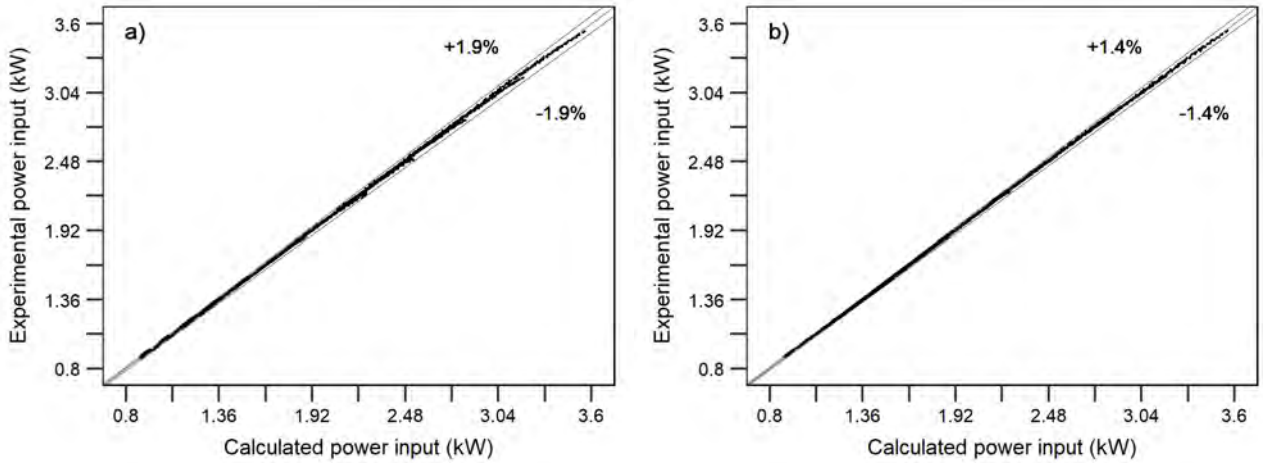

Figure 3: IMST-ART unit consumption vs consumption calculated with polynomials: a) eq (3) and (2), b) eq. (4)

The same polynomial was applied with also very good results to the condenser and evaporator capacities (eq. 5 and eq. 6). It turned out that one of the terms had not sufficient significance so it was removed and the proposed polynomials have in this case 1 coefficient less, total 11. The prediction results were again very good: Qc (max. error ±1.9%) and Qe (max. error ±3.2%).

$$\frac{Q_c}{f_c} = k_0 + k_1 T_{co}^2 + k_2 T_{co} + k_3 T_{co} T_{eo} + k_4 T_{eo}^2 + k_5 T_{eo} + k_6 dT_c + k_7 dT_e + k_8 f_c + k_9 \frac{1}{f_c} + k_{10} f_c T_{eo} \quad \text{Eq. (5)}$$

$$\frac{Q_e}{f_c} = k_0 + k_1 T_{co}^2 + k_2 T_{co} + k_3 T_{co} T_{eo} + k_4 T_{eo}^2 + k_5 T_{eo} + k_6 dT_c + k_7 dT_e + k_8 f_c + k_9 \frac{1}{f_c} + k_{10} f_c T_{eo} \quad \text{Eq. (6)}$$

4. DOE METHODOLOGY

Once we have accurately characterized the response surfaces corresponding to the heat pump performance, we are able to assess the effectivity of different DOE methodologies to determine the unit performance maps with a reduced number of test points. The following well known DOE methodologies were tested:

- Central Composite Design, Box and Wilson (1951)
- Box & Behnken, Box and Behnken (1960)

- Hyper-Graeco-Latin-Square (HGLS), Fisher (1971)
- Taguchi's matrix L16b, Taguchi (1987)

Different Experiment Designs were defined following these methodologies. The developed polynomials (Eqs. 4 5 and 6) where fitted to the selected set of points, and then the prediction from those fitted polynomials were compared with the 3125 performance values covering the entire domain. This gave us a criterion to quantitatively compare the different methodologies and, additionally investigate further reduction of the corresponding test matrixes by taking only part of their orthogonal blocks.

Table 3 shows the maximum deviation, the RMS error and the Standard deviation for each performance parameter. As can be observed, the maximum deviation is considerable low for most of the methodologies, taking into account the small number of points of the test matrix employed to adjust the polynomials and the broadness of the 5D solution domain considered.

Table 3. DoE methodology results

error (%)	Qc			Qe			Wc			Test points
	Max.	Mean	STD	Max.	Mean	STD	Max.	Mean	STD	
CCD (Blocks I+III)	1.98	0.43	0.36	3.05	0.55	0.49	1.42	0.28	0.26	30
Box & Behnken	2.63	0.48	0.43	4.84	0.61	0.58	1.55	0.27	0.22	46
Hyper-Graeco-Latin-Square (HGLS)	1.98	0.45	0.36	3.08	0.57	0.48	1.51	0.29	0.24	25
Taguchi	2.44	0.54	0.45	4.81	0.69	0.57	6.49	1.01	0.87	16

As can be seen, the solution provided by the CCD methodology taking into consideration only blocks I and III, what means utilizing only 30 test points, lead to a very good accuracy in the determination of the surface response. This is in line with the results obtained in Marchante et al., (2018a). Also, the Hyper-Graeco-Latin Square provides outstanding results with only 25 points. For this methodology, we selected the frequency as the main variable, the temperatures as the blocking variables, and the temperature differences as noise variables. Still, the authors recommend the use of the CCD methodology with orthogonal blocks I and III for the characterization of the heat pump performance, given that it is a very well stablished and perfectly defined methodology providing very clear and ordered test matrixes. Just as an example, figure 4 shows the results of the unit consumption for the CCD and Taguchi methodologies, which clearly shows how the polynomial fitted to the points defined by the CCD methodology is able to perfectly describe the whole response surface of 3125 points.

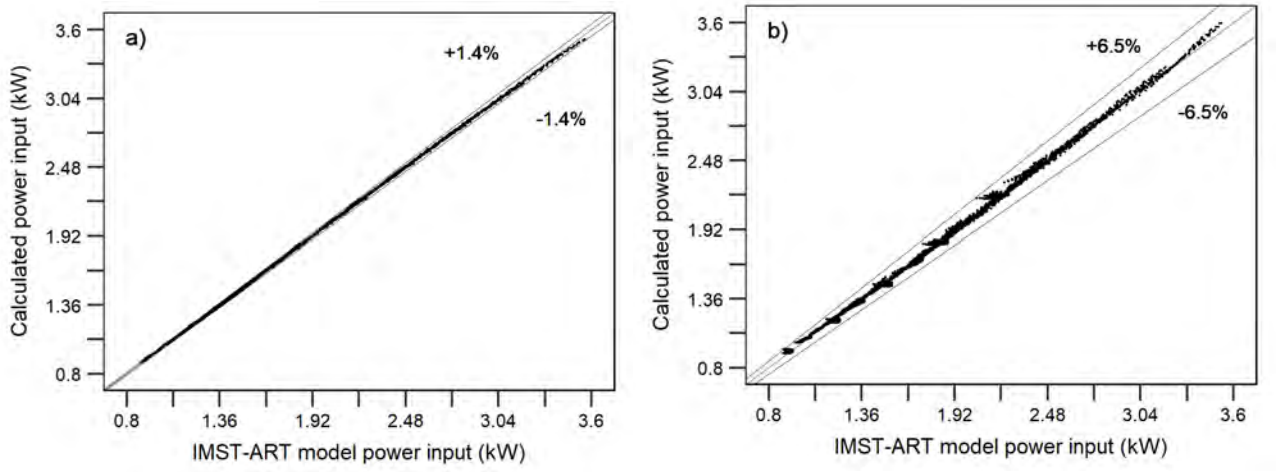

Figure 4: IMST-ART heat pump consumption vs calculated values with the polynomial (eq. 4) fitted to a) blocks I and III of CCD, and b) Taguchi

4.1. COMPARISON WITH THE EXPERIMENTAL DATA

The dual heat pump described was experimentally tested at the set of tests points corresponding to blocks I and III of the CCD methodology. The results predicted by the developed polynomials, fitted

to the IMST-ART calculations, were in very good agreement with the experimental results for the 7 operation modes. This agreement confirms first the validity of IMST-ART to predict the performance of this kind of equipment with high accuracy, and at the same time, proves that only 25 or 30 test points are necessary to fit adequate polynomials, which are then able to very accurately predict the unit performance all across the entire 5D considered domain. Just as an example, figure 5 shows the results comparison for the ground source heat pump case. In previous studies we had had to slightly readjust just the intercept of the polynomial in order to get a better fit. In this case, no readjustment was necessary so the calculated results are exactly the ones obtained with the polynomials fitted to the performance predicted by IMST-ART at the considered test points. It should be highlighted that the very good accuracy attaint, especially in the unit consumption, is also due to the fact that we had previously adjusted the compressor model in IMST-ART to experimental results, as described in Section 2.1. Anyhow, this proves that IMST-ART provides a very accurate prediction of the processes at both evaporator and condenser.

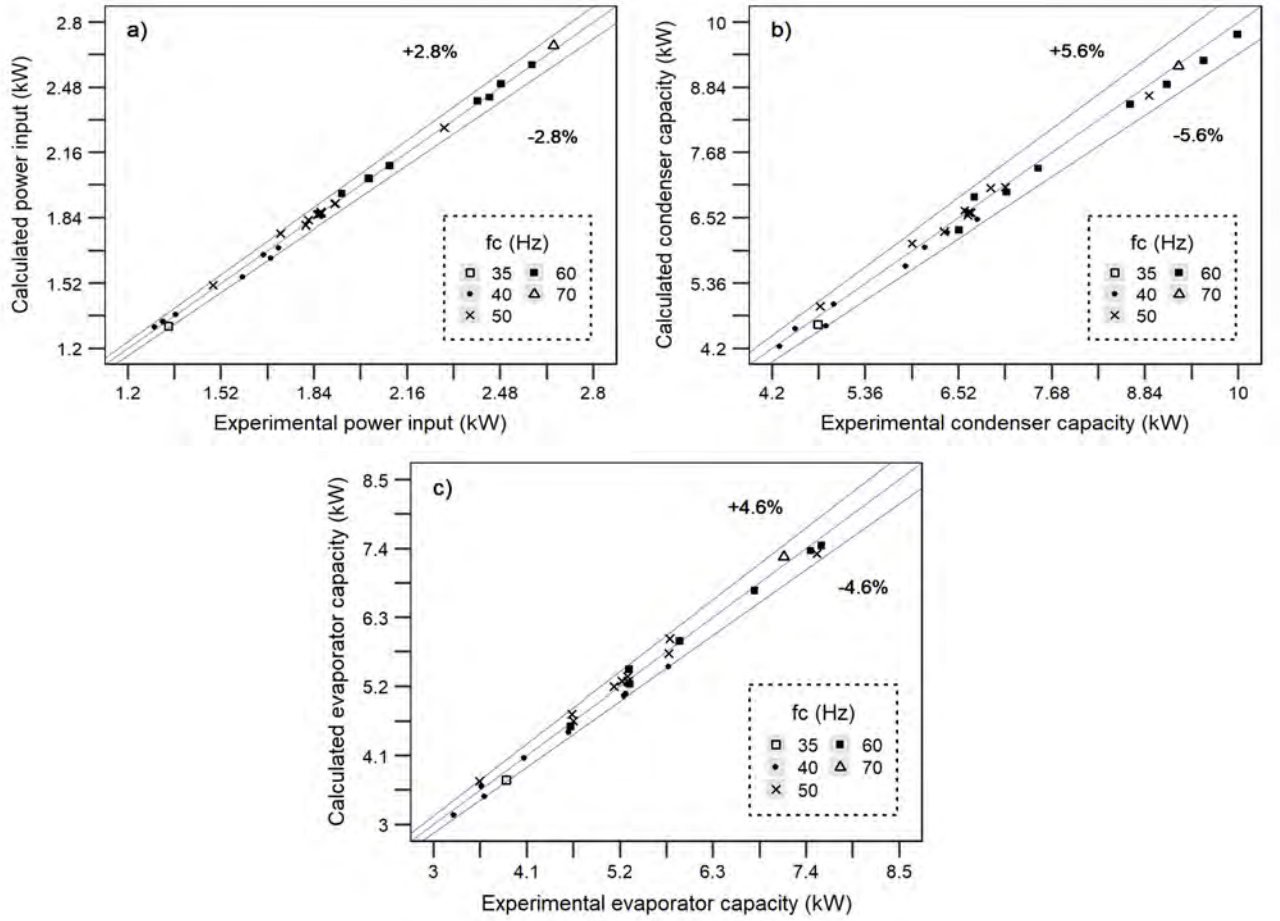

Figure 5: Calculated vs experimental condenser capacity, evaporator capacity and power input for the ground source heat pump case

5. CONCLUSIONS

The main conclusions drawn from this study are the following:

- The performance of a vapour compression heat pump/refrigeration unit with a variable speed compressor has in general 5 independent variables, for instance: inlet temperature and mass flowrate of the secondary flow at the evaporator and at the condenser, plus the compressor frequency. Therefore, the response surfaces for the evaporator capacity, condenser capacity and unit consumption lie on a 5D domain.
- A testing campaign following a full factorial plan would require a huge number of test points, e.g. 3150 points with 5 levels for each independent variable. Therefore, some DOE methodology must be applied to reduce the test matrix to a reasonable size.
- The performance of the unit can be characterized very efficiently by adequate polynomials. We have obtained a very good surface response for Qe and Qc with a 11 coefficients polynomial, and

with 12 for the unit consumption. The error of the prediction is very small all across the entire 5D domain, Qc (max. error ±1.9%), Qe (max. error ±3.2%) and Wc (max. error ±1.4%).

- These well defined response surfaces have been employed to study which DOE methodology leads to a good compromise between number of points for the fitting of the surface and accuracy of the prediction. CCD and HGLS are very good, requiring 30 and 25 test points respectively, and allowing a very good characterization of the compressor performance across the whole domain.
- The developed polynomials were compared with the experimental performance and they provided such a good prediction that no readjustment of the coefficients was necessary: Qc (max. error ± 5.6%), Qe (max. error ±4.6%) and Wc (max. error ±2.8%) for the GSHP case.

ACKNOWLEDGEMENTS

The present work has been partially funded by the Ministerio de Educación, Cultura y Deporte through the 'Formación de Profesorado Universitario' programme ref. FPU15/03476. The authors also want to acknowledge the financial support provided by the project "ENE2017-83665-C2-1-P" funded by the "Ministerio de Ciencia, Innovación y Universidades" of Spain.

REFERENCES

Allen, J.J., Hamilton, J.F., 1983. Steady-state reciprocating water chiller models, in: ASHRAE Transactions 89(2A). pp. 398–407.

ANSI/AHRI, 2015. AHRI 540 - Standard for performance rating of positive displacement refrigerant compressors and compressor units.

Box, G.E.P., Behnken, D.W., 1960. Some new three level designs for the study of quantitative variables. Technometrics 2, 455–475.

Box, G.E.P., Wilson, K.B., 1951. On the Experimental Attainment of Optimum Conditions. J. R. Stat. Soc. Ser. B 13(1), 1–45.

Corberan, J.M., Gonzalvez, J., Montes, P., Blasco, R., Corberán, J.M., Gonzálvez, J., Montes, P., Blasco, R., 2002. 'ART' A Computer Code To Assist The Design Of Refrigeration and A/C Equipment, in: International Refrigeration and Air Conditioning Conference.

EnergyPlus Documentation – Engineering Reference, Simulation Models, Electric Chiller Model Based on Condenser Entering Temperature, https://energyplus.net/.

Fisher, S.R.A., 1971. The Design of Experiments, 9th ed.

Geothermal Technology for €conomic Cooling and Heating, GEOT€CH (subprogramme H2020-LCE-2014-2, 656889), http://www.geotech-project.eu/.

Jin, H., Spitler, J., 2003. Parameter estimation based model of water-to-water heat pumps with scroll compressors and water/glycol solutions. Build. Serv. Eng. Res. Technol. 24, 203–219.

Li, X., Shao, S., Shi, W., Chen, H., 2004. Performance representation of variable-speed compressor for inverter air conditioners based on experimental data. Int. J. Refrig. 27, 805–815.

Marchante-Avellaneda, J., Corberán, J.M., Cazorla-Marin, A., Montagud, C., 2018a. Initial Test Campaign of an Innovative Dual Source Heat Pump, in: CYTEF 2018 − IX Congreso Ibérico | VII Congreso Iberoamericano de Las Ciencias y Técnicas Del Frío Valencia, España, 19-21 Junio, 2018. Valencia.

Marchante-Avellaneda, J., Corberán, J.M., Cazorla-Marin, A., Montagud, C., 2018b. Diseño de una bomba de calor de 8 kW con foco de calor dual: aerotermia y geotermia, in: CYTEF 2018 − IX Congreso Ibérico | VII Congreso Iberoamericano de Las Ciencias y Técnicas Del Frío Valencia, España, 19-21 Junio, 2018. Valencia.

Taguchi, G., 1987. System of Experimental Design: Engineering Methods to Optimize Quality and Minimize Cost., UNIPUB, White Plains, NY.

Team, R.C., 2018. R: A Language and Environment for Statistical Computing. Vienna, Austria.

Manuscript ID: 1165
DOI: 10.18462/iir.icr.2019.1165

Experimental analysis of the intermediate conditions of a variable speed vapor-injection scroll compressor working with R-410A

Fernando M. TELLO-OQUENDO[(a,*)], Bertrand DECHESNE[(b)], Emilio NAVARRO-PERIS[(a)], José GONZÁLVEZ-MACIÁ[(a)], Vincent LEMORT[(b)]

[(a)] Universitat Politècnica de València, University Institute of Energy Engineering Research, Camino de Vera s/n, Valencia, 46022, Spain.
[*] E-mail: fertelo1@upvnet.upv.es
[(b)] University of Liège, Thermodynamics Laboratory, Allée de la découverte 17, Liège, 4000, Belgium.
E-mail: bdechesne@uliege.be

ABSTRACT

This paper presents an experimental analysis of the intermediate conditions for a variable speed (VS) vapor-injection scroll compressor (SCVI) under several working conditions and speeds.
A set of experimental tests was conducted for a VS-SCVI working with R-410A as a refrigerant. From the experimental data and based on previous correlations obtained for constant speed SCVI, a correlation for VS-SCVI was obtained to estimate the injection ratio depending on the compressor speed with an error lower than 10%. Results showed differences in the intermediate conditions of the compressor for low and high compressor speeds.
Keywords: Variable speed, Vapor-injection, Scroll compressor, Correlation, Experimental, Optimization.

1. INTRODUCTION

Nowadays, scroll compressors are widely used in residential and commercial air-conditioning, refrigeration and heat pump applications as well as in automotive air conditioning. This kind of compressor technology is orbital motion, positive-displacement machines that compress with two inter-fitting, spiral-shaped scroll members. They have no dead space, the contact between the flanks of scrolls and in their bases and upper edges is almost perfect and constant; therefore, it has very good axial and radial compliance. Consequently, scroll compressors present advantages such as high compressor and volumetric efficiencies, low vibrations and noise, low torque variations and leakage (ASHRAE Handbook, 2008). Several advanced technologies have been studied in order to enhance the compressor performance and save energy. One of these technologies is the vapor-injection and the other is the use of the variable speed motor.
Vapor-injection technic in scroll compressors has rapidly developed in recent years. The refrigerant injection can either increase the capacity and performance efficiency of the system or decrease the discharge temperature of the compressor to extend the working envelope, especially for refrigeration and heat pump systems working with low evaporating temperatures or high condensing temperatures.
The efficiency of a variable speed compressor with refrigerant injection depends on ambient conditions and compressor frequency as well. Therefore, characterization analysis of a variable speed compressor with refrigerant injection should include the effects of compressor frequency on the performance. This analysis should lead to find a fitting equation that help designers to calculate the compressor performance in a vapor compression cycle in a simple way.
Several researchers studied this problem and tried to develop a correlation to predict compressor performance.
Park et al. (2002) developed a model of a variable speed scroll compressor with vapor-injection working with R22.

The model was validated considering only the no injection condition showing deviations of the predicted compressor capacity and electrical power lower than 10 % with respect to the experimental ones. The model was then used to investigate the influence of geometrical (injection hole diameter and position) and thermodynamic (refrigerant pressure and quality or superheat) injection parameters on compressor working parameters as a function of rotational frequency. An optimal configuration leading to an increase of COP equal to 12 % COP was found.

Dardenne et al. (2015) developed a semi-empirical model of a hermetic, variable-speed vapor-injected R-410A scroll compressor based on the semi-empirical model of a fixed speed scroll compressor presented by Winandy and Lebrun (2002). The model was validated using 63 experimental test conditions. The model requires 10 parameters fitted from experimental data to simulate the process that the refrigerant undergoes from suction and injection ports to discharge port. The model includes the leakage in the compression process and computes the suction and injection refrigerant mass flow rates, the compressor power, and the discharge temperature within ±5 %, ±10 %, ±5 %, ±5 K, respectively.

Lumpking et al. (2018) and Sun et al. (2018) used experimental data from Dardenne et al. (2015) for validate its own characterization models.

Lumpking et. Al. (2018) proposed a correlation for the calculation of injection mass flow rate that uses 10 fitting exponents of dimensionless group numbers derived by the Buckingham-PI theorem. The proposed correlation was validated based in the 63 data points obtained by Dardenne et. Al (2015) and predicts the injection ratio with an average error of ±9.8% and a RMSE of ±6.7%.

Sun et al. (2018) presented a theory based explicit compressor model that consists in a series of models for the suction and injection mass flow rate, total power input and outlet enthalpy. The model needs 26 fitting parameters. Model is validated against experimental data by Dardenne et al. (2015). Predicted injection mass flow rate can describe 83% of the experimental data within deviation of ±10 %.

Authors of this papers presented previous studies in this field. Tello-Oquendo et. al. (2018a) studied the set of equations in two stage vapour compression cycles with economizer to conclude that there are three degrees of freedom namely injection superheat, injection ratio and injection pressure. These parameters are fixed in the cycle by using an injection valve, economizer size and injection compressor characteristics. In case that economizer is replaced by a flash tank, the only degree of freedom is the injection pressure that is determined by the compressor characteristics.

Tello-Oquendo el al. (2017) presented a new methodology for measuring vapour injection compressors. They observed a linear dependence of the injection ratio with the injection pressure ratio and proposed a simple linear correlation between these variables:

$$\frac{\dot{m}_{inj}}{\dot{m}_e} = A + B\frac{P_{inj}}{P_e} \qquad \text{Eq. (1)}$$

Where $\dot{m}_e$ is the evaporator mass flow rate in $kg\ s^{-1}$, $\dot{m}_{inj}$ is the injection mass flow rate in $kg\ s^{-1}$, P_e is the evaporation pressure in Pa and P_{inj} is the injection pressure in Pa.

The correlation predicts the injection mass flow rate with a maximum error of -1.80% and an average error of -0.79%.

Tello-Oquendo et. al. (2018b) extends the correlation with new data for a variable speed compressor working with propane. Compressor was tested at 3 different frequencies (50 Hz, 100 Hz and 120 Hz) and using the data provided by Dardenne et al. (2015) of the R-410A compressor. Equation 1 is adapted making the lineal coefficients dependent on the frequency in a linear form. Proposed correlation agrees very well with both experimental data sets having a maximum absolute error of 7.36% and a RMSE of 5.6%.

Dechesne & Lemort (2018) developed a model for the whole two-stage cycle that uses an equation of the injection ratio as a logarithmic function of the injection pressure ratio. The compressor model was validated using measurements of an air to water heat pump under different compressor speeds and temperatures of the sink/source. The system model is capable to predict the heating capacity and compressor power input with an error less than 2.6% and 6.8% respectively.

2. EXPERIMENTAL SETUP

A schematic representation of the test bench is given in **Error! Reference source not found.**.
The refrigerant loop is controlled by means of a ModBus Interface, which implies the adjustment of the rotational speed of the air evaporator fan, of the scroll compressor, as well as the openings of the expansion valves. Both expansion valves, evaporator and injection, controls the inlet superheat of evaporator and injection compressor port to 5 K respectively.
The drive cooler is an additional heat exchanger installed to cool down the power electronic used for the variation of the compressor speed.

- Conditions in terms of temperature and absolute pressure are measured at the supply/exhaust of each component of the refrigerant loop. Temperatures are determined by means of sensor pocket (type T thermocouple) with accuracy of ±0.3 K. Used absolute pressure sensors show the following characteristics:Operating range of 0-20 bar for the sensor used at the supply of the compressor with an accuracy of 1% of the full scale range
- Operating range of 0-30 bar for sensors used for measuring the low and intermediate pressure level with an accuracy of ±1% of the full scale range,
- Operating range of 0-50 bar for sensors used for measuring the high pressure with an accuracy of ±0.5% of the full scale range.

The refrigerant flow rate at the exhaust of the liquid receiver is measured by means of a Coriolis flow meter with a relative error of 0.1%. A heat exchanger (subcooler, SC) has been added in order to insure a small degree of subcooling under any working conditions and thus assure a better flow rate measurement. This subcooler is a 10 cm long concentric tube heat exchanger where the refrigerant in the inner tube can be cooled down with tap water.
The relative error related to the use of flow meter used for the determination of the refrigerant flow rate passing through the high pressure side economizer is also equal to 0.1%.

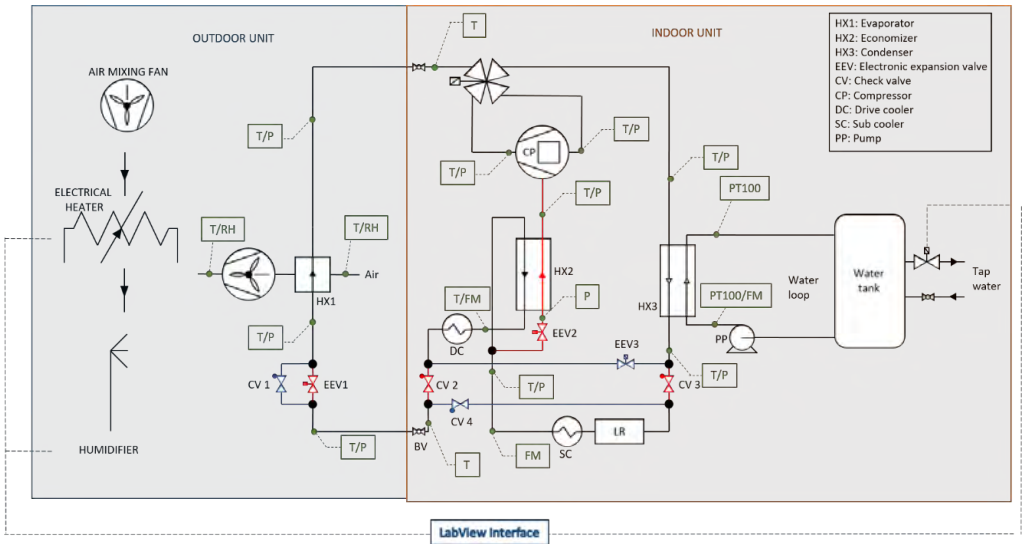

Figure 1: Experimental setup

Water flow rate passing through the condenser is controlled by adjusting the rotational speed of the water pump. The water temperature at the supply of the condenser is adjusted by a PID controlling the opening of a valve on the tap water loop. This latter is used to cool down the water tank that acts as a buffer and helps to maintain steady conditions at the inlet of the condenser. This water tank is thus used as a heat sink that can be either cooled continuously by means of tap water or heated up via variable electrical resistances. Given the low temperature difference between the supply and the exhaust of the condenser (between 3 and 10K), PT100 with accuracy of ±0.1 K have been preferred instead of type T thermocouple. Water flow rate is determined by means of an impulse water meter (4 pulses per litter).

3. TEST CAMPAIGN

Compressor tested is the Copeland model ZHW08 with a swept volume of $2.8\ m^3/h$ at $50\ Hz$ working with the refrigerant R-410A.
Compressor is tested in the experimental setup with and without injection in the operation points shown in Figure 2 and Figure 3. A total number of 68 points are tested in the central operation points of the compressor. For each operation point, 7 different frequencies are tested ranging from 30 Hz to 120 Hz.

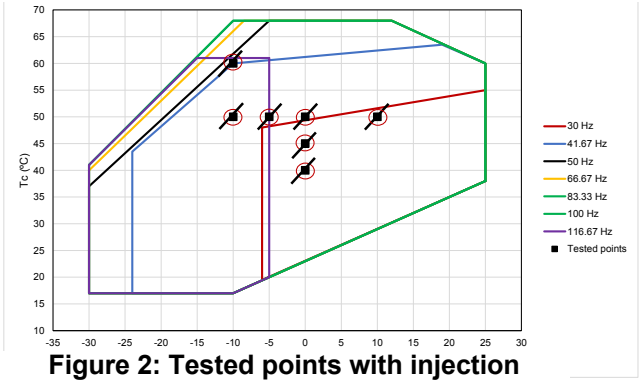

Figure 2: Tested points with injection

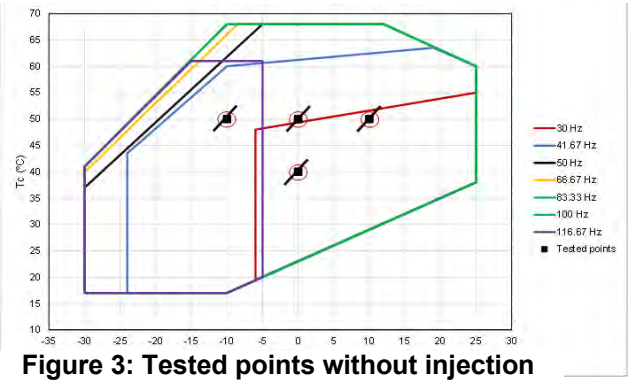

Figure 3: Tested points without injection

After testing, values of volumetric efficiency and isentropic efficiency are calculated.
Volumetric efficiency is defined in the following way:

$$\eta_v = \frac{\dot{m}_{ev}}{\rho_i V n} \qquad \text{Eq. (2)}$$

Where ρ_i is inlet density in $kg\ m^{-3}$, V is the swept volume in $m^3\ rev^{-1}$, and n is compressor speed in $rev\ s^{-1}$.

And compressor isentropic efficiency is calculated as:

$$\eta_c = \frac{\dot{m}_{ev}(h_{is,i} - h_i) + \dot{m}_{inj}(h_{is,inj} - h_{inj})}{\dot{E}} \qquad \text{Eq. (3)}$$

Where h_i and h_{inj} are the inlet and injection enthalpies in $J\ kg^{-1}$, $h_{is,i}$ and $h_{is,inj}$ are the enthalpies with the inlet entropy and injection entropy respectively calculated at outlet compressor pressure and $\dot{E}$ is the compressor electrical power input in W. Injection mass flow rate is calculated with the total mass flow rate measured after liquid receiver and evaporator mass flow rate measured after high side pressure economizer.

4. RESULTS

Figure 4 shows the volumetric efficiency obtained for the injection compressor where the labelling 0/40 means the operating point measured at 0°C evaporation temperature and 40°C condensation temperature. Clearly, there are two different zones defined above and below the nominal frequency of 50 Hz.

At frequencies above 50 Hz, volumetric efficiencies increases at higher speeds. Main reason of this observed trend is due to lower relative influence of leakage at higher speeds. Curves trends are similar at the different points measured and total pressure ratio between condenser and evaporator is the reason of different volumetric efficiencies between points, i.e. 0/40 curve has the lowest pressure ratio ($p_r = 3$) and -10/60 curve has the highest pressure ratio ($p_r = 6.7$).

At frequencies below 50 Hz, there is a sudden jump in the volumetric efficiency and isentropic efficiency at 40 Hz. This phenomenon is observed for all conditions except 10/50. This point out of the trend has been analyzed in deep (data analysis calculation, sensors signal, etc.) and replication of the experiment is made. No mistake or errors have been found and measurement replication is giving the same result. Authors cannot propose a clear explanation of the phenomenon, there is some speculations about oil seal or supercharging injection effects that have to be confirmed in future research.

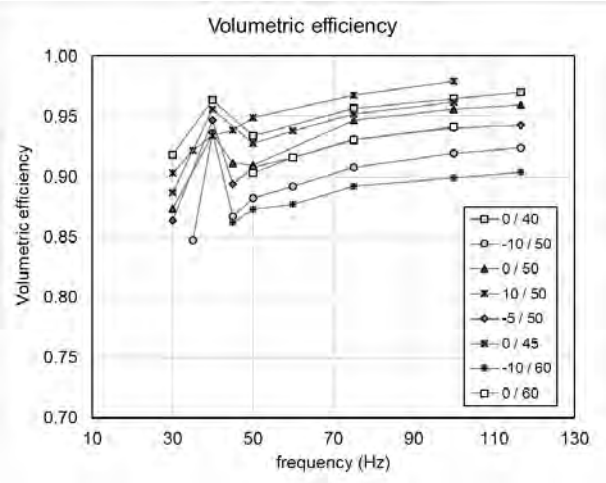

Figure 4: Injection compressor volumetric efficiency

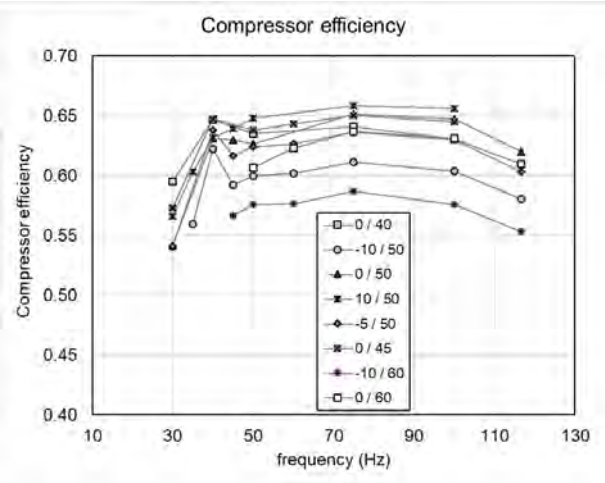

Figure 5: Injection compressor isentropic efficiency

Next figures (Figure 6 and Figure 7) shows comparison of the compressor working with and without injection. Peak values at 40 Hz are not detected in the no-injection mode, giving a clue that the phenomenon is related with the injection process.

Volumetric efficiency values are similar for both cases (injection and no-injection) as the injection process has no big influences in the evaporator mass flow rate as expected.

In the other side, isentropic efficiency values drop with injection compressor at condition 10/50 in all the frequency range and at condition 0/40 only at higher frequencies than nominal. In the 0/50 case, injection compressor performs with better efficiency. This performance is related with pocket pressure matching with intermediate injection pressure. There are phenomena of over-compression or under-compression when injection hole opens.

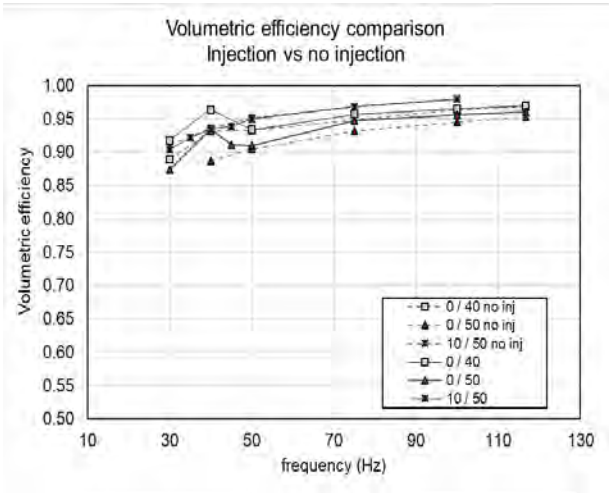

Figure 6: Volumetric efficiency comparison

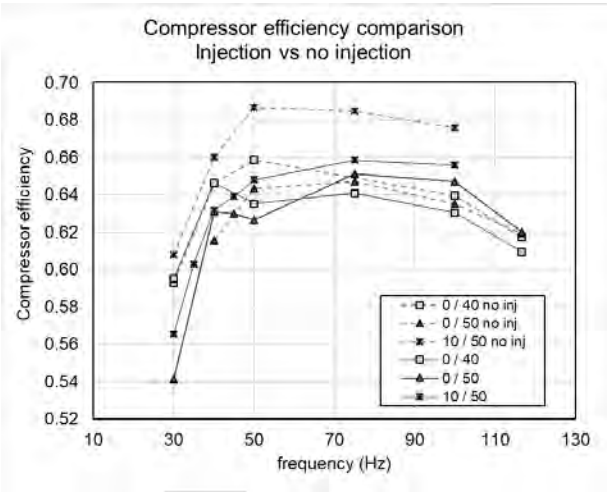

Figure 7: Isentropic efficiency comparison

Injection mass flow rate performance is shown in Figure 8 and Figure 9.
Intermediate pressure ratio shown in Figure 8 presents low influence with compressor frequency. A positive relationship is detected between total pressure ratio and intermediate pressure ratio. Higher values of total pressure ratio leads to higher values of intermediate pressure ratio.
Injection ratio, defined as the ratio of injection mass flow rate over evaporator mass flow rate, shows also a slight dependence with compressor frequency, being the evaporation and condensation temperatures the main dependence factor. Examining both figures, a direct dependence between intermediate pressure and injection ratio is found as stated by Tello-Oquendo (2017) for constant speed injection compressors.

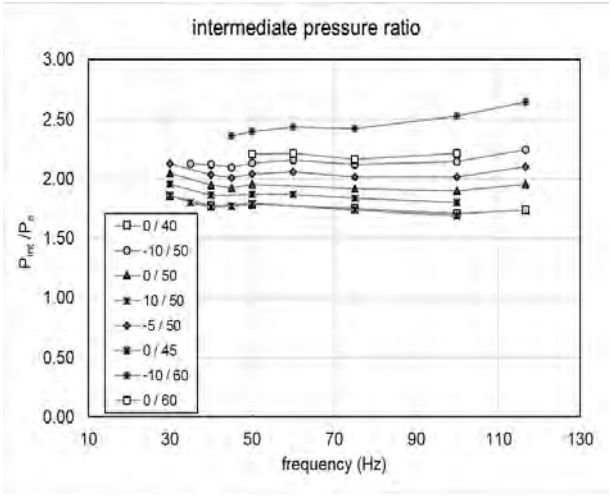

Figure 8: Intermediate pressure as function of compressor conditions

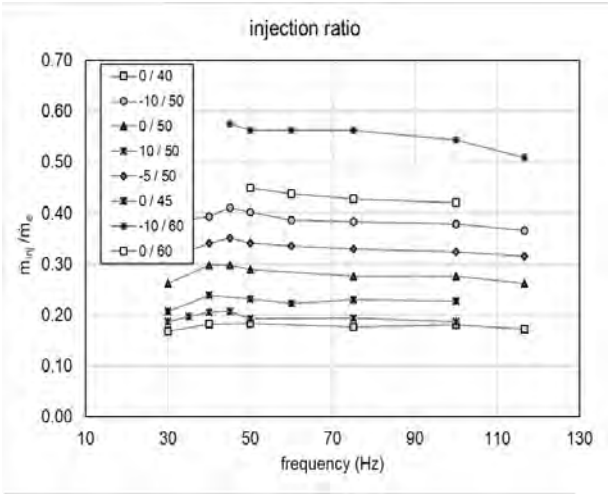

Figure 9: Injection ratio dependence on compressor conditions

Eq. (1) is fitted for each frequency and results are shown in Figure 10. Equations fits perfectly data for each frequency obtaining R-squared values between 0.98 and 1. Figure 11 shows dependence of intercept (A factor in equation (1)) and slope (B factor in Eq. (1)). Both factors shows the same behavior: two straight lines with the common point centered in the nominal frequency of 50Hz.

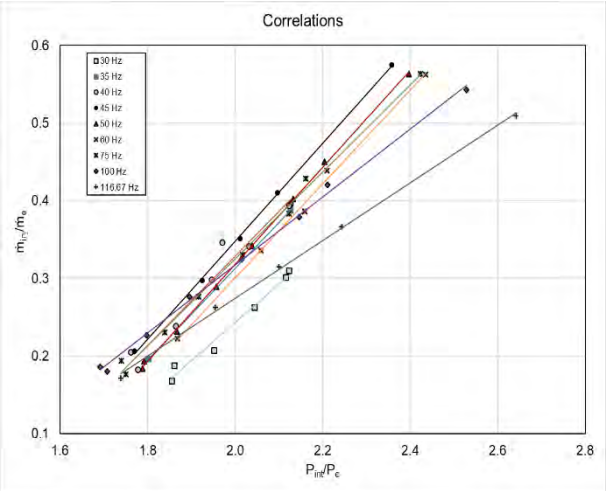

Figure 10: Injection mass flow rate correlation at different frequencies.

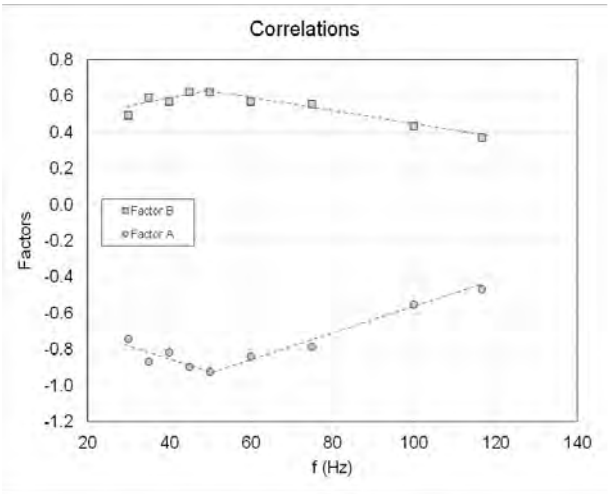

Figure 11: Slope and intercept dependence on frequencies

After examining these results presented, the following correlation is proposed in order to estimate the injection mass flow rate of the compressor:

$$\frac{\dot{m}_{inj}}{\dot{m}_e} = (A_0 + fA_1) + (B_0 + fB_1)\frac{P_{inj}}{P_e} \qquad \text{Eq. (4)}$$

Where coefficients are given in the following table:

Table 1. Coefficients fitted for Equation (4)

	$f < 50\ Hz$	$f \geq 50\ Hz$
A_0	$-5.162 \cdot 10^{-1}$	-1.332
A_1	$-8.462 \cdot 10^{-3}$	$7.468 \cdot 10^{-3}$
B_0	$3.391 \cdot 10^{1}$	$8.361 \cdot 10^{-1}$
B_1	$6.078 \cdot 10^{-3}$	$-3.942 \cdot 10^{-3}$

5. CONCLUSIONS

This paper presents an analysis of variable speed scroll compressors with vapor-injection (VS-SCVI). The following conclusions can be drawn from the study:

- Intermediate injection pressure and injection ratio is weak dependent on the compressor frequency.
- Two different compressor performance is detected depending on the frequency range: below or above nominal frequency of 50 Hz.
- An increase of volumetric and isentropic compressor efficiency is detected in around the frequency of 40Hz. This phenomenon can be related with the injection process flow dynamics.
- A correlation between the intermediate conditions of VS-SCVI has been obtained from experimental data. The injection ratio was correlated with the injection pressure ratio and the frequency.

ACKNOWLEDGEMENTS

Fernando M. Tello-Oquendo acknowledges the financial support provided by the CONVOCATORIA ABIERTA 2013-SEGUNDA FASE program, which was funded by the SENESCYT (Secretaría de Educación Superior, Ciencia, Tecnología e Innovación) (Grant No 2015-AR37665) of Ecuador.
Author acknowledges the financial support provided by the project "ENE2017-83665-C2-1-P" funded by the "Ministerio de Ciencia, Innovación y Universidades" of Spain.

REFERENCES

ASHRAE (2008), ASHRAE HANDBOOK:*HVAC Systems and Equipment.* Atlanta: American Society of Heating, Refrigerating and Air-Conditioning Engineers, Inc.

Dardenne, L., Fraccari, E., Maggioni, A., Molinaroli, L., Proserpio, L., & Winandy, E. (2015). Semi-empirical modelling of a variable speed scroll compressor with vapour injection. *Int. J. Refrig., 54*, 76-87.

Dechesne, B. & Lemort, V. (2018). Modelling and experimental results of a residential heat pump with vapor injection and variable speed scroll compressor, In*: Proceedings of the REHVA Annual Meeting Conference 2018, Low Carbon Technologies in HVAC.*

Lumpkin, D. R., Bahman, A. M., & Groll, E. A. (2018). Two-phase injected and vapor-injected compression: Experimental results and mapping correlation for a R-407C scroll compressor. *Int. J. Refrig., 86*, 449-462.

Park, Y. C., Kim, Y., & Cho, H. (2002). Thermodynamic analysis on the performance of a variable speed scroll compressor with refrigerant injection. *Int. J. Refrig., 25*, 1072–1082.

Sun, H. et. al. (2018). A theory-based explicit calculation model for variable speed scroll compressors with vapor injection. *Int. J. Refrig., 88*, 402–412.

Tello-Oquendo, F. M., Navarro-Peris, E., & Gonzálvez-Maciá, J. (2017). New characterization methodology for vapor-injection scroll compressors. *Int. J. Refrig., 74*, 526-537.

Tello-Oquendo, F.M., Navarro-Peris, E., & Gonzálvez-Maciá, J., (2018a). A comprehensive study of two-stage vapor compression cycles with vapor-injection for heating applications, taking into account heat sink of finite capacity. *Int. J. Refrig., 93*, 52-64.

Tello-Oquendo, F. M., Navarro-Peris, E., & Gonzálvez-Maciá, J. (2018b). Analysis of variable speed injection scroll compressors working with several refrigerants: Empirical correlation for the characterization and optimization of the intermediate conditions. In*: International Compressor Engineering Conference at Purdue University, West Lafayette*, *U.S.A, Paper 2536.*

Winandy, E.L. & Lebrun, J. (2002). Scroll compressors using gas and liquid injection: experimental analysis and modelling. *Int. J. Refrig.*, *25*, 1143-1156.

Manuscript ID: 1183
DOI: 10.18462/iir.icr.2019.1183

Prediction of Two-Phase Flow Boiling Heat Transfer Coefficient of Refrigerants in Minichannel Multiport Tubes

Nguyen Ba CHIEN[(a)], Pham Quang VU[(b)], Jong-Taek OH[(c)*]

[(a)] School of Heat Engineering and Refrigeration, Hanoi University of Science and Technology, 1st Dai Co Viet, Hanoi, Vietnam, chien.nguyenba@hust.edu.vn
[(b)] Graduate School, Chonnam National University, 50 daehak-ro, Yeosu-si, 59626, Republic of Korea
[(c)] Dept. of Refrigeration and Air-conditioning Engineering, Chonnam National University, 50 daehak-ro, Yeosu-si, 59626, Republic of Korea, ohjt@chonnam.ac.kr

ABSTRACT

In this study, we demonstrate the prediction method for two-phase flow boiling heat transfer coefficient of R410A inside various minichannel multiport tubes. The experimental data were conducted in four tube types with the hydraulic diameters of 0.96 mm, 1.07 mm, 1.14 mm and 1.16 mm, and the aspect ratio from 1.6 to 2.5. The data were collected under the heat fluxes of 3 and 6 kW/m2, the mass flux ranging from 50 to 500 kg/m-2 s-1, the vapor quality up to 1.0 and the saturation temperature of 6 ºC. The effect of the heat flux, mass flux, vapor quality and the geometry on heat transfer coefficient are analyzed. The comparison with several heat transfer coefficient correlations was also established. Finally, a new heat transfer coefficient correlation was proposed including the effect of aspect ratio. The validation with present data and the data in open literature shows a good prediction of new correlation.
Keywords: Multiport Tube, Minichannel, R410A, Heat Transfer Coefficient, Correlation.

1. INTRODUCTION

In recent decades, minichannel multiport tubes have been applied widely in designing heat exchanger for various systems including electronics cooling, automotive and modern domestic devices due to its effectiveness and compactness. Several studies of heat transfer characteristics of fluids inside multiport tubes were performed in the literature. Huai et al., (2004) demonstrated the flow boiling of carbon dioxide in ten parallel circular channels tube with inner diameter of 1.31 mm. They reported that both the mass velocity and the heat flux strongly effect on flow boiling heat transfer coefficient, and suggested that the suppression factor (Chen, 1969) need to be modified to predict the data in their work. Vakili-Farahani et al., (2013) reported the flow boiling heat transfer of R245fa and R1234ze in multiport tubes with 7 channels of 1.4 mm inner diameter. They also proposed the flow pattern-based approach to predict the heat transfer coefficient. Li et al., (2016) showed the flow boiling of R-1234yf in vertical aluminum multiport tube with 16 and 40 parallel channels. The data showed that the experimental heat transfer decreased linearly with the increase of vapor quality. More importance, the geometry, especially aspect ratio, strongly affects to the heat transfer performance.
On the other hand, the research on heat transfer of refrigerants in rectangular tubes from Yang et al., (2004) and Tanaka et al., (2014) illustrated that the tendency of heat transfer coefficient cannot be explained by conventional flow boiling model or combination of nucleate and forced-convective boiling mechanism.
Therefore, in this study, we analyzed the effect of heat flux, mass flux and aspect ratio of rectangular tube on the heat transfer coefficient of R410A in four tube types. Base on that, a new heat transfer coefficient correlation is proposed that predicts well the present experimental data.

2. MAIN SECTION

2.1. Experimental Models

2.1.1. Experimental apparatus
The schematic diagram of the experimental apparatus was shown in Fig. 1. The model mainly consists

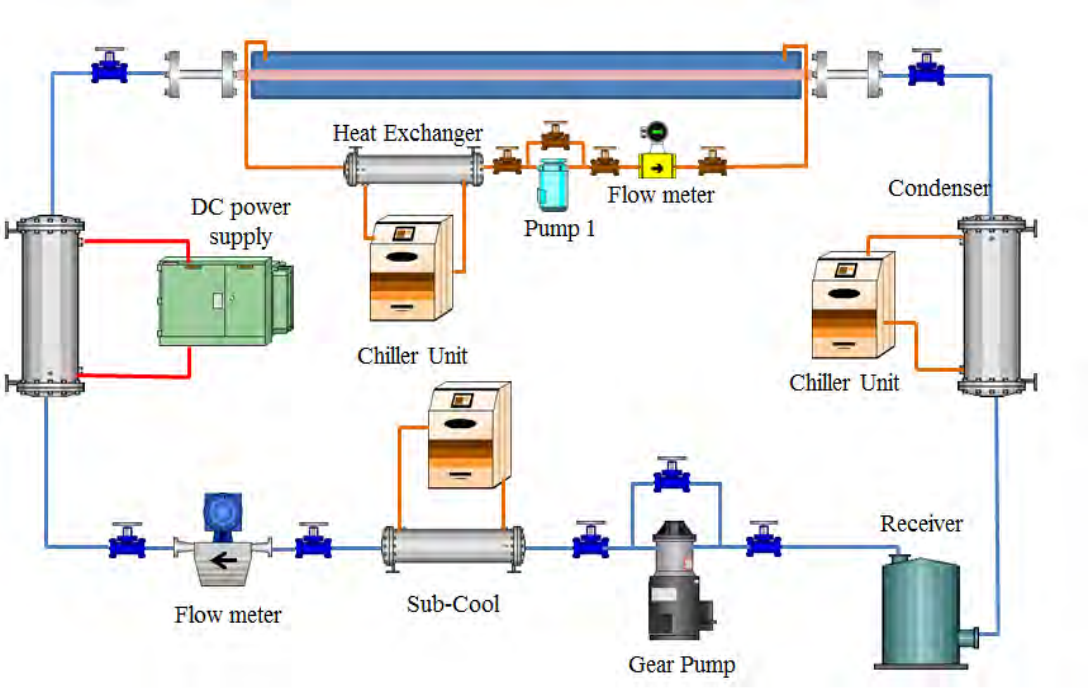

Figure 1: The experimental apparatus

the refrigerant loop, three water loops and the data acquisition system. The refrigerant loop included a magnetic gear pump, a sub-cooler, a mass flow meter, a pre-heater, an evaporator, a test section, a condenser and a receiver. When the test facility was operated for evaporation, the refrigerant was delivered into the test section by the gear pump. The mass flow rate of refrigerant was measured by the Coriolis mass flow meter and could be adjusted by changing the pump speed. The quality of the refrigerant at the inlet of test section was controlled by setting power consumption in pre-heater. The test section was heated by the water loop as shown in Fig. 1. The heat capacity could be varied by mastering the mass flow rate and working temperature of water. The vapor at the outlet of test section was condensed by a condenser unit then accumulating in the receiver for a new testing cycle. The experimental apparatus was insulated with foam to minimize heat transfer between the system and environment.

The detail of test sections was depicted in Fig. 2. The heat flux applied on test sections by a water loop. The T-type thermocouples were attached at top and bottom sides every 50 mm along the test sections from the inlet. The effective length was 200mm. Thermocouples and pressure transducers were also set up at the adiabatic pipes between the inlet and outlet. Moreover, two sight glasses

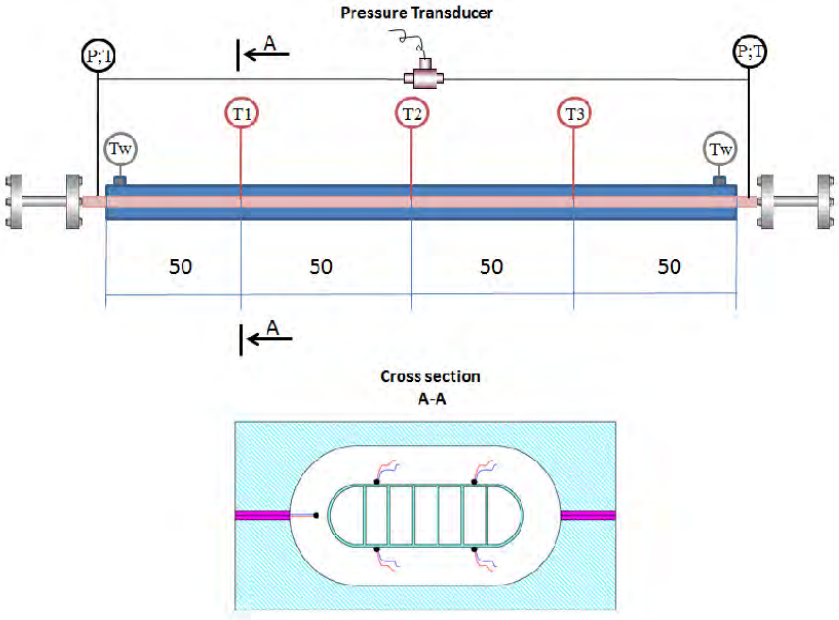

Figure 2: Test section and sample cross-section

were installed at the beginning and the end of test tubes to visualize the flow pattern. The dimensions of test tubes are described in Table 1.

Table 1. Dimensions of multiport tube

Parameter	Height (mm)	Width (mm)	Number of channel	Aspect Ratio	Hydraulic Diameter (mm)
Type A	2.00	0.79	7	2.531	1.16
Type B	2.00	0.77	11	2.597	1.14
Type D	1.40	0.87	16	1.609	1.07
Type E	1.42	0.70	9	2.028	0.96

2.1.2. Data reduction

The data were collected using a data acquisition equipment (MX100 Yokogawa) and analysed by a data reduction program. The physical properties of the refrigerant were obtained from REFPROP 8. All the information included the testing conditions and real-time data were monitored from the PC.

The heat flow rate is calculated from mass flow rate and temperature change of heating water flowing inside the water jacket as follows:

$$Q = \dot{m} c_p (T_{in} - T_{out}) - Q_{loss} \quad \text{Eq. (1)}$$

where ṁ, cp and T are the mass rate of flow, specific heat and temperature of the heating water loop. Q_{loss} is the heat loss on the test section which was determined on the calibrating process. The local heat transfer coefficient inside the channel can be evaluated as the ratio of the heat flux to saturation minus the inside wall temperature:

$$h = \frac{Q}{A.(T_{wi} - T_{sat})} \quad \text{Eq. (2)}$$

The inside tube wall temperature, T_{wi}, which was the average temperature of the top and the bottom wall temperatures, was determined based on the steady-state one-dimensional radial conduction heat transfer through the wall without internal heat generation.

The average vapor quality, x, at the measurement locations, z, were determined based on the thermodynamic properties:

$$x = \frac{i - i_{fi}}{i_{fg}} \quad \text{Eq. (3)}$$

where i is the enthalpy of flow at the measured point; i_{fi} and i_{fg} are the enthalpies of inlet fluid and latent heat of refrigerant at saturation state, respectively.

The experimental uncertainties were then analysed as described in the ISO guidelines (1995). Following that, the standard uncertainty of a measured parameter is composed of type A and type B evaluations of uncertainty. Type A evaluation is conducted from the statistical analysis of repeated measurements taken under steady state conditions during the recording time interval. Type B uncertainty comes from the instrument and data logger that are provided by the manufacturers or specific calibration procedures. Table 2 demonstrates the type B evaluation of sensors and measured devices. In present work, the uncertainty of heat flux, vapor quality and the heat transfer coefficient are approximately 3%, 5% and 9.91%, respectively. All the uncertainties were reported with the confident level of 95%.

Table 2. Summary of type B uncertainty

Parameter	Expanded uncertainty
Temperature	±0.15 K
Absolute pressure	±1 kPa
Different pressure	±2.5 kPa
G refrigerant	±0.2 %
G water	±0.2 %

2.2. Results and Discussions

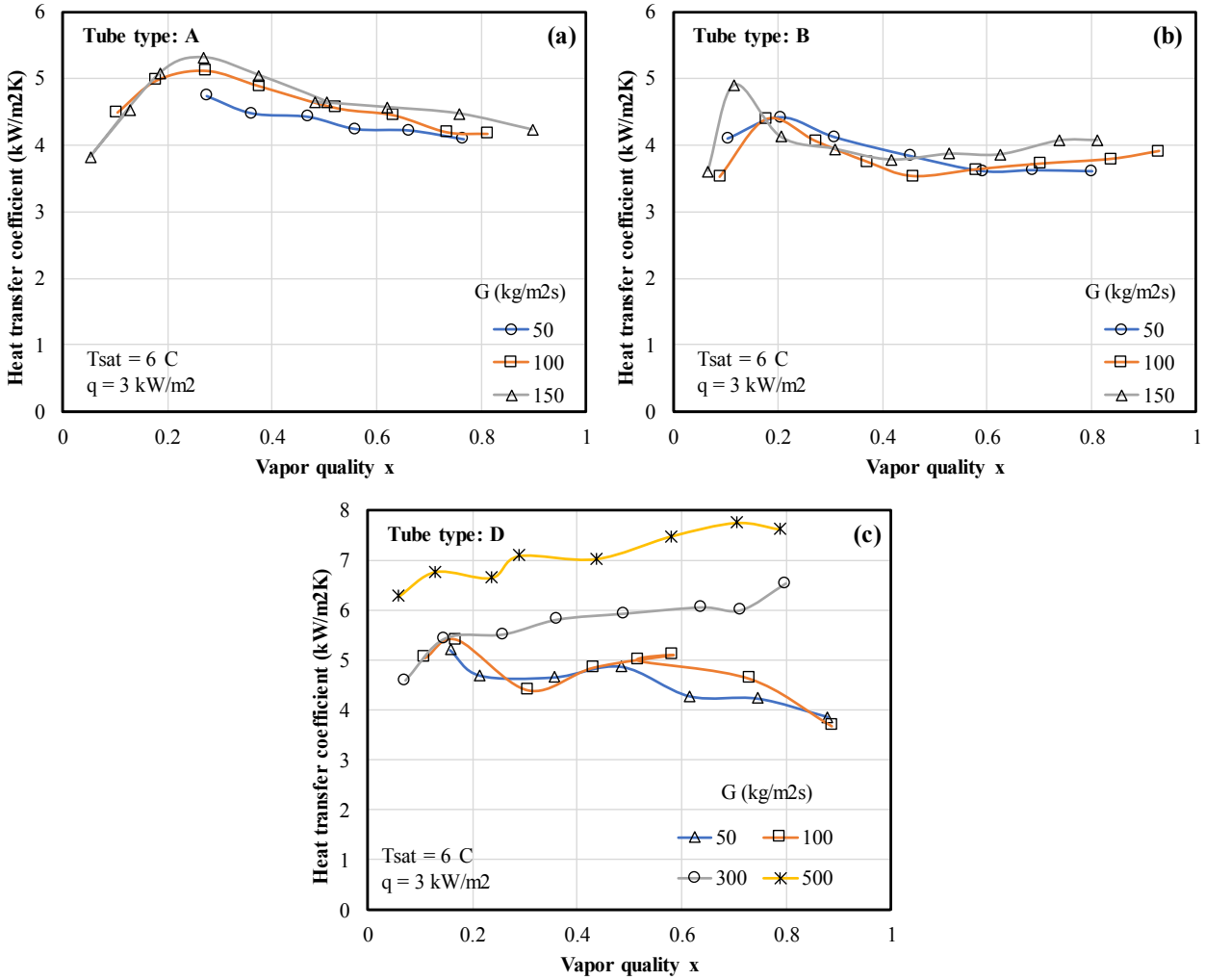

Figure 3: The effect of mass flux on heat transfer coefficient of R410A

The effect of mass flux on heat transfer coefficient of R410A is shown in Fig. 3. The heat transfer coefficient of R410A is higher in higher mass flux conditions. However, at quality of around 0.2, heat transfer coefficient decrease when mass flux is less than 150 kg/m^{2}s. It can be explained that in the low aspect ratio tube, when the mass flux is small, liquid film at the flat side of rectangular tube is thinner than the one in circular tube since the liquid detains in the corner. The observation of this phenomenon is demonstrated in the study of Tanaka et al. (2014). Also, this phenomenon is suppressed at high mass flux condition.

The effect of heat flux is illustrated in Fig. 4. The heat transfer coefficient also increases with the increasing of heat flux. At some conditions, the effect of heat flux on heat transfer coefficient is not

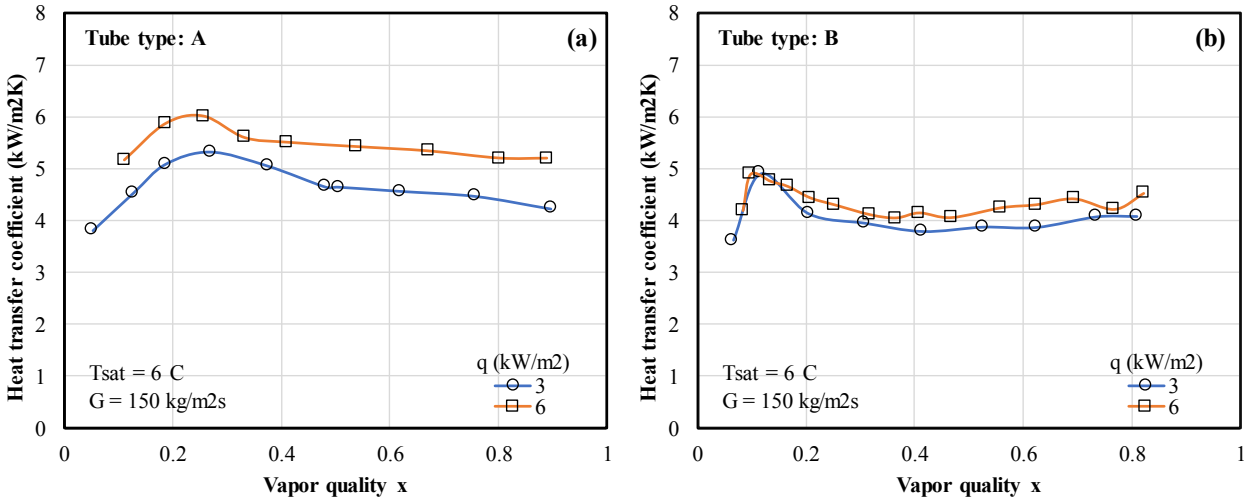

Figure 4: The effect of heat flux on heat transfer coefficient of R410A

significant at smallest vapor quality compared to that at larger vapor quality.

Table 3. Summary of HTC comparison

Types	A		B		D		E		OVERALL	
Correlations	MD	AD	MD	AD	MD	AD	MD	AD	MD	AD
Lazarek & Black (1982)	62.87	-62.87	55.15	-55.15	66.69	-60.88	53.30	-51.65	59.47	-57.59
M. Shah (1976)	55.48	-55.48	47.09	-47.09	43.30	-30.10	48.69	5.18	48.44	-32.32
Copper (1984)	63.06	-63.06	55.78	-55.78	62.49	-60.35	57.03	-56.16	61.32	-59.70
Gungor & Winterton (1987)	20.64	-20.05	14.82	-4.19	25.27	-0.34	41.09	37.52	25.07	2.98
Liu & Winterton (1991)	61.28	-61.28	53.88	-53.88	54.91	-50.71	42.23	-39.37	53.07	-51.31
Tran et al. (1996)	71.00	-71.00	65.60	-65.60	75.86	-72.54	67.38	-67.38	69.92	-69.06
Warrier et al. (2002)	81.15	-81.15	79.32	-79.32	76.40	-76.26	80.79	-80.79	79.34	-79.31
Bertsch et al. (2009)	27.86	-24.87	26.59	-11.00	31.64	-21.99	41.42	21.22	31.69	-9.44
Li and Wu (2010)	39.24	39.24	63.09	61.45	40.62	22.25	59.21	51.27	50.86	43.80
Oh and Sun (2011)	56.11	-54.85	47.06	-44.78	52.84	-22.01	62.84	24.39	54.38	-24.91
Sun and Mishima (2009)	31.17	-31.17	18.27	-17.74	41.10	-28.35	27.62	-10.57	29.35	-21.89
Choi et al. (2007)	48.02	-35.90	56.64	-5.30	65.04	0.92	75.55	41.49	61.27	0.26
Chien et al. (2015)	69.36	68.37	80.17	-80.17	79.76	-79.76	77.66	-77.66	80.11	-80.11

2.3. Proposing new heat transfer coefficient correlation

Table 3 shows the comparison of experimental data with some well-known heat transfer coefficient correlations includes the ones proposed by Cooper, (1984), Bertsch et al., (2009); Lazarek and Black, (1982); Li and Wu, (2010); Gungor and Winterton, (1987); Liu and Winterton, (1991); Shah, (1982), Chien et al., (2015); Li and Wu, (2010); Oh and Son, (2011); Tran et al., 1996; Warrier et al., (2002), Choi et al., (2007) and Sun and Mishima, (2009). The trends show the overall deviation of four tube types. The best prediction is a correlation of Gungor and Winterton (1986) which shows the overall mean deviation of about 25%. The other correlations proposed by Bertsch et al. (2009) and Sun and Mishima (2009) also show the good prediction with overall mean deviations of about 30%. Most of heat transfer coefficient correlations are under predicted, exception is the one proposed by Li and Wu (2010), which is much over predicted against the present experimental data.

From the observation of experimental data, we found that, the effect of mass flux, heat flux and aspect ratio on the heat transfer coefficient of refrigerants should be consider simultaneously. Moreover, Tanaka et al. (2014) reported that most the nucleate bubbles coalesce in corners while the thin liquid appears soon at the flat side. The flow pattern in rectangular channel, in consequence, may differ than flow pattern in circular tubes. The work reported by Yang et al. (2004), in addition, well demonstrated the contrary heat transfer phenomenon of mini rectangular channel compared to conventional tube such as the existence of heat flux effect in annular regime. Thus, we proposed that, for rectangular tube, the heat transfer coefficient should be considered as follows:

$$h_{tp} = F \times h_{lo} \qquad \text{Eq. (4)}$$

Where F is the enhanced factor and h_{lo} is the single-phase liquid heat transfer coefficient, which is defined by the Dittus–Boelter correlation.

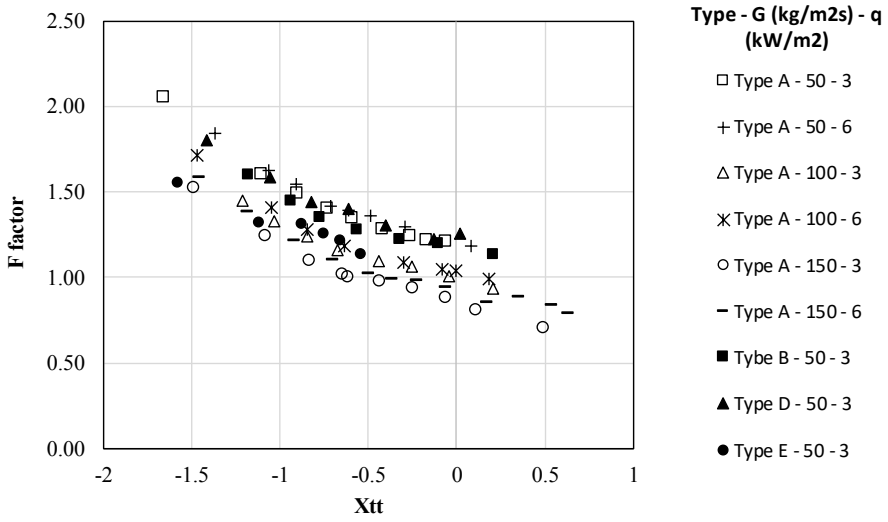

Figure 5: F factor versus the X_{tt} Parameter

$$h_{lo} = 0.023 \frac{k_f}{D}\left[\frac{G(1-x)D}{\mu_f}\right]^{0.8}\left(\frac{c_{pf}\mu_f}{k_f}\right)^{0.4} \quad \text{Eq. (5)}$$

The relation of ratio heat transfer coefficient (h_{tp}/h_{lo}) versus the Martinelli parameter is described in Fig. 5. The results show the strong relation of enhancement factor F and Xtt.which is determined as follows:

$$X_{tt} = \left(\frac{1-x}{x}\right)^{0.9}\left(\frac{\rho_l}{\rho_v}\right)^{0.5}\left(\frac{\mu_l}{\mu_v}\right)^{0.1} \quad \text{Eq. (6)}$$

Using the regression method, we finally found the form of F factor as follows:

$$F = 0.2655 \times \left(\frac{G}{G_{base}}\right)^{-0.682} \times \left(\frac{q}{q_{base}}\right)^{0.135} \times 10^{B+C}$$
$$B = 2.41\beta - 0.672\beta^2$$
$$C = 0.182\log\left(\frac{1}{X_{tt}}\right) + 0.2\log\left(\frac{1}{X_{tt}}\right)^2 \quad \text{Eq. (7)}$$

The comparison between the experimental data and proposed heat transfer coefficient correlation is shown in Figure 6. When compare with the whole data, the overall mean deviation and average deviation

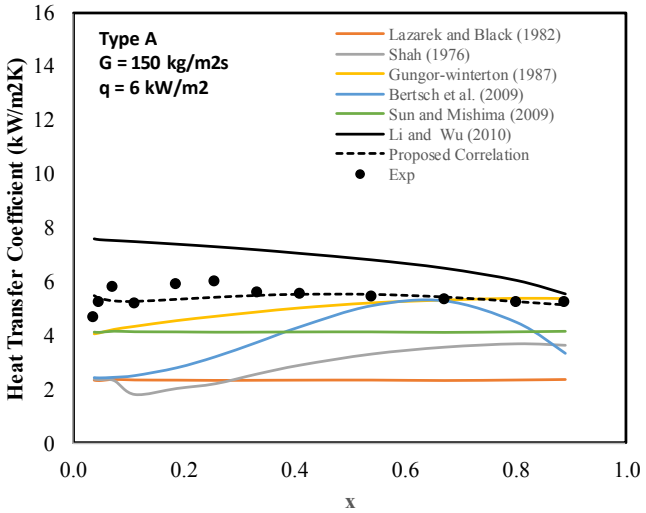

Figure 6: comparison between the experimental data and proposed heat transfer coefficient correlation

of new correlation are 10.7% and -2.5%. Also, to validate the new correlation, Total 81 data points from the work of Keaw-On et al. (2009) are collected. The proposed correlation performs a good prediction with the mean deviation of 15.5% and most of data fall in the ±30% MAE region.

3. CONCLUSIONS

The two-phase flow boiling heat transfer coefficients of R410A in four types of minichannel multiport tube and a new heat transfer coefficient correlation were investigated in this study. The heat transfer coefficient in rectangular was found to be strongly influenced by the aspect ratio as well as the heat flux and mass flux. The balance of those factors is important when design the heat exchanger using the multiport rectangular tube. Also, the new heat transfer coefficient correlation shows the good prediction against the experimental data and the existing data in literature.

ACKNOWLEDGEMENTS

This research was supported by Basic Science Research Program through the National Research Foundation of Korea (NRF) funded by Ministry of Education, Science, and Technology (NRF-2016R1D1A1A09919697)

NOMENCLATURE

A	Area (m^2)	$\dot{m}$	Mass flow rate (kg/s)
Cp	Specific heat (kJ/kg.K)	*T*	Temperature (K)
i	Enthalpy (kJ/kg)	*x*	Vapor quality (-)

REFERENCES

Bertsch, S.S., Groll, E. a., Garimella, S. V., 2009. A composite heat transfer correlation for saturated flow boiling in small channels. Int. J. Heat Mass Transf. 52, 2110–2118. Chen, J.C., 1966. Correlation for boiling heat transfer to saturated fluids in convective flow. Ind. Eng. Chem. Process Des. Dev. 5, 322–329. doi:10.1021/i260019a023

Chien, N.B., Vu, P.Q., Choi, K.-I., Oh, J.-T., 2015. A general correlation to predict the flow boiling heat transfer of R410A in macro-/mini-channels. Sci. Technol. Built Environ. 21, 526–534. doi:10.1080/23744731.2015.1035603

Choi, K.-I., Pamitran, a. S., Oh, J.-T., 2007. Two-phase flow heat transfer of CO2 vaporization in smooth horizontal minichannels. Int. J. Refrig. 30, 767–777. doi:10.1016/j.ijrefrig.2006.12.006

Cooper, M.G., 1984. Saturation nucleate pool boiling - a simple correlation, in: First U.K. National Conference on Heat Transfer. Elsevier, pp. 785–793. doi:10.1016/B978-0-85295-175-0.50013-8

Copetti, J.B., de Sá Bekerle, B., Macagnan, M.H., Passos, J.C., Oliveira, J.D., 2017. Flow Boiling Heat Transfer Characteristics of R600a in Multiport Minichannel. Heat Transf. Eng. 38, 323–331. doi:10.1080/01457632.2016.1189271

Fernando, P., Palm, B., Ameel, T., Lundqvist, P., Granryd, E., 2008. A minichannel aluminium tube heat exchanger – Part II: Evaporator performance with propane. Int. J. Refrig. 31, 681–695. doi:10.1016/j.ijrefrig.2008.02.012

Gungor. K. E. and Winterton, R. H. S., 1987, Simplified General Correlation for Saturated Flow Boiling and Comparisons of Correlations with Data, Chem. Eng. Res Des., 65, pp. 148-156.

Huai, X., Koyama, S., Zhao, T.S., Shinmura, E., Hidehiko, K., Masaki, M., 2004. An experimental study of flow boiling characteristics of carbon dioxide in multiport mini channels. Appl. Therm. Eng. 24, 1443–1463. doi:10.1016/j.applthermaleng.2003.10.032

Kaew-On, J., Wongwises, S., 2009. Experimental investigation of evaporation heat transfer coefficient and pressure drop of R-410A in a multiport mini-channel. Int. J. Refrig. 32, 124–137. doi:10.1016/j.ijrefrig.2008.06.010

Lazarek, G., Black, S., 1982. Evaporative heat transfer, pressure drop and critical heat flux in a small vertical tube with R-113. Int. J. Heat Mass Transf. 25.

Lee, H.J., Lee, S.Y., 2001. Heat transfer correlation for boiling flows in small rectangular horizontal

channels with low aspect ratios. Int. J. Multiph. Flow 27, 2043–2062. doi:10.1016/S0301-9322(01)00054-4

Li, Jiyang; Dang, Chaobin; and Hihara, E., 2016. Experimental investigation on up-flow boiling of R1234yf in aluminum multi-port extruded tubes, in: International Refrigeration and Air Conditioning Conference. p. 8.

Li, W., Wu, Z., 2010. A general correlation for evaporative heat transfer in micro/mini-channels. Int. J. Heat Mass Transf. 53, 1778–1787. doi:10.1016/j.ijheatmasstransfer.2010.01.012

Liu, Z., Winterton, R., 1991. A general correlation for saturated and subcooled flow boiling in tubes and annuli, based on a nucleate pool boiling equation. Int. J. Heat Mass Transf. 34, 2759–2766.

Lockhart, R.W., Martinelli, R. c., 1949. Proposed correlation of data for isothermal two-phase, two-component flow in pipes. Chemecal Eng. Prog. doi:http://dx.doi.org/10.1016/0017-9310(67)90047-6

Mishima, K., Hibiki, T., 1996. Some characteristics of air-water two-phase flow in small diameter vertical tubes. Int. J. Multiph. Flow 22, 703–712. doi:10.1016/0301-9322(96)00010-9

Oh, H.-K., Son, C.-H., 2011. Evaporation flow pattern and heat transfer of R-22 and R-134a in small diameter tubes. Heat Mass Transf. 47, 703–717. doi:10.1007/s00231-011-0761-4

Shah, M.M., 1982. Chart correlation for saturated boiling heat transfer: equations and further study. ASHRAE Trans.;(United States) 88, 185–196.

Sun, L., Mishima, K., 2009. An evaluation of prediction methods for saturated flow boiling heat transfer in mini-channels. Int. J. Heat Mass Transf. 52, 5323–5329. doi:10.1016/j.ijheatmasstransfer.2009.06.041

Tanaka, C., Dang, C., Hihara, E., 2014. Characteristics of Flow Boiling Heat Transfer in Rectangular Minichannels, in: Proceedings of the 15th International Heat Transfer Conference. Begellhouse, Connecticut, pp. 1–15. doi:10.1615/IHTC15.fbl.009589

Tran, T., Wambsganss, M., France, D., 1996. Small circular-and rectangular-channel boiling with two refrigerants. Int. J. Multiph. Flow 3, 485–498.

Vakili-Farahani, F., Agostini, B., Thome, J.R., 2013. Experimental study on flow boiling heat transfer of multiport tubes with R245fa and R1234ze(E). Int. J. Refrig. 36, 335–352. doi:10.1016/j.ijrefrig.2012.12.007

Warrier, G.R., Dhir, V.K., Momoda, L. a., 2002. Heat transfer and pressure drop in narrow rectangular channels. Exp. Therm. Fluid Sci. 26, 53–64. doi:10.1016/S0894-1777(02)00107-3

Y. Yang, Y. Fujita, 2004. Flow Boiling Heat Transfer and Flow Pattern in Rectangular Channel of Mini-Gap, in: ASME. International Conference on Nanochannels, Microchannels, and Minichannels, ASME 2nd International Conference on Microchannels and Minichannels. pp.573–580

Manuscript ID: 1185
DOI: 10.18462/iir.icr.2019.1185

Cesium and ammonium salts as low temperature secondary fluids

Monika IGNATOWICZ[(a)], Lorenzo BARCAROLO[(b)], Åke MELINDER[(a)], Luca MOLINAROLI[(b)], Björn PALM[(a)]

[(a)] KTH Royal Institute of Technology
Stockholm, 100 44, Sweden, monikai@kth.se
[(b)] Politecnico di Milano
Milano, 201 33, Italy

ABSTRACT

Potassium formate and potassium acetate, as well as their blends are known as environmentally friendly secondary fluids with good thermophysical properties. The aim of this work was to investigate properties of cesium formate, cesium acetate and ammonium acetate solutions. Results showed that various alkali metal ions such as potassium, sodium, cesium or ammonium are affecting the freezing point, thermal conductivity, viscosity and specific heat capacity in different ways. Among examined salts, ammonium formate showed the best performance by giving the highest specific heat capacity and highest thermal conductivity and the lowest dynamic viscosity compared to potassium formate and other salts. Cesium formate solutions had the lowest viscosity among all tested salts. This study shows that both cesium formate and sodium formate could be used as different additives to enhance different properties of potassium formate and potassium acetate secondary based fluids.
Keywords: Cesium Formate, Cesium Acetate, Potassium Formate, Potassium Acetate, Ammonium Formate, Ammonium Acetate, Secondary Fluid, Indirect Refrigeration System, Thermophysical Properties.

1. INTRODUCTION

Potassium formate (KF) is a monovalent alkali formate salt that has been used for many decades in various cooling and ventilation applications. Potassium formate solutions at low concentrations up to 50 wt-% are mostly used as low temperature secondary fluids for indirect refrigeration systems (Aittomäki and Lahti, 1997) and biodegradable de-icing solutions (Lowenstein, 2008). Moreover, highly concentrated potassium formate solutions, 60 – 80 wt-%, in temperature range between 1 and 80 °C have been investigated as new liquid-desiccants (Longo and Gasparella, 2016). Potassium formate has been known as cheap, environmentally friendly and less corrosive than chloride based secondary fluids (Aittomäki and Lahti, 1997). It can create a highly concentrated solution of 76 wt-% near the saturation conditions (Balarew et al., 2001). Another well-known organic salt used as secondary fluid is potassium acetate (KAc). Potassium acetate is a less corrosive salt for low temperature applications giving a 70 wt-% concentrated solution (Stephen and Stephen, 1963). The biggest drawback of potassium acetate solutions is higher viscosity compared to potassium formate solutions (Melinder, 2007). Therefore, blends of potassium formate and potassium acetate were introduced to the market to overcome problems related to corrosion and thermophysical properties (Ure, 2003) and (Melinder, 2007). Both potassium formate and potassium acetate solutions have good thermophysical properties compared to aqueous solutions of alcohols and glycols. An extensive review of thermophysical property data for both pure and commercial potassium formate and potassium acetate solutions at salt concentration up to 48 wt-% were presented in (Melinder, 1998), (Melinder, 2007) and (Melinder, 2010). Most recent experimental results for some thermophysical properties of pure solutions of potassium formate for cooling applications can be found in Ignatowicz et al. (2017) and Wåhlin and Klein-Paste (2017).
Monovalent formate salts such as potassium formate, sodium formate (NaF) and cesium formate (CsF) have been used as the drilling and completion fluids for oil industry since early 1990's and the collaboration between oil and refrigeration industry resulted in new generation

of organic salt based secondary fluids in late 1990's. These alkali metal formates have very high solubility levels in water and create dense, thermally stable and relatively low viscous alkaline solutions ideally suited for extreme conditions as reported by Downs (1992) and Downs (1993). A drawback of these highly concentrated formate blends (between 40 and 97 wt-%) is rather high crystallization temperature above 8 ºC limiting its use only to high temperature and high pressure applications (Caenn et al., 2017). The thermophysical properties in the temperature range between 10 and 70 ºC for highly concentrated blends of potassium formate and sodium formate; cesium formate and potassium formate as well as sodium formate (15.7; 29.9; 42.9 and 49 wt-%) have been found in Cabot Corp (2016). Among all formate salts, pure solutions of sodium formate showed the most promising thermophysical properties at high temperatures (Cabot Corp, 2016). Frolova et al., (2015) reported that sodium formate solutions experience rather high eutectic temperature of about -16 ºC at the concentration of 24.7 wt-%, which limits its possible low temperature application to additive only. Some experimental results for density and dynamic viscosity at 25 ºC for low concentration sodium formate solutions up to 8.2 wt-% has been reported by Chmielewska et al., (2005). Cesium formate has even higher solubility compared to potassium formate that can reach the freezing point temperature of -60 °C (Caenn et al., 2017). Cabot Corp (2016) has published the density data at temperature of 25 °C as well as the dynamic viscosity data in the temperature range between 0 and 100 °C for cesium formate solutions between 22 and 87 wt-%. Cesium acetate (CsAc) is another interesting highly soluble acetate salt creating a highly concentrated solution of 91 wt-% close to saturation condition at temperature of 20 °C (Stephen and Stephen, 1963). Nowadays, cesium acetate salt is often used in various chemical and biochemical processes, ion sensors for combustion processes (Butt et al., 2015) as well as a modifier in thin layer solar cells (Mahmud et al., 2018). Due to lack of literature thermophysical property data it was decided to investigate cesium acetate solutions as a possible new secondary fluid.

Ammonium formate (NH_4F) and ammonium acetate (NH_4Ac) are other interesting salts having very similar molar mass as sodium formate. Literature data for aqueous ammonium formate and ammonium acetate solutions are very limited. Ammonium formate and ammonium acetate are mostly used as a buffering agent, solvent and food preservatives. Nevertheless, the experimental data for molten ammonium formate show rather high thermal conductivity and specific heat capacity values (Osman et al., 1996). Ammonium formate solution can give a 50 wt-% concentrated solution close to the saturation conditions as found in Balarew et al., (2001). Latest results show that different alkali metal ions such as sodium, lithium or ammonium are affecting the solubility level, freezing point, thermal conductivity, viscosity and specific heat capacity in different way (Ignatowicz et al., 2017). Thus, the purpose of this work is to investigate the thermophysical properties of various cesium, ammonium and potassium salts at low temperatures in order to investigate possibilities of using these salts as a new generation of secondary fluids for low temperature applications.

2. METHODOLOGY

Ammonium formate (purity 98%), ammonium acetate (purity 99%) and sodium formate (purity 99%) were purchased from Merck Co., whereas potassium formate (purity 99%), potassium acetate (purity 99%), cesium formate (purity 99%) and cesium acetate (purity 99%) were supplied by Alfa Aesar. Note that all solutions were prepared directly using de-ionized water. Various cesium formate, cesium acetate, sodium formate, ammonium formate and ammonium acetate solutions having concentration each 10 wt-% up to the highest possible concentration just below the saturation level were prepared in order to study the freezing point due to the very limited reference data. Afterwards, solutions of the representative freezing point of about -10 ºC, -20 ºC and -30 ºC were prepared.

2.1. Freezing Point and Specific Heat Capacity

The freezing point temperature and specific heat capacity were measured using microDSC7 evo from Setaram Instrumentation with a temperature accuracy of ±0.01 ˚C and specific heat capacity accuracy of ±1%. The testing input parameters were defined based on measurements obtained for water at four different continuous mode heating and cooling scanning rates (0.025; 0.05; 0.1 and 0.15 $K \cdot min^{-1}$). The results showed that the continuous heating scanning rate of 0.1 $K \cdot min^{-1}$ and 0.05 $K \cdot min^{-1}$ were most suitable for the freezing point temperature and specific

heat capacity tests, respectively. Sample volume was always kept constant (750 µl) and all tests were performed in the temperature range between -45 and 40 °C. The freezing point measurements for samples having lower freezing point than -45 ˚C were performed using a specially built apparatus consisting of Sanyo Ultra Low freezer (temperature range between -15 and -90 ˚C), an Agilent 34970A Data Acquisition unit, a computer and a designed freezing unit with thermocouples (type TT-T-30-SLE) having accuracy of ±0.1°C. The freezing unit consisted of nine identical containers (volume 100ml) arranged in the circle, fitted to a Plexiglas plate and enclosed from the top with a closing plate. Additional two thermocouples were attached to the freezing unit to measure the conditions in the freezer. All eleven thermocouples were calibrated each 5K in temperature range between -20 and 25 ˚C with accuracy of ±0.01°C. Note that tests were repeated three times and sample temperature was recorded every second and freezer temperature was set to maximum 5K below the expected freezing point.

2.2. Density

The density measurements were performed using pycnometer with and without thermometer. The pycnometer is a glass bottle with a stopper having a capillary tube through it. By knowing the total volume and by measuring the mass of empty as well as of full pycnometer with a Mettler Toledo high accuracy analytical balance (accuracy of ± 0.0001 g), the density of solutions at 20 °C was determined. The accuracy of the density measurement at 20 °C using calibrated pycnometer (volume 25.131 cm^3) is set to be ± 0.2 %. The density gradient in temperature range between 10 and 25 °C was obtained using the calibrated pycnometer with thermometer having similar volume of 25.156 cm^3 and the thermostat bath. Note that the correction of the certified volume of pycnometer for a given temperature was done according to ISO specifications.

2.3. Dynamic Viscosity

Brookfield rotational viscometer DV-II Pro with special low viscosity adapter (UL-adapter) was used to perform dynamic viscosity measurements in the temperature range between -18 and 40 °C. All measurements were done using the same UL-adapter and spindle to reduce the uncertainty of measurements. The dynamic viscosity value at given temperature was obtained as the slope of shear stress versus shear rate function for the torque range between 10 and 90 % and the instrument accuracy of ± 1 %.

2.4. Thermal Conductivity

Thermal conductivity measurements were performed using Transient Plane Source (TPS) method by means of Hot Disk Thermal Constants Analyser TPS-2500S having the accuracy of ± 2 %. Kapton sensor 7577 (radius 2.001 mm) was chosen and tests for a given temperature were repeated six times at different measuring time (2 - 3 s) and output power (20 - 32 mW) in the temperature range between -28 and 40 °C.

3. RESULTS

Fig. 1 presents the freezing point temperature results. The measurement error of the freezing point between each single test was about ± 0.1°C. Note that the freezing point reference values for potassium acetate solutions found in Melinder (2007) are mainly based on Timmermans (1960), Florian (1997), Melinder (1998), as well as commercial products. Moreover, the reference data for potassium formate found in Melinder (2007) and Cabot Corp., (2016) are based on commercial products containing different additives. No reference data for ammonium formate, ammonium acetate and cesium acetate solutions were found. As seen, the reference and experimental values for potassium formate solutions up to concentration of 40 wt-% (respective freezing point of -35 °C) are in rather good agreement. At higher concentrations, the freezing point results was about 1-2 K lower than expected. Thus, lower potassium formate concentration of 45 wt-% and 47 wt-% is needed to obtain the freezing point of -45 °C and -50 °C, respectively. Higher discrepancies in terms of both concentration and freezing point were found in case of potassium acetate solutions.

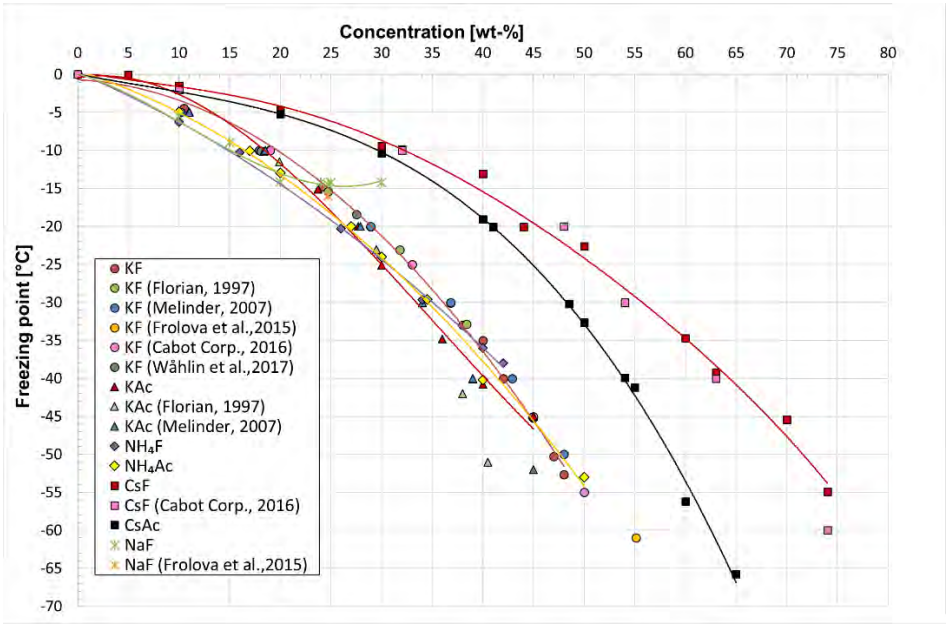

Figure 1: The freezing point temperature results for different formate and acetate salts

The deviation in the freezing point results for potassium acetate solutions was about 2-7 K at concentrations over 34 wt-%. Therefore, lower potassium acetate concentration (39 wt-% and 45 wt-%) are needed to obtain the freezing point of -40 °C and -45 °C, respectively. These differences can partly be explained by the fact that the different additives found in commercial products can significantly affect the freezing point temperatures. Thus, this study presents for the first time the concentrations of pure potassium formate and potassium acetate solutions required to obtain the respective freezing point temperatures of -30; -35; -40; -45 and -50 °C. Moreover, first freezing curves for cesium acetate, ammonium formate and ammonium acetate solutions have been published. As seen, 42 wt-% ammonium formate and 50 wt-% ammonium acetate solutions had the lowest freezing point temperature of -38 °C and -53 °C, respectively. The lowest temperature of about -66 °C was reached for 60 wt-% cesium acetate solution while 80 wt-% cesium formate solution gave the freezing point of around -56 °C. The extrapolated freezing curve for commercial cesium formate solutions found in Cabot Corp., (2016) show that the lowest freezing point temperature of -60 °C for 74 wt-% cesium formate commercial product. The experimental results for 24.7 wt-% sodium formate solution was in a good agreement with reference values found in Frolova et al., (2015). Note that solutions of sodium formate had rather high freezing point temperature and only 15 wt-% sodium formate solution was included in this study.

Fig. 2 shows the density results obtained for cesium, ammonium, sodium and potassium salts. The experimental density results for potassium acetate were in rather good agreement with references (± 0.2 %). However, the density results for 19 wt-% and 36.8 wt-% potassium formate solutions were about 0.5 % lower than references. Only density results for 29 wt-% potassium formate solution were in rather good agreement with reference values. Note that the reference values for potassium formate solutions found in Melinder (2007) and Melinder (2010) are mainly based on commercial product data having different additives that affect property values. As seen, cesium formate and cesium acetate solutions had the highest density due to the significantly higher concentrations. Additionally, potassium formate and potassium acetate solutions had higher density compared to sodium formate, ammonium formate and ammonium acetate solutions.

Fig. 3 presents the results of dynamic viscosity measurements for different salt solutions. The experimental results obtained for water were higher by up to 3 % than NIST reference values. As seen, similar trends were observed for chosen salts solutions with different freezing point temperatures. Results show the outstanding low dynamic viscosity results for all cesium formate solutions.

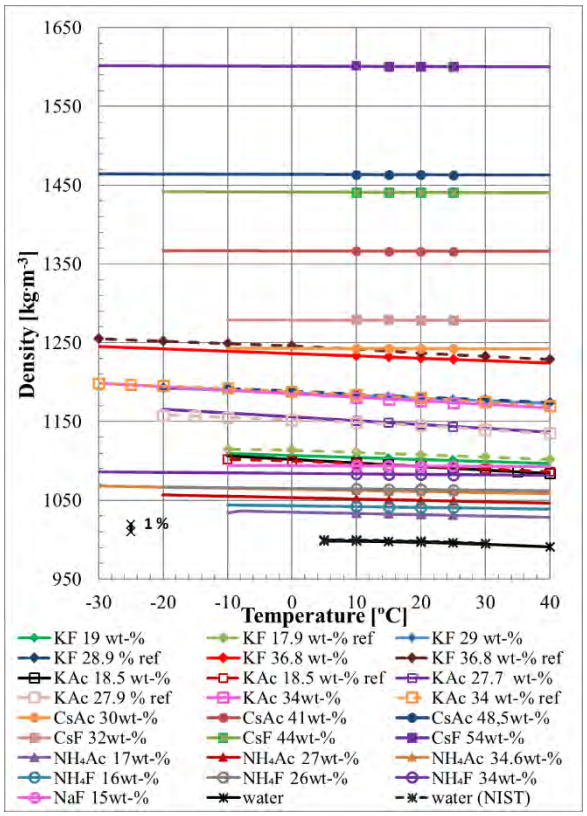

Figure 2: Density results

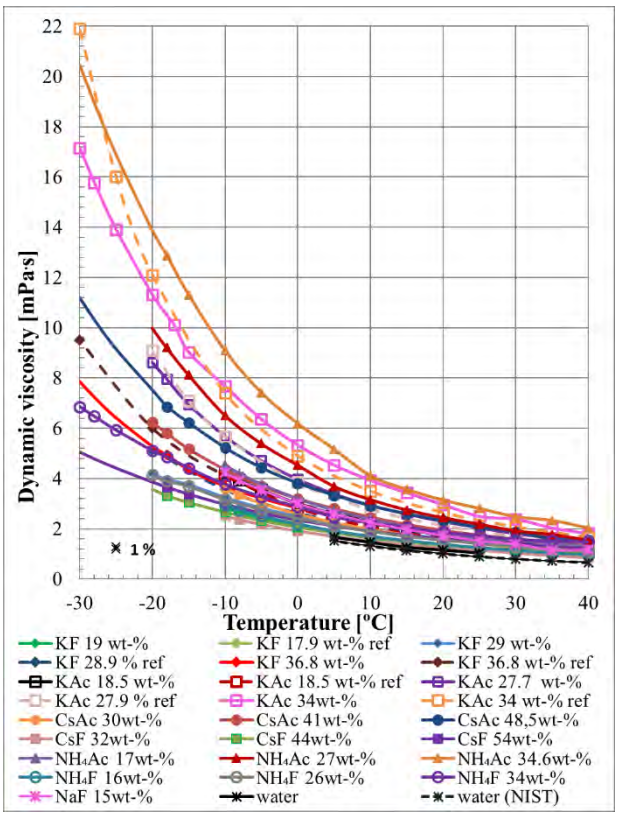

Figure 3: Dynamic viscosity results

Both 19 wt-% potassium formate and 16 wt-% ammonium formate solutions had higher viscosity than 32 wt-% cesium formate solution at temperature of -8 °C by 12 % and 16 %, respectively. Furthermore, 30 wt-% cesium acetate had higher viscosity by up to 41 % compared to 32 wt-% cesium formate solution. Solutions of 15 wt-% sodium formate and 18.4 wt-% potassium acetate had very similar viscosity values in full temperature range. Additionally, 17 wt-% ammonium acetate had the highest viscosity values among all samples. Both 26 wt-% ammonium formate and 29 wt-% potassium formate solutions had higher viscosity than cesium formate at temperature of -18 °C by 17 % and 19 %, respectively. 41 wt-% cesium acetate, 27.7 wt-% potassium acetate and 27 wt-% ammonium acetate had higher viscosity than 44 wt-% cesium formate by up to 42%, 58 % and 64 %, respectively. 27 wt-% ammonium acetate solution showed the highest viscosity values among all tested samples. 36.8 wt-% potassium formate and 34 wt-% ammonium formate had higher dynamic viscosity than 54 wt-% cesium formate at temperature of -18 °C by up to 33 % and 34 %, respectively. Instead, 48.5 wt-% cesium acetate solution had higher viscosity by up to 51 % compared to 54 wt-% cesium formate solution. Again, 34.6 wt-% ammonium acetate showed the highest viscosity values among all samples.

Fig.4 presents the specific heat capacity results. The experimental results for water were up to 1.5 % higher than NIST reference values. Note that the reference values for potassium formate and potassium acetate found in Melinder (2007) and Melinder (2010) were mainly based on different commercial products. As seen, 18.4 wt-% potassium acetate had higher specific heat capacity than 19 wt-% potassium formate by up to 2 %. Moreover, 17 wt-% ammonium acetate, 15 wt-% sodium formate and 16 wt-% ammonium formate solutions had higher specific heat capacity than 19 wt-% potassium formate by up to 8%, 6.5% and 6 %, respectively. Both 30 wt-% cesium acetate and 32 wt-% cesium formate had 8 % and 18% lower specific heat capacity than 19 wt-% potassium formate. Similar tendencies were observed for solutions having the freezing point of -20 °C and -30 °C. Again, potassium acetate solutions had higher specific heat capacity than potassium formate solutions by up to 6 %. 27 wt-% ammonium acetate and 26 wt-% ammonium formate had the highest specific heat capacity than 29 wt-% potassium formate by up 11 % and 10 %, respectively.

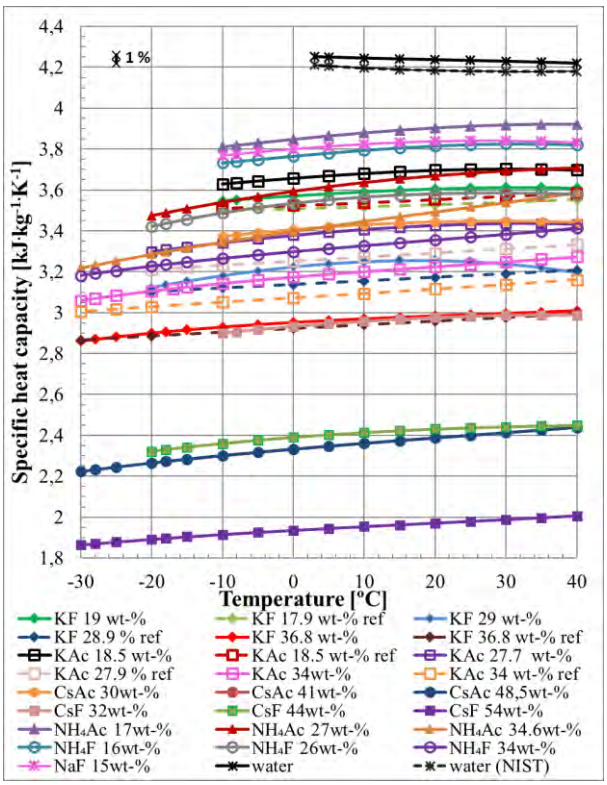

Figure 4: Specific heat capacity results

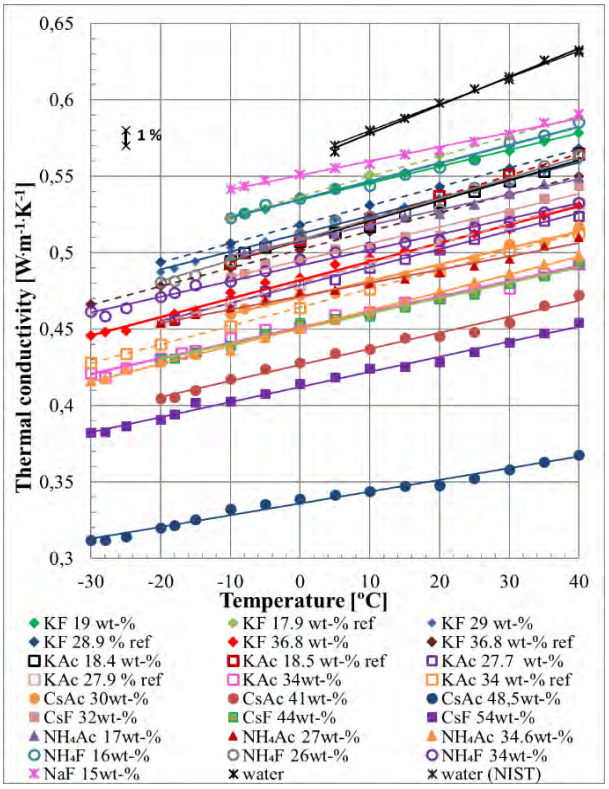

Figure 5: Thermal conductivity results

Whereas, 41 wt-% cesium acetate and 44 wt-% cesium formate had the lowest specific heat capacity than 29 wt-% potassium formate by up to 19 % and 26 %, respectively. 34.6 wt-% ammonium acetate and 34 wt-% ammonium formate solutions had the highest specific heat capacity among all solutions having the freezing point of -30 °C. Instead, 48.5 wt-% cesium acetate and 54 wt-% cesium formate had lower specific heat capacity than 36.8 wt-% potassium formate by up to 3.8 % and 30 %, respectively.

Fig. 5 shows the results of thermal conductivity tests. The difference between the experimental results and NIST reference values for water was less than 0.7 % which is significantly below the measurement error of instrument set to be ± 2 %. It is important to underline that the comparison of different salt solutions was based on the experimental results obtained for potassium formate and potassium acetate solutions. Note that the density and specific heat capacity are input values for post processing of thermal conductivity results since knowledge of the volumetric heat capacity, ρcp, decreases the measurement error below 2 %. As seen, the obtained results for potassium formate and acetate were up to 1 % lower than reference values in Melinder (2007). Experimental results for 36.8 wt-% potassium formate and 34 wt-% potassium acetate were by up to 5 % and 2 % lower than the reference values found in Melinder (2007). The difference between experimental and reference values could be explained by the fact that most reference values are based on commercial products data. As seen, 15 wt-% sodium formate had higher thermal conductivity values than 19 wt-% potassium formate and 16 wt-% ammonium formate. Instead, 32 wt-% cesium formate and 30 wt-% cesium acetate had lower thermal conductivity than 17.9 wt-% potassium formate by up to 7 % and 11 % at temperature of -8 °C, respectively. Both 17 wt-% ammonium acetate and 18.7 wt-% potassium acetate solutions had rather similar results. 29 wt-% potassium formate and 26 wt-% ammonium formate had the highest thermal conductivity among solutions having the freezing point of -20 °C. 44 wt-% cesium formate and 41wt-% cesium acetate solutions had lower thermal conductivity than 29 wt-% potassium formate at temperature of -18 °C by up to 11 % and 16 %, respectively. Moreover, 27.7 wt-% potassium acetate had slightly higher thermal conductivity values than 27 wt-% ammonium acetate. Similar results were observed for solutions having the freezing point of -30 °C. Again, 36.8 wt-% potassium formate and 34 wt-% ammonium formate had the highest thermal conductivity among all investigated

solutions. Both 54 wt-% cesium formate and 48.5 wt-% cesium acetate solutions had lower thermal conductivity than 36.8 wt-% potassium formate at temperature of -28 °C by up to 13 % and 30 %, respectively.

4. CONCLUSIONS

Results showed that different alkali metal ions such as potassium, sodium, cesium or ammonium are affecting the freezing point, thermal conductivity, viscosity and specific heat capacity in different ways. Among examined salts, ammonium formate showed the best performance by giving the highest specific heat capacity and highest thermal conductivity and the lowest dynamic viscosity compared to potassium formate and other salts. However, the lowest freezing point measured for ammonium formate solution (42 wt-%) was -38 °C. Cesium formate solutions had the lowest viscosity among all salts. Moreover, first freezing curves for cesium acetate, ammonium formate and ammonium acetate solutions have been published. This study shows that both cesium formate and sodium formate could be used as additives to enhance different properties of potassium formate and potassium acetate secondary based fluids. Further studies are planned to investigate new formate and acetate blends.

ACKNOWLEDGEMENTS

The Swedish Energy Agency, Termo program, Swedish Refrigeration Foundation (Kylbranchens Samarbetsstiftelse) and all industrial partners are greatly acknowledged for financing this project.

NOMENCLATURE

c_p	specific heat capacity ($J \cdot kg^{-1} \cdot K^{-1}$)	*NaF*	sodium formate
CsAc	cesium acetate	NH_4F	ammonium formate
CsF	cesium formate	NH_4Ac	ammonium acetate
f	freezing	*T*	temperature (ºC)
k	thermal conductivity ($W \cdot m^{-1} \cdot K^{-1}$)	*wt-%*	weight concentration (-)
KAc	potassium acetate	μ	dynamic viscosity ($mPa \cdot s$)
KF	potassium formate	ρ	density ($kg \cdot m^{-3}$)

REFERENCES

Aittomäki, A., Lahti, A., 1997. Potassium formate as a secondary refrigerant. Int. J. Refrigeration 20, 276–282.

Balarew, Ch., Dirkse, T.P., Golubchikov, O.A., Salomon, M., 2001. IUPAC-NIST Solubility data series: metal and ammonium formate systems. J. Physical Chem. Ref. Data 30, No. 1, 1-163.

Barcarolo L., 2018, Alternative salt based secondary fluids for indirect refrigeration systems. Thesis, Royal Institute of Technology, KTH, Stockholm, Sweden.

Butt, R.H., Chen, Y., Mack, J.H., Saxena, S., Dibble, R.W., Chen, J.Y., 2015. Improving ion current of sparkplug ion sensors in HCCI combustion using sodium, potassium, and cesium acetates: Experimental and numerical modeling, Proceedings of the Combustion Institute 35, 3107–3115.

Cabot Corp, 2016. Formate technical manual, Cabot Specialty Fluids, Aberdeen, Scotland.

Caenn, R., Darley, H. CH., Gray G. R., 2017. Composition and properties of drilling and completion fluids. Gulf Professional Publishing, Elsevier, ISBN 978-0-12-804751-4.

Chmielewska, A., Wypych-Stasiewicz, A., Bald, A., 2005. Viscosimetric studies of aqueous solutions of salts of carboxylic acids. J. Molecular Liquids 122, Issue 1-3, 110-115.

Downs, J.D., 1992. Formate brines: new solutions to deep slim-hole drilling fluid design problems. paper SPE 24973, European Petroleum Conference, Cannes, France.

Downs, J.D., 1993. Formate brines: novel drilling and completion fluids for demanding environments. paper SPE 25177, SPE International Symposium on Oilfield Chemistry, New Orleans, USA.

Evenmo, K., 1998. A new secondary fluid. IIR Gustav Lorentzen Conference on Natural Working Fluids, Oslo, Norway.

Florian O., 1997, Heat transfer and pressure drop of liquid secondary refrigerants - experiments and theory. Thesis, Royal Institute of Technology, KTH, Stockholm, Sweden.

Frolova, E.A., Kondakov, D.F., Nikolaev,V.V., Tin'gaev O. P., Danilov V. P., 2015. Phase equilibria in the sodium formate–potassium formate–water system below 0°C and the anti-icing properties of salt compositions, Theoretical Foundations of Chemical Engineering 49, No. 5, 719–720.

Ignatowicz, M., Melinder, Å., Palm, B., 2017. Alternative formate salts as low temperature secondary fluids. 5th IIR International Conference on Thermophysical Properties and Transfer Processes of Refrigerants, Seoul, South Korea.

Lemmon, E.W., Huber, M.L., McLinden, M.O., 2013. NIST Standard reference database23: Reference fluid thermodynamic and transport properties – REFPROP Version 9.1. NIST, Gaithersburgh, MD.

Longo, G.A., Gasparella, A., 2016. Experimental measurement of thermophysical properties of H2O/KCOOH (potassium formate) desiccant. Int. J. Refrigeration 60 106–113.

Lowenstein, A., 2008. Review of liquid desiccant technology for HVAC applications. HVAC&R Res. 14, 819–839.

Mahmud, M.A., Elumalai, N.K., Upama, M.B., Wang D., Gonçales, V.R., Wright, M., Gooding, J.J., Haque, F., Xu, C., Uddin, A., 2018. Cesium compounds as interface modifiers for stable and efficient perovskite solar cells, Solar Energy Materials and Solar Cells 174, 172-186.

Melinder, Å., 1998, Thermophysical properties of liquid secondary refrigerants, a critical review on literature references and laboratory measurements, Engineering Licentiate Thesis, Royal Institute of Technology, KTH, Stockholm, Sweden.

Melinder, Å., 2007. Thermophysical properties of aqueous solutions used as secondary working fluids, Doctoral thesis, Royal Institute of Technology, KTH, Stockholm, Sweden.

Melinder, Å., 2010. Properties of secondary working fluids for indirect systems, International Institute of Refrigeration, IIR, Paris.

Osman, M.B.S., Dakroury, A.Z., Dessouky, M.T., Kenawy, M.A., El-Sharkawy, A.A., 1996. Measurements of thermophysical properties of ammonium salts in the solid and molten states. J. Thermal Analysis 46, 1697-1703.

Söhnel, O., Novotny, P., 1985. Densities of solutions of inorganic substances, Physical Science Data.

Stephen, H., Stephen,T., 1963. Solubilities of inorganic and organic compounds, 1, Part 1, Macmillian, New York, 107-212.

Timmermans, J., 1960, The physico-chemical constants of binary systems in concentrated solutions, Vol. 4, Interscience Publishers, New York, USA.

Ure, Z., 2003. Secondary refrigeration European experiences. 2003 ASHRAE WINTER Meeting, Chicago, USA.

Wåhlin, J., Klein-Paste, A., 2017. The effect of mass diffusion on the rate of chemical ice melting using aqueous solutions. Cold Regions Science and Technology 139, 11-21.

Manuscript ID: 1201
DOI: 10.18462/iir.icr.2019.1201

Comparison of efficiency increasing methods in transcritical CO2 refrigeration systems

Christian DOERFFEL[(a)], Thomas TANNERT[(a)], Ullrich HESSE[(a)]

[(a)] Technische Universität Dresden
01062 Dresden, Germany, christian.doerffel@tu-dresden.de, ullrich.hesse@tu-dresden.de

ABSTRACT

CO_2 refrigeration systems often encounter a drastical decrease of COP during transcritical operation. Most commonly used methods for increasing the system efficiency are parallel compression, ejectors or other work recovery expansion devices and mechanical subcooling. The comparison of those methods in reference to the same refrigeration cycle is subject of the current research work.
Previous publications are presented considering the comparison of single methods usually in reference to a specific base cycle. To obtain the comparability of the mentioned methods a system simulation is performed within this paper with respect to the prospective applicability of all methods on one existing refrigeration cycle.
As result of the simulations the system's efficiency improvement potential of each method is presented considering the corresponding operation conditions. Finally, a direct comparison between all methods is done.
In conclusion the applicability of different efficiency increasing methods for transcritical operated CO_2 refrigeration systems is stated.
Keywords: Refrigeration, Carbon Dioxide, Compressors, COP, Energy Efficiency, Expander, R744, Subcooling.

1. INTRODUCTION

Refrigeration systems using carbon dioxide (R-744) as refrigerant have experienced a rising interest and spreading in the recent years. This is a result of restrictions within common HFC refrigerants due to the EU F-Gases Regulation (European Commission, 2014), the good availability and low costs of this refrigerant as well as advances in CO_2 refrigeration technologies (Nordtvedt, 2012). The environmental impact of carbon dioxide as a refrigerant is very low as it has a global warming potential (GWP) of 1 and no ozone depletion potential (ODP) (Lorentzen, 1994). Disadvantages of CO_2 as refrigerant are its high critical pressure (7.4 MPa) at a low temperature (31°C) and the low energetic efficiency of refrigeration systems during transcritical operation. There are several concepts for improving the energetic efficiency (Gullo, 2018): the exergy loss of throttling high pressure refrigerant can be utilized by ejectors (Hafner, 2014; Elbel, 2008) or expanders, flash gas at an intermediate pressure can be recompressed to high pressure and after leaving the gas cooler refrigerant can be subcooled below ambient temperature by an additional refrigeration cycle. This cycle is usually a separate cycle with a different refrigerant. It is called external subcooling, sometimes also referred to as mechanical subcooling (Llopsis, 2015). It is also possible, to perform subcooling by using an internal subcooler with an expander-compressor unit (Nickl, 2016). In this work, the energetic efficiencies of these concepts are compared with each other by means of a simulation.

2. INVESTIGATED SYSTEM DESIGNS

In Fig. 1 a simple refrigeration system for medium temperature cooling is shown. Carbon dioxide refrigeration systems in supermarkets for transcritical operation are set up as a booster system, which includes a low temperature stage. This additional stage is neglected here as its impact on this

investigation is very small. The system set-up is denoted as flash gas bypass system and represents the baseline system for the comparison of the improvements.
Fig. 2 shows a system, that includes both parallel compression and subcooling with an external refrigeration circuit. At the same boundary conditions and pressures, subcooling of the refrigerant leads to a lower flash gas amount in the receiver and improves the efficiency of the system. Using parallel compression (9-11) instead of throttling flash gas (9-10) further improves the systems efficiency. This benefit results from the lower specific compression work of the parallel compressor compared to the specific compression work of the main compressor. Besides the parallel compressors a flash gas bypass is still contained in the system. Thereby the influence of parallel compression on a system with external subcooling can be derived.

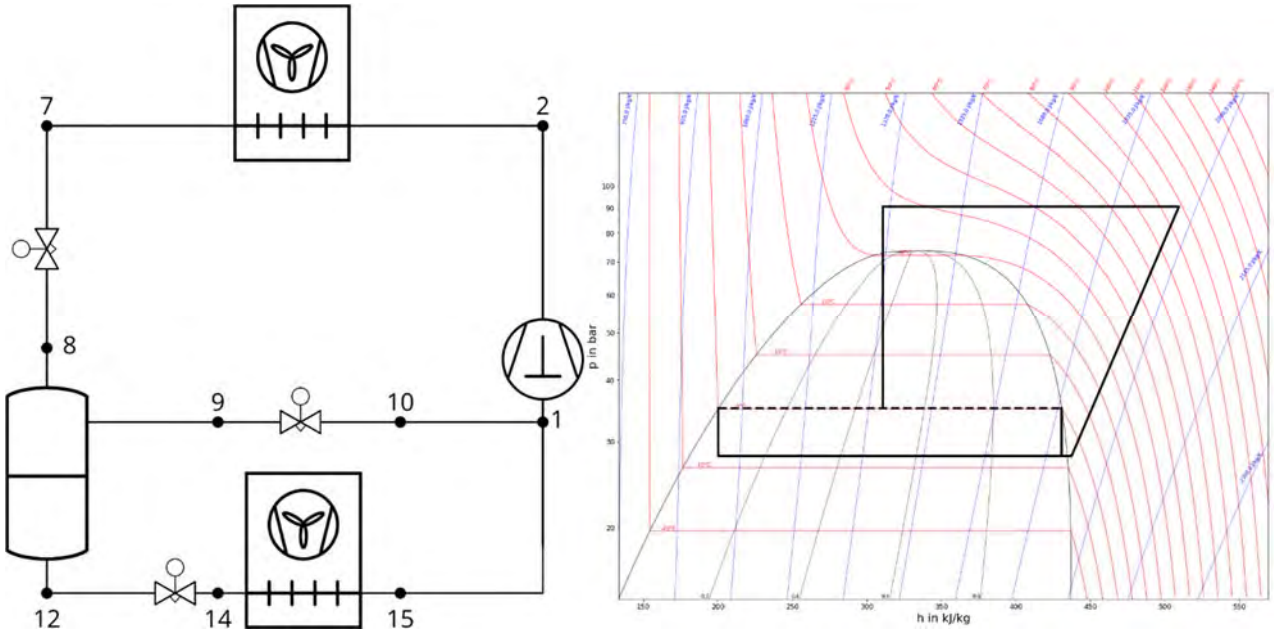

Figure 1: scheme of simulated flash gas bypass system as reference system and associated log(p)-h-diagram

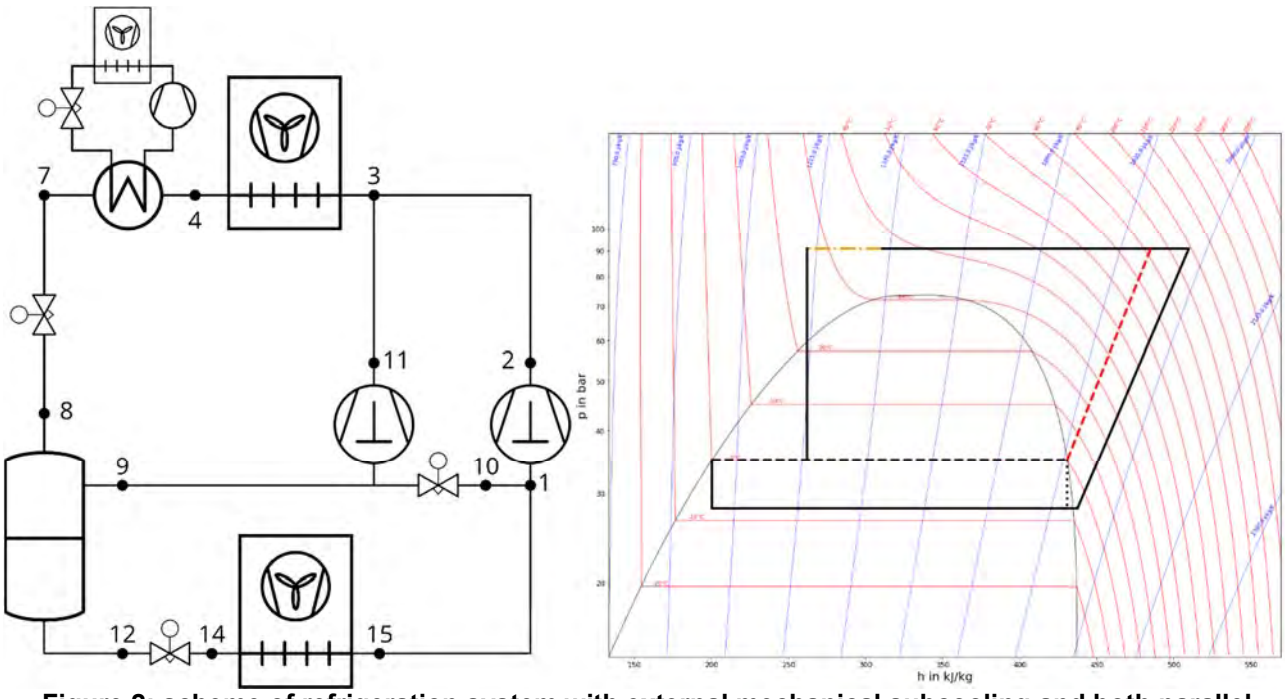

Figure 2: scheme of refrigeration system with external mechanical subcooling and both parallel compression and flash gas bypass with associated log(p)-h-diagram

Instead of external mechanical subcooling, refrigerant at the gas cooler exit can be subcooled by an internal subcooler circuit, as shown in Fig. 3. The expander compressor unit utilizes the expansion work when expanding the CO_2 from gas cooler pressure to intermediate pressure in the receiver. The recovered work is used to recompress a subcooler mass flow from subcooler-evaporation pressure to gas cooler pressure. By subcooling the refrigerant and expansion work recovery the system gains additional refrigeration capacity and therefore the efficiency increases. This system also contains both a flash gas bypass and parallel compression for comparison.

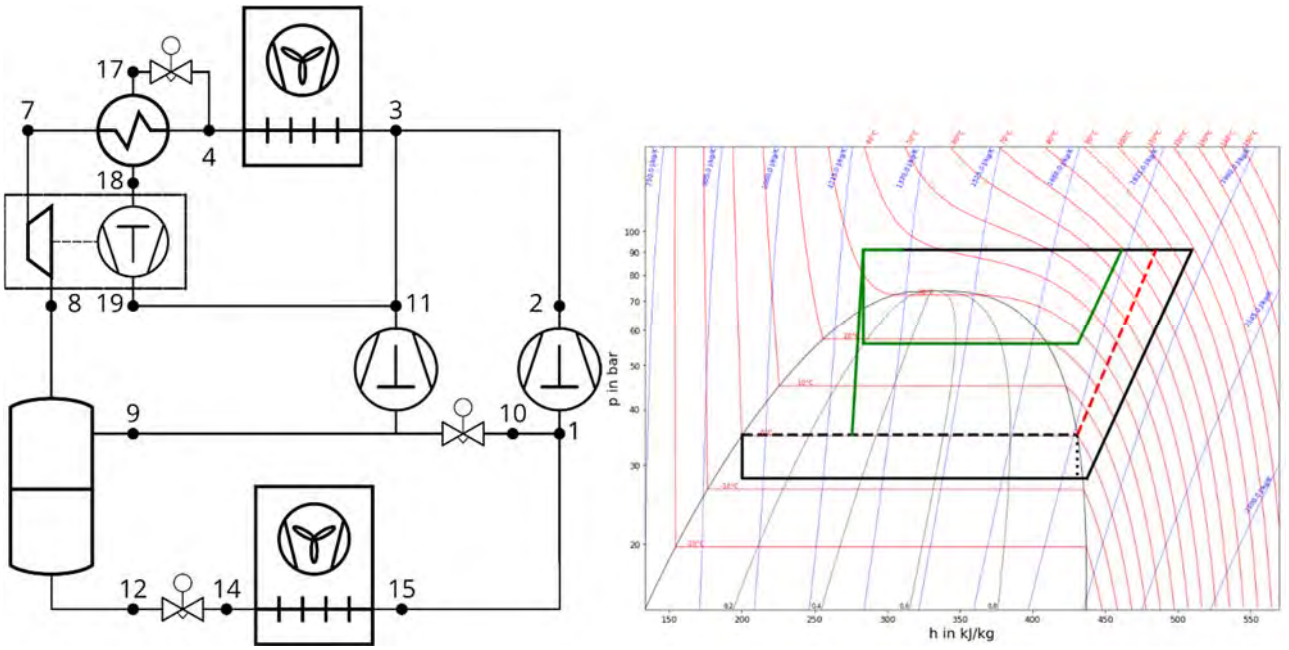

Figure 3: scheme of expander-subcooler system and associated log(p)-h-diagram

3. SIMULATION SET-UP

For investigations on R-744 refrigeration systems an object oriented system simulation was set up in the programming language Python. Each component in the refrigeration cycle is represented by an object and need different input values for computing the corresponding outlet values.
For the compressors model certain values for the inlet and outlet pressure, the inlet enthalpy and the frequency are used to calculate the output enthalpy and the mass flow rate as will be described later.
Expansion valves are modeled by an isenthalpic change of state and a flow function, which needs the inlet density and both the inlet and the outlet pressure for calculating the mass flow rate.
Vessels like receivers or suction line accumulators are described by mass- and energy balances. If there is two phase state (gas and liquid) inside the vessel, the exiting gas is considered as saturated vapour and the liquid phase as saturated liquid. Otherwise the outlet enthalpy is calculated by the energy balance assuming an ideal mixture of the containing and incoming refrigerant mass.
In the simulation an exemplary rack of five compound compressors is used in place of the depicted single compressor in Figure 1 respectively the parallel compressor in Figs. 2 and 3. This rack maps the behaviour of capacity control of a real compressor compound by varying the frequency of one compressors and switching other compressors on or off. Additionally, PID controllers are used, which control suction pressures with the racks capacity control. The high pressure as well as the intermediate pressure in the flash gas bypass system is adjusted by controlling the valve lift of the expansion valves.
For the simulations an evaporation temperature of temperature $t_{ev} = -8\,°C$ was chosen, as a typical evaporation temperature for medium temperature cooling in existing supermarket refrigeration systems.
The coefficient of performance is calculated as follows:

$$COP = \frac{\dot{Q}_{ev}}{\sum P_c} \quad \text{Eq. (1)}$$

$\dot{Q}_{ev}$ in equation 1 is the cooling capacity, which is calculated by:

$$\dot{Q}_{ev} = \dot{m}_{ev}(h_{15} - h_{14}) \quad \text{Eq. (2)}$$

where $\dot{m}_{ev}$ is the mass flow rate through the evaporator and h_8 and h_9 are the enthalpy values at the evaporator inlet and outlet respectively. P_c in Eq. (3) is the shaft power of the (main) compressor calculated by:

$$P_c = \dot{m}_c(h_2 - h_1) \quad \text{Eq. (3)}$$

with the compressor mass flow rate $\dot{m}_c$ and the compressor inlet enthalpy h_1. The value h_2 denotes the compressor outlet enthalpy, which is calculated by the isentropic compression outlet enthalpy $h_{2,is}$, the compressor inlet enthalpy h_1 and the isentropic efficiency η_{is}:

$$h_2 = h_1 + \frac{h_{2,is} - h_1}{\eta_{is}} \quad \text{Eq. (4)}$$

As the compressor model of the parallel compressor is the same, the input power is calculated accordingly.
The expander-compressor was modelled in the way, that the whole expander power is used for compression of the subcooler-cycle:

$$P_{exp} = \dot{m}_{exp}(h_7 - h_8) = \dot{m}_{18}(h_{19} - h_{18}) \quad \text{Eq. (5)}$$

$$h_8 = h_7 - \eta_{is}(h_{8,is} - h_7) \quad \text{Eq. (6)}$$

For the following comparison of the COPs, only the gas cooler pressures with the highest COP value were taken into account. These optimum gas cooler pressures vary slightly in each system. In general they are slightly lower than the optimum gas cooler pressures of the flash gas bypass system at the same gas cooler outlet temperature. The pressure in the receiver $p_9 = 3.5\,MPa$ was kept constant.
The external subcooling was calculated for the refrigerant R-290, as this natural refrigerant with a very low GWP of 3 is assumed as a state of the art available component.

4. RESULTS

Fig. 4 shows, that each method improves the systems efficiency compared to the flash gas bypass system by a certain amount. Parallel compression shows the smallest increase of the overall systems efficiency whereas the subcooling-expansion-compression-cycle combined with parallel compression shows the highest efficiency improvement potential.
Each system's COP relative to the COP of the Flash gas bypass system is shown in Fig. 5.
The parallel compression shows an improvement of about 10 % in COP over the whole range of gas cooler outlet temperatures. A system with external subcooling at a subcooling temperature difference of 10 K has a up to 30 % higher COP value than a flash gas bypass system, depending on the ambient temperature. When subcooling the CO_2 by 20 K, the improvement in COP rises over 40 % at gas cooler oulet temperatures over 43 °C. Finally, with internal subcooling and usage of an compressor-expander-unit, the COP increases over a wide range of ambient temperatures by about 35 %. Combined with parallel compression the COP is up to 45% higher.
The own results matches to the results given by other authors: Ferrara demonstrated an improvement in COP of 34,5 % by use of an expander, whereas there the electrical expander output energy was used for compression, so the system's COP is calculated as follows (Ferrara, 2016):

$$COP_{EXP} = \frac{Q_{ev}}{W_C - W_{EXP}} \quad \text{Eq. (7)}$$

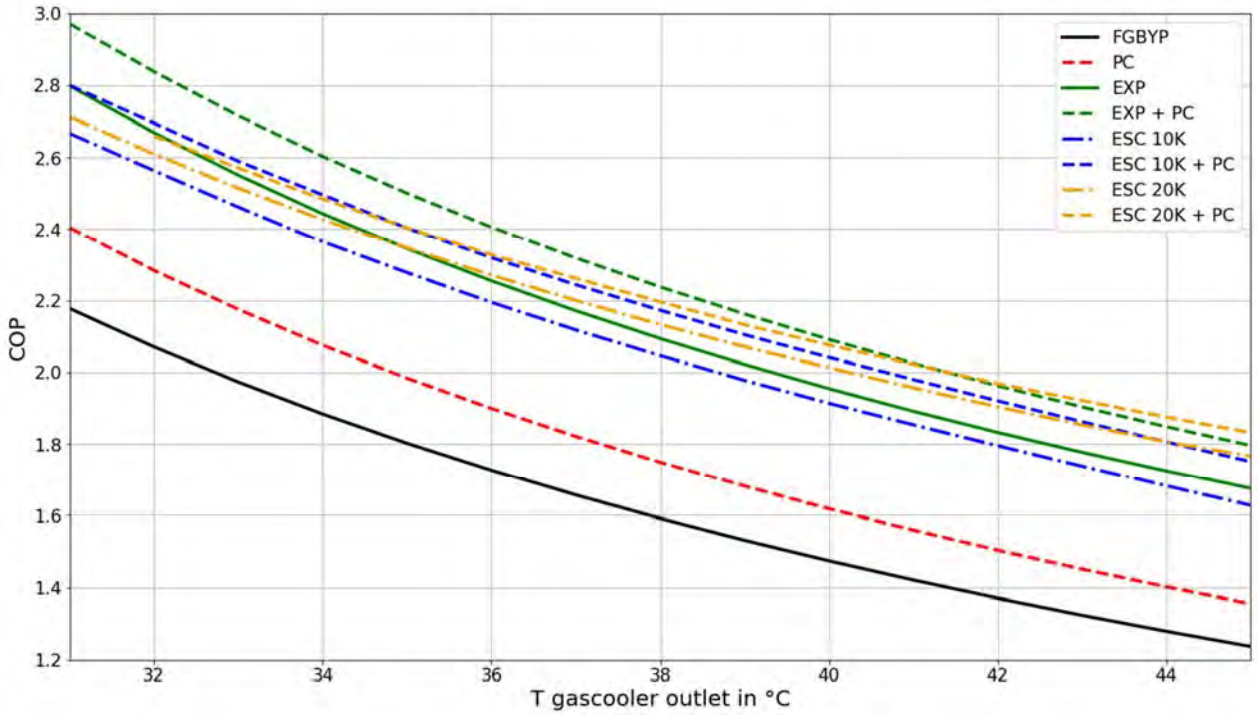

Figure 4: Calculated COPs of a flash gas bypass system (FGBYP), parallel compression system (PC), expander-compressor-system (EXP) and systems with exteneral subcooling (ESC) by 10 K respectively 20 K vs. gas cooler outlet temperature

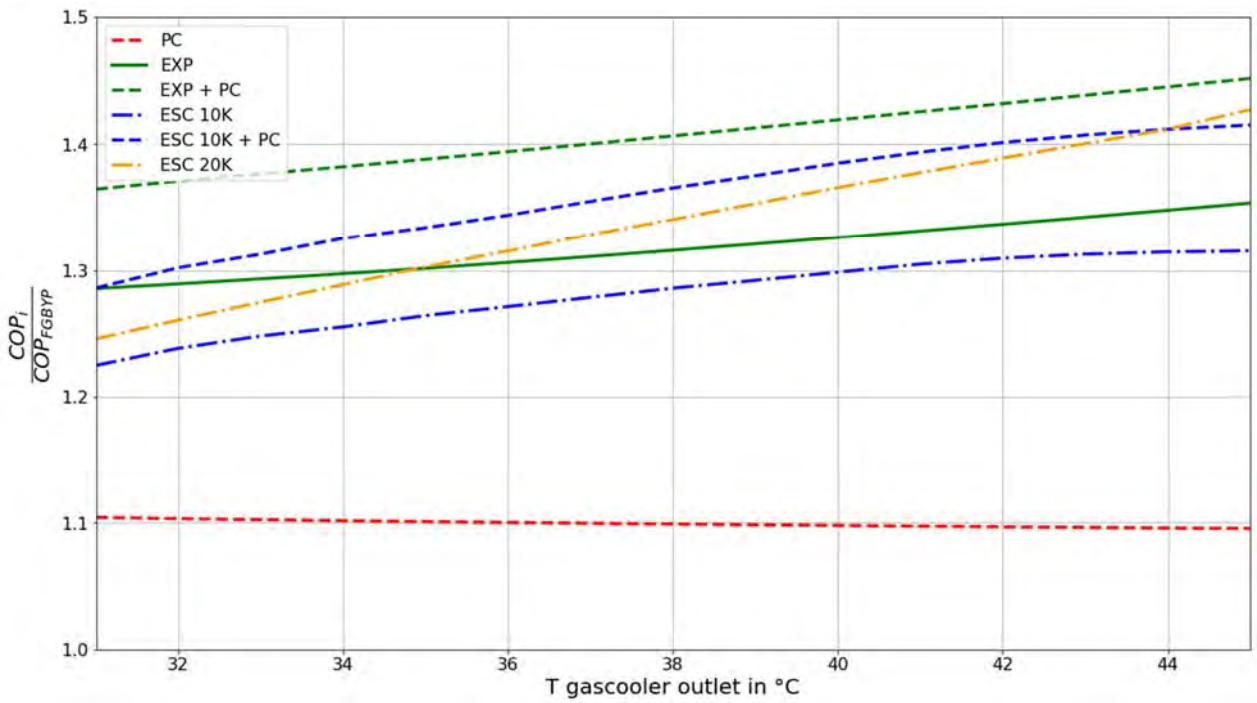

Figure 5: COPs of improved systems relative to COP of the flash gas bypass system vs. gas cooler outlet temperature

Additionally, by using a three-stage expander Nickl (2005) reports about an efficiency increase of 40 % and Wenzel demonstrated about 10 % (2012) with a two-stage-expander and up to 25 % for mobile air conditioning.

The calculated increase of energetic efficiency by external subcooling is in the same order as Hanslik (2018) reports for subcooling with water as refrigerant (R-718). There it is stated, that the COP can be improved by 35 % at an evaporation temperature of -5 °C and 7.5 K subcooling temperature difference. Sanchez (2016) demonstrated an improvement potential of 17.3 % in COP for

mechanical subcooling with R-600a in a test rig at 35 °C cooling water inlet temperature. Here for similar conditions an improvement of 27 % was calculated. The different increase of COP may result from a different assumption of the isentropic efficiency of the compressor in the external subcooling cycle.
The additional costs of each system are estimated by price lists of required components and include only the additional investment costs (based on a 100 kW cooling capacity system). Implementing parallel compression is estimated up to a 20 %; implementing external subcooling (10K) also 15 to 20 % increase in investment costs. A higher subcooling capacity for 20 K subcooling can make up 25 %. Combining parallel compression and external subcooling may lead to approximately 30 % higher investment costs and in the case of 20 K external subcooling system approximately 35 %. There is no price information regarding expanders. It can be assumed, that they will cost less than an external subcooling system (e.g. less than 20 % of the total invest volume).

5. CONCLUSIONS

In this paper the energetic efficiency of different R-744 refrigeration system designs is examined by means of a system simulation. The energetic efficiency rises with additional efforts such as parallel compression, external subcooling or application of an expander-compressor subcooler cycle in a certain way. The additionally integration of parallel compression in each system, further increases the energetic efficiency by a nearly constant benefit of about 10 %. The increase in efficiency when using external subcooling depends on the gas cooler outlet temperature. The expander-compressor subcooling cycle in combination with parallel compression reaches the highest efficiency values of the investigated systems.

ACKNOWLEDGEMENTS

The authors gratefully acknowledge the Bundesministerium für Wirtschaft und Energie, who funded this work within the project 03ET1541A.

NOMENCLATURE

p	pressure (MPa)	h	specific enthalpy ($\mathrm{kJ \cdot kg^{-1}}$)
T	temperature (K)	t	temperature ($\mathrm{°C}$)
COP	coefficient of performance	$\dot{Q}$	cooling/heating capacity
FGBYP	flash gas bypass (system)	PC	parallel compression (system)
ESC	external mechanical subcooling	EXP	expansion-compression subcooling circuit
GC	gascooler	ev	evaporation

REFERENCES

Elbel, S., Hrnjak, P., 2008. Experimental validation of a prototype ejector designed to reduce throttling losses encountered in transcritical R744 system operation. Int. J. Refrig. 31 () (2008) 411-422.

European Commission, 2014. Regulation (EU) No 517/2014 of the European Parliament and of the Council of 16 April 2014 on Fluorinated Greenhouse Gases and Repealing Regulation (EC) No 842/2006.

Ferrara, G. et. al., 2016. Energy recovery by means of a radial piston expander in a CO2 refrigeration system. Int. J. Refrigeration 72(07), 147-155.

Gullo, P., Hafner, A., Banasiak, K., 2018. Transcritical R744 refrigeration systems for supermarket applications: Current status and future perspectives. Int. J. Refrigeration 93(07), 269-310.

Hafner, A., Försterling, S., Banasiak, K., 2014. Multi-ejector concept for R-744 supermarket refrigeration. Int. J. Refrigeration 43(1), 1-13.

Hanslik, F., Suess, J., Koehler, J., 2018. Efficiency Enhancement by Subcooling the Carbon Dioxide Process with Water as Refrigerant. Proceedings of the International Refrigeration and Air Conditioning Conference at Purdue 2018, paper No. 2149.

Llopis, R., Cabello, R., Sanchez, D., Torrella, E., 2015. Energy improvements of CO2 transcritical refrigeration cycles using dedicated mechanical subcooling. Int. J. Refrigeration 55(03), 147-155.

Lorentzen, G., 1994. Revival of carbon dioxide as a refrigerant. Int. J. Refrig. 17 (5) (1994) 292–301.

Nickl, J., Will, G., Quack, H., Kraus, W.E, 2005. Integration of a three stage expander into a CO2 refrigeration system. Int. J. Refrigeration 28(08), 1219-1224.

Nickl, J., Bartzsch, R., Hesse, U., 2016. CO2-Anlage mit neuer Generation ECU. Proceedings of the conference Deutsche Kälte-Klima Tagung 2016, paper No. III-05.

Nordtvedt, T. S., Hafner, A., 2012. Integration of Refrigeration and HVAC in Supermarkets. Proceedings of the 10th IIR Gustav Lorentzen Conference on Natural Refrigerants, Delft, paper No. 184.

Sanchez, D., Catalan-Gil, J., Llopis, R., Nebot-Andres, L., Cabello, R., Torrella, E., 2016. Improvements in a CO2 transcritical plant working with two different subcooling systems. Proceedings of the 12th IIR Gustav Lorentzen Natural Working Fluids Conference, 21st - 24th August. Edinburgh. paper No. 1170

Sawalha, S., 2008. Theoretical evaluation of trans-critical CO2 systems in supermarket refrigeration. Part I: Modeling, simulation and optimization of two system solutions. Int. J. Refrigeration 31(3), 516-524.

Wenzel, M., Hesse, U., 2012. COP Improvement of a CO2 Refrigeration System with an Expander-Compressor-Unit (ECU) in Subcritical and Transcritical Operation. Proceedings of the International Refrigeration and Air Conditioning Conference at Purdue 2012, paper No. 2183.

Wenzel, M., Nickl, J., 2009. CO2-Expander-Kompressoreinheit: Weiterentwicklung, Einbindung in Kälteanlagen und Regelung. Proceedings of the conference DKV Tagung 2009, paper No. II2-10.

Manuscript ID: 1202
DOI: 10.18462/iir.icr.2019.1202

Design and experimental results of a hybrid water/lithium bromide absorption-compression chiller

Martin HELM, Thomas ECKERT, Christian SCHWEIGLER

CENERGIE Research Center Energy-efficient Buildings and Districts,
Munich University of Applied Sciences, Department of Building Services Engineering,
Lothstr. 34, Munich, D-80335, Germany, christian.schweigler@hm.edu, +49 89 1265-1501

ABSTRACT

Application of absorption chillers and heat pumps based on the working pair water/lithium bromide is limited by the requirement of high driving temperatures, limited temperature lift due to the risk of crystallization, and weak peak load capability at raised ambient temperatures. Increased flexibility is achieved when a mechanical vapor compressor is integrated in a conventional absorption cycle, forming a hybrid absorption/compression chiller.
A pre-commercial design of the hybrid absorption/compression chiller is presented which can be operated in pure absorption mode and hybrid operation with variable contribution of a mechanical turbo compressor. Starting from the conventional design, the configuration of evaporator and absorber have been refined in order to avoid pressure drops in the vapor flow and entrainment of liquid refrigerant at the inlet of the compressor. Experimental results confirm the potential of the hybrid concept. Operating temperatures, electrical and thermal COP are used as figures of merit.
Keywords: Absorption, Centrifugal Compressor, Chiller, Compression, Heat Pump, Hybrid System, Water/Lithium Bromide, Natural Refrigerant R718.

1. INTRODUCTION

The environmental compatibility of refrigerants and the decarbonization of primary energy demand for cooling and heating purposes in buildings is a great challenge for the future. While the use of fluoro chlorinated hydrocarbons CFC with significant ozone depletion potential (ODP) has declined sharply due to the Montreal Protocol in 1989, the focus is currently on the global warming potential (GWP) of the replacement refrigerants used. However, these refrigerants are now often subject to the 2014 tightened Regulation (EU) No.517 / 2014 on fluorinated greenhouse gases, as well as the aspired phase-out until 2030 or simply very expensive. Not least because of that, natural refrigerants are currently experiencing a renaissance. Table 1 lists indicative properties of some currently used refrigerants assuming an idealized vapor compression refrigeration cycle between 45 ° and 6 °C. Especially, specific volume, maximum process pressure and isentropic coefficient pose specific challenges for refrigeration technology to obtain safe and efficient operation.

Table 1. Thermodynamic properties of some refrigerants in an idealized cooling cycle (6/45 °C)

ASHRAE, trivial name	formula	GWP -	T_{crit} °C	p_{vap} bar	p_{cond} bar	Π -	$r \cdot c_p^{-1}$ K	κ -	q_{ov} $kJ \cdot m^{-3}$	v $m^3 \cdot kg^{-1}$
R717 Ammonia	NH_3	0	132	5.3	17.8	3.3	267	1.41	4484	0.23
R718 Water	H_2O	0	374	0.009	0.096	10.3	592	1.33	17	137.60
R744 Carbon dioxide	CO_2	1	31	40.7	tr.crit	N/A	76	2.42	25053	0.01
R22 Chlorodifluoromethane	$CHClF_2$	1810	96	6.0	17.3	2.9	168	1.31	3852	0.04
R290 Propane	C_3H_8	3	97	5.7	15.3	2.7	143	1.23	3190	0.08
R600a Isobutane	C_4H_{10}	3	135	1.9	6.0	3.1	150	1.13	1309	0.19
R134a Tetrafluorethane	$C_2H_2F_2$	1430	101	3.6	11.6	3.2	143	1.19	2449	0.06
R407C R32/R125	Blend	2088	86	5.7	19.7	3.5	142	1.26	3458	0.04
R1234yf Tetrafluoropropene	$C_3H_2F_4$	4	95	3.9	11.5	3.0	122	1.16	2249	0.05

Beside climate friendly refrigerants, new innovative system concepts for optimized integration of renewable energies and/or waste heat have to be realized and tested for promising applications.
This paper describes the concept and technical execution of a combined absorption-compression cycle with the natural refrigerant R718 and lithium bromide as sorbent. Furthermore, an investigation on the intake pressure losses of the turbo compressor is carried out and measuring results for low driving heat return temperatures are presented.

2. CONCEPT OF A HYBRID ABSORPTION-COMPRESSION CYCLE

In general, R718 absorption and compression cycles can be combined in parallel or serial arrangement in order to form a hybrid cycle. In parallel the pressure difference between evaporator and condenser has to be fulfilled by both technologies. Standard temperature levels (6 to 40 °C) effect a huge suction volume and a compression ratio of 8 and more, which is fluid dynamically out of scope of single stage vapor compressors. Moreover, these temperature levels request high driving heat temperatures and thus lithium bromide concentrations of the absorption process with increased danger of crystallization. As great advantage of the parallel arrangement, both technologies operate independently with variable share of the overall chilled water capacity. If compression and absorption cycle work in serial, the thermodynamic process conditions change with varying contribution of both technics to the overall temperature lift between evaporator and condenser. Nevertheless, the two processes themselves operate at moderate conditions far away from any constraint. But in that case, to operate the compression or absorption cycle solely, additional bypasses are needed.
Here, a serial single stage hybrid absorption-compression cycle is proposed, wherein the turbo-compressor merely supports the absorption process. As defined earlier by Eckert et al. (2015) and depicted in Figure 1, the mechanically driven compressor operates either between evaporator and condenser in EVA configuration, or in the DECO configuration, where the compressor is arranged between desorber and condenser. The graphical position of the main components qualitatively shows the logarithmic pressure level (ordinate) and negative inverse temperature level (abscissa) of the working fluid lithium bromide as sorbent and water as refrigerant. An isenthalpic throttle depressurizes the liquid refrigerant from the condenser to evaporator equilibrium conditions. In the absorption section, a pump circulates lithium bromide solution between the externally cooled absorber and the heat driven desorber. In between, a single phase heat exchanger recovers heat for improved system efficiency. Here, the cooling water first enters the absorber and flows through the condenser afterwards. Alternatively, a parallel or reverse connection is conceivable, but not considered here.

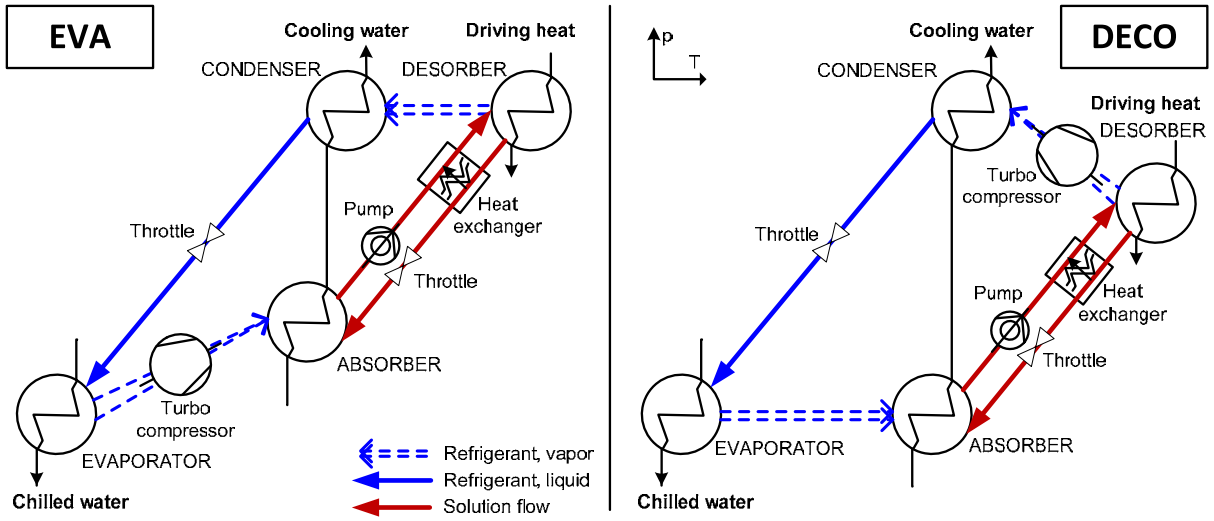

Figure 1: Scheme of the serial hybrid cycle with integrated compressor between evaporator and absorber (EVA configuration) or desorber and condenser (DECO configuration)

The thermodynamic performance and different operation modes describes Helm et al. (2015) by means of a simplified absorption-compression model with additional mechanical compression ratios up to Π=3 for both configurations.

While a given mechanical compression ratio Π induces a slightly better process improvement in the DECO configuration, the required specific shaft power P_{spec} in that case is much higher due to the super-heated vapor released from the desorber. This might be eliminated by an additional inlet cooling, but has not yet been analyzed in depth. Moreover, the isentropic efficiency η of the mechanical compression significantly decreases the mechanical power consumption, but has a only minor effect on the desired process improvement. In general as shown in Figure 2, the temperature lift ΔT_{lift}, provided by the mechanical compression, increases with rising compression ratio Π, but is also positively affected by the suction pressure p_s . Additionally, for a given impeller diameter and displacement volume the refrigerant mass flow through the turbo compressor is much higher in DECO, as there is a massive change in vapor density and specific volume v for rising suction pressure, as shown in Figure 3. Figure 4 depicts the rising specific heat of solution l with increasing lithium bromide concentration w in the solution for both configurations. The pressure level plays a rather subordinate role, but it increases slightly with higher pressures as well.

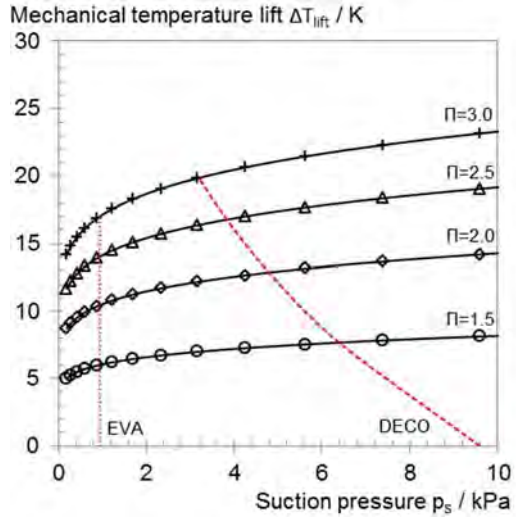

Figure 2: Mechanical temperature lift ΔT_{lift} vs. compression ratio Π and suction pressure p_s

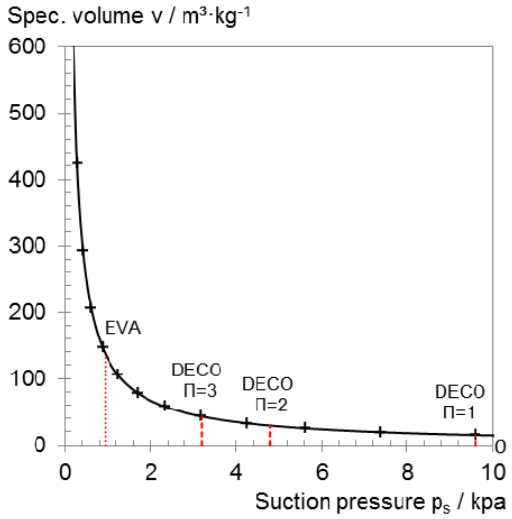

Figure 3: Specific vapor volume at given compressor suction pressure p_s

In a nutshell, the DECO configuration requires more heat in the desorber to separate the refrigerant from the lithium bromide solution, resulting in a lower thermal efficiency. But, signifycantly more refrigerant throughput and a slightly improved ΔT_{lift} of the compressor are obtained. Nevertheless, with regard to the heat ratio ζ_C, of usable cooling capacity Q_E in relation to the necessary heat input, the EVA configuration is more effective and offers higher flexibility for application.

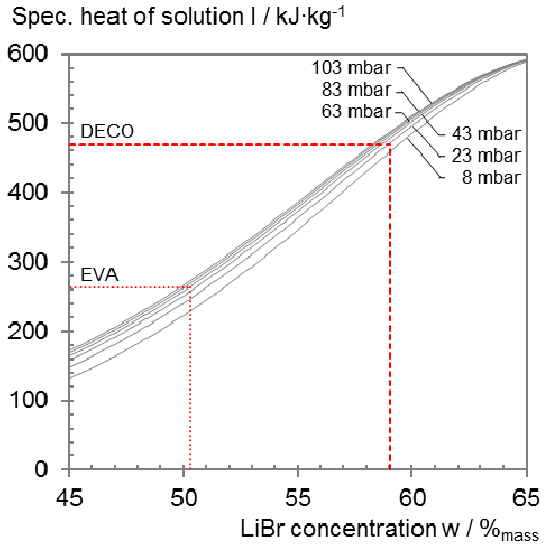

Figure 4: Specific heat of solution l as a function of lithium bromide concentration w and the prevailing pressure level during absorption or desorption in EVA and DECO configuration

3. HYBRID CHILLER PRE-COMMERCIAL DESIGN

Thanks to improvements in turbo compressor technology operating with the natural refrigerant water (Meier-Staude and Kniffler, 2013; Efficient energy GmbH, 2016) the technical proof of concept of a hybrid absorption-compression chiller has now become feasible. Therefore, a laboratory test plant has been set up at Munich University of Applied Sciences in order to evaluate its performance under different boundary conditions for selected application scenarios. The development aims at a hybrid chiller providing 15 kW of chilled water at 6 °C with a maximum driving temperature of 90 °C and cooling water inlet temperatures between 35 and 40 °C.
Basically, the thermodynamic properties of the natural refrigerant water require a revised absorption chiller design to ensure undisturbed transonic vapor flow into the turbo compressor. Furthermore, flow losses and the danger of entrainment of refrigerant droplets have to be minimized. Finally, a concept with falling film over side by side horizontal tube bundles for the main heat exchangers (Evaporator, Absorber, Condenser and Desorber) promises best thermodynamic and fluid dynamic performance as well as scalability to higher capacities. Figure 5 shows a photo of the chiller (LxHxW, 160x200x80 cm) and the rendered 3D-CAD Model with upper Desorber-Condenser vessel and lower Absorber-Evaporator vessel with turbo compressor on top. An automatized purge system continuously removes non-condensable gases from the sub-atmospheric refrigeration process to ensure equilibrium test conditions at any time.

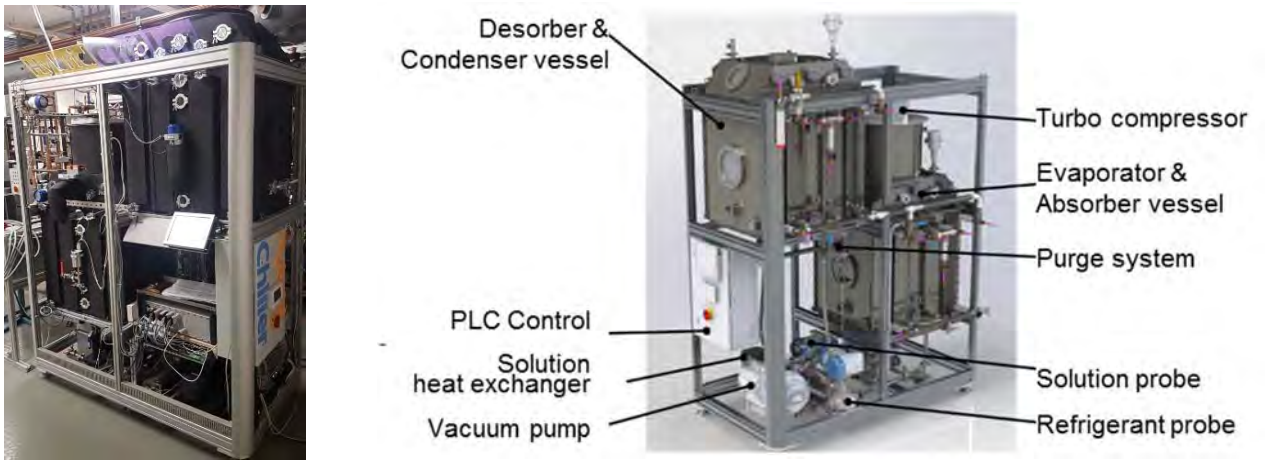

Figure 5: Front view of the hybrid chiller demonstrator (left) and rear view of 3D CAD Model (right)

For improved flexibility, an additional one-way opening bypass flap between Evaporator and Absorber allows a pure sorption mode without compressor input. Figure 6 shows this yellow high-lighted plastic flap around the conic suction dome in the center. Another fast opening anti-surge motor valve in a bypass between absorber and evaporator avoids unstable operation conditions of the turbo compressor during startup and fast load changes. This device (see Figure 7), ensures the minimum flow through the compressor at any time, avoiding surge and thus improving plant safety.

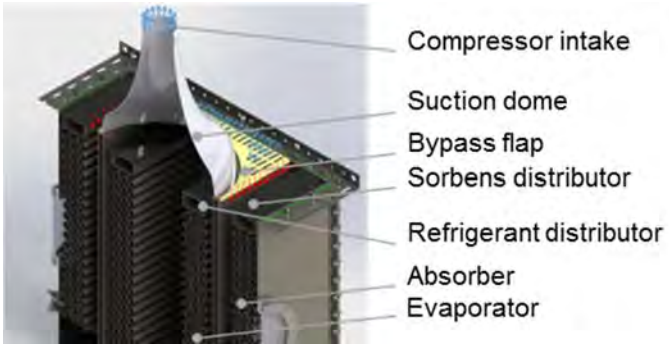

Figure 6: Cross sectional view of low pressure vessel with centered evaporator, side facing absorber and suction dome with bypass on top

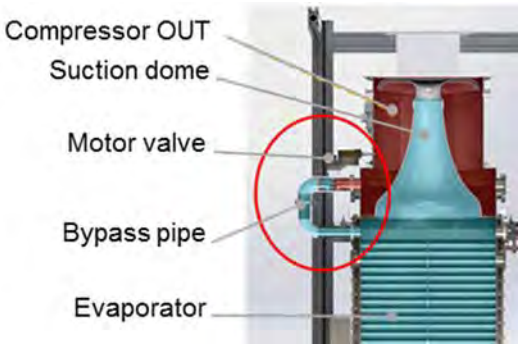

Figure 7: Fast opening ball valve in bypass connecting compressor discharge and suction side to prevent surge at any operation condition

4. SUCTION DOME INVESTIGATION

The main goals of the inlet dome are an efficient flow from the evaporator outlet to the turbo compressor inlet, minimized construction volume and minor pressure drop between evaporator outlet and compressor inlet. In this inlet duct investigation, a droplet separation is applied to eliminate liquid drops in compressor inlet to prevent damage of the impeller.

$$\zeta = \frac{p_{tot.In} - p_{tot.Out}}{p_{tot.Out} - p_{Out}} \quad (1)$$

Figure 8 shows different simulation results of various inlet domes for hybrid chiller concepts.

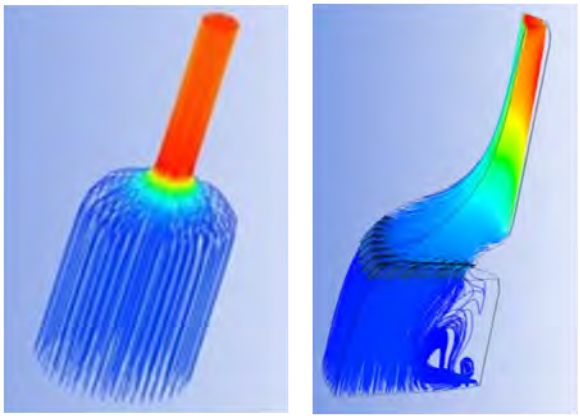

Figure 8: Ideal straight inlet dome (left) and inlet dome with evaporator tubes inside circle (right)

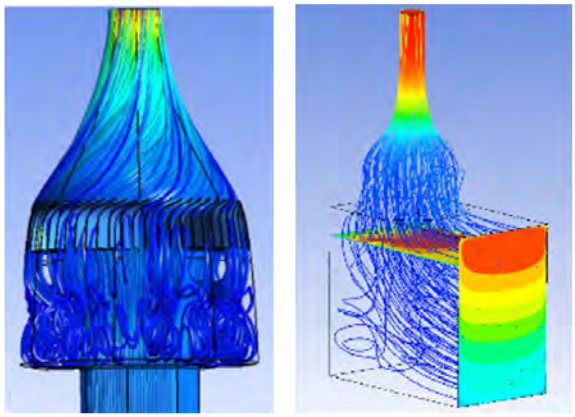

Figure 9: Inlet dome with evaporator tubes outside circle (left) and lateral inflow (right)

Figure 10 shows the pressure drop coefficient ζ for the concept figure 9 (right) lateral inflow for different evaporator temperatures from 10 °C to 25 °C for the volume flow of 0,77 m³·s^{-1}. For rising inlet temperatures, the Reynolds number of water is decreasing; therefore, losses through friction and viscosity decrease and result in lower pressure loss. In contrary, low evaporator temperatures around 5 and 10 °C yield higher loss coefficients for the inlet dome.

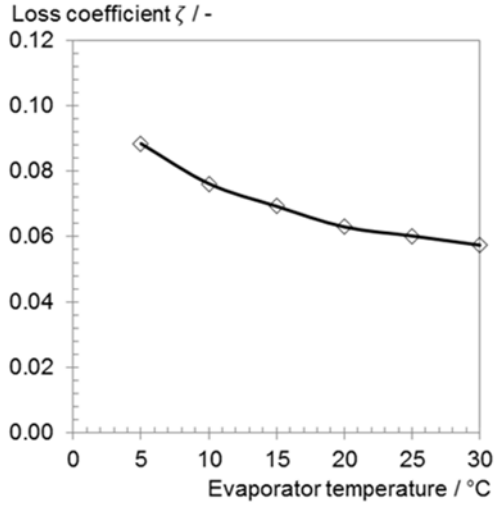

Figure 10: Inlet dome with side inflow for a volume flow of 0,77 m³/s

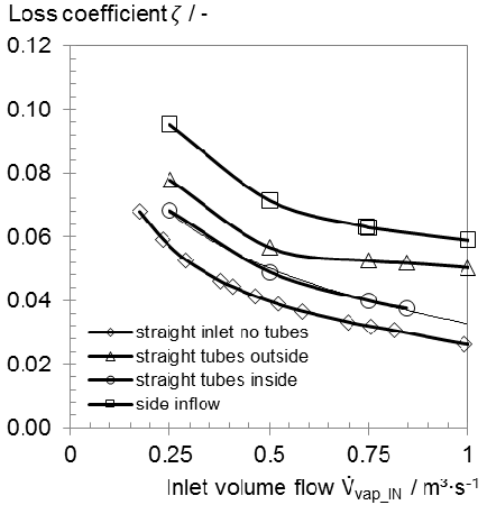

Figure 11: Loss coefficients for the inlet dome in figure 8 and 9 for different volume flows

In Figure 11 the loss coefficient for different inlet dome concepts of figure 7 and 8 is given. All concepts are characterized by a decrease of the pressure drop for increasing volume flows. Low volume flows lead to higher turbulence and detached inlet flow. The straight inflow with no tubes is the theoretic ideal solution, but an inlet guide vane IGV is needed to separate liquids. Evaporator tubes in the center result in a lower pressure drop than the tubes outside. The reason is a higher flow velocity in the outer impeller leading to higher velocities in the inflow duct near the outer wall.

5. TEST RESULTS FOR REDUCED DRIVING HEAT RETURN TEMPERATURES

As earlier described by Helm at al. (2018), the integration of a mechanical turbo compressor between the evaporator and absorber of an absorption chiller (EVA-Configuration) helps to overcome the limitations of the chosen working fluid and allows for the following relevant process improvements:

a) Increased cooling water temperatures for dry heat rejection under hot climate conditions
b) Lower driving heat inlet temperatures for utilization of low-tempered waste or solar heat
c) Capacity booster for peak load conditions and integration of abundant renewable electricity

Furthermore, especially in Combined Heat and Power (CHP) applications with combustion engines a relatively low driving heat return temperature of 75 °C or less is questioned in order to ensure proper oil cooling. Additionally, district heating networks often require low return temperatures as well. So eventually, a high temperature difference in the driving heat circuit is targeted.
For that scenario, Table 2 gives the main test parameters of the combined absorption-compression process providing 6.3 °C of chilled water (E1#T_brine_OUT) with a relatively high Absorber cooling water inlet temperature A1#T_cool_IN = 34.8 °C at constant cooling water flowrate A1#$\dot{V}$_cool of 3.6 $m^3 \cdot h^{-1}$. In that case, the turbo compressor adds an additional internal temperature lift of 12 K, which corresponds to a compression ratio of Π=2.2 respectively. This mechanical compression support allows a driving heat utilization from 89.9 °C at the desorber Inlet (D1#T_heat_IN) down to 66.3 °C at the desorber outlet (D1#T_heat_OUT). Simultaneously, about 0.155 Watts of electricity are consumed per Watt external chilled water capacity including refrigerant flash loses, called specific compressor rating P_{spec}. The concentrations in the lithium bromide circuit of 49.9 % and 52.7 % are quite low. Thus, a good heat ratio ζ_C between chilled water and driving heat capacity of 0.753 is obtained. As the parameters standard deviation of the sample σ after the tuning phase is quite low, quasi-stationary conditions are assumed during the entire measuring phase of 10 minutes.

Table 2. Parameters of the absorption-compression process for low driving heat return temperatures

Parameter	Unit	Value	σ
E1#T_brine_IN	°C	12.0	$\pm 2.5 \times 10^{-1}$
E1#T_brine_OUT	°C	6.3	$\pm 1.2 \times 10^{-1}$
A1#T_cool_IN	°C	34.8	$\pm 2.0 \times 10^{-1}$
A1#V_cool	$m^3 \cdot h^{-1}$	3.602	$\pm 1.6 \times 10^{-2}$
A1#V_sol_OUT	$m^3 \cdot h^{-1}$	0.2	$\pm 1.0 \times 10^{-2}$
A1#w_sol_OUT	$\%_{mass}$	49.9	$\pm 8.3 \times 10^{-1}$
D1#T_heat_IN	°C	89.9	$\pm 3.5 \times 10^{-2}$
D1#T_heat_OUT	°C	66.3	$\pm 8.0 \times 10^{-2}$
D1#w_sol_OUT	$\%_{mass}$	52.7	$\pm 2.7 \times 10^{-1}$
P_{spec}	-	0.155	$\pm 1.4 \times 10^{-1}$
ζ_C	-	0.753	$\pm 3.3 \times 10^{-2}$

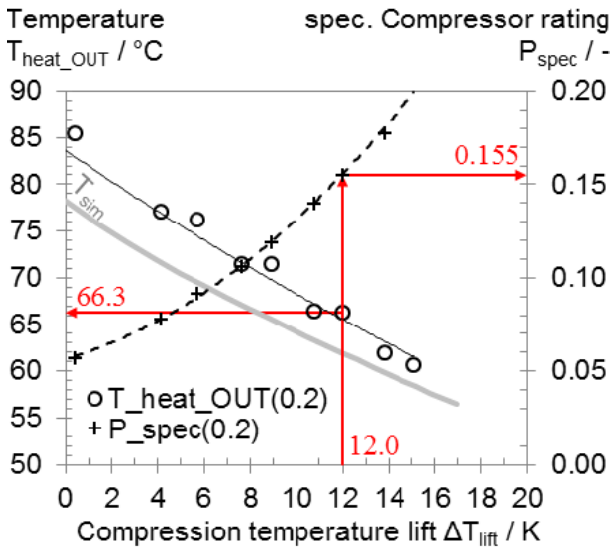

Figure 12: Effect of the temperature lift ΔT_{lift}, provided by mechanical turbo compressor, on driving heat return temperature T_{heat_out} and specific compressor rating P_{spec} with constant H_2O/LiBr-flow rate

By adjusting the revolution speed of the turbo compressor at unchanged boundary conditions, the additional compression temperature lift ΔT_{lift} varies between 0 and 15 K. Figure 12 indicates this impact on driving heat return temperature and specific compressor rating for a constant solution flow rate of A1# $\dot{V}$_sol_OUT = 0.2 $m^3 \cdot h^{-1}$. While the desorber inlet temperature D1#T_heat_IN remains constant at 90 °C the driving heat return temperature, leaving the desorber, drops down to almost 60 °C with corresponding reduction in driving heat volume flow through the desorber. Without turbo compressor support the return temperature increases to more than 85 °C.

6. PERFORMANCE CHART

The “characteristic equation method” based on Ziegler (1999), Schweigler (1999) and recently refined by Albers (2017) describes the part-load performance of absorption chillers and heat pumps in a simplified analytical way. Here, the parameter “total temperature difference” ΔΔT as defined in equation (2) establishes a linear link of the attainable chilled water capacity to the easy to measure external temperature levels in the different heat transfer components. Thereby, the variable t represents the average temperature of the external heat carrier medium of each component. Additional input from the mechanical compressor is represented by ΔT_{lift}, describing the difference of equilibrium temperatures based on the evaporator and absorber pressure. The correction factor R, namely Dühring coefficient, is determined from the average lithium bromide solution concentration circulating between absorber and desorber, likewise reciprocal slope of the corresponding isostere in the Dühring chart.

$$\Delta\Delta T = (t_D - t_A) - \left(t_C - (t_E + \Delta T_{lift}\right) \cdot \mathrm{R} \tag{2}$$

Most of the 40 measured values in the different operation modes are in good accordance with the theoretical reflection. Only at high ΔΔT values, in the “LowReturn” mode as previously described, the huge temperature difference in the external driving heat circuit and related low flow rate cause greater deviations. This is attributable to a simplified logarithmic temperature difference approach of the method. By neglecting these values, Figure 13 depicts a linear dependency between chilled water capacity Q_E and total temperature difference ΔΔT. The root of the linear function shows the minimum temperature difference $\Delta\Delta T_{min}$ to overcome the internal losses of the process. Particularly, this includes solution heat exchanger effectiveness and heat losses and gains in between the components and the ambient.

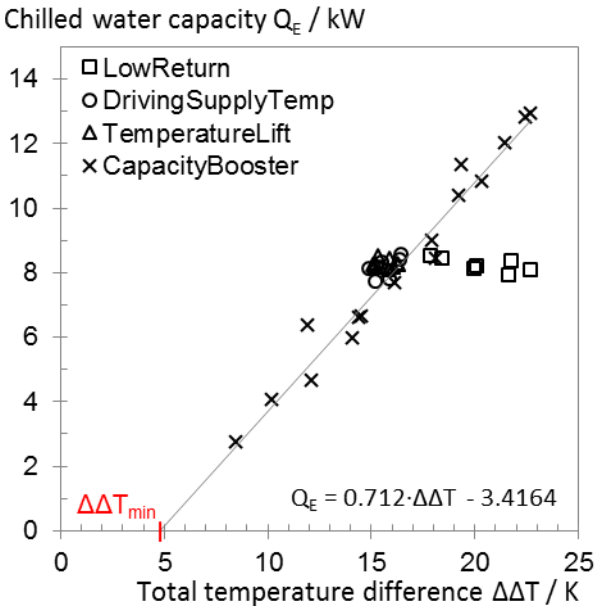

Figure 13: Attainable chilled water capacity Q_E from total temperature difference ΔΔT supplied to absorption-compression process

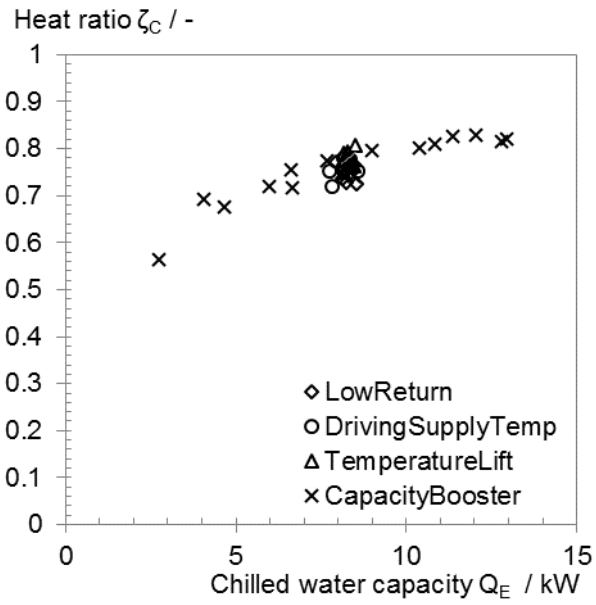

Figure 14: Heat ratio ζ_C of the four operation modes with variable ΔΔT dependent on external chilled water capacity Q_E

Figure 14 shows the quotient of produced chilled water capacity versus consumed driving heat, so called heat ratio ζ_C, for a variable total temperature difference in part-load performance. While the variance is quite small with changing ΔΔT and mechanical compressor input ΔT_{lift}, the heat ratio degrades moderately with decreasing chilled water capacity from over 0.8 at full load to less than 0.6 at 15 % of design chilled water capacity. To further improve the part load characteristic, the solution flow rate circulating between absorber and desorber may be adapted to the current chilled water capacity. Yet, this measure is limited by the minimum flow rate required for sufficiently wetting the horizontal tube heat exchangers.

7. CONCLUSION

Future climate friendly cold and heat supply systems for buildings necessitate efficient heat pumps and chillers with minimal global warming potential over the entire lifespan. Beside low cost and easily available natural refrigerants, this will incorporate efficient heat transformation processes with a high share of renewable driving energy and/or waste heat. In this context, a combination of the thermal absorption and mechanical vapor compression process with the natural refrigerant water (R718) and lithium bromide as sorbent in a compact Hybrid Chiller cycle seems promising. For thermodynamic performance and flexibility reasons, the mechanical compressor preferentially supports the sorption process between evaporator and absorber. If a high power density is the dominating criterion, the compressor performs best between desorber and condenser. With respect to the special refrigerant conditions and operation envelope of the mechanical compressor, the hybrid chiller demonstrator design has to be revised concerning optimal incident flow, pressure drop and safety equipment. In total, four relevant operation modes have been identified, which show a significant improvement of the sorption process regarding temperature levels and power output by means of the additional temperature lift provided by the mechanical turbo compressor. In total, good conversion ratios of heat to cold are achieved. Finally, a simple extension of the established “characteristic equation method” of absorption technology to characterize the operation of hybrid chiller is in good agreement with most measuring results in the different operation modes.

ACKNOWLEDGEMENT

This project has been funded by the German Ministry of Education and Research, grant 13FH023I.

NOMENCLATURE

p_s	suction pressure of compressor (kPa)	v	specific volume ($m^3 \cdot kg^{-1}$)
l	spec. heat of solution ($kJ \cdot kg^{-1}$)	ΔT_{lift}	mechanical temperature lift (K)
Q_E	chilled water capacity (kW)	$\Delta\Delta T$	total temperature difference (K)
P_{spec}	spec. power per cooling (-)	κ	isentropic exponent (-)
q_{ov}	volumetric cooling power ($kJ \cdot m^{-3}$)	Π	pressure ratio of compressor (-)
R	Dühring coefficient (-)	ζ_C	heat ratio in chiller mode (-)
w	lithium bromide concentration (%)	ζ	pressure loss coefficient (-)
T_{crit}	critical point temperature (°C)		

REFERENCES

Albers J, 2017. Präzisierungen zur Methode der charakteristischen Gleichung. DKV-Jahrestagung, 22.-.24.Nov.2017, Bremen, Paper AA.II.1.15.

Eckert T, Helm M, Schweigler C, 2015. Hybrid sorption/compression cycle with the working fluid water for increased flexibility of tri-generation, cooling or heating. 24th IIR International Congress of Refrigeration (ICR2015), 16.-22.8.2015, Yokohama, Japan.

Efficient energy GmbH, 2016. Technical data eChiller 2-35, Feldkirchen, Germany.

Helm, M., Eckert, T. & Schweigler, C., 2015. Hybrid Water/LiBr Absorption chiller boosted by high-speed turbo compressor. Rome, Italy: 6th International Conference Solar Air-Conditioning.

Helm M, Eckert T Schweigler C, 2018. Design and Practical Validation of a Hybrid Absorption/Compression Chiller Driven by Low-Grade Heat. 8th International Conference on Solar Air Conditioning, September 12-13, 2018 - Rapperswil, Switzerland.

Meier-Staude, R. & Kniffler, O., 2013. Entwicklung und Herstellung von Prototypen der Verdampfer und Verflüssiger für die ct-turbo Wärmepumpe. Feldkirchen: Efficient Energy GmbH.

Schweigler C, Storkenmaier F, Ziegler F, 1999. Die charakteristische Gleichung von Sorptionskälteanlagen. Tagungsband der Deutschen Klima-Kälte-Tagung.

Ziegler F, Hellmann H. M, Schweigler C, 1999. An approximative method for modelling the operating characteristics of advanced absorption chillers. 20th Int. Congr. of Refrigeration, Sydney

Manuscript ID: 1203
DOI: 10.18462/iir.icr.2019.1203

Design considerations for dynamically operated large-scale ammonia heat pumps

Wiebke MEESENBURG[(a)], René KOFLER[(a)], Torben OMMEN[(a)], Wiebke Brix MARKUSSEN[(a)], Brian ELMEGAARD[(a)]

[(a)] Technical University of Denmark, Department of Mechanical Engineering
Kongens Lyngby, 2800, Denmark, wmeese@mek.dtu.dk

ABSTRACT

Large-scale heat pumps (HPs) are being implemented to provide heat for district heating (DH) systems from renewable heat sources. They are further expected to play a key role in integrated energy systems as flexible loads that can be used to balance the electricity grid. However, most large-scale HPs installed are designed for base load operation and are thus not optimized with regard to dynamic behaviour. Within this work, the dynamic behaviour of different HP configurations was assessed with regard to performance during load change. For this purpose, a two-stage and a one-stage ammonia HP were modelled using Modelica. Further, different adaptions of the two-stage HP to avoid condensation in the suction line were assessed. Fast ramping resulted in oscillation of the liquid level in the receivers. It would thus be necessary to design receivers carefully and include suction traps to avoid entrainment of droplets into the suction lines. The results indicated that condensation in the low-pressure suction line was a limiting factor for how fast the HPs may ramp down. This could be avoided by preheating of the suction line. In that case, the HPs under assessment were able to regulate between 100 % and 40 % load in less than five minutes, and they would thus be capable of providing secondary regulation power.

Keywords: Large-scale heat pump, dynamic operation, dynamic model, ammonia, regulation power

1. INTRODUCTION

Denmark has decided to reduce CO2 emissions drastically in order to comply with international climate change mitigation targets and national energy targets. The target is to supply all heating and electricity from renewable energy sources in 2035 (The Danish government - Energi-Forsynings- og Klimaministeriet, 2013).Renewable energy sources such as wind or solar power are fluctuating and difficult to predict. In order to secure grid stability even with high shares of fluctuating power production, flexible units on the production and demand side can be used to balance out the frequency in the grid.

Heat pumps (HPs) enable the use of ambient or low-grade heat sources for heating purposes by lifting the temperature from the source temperature to values high enough to supply the required heating service. The fuel for the cycle is most cases electricity. Thus, HPs provide a link between the electricity and the heating sector, and thereby they may act as flexible loads while supplying renewables-based heat. The flexibility is provided by the possibility to store heat in storages, the buildings or in the district heating (DH) grid.

Flexible operation of heat pumps may results in additional losses on the heating side (Meesenburg et al., 2018). However, the flexibility to adapt the electric capacity of HPs can be used to provide frequency regulation and thus act on the reserve markets. This may offer additional income for plant operators. In order to do so the regulation rate needs to be fast enough in order to comply with the standards of the transmission system operator (TSO).

While small-scale HPs can switch on and off rather quickly, large-scale HPs for DH supply are usually designed for base load operation and thus, not optimized for fast regulation (David et al., 2017). Accordingly, ramping rates in many applications are limited (Averfalk et al., 2014). In order to improve the ability of large-scale HP systems to deliver regulation services, it has to be identified what causes the limitations with regard to ramping rates and thereby, how the HP design and control can be improved (Fischer and Madani, 2017).

Danish law forbids the use of HFC refrigerants in large-scale applications because of their high global warming potential (Miljøstyrelsen, 2016). Natural refrigerants such as ammonia are mostly used for large-scale applications in Denmark today and accordingly, we chose to focus on ammonia as a refrigerant for this study.
This study focused on the description of dynamic behaviour during load change of large-scale ammonia HPs in a one-stage and a two-stage configuration. The aim was to identify what limits fast ramping up and down of the HP. Liquid formation in the suction line during ramp-down has been identified as a limitation to fast ramping. Accordingly, different strategies to avoid this were assessed. The study was based on a dynamic simulation of the HP configurations, which is further described in section 2. The results are presented in section 3 and discussed in section 4, before conclusions are presented in section 5.

2. METHOD

2.1. Heat pump application case

The HPs simulated in this study were designed to fit a real HP application, supplying DH to a small grid in the development area of Nordhavn in Copenhagen, Denmark. The design heating capacity of the system was 800 kW. As heat source groundwater at 10.5 °C was used. It was cooled down in the evaporator and ejected into the sea. This was possible as the groundwater reservoir is infiltrated by seawater anyway. The HP was able to deliver forward temperatures of 65 °C to 84 °C. For this study, we assumed a forward temperature set point of 70 °C and a constant return temperature of 35 °C. The assessed system was a two-stage ammonia HP, which comprises a flooded evaporator, separator, low-stage compressor, open flash intercooler, high-stage compressor, desuperheater, condenser, subcooler and two expansion valves as main components. Pipe models were included for both suction lines of the compressors. For better understanding of the nature of limitations during ramping of the HP, the results for the two-stage HP were compared to a one-stage ammonia HP, supplying the same services. This was comprised of flooded evaporator, separator, compressor, desuperheater, condenser, subcooler and one expansion valve. A sketch of the two configurations is shown in Figure 1.

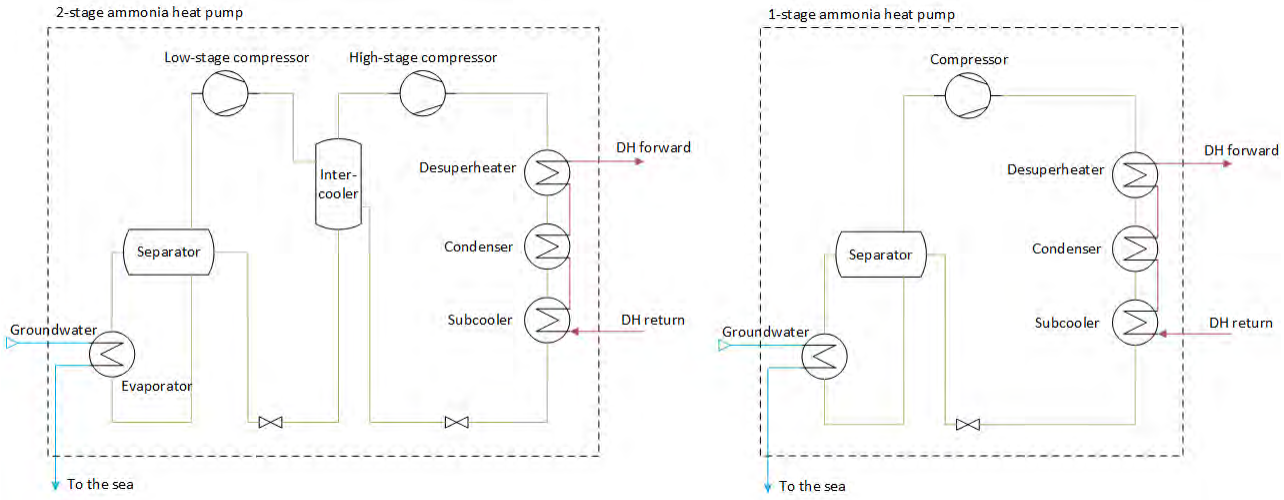

Figure 1 Sketch of 2-stage and 1-stage ammonia HP

2.2. Dynamic model

In order to simulate the behaviour of the system during up- and down ramping a dynamic model of the system was built in the object-oriented programming language Modelica (Modelica Association, 2017) using Dymola software (Dassault Systèmes, 2017) and the TIL library (TLK Thermo GmbH & IfT, 2017). The latter includes validated component models for the simulation of refrigeration systems. All components were modelled using dynamic energy and mass balances. Momentum balances were modelled using steady state equations, as the time constants for momentum balances are relative small compared to energy and mass balances.
The heat exchangers were modelled as corrugated plate heat exchangers using heat transfer correlations of Steiner (VDI, 2010) for evaporation, of Shah (VDI, 2010) for condensation and of

Gnielinski, Dittus & Boelter (Baehr and Stephan, 2011) for one-phase flow and a quadratic mass flow dependent pressure drop for ammonia. The pressure drop on the water side was neglected and the heat transfer coefficient was calculated according to (VDI, 2010). The pipe model included Dittus & Boelter heat transfer model and Konakov's pressure drop correlation for smooth pipes (VDI, 2010). Heat conduction from the ambient through steel pipe and insulation was considered.
The compressors were piston compressors equipped with variable speed drive for part-load operation. The oil-cooling was not modelled in detail, but was considered as a heat loss from the compressor. The compressor efficiencies were calculated from compressor polynomials, which were functions of condensation temperature, temperature lift, pressure ratio and compressor frequency. The displacement volumes were assumed to be 0.009425 m³ and 0.0044 m³ for the low-stage and high-stage compressor of the two-stage HP. The high-stage compressor polynomial was also used for the compressor in the one-stage HP, due to the high temperature tolerance (Johnson Controls, 2019). The displacement volume was 0.0088 m³.
The separators and open-flash intercooler were modelled as ideal tanks, i.e. equilibrium between the gaseous phase and the liquid phase and uniform pressure and temperature in the tank were assumed. As the liquid levels were assumed to be low, the pressure difference between gas- and liquid outlet was neglected.

2.3. Control of the heat pumps

The aim of controlling the HPs was to ensure a certain DH forward temperature and heat output at high efficiency and safe operation of the HPs.
In the case of the two-stage HP there were 6 manipulating variables, namely the rotational speed of both compressors, the source water flow, the DH water flow and the cross sectional area of both expansion valves. The pairing of manipulating and controlled variables was deducted from a relative gain array (RGA) analysis for the two-stage and one-stage HP (Seborg et al., 2010). Resulting in the following control structures:

- *Two-stage HP*: The source water flow was fixed and the water temperature at the evaporator outlet was controlled with the low-stage compressor rotational speed. Thereby, the capacity of the HP was controlled indirectly. The rotational speed of the high-stage compressor controlled intermediate pressure level, ensuring similar pressure ratios for both compressors. The DH flow was altered to control the condensation temperature and thereby indirectly the DH forward temperature. The high-stage expansion valve controlled the fluid quality at the condenser outlet, and the low-stage expansion valve was used to control the liquid level in the separator.
- *One-stage HP*: the forward temperature was controlled by the DH water flow directly and the heat output was controlled by the compressor rotational speed. The separator level was not controlled, but the valve was used to control the condenser outlet quality of the fluid.

All controls were implemented as PI-controllers into the model. The parametrization was conducted according to the method described by Kuhn (1995).The integration time constants for the 1-stage system were reduced slightly to match those found for the two-stage cycle, in order to ensure that the results are comparable. This resulted in slightly faster regulation of the one-stage HP.

2.4. Operation strategy

In order to deliver frequency regulation, the HPs need to adapt their electricity consumption quickly. It was assumed that only upward regulation defined from an electricity supply perspective was provided. Accordingly, the HP can supply upward regulation by reducing electricity consumption. This could be achieved either by

- ramping down into part-load and ramping up again when the regulation period is over
- shutting down the HP completely and starting up again afterwards.

To avoid the necessary dead times before restart of the compressors and increased wear through recurrent starts and stops the first option was considered. Tests with the existing two-stage HP have shown that the HP can operate at part loads of down to 40 % of full load. We thus assumed that the HP capacity can be reduced by 60 % during regulation periods. The response time for frequency normal reserve (primary reserve), secondary reserve and tertiary reserve in Eastern Denmark is 150 s and 5 min and 15 min, respectively (Energinet.dk, 2017).. The frequency (normal) reserve market is the economically most attractive option and thus the aim of this study was to find out whether it could be possible to deliver the regulation power within 150 s. The electric capacity of the assessed HP is too low to bid into the markets. That means an exceptional allowance would be needed or the HP could be clustered with other flexible assets.

2.5. Evaluation criteria

The ramping time was defined as the time during which the set point of the heat load was changed, thus forcing the system to a slower or faster change of load. This value was varied to be 150 s, 100 s, 50 s and 10 s. The time between start of the ramping and reaching steady state (ss) was defined as the response time Δt_{r}

$$\Delta t_{\mathrm{r}} = t_{\mathrm{start}} - t_{\mathrm{ss}} \qquad \text{Eq. (1)}$$

Steady-state was assumed to be reached when the heat output was within a tolerance of 0.1 % of the overall heat output. This corresponded to a tolerance of < 0.2 % of the steady-state value for the power uptake.

The steady-state COP was defined as the ratio of the steady state heat output $\dot{Q}_{\mathrm{ss}}$and power consumption $\dot{W}_{\mathrm{ss}}$.

$$\mathrm{COP}_{\mathrm{ss}} = {\dot{Q}_{\mathrm{ss}}}\Big/{\dot{W}_{\mathrm{ss}}} \qquad \text{Eq. (3)}$$

2.6. Strategies to avoid condensation in the suction line

The observed condensation in the suction line was a limiting factor to how fast the HP may be ramped down. There are a couple of possible technical solutions that may avoid condensation in the suction line during fast ramp-downs. These could help to allow a faster ramping of the HP. Here, we assessed four different strategies for the two-stage HP:

- Controlling the source outlet temperature from the evaporator to a constant temperature

The idea is to reduce the increase of evaporation pressure during fast ramp down by keeping the mean source temperature constant. This may be obtained by controlling the source outlet temperature by changing the source mass flow through the evaporator.

- Replacement of the flooded evaporator with a direct expansion evaporator (DEX)

In this case, the superheat after the evaporator could be controlled, to a value high enough to avoid liquid entering the compressor during ramp-down. The heat exchanger size of the evaporator was increased for this simulation by a factor 2, which was large enough to ensure superheating at the outlet, but it was not optimized. The superheat was controlled by the low-stage expansion valve.

- Implementation of an internal heat exchanger (IHX) to superheat the fluid in the suction line

This design would keep the flooded evaporator by installing an IHX to preheat the suction line using the liquid exiting the open-flash intercooler as heat source. The IHX was designed using manufacturer software to provide a superheating of 5 K. No further control was considered.

- Implementation of an electric preheating (el. PH) of the suction line

Ensuring superheated gas in the suction line by external electric heating is a flexible option, which may easily be added to existing systems and may allow adapting the superheating to the requirements of different operation modes. Due to simplicity for this study, we assumed a constant heating power of 2 kW throughout the simulation time.

3. RESULT

This section presents the simulation results regulation of the two-stage HP and compares them to the one-stage HP. Different possibilities of avoiding condensation in the suction line are compared.

3.1. Two-stage heat pump

The dynamic behaviour of the two-stage HP was simulated for four different ramping times. The power uptake and heat output for an exemplary case is depicted in Figure 2 and the steady state COPs were calculated as 3.45 during full-load and 3.43 at 40 % part-load. The response times of the system until steady-state are listed in Table 1.

It can be seen that the given system was not able to reach steady state in less than 150 s, which corresponds to the necessary reaction time for primary reserve in Denmark. The full regulation capacity might be delivered within 182 s to 306 s. That means that under the implemented control strategy, the system reacted too slowly to provide primary reserve, but it might be possible to provide secondary regulation power. The integration time constants of the controllers had a large influence on the system response time, i.e. optimizing the controller would allow faster ramping.

Table 1 Response time for different ramping times (change of set value) for the two- and one-stage ammonia HP cycle

Ramping time [s]	Two-stage HP		One-stage HP	
	Δt_r ramp-down [s]	Δt_r ramp up [s]	Δt_r ramp-down [s]	Δt_r ramp up [s]
150	278	306	285	303
100	238	270	240	265
50	205	221	203	232
10	182	190	179	209

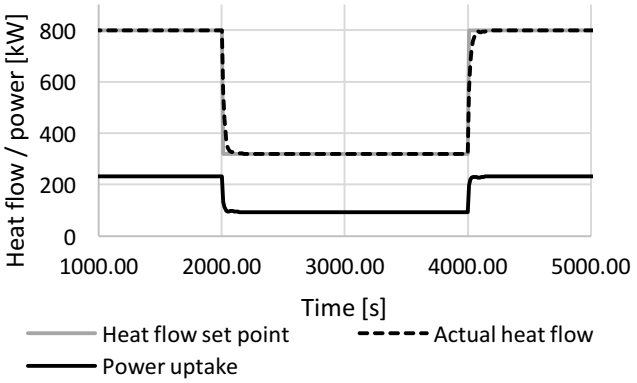

Figure 2 Operation scheme for the provision of regulation power. Depicted is the set value for the heat flow, the actual heat flow and the power uptake

The limiting factor was found to be a thermodynamic effect. As can be seen in Figure 4 the fast ramp-down from full-load into part-load led to formation of liquid in the suction line. The effect was stronger the faster the HP ramped down. This was due to a sudden increase in pressure on the low-pressure side, which caused the saturation temperature of the fluid to increase. The walls of the suction line warm up more slowly than the fluid due to the thermal inertia of the piping material. Accordingly, the wall temperature was below the saturation temperature of the fluid, which would lead to condensation along the pipe walls. The suction line in the model is only discretized in one dimension, i.e. the quality values given here are averaged over the control volumes and it is uncertain how much fluid would actually condense on the cold surface. Potentially, any droplet may however harm the reciprocating compressor and condensation in the suction line should be avoided. This limited how fast the HP capacity can be ramped down. Thus, an ammonia HP that should adapt its load quickly needs to be designed in a way that condensation in the suction line is avoided. During ramp-up, the suction line is warmer than the saturation temperature and thus there is no problem with regard to condensation.

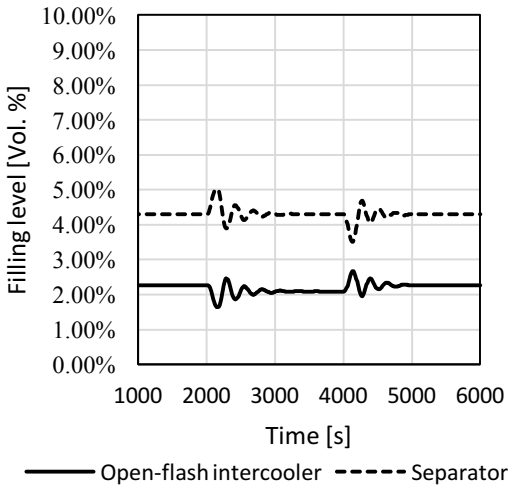

Figure 3 Filling level of intercooler and separator. Ramp-down start at 2000 s. Ramp-up starts at 4000 s.

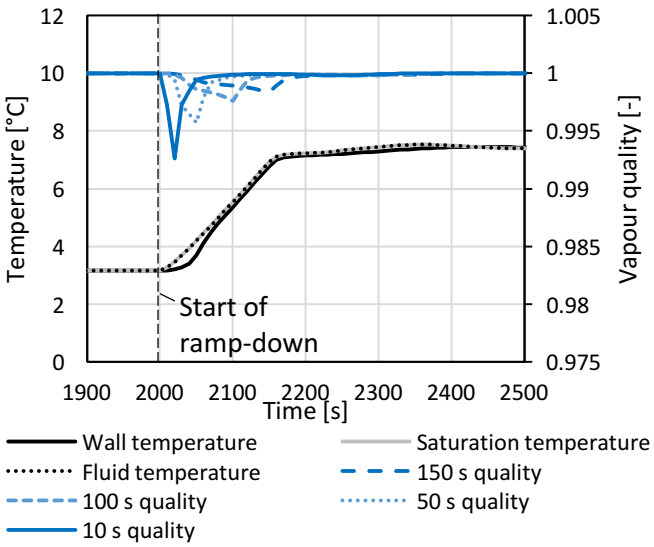

Figure 4 Fluid temperature, wall temperature, saturation temperature of the fluid and vapour quality at the end of the low-pressure suction line in a two-stage ammonia heat pump. Ramp-down into part load starts at 2000 s. Ramp-up to full load starts at 4000 s.

Figure 3 shows the liquid level of the open-flash intercooler and the separator. The fast load change induced large peaks in the filling level compared to steady-state level. This was especially critical for relatively high filling levels in steady-state, as the absolute peaks in filling level were high, too. This means that under the assumed control strategy the fast ramp down led to large agitation, which could influence the separation of liquid and vapour in the vessel negatively, and

which also influences the low and high stage pressure level - and thus the operation conditions of the heat pump. The dynamic response of the filling level depended mainly on the controller parameters chosen for the low-pressure expansion valve controller. This indicated that the applied controller design method was not sufficient for this control pair and that a more elaborate controller design is necessary.

3.2. One-stage heat pump

In order to assess whether the more simple cycle design of a one-stage HP can lead to faster response time of the HP system during ramping, a one-stage cycle with the same nominal heating capacity as the two-stage cycle was simulated.
The response time for different ramping times of the one-stage HP are presented in Table 1. The response times obtained did not differ significantly from the response times of the two-stage system. This was due to the similar time constants of the controllers.
The filling level in the separator was not controlled in the one-stage cycle. Nonetheless, the induced oscillations were as low as 3 % of the steady state filling level in full load and thus significantly lower than for the two-stage cycle. Even though no advantage in terms of response time was observed, the system reaction was more robust and fewer oscillations were induced. Thus, a more simple cycle might be well suited for flexibly operated heat pumps. However, the forward temperatures that may be delivered with a one-stage ammonia HP are limited.
As with the two-stage HP the fluid state in the suction line was in the two-phase region under fast ramp-down of the HP capacity, i.e. condensation might occur. The effect was stronger for faster ramping times.

Table 2 Results for different cycle adaptions to avoid condensation in the suction line

Design	Risk of fluid in suction line [yes/no]	Δt_r down [s]	Δt_r up [s]	COP_{ss} full-load [-]	COP_{ss} part-load [-]
Base case	yes	182	190	3.45	3.43
Source control	yes	176	159	3.41	3.24
DEX	no	205	182	3.42	3.31
IHX	no	193	206	3.40	3.39
El. PH	no	254	176	3.41	3.35

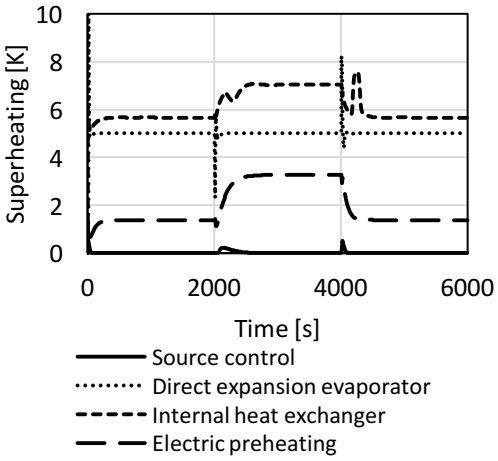

Figure 5 Superheating for four different strategies to avoid condensation in the suction line

3.3. Strategies to avoid condensation in the suction line

The results for these four adaptions to avoid condensation in the suction line are summarized in Table 2. The response times were in a similar range as for the two-stage cycle without adaption. The first option resulted in condensation in the suction line, too. Even though the increase in the evaporation pressure was less than with the original control strategy, it still increased and even peaked during ramp down. This meant that the same phenomenon as in the original cycle design occurred.
The COP in full load was highest for DEX and el. PH. In both configurations the part-load COP was comparably low. Further, Figure 5 shows that the superheating for DEX and el.PH decreased shortly during ramp-down, this means that it is crucial to design the control in a way that the superheating is large enough to accommodate this negative peak. The part-load COP of the el. PH configuration might be increased to the value of the two-stage HP base case by shutting the preheating off during part-load operation. The COP in part-load was highest for the internal heat exchanger configuration. This was advantageous in the case of the proposed operation strategy, as the heat pump would be operated in part-load during regulation periods. Thus, the loss due to

regulation would be smaller and the cost of regulation would be lower. The full-load COP in the IHX case was slightly lower than for the alternative adaptions. As shown in Figure 5, this was due to the larger superheating compared to the other technologies. The superheating increased in part load and did not show any downward peaks during ramp-down of the heat pump. It might be possible to reduce the IHX size, and thereby the set point for the superheating, and thus reduce the decrease in COP compared to the base case. In the IHX case, the reduction in COP due to superheating was partly outbalanced by the effect of additional subcooling of the liquid before entering the low-pressure expansion valve. This explains the better COP in part-load compared to the other cases.

4. DISCUSSION

The results indicated that the thermal inertia of the components as well as inertia of the system due to refrigerant migration actually had a minor impact on the system dynamics, as the system was not ramped down completely and started up again, but only the load was changed. It was observed that the dynamic behaviour is strongly influenced by the controller design. In the present study, only PI controllers were considered. It is expected that the controller design may be improved by advanced controller design methods, which may possibly reduce the reaction time of the two-stage system far enough to be able to provide frequency normal reserve (150 s response time). It should however be noted that the presented simulation results did not consider dead-times of actuators or waiting times during compressor ramping. The latter was especially relevant for the two-stage cycle, as the compressor load needs to be changed in an orchestrated way during ramping. This may possibly lead to longer actual regulation times for the two-stage HP. Further, the heat pump was controlled according to the desired heating capacity, as this is the main purpose of the heat pump. In future applications, it might be considered to control the heat pump according to the power uptake and thereby force the heat pump to follow the desired power consumption profile for frequency regulation.

The results for the one-stage cycle did not show faster regulation performance than the two-stage cycle model. However, during load change fewer oscillations occurred and the overall system performance seemed to be more robust. The one-stage ammonia cycle is usually not chosen for DH applications due to the limited supply temperatures. For 70 °C forward temperature the discharge temperature exiting the compressor in the one-stage case was calculated to be ca. 172 °C. This might still be allowable with regard to thermal stability of the lubrication oil (Ommen et al., 2015), but it is at the upper end of discharge temperatures tolerated in state-of-the-art compressor technology. However, it seems promising to investigate whether one-stage cycles with other working fluids may be more suitable for flexible operation.

Additionally, fast regulation led to sudden changes in the hold up of vessels in the system, such as receivers, open flash intercooler and separators. This can lead to increased agitation of the vapour and liquid flow, which may in extreme cases lead to two-phase flow in the lines towards compressor or valve. Both should be avoided. The effect may be decreased by improved control of the valves during the ramping routine. Further, the layout of vessels as suction traps (ASHRAE, 2006) can help to secure that no liquid enters the compressors during fast load changes.

The results showed that the crucial factor when ramping the HP down quickly was the danger of condensation in the suction line due to sudden increase of evaporation pressure. It should however be noted, that from this system level analysis it cannot be determined how much fluid actually condensates in a real system, as the flow characteristics and heat conductions along the pipe might have an influence, as well. Thus, the results only can give an indication on whether there is a risk of condensation or not. Different possible strategies to avoid this risk were compared in the results of this study. Among those, the implementation of an IHX and electric preheating of the suction line seemed most promising. The first is preferable, if the system is supposed to ramp up and down frequently, as condensation in the suction line can safely be avoided under all conditions. The part load COP is comparably high for this system. The benefit of el. PH is that the superheating control is very flexible and may be switched off during part-load or when the HP is not delivering regulation power. Further, el.PH can be added relatively easy to existing HP systems. The necessary heating power needs to be chosen carefully in order to deal with the downward peaks in superheating that were observed. Another option would be to combine the flexible approach and the IHX, by bypassing the IHX during part load operation or when no flexible operation is scheduled. This would need further implementation of three-way-valves and controllers. The influence of these on the system should be assessed further.

5. CONCLUSION

This paper assessed the dynamic behaviour of a two-stage ammonia heat pump during ramping from full-load into part-load and up to full-load again. The results were compared to a one-stage cycle. The response times for both systems was comparable, but the one-stage cycle showed less oscillation during fast ramping. By ramping the heat pump down quickly, large oscillations were observed in the filling levels of intercooler and separator in the two-stage cycle. This should be considered in controller design. Further, suction traps could avoid liquid entering the suction line.
Condensation in the low-pressure suction line was identified as a major limiting factor with regard to possible ramping times. Condensation was more likely to happen the faster the heat pump was ramped down. In order to avoid this, several possible adaptions were assessed. Out of these, an internal heat exchanger between the liquid outlet from the intercooler and the suction line and electric preheating seemed to be most feasible. If condensation could be avoided, the heat pump set up would be able to deliver secondary regulation power, i.e. response time below five minutes.

6. ACKNOWLEDGEMENT

This research project is financially supported by the Danish Energy Agency EUDP (Energy Technology Development and Demonstration Program) under the project ”EnergyLab Nordhavn - New Urban Energy Infrastructures” (project number: 64014-0555).

7. BIBLIOGRAPHY

Averfalk, H., Ingvarsson, P., Persson, U., Werner, S., Industry, D., 2014. On the use of surplus electricity in district heating systems 7–12.

Baehr, H.D., Stephan, K., 2011. Heat and mass transfer, 3rd Editio. ed, Heat and Mass Transfer. Springer- Verlag. https://doi.org/10.1007/978-981-10-1557-1

Dassault Systèmes, 2017. Dymola Systems Engineering [WWW Document]. URL https://www.3ds.com/products-services/catia/products/dymola/ (accessed 10.31.17).

David, A., Mathiesen, B.V., Averfalk, H., Werner, S., Lund, H., 2017. Heat Roadmap Europe: Large-Scale Electric Heat Pumps in District Heating Systems. Energies 10, 578. https://doi.org/10.3390/en10040578

Fischer, D., Madani, H., 2017. On heat pumps in smart grids: A review. REHVA J. https://doi.org/http://dx.doi.org/10.1016/j.rser.2016.11.182

Johnson Controls Denmark ApS, n.d. SABROE ® HPO / HPC / HPX high-pressure reciprocating compressor units [WWW Document]. URL www.sabroe.com (accessed 1.24.19).

Kuhn, U., 1995. Eine praxisnahe Einstellregel für PID-Regler: Die T-Summen-Regel (A practical parametrization rule for PID-conrollers: The T-sum-rule). Autom. Prax. 37, 10–16.

Meesenburg, W., Ommen, T., Elmegaard, B., 2018. Dynamic exergoeconomic analysis of a heat pump system used for ancillary services in an integrated energy system. Energy 152, 154–165. https://doi.org/10.1016/j.energy.2018.03.093

Miljøstyrelsen, 2016. Bekendtgørelse om regulering af visse industrielle drivhusgasser (BEK nr 1326 af 19/11/2018). Denmark.

Modelica Association, 2017. Modelica and the Modelica Standard Library [WWW Document]. URL http://www.modelica.org (accessed 10.31.17).

Ommen, T., Jensen, J.K., Markussen, W.B., Reinholdt, L., Elmegaard, B., 2015. Technical and economic working domains of industrial heat pumps: Part 1 - Single stage vapour compression heat pumps. Int. J. Refrig. 55, 168–182. https://doi.org/10.1016/j.ijrefrig.2015.02.012

Seborg, D.E., Edgar, T.F., Mellichamp, D.A., Doyle, F.J., 2010. Process dynamics and control. Wiley.

The Danish government - Energi- Forsynings- ogKlimaministeriet, 2013. The Danish Climate Policy Plan Towards a low carbon society

TLK Thermo GmbH & IfT, 2017. TIL 3.4 – Model library for thermal components and systems.

VDI - Gesellschaft Verfahrenstechnik und Chemieingenieurwesen (Ed.), 2010. VDI Heat Atlas, 2nd Editio. ed, VDI Heat Atlas. Springer-Verlag, Berlin Heidelberg. https://doi.org/DOI 10.1007/978-3-540-77877-6

Manuscript ID: 1208
DOI: 10.18462/iir.icr.2019.1208

Transient Thermal Management of Vapor Cycles to Simulate Aircraft Electrical Environment Control Systems

Nicolás ABLANQUE[(a,*)], Santiago TORRAS[(a)], Carles OLIET[(a)], Joaquim RIGOLA[(a)], Carlos-David Pérez-Segarra[(a)]

[(a)] Universitat Politècnica de Catalunya – Barcelona Tech (UPC), Heat and Mass Transfer Technological Center (CTTC),
Terrassa, Barcelona, Spain, cttc@cttc.upc.edu

ABSTRACT

A Modelica library has been developed to simulate thermal management architectures of Electrical Environmental Control Systems (E-ECS) in new generation aircrafts. The modeling of these architectures requires significant efforts to overcome the non-negligible number of numerical difficulties related to the steady-state and dynamic resolution of both particular components and subsystems. The library main goal is to conduct accurate and robust simulations with optimized computational time based on an appropriate trade-off between component model simplicity and ability to represent its behavior accurately.
The work presented herein is focused on the resolution of the Vapor Compression System (VCS) and its integration within the aforementioned E-ECS architectures. The VCS has been modeled together with other relevant subsystems in order to assess the library numerical capacities and to study the influence of some relevant parameters such as the environment temperature or the VCS compressor working frequency.
Keywords: Modeling, Vapor Compression Systems, Dynamic Simulations, Environmental Control System.

1. INTRODUCTION

The design of new environmental control system architectures in the aeronautical industry is usually conducted with the support of numerical modeling and simulations. However, the analysis of such architectures is a complex task and their modeling is a challenging goal. The present work derives from an on-going project within the CleanSky2 European research program whose aim is to develop a complete set of Modelica libraries to simulate E-ECS with the following requirements: high accuracy (numerical predictions close to correct values), robustness (numerical reliability within a wide range of operating conditions), and minimized computational time (to guarantee reasonable computational time of large architectures).
Modelica is an object-oriented and an equation-based language where large and complex system architectures involving multiple physics can be handled with relative ease. The whole set of system equations are internally rearranged and manipulated to generate an optimized code prior to the execution of simulations so that the user can concentrate the efforts on the modeling aspect instead of the solving procedures. The use of such language approach has been used and recommended for the modeling and simulation of combined systems (Wetter et al., 2016).
The E-ECS architectures being currently studied usually include a VCS unit to provide additional power to cool down the cabin when needed (unlike prior architectures where the cabin cooling was mainly achieved by means of simpler but less efficient air cycles). In the particular E-ECS architecture tackled herein, the VCS is directly linked to a liquid circuit that serves as a heat bridge between the VCS evaporator and the cabin recirculation air flow, and indirectly related to another liquid circuit whose main function is to cool down some electronic devices.

Many difficulties have been faced during the development of the libraries. On the one hand, the complex phenomena involved in some components (i.e. the phase changes in heat exchangers, the consideration of moist air in heat exchangers, the surge conditions in centrifugal compressors), and on the other hand, the numerous numerical problems when solving systems (i.e. the appropriate arrangements for initialization procedures, the management of fluid charge in closed circuits, the handling of near-zero and reverse mass flow rates). All these aspects where meticulously tackled in order to get an acceptable compromise between prediction accuracy, robustness, and computational time consumption.
In the present work an E-ECS model based on the Modelica libraries developed is presented and analyzed. In the following sections the main E-ECS components and subsystems are described from both the mathematical and numerical point of views. The model is tested at both transient and steady-state conditions to assess its numerical robustness and the influence of some relevant parameters.

2. SYSTEM CONFIGURATION

The basic scheme of the E-ECS model analyzed is presented in Fig. 1 and consists of three main circuits, namely, a vapor compression system and two liquid loops.

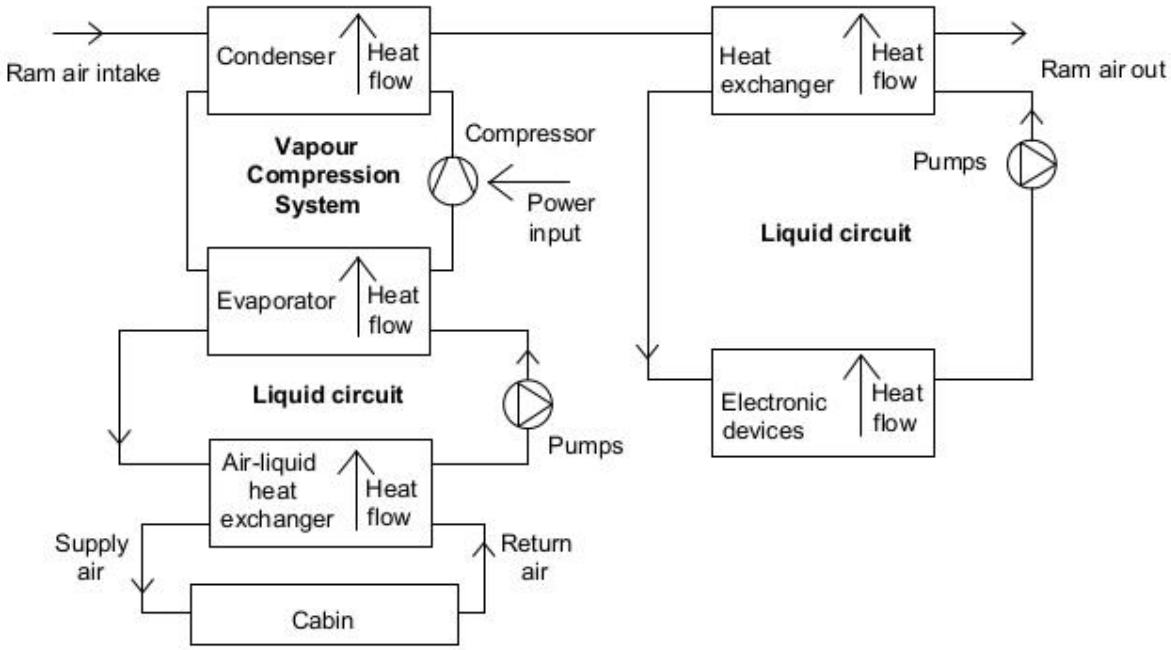

Figure 1: Simplified E-ECS architecture scheme

The VCS is at the core of the E-ECS. Its main task is to generate cooling power from its work input. It is made up of a centrifugal compressor (to heat, pressurize, and drive the refrigerant), a condenser (to evacuate the heat), an evaporator (to extract heat from the adjacent liquid loop), and a thermostatic valve (to regulate the flow conditions). This circuit includes other minor components such as ducts, by-pass valves, and a reservoir (to store/release refrigerant according to the VCS cooling demand).
The cold liquid circuit is directly linked to the vapor compression system as they both share the evaporator component. Its task is to remove heat from the aircraft cabin recirculation air and to transfer it to the VCS evaporator. This circuit is composed of pumps placed in parallel (to produce fluid flow), ducts, valves (to regulate the flow), and a tank (to handle liquid expansion/contraction).
The hot liquid circuit is indirectly linked to the VCS as the incoming ram air temperature is modified at the condenser when the VCS is working. Its assignment is to keep the on-board electronic devices at appropriate temperatures to prevent them from overheating failures. The heat is extracted by means of multiple heat exchangers connected in parallel and then drained into the ram air duct.

It is worth mentioning that the cabin temperature is regulated by both an air cycle (which has not been modeled for this work) and the VCS system. However, the VCS is only activated when additional cooling power is needed (i.e. when the environment temperatures are relatively high).

3. COMPONENTS AND SYSTEMS

This section is devoted to introduce the most relevant components developed for the E-ECS libraries together with the main numerical aspects considered for circuits resolution.

3.1. Components

The primary goal was to provide low time consuming components to prevent from having bottlenecks during the global numerical resolution (most components are based on simplified mathematical formulations and fed with performance maps).

3.1.1. Turbo machines

On the one hand, the vapor compression system is driven by a centrifugal type compressor with variable speed. The compressor is calculated from performance maps which in turn are derived from experimental data or higher detailed models. Both the pressure drop and the work consumption are expressed as a function of both the compressor working frequency and de volumetric flow rate. A characteristic curve is also provided to prevent the compressor from working at surge conditions (e.g. by means of a by-pass duct). A dynamic relaxation is applied over the mass flow rate to facilitate the match between the actual system variables and the performance map readings. Besides the compression itself, a physical volume is located upstream of the compressor to account for flow dynamics.
On the other hand, the flow through both liquid circuits is driven by two pumps connected in parallel. The performance maps for pumps are calculated and obtained in a similar manner than for the centrifugal compressors

3.1.2. Heat exchangers

The E-ECS system studied herein is made up of several heat exchanger types, namely, condenser, evaporator, and liquid-to-air heat exchanger. The models for all these cases have been developed following a similar approach based on differentiated fluid subcomponents for air, liquid, and two-phase refrigerant. In each heat exchanger two fluid subcomponents share a common solid subcomponent that stands for the interface between them.

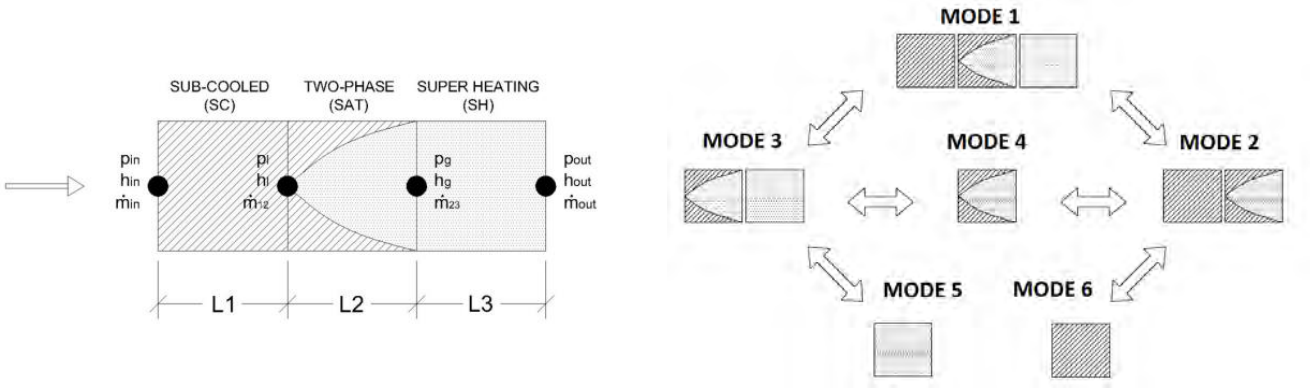

Figure 2: SMB approach: evaporator scheme (left) and transitions (right)

The liquid fluid model is based on an ε-NTU approach in order to optimize the calculation speed and to prevent the emergence of unreal temperature values. The moist air flow model is based on a similar approach but heat transfer due to water condensation is also considered. The refrigerant model is based on a switching moving boundary approach (SMB) with low computational time as only three control volumes are used (unlike distributed models where many control volumes are needed). These models allow to consider the three possible fluid phases but possess added

numerical complexity. Fig. 2 shows the typical scheme of an evaporator together with its operating modes and transitions in the SMB method.

3.1.3. Minor components

Additional models for minor components were also developed. In expansion devices the mass flow rate is calculated as a function of the pressure drop, the flow coefficient and the effective cross-sectional area which can be adjusted from an external signal. Tanks are important components present in all the studied fluid circuits. Their formulation is based on a unique temperature, common to the whole tank, and the assumption that phase separation is complete in the case of two-phase flow tanks. Ducts are less complex components but may account for important pressure losses between major components and imply some delay between inlet and outlet flows.

3.2. Systems

Many difficulties arise when closed circuits are addressed with Modelica, namely, the initialization procedure, the strategy to reach a steady-state operating point, the handling of start-up/shut-down events, the flow at low/null mass flow rate conditions, the self-regulation thermostatic valve in the VCS, and the management of the system fluid charge. These critical aspects were tackled in the present work focusing on achieving robustness and minimum computational time.

3.2.1. Initialization

The system resolution at time equal to zero is a critical numerical task as no information on the previous time step is available. Appropriate initial values could be difficult to obtain specially for closed systems. To facilitate the resolution of components during the initialization both homotopy transformations and dynamic relaxation of certain variables were implemented. In addition, the variables initial values were automatically defined from a dedicated global component that was developed for each specific circuit.

3.2.2. Steady-state resolution

A direct calculation of the initial steady-state cannot be achieved by setting all derivatives equal to zero because it leads to a singularity. This difficulty was addressed by reaching the steady-state by means of a meaningless transient relaxation starting from a set of guessed initial values.

3.2.3. Start-up/shut-down operations

The system simulation at (near) zero mass flow rates is a considerable challenge. At such conditions oscillations appear due to the fast dynamics in the model that force the solver time step to be significantly reduced. Equations were rearranged to avoid any possible division by zero and regularization was added to all the pressure drop equations.

3.2.4. Refrigerant charge management

The refrigerant mass amount conservation is a critical aspect to consider for simulations, specially for the VCS. The charge amount value can be defined at the initial condition but can experience non-negligible variations during the simulation execution as long as the mass conservation undergoes small deviations in time due to the lumped nature of the two-phase flow heat exchanger models. The approach used in the present model consist in correcting the refrigerant mass amount whenever its value deviates too much from the reference value by artificially injecting or extracting tiny amounts of mass into or from the circuit, respectively.

3.2.5. Transient resolution

The system transient response throughout time can produce numerical issues when extreme modifications of the boundary conditions occur. The model has been tested at these conditions to assure robustness.

3.2.6. Thermostatic valve operation

As mentioned previously the VCS superheating is controlled by means of a thermostatic valve located between the condenser and the evaporator. This type of self-controlling systems can

generate several numerical instabilities. The proposed approach consisted in using an adjustable valve combined with a PID controller that compares the reference superheating value against the measured one (PID parameters are adjusted from experimental data).

4. RESULTS

The E-ECS architecture presented in Fig. 1 has been assembled using the Dymola/Modelica environment and the recently developed libraries. The assembly includes all the circuits involved with all their corresponding components.

4.1. Steady-State Simulations

Two sets of steady-state simulations of the whole E-ECS have been carried out to analyze the influence of two relevant parameters: the ram air inlet temperature (which represents the aircraft surrounding conditions) and the VCS compressor working frequency (which represents a major control action). These two parameters were modified over a wide range starting from a reference case defined by an inlet ram air of 40 ºC and a compressor dimensionless frequency of 1. The other boundary variables were kept constant for all the simulations, namely, the ram air mass flow rate, the cabin recirculation air circuit mass flow rate, the VCS superheating reference value, the working speed of pumps, the heat gain due to all electronic devices, and the cabin air return temperature (30ºC). The results presented in this document are based on dimensionless parameters:

$$Q^* = Q/Q_{ref} \quad \text{eq. (1)}$$

$$COP^* = COP/COP_{ref} \quad \text{eq. (2)}$$

$$\dot{m}^* = \dot{m}/\dot{m}_{ref} \quad \text{eq. (3)}$$

$$f^* = f/f_{ref} \quad \text{eq. (4)}$$

Where *Q* is the VCS cooling power, *COP* is the VCS coefficient of performance, $\dot{m}$ is the VCS refrigerant mass flow rate, and *f* is the VCS compressor working frequency. The index *ref* stands for the reference case while the asterisk stands for non-dimensionality.

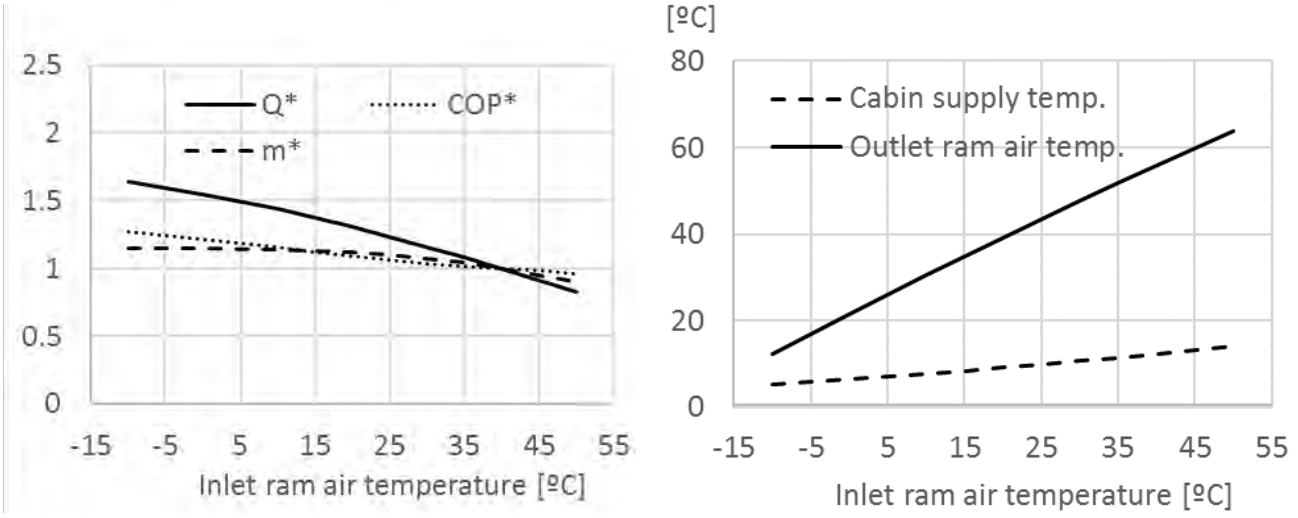

Figure 3: VCS characteristics and ECS relevant temperatures (steady-state simulation with different inlet ram air temperatures)

Fig. 3 shows the E-ECS response according to the ram air inlet temperature value. The value of the ram air temperature is closely related to the altitude and geographical zone of the airplane location. For instance, the selected reference value of 40 ºC can represent the surrounding air temperature at sea level during a hot summer day. The increase of the environment temperature forces the VCS to augment its discharge pressure together with its condensation temperature to

enable heat rejection. Therefore the compressor power consumption grows and the VCS coefficient of performance deteriorates as seen in Figure 3. The overall cooling power diminishes and the cabin supply temperature rises. The ram outlet temperature increases accordingly.

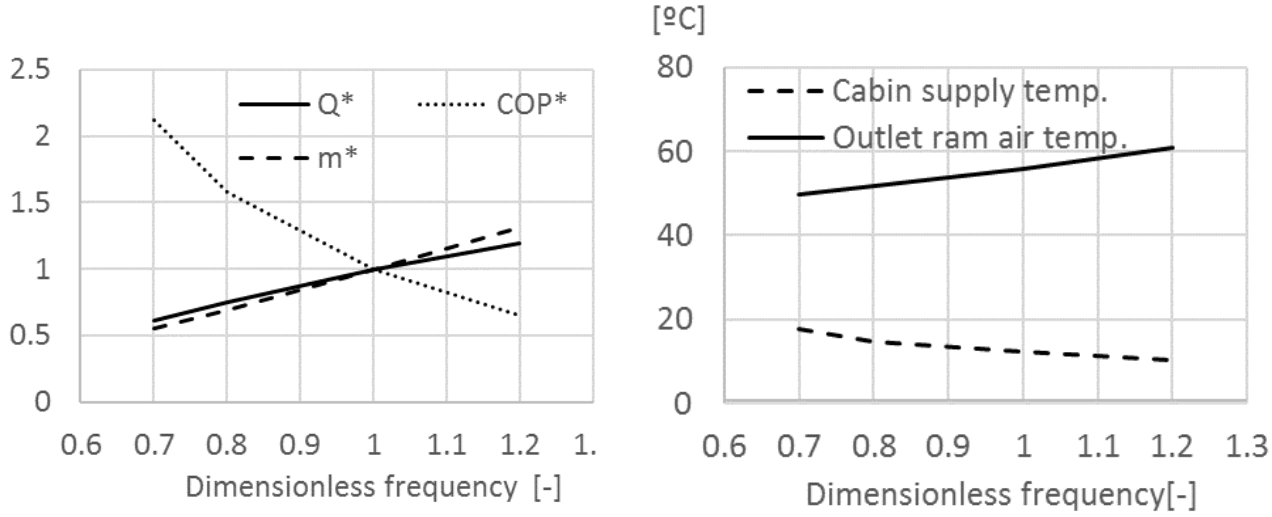

Figure 4: VCS characteristics and ECS relevant temperatures (steady-state simulation with different compressor working frequencies)

Fig. 4 presents the E-ECS behavior as the compressor frequency is increased. Both the compressor power consumption and the VCS refrigerant mass flow rate increase as well as the heat extracted by the VCS evaporator. However, the latter parameter increases at a lower rate so that the coefficient of performance decreases. The cabin supply temperature diminishes in accordance to the cooling power increase while the outlet ram air temperature increases due to the higher heat expelled through the condenser.

More than 20 steady-state cases were run to produce the present parametric study. The computational time for each particular test ranged between 25 and 40 seconds. These calculation times are relatively low considering that the complete assembly from Fig. 1 has been fully simulated considering the real configuration of all circuits and all the components involved. The time values mentioned in this document stand for the CPU integration time provided by Dymola (version 17). The specifications of the PC used to run all cases presented herein are: Intel(R) Core (TM) i5-2540M CPU @ 2.60GHz with 8192MB RAM.

4.2. Transient Simulations

In this section an illustrative test of the E-ECS response to a progressive increase in the environment temperature is presented. This particular temperature increase could represent the aircraft surrounding conditions according to the following sequence during a summer day: aircraft starting at the sea level in an airport, taking off, and initial climbing (progressive decrease of temperature).

The E-ECS has been subjected to a linear decrease of the surrounding temperature. As seen in Fig. 5, the whole E-ECS is initialized from guessed values, and after 1000 seconds, when the steady-state condition is reached, the inlet ram temperature is linearly decreased from 55 to 20 ºC during 500 seconds. The simulation finishes after 3000 seconds. It is observed how the VCS generates more cooling power as the environment temperature decreases leading to lower cabin supply temperatures.

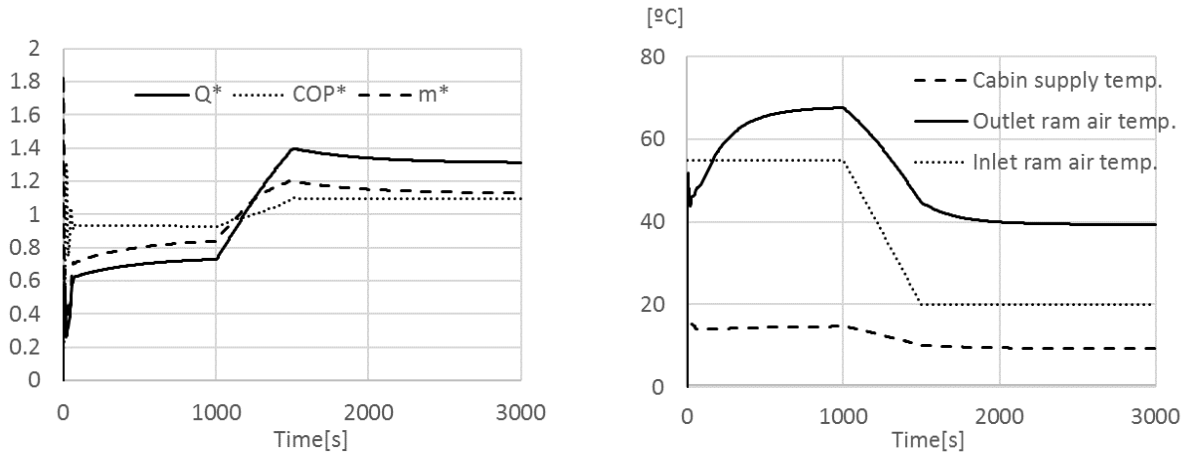

Figure 5: VCS characteristics and ECS relevant temperatures (transient simulation: inlet ram air temperature decrease)

Fig. 6 shows the same exact change of the inlet ram air temperature but in this case the VCS compressor speed is linearly decreased during the same interval (the dimensionless frequency value is changed from 1 to 0.55). This action allows the VCS to adjust its operation to a more appropriate condition in order to keep the same cooling power. As seen in Fig. 6 the supply temperature remains almost constant as no excess cooling is provided, furthermore, the VCS power consumption is drastically reduced, leading to a clear increase of the COP. The CPU time for integration of the transient cases plotted in Figs. 5 and 6 ranged between 60 and 80 seconds.

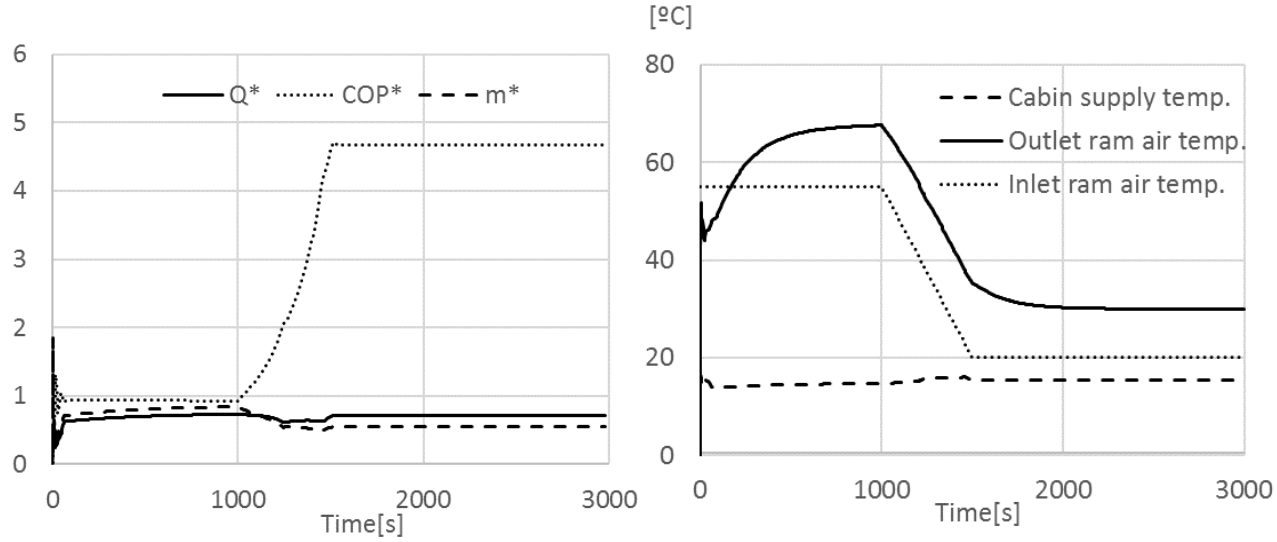

Figure 6: VCS characteristics and ECS relevant temperatures (transient simulation: inlet ram air temperature decrease combined with compressor speed decrease)

4.3. Start-Up/Shut-Down Simulations

This section is devoted to test a more challenging numerical condition that must be faced by the E-ECS: shut-downs and start-ups. The illustrative case presented herein consists of a transient case lasting 6000 seconds where the compressor was subjected to consecutive start-ups and shut-downs. The CPU integration time spent for this simulation was 200 seconds.

The results presented in Fig. 7 show the evolution of the VCS most relevant parameters, namely, cooling power, and refrigerant mass flow rate, together with the resulting cabin supply and outlet ram air temperatures. During the first compressor shut-down (between 1600 and 2600 seconds) both the VCS mass flow rate and its cooling power drop to zero as expected, while the cabin supply temperature increases progressively in an asymptotical way towards 30 ºC which is the

cabin return temperature value. The outlet ram air temperature is also heavily affected when the VCS is not operative as its value drops about 10 ºC due to the condenser inactivity.

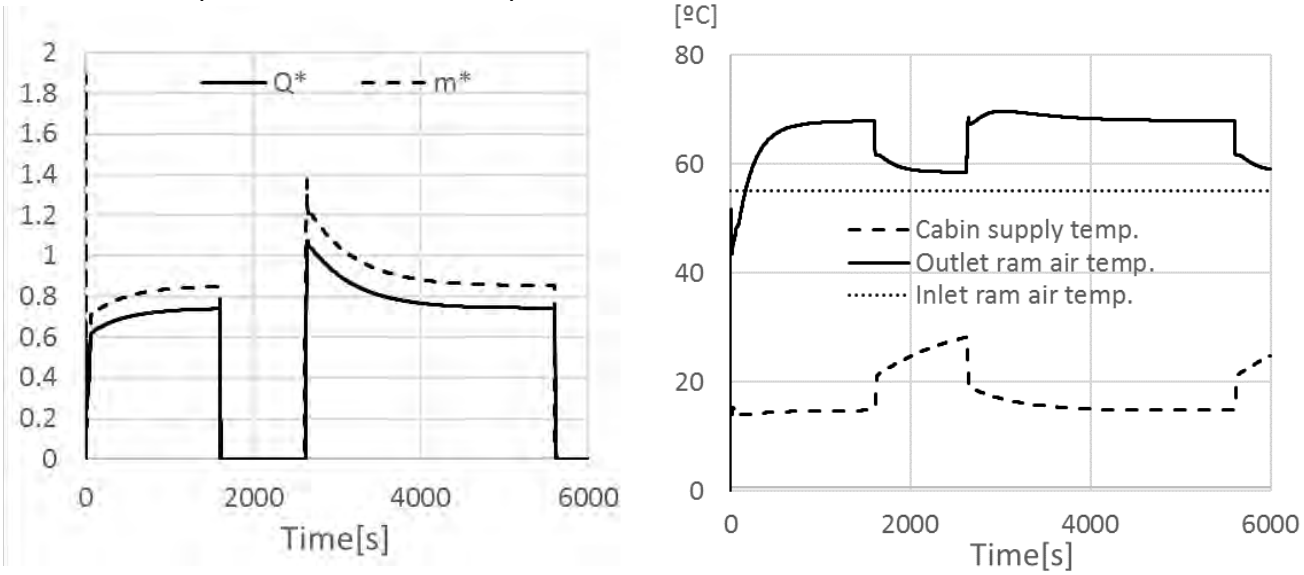

Figure 7: VCS characteristics and ECS relevant temperatures (transient simulation considering compressor shut-down and start-up)

5. CONCLUSIONS

The Modelica library developed and presented has been numerically tested with success. A particular E-ECS architecture including multiple components and fluid circuits has been modelled and simulated at both steady-state and transient conditions.

A significant number of numerical difficulties were addressed during the development of the aforementioned library concerning both component modeling and system resolution aspects. The solutions applied for each particular issue where based on an appropriate compromise between the main library requirements of robustness and time consumption.

Many aspects of the developed numerical tool can be highlighted. First, the modeling and simulation of a system made up of complex circuits combinations was properly achieved (i.e. a partial configuration of an E-ECS architecture consisting of a vapor compression cycle directly and indirectly associated with two liquid circuits respectively). Second, the computational time consumption when conducting the numerical integration was relatively low (steady-state cases were calculated in about 35 seconds while demanding transient cases lasting 6000 seconds were calculated in about 200 seconds). Third, the library is now ready to study and integrate more advanced control procedures in order to optimize the system performance during all the aircraft journey phases.

ACKNOWLEDGEMENT

This work has been developed within the research project “MALET – Development of Modelica Libraries for ECS and Thermal Management Architectures” within the CleanSky2 framework.

REFERENCES

Wetter, M., Bonvini, M., Nouidui, T.S., 2016. Equation-based languages – A new paradigm for building energy modeling, simulation and optimization. Energy and Buildings 117(1), 290-300.

Manuscript ID: 1211
DOI: 10.18462/iir.icr.2019.1211

Thermal system oriented heat exchanger models. Focus on moist air liquid cooled units with dehumidification

Santiago TORRAS[(a,*)], Carles OLIET[(a)], Nicolás ABLANQUE[(a)], Joaquim RIGOLA[(a)]

[(a)] Universitat Politècnica de Catalunya – Barcelona Tech (UPC), Heat and Mass Transfer Technological Center (CTTC),
Terrassa, Barcelona, Spain, cttc@cttc.upc.edu

ABSTRACT

The simulation of complex thermal systems including an increasing number of components, and specifically heat exchangers, is still attracting the attention of the researchers, both to reduce the time needed for the resolution and to improve the accuracy for such simplified models. In the heat exchanger field, simplified models are typically based on semi-analytical methods such e-NTU (for steady state analysis), or by using single volume transient models (with strong limitations to cover temperature crossing within the exchanger). The current paper describes the work of the authors in the development of simplified models for heat exchangers under the Modelica platform, trying to find a compromise between accuracy in steady state conditions, while maintaining the transient response of the component. In this case, the focus is given to liquid cooled air heat exchangers in an aircraft application, where the water condensation on the airside is of importance to characterize the performance.
Keywords: Heat Exchanger, Dehumidification, Modelica.

1. INTRODUCTION

The liquid cooled air heat exchangers are widely used in air cooling systems. They have been extensively studied from a numerical and experimental point of view. However, is still attracting the attention of the researchers, both to reduce the time needed for the resolution and to improve the accuracy for such simplified models. If industrial applicability is desired, effort must focus on these aspects. In this regard, an accurate simulation model for liquid cooled air heat exchanger is the perfect tool to conduct studies on both design and optimization to achieve better cost-effective solutions. The focus of this work is to develop simplified heat exchanger models with a low computational consumption, focusing the attention in the air-side, specially in dehumidifying conditions. The model of the liquid cooled air heat exchanger and the other components shown in this work to form the air cooling system are being developed using the Modelica language and consists of several libraries that account for all components and fluids present in such systems. Modelica is an equation-based language. This characteristic implies that component models are based on equations where assignments are not needed unlike imperative programming languages. The whole set of components and links equations are systematically rearranged and algebraically manipulated to generate an optimized code prior to simulation so that Modelica users or programmers do not have to deal with this task. Modelica is also an object-oriented language where models can be associated following real physical connections and where multi-physics simulations can be handled with ease. The use of such approach for thermal systems has been recommended (Wetter, 2016). The development of the aforementioned libraries for air cooling systems is currently focused on modeling the liquid circuit and the vapor compression system (VCS). Three main attributes are required for individual components and components assemblies: robustness (numerical reliability within a wide range of operating conditions), accuracy (numerical predictions close to measured values), and minimized computational time. This latter attribute is

crucial to guarantee reasonable computational time in air cooling systems with large and complex configurations but also to conduct control procedures over large periods of time.
This work presents two types of simulations, individual component and the whole system. The individual simulations of the liquid cooled air heat exchanger where the information obtained with more detailed models are used for a comparison of the numerical model develop for the liquid cooled air heat exchanger with different dehumidifying situations. In the other type, the air cooling system made up of a vapor compression cycle combined with a liquid loop that cools down a cabin through an air-to-liquid heat exchanger. In the following sections the mathematical formulation of the most important components and systems is briefly described and the most relevant numerical results of the studied system are shown.

2. SYSTEM CONFIGURATION

The system studied herein consists of two different flow circuits interacting between each other. The liquid circuit interacts with the vapor compression loop through the refrigerant-to-liquid heat exchanger which is a shared component. It also contains a pump, a liquid-to-air heat exchanger (to cool down the indoor environment), and other additional components like valves, tubes and tanks. The other system is the vapor compression cycle which is made up of several elements, namely, a centrifugal compressor, a refrigerant-to-air condenser (to eject heat towards the environment), a refrigerant-to-liquid evaporator (to extract heat from the liquid loop), and some additional minor elements. The system layout scheme is presented in Fig. 1 (left).

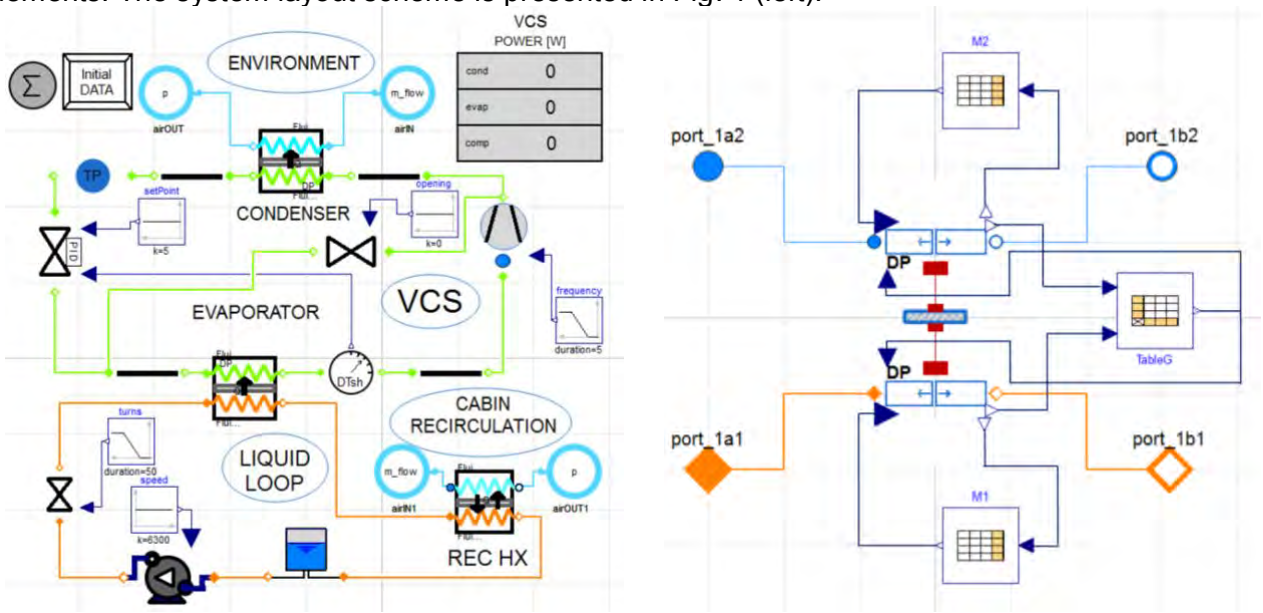

Figure 1: Dymola simulation environment. On the left, the air cooling system layout; on the right, the heat exchanger internal scheme

3. COMPONENTS

This section is devoted to introduce the models of components that have been developed and included in the Modelica libraries created. The primary goal was to provide low time consuming components to prevent from having bottlenecks during the numerical resolution. Therefore, the modeling of most components has been based on simplified mathematical formulations and fed with performance maps. The mathematical formulation of the most determinant components is presented in this section.

3.1. Turbo Machines

The vapor compression system and the liquid loop are driven by a compressor and a pump, respectively.

3.1.1. Compressor

The compressor used in the vapor compression system is of the centrifugal type. The compression process is considered instantaneous as its time scale is significantly smaller compared to the whole vapor cycle thermal and fluid-dynamic time scale. Both the mass flow rate produced and the compressor work done are expressed via the volumetric and the isentropic efficiencies. These efficiencies are also defined as a function of the compression ratio from experimental data or high detailed simulations.

3.1.2. Pump

The pump model calculates the pressure gain together with the consumed power by means of performance maps. These two variables are expressed as a function of the volumetric flow and the working frequency. The maps are previously generated from empirical data, or alternatively, from more advanced models.

3.2. Heat Exchangers

Heat exchangers are probably the most challenging components of the whole system. Three types of heat exchangers were implemented, namely, a condenser (refrigerant vs. dry air), an evaporator (refrigerant vs. liquid), and the air-to-liquid heat exchanger (liquid vs. moist air). These components share a common internal structure where two fluid flow models are thermally linked through a specific component that stands for the physical solid between them (see Figure 1 (right)). This simple approach allows to easily build a large variety of heat exchangers by combining different fluid models. The most relevant aspects of these crucial components are detailed in the following. Fluid flows are calculated from lumped heat transfer analyses in order to optimize the computational time, which is a critical requirement for the simulation of large and complex systems. The model accuracy relies on the empirical information provided (e.g. heat transfer coefficients) due to its lumped nature. The acquisition of appropriate heat transfer coefficients is essential for the model accuracy.

3.2.1. Liquid flow model

The prediction of the heat transfer between the liquid flow and the solid interface is carried out considering a single control volume. The method implemented is based on an ε-NTU approach in order to optimize the calculation speed and also to prevent the calculation of unreal temperature values. The sensible heat is calculated by:

$$Q_s = \varepsilon C\left(T_{solid} - T_{fluid,in}\right)A \qquad \text{eq. (1)}$$

3.2.2. Refrigerant flow model

In this work, the implemented refrigerant model is based on the switching moving boundary approach SMB (Jensen, 2002), this approach has low computational time compared to fixed volumes approach. However, SMB models add difficulties such as the calculation of the mean void fraction, the variation of the length of the zones and the activation and deactivation of the different zones. In the refrigerant flow three different zones are distinguished: sub-cooled, two-phase, and super heating. The conservation equations of mass and energy are calculated at each zone. Depending on the current flow conditions, the model switches between different operating modes so that zones are activated or deactivated. The model for the refrigerant flow has been presented in a previous work (Ablanque et al., 2019), where more details can be found.

3.2.3. Moist air flow model

The dry air flow calculation is conducted in a similar way to the liquid case presented in section 3.2.1. However, when moist air is considered the heat transfer due to water condensation should be also considered. The total heat transferred by the fluid is now calculated from both its sensible (Q_s) and latent (Q_s) terms, see equations (2) and (3). The sensible heat term is calculated as in section 3.2.1, while the humidity at the exit is expressed as is shown in equation (4), where β is the ratio between thermal diffusivity and mass diffusivity of humid air.

$$Q = Q_s + Q_l \quad \text{eq. (2)}$$

$$Q_l = \dot{m}_{air} h_{fg} (w_{out} - w_{in}) A \quad \text{eq. (3)}$$

$$w_{out} = w_{sat,solid} + \left(w_{in} - w_{sat,solid}\right) e^{(-A\beta/\dot{m}_{air})} \quad \text{eq. (4)}$$

3.2.4. Empirical information

The heat exchangers level of accuracy depends on the calibration process done prior to simulations. Both the thermal performance and the pressure drop calculation are based on performance maps. These maps are previously obtained from a more advanced model, or alternatively, from experimental tests. The calibration used is scalable and can be used between heat exchangers with similar geometry and configuration.

3.3. Minor Components

In addition to the most important components other devices such as valves, ducts, tanks, sensors, and controllers are also included in the libraries. The models for the minor components have been presented in a previous work (Ablanque et al., 2019), where more details can be found.

4. SYSTEMS

Several difficulties appear when complex systems are numerically solved. The complications increase when some specific characteristics are present such as closed loops, and the use of fluids with different phenomena, such as the phase changes in the refrigerant or the humidity in the air. In addition to many other aspects that require special attention, namely, the initialization stability of the system, the strategy to reach a steady-state operating point, the flow at low mass flow rate conditions, and the management of the system refrigerant charge. These aspects have been worked to perform the system simulation. For example to facilitate the resolution of components during the initialization both homotopy transformations (Casella, 2011) and dynamic relaxation of certain variables were implemented inside the different models. More details of how these aspects were tackled can be found in Ablanque et al. (2019).

5. RESULTS

The air conditioning system presented in section 2 and detailed in section 3 has been assembled using the Dymola/Modelica simulation environment and the recently developed libraries. A comprehensive study has been carried out in order to test the system numerical robustness and computational time at different operating conditions. The system graphical scheme is shown in Figure 1 (right) where the two main fluid closed circuits are observed. On the one hand, the liquid circuit is composed of two heat exchangers, one centrifugal pump, a tank, and a regulation valve. The liquid mass flow rate is managed through both the valve level of contraction and the pump working speed. The role of the liquid-to-air heat exchanger (recirculation heat exchanger, RECHX) is to cool down the cabin, which is in turn characterized with the air flow operating conditions. Water condensation is considered in the aforementioned heat exchanger model. On the other hand, the VCS which is made up of two heat exchangers, an centrifugal compressor, two valves, four ducting tubes and a reservoir located between the condenser and the main expansion valve. The VCS role is to extract heat from the evaporator and eject it on the environment. The environment is characterized with the condenser air flow operating conditions. The VCS performance can be regulated either by modifying the by-pass valve opening degree or by reducing/incrementing the compressor working speed. The evaporator, which is shared by both circuits, sucks heat from the liquid loop. The VCS is self-regulated as its operating point is

controlled by the expansion valve whose level of aperture is determined by the super heating degree at the evaporator outlet. The focus of this work is given to the liquid cooled air heat exchanger for aircraft application, where the water condensation on the airside is of importance to characterize the performance. For this reason, in sections 5.1 and 5.2 several tests have been performed in order to visualize the heat exchanger and the system response for different humidity ratios (x1, x2 and x3). The system variables shown in the results section include three different dimensionless values, namely, the heat extracted by RECHX, its sensible heat factor (SHF), and the VCS coefficient of performance (COP). The dimensionless values shown in the results are calculated with equation (5), using a specific reference case for each results section. Depending on the case, different variables can be shown.

$$Q^* = Q_{RECHX}/Q_{REF} \qquad SHF = Q_s/Q_{RECHX} \qquad COP^* = COP/COP_{REF} \qquad \dot{m}^* = \dot{m}/\dot{m}_{REF} \qquad \text{eq. (5)}$$

5.1. The Moist Air-Liquid Heat Exchanger Calibration

Some numerical procedures have been performed by the authors in order to calibrate the numerical model developed for the RECHX. The calibration process required a great effort and is briefly below. The initial numerical outcomes were compared to the data obtained from a more advanced model, showing coherent results but with important different. The impact of several aspects was investigated, including the flow configuration and the humidity ratio effects. From the study carried out, a calibration has been generated that takes into account these aspects. In addition, it has been implemented in the simplified model developed. A full set of steady-state simulations has been conducted for different flow rates to validate the moist air-liquid heat exchanger. Each simulation (test) has a different combination of mass flow rate between both fluids. And they have been carried out for three different humidity ratios. The reference case was defined using the test number 31, where: the cabin return air temperature of 29 ºC, the liquid inlet temperature of 0 ºC, the dimensionless mass flow rate for the liquid and the air are 1.0 and 3.2, respectively, and a defined mass flow rate compressor working frequency.. The dimensionless mass flow rates in the liquid side were in the range of (0.2 to 1.6), and for the air side were in the range of (0.8 to 3.2). A comparison between the numerical and the data obtained from a more advanced model has been carried out for the different combination of mass flow rate and humidity ratios considered. Fig. 2 shows the heat extracted by RECHX and its sensible heat factor for the different tests. In general, good agreement can be appreciated between the results obtained from a more advanced model and the numerical results. It can be observed that the heat extracted by the RECHX is increased as a consequence of the increase in the mass flow rate. It is also appreciated that with increase of the humidity ratio the amount of the heat extracted is greater. To produce these studies 52 steady-state simulations were carried out for each humidity ratio.

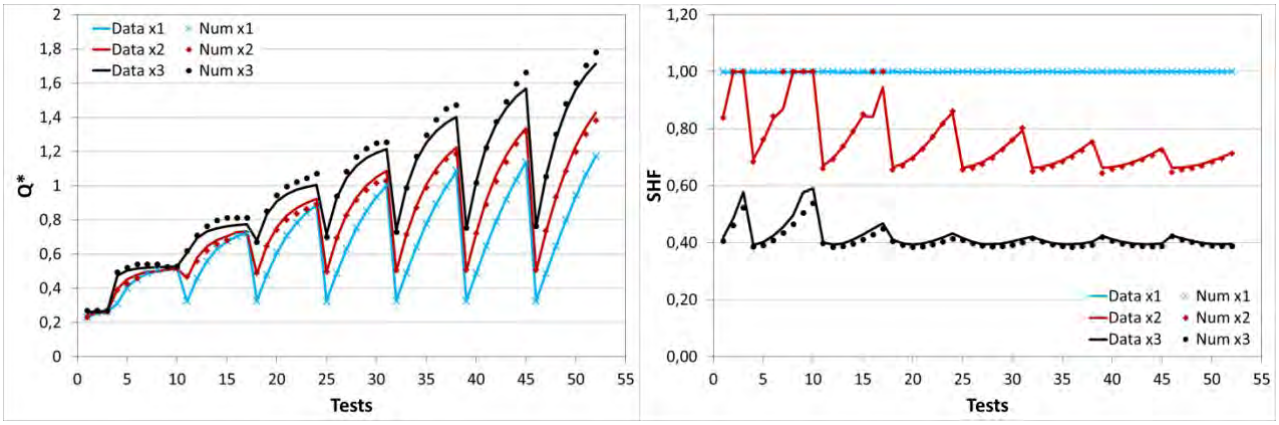

Figure 2: The moist air-liquid heat exchanger validation. On the left, the heat extracted (Q*); on the right, the sensible heat factor (SHF)

5.2. Steady-State Simulations

Steady-state simulations were conducted to analyze the effect of the cabin return air temperature, the environment air temperature, and the VCS compressor working frequency in the air cooling system. These variables were modified over a wide range starting from a reference case defined in the following way: cabin return air temperature of 28 ºC, environment air temperature of 35 ºC, a defined compressor working frequency, and a specific humidity ratio (x1). Fig. 3 shows the system response according to the cabin return air temperature value for different humidity ratios (x1, x2 and x3). In Fig. 3 (left), it is observed that the rise in the cabin return air temperature increase the heat extracted by the RECHX. It is also appreciated that with increase of the humidity ratio the amount of the heat extracted is greater. Another interesting variable to show is the sensible heat factor of the RECHX for the different cabin return air temperatures considered (Fig. 3 (right)). It can be observed the portion of the total cooling capacity that is providing by the dehumidification for the different tests. Fig. 3 (right) also shows that the portions of heat extracted by dehumidification are more significant for the lower cabin return air temperature. This is due to the lower wall temperature in the moist air side.

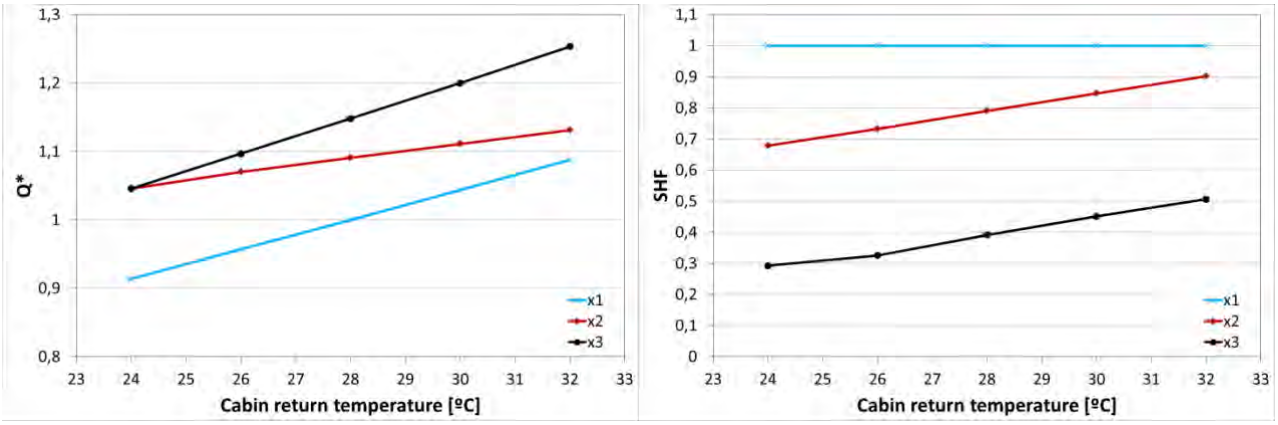

Figure 3: Cabin return air temperature effect (T_{env} =35 ºC). On the left, the heat extracted (Q*); on the right, the sensible heat factor (SHF)

The influence of increasing the environment temperature is shown in Fig. 4. In this case the VCS high pressure must increase to enable heat rejection to the ambient. Therefore, the overall cooling power decreases as shown in Fig. 4 (left). As in the previous cases, there is also an increase in the heat extracted by the RECHX for a higher humidity ratio. The compressor power consumption grows and the VCS coefficient of performance deteriorates as shown in Fig. 4 (right).

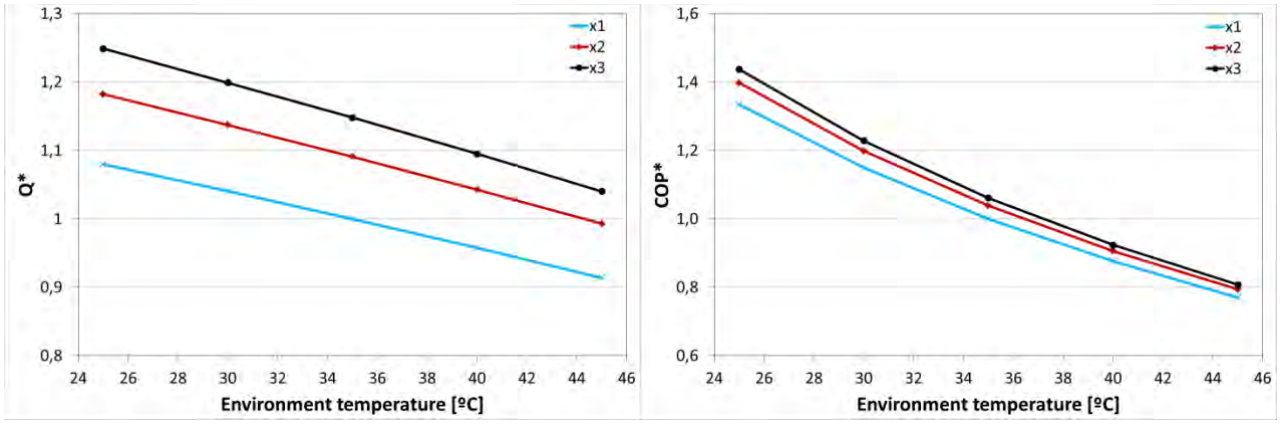

Figure 4: Environment air temperature effect (T_{cabin} =28 ºC). On the left, the heat extracted (Q*); on the right, the VCS coefficient of performance (COP)

Fig. 5 shows the system behavior as the compressor frequency is increased. In this case, the increase of the compressor frequency causes the heat extracted by the RECHX and the power consumption to increase. Although the heat extracted in the evaporator increases, it is a lower rate that the power consumption, so that the coefficient of performance is reduced as is shown in Fig. 5

(right). To produce these studies more than 45 steady-state simulations were carried out. The computational time for each particular test ranged between 6 and 10 seconds. The time values mentioned in this document stand for the CPU time for integration provided by Dymola (version 17). The specifications of the PC used to run all cases presented herein are: Intel(R) Core (TM) i5-2540M CPU @ 2.60GHz with 8192MB RAM.

5.3. Transient Simulations

In this section an illustrative test of the air cooling system response to several changes of the operating conditions is detailed with the aim of showing the flexibility of the simulation model developed. The system transient behavior has been studied for a period of 1800 seconds and has been subjected to multiple adjustments/events at different moments of the simulation.

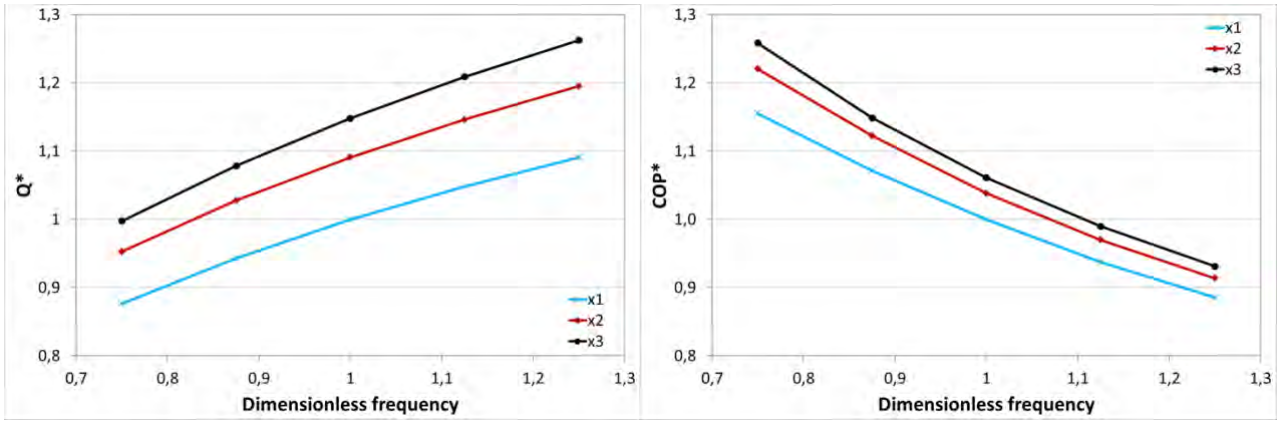

Figure 5: Compressor working frequency effect (T_{env} =35 ºC, T_{cabinr} =28 ºC). On the left, the heat extracted (Q*); on the right, the VCS coefficient of performance (COP)

The system events sequence is listed as follows: (1) system is initialized from guessed values; (2) at 200 seconds: system reaches steady-state; (3) at 300 seconds: the environment temperature is suddenly reduced from 35 ºC to 30 ºC; (4) at 500 seconds: the environment temperature is suddenly increased from 30 ºC to 35 ºC; (5) at 700 seconds: compressor frequency is reduced (75% of the initial working frequency); (6) at 900 seconds: the VCS by-pass valve is opened up to a certain degree; (7) at 1200 seconds: the cabin return temperature is increased from 28 ºC to 32 ºC, (8) at 1400 seconds: the cabin return temperature is reduced from 32 ºC to 28 ºC, (9) at 1600 seconds: the cabin return temperature is increased from 28 ºC to 32 ºC.

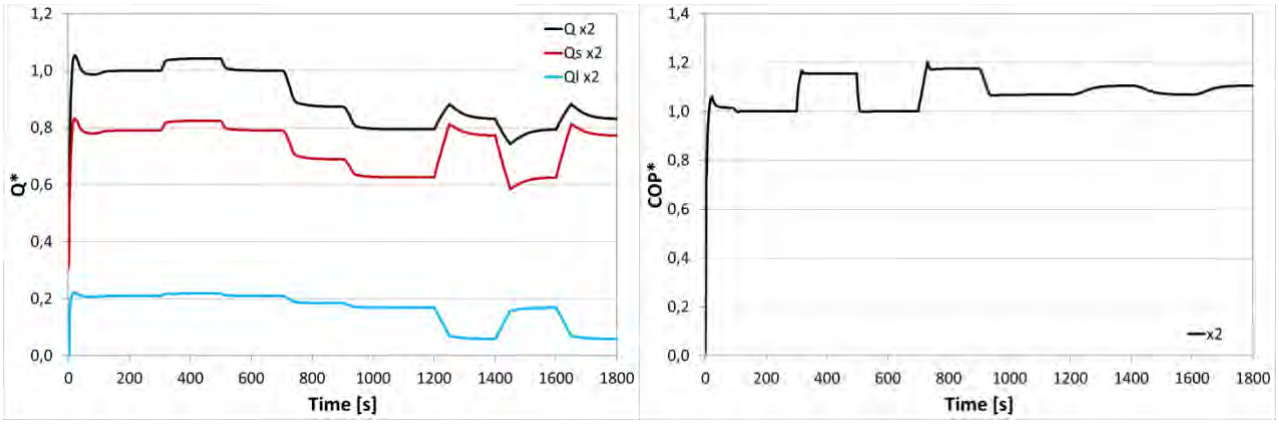

Figure 6: Transient evolution of: on the left, the total, sensible and latent heat extracted (Q*); on the right, the VCS coefficient of performance (COP)

The complete simulation took about 18 seconds and the evolution of the total, sensible and latent heat extracted by the RECHX, and the VCS coefficient of performance are plotted in Fig. 6. These variables were modified from a reference state that is selected when the system reaches steady-

state (at 250 seconds) defined in the following way: cabin return air temperature of 28 ºC, environment air temperature of 35 ºC, a defined compressor working frequency, and a specific humidity ratio (x2). This humidity ratio has been selected in order to appreciate the importance of the dehumidification on the airside to characterize the performance. In Fig. 6 it is observed how the system initializes from unreal values and reaches the steady-state condition after about 200 seconds. At 300 seconds, the environment temperature is reduced, the heat extracted by the RECHX and the VCS coefficient of performance are increased. At 500 seconds, the environment temperature is increased to the initial temperature. In this case, the heat extracted by the RECHX and the VCS coefficient are reduced while the RECHX outlet air temperature grow accordingly. At 700 seconds, when the compressor working frequency is decreased, the mass flow rate in the VCS system is reduced together with the heat extracted by the RECHX. In addition, the VCS coefficient of performance is increased. At 900 seconds, the opening of the by-pass valve in the VCS system conducts to a recover the mass flow rate. However, the cooling capacity of the VCS is degraded. At 1200 seconds, the cabin return temperature is increased from 28 ºC to 32 ºC. As a result, the heat extracted by the RECHX and the VCS coefficient of performance are increased. Also, the portion of heat extracted by dehumidification is reduced. The following changes lead to previously commented situations.

6. CONCLUSIONS

The focus of the present work was to develop a robust and accurate simplified model to simulate air cooling systems, specifically models for heat exchangers under the Modelica platform. A liquid cooled air heat exchanger composed of three models (liquid flow, solid and a moist air flow) has been developed. A data obtained with more detailed models were used to calibrate and validate the heat exchanger. Different results of the heat exchanger are shown, such as the heat extracted by the RECHX and its sensible heat factor, where the numerical results presents a good agreement against the data obtained from a more advanced model for both dry air and wet air cases. The model has been extensively tested to ensure the aforementioned capacities. The air cooling system presented in this work has shown to consume low computational time for steady-state simulations. For instance, the time needed to predict the steady-state of the system configuration studied in the present work was less than 10 second. The air cooling system has been satisfactorily tested at demanding transient conditions including several changes of the operating conditions. The computational time for the transient case was about 18 second. The models developed and used in the air cooling system are ready to study cases during short or long periods of time due to the robustness and it low calculation time. According to the results, the capabilities of the heat exchanger model developed have been demonstrated, allowing the use of this model for prediction purposes of liquid cooled air heat exchangers in an aircraft application.

ACKNOWLEDGEMENT

This work has been developed within the research project “MALET – Development of Modelica Libraries for ECS and Thermal Management Architectures” within the CleanSky2 framework.

NOMENCLATURE

A	area	C	lowest capacity rate
h_{fg}	latent heat vaporization of water	$\dot{m}$	mass flow rate
Q	heat transfer	T	temperature
w	humidity ratio	ε	efficiency
Subscripts			
air	air	$fluid$	liquid
in	inlet	out	outlet
sat	saturated	$solid$	solid between the fluids

REFERENCES

Ablanque, N., Torras, S., Oliet, C., Rigola, J., 2019. Dynamic simulation of indirect air conditioning systems with optimized computational time. Proceedings of the 13th REHVA World Congress CLIMA 2019, Bucharest, Romania.

Casella, F., Sielemann, M., Savoldelli, L., 2011. Steady-state initialization of object-oriented thermo-fluid models by homotopy methods. Proceedings of the 8th Modelica Conference, Dresden, Germany, 86-96.

Jensen, J.M., Tummescheit, H., 2002, Moving boundary models for dynamic simulation of two-phase flows. Proceedings of the 2th Modelica Conference, Oberpfaffenhofen, Germany, 235-244.

Wetter, M., Bonvini, M., Nouidui, T.S., 2016. Equation-based languages – A new paradigm for building energy modeling, simulation and optimization. Energy and Buildings 117, 290-300.

Manuscript ID: 1221
DOI: 10.18462/iir.icr.2019.1221

Monitoring energy efficiency of refrigerating systems under real operating conditions – methods and recommendations

Stefan Hudjetz[(a)], Peter Köhler[(b)], Martin Becker[(a)]

[(a)] Biberach University of Applied Sciences
88400 Biberach an der Riss, Germany, hudjetz@hochschule-bc.de
[(b)] KKE-Plan
55545 Bad Kreuznach, Germany

ABSTRACT

A multitude of different figures exist that can be used to assess energy efficiency in refrigerating systems. However, most of these figures are only applicable to standardized test conditions. German specification VDMA 24247-7 offers an efficiency metrics aimed specifically at the evaluation of energy efficiency of refrigerating systems under real operating conditions. So far, experience with this metrics mainly stems from investigations on a laboratory scale. Little has been published on its applicability to more complex real-world refrigerating systems. Therefore, several field sites have been prepared for closer investigation. The field sites are introduced in a compact form. Preliminary results are shown. Results obtained so far lead to the conclusion that an assessment of energy efficiency of more complex systems only based on the whole system alone might not be enough. For an improved metrics, these user experiences are fed to the committee revising the VDMA specification.
Keywords: Refrigeration, TCOP, VDMA 24247, Energy Efficiency, Monitoring, Field Sites, Supermarket, Cafeteria, Laboratory

1. INTRODUCTION

According to a study by the Research Council for Refrigeration Technology (Forschungsrat Kältetechnik, 2011), refrigeration accounts for approximately 14 % of the total electrical end energy use in Germany. In its position paper on the contribution of refrigerating and air conditioning systems to climate protection (Forschungsrat Kältetechnik, 2008), the Research Council for Refrigeration Technology estimated potential energy savings of 40 % until 2020 if accompanying political measures are taken. This energy savings potential was confirmed in a superseding position paper (Forschungsrat Kältetechnik, 2012). The German government (2007) adopted an energy and climate programme with 29 key elements which is presented in more detail in a report of the Federal Ministry of Economic Affairs and Energy as well as the Federal Ministry of the Environment, Nature Conservation and Nuclear Safety (2007). Among these key elements are several which can be regarded as relevant for the refrigeration sector, for example the introduction of modern energy management systems, support programmes for climate protection and energy efficiency, energy-efficient products as well as the reduction of emissions of fluorinated greenhouse gases.
In order to tap the full savings potential mentioned above, a suitable metrics is needed which enables owners and operators respectively to assess the energy efficiency of existing refrigerating systems during operation.
A multitude of different figures exist that can be used to assess energy efficiency. However, most of these figures are only applicable to standardized test conditions (q.v. Becker (2008) as well as Köberle and Becker (2013)).
The German Mechanical Engineering Industry Association (Verband Deutscher Maschinen- und Anlagenbau e.V., VDMA) tries to address these issues with several measures. Among them is the publication of German specification VDMA 24247 (2011) which deals with energy efficiency of refrigerating systems and comprises eight parts.
VDMA 24247-7 (2011) offers an efficiency metrics aimed specifically at the evaluation of energy efficiency of refrigerating systems under real operating conditions.

Eight years later, still only little is known about the applicability of VDMA 24247 to real-world refrigerating systems and published results are scarce. Cheung and Braun (2014) use process efficiencies as introduced in VDMA 24247-2 (2011) in a modified method to study the performance of residential heat pump systems. Köberle and Becker (2011) applied the methodology of VDMA 24247-7 (2011) to two chillers – one was an experimental setup in a laboratory. Nothing could be found about the applicability of aforementioned method to direct refrigerant cooling applications as found in commercial refrigeration, e.g. supermarket refrigeration.
Hence, the methodology of VDMA 24247-7 (2011) will be presented in the next section. Afterwards, field sites available for the experimental investigation and preliminary results from first measurements will be shown. At the end, first conclusions are drawn and relevant next actions are highlighted.

2. METHODOLOGY

VDMA 24247-7 (2011) recommends to establish a continuous monitoring with a suitable data acquisition strategy and an adequate energy management concept. Besides general recommendations for improved control and operation of refrigerating systems, three different balancing boundaries for the assessment of energy efficiency under operating conditions are given (shown in figure 1). The innermost boundary (I) is drawn around the refrigerant circuit with compressors and heat exchangers. Auxiliary devices like oil sump heating, control, and defrost systems should also be included within this boundary. In order to balance according to balancing boundary II, the heat sink has to be added to the evaluated components. Finally, the complete system with all its components is assessed within balancing boundary III. This balancing concept of VDMA 24247-7 (2011) is also described in the report of Becker et al. (2017).
Having chosen a desired balancing boundary, energy efficiency can be described by the Total Coefficient of Performance (TCOP) or the Total Energy Performance Factor (TEPF), which are used as key performance indicators and defined as given below.

$$TCOP = \frac{\dot{Q}o,balancing\ boundary}{\sum P_{el,i}} \quad \text{(Eq. 1)}$$

$$TEPF = \frac{\dot{Q}o,balancing\ boundary * t}{\sum P_{el,i} * t_i} = \frac{\int_{t_1}^{t_2} \dot{Q}o,balancing\ boundary\ dt}{\sum_i (\int_{t_1}^{t_2} P_{el,i} dt_i)} \quad \text{(Eq. 2)}$$

where $Q_{0,\ balancing\ boundary}$ is the usable cooling capacity and $P_{el,i}$ is the total electric power consumption.

Dai et al. (2001), Liu et al. (2006), Li et al. (2012) and Abdel-Salam et al. (2013), to name just a few, deal with dessicant cooling and use TCOP as an acronym for Thermal Coefficient of Performance which is defined as usable cooling capacity divided by thermal energy input to the system. Yang et al. (2012) investigated the performance of a transcritical carbon dioxide two-stage compression cycle and used TCOP to abbreviate two-stage compression at optimal intermediate pressure. In this paper, solely the definition according to VDMA 24247-7 (2011) shown above is used and must not be mistaken with any of the other definitions.
VDMA 24247-7 (2011) does not specify closer how usable cooling capacity or electrical power consumption have to be determined. These values can be measured directly – an approach which is often not possible due to the absence of a mass flow sensor in most commercial refrigerating systems – or they can be deduced from several available indirect methods, which have also been presented further by Becker et al. (2017).
Köberle and Becker (2011) used the methodology of VDMA 24247-7 (2011) to investigate energy efficiency of two chillers. In order to find out more about the applicability of this method to direct refrigerant cooling applications, several new field sites have been equipped with sensors.
In the next section, each system that is meanwhile available for further investigation will be presented in compact form.

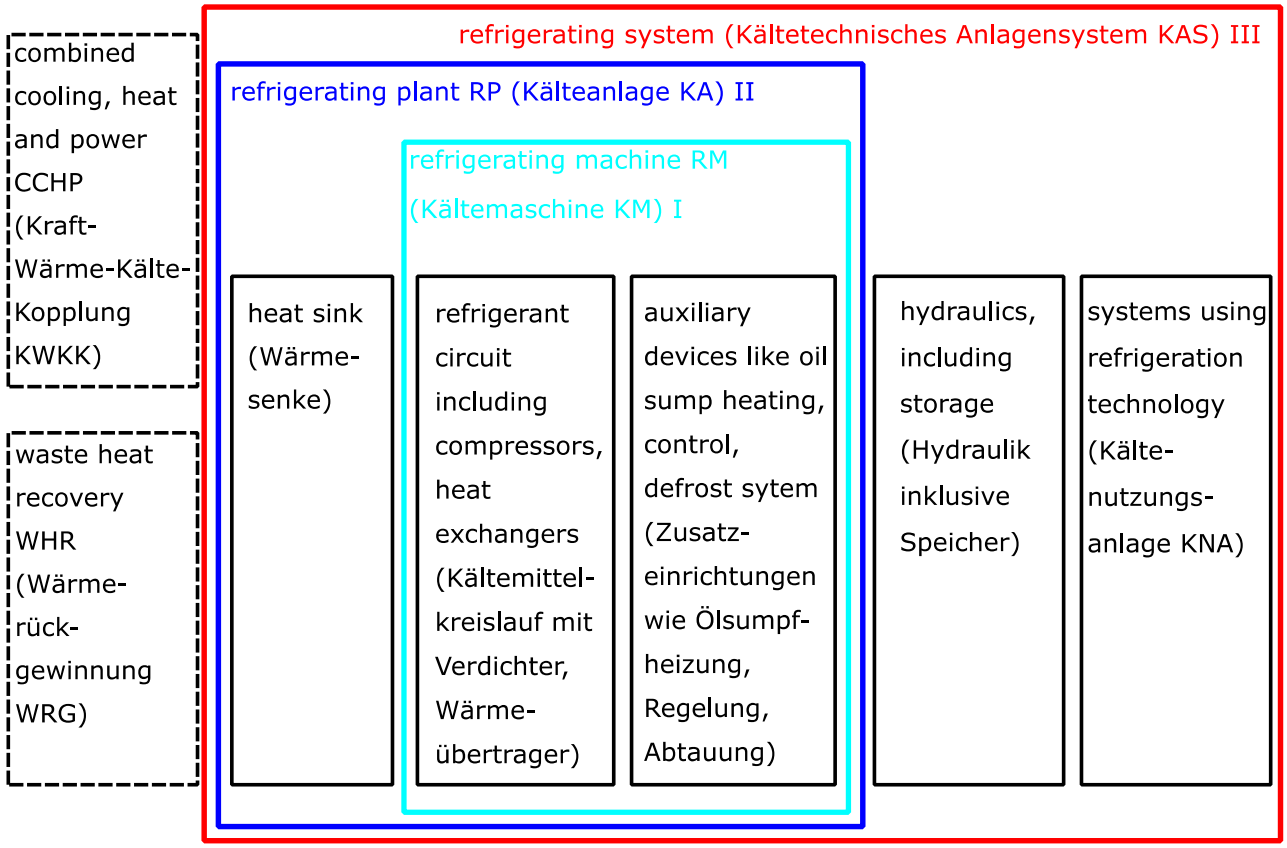

Figure 1: Balancing boundaries I, II and III (taken from VDMA 24247-7 (2011) with English translations added and original German text given in brackets).

3. FIELD SITES

Four different refrigerating systems – one small laboratory system with freely controllable boundary conditions and three real-world systems of different sizes under regular operating conditions as requested by the customer – have been prepared so that energy efficiency of refrigerating systems can be investigated further. The purpose of this paper is to provide an introductory first glance of the entirety of systems and the preliminary results obtained so far. For the laboratory-scale refrigerating system, a detailed presentation can be found in the report of Becker et al. (2017). For the additional three field sites, a more detailed presentation will follow.

As can be seen, field sites range from a basic system configuration to complex ones. The refrigerating system installed in the laboratory at Biberach University of Applied Sciences starts with the most basic system. It consists of one compressor, one condenser, an electronic expansion valve and one evaporator installed inside a walk-in cooler. Furthermore, the system is equipped with a vast number of sensors for measuring temperature and pressure as well as refrigerant mass flow and electrical power. Due to the basic system configuration, no schematic is shown in this case. Instead, the reader is referred to the report of Becker et al. (2017) for more details, e.g. on data acquisition.

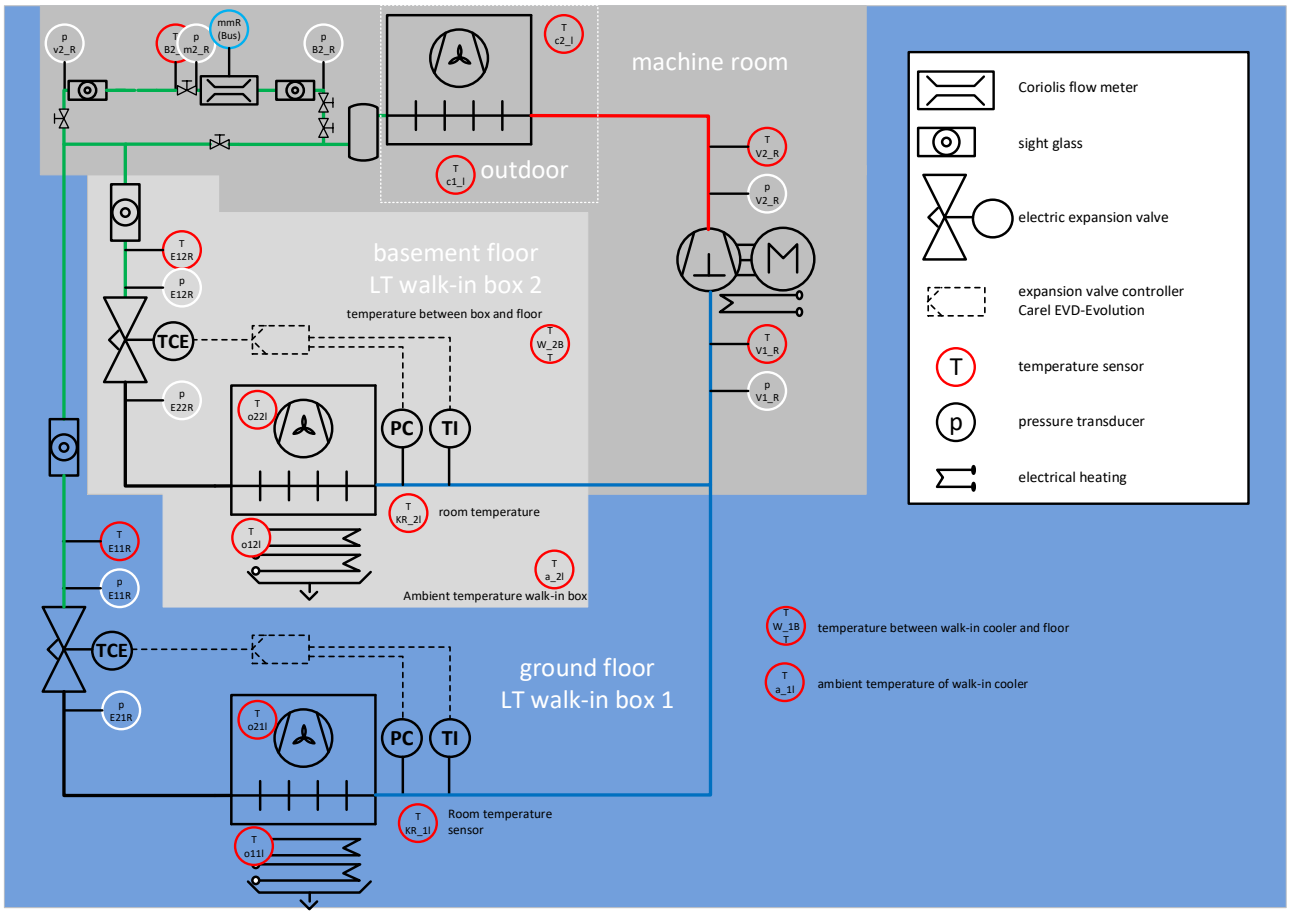

Figure 2: Simplified schematic diagram of a cafeteria low temperature refrigerating system.

The first real-world refrigerating system with regular operating conditions is shown in Fig. 2.
It is a low temperature refrigerating system of a cafeteria. This setup differs from the laboratory system primarily in the number of evaporators and the sizing of the components. In this system, there are two walk-in coolers with one evaporator in each of the boxes.
Fig. 3 shows a medium temperature refrigerating system of the same cafeteria with three walk-in coolers and a parallel rack of three compressors instead of only one single compressor as in the first two systems. The dotted line leads to several small cooling cabinets which are not monitored. Therefore, only balancing boundaries I and II according to VDMA 24247-7 (2011) can be used in this case.
Each of these first three systems is equipped with a permanently installed Coriolis flow meter so that refrigerant mass flow can be measured directly.

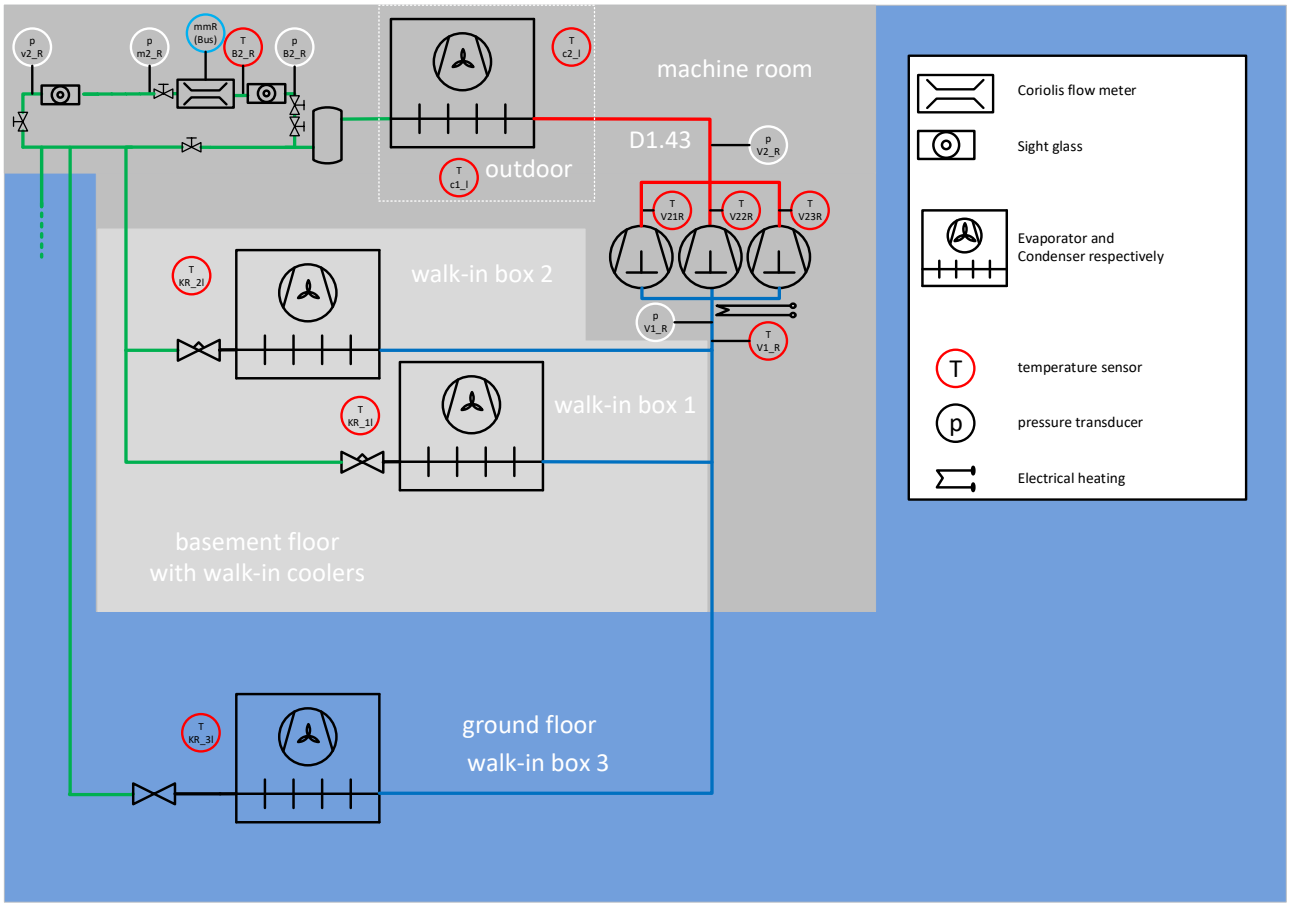

Figure 3: Simplified schematic diagram of a cafeteria medium temperature refrigerating system.

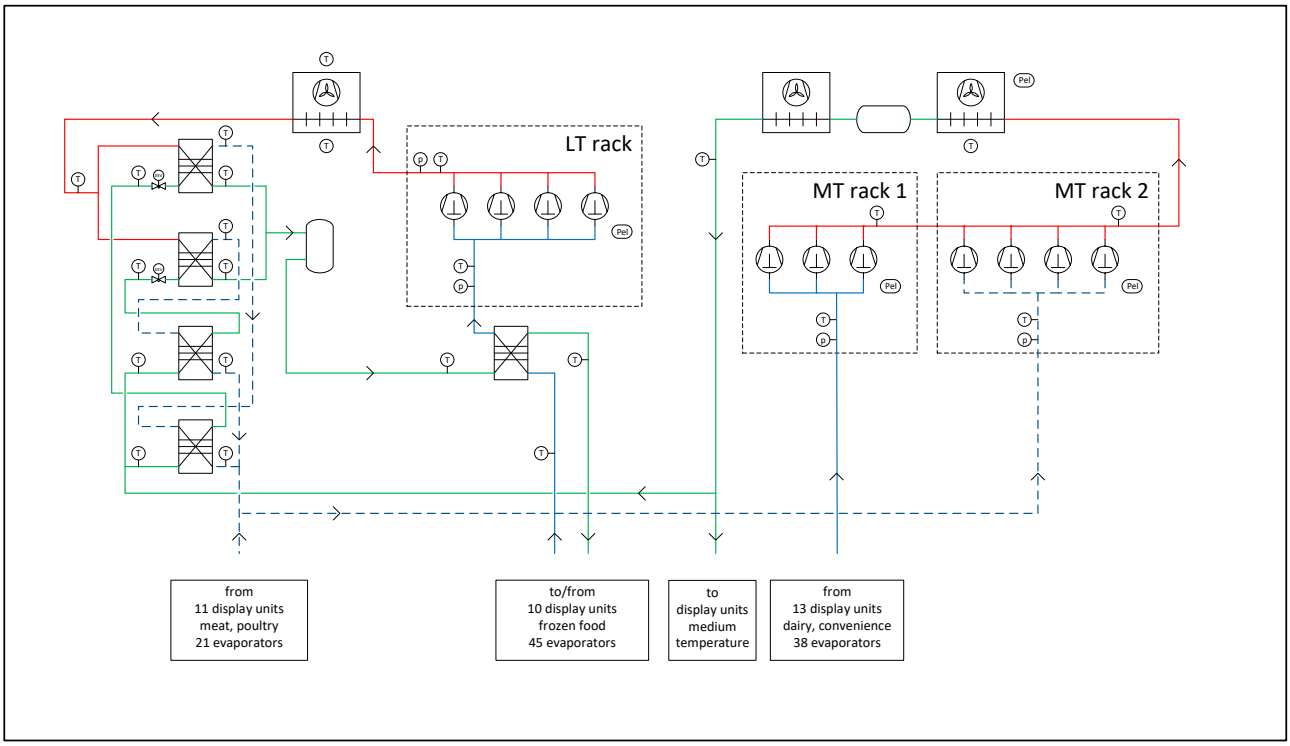

Figure 4: Simplified schematic diagram of a supermarket refrigerating system

The last and most complex refrigerating system is a commercial refrigeration system in a supermarket in Germany (Fig. 4). Two parallel racks for medium temperature (MT) refrigeration (R134a as refrigerant) and one parallel rack for low temperature (LT) refrigeration (subcritical process with carbon dioxide as refrigerant) provide cooling to more than 30 cabinets and walk-in coolers, with a total of more than 100 evaporators installed. Here, refrigerant mass flow can only be measured directly with a temporarily available clamp-on ultrasonic flow meter.

4. PRELIMINARY RESULTS

Preliminary results from the supermarket refrigerating system are shown in the figure below. TCOP has been calculated for balancing boundary I in each case using an indirect method based on compressor polynomials over a period of 24 hours. Since the chosen method may lead to unrealistically large values for TCOP when the load increases significantly and suddenly, startup processes of compressor 1 of MT rack 1 (load change from 0 % to more than 90 % max.) have been filtered out. 34 values (appr. 2 % of the observed values) are concerned. No filtering was applied to MT rack 2 and the LT rack due to different control strategies of these racks.
TCOP values of the subsystems (LT rack, MT 1 and MT 2 racks) are calculated according to equation 1 in section 2. In this balancing boundary, only electric power consumption of the compressors is used. Additional components like heaters, defrost systems etc. have not been taken into consideration so far. $TCOP_I$ of the whole system (consisting of the low temperature rack and the two medium temperature racks) is calculated by summing up the cooling capacities of the subsystems and dividing this total capacity by the sum of the electric power consumption of each subsystem.

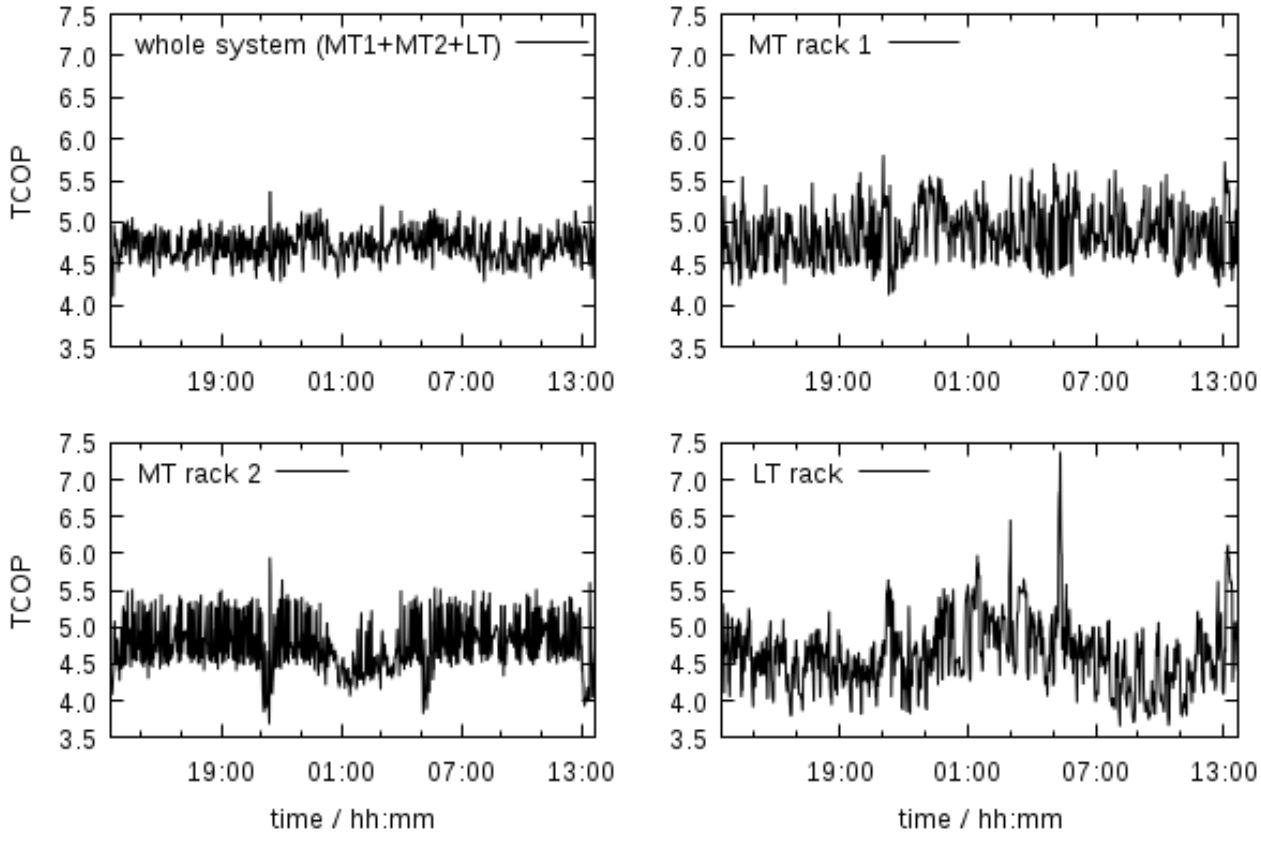

Figure 5: TCOP of the supermarket refrigerating system from an indirect calculation method for balancing boundary I

A graphical representation of both the whole system and the subsystems is given in figure 4. From a first glance at the top left diagram, one could assume that the whole system is running within acceptable conditions due to only minor fluctuations in the calculated TCOP. However, having a second glance at the TCOP values of the subsystems in the other diagrams of figure 4, one can see that there is a drop in the TCOP of medium temperature parallel rack 2 (bottom left) during the middle

of the night while at the same time TCOP of the LT rack (bottom right) rises to values of up to 7. MT rack 1 (top right) shows a characteristic during this time similar to its daytime behaviour. The two racks have a common condenser but different suction line temperatures due to different evaporation temperatures caused by the required temperature of the content of the cabinets.
These peculiar values must be investigated further and possible causes must be identified. The observed behaviour leads to the hypothesis that an assessment of energy efficiency based on only the whole system might not be enough.

5. CONCLUSIONS

An interesting mix of field sites of different sizes could be found for the planned investigations. The commissioning of the additional data acquisition systems in the presented field sites has shown that a precise measurement of electrical power is of vital importance. However, existing data acquisition is often not sufficient and upgrading these systems is constrained by various factors, e.g. limited available space in electrical enclosures for additional transformers for current sensing or large cable-cross sections. Thus, upgrading electrical power measurement was a challenge in nearly each field site. First results are promising, e.g. in terms of the applicability of indirect methods and the resulting calculation effort. TCOPs for balancing boundary I could be analysed for three of the four refrigerating systems and have been shown for the supermarket refrigerating system.
One relevant next action is the calculation of TCOPs for the remaining balancing boundaries in order to find out more about the applicability of the balancing concept presented in VDMA 24247-7. Furthermore, alternative indirect methods must be tested. These indirect methods will be compared to results from direct measurements which serve as a reference.

ACKNOWLEDGEMENTS

The authors acknowledge the financial support by the Federal Ministry for Economic Affairs and Energy on the basis of a decision by the German Bundestag (project number 03ET1449A).

REFERENCES

Abdel-Salam, A. H., Ge, G., Simonson, C. J., 2013. Performance analysis of membrane liquid desiccant air-conditioning system. Energy and Buildings (62), p. 559-569

Becker, M., 2008. Energetische Bewertung und optimierte Betriebsführung von Kälteanlagen aus automatisierungstechnischer Sicht, Tagungsband Bd. II, DKV-Tagung Ulm, 19-21 November 2008

Becker, M., Köberle, T., Rettich, D., Pfeiffer, D., 2017. Energieeffizienz und optimierte Betriebsführung von gewerblichen Kälteanlagen: Forschungsprojekt EnBeKa. Report. Hochschule Biberach. https://doi.org/10.2314/GBV:1008761230

Cheung, H., Braun, J. E., 2014. Performance comparisons for variable-speed ductless and single-speed ducted residential heat pumps. International Journal of Refrigeration (47), p. 15-25

Dai, Y. J., Wang, R. Z., Zhang, H. F., Yu, J. D., 2001. Use of liquid desiccant cooling to improve the performance of vapor compression air conditioning. Applied Thermal Engineering (21), p. 1185-1202

Federal Ministry for Economic Affairs and Energy, Federal Ministry for the Environment, Nature Conservation and Nuclear Safety, 2007. Report on implementation of the key elements of an integrated energy and climate programme adopted in the closed meeting of the Cabinet on 23/24 August 2007 in Meseberg. Berlin, 5 December 2007

Forschungsrat Kältetechnik, 2008. Contribution to climate protection of air conditioning plants, improvement of energy efficiency, reduction of greenhouse-related emissions. Forschungsrat Kältetechnik e.V., Frankfurt am Main, June 2008

Forschungsrat Kältetechnik, 2011. Energiebedarf für Kältetechnik in Deutschland – Eine Abschätzung des Energiebedarfs von Kältetechnik in Deutschland nach Einsatzgebieten. Forschungsrat Kältetechnik e.V., Frankfurt am Main, 04.04.2011

Forschungsrat Kältetechnik, 2012. Contribution of refrigerating and air conditioning systems to climate protection, improvement of energy efficiency, reduction of greenhouse-related emissions. Forschungsrat Kältetechnik e.V., Frankfurt am Main, March 2012

German Government, 2007. Key Elements of an Integrated Energy and Climate Programme. Decision of German Cabinet. Closed meeting, 23/24 August 2007. Meseberg

Köberle, T., Becker, M., 2011. A method for calculating the energy efficiency of refrigeration systems during ongoing operation. 23rd IIR International Congress of Refrigeration, Prague, Czech Republic. Volume 3, p. 1763-1770

Köberle, T., Becker, M., 2013. Übersicht zu Energieeffizienzkenngrößen und Bewertung der Energieeffizienz in der Kältetechnik. GI – Gebäudetechnik / Innenraumklima, 1-2013, p. 54-64

Li, H., Dai, Y. J., Li, Y., La, D., Wang, R. Z., 2012. Case study of a two-stage rotary desiccant cooling/heating system driven by evacuated tube solar air collectors. Energy and Buildings (47), p. 107-112

Liu, X., Li, Z., Jiang, Y., Lin, B., 2006. Annual performance of liquid desiccant based independent humidity control HVAC system. Applied Thermal Engineering (26), p. 1198-1207

VDMA 24247, 2011. Energy efficiency of refrigerating systems, Parts 1-8. Verband Deutscher Maschinen- und Anlagenbauer e.V., www.vdma.org

VDMA 24247-2, 2011. Energy efficiency of refrigerating systems – part 2: Requirements for system design and components. 27 p.

VDMA 24247-7, 2011. Energy efficiency of refrigerating systems – part 7: Control, energy management and efficient system management. 16 p.

Yang, J. L., Ma, Y. T., Liu, S. C., 2007. Performance investigation of transcritical carbon dioxide two-stage compression cycle with expander. Energy (32), p. 237-245

Manuscript ID: 1227
DOI: 10.18462/iir.icr.2019.1227

Performance monitoring of closed cooling towers for fouling detection

Björn NIENBORG[(a)], Subramanian SANTHANAM[(a)], Marc MATHIEU[(b)], Alexander SCHWÄRZLER[(b)], Katharina CONZELMANN[(b)], Lena SCHNABEL[(a)]

[(a)] Fraunhofer ISE – Institute for Solar Energy Systems, Heidenhofstr. 2, 79110 Freiburg, Germany
bjoern.nienborg@ise.fraunhofer.de

[(b)] Dr. O. Hartmann GmbH & Co. KG, Uhlandstrasse 30, 71665 Vaihingen/Enz, Germany

ABSTRACT

Fouling is a permanent problem in process technology and is estimated to cost 0.25% of the gross national product. Evaporative cooling systems, which are often used in refrigeration systems to dissipate condenser heat to the environment, are also susceptible to fouling: as they work with untreated outside air, they are exposed to both natural (e.g. pollen) and human-made (e.g. industrial dust) contaminants. Also suspended solid particles and dissolved salts in the spray water are an issue

Since hardly any congruent data on the quantitative influence of fouling on the thermal performance of cooling towers (CT) are available, Fraunhofer ISE conducted a corresponding series of tests. For this purpose, a closed CT was tested under a variety of operating conditions and with different calcification conditions of the tube bundle. For the evaluation of the results, a graphical and a model-based method were compared, of which the latter turned out to be more suitable. With an average scaling thickness of around 1mm on the tube bundle, the reduction in performance is approx. 15%.

Keywords: Fouling, Scaling, Closed Cooling Tower, Performance, Heat Transfer Rate, Fouling Resistance.

1. INTRODUCTION

Fouling is a permanent problem in process engineering and is estimated to cost 0.25% of GDP due to oversizing, downtime and increased energy consumption (Heat Exchanger Fouling and Cleaning 2018). Evaporative cooling systems, which are frequently used in refrigeration systems and industry processes to dissipate condenser or waste heat to the environment, are also subject to fouling: due to contaminants in the ambient air (e.g. dust, pollen, etc.) as well as suspended and diluted solids in the spray water. In the following we evaluate wether a detection of fouling based on its impact on the thermal performance is possible. We concentrate on closed-type cooling towers, i.e. cooling circuits decoupled by heat exchangers and separate spray circuits.

In literature little reliable and congruent data on the influence of air-side fouling on the performance of closed cooling towers are available. While (Qureshi und Zubair 2005) Qureshi reports a performance decrease of ~5% for a scaling thickness of 0.1mm on the air-side of the tube bundle, (Hartvig 2015) claims it to be around 30% under these conditions. Therefore we carry out a test series with fouling (scaling) in a small cooling tower unit and measured the increase of the lime layer on the tube bundle as well as the resulting performance decrease.

2. METHODOLOGY

2.1. Description of the Experimental Setup

In order to evaluate the influence of fouling on thermal performance, a closed cooling tower is continuously measured during operation on a test rig. It is a market-available Gohl VK8/5 (specifications see Table 1). On the cooling fluid side, the volume flow can be varied up to approx. 5300l/h and the inlet temperature into the cooling tower up to approx. 60°C. On the air side, the cooling tower is supplied with ambient air, i.e. temperature and humidity cannot be influenced. However, the cooling tower fan can be controlled via a frequency converter in the range from 20% to 100%. The spray pump can be switched on or off but not controlled. Figure 1 shows a scheme of the setup.

Table 1. Characteristics of the investigated cooling tower and the heat exchanger installed therein

Description	Unit	Value
Nominal capacity	kWth	35
Fan electric power	kWel	1.5
Spray pump electric power	kWel	0.7
Nominal air volume flow rate	m³/h	5350

Description	Unit	Value
Vertical passes	-	18
Horizontal tubes	-	10
Tube distance horizontal/vertical	mm	30
Tube diameter	mm	26.3

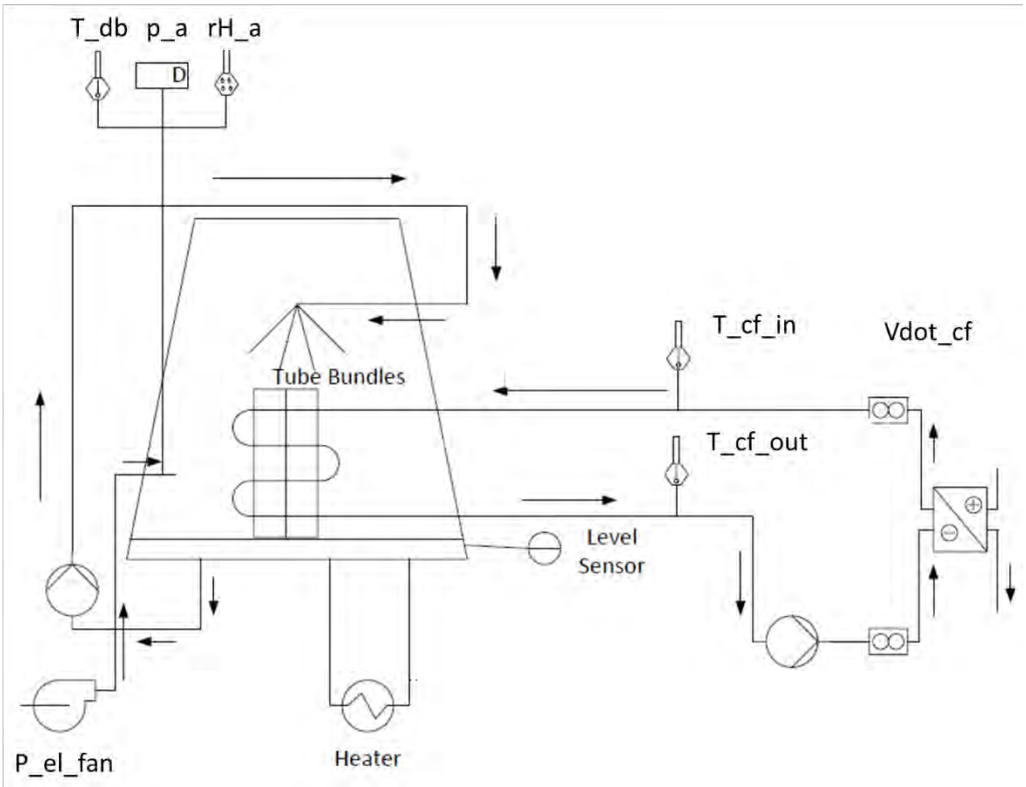

Figure 1: Scheme of the cooling tower test setup including sensor positions

The installed sensors record 1-minute values. The measuring points are located in the cooling circuit (input/output temperature and volume flow), the supply air conditions (temperature, humidity, pressure) as well as the operating status of the spray pump (on/off) and the electrical power consumption of the fan are also measured. The most important technical data of the measurement technology are listed in Table 2.

Table 2. Description of measuring points; * (sensor + data acquisition)

Quantity	Type of sensor	Max. error	Resolution	Short name
Dry bulb temperature	Combinded T/H-Probe (Pt100 + capacitive sensor)	+/- (0.3K + 0.3K)*	0.02K	T_db
Relative humidity		+/- (2% + 0.3%)*	0.02%	rH
Air pressure	Piezoresistive pressure sensor	+/- (1hPa + 0.5hPa)*	0.04hPa	p_a
Temperature cooling fluid (in/out)	Pt100, 4-wire	+/- 0.05K	0.005K	T_cf_in/out
Volume flow cooling fluid	magnetic-inductive	+/- (0.5% + 0.3%)*	0.1l/h	Vdot_cf
Fan electric power		+/- 1.5%	10mW	P_el_fan

The blowdown control is based on the conductivity via a measuring device from Dr. Hartmann Chemietechnik. This also continuously records the pH value and the redox potential. To control biological growth, biocide is regularly added to the spray water. Naturally, the requirements of the latest German Federal Emissions Control Regulation are also complied with.

2.2 Description of the Test Procedure

2.1.1. Characterization in unpolluted conditions

At the beginning of the measurement campaign, the cooling tower was tested under a number of operating conditions without fouling, in order to record the clean characteristics as reference. Therefore softened water was used in wet operation. The following parameters were varied.

Table 3: Set values for cooling water inlet temperature and volume flow as well as the fan signal during measurements in the unpolluted as-delivered condition; the reference conditions are highlighted (described in chapter 2.2.2)

Mode of operation	Water inlet temperature [°C]	Cooling water volume flow [l/h]	Fan signal [%]
Dry	30, 33, 36, **39**	3200, **4200**, 5200	**25, 50, 75, 100**
Wet	20, 23 27, **30**, 33, 36	3200, **4200**, 5200	**25, 50, 75, 100**

2.2.2 Tests with scaled tube bundle

Following the measurements in the unpolluted state, the cooling tower was put into continuous operation. City water at ~12°dH and a thickening of 4 were chosen initially used for the spray water. Since the growth of scaling was slower than expected, higher thickening and addition of sodium hydrogen carbonate and calcium chloride solution to the makeup water were later experimented with.

To check the thermal performance in wet operation with a graphical method presented in (Fugmann et al. 2015), a reference measuring sequence was run twice a week, which was also measured in the unpolluted state (30°C water inlet temperature, 4200l/h cooling water volume flow, all 4 fan stages). In addition, a reference sequence (39°C water inlet temperature, 4200l/h cooling water volume flow, all 4 fan stages) was measured once a week in dry operation.

3. RESULTS AND INTERPRETATION

3.1 Description of Operating Period

Measurements were carried out during approximately one year, from September 2017 until September 2018, with short downtimes due to modifications in the setup or annual closing. Initially the cooling fluid loop was operated with pure water as heat transfer medium. In the end of November 2017 it was replaced by a glycol mixture for frost protection. After a leakage in June 2018 water was used as heat transfer fluid again.

During the test period the thickness of the scaling layer was measured after every reference sequence in wet operation (twice weekly, see 2.2.2). The results of four tubes at the top of the bundle (accessible via a service hatch at the side of the cooling tower housing, counting from the top) and the average over all ten tubes at the bottom (accessible via a second service hatch) are plotted in the following Fig. 2. Fig. 3 shows photos of the top tubes at different stages of scaling.

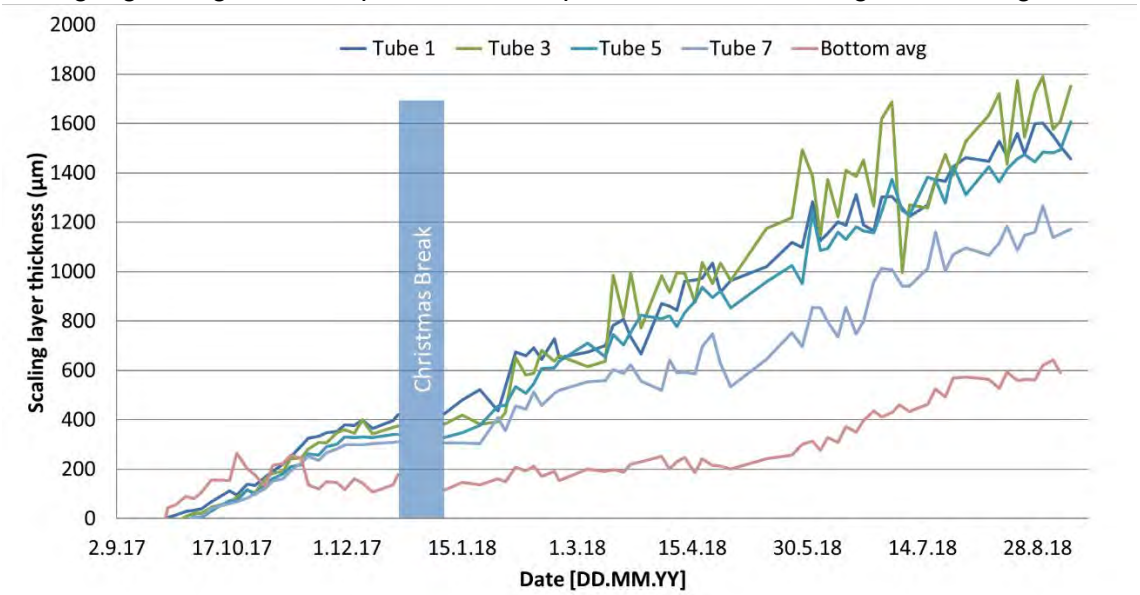

Figure 2: Thickness measurement at 4 tubes at top and all bottom tubes (averaged)



Figure 3: Top tubes after measurements with softened water (left) and after 1 (middle) and 12 (right) months of operation with hard water, respectively

3.2 RESULTS FOR DRY OPERATION

Fig. 4 shows the data recorded at different sensors during the initial (unpolluted) measurements in dry operation. The four fan speeds are clearly visible by the step-shaped profile of the fan electricity consumption (green line). The ambient temperature (blue line) shows the expected daily fluctuations, jumps are due to interruptions in operation or filtered, strongly unstationary operation. The set values for the cooling water are kept stable by the test setup.

The evaluation of the data showed that the ambient temperature sensor was initially not sufficiently shielded against radiation influences. Therefore, measurement data during sunshine hours were filtered out and the sensor was equipped with a ventilated radiation shield for the subsequent measurements. Clearly unsteady operating states due to setpoint changes were also removed from the data. For the ambient temperature and the cooling water inlet temperature, the standard deviation is calculated over three successive values and measured values that are above twice the mean standard deviation are filtered out. After this processing, 2340 1-minute values remain.

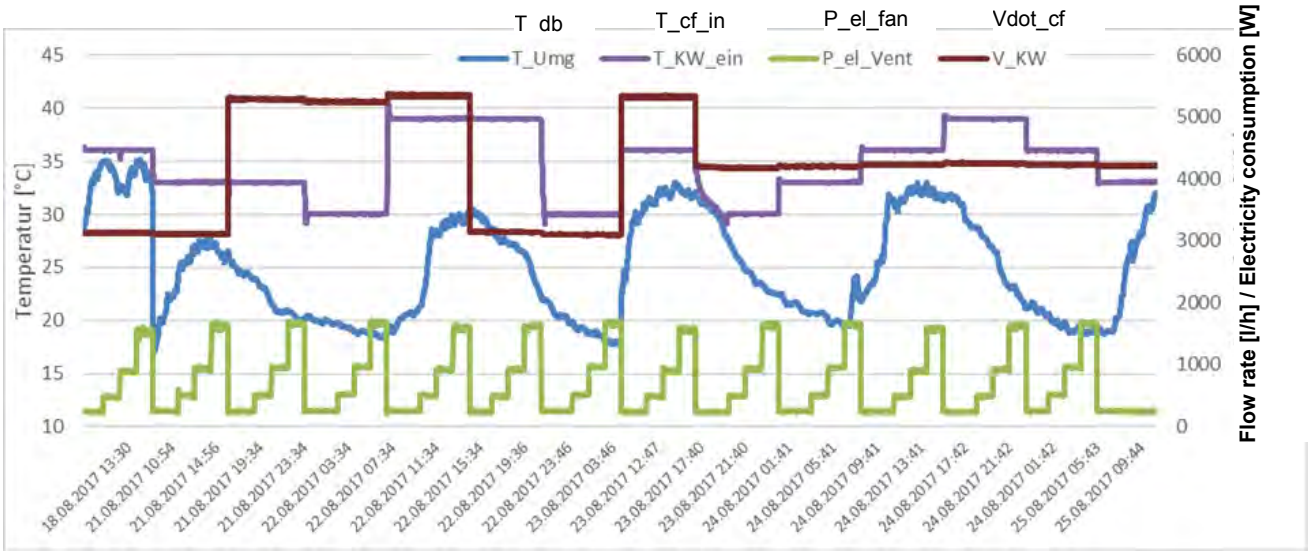

Figure 4: Measured values of ambient and cooling water inlet temperature (T_db / T_cf_in), fan current consumption (P_el_fan) and cooling water volume flow (Vdot_dc) over the entire measurement time with dry operation; minutely values, only periods with measurement operation are shown

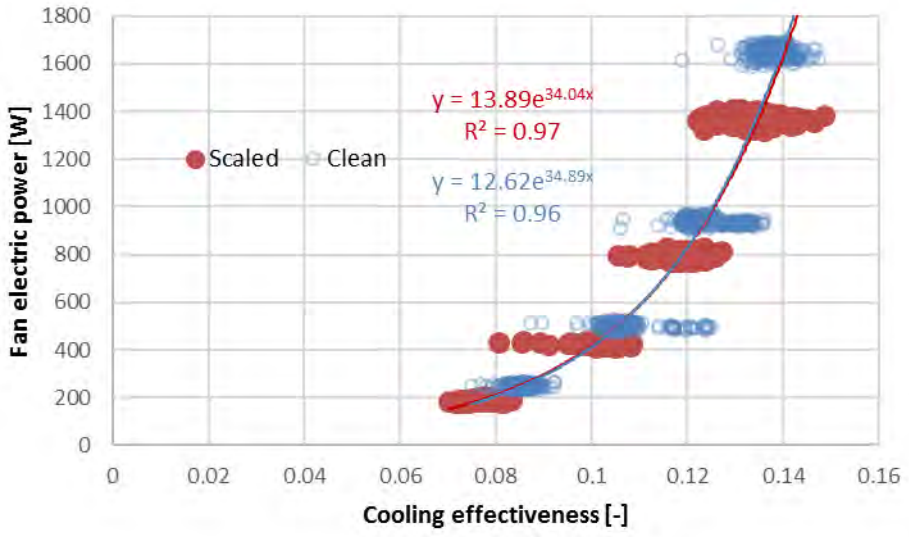

Figure 5: Correlation between fan electricity consumption and cooling effectiveness under clean (blue) and scaled (red) conditions

The method presented by (Fugmann et al. 2015) was used for an initial evaluation of the measurement data quality. Accordingly, for air-water heat exchangers with forced air flow, a defined relationship between achievable cooling effectiveness (=benefit) and required fan power (=cost) can be expected, independently of the absolute operating conditions (in particular air and water temperatures, provided that the volume flow on the water side is constant). For polluted/fouled heat exchangers a decrease in cooling effectiveness can be expected. Fig. 5 shows this correlation for the measurements with 4200l/h cooling water volume flow under clean conditions (blue), in the beginning of the measurement campaign, and during the last month of tests, with the scaled tube bundle (red).
Contrarily to the expectations, no decrease of the cooling effectiveness (shift to the left) can be observed. However the electricity consumption of the fan is lower at the end of the measurement period, presumably because the increased pressure drop leads to a reduced air flow rate.
Therefore, in the next step a simple calculation model for dry and wet coolers based on (Stabat and Marchio, 2004) was calibrated using the data measured under clean conditions. The air volume flow, which is not measured but required for the model, is calculated from the control signal for the fan frequency converter and the nominal air volume flow from the data sheet, assuming a linear correlation. As shown in figure 6, 95% of the calculated values show a relative deviation from the measured values of less than 10% (min: -16%, max. +17%). When the model is run with data of the last month of the tests (scaled tube bundle), it significantly overestimates the thermal capacity. Evidently this deviation corresponds to the capacity decrease due to fouling. The fact that the deviation correlates to the fan speed under scaled conditions (right figure) suggests, that the assumption of a linear function between fan signal and air flow rate is deficient.

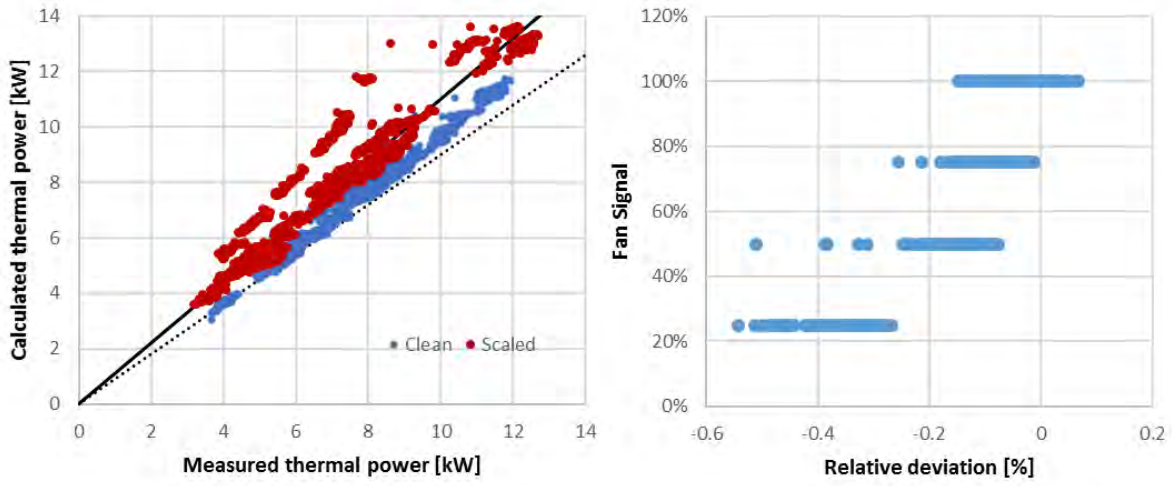

Figure 6: Left: Comparison of calculated and measured thermal power in dry mode under clean (blue) and scaled (red) conditions; right: relative deviation as a function of the fan signal under scaled conditions

3.2 RESULTS FOR WET OPERATION

Data for operation periods with water and brine have to be evaluated separately. Therefore, in a first step the influence of maximum scaling at the end of the test period in comparison to a clean tube bundle is studied. The data with water as cooling fluid are used therefore. In a second step the trend of the performance change is shown based on the data with brine as cooling fluid, as they are continuous over a period of 7 months.

3.2.1 Difference between clean and maximum scaled tube bundle

Fig. 7 again shows the selected measured values of the characterization under clean conditions in wet operation. The wet bulb temperature (T_wb), which now represents the cooling limit temperature,

replaces the dry bulb temperature (T_db) shown for the dry measurements. Again the presented data is filtered for quasi-stationary values, as described above.

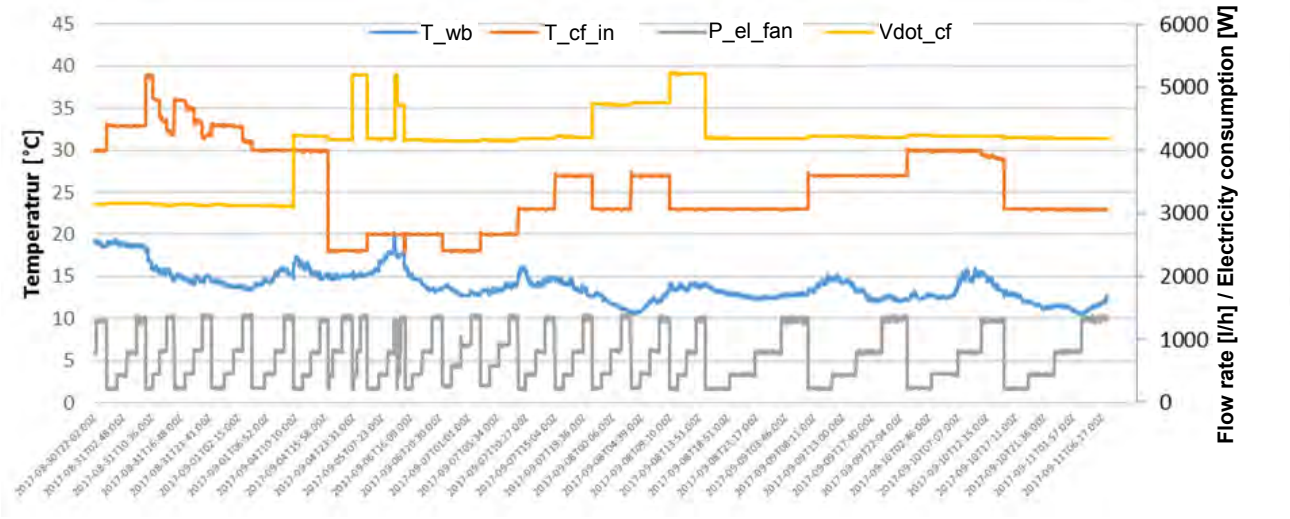

Figure 7: Measured values of wet bulb and cooling water inlet temperature (T_wb / T_cf_in), fan current consumption (P_el_fan) and cooling water volume flow (Vdot_cf) over the entire measurement time with wet operation; minute values, only periods with measurement operation are shown

This data was then used to calibrate the cooling tower mode. In order to reduce the error in determining the air flow rate, it is now determined as a function of the fan electricity consumption. Compared to the dry measurements, the scattering is somewhat greater (see Fig. 8, min: -23%, max: +33%). However, the deviation of the calculated values from the measured values is below 10% in over 99% of cases. One possible reason for this better result compared to dry operation is the larger database used for calibration (8365 versus 2340 values).

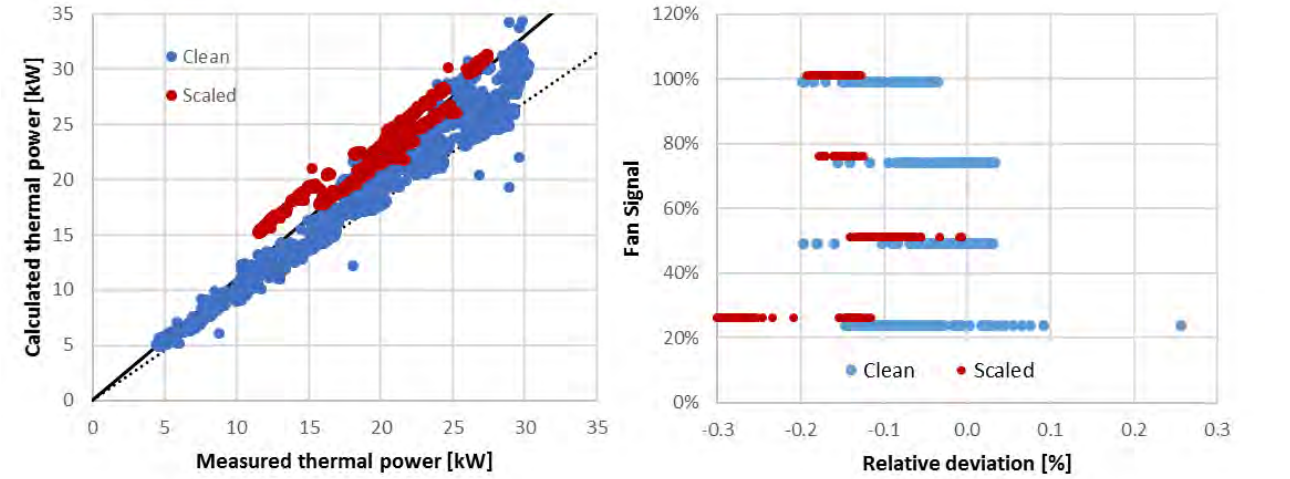

Figure 8: Left: Comparison of calculated and measured thermal power in wet mode under clean (blue) and scaled (red) conditions; right: relative deviation of the thermal power as a function of the fan signal under clean conditions.

When the model is run with the data of the scaled cooling tower, analogously to the results in dry operation, there is a decrease in thermal power compared to the values forcasted with the clean model by approximately 12%. Under clean conditions the scattering of the deviation between measured and calculated thermal power ist rather independent of the fan speed. For the scaled data, deviations at the lowest fan speed stand out.

3.2.2 Influence of scaling during continuous operation

Finally the model is calibrated with the initial measurement data after switching to brine as heat transfer fluid. Then it is run with all the measured data in this configuration. Figure 9 shows the resulting performance decrease in correlation to the measured scaling thickness at the tube bundle (normalized to zero thickness at the beginning). In both graphs a performance reduction with increasing scaling layer thickness can be identified. Yet it is strongly superposed by fluctuations which suggest the need for additional data preparation and/or a refined model.

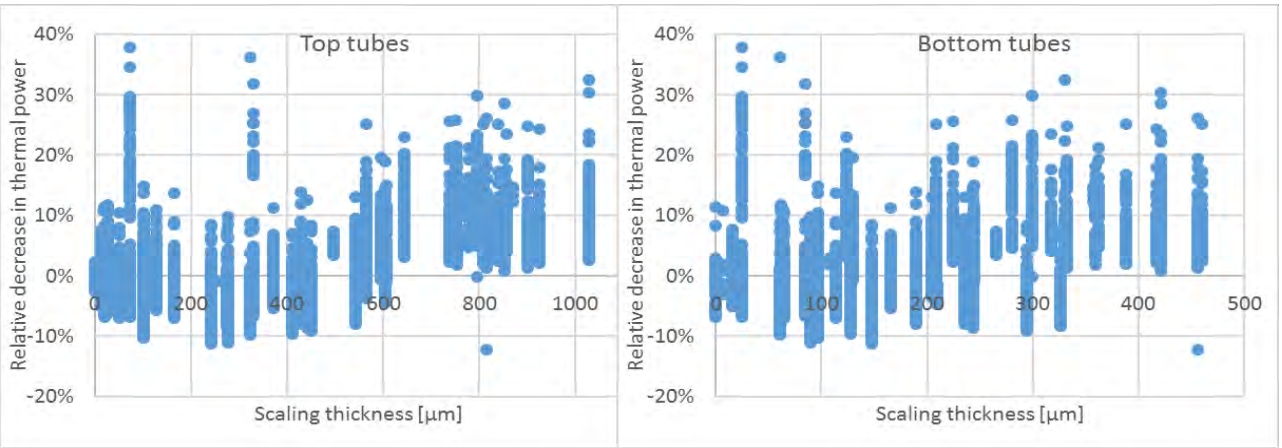

Figure 9: Correlation between thickness of the scaling layer on the top (left) / bottom (right) tubes and the decrease in thermal power (positive value means measured power decrease compared to model)

3. CONCLUSIONS

At Fraunhofer ISE, a closed cooling tower was operated and measured over a period of several months in order to investigate the influence of typical crystallization fouling (scaling) on the heat transfer performance. After a characterisation of the unpolluted cooling tower at the beginning of the test period, it was purposely operated with calcium carbonate-containing water up to a thickness of ~0.6mm and 1.6mm (bottom and top tubes, respectively) on the tube bundle.

The model-based evaluation showed that this scaling layer reduced the thermal power by around 15% in both wet and dry operation. This value is well below the figures published in the literature. The graphical evaluation method according to (Fugmann et al. 2015), on the other hand, has proved to be unreliable. The detection of fouling due to performance decrease by continuous monitoring seem possible based on the test rig data. Yet, the current results suggest the need for improved data processing and/or refining the cooling tower model. Taking into account additional data, such as water consumption, can also help clarify the results.

In a next step this approach will be applied to measurement data from the field and extended to other evaporative cooling systems. If necessary, the operation monitoring can also be extended to other operating parameters.

ACKNOWLEDGEMENTS

The presented work is funded by the Federal Ministry of Education and Research (FKZ01LY1618) as part of the WCS-energy project.

REFERENCES

Fugmann, H.; Nienborg, B.; Trommler, G.; Dalibard, A.; Schnabel, L. (2015): Performance Evaluation of Air-Based Heat Rejection Systems. In: *Energies* 8 (2), S. 714–741. DOI: 10.3390/en8020714.

Hartvig, A. (2015): Biofilm effect on Cooling Towers for industrial purpose, Report by Danish Clean Water

Heat Exchanger Fouling and Cleaning (2018). Accessible online http://www.heatexchanger-fouling.com/, last accessed 09.02.2018

Qureshi, B. A.; Zubair, S. M. (2005): The impact of fouling on performance evaluation of evaporative coolers and condensers. In: *Int. J. Energy Res.* 29 (14), S. 1313–1330. DOI: 10.1002/er.1120.

Stabat, P.; Marchio, D. (2004): Simplified model for indirect-contact evaporative cooling-tower behaviour. In: *Applied Energy* 78 (4), S. 433–451. DOI: 10.1016/j.apenergy.2003.09.004.

Manuscript ID: 1231
DOI: 10.18462/iir.icr.2019.1231

Energy improvements in a stand-alone transcritical refrigeration system using a low-GWP mixture of CO_2/R1270

Daniel Sánchez[(a)], Ramón Cabello [(a)], Rodrigo Llopis [(a)]
Jesús Catalán[(a)], Laura Nebot[(a)], Daniel Calleja[(a)], Eduardo Gil[(a)]

(a) Jaume I University, Dep. of Mechanical Engineer and Construction, E-12017, Castellón, Spain, sanchezd@uji.es

ABSTRACT

The performance of CO_2 transcritical cycles is widely affected by the heat rejection temperature due to its low critical temperature. Due to this, basic cycles are modified by adding new configurations and components that increase their complexity and cost. Blends of CO_2 with other fluids as hydrocarbons, can improve the performance of these cycles by increasing their critical point and latent heat while reducing the working pressure of the compressor. Accordingly, the aim of this communication is to show the energy benefits obtained with a theoretical non-flammability blend of CO_2/R1270 (91/9% by mass) when it is tested in a beverage cooler system adapted for CO_2. Using a transcritical basic cycle with an IHX and one expansion-stage, the energy savings obtained with the new bled, maintaining an average can temperature of 3.3ºC, are 10.3% at the climate conditions of 25ºC and 60% of RH (class 3).

Keywords: Zeotropic Mixture, Carbon Dioxide, Commercial Refrigerator, COP, Low-GWP, R1270, Refrigerating System, Transcritical Cycle.

1. INTRODUCTION

The Worldwide extended prohibitions about using fluorinated gases in commercial and domestic refrigeration have been the principal starting point of the progressive increase in the use of natural refrigerants as hydrocarbons (HCs) and carbon dioxide (CO_2). Despite their excellent thermophysical properties and economical costs, natural refrigerants have intrinsic drawbacks that must be solved when they are used in a refrigeration facility (Elbel et al., 2017). Thus, flammability (HCs), high working pressure (CO_2) and low critical temperature (CO_2) are the most relevant issues that affect, respectively, the maximum refrigerant mass charge (IIR, 2017), the design of the components (DeAngelis and Hrnjak, 2005) and the energy performance of the refrigerating facility, especially in warm climates (Cecchinato and Corradi, 2011; Sánchez *et al.* 2018). Stand-alone refrigeration units are one of the most affected by these challenges due to their low manufacturing cost and their relative high replacement rate. At present, commercial plug-in systems with a refrigerant mass charge between 150 and 1000 g use basically R134a or R404A as refrigerants, with a GWP higher than the values allowed by the F-Gas regulation (EU Nº 517/2014). For these units, CO_2 seems to be the unique long-term solution if the hydrocarbon limits are not raised. However, the use of CO_2 increases the manufacturing complexity as well as the total cost of the refrigerating plant in order to be energy competitive with the current artificial refrigerants.

As a simple solution, some researchers proposed the use of refrigerant mixtures of CO_2 and low-GWP refrigerants (hydrocarbons or HFCs) with the goal of obtaining a hybrid refrigerant which minimizes the main problems stressed above. Hence, authors as Niu and Zhang (2007), Kim et al.

(2008), Zhang et al. (2013), Zhang et al. (2017a), Ju et al. (2018), Yu et al. (2018) have analyzed the use of zeotropic blends with propane (R290) for cascade systems, heat pumps and automobile air conditioning. Similarly, Sarkar and Bhattacharyya (2009) studied the use of butane (R600) and isobutane (R600a), Cox et al. (2008) proposed the use of HFC-R41 for a near-azeotropic refrigerant blend, and Zhang et al. (2017b) investigated about using DME (dimethyl-ether) as binary mixture. Others authors, such as Di Nicola et al. (2011) and Dai et al. (2015), studied several binary blends of CO_2 for their use as low-temperature working fluids in cascade systems and in heat pump applications, respectively. In all cases, the mass rate of both fluids (expressed as % of mass) is optimized for a specific application attending to the maximization of the COP.

Benefits of carbon dioxide blends are promising since they increase the critical point, reduce the high operation pressure of the CO_2 system, improve the energy efficiency and minimize (or remove) the flammability of the blend maintaining a low GWP value (Dai et al., 2015). However, most of them are zeotropic with a non-negligible glide which difficults the design of the heat exchangers as well as the expansion systems. On the other hand, there is no data neither information about their security classification or chemical interaction between components.

In this work, the preliminary energy improvements reached using the virtually non-flammable binary mixture of CO_2 and propylene (R1270), are presented and discussed. The mixture of R744/R1270 (91/9% by mass) has been tested in a CO_2 beverage cooler when it is tested at the climate conditions of 25ºC and 60% RH and maintaining an average temperature of 3.3ºC in 15 test cans placed inside. The results obtained with a slight-optimized system, show an energy reduction of 10.3% with regard to pure CO_2 working in a base-cycle with IHX.

2. TEST BENCH AND EXPERIMENTAL METHODOLOGY

2.1. Refrigerant Blend

As was stated before, the proper blend selection depends on the application and it is each time optimized to maximize the COP of the cycle. However, some other aspects should be taken into account if the mixture is devoted to replace pure-CO_2 in commercial applications. At first, non-flammable condition is mandatory to avoid refrigerant mass charge limitations. Secondly, the value of GWP_{100} should be kept below 150 in order to be consistent with the current regulations. And finally, the glide of the new mixture should be “acceptable” (for example, below 10 K) in order to make easier the design of the refrigerating cycle. As can be show in Table 1, carbon dioxide and propylene are ultra-low-GWP refrigerants, so their blends, regardless the composition, will be always lower than 2. Therefore, these mixtures will be accepted by the current regulations. Regarding the flammability, carbon dioxide is classified by ASHRAE standard 34 as A1 while the hydrocarbon propylene, is labeled as A3. A mixture of both can provide blends with flammable conditions, so it is necessary to determine the maximum mass of propylene that can be mixed with carbon dioxide to ensure non-flammability. Kondo et al. (2006) defined the Fuel Inertization Point (FIP) as *the point on the envelope of flammable region in the triangular system of fuel-air-diluent which defines the maximum ratio of fuel to diluent concentration that never gives flammable mixtures whatever the amount of air is added to or subtracted from the mixture*. At this point, the upper and lower flammability limit mixture becomes coincident, so it is possible to determine which the maximum propylene concentration is in the blend R744/R1270 that ensures non-flammability. Using the data presented at the Table 1 and the expressions adjusted by Kondo et al. (2006), the maximum percentage in mass of propylene in the mixture is 9%. Finally, the total glide of the mixture depends on the operating conditions of the refrigerating facility. Assuming an evaporating temperature of -8ºC and a condensing temperature of 28ºC, values of glide (ΔT_{GL}) are 4.2 K and 2.6 K, respectively, assuming a vapor quality of 0.5 according to the assumptions presented by Radermarcher and Hwang (2005). Table 2 includes the critical temperature and pressure (T_{crit}) (P_{crit}), the latent heat (λ), the volumetric capacity (q_V), the molar weight (M_W) and the pressure levels (P) of R744, R1270 and the blend R744/R1270 (“Blend”) at the temperatures of -8ºC and 28ºC. All thermophysical properties are obtained using the software REFPROP v.9.1.

Table 1. Refrigerant properties. Part I [(1)] IPCC (2014)

	GWP_{100} [(1)]	LFL (vol%)	UFL (vol%)
R744	1	-	-
R1270	2	2.16	11
Blend	1.09	-	-

Table 2. Refrigerant properties. Part II

	M_W (g/mol)	T_{crit} (ºC)	P_{crit} (bar)	$P_{K\ (x=0.5)}$ (bar)	$P_{O\ (x=0.5)}$ (bar)	q_V (kJ/m^3)	λ_O (kJ/kg)	λ_K (kJ/kg)
R744	44.0	31.0	73.8	68.9	28.0	19216.0	253.4	91.6
R1270	42.1	91.1	45.6	12.4	4.6	3782.5	389.4	329.0
Blend	43.8	38.1	76.5	61.5	25.4	17422.0	266.8	138.0

Comparing pure CO_2 with the blend of R1270, the use of the zeotropic mixture increases the latent heat of evaporation 5.3% and enhances the critical temperature up to 7.1ºC. In terms of pressure levels, the mixture reduces the high-side and the low-side pressure up to 7.4 bar and up to 2.7 bar, respectively. However, the pressure ratio is almost similar presenting a slight reduction of 1.8%. Regarding the latent heat of condensation, the use of propylene increases this value up to 50.7% which is determinant in the design of the heat exchanger used as condenser or gas-cooler, depending on the working conditions.

2.2. Experimental Test Bench

To perform the energy analysis a commercial beverage cooler adapted for CO_2 has been used. This stand-alone unit is 620 (L) x 2000 (H) x 655 (D) mm with an inner capacity of 440 liters and a glass door at the front. The system is equipped with a temperature controller that maintains the indoor air temperature at 1ºC using and ON/OFF control. The controller also manages the defrosting process which is performed each 8 hours with hot gas until the temperature at the evaporator surface reaches 5ºC.

The schematic diagram of the refrigeration cycle is depicted in Fig.1. Starting from the compressor suction port, the vapor is compressed by a hermetic compressor (A) with a cubic capacity of 1.1 cm^3 running at 50 Hz (~2900 rpm). The compressor uses DAPHNE PZ68S as lubricant and is cooled by the gas-cooler/condenser air fan (D). From the discharge point, the refrigerant is cooling down by a wire-on-tube heat exchanger (B) positioned vertical with natural convection. This heat exchanger has an inner heat transfer area of 0.185 m^2 with a tube diameter of 3.5 mm (id). After that, the refrigerant is cooled again with a fined-tube heat exchanger (C) installed at the bottom of the unit with forced convection by means of an air-fan that also cools down the compressor. The inner heat transfer area of this heat exchanger is 0.089 m^2 with a tube diameter of 6.5 mm (id). The refrigerant at the exit of the condenser/gas-cooler runs through the Coriolis mass flow meter (D) to a counter-current IHX (E) with a heat transfer area of 0.01 m^2 and an outer/inner diameter tube of 11.1/8.0 mm. To make easier the experimental tests, a micrometer needle valve (F) has been used as expansion device. The expanded refrigerant goes into the fined-tube evaporator (G) installed inside the beverage cooler with an inner heat transfer area of 0.186 m^2 with a tube diameter of 7 mm (id). Finally, the vapor from evaporator is superheated by the IHX before entering the compressor.

All the pipe-lines, excepting the discharge one, are insulated with a foam with an average thermal conductivity of 0.036 W/m·K. The ambient test conditions are maintained with a climatic chamber of 31.5 m^3 where temperature and relative humidity are kept at 25 °C ± 0.4 °C and 60% ± 5%, respectively (class 3 according to UNE-EN ISO 23953-2:2005+Amd.1:2012)

The system is fully instrumented with 10 T-thermocouples with an uncertainty of ±0.5 K, 2 pressure transducers with range of 0-160 bar and uncertainty of ±0.48bar placed at the high side pressure, 2 pressure transducers with range of 0-60 bar and uncertainty of ±0.18bar placed at the low side

pressure, 1 relative humidity transducer with a measurement error of ±2% RH, a digital power meter with an uncertainty of ±0.5% and a Coriolis mass flow meter placed at the liquid line with an uncertainty of ±0.1%. Moreover, 15 test cans have been placed inside the unit distributed in 3 heights. These test cans are made with a mixture of water/propylene-glycol 67/33% by volume and have an immersion T-Thermocouple placed inside. All data are gathered by a DAQ-system each 5 seconds and stored in a computer. Fig. 1 shows the location of all transducers. Excepting the test cans, all temperature sensors are placed on the pipes and are insulated from the environment with the foam indicated above.

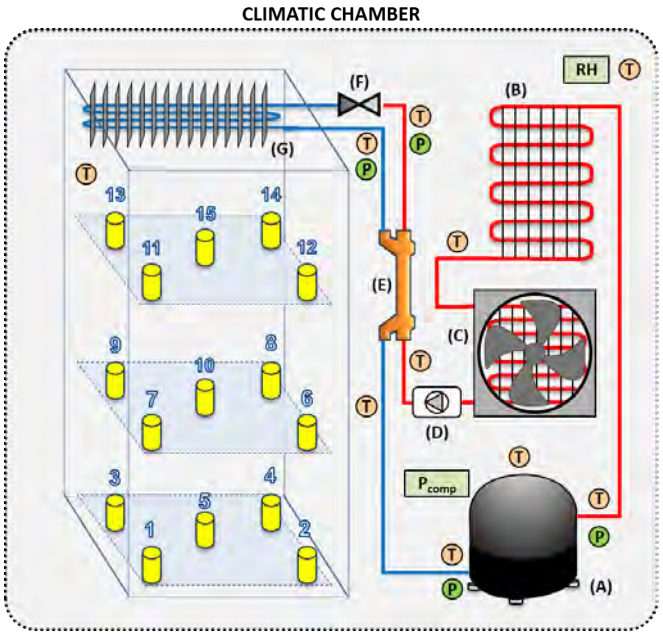

Figure 1: Schematic diagram of the refrigeration facility

2.3. Test Methodology

2.3.1. Reference parameters

As previously mentioned, the ambient conditions have been fixed to 25ºC and 60% of RH, which correspond to class 3 according to the ISO23953. The inner temperature of the unit is modified to obtain an average can temperature of 3.3ºC by changing the set point of the temperature controller. Finally, the superheat at the evaporator was maintained below 4K by changing the position of the micrometer needle valve. Table 3 summarizes the average and the standard deviations of the reference parameters during the 10-h tests.

Table 3. Reference Parameters

	RH_{cham} (%)	T_{cham} (ºC)	$T_{avg\ can}$ (ºC)
R744	58.72 ± 3.53	24.94 ± 0.44	3.37 ± 0.58
Blend	58.91 ± 3.15	25.09 ± 0.39	3.15 ± 0.25

2.3.2. Mass charge process

The mass charge process was started at 400 g for CO_2 and 300 g for the zeotropic mixture with increments of ~20 g. In both cases, the charge has been carried out with liquid phase to maintain the blend composition. After each charge, the unit has been left running for 1 hour modifying the micrometer valve to adjust the average test can temperature and the superheat. Once it is adjusted, the unit runs for at least 5 hours to determine the energy consumption. If the consumption is lower than the previous one, a new mass charge is done. If not, the previous mass introduced is used to perform the energy analysis. Using this methodology, the optimal mass charge of CO_2 was 482 g and that of the R744/R1270 blend was 400 g. Once the refrigerant mass charge is adjusted, the experimental tests of pull-down and energy utilization are performed.

2.3.3. Experimental tests

In beverage coolers two kinds of tests are performed: the pull-down test and the energy utilization test. The pull-down test determines the time necessary to obtain a specified product temperature. It aims to give us evidence about the speed of cooling starting from the same conditions. For this test, the beverage cooler and the can tests were stabilized to the climatic chamber conditions during 10 hours with the optimal mass charge and the optimal micrometer position determined in section 2.3.2. After that, the door was closed and the unit was switched on during at least 6 hours. If the pull-down test is ok, the energy utilization tests can be performed. In this case the beverage cooler is running at least 10 hours at the same conditions stated before maintaining the temperature of the product. The energy utilization tests include the defrosting periods.

2.3.4. Energy consumption

For the comparison between pure CO_2 and the mixture of CO_2 and propylene, an energy evaluation was implemented considering the energy consumption of the whole system excluding the data acquisition system and transducers. This energy consumption includes the compressor, the evaporator and condenser air-fans, the controller and the external/internal LED lights of the unit. Eq. (1) determines the energy consumption of the whole system during a specific time-range test where *P* is the power consumption and *j* represents each sampled data.

$$E = \frac{1}{36 \cdot 10^5} \cdot \int_0^{24h} P(t) \cdot dt \simeq \frac{1}{36 \cdot 10^5} \cdot \sum_{j=1}^{24h} \left\{ \left[\frac{P(j)+P(j-1)}{2} \right] \cdot [t(j) - t(j-1)] \right\} \quad \text{Eq. (1)}$$

3. EXPERIMENTAL RESULTS

3.1. Pull-down test

Fig.2 graphically presents the average temperature of cans with regard to the time of operation. Taking into account the target temperature of 3.3ºC, the time and the trend of the pull-down is similar for both refrigerants. Moreover, if the energy consumption of the pull-down test is obtained with the Eq. (1) at the time of 300 min, the results from pure CO_2 and the blend are quite similar.

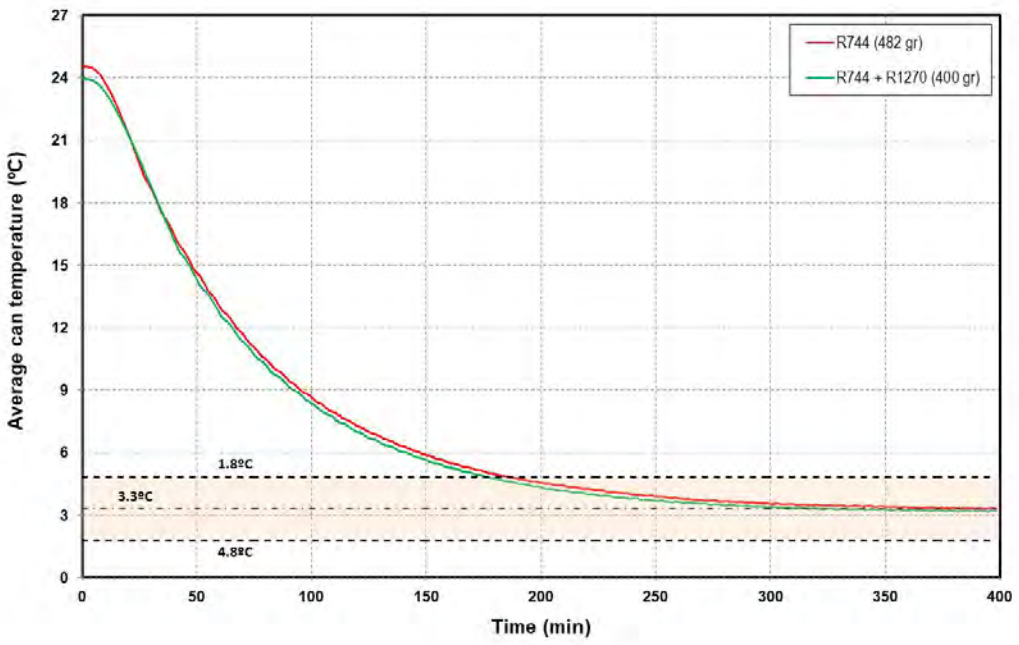

Figure 2: Pull-down test

3.2. Energy utilization test

3.2.1. Temperature and pressure Indicators

Table 4 gathers the representative temperatures and pressures of the refrigerating cycle including the discharge (P_{dis}) and the suction pressure (P_{suc}), the condensation (T_k) and evaporating (T_{ev}) temperatures obtained with the average pressure at the high and low side, the discharge temperature (T_{dis}) and the useful superheat (SH). The data is presented as an average value during the 10-h test when the compressor is running. Table 3 also includes the standard deviation obtained in the same period of time.

Table 4. Temperature and Pressure indicators

	P_O (bar)	T_O (ºC)	P_K (bar)	T_K (ºC)	T_{dis} (ºC)	SH (K)
R744	28.51 ± 0.87	-7.44 ± 1.09	73.53 ± 1.16	30.53 ± 0.50	70.07 ± 2.59	3.55 ± 1.86
Blend	26.63 ± 0.56	-7.38 ± 0.77	61.40 ± 0.87	26.77 ± 0.66	64.54 ± 2.50	5.78 ± 1.83

As it is shown in the latter table, the use of the mixture R744/R1270 reduces the high rejection pressure in 12.13 bar and the evaporation level in 1.88 bar, resulting in a reduction of 10.6% in the pressure ratio. Regarding the phase-change temperatures, both refrigerants have similar evaporating levels but different condensing ones. CO_2 performs higher condensation level than the zeotropic mixture. These results could be further improved increasing the heat transfer area of the condenser. Finally, the discharge temperature for pure CO_2 is +5.53K higher than the zeotropic mixture due to the high pressure ratio of CO_2.

3.2.2. Power consumption, energy consumption and compressor duty cycle

As mentioned in Subsection 2.3.3, the active elements of the unit are the compressor, the air-fans, the temperature controller and the LED lights of the unit. The controller and LED lights are always running whatever the conditions of the refrigerating unit are. The average power consumption of both is 18.41 W. The evaporator air-fan, the compressor and the condenser air-fan, are switch on/off according to the inner temperature. All of them are switched off during a defrosting process excepting the evaporator air-fan which is running until the temperature at the evaporator surface reaches 5 ºC. The average power consumption of each air-fan is 30.42 W. Finally, the power consumption of the compressor represents the largest portion of the beverage electrical power.

Table 5 reports the average value for the power consumption and its standard deviation, as well as the energy consumption of the beverage cooler (E) during 10 hours and the compressor duty cycle (D_{comp}).

Table 5. Electrical power, energu consumption and compressor duty cycle

	$\mathbf{P_{elec}}$ (W)	$\mathbf{E}$ (kW·h)	D_{comp} (-)
R744	332.79 ± 2.67	1.91	58.5 %
Blend	295.87 ± 2.70	1.71	58.6 %

From the results presented in Table 5 it can be affirmed that compressor duty cycle is similar in both refrigerants, but the electrical power consumed by the blend is about 11% lower than pure-CO_2. This effect reduces the energy consumption of the refrigerating plant up to 10.3%.

4. CONCLUSIONS

In this work an energy comparison between pure-CO_2 an alternative low-GWP blend is experimentally analyzed and discussed. The new zeotropic mixture of CO_2 and propylene has been tested in a stand-alone refrigeration facility designed for CO_2 at the ambient conditions of 25ºC and 60% RH. The slight-optimized results show energy savings of 10.3% maintaining a temperature target of 3.3ºC in 15 test cans placed inside the unit.

ACKNOWLEDGEMENTS

Authors gratefully acknowledge Conselleria d'Educació, Investigació, Cultura i Esport de la Generalitat Valenciana for financing this research work (project AICO/2018/058).

REFERENCES

Cecchinato L., Corradi M., 2011. Transcritical carbon dioxide small commercial cooling applications analysis, International Journal of Refrigeration, 34, 50-62.

Cox N., Mazur V., Colbourne D., 2008, New High Pressure Low-GWP Azeotropic and Near Azeotropic Refrigerant Blends, International Refrigeration and Air Conditioning Conference. Paper 987. http://docs.lib.purdue.edu/iracc/987

Dai B., Dang C., Li M., Tian H., Ma Y., 2015. Thermodynamic performance assessment of carbon dioxide blends with low-global warming potential (GWP) working fluids for a heat pump water heater, International Journal of Refrigeration, 56, 1-14.

DeAngelis J.M., Hrnjak P., 2005. Experimental study of system performance improvements in transcritical R744 systems with applications to bottle coolers. Air Conditioning and Refrigeration Center (ACRC). University of Illinois at Urbana-Champaign.

Di Nicola G., Polonara F., Stryjek R., Arteconi A., 2011. Performance of *cascade* cycles working with blends of CO_2 + natural refrigerants, International Journal of Refrigeration, 34 (6), 1436-1445.

Elbel S., Visek M., Hrnjak P., 2017. A fair comparison of CO_2 and propane used in light commercial applications featuring natural refrigerants. International Refrigeration and Air Conditioning Conference. Paper 1748. http://docs.lib.purdue.edu/iracc/1748

IIR, 2017. Flammable refrigerants. 36th Informatory note on refrigeration technologies. http://www.iifiir.org/userfiles/file/publications/notes/NoteTech_36_EN_nkyix2fcj7.pdf

IPCC, 2014. Climate Change 2014: Synthesis Report. Contribution of Working Groups I, II and III to the Fifth Assessment Report of the Intergovernmental Panel on Climate Change [Core Writing Team, R.K. Pachauri and L.A. Meyer (eds.)]. IPCC, Geneva, Switzerland.

Ju F., Fan X., Chen Y., Ouyang H., Kuang A., Ma S., Wang F., 2018. Experiment and simulation study on performance of heat pump water heater using blend of R744/R290. Energy and buildings, 169, 148-156.

Kim J. H., Cho J. M., Kim M. S., 2008. Cooling performance of several CO_2/propane mixtures and glide matching with secondary heat transfer fluid, International Journal of Refrigeration, 31 (5), 800-806.

Kondo S., Takizawa K., Takahashi A., Tokuhashi K., 2006. Extended Le Chatelier's formula for carbon dioxide dilution effect on flammability limits, Journal of Hazardous Materials, 138 (1), 1-8.

Niu B., Zhang Y., 2007. Experimental study of the refrigeration cycle performance for the R744/R290 mixtures, International Journal of Refrigeration, 30 (1), 37-42.

Radermacher R, Hwang Y., 2005. Vapor Compression Heat Pumps with Refrigerant Mixtures, CRC Press. ISBN: 9780849334894.

Sánchez D., Catalán-Gil J., Llopis R., Nebot-Andrés L., Cabello R., Torrella E., 2018. CO_2 vs. fluorinated refrigerants. Energy evaluation in a MT cabinet with DX-system. Refrigeration Science and Technology, 149 – 156.

Sarkar J., Bhattacharyya S., 2009. Assessment of blends of CO_2 with butane and isobutane as working fluids for heat pump applications. International Journal of Thermal Sciences, 48 (7), 1460-1465.

Yu B., Wang D., Liu C., Jiang F., Shi J., Chen J., 2018. Performance improvements evaluation of an automobile air conditioning system using CO_2-propane mixture as a refrigerant, International Journal of Refrigeration, 88, 172-181.

Zhang L., Yang C., Liu H., Du P., Gao H., 2017a. Theoretical Investigation on the Properties of R744/R290 Mixtures, Procedia Engineering, 205, 1620-1626.

Zhang X., Wang F., Liu Z., Gu J., Zhu F., Yuan Q., 2017b. Performance research on heat pump using blends of R744 with eco-friendly working fluids, Procedia Engineering, 205, 2297-2302.

Zhang X. P., Wang F., Fan X. W., Wei X. L., Wang F. K., 2013. Determination of the optimum heat rejection pressure in transcritical cycles working with R744/R290 mixture, Applied Thermal Engineering, 54 (1), 176-184.

Manuscript ID: 1241
DOI: 10.18462/iir.icr.2019.1241

A theoretical and experimental analysis of n-butane application for household refrigerators

Adriano F. RONZONI[(a)], André A. FURLAN[(a)], Gustavo P. MONTAGNER[(a)], Mario STRAUB[(b)], Didier SIEGEL[(b)]

[(a)]Embraco, Research and Development Department
Joinville, 89219580, Brazil,
adriano.f.ronzoni@embraco.com
[(b)]Liebherr Hausgeräte, Research and Development Department
Ochsenhausen, Germany
mario.straub@liebherr.com

ABSTRACT

This paper presents a theoretical and experimental comparison between the performance of isobutane (R600a) and n-butane (R600) for a built-in household refrigerator. Energy consumption tests were performed at two ambient temperatures (16°C and 32°C) and two thermostat positions (hot and cold). Second law efficiency was used to evaluate the performance inventory for both fluids under different system configurations. Results have shown an overall energy consumption saving up to 14% when a system originally designed to run on isobutane is optimized to run on n-butane. It was observed that due to its lower volumic refrigerant effect, the application of n-butane is beneficial for low thermal load systems such as small household refrigerators required to comply with new energy consumption policies.
Keywords: Butane, Hermetic Compressor, Household Refrigerator, R600, R600a, Variable Speed.

1. INTRODUCTION

A household refrigerator is typically composed of thermally insulated cabinets used to store frozen and fresh goods. A vapour-compression refrigeration loop is responsible for keeping the compartments at desired temperature. Although the energy consumption of a single household refrigerator is low, these systems consume a large amount of energy since hundreds of millions are currently in use and their thermodynamic efficiency is intrinsic low, typically around 20% of Carnot's COP (Negrão and Hermes, 2011). Such appliances respond for approximately 6% of total electrical energy produced worldwide (Melo and Silva, 2010). For this reason, international policy makers are constantly pushing appliance manufacturers to increase the efficiency of the refrigeration units. During last decades, efficiency regulations have been constantly updated to keep pace with advancing technology. As a result, refrigerators energy consumption in the USA market decreased by 50% in the last 25 years. The average energy efficiency level of refrigerators sold in China has been upgraded by around 42% between 1999 and 2013 (AHAM, 2015). In the European market, a typical 330 L fridge-freezer energy consumption dropped by 72% in the last 16 years (Straub, 2018). These improvements were only possible due to the application of state of art technology such as high efficiency variable speed compressor, vacuum insulation panels and alternative refrigeration cycles such as dual evaporator systems.

In addition to efficiency standards, appliance manufacturers are also challenged to comply with environmental regulations such as recent hydrofluorocarbon (HFC) phase-down. Natural low GWP refrigerants such as hydrocarbons (HC) are not affected by phase-down policies and their use is expected to increase exponentially. Therefore, it is important to understand how to select the suitable natural refrigerant for each application in order to address the current high standards for energy efficiency.

For this reason, this paper presents a theoretical and experimental comparison between the performance of n-butane (R600) and isobutane (R600a) refrigerants for a built-in household refrigerator. A semi-empirical mathematical model was put forward to predict system energy consumption and its second law efficiency for different system configurations.

2. EXPERIMENTAL WORK

2.1. Refrigeration Circuit

Tests were performed with a typical built-in household fridge originally designed to run on isobutane (R600a) as a working fluid. The refrigeration circuit (Fig. 1a) was comprised of a variable speed 5 cm^3 displacement hermetic reciprocating compressor. A natural draft plate-type roll-bond heat exchanger was used as an evaporator while a natural draft wire-on-tube heat exchanger was used as a condenser. Suction (point 1) and discharge (point 2) pressures were measured by strain-gage absolute pressure transducers with a measurement uncertainty of 0.1% of the full scale. In addition, suction and discharge temperatures were measured by T-type thermocouples (±0.2°C uncertainty) both installed at 100 mm from compressor shell. Additional T-type thermocouples were used to measure the refrigerant temperature at condenser inlet (point 3), condenser outlet (point 4), capillary tube inlet (point 5), evaporator inlet (point 6), and evaporator outlet (point 7).

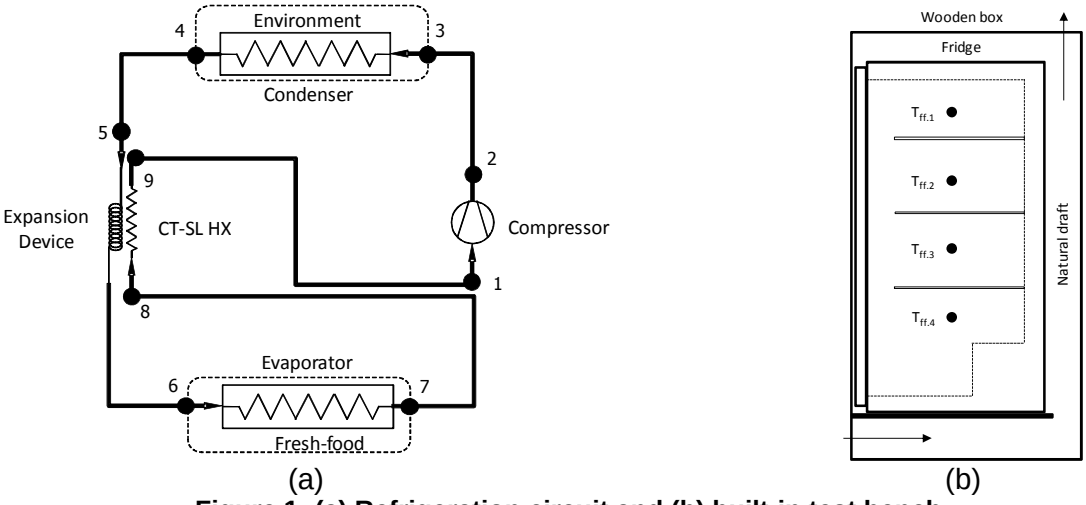

Figure 1: (a) Refrigeration circuit and (b) built-in test bench

The fresh-food compartment temperature was measured by four T-type thermocouples placed in cabinet shelves (Fig. 1b). The refrigerator was mounted inside a wooden box and placed in an environmental chamber with controlled air temperature (±0.5°C uncertainty) and relative humidity (±2.7% uncertainty). The chamber temperature was measured by 4 T-type thermocouples installed around the wooden box. System power consumption was measured by a digital power analyzer with an uncertainty of 0.1% of the full scale.

2.2. Experimental Procedure

Energy consumption tests were performed at two ambient temperatures (16°C and 32°C) and two thermostat positions (hot and cold) in accordance with IEC62552-3/2015. The energy consumption was computed by integrating the overall power consumption during running time. For each ambient temperature, all relevant variables (e.g.: energy consumption, running time ratio, evaporating and condensing pressures) were computed at a reference value of T_{ff} = 4°C by a linear interpolation between results gathered at each thermostat position (hot and cold). The overall energy consumption result was then computed as an average between results gathered at 16°C and 32°C. Additional tests were performed to investigate the influence of (i) compressor speed, (ii) refrigerant fluid (n-butane or isobutane) and (iii) evaporator overall heat transfer coefficient. The test matrix is presented on Table 1.

Table 1. Test matrix

Run	T_{amb} [°C]	N_{comp} [RPM]	Refrigerant	Evap. Fan [Y/N]
1	16	1300	isobutane	No
2	32	1300	isobutane	No
3	16	950	isobutane	No
4	32	950	isobutane	No
5	16	950	n-butane	No
6	32	950	n-butane	No
7	16	950	n-butane	Yes
8	32	950	n-butane	Yes

3. MATHEMATICAL MODEL

A semi-empirical steady-state mathematical model was put forward to assess the performance of typical household built-in refrigerator. The model consists on first principle algebraic equations adjusted with experimental data to the system under investigation. The formulation for the vapour compression model follows closely that proposed by Hermes et al. (2009). The model was used to perform a loss inventory for the baseline system in order to identify what are the main parameters which depreciate system performance. In addition, the model was used to investigate the influence of compressor speed, refrigerant fluid and heat exchangers overall heat transfer coefficient on the system performance represented here by its second law efficiency as show on Eq. (1).

$$\eta_{2nd} = \frac{COP_{actual}}{COP_{carnot}} \quad \text{Eq.(1)}$$

The coefficient of performance of the actual system, COP_{actual} [-], was defined as the ratio between the cooling capacity, $\dot{Q}_{ev}$ [W], and the system power consumption, $\dot{W}_{sys}$ [W], as shown on Eq.(2).

$$COP_{actual} = \frac{\dot{Q}_{ev}}{\dot{W}_{sys}} \quad \text{Eq.(2)}$$

3.1. Vapor Compression System Model

The refrigeration system was divided into four component sub-models: (i) compressor, (ii) capillary tube-suction line heat exchanger (CT-SL HX), (iii) condenser and (iv) evaporator (Hermes et al., 2009). The simulation model was devised assuming that the refrigeration system operates at steady-state conditions while the effect of thermostat is accounted for by the compressor running time ratio (ratio between total thermal load and cooling capacity) assessed by a global energy balance in the compartment. The components sub-models are presented as follows:

3.1.1. Reciprocating compressor

The main compressor parameters to be assessed by the sub-model are compressor mass flow rate, $\dot{m}_k$ [kg·s^{-1}] and power consumption $\dot{W}_k$ [W]. The former is calculated as follows:

$$\dot{m}_k = \frac{NV_k}{v_1}\eta_v \quad \text{Eq. (3)}$$

where V_k [m^3] is the compressor displacement, N [s^{-1}] the compressor frequency, v_1 [m^3·kg^{-1}] the refrigerant specific volume at compressor suction line evaluated at evaporating pressure p_{ev} [Pa] and suction line temperature T_1 [°C]. The volumetric efficiency η_v[-], is expressed by a polynomial equation whose coefficients were fitted to the manufacturer calorimeter test data.

Compressor power consumption can be computed as a function of compressor specific isentropic work $w_s = h_{2s} - h_1$ [J·kg^{-1}], mass flow rate and compressor overall efficiency η_g [-] (which accounts for thermodynamic, mechanical and motor efficiencies):

$$\dot{W}_k = \dot{m}_k \frac{(h_{2s} - h_1)}{\eta_s} + UA_k(T_2 - T_{amb}) \quad \text{Eq. (4)}$$

where h_1 [J·kg^{-1}] and h_{2s} [J·kg^{-1}] are, respectively, the refrigerant specific enthalpies at the beginning and at the end of the isentropic compression process, UA_k [W·°C^{-1}] the compressor shell overall heat transfer coefficient, T_2 [°C] the refrigerant temperature at compressor discharge line and T_{amb}[°C] the climate test ambient temperature.

3.1.2. Capillary tube suction-line heat exchanger

An overall energy balance in the capillary tube suction line heat exchanger (CT-SL HX) provides an expression for the refrigerant specific enthalpy at evaporator inlet h_6 [J·kg^{-1}].

$$h_6 = h_7 - (h_1 - h_5) \quad \text{Eq. (5)}$$

where h_5 [J·kg^{-1}] is the specific enthalpy of refrigerant at capillary tube inlet, assessed by discharge pressure p_{cd} [Pa] and refrigerant temperature at capillary tube inlet $T_5 = T_{cd} - \Delta T_{sub}$. The sub cooling degree, ΔT_{sub} [°C], was measured during the baseline energy consumption tests and kept constant during all simulations. In a similar way, h_7[J·kg^{-1}], the specific enthalpy of refrigerant at evaporator outlet was computed considering the evaporating pressure p_{ev} [Pa] and refrigerant temperature at evaporator outlet $T_7 = T_{ev} + \Delta T_{sup}$. T_{ev} [°C] is the evaporating temperature and the superheating degree, ΔT_{sup} [°C], was measured during the baseline energy consumption tests and kept constant during all simulations. Finally, the specific enthalpy at compressor inlet was evaluated considering the evaporating pressure and the refrigerant temperature at compressor suction line (point 1 – Fig. 1). The CT-SL HX effectiveness ε_{iHX} [-], calibrated during baseline energy consumption, was used to calculate the refrigerant temperature at compressor suction line T_1 [°C] as follows:

$$T_1 = \varepsilon_{iHX} T_5 + (1 - \varepsilon_{iHX}) T_7 \quad \text{Eq. (6)}$$

3.1.3. Heat exchangers: condenser and evaporator

Both condenser and evaporator are natural-draft heat exchangers. The heat exchangers mathematical model was based on mass and energy conservation principles applied to refrigerant and air side. The mathematical model was devised in a way that the heat exchangers overall heat transfer coefficients (UA) could be calibrated based on experimental measurements gathered when the energy consumption test was carried out. The heat rejected by the condenser was computed as follows:

$$\dot{Q}_{cd} = \dot{m}_k(h_3 - h_4) = UA_{cd}(T_{\mathrm{cd}} - T_{\mathrm{amb}}) \quad \text{Eq. (7)}$$

where h_3 [J·kg^{-1}] and h_4 [J·kg^{-1}] are, respectively, the specific enthalpies at condenser inlet and outlet. Specific enthalpy at condenser outlet is assessed using the temperature at condenser outlet $T_4 = T_{cd} - \Delta T_{sub}$. During model calibration, the specific enthalpy at condenser inlet h_3 [J·kg^{-1}] was computed by considering the pressure and temperature measurements at condenser inlet. In a similar way, the heat absorbed by the evaporator (a.k.a. cooling capacity) was computed from mass and energy balances on the refrigerant side as follows:

$$\dot{Q}_{ev} = \dot{m}_k(h_7 - h_6) = UA_{ev}(T_{\mathrm{ff}} - T_{\mathrm{ev}}) \quad \text{Eq. (8)}$$

Where h_6 [J·kg^{-1}] and h_7 [J·kg^{-1}] are respectively the specific enthalpies at the evaporator inlet and outlet. The specific enthalpy at evaporator outlet is assessed considering temperature at evaporator outlet $T_7 = T_{ev} + \Delta T_{sup}$, where T_{ev}[°C] is the evaporating temperature and ΔT_{sup} the

superheating degree. The specific enthalpy at evaporator inlet, h_6 [J·kg^{-1}], was computed based on the energy and mass balance on the CT- SL HX as shown on the previous section. Equations (3) and (5) can be combined to equation (8) in order to derive empirical values to the overall heat transfer coefficient, UA_{ev}[W·°C^{-1}].

4. RESULTS AND DISCUSSION

The mathematical model was used to assess the performance inventory of the refrigeration unit when moving from an ideal reverse Carnot cycle configuration to the actual baseline system running with R600a. For each case, the second law efficiency was evaluated considering the following assumptions:

i. Carnot cycle ($T_{H,carnot}$ = 305.15 K and $T_{C,carnot}$ = 277.15 K)
ii. Internally reversible system's COP ($T_H = T_{H,carnot}$ + 15 K and $T_C = T_{C,carnot}$ - 12 K)
iii. Reverse Rankine cycle (T_{cd} = 47°C, T_{ev} = -8°C, ΔT_{sub} = 0°C, ΔT_{sup} = 0°C, $s_6 = s_5$, $T_1 = T_{ev}$).
iv. Non-isentropic compression (η_g = 0.68)
v. Isenthalpic expansion ($h_6 = h_5$)
vi. Actual baseline system with non-adiabatic capillary tube ($\varepsilon_{iHX} = 0.83$)

The evaporating and condensing temperatures, the refrigerant temperature at compressor suction line, the compressor efficiency and the internal heat exchanger effectiveness were all evaluated considering the average tests results gathered during the experimental investigation (run 2 on Table 1). As one can see on Fig. 2, the adoption of a natural draft plate-type roll-bond heat exchanger as an evaporator and a natural draft wire-on-tube heat exchanger as a condenser led to a relevant temperature difference on both heat exchangers (ΔT_{cd} = 15°C and ΔT_{ev} = 12°C). As a consequence, the second law efficiency dropped to 49% of its ideal value when the actual heat exchangers were taken into account. Additional efficiency cutback was also observed when considering the reverse Rankine cycle ($\eta_{2nd} = 0.39$), non-isentropic compression ($\eta_{2nd} = 0.26$) and isenthalpic expansion ($\eta_{2nd} = 0.25$). It is worth to mention that the increase in the second law efficiency when the internal heat exchanger is applied ($\eta_{2nd} = 0.26$) was caused by the additional cooling capacity due to the reduction in the refrigerant specific enthalpy at evaporator inlet caused by the non-adiabatic expansion.

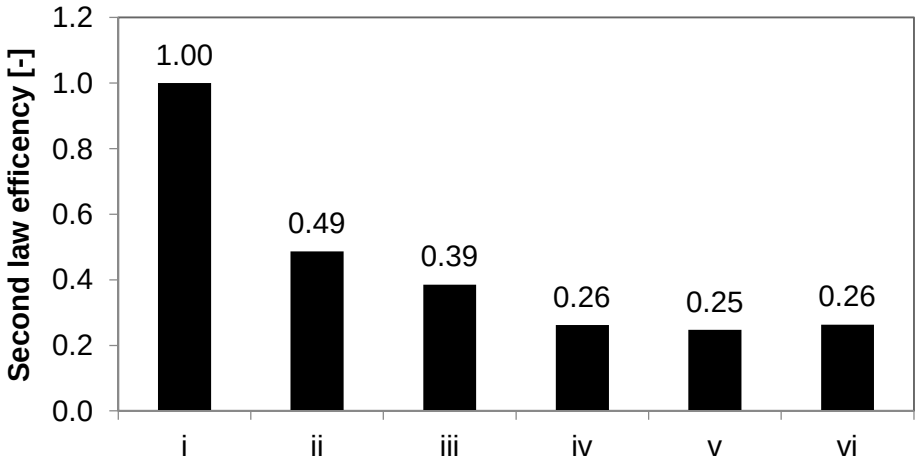

Figure 2: System performance inventory

In order to recovery system efficiency, it is important to understand how each system configuration parameter affects the system performance. As shown on Fig. 2, the most relevant irreversibility on the actual system is caused by the temperature differences on the heat exchangers. In general, there are basically four main parameters that can affect the temperature difference between the hot and cold side heat exchangers during compressor operation: (i) compressor displacement, (ii) compressor speed, (iii) refrigerant and (iv) heat exchanger overall heat transfer coefficient. The influence of each parameter was evaluated as follows.

Fig. 3a presents the influence of compressor speed on the evaporating and condensing temperatures of the actual system running with both isobutane (R600a) and n-butane (R600). As the compressor speed drops, the instantaneous cooling capacity, compressor power and heat rejected by the condenser will decrease. As a consequence, the energy can now be transferred on both heat exchangers over a longer period of time due to the increase in the compressor running time ratio caused by the speed reduction. Assuming that the overall heat transfer coefficient of both heat exchangers are unaffected by the compressor speed, the lower heat transfer rates can now be accomplished by a lower temperature difference between the heat exchangers and the medium from/to where it absorbs/releases energy, leading to an increase in the evaporating temperature and a decrease in the condensing temperature.

System efficiency can be improved by decreasing compressor speed (or displacement) in order to match system cooling capacity with its thermal load. This scenario would lead to the lowest condensing temperature, the highest evaporating temperature and the highest system efficiency considering no additional energy consumption devices (e.g. fans). In practice, however, it is not possible to decrease compressor displacement and speed indefinitely. The first is typically limited by the influence of piston-cylinder leakage on compressor volumetric efficiency while the later by lubricating issues. Therefore, for very low thermal load systems (such as small household refrigerators) even small displacement variable speed compressors running at minimum speed can present excess of capacity (especially at T_{amb} = 16°C). In this scenario, the lower volumic cooling capacity of butane refrigerant (approximately 30% lower than isobutane) can be used as an alternative to a better matching between thermal load and cooling capacity for low thermal load systems. Butane lower volumic cooling capacity has an effect similar to displacement or speed reduction. It increases system running time ratio allowing an even lower temperature difference on both heat exchangers. As a result, the system second law efficiency increases by approximately 3% when replacing isobutane (R600a) by butane (R600).

Another alternative to decrease the temperature difference between both heat exchangers is by increasing condenser and evaporator overall heat transfer coefficients. This result can be accomplished by both area or heat transfer coefficient increase (e.g. forced draft HXs). Fig. 3b presents the influence of evaporator overall heat transfer coefficient on system energy consumption. A similar behavior is observed for the influence of condenser overall heat transfer coefficient on system energy consumption.

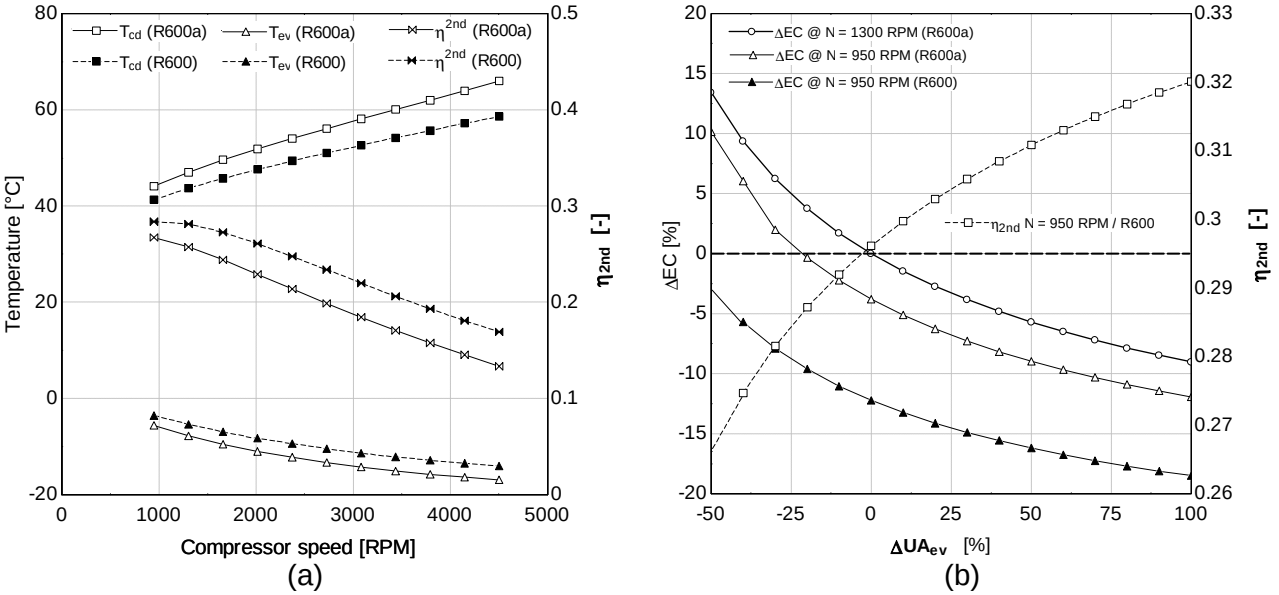

Figure 3: (a) Effect of compressor speed and refrigerant on system performance and (b) effect of UA_{ev} on system performance.

A set of tests (Table 1) was performed in order to validate the conclusions found during the theoretical investigation. The experimental procedure was used to assess the influence of (i) compressor speed, (ii) refrigerant (butane vs. isobutane), (iii) evaporator overall heat transfer coefficient on system energy consumption (Fig. 4a) and running time ratio (Fig. 4b). As one can

see on Fig. 4, when the compressor speed drops from 1300 RPM to 950 RPM, an energy consumption saving about 3% and a RTR increase about 10% percentage points are observed, confirming the predictions found during the theoretical investigation.

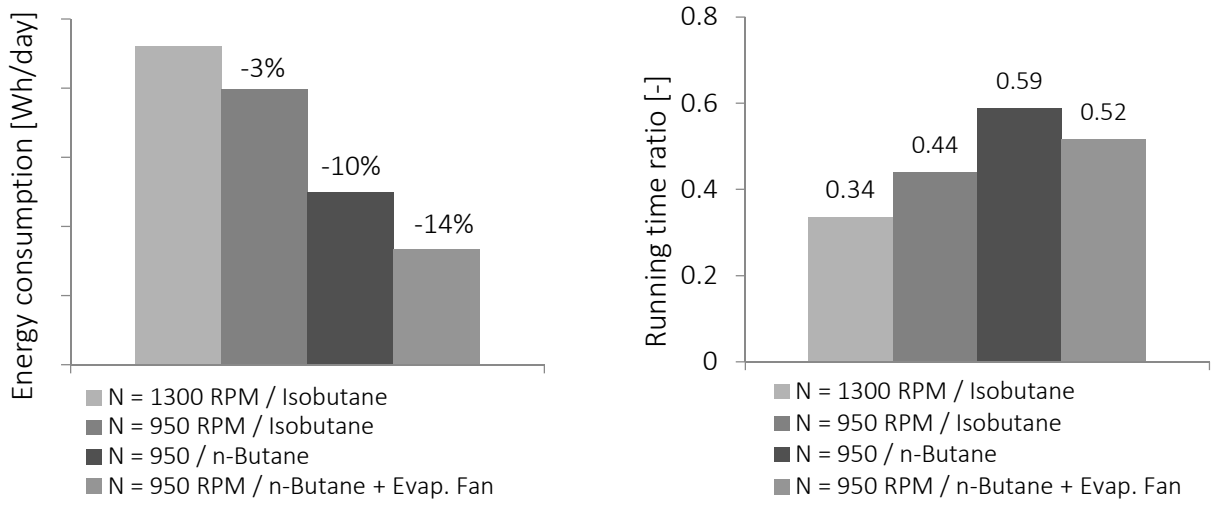

(a) (b)

Figure 4: (a) Energy consumption and (b) running time ratio

When running with butane, the lower system cooling capacity leads to an additional increase in RTR (from 0.44 to 0.59). As a result, the temperature differences in the HXs drop, increasing system second law efficiency resulting in an additional energy consumption reduction about 7%. Finally, the effect of evaporator overall heat transfer coefficient was evaluated by adding a 0.5 W fan to the fresh food compartment. Despite of fan energy consumption, the increase in the evaporator overall heat transfer coefficient surpassed the drawback caused by the fan power consumption. The net result was an energy saving about 4%. In total, an overall energy consumption saving up to 14% was found.

5. CONCLUSIONS

This paper presented a theoretical and experimental analysis of the performance of a built-in household refrigerator originally designed to run with isobutane as a working fluid. A mathematical model was put forward to assess the system performance loss inventory as a function of different system arrangements. It was found that system second law efficiency drops approximately by half when actual natural draft heat exchangers (evaporator and condenser) are taken into account.

The mathematical model was then used to predict the influence of (i) compressor speed, (ii) refrigerant (isobutane vs. butane) and (iii) heat exchangers overall heat transfer coefficient on the evaporating and condensing temperatures and their impact on system performance. It was observed that for low thermal load systems, even low displacement variable speed compressors running at minimum speed may present excess cooling capacity. It was also stated that since compressor speed and displacement cannot be reduced indefinitely, the choice of refrigerant must be taken into account in order to better match system thermal load and compressor cooling capacity. It was observed that due to its lower volumic refrigerant effect, butane refrigerant becomes more suitable for lower thermal load systems such as small household refrigerators, especially those to be tested at low ambient temperatures (T_{amb} = 16°C).

In order to validate the conclusions found during the theoretical investigation, EC tests were performed at two ambient temperatures and two thermostat positions at different system configurations. It was shown that an energy consumption saving about 7% can be achieved by only replacing isobutane (R600a) by butane (R600) as working fluid for low thermal load refrigerators where isobutane compressors present excess of capacity.

ACKNOWLEDGEMENTS

This study was carried out at the Embraco R&D facilities by the Thermal Systems Engineering team. The authors are grateful to Mr. Fabian Fagotti for his contributions to the quality of the manuscript. Thanks are also addressed to Liebherr Hausgeräte Ochsenhausen GmbH.

NOMENCLATURE

Nomenclature

CT	capillary tube
COP	coefficient of performance (-)
EC	energy consumption (Wh·day^{-1})
HX	heat exchanger
h	specific enthalpy (J·kg^{-1})
$\dot{m}$	mass flow rate (kg·s^{-1})
N	compressor frequency (s^{-1})
p	pressure (Pa)
$\dot{Q}$	heat transfer rate (W)
RTR	running time ratio (-)
SL	suction line
s	specific entropy (J·kg^{-1}·K^{-1})
T	temperature (°C)
t	time (s)
UA	overall heat transfer coefficient (W/°C)
V	compressor displacement (m^3)
v	refrigerant specific volume (m^3·kg^{-1})
w	specific work (J·kg^{-1})
$\dot{W}$	power (W)

Greek

η	efficiency (-)
Δ	difference
ε	effectiveness (-)

Subscripts

amb	ambient
C	cold
cd	condenser
ev	evaporator
ff	fresh-food compartment
g	global
H	hot
iHX	internal heat exchanger
k	compressor
on	compressor on time
off	compressor off time
s	isentropic
sys	system
sub	sub cooling
sup	superheating
v	volumetric

REFERENCES

Hermes, C. J. L., Negrão, C. O. R., 2011. Energy and cost savings in household refrigerating appliance: A simulation based design approach. Applied Energy, 88, 3051-3060.

Melo, C., Silva, L.W., 2010. A perspective on energy savings in household refrigerators. Sustainable refrigeration and heat pump technology conference, Stockholm, Sweden.

Straub, M., 2018. Alternative Refrigerants For Household Refrigerators. International Refrigeration and Air Conditioning Conference, West Lafayette,

IEC62552-3. Household refrigerating appliances – Characteristics and test methods – Part 3: Energy consumption and volume. International Electrotechnical Commission, Geneva, Switzerland, 2015.

Hermes, C. J. L., Melo, C., Knabben, F. T. & Gonçalves, J. M., 2009. Prediction of the energy consumption of household refrigerators and freezers via steady-state simulation. Applied Energy, 86, 1311-1319.

Association of Home Appliance Manufacturers, 2015. Promote Market Based Solutions to Increase Efficiency,http://www.aham.org/AHAM/News/Latest_News/Promote_Market_Based_Solutions_to_Increase_Efficiency_says_IRHMA.aspx. (accessed on 26 January 2019).

Manuscript ID: 1273
DOI: 10.18462/iir.icr.2019.1273

Characterisation of the behaviour of a CO_2 water/water heat pump for hot water generation

J.R. GARCÍA-CASCALES, R. MOLINA-VALVERDE, F. ILLÁN-GÓMEZ, F.J. SÁNCHEZ-VELASCO, V.F. SENA-CUEVAS

DITF, ETSII, Universidad Politécnica de Cartagena, Dr Fleming, s/n
30202 Cartagena, Murcia, Spain
e-mail: jr.garcia@upct.es, rmolinavalverde@gmail.com, fernando.illan@upct.es, fjavier,sanchez@upct.es, victor.sena@edu.upct.es

ABSTRACT

In this work, a model to analyse a CO_2 water/water heat pump for the generation of hot water is described. Once the heat pump has been presented, the models employed to characterise the different components of the system will be introduced paying special attention to the heat exchangers modelling. Its originality resides in that the model is a cell-by-cell method which relies in the iterative calculation of the heat transfer area of each cell. The model is validated with experimental data. These models are included in several TRNSYS components which allow dynamically simulating the heat pump and obtaining its seasonal performance. After presenting these results, some conclusions are finally drawn.
Keywords: Refrigeration, Carbon Dioxide, Compressors, COP, Evaporators, Energy Efficiency.

1. INTRODUCTION

The use of heat pumps for domestic hot water generation has been the objective of several researchers over the last years. The high COP makes them quite appealing as they are a competitive technology when they are compared to conventional system even those including renewable energies. This work is structured as follows. Firstly, the model proposed to characterise the heat pump is presented, after that the model is integrated in a Trnsys model for a system for the generation of domestic hot water. This is compared with a conventional system formed by a set of solar collectors assisted by a natural gas heater. The comparison is done from the point of view of the primary energy consumption and de CO_2 emission. Some conclusions are finally drawn.

2. HEAT PUMP MODEL

The heat pump considered in this work corresponds to a transcritical cycle with CO_2 working as refrigerant with a tank at mid pressure which allows vapour injection before the compressor inlet (Fig. 1). A liquid-to-vapour heat exchanger let increase the subcooling/superheating if necessary. The compressor is a Dorin CD 300H, the heat exchangers are Swep plate heat exchangers, the evaporator is a BX8Tx26, the gas cooler is a B16Hx4, the liquid to vapour heat exchanger is a B17Hx4, the back pressure and the thermostatic pressures are Carel electronic valves.

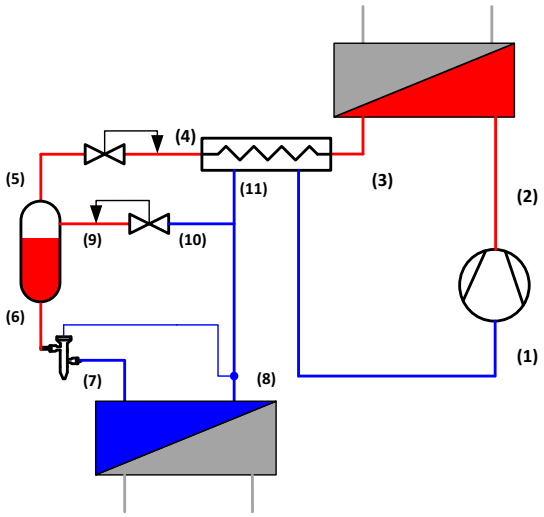

Figure 1: Schematic of the heat pump studied

The models adopted for each component is described in what follows. Firstly, the inlets and outlets in each component have to be identified as they will condition the approach adopted for each device.

In the compressor, the inputs are the suction and discharge pressures, the first one is imposed by the evaporator and the second by the back pressure valve after the gas cooler. The inlet enthalpy is also known. The outputs are the mass flow rate and the outlet enthalpy. Considering the AHRI polynomials provided by the manufacturer mass flow rate and power supplied to the fluid may be determined by means of

$$y = C1 + C2 \cdot T_o + C3 \cdot P_c + C4 \cdot T_o^2 + C5 \cdot T_o \cdot P_C + C6 \cdot P_C^2 + C7 \cdot T_O^3 + C8 \cdot T_o^2 \cdot P_C + C9 \cdot T_o \cdot P_C^2 + C10 \cdot P_C^3 \quad \text{Eq. (1)}$$

where T_o is evaporation temperature (°C), P_c is discharge pressure (bar), and the coefficients are given in Table 1.

Table 1. Polynomial coefficient for characterisation of the compressor behaviour.

	C1	C2	C3	C4	C5
$\dot{m}_r$ (kg/s)	0.0400442	0.0011412	-0.000197	1.08E-05	-1.76E-06
$\dot{P}$ (W)	-1904.943	-77.20901	78.168193	-1.032906	1.1945615
	C6	C7	C8	C9	C10
$\dot{m}_r$ (kg/s)	5.48E-07	0	0	0	0
$\dot{P}$ (W)	-0.529691	-0.004792	0.0052196	-0.003218	0.0013893

this values are given at saturation, so they are density corrected by using

$$\frac{\dot{m}_r}{\dot{m}_{r\,sat}} = 1 + 0.75\left(\frac{\rho}{\rho_{g_{sat}}} - 1\right) \quad \text{Eq. (2)}$$

$$\frac{\dot{P}}{\dot{P}_{sat}} = 1 + 0.75\left(\frac{\rho}{\rho_{g_{sat}}} - 1\right) \quad \text{Eq. (3)}$$

so enthalpy at the outlet is determined by

$$h_{out} = h_{in} + \frac{\dot{P}}{\dot{m}} \quad \text{Eq. (4)}$$

The model used for the evaporator is that introduced in (García-Cascales et al., 2019), its inputs are the inlet enthalpies of the fluids, inlet pressure of the secondary fluid, mass flow rates of the fluids and the superheating. In this model, the heat exchangers are discretised into two parts, the two-phase part and the single phase part. The two phase part is divided into N cells of equal quality

difference and the single phase part is divided into N cells of equal temperature difference. Pressure at the inlet is initially assumed as the average value between a theoretical maximum pressure corresponding to the saturation pressure at the secondary fluid inlet temperature (p_{low}) and an arbitrary low temperature (p_{high}).
Thus, with this pressure at the inlet and the inlet enthalpy, pressure drop is evaluated and therefore outlet pressure and enthalpy considering that quality difference is known, thus the heat exchanged in the cell is calculated. The outputs of each cells are the inlet of the following one. So, all variables are evaluated at the nodes. Assuming that the heat absorbed by the refrigerant is the same as that given by the secondary fluid, the temperatures (enthalpies) of the secondary fluid at the different nodes are calculated. After this, the heat transfer coefficients are determined and the heat transfer area is calculated ($A_{calculated}$) and compared with the actual one (A_0), and finally refrigerant pressure at the inlet is evaluated considering the following criterion

$$p_{high} = p_{ri}\ if\ A_0 > A_{calculated}$$
$$p_{low} = p_{ri}\ if\ A_0 < A_{calculated}. \quad \text{Eq. (5)}$$

$$p_{ri} = \frac{p_{low} + p_{high}}{2} \quad \text{Eq. (6)}$$

so the process is repeated until convergence is reached.
The liquid to vapour heat exchanger and the gas cooler are both single phase heat exchangers in which the inputs are the inlet enthalpies, pressures and the mass flow rates of both fluids. In this model, the hot fluid outlet temperature is assumed as the average value between the maximum temperature (inlet temperature) and the minimum possible temperature (the cold fluid inlet temperature). Following the methodology introduced in (Molina-Valverde, 2019) the enthalpy of the hot fluid at the outlet is also determined (at the assumed outlet temperature), so the heat exchanged in the heat exchanger can be evaluated. After dividing the exchanger into N elements which exchange the same amount of heat, the pressure drop at each cell and the enthalpies at each node at refrigerant side are calculated. Then, the secondary fluid enthalpy at each node can be evaluated as well. As was did with the evaporator, the htc of each cell can be determined and so the heat transfer area. Finally, the evaluated area is compared to the actual one and the outlet enthalpy of the hot fluid is recalculated considering

$$h_{high} = p_{ri}\ if\ A_0 < A_{calculated}$$
$$h_{low} = p_{ri}\ if\ A_0 > A_{calculated}. \quad \text{Eq. (7)}$$

$$h_{ri} = \frac{h_{low} + h_{high}}{2} \quad \text{Eq. (8)}$$

The rest of the elements composing the heat pump are easily determined. Pressure valves impose the pressure at the gas cooler outlet and at the tank. The thermostatic expansion valve imposes superheating.
The mass flow rates and enthalpies at the tank outlets are determined by means of a mass and an energy balances, considering, that the enthalpy, pressure and mass flow rate at the tank inlet are all known.
The heat transfer coefficients correlations used in the calculations presented in this work are Cooper correlation (1984) for the two phase boiling htc and Bogaert and Bölcs (1995) for single phase one.
The pressure drop correlations considered are Churchill correlation (1972) and Chisholm (1991) for single and two phase flow respectively. All the models presented have been implemented in different Trnsys17 components and linked to model the heat pump presented in Fig. 1.

3. HEAT PUMP MODEL VALIDATION

Several tests have been performed in a heat pump instrumented in our lab. The conditions of the tests used here for validation are included in Table 2. The tests are defined by the temperature

difference in the both cold and hot sinks, the gas cooler pressure and liquid receiver pressure.

Table 2. Tests considered in this study.

Test	Tsec in	Tsec out	Tsec in	Tsec out	pgc in	ptank
1	12	7	30	35	75	45
2	12	7	20	40	80	45
3	12	7	30	40	80	45
4	20	15	20	30	80	45
4 repeat.	20	15	20	30	80	45
6	12	7	20	30	80	45
7	12	7	30	40	80	45

In Fig. 3, the estimated values of the heating capacity, cooling capacity compressor power consumption, and COP of the heat pump are represented against the experimental ones. In Figure 4, values provided be the model of the outlet temperature of the gas cooler, the evaporation temperature, and the inlet pressure at the evaporator are compared with the experimental ones. All predicted values are between the ±10% lines also depicted in these Figures. Only two values of the COP show a difference a little bit greater than 10%. The results obtained are good enough and make think that the model of the heat pump is suitable to be introduced in a more complex one that let us model a domestic hot water system.

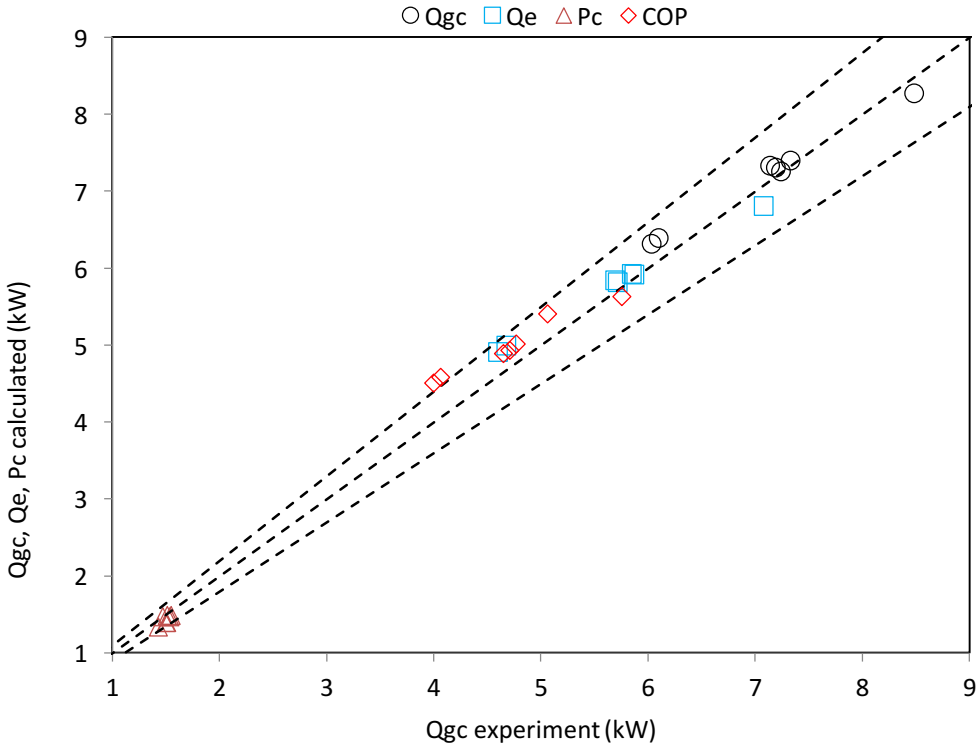

Figure 3: Comparison between the experimental values and calculated the calculated ones of the heating capacity, Q_{gc}, cooling capacity, Q_e, the compressor consumption, P_c, and the COP

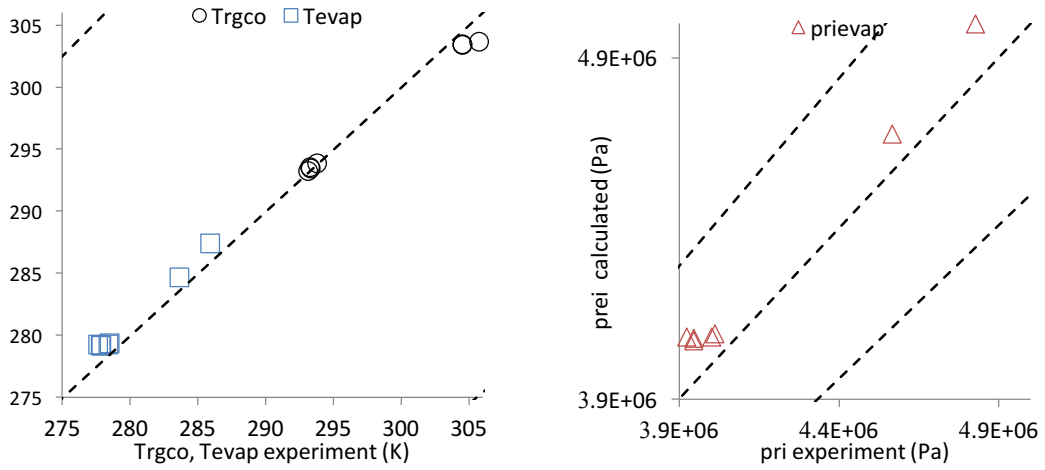

Figure 4: Comparison between the experimental values and the calculated ones of: Left: outltet refrigerant temperature in the gas cooler, T_{rgco}, and evaporation temperature, T_{evap}, right: inlet pressure at the evaporator p_{rievap}

4. DOMESTIC HOT WATER GENERATION SYSTEMS

The previous model is used to compare the consumption of a DHW system based on a heat pump and an already conventional system based on thermal solar energy. Both systems are supported by a natural gas heater. They have been designed to satisfy the needs of a single-family home. In Figure 5, the system based on the CO_2 heat pump modelled with Trnsys is depicted. In Figure 6 the system based on Solar Energy is displayed.

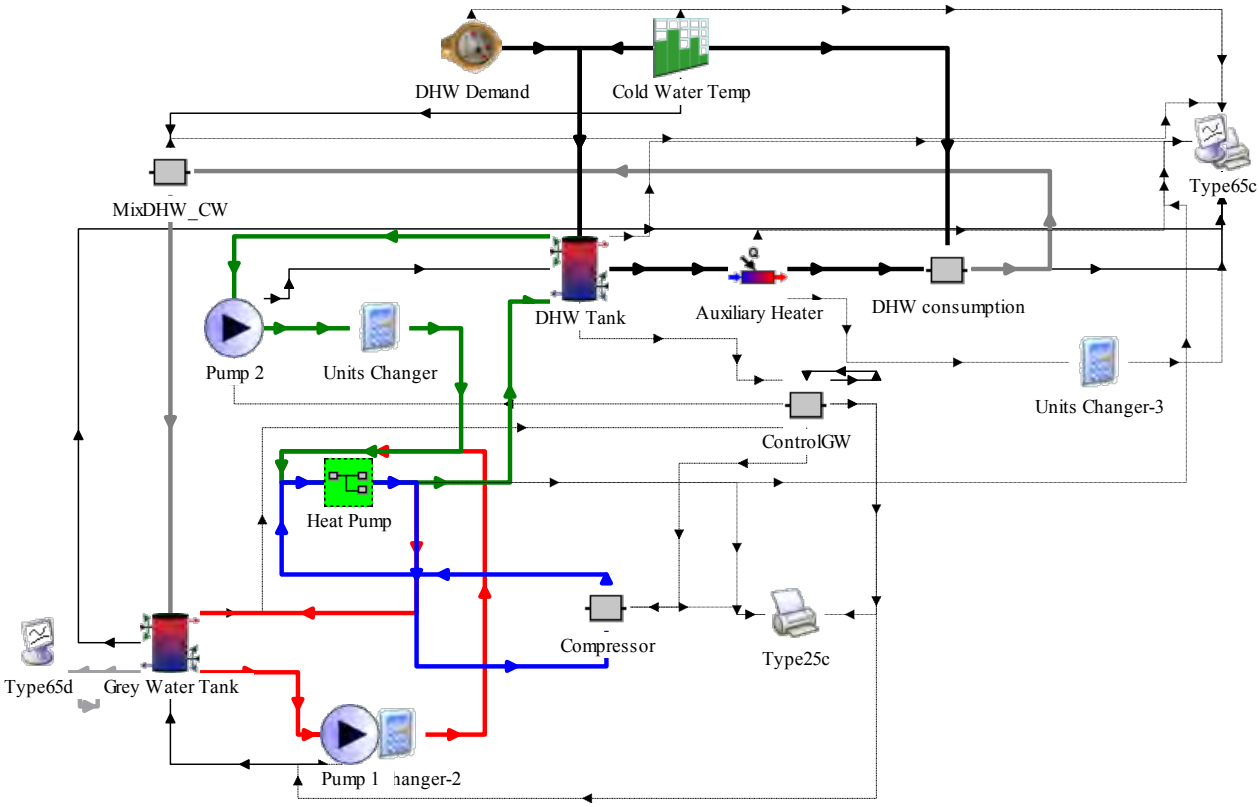

Figure 5: DHW system based on a heat pump assisted by an auxiliary heater

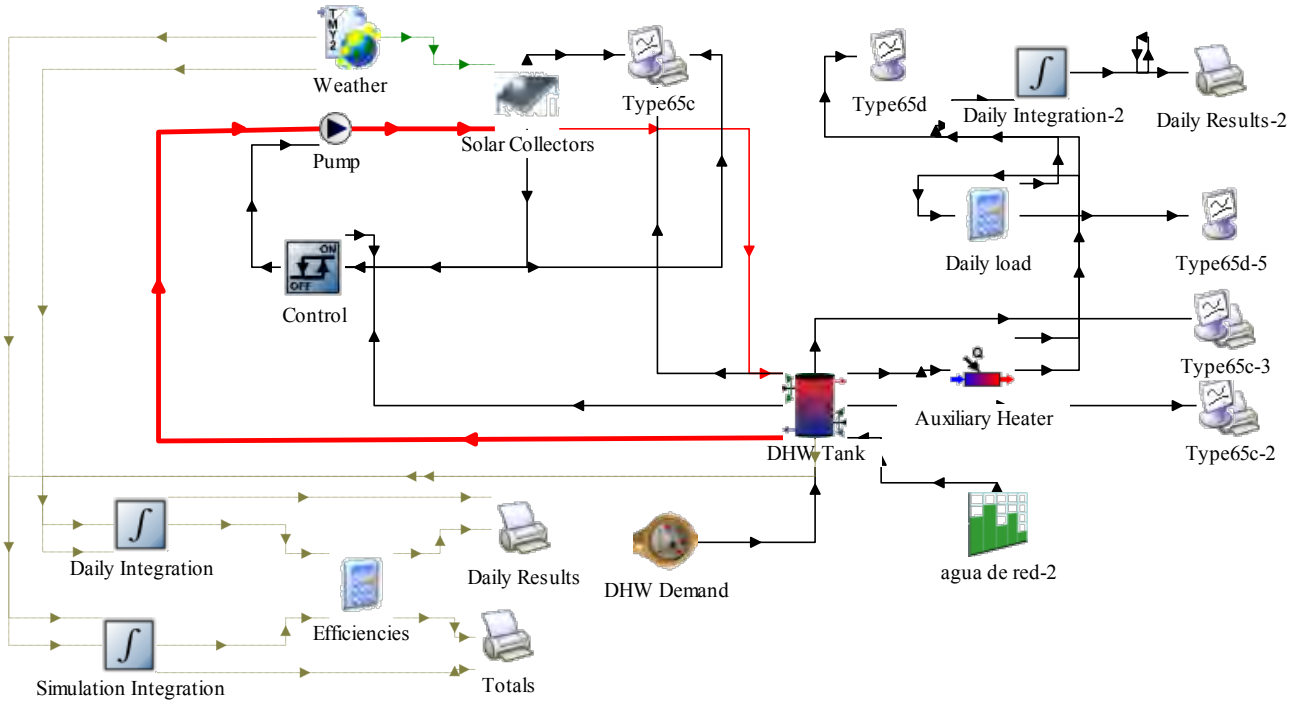

Figure 6: DHW system based on a solar system assisted by an auxiliary heater

The demand considered in this problem is that shown in Figure 7. This is an arbitrary distribution considering Spanish standards. The temperature of drinking water coming from the network is that in Fig. 8. The values in the Figure correspond to the uniform distribution considered by Trnsys in the simulations which is obtained by means of the monthly average values registered for the Region of Murcia, Spain.

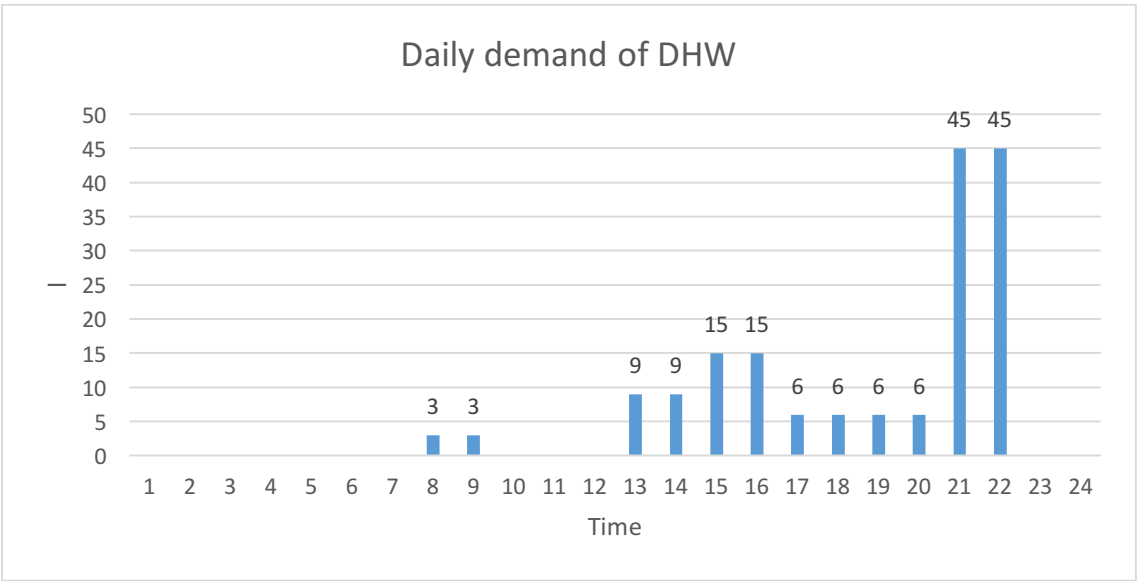

Figure 7: Daily demand considered in the simulations

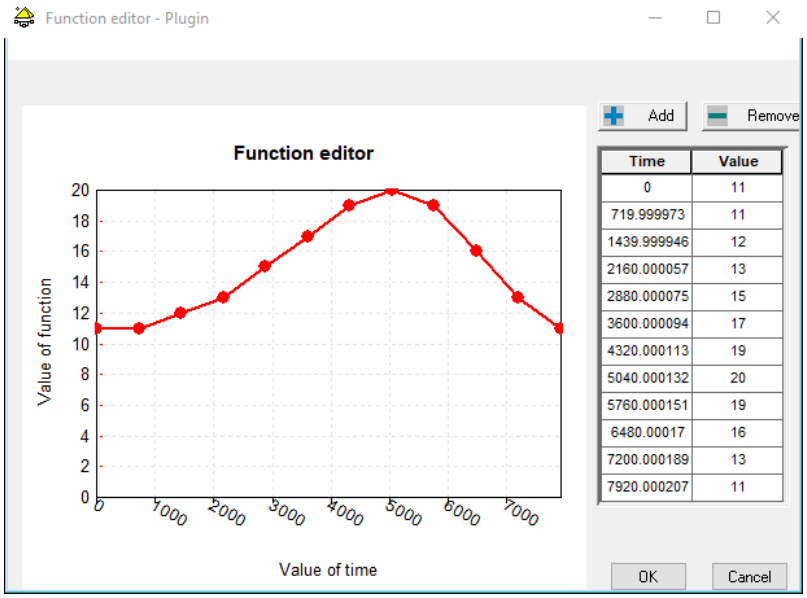

Figure 8: Network water temperature in the Region of Murcia

Both systems have been studied for a whole year and have been compared in terms of primary energy consumption and CO_2 emissions. The indexes used to calculate the primary energy consumed and the CO_2 emissions produced by each system are those published by the Spanish Ministry of Industry, Energy and Tourism in 2016 according to the yearly energy consumption of the country. The coefficients are in Table 3. The results displayed in Figure 9 and 10 show that the primary energy consumption and the CO_2 emissions are greater in the case of the solar system and the heat pump modelled in this study.

Table 3. Conversion factors for the calculation of primary energy consumption and CO_2 emissions

	Conversion factors
Conventional electricity in the peninsula	2.368 kWh primary energy/kWh final energy
Natural gas	1.195 kWh primary energy/kWh final energy
CO_2 coefficient for electricity	0.28 kg CO_2/kWh
CO_2 coefficient for natural gas	0.22530522 kg CO_2/kWh

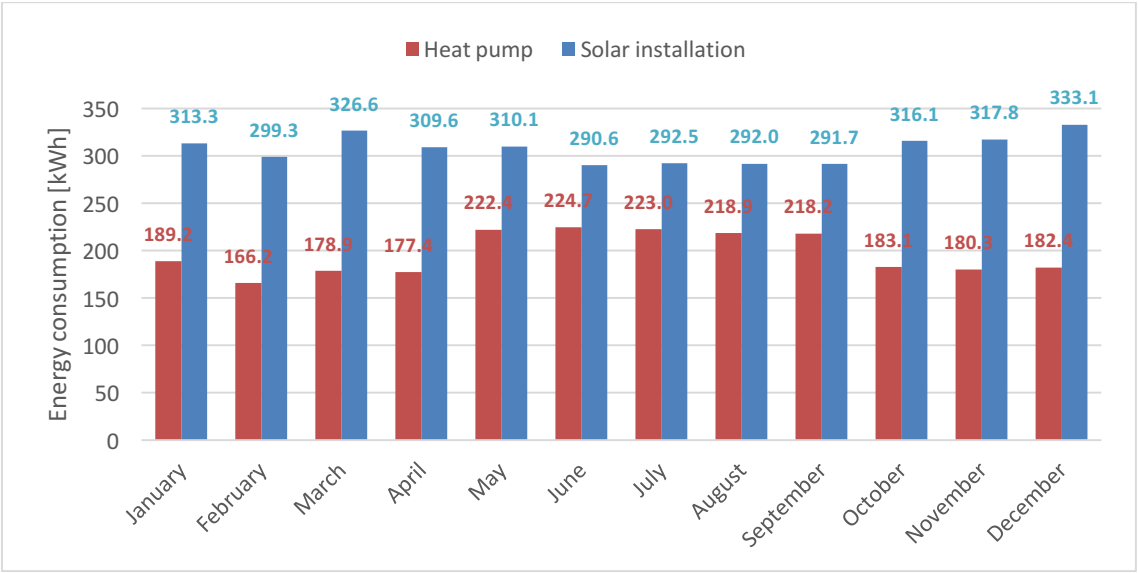

Figure 9: Comparison between the primary energy consumed by the DHW installations

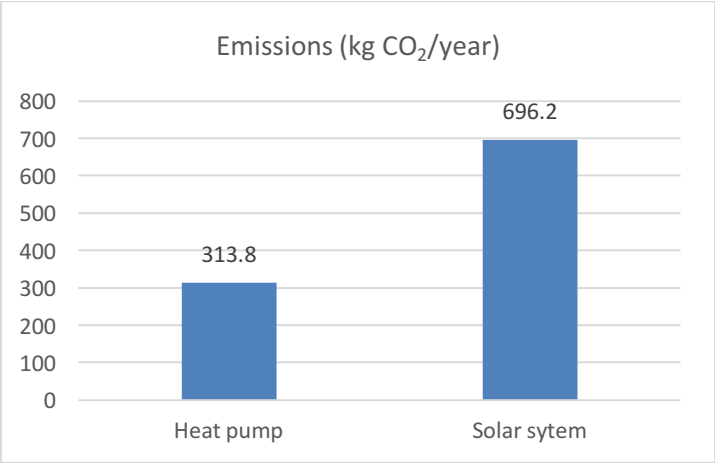

Figure 10: Annual CO_2 emissions of the DHW installations

5. CONCLUSIONS

In this work, a model to characterise the behaviour of a heat pump have been presented. This has been programmed in fortran to create several Trnsys components which has allowed its validation against some experimental values obtained in our lab. After, it has been used to model a heat pump for the production of domestic hot water for a single-family home and compared to a conventional solar system. The solutions studied consider a support heater to satisfy the demand whenever the heat pump or the solar system are not capable. The results show that the heat pump system consumption in terms of primary energy and the CO_2 emissions are both greater in the case of the solar system. As final conclusion, this contribution demonstrates that the heat pump for the production of DHW is a competitive technology at least as far as the systems considered here is concerned.

ACKNOWLEDGEMENTS

This work has been financed by the the Ministry of Economy, Industry and Competitiveness and the European Regional Development Fund through projects ENE2014-53311-C2-1-P and ENE2017-83665-C2-2-P.

REFERENCES

Bogaert, R. Bölcs, A., 1995. Global performance of a prototype brazed plate heat exchanger in a large Reynolds number range, Experimental Heat Transfer 8, 293-311.

Chisholm, D., Wanniarachchi, A., 199.1Layout of plate heat exchangers, ASME/JSME Thermal Engineering Proceedings, vol. 4, New York, pp. 433-438.

Churchill, S. W., 1972. Friction-factor equation spans all fliud-flow regimes.

Cooper, M.G., 1984, Heat flow rates in saturated nucleate pool boiling, Advances in Heat Transfer 16, 157-239.

García-Cascales, J.R., Molina-Valverde R., Illán-Gómez, F., Sánchez-Velasco, F.J., Sena-Cuevas, V., 2019. To be published.

Manuscript ID: 1287
DOI: 10.18462/iir.icr.2019.1287

Active control of external volume flow rates for single effect absorption chillers

Stefan PETERSEN, Walther HÜLS, Christopher PAITAZOGLOU, Jan ALBERS

Technische Universität Berlin,
Berlin, 10587, Germany, stefan.petersen@tu-berlin.de

ABSTRACT

Energy efficient absorption chiller cooling assemblies (ACCA) ought to include active speed control of pumps and fans and heat rejection devices as well. Three external circuit pumps can be controlled actively to minimize auxiliary energy consumption. According to monitoring data of a field test with 25 absorption chillers in 16 installations, up to 80 % of auxiliary electric energy consumption is caused by the cooling water pump and the cooler.
Reducing a volume flow rate by reducing fan or pump speed by 50% leads theoretically to a reduction of 87% in electricity consumption for the pump/fan. In practice within the field test, a reduction of up to 65% is attained and has been proven successfully by control of reject heat and chilled water cycle pump. Control of hot water flow has a more complex, but promising potential. Lowering e.g. hot water flow rate leads to higher set temperatures for the cooler and/or lower cooling water flow rates, thus saving electric energy.
Keywords: efficiency, cooling, sorption, field test, measurement, electricity, cooler, pump

1. INTRODUCTION

Absorption chillers, in the second half of last century were well known as energy efficient, environmentally friendly, long durable and base load supplying chillers. Nevertheless, investment costs were extremely high, space effort was much higher than for compression chillers and dynamic behaviour was meant to be absent. None of these characteristics may still prove reliability.
Based on the upper mentioned qualities, especially environmental friendliness, sorption technologies went in the focus of research and development, increasing the market share in Europe for solar cooling and multi-generation energy systems, such as combined heat, power and cooling applications (PolySMART, 2010), (Henning, 2004). Besides thermal efficiency improvements and cost reduction of absorption chillers, system efficiency is a main target to cope with. Therefore recent development projects have included low hydronic efforts (i.e. pressure differences) in the heat exchanger design and high flexibility due to wide range of possible supply volume flows (Petersen et al., 2013). Although speed controlled pumps are state of the art in heating systems, in cooling systems they are still not commonly used discarding the potential offered by load adjusted volume flow rates. Theoretical analysis point out a potential of nearly 75% of energy savings for the chilled water circuit based on senseful and constant temperature difference control of the chilled water pump (Petersen et al., 2019). Based on actual figures for state of the art efficiencies of compression chiller systems (including reject heat efforts and chilled water pumping) and load spreading in building application according to (DIN18599-7, 2018), (Eurovent, 2018), approximately 75% of electricity consumption can directly be saved by operating the chilled water pump with variable speed. Although theoretically hydronic effort and volume flow rate have a cubic dependency, a decreasing pump efficiency in part load has to be taken into account. Nevertheless, the net electrical effort can be reduced due to the lower pressure difference in part load as compared to full load conditions (see table 1).

Table 1: potential of electricity saving, chilled water pump (Petersen et al., 2019)

		Without flow rate control (constant speed)	With flow rate control (load distribution related to Eurovent)			
Load	%	100	100	75	50	25
Operating hours	h	1500	45	495	615	345
Volume flow rate	m³/h	27,7	27.7	20.8	13.9	6.9
Pressure drop	kPa	6	60	34	15	4
Efficiency	%	67	67	58	45	25
Electric power	W	689	689	338	129	29
Electric energy	kWh/a	1034	31	167	80	10
			288			
Saving	kWh/a		747			

In an ACCA there are three supply circuits and therefore three flow rates to control: hot, reject heat and chilled water flow. During a field test for absorption chillers, including 25 chillers being installed in 16 different locations throughout Germany, control strategies for variable volume flow rates were tested (Petersen et al., 2019), (Paitazoglou et al., 2018). Due to a special heat exchanger design a wide range of flow rates between 20 % and 150 % of the nominal flow rates are allowed by the chillers under investigation (BINE, 2012).

2. CONTROL STRATEGIES

After introducing the general control algorithm for the chiller in section 2.1 some project and operation control results are highlighted in section 2.2, focusing on the reject heat circuit. In section 2.3 research and development of a controlled hot water pump to safe energy on the reject heat side also is explained.

2.1. ACCA-Control with Variable Flow Rates

During the research and demonstration project a model based multivariable control strategy for the control of ab- and adsorption chillers has been developed and implemented into a programmable logic controller (PLC). The so-called CE-controller uses an improved characteristic equation method (Albers, 2018; Albers and Ziegler, 2016). According to this method the cooling capacity $\dot{Q}_E$ of an absorption chiller is a linear function of a modified characteristic temperature difference $\Delta\Delta t^*$.

$$\Delta\Delta t^* = t_{Di} \cdot (1 - K_1) - t_{Ai} \cdot (1 - K_2) + t_{Eo} \cdot (1 - K_3) \quad \text{Eq. (1)}$$

$$\dot{Q}_E = K_4^* \cdot \Delta\Delta t^* \quad \text{Eq. (2)}$$

$$\dot{Q}_D = K_5^* \cdot \Delta\Delta t^* + K_6 \cdot \Delta\Delta t_{min}^* \quad \text{Eq. (3)}$$

$$\Delta\Delta t_{min} = K_1 \cdot t_{Di} - K_2 \cdot t_{Ai} + t_{Eo} \cdot (K_3 - 1) \quad \text{Eq. (4)}$$

The modified characteristic temperature difference $\Delta\Delta t^*$ combines hot and cooling water inlet temperature (i.e. t_{Di}, t_{Ai}) and chilled water outlet temperature t_{Eo}. The coefficients K_1 to K_3 in equation (1) account for the phase equilibrium data of the working pair in combination with the heat capacity flow rates $\dot{W}_X = c_p \cdot \dot{m}_X$ and heat transfer capabilities $Y_X = U_X \cdot A_X$ (where $X = D, E, C, A$ holds for the main heat exchangers, desorber, evaporator, condenser, and absorber). Hence $\Delta\Delta t^*$ includes all information of load dependent losses. The capacity potential of the chiller (i.e. its 'thermal size') is described by the slope parameters K_4^* and K_5^*, respectively. The coefficient K_6 scales the minimum driving heat $\dot{Q}_{D,min} = K_6 \cdot \Delta\Delta t_{min}$ which results mainly from limited internal heat recovery in the solution heat exchanger. The variable minimum driving heat flow $\dot{Q}_{D,min}$ can be calculated by means of a second characteristic temperature difference

$\Delta\Delta t_{min}$ which is a function of the same independent external temperatures and coefficients K_1 to K_3 (Albers, 2018). At constant flow rates all K_N and K_N^* can be assumed constant also. With respect to a certain load case (where $\dot{Q}_E = \dot{Q}_E^{set}; t_{Eo} = t_{Eo}^{set}$) the necessary value for $\Delta\Delta t_{set}^*$ is fixed (see figure 1). Nevertheless, there is still one degree of freedom since t_{Di} and t_{Ai} are both not fixed yet. For the economic operation of CHPC-plants compliance of a minimal hot water outlet temperature from the desorber of an absorption chiller (i.e. $t_{Do} \leq t_{Do}^{set}$) is an interesting third objective because a reduction of primary energy efficiency (e.g. by wasting heat in an emergency cooler) can be avoided. The CE-controller calculates the required hot and cooling water temperatures $t_{Di} = t_{Di}^{set}$ and $t_{Ai} = t_{Ai}^{set}$ which are necessary to reach all three objectives concurrently (i.e. $\dot{Q}_E = \dot{Q}_E^{set}; t_{Eo} = t_{Eo}^{set}$ and $t_{Do} = t_{Do}^{set}$).

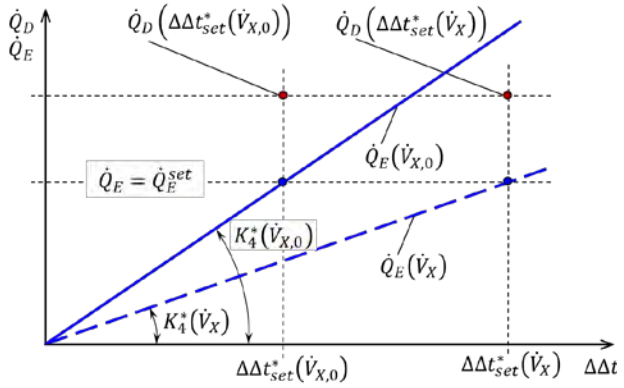

Figure 1: Effect of $\dot{V}_X < \dot{V}_{X,0}$ on part load behaviour

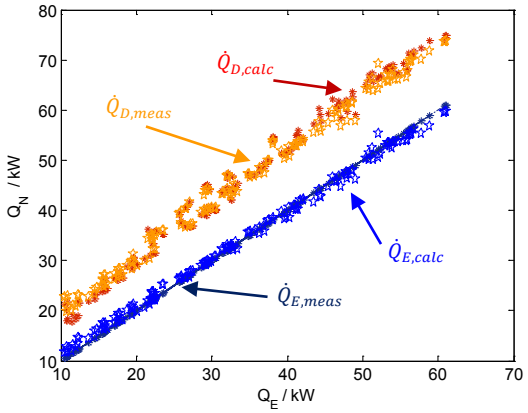

Figure 2: Predicted and measured data, $\dot{Q}_D$ and $\dot{Q}_E$

By definition all K_N and K_N^* are directly influenced by the external volume flows $\dot{V}_X$ since they affect the overall heat transfer coefficient U_X. In Fig. 1 the effect of a flow rate $\dot{V}_X$ lower than the rated value $\dot{V}_{X,0}$ is shown for any supply circuit ($X = D, H$ or E). In both cases (i.e. at nominal or reduced flow rate) the cooling capacity is a linear function of $\Delta\Delta t^*$ but with different values for K_N and K_N^*. Due to a lower flow velocity inside the heat exchanger tubes at $\dot{V}_X < \dot{V}_{X,0}$ the process external heat transfer coefficient $\alpha_{ext,X}$ and consequently the overall heat transfer coefficient U_X is reduced. The resulting lower heat transfer capability $Y_X = U_X \cdot A_X$ leads to lower slope parameters K_4^* and K_5^* (i.e. a lower thermal size of the chiller). Therefore the characteristic temperature difference has to be increased from $\Delta\Delta t_{set}^*(\dot{V}_{X,0})$ to $\Delta\Delta t_{set}^*(\dot{V}_X)$ either by a higher t_{Di} or a lower t_{Ai} or both to reach all three set values $\dot{Q}_E^{set}, t_{Eo}^{set}$ and t_{Do}^{set}. Due to $\dot{Q}_{D,min}$ the driving heat $\dot{Q}_D$ is not a linear function of $\Delta\Delta t^*$. However, when all three set values are reached either with $\dot{V}_{X,0}$ or $\dot{V}_X$ the load dependent and load independent losses are nearly the same and therefore $\dot{Q}_D\left(\Delta\Delta t_{set}^*(\dot{V}_X)\right) \approx \dot{Q}_D\left(\Delta\Delta t_{set}^*(\dot{V}_{X,0})\right)$, see Fig. 1.

The developed CE-algorithm is not only used for control but also to predict chiller capacity as shown in Fig. 2. The measurement data used to define all K_N and U_X values for the CE-model consist of 172 steady state operation points with cross variation of all three set temperatures (t_{Di}, t_{Ai}, t_{Eo}) and the three volume flow rates ($\dot{V}_D$, $\dot{V}_H$, $\dot{V}_E$) according to Table 2. In Fig. 2 driving heat and cooling capacity, measured and calculated values are depicted in a range of 20 % to 120 % of cooling capacity. While $\dot{Q}_E$ is above 20 kW the deviation between predicted and measured values of driving heat and cooling capacity is less than 5 % and within the whole range deviation is always less than 5 kW.

Table 2: operation range for CE algorithm analysis in figure 2

	t_{Eo} in °C	$\dot{V}_E$ in m^3/h	t_{Ai} in °C	$\dot{V}_H$ in m^3/h	t_{Di} in °C	$\dot{V}_D$ in m^3/h
Min	6	4	22	5.4	70	1.4
Max	18	10	38	14	90	4

2.2. Field Test Results and First Volume Flow Control Strategies

Within the field test all kind of electricity (pumps, fans, control units, etc.) and heat consumption have been measured in 5 sec. intervals and analysed in order to identify the main energy consumers and the differences of their contribution due to different load conditions. In Fig. 3 the total specific electricity consumption w_{ACCA} of the absorption chillers installed in various sites of the field test and the share for chiller control, hot, cooling, and chilled water pump as well as the reject heat device are shown. More than 80 % of the consumption is related to the reject heat circuit in most sites with slight differences in the share between pump and reject heat device. Electricity consumption for hot water pump reaches rarely values above 5%, mostly being below a share of 2%.

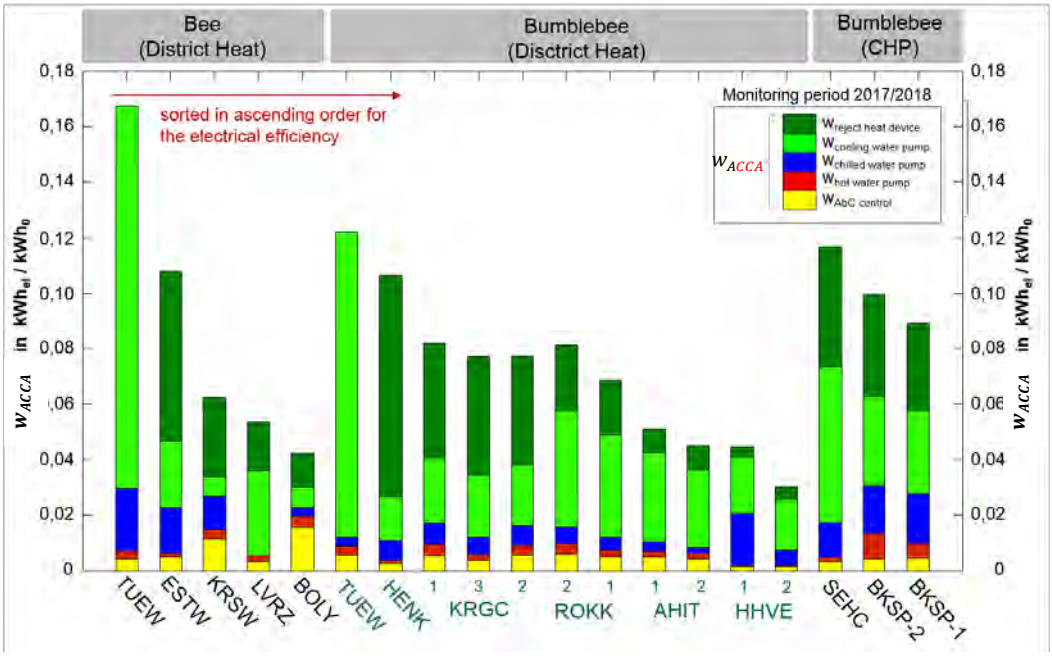

Figure 3: specific electricity consumption ACCA$_{th}$

During the final year of the project, the control strategies for a variable flow rate control and/or variable temperature setpoint for dry coolers were implemented and tested in selected field tests. (Paitazoglou et al., 2018) highlights the achieved operation results that in addition to an increase of the electrical efficiency by a factor of approx. two, the strategies promise to reduce operation costs and the economic feasibility of the thermally driven chillers. The operation of the cooling water pump accounts for a high electricity demand especially when absorption chillers are operated at part-load. The applied volume flow rate control strategy adjusts the flow rate depending on a setpoint temperature difference ($\Delta t_{H,set}$) between condenser outlet and absorber inlet. The strategy was tested in the project at multiple sites during late summer period. In a field test with a constant cooling load the overall performance of the absorption chiller was evaluated for various $\Delta t_{H,set}$ values between 4 K and 11 K and reported in (Paitazoglou et al., 2018). It has been assured, that the demanded cooling load was continuously covered. Thus, the strategy was leading to an electrical efficiency increase to values above 40 kWh$_0$/kWh$_{el}$ in comparison to 20 kWh$_0$/kWh$_{el}$ which was reached without an active flow rate control. Although lower heat transfer capabilities Y_A and Y_C as a result of decreased flow rates have to be compensated by lower t_{Ai} and therefore by a slightly higher cooler effort the benefits in the sum of electricity consumption have been advantageous. During the measurement period the cooler fans were operated in medium speed or even low speed.

If the cooler already operates at high fan speed with low temperature glide, results may be different. At the given circumstances the results are expected to be transferable to most year operation, dependencies between w_H, t_{Ai} and $w_{reject\ heat\ device}$ are obvious. Due to high share of electricity consumption for ACCA pump speed of cooling water should not be operated anymore without active control or fixed at nominal conditions.

2.3. Electricity Savings by Flow Rate Control in Hot Water

In Fig. 4, driving heat temperatures in an installation connected to a district heating network for a whole year are presented. The values are sorted by driving temperature t_{Di} on an hourly averaged base. Smoothened and coloured thick lines in front of the momentary values (thin grey lines) show the general tendencies. Desorber volume flow $\dot{V}_D$ was hold constant at 8.9 m³/h during the whole year. The values between operating hours 8260 and 8760 are mainly related to start-up periods, the hot water temperatures are low (i.e. $t_{Do} < t_{Di} < 70$ °C) but the temperature glide is high (i.e. $\Delta t_{D,AKA} > 10$ K) as the cycle is warming up. Values on the left side, operating hours 0 to 260 are belonging to other particularities and will even not being included in further discussion. The lasting 8000 operating hours, between 260 and 8260 are indicated as case M. To satisfy load condition ($\dot{Q}_E^{set}; t_{Eo}^{set}$) and to keep hot water outlet temperature t_{Do} at the set-point t_{Do}^{set} the necessary inlet temperature t_{Di}^{set} at given $\dot{V}_D = \dot{V}_{D,0}$ is always lower than the available supply temperature of the district heating network $t_{FW,max}$.

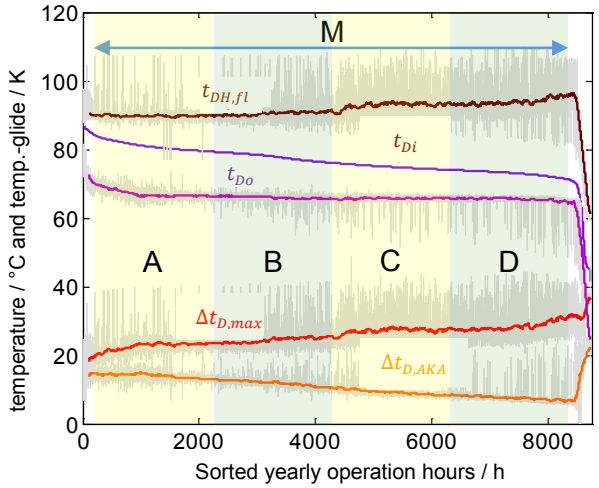

Figure 4: sorted annual temperature curves of driving heat at HENK installation, FAKS 2017

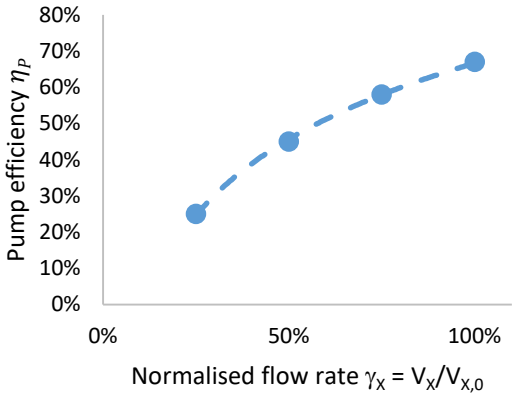

Figure 5: Pump efficiency, Data: Wilo Stratos

If the maximum available temperature could be used to match the same load condition ($\dot{Q}_E^{set}; t_{Eo}^{set}$) the hot water flow rate can be reduced in order to keep t_{Do} constant, also. This reduced flow rate has two main effects: at first, the electricity consumption of the hot water pump is reduced, second the characteristic temperature difference $\Delta\Delta t_{set}^*$ is increased due to the higher driving temperature, while at the same time the thermal size of the chiller (i.e. the slope parameter K_4^*) is reduced as explained in section 2.1. Within the main range of operation the increase of $\Delta\Delta t_{set}^*$ overcompensates the effect of $\dot{V}_D < \dot{V}_{D,0}$ on K_4^* . Therefore and in order to keep $\dot{Q}_E$ constant either the reject heat water temperature t_{Ai} has to be increased or an additional decrease of the thermal size of the chiller (i.e. the slope parameter K_4^*) has to be forced. The latter can be achieved by reducing $\dot{V}_H$. A combination of both control measures is also possible and described by (Mittermaier et al., 2010), and beneficial.

Table 3: Possible savings for t_{Do}^{set} = 67 °C

	t_{Di}	$t_{DH,fl}$	Load	V_D	γ_D	Δp_D	$\Delta\Delta t^*$	V_H	γ_H	Δp_H	$\eta_{P,D}$	$\eta_{P,H}$	$L_{P,D}$	$L_{P,H}$	b_{ACCA}	$W_{P,D}$	$W_{P,H}$	ΣW_P
	°C	°C	%	m³/h	%	kPa	K	m³/h	%	kPa	%	%	kW	kW	h/a	kWh	kWh	kWh
M	81	81	100	8.9	100	7.8	30.8	46.0	100	81.8	67	67	0.03	1.57	8000	231	12538	12770
A	81	90	100	5.5	62	3.4	37.9	39.5	86	62.2	52	62	0.01	1.10	2000	20	2199	2219
B	79	91	88	4.9	55	2.8	34.8	30.0	65	38.3	49	54	0.01	0.59	2000	16	1188	1204
C	76	93	72	3.5	39	1.6	33.6	23.4	51	25.0	38	46	0.00	0.35	2000	8	703	712
D	73	93	57	2.6	29	0.9	31.3	21.1	46	20.9	29	43	0.00	0.28	2000	4	569	573
											Sum A to D					48	4659	4707
											relative savings ($W_{P,X}/\Sigma W_P$)					1%	62%	63%

The results of decreasing $\dot{V}_D$ to make use of $t_{DH,fl}$ and the possible reduction in electricity demand, as consequence of this operation strategy is summarized in eff 3. Savings are calculated due to reducing the thermal size by adapting the volume flow rates $\dot{V}_D$ and $\dot{V}_H$. No changes are done to t_{Ai}. Input data are taken from Fig. 4. Case M is inheriting the measured reference operation data. Cases A to D cover the same variable cooling load as measured. The values of cases A to D in table 3 are determined as mean values of the marked sections in Fig. 4 with a duration of 2000 h each.

The comparison of case M (which holds for the mean of measured values during sorted operating hours 260 and 8260 in figure 4) and case A with reduced hot water flow rate for the first quarter (2000h) of the same duration highlights the advantage of hot water flow rate control even under full load conditions. Using the available driving temperature of 90.3 °C instead of 81.0 °C and reducing the hot water flow rate from 8.9 to 5.5 m³/h to keep $t_{Eo} = t_{Eo}^{set}$ and $t_{Do} = t_{Do}^{set}$ = 67 °C constant, increases the characteristic temperature difference from 30.8 K to 37.9 K. According to the characteristic equation (2) a constant cooling capacity $\dot{Q}_E = \dot{Q}_E^{set}$ at higher characteristic temperature difference is only possible with a lower slope parameter K_4^* (see also figure 1). Hence, in addition to $\dot{V}_D$ also $\dot{V}_H$ has to be reduced from the nominal value of 46.0 m³/h to 39.5 m³/h. The lower flow rates lead to lower pressure drops Δp_D and Δp_H. Thus the necessary electric power for the pumps ($X = D, H$)

$$L_{P,X} = \frac{\Delta p_X \cdot \dot{V}_X}{\eta_{P,X}} \tag{5}$$

is 31 % lower for full cooling load condition in case A with reduced hot and cooling water flow rate (Σ = 1.11 kW_{el}) as compared to first quarter of case M with nominal flows (Σ = 1.60 kW_{el}). Under part load conditions the possible savings are even higher. This is illustrated by case B to D where again the measured available temperature $t_{DH,fl}$ is used as driving temperature in the characteristic equations (1) to (4) (instead of t_{Di}) to match the case related cooling load ($\dot{Q}_E = \dot{Q}_E^{set}; t_{Eo} = t_{Eo}^{set}$) and the third objective ($t_{Do} = t_{Do}^{set}$). From this (higher) driving temperature the necessary (lower) hot and cooling water flow rates are calculated to reach the same values for $\dot{Q}_E$, t_{Eo} and t_{Do} as measured. Taking the decreased pump efficiencies, according to figure 5, pressure drops and volume flows into account, the electric energy consumption can be calculated for each case with a duration of b_{pl} = 2000 h as

$$W_{P,X} = \frac{\Delta p_X \cdot \dot{V}_X}{\eta_{P,X}} \cdot b_{ACCA} = L_{P,X} \cdot b_{pl} \tag{6}$$

The total amount of electricity with variable flow rates during 4·2000 h = 8000 h of operation is 4707 kWh. This is 63 % below the value of 12770 kWh for the same load characteristic but with nominal and fixed flow rates over 8000 h in case M.

3. CONCLUSIONS

New control strategies for absorption chiller cooling assemblies, not only satisfying cooling load ($\dot{Q}_E = \dot{Q}_E^{set}; t_{Eo} = t_{Eo}^{set}$) but also ensuring an additional objective, such as a minimal or set driving heat outlet temperature have been successfully tested in an extensive field test. In combination with a new generation of absorption chillers, which can operate at a huge variety of volume flow rates from 20% to 150% in driving heat, reject heat and chilled water cycle and new control strategies lead to electrical energy savings for pumps within the system, where 80% are related to the reject heat cycle (pump and cooler). Therefore, the yearly electrical consumption can be reduced significantly by reducing pump speed in the reject heat cycle directly. Most state of the art of absorption chiller systems operate on the hot water/driving heat side using a valve to adjust hot water inlet temperature t_{Di} at fixed pump speed to match cooling load by mixing colder hot water from the return line of the chiller and hot water from the hot water network. By reducing pump speed of the hot water pump, the direct electricity savings for this pump are below 1% of overall consumption, which is consequently due to low share of overall electricity consumption by this pump. But the indirect effect causes a range of savings in the reject heat cycle of approx. 60% as pump and/or fan speed in this cycle can be reduced in addition. The potential is proven theoretically. The concept should be proven in the field installations by summer of 2019.

ACKNOWLEDGEMENTS

We acknowledge financial support by the EnEff:Wärme Projects 03ET1171A and 03ET1583 grant funded by the Federal Ministry for Economic Affairs and Energy (BMWi).

NOMENCLATURE

Code letters

A	Area [m²]
ACCA	Absorption chiller cooling assambly
CE	Characteristic equation
K	Coefficient of CE (1 to 6)
L	Electrical power [kW]
U	Heat transfer coefficient [kW/K/m²]
W	Electrical / mechanical energy [kWh]
Y	Heat transfer capability [kW/K]
p	Pressure [hPa]
t	temperature [°C]
b	operation hours
$\dot{Q}$	Heat capacity of component X
$\dot{V}$	Volume flow [m³/h]
$\Delta\Delta t$	Characteristic temp. difference
η	efficiency
γ	normalized flow rate

Indexes

A	Absorber
C	Condenser
D	Desorber
DH	District heat
E	Evaporator
H	Absorber & Condenser
P	Pump
X	Component indicator (A, C, D, E, H)
calc	calculated
el	electrical
fl	feedline
i	in
meas	measured
pl	part load
o	out
*	modified
0	reference status *or* cold

REFERENCES

Albers, J., 2018. Improvement of a calculation method for the control of absorption chillers. PhD thesis, TU Berlin, Fakultät III Prozesswissenschaften, Institut für Energietechnik.

Albers, J. & Ziegler, F., 2016. Control Strategies for Absorption chillers in CHPC-plants ensuring low hot water return temperatures. Proceedings of Heat powered cycles conference, Nottingham, Great Britain, paper ID: 800.

BINE, 2012. Cooling with heat - A new generation of compact chillers cools and heats with low-temperature heat. http://www.bine.info/fileadmin/content/Presse/Projektinfos_2012/Projekt_07-2012/ProjektInfo_0712_engl_internetx.pdf

DIN18599-7, 2018. Energetische Bewertung von Gebäuden - Berechnung des Nutz-, End- und Primärenergiebedarfs für Heizung, Kühlung, Lüftung, Trinkwarmwasser und Beleuchtung - Teil 7: Endenergiebedarf von Raumlufttechnik- und Klimakältesystemen für den Nichtwohnungsbau. DIN Standard, Germany

Eurovent, 2018. Rating standard for the certification of liquid chilling packages, Eurovent

Henning, H.-M., 2004. *Solar-assisted air conditioning in buildings - a handbook for planners*. Springer, Wien, New York.

Mittermaier, M., Petersen, S. & Ziegler, F., 2010. Primary Energy optimized operating strategies of Absorption Systems in CHCP networks. Proceedings of Sustainable Refrigeration and Heat Pump Technology Conference, Stockholm, Sweden.

Paitazoglou, C., Hüls, W., Albers, J. & Petersen, S., 2018. Betriebsführungsstrategien zur Steigerung der elektrischen Energieeffizienz bei der thermischen Kälteerzeugung. Proceedings of Tagungsband Deutsche Klima-Kälte-Tagung, DKV, Aachen, Germany, p. paper III.21.

Petersen, S., Albers, J., Graf, R., Hausherr, C., Hennrich, C., Hüls, W., Hunt, S., Lanser, W., Paitazoglou, C., Schröder, M. & Ziegler, F., 2019. EnEff:Wärme - Feldtest Absorptionskälteanlagen für KWKK Systeme, FKZ 03ET1171A. Final Project Report, TU Berlin, Inst. f. Energietechnik, FG Maschinen u. Energieanlagentechnik, Berlin, Germany.

Petersen, S., Ziegler, F., Albers, J. & Lanser, W., 2013. EnEff:Wärme – Absorptionskältetechnik für Niedertemperaturantrieb - Grundlagen und Entwicklung von Absorptionskältemaschinen für die fernwärme- und solarbasierte Kälteversorgung, FKZ 0327460B. Final Project Report, TU Berlin, Inst. f. Energietechnik, FG Maschinen u. Energieanlagentechnik, Berlin, Germany.

PolySMART, 2010. PolySMART - Polygeneration with advanced Small and Medium scale thermally driven Air-conditioning and Refrigeration Technology. Final Project Report, EU, 6th FRP

Manuscript ID: 1289
DOI: 10.18462/iir.icr.2019.1289

Heat rejection coolers for absorption chillers – theory and field test results

Wolfgang LANSER[(a)], Rupert GRAF[(a)], Martin SCHRÖDER[(a)], Carsten HAUSHERR[(a)]

[(a)] Technische Universität Berlin,
Berlin, 10587, Germany, wolfgang.lanser@tu-berlin.de

ABSTRACT

Coolers are the most relevant components of absorption chiller systems regarding electricity and water consumption as well as operational costs, space requirement, and noise emission. While evaporative cooling towers can supply lower temperatures, package type dry coolers are significantly cheaper in investment, operation and maintenance. In the last few years, single effect absorption chillers have been developed to operate with dry coolers. In a field test 25 chillers were tested in 16 different locations throughout Germany.
Using dry coolers instead of wet coolers facilitates the overall installation. Project results show the energy efficiency potential of absorption chillers in combination with dry coolers. Three strategies reduced the electrical energy consumption by 70 % on average, without negative side effects for absorption chillers. The annual specific electricity demand of 0.028 $kW_{el}/kW_{th,0}$ was even lower than typical values for wet cooling towers.
Keywords: Absorption Cooling, Energy Efficiency, Experimental Results, Control Strategies.

1. INTRODUCTION

A main advantage of absorption chillers (ACh) is their ability to use low grade heat as driving energy instead of electricity. However, compared to vapor-compression chillers (CCh), more driving energy is necessary for the same cooling energy. As a result, more heat is rejected, which in turn requires a larger cooling tower (CT) or increased auxiliary expenditures, such as electrical energy demand of the fans or water consumption. The former leads to higher capital costs, the latter to increasing operating costs. From an economical point of view, the savings in operating expenditures for driving heat (e.g. waste heat instead of electricity) have to overcompensate the higher amount of driving energy and costs (capital and/or operating) for the chiller and its cooling tower. Typically, most of the auxiliary electrical energy consumption is caused on the heat rejection side (Eicker et al., 2012). Besides providing profitable cooling energy, a secondary objective for absorption chiller installations is to substitute electrical energy consumption, e.g. reducing the overall primary energy consumption of a tri-generation system. Therefore, efficient heat rejection is a key factor for economic and primary energy efficient absorption chiller systems.
Evaporative cooling systems allow lower cooling water temperatures, which affects heat driven chillers positively (Buchin and Ziegler, 2011). However, preventing Legionnaires' disease and precautions against freezing in cold seasons result in additional costs, which may exceed the capital costs of the chiller in small scaled installations. Hence, for small and medium load applications, dry cooling towers are getting more and more interesting in temperate and even Mediterranean climate zones (Paitazoglou et al., 2015).
In the field test project FAkS (Feldtest Absorptionskälte für Kraft-Wärme-Kälte-Kopplung-Systeme funded by BMWi with project ID FKZ 03ET1171a-d) a total of 25 absorption chillers, designed for high reject heat temperatures, were installed and - over the period of 5 years - monitored in 16 different locations throughout Germany. Among others, a main objective of the field tests was to demonstrate a low specific electrical energy consumption for the overall cooling system $w_{el} = 0.05\ kWh_{el}/kWh_0$.
This paper presents the motivation and field test results for three different measures of decreasing the electrical consumption of dry cooling towers (DCT). The field test results show measurement

data of a cooling system consisting of three absorption chillers and one compression chiller in Karlsruhe, Germany ('KRGC').

2. MEASURES TO REDUCE THE ELECTRICITY EXPENDITURES

2.1. Cooling Tower Technologies

The minimal cooling water temperature for dry cooling towers is limited by the dry bulb temperature. However, low approach temperatures[1] ($t_{appr} = t_{HTM,o} - t_{amb}$) result in high capital costs, fan energy consumption and relatively large required floor space. In order to operate DCT economically, the design cooling water temperature is recommended to be within around 11 K of the dry bulb temperature (ASHRAE, 2016). Modern variable frequency driven fans allow efficient capacity controlling for DCT during part load operation.

Evaporative cooling systems can be classified in wet (open and closed circuit) and in so called *adiabatic* cooling towers. In efficient cooling towers the water temperature can approach the wet bulb temperatures to about 2-3 K (ASHRAE, 2016). In closed circuit cooling towers the ambient air is not in direct contact with the heat transfer medium. Due to the additional heat exchanger, the minimum reachable temperature is higher than in open circuit heat exchangers. Hybrid cooling towers are a combination of dry and wet cooling tower (WCT) and are operated in both modes, either simultaneously or separately. Additionally, the term *adiabatic* cooling tower is often used for cooling towers where the supplied air is pre-cooled adiabatically by humidification without wetting the heat exchanger surfaces. In all evaporative cooling systems, the evaporated water needs to be replaced continuously and added to the operational costs. Water flow rates may be specified strictly by the manufacturer, which can restrict control strategies for efficient part load operation as suggested by Petersen et al. (2019). Furthermore, specific requirements in terms of hygiene have to be fulfilled. This often means inspections, monitoring, and water treatment facilities (VDI, 2013). The latter is also necessary to avoid fouling, since this affects the heat transfer (VDI, 2013).

To prevent the heat transfer medium in DCT from freezing antifreeze agents (ethylene glycol) can be added. In contrast to this, special precautions are required to prevent evaporative cooling towers from freezing in temperate climate zones. Altogether, the water treatment and (anti)-freezing precautions for evaporative cooling systems can significantly affect the overall system efficiency, degree of maintenance, and operational life span of components (ASHRAE, 2016). This adds to both the capital and operational costs.

2.2. Project Context and Problem Description

In about 2/3 of the systems within FAkS, the absorption chillers provide the base load and additional compression chillers cover the peak demand. In this case the goal for the absorption chillers is to achieve a high share of the overall cooling energy output.

Feasible cooling tower types were chosen based on capital and expected operational costs[2]. Capital costs for water treatment facilities were at about 50 to 100 % of the capital costs for the WCT. Furthermore, operational costs for inspections and maintenance per year add up to about 50 % of the capital costs for the WCT.

Since the degree of maintenance is much lower and controlling is more flexible, (large scale) dry cooling towers were often in favour over other CT types, see Table 1.

Table 1: Overview of different heat rejection methods

ID[3]	AHIT	BKSP	BOLY	BVES	DUBA[4]	ESTW	GKIT	HENK[2]
location	Aachen	Berlin			Dessau	Essen	Garmisch-Partenk.	Hannover
type	wet	dry	dry	dry	adiabatic	adiabatic	dry	wet

[1] Temperature difference between the ambient temperature t_{amb} and the heat transfer medium outlet temperature $t_{HTM,o}$.

[2] In some locations already existing cooling towers were utilized.

[3] Each field test location is abbreviated with a four letter ID.

[4] Existing cooling tower.

ID	HHVE	KFWK[2]	KRGC	KRSW	LVRZ	ROKK	SEHC[2]	TUEW[2]
location	Hamburg	Kassel	Karlsruhe		Lever-kusen	Rosen-heim	Stuttgart	Berlin
type	dry	river	dry	dry	adiabatic	dry	dry	wet

Despite higher capital costs, typical design points of the approach temperatures in *FAkS* were between 2 and 5 K.
These low approach temperatures usually go along with a high fan speed to further increase the heat transfer. Thus, on the one hand these dry cooling towers consume a high amount of electrical energy during peak load hours. On the other hand, the larger surface areas result in a more efficient part load behaviour.
The largest DCT (~1600 kW) in the field test site 'KRCG', is designed to reject the waste heat of four chillers. Three district heat driven ACh (design capacity of 50 kW[5]) cover the base load and a larger CCh (design cooling capacity of 1100 kW) covers the peak load. During the planning phase the cooling load of the newly constructed building could only be estimated roughly. Therefore, the optimization measures in this paper are based on the first year of regular operation, which is 2016. Fig. 1 (top) shows the corresponding load distribution as a function of the ambient temperature.
Each marker represents an hourly mean value of the produced or consumed cooling capacity. The latter increases with the ambient temperature to about 500 kW at 35°C.

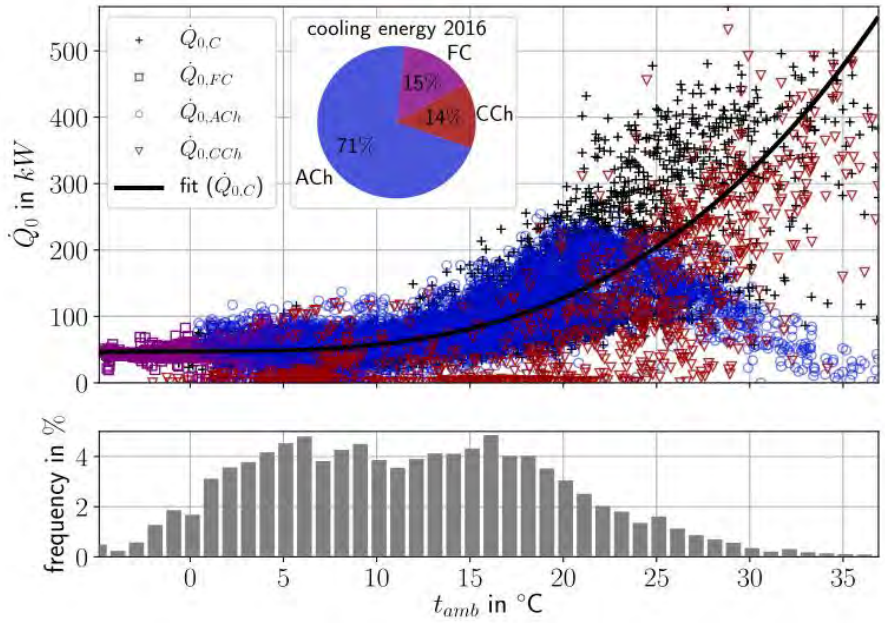

Figure 1: supplied and consumed cooling load as a function of the ambient temperature and ambient temperature frequency (1 h mean value of 2016)

At low ambient temperatures, the base load of about 50 kW is covered by the DCT in free cooling (FC) mode. To about 25 °C and 200 kW the compound of three ACh supplies the entire cooling demand. Higher ambient temperatures in combination with low district heat temperatures during the summer period significantly reduce the cooling capacity of the ACh. Consequently, the CCh covers the difference. Most of the yearly cooling consumption is required during moderate ambient temperatures (see frequency in Fig. 1 bottom), where the ACh are able to supply the entire demand. Therefore, their cooling energy share is more than 2/3 of the overall produced cooling energy per year, although the design cooling capacity in total is only about 10% of the designd peak load.
Since the ACh are the main suppliers and the DCT rejects heat for all four chillers, those two components are most important for the overall system efficiency. However, the efficiency was below expectations in this first year, for which three main reasons were identified. Parallel operation of all three ACh during hours with low loads ($\dot{Q}_{0,C} < 100$ kW) led to a high degree of part load operation and as a consequence to thermal coefficient of performance values $COP_{th} = \dot{Q}_0/\dot{Q}_2$ below 0.6.

[5] The nominal capacity of this chiller model is 160 kW. Under these specific design conditions (high heat sink - and low driving heat source temperature) the resulting capacity is only 50 kW.

Specific electrical efficiency values w_{el} were between 0.1 and 0.2 during ACh operation, which were mainly caused by the DCT controller and lead to an unnecessary high fan speed, especially during moderate ambient temperatures and medium cooling load (75 kW < $\dot{Q}_{0,C}$ < 250 kW).
The cooling capacity as well as the chilled and the hot water outlet temperature of the absorption chillers are simultaneously controlled by setting the hot and also cooling water inlet temperature (see Albers and Ziegler 2016). The latter affects the efficiency of the DCT, particularly at high ambient temperatures when the ACh controller requires low cooling water temperatures to cover high cooling load ($\dot{Q}_{0,C}$ > 200 kW).

2.3. Improving the Thermal Efficiency (COP_{th}) of Absorption Chillers in Low Load Cases

Reducing the amount of rejected heat is an obvious way to improve the efficiency of cooling towers. The less an absorption chiller is working at full capacity, the lower usually is its thermal efficiency. In 'KRGC' minimal load cases of less than 100 kW ocoure for more than 70 % per year (cf. Fig.1). Therefore, the number of simultaniously operating absorption chillers is important. Fig. 2 shows measurement data of two months before and after the implementation of a new control strategy, which significantly improved the overall thermal efficiency of the three chillers. The new control strategy successively turns chillers on or off, depending on several conditions. For example, if a cooling load of 100 kW is supplied by three chillers in equal parts, the resulting overall coefficient of performance is 0.65. If only two chillers provide the same cooling load, the overall COP_{th} of the two chillers can be increased up to 0.75. Even though this is still a low utilization of the chillers, the nominal COP_{th} (~0.8) is almost reached. Thus, the amount of reject heat can be reduced by ~8 % (and driving heat by 13 %) for fulfilling the same cooling load. With a cooling load of 55 kW the thermal efficiency of the ACh system was improved from ~0.5 to 0.75, which leads to a reduction of waste heat of ~22 % (and driving heat by 1/3). Besides the cooling load, t_{amb}, and the chiller size, the new control strategy considers additional variables, such as cold-water inlet temperature to the consumers, cold-water storage temperatures, cold-water volume flow rates of the consumers and the electricity consumption of the cooling towers. All these variables are processed by the controller to prevent undesirable effects, such as higher electricity demand due to increasing fan and pump speed. Thus, the thermal as well as the electrical performance of the whole system was improved for the low load period, which is the predominant part throughout the year in 'KRGC'.

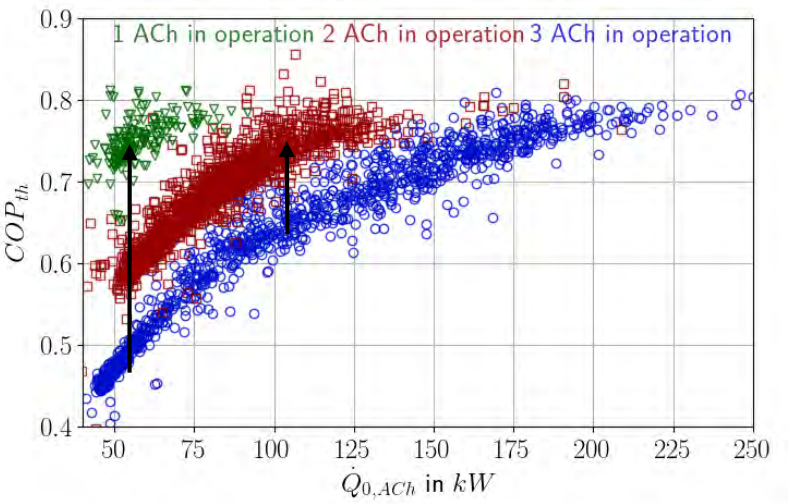

Figure 2: COP_{th} as a function of cooling capacity

2.4. Using the Heat Exchanger Surface to Full Capacity in Medium Load Cases

The heat transfer medium (HTM) outlet temperature of a DCT is commonly controlled by adjusting the air mass flow through the heat exchanger. The air mass flow is varied either by switching individual fans on and off or by controlling the fan speed. In the following, only DCT with variable speed driven fans are considered.
A DCT equipped with more than one fan can be operated in two different ways: either with uniform fan speed (parallel) or with individually controlled fan speed (serial). While the parallel control strategy changes the velocity of all fans simultaneously, so that all fans have the same rotational speed, the serial strategy controls the fan velocity in sequence. To increase the air mass flow, the fans are controlled one after another. As soon as a fan reaches its maximum velocity, the next one is switched on. Decreasing the air mass flow works the other way around. The velocity of only one fan at a time is reduced until it is switched off. Thereafter the velocity of the next fan is reduced and so forth. Both strategies are also applicable for a group of DCT, which are connected in parallel on the HTM side. The heat rejection system in 'KRGC' consists of six DCT in two groups of three units each (cf. Fig. 3). Both groups have a dedicated control system for load regulation.

By default, the serial control strategy was set for the DCT. When the extensive electricity consumption became apparent, a reliable estimation of the potential savings was required in order to convince the operator to commission a change to the control strategy by the manufacturer. Therefore, both control strategies have been simulated in python using an extended model based on the TRNSYS Type511 for the thermal behaviour of the DCT (Albers et. al 2011). Since both groups A and B are equal in construction and controlled individually, only one group had to be simulated. In summer 2016, the control strategy of the DCT was changed. In Fig. 4, where the electric power consumption of the fan motors is plotted against the approach temperature, the simulation results are compared to measurement data[6]. In the range of medium cooling loads in 'KRGC', the corresponding rejected heat loads of the DCT compounds vary between 100 and 300 kW each. Therefore, this range was used for the simulation, so that the leftmost and the rightmost edge of the area correspond to a recooling load of 100 and 300 kW respectively. For higher approach temperatures the measured electricity consumption using the parallel strategy is higher than predicted by the simulation. This could be caused by oscillations of the PID controller at low fan speeds which lead to a higher mean power consumption.

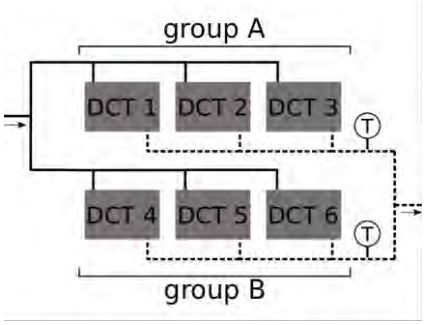

Figure 3: arrangement of DCT units in 'KRGC'

For low approach temperatures, when the DCT compound is at maximum load, there is no difference between the two strategies. For very high approach temperatures of more than about 12 K, on the other hand, the difference in energy consumption is negligibly.

According to Fig. 4, the greatest savings were achieved for approach temperatures between about 2.5 K and 10 K, where the DCT group is at medium capacity. In this range representing the typical medium cooling load cases in 'KRGC', the electrical power consumption of the DCT decreased by up to 80 % by using the parallel instead of the default serial control strategy. In 2016, this covered about 40 % of all load cases.

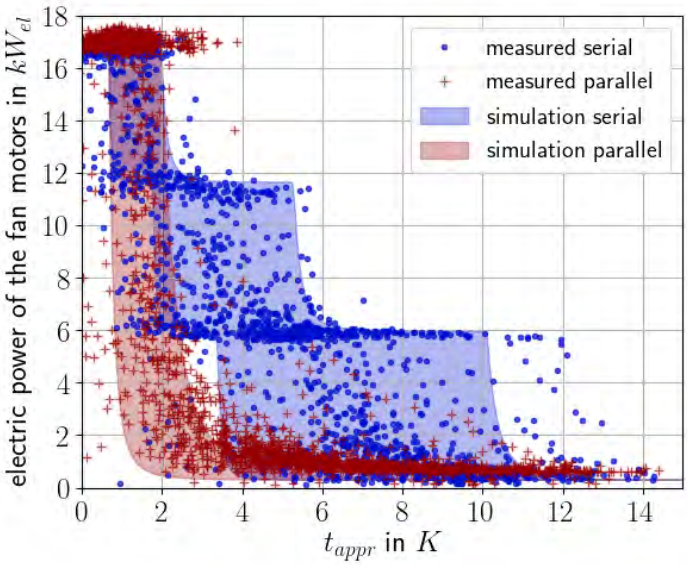

Figure 4: comparison of two control strategies for the fan control of a dry cooler compound

2.5. Identification of Inefficient Operating Points in High Load Cases and Strategies of Avoiding Them

Low t_{appr} lead in dry cooling towers to high electrical energy consumption, independent of the cooling output of the chillers. If in addition t_{amb} gets very high, the electrical power consumption of the fans can even exceed the cooling capacity of the chiller. This is due to the decreasing capacity of chillers and absorption chillers in particular by increasing cooling water temperatures. In case of 'KRGC', low t_{appr} can appear from t_{amb} > ~20 °C when the cooling load overruns the design cooling capacity of the ACh, which still tries to cover the load completely by decreasing its set value for the cooling water circuit. This led to inefficient operation points and, as they occurred many hours a year, they affected the annual average. Fig. 5 visualises the way this problem was solved, simply but effectively, in the project. While t_{amb} is increasing during the early hours (with a short-time artificial peak of t_{amb} due to solar irradiation at 7:30 am), the consumers cooling load increases and t_{appr} gets smaller. In order to avoid the fans running with maximum electricity consumption, the set value is limited by t_{amb}

[6] The presented measured data is filtered to periods where only the absorption chiller is in operation, and averaged with a window of 10 minutes.

with an offset Δt of 2 K between 11 am and 9 pm. Consequently, almost the maximum ACh contribution to cold production can be realised, and shutting off the ACh is avoided.
The temperature difference Δt is crucial to both, ACh contribution to cold production and reduction of electrical energy consumption. Both targets are inbetween a stress field. The decision of the operator, which objective is more important, determines the offset. In case of 'KRGC' a Δt of 2 K proved to be sufficient, limiting the electricity consumption of the DCT to 15 % for typical rejection heat capacities.
It is important to mention, that the plausibility and a high precision of the ambient temperature sensor are of utmost necessity for adopting this logic sensibly and promising. Unfortunately, this is not always given in real installations outside of laboratory conditions.
The resulting specific energy demand of the DCT to produce one kWh of cold is shown in Fig. 6. Before implementing the strategy, $w_{el,DCT}$ was typically greater than 0.2 for ambient temperatures above 20 °C and could reach values of up to 1 at about 35 °C. By this simple restriction of the cooling water set values, the specific energy demand was limited to mostly less than 0.05. Thus, a good electrical performance of the ACh was realised for the entire temperature range at the field site. As a matter of course, even with this slight increase of the heat sink temperature the cooling capacity of the ACh must be reduced. This is a thermodynamically given law. But compared to the electrical energy savings, this effect proved to be negligible under the field conditions.

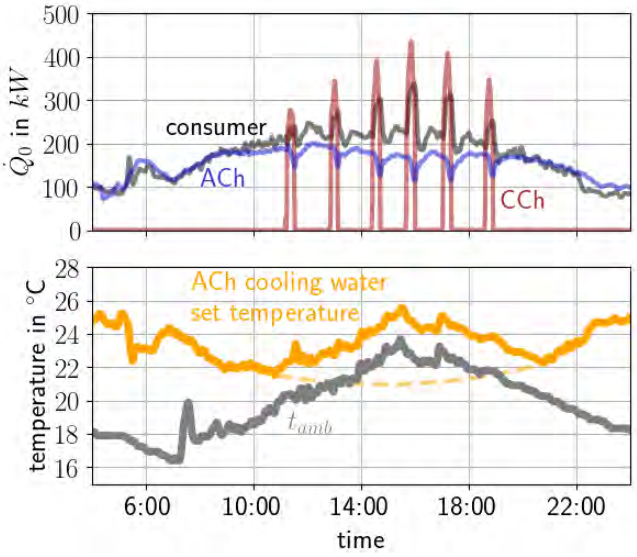

Figure 5: temperature and cooling capacity profiles on June 16th, 2017

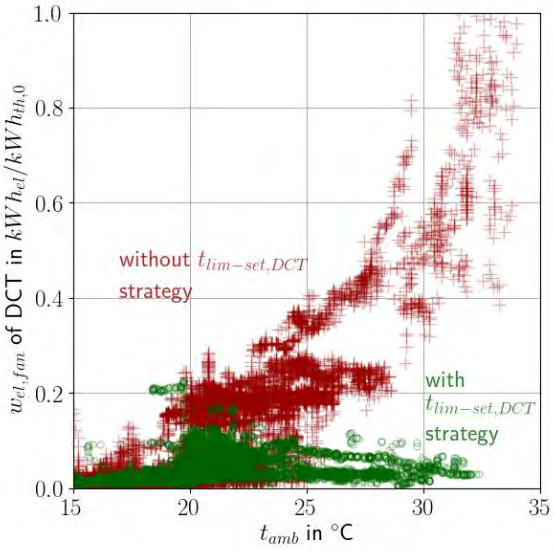

Figure 6: effect of the $t_{lim\text{-}set,DCT}$ strategy

2.6. Annual Performance Results

The first measure applied in July 2016 was the parallel control strategy of the DCT, which is most effective in medium load range. The improvements for low load cases followed in April 2017, before in June 2017 the cooling water set temperature was limited by t_{amb} and Δt (high load cases). Due to the field test nature, it is barely possible to precisely quantify the energy saving potential of each measure. Moreover, all three measures influence each other and were overlapping with other modifications and optimizing measures. As a result, the measures cannot be evaluated separately. For example, the measure for high load cases prevents the DCT from running with inefficient high fan speed. This way the number of operating hours, where the parallel fan control yields significant energy savings, is increased. It should be highlighted, that the parallel fan control is simple to implement and improves not only the ACh, but also the CCh and FC efficiency. However, the tendency with respect to long term periods is very clear. To ensure, that temporary modifications and specific field test characteristics have a marginal impact on the statement, only the specific electrical energy demand of the DCT on annual basis is evaluated. As shown in Fig. 7, in 2018 the specific electricity consumption $w_{el,DCT}$ could be reduced by 70 % in comparison to 2016. It should be noted that the efficiency of the initial phase in 2016 was already better than the expectations

corresponding to DIN V 18599 (2011) for DCT in combination with ACh[7]. The specific electricity demand in 'KRGC' for the DCT in 2018 amounts to $w_{el,DCT}$ = 0.028 and is therefore even lower than the expectations for a WCT according to DIN V 18599 of 2011. Recently, the estimation of DIN V 15899 has been significantly reduced. Due to the monitoring and the optimization efforts, the measured specific electricity consumption of the DCT in 2018 is still less than half, compared to the new guideline. On the one hand the results show how efficient the combination of DCT and ACh can be. On the other hand, it shows once again that energy efficiency of chilling installations is not only a question of the components efficiency. Other field test installations of FAkS confirm these results.

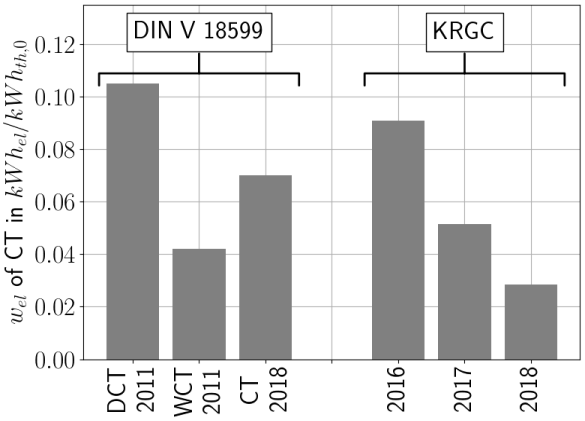

Figure 7: reference and measured values of the spec. electricity consumption

It should be noted that the measures did not have any detectable influence on the share of the annual cold production of the ACh. For some of the more complex systems, monitoring, data analysis and improvement measures will be continued in the recently started project "ReKs: Regelung für energieaufwandsoptimierte Kälteerzeugungssysteme zur Primärenergieeinsparung".

3. CONCLUSION

It has been pointed out that dry cooling towers have several economical and operational advantages compared to evaporative coolers. The main disadvantage, however, are the higher heat rejection temperatures, which, in times of peak load at high ambient temperatures, may drastically reduce the electrical efficiency of the overall cooling system.

In the field test site 'KRGC', which has been monitored over the course of 3 years within the FAkS project, significant savings were achieved in the specific electrical energy consumption of the DCT. The main part of these savings results from the three measures presented above, which have a direct or indirect effect on the DCT.

By improving the thermal efficiency of ACh compounds in low load cases, the amount of reject heat was decreased significantly, for instance by more than 20 % at a cooling load of 55 kW. Applying a parallel rather than a serial control strategy for DCT compounds yielded a reduction of the electricity consumption of up to 80 % on a wide range of medium cooling load cases. And finally, by identifying and avoiding inefficient operating points in high load cases, the specific energy demand of the DCT could be reduced to typically less than 0.05 kW_{el} / $kW_{th,0}$ even at high ambient temperatures.

As a result, the specific electrical energy consumption of the DCT installed in 'KRGC' has been reduced from 2016 to 2018 by about 70 %. In 2018 the DCT in 'KRGC' was more efficient than a WCT according to DIN V 18599.

ACKNOWLEDGEMENTS

We acknowledge financial support by the EnEff:Wärme Projects 03ET1171A and 03ET1583 grant funded by the Federal Ministry for Economic Affairs and Energy (BMWi).

[7] A COP_{th} is necessary, to reference the electrical consumption of the DCT to the cooling production in DIN V 18599. In this case a COP_{th} of 0.75 is assumed.

NOMENCLATURE

Variables

COP	coefficient of performance (-)
$\dot{Q}$	capacity (kW)
t	temperature (°C)
w	specific electrical energy demand (kWh_{el}/kWh_{th})

Abbreviations

ACh	absorption chiller
CCh	compression chiller
CT	cooling tower
C	consumer
DCT	dry cooling tower
FC	free cooling
HTM	heat transfer medium
WCT	wet cooling tower

Indices

amb	ambient temperature
appr	approach temperature
el	electrical
o	outlet
th	thermal
0	chilled water temperature level
1	cooling water temperature level

REFERENCES

Albers, J., Ziegler, F., 2016. Control Strategies for Absorption chillers in CHPC-plants ensuring low hot water return temperatures. Proceedings of the heat powered cycles conference, Nottingham, paper ID 080.

Albers et al., 2011. Optimierung der Einbindung der Aquiferspeicher in die Wärme- und Kälteversorgung der Parlamentsbauten im Berliner Spreebogen; Teilprojekt: Charakterisierung und Modellierung der Systemkomponenten.

ASHRAE, 2016. Ashrae handbook: heating, ventilating, and air-conditioning systems and equipment. ASHRAE, Atlanta GA, USA, 950.

Buchin, O., Ziegler, F., 2011, Valorization of low-temperature heat: Impact of the heat sink on performance and economics, Appied thermal Engineering 50(2013), 1543-1548.

Deutsches Institut für Normung e.V., 2011. DIN V 18599-7:2011-12, Energetische Bewertung von Gebäuden - Berechnung des Nutz-, End- und Primärenergiebedarfs für Heizung, Kühlung, Lüftung, Trinkwarmwasser und Beleuchtung – Teil 7: Endenergiebedarf von Raumlufttechnik- und Klimakältesystemen für den Nichtwohnungsbau. Beuth Verlag.

Deutsches Institut für Normung e.V., 2018. DIN V 18599-7:2018-09, Energetische Bewertung von Gebäuden - Berechnung des Nutz-, End- und Primärenergiebedarfs für Heizung, Kühlung, Lüftung, Trinkwarmwasser und Beleuchtung – Teil 7: Endenergiebedarf von Raumlufttechnik- und Klimakältesystemen für den Nichtwohnungsbau. Beuth Verlag.

Eicker, U., Pietruschka, D., Pesch, R., 2012. Heat rejection and primary efficiency of solar driven absorption cooling systems. Int. J. Refrigeration 35, 729-738.

Paitazoglou, C., Petersen, S., Lanser, W., 2015. First performance results of solar cooling in Jordan based on highly efficient absorption chillers. Proceedings of the 6th International Conference on Solar Air-Conditioning, Rome, Italy, OTTI, 258-263.

Petersen, S., Hüls, W., Paitazoglou, C., Albers, J., 2019. Active control of external volume flow rates for single effect absorption chillers. Proceedings of the 25th IIR International Conference of Refrigeration, Montréal, Canada, IIR, unpublished (January 2019).

VDI, 2013. VDI-Wärmeatlas. Imprint Springer Vieweg, Berlin, Heidelberg, Germany, Vol. 11, 1784.

Manuscript ID: 1321
DOI: 10.18462/iir.icr.2019.1321

Multi-input multi-output (MIMO) artificial neural network (ANN) models applied to economized ccroll compressors

Davide ZIVIANI[(a,*)], Ammar BAHMAN[(b)], Eckhard GROLL[(a)]

[(a)] Ray W. Herrick Laboratories, School of Mechanical Engineering, Purdue University
West Lafayette, IN 47907-2099, USA, dziviani@purdue.edu[(*)], groll@purdue.edu
[(b)] Mechanical Engineering Department, College of Engineering and Petroleum, Kuwait University
P.O. Box 5969, Safat 13060, Kuwait, a.bahman@ku.edu.kw

ABSTRACT

Predicting the compressor performance is an essential part in the design and optimization of HVAC&R equipment. The AHRI standard polynomial equations are well suited to map the performance of single-stage fixed-speed positive displacement machines, but present a number of well documented shortcomings especially in the case of compression enhancements (e.g. oil-flooding, injection, variable-speed). To this end, a Multi-Input Multi-Output Artificial Neural Network (ANN) model has been developed to map the performance of single-phase and two-phase injected scroll compressors. The ANN models are based on a multi-layer structure whose number of neurons has been optimized to obtain high-accuracy predictions. The models have been developed by using the open-source Keras package. The trained ANN models have been compared with the current state-of-the-art correlations available and they outperformed the existing correlations in terms of accuracy.
Keywords: Deep Learning, ANN, Modeling, Two-phase Injection, Vapor-Injection, Scroll Compressor.

1. INTRODUCTION

Current vapor compression systems for residential, commercial, and industrial applications heavily rely on positive displacement compressors. Accurate compressor models to predict the performance within and outside their operating envelopes are very important to optimize the systems in which they will be installed. Although, gray-box and white-box model categories are able to provide deeper insights on the physics of the compressors, black-box models are still de-facto standard in industry. Among black-box models, the third-order 10-coefficient polynomials suggested by AHRI Standard 540 (2015) are still the preferred method by manufacturers to fit the performance data of compressors in spite the fact that their limitations are well-known and proven. In particular, by having no physical meaning, the extrapolation of the compressor performance could lead to erroneous values. In addition, such models are fitted by fixing the compressor suction superheat and subcooling before the expansion valve as well as the rotational speed. If the operating conditions vary the superheat and subcooling, corrections are necessary (e.g., Dabiri and Rice, 1981). Cheung and Wang (2018) provided a critical discussion about the extrapolation capability of empirical and semi-empirical compressor models and associated uncertainties.
These considerations are particularly true when vapor compression enhancements such as liquid flooding or single (vapor or liquid)/two-phase injection need to be captured by compressor mapping methodologies. By limiting the discussion to economized injection cycles, the shortcomings of AHRI polynomials in predicting the injected compressor performance have been investigated by Tello-Oquendo et al. (2016) and Lumpkin et al. (2018). To this end, a number of authors have addressed the need for accurate models to predict the performance benefits of single and two-phase injection processes especially applied to fix and variable-speed compressors. Dardenne et al. (2015) and Sun et al. (2018) developed semi-empirical models of vapor injected scroll compressors by including essential physical elements to better capture the compressor behavior. The added complexity to the models has been justified by the improved accuracy, increased level of insights on internal losses, and reasonably fast models. Yet, these type of models require

adjustments prior being able to be used for different compressor types and, therefore, hard to be included within a standard.

Machine learning techniques such as Artificial Neural Network (ANN) models represent an alternative to common empirical and semi-empirical models and have been widely used to map the performance of positive displacement machines, as summarized in Table 1. The reliability of such models depends on the data set used for training the model and the extrapolation capabilities can be challenging, as shown by Ziviani et al. (2018). Nevertheless, a general mapping methodology based on an ANN model could be developed and included into a standard.

Until now, limited work can be found on performance mapping applied to liquid, vapor, and two-phase injected compressors. For instance, Kim B.G. et al. (2017) and Kim D. at el. (2018) employed detailed compressor models to perform in-depth analyses, but only Lumpkin et al. (2018) proposed a general correlation to cover single and two-phase injection states.

The main contributions of the present work with respect to the available literature are as follows:

- develop of a MIMO (Multi-Input Multi-Output) ANN model of a vapor- and two-phase injected scroll compressor;
- train and test the ANN model with both compressor calorimeter and in-system data;
- compare the ANN model with a state-of-art dimensionless correlation available in the literature;
- assess extrapolation capabilities of the ANN model.

Table 1. Review of ANN model-based compressor mapping

Reference	Compressor type	Working fluid	Notes
Yang et al. (2009)	Fixed-speed scroll, reciprocating, twin-screw compressors; Variable-speed scroll compressor	R-410A (scrolls) R-134a (recip., twin- screw)	Data: scroll compressor 57 data points; recip. Compressor 33 data points; screw compressor 29 data points; variable-speed scroll compressor 175 data points; ANN: MIMO model Software: MATLAB
Sanaye et al. (2011)	Open-drive rotary vane compressor	R-134a	Single hidden layer ANN; 80 data points (80% training; 20% testing); Output layer: $T_{\mathrm{dis}}, \dot{m}_{\mathrm{r}}$
Ledesma et al. (2014)	Open-drive variable speed reciprocating compressor	R-134a R-1234yf	Single hidden layer ANN; Output layer: COP
Belman-Flores et al. (2015) Ledesma et al. (2015)	Open-drive variable speed reciprocating compressor	R-134a	Single hidden layer ANN; Three ANN models: $T_{\mathrm{dis}}, \dot{m}_{\mathrm{r}}, \dot{W}$
Zendehboudi et al. (2017)	Variable-speed scroll compressor	R-410A	63 data points (70% training; 30% testing); Comparison ANN and ANFIS; ANN model: single hidden layer; Optimized neurons: 6-8-5 Software: MATLAB
Ziviani et al. (2018)	Vapor-injected hermetic scroll	R-407C	ANN model: multi-hidden layer; optimized

	compressor		neurons; Package: Keras[1], Theano

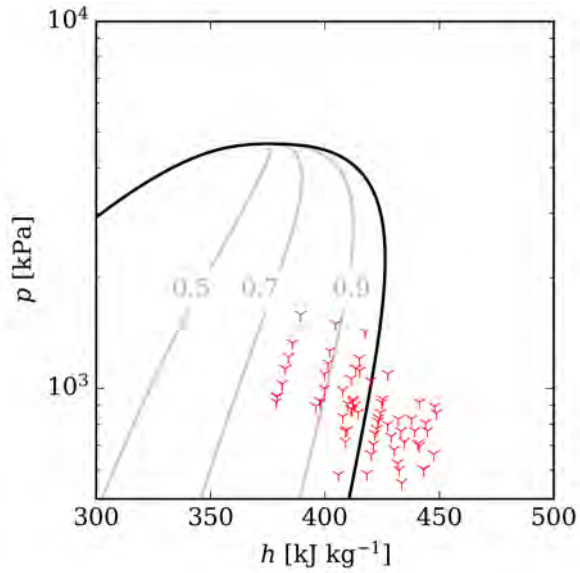

Figure 1: Experimental injection state points visualized on the *p-h* diagram of R-407C where the iso-quality lines (0.5, 0.7, 0.9) are overlaid for completeness

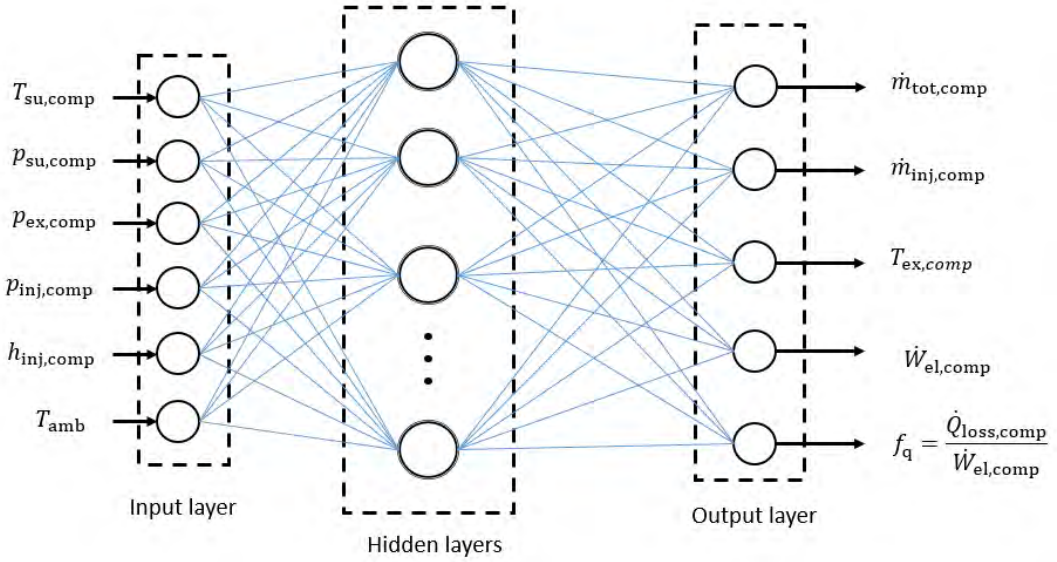

Figure 2: Schematic of the MIMO ANN model

2. EXPERIMENTAL DATA AND MODEL DEVELOPMENT

2.1. Experimental Data

To carry on the present study, experimental data of an R-407C hermetic scroll compressor (model: ZF13KVE-TF5) with a single-port injection and a volumetric displacement rate of 14.1 m^3 h^{-1} has been obtained by installing the compressor in a compressor calorimeter as well as in a retrofitted Environmental Control Unit (ECU) for military applications. Details regarding the compressor calorimeter testing and the in-system compressor testing can be found in Lumpkin et al. (2018) and

[1] Keras: The Python Deep Learning library (https://keras.io/)

Bahman et al. (2018). It is important to mention that both systems included a plate heat exchanger economizer with a down-stream extraction to allow refrigerant injection to the compressor. A control strategy was implemented to control the refrigerant quality in the injection line. Fig. 1 shows an overview of all the vapor and two-phase injection state points recorded (67 in total). An in-depth discussion about the influence of single- and two-phase injection on the compressor performance is provided in a companion paper (Bahaman et al., 2019).

2.2. ANN Model Implementation

One of the objectives of this paper is to develop a MIMO ANN model to predict the performance of a single- and two-phase injected scroll compressor. It is of particular interest to consider a shallow neural network model, i.e. single hidden later, and optimize its number of neurons to achieve high-accuracy in the predictions. Additional background on ANN models can be found in Haykin (2009). A schematic of the ANN model with input and output variables is shown in Fig. 2. The model has been developed by employing the Keras API with Tensor Flow backend in the Python 3.6 programming language. The ANN model has been trained with 80% of the data points and the remaining 20% has been used for testing. Due to the fact that the inputs to the ANN have different nature (temperature, pressure, enthalpy), both training and testing data sets have been normalized between 0.1 and 0.9:

$$x_n = 0.8\frac{x - x_{min}}{x_{max} - x_{min}} + 0.1 \qquad \text{Eq. (1)}$$

where $\boldsymbol{x}$ is the actual data point, $\boldsymbol{x_n}$ is the normalized data point, $\boldsymbol{x_{max}}$ and $\boldsymbol{x_{min}}$ are the minimum and maximum values defined according the input type. The training process has been carried out with the *AdaMax* algorithm by using the mean square error (MSE) as the objective function to be minimized. Particular attention has been given to prevent overfitting during the training and testing of the neural network model. In particular, optimization of the capacity of the network (number of neurons), add weight regularization, and control the dropout rate are the major aspects considered while developing the model. History plots of the training and testing processes allowed to optimize the ANN model properly.

3. RESULTS AND DISCUSSION

The following sections discuss the accuracy of the developed ANN, compare the ANN model with a state-of-art dimensionless correlation, and assess the extrapolation capabilities of the ANN model.

3.1. ANN model: Training vs. Testing

The ANN model has been trained with randomly-selected 80% of the total test points. Hyperbolic tangent and linear functions have been used to activate the input layer and the output layer, respectively. The selected number of neurons within the single hidden layer was 18, which gave the minimum value of the MSE. Fig. 3 and Fig. 4 shows the resulting parity plots to compare ANN model predictions with experimental data in terms of injected and total mass flow rate, discharge temperature, and compressor input power. With the exception of the injected mass flow rate, the other output parameters have been predicted with extremely high accuracy throughout the operating range. The training results of the injected mass flow rate present a few points with higher relative errors. It is suspected that the associated experimental points were affected by uncertainty measurements due to the two-phase inlet conditions. The single hidden layer MIMO AAN model has been proven to be accurate enough for the purpose of this study. Deeper networks have been previously investigated by the authors (Ziviani et al., 2018) and resulted in similar overall accuracy.

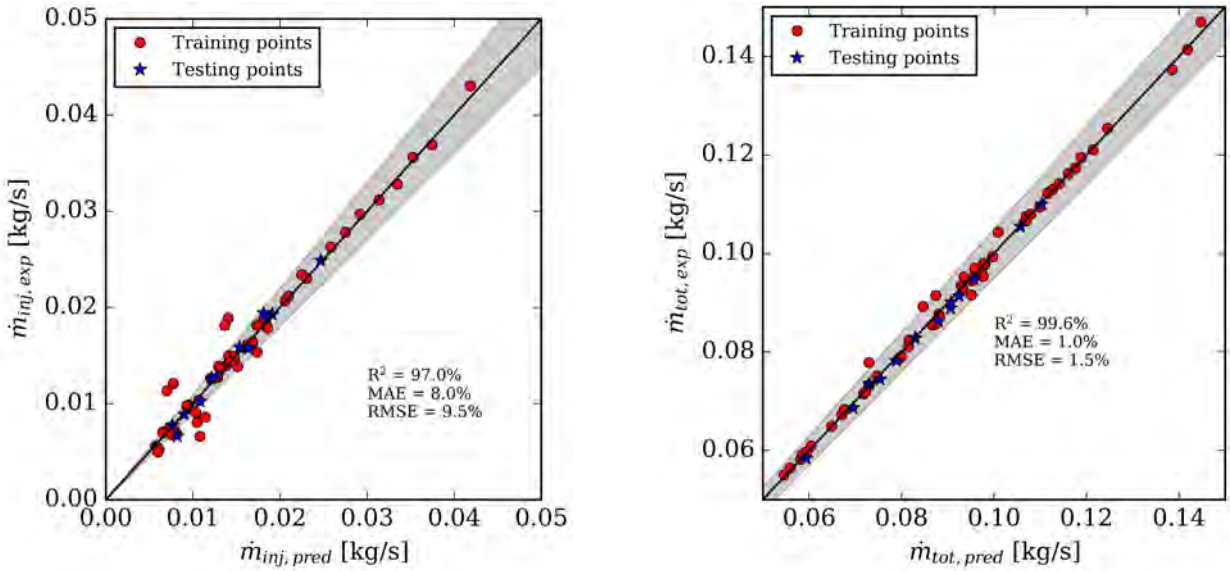

Figure 3: Comparison between measured and predicted values with ANN model for the injected mass flow rate (left) and total compressor mass flow rate (right) where training and testing points are shown.

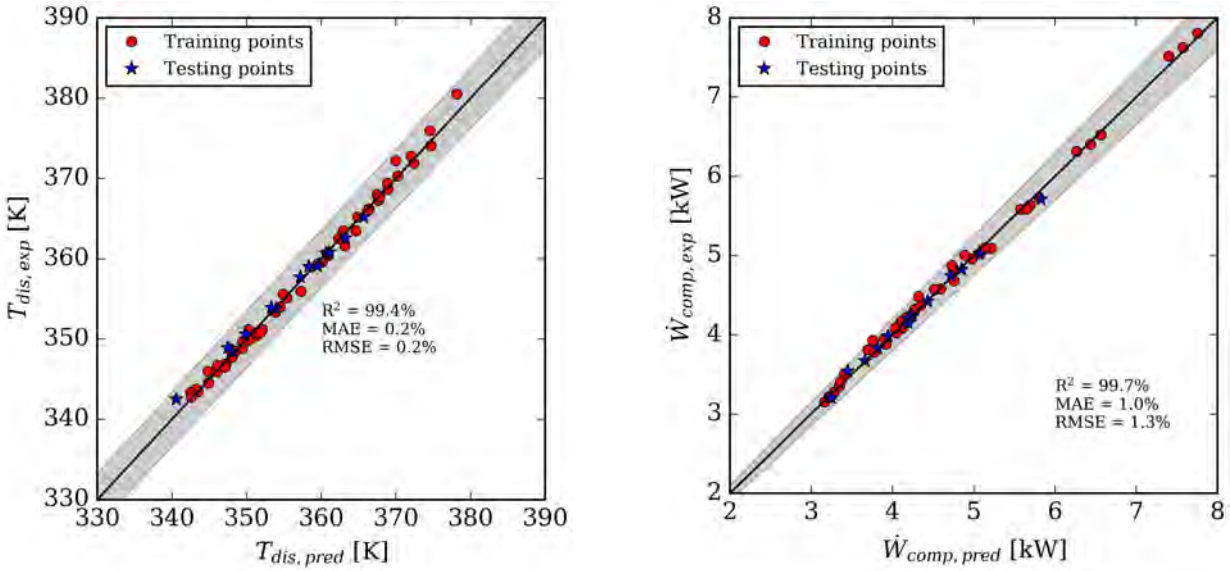

Figure 4: Comparison between measured and predicted values with ANN model for the compressor discharge temperature (left) and compressor input power (right) where training and testing points are shown

3.2. Dimensionless Correlation vs. ANN Model

Besides the accuracy of the ANN model predictions, it is interesting to compare such model with a state-of-art dimensionless correlations developed to map the performance of single- and two-phase injected compressor with fixed and variable-speed drives and different working fluids. As described by Lumpkin et al. (2018), the correlations were developed by employing the Buckingham-π theorem to determine the most important functional groups. The correlations have been calibrated on the same data sets and using 80% of the total data, for consistency.

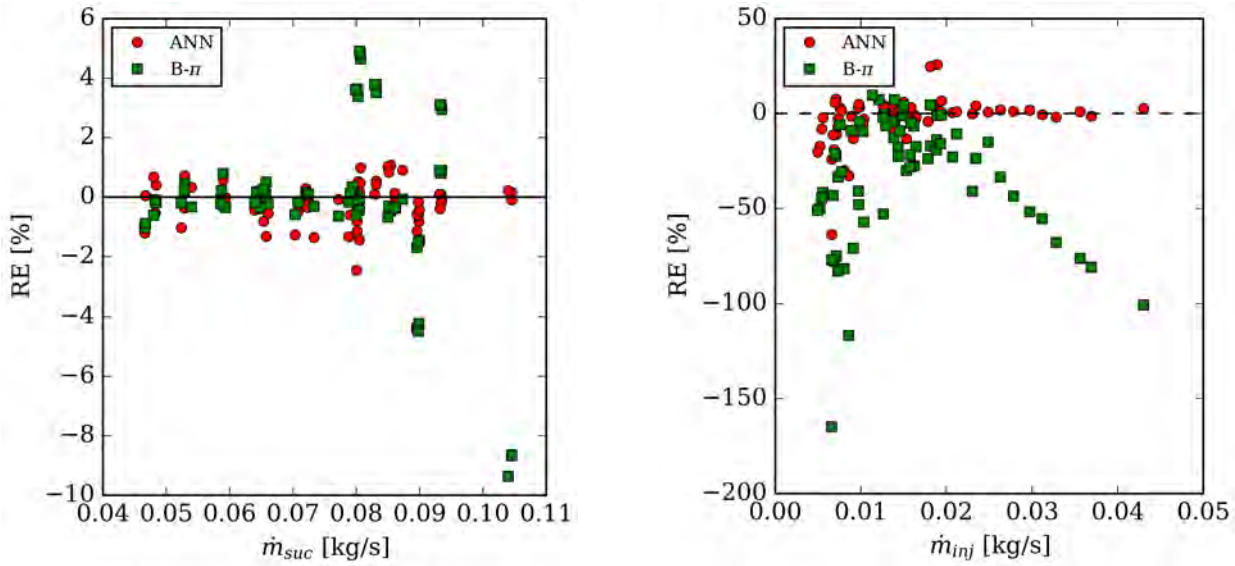

Figure 5: Relative errors of ANN model and Buckingham- π correlations in predicting suction mass flow rate and injected mass flow rate

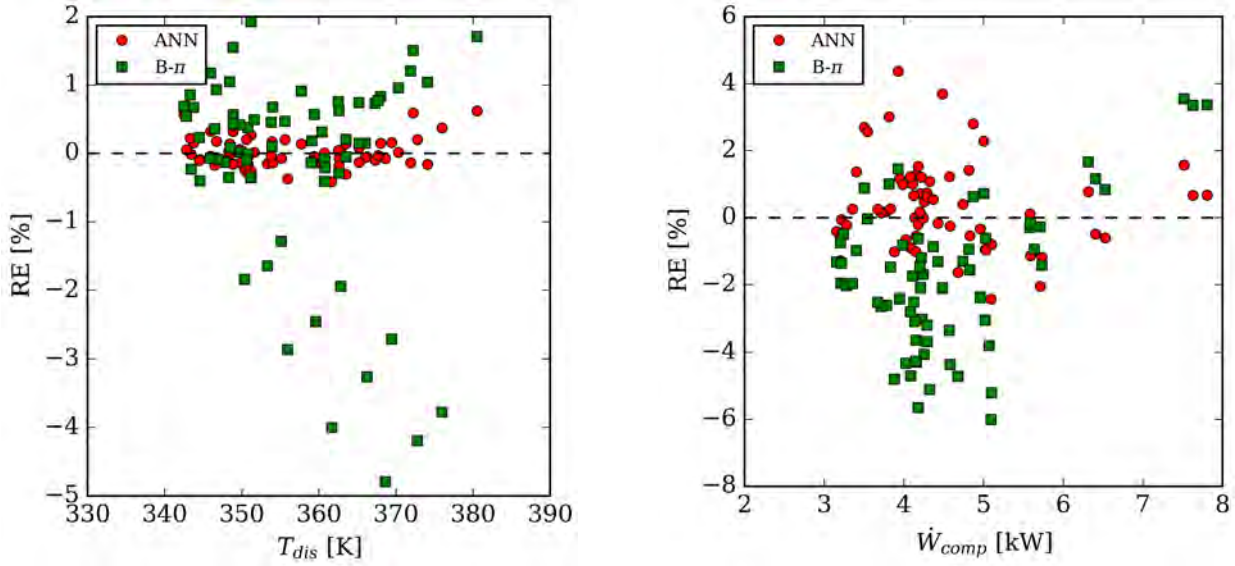

Figure 6: Relative errors of ANN model and Buckingham- π correlations in predicting compressor discharge temperature and compressor input power

By looking at Fig. 5 and Fig. 6, the ANN model is able to predict compressor calorimeter data and in-system data fairly consistently. Whereas, the dimensionless correlations struggle in achieving high accuracy with in-system data, especially with respect to the injected mass flow rates.

3.3. Considerations on ANN Model Extrapolation Capabilities

The usefulness of the developed models is related to the possibility of integrating the compressor performance within a cycle model in order to predict the system performance under different conditions. To this end, it is important to ensure that the models can handle extrapolations. To test the two models, a reference experimental data point has been selected. In particular, a data point having high ambient temperature (324.8 K) and nearly saturated injection quality (0.96) has been selected. By fixing the evaporating and condensing pressures, the injection quality has been varied to evaluate the impact of vapor- and two-phase injection on the compressor discharge temperature and input power. The results are shown in Fig. 7. To be noted is that both figures reports the results for both ANN model and dimensionless correlations, and the reference data point is overlaid.

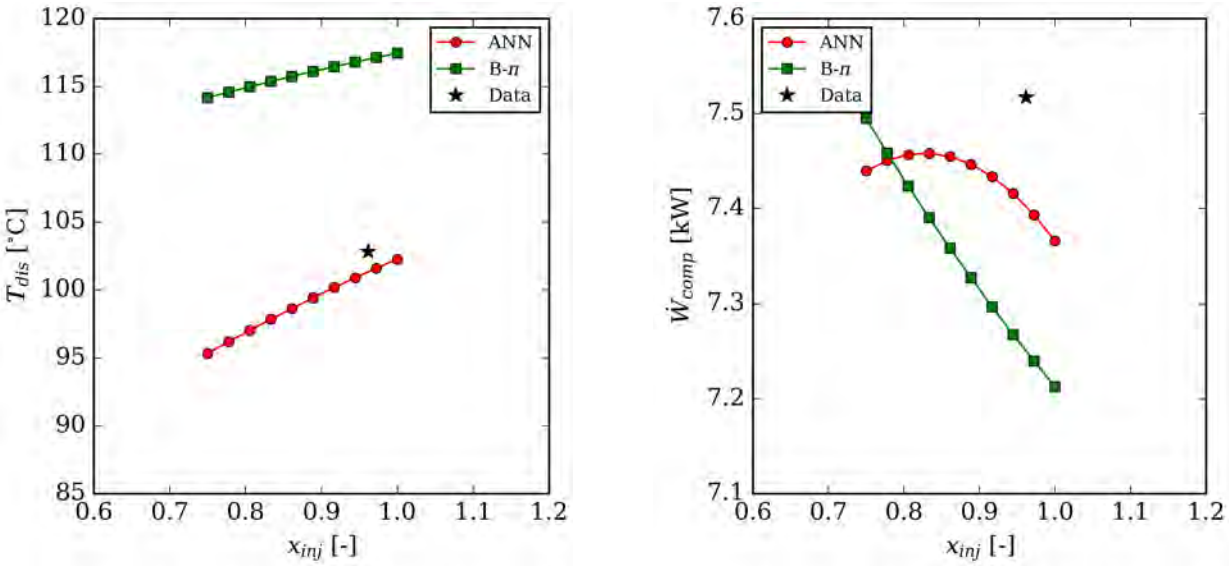

Figure 7: Parametric studies to evaluate the effect of injection inlet quality to the compressor discharge temperature and input power where the reference data point used is overlaid

By analyzing the plots, it appears that the ANN models provide more reliable predictions than the dimensionless correlations. In fact, the discrepancy between the numerical results and the reference experimental data point is 1 K and 100 W for the discharge temperature and the input power respectively. Whereas, the dimensionless correlations are significantly off and related to the calibration process. The ANN model can also capture the behavior of the compressor power when decreasing the injection quality. In fact, such trend has been experimentally captured by Bahman et al. (2019).

4. CONCLUSIONS

This paper presents an assessment of employing MIMO ANN models to predict the performance of compressors with single- and two-phase injection and both calorimeter and in-system test data. Besides the accuracy of the ANN model which is typically well known, the study focused on the comparison with state-of-art correlations for compressor mapping as well as extrapolation capabilities. The results yielded the following conclusions:

- The ANN model was able to predict the compressor performance throughout the testing conditions with both calorimeter and in-system data.
- The dimensionless correlations struggled with in-system data especially in predicting the injected mass flow rate. The reasoning behind can be explained with the two-phase inlet conditions that are affected by uncertainties. The ANN model was able to better handle variations of physical behaviors related to measurement uncertainties.
- The ANN model showed reliable results while performing parametric studies.

As a closing remark, it is necessary to quantify the minimum number of data set required to effectively train an ANN model and establish a numerical procedure to select data points within a compressor envelope. The results of this study could lead to a new compressor mapping procedure to be used by compressor manufacturers and HVAC&R industry.

ACKNOWLEDGEMENTS

The authors would like to acknowledge the support from the Center for High Performance Buildings (CHPB) at the Ray W. Herrick Laboratories.

NOMENCLATURE

h	enthalpy (kJ·kg^{-1})	ECU	environmental control unit (–)
$\dot{m}$	mass flow rate (kg s^{-1})	**Subscript**	
p	pressure (kPa)	amb	ambient
$\dot{W}$	work rate (kW)	comp	compressor
T	temperature (°C/°F)	el	electric
x	quality (-)	ex	exhaust
API	Application Program Interface	in	inlet
ANN	artificial neural network	inj	injection
ANFIS	adaptive neuro-fuzzy inference system	su	supply

REFERENCES

AHRI, 2015, Standard 540. Performance rating of positive displacement refrigerant compressors and compressor units.

Bahman, A.M., Ziviani, D. and Groll, E.A., 2019. Investigation of two-phase injected compression with economization for high temperature applications. In Proceedings: 25th IIR International Congress of Refrigeration, Montreal, Quebec, Canada. Paper ID: 292.

Bahman, A.M., Ziviani, D. and Groll, E.A., 2018. Vapor injected compression with economizing in packaged air conditioning systems for high temperature climate. International Journal of Refrigeration, 94, pp.136-150.

Belman-Flores, J.M., Ledesma, S., Barroso-Maldonado, J.M. and, Navarro-Esbri, 2015. A comparison between the modeling of a reciprocating compressor using artificial neural network and physical model. International Journal of Refrigeration, 59, pp.144-156.

Cheung, H. and Wang, S., 2018. A comparison of the effect of empirical and physical modeling approaches to extrapolation capability of compressor models by uncertainty analysis: A casa study with common semi-empirical compressor mass flow rate models. International Journal of Refrigeration, 86, pp. 331-343.

Dabiri, A.E. and Rice, C.K., 1981. A compressor simulation method with corrections for the level of suction gas superheat. AHRAE Transaction, 87(2), pp.771-782.

Dardenne, L., Fraccari, E., Maggioni, A., Molinaroli, L., Proserpio, L. and Winandy, E., 2015. Semi-empirical modelling of a variable-speed scroll compressor with vapour injection. International Journal of Refrigeration, 54, pp. 76-87.

Haykin, S. (2009). Neural Networks and Learning Machines (3rd Edition). Pearson Practice Hall.

Ledesma, S. and Belman-Flores, J.M., 2014. Application of artificial neural networks for generation of energetic maps of a variable speed compression system working with R1234yf. Applied Thermal Engineering, 69, pp.105-112.

Ledesma, S., Belman-Flores, J.M. and Barroso-Maldonado, J.M., 2015. Analysis and modeling of a variable speed reciprocating compressor using ANN. International Journal of Refrigeration, 59, pp.190-197.

Lumpkin, D.R., Bahman, A.M. and Groll, E.A., 2018. Two-phase injected vapor-injected and vapor-injected compression: Experimental results and mapping correlation for a R-407C scroll compressor. International Journal of Refrigeration, 86, pp.449-462.

Kim, B.G., Kim, D., Lee, D. and Kim, Y., 2017. Performance of a two-phase injection heat pump with the variation of injection quality and pressure. International Journal of Air-Conditioning and Refrigeration, 25(02), p.1750018.

Kim, D., Jeon, Y., Jang, D.S. and Kim, Y., 2018. Performance comparison among two-phase, liquid, and vapor injection heat pumps with a scroll compressor using R410A. Applied Thermal Engineering, 137, pp.193-202.

Sun, H., Hu, H., Wu, J., Ding, G., Li, G., Wu, C., Wang, X. and Lv. Z., 2018. A theory-based explicit calculation model for variable scroll compressors with vapor injection. International Journal of Refrigeration, 88, pp. 402-412.

Tello Oquendo, F. M., Peris, E. N., Macia, J. G., Corberán, J. M., 2016. Performance of a scroll compressor with vapor-injection and two-stage reciprocating compressor operating under extreme conditions. International Journal of Refrigeration, 63, 144-156.

Yang, L., Zhao, L.X., Zhang, C.L. and Gu, B., 2019. Loss-efficiency model of single and variable-speed compressors using neural networks. International Journal of Refrigeration, 32(6), 1423-1432.

Zendehboudi, A., Li, X. and Wang, B., 2017. Utilization of ANN and ANFIS models to predict variable speed scroll compressor with vapor injection. International Journal of Refrigeration, 74, 475-487.

Ziviani, D., Bahman, A.M., James, N.A., Lumpkin, D.R., Braun, J.E. and Groll, E.A., 2018. Machine Learning Applied to Positive Displacement Compressors and Expanders Performance Mapping. Proceedings of International Compressor Engineering Conference at Purdue. Paper 2533.

Manuscript ID: 1346
DOI: 10.18462/iir.icr.2019.1346

Compressor characteristics of an oil-free, two phase rotary vane motor for water-steam applications

Espen VERPE[(a)], Michael BANTLE[(a)], Steinar FAANES[(b)], Nikolai SLETTEBØ[(b)], Trygve M. EIKEVIK[(c)]

[(a)] SINTEF Energy Research P.O. Box 4761 Torgården, NO-7465 Trondheim, Norway, michael.bantle@sintef.no
[(b)] Tocircle Industries AS, 0160 Oslo, Norway
[(c)] Norwegian University of Science and Technology, Trondheim, Norway

ABSTRACT

The development of high temperature heat pumps is often limited by the quality of the excess waste stream. For processes like drying, distillation, frying, pasteurization or evaporators the excess stream is often a combination of different phases (liquid water and saturated steam) which makes the system integration of a heat pump challenging.
Rotary vane motors can handle two phase flows, which enables especially steam application to compress the excess stream directly to higher pressure and temperature levels while the liquid water phase is used to cool the compressor simultaneously. Experimental results from a prototype oil-free rotary vane machine is presented, and its performance indicators are presented and discussed in detail. Two approaches to determine the isentropic efficiency is presented, due to unconventional two-phase mechanisms. The vane compressor is evaluated with respect to industrial implementation.
Keywords: Steam Compression, Two-Phase Compression, Heat Recovery.

1. INTRODUCTION

Heat pumps has been identified as a possible technology to reduce the total greenhouse gas emissions (Arpagaus et al., 2018). One possible application of heat pump technology is to increase the proportion of utilized waste energy from the industry, by increasing the waste stream pressure and temperature to a re-useable level. For the current and near-future heat pump technology, the food & drink, paper and chemical industry has the largest potential for waste heat recovery (Wolf, S., et al. (2014). By introducing heat pump systems such as MVR or direct/indirect waste heat compression, the main energy source for the facility, often natural gas, can be significantly reduced. There is a lack of small-scale heat recovery heat pumps in the range of 0.5 to 4 MW as most systems are above 5MW, especially MVR systems (Tolstorebrov et al., 2014). Fans or blowers are often used, which has limited temperature lift, often no more than 10K. More recently, turbo compressors are used for steam compression which has high volumetric flow and temperature lift of approximately 20K (Larminat, 2015). They are, however, very sensitive to particles and droplets, thereby requiring superheated steam.
Industrial waste streams are often governed by unstable, particle infested, two-phase flow which makes it problematic to recover the heat directly. However, vane compressors are suitable for these conditions due to their robust construction and relatively low RPM. In fact, the compressor described in this paper relies on liquid water on the suction side for lubrication, sealing and internal cooling.
This paper portrays experimental prototype results for an oil-free, two-phase-water rotary vane compressor which is intended to use in a future waste heat recovery heat pump for the industry.

2. METHOD AND MATERIALS

2.1 The compressor

The investigated compressor is based on expander technology from Kjell Vadings patented principle (Vading, 2011)

Conventional rotary vane devices are positive displacement machines in which the drive shaft are driven by a cylindrical rotor, supported eccentrically within a cylindrical casing having a larger diameter then the rotor, so that the rotor and the stator tangents in one line. A volume is then formed between the rotor and the stator, and this volume is divided into smaller chambers by vanes that are free to slide radially in and out of the rotor. The vanes are pushed outwards by springs or simply by centrifugal forces, and their extension is limited only by the vane tip contacting the inner casing wall. A closed compression or expansion chamber is then formed between 2 vanes, the rotor and the casing wall, and the volume of this chamber decreases as the rotor rotates; the closer the chamber comes to the rotor-stator tangent line, the smaller it gets.

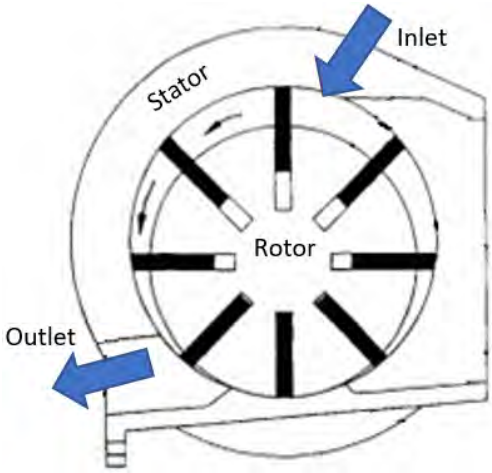

Figure 1: Principal sketch for a vane compressor

Rotary vane compressors are known to be simple, effective and robust machines, being highly tolerant to liquid droplets in the process. However, the friction occurring in the contact between the moving vanes and the static casing sets limits the size and volumetric capacity that can be obtained without allowing the working fluid to be contaminated by lubricating oil.

The newly developed machine, presented in this paper, is similar to conventional rotary vane machines in that they have a similar arrangement of rotor, stator and vanes, and therefore maintain the advantages of the conventional rotary vane machines. However, in the new machines the problem of vane tip friction is solved by moving the control of the vane extension to the center of the machine. This means there is no contact between the vane tips and the casing. The geometric principle of the new machine ensures that the vane tip always follows the casing wall with a small and constant clearance to the stator wall.

Through testing the compressors, they have been proven to be very tolerant to liquid in the working media, and it has shown that so-called evaporative compression can be realized in the machines by injecting liquid at the inlet, in the compression chamber, or through liquid supported hydrostatic bearings, which is a key enabling technology in the current designs. Evaporative compression is compression of a two-phase working fluid, so that the liquid is evaporated during the compression prosses. If the working fluid is still in the two-phase region after the compression, the working media is never superheated, which is beneficial both for the compressor itself and for the heat pump process efficiency. Fig. 2 illustrates how the ideal and the actual compression looks like in the T-S diagram. The ideal case being just enough liquid on the suction side so that saturated gas is formed at the outlet, resulting in pure saturated gas in the condenser. However, the actual process requires more liquid for sealing and cooling, resulting in two-phase outlet conditions. This is not ideal as compressor energy is used to increase the pressure and temperature of the liquid, which delivers very little to no energy in the condenser.

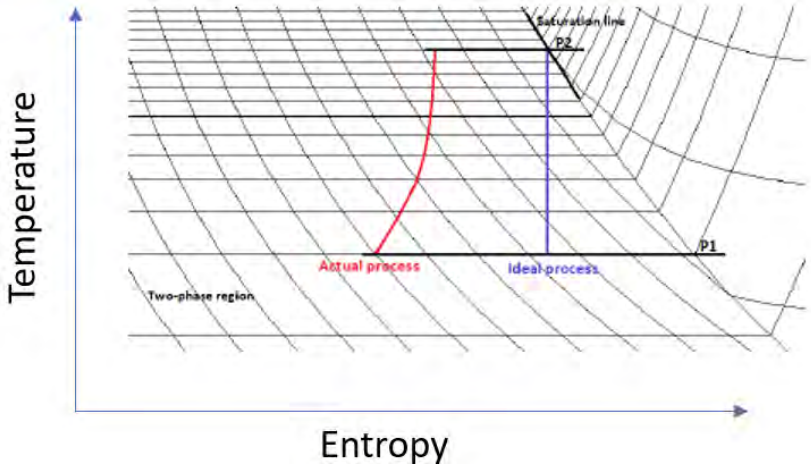

Figure 2: Evaporative compression. Ideal case and actual

2.2 The test rig

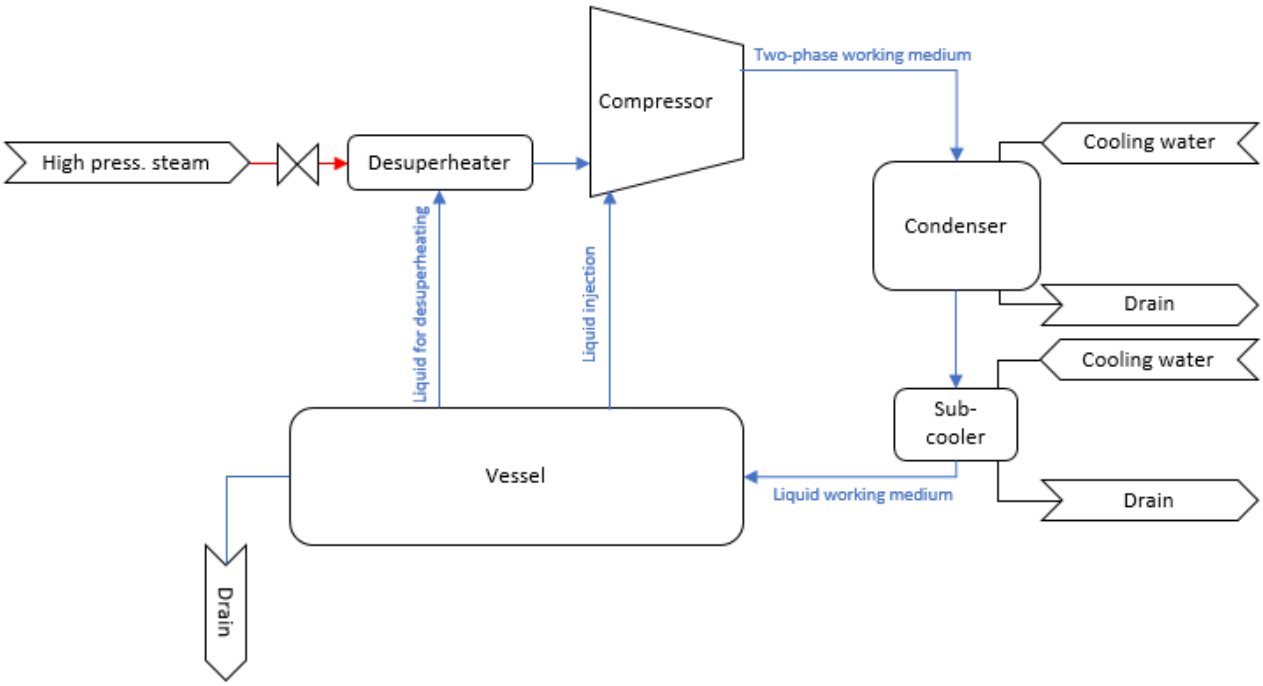

Figure 3: Schematics for the compressor test rig

The working medium of the heat pump is water, which is circulated in an open-loop system with a buffer vessel. Heat is supplied to the heat pump by a high-pressure steam feed, which is expanded to a lower pressure and desuperheated before being supplied to the compressor. Compressed working medium, normally in the two-phase state, is condensed in the condenser by a supply of cooling water, before being subcooled, throttled to low pressure and returned to the vessel. There is also a liquid water injection from the vessel to the compressor inlet, resulting in two-phase flow at the compressor inlet.

There are additional streams between the compressor and the vessel, representing liquid working media to be injected in the process (both directly, and indirectly as cooling, bearing and sealing liquid) and liquid separated from the process during or after compression.

Pressure and temperature sensors are placed before and after the important components. In addition, flow sensors are placed at the compressor inlet, after the heat exchangers and on the compressor draining streams. The flow sensors are of the type vortex meters, temperature sensors of the type PT100 and pressure sensors of the type piezoresistive element. The test rig is well insulated in order to avoid heat loss from the components and piping.

The usual procedure for calculating isentropic efficiency may not be applicable to the compression process of the heat pump, due to the challenge of defining actual inlet and outlet enthalpies, as well as defining a reversible (ideal) process to compare with. The authors could not find any data in the literature on isentropic efficiency for two-phase compressors. Therefore, regular single-phase compressors is used for comparison

While inlet enthalpy may be determined by summing up the enthalpy f lows of all vapor and liquid inlets, mixing them at constant pressure, this will not provide a good representation of actual inlet conditions as vapor-liquid equilibrium (VLE) is not achieved instantly. Furthermore, parts of the liquid may not be introduced to the vapor until later in the compression process and is thus not present in the supposed inlet equilibrium mixture.

Any reversible process requires the fluid to be in thermal equilibrium throughout the process. While the ability to achieve VLE may be a relevant property of the compressor, VLE may not necessary be desirable to the overall performance of the heat pump, and a part of the liquid passing through the compressor may deliberately be kept from reaching equilibrium with the vapor phase. The idea l process to compare with is therefore not necessarily compression of a mixture of all streams entering the compressor at continuous equilibrium.

The challenge of determining inlet and outlet enthalpy is purely caused by limitations in measuring techniques. Practical and robust measuring techniques are not available to measure vapor fraction, except for vapour quality sensors from HB (HBproducts, 2019). However, these sensors do not operate at temperatures above 100 °C.

2.3 Compressor isentropic efficiency calculation

Heat transfer in the condenser can be calculated with high certainty from flow and temperature measurements on the cold side, to yield the amount of heat that is received on the cold side. Heat- and mass balance can be used to calculate hot side heat transfer, i.e. the amount of heat that is removed from the hot side. This will however require knowledge of all heat- and mass flows to and from the compressor and is thus inherently more sensitive to measurement errors.
Valid for all heat transfer in the condenser:

$$Q_{cond} = \dot{m}_{tot} \Delta h_{cond} \quad \text{Eq. (1)}$$

Where $\dot{m}_{\mathrm{tot}}$ is the total mass flow in the condenser hot side and Δh_{cond} is the change of enthalpy in the condenser. If one assumes two-phase flow on the inlet of the condenser, the following equations apply:

$$Q_h = \dot{m}_{vap} \Delta H + \dot{m}_{tot}\left(h_{sat,liq} - h_{out}\right) \quad \text{Eq. (2)}$$

$$Q_c = \dot{m}_c \cdot c_{p,c} \cdot \Delta T_c \quad \text{Eq. (3)}$$

$$Q_h = Q_c + Q_{loss} \quad \text{Eq. (4)}$$

Eqs. (2) and (3) constitutes two different methods of measuring the condenser heat, from the hot side (h) and the cold side (c). The condenser is designed to maintain saturated liquid at the outlet, by controlling the amount of cooling water. On the cold side, an energy meter is used to measure mass flow and change in temperature of the cooling water. Q_{loss} is estimated by measuring the surface temperature on the outside of the insulation around the condenser.
For an ideal process, see Figure 2, the isentropic compressor energy, W_{is}, can be defined:

$$W_{is} = \dot{m}_{\mathrm{tot}}\left(h_{P2,sat} - h_{P1,is}\right) = \dot{m}_{\mathrm{tot}} \Delta h_{comp,is} = \dot{m}_{\mathrm{vap}} \Delta h_{comp,is} \quad \text{Eq. (5)}$$

Where Δh_{comp} can be determined by knowing the two pressure levels and $h_{P1,is}$, which is known from assuming equal entropy through the compressor. In the ideal case $\dot{m}_{\mathrm{vap}} = \dot{m}_{\mathrm{tot}}$ due to saturated steam on the outlet. The definition of isentropic efficiency is:

$$\eta_{is} = \frac{W_{is}}{W} \quad \text{Eq. (6)}$$

Where W is the measured compressor work. If one assumes no subcooling in the condenser, the second term in Eq. (2) is eliminated. Inserting the expression for the mass flow from Equation 2 into Eq. (5), a new expression for isentropic efficiency is formed:

$$\eta_{is} = \frac{Q_h \cdot \Delta h_{comp,is}}{W \cdot \Delta H} \quad \text{Eq. (7)}$$

The COP for a heat pump is defined by:

$$COP = \frac{Q_h}{W} \quad \text{Eq. (8)}$$

And the ideal COP, equal to Carnot COP if the temperature levels are set to condensing and evaporating temperatures, is defines as:

$$COP_{ideal} = \frac{\Delta H}{\Delta h_{comp,is}} \quad \text{Eq. (9)}$$

Eq. (7) can therefore be re-written to:

$$\eta_{is} = \frac{COP}{COP_{ideal}} \quad \text{Eq. (10)}$$

Equation 10 essentially says that the deviation in obtainable COP, compared to the ideal case, are inefficiencies in the compressor. In a real system, other factors like heat loss, pressure loss and superheated steam loss also contribute to a decreased COP. However, for a two phase-compressor, the latter is non-existing. Therefore, by estimating heat loss in the compressor, condenser and piping, the isentropic efficiency is well estimated.
Furthermore, the isentropic efficiency will also be estimated by using more conventional methods, Equation 6. Here, the isentropic compressor work is calculated by assuming VLE at the compressor inlet and outlet.

3. RESULTS AND DISCUSSION

In this part, various measurement data of the compressor will be presented, starting with pressure.

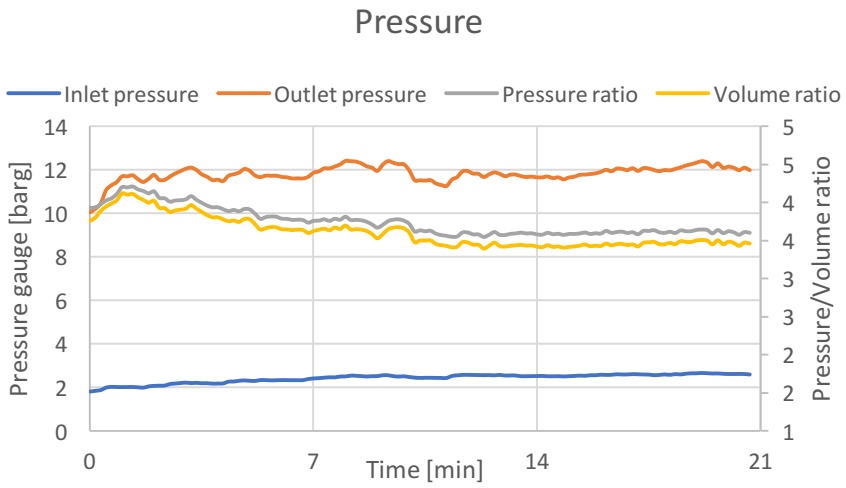

Figure 4:Pressure measurement (gauge) at the inlet and outlet of the compressor

The suction pressure is held quite stable at 2.4 barg, while the discharge pressure is varying between 11 and 12.5 barg, resulting in a varying pressure ratio between 4.5 and 3.5, stabilizing at 3.6 towards the end of the experiment. The mean saturated temperature elevation is measured to be 53K at the inlet conditions presented above. However, for lower inlet pressure the temperature elevation is

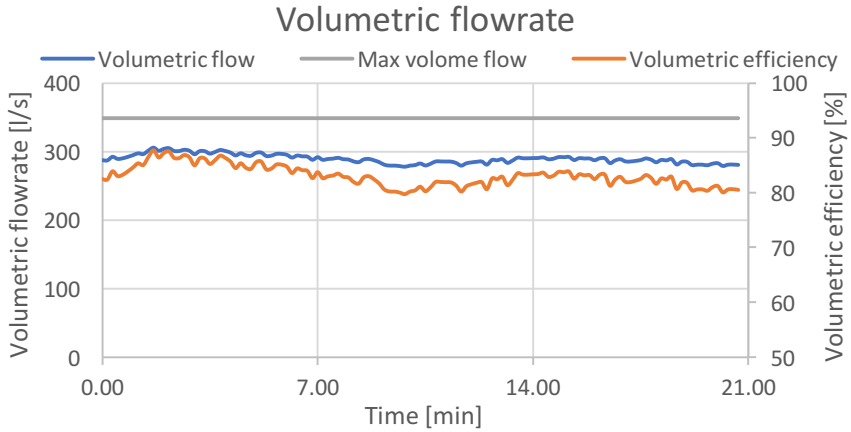

Figure 5: Designed and actual volumetric flowrate at the compressor

expected to be less due to fixed compressor volume ratio and steam properties.

The designed volumetric flowrate is 360 $L \cdot s^{-1}$, at 1000 RPM, while the measured flowrate varies just below 300 $L \cdot s^{-1}$, resulting in a volumetric efficiency of 83%. Volumetric losses occur due to migrating steam and liquid water from a high-pressure chamber to the neighboring low-pressure chamber. Smaller clearance between stator and the vane tips together with better vane tip design is thought to increase the volumetric efficiency, which in turn will increase the thermal capacity of the

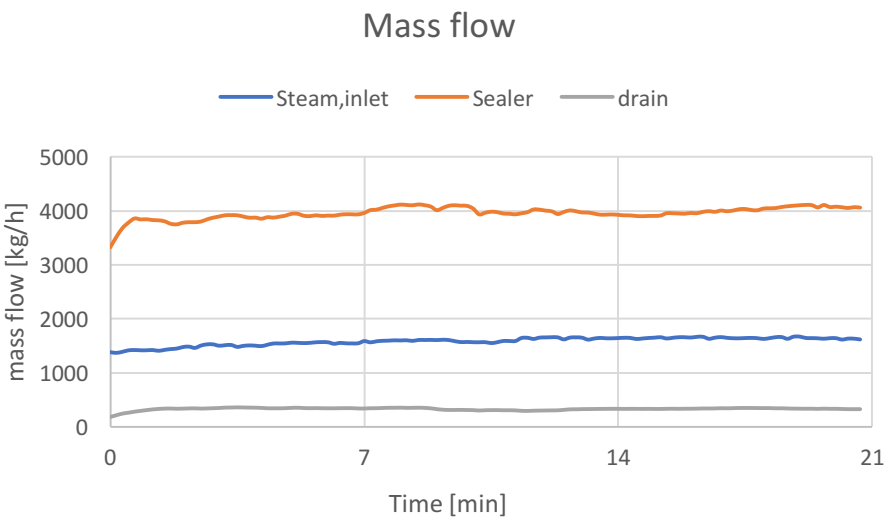

Figure 6: Mass flow of suction steam, liquid water (sealer) and draining fluid

compressor.

The mass flow balance is a little more complex due to multiple inlets and outlets. Even though the mass fraction of vapor is around 1/3 of the total flow, it dominates the volumetric fraction due to much lower steam density compared to liquid water. At the inlet conditions presented in Figure 4, the compressor steam mass flow is measured to be around 1600 kg/h. Notice a considerably higher mass flow of liquid water which is used to lubricate, seal and cool the compressor. Around 300 kg/h of water is drained from the compressor, in addition to other smaller liquid inlet and outlets.

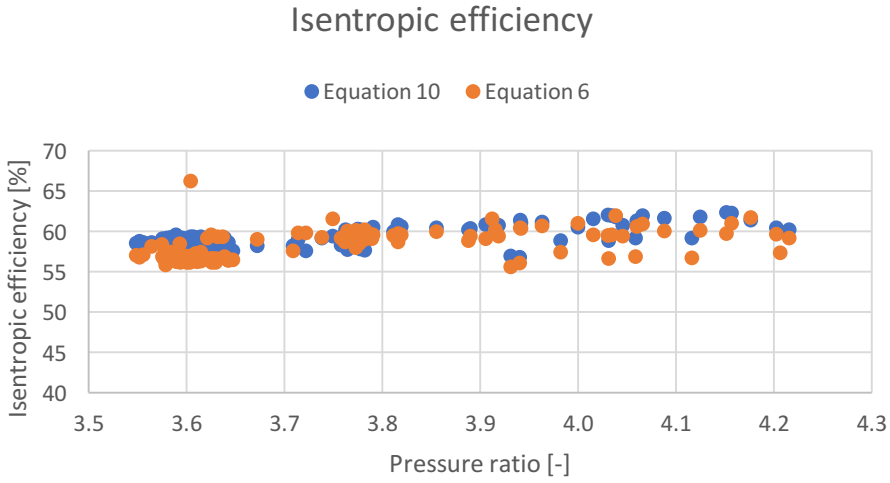

Figure 7: The isentropic efficiency of the compressor by two different approaches

Isentropic efficiency can be calculated by methods explained in chapter 2.3. The two methods yield very similar results, just below 60 %. Furthermore, methods are currently being developed to increase the isentropic efficiency and will be tested in the near future.

Table 1:Averaged experimental KPIs for the vane compressor

Averaged KPIs		
Mean suction pressure	2.4	barg
Discharge pressure	11.8	barg
Saturated discharge temperature	190	°C
Pressure ratio	3.8	-
Volume ratio	3.6	-
Saturated temperature lift	53	K
Suction steam mas flow	1584	kg/h
Sealer mas flow	3957	kg/h
Volumetric suction flowrate	289.7	l/s
Volumetric efficiency	83.0	-
Isentropic efficiency (eq. 6)	59.2	-
Isentropic efficiency (eq. 10)	58.3	-
Shaft power	217.5	kW
Condensator capacity	903.2	kW

Table 1 provides an overview of the test results in the figures above. If the compressor were to be used in a heat pump, it could deliver 900 kW of heat at 190 °C, or close to 1600 kg/h condensable steam, from 3.4 bar to 12.8 bar. One could argue that even though the compressor efficiency of 59 % is not that high, compared to other single-phase compressors on the market, the overall system COP will be improved due to no superheating at the compressor discharge. In addition, water generally suffers from high discharge temperatures, which leads to compressor sealing difficulties and decreased condenser efficiency. This problem is avoided due to two-phase flow in the compressor, leading to higher obtainable condensing temperatures than other compressors. For comparison, the isentropic efficiency for rotary screw and centrifugal compressor is generally in the range of 65 % -75 % and 70 % -85 %, respectively (Campbell, 2014).
It is, however, difficult to directly compare efficiency of a two-phase compressor to that of a single-phase compressor, as the heat transfer between vapor and non-evaporated liquid will appear as an additional mechanism that effects the efficiency of the two-phase compressor. The mass flow of steam might not be constant through the compressor. Further experiments are needed to properly define the relation between surplus/deficient gas mass flow, which directly influence the thermal capacity of the compressor.

4. CONCLUSION

Compressor characteristic of a steam based, two-phase vane compressor has been established by an experimental approach. The suction and discharge pressure were measured to be around 3.4 and 12.8 bar, resulting in a pressure ratio of 3.8. The actual suction volume flow was measured to be 290 l/s, corresponding to 1600 kg/s steam and 900 kW condensable thermal power at 3.4 bar. The isentropic efficiency was estimated to be around 59 %, from two different approaches, resulting in nearly the same outcome. The first method (eq.6) is based on measured compressor work compared to isentropic work, assuming LVE (liquid/vapour equilibrium) at the compressor inlet and trough the evaporative compression cycle. The second compares actual heat pump COP, including heat loss, with ideal COP and states that the rest of losses must come from the compressor.
The compressor is designed to be installed in a steam generating heat pump. Steam is the preferred heat carrier in many industries and is mostly generated by natural gas boilers today. A steam generating heat pump can therefore help the industry with reducing its carbon footprint. In addition, if the heat pump has a higher COP than the energy price ratio for electricity/natural gas, the steam generating heat pump will also reduce the total energy cost for the company. Results in this paper demonstrates that this compressor has the potential to be used in heat pumps to elevate waste

streams more than 50K in a single stage. Even higher lifts are possible when using a bottom stage heat pump, or a two-stage setup.

ACKNOWLEDGEMENTS

The authors would like to acknowledge the support of The Research Council of Norway and the industrial partner ToCircle Industries AS through the grant NFR-282123 (Free2Heat).

NOMENCALTURE

Q	Heat [W]	$\dot{m}$	Mass flow [kg/s]	W	Compressor work [kW]
h	Enthalpy [kJ/kg]	ΔH	Heat of fusion [kJ/kg]	η	Efficiency [-]
T	Temperature [K]	c_p	Heat capacity [kJ/kgK]	COP	Coefficient of performance

REFERENCES

Arpagaus, C., Bless, F., Uhlmann, M., Schiffmann, J., & Bertsch, S. (2018). High temperature heat pumps: Market overview, state of the art,research status, refrigerants, and application potentials. *Energy*, 985-1003.

Campbell, J. M., & Larry, L. L. (2014). *Gas conditioning and processing Volume 2: The equipment modules* (6 ed.). Campbell Petroleum Series.

HBproducts. (2019). *HBX sensors*. Retrieved from https://www.hbproducts.dk/en/products/hbx-sensors.html

Larminat, P. (2015). A High Temperature Heat Pump Using Water Vapor as Working Fluid . Brussel: ATMOsphere.

Tolstorebrov, I., Bantle, M., Hafner, A., Kuz, B., & Eikevik, T. M. (2014). Energy efficiency by vapor compression in superheated steam drying systems. *11th IIR-Gustav Lorentzen Conference on Natural Refrigerants.*

Vading, K. (2011). *Unite States of America Patent No. US9376914B2.*

Wolf, S., Fahl, U., Blesl, M., & Vos, A. (2014). *Analyse des Potenzials von Industriewärmepumpen in Deutschland.* Universität Stuttgart.

Manuscript ID: 1361
DOI: 10.18462/iir.icr.2019.1361

Development of a dynamic model for ice-on-coil external melt storage systems

Jasper NONNEMAN[(a,b)], Michiel DE VOS[(a)], Hugo MONTEYNE[(a)], Wim BEYNE[(a)], Michel DE PAEPE[(a,b)]

[(a)] Department of Flow, Heat and Combustion Mechanics, Ghent University, Sint-Pietersnieuwstraat 41, 9000 Ghent, Belgium, Jasper.Nonneman@UGent.be
[(b)] Flanders Make, Core Lab MotionS, Gaston Geenslaan 8, 3001, Leuven, Belgium

ABSTRACT

Ice storage systems are commonly used to balance the intermittency of renewable energy and decrease the peak load by switching to off-peak hours. An adequate model is necessary to predict the behaviour of these systems. However, there is a scarce in detailed models available used to describe the performance of an ice storage evaporator and its use in a refrigeration cycle. Most existing models approximate the working principles with a steady analysis, not considering the sub cooling of ice and thickness distribution along the length. The developed model in this article uses a discretisation in length and radial direction together with an adapted thermal resistance matrix method to limit the calculation time. It has a great variability of boundary conditions and the ability to implement different types of refrigerants. The simulation results are in good agreement with the data of the manufacturer. The model shows that switching from R404A to R449A reduces the total electricity consumption.
Keywords: Cold Storage, Evaporator, Ice Bank, Modelling, R404A, R449A

1. INTRODUCTION

Present day, renewable power generation is quickly growing all over the world. Questions arise about their intermittent generation and as a result the continuous need of backup systems which are more polluting (Steinke et al., 2013). Moreover, the boost of air conditioning systems with a growth from 1.6 billion today to an expected 5.6 billion by 2050 requires a new electricity capacity equivalent to the combined electricity capacity of US, EU and Japan today. Together with this, air conditioning systems are also responsible for a major part of the peak loads, especially during the summer and/or in hot climates (Goetzler et al., 2016). During these peak moments, less efficient and more polluting peak plants are required. To balance both the demand and the intermittent generation of renewable energy methods, a storage method can be used to introduce both a spatial as well as a temporal dissociation between production and usage. This paper focuses on the use of a cool thermal storage. The charging during off-peak hours or when there is a surplus of renewable energy has the possibility to drastically reduce the peak load and consequently electricity costs by switching parts from on- to off-peak hours (Cárdenas & León, 2013; Saito, 2002).
Different cool thermal storage options exist, but the focus in this paper is on ice thermal storage which benefits from the large value of the latent heat of fusion compared to the sensible heat. In a narrow temperature range, a high volumetric capacity can be reached with these systems (Biosca-Taronger et al., 2012). An ice-on-coil external melt system will be discussed in this work, which is charged by a refrigerant flowing inside the coils and discharged by water flowing over the ice coils (see Figure 1). Consequently, no ice bridging between the different coils is allowed to ensure the circulation of the water over the ice coils during discharging. Ice is formed outside of the coils and due to the increased thickness of the ice, the thermal resistance of the ice rises and as a result, the effectiveness decreases. This is a characteristic of a static thermal energy storage; the ice is built and stored at the same location and no complex harvesting techniques are required in contrast to a dynamic thermal energy storage (Saito, 2002).

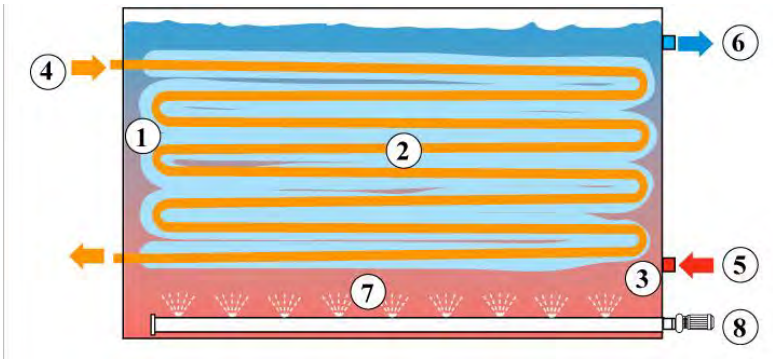

Figure 1: Ice-on-coil external melt working principle (Baltimore, 2019)

With a constant evaporator temperature, the ice thickness increases non-linearly with a decreasing slope due to the increased thermal resistance with ice thickness. Consequently, the evaporating temperature has to be decreased to ensure the uniform continuation of the ice formation when connected to a condensing unit. Due to the decrease in evaporating temperature, the cooling power delivered by the condensing unit/refrigerant decreases as well. Most numerical models approach the working principle of the ice storage as a perfect heat transfer of two flows. The ice formation is obtained by $Q_{ice} = \Delta T_f \dot{m}_f c_{p,f}$ in the case of a single phase coolant, with Q_{ice} the cooling capacity, ΔT_f the difference between the inlet and outlet temperature of the charge flow, $\dot{m}_f$ the mass flow rate of the charge flow and $c_{p,f}$ the specific heat capacity of the charge flow (Vetterli & Benz, 2012). Moreover, environmental conditions and consequently losses to the environment are not taken into account in most models found in scientific literature. To take into account the increase of ice resistance and therefore the decrease in effectiveness, an effectiveness curve ε in function of the fraction of ice is implemented in the majority of the models. This curve is obtained from experimental data and is added to the equation for the cooling power: $Q_{ice} = \varepsilon \Delta T_f \dot{m}_f c_{p,f}$. This equation is used both for the charging and the discharging process with a different slope (Candanedo et al., 2013). This gives an idea about the cooling power, but no further insights in the working principle or possible adaptations/optimisations can be obtained from these models.
Furthermore, a switch from R404A to R449A is recently proposed in the refrigeration systems due to its lower global warming potential which is almost three times smaller. As with R404A, no chlorine is present in R449A and consequently, the ozone depletion potential is zero. Little research has been done, but the results are promising: similar energy performances are obtained after the switch. The major drawback is found in the temperature glide of 5.8 °C at 0.1 MPa for R449A which is only 0.8 °C at the same pressure for R404A (Makhnatch et al., 2017; Tecumseh, 2016). Because of the lack of adequate models to predict the performance of ice-on-coil external melt storage systems, a dynamic model is developed in this work, with a great variability of boundary conditions and the ability to implement different types of refrigerants. With this model, the two refrigerants R404A to R449A will be investigated.

2. DYNAMIC NUMERICAL MODEL

The numerical model is based on the thermal resistance matrix method for one phase materials/fluids, although adapted to account for phase changes. The different nodes *i* are thermally connected to each other and as a result, this method is based on the discretized energy balances between the nodes. The node temperatures are obtained in the regular thermal resistance matrix method by $T=K^{-1}b$ with K the conductance matrix, T the array of node temperatures and b the array of heat inputs:

$$K_{ij} = K_{ji} = R_{ij}^{-1} = R_{ji}^{-1} \quad \text{Eq. (1)}$$

$$K_{ii} = -(\Sigma_{j \neq i} K_{ij} + \Sigma R_{ext,i}^{-1} + m_i c_{p,i} \Delta t^{-1}) \quad \text{Eq. (2)}$$

$$b_i = -(Q_i + \Sigma T_{ext,i} R_{ext,i}^{-1} + m_i c_{p,i} \Delta t^{-1} T_{i,t-1}) \quad \text{Eq. (3)}$$

Where R is the thermal resistance, i and j represent the different nodes, m_i the mass in node i, Δt the discretised time step and *ext* refers to external nodes. When a phase change occurs, the temperature stays constant and only the enthalpy changes. As a result, the previously defined equations can no longer be used for this node. The array of node temperatures T is changed to an array of node temperatures and/or enthalpies TH where TH_k is the enthalpy in node k; the node where ice is formed or melted. The other elements still represent the corresponding node

temperature. Consequently, column k in the K matrix that interacts with TH_i has to be adapted. A characteristic of node k with an enthalpy in the range $[-H_{lat};0]$ is that the temperature is equal to the melting temperature until the enthalpy exceeds the limits of the range defined. An enthalpy of zero is considered for water at melting temperature and an enthalpy of $-H_{lat}$ corresponds to ice at melting temperature. The regular resistance matrix method can be used with the following additions to account for the change from temperature to enthalpy for one node:

$$K_{kk} = -m_k \, \Delta t^{-1} \quad \text{Eq. (4)}$$

$$K_{k\pm1,k} = 0 \quad \text{Eq. (5)}$$

$$b_k = \Sigma_{i\neq k} K_{ki} \, T_{melt} + \Sigma \, T_{melt} \, R_{ext,k}^{-1} - (Q_k + \Sigma \, T_{ext,k} \, R_{ext,k}^{-1} + m_k \, \Delta t^{-1} H_{k,t-1}) \quad \text{Eq. (6)}$$

$$b_{k\pm1} = -K_{k,k\pm1} \, T_{melt} - (Q_{k\pm1} + \Sigma \, T_{ext,k\pm1} \, R_{ext,k\pm1}^{-1} + m_{k\pm1} \, c_{p,k\pm1} \, \Delta t^{-1} T_{k\pm1,t-1}) \quad \text{Eq. (7)}$$

The energy balances are based only on sensible heat for layers with only ice or only water. A layer which is partially filled with ice is based on the latent heat and consequently, the enthalpy difference with a known temperature and state.

A division into different layers and in sections of length is proposed in this model. The outer radius of the last layer is defined by the maximum radius the ice can reach to ensure no ice bridging. Due to the division into different layers, a thermal capacitance per layer is taken into account and every time step the total ice layers are calculated to update the ice resistances. This division in sections of length is introduced to take into account the effect of the temperature glide of the refrigerant which is not negligible for R449A, and consequently resulting in a different ice thickness over the length of the coil. The energy balances obtained from this division into different layers are visualized by the thermal equivalent circuit shown in Figure 2 for an example with two full ice layers and a division into four equivalent layers.

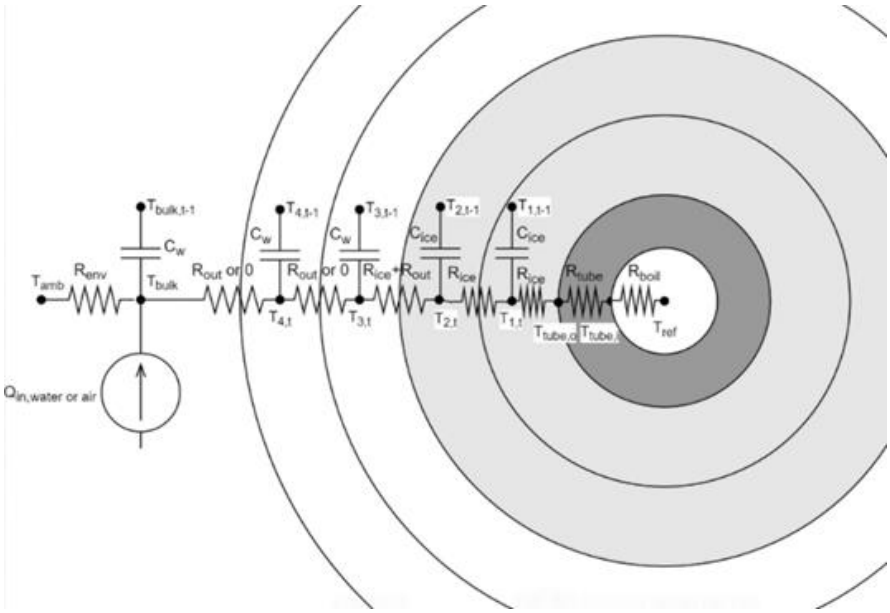

Figure 2: Thermal equivalent circuit for two full ice layers.

The heat transfer of the refrigerant at the inside of the coil which is a two-phase flow, is calculated with the Shah correlation (Shah, 1976) for heat transfer during boiling flow through pipes (Lee & Jones, 1996). This correlation is based on the consideration that the nucleate boiling and the convective boiling are the two most important heat transfer mechanisms where the larger one is chosen as the value to approach the local two-phase boiling heat transfer coefficient. The heat transfer at the outside of the coil is dependent on the mass flow rate of the water or in general when charging or discharging occurs. In case of a mass flow of water (during discharging), forced convection correlations are used which are based on the Reynolds number, $Re=v \, \rho \, (2r) \, \mu^{-1}$, with v the fluid velocity, ρ the density, r the ice radius and μ the fluid viscosity. During charging, there is no incoming mass flow rate of water, so natural convection occurs and this is based on the Rayleigh number Ra. The Rayleigh number (a dimensionless number defining whether heat in a fluid is transferred primarily by free convection or conduction) is expressed by $Ra=(2r)^3 g\beta(T_{wall} - T_\infty) \, \rho^2 c_p \mu^{-1}$

with β the thermal expansion coefficient, T_{wall} the outer temperature of the (ice) coil and T_{∞} the average tank temperature. The density curve of water has its maximum point around 4 °C so further cooling down shows a negative thermal expansion coefficient and a switch of the stratification of the water inside the tank.
Convection correlations from scientific literature are compared which are able to handle this sign difference and the correlation of Merk is chosen in the model. This correlation is based on a cylinder in a tank with a certain bulk water temperature similar to an ice storage tank and experimental results found in literature showed a small deviation for a large range of conditions (Yen, 1990). This correlation only describes the heat transfer from bulk fluid temperature to the tube wall, but does not provide a temperature distribution of the fluid around the coil. The flow characteristic per layer and consequently the temperature in the middle of this water layer is approached by a division of the outer resistance equally between every node. As a result, a temperature gradient is obtained between the bulk temperature and the water layer temperature closest to the coil. For the discharging process, on the other hand, the whole tank is assumed to be perfectly mixed due to the circulating water and no temperature gradient is present close to the coil. With this approach, every node has the same temperature as the tank temperature on that height level. The ambient conditions are taken into account by the calculation of the losses to the environment. At the outside this is based on natural convection of the air. Dependent on the mass flow rate of water, forced or natural convection correlations are used at the inside of the wall.
During the discharging, water is circulated through the tank with a certain mass flow rate and to facilitate this discharging process, air is introduced from an air blower. This air is released at the bottom of the tank through pipes with a small perforation. Two sources of heat inputs (incoming water and air flow) are present and are taken into account, but only the water flow is taken into account to calculate the forced convection resistance. Nevertheless, air will promote the heat transfer, so an enhancement factor can be estimated based on experiments to reduce the deviations between the simulations and the experiments.

3. SIMULATION RESULTS

3.1. Evaporator model

The described model is further used to simulate a 1.28 m high, 1.15 m wide and 1.8 m long ice storage tank with five evaporator coils of 13.85 m long and with an outer diameter of 6.25 mm. The coils are made of copper and are positioned such that the maximum ice radius on a coil before ice bridging is 38 mm. The simulations are done for only one coil, so the total length of the tank (1.8 m) is divided by 5. In this part (evaporator model), a constant refrigerant inlet temperature and mass flow rate are assumed. Both a charging cycle and discharging cycle are investigated.

3.1.1. Charging cycle

First, the charging of the ice tank is evaluated with the refrigerant R449A at 270 K inlet temperature and a mass flow rate of 0.0084 kgs^{-1}, which is equally distributed over the 5 coils. The water in the tank is initially at 278 K and the ambient temperature is 293.15 K. The simulations are done with a time step of 180 s and the total charging time is 5 h. In Figure 3 and Figure 4 a comparison is shown between the total ice capacity after 5 h of charging and the amount of respectively layer or section divisions that were used in the simulation. The temperature glide has been neglected if the length is not divided into different sections. As a result, this case is an overestimation of the cooling capacity. This error drops quite fast and from the moment the length is divided into 15 sections the relative error is below 1 % compared to the defined limit value of 40 which is visualized in Figure 3.
A small amount of different layers is expected to be an overestimation of the system because the temperatures taken are only an average over the entire layer, which introduces an error on the ice formation. With a division into layers, a relative error of less than 0.2 % is reached with a division into 25 layers compared to the defined limit value of 60 divisions. The defined limit values are visualized in the graphs by the dashed line (Figure 4). The evaporator model for charging is further validated by the evaluation of the equality of the energy balances. The cooling power supplied by the refrigerant should be equal to the energy used to cool the ice/water and the losses to the environment. The difference does not exceed 0.2 W in absolute terms, which is a consequence of the iterations that are done to converge the model.

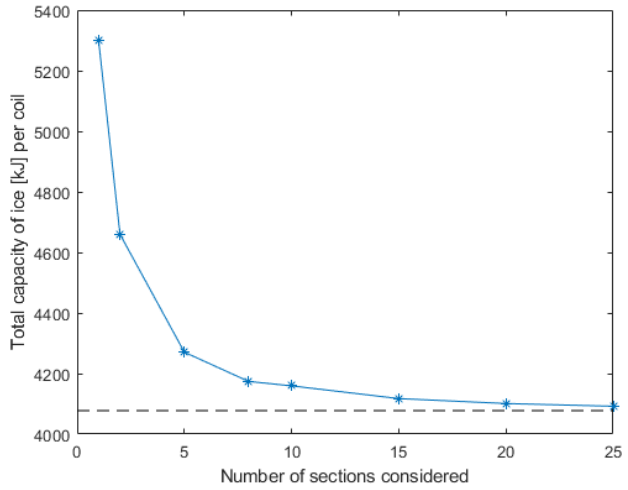

Figure 3: Influence of the total amount of section divisions on the total capacity of ice per coil after 5 hours of charging.

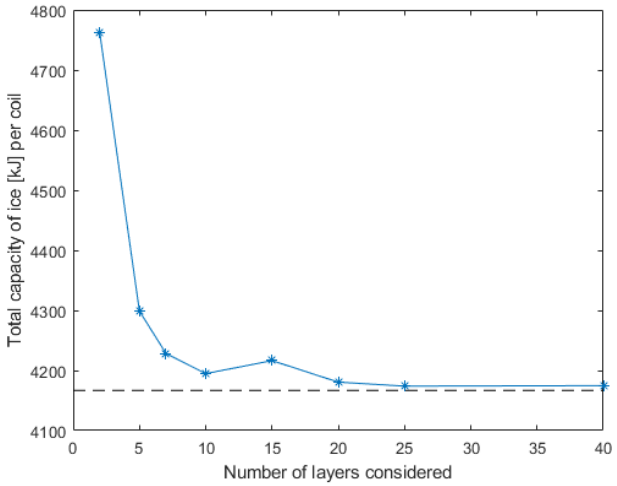

Figure 4: Influence of the division into different layers on the total mass of ice after 5 hours charging.

3.1.2. Discharging cycle

The discharging time is evaluated to validate the time span of discharging which should be in the range of 30 to 60 min according to the manufacturer. At the start of the discharging, the tank and content are at a temperature of 273.65 K and with a 55.4 kg initial mass of ice. The mass flow rate of the hot water entering the tank is 1.933 kgs^{-1} and is assumed to be divided equally over the 5 coils. With a varying inlet temperature of the water, the mass of ice per coil is visualized within time in Figure 5. In Figure 6 the effectiveness curve in function of the fraction of ice of the discharge simulation is compared to one from Henze and Krarti (Ihm et al., 2004), and they show a similar trend. Next to these validations, the energy balances are compared to ensure no energy is lost. No iterations occur here, because the forced convection correlation is independent of unknown temperatures in contrast to the charging process. As a result, the absolute error is at its maximum $12x10^{-5}$ W.

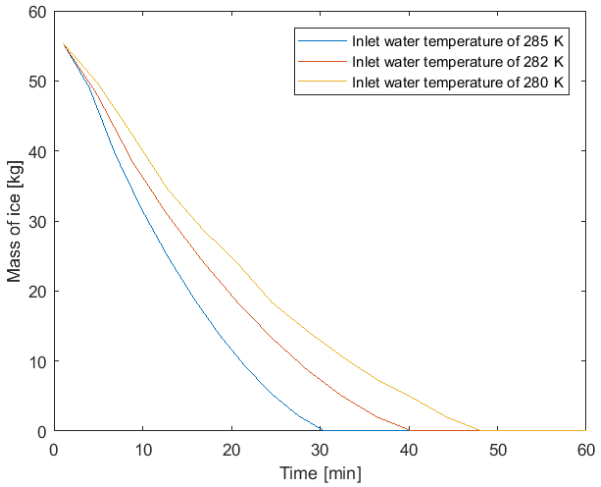

Figure 5: Mass of ice during a discharging process with a varying inlet water temperature.

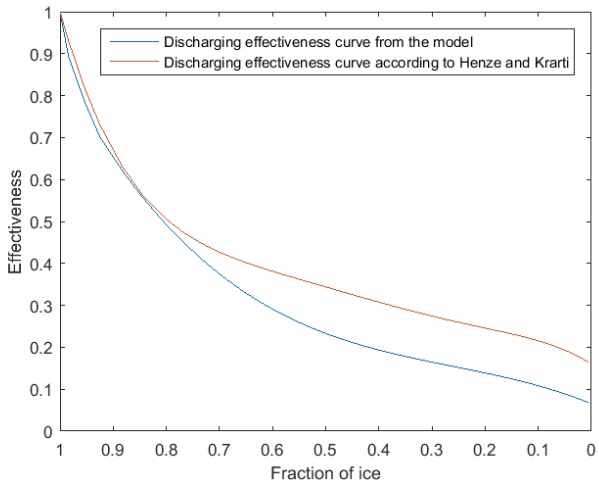

Figure 6: Effectiveness curve in function of the fraction of ice obtained from the model and according to Henze and Krarti. (Ihm et al., 2004)

3.2. Evaporator model coupled to condensing unit

Next the evaporator model is coupled to a condensing unit. Based on data of the condensing unit TFHT4531ZHR from Tecumseh (Tecumseh, 2016), polynomials are obtained by data fitting for the cooling power and mass flow rate of the refrigerant. The model is connected to these data and iterated till the cooling power in the model is equal to the cooling power delivered by the condensing unit. The cooling power delivered by the refrigerant drops after time due to the increased thermal

resistance of ice. To ensure the ice formation, the evaporating temperature and mass flow rate of the refrigerant decreases as well. With initially no ice in the tank and an initial temperature of 273.65 K, a charging time of 5.9 h is achieved.

3.2.1. Comparison R404A and R449A

Recently, a switch from R404A to R449A in air conditioning systems is proposed. A lower GWP and ODP are the reasons for this switch but little research has been done on the effect on the performances of this switch. Based on simulations of a charging cycle with both refrigerants, they can be compared under the same conditions and with the same condensing unit. The differences in performance after a charging cycle of 5.9 h are shown in Table 1 for the two refrigerants. The total mass and capacity of ice is larger with the use of R404A, which can be explained by the more even distribution of the ice thickness along the length. This can be seen in Figure 7 where the thickness distribution along the length is shown. The more even distribution results in a higher total mass of ice when one point reaches the maximum radius. Furthermore, the opposite sign of the slopes is clearly noticed. This phenomenon is explained by the combination of a different temperature glide and the convection coefficient by boiling along the length.

Table 1: Performance comparison after a complete charging cycle.

Parameter	Theoretical maximum	R449A	R404A
Ice mass [kg]	*55.4*	*51.1*	*52.8*
Ice capacity [MJ]	*18.5*	*17.3*	*17.9*

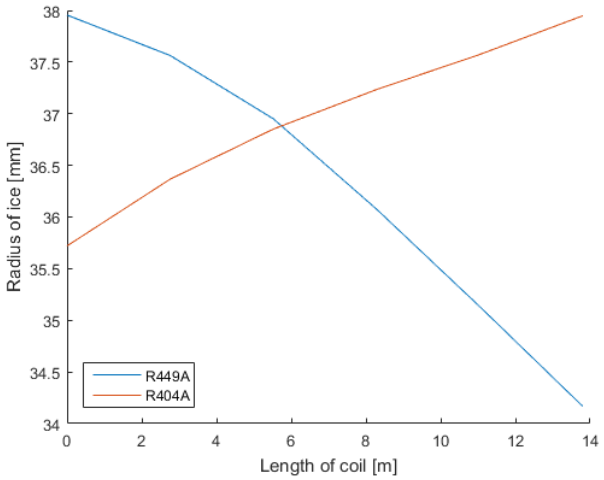

Figure 7: Ice radius distribution along the length.

The convection coefficient increases along the length because the boiling phenomenon is more profound when a larger vapour fraction of the refrigerant is present. As a result, the ice formation is expected to be enhanced along the length which is the case for R404A. However, the heat transfer is also dependent on the temperature difference between fluid and wall. The temperature glide of R449A is larger than the decrease in temperature difference between the refrigerant and the tube wall due to an increase in convection coefficient. The difference of the temperature glide between the two refrigerants is shown in Figure 8.
A drop of the evaporating temperature, visualized in Figure 8, is needed to ensure the continuation of the ice formation. Moreover, it also corresponds to a drop of the mass flow rate, which is a result of the constant volumetric flow rate of the compressor. Based on the storage capacity after the complete charging cycle, the switch from R404A to R449A would not be suggested. However, some additional benefits next to the decreased environmental impact are obtained. We can also determine the performance of the condensing unit by its coefficient of performance (COP):

$$COP = Q\ W^{-1} \qquad \text{Eq. (8)}$$

With Q the supplied cooling power and W the needed electric power input. The COP decreases with time as a result of the decreased evaporating temperature. The COP, visualized in Figure 9, is continuously larger (on average 10%) for R449A compared to R404A. As a result, the electricity consumption is lower.

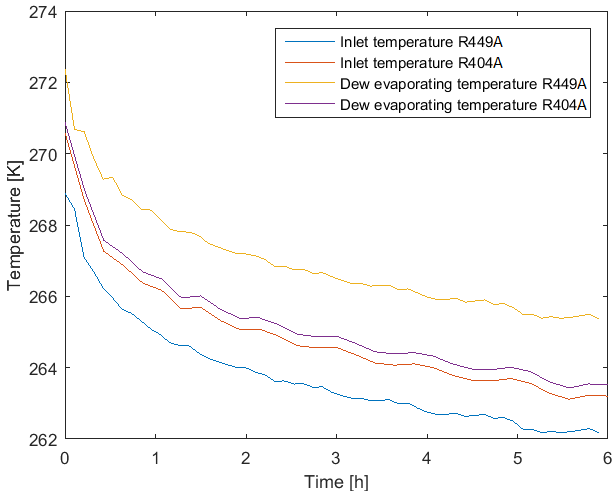

Figure 8: Inlet and dew evaporating temperatures during a complete charging cycle.

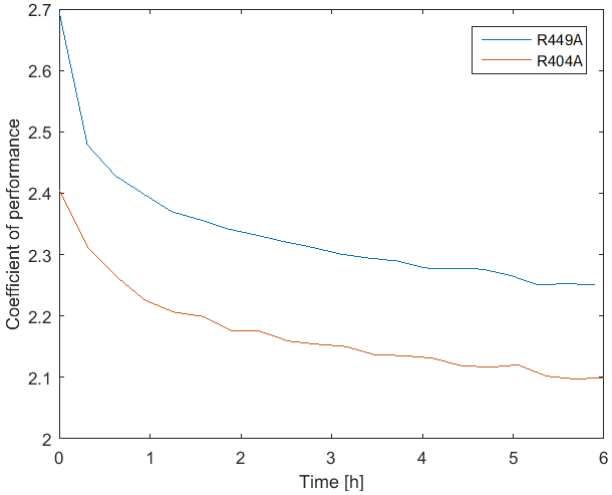

Figure 9: Coefficient of performance during a complete charging cycle.

4. CONCLUSIONS

A dynamic numerical model is developed in this work, based on the thermal resistance matrix method. It is capable to perform simulations on both the charging as well as the discharging process of an ice-on-coil external melt system and shows great similarity with data provided by the manufacturer and effectiveness curves from scientific literature. Numerical results indicate that an increased division in sections and layers converges to a defined limit value. The charging cycle is evaluated with the connection of the evaporator model to a condensing unit to study the effect of different refrigerants. To ensure the continuation of the ice formation with the increased ice thermal resistance, the inlet refrigerant temperature drops from 269.1 K to 263 K and as a result, the COP of the system decreases from 2.7 to 2.25. In the end a cooling capacity of 86.5 MJ is obtained (with five coils) and a total mass of ice of 255.08 kg. This is a deviation of 6.74 % in total ice capacity and 7.92 % in total mass compared to the theoretical maximum values. Furthermore, it was found that the switch of refrigerant from R404A to R449A is not only supported by its lower GWP and ODP value, but also by the increase in COP of around 10 %. However, numerical simulations showed a more uneven thickness distribution of R449A compared to R404A. As a result, the mass of ice is 1.823 kg lower and the corresponding ice capacity is 617 kJ lower per coil. To support the findings in this paper, an experimental setup is being constructed to validate the model thoroughly. With this validated model, it will be possible to design more efficient ice storage tanks.

NOMENCLATURE

b	input array (W)
c_p	heat capacity (J kg^{-1} K^{-1})
COP	coefficient of performance (-)
ext	external nodes
g	gravitational acceleration (m s^{-2})
GWP	global warming potential (-)
H	enthalpy (J kg^{-1})
H_{lat}	latent heat (J kg^{-1})
i,j,k	node indices
K	thermal conductance (W K^{-1})
m	mass (kg)
$\dot{m}_f$	fluid mass flow rate (kg s^{-1})
ODP	ozone depletion potential (-)
Q_{ice}	cooling capacity (W)
Q	heat (transfer) (W)
r	radius (m)
R	thermal resistance (K W^{-1})
Ra	Rayleigh number (-)
Re	Reynolds number (-)
T	temperature (K)
T_{melt}	melting temperature (K)
T_{wall}	outer temperature of the (ice) coil (K)
T_∞	average tank temperature (K)
v	fluid velocity (m s^{-1})
W	electric power input (W)
β	thermal expansion coefficient (K^{-1})
Δt	discretised time step (s)
ΔT	temperature difference (K)
ε	effectiveness (-)
μ	dynamic viscosity (Pa s)
ρ	density (kg m^{-3})

REFERENCES

Baltimore. 2019. Ice-on-coil external melt. Retrieved from https://www.baltimoreaircoil.eu/

Biosca-Taronger, J., Payá, J., López-Navarro, A., & Corberán, J., 2012. Ice formation modelling around the coils of an ice storage tank. Journal of Physics: Conference Series, 012133.

Candanedo, J., Dehkordi, V., & Stylianou, M., 2013. Model-based predictive control of an ice storage device in a building cooling system. Applied Energy 111, 1032-1045.

Cárdenas, B., & León, N., 2013. High temperature latent heat thermal energy storage: Phase change materials, design considerations and performance enhancement techniques. Renewable and Sustainable Energy Reviews 27, 724-737.

Goetzler, W., Guernsey, M., Young, J., Fuhrman, J., & Abdul-Aziz, O., 2016. The future of air conditioning for buildings. US Department of Energy, Office of Energy Efficiency and Renewable Energy Building Technologies Office report.

Ihm, P., Krarti, M., & Henze, G. P., 2004. Development of a thermal energy storage model for EnergyPlus. Energy and Buildings 36(8), 807-814.

Lee, A. H., & Jones, J. W., 1996. Modeling of an ice-on-coil thermal energy storage system. Energy Conversion and Management 37(10), 1493-1507.

Makhnatch, P., Mota-Babiloni, A., Rogstam, J., & Khodabandeh, R., 2017. Retrofit of lower GWP alternative R449A into an existing R404A indirect supermarket refrigeration system. International Journal of Refrigeration 76, 184-192.

Saito, A., 2002. Recent advances in research on cold thermal energy storage. International Journal of Refrigeration 25(2), 177-189.

Shah, M. M., 1976. A new correlation for heat transfer during boiling flow through pipes. Ashrae Trans. 82(2), 66-86.

Steinke, F., Wolfrum, P., & Hoffmann, C., 2013. Grid vs. storage in a 100% renewable Europe. Renewable Energy 50, 826-832.

Tecumseh. 2016. Guidelines for using R449A and R452A in new and existing commercial refrigeration.

Vetterli, J., & Benz, M., 2012. Cost-optimal design of an ice-storage cooling system using mixed-integer linear programming techniques under various electricity tariff schemes. Energy and Buildings 49, 226-234.

Yen, Y.-C., 1990. Natural convection heat transfer in water near its density maximum. U.S. Army Corps of Engineers, Cold Regions Research & Engineering Laboratory.

Manuscript ID: 1404
DOI: 10.18462/iir.icr.2019.1404

Fuzzy logic in a refrigerating laboratory

Thomas SUQUET[(a)], Frantz LATCHAN[(a)], Xining WU[(a)], Nicolas BOUDET[(a)]

[(a)] Cemafroid
5 Avenue des Prés, Fresnes, 94266, France, contact@cemafroid.fr

ABSTRACT

Our daily life is overwhelmed by artificial intelligence. This technology performs extremely well, so we look towards in its implementation in thermal regulation processes. What gains can we expect between a conventional PID regulator and a fuzzy logic one? To get an idea, we used as an experimental work a condensing unit used for testing display cabinets according to EN ISO 23953 regulation. This condensing unit was chosen due to its transient respond where usual regulation systems failed to ensure stabilisation.
Keywords: Control, Regulation, Neuronal Network, Tests, Laboratory, Optimization.

RESUMÉ

Notre quotidien est envahi par l'intelligence artificielle. Cette technologie réalise des prouesses et c'est naturellement que nous nous sommes intéressés à son implémentation dans des processus de régulation thermiques ? Quels gains peut-on penser espérer obtenir entre une régulation dite classique avec les PID et logique floue. Les critères considérés portent sur la susceptibilité de ces systèmes de régulation vis-à-vis des objets soumis à essai, sur le temps nécessaire pour obtenir une stabilité thermique et sur l'écart de consigne obtenu. Le banc d'essais pris en exemple est celui utilisé pour réaliser des essais sur des meubles frigorifiques de vente selon la norme EN ISO 23953.
Mots clefs : Contrôle, régulation, réseau neurones, essais, laboratoire, optimisation.

1. INTRODUCTION

The vast majority of industrial installations prefers the use of proven regulation technologies. As such, the PID regulator (Proportional, Integral, Derivative) is the most widely used in industrial processes for its simplicity of application and its correction qualities that apply to lots of physical quantities. The optimum of this regulation is defined by the operator who chooses a balance between the robustness, the speed and the precision. Robustness describes the regulation ability to function satisfactorily even if the process' transfer function varies a little. Speed describes the ability of the controller to reach and maintain the controller near the setpoint. The accuracy describes the static error of the process value in relation to the controller setpoint. In the case where the process is composed only by a single servocontrol structure, several known methods can be successfully exploited including those of Ziegler-Nichols, Naslin, etc to find out how to adjust the PID regulatorin. In the case where the process consists of several structures of PID regulator who can interact one to another, then the usual adjustment methods become difficult to implement and / or require the use of other regulation technologies. In the last case, will such systems be able to propose an acceptable solution for regulation? What about fuzzy logic? What gains can we draw? In order to answer these questions, a test bench used in the laboratory was selected where PID regulator and fuzzy logic was intended to be fit in.

2. THE TEST BENCH

The chosen test bench has been developed in order to meet the requirements described in the test standard NF EN ISO 23953 for remote refrigerated display cabinets. The test laboratory already has a HFC condensing unit that requires the simultaneous operation of four independent PID regulators. The new test-bench operates with CO_2 (R744) and requires eight regulators. The fundamental differences between the HFC bench and the CO_2 bench are the stronger regulators mutual interaction (process-related), a lower ratio between the actuators' speed compared to the processes values and a greater internal bench pressures susceptibility in regards of the compressors frequency.

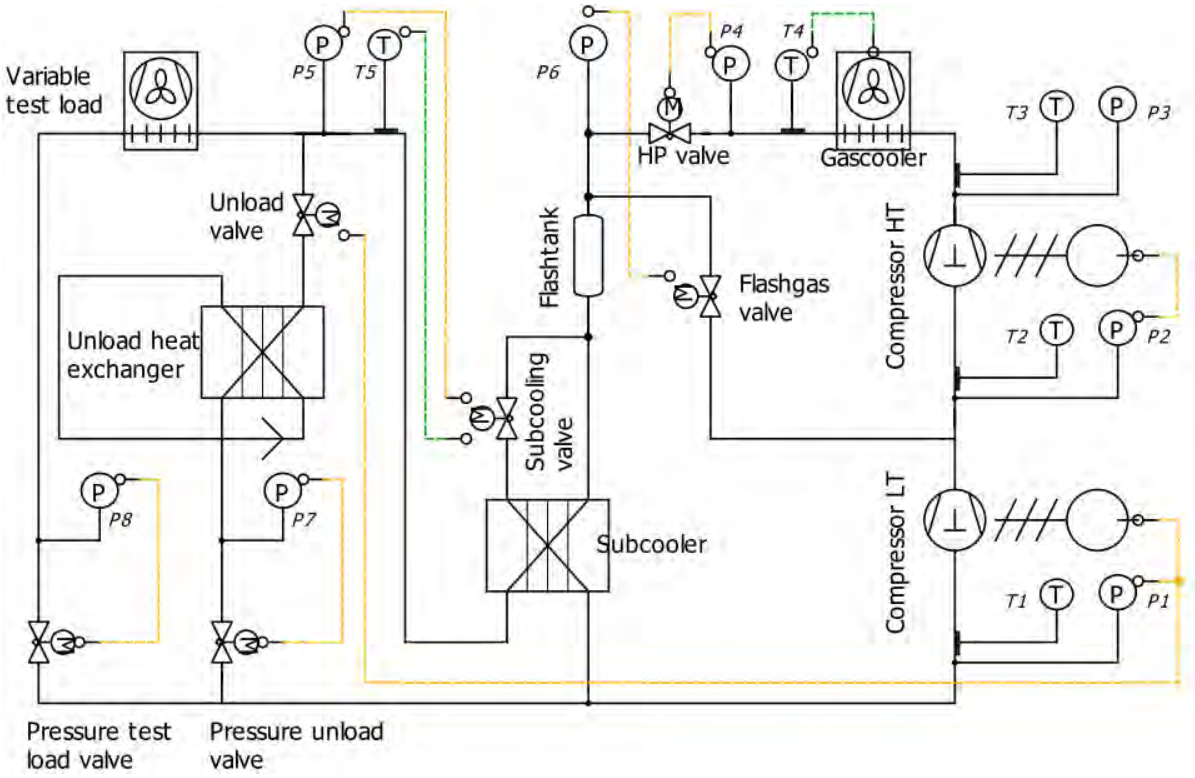

Figure 1: CO2 test bench diagram

The test bench is a booster type refrigerating compressor with two compressors in series. A compressor passes the gaseous CO_2 from an evaporation pressure of 26bar (-10°C) to a pressure of 90bar at which the CO_2 is in the transcritical state and will cool down. The second compressor compresses the CO_2 from 12 bar (-35°C evaporation pressure) to 26 bar (-10°C intermediate pressure between the two compressors). A flash-gas valve evacuates the gases present in the bottles (flash tank) to maintain a supply pressure of 40 to 45 bar. Since the cooling capacity of each display cabinet to be tested differs, an off-load exchanger is installed to ensure operation even if no heat load is apply to the test bench. The display cabinets are connected on the low pressure part, the two compressors operating continuously in series with an adjustment of the evaporation pressures by the use of pressure maintaining valves.
Any condensing unit conforming to EN ISO 23953 test standard specifications shall ensure the following conditions:

- The refrigerant is at the evaporating pressure or at the temperature at the outlet of the cabinet specified by the display cabinet manufacturer,
- The display cabinet is supplied with liquid without any steam or at a temperature no higher than 10°C above the specified test chamber temperature or, if applicable, to the subcooled liquid temperature if specified.

Each functional parameter of the CO_2 condensing unit to be regulated is sensitive to several actuators but only one of them has a major effect. In the interest of simplification and representation, the links between parameter and actuator are shown in the table below.

Table 1: Links between the transducers and actuators

Where	Low pressure LT		Intermediate pressure	Gascooler pressure	Flashgas pressure
Transducer label (cf. figure 1)	*P1*		*P2*	*P4*	*P6*
Actuator (cf. figure 1)	Compressor LT	Unload valve	Compressor HT	HP valve	Flashgas valve
Where	Liquid line pressure	Liquid line temperature	Variable test load pressure	Gascooler outlet temperature	Unload heat exchanger outlet pressure
Transducer label (cf. figure 1)	*P5*	*T5*	*P8*	*T4*	*P7*
Actuator (cf. figure 1)	Subcooling valve		Pressure test load valve	Gascooler	Pressure unload valve

The regulation of the CO_2 condensing unit is a copy of the one use in the HFC condensing unit. In other words, the regulation of each parameter is entrusted to a dedicated PID regulator independent of the others.

3. PID REGULATOR

The HFC condensing unit tests have shown that the performance of PID regulation makes it possible to comply with the specifications of the EN ISO 23953 standard. The rendering of one of the condensation group acceptance tests is proposed below:
The display cabinet manufacturer specifies the operating conditions of the furniture:

- Refrigerant fluid : R404A,
- Evaporating pressure : 5barr,
- Superheat : 5K,
- Liquid subcooled temperature: 40°C.

During the test, there was never any visible vapor in the sight glass at the output of the flowmeter: The refrigerant charge has been adjusted to ensure sufficient subcooling to avoid any presence of vapor bubble on the supply line of the display cabinet. A data acquisition rate of 10 seconds was chosen and the measurements made are presented below.

Table 2: Operating parameters of the HFC condensing unit table.

12/01/2017		Evaporating pressure	Superheat	Liquid subcooled temperature
		(bar relatif)	(K)	(°C)
display cabinet manufacturer conditions		5	5	40
Test conditions	Mean	4.88	5.73	40.58
	Minimum	4.81	1.08	38.80
	Maximum	5.32	8.46	42.56
	Standard-déviation	0.04	0.64	0.35
Conditions déviation manufacturer vs test conditions		0.12	0.73	0.58

The evaporation pressure average deviation between the one required by the display cabinet manufacturer and the one measured is equal to 0.12 bar. This variation can be explained by a refrigerating power call when the display cabinet is in cooling down the goods following a defrost, which momentarily generates high pressure. The uprising frost in the exchanger causes a decreasing of the evaporation pressure due to the reduction of the heat exchange. These two characteristics are therefore intrinsic to the operation of the refrigerated display cabinet.

The display cabinet superheat is controlled by an internal expansion valve fit in the cabinet and the superheat is function of the evaporation pressure. This parameter can be set by the user of the display cabinet. In this test, it has been set to obtain good operating conditions, but hasn't been readjusted as soon as the display cabinet was under tests.

Liquid subcooled temperature is fully controlled by the HFC condensing unit, there is a difference of ± 0.58K between the average temperature and the desired set-point by the customer.

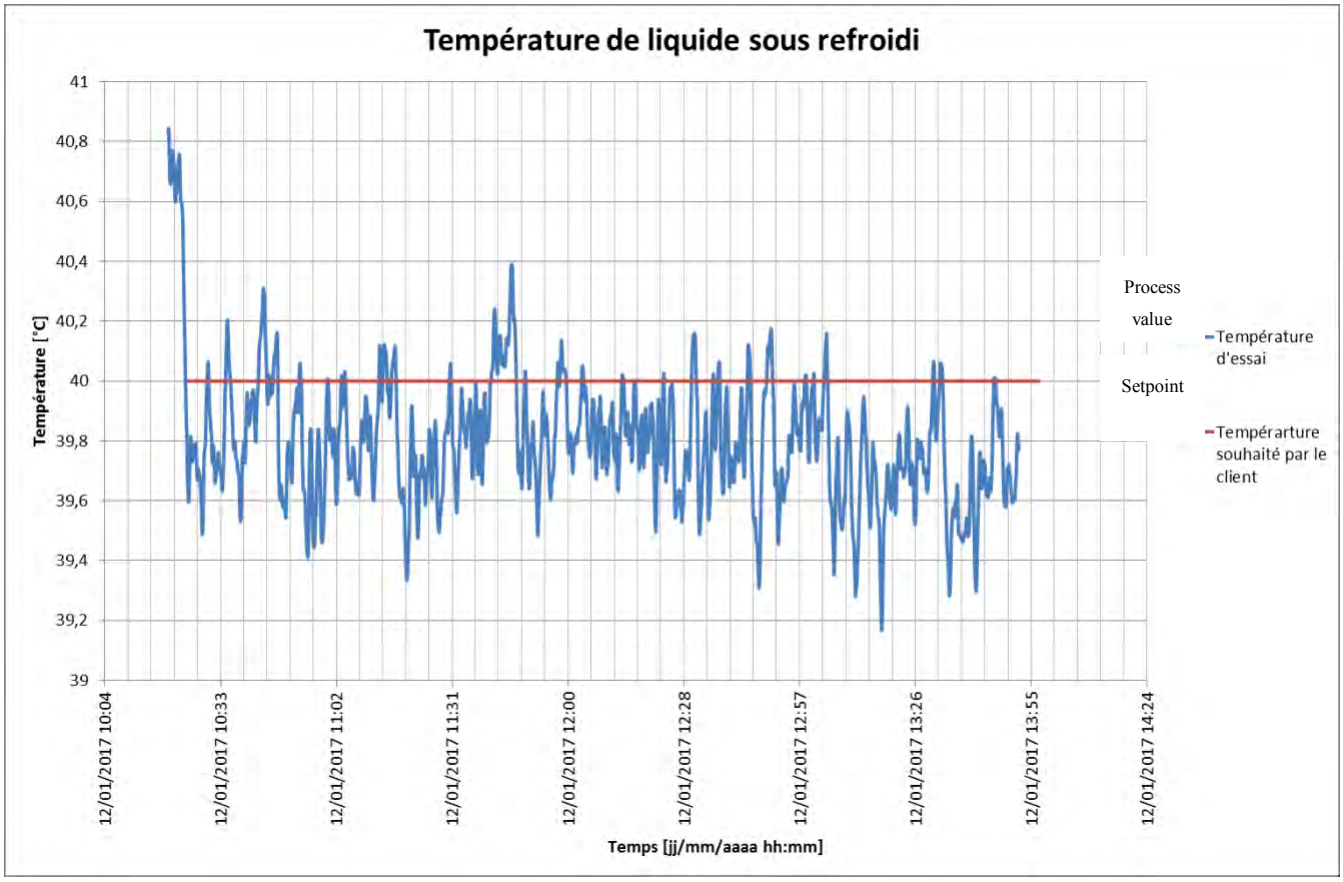

Figure 2: Liquid subcooled temperature evolution.

The HFC condensing unit regulation transposed to the CO_2 condensing unit does not give the same result. The functional parameters of the bench can be maintained once the stabilization has been reached by a manual override. It is important to note that the parameterization method was carried out in the same way as for the CO_2 bench using the so-called "Auto-tune" mechanisms integrated into the regulator. Further parameterization tests were carried out using the step studies or by the method of Broida. The stability of the bench has not been improved or even its ability to reach a stability point after starting. As such it seems that PID controllers are not suitable for this type of editing where different constants of time and dynamic behaviors occur.

Table 3: PID parameters according to the Broida method Château et al. (2011)

Regulator type	P	PI	PID
K	$\frac{0.8\tau}{TK}$	$\frac{0.8\tau}{TK}$	$\frac{\tau + 0.4T}{1.2TK}$
T_i	-	$K\frac{T}{0.8}$	$K\frac{T}{0.75}$
T_d	-	-	$\tau\frac{0.35}{K}$

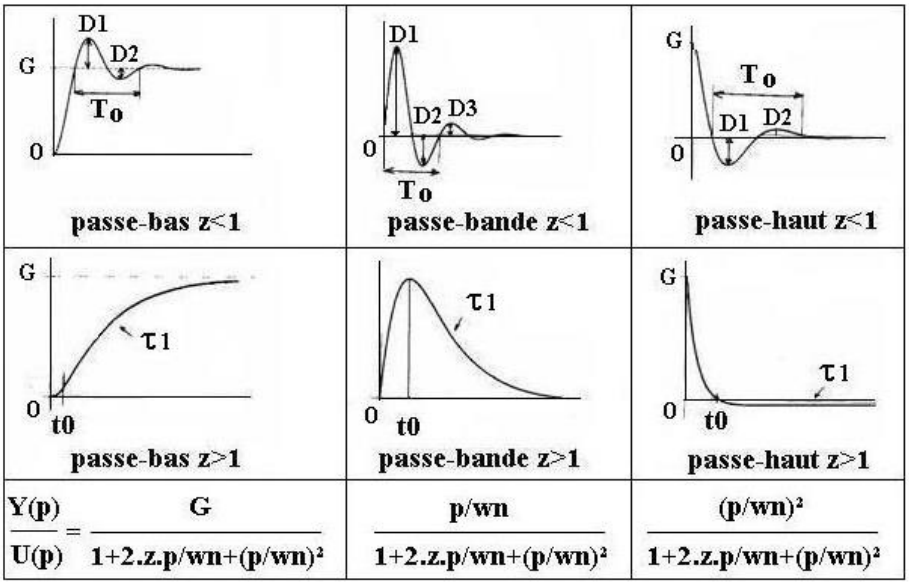

Figure 3: Steps answers for 2nd order systems Curtil (2007)

The CO_2 condensing unit regulation by PID regulators was not convincing. It was necessary to turn to other regulation techniques. Knowing that, by experimenting on the condensing bench, the human drivers had acquired good abilities to anticipate the behavior of the parameters, the choice naturally fell on a regulation by the fuzzy logic which makes it possible to transcribe the human actions in a functional logic diagram. The interest is to valorize the analysis of human by injecting it into an automaton taking into consideration that an automaton can observe at every moment the operating parameters and thus obtain a much better regulation.

4. FUSSZ LOGIC

Fuzzy logic can be deployed when there is human know-how. If this is the case, it can be transposed into fuzzy rules which are themselves easily understood by the user. The collection of know-how is therefore an important step in the implementation of fuzzy logic regulation. The other interest of fuzzy logic also lies in the fact that it is not necessary to get the transfer function of the condensing unit to implement efficient regulation. As it seems that the impact of the CO_2 condensing unit actuators have global impacts more or less weighted on the quantities to be regulated, the fuzzy logic seems to provide a valid solution.

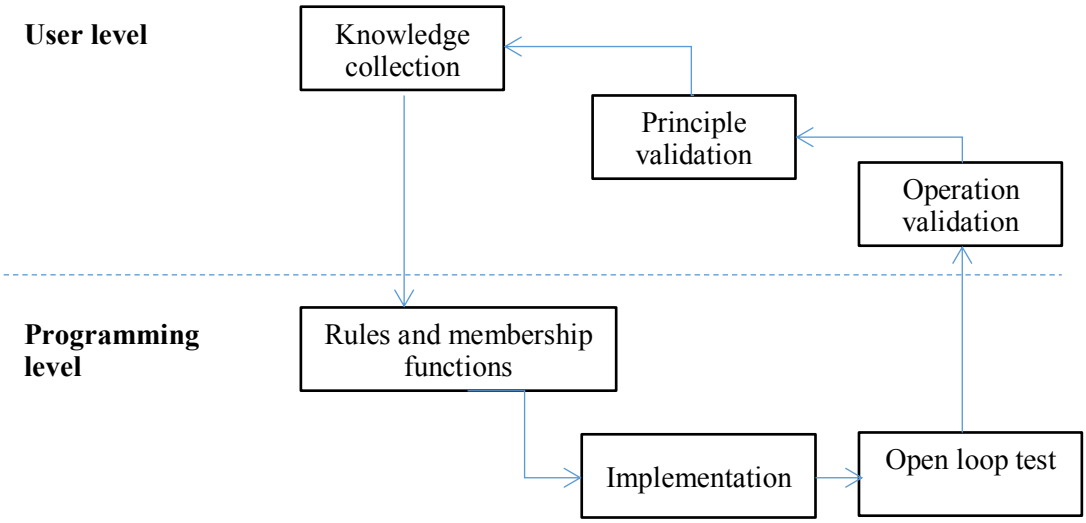

Figure 4: Methodology of conception Chevrie et al. (1998)

The primary elements of a fuzzy logic model are (1) fuzzy sets, (2) membership function (3) IF-THEN rules AZIZ (2015). A fuzzy set is labeled by a linguistic term, and the linguistic term is a word such as Negative Big (NB), Negative Small (NS), Zero Low (ZL), Zero (Z), Positive Small (PS), Positive Big (PB), etc… The fuzzy sets and IF-THEN rules construct a rule base of fuzzy logic model. Membership function is the effective method for comprehensive evaluation based on multi factors. Membership function is a curve that defines how each point in the input space is mapped to a membership value between 0 and 1. It provides a measure for the degree of an element to a fuzzy set. It fully defines fuzzy set and it can take any form, but there are some common examples that appear in real applications. There are different shapes of membership functions: triangular, trapezoidal, piecewise-linear, Gaussian and so on. In most literature, triangular membership functions are used due to having flexible formula to calculate KUMAR ET AL. (2014), YANG ET AL. (2016).

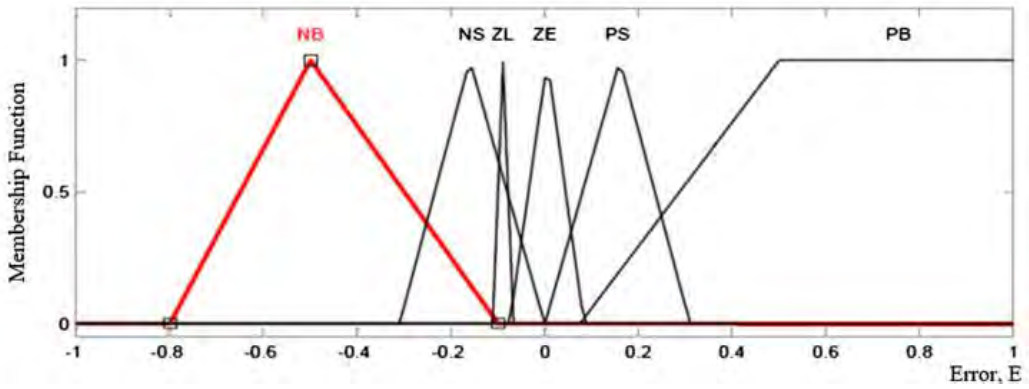

Figure 5 : Input variable, Error Zainal et al. (2019) .

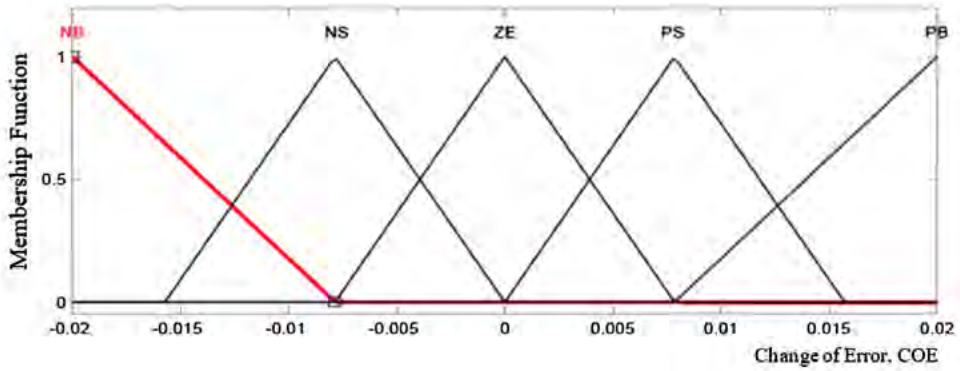

Figure 6. Input variable, change of error Zainal et al. (2019).

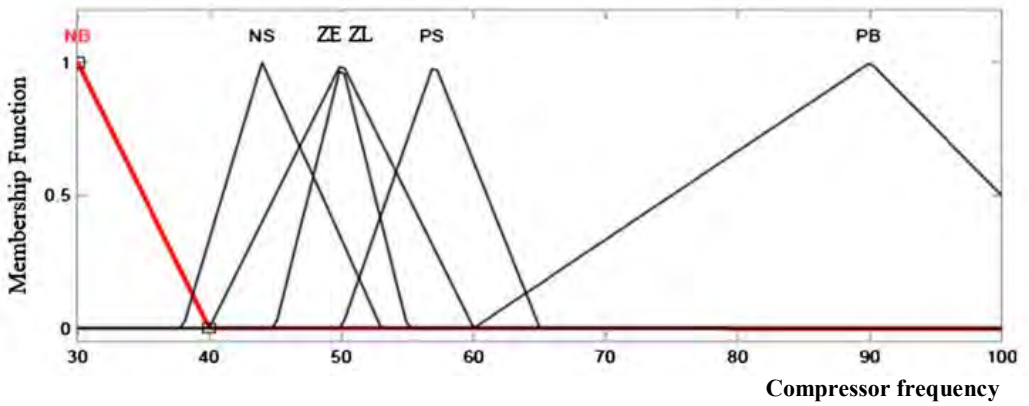

Figure 7. Output variable, actuator positioning.

5. CONCLUSION

Unfortunately, the laboratory was unable to implement the fuzzy logic in the CO_2 condensing bench as specific component came to break, prevented its completion. Nevertheless, the laboratory's appropriation of fuzzy logic enabled it to perceive its interest for at least one good reason: It is societal aspect thanks for the preservation of the know-how.

REFERENCES

Aziz, A., 2015, A new perspective on the choice of fuzzy membership functions in multitarget tracking systems, Aerospace Conference, 2015 IEEE. 1-8

Chevrie, F., Guély, F., 1998, Cahier technique Schneider N°191, Schneider, 16-17

Château T., Adouane, L., 2011, Régulateur PID de Polytech'Clermont-Ferrand, Polytech'Clermont-Ferrand, 3

Curtil, D., 2007, Introduction à l'Automatique de l'INP Grenoble, INP Grenoble, II - Étude et description des systèmes automatiques

Kumar, E., Sundaresan, M., 2014, Edge detection using trapezoidal membership function based on fuzzy's mamdani inference system, 2014 International Conference on. IEEE, Computing for Sustainable Global Development (INDIACom), 515-518.

Yang, L., Tai, N., Fan, C., Meng, Y., 2016, Energy regulating and fluctuation stabilizing by air source heat pump and battery energy storage system in microgrid, Renewable Energy 95, ELSEVIER, 202-212.

Zainal, N., Yusoff, A., Apen, A., 2019, Integrated cooling systems and maximum power point tracking of fuzzylogic controller for improving photovoltaic performances, Measurement 131, ELSEVIER, 100-108.

Manuscript ID: 1431
DOI: 10.18462/iir.icr.2019.1431

Experimental comparison of the heat transfer performance of R134a and R1234ze(E) in a hybrid film evaporator

Giuseppe CENSI[(a)], Loris GIANCOTTI[(a)], Andrea PADOVAN[(a)]

[(a)] Onda S.p.A., R&D Department
Lonigo, I-36045, Italy, gcensi@onda-it.com

ABSTRACT

Environmental and cost issues in vapour compression systems call for new high efficiency evaporators with reduced refrigerant charge.
This paper presents a new concept of shell-and-tube heat exchanger, named hybrid film evaporator. In this, a liquid film falls down from the top to the bottom and it is re-distributed on each row of tubes by means of special drilled plates. The heat transfer mechanism is a combination of falling film evaporation and pool boiling. When compared to a flooded evaporator, the refrigerant charge is significantly lower, almost 40% for the entire chiller, while maintaining the same heat transfer capacity and overall dimensions.
The experimental heat transfer performances of a hybrid film evaporator prototype, working with R134a and R1234ze(E), are presented and discussed.
The results show that nucleate boiling is not the only heat transfer mechanism and, at the same heat flux, the measured heat transfer coefficient of R1234ze(E) is even 20% lower than that of R134a.
Keywords: Evaporators, Falling film, R1234ze(E), R134a, Refrigerant Charge, Shell-and-Tube Heat Exchangers.

1. INTRODUCTION

The global warming in the earth climate system is greatly influenced by greenhouse gas emissions (Stocker et al., 2013), as known for some decades (Lashof and Ahuja, 1990). The increased worldwide sensitivity and the relative regulations are forcing more and more to consider refrigerants alternative to the currently used hydrofluorocarbons (HFC), which are very common and in general present an unacceptable global warming potential (GWP). In particular, the hydrofluoro-olefin (HFO) fluid R1234ze(E) is, at present, the main long-term candidate to replace the HFC fluid R134a. The choice of R1234ze(E) is primarily due to the lower GWP (less than 1, versus 1430), but also to the atmospheric lifetime (about 2 weeks, compared to 13 years) (Hodnebrog et al., 2013), with both characteristics linked to the high reactivity of its molecule. For this reason, moreover, R1234ze(E) belongs to A2L safety classification, meaning low toxicity and slight flammability, whereas R134a is classified as A1, having no safety issue. Together with this problem, there is also a reduction of the thermodynamic efficiency. A direct drop-in replacement of R134a with R1234ze(E), in an existing plant at the same saturated temperatures, implies almost the same coefficient of performance (COP), but the maximum cooling capacity obtainable is significantly reduced. Indeed, at the same conditions, the volumetric capacity of R1234ze(E) is 25 % lower than the one of R134a. A comprehensive detailed theoretical study on thermodynamic efficiency and the role of the thermo-physical properties of R1234ze(E) (together with other low GWP fluids) can be found in McLinden et al. (2017). The safety classification, and the high cost in the market, force to consider limiting the amount of the charge of this refrigerant in vapour compression cycles, especially for systems using flooded evaporators. An increasingly adopted option for the charge reduction consists of horizontal falling film or spray evaporators, whose tubes, instead to be flooded in a liquid pool, are wet one-by-one by a thin film of liquid.
As regards a direct comparison of R134a and R1234ze(E) during pool boiling on enhanced surfaces, Van Rooyen and Thome (2013) and Gorgy (2016) evaluated the pool boiling performances of R134a and R1234ze(E) in enhanced tubes with structured surface. At saturation temperatures around 5 °C, and with heat fluxes below 100 kW m^{-2}, the measured heat transfer coefficients of R1234ze(E) and R134a were very similar. Byun et al. (2017), on the other hand, found some differences between the

two fluids. For two different evaporation temperatures (4.4 °C and 26.7 °C), with heat fluxes from 10 to 50 kW m^{-2}, the heat transfer coefficient of R1234ze(E) was found lower than that of R134a of an amount variable between 10 and 20 %.
With respect to falling film evaporation, in the open literature the fluid R134a is widely studied, whereas no work regarding R1234ze(E) is at present authors' knowledge. Roques and Thome (2007) tested R134a, and Christians and Thome (2012) tested R134a and R236fa, during pool boiling and falling film on structured surfaces at a saturated temperature of 5 °C and heat fluxes of less than 100 kW m^{-2}. Their results show, for falling film evaporation, higher heat transfer coefficients than for pool boiling, in a measure depending on the characteristics of the surface: in some cases, the performances tend to approach at high heat fluxes. Ji et al. (2019), who studied R134a evaporating on structured surface tubes at 11 °C, achieved better results in falling film evaporation when the heat flux was less than 30 kW m^{-2}, whereas the performances started to worsen compared to pool boiling at higher heat fluxes.
Considering a whole bundle of tubes, spray or falling film evaporators present some complications with respect to flooded evaporators. They require a complex distribution system for the liquid inlet and for the dissipation of the flash gas, and particular care in the alignment of the tubes, in order to guarantee uniformity in the liquid supply and avoid dry patches on the tubes wall. Furthermore, dryout can occur when the flow rate is reduced, for example at partial loads, starting from the lowest tube rows of the bundle. Depending on geometry, operating conditions and fluid properties, it is possible to identify up to five different flow patterns, and, among them, mainly three are distinguished: sheet, jet (column), and droplet modes. In particular, the sheet mode seems to develop the highest heat transfer coefficient (Fernández-Seara and Pardiñas, 2014). In classical falling film evaporators, moreover, a big volume of the shell is usually required to avoid liquid entrainment to the compressor by the vapour flow. Besides, the local ascending vapour can modify the trajectory of the falling liquid, affecting the heat transfer performance. Detailed reviews of the studies focused on the distribution systems and tube layouts, and on the influence of flow pattern and vapour flow, can be also found in Ribatski and Jacobi (2005) and Abed et al. (2014).
The hybrid film evaporator, described in this work, owes its name to the mixing of the falling film and of the pool boiling processes involving each tube. Censi et al. (2018) conducted an experimental study in a hybrid film evaporator prototype, with R134a at 6 °C from 15 to 35 kW m^{-2}, finding refrigerant heat transfer coefficients similar or slightly higher than those of the flooded evaporator. In the present work, the investigation of the performances of the hybrid film evaporator is extended to the fluid R1234ze(E). After introducing the operating concept of the evaporator, the experimental study is focused on the heat transfer comparison between fluids R134a and R1234ze(E).

2. EXPERIMENTAL PROTOTYPE

2.1. Operating Description

The heat exchanger described in this work, named “hybrid film evaporator”, belongs broadly to the family of the falling film evaporators, as can be noted from Fig. 1.

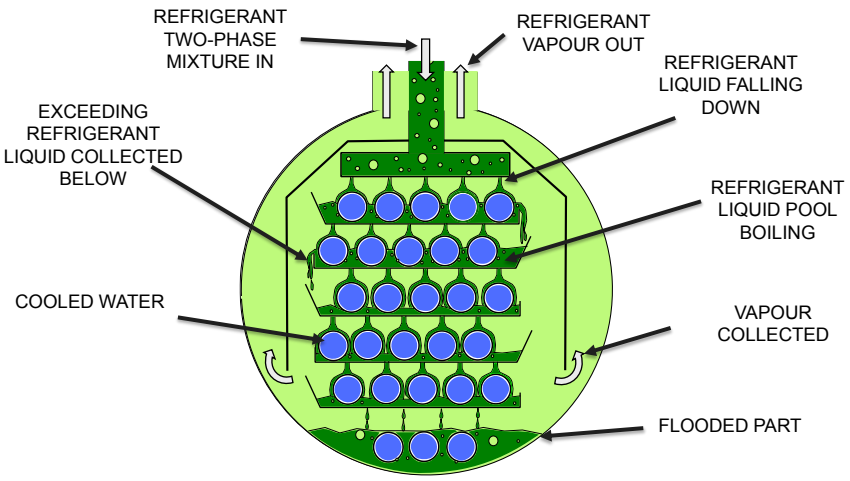

Figure 1: Schematic view of the hybrid film evaporator

Like falling film evaporators, indeed, it starts from the need to keep the refrigerant charge as low as possible and to achieve, or to improve, the performances of the flooded evaporator. Besides, it aims to avoid some of the classical problems of falling film: the difficult distribution, the dryout occurring at non-nominal conditions, and the large dimensions, all discussed in the Introduction.
The resulting final design is illustrated in Fig. 1, and the detailed operating principles are reported by Censi et al. (2018). Unlike the classical film evaporators, the hybrid film evaporator includes special perforated plates with vertical longitudinal borders placed below each tube row. The plates are designed to solve two of the above-mentioned problems. First, they help to supply liquid to the lower tubes and to minimize or avoid dryout phenomena: thus, they work as "liquid catchers", similarly to the devices described by Chang and Chiou (1999). Additionally, they prevent liquid maldistribution, both along the width direction and the length direction, whose effects are studied and illustrated, for example, by Yang and Wang (2011).
It is worth noting that, due to the plate drilling, the liquid flow pattern from the upper plate to the lower row of tubes can be classified mainly as column mode. This flow regime was confirmed by visualizations carried out in a separate prototype with water in adiabatic single-phase flow.

2.2. Characteristics of the Prototype

The present work, and the works cited in the Introduction, consider only tubes with structured external surface, specifically designed for pool boiling. The surface is enhanced by fins with a dedicated shape, in order to create sites that promote nucleate boiling at low temperature differences, of the type, for example, presented by Bergles (1997). Under moderate heat fluxes, they are the best choice for flooded evaporators.
As regards falling film, instead, no specific enhanced tubes exist. Anyway, the structured surfaces seem the most suitable, as, in general, they let the liquid flow longitudinally and promote the sheet flow mode. The hybrid film design, which works under column flow mode but with a pool boiling part, present in almost each row of tubes, suggests using structured surfaces. In particular, the tube model of the present prototype is Gewa-B6H, provided by Wieland, with outside nominal diameter 19.05 mm. Possible future studies will show if other surfaces, for example low-finned, are suitable for the hybrid film.
The geometry of the prototype is summarized in Table 1. It is very compact, and the tube pass configuration is chosen in order to reduce the water pressure drop as much as possible.

Table 1. Characteristic of the hybrid film prototype

Parameter	Value	Parameter	Value
Tube name	Gewa-B6H	Tube length	1016 mm
Tube surface	Structured	N. of tube passes	4
Tube outside diameter	19.05 mm	Shell outside diameter	610 mm

3. EXPERIMENTAL STUDY

3.1. Experimental Apparatus

The experimental tests were run on the test facility set up at the laboratory of Onda S.p.A., Italy, schematic of which is depicted in Fig. 2. It represents a classical vapour compression system (compressor, condenser, expansion device, evaporator), with an additional subcooler downstream of the condenser. The compressor is centrifugal and oil free, with axial and radial magnetic bearings. For the tests, the system was charged with R134a first, and then with R1234ze(E); between the two operations, the plant was cleaned with nitrogen and the electronic regulation system of the compressor was re-set.
The superheated vapour at high pressure flows from the compressor to the shell-and-tube condenser, where it is fully condensed and then further subcooled in a brazed-plate heat exchanger. The subcooling level can be independently controlled, varying the cooling water temperature and flow rate. As a result, it is possible to achieve the set vapour quality at the inlet of the test evaporator. The expansion device is a step motor electronic valve, whose opening is varied manually according to the required liquid level at the evaporator, maintained constant. After reducing pressure through the expansion valve, the refrigerant flows to the evaporator and finally to the compressor, again. A sight glass is placed between the evaporator and the compressor to check that there is not

entrainment of liquid drops in the vapour flow. Furthermore, in order to make sure of that, the isentropic efficiency of the compressor is measured and compared to that declared by the compressor manufacturer.

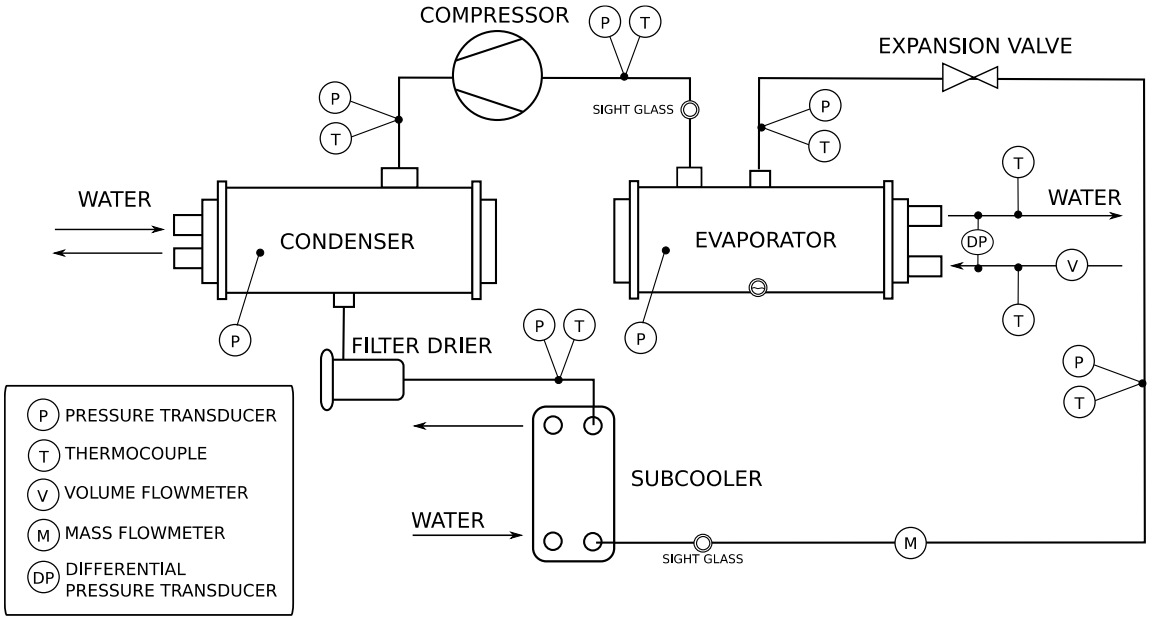

Figure 2: Schematic drawing of the experimental test rig

Water is used as secondary fluid to vaporise R134a and R1234ze(E). The water temperature at the inlet and outlet of the test evaporator is measured by thermocouples inserted in adiabatic sections, where perfect mixing is assured. Type J thermocouples connected to a Kaye ice point instrument as zero reference system are used. Thermocouples were calibrated on site using a primary Pt100 probe and a reference bath to get the accuracy value reported in Table 1. The water volume flow rate and pressure drop through the evaporator are measured with an electromagnetic flow meter and a differential pressure transducer, respectively. Thermocouples and pressure transducers are also installed in different sections of the refrigerant loop to get all the measurements needed for the data reduction. In particular, saturation temperature at the evaporator is obtained by the pressure, which is taken both inside the shell and at the evaporator outlet. A Coriolis effect flow meter measures directly the refrigerant mass flow rate. In this way, the thermal balances on both water and refrigerant side are compared and checked. The mean deviation is found to be around 3%. The accuracies for sensors and parameters (described in the next section) are listed in Table 2.

3.2. Data reduction and operative conditions

In order to understand the behaviour at different loads, the compressor capacity was varied by means of an inverter, maintaining constant the evaporator inlet vapour quality. The value was fixed at 0.18 kg kg^{-1}. In a different set of tests, the vapour quality was varied at constant heat flow rate.
The average heat flux at the evaporator, $\bar{q}$, is given by the water side heat flow rate divided by the reference area A_{ext}, that is the external envelope plain tube surface area at the nominal diameter. It ranges from 19 to 33 kW m^{-2}; the heat flux on each water passage, instead, varies from 9 to 55 kW m^{-2}.
The first performance parameter considered is the water-to-saturation temperature approach Δt_{app} at the outlet nozzle. This parameter is the difference between the leaving water temperature and the saturation temperature, as calculated by the pressure measured just after the evaporator outlet: it ranges from 1.1 to 1.9 K. Another performance parameter considered is the average global heat transfer coefficient K, measured at the shell. Indeed, K is given by the water side heat flow rate divided by A_{ext} and by Δt_m, which is the water-to-saturation mean temperature difference where the saturation temperature comes from the pressure measured inside the shell. The range for K is 6.5 ÷ 8.5 kW m^{-2} K^{-1}. The final parameter considered is the average external heat transfer coefficient α_{ext}, obtained by a thermal resistance subtraction. The tube-side heat transfer coefficient is obtained by means of an empirical based correlation provided by the tube manufacturer, and verified by means

of ad hoc single-phase tube-in-tube experimental tests. The present procedure is affected by up to almost 20 % uncertainty (Table 2).
All thermo-physical properties of R134a, R1234ze(E) and water are calculated by means of the Refprop 9.1 software (Lemmon et al., 2013).

Table 2: Accuracy for sensors and parameters (at typical test conditions)

Parameter	Accuracy	Parameter	Accuracy
Temperature	±0.05 K	Temp. difference	±0.10 K
Volumetric flow rate	±0.5 %	Temperature approach	±0.12 K
Mass flow rate	±0.5 %	Heat flux	±3 %
Absolute pressure	±1 kPa	Global heat transf. coeff.	±5 %
Differential pressure	±200 Pa	Refrigerant heat transf. coeff.	±18 %

3.3. Experimental Results

In Fig. 3 the water-to-saturation temperature approach at the outlet nozzle is plotted as a function of the average heat flux. In Fig. 3a, the data are taken at fixed values of water inlet and outlet temperatures ($t_{W,in}$ and $t_{W,out}$), namely 12 and 7 °C, and consequently at constant temperature drop (5 K) of the chilled fluid. In Fig. 3b, instead, the data are taken with water at constant flow rate and constant outlet temperature, respectively 14 kg s^{-1} and 7 °C. Such values allow to obtain the value of 12 °C for the water inlet temperature, for R1234ze(E) at full capacity. Then, the points at maximum heat flux (25 kW m^{-2}) on R1234ze(E) curves in Fig. 3a and in Fig. 3b must coincide (within the measurement uncertainty). Anyway, it is evident that even the whole curves almost coincide, both for R134a and for R1234ze(E).

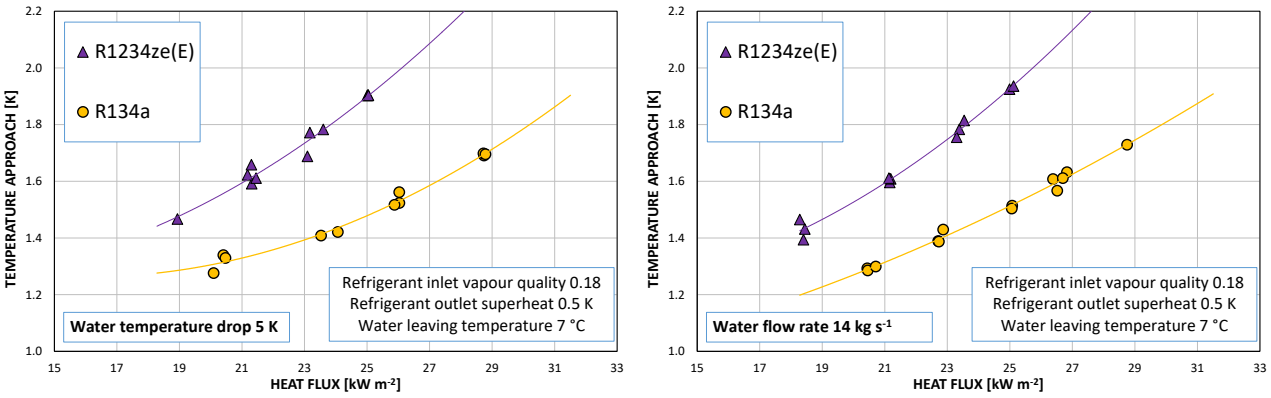

a) b)

Figure 3: Water-to-saturation temperature approach at the outlet nozzle Δt_{app}: a) at constant water temperature drop ($t_{W,in}$=12 °C, $t_{W,out}$=7 °C); b) at constant water flow rate ($\dot{m}_W$=14 kg s^{-1}, $t_{W,out}$=7 °C)

The explanation is as follows. At constant water temperatures (Fig. 3a), an increase of the heat flux implies an increase of the water flow rate and then of the in-tube heat transfer coefficient. Being the water-side heat resistance the dominant one, the global heat transfer coefficient grows, even if not enough to supply all the heat flux increase. The remaining contribute is given by the water-to-refrigerant mean temperature difference, whose increase can only be given by a decrease of the refrigerant saturation pressure, resulting in an increase of the approach. On the contrary, at constant water flow rate (Fig. 3b), the global heat transfer coefficient remains almost constant with the heat flux, as the water-side heat transfer coefficient is constant and its resistance is dominant. Then, the water-to-refrigerant mean temperature difference must supply alone the heat flux increase, but only a limited decrease of the refrigerant saturation pressure is required, as the inlet water temperature grows. The increase of the approach is consequently limited.
In this special case, with the final contribution of the vapour pressure drop, the approach varies with the heat flux almost in the same way at water temperature drop constant and at water flow rate constant. Thus, in the two graphs reported in Fig. 3 there is an accidental concurrence of the curves.

The main indication coming from Fig.3 is that the temperature approaches obtained with R1234ze(E) are higher than those obtained with R134a (with a difference of 0.2 ÷ 0.4 K). Anyway, the average reduced pressure of R1234ze(E) is 19 % less than the one of R134a, and it is a disadvantage, assuming that pool boiling plays an important role in this evaporator. For example, the Cooper (1984) formula for nucleate boiling heat transfer coefficient α_{NB} can be taken as reference:

$$\alpha_{NB} = C \cdot p_{red}^{0.12-0.2\log_{10} R_p} (-\log_{10} p_{red})^{-0.55} M^{-0.5} \bar{q}^{0.67} \qquad \text{Eq. (1)}$$

where C is a constant independent of the fluid, p_{red} is the reduced pressure, M is the molar mass, and R_p is the surface roughness. Being the molar mass of R1234ze(E) 12 % higher than the one of R134a, the HFO fluid is even more penalized. In order to try out this prediction, the graphs of Fig. 4 report the previous data sets (R134a at p_{red} = 0.089 and R1234ze(E) at p_{red} = 0.073) together with two new R1234ze(E) data sets. For one new set, the reduced pressure is the same as the one of R134a (0.089), and for the other one, the reduced pressure is 0.101, a value such that the group $p_{red}^{0.12-0.2\log10(Rp)}$ $(-\log_{10} p_{red})^{-0.55} M^{-0.5}$ assumes the same value for both fluids. The value of R_p, in the typical range for commercial tubes, has a negligible effect when the above group is equalled for the two fluids. Consequently, a similar value of α_{NB} should be expected. The reduced pressure of R1234ze(E) is changed modifying the value of the leaving water temperature, which is constant for each data set. The flow rate is constant too, with a value that allows to achieve the same in-tube heat transfer coefficient for all. The experimental global heat transfer coefficient is reported in Fig. 4a. For all the data sets, the global heat transfer coefficient increases with the heat flux, due to the increase of the refrigerant heat transfer coefficient, as shown in the graph of Fig. 4b. Data for R134a at 0.089 reduced pressure and for R1234ze(E) at 0.073 reduced pressure are at the same operating conditions as discussed in Fig. 3b. At the same value of heat flux, for instance 26.5 kW m^{-2}, the external heat transfer coefficient of R134a can be even 20% higher than that of R1234ze(E), and the global heat transfer coefficient around 7% higher. From Fig. 4b, when the reduced pressure increases from 0.073 to 0.089 for R1234ze(E), the refrigerant heat transfer coefficient slightly increases in the whole range of the heat flux investigated, although such variation is within the estimated experimental uncertainty. When further increasing the reduced pressure to the value 0.101, the external heat transfer coefficient does not increase. Thus, it results that the R1234ze(E) external heat transfer coefficient remains lower than that of R134a, even when its reduced pressure is equal or higher. This behaviour suggests that nucleate boiling is not the only mechanism driving heat transfer.

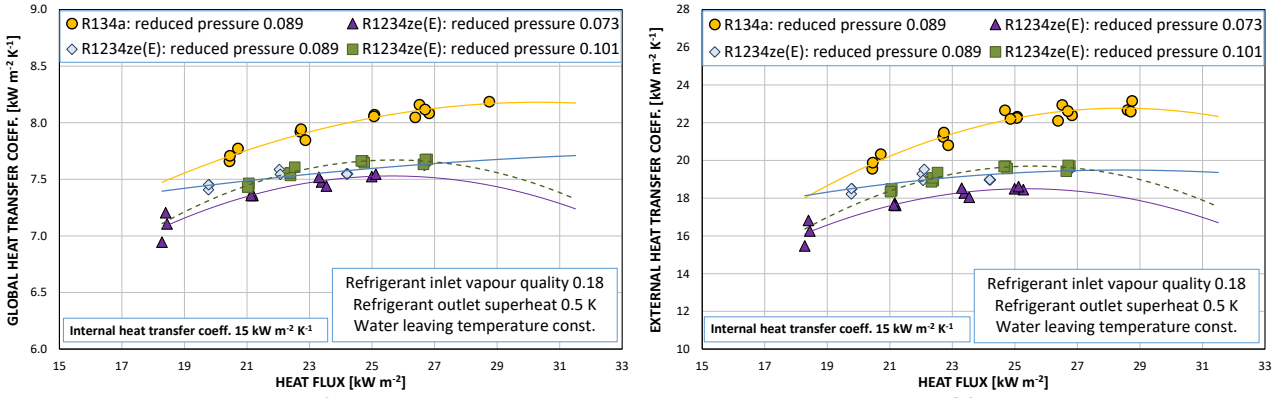

Figure 4: Comparison of the performances of R134a at 0.089 reduced pressure with those of R1234ze(E) at 0.073, 0.089, and 0.101 reduced pressure, with the same in-tube coefficient: a) global heat transfer coefficient; b) shell-side heat transfer coefficient

In Fig. 5 the influence of the inlet vapour quality is investigated, in term of the global and of the external heat transfer coefficient. Some test facility limitations prevented to reach the same water conditions for both fluids; therefore, the two graphs must be read as indicative of a comparison of the trend of the heat transfer coefficients, but not of the absolute values. The R134a heat transfer coefficient slightly decreases with increasing vapour quality; however, this variation has not consequences in the global heat transfer coefficient. Differently, the R1234ze(E) heat transfer coefficient does not exhibit any dependence on inlet vapour quality. Finally, Fig. 6 illustrates the saturation temperatures at different heat exchanger locations. The temperature directly connected

to the heat transfer is the one in the shell; the difference with the inlet nozzle is mainly due to the pressure drop in the distribution system, while the difference with the outlet nozzle is due to the vapour stream pressure drop.

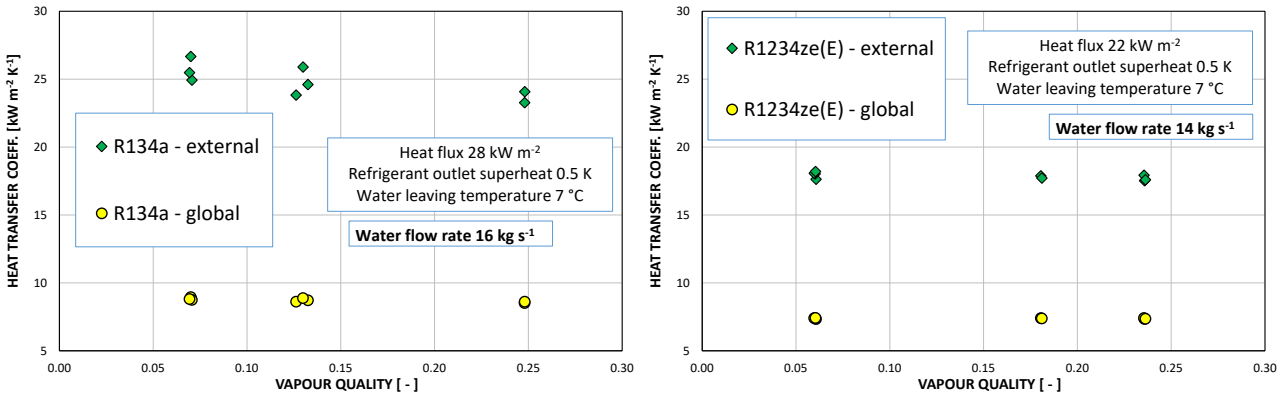

a) b)

Figure 5: Global and shell-side heat transfer coefficient versus vapour quality at constant heat flux: a) R134a; b) R1234ze(E)

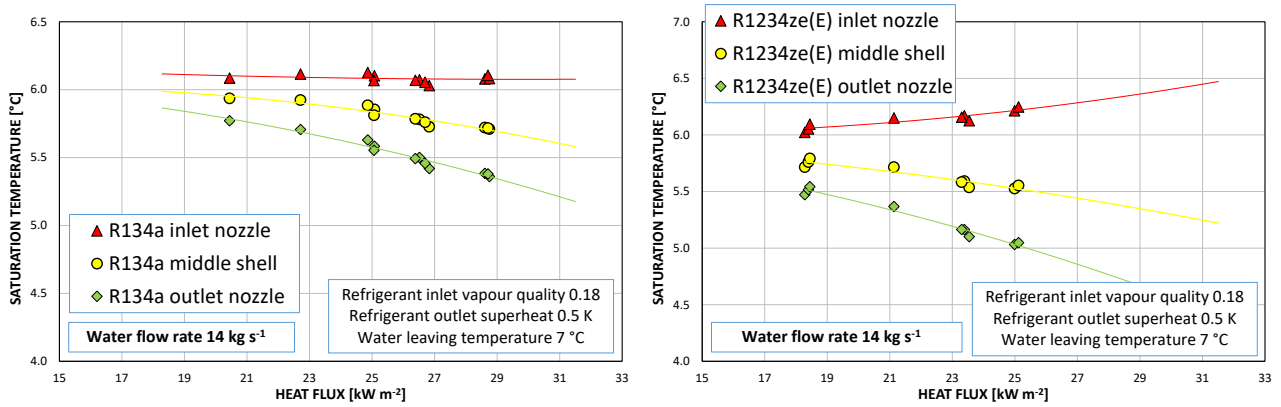

a) b)

Figure 6: Saturation temperatures at water flow rate 14 kg s^{-1}: a) R134a; b) R1234ze(E)

For both fluids, the curves diverge, as the pressure drops increase with the heat flux; for R1234ze(E) the differences between the curves are sensibly higher. Indeed, R1234ze(E) is strongly penalized: first, at same heat flux, its mass flow rate is higher than R134a, as the latent heat is lower (- 7 % at 5.5 °C). Second, the derivative of the saturation temperature as a function of the pressure $(dt/dp)_{sat}$ is higher (+33 % at 5.5 °C), meaning that, at the same pressure drop, the temperature drop is higher. Moreover, the vapour density is 19 % lower at 5.5 °C: at the same mass flow rate, the vapour phase pressure drop (between shell and outlet nozzle, for example) results higher.

4. CONCLUSIONS

The hybrid film evaporator is a low-charge alternative to the flooded evaporator; its design derives from the falling film concept, refining it with solutions to avoid the dryout and to improve the distribution. The experimental results of comparative tests with R134a and R1234ze(E) on the same hybrid film prototype show that:

- at typical air conditioning operative conditions, the water-to refrigerant approach obtained with R1234ze(E) is 0.2 ÷ 0.4 K higher than that obtained with R134a;
- the shell-side heat transfer coefficient of R1234ze(E) can be even 20% lower than that of R134a, for example, 18 versus 22 kW m^{-2} K^{-1} at 25 kW m^{-2} heat flux;
- nucleate boiling is not the only mechanism driving heat transfer;
- the inlet vapour quality has a weak influence on the heat transfer coefficient for both fluids;
- the saturation temperature drop of R1234ze(E), although still admissible for vapour compression systems, is even two times that of R134a, mainly due to the distribution system.

REFERENCES

Abed, M.A., Alghoul, M.A., Yazdi, M.H., Al-Shamani, A.N., 2015. The role of enhancement techniques on heat and mass transfer characteristics of shell and tube spray evaporator: a detailed review. Appl. Therm. Eng. 77, 923-940.

Bergles, A.E., 1997. Heat Transfer Enhancement - The Maturing of Second-Generation Heat Transfer Technology. Heat Transfer Eng., 18(1), 47-55.

Byun, H.-W., Kim, D.H., Yoon, S.H., Song, C.H., Lee, K.H., Kim, O.J., 2017. Pool boiling performance of enhanced tubes on low GWP refrigerants. Appl. Therm. Eng. 123, 791-798.

Censi, G., Giancotti, L., Padovan, A., 2018. Experimental investigation of a new low-approach evaporator with reduced refrigerant charge. International Refrigeration and Air Conditioning Conference at Purdue, West Lafayette, Indiana, USA.

Chang, T.B., Chiou, J.S., 1999. Spray evaporation heat transfer of R-141b on a horizontal tube bundle. Int. J. Heat Mass Transf. 42, 1467-1478.

Christians, M., Thome, J.R., 2012. Falling film evaporation on enhanced tubes, part 1: Experimental results for pool boiling, onset-of-dryout and falling film evaporation. Int. J. Refrigeration 35, 300-312.

Cooper, M.G., 1984. Heat flow rates in saturated nucleate pool boiling - a wide-ranging examination using reduced properties. Adv. Heat Transfer 16, 157-239.

Fernández-Seara, J., Pardiñas, Á. Á., 2014. Refrigerant falling film evaporation review: Description, fluid dynamics and heat transfer. Appl. Therm. Eng. 64(1), 155-171.

Gorgy, E., 2016. Nucleate boiling of low GWP refrigerants on highly enhanced tube surface. Int. J. Heat Mass Transf. 96, 660-666.

Hodnebrog, Ø., Etminan, M., Fuglestvedt, J.S., Marston, G., Myhre, G., Nielsen, C.J., Shine, K.P., Wallington, T J., 2013. Global Warming Potentials and Radiative Efficiencies of Halocarbons and Related Compounds: A Comprehensive Review. Rev. Geophys. 51(2), 300-378.

Ji, W.-T., Zhao, E.-T., Zhao, C.-Y., Zhang, H., Tao, W.-Q., 2019. Falling film evaporation and nucleate pool boiling heat transfer of R134a on the same enhanced tube. Appl. Therm. Eng. 147, 113-121.

Lashof, D.A., Ahuja, D.R., 1990. Relative contribution of greenhouse gas emissions to global warming. Nature 344, 529–531.

Lemmon, E.W., Huber, M.L., McLinden, M.O., 2013. NIST Standard Reference Database 23: Reference Fluid Thermodynamic and Transport Properties - REFPROP, Version 9.1, National Institute of Standards and Technology, Standard Reference Data Program, Gaithersburg.

McLinden, M.O., Brown, J.S., Brignoli, R., Kazakov, A.F., Domanski, P.A., 2017. Limited options for low-global-warming-potential refrigerants. Nature Comm. 8: 14476.

Ribatski, G., Jacobi, A.M., 2005. Falling-film evaporation on a horizontal tubes a critical review. Int. J. Refrigeration 28, 635-653.

Roques, J.F., Thome, J.R., 2007. Falling Films on Arrays of Horizontal Tubes with R-134a, Part I: Boiling Heat Transfer Results for Four Types of Tubes. Heat Transfer Eng., 28(5), 394-414.

Stocker, T.F., Qin, D., Plattner, G.K., Tignor, M., Allen, S.K., Boschung, J., Nauels, A., Xia, Y., Bex, V., Midgley, P.M., 2013. IPCC, 2013: Climate Change 2013: The Physical Science Basis. Contribution of Working Group I to the Fifth Assessment Report of the Intergovernmental Panel on Climate Change. Cambridge University Press, Cambridge, United Kingdom and New York, NY, USA, pp. 1535.

Van Rooyen, E., Thome, J.R., 2013. Pool boiling data and prediction method for enhanced boiling tubes with R-134a, R-236fa, and R-1234ze(E). Int. J. Refrigeration 36 (2), 447-455.

Manuscript ID: 1439
DOI: 10.18462/iir.icr.2019.1439

Experimental and numerical study of heat transfer in evaporation and condensation with R410A, R32 and R454B in a finned tube heat exchanger

Pierre PARDO[(a)], Nicolas GAILLARD[(a)], Michèle MONDOT[(a)]

[(a)]CETIAT, Centre Technique des Industries Aérauliques et Thermiques
Villeurbanne, 69100, France, pierre.pardo@cetiat.fr

ABSTRACT

The progressive phase-out of HFCs and their replacement by the 4th generation of refrigerants require identifying the performance of these alternative refrigerants in heat exchangers. The objective of this study was to assess the heat transfer performance during evaporation and condensation of R410A, R454B and R32 in a finned tube heat exchanger. A 30 kW experimental setup was built to assess the heat exchanger performance with these three refrigerants. For each refrigerant, 6 tests were carried out in evaporation and 5 tests in condensation. During the tests, energy balance between the thermal capacities measured on the air and refrigerant sides was found to be less than 5%, which confirmed a good accuracy of measurements. A good agreement (+/-2.5%) between experimental data and simulations allowed using EVAP-COND software for comparison of the performance of a same heat exchanger design with the 3 refrigerants. The simulations show that the same design of finned tube heat exchanger can be used for R410A and R454B but a design optimization will be necessary with R32.
Keywords: Low GWP Refrigerants, Finned Tube Heat Exchanger, R410A, R32, R454B.

1. INTRODUCTION

New refrigerants with low GWP are now offered by the chemical industry. Some of these refrigerants will be the solutions of tomorrow and HVAC manufacturers have to be ready to use them. Studies conducted on this transition essentially dealt with the thermal performances of low GWP refrigerants in existing equipment with drop-in tests or soft optimization tests (Amrane, 2015; Wang and Amrane, 2016; Pardo and Mondot, 2018). Some also looked at the compatibility between low GWP refrigerants and materials (Majurin et al., 2014). Studies on heat transfer of low GWP refrigerants in evaporation and in condensation have been published (Azzolin et al., 2016; Del Col et al., 2010; Diani et al., 2014; Diani et al., 2015; Jige et al., 2016; Jige et al., 2017; Longo et al., 2018a; Longo et al., 2018b). Most of these works focused on the heat transfer coefficient in evaporation or in condensation in smooth tubes, microchannels and microfin tubes. The evaluation of the heat transfer coefficient is essential for the heat exchanger design.
The objectives of this work are to assess experimentally the thermal performance, capacity and pressure drop, in condensation and in evaporation, of R32 and R454B, as alternatives to R410A, in a finned tube heat exchanger and to use a reliable software tool for performance comparison of the refrigerants.
The paper is divided in three parts:

- presentation of the main refrigerant properties;
- experimental investigation: method and results;
- numerical investigation: validation of EVAP-COND software (Domanski and Yashar, 2016) and simulations in evaporation and condensation modes.

2. REFRIGERANT PROPERTIES

The choice of the alternative refrigerants to R410A is based on the result analysis of the AHRI Low GWP AREP program (Wang and Amrane, 2016) and on the experimental results of drop-in tests

previously carried out in an air-to-water heat pump by CETIAT (Pardo and Mondot, 2018). Table 1 presents the main properties of the selected refrigerants. The data source is the software REFPROP V10 (Lemmon et al., 2018).

Table 1: Refrigerant properties

Refrigerant	Composition	GWP_{100}	Latent heat (kJ/kg) (at 0 °C)	Critical temperature (°C)	Normal boiling point (°C)	Glide (K)	Safety class
R410A	R32/R125 (50/50%w)	2088	221.3	70.2	-51.6	0.1	A1
R32	R32 (100%w)	675	315.3	78.0	-52.0	0	A2L
R454B	R32/R1234yf (68.9/31.1%w)	466	260.9	78.1	-50.4	1.3	A2L

Alternative refrigerants have a lower GWP than R410A, -67% for R32 and -78% for R454B. R32 is a pure refrigerant and R454B is a mixture composed of R32 (~69%w) and R1234yf (~31%w). The phase change enthalpies of R454B and R32 are higher than that of R410A by +18% and +42%, respectively. The safety class of alternative refrigerants is A2L, which means they have a low flammability and are non-toxic. The saturation properties (pressure-temperature) are shown in Fig. 1. The three refrigerants have equivalent saturation properties. R454B remains slightly less volatile than R410A and R32.

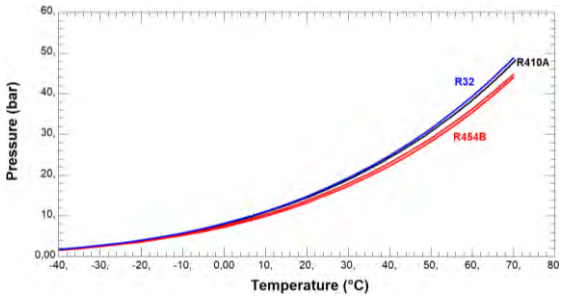

Figure 1: Saturation properties: Pressure-Temperature

3. EXPERIMENTAL INVESTIGATION

3.1. Finned Tube Heat Exchanger Description

The main characteristics of the finned tube heat exchanger are presented in Fig. 2. The finned tube heat exchanger was designed to operate either as an evaporator or as a condenser in a reversible air-to-water heat pump for an optimal heating performance. During tests, two flow patterns were thus used (see Fig. 2d):

- Evaporation mode: counter-current;
- Condensation mode: co-current.

a)

ROW DATA	
Number of rows	3
Number of tubes per row	32
Number of circuits	8
FIN DATA	
Fin type	Louver
Pitch	2,5 mm
Thickness	0,08 mm
Material	Aluminium
TUBE DATA	
Tube length	813 mm
Inner diameter	7,81 mm
Outer diameter	8,37 mm
Tube pitch	25,5 mm
Depth row pitch	20 mm
Inner surface	Smooth
Material	Copper


b)


c)

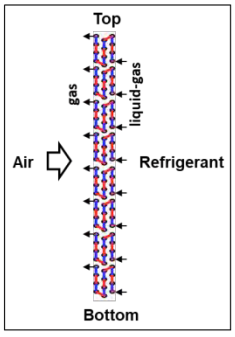

d) Evaporation mode

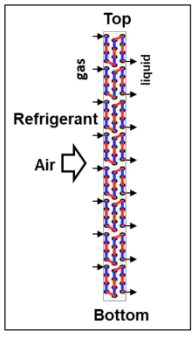

Condensation mode

Figure 2: Main characteristics of the tested finned tube heat exchanger: a) Geometry characteristics; b) Overview photography; c) Fins close-up; d) Flow patterns

In evaporation mode, the refrigerant flows through a distributor at the upstream side of the heat exchanger, in which a diaphragm is placed. This element generates an additional pressure drop downstream of the expansion device. Then, the distributor is connected to eight capillary tubes which each feeds a circuit. At the outlet, the eight circuits are connected to a collector. In condensation mode, the refrigerant flows in the other way with a by-pass of the diaphragm through a non-return valve; the circuit thus generates less pressure drop than in evaporation mode (see Fig. 4).

3.2. Experimental Set-Up

A 30 kW thermodynamic loop was designed and built to test the finned tube heat exchanger. It is composed of an inverter driven compressor, an oil separator, a plate heat exchanger and a manual expansion device. Pt100 contact probes (-20 to 100°C, +/-0.1°C) and pressure transducers (0-40 barg, +/-0.01 barg) are installed at the inlet and outlet of each component of the refrigerating circuit. In addition, a Coriolis mass flow meter (0-720 kg/h, +/-1%) in the liquid line, at the outlet of the condenser, allows measuring the refrigerant flow. This loop allows controlling the test conditions at the inlet of the finned tube heat exchanger on the refrigerant side. On the air side, the finned tube heat exchanger is installed between straight ducts of 2500 mm length, having the same rectangular section as the heat exchanger frontal surface (813 mm × 813 mm) and a 20 mm thick thermal insulation (λ = 0.022 W/m.K). The inlet air is the ambient air of a climatic room which is controlled in temperature and humidity by an air handling unit. The air volumetric flow rate is adjusted and measured thanks to a multi-nozzle chamber coupled to a fan (0-6000 m^3/h, +/-3.5%). Pt100 probes (-20 to 100°C, +/-0.1°C), mirror hygrometers (-20 to 60°C, +/-0.3°C) and Pitot probes (0-100 Pa, +/-1Pa) are placed upstream and downstream to measure, the air dry bulb and the dew point temperatures and the pressure drop, respectively. The schematic diagram in Fig. 3 shows the installation and the instrumentation in evaporation mode.

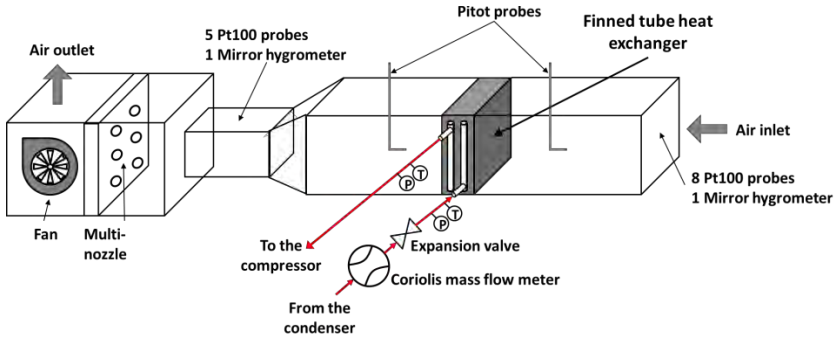

Figure 3: Schematic diagram of the installation and the instrumentation in evaporation mode

In addition, the inlet and outlet of the finned tube heat exchanger were instrumented with pressure transducers and Pt100 contact probes. The fifth circuit from the top of the finned tube heat exchanger was instrumented with 3 pressure transducers (red squares) and 10 Pt100 contact probes (blue hexagons) (see Fig. 4).

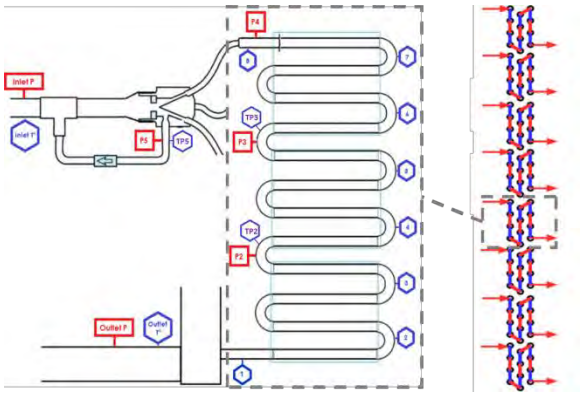

Figure 4: Specific instrumentation placed at inlet/outlet and on the 5th circuit from the top of the finned tube heat exchanger

3.3. Test Conditions

3.3.1. Evaporation Mode

The test conditions in evaporation mode are shown in Table 2.

Table 2: Test conditions in evaporation mode

Run	Flow	Air	Air dry bulb temperature (wet bulb temperature) (°C)	Air frontal velocity ($m.s^{-1}$)	Refrigerant mass flow rate ($kg.h^{-1}$)	Refrigerant liquid temperature (°C)
1	Counter-current	Dry	20(10)	2.25	230	30
2	Counter-current	Dry	20(10)	2.25	270	30
3	Counter-current	Dry	20(10)	2.25	330	30
4	Counter-current	Wet	16(14)	2.25	230	30
5	Counter-current	Wet	16(14)	2.25	270	30
6	Counter-current	Wet	16(14)	2.25	330	30

Two air dry and wet bulb conditions are defined. For each, the refrigerant flow is set at three different values. To obtain an air frontal velocity of 2.25 $m.s^{-1}$, the inlet volumetric air flow rate is adjusted close to 5350 $m^3.h^{-1}$ (+/-50 $m^3.h^{-1}$). 2.25 $m.s^{-1}$ is the maximal frontal air velocity reachable by the experimental set-up, due to the fan downstream of the multi-nozzle chamber.

3.3.2. Condensation Mode

The test conditions in condensation mode are shown in Table 3.

Table 3: Test conditions in condensation mode

Run	Flow	Air	Air dry bulb temperature (wet bulb temperature) (°C)	Air frontal velocity ($m.s^{-1}$)	Refrigerant mass flow rate ($kg.h^{-1}$)	Refrigerant inlet condenser temperature (°C)
1	Co-current	-	30(-)	2.15	230	80
2	Co-current	-	30(-)	2.15	270	80
3	Co-current	-	30(-)	2.15	330	80
4	Co-current	-	30(-)	2.15	360	80

One air condition is tested with four refrigerant flow rates. To obtain an air frontal velocity of 2.15 m/s, the inlet volumetric air flow rate is adjusted close to 5115 $m^3.h^{-1}$ (+/-50 $m^3.h^{-1}$). The frontal air velocity is lower than in evaporation because the air specific volume at the inlet of the heat exchanger is slightly higher: 0.9 against 0.85 (at 16°C) $m^3_{wet\_air}.kg_{dry\_air}^{-1}$. Thus, 2.15 $m.s^{-1}$ is the maximal reachable frontal air velocity.

3.4. Experimental Results

In this section, the evaporating or condensing temperatures, the thermal capacities and the pressure drops measured during the tests are presented.

3.4.1. Evaporation Mode

During the evaporation tests, the heat balance between the thermal capacities measured on the air and refrigerant sides is comprised between:

- 0.4% and 2.5% in dry air condition;
- 3.4% and 9.3% in wet air condition.

Three tests with wet air (among a total of nine) have a heat balance between 6.1% and 9.3%. There is only one dew point temperature measurement in the downstream duct against five for the dry temperature (mean value from 5 Pt100 probes). It can thus be considered that the dew point temperature measurement probably generates these heat balance deviations. Nevertheless, the measurements can be considered as reliable enough in the context of this study.

The evaporating temperatures, the superheating (SH), the cooling capacity and the pressure drop (P4 – Outlet P; see Fig. 4) are presented in Table 4 for the three refrigerants.

Table 4: Main results measured on the refrigerant side in evaporation mode

Refrigerant	Run	Evaporating temperature (°C)		SH (K)	Cooling capacity (kW)	Pressure drop (kPa)
		Bubble point	Dew point			
R410A	1	2.2	1.4	16.6	12.2	22
	2	1.1	-0.3	17.6	14.3	36
	3	-0.7	-2.8	18.5	17.5	52
	4	3.4	2.6	11.7	11.9	20
	5	0.4	-1.0	15.1	14.1	37
	6	-0.5	-2.7	16.0	17.3	52
R454B	1	1.8	0.4	16.7	14.6	33
	2	0.5	-1.3	17.3	17.0	46
	3	-0.3	-3.3	15.6	20.8	69
	4	0.4	-1.1	15.2	14.3	36
	5	0.2	-1.8	15.2	17.1	47
	6	0.3	-2.7	14.6	20.6	69
R32	1	2.2	1.0	12.7	17.4	29
	2	-3.7	-4.7	20.9	21.1	59
	3	-3.5	-7.1	12.5	25.1	78
	4	2.2	1.0	11.0	17.5	29
	5	0.6	-1.4	12.4	20.6	46
	6	-1.7	-5.1	14.0	25.2	77

It should be noted that the evaporating temperatures of the three refrigerants are not the same. The differences can reach up to 5 K (see runs 2, 3 and 4). This is due to the difficulty in adjusting this parameter during the test. Some of the differences in cooling capacity are due to better heat transfer coefficient values and some due to large temperature differences between air and refrigerant. Similarly on pressure drop, most of the increase in pressure drop for R32 and R454B seem to be due to lower evaporation temperature (and pressure) so lower density vapour and higher vapour velocities for the same mass flow. This means that we cannot directly conclude on the benefit of using one refrigerant in comparison to another.

3.4.2. Condensation Mode

During the condensation tests, the heat balance between the thermal capacities measured on the air and refrigerant sides is comprised between 0.5% à 2.1%. The measurements are reliable.
The condensing temperatures, the subcooling (SC), the heating capacity and the pressure drop (Outlet P – P4; see Fig. 4) are presented in Table 5 for the three refrigerants.

Table 5: Main results measured on the refrigerant side in condensation mode

Refrigerant	Run	Condensing temperature (°C)		SC (K)	Heating capacity (kW)	Pressure drop (kPa)
		Dew point	Bubble point			
R410A	1	46.6	46.3	6.2	13.31	18
	2	48.3	48.1	6.6	15.29	18
	3	50.2	49.9	4.8	17.8	23
	4	51.1	50.7	4.0	19.25	21
R454B	1	50.3	48.5	7.3	15.29	16
	2	52.1	50.3	7.7	17.34	19
	3	53.8	52.0	6.2	20.39	20
	4	55.0	53.2	5.9	21.88	22

R32	1	49.4	49.3	4.4	17.78	16
	2	51.5	51.3	4.3	20.10	17
	3	54.0	53.8	3.3	23.44	20
	4	56.3	56.1	5.7	25.45	21

As previously, the condensing temperatures of the three refrigerants do not have the same value. The differences can reach up to 5 K. We cannot directly conclude on the benefit of using one refrigerant in comparison to another.

4. NUMERICAL INVESTIGATION

4.1. Software Validation

The objective of this part is to compare the experimental results with the results of the EVAP-COND software. The geometrical parameters of the finned tube heat exchanger and the inlet operating conditions have been used as input data in the software. The 30 experimental tests were simulated and compared. The calculated versus experimental capacities of R410A, R454B and R32, in evaporation and condensation modes, are plotted in Fig. 5.

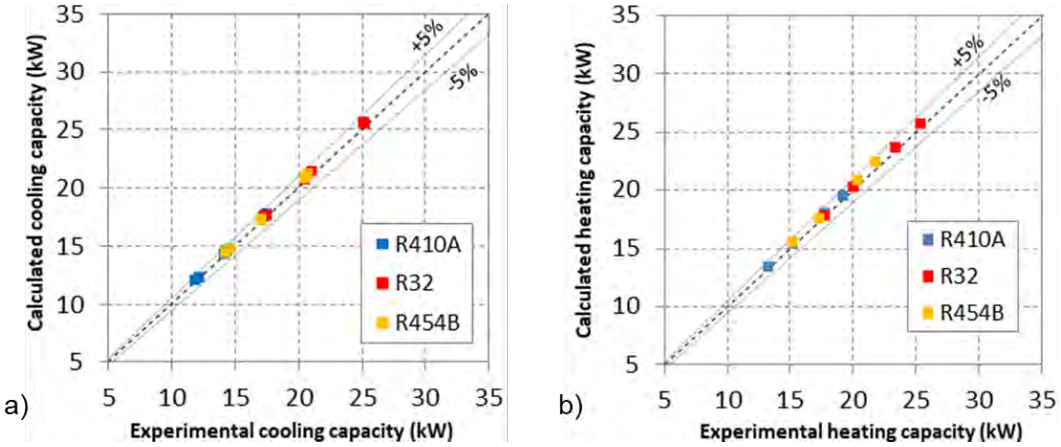

Figure 5: Calculated capacity versus experimental capacity of R410A, R454B and R32, for both modes: a) Evaporation mode; b) Condensation mode

According to Fig. 5, the comparison shows that the EVAP-COND software is a reliable tool to simulate the thermal capacity of finned tube heat exchangers. The maximal deviation observed is less than 2.5%. As a reminder, the fifth circuit from the top of the finned tube heat exchanger was instrumented with 10 Pt100 contact probes and 3 pressure transducers. The comparisons between the simulated and the experimental temperature and pressure evolutions along the 5th circuit of the run 1, in evaporation and in condensation, are shown in Fig. 6 and Fig. 7, respectively. The horizontal axis refers to the inlet and outlet of each of the 12 tubes of the circuit.

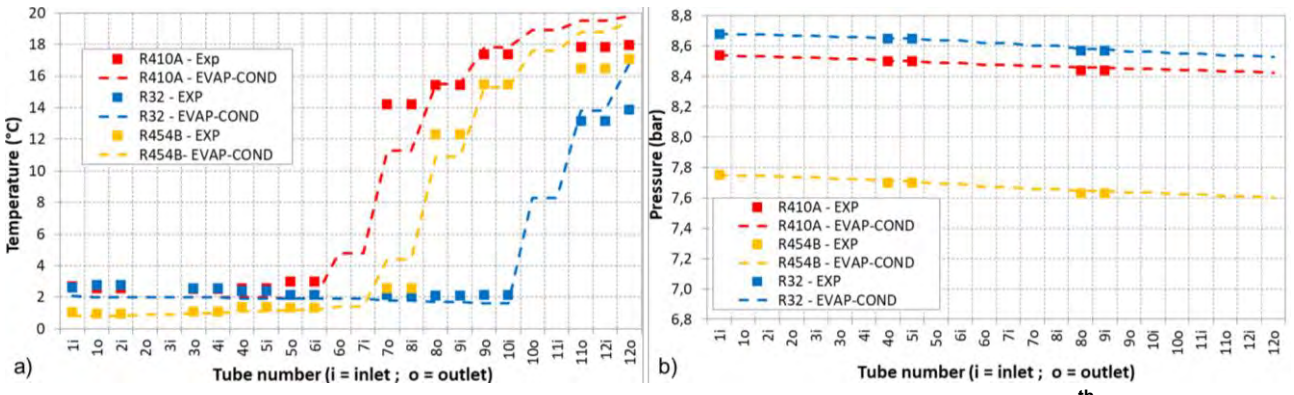

Figure 6: Calculated and experimental temperatures and pressures along the 5th circuit in evaporation: a) Refrigerant temperature; b) Refrigerant pressure

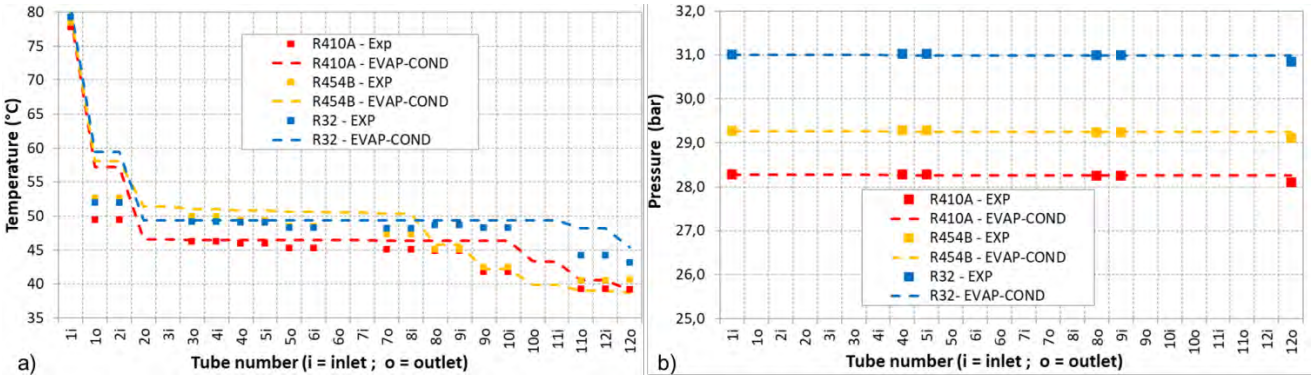

Figure 7: Calculated and experimental temperatures and pressures along the 5th circuit in condensation: a) Refrigerant temperature; b) Refrigerant pressure

The temperature and pressure evolutions of the three refrigerants in the simulated circuit are close to those observed during experimental tests. The same conclusions are drawn from all other runs of the tests (not presented in details in this paper). We can conclude that EVAP-COND software is a reliable tool to design the finned tube heat exchanger; however its robustness has not been fully validated in this study. Since most of the HFC alternatives have a high temperature glide, a comparison between experimental results obtained with a higher temperature glide refrigerant (>5 K) and the EVAP-COND simulations could be of interest.

4.2. Numerical Analysis

EVAP-COND software is then used to simulate the performance in evaporation mode and in condensation mode of the same heat exchanger design with the different refrigerants. For that purpose, the refrigerant mass flow rate is not fixed as it was for the experimental approach.
In evaporation mode, the SC1 condition of the NF EN 328 standard (see Table 6) is used with an air frontal velocity of 2.25 $m.s^{-1}$. The main results are presented in Table 7.

Table 6: SC1 condition of the NF EN 328 standard

Air dry bulb temperature (°C)	Dew point temperature (°C)	Evaporating temperature (Dew point) (°C)	Superheating (K)	Refrigerant liquid temperature (°C)
10	< -2	0	6.5	30

Table 7: Main simulation results: Evaporation mode – SC1

Refrigerant	Evaporating temperature (°C)		Refrigerant mass flow rate ($kg.h^{-1}$)	Cooling capacity (kW)	Pressure drop (kPa)
	Bubble point	Dew point			
R410A	0.2	0	195	9.7	8.7
R32	0.1	0	125 (-36%)	9.3 (-5%)	5.2 (-40%)
R454B	-0.7	0	170 (-13%)	10.3 (+5%)	8.7 (0%)

In comparison to R410A, R454B shows a higher cooling capacity (+5%) and an equivalent pressure drop. In comparison to R410A, R32 shows a lower cooling capacity (-5%), but also a lower mass flow rate (-36%) and a lower pressure drop (-40%).
In condensation mode, the SC1 condition of the NF EN 327 standard (see Table 8) is used with an air frontal velocity of 2.15 $m.s^{-1}$. The main results are presented in Table 9.

Table 8: SC1 condition of the NF EN 327 standard

Air dry bulb temperature (°C)	Condensing temperature (Bubble point) (°C)	Subcooling (K)	Superheating (K)
25	40	< 3	40

Table 9: Main simulation results: Condensation mode – SC1

Refrigerant	Condensing temperature (°C)		Refrigerant mass flow rate ($kg.h^{-1}$)	Heating capacity (kW)	Pressure drop (kPa)
	Bubble point	Dew point			
R410A	39.9	40.1	212	12.9	2.4
R32	40.0	40.0	151 (-29%)	12.7 (-1%)	1.8 (-25%)
R454B	39.9	41.2	186 (-12%)	13.3 (+3%)	2.4 (0%)

In comparison to R410A, R454B shows a slightly higher heating capacity (+3%) and an equivalent pressure drop. In comparison to R410A, R32 shows an equivalent heating capacity (-1%), a lower mass flow rate (-29%) and a lower pressure drop (-25%).
For the replacement of R410A, the same finned tube heat exchanger could be designed with R454B and a design optimization will be necessary with R32.

5. CONCLUSIONS

In the first part of this study, the thermal performances of R410A, R32 and R454B were measured in a finned tube heat exchanger, in condensation and in evaporation. 30 tests were carried out. In the second part of the study, the experimental results were used to validate the simulation results from the EVAP-COND software. The differences between experimental and calculated capacities are less than 2.5% for all tests. The temperature and pressure evolutions of the three refrigerants in the simulated circuit are also close to those observed during experimental tests. These comparisons for a pure, a quasi-azeotrope and a small temperature glide (<2 K) refrigerants, allow considering EVAP-COND software as a reliable tool for the simulation of finned tube heat exchangers. The simulations of a same heat exchanger design with the 3 refrigerants show that the same design of finned tube heat exchanger can be used for R410A and R454B but a design optimization will be necessary with R32.

REFERENCES

Amrane, K., 2015. Participants Handbook: ARHI Low-GWP Alternative refrigerants evaluation program (Low-GWP AREP). Retrieved from http://www.ahrinet.org/site/1/Home.

Azzolin, M., Bortolin, S., Del Col, D., 2016. Flow boiling heat transfer of a zeotropic binary mixture of new refrigerants inside a single microchannel. Int. J. Thermal Sciences 110, 83-95.

Del Col, D., Torresin, D., Cavallini, A., 2010. Heat transfer and pressure drop during condensation of the low GWP refrigerant R1234yf. Int. J. Refrigeration 33, 1307-1318.

Diani, A., Tamura, M.T., Mancin, S., Barbosa, J., Rossetto, L., 2014. R1234yf flow boiling heat transfer inside a 3.4 mm ID microfin tube. 15th International Refrigeration and Air Conditioning Conference at Purdue, paper number 2460.

Diani, A., Mancin, S., Cavallini, A., Rossetto, L., 2015. R1234ze(E) flow boiling heat tranfer and pressure drop inside a 2,4 mm microfin tube. 24th International Congress of Refrigeration, Yokohama, paper number 549.

Domanski, P. A., Yashar, D. A., 2016. EVAP-COND V4.0, Simulation models for finned-tube heat exchangers with circuitry optimization. Retrieved from https://www.nist.gov/services-resources/software/evap-cond.

Jige D., Sagawa, K., Inoue, N., 2016. Flow boiling heat transfer characteristics of R32 inside a horizontal small-diameter microfin tube. 16th International Refrigeration and Air Conditioning Conference at Purdue, paper number 2371.

Jige D., Sagawa, K., Inoue, N., 2017. Effect of tube diameter on boiling heat transfer and flow characteristic of refrigerant R32 in horizontal small-diameter tubes. Int. J. Refrigeration 76, 206-218.

Lemmon, E.W., Bell, I.H., Huber, M.L., McLinden, M.O., 2018. REFPROP, Reference Fluid Thermodynamic and Transport Properties, Database 23, V10.

Longo, G. A., Mancin, S., Righetti, G., Zilio, C., 2018a. R134a and its low GWP substitutes R1234yf and R1234ze(E) flow boiling inside a 4 mm horizontal smooth tube. 17th International Refrigeration and Air Conditioning Conference at Purdue, paper number 2204.

Longo, G. A., Mancin, S., Righetti, G., Zilio, C., 2018b. R134a and its low GWP substitutes R1234yf and R1234ze(E) condensation inside a 4 mm horizontal smooth tube. 17th International Refrigeration and Air Conditioning Conference at Purdue, paper number 2205.

Majurin, J., Gilles, W., Staats, S.J., 2014. Material Compatibility of HVAC&R System Materials with Low GWP Refrigerants. 15th International Refrigeration and Air Conditioning Conference at Purdue, paper number 2132.

Pardo, P., Mondot, M., 2018. Experimental evaluation of R410A, R407C and R134a alternative refrigerants in residential heat pumps. 17th International Refrigeration and Air Conditioning Conference at Purdue, paper number 2498.

Wang, X., Amrane, K., 2016. AHRI low global warming potential alternative refrigerants evaluation program (Low-GWP AREP) – summary of phase II testing results. 16th International Refrigeration and Air Conditioning Conference at Purdue, paper number 2064.

Manuscript ID: 1440
DOI: 10.18462/iir.icr.2019.1440

Thermal resistance analysis for fin-and-tube phase change thermal energy storage unit

Hao CHEN[(a)], Xiangfei LIANG[(a),(b)*], Yingwen WU[(a),(b)]

[(a)] Refrigeration Institute, Gree Electric Appliances, Inc. of Zhuhai, Zhuhai, 519070, China
[(b)] National Engineering Research Center of Green Refrigeration Equipment, Zhuhai, 519070, China
* E-mail: liangxf@cn.gree.com

ABSTRACT

Considering that the thermal resistance is significant to the thermal performance evaluation of the phase change thermal energy storage (PCTES) unit, a thermal resistance model of the fin-and-tube PCTES unit is established in this work. The model is used to investigate the effects of the structure parameters for the PCTES unit, the thermal conductivity of phase change material (PCM) and the Reynolds number. A comparison for the thermal resistance outside the tube between the PCTES unit filled with composite PCM and the fin-and-tube PCTES unit filled with single PCM is also discussed under the same condition.
Keywords: Finned Tube, Phase Change Material, Thermal Energy Storage, Thermal Resistance Model.

1. INTRODUCTION

Considering that thermal energy storage is one of the effective methods to overcome the problem of the mismatch between supply and demand of energy, the study for the thermal energy storage (TES) unit has attracted much attention. The thermal energy storage unit is usually classified as the sensible heat storage unit, the latent heat thermal energy storage unit and the thermo-chemical storage unit. Since the latent heat energy storage unit has the advantages of high energy storage density and small temperature fluctuation during the charging and discharging processes by comparing with other thermal energy storage units, this work mainly focuses on the study of the latent heat energy storage unit. The pure phase change material (PCM) used in the latent heat energy storage unit has a drawback of the poor thermal conductivity, which significantly influences the heat exchange between the heat transfer fluid (HTF) and the phase change material (PCM) as well as the charging and discharging efficiencies. To overcome that limitation, several heat transfer enhancement methods were applied including the finned tubes as presented by Agyenim and Hewitt (2010) and Merlin et al. (2016), the metal foam as presented by Yao et al. (2018) and Abishek et al. (2018), the high thermal conductivity nanoparticle as presented by Hossain et al. (2015) and the expanded graphite by Wu and Wang (2015) and Xia et al. (2010). The finned tube is used to solve the problem of the low thermal conductivity of the PCM here because of its high thermal conductivity, low cost and large extended surface.
Numerous experimental and numerical researches (Dhaidan et al., 2013; Li et al., 2014; Zauner et al., 2016; Riahi et al., 2018.) were performed to investigate the performance of the thermal energy storage unit. Although the numerical method can be used to predict the phase change behavior of the PCM in detail, a serious drawback is that the relevant numerical simulation was rather time-consuming. Besides, it is difficult to evaluate the thermal performance of a new thermal energy storage unit by using previous experimental data. Therefore, the thermal resistance model of the phase change thermal energy storage unit is necessary to be established by using theoretical

method, which can be applied to guide the design of the thermal energy storage unit. Tay et al. (2014) firstly proposed a thermal resistance model of the fin-and-tube PCTES unit, which was composed by the isothermal heat flow and the parallel heat flow models. An adjustable parameter, which was normally determined by the experiment or the numerical simulation, was required to weight the effects of two models. The motivation for this work is to establish a simple thermal resistance model of the fin-and-tube PCTES unit, which can be used to predict the thermal performance of the PCTES unit conveniently.
In this work, a new thermal resistance model of the fin-and-tube PCTES unit is established to study the influences of the structure parameters, the thermal conductivity of the PCM and the flow rate of the heat transfer fluid on the thermal performance of the fin-and-tube PCTES unit. In addition, the effect of the fin on the thermal resistance of the energy storage unit is also discussed.

2. PHYSICAL AND MATHEMATICAL MODELS

The schematic of the fin-and-tube PCTES unit is depicted in Fig. 1, in which the symbols r_1, r_2, r_3, r_4 and L are the inner radius of the tube, the outer radius of the tube, the outer radius of the collar, the half tube pitch and the tube length. Besides, the phase change front denotes the interface between solid and liquid phases of the phase change material.

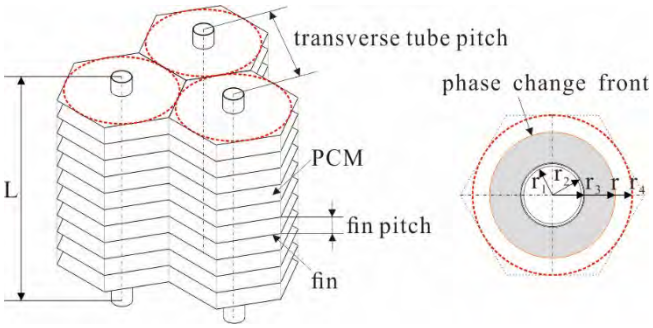

Figure 1: Schematic of the fin-and-tube PCTES unit structure

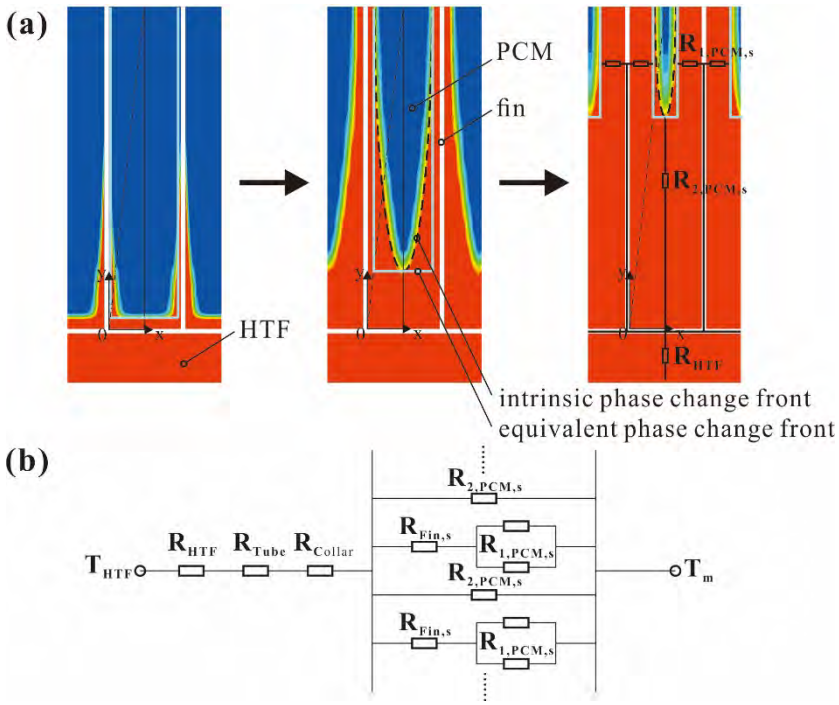

Figure 2: (a) Evolution of the phase change front
(b) Thermal resistance network of the fin-and-tube PCTES unit

The phase change front for the melting process is shown in Fig. 2a, which is simplified as straight line in this work. Therefore, the evolution rule of the phase change front can be described by using

Eq. (1). It is assumed that the phase change fraction along the tube length and the thermal properties of the materials involved are constant, and the effect of the natural convection on the phase change front is neglected. The phase change temperature remains the same in the process of the phase change. Under these assumptions, the thermal resistance network of the fin-and-tube PCTES unit shown in Fig. 2b can be obtained by analyzing Fig. 2a. Note that the evolution process of the phase change front shown in Fig. 2a is simulated by the authors of the present paper for analyzing that process.

$$\begin{cases} y = \gamma\left(r_4 - r_3\right) \\ x = \dfrac{\gamma\left(F_p - \delta_{Fin}\right)}{2}, \quad 0 \le \gamma \le 1 \end{cases} \qquad \text{Eq. (1)}$$

where γ denotes the phase change fraction, and the value of γ varies from 0 to 1. The symbols F_p and δ_{Fin} are the fin pitch and the fin thickness respectively.

As shown in Fig 2b, the thermal resistance outside the tube is composed by several thermal resistances, which mainly caused by the different heat flux paths. In addition, the symbols T_{HTF} and T_m denote the heat transfer fluid temperature and the phase change temperature respectively. Different from the thermal resistance model proposed by Tay et al. (2014), the thermal resistance model established in this work can be briefly described by using single mathematical model.

The calculation formulas of the thermal resistance shown in Fig. 2b are given as follows:

$$R_{HTF} = \frac{1}{2\pi r_1 L h_f}, \quad R_{Tube} = \frac{ln\left(r_2/r_1\right)}{2\pi L \lambda_{Tube}}, \quad R_{Collar} = \frac{ln\left(r_3/r_2\right)}{2\pi L \lambda_{Collar}} \qquad \text{Eq. (2)}$$

$$R_{Fin,s} = \frac{ln\left(r_4/r_3\right)}{2\pi\delta_{Fin}\lambda_{Fin}} \qquad \text{Eq. (3)}$$

$$R_{1,PCM,s} = \frac{\gamma\left(F_p - \delta_{Fin}\right)/2}{\pi\left(r_4^2 - r_3^2\right)\lambda_{PCM}} \qquad \text{Eq. (4)}$$

$$R_{2,PCM,s} = \frac{ln\left[1 + \gamma\left(r_4 - r_3\right)/r_3\right]}{2\pi\left(F_p - \delta_{Fin}\right)\lambda_{PCM}} \qquad \text{Eq. (5)}$$

where h_f and λ_{PCM} are the heat transfer coefficient inside the tube and the thermal conductivity of the phase change material respectively. λ_{Tube}, λ_{Collar} and λ_{Fin} are the thermal conductivities of the tube, the collar and the fin respectively.

$$L_T = L_B = \frac{F_p - \delta_{Fin}}{2} \qquad \text{Eq. (6)}$$

$$R_{2,PCM,T} = \frac{ln\left[1 + \gamma\left(r_4 - r_3\right)/r_3\right]}{2\pi L_T \lambda_{PCM}} \qquad \text{Eq. (7)}$$

$$R_{2,PCM,B} = \frac{ln\left[1 + \gamma\left(r_4 - r_3\right)/r_3\right]}{2\pi L_B \lambda_{PCM}} \qquad \text{Eq. (8)}$$

$$R_{Fin\&PCM}=\left[\frac{n_{Fin}}{R_{Fin,s}+R_{1,PCM,s}/2}+\frac{n_{Fin}-1}{R_{2,PCM,s}}+\frac{1}{R_{2,PCM,T}}+\frac{1}{R_{2,PCM,B}}\right]^{-1} \quad \text{Eq. (9)}$$

where n_{Fin} and $R_{Fin\&PCM}$ are the fin number and the equivalent thermal resistance of the fin and the PCM respectively. The subscripts 'T' and 'B' denote the marginal parts of the finned tube.
The total thermal resistance can be calculated by using Eq. (10).

$$R_{Total}=R_{HTF}+R_{Tube}+R_{Collar}+R_{Fin\&PCM} \quad \text{Eq. (10)}$$

The average value of total thermal resistance and the average effectiveness are given by:

$$R_{Total,ave}=\int_0^1 R_{Total}d\gamma \quad \text{Eq. (11)}$$

$$\varepsilon_{ave}=1-e^{-NTU_{ave}}=1-e^{-\frac{1}{R_{Total,ave}}\frac{1}{m_{HTF}c_{p,HTF}}} \quad \text{Eq. (12)}$$

where ε_{ave}, m_{HTF} and $c_{p,HTF}$ are the average effectiveness, the mass flow rate and the specific heat respectively.
Besides, the average thermal resistance outside the tube is given by:

$$R_{Eff,ave}=R_{Total,ave}-R_{HTF}-R_{Tube} \quad \text{Eq. (13)}$$

The following heat transfer correlations (Tay et al. 2012) are used to determine the Nusselt number inside the heat transfer tube under different flow types, and the heat transfer coefficient h_f is given by $h_f=Nu\lambda_{HTF}/d_1$.

$$Nu=3.66+\frac{0.0668\left(\frac{d_1}{L}\right)\mathrm{Re}\,\mathrm{Pr}}{1+0.04\left[\left(\frac{d_1}{L}\right)\mathrm{Re}\,\mathrm{Pr}\right]^{\frac{2}{3}}} \quad \text{(Laminar flow, Re≤2300)} \quad \text{Eq. (14)}$$

$$Nu=\frac{(f/8)(\mathrm{Re}-1000)\mathrm{Pr}}{1+12.7\sqrt{f/8}\left(\mathrm{Pr}^{2/3}-1\right)}\left[1+\left(\frac{d_1}{L}\right)^{2/3}\right] \quad \text{(Transition flow or turbulent flow, Re>2300)} \quad \text{Eq. (15)}$$

where $\mathrm{Re}=\rho_{HTF}ud_1/\mu_{HTF}$, $\mathrm{Pr}=\mu_{HTF}c_{p,HTF}/\lambda_{HTF}$, and $f=(1.82\lg\mathrm{Re}-1.64)^{-2}$.

3. RESULTS AND DISCUSSION

3.1. Validation of the Thermal Resistance Model

A comparison between the result obtained by present work and the result obtained by Tay et al. (2014) is shown in Fig. 3, and the structure parameters used in this validation for the TES unit are $d_2=d_3=12$ mm, $d_4=53$ mm, $\delta_{Tube}=2$ mm, $L=280$ mm, $\delta_{Fin}=1.5$ mm and $F_p=20$ mm. Fig. 3 shows that a small deviation between present result and reference result is found in the case of the charging process. Considering that the simple thermal resistance model established in this work without any adjustable parameters, this model can be conveniently used to analyze the influence factors, and optimize the structure for the fin-and-tube PCTES unit. Note that the symbol 'A' shown in Fig. 3 denotes the heat transfer area without extended surface.

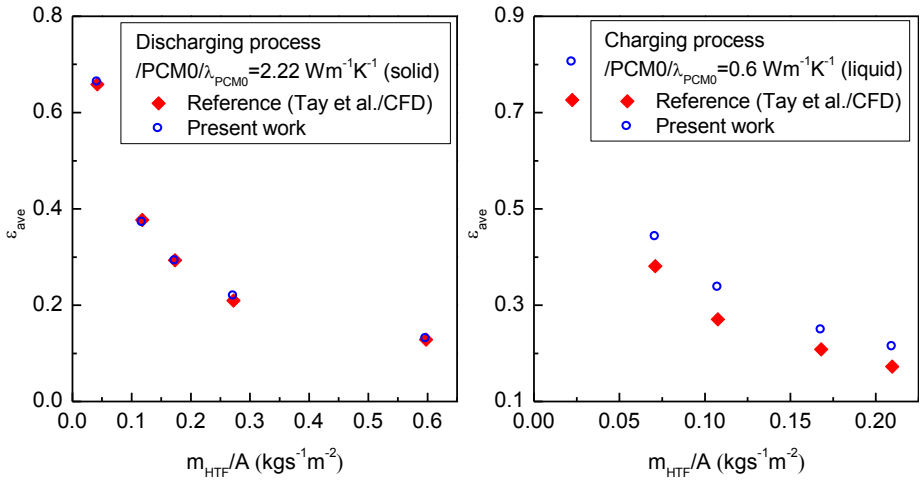

Figure 3: Validation of thermal resistance model

3.2. Influent Factors of Thermal Performance of the Fin-and-Tube PCTES Unit

In this section, the thermal resistance model aforementioned is used to analyze the effects of several influence factors on the thermal performance of the fin-and-tube PCTES unit. Besides, the thermal resistances of the plain tube TES unit with the composite PCM and the finned tube TES unit with the pure PCM are also discussed, in which the thermal resistance model of the plain tube TES unit was proposed by Tay et al (2012). The structure parameters used in following discussion for the finned tube TES unit and the plain tube TES unit are listed in Table 1. Furthermore, the thermal conductivities for the PCM1 are 0.7 $Wm^{-1}K^{-1}$ for the solid phase and 0.4 $Wm^{-1}K^{-1}$ for the liquid phase. The thermal properties of the heat transfer fluid, including the density, the thermal conductivity, the specific heat and the dynamic viscosity, are ρ_{HTF}=998.2 kgm^{-3}, λ_{HTF}=0.599 $Wm^{-1}K^{-1}$, $c_{p,HTF}$=4183 $Jkg^{-1}K^{-1}$, and μ_{HTF}=0.001003 Pas. The thermal conductivities of the heat transfer tube and the fin are 387.6 $Wm^{-1}K^{-1}$ and 202.4 $Wm^{-1}K^{-1}$ respectively.

Table 1. Structure parameters for the finned tube TES unit and the plain tube TES unit

TES unit	d_2 (mm)	δ_{Tube} (mm)	L (mm)	δ_{Fin} (mm)	F_p (mm)	d_4 (P_t) (mm)
Finned tube TES unit	7.4	0.279	381.5	0.105	1.7	22
Plain tube TES unit	7	0.3	381.5	-	-	-

As shown in Figs. 4a, 4b and 4c, when the fin pitch decreases or the fin thickness increases or the PCM thermal conductivity enhances, the thermal resistance outside the tube decreases. Besides, when the fin pitch is decrease from 1.7 mm to 1 mm, the thermal resistance outside the tube is decrease from 0.0342 KW^{-1} to 0.0203 KW^{-1}. When the fin thickness is increase from 0.105 mm to 0.2 mm, the thermal resistance outside the tube is decrease from 0.0342 KW^{-1} to 0.0202 KW^{-1}. When the thermal conductivity of the PCM is increase from 0.7 $Wm^{-1}K^{-1}$ to 4.9 $Wm^{-1}K^{-1}$, the thermal resistance outside the tube is decrease from 0.0342 KW^{-1} to 0.0203 KW^{-1}. Therefore, the increment of the total cost and the decrement of the energy storage density can be selected as an evaluation criterion, when several heat transfer enhancement methods are used to improve the thermal performance of the fin-and-tube PCTES unit.

As shown in Fig. 4(d), with the decrease of the transverse tube pitch, the fin area and the mass of the filling PCM decrease. When the thermal resistance increment caused by the decrement of the fin area is small than the thermal resistance decrement caused by the decrement of the filling PCM mass, the thermal resistance outside the tube decreases. On the contrary, the thermal resistance increases. Therefore, the thermal resistance outside the tube decreases first and then increases with the increase of the transverse tube pitch. There exists an extreme point in the $R_{Eff,ave}$-P_t variation curve.

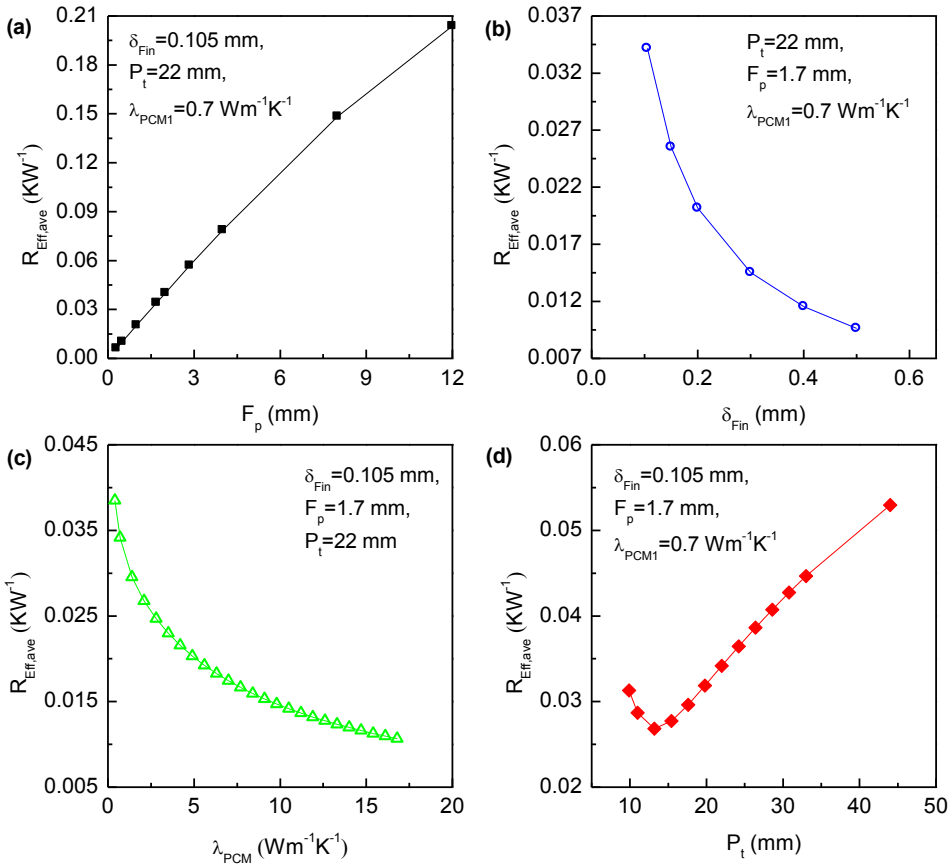

Figure 4: Effect of the fin pitch, the fin thickness, the thermal conductivity of PCM and the tube pitch on the thermal resistance outside the tube under the conditions of the discharging process and m_{HTF}=0.1 kgs^{-1}

Fig. 5 indicates that with the increase of the Reynolds number, the thermal resistance inside the tube decreases, the thermal resistance outside the tube keeps constant, and the average effectiveness of the PCTES unit decreases. However, when the flow type inside the tube is beginning to transform from the laminar flow to the turbulent flow, the average effectiveness increases first. Furthermore, the thermal resistance inside the tube may higher than the thermal resistance outside the tube even if the flow type is the turbulent flow.

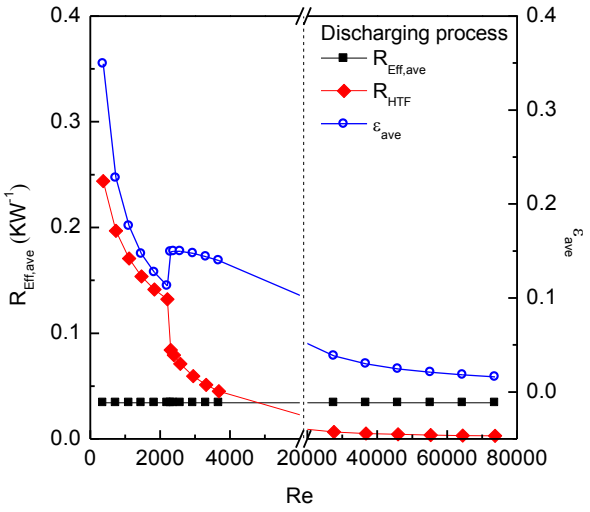

Figure 5: Variations of the effective thermal resistance and the average effectiveness with the Reynolds number

As shown in Fig. 6, when the thermal conductivity of the composite PCM filled in the plain tube TES unit is 9.45 Wm^{-1}K^{-1}, the thermal resistance outside the tube of this unit is similar to that of the finned

tube TES unit filled with the pure PCM1. Note that the fin pitch and the thermal conductivity of the pure PCM1 for the finned tube TES unit are 1.7 mm and 0.7 $Wm^{-1}K^{-1}$ respectively.
In addition, when the thermal conductivity of the composite PCM filled in the plain tube TES unit is 7 $Wm^{-1}K^{-1}$, the thermal resistance outside the tube of this unit is similar to that of the finned tube TES unit filled with the pure PCM2. Note that the fin pitch and the thermal conductivity of the pure PCM2 for the finned tube TES unit are 1.7 mm and 0.2 $Wm^{-1}K^{-1}$ respectively. From above analysis, a conclusion can be proposed that when the composite PCM with high thermal conductivity is very expensive, the finned tube can be adopted for the heat transfer enhancement of the PCTES unit.

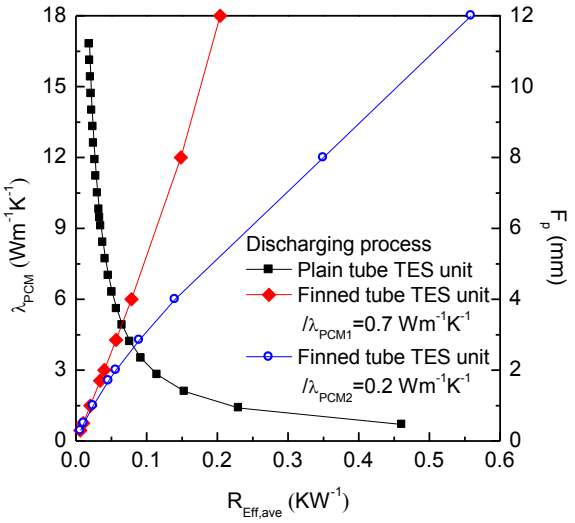

Figure 6: Comparison for the thermal resistances outside the tube of the plain tube TES unit filling with the composite PCM and the finned tube TES unit filling with the pure PCM

4. CONCLUSIONS

In this work, a new thermal resistance model of the fin-and-tube PCTES unit is established to analyze the effect of the fin thickness, the fin pitch, the tube pitch, the thermal conductivity of the PCM, the Reynolds number on the thermal resistance outside the tube. In addition, the thermal performances of two kinds of the TES unit are also discussed. The major results presented in this work reveal that the thermal resistance outside the tube decreases first and then increases with the increase of the tube pitch. The thermal resistance outside the tube decreases when the fin pitch decreases, the fin thickness increases or the PCM thermal conductivity improves. Normally, the dominated thermal resistance of the PCTES unit is the thermal resistance outside the tube. The finned tube can be adopted for the heat transfer enhancement of the PCTES unit when the composite PCM with high thermal conductivity is very expensive.

NOMENCLATURE

A	Heat transfer area
c_p	Specific heat ($Jkg^{-1}K^{-1}$)
d	Diameter (m)
F_p	Fin pitch (m)
h_f	Heat transfer coefficient ($Wm^{-2}K^{-1}$)
L	Tube length (m)
m	Mass flow rate (kgs^{-1})
n_{Fin}	Fin number
NTU	Number of transfer units
Pr	Prandtl number
P_t	Transverse tube pitch
R	Thermal resistance (KW^{-1})
Re	Reynolds number
r	Radius (m)
u	Velocity (ms^{-1})
W	Weighted factor

Greek symbols

δ_{Fin}	Fin thickness (m)
ε	Effectiveness
γ	Phase change fraction
λ	Thermal conductivity ($Wm^{-1}K^{-1}$)
μ	Dynamic viscosity (Pas)
ρ	Density (kgm^{-3})

Subscripts

ave	Average value
HTF	Heat transfer fluid

T_m Phase change temperature (K) PCM Phase change material

REFERENCES

Abishek, S., King, A.J.C., Nadim, N., Mullins, B.J., 2018. Effect of microstructure on melting in metal-foam/paraffin composite phase change materials. Int. J. Heat Mass Transfer, 127, 135-144.

Agyenim, F., Hewitt, N., 2010. The development of a finned phase change material (PCM) storage system to take advantage of off-peak electricity tariff for improvement in cost of heat pump operation. Energy Build, 42, 1552-1560.

Dhaidan, N.S., Khodadadi, J.M., Al-Hattab, T.A., Al-Mashat, S.M., 2013. Experimental and numerical investigation of melting of phase change material/nanoparticle suspensions in a square container subjected to a constant heat flux. Int. J. Heat Mass Transfer, 66, 672-683.

Hossain, R., Mahmud, S., Dutta, A., Pop, I., 2015. Energy storage system based on nanoparticle-enhanced phase change material inside porous medium. Int. J. Therm. Sci., 91, 49-58.

Li, W.Q., Qu, Z.G., He, Y.L., Tao, Y.B., 2014. Experimental study of a passive thermal management system for high-powered lithium ion batteries using porous metal foam saturated with phase change materials. J. Power Sources, 255, 9-15.

Merlin, K., Delaunay, D., Soto, J., Traonvouez, L., 2016. Heat transfer enhancement in latent heat thermal storage systems: Comparative study of different solutions and thermal contact investigation between the exchanger and the PCM. Appl. Energy, 166, 107-116.

Riahi, S., Saman, W.Y., Bruno, F., Belusko, M., Tay, N.H.S., 2018. Performance comparison of latent heat storage systems comprising plate fins with different shell and tube configurations. Appl. Energy, 212, 1095-1106.

Tay, N.H.S., Belusko, M., Castell, A., Cabeza, L.F., Bruno, F., 2014. An effectiveness-NTU technique for characterising a finned tubes PCM system using a CFD model. Appl. Energy, 131, 377-385.

Tay, N.H.S., Belusko, M., Bruno, F., 2012. An effectiveness-NTU technique for characterising tube-in-tank phase change thermal energy storage systems. Appl. Energy, 91, 309-319.

Wu, Y., Wang, T., 2015. Hydrated salts/expanded graphite composite with high thermal conductivity as a shape-stabilized phase change material for thermal energy storage. Energy Convers. Manage, 101, 164-171.

Xia, L., Zhang, P., Wang, R.Z., 2010. Preparation and thermal characterization of expanded graphite/paraffin composite phase change material. Carbon, 48, 2538-2548.

Yao, Y., Wu, H., Liu, Z., Gao, Z., 2018. Pore-scale visualization and measurement of paraffin melting in high porosity open-cell copper foam. Int. J. Therm. Sci., 123, 73-85.

Zauner, C., Hengstberger, F., Etzel, M., Lager, D., Hofmann, R., Walter, H., 2016. Experimental characterization and simulation of a fin-tube latent heat storage using high density polyethylene as PCM. Appl. Energy, 179, 237-246.

Manuscript ID: 1498
DOI: 10.18462/iir.icr.2019.1498

Development of macroscopic two-phase flow model based on equivalent porous media approach for plate and fin heat exchanger

Cédric SEPTET[a,b], Jean-Michel HUGO[b], Olivier LEMETAYER[a], Georges EL ACHKAR[c]

(a) Laboratoire IUSTI - CNRS UMR 7343
Marseille Cedex 13, 13453, France, cedric.septet@etu.univ-amu.fr
(b) TEMISTh SAS
Marignane, 13700, France, contact@temisth.com
(c) Tianjin Key Laboratory of Refrigeration Technology
Tianjin, 300134, China, georges.elachkar@tjcu.edu.cn

ABSTRACT

In this paper, a numerical model based on a macroscopic approach and developed to describe flows, heat and mass transfer phenomena in two-phase heat exchangers, is presented. The two-phase flow model is first established and the basics of macroscopic approach at the volume integration step are introduced. As for the model's approach, the fluid and solid phases were represented by a homogeneous media, and the governing equations were obtained by a volume averaging of local equations. Physical interactions between the phases were modelled by source terms, whose some parameters formulation could be found either numerically or experimentally. The important parameters that must be characterized are then identified. Therefore, an experimental set-up has to be developed to define the formulations of global and local parameters and then enable the macroscopic simulation of plate and fin heat exchangers.

Keywords: Heat exchangers, porous media, boiling and condensation, changes of state of refrigerants.

1. INTRODUCTION

Heat exchangers are progressively taking a dominating place in industrial applications. In a general context of reducing energy consumptions and production costs, they have become a key component in improving energy system efficiency. Also, the current needs in terms of thermal efficiency and compactness imply increasing heat flux densities values, which can reach values of 50W/cm² in electronic cooling and 1000W/cm² in solar energy systems. At these levels of heat flux, the use of phase-change fluids in cooling systems may become necessary to reduce temperature gradients inside the component and the mechanical energy needs at the pump to overcome the pressure drop. To overcome these constrains, engineers need to reconsider their methods and use appropriated tools to assist them in heat exchangers design, optimization and manufacturing.

In design, they can rely on a database of experimental correlations that are satisfying for the description of heat transfer and pressure drop phenomena in flow boiling or flow condensation at the scale of the component and useful for the global design of two-phase heat exchangers. Also, it exists several passive and active methods to enhance heat and mass transfer (Webb and Kim, 2005). Algorithms based on parametric, shape and topology optimization methods, widely developed and employed for mechanical structure applications at first, are now interesting industry for thermohydraulic systems (Gosselin and al., 2009) (Dbouk, 2017). Combined to Computational Fluid Dynamic (CFD) and Computer-Aided Design (CAD) softwares, these approaches can be used as reliable optimizer tools in engineering that could generate optimized complex and evolutive structures adapted to heat transfer and fluid flow variations inside thermal devices.

However, each passive method and experimental correlations are applied to specific heat exchanger architectures, flow regimes and heat exchange modes, and corresponds to particular

mechanisms of intensification that are still in study. It forces manufacturers to build their own database of correlations when they develop a new product. Besides, the optimization process requires appropriate numerical models and solvers to describe fluid flow and heat transfer in the domain and evaluate the thermos-hydraulic performances, which remains an important subject in academic research. Obtaining a reliable and cost effective numerical tool to simulate the functioning of fluid systems including phase change due to boiling or condensation phenomena remains a major challenge for the industry. Yet, the knowledge of spatial and temporal fluctuations of flow variables could enable the structural optimization of heat exchangers.

In this paper, we propose a numerical method to solve fluid flows, heat and mass transfer in thermal components using the principle of equivalent porous media. The principle of this method consists in describing the flow and interacting phenomena between a fluid flow through a solid matrix at macroscale without representing the surface, creating an immediate reducing of the computational cost. This approach has been studied for a long time and has shown good capacities in solving fluid flows and heat transfer in complex structures but principally using monophasic fluids. Some research studies have been done to find physical models that can solve multiphase flows using the approach of porous media (Duval and al., 2004). Experimental works have also been done with adiabatic two-phase flows (Bonnet, 2007) and a few with flow boiling in metal foam (Madani and al., 2013) and other complex structures. The complete physical models proposed for two-phase flows with phase change in porous media are complex and still in study. We will propose a simplest physical model, user-friendly, cost effective and avoiding a long process of mathematical development.

2. PHYSICAL MODEL

A physical model has been developed to describe flow of a fluid-mixture in a domain with the presence of a solid matrix. The matrix solid will represent the extended surface, which can be compared to fins, enhancing heat and transfer to the fluid-mixture. The phases are assumed as non-miscible and the solid matrix as non-deformable and fixed. In our cases, we will consider a mixture of two components: a liquid and a vapor/gaseous phase. We use here the hypothesis that the two phases constituting the fluid-mixture obey the mixture Euler equations with species. This is a 4-equations model where we suppose a thermal and dynamic equilibrium between the constituting phases. It means the phenomena we observe occur with a rapid dynamic. As a consequence, the constituting phases share the same temperature, velocity and pressure. These assumptions are often used in physical problems such as flashing flows.

2.1. System of governing equations

The governing equations of the inviscid flow model (Eq. (1)-(4)) are given in the general conservative form as below:

Mass of liquid phase

$$\frac{\partial \rho Y_1}{\partial t} + \vec{\nabla}.\left(\rho \vec{u} Y_1\right) = 0 \qquad \text{Eq. (1)}$$

Mass of vapour phase:

$$\frac{\partial \rho Y_2}{\partial t} + \vec{\nabla}.\left(\rho \vec{u} Y_2\right) = 0 \qquad \text{Eq. (2)}$$

Momentum:

$$\frac{\partial \rho \vec{u}}{\partial t} + \vec{\nabla}.\left(\rho \vec{u} \otimes \vec{u} + P\bar{\bar{I}}\right) = 0 \qquad \text{Eq. (3)}$$

Total energy:

$$\frac{\partial \rho E}{\partial t} + \vec{\nabla}.\left(\left(\rho E + P\right)\vec{u}\right) = 0 \qquad \text{Eq. (4)}$$

The mass fraction of the liquid and vapor phase are considered with respect to the total mass balance (Y_1+Y_2=1). The velocity and pressure are defined at the dynamic equilibrium. In Eq. (4), the mixture total energy is calculated by:

$$E = e + \frac{\|\vec{u}\|^2}{2} \quad \text{Eq. (5)}$$

2.2. Closing laws

Including the internal mixture energy of the fluid which is defined as below:

$$e = Y_1 e_1 + Y_2 e_2 \quad \text{Eq. (6)}$$

The mixture density is defined as follows:

$$\frac{1}{\rho} = \frac{Y_1}{\rho_1} + \frac{Y_2}{\rho_2} \quad \text{Eq. (7)}$$

To close the system, equations of state for each phase are introduced. In many cases, the liquids have low compressibility and low sensibility to temperature fluctuations. We use the Murnaghan-Tait equation of state in the linear form (MacDonald, 1966) to calculate the density of the liquid phase. This is one of main equations of state that have been used in earth sciences and shock physics:

$$P = P_0 + \kappa_0 \left(\frac{\rho_1}{\rho_0} - 1 \right) \quad \text{Eq. (8)}$$

The bulk modulus of a liquid phase can be evaluated using the standard definition:

$$\kappa = \rho \frac{\partial P}{\partial \rho} \quad \text{Eq. (9)}$$

Considering an isentropic process, the reference bulk modulus in Eq. (8) is calculated as follows:

$$\kappa_0 = \rho_0 c_0^2 \quad \text{Eq. (10)}$$

The reference pressure, density and speed of sound (P_0,ρ_0 and c_0) are evaluated at the standard conditions for temperature and pressure.

The density of the vapor phase calculated with the ideal gas law:

$$P = (\gamma_2 - 1)\rho_2 C_{V,2} T \quad \text{Eq. (11)}$$

3. NUMERICAL METHODS

Considering two-dimensional cases, the system of equations (1)-(4) can be rewritten in the following conservative form:

$$\frac{\partial U}{\partial t} + \frac{\partial F(U)}{\partial x} + \frac{\partial G(U)}{\partial y} = 0 \quad \text{Eq. (12)}$$

Where the extended system of conservative variables is $U=(\rho Y_1, \rho, \rho u, \rho v, \rho E)^T$; and the corresponding vectors of conservative fluxes in the two directions are $F(U)=(\rho u Y_1, \rho u, \rho u^2+P, \rho uv, (\rho E+P)u)^T$ and $G(U)=(\rho v Y_1, \rho v, \rho uv, \rho v^2+P, (\rho E+P)v)^T$.

This system is integrated in a two-dimensional domain discretized with a regular Cartesian computational mesh constituted of n_X*n_Y control volumes. Each element in the domain is defined by a volume $V=\Delta x \Delta y$, a center with local coordinates (i,j) and four boundaries (see Fig. 1).

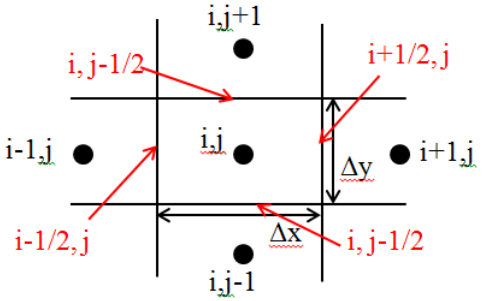

Figure 1: Definition of the Cartesian computational mesh, control volume and boundaries

Each control volume includes a volume of solid matrix V_S with an arbitrary topology and a surrounding volume of fluid V_F. The matrix solid is assumed as fixed, non-deformable and with constant thermo-physical properties, including thermal conductivity, density and specific heat. The fluid and solid matrix can also be characterized by their respective volume fraction $\varepsilon_1=V_S/V$ and $\varepsilon_2=V_F/V$. The volume fraction of fluid is also called porosity and is an important parameter in study of porous media. We will use the following definition of the porosity for the rest of the document $\varepsilon=V_F/V$.

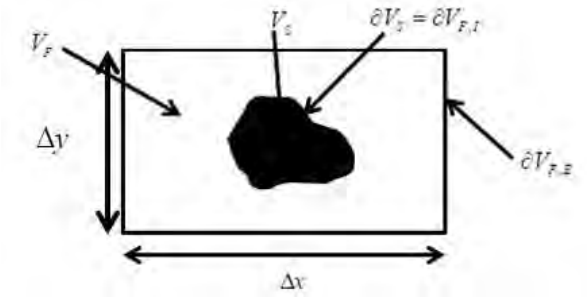

Figure 2: Schematic representation of the solid and fluid volume and boundaries inside a control volume, defining the porous media

The spatial integration using two-dimensional regular Cartesian mesh and temporal integration using a first order explicit Euler scheme of the system (10) give the following discrete formulation:

$$(\varepsilon U)_{i,j}^{n+1} = (\varepsilon U)_{i,j}^{n} - \Delta t \left(\frac{F^*(U)_{i+\frac{1}{2},j}^{n} - F^*(U)_{i-\frac{1}{2},j}^{n}}{\Delta x} + \frac{G^*(U)_{i,j+\frac{1}{2}}^{n} - G^*(U)_{i,j-\frac{1}{2}}^{n}}{\Delta y} \right) \qquad \text{Eq. (13)}$$

This hyperbolic system of partial differential equations can be solved using a Godunov's scheme. In numerical analysis and computational fluid dynamics, this scheme corresponds to a conservative finite-volume method. Exact or approximate Riemann problems are solved at each inter-cell boundary to evaluate the values in the vectors of conservative fluxes (Toro, 2009). In its basic form, Godunov's method is first order accurate in both space, and time. This system describes only the transport and the compression waves. It is important to notice that this step only solve the hyperbolic system of equations. To introduce the effect of interaction phenomena between the fluid and solid matrix, an additional numerical step is necessary. All the interaction phenomena between the solid and the fluid matrix in the domain are taken into account by additional source terms after solving the discrete formulation (Eq. (13)).

The temporal and spatial integration of source terms are made using the Splitting method. It assumes the variables constituting the source can be considered as constants during the time step. Finally, the complete numerical method is presented as a 2-step method. Each step is successively performed in order to circumvent specific numerical problems:

- First, the discrete conservative system of equations (Eq. (13)) is solved using a Godunov type numerical scheme and a HLLC solver (Toro, 2009) to resolve Riemann problem at the boundaries, giving an intermediate solution:

$$\left(\varepsilon U\right)_{i,j}^{n} = \left(\varepsilon U\right)_{i,j}^{n} - \Delta t\left(\frac{\Delta F^{*}\left(U\right)_{i,j}^{n}}{\Delta x} + \frac{\Delta G^{*}\left(U\right)_{i,j}^{n}}{\Delta y}\right) \quad \text{Eq. (14)}$$

- Second, the intermediate solution is modified by adding the additional source terms in source terms vector S(U) one by one using a splitting method, giving the new temporal solution:

$$\left(U\right)_{i,j}^{n+1} = \left(U\right)_{i,j}^{n} - \Delta t\, S\left(U\right)_{i,j}^{n} \quad \text{Eq. (15)}$$

As we use an explicit temporal formulation, the time step is evaluated considering the maximum wave velocity σ inside the domain. We introduce a Courant number (CFL) value to ensure convergence and stability to the solution. The time step is calculated at each iteration as it follows:

$$dt = CFL\frac{\min\left(\Delta x, \Delta y\right)}{\max\left(\sigma_{i,j}\right)} \quad \text{Eq. (16)}$$

4. DEFINITION OF SOURCE TERMS

4.1. Pressure drop

The momentum losses can be calculated using an appropriate flow law. At the macroscopic scale, three forms of flow laws are mainly used to describe the pressure drop when a fluid flows in a porous medium. The laws of Darcy and Forchheimer are two most common laws that have been used in porous media. Historically, they have both been experimentally validated but the Darcy law has been validated analytically also by using the method of volume averaging on Stokes equation (Whitaker 2013). There is a transition where viscous forces become non dominant and inertial effect must be taken into account. In our cases, the source term in momentum equation describing the viscous and inertial forces due to the fluid flow uses the formulation of the Darcy-Forchheimer law (Bejan & Nield 2013):

$$\vec{\nabla}P = -\mu\overline{\overline{K}}^{-1}\vec{u} - \rho\overline{\overline{\beta}}\vec{u}\left\|\vec{u}\right\| \quad \text{Eq. (17)}$$

Where μ is the dynamic viscosity of the mixture fluid. In general form, permeability and resistance inertia coefficient are expressed as tensors. We can notice they can be expressed as simple scalars in case of isotropic porous media. The tensor values can be determined either by numerical method or by experimental method (Hugo, 2012) (Kumar, 2014).

4.2. Fluid-solid heat transfer

We introduce heat transfers between the solid matrix and the fluid flow using the thermal non-equilibrium model (Bejan and Nield, 2013). We introduce a conservation equation on energy for the solid matrix. Heat transfer at fluid-solid interface and thermal dissipation are defined for solid and fluid volume as below:

Fluid volume:

$$\frac{\partial\varepsilon\rho E}{\partial t} = \vec{\nabla}.\left(\overline{\overline{k_f}}^{eff}\vec{\nabla}T\right) + h_{sf}\alpha_{sf}\left(T_s - T\right) \quad \text{Eq. (18)}$$

Solid volume:

$$\left(1-\varepsilon\right)\rho_s C_{P,s}\frac{\partial T_s}{\partial t} = \vec{\nabla}.\left(\overline{\overline{k_s}}^{eff}\vec{\nabla}T_s\right) - h_{sf}\alpha_{sf}\left(T_s - T\right) \quad \text{Eq. (19)}$$

In a porous media, the specific surface area is the ratio between the fluid-solid interface area and the volume of the media. As numerous researchers have proved, the effective thermal conductivity of the solid and fluid matrix and the heat transfer coefficient at fluid-solid surface can be easily determined numerically and experimentally for monophasic flow. The thermal dissipation in solid and fluid domain (first part of the right hand side in (16) and (17)) is solved with a secondary finite volume solver (Patankar, 1980).

4.3. Mass transfer due to boiling or condensation

The phase change occurring in the fluid-mixture is introduced in the liquid mass conservation equation:

$$\frac{\partial \rho Y_1}{\partial t} = -\dot{m} \qquad \text{Eq. (20)}$$

The local volume mass transfer rate "m" in Eq. (18) is evaluated considering equivalence between local latent heat and sensible heat between the two phases constituting the fluid-mixture:

$$\dot{m} = \frac{\left(h_{TV} + h_{TL}\right)\left(T - T_{sat}\right)}{L_{VL}\left(T_{sat}\right)} \qquad \text{Eq. (21)}$$

4.3.1. Saturation conditions

The temperature saturation can be obtained from the local pressure using the Antoine equation. The equation parameters A, B and C are taken from (Osborn and Douslin, 1974).

$$T_{sat}\left(P\right) = \frac{B}{A - \log_{10}\left(P\right)} - C \qquad \text{Eq. (22)}$$

The latent heat of vaporization $L_{VL}(T_{sat})$ is calculated as a function of the saturation temperature with the following thermodynamic definition:

$$L_{VL}\left(T_{sat}\right) = H_{sat,2}\left(T_{sat}\right) - H_{sat,1}\left(T_{sat}\right) \qquad \text{Eq. (23)}$$

In this equation, the enthalpies of vapor and liquid phases are defined as it follows:

$$H_{sat,2}\left(T_{sat}\right) = C_{P,2}T_{sat} + q_2 \qquad \text{Eq. (24)}$$

$$H_{sat,1}\left(T_{sat}\right) = C_{V,1}T_{sat} + q_1 + \frac{P_{sat}}{\rho_{sat,1}} \qquad \text{Eq. (25)}$$

The constants q_1 and q_2 are used to adjust the value of internal energy and enthalpy of each phase to fit with the latent heat of vaporization data in the literature for any fluid.

The interfacial heat transfer coefficients between the phase k and the interface are defined by $h_{Tk}=H_{Tk}\,A_I$, where H_{Tk} the volume heat transfer coefficient between the phase k and the liquid-vapor interface and A_I corresponds to the interfacial surface area between the liquid and vapor phase. The interface surface area highly depends on the flow topology we consider. In many cases, this information is not directly available and requires appropriated experimental methods. If flow topologies can be easily predicted for simple cases such as flow in tubes, it becomes more complicated when considering flow through complex structures. Previous works have been done to study the distribution of fluid phases inside porous materials or metal foams in presence of adiabatic fluid-mixtures flows or flow boiling (Bonnet, 2007) (Abadi and al., 2016). In addition to the strong dependence on quality, mass flux, velocity ratio, void fraction and working conditions, the models of flow topology are hardly transposable form one case to another.

4.3.2. Considerations for flow topology

In our case, we will attempt to evaluate the interface surface area using schematic models of flow topology, which are illustrated in Fig. 3. The volume heat transfer coefficients of each phase are

assumed as constants. Other models can be found in literature to estimate the local Nusselt number and may be used to fit with experimental results.

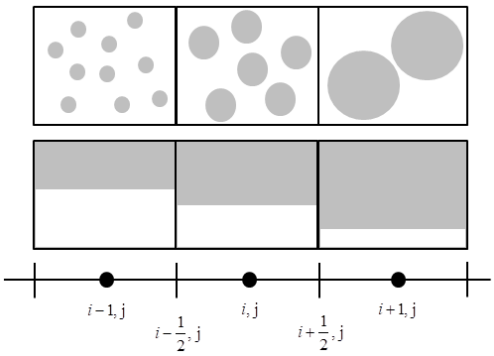

Figure 3: Schematic representation of flow topologies and phases distribution: at the top, bubble or droplet flow topology; at the bottom, stratified flow topology.

The number of bubbles/droplets per unit of volume N is fixed at the initialization which means there is neither coalescence nor interpenetration between the bubbles/droplets. We also use an additional conservative equation on the number of bubbles/droplets per unit of volume:

$$\frac{\partial N}{\partial t}+\vec{\nabla}.\left(N\vec{u}\right)=0 \qquad \text{Eq. (26)}$$

This equation is solved after the resolution of the first numerical step considering the velocities calculated at the mesh boundaries. The bubbles are supposed perfectly spherical and with an identical radius in each element of the domain. With this consideration, the volume fraction of the phase constituting the bubbles/droplets can be calculated by:

$$\alpha_k=\frac{\rho\left(1-Y_k\right)}{\rho_k}=\frac{4}{3}\pi r^3 N \qquad \text{Eq. (27)}$$

The mean radius r of the bubbles/droplets can be obtained with the previous equation:

$$r=\left(\frac{3\alpha_k}{4\pi N}\right)^{1/3} \qquad \text{Eq. (28)}$$

Then, the interface surface area A_I is calculated by the following equation:

$$A_I=4\pi r^2 N \qquad \text{Eq. (29)}$$

5. CONCLUSION AND PERSPECTIVES

In this article, a physical model has been proposed to solve two-phase flows including heat and mass transfer in thermal components. The governing equations and physical models are defined at macroscale using the approach of equivalent porous media. All the interaction phenomena occurring at microscale are modeled at macroscale by additional source terms. Appropriated formulations are essentials to reproduce the physical interaction between an heat transfer surface and the mixture fluid. Source terms chosen in momentum, energy and mass conservation equation have been presented. Most of the variables used in source term formulations can be determined analytically (porosity, specific surface area, etc.) or some can be estimated numerically using CFD software (permeability, effective thermal conductivity, etc.). The experimental results obtained enable us to build heat transfer coefficient laws we can coupled with our numerical method to simulate fluid flows with phase change. The combination of numerical model and experimental set-up enable us to generate a new database of properties, flow and heat transfer laws.

REFERENCES

Bejan, A. & Nield, D. A., 2013. Convection in porous media, 4th edition, New-York: Springer.

Bonnet, J. P.,2007. Phénomènes de transport dans les mousses métalliques: approche expérimentale des écoulements monophasiques et liquid-gaz, PhD thesis.

Dbouk, T., 2017. A review about the engineering design of optimal heat transfer systems using topology optimization, Applied Thermal Engineering, 112, pp. 841-854.

Duval, F., Fichot, F. & Quintard, M., 2004. A local thermal non-equilibrium model for two-phase flows with phase-change in porous media, International Journal of Heat and Mass Transfer, 47(3), pp..613-639.

Gosselin, L., Tye-Gingras, M. & Mathieu-Potvin, F., 2009. Review of utilization of genetic algorithms in heat transfer problems, International Journal of Heat and Mass Transfer, 52(9-10), pp.2169-2188.

Hugo, J. M., 2012. Transferts dans les milieux cellulaires à forte porosité : Application à l'optimisation structurale des échangeurs à ailettes. PhD thesis.

Kumar, P., 2014. Investigation of Kelvin-like solid foams for potential engineering applications: An attractive set of geometrical and thermo-hydraulic properties, PhD thesis.

MacDonald, J., 1966. Some simple isothermal equations of state. Review of Modern Physics, vol. 38, pp. 669-679.

Osborn, A. G., & Douslin, D. R., 1974. Vapor-Pressure Relations for 15 Hydrocarbons. Journal of Chemical & Engineering Data, vol. 19 (2), pp. 114-117.

Patankar, S. V.,1980. Numerical heat transfer and fluid flow, 1st edition, CRC Press

Saraf, K., Launay, S., El Achkar, G. & Tadrist, L., 2015. Local vs global heat transfer and flow analysis of hydrocarbon complete condensation in plate heat exchanger based on infrared thermography, International Journal of Heat and mass Transfer, 90, pp. 878-893.

Thompson, P. A., & Beavers, G. S., 1972. Compressible-fluid dynamics. Journal of Applied Mechanics, vol. 39 issue 2.

Toro, E. F., 2009. Riemann solvers and numerical methods for fluid dynamic: A practical introduction, 3rd Edition. Springer-Verlag Berlin Heidelberg.

Webb, R. L., Kim, N.-H., 2005. Principles of enhanced heat transfer, 2nd edition, Taylor & Francis.

Whitaker, S., 2013. The method of volume averaging, Vol. 13, Springer Science & Business Media.

NOMENCLATURE

A_I	Interfacial surface area (m²)	*Cv*	Specific heat at constant volume (J/(kg.K))
Cp	Specific heat at constant pressure (J/(kg.K))	*e*	Internal energy (J/kg)
E	Total energy (J/kg)	*h*	Heat transfer coefficient (W/m².K)
H	Enthalpy (J/kg)	*k*	Thermal conductivity (W/m.K)
K	Permeability of the porous media (m²)	*m*	Liquid/vapor mass transfer rate per unit of volume (kg/m^3.s)
N	Number of bubbles/droplets per unit of volume	*P*	Pressure (Pa or bar)
r	Average radius of bubbles/droplets	*T*	Temperature (K)
u,v	X and Y component of the velocity vector (m/s)	*Y*	Mass fraction
Δt	Time step (s)	Δx,Δy	Spatial step in X and Y direction (m)
Greek letters			
α	Specific surface area (m²/m^3)	*β*	Inertial resistance coefficient (m-1)
ε	Volumic porosity	*ρ*	Density (kg/m^3)
κ	Fluid bulk modulus (Pa)	*γ*	Polytropic coefficient

Manuscript ID: 1522
DOI: 10.18462/iir.icr.2019.1522

Modeling of spray evaporators for salt solutions

Daniel B. BOMAN[(a)], Srinivas GARIMELLA[(a)]

[(a)]Sustainable Thermal Systems Laboratory,
GWW School of Mechanical Engineering,
Georgia Institute of Technology,
Atlanta, GA, 30332, sgarimella@gatech.edu

ABSTRACT

Evaporation is critical for cooling and water purification. Spray evaporators demonstrate advantages over conventional evaporators, including higher rates of heat and mass transfer. In this study, a model for evaporation of saltwater is developed and applied to an evaporator. Energy and species equations are solved in a spherical coordinate system with a moving boundary to determine the temperature and salt concentration within an evaporating droplet. A droplet distribution function is used in conjunction with the model to elucidate the characteristics of the entire flow. Evaporator performance is calculated as a function of inlet temperature, salt concentration, and spray properties. Evaporator size and power requirements are compared with those of conventional evaporators. Based on the simulations, it is shown that using a spray evaporator in a refrigeration cycle using salt water in the evaporator delivers water to the conditioned space heat exchanger at a lower temperature while still requiring low pumping power.
Keywords: Evaporator, Droplets, Heat Exchanger, Water Purification.

1. INTRODUCTION

As conventional refrigerants fall out of favor due to concerns about their global warming potential, researchers have started considering alternative refrigerants, including water. One of the challenges with refrigeration cycles that use water as a refrigerant, however, is that they must operate at sub-atmospheric pressures, which results in a very low pressure drop budget for the heat exchangers in the cycle. Due to this, evaporators for these cycles are typically liquid-coupled falling film designs or pool boiling designs, with the chilled heat transfer fluid being routed to a conditioned space heat exchanger. While efficient in terms of pressure drop, these designs tend to have lower heat transfer coefficients than those of forced convective designs, which results in larger heat transfer area requirements. One way to increase the heat exchange area is through the use of spray evaporators, in which a spray of droplets into a low pressure zone undergoes partial evaporation.

Spray evaporation has been studied over the past few decades for use in desalination, where it has been shown to increase heat and mass transfer over flowing water or pool boiling in multi-stage flash and multi-effect distillation (Miyatake et al., 1981). Therefore, combined cycles, in which water purification and cooling are both achieved, are potential candidates for the application of this technology. The water left over after evaporation can be routed directly to a conditioned space heat exchanger, removing the thermal resistance between the evaporating water and the coupling fluid used in the conditioned space heat exchanger. The material required to fabricate the evaporator can also be reduced, resulting in a lower first cost. In this work, a spray evaporator using either pure water or a salt water solution up to 15 wt% is modeled for water purification and cooling applications.

2. MODEL DEVELOPMENT

A model of a spray evaporator for water and saltwater is developed by first modeling the trajectories and heat and mass transfer behavior of a single droplet of each size. A size distribution function is then used to determine the number of droplets of each size in the spray and the results of the single droplet model are distributed accordingly. The spray evaporator considered in this work is for use in refrigeration systems that use water as a refrigerant; thus, it is maintained at low pressure. The

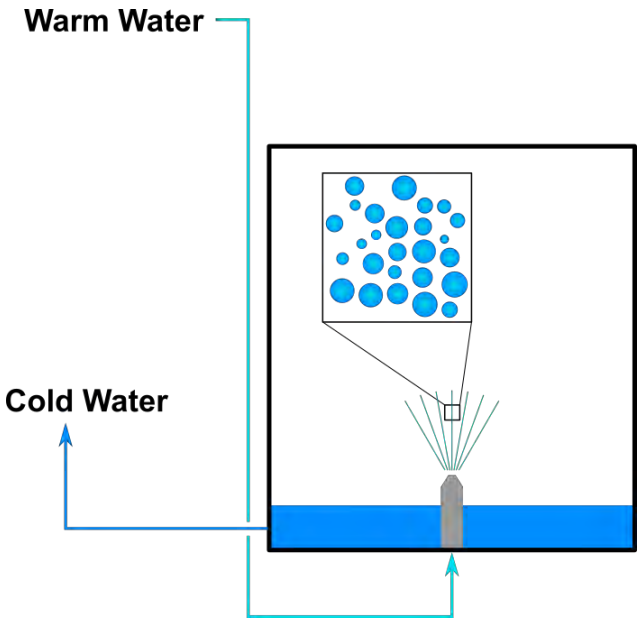

Figure 2: Schematic of the studied spray evaporator

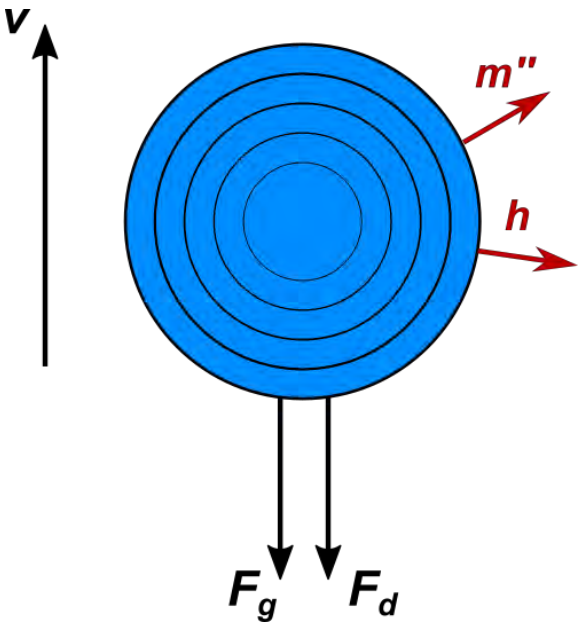

Figure 1: Droplet with finite volume shells identified

nozzle is mounted at the bottom of the evaporator with the spray injected upward to allow for improved performance and a more compact evaporator (Ikegami et al. 2006). A schematic of the evaporator modeled is shown in Fig. 2. The general method of combining a droplet model with a spray evaporator model is similar to that reported by Chen et al. (2016). Once the model is developed, parametric studies are conducted to determine the outlet temperature and concentration and the required evaporator height as a function of several flow parameters.

2.1. Droplet Model

The following model describes the behavior of a spherical droplet of water containing dissolved salt as it undergoes partial evaporation due to exposure to a low-pressure environment while moving through that environment under the influence of drag and gravity. The model treats the droplet as a series of finite shells, each of which is considered to have uniform intensive properties. This conception of the droplet, along with the major effects on the droplet, including forces and heat transfer, can be seen in Fig. 1. Advective effects within the droplet are neglected because of the small size of the droplet; therefore, mass transfer occurs due to diffusion and heat transfer occurs due to conduction.

As the volume of the droplet changes due to evaporation, water is removed from the outermost shell. With sufficient evaporation and no resizing of the shells, the outermost shell disappears, resulting in errors in the simulation. Therefore, mass is removed from each shell (and placed into the next larger shell) in such a way that each shell loses the same fraction of its mass. The mass removed from shell i is:

$$m_{r,i} = 4\pi R^2 \dot{m}'' \frac{\sum_{j=1}^{i} m_j}{\sum_{j=1}^{N} m_j} \qquad \text{Eq. (1)}$$

where $\dot{m}''$ is the mass flux off the outer surface of the droplet and is calculated using kinetic theory (Kazemi et al., 2017), R is the radius of the droplet, and m_i is the mass of shell i. Mass balances are performed for each species on each shell. The mass balance for either species is:

$$\frac{dm_{k,i}}{dt} = -D\rho_{i-1}A_{i,i}\frac{w_{k,i}-w_{k,i-1}}{\frac{r_{o,i}-r_{i,i-1}}{2}} + D\rho_i A_{o,i}\frac{w_{k,i}-w_{k,i-1}}{\frac{r_{o,i+1}-r_{i,i}}{2}} + m_{r,i-1}w_{k,i-1} - m_{r,i}w_{k,i} \quad \text{Eq. (2)}$$

where the subscript k can represent either water or salt, w is the mass fraction of a given component, and A is the surface area of a given shell on either the inner (subscript i) or outer surface (subscript o). The first and second terms represent Fickian diffusion, while the third and fourth terms represent mass flows associated with changes to the size of the shell. In the innermost shell, the first and third terms are not included, while for the outermost shell, the second term is not included for both water and salt, and the fourth term is not included for salt.

In keeping with the previous calculations, which use extensive quantities, the energy is calculated for each shell. For the interior shells, the energy equation is:

$$\frac{dU_i}{dt} = -kA_{i,i}\frac{T_i - T_{i-1}}{\frac{r_{o,i}-r_{i,i-1}}{2}} + kA_{o,i}\frac{T_i - T_{i-1}}{\frac{r_{o,i+1}-r_{i,i}}{2}} + m_{r,i-1}u_{i-1} - m_{r,i}u_i \quad \text{Eq. (3)}$$

The first and second terms are the conduction terms, while the third and fourth terms represent the energy flows associated with changes in the size of the shell. For the innermost volume, the first and third terms are neglected. The energy equation for the outermost shell is:

$$\frac{dU_N}{dt} = -kA_{i,N}\frac{T_N - T_{N-1}}{\frac{r_{o,N}-r_{i,N-1}}{2}} + m_{r,i-1}u_{i-1} - \dot{m}''A_{o,N}\left(h_{vapor} - h_N\right) - A_{o,N}\alpha\left(T_N - T_\infty\right) \quad \text{Eq. (4)}$$

where α is the convective heat transfer coefficient, calculated using the correlation of Ranz and Marshall (1952). The third term represents energy transfer out of the droplet due to evaporation.

The mass and energy balances are solved for all shells simultaneously, and then property relations are used to compute the density and temperature. The mass and density of each shell are used to calculate the volume, and this, along with the requirement that the outer diameter of one shell must be the inner diameter of the next, is used to calculate the radii of the shells.

The motion of the droplet is determined using a kinematic model that takes inertial drag and gravity into account and is used to determine the convective heat transfer coefficient. Each droplet is considered to be launched upwards from a nozzle with an initial velocity v_0. Performing a force balance on the droplet, and assuming that the rate of change of mass of the droplet is small relative to the acceleration gives:

$$\frac{dv}{dt} = \frac{1}{m}\left(-mg + F_D\right) \quad \text{Eq. (5)}$$

where F_D is the drag force on the droplet and is computed following the work of Lapple and Shepherd (1940).

2.2. Spray Distribution Model

Throughout the literature, the droplet distribution function for a flashing spray or spray from a nozzle is commonly modeled by a lognormal distribution:

$$f(D) = \frac{1}{D\ln(\delta)\sqrt{2\pi}}\exp\left(-0.5\left[\frac{\ln\left(D/D_{mean}\right)}{\ln\delta}\right]^2\right) \quad \text{Eq. (6)}$$

Table 1. Cycle baseline operating parameters

Parameter	Value
Inlet temperature (T_{in})	20°C
Inlet velocity (v_{in})	5 m·s^{-1}
Inlet salt concentration (w_{in})	0, 5, 10, 15 wt%
SMD	200 µm
Vapor pressure	0.86 kPa

Two cutoffs are used to determine the range over which the droplet distribution function is investigated. The first is that the value of f is greater than 10^{-10} for the diameter of interest. The second is that the droplets are at least 100 nm in diameter for both physical and numerical reasons. Because the nozzle for this application is not specified, two parameters are required to specify the distribution. The first of these is the Sauter mean diameter (SMD), which is the average volume of a droplet in the spray divided by the average surface area of a droplet in the spray.

$$SMD = \frac{\int f(D) D^3 \, dD}{\int f(D) D^2 \, dD} \qquad \text{Eq. (7)}$$

The second parameter, which is δ in Eq. 6, is determined through simulation as follows. Initial simulations indicated that the larger droplets in the spray had a disproportionate effect on the performance of the evaporator and that the largest droplet size in the spray exhibited a maximum as a function of δ for a given SMD (D_{mean} in Eq. 6 is calculated based on the specified values of SMD and δ). Therefore, to provide a conservative estimate of the performance of the evaporator, the value of δ that provides the largest maximum droplet diameter is selected.

2.3. Spray Evaporator Model

The performance of the spray evaporator is calculated by combining the droplet evaporation model with the spray distribution model. The inlet salt concentration, inlet temperature, inlet velocity, vapor pressure, and spray distribution parameters are determined. Next, the number of droplets of each size is determined using the spray distribution, and the droplet model for that diameter is simulated. An energy balance is then performed on the vapor, and the temperature of the vapor is adjusted until that energy balance is satisfied. The model assumes that the droplets do not interact, and thus, the performance of the evaporator can be determined by linear combination of the performance of the individual droplets.

The baseline parameters for the model are given in Table 1. The baseline inlet temperature is one that reflects the ambient temperature of seawater in lower latitudes, and the baseline SMD is selected such that the largest droplets have diameters less than 2 mm. The baseline vapor pressure is the vapor pressure of pure water at 5°C, which is a reasonable evaporator temperature for a cooling cycle that uses water as a refrigerant. Parametric studies are conducted on the SMD, inlet temperature, and inlet velocity, with all baseline salt concentrations studied at all cases.

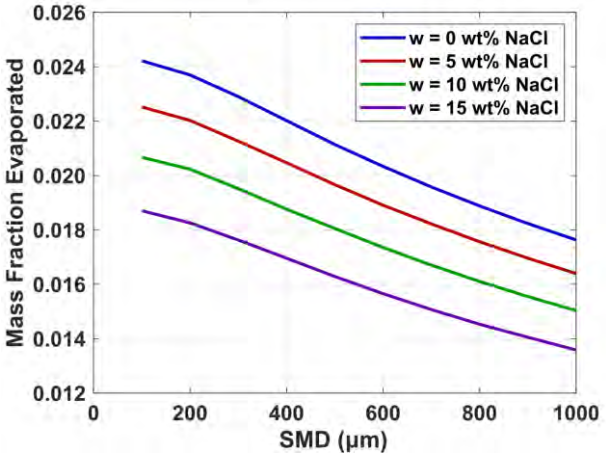

Figure 3: Effect of SMD on mass fraction evaporated

3. RESULTS AND DISCUSSION

One of the most important parameters for describing any spray is the SMD, as lower SMDs reflect higher surface area-to-volume ratios. The larger the surface area in a given spray, the more the evaporation that occurs

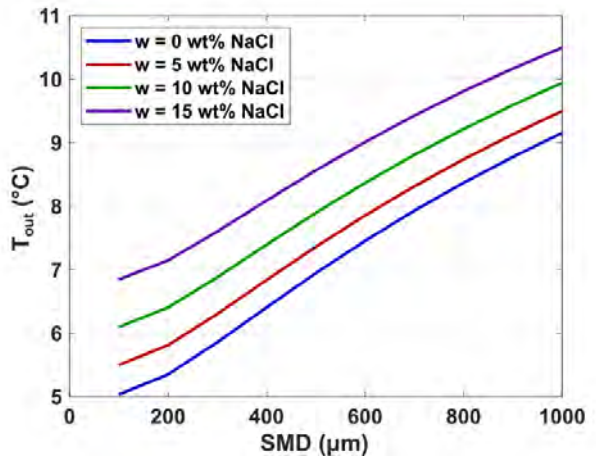

Figure 4: Effect of SMD on outlet temperature of the spray

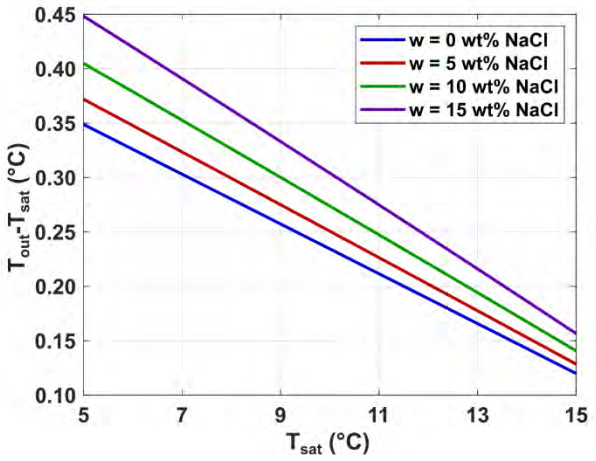

Figure 5: Effect of evaporator saturation temperature on flow outlet temperature

with the same inlet conditions. This can be seen in Fig. 3, which shows the mass fraction of the spray evaporated (i.e., kg/s of vapor generation per kg/s of flow) as a function of SMD for the four studied salt concentrations. As the SMD increases, the vapor generation rate decreases almost linearly and quite severely. The mass fraction evaporated decreases by more than 25% at all salt concentrations as the SMD is increased from 100 μm to 1000 μm.

The vapor generation rate decreases with increasing salt concentration. As the salt concentration increases, the saturation temperature for the vapor pressure in the chamber increases, resulting in less sensible energy being available to drive the evaporation. In addition, evaporation of water from the droplet surface increases the salt concentration there, exacerbating this effect as evaporation progresses.

The SMD and salt concentration both affect the temperature at which the remaining liquid exits the evaporator. This can be seen in Fig. 4. As the SMD increases, the aforementioned decrease in evaporation seen in Fig. 3 results in more energy remaining in sensible form, which leads to a higher temperature. As with the evaporated mass fraction, there is a strongly detrimental effect on the outlet temperature when increasing the mass fraction. Therefore, it is recommended that when designing spray evaporators for cooling and water purification applications, the SMD for the spray be 400 μm or less.

The effect of salt buildup at the liquid-vapor interface on the outlet temperature can be seen in Fig. 5, which plots the difference between the outlet temperature and saturation temperature as a function of the saturation temperature of the vapor in the chamber at the salt concentration of the spray. For these simulations, the vapor pressure in the chamber was varied to match the selected saturation temperature for the given salt concentration. For all salt concentrations studied, the difference between the outlet temperature and the saturation temperature decreases slightly with increasing saturation temperature. The most likely reason for this is that with a smaller temperature difference between the inlet temperature and the saturation temperature and the same time to undergo evaporation, the droplets are able to more closely approach the saturation temperature. The effect of salt concentration on the outlet temperature is much less pronounced in this case than in the cases where other parameters are varied, but it can still be seen that the buildup of salt at the interface results in a decrease in evaporation and a subsequent increase in outlet temperature, even when the spray has the potential to reach the same temperature.

The inlet temperature of the spray has a much smaller effect on the outlet temperature. Fig. 6 shows the outlet temperature of the spray evaporator as a function of inlet temperatures ranging from 10°C to 50°C. Over this 40°C temperature range, the outlet temperature only increases by about 0.9°C at the lowest salt concentration and by about 1.2°C at the highest salt concentration. This suggests that if the intent of the evaporator is to provide cooling, it can be operated with almost any inlet temperature.

From a design perspective, one of the concerns in the design of any heat pump is its footprint. The spray evaporator is relatively compact laterally (depending on the nozzle used), but due to the

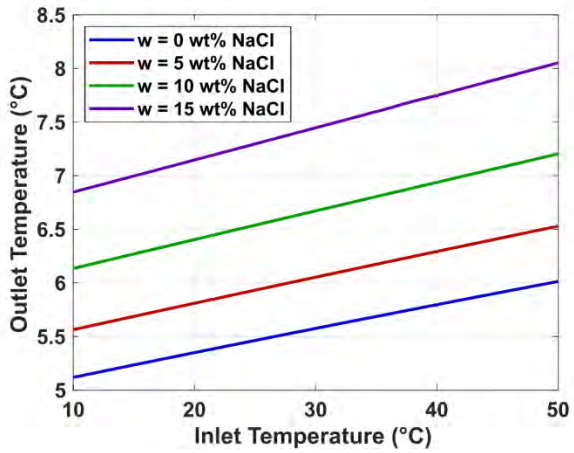

Figure 6: Outlet temperature as a function of inlet temperature

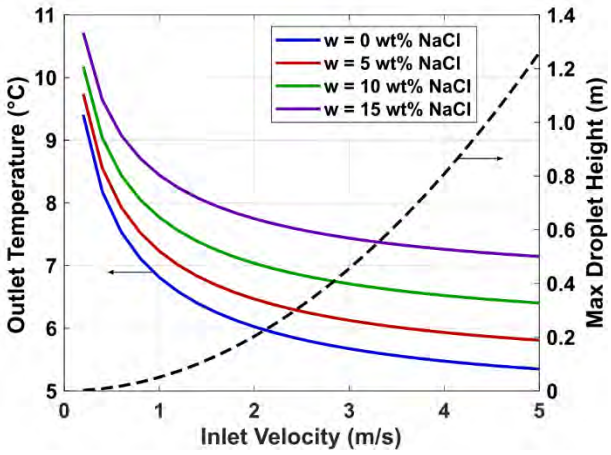

Figure 7: Outlet temperature and maximum droplet height as a function of velocity

upward spraying design considered here, the height is determined directly by the velocity of the droplets at the nozzle. Because changing the velocity changes the residence time of the droplets in the evaporator, this has a direct effect on the performance of the cycle, as shown in Fig. 7. The maximum height achieved by a droplet in the cycle is shown as a dashed line on the secondary y-axis. It becomes immediately apparent from the figure that for the evaporator to be vertically compact, the velocity must be decreased from the 5 m/s baseline to a value closer to 3 m/s. The result of this decrease, however, is a decrease in residence time for all droplets, which leads to an increase in the outlet temperature.

A comparison can be made between the spray evaporator and a conventional falling-film evaporator at the same capacity. A horizontal-tube falling-film evaporator with a 300 W capacity, saltwater inlet temperature of 13°C, and inlet salt concentration of 1 wt% was designed separately with 36 rows of tubes with two tubes per row. Each tube is 23 cm long, and the overall height of the evaporator is 0.5 m. The heat transfer fluid enters the evaporator at 22°C and leaves at 7°C. The pressure in the evaporator is set so that the 1 wt% solution has a saturation temperature of 5°C. A simulation of a spray evaporator is conducted with the saltwater being evaporated serving as the heat transfer fluid in the external heat exchanger, so the inlet temperature for the spray evaporator is 22°C. The velocity is set so the evaporator height is less than 0.5 m. The results for the two evaporators are compared in Table 2. Due to the removal of the heat transfer resistance associated with the tubes, the outlet temperature of the heat transfer fluid in the spray evaporator is reduced by over 1°C while simultaneously simplifying fabrication of the heat exchanger. The reduced temperature provides a larger temperature difference across the conditioned space heat exchanger, which allows a lower flow rate for the same heat transfer.

The spray evaporator does have a higher pumping power requirement. The pumping power requirement is calculated by assuming an ideal pump, a 10 kPa pressure drop through the loop including the external heat exchanger, and that any liquid leaving the evaporator at low pressure must be pumped back up to atmospheric pressure. Although the heat transfer fluid flow rate in the spray evaporator is lower than that of the falling film, it is at the low pressure associated with the evaporator and must be pumped back to atmospheric pressure. It should be noted, however, that the pumping power still remains less than 0.5% of the cooling delivered.

The separation between the evaporator and the external heat exchanger in the above discussion is not seen in most space-conditioning units. This design choice is due to the small pressure drop

Table 2. Comparison between falling film and spray evaporator

-	Falling Film	Spray
HTF outlet temperature (°C)	7.00	5.74
HTF flow rate (g/s)	4.79	4.5
Max ideal pumping power (W)	0.1	0.5

available for water as a refrigerant and the large two-phase pressure drops associated with operation of internal flow evaporators. It is this split nature of the heat exchangers and the ability of the evaporating fluid to serve as the heat transfer fluid that affords the spray evaporator the advantages discussed above. A single nozzle can accommodate up to 340 mL min^{-1} of flow and 6.8 mL min^{-1} of water production, but this can be increased by increasing the number of nozzles.

4. CONCLUSIONS

A droplet-based model for a spray evaporator with a nozzle directed upwards has been developed. The model assesses heat and mass transfer within a droplet and the kinematics of the droplet motion using a finite volume formulation with variable-volume shells. A statistical spray model is applied in conjunction with the droplet model to enable modeling of the complete spray. The performance of the evaporator is simulated at baseline conditions to determine the fraction of the spray evaporated and the outlet temperature, and parametric studies are conducted to determine the variation in performance based on the SMD of the spray and the inlet velocity. The performance of a spray evaporator is compared with that of a falling film evaporator, and the spray evaporator is found to have lower outlet temperature and flow rate but higher required pumping power.

NOMENCLATURE

A	area (m^2)	SMD	Sauter mean diameter (m)
D	mass diffusivity (m^2 s^{-1}), diameter (m)	T	temperature (°C)
h	specific enthalpy (kJ kg^{-1})	U	internal energy (J)
k	thermal conductivity (W m^{-1} K^{-1})	u	specific internal energy (J kg^{-1})
m	mass (kg)	w	weight fraction
$\dot{m}$	mass flow rate (kg s^{-1})	α	convective heat transfer coefficient (W m^{-2} K^{-1})
$\dot{m}''$	mass flux (kg m^{-2} s^{-1})	δ	spray distribution parameter
m_r	mass removed (kg s^{-1})	ρ	density (kg m^{-3})
R, r	radius (m)		

Subscripts

i	inner	N	number of volumes
o	outer	∞	ambient

REFERENCES

Chen, Q., Thu, K., Bui, T.D., Li, Y., Ng, K.C., Chua, K.J., 2016. Development of a model for spray evaporation based on droplet analysis. Desalination 399, 69-77.

Ikegami, Y., Sasaki, H., Gouda, T., Uehara, H., 2006. Experimental study on a spray flash desalination (influence of the direction of injection). Desalination 194(1-3), 81-89.

Kazemi, M.A., Nobes, D.S., Elliott, J.A.W., 2017. Experimental and Numerical Study of the Evaporation of Water at Low Pressures. Langmuir 33(18), 4578-4591.

Lapple, C.E., Shepherd, C.B., 1940. Calculation of Particle Trajectories. Industrial & Engineering Chemistry 32(5), 605-617.

Miyatake, O., Tomimura, T., Ide, Y., Fujii, T., 1981. An experimental study of spray flash evaporation. Desalination 36(2), 113-128.

Ranz, W., Marshall, W.R., 1952. Evaporation from drops. Chem. Eng. Prog 48(3), 141-146.

Manuscript ID: 1564
DOI: 10.18462/iir.icr.2019.1564

Experimental investigations of the single-phase flow distribution in brazed plate heat exchangers and its impact on the heat exchanger

Wenzhe LI[(a)], Pega HRNJAK [(a), (b), *]

[(a)] Air-Conditioning and Refrigeration Center (ACRC), University of Illinois Urbana-Champaign
Urbana, 61801, IL, USA, liwz310@illinois.edu, pega@illinois.edu
[(b)] Creative Thermal Solutions In. (CTS)
Urbana, 61802, IL, USA

ABSTRACT

Maldistribution of fluid among parallel channels is one of the main issues in applications of brazed plate heat exchangers (BPHEs).
This paper presents an experimental investigation of the single-phase flow distribution in BPHEs and its impact on the heat exchanger performance.
In the experiments, water is used as the working fluid on both sides. Probes are placed into the headers of the BPHEs to measure the pressure change along the headers, as well as the pressure drop and temperature change across different channels.
The results show that the maldistribution is more significant as the number of plates and total mass flow rate increase. The entrance effect would decrease the flow rate in first several channels. The maldistribution in channel flow rate results in the non-uniformity of the channel heat capacity.
Keywords: Brazed Plate Heat Exchangers, Single-phase, Distribution.

1. INTRODUCTION

Brazed plate heat exchangers (BPHEs) have been widely used in the heating, ventilating, air conditioning, and refrigeration industry. But the maldistribution of working fluid among parallel channels is still one of the main issues. For single-phase flow, the distribution of fluid among parallel channels is basically determined by the header induced pressure drop, as well as the pressure drop cross the channels. The maldistribution would generally decrease the performance of BPHEs by causing a higher pressure drop and a poor utilization of heat transfer area.
Several researchers have worked on the experimental study of single-phase flow distribution in plate heat exchangers and similar structures. Rao and Das (2004) investigated the influence of flow distribution on the hydraulic performance of plate heat exchangers by measuring the pressure drop across the heat exchangers with different number of plates. Their results show that flow maldistribution generally increases the total pressure drop of the heat exchanger and the pressure increase is depending on the flow rate, number of plates and port size. The authors also compared their measurements with the predictive results by the analytical pressure drop model proposed by Bassoiuny and Martin (1984a, 1984b) and found they agree well with each other. Later, the same group (Rao et al., 2005) studied the effects of flow maldistribution on the thermal performance of plate heat exchangers by both experimental and theoretical approaches. The authors concluded that the flow maldistribution would decrease the effectiveness of the heat exchangers, and the parameters which are found to influence the maldistribution (flow rate, number of plates and port size), as a consequence, affect the thermal performance of plate heat exchangers. Instead of just recording the overall performance of the heat exchangers, Bobbili et al., 2006 tested the port flow maldistribution by inserting mobile static pressure tubes into the inlet and outlet ports to measure the pressure drop across each channel. Their experimental data verified that the heat exchangers with more plates present higher non-uniformity in pressure profile and channel mass flow rate. In addition, Wang et al. (2011) characterized liquid flow distribution in compact parallel flow heat exchangers and found that the jet flow at the entrance of heat exchangers, induced by the abrupt expansion of flow area, would decrease the flow mass in the first several tubes. Taking this entrance effect into

the consideration, Li and Hrnjak (2018) developed an analytical single-phase flow distribution model for BPHEs and the model has been validated by the vapor tests.
The objective of this paper is to experimentally explore the single-phase flow distribution in brazed plate heat exchangers and its impact on the heat exchanger.

2. EXPERIMENTAL SETUP

2.1. Experimental Apparatus

Fig. 1 shows the schematic of the experimental apparatus. It consists of two independent loops: hot and cold water loop. Two centrifugal pumps with variable frequency drivers are used to circulate the distilled water for two loops, respectively. Water is charged from the highest location of each loop and the system is held vacuum until fully charged, so that no pocket of air is trapped inside. Micro-motion flow meter, absolute and differential pressure transducers, and type T (copper-constantan) thermocouples are installed at locations as indicated in Fig 1. The sensors have been calibrated and their range and uncertainty are listed in Table 1.

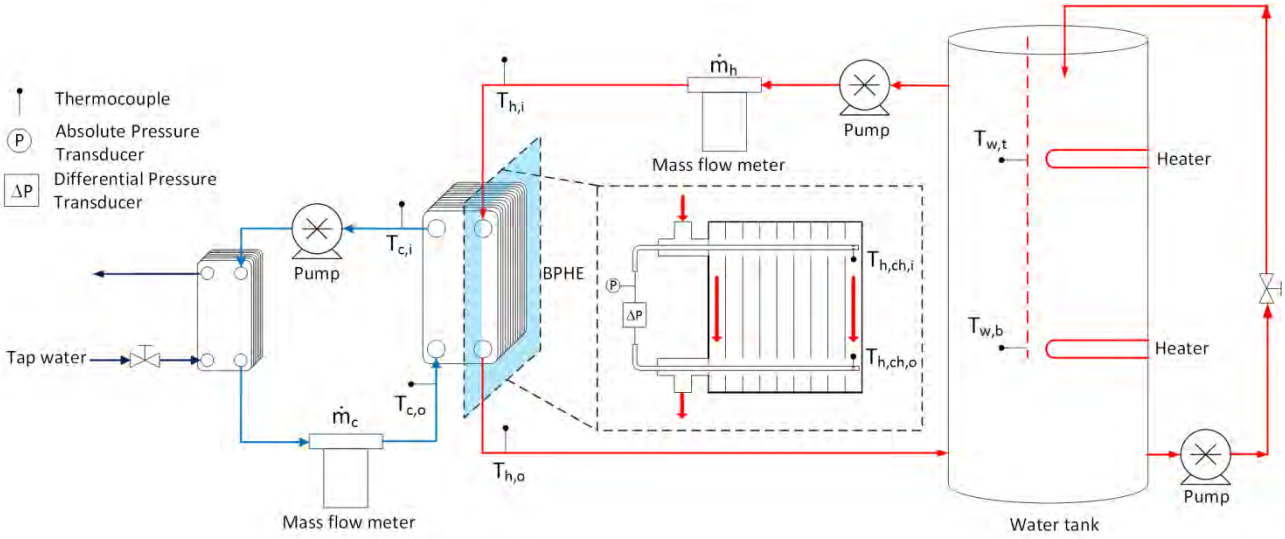

Figure 1: Experiment facility

Table 1. Measurement uncertainty

Measured Parameter	Uncertainty
Temperature (T type)	0.1 (°C)
Absolute pressure (0-172 kPa)	0.11 % (full scale)
Differential pressure (0-7.5 kPa)	0.25 % (full scale)
Differential pressure (0-6.9 kPa)	0.25 % (full scale)
Mass flow rate	0.15 % (reading)

One unique feature of this experiment is placing four probes into the inlet/outlet headers of the BPHE to measure the temperature change and pressure drop across different channels, as well as the pressure profile in the headers. Fig. 2 shows the structure of the probe and its relative position in the BPHE. The probes are designed as inserting a lengthened thermocouple (outer diameter: 1.59 mm) into a piece of steel tube (outer diameter: 3.18 mm, inner diameter: 2.36 mm). One end of the steel tube is blocked and a through hole is drilled on the side surface close to that end, to measure the static pressure in headers. The tip of the thermocouple is bent into the channel through the open hole of the steel tube, to record the temperature change across a channel. By moving the probes forward and backward, the temperature change and pressure drop of different channels could be measured.
The test section is well insulated, with heat loss calibrated so that the energy balance (measured heat load between hot and cold stream) is within ±4 %. The BPHEs with the identical plate geometry

but different number of plates have been tested in the experiments. They are all of 1pass-1pass U-type configuration. The geometric parameters of the BPHEs are summarized in Table 2.

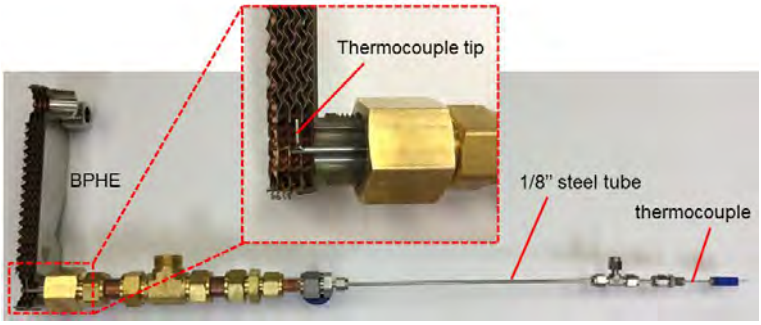

Figure 2: Pressure and temperature probes

Table 2. Geometric parameters of the BPHE

Parameter	
Chevron angle, φ=90°-β, °	60
Corrugation depth, b, mm	2.0
Corrugation pitch, P_c, mm	7.0
Plate thickness, t, mm	0.30
Port length, L_p, mm	172
Total length, L_v, mm	206
Port width, L_h, mm	42
Total width, L_w, mm	76
Heat transfer area per plate, A_p, m^2	0.014
Port diameter, D_p, mm	20.0

2.2. Data Reduction

Three BPHEs with different number of plates (4, 10，50 plates) have been tested in this study. In the tests, the inlet temperature of the hot and cold stream is maintained at 50 and 30 °C respectively. For each test, the primary measurements of each flow stream are: total mass flow rate; the inlet and outlet temperature of the entire heat exchanger; the temperature change and pressure drop across different channels. By moving the probes, the pressure change along the inlet/outlet header is also obtained.

For the data reduction, fluid properties are calculated at the bulk mean temperature given by：

$$T_{h,b} = \frac{T_{h,i} + T_{h,o}}{2};\ T_{c,b} = T_{h,b} - LMTD \qquad \text{Eq.(1)}$$

Where LMTD is calculated by:

$$LMTD = \left[\left(T_{h,i} - T_{c,o}\right) - \left(T_{h,o} - T_{c,i}\right)\right] / ln\left[\left(T_{h,i} - T_{c,o}\right) / \left(T_{h,o} - T_{c,i}\right)\right] \qquad \text{Eq.(2)}$$

The heat transfer is obtained from the average of hot side and cold side energy balance, whose difference is less than 4 %.

$$Q_h = \dot{m}_h \cdot c_p \cdot \left(T_{h,i} - T_{h,o}\right);\ Q_c = \dot{m}_c \cdot c_p \cdot \left(T_{c,o} - T_{c,i}\right);\ Q_{avg} = (Q_h + Q_c)/2 \qquad \text{Eq.(3)}$$

The purpose of testing the 4-plate (3-channel) BPHE is to characterize the liquid flow in a single plate channel and develop correlations of the heat transfer coefficient and friction factor for this specific plate geometry. In such a BPHE, the hot fluid is flowing downward in a single channel in the middle; the cold fluid is flowing upward in two outer channels. To calculate heat transfer coefficient, the heat transfer data from this BPHE is further processed by following equations:

$$Q_{avg} = UA \cdot LMTD \qquad \text{Eq.(4)}$$

$$\frac{1}{(UA)} = \frac{1}{(h_h A_h)} + \frac{t}{(k_p \cdot 2A_p)} + \frac{1}{h_c A_c} \quad \text{Eq.(5)}$$

$$Q_{avg} = h_h A_h \cdot (T_{h,b} - T_{w,h}) = k_p \cdot 2A_p \cdot (T_{w,h} - T_{w,c}) = h_c A_c \cdot (T_{w,c} - T_{c,b}) \quad \text{Eq.(6)}$$

The wall temperatures above are determined iteratively through heat balance of Eq. (6). In such a 4-plate (3-channel) BPHE, ideally, the heat transfer area in two streams is identical: $A_h = A_c = 2A_p$. However, the two end plates, which are ideally adiabatic, actually function as fins and transfer heat due to the heat conduction through the contact with the adjacent thermal plates. Therefore, the active heat transfer area in cold stream is enlarged. This is known as the "end-plate effect" (Jin and Hrnjak, 2016). The heat transfer area in two streams is corrected as:

$$A_h = 2A_p;\ A_c = 2 \cdot (1 + \eta) \cdot A_p \quad \text{Eq.(7)}$$

Here, η is the fin efficiency of the end plate, which is defined as the ratio between the heat dissipation through the end plate and that through the adjacent thermal plate. η is depending on the plate geometry, temperature profiles of two streams and convective heat transfer coefficient. The detailed analysis and quantification of the end-plate effect could be found on authors' another ICR2019 conference paper (Li and Hrnjak, 2019).

In the tests, equal mass flux is maintained for both hot and cold stream. Since water is used for both sides and each plate channel is geometrically identical, it is reasonable to assume that the heat transfer coefficients of two streams are governed by the same correlation. Therefore, the modified Wilson plot (Shah, 1990) is used to correlate Nu as a power-law function of Re, Pr, and Sieter-Tate factor, as Eq. (8) shows.

$$Nu = C_1 \cdot Re^{C_2} \cdot Pr^{1/3} \cdot (\mu/\mu_w)^{0.14} \quad \text{Eq.(8)}$$

The channel Reynolds number, Re, is defined as:

$$Re = \frac{\dot{m}_{\mathrm{ch}} \cdot D_e}{\mu \cdot A_{cs}} \text{ with } D_e = 2 \cdot b;\ A_{cs} = b \cdot L_w \quad \text{Eq.(9)}$$

As mentioned above that, the fin efficiency of the end plate is convective heat transfer coefficient dependent. Iteration is thus necessary to develop a reliable heat transfer correlation. The procedure is: first assume zero fin efficiency (η=0) to obtain a heat transfer correlation by the Wilson plot, and this correlation is also denoted as the "correlation without end-plate effect correction"; then, use the developed correlation to calculate the heat transfer coefficient and renew the fin efficiency through the theoretical solutions in Li and Hrnjak (2019); correct the cold side active heat transfer area by the fin efficiency and re-use the Wilson plot to update the heat transfer correlation; repeat until the fin efficiency and heat transfer coefficient are converged.

The Fanning friction factor for a single channel is calculated through Eq. (10):

$$f = \frac{\rho \cdot D_e \cdot \Delta P_{ch}}{2L_p \cdot (\dot{m}_{ch}/A_{cs})^2} \quad \text{Eq.(10)}$$

The friction factor is then correlated with Re in the form as Eq. 11 shows. In later tests of the BPHEs with more plates, this developed friction factor correlation is used to calculate the mass flow rate from the channel pressure drop measurements.

$$f = C_3/Re^{C_4} \quad \text{Eq.(11)}$$

3. RESULTS AND DISCUSSIONS

3.1. Single Channel Liquid Friction Factor

Fig. 3 shows the liquid friction factor characteristics in a single channel. The tested range is: 180 ≤ Re ≤ 1100. Several studies (Jin and Hrnjak, 2016; Focke, et al., 1985) demonstrated that the transition from laminar to turbulence in the channel of BPHE usually happens a low Re (100~400). The tested conditions should be in early turbulence regime.

It is interesting to notice that there is a slight difference between the friction factor characteristics of hot and cold stream. Under the same Reynolds number, the friction factor of the hot stream is slightly higher than that of the cold stream. This may be a result of the different flowing direction of two streams (hot stream downward flow; cold stream upward flow). Under the influence of the gravitational force, two streams in opposite flowing direction might present different flow pattern in the channel which leads to the different pressure drop feature.
For the comparison, the friction factor correlation proposed by Focke et al. (1985) is also plotted. The Focke's correlation gives the similar results as the measurements in this study. The small difference in value may be attributed to the variation in the geometry. Instead of being a general correlation, the obtained friction factor was only a characterization of the plate used in this study.

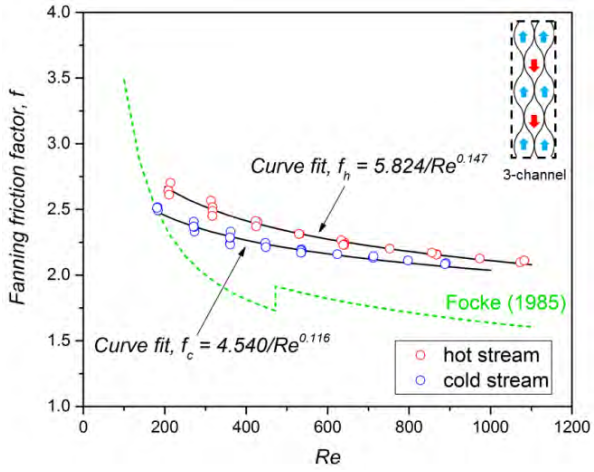

Figure 3: Single channel friction factor

3.2. Single Channel Heat Transfer Coefficient

Fig. 4 shows the developed heat transfer correlations for the BPHEs in this study. For the comparison, both the correlation without end-plate effect correction and the correlation corrected by the numerical solution in Li and Hrnjak (2019) are plotted. As shown in Fig. 7, there would be an overestimation of 17 ~ 33% in the heat transfer coefficient if no correction is made in this case. Fig. 7 also gives the calculated fin efficiency of the end plate in the tests. The results show that the end plate contributes 40 ~ 95% of its surface area as the active heat transfer area.

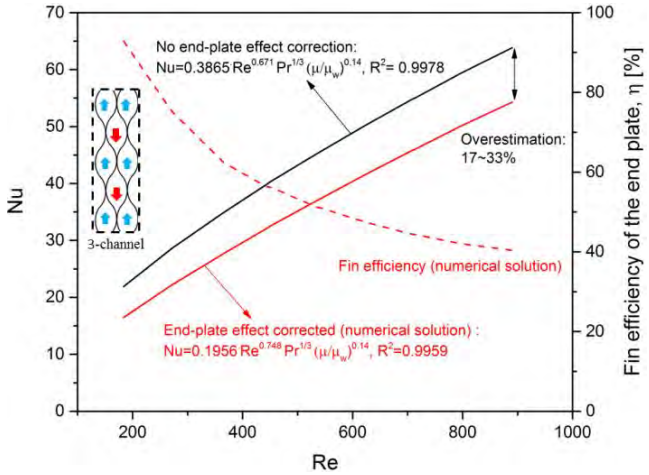

Figure 4: Single channel heat transfer correlation

3.3. Multi-Channel BPHEs Pressure Drop and Distribution

Experimental results in two BPHEs with different number of plates (10 plates and 50 plates) are compared in this section to demonstrate the flow maldistribution in the BPHE. Each heat exchanger is tested under three average channel mass flow rates: 5 g·s^{-1}, 7.5 g·s^{-1} and 10 g·s^{-1} (Corresponding channel Re ≈ 200 ~ 400).

The pressure change along the headers, as well as the mass flow rate distribution in the 10-plate BPHE is shown in Fig. 5a and 5b. The mass flow rate is calculated based on the measured pressure drop across the channel and the previously developed friction factor correlation. By adapting this approach, the summation of calculated channel flow rate is within a difference of 5 % compared with the measured total flow rate in the 10-plate heat exchanger. To compare the results with three average channel mass flow rates, the non-dimensionalized parameters, defined in Eq. (12), are used. Basically, the pressure in the headers is represented by the difference with the exit pressure of the heat exchanger (P_{exit}) and non-dimensionalized by the total pressure drop of heat exchanger ($|\Delta P_{BPHE}|$); the channel mass flow rate is plotted as the percentage of the average channel flow rate.

$$P^* = \frac{P - P_{exit}}{|\Delta P_{BPHE}|};\ \dot{m}^*_{ch} = \frac{\dot{m}_{ch}}{\dot{m}_{ch,avg}} \qquad \text{Eq.(12)}$$

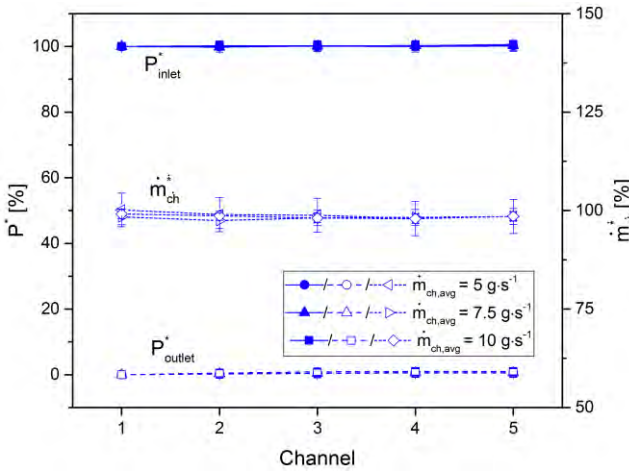

Figure 5a: Pressure in the headers and flow rate distribution- 10 plates, cold stream

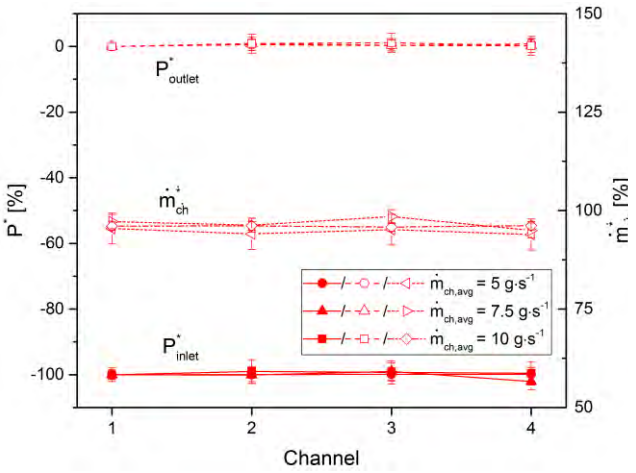

Figure 5b: Pressure in the headers and flow rate distribution- 10 plates, hot stream

As Fig. 5 shows, it seems that the pressure in the headers is almost constant for both streams in the 10-plate BPHE under the test conditions. The impact of the average channel mass flow can also be ignored since the pressure curves under the different flow rates are almost overlapping. Since the header induced pressure drop is almost negligible, the mass flow rate distribution is quite uniform for all three test conditions. It is worthwhile noticing that because the hot stream is flowing downward, the absolute pressure in the inlet header is actually smaller than that in the outlet header due to the hydraulic pressure, which gives a negative channel pressure drop.

Figs. 6a and 6b show the results of 50-plate BPHE. As Fig. 6 shows, there is a significant pressure change in the header. Along the flowing direction, the static pressure generally increases in the inlet header and decreases in the outlet headers. In the inlet header, the dynamic pressure is converted to the static pressure due to the fluid continuously branches out through channels and the flow rate in the header decreases. In the outlet headers, with the fluid continuously entering the header through channels, the flow in the header accelerates and the static pressure is converted to the dynamic pressure which causes pressure decrease in flowing direction. It is also noticeable that, due to the entrance effect (abrupt expansion of flow area at the entrance of the BPHE), the inlet header pressure rise at the first several channels is much more rapid than that of the rear part. This effect has not been observed in Fig. 5 since the tested total flow rates are not sufficiently high in the cases of the 10-plate BPHE. The effect of the average channel mass flow rate is also obvious in this case. With a higher average channel mass flow rate, the pressure change in the headers is larger. Comparing Figs. 6a and 5b, it seems that the header pressure change is more significant in hot stream. One reason is the total pressure drop of heat exchanger ($|\Delta P_{BPHE}|$) is relatively smaller in the hot stream, where the frictional force and gravitational force are acting in opposite direction.

As discussed previously, the channel flow rate distribution is mainly the results of header induced pressure drop. As demonstrated in Fig. 6, along the flowing direction in the inlet header, the channel flow rate first increases for the first several channels due to the entrance effect. For the rest channels, the flow rate generally decreases with the distance away from the entrance/exit of the heat exchanger. This may be because the flow path through the channels away from the entrance/exit,

would have a larger flow resistance, thus receives less mass flow rate. It also could be observed that the higher average channel flow rate would lead to a more mal-distributed flow distribution.

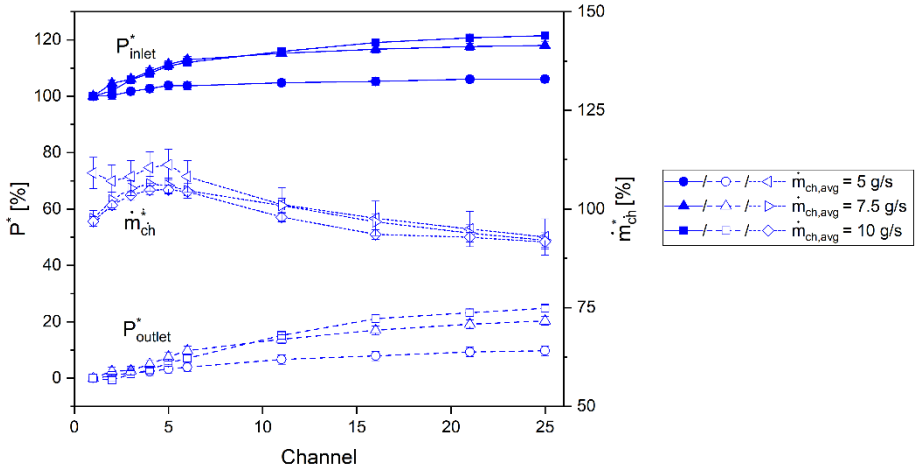

Figure 6a: Pressure in the headers and flow rate distribution- 50 plates, cold stream

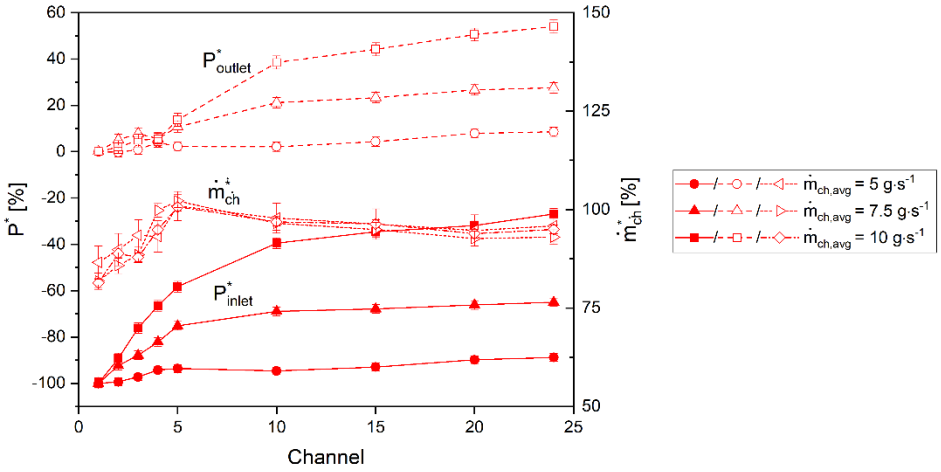

Figure 6b: Pressure in the headers and flow rate distribution- 50 plates, hot stream.

3.4. Impact of Maldistribution on the Thermal Performance of BPHEs

Fig. 7 shows the channel heat capacity distribution in the 50-plate BPHE under three different flow rates.

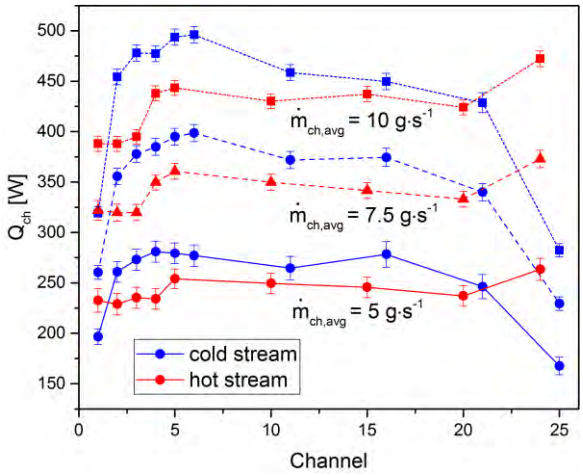

Figure 7: Channel heat capacity- 50 plates

Compared with Fig. 6, it can be observed that the heat capacity distribution is quite similar to the mass flow rate distribution. The channel receiving more flow rate would have a higher heat capacity. The exceptions are the channels at two ends: two cold channels at ends have less heat capacity

since heat is only transferred from one neighboring hot channel; two hot channels at ends have higher heat capacity due to a larger temperature difference with two outer cold streams. The heat capacity distribution seems to be more sensitive to the flow rate. With a higher flow rate, the maldistribution in channel heat capacity is more obvious. The non-uniformity of the channel heat capacity may lead to a poor utilization of the heat transfer area.

4. CONCLUSION

Single-phase flow distribution in BPHEs has been experimentally investigated. Water is used as the working fluids. Probes are placed into the headers of the BPHEs to measure the pressure change along the headers, as well as the pressure drop and temperature change across different channels. The results show that the maldistribution is more significant as the number of plates and total mass flow rate increase. The entrance effect would decrease the flow rate in the channels near the entrance/exit of the heat exchanger. The maldistribution in channel flow rate results in the non-uniformity of the channel heat capacity.

ACKNOWLEDGEMENTS

The authors thankfully acknowledge the support provided by the Air Conditioning and Refrigeration Center at the Univ. of Illinois at Urbana-Champaign and CTS (Creative Thermal Solutions Inc.).

REFERENCES

Bassiouny, M. K., Martin, H., 1984a. Flow distribution and pressure drop in plate heat exchangers-I: U-type arrangement. Chemical Engineering Science, 39(4), 693-700.

Bassiouny, M. K., Martin, H., 1984b. Flow distribution and pressure drop in plate heat exchangers-II: Z-type arrangement. Chemical Engineering Science, 39(4), 701-704.

Focke, W. W., Zachariades, J., and Olivier, I., 1985. The effect of the corrugation inclination angle on the thermohydraulic performance of plate heat exchangers. International Journal of Heat and Mass Transfer, 28(8), 1469-1479.

Jin, S., Hrnjak, P., 2017. Effect of end plates on heat transfer of plate heat exchanger. Int. J. Heat and Mass Transfer, 108, 740–748.

Li, W., Hrnjak, P., 2018. An experimentally validated model of single-phase flow distribution in brazed plate heat exchangers. International Refrigeration and Air Conditioning Conference at Purdue. Paper 1907. https://docs.lib.purdue.edu/iracc/1907.

Li, W., Hrnjak, P., 2019, Theoretical analysis of the end-plate effect on heat transfer in brazed plate heat exchangers. The 25th IIR Int. Congress of Refrigeration ICR 2019, Montreal, Paper 1565.

Rao, B. P., Das, S. K., 2004. An experimental study on the influence of flow maldistribution on the pressure drop across a plate heat exchanger. Journal of Fluids Engineering, 126, 680-691.

Rao, B. P., Bwngt, S. and Das, S. K., 2005. An experimental and theoretical investigation of the effect of flow maldistribution on the thermal performance of plate heat exchangers. Journal of Heat Transfer, 127, 332-343.

Shah, R.K., 1990. Assessment of modified Wilson plot techniques for obtaining heat exchanger design data heat transfer, in: Proceedings of the International Heat Transfer Conference.

Wang, C. C., Yang, K., S., Tsai, J. S. and Chen, I. Y., 2011. Characteristics of flow distribution in compact parallel flow heat exchangers, part I: Typical inlet header. Applied Thermal Engineering, 31, 3226-3234.

Manuscript ID: 1565
DOI: 10.18462/iir.icr.2019.1565

Theoretical analysis of the end-plate effect on heat transfer in brazed plate heat exchangers

Wenzhe LI[(a)], Pega HRNJAK [(a), (b), *]

[(a)] Air-Conditioning and Refrigeration Center (ACRC), University of Illinois Urbana-Champaign
Urbana, 61801, IL, USA, liwz310@illinois.edu, pega@illinois.edu
[(b)] Creative Thermal Solutions In. (CTS)
Urbana, 61802, IL, USA

ABSTRACT

In brazed plate heat exchangers (BPHEs), two end plates function as fins due to the heat conduction with the adjacent thermal plates. This effect brings difficulties in the development of reliable heat transfer correlations.
This paper presents a theoretical analysis of the end-plate effect on heat transfer in BPHEs.
In the analysis, the governing equation is obtained by the energy balance of an elementary cell of the end plate. Then, both numerical and analytical approaches are adopted to solve the governing equation.
The results show that the numerical solution and analytical solution agree well with each other. The end-plate effect enlarges the active heat transfer area and leads to an overestimation of the heat transfer coefficient. An equation for the fin efficiency of the end plates is also proposed.
Keywords: Brazed Plate Heat Exchangers, End-plate Effect, Fin Efficiency.

1. INTRODUCTION

Brazed plate heat exchangers (BPHEs) have been widely used in the heating, ventilating, air conditioning, and refrigeration industry. A BPHE essentially consists of multiple thin metal plates that are stamped with a wavy chevron or herringbone pattern. Two working fluids flow through the alternating channels which are constructed by brazing or welding the plates with opposite chevron direction together. In such a structure, the “end plate” refers to the “two outer plates that ideally do not transfer heat”. Since two end plates are usually assumed to be adiabatic, only the interior plates, also known as the “thermal plates”, are counted in most cases when calculating the active heat transfer area.
However, the contribution of the end plates to heat transfer is not always trivial, especially when the plate number is small. For instance, Heggs and Scheidat (1992) suggested that the effect of the end plates would be beyond 2.5% if the plate number is less than 19. To characterize and compensate such an effect, most work in open literature have taken the method of adding a correction factor on log mean temperature difference (LMTD) or plotting ε-NTU for different configurations and operating conditions. Kandilikar and Shah (1989) investigated the influence of the number of plates on heat exchanger performance through the numerical analysis for different flow arrangements. They tabulated the correction factor F for LMTD as a function of capacitance ratio R, number of heat transfer unit (NTU), temperature effectiveness P and number of plates N. The authors also concluded that the end-plate effect is negligible only for N > 40. The approach of using the correction factor has provided a good guideline for some practical purposes. Yet the idealized assumption renders it insufficient under certain circumstances. Jin and Hrnjak (2017) regarded the end plate as a fin which transfers heat through the contact with the corrugated surfaces of adjacent thermal plates. The authors also developed a thermal conduction model to quantify the end-plate effect and validated their model by the single-phase heat transfer experiments using heat exchangers with different number of plates. Their results showed that the fin efficiency of the end plate is a function of the convective heat transfer coefficient and conductive thermal resistance.

The effect of the end plate is quickly diluted with an increased number of plates in real applications. But its influence cannot be ignored when the plate number is small, which is often the case in laboratory settings for the development of heat transfer correlations. The objective of this paper is to theoretically quantify the end-plate effect and provide a general equation to correct the measurements, and eventually model for the BPHEs.

2. THEORETICAL ANALYSIS

2.1. Description of the Problem

Fig. 1 shows the schematic of the end-plate effect. It is convenient to assume the cold fluid (inner stream) flows upward between the end plate and the adjacent thermal plate; the hot fluid (outer stream) flows downward in the next channel. The end plate, which is ideally adiabatic, actually functions as a fin and transfers heat due to the heat conduction through the contact with the adjacent thermal plate. In Fig. 1, the primary heat flow path is directly through the thermal plate (straight arrow); for the secondary heat flow path, heat is first conducted through the contact area and then transferred to the inner stream by convection through the end plate (curved arrow).

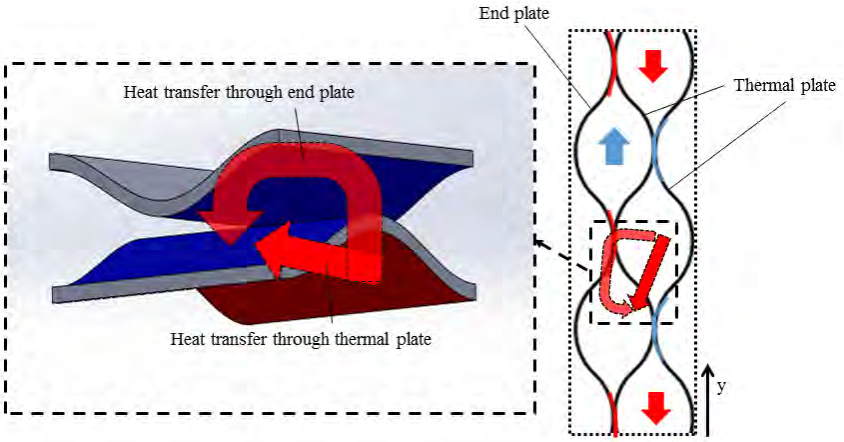

Figure 1: End-plate effect

2.2. Assumptions

Following assumptions are made to simplify the problem:

1. Fluid flow in a plate channel is one-dimensional, along the length of the BPHE ($T_f = f(y)$);
2. Neglect the thermal resistance in plate thickness direction due to the thin plate;
3. Neglect the thermal resistance of the contact area due to the high thermal conductivity of the brazing material. This assumption also indicates that the temperature of the contact area is very close to the local temperature of the outer stream ($T_{contact} \approx T_{f,o}$);
4. Constant convective heat transfer coefficient ($h = C$);
5. Constant thermal conductivity of the plate ($k = C$).

2.3. Governing Equation

Due to the geometric symmetry of the plate and 1-D flow assumption, it is rational to take half of the end plate (more precisely, half of the corrugated region) as the object of analysis, as shown in Fig. 2. For this object of analysis, the four edges are assumed to be adiabatic. There are multiple interior contact areas, of which the temperature is approximated to be the local temperature of the outer stream. In Fig. 2, there are two sets of rectangular coordinates: (x, y) are along the plate width (L_w) and length (L_p) direction; (t, n) denote the direction along the corrugated groove and the direction normal to the corrugated groove. (t, n) is obtained by rotating (x, y) an angle β.

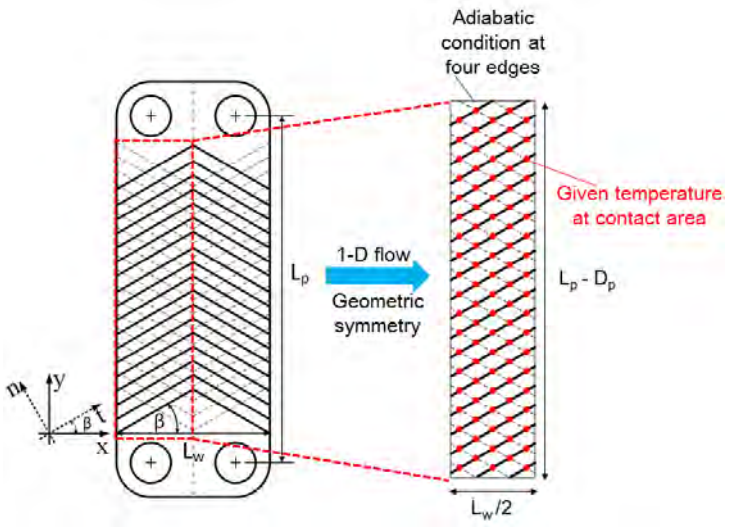

Figure 2: Object of analysis

Similar to the fin analysis, the essence of the end-plate effect is the balance between the heat conduction within the plate, with the heat convection between the end plate and the inner stream. An element of the end plate is taken to analyze the energy balance, as Fig. 3 shows. In Fig. 3, another coordinate (*s*) is introduced to represent the curve of the corrugated pattern.

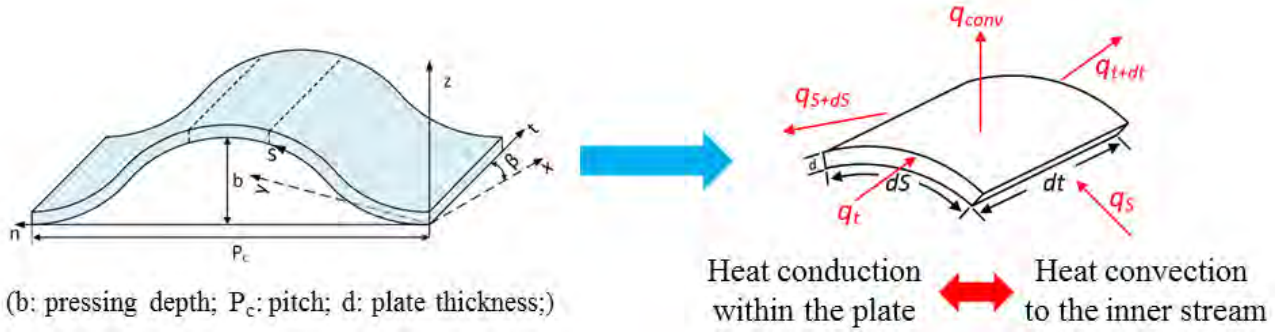

Figure 3: Heat balance of an element of the end plate

For an element of the end plate, the heat conduction is within the corrugated plate and it can be decomposed into two directions: along the corrugated groove (*t*) and along the corrugated curve (*s*). By using the Fourier's law and Taylor expansion, the heat conduction terms in Fig. 3 can be expressed as:

$$q_t = -k \cdot ds \cdot d \cdot \frac{\partial T}{\partial t} \quad \text{Eq.(1)}$$

$$q_{t+dt} = q_t + \frac{\partial q_t}{\partial t} \cdot dt + O(dt^2) \quad \text{Eq.(2)}$$

$$q_s = -k \cdot dt \cdot d \cdot \frac{\partial T}{\partial s} \quad \text{Eq.(3)}$$

$$q_{s+ds} = q_s + \frac{\partial q_s}{\partial s} \cdot ds + O(ds^2) \quad \text{Eq.(4)}$$

The convective term is calculated by the Newton's law of cooling:

$$q_{conv} = h \cdot dt \cdot ds \cdot (T - T_{f,i}) \quad \text{Eq.(5)}$$

Where $T_{f,i}$ denotes the temperature of the inner stream. Put Eq. (1) ~ (5) into the energy balance:

$$q_{conv} = q_t + q_{t+dt} + q_s + q_{s+ds} \quad \text{Eq.(6)}$$

Neglect the higher order terms ($O(dt^2), O(ds^2)$), and re-arrange the equation:

$$\frac{\partial^2 T}{\partial s^2}+\frac{\partial^2 T}{\partial t^2}-\frac{h}{k\cdot d}\left(T-T_{f,i}\right)=0 \quad \text{Eq.(7)}$$

Further, let: $\theta = T - T_{f,i}$, and assume $T_{f,i}$ is varying linearly in *y* direction: $T_{f,i} = T_{f,i}\big|_{y=0} + a \cdot y$, then Eq. (7) becomes:

$$\frac{\partial^2 \theta}{\partial s^2}+\frac{\partial^2 \theta}{\partial t^2}-\frac{h}{k\cdot d}\theta=0 \quad \text{Eq.(8)}$$

Eq. (8) is a partial differential equation (PDE) about θ and it is the governing equation of the end-plate effect. The first two terms in Eq. (8) represent the heat conduction in two directions; the last term represents the heat convection.

Along with the PDE, the physical boundary conditions are given as following:

$$x=0 \; and \; x=\frac{L_w}{2},\ \frac{\partial \theta}{\partial x}=0; \quad \text{Eq.(9)}$$

$$y=0 \; and \; y=\left(L_p-D_p\right),\ \frac{\partial \theta}{\partial y}=-a; \quad \text{Eq.(10)}$$

$$\theta(x_i,y_i)=\theta_i,(x_i,y_i)\in contact\ areas; \quad \text{Eq.(11)}$$

The first two conditions are for the four adiabatic edges; the last one accounts the given temperature at the contact areas.

It is noticeable that the PDE (Eq. (8)) is in (*t*, *s*) coordinates but the boundary conditions are in (*x*, *y*) coordinates. Since the *s* coordinate is not in the (*x*, *y*) plane, it is beneficial to convert *s* in the PDE into *n*, which is coplanar with (x, y). The sinusoidal curve of the corrugated pattern can be described by:

$$F(n)=\frac{b}{2}sin\left[\frac{2\pi}{P_c}n-\frac{b}{2}\right]+\frac{b}{2} \quad \text{Eq.(12)}$$

Then, the measure of the curve (s), is expressed as:

$$ds=\sqrt{F'(n)^2+1}\cdot dn=\sqrt{\frac{b^2\pi^2}{{P_c}^2}cos^2\left[\frac{2\pi}{P_c}n-\frac{b}{2}\right]+1}\cdot dn \quad \text{Eq.(13)}$$

By Eq. 13, the PDE (Eq. 8) is converted to:

$$\frac{\partial^2 \theta}{\partial n^2}\cdot\frac{1}{\frac{b^2\pi^2}{{P_c}^2}cos^2\left[\frac{2\pi}{P_c}n-\frac{b}{2}\right]+1}+\frac{\partial^2 \theta}{\partial t^2}-\frac{h}{k\cdot d}\theta=0 \quad \text{Eq.(14)}$$

Eq. (14) is the governing equation in (t, n) coordinates.

2.4. Solution of the Governing Equation

2.4.1. Numerical solution

The first option is to solve the governing equation by the numerical approach, or to be more precise, the finite element method. To implement the finite element method, a mesh is first generated in the computational domain, which is the projection of the object of analysis on (*x*, *y*) plane (or (*t*, *n*) plane). Then, the target PDE is discretized and solved by the numerical solver in the computational domain. Fig. 4 gives a specific example of a certain BPHE. Table 1 gives the geometric parameters of the target BPHE. As Fig. 4 shows, the contact areas in the plate are approximated to be elliptical. In this calculation, the BPHE has two channels; inlet temperature of the inner and outer stream is 30 °C and 50 °C respectively; the convective heat transfer coefficient is taken as 2000 W/ m^2 ·K.

From the temperature profile of the end plate in Fig. 4, there is a clear temperature gradient around the contact areas which drives the heat dissipate within the plate.

The heat dissipation through the end plate can be calculated by following numerical integration:

$$Q_{end\ plate} = \iint h \cdot \theta(x,y) \cdot \sqrt{\frac{b^2\pi^2}{{P_c}^2} cos^2\left[\frac{2\pi}{P_c}(y \cdot cos\beta - x \cdot sin\beta) - \frac{b}{2}\right] + 1} \cdot dxdy \quad \text{Eq.(15)}$$

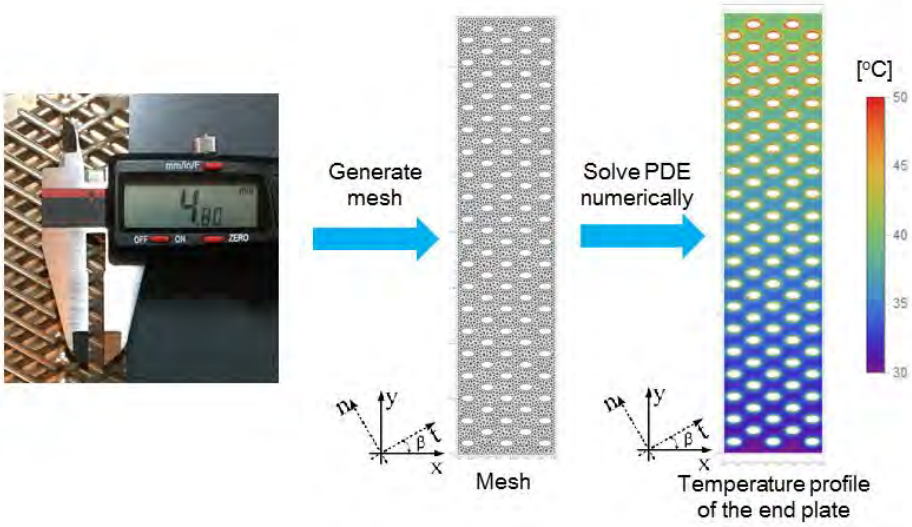

Figure 4: Numerical solution of the end-plate effect

Table 1. Geometric parameters of the BPHE

Parameter	
Chevron angle, φ=90°-β, °	60
Corrugation depth, b, mm	2.0
Corrugation pitch, P_c, mm	7.0
Plate thickness, d, mm	0.30
Port length, L_p, mm	172
Total length, L_v, mm	206
Port width, L_h, mm	42
Total width, L_w, mm	76
Heat transfer area, A_{plate}, m^2	0.014
Port diameter, D_p, mm	20.0

2.4.2. Analytical solution

The second option is to seek further simplification of the governing equation and solve analytically. As mentioned above, one difficulty of this problem is that the PDE and the boundary conditions are in different coordinates and the conversion between two coordinates would make either PDE or the boundary conditions quite complicated. To resolve this issue, “flat plate approximation” is adopted. In this approximation, the corrugated end plate is assumed to be flat and the heat dissipation through the end plate is approximated by:

$$Q_{end\ plate} \approx Q_{flat} \cdot \emptyset \quad \text{Eq.(16)}$$

In Eq. (16), ∅ is the area enlargement factor, which is defined as the area ration of the corrugated plate to the flat plate. It can be estimated by:

$$\emptyset = \frac{A_{corrugated}}{A_{flat}} \approx \frac{1}{6}\left(1 + \sqrt{1+X^2} + 4\sqrt{1+\frac{X^2}{2}}\right), X = \frac{\pi b}{P_c} \quad \text{Eq.(17)}$$

For a flat plate, the PDE is reduced to:

$$\frac{\partial^2\theta}{\partial x^2} + \frac{\partial^2\theta}{\partial y^2} - \frac{h}{k \cdot d}\theta = 0 \quad \text{Eq.(18)}$$

Now, the PDE (Eq. (18)) and boundary conditions (Eq. (9) ~ (11)) are all in (*x*, *y*) coordinates and their forms are relatively simple.
Dealing with the given temperature at multiple interior contact areas is another difficulty. Based on the previous assumption (1) and (3), one could infer that the temperature of the contact areas is only a function of *y* coordinate: $T_{contact} \approx T_{f,o} = f(y)$. That means the contact areas at the same level (same *y*) have the same temperature. Therefore, the heat conduction in x-direction is much smaller than that in y-direction. That allows making the "1-D strip simplification": dividing the end plate into multiple strips and make 1-D assumption in each strip: $\theta \approx \theta(y)$.
Schematic of the" 1-D strip simplification" is given in Fig. 5.

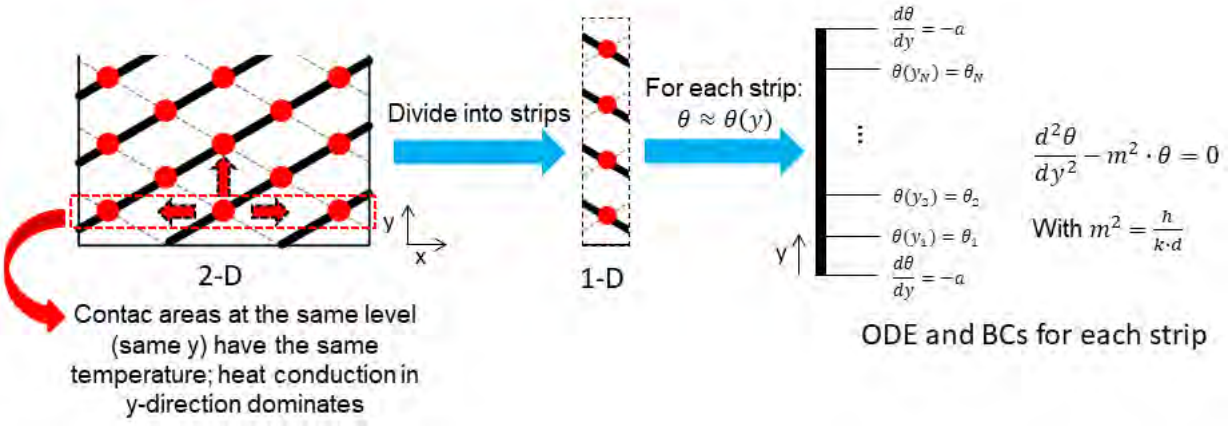

Figure 5: 1-D strip simplification

With this simplification, a 2-D PDE is converted into multiple 1-D ordinary differential equations (ODE):

$$\frac{d^2\theta}{dy^2} - m^2 \cdot \theta = 0 \qquad \text{Eq.(19)}$$

With: $m^2 = \frac{h}{k \cdot d}$. The boundary conditions are:

$$y = 0 \; and \; y = (L_p - D_p), \; \frac{d\theta}{dy} = -a; \qquad \text{Eq.(20)}$$

$$\theta(y_i) = \theta_i, y_i \in contact \; areas; \qquad \text{Eq.(21)}$$

The boundary conditions separate each strip into multiple segments, in each segment, the ODE can be solved analytically with two boundary conditions at two ends. The heat dissipation through the flat plate is then obtained from the following equation:

$$Q_{flat} = \sum_{strip} \left(\sum_{segment} h \cdot \Delta x \cdot \int \theta(y) \cdot dy \right) \qquad \text{Eq.(22)}$$

$$= \sum_{strip} \frac{\sqrt{h \cdot k \cdot d} \cdot P_c}{2 \cdot sin\beta} \left\{ 2tanh\left(\frac{P_c \cdot m}{4 \cdot cos\beta}\right) \cdot \sum_{1}^{N} \theta_i + \left(tanh\left(\frac{P_c \cdot m}{2 \cdot cos\beta}\right) - tanh\left(\frac{P_c \cdot m}{4 \cdot cos\beta}\right) \right) \cdot (\theta_1 + \theta_N) \right\}$$

If the convective heat transfer coefficient (h) is sufficiently large, all the hyperbolic tangent terms (tanh) in above equation would be approximately 1, and Eq. (22) can be simplified as:

$$Q_{flat} \approx \sum_{strip} \left(\frac{\sqrt{h \cdot k \cdot d} \cdot P_c}{sin\beta} \sum_{i=1}^{N} \theta_i \right) \qquad \text{Eq.(23)}$$

Then, heat dissipation through the actual corrugated plate could be estimated by Eq. (16)

2.4.3. Numerical vs. analytical solution

To compare the numerical and analytical solution, the same example (discussed in 2.4.1) is calculated by the analytical method. The fin efficiency of the end plate, defined as the ratio between the heat dissipation through the end plate and that through adjacent thermal plate, is used to quantify the end-plate effect.

$$\eta = \frac{Q_{end\ plate}}{Q_{adjacent\ thermal\ plate}} \qquad \text{Eq.(24)}$$

Fig. 6 gives the fin efficiency of the end plate as the function of the convective heat transfer coefficient.

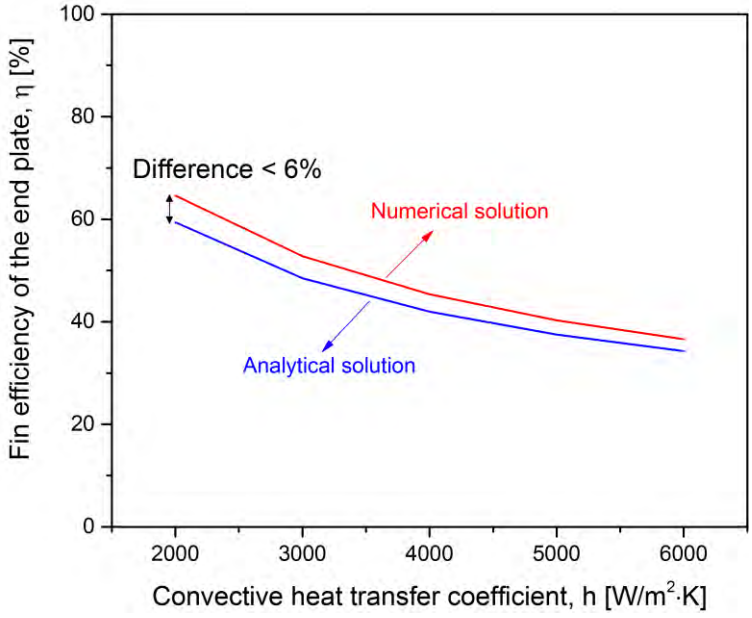

Figure 6: Numerical vs. analytical solution

Fig. 6 shows that the numerical and analytical solution agrees well with each other. The difference in the fin efficiency of the end plate by these two solutions is within 6 %. In this specific case, the fin efficiency could reach up to 65 %, which means the end plate contributes up to 65 % of its surface area as active heat transfer area. Similar to the classical fin theory, the fin efficiency of the end plate generally decreases with the convective heat transfer coefficient.

3. APPLICATION: CORRECTION OF EXPERIMENTAL DATA

As mentioned previously, one objective of this analysis is to correct the measurements in the development of heat transfer correlations. An experiment has been conducted to develop a single-phase heat transfer correlation for the BPHE as Table 1 described. In the experiments, 3-channel BPHE is used (two cold fluid channels at outside, one hot fluid channel in the middle). Water is the working media for both sides. The temperature change, as well as the pressure drop across the heat exchanger is recorded during the tests. Modified Wilson plot (Shah, 1990) is used to develop the heat transfer correlation. The detailed description of the experimental facility can be found in authors' another ICR2019 conference paper (Li and Hrnjak, 2019).

In such a 3-channel heat exchanger configuration, the cold side heat transfer area is enlarged by the end plate effect; the hot side heat transfer area keeps unchanged. To correct this effect, the iteration is necessary: first assume zero fin efficiency to obtain a heat transfer correlation by the Wilson plot; then, use the developed correlation to calculate the heat transfer coefficient and renew the fin efficiency through the solutions; correct the active heat transfer area by the fin efficiency and re-use the Wilson plot to update the heat transfer correlation; repeat above procedure until the fin efficiency and heat transfer coefficient is converged.

Fig. 7 shows the results of the correction by two solutions. The calculated fin efficiency of the end plate is also plotted.

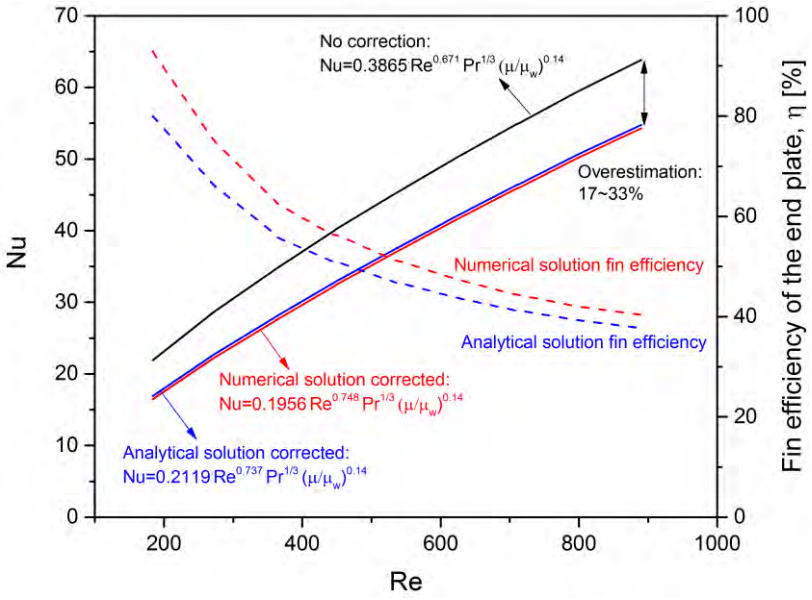

Figure 7: Correction of the heat transfer coefficient

In Fig.7, the numerical and analytical solutions give similar results again in both heat transfer correlation and fin efficiency. Fig. 7 also demonstrates that there would be an overestimation of 17 ~ 33% in the heat transfer coefficient if no correction is made in this case.

4. CONCLUSIONS

The end-plate effect is theoretically analysed in this paper. The governing equation of the end-plate effect is derived through the energy balance. Two solutions are developed for the governing equation: numerical and analytical. The calculation aiming at one specific example shows that these two solutions agree well with each other. The obtained solutions are used to correct the measurements in the development of heat transfer correlations. The results show that there would be a significant overestimation in the heat transfer coefficient if the end-plate effect is not corrected.

ACKNOWLEDGEMENTS

The authors thankfully acknowledge the support provided by the Air Conditioning and Refrigeration Center at the Univ. of Illinois at Urbana-Champaign and CTS (Creative Thermal Solutions Inc.).

REFERENCES

Heggs, P.J., Scheidat, H.J., 1992. Thermal performance of plate heat exchanger with flow maldistribution, in: R.K. Shah, T.M. Rudy, J.M. Robertson, K.M. Hostetler (Eds.), Compact Heat Exchangers for Power and Process Industries, HTD, vol. 201, ASME, New York, 87–93.

Jin, S., Hrnjak, P., 2017. Effect of end plates on heat transfer of plate heat exchanger. Int. J. Heat and Mass Transfer, 108, 740–748.

Kandlikar, S.G., Shah, R.K., 1989. Multipass plate heat exchangers—effectiveness-NTU results and guidelines for selecting pass arrangements. J. Heat Transfer, 111(2), 300–313.

Li, W., Hrnjak, P., 2019, Experimental investigations of the single-phase flow distribution in brazed plate heat exchangers and its impact on the heat exchanger, The 25th IIR International Congress of Refrigeration ICR 2019. Montreal, Paper ID 1564.

Shah, R.K., 1990. Assessment of modified Wilson plot techniques for obtaining heat exchanger design data heat transfer, in: Proceedings of Ninth International Heat Transfer Conference, vol. 5, 1990, pp. 51–56.

Manuscript ID: 1597
DOI: 10.18462/iir.icr.2019.1597

Influence of commercial refrigeration system design and refrigerant options on life cycle climate performance

Michael PETERSEN[(a)], Gustavo POTTKER[(a)], Brian A. FRICKE[(b)]

[(a)] Honeywell, Buffalo, NY, 14210, USA, michael.petersen4@honeywell.com, gustavo.pottker@honeywell.com

[(b)] Oak Ridge National Laboratory[1]
Oak Ridge, TN, 37831, USA, frickeba@ornl.gov

ABSTRACT

Ongoing efforts to reduce direct and indirect emissions of commercial refrigeration systems include using leak reduction measures, refrigerant charge minimization, low global warming potential (GWP) refrigerants and energy efficiency measures. In this paper, Life Cycle Climate Performance (LCCP) analysis is used to estimate the lifetime carbon dioxide equivalent emissions of commercial refrigeration system designs and refrigerant options. Commercial refrigeration systems investigated in this study include the centralized direct expansion (DX) system with hydrofluorocarbon (HFC) and hydrofluoroolefin (HFO) refrigerant blends, the transcritical R-744 booster system, and self-contained systems using R-290. The results of the LCCP analysis are presented for a variety of cities around the world, and recommended systems and refrigerant options are provided based on direct and indirect carbon emissions.
Keywords: Commercial Refrigerator, Global Warming, Life Cycle Climate Performance, Refrigerant.

1. INTRODUCTION

The traditional centralized direct expansion (DX) refrigeration system used in commercial applications is known to suffer from significant refrigerant leakage, especially in older existing systems. EPA (2012) estimates that the U.S. supermarket industry-wide average refrigerant emission rate is on the order of 25%. The use of high Global Warming Potential (GWP) refrigerants in these systems, combined with high refrigerant leakage, can result in considerable direct carbon dioxide equivalent (CO_{2e}) emissions. In addition, commercial refrigeration systems consume a substantial amount of electrical energy, resulting in high indirect CO_{2e} emissions. Thus, there are ongoing efforts to reduce the direct and indirect environmental effects of commercial refrigeration systems through the use of leak reduction measures, refrigerant charge minimization, low GWP refrigerants and energy efficiency measures.

With the phase-out of chlorofluorocarbon (CFC) and hydrochlorofluorocarbon (HCFC) refrigerants, manufacturers turned to hydrofluorocarbons (HFC) as substitutes. These HFC refrigerants are commonly used in air-conditioning, heat pumping and refrigeration applications, and while they have zero ozone-depleting potential (ODP), many HFC refrigerants have relatively high GWPs. The need to be compliant with the Montreal Protocol and related governmental mandates has driven the industry to revisit the use of long-term alternative refrigerants that are favorable for the environment and exhibit better thermodynamic cycle efficiency. Alternative refrigerants with lower or near zero GWP are available, including hydrocarbons such as propane (R-290) and isobutane (R-600a), ammonia (R-717), carbon dioxide (R-744) and hydrofluoroolefin (HFO) refrigerants such as R-1234yf and R-1234ze(E) and their blends (UNEP, 2010a,b).

Hydrofluoroolefin refrigerants are a relatively new class of refrigerant and they have very low GWPs; however, many of them are classified as mildly flammable. Nevertheless, refrigerant blends

[1] Notice: This manuscript has been authored by UT-Battelle, LLC, under Contract No. DE-AC05-00OR22725 with the U.S. Department of Energy. The United States Government retains and the publisher, by accepting the article for publication, acknowledges that the United States Government retains a non-exclusive, paid-up, irrevocable, world-wide license to publish or reproduce the published form of this manuscript, or allow others to do so, for United States Government purposes.

consisting of the proper concentrations of HFOs and HFCs can be made non-flammable, resulting in alternative refrigerants with GWP values significantly lower than HFCs alone. Such lower GWP HFO refrigerant blends have the potential to be direct replacements for commonly used high GWP HFC refrigerants, thereby extending the useful life of HFC-based refrigeration systems.

Hydrocarbon refrigerants have zero ODP and relatively low GWP; however, their flammability poses a significant safety concern. Therefore, application of hydrocarbon refrigerants is limited to smaller equipment with limited charge sizes. In commercial refrigeration applications, small self-contained refrigerated display cabinets which consist of a thermally insulated compartment for the storage of foods and beverages and an integrated compact refrigeration system can utilize hydrocarbon refrigerants.

Another refrigerant which has recently gained the attention of the commercial refrigeration industry is carbon dioxide (R-744). Since R-744 has zero ODP and a GWP value of 1, it is considered an environmentally-friendly refrigerant option. R-744 is non-flammable and nontoxic, and, it has great heat transfer characteristics. However, operating pressures for R-744 are significantly higher compared to commonly used HFC refrigerants. In addition, the critical temperature of R-744 is low, which indicates that at high ambient temperatures, R-744 will operate in a supercritical cycle. Thus, transcritical R-744 booster refrigeration systems are currently sought for commercial refrigeration applications. These systems are currently being designed to maximize performance and safety. In cool and moderate climates, the on-going developments in transcritical R-744 booster refrigeration technology have resulted in systems which are competitive with HFC systems (Ge and Tassou, 2011).

The selection of an appropriate refrigeration system and/or refrigerant should be based on several factors, including the GWP of the refrigerant, the energy consumption of the refrigeration system over its operating lifetime, and leakage of refrigerant over the system lifetime. For example, focusing on energy efficiency alone may overlook the significant environmental impact of refrigerant leakage; while focusing on GWP alone might result in lower efficiency systems that result in higher indirect impact over the equipment lifetime. Therefore, in this paper, Life Cycle Climate Performance (LCCP) is used to estimate the lifetime direct and indirect carbon dioxide equivalent emissions of various commercial refrigeration system designs and refrigerant options for a variety of cities around the world, with the goal of providing guidance on lower GWP refrigerant solutions with improved LCCP compared to baseline systems. Commercial refrigeration systems investigated in this study include the centralized direct expansion (DX) system with hydrofluorocarbon (HFC) and hydrofluoroolefin (HFO) refrigerant blends, the transcritical R-744 booster system, and self-contained systems using R-290.

Systems investigated in this study include the baseline centralized direct expansion (DX) system with R-404A, and alternative systems and refrigerant options such as the centralized DX system with R-448A, the transcritical CO_2 (R-744) booster system and the self-contained R-290 system.

2. REFRIGERATION SYSTEMS

The energy and LCCP impacts of several refrigeration system architectures and refrigerant options were investigated in this study. The baseline refrigeration system consists of a centralized direct expansion (DX) system utilizing R-404A. Other refrigeration system options included a centralized DX system utilizing R-448A, a transcritical R-744 booster system, and the self-contained R-290 system. In general, all of the refrigeration systems had a nominal medium-temperature refrigeration load of 207 kW and nominal low-temperature refrigeration load of 103 kW. The refrigeration systems provided cooling for 184 m of low-temperature (frozen food) display cabinets, including reach-in multi-deck cabinets and coffin cabinets, as well as 138 m of medium-temperature (chilled food) display cabinets, including open single- and multi-deck cabinets and coffin cabinets. In addition, the refrigeration systems cooled 139 m^2 of walk-in freezer storage space and 399 m^2 of walk-in cooler storage space. A list of design parameters and assumptions for each refrigeration system type and refrigerant option are shown in Table 1.

Table 1. Refrigeration system design parameters and assumptions

System Parameter	Centralized DX, baseline	Centralized DX	Transcritical R744 booster	Self-contained
Refrigerant (GWP)	R-404A (3943)	R-488A (1273)	R-744 (1)	R-290 (3)
Refrigerant charge (kg)	1400 kg	1400 kg	750 kg	50 kg
Annual refrigerant leak rate (including service)	18%	18%	18%	5%
Refrigerant loss at end-of-life	10%	10%	10%	15%
MT suction temperature	-6.7°C	-6.7°C	-5.5°C	-6.7°C
LT suction temperature	-28.9°C	-28.9°C	-27.7°C	-28.9°C
MT and LT superheat	5 K	5 K	5 K	5 K
MT return gas temperature	15°C	15°C	15°C	10°C
LT return gas temperature	5°C	5°C	5°C	0°C
Minimum condensing temperature	21°C	21°C	10°C	N/A
LT subcooling or subcooler outlet temperature	4.4°C outlet	4.4°C outlet	0°C	3°C
Condenser or gas cooler approach temperature	4°C	4°C	4°C	4°C

3. ENERGY MODELING

The whole-building energy modelling tool, EnergyPlus, was used to estimate the annual energy consumption of a prototypical supermarket with the various refrigeration systems. The energy analysis was performed for 12 cities across the world, as shown in Table 2. The average, minimum and maximum temperatures shown in Table 2 for each city were obtained from the weather files used as input to the EnergyPlus simulations. The prototypical supermarket used in the EnergyPlus simulations has a floor area of 4181 m^2 and is based on the new construction reference supermarket model developed by the US Department of Energy (Deru et al., 2011).

Table 2. Cities and their annual average temperatures, as used in the energy and LCCP analyses

City, Country	Annual average temperature (°C)	Minimum temperature (°C)	Maximum temperature (°C)
Athens, Greece	17.9	2.0	37.2
Atlanta, USA	16.7	-12.8	36.7
Cairo, Egypt	21.7	7.0	43.0
Guangdong, China	22.3	6.0	37.0
Melbourne, Australia	13.8	0.0	39.0
Mexico City, Mexico	16.9	2.5	30.0
Miami, USA	24.5	5.0	35.6
Minneapolis, USA	7.7	-31.1	37.2
New Delhi, India	24.5	4.2	43.6
Phoenix, USA	23.8	2.2	44.4
Riyadh, Saudi Arabia	26.2	4.0	46.0
Sao Paulo, Brazil	19.9	8.0	35.0

4. LIFE CYCLE CLIMATE PERFORMANCE (LCCP)

The Life Cycle Climate Performance (LCCP) of a refrigeration system is defined as the sum of the direct and indirect carbon dioxide equivalent (CO_{2e}) equivalent emissions resulting from system construction, operation and decommissioning. Direct emissions include the environmental effects of leakage of refrigerant which occurs during system operation, servicing, and at the end-of-life as well as during refrigerant production and transportation. Indirect emissions include the environmental effects associated with the production and distribution of the energy required to operate the

refrigeration system as well as energy associated with production, transportation and disposal of the system.
The Life Cycle Climate Performance, *LCCP*, of a refrigeration system may be determined as follows:

$$LCCP = E_{dir} + E_{indir} \quad \text{Eq. (1)}$$

where E_{dir} is the direct emissions and E_{indir} is the indirect emissions. The direct emissions are determined as follows (IIR, 2016):

$$E_{dir} = \mathrm{C}(L \cdot ALR + EOL)\left(GWP + GWP_{adp}\right) \quad \text{Eq. (2)}$$

where *C* is the refrigerant charge (kg), *L* is the average lifetime of the refrigeration system (yr), *ALR* is the annual refrigerant leak rate (in percentage of refrigerant charge), *EOL* is the end-of-life refrigerant leakage (in percentage of refrigerant charge), *GWP* is the global warming potential of the refrigerant (kg CO_{2e}·kg^{-1}) and GWP_{adp} is the global warming potential of the atmospheric degradation products of the refrigerant (kg CO_{2e}·kg^{-1}). The indirect emissions are determined as follows (IIR, 2016):

$$E_{indir} = \mathrm{L} \cdot \mathrm{AEC} \cdot \mathrm{EM} + \sum(m \cdot MM) + \sum(mr \cdot RM) + \mathrm{C} \cdot (1 + L \cdot ALR) \cdot \mathrm{RFM} + \mathrm{C} \cdot (1 - EOL) \cdot \mathrm{RFD} \quad \text{Eq. (3)}$$

where *AEC* is the annual energy consumption of the refrigeration system (kWh), *EM* is the carbon dioxide emissions associated with energy production (kg CO_{2e}·kWh^{-1}), *m* is the mass of the refrigeration system (kg), *MM* is the carbon dioxide emissions associated with material production (kg CO_{2e}·kg^{-1}), *mr* is the mass of recycled material (kg), *RM* is the carbon dioxide emissions associated with recycled material production (kg CO_{2e}·kg^{-1}), *RFM* is the refrigerant manufacturing carbon emissions (kg CO_{2e}·kg^{-1}) and *RFD* is the refrigerant disposal emissions (kg CO_{2e}·kg^{-1}). Table 3 provides emissions factors used for the LCCP analysis (Deru and Torcellini, 2007; Brander et al., 2011).

Table 3. Emission factors for electricity production

City, Country	Emission factor for electricity production (kg CO_{2e}·kWh^{-1})
Athens, Greece	2.107
Atlanta, USA	0.788
Cairo, Egypt	0.573
Guangdong, China	1.076
Melbourne, Australia	1.076
Mexico City, Mexico	0.549
Miami, USA	0.788
Minneapolis, USA	0.788
New Delhi, India	1.801
Phoenix, USA	0.594
Riyadh, Saudi Arabia	0.877
Sao Paulo, Brazil	0.110

5. RESULTS AND DISCUSSION

5.1. Energy Consumption

The annual energy consumption for the four refrigeration systems is summarized in Fig. 1. As expected, the annual energy consumption correlated well with the annual average ambient temperature, with the warmer cities exhibiting higher annual refrigeration system energy

consumption (see Fig. 2). For all cities modelled, it was found that the centralized R-448A DX system consumed less energy than the baseline centralized R-404A system. On average, the R-448A DX system consumed 7.2% less energy than the baseline R-404A system. Both the transcritical CO_2 booster system and the self-contained R-290 system consumed on average approximately 6% more energy than the baseline R-404A DX system. The transcritical CO_2 booster system showed greater energy efficiency for the colder climate (Minneapolis, USA), while the self-contained R-290 systems performed slightly better than the baseline system for the hottest climate (Riyadh, Saudi Arabia).

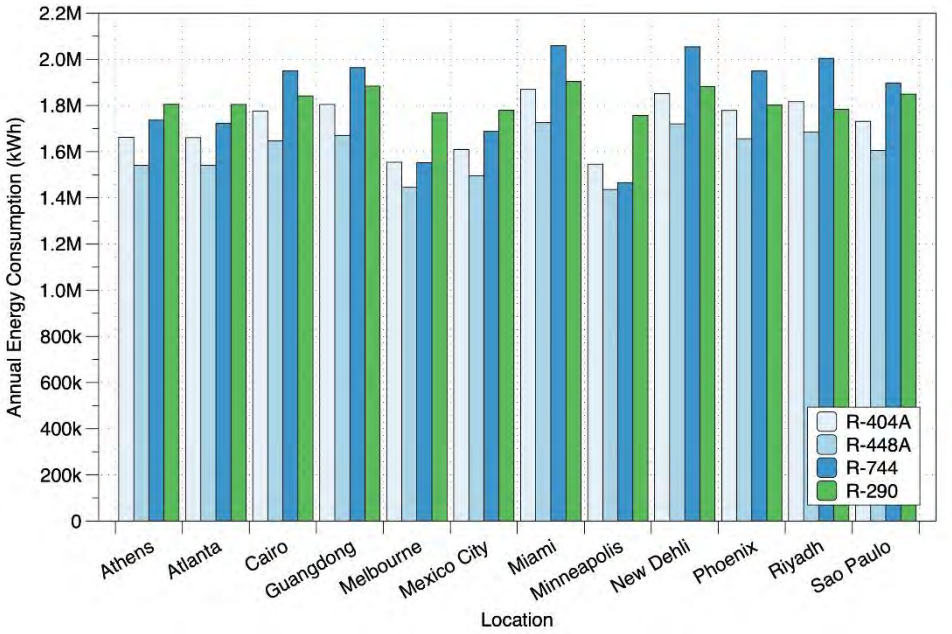

Figure 1: Annual energy consumption of the four refrigeration systems

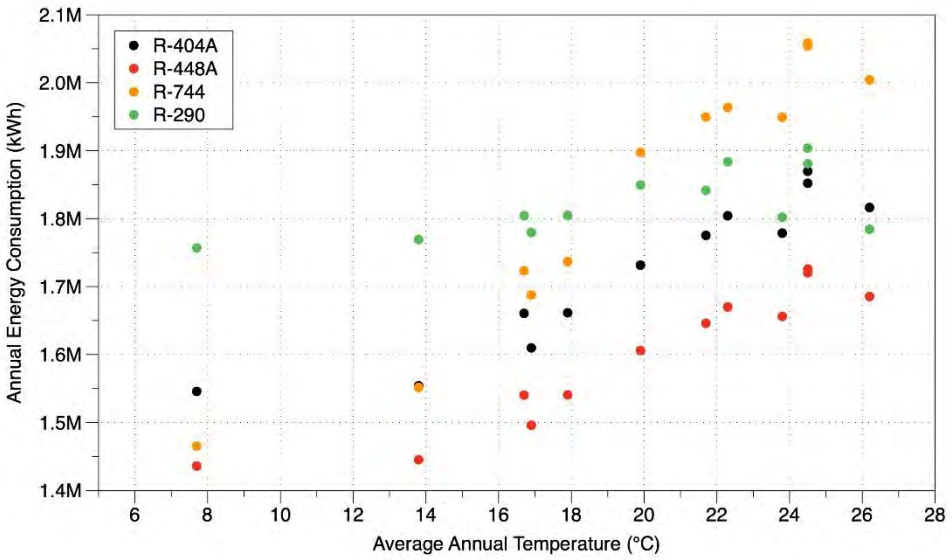

Figure 2: Annual energy consumption versus average annual temperature

5.2. Life Cycle Climate Performance (LCCP)

The total lifetime carbon dioxide equivalent emissions of each of the four refrigeration systems in the various cities is shown in Fig. 3. Note that the total emissions shown in Fig. 3 are divided into the direct and indirect contributions. It can be seen that the R-448A DX system, the transcritical CO_2 booster system and the self-contained R-290 systems all exhibit lower total carbon dioxide equivalent emissions than the baseline R-404A DX system. Direct emissions associated with the baseline R-404A system are significant, and many times represent nearly half of the total carbon emissions. Compared to the baseline R-404A DX system, direct carbon dioxide equivalent emissions

are reduced by 67% with the R-448A DX system. Direct emissions from the transcritical CO_2 booster system and the self-contained R-290 systems are negligible. Furthermore, the indirect emissions which are associated with energy consumption generally dominate the total emissions for all the refrigeration systems investigated.

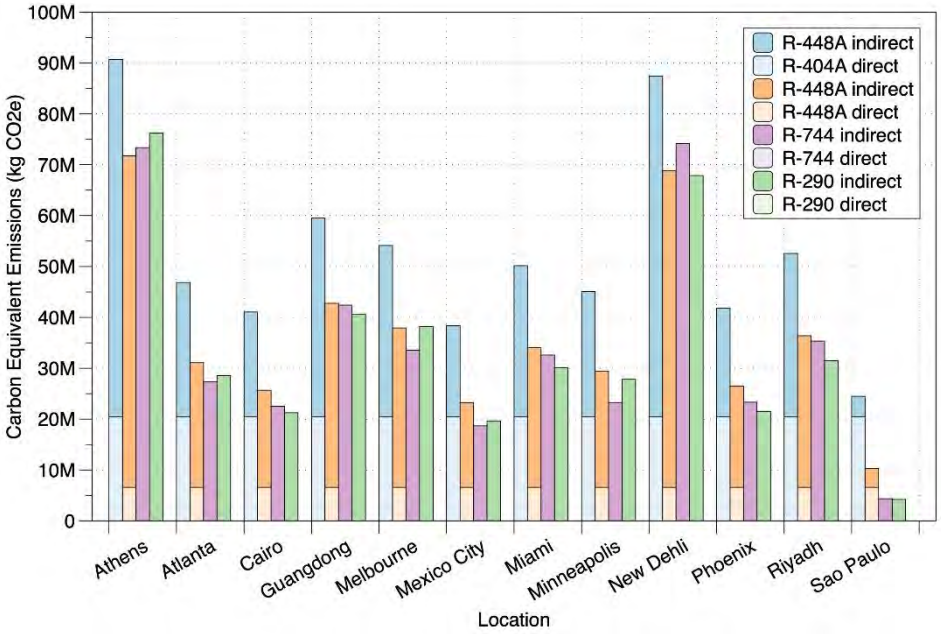

Figure 3: Total lifetime carbon dioxide equivalent emissions of the four refrigeration systems

The influence of sources of electric power generation on indirect emissions is illustrated in Fig. 4. Renewable energy, consisting mainly hydroelectric power with smaller contributions from wind and solar, account for nearly 80% of Brazil's electrical energy generation (EIA, 2017a). Thus, Brazil's carbon emissions associated with electrical power generation are very low compared with the other countries considered in this study. Therefore, the total lifetime carbon dioxide equivalent emissions associated with the four refrigeration systems is by far the lowest for Sao Paulo. Greece and India, on the other hand, rely almost totally on fossil fuel fired plants for electrical energy production (EIA, 2016), resulting in large indirect and total carbon dioxide equivalent emissions.

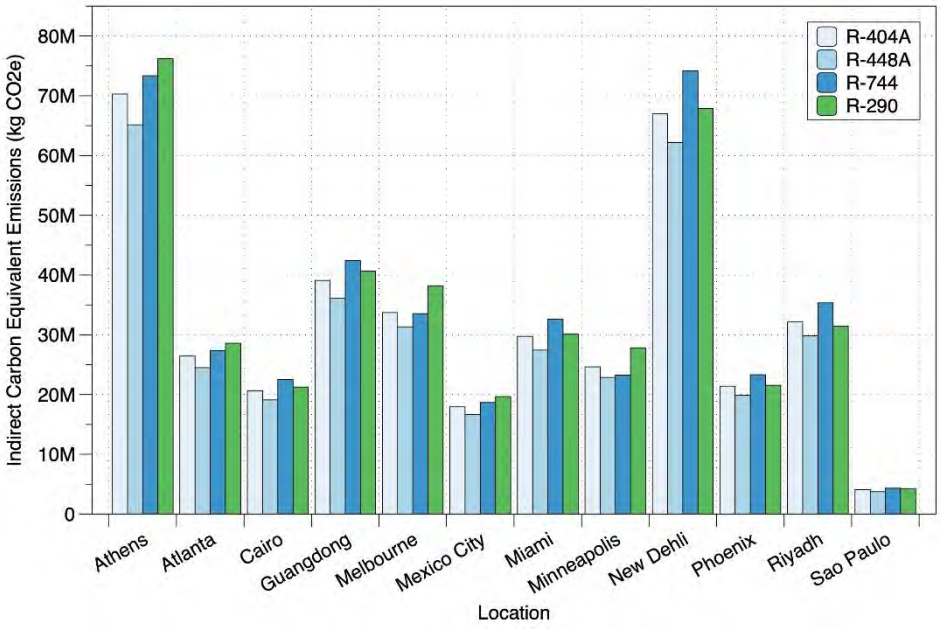

Figure 4: Indirect carbon dioxide equivalent emissions of the four refrigeration systems

The cities of Atlanta, Miami, Minneapolis and Phoenix in the United States produced similar levels of emissions, where on average, 63% of US electricity is produced by fossil fuelled power plants. Cairo, Egypt and Riyadh, Saudi Arabia rely heavily on natural gas for electrical energy production (EIA, 2017b; EIA, 2018) and showed similar levels of carbon dioxide equivalent emissions, with Riyadh producing higher levels than Egypt due its slightly warmer climate.

On average, the total lifetime carbon dioxide equivalent emissions for the R-448A DX system was 34% lower than that of the baseline R-404A DX system for the cities investigated. In addition, the total lifetime carbon emissions for the transcritical CO_2 booster system and the self-contained R-290 systems were approximately 40% lower than that of the baseline R-404A DX system.

6. CONCLUSIONS

In this paper, energy analyses and life cycle climate performance (LCCP) analyses were performed on four different commercial refrigeration systems for 12 cities across the world. The four commercial refrigeration systems included the R-404A DX system, the R-448A DX system, the transcritical CO_2 booster refrigeration system, and the self-contained R-290 system. The energy and LCCP analyses provided insight into the environmental effects associated with refrigeration system design and refrigerant selection across the world.

Compared to the baseline R-404A DX refrigeration system, the R-448A DX refrigeration system was found to have 67% less direct emissions, which is attributed to the lower GWP of the refrigerant, and 7.4% less indirect emissions due to increased system efficiency. The direct emissions of the transcritical CO_2 booster system and the self-contained R-290 system were found to be negligible due to the very low GWP of R-744 and R-290. However, the indirect emissions of the transcritical CO_2 booster system and the self-contained R-290 system were found to be approximately 5% to 6% higher on average than the baseline R-404A DX system due to their higher energy consumption. Nevertheless, all three refrigeration system designs/refrigerant options (R-448A DX, transcritical R-744, and self-contained R-290) produced lower total carbon dioxide equivalent emissions than the baseline R-404A DX system.

It was found that the sources of the electric power generation greatly influenced the total carbon dioxide equivalent emissions of the refrigeration systems. In regions where the electricity is generated primarily from fossil fuel fired power plants, the total carbon dioxide emissions are the greatest and the centralized R-448A DX system provided the lowest total carbon dioxide equivalent emissions for these regions. However, for regions with higher renewable energy sources and less fossil fuel fired power plants, the total carbon dioxide emissions are the lowest and the transcritical CO_2 booster system and the self-contained R-290 systems provided the lowest total carbon dioxide equivalent emissions in these regions.

NOMENCLATURE

AEC	Annual energy consumption (kWh)	L	Refrigeration system lifetime (yr)
ALR	Annual refrigerant leak rate (% total charge)	LCCP	Life cycle climate performance (kg CO_{2e})
C	Refrigerant charge (kg)	m	Mass of refrigeration system (kg)
E_{dir}	Direct emissions (kg CO_{2e})	MM	Emissions for material production (kg CO_{2e}·kg^{-1})
E_{indir}	Indirect emissions (kg CO_{2e})	mr	Mass of recycled material (kg)
EM	Emissions due to energy production (kg CO_{2e})	RFD	Refrigerant disposal emissions (kg CO_{2e}·kg^{-1})
EOL	End-of-life refrigerant leakage (% total charge)	RFM	Refrigerant manufacturing emissions (kg CO_{2e}·kg^{-1})
GWP	Global warming potential (kg CO_{2e}·kg^{-1})	RM	Emissions for recycled material production (kg CO_{2e}·kg^{-1})
GWP_{adp}	GWP of atmospheric degradation products (kg CO_{2e}·kg^{-1})		

REFERENCES

Deru, M., Torcellini, P., 2007. Source Energy and Emission Factors for Energy Use in Buildings. Technical Report NREL/TP-550-38617, National Renewable Energy Laboratory, Golden, Colorado.

Deru, M., Field, K., Studer, D., Benne, K., Griffith, B., Torcellini, P., Liu, B., Halverson, M., Winiarski, D., Rosenberg, M., Yazdanian, M., Huang, J., Crawley, D., 2011. U.S. Department of Energy Commercial Reference Building Models of the National Building Stock. National Renewable Energy Laboratory, Golden Colorado.

EIA, 2016. Country Analysis Brief: India. U.S. Energy Information Administration (EIA), Washington, D.C.

EIA, 2017a. Country Analysis Brief: Brazil. U.S. Energy Information Administration (EIA), Washington, D.C.

EIA, 2017b. Country Analysis Brief: Saudi Arabia. U.S. Energy Information Administration (EIA), Washington, D.C.

EIA, 2018. Country Analysis Brief: Egypt. U.S. Energy Information Administration (EIA), Washington, D.C.

EPA, 2012. Progress Report 2011 - GreenChill, a Partnership at Work, U.S. Environmental Protection Agency, Washington, D.C. (http://www.epa.gov/greenchill/downloads/ GreenChill_ProgressReport2011_2012-09-24.pdf)

Ge, Y.T., Tassou, S.A., 2011. Performance Evaluation and Optimal Design of Supermarket Refrigeration Systems with Supermarket Model “SuperSim”, Part II: Model Applications. International Journal of Refrigeration 34(2), 540-549.

IIR, 2016. Guidelines for Life Cycle Climate Performance. International Institute of Refrigeration (IIR), Paris, France.

UNEP, 2010. Alternatives to HCFCs in the Refrigeration and Air-conditioning Sector: Practical Guidelines and Case Studies for Equipment Retrofit and Replacement. United Nations Environment Programme, Division of Technology, Industry and Economics, Paris, France.

UNEP, 2010. Barriers to the use of Low-GWP Refrigerants in Developing Countries and Opportunities to Overcome These. United Nations Environment Programme, Division of Technology, Industry and Economics (UNEP DTIE), Paris, France.

Manuscript ID: 1669
DOI: 10.18462/iir.icr.2019.1669

Adsorption dynamics of MOF coatings for waste heat driven cooling

Eric LAURENZ[(a)], Andreas VELTE[(a)], Harry KUMMER[(a)], Gerrit FÜLDNER[(a)], Lena SCHNABEL[(a)]

[(a)] Fraunhofer Institute for Solar Energy Systems ISE
79110 Freiburg, Germany, eric.laurenz@ise.fraunhofer.de

ABSTRACT

Adsorption chillers are a promising option for environmentally friendly data centre cooling allowing for high energy efficiency. Waste heat from liquid cooled CPUs (~60 °C) drives the cooling for auxiliary loads (~20 °C) with heat rejection around 30 °C. Adsorption properties of the metal-organic frame work (MOF) aluminium fumarate largely outperform the state-of-the-art material silica gel at these temperatures. With adsorbent coatings, volume and mass specific cooling power may be increased to reduce specific costs.
Samples were prepare with a binder-based aluminium fumarate coating in three different thicknesses (140–610 µm) and measured for adsorption dynamics with large-temperature-jump-experiments. Uptake-times (15-85%) are in the range of 9–78 s. On a full scale heat exchanger expected volume and adsorbent mass specific cooling powers are 200–700 W l^{-1} and 1.3–14 kW kg^{-1} – an increase to state-of-the-art of 3–10 times and >10 times at reasonable cooling COPs of 0.47–0.57.
Keywords: Adsorption Cooling, Data Centre Cooling, Energy Efficiency, Metal Organic Frameworks, Aluminium Fumarate, Adsorbent Coating.

1. INTRODUCTION

Adsorption chillers are an environmentally friendly solution for the valorisation of waste heat for cooling demands. The working principle allows a simple, robust and scalable design. Adsorption chillers and heat pumps have been applied successfully for different applications like solar thermal cooling of buildings (Meunier, 2013) or gas adsorption heat pumps (Metcalf et al., 2012). A possible application that has attracted rising interest in recent years is the provision of data centre cooling driven by heat yielded from water cooled CPUs. Current high performance CPUs allow cooling water temperatures of up to 60 °C or more (Wilde et al., 2017; Zimmermann et al., 2012) that can be used to drive adsorption chillers.
An adsorption chiller (Figure 1) consists of two adsorption heat exchangers, a condenser and an evaporator in a pure working fluid atmosphere. If temperatures below 0 °C can be excluded, usually water is used as working fluid due to its high evaporation enthalpy. The adsorption heat exchangers (Ad-HX) have a heat transfer fluid on the primary and a stationary adsorbent material or composite on the secondary side. The process is cyclic: In the first half-cycle the CPU's waste heat is used to regenerate the first Ad-HX. The desorbed working fluid is condensed in the condenser which is cooled to the ambient at e.g. 30 °C. In the second half-cycle working fluid is adsorbed on the Ad-HX which is again cooled to the ambient. The resulting pressure drop induces the evaporation in the evaporator at about 20 °C. For continuous provision of cold, two Ad-HXs are operated alternately.

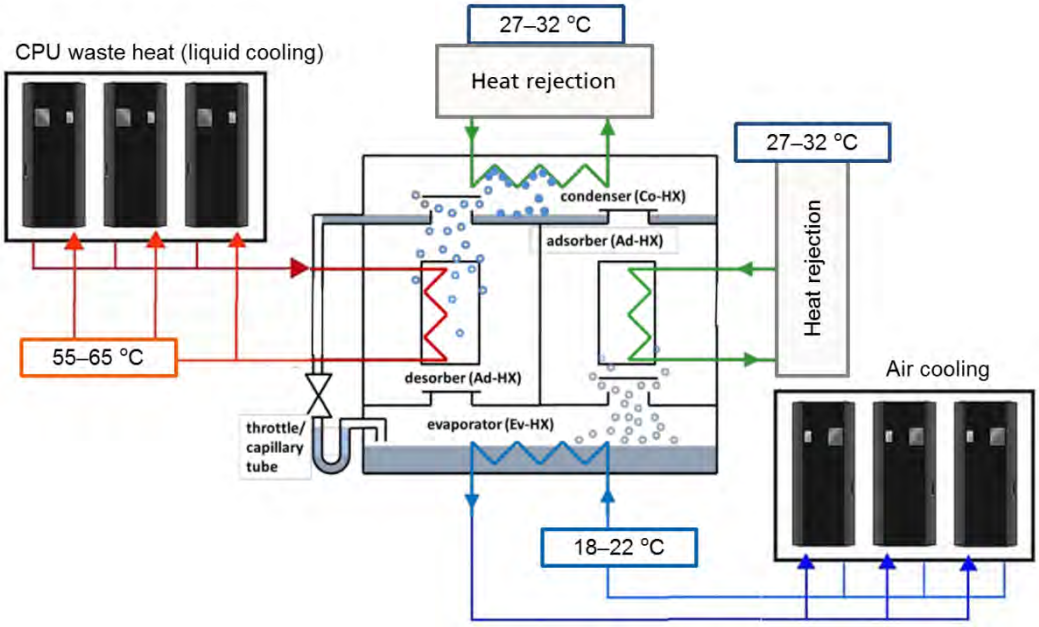

Figure 1: Working principle of an adsorption chiller for data centre cooling.

Aluminium fumarate, a metal-organic framework (MOF) that attracted increasing interest for thermal applications in recent years, exhibits adsorption equilibrium properties that fit well to the boundary conditions of this cycle. Compared to the state of the art material silica gel it allows considerably more efficient cycles with a good hydrothermal cycle stability (Jeremias et al., 2014; Kummer et al., 2017). The material is potentially a low cost material due to widely available educts (Al-salts and fumaric acid) and water based synthesis route (Kiener et al.).

The increase of volume specific cooling power (VSCP) – thus reduction of specific costs – while keeping a reasonably high COP is one of the major development challenges for adsorption chillers (Schnabel et al., 2018). Typical values for COPs of market available adsorption chillers are in the order of 0.5 to 0.65 (ASUE, 2017). In the case of data centre cooling the target COP is determined by the ratio of low temperature cooling demand and available waste heat from CPUs which typically is in the same range (Wilde et al., 2017). A promising approach to increase VSCP is to use binder based adsorbent coatings to allow for a substantially better heat transfer to the heat exchanger structure in comparison to loose grain bed, the state of the art solution (Freni et al., 2015).

The aim of this study is to evaluate the potential of binder based aluminium fumarate coatings in adsorption chillers for data centre cooling. Based on a variation of the coating thickness particular attention will be paid to the effect of this key design parameter.

2. MATERIAL

The aqueous dispersion (26.8 wt% aluminium fumarate Basolite® A520, BASF; 17.9 wt% SilRes® MP50E, Wacker Silicones) was processed by a knive coating applicator on 50x50x2 mm AlMg3 sample plates. The wet film thickness was varied by an octagonal stainless steel mask with a defined thickness (200, 350, 600 µm) and constant coating surface A_{ct} (18.7 cm^2). Samples were oven dried at 200 °C for 3 h before measuring coating thicknesses d_{ct} of final samples (Table 1, Figure 2) at five points with a probe indicator. Total dry adsorbent content $w_{\mathrm{s,dry}}$ and sample adsorbent dry mass m_{s} were calculated based on experimentally determined dry mass of dispersion components and final samples, as shown by Kummer et al. (2015).

Table 1: Sample properties

Sample	m_s (mg)	d_{ct} (µm)	$w_{s,dry}$ (-)
Ct_140	100	140±40	0.749
Ct_240	163	240±50	0.749
Ct_610	422	610±70	0.749



Figure 2: Sample with 610 µm coating

3. EXPERIMENTAL

The measurement set-up for the experiments carried out is described in detail in recent publications by Sapienza et al. (2017) and Velte et al. (2017). It consists mainly of two vacuum chambers with pressure sensors (MKS Baratron 627B), an infrared temperature sensor (Heitronics KT15.82 IIP) for sample surface temperature, and three Pt-100 temperature sensors to measure the vapour temperature in the dosage chamber and the carrier plate temperature, respectively. The samples are placed on the carrier plate with thermal grease (TG20032) for a good thermal contact. Two independent thermostats are operated in parallel and each of them can be coupled to the carrier plate via the hydraulic circuit. The switching between the two thermostats is very fast (switching time < 0.5 s) due to pneumatically actuated valves. For the large temperature jump (LTJ) experiments the sample is heated up while the measurement chamber is connected to the vacuum pump. After this pre-conditioning dosage chamber and measurement chamber are filled with water vapour at a certain pressure. After reaching equilibrium, the thermostats are switched. The sample starts to ad- or desorb water vapour to reach the new equilibrium. The mass of water vapour that is ad- or desorbed can be calculated by applying the law of the ideal gas to the closed system (volumetric measurement).
LTJ experiments from 45 to 35 °C and from 50 to 30 °C were performed (carrier plate temperatures). Given a driving temperature difference of 5 K, this simulates boundary conditions of about 60 °C for driving heat and 30 or 25 °C respectively for heat rejection. The earlier is easier met in actual application while the latter is expected to allow for better performance. To keep the average pressure at about 23.4 mbar (i.e. 20 °C evaporator temperature) for all measurements, the initial pressure in measurement chamber and dosage chamber was slightly lower for larger samples than for smaller samples.

4. RESULTS

In this section we first report the large temperature jump experiment results followed by an extrapolation to the performance of a full adsorber heat exchanger.

4.1. Large Temperature Jump

The temperature jump experiments show fast adsorption kinetics of all samples with the larger temperature jumps (50 → 30 °C) slightly faster than the smaller jumps (45 → 35 °C). As expected the adsorption time increases with coating thickness. The uptake over time (Figure 3) shows the exponential form typical for adsorption kinetic experiments (Velte et al., 2017). The significantly delayed surface temperature response indicates heat transfer to be among the rate limiting steps, especially for thicker coatings.

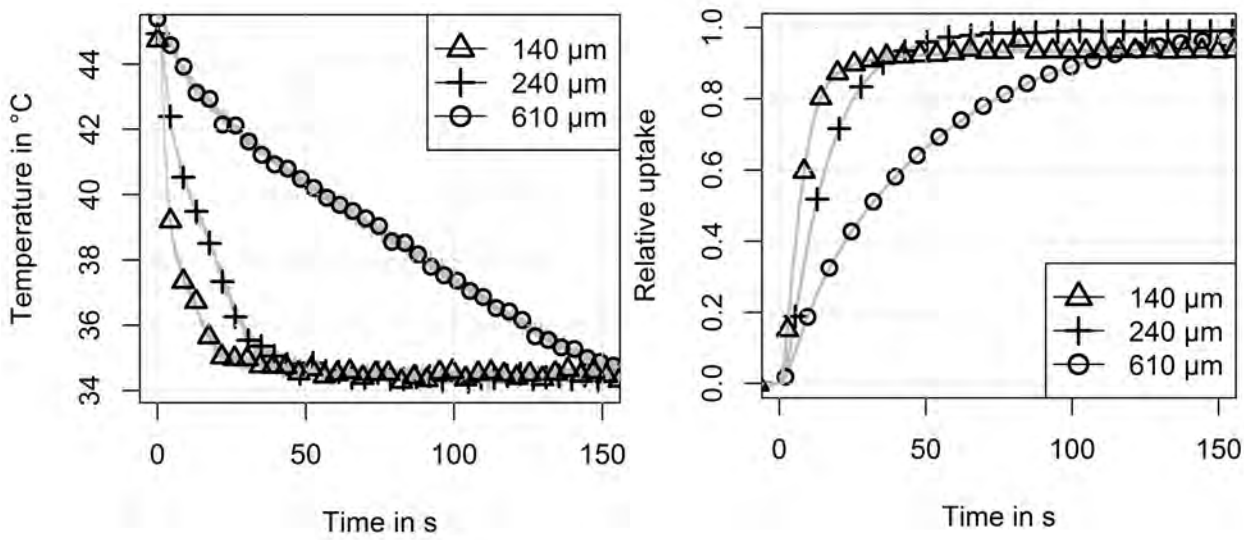

Figure 3: Surface temperature (left) and relative uptake (right, determined volumetrically) over time after rapid jump (τ < 1 s) of the carrier plate temperature for different coating thicknesses. Here the data for the jump from 45 to 35 °C is shown.

The absolute uptake (Figure 4) does not change much with the jump temperature boundary conditions. This can be explained by the form of the isotherm with a step at about p_{rel} = 0.3 (Splith et al., 2018): Both, the small and the large jump cover this step as shown by the step initial and end state in Table 2. The relative uptake shows a good comparability between the different samples. The remaining differences are due to slight deviations in experimental conditions and small errors of dry mass determination.

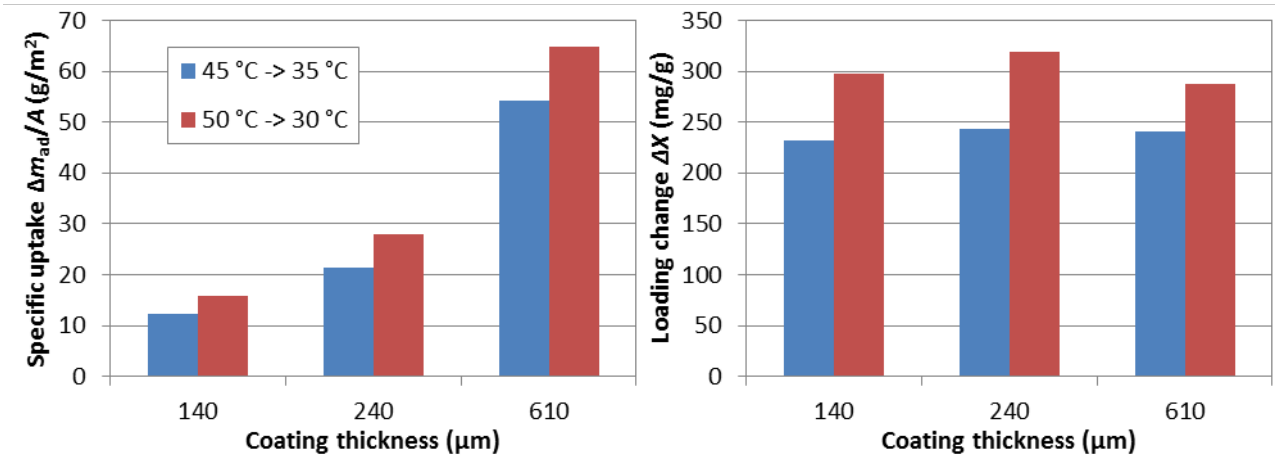

Figure 4: Area specific uptake and loading spread for different coating thicknesses and measurement conditions.

Table 2: Initial (0), final (∞) and integral results of LTJ experiments for differently coated samples

d_{ct} (µm)	$T_0 \rightarrow T_\infty$ (°C)	$p_0 \rightarrow p_\infty$ (mbar)	$p_{rel,0} \rightarrow p_{rel,\infty}$	Δm_{ad} (mg)	ΔX (mg/g)	Δt_{15-85} (s)
140	44.9 → 34.8	24.1 → 23.3	0.25 → 0.42	23.2	232	11
140	49.8 → 30.0	24.1 → 23.1	0.20 → 0.54	29.8	298	9.3
240	44.9 → 34.9	24.4 → 23.0	0.26 → 0.41	39.8	244	24
240	49.8 → 30.0	24.4 → 22.6	0.20 → 0.53	52.1	320	20
610	45.5 → 34.9	24.3 → 20.8	0.25 → 0.37	102	241	78
610	49.8 → 30.0	24.4 → 20.2	0.20 → 0.48	121	288	57

For further evaluation the 15-85% uptake time constant Δt_{15-85} is evaluated in Figure 5, being the range of 9 to 57 s and 11 to 78 s for the larger and the smaller jumps. The faster kinetics of the larger jump is again a result of the step like isotherm. For experiment's pressure level (23.4 mbar) the equilibrium temperature at the step position is of about 40 °C. This results in higher driving temperature differences for the larger jumps.
To what extent heat or mass transfer resistances govern the overall kinetics and whether this mass transfer is macropore diffusion in the coating or micropore diffusion in the adsorbent particle may not be answered from these results straight away. As discussed above, a tendency towards heat transfer limitations can be seen. However, for further targeted improvements this information would be highly valuable.

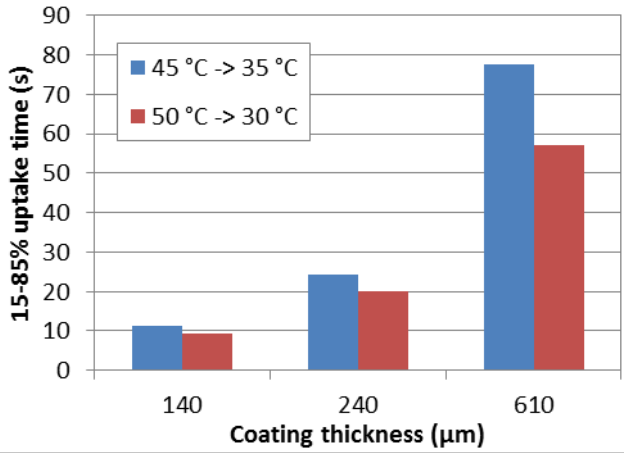

Figure 5: Duration between 15% and 85% uptake for different coating thicknesses and operation conditions as basis for all power and efficiency estimations.

4.2. Extrapolation to Full Scale Adsorption Heat Exchanger

To judge the application relevance of results from small scale kinetic experimental they need to be extrapolated to the performance of a full scale heat exchanger (Wittstadt, 2018). In the following this will be done based on a simple adsorption cooling cycle with passive heat recovery (delayed valve switching (Wang et al., 2005)) for a fin-and-tube heat exchanger as described in detail by Wittstadt (2018, p. 141). Tubes (copper, Ø9.5×0.3 mm) have a spacing of 25×21.6 mm, fins (aluminium, 0.2 mm thickness) are arranged in spacing allowing for 2 mm free vapour channels. Headers and tube bends outside the fin package are assumed to occupy 20% of the total HX volume and to account for additional 25% of the tube's thermal mass. We assume the resistance from heat transfer in the tubes and fins as well as from the vapour flow to be negligible. Thus, the expected average evaporator heat flux (per coated area) for a single Ad-HX:

$$\dot{q}_{\mathrm{evp}} = \frac{q_{\mathrm{evp}}}{\Delta t_{\mathrm{cyc}}} = \frac{-(0.85-0.15)\Delta m_{\mathrm{ad}}}{A_{\mathrm{ct}} 2\Delta t_{15-85}} \left(\Delta h_{\mathrm{v}}(T_{\mathrm{evp}}) - c_{\mathrm{w}}(T_{\mathrm{cnd}} - T_{\mathrm{evp}})\right) \quad \text{Eq. (1)}$$

can be directly deduced from the measurement results and material properties of water (Wagner et al., 2000) under the assumption that the total cycle time Δt_{cyc} is twice Δt_{15-85}. With the above mentioned geometry the volume specific cooling power can be derived straightforwardly:

$$\mathrm{VSCP} = \dot{q}_{\mathrm{evp}} \frac{A_{\mathrm{ct}}}{V_{\mathrm{HX}}}. \quad \text{Eq. (2)}$$

Similarly, the COP for an adsorption cooling cycle is:

$$\mathrm{COP} = \frac{-q_{\mathrm{evp}}}{(0.85-0.15)\Delta m_{\mathrm{ad}}/A_{\mathrm{ct}}\Delta h_{\mathrm{s}} + c_{\mathrm{A,HX}}(T_{\mathrm{des}} - T_{\mathrm{ads}})} \quad \text{Eq. (3)}$$

Where the specific heat capacity (per coated area) of the Ad-HX is $c_{A,HX}$ derived from the geometry and material properties of the heat exchanger metals ($(\rho c_p)_{Al}$ = 2.43 MJ m^{-3}K^{-1}, $(\rho c_p)_{Cu}$ = 3.42 MJ m^{-3}K^{-1}) and the adsorbent coating (ρ = 400 kg m^{-3}, c_p = 2.27 kJ kg^{-1}K^{-1}). The adsorption enthalpy is approximated following Dubinin and Astakhov (1971) for the steepest position in the isotherm (Δh_s = 2.51 MJ kg^{-1}).
The expected VSCP of a supposed coated Ad-HX is in the order of 200 to 700 W l^{-1} for the different coatings and temperature conditions (Figure 6). With respect to the cost relevant aluminium fumarate input the expected adsorbent mass specific cooling power (MSCP) ranges between 1.3 and 14 kW kg^{-1}. The dependency on coating thickness and temperature conditions reflects mainly the results for uptake time and total uptake (Table 2) damped by the decreased volume usage of the thin samples (less sorption material per HX volume).
Measurements with state of the art silica gel loose grains (single layer) as described by Aristov et al. (2012) at conditions comparable to the larger jump (LTJ 48 → 30 °C, evaporator temperature: 20 °C) results in expected values of 70 W l^{-1} and 0.11 kW kg^{-1} for VSCP and MSCP. This underlines the high performance of the aluminium fumarate coating for data centre cooling applications. With the same material Kummer et al. (2017) reported values of 100 W l^{-1} and 1.4 kW kg^{-1} indicating the potentially high performance increase from coating and heat exchanger optimization.

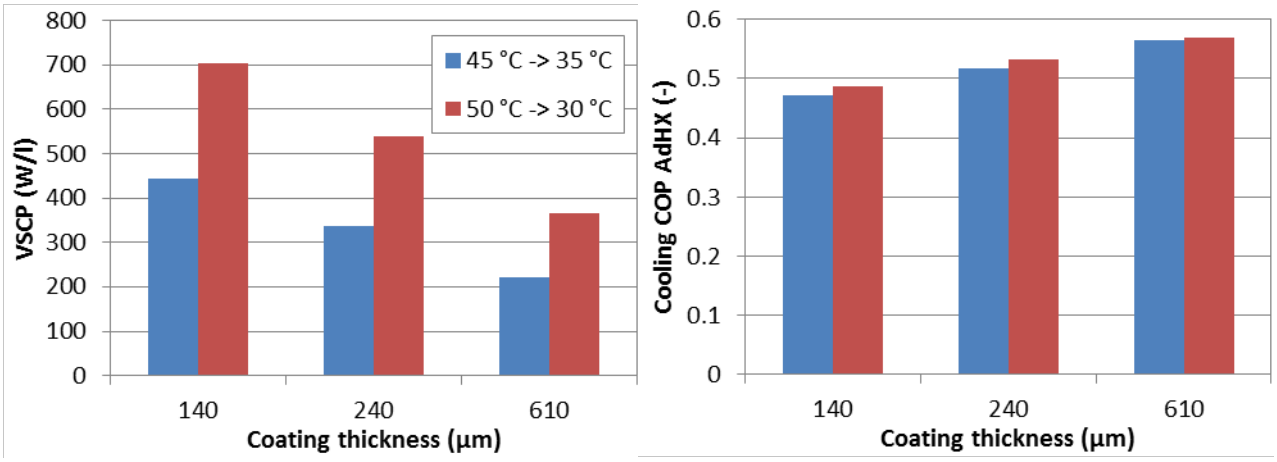

Figure 6: Expected volume specific cooling power and COP with respect to adsorber heat exchanger volume and thermal mass for different coating thicknesses and operation conditions with 20 °C evaporation temperature under assumption given in the text.

The expected COP is between 0.47 and 0.57 – the required order for data centre cooling (Wilde et al., 2017). As expected (Schnabel et al., 2018) thicker coatings are more preferable in terms of efficiency due to a better mass ratio between sorption material and heat exchanger metal. For the temperature conditions, the difference vanishes. The positive effect of higher uptakes is compensated by larger temperature differences between de- and adsorption (25 and 30 K for small and the large temperature lift, respectively) which increases the amount of heat required for sensible heating.
It should be noted that the assumption are rather conservative. In practise thinner fins with narrower vapour channels might prove to be preferable as the increased transport resistance could be balanced out by the gains in volume and thermal mass. However, for this kind of targeted design and optimization a more detailed understanding and modelling of the underlying heat and mass transfer resistances is necessary in order to avoid costly and time consuming parameter variations on prototype level.

5. CONCLUSIONS

In this study we evaluated the potential of a novel adsorbent coating for waste heat valorisation in data centre applications. The metal organic framework aluminium fumarate could be applied in stable coating from a water based suspension in different layer thicknesses between 140 and 610 µm. The results from large temperature jump experiments under two different temperature boundary conditions showed time constants (15-85% uptake) of 9 to 78 s for different coating

thicknesses. Extrapolation to full scale heat exchanger reveals a high potential for application with adsorber volume specific cooling power between 200 and 700 W l^{-1} and adsorbent mass specific cooling power between 1.3 and 13 kW kg^{-1}. Compared to state of the art silica gel loose grain configurations this means an increase of about 3 to 10 times for volume and more than 10 times for mass specific cooling power at reasonable COPs.
From a qualitative assessment of surface temperature and uptake over time there is evidence that heat transfer in the coating becomes more relevant for thicker layers. For further optimisation a more detailed quantitative understanding of the underlying heat and mass transfer limitation appears necessary.

ACKNOWLEDGEMENTS

Funding of the project HARVEST from Fraunhofer-Zukunftsstiftung and the PhD scholarship for Eric Laurenz from Heinrich-Böll-Stiftung is gratefully acknowledged. The authors thank Raffael Wolff for practical support in preparation and characterisation of the samples.

NOMENCLATURE

A_{ct}	coated area (m^2)	$\dot{q}$	heat flux ($W \times m^{-2}$)
c_{A}	heat capacity per coated area ($J \times m^{-2} \times K^{-1}$)	t	time (s)
d_{ct}	coating thickness (µm)	T	temperature (°C)
m_{ad}	adsorbed mass (kg)	V	volume (m^3)
p	pressure (kPa)	V_{HX}	heat exchanger volume
p_{rel}	relative pressure (-)	X	loading ($kg_{ad} \times kg_{dry}^{-1}$)
q	amount of heat per cycle per coated area ($J \times m^{-2}$)		

Ad-HX	adsorber heat exchanger	MSCP	adsorbent mass specific cooling power ($W \times kg_{dry}^{-1}$)
COP	coefficient of performance (-)	VSCP	volume specific cooling power ($W \times l^{-1}$)
MOF	metal-organic framework		

REFERENCES

Arbeitsgemeinschaft für sparsamen und umweltfreundlichen Energieverbrauch e. V., 2017. Marktübersicht Gaswärmepumpen 2017/18. https://asue.de/sites/default/files/asue/themen/gaswaermepumpe_kaelte/2017/broschueren/ASUE_Marktuebersicht-Gaswaermepumpen_2017.pdf. Accessed 6 February 2019.

Aristov, Y.I., Glaznev, I.S., Girnik, I.S., 2012. Optimization of adsorption dynamics in adsorptive chillers: Loose grains configuration. Energy 46, 484–492. 10.1016/j.energy.2012.08.001.

Dubinin, M.M., Astakhov, V.A., 1971. Description of Adsorption Equilibria of Vapors on Zeolites over Wide Ranges of Temperature and Pressure, in: Flanigen, E.M., Sand, L.B. (Eds.), Molecular sieve zeolites. 2. International conference on molecular sieves 2, vol. 102. American Chemical Society, Washington, D.C., pp. 69–85.

Freni, A., Dawoud, B., Bonaccorsi, L., Chmielewski, S., Frazzica, A., Calabrese, L., Restuccia, G., 2015. Adsorption Heat Exchangers, in: Freni, A. (Ed.), Characterization of zeolite-based coatings for adsorption heat pumps. Springer, Cham, pp. 35–53.

Jeremias, F., Fröhlich, D., Janiak, C., Henninger, S.K., 2014. Advancement of sorption-based heat transformation by a metal coating of highly-stable, hydrophilic aluminium fumarate MOF. RSC Adv. 4, 24073. 10.1039/C4RA03794D.

Kiener, C., Müller, U., Schubert, M. Organometallic Aluminum Fumerate Backbone Material.

Kummer, H., Füldner, G., Henninger, S.K., 2015. Versatile siloxane based adsorbent coatings for fast water adsorption processes in thermally driven chillers and heat pumps. Appl. Therm. Eng. 85, 1–8. 10.1016/j.applthermaleng.2015.03.042.

Kummer, H., Jeremias, F., Warlo, A., Füldner, G., Fröhlich, D., Janiak, C., Gläser, R., Henninger, S.K., 2017. A Functional Full-Scale Heat Exchanger Coated with Aluminum Fumarate Metal–

Organic Framework for Adsorption Heat Transformation. Ind. Eng. Chem. Res. 56, 8393–8398. 10.1021/acs.iecr.7b00106.
Metcalf, S.J., Critoph, R.E., Tamainot-Telto, Z., 2012. Optimal cycle selection in carbon-ammonia adsorption cycles. International Journal of Refrigeration 35, 571–580. 10.1016/j.ijrefrig.2011.11.006.
Meunier, F., 2013. Adsorption heat powered heat pumps. Appl. Therm. Eng. 61, 830–836. 10.1016/j.applthermaleng.2013.04.050.
Sapienza, A., Velte, A., Girnik, I., Frazzica, A., Füldner, G., Schnabel, L., Aristov, Y., 2017. "Water - Silica Siogel" working pair for adsorption chillers: Adsorption equilibrium and dynamics. Renewable Energy, 40–46. 10.1016/j.renene.2016.09.065.
Schnabel, L., Füldner, G., Velte, A., Laurenz, E., Bendix, P., Kummer, H., Wittstadt, U., 2018. Innovative Adsorbent Heat Exchangers: Design and Evaluation, in: Bart, H.-J., Scholl, S. (Eds.), Innovative Heat Exchangers. Springer International Publishing, Cham, pp. 363–394.
Splith, T., Fröhlich, D., Henninger, S.K., Stallmach, F., 2018. Development and application of an exchange model for anisotropic water diffusion in the microporous MOF aluminum fumarate. Journal of magnetic resonance 291, 40–46. 10.1016/j.jmr.2018.04.009.
Velte, A., Füldner, G., Laurenz, E., Schnabel, L., 2017. Advanced Measurement and Simulation Procedure for the Identification of Heat and Mass Transfer Parameters in Dynamic Adsorption Experiments. Energies 10, 1130. 10.3390/en10081130.
Wagner, W., Cooper, J.R., Dittmann, A., Kijima, J., Kretzschmar, H.-J., Kruse, A., Mareš, R., Oguchi, K., Sato, H., Stöcker, I., Šifner, O., Takaishi, Y., Tanishita, I., Trübenbach, J., Willkommen, T., 2000. The IAPWS Industrial Formulation 1997 for the Thermodynamic Properties of Water and Steam. Journal of Engineering for Gas Turbines and Power 122, 150. 10.1115/1.483186.
Wang, X., Chua, H.T., Ng, K.C., 2005. Experimental investigation of silica gel–water adsorption chillers with and without a passive heat recovery scheme. International Journal of Refrigeration 28, 756–765. 10.1016/j.ijrefrig.2004.11.011.
Wilde, T., Ott, M., Auweter, A., Meijer, I., Ruch, P., Hilger, M., Kuhnert, S., Huber, H., 2017. CooLMUC-2: A supercomputing cluster with heat recovery for adsorption cooling, in: Thirty-third Annual Semiconductor Thermal Measurement and Management Symposium. Proceedings 2017, San Jose, CA, USA, March 13-17, 2017. 2017 33rd Thermal Measurement, Modeling & Management Symposium (SEMI-THERM), San Jose, CA, USA. IEEE, Piscataway, NJ, U.S.A., pp. 115–121.
Wittstadt, U., 2018. Experimentelle und modellgestützte Charakterisierung von Adsorptionswärmeübertragern. Dissertation. Technische Universität Berlin, Berlin.
Zimmermann, S., Meijer, I., Tiwari, M.K., Paredes, S., Michel, B., Poulikakos, D., 2012. Aquasar: A hot water cooled data center with direct energy reuse. Energy 43, 237–245. 10.1016/j.energy.2012.04.037.

Manuscript ID: 1698
DOI: 10.18462/iir.icr.2019.1698

Replacement of R-404A refrigerant in supermarkets

Olivier CALMELS[(a)], Thomas MICHINEAU[(a)], Thomas SUQUET[(a)]

[(a)]Cemafroid
Fresnes, 94260, France, Olivier.calmels@cemafroid.fr

ABSTRACT

F-Gas regulation imposes a gradual reduction of greenhouse gases emissions, among which fluorinated refrigerants with high global warming potential (GWP).The most used refrigerant in commercial refrigeration, the R-404A, will be banned from 2021. Users shall consider the replacement of this refrigerant. This paper presents a study for the replacement of R-404A by R-442A in a supermarket low temperature refrigeration unit. A two weeks registration campaign was conducted. One week before replacement (R-404A utilization) and one week after (R-442A utilization). The instrumentation of the refrigerated display cabinets and the refrigeration units by temperature sensors and electric analyser allows measuring the refrigeration consumption in the supermarket. Consumptions obtained using the R-404A are compared to the ones obtained using the R-442A.Results show a good conservation of the performance of the installation and a decrease in operating time and power consumption of around 5% with the R-442A.
Keywords: Refrigeration, R-404A, R-442A, Retrofit, COP, Energy Efficiency.

1. INTRODUCTION

Since 2015, the HCFC emissions are almost zero in Europe (Graziosi et al, 2015), so the next big step is the decrease of HFC's global warming effect. This is goal of the entry into force of the European Regulation N°517/2004 on January 1st 2015 ("F-Gas"). New refrigerants appear for each refrigeration application, some of them are mixtures created to replace the existing refrigerant directly, with only few adaptations of the refrigeration systems. The physical characteristics of these refrigerants, like the pressure-temperature relationship or the low pressure density, impact the operating parameters. Thus, the efficiency of the system and the energy consumption can be reduced or increased depending on the nature of the replacement refrigerant and the operating conditions of the system.

Supermarket refrigeration systems have the highest leakage rates among the different refrigeration applications. The main leaks are related to problems of joints and valves (Francis et al, 2017). A test campaign was conducted to compare the operation of a commercial refrigeration system with R-404A and then with R-442A under the "drop-in" conditions. A drop-in is the procedure when replacing a refrigerant with another one, generally less harmful for the environment, in refrigeration plants of any kind, without any important modifications. (IIR, 2019) (like expansion valve adjustment).

2. CONTEXT, PROGRESS AND RESULTS OF THE STUDY

2.1. Theoretical Impact of Refrigerant Replacement

All replacement refrigerants are mixtures. This induces:

- A link between physical characteristics and refrigerant composition.
- The respect of special precautions for refrigerant transfer and monitoring.

Fig. 1 contains the principal substitution refrigerants (for R-404A), their security class (according to EN NF 378) and their composition. It appears that each substitution refrigerant contains R-32 refrigerant. This component induces high discharge temperatures.

Refrigerant	Family	Class	Composition							
			R1234yf	R1234ze	R125	R134a	R143a	R152A	R227ea	R32
R404A	HFC	A1			44%	4%	52%			0%
R407A	HFC	A1			40%	40%				20%
R407C	HFC	A1			25%	52%				23%
R407F	HFC	A1			30%	40%				30%
R442a	HFC	A1			31%	30%		3%	5%	31%
R448A	HFC (with HFO)	A1	20%	7%	26%	21%				26%
R449A	HFC (with HFO)	A1	25%		25%	26%				24%
R452A	HFC (with HFO)	A1	30%		59%	0%				11%

Figure 1. Mixtures compositions

2.1.1. Glide

All the mixtures proposed to replace R-404A are zeotropic. The components of these mixtures have different volatilities. So, under constant pressure, the liquid-vapor phase change of a zeotrope is made at non-constant temperature and composition.

Refrigerant	P	Tsat liq	Tsat vap	Glide	Zeotropic / azeotropic	GWP
	[bar]	[°C]	[°C]	K		
R404A	4,3	-10,6	-10	0,6	Quasi-azeotropic	3922
R407A	3,5	-15,9	-10	5,9	Zeotropic	2107
R407C	3,2	-16,5	-10	6,5		1770
R407F	3,6	-15,9	-10	5,9		1824
R442A	3,6	-16,2	-10	6,2		1273
R448A	3,6	-15,9	-10	5,9		1387
R449A	3,6	-15,4	-10	5,4		1397
R452A	4,0	-13,9	-10	3,9		2141

Figure 2. Mixtures glide

As you can see in Fig. 2, the glide varies between 3.9°C and 6.5°C (with a -10°C vapor saturated temperature). This important glide requires liquid phases transfers to maintain good proportions of each component in the mixture. In the same way, the composition can be distorted in case of leakage on vapor side. In the F-gas, and in Fig. 2, all GWP values come from the IPCC Fourth assessment report (IPCC, 2007).

2.1.2. Energetic performances

We define the following hypothesis to compare refrigerants with each other theoretically:

- Evaporation temperature at -10 ° C (corresponding to the vapor saturation temperature at low pressure, evaporator outlet)
- Overheating at suction of 10 K
- All overheating is useful
- Condensation temperature of 45 K (corresponding to the saturation temperature of the liquid at high pressure, condenser outlet)
- Under cooling of 3 K
- No loss of charges
- Isentropic compression
- Calculations made with RefProp / Excel
- R-404A values are taken for reference (=100%).

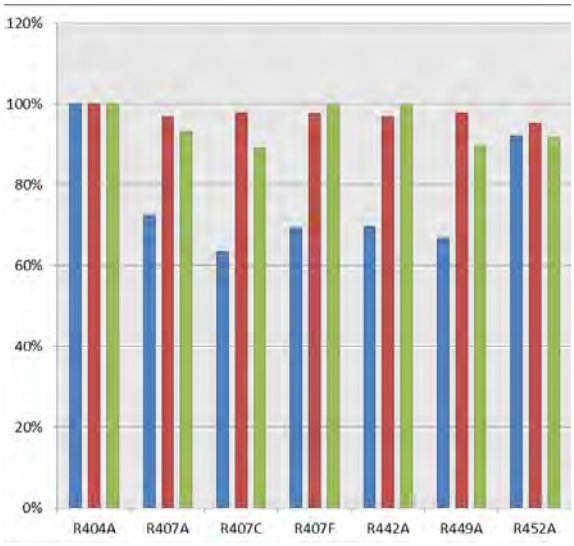

Figure 3. Comparative results. Blue: density in suction line. Red: COP. Green: cooling power.

It can be seen from Fig. 3 that R407F and R-442A offer cooling capacities close to those of R404A. The R407a, R407C, R449A and R452A induce a power loss of almost 10%. These figures are the results of theoretical calculations, not taking into account the pressure drop, the presence of oil in the exchangers, or the transient stop and start phases of systems when they regulate.

2.2. Test Campaign

2.2.1. Refrigeration systems

The installation studied is a commercial positive temperature system located in the south of France (near Toulouse). The refrigeration production is centralised in an engine room and composed by 4 piston compressors. Each compressor is equipped with an oil separator.
The production feeds 59 frigorific cabinets and 18 cold rooms.
All the refrigeration utilities are supplied by electronics expansion valves.
The production and the utilization are both controlled by a centralised system which allows changing set points and controlling the production.
The system is equipped with floating high pressure regulation, but this is not activated during the tests period.
The condensers are outside, on the roof above the engine room.

2.2.2. Instrumentation

The purpose of the instrumentation is to check the correct operation of the installation (good temperatures in the utilities) and to measure its performance. Thus, temperature recorders are placed in the refrigerated cabinets, in cold rooms and at different points of refrigeration production.
The recorders installed on the pipes in the engine room are put in direct contact with the piping, then fixed with metal tape and insulated with refrigerant insulation. This method allows to measure the refrigerant's temperature. The discharge pipes are instrumented because their temperature variations will indicate stops and starts of the compressors.
Each temperature recorder measuring an air temperature in a refrigerating cabinet or a cold room is inserted in a perforated box (to protect it from shocks and limit the exchanges by radiation and conduction) while leaving the air circulate. Each temperature is recorded by a 2 minutes period.
An electric network analyser is connected to the refrigeration production's power supply. It calculates and records the instantaneous active power.

2.2.3. Test campaign steps

The campaign started at the end of August by the instrumentation of refrigeration installation, when the refrigerant used is yet R-404A. The sensors recorded for one week then R-404A was replaced by R-442A. The recording lasted one more week before sensors were removed.

Every day of the week does not lead to the same consumption. In particular, Sunday is the only day with a closing time at 1PM. Therefore it's a day when the refrigerant cabinets are closed and the lights off for longer than the other days. The result is lower daily energy consumption than other days. The two periods selected for this study:

- cover the same duration: 4 full days each (24h)
- same hours: midnight to midnight
- with a Sunday included: 03/09 and 10/09
- with 3 days other than Sunday
- The difference between mean temperature of first and second week is 0.4°C.

2.3. Results Analysis

2.3.1. Cold rooms and frigorific cabinets temperatures

The 4 days before drop-in (first testing period) and the 4 days after it (second testing period) are nearly equivalent following internal cold-rooms and cabinet temperatures. More of that, all temperature ranges are similar regardless of the testing period. For example, the average temperature of the bakery cold room and deli frigorific cabinets temperature was, respectively, at 3,54°C and 3,27°C during the first testing period. At the second period, average temperatures drops, respectively, at 3,08°C and 3,13°C.

2.3.2. Oil return

The first observation is that in the hour following the restart of the plant after the refrigerant replacement, the oil tank has filled up several times. Each time it was full, a quantity of oil was recovered. A total quantity of 10kg of oil has been removed from the installation. In addition, the oil separators of the compressors were drained during the refrigerant change. These have some internal volume. The total amount of oil "returned" to the positive plant is therefore significantly greater than 10 kg.
This sudden oil return can be explained by the difference in miscibility in the oil between R-404A and R-442A. The best miscibility of the R-442A makes it possible to return the oil previously trapped and accumulated in the pipes and heat exchangers of the circuit. The return of this oil can theoretically allow a better heat exchange in the exchangers.

2.3.3. Discharge temperatures

Fig. 4 graphically shows the temperature record taken at the discharge of the compressor 1. Prior to the work, the discharge temperature oscillated around 82.5°C. After the drop-in, this value increased by more than 6°C. In fact, the values that have been recorded correspond to the maximum value that can be measured by the recorder: 86.75°C. This explains the fact that the measured temperature ceases to oscillate. In reality, the discharge temperature oscillates above 86.7° C.

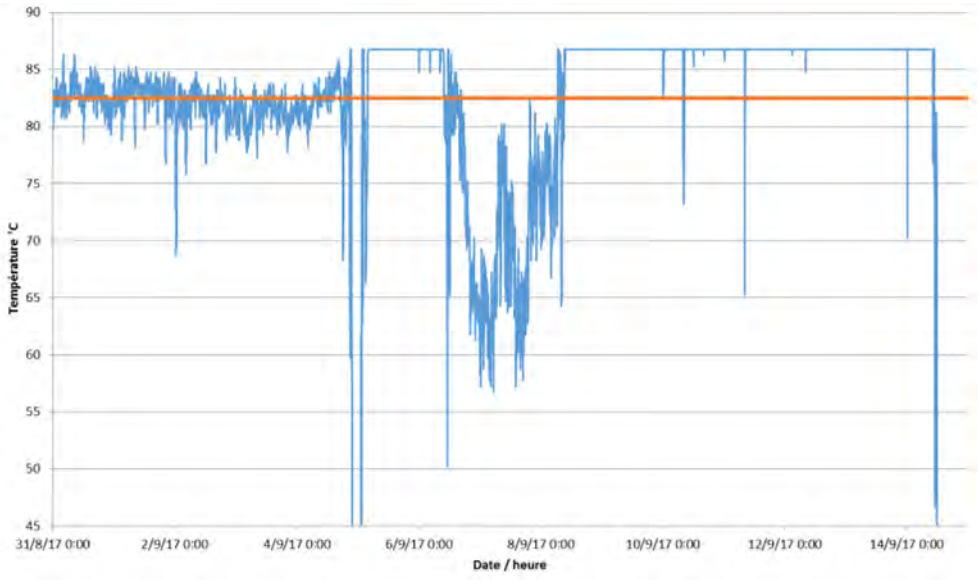

Figure 4. Discharge temperature, compressor 1

2.3.4. Consumption and operating rates

Figs. 5 and 6 show the daily electricity consumption, the daily operating rate and the average operating rate for each period. All of those three values are named as operating ratio.
In both of them, the day with lower consumption corresponds with Sunday.

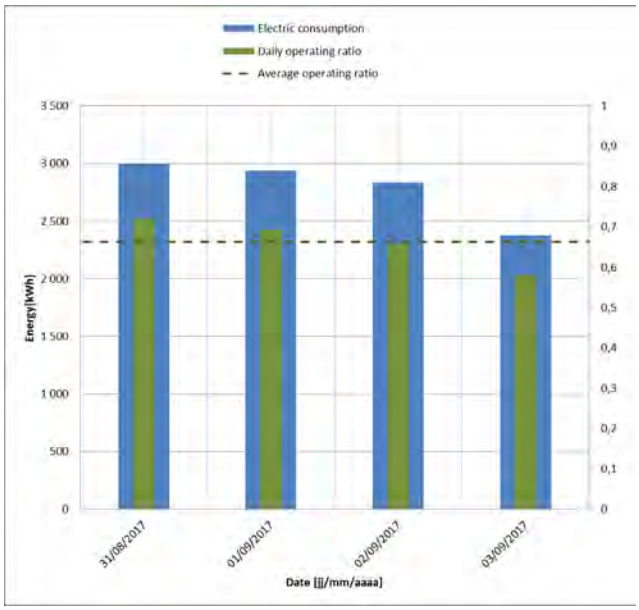

Figure 5. Operating ratio before drop in

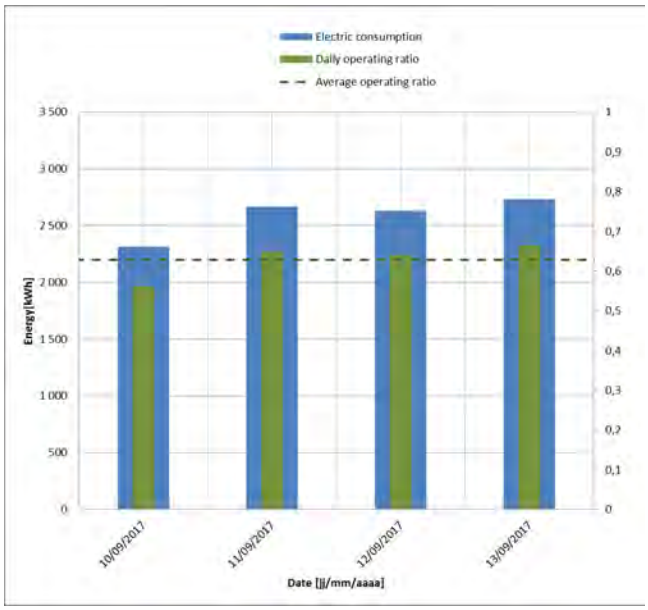

Figure 6. Operating ratio after drop in

Fig. 5 and Fig. 6 show that the operating rate of the positive power station decreases from 66% to 63%. This can be due to a refrigeration power increase. If the refrigeration power increases, the system needs to work less time for the same result.
The calculation of the average daily electric consumption indicates a drop from 2735 kWh to 2555 kWh, i.e. a decrease of 6.5% of the daily consumption. This decrease includes, de facto, the power change consumed instantly and the difference in operating rate.

3. CONCLUSIONS

The comparison of the installation behavior before and after Drop-in resulted in the following conclusions.
Firstly, the Drop-in from R-404A to R-442A is equivalent in regards of the cold rooms and frigorific cabinets internals temperatures.
Secondly, a lot of oil trapped in the heat exchangers came back after the refrigerant replacement.
Thirdly, after changing the refrigerant, the operating time decreases by 3% and the consumption by 6.5%. These improvements are influenced for the reasons outlined above.
Fourthly, the discharge temperature has increased significantly. This increase can have an impact on the life of the compressors. The use of a high floating pressure, in addition to energy savings achieved, would limit this discharge temperature.

REFERENCES

AFCE, 2018, Energy efficiency state of the art of available low GWP refrigerants and systems

Francis, C., Maidment, G., Davies, G., 2017. An investigation of refrigerant leakage in commercial refrigeration. International journal of Refrigeration 74, 12–21.

Graziosi, F., Arduini, J., Furlani, F., Giostra, U., Kujpers, L., Montzka, S., Miller, B.R., O'Doherty, S., Stohl, A., Bonasoni, P., Maione, M., 2015. European emissions of HCFC-22 based on eleven years of high frequency atmospheric measurements and a Bayesian inversion method. Atmospheric Environment. 112, 196–207.

IIR, International Dictionary of Refrigeration

http://dictionary.iifiir.org/search.php, consulted on January 20th, 2019.

IPCC, 2007, IPCC Fourth Assessment report.

Manuscript ID: 1702
DOI: 10.18462/iir.icr.2019.1702

Refrigerant handling practices and their evolution over the last decade

Olivier VALET[(a)], Francis LANAUD[(b)], Gérald CAVALIER[(a)]

(a) Cemafroid, 5 Avenue des Prés – 94266 Fresnes cedex – France

(b) Tecnea Italia, Viale Ottavio Marchino, 15 – 15033 Casale Monferrato - Italy

gerald.cavalier@cemafroid.fr, olivier.valet@cemafroid.fr, francis.lanaud@cemafroid.fr

ABSTRACT

The French regulation applicable to the handling of refrigerants is intended to prove the proper containment of halogenated gases and their traceability. Every company wishing to handle refrigerants shall undergo from an accredited body an on-site verification of its practices.

Issues are treated individually for each single company; however a summary would help the stakeholders to prioritize actions and achieve targets more efficiently.

Cemafroid gathered information from more than 6000 operators. The non-conformities detected during on-site audits have been categorized and analyzed; moreover, the good practices have been summarized.

Both information lead to a better knowledge of the evolution of practices over the last decade, and will make it possible to define areas for improvement and share good practices.

Keywords: Refrigerant, F-gas, HFC, French Regulation, Certification, Audits, Best Practices.

INTRODUCTION

Following the French regulation of 1992, the European regulation called F-Gas carried by the regulations n°842/2006 then 517/2014 instituted certification of people and establishments handling refrigerants. France has been implementing this regulation since 2008 and issuing certificates of competence for people, then called “certified personnel”, and issuing certificates of ability to handle refrigerants for companies, then called “operators”.

These European and French regulations are intended to reduce the environmental impact of refrigerants by controlling their containment and traceability. This control is based firstly on documentary and on-site audits to verify the human and material resources of the company and its refrigerant handling practices, and secondly on the declared annual balance of quantities between the purchase, sale, use and recycling of refrigerants. Since 2008, thousands of audits of companies handling refrigerants have been carried out in France and thousands of refrigerants reports have been analyzed to maintain, suspend or withdraw the certificates of ability of the operators.

The results of audits and refrigerant balances represent a wealth of information on the behavior of companies, their evolution and their impact on refrigerant containment and on the environment. Knowing them would help improve the performance of operators and reduce their environmental impact. It would improve the efficiency of French and European regulations and achieve CO_2 emission targets. Nevertheless, up to now, no analysis of the results of these audits and reviews has been published. The individual treatment of the non-conformities identified for each operator does not show the scope of the difficulties encountered on the field, whereas a global approach would make it possible to more effectively achieve the objectives set by the regulations.

Cemafroid, with its 10 years of experience as an accredited body, has gathered and analyzed information from processed refrigerant balances and on-site audits of a representative sample of companies since 2008 in order to provide data to better support its customers and to contribute more strongly to the efficiency of the system of certification of ability to handle refrigerants.

This article describes the analytical method and the sample selected, then presents the results of the analysis of refrigerant balances and on-site audits of certified companies certified, and finally suggests ways to improve practices.

SCOPE OF THE STUDY

2.1. On-Site Audits and Declared Refrigerant Quantities Studied

Cemafroid, as the first organization accredited in 2008 by the ministries of ecology and industry for the issuance of certificates of ability and the first organization accredited by COFRAC according to the ISO 17 065 standard, delivered over the period from June 2009 to June 2018 more than 11,000 certificates of ability to handle refrigerants.

In France, the application of European regulations requires that each operator is subject to at least one on-site audit during the period of validity of the 5-year certificate. The company is no longer certified as a whole, but each of its establishments handling refrigerants shall be certified. Since 2008, thousands of audits have been conducted on site. For the purpose of the study, a random sample, representative of more than 4,500 audits conducted by Cemafroid, has been analyzed.

At the same time each year, the operators provide their certification body with their quantities of refrigerant balance sheet, for each of their establishments concerned. The certification body is then in charge of analyzing the data and validating the balance sheets. Tens of thousands of reports have been produced and processed since 2008. For the purposes of this study, a random sample of more than 5,000 refrigerants reports has been analyzed.

2.2. Types of Companies and Establishments Studied

The study deals with all types of certificate of ability issued by Cemafroid, consisting in all categories of the regulation from I to V, as described in Table 1. The category determines the regulatory requirements to be audited. In the scope of the audits studied, as in the real situation, the types of certificates of ability issued are mainly categories I and V.

Table 1: Description of the categories of certificates of ability

Category	Activity of the establishment
I	Leakage testing, equipment maintenance, commissioning, refrigerant recovery of all refrigeration, air conditioning and heat pump equipment
II	Maintenance and servicing, commissioning, recovery of refrigeration, air conditioning and heat pump fluids containing less than 2 kg refrigerant and leak testing of refrigeration, air conditioning and heat pump equipment
III	Recovery of fluids from refrigeration, air conditioning and heat pump equipment containing less than 2 kg of refrigerant
IV	Leakage test of refrigeration, air conditioning and heat pump equipment
V	Leakage testing, maintenance and servicing, commissioning, recovery of vehicle air conditioning system fluids, machinery and equipment mentioned in Article R. 311-1 of the traffic laws
V VHU only	Recovery of fluids from refrigeration equipment, containing less than 2 kg of refrigerant whose regulation is linked to the traffic laws

The sample consists in all types of companies, from very small businesses to the multinational through small and medium enterprises. The size of the establishments is also very variable, from establishments with only one worker to sites of several thousand people with several dozen people handling refrigerants.
The number of certified personnel is verified during the audits and this number determines the number of tools that the establishment must have for its activity and which must be consistent with the number of people handling refrigerants.
On average, the number of certified personnel is on the sample of 2.9 people per operator. But more than a half of the firms have only one stakeholder as shown in Fig. 1. The number of stakeholders is less than or equal to 2 in 74% of the establishments concerned.

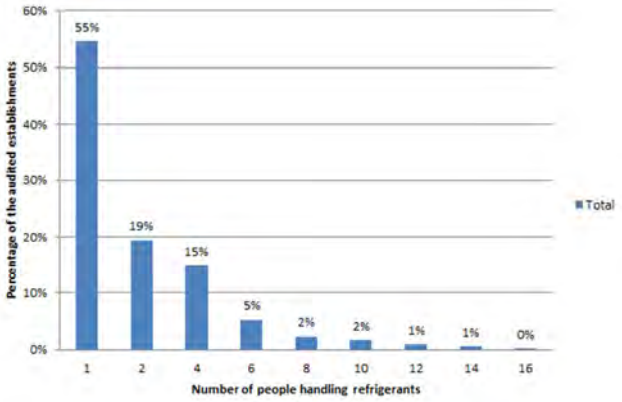

Figure 1: Distribution of the average number of stakeholders handling refrigerants in the certified establishments

2.3. Analyzing Method

The study is based on the gathering of the results of 4,500 on-site audits carried out for Cemafroid between 2012 and 2018, by a sample of about ten different experienced auditors. The non-conformities found on site by the auditors have been sorted by type and the regulatory requirements have been classified into 5 categories:

- The activity: the matching between the category of the certificate and the activity of the company.
- The details of the establishment: the accuracy and completeness of the company name, registration number, etc. ...
- People: the number of certified personnel with a certificate of competence for the appropriate category of activity.
- Tooling: the type of tools required by the regulations, the number of tools in accordance to the number of people handling refrigerants and the organization of work, the declaration of conformity for certain tools, and the verification of tools done on a 12 months frequency.
- Traceability: all the traceability documents required by the regulations.

The analysis of the refrigerant balance sheets was carried out on the balance sheets 2009 and the balance sheets 2017 in order to quantify the evolution over a period of 8 years.

3. ANALYSIS OF THE RESULTS OF THE AUDIT

3.1. Conformity Rate of the Audited Operators

Considering all the audits performed between 2012 and 2018, the average compliance rate for establishments is 40% as shown in Fig. 2. That is, at least one critical deviation was detected in 60% of the establishments audited.

This compliance rate evolves over time as controlled points and regulatory requirements. Fig. 3 shows the evolution of the audit compliance rate over the last four years. It is around 40% in 2015, down to 30% in 2016-2017 and in 2018, to 37% from January to June 2018.

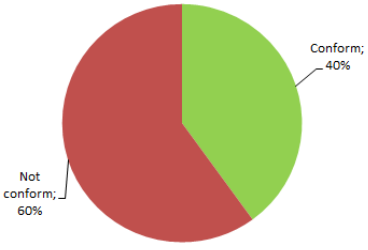

Figure 2: Average compliance rate of the audited establishments

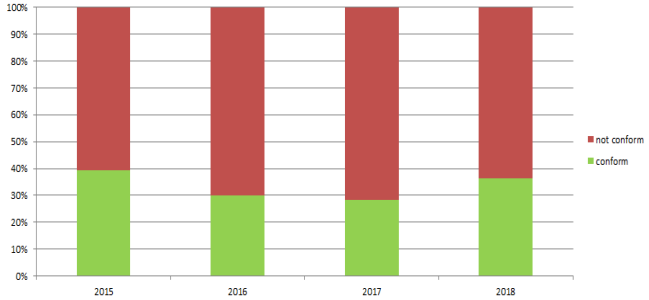

Figure 3: Evolution of the average compliance rate of the certified establishments audited between 2015 and 2018

3.2. Typology of Non-Conformities of the Operators

The classification of the non-compliances of the establishments audited according to the five categories selected shows that two of them stand out clearly in Fig. 4.

Considering the average data since 2015, more than half of the audited operators (52%) have a non-compliance at least on their tools, and 44% of them have been the subject of a lack of traceability of refrigerants. Over the last 4 years, there is no clear trend towards improving these two categories. Non-compliance with people competence and institutions is secondary, with 7% and 14% respectively of non-compliant establishments and a clear improvement trend with a decrease in non-compliance related to the establishment. Finally, non-conformities related to the activity are decreasing and only 1% of the establishments are concerned today.

Catégory	2012	2013	2014	2015	2016	2017	2018	Average since 2015
Activity	1%	1%	2%	2%	3%	1%	1%	2%
Establishment	1%	8%	17%	18%	14%	14%	9%	14%
People	10%	7%	10%	7%	5%	7%	11%	7%
Tooling	1%	19%	34%	44%	54%	57%	54%	52%
Traceability	1%	17%	24%	36%	47%	53%	35%	44%

Figure 4: Rate of non-compliance linked to each category of regulation specification in the establishments audited between 2012 and 2018

The following chapters deal with the details of the non-conformities of each category.

3.3. Non-Conformities Linked to the Activity

For the requirement category "Activity", the audits revealed a discrepancy between the category of attestation issued and the activity of the company.

3.4. Non-Conformities Linked to the Establishment

Establishment-related non-conformities are administrative in nature, and are mainly due to people forgetting or neglecting to update the files following changes. The quantity is decreasing and the auditors detect an improvement in the management of administrative files by the operators as shown in Fig. 5. These mistakes may lead to legal and commercial consequences, because the address of the operators is incorrect in 8% of the cases.

	2012	2013	2014	2015	2016	2017	2018	Average since 2015
Wrong legal status	0%	1%	1%	1%	0%	1%	0%	1%
Wrong company name	1%	2%	5%	4%	3%	2%	1%	3%
Wrong registration number	1%	4%	8%	10%	6%	7%	6%	7%
Wrong address	1%	3%	9%	10%	7%	10%	6%	8%

Figure 5: Evolution of the average compliance rate (number of raised non conformities / number of audits) for each type of non-conformity linked to the category « Establishment »

3.5. Non-Conformities Linked to People Competences

Human resources are one of the pillars of the regulatory system with the requirement of attestation of competence for all people handling refrigerants since July 2011 (Decree of 18 March 2009). Until 2015, the identified non-compliances are mainly linked to the absence of a certificate of competence for the personnel of the operator. The Fig. 6 below shows that the number of deviations is, however, steadily decreasing compared to the number of audits carried out. It can be seen that in 2018, 7 years after the entry into force of the regulation, 3% of the audited operators still handle refrigerants by non-certified people.

From 2016, the lack of registration of personnel represents an important and growing part of the discrepancies identified during the audits. This requirement appeared in 2016 (decree of 2016, February 29th), and stipulates that the personnel register must be the subject of a comprehensive

audit: registered personnel and competence. In 2018, 8% of the audited establishments did not comply with this regulation requirement.



Figure 6: Evolution of the average compliance rate (number of raised non conformities / number of audits) for each type of non-conformity linked to the category «People »

3.6. Non-Conformities Linked to the Tools

Non-conformities concerning tooling management can be divided into 3 groups of deviations:

- The inventory and the conformity of the material including the proofs of ownership, in blue in the Fig. 7,
- The regular regulatory verification of tools internally or externally both on the verification method and its implementation, in green in Fig. 7,
- The use of transfer and recovery bottles, in red in Fig. 7.

The rate of non-conformity of tooling declarations is high and stable. They concern on the one hand their conformity for the charging station and / or the leak detector and on the other hand the proof of their detention. The rate of non-compliance related to misuse of transfer and recovery cylinders is also stable.

The proportion of establishments not verifying correctly is around 50% over the years 2017 and 2018. The discrepancies used to be linked to the adequacy of the procedures; today they relate more to their implementation. Tooling management, including the annual verification, is therefore only poorly controlled by the operators.

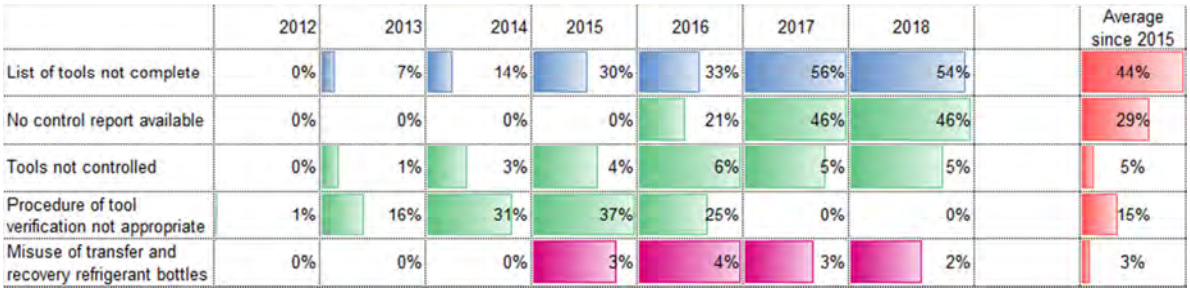

Figure 7: Evolution of the average compliance rate (number of raised non conformities / number of audits) for each type of non-conformity linked to the category «Tooling »

3.7. Non-Conformities Linked to the Traceability

Deviations in traceability management can be divided into 2 groups of deviations:

- The use of regulatory documents,
- The annual declaration of the quantity of refrigerants that have been purchased and used.

Regarding regulatory documents, they are systematically verified during an initial application or renewal of certification. Their use is verified through on-site audits. The lack of formal record of the handled quantities of refrigerants and wastes is still an important part of the discrepancies, as shown in Fig. 8. The high non-compliance rate in 2016-2017 is improving in 2018. On average over 4 years, nearly 30% of the audited establishments are non-compliant.

The marking equipment indicating the GWP of the refrigerant, the leakage control labels and the complaints register have been mandatory since 2016 (decision of February March 2016). The

differences related to the use of these documents have been recorded since 2016. On average over 4 years, 12% of the audited institutions are non-compliant as shown in Fig. 8.

	2012	2013	2014	2015	2016	2017	2018	Average since 2015
No record of the handling of refrigerant and wastes	0%	0%	0%	18%	36%	39%	21%	29%
No GWP marking label and leakage test label available				0%	10%	23%	14%	12%
No customer complaint follow-up document available	0%	0%	0%	0%	0%	2%	6%	2%
Balance sheet of refrigerant quantities not conform	1%	15%	22%	20%	25%	23%	19%	22%
No leak declaration	0%	0%	1%	0%	2%	0%	1%	1%
Absence de certificat de contrôle d'étanchéité	0%	0%	2%	10%	15%	0%	0%	0%
No GWP marking label available	0%	1%	2%	15%	12%	0%	0%	6%

Figure 8: Evolution of the average compliance rate (number of raised non conformities / number of audits) for each type of non-conformity linked to the category «Traceability »

4. STUDY OF THE REFRIGERANT ANNUAL DECLARATION

Operators are companies and bodies carrying out, in a professional capacity, all or part of the following operations on equipment containing refrigerants:

- Commissioning,
- Maintenance and repair, as long as these operations require intervention on the circuit containing refrigerants,
- The tightness test,
- The dismantling,
- Recovery and charging of refrigerants,
- Any other operation carried out requiring the handling of refrigerants.

Operators must obtain a certificate of ability issued by an approved organization in order to handle refrigerants and have the obligation to provide the distributors with recovered refrigerants that cannot be reintroduced into equipment (or whose reuse is prohibited), as well as packaging that has contained refrigerants. They also have the opportunity to treat used refrigerants and packaging under their responsibility.

They are also required to declare each year, before January 31st, the balance of the refrigerants they handled to the certification body that issued them the certificate of ability. On the certification body side, the annual refrigerant balance starts on January 1st and ends on March 31st.

4.1. Refrigerants Purchased and Stored by the Operators

Overall, the quantities of HFC refrigerants purchased per operator averaged 167 kg of refrigerants in 2017, an increase of 41% compared to 2009. Fig. 9 shows that 80% of operators bought less than 85 kg of HFC refrigerants in 2017.

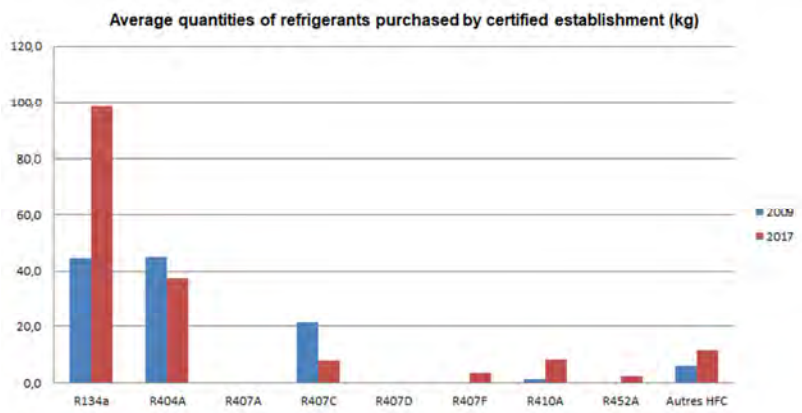

Figure 9: Average quantities of refrigerants purchased in 2009 and 2017 (declared in 2010 and 2018) per operator

	2009	2017
R134a	38%	58%
R404A	38%	22%
R407A	0%	0%
R407C	18%	5%
R407D	0%	0%
R407F	0%	2%
R410A	1%	5%
R452A	0%	1%
Autres HFC	5%	7%
	100%	100%

Figure 10 : Quantities of refrigerants purchased in 2009 and 2017

The "average shopping cart" of refrigerants is heterogeneous as shown in Fig 10. R-134a represents nearly 60% of the quantities of refrigerants purchased in 2017. But the R-404A, whose ban is approaching, is still the second most purchased refrigerants by operators certified by Cemafroid. It should be noted that while the mandatory HFC declarations are made, voluntary declarations of other refrigerants are almost non-existent.

Since 2009, the average refrigerants stock of operators certified at the end of the year has increased by 150% and the increase concerns all refrigerants. It has increased by 21% in 2017 as shown in Fig. 11 and Fig. 12.

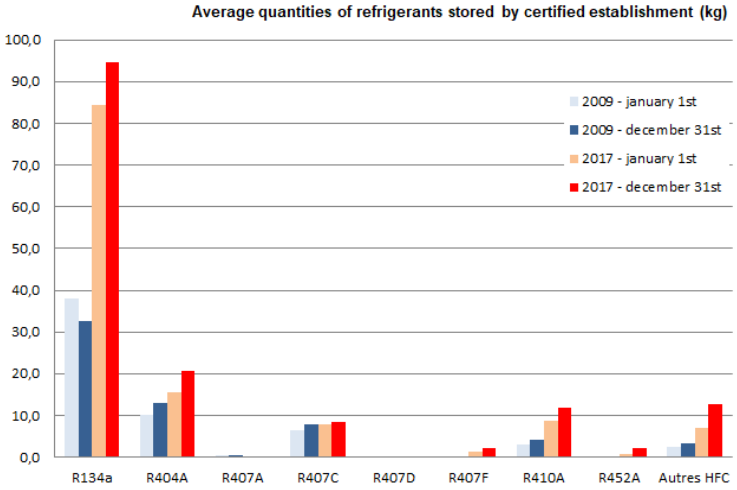

Figure 11: Average quantities of refrigerants stored in 2009 and 2017 by certified establishment

	2009 - jan 1st	2009 - dec 31st	2017 - jan 1st	2017 - dec 31st
R134a	63%	53%	67%	62%
R404A	17%	21%	12%	13%
R407A	1%	1%	0%	0%
R407C	11%	13%	6%	6%
R407D	0%	0%	0%	0%
R407F	0%	0%	1%	1%
R410A	5%	7%	7%	8%
R452A	0%	0%	1%	1%
Other HFC	4%	6%	6%	8%
	100%	100%	100%	100%

Figure 12: Quantities of refrigerants stored in 2009 and 2017

4.2. Use of Refrigerants by the Certified Establishments

The evolution of the refrigerants balance rules in 2016 now makes it possible to distinguish the various uses of refrigerants by the operators. The majority of the refrigerants are used in maintenance according to the Fig. 13. Only 17% of refrigerants are loaded in new machines. It is surprising to note that still 13% of the R-404A is loaded in new machines whose maintenance will inevitably raise a concern in a very short time because of the very close ban of the R-404A at the end of 2020 as shown in the Fig. 14.

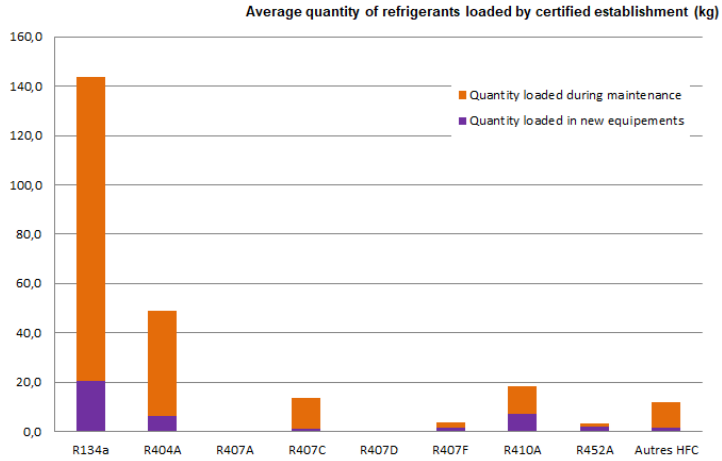

Figure 13: Average quantities of refrigerants loaded in 2017 (declared in 2018) by certified establishment

	Quantity loaded in new equipements	Quantity loaded during maintenance
R134a	14%	86%
R404A	13%	87%
R407A	8%	92%
R407C	8%	92%
R407F	47%	53%
R410A	38%	62%
R452A	65%	35%
Other HFC	14%	86%
TOTAL	17%	83%

Figure 14. Quantities of refrigerants loaded 2017

The reuse of refrigerants has increased significantly in recent years. In 2017, 28% of recovered refrigerants are handed over to distributors and 6% are sold for reuse according to Fig. 15.

Figure 15: Rate of refrigerants returned to distributors or given to another certified establishment in 2017

	Rate of refrigerants returned to distributors	Rate of refrigerants provided to an other certified establishment
R134a	12%	4%
R404A	54%	6%
R407C	75%	3%
R410A	59%	13%
Other HF	47%	28%
TOTAL	28%	6%

Between 2009 and 2017, the average quantities of HFCs recovered per operator per year has more than doubled while the quantities purchased were multiplied by only 1.4 and the quantities loaded by 1.6 over the same period as shown on Fig. 16. On the other hand, the quantities destroyed were halved because of a sharp increase in the reuse of refrigerants.

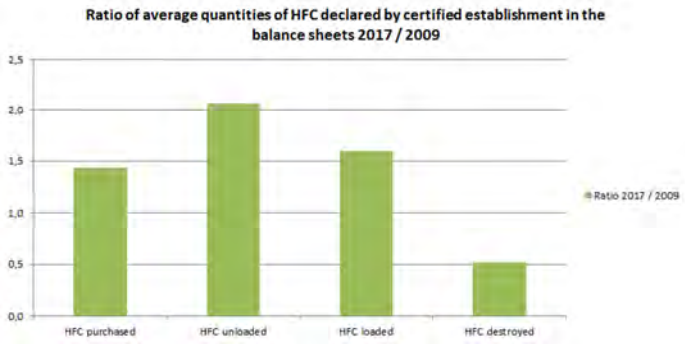

Figure 16: Ratio of average quantities of HFC declared by certified establishment in the balance sheets 2017 / 2009

Loaded quantities rose sharply for R-134a in 9 years, but only slightly decreased for R-404A. New refrigerants such as R-407F, R-410A, R-449A or R-452A have appeared or taken a larger share, but they remain a minority as shown in Figure 13.

5. CONCLUSION

The data of the refrigerant balances and the audits carried out within the framework of the certificates of ability of the operators handling refrigerants provide a wealth of information. The summary produced by Cemafroid highlights a certain number of critical points allowing to suggest ways of improvement.

Generally speaking, operators are increasingly qualified, the number of uncertified workers decreases sharply. The regular checking and the use of tools are poorly managed. The traceability of operations and refrigerants is still poorly controlled and, before computerizing it, it is important to implement it in practice. Quality is improving, but there is still room for significant progress in achieving environmental and economic goals. The study also shows that alternatives are still slow to break through. R-404A machine commissioning remains high at two years of its ban.

Improved tooling management and control, continued training of operators and awareness of alternatives should further reduce the environmental impact of the refrigerant handling.

NOMENCLATURE

GWP	Global Warmth Potential
HFC	Hydrofluorocarbon
Operator	means the natural or legal person exercising actual power over the technical functioning of the equipment and systems covered by the F-Gas

REFERENCES

Regulation of the European Parliament and of the council: No 842/2006 of 17 May 2006, No 517/2014 of 16 April 2014.

French Regulation : Section R.543-75 to R.453-123 of the Environmental Act, section of 20 December 2007, section of 30 june 2008, section of 7 may 2007.

Manuscript ID: 1738
DOI: 10.18462/iir.icr.2019.1738

Effects of cooling method for condensation heat transfer in plate-fin heat exchanger

Sho Fukuda[(a)], Takahiko Miyazaki[(b,c)], Nobuo Takata[(b)], Shigeru Koyama[(b,c)]

[(a)]Department of Mechanical Engineering, Faculty of Science and Engineering,Kyushu Sangyo University, 3-1 Matsukadai 2-chome, Higashi-ku, Fukuoka 813-8503, Japan
s.fukuda@ip.kyusan-u.ac.jp
[(b)]Faculty of Engineering Sciences, Kyushu University, 6-1 Kasuga-koen, Kasuga, Fukuoka 816-8580, Japan
[(c)]International Institute for Carbon-Neutral Energy Research, Kyushu University, 744 Motooka, Nishi-ku, Fukuoka 819-0395, Japan

ABSTRACT

Recently, the development of high temperature heat pump systems for heat recovery from industrial waste heat below 100 °C is one of important subjects to reduce primary energy consumption.
However, in order to develop such systems, it is indispensable to use an environmentally acceptable refrigerant, highly efficient heat exchangers and highly efficient compressors.
From this viewpoint, in the present study, the condensation of low GWP refrigerant R1234ze(Z) in vertical channels is investigated experimentally in order to establish optimum design method of plate-fin heat exchanger. Then, heat transfer coefficients are measured by two type cooling methods. One type is one side cooling method, another type is both cooling method.
As the results, the heat transfer coefficient in consideration of fin efficiency of one side cooling method is higher than that of both cooling method in high quality.
Keywords: Plate-fin heat exchanger, condensation, heat transfer coefficient

1. INTRODUCTION

In recent years, in the civilian, the industrial and the transportation sectors, effective use of energy is one of the most important issues in order to reduce the greenhouse gas emissions and save the primary energy consumption. Especially, in the industrial sector, the development of high temperature heat pump systems for heat recovery from industrial waste heat below 100 °C is one of important subjects. However, in order to develop such systems, it is indispensable to use environmentally acceptable refrigerant, highly efficient heat exchangers and highly efficient compressor. In this situation, recently, hydro-fluoro-olefins (HFOs) and hydro-chloro-fluoro-olefins (HCFOs) such as R1234yf, R1234ze(E), R1234ze(Z) and R1233zd(E) were developed as environmentally acceptable refrigerants with extremely low global warming potential (GWP). Among these refrigerants, R1234ze(Z) and R1233zd(E) are expected as working fluids of high temperature heat pump system recovering the waste heat below 100 °C as the more useful and effective heat above 160 °C. Meanwhile, plate-fin heat exchangers are expected as highly efficient heat exchangers for high temperature heat pump system. The heat transfer characteristics of newly developed refrigerants condensing and evaporating in plate-fin heat exchanger are, however, not clarified sufficiently yet.
In the present study, in order to develop highly efficient condenser for high temperature heat pump system, the condensation of low-GWP refrigerant R1234ze(Z) in a vertical plate-fin heat exchanger is investigated experimentally. In the experiment, the local condensation heat transfer characteristics of R1234ze(Z) flowing downward vertically inside serrated-fin path made of SUS 316 are measured. Then, heat transfer coefficients are measured by two type cooling methods. One type is one side cooling method, another type is both cooling method.

2. EXPERIMENT METHOD

2.1. Experimental Set-Up and Conditions

In the present experiment, serrated-fin and plane-fin, which are widely used in plate-fin heat exchangers, are tested. Fig. 1 shows a schematic view of a test serrated-fin, and Table 1 shows its dimensions.

Fig. 2a shows a schematic view of the test section of one side cooling method, which consists mainly of the serrated-fin path and a cooling jacket. The cooling jacket is attached on the back side of serrated-fin path or plane-fin path. The refrigerant flows downward vertically, and it is cooled by the cooling jacket, to which the compressed water used as coolant is supplied. It is noted that the serrated-fin path is only cooled from the back side. The width of the serrated-fin path is 100 mm, and its effective heat transfer length is 400 mm. Eight heat flux sensors of 50 mm in length are inserted between the serrated-fin path and the cooling jacket to measure the sectional average heat flux. Eight K-type thermocouples are inserted in the ditch of the serrated-fin path to measure the outside wall temperature at the central positions of heat flux sensors. Two mixing chambers are installed at the inlet and outlet of the serrated-fin path to measure the refrigerant pressure and temperature. On the front side of the serrated-fin path, four pressure taps are set to measure the local pressure distribution, and two glass windows are installed to observe the refrigerant flow. Fig. 2b shows a schematic view of the test section of both cooling method. The serrated fin path is cooled and sandwiched between two cooling jackets. The heat sensors and K-type thermocouples are inserted between the serrated-fin path and the cooling jacket as with one side cooling method. The refrigerant pressure are measured inlet and outlet of serrated-fin path.

The test sections are installed in a test loop, a schematic view of which is shown in Fig. 3. The refrigerant in a liquid state discharged from a liquid pump (1) flows into an electric pre-heater (3) and a pre-heater using a silicon oil as heat source (4) through a mass flow meter (2). In these pre-heaters, the refrigerant in a liquid state is vaporized partly or completely to a vapor-liquid two phase state or to a superheated vapor state. Then, it flows into a test section (5). In the test section the refrigerant is cooled and the part of vapor is condensed. After that, the refrigerant returns to the pump through a sub-cooler (6) and a liquid receiver (7). Five mixing chambers and two sight glasses are installed at the pertinent positions in the test loop.

The test fluid is R1234ze(Z). Table 2 lists the experimental conditions.

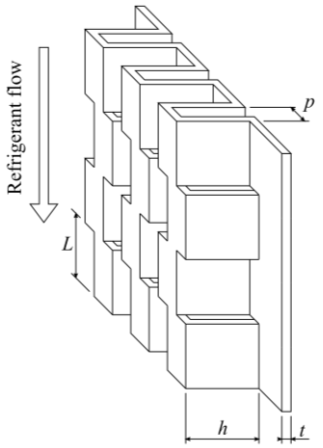

Figure 1.: Test serrated fin

Table 1 Dimension of Serrated fin

Fin dimensions		Cooling method	
		Oneside cooling	Both cooling
Fin pitch	p [mm]	2.117	2.117
Fin height	H [mm]	3.200	3.200
Fin thickness	t [mm]	0.203	0.203
Serration pitch	L [mm]	3.175	3.175
Hydraulic diameter	d_h [mm]	2.34	2.34
Increasing ratio of surface area	η [-]	3.86	2.38

2.2. Data Reduction Method

The experiments of types A and B are carried out. In the experiment of type A, the refrigerant states at the inlet and outlet of the serrated-fin path are in a superheated vapor state and in a vapor-liquid two phase state, respectively. In the experiment of type B, the refrigerant states at the inlet and outlet of the serrated-fin path are in a vapor-liquid two phase state and in a subcooled liquid state, respectively.

In the experiment of type A, the data reduction is carried out as follows:

(1) The refrigerant pressure distribution in the serrated-fin path is obtained by the interpolation method using the measured pressure.

(2) The saturation temperature distribution is calculated from the pressure distribution.

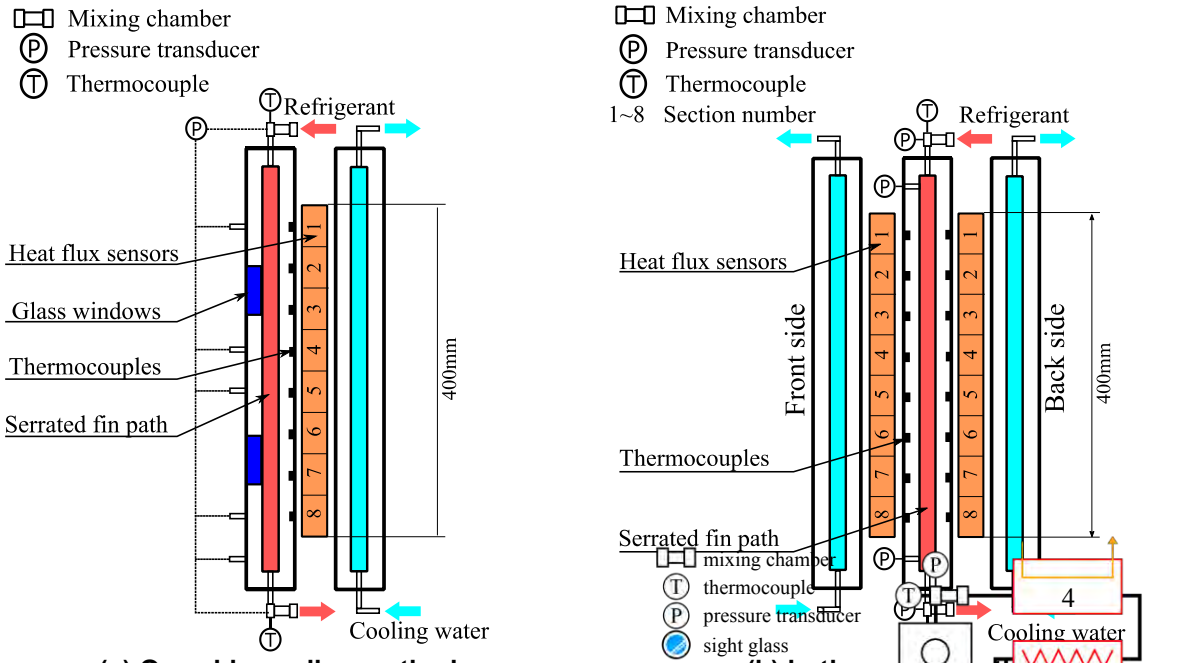

(a) One side cooling method (b) both co... meth...

Figure 2: Schematic view of test sect...

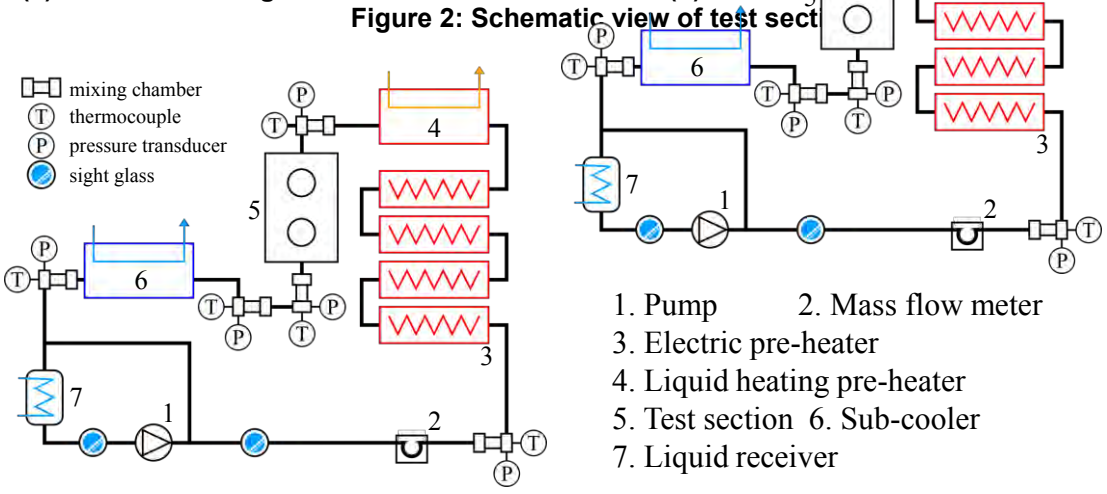

Figure 3: Schematic view of test loop

Table 2. Experimental conditions

saturation temperature [°C]	100,120,140
refrigerant velocity [kg·m^{-2}·s^{-1}]	25,50
saturation temp. - wall temp. [K] (degree of subcooling)	2,5,10

(3) The refrigerant bulk enthalpy and quality at the inlet of the serrated-fin path are calculated from the refrigerant pressure and temperature measured at the inlet mixing chamber.
(4) The distributions of refrigerant bulk enthalpy and quality are obtained from the energy balance equation using the measure refrigerant mass flow rate and the measured heat flux.

In the experiment of the type B, the data reduction method is almost similar to that of the type A experiment, except that the energy balance equation is solved from the outlet to the inlet. In the above-mentioned data reduction, thermophysical properties of R1234ze(Z) are calculated using NIST REFPROP Ver. 9.1 (2013) modified by Akasaka et al. (2014).

The representative inner wall temperature, T_{wi}, at the central position of each heat flux sensor is calculated by the Fourier law from the measured outer wall temperature and heat flux as follows:

$$T_{wi} = T_{wo} + \frac{q\lambda_w}{\delta_w} \quad (1)$$

where q is heat flux based on the projected heat transfer area in W·m^{-2}, T_{wi} is inner wall temperature in °C, T_{wo} is inner wall temperature [°C], δ_w = plate thickness [m], λ_w = plate thermal conductivity [W·m^{-1}·K^{-1}].

The sectional average heat transfer coefficient in consideration fin efficiency, αfin, corresponding to each heat flux sensor is defined as:

$$\alpha_P = \frac{Q_S}{[A_R-(1-\varphi_R)A_{Rf}]\Delta T_{sub}} \quad (2)$$

$$\varphi_R = \frac{thah\left(\sqrt{\frac{\alpha_{fin}s}{\lambda_w F}}H'\right)}{\sqrt{\frac{\alpha_{fin}s}{\lambda_w F}}H'} \quad (3)$$

where

s is surface area of fin and F is cross-sectional area of fin.

3. EXPRIMENTAL RESULT

3.1. Effect of Degree of Subcooling

Fig. 4 show the relationship between the heat transfer coefficient and quality at refrigerant saturation temperature 100 °C, refrigerant velocity 25 kg·m^{-2}·s^{-1}. In the Fig. 4, the red, blue and green represent the degree of subcooling 2K, 5K and 10K, respectively. The vertical and horizontal bars appended to symbol show the propagated measurement uncertainty and the quality change in each measured area of heat flux sensor, respectively. Fig. 4 (a) and (b) are results of both cooling method and one side cooling method.

In high quality area, the results of degree of subcooling 2 K are higher than that of 5 K and 10 K. This main cause is balance between surface tension and local condensation amount. Compare with Fig. 4 (a) and (b), the results of one side cooling method are higher than that of both cooling method in high quality area. This cause is that, in the one cooling method, condensation liquid assembles on the not cooling side wall.

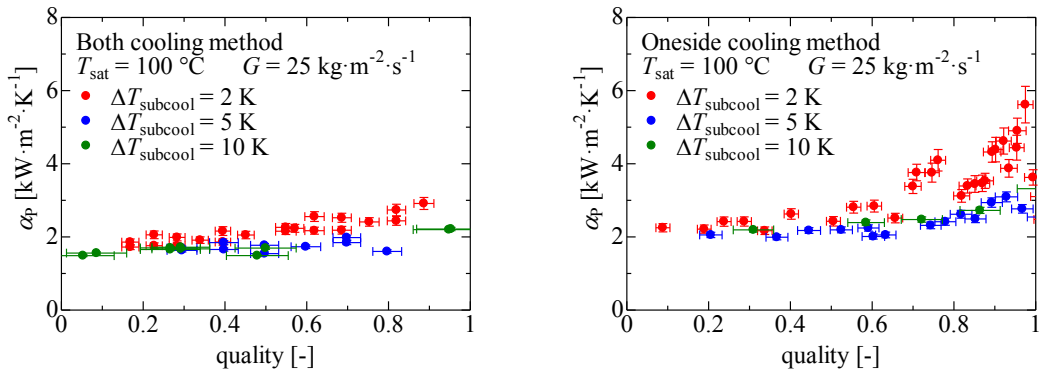

(a) Both cooling method **(b) Oneside cooling method**

Fig.4 Effect of degrees of wall subcooling for condensation heat transfer coefficient

3.2. Effect of Saturation Temperature

Fig. 5 show the relationship between the heat transfer coefficient and quality at refrigerant velocity 25 kg·m^{-2}·s^{-1}, degree of subcooling 2 K. In the Fig. 5, the red, blue and green represent the refrigerant saturation temperature 100 °C, 120 °C and 140 °C, respectively. The vertical and horizontal bars appended to symbol show the propagated measurement uncertainty and the quality change in each measured area of heat flux sensor, respectively. Fig. 5 (a) and (b) are results of both cooling method and one side cooling method.
The higher saturation temperature, the lower the heat transfer coefficient, because the higher saturation temperature, the lower the thermal conductivity, the lower the surface tension.

3.3. Effect of Refrigerant Velocity

Fig. 6 show the relationship between the heat transfer coefficient and quality at refrigerant saturation temperature 100 °C, degree of subcooling 5 K. In the Fig. 5, the red, blue and green represent the refrigerant velocity 25 kg·m^{-2}·s^{-1} and 50 kg·m^{-2}·s^{-1}, respectively. The vertical and horizontal bars appended to symbol show the propagated measurement uncertainty and the quality change in each measured area of heat flux sensor, respectively. Fig. 6 (a) and (b) are results of both cooling method and one side cooling method.
Effect of refrigerant velocity in not confirmed.

4. CONCLUSIONS

The condensation heat transfer characteristics in vertical plate-fin heat exchanger has been experimentally evaluated using low-GWP refrigerant R1234ze(Z).

(1) In high quality area, the results of degree of subcooling 2 K are higher than that of 5 K and 10 K. This main cause is balance between surface tension and local condensation amount.
(2) The higher saturation temperature, the lower the heat transfer coefficient, because the higher saturation temperature, the lower the thermal conductivity, the lower the surface tension.
(3) The results of one side cooling method are higher than that of both cooling method in high quality area. This cause is that, in the one cooling method, condensation liquid assembles on the not cooling side wall.

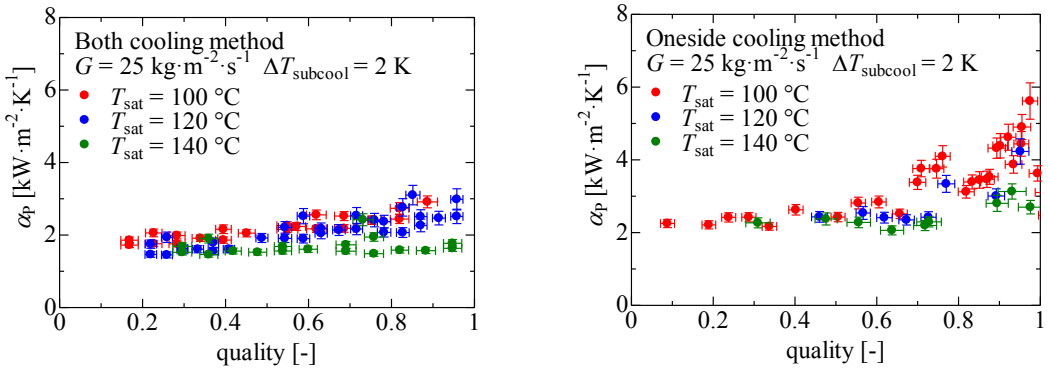

(a) Both cooling method **(b) Oneside cooling method**

Fig.5 Effect of saturation temperature of HFO-1234ze(Z) for condensation heat transfer coefficient

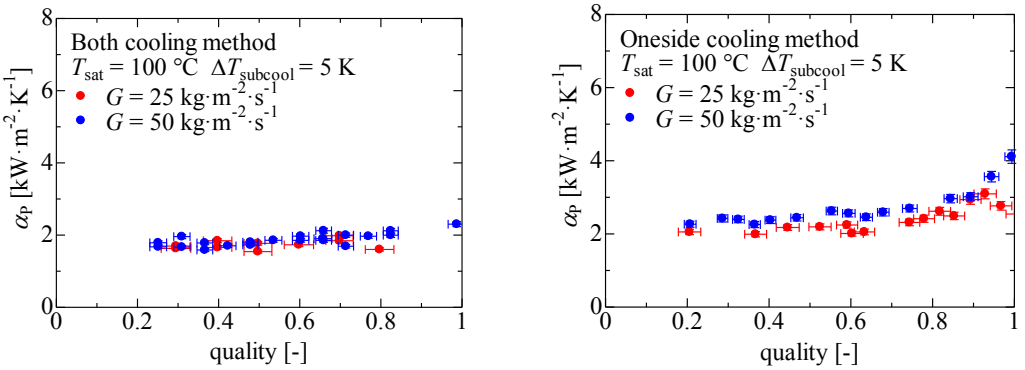

(a) Both cooling method **(b) Oneside cooling method**

Fig.6 Effect of mass velosity of HFO-1234ze(Z)

5. ACKNOWLEDGMENT

The present study was conducted as one of national projects supported financially by Thermal Management Materials and Technology Research Association (TherMAT), Japan.

6. REFERENCES

Lemmon, E.W,, Huber, M.L,, McLinden, M.O., 2013. NIST Standard Reference Database23: Reference Fluid Thermodynamic and Transport Properties-REFPROP, Version 9.1, National Institute of Standards and Technology, Standard Reference Data Program, Gaithersburg.

Akasaka, R, Higashi, Y., Miyara, A., Koyama, S., 2014. A fundamental equation of state for cis-1,3,3,3-tetrafluoropropene (R-1234ze(Z)), Int. J. Ref. 44,168-176.

Manuscript ID: 1757
DOI: 10.18462/iir.icr.2019.1757

Numerical simulation on characteristics of cooling heat transfer and pressure drop of supercritical pressure fluids flowing in a chevron-type plate heat exchanger

Yuki YAMASAKI[(a)], Naoto WATANABE[(a)], Kazushi MIYATA[(b)], Hideo MORI[(b)], Yoshinori HAMAMOTO[(b)], Shuichi UMEZAWA[(c)], Katsuhiko SUGITA[(c)], Kizuku KUROSE[(a)]

(a) Department of Mechanical Engineering, Graduate school, Kyushu University
Fukuoka, 819-0395, Japan, yamasaki@therme.mech.kyushu-u.ac.jp
(b) Department of Mechanical Engineering, Kyushu University
Fukuoka, 8190395, Japan
(c) TEPCO Research Institute, Tokyo Electric Power Company Holdings, Inc.
Yokohama, 2308510, Japan

ABSTRACT

In industrial fields, heat source over 130°C are widely needed, and for this the development of industrial high-temperature heat pump systems has been promoted. For the heat release process in such the heat pump systems, the authors have studied on cooling heat transfer of refrigerants at supercritical pressures in chevron-type plate heat exchangers (PHEs). In this study, to establish a simulation model which estimates the cooling heat transfer coefficient of supercritical pressure refrigerants flowing in the chevron-type PHEs, a CFD analysis was carried out. The results of this analysis agreed well with the experimental results including the data in pseudocritical region where the physical properties of the refrigerant change rapidly with temperature. From the simulation results, characteristics of temperature distribution and heat flux distribution in the chevron PHE were discussed.
KeyWords: CFD, Chevron-type Plate Heat Exchanger, Supercritical Pressure Refrigerants.

1. INTRODUCTION

In industrial fields, currently fossil fuel boilers are used for supplying high-temperature heat source, however, increasing the use of heat pump systems is desired from the viewpoints of suppression of energy resource consumption and reduction of greenhouse gas emission. For consumer use, heat pump systems that supply hot water at around 90 °C are widely used. However, heat sources over 130 °C are required in the industrial processes. Therefore, the development of industrial high-temperature heat pump systems operated in transcritical heat pump cycle has been advanced. The authors studied on cooling heat transfer of refrigerants at supercritical pressures (Mori, 2016, Miyata, 2017a, Miyata, 2018a) and condensation heat transfer at high subcritical pressures (Miyata, 2017b, Miyata, 2018b) in chevron-type plate heat exchangers (PHEs).
The use of refrigerants with low global warming potential (GWP) in the industrial heat pump systems is being considered. Since there is a possibility that a more workable low GWP refrigerant will be developed in the future, it is beneficial to establish a simulation model that predicts the heat transfer performance of the refrigerant with only its thermophysical properties data. Therefore, in this study, a CFD model simulating a chevron PHE were created and numerical calculations were performed for cooling heat transfer of refrigerants at supercritical pressures. The validity of the model was confirmed by comparing with the experimental results (Mori, 2016, Miyata, 2017a). In addition, based on the calculation results, characteristics of temperature distribution and heat flux distribution inside the chevron PHE were discussed. These results are shown below.

2. CALCULATION METHOD

A 3D model simulating the chevron PHE used in the previous experiment (Mori, 2016; Miyata, 2017a) was prepared and the heat exchange in the PHE were analyzed using ANSYS Fluent 17.1. The model was composed of three identical flow channels which were separated by two chevron patterned metal plates. Fig. 1 shows the three flow channels. The supercritical pressure refrigerant flowed in the middle channel and pressurized water flowed in the other channels. The refrigerant was cooled by the pressurized water through the metal plates. Fig. 2 shows the configuration of the one flow channel formed between two chevron patterned metal plates. The refrigerant or the pressurized water flowed into the chevron patterned flow channel through the inlet header connected one side of the flow channel, and flowed away through the outlet header. The boundary conditions on the inlet and outlet faces were uniform velocity and uniform pressure, respectively. The specifications of the flow channel are listed in Table 1.

The refrigerants used in the simulation were HFC134a and HFO1234ze(E). Governing equations were continuity, momentum conservation and energy conservation equations, and steady-state calculations were made. Besides, the buoyancy was not taken into account because the physical properties change in the channel cross section perpendicular to main flow direction is considered small (Miyata, 2018a). Computational mesh was created by ANSYS Meshing. The shape of the mesh in the flow cannel except for near-wall region were tetrahedral, and those in the near-wall were 17 layers of thin layered mesh so as to resolve the rapid change in physical properties with temperature of supercritical pressure refrigerant. The total mesh number was about 40 million. The physical properties of the refrigerant were given as a function of the representative pressure in the channel and the local temperature of each mesh because the effect of pressure drop on the properties was smaller than that of temperature change. Since the temperature dependence of physical properties

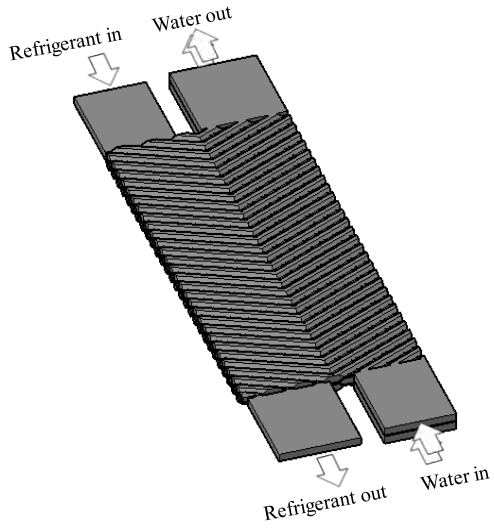

Fig. 1 Calculation model of three channels PHE

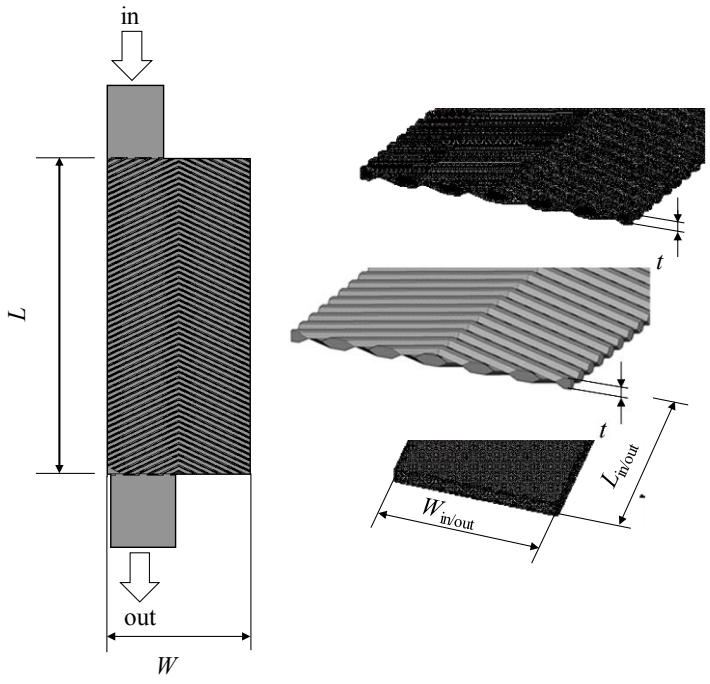

Fig. 2 Calculation model of one flow channel in PHE

Table 1. Dimensions of calculation model

Chevron angle, β [°]	65
Test section length, L [mm]	220
Chevron channel width, W [mm]	99.4
Channel thickness, t [mm]	3.7

of pressurized water was small, the appropriate constant properties were given for them. The physical properties of HFC134a, HFO1234ze(E) and water were calculated with RRFPROP Ver. 9.1 (Lemon, 2013). The turbulence model of SST k-ω was used for analysis. Calculation conditions are listed in Table 2. The specific enthalpy change of the refrigerants in the PHE was adjusted to a target range from 25 to 30 kJ·kg^{-1}. In the same way as the experiments, the heat transfer coefficient of the refrigerant α_{ref} was determined from the heat transfer resistance on the refrigerant side $1/\alpha_{ref}$. The refrigerant-side heat transfer resistance $1/\alpha_{ref}$ was obtained by subtracting the sum of pressurized water-side heat transfer resistance $1/\alpha_{pw}$ and plate heat conduction resistance δ/k from the overall heat transfer resistance $1/K$ between the test refrigerant and the pressurized water, as written in Eq. (1).

$$\frac{1}{\alpha_{ref}} = \frac{1}{K} - \left(\frac{1}{\alpha_{pw}} + \frac{\delta}{k} \right) \quad \text{Eq. (1)}$$

where K is the overall heat transfer coefficient, α_{pw} is the pressurized water-side heat transfer coefficient, δ is the plate thickness, and k is the thermal conductivity of the plate material. The overall heat transfer coefficient K was evaluated by Eq. (2):

$$K = \frac{Q}{\Delta T \, A} \quad \text{Eq. (2)}$$

where Q is the heat transfer rate from the refrigerant to the pressurized water in the PHE. ΔT is the mean temperature difference between the refrigerant and the pressurized water in the PHE, and A is the total projected heat transfer surface area of the PHE. In this study, the mean temperature difference ΔT was evaluated by an integral method (Utamura, 2007) because isobaric specific heat of the supercritical pressure refrigerant changes rapidly with temperature especially in the pseudocritical region.
The pressurized water-side heat transfer coefficient α_{pw} was obtained from preliminary calculations for heat exchange between waters in the PHEs model.

3. RESULTS AND DISCUSSION

3.1 Heat Transfer Coefficient and Pressure Drop

The refrigerant heat transfer coefficients obtained from the simulation are plotted against the arithmetic mean specific enthalpy of inlet and outlet in Figs. 3 and 4, comparing with the experimental data (Mori, 2016; Miyata, 2017a). Figs. 3 and 4 show the results for HFC134a and HFO1234ze(E), respectively. The left figures of Figs. 3 and 4 show the different pressure conditions and the right ones show the different mass velocity conditions. The pseudocritical enthalpy h_{pc}, where the isobaric specific heat takes a maximum value, is shown by vertical solid line for every pressure condition. As shown in the figures, the simulation predicts well the experimental data not only for the change in the heat transfer coefficient with specific enthalpy but also for those with pressure and mass velocity. That is, heat transfer coefficient takes a maximum value at a specific enthalpy which is slightly higher than the pseudocritical enthalpy; pressure dependence of heat transfer coefficient is seen at pseudocritical region and the heat transfer coefficient increases with pressure approaching the critical pressure; the effect of mass velocity is found in a wide range of enthalpy.
Figure 5 shows the comparisons between the simulation and the experiment in frictional pressure drop at the supercritical pressures. The left and right figures in Fig. 5 show the comparison results

Table 2. Calculation conditions

Refrigerant	HFC134a			HFO1234ze(E)		
Pressure, P [MPa]	4.09	4.49	4.95	3.67	3.94	4.31
(Reduced pressure, P/P_c)	(1.01)	(1.11)	(1.22)	(1.01)	(1.08)	(1.22)
Mass velocity, G [kg·m^{-2}·s^{-1}]	105, 165					

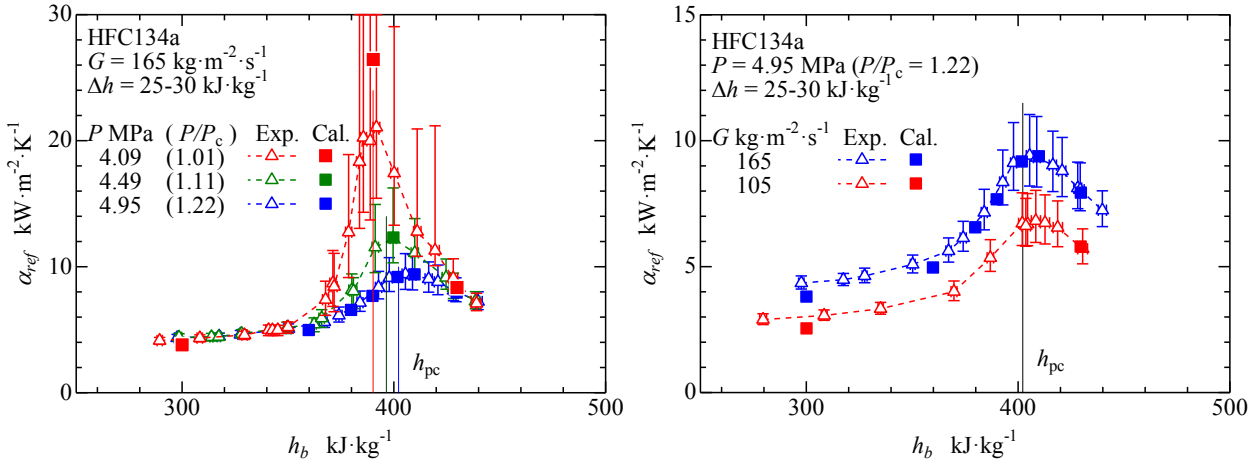

Figure 3: Comparison in heat transfer coefficient of HFC134a between CFD and experiment

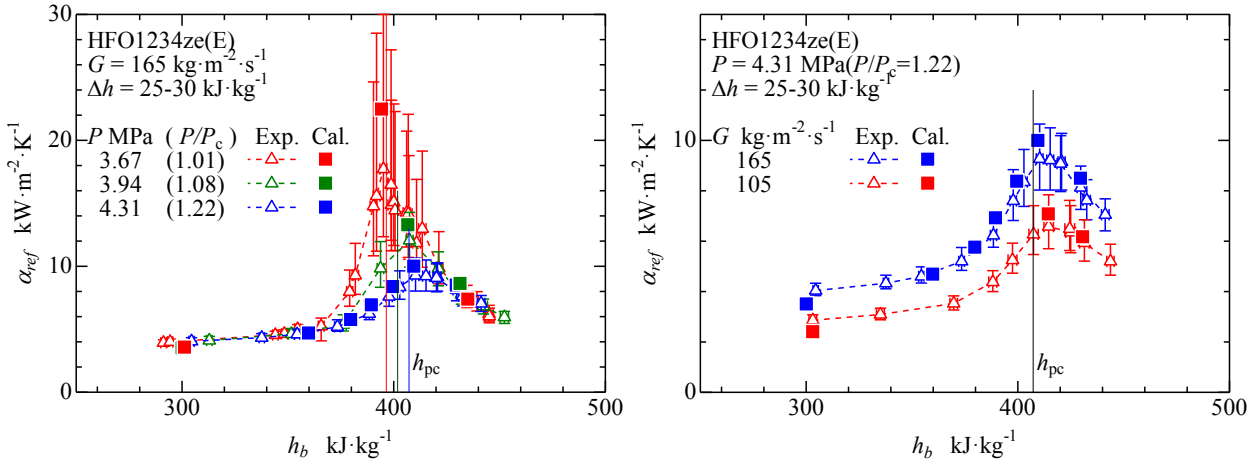

Figure: 4 Comparison in heat transfer coefficient of HFO1234ze(E) between CFD and experiment

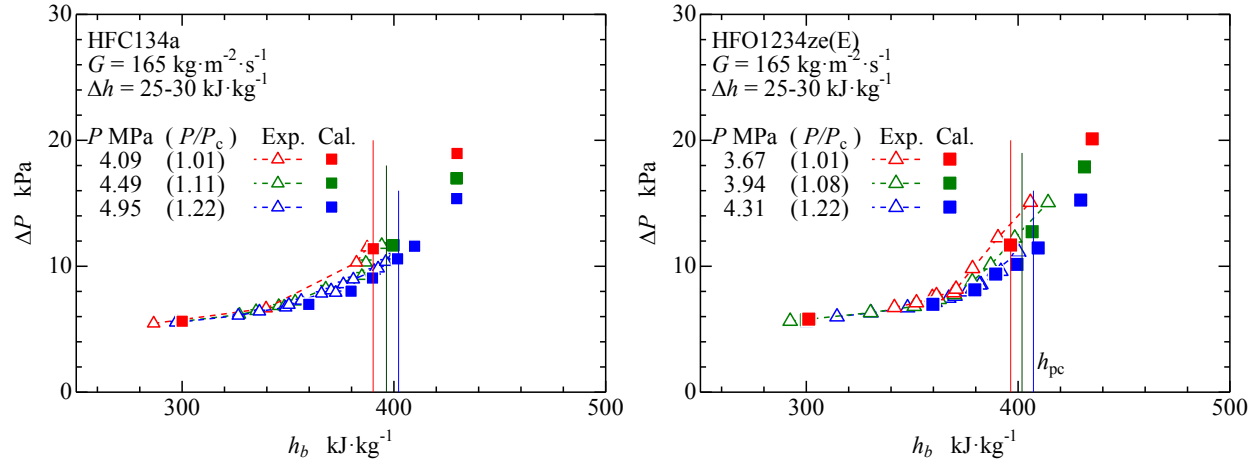

Figure: 5 Comparison in pressure drop between CFD and experiment for HFC134a and HFO1234ze(E)

for HFC134a and HFO1234ze(E), respectively. As shown in the figure, the simulation predicts the measured friction pressure drop accurately for both the refrigerants.

3.2 Heat Transfer Characteristic at Pseudocritical Region

It has been confirmed that the cooling heat transfer coefficient of the supercritical pressure refrigerant shows a maximum at a specific enthalpy which is somewhat higher than the pseudocritical point, by

the previous experimental study (Miyata, 2017a). It is considered that the maximum of the heat transfer coefficient is achieved when the fluid temperature in the thermal boundary layer on the heat transfer wall reaches the pseudocritical temperature because the large peak of isobaric specific heat significantly contributes to heat transfer through turbulent mixing. On this occasion, bulk fluid temperature is still higher than the pseudocritical temperature, hence the maximum heat transfer coefficient appeared at a specific enthalpy which is somewhat higher than the pseudocritical point. As seen from the simulation results for HFC134a at 4.95 MPa and 165 kg·m^{-2}·s^{-1} in Fig. 3, the present simulation predicts well the enthalpy where the heat transfer coefficient takes the maximum.
Figure 6 shows the fluid temperature distribution in the central section in the thickness direction of the channel, and Fig. 7 shows the temperature distribution on the heat transfer surface, for HFC134a at 4.95MPa and 165 kg·m^{-2}·s^{-1}. The parametric enthalpies in these figures are the mean specific enthalpy of inlet and outlet, and the value of 400 kJ·kg^{-1} is near the pseudocritical enthalpy and 410 kJ·kg^{-1} is the enthalpy where the heat transfer coefficient takes the maximum. In both figures, the boundary between yellow and yellowish green regions is the pseudocritical temperature of 111.1 °C. As shown in Fig. 6, at the central section in the thickness direction of the channel, the pseudocritical temperature is located in the middle of the main flow direction at 400 kJ·kg^{-1} while in a downstream region at 410 kJ·kg^{-1}, as expected. At this time, as seen in Fig. 7, the heat transfer surface temperature is lower than the central section, and the pseudocritical temperature is located in an upstream region at 400 kJ·kg^{-1}, and in the middle at 410 kJ·kg^{-1}. That is, the temperature range near the pseudocritical point where the specific heat shows a markedly high value occupies a wide region of heat transfer surface at 410 kJ·kg^{-1}. In this way, it is confirmed that the peak of the heat transfer coefficient appears when the temperature of the heat transfer surface, which is close to the boundary layer temperature, reaches the pseudocritical temperature.

3.3 Heat Flux Distribution

An example of the heat flux distribution on the refrigerant side heat transfer surface is shown in Fig. 8. From a macroscopic standpoint, the heat flux distribution is nearly uniform. That is, the entire surface of the plate is used effectively. In the previous study (Kurose, 2018), it was confirmed that the dead water region in the 65° PHE is small, and the velocity distribution in the width direction of

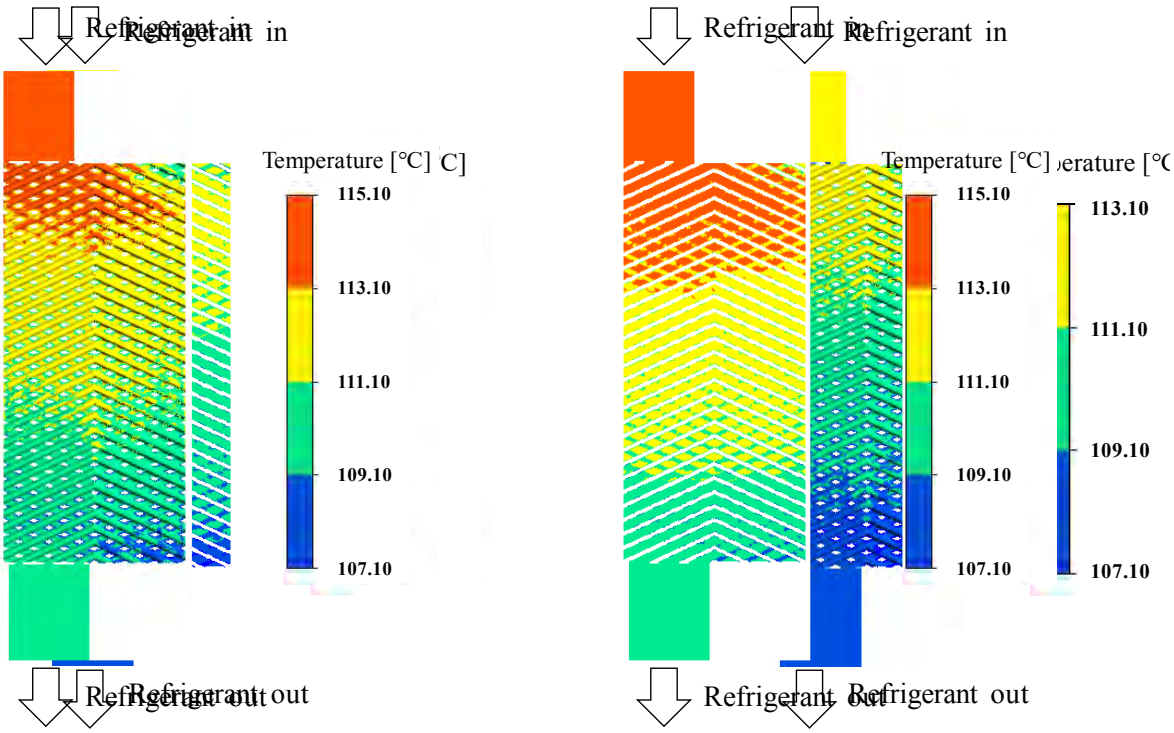

(a) h_b = 400 kJ·kg^{-1} (b) h_b = 410 kJ·kg^{-1}

Fig. 6 Temperature distribution of refrigerant in central section in thickness direction in the refrigerant flow channel for HFC134a at 4.95 MPa and 165 kg·m^{-2}·s^{-1}

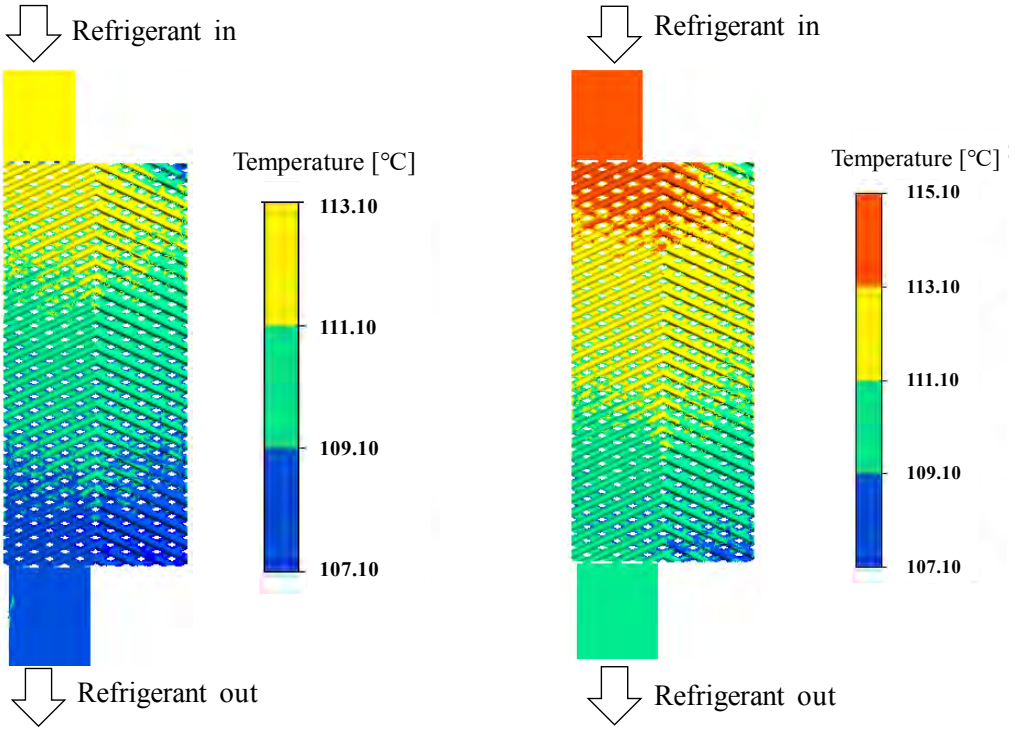

(a) h_b = 400 kJ·kg^{-1} (b) h_b = 410 kJ·kg^{-1}

Fig. 7 Temperature distribution on the heat transfer surface in the refrigerant channel for HFC134a at 4.95 MPa and 165 kg·m^{-2}·s^{-1}

the flow channel is uniform. In the present study, it is also confirmed that the distribution of the heat flux is uniform in the width direction of the flow channel.
In Fig. 8, by enlarging a part of the flow channel, the local heat flux distribution is also shown in detail. From a microscopic point of view, the heat flux through the wall surface standing against the main flow direction is larger than the other surfaces. That is, when the flow gets over the convex part of the corrugated plate, the boundary layer becomes thin and heat transfer is enhanced. Similar results were obtained for the case of HFO1234ze(E).

4. CONCLUSION

A CFD model for the chevron-type plate heat exchanger (PHE) with a chevron angle of 65° was developed and simulation of cooling heat transfer of supercritical pressure refrigerants HFC134a and HFO1234ze(E) were carried out. The simulation results of heat transfer coefficient and pressure drop were in good agreement with experimental values. Based on the simulation results, the characteristics of temperature distribution and heat flux distribution were examined.

REFERENCES

Mori, H., Nakamura, S., Ono, F., Kariya, K. Umezawa, S., 2016. A Study on Characteristics of Cooling Heat Transfer of Supercritical Pressure Fluids in a Plate Heat Exchanger, Heat Transfer Engineering 37(7-8), pp.659-667.

Miyata, K., Mori, H., Taniguchi, T., Umezawa, S., Sugita, K., 2017a. Cooling Heat Transfer of Supercritical Pressure HFO1234ze(E) in a Plate Heat Exchanger, Transactions of the JSME 83(855), p. 17-00280 (in Japanese).

Miyata, K., Yanagihara, S., Taniguchi, T., Mori, H., Hamamoto, Y., Umezawa, S., Sugita, K., 2017b, Condensation heat transfer of a refrigerant at near-critical pressures in a chevron-type plate

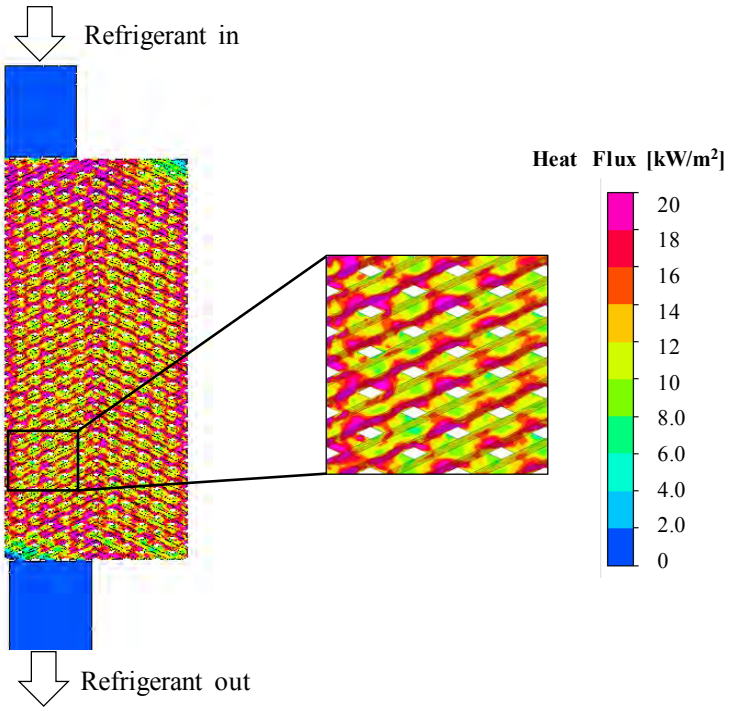

Fig. 8 Distribution of heat flux on heat transfer surface in refrigerant flow channel for HFC134a at 4.95MPa, 165 kg·m^{-2}·s^{-1} and 410 kJ·kg^{-1}

heat exchanger, Transactions of the Japan Society of Refrigerating and Air Conditioning Engineers 34(4), pp. 443-452 (in Japanese).

Miyata, K., Mori, H., Taniguchi, T., Umezawa, S., Sugita, K., 2018a, Effect of the Chevron Angle on Cooling Heat Transfer Characteristics of Supercritical Pressure Fluids in Plate Heat Exchangers, Heat Transfer Engineering, DOI:10.1080/01457632.2018.1450334.

Miyata, K., Yanagihara, S., Watanabe, N., Mori, H., Hamamoto, Y., Umezawa, S., Sugita, K., 2018b, Effect of chevron angle on condensation heat transfer of refrigerants at high pressures in plate heat exchangers, Transactions of the Japan Society of Refrigerating and Air Conditioning Engineers 35(4), DOI: https://doi.org/10.11322/tjsrae.18-42AC_OA

Lemon, E. W., Huber, M. L.,McLinden, M. O. 2013, NIST Standard Reference Database 23 Version 9.1

Utamura, M., Nikitin, K. Kato, Y., 2007, Generalization of Logarithmic Mean Temperature Difference Method for Heat Exchanger Performance Analysis, Thermal Science and Engineering 15(3), pp. 163-173 (in Japanese).

Kurose, K., Yanagihara, S., Miyata, K., Hamamoto, Y., Mori, H., 2018, Experiment and numerical simulation of flow characteristics in plate heat exchangers, Trans of the JSME 84(862), DOI:10.1299/transjsme.17-00593(in Japanese).

Manuscript ID: 1772
DOI: 10.18462/iir.icr.2019.1772

Amorphous silica nanosprings: a candidate for improving condensation heat transfer performance

Nickolas C. SCHMIESING[(a)], Andrew D. SOMMERS[(b)*], Giancarlo CORTI[(c)*]
[(a)] Department of Mechanical and Manufacturing Engineering, Miami University
Oxford, OH, 45056, United States, schmienc@miamioh.edu
[(b)] Department of Mechanical and Manufacturing Engineering, Miami University
Oxford, OH, 45056, United States, sommerad@miamioh.edu
[(c)] Department of Mechanical and Manufacturing Engineering, Miami University
Oxford, OH, 45056, United States, corticlg@miamioh.edu

ABSTRACT

In this work, heat transfer data are presented for water vapor condensing on the outside of aluminum tubes in a purpose-built environmental chamber. Testing was performed both before and after coating the tube with an amorphous silica nanospring coating of prescribed thickness. Silica nanosprings offer several advantages over other one-dimensional nanostructures including high surface area (350 $m^2 g^{-1}$), mild growth conditions (350°C and atmospheric pressure), thermal stability < 1000°C in air, innate hydrophilicity, and photolithography compatibility. Depending on the functionalization that is performed, either hydrophilic or super-hydrophobic conditions can be achieved. Special focus is given to baseline testing, benchmarking the experimental setup, and the performance of the silica nanospring coating. Data are interpreted in terms of coating thickness, wettability, and other environmental factors with the overall aim of improving condensation heat transfer performance.
Keywords: Coating (Materials), Condensation, Heat Exchanger, Heat Transfer Coefficient, Horizontal Tube, Nanotechnology, Water.

1. INTRODUCTION

Heat exchangers have a wide range of applications and industries including the automotive, aerospace, heating, ventilation, air conditioning, and refrigeration (HVAC&R), and steam power production. Because of the prevalence of these applications in the world today, it is crucial to make them as efficient as possible in order to reduce the associated costs. One common area of focus for improving efficiency is heat exchanger surface design including geometric modifications, surface roughness, and coatings. Heat exchangers are commonly made of conducting materials such as copper and aluminum, which have high thermal conductivities. However, both of these metals are also naturally hydrophilic, so water retention can be problematic and become a source of inefficiency. This condensation can block the airflow within the heat exchanger, while also posing an additional thermal resistance to air-side heat transfer. In addition, retained condensate on the fin surface can also become a repository for harmful bacteria such as Legionella, which can lead to Legionnaires' disease or other respiratory infections (Bèdard et al. (2016) and Martinelli et al. (2000)).
A common strategy for addressing these problems involves altering the natural wettability (i.e. degree of hydrophobicity or hydrophilicity) of the surface in order to affect the mode of condensation as well as the quantity of retained condensate during operation. Typically, hydrophobic surfaces are more likely to promote dropwise condensation (DWC), while hydrophilic surfaces are more likely to promote filmwise condensation (FWC). In a review by Rose (2002), it was shown that the promotion of DWC is beneficial for improving heat transfer performance, whereas in FWC, a liquid film is formed such that droplets are less likely of shedding from the surface, resulting in an additional resistance to heat transfer. In contrast, in DWC, many individual droplets nucleate on the surface, leaving areas of the underlying surface

exposed to the surroundings. The hydrophobic nature of the surface also allows for easier droplet removal. As a result, there is typically less resistance to heat transfer in DWC than FWC.

A number of studies have investigated different surface modifications with the intention of improving condensation heat transfer by means of promoting dropwise condensation. In a recent study by Preston et al. (2015), a graphene coating on horizontal copper tubes showed promising results. It is important to note, however, that the high temperatures of the application process for this coating limit the materials on which this coating can be applied. Other chemical coatings evaluated for this purpose include a hexadecylthiol self-assembled monolayer (SAM) coating by Das et al. (1999) and oil-infused surfaces by Tsuchiya et al. (2017). The surface wettability can also be adjusted by altering the surface topology. In a study by Wen et al. (2017), heat transfer improvements were observed after depositing copper nanowires on planar surfaces. Zhao et al. (2017) investigated the impact of two- and three-dimensional fins on horizontal tubes, while Miljkovic et al. (2018) etched silicon nanopillars into planar silicon substrates. A study by Rajkumar et al. (2018) combined topological alterations with chemical coatings by depositing a lead coating onto vertical copper tubes containing milled grooves parallel to the tube axis.

Other studies have also been conducted to determine if wettability patterns provide heat transfer advantages over surfaces with homogenous wettability. With these patterned surfaces, localized regions of relative hydrophobicity are positioned adjacent to regions of relative hydrophilicity. By doing so, it is possible to force droplets to move from the hydrophobic region to the hydrophilic region, where the droplets can then coalesce with other neighboring droplets since it is more likely for the resulting larger droplet to shed from the surface. In another study with a patterned tube with alternating rings of hydrophobicity and hydrophilicity, Alwazzan et al. (2017a, 2017b) were able to obtain improvements in the heat transfer coefficient over both a purely hydrophobic tube and a purely hydrophilic one. In other work, studies by Yang et al. (2017) and Ghosh et al. (2014) evaluated wettability patterns on planar surfaces; however, relatively few other studies could be found.

In this paper, an amorphous silica nanospring (SN) coating is proposed as a candidate for improving the condensation heat transfer performance of horizontal aluminum tubes. SN have not yet been evaluated from a condensation heat transfer perspective. This coating is in the early stages of testing, but characterization from previous studies and early testing have both suggested that this coating may be a suitable candidate for heat transfer improvement. This paper will highlight some of these previously discovered characteristics, while also providing some preliminary results. Further testing however is needed to better understand the effect that the coating has on heat transfer performance.

2. METHODOLOGY

2.1 Nanospring Growth and Sample Fabrication

Silica nanosprings (SN) are a one-dimensional nanomaterial discovered in the laboratory of Dr. David McIlroy as documented by Wang et al. (2006). SN are comprised of multiple amorphous silica nanowires that intertwine around one another to form a high-surface area 3-D coating, as shown in the scanning electron microscope (SEM) image in Fig. 1a. A vapor-liquid-solid (VLS) mechanism, discussed in detail by McIlroy et al. (2004), is used to grow the nanosprings. One advantage of this growth process is that it occurs at atmospheric pressure and a relatively mild temperature of 350ºC. This allows a wide range of materials with lower melting temperatures, namely aluminum, to be coated with the SN without being harmed. Briefly, the growth procedure is as follows: first, the desired substrate is sputter coated with a thin layer of gold. The gold acts as a catalyst to promote the growth of the coating, with each gold particle becoming a nucleation site for a nanostructure. In this work, Al tubes were coated with the SN. In order to ensure a uniform coating around the circumference of the tube, the tubes are rotated using a DC motor throughout the sputtering process. After sputtering with gold, the sample is then exposed to a silane precursor within a chemical vapor deposition (CVD) reactor. Using the programmable reactor, specified temperatures and precursor exposure times can be applied, allowing for control over the resulting coating thickness. Increasing the precursor exposure time results in a thicker coating growing

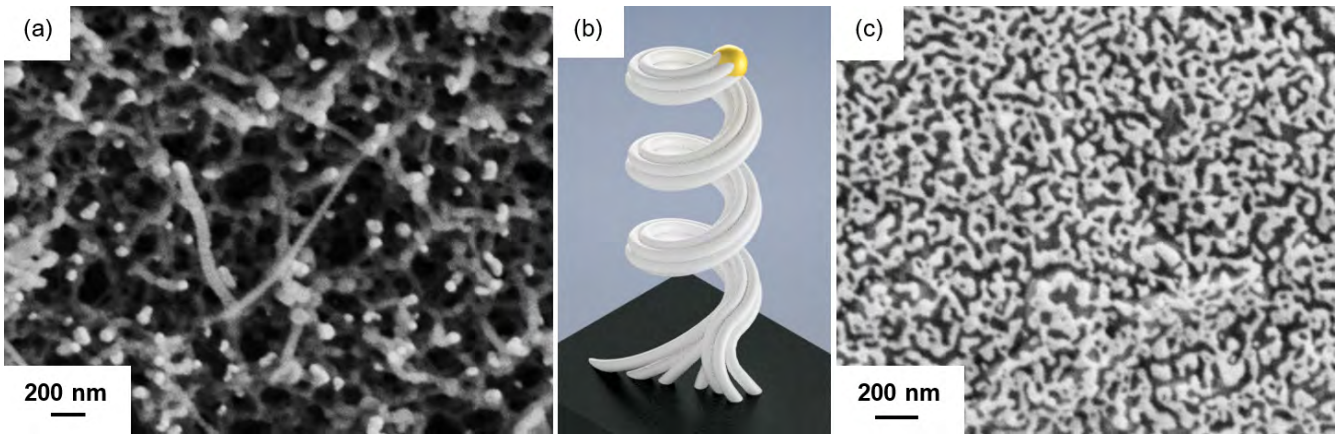

Figure 1: (a) SEM micrograph of a representative nanospring mat, (b) rendering of an individual nanospring model, and (c) islands of gold (Au) that form prior to nanospring growth.

on the surface. Finally, hydrophilic SN coated tubes are functionalized with hexamethyldisiloxane (HMDSO) at 200°C for 30 min to render them hydrophobic.

Work by Wojcik et al. (2017) captured the early stages of the nanospring growth using advanced microscopy techniques. From the images gathered, the group was able to show that each nanospring begins as multiple individual nanowires that eventually come together and intertwine to form a helical spring with the gold catalyst at the tip. Figure 1b shows a rendering of a model of an individual nanospring to help demonstrate this structure. Anywhere from 5 to 8 nanowires can join to create a nanospring (Wang et al., 2006). The amorphous nature of these nanosprings may be beneficial to the durability of this coating, especially in a low abrasion condensation environment. During the growth process, the gold particles shift to form islands of gold, as shown in the bright regions of the SEM micrograph in Fig. 1c. These islands determine where the silica nanowires will form. The dark areas show the underlying uncoated surface, which will remain exposed to the surroundings. As a result, any thermal resistance posed by the coating is reduced, and the beneficial thermal properties of the underlying aluminum substrate can still contribute to the heat transfer performance.

A number of other studies have also identified characteristics of the SN coating that suggest it may be suitable for promoting heat transfer enhancement. Schilke et al. (2010) determined that the coating is capable of being functionalized and is thermally stable at temperatures below 1000ºC. With proper functionalization, the wettability of the SN mat can be altered, which could also potentially further improve the heat transfer performance. The silica nanosprings grow at a rate of approximately 2.5 μm per minute, which was shown to be about 40 mg per hour for a 24 cm^2 sample, as demonstrated by Corti et al. (2018). Brunauer-Emmett-Teller (BET) measurements also revealed that the SN have ~350 $m^2\ g^{-1}$ of accessible surface area (Corti et al., 2013). Cantrell et al. (2010) and Bakharev et al. (2014) conformally coated a variety of two- and three-dimensional surfaces, including complex geometries, showing that the SN can be grown on a wide range of objects given that they are capable of withstanding the growth conditions. Finally, the SN coating has been shown to be photolithography compatible, allowing for control over where the coating is applied (Corti et al., 2007; Sai et al., 2011; Timalsina et al., 2010). All of these characteristics provide insight on how the SN coating should perform and suggest that the coating could be a viable option for improving condensation heat transfer performance.

2.2 Condensation Heat Transfer Experiments

Condensation heat transfer testing was performed on both uncoated and silica nanospring coated samples in order to determine the effectiveness of the coating. All samples were created using identical aluminum 6061-T6 tubes with 6.35 mm and 5.10 mm outer and inner diameters, respectively. The length of the tube used during testing was approximately 152.4 mm in length. It has been shown by Tanner et al. (1968) that the presence of non-condensable gases in a condensing environment can influence the condensation heat transfer performance. As a result, a well-insulated, controlled-environment vacuum chamber, shown in Fig. 2, was designed and constructed to carry out the experimental testing. This

setup includes an isothermal bath (A) to control the inlet temperature of the cooling water, which flows through the system by means of a pump (B). The flowrate of the cooling water was monitored with a digital flow meter (C). The cooling water then flows through the test sample which is housed inside the environmental chamber (D), which was evacuated using a mechanical vacuum pump (E) to remove the non-condensable gases from the test environment. The test sample, wiring for the interior LED lighting, and *T*-type thermocouples enter the chamber through vacuum-suitable fittings. A data acquisition unit (DAQ) (F) was used to record the temperature, pressure, and flowrate data measured during testing. In order to ensure that condensation only occurred on the test sample, a wrap heater controlled by a PID controller (G) was placed on the exterior of the chamber to keep the chamber wall temperature sufficiently high, preventing condensation on these surfaces.

Inside the evacuated chamber, two *T*-type thermocouples were used to record the surface temperature of the test sample (H) during testing. The thermocouples were calibrated using a high-precision RTD and found to have an experimental uncertainty in the range of 0.03 to 0.04°C with 95% confidence. These thermocouples (I) were held firmly to the surface of the Al tube using plastic hose clamps. Prior to pulling a vacuum, deionized water (J) was placed inside the chamber to ensure that the surrounding environment was saturated during testing. A digital pressure transducer was used to record the pressure inside the chamber, which in turn was used to calculate the environmental chamber temperature. A viewport on the vacuum chamber allowed for the collection of still images and video during testing. The testing procedure was as follows: first, the prescribed testing conditions were established within the test setup (i.e. cooling fluid flow rate, degree of subcooling, etc.). After setting these conditions, a sufficient period of time was then allotted to allow the setup to reach thermal equilibrium. Once equilibrium was established, the aforementioned data were collected using the DAQ system for 120 seconds with a frequency of 1 Hz. Upon completion, a test parameter (i.e. flow rate, etc.) was altered, and the chamber was again allowed to reach a new thermal equilibrium. This process was repeated until all necessary data had been acquired. The collected data were then used to calculate the condensation heat transfer coefficient using Newton's law of cooling and the measured heat transfer rate to the water to calculate Q. In this study, the condensation heat transfer coefficient was chosen as the primary means for making comparisons between test samples.

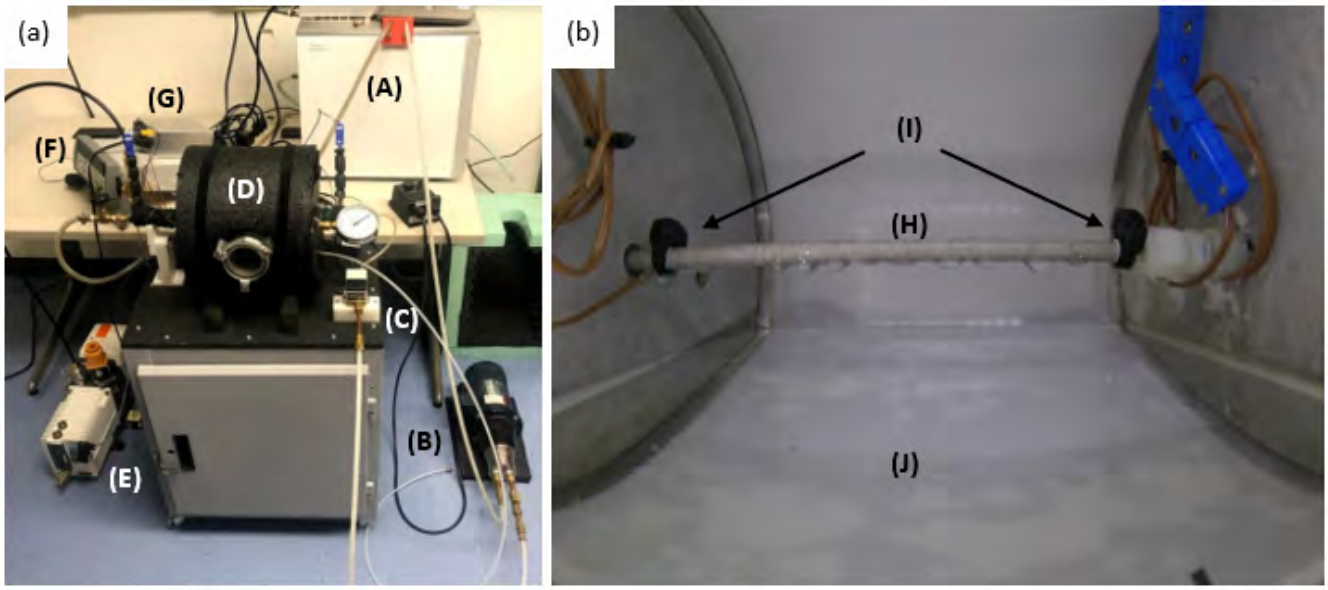

Figure 2: Images of the (a) exterior and (b) interior of the controlled environment vacuum chamber for carrying out the condensation heat transfer testing.

3. PRELIMINARY RESULTS

3.1 Contact Angle Measurements

In order to quantify the surface wettability, both static and dynamic contact angle measurements were recorded for planar surfaces in previous works by Schmiesing and Sommers (2017) and Corti et al. (2019). The sessile drop method was applied using a ramè-hart goniometer to inject the water droplets onto each sample. These contact angle measurements and their associated contact angle hysteresis $(\theta_{advancing} - \theta_{receding})$ can be found in Table 1. As a reminder, longer growth periods for the SN coating result in a thicker nanospring mat. Table 1 shows that the surfaces coated in SN have higher static contact angles, while also possessing lower contact angle hysteresis values. This indicates that the silica nanospring coating, as expected, is significantly more hydrophobic than the uncoated baseline sample. Moreover, all of the SN coated surfaces would be considered superhydrophobic (θ_{static} >150º). This table also reveals that SN samples with thinner mats tend to be more hydrophobic than samples with thicker SN mats. This was an interesting discovery and could be especially advantageous in a condensation heat transfer context since thinner coatings should pose a smaller overall thermal resistance to heat transfer. Additional contact angle measurements are planned to more accurately characterize the samples being created for condensation testing.

Table 1. Mass and contact angle measurements on planar samples

Surface	Au (mg)	SN (mg)	θ_{static}	$\theta_{advancing}$	$\theta_{receding}$	Hysteresis
Baseline surface	0	0	99.0º	110.4º	70.5º	39.9º
SN coating (30 min of growth)	0.69	15.7	154.6º	161.4º	130.6º	30.8º
SN coating (5 min of growth)	0.59	5.4	164.7º	166.9º	156.7º	10.2º
SN coating (2 min of growth)	0.63	1.1	165.8º	166.9º	160.0º	6.9º

3.2 Condensation Testing

To date, early condensation heat transfer testing, primarily focused on characterizing an uncoated baseline sample, has been conducted. As expected, the bare aluminum 6061-T6 tube exhibited a filmwise condensation (FWC) mode, which can be seen in Fig. 3a. Although a full data set has not yet been collected for a silica nanospring coated tube, sample images of condensation on a SN-coated tube have been recorded (see Fig. 3b), which show the dropwise nature of the condensation (DWC) on the superhydrophobic surface. The coated tube has 1.1 mg of SN, which increase the overall tube surface

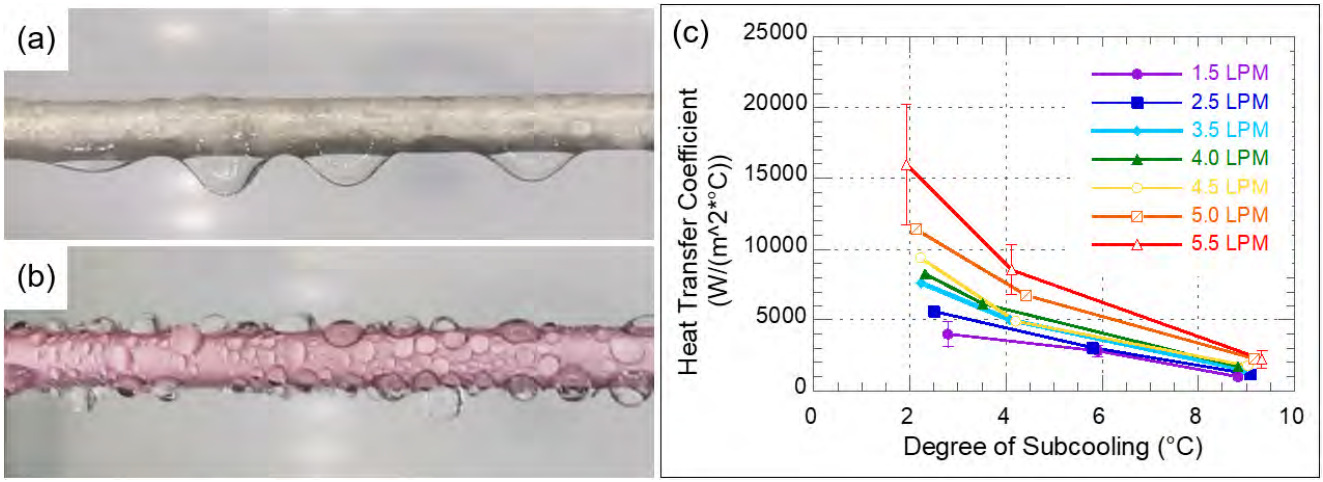

Figure 3: Condensation modes on (a) a baseline tube and (b) a silica nanospring-coated tube. (c) A plot of the baseline condensation heat transfer coefficient with respect to the degree of subcooling.

area by ~12 times at an estimated cost increase of 10 cents per tube. The exposed area of the underlying substrate is present between the condensation droplets. When comparing Fig. 3a and Fig. 3b, the droplets on the baseline tube appear much larger than the droplets on the SN-coated tube. Videos of each sample also show that the SN sample sheds droplets at a higher rate (i.e. frequency) than the baseline surface. Figure 3c contains a plot of the condensation heat transfer coefficient data that has been calculated for the baseline tube. These data have been plotted with respect to the degree of subcooling between the environmental chamber temperature and the inlet cooling water temperature. Representative error bars are provided on the basis of error propagation for the uncertainties of the data measurement devices. Moving forward, these data will serve as the primary basis for comparison with the enhanced SN-coated tube data in order to draw conclusions on the effect of the coating.

3.3 SEM Imaging

In order to better characterize the nano-scale features of the silica nanospring coatings, scanning electron microscopy (SEM) images were also gathered using a Zeiss Supra 35VP microscope. These micrographs provide information on the uniformity of the coating, dimensions of the coating and springs, and can also provide information on the durability of the coating by examining the samples both before and after testing. Using the growth process methodology previously explained, a uniform coating on the circumference of each tube sample can be fabricated as shown in Fig. 4a. By increasing the magnification, the helical structure of individual springs can also be seen, as shown in Fig. 4b. These high magnification images also allow for the determination of the spring diameters and how much area is occupied by springs as opposed to the surrounding environment. The mat thickness is another critical dimension that can be measured with the help of the SEM. These imaging techniques provide a better understanding of the coating itself and may help to also explain and interpret certain results.

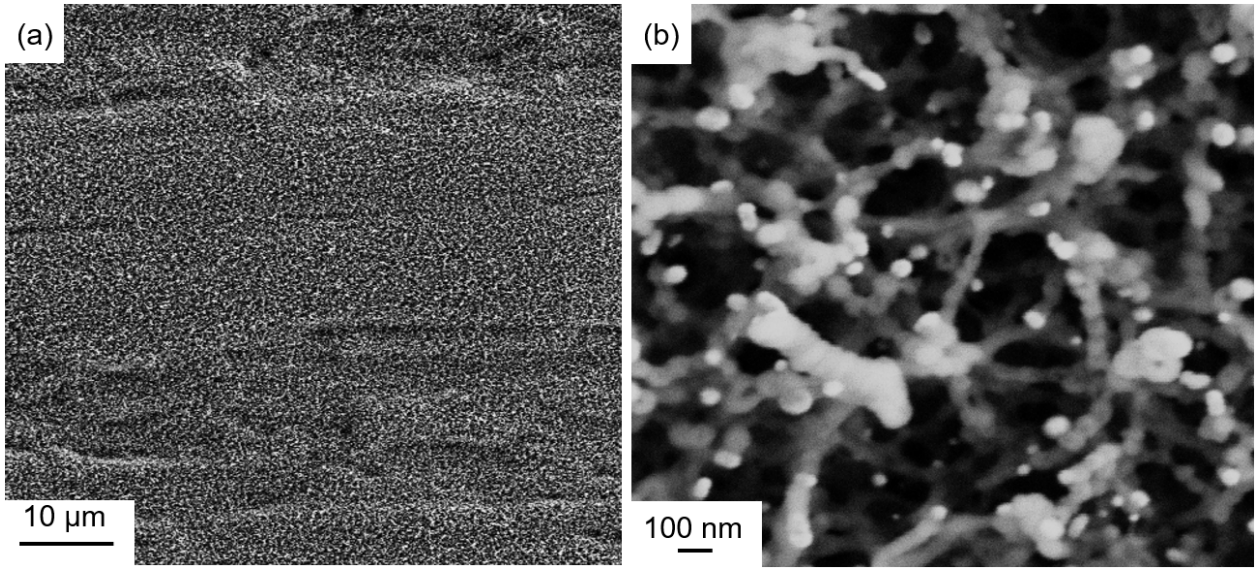

Figure 4: Scanning electron microscopy images showing (a) the uniformity of the silica nanospring coating, and (b) the helical structure and intertwinement of individual nanosprings in the mat

4. CONCLUSIONS

In this work, an amorphous silica nanospring coating was proposed as a possible candidate for improving condensation heat transfer performance. Although the coating is still in the early stages of testing, a number of previous studies and the gathered preliminary data to date have supported this idea and additionally provided some insight into the characteristics of the coating that might aid in the heat transfer process. Contact angles measured on SN-coated surfaces have exceeded 150° which classifies the coating as being superhydrophobic. Furthermore, the coating has been shown to promote

dropwise condensation (DWC), which is favorable over filmwise condensation in heat transfer applications. The high surface area coating is also capable of being functionalized, which allows for further alterations to the wettability and customization, if desired. A unique feature of the coating is that the areas of the underlying substrate remain exposed to the surrounding environment, allowing the aluminum (and its beneficial thermal properties) to still participate in the heat transfer process. Because the nanosprings are made of amorphous silica, they are capable of moving without breaking. This suggests the possibility of a reasonably high durability for the coating, especially in a non-abrasive condensation environment. Preliminary baseline condensation heat transfer data have been collected in a controlled environmental chamber, which will serve as a benchmark for evaluating the performance of the SN-coated tubes. Heat transfer coefficients in the range of 1,000 – 16,000 W m^{-2} K^{-1} have been measured, depending on the flow rate and degree of subcooling. Moving forward, the SN samples will also be evaluated. SEM imaging will be used to determine key surface dimensions and to address the issue of the durability of the coating. In addition, various media will be collected in order to gather information on differences in the condensation behavior including the shedding rate and average dimensions of condensed droplets. To date, the information gathered suggests that silica nanosprings are a promising idea for improving condensation heat transfer performance on round tubes.

NOMENCLATURE

CVD	Chemical vapor deposition	SEM	Scanning electron microscope
DAQ	Data acquisition unit	SN	Silica nanosprings
DWC	Dropwise condensation	VLS	Vapor-liquid-solid
FWC	Filmwise condensation	θ	Contact angle

REFERENCES

Alwazzan, M., Egab, K., Peng, B., Khan,J., Li, C., 2017a. Condensation of Hybrid-Patterned Copper Tubes (I): Characterization of Condensation Heat Transfer. Int. J. Heat Mass Transf. 112, 991-1004.

Alwazzan, M., Egab, K., Peng, B., Khan,J., Li, C., 2017b. Condensation of Hybrid-Patterned Copper Tubes (II): Visualization Study of Droplet Dynamics. Int. J. Heat Mass Transf. 112, 950-958.

Bakharev, P., Dobrokhotov, V., McIlroy, D., 2014. A Method for Integrating ZnO Coated Nanosprings into a Low Cost Redox-Based Chemical Sensor and Catalytic Tool for Determining Gas Phase Reaction Kinetics. Chemosensors 2(1), 56-68.

Bèdard, E., Lèvesque, S., Martin, P., Pinsonneault, L., Paranjape, K., Lalancette, C., Dolcè, C.-È., Villion, M., Valiquette, L., Faucher, S.P., Prèvost, M., 2016. Energy Conservation and the Promotion of Legionella Pneumonia Growth: The Probable Role of Heat Exchangers in a Nosocomial Outbreak. Infect. Control Hosp. Epidemiol. 37(12), 1475-1480.

Cantrell, T., Corti, G., Beaux, M., Prakash, T., McIlroy, D., Turba, T., Norton, G., 2010. Next Generation Nanospring-Enhanced Catalytic Converters. Clean Technology, Clean Technology and Sustainable Industries Organization, 267-270.

Corti, G., Wang, L., Major, D., Branen, J., Jabal, J., Branen, L., Nagler, J., Aston, E., Norton, G., McIlroy, D., 2007. Nanospring-Based Biosensors for Electrical DNA Microarrays. Materials Research Society Symposia Proceedings, Materials Research Society, V05-03.

Corti, G., Zhan, Y., Wang, L., Hare, B., Cantrell, T., Beaux II, M., Prakash, M., Ytreberg, M., Miller, M., McIlroy, D., 2013. Nanoscale Geometry and Spillover on Room Temperature Storage of Hydrogen on Silica Nanosprings. J. Phys. D: Appl. Phys. 46, 505307.

Corti, G., Brown, J., Rajabi, N., McIlroy, D., 2018. Threefold Growth Efficiency Improvement of Silica Nanosprings by Using Silica Nanosprings as a Substrate. Nanotechnology 29(11), 115604.

Corti, G., Schmiesing, N., Barrington, G., Humphreys, M., Sommers, A., 2019. Characterization of Methyl-Functionalized Silica Nanosprings for Superhydrophobic and Defrosting Coatings. ACS Appl. Mater. Interfaces 11, 4607-4615.

Das, A., Kilty, H., Marto, P., Andeen, G., Kumar, A., 1999. The Use of an Organic Self-Assembled Monolayer Coating to Promote Dropwise Condensation of Steam on Horizontal Tubes. J. Heat Transf. 122(2), 278-286.

Ghosh, A., Beaini, S., Zhang, B., Ganguly, R., Megaridis, C., 2014. Enhancing Dropwise Condensation through Bioinspired Wettability Patterning. Langmuir 30(43), 13103-13115.

Martinelli, F., Caruso, A., Moschini, L., Turano, A., Scarcella, C., Speziani, F., 2000. A Comparison of Legionella Pneumophila Occurrence in Hot Water Tanks and Instantaneous Devices in Domestic, Nosocomial, and Community Environments. Curr. Microbiol. 41(5), 374-376.

McIlroy, D., Alkhateeb, A., Zhang, D., Aston, D., Marcy, A., Norton, G., 2004. Nanospring Formation – Unexpected Catalyst Mediated Growth. J. Phys. Condens. Matter. 16(12), R415-R440.

Miljkovic, N., Enright, R., Wang, E., 2012. Effect of Droplet Morphology on Growth Dynamics and Heat Transfer during Condensation on Superhydrophobic Nanostructured Surfaces. ACS Nano 6(2), 1776-1785.

Preston, D., Mafra, D., Miljkovic, N., Kong, J., Wang, E., 2015. Scalable Graphene Coatings for Enhanced Condensation Heat Transfer. Nano Lett. 15(5), 2902-2909.

Rajkumar, M., Praveen, A., Arun Krishna, R., Asirvatham, L., Wongwises, S., 2018. Experimental Study of Condensation Heat Transfer on Hydrophobic Vertical Tube. Int. J. Heat Mass Transf. 120, 305-315.

Rose, J., 2002. Dropwise Condensation Theory and Experiment: A Review. Proc. Inst. Mech. Eng. Part A J. Power Energy 216(2), 115-128.

Sai, V., Gangadean, D., Niraula, I., Jabal, J., Corti, G., McIlroy, D., Aston, D., Branen, J., Hrdlicka, P., 2011. Silica Nanosprings Coated with Noble Metal Nanoparticles: Highly Active SERS Substrates. J. Phys. Chem. C 115(2), 453-459.

Schilke, K., Wilson, K., Cantrell, T., Corti, G., McIlroy, D., Kelly, C., 2010. A Novel Enzymatic Microreactor with Aspergillus Oryzae β-Galactosidase Immobilized on Silicon Dioxide Nanosprings. Biotechnol. Prog. 26(6), 1597-1605.

Schmiesing, N., Sommers, A., 2017. Defrosting Performance on Hydrophilic, Hydrophobic, and Micro-Patterned Gradient Heat Transfer Surfaces. Sci. Technol. Built Environ. 23(6), 946-959.

Tanner, D., Pope, D., Potter, C., West, D., 1968. Heat Transfer in Dropwise Condensation at Low Steam Pressure in the Absence and Presence of Non-Condensable Gas. Int. J. Heat Mass Transf. 11(2), 181-190.

Timalsina, Y., Oriero, D., Cantrell, T., Prakash, T., Branen, J., Aston, D., Noren, K., Nagler, J., Rastogi, S., McIlroy, D., Corti, G., 2010. Characterization of a Vertically Aligned Silica Nanospring-Based Sensor by Alternating Current Impedance Spectroscopy. J. Micromech. Microeng. 20(9), 095005.

Tsuchiya, H., Tenjimbayashi, M., Moriya, T., Yoshikawa, R., Sasaki, K., Togasawa, R., Yamazaki, T., Manabe, K., Shiratori, S., 2017. Liquid-Infused Smooth Surface for Improved Condensation Heat Transfer. Langmuir 33(36), 8950-8960.

Wang, L., Major, D., Paga, P., Zhang, D., Norton, M., McIlroy, D., 2006. High Yield Synthesis and Lithography of Silica-Based Nanospring Mats. Nanotechnology 17(11), S298.

Wen, R., Li, Q., Wu, J., Wu, G., Wang, W., Chen, Y., Ma, X., Zhao, D., Yang, R., 2017. Hydrophobic Copper Nanowires for Enhancing Condensation Heat Transfer. Nano Energy 33, 177-183.

Wojcik, P., Bakharev, P., Corti, G., McIlroy, D., 2017. Nucleation, Evolution, and Growth Dynamics of Amorphous Silica Nanosprings. Mater. Res. Express 4(1), 015004.

Yang, K.-S., Lin, K.-H., Tu, C.-W., He, Y.-Z., Wang, C.-C., 2017. Experimental Investigation of moist Air Condensation on Hydrophilic, Hydrophobic, Superhydrophilic, and Hybrid Hydrophobic-Hydrophilic Surfaces. Int. J. Heat Mass Transf. 115, 1032-1041.

Zhao, C.-Y., Ji, W.-T., Jin, P.-H., Zhong, Y.-J., Tao, W.-Q., 2017. The Influence of Surface Structure and Thermal Conductivity of the Tube on the Condensation Heat Transfer of R134a and R404A over Single Horizontal Enhanced Tubes. Appl. Therm. Eng. 125, 1114-1122.

Manuscript ID: 1870
DOI: 10.18462/iir.icr.2019.1870

CO_2 ejector modelling using CFD: current status

Knut RINGSTAD[(a)], Yosr ALLOUCHE[(a)], Paride GULLO[(a)], Krzysztof BANASIAK[(b)], Armin HAFNER[(a)]

[(a)] Norwegian University of Science and Technology, Kolbjørn Hejes vei 1B, 7491 Trondheim, Norway,
[(b)] SINTEF Energy, Kolbjørn Hejes vei 1d, 7465 Trondheim, Norway
knut.e.ringstad@ntnu.no, armin.hafner@ntnu.no

ABSTRACT

This paper presents the current status of CFD modelling applied to CO_2 two-phase ejectors for refrigeration applications. Previous reviews on CO_2 ejector technology have provided detailed analysis and thorough discussion about the optimal design and performance parameters. However, there is still a lack of information about CFD modelling of CO_2 ejectors, mainly when it comes to the accuracy of the two-phase ejector models. The ultimate goal of this paper is to provide a complete overview about CFD modelling of two-phase CO_2 ejectors for refrigeration applications, as mainly analytical approaches were previously discussed. The fundamental background for the research work carried out within CO_2 two-phase modelling using CFD is presented through this review. Moreover, it highlights the main challenges that are still needed to be overcome mainly related to turbulence modelling, fluid properties and 3D-effects in multi-phase flows.
Keywords: CFD, Expansion Work Recovery, Multi-Phase Flow, R744, Trans-Critical Refrigeration System, Two-Phase Ejector.

1. INTRODUCTION

The entry into force of the EU F-Gas Regulation 517/2014 (European commission, 2014) has led CO_2 (R744) to take centre stage as the most promising refrigerant for many applications. Also, despite its low critical temperature, nowadays trans-critical R744 vapour-compression systems offer great energy efficiencies even at high cooling medium temperatures. This result can be achieved by recovering part of the available expansion work with the aid of two-phase ejectors. As an example, it was found that commercial R744 refrigeration units consume up to 25% less electricity than the solutions relying on man-made working fluids in warm climates (Gullo et al., 2018). Furthermore, ejector-equipped CO_2 vapour-compression systems are expected to attain similar energy benefits to those experienced in supermarkets in other applications too (Hafner et al., 2014). However, the potential improvements in performance offered by an ejector are highly sensitive to its four characteristic dimensions, i.e. suction nozzle, motive nozzle, mixing chamber and diffuser. Therefore, methods for efficient and accurate design of ejectors has gained interest from industry and academia. A promising tool for enhancing ejector performance is the advanced computational fluid dynamics (CFD). CFD offers insights into the complex flow in the ejector device and has already been applied to single-phase ejector with satisfactory results (Grazzini et al., 2018). An overview of R744 two-phase ejector CFD models was presented by Nowak et al. (2016) and also discussed by Elbel and Lawrence (2016). These investigations revealed that currently state of the art CFD models can quite accurately predict certain flow parameters in R744 two-phase ejectors. However, the comparison with the limited experimental results uncovers significant errors, especially at off-design conditions. In addition, the limitations and advantages of different models as well as recent developments and challenges in flash models for R744 have not lately been described. Therefore, the aim of this paper is to bridge the aforementioned knowledge gaps by carrying out a comprehensive review on the developments of CFD models for R744 two-phase ejectors. Special attention has been given to two-phase flashing models, as this has been the discussion focus in recent literature.

2. EVALUATION OF CURRENT STATUS

CO_2 two-phase ejectors were primarily designed and investigated mainly based on experimental studies (Elbel and Lawrence, 2016). The experimental work by Nakagawa et al. (2011) revealed improvements in Coefficient of Performance (COP) of up to 26% compared to systems without ejectors. However, design of ejectors can be carried out more efficiently with models, as the time and resource costs of experimental studies heavily outweigh those of models. Furthermore, accurate models can give insights into the flow physics that can allow for improved and new designs. Still, unobtrusive experimental results for the validation of these models is lacking due to the difficulty involved. While much progress has been made on R744 ejector modelling, the treatment of multiphase flows is not well understood and many simplifying assumptions have been considered. Several theoretical frameworks have been presented for such models The development started with one dimensional models with the homogeneous equilibrium model (Liu and Groll, 2012), which was later furthered with more advanced non-equilibrium approaches (Banasiak and Hafner, 2011; Brown et al., 2013). While able to capture much of the flow physics, 3D effects were found to be non-negligible (Smolka et al., 2013). These limitations ushered in a much research in the multidimensional CFD models. The paper is organized as follows, the homogeneous equilibrium model, homogeneous relaxation model and the mixture models are presented in Subsection 2.1-2.3. Some applications of these models are described in Subsection 2.4, further model reduction is discussed in Subsection 2.5. The advantages and limitations of the aforementioned models are summarized in Section 3. Finally, main conclusions are given in Section 4.

2.1. Homogeneous Equilibrium Model

The high accuracy and relative simplicity of the homogeneous equilibrium model (HEM), where two-phase pure CO_2 mixture is modelled as a pseudo-single-phase fluid, has been demonstrated for one-dimensional models (Elbel and Lawrence, 2016). The HEM approach assumes instantaneous thermodynamic and mechanical equilibrium between liquid and vapour. With these assumptions both phases are described with a single velocity-($\vec{u}$), temperature- (T) and pressure-field (P). Smolka et al. (2013) implemented such a homogeneous equilibrium model (HEM) into a 3D CFD model using ANSYS Fluent (ANSYS, 2019) to capture two-phase effects in R744 ejectors. They used an enthalpy formulation (Equation 1) in the Energy equation, treating enthalpy, instead of temperature, as the transported variable in the energy equation. The energy equation is then re-written into:

$$\nabla \cdot (\rho \vec{u} h) = \nabla \cdot (\Gamma_{eff} \nabla h) + \dot{S}_{h1} + \dot{S}_{h2} + \dot{S}_{h3} \qquad \text{Eq. (1)}$$

The source terms $\dot{S}_{h1-3}$ describe the mechanical energy, the irreversible dissipation of the kinetic energy variations and the dissipation of the turbulent kinetic energy (Smolka et al., 2013), respectively. Under the equilibrium assumption the pressure and enthalpy uniquely define the thermodynamic state in the two-phase dome:

$$\rho, \mu, k, c_p = f(P, h) \qquad \text{Eq. (2)}$$

The two-phase equilibrium properties were in Smolka et al. (2013) found using the REFPROP library (Lemmon et al., 2013), and implemented into Fluent using user-defined functions (UDFs). Experimental results performed at the SINTEF Energy Research laboratory in Trondheim (Norway) were presented and used to validate the model. Their findings indicate that 3D effects are non-negligible as was commonly assumed in previous simulations (Colarossi et al., 2012). The HEM approach produced results that could accurately describe the global parameters (e.g. mass flow rate) for conditions near the critical point. A maximum deviation of about 12% for the mass flow rate was computed. A similar approach to the work by Smolka et al. (2013) was proposed by Lucas et al. (2014). A 3D CFD model using the HEM approach was implemented in the open source CFD framework OpenFOAM (Weller et al, 1998), using the TEMO-media library. The results were compared with the experimental data collected by Lucas et al. (2013). The comparison showed 20% and 10% discrepancy in pressure recovery when operating with and without suction flow, respectively. They concluded that this error difference was due to the model's inaccurate description of mixing losses. Further studies with the HEM were implemented by Giacomelli et al. (2016, 2018a).

In these works, the HEM was implemented with look-up tables generated from the REFPROP library for speed of sound and density.
Palacz et al. (2015) evaluated the application range of the HEM approach for R744 ejectors within typical supermarket refrigeration operational conditions. Here, a multi-ejector block was investigated with experimental validation for 24 different running modes. Their findings indicate that the HEM approach can produce accurate results when the operating conditions are close to or above the critical pressure of CO_2. However, as the motive pressure and temperature is decreased the accuracy of the HEM approach is dramatically lowered when compared to their experimental results. These significant errors were attributed to the non-equilibrium effects at operating conditions away from the critical point. These effects are discussed in the next paragraph.
The limitations of the HEM have previously been discussed in the literature (Wallis, 1980, Liao and Lucas, 2017). In general, states further away from the critical point have a wider meta-stable region. This translates to slower meta-stable transition and larger significance for non-equilibrium effects. Further limitations concerning the homogeneous approaches is discussed in Section 3.

2.2. Homogeneous Relaxation Model

Palacz et al. (2015) concluded that non-equilibrium models are necessary to properly model a R744 ejector for the whole range of common supermarket operating conditions. Bilicki and Kestin (1990) introduced the homogeneous relaxation model, a relaxed version of the HEM. The homogeneous relaxation model (HRM) assumes, similarly to the HEM approach, a single pseudo fluid representing the mixture of the two-phases. However, meta-stability effects are treated by applying a relaxed vapour quality transport equation (Eq. 3).
This relaxation delays the onset of phase change in the meta-stable region. Downar-Zapolski et al. (1996) defined a relation for the relaxation time, θ, formulated in Eq. 4. The parameters of Eq. 4 are the mixture void fraction defined in Eq. 5, and φ is a non-dimensionalized pressure parameter. This latter parameter was defined for supercritical parameters in Angielczyk et al. (2010) stated in Eq. 6. The exponents a and b were empirically fit for CO_2 in Angielczyk et al. (2010). Among the first works with CFD simulations of R744 ejectors using the HRM is the model used by Colarossi et al. (2012). In this work, the HRM was implemented in a 2D CFD model using the OpenFOAM framework. As a starting point, they used the empirical relations for the relaxation factor for flashing water (Downar-Zapolski et al., 1996). Colarossi et al. (2012) compared the resulting pressure recovery from their simulations with the experimental results in Nakagawa et al. (2011). The comparison showed up to 50% deviation, with an average error of 18.6%. They concluded that the non-equilibrium effects were negligible, this was however evaluated near the critical point of R744.

$$\frac{Dx}{Dt} = \frac{\bar{x} - x}{\theta} \qquad \text{Eq. (3)}$$

$$\theta = \theta_0 \alpha^a \varphi^b \qquad \text{Eq. (4)}$$

$$\alpha = \frac{\rho_{sl} - \rho}{\rho_{sl} - \rho_{sv}} \qquad \text{Eq. (5)}$$

$$\varphi = \left| \frac{P_{sat}(s_{motive}) - P}{P_{crit} - P_{sat}(s_{motive})} \right| \qquad \text{Eq. (6)}$$

The results by Palacz et al. (2015) were contrasted with those obtained by Palacz et al. (2017a), which were based on the HRM approach relying on the constant relaxation time for CO_2 presented by Angielczyk et al. (2010). The comparison revealed that the HRM was able to improve model prediction compared to HEM when the operating regime is far away from the critical point. However, at supercritical inlet conditions the HEM approach would perform better than their HRM. Overall, the authors found that their current HRM only improved model accuracy by up to 5% compared to the HEM. This improvement was found unsatisfactory which prompted further investigation into the choice of relaxation time.

The conclusions from Palacz et al. (2017a) were that a constant relaxation time is not appropriate when a large range of operating conditions is considered. Much investigation went into the different parameters of equation (4) in the study by Haida et al. (2018d). The effect of the different parameters θ_0, a and b on the nozzle expansion process was discussed. In the mentioned study an optimization algorithm was used to find optimal relaxation time parameters for different operational ranges. The authors divided the motive nozzle pressure into a high, medium and low pressure range. In each pressure range the RT-parameters that minimized the mass flow rate error were found. The modified HRM showed improved results with below 15% error for the mass flow are for the extended operating range.

2.3. Mixture Models

The physical mechanisms of phase change are only indirectly treated by the HEM and HRM, as the two-phase properties are determined based on equilibrium states. An alternative approach to evaluate the phase fractions is using mixture models. Similar to the homogeneous approaches, an averaged mass, momentum and energy equation are solved with the single pseudo fluid approach (Eqs. 7-9). However, an additional equation governing the transport of the phase fraction is included, Eq. 10. Here, additional submodels for the phase mass transfer mechanisms (Λ) allow for more accurate estimates of the phase fraction (α). The state of each phase is then evaluated separately and thermodynamic properties are found by volume and mass averaging from the vapour and liquid properties. This contrasts the HEM and HRM, where the phase fraction and other fluid properties are evaluated based on the equilibrium state in the two phase region (Eq. 2).

$$\frac{\partial \rho_m}{\partial t} + \frac{\partial}{\partial x_j}\left(\rho_m u_{m,j}\right) = 0 \qquad \text{Eq. (7)}$$

$$\frac{\partial \rho_m u_{m,i}}{\partial t} + \frac{\partial}{\partial x_j}\left(\rho_m u_{m,j} u_{m,i} + P\delta_{ij} - \tau_{ij,eff}\right) = 0 \qquad \text{Eq. (8)}$$

$$\frac{\partial \rho_m E_m}{\partial t} + \frac{\partial}{\partial x_j}\left(\rho_m u_{m,j} h_m - q_{j,eff} + u_{m,i}\tau_{ij,eff}\right) = 0 \qquad \text{Eq. (9)}$$

$$\frac{\partial \rho_k \alpha_k}{\partial t} + \frac{\partial}{\partial x_j}\left(\rho_k u_j \alpha_k\right) = \Lambda_e - \Lambda_c \qquad \text{Eq. (10)}$$

the subscript k is the phase index, summing over the N number of phases. To the best of the authors' knowledge, the first use of a mixture model for the R744 ejector was presented in Yazdani et al. (2012). In the mentioned paper, a non-equilibrium mixture model was implemented into a 3D CFD model in ANSYS Fluent. Yazdani et al. (2012) found the thermodynamic properties using the REFPROP libraries for supercritical fluid and subcooled fluid. States inside the saturation region were interpolated from the saturation lines in the REFPROP library. Mass transfer was considered through condensation and evaporation mechanisms, where meta-stability was treated by introducing a time delay analogous to the relaxation time of the HRM. The model of Yazdani et al. (2012) also included additional terms for velocity slip between the phases in Equation 8.
Recently, Giacomelli et al. (2018b) implemented a mixture model in ANSYS Fluent to simulate supersonic nozzle flow. In this model the compressibility of both the liquid and gas phase was considered with user-defined real gas models. Here, the two-phases were treated computationally as two interacting fluids of different species, allowing their better description. The model uses look-up tables based on the NIST REFPROP library to define the properties of both phases. Furthermore, the presented method is applicable for a wide range of multiphase and compressible flows.

2.4. Applications

The presented CFD models have been extensively used for investigations of designs and concepts. The CFD model by Smolka et al. (2013) was used to investigate irreversibility in the ejector in

Banasiak et al. (2014). The entropy increase in different sections of the ejector was evaluated with different ejector geometries. The analysis shows that the mixing section is one of the most significant contributors to entropy generation due to the complex shock- and turbulent structures. Furthermore, the authors argue that geometric optimization should focus on the interactions between different geometric parameters, as individual optimization of these parameters in isolation yields suboptimal results. Entropy generation in ejectors was further investigated by Sierra-Pallares (2016), where a direct method was applied to investigate entropy generation in three R134a ejectors. The authors novel approach involved solving the differential equations of entropy transport, identifying four mechanisms of entropy generation. Their investigation revealed that the primary contributor is the turbulent viscous dissipation produced in the shock train and nozzle exit shear layer.
Later, this model was applied for the investigation of an optimized shape of R744 two-phase ejectors by Palacz et al. (2016). The optimization tool was developed with the *ejectorPL* software. This is a script that automates most of the CFD workflow in the pre- and post-processing, and feeds the resulting model into the optimization algorithm. The optimization was done using both a genetic algorithm and an evolutionary algorithm for six geometrical parameters to maximize the ejector efficiency. The results show that these methodologies can effectively be used for shape optimization when the operating conditions are within the CFD model's range of validity. The shape investigations were furthered in Palacz et al. (2017b) with 3 more geometric parameters and for two additional ejector geometries than in Palacz et al. (2016). Here the genetic algorithm was applied. This procedure improved the ejector efficiencies by 6% in a robust and efficient way. A comparative study of the controllable needle ejector (Liu et al., 2012) and the fixed geometry ejector (as used in the multi-ejector block concept formulated by Hafner et al., 2014) was done by Smolka et al. (2016). The previously mentioned model using the HEM approach was used. The simulation results showed high and predictable ejector efficiency for the fixed-geometry setup for all investigated operating conditions. On the one hand, the controllable-geometry case was able to outperform the fixed-geometry case for certain needle positions. On the other hand, it was shown that these positions were difficult to evaluate, and gave less predictable efficiency. Simulations of ejector operation of three different ejectors in a multi-ejector block were presented by Bodys et al. (2016). The investigation focuses on the use of swirl-motion generator on ejector performance. The authors suggest that improvements to the mass entrainment ratio could be achieved at very high motive inlet rotational speeds. Furthermore, a full-scale 3D CFD investigation of the multi-ejector block was carried out by Bodys et al. (2017). The authors demonstrated the stable operation of the multi-ejector based refrigeration unit and indicated the possibility of shape optimization for pressure loss reduction.
The HRM model presented by Palacz et al. (2017a) was implemented together with a heat transfer model (coupled with the CFD solver) for the ejector walls by Haida et al. (2018a). An extensive sensitivity analysis of the mesh was also performed. The experimental and numerical investigation demonstrated high accuracy of the model, being capable of reproducing the wall temperature distribution within ± 5K. The accuracy of different turbulence models for the prediction of near wall temperature distribution as well as of mass entrainment ratio was presented. Four turbulence models were compared: (i) k−ε Realizable model, (ii) k−ω SST model, (iii) Transition SST model and (iv) Reynold stress model. The comparison showed that choice of turbulence models had a significant effect on the results. The Transition SST turbulence model yielded the most accurate prediction of mass entrainment ratio and wall temperature distribution. Furthermore, the investigation showed that the effect of ambient temperature and non-adiabatic boundary conditions on the ejector outer wall was negligible. However, the non-adiabatic boundary conditions on the inner ejector wall had a significant impact on the flow parameters. This implies that the use of non-adiabatic ejector wall boundary conditions may be important to capture the correct flow physics. The authors also suggest that the use of materials with low thermal conductivity may improve ejector performance.

2.5. Model Reduction

The large computational time expense of CFD models are, in general, prohibitive for large scale optimization procedures. Computational tools such as *ejectorPL*, that can quickly generate CFD models are important for rapid investigation of potential improvements. Therefore, reducing the model size while maintaining the high accuracy of the CFD models have recently been discussed. The authors would like to point to two methods that have recently been applied for the reduction of ejector CFD models, reduced order modelling and lumped parameter modelling. Reduced order models attempts to find an optimal basis for a model by looking at previous results. These results are typically outputs from a high accuracy CFD model or an experimental investigation. The

investigations by Haida et al. (2018b, 2018c) brought to light that the reduced order model ensures high accuracy results (i.e. within 10% mass flow rate error) for a R744 ejector over most of the investigated conditions.
Besagni (2019) presented a thorough discussion on the current and future state of ejector modelling. Here, emphasis was put on the lumped parameter approach. The integration of CFD models with lumped parameter models was previously described by the mentioned author. While not yet applied to R744 systems, this should be considered for future investigations. Still, research into more accurate CFD models will continue to be important as these directly impact the quality of these reduced models.

3. DISCUSSION

A summary of the different two-phase methods described in this paper is presented in Table 1. The HEM approach has the advantage of simplicity and stability, and can yield accurate results for supercritical conditions. It is well suited for initial designs and optimizations, however has limited accuracy for subcritical conditions. The HRM has been developed to overcome the main limitations of the HEM, while retaining much of the benefits of the HEM. The HRM considers meta-stable effects, and using variable relaxation times can yield accurate results for sub- and supercritical conditions. The mixture model is a more advanced model that solves an additional conservation equation for the phase fraction, however this requires further sub-modelling for closure of the equations. Here, separate evaluation of the liquid and gas states gives a more accurate average value for the fluid transport properties. Both the HRM and the mixture model have parameters of non-equilibrium that needs to be tuned, based on substantial experimental effort. This may help generate results with higher reliability, however requires detailed knowledge of the flow conditions.
All discussed models for the R744 ejector treat the two-phase flow as a single phase fluid with some notion of average transport properties. This assumption is severely limiting as all information about phase interfaces are lost, furthermore transport properties such as an averaged fluid viscosity and speed of sound are not well defined. Some discussion on the current modelling of these properties can be found in Awad and Muzychka (2008). However, due to the lack of experimental, tuning an accurate two-fluid model is beyond the current state of the art.

Table 1. Summary of two-phase models used for R744 ejector CFD modelling

Model	Advantages	Challenges and limitations
Homogeneous Equilibrium model Smolka et al. (2013), Lucas et al. (2014), Giacomelli et al. (2016)	-Simplicity and stability, -Accurate at supercritical conditions, -Extensively tested in literature	-Does not consider meta-stability (underestimates flashing flows)
Homogeneous Relaxation model Colarossi et al. (2012), Palacz et al. (2017a), Haida et al. (2018a)	-Considers meta-stability, -Extended with variable relaxation time for subcritical conditions	-Empirically based parameters for relaxation time, -Requires tuning of parameters
Mixture model Yazdani et al. (2012), Giacomelli et al. (2018b)	-Considers meta-stability, -Can more accurately evaluate the phase fractions by mass transfer modelling -Highly accurate results for motive flows	-Increased complexity, -Requires tuning of model parameters, -Less profound literature database on R744 ejectors

All mentioned methods are based on a pseudo-fluid approach. While more advanced two-phase models have been proposed and utilised in the literature for flashing water (Liao and Lucas, 2017), this has not yet been feasible for R744 ejectors. Mainly, this is due to the small dimensions of the

R744 ejectors, which limit experimental investigations. Many other research questions remain unanswered and is beyond the scope of this review. One of the toughest challenges is proper understanding of turbulent effects. While model tests have been performed with different Reynolds Averaged Navier-Stokes models, little is known about the two-phase effects on turbulence. Furthermore, the effects of wall heat transfer (Haida et al., 2018a) and wall surface roughness (Brezgin et al., 2017) have been shown to have an effect on the flow. Also, it has never been quantitatively estimated how much the presence of lubricants dissolved/mixed with R744 could influence first the fluid properties and second the validation procedures performed in all the reported papers. Other aspects of modelling including mesh design, solvers, 3D-effects, shock-capturing and computational requirements should be further addressed. Lastly, the interactions between the aforementioned factors may be important, and understanding if we are tuning the correct physical phenomenon with the available experimental results remains a major challenge.

4. CONCLUSIONS

The transition to more environmentally friendly refrigeration systems has brought about a great interest in ejector-equipped CO_2 systems for several applications and operating in any climate context. Much due to the size of this component accurate CFD models have been used to improve its design. The HEM approach has been the most prominently used model, and has been applied for design applications. Due to inherent limitations of the equilibrium assumption, the HRM and mixture models have been implemented into commercial CFD software. These models include meta-stability effects, which have been found to be important for R744 refrigeration applications. These methods have been applied for investigations of heat transfer, swirl generation, entropy generation and controllable geometries. Furthermore, methods for reducing computational cost of these models have recently been discussed. While the currently available models are able to reproduce experimental results with satisfactory accuracy, further research into turbulence, multiphase effects and shock structures may improve model accuracy and enable improved design procedures for R744 ejectors. Further discussion on the different aspects in CFD modelling of R744 ejectors will be presented in future review work.

ACKNOWLEDGEMENTS

The work is part of HighEFF - Centre for an Energy Efficient and Competitive Industry for the Future, an 8-year Research Centre under the FME-scheme (Centre for Environment-friendly Energy Research, 257632/E20). The authors gratefully acknowledge the financial support from the Research Council of Norway and user partners of HighEFF.

NOMENCLATURE

CFD	Computational fluid dynamics	*COP*	Coefficient of Performance
HEM	Homogeneous equilibrium model	*HRM*	Homogeneous relaxation model
UDF	User defined function		
a,b	Dimensionless exponents	c_p	Heat capacity ($kJ \cdot kg^{-1} \cdot K^{-1}$)
E	Total energy ($kg \cdot s^{-2} m^{-1}$)	*h*	Specific enthalpy ($kJ \cdot kg^{-1}$)
k	Thermal conductivity ($kJ \cdot s^{-1} \cdot m^{-2} K^{-1}$)	*P*	Pressure (bar)
s	Specific entropy ($kJ \cdot kg^{-1} \cdot K^{-1}$)	*S*	Enthalpy source term
T	Temperature (K)	*u*	Velocity (ms^{-1})
x	Vapour quality		
	Greek letters		
α	Phase fraction	Γ	Diffusion coefficient
θ	Relaxation time	Λ	Mass transfer coefficient
μ	Dynamic viscosity ($kg \cdot m^{-1}\ s^{-1}$)	ρ	Density ($kg \cdot m^{-3}$)
τ	Shear stress	φ	Non-dimensionalized pressure parameter
	Subscripts		
c	Condensation	*crit*	Critical condition

e	Evaporation	*eff*	Effective
k	Phase index	*m*	Mixture property
motive	Motive nozzle condition	*sat*	Saturated
sv	Saturated vapour	*sl*	Saturated liquid

REFERENCES

Angielczyk, W., Bartosiewicz, Y., Butrymowicz, D., Seynhaeve, J.-M., 2010. 1-D Modeling of Supersonic Carbon Dioxide Two-Phase Flow Through Ejector Motive Nozzle, Int. Refrig. Air Cond. Conf, 1-8

ANSYS® Fluent, 2019. Latest Release 19.2

Awad, M.M., Muzychka, Y.S., 2008. Effective property models for homogeneous two-phase flows, Exp. Therm Fluid Sci. 33 (1), 106-113

Banasiak, K, Hafner, A., 2011, 1D Computational model of a two-phase R744 ejector for expansion work recovery, Int. J. Therm. Sci. 50(11), 2235-2247

Banasiak, K., Hafner, A., Kriezi, E.E., Madsen, K.B., Birkelund, M., Fredslund, K., Olsson, R., 2015. Development and performance mapping of a multi-ejector expansion work recovery pack for R744 vapor compression units. Int. J. Refrig 57, 265–276.

Banasiak, K., Palacz, M., Hafner, A., Bulinski, Z., Smołka, J., Nowak, A.J., Fic, A., 2014. A CFD-based investigation of the energy performance of two-phase R744 ejectors to recover the expansion work in refrigeration systems: An irreversibility analysis. Int. J. Refrig 40, 328–337.

Besagni, G., 2019. Ejectors on the cutting edge: the past, the present and the perspective. Energy 170, 998-1003.

Bilicki, Z., Kestin, J., 1990. Physical Aspects of the Relaxation Model in Two-Phase Flow. Proc Math Phys Eng Sc 428 (1875), 379–397.

Bodys, J., Palacz, M., Haida, M., Smolka, J., Nowak, A.J., Banasiak, K., Hafner, A., 2017. Full-scale multi-ejector module for a carbon dioxide supermarket refrigeration system: Numerical study of performance evaluation. Energy Convers. Manage. 138, 312–326.

Bodys, J., Smolka, J., Palacz, M., Haida, M., Banasiak, K., Nowak, A.J., Hafner, A., 2016. Performance of fixed geometry ejectors with a swirl motion installed in a multi-ejector module of a CO_2 refrigeration system. Energy 117, 620–631.

Brezgin, D. V., Aronson, K. E., Mazzelli, F., & Milazzo, A. (2017). The surface roughness effect on the performance of supersonic ejectors. Thermophys. Aeromech., 24(4), 553-561.

Brown, S., Martynov, S., Mahgerefteh, H., Proust, C., 2013. A homogeneous relaxation flow model for the full bore rupture of dense phase CO_2 pipelines. Int. J. Greenhouse Gas Control 17, 349–356.

Colarossi, M., Trask, N., Schmidt, D.P., Bergander, M.J., 2012. Multidimensional modeling of condensing two-phase ejector flow. Int. J. Refrig 35 (2), 290–299.

Downar-Zapolski, P. Bilicki, Z. Bolle, L., Franco, J., 1996. The non-equilibrium relaxation model for one-dimensional flashing liquid flow. Int. J. Multiphase Flow 22 (3), 473–483.

Elbel, S., Lawrence, N., 2016. Review of recent developments in advanced ejector technology. Int. J. Refrig 62, 1–18.

European Commission, 2014. Regulation (EU) No 517/2014 of the European Parliament and of the Council of 16th April 2014 on fluorinated greenhouse gases and repealing Regulation (EC), No 842/2006. Brussels, Belgium.

Giacomelli, F., Mazzelli, F., Milazzo, A., 2018b. A novel CFD approach for the computation of R744 flashing nozzles in compressible and metastable conditions. Energy 162, 1092–1105.

Giacomelli, F., Banasiak, K., Hafner, A., 2018a. Experimental and Numerical Investigation on an Ejector for CO_2 Vapor Compression Systems, 13th IIR Gustav Lorentzen Conference, IIR, 1179-1187

Giacomelli, F., Mazzelli, F., Milazzo, A., 2016. Evaporation in supersonic CO_2 ejectors: analysis of theoretical and numerical models. 9th International Conference on Multiphase Flow, ICMF, 22-27

Gullo, P., Hafner, A., Banasiak, K., 2018. Transcritical R744 refrigeration systems for supermarket applications: Current status and future perspectives. Int. J. Refrig 93, 269-310,

Grazzini, G., Milazzo, A., Mazzelli, F., 2018. Ejectors for efficient refrigeration: Design, applications and computational fluid dynamics. Springer International Publishing.

Hafner, A., Forsterling, S., Banasiak, K., 2014. Multi-ejector concept for R-744 supermarket refrigeration. Int. J. Refrig 43, 1–13.

Haida, M., Smolka, J., Hafner, A., Palacz, M., Banasiak, K., Nowak, A. J., 2018d. Modified homogeneous relaxation model for the R744 trans-critical flow in a two-phase ejector. Int. J. Refrig 85, 314–333.

Haida, M., Smolka, J., Hafner, A., Ostrowski, Z., Palacz, M., Nowak, A.J., Banasiak, K., 2018c. System model derivation of the CO_2 two-phase ejector based on the CFD-based reduced-order model. Energy 144, 941–956.

Haida, M., Smolka, J., Hafner, A., Ostrowski, Z., Palacz, M., Madsen, K.B., Forsterling, S., Nowak, A.J., Banasiak, K., 2018b. Performance mapping of the R744 ejectors for refrigeration and air conditioning supermarket application: A hybrid reduced-order model. Energy 153, 933–948.

Haida, M., Smolka, J., Hafner, A., Mastrowski, M., Palacz, M., Madsen, K.B., Nowak, A.J., Banasiak, K., 2018a. Numerical investigation of heat transfer in a CO_2 two-phase ejector. Energy 163, 682–698.

Lemmon E.W., Huber M.L., McLinden M.O., 2013, Nist standard reference database 23: reference fluid thermodynamic and transport properties - refprop, National Institute of Standards and Technology, Standard Reference Data Program.

Liao, Y., Lucas, D., 2017. Computational modelling of flash boiling flows: A literature survey. Int. J. Heat Mass Transfer 111, 246–265.

Liu, F., Li, Y., Groll, E. A., 2012. Performance enhancement of CO_2 air conditioner with a controllable ejector. Int. J. Refrig 35 (6), 1604–1616.

Lucas, C., Rusche, H., Schroeder, A., Koehler, J., 2014. Numerical investigation of a two-phase CO_2 ejector. Int. J. Refrig 43, 154–166.

Lucas, C., Koehler, J., Schroeder, A., Tischendorf, C., 2013. Experimentally validated CO_2 ejector operation characteristic used in a numerical investigation of ejector cycle. Int. J. Refrig 36(3), 881–891.

Nakagawa, M., Marasigan, A., Matsukawa, T., Kurashina, A., 2011. Experimental investigation on the effect of mixing length on the performance of two-phase ejector for CO_2 refrigeration cycle with and without heat exchanger. Int. J. Refrig 34 (7), 1604–1613.

Nowak, A.J., Palacz, M., Smolka, J., Banasiak, K., Bulinski, Z., Fic, A., Hafner, A., 2016. CFD simulations of transport phenomena during transcritical flow of real fluid (CO_2) within ejector. Int. J. Numer. Method H. 26(3/4), 805–817.

Palacz, M., Smolka, J., Nowak, A.J., Banasiak, K., Hafner, A., 2017b. Shape optimization of a two-phase ejector for CO_2 refrigeration systems. Int. J. Refrig 74, 212–223.

Palacz, M., Haida, M., Smolka, J., Nowak, A. J., Banasiak, K., Hafner, A., 2017a. HEM and HRM accuracy comparison for the simulation of CO_2 expansion in two phase ejectors for supermarket refrigeration systems. Appl. Therm. Eng. 115, 160–169.

Palacz, M., Smolka, J., Kus, W., Fic, A., Bulinski, Z., Nowak, A.J., Banasiak, K., Hafner, A., 2016. CFD-based shape optimization of a CO_2 two-phase ejector mixing section. Appl. Therm. Eng. 95, 62–69.

Palacz, M., Smolka, J., Fic, A., Bulinski, Z., Nowak, A. J., Banasiak, K., Hafner, A., 2015. Application range of the HEM approach for CO_2 expansion inside two-phase ejectors for supermarket refrigeration systems. International Journal of Refrigeration 59, 251–258.

Sierra-Pallares, J., García del Valle, J., García Carrascal, P., Castro Ruiz, F., 2016. A computational study about the types of entropy generation in three different R134a ejector mixing chambers, Int. J. Refrig 63, 199-213

Smolka, J., Palacz, M., Bodys, J., Banasiak, K., Fic, A., Bulinski, Z., Nowak, A.J., Hafner, A., 2016. Performance comparison of fixed- and controllable-geometry ejectors in a CO_2 refrigeration system. Int. J. Refrig 65, 172–182.

Smolka, J., Bulinski, Z., Fic, A., Nowak, A.J., Banasiak, K., Hafner, A., 2013. A computational model of a transcritical R744 ejector based on a homogeneous real fluid approach. Appl. Math. Modell. 37 (3), 1208–1224.

Wallis, G. B., 1980. Critical two-phase flow. Int. J. Multiphase Flow 6 (1-2), 97–112.

Weller, H.G., Tabor, G., Jasak, H., Fureby, C., 1998. A tensorial approach to computational continuum mechanics using object-oriented techniques. Comput. Phys. 12 (6), 620.

Yazdani, M., Alahyari, A. A., Radcliff, T. D., 2012. Numerical modeling of two-phase supersonic ejectors for work-recovery applications. Int. J. Heat Mass Transfer 55 (21-22), 5744–5753.

Manuscript ID: 1872
DOI: 10.18462/iir.icr.2019.1872

Optimization of water cooled low charge propane integral display cabinet with dedicated variable speed compressor solution

Kristian HUCHTEMANN [(a)], Eric WINANDY[(a)],Stéphane BERTAGNOLIO [(a)]

[1]Emerson Commercial & Residential Solutions
Aachen – Germany
kristian.huchtemann@emerson.com

ABSTRACT

Within the scope of the F-gas regulation there is a trend towards future proof technologies using hydrocarbons, CO2 or other low GWP refrigerants. In supermarket refrigeration, the integral display case architecture is one of these technologies because it allows for using the flammable hydrocarbon propane (R290).
The integral display case architecture consists of refrigerant circuits for each display case which reject heat to a water or brine loop. For the application with R290 it uses multiple circuit systems with low charge each (<150 g) to comply with international product standards (IEC60335-2-89). With safety regulations allowing for larger quantities of R290 per refrigerant circuit, it will be possible to use single circuit designs and therefore benefit from the variable speed compressor technology.
The paper presents an integrated solution for water cooled integral display cases that supports manufacturers in dealing with the technical challenges associated with new refrigerants such as hydrocarbons and variable speed technology. The solution includes a variable speed scroll compressor designed for the use of R290, a variable frequency drive, electronic expansion valve, safety devices and a system controller. The focus is on the optimization of the system efficiency and control as well as the design for limited refrigerant charge.
Keywords: R290, Integral Display Case, Water Loop, Low Charge, Variable Speed.

1. INTRODUCTION

As alternatives to HFCs are considered, there are two primary natural alternatives available, CO2 and hydrocarbons such as propane, and other low GWP refrigerants. In supermarket refrigeration, the integral display case architecture is a technology that allows for using the flammable hydrocarbon propane (R290).
'Integral' refrigeration describes stand-alone display cabinets and freezers that each contain their own cooling system – much like a domestic fridge. Integral units predominate in the drinks vending machines and ice cream freezers found in corner shops around the world. Most supermarkets have some integral units, even if their main system is remote. But integral systems can also be used to provide refrigeration for entire stores provided the heat generated is removed to an external chiller or heat exchanger through a simple pipe containing water or brine. These are referred to as water cooled integral systems.
Benefits of such architecture can include improved energy efficiency, reduced refrigerant leakage and lower maintenance requirements, that can contribute to better environmental performance and significant cost savings in the right application (Peters, 2017).
For the application with R290 it uses multiple circuit systems with low charge each (<150 g) to comply with international product standards (IEC60335-2-89, 2010). However, with safety regulations allowing for larger quantities of R290 per refrigerant circuit, it will be possible to use single circuit designs and therefore benefit from the variable speed compressor technology.

A seasonal calculation can show the advantage of using a variable speed compressor for the display case application. The main benefit is generated through the capacity control according to different cooling loads occurring. The calculation procedure used is described in Fig. 1:

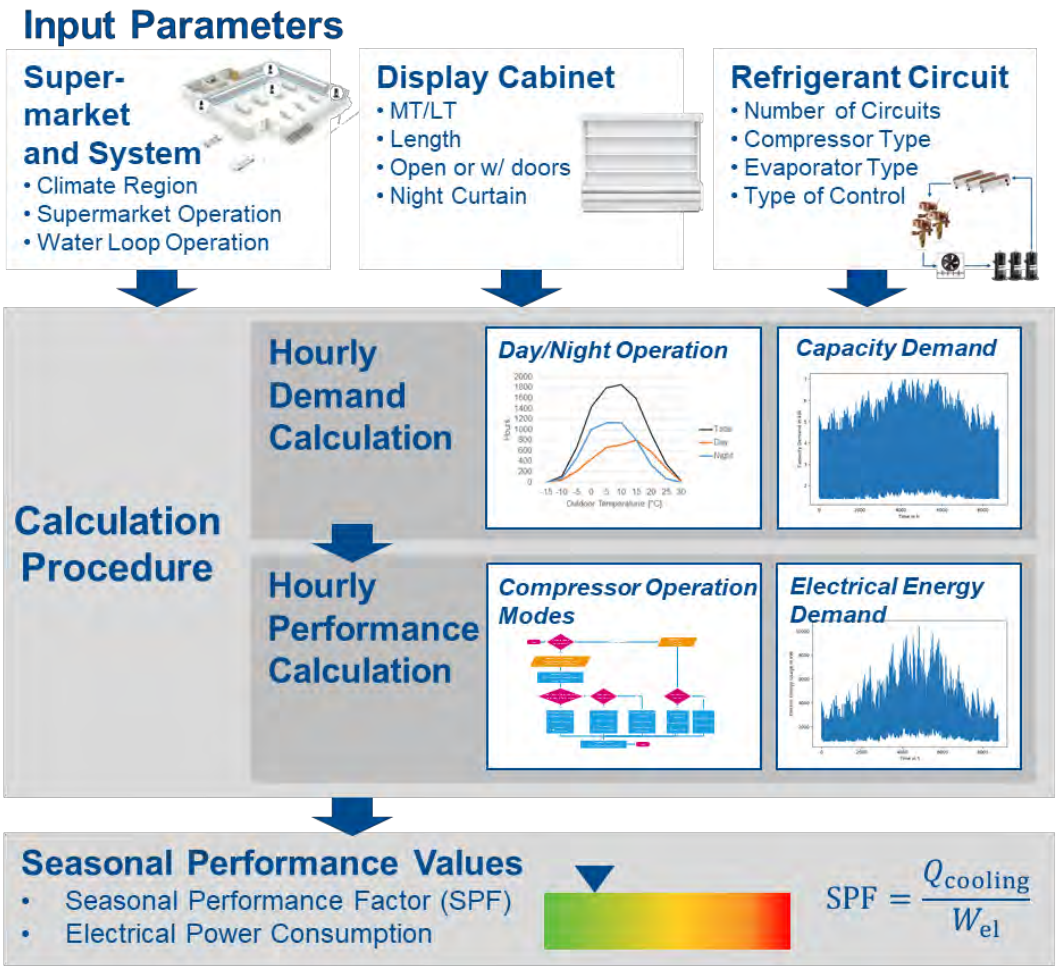

Figure 1: Flow chart of seasonal calculation procedure

We start with the demand calculation which calculates the display cooling load for every hour in one year. We assume the supermarket indoor conditions (air temperature and relative humidity) to linearly correlate with the outdoor air temperature. Ming described the load variation of a display case depending on these indoor conditions (Zhang Ming, 2006). The load also depends on the usage of night curtains during the hours that the supermarket is closed. For the water or brine loop temperature we use a fixed difference to the outdoor temperature describing the efficiency dry cooler. With the capacity demand and water temperature for each hour the refrigerant circuit can be computed. For each hour the compressor operation (on/off cycling, capacity control) is calculated. Therefore, the compressor polynomial and a linear evaporator characteristic is used. The annual cooling demand and the annual electrical energy consumption are the sum of the hourly values and are used to compute the seasonal performance factor of the solution.
For a typical configuration in a western European climate we calculate an improvement of the variable speed technology over fixed speed compressors of more than 10%. The main benefit is through the improved temperature differences in the evaporator during part load operation.
This paper presents the development of the integrated solution including variable speed compressor with focus on energy efficiency optimization and low charge of refrigerant.

2. INTEGRATED SOLUTION FOR SYSTEMS USING VARIABLE SPEED COMPRESSOR

2.1. Horizontal variable speed scroll technology

Since 2012, cooling and heating optimized high efficiency variable speed scroll compressors have been released and were very successful on European residential heat pump market and shortly after on the commercial AC market (Dardenne et al., 2014; Bertagnolio et al, 2016).,
Variable speed scroll compressors provide the following advantages

- Extensive 900-7200 RPM speed range for enhanced light load efficiency
- Optimized scroll elements for variable speed performance and efficiency boost in part load operation
- Low oil circulation compressor plus scroll oil injection for low speed performance and reliability
- Permanent magnet motor technology for highest efficiency

Variable speed scroll technology brings also many other system advantages, such as: enhanced control accuracy, continuous capacity management, reduced start-up current, low sound emissions at part load and during cycle reverse transitions of reversible systems.
Horizontal compressors (figure 2) are of interest in integral display case applications since they can be installed on top of the display case while remaining below the max allowable typically in supermarkets. It is an advantage indeed not to alter the rest of the design of the cabinet that otherwise could influence the air stream, air temperature and humidity controls.



Figure 2: Horizontal Variable speed scroll compressor dedicated to integral display cabinet

Compressor-drive matching is also critical and requires particular attention in order to deliver the best performance in terms of motor and inverter drive efficiency and reliability. Active protection algorithms incorporated into the motor control drive safeguard the compressor and drive from many adverse operating conditions, including:

- Motor & scroll temperature protection
- Locked rotor detection
- Phase protection and correction
- Maximum operating current detection
- Anti-short cycling

2.2. Integrated Solution for IDC

Implementation of variable speed technology in an integral display cabinet represents a significant challenge for system manufacturers, in terms of system design, control and qualification. For that reason, some integrated solutions have been developed to:

- Allow easier and effective implementation of variable speed technology in systems by proposing pre-qualified sets of optimized components (compressors, drive, expansion valve and controls), ready for assembly, to system manufacturers
- Increase performance of systems, not only through the use of variable speed technology, but also through more efficient system control and management in steady-state and transient operation
- Reach maximal reliability by integrating active protection and fault detection capabilities

Typically, the integrated solution includes (Fig. 3):

- the variable speed scroll compressor
- the inverter drive with Modbus communication capability
- the bipolar stepper motor electronic expansion valve
- the pressure transducers and temperature sensors
- the circuit controller, managing the main components of the refrigerant circuit

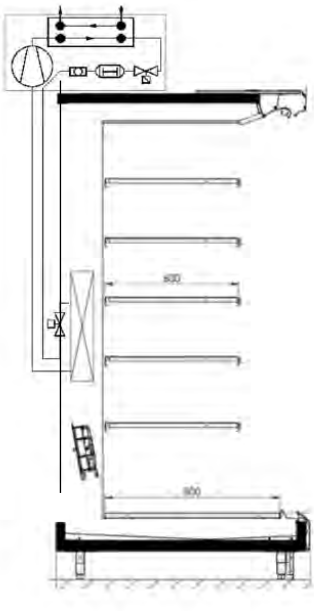

Figure 3: Typical arrangement of the main elements of the integrated solution for an integral display cabinet

3. SOLUTION PROTOTYPING AND TESTING

A prototype of the solution has been set-up and tested in our laboratory, see figures 4 and 5 for the schematics. A particular care has been given to the water loop where a configuration with recirculating 3 way valve and pump has been installed in order to increase the Delta T on the primary water flow and hence maintain good accuracy even at part load (see Fig. 4).



Figure 4: Solution prototype testing on display case

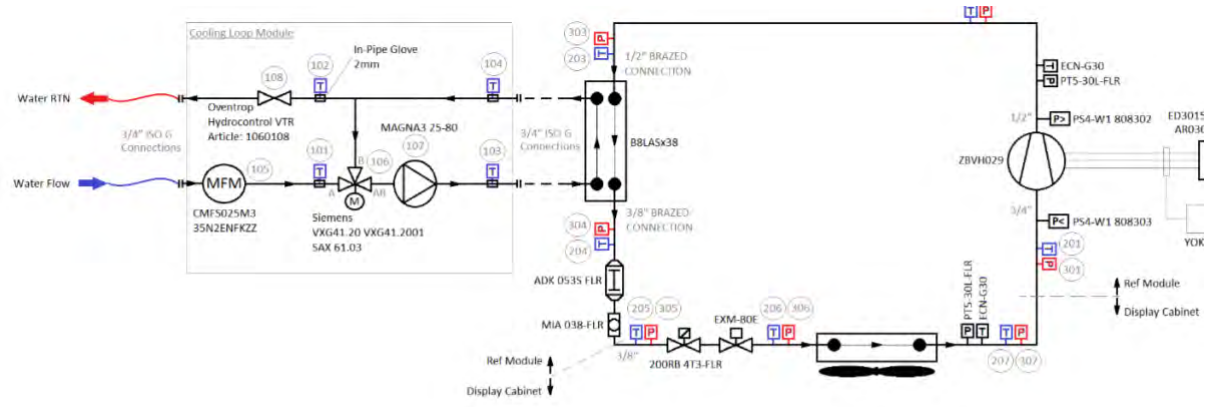

Figure 5: Test stand schematic including the water loop controls

As can be seen in Fig. 6, normalized silicon modules have been installed in order to monitor the product temperature according to EN 23953 (2015). Resulting temperatures at the different places in the display cabinet need to remain in a certain temperature band according to the class of the cabinet, see figure z.

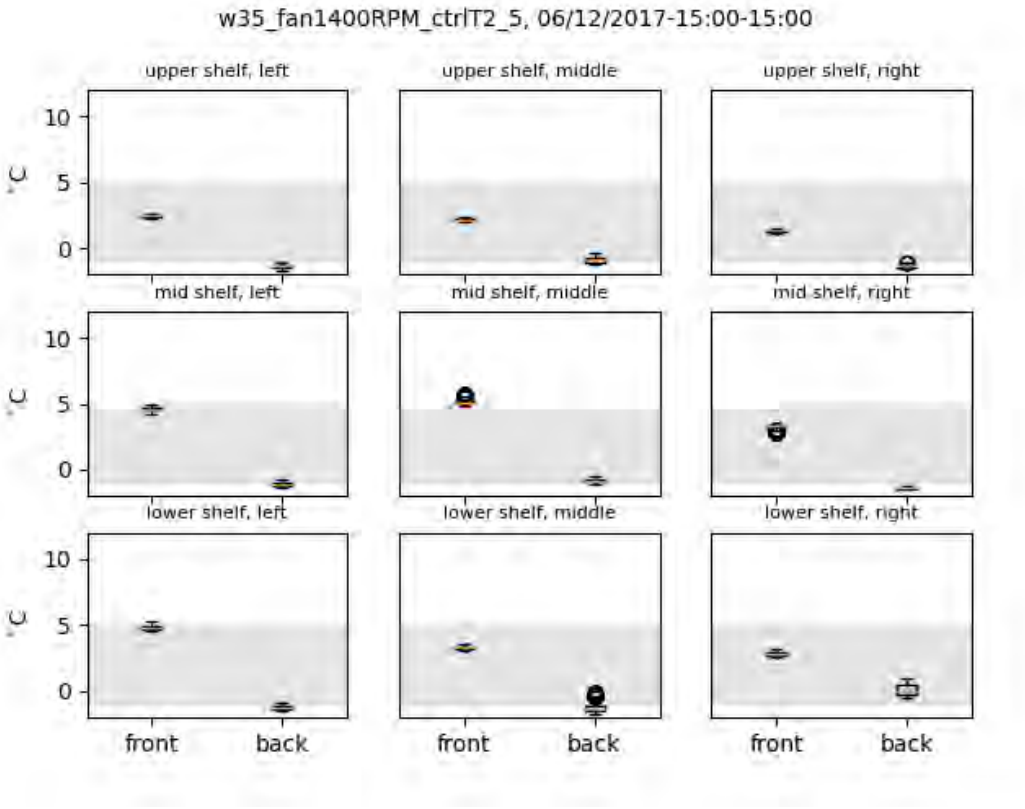

Figure 6: Reference silicone module temperature measurements representing product temperature

4. SOLUTION OPTIMISATION

4.1 Variable Speed Compressor and Electronic Valve

The peculiarity of the solution resides in the synchronised management of the compressor and the electronic expansion valve. The control uses predictive algorithms relying on compressors and valve performance mapping data allows achieving more accurate and dynamic control of the system as well as active protection of the system.

The circuit control ensures variable speed compressor envelope management and drives the compressor in a smooth way across the different regions of its operating envelope (Figure 6).

In parallel, the electronic expansion valve (EEV) is driven to maintain compressors suction state within acceptable range to ensure efficient and reliable operation, avoiding too high superheat (typically >20K) or liquid floodback. EEV control during transient is crucial and has to match fast systems capacity variations (speed ramp-up/ramp-down, compressor cycling at very low load, oil recovery cycles). To this end, smart control logics, including fuzzy logic, adaptive PID and dynamic valve prepositioning, have been implemented. Figure 7 shows the control of two different superheat setpoints.

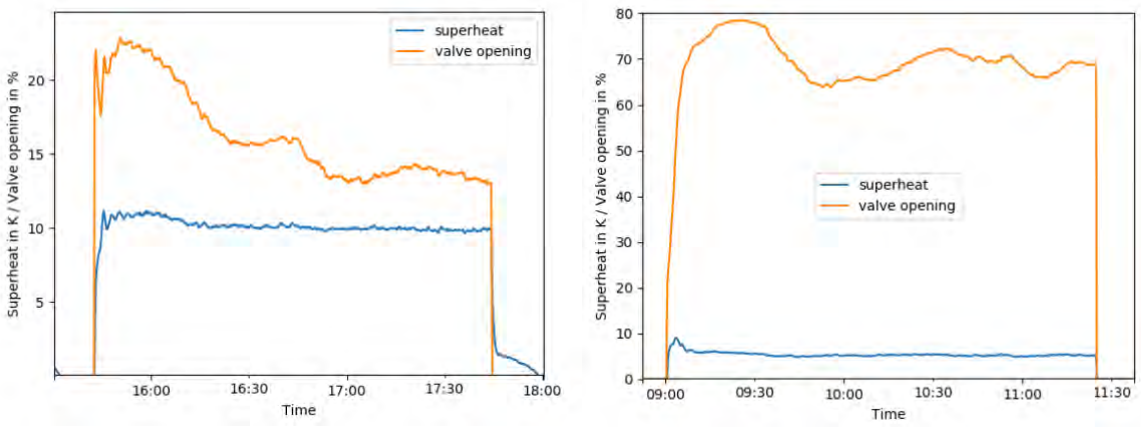

Figure 7: Superheat temperature difference and valve opening for two different superheat set points (10 K – left graph, 5 K – right graph)

EEV control is critical to ensure optimal system efficiency in steady-state operation. Indeed, too high superheat may quickly lead to inefficient operation due to excessive approach temperature in evaporator plate heat exchanger, leading to lower evaporating temperature levels and higher compressor power consumption. While lowering evaporator superheat is beneficial for system overall performance, it also increases the risk of liquid floodback to the compressor. Then, smart control algorithms relying on compressor and valve performance mapping equations are used to increase control robustness and achieve optimal superheat levels, in a safe and reliable way.
Of course, integrating compressors and EEV control can bring significant advantages in terms of active compressor protection, such as anticipation of high/low evaporating or high condensing limits crossing or flood-back and activation of adapted corrective actions (compressor speed or valve opening adjustment)
Beyond the compressor and valve controls, the main components like the evaporator need to be considered in the optimisation process. Particularly in this case where the limitations on the total refrigerant charge in the system can affect heavily the display case performance.

4.2 Evaporator

The evaporator is the component that contains the highest part of the total charge in the system. Reducing the coil pipe diameter is an important way to achieve lower charge. By doing so though, pressure drop increase needs to be compensated by an increased number of circuits. Also, reduction of the surface area needs to be compensated by an increased number of lengths of tube. Void fraction analysis and heat exchanger heat transfer model was used in this case to optimise the solution. Reference. Purdue
As mentioned above, compressor speed modulation influences evaporation temperature, see Figure 8, and has a notable effect on system efficiency.

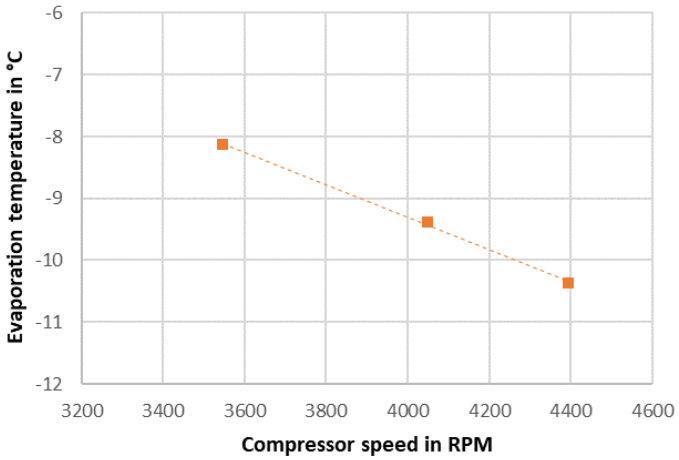

Figure 8: Evaporation temperature depending on compressor speed

4.4 Fan Speed

Fixed speed display case fans were changed to variable speed ones with Modbus connectivity to the electronic board. This allows to optimise the air curtain in order to achieve the required product temperature conditions at the lowest power as possible. Here a display case approach needs to be taken as an optimum air speed at the evaporator level can be negative at the display case level because of its impact on the air curtain and the consequent mixing of hot and wet air with the recirculating air in the display cabinet.
A too high fan speed increases the cooling demand of the display case through a high infiltration rate. With the variable speed compressor, the cooling capacity is controlled to ensure a constant product temperature with varying cooling demands. Fig. 9 shows that the compressor speed increases with increasing fan speed.

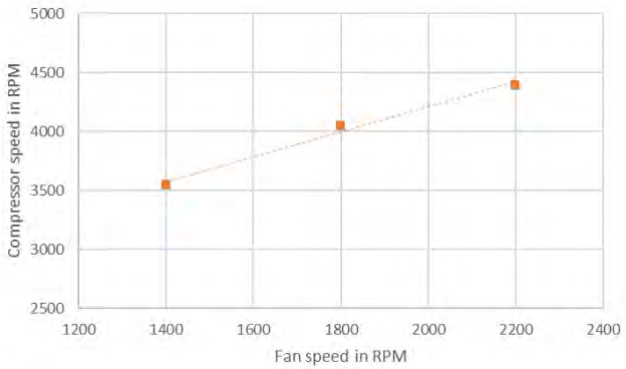

Figure 9: Compressor speed vs. fan speed for tested display case with variable speed compressor

4.3 Condenser

A plate heat exchanger was used with minimization of charge in mind. Given the length of such heat exchanger and the space available (mainly the height is constrained), there is an optimum in terms of number of plates and tilt angle for achieving the highest performance at the lowest charge.

5. CONCLUSIONS

The benefits of the water loop integral display cabinets have been discussed in this paper in the context of the F-gas phase down, the subsequent need for future proof refrigerants and the usage of propane in supermarket refrigeration.
The regulatory change soon allowing higher charge, the paper shows the energy benefit of using variable speed modulation at the compressor level. A seasonal efficiency analysis taking into account the different parameters of the supermarket, the display cabinet and the refrigerant circuit shows up to 10% higher efficiency when using variable scroll technology.
A display case prototype has been equipped with the horizontal scroll compressor technology allowing the optimization process of the developed integrated solutions including the controls of the frequency drive, the electronic expansion valve and the safety devices. Besides the controls part, the other components including the evaporator, the condenser and the fans have also been discussed in the scope of the requirement of a low charged system.

6. REFERENCES

IEC 60335-2-89,2010, Household and similar electrical appliances - Safety - Part 2-89: Particular requirements for commercial refrigerating appliances with an incorporated or remote refrigerant unit or compressor.

Peters T., 2017, Retail refrigeration – Making the Transition to Clean Cold, White Paper, University of Birmingham

EN 23953, 2015, Refrigerated display cabinets Parts 1 & 2

Dardenne, L., Fraccari, E., Maggioni, A., Molinarolli, L., Proserpio, L., Winandy, E. 2014. A Wet Vapour Injection and Variable Speed Scroll Compressor Air to Water Heat Pump Model and its Field Test Validation. Proceedings of the 11th IEA Heat Pump Conference, Montreal, Canada

Bertagnolio S, Winandy E. and Koepke D., 2016 An Integrated Solution for Commercial AC Chillers Using Variable Speed Scroll Compressors Proceedings of the Refrigeration Conference at Purdue,

Zhang Ming, 2006, Energy Analysis of Various Supermarket Refrigeration Systems,https://docs.lib.purdue.edu/cgi/viewcontent.cgi?article=1855&context=iracc

Manuscript ID: 169
DOI: 10.18462/iir.icr.2019.0169

Loss of mitochondrial function and accumulation of acidic vesicular organelles under low-temperature incubation in HaCaT cells

Yukitoshi NAGAHARA, Natsumi UCHIDA, Tomoki MIDORIKAWA, Norio MURASE, Takahisa SHINOMIYA

School of Science and Engineering, Tokyo Denki University
Hatoyama, Hiki-gun, Saitama, 350-0394, Japan, yuki@mail.dendai.ac.jp

ABSTRACT

Compared to plants, response to cold stress in animals is regarded as less important; however, in animals, peripheral tissues like skin are sensitive to cold and induce shivering. In this study, we focused on the mitochondrial damage resulting from exposure to low temperature using HaCaT cells as a human epidermal cell model.
HaCaT cells were incubated at 4 °C. Mitochondrial membrane potential was observed by a membrane potential indicator dye, JC-1. Reactive oxygen species (ROS) was detected by H_2DCFDA and MitoSOX dyes. Acidic vesicular organelles were stained with acridine orange.
After incubating the HaCaT cells at 4 °C, the mitochondrial membrane potential decreased and ROS generation increased, leading to cell death. Moreover, accumulation of acidic vesicular organelles was observed and lysosomes were co-localized to the mitochondria.
These data suggest that lysosomes degraded the damaged mitochondria for cell survival in cold stress.
Keywords: Low-temperature stress, Mitochondria, Lysosome, ROS.

1. INTRODUCTION

Cells are generally exposed to stress caused by external and internal factors (Neutelings et al., 2013; Muriach et al., 2014). Therefore, cells have developed mechanisms to adapt to various forms of stress, wherein, they induce reactions that maintain homeostasis. Therefore, elucidating this stress response would provide insight into the maintenance of homeostasis in the cells.
Various external stress factors exist, one of them being low-temperature stress. Study on low-temperature stress signaling was carried out in plants (O'Kane et al., 1996). When the chloroplasts and mitochondria are damaged by low-temperature stress, reactive oxygen species (ROS) is produced and it accumulates in the cell. Upon ROS upregulation, the cell membranes are destroyed and cell death is induced. Plants synthesize antioxidants to protect the cell membranes and prevent the damage caused by low-temperature stress (Zhang et al., 2013). Thus, in plants, the stress response mechanism via reduction of ROS is crucial in low-temperature stress.
Nevertheless, few reports were obtained only regarding the low-temperature stress response in mammals, because they are homoeothermic; however, the skin covering the entire body in homoeothermic animals is easily susceptible to external temperature changes. In particular, by swimming in cold water or working in deep cold storage room, the skin surface temperature could be dropped to 10 °C (Baldus et al., 2012; Rust et al., 2012), leading to low-temperature stress. In the previous study, we revealed that mammalian cells provoked ROS generation after low-temperature incubation and resulted in cell death. Inhibition of ROS attenuated low-temperature incubation-induced cell death, suggesting that low-temperature incubation induces ROS generation (Yazawa et al., 2015).
In this study, we elucidated a possible mechanism in response to the low-temperature-induced ROS generation with human keratinocyte HaCaT cells as an epidermal cell model.

2. MATERIALS AND METHODS

2.1. Cell line

The human keratinocyte cell line HaCaT was provided by Professor P. Boukamp and Dr. N. Fusenig (German Cancer Research Center, Heidelberg) (Boukamp et al., 1991). Cells were cultured in Dulbecco's Modified Eagle's Medium (DMEM; Sigma, Missouri, USA), supplemented with 10% fetal bovine serum (Biofill, Elsternwick, Australia) and 10 mL/L × 100 Streptomycin/Penicillin solution (Wako, Osaka, Japan) at 37 °C, in a 5% CO_2 incubator (ESPEC, Osaka, Japan). For incubation at 4 °C, DMEM with 25 mM HEPES (25 mM HEPES/DMEM) and 10% fetal bovine serum and 10 mL/L × 100 Streptomycin/Penicillin solution was used as a medium to control pH and the cells were cultured in the refrigerator.

2.2. Analysis of mitochondria membrane potential ($\Delta\Psi_m$)

Cells (1×10^6) were incubated for 15 min with a medium containing 1 µg/mL cation dye, that is, 5,5',6,6'-tetrachloro-1,1',3,3'-tetraethylbenzimidazolylcarbocyanine iodide (JC-1, Sigma). Thereafter, the cells were incubated for the indicated times at 4 °C with 25 mM HEPES/DMEM. The cells were then centrifuged and collected, washed, and resuspended in PBS. The fluorescence of mitochondria localized in the aggregated form (red) and in the cell-incorporated monomer form (green) was observed via confocal microscopy. In contrast, the cells (1×10^6) were incubated for the indicated times at 4 °C with 25 mM HEPES/DMEM. The cells were then collected, washed, and resuspended in PBS. Thereafter, they were incubated for 15 min in a medium containing 100 nM 3,3'-dihexyloxacarbocyanide iodide (DiOC6 (3); Molecular Probes, Eugene, OR). After incubation, the cells were washed with PBS, resuspended in PBS and the $\Delta\Psi_m$ value was examined via flow cytometry (FACS) (Becton Dickinson, Franklin Lakes, USA).

2.3. Analysis of ROS generation

For estimating the cellular ROS, cells (1×10^6) were incubated for 30 min in a medium containing 25 µM 2',7'-dichlorodihydrofluorescein diacetate (H_2DCFDA). Thereafter, they were incubated for the indicated times at 4 °C with 25 mM HEPES/DMEM. The cells were then collected, washed, and resuspended in PBS. Fluorescence intensity of H_2DCFDA was then measured via confocal microscopy. For estimating the mitochondrial ROS, cells were incubated for the indicated times at 4 °C with 25 mM HEPES/DMEM. Thereafter, they were incubated with 5 µM MitoSOX Red mitochondrial superoxide indicator (Molecular Probes), for 15 min at 37 °C, in the dark, according to manufacturer's instructions. Fluorescence intensity of MitoSOX Red was then measured via flow cytometry.

2.4. Cellular viability analyzed by calcein-AM and propidium iodide (PI) assay

A 0.1% poly-L-lysine-coated 12-mm Φ microscope cover glass (Thermo Fisher Scientific, Waltham, USA) was placed in a 24-well plate (Corning, NY, USA) base. About 2.0×10^5 HaCaT cells were seeded into each well, and cultured overnight at 37 °C in a 5% CO_2 incubator. These cells were adhered to a 12-mm Φ microscopic cover glass. The cellular viability was evaluated by double staining: 3 µg/mL calcein-AM, and 1-µg/mL PI containing PBS. After cultivation for 6, 12, 18, and 24 h at 4 °C, DMEM was removed from the 24-well plates. Thereafter, 500 µL of prepared calcein-AM and PI staining solution was added to each well, and the plates were incubated for 15 min at 37 °C in a 5% CO_2 incubator. When cover glasses were removed, approximately 100 cells were observed in the field via a fluorescence microscope (BX51, Olympus, Tokyo, Japan). Cellular viability (%) was calculated by the number of viable cells divided by the viable and dead cell count.

2.5. Observation of lysosome (acidic vesicular organelle) by using acridine orange staining

Cells (1×10^6) were incubated for the indicated times at 4 °C with 25 mM HEPES/DMEM. Thereafter, the cells were incubated for 15 min with acridine orange at 37 °C in a 5% CO_2 incubator. The fluorescence was observed via confocal microscopy.

3. RESULTS

3.1. Loss of mitochondrial function

In our previous study, we revealed that 4 °C treatment of HaCaT cells increases the mitochondrial ROS, suggesting that mitochondrial function is perturbed by low-temperature treatment (Yazawa et al., 2015). Therefore, we focused on the $\Delta\Psi_m$, which is decreased during the mitochondrial damage. We used cationic dye JC-1 to estimate the $\Delta\Psi_m$ in confocal microscopy. When $\Delta\Psi_m$ is high, JC-1 concentrates in the mitochondrial matrix and aggregates to form bright red fluorescence. When $\Delta\Psi_m$ is low, JC-1 disperses to the cytoplasm and shifts to green florescent monomers. As presented in Figure 1, after the treatment to HaCaT cells at 4 °C, fluorescence of JC-1 shifted the from red to green, which indicates the time-dependent loss of $\Delta\Psi_m$. Similar results were obtained by using a different cationic mitochondrial dye, DiOC6 (data not shown). Upon $\Delta\Psi_m$ occurrence, we checked whether ROS was also generated. In Figure 2, confocal microscopic analysis clearly indicated that the ROS generation was increased after culture at 4 °C. Precise ROS detection was measured using mitochondrial ROS indicator and flow cytometric analysis, and we concluded that mitochondrial ROS was increased after cultivation at 4 °C (Fig. 3). This data suggested that cultivation at 4 °C induced loss of mitochondrial function.

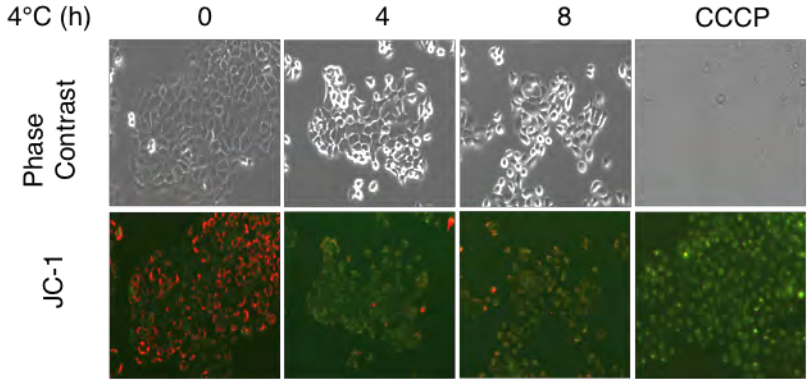

Figure 1. Mitochondrial membrane loss after cultivation at 4 °C

Confocal microscopy images of HaCaT cells treated with $\Delta\Psi_m$ indicator JC-1. Protonophore CCCP was used as a positive control.

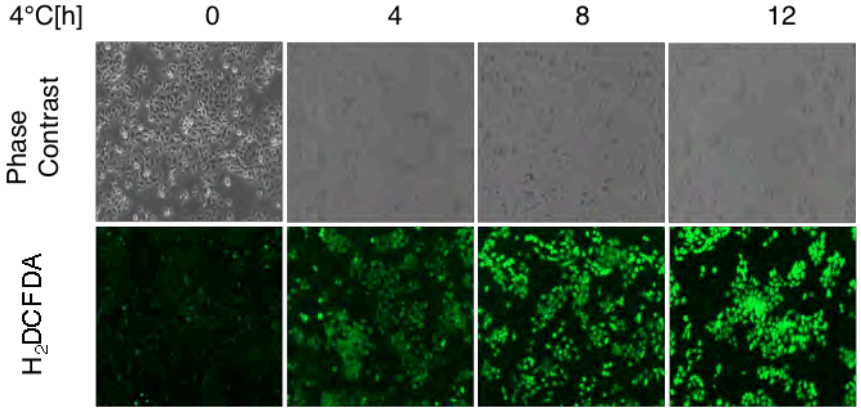

Figure 2. ROS generation after cultivation at 4 °C

Confocal microscopy images of HaCaT cells treated with ROS indicator H_2DCFDA.

3.2. Cell death induced by mitochondrial loss of function

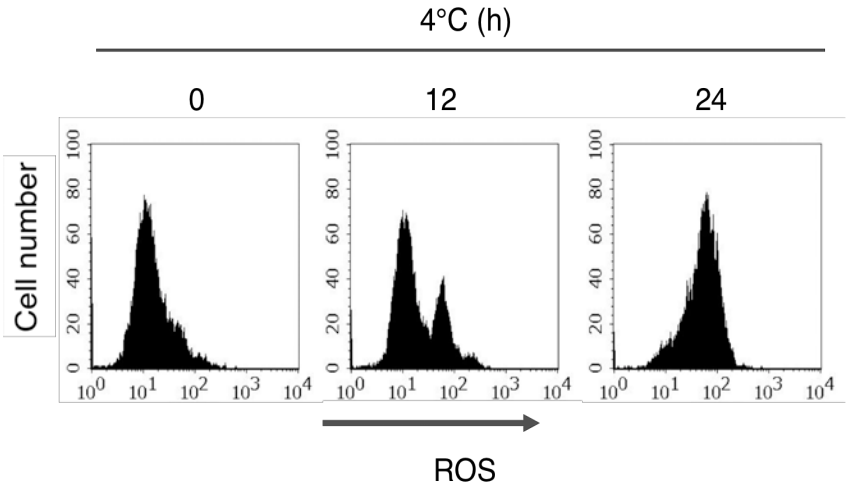

Figure 3. Mitochondrial ROS after cultivation at 4 °C

Flow cytometric analysis of HaCaT cells treated with the mitochondria ROS indicator MitoSOX Red.

After a certain period of time at 4 °C, HaCaT live cells were stained green by calcein-AM, whereas dead cells were stained red by PI. Figure 4 shows that cell viability did not change during 0–6 h of culture at 4 °C; however, cell viability dropped after 12 h of culture. After adding 10 mM N-acetyl-L-cysteine (NAC) as an antioxidant, the cell viability was higher than that observed with no addition in the control after cultivation at 4 °C for over 12 h. From these results, we conclude that cell death after cultivation at 4 °C was induced by mitochondrial damage.

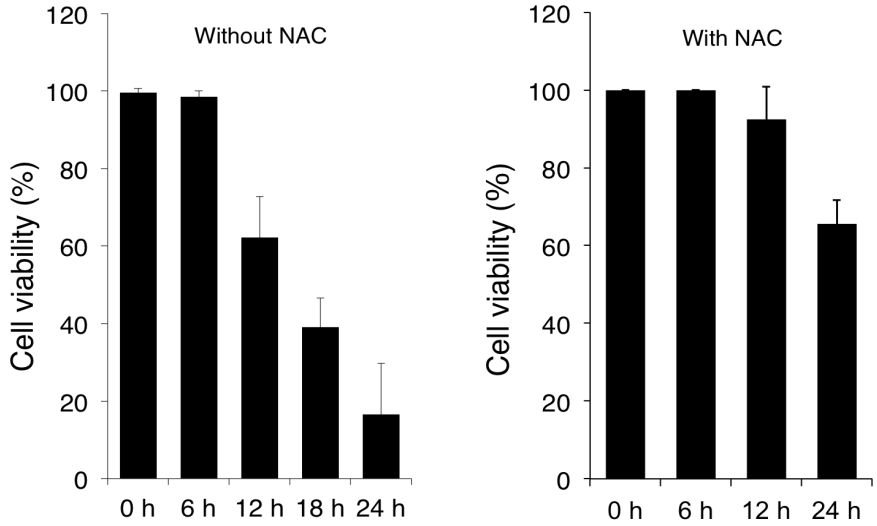

Figure 4. Cell viability loss after cultivation at 4 °C was occurred by mitochondrial ROS generation

HaCaT cells treated with calcein-AM (live cells) and PI (dead cells) after cultivation for indicated times at 4 °C with/without 10 mM NAC. Cellular viability (%) was calculated as the number of viable cells divided by the sum of viable and dead cells.

3.3. Accumulation of acidic vesicular organelles

Damaged mitochondria are excluded by inducing autophagy. We, therefore, determined the involvement of lysosomes for the exclusion of damaged mitochondria. We used the dye acridine orange as its protonated red fluorescent form accumulates in acidic vesicles such as lysosomes. In Figure 5, control cells exhibited only green fluorescence, and culture at 4 °C displayed considerable red fluorescence, suggesting that acidic vesicular organelles such as lysosomes were accumulated.

Moreover, co-localization of mitochondria and lysosomes were observed after culture at 4 °C (data not shown).

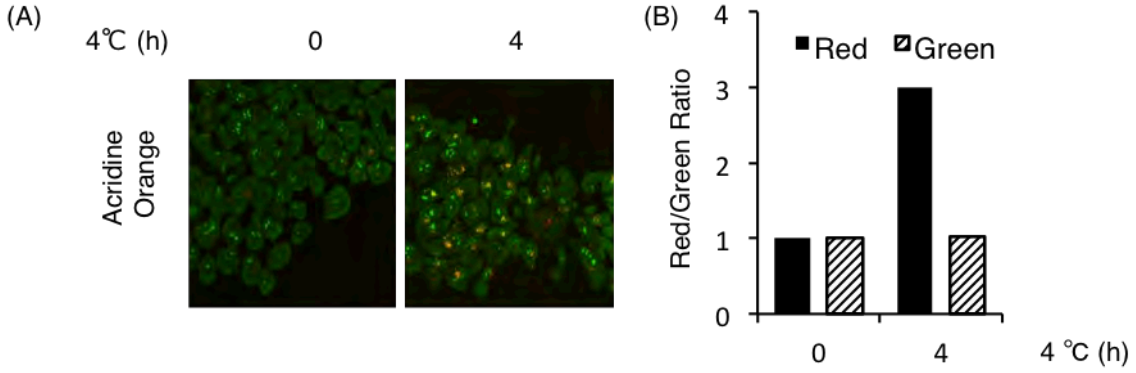

Figure 5. Accumulation of acidic organelle after cultivation at 4 °C

(A) Confocal microscopy images of HaCaT cells treated with acridine orange. (B) Red/Green ratio of (A) was calculated.

4. DISCUSSION

Cell death increased in the HaCaT cells after 12 h of culture at 4 °C. Reduction of $\Delta\Psi_m$ and increase of mitochondrial ROS was observed, suggesting that cultivation at 4 °C induced loss of mitochondrial function. We thus considered that HaCaT cells received oxidative stress by low-temperature. Indeed, addition of anti-oxidant NAC reduced the cell damage by low-temperature.
Abnormal mitochondria promote ubiquitination. It is widely accepted that this ubiquitination signals abnormal mitochondrial elimination by autophagy, which is a cytoprotective action that decomposes its intracellular constituent to the amino acid level and reuses it when the cell falls into a starvation state. Moreover, autophagy allows the turnover of organelles in eukaryotic cells. This process initially occurred by the formation of membrane vesicles called autophagosomes, which sequesters macromolecules and organelles before fusing with lysosomes. Second, lysosomes were fused to autophagosomes and formed autolysosomes on degradation. In the present study, we found that acidic organelles were accumulated by low-temperature induction, suggesting that lysosomes were increased. However, to prove autophagy occurred by low-temperature progression, autophagosome formation as well as autolysosome formation was observed. We will be addressing this issue in future studies.

5. CONCLUSIONS

Loss of mitochondrial function was induced by low-temperature stress in HaCaT cells. Addition of antioxidant NAC reduced cell damage by low-temperature. Moreover, accumulation of acidic vesicular organelles induced by low-temperature treatment was observed. These data suggest that lysosomes degraded damaged mitochondria for cell survival in cold stress.

REFERENCES

Boukamp, P., Petrussevska, R.T., Breitkreutz, D., Hornung, J., Markham, A., Fusenig, N.E., 1991. Normal keratinization in a spontaneously immortalized aneuploid human keratinocyte cell line, J. Cell. Biol. 106(3), 761-771.

Baldus, S., Kluth, K., Strasser, H., Order-picking in deep cold – physiological responses of younger and older females. Part 2: body core temperature and skin surface temperature, 2012. Work, 41(2012), 3010-3017.
Goldman, S.J., Taylor, R., Zhang, Y., Jin, S., 2010. Autophagy and the degradation of mitochondria, Mitochondrion, 10(4), 309-315.
Neutelings, T., Lambert, C.A., Nusgens, L.B., Cologe, A.C., 2013. Effects of mild cold shock (25°C) followed by warming up at 37°C on the cellular stress response, PLoS ONE, 8(7), e69687.
Muriach, M., Flores-Bellver, M., Romero, F.J., Barcia, J.M., 2014. Diabetes and the brain: oxidative stress, inflammation, and autophagy, Oxid. Med. Cell Longev., 2014, 102158.
O'Kane, D., Gill, V., Boyd, P., Burdon, R., 1996. Chilling, oxidative stress and antioxidant responses in Arabidopsis thaliana callus, Planta 198(3), 371-377.
Rust, C.A., Knechtle, B., Rosemann, T., 2012. Changes in body core and body surface temperatures during prolonged swimming in water of 10°C—a case report, Extrem. Physiol. Med., 1(1), 8.
Yazawa, T., Sekine, H., Murase, N., Nagahara, Y., 2015. Mitochondrial reactive oxygen spicies involved in cold stress in HaCaT cells, Proceedings of the ICR, Yokohama, Japan, ICR, 473.
Zhang, Q., Jiang, N., Wang, G.L., Hong, Y., Wang Z, 2013. Advances in understanding cold sensing and the cold-responsive network in rice, Adv. Crop Sci. Tech., 1, 104.

Manuscript ID: 498
DOI: 10.18462/iir.icr.2019.0498

Ultra-Fast Vitrification Experiment of Hamster Ovary Cells utilizing Thin Film Evaporation

Fengmin SU[(a)], Yiming FAN[(a)], He XU[(a)], Nannan ZHAO[(a)], Yulong JI[(a)] Hongbin MA[(b)]

[(a)]Institute of Marine Engineering and Thermal Science, Dalian Maritime University, Dalian, 116023, China, fengminsu@dlmu.edu.cn
[(b)]Department of Mechanical & Aerospace Engineering, University of Missouri Columbia, MO 65211, USA

ABSTRACT

Vitrification is one of effective methods for cells cryopreservation. An ultra-fast cooling rate is beneficial to improve the vitrification level of the extra and intracellular solution and increase cell survival rates. Thin film evaporation is an efficient phase change heat transfer mode, and can achieve the ultra-fast cooling rate if it is utilized for cell vitrification. In this paper, a novel ultra-fast cooling method utilizing thin film evaporation was developed, and used for the vitrification of hamster ovary cells. Contrast experiments among this novel method, slow freezing method and open pulled straw vitrification were conducted. The experimental results showed that the novel method achieved a highest cooling rate and cell survival rate than the other two conventional methods. The reason why the novel method achieved the ultra-high cooling rate was mainly that thin film evaporation of liquid nitrogen can avoid the forming of "vapor blanket" and improve the heat transfer coefficient of cell vitrification. The current investigation proved preliminarily the feasibility of this novel cell vitrification method.

Keywords: Cell Cryopreservation, Ultra-fast Cooling, Vitrification, Thin Film Evaporation

1. INTRODUCTION

Cell vitrification has been widely used in many biological fields such as biodiversity conservation, livestock species improvement, and human assisted reproduction. In this process, an ultra-fast cooling rate is a key parameter. ultra-fast cooling can offer two advantages(Vajta et al., 1998): 1) the required cryoprotectant concentration can be decreased with a consequent decrease in the associated potential toxicity; 2) a more rapid passage through the dangerous temperature zone results in reduced freezing injury. In conventional vitrification procedure, such as, electron microscopic(EM) grip method(Steponkus et al., 1990 and Martino et al., 1996), open pulled straws (OPS) method(Vajta et al., 1998 and Isachenko et al., 2001), method using cryoloops (Mukaida, et al., 2001), and slush nitrogen method(Steponkus et al., 1993and Yoon et al., 2007),a typical cooling rate applied to samples is approximately 25000°C/min. Although these methods achieve complete or partial vitrification of cell suspensions, highly concentrated cryoprotectants are required. The highly concentrated cryoprotectants have certain toxic and permeability damage to the cells, and that results in reduced cell survival rates. Besides, the procedure for adding and removing it during cell freezing and resuscitation is very complicated. If the cooling rate was improved further, the concentration of cryoprotectants could be decreased.

Thin film evaporation is an efficient phase change heat transfer style, and its heat transfer coefficient far exceeds other heat transfer forms(Bau et al., 1982, Kaviany et al., 1995,Demskyet al., 2004, and Saitet al., 2009). process of liquid nitrogen as the evaporation liquid. The results showed that the average evaporation heat transfer coefficient of liquid nitrogen in the thin film evaporation zone can reach 10^6W/m^2°C.If it was used to freeze 0.1mm thick cell suspension liquid, the cooling rate could theoretically reach 10^6 °C/min. On the basis of the theoretical analysis, Su et al. (2012) constructed the experimental system that can realize thin liquid film evaporation of liquid nitrogen. The cooling rate reached 50000 °C/min, and is 2 times that of the current vitrification method.

To examine the practicability of this method for cell vitrification, an experiment for hamster ovary cells vitrification will be done in this paper. It is based on thin film evaporation of liquid nitrogen. Furthermore, the

comparison experiments, in which the other two generic approaches of cell cryopreservation are used, will be done. The methods are respectively the equilibrium freezing method and the open pulled straws vitrification method. Besides, the mechanism for the improvement of the cooling rate in the novel method will be analysed from the view of heat transfer.

2. EXPERIMENTAL SYSTEM AND PROCEDURE

2.1. Cell vitrification method based on thin film evaporation

The experimental system is illustrated in Fig. 1. This system includes a chamber, a frozen carrier, two liquid nitrogen containers (CRY-AC®B-700, Brymill Cryogenics Systems) connected with liquid nitrogen jet tubes(2mm inner diameter, 291mm length), a pressure sensor(Series 910, MKS Instruments Inc.), a fine thermocouple of 70 μm in diameter(OMEGA Engineering Inc.), and a data acquisition system(National Instruments Inc.).The frozen carrier refers to a carrier used to carry cell suspension liquid during cell vitrification. In the thin liquid film evaporation cooling process of liquid nitrogen, it also plays a role in forming thin liquid film region. It is shown in Fig.2. It is made from two pieces of the 10 mm×10 mm×0.15 mm silicon chips as the basal sheets. A microstructured layer with a thickness of 100 μm, which consisted of 100 μm×100 μm×100 μm pillars, was etched on its outside surface. The distance between these cubes on the microstructured surface is 200 μm. Between two silicon chips, there is a 5mm×5mm×0.1 mm storage space to place cell suspension. Liquid nitrogen serves as the working fluid. The two liquid nitrogen containers with jet tubes inject liquid nitrogen on the micro structured surface of the frozen carrier. The pressure sensor and the fine thermocouple measure the actual pressure and temperature and sent the signal to the data acquisition system. The thermocouple is fixed among two pieces of the silicon chips. Because the diameter of the thermocouple is only 70 μm, its time constant is 18.5μs. The temperature sampling time interval is 100μs. The thermal inertia of the thermocouple does not significantly influence the transient temperature measurements. The uncertainty of the measured temperature is ±0.3°C. The uncertainty of the measured pressure is ±50 Pa.

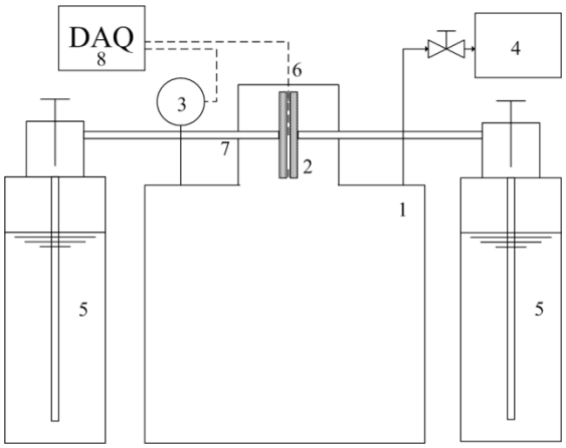

1. chamber,2. frozen carrier, 3. pressure sensor, 4. vacuum pump, 5. liquid nitrogen container,6. thermocouples, 7.liquidnitrogen jet tubes, and 8. data acquisition system

Figure 1: Vitrification freezing experimental system based on thin liquid film evaporation

In the experiment, the hamster ovary cells are suspended in the cryopreservation solution (including 80% F12K medium which contains a certain amount of nutrients such as Amino acid, Nucleoside, sugar, Peptide growth factors, hormones, inorganics, lipids, 10% fetal bovine serum, and 10% Dimethyl sulfoxide). Fig. 3 show the photo of the prostate cancer cells using a laser scanning confocal microscopy. The cell suspension with the prostate cancer cells is first placed in the storage space between the two silicon chips. The frozen carrier is put vertically between the two liquid nitrogen containers. The data acquisition system opened and start recording the temperature of the frozen carrier; Then, the liquid nitrogen injector valve is opened. liquid nitrogen arrives on the frozen carrier microstructure surface and evaporates. Due to this quick evaporation and heat absorption, the frozen carrier was ultra-fast cooled from 20°C to -196°C.Finally, the valve of the liquid nitrogen injector and the NI data acquisition system are closed, and the freezing carrier with the cell suspension liquid is placed in a liquid nitrogen tank for storage.

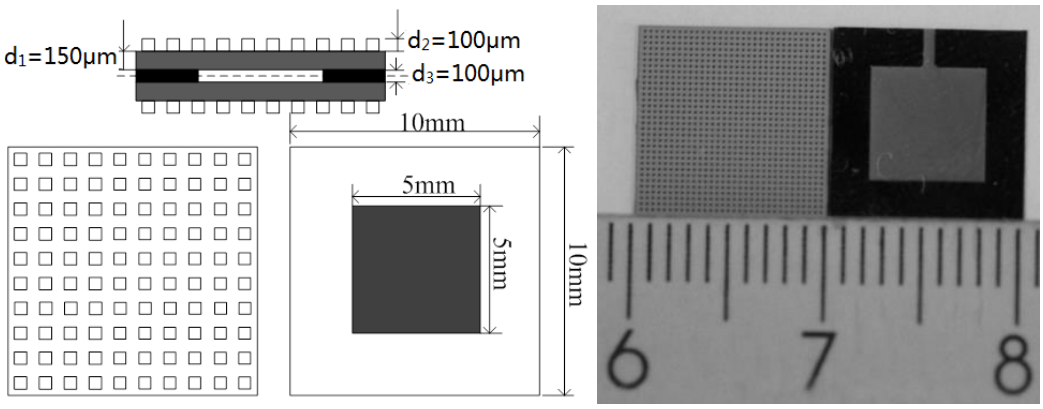

Figure 2: Frozen carrier diagram



Figure 3: Photo of hamster ovary cells

2.2. Equilibrium freezing method

Equilibrium freezing method is a slow freezing method. Its experimental procedure is as follows: 1. the frozen storage tube containing the cell suspension with hamster ovary cells is placed in a refrigerator at 4 °C for 1 hour; 2. it is transferred into a refrigerator at -20 °C for 4 hours; 3. it is transferred to a -70 °C refrigerator for 12 hours; 4. It is sunk into liquid nitrogen sank for storage finally.

2.3. Opening Pulled Straw vitrification method

The opening pulled straw vitrification method of Vajtaet et al. (1998) is cited in this paper. The inside diameter of the straw is 0.9mm, and the wall thickness is 0.15mm. A fine thermocouple whose diameter is 70 μm is fixed in the straw to measure the temperature variation in the cooling procedure. The experiment procedure is shown in Fig. 4. The cell suspension with hamster ovary cells is firstly sucked into the straw by capillary force, then directly immersed in liquid nitrogen. The straw with the cells suspension is cooled to the liquid nitrogen temperature. Finally, the straw is transferred into a liquid nitrogen tank for storage.

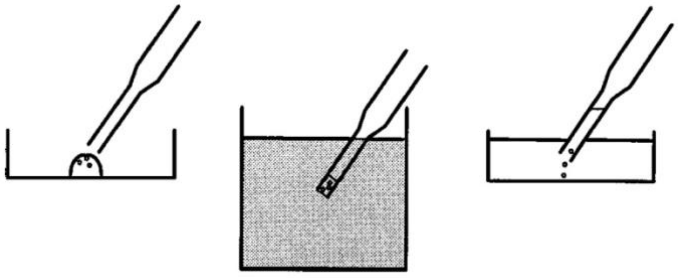

(1. cell suspension with hamster ovary cells is sucked into the straw by capillary force; 2. it is immersed in liquid nitrogen. 3. It is placed in a 37 ℃ constant temperature water bath.)

Figure 4: Opening pulled straw vitrification method (Vajta et al., 1998)

2.4. Cell viability detection

In the paper, the same cell viability detection method is used in the above three cell cryopreservation methods. It is the trypan blue exclusion test. The cell suspension is taken out from the liquid nitrogen tank together with the respective freezing carrier, then directly placed in a 37 °C constant temperature water bath. The cells sample melts for about 90 s. It is washed and centrifuged to remove the cryoprotectant. The cell suspension of 10μL is removed into a test tube, and added into the trypan blue solution of 10μL. The mass concentration of the trypan blue solution is 0.4%. The cell suspension with the trypan blue is removed on a piece of cell counting plate. It is tested by a laser scanning confocal microscopy (LEXT3100, Olympus Corporation). Living cells are not stained with trypan blue, so they are translucent under the microscope. Dead cells are changed into blue. The total number of all cells on the cell counting plate and the number of cells stained with trypan blue were counted separately. Cell Survival rate, R_S is calculated by:

$$R_S = \frac{N_1}{N_2} \times 100\% \qquad \text{Eq. (1)}$$

Where N_1 represents the number of viable cells, and N_2 represents the total number of all cells.

3. DATA ANALYSIS METHODOLOGY

To achieve more heat transfer information of the novel cells freezing method, the lumped capacitance method was used. This method assumes that the temperature of the frozen carrier is spatially uniform at any instant during the transient process. The temperature of the carrier was measured by the thermocouple in the experiments. The amount of heat transfer, Q, from the carrier was absorbed in the evaporation of liquid nitrogen at the moment of (t-1) and (t) with a differential time of Δt. Therefore, Q, is expressed as,

$$Q = mC_p[T(t-1) - T(t)] \qquad \text{Eq. (2)}$$

T(t-1) is the temperature of the carrier at the moment of (t-1), and T(t) is the temperature of the carrier at the moment of (t).With energy conservation, Q could be expressed as,

$$Q = qs\Delta t \qquad \text{Eq. (3)}$$

The heat flux, q, at time t, could be obtained by combining Eqs. (2) and (3), which gives

$$q = \frac{mC_p[T(t-1) - T(t)]}{s\Delta t} \qquad \text{Eq. (4)}$$

The heat flux, q, at time t, can be represented by the following expression of

$$q = \frac{\Delta T}{R_t} = \frac{T(t) - (-196)}{R_t} \qquad \text{Eq. (5)}$$

where ΔT is the temperature difference between the frozen carrier and liquid nitrogen, and-196 °C is the liquid nitrogen saturation temperature. Because the cooling process happened in a second, and the liquid nitrogen was injected from the atmosphere, which resulted in -196 °C of liquid nitrogen saturation temperature for a quasi-steady state process.

Combining Eqs. (4) and (5), the total heat resistant, R_t, can be obtained as

$$R_t = \frac{[T(t)-(-196)]\Delta ts}{mC_p[T(t-1)-T(t)]} \quad \text{Eq.(6)}$$

The total heat resistance includes four parts: the conductive resistance of the silicon base, R_1, the conductive resistance of the micro structured layer, R_2, the evaporation heat resistance of the liquid nitrogen,R_3,andthe conductive resistance of the cells suspension, R_4.

$$R_T = R_1 + R_2 + R_3 + R_4 \quad \text{Eq.(7)}$$

The conductive resistance of the silicon base, R_1, can be found as

$$R_1 = \frac{d_1}{k_1} \quad \text{Eq.(8)}$$

The conductive resistance of the microstructured layer, R_2, can be expressed as

$$R_2 = \frac{d_2}{k_2} = \frac{d_2}{\varepsilon k_N + (1-\varepsilon)k_1} \quad \text{Eq.(9)}$$

The microstructured layer is made from silicon and liquid nitrogen. Its thermal conductivity could be calculated by the spatial mean. The evaporation heat resistance of liquid nitrogen, R_3, can be expressed as,

$$R_3 = \frac{1}{h} \quad \text{Eq.(10)}$$

The conductive resistance of the cells suspension, R_4, can be expressed as

$$R_4 = \frac{d_3}{2k_3} \quad \text{Eq.(11)}$$

Combining Eqs. (7-11), the evaporation heat transfer coefficient of liquid nitrogen, h, can be obtained as

$$h = \frac{1}{\frac{[T(t)-(-196)]\Delta ts}{mC_p[T(t-1)-T(t)]} - \frac{d_1}{k_1} - \frac{d_2}{\varepsilon k_N + (1-\varepsilon)k_1} - \frac{d_3}{2k_3}} \quad \text{Eq. (12)}$$

4. RESULTS AND DISCUSSION

The contrast tests of the cryopreservation practicability of hamster ovary cells using the equilibrium freezing method, the open pulled straws vitrification method(OPS method), and the vitrification method based on thin

film evaporation(TFE method)are done. Fig.5 shows the survival rate of cells in the above three methods. The cell viability of TFE method is highest and 82.9%. The open pulled straw vitrification method is 71.7%. The equilibrium freezing method is 75%.This initially demonstrates the feasibility of thisnew vitrification method based on thin film evaporation in cell freezing.

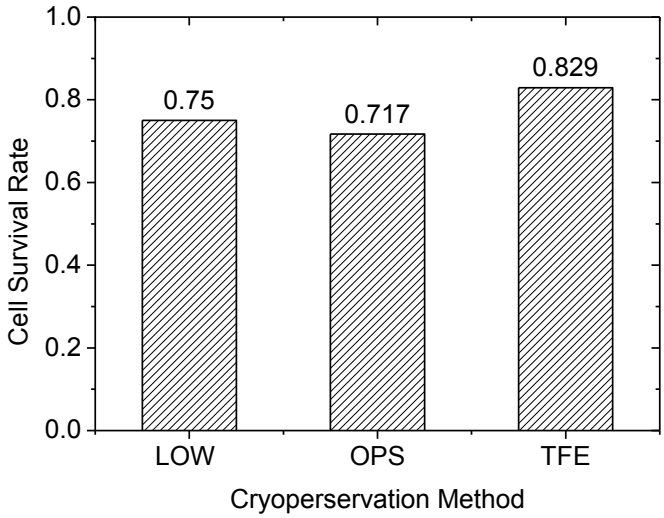

(LOW is the balance freezing method, TFE method is the vitrification method based on thin film evaporation, OPS is the open pulled straw Vitrification method)

Figure 5: Survival rate of cells in three methods

The OPS method and the TFE method belong to vitrification freezing methods. The cooling rate in the freezing procedure is a key for the survival rate of cells after freezing. The higher cooling rate can improve the survival rate. Because intracellular and extracellular liquid changes ice in the temperature range of -60-0 ℃, the temperature range is a dangerous and key area for cells cryopreservation. Fig.6 shows the temperature histories of the cells samples in the two vitrification methods when the temperature changes from 0℃ to -60℃. The average cooling rate of the TFE method can reach 50059℃/min, while that of the OPS method is only 25200℃/min. The former is nearly twice as high as the latter.

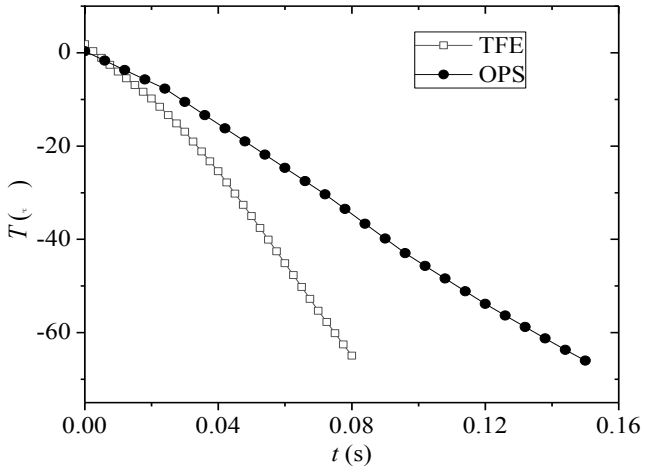

(TFE method is the vitrification method based on thin film evaporation, OPS is the open pulled straw Vitrification method)

Figure 6: Temperature histories in two vitrification methods

From the view of heat transfer, the main reason for the lower cooling rate of the OPS method is the low heat transfer coefficient of liquid nitrogen film boiling. The carrier (the straw) with cell suspension is directly plunged into liquid nitrogen in this method. Film boiling takes place because of the huge temperature difference between the carrier surface and the liquid nitrogen. The evaporation forms a “vapor blanket,” which acts as a heat-

insulation layer as shown in Fig.7. As a result, the evaporation heat transfer coefficient of liquid nitrogen is limited due to the poor thermal conduction of the “vapor blanket”. However, liquid nitrogen only consists of the microstructured surface of the freezing carrier in the TFE method, and the nitrogen vapor that is formed by evaporation easily departs from the liquid-vapor interface, therefore, the “vapor blanket” is avoided. Besides, Liquid nitrogen forms a thin film at a micro meter level due to the interaction of the capillary pressure and disjoining pressure in the microstructured surface(Su et al., 2012). The heat transferred from the evaporating surface is absorbed at the liquid-vapor interface by the latent heat of the liquid film and transferred through heat conduction in the thin film to the vapor phase. Because the thickness of the evaporating thin film is very thin, the total thermal resistance in the cooling procedure is very small. Fig. 8 shows the thermal resistances of the two methods in the experiments. That of the TFE method is obviously lower than that of the OPS method.

Figures 8 and 9 shows the heat flux and the evaporation heat transfer coefficient of liquid nitrogen in the two method. The abscissa of the two figures is the temperature of the frozen carrier, T. As previously analyzed, the heat flux and the evaporation heat transfer coefficient of the TFE method are both higher obviously than those of the OPS method. The heat flux of the TFE method decreases gradually with the temperature of the frozen carrier decreasing. The average heat flux is 315291W/m^2. However, that of the OPS method first increases, then decreases. The average heat flux is 139387W/m^2. The evaporation heat transfer coefficient of the TFE method increases slightly with the temperature of the frozen carrier decreasing. The evaporation heat transfer coefficient is 1965W/m^2℃.The evaporation heat transfer coefficient of the OPS method first increases, then decreases. The evaporation heat transfer coefficient is 904W/m^2℃.

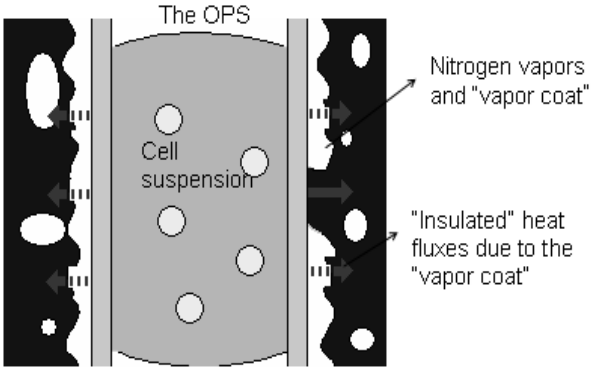

Figure 7: Formation process of gas film during pool boiling of OPS cooling

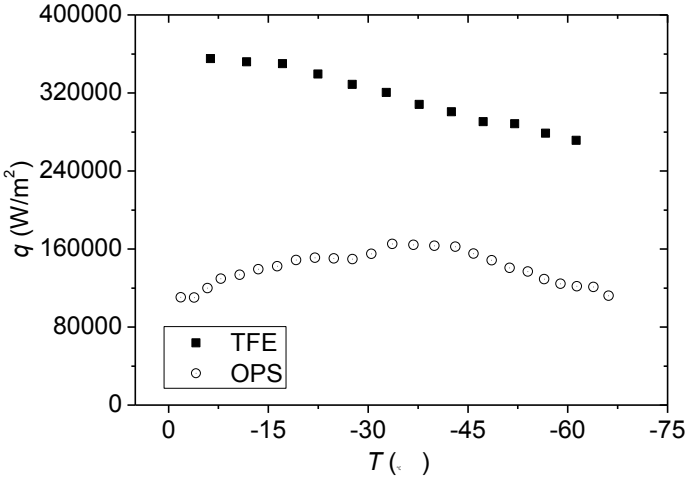

(OPS is the open pulled straw vitrification method, TFE is a vitrification method based on thin film evaporation)

Figure 8: Heat flux in two vitrification method

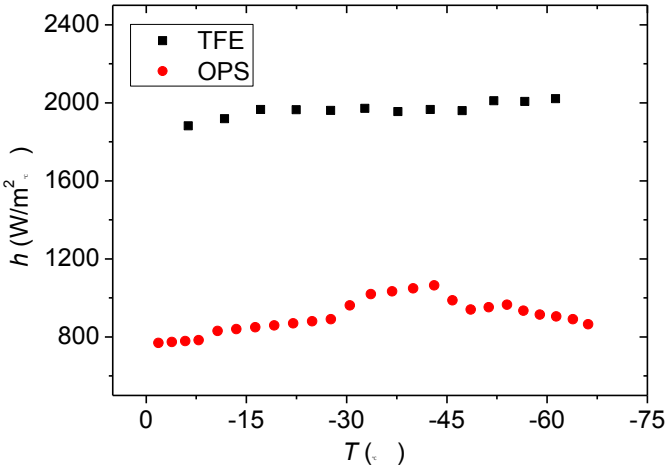

(OPS is the open pulled straw vitrification method, TFE is a vitrification method based on thin film evaporation)

Figure 9 Evaporation heat transfer coefficient of liquid nitrogen in two vitrification methods

5. CONCLUSIONS

In this paper, the ultra-fast freezing method based on thin film evaporation was used for the vitrification freezing of hamster ovary cells, and compared with the equilibrium freezing method and the open pulled straw vitrification method. At the same time, the mechanism for the improvement of the cooling rate in the thin film evaporation method was analysed in detail from the view of heat transfer. Two major conclusions can be drawn from the experimental results:

1. The cell vitrification method utilizing thin film evaporation can greatly improve the cooling rate, and obtain higher cell survival rate. This initially demonstrates the feasibility of this method in the cell vitrification process.

2. Thin film evaporation of liquid nitrogen on the micro-structured surface of the frozen carrier avoids forming of “vapor blanket”, and achieves the higher evaporation heat transfer coefficient than that of film boiling.

ACKNOWLEDGEMENTS

The authors are grateful for the financial support provided by National Natural Science Foundation of China (Contract No. 51376027)

NOMENCLATURE

C_p	specific heat capacity of silicon, J/kg°C	d_1	thickness of silicon base, m
d_2	thickness of microstructured layer, m	d_3	thickness of cell suspension, m
h	evaporation heat transfer coefficient, W/m^2 °C	k_1	conductivity of silicon, W/m°C
k_2	conductivity of microstructured layer, W/m°C	k_3	conductivity of cell suspension, W/m°C
k_N	conductivity of liquid nitrogen, W/m°C	m	mass of frozen carrier, kg
N_1	number of viable cells	N_2	total number of all cells
Q	heat quantity, J	q	heat flux, W/m^2
R_S	Cell Survival rate	R_t	total heat resistance, m^2°C/W
R_1	conductive resistance of silicon base, m^2°C/W	R_2	conductive resistance of micro structured layer, m^2°C/W
R_3	evaporation heat resistance of liquid nitrogen, m^2 °C/W	R_4	The conductive resistance of the cells suspension, m^2°C/W
s	evaporation heat transfer area, m^2	T	Temperature, °C
t	time, s	ε	proportion of liquid nitrogen in microstructured layer

REFERENCES

Bau, H. H., Torrance, K. E., 1982, Boiling in low-permeability porous materials, International Journal of Heat and Mass Transfer 25(1) 45-55.

Demsky, S. M., Ma, H. B., 2004, Thin film evaporation on a curved surface, Nanoscale and Microscale Thermophysical Engineering 8(3) 285-299.

Han, X., Ma, H. B., Jiao, A., Critser, J. K., 2008, Investigations on the Heat Transport Capability of a Cryogenic Oscillating Heat Pipe and its Application in Achieving Ultra-Fast Cooling Rates for Cell Vitrification Cryopreservation, Cryobiology, 56: 195-203.

Isachenko, V., Alabart, J. L., Nawroth, F., Isachenko, E., Vajta, G, Floch, J., 2001, The open pulled straw vitrification of ovine GV-oocytes: positive effect of rapid cooling or rapid cooling or rapid thawing or both,Cryo Letter 22(3) 157-162.

Jiao A J, Han X, Critster K J, Ma H B. 2006, Numberical investigations of transient heat transfer characteristics and vitrification tendencies in ultra-fast cell cooling processes. Cryobiology, 52(3): 386-392.

Kaviany, M., 1995, Principles of heat transfer in porous media, Springer-Verlag, New York, 626-628.

Martino, A., Songsasen, N., Leibo, S. P., 1996, Development into blastocysts of Bovine occytes Cryopreserved by ultra-rapid cooling, Biology of Reproduction 54(5) 1059-1069.

Mukaida, T., Nakamura, S., Tomiyama, T., Wada, S., Kasai, M., Takahashi, K., 2001, Successful birth after transfer of vitrified human blastocysts with use of a cryoloopcontainerless technique, Fertility and Sterility 76(3) 618-620.

Sait, H., Ma, H. B., 2009, An experimental investigation of thin film evaporation. Nanoscale and Microscale Thermophysical Engineering 13(4) 218-227.

Steponkus,P. L., Myers,S. P.,Bronshteyn,V.,Leibo,S. P.,Rall,W. F., Pitt,R. E., Lin,T. T.,MacIntyrell, R. J., 1990, Cryopreservation of drosophila melanogaster embryos, Nature 345(6271) 170-172.

Steponkus, P. L., Caldwell, S., 1993, An optimized procedure for the cryopreservation of Drosophila melanogaster embryos,Cryo Letter 14(6) 375-380.

Su, F. M., Ma, H. B., Han, X., Chen, H. H., Tian, B. H., 2012, Ultra-high cooling rate utilizing thin film evaporation, Applied Physics Letters 101(11) 113702.

Vajta,G., Holm,P., Kuwayama,M.,Booth, P. J., Jacobsen, H.,Greve,T.,Callesen,H., 1998, Open pulled straw(OPS) vitrification: a new way to reduce cryoinjuries of bovine ova and embryos, Molecular Reproduction and Development 51(1)53-58.

Yoon, T. K., Lee, D. R., Cha, S. K., Chung, H. M., Lee W. S., Cha, K. Y., 2007, Survival rate of human oocytes and pregnancy outcome after vitrification using slush nitrogen in assisted reproductive technologies, Fertility and Sterility 88(4) 952-956.

Manuscript ID: 572
DOI: 10.18462/iir.icr.2019.0572

Instant cryopreservation of porcine heart valves and aortic segments in low-viscous polydimethylsiloxane – first results

Stanislav LAUK-DUBITSKIY[(a)], Lyubov SEVERGINA[(b)], Igor KOROVIN[(c)], Alexey SHAKUROV[(a)], Alexander PUSHKAREV[(a)], Roman KOMAROV[(d)], Dmitrii BRITIKOV[(e)], Ivan NOVIKOV[(f)]

[(a)] The Bauman Moscow State Technical University, Moscow, 105005, bauman@bmstu.ru
[(b)] Anatomic pathology department, I.M. Sechenov First Moscow State Medical University, Moscow, 119435, losevergina@gmail.com
[(c)] 5th year student, medical school "Medicine of the future", I.M. Sechenov First Moscow State Medical University, Moscow, 119435, project14@bk.ru
[(d)] Clinic of cardiovascular surgery, I.M. Sechenov First Moscow State Medical University, Moscow, 119435, clinic@1msmu.ru
[(e)] A.N. Bakulev National Medical Research Center of Cardiovascular Surgery, Moscow, 121552, info@bakulev.ru
[(f)] FGBU «NII Eyes disease», Moscow, 119021, info@eyeacademy.ru

ABSTRACT

The aim of study was to evaluate the safety of heart valves cryopreservation in low-viscous polydimethylsiloxane (PDMS). 15 porcine heart valves (mitral and aortic / 1.0 cm) and aortic segments (2.0 cm) were cryopreserved in PDMS (1cSt, -75°C, 1L, temperature control) with stirring (150 turns per minute) for 40 sec, and then thawed in the PDMS (5cSt, +24°C, 1L, 1 min). The cryopreservation protocol was applied with speed of freezing and thawing close to 200°C/min without cryoprotectants and LN2. The quality of cryopreservation was assessed by histological methods (Orcein, Van Gieson, H&E). There were no critical differences between the valves and aortic segments of experimental and control groups. Using of PDMS is feasible for instant cryopreservation of vascular tissue for their implantation as homografts or biobanking with possible additional usage of the inner hydrophilic covering of tissue to prevent hydrophobization.

Keywords: Vitrification, Ice-free cryopreservation, Polydimethylsiloxane, Porcine heart valves, Porcine aortic segments

1. INTRODUCTION

Congestive heart failure is a leading cause of death worldwide. For many patients with that disease, one of the main definitive treatment options is cardiac allotransplantation with a cryopreserved homograft. Such replacement is a safe and desirable surgical option especially for high-risk patients with infective endocarditis and aortic root abscess. Safety cryopreserved homograft with preserved ECM components, elastin and collagen generally shows good hemodynamic performance and reduced T-cell infiltration in the valve stroma (Sultan, 2018). But the main problem of homografts using is their limitation by the number of donor tissues accessible by the local surgeon and lack of appropriate modern protocols for instant cryopreservation of cadaveric vascular tissue to create homografts.

The relevance of the research topic is related to the necessity of developing a new basic protocol of cryopreservation and thawing of vascular tissues just after their retrieval from a donor for their further implantation as homograft or biobanking. This protocol should be safe enough, simple and modifiable by changing freezing/thawing rate for both single and bulk processing of tissues and their repeated freezing. For this purpose, in the course of ongoing research (Lauk-Dubitsky, 2017; Lauk-Dubitsky, 2017; Lauk-Dubitsky, 2018), the polydimethylsiloxane (PDMS) was used as a basic cryopreservation media with hydrophobic properties.

2. CRYOPRESERVATION IN PDMS

Low-viscous polydimethylsiloxane (PDMS) is widely used as a coolant for medical and other equipment, and ultra-viscous PDMS is used as a non-toxic media for hydrophobization, basic compound to make bio-chips in microfluidics, and some medical drugs. PDMS used in current research as heat and cold transfer fluid and non-penetrating protector is characterized by its high hydrophobicity (contact angle 90-120°), low viscosity, high rate of evaporation, low pour point (-100°C), low VTC (viscosity change at temperature) and low surface tension. Its thermal conductivity is 0.00024 cal/cm. sec. x10-4 °C, a coefficient of thermal expansion - 0,00134 K^{-1}, flash point - 37°C, pour point -100°C. Verification of PDMS coolant capabilities was performed in a previous work with mathematical modelling in CFX Ansys 17.0 Academic software and tests with an electronic thermometer (UT325 UNI-T, China, 6 values per second) fixed in the internal lumen of the iliac artery segment, freezing rates were - from 35 °C/min in statics to ~155 °C / min and above with rotating the vessel in PDMS at a speed of 150-200 RPM.

For the study 15 porcine hearts were isolated aseptically via thoracotomy from euthanized physically healthy pigs (70-100 kg, 1-1.5 years of age, «German landrace» pigs; equal gender distribution), they were acquired from a locally approved abattoir (Meat House, Pushkino city, MO) according to EU Council Directive 93/119/EC on the protection of animals at the time of slaughter or killing. No animals were sacrificed specifically for this study. Ethical approval was granted for this study by the I.M. Sechenov First Moscow State Medical University. Ten minutes later after slaughter hearts (350-450 g) were perfused with a heparinised 0.9% saline solution to clear residual blood and placed in a cryo-container (+4 °C) for transportation to the pathoanatomical department of Pushkino Central Hospital. All further actions were performed in a dissecting room on a sterilized table not later than 30 minutes after slaughter. Cadaveric hearts valves were used as controls.

All valves (mitral and aortic) and aortic specimens (n = 90 incl. native) were immediately excised aseptically and dissected free as 1.0x1.0x0.1 cm for valvular and 2.0x0.5x0.2 cm – for thoracic ones; then rinsed three times in cold phosphate-buffered saline (PBS; Lonza, Cologne, Germany).

Low-viscous PDMS-1 (PSF-1cSt - Octamethyltrisiloxane, Clearco Products Co., Inc., USA) was used as the cold-transfer fluid for freezing and PDMS-5 (PSF-5cSt) as heat transfer fluid for thawing. LogTag TREL-8 temperature sensor with a remote probe (LogTag records, USA) was used for temperature control. Refrigeration chamber (Bychkov 2017) was used for PDMS preparing. For all the valves cryopreservation was performed in a plastic container (2L) filled with PDMS-1 (-75°C, 1L) and with carbon dioxide ice (757 g) out of its contour for thermal stability. Each valve was

cryopreserved once by immersion in PDMS and rotation (140 turns per minute) for 40 seconds and then immediately thawed in another plastic container (2L) filled with PDMS-5 (+30°C, 1L) for 1 min with the same rotation. All thawed segments were washed in saline and fixed in 10% buffered formalin for at least 24 hours for further transportation to the laboratory for histology tests with comparing to control. Samples of valves were embedded in paraffin, sliced into 5 µm-thick sections and stained with Hematoxylin and Eosin for histomorphology, with Orcein for elastic fibers and with Van Gieson (EVG) to distinguish collagen fibers and to characterize the density and structure of connective tissue and vascularity. Analysis of tissue microstructure was performed using routine bright field microscopy (Olympus BX40, Olympus, Tokyo, Japan; with color camera AxioCam MRc, Carl Zeiss, Jena, Germany). Sections of an untreated valve were also stained and served as a positive control.

As a result, according to histological slides of cryopreserved valves and aortic segments in comparison with control, no significant difference was observed at the light-optical level of examination (Fig.1-4). All valves and segments were free from cracks or other gross and minor damages after thawing, and this fact may indirectly indicate the safety of the cryopreservation process in PDMS.

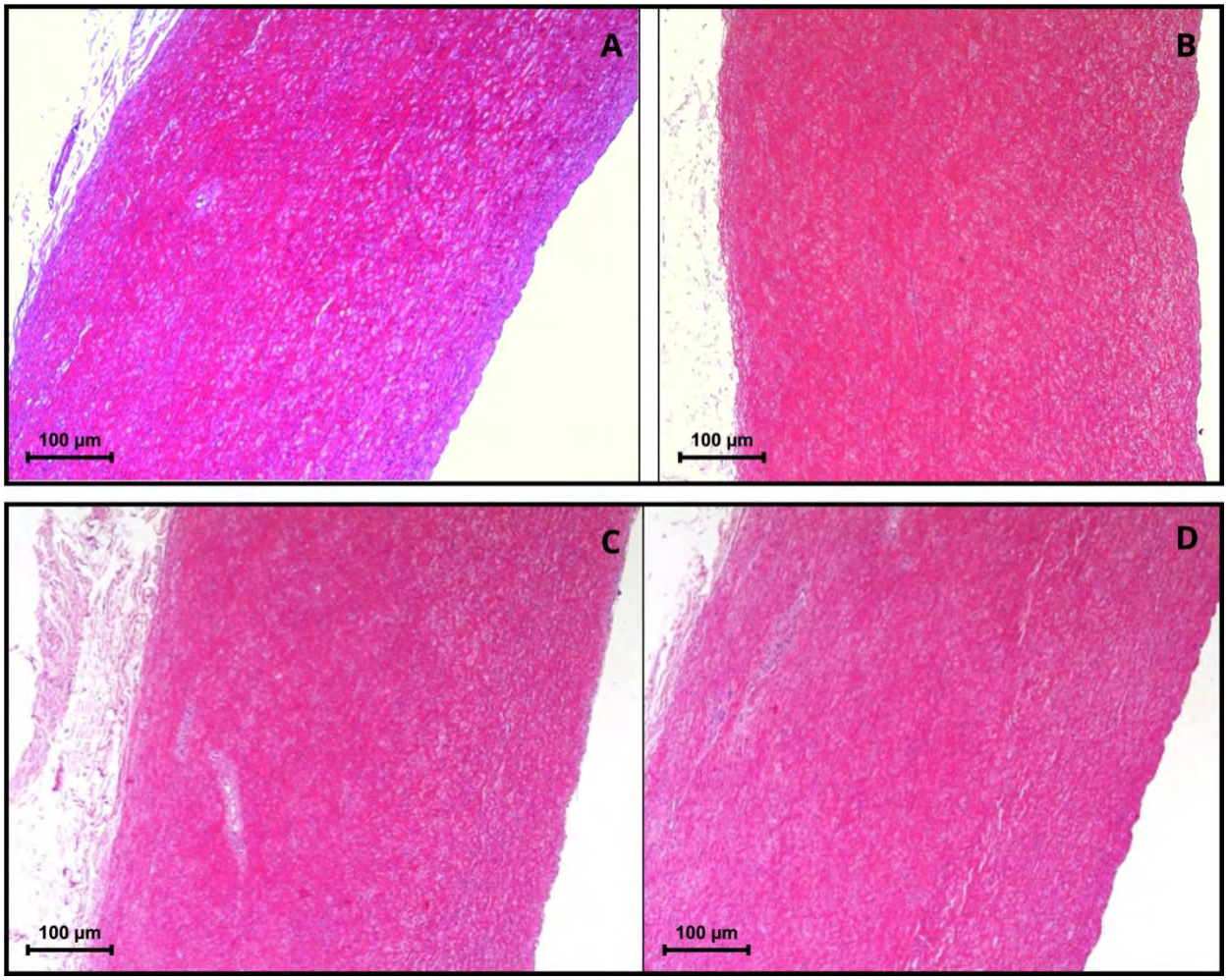

Figure 1: H&E staining of aorta (x200). A/C. Cryopreserved segment B/D. Native segment

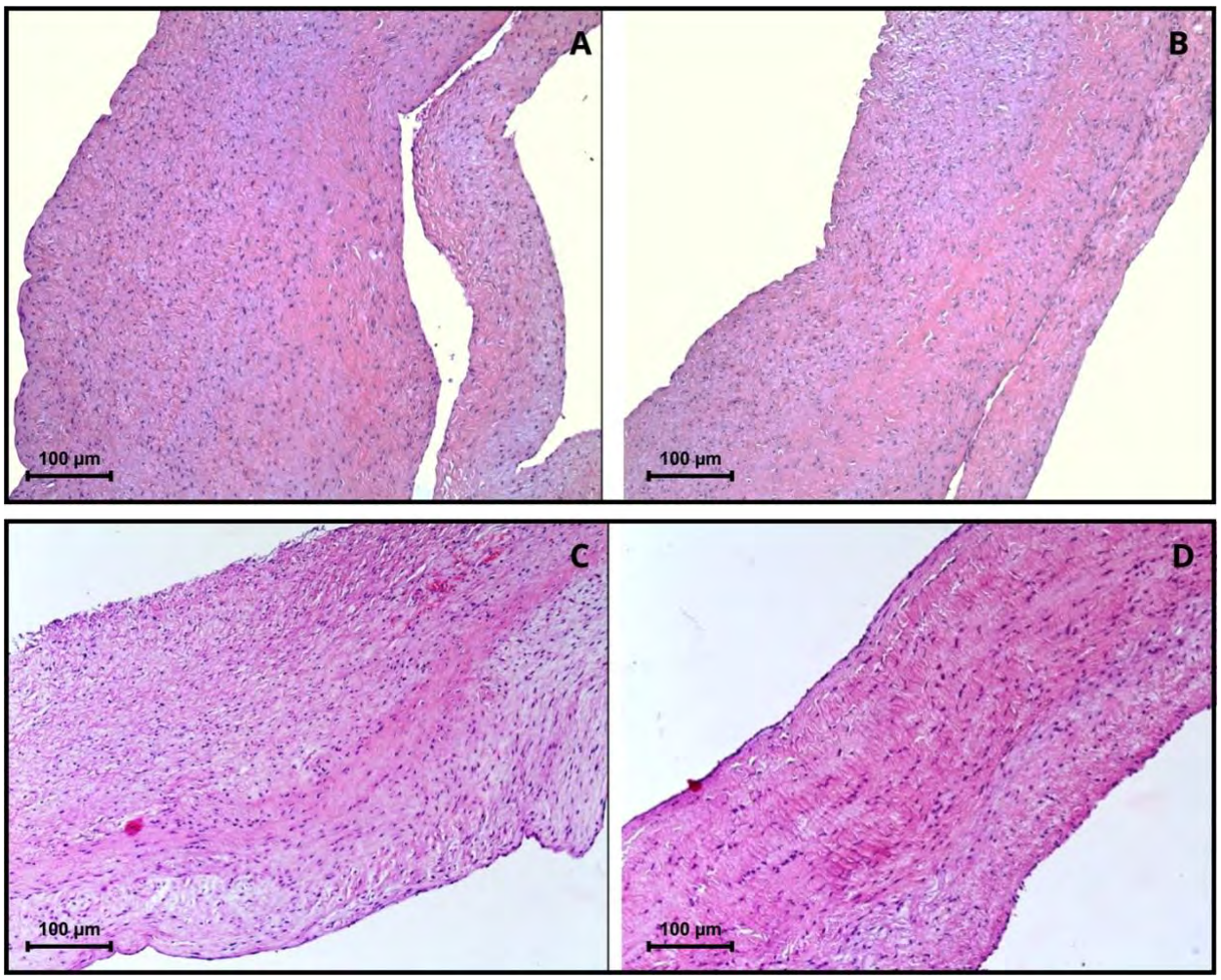

Figure 2: H&E staining of aortic valves with adjacent chordae (x200). A/C. Cryopreserved valve B/D. Native valve

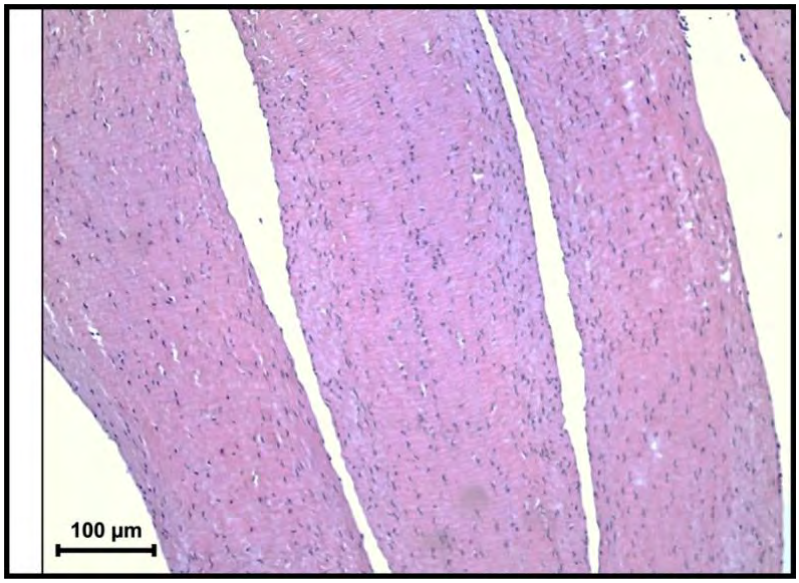

Figure 3: H&E staining of cryopreserved chordae of the mitral valves (x200)

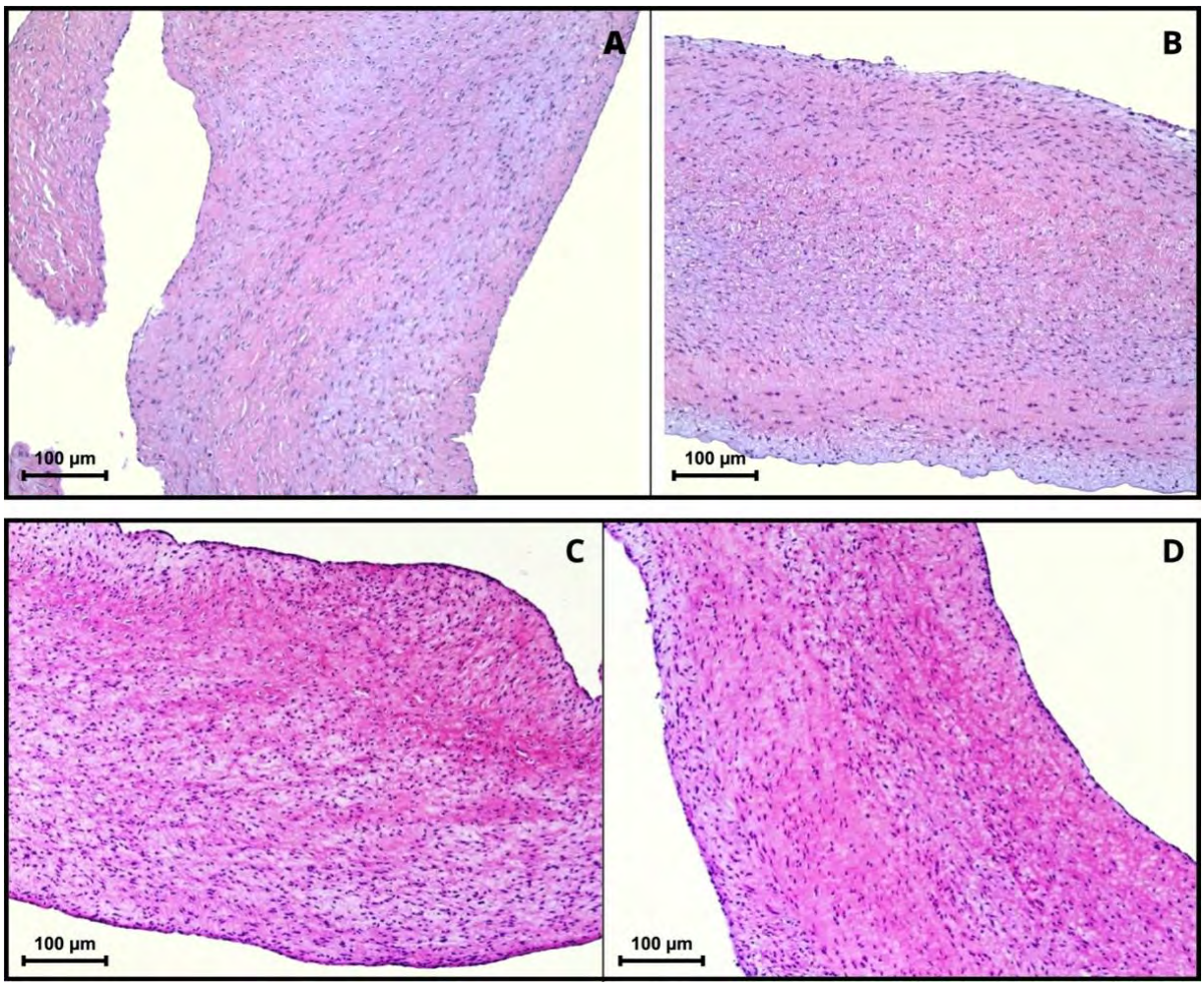

Figure 4: H&E staining of mitral valves (x200). A/C. Cryopreserved valve B/D. Native valve

In particular, van Gieson staining has shown organisation in a layer-ordered collagen fibers, without any signs of disruption, completely similar to the native ones (Fig.5); and Orcein staining – that elastic fibers in valves appeared to be well-organized and distributed throughout the lamina (Fig.6). All fibers show a general alignment in the circumferential direction, agreeing with the observed mechanical anisotropy. Endothelium on surfaces of aorta and valves as well as in vasa vasorum and in intervalvular vessels was preserved.

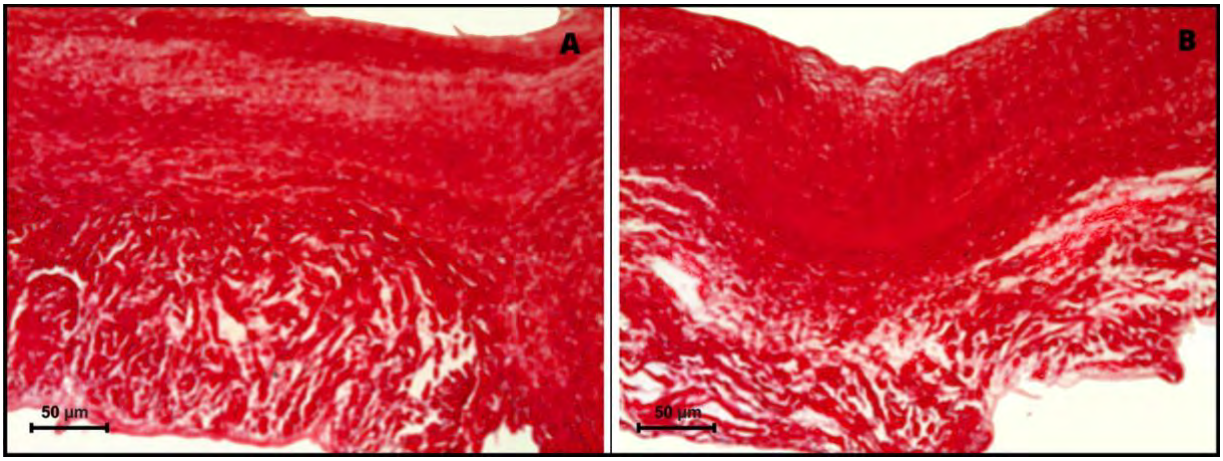

Figure 5: van Gieson staining of aortic segments (x100). A. Cryopreserved segment B. Native segment

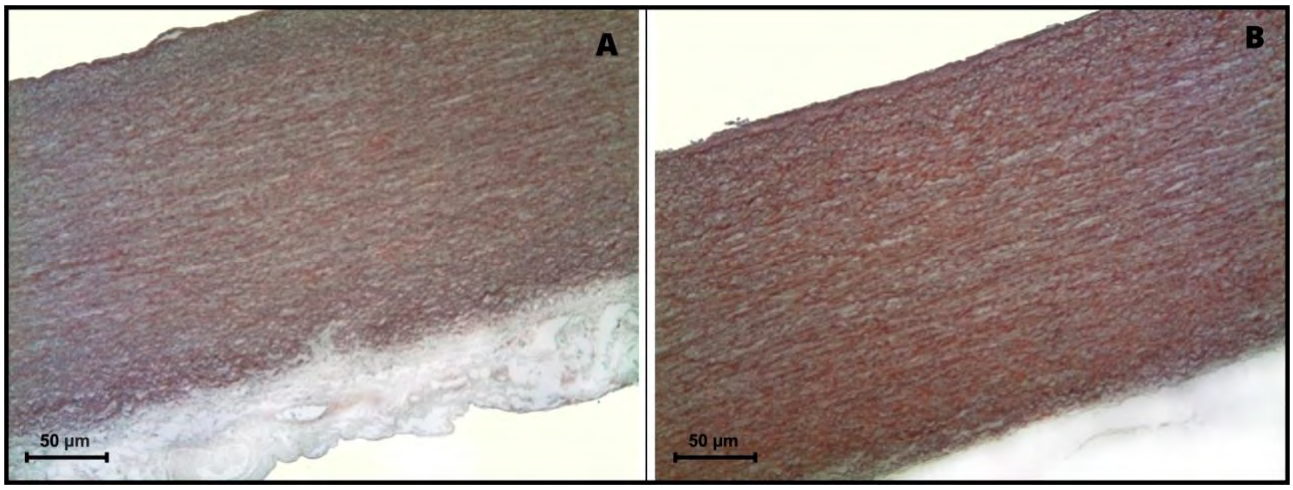

Figure 6: Orcein staining of aortic segments (x100). A. Cryopreserved segment B. Native segment

CONCLUSION

After the performance of the experiment we tested the cooling rate of cryopreservation processes using mathematical modelling. Cooling and thawing of biological objects - heart valves and aortic fragments was modelled in the CFX application in the Ansys 19.2 Academic software using the iterative approximation method for calculating the equations of hydro and thermodynamics (equations of continuity, Navier-Stokes and thermal conductivity) and given thermal properties of biological objects and PDMS. According to the modelling biological objects were cooled to -50 ºC for 6 s (~900ºC/min, the cooling rate is close to vitrification standard) and heated to 0 ºC for 5 s (~ 900ºC/min). In the future, this approach should be tested for larger samples.

As mentioned before there were no significant differences in ultrastructure between control valves and valves cryopreserved in PDMS indicating the prospects of polydimethylsiloxane using as a cold and heat transfer agent with hydrophobic properties mainly because of achievable and controllable cooling rate of biological tissues for volumes over 50 ml, that can reduce intracellular and extracellular ice formation without osmotic shifts, which is considered to be fundamental to all cryoinjuries.

The cooling and thawing rate close to vitrification, uniformity, ultra-high heat transfer coefficient without effect similar to film boiling of LN on an outer layer of biological tissue achieved during the protocol is based on a direct contact of the vascular tissue with hydrophobic PDMS from the outside and the inside, which positively affects the rate of cooling and heating and reduces the risks of cracking, also reducing the intensity of the negative mechanical effect on the vascular tissue during heat exchange processes. In the future, it is necessary to carry out experimental and calculated verification using the following approaches (Dombrovsky 2015, Zhang 2017, Katyba 2018).

The problem of the inevitable formation of a hydrophobic film on the valves and its possible delamination during thawing can be solved by using a hydrogel water-soluble coating based on a crosslinked copolymer of chitosan, collagen and hyaluronic acid. Hydrogel coating forms an adhesive thin film with high thermal conductivity, which additionally allows equalizing temperature gradients.

In summary, we developed an approach of using of low-viscous PDMS for intensive one-stage cryopreservation which provides uniform and rapid freezing. Hydrophobic properties of PDMS allow reducing the negative effect of crystallization during cooling and recrystallisation effect during thawing. The wide possibilities for choosing the cooling and thawing rates, as well as the

compatibility with penetrating cryo-protectors make PDMS based protocol suitable for further modification for the preservation of the cellular component in the biological tissues, both native and tissue-engineered.

The computational model and the gauze wrapping technology developed in this study may be valuable to facilitate cell cryopreservation by vitrification with negligible ice formation.

NOMENCLATURE

cSt	santistocks (kPa)
L	litre
LN	liquid nitrogen
H&E	Hematoxylin and eosin staining

ACKNOWLEDGEMENTS

The authors would like to thank the Bauman Moscow State Technical University for obtaining access to Ansys. Mathematical modeling was supported by the Russian Science Foundation (project 19-19-00359).

REFERENCES

Lauk-Dubitsky, S., 2017. Scheme of the emergency mobile cryopreservation of vascular allotransplants. Medicine of extreme situations 2(60), 181-186.

Lauk-Dubitsky, S., 2017. Elaborating of a complex cryoconservation protocol of blood vessels for the tissue-specific matrices. Saratov Journal of Medical Scientific Research 13(4), 891-900.

Lauk-Dubitsky S., 2018. Complex approach for portable cryopreservation of segments of blood vessels with polydimethylsiloxane. Russian Journal of Transplantology and Artificial Organs 20(1), 86-95.

Sultan, I., Bianco, V., Kilic, A., Chu, D., Navid, F., Gleason, T., 2018 / Aortic root replacement with cryopreserved homograft for infective endocarditis in the modern North American opioid epidemic. The Journal of Thoracic and Cardiovascular Surgery 157(1), 45-50.

Bychkov, E.G., Samokhvalov, Y.V., Makarov, B.A., Yakovlev, V.I., 2017. Experimental research of low-temperature throttling refrigerator for cryoconservation of medical and biological objects. Journal of Physics: Conference Series, 891 (1), № 012109.

Dombrovsky, L.A., Nenarokomova, N.B., Tsiganov, D.I., Zeigarnik, Y.A., 2015. Modeling of repeating freezing of biological tissues and analysis of possible microwave monitoring of local regions of thawing/ (2015) International Journal of Heat and Mass Transfer, 89, pp. 894-902.

Zhang, Y., Zhao, G., Chapal Hossain, S.M., He, X.Modeling and experimental studies of enhanced cooling by medical gauze for cell cryopreservation by vitrification (2017) International Journal of Heat and Mass Transfer, 114, pp. 1-7.

Katyba, G.M., Zaytsev, K.I., Dolganova, I.N., Shikunova, I.A., Chernomyrdin, N.V., Yurchenko, S.O., Komandin, G.A., Reshetov, I.V., Nesvizhevsky, V.V., Kurlov, V.N. Sapphire shaped crystals for waveguiding, sensing and exposure applications (2018) Progress in Crystal Growth and Characterization of Materials, 64 (4), pp. 133-151.

Manuscript ID: 1555
DOI: 10.18462/iir.icr.2019.1555

Study on proline as cryoprotectant in cryopreservation

Ziqiao SUN[(a)], Yazhou LI[(a)], Wei RAO[*(b)]

[(a)] Beijing Engineering Research Center of Sustainable Energy and Buildings, Beijing University of Civil Engineering and Architecture, Beijing, 100044, China, Sunziqiao@bucea.edu.cn

[(b)] Technical Institute of Physics and Chemistry of the Chinese Academy of Sciences (TIPCCAS), Beijing, 100190, China, weirao@mail.ipc.ac.cn

ABSTRACT

This study is aimed at evaluating the performance of proline as a green protectant in cryopreservation. The freezing temperatures of four kinds of cryoprotectants were compared with the one of proline by DSC tests, and four kinds of composite cryoprotectants based on proline also presented a contrast. Then, four groups of living ants have implemented the freezing experiments, the ants fed by the higher concentration of proline held the higher survival rate after freezing. Also, the results indicated that proline was provided with the stronger anti-icing effect and could significantly improve ants' freezing inhibition ability. This work would provide useful experience for cryopreservation solutions in vivo of microorganisms.
Keywords: Cryopreservation, Proline, Differential Scanning.

1. INTRODUCTION

Cryopreservation, as clinical practice has shown, is the only feasible way of biomaterials' long-term preservation. This low temperature conservation technology focuses on to investigate the damage discipline of cells, tissues or organisms at low-temperature, especially the crystallization of intracellular and external water during freezing process(Hua and Ren 1994, Liu 2007).

Polge et al. (1949) found that the sperm could be cryopreserved in glycerol solution without death. Since then, cryopreservation technology has been dramatically developed with the research and exploration more than half a century. In the 1960s to 1980s, the cryopreservation of blood cells, cattle and sheep embryos, and islet cells were achieved step by step (Zhang and Zhou 2007). And researchers have achieved a long-term cryopreservation of most cells successfully, such as sperm, oocytes, human bone marrow mesenchymal stem cells, and hepatocytes(Broxmeyer et al. 1989; Fuller et al. 2013; Gaucher et al. 2012; Liu et al. 2010; Pallotta et al. 2012; Justice and Christensen 2013). Some progress has also been made in short-term cryopreservation of complex tissues and organs, like skin, cornea, ovaries, liver, and kidneys (Hua and Ren, 1994; Liu and Liu 1993). To date, cryopreservation technology has been widely used in many fields, including food sciences, medicine, biology, etc.

However, for slightly complicated cells, the most advanced cryogenic cryopreservation technology is even difficult to guarantee a 100% successful cryopreservation rate, not to mention achieving cryopreservation of tiny life, such as ants which is non-cold-resistant. By Contrast, many lives can survive in low-temperature environments in nature. For example, Antarctic nematodes can maintain their vital activity after rewarming from freezing with 82% body water frozen (Raymond and Wharton 2013). Alaska wood frog can endure a two-month freezing period at -4 °C (Costanzo et al. 2015). Are there some particular anti-icing substances in their bodies?

As an attempt, the researchers fed a proline-rich food to the larvae of Chymomyza crostatas in the Arctic and the larvae of cold-sensitive Drosophila melanogasters in the tropics, in order to enhance the proline content in the bodies before cryopreservation. The results showed that both the two kinds of larvae could survive from frozen after rewarming, even produce normal offspring (Kostál et al. 2012; Vladimír et al. 2011). It seems that proline acts as a cryoprotectant (CPAs).

Withers and King (1979) preserved corn cells successfully with a 10% ($w.v^{-1}$) proline solution. It was the first-time that proline employed as a cryo-protectant. Some studies on proline cryopreservation have achieved some progress. Sánchez-Partida et al. (1998) preserved goat sperm using a 27 mM proline solution. Denise et al. (2011) preserved human stem cells with 1% ($w.v^{-1}$) proline in combination with 10% ($w.v^{-1}$) of ectoin. In the same period, Kostál et al. (2012) and Vladimír et al.

(2011) demonstrated that proline could be used as a cryoprotectant by the study of the two species of cold tolerance flies directly. Further, research showed that the addition of proline reduced the concentration of DMSO from 10% to 2.5 % in human endothelial cell cryopreservation (Sun et al. 2012). Zhang et al. (2016) found that proline can protect mitochondrial function and increase the revitalization rate of vitrified cryopreserved oocytes. It indicates that proline can be used as a novel cryoprotectant for vitrification of mouse oocytes.
In this paper, the advantages of proline as a cryoprotectant in vivo was clarified by comparison with other cryoprotectants. Then, the feasibility of proline as a cryoprotectant was demonstrated by in vivo experiments based on ants.

2. METHODS AND MATERIALS

2.1. Freezing Temperature Analysis Experiment of Cryoprotectant Based on DCS Test

The formation of ice crystal nucleus depends on thermal factors, and its growth/extension is dependent on kinetic factors. The temperature of the liquid must be cooled to a temperature T_s, below the T_f (solution equilibrium freezing point), so that the liquid could change from liquid phase to solid spontaneously. Also, T_s is so-called freezing temperature (Hua and Ren 1994).
The freezing temperature, to a certain extent, reflects the inhibitory effect of the cryoprotectant on the nucleation and growth of the ice crystal in the solution.
The cryoprotectant solution reduces the damage of intracellular icing by helping cells to ooze water out before freezing. The lower freezing temperature of the cryoprotectant solution indicates the harder to freeze and the stronger low-temperature protection ability— instead, the more easily to freeze and the weaker protection ability.
In following, the potentiality of proline was investigated where proline acted as a low-temperature cryoprotectant. Proline was compared with four common cryoprotectants: Trehalose, Sucrose, Glucose, and DMSO by DSC test. Further, proline was mixed with Glucose, Sucrose and Trehalose solution separately, and three composite cryoprotectants were prepared. The ice-suppressing ability of these three solutions would also be evaluated. As it is known that, during the freezing process of an organism, the low-temperature protection effect of cryoprotectant is not the result of a single substance action, and the combination of green cryoprotectants would reduce the toxicity of a single cryoprotectant.
The reagents of Proline, Trehalose, Sucrose, Glucose, DMSO solution in this study are provided by the Beijing Chemical Reagent Company.
The variation of the sample's temperature in DSC equipment sets up as below:
a) set the initial temperature to 30 ° C, the temperature difference between the device and the sample reduces to 1.7 °C, the subsequent procedure will carry out automatically.
b) Cooling the temperature of the sample from 30°C to 20°C with a rate of 10°C.min^{-1}.
c) Maintain a constant temperature at 20°C for 5 minutes.
d) Cooling the temperature of the sample from 20°C to -150°C with a rate of 10°C.min^{-1}.
e) Maintain a constant temperature at -150 °C for 5 minutes.
f) Raising the temperature of the sample from -150°C to 20°C with a rate of 10°C.min^{-1}.
g) Maintain a constant temperature at 20 °C for 5 minutes;
The software of DSC equipment will record the data such as the temperature of the sample, time and heat flow data, automatically.

2.1.1 Anti-icing effect of different single cryoprotectants:

Dissolve 100 mg.mL^{-1} mixture of proline, trehalose, sucrose, glucose, and DMSO with phosphate buffer solution (PBS)separately, and take 12 mg of each solution for thermal analysis on DSC 200 F3 differential scanning calorimeter. The freezing temperature of cryoprotectant would be evaluated.

2.1.2 Anti-icing effect of composite cryoprotectants:

Composite cryoprotectants would be prepared with two steps: mixing proline with a cryoprotectant by a mass ratio of 1:1and dissolving the mixture in the phosphate buffer solution (PBS) at a concentration of 100 mg.mL^{-1}. In this test, four kinds of samples will be used: proline-PBS solution (abbreviated as PP solution below), Glucose-proline-PBS solution (abbreviated as GP solution below), Sucrose-proline-PBS solution (abbreviated as SP solution below) and Trehalose-proline-PBS solution(abbreviated as TP solution below).

2.2. Carpenter Ants Freezing-Rewarming Experiment in Vivo

The experiment used artificially fed carpenter ants as the research object. Ants are divided into four groups randomly and fed with different feed diets. Three kinds of proline-enriched diets were prepared by mixing proline with a standard diet (a mixture of agar and honey water). For example, the diet for Group Pro10 is prepared by mixing 10 mg proline with 90 mg agar powder and 900 mg honey water. Table 1 shows the proline content in the diet for each group of ants and the mixing ratio of various substances. All ants were housed in 2000 mL beakers and fed twice a day in the morning and evening for five days.

Table 1. Proline content in diets of different groups

Group name	Pro 0	Pro10	Pro 20	Pro 30
Proline content in each group diet C_{pro}	0 mg.g^{-1}	10 mg.g^{-1}	20 mg.g^{-1}	30 mg.g^{-1}
mixing ratio (proline: agar powder: honey water)	0 mg :100 mg: 900 mg	10 mg :90 mg: 900 mg	20 mg :80 mg: 900 mg	30 mg :70 mg: 900 mg

The experiment is implemented by the Advatntage Series freeze dryer. A certain number of ants were placed in a plastic petri dish and placed in freeze dryer which would perform freezing and rewarming process according to a set temperature program. The Agilent 34902A data acquisition system was used to collect the temperature variation of ants during the experiment.
In the experiment, each group of ants would be cooled down to -25 °C as a rate of 0.021 °C per minute and stay at -25 ° C for an hour, then be rewarmed at 18 °C in the next 24 hours. Fig. 1 illustrates the experimental process.

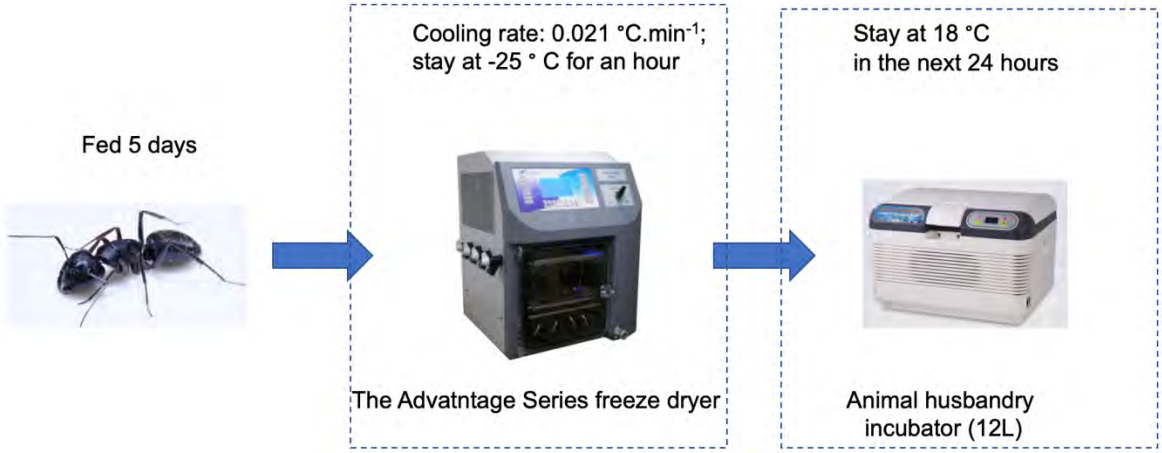

Figure 1: Sketch map of carpenter ants freezing-rewarming experiment in vivo

3. RESULTS AND DISCUSSION

3.1. Freezing Temperature Analysis Experiment of Cryoprotectant based on DCS Test

3.1.1 Anti-icing effect of different single cryoprotectants

To confirm the superior icing-inhibition of proline, proline and various typical cryoprotectants were detected by DSC test. Also, the freezing temperatures obtained were compared. PBS was employed as a solvent to simulate the ants' body fluid environment. DMSO, glucose, sucrose, trehalose, and proline was dissolved in PBS at the same concentration separately. Fig. 2 shows a typical DSC curve for 100 mg.mL^{-1} DMSO, Glucose, Sucrose, Trehalose, Proline in PBS.

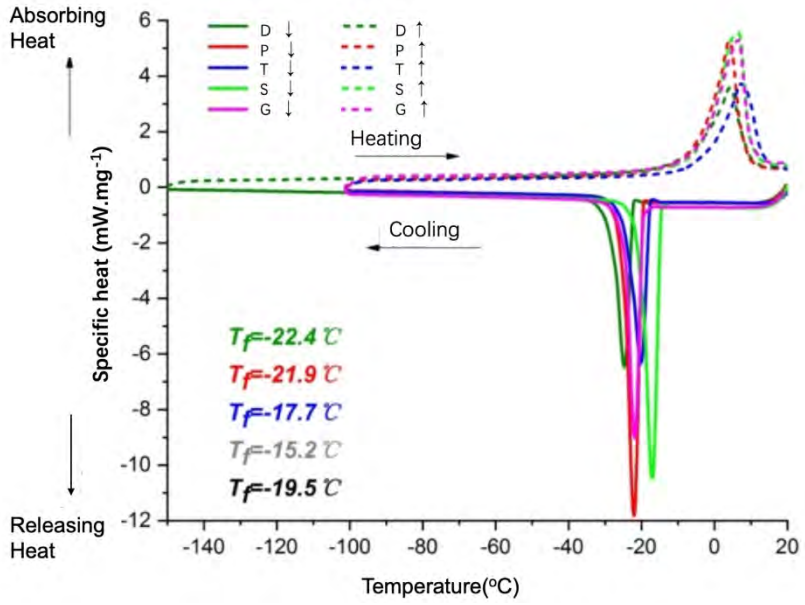

Figure 2 Typical DSC curve of cryoprotectant in PBS solution (100 mg.mL $^{-1}$). The temperature varies during the freezing and rewarming process. D stands for DMSO solution, P stands for proline solution, T stands for trehalose solution, G stands for glucose solution, and S stands for sucrose solution

The freezing temperatures of glucose, sucrose, and trehalose in PBS were -19.5 °C, -15.2 °C, -17.7 °C, respectively, which was significantly higher than -20.9 °C for proline and -22.4 °C for DMSO. That means proline holds the stronger ability to inhibit ice crystal formation than Sucrose, Glucose, Trehalose, but weaker than DMSO. However, from the perspective of adding a single cryoprotectant, proline would be a suitable candidate cryoprotectant to cryopreservation in vivo, for DMSO is toxic to organisms.

3.1.2 Anti-icing effect of composite cryoprotectants

The mixed cryoprotectants based on proline were used to verify the anti-icing performance of proline. As shown in Fig. 3, the freezing temperatures of GP solution, SP solution and TP solution were -20.4 °C, -15.3 °C, -18.7 °C, respectively, which are significantly higher than -20.9 ° C of PP solution. The freezing temperature of PP solution is the lowest among all four solutions. This result proved that PP solution is provided with the much stronger Anti-ice crystal nucleation ability than the other three composite cryoprotectants. It also indicated that proline was the better cryoprotectant for cryopreservation in vivo.

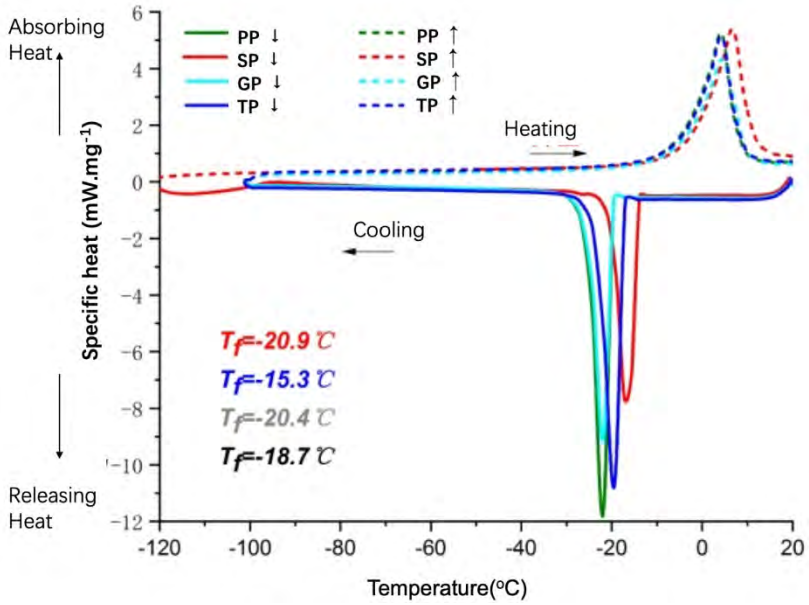

Figure3: Typical DSC curves of various mixed cryoprotectant with PBS solution (100 mg.mL $^{-1}$) during the temperature rise and fall process. PP stands for proline-PBS solution, TP stands for trehalose-PBS solution, GP stands for glucose-PBS solution, and SP stands for sucrose-PBS solution

3.2. Effect of Proline Concentration on Ant Survival Rate

According to the concentration of proline fed, ants were divided into four groups, namely 10 mg.g^{-1} (Pro 10 group), 20 mg.g^{-1} (Pro 20 group), 30 mg.g^{-1} (Pro 30 group), 0 mg.g^{-1} (Pro 0, control group). For each group, the experiment would repeat three times by ants samples fed, in other words, the freezing and rewarming process would be implemented by three parallel groups of ants.

Fig. 4 illustrates that the ants fed with proline will have a higher survival rate, and proline has a significant effect on improving the freezing tolerance of ants. As the concentration of proline fed increases, the survival rate of ants raised from 37.5% in Pro0 group to 83.889% in the Pro30 group. The survival rate increased considerably, and the data is believable statistically ($p<0.01$). Thus, it can be inferred that the increase in proline content has a significant effect on improving the freezing tolerance of ants.

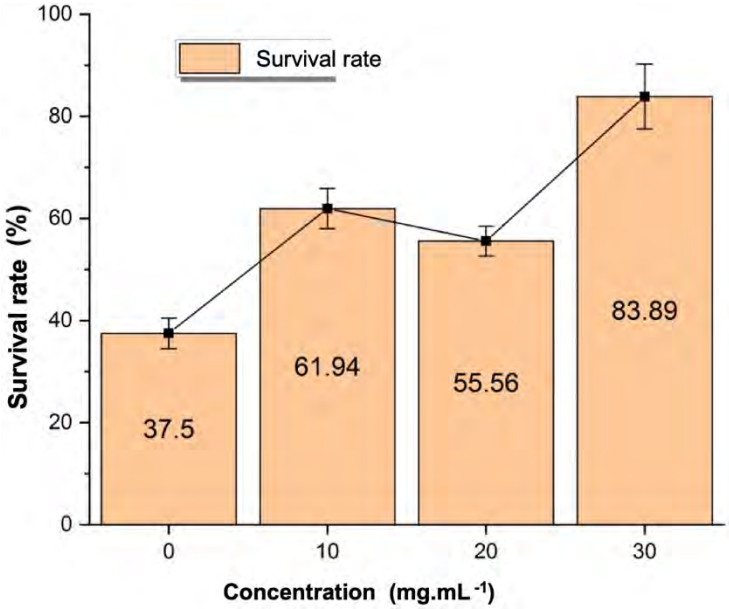

Figure 4: The ants survive rate of four group with different proline feeding concentrations

4. CONCLUSIONS

In this paper, the cryopreserved potential of proline was evaluated by comparing with four traditional cryogenic cryoprotectants. DSC test results show that proline is more suitable in cryopreservation in vivo than Trehalose, Sucrose, Glucose, and DMSO. Then the survival rate of ants with various proline content were statistics after a subject freezing and rewarming process. The ants fed with 30 $mg.g^{-1}$ mixed diet held the highest survival rate, this indicates that the anti-freezing ability of ants increases with the proline content raise of ants. All the pieces of evidence proved that the increase of proline concentration can improve the ant's low-temperature resistance and help the ants survive in the low temperature. All work is expected to provide more inspiration for cryogenic cryopreservation technology.

ACKNOWLEDGEMENTS

This work is supported by the NSFC Grant (No.51605472). Also, thanks to the support of Beijing Engineering Research Center of Sustainable Energy and Buildings and National Virtual Simulation Experimental Teaching Center of Energy and Buildings.

NOMENCLATURE

C_{pro}	concentration of proline in ant's diet ($mg.g^{-1}$)	T_s	freezing temperature (K)
T_f	temperature of solution equilibrium freezing point (K)		

REFERENCES

Costanzo, J.P., et al., 2015. Cryoprotectants and Extreme Freeze Tolerance in a Subarctic Population of the Wood Frog. PLOS ONE. 10(2), e0117234.

Denise, F., et al., 2011. Systematic parameter optimization of a Me(2)SO- and serum-free cryopreservation protocol for human mesenchymal stem cells. Cryobiology. 63(2), 67-75.

E Broxmeyer, H., et al., 1989. Human umbilical cord blood as a potential source of transplantable hematopoietic stem/progenitor cells, 3828-32.

Fuller, B., et al., 2013. Biopreservation of hepatocytes: Current concepts on hypothermic preservation, cryopreservation, and vitrification, 432-452.

Gaucher, S., et al., 2012. Viability of cryopreserved human skin allografts: effects of transport media and cryoprotectant. Cell and Tissue Banking. 13(1), 147-155.

Hua, Z. and Ren, S., 1994. Cryogenic biomedical technology(in Chinese). Science Press, Beijing

Kostál, V., et al., 2012. Conversion of the chill susceptible fruit fly larva (Drosophila melanogaster) to a freeze tolerant organism, 3270-4.

Liu, J. and Liu, Z., 1993. Cryonic medicine(in Chinese). People's Health Publishing House.

Liu, J., 2007. Principles of cryogenic biomedical engineering(in Chinese). Science Press, Beijing.

Liu, Y., et al., 2010. Cryopreservation of human bone marrow-derived mesenchymal stem cells with reduced dimethylsulfoxide and well-defined freezing solutions. Biotechnol Prog. 26(6), 1635-43.

Pallotta, V., et al., 2012. Red blood cell processing for cryopreservation: from fresh blood to deglycerolization. Blood Cells Mol Dis. 48(4), 226-32.

Polge, C., Smith, A.U., and Parkes, A.S., 1949. Revival of Spermatozoa after Vitrification and Dehydration at Low Temperatures. Nature. 164, 666.

Raymond, M.R. and Wharton, D.A., 2013. The ability of the Antarctic nematode Panagrolaimus davidi to survive intracellular freezing is dependent upon nutritional status. Journal of Comparative Physiology B. 183(2), 181-188.

Sánchez-Partida, L.G., Setchell, B.P., and Maxwell, W.M., 1998. Effect of compatible solutes and diluent composition on the post-thaw motility of ram sperm. Reproduction Fertility & Development. 10(4), 347.

Sun, H., Glasmacher, B., and Hofmann, N., 2012. Compatible solutes improve cryopreservation of human endothelial cells. Cryo Letters. 33(6), 485-493.

T. Justice and Christensen, G., 2013. Sperm cryopreservation methods. Humana Press.

Vladimír, K., Helena, Z., and Petr, I., 2011. Hyperprolinemic larvae of the drosophilid fly, Chymomyza costata, survive cryopreservation in liquid nitrogen. Proceedings of the National Academy of Sciences of the United States of America. 108(32), 13041-13046.

Withers, L.A. and King, P.J., 1979. Proline: A Novel Cryoprotectant for the Freeze Preservation of Cultured Cells of Zea mays L. Plant Physiology. 64(5), 675-678.

Zhang, L., et al., 2016. L-proline: a highly effective cryoprotectant for mouse oocyte vitrification. Sci Rep. 6(1), 26326.

Zhang, S. and Zhou, Y., 2007. Effects of Temperature, Time and Glucose Loading on Resuscitation of Frozen Ants at Deep Low Temperature (near -15 °C)(in Chinese). Science and technology guide. 25(5), 4.

Manuscript ID 1574
DOI: 10.18462/iir.icr.2019.1574

Difference in skin temperature variation between whole- and partial-body cryotherapy devices - A new approach to optimized treatment protocols

Romain BOUZIGON[(a,b)*], Thibaud MIHAILOVIC[(b)], Guillaume LAFRANCE[(b)], Charles FOSTEL[(b)]

[a] Université de Franche Comté, Laboratoire « Culture Sport Santé Société (C3S) », EA 4660, Unité de Promotion, de Formation et de Recherche (UPFR) des Sports, 31 rue de l'Épitaphe, 25000 Besançon, France.

[b] Université de Franche Comté, Unité de Promotion, de Formation et de Recherche (UPFR) des Sports de Besançon, 31 rue de l'Épitaphe, 25000 Besançon, France.

Corresponding author*: Romain BOUZIGON, 20 rue des vergers dessous, 25320 Vorges les pins, France. E-mail address: romain.bouzigon@gmail.com.

ABSTRACT

Whole- (WBC) and partial-body cryotherapy (PBC) are today highly developed treatment methods used in several domains like pain relief, sport recovery and well-being. In recent years, there are more and more device manufacturers. However, although more and more studies are published on WBC and PBC, the two technologies are not always well demarcated in the literature. In several articles, the technology used is not indicated. It is very important because it appears that these two technologies have different effects on human. In this context, it is difficult to standardized precisely the exposure protocols according to the desired effects. The aim of this study is to compare the effects of a 3-min exposure in WBC and in a PBC on skin temperature variation.

Skin temperature of four healthy men was measured 5 minutes before, immediately after (post 10 s) and within 5 minutes after the exposure with a VarioCAM® hr head thermal camera (Jenoptik, Jena, Germany) and connected to the IRBIS3® Infratec software.

The whole-body mean temperatures after exposure are significantly different ($p = 0.001$) between the cryotherapy technologies (PBC: 23.17 ± 0,35 °C; WBC: 26.70 ± 0.49 °C). The temperature decrease after WBC session was -24.17 ± 1.67 % and after PBC exposure -15,03 ± 0,74 %. The skin temperature variation of upper and lower limb had the same results. The decrease was higher with WBC than PBC.

These results highlight the interest of adapting exposure protocols. It demonstrates the interest of adapting the duration of exposure in function of the cryotherapy device used.

1. INTRODUCTION

Whole- (WBC) and partial-body cryotherapy (PBC) are today highly developed treatment methods used in several domains like pain relief, sport recovery and well-being. These methods consist of exposing a person to a very intense cold (-40 °C to -195 °C depending on the manufacturer) for a short time (2 to 4 minutes). It was invented in 1979 by Professor Yamauchi and was later developed in Europe by Professors Fricke and Zagrobelny in the 1980's and 1990's. It was first used to relieve rheumatic and inflammatory pain, and now to accelerate sports recovery (Bouzigon et al, 2016). Expositions are performed in underwear with protections at the ends of the body (gloves, slippers, headband covering the ears and mask covering the mouth and nose). Chambers can be composed of one to three pieces with different temperatures (e.g. -10, -60 and -110 °C according to the manufacturers).

There are two types of technology: WBC (5 European and 1 Asian manufacturers) and partial body cryotherapy (PBC) (more than a dozen manufacturers around the world). The difference between these two technologies is the cold exposure method. WBC chambers allow to be fully exposed with electrically cooled chambers or with nitrogen (gas between -110 and -195 °C) flowing through the chamber walls. PBC cabins are open at the head ("partial body") because cold is created with a direct injection of nitrogen into the cabin.

The known effects of the WBC and PBC, in link with sports recovery, are multiple. Exposures reduce the imbalance of the pro-antioxidant balance by neutralizing the production of free radicals and stimulating the activity of antioxidant enzymes (Lubkowska et al., 2008 & 2010). The inflammatory syndrome is decrease with a peripheral vasoconstriction, the increase in anti-inflammatory cytokine production (IL-6, IL-10, IL-1ra) and the decrease in pro-inflammatory cytokine and marker concentration (IL-1α, IL-1β, IL-2, IL-8, TNF -α, PGE2). Exposition also have an analgesic effect to (Banfi et al, 2009 ; Pournot et al, 2011). The activity of the autonomic nervous system will be increased, resulting in a decrease of the heart rate (Hausswirth et al., 2013). Finally, it has been demonstrated that exposures allows the improvement of well-being and quality of sleep (Schaal et al., 2014, Douzi et al. 2018, Bouzigon et al. 2014).

However, although more and more studies are published on WBC and PBC, the two technologies are not always well demarcated in the literature. In several articles, the technology used is not indicated. The differentiation between the two terminologies "WBC" and "PBC" appeared in 2011 (Hausswirth et al., 2011). It is very important because it appears that these two technologies have different effects on human (Bouzigon et al., 2016; Hausswirth et al., 2011; Louis et al., 2015). Moreover, the difference in cold production between technologies probably have different responses in skin temperature variation. The decrease in skin temperature which activated the skin thermoreceptors is the basis of the effects of WBC and PBC. The measure of the skin temperature variation with an exposure is essential to assess technological efficiency of cryotherapy device (Bouzigon et al., 2017). Local analgesia is achieved when the temperature was below 13.6 °C (Bugaj, 1975). The nerve conduction velocity decreases by 10% when the skin temperature is below 12.5 °C degrees (McMeeken et al., 1984) and metabolic enzyme activity is reduce of 50% when the skin temperature is between 10 and 11 °C (Zachariassen, 1991).

It seems interesting to measure the skin temperature variation in function of each existing technology. Thus it would be possible to obtain a frame of reference in skin temperature variations to standardize more precisely the protocol of exposure. The beneficial effects could be optimized and the risks of accidents decreased. The aim of this study is to compare the effects of a 3-min exposure in WBC and in a PBC on skin temperature variation. The validation of the protocol of skin temperature measurement could allow its used with the others cryotherapy technologies.

2. METHOD

2.1. Study design

This study was performed in France. The aim was the assessment of skin temperature variation between before and after a 3-min WBC and PBC exposures. Skin temperature was assessed during 5 minutes before and during 5 minutes immediately after exposure in the same position. The mean temperature of the different rooms, during the investigations of the skin temperature, was 18,2 ± 0,4 °C, and the mean hygrometry was 42,5 ± 10,6 %. The investigations were performed at the same hour (between 10:30 am and 12:00 am) of the day for each subject and for each technology tested to limit bias induced by the chronobiological variations of body temperature.

2.2. Cryotherapy devices

In this study, two types of cryotherapy technologies have been tested: 1) a WBC chamber based on forced convection (model Cryowind, Aurore Concept, Noisiel, France) ; and 2) a PBC cabin based

on nitrogen sprayed (model Cryonext, Cryoness, Gliwice, Poland) (Figure 1). The WBC chamber was composed of two chambers, the first was used to dry air and to isolate the second chamber. The second chamber was the main exposure compartment. In the two chambers, two fans combined with cold temperature allowed even colder conditions. In the PBC cabin, the cooling system is based on nitrogen injection directly inside the compartment.

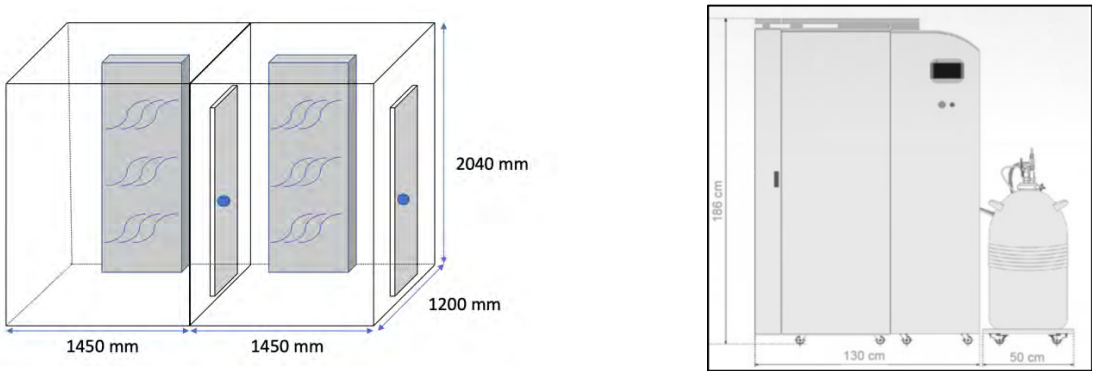

Figure 1: Left: WBC chamber ; Right: PBC cabin

2.3. Participants

Four healthy men (Age: 25,0 ± 4,0 years ; Height: 175,5 ± 4,8 cm ; Weight: 72,5 ± 7,7 kg ; BMI: 23,5 ± 1,5 kg/m^2 ; Bodyfat: 13,6 ± 1,0 %) participated in this study. Body fat percentage was assessed using the sum of skinfold measures (biceps, triceps, subscapular and supra-iliac) with a Harpenden skinfold calliper. All of the participants volunteered and signed a statement of informed consent at their enrolment. They didn't present any contraindications for the use of cryotherapy technologies. The study was conducted in professional cryotherapy centres with certified technologies, and in accordance with the Declaration of Helsinki (2001).

2.4. Exposure protocol

For the WBC technology, subjects were exposed 30 seconds at -24 °C in the first chamber and then 3 minutes at -48 °C in the main chamber. For the PBC technology subjects were exposed during 3 minutes at -190 °C. The temperatures which is mentioned are those indicated on the devices. For each technology the time to exposure was standardized at 3 minutes. It's the most common time to exposure which is used on scientific literature for WBC and PBC (Bouzigon 2016). During all the duration of exposure, subjects had to turn on themselves. During the two exposures, subjects wore briefs, gloves, socks and slippers. In addition, for the WBC technology, subjects wore a headband over their ears and a surgical mask. For the PBC technology, subjects didn't need to wear these protections because the head is outside of the cryotherapy compartment. At the end of the exposure, they had to leave the chamber within 10 seconds and were instructed not to rub their skin. They removed quickly their protections and situated themselves in the same position as before the exposure.

2.5. Measurements

Skin temperature was measured 5 minutes before, immediately after (post 10 s) and within 5 minutes after the exposure with a VarioCAM® hr head thermal camera (Jenoptik, Jena, Germany) and connected to the IRBIS3® Infratec software. The infrared thermal camera is a non-invasive tool for measuring temperature and provides the surface temperature of a body. Thermal imaging was considered a safe and suitable method for monitoring skin temperature during and after a cryotherapy treatment at both clinical and sports levels (Matos et al., 2015). On the camera, we installed a type 1 lens with a focal length of 50 mm (Infratec, Infrared). The range of temperature measurement of the VarioCAM® hr was between −40 °C and 1200 °C with an accuracy of ± 2% in the measurement range. The radiometric thermographic system was based on an uncooled

microbolometer FPA detector at 640 × 480 IR pixels. The camera spectral range was between 7.5 and 14 µm.

Participants were instructed to stand still in the same posture before and after the exposure. They were instructed to stand in front of the thermal camera with palms open and head straight. A black sheet was placed behind the subjects. The distance between the camera and the participants was 4.45 m to have a complete vision of body subject's (from top of the forehead to top of the ankle). Thermal captures were performed every 10 seconds before and after the exposure during 5 minutes. The measurement zone was between the forehead and the shinbone. The zones of interest were the right and left: Shoulders, chest, arms, forearms, abdomen, thighs and shinbones (Figure 2). The mean skin temperatures corresponded to the mean values calculated from all these zones. To compare evolution to mean skin temperatures of lower limbs and upper limbs the values of different zones have been regrouped (upper limb: Shoulders, chest, arms, forearms and abdomen ; lower limb: Thighs and shinbones).

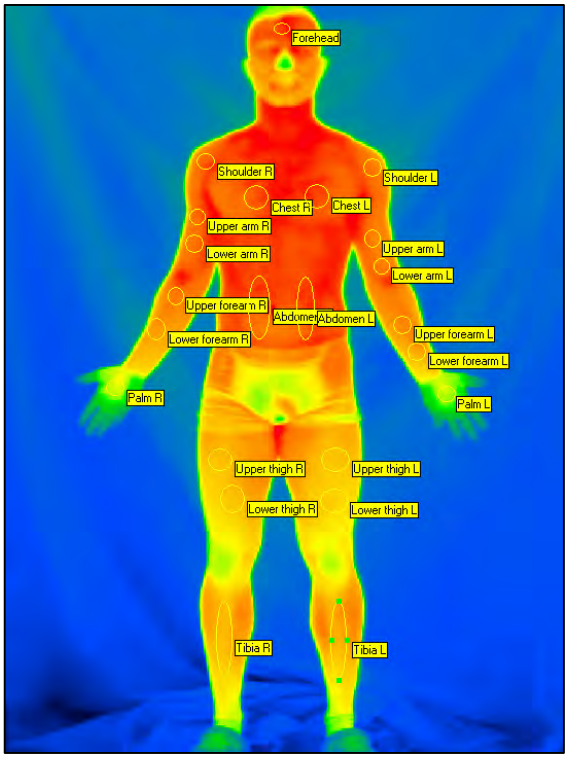

Figure 2: Measurement zones

2.6. Statistical analysis

The statistical program used was SigmaPlot 12.0 Software (Systat Inc., San Jose, CA, USA). Results were expressed in average and standard deviation. Skin temperature variation according to the time and the technologies was analyzed with a two way analysis of the variance (ANOVA) with repeated measures. Post-hoc comparisons were realized with a Holm-Sidak statistical test.

3. RESULTS

ANOVA statistical test with repeated measures shows several results in terms of skin temperature. The whole body mean temperatures before exposure are not significantly different between the WBC and PBC session ($p>0.05$). Nevertheless, the whole body mean temperatures after exposure are significantly different ($p = 0.001$) between the cryotherapy technologies (23.17 ± 0,35 °C vs 26.70 ± 0.49 °C, respectively). Therefore, the temperature decrease after WBC session was -24.17 ± 1.67 % and after PBC exposure -15,03 ± 0,74 %. The evolution of whole-body temperatures during all the measures (before and 5 minutes after exposure) according to cryotherapy technologies shows

significant difference (p<0.001). The comparison of the technologies effects in skin temperature by bout of duration also demonstrate significant differences (Figure 3). Whole-body mean skin temperature was lower after WBC than PBC.

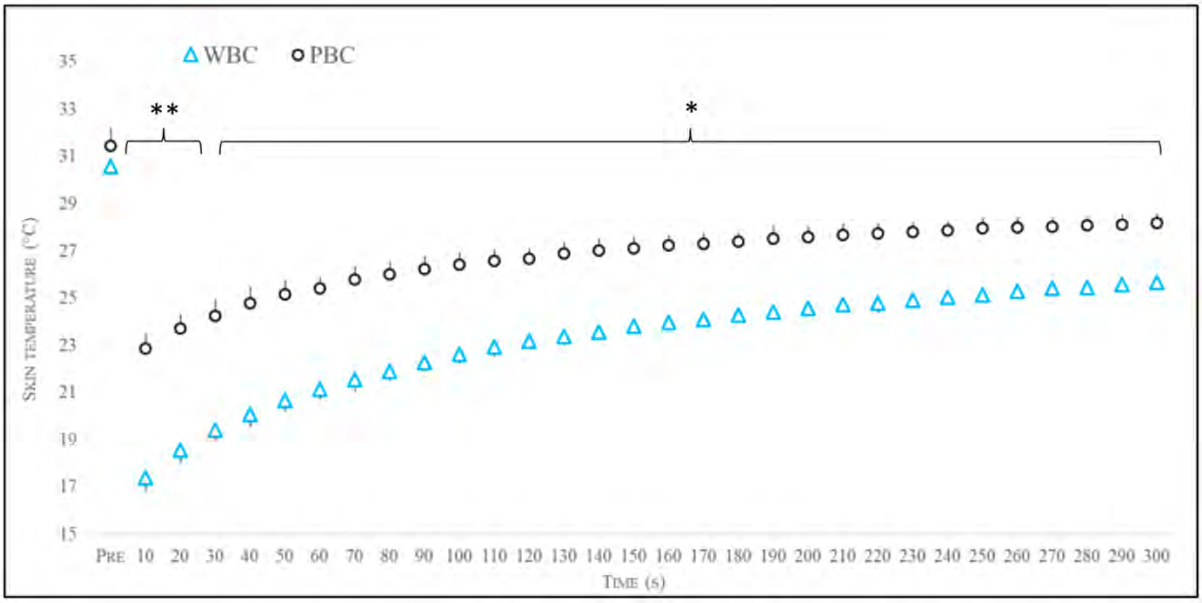

Figure 3: Variation of whole-body temperature according to cryotherapy technologies. (Significant difference between technologies: * = p<0,05 ; ** = p<0,01)

The skin temperature variation of upper and lower limb had the same results. Effectively, the upper and lower limb mean temperatures before exposure are not significantly different between WBC and PBC session (p>0.05). Like for the whole-body mean temperature, WBC allowed a better skin temperature decrease than PBC (upper body: -24.74 ± 2,26 % vs -13.20 ± 0.22 %, respectively; Lower body: -28.79 ± 0.77 vs -23.45 ± 2.90 %, respectively). There was a significant difference between the evolution on skin temperature in upper and lower limb in function of the cryotherapy technologies (p=0.001 and p<0,05, respectively). To finish, the comparison of technologies effects in skin temperatures by bout of duration, for each body parts, also demonstrated significant differences (Figure 4 and Figure 5).

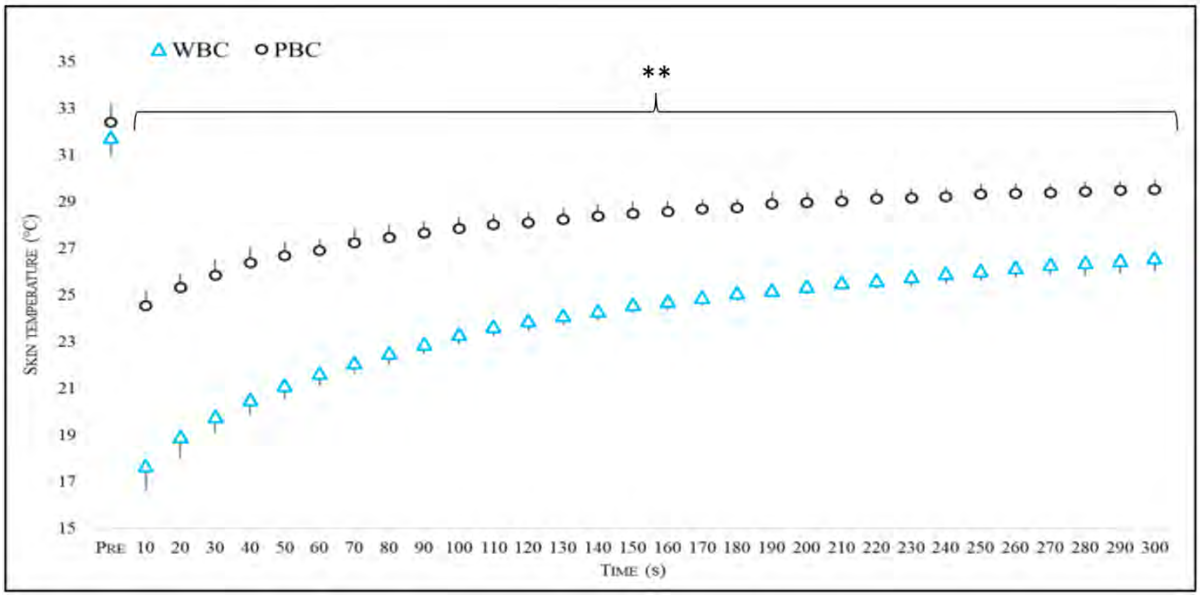

Figure 4: Variation of upper limb temperature according to cryotherapy technologies. (Significant difference between technologies: ** = p<0,01)

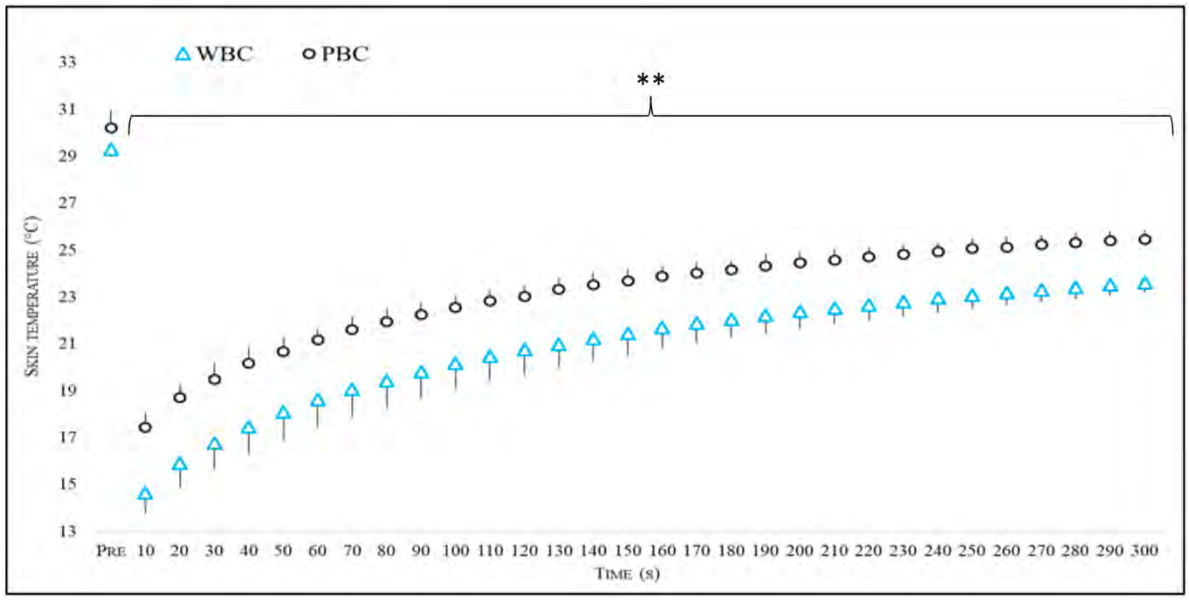

Figure 5: Variation of lower limb temperature according to cryotherapy technologies. (Significant difference between technologies: ** = p<0,01)

With descriptive statistical analysis, thermal discomfort seemed less important during WBC than PBC (7,5 ± 0,4 UA vs 8,1 ± 1,4UA, respectively). However, participants had colder sensation in WBC than in PBC (-3,6 ± 0,5 UA vs -2,1 ± 0,3 UA, respectively).

4. DISCUSSION

The aim of this study was to compare skin temperature variation after a 3-min exposure on two types of cryotherapy technology.

The main important finding of this study is the difference in skin temperature decrease between the two technologies. After a 3-min of exposure, whole-body, upper limb and lower limb mean skin temperature had a greater variation with WBC than with PBC. However, the exposure temperature in the WBC technology (-48 °C) were higher than in PBC technology (-190 °C). It seems that the body heat extraction allows by the forced convection is more effective to decrease skin temperature. On the other hand, WBC chamber allows greater body exposition and maybe a better homogeneity of the temperature of exposure. Indeed, the open cabin of PBC lead to an heterogeneity of the temperature between the top and the bottom of the tank. Cold always go down and the top of the cabin is warmer than the bottom during exposure (Savic et al., 2014). So, the WBC technology allow a better global cooling of the body than PBC, especially on the upper limb.

At the end of exposure protocol, the mean whole-body skin temperature is of 18 °C for WBC and of 23 °C for PBC. Focused on upper limb, the mean skin temperature after exposure protocol is of 17 °C for WBC and 24 °C for PBC. Focused on lower limb, the mean skin temperature after exposure protocol is of 14 °C for WBC and of 17 °C for PBC. The skin temperature decrease after WBC could allow to trigger some known physiological responses, specifically on the lower limb. Indeed, as we see on some works, it's necessary to reach skin temperature between 10 to 13,5 °C to trigger some responses like analgesia, decrease of the nerve conduction velocity and of the reduction of metabolic enzyme activity (Bugaj, 1975; McMeeken et al., 1984; Zachariassen, 1991). For PBC, it appears that the skin temperature achieved is not enough cold to allow these responses. However, we must remain cautious because the temperature inside the cabin or chamber is probably colder than outside. It is important to precise that currently we don't know the targeted skin temperature to allow several desired effects. Even if the mean skin temperature after PBC was 23°C, lots of benefits heave already been demonstrated with PBC exposures in inflammatory diseases, in sport recovery and in sleep quality (Bouzigon et al., 2014; Fonda and Sarabon, 2013; Hausswirth et al., 2013; Jastrzabek et al., 2013).

These results highlight the interest of adapting exposure protocols. Indeed, it seems that a 3-min WBC exposure is more effective in skin temperature variation than a 3-min PBC exposure. Theses finding demonstrate the interest of adapting the duration of exposure in function of the cryotherapy device used. To have the same effects in both devices, it may be necessary to have a longer duration of exposure in PBC. This finding is really important because the actual temperature given by the manufacturer and displayed on the devices could suggest that PBC induces higher variation in skin temperature than WBC (-190 °C vs -48 °C in this study, respectively). At the sight of these data, it is now essential to measure the actual temperature inside each devices during exposure.

The lack of measures of the actual temperatures inside the two technologies is a limit of this study. Planned at the base, they could not be performed in time. The temperatures given by the manufacturers displayed in the devices were used. But these temperatures could change from an exposition to another, so it will be essential to measure the exposure temperature before and during each exposure protocol. For the PBC, it will be interesting to measure the temperature at different levels of the compartment (level of lower limbs, level of the abdomen, level of upper limbs) to check if the descent of nitrogen induces a lower temperature at the bottom of the compartment in comparison to the middle and the upper part of this one. Furthermore, for future studies, it could be interesting to assess the effects of these two types of technologies (WBC and PBC) on the internal temperature.

5. CONCLUSION

To conclude, this study demonstrates that two different types of cryotherapy technology (WBC and PBC) have not the same effects on skin temperature variation. These findings allow to have first indications concerning the adaptation to take into account according to the technology used. Now, it's essential to compare all the WBC and PBC technologies which exists in the world to create a frame of reference in skin temperature variation between pre and post exposure in each device.
To finish, it will be interesting to ask the question of the division of technologies according to the desired effects. Maybe PBC could use in some domains (e.g. sport which lower limb is mainly use, lower limb injuries, ...) and WBC in other domains (e.g. sport which whole-body is use, pathologies, ...).

ACKNOWLEDGMENTS

We warmly thank William BERTUCCI, Ahlem ARFAOUI and Benoit JARLOT of the PSMS laboratory of Reims (EA 7507), the centres Zen Home of Besancon and Aurore concept of Noisiel.

REFERENCES

Bouzigon, R., Arfaoui, A., Grappe, F., Ravier, G., Jarlot, B., Dugue, B., 2017. Validation of a new whole-body cryotherapy chamber based on forced convection. J. Therm. Biol. 65, 138-144.

Bouzigon, R., Grappe, F., Ravier, G., Dugue, B., 2016. Whole- and partial-body cryostimulation/cryotherapy: Current technologies and practical applications. J. Therm. Biol. 61, 67-81.

Bouzigon, R., Ravier, G., Dugue, B., Grappe, F., 2014. The use of whole-body cryostimulation to improve the quality of sleep in athletes during high level standard competitions. Brit. J. Sport. Med. 48, 572.

Bugaj, R., 1975. The cooling, analgesic, and rewarming effects of ice massage on localized skin. Phys. Ther. 55, 11-19.

Fonda, B., Sarabon, N., 2013. Effects of whole-body cryotherapy on recovery after hamstring damaging exercise: A crossover study. Scand. J. Med. Sci. Spor. 270-278.

Hausswirth, C., Louis, J., Bieuzen, F., Pournot, H., Fournier, J., Filliard, J.R., Brisswalter, J., 2011. Effects of whole-body cryotherapy vs. far-infrared vs. passive modalities on recovery from exercise-induced muscle damage in highly-trained runners. PloS one 6, e27749.

Hausswirth, C., Schaal, K., Le Meur, Y., Bieuzen, F., Filliard, J.R., Volondat, M., Louis, J., 2013. Parasympathetic activity and blood catecholamine responses following a single partial-body cryostimulation and a whole-body cryostimulation. PloS one 8, e72658.

Jastrzabek, R., Straburzynska-Lupa, A., Rutkowski, R., Romanowski, W., 2013. Effects of different local cryotherapies on systemic levels of TNF-alpha, IL-6, and clinical parameters in active rheumatoid arthritis. Rheumatol. Int. 33, 2053-2060.

Louis, J., Schaal, K., Bieuzen, F., Le Meur, Y., Filliard, J.R., Volondat, M., Brisswalter, J., Hausswirth, C., 2015. Head Exposure to Cold during Whole-Body Cryostimulation: Influence on Thermal Response and Autonomic Modulation. PloS one 10, e0124776.

Matos, F., Neves, E.B., Norte, M., Rosa, C., Reis, V.M., Vilaça-Alves, J., 2015. The use of thermal imaging to monitoring skin temperature during cryotherapy: A systematic review. Infrared Phys Techn 73, 194-203.

McMeeken, J., Lewis, M.M., Cocks, S., 1984. Effects of Cooling with Simulated Ice on Skin Temperature and Nerve Conduction Velocity. Aust. J. Physiother. 30, 111-114.

Zachariassen, K.E., 1991. Hypothermia and cellular physiology. Arctic Med. Res. 50 Suppl 6, 13-17.

Manuscript ID: 1859
DOI: 10.18462/iir.icr.2019.1859

What everybody should know about whole-body cryotherapy/cryostimulation: an up-dated mini review

Benoit DUGUE[(a)], Wafa DOUZI[(a)], Pierre CARETTE[(a)], Olivier DUPUY[(a)]

[(a)] Faculty of Sport Sciences, Laboratory "Mobilité, Vieillissement, Exercice (MOVE)", University of Poitiers, 86000 Poitiers, France, benoit.dugue@univ-poitiers.fr

ABSTRACT

Cold therapy or cryotherapy has long been used to relieve pain and inflammatory symptoms. Nowadays, whole-body cryotherapy - an extreme cold therapy- which lasts 1-3 min, and given in a cold room in which the air temperature maybe -110°C or less is also used.
Important series of data have been collected in the context of injury prevention, recovery after injuries or surgery, recovery improvement after physical exercise in athletes and patients. Cryotherapy/cryostimulation is also used as a complementary treatment in different kinds of chronic disease patients, in patients having pain and/or inflammatory problems, and with subjects with mobility difficulties. However, there are nowadays several reports expressing the absence of benefits with the use of cryotherapy/cryostimulation and also safety problems.
The purpose of this work is to summarize what is really known on the effects of whole body cryotherapy/cryostimulation, to present the main physiological mechanisms involved and to suggest possible developments.
Keywords: Cryotherapy, Cryostimulation, Pain Relief, Recovery.

1. INTRODUCTION

Local cold therapy or cryotherapy has long been used to relieve pain and inflammatory symptoms through cold-induced analgesia. Nowadays, whole-body cryotherapy (WBC) - an extreme cold therapy- given in a cold room in which the air temperature maybe -110°C or less is also used where subjects, wearing minimal clothing, are usually exposed during to 1-3 min. Former forms of WBC consist in bathing in ice-cold water. Such practices are quite common in Northern countries where seas, lakes and rivers freeze during the wintertime and are thought to be healthy through body hardening and improving general well-being. Being regularly exposed briefly in the cold may also bring benefits for patients suffering inflammation and pain in, for example, arthrosis, osteoarthritis, fibromyalgia, respiratory tract infections and musculoskeletal pains (Bouzigon and al., 2016). Such possible impacts have been suggested more than 20 years ago. Quite surprisingly, scientific evidence have been release only few years ago concerning some of these items and important series of data have been collected during the recent years in the context of injury prevention, recovery after injuries or surgery, recovery improvement after physical exercise in athletes and patients (e.g. physical exercise organised in rehabilitation centres). Cryotherapy/cryostimulation is also used as a complementary treatment in different kinds of chronic disease patients, in patients having pain and/or inflammatory problems, and with subjects with mobility difficulties (Bouzigon and al., 2016). However, there are nowadays several reports expressing the absence of benefits with the use of cryotherapy/cryostimulation and safety problems.
In this short review, we will present the main physiological mechanisms involved in cold-induced adaptations, explain the peculiarities of the research performed in WBC and emphasize the difficulties that we are facing, and suggest possible research developments.

2. MAIN SECTION

WBC is used both in healthy subjects and patients in two contexts: one per se as some kind of treatment for well being and health improvement and/or after exercise for improving recovery.

2.1. Cold and Physiological Adaptations

When subjects are exposed to cold temperature, thermo-sensitive receptors located in skin and internal organs are stimulated and send messages to the hypothalamic integrator in brain. Depending of the stimulus intensity, circulatory adaptation (e.g. vasoconstriction) and shivering occur.

During and after WBC exposure, the current view is the following: there is a strong stimulation of the sympathetic system accompanied with the release of noradrenalin. Noradrenalin is known to have an impact on pain and this may explain how WBC help in relieving pain symptoms. Other compounds like endorphins may also have an impact. Also, it seems there is a decrease in the production of pro-inflammatory and oxidative substances whereas anti-inflammatory and anti-oxidative compounds are produced in larger quantities. The vasoconstriction that is induced after cold exposure may have effects in decreasing the amount of blood in and around muscles and in some organs, in decreasing cell permeability and leaking, in diminishing fluid diffusion in interstitial space, in reducing oedema development and in reducing inflammation. In the context of recovery after physical exercise, a WBC exposure induces a lower muscle temperature that may decrease muscle enzyme activities, metabolism, inflammation and secondary degradation after hypoxia (lowering ischemia/reperfusion problems) that may help to recover (Bouzigon and al., 2016). A recent work also provided strong evidence that an improved recovery through WBC could be linked to a better sleep quality the night following the cold stimulus (Douzi and al., 2019).

2.2. Peculiarities of the Research Performed in WBC

2.2.1. Lot of beliefs at the beginning and few scientific evidences but WBC succeeded to develop.

It has been believed for a very long time that WBC provides benefits concerning cold tolerance, mood, sleep quality, coping with stress situations, pains and aches, lower respiratory infections, health status and quality of life. Therefore WBC has been used to help patients suffering from rheumatic diseases, fibromyalgia, arthritis, back disorders, psoriasis, depression, spasticity diseases, sports injuries, and also has been used to help for recovery purposes after exercise. Surprisingly, the evidences that WBC may provide such benefits are quite recent, mainly in the few last years. For instance, the first evidence concerning the positive impact of WBC in depression have been published in 2008 (Rymaszewska et al, 2008), in fibromyalgia and multiple sclerosis in 2013 (Bettoni et al, 2013; Miller et al., 2013), in low back pain in 2014 (Giemza et al, 2014), in sleep quality in 2014 (Schaal et al, 2014; Bouzigon et al., 2014), in mental state and quality of life in 2014 (Szczepańska-Gieracha et al., 2014), in obesity in 2015 (Dulian et al, 2015), in ankylosing spondylitis (Stanek, 2015), etc.

2.2.2. Difficulties for experimental research design

The main drawback in the research design for WBC studies is the absence of possibility for organising double-blind experiments. However, some other problems are also present as many biological factors may interact with short and long term cold-induced physiological adaptations. Among others, body size, BSA/mass-ratio, fatness, physical fitness, gender, age, state of cold adaptation, health status have been shown to be important factors (Bouzigon and al., 2016; Bouzigon and al., 2018). Therefore, due to this very large inter-individual biological variation it is more difficult to find out statistical significance due to WBC impact in a series of data unless using very stringent inclusion criteria and recruiting large number of volunteers. Globally, in the scientific literature there are many studies with limited number of subjects, some have problems with procedure standardization, too often a control group is missing. Altogether, in the literature results are too often at variance.

2.3. Results are Sometimes at Variance but Meta-Analyses may help

Though many studies have shown positive impacts of WBC, there are quite often reports expressing that WBC is of no use or even detrimental (Krueger et al., 2019; Peake, 2017). It is therefore complicated to have a clear picture on the real impact of WBC. A way to solve the problem is the use of meta-analysis when sufficient amount of data is available and rather similar investigations have been conducted (even though meta-analysis also have drawbacks). Recently, we were able to

show that WBC has a significant impact on lowering delayed onset muscle soreness after physical exercise (Dupuy et al, 2018) and a positive impact on rheumatic diseases (Guillot et al, 2014).

2.4. Safety Issues

There are subjects that seem to be at risk and who should retain from using WBC until evidence of limited risks is provided. For instance, subjects with serious hypertension, serious cardiopathies, cold allergy, Raynaud syndroma, drepanocytose, cryoglobulinemia, claustrophobia, skin problems, frostbites, severe hypothyroid disease should not be exposed to WBC. In some countries, medical checking of the subjects that are going to be exposed is compulsory and in some other countries such checking is not. Also, blood pressure is sometimes measured but there are no agreements on the cut-off values for allowing subjects to go or not to go to the chamber. In Poland, the cut-off value has been rather strict and subjects over a systolic blood pressure of 140 mmHg are not allowed to be exposed. Protocols should be defined and validated for limiting the risks of health problems during and after exposure. There has been, unfortunately, few cases where significant health problems occurred during and after the exposure (Cámara-Lemarroy et al, 2017; Carrard et al., 2017; Greenwald et al., 2018).

3. CONCLUSIONS AND PERSPECTIVES

Basically, we need more data. One of our problem is the diversity of the cold chambers we use, the different protocols we use, the different kind of subjects we study. The difficulties we have is to compare data obtained from sometimes very different circumstances. Some works concerning the temperature that is obtained with the different chambers should be organised (with and without the subject inside the device), some studies concerning dose effect of the stimulation(s) should be conducted, the effects of one vs a series of cryostimulation should be compared, safety issues should also be addressed. Optimal protocol should be defined depending of the treatment desired effect and the subject characteristics (age, gender, body-mass index, etc). These issues are quite urgent and are in the list of tasks we need to handle effectively in the very near future.

Several recent publications expressed that whole body cryotherapy is of no use or even detrimental. Reporting such information is correct only if the design of the work, the statistical approach, the statistical power, and the interpretation are also correct. Unfortunately, this is not always the case. Maybe we should be more active in smoothing the conclusion of those publications in providing polite but smart comments.

Nowadays, in Pubmed the number of papers concerning whole-body cryotherapy or cryostimulation is around 600. This number is globally quite low but interestingly one third of the articles have been published in the five past years reflecting growing understanding of the importance of the field. The community interested in cryotherapy or cryostimulation is clearly developing. Through this congress and through the International Institute of Refrigeration Working Group on Whole body cryotherapy we are starting to know each other a bit better. This may help in solving some issues for instance by stimulating collaborative works, enabling the development of multi centric investigations, sharing similar investigation material, etc. In that context we should be able to conduct studies with a higher number of subjects, with fine design and statistical approach, with appropriate and unassailable interpretation, and to reach publications with respected impacts (scientifically and in the media). Our work is of importance and present interest both for basic and applied research. The applications that may stem from this research may also have practical impacts for the health and the recovery of many subjects and patients.

REFERENCES

Bettoni, L., Bonomi, F., Zani, V., Manisco, L., Indelicato, A., Lanteri, P., Banfi, G., Lombardi, G., 2013. Effects of 15 consecutive cryotherapy sessions on the clinical output of fibromyalgic patients. Clin Rheumatol, 32:1337-1345.

Bouzigon, R., Ravier, G., Dugué, B., Grappe, F., 2014.The use of whole-body cryostimulation to improve the quality of sleep in athletes during high international competitions. Br J Sports Med, 48,572.

Bouzigon, R., Grappe, F., Ravier, G., Dugué, B., 2016. Whole- and partial-body cryostimulation/cryotherapy: Current technologies and practical applications. J Therm Biol, 61:67–81.

Bouzigon, R., Ravier, G., Dugué, B., Grappe, F., 2018. Thermal sensations during a partial-body cryostimulation exposure in elite basketball players. J Hum Kinet 62:55-63.

Cámara-Lemarroy C.R., Azpiri-López, J.R., Vázquez-Díaz, L.A., Galarza-Delgado, D.A., 2017. Abdominal aortic dissection and cold-intolerance after whole-body cryotherapy: A case report. Clin J Sport Med, 27:e67-e68

Carrard, J., Lambert, A., Genné, D., 2017. Transient global amnesia following a whole-body cryotherapy session. BMJ Case Rep, 2017.

Douzi, W., Dupuy, O., Tanneau, M., Boucard, G., Bouzigon, R., Dugué, B., 2019. 3-min whole body cryotherapy/cryostimulation after training in the evening improves sleep quality in physically active men. Eur J Sport Sci, in press.

Dulian, K., Laskowski, R., Grzywacz, T., Kujach, S., Flis, D., Smaruj, M., Ziemann, E., 2015. The whole body cryostimulation modifies irisin concentration and reduces inflammation in middle aged, obese men. Cryobiology 71:398-404.

Dupuy, O., Douzi, W., Theurot, D., Bosquet, L., Dugué, B., 2018. An evidence-based approach for choosing post-exercise recovery techniques to reduce markers of muscle damage, soreness, fatigue and inflammation: a systematic review with meta-analyses. Front Physiol, 9:403.

Giemza, C., Matczak-Giemza, M., Ostrowska, B., Bieć, E., Doliński, M., 2014. Effect of cryotherapy on the lumbar spine in elderly men with back pain. Aging Male 17:183-188.

Greenwald, E., Christman, M., Penn, L., Brinster, N., Liebman, T., 2018. Cold panniculitis: Adverse cutaneous effect of whole-body cryotherapy. JAAD Case Rep 4:344-345.

Guillot, X., Tordi, N., Mourot, L., Demougeot, C., Dugué, B., Prati, C., Wendling, D., 2014. Cryotherapy in inflammatory rheumatic diseases: a systematic review. Expert Rev Clin Immunol 10: 281-294.

Krueger, M., Costello, J.T., Achtzehn, S., Dittmar, K.H., Mester, J., 2019. Whole-body cryotherapy (-110 °C) following high-intensity intermittent exercise does not alter hormonal, inflammatory or muscle damage biomarkers in trained males. Cytokine 113:277-284.

Miller, E., Saluk, J., Morel, A., Wachowicz, B., 2013. Long-term effects of whole body cryostimulation on uric acid concentration in plasma of secondary progressive multiple sclerosis patients. Scand J Clin Lab Invest 73:635-640.

Peake, J.M., 2017. Cryotherapy: Are we freezing the benefits of exercise? Temperature (Austin), 4:211-213.

Rymaszewska, J., Ramsey, D., Chładzińska-Kiejna, S., 2008. Whole-body cryotherapy as adjunct treatment of depressive and anxiety disorders. Arch Immunol Ther Exp (Warsz) 56:63-68.

Schaal, K., Le Meur, Y., Louis, J., Filliard, J.R., Hellard, P., Casazza, G., Hausswirth, C., 2015. Whole-Body Cryostimulation Limits Overreaching in Elite Synchronized Swimmers. Med Sci Sports Exerc 47:1416-25.

Stanek, A., Cholewka, A., Gadula, J., Drzazga, Z., Sieron, A., Sieron-Stoltny, K., 2015. Can whole-body cryotherapy with subsequent kinesiotherapy procedures in closed type cryogenic chamber improve BASDAI, BASFI, and some spine mobility parameters and decrease pain intensity in patients with ankylosing spondylitis? Biomed Res Int. 404259.

Szczepańska-Gieracha, J., Borsuk, P., Pawik, M., Rymaszewska, J., 2014. Mental state and quality of life after 10 session whole-body cryotherapy. Psychol Health Med. 19:40-46.

Manuscript ID: 1864
DOI: 10.18462/iir.icr.2019.1864

What is the future of using WBC in medicine?

Miller Elzbieta, DOROTA [(a,b)], Zielinska EWA [(a)]

[(a)]Department of Physical Medicine Medical University of Lodz, Poland, Pl. Hallera 1, Lodz 90-647, Poland, elzbieta.dorota.miller@umed.lodz.pl
[(b)] Neurorehabilitation Ward III General Hospital of Lodz, Poland, Milionowa 14, Lodz 93-113, Poland.

ABSTRACT

Currently, people are living longer and healthier than in the past and therefore, the prevention of illnesses is playing an ever-larger part in medicine. Intervention to protect people from long-term diseases is crucial topic in current medicine. Although a decline in quality of life and health status of older people might seem normal, there is an ongoing debate about where healthy ageing ends and disease begins. The idea of maintaining people's wellbeing rather than reacting to the symptoms is a key point of preventive medicine. The rehabilitation in the future should be definitely oriented towards new priorities and re-organization to meet demands of the growing population of neurological patients. New health policy should be implemented immediately in order to develop modern neuro-rehabilitation medicine. Whole-body cryostimulation (WBC), is becoming more and more popular not only in sports but also in clinical applications. Therefore, the aim of this presentation was to review the current state of knowledge about potential using WBC in medicine.
.
Keywords: Whole-Body Cryostimulation, Neurorehabilitation, Multiple Sclerosis, Neurology.

1. INTRODUCTION

Nowadays, life expectancy is much higher than ever before, but still the main cause of morbidity and mortality all over the world are noncommunicable diseases (NCDs), also called chronic or lifestyle diseases. In the group of NCDs there are heart diseases, stroke, cancer, diabetes, lung disease and neurodegenerative diseases. This is not only a medical problem but also very high cost from an economic point of view. One of the key reasons of this situation is reduced physical activity due to widely available means of transport and mechanization of labor. Regular physical activity is crucial to maintain a healthy weight, reduce the risk of stroke, type 2 diabetes, colon and breast cancer, osteoporotic fractures, osteoarthritis, depression, and neurodegenerative diseases. The medical system in most of countries is still focused on treating diseases and not preventing them or promoting wellness in the first place. Prevalence of NCDs is constantly growing. Therefore, the World Health Organization (WHO) and the Centers for Disease Control and Prevention (CDC) have labeled lifestyle diseases both epidemic and pandemic. However, the WHO definition of health was created in 1940s as: "a state of complete physical, mental and social well-being and not merely the absence of disease." On the other hand wellness is defined as "the sense that one is living in a manner that permits the experience of consistent, balanced growth in the physical, spiritual, emotional, intellectual, social, and psychological dimensions of human existence."
There is the need to find effective tool that can be use as safe procedure to enhance our physiological functioning especially in the group of older people.
The standard treatment of most diseases are medications, yet not all of the patients respond to them positively. In such cases, alternative, non-pharmalogical forms of therapy have found their application. When standard treatment is no longer effective, a place for holistic therapies

with low risk of side-effect therapies occurs. There are many additional therapies used in medicine and rehabilitation with positive outcomes and one of them is cryotherapy, which is becoming more and more popular in sports and rehabilitation.

2. LOW TEMPERATURES AND ITS CLINICAL APPLICATIONS

2.1. Physiological and Molecular Response to Low Temperatures

Physiological response of human body to low temperatures manifests itself in changes in the endocrine, circulatory, neuro-muscular, and immunological systems. The cutaneous circulation is the major effect of thermoregulation. Temperature is detected by peripheral sensory nerves. They can be classified according to degree of myelination and the velocity at which action potentials conduct through afferent fibers. On this basis there are fast conducting, myelinated (large) A nerve fibers and the slow conducting, unmyelinated (small) C fibers. There are 4 types of A fibers: alpha, beta, gamma and delta (Aδ). C fibers can react to different stimuli such as chemical, mechanical and temperature changes. The C fibers are the predominant nerve pathway for thermo-perception of warmth. A Aδ fibers carry gentle cold, whereas fibers C are activated in cryogenic temperatures. Generally, the perception of cool temperature occurs when the skin is cooled as little as 1°C from normal body temperature. Temperatures in the range between 30°C and 15°C can activate both Aδ and C fibers. However, below either 25°C or 15°C there can be a difference in their activity. When the temperature is reaching approximately 15°C, the perception of cold is closer to pain sensation. Cold-induced pricking sensation is largely reduced when Aδ fibers are blocked. During the block of the Aδ fiber, when C afferents are still active, the perception of noxious cold stimulus is experienced as burning or heat. This suggests that input from the Aδ fibers that signals the 'cool' sensation either blocks or modifies the C fiber input into the central nervous system. Therefore, the sensory experience induced by noxious cold stimuli depends on the integration of neuronal activity from both small myelinated and unmyelinated afferents (Bomi and Seong, 2013).
Recently, advances in understanding the temperature sensation have been made after discovering and characterizing TRP (Transient Receptor Potential) ion channel in 1997. The Activity of thermo TRP depends on the current temperature. The mammalian TRPV channels are thermo- and chemo-sensitive channels which are composed of 6 components. The best known is TRPV1. It can be activated by different stimuli and plays key role in pain and neurogenic inflammation. TRP channels are gated by heat and capsaicin (>43°C; TRPV1), noxious heat (>52°C; TRPV2), and cooling (<22°C; TRPM8) (Patapoutian et al., 2003). Recently, the cooling sensation generated especially by TRPM8 and/or cold and menthol receptor 1 (CMR1) has drawn attention for its potential usefulness.

2.2. Cryotherapy in Medicine

Normal body temperature known as normothermia ranges between 36.5-3.7.5°C. However, some changes can be observed depending on health status, sex, hormonal disturbances, the time of day, emotional state, physical activity, external factors etc. The first medical recommendations for induced hypothermia are from the Ancient World, mainly as a therapy for battle injured man and brain disturbances. In 60s there have been several clinical studies with brain cooling conducted to reduce intracell metabolism. Moreover, mild to moderate hypothermia might reduce abnormal blood-brain barrier permeability after stroke and traumatic brain injuries.
Cryotherapy is a medical procedure which uses an extremely cold liquid to lower the body temperature locally or systemically. This kind of therapy is widely used to bring relief in different diseases and sport injures. Triggering physiological defensive mechanisms in response to repeated external stressor (cold) has a potential to be more commonly used in medicine, physiotherapy, sports and athlete recovery. However, it is important to apply an appropriate duration, form and number of cryostimulations, based on individual needs of each patient. In conclusion, this presentation tries to review the potential benefits of using WBC in neurorehabilitation and answer the question: How can WBC impact clinical practice in

the near future?

2.3. Whole Body Cryostimulation (WBC) Procedure.

Currently, whole body cryotherapy (WBC) is becoming more and more popular not only in sport but also in clinical studies. The procedure of the WBC therapy consists of the short exposure to cold air (in cryogenic temperature) in special cryochambers. The air temperature is between -100°C and -140°C and single exposure usually lasts about 2-3 minutes. It can be performed in a single cryochamber or, more often, in much bigger one, where 3 to 5 persons are walking inside in the circle one by one. To adapt organism to cryogenic temperatures, in most protocols, each exposure in cryochamber is preceded by spending 30 seconds in a vestibule room with higher temperature of -60°C. During WBC special outfit, consisting of bathing suit, long socks, clogs or shoes, surgical mask (to protect upper part of respiratory system from very cold air), gloves, and a hat (or headband) is required. Using protection to cold sensitive parts of our body including feet, hands, auricles, nose is very important. Any sweat should be removed from the body of participants before WBC. Inside cryochamber, the subjects have to move step by step without any touching or talking. To control safety inside cryochamber, there is a camera and microphone which enables permanent contact with therapist, who is remaining outside.
This procedure is safe, however the medical examination before starting therapy should not be omitted. In most countries WBC is carried out only by private sector, mainly to improve well-being or as an alternative recovery tool after overtraining. It is rather expensive procedure, for example in the USA single exposure costs about 60 dollars, so full series of treatments consisted of 10 exposures costs about 600 dollars without any medical support or examination. In Poland WBC is refunded by National Health Fund in amount of 2 series of treatments per year. However, only medical doctor can write the prescription for WBC. It's recommended for patients to have at least 3 months break between series. One series consist of total number of 10 exposures (1 exposure per day). Therefore, the huge amount of people use this kind of therapy as one of the possible rehabilitation procedures. All the patients are obligated to have a medical checkup with blood pressure measurements and other basic examinations (Banfi et al., 2010).

2.4. Whole Body Cryostimulation (WBC) in Sports Medicine

WBC is widely used in sport medicine mainly as a therapy that can accelerate recovery from muscle injury and prevent overtraining symptoms. Cryotherapies have been used for post-exercise recovery in a variety of sports to help coping with fatigue, muscle overtraining and/or delayed-onset muscle soreness (DOMS). Exercising with different intensity induces many medical problems including pain, fatigue, depression, muscle injury. Exercising is also associated with microscopic tears in the muscle tissue. These micro tears are necessary for the muscles to grow, as without damage (a stimulus), there can be no response from the body. Although, it cannot be forgotten overtraining can induce muscle damage and lead to DOMS (Bleakley et al., 2012).

In sports medicine, cryotherapy is commonly used as a post-training intervention. WBC has been studied by means of subjective ratings of DOMS and general ratings of perceived exertion (RPE), objective attenuations of blood plasma markers such as creatine-kinase (CK) and lactate-levels or blood plasma cytokines encompassing Interleukines (IL) and C-reactive protein (CRP). Commonly cryotherapy is described as an analgesic therapy that can decrease inflammation in musculoskeletal problems. The physiological mechanism of using WBC for recovery after strenuous exercises is mainly related to vasoconstrictive effect, which reduces the inflammation reactions through a decrease of the cell metabolism (Hohenauer et al., 2015).
Recently, Banfi et al. (2009) has observed beneficial effects of a one week course of daily sessions of WBC in professional rugby players. Results indicate a significant reduction in muscular enzymes (creatine kinase [CK] and lactate dehydrogenase [LDH]) and pro-inflammatory cytokines into the plasma, associated with an increase of anti-inflammatory cytokines. Additionally, Pournot et al. (2001) reported that a single exposure to WBC significantly alleviated inflammation after a strenuous exercise run mainly composed of

eccentric contractions. According to these results, WBC could hasten muscular recovery after exercise by reducing inflammatory processes, vascular permeability and subsequent edema development. Practically, it seems that a sufficient number of WBC sessions (at least 10 sessions) are necessary to stimulate an immunological response, while antioxidant and anti-inflammatory effects could be obtained in the first session. Such reactions could be particularly beneficial during the recovery period following exercise and reinforce the significance of WBC in a sporting context. Banfi et al. (2009) reported a significant, 40%, reduction in CK level after five days of daily WBC sessions in rugby players. Wozniak et al. (2007) reported a 34% decline in CK concentration after 10 WBC sessions performed by 21 kayakers before each training session. The repeated cold-related stimulations of noradrenalin could partly explain the decrease in CK concentration after WBC sessions, associated with a decline in prostaglandin PGE2 (i.e. an inflammatory mediator and vasodilator) which could reduce vascular permeability (Banfi et al., 2009).
According to these results, it seems that repeated expositions (a minimum of 5 to 10 sessions) to WBC are required to stimulate recovery from muscle fiber damage by reducing muscle membrane breakdown or increased cell permeability induced by physical exercise (Hausswirth et al., 2011). The enhancement of the cardiovascular system, amelioration of muscular activation, limitation of sport-induced haemolysis, potential anti-inflammatory effect and additional potentially beneficial effects of WBC could be useful for athletes. Furthermore, post-WBC treatment changes in biochemical and haematological parameters could lie outside the threshold range imposed by sports federations and official control agencies for athletes classified as being doped or they could be interpreted as an attempt to mask changes caused by illicit treatment.

2.5. Whole Body Cryostimulation (WBC) as a Pain Killer

It can be observed, that pain is one of the most common and hence almost all adults have experienced episodes of musculoskeletal pain associated with injury or overuse. It affects over one-third of persons over 60 years of age (Lawrence et al., 2008). Aging predispose to recurrent or chronic musculoskeletal pain connected with multi joints osteoarthritis (OA). Radiographic changes of OA, in multiple joints (hands, spine, hips and knees) reveal OA in at least one joint in over 80% of older adults (Loeser, 2010).
The most commonly complaint pain is located in lower back, approximately 30–40% of adults in the general population have suffered from it. Low back pain can result from injury or systematic overuse and it can lead to osteoarthritis. The main determinant of disability in patients with osteoarthritis is pain, especially chronic pain. Chronic (persistent) pain lasts more than 3 months and it/s pathophysiology is not entirely understood. However, there are 3 main components: inflammation, joint damage which prolong inflammation and, as a result of 2 factors mentioned before, pain sensitization.
Cold therapy has multiple physiological effects on injured, damaged tissues. When skin temperature is decreasing, muscles reduce blood flow to the cooled tissues as a result of activation of sympathetic vasoconstrictive reflex. Low temperature decreases blood flow and it leads to reduction of edema as well as the generation of proinflammatory mediators including cytokines, chemokines, free radicals etc. Moreover, decreasing tissue temperature also reduces the metabolic demand of hypoxic tissues, potentially preventing secondary hypoxic damage in injured tissue. Cold therapy induces a local anesthetic effect, referred to as cold-induced neurapraxia, by decreasing the activation threshold of tissue nociceptors and the conduction velocity of nerve signals conveying pain (Malanga et al., 2015), (Samanta et. al., 2018).
WBC has also proven to be an effective therapy among patients with fibromyalgia, who are struggling with widespread musculoskeletal pain and decreased quality of life and functional status. Vitenet et al. (2018) reported positive impact of WBC on psychological and physical dimension of quality of life among fibromyalgic patients.

2.6. Whole Body Cryostimulation (WBC) in Neurology

A recent studies have found observational evidence that WBC can cause a positive effect on many key biochemical and physiological parameters. What is more, it can induce adaptive changes in antioxidant status, and positive effects on inflammatory and immunological

processes, which are the hallmark of neurodegeneration. Therefore, WBC is being considered as a therapy with the huge potential in neuroprotection of neurodegenerative disorders. It also seems that cryostimulation may be used as an adjuvant therapy in the treatment of diseases with oxidative stress background.
Multiple sclerosis (MS) is a neurological disease diagnosed among young adults with fatigue and difficulty with walking as the most burdensome symptoms, which can be intensified by increased temperature and humidity. Therefore, lower temperatures are more suitable for MS patients, hence they are often used during rehabilitation process. Our last study reported the positive effect of WBC on fatigue and functional status in MS patients. However, greater improvement was observed in high fatigue group (Miller et al., 2016). Another study showed positive effect of WBC on MS patients mood and functional status (Miller et al., 2013).

2.7. Whole Body Cryostimulation (WBC) in Rheumatic Diseases

Rheumatoid arthritis (RA) is the most common inflammatory arthritis, which affects 1-2 percent of population. The onset of RA mainly occurs between the ages of 30 and 50. The pathophysiology of RA is characterized by constant inflammatory processes that lead to proliferation of synovial cells in joints, moreover in mature form of RA cartilage destruction and bony erosions may occur. These destructive processes are connected with the overproduction of proinflammatory cytokines (Wasserman, 2011).
The main symptom of RA is pain, which significantly decreases patients quality of life. In order to treat patients suffering from RA , in Japan in1970s the first cryochamber was built. Last meta-analysis of studies reported that WBC can be used as an effective pain therapy in RA patients which is not only improving mobility but also quality of life (Guillot et al. 2014). Nevertheless, a study performed by Gizińska at al. (2015) has reported positive effects of a 2-week rehabilitation program for patients with RA regardless of the kind of the applied physical procedure.

2.8. Hypothesis About WBC's Future

In the present state of knowledge, it can be hypothesized that WBC is potentially effective therapy that can prevent neurodegenerative diseases in preclinical course of dementia or mild cognitive impairment. It is also potential antioxidative therapy that can prevent chronic or lifestyle diseases (Misiak and Kiejna, 2012). Moreover, there is also convincing evidence supporting the neuroprotective role of low temperatures, which originates from experimental studies on the application of therapeutic hypothermia in infants and adults with hypoxic-ischemic cerebral injury (Drury et al., 2010).
Interesting conclusions supporting potentially beneficial influence of WBC on oxidative stress and antioxidant function have been drawn. There is an evidence that series of 10 WBC exposures increased total antioxidant status and uric acid level in plasma, consequently extremely low temperatures improve the antioxidant capacity in human organism (Miller, 2012).
Rymaszewska et al found that WBC has a positive impact on treatment of patients with affective and anxiety disorders, therefore WBC can be also considered as an alternative, non-pharmalogical form of treatment for neurological patients struggling with such symptoms and also with depression (Rymaszewska et al., 2008).

3. CONCLUSIONS

Recently short-term cryostimulation has become a popular topic in different fields of medicine especially in musculo-sceletal and neurodegenerative diseases. However, there is also a need to answer on several questions concerning safety and possible side-effects of using cryogenic temperature applications.
The key problem in comparing different studies and their effectiveness is the heterogeneity among the exposure protocols that have been performed. WBC is a therapy with a huge potential in medicine. However, medical examination before starting cryogenic temperatures is obligatory to avoid side effects. Currently, many studies reported many benefits after series of WBC but there is the demand for randomized controlled clinical studies.

REFERENCES

Banfi, G., Lombardi, G., Colombini, A., Melegati, G., 2010. Whole-body cryotherapy in athletes. Sports Med. 40(6), 509-17

Banfi, G., Melegati, G., Barassi, A., d'Eril, G.M., 2009. Effects of the whole-body cryotherapy on NT proBNP, hs CRP and troponin I in athletes. J. Sci. Med. Sport. 12(6), 609–610.

Banfi, G., Melegati, G., Barassi, A., Dogliotti, G., d'Eril, G.M., Dugué, B., Corsi, M.M., 2009. Effects of whole-body cryotherapy on serum mediators of inflammation and serum muscle enzymes in athletes. J. Thermal. Biol. 34(2), 55 – 59.

Bleakley, C., McDonough, S., Gardner, E., Baxter, G.D., Hopkins, J.T., Davison, G.W., 2012. Cold-water immersion (cryotherapy) for preventing and treating muscle soreness after exercise. Cochrane Database Syst. Rev. (2):CD008262

Bomi, P., Seong, J.K., 2013. Cooling the Skin: Understanding a Specific Cutaneous Thermosensation. J. Lifestyle Med. 3(2), 91-97.

Drury, P.P., Bennet, L., Gunn, A.J., 2010. Mechanisms of hypothermic neuroprotection. Semin. Fetal. Neonatal. Med. 15(5), 287–92.

Guillot, X., Tordi, N., Mourot, L., Demougeot, C., Dugue, B., Prati, C., Wendling, D., 2014. Cryotherapy in inflammatory rheumatic diseases: a systematic review. Expert. Rev. Clin. Immunol. 10(2), 281-94

Gizińska, M., Rutkowski, R., Romanowski, W., Lewandowski, J., Straburzyńska -Lupa, A., 2015. Effects of whole-body cryotherapy in comparison with other physical modalities used with kinesitherapy in rheumatoid arthritis. Biomed. Res. 2015 doi: 10.1155/2015/409174.

Hausswirth, C., Louis, J., Bieuzen, F., Pournot, H., Foumier J., Filliard, J.R., Brisswalter, J., 2011. Effects of whole-body cryotherapy vs far-infrared vs passive modalities on recovery from exercise-induced muscle damage in highly-trained runners. PloS ONE. 6(12):e22749. doi: 10.1371/journal.pone.0027749

Hohenauer, E., Taeymans, J., Baeyens, J.P.,Clarys, P., Clijsen, R., 2015. The Effect of Post-Exercise Cryotherapy on Recovery Characteristics: A Systematic Review and Meta-Analysis. PLoS One. 10(9).

Lawrence, R.C., Felson, D.T., Helmick, C.G., Arnold, L.M., Choi, H., Deyo, R.A., Gabriel, S., Hirsch, R., Hochberg, M.C., Hunder, G.G., Jordan, J.M., Katz, J.N., Kremers, H.M., Wolfe F., 2008. Estimates of the prevalence of arthritis and other rheumatic conditions in the United States: Part II. Arthritis Rheum. 58(1), 26–35

Loeser, R.F., 2010. Age-related changes in the musculoskeletal system and the development of osteoarthritis. Clin. Geriatr. Med. 26(3), 371–386.

Malanga, G.A., Yan, N., Stark, J., 2015. Mechanisms and efficacy of heat and cold therapies for musculoskeletal injury. Postgrad Med. 127(1), 57-65.

Miller, E., Kostka, J., Włodarczyk, T., Dugue, B., 2016. Whole – body cryostimulation (cryotherapy) provides benefits for fatigue and functional status in multiple sclerosis patients. A case – control study. Acta Neurol. Scand. 134(6), 420-426.

Miller, E., Markiewicz, L., Saluk, J., Majsterek, I., 2012. Effect of short-term cryostimulation on antioxidative status and its clinical applications in humans. Eur. J. Appl. Physiol. 112(5), 1645–1652

Miller, E., Saluk, J., Morel, A., Wachowicz, B., 2013. Long-term effects of whole body cryostimulation on uric acid concentration in plasma of secondary progressive multiple sclerosis patients. Scand. J. Clin. Lab. Invest. 73, 635-40.

Misiak, B., Kiejna, A., 2012. Translating whole-body cryotherapy into geriatric psychiatry – A proposed strategy for the prevention of Alzheimer's disease. Med. Hypotheses. 79(1), 56-8.

Patapoutian, A., Peier A.M., Story G.M., Viswanath V., 2003. ThermoTRP channels and beyond: mechanisms of temperature sensation. Nat. Rev. Neurosci. 4(7), 529–39.

Pournot, H., Bieuzen, F., Louis, J., Fillard, J.R., Barbiche, E., Hausswirth C., 2011. Time-course of changes in inflammatory response after whole-body cryotherapy multi exposures following severe exercise. PLoS One. 6(7).

Rymaszewska, J., Ramsey, D., Chladzinska-Kiejna, S., 2008. Whole Body Cryotherapy as adjunct treatment of depressive and anxiety disorders. Arch. Immun. Therap. Exp. 56 (1), 63-68

Samanta, A., Hughes, T.E.T., Moiseenkova-Bell, V.Y., 2018. Transient Receptor Potential (TRP) Channels. Subcell. Biochem. 87, 141 – 165.
Vitenet, M., Tubez, F., Marreiro, A., Polidori, G., Taiar, R., Legrand, F., Boyer, F.C., 2018. Effect of whole body cryotherapy interventions on health – related quality of life in fibromyalgia patients: A randomized controlled trial. Complement. Ther. Med. 36, 6-8.
Wasserman, A.M., 2011. Diagnosis and management of rheumatoid arthritis. Am. Fam. Physician. 84(11), 1245-52.
Wozniak, A., Wozniak, B., Drewa, G., Mila-Kierzenkowska, C., Rakowski A., 2007. The effect of whole-body cryostimulation on lysosomal enzyme activity in kayakers during training. Eur. J. Appl. Physiol. 100(2), 137– 42.

Manuscript ID: 49
DOI: 10.18462/iir.icr.2019.0049

A simplified heat transfer model of a closed refrigerated display cabinet

Nattawut CHAOMUANG[(a)(b)(c)], Onrawee LAGUERRE[(a)], Denis FLICK[(b)]

[(a)] UR GPAN, Refrigeration Processing Engineering Research Unit, Irstea
1 rue Pierre-Gilles de Gennes, Antony, 92160, France, nattawut.chaomuang@irstea.fr
[(b)] AgroParisTech, Inra, Université Paris-Saclay, UMR Ingénierie Procédés Aliments
Massy, 91300, France
[(c)] Department of Food Engineering, King Mongkut's Institute of Technology Ladkrabang
Bangkok, 10520, Thailand

ABSTRACT

A simplified heat transfer model for a closed refrigerated display cabinet was developed based on a zonal approach. The developed model allows the prediction of time-averaged air and load temperatures at various positions in the display cabinet. These predicted values were compared with measured air and load temperatures. Good agreement was found between them with the maximum difference of 0.5°C for every studied position and the overall mean absolute error of 0.2°C. Air and load temperatures vary with positions. High temperature was observed at the front (highest value at the front top) and low at the back (lowest value at the back bottom). Based on the simulation, the cabinet thermal performance can be enhanced by minimizing the size of door gaps.
Keywords: Closed refrigerated display cabinet, Simplified model, Heat transfer, Temperature

1. INTRODUCTION

It is well known that air infiltration across an air curtain is one of the major drawbacks of open refrigerated display cabinets. It accounts for about 66-77% of total refrigeration loads (Gaspar et al., 2011) and also causes temperature heterogeneity in the cabinets (Laguerre et al., 2012b). High temperature is mostly at the front areas and low temperature at the rear (Evans et al., 2007). As temperature is one of the most important factors affecting food quality and safety, minimizing the air infiltration would prolong product shelf life.
Installation of doors on the open cabinets is one of the simple and effective solutions for the air infiltration reduction. Many achievements were demonstrated by various studies: energy saving potential (Faramarzi et al., 2002; Fricke and Becker, 2010), better temperature homogeneity (Chaomuang et al., 2019; Lindberg et al., 2010) and slower quality decay (Atilio de Frias et al., 2015). As a result, the use of display cabinets with doors is increasingly used in retail stores worldwide. Closed display cabinets will account for about 75% of all operating display cabinets by 2020 in France (RPF, 2016).
Because door installation can modify airflow pattern and temperature distribution inside the cabinet (Faramarzi et al., 2002), an understanding of mechanism of heat transfer and airflow in the equipment becomes necessary to ensure food quality and safety. Although numerical simulation with CFD (Computational Fluid Dynamics) models is widely used to investigate the thermal phenomena in many refrigerating equipment (Smale et al., 2006), this approach entails some limitations because of the requirement of calculation time and computational resources. A simplified heat transfer model based on a zonal approach becomes a complementary option as demonstrated by Laguerre et al. (2012a). They applied such a model to assess the influence of operating conditions and equipment design on temperature of products stored in an open display cabinet under steady state.

This work on a closed display cabinet is a continuity of the previous studies of which the objective is to present a simplified heat transfer model based on the zonal approach. This developed model enables the understanding of the heat transfer phenomena in the equipment as well as the prediction of internal temperature distribution.
This developed heat transfer model will be further integrated with the other models already developed by our teams for several refrigerating equipment. By this mean, it allows the prediction of time-temperature history of food products from a production plant to a household refrigerator. Furthermore, these models linked with predictive microbiological and/or quality models can be used as an evaluation tool for consumer risk (Duret et al., 2015).

2. MATERIALS AND METHOD

2.1. Experimental setup

Temperature measurement was carried out in a closed refrigerated display cabinet loaded with test packages made of methylcellulose. This cabinet was installed in a test room in which the ambient temperature was controlled at 19.5°C. The lights in the test room and in the cabinet were switched on to represent the real-use condition in supermarket and the cabinet doors were always closed during the experiment. As shown in Fig.1, calibrated thermocouples (T-type, accuracy ±0.2°C) were placed at various positions in the cabinet for the measurement of air and load (core and surface) temperatures. Perforation pattern of the back panel (PBP) of the studied cabinet is also depicted in this figure. According to the total plate area over each shelf, there are 2.3% of holes at the top shelf, 8.3% at the bottom shelf and 3.8% at all intermediate shelves.The temperatures were recorded every 10 s using a data logger for 24 hours. The time-averaged values were then calculated over 5 h of the quasi-steady state during which the defrosting period was excluded from the calculation. These results were then used for the model validation.

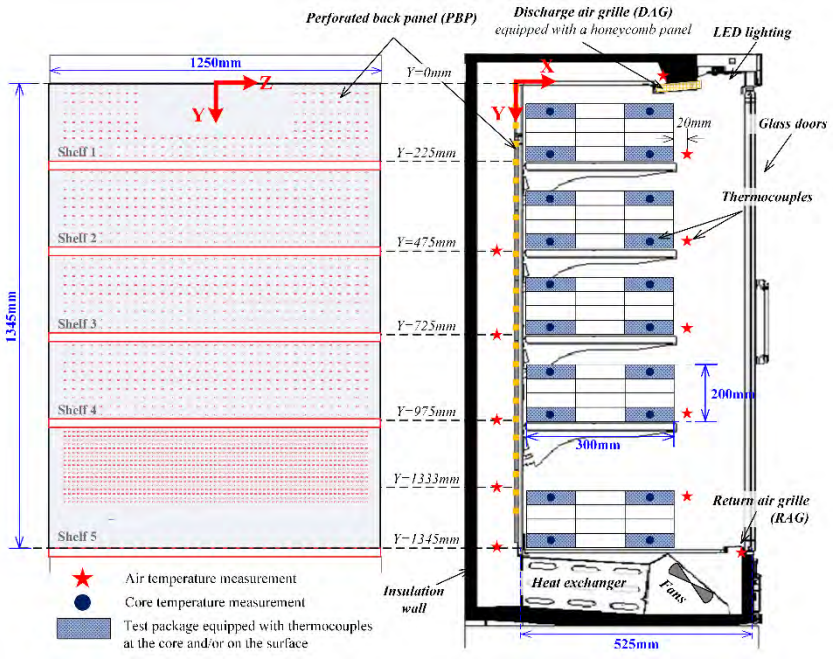

Figure 1: Experimental setup for the temperature measurement

2.2. Model development

2.2.1. Model description

A steady state model is developed in the present study to predict the time-averaged air and load temperatures in the closed refrigerated display cabinet. The air temperature just after the

heat exchanger at which the thermostat sensor is located (T_{th}) and the external air temperature (T_{ext}) are the input parameters which are assumed constant. To generalize the model, dimensionless temperature (θ_i) based on these temperatures is defined as follows:

$$\theta_i = \frac{\overline{T}_i - \overline{T}_{th}}{T_{ext} - \overline{T}_{th}} \quad \text{Eq. (1)}$$

2.2.2. Zone definition

Based on the zonal approach, heat exchange zones at different positions in the cabinet were established (Fig.2). Two main domains were considered, the first one represents the heat transfer in the rear duct where cold air exchanges heat with the ambient air through the rear wall while the second one represents the heat transfer in the shelf space.

2.2.3. Heat balance equations

For every zone in both domains, algebraic heat balance equations were derived to describe the heat transfers in the display cabinet.

Starting from Domain I and Position 1 (denoted by EZ [1,1], Fig. 2), the supply air (mass flow rate $\dot{m}_t$ and temperature θ_{th}) exchanges heat with the external air (θ_{ext}) through the rear wall by conduction and by convection (overall heat transfer coefficient U_{ovw}). The air temperature then increases to θ_{ard1}. By integration along the rear duct located at this position, the heat balance equation becomes:

$$\theta_{ard1} = \alpha_{rd1}\theta_{th} + (1 - \alpha_{rd1})\theta_{ext} \text{ where } \alpha_{rd1} = \exp\left(-\frac{U_{ovw}S_{w1}}{\dot{m}_t C_{pa}}\right) \quad \text{Eq. (2)}$$

A part of air flows into the shelve space through the perforated back panel (PBP) while the remaining part (mass flow rate $\dot{m}_{ard}$) continues flowing towards the discharge air grille (DAG), along which the air temperature increases successively to θ_{ard7}. The heat balance of EZ [1,2…7] was therefore carried out in the same manner as that of EZ [1,1].

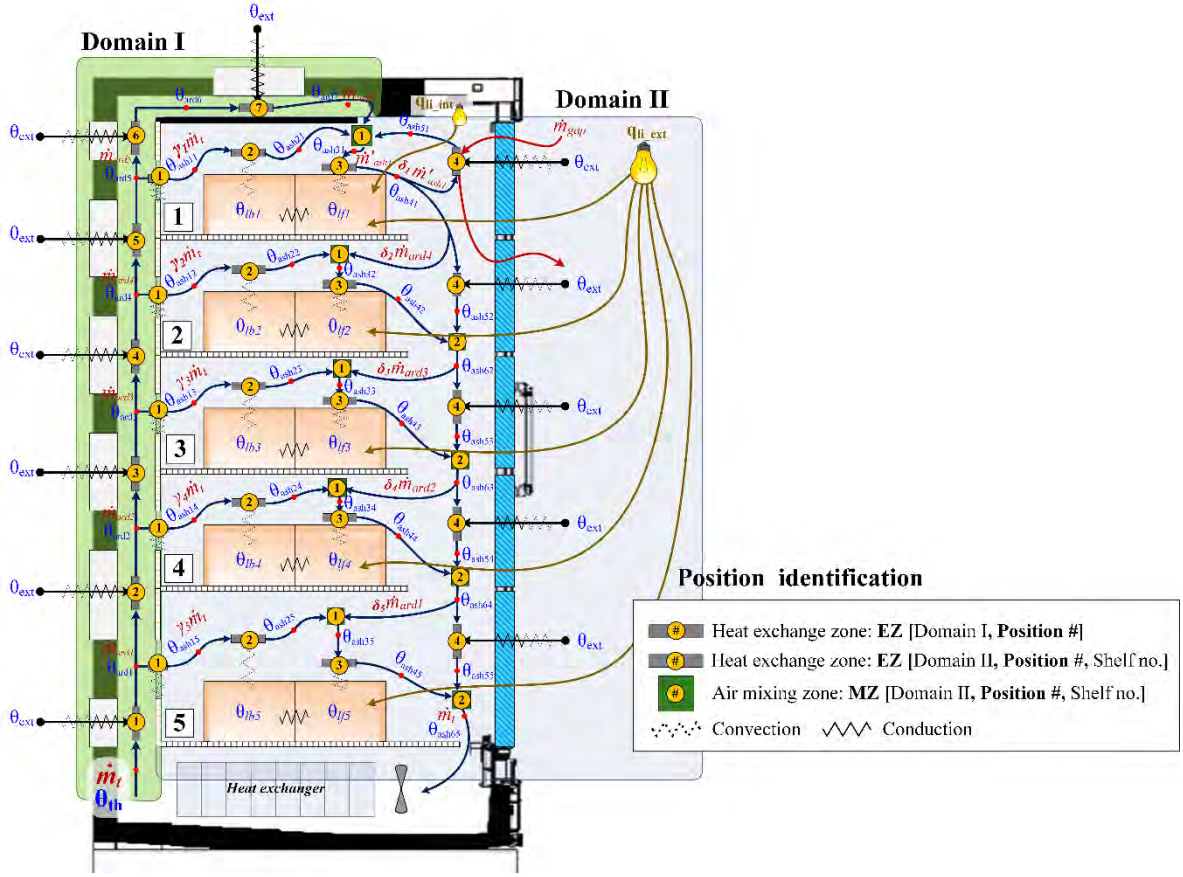

Figure 2: Schematic view of the simplified heat transfer model of a closed refrigerated display cabinet.

Domain II is composed of five shelves. Each shelf has four heat exchange zones (EZ [2,1…4,1…5]) and one or two air mixing zones (MZ [2,1…2,1…5]). At Position 1 Shelf 1, i.e. EZ [2,1,1] (see Fig. 2), a part of the air (mass flow rate $\dot{m}_{ash1} = \gamma_1 \dot{m}_t$ and temperature θ_{ard5}) flows horizontally through PBP at the mid height of Shelf 1. At the steady state, the air temperatures before and after flowing through PBP are the same:

$$\theta_{ash11} = \theta_{ard5} \quad \text{Eq. (3)}$$

At EZ [2,2,1], the air (temperature θ_{ash11}) exchanges heat by convection (heat transfer coefficient U_{lb1}) with the back load (temperature θ_{lb1}). The air temperature becomes θ_{ash21}.

$$\theta_{ash21} = \alpha_{sh11}\theta_{ash11} + (1 - \alpha_{sh11})\theta_{lb1} \text{ where } \alpha_{sh11} = \exp\left(-\frac{U_{lb1}S_{l1}}{\dot{m}_{ash1}C_{pa}}\right) \quad \text{Eq. (4)}$$

In addition to this convective heat exchange with air, the back load also exchanges heat with the front one by conduction (heat transfer coefficient U_{ll1}) because of the contact between these two loads.

$$\theta_{ash21} = \theta_{ash11} + \beta_{sh11}(\theta_{lf1} - \theta_{lb1}) \text{ where } \beta_{sh11} = \frac{U_{ll1}S_{ll1}}{\dot{m}_{ash1}C_{pa}} \quad \text{Eq. (5)}$$

A similar heat balance was developed for other shelves.
The air then mixes with other two air streams at MZ [2,1,1] (Fig. 2) including air from DAG (mass flow rate $\dot{m}_{ard5}$ and temperature θ_{ard7}) and a part of the recirculating air (mass flow rate $\delta_1 \dot{m}'_{ash1}$ and temperature θ_{ash51}).

$$\dot{m}'_{ash1}\theta_{ash31} = \dot{m}_{ard5}\theta_{ard7} + \dot{m}_{ash1}\theta_{ash21} + \delta_1\dot{m}'_{ash1}\theta_{ash51} \text{ where } \dot{m}'_{ash1} = \frac{\dot{m}_{ash1}+\dot{m}_{ard5}}{1-\delta_1} \quad \text{Eq. (6)}$$

This mixed air then exchanges heat with the front load, EZ [2,3,1], and its temperature becomes θ_{ash41}.

$$\theta_{ash41} = \alpha_{sh21}\theta_{ash31} + (1 - \alpha_{sh21})\theta_{lf1} \text{ where } \alpha_{sh21} = \exp\left(-\frac{U_{lf1}S_{l1}}{\dot{m}'_{ash1}C_{pa}}\right) \quad \text{Eq. (7)}$$

In addition to this convective heat exchange with the air, the front load also exchanges heat with the back load by conduction (heat transfer coefficient, U_{ll1}) and receives heat from the conversion of the room and cabinet lighting powers (q_{li}). At steady state:

$$\theta_{ash41} = \theta_{ash31} + \beta_{sh21}(\theta_{lb1} - \theta_{lf1}) + q''_{li1} \text{ where } \beta_{sh21} = \frac{U_{ll1}S_{ll1}}{\dot{m}'_{ash1}C_{pa}};\ q''_{li1} = \frac{q_{li1}}{\dot{m}'_{ash1}C_{pa}(T_{ext}-\bar{T}_{th})} \quad \text{Eq. (8)}$$

Unlike Shelf 1, different heat balance is applied to the other shelves. The heat transfer mechanism on Shelf 2 was selected as a sample of the model development. The air flowing through PBP (mass flow rate $\dot{m}_{ash2}$ and temperature θ_{ash22}) mixes with a part of the air curtain from the upper shelf (mass flow rate $\delta_2\dot{m}_{ard4}$ and temperature θ_{ash41}).

$$\dot{m}'_{ash2}\theta_{ash32} = \dot{m}_{ash2}\theta_{ash22} + \delta_2\dot{m}_{ard4}\theta_{ash41} \text{ where } \dot{m}'_{ash2} = \dot{m}_{ash2} + \delta_2\dot{m}_{ard4} \quad \text{Eq. (9)}$$

Then, the mixed air exchanges heat with the front load, EZ [2,3,2], and its temperature becomes θ_{ash42}.

$$\theta_{ash42} = \alpha_{sh22}\theta_{ash32} + (1 - \alpha_{sh22})\theta_{lf2} \text{ where } \alpha_{sh22} = \exp\left(-\frac{U_{lf2}S_{l2}}{\dot{m}'_{ash2}C_{pa}}\right) \quad \text{Eq. (10)}$$

The load located at the front of Shelf 2 is subjected to the convection with the mixed air, the conduction with the adjacent load at the back (heat transfer coefficient U_{ll2}) and the heat conversion of visible radiation from the room lighting power (q_{li2}), thus

$$\theta_{ash42} = \theta_{ash32} + \beta_{sh22}(\theta_{lb2} - \theta_{lf2}) + q''_{li2} \text{ where } \beta_{sh22} = \frac{U_{ll2}S_{ll2}}{\dot{m}'_{ash2}C_{pa}};\ q''_{li2} = \frac{q_{li2}}{\dot{m}'_{ash2}C_{pa}(T_{ext}-\bar{T}_{th})} \quad \text{Eq. (11)}$$

After exchanging heat with the front load, a part of the air at Shelf 1 (mass flow rate $\delta_1 \dot{m}_{ash1}$ and temperature θ_{ash41}) flows toward the doors and is submitted to heat losses through the doors (overall heat transfer coefficient U_{ovd}). This air also interacts with the air infiltration through the door gaps (mass flow rate $\dot{m}_{gap}$). These exchanges at EZ [2,4,1] result in an air temperature increase to θ_{ash51}.

$$\theta_{ash51} = \alpha_{sh31}\theta_{ash41} + (1-\alpha_{sh31})\theta_{ext} \text{ where } \alpha_{sh31} = \exp\left(-\frac{C_{eq}S_{d1}}{\delta_1 \dot{m}'_{ash1} C_{pa}}\right) \quad \text{Eq. (12)}$$

For simplification and as a first approach, it is considered that there is no air recirulation and air infiltration through the door gaps for the other shelves. A part of the air at these shelves, e.g. Shelf 2, is mixed with the air from the top shelf (mass flow rate $(1-\delta_2)\dot{m}_{ard4}$ and temperature θ_{ash41}) and exchanges heat with the external ambient air through the glass doors (overall heat transfer coefficient U_{ovd}).

$$\theta_{ash52} = \alpha_{sh32}\theta_{ash41} + (1-\alpha_{sh32})\theta_{ext} \text{ where } \alpha_{sh32} = \exp\left(-\frac{U_{ovd}S_{d2}}{(1-\delta_2)\dot{m}_{ard4}C_{pa}}\right) \quad \text{Eq. (13)}$$

This air then mixes with the air which exchanged heat with the load located at the front of the shelf at MZ [2, 2, 2].

$$\dot{m}_{ard3}\theta_{ash62} = \dot{m}'_{ash2}\,\theta_{ash42} + (1-\delta_2)\dot{m}_{ard4}\theta_{ash52} \quad \text{Eq. (14)}$$

A similar heat and mass balances at EZ [2, 4, 2] and MZ [2, 2, 2] were applied to Shelf 3 to 5. Input parameters used in the developed model were obtained from several sources: physical measurement, calculation based on literature and material properties and model fitting as summarized in **Table 1**. The simulation was run on MATLAB environment.

Table 1 Values of input parameters used in the simplified heat transfer model

Parameter		Value	Source		Value	Source
Mass flow rate (kg·s^{-1})	$\dot{m}_t$	0.1120	Measurement	$\dot{m}_{gap}$	0.0051	Model fitting
Air distribution coefficient (-)	γ_1	0.02	Measurement	δ_1	0.90	Model fitting
	γ_2	0.02		δ_2	0.70	
	γ_3	0.04		δ_3	0.70	
	γ_4	0.05		δ_4	0.70	
	γ_5	0.36		δ_5	0.70	
Heat transfer coefficient (W·m^{-2}·K^{-1})	U_{lb}	15	Model fitting	U_{ovw}	0.77	Calculation
	U_{lf}	24	Model fitting	U_{ovd}	1.02	Calculation
	U_{ll}	3.4	Calculation	C_{eq}	17.6	Calculation
Exchange area* (m^2)	S_{w1}	0.216	Measurement	S_c	0.500	Measurement
	$S_{w2\ldots5}$	0.313	Measurement	$S_{d1\ldots4}$	0.313	Measurement
	S_{w6}	0.156	Measurement	S_{d5}	0.431	Measurement
Lighting power (W)	q_{li1}	10	Calculation	$q_{li2\ldots5}$	0.25	Calculation
**The cabinet is 1.25 m in length.*						

3. RESULTS AND DISCUSSION

Fig. 3a shows the predicted and measured air and load temperatures inside the closed display cabinet for the ambient temperature of 19.5°C. It was observed that the air temperature in the rear duct increased progressively from the duct upstream to the DAG (Fig.3a) because of heat losses through the rear wall. As a part of this cold air also infiltrated into the cabinet through PBP, it explains higher temperature of back load at the top shelf compared to the lower shelves. Similarly, higher temperature of the load at the front top shelf was observed compared to that at the lower shelves. On the same shelf, the front load temperature was relatively higher (average difference of about 1.4°C) compared to the one at the back because of heat losses through the glass doors. The maximum difference (2.1°C) at the top shelf can be explained by additional heat loads from the warm air infiltration through the door gaps and the heat

conversion of visible radiation from the room and cabinet lightings. The highest and lowest load temperature positions were located at the front of the top shelf and the back of the bottom shelf, respectively.

As shown in Fig.3b, the calculated air and load temperatures agreed with the measured ones with an overall mean absolute error of about 0.2°C. A slight over-estimated air temperature at the front can be explained by the measurement position which may not be a good representation of the entire air across the front area. Nevertheless, the load temperature is well predicted. The maximum difference of the calculated and measured load temperatures was less than 0.5°C for every studied position. It is worth to remind that the developed model does not take into account the air infiltration due to door openings because the airflow during door openings is too complex to be predicted by the simplified model.

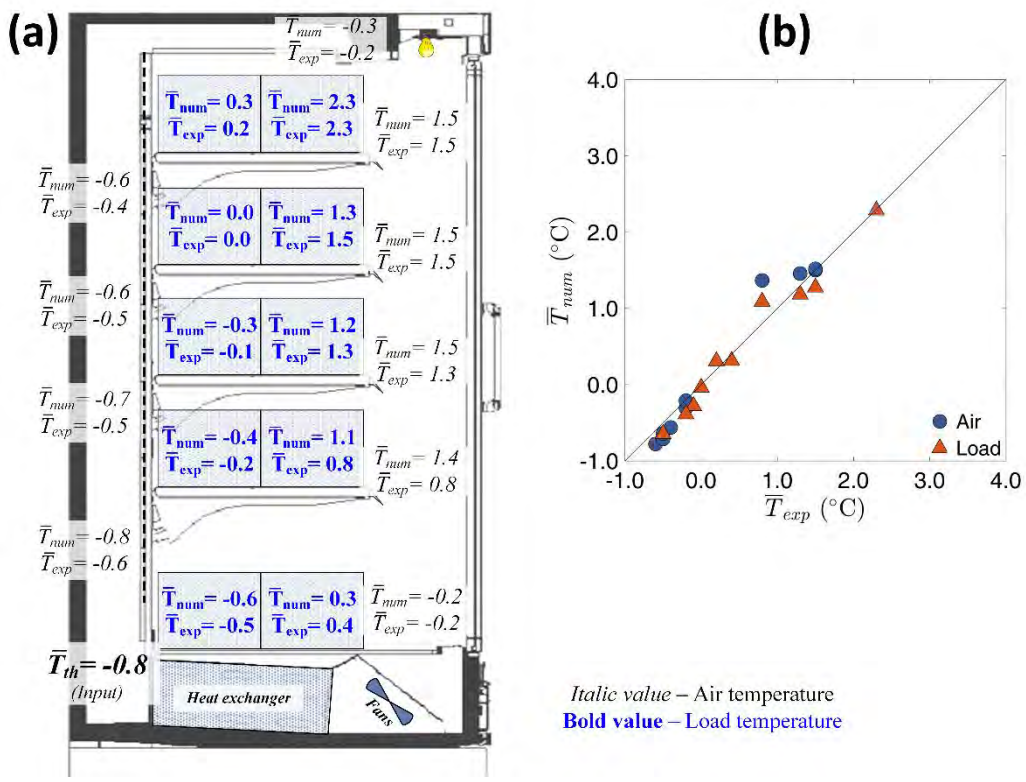

Figure 3: (a) Temperature distribution obtained from the numerical simulation ($\bar{T}_{num}$) and measurement ($\bar{T}_{exp}$) in a closed display cabinet for ambient temperature of 19.5°C (b) comparison between the predicted and measured air and load temperatures.

The validated model was further used to investigate the effect of design parameters on the load temperature in the closed display cabinet including rear wall insulation thickness (e) and air infiltration rate through the door gaps ($\dot{m}_{gap}$). As shown in Fig.4a, doubling insulation wall thinkness resulted in a slight decrease of load temperatures (about 0.2°C). Load temperatures could be notibly decreased (up to 0.7°C) when the air infiltration through the door gap reduced by half (Fig.4b). These findings suggested that the temperature performance of closed refrigerated display cabinets could be improved by minimizing the door gaps of the cabinets.

4. CONCLUSIONS

A steady state simplified heat transfer model was developed for a closed refrigerated display cabinet. Based on a zonal approach, the display cabinet was decomposed into various heat exchange zones allowing the prediction of air and load temperatures at different positions. In the shelves-space storage, time-averaged load temperatures at 10 positions (front and back

of the five shelves) were predicted and compared with the experimental results. It was observed that the load temperatures were well predicted by the model whereas the air temperature in the air curtain was slightly over-estimated. Possible explanation of the discrepancy between the model and the experiment is that the air temperature was measured only at one position which may not be representative of the average air temperature inside the curtain . Nevertheless, the load temperature ranges and trends in the closed display cabinet are well represented by the proposed model with a short calculation time (less than 1 s). The overall mean absolute error was less than 0.2°C, and the maximum difference of the calculated and measured load temperatures never exceeds 0.5°C for every studied position. Moreover, this validated model can be used to study the influence of display cabinet design on the thermal performance.

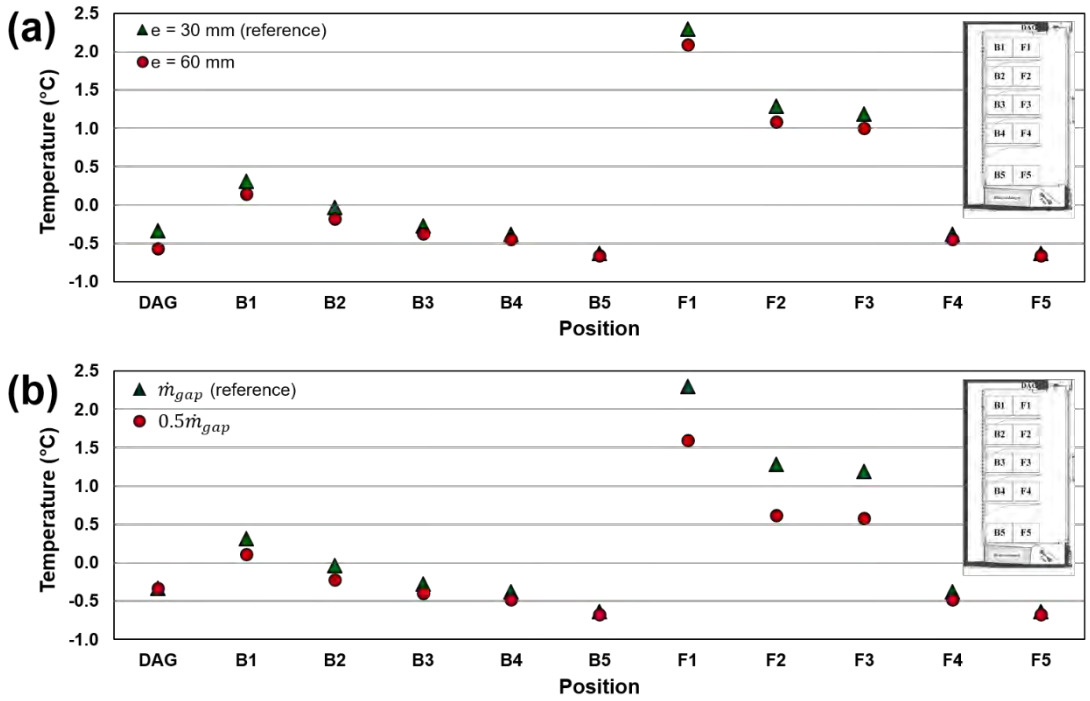

Figure 4: Numerical results showing the variation of air temperature at discharge air grille (DAG) and load temperatures with (a) wall insulation thickness and (b) air infiltration rate through the door gaps

ACKNOWLEDGEMENT

This research was granted by King Mongkut's Institute of Technology Ladkrabang, Thailand, National Research Institute of Science and Technology for Environment and Agriculture, France and the French Embassy in Thailand.

NOMENCLATURE

C_{eq}	Equivalent thermal conductance, W·m^{-2}·K^{-1}	T	Temperature, °C or K
e	thinkness, m	U	Overall heat transfer coefficient, W·m^{-2}·K^{-1}
h	Convective heat transfer coefficient, W·m^{-2}·K^{-1}	α, β	Exponential dimensionless heat transfer coefficient
$\dot{m}$	Mass flow rate, kg·s^{-1}	δ, γ	Air distribution coefficient
q	Heating power, W	θ	Dimensionless time-averaged temperature
S	Exchange area, m^2		

REFERENCES

Atilio de Frias, J., Luo, Y., Kou, L., Zhou, B., Wang, Q., 2015. Improving spinach quality and reducing energy costs by retrofitting retail open refrigerated cases with doors. Postharvest Biology and Technology 110, 114-120.

Chaomuang, N., Flick, D., Denis, A., Laguerre, O., 2019. Experimental analysis of heat transfer and airflow in a closed refrigerated display cabinet. Journal of Food Engineering 244, 101-114.

Duret, S., Gwanpua, S.G., Hoang, H.-M., Guillier, L., Flick, D., Laguerre, O., Jabri, M.E.L., Thuault, D., Hezard, B., Lintz, A., Stahl, V., Geeraerd, A., (2015). Identification of the significant factors in food quality using global sensitivity analysis and the accept-and-reject algorithm. Part II: Application to the cold chain of cooked ham. Journal of Food Engineering 148, 58-65.

Evans, J.A., Scarcelli, S., Swain, M.V.L., 2007. Temperature and energy performance of refrigerated retail display and commercial catering cabinets under test conditions. International Journal of Refrigeration 30, 398-408.

Faramarzi, R.T., Coburn, B.A., Sarhadian, R., 2002. Performance and energy impact of installing glass doors on an open vertical deli/dairy display case. ASHRAE Transactions 108, 673.

Fricke, B., Becker, B., 2010. Energy use of doored and open vertical refrigerated display cases, International Refrigeration and Air Conditioning Conference. Purdue University, West Lafayette, IN, USA.

Gaspar, P.D., Carrilho Gonçalves, L.C., Pitarma, R.A., 2011. Experimental analysis of the thermal entrainment factor of air curtains in vertical open display cabinets for different ambient air conditions. Applied Thermal Engineering 31, 961-969.

Laguerre, O., Hoang, M.H., Flick, D., 2012a. Heat transfer modelling in a refrigerated display cabinet: The influence of operating conditions. Journal of Food Engineering 108, 353-364.

Laguerre, O., Hoang, M.H., Osswald, V., Flick, D., 2012b. Experimental study of heat transfer and air flow in a refrigerated display cabinet. Journal of Food Engineering 113, 310-321.

Lindberg, U., Axell, M., Fahlén, P., 2010. Vertical display cabinets without and with doors–a comparison of measurements in a laboratory and in a supermarket, 1st IIR International Conference on Sustainability and the Cold Chain, Cambridge, United Kingdom.

RPF, 2016. Fermeture des meubles réfrigérés: du positif pour les clients, La Revue Pratique du Froid et du Conditionnement d'Air. Imprimerie Chirat, St-Just-la-Pendue, pp. 26-28.

Smale, N.J., Moureh, J., Cortella, G., 2006. A review of numerical models of airflow in refrigerated food applications. International Journal of Refrigeration 29, 911-930.

Manuscript ID: 178
DOI: 10.18462/iir.icr.2019.0178

Modelling the fluid flow inside a refrigerated trailer loaded with pork carcasses

Mouna MERAI[(a)], Steven DURET[(a)], Jean MOUREH[(a)], Onrawee LAGUERRE[(a)], Denis FLICK[(b)]

[(a)] Irstea, Refrigeration Process Engineering RU
Antony, 92761, France, steven.duret@irstea.fr

[(b)] AgroParisTech, Inra, Université Paris-Saclay, Food Process Engineering JRU
Massy, 91300, France, denis.flick@agroparistech.fr

ABSTRACT

When pork carcasses are transported in a refrigerated trailer, all of them should be correctly ventilated. CFD simulations were performed to assess the homogeneity of air circulation around the carcasses. From an Xray scanner of a carcass, a simplified geometry was deduced. The air volume inside a semitrailer containing 430 pork half-carcasses was then meshed (21.10^6 cells). The Reynolds Averaged Navier Stokes equations were solved with the k-ε turbulence model. The flow pattern is very complex: air is blown at high velocity on the top of the container front, forming a wall jet. There is an air entrainment by this jet whose section increases whereas its velocity decreases. Part of the blown air flows throughout the 'porous' zone constituted by the carcasses while another part reaches the gap between the carcasses and the doors at the rear of the container. Finally air flows back toward the outlet. Zones of low velocity between half-carcasses were identified.

Keywords: Aeraulics, Carcass, Computational Fluid Dynamics, Refrigerated vehicle

1. INTRODUCTION

When pork carcasses are transported in a refrigerated trailer, all of them should be correctly ventilated. But in fact, it has be shown both by experimentation and computational fluid dynamics (CFD) that air flow can be very heterogeneous in refrigerated trailers. Up to now, the studies concerned empty trailers (Moureh and Flick 2005), trailers loaded with impermeable or porous pallets (Tapsoba et al. 2007, Moureh et al. 2009) or a single carcass (Pham et al. 2009, Kuffi et al. 2016).

The present study concerns the case of a long trailer (13.3 m) loaded with 430 pork half-carcasses. The air inlet and outlet are both located at the front of the container, this generally implies a better ventilation in the front part than in the rear part. The air is blown at high velocity (11 m/s) near the ceiling of the container front, forming a turbulent wall jet. The particularity of this configuration in comparison with previous studies is the very complex geometry of the load. A numerical approach is here presented.

Many CFD studies of air flow in refrigeration equipment use the Reynolds Averaged Navier Stokes (RANS) approach. The objective is to predict the time-averaged mean velocity ($\vec{v}$). Most often the Reynolds stresses, due to the velocity fluctuations ($\vec{v}'$) are expressed with the Boussinseq approximation by introducing the turbulent viscosity (ν_t). This way, the eddies are not directly solved but only characterized by their turbulent kinetic energy (k). Following Kolmogorov's point of view, mechanical energy of the mean flow is transformed into turbulent kinetic energy (because of the mean velocity gradients) and the energy of the smallest eddies is transformed into heat (molecular agitation) with a specific dissipation rate (ε). For complex geometries, an algebraic estimation of the turbulent viscosity cannot be used; the most popular approach relates ν_t to k and

ε (taking into account indirectly of the turbulence length scale l_t). Different versions are available which differ by some energy redistribution terms and near wall treatment (standard k-ε. realizable k-ε, k-ε RNG, k-ω SST). Near wall treatment is especially important if heat transfer has to be predicted. Sometimes the Boussinesq approximation cannot be applied because eddies are highly anisotropic and more sophisticated model (e.g. RSM) have to be used (Defraeye et al. 2013).

Near the walls, $\vec{v}$ varies very rapidly in a nonlinear way, so that a very fine mesh should be employed near the walls. But this becomes very expensive in term of memory and computing time. Therefore, assuming that the flow is almost parallel to the wall in the first cell near a wall, the boundary layer theory can be employed to estimate the wall shear stress. In the software the employed near wall relations are called 'wall functions'.

The present study aims to predict the homogeneity of the fluid flow around the carcasses. No precise velocity field or estimation of the heat transfer intensity is expected; therefore the standard k-ε model (with wall functions) was used.

2. GEOMETRY AND MESH

Fig.1 presents the dimensions of the trailer and of the zone occupied by the carcasses.

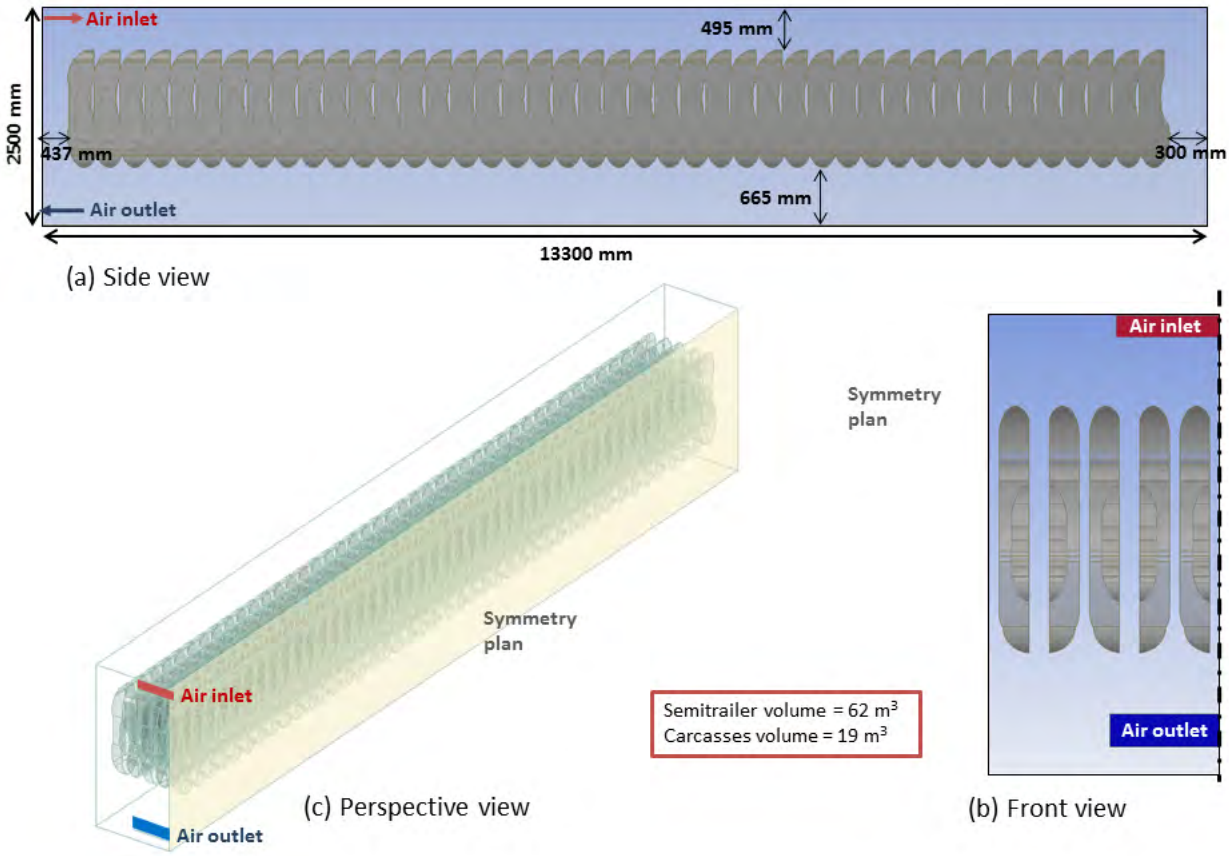

Figure 1: Dimensions of the trailer (real scale)

From an Xray scanner of a carcass, a simplified geometry was deduced as shown on Fig. 2.

The simplified geometry was developed in order to have the same volume ensuring the same porosity of the zone occupied by the carcasses. The horizontal section at a given height is also about the same for the real carcass and the simplified geometry, ensuring almost the same convergent or divergent flow in the vertical direction.

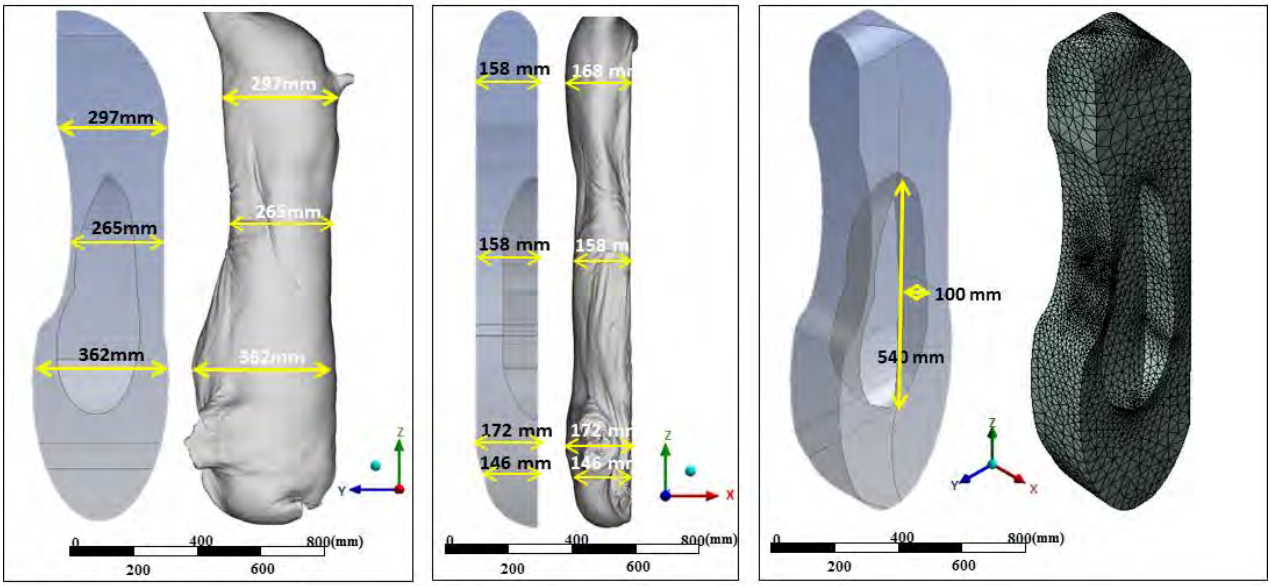

Figure 2: Simplified geometry of the carcasses

The air volume inside a semitrailer containing 430 pork half-carcasses was then meshed using 21 009 342 cells (Fig. 3). Near the top wall, the mesh is prismatic in order to better take into account the wall jet development.

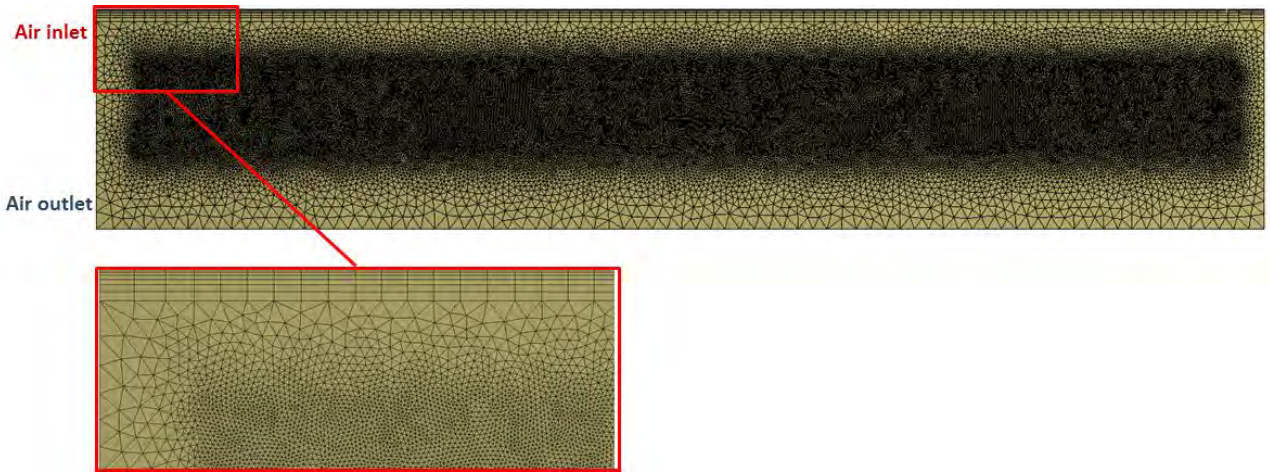

Figure 3 View of the mesh

3. MAIN HYPOTHESES AND BOUNDARY CONDITIONS

The fluid was assumed incompressible and isothermal. Properties of air at 4°C were used.

The steady state Reynolds Averaged Navier Stokes (RANS) equations with the standard k-ε model of turbulence and the standard (logarithmic) wall function (smooth walls) were solved using the finite volume method (Fluent).

The inlet conditions are:
- section 1.100 m x 0.16 m (hydraulic diameter: 0.28 m)
- normal mean velocity: 11 m/s (Reynolds number: $2.2\ 10^5$)
- turbulence intensity: 10 %
- turbulence length : 7% of hydraulic diameter

At outlet, uniform pressure was imposed (without viscous stress).

The simulation converged after 3500 iterations which needed 48 hours of computation on a 12 cores computer with 130 Go RAM.

4. RESULTS AND DISCUSION

Fig. 4 present some computed stream lines inside the loaded trailer (the carcasses are not represented in this figure but where taken into account in the simulation). This highlights the complexity of the 3D flow pattern. Globally air blown near the ceiling forms a wall jet. Its section increases whereas its velocity decreases (1). It adheres to the top wall (by Coanda effect) nearly up to the rear of the trailer. Part of the blown air flows throughout the ‘porous’ zone constituted by the carcasses while another part reaches the gap between the carcasses and the doors at the rear of the container (2). Finally air flows back toward the outlet near the bottom (3). There is an air entrainment by the jet which explains an upward flow on the front of the trailer (4).

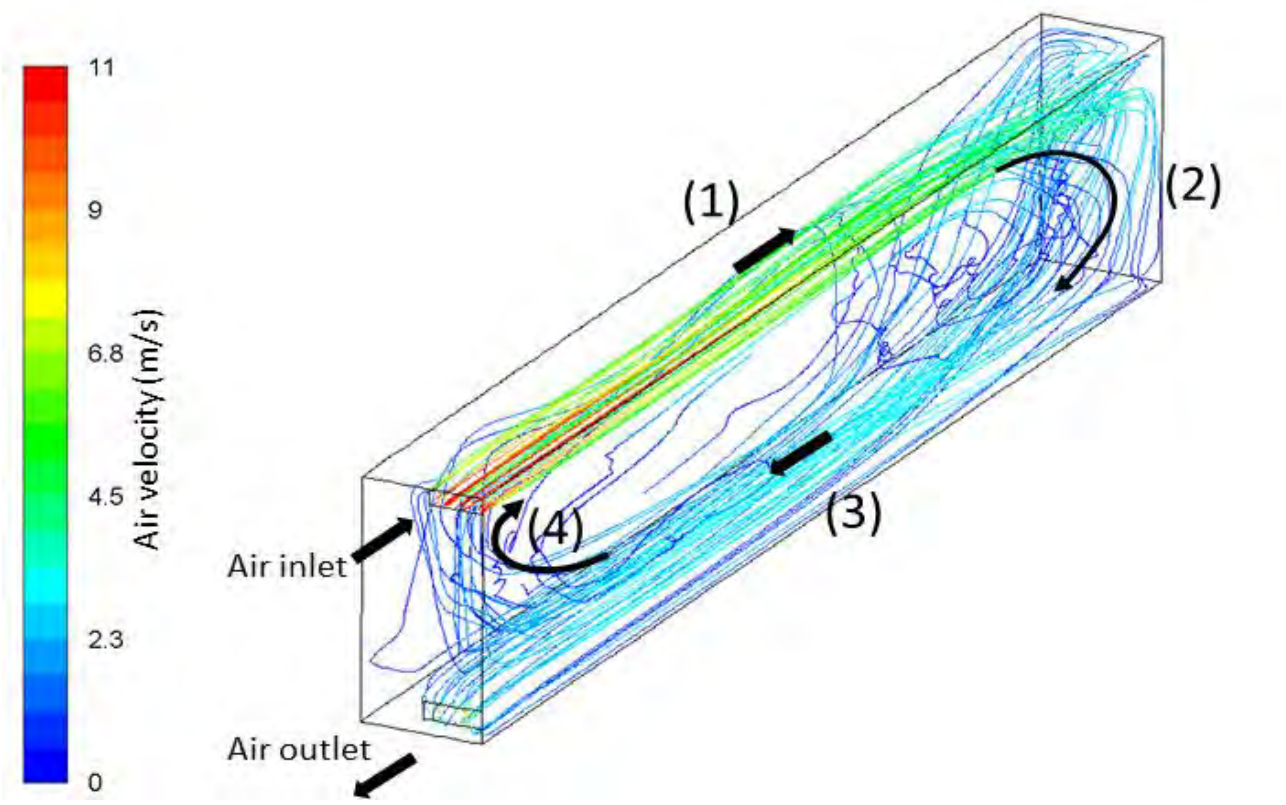

Figure 4 : Stream lines issued from the inlet section

Fig. 5a presents the computed velocity magnitude in the symmetry plan. This velocity field can be compared outside the zone of carcasses with the experimental one (Fig. 4b) which was obtained on a reduced scale trailer loaded with reduced scale carcasses made of polyurethane foam (Merai et al. 2018) by 2D Laser Doppler Velocimetry (LDV).

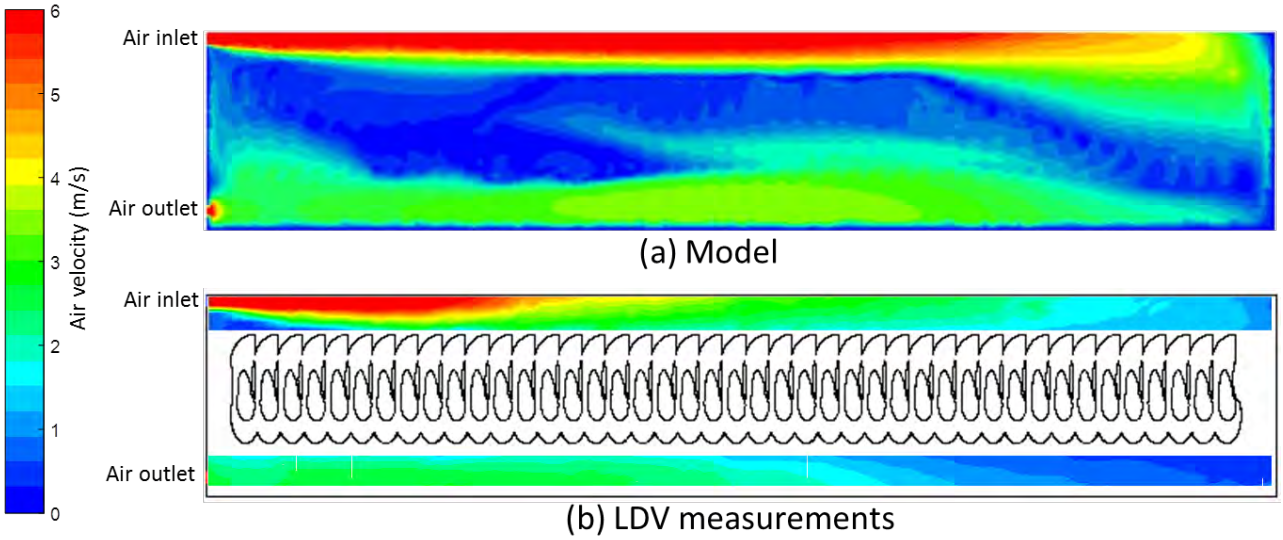

Figure 5: velocity magnitude in the symmetry plan (red color represents velocities ranging from 6m/s to 11 m/s which is the value at inlet)

Fig. 6 compares the evolution along the jet axis (longitudinal axis passing by the center of the inlet section) of the numerical and experimental axial velocities.

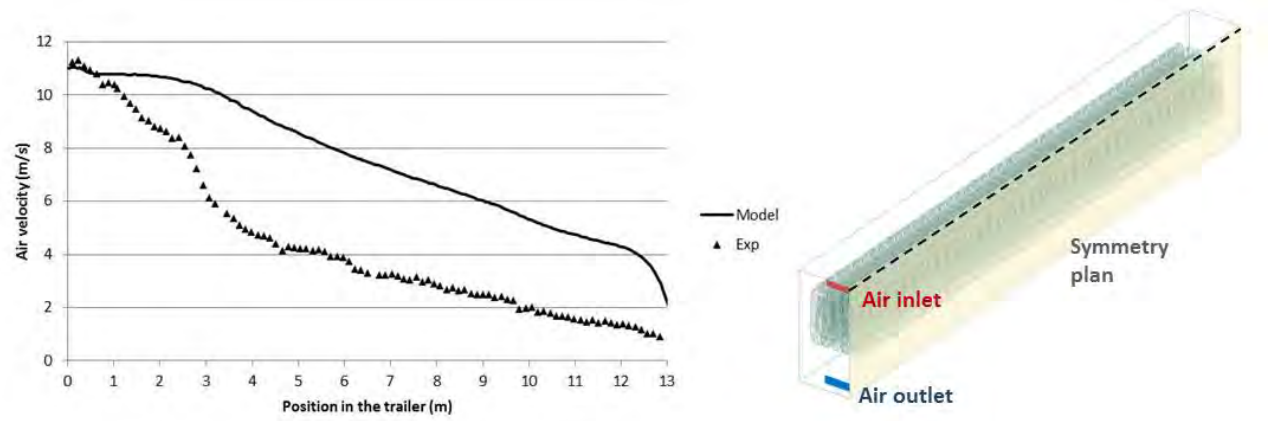

Figure 6 : Velocity along the jet axis

The main difference is that the predicted velocity decreases less rapidly along the jet axis than the measured one. This can be explained by several reasons. The simulated geometry does not take into account the presence of the hooks and the extremity of the feet. Also the heights at which the carcasses are hanged is not exactly the same in the experiment (and in real configuration) to the contrary of simulation. All these aspects could contribute to produce turbulence and increase the jet diffusion in the lateral and vertical directions. The k-ε model is also known to predict incorrectly flows with adverse pressure gradients. This explained that for of an empty trailer, the k-ε was unable to predict the experimentally observed separation of the jet from the wall (Moureh and Flick 2005) whereas the RSM model, which better takes into account of turbulence anisotropy, predicted it well. More realistic geometry and more advanced turbulence models will be tested in future work.

Nevertheless, even taking in mind the limitations of the present numerical results, the interest of the CFD approach is that, contrarily to the experimental approach, it is possible to estimate the air flow around the carcasses.

Fig. 7 presents the velocity magnitude at different position between the half carcasses. Some zones of low velocity between half carcasses can be identified.

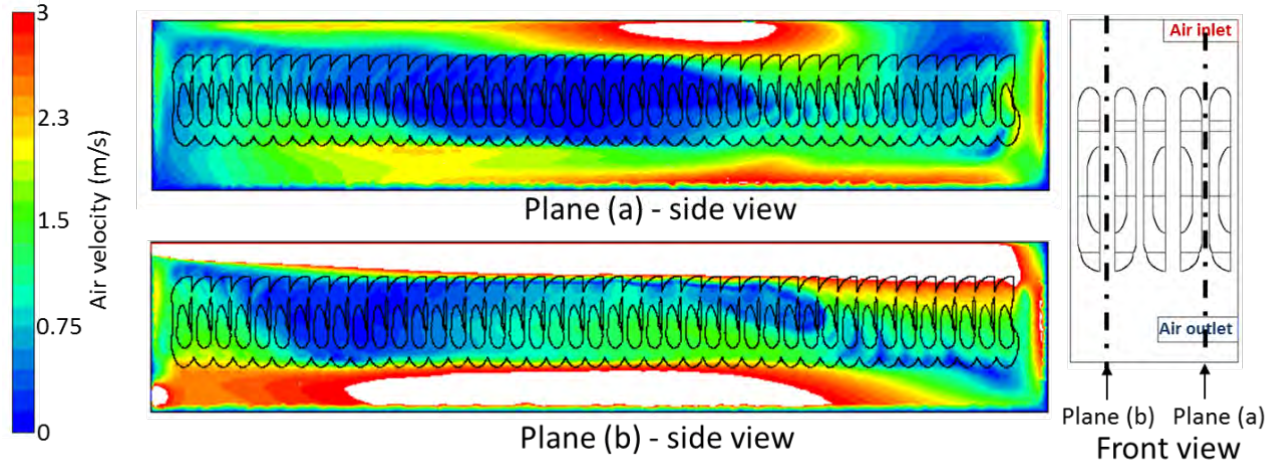

Figure 7 : Velocity magnitude between half carcasses

In plane (a) notably, a nearly stagnant zone at mid length of the trailer was predicted because the simulated jet wall continued flowing along the top wall until the rear of the trailer. In fact, according to the experimental velocity evolution on the jet axis, is seems that less air reaches the trailer rear and more air flows downward through the carcasses.

Fig. 8 present the vertical velocity component at mid height of the trailer. One could imagine that the carcasses form a porous medium of relative high pressure drop and that since the air is blown on the top, a relative homogenous downward airflow would occur throughout the carcass zone. But in fact, near the trailer rear the flow is indeed downward but near the front, the entrainment effect of the wall jet induces a suction effect and air flows upward throughout the carcasses in the front zone. In the intermediate region, there is sometimes neither downward and neither upward flow leading to low velocity zones.

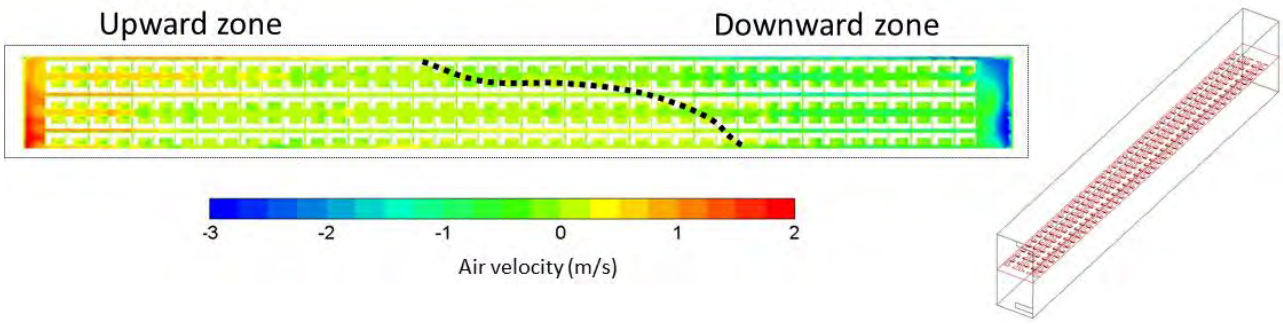

Figure 8: Vertical velocity (positive upward) at mid height of the trailer

In the zones of low velocity, the refrigeration will be of low intensity. Thus, if the carcasses are loaded while there are still warm at core (e.g. 15°C at core and 7°C at surface), they could take a long time to reach everywhere the recommended temperature (<7°C). Even the surface temperature could slightly increase. This can be problematic for sanitary risk (pathogenic microorganism growth). In fact, the smallest velocities are observed in the loan region of the carcasses (at mid height of the carcasses). Since the loan thickness is small (compared to the jam for example) the loan is generally rapidly cooled down in the cold room of the slaughterhouse. So, microbial risk should be limited for the loan part. In opposite, the jam core is often the warmest part at the exit of the slaughterhouse but the velocity is rather high all along the trailer at the top of the carcasses (jam part). The shoulder regions are also quite well ventilated.

5. CONCLUSIONS

Numerical simulations were performed to determine the air flow distribution in a refrigerated trailer loaded with pork half carcasses using the standard k-ε model. In the studied configuration, some low velocity zones were located in the loan region of the carcasses but this should not be problematic for sanitary risk.

These numerical results are specific of the trailer geometry (inlet and outlet section and location, number of rails) and of the load (here 215 pork carcasses about 75 kg each). The numerical approach could be used to see the influence of the trailer configuration, including the effect of air ducts, and of load (lower or higher number of carcasses) on the airflow distribution.

Nevertheless, the numerical model should be improved, because it overestimates the flow rate which reaches the rear of the trailer. In further work, a more realistic geometry and more sophisticated turbulence model (e.g. RSM or k-ω SST) will be tested and the simulation will also integrate unsteady heat transfer.

ACKNOWLEDGEMENTS

This research work was carried out within the framework of a DIM ASTREA grant by the Regional Council of Ile-de-France (France).

REFERENCES

Defraeye T., Verboven.P. Nicolai B. (2013) CFD Modeling of flow and scalar exchange of spherical food products; turbulence and boundary layer modelling. Journal of food engineering 114, 495-504.

Kuffi K.D., Defraeye T., Nicolai B., De Smet S., Geeraerd A., Verboven P. (2016) CFD modelling of industrial cooling of large beed carcasses. International Journal of Refrigeration 69, 324-339.

Merai M., Flick D., Guiller L., Duret S., Laguerre O. (2018) Experimental characterization of airflow inside a refrigerated trailer loaded with carcasses. International Journal of Refrigeration, 88, 334-346.

Moureh J. Flick D. (2005) Airflow characteristics within slot ventilated enclosures. International journal of heat and fluid flow, 26, 12-24.

Moureh J., Tapsoba M.S., Derens E., Flick D (2009). Air velocity characteristics within vented pallets loaded in a refrigerated vehicle with and without air ducts. International Journal of Refrigeration 32, 220-234

Pham Q.T., Trujillo F.J,. McPhail N. (2009) Finite element model for beef chilling using CFD-generated heat transfer coefficients. International Journal of Refrigeration 32, 102-113.

Tapsoba M.S., Moureh J., Flick D (2007). Airflow patterns in a slot-ventilated enclosure partially loaded with empty slotted boxes. International Journal of Heat and Fluid Flow 28, 963-977.

Manuscript ID: 215
DOI: 10.18462/iir.icr.2019.0215

Study of freezing process and short-term storage of meat using electroconvection

Boris S. BABAKIN[(a)], Mikhail I. VORONIN[(a)], Georgy A. BELOZEROV[(b)], Sergey B. BABAKIN[(c)]

[(a)] Moscow State University of Food Factories, FGBOU VO "MGUPP"
Moscow, 125080, Russian Federation, holod@mgupp.ru
[(b)] VNIKHI - Branch of V.M. Gorbatov Research Center of Food Systems, RAS

Moscow, 127422, Russian Federation. mail@vnihi.ru

[(c)]Federal Scientific Center of Food Systems
Moscow, 109316, Russian Federation, pr@vniimp.ru

ABSTRACT

The process of freezing and short-term storage (3 months) of meat with different autolysis development is examined; meat is processed in big food complexes using a low-power consuming method, in particular electroconvection. Comparative results of study of the processes of freezing and short-term storage of meat samples using the conventional method and a combined method of refrigeration with air electroconvection applied are cited. A significant shortening of duration of freezing process of meat at different autolysis using electroconvection as well as the increase of the external heat transfer coefficient were defined. Meat shrinkage reduced at freezing and short-term storage. Qualitative characteristics of meat were of high level.
Keywords: Freezing, Autolysis, Electroconvection, DFD, PSE, NOR Meat, Short-Term Storage.

1. INTRODUCTION

In Russia the refrigeration enterprises are forced to operate under conditions of irregular deliveries of foods by small parcels for short period of storage (up to 3 months). At the same time, frequent shipping and delivery of foods cause shrinkage of meat products. A short-term storage at higher temperature (-12°C) in comparison with conventional temperature regime (-18°C and lower) gives the possibility to reduce power consumption, to increase an enterprise's efficiency as well as the turnover rate of freezing chambers (Babakin et al., 1999). About 60% of energy consumed by meat industry is spent for cold production. The increase of temperature of meat refrigeration treatment from -18°C to -12°C allows saving energy up to 24%. World energy consumption by refrigeration systems is constantly growing. In particular, if recently it was 15%, now it has risen to 18%. Pale Soft Exudative (PSE) and Dark Firm Dry (DFD) meats are two of the major quality defects facing the meat industry. According to data of the Federal State-Financed Scientific Institution "Federal Scientific Center of Food Systems" (Russia) from 20 to 80% of meat raw materials delivered to industrial plants have DFD and PSE defects (Tsvetkov et al., 2003). Meat at low autolysis process (PSE, pH < 5.6) has pale, mucilaginous structure with dense consistence. The causes of PSE are stress factors before slaughtering. An animal's muscle glycogen reserves are not yet depleted; also the conditions of handling and feeding of animals influence much the meat quality. Meat at high pH (6.3 ÷ 6.6) – DFD meat has dark, firm, mucilaginous structure with dense consistence. Its water binding capacity is higher. NOR meat is meat at normal process of autolysis (pH = 5.7 ÷ 6.2).

The authors have developed a low energy consumption method to process animal raw materials by electroconvection, which allowed shortening the duration of refrigerating treatment and reducing packed products shrinkage. Electroconvection occurs at corona discharge due to the action of the electric wind. The movement of the electric wind represents a deeply turbulent air flow because of ions formed. The freezing and storage process intensification is provoked by high ions mobility in air that destructs the thermal resistance on the product surface (Rogov et al., 1996; Babakin et al.,

1992). The authors were granted a number of patents of Russia (#2141208, #2623242 and others).

2. METHODS AND RESULTS OF INVESTIGATIONS

The beef samples taken from the longest spinal muscle sized 130x30x30 mm were studied. The final DFD meat pH was 6.4, PSE meat pH was 5.3, NOR meat pH – 5.7. The temperature in the cold chamber was -12°C. The refrigeration aggregate operated on HFC ozone friendly refrigerant at ODP=0 (Babakin et al., 2017). The heat flow density was measured by the electronic density gauge of ITP-MG4 "POTOK" type with sensors at 10% admissible error limit. At the same tyme the gauge fixed the temperatures of air and on the sample surface. The temperature of the sample center was measured using thermocouples XK and potentiometer PP-63.

The heat transfer coefficient was defined by Newton-Richman equation (Lykov, 1967). The standard methods were applied to define pH, water binding capacity, peroxide number, myofibrillar protein content and microstructure changes (Zhuravskaya, 1985).

To define meat samples pH Testo-206 was used; the water binding capacity – the Grau method. The protein content was determined by Kjeldahl method (GOST 25011—2017). The peroxide number was defined according to GOST 34118-2017.

To define the loss of product mass the samples were weighted using the VLTK-500 electronic balance.

The working parameters of test samples refrigerated by applying electroconvection were compared with the control samples cooled by air. The rate of air flow was the same in both cases. In the first case the flow rate was provided by the electric wind, in the second – by the ventilator. The constant electric field strength was E = (7.5÷9.0)·10^5 V/m.

Figs. 1a and 1b show that the shortening of duration of freezing process of DFD meat test samples on the surface and in the center was 28-35%, of NOR meat – 24-36%, of PSE meat – 29-41% on the average as compared with control samples.

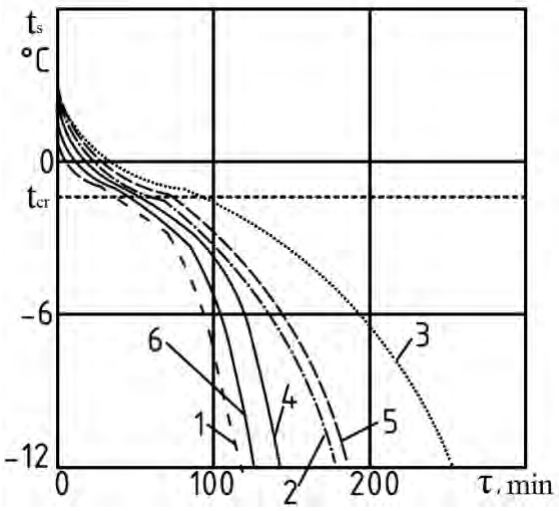

Figure 1a:Temperature change on meat samples surface at freezing: 1, 4, 6, - test samples; 2, 3, 5 – control samples; 1, 2 – DFD meat; 3, 4 – PSE meat; 5, 6 – NOR meat

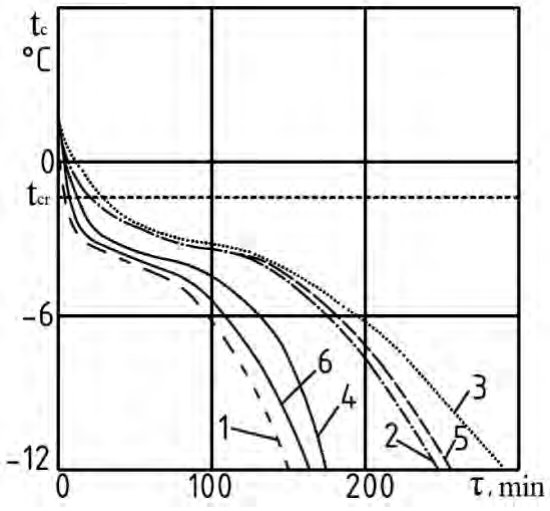

Figure 1b: Temperature change in meat samples center: 1, 4, 6, - test samples; 2, 3, 5 – control samples; 1, 2 - DFD meat; 3, 4 – PSE meat; 5, 6 – NOR meat

The analytical description of freezing process is given by Eq.(1)

$$t_i = A_i + B_i\tau + C_i\tau^2 + D_i\tau^2 \qquad \text{Eq. (1)}$$

where A_i, B_i, C_i, D_i are constant coefficients for each experimental curve correspondingly, τ is duration of freezing process in minutes.

The change of the heat flow density when samples are frozen is characterized by three sectors as shown in Fig. 2.

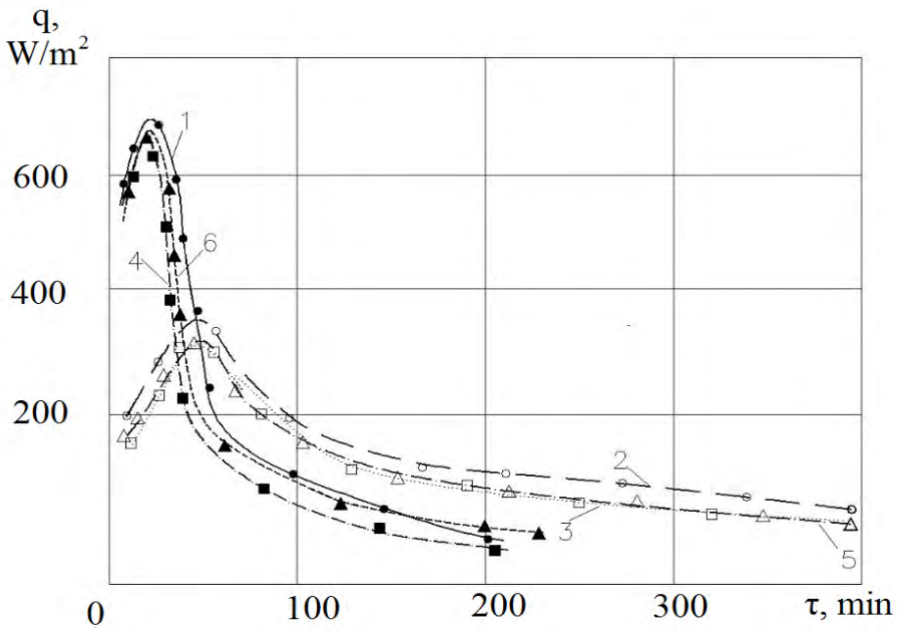

Figure 2: Change of density of heat flux from freezable meat samples: 1, 4, 6 – test samples; 2, 3, 5 – control samples; 1, 2— DFD meat; 3, 4 – PSE meat; 5, 6 — NOR meat

During 20-40 minutes of the initial period the heat flow density of test samples increased from 520 W/m^2 to 690÷700 W/m^2; the heat flow density of control samples increased from 180 W/m^2 to 350÷380 W/m^2. The product thermal capacity at this time was maximal, but during freezing it decreased (Ginzburg et al., 1980). The second sector is characterized by an abrupt decrease of heat flow caused by formation of a frozen crust on the test meat sample surface.

The third sector is specified by a slow decrease of heat flow density, whereupon the lower “q” value of the test samples is due to the fact that a drying crust was formed on the surface of the meat for a shorter period of time as compared with the control samples. So, the heat flow density decreased.

When determining the “α” external coefficient of heat transfer a significant increase of this coefficient of the test samples was noted in comparison with the control samples, as shown in Fig. 3. In particular, the “α” coefficient of DFD meat increases 2.2 times, of PSE meat 1.8 times, of NOR meat – 1.9 times.

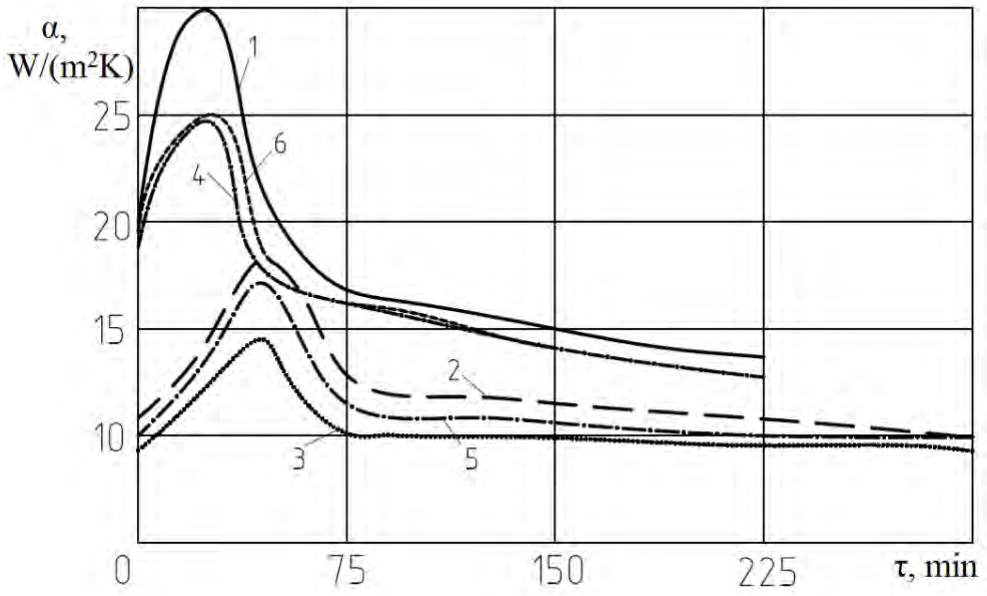

Figure 3: Dependence of the heat transfer coefficient on meat sample freezing duration: 1, 4, 6 – test samples; 2, 3, 5 – control samples. 1, 2 – DFD meat, 3,4 – PSE meat, 5, 6 – NOR meat

Fig. 4 shows mass shrinkage losses of meat samples during 3 months storage. It was evident that the shrinkage of test samples was less pronounced during all period of storage. In particular, the shrinkage of DFD meat test samples was less by 0.3÷0.35%; the shrinkage of PSE meat samples by 0.1÷0.17%, and NOR meat samples by 0.19÷0.21 % as compared with control samples. It was due to the earlier formation of the crust drying up on the surface as well as to the decrease of moving forces of shrinkage, i.e. to the partial pressure difference between the product surface and its structure (Tsvetkov et al., 2003; Babakin et al., 1999).

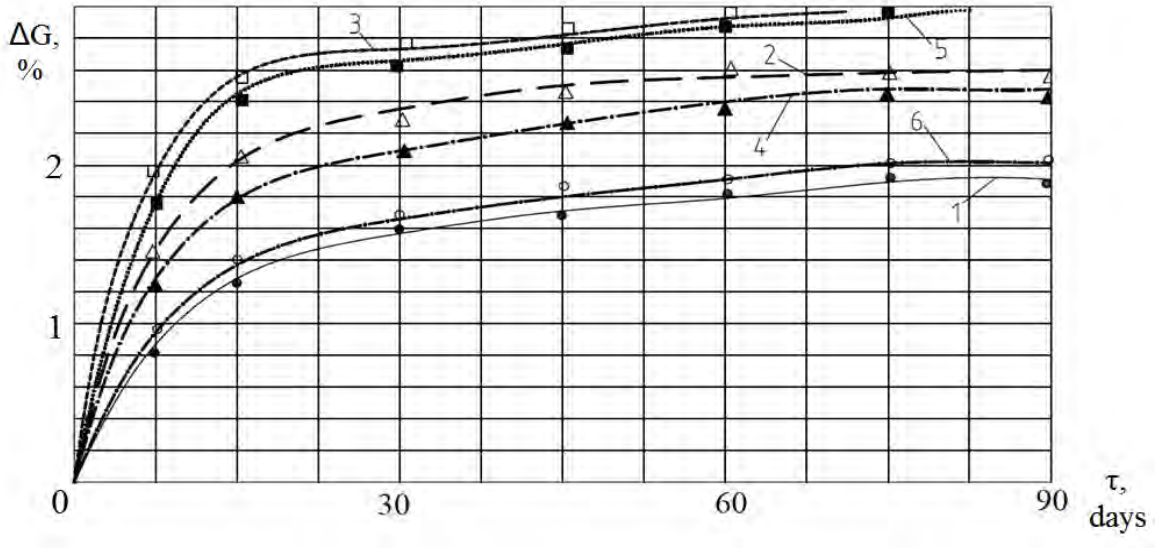

Figure 4: Mass shrinkage losses of meat raw material during short-term storage: 1, 4, 5 – test samples; 2, 3, 6 – control samples; 1, 6 – DFD meat, 2, 4 – NOR meat, 3, 5 – PSE meat

The indices of meat water binding capacity during storage, after freezing under electroconvection conditions of test samples were better than that of control ones. In particular, they were 2-3% higher during all period of short-term storage of DFD meat samples. As regards PSE meat samples the indices were 0.5-1%, NOR meat samples – 1.5-1.7%. The change of dissolubility of myofibrillar proteins in solutions of high ionic strength during short-term storage was investigated. The

investigations showed that the dissolubility indices of DFD test samples were 1-1.3% higher, of PSE test samples 0.8-0.95% higher, and of NOR meat samples 0.9-1.0% higher. It was due to the higher rate of freezing. The oxidation development was less expressed in meat samples frozen under electroconvection conditions. The application of electroconvective air medium at product freezing practically didn't influence the oxidation level during short-term storage. When studying the meat microstructure it was revealed that at freezing of control samples a local damage of muscle fibers occurred; deformation and rupture of myofibrils, local rupture of sarcolemmas, decondensation of corrugate structures of the connective tissue took place. As regards the test samples, at ice formation lesser damages of sarcolemmas were observed; and a fine-grained protein mass passed into the interfibrillar space. After three months storage larger crystals were formed between muscle fibers in endomysium and perimysium interlayers of control samples. The crystals were of different forms and sizes and contributed to deformation and rupture of muscle fibers; it was due to the phenomenon of recrystallization during storage. The test samples had a regular disposition of muscle fibers; they had identical forms and sizes. A significant deformation and ruptures were not observed.

3. CONCLUSIONS

The results of investigations showed that the use of electroconvective air flow (electrocovection) at freezing and short-term storage (3 months) allowed shortening freezing process duration of DFD meat by 28-37%, NOR meat by 23-29%, PSE meat by 27-44% on the average as compared with conventional methods of freezing. Also the external coefficient of heat transfer increased almost 1.8-2.2 times, the shrinkage decreased by 0.1-0.35%. Quality characteristics of meat at different autolysis (DFD, PSE, NOR) were of high level. After 3 months storage a significant deformation and the rupture of muscle fibers were not observed.

NOMENCLATURE

τ	duration of freezing process (storage) (min.,days)	t_s	temperature of product surface (^{0}C)
q	Heat flow density (W/m^2)	t_a	air ambient temperatures (^{0}C)
α	Heat transfer coefficient (W(m^{2}K)	ΔG	sample mass loss(%)

REFERENCES

Babakin, B.S., Bovkun, M.P., Amerkhanov, R.M. 1992. Meat freezing under conditions of electroconvective heat exchange. Publishers Kholodilnaya Tekhnika, 5, 16-18

Babakin, B.S., Babakin, S.B., 2017. Refrigerants and refrigerator oils. DeLi plus publishers, Moscow, 390 p.

Babakin, B.S., Vygodin, V.A., Tsvetkov, M.M., 1999. Modification of meat microbial semination at non-traditional autolysis development. Collected papers "Problems of improvement of refrigerating engineering and technology", Moscow, Russia, 94-95

Babakin, B.S., Vygodin, V.A., Tsvetkov, M.M., 1999. Choice of conditions of meat refrigeration treatment. Collected papers "Problems of improvement of refrigerating engineering and technology", Moscow, Russia, 94-95

Ginzburg, A.S., Gromov, M.A., Krasovskaya G.I., 1980. Thermal characteristics of foods. Reference book. Publishers "Pischevaya promyshlennost", Moscow, 288 p.

GOST 25011-2017 Interstate Standard. Meat and meat products. Methods of protein testing

GOST 34118-2017 Meat and meat products

Lykov, A.V. 1967. Heat conductivity theory. Higher school. Moscow, 599 p.

Rogov, I.A., Babakin, B.S., Vygodin, V.A., 1996. Electrophysical methods in refrigeration engineering and technology. Kolos publishers, Moscow, 336 p.

Tsvetkov, M.M., Mizeretskiy, N.N., Babakin, B.S., 2003. Study of heat transfer of refrigeration processing of meat at different autolysis using electroconvective movement of air medium. In: Collected papers – Problems of improving refrigeration engineering and technology, Moscow, Russia, 71-74.

Zhuravskaya, N.K., Alekhina, L.T., Otryashenkova, L.M., 1985. Study and control of meat products quality. Publishers Agropromizdat, Moscow, 296 p.

Manuscript ID: 216
DOI: 10.18462/iir.icr.2019.0216

Control of the process of structure formation of "premium" class ice cream using monostabilizers

Antonina A. TVOROGOVA, Natalia V. KAZAKOVA, Tatyana V. SHOBANOVA, Georgy A. BELOZEROV

VNIKHI - Branch of V.M. Gorbatov Research Center of Food Systems, RAS
Moscow, 127422, Russian Federation, mail@vnihi.ru

ABSTRACT

The objective of the present study is substantiation of the technology of "premium" ice cream without food additives of structure stabilizers. A technologically functional fat content of ice cream to be not less 15% and effective using monostabilizers (MS) that are products of the physically modified tapioca starch and cellulose were experimentally proved. It was established that MS provided an optimal 400-600 mPa·s mixture viscosity at 0.83 1/s shear rate, initiated nucleation, and contributed to ice crystals dispersion maintaining at temperature fluctuations. The fat phase participation in the formation of the product structure was proved. Micro-structural and structural-mechanical research methods allowed basing the modes of control of the ice cream structure formation process. Concerning structural elements stability ice cream with MS is lightly inferior to ice cream with effective stabilizers-emulsifiers (ESE), but it keeps high dispersion of structural elements not less 6 months.
Keywords: Premium Class Ice Cream, Physically Modified Monostabilizers, Nucleation Intensification, Structural Elements Dispersion.

1. INTRODUCTION

Premium ice cream is a full-value food, it contains 40 –60 % of milk dry substances. To produce one ton of premium ice cream 2.2-2.5 tons of milk are needed. In Russia this kind of ice cream is considered as a national food, its production is more than 50% of the total production. The particularity of traditional Russian premium ice cream is a balanced chemical composition as well as the presence of the bulk milk fat in the state of emulsion (in mixture) and high dispersed suspension (in ice cream). Since 1990s the emulsifiers have been applied in full-cream ice on a large scale, they provoked demulsification and agglomeration of the fat phase that led to formation of new consumer characteristics (Goff and Hartel, 2016). But now the demand in traditional full-cream ice without emulsifiers and other food additives has increased. 3-5 food additives in composition of stabilizers-emulsifiers are needed to produce ice cream; they contribute to formation and keeping the product structure (Tvorogova, 2003; Tvorogova, 2014; Williams et al., 2002). At production of traditional full-cream ice the use of chemically modified starches and gelatin will lead to shortening of the expiration date 2-4 times due to decrease of structural elements dispersion at storage. Hence, the physically modified MS were selected because of their high water-bound properties as well as their ability to pass into a suspension state when contacting with water leading to nucleation intensification.

2. METHODS AND AIMS OF RESEARCHES

The study deals with grounding the technology of "premium" class ice cream without food additives as structure stabilizers. In order to determine the mixture viscosity the method of rotational viscometry using the viscometer BrookFieldDV2+Pro (USA) with Rheocalc software V3. 1-1 was applied. The precision of results obtained was not less+/- 1 % of the range used and reproducibility not less 0.2 %. The microstructural method was applied using the microscope CX41RF (Japan) with program control to study the state of air phase and ice crystals. The sizes of air bubbles and ice crystals were defined, their average sizes were calculated. To improve the precision and

validity of measurements up to 10 photographs were taken and treated for each sample. The results were processed using the ImageScope program. The resistance of ice cream samples to thawing was defined. The ice cream capability to resist to thawing when maintaining ice cream at 20°C was studied. The thermostat and electronic balance were used; the sample temperature was minus 18°C in the beginning of study.

2.1. Substantiation of efficiency of monostabilizers use in full-cream ice production

The study is based on the hypothesis of possible formation and keeping high dispersion of ice crystals in ice cream at fat content not less that 15% when using physically modified stabilizers (PMS) that intensify nucleation and retain water well in the product structure even at temperature fluctuations.

2.2. Substantiation of selection of ice cream and stabilizers as subjects of inquiry

First, basing on analytical researches and experience the subjects of inquiry were selected. Ice cream at 15% fat content fabricated using MS was chosen. Thanks to a high fat content at optimal homogenization pressure it is possible to obtain a high dispersion of fat particles that may intensify nucleation in suspension state after thermomechanical treatment in a freezer. In addition, at 7%-10% dry skimmed-milk residue (DSMR) of full-cream ice the ratio of DSMR/fat will be 0.46-0.67 that is less than an optimal ratio (0.7). Hence, when processing in a freezer a partial destabilization and agglomeration of the fat phase is possible (Goff and Hartel, 2016). The emulsifiers are just purposely used in stabilization systems to reach these effects. Moreover, the structurization of the fat phase of full-cream ice is possible due to a high fat content in the product. The fat content remaining in the full-cream ice structure was defined experimentally by means of the fat content of ice cream melt using 20 samples. As it follows from the data cited in Table 1 most of the fat (not less 50%) was involved in the product structure formation when producing ice cream at 15% fat content.

Table 1. Fat content in test samples (with food fibers)

Fat content of ice cream, %	Fat content of melt, %	Fat content retained in ice cream structure, %
12	9	25
15	7	53
18	5	72
20	3	85

The selection of PMS is linked with their high water retaining and water absorbing capabilities as well as their ability to form the suspension and granulated substances intensifying nucleation in water solutions. It was defined that at 1.0-1.5 % content of the physically modified starch (PMSt) and at 0.2-0.35 % content of food fibers (FF) in the mixtures for full-cream ice an optimal level of dynamic viscosity 400-600 mPa·s at 0.83 1/s shear rate was reached (Tvorogova, 2003). In particular, when using FF the value of viscosity was close to the value of viscosity of the mixtures with ESE (as illustrated by Table 2).

Table 2. Effective viscosity of ice cream mixtures

Ice cream mixture with FF			Ice cream mixture with ESE		
Fat content, %	Fat content FF, %	Mixture viscosity, mPa·s	Fat content, %	Content of stabilizer-emulsifier	Mixture viscosity, mPa·s
12	0.45-0.6	207	10	0.5-0.55	200-300
			12	0.45	350-450
15	0.3-0.35	435	15	0.35-0.4	450-520
18	0.2-0.25	525	18	0.3	550-650
20	0.15-0.2	630	20	0.2-0.25	650-800

2.3. Study of PMSt and FF influence on ice crystals and air bubbles dispersion

The influence of MS on dispersion of ice crystals and air phase was investigated. The studies showed that the dispersion of ice crystals increased slightly as far as the fat content (12%, 15 %, 18 % and 20 %) of full-cream ice with FF increased, as illustrated by Fig. 1. In particular, the proportion of ice crystals of 20 μm size after hardening was 4% in sample 1 and 8% in sample 4.

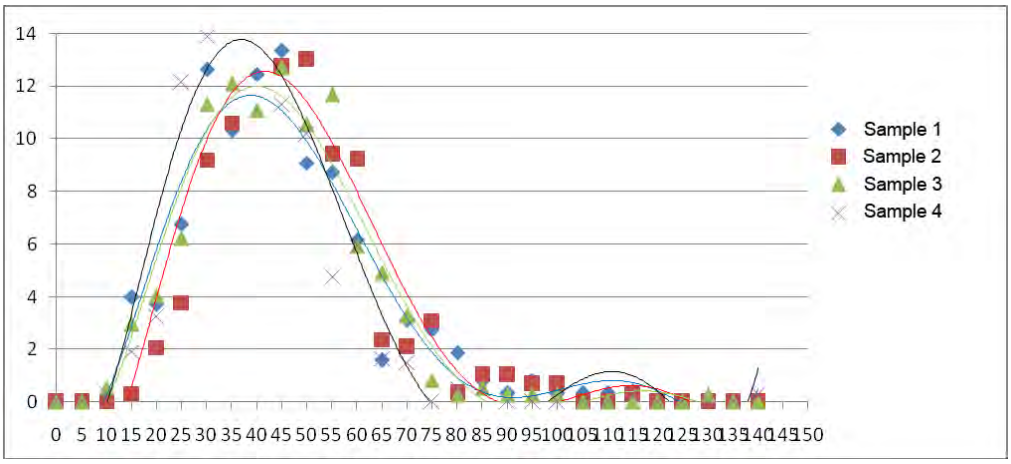

Figure 1: Ice crystals size distribution in full-cream ice at fat content 12% (sample 1), 15% (sample 2), 18% (sample 3) and 20% (sample 4) after 1 month storage at -18°C

When estimating the influence of PMSt on dispersion of ice crystals, their high dispersion was noted during storage; and it differed only slightly from dispersion at using ESE, as shown in Fig. 2.

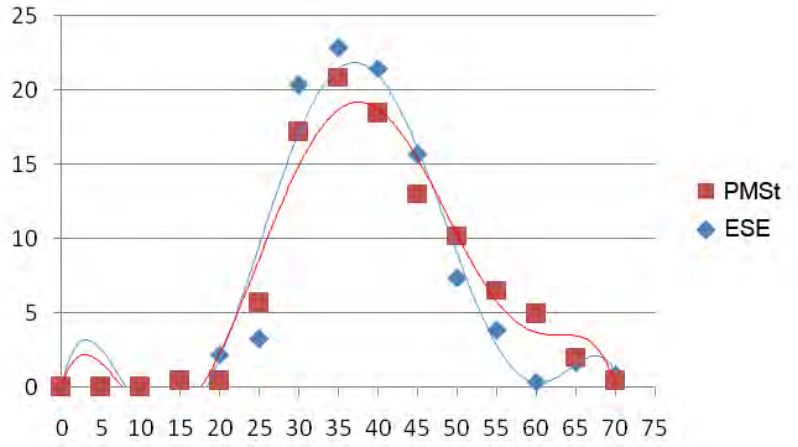

Figure 2: Ice crystals size distribution in full-cream ice after 6 months storage.

As expected, the index “air phase dispersion” of ice cream with MS was found less competitive in comparison with ice cream with ESE as illustrated by Fig. 3. It is to note a significant dispersion decrease when using PMSt in ice cream.

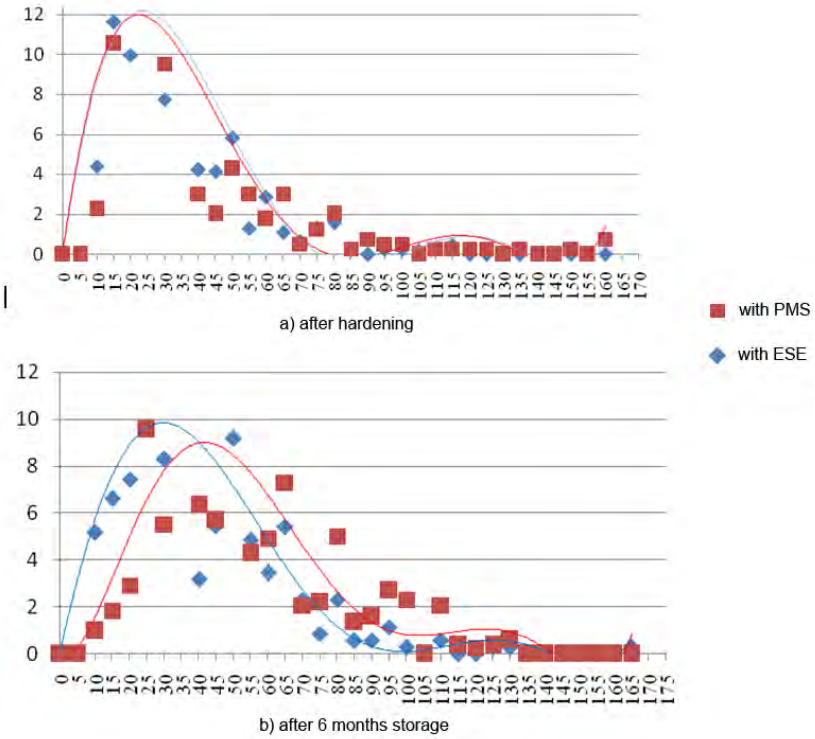

Figure 3: Air bubbles size distribution.

Fig. 4 demonstrates the microphotography showing a high content of tiny air bubbles in ice cream with an integrated stabilizer-emulsifier.

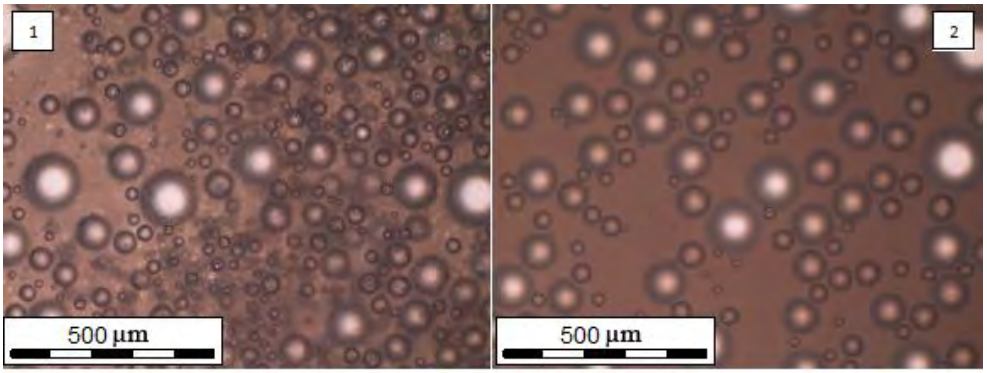

Figure 4: State of air phase after 6 months storage in ice cream at 15% fat content: 1 – ESE, 2 - PMSt

2.4. Study of ice crystals dispersion in full-cream ice with PMSt at temperature fluctuations

The data given in Fig. 5 show better keeping of ice crystals dispersion of full-cream ice with PMSt at temperature fluctuations in comparison with traditional ice cream. In particular, even after three temperature fluctuations the value of the peak of the distribution derived curve is 47-48 µm in full-cream ice with ESE and PMSt that is lower than the threshold of organoleptic perception (50 µm). But this index changes at temperature fluctuations are more expressed in traditional ice cream (Tvorogova et al., 2016; Shobanova and Tvorogova, 2018).

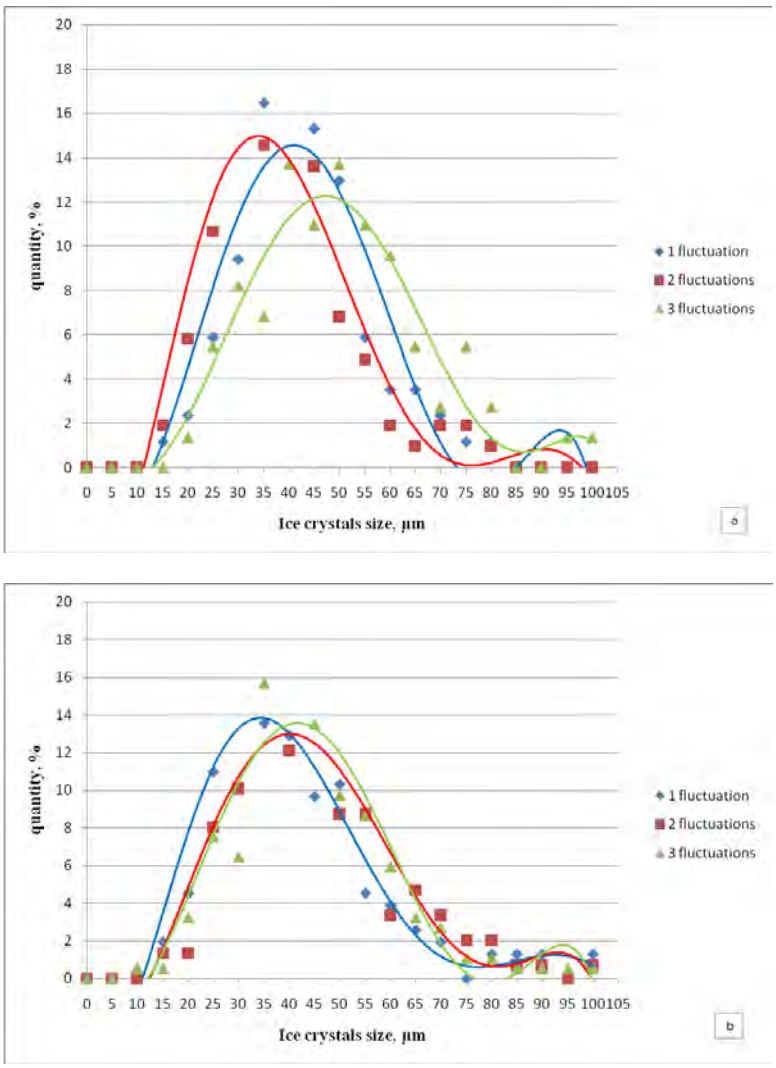

Figure 5: Ice crystals size distribution in full-cream ice: a) with ESE b) with PMSt

The capability of PMSt to retain water in a gel structure exerts a stabilizing action on ice crystals dispersion at temperature fluctuations. This capability was defined when studying the viscosity of water solutions after thawing. It was determined that the viscosity of water solutions after thawing increased 4-10 times depending on varieties of PMSt as shown in Fig. 6.

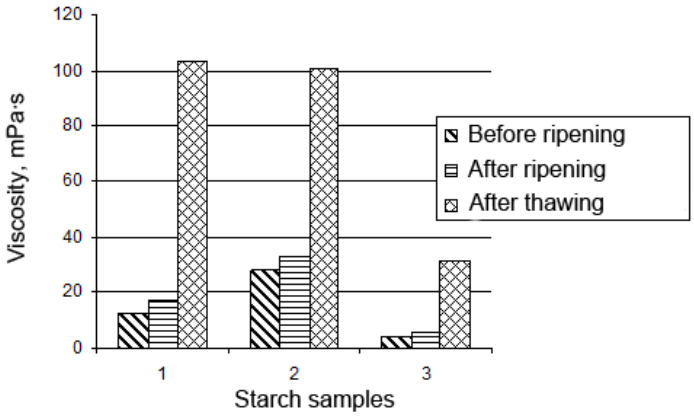

Figure 6: Effective viscosity of PMSt water solutions

2.5. Study of PMSt and FF influence on full-cream ice thermal stability

An ice cream thermal stability is indicative of a stable state of this product. As expected, the absence of an emulsifier when using PMSt and FF affects adversely the thermal stability of ice cream as Fig.7 shows. Specifically, a melt content of ice cream with PMSt was 20%, with FF was 8%, but the melt was not observed in the sample with ESE. Consideration must be given to the choice of the type of package. The package with a rigid surface is preferable.

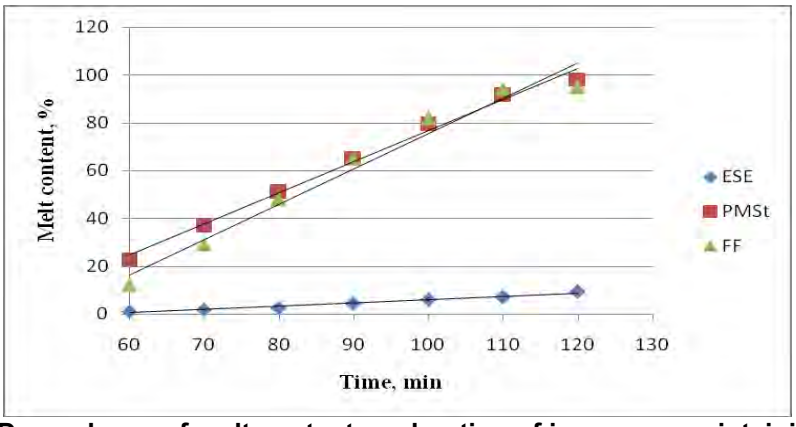

Figure 7: Dependence of melt content on duration of ice cream maintaining at 20°C

3. CONCLUSIONS

1. The requirements for the fat content of “premium” class ice cream produced with monostabilizers (not less 15%) and for monostabilizers used (ability to intensify nucleation and to retain water in the product structure including possible temperature fluctuations) were defined and proved experimentally. The use of “SenseFi” food fibers in the product in the form of suspension and “Novation” physically modified starches as effective monostabilizers was grounded.

2. It was proved that monostabilizers affected much less a stable state of structural elements as compared with effective stabilizers-emulsifiers. Therefore, the expiration date of ice cream produced with physically modified monostabilizers should be fixed 6 months not more at temperature not higher minus 18°C.

3. New factors of impact on structural elements stability in premium class ice cream were revealed. These are: capability of monostabilizers to keep an initial viscosity of solutions after thawing and to intensify nucleation in suspension state and the quantity of structure-forming fat remaining in the product structure after thawing.

NOMENCLATURE

PMSt	physically modified starch	*FF*	food fibers
MS	monostabilizers	*ESE*	effective stabilizer/emulsifier

REFERENCES

Goff, H.D., Hartel, R.W. (2016) Ice Cream. Transl. from English to Russian, SPb: Profession, 540 p. ISBN978-5-904757-90-8

Tvorogova, A.A., 2003. Scientific and practical recommendations on ice cream structure stabilization. Rosselkhozakademia publishers, Moscow, 46 p.

Tvorogova, A.A., Konovalova, T.V., Spiridonova, A.V., Gurskiy, I.A., 2016. State of ice crystals in traditional ice cream at storage. Molochnaya promyshlennost, 8, 57-58.

Tvorogova, A.A., 2014. On using ingredients in production of ice cream, whipped frozen desserts and food ice. Food ingredients in creation of modern foods. DeLi plus Publishers, Moscow, 412-432.

Shobanova, T.V., Tvorogova, A.A., 2018. Impact of the fat phase on technologically important indices of full-cream ice without emulsifiers. Pischevye sistemy, 1(2), 4-11.

Williams, P. A., Phillips, G.O., Norton, I.T, Foster T. J. (2002). Hydrocolloids in Real Food Systems. Proceedings of the Eleventh Gums and Stabilizers for the Food Industry Conference, Eds. - Royal Society of Chemistry Special Publication, (278), 187-200. ISBN0854048367.

Manuscript ID: 250
DOI: 10.18462/iir.icr.2019.0250

Development of multi-criteria analysis approach considering food quality and energy consumption: Application to production process of puff pastry

Steven DURET[(a)], Hong-Minh HOANG[(a)], Evelyne DERENS-BERTHEAU[(a)], Erwann HAMON[(b)], Valérie STAHL[(b)], Laurent GUILLIER[(c)], Jean-Christophe AUGUSTIN[(c,d)], Anthony DELAHAYE[(a)], Onrawee LAGUERRE[(a)]

[(a)] Irstea, UR GPAN, Refrigeration Process Research Unit, 1 rue Pierre-Gilles de Gennes, 92761 Antony, France, steven.duret@irstea.fr
[(b)] Aerial, Parc d'Innovation, rue Laurent Fries, F-67412 Illkirch, France
[(c)] Anses, French Agency for Food, Environmental and Occupational Health & Safety, Laboratory for Food Safety, Université Paris-Est, Maisons-Alfort F-94701, France
[(d)] Ecole Nationale Vétérinaire d'Alfort, Maisons-Alfort F-94704, France.

ABSTRACT

The preservation of perishable food *via* cold supply chain is essential to extend shelf life and ensure food safety. However, the use of refrigeration processes involves energy consumption with economic and environmental impact. Increasing the temperature set point in cold equipment could save energy, but the global cost may increase due to food waste or safety issues.

This study focuses on the modeling of the energy consumption of cold facilities, food temperature and bacterial growth in a puff pastry plant. Main components of production line (kneader, cooling spiral and cold room) were considered. Different scenarios were tested to evaluate the impact of operating conditions (setting temperature and duration) on energy consumption, food waste and food safety.

This methodology helps manufacturers in decision making to optimize operating conditions and reduce energy consumption with a limited impact on food waste and safety.

Key words: Multi-criteria analysis, energy consumption, temperature, food quality, refrigeration process

1. INTRODUCTION

Refrigeration is crucial to ensure optimal preservation of perishable food products, extend shelf life and provide consumers with safe food of high organoleptic quality. The use of refrigeration for food is in constant growth in developed and developing countries and this requires important energy consumption to cool down and to maintain food product at desired temperatures. In EU states, cooling and freezing represent about 30 % of electricity consumption in the food industry, a relatively high rate compared to other industrial sectors.

Public authorities and industrials are looking for solutions to reduce the impact of the refrigeration facilities such as implementing new regulation to limit the use of high GWP (Global Warming Power) fluids (Anonymous 2014), installation of doors on opened display cabinet in supermarkets (Anonymous 2015), developing more efficient new technologies.

Another solution to reduce the impact of refrigeration process consists in modifying the operating conditions, for example, by increasing the thermostat setting temperature of

refrigerated equipment (Duret et al. 2019). However, because of accelerated product quality alteration caused by higher temperatures, the global cost due to food waste or safety issues may increase (Zanoni and Zavanella 2012). While numerous experimental and numerical studies were conducted on food product temperature and energy consumption in cold chain facilities: refrigerated transport (Merai et al. 2018), storage cold room (Duret et al. 2014, Gruyters et al. 2018), display cabinet (Chaomuang et al. 2017, Ben-abdallah et al. 2018) and domestic refrigerator (Laguerre and Flick 2010), few studies were conducted on food plants (Lecoq et al. 2017, Parpas et al. 2017, Parpas et al. 2018). Moreover, these studies focused on surface drying or on air distribution in food facilities but do not address the relationship between food plant operating conditions, energy consumption, food temperature and food quality.

The objective of this study is to propose an original multidisciplinary approach linking prediction of food temperature, food quality and energy consumption of refrigeration processes in a food plant. The proposed methodology was applied to a puff pastry plant. The daily-recorded temperatures and energy consumption provided by an industrial manufacturer and the data measured on site by our team were used in model development and validation. The developed models were used to study the influence of operating conditions on the product temperature, quality and energy consumption of cold facilities. In such a way, the potential efficient measures to reduce energy consumption with a limited impact on food quality can be identified.

2. MATERIALS AND METHODS

2.1 Product, production line and plant description

The studied product is a puff pastry of 0.23 kg per unit. The thermal heat capacity is 2760 $J.kg^{-1}°C^{-1}$. The production line described in Fig. 1 includes kneading, folding and lamination, cutting, wrapping, cooling spiral, packing and storage in a cold room. A pending step between packing and storage in the cold room is also included. The product flows through the different steps by conveying line. Rooms' dimensions, volume, operating conditions are presented in Table 1. The air is distributed in the process room by blowing through textile ducts. Cold air is provided in the cooling spiral and in the cold room by direct expansion coils.

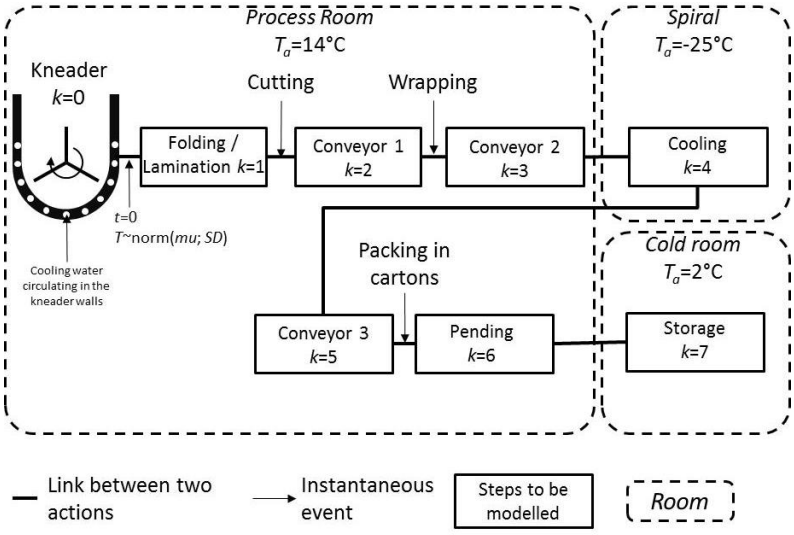

Figure 1: Overview of the food plant

Table 1. Dimensions (estimated from site plan) and current operating conditions (data provided by the manufacturer)

Room	Floor Surface Area (m²)	Wall Surface Area (m²) (including floor and ceiling)	Volume (m^3)	Setting temperature (°C)	Air distribution system
Process	2325	5600	10460	14°C	textile ducts
Spiral	NE*	NE*	NE*	-25°C	Direct expansion coils
Cold room	320	970	1450	2°C	Direct expansion coils

* (NE) Non Estimated

2.2. Model development

Products were modeled individually for each production step from the kneader (*k*=0) to the cold room (*k*=7). The product temperature was assumed uniform at each step. Because of a short duration at each step, water transfer was considered as negligible. A discrete event framework was used to describe the consecutive element of the processing line (i.e. kneader, conveyor, cooling spiral...). In such a manner, the inclusion of additional events or the modification of event sequences is possible, for example, refrigeration process breakdown or periods of standstill which are difficult to manage. A first-order Monte Carlo simulation was implemented to describe the variability of the operating conditions such as product initial temperature, product cooling rates in the storage cold room. The model was implemented in the Matlab software R2016b (MathWorks Inc., Natick, MA, USA) and is available on request to the corresponding author.

2.2.1. Product temperature

2.2.1.1. Product initial temperature.

According to the manufacturer, dough temperature during and after the kneading (*k*=0) is highly heterogeneous and depends on many parameters such as the external temperature T_{ext}, the process room temperature $T_{a,p}$ and the temperature of the cooling water flowing in the double envelope of kneader walls T_{water}. These operating condition temperatures were recorded every 10 minutes over 1 year (manufacturer data, 51408 measurements) while one temperature per batch over 1 year was recorded (manufacturer data, 20899 measurements). Because of the difficulty to develop heat transfer model to predict the product temperature due to the complexity of the kneader (mixing of several ingredients of different initial temperature, heat generation because of reactions between ingredients and mechanical energy during mixing with variable speeds), a statistical approach was used assuming a normal distribution of the dough temperature of one batch after the kneading (*k*=0). Considering that conduction and convection are the main heat transfer modes while radiation is negligible in the kneader, a linear correlation was considered between the batch average temperature after kneading $\overline{T}_0$ and the other known temperatures ($T_{ext}, T_{a,p}, T_{water}$). For these reason, the three known temperatures were considered as fixed effects while the batch was considered as a random effect to predict the initial dough temperature after the kneading (*k*=0).

$$T_0 \sim N\left(\overline{T}_0\left(T_{a,p}, T_{ext}, T_{water}\right), SD\right) \quad \text{Eq. (1)}$$

Where $\overline{T}_0$ is the batch average temperature (Eq. 2) and SD the standard deviation (*SD*=1.2).

$$\bar{T}_0 = 16.82 + 0.12 \times T_{ext} + 0.20 \times T_{a,p} + 0.10 \times T_{water} \quad \text{Eq. (2)}$$

2.2.1.2. Product temperature change along the production line.

For each step of the production line from k=1 to k=7, the product temperature $T_k(t)$ tends to reach the ambient temperature $T_{air,k}$. The product temperature evolution can be represented by Eq. 3.

$$T_k(t) = T_{air,k} + \left(T_{0,k} - T_{air,k}\right) \times e^{-t/\tau_k} \quad \text{Eq. (3)}$$

where $T_{0,k}$ the product initial temperature at the step k, t the time and τ_k the characteristic time of the product in the step k. The characteristic time τ_k is defined as:

$$\tau_k = m \times C / h_k \times A_k \quad \text{Eq. (4)}$$

With m product mass (kg), C product heat capacity (J.kg^{-1}.°C^{-1}), h_k convective heat transfer coefficient between product and air at step k (W.m^{-2}.°C^{-1}), A_k, exchange surface area between product and air at step k.

For certain steps where the experimental product temperature change was available (Fig. 2a), the characteristic times of the product τ_k was determined from the slope of the dimensionless temperature (T*, $T^* = \frac{T_{p,k}(t) - T_{0,k}}{T_{air,k} - T_{0,k}}$) as a function of time (Fig. 2b).

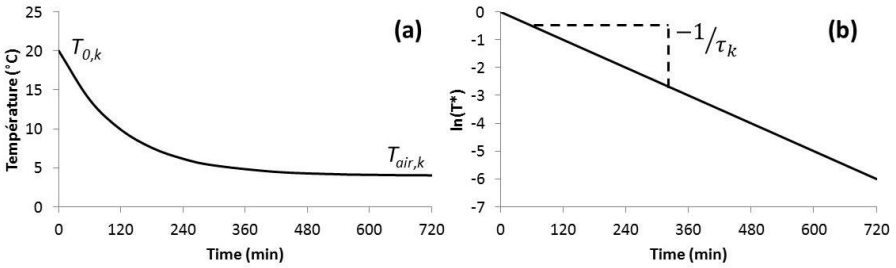

Figure 2: Illustration of the method to calculate the characteristic time. (a) Temporal evolution of product temperature. (b) The characteristic time τ_k can be calculated from the slope of the curve (Hoang et al., 2012)

Calculated τ_k values of the products at the different steps are presented in Table 2.

Table 2. Calculated τ_k values of the products at the different steps

Step	τ (min)	Determination method
Lamination and folding	+∞	No temperature variation
Conveyor 1	15 min	Calculation (Eq. 4)
Conveyor 2	54 min	Experimental temperature (Fig. 2)
Cooling spiral	55 min	Experimental temperature (Fig. 2)
Conveyor 3	54 min	Experimental temperature (Fig. 2)
Pending	[202; 299] min	Experimental temperature (Fig. 2)
Cold room	[275; 805] min	Experimental temperature (Fig. 2)

2.2.2. Energy consumption

The energy consumption model was developed to evaluate the energy required for the refrigeration of the food plant in function of the operating conditions (i.e. setting temperature, external temperature, production throughput…). The total heat generation P_T (W) is composed of heat generation from the walls (P_w), product (P_p), air renewal (P_{air}), lights (P_f), machines (P_m), fans (P_f) and doors (P_d) (Evans et al. (2014) :

$$P_T = P_w + P_p + P_{air} + P_l + P_m + P_f + P_d \quad \text{Eq. (5)}$$

The electrical consumption Q_T (J) of the equipment was calculated using Eq. 5:

$$Q_T = \frac{P_T \times dt}{\eta \times COP} \quad \text{Eq. (6)}$$

With η the global performance coefficient of the cooling unit (η is considered to be 0.5) and COP the coefficient of performance of Carnot. The COP corresponds to the ratio of the provided cooling to the work required (not including thermodynamic irreversibility in the refrigerating machine) and can be calculated as below:

$$COP = \frac{T_{cold}}{T_{hot} - T_{cold}} \quad \text{Eq. (7)}$$

with T_{cold} and T_{hot} the temperatures of the cold and hot sources, respectively. These temperatures can be estimated from the thermostat temperature (T_{th}), and the ambient temperature (T_a) considering a temperature pinch of 10°C (temperature difference between the air and the refrigerant in the evaporator), i.e. T_{cold} = T_{th}-10 and T_{hot}=T_{ext}+10. For the majority of the cold production system, the air temperature at the evaporator outlet is close to the thermostat temperature T_{th}.

2.2.3. *Microbiological quality change along the production line*

A generic microbial growth without lag time is proposed to evaluate the log increase of the bacterial population in function of the product temperature is proposed as below.

$$\frac{dQ}{dt} = \mu_{Ref} \times \left(\frac{T - T_{min}}{T_{ref} - T_{min}} \right) \quad \text{Eq. (8)}$$

with μ_{ref} the reference growth rate (=0.3 h^{-1}), T_{ref} and T_{min} the reference and minimal growth temperatures, respectively set at 25°C and 0°C. Validated growth models for *Listeria monocytogenes* and lactic acid bacteria will be integrated in further study.

2.3. Description of studied scenarios

Six scenarios are proposed to evaluate the impact of the operating conditions on the energy consumption and products quality (Table 3). Results were expressed relatively to the reference scenario (#1). Results of each scenario were normalized to the scenario 1 (Reference of this study), to provide a relative measure (Table 4).

Table 3. Studied scenarios

Scenario number	T° ext	T° process room	T° air in spiral	T° air in cold room	Description
Ref (#1)	20°C	14°C	-25°C	2°C	Reference condition
#2	20°C	14°C	-25°C	4°C	Increased air temperature in cold room
#3	20°C	16°C	-25°C	4°C	Increased air temperature in cold room and in process room
#4	20°C	14°C	14°C	2°C	Cooling spiral outage
#5	40°C	14°C	-25°C	2°C	Hot day without technical issue
#6	40°C	20°C	-20°C	4°C	Hot day with limited power of refrigeration processes

3. RESULTS AND DISCUSSION

3.1. Product temperature change along the production line.

The reference scenario (**#1,** Table 3) was used for the simulation and the results are reported in Fig. 3 for six random initial product temperatures (after kneading). These temperatures were obtained by Eq. 1 considering normal distribution of the known temperatures ($T_{ext}, T_{a,p}, T_{water}$). As expected the cooling spiral (k=4) can easily be identified on the temperature profiles. The temperature tends to increase after the spiral (k=5) and in the pending zone, with a slow decrease in the cold room. Precautions on the duration of the pending during product packing have to be made by the manufacturer to avoid product temperature increase.

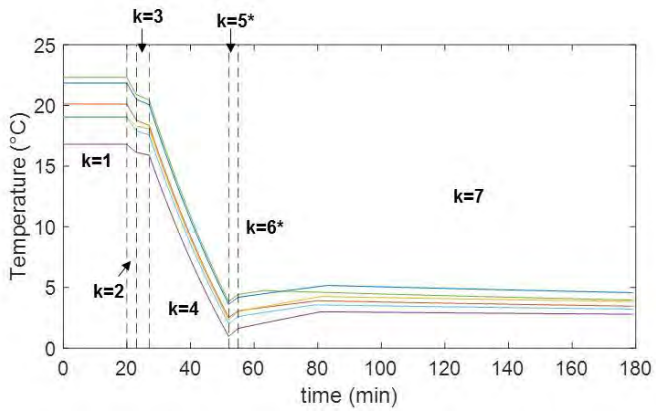

Figure 3: Temperature evolution along the chain of six random products of one batch; time = 0 min corresponds to step *k*=0 (after kneading). *Products in pending zone (*k*=6) have different durations, e.g. if a palette loading is starting or about to end, duration of products varies

3.2. Influence of operating temperatures on energy consumption and quality loss

The six scenarios (Table 3) were used for the simulation and the results are reported in Table 4 in terms of daily energy consumption relative to the reference scenario, % of products with temperature < 6°C at the entrance and exit of the cold room and the microbiological quality loss compared with the reference scenario. It is to be emphasized that the recommended temperature is 6°C. The analysis of the scenario 6 shows that 42% of product with temperature < 6°C after 6h, 94.5% after 12h and all of them (100%) after 18h.

Increasing temperature in the process room and the cold room (scenarios 2 and 3, decreases energy consumption by 12 and 18% with a limited impact on food quality (<1%).

Table 4. Results of simulation of scenarios

Scenario number	% Reference daily energy consumption (normalized)	% of products <6°C at the entrance of the cold room	% of products <6°C at the exit of the cold room (1 day)	% Reference microbiological quality loss (normalized)
Ref		98.5%	100%	
#2	-12%	98.5%	100%	-0.4%
#3	-18%	84.3%	100%	-0.5%
#4	*	0%	100%	-2.8%
#5	+72%	92.83%	100%	-0.2%
#6	+33%	0.2%	100%	-1.5%

*Comparison is not relevant because of the outage of the cooling spiral.

3.3. Influence of season on energy consumption

Simulations were carried out by using the external air temperature (T_{ext}) recorded every 10 minutes by the manufacturer in summer, fall and winter. The results of the daily energy consumption of the production line room and cold room are presented in Table 5. Information on the energy consumption of the cooling spiral could not be retrieved. While differences can be observed between predicted and measured data, overall, the trend is acceptable with higher energy consumption during the summer and lower energy consumption during the winter. These differences might be explained by the uncertainty of the model and the difficulty to include all characteristics of the food plant (air infiltration, machines, deterioration of the isolation). For example, the model largely underestimates energy consumption in the cold room during the winter with a total of 56 kWh per day while a total of 215 kWh per day was measured. More detailed onsite investigation will be conducted to characterize these differences.

Table 5: Influence of the external air temperature on the energy consumption of production line and cold room (comparison between predicted and measured results)

	Summer day 06/21/2017 (Average T_{ext} = 27°C)		Fall Day 10/02/2017 (Average T_{ext} = 15°C)		Winter Day 02/28/2018 (Average T_{ext} = -1.8°C)	
	Predicted (kWh / day)	Measured (kWh / day)	Predicted (kWh / day)	Measured (kWh / day)	Predicted (kWh / day)	Measured (kWh / day)
Production line room	1258	928	786	669	201	349
Cold room	699	803	531	547	56	215

4. CONCLUSION

This study proposes an original multidisciplinary approach linking prediction of food temperature, food quality and energy consumption of refrigeration processes in a food plant. More precisely, this study focuses on a production line of puff pastry including kneading, folding and lamination, cutting, wrapping, cooling spiral, packing and storage in a cold room. Temperature and energy consumption data provided by the manufacturer and measured by our team were used to develop and validate the model. Six scenarios simulating issues encountered by the manufacturer (hot days, equipment failures) and solution to reduce energy consumption were tested. The impact of these scenarios on the food quality was

evaluated. The slight increase of temperature setting of the air in the process room and in the cold room could reduce energy consumption with a limited effect on food quality degradation.

REFERENCES

Anonymous, 2014. Regulation (EU) No 517/2014 of the European Parliament and of the Council of 16 April 2014 on fluorinated greenhouse gases.

Anonymous. (2015). "Fermeture des meubles frigorifiques de vente à température positive. BAT-EQ-124. Journal officiel de la république française - N°75 du 29 mars 2015." Retrieved April 04, 2018, from http://atee.fr/sites/default/files/bat-eq-124-fermeture_meubles_frigorifiq_de_vente_a_temperature_positive.pdf.

Ben-abdallah, R., D. Leducq, H. M. Hoang, O. Pateau, B. Ballot-Miguet, A. Delahaye and L. Fournaison, 2018. Modelling and experimental investigation for load temperature prediction at transient conditions of open refrigerated display cabinet using Modelica environment. Int. J. Refrigeration.

Chaomuang, N., D. Flick and O. Laguerre, 2017. Experimental and numerical investigation of the performance of retail refrigerated display cabinets. Trends Food Sci Technol, 70,(95-104.

Duret, S., H.-M. Hoang, E. Derens-Bertheau, A. Delahaye, O. Laguerre and L. Guillier, Combining Quantitative Risk Assessment of Human Health, Food Waste, and Energy Consumption: The Next Step in the Development of the Food Cold Chain? Risk Anal, 0,(0).

Duret, S., H. M. Hoang, D. Flick and O. Laguerre, 2014. Experimental characterization of airflow, heat and mass transfer in a cold room filled with food products. Int. J. Refrigeration, 46,17-25.

Evans, J. A., A. M. Foster, J. M. Huet, L. Reinholdt, K. Fikiin, C. Zilio, M. Houska, A. Landfeld, C. Bond, M. Scheurs and T. W. M. van Sambeeck, 2014. Specific energy consumption values for various refrigerated food cold stores. Energ Buildings, 74,(Supplement C), 141-151.

Gruyters, W., P. Verboven, M. Delele, S. G. Gwanpua, A. Schenk and B. Nicolaï, 2018. A numerical evaluation of adaptive on-off cooling strategies for energy savings during long-term storage of apples. Int. J. Refrigeration, 85,431-440.

Hoang, H. M., D. Flick, E. Derens, G. Alvarez and O. Laguerre, 2012. Combined deterministic and stochastic approaches for modelling the evolution of food products along the cold chain. Part II: A case study. Int. J. Refrigeration, 35,(4), 915-926.

Laguerre, O. and D. Flick, 2010. Temperature prediction in domestic refrigerators: Deterministic and stochastic approaches. Int. J. Refrigeration, 33,(1), 41-51.

Lecoq, L., E. Derens, D. Flick and O. Laguerre, 2017. Influence of air dehumidification on water evaporation in a food plant. Int. J. Refrigeration, 74,435-449.

Merai, M., D. Flick, L. Guillier, S. Duret and O. Laguerre, 2018. Experimental characterization of airflow inside a refrigerated trailer loaded with carcasses. Int. J. Refrigeration, 88,(337-346.

Parpas, D., C. Amaris and S. A. Tassou, 2017. Experimental investigation and modelling of thermal environment control of air distribution systems for chilled food manufacturing facilities. Appl. Therm. Eng, 127,1326-1339.

Parpas, D., C. Amaris and S. A. Tassou, 2018. Investigation into air distribution systems and thermal environment control in chilled food processing facilities. Int. J. Refrigeration, 87, 47-,64.

Zanoni, S. and L. Zavanella, 2012. Chilled or frozen? Decision strategies for sustainable food supply chains. Int. J. Prod. Econ, 140,(2), 731-736.

Manuscript id: 303
DOI: 10.18462/iir.icr.2019.0303

Freezing and storage of seaweed

Tom S. NORDTVEDT[a], Pierrick STEVANT[b], Erlend INDERGÅRD[a]

[a] SINTEF Ocean,
7465 Trondheim, Norway, Tom.S.Nordtvedt@sintef.no
[b]Møreforskning,
6021 Ålesund, Norway

ABSTRACT

Industrial utilization of macroalgae is in a rapid development in Europe, where the final products have several applications such as food and health, feed, manure, biofuels and chemicals. Norway has an extensive coastline and an existing know-how on processing of marine raw material and related infrastructure, thus, is a prime candidate for developing a bio-economy based on cultivation and processing of seaweeds. Many studies have focused on improving the quality of biomaterials (e.g. fruits, meat, fish) however, little efforts were committed to optimize the quality of frozen seaweeds.
The effect of refrigerated seawater (RSW) storage and frozen storage and thawing methods on the biomass quality of cultivated S. latissimi shows prolonged shelf life but also some challenges. Indicators commonly employed in food research, i.e. weight variations, texture, colour, bacterial load, were used to assess the quality of the biomass.

1. INTRODUCTION

Industrial utilization of macroalgae is in a rapid development in Europe, where the final products have several applications such as food and health, feed, manure, biofuels and chemicals. Seaweeds can be cultivated on large scale in costal areas and may therefor offer superior alternatives to the production of terrestrial biomass and related challenges, such as high demand on fresh water resources. Norway has an extensive coastline and an existing know-how on processing of marine raw material and related infrastructure, thus, is a prime candidate for developing a bio-economy based on cultivation and processing of seaweeds. Recent efforts from research, industry and public authorities have been committed to develop a bio economy based on seaweed biomass and future perspectives for industrial development are positive (Stevant et al. 2017b). One of the main challenges for industrial players is to preserve the biomass since seaweeds are characterized by a rapid microbial decomposition once harvested (Enriquez et al. 1993). Substantial volumes are typically harvested within a limited time frame in the kelp cultivation (approximately 4-6 weeks for *Sachharinalatissima* and *Alaria esculenta*), setting standards for efficient processing strategies (Stevant et al. 2017b). Preservation methods that (i) minimize losses of valuable compounds, (ii) ensure product safety and (iii) limit the energy use and associated costs, are key to increase profitability of the industry. Despite a large body of literature reporting on the bioactive content of various seaweed species (Holdt and Kraan 2011; Schiener et al 2015; MacArtain et al. 2017), relatively few studies on preservation techniques and their impact on the valorisation of valuable compounds have been undertaken. Primary processes of harvested seaweeds using convective air-drying can effectively stabilize the biomass but require technology and may be difficult to implement close to harvesting sites.
Freezing is one of the most widely used method of long-term food storage. By changing the physical state of the liquid water in the food into ice, the growth of microorganisms is stopped, and the rate of biochemical reactions governing food deterioration is limited. The loss of quality in

frozen foods depends primarily on storage temperature and duration, as well as thawing procedures (Rahman and Velez-Ruiz 2007). Many studies have focused on improving the quality of biomaterials however, little efforts were committed to optimize the quality of frozen seaweeds. Choi et al. (2012) suggested freezing at -30°C in polyethylene bags containing 50% seawater then thawing in running tap water for 6 hours as a simple method for the long-term storage of freshly harvested *wakame* (*Undaria pinnatifida*), preventing from significant losses of quality compared to the fresh material. However, using seawater as a freezing medium will considerably increase the energy requirements of the processes along with the costs associated to the transport and storage of the frozen material in a commercial setting. The present work reports report on the effect of frozen storage and thawing methods on the biomass quality of cultivated *S. latissima*. Indicators commonly employed in food research, i.e weight variation, texture, color, bacterial load, were used to assess the quality of the biomass. Technical aspects and energy requirements related to the studied process are also studied.

2. MATERIAL AND METHODS

2.1 Seaweed material

Biomass of *S. latissima* was harvested at Seaweed Energy Solution (SES) at Frøya on June 7, 2017, then 200 kg was transported to SINTEF Oceans laboratory facilities in a tank filled with seawater. The seaweeds were stored overnight in a large tank (2 m^3) provided with a (9 °C) flow-through system. The biomass entered two separate experiments studying the effects of i) RSW storage and ii) freezing and subsequent thawing methods on the biomass quality. The latter is reported in this paper.

2.2 Freezing and thawing

Individual bags containing at least 3 kg of *S. latissima* blades were prepared and weighted. The samples were frozen at -25 °C using impingement freezing technology (Frigoscandia, ADVANTEC) then stored in a freezer warehouse at -25 °C. The sample bags were taken after 1, 3, 6 months and 11-months storage, then either thawed in a laboratory incubator maintained at 20 °C during 24 h or in running tap water at 13 °C and 1 L min^{-1} during 10 h. Both thawing methods at each sampling time were tested in triplicates and the samples analyzed for their color, texture, drip loss, dry matter content and microbial load.

2.3 Quality parameters

Wet weight (WW) In each of the three RSW tanks, 12 blades of *S. latissima* were marked and weighed to monitor the variations in FW of the biomass. Prior to weighing, the seaweed blades were hanged from their stipe for 30 seconds to remove the excess water and standardize the measurement. The results were expressed in % of the initial blade weight.

Dry weight (DW) The DW was determined gravimetrically as the residue remaining after drying in a laboratory oven at 105 °C for 24 h. Each measurement was performed in triplicate.

Surface color The surface color of the samples was analyzed by a computerized image technique known as computer vision system (CVS) as described in Stévant et al. (2017a).

Texture The tensile strength of thawed *S. latissima* blades was measured using a TA.XT plus texture analyzer (Stable Micro Systems Ltd, Godalming, UK) following the method adapted from Choi et al (2012).

Drip loss following freezing and thawing reflects the amount of liquid lost from the seaweed blades after thawing and was calculated as following (1):

$$\frac{W_L}{W_i} \times 100 \qquad \text{Eq. 1}$$

Where W_L is the weight of the liquid fraction from the thawed samples and W_i is the initial weight of the samples.

Microbial load Approximately 5 g of seaweed samples were diluted in a ratio 1 to 10 using peptone water (pH 7.0 ± 0.2) and homogenized in a stomacher (Seward Ltd, Worthing, UK). Five serial dilutions were then plated (1 ml) onto distinct types of count plates, namely aerobic, coliform, and yeast and mold count plates (3M Petrifilm, Maplewood, MN, USA). The microbial load of the samples was expressed in colony forming unit (CFU) per g of fresh sample.

Statistical analysis
All statistical analyses were performed on R software (version 3.4.4, R Development Core Team 2018) including functions from the nlme package (Pinheiro et al. 2017). Raw data were pre-processed for descriptive statistics and the results expressed as mean ± standard error (n = 3, unless stated otherwise). The differences among treatments (between-subject variable) over time (within-subject variable) in quality parameters were analyzed by repeated measures analysis of variance (RM ANOVA, R function lme) at $p < 0.05$.

Energy requirements
The freezing process can be divided into 3 stages, a first stage where the temperature of the product is lowered down to the initial freezing point (approximately -1 °C), then a phase change of the water from liquid to ice and the final stage where the temperature is lowered down to the storage temperature (-25 °C). While the energy requirements associated to the first and final stages can be estimated using the equation (2), the energy to be removed during the phase change was calculated using the equation (3):

$$Q = m \times C_p \times \Delta T \quad \text{Eq. 2}$$

$$Q_{ice} = m \times l_{ice} \quad \text{Eq. 3}$$

Where l_{ice} is the latent heat of ice, m is the mass (in kg), C_p is the specific heat (in kJ kg.K^{-1}) and ΔT is the temperature change (in K). The estimation of the energy needed for frozen storage at -25°C is described in Magnussen and Nordtvedt (2006).

The energy consumption (W, in kWh) of a cooling or freezing process highly depends on the coefficient of efficiency (COP) of the system (RSW unit or freezer) defined by the equation (4):

$$COP = \frac{Q}{W} \quad \text{Eq. 4}$$

For the frozen storage processes, a COP of 3 was used to estimate the associated electrical energy requirements. The values used for the calculation of the energy requirements of both processes and the costs associated are given in table 1.

Table 1: Values used for the calculation of the energy requirements frozen storage of *S. latissima* and associated costs

Variable	Value	Definition
C_p	4.2 kJ kg.K^{-1}	Specific heat of seawater
C_p	3 kJ kg.K^{-1}	Specific heat of fresh *S. latissima*
C_p	2 kJ kg.K^{-1}	Specific heat of frozen *S. latissima*
l_{ice}	335 kJ kg^{-1}	Latent heat of ice
d_s	300 kg m^{-3}	Density of frozen and packed *S. latissima*
	0.4 NOK kWh^{-1}	Estimated energy costs for the industry in Norway

3. RESULTS AND DISCUSSION

Table 2: Results (*p*-values only) from RM ANOVAs for individual quality parameters measured on *S. latissima* samples following freezing and two thawing methods. Significant results ($p < 0.005$) are indicated in bold.

Independent variable	Thawing	Time	Thawing * Time
Dependent variable			
DW	0.411	**< 0.001**	**0.664**
Drip loss	0.593	**0.003** [a]	0.341
Color (Δ*E*)	0.388	0.150 [a]	0.053
Texture (peak load)	0.082	**< 0.001**	**< 0.001**

Independent variables are (i) thawing (2 levels: air, running water), (ii) time (5 levels: 0, 32, 110, 187, 308 days, except for [a], 4 levels: 32, 110, 187 308). Within-group replication: n = 3.

Dry weight

The quality of frozen *S. latissima* stored over a 10 months-period and thawed using two different methods was investigated. The initial DW of the biomass was 9.29 % as mentioned in the previous section. The DW of the biomass increased during the experiment (fig. 1) up to over 15 % of the initial DW after 10 months of storage, indicating fluid losses from the seaweed material following freezing and subsequent thawing. The observed variations in DW did not differ with regard to the thawing method employed (table 2). These results were confirmed by considerable drip losses observed at each sampling time, exceeding 40 % of the initial weight of the samples (fig. 2). The extent of the losses and the aspect of the liquid fraction from the thawed samples, i.e. a viscous brown solution, suggest that the fluids lost during the process also contained phytochemical compounds.

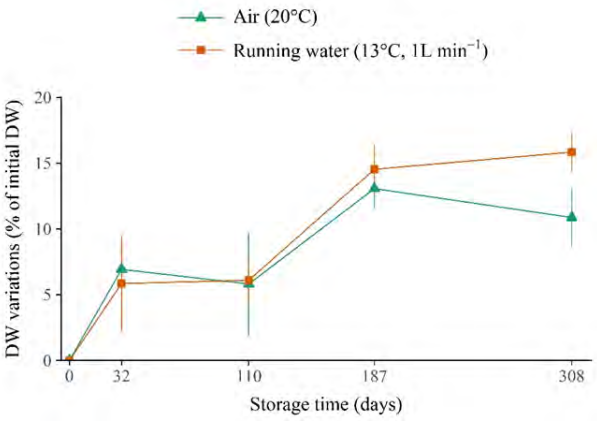

Figure. 1: Variations in DW of *S. latissima* following freezing storage and two thawing methods. Values are given as mean ± standard error (*n* = 3)

Drip loss

Drip loss reflects structural damages within a biomaterial and is influenced by several factors intrinsic to the food product and the conditions of both the freezing and thawing processes. In plant tissue, ice generally forms in the extracellular matrix because cell walls constitute a physical barrier to crystal growth. This leads to an increase in solute concentration in the unfrozen portion of the

matrix during the freezing process (Reid and Barett 2004; Rahman and Velez-Ruiz 2007). Due to the osmotic potential between the intra- and extracellular spaces, water migrates out of the cell contributing to the growth of extracellular ice and resulting in cell dehydration and shrinkage, and subsequent membrane damage. This water does not return to the cell upon thawing, resulting in drip loss. (fig. 8, table 2).

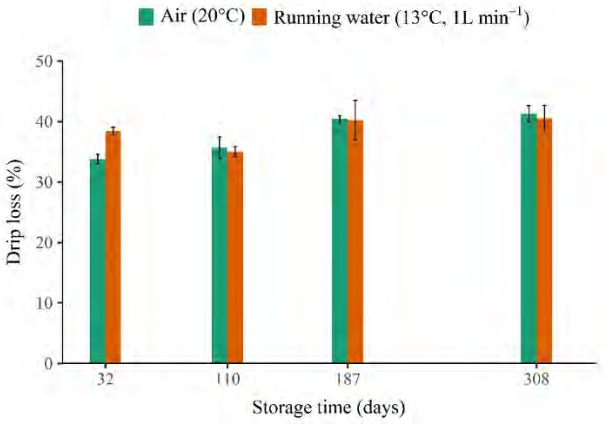

Figure. 2: Drip losses in *S. latissima* following freezing storage and two thawing methods. Values are given as mean ± standard error (*n* = 3)

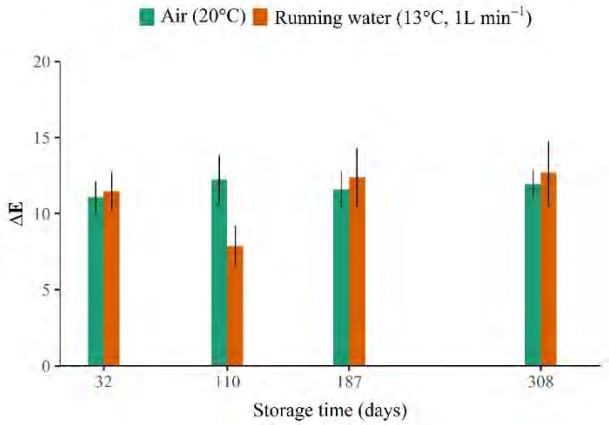

Figure. 3: Total color variation (Δ*E*) of *S. latissima* following freezing storage and two thawing methods. Values are given as mean ± standard error (*n* = 3)

Colour of the seaweed

The variations in the surface colour of the samples (defined by the color coordinates *L**, *a** and *b**) were recorded using a computerized image analysis and the total colour variation (Δ*E*) reflected the variation in each of the three coordinates during the storage period as compared to the initial values measured on the samples prior to freezing and storage. No significant differences in Δ*E* were detected either across sampling times or thawing methods (fig. 3, table 2).

Texture

In this study, the tensile strength of S. latissima, i.e. the force required to disrupt the blade, was significantly reduced by the freezing process, regardless of the thawing method employed (fig. 4, table 2). This textural property may be influenced by the blade size which was highly variable among the individuals analyzed (blade width in the range of 9 to 23 cm) hence, potentially acting as a confounding factor. However, this hypothesis was rejected following the lack of correlation between blade width and tensile strength (r^2 = 0.01, n = 140). The decrease in tensile strength is likely the result of cell damage and extensive structural alteration. In kelp species, cell walls are mainly composed of alginates which is also the main skeletal compound of the intercellular matrix in brown algae, giving the plant both mechanical strength and flexibility. Alginates are widely used in the industry because of its ability to retain water, and its gelling and stabilizing properties. The loss of tensile strength in S. latissima observed in this study, may be the result of the degradation of the alginate matrix. Furthermore, the viscosity of the liquid fraction indicates the release of large molecules, possibly alginates, through drip losses. Fucoidans, another group of water-soluble polysaccharides, are considered as cell-wall reinforcing molecules (Stiger-Pouvreau et al. 2016). Their degradation and loss following the freezing and thawing processes may also contribute to the reduction in mechanical strength, although the amount of fucoidan in S. latissima harvested in May-June is reported low (Stévant et al. 2017a).

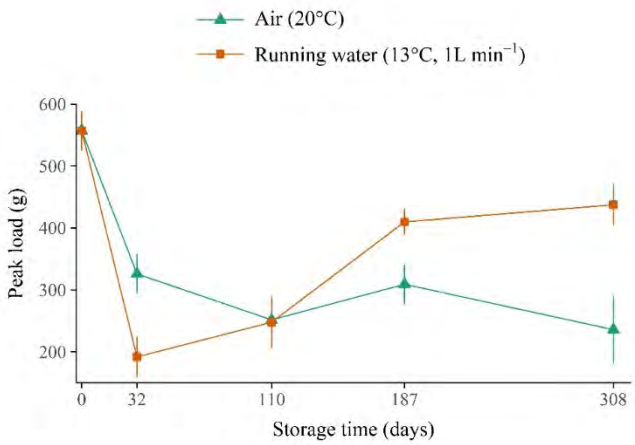

Figure. 4: Variation in tensile strength (peak load) of *S. latissima* following freezing storage and two thawing methods. Values are given as mean ± standard error (*n* = 3).

Microbial load on seaweed

Frozen and thawed *S. latissima* samples were analysed for their microbial load, including the total number of aerobes, yeasts and molds, and coliforms, using standard culture-based techniques in food control. The results were compared to those from fresh samples after harvest. Freezing greatly reduced to the microbial load of *S. latissima* which remained stable at low levels during the entire storage period (10 month). Although yeasts and molds were detected in low number in the initial biomass (< 100 CFU g^{-1}), they were not observed in the frozen and thawed samples (< 10 CFU g^{-1}). No coliforms (< 10 CFU g^{-1}) were detected in any of the analyzed samples. In vegetables, freezing causes the apparent death of 10 to 60 % of the viable microbiota, a percentage that gradually increases during frozen storage (Rahman and Velez-Ruiz 2007). There is considerable variation in the ability of bacteria to resist damage by freezing. Freeze injury of bacterial cells involves damage to the membrane from crystallisation, especially upon rapid cooling, and osmotic stress caused by extracellular ice formation hence, increasing solute concentration (Archer et al. 1995). Osmotic stress likely played an important role in the drastic reduction of the bacterial load of *S. latissima* samples in this study, given the high mineral content reported in this kelp species (Schiener et al. 2015; Stévant et al. 2017a). The main concern regarding food safety, come from micro-organisms that are likely to survive the freezing treatment and grow following thawing of the product, such as spores of the genus *Clostridium* and *Bacillus*.

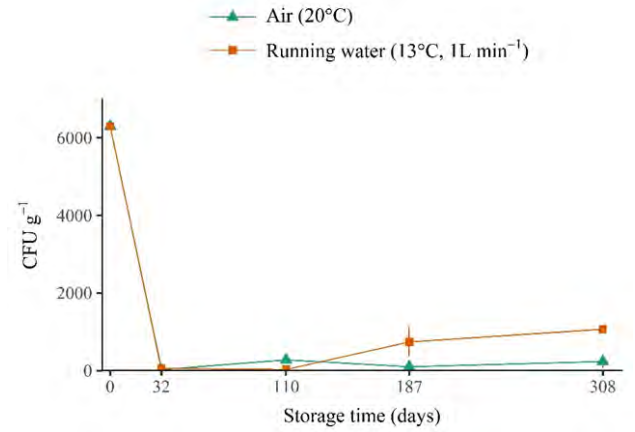

Figure 5: Microbial load (total aerobes) of *S. latissima* following freezing storage and two thawing methods. Values are given as mean ± standard error (n = 3).

Energy requirements associated with frozen storage

As the freezing process is divided in three stages (see material and methods section), the energy requirements associated to each of the stages must be calculated separately. Using the equation (2), the energy needed to cool down the biomass from 8 °C to -1 °C and from -1 °C to -25 °C are estimated to 27 and 48 kJ kg^{-1} respectively (using C_p = 3 kJ kg K^{-1} for fresh and C_p = 2 kJ kg K^{-1} for frozen seaweeds). The energy need associated to the phase change of water from liquid to ice is 335 kJ kg^{-1}, resulting in a total 410 kJ kg^{-1} (or 0.114 kWh) required for the entire freezing process. Given a COP of 3 for the equipment (i.e. impingement freezer), the electrical energy demand associated to the freezing process of *S. latissima* will be 0.038 kWh kg^{-1} or 38 kWh t^{-1}.

The energy requirement for frozen storage at -25 °C is described by Magnussen and Nordtvedt (2006) and estimated to 0.12 kWh m^{-3} day^{-1}. The scenario of packing 10 kg of seaweed biomass in standard storage boxes (0.4 x 0.4 x 0.2 m) was used to provide a realistic estimate of the density of frozen *S. latissima* (300 kg m^{-3}, table 1). Given this estimate, the energy use for the frozen storage of *S. latissima* at -25 °C will be 0.4 kWh t^{-1} day^{-1}, hence, 123.2 kWh t^{-1} over a 10-months period (308 days). The costs associated to both the freezing process and the frozen storage for 10 months will then be 64.5 NOK t^{-1}.

Another storage method for seaweed is drying. In NFR 244244 PROMAC project, investigations have been made on how much energy is needed to dry and store *S. latissima*. Assuming it is necessary to dry to 10 % moisture content, 1,16 kWh/kg (raw) has then to be removed from the seaweed according to Walde (2017). A storage of this dried algae at 12°C for 10 months will require 207 kWh t^{-1} (from PROMAC Memo T2.5 Energy requirement Storage of Seaweed, 2018). The cost associated for drying and storage will then be 629.7 NOK t^{-1}.

4. CONCLUSIONS

Freezing and subsequent thawing of *S. latissima* resulted in considerable drip loss (over 40 % of the initial samples' weight) regardless of the thawing method employed. This is likely due to the high mineral content of the biomass (25 to 45 % DW reported in the literature) resulting in extensive osmotic damage to the cell membranes as a direct consequence of freeze-concentration during the process. In addition, enzymatic degradation during frozen storage may have occurred during the storage period. The extent of the losses clearly compromises the quality of the product to be used in fresh form after thawing. A pre-treatment step consisting of fresh water soaking at high temperature (i.e. blanching) will both reduce the mineral content of the biomass and inactivate enzyme responsible for the quality alterations during storage. While optimal freezing protocols of foods aim at maintaining tissue integrity, textural and sensory attributes of the biomaterial, radical alterations such as extensive cell rupture, may facilitate the recovery of intracellular compounds in biorefinery processes. The characterization of both the solid and liquid fractions from thawed *S. latissima* is envisaged which will give information on the possible advantage of implementing this process as a pre-treatment step for the recovery of multiple compounds on a commercial scale. Besides, future studies should determine the optimal conditions during the freezing processes of *S. latissima* in order to i) maintain the quality and integrity of *S. latissima* as food and ii) facilitate the extraction of valuable phytochemical compounds.

ACKNOWLEDGEMENT

This work has been financed by Regional Research Council of Norway under the project 2721 RFF MN ISBIT.

REFERENCES

Archer GP, Kennedy CJ & Wilson AJ (1995) Position paper: Towards predictive microbiology in frozen food systems – a framework for understanding microbial population dynamics in frozen structures and in freeze-thaw cycles. International Journal of Food Science & Technology. 30(6), 711-723.

Choi J-S, Lee B-B, An S, Sohn J, Cho K & Choi I (2012) Simple freezing and thawing protocol for long-term storage of harvested fresh Undaria pinnatifida. Fisheries Science. 78(5), 1117-1123.

Enríquez S, Duarte CM & Sand-Jensen K (1993) Patterns in decomposition rates among photosynthetic organisms: the importance of detritus C:N:P content. Oecologia. 94(4), 457-471.

Holdt SL & Kraan S (2011) Bioactive compounds in seaweed: functional food applications and legislation. Journal of Applied Phycology. 23(3), 543-597.

Kaale LD, Eikevik TM, Rustad T & Kolsaker K (2011) Superchilling of food: A review. Journal of Food Engineering. 107(2), 141-146.

MacArtain P, Gill CIR, Brooks M, Campbell R & Rowland IR (2007) Nutritional Value of Edible Seaweeds. Nutrition Reviews. 65(12), 535-543.

Magnussen OM & Nordtvedt TS (2006) Kuldeanlegget - ENØK i fiskeindustrien. In, vol Teknisk rapport A6287. pp. SINTEF.

Pinheiro J, Bates D, DebRoy S, Sarkar D & Team RC (2017) nlme: linear and nonlinear mixed effects models. In., R package version 3.1–131 edn. pp.

Rahman MS & Velez-Ruiz JF (2007) Food Preservation by Freezing. In: Rahman MS (ed) Handbook of Food Preservation, Second Edition. Food Science and Technology. pp 635-665. CRC Press.

Schiener P, Black KD, Stanley MS & Green DH (2015) The seasonal variation in the chemical composition of the kelp species Laminaria digitata, Laminaria hyperborea, *Saccharina latissima* and *Alaria esculenta*. Journal of Applied Phycology. 27(1), 363-373.

Stévant P, Indergård E, Ólafsdóttir A, Marfaing H, Larssen WE, Fleurence J, Roleda MY, Rustad T, Slizyte & Nordtvedt TS (2018) Effects of drying on the nutrient content and physico-chemical and sensory characteristics of the edible kelp Saccharina latissima. Journal of Applied Phycology.

Stévant P, Rebours C & Chapman A (2017b) Seaweed aquaculture in Norway: recent industrial developments and future perspectives. Aquaculture International. 25(4), 1373–1390.

Stiger-Pouvreau V, Bourgougnon N & Deslandes E (2016) Chapter 8 - Carbohydrates From Seaweeds. In: Seaweed in Health and Disease Prevention. pp 223-274. Academic Press, San Diego.

Walde P, (2017) Prosjekt report Promac " Excess energy from waste to energy conversion plant.

Manuscript ID: 305
DOI: 10.18462/iir.icr.2019.0305

Chilling of pelagic fish onboard Norwegian fishing vessels

Tom S. NORDTVEDT[a], Kristina N. WIDELL[a]

[a] SINTEF Ocean,

7465 Trondheim, Norway, Tom.S.Nordtvedt@sintef.no

ABSTRACT

Wild caught fish is divided into pelagic (Herring, Mackerel) and demersal fish (Cod, Saithe and Haddock). Pelagic fish is caught in large quantities and transported fresh to processing on land. Ice was earlier used for chilling of fish, but because of large amounts of fish onboard, tanks with refrigerated sea water (RSW) has been used since the 1960s for chilling of pelagic fish. The water is chilled in a refrigeration system and circulated through the fish tanks. The efficiency of the chilling is dependent of the ratio of water and fish, species and water flow. The most common pelagic species caught are mackerel, herring and blue whiting. Each of them has different floating pattern in the tanks and the ratio of fish and water is also different depending on species.

To investigate the efficiency of chilling, a fishing vessel has been equipped with temperature sensors in two identical tanks, where one of them has possibility to change the flow pattern. Temperature profiles and flow pattern from research cruises where blue whiting was caught show that small changes in flow pattern has a large impact on average fish temperature. It has given input to improved management of the RSW system.

1. INTRODUCTION

The pelagic fish industry is the largest industry based on wild caught fish. Norway's share of herring and mackerel in 2018 was 874 800 tonnes. The fish is caught mainly with purse seiner and is transported fresh to processing on land. The development within the pelagic fish industry has increased since the 1960s. The fishing vessels has increased and are more effective in catching fish. The traditional way of storing the fish are boxes with ice that were labour intensive and often led to elevated fish temperatures during transportation. This results in poor quality and a large share of the catch had to be processed to oil and fishmeal with low profit. During the 1980s fish tanks with refrigerated seawater (RSW) was introduced and became the preferred method for preserving pelagic fish onboard. The requirements for the fishing vessel are insulated tanks, enough cooling capacity to chill and keep the temperature at -1 °C and circulation in the tanks to ensure even temperature. These requirements for equipment's and methods differs between vessels, but it still resulted in higher quality of the products. The onboard RSW chilling resulted in that almost all pelagic fish were frozen in onshore processing plants and sold for human consumption and not for fishmeal and oil production. Today, this industry stands for about 25% of Norway's fish export (Statistics Norway 2018).

The efficiency of refrigerated seawater (RSW) chilling is dependent the ratio of water and fish, species and flow. The most common pelagic species caught are mackerel, herring and blue whiting. Each of them has different behaviour in water and ratio of fish and water.

To improve the quality and get better price it is important to have control of the circulation in the tanks. Especially when catching blue whiting and herring there is a problem with clogging of the fish. This happens if the temperature is not lowered fast enough and if the ratio of fish and water is to high. To avoid this, it has been searched for measures which can improve the circulation in the tanks.

2. DESCRIPTION OF THE FISHING VESSEL

To investigate the efficiency of chilling and other aspects, the fishing vessel Selvåg Senior has been equipped with temperature sensors in two equally tanks where one of them has possibility to change the flow pattern. Selvåg Senior is a combined vessel from the Meløy municipality of Nordland, equipped with purse sein and pelagic trawl. The boat is owned by the shipping company Selvåg Senior AS. The vessel was built in 1999, the length and width are 67.4 x 13 m and has a gross tonnage of 1969 tons. The main engine is a Wärtsilä NSD 21V32.

Purse sein is used for the fishing of herring (NVG and North Sea Herring), mackerel and caplin, while trawling is used in fishing for greater silver smelt and blue whiting.

All fish go to human consumption, apart from blue whiting and sometimes caplin, which is essentially going to industry application (fishmeal and oil). However, there are previously attempted fishing for human consumption of blue whiting with varying experience and result. When fishing for human consumption, special considerations are taken to ensure fish quality, including the degree of fill in the tanks (fish/water) is typically approx. 60%, while the degree of fill of blue whiting fishing for fishmeal and oil use typically is around 90%.



Figure 1: Selvåg Senior

Approximately 45 % of the cargo capacity are in the 3 main tanks in section 3, furthest aft of the vessel (see Fig. 2). Challenges with uneven cooling occurs according to the machinist primarily in section 3, Tank BB 3 (left side), S 3 (center) and SB 3 (starboard), each on respectively. 294, 300 and 294 m^3.

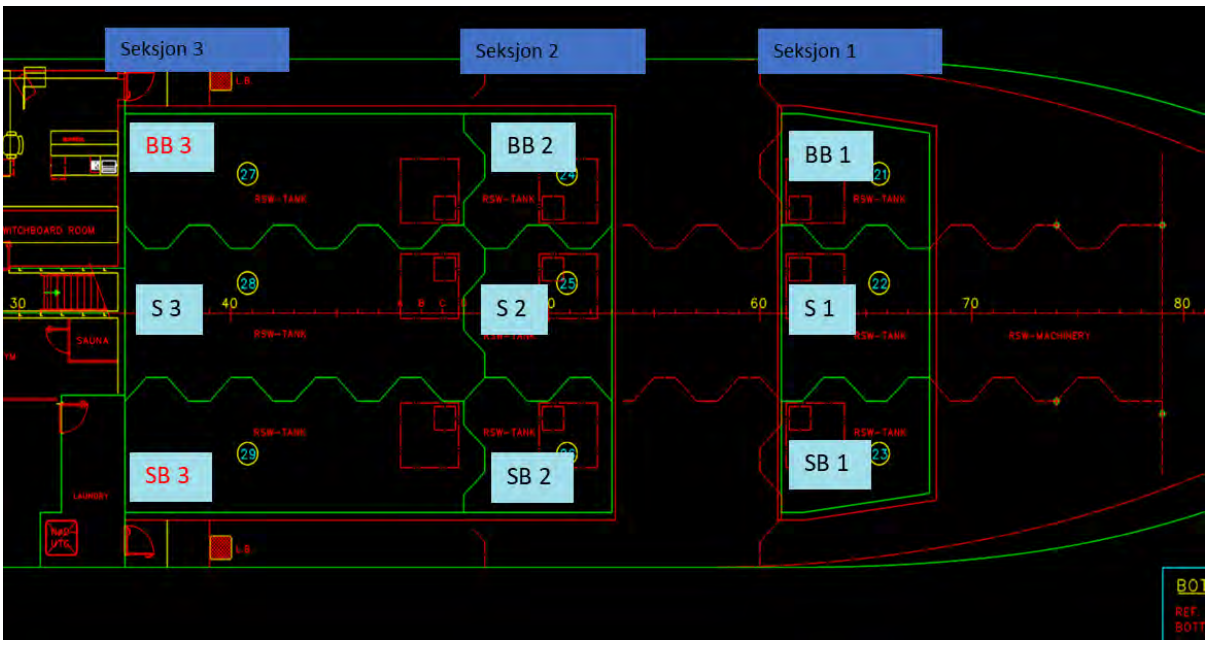

Figure 2: Overview of RSW tanks (green and red lines indicates walls of the tanks).

2.1 Refrigeration

The refrigeration plant consists of 2 separate vapor compression systems with 100 kilograms of ammonia in each system. Separate systems ensure cooling of the cargo even if one system would fail. There are two compressors (Howden), each having a cooling capacity of 1020 KW. Fig. 3 shows one of the compressor units in the refrigeration system. The refrigeration system is 2 years old.

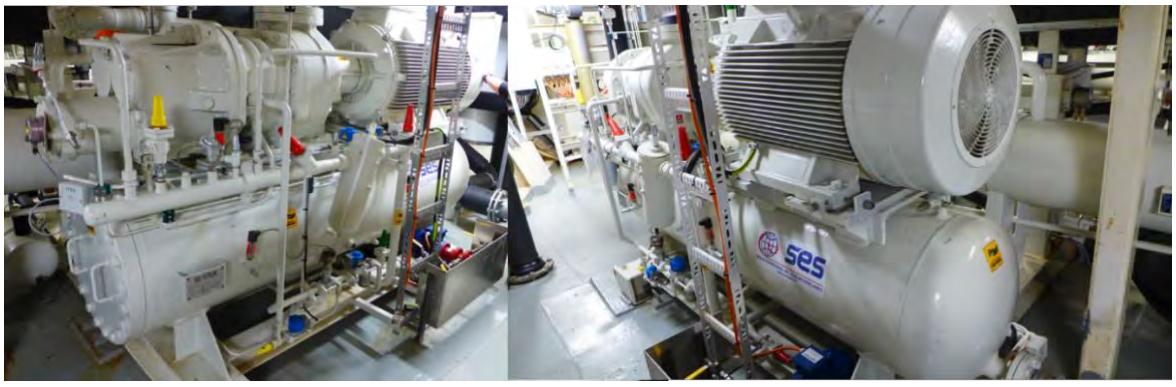

Figure 3. Compressor units.

The chief engineer is pleased with the plant as it offers good flexibility, good capacity and good reliability. Compressors, RSW-circulation pumps and condenser pumps have all frequency converters. The frequency converters are assembled by the engine compartment but can also be controlled from control rooms.

The two RSW circulation pumps each have a capacity of 720 m^3/hour. Circulation to sections 1-3 can be done separately. Fig. 4 shows the management of the circulation pumps in section 3 covering tank BB3, SB3 and S3. The pumps can be controlled from control rooms manually. Regarding the refrigeration plant, the energy consumption measured during the cruises can be used to compare with a system running on CO_2 under the same conditions. This will be a continuation of the work described in (Widell et al. 2016).



Figure 4. Management of circulation pumps in section 3 with the three biggest tanks of 300 m3

The flow of water in the RSW plant can run either way, i.e. one can run in water where the water is usually taken out, and out where it usually goes into the tanks, but this must be done manually. This is done occasionally when the drains are clogged to "flush" them clean.

3. MEASUREMENT AND METHODS

3.1 Chilling procedure during research cruises

Before fishing, 520 m^3 of fresh water was chilled to approx. 0-1°C. Two tonnes of acetic acid was added to the water for preservation of fish and for reduction in clogging. The fresh water fills the three tanks in section 2. Just prior to clearing the first cod end, the cooled fresh water was distributed in all 9 tanks on board. The circulation of RSW was started one hour after a tank was filled with fish, because the air must get out of the fish to enable good circulation. When the tanks were filled from a single haul, the surplus water was drained before the next catch. Fish/water fill rate was at full tank approximately 90 %. The residual water (approximately 10% of the tank volume) was circulated in the RSW and the cooling was done until delivery.

3.2 Instrumentation

To get an overview of the flow pattern it was important to get the entire tank volume covered with temperature sensors. In addition, mass flow meters were installed at the water inlet and outlet of both tanks. The chart (Fig. 5) shows where the temperature sensors were placed in the tank BB3 and SB3

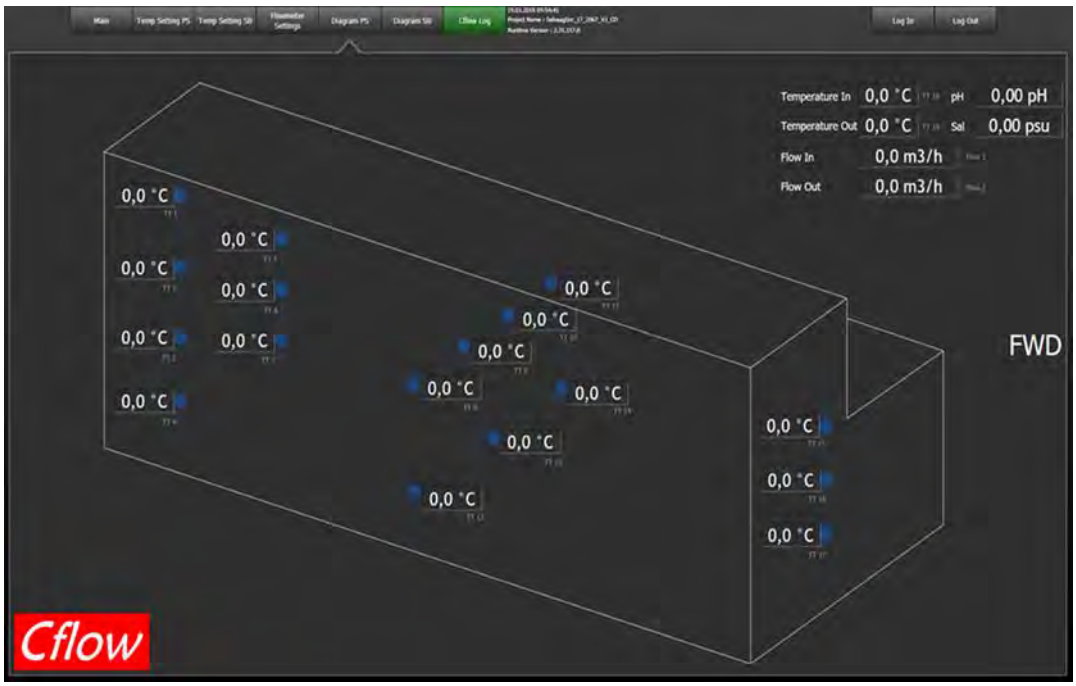

Figure 5: Instrumentation of tank BB3. SB3 instrumentation is mirrored.

Some changes to the suction side for tank SB3 was made, to be able to change the flow direction, so that water could be sucked from the grating on top or rear, or both.

Measurements were conducted during two research cruises in the period March – April 2018. The catches were made west of Ireland. In the first cruise both tanks (BB3 and SB3) were filled and operated identical during the whole cruise. The inlet of the RSW was at the bottom of the tank (indicated as blue arrows in figure 6) and the outlet was through the "Cigar" and pipe suction at lid and rear. In the second cruise both tanks were filled identical but had a different operation of the in- and outlet during transportation after catch. During the second cruise, water was sucked from the rear grating and "Cigar" from tank SB3 after the last catch and not the pipe suctions. Fig. 6 shows the in- and outlet in the tanks.

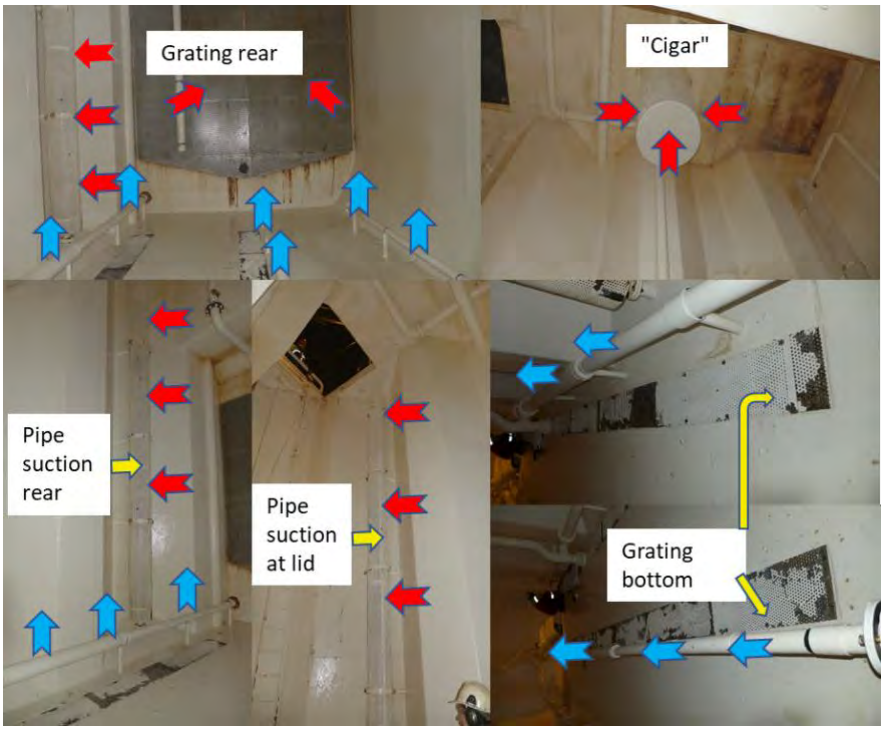

Figure 6: Overview of SB3 tank

4. RESULTS AND DISCUSSION

The blue whiting was caught at approximately 400 m depth. It had a temperature of about 10°C. From the cod end the fish was pumped into the tanks over a grid to drain of the seawater before in was put into the mixture of cooled fresh water an acetic acid. The tank was filled up with 90% of fish and the circulation in the tank was started approximately 1 hour after, when the fish had settled. In fig. 7 and fig. 8 the water temperatures in tank BB3 and SB3 from cruise 1 are shown. Fig. 9 and fig. 10 show water temperatures from tank BB3 and SB3 from cruise 2

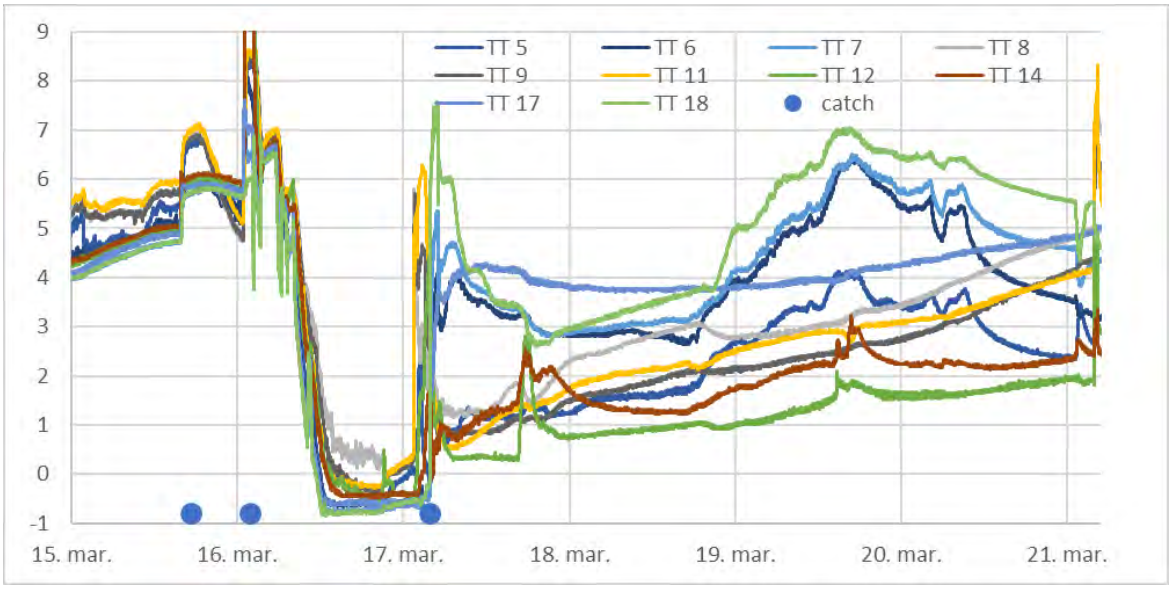

Figure 7: Water temperatures from tank BB3 from cruise 1.

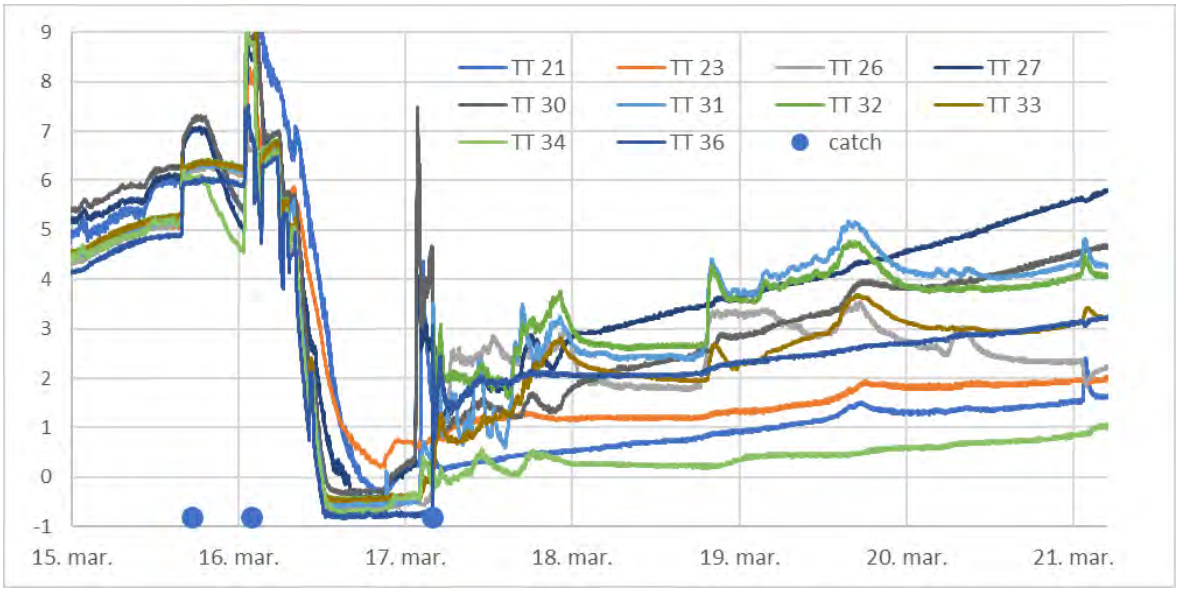

Figure 8: Water temperatures from tank SB3 from cruise 1.

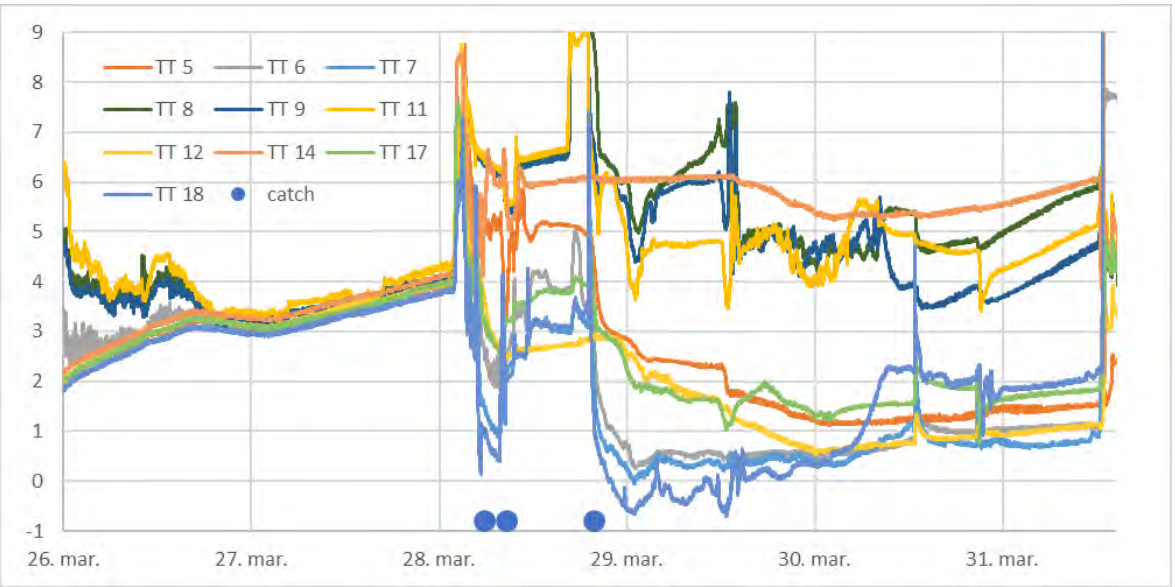

Figure 9: Water temperatures from tank BB3 from cruise 2

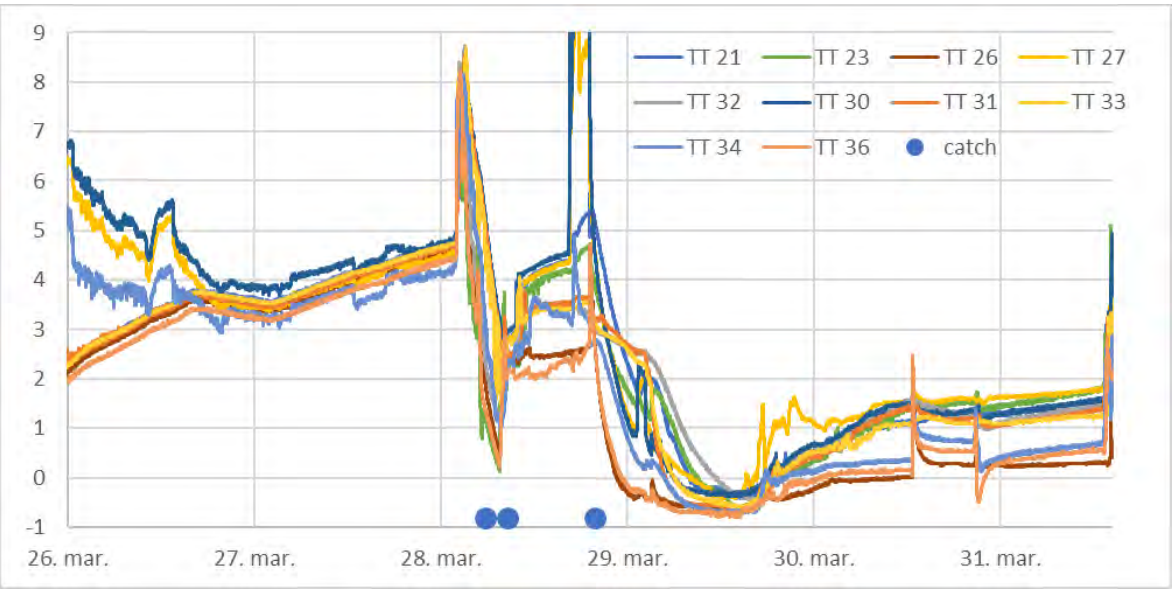

Figure 10: Water temperatures from tank SB3 from cruise 2

Both tanks SB3 and BB3 were full at both cruises. Dots in the graphs indicates when fish were loaded into the tanks. For cruise 1 (both tanks) and cruise 2 in the BB3, the water temperature was at unloading between 1 and 6 °C, while those for cruise 2, SB3 are between 0 and 2 °C. The flow pattern was identical in both tanks during cruise 1, but different during the cruise 2. At cruise 2 there where normal operation of the BB3, while SB3 had suction from top and rear gratings.

This resulted in a more even temperature profile in tank SB3 compared to the others and resulted in lower temperature of the fish. The average water temperature at unloading for cruise 1 was 3.7 °C in tank SB3 and 4.1 °C in tank BB3. For the cruise 2 the numbers were 1.2 °C for tank SB3 and 2.9 °C for tank BB3.

A mixture of 90% Blue Whiting and 10% water has fluid consistency and it is difficult to obtain a good circulation. The result from cruise 2 indicate that a perpendicular in- and outlet of the RSW gives a more even temperature in the tanks.

5. CONCLUSIONS

There is a distinct gain of altered operating patterns and this is to be tested further in the future cruises for other species and had to be implemented in how the refrigeration plant and pumps are

managed. One of the main goals is to make an automated management of the refrigeration plant where both the circulation system and the energy consumption are optimal for different pelagic fish species. This will be obtained through numerical modelling, simulation and verification in test cruises. This work will also give input to how new vessels are build and how tanks are designed.

ACKNOWLEDGEMENTS

The authors gratefully acknowledge the Norwegian Seafood Research Fund and the Research Council of Norway for the financial support for carrying out the present research [NFR project No. 269253].

REFERENCES

Statistics Norway (2018). External trade in goods. Export of fish, by species. http://ssb.no/en/

Kristina N. Widell, Tom Ståle Nordtvedt, Trygve M. Eikevik (2016). *Natural refrigerants in refrigerated seawater system on fishing vessels.* 12th IIR Gustav Lorentzen Natural working Fluids Conference, Edinburgh.

Manuscript ID: 322
DOI: 10.18462/iir.icr.2019.0322

Development of prediction model of leaf vegetable product coupled photosynthetic rate and growth curve of leaf area under air-conditioning environment in plant factory

Atsumasa YOSHIDA[(a)], Koji MORIUCHI[(b)], Yasushi UEDA[(c)], Shinichi KINOSHITA[(d)]

[(a)] Department of mechanical engineering, Osaka Prefecture University
Sakai, 599-8531, Japan, ayoshida@me.osakafu-u.ac.jp
[(b)] Technology and Development Department, Seiken Co., Ltd.
Toyonaka, 561-0894, Japan, moriuchi@seikenn.co.jp
[(c)] Technology and Development Department, Seiken Co., Ltd.
Toyonaka, 561-0894, Japan, ueda.y@seikenn.co.jp
[(d)] Department of mechanical engineering, Osaka Prefecture University
Sakai, 599-8531, Japan, kinosita@me.osakafu-u.ac.jp

ABSTRACT

Growth prediction method depending on a cultivation condition is important for planning and operating vegetable production in a plant factory. In this paper, it was proposed to incorporate the growth prediction method based on plant physiology into the air conditioning simulation tool. Photosynthetic rate equation was expanded by incorporating light intensity, air temperature, carbon dioxide concentration and wind speed dependency. Plant characteristic values necessary for photosynthetic rate were identified by cultivation experiments. Growth amount of leaf area was modeled as a growth curve and coupled with photosynthetic rate. Comparing the prediction results with cultivation experiment results, it was confirmed that this prediction method has accuracy for practical use.
Keywords: Air conditioning system, Plant factory, Cultivation test, Photosynthesis, Crop yield, Leaf area, Growth curve, Water content.

1. INTRODUCTION

A plant factory is a cultivation facility capable of planned production of plants such as vegetables annually by precisely grasping the environmental control conditions and the growth conditions by the monitoring techniques. It is easier to control cultivation conditions in a completely artificial light plant factory planted in a closed environment without sunlight (Kozai, 2012).
Plant growth is known to be affected by various cultivation environments such as light intensity, air temperature, humidity, CO_2 concentration and wind speed. For example, there is a temperature at which the growth amount becomes the largest (Oda et al., 1987). Increased growth due to CO_2 manuring has also been observed (Kawashima and Kurozumi, 1990).
In order to carry out an optimum air conditioning control in a plant factory, a growth prediction method according to the cultivation environment is necessary. This makes it possible to control for more economical production and environmental diagnosis in plant factories in operation.
Various methods are used as plant growth prediction methods. Effective cumulative temperature method (Iwata and Okubo, 1969, Ebata, 1990(1)(2)) that predicts growth from values obtained by integrating effective temperatures above the minimum growth temperature can be mentioned. There is also a method called DVR (DeVelopmental Rate) method (Horie and Nakagawa, 1990) that takes into consideration not only the air temperature but also the sunshine duration. There is a growth prediction method obtained from multiple regression analysis of the measurement results of air temperature, humidity, light intensity, CO_2 concentration, and pH, concentration and temperature of nutrient solution during cultivation period (Itoh and Yamashita, 1999). On the other hand, as a monitoring method of growing situation during cultivation, an attempt has also been made to diagnose the photosynthetic function of cultivated plants by measuring chlorophyll fluorescence of leaves with images (Sakai et al., 2011).

As described above, several growth prediction methods and growth situation diagnosis methods have been proposed and used. Growth of plants is considered to be linked with growth based on plant physiology such as photosynthesis, and growth of plant leaves and stem size. There is no reports to deal with both the photosynthesis rate and the exponential growth of leaves. Therefore, in the present study, a growth prediction method is proposed in which photosynthetic rate and leaf exponential growth are coupled.

2. CULTIVATION EXPERIMENT

Cultivation experiments were conducted to identify the plant characteristic values of photosynthetic rate, leaf area growth rate and watere content described later. The experiment site was the environmental simulator room of C20 building of plant factory research center, Osaka Prefecture University. In this cultivation room, blower, nutrient solution tank, lighting device were installed on each cultivation shelf. Nine stocks of lettuce per shelf were settled on a cultivation board and placed on a water tank. The actual measurement after cultivation was carried out using five strains. Leaf lettuce (variety: frill ice) cultivated in many fully artificial light type plant factories as cultivars was used. In order to investigate the effects of air temperature, wind speed, light intensity and CO_2 manuring application, cultivation was carried out with each condition changed. Table 1 shows actual measurement conditions of the cultivation environment. In the light intensity, the LED indicates LED illumination, and Hf 3, Hf 4 and Hf 7 indicate cases where the number of Hf fluorescent lamps is 3, 4 and 7. In order to experiment under different light intensity, cultivation conditions other than light intensity were the same, and four shelves of cultivation racks were used. The light period was 14 hours, the dark period was 10 hours, and CO_2 was not applied during the dark period.

After seeding, the plant stocks nursed for 3 weeks was planted in a cultivation pallet and cultivated for 14 days under predetermined conditions. For comparison, it may have been harvested for 7 days of cultivation. After harvesting, all the lettuce leaves were removed, leaf image data was taken into a PC with a scanner, and the leaf area was measured. The fresh weight was measured excluding the roots of the harvested lettuce and then dried in a constant temperature drier set at 80 ℃ for 24 hours and then the dry weight was measured. The photosynthetic rate was calculated by converting the increment of dry weight from planting time to harvest time into the increase amount of CO_2 (National Institute for Agro-Environment Sciences, 2003) and dividing by the average leaf area and cultivation period. It could be confirmed that the leaf area grew exponentially.

Table 1. Environmental condition of cultivation experiment

	Air Temperature	Relative Humidity	Wind Speed	Cultivation Period	CO_2 Concentration	Light intensity [μmol·m^{-2}·s^{-1}]			
						LED	Hf fluorescent lamp		
	[°C]	[%RH]	[m·s^{-1}]	[day]	[ppm]		Hf3	Hf4	Hf7
Case 1	24.0	72.7	0.55～1.22	14	340	183 ～ 238	182 ～ 236	254 ～ 316	465 ～ 628
Case 2	23.0	75.4		14	943				
Case 3	22.9	74.9	0.01～0.80	14	924				
Case 4	22.4	76.4	0.55～1.22	7	858				
Case 5	30.2	71.4		7	929				
Case 6	30.3	73.4		14	888				
Case 7	22.6	70.5	1.76～2.55	14	897				
Case 8	26.1	71.6	0.55～1.22	14	896				

3. PREDICTION MODEL OF LEAF VEGETABLE PRODUCT

3.1. Photosynthetic rate

The effective light wavelength for photosynthesis is in the range of 400 to 700 nm, the number of photons within that wavelength is called the effective photon flux density PPFD (photosynthetic photon flux density), and the unit is μmol·m^{-2}·s^{-1}. It is known that the relationship between PPFD and photosynthetic rate can be represented by nonorthogonal hyperbola (Johnson and Thornley, 1984). The photosynthetic rate V_p [mg CO_2 · m^{-2} · s^{-1}] is expressed by Eq. (1).

$$V_p = V_d + \frac{g_p I_R + V_{pmax}}{2\varphi_p} - \frac{\sqrt{\left(g_p I_R + V_{pmax}\right)^2 - 4 g_p \varphi_p V_{pmax} I_R}}{2\varphi_p} \quad \text{Eq. (1)}$$

Where, I_R indicates PPFD. V_d is the respiration rate at PPFD = 0, called the dark respiration rate. g_p shows the slope in the initial section where the photosynthetic rate linearly increases with increasing PPFD. In addition, the maximum photosynthetic speed V_{pmax} indicates the photosynthesis speed converged to a constant value in the light intensity exceeding the light saturation point. Φp represents the curvature of the light-photosynthetic curve. The above V_d, Φ_p, g_p, V_{pmax} are inherent values of plants. g_p, V_{pmax} are influenced by cultivation environments such as air temperature, wind speed and CO_2 concentration. In this paper, V_d and φ_p are assumed to be constant without being influenced by the cultivation environment.

Regarding the influence on the air temperature of photosynthesis rate, it is said to have an upwardly convex relationship with optimum air temperature (Johnson and Thornley, 1984). In the temperature condition of the cultivation experiment of this study, the photosynthetic rate tended to be larger as the air temperature was lower, and the optimum temperature could not be found. According to the findings of the previous study, the initial slope g_p and the maximum photosynthetic rate V_{pmax} were determined by quadratic functions with air temperature as a variable. As shown in Fig. 1, photosynthetic rate tended to increase due to fertilization of CO_2, and significant difference was confirmed even at the 5% level significant difference test. Previous studies (Kawashima and Kurozumi, 1990) were similar to the results in Fig. 1. This fact means that the CO_2 concentration in this study has not reached saturation in the photosynthetic reaction (Onoda, 2007). In addition, the photosynthesis rate increases with increasing CO_2 concentration in the range where CO_2 concentration is small, and it becomes constant value in the range where CO_2 concentration is large have been reported (Onoda, 2007 and Morison et al., 1983). From the above, the relationship between photosynthesis rate and CO_2 concentration is treated as the photosynthesis rate increases with increasing CO_2 concentration in the range where CO_2 concentration is small, and converges to constant value in the range where the CO_2 concentration is large. Fig. 2 shows the relationship between wind speed and photosynthetic rate. It is reported that this relationship becomes convex upward in the past study (Yabuki and Miyagawa, 1970). As the wind speed increases, the leaf boundary layer becomes thinner, CO_2 absorption from the outside air becomes easier, and photosynthesis is promoted. However, transpiration is promoted in the same way, so it is stated that because the moisture in the leaves is insufficient above a certain wind speed, photosynthesis is suppressed. Following this idea, the relationship between wind speed and photosynthetic rate is not clear in this report, but it is treated as a quadratic function convex upward. In view of the above, we propose Eqs. (2) - (9) for g_p and V_{pmax} in Eq. (1), taking into consideration the effects of air temperature T_a, CO_2 concentration c and wind speed u.

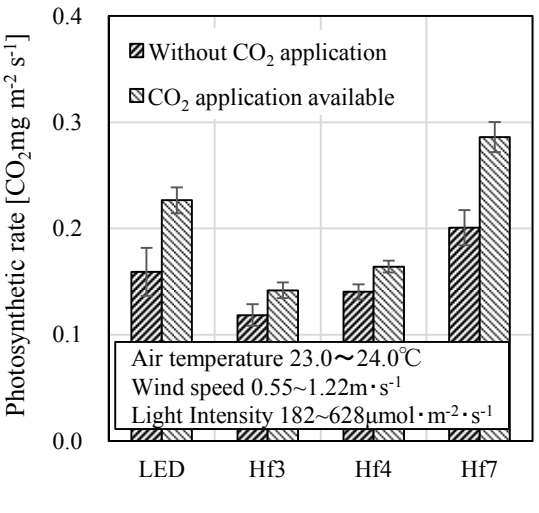

Figure 1: Difference in photosynthesis rate due to CO_2 fertilization

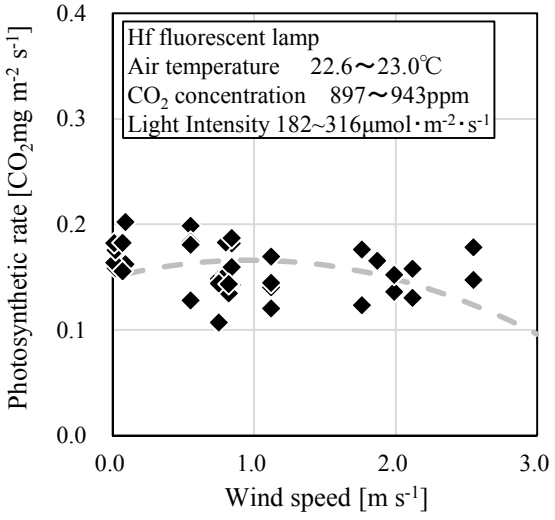

Figure 2: Relationship between photosynthesis rate and wind speed

$g_p(T_a, c, u) = f_1(T_a) \cdot f_2(c) \cdot f_3(u)$ Eq. (2) $V_{p\max}(T_a, c, u) = f_4(T_a) \cdot f_5(c) \cdot f_6(u)$ Eq. (3)

$f_1(T_a) = E_1 \cdot T_a^2 + E_2 \cdot T_a + E_3$ Eq. (4) $f_2(c) = E_4 \cdot c + E_5$ Eq. (5) $f_3(u) = E_6 \cdot u^2 + E_7 \cdot u + E_8$ Eq. (6)

$f_4(T_a) = F_1 \cdot T_a^2 + F_2 \cdot T_a + F_3$ Eq. (7) $f_5(c) = F_4 \cdot c + F_5$ Eq. (8) $f_6(u) = F_6 \cdot u^2 + F_7 \cdot u + F_8$ Eq. (9)

Where, E_1 to E_8 and F_1 to F_8 are plant-specific values and are identified from the results of cultivation experiments. Note that the mutual dependency on air temperature, CO_2 concentration and wind speed in photosynthetic rate is not known from cultivation experiment results and has not been reported in past studies. Therefore, in this study, it is treated as having no mutual dependence on air temperature, CO_2 concentration, wind speed. In addition, the relative humidity did not differ greatly in each cultivation experiment, and was set to 70-77%.

3.2. Leaf area

Although there are individual differences in plants, growth analysis has been proposed in consideration of the feature that their growth is exponential (Nagashima, 2009). In this method, the growth process of plants is represented by the relative growth rate (RGR) defined by Eq. (10).

$$RGR = \frac{1}{W_d} \cdot \frac{dW_d}{dt} = \frac{d(\ln W_d)}{dt} \quad \text{Eq. (10)}$$

W_d is the dry weight [g] of the whole individual, and t is the cultivation period. In this study, we considered that growth of leaf area was also exponential and growth analysis could be applied, and the relative growth rate and growth curve of leaf area were modeled. The growth curve of the leaf area is obtained by Eq. (11), and the relative growth rate RGR_{LA} of the leaf area in this equation is defined by Eq. (12).

$$S_{plant}(d) = S_{plant}(0) \cdot e^{(RGR_{LA} \cdot d)} \quad \text{Eq. (11)} \qquad RGR_{LA} = \frac{1}{S_{plant}} \cdot \frac{dS_{plant}}{dt} = \frac{d(\ln S_{plant})}{dt} \quad \text{Eq. (12)}$$

Where S_{plant} is the leaf area [m^2] of one plant and t is the cultivation period.
The relationship between the relative growth rate of leaf area and the number of cultivation days is discussed for each illumination condition. The relative growth rate of the leaf area in LED, Hf 3, Hf 4, Hf 7 was 7 days and 14 days on the cultivation day, and as a result of a significant difference test of 5% level, no significant difference was found. From this, it is considered that the relative growth rate of the leaf area does not depend on the cultivation days. Also, no significant difference was observed even if a significant difference test of 5% level was performed among Hf 3, Hf 4, and Hf 7. From these results, we cannot confirm the influence of the light intensity on the relative growth rate of the leaf area. There was no significant difference in the 5% level significant difference test for LED and Hf 3. Although the light intensity is the same for the LED and Hf 3, the spectral distribution of the light is different (Kotani, 2011), but the influence of the kind of light on the relative growth rate of the leaf area could not be confirmed within the scope of this study. From the above, in this report, we cannot confirm the influence of cultivation days, light intensity and kind on the relative growth rate of leaf area, and treat it as constant within the range of this study.
Fig. 3 shows the relationship between the CO_2 concentration and the relative growth rate of the leaf area for each illumination condition. When applying CO_2 fertilizer with the same light intensity from this, the relative growth rate of the leaf area is increasing. A significant difference was observed in the presence or absence of CO_2 fertilization in the significance test of 5% level. It is considered that the relative growth rate of leaf area increases with CO_2 concentration. The relationship between air temperature and relative growth rate of leaf area is also discussed. In Hf 3 and Hf 4, the relative growth rate of leaf area tended to decrease as the air temperature increased. In LED and Hf 7, there is no significant difference in the relative growth rate of leaf area, and the influence of the air temperature on the relative growth rate of leaf area is unknown. No significant difference in temperature was observed even with a significant difference test of 5% level. From the above, in this study the influence of the air temperature on the relative growth rate of leaf area is treated as constant. Fig. 4 shows the relationship between wind speed and relative growth rate of leaf area. As indicated by the correlation curve (broken line), the relative growth rate of leaf area tended to decrease as the wind speed increased. In this study, the relative growth rate of leaf area is treated as decreasing with increasing wind speed.

Based on the above results, the relative growth rate of leaf area RGR_{LA} is expressed by Eq. (13) by multiplex analysis based on the results of the cultivation experiment.

$$RGR_{LA} = H_1 \cdot u + H_2 \cdot c + H_3 \quad \text{Eq. (13)}$$

Where, H_1 to H_3 are inherent values of plants and are identified from the results of cultivation experiments.

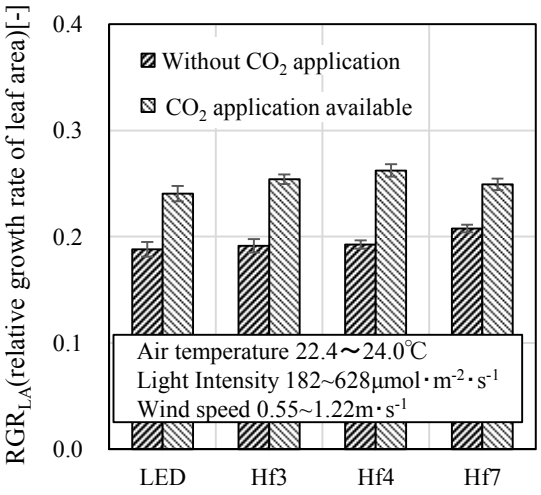

Figure 3: Relationship between RGR of leaf area and CO_2 concentration

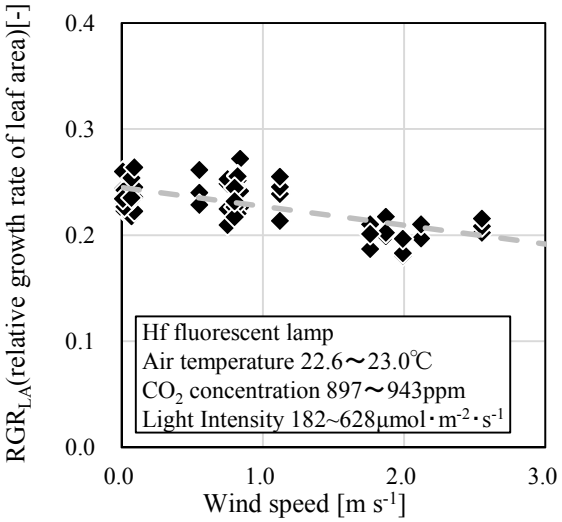

Figure 4: Relationship between RGR of leaf area and wind speed

3.3. Dry weight and fresh weight

The growth rate is predicted by combining the photosynthetic rate equation and the growth curve of leaf area determined in the previous section. The amount of CO_2 absorbed per share by photosynthesis is calculated by Eq. (14). The photosynthetic rate was not affected by the cultivation days.

$$\Delta W_{CO2}(D) = \sum_{d=1}^{D} V_p \cdot S_{plant}(d) \quad \text{Eq. (14)}$$

About 40% of the increase in dry weight during the cultivation period is carbon (National Institute for Agro-Environment Sciences, 2003), the increment of dry weight per share can be obtained by Eq. (15).

$$\Delta W_d(D) = \Delta W_{CO2}(D) \times \frac{12}{44} \times \frac{1}{0.4} \quad \text{Eq. (15)}$$

For conversion from dry weight to fresh weight, Eq. (16) is used. It is conceivable that the water content w required at that time may be different if the cultivation environment is different. As shown in Fig. 5, the water content tends to decrease as the light intensity increases. It has been reported that the water content decreases with the increase of the light intensity in the previous study (Ikeda, 1984). In the range where the light intensity is small, the water content tends to rise due to CO_2 fertilization, but no significant difference was found in the 5% level significant difference test. Therefore, in this study, CO_2 fertilization is treated as not affecting the water content. Based on the relationship between the air temperature and water content in Fig. 6, the water content tends to

decrease as the air temperature rises. In this study, the water content is treated as decreasing with air temperature rise. On the other hand, the water content shows a tendency to decrease as the wind speed increases. It is thought that the wind speed has an influence on the water content. Therefore, the water content used for converting the dry weight to the fresh weight is not a constant value, and $w\ (I_R,\ T_a,\ u)$ expressed by Eq. (17) is used.

$$\Delta W_{\mathrm{F}}(D) = \{\Delta W_d(D) + \Delta W_d(0)\} \times \frac{100}{100-w} \quad \text{Eq. (16)} \qquad w(I_R, T_a, u) = J_1 \cdot I_R + J_2 \cdot T_a + J_3 \cdot u + J_4 \quad \text{Eq. (17)}$$

From the above, the CO_2 absorption amount $\Delta W_{CO2}(D)$ is obtained by substituting the leaf area obtained from Eq. (11) and the photosynthetic rate obtained from Eq. (1) into Eq. (14). By substituting this value into Eq. (15), the increase in dry weight $\Delta W_d(D)$ can be calculated. The dry weight at the time of harvest is obtained by adding dry weight $W_d(0)$ at the time of planting separately measured to the increment of dry weight. By using the dry weight and the water content obtained from Eq. (17), it is possible to convert from Eq. (16) to the fresh weight $\Delta W_F(D)$. Table 2 shows the values used for each equation.

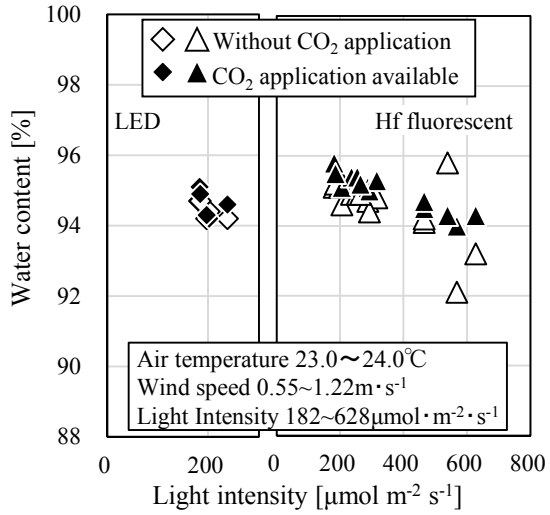

Figure 5: Relationship between water content and light intensity

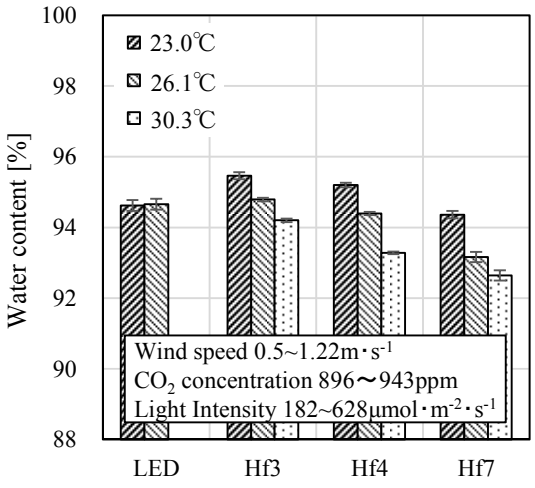

Figure 6: Relationship between water content and air temperature

Table 2. Numerical values used for analysis

Coefficients of photosynthesis	g_p	$mgCO_2 \cdot \mu mol^{-1}$	$f_1(T_a)=(-0.002T_a^2+2.7T_a+0.1)\times10^{-5}$
			$f_2(c)=(0.00466\times10^{-3}c+4.45)\times10^{-4}$
			$f_3(u)=(-0.3u^2+0.08u+9.0)\times10^{-4}$
	V_{pmax}	$mgCO_2 \cdot m^{-2} \cdot s^{-1}$	$f_4(T_a)=(-0.75T_a^2+22.5T_a+210)\times10^{-3}$
			$f_5(c)= 1.38\times10^{-3}c+0.13$
			$f_6(u)=(-1.83u^2+2.40u+22.9)\times10^{-2}$
	V_d	$mgCO_2 \cdot m^{-2} \cdot s^{-1}$	-0.02
	φ_p	-	0.85
	RGR_{LA}	-	$(-21.91u+0.068c+217.4)\times10^{-3}$
	w	%	$-4.24\times10^{-3}I_R-12.78\times10^{-2}T_a-8.77\times10^{-2}u+99.3$

Fig. 7 shows the relationship between dry weight predicted using Eq. (15) and measured values when cultivated for 14 days under irradiation with Hf fluorescent light. The correlation coefficient between them is 0.90. Similarly, the relationship between the fresh weight predicted using Eq. (16) and the measured value is shown in Fig. 8. The correlation coefficient between them was 0.90. From the above results, the growth prediction method proposed in this study can be applied to

fluctuation of the cultivation environment by treating the leaf area as a growth curve, so that this method is considered to be practical.

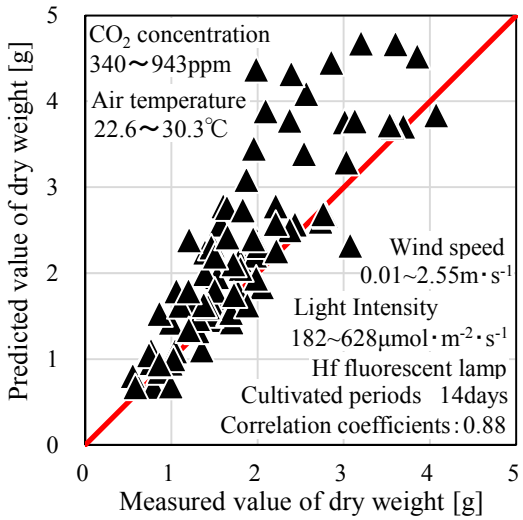

Figure 7: Comparison of measured and predicted values in dry weight

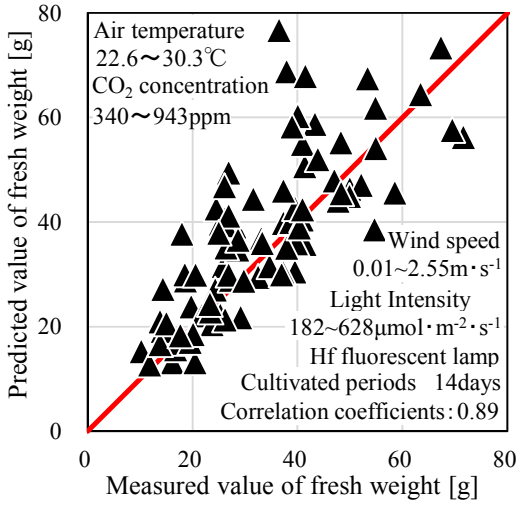

Figure 8: Comparison of measured and predicted values in fresh weight

4. CONCLUSIONS

We aimed to predict the growth in a plant factory in accordance with plant physiology and derived a growth prediction method that combines the leaf area growth curve and photosynthetic rate. The main contents and conclusions are listed below.

(1) Modeling of growth curve of leaf area derived from cultivation experiment was conducted.
(2) Light intensity, air temperature, CO_2 concentration and wind speed dependence were incorporated, and the photosynthetic rate formula was formulated.
(3) The leaf area growth curve and the photosynthetic rate equation were coupled.
(4) Conversion to fresh weight was carried out using water content incorporating environmental condition dependency.
(5) By the expansion of the photosynthetic curve and the modeling of the growth curve of the leaf area, it was confirmed that this proposed growth prediction method could cope with changes of cultivation environment such as light intensity, air temperature, wind speed, CO_2 concentration and cultivation period .

ACKNOWLEDGEMENTS

In carrying out this study, we gave a great help and advice to the consortium's optimization air conditioning project of the plant factory research center attached to Osaka Prefecture University. Also, Mr. Nobuyuki Okamura of Daiwa House Industry Co., Ltd. received much effort in cultivation experiments. We deeply appreciate everyone in the relationship.

REFERENCES

Ebata M., 1990. Effective heat unit summation and base temperature on the development of rice plant I. a method determining base temperature and its application to the vegetative development of rice plant, Japanese J. Crop Science, 59(2), 225-232.

Ebata M., 1990. Effective heat unit summation and base temperature on the development of rice plant II. on heading, flowering, kernel development and maturing of rice, Japanese J. Crop Science, 59(2), 233-238.

Horie T. and Nakagawa H., 1990. Modelling and pediction of developmental process in rice I. sructure and method of parameter estimation of a model for simulating developmental process toward heading, Japanese J. Crop Science, 59(4), 687-695.

Ikeda A., Esaki K. and Nakayama S., 1984. Plant growth characteristics under all direction illumination. I. Effects of light untensity, CO_2 concentration and air temperature on growth rate of lettuce, Environment Control in Biology, 22(4), 71-77.

Itoh H. and Yamashita R., 1999. An analysis of lettuce growth in a plant factory –multivariate analysis on time course of fresh weight-, J. Soc. High Technology in Agriculture, 11(1), 50-58.

Iwata F. and Okubo T., 1969. Physiological and ecological studies on corn growth and yield I. on the constancy of heat-unit accumulation in the effective degrees required for the growth of corn planted at various dates, Japanese. J. Crop Science, 38(1), 91-94.

Johnson I. R. and Thornley. J. H. M., 1984. A model of instaneous and daily canopy photosynthesis, J. Theoretical Biology, 107(4), 531-545.

Kawashima N., and Kurozumi, T., 1990. Studies on the CO_2 enrichment in a greenhouse (2) effect on the growth of leaf vegetables, Bull. Nara Agricultural Experiment Station, 21, 15-23.

Kotani T., 2011. Color rendering of LED lighting, J. Society of Photographic Science and Technology of Japan, 74(5), 210-214.

Kozai T., 2012. Plant Factory with Artificial Light, Ohmsha, Tokyo, 11-20.

Morison J. I. L. and Gifford R. M., 1983. Stomatal sensitivity to carbon dioxide and humidity, Plant Physiol., 71, 789-796.

Nagashima H., 2009. Plant growth analysis, Low Temperature Science, 67**,** 113-118.

National Institute for Agro-Environmental Sciences, 2003. Manual for life cycle assessment of agricultural practices in Japan, National Institute for Agro-Environmental Sciences, Tsukuba, 16.

Oda M., Nonaka M., and Hoshino, K., 1987. Application of nondestructive and continuous measurement of fresh weight to analyzing growth response of leaf lettuce to air temperature. J. Agricultural Meteorology, 43(1), 37-39.

Onoda Y., Natural CO_2 springs, 2007. Natural Laboratory to study long-term response to elevated CO_2., The Ecological Society of Japan, 57, 145-158.

Sakai Y, Takayama K. and Nishina H., 2011. Diagnosis of photosynthetic functions of grafted tomato seedlings with chlorophyll fluorescence measurement techniques, J. Soc. High Technology in Agriculture, 23(3), 101-106.

Yabuki K. and Miyagawa H., 1970. Studies on the effect of wind speed upon the photosynthesis (2) the relation between wind speed and photosynthesis, J. Agricultural Meteorology, 26(3), 137-141.

Manuscript ID: 385
DOI: 10.18462/iir.icr.2019.0385

Effect of permanent magnetic field and alternating magnetic field on the cherry quality during the freezing process

Junyan TANG[(a),(b),(c)] , Shuangquan SHAO[(a),(b)*], Huiming ZOU[(a),(b)], Changqing TIAN[(a),(b),(c)*]

[(a)]CAS Key Laboratory of Cryogenics, Technical Institute of Physics and Chemistry, Chinese Academy of Sciences, Beijing, China
[(b)]Beijing Key Laboratory of Thermal Science and Technology, Technical Institute of Physics and Chemistry, Chinese Academy of Sciences, Beijing, China
[(c)]University of Chinese Academy of Sciences, Beijing, China
* Corresponding author. Tel.: +86-10-82543433.
E-mail address: shaoshq@mail.ipc.ac.cn (S Shao), chqtian@mail.ipc.ac.cn (C Tian)

ABSTRACT

Cherry is very popular depending on its great taste and nutrition, but the perishable characteristic increases the difficulties to store. Traditional freezing methods can extend the shelf life while it still needs to be optimized. Many innovative assisted freezing methods are proposed to improve the food quality. The magnetic field is one of the physical fields which can influence the freezing process. In this paper, the permanent magnetic field (0~15mT) and alternating magnetic field (0~20Gs) are applied on the cherries respectively. The cherry samples are freezing to -30℃ at the freezing rate of 4℃/min. The objective is to evaluate the effect on the ice crystal size with different magnetic field. The result shows that both the permanent magnetic field and the alternating magnetic field can reduce the ice crystal size. And the cell structure maintains more complete compared with the control group. Especially, the effect seems more significantly in the case of the alternating magnetic field.
Keywords: Permanent Magnetic Field, Alternating Magnetic Field, Freezing, Ice Crystal Size, Food Quality.

1. INTRODUCTION

In order to extend the shelf life of the perishable foods, many methods such as freezing (Le-Bail et al., 2008; Holzwarth et al., 2012) and hot treatment are adopted. However, the traditional treatment methods cannot satisfy the high quality requirement of the consumers (James et al., 2015). In recent years, some innovative assisted freezing methods such as electric field assisted freezing (Dalvi-Isfahan et al., 2016; Xanthakis et al., 2013), radiofrequency assisted freezing (Anese et al., 2012) and magnetic field assisted freezing (Dalvi-Isfahan et al., 2017) attract extensive attention. Among these freezing methods, the researches on the magnetic field assisted freezing are increasing gradually, while the effects of the magnetic field on the food quality still exist some controversies (Kaku et al., 2012).

The studies about the effect on the water and saline solution with the magnetic field are relatively more (Cai et al., 2009; Holysz et al., 2007; Mok et al., 2015). The molecular dynamics simulations are utilized to investigate the effects of magnetic field (intensity: 1~10T) on aqueous NaCl electrolyte solutions. The result shows that the effect on the average number of hydrogen bonds is related to the solution concentration and the magnetic field intensity, which can be used to explain the micro-mechanism of the food freezing (Chang and Weng, 2008). Except the investigations on the water and saline solution, the magnetic field is used very common in the medicine science (Abedini et al., 2011; Kaku et al., 2010; Kamada et al., 2011; Kojima et al., 2013). Kojima et al. use the programmed freezer with a magnetic field (Cells Alive System) to examine the MSC (mesenchymal stem cell) viability and tissue regenerative ability after long-term cryopreservation (Kojima et al., 2015). The result indicates that the MSCs survival and proliferation rates are

significantly higher in the Cells Alive System group than in the direct group. Choi et al. (Choi et al., 2015) compared the ultrastructure in the beef muscle with the electro-magnetic resonance and air blast freezing during the frozen storage. As a result, not only the increase rate of the ice crystal size is lower by the electro-magnetic resonance freezing but also the thawing loss is significantly lower than the air blast freezing. Although some investigations indicate that the magnetic field has a positive effect on the food freezing (Kim et al., 2013; Mok et al., 2017), some contrary viewpoints are proposed in these years (Fernández-Martín et al., 2017a, b; James et al., 2015; Wowk, 2012). Otero et al. (Otero et al., 2017) indicate that no advantage of electro-magnetic freezing over air-blast freezing is detected at the conditions tested. In order to find out the exact effect and mechanism of the magnetic field, more investigations should be made in the future.

In this paper, the permanent magnetic field (PMF) and alternating magnetic field (AMF) are applied on the cherry cut sections respectively. The optical microscope and the CCD camera are used to observe the whole freezing process of the cherries. The cooling stage temperature when the phase change process occurs is recorded to represent the nucleation temperature of the cherries to some extent. In addition, the ice crystal area is analysed to compare the effect of magnetic field assisted freezing and the control groups.

2. MATERIALS AND METHODS

2.1. Sample Preparation

The fresh cherry samples are purchased from a fruit supermarket in Beijing and they are preserved under the environment temperature of 25℃ immediately after transported to the laboratory. The cherries of the similar size, shape and maturity are chosen to cut into small slices (10mm×3mm×0.1mm). In order to reduce the experimental error, the small slices are chosen from the same position of the individual cherry. In addition, all treatments are carried out on the day of purchase. After cutting into small slices, the cherry slice sample is placed on the cooling stage to observe the microstructure changes during the freezing process.

2.2. Experimental Equipment

The schematic diagram of the whole experimental equipment is shown in Fig.1. The experimental equipment is designed and fabricated including the refrigeration system, the microscopy imaging system and the magnetic field generation system. The refrigeration system consists of the cooling stage (temperature resolution ratio≤0.001℃), the liquid nitrogen tank and the controller. The cooling capacity of the cooling stage is provided by the liquid nitrogen, the cooling rate and the target temperature are set by the controller. The microscopy imaging system consists of the optical microscope (magnification:500×), the CCD camera (five million pixel) and the computer. The optical microscope fitted with a CCD camera can transfer the real-time image during the freezing process to the computer. The magnetic field generation system consists of the permanent magnets and the alternating current coils. The permanent magnets are placed between the sample area and the shell of the cooling stage. And the two alternating current coils are supported on both side of the cooling stage symmetrically. In addition, all the magnetic field intensity values of the cooling stage centre are measured by the gauss meter (resolution ratio: 0.0001mT) before the freezing process. Fig.2 shows the real picture of the experimental device.



Figure 1: The schematic diagram of the whole experiment equipment

(1 cooling stage, 2 optical microscope, 3 CCD camera, 4 section sample, 5 permanent magnets, 6 nitrogen tank, 7 controller, 8 alternating current coil, 9 alternating power source, 10 Gauss meter, 11 computer)

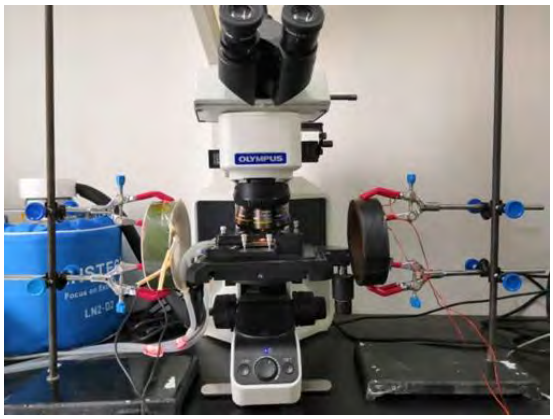

Figure 2: The picture of the real experimental device

2.3. PMF and AMF Treatments

The permanent magnetic field and alternating magnetic field are generated respectively. The permanent magnetic field is generated by the permanent magnet. The size of the single permanent magnet is 30mm×10mm×2mm. The magnetic field intensity of one permanent magnet is about 1.50mT in the cooling stage centre, so the magnetic field intensity can be adjusted by increasing or reducing the number of permanent magnet. Because the space limitation of the two sides between the sample area and the shell of the cooling stage, at most 5 permanent magnets can be placed on one side of the gap. Therefore, the magnetic field intensities in the cooling stage centre range from 0.00mT to 15.00mT at intervals of 1.50mT when the number of the permanent magnets is varied. The alternating magnetic field is generated by the alternating current coil that is energized. When the current intensities are varied from 0.00A to 2.50A at intervals of 0.25A, the corresponding peak values of the magnetic field intensity in the cooling stage centre are 0.00Gs, 0.21Gs, 0.46Gs, 1.29Gs, 2.81Gs, 5.40Gs, 6.43Gs, 7.64Gs, 12.63Gs, 16.04Gs, and 17.44Gs respectively. And the frequency of the alternating magnetic field is 50Hz.

2.4. Freezing Experiment

In order to investigate the microstructure changes of the cherry cells with PMF and AMF treatment respectively, the cherry slice is placed on the centre of the cooling stage. The cooling rate and the target temperature are set as 4℃/min and -30℃ respectively. The magnification of the microscope is set as 200× which is enough to observe the whole change process. The PMF ranged from 0.00mT to 15.00mT and AMF ranged from 0.00Gs to 17.44Gs are applied to the cherry slice during the freezing process respectively. Each trial of different condition is repeated 4 times to reduce the occasional error. The cooling stage temperature when the phase change process occurs is recorded to represent the nucleation temperature of the cherry. The changes of the cell structure are described by the real-time microscopic images which are saved in the computer. The ice crystal area is calculated from the final freezing microscopic images under each experiment condition to reflect the food quality indirectly.

3. RESULTS AND DISCUSSION

3.1. Cooling Stage Temperature

The index of the cooling stage temperature refers to the temperature of the cooling stage when the phase change process occurs. When the water turned into ice, the visual field of the microscope will be black suddenly. It can be ascribed to the optical property changes of the sample. The cooling stage temperature can represent the nucleation temperature to some extent. So it can be used as an index to reflect the food quality. When the nucleation temperature is lower, the

supercooling degree is higher when the freezing point remains constant. Supercooling is a metastable state of water. When the temperature of the object is below its usual freezing point, the phenomenon of no ice crystals formation is perceived as supercooling. Generally speaking, the tinier ice crystals can be obtained when the supercooling degree is higher.

When the permanent magnetic field is applied on the cherry sample, the cooling stage temperature is varied when the PMF intensity is different. The corresponding change tendency is shown in Fig.3. Compared with the control group without the magnetic field, the cooling stage temperature is lower in most cases. The lowest cooling stage temperature and the control group temperature are -15.92℃ and -13.08℃ respectively. This is equivalent to the nucleation temperature decreases 2.84℃ which can improve the freezing food quality significantly. As the magnetic field intensity changes, the degree of the cooling stage temperature reduction is different. As Fig.3 shows, the regularity of the cooling stage temperature change is not obvious through the experiments.

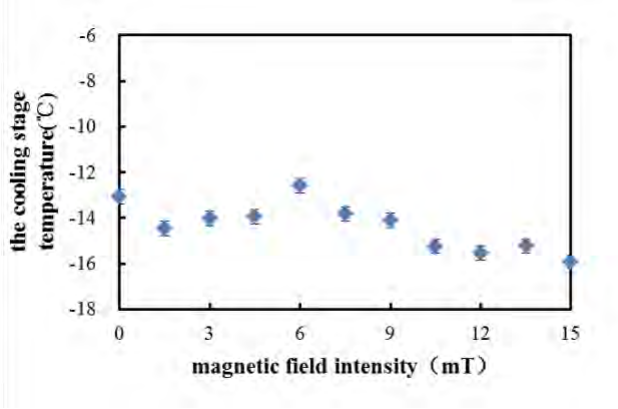

Figure 3: The cooling stage temperature change tendency with PMF

When the alternating magnetic field is applied on the cherry sample, the cooling stage temperature is varied as Fig.4 shows. It shows that the cooling stage temperature is decreased in some degree. The cooling stage temperatures in most cases are lower than the control group except some special circumstances. The maximum difference of the cooling stage temperature appears when the alternating current intensity is 1.50A. The difference value between the experimental group and the control group reaches 4.64℃. Compared with the PMF treatment, the degree of the cooling stage temperature reduction is relatively higher. Meanwhile, the fluctuation of the temperature is intense and 1.50A may be the best current intensity which can obtain the lowest temperature.

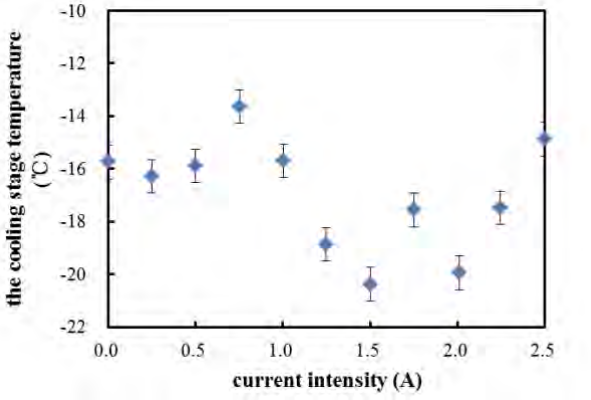

Figure 4: The cooling stage temperature change tendency with AMF

3.2. Cellular Structure

During the freezing process, the ice crystals are formed intracellular and extracellular. When the freezing rate is low, the ice crystal is formed extracellular first. With the increasing of the ice crystals extracellular, the extracellular solution concentration increases at the same time which leads to a high osmotic pressure. Under this circumstance, the cell wall may be torn. If the ice

crystals can be formed intracellular and extracellular simultaneously, the ice crystals are small and homogeneous. In this way, the structure damage can be avoided and the large drip loss can be reduced to some extent. Generally speaking, the integrity of the cell structure is very important for high quality foods during the freezing process. In this study, the images of the whole freezing process are photographed by the CCD camera in real time. By comparing the images recorded, the effect of the magnetic field can be observed.

When the permanent magnetic field is applied on the cherry sample, the freezing images are shown in Fig.5. As for the control group, the size of the ice crystal is not uniform, some large ice crystals can puncture the cell wall which destroy the cell structure. So the cell boundaries are not very clear which indicate the deterioration of the food quality. As for the samples with the PMF treatment, the size of the ice crystal is not consistent completely, but there are no particularly large ice crystals. It is obvious that the shape of the ice crystal is changed from the irregular column to the small column. Most of the ice crystals are formed in the cells evenly, and the puncture to the cell wall is infrequent. So as the right picture shows, the cell boundary is very clear and the cell structure remains pretty well. Above all, the PMF treatment can improve the food quality to some extent from the aspect of the freezing images.



Control group **PMF treatment**

Figure 5: The comparison of the cell structure with and without PMF
(The blue line represents the ice crystal boundary and the red line represents the cell wall)

When the alternating magnetic field is applied on the cherry sample, the freezing images are shown in Fig.6. The effect is similar to the PMF treatment from the aspect of the microstructure. From the two pictures below, the shape of the ice crystal transfers from large column to small graininess when AMF is applied. The cell boundary is very clear and the cell structure remains pretty well with AMF. Compared with the PMF treatment, the size of the ice crystal is much smaller. In addition, the ice crystal boundaries are very clear. So the effect of the AMF assisted freezing is better than the PMF assisted freezing.



Control group **AMF treatment**

Figure 6: The comparison of the cell structure with and without AMF
(The blue line represents the ice crystal boundary and the red line represents the cell wall)

3.3. Ice Crystal Size

The size of the ice crystal is related to the food quality closely. When the size of the ice crystal is smaller, the food quality is better. So in this paper, the ice crystal area is investigated as an important index of the food quality. The ice crystal size is evaluated from a quantitative perspective, and the ice crystal areas are calculated from the pictures which are chosen from the freezing process.

When the permanent magnetic field is applied on the cherry sample, the relationship of the average ice crystal areas and the magnetic field intensity is shown in Fig.7. When PMF is applied, the ice crystal areas reduce by 50% maximally. It is clear that the ice crystal areas decrease significantly when PMF is applied. But the magnetic field intensity has little influence on the ice crystal area, because the variation tendency of the ice crystal area is flat with the increasing of the magnetic field intensity.

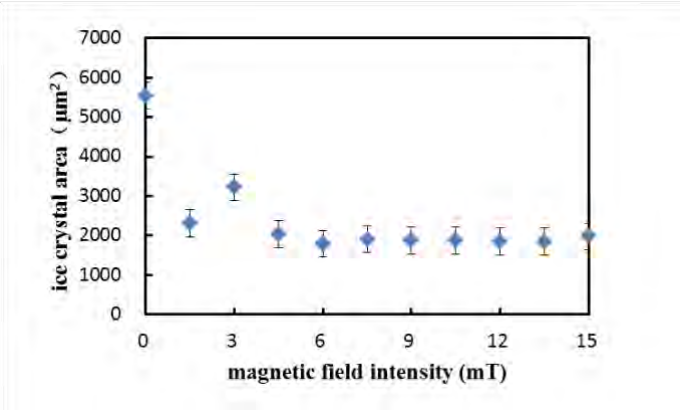

Figure 7: The icy crystal area with the PMF treatment

When the alternating magnetic field is applied on the cherry sample, the relationship of the average ice crystal areas and the current intensity is shown in Fig.8. The ice crystal areas reduce by 70% maximally, so the degree of the ice crystal reduction is higher compared with the PMF treatment. Meanwhile the fluctuation of the ice crystal area is relatively higher than the PMF treatment.

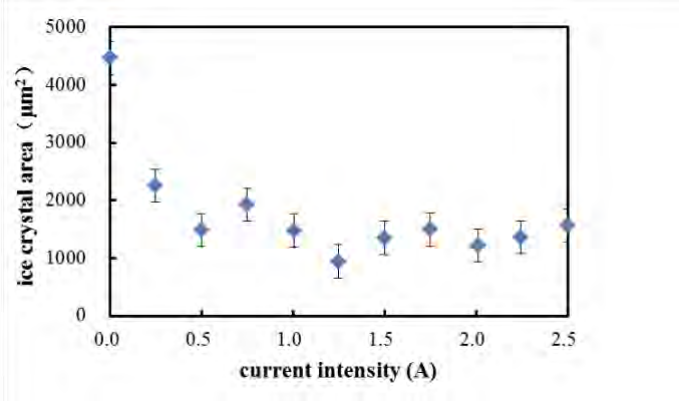

Figure 8: The ice crystal area with the AMF treatment

4. CONCLUSIONS

In this paper, the effect of the permanent magnetic field and alternating magnetic field on the food quality are investigated respectively. The food quality is reflected from three aspects: the cooling stage temperature which represents the nucleation temperature, the microscopic cellular structure and the average ice crystal size. The three indexes can represent the food quality during the freezing process in some degree. From the repeated experiments and subsequent analysis, some conclusions are drawn as follows:(1) when PMF and AMF are applied on the cherry section sample, the cooling stage temperature is lower than the control group, the cellular structure remains better especially with the AMF assisted freezing, the average ice crystal area reduced about 50% and 70%

when PMF and AMF are applied respectively (2) both the permanent magnetic field and alternating magnetic field have positive effect on the food quality during the freezing process, but the alternating magnetic field has a better effect than the permanent magnetic field (3) although the PMF and AMF assisted freezing have positive effect on the food quality, the variation tendency with the magnetic field intensity is not obvious.

Up to now, it is difficult to find the best magnetic field intensity because the individual difference and other factors. There are still some problems to be solved in the following investigations. The greater range of the magnetic field intensity and different frequency of the alternating magnetic field still need further research. More repeated experiments are needed to find out the universal law. In addition, the temperature measurement technique should be explored to measure the temperature of the very thin biological sections.

ACKNOWLEDGEMENTS

The authors gratefully thank the financial supports from Beijing Science and Technology Plan (Z171100001317016) and National Natural Science Foundation of China (51676199).

REFERENCES

Abedini, S., Kaku, M., Kawata, T., Koseki, H., Kojima, S., Sumi, H., Motokawa, M., Fujita, T., Ohtani, J., Ohwada, N., Tanne, K., 2011. Effects of cryopreservation with a newly-developed magnetic field programmed freezer on periodontal ligament cells and pulp tissues. Cryobiology 62(3), 181-187.

Anese, M., Manzocco, L., Panozzo, A., Beraldo, P., Foschia, M., Nicoli, M.C., 2012. Effect of radiofrequency assisted freezing on meat microstructure and quality. Food Research International 46(1), 50-54.

Cai, R., Yang, H., He, J., Zhu, W., 2009. The effects of magnetic fields on water molecular hydrogen bonds. Journal of Molecular Structure 938(1-3), 15-19.

Chang, K.-T., Weng, C.-I., 2008. An investigation into the structure of aqueous NaCl electrolyte solutions under magnetic fields. Computational Materials Science 43(4), 1048-1055.

Choi, Y.S., Ku, S.K., Jeong, J.Y., Jeon, K.H., Kim, Y.B., 2015. Changes in Ultrastructure and Sensory Characteristics on Electro-magnetic and Air Blast Freezing of Beef during Frozen Storage. Korean J Food Sci Anim Resour 35(1), 27-34.

Dalvi-Isfahan, M., Hamdami, N., Le-Bail, A., 2016. Effect of freezing under electrostatic field on the quality of lamb meat. Innovative Food Science & Emerging Technologies 37, 68-73.

Dalvi-Isfahan, M., Hamdami, N., Xanthakis, E., Le-Bail, A., 2017. Review on the control of ice nucleation by ultrasound waves, electric and magnetic fields. Journal of Food Engineering 195, 222-234.

Fernández-Martín, F., Pérez-Mateos, M., Dadashi, S., Gómez-Guillén, C.M., Sanz, P.D., 2017a. Impact of magnetic assisted freezing in the physicochemical and functional properties of egg components. Part 1: Egg white. Innovative Food Science & Emerging Technologies 44, 131-138.

Fernández-Martín, F., Pérez-Mateos, M., Dadashi, S., Gómez-Guillén, C.M., Sanz, P.D., 2017b. Impact of magnetic assisted freezing in the physicochemical and functional properties of egg components. Part 2: Egg yolk. Innovative Food Science & Emerging Technologies.

Holysz, L., Szczes, A., Chibowski, E., 2007. Effects of a static magnetic field on water and electrolyte solutions. J Colloid Interface Sci 316(2), 996-1002.

James, C., Purnell, G., James, S.J., 2015. A Review of Novel and Innovative Food Freezing Technologies. Food and Bioprocess Technology 8(8), 1616-1634.

James, C., Reitz, B., James, S.J., 2015. The freezing characteristics of garlic bulbs (Allium sativum L.) frozen conventionally or with the assistance of an oscillating weak magnetic field. Food and Bioprocess Technology 8(3), 702-708.

Kaku, M., Kamada, H., Kawata, T., Koseki, H., Abedini, S., Kojima, S., Motokawa, M., Fujita, T., Ohtani, J., Tsuka, N., Matsuda, Y., Sunagawa, H., Hernandes, R.A., Ohwada, N., Tanne, K., 2010. Cryopreservation of periodontal ligament cells with magnetic field for tooth banking. Cryobiology 61(1), 73-78.

Kaku, M., Kawata, T., Abedini, S., Koseki, H., Kojima, S., Sumi, H., Shikata, H., Motokawa, M., Fujita, T., Ohtani, J., Ohwada, N., Kurita, M., Tanne, K., 2012. Electric and magnetic fields in cryopreservation: A response. Cryobiology 64(3), 304-305.

Kamada, H., Kaku, M., Kawata, T., Koseki, H., Abedini, S., Kojima, S., Sumi, A., Motokawa, M., Fujita, T., Ohtani, J., Ohwada, N., Tanne, K., 2011. In-vitro and in-vivo study of periodontal ligament cryopreserved with a magnetic field. Am J Orthod Dentofacial Orthop 140(6), 799-805.

Kim, Y.B., Woo, S.M., Jeong, J.Y., Ku, S.K., Jeong, J.W., Kum, J.S., Kim, E.M., 2013. Temperature changes during freezing and effect of physicochemical properties after thawing on meat by air blast and magnetic resonance quick freezing. Korean Journal for Food Science of Animal Resources 33(6), 763-771.

Kojima, S., Kaku, M., Kawata, T., Sumi, H., Shikata, H., Abonti, T.R., Kojima, S., Fujita, T., Motokawa, M., Tanne, K., 2013. Cryopreservation of rat MSCs by use of a programmed freezer with magnetic field. Cryobiology 67(3), 258-263.

Kojima, S.I., Kaku, M., Kawata, T., Motokawa, M., Sumi, H., Shikata, H., Abonti, T.H., Kojima, S.T., Yamamoto, T., Tanne, K., Tanimoto, K., 2015. Cranial suture-like gap and bone regeneration after transplantation of cryopreserved MSCs by use of a programmed freezer with magnetic field in rats. Cryobiology 70(3), 262-268.

Le-Bail, A., Chapleau, N., Anton-De Lamballerie, M., Vignolle, M., 2008. Evaluation of the mean ice ratio as a function of temperature in a heterogeneous food: Application to the determination of the target temperature at the end of freezing. International Journal of Refrigeration 31(5), 816-821.

Mok, J.H., Choi, W., Park, S.H., Lee, S.H., Jun, S., 2015. Emerging pulsed electric field (PEF) and static magnetic field (SMF) combination technology for food freezing. International Journal of Refrigeration 50, 137-145.

Mok, J.H., Her, J.-Y., Kang, T., Hoptowit, R., Jun, S., 2017. Effects of pulsed electric field (PEF) and oscillating magnetic field (OMF) combination technology on the extension of supercooling for chicken breasts. Journal of Food Engineering 196, 27-35.

Otero, L., Pérez-Mateos, M., Rodríguez, A.C., Sanz, P.D., 2017. Electromagnetic freezing: Effects of weak oscillating magnetic fields on crab sticks. Journal of Food Engineering 200, 87-94.

Wowk, B., 2012. Electric and magnetic fields in cryopreservation. Cryobiology 64(3), 301-303; author reply 304-305.

Xanthakis, E., Havet, M., Chevallier, S., Abadie, J., Le-Bail, A., 2013. Effect of static electric field on ice crystal size reduction during freezing of pork meat. Innovative Food Science & Emerging Technologies 20, 115-120.

Manuscript ID: 421
DOI: 10.18462/iir.icr.2019.0421

Optimizing design and operation of chilling tank for Atlantic salmon

Kristina N. WIDELL[(a)], Tom Ståle NORDTVEDT[(a)], Ignat TOLSTOREBROV[(b)], Inge FOSSEN[(c)]

[(a)] SINTEF Ocean, 7465 Trondheim, Norway, kristina.widell@sintef.no
[(b)] Norwegian University of Technology and Science, 7491 Trondheim, Norway
[(c)] Stranda Prolog AS, 6518 Kristiansund N., inge@stranda.net

ABSTRACT

Farmed salmon is a large export product from Norway. After the salmon is stunned and killed, it is often transported to large tanks for bleeding, chilling and buffering before gutting and further processing. The temperature of the fish into the processing plant is varying, but it is necessary to cool down the fish fast, both to reduce bacterial growth and to maximize yield. In this paper, a demonstration tank was set up and different operational regimes were tested. Refrigerated sea water (RSW) was used for chilling of the fish. Killed and bled salmon was used to see how the fish was located inside the tank, something which can be very difficult in a production tank where the chilling water is unclear because of blood. The flow pattern through the tank was registered. Operation which resulted in lowest contact between the fish gave best heat transfer and therefore best chilling.

Keywords: Atlantic Salmon, RSW, measurements, heat transfer

1 INTRODUCTION

Norway produces large amount of Atlantic Salmon each year. In 2018 exported 1.1 million tonnes of salmon, worth NOK 67.8 billion. This is a 5 % volume and value increase from 2017. There is a large potential in increasing the salmon production in Norway, but there are several biological issues that must be solved first (for example lice and feed production). A rapid and efficient processing of the fish is necessary, both today and with increased future production. (Almås & Ratvik, 2017), (Norwegian seafood council, 2019)

The salmon is produced in sea cages and often transported live in well boats to processing plants onshore. Before the salmon is slaughtered it is often kept either in holding cages or in a wellboat , to reduce stress levels and increase product quality. Processing factories include some main processing and handling stages. The fish are often slaughtered by stunning and bleeding. Sometimes, it is first live chilled for 30-60 min. After that it bleeds and die in another chilling tank and is then transported to gutting, before they are either packed as gutted fish into polystyrene boxes or filleted and packed into boxes of expanded polystyrene (EPS) containing >10 % ice. Fish and fillets are then packed into semitrailers and shipped to the market directly or by plane (US and Asia). (Ates, Widell, Nordtvedt, & Cojocaru, 2017), (Borderias & Sanchez-Alonso, 2011)

An effective chilling of salmon depends on the temperature difference between fish and chilling water, the flow of water, mass of fish and water and of stirring. Live fish cool more rapidly than dead fish, because of higher thermal conductivity and higher convection, but is seldom used because of fish welfare (Bantle et al., 2015). Dead fish sink to the bottom of the tank, which could lead to cold water passing above the fish, instead of between, resulting in less efficient chilling. It is necessary to have and to develop equipment for effective and rapid chilling of the fish.

Chilling of salmon to a low and stable temperature is important for the quality and the shelf life of the product. A reason for increased shelf life with decreasing product temperature is that the growth of

microorganisms is slower when the temperature is low. Another consequence of low temperature is slower protein denaturation and protein degradation (Gallart-Jornet et al 2007).

In previous work, Widell et al (2018) studied one full scale helix fish chilling tank at a salmon processing plant. The results showed that temperatures of both fish and chilling water had large variations. It was not possible to test different operational patterns because it would interrupt the production. In this paper, a demotank was therefore set up for testing of specific operation patterns. The demotank was set up in a processing plant, to have easy access to RSW water and salmon. Results from tests and measurements are presented in this paper, together with suggestions for further work.

2 MEASUREMENTS AND METHODS

Two days were spent at a salmon processing plant, measuring temperatures with different instruments and in different locations. One HeliX chilling tank (described in section 2.1) was used for the experiments. The different methods were selected based on previous research in similar facilities. The project is ongoing, and evaluation of the methods will be conducted in further tests as well. The experimental setups are described in section 2.1 and the measuring equipment in section 2.2.

2.1 Description of demo tank, procedures and test setup

The chilling tank used in this study (shown in Fig. 1) is a smaller version of a HeliX tank, approximately 10 vol.% of the tanks that are common in salmon processing plants. It has 4 chambers divided by a Helix screw. Water is circulated from right to left and the water flow can be regulated. The common settings for water flow in full scale Helix tanks are 1-1.5 cm s^{-1}, with a maximum flow of about 250 m^3 h^{-1}, to avoid damage of the helix screw. A flow in the demo tank of 1 cm s^{-1} is about 14 m^3 h^{-1} with normal filling of fish. There is no refrigeration system connected to the circulated water, but the tank was filled each day with new RSW water of 1 °C. There are two water inlets, one top right in the figure and one underneath the tank, in chamber 2. There is a flow meter at the water outlet. The HeliX screw blades contains many holes (see Fig. 1 right), so that the chilling water can flow from chamber to chamber. There is also a thin clearance between the screw and the tank.

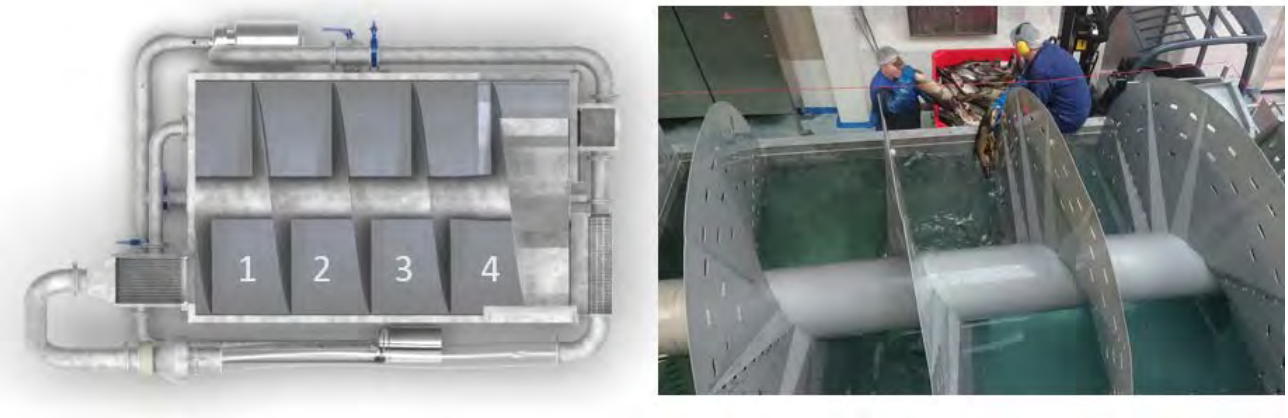

Figure 1. Layout from above of Helix demo tank (left), photo of the tank when fish was inserted (right).

The fish were thrown into chamber 2 up to a charge level similar to what is used in full scale tanks (app 45 vol %). The fish were chilled in the tank for 60-140 minutes, before it was removed from the tank. To empty the fish from the tank, the helix screw was turned until the fish was pushed out of the tank at the lower right part in the figure.

Four tests were run during the field trip, two each day, summarized in Table 1. Salmon chilled in the demo tank were fish not approved for the regular processing line, mainly because of size and spawning conditions. Because of that the amount of fish was limited. The same fish were used for test 2 and test 3. Water flow was set to 14 m^3 h^{-1}, which represented normal flow, or 32 m^3 h^{-1}, which

represented high volume flow. The flow was constant during each test. Water inlet was either only at the end of the tank (top right), or both there and from the bottom of the tank, in bottom of chamber 3. Water inlet from underneath one chamber is in this way not common in industry. The objective was to have water passing the fish from an extra direction, which should result in better chilling. The tank had 24 air nozzles in the bottom of the tank, positioned in two lines (2x12). Pressure was set to 2 bars and when used for air bubbling in the tank, the valves were opened with a certain interval, from every minute to every 5th minute. The reason for the air bubbling was to create turbulence in the water for better mixture of both water and fish.

Table 1. Experimental setup

Test	Day	Water flow, $m^3 h^{-1}$	Water inlet	Air inlet
1	1	14	At end	no
2	1	32	At end + middle	Every minute
3	2	14	At end	Every 5th minute
4	2	14	At end	Every 3rd minute

2.2 Measuring equipment

Thermocouples were installed in line at three locations in the bottom of the tank, located in chambers 2 and 3. A sketch of the installation of one thermocouple is shown in Fig. 2 (left).

Height and width were measured with a specially built equipment, with scales, see Fig. 2 (middle).

A **Testo temperature measuring instrument** (Testo, 2017), with a 23 cm long probe, was used for measuring temperatures inside the fish, both before and after they were in the tank. Accuracy: ± 0.2 °C.

A **GoPro camera** was mounted on a long pole and used for filming inside the tank, to find the positioning of the fish. The distance between the water surface and the fish was measured with a metal tape measure.



Figure 2. Illustration of measuring equipment and methods. Installation of thermocouples through the bottom of the tank (left). Measuring temperature and size of salmon (middle). A testo temperature instrument (right).

3 CHILLING INDEX CALCULATIONS

During the project, several experiments were conducted, with the demo tank but also with full-scale tanks used in industry for chilling and bleeding of salmon before further processing. Each experiment has unique parameters, which can vary significantly. Here are some examples:

- Initial and final temperature of fish
- Geometry of fish (weight)
- RSW temperature
- Exposition time in Helix tank
- Flow of RSW in Helix tank chambers

Since conditions vary between different tests it was necessary to find a common index for grading the effect of chilling. It was named *chilling index (Ch.I)* and was calculated with this formula:

$$Ch.I = \frac{T_0 - T_{fish,measured}}{T_0 - T_{fish,model}} \quad \text{Eq. (1)}$$

Temperatures of fish relates to in the thermal centre of the fish. T_0 was initial temperature of fish before it entered the tank, $T_{fish,measured}$ temperature of fish after chilling inside tank. $T_{fish,model}$ was calculated using analytical solution based on a model developed in MATLAB 2017a. The model used initial temperature of fish, dimensions of fish, chilling time, heat transfer coefficient, thermal properties of salmon and chilling water temperature to calculate $T_{fish,model}$. $T_{fish,model}$ gives an ideal temperature of the fish exiting the tank, assuming that the fish is fully surrounded by chilling water and not in contact with other fish. The chilling index will be a percentage showing how close to ideal chilling the fish has been exposed to.

The internal heat resistance is very high for Atlantic salmon (thermal conductivity is typically 0.4-0.5 W m^{-1} K^{-1}) (Flesland & Magnussen, 1990) (Bantle et al., 2015) and because of that, the RSW temperature is the most important factor for calculating $T_{fish,model}$.

However, the RSW temperature was not uniform inside the tank and it both varied along the tank and within each chamber. It also varies with time. In similar modelling, it is common to use one reference temperatures for each chamber based on a linear approximation between inlet and outlet temperatures. In the Helix chilling tank cases, another approach was selected. $T_{fish,model}$ was calculated with this formula:

$$T_{ref} = \frac{\sum_{i=1}^{n} T_{RSW\ out,i}\tau_i}{\tau_{total}} \quad \text{Eq. (2)}$$

4 RESULTS AND DISCUSSION

Different operational patterns in a demo tank was tested in this work. Measurement data and modelling results are presented in this paper. The objective of the work was to be able to rate the chilling and evaluate how to optimize the processes in full scale tanks.

4.1 Temperatures in fish

Four tests were run during the field trip, two each day, summarized in Table 1. Salmon chilled in the demo tank were fish not approved for the regular processing line, mainly because of size and spawning conditions. Because of that the amount of fish were limited. For test 3 the same fish were used as for test 2 from the day before. As a result of that, the variation in temperatures of the fish going into the tank varied much more than for the other tests. Before the fish was put into the tank it was kept in vessels in the size of 0.5-1 m^3, standing next to the tank. The room temperature was about 10 °C.

Table 2. Experimental setup

Test	Day	Number of fishes	Average weight, kg	Fish density, % of water volume	Initial temperature of fish, ºC	Water flow, $m^3\ h^{-1}$	Water inlet	Air inlet
1	1	158	3.7 (1.04)	27.8	10.6 (0.2)	14	At end	no
2	1	106	3.4 (0.9)	17.2	10.5 (0.2)	32	At end + middle	Every minute
3	2	106	3.4 (0.9)	17.2	Big variation in fish temperature	14	At end	Every 5th minute
4	2	105	2.8 (1.1)	14.0	10.4 - 11.3	14	At end	Every 3rd minute

The temperature differences calculated from measured inlet and outlet temperatures of the fish are shown in Fig. 3. The time in the tank was longest for the fish in the first test and shortest for fish in the last test. Temperature differences in fish were slightly higher for test 1 (6.2 °C) than for test 2 (5.9 °C). Test 4 had an average temperature difference of 2.8 °C.

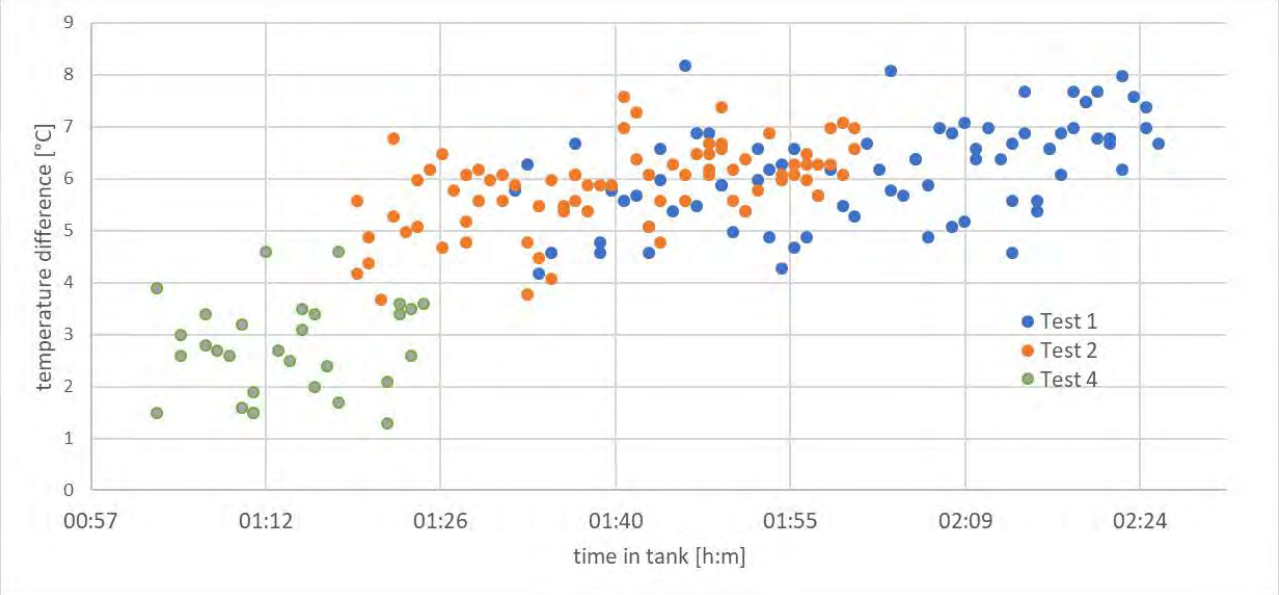

Figure 3. Temperature differences in salmon, for three of the tests.

4.2 Logged water temperature inside the tank

Temperatures measured at the bottom of the tank by thermocouples are shown in Fig. 4 for test 1 and Fig. 5 for test 2. Blue lines show temperature in the chamber that was filled with fish (Ch2), orange line shows temperature in the next chamber (Ch3), where the water flows after. Filling of fish into chamber 2 caused a significant increase in RSW temperature at the bottom of the tank. This temperature remained at a higher value when compared with RSW temperature in chamber 3. The temperature decreased again when the screw started. Temperature measured after the chamber

with fish, did not increase so dramatically. This implies that there was not much mixture of water and fish in the tank. The colder water passed over the fish and not between or under the fish.

In test 2 there was bubbling of air every minute and higher water velocity. From Fig. 5 (right) it can be seen that the temperatures in the chambers are more even and therefore much better mixture of water and fish. RSW temperatures were higher in test 2 than in test 1 because there was no refrigeration system connected with the tank.

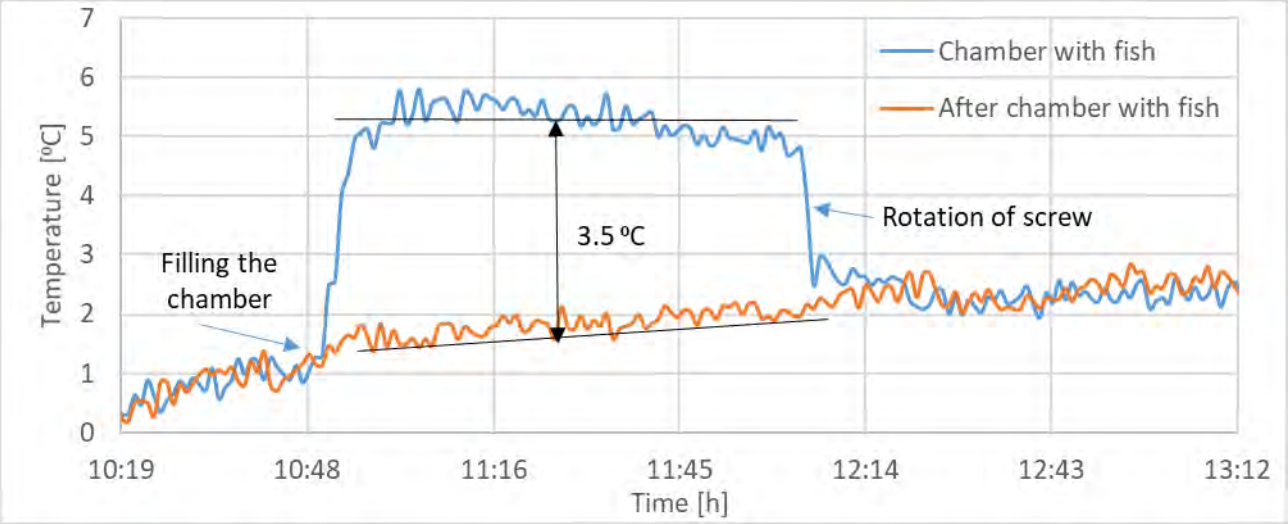

Figure 4 Time temperature chart from temperature loggers mounted on the bottom of Helix Demo-tank, Test 1. Water flow in one direction from chamber 4 to chamber 1.

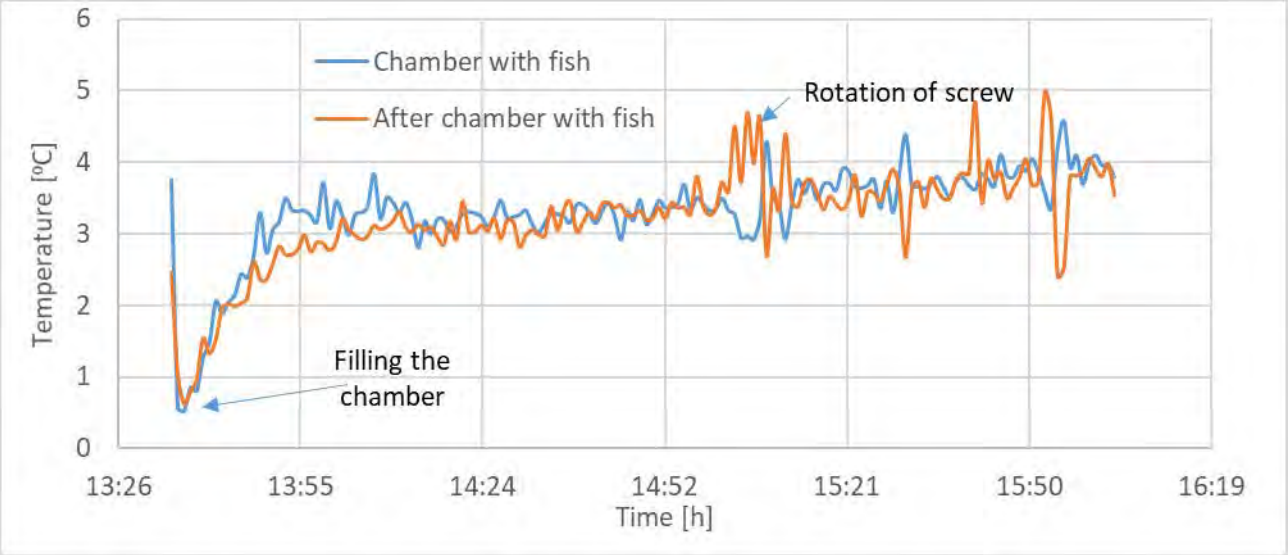

Figure 5. Time temperature chart from temperature loggers mounted on the bottom of Helix Demo-tank, Test 2. Water flow in one direction from chamber 4 to chamber 1.

4.3 Chilling index

Fig 6. shows the chilling index with respect to experimental parameters. The highest chilling index of 99.0 % was observed for intensive mode of fish agitation in chamber, Test 2. The standard flow of RSW (Test 1) in one direction without additional agitation resulted in 86.78 %. This chilling index is similar to a test in a full-scale tank at a fish processing industry, where the density of fish in tank was 34 %. That tank did not have air bubbling, but water injected at several locations in the bottom. Periodic agitation of fish in a chamber with compressed air bubbling (Test 2, Test 4) resulted in

significant increasing of chilling index when compared with normal flow. The chilling index of Test 3 were the lowest, even though it had some agitation. The reason for the low chilling index of Test 3 were likely the varying inlet temperatures of the fish.

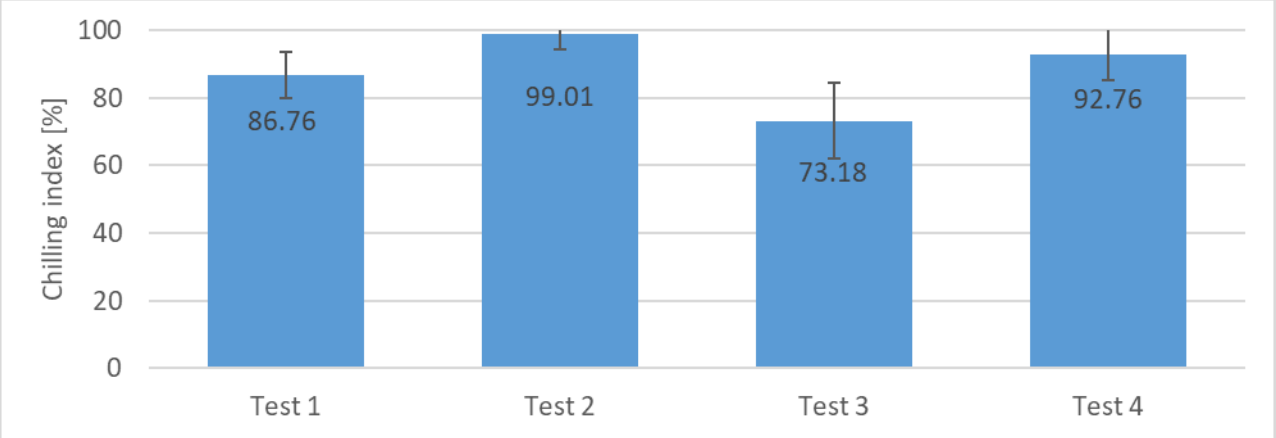

Figure 6. Modelled chilling index in chamber 2 during chilling, overview of all sets.

4.4 Positioning of fish inside the tank

The water in the tanks were clear in the beginning of the day (as can be seen in Fig. 1, right). However, as soon as the fish went into the tank the water went unclear, and it was not possible to see the fish. Measurements with a metal tape measure showed that the fish sink to the bottom, leaving half a meter of water without fish above. Poking with a stick also gave an indication that the fish is lumped together rather than having space between for water to flow.

Filming with GoPro gave some indication that the fish was stacked together, but it was difficult to see more exactly how the fish was positioned and stacked inside the tank.

5 CONCLUSIONS AND FURTHER WORK

Rapid and efficient chilling of the fish is essential at a salmon processing plant, to maximise quality and shelf life. In this paper, different operational patterns in a demotank has been tested. The demotank is 10 % of a common industrial full-scale tank for chilling of salmon. Temperature measurements of fish and chilling water were conducted, and the data was evaluated. This work is done within a larger project, where the goal is to increase the effectiveness of the Helix chilling tanks and to let the user of the tanks have more control of the parameters of chilling. Similar measurements have been conducted at full-scale tanks at processing plants.

The results showed that agitation is necessary to have better mixture of fish and water and to reduce the temperature of the fish. Agitation with air bubbling showed good chilling index. However, only four tests were conducted, where one of the tests must be excluded because of varying fish inlet temperatures. Doing experiments at an industrial site is always challenging, because of limitations in product and RSW supply, in addition to other uncontrollable factors.

The temperature measurements resulted in the following statements:

- Temperature field is not uniform in chambers, the deviations can be observed in different parts of a chamber and the flow pattern of RSW is complicated.
- Increasing of the RSW flow and decreasing of fish filling densities can decrease the temperature gradient significantly.
- Temperature in the bulk of the fish were higher than RSW outlet temperature, showing that there is more potential for chilling by installing equipment for agitation of fish and water.

- Movement of the screw influenced the temperature variation, which lead to redistribution of the temperature field in the chamber and subsequent decreasing of the temperature.
- Agitation of fish by compressed air decrease the temperature variation in chambers, but frequency of air injection is also of a high importance.

Air bubbling and extra water inlets will give better chilling of the salmon inside these tanks. There will be further tests with the demo tank, and it is then necessary to keep RSW temperature stable and to test more alternatives with water and air inlets, in addition to varying the frequency.

ACKNOWLEDGEMENTS

The authors gratefully acknowledge the Research Council of Norway for the financial support for carrying out the present research [NFR project No. 269175].

REFERENCES

Almås, K. A., & Ratvik, I. (2017). Sjøkart mot 2050 - Tiltak for utvikling av biologisk baserte marine næringer mot 2050 [in Norwegian] (OC2017 A-092, ISBN 978-82-7174-283-6).

Ates, M. B., Widell, K. N., Nordtvedt, T. S., & Cojocaru, A.-L. (2017). Energy consumption for salmon slaughtering processes. Paper presented at the 7th Conference on Ammonia and CO2 Refrigeration Technology, Ohrid, Macedonia.

Bantle, M., Digre, H., & Tobiassen, T. (2015). Optimalisering av slakteprosess for laksefisk [in Norwegian. Optimizing the salmon slaughtering process]. Retrieved from https://goo.gl/Ew9xYi

Borderias, A. J., & Sanchez-Alonso, I. (2011). First processing steps and the quality of wild and farmed fish. Journal of food science, 76(1).

Flesland, O., & Magnussen, O. (1990). Chilling of farmed fish. Paper presented at the International congress of refrigeration Aberdeen UK.

Gallart-Jornet, L., Rustad, T., Barat, J. M., Fito, P., & Eschriche, I. (2007). Effect of superchilled storage on the freshness and salting behaviour of Atlantic salmon (Salmo salar) fillets. Food Chemistry.

Norwegian seafood council (2019), Norwegian seafood exports, retrieved 2019.01.21 from https://en.seafood.no/news-and-media/news-archive/norwegian-seafood-exports-total-nok-99-billion-in-2018/

Testo. (2017). Temperature measurement / Thermometer. Retrieved from https://goo.gl/XEzCzA

Widell, K. N., Nordtvedt, T. S., Tolstorebrov, I., Fossen, I. (2018). Experimental investigation of chilling tank for Atlantic Salmon. In proceedings of 5th IIR Conference on Sustainability and the Cold Chain, Beijing, China.

Manuscript ID: 424
DOI: 10.18462/iir.icr.2019.0424

Refrigeration to prevent food losses

Kristina N. WIDELL[(a)], Pranab R. DHAKAL[(b)], Maitri THAKUR[(a)], Armin HAFNER[(b)]

[(a)] SINTEF Ocean, 7465 Trondheim, Norway, kristina.widell@sintef.no
[(b)] Norwegian University of Science and Technology, 7491 Trondheim, Norway

ABSTRACT

Globally, it is estimated that 1.3 billion tonnes of edible food are lost every year, which is one-third of the food available. Food is lost throughout various stages of the food supply chain (production and harvesting, postharvest handling, processing, distribution and consumption), but where the main losses are, differs between countries. In medium- and high-income countries, food is mostly wasted in the kitchen or at the end of the supply chain by consumers. In low-income countries, food is mainly lost during the early and middle stages of the food chain because of the drawbacks in the farming, harvesting, packaging and often a non- existing or poor cold chain. This paper gives data for the food losses in the world, with special focus on China and India. Examples of measures to reduce food losses are given, with focus on improved cold chain.

Keywords: Food loss, Cold chain, India, China

1 INTRODUCTION

Globally, 1.3 billion tonnes of food are lost every year (Gustavsson et al. 2011). Food loss refers to the food resources that go unutilized during the production, handling and processing stages while waste refers to the food thrown away by the consumers. Majority of food waste occurs at the consumption stage in Europe, but in many countries in Asia, most of the loss occurs at the post-harvest stage due to improper handling and cold chain management.

There is an urgent need to provide enough and safe food (not harmful and with all nutrients preserved) for the growing world population, which is expected to increase from 7.6 billion today to 9-11 billion in 2050 (World Population Trends 2017), (FAO 2016). Optimum storage condition for high quality and long shelf life of products in a cold chain depends on temperature and relative humidity of the storage chamber. Fluctuation of these parameters during storage, transportation and shipment is responsible for growth and survival of pathogenic microorganisms. Food is lost or wasted throughout various stages of the food supply chain (shown in Fig. 1):

i. **Production and harvesting**: Agricultural produce and harvest are damaged or spilled, animals may die or be diseased, milk could be lost due to cattle ailments, and fish may be thrown away.
ii. **Postproduction handling**: Spoilage during storage, transportation and other postharvest handling activities. Reasons can be high temperature exposure, bacterial infections, mold, pests, insects, etc.
iii. **Processing:** The quality and shelf life of the food can be lost or degraded during washing, peeling, slicing, canning, packaging etc., or during slaughtering, smoking, freezing or pasteurizing.
iv. **Distribution:** Wholesale markets, supermarkets, retailers and other stakeholders in food distribution also experience some food loss and waste (e.g., when cans and packages etc. are accidentally opened or destroyed) during the transportation activities.
v. **Consumption:** The consumers usually waste food by throwing it away. Cooking more food than is necessary, over-shopping for convenience and even overfeeding is listed in this category.

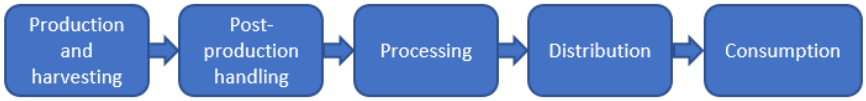

Figure 1. Different stages of food supply chain

2 GLOBAL VIEW ON FOOD LOSS AND WASTE

Several international targets have been set to end hunger and reduce the food wastage. United Nations Sustainable Development Goals (SDG) are probably one of the largest and ambitious targets in human history. The 2nd SDG goal sets its sight towards zero hunger and the 12th goal on responsible consumption and production. The target 2.1 and 2.2 aims at ending hunger and malnutrition by 2030. Similarly, the target 12.3 aims at reducing the food waste and loss by 50 % along the production and supply chains (with post-harvest losses) within 2030. (Lipinski et al, 2017)

2.1 Food loss and waste

According to *Momagri*, China, European Union (EU), United States (USA) and India are the four major food producers in terms of economic values. Fig. 2 illustrates that the total per capita food loss in Europe and North-America is 280-300 kg/year. In sub-Saharan Africa and South/Southeast Asia, it is 120-170 kg/year. The total per capita production of edible parts of food for human consumption is, in Europe and North America, about 900 kg/year and, in sub-Saharan Africa and South/Southeast Asia, 460 kg/year. Similarly, the per capita food wasted by consumers in Europe and North America is 95-115 kg/year, while the figure in sub-Saharan Africa and South/Southeast Asia is only 6-11 kg/year. FAO estimates that 30 % of cereals, 20 % of the dairy, 35 % of fish and seafood, 45 % of fruits and vegetables, 20 % of meat products, 20 % of oil seeds and pulses, and 45 % of roots and tubers are wasted. Looking at the various stages of the food supply chains worldwide, the major producer of food wastage is the phase of agricultural production followed by the postharvest handling and storage and final consumption. (FAO 2012) (Gustavsson et al, 2011)

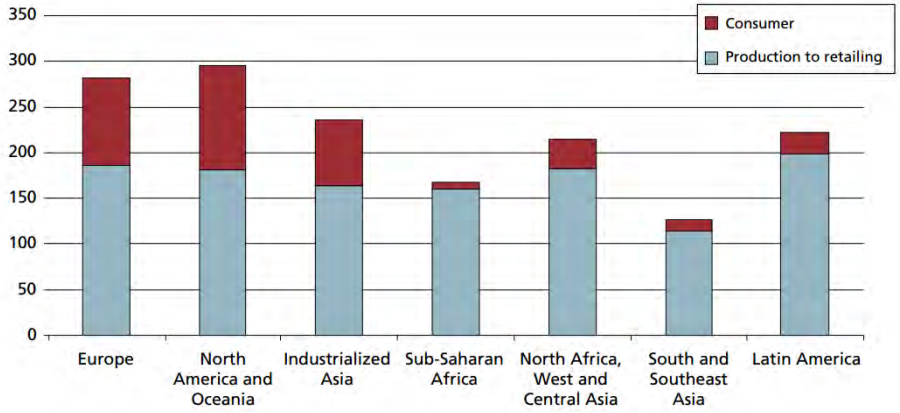

Figure 2. Per capita food losses and waste (Kg/year) (Gustavsson et. al., 2011)

2.2 Case: China

China is the largest producer of food in the world. As of 2010, China produced food worth about € 740 trillion and the food worth € 32 billion was exported, the import was worth € 72 billion. Most of the estimates of the food loss and waste in China are primarily based on the Chinese staple food maize, rice and wheat. Thus, the information on food loss and waste along the various stages of food supply chain is insufficient. Chinese agriculture arrangement is highly decentralized, so a significant percentage of post-harvest losses (5.7-8.6 % grains, 2.5-3.7 % meat, and 10-15 % for perishable food) occur during storage. There is about 6 % food loss during the storage of the food. Even if the governmental storage systems are efficient, it is difficult to use such facilities in a country where farms are dispersed. The on-farm grain storage facilities had losses more than 8 % while the central facilities had losses less than 0.5 % of the grain storage. There are also problems in the controlling of pests, rodents and moulds due to the lack of strong pesticides in the farms and the basic knowledge for storage and technology is lacking for grains storage in many farmers.

In recent years, the industrial development has cut short the harvest and post-harvest losses but the food waste habits in consumers has increased dramatically, due to the increasing affluence in the Chinese society. Consequently € 27-38 billion worth or 17-18 million tonnes of food is wasted annually in China. (Liu, 2013). The Chinese catering and restaurant businesses have been the major source of food waste and not the households. The food loss is as high as 19% in the restaurants, which is surprisingly higher than the 7% of food loss happening in the households. However, only 5% of the food is lost when people eat in the canteens.

2.3 Case: India

India is a major producer and exporter of food products and food processing is recognised as a priority sector in their new manufacturing policy. India is also a major exporter of fruits and vegetables to Europe. Fruits and vegetables losses in India range from 15% for potatoes to up to 50% for citrus fruits (Jakhar, et al. 2015). The total food loss in India amounts to over 26 billion Euros annually, as about 30 percent of all food produced is spoiled after harvesting due to lack of cold chain management and proper food processing units (Dhakal et al 2014). The Indian agricultural sector is highly dispersed compared to other countries. The average farmers have just 2-4 acres of land and 70% of the farmers have less than 1 or 2.5 acres of land. (The CSR Journal, 2015). It is difficult to apply the modern and efficient techniques and technologies in each of these farms because it could be costly. (Artiuch & Kornstein, 2012)

In aquaculture, the total loss in farm operation was about 10%. The losses in the catch of marine fish is because the low value fish is discarded and only the high value fish is taken by the fishermen. However, this is changing now a days as the fishermen bring the low value fish home. The overall total loss of 11 % was observed in which is significantly higher than the previous study (3%) of 2005-07, mainly because the catch operation was not covered in the previous study.

In case of meat, the total loss in farm operations was found to be about 2% due to loss during slaughtering. About 1% of loss happened in the process of storage at the retailers and wholesalers. The overall total loss of meat at national level is about 3%. The poultry meat loss at the national level is about 7% and the losses during the storage of poultry meat is about 4%. It is due to the lack of proper distribution, cold chain system and refrigerated display in the market. Further, the overall total loss of milk in the national level is about 1% only.

3 REFRIGERATION TO PREVENT FOOD LOSSES

Refrigeration includes both chilling and freezing and is one of the best ways of preserving food as close to its original state as possible. When the product temperature is reduced, microbiology activity and chemical and physical changes are slowed down, and shelf life is extended. Improvements to the food cold chain and better use of refrigeration will help to reduce some of the food losses in the world. With a growing population in need of more food, it is necessary to improve the cold chains especially where it is poor today. (IIR, 2009). In the introduction of this paper, the food value chain was divided into 5 stages. In this section, possibilities of improving the cold chain for each stage will be given.

3.1 Production and harvesting

During production and harvesting, there is seldom a need for refrigeration, but it is important that some highly perishable food stuffs, for example fish and seafood, are quickly chilled or frozen after production and harvesting. If not, the quality degradation starts, and it is not possible to go back to the original state. Handling of food after production and harvesting is described in the following section.

3.2 Postproduction handling

Many **fruits, vegetables, tubers and roots** must be stored above freezing temperatures to avoid damage. Examples are bananas (13-15 °C), lemons (10-13 °C), cucumber (10-12 °C), mangos (13 °C), tomatoes (8-13 °C), sweet potatoes (13-15 °C) and potatoes (4-15 °C) (ASHRAE, 2006, chap. 11). However, chilling of these products is still important to prevent them from becoming overripe, especially at high ambient temperatures. A refrigeration system will mainly control the temperature,

but also humidity when necessary. When transporting unwrapped products, more focus should be on humidity control because unwrapped products will dry faster than products that are packed.

Cold water **fish and seafood** will degrade fast if not chilled quickly after harvesting. Fish and seafood from warmer waters will not have the same degradation rate but must also be chilled to preserve quality and shelf life. An example is the development within the pelagic fish industry in Norway, which increased drastically during the 1960s. The fishing vessels became larger and more effective in catching fish. The fishing grounds were also farther away from the shore. However, the traditional way of storing the fish in boxes with ice turned out to be too labour-intensive which often led to increased fish temperatures during transportation. This resulted in poor quality and a lot of the catch had to be sold as oil or fishmeal, with very low profit. After some time with searching and testing, fish tanks with refrigerated seawater (RSW) were selected as the best method for preserving the products on the fishing vessels. In Norway, the primary requirements included insulated tanks, chilling to -1 °C, circulation, cleaning equipment, loading equipment and temperature controlling equipment. The onboard RSW chilling resulted in that almost all mackerel and herring were sold to consumers and not being processed to fish oil or meal. (Widell et al, 2016). Other types of fish, like cod and saithe, are typically stored fresh on ice in the ship. In most cases, there is not a refrigeration system onboard, so the ice is brought from land. Enough ice should be brought to last for the complete journey. These types of fish can also be frozen onboard, typically in plate freezers or filleted and single-frozen.

Animals for **meat** production are mainly transported alive to the slaughterhouse. Chilling of the meat after slaughter and partitioning is necessary, but the rate of chilling affects the quality of the product. Chilling too rapidly will decrease the tenderness of the meat (cold-shortening), especially for beef, pork and lamb. However, electrical stimulation of the meat can be used for avoiding this issue. Studies show that the weight loss can be reduced by fast chilling of meat. (Johannessen, Paulsrud, 2000)

Milk cooling and storage at farms has been provided by innovative R744 refrigeration units in Norway and elsewhere (Fig. 3, left). Such units provide a fast cooling of fresh milk, while the hot side of the refrigeration circuit is applied to produce sanitary hot water at 90°C, applied for cleaning purposes of the milk handling equipment.

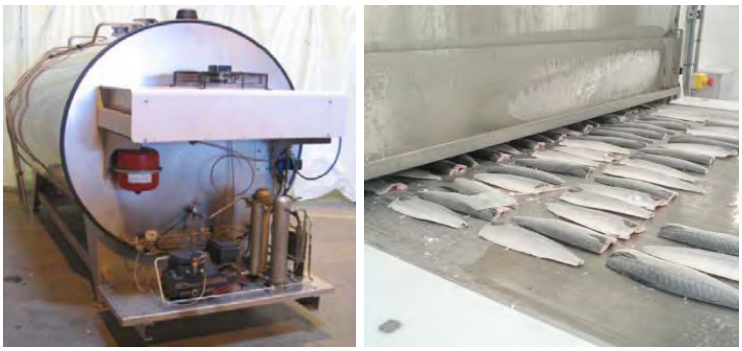

Figure 3. Milk cooling unit with CO_2 refrigeration system (left). Mackerel fillets frozen in belt freezer (right)

3.3 Processing

Many different food products are further handled in an industrial processing plant, before being distributed to the consumers. Typical processing includes peeling, cutting and chilling/freezing of **fruits, vegetables, tubers and roots** and slaughtering, gutting, partitioning, filleting of **fish and meat**. Refrigeration during all steps of processing will increase quality and could also reduce food loss.

Superchilling is a process where the temperature of a product is reduced below regular chilling, but still higher than freezing store temperatures. The product is partly frozen, but the consumer will experience it as a fresh product. Chilling a product below initial freezing point will result in a frozen surface layer of 1-3 mm (Kaale, 2014), which creates a cold storage within the product. This can be compared with chilling with ice, where the cold storage is outside of the product. The shelf life of the product increases with decreasing temperature, especially at lower temperatures. During transport, the temperature of the product will level out, resulting in a low temperature within the product and

less or no ice. In general, fast cooling results in smaller and more even distribution of the ice crystals than slow cooling, which will give a better product quality. Fast cooling can also give higher production capacity. Other factors that affect the quality of the products are the initial quality of the product, packing and storage temperature. The complete cold chain should therefore be evaluated, to get the best possible product.

Superchilling can be a less energy demanding alternative to a freezing/thawing, with less liquid loss. It also includes fewer handling elements and thus lower labour costs (Magnussen, Haugland et al. 2008). When storing and transporting chilled products, it is common to do this with ice together with the fish inside the boxes. A typical ratio is 1/3 of ice and 2/3 of fish. When superchilling the fish, ice is not necessary, since parts of the products are frozen. That means more product within each transport, which is beneficial both financially and environmentally. The challenge with superchilling is to control the quantity of ice in the product, the ice fraction, so that it is neither too low, nor too high.

Frozen food products are mainly stored between -20 °C and -30 °C. The lower temperature levels are necessary for fish and ice cream. There are several different food freezing methods. Air is often used because it is easily available, even though it has poor heat transfer properties. Air blast fans increase heat transfer, but they also use electricity and add heat to the freezing tunnel. Large products are often frozen in air blast freezing tunnels, while smaller products are frozen in belt freezers (see Fig. 3, right) or fluidized bed freezers. If the product is unwrapped, a disadvantage is evaporation from the surface. Packaging, on the other hand, results in poorer heat transfer and longer freezing times. There is a risk of uneven air distribution and uneven freezing times in a blast freezer, which can partly be avoided if the products are continuously loaded and unloaded. Proper tunnel design and loading is essential. Unpacked, single products can be frozen in impingement freezers at high production rates. In these, air jets (20-40 m/s) are directed at the products, which provides higher heat transfer than in blast freezers. (Kaale et al., 2014) (Widell, 2012)

Another type of freezing system is the plate freezer, where the refrigerant is circulated inside plates and the products are pressed between the plates. The products are frozen into equally shaped boxes, which is beneficial for stacking and transport. These freezers are energy efficient because no fan energy is needed, and higher evaporation temperatures can be used than in air blast freezers. Liquid as a cooling media is used in cryogenic freezers. The products are sprayed with, for example, liquid carbon dioxide resulting in high temperature differences and high production rates. A refrigeration plant is not needed, but the cooling media is expensive, and large quantities are necessary. All types of freezers should be insulated from surrounding (warmer) areas to prevent heat leakage into the freezer.

Heat absorbed by the refrigeration unit during the cooling / freezing process can be upgraded to e.g. useful hot water/steam applied to clean and sterilize the process equipment after usage. Depending on the simultaneity of cooling and heating demands, compact thermal cold/hot storage devices can be integrated into the energy systems.

3.4 Distribution

To secure food quality and at the same time achieve a high seasonal energy efficiency of the refrigeration systems, the performance requirements should be described over a wide range of operating conditions. High part load efficiency is important for both stationary equipment as well as for transport refrigeration units. Implementation of capacity control devices and thermal energy storage (for example phase change materials) to avoid on-off operation are examples to secure constant foodstuff temperatures. Reliability and redundancy options are important factors to secure the process plant operation.

Transport of food between the production sites, after processing and storage towards the end-users must be performed in well designed and refrigerated containments. Temperature fluctuations should be avoided.

The supermarket or local grocery store is the final distribution centre for food towards the end-users. To avoid food wastage of chilled and frozen foodstuff at this stage of the food chain, the temperature distribution and variations within the cold rooms and display cabinets are the essential parameters (Minetto et al. 2014). Novel CO_2 refrigeration units enable uniform temperature distribution and

eliminate the need for long defrosting cycles. Long cycles of defrosting could lead to several degrees of increased product temperatures, reducing product quality and shelf life.

3.5 Consumption

To achieve SDG, appropriate food waste mapping techniques and technologies are being developed and the proper reporting and the compilation of the statistics has been carried out. The 'ForMat' project in Norway carried out 2010-2015 shows a decrease of food waste by 25500 tonnes. Consumers were for example instructed to have the right temperatures in refrigerators, information was given about food waste and that food can be edible also after the "best before"-date. After the focus on consumers in the *ForMat* project, the focus has now shifted towards processing phase, for example a SINTEF Ocean is leading a project on mapping of food loss in seafood industry.

In China, some steps have been started by the central and local government to decrease and manage food wastage. For example, "Empty your plate" campaign in 2013 for highly grassroots level has encouraged the consumers to avoid food waste. A blog of posts in Weibo (a Chinese social media) has enhanced awareness all over the country and changes in the policies so that the restaurants had to change the size of the plates, etc. (Liwei et al., 2013)

Some creative ideas have been implemented in India. For example, the employees of municipality of Kolkata collect the waste directly from the homes and recover 80% of the waste. Women's associations collect and dry the food waste for recycling with minimal charge in cities of Bangalore and Pune. The 419 slums of Mumbai have adopted a system of waste collection effectively. The leftovers from the hotels are distributed to the homeless and orphans. The food not suitable for human consumption is given to the pig farms, the pig farmers collect the remains from the hotels and restaurants.

Many small vendors in India take fruits and vegetables to the doors and sell them. In this process the food is exposed to high temperature, which is the cause of short life of the food products. To cool the vegetables, they sprinkle cold water, but it also leads to faster spoilage of the vegetables. Indian Agricultural Research Institute (IRAI), New Delhi has developed a solar powered vending cart-technology to boost the economy of poor vegetable vendors. It is expected to store the fresh fruits and vegetables for 2-5 days. The extended shelf life of the food can hence help the vendors generate more income. There is a large potential for further development in this area.

3.6 Monitoring environmental parameters

Monitoring environmental parameters such as temperature and humidity in the supply chain of perishable foods is essential to track quality deterioration and thus reduce losses. Real-time monitoring of food quality has a lot of prospect, but it is yet to come to actual practice. However, recent initiatives in this direction indicate the possibilities of real time monitoring and building models to predict and improve quality and shelf life. (Abad et al 2009). Initial conditions of the product also play a key role to assure durability. Often, fruits and vegetables are bruised and damaged due to improper handing during harvesting and transportation (FAO 2017). In this regard, visible and near-infrared (Vis/NIR) spectroscopy has been one of the most successful techniques for non-destructive measurement of chemical constituents and quality attributes (such as damage, internal quality, total soluble solids, titratable acidity and maturity index) of horticultural and food products (Pu et al 2015) (Hu et al 2017).

More attractive solutions than conventional RFID have been proposed in some pilot business research. An example is wireless sensor network (WSN), which can be used to detect different kinds of environment parameters, such as the temperature, humidity, carbon dioxide, ethylene, and vibration (Wang et al 2015). This can help real time tracking and remote monitoring in food traceability. Many authors have proposed optimization models for maximizing the profit in such supply chains, while maintaining quality and reducing losses.

Other factors that can be studied are the degree of impact the products have on the climate and the environment. Winther et al (2009) showed that seafood products exported as frozen or superchilled (shipped) had lower environmental impact than fresh, transported with air freight. Increasing the amount of processed fish, leaving the rest raw material for other production, would also reduce the environmental impact, compared to transporting the whole fish.

3.7 Refrigerants

Refrigeration systems should only apply working fluids with lowest possible climate and environmental impact, therefore, natural working fluids are a safe and sustainable option, due to their well-known behaviour when released into the environment. When developing new heat pumping system, focus should be: energy efficiency also during part load and integration of multi-functionalities. This means that advanced integrated units can provide freezing, cooling, air-conditioning, space heating, hot water, and process steam.

Due to the Kigali Amendment of the Montreal Protocol, and the EU F-gas regulation, the traditional HCFC and HFC refrigeration equipment in the supermarket sector is nowadays replaced by the end-users with units applying natural working fluids. The environmental impact of working fluids like propane (self-contained cabinets) and carbon dioxide (centralised units) are well known and no restrictions will appear in the future. This makes this technology attractive to end-users whenever they can find a local vendor to install and maintain the units. A UNIDO supported demonstration supermarket in the capital of Jordan (Jordan is defined as a High Ambient Temperature HAT country) is an example, that a leapfrog in refrigeration technology from HCFC to CO_2 is possible. The feedback from the supermarket owner after the first year of operation (January 2018 to January 2019):

- No extraordinary maintenance visits, i.e. no failure in the system nor the cabinets
- Zero food wastage due to stable temperature levels in the display cabinets
- Reduction of energy demand related to the refrigeration unit by more than 30% compared to similar new HFC installations in the region

Training and knowledge transfer are important for a successful and fast phase in of natural refrigerants within the food sector and supermarkets globally. Relatively high first costs to install integrated CO_2 refrigeration systems are still the main barrier to a fast phase in of this technology on a global scale, especially when none of the local vendors has delivered such units before.

4 CONCLUSION

With the world population set to approach an estimated 9 billion by 2050, against a background of finite natural resources, we need renewable biological resources for securing healthy food and animal feed to meet the nutritional requirements of the growing population.

Most of high-income areas have good infrastructure and technologies for cold chain management. It is in low-income countries and especially within agriculture that substantial improvements can be made to the cold chains to reduce food loss as a result.

If food wastage was a country, it would be the third largest GHG emitter in the World after China and the USA. Environmental impact of the food chains will be reduced if the overall losses are reduced. Food production requires energy, so reducing food losses will also result in reduction in energy use per tonne of food produced. Energy use has different environmental impacts depending on how it is produced and transferred, but it is seldom zero and improving the energy efficiency of a process is always positive for the environment. Refrigerant systems still use working fluids that, if released to the atmosphere, deplete the ozone layer and increase the global warming potential. During the last decades, there has been a focus on reducing these emissions and finding more environmentally friendly replacements. However, there are still too many refrigeration systems in place that use harmful refrigerants. In further research and development, it is necessary to:

- Reduce food losses along food value chains by:
    - Increasing awareness of the benefits of high-performance cold chains
    - Increasing collaboration between politicians, refrigeration stakeholders and food producers to improve cold chain technology and management
    - Transfer of high-performance, environmentally friendly and cost-effective technology to areas where food loss is high
    - Training of technicians and users for proper and efficient operation of refrigeration systems
- Reduce energy consumption and carbon footprint in the cold chain

REFERENCES

Abad et al . (2009). RFID smart tag for traceability and cold chain monitoring of foods: Demonstration in an intercontinental fresh fish logistic chain. Journal of food engineering 93(4), 394-399.

Artiuch, P., & Kornstein, S. (2012). Sustainable approaches to reducing food waste in India. mit.edu.

CSR Journal (2015). The CSR Journal. Retrieved from http://thecsrjournal.in/food-wastage-in-india-a-serious-concern/

Dhakal et al. (2014). Effect of Inadequate Processing and Cold Storage Unit on the Horticultural Crops of India. 48th Annual Convention of Indian Society of Agricultural Engineers.

FAO (2012). Food and Agriculture Organization. Retrieved from http://www.fao.org/save-food/resources/keyfindings/infographics/en/

FAO (2016). The State of Food and Agriculture. Rome: FAO. Retrieved from http://www.fao.org/3/a-i6030e.pdf

FAO (2017). Food loss prevention in perishable crops. Retrieved from FAO Corporate Document Repository.

Gustavsson et al. (2011). Global food losses and food waste – Extent, causes and prevention. Rome: FAO.

Hu et al. (2017). Development of a multichannel hyperspectral imaging probe for property and quality assessment of horticultural products. Postharvest Biology and Technology 133, 88-97.

Jakhar, N., Rudra, S., Nishad, J., & Walia, K. K. (2015). Waste utilization from fruits and vegetable industry. Biotechnology for food and fuel. New Delhi: TERI Press.

Johannessen, Paulsrud (2000). The effects of suspension method and chilling regime on pork eating quality. [in Norwegian] Master, Ås, Norway, Norges Landbrukshøgskole

Kaale, L. D. (2014). Modelling and ice crystallization/recrystallization of foods in superchilling technology, Norwegian University of Science and Technology. PhD.

Minetto S., Brignoli R., Zilio C., Marinetti S. (2014) Experimental analysis of a new method for overfeeding multiple evaporators in refrigeration systems. International journal of refrigeration 38 (2014) 1 9

IIR (2009). 5th Informatory note on refrigeration and food: The role of refrigeration in worldwide nutrition.

Lipinski, B., Clowes, A., Goodwin, L., Hanson, C., Swannell, R., & Mitchell, P. (2017). SDG TARGET 12.3 ON FOOD LOSS AND WASTE: 2017 PROGRESS REPORT.

Liu, G. (2013). Food losses and food waste in China. Trondheim.

Liwei, G., Shengkui, C., Xiaochang, C., Dan, Z., Xiaojie, L., Qi, Q., & Yao, L. (2013). An overview of the resources and environmental issues from wasted food in urban catering across China. Journal of resources and ecology 4(4), 337-343.

Magnussen, O., et al. (2008). "Advances in superchilling of food - Process characteristics and product quality." Trends in Food Science & Technology.

Pu et al. (2015). Recent Progress of Hyperspectral Imaging on Quality and Safety Inspection of Fruits and Vegetables: A Review. Comprehensive Reviews in Food Science and Food Safety, Volume 14, Issue 2, 176-188.

Wang, X., & Li, D. (2012). A dynamic product quality evaluation based pricing model for perishable food supply chains. Omega, 40(6), 906-917.

Widell, K. N. (2012). PhD thesis: Energy efficiency of freezing tunnels: towards an optimal operation of compressors and air fans. (Doctoral), Norwegian University of Science and Technology, Trondheim, Norway.

Winther, U., Ziegler, F., Hognes, E. S., Emanuelsson, A., Sund, V., & Ellingsen, H. (2009). Carbon Footprint and energy use of Norwegian seafood products, Report SFH80 A096068. Retrieved from sjomatnorge.no

World Population Trends (2017). Retrieved from United Nations Population Funds: http://www.unfpa.org/world-population-trends

Manuscript ID: 450
DOI: 10.18462/iir.icr.2019.0450

Numerical heat transfer model for industrial chilling installations

Duy K. HOANG [(a)], Simon J. LOVATT [(a)], Jamal R. OLATUNJI [(b)], James K. CARSON [(a)]

[(a)] University of Waikato, Private Bag 3105, Hamilton 3240, New Zealand
[(b)] Massey University, Private Bag 11222, Palmerston North 4442, New Zealand

ABSTRACT

A computational fluid dynamics (CFD) simulation was developed to model heat transfer of six blocks of agar in a forced air chilling process. The flow field was solved at steady-state and decoupled from the heat transfer processes. The six blocks of agar were placed in a polystyrene test chamber that mimics the airflow and product arrangement in an industrial cheese chilling tunnel. Temperatures were measured at the surfaces and the geometric centre of the tested blocks of agar. Good agreement was observed between predicted and experimental data. The local heat transfer coefficient across blocks of agar surface varied by a factor of five at the high air velocity.
Keywords: CFD, heat transfer, chilling, industrial application.

1. INTRODUCTION

Food technology continues to develop as new refrigeration equipment becomes available and as consumer preferences continue to change (Bogh-Sorensen, 2006). On the industrial scale, food refrigeration equipment is often made to order for a given end user, and may be designed either for a single type of product or multiple products. With such a high degree of customisation in modern refrigeration equipment, it is necessary to have a design optimisation tool to evaluate the performance of the refrigeration system. The rate of cooling for a given chilling operation depends on the refrigeration air temperature and airflow characteristics (turbulence intensity, velocity), packaging, and packing arrangement, as well as the dimensions, morphology and physical properties of the food product (ASHRAE, 2006; O'Sullivan et al., 2014).

The experimental assessment of the cooling performance of different package systems is not only costly and time consuming, but also limited in scope. The growth of computer power in recent years has led to an increased use of numerical models to the predict airflow patterns and cooling profiles of food products during forced-air cooling (Defraeye, Verboven, & Nicolai, 2013; Ferrua & Singh, 2009; Gruyters et al., 2018; Kuffi et al., 2016; O'Sullivan et al., 2016). The use of numerical modelling provides detailed information on the local airflow behaviour and temperature profile within the product at different operating conditions. This assists the design process and improves cooling performance of food processing equipment.

This paper details a CFD based numerical model for six blocks of agar in a chilling tunnel. The model was then validated using measured temperatures profile of agar at different air velocities.

2. MATERIALS AND METHODS

2.1 Experiments

Chilling experiments were conducted at AgResearch Ltd. Six blocks of agar gel (food analogue) were place in a polystyrene test chamber (PTT) (Fig. 1a) which was in turn in an environmental testing chamber (ETC). A transition section (Fig. 1b) was created to guide the air flow from the inlet

through the product due to suction created by a fan at the tunnel outlet. The experimental system allowed for precise control of the temperature and air velocity of the cooling air passing through the PTT.

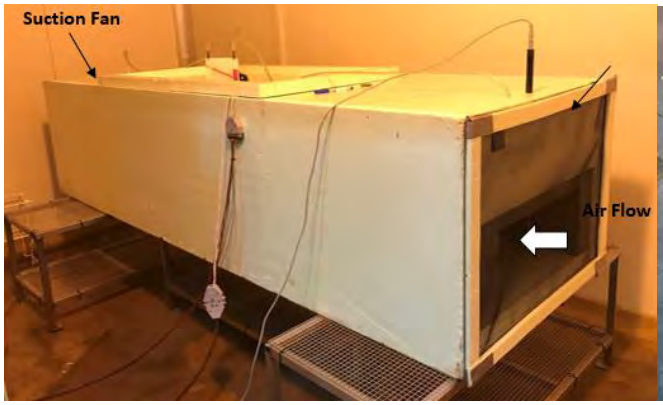

Figure 1a: The Styrene Test Chamber

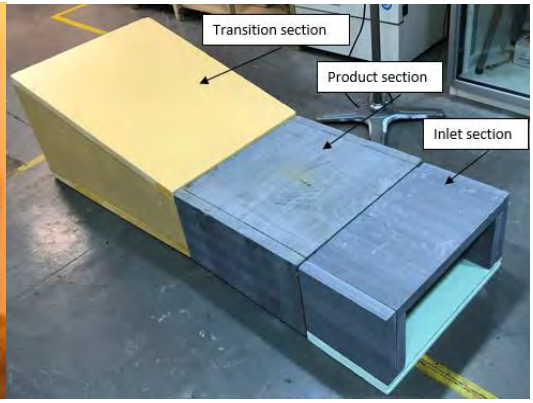

Figure 1b: The transition section

Six blocks of agar were placed in the PTT, arranged (Fig. 2) to create an airflow pattern similar to an industrial cheese chilling tunnel. The four blocks on the two sides of the central pair were cut by the symmetry plane and were bordered by insulated walls to reduce the air flow cross-section. The dimensions of the two test blocks in the middle were 135 x 210 x 270 mm, while the dimensions of the half blocks on the sides were 135 x 105 x 270 mm.





Figure 2: Six blocks of agar arrangement

Temperatures were measured with T-type thermocouples connected to a Keysight 24982A data acquisition unit and were recorded every 60 seconds. Fig. 3 indicates the thermocouple positions in the agar blocks. Thermocouple Numbers 1 and 11 measured the cooling air temperature. The multipoint thermocouple probes supporting thermocouple Numbers 3, 4, 5 and 13, 14, 15 were placed along the shortest axes of Block A and Block B respectively. Thermocouple Numbers 4 and 14 were at the geometric centre of the blocks and the two other thermocouples on the multipoint probes were 2 cm from the geometric centre. The other thermocouples were at the middle of each surface of the agar blocks. The thermocouples were calibrated with an ice-point reference prior to the experiments.

Prior to each chilling trial the six blocks of agar were equilibrated at 20 °C for 24 hours. The ETC temperature was set and maintained at 0 °C during the trials. Three different inlet air velocities (1 m s^{-1}, 3 m s^{-1}, 4.5 m s^{-1}) were tested, and each trial was repeated three times.

Air velocity was measured by a hot-wire anemometer (Dantec 54N60 FlowMaster) before and after each trial at the inlet of the tunnel and at 2 cm above the top surface of the test blocks. The sample time of each velocity measurement was five minutes. The air velocity was kept constant during

each experiment. The inlet and outlet pressures of the airflow through the PTT were measured before and after each trial using an inclined fluid manometer (RS Pro, RS 730-2937)

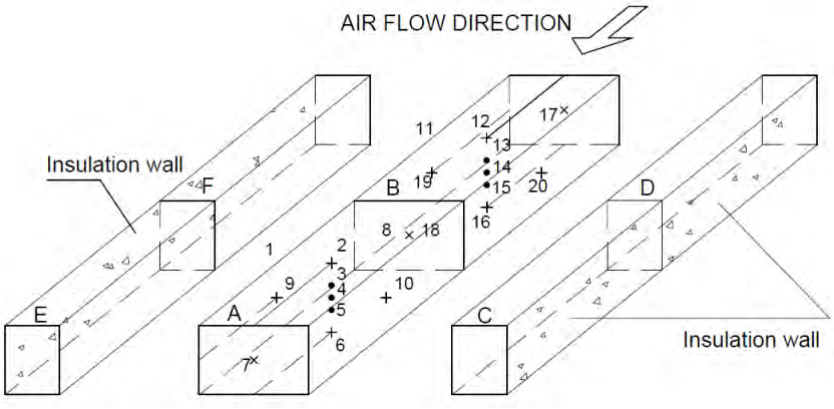

Figure 3: Thermocouples position in the agar chilling trials

2.2 Numerical CFD Model

2.2.1 Geometrical model

Based on a symmetry plane, the computational domain of the agar chilling model was reduced by a factor of 2 (Fig. 4). The geometrical model was created using Ansys Design Modeller, with half of the centre blocks, and the two half-blocks on the left side included in the geometrical model.

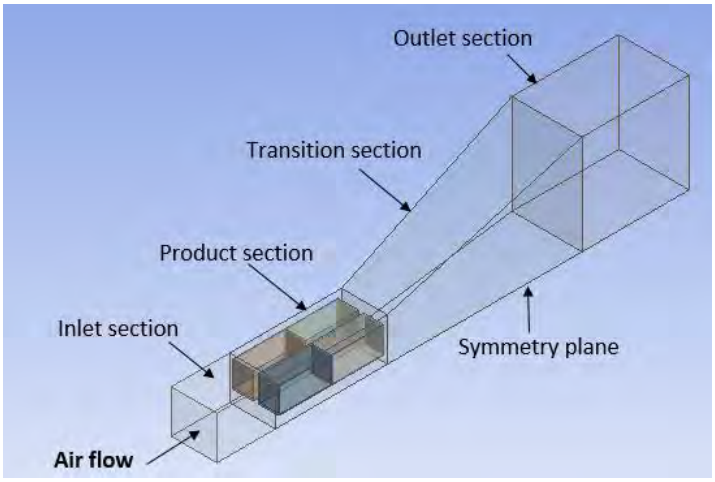

Figure 4: The computational domain of agar chilling

The inlet boundary was located 30 cm upstream of the product section and the outlet boundary was 155 cm downstream of the product section to prevent the inlet and outlet boundary conditions from influencing the airflow distribution over the product section.

2.2.2 Numerical setup

Heat transfer mechanisms during agar chilling include: forced convection between the refrigerated air flow and the blocks of agar surface, conduction inside the blocks of agar, and radiation between the blocks of agar surface and the insulated walls. Typically, in the forced air cooling of food product, the influence of radiation is expected to be small compared to the convective heat transfer (Defraeye, Lambrecht, et al., 2013). Therefore, radiation was neglected in the CFD model.

The momentum and energy transport equations were solved using the Reynolds-averaged Navier-Stokes equations (Versteeg & Malalasekera, 2007). The turbulence model used was the standard k-ε combined with the Enhanced Wall Treatment function.

The thermo-physical properties of the agar, plastic boxes and air are listed in Table 1, and were kept constant throughout the simulation, since they have negligible dependence on temperature in the range between 0°C (cooling air temperature) and 20°C (the initial agar temperature) (Ferrua & Singh, 2009; O'Sullivan et al., 2016). Air properties were evaluated at 0°C while agar and plastic properties were evaluated at 20 °C.

Table 1. Material thermo-physical properties

Materials	Density kg m $^{-3}$	Specific heat J kg $^{-1}$K $^{-1}$	Thermal cond, $Wm^{-1}K^{-1}$	Dynamic Viscosity kg m^{-1} s^{-1}	Reference
Air	1.292	1006	0.02364	1.729 x 10^{-5}	(Yunus & Afshin, 2011)
Plastic	1190	1470	0.2	-	(EngineeringToolbox)
Agar	998	4182	0.543	-	(Zhang et al., 2010)

A hybrid mesh with tetrahedral and hexahedral elements was generated using ANSYS mesh generation software. The element size in the product section was 10 mm while the maximum face size was kept as default (36.5 mm). The fluid region close to the agar block surface was meshed with a small mesh size. From the surface of the agar blocks outwards, 10 layers of hexahedral element were placed with the first layer thickness of 0.1 mm and the growth rate of 1.2. A mesh sensitivity study was performed by running simulations at three different mesh sizes to estimate the spatial discretization error from the difference in the average surface heat transfer coefficient (*SHTC*) of two test blocks of agar (Table 2).

The mesh independent solution was determined by Richardson extrapolation (Roache, 1997), and the value of the average *SHTC* was 42.44 $Wm^{-2}K^{-1}$. The error of the average *SHTC* for a mesh size of 0.1 mm of 1.2% was considered sufficiently low. Therefore, the mesh with 273258 elements was chosen for these computations.

Table 2. Effect of different mesh size on average SHTC of two test blocks of agar

Mesh size on product surface, mm	Number of elements	Y plus (average)	SHTC (average), W m^{-2} K^{-1}
0.4	262923	5.06	46.05
0.2	266901	2.52	44.12
0.1	273258	1.25	42.94

The surfaces of the blocks of agar were modelled as no-slip walls with zero roughness. A zero heat flux boundary condition was used for the side walls of the PTT. The coupled thermal condition was applied for the interfaces between air flow and plastic, plastic and agar, and plastic and plastic. The inlet of the computational domain was modelled with a uniform velocity boundary condition with a turbulence intensity of 1%. The outlet of the computational domain was defined as a pressure outlet with an underpressure measured by the inclined manometer to represent the pressure drop created by the suction fan. The outlet pressure of -85, -35 and -5 Pa produced inlet velocities of 4.5 m s^{-1}, 3 m s^{-1} and 1 m s^{-1}, respectively.

In this study, the simulations were performed with the ANSYS fluent 18.2 software which uses the finite volume technique. Second-order discretisation was used throughout. The SIMPLE algorithm was used for pressure-velocity coupling. To speed up the simulation, the momentum equations were decoupled from heat transfer equations. A converged steady-state solution for airflow was used as an initial condition for the transient heat transfer equations. The transient simulation was run with a time step of 60 s. The computational time for 800 minutes cooling took 33 minutes on a 64 bit Intel ® Xeron ® CPU E5-1620, 3.5 GHz, 16 GB RAM.

3. RESULTS AND DICUSSIONS

3.1 Local surface heat transfer coefficient

In this study, the surface heat transfer coefficient (*SHTC*) was calculated from Eq. (1):

$$SHTC = \frac{q_{wall}}{T_{in} - T_{air}} \quad \text{Eq. (1)}$$

where q_{wall} (W m^{-2}) is the steady state wall heat flux, T_{in} (K) is the initial temperature of the blocks of agar, and T_{air} (K) is the cooling air temperature. Fig. 5 shows a contour plot of the heat transfer coefficient on the surface of two test blocks of agar, at the inlet air velocity of 4.5 m s^{-1}. The *SHTC* across the agar block surface varied by factor of 5, with the maximum value at the four corners of the surface on the upstream side and minimum values at the opposite surface. The surface-averaged *SHTC* over the agar blocks at inlet air velocities of 1 m s^{-1} , 3 m s^{-1}, and 4.5 m s^{-1} were 15.3 W m $^{-1}$ K $^{-2}$, 32.5 W m $^{-1}$ K $^{-2}$ and 42.9 W m $^{-1}$ K $^{-2}$ respectively.

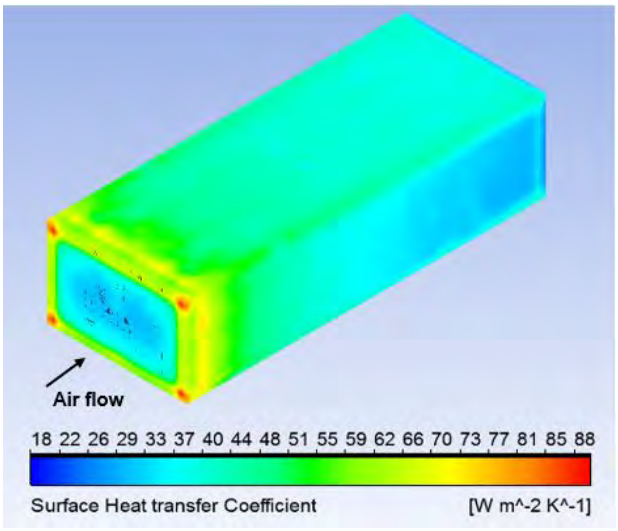

Figure 5: Surface heat transfer coefficient distribution on the surface of two test blocks of agar at the inlet air velocity = 4.5 m s^{-1}

3.2 Comparison of measure and predicted temperature

3.2.1 Uncertainty analysis of the empirical data

The temperature profile of the agar blocks of was computed by averaging the temperature history of the three replicates of the experimental trials Eq. (2):

$$\overline{T_i}(t) = \frac{\sum_{j=1}^{n} T_{i,j}(t)}{n} \quad \text{Eq. (2)}$$

The experimental standard deviation in $\overline{T_i}(t)$ at 95% confidence level and a normal distribution, was computed by Eq. (3):

$$P_{\overline{T_i}} = t_{n-1,0.025} \times \frac{1}{\sqrt{n}} \left[\frac{1}{n-1} \sum_{j=1}^{n} \left(\overline{T_i} - T_{i,j} \right)^2 \right]^{1/2} \quad \text{Eq. (3)}$$

In general, the standard deviation of all monitored temperatures was lower than 0.5°C, except for the surface temperatures (T8 and T18) at the interface of the two test blocks. This could be explained by the imperfect thermal contact of the two test blocks, as there was a small air gap between them.

3.2.2 Comparison of measured and predicted temperatures

Fig. 6 shows the comparison between the predicted and experimental temperatures of the two test blocks, in which Block B was at the front and Block A was at the rear along the flow direction. Overall, the model predictions fit well with the experimental data.

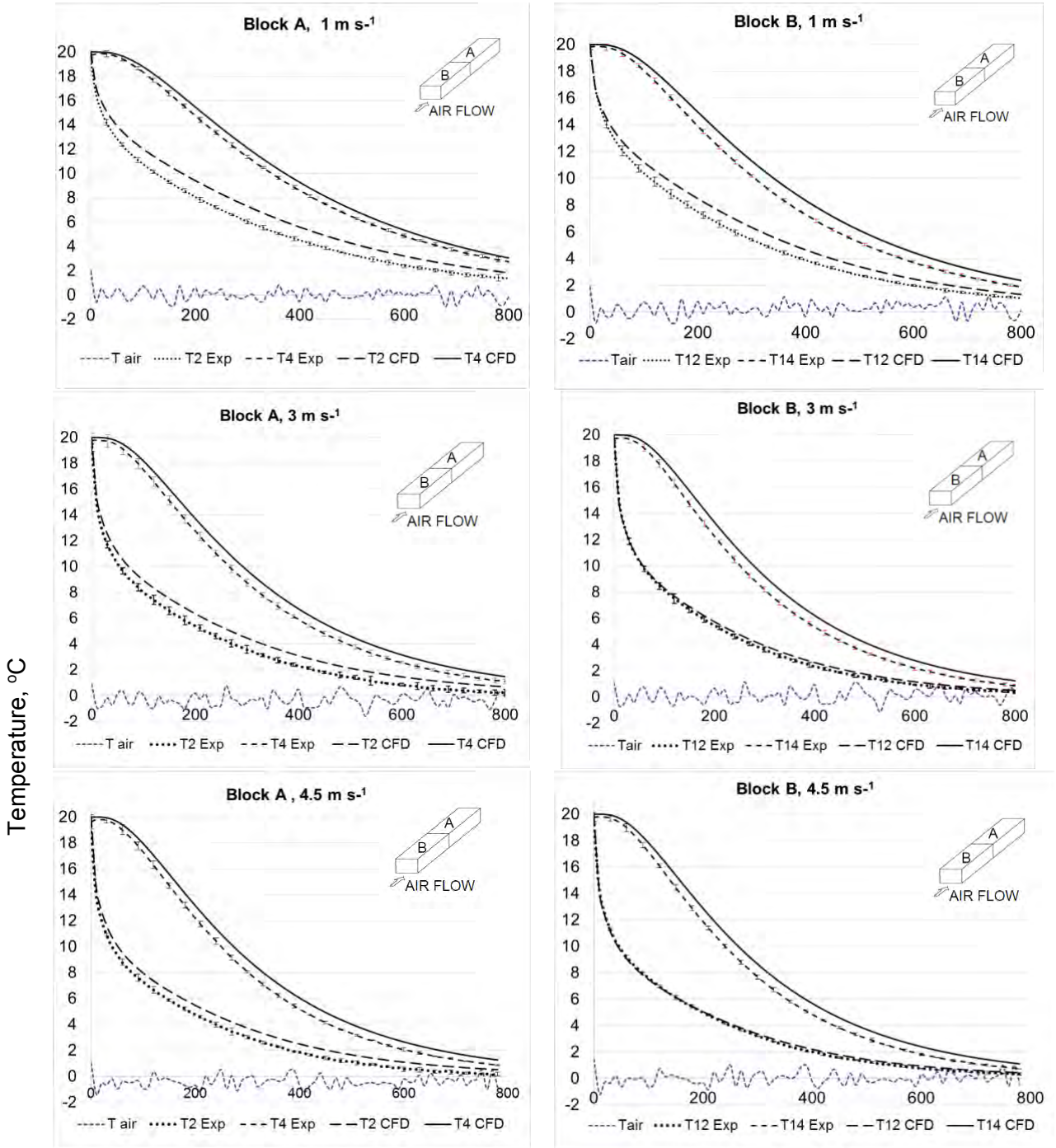

Figure 6: Comparison between predicted and measured temperatures in the two test blocks

For the three air velocities tested, the mean absolute differences between the measured and predicted temperatures (ΔT_{mean}) during the chilling process were lower than 1.0 °C. At the lowest inlet air velocity (1 m s^{-1}), the largest difference between predicted and measured temperatures was at the top surface (T2 and T12) with ΔT_{mean}= 0.98 °C and 0.77 °C, respectively. At the highest

air speed (4.5 m s^{-1}), the largest differences were at the centre temperatures (T4 and T14), with ΔT_{mean}= 0.68 °C and 0.69 °C, respectively.

At low air velocity (low Reynolds number) the contribution of natural convection, and radiation (which were not included in the model) to the overall heat transfer between the air flow and the product surface would have been more significant than that at the high air velocity, which could explain why the agreement between measured and modelled temperature was better at higher air velocities.

Fig. 7 illustrates the predicted temperature differences at the same positions on the surface (T2 vs T12, T10 vs T20) and at the geometrical center (T4 vs T14) of the two test blocks of agar at the inlet air velocity of 4.5 m s^{-1}. The temperature decreased faster in block B (in the front along the air flow direction) than in block A (at the back along the air flow direction). This trend is more obvious at the surface temperatures at the beginning of the chilling process. This observation was to be expected since the *SHTC* decreased along the flow direction (Fig. 5). At the end of the process, the driving force of the heat transfer process (temperature difference between the product surface and the refrigerated air) was decreased and the temperature of the two blocks was almost the same.

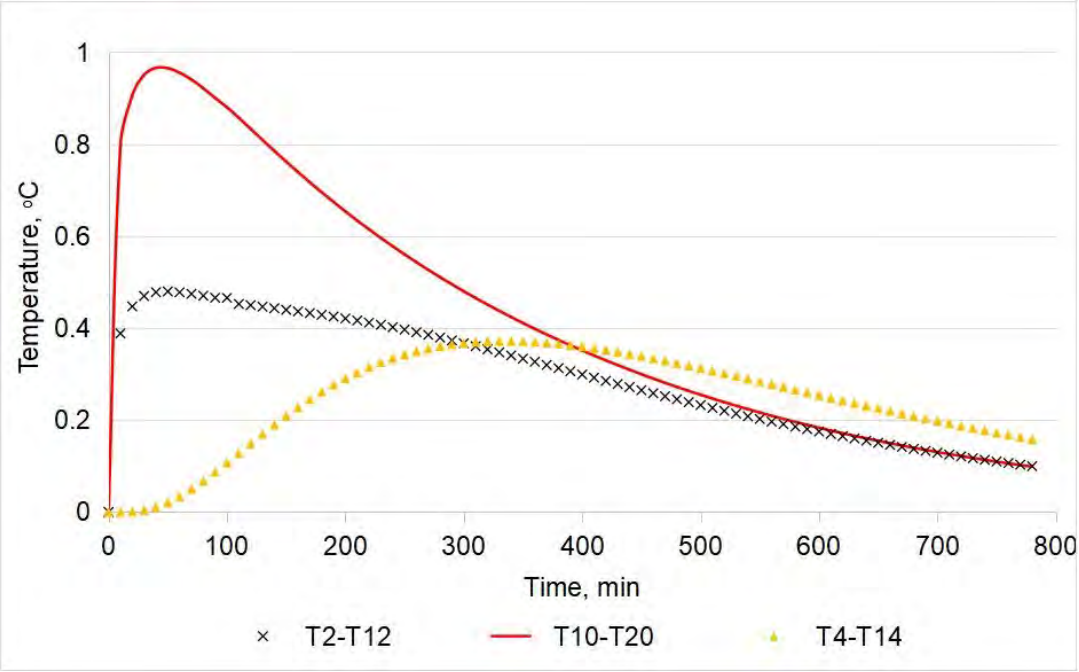

Figure 7: Temperature difference of the two test blocks at the same positions at the inlet air velocity of 4.5 m s^{-1}

5. CONCLUSIONS

The use of standard k-ε turbulence model with the Enhanced Wall Treatment function can predict, to within 1 °C, the forced air chilling of agar blocks in an arrangement that was representative of an industrial cheese chiller. The model presented in this study can be used to evaluate the cooling performance at different operating conditions of the cheese chilling which has similar airflow pattern and products arrangement as the experiment.

NOMENCLATURE

$P_{\overline{T}}$	Standard deviation in $\overline{T_i}(t)$ (K)	T_{air}	The cooling air temperature (K)
q_{wall}	The steady state wall heat flux (W m^{-2})	$\overline{T_i}$	Average temperature at thermocouple

			number *i*-th (K)
t	Time (s)	$T_{i,j}$	Temperature thermocouple number *i*-th in the *j*-th trial (K)
$t_{n-1,\ \alpha/2}$	Student's t-statistic with (*n*-1) degrees of freedom at a (1-α) confidence level	n	Number of the experimental trial, $n = 3$
T_{in}	The initial temperature of the blocks of agar (K)	$SHTC$	Surface heat transfer coefficient (W m^{-2} K^{-1})

REFERENCES

ASHRAE, A. H. (2006). Refrigeration. *American Society of Heating, Refrigerating and Air-Conditioning Engineers, Atlanta, GA*

Bogh-Sorensen, L. (2006). *Recommendations for the processing and handling of frozen foods* (4th ed.): International Institute of Refrigeration, Paris.

Defraeye, T., Lambrecht, R., Tsige, A. A., Delele, M. A., Opara, U. L., Cronjé, P., . . . Nicolai, B. (2013). Forced-convective cooling of citrus fruit: package design. *Journal of Food Engineering, 118*(1), 8-18.

Defraeye, T., Verboven, P., & Nicolai, B. (2013). CFD modelling of flow and scalar exchange of spherical food products: Turbulence and boundary-layer modelling. *Journal of Food Engineering, 114*(4), 495-504.

EngineeringToolbox. Thermal Conductivity of common Materials and Gases. Thermal Conductivity of common Materials and Gases

Ferrua, M., & Singh, R. (2009). Modeling the forced-air cooling process of fresh strawberry packages, Part I: Numerical model. *International Journal of Refrigeration, 32*(2), 335-348.

Gruyters, W., Verboven, P., Diels, E., Rogge, S., Smeets, B., Ramon, H., . . . Nicolaï, B. (2018). Modelling Cooling of Packaged Fruit Using 3D Shape Models. *Food and Bioprocess Technology, 11*(11), 2008-2020.

Kuffi, K. D., Defraeye, T., Nicolai, B. M., De Smet, S., Geeraerd, A., & Verboven, P. (2016). CFD modeling of industrial cooling of large beef carcasses. *International Journal of Refrigeration, 69*, 324-339. 10.1016/j.ijrefrig.2016.06.013

O'Sullivan, J., Ferrua, M., Love, R., Verboven, P., Nicolaï, B., & East, A. (2014). Airflow measurement techniques for the improvement of forced-air cooling, refrigeration and drying operations. *Journal of Food Engineering, 143*, 90-101.

O'Sullivan, J., Ferrua, M. J., Love, R., Verboven, P., Nicolaï, B., & East, A. (2016). Modelling the forced-air cooling mechanisms and performance of polylined horticultural produce. *Postharvest Biology and Technology, 120*, 23-35.

Roache, P. J. (1997). Quantification of uncertainty in computational fluid dynamics. *Annual review of fluid Mechanics, 29*(1), 123-160.

Versteeg, H. K., & Malalasekera, W. (2007). *An introduction to computational fluid dynamics: the finite volume method*: Pearson Education.

Yunus, C. A., & Afshin, J. G. (2011). Heat and mass transfer: fundamentals and applications. *Tata McGraw-Hill, New Delhi, India*

Zhang, M., Che, Z., Chen, J., Zhao, H., Yang, L., Zhong, Z., & Lu, J. (2010). Experimental Determination of Thermal Conductivity of Water− Agar Gel at Different Concentrations and Temperatures. *Journal of Chemical & Engineering Data, 56*(4), 859-864.

Manuscript ID: 451

DOI: 10.18462/iir.icr.2019.0451

Experimental study on effects of packing arrangement and plastic liner bag on freezing rates of bulk packed chicken drumsticks

Duy K. HOANG[(a)], Jamal R. OLATUNJI[(b)], Simon J. LOVATT[(a)], James K. CARSON[(a)]

[(a)] University of Waikato, Private Bag 3105, Hamilton 3240, New Zealand
[(b)] Massey University, Private Bag 11222, Palmerston North 4442, New Zealand

ABSTRACT

Accounting for voids within food packages remains a significant challenge for designers of industrial refrigeration equipment. The aim of this work was to assess the impact of the packing arrangement (regular arrangement versus random/irregular arrangement) and the presence of a carton liner bag on freezing rates of trays of chicken legs ('drumsticks'). The freezing experiments showed that when contained within the liner bag, the packing arrangement of the chicken drumsticks within the tray did not have a significant impact on freezing rate for any of the air velocities investigated based on a 95 % confidence interval. However, the presence of the liner bag had a significant impact on freezing times, increasing them by more than a factor of three at high air velocity (4.3 m s^{-1}).

Keywords: Industrial Refrigeration, Food Freezing, Chicken

1. INTRODUCTION

Food freezing technology continues to develop as new refrigeration equipment becomes available and as consumer preferences continue to change (Bogh-Sorensen, 2006; Singh & Heldman, 2009) On the industrial scale, food refrigeration equipment is often made to order for a given end user, and may be designed either for a single type of product or multiple products. While modular, bulk-produced refrigeration components such as compressors and condensers may be incorporated into the overall refrigeration installation, the cold side (evaporator) is likely to be highly customised. With such a high degree of customisation, it is important that the freezing process may be modelled accurately to allow for design optimisation.

Factors affecting freezing time of food products include the refrigeration air temperature and air-flow characteristics (turbulence intensity, velocity), packaging, and packing arrangement, as well as the dimensions, morphology and physical properties of the food product (ASHRAE, 2006; O'Sullivan et al., 2014). Many primary (i.e. minimally processed) products such as meat/poultry cuts, fruit and vegetables have irregular shapes and, when packed in bulk (e.g. within cartons, bag or trays) air voids typically exist between individual food items, which can have a significant effect on freezing rates. Despite research to account for the effect of voids on heat transfer rates (Datta, 2007; James, Vincent, de Andrade Lima, & James, 2006; North, 2000; O'Sullivan, 2016; O'Sullivan et al., 2016) a general approach for dealing with the problem has yet to be established. As such, accounting for voids within food packages remains a significant challenge for designers of industrial refrigeration equipment (Smitheram, 2018).

While several research articles report results on the refrigeration of whole chicken carcasses (James et al., 2006; Mannapperuma, Singh, & Reid, 1994), there does not appear to be as many data for chicken pieces (portions) and none on chicken legs (commonly referred to as 'drumsticks') in particular. Chicken legs represent an interesting problem due to their shape and the significance

of bone, which has the potential to act as a conduction pathway to the thermal centre of the drumstick. Air voids of different shapes and sizes exist when drumsticks are packed in bulk, due to the irregular shapes of the drumsticks. On the industrial scale, chicken portions are typically cooled within a plastic carton liner bag, which has the effect of restricting air movement within the voids and also results in a larger air void within the bag on top of the chicken (Delele, Ngcobo, Opara, & Meyer, 2013; O'Sullivan, 2016). This research focused on the effects of air voids in bulk-packed chicken drumsticks on freezing times. The aim was to determine the extent to which the packing arrangement (or structure) of chicken drumsticks (and associated voids) and the presence of a liner bag affect freezing rates.

2. METHODS AND MATERIALS

2.1 Experimental Systems

Freezing trials were conducted in the Environmental Test Chamber (ETC) at AgResearch Ltd, Hamilton, New Zealand. Two polystyrene test tunnels (PTT) 2500 mm long x 720 mm height and 510 mm wide (Fig. 1) each with a variable speed fan at the downstream end and a fine mesh at the upstream end to act as a flow diffuser were used. A transition section was placed inside the PTT to guide the air-flow and reduce the cross sectional area to 300 mm x 510 mm. The experimental setup allowed for precise control of the temperature and velocity of the cooling air being forced through the PTT.



Figure 1: Polystyrene Test Tunnels (PTT) in the Environmental Testing Chamber (ETC)

Cardboard trays, as used by chicken processors, measuring 320 mm x 590 mm x 150 mm with open tops (Fig. 2a) were used in this study. Each tray was loaded with 11.5 kg of drumsticks. In each run, one tray was put in the top tunnel and another tray was put in the bottom tunnel such

that two trials could be run at the same time. In each tunnel a metal platform was used to support the tray of drumsticks. This arrangement allowed the bottom surface of the cardboard tray to be exposed to the cold air.

In the first set of experiments, a tray of regularly arranged drumsticks within the plastic liner (Fig. 2b) was frozen at three different air velocities (1 m s^{-1}, 2.5 m s^{-1}, and 4.3 ms^{-1}). Seventy two drumsticks weighing from 140 g to 190g were arranged in four layers. Eight drumsticks each having a mass of 160 g (the average weight of drumsticks in a tray) distributed along the two diagonals at both high and low, central and peripheral positions were chosen for temperature measurement (Fig. 3). In the second set of experiments, a tray of drumsticks arranged randomly within the liner bag was used (Fig 2c). The drumsticks selected for temperature measurement also weighed 160 g and were carefully placed at similar locations to the measurement positions in the first set of experiments. In the third experiment, a tray of regularly arranged drumsticks without the plastic bag was used (Fig. 2d) and thermocouple placement was selected as for the first set of experiments.

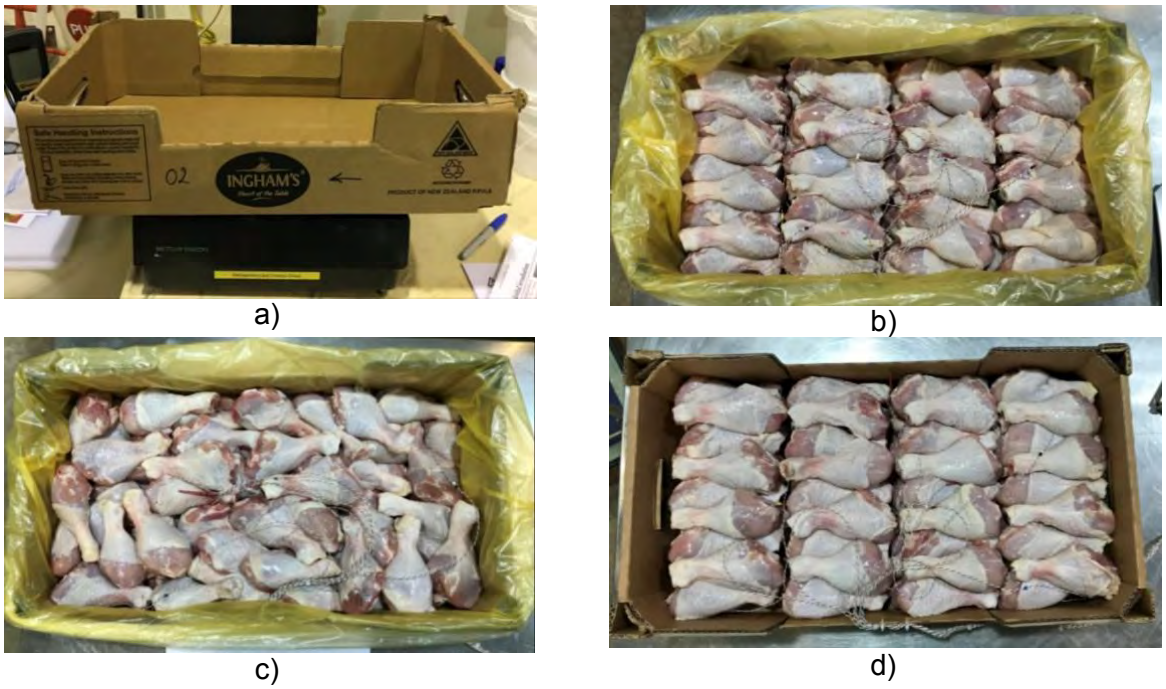

Figure 2: Cardboard trays and chicken used in freezing experiments: a) empty tray, b) regularly arranged drumsticks with liner bag, c) randomly arranged drumsticks with liner bag, d) regularly arranged drumsticks without liner bag

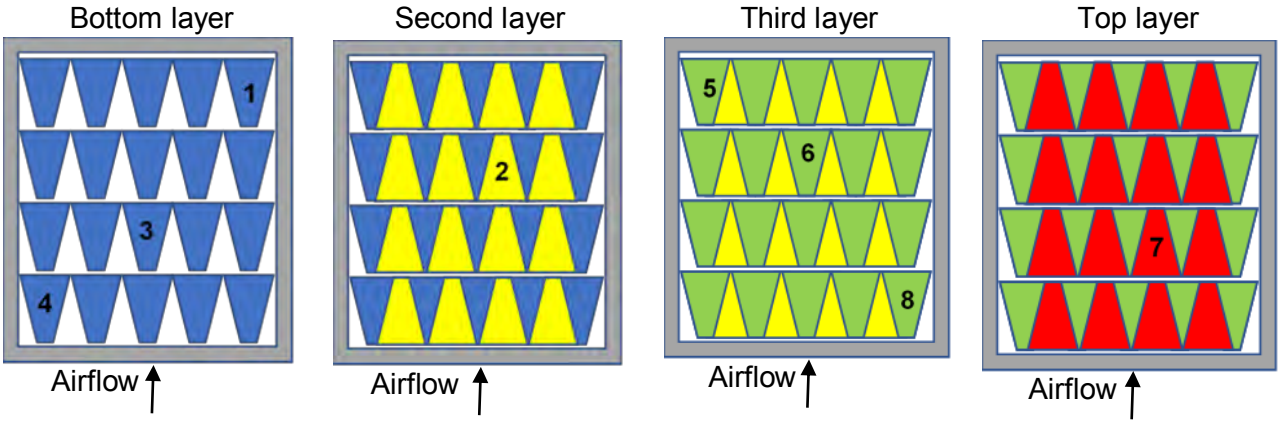

Figure 3: Chicken drumsticks distribution and thermocouple location in a tray

2.2 Measurements

T-type thermocouples were placed at in the thickest part (approximately 3 cm deep, Fig. 4) of the leg at the eight selected locations within the tray. All the thermocouples were calibrated using ice-point reference before and after the measurements. The temperatures were recorded on a Keysight 24982A data acquisition unit every 60 seconds during the freezing trials. The cooling air temperatures above the tray, and the air temperature inside the plastic liner bag were also monitored during the experiments.

The air velocities at the inlet of the PTT and at a position 5 cm above the tray of drumsticks were measured before and after each trial using a hot-wire anemometer (Dantec 54N60 FlowMaster). The sample time for each velocity measurement was five minutes. The air velocity was held constant during the experiment.

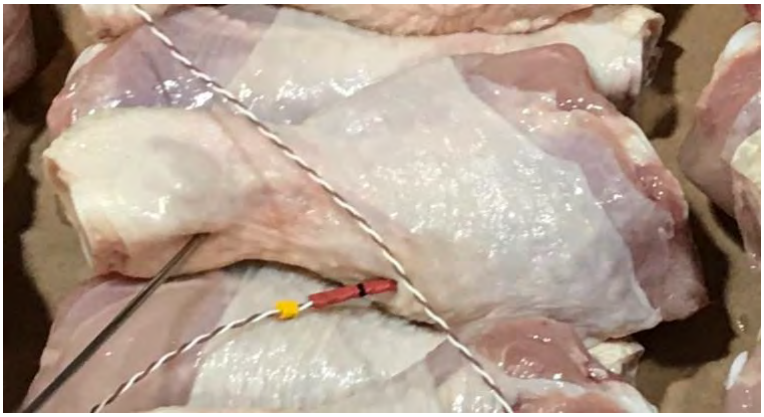

Figure 4: Thermocouple placement in chicken drumstick

2.3 Procedure

Chicken drumsticks were purchased fresh from a local retailer on the day of delivery. The drumsticks were then sorted, scaled and positioned individually in the tray and the thermocouples were inserted into the selected drumsticks. The plastic liner was then tied to enclose the drumsticks and thermocouples (other than for the experiments without the plastic liner bag). The loaded trays were then placed in the ETC to equilibrate at 10°C for 24 hours. The drumstick temperatures were monitored during the equilibration process to ascertain when the trays reached uniform temperatures.

All freezing trials started with chicken at uniform initial temperature of 10°C (equilibration temperature) and the ETC air temperature was maintained at -25°C. The inlet air velocity was adjusted to the desired speed (1 m s^{-1}, 2.5 m s^{-1}, or 4.3 ms^{-1}). The thermally equilibrated drumstick trays were placed in the tunnels and the trial was started. Each trial was terminated when all the monitored drumstick temperatures fell below -20°C.

After the freezing process was completed, the drumsticks were thawed for 12 hours, before being re-equilibrated at 10°C. Two subsequent trials were performed on the each batch of drumsticks, with the exception of the eight drumsticks that contained the thermocouples, which were replaced by fresh 160 g drumsticks for each replicate. Thus there were three replicates for each air velocity for each type of experiment (regular arrangement in liner bag, irregular arrangement in liner bag and regular arrangement without liner bag). No drumsticks were used for more than three trials.

3. RESULTS AND DICUSSION

3.1 Uncertainty Analysis

The average temperature profile of a tray of drumsticks during each of the three replicated trials was computed by averaging the temperature history of all monitored drumsticks within the tray (Eq. 1)

$$T_j(t) = \frac{\sum_{s=1}^{N} T_{s,j}(t)}{N} \quad \text{Eq. (1)}$$

The final average-temperature of the tray of drumsticks was computed by averaging the temperature history of the three replicated experimental trials Eq. (2)

$$\overline{T}(t) = \frac{\sum_{j=1}^{n} T_j(t)}{n} \quad \text{Eq. (2)}$$

The experimental standard deviation in $\overline{T}(t)$at a 95% confidence level and a normal distribution of the measurements, was computed by Eq. (3):

$$P_{\overline{T}} = t_{n-1,0.025} \times \frac{1}{\sqrt{n}} \left[\frac{1}{n-1} \sum_{j=1}^{n} \left(\overline{T} - T_j \right)^2 \right]^{\frac{1}{2}} \quad \text{Eq. (3)}$$

In general, the standard deviation of the average temperature of a tray of drumsticks ranged from 0.5°C to 3.0°C except for the case of the experimental data of the irregular arrangement at the inlet air velocity of 4.3 m s^{-1}.

3.2 Temperature profile of individual drumsticks within a tray

Fig. 5 shows the heterogeneity of the freezing process within the tray in case of regularly packed drumsticks at the medium inlet air velocity (2.5 m s^{-1}). The temperature profile of the individual drumsticks were determined by averaging temperature of the three replicated trials. The maximum difference between individual drumsticks increased at the beginning of the process until the first phase change happened in the drumstick number 5, and reach the first peak of 7°C. This value then decreased until the last phase change period started in drumstick number 7, before raised up again and accomplished a second peak of 17°C when the last phase-change period ended in drumstick number 7. The maximum difference temperature declined when the sub-cooling period started at all of the monitored drumsticks.

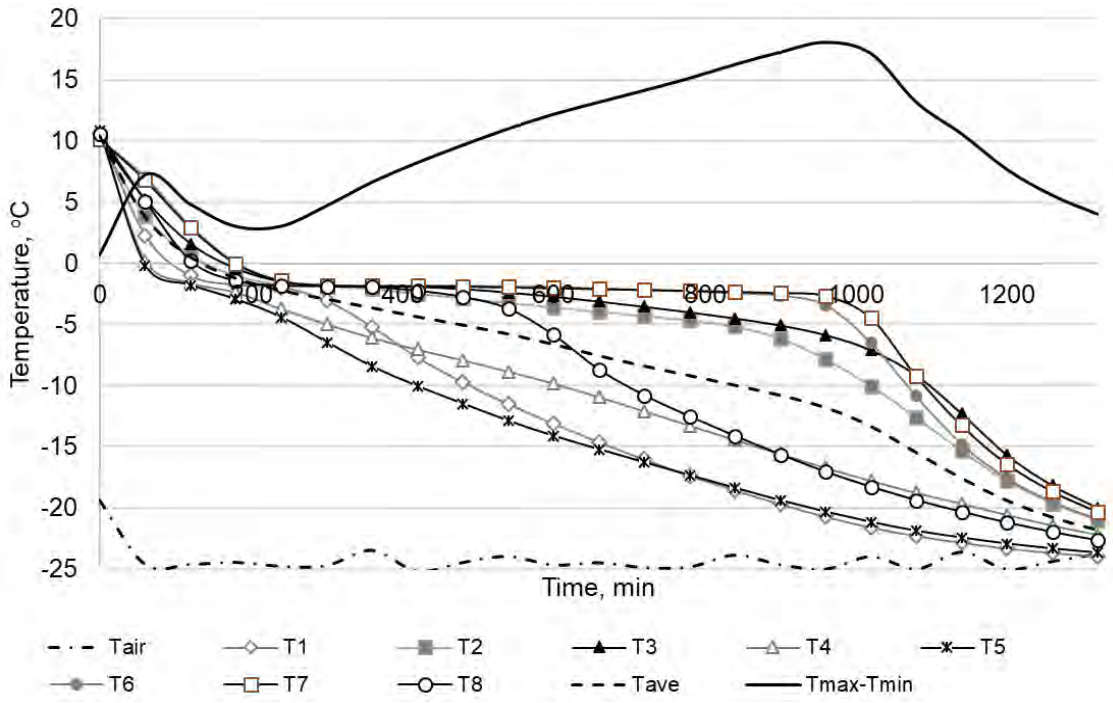

Figure 5: Temperature profile of the monitored drumsticks and the maximum temperature difference between individual drumsticks (the continuous line) within a tray at the air velocity inlet of 2.5 m s^{-1}

3.3 Comparison of Cooling Times between Regular and Irregular Packing of Drumsticks

Fig. 6 shows cooling histories of trays of regularly packed and randomly packed drumsticks, where error bars indicate 95% confidence intervals of the average temperature of the tray. Although the randomly packed drumsticks appeared to have cooled slightly faster on average than the regularly packed drumsticks, the difference between the two packing arrangements was less than the uncertainty in the measurements at both low and high air-speeds. This suggests that the packing arrangement and alignment of the leg-bone within the drumstick did not have a significant impact on freezing time when the drumsticks are contained within the bag. Consequently, it is probable that accounting for packing structure in chicken drumsticks is unnecessary when modelling freezing times.

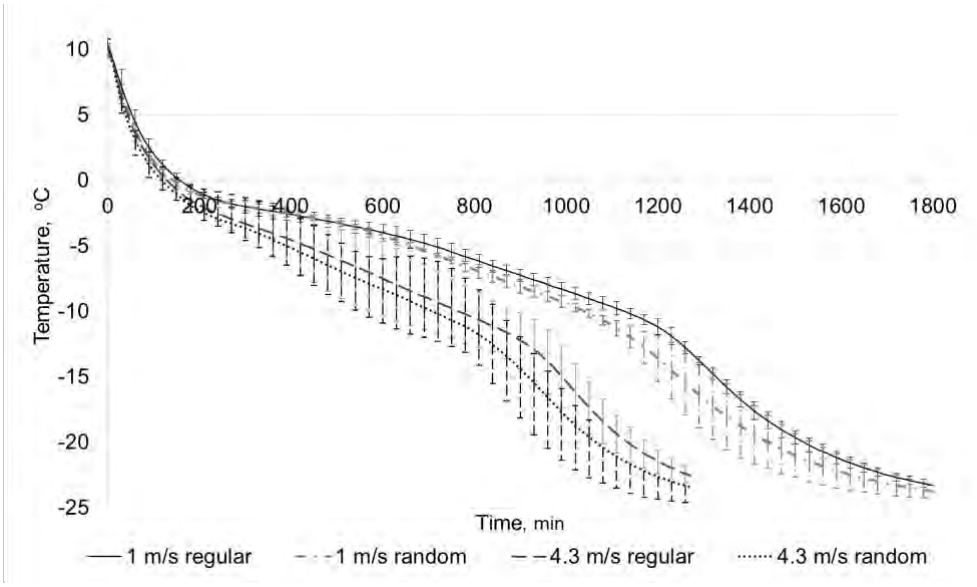

Figure 6: Cooling histories of regularly packed and randomly packed drumsticks at different air velocities

3.4 Comparison of Cooling Times of Regularly Packed Drumsticks with and without Liner Bag

Fig. 7 shows cooling histories of regularly packed chicken drumsticks both with and without the liner bag. As expected, the drumsticks without the liner bag cooled significantly faster than those packed within the liner bag for all three air velocities.

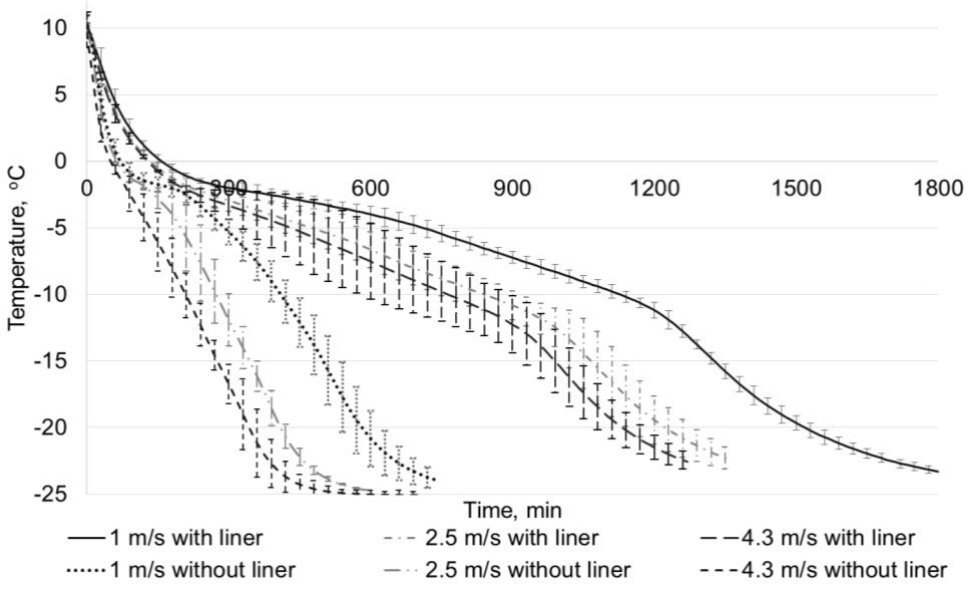

Figure 7: Cooling histories of regularly packed drumsticks with and without the liner bag

In order to quantify the effect of the liner bag on cooling time the seven-eighths cooling time (SECT) (i.e. the time required for the temperature to reach seven eighths of the difference between initial and cooling air temperatures) were calculated, and results are shown in Table 1. The effect of the liner bag on cooling time increases as the air velocity increases, the SECT for the plastic lined chicken more than three times greater than for the unlined case when the air velocity was 4.3 m s^{-1}.

Table 1. Experimental SECT of the tray of drumsticks

Configuration	SECT, min		
	1m s^{-1}	2.5 m s^{-1}	4.3 m s^{-1}
With liner	1520	1250	1160
Without liner	600	420	350

Evaporative cooling would have been much more significant for the chicken without the liner, and hence would have contributed to some of the increase in the cooling rate. However, it was estimated that the effect of evaporation accounted for less than 11 % of the total cooling. The liner bag is required to minimise moisture loss during the refrigeration process, which could have a detrimental impact on product quality, so it is unlikely that processors would remove the bag to increase throughput. However, these results clearly indicate that the presence of the liner bag has a much greater impact on freezing time than the orientation of the chicken drumsticks within the bag. Since the orientation of the drumsticks did not appear to affect freezing time, it is possible that only the total fraction of air voids within the package may be required as a model input, with no requirement to account for size or shape of the air voids.

4. CONCLUSIONS

The freezing experiments showed that the packing structure of the chicken drumsticks within the plastic liner bag did not have a significant impact on freezing rate for any of the air velocities investigated based on a 95% confidence interval. However, the presence of the plastic liner bag increased freezing times by more than a factor of 3 at high air velocities.

NOMENCLATURE

$P_{\overline{T}}$	Standard deviation in $\bar{T}(t)$ (K)	$\overline{T_j}$	Average temperature of a tray of drumsticks during the *j*-th trial (K)
t	Time (s)	$T_{s,j}$	Temperature of drumstick – *s* within the tray (K)
$t_{n-1,\ \alpha/2}$	Student's t-statistic with (*n*-1) degrees of freedom at a (1-α) confidence level	*n*	Number of the experimental trial, *n* = 3
$\bar{T}$	Average temperature of a tray of drumsticks (K)		

REFERENCES

ASHRAE, A. H. (2006). Refrigeration. *American Society of Heating, Refrigerating and Air-Conditioning Engineers, Atlanta, GA*.

Bogh-Sorensen, L. (2006). *Recommendations for the processing and handling of frozen foods* (4th ed.): International Institute of Refrigeration, Paris.

Datta, A. (2007). Porous media approaches to studying simultaneous heat and mass transfer in food processes. I: Problem formulations. *Journal of Food Engineering, 80*(1), 80-95.

Delele, M. A., Ngcobo, M. E., Opara, U. L., & Meyer, C. J. (2013). Investigating the effects of table grape package components and stacking on airflow, heat and mass transfer using 3-D CFD modelling. *Food and Bioprocess Technology, 6*(9), 2571-2585.

James, C., Vincent, C., de Andrade Lima, T., & James, S. (2006). The primary chilling of poultry carcasses—a review. *International Journal of Refrigeration, 29*(6), 847-862.

Mannapperuma, J., Singh, R., & Reid, D. (1994). Effective surface heat transfer coefficients encountered in air blast freezing of single plastic wrapped whole turkey. *International Journal of Refrigeration, 17*(4), 273-280.

North, M. F. (2000). *Prediction of chilling rates for food product packages: PhD thesis, Massey University, New Zealand, .*

O'Sullivan, J. (2016). *Significant factors affecting the forced-air cooling process of polylined horticultural produce: PhD thesis. Massey University, New Zealand.*

O'Sullivan, J., Ferrua, M., Love, R., Verboven, P., Nicolaï, B., & East, A. (2014). Airflow measurement techniques for the improvement of forced-air cooling, refrigeration and drying operations. *Journal of Food Engineering, 143*, 90-101.

O'Sullivan, J., Ferrua, M. J., Love, R., Verboven, P., Nicolaï, B., & East, A. (2016). Modelling the forced-air cooling mechanisms and performance of polylined horticultural produce. *Postharvest Biology and Technology, 120*, 23-35.

Singh, R. P., & Heldman, D. R. (2009). *Introduction to food engineering*. Elsevier/Academic Press, Amsterdam Gulf Professional Publishing.

Smitheram, D. (2018). *Design engineer for Milmeq, Personal communication.*

Manuscript ID: 457
DOI: 10.18462/iir.icr.2019.0457

Cold-chain monitoring of fresh food distribution converging internet of thing and dynamic prediction technology

Byeongsam KIM[(a)], Jiyoung KIM[(a)], Samuel M. YIMENU[(b)], Jonghoon KIM[(a)], Seungil OH[(a)], Junemo KOO[(c)]

[(a)] Research Division of Strategic Technology, Korea Food Research Institute Wanju-gun, 55365, Republic of Korea, bskim@kfri.re.kr
[(b)] Department of Food Biotechnology, University of Science and Technology (UST) Daejeon, 305-350, Republic of Korea, Samuelmezemir2@gmail.com
[(c)] Department of Mechanical Engineering, Kyung Hee University, Yongin, Gyeonggi-do,17104, Republic of Korea, jmkoo@khu.ac.kr

ABSTRACT

This study was conducted to monitor quality indices and distribution history during cold-chain distribution of fresh food such as chicken meat. In order to monitor quality indices, temperature data during distribution process were collected in real time by using 424MHz Radio Frequency sensor tag and wireless sensor network (WSN). We constructed the quality monitoring system that embedded the quality prediction algorithm. The quality monitoring system contains quality prediction model and calculates and saves quality index in real time, inter-working with quality prediction algorithm according to transmission of environmental information through WSN/CDMA. Various quality prediction algorithms were developed using specific prediction tools such as predictive microbiology, Arrhenius equation and Weibull distribution, and so on. When applying real time quality monitoring system to actual field, prediction was excellent within the 95% prediction interval.
Keywords: Quality monitoring, Dynamic prediction, Internet of Thing, Fresh food, Cold-chain.

1. INTRODUCTION

Most food today requires refrigerated transportation. While break-downs in machinery, delays in transportation, and inconsistencies in optimal refrigeration temperatures due to cost-reduction factors may cause massive food spoilage, it is nearly impossible to check the freshness of most food products without opening their packaging. It is reported that more than 30% of fresh food is impaired and lost during distribution process because of lack of the proper management. In particular, quality of fresh refrigerated foods depends on the temperature history which food experiences. Recently, supply of small-packed or fresh chicken breast meat has increased to facilitate efficient diet and convenience of distribution. However, the improper temperature management may end up with food quality impairment to result in food borne disease. Therefore, to supply safe and high-quality refrigerated food, it requires real-time management of temperature and food quality during distribution process(Kim, 2014, Kim et. al., 2016).

2. FOOD QUALITY MONITORING TECHNOLOGY

2.1. Cold-chain Monitoring System

In this study, RFID (Radio Frequency Identification) sensor tag and WSN (wireless sensor network)/CDMA technologies were applied to monitor temperature and food freshness in real-time. The cold-chain monitoring and freshness prediction in real-time was done through its own built below monitoring system (Fig. 1).



Figure 1: Real-time cold-chain monitoring system

The monitoring system is a combination of the real-time quality management system, which assesses and predicts the changes in food freshness according to changes in temperature and humidity, and the transportation management system (u-TMS), which controls, in real-time, the transportation status of food based on LBS/GPS. Food production information is registered to the server immediately after production. The QR code and RFID sensor tags (424~433MHz, data transportation speed 2.4~32kbps, KFRI.ST.2018.LTE, ASN Co., Korea), both mapped with the registered information, are attached to each product unit and to the package box. While in transport, the communication device installed within the delivery vehicle records the temperature and humidity information measured by the RFID sensor tags on the food package and sends it to the server in real-time. Once transmitted to the server, this information is input into the quality prediction (forecast) model and algorithm by the u-Food RQMS according to food type to calculate the freshness of the products in real-time. This, in turn, is communicated to the managers and the consumers. u-TMS provides all the necessary information related to the location of the delivery vehicles in real-time for quality control.

The consumers can either use their Smart devices or the kiosks located within the store to scan the QR code or the RFID tags on the food products and check their freshness before purchasing or receiving their goods. Once the required information is identified, it is linked to the server via wireless Internet. The server traces the ID of the QR code, processes and transmits the required information, such as food quality index, remaining shelf life, production and transportation history in the desired quantity format, thus allowing the consumers to easily and quickly check the freshness of their purchases.

2.2. Dynamic Prediction Model Development

2.2.1. Storage and distribution simulation test of chicken meat

Packaged chicken meat real-time simulation experiment, starting at the poultry processing plant and ending at the end of shelf-life on display shelf, was conducted. The real-time simulation experiment was conducted in October-November, 2018. Chicken breast samples produced at fresh chicken meat packing factory in Chungbuk province, South Korea were obtained and transported to Korea Food Research Institute in a cold delivery vehicle (from 2:30 pm to 5:00 pm, at 2°C). Storage at Mart warehouse was simulated (from 5:00 pm on October 30, 2018 to 9:00 am on October 31, 2018, at 0 °C). Then the chicken meat samples were unloaded at their final destination, and the samples were immediately transferred to display showcase set at 2°C.

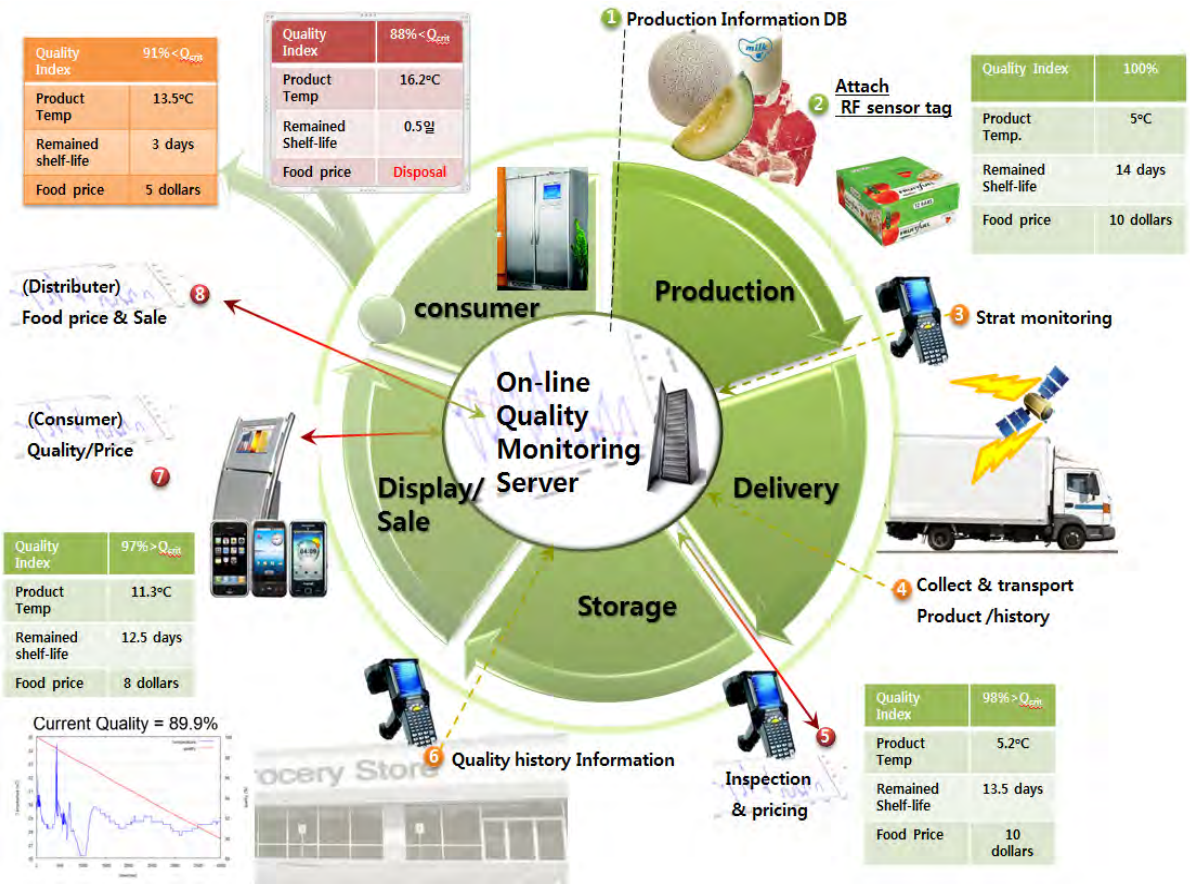

Figure 2: Freshness monitoring during food-chain from producer to consumer

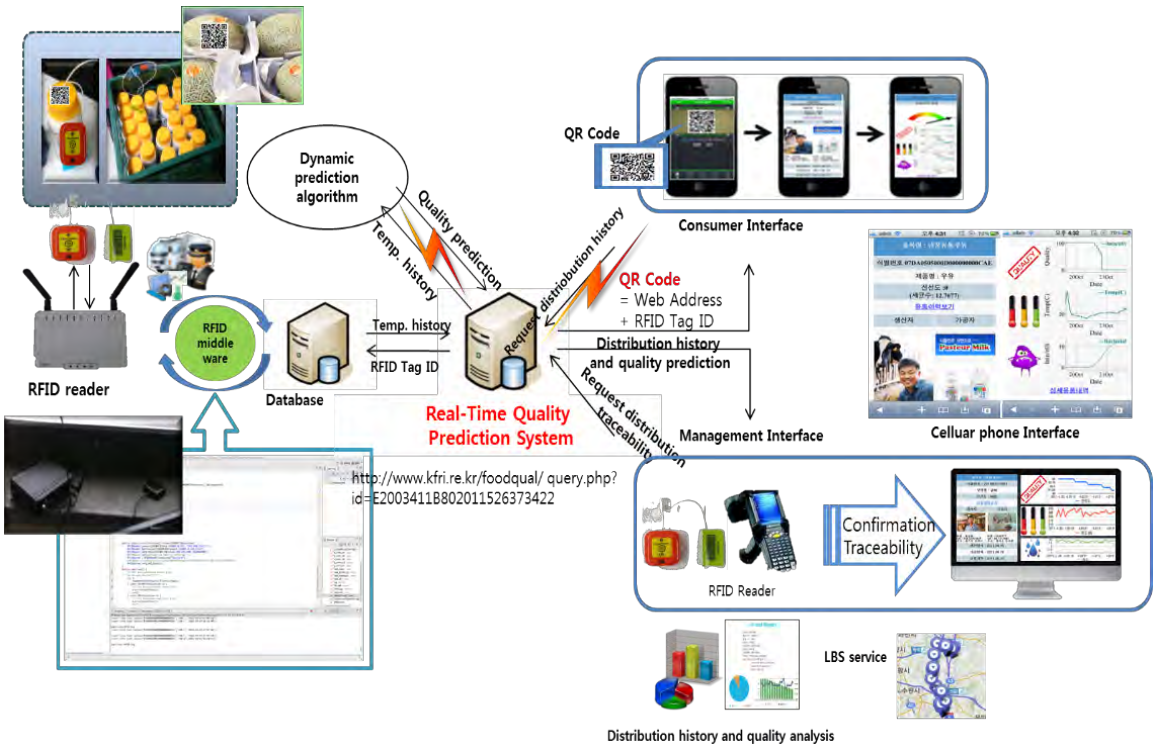

Figure 3: u-Food smart quality monitoring system

2.2.2. Microbial analysis

During each storage test, three packs of breast fillets were randomly drawn from shelves and a representative 10 g meat sample was aseptically weighed and placed in to a sterile stomacher filter bag, and 90 mL of saline peptone diluent (3M, St. Paul, MN, USA) was added. The samples were blended using a Bag Mixer 400 CC (interscience, 30, ch. du bois des arpents 78860 Saint Nom, France) for 60 s at room temperature.The microbial analysis was performed using PetrifilmTM (3M, St. Paul, MN, USA) media for total plate count (TPC) according to a standard method (KFDA, 2011). Plates were incubated aerobically at 35°C for 48 h. All measurements were performed in triplicates, each from separate breast packages. Microbiological data were transformed into logarithms of the number of CFU/g.

2.2.3. Measurement of chicken meat temperature

Temperature conditions were continuously controlled and recorded every five minutes by data loggers (TR-52*i*, T&D Corporation, Japan), that contain wires to which needle probes were attached. Three meat packs were randomly taken from shelves and instrumented with data loggers by piercing the polyvinylidene film wrap and then inserting the probe in to one of the fillets' core. Then the pierced area on the film was sealed with glue. The average chicken meat core temperature data were used during mathematical prediction model development.

2.2.4. Mathematical model

The differential equation form of the primary model (Baranyi & Roberts, 1994; Swinnen et al., 2004) is shown in Eqs. (1) and (2).

$$\frac{\mathrm{dN}}{\mathrm{dt}} = \frac{Q(t)}{1+Q(t)} \cdot \mu_{max} \cdot \left[1 - \frac{N(t)}{N_{max}}\right] \cdot N(t) \qquad \text{Eq. (1)}$$

$$\frac{\mathrm{dQ}}{\mathrm{dt}} = \mu_{max} \cdot \mathrm{Q(t)} \qquad \text{Eq. (2)}$$

$$\mu_{max}(\mathrm{T}) = \mathrm{c}_0 + c_1 \cdot T + c_2 \cdot T^2 \qquad \text{Eq. (3)}$$

Table 1. Determination model parameters

N_{max}	c_0	c_1	c_2	c_3
2.379×10^{8}	9.716×10^{-1}	5.935×10^{-2}	2.455×10^{-2}	2.456×10^{-1}

Where *N*, N_{max}, μ_{max}, and *t* represent microbial concentration at the stationary phase, microbial maximum growth rate and time, respectively. *Q* is a parameter representing the physiological state of the food. Here, the model parameters N_{max}, Q_0, c_0, c_1 and c_2 were determined in the process of residual minimization which searched for the best values of model parameters to minimize the deviations between the measured microbial concentrations and the model estimated ones. The measured initial values for each test condition were used as the initial value of the concentration, N_0. The measurement data for four different temperatures (0, 4, 10, and 15°C) were fitted into the Baranyi and Roberts growth curves using Eqs. (1) and (2) in order to obtain the temperature dependence of the model parameters. To determine the specific growth rate, the quadratic polynomial model (Eq. 3) was used as a secondary model. The best dynamic model is the one that has a good fit in both primary and secondary models.

Coefficients of the model equations were determined using the open source statistics program, R for Windows 3.3.1 (R Development Core Team, 2011). The statistical indices of bias factor (B_f) and accuracy factor (A_f) (Ross, 1996) were used to evaluate model performance.

$$A_f = 10^{\frac{\sum\left|\log\left(C_{predicted}/C_{observed}\right)\right|}{n}}, \quad B_f = 10^{\frac{\sum\log\left(C_{predicted}/C_{observed}\right)}{n}} \qquad \text{Eq. (4)}$$

Where $\boldsymbol{C_{observed}}$ is the value of each experimentally observed data, $\boldsymbol{C_{predicted}}$is the predicted value at the same time, and *n* is the number of observations.

2.2.5. Validation of dynamic prediction model

The microbial growth of chicken was measured under a fluctuating temperature condition, and it was compared with the estimations by the developed model. The comparison between predicted and observed growth of TPC in chicken meat samples stored under fluctuating temperature condition is graphically illustrated in Fig. 3. The A_f and B_f were estimated to be 1.045 and 0.991 respectively, and they matched well each other. The value of the B_f index showed that the predictions were 1% shorter than the observations resulting in a systematic under estimation of the model. This implied that the model of which parameters were determined by using the data from constant temperature experiments could be applied to the cases of fluctuating temperature conditions.

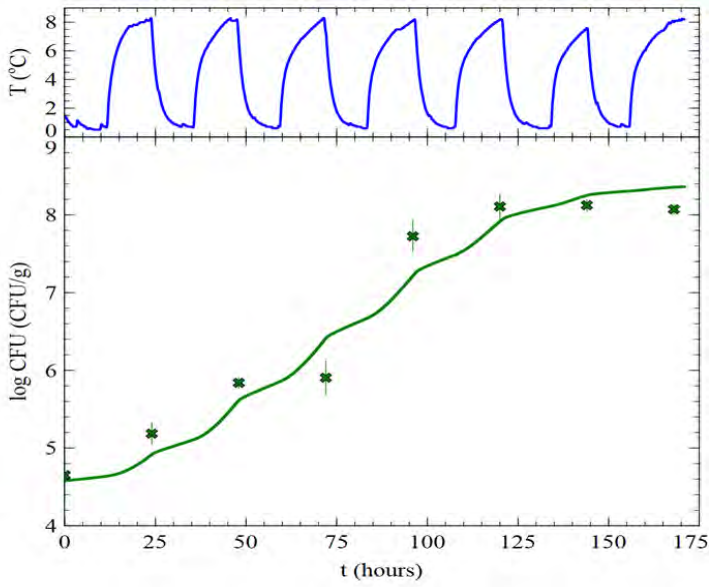

Figure 4: Comparison of the measured microbial concentrations with the model estimated results for packaged chicken meat samples stored at 0-8ºC fluctuating temperature condition; (✖) observed growth data, (—) predicted growth, (blue line: temperature profile)

2.2.6. Remaining shelf-life estimation

Shelf-life is the recommended maximum storage time for the safe consumption of food, and it is determined depending on the degradation mechanism of the interested food. For chicken meat, the microbial growth count is usually used and it should not exceed the upper limit of microbiological acceptability of 7 log CFU/g (Silliker et al., 1988; Tuncer and Sireli, 2008).

If the storage temperature is fixed, the shelf-life could be easily estimated by the developed model. For example, if the chicken meat is stored at the constant temperature of 4 °C as shown in Fig. 4, the total shelf-life will be estimated to be around 120 hours. If the initial microbial counts are different the total shelf-life will be different as shown in Fig. 4, where the chicken of lower initial microbial count would have 10 more hours of shelf-life. The remaining shelf-life could be estimated simply by the difference between the total shelf-life and the elapsed time at the moment of estimation as shown in Eq. (5).

$$\text{Shelf-life}_{\text{remaining}} = \text{Shelf-life}_{\text{total}} - t_{\text{current}} \qquad \text{Eq. (5)}$$

However, it would be hard to estimate the change of shelf-life under the fluctuating temperature condition, since the total shelf-life changes with the shifting temperature. If the food temperature was shifted to lower after spending a long time at a higher temperature and the shelf-life is estimated using the recent temperature, then the shelf-life suddenly extends longer, and vice versa. The dashed blue line in Fig. 5 represents the estimation of the remaining shelf-life of the chicken meat under fluctuating temperature condition used for validation using the temperature history and assuming the storage temperature to remain at the recent temperature for the time to come. It starts with very long remaining shelf-life because the storage temperature is low at the beginning, then it decreases sharply with the temperature shift-up. The remaining shelf-life increases sharply again

with the next temperature shift-down indicating excessive sensitivity with temperature change, which is caused by the assumption that the food temperature will be the same as the recent temperature monitored throughout the remaining time. This might transfer false information to the customers.

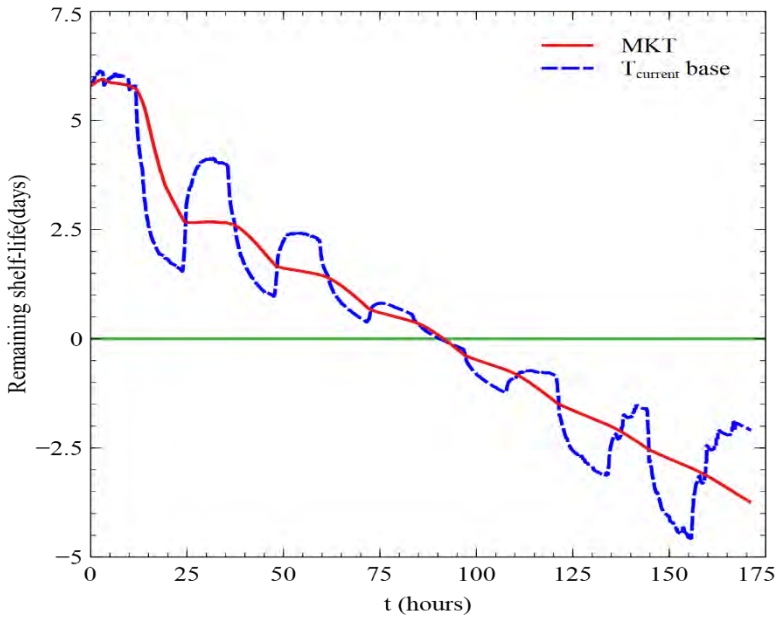

Figure 5: Comparison of the remaining shelf-life estimations using the mean kinetic temperature and the temperature histories under the 0-8℃ fluctuating temperature condition during storage; (—) based on mean kinetic temperature, (- -) based on fluctuating temperature, (green line) shelf-life limit

As a remedy for this, the mean kinetic temperature was tested as the food temperature to remain for the remaining of the time of circulation. The mean kinetic temperature is the effective constant temperature to represent the impact of the fluctuating temperature history on the food quality degradation. It indicates the constant temperature $T = T_{\text{MKT}} = const.$ at which the food quality becomes at the level of the inspecting moment t_{current} under fluctuating temperature $T(t)$ condition as shown in Eq. (6). Since N in Eq. (6) shows the food quality, it could be obtained by integrating the equation as in Eq. (7)

$$N(t_{\text{current}}, T = T_{\text{MKT}} = const.) = N(t_{\text{current}}, T(t)) \qquad \text{Eq. (6)}$$

$$N = N_0 + \int_0^{t_{\text{current}}} \frac{dN}{dt}(t, T(t))\, dt = N_0 + \int_0^{t_{\text{current}}} \frac{dN}{dt}(t, T = T_{MKT} = const.)\, dt \qquad \text{Eq. (7)}$$

2.3. Real-time monitoring of freshness and distribution history

Manufacturers and logistics companies can manage their operations more rationally as a result of the detailed information provided by the system, including food status data such as quality index, remaining shelf life, number of microbes, mean kinetic temperature, history of in-transport temperatures, production history, and abnormal temperature warnings. Detailed information on the delivery vehicles, such as the travel status, location tracing function, and delivery completion status, as well as a warning system for abnormal qualities or conditions is also provided. Fig. 6 shows the concept of monitoring of freshness and distribution history during chicken meat distribution.



Figure 6: The concept of real-time monitoring of freshness and distribution history during chicken meat distribution

The quality monitoring system will provide accurate information for consumer purchasing decisions, allow rational food management and price policies based on freshness, raise the sense of accountability on the part of the food distribution industry, and lead innovation in logistics and distribution.

3. CONCLUSIONS

The results of the current study, when applying real time freshness monitoring system to actual field, during distribution in both constant temperature and fluctuated temperature, showed prediction was excellent within the 95% prediction interval (PI). Therefore, we can conclude that the on-line quality monitoring technology for refrigerated chicken meat during distribution process could be applied effectively and reliably for the food quality management.

ACKNOWLEDGEMENTS

This research was supported by Main Research Program (E0122500, E0162501) of the Korea Food Research Institute (KFRI) funded by the Ministry of Science and ICT.

REFERENCES

Baranyi, J., and Roberts, T. A., 1995. Mathematics of predictive food microbiology. International Journal of Food Microbiology, 26, 199–218.

Silliker, J. H., Baired-Parker, A. C., Bryan, F. L. , Christian, J. H. B., Roberts, T. A. and Tompkin, R. B., 1988. HACCP in Microbiological Safety and Quality. ICMSF (Int. Commission Microbiological Specifications for Foods), Great Britain. Blackwell, London, U.K. pp 7–12

KFDA. Korean Food Standards Codex. Korea Food and Drug Administration, 2011. Seoul, Korea. pp. 5.11.2-5.11.3, 10.3.1

Kim, B. S., 2014. Establishment of platform for u-Food system. A research report R14-E0142053305-48, Korea Food Research Institute, Wanju-gun, Republic of Korea.

Kim, B.S., Lee, M., Kim, J.Y., Jung, J.Y. and Koo. J., 2016. Development of a freshness-assessment model for a real-time online monitoring system of packaged commercial milk in distribution. LWT - Food Sci. Technol., 68, 532–540.

Koseki, S. and Isobe, S., 2005. Prediction of pathogen growth on iceberg lettuce under real temperature history during distribution from farm to table. Int. J. Food Microbiology 104(3), 239-248.

Labuza, T., Fu, B., 1993. Growth kinetics for shelf-life prediction: theory and practice Int. J. Food Microbiology 12(3), 309-323.

R Development Core Team. 2011. R: A Language and Environment for Statistical Computing. R Foundation for Statistical Computing, Vienna, Austria. ISBN 3-900051-07-0, URL http://www.R-project.org.

Ross, T., 1996. ndices for performance evaluation of predictive models in food microbiology. Journal of Applied Bacteriology 81(5), 501– 508.

Samuel , M. Yimenu., 2019. Dynamic prediction modeling for real-time freshness management in poultry products supply chain. Ph.D Thesis. Daejeon. Republic of Korea. 190-204.

Swinnen, I. A. M., Bernaerts, K., Dens, E. J. J., Geeraerd, A. H. and Van,J. F. I., 2004. Predictive modeling of the microbial lag phase: a review. *International Journal of Food Microbiology*, 94, 137 - 159.

Tuncer, B. and Sirel, U. T. i., 2008. Microbial growth on broiler carcasses stored at different temperatures after air- or water-chilling. *Poult. Sci.*, 87, 793 – 799.

Vankerschaver, K., Willocx, F., Smout, C., Hendrickx, M. .and Tobback, P., 1996. Modeling and prediction of visual shelf-life of minimally processed endive. Journal of food Science 61(5), 1094-1098.

Manuscript ID: 560
DOI: 10.18462/iir.icr.2019.0560

Numerical modelling of thermal processes in Chinese cabbage cold storage chamber using variable turbulence models

Kamil ŚMIERCIEW[(a)], Mirosława KOŁODZIEJCZYK[(a)], Jerzy GAGAN[(a)] Dariusz BUTRYMOWICZ[(a)]

[(a)] Bialystok University of Technology
Bialystok, 15351, Poland, k.smierciew@pb.edu.pl

ABSTRACT

Losses of stored fruits and vegetables may occur mainly due to non-uniformity of the environmental conditions. Cooling air flow pattern in the cold storage chamber strongly depends on the turbulence model applied. In modelling of mechanical ventilation standard k-ε model turbulence models is used routinely because of good convergence. However, this model is not able to predict the flow rate of the air stream and is unable to reproduce the Coanda effect. In the paper the results of numerical modelling of processes in cold storage chamber for vegetables are presented. The RANS turbulence models have been tested to determine the most appropriate ones for the studied configuration. The highest difference of measured and computed temperature in the bulk of vegetables is 0.40 K regardless of the turbulence model. Relative humidity difference varies between 4 and 13%. Tested turbulence models led to overprediction of air temperature and velocity, however the SST k-ω model gives the best results.
Keywords: Refrigeration, CFD, turbulence, comparison, RANS, vegetables, relative humidity, simulations

1. INTRODUCTION

The need for refrigerated storage of fruits and vegetables causes significant energy consumption and greatly influences the cost of postharvest handling of agricultural products. Storage facilities should then be designed and maintained with low energy demands together with care to ensure the high product quality. Bad storage conditions in cold stores of fruit and vegetables may induce drying of the commodities or its low temperature injuries, therefore usually strongly affect the stored products quality. Quantitative and qualitative losses may occur mainly due to non-uniformity of the environmental conditions in the packed bed of stored products. The most important factors affected the homogeneity in the bulk of vegetables are velocity, temperature and humidity of air blown from the cooling unit, load arrangements and physical properties of stored vegetables and fruit. A geometric model of the cold store cannot retain the shape of all of its relatively small components. For that reason, a porous media model of large pores is widely used in modelling the bed of the stored products and the fan cooler. A space occupied by a large number of small objects is treated as a fictitious continuum of resistance to flow equal to the resistance of real obstacles, taken into account by means of the additional negative source term in the momentum equation. Containers of the stored vegetables are usually modelled by a packed bed including both viscous and inertia resistance terms calculated according to the Ergun equation (Nahor et al. 2005). However, in Tapsoba et al. (2006) the containers were regarded as impenetrable solid areas with specified boundary conditions on the walls. The resistance of the packed bed of vegetables is calculated on the base of the measurements in Moureh et al. (2002). There are additional problems associated with complex geometry of the flow through the containers with stored products, the confinement effect of the porous medium, causing different flow conditions in the vicinity of the walls and in the core of the bed, and narrow gaps between containers, strongly increasing the number of computational cells. These problems were studied by Moureh et al. (2002,2009a,b).

The fan air cooler is usually modelled with use of the simplified geometry and physics. The fans, making the air to move in the chamber, are included into the model in many ways, mostly in 3D approaches as infinitely thin plates for which pressure jump is assumed (Delele et al. 2009a,b), and in 2D approaches as line segments (Chourasia and Goswami, 2007). Earlier, the effects of pressure rise in the fan and pressure drop in the air cooler were modelled as a combined dynamic

source in momentum equation in the direction of the local flow in the cooler (Hoang et al. 2000). The performance of the fan and the flow resistance of the cooler were applied to obtain the operation point of the fan. In paper (Nahor et al., 2005) the fan and the cooler were represented by the distributed body forces and resistance which were taken from the characteristics of these devices and applied to the block of cooler dimensions. Hoang et al. (2015) modelled the swirling air jets blown out by the fans by means both nominal data and measurements of air velocity at the outflow of the fans. The varying supply air temperature was modelled by exponential function with adjustments taken from the measurements. It should be noted that flow pattern inside the storage chambers strongly depends on the turbulence model applied



Figure 1: Experimental cold storage chamber of Chinese cabbage (a view from the cooler side)

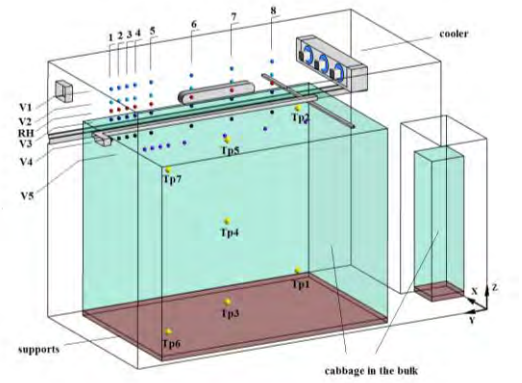

Figure 2: Geometric model of the cold storage chamber

In modelling of mechanical ventilation of the cold storage chambers, turbulence models based on Bousinesq approximation were mainly used. Standard model k- ε is used routinely because of good convergence. However, this model is not able to predict the flow rate of the air stream blown by the fan. It also fails in flow calculations with large areas of detachment and recirculation and is unable to reproduce the Coanda effect. Using more advanced turbulence models is limited due to worse convergence compared to the convergence of the standard k- ε model. However, the k- ε model is still used, mainly as a compromise between computational costs and relatively good prediction of the flow. In most cases for CFD analysis the RNG k- ε turbulence model is applied. Hoang et al. (2000) presents results of simulation of airflow inside empty and fully loaded storage chambers. The standard k- ε and RNG k- ε models were used. Maximum error between calculated and measured velocity was 26% for both models. Later, Nahor et al. (2005) obtained accuracy of 22% for empty and 20% for loaded cold store for standard k- ε turbulence model. Mirade et al. (2006) conducted an experimental validation of flow simulation with the k- ε, RNG k- ε and k-ω models in cheese ripening chambers. The k- ε gives relatively good agreement with experiments while for the rest of the tested models simulations did not converged. The RNG k- ε was also used in Chourasia and Goswami (2007). The realizable k- ε turbulence model is used very rarely. Delele et al. (2009a, b) applied the SST turbulence model, and later other models: SST k-ω, standard k-ω, standard k- ε, RNG k- ε, and realizable k- ε. The results obtained with application of these models were compared with experiments. Model SST k-ω was considered as the most accurate. Moureh et al. (2002, 2009a) used 6 equations Reynolds RSM stress model, applied due to the closest real effect of modeling the detachment area of the free-stream from the cooler. In general, RSM model is recommended for high swirling flows, with large volume deformations and high curvature lines and detachment. It is estimated that the use of the RSM model increases the iteration time by approximately 50-60% and the memory usage by approximately 20%. The use of this model also aggravates the convergence, due to the strong coupling of the Reynolds stress tensor components with the main flow parameters. RSM turbulence model was used in simulation of airflow inside refrigerated vehicle Moureh et al. (2009a,b). According the authors only RSM is able to predict the detachment points. Modeling the airflow, heat and mass transfer in the storage chamber with consideration of the cooling unit and the bulk of vegetables due to non-uniformity of parameters inside the chamber may be thought as a very complex issue. Many parameters can be considered as crucial. Therefore, the obtained results of the modelling of processes occurring in the cold storage chamber are presented as separate issues, e.g. Kolodziejczyk et al. (2016),

Śmierciew K. et al. (2016). In this paper the numerical results obtained with use of various turbulence models were compared with the experimental results.

2. NUMERICAL MODEL

View from the cooler side of the investigated experimental storage chamber in Fig. 1. The geometry of the chamber and the load arrangement are shown in Fig. 2. The overall dimensions were 2.05 × 4.33 × 2.93 m. The chamber was loaded with 2629 kg of Chinese cabbage, packed in the plastic boxes, arranged as one block of dimensions 1.8 × 2.8 × 2.17 m that occupies most of the space. Boxes of cabbage were placed on wooden supports. There was also a column of boxes in the antechamber. The ceiling-type unit cooler was operating with glycol solution. The nominal capacity of the cooler is 1148 W, and nominal air flow rate is 1105 m3/h. The airflow was generated by three axial fans of 20 cm of diameter rotating at 1300 rpm, placed at the outflow of the cooler.
The geometry of the cooling unit was simplified. The heat exchanger shape was assumed as a box of porous medium and fans - infinitely thin plates with pressure jump depending on the local normal velocity component according to the fan performance curve taken from manufacturer data+

$$p = -0.085\ V_n^3 + 1.9046\ V_n^2 - 14.998\ V_n + 60.604 \qquad \text{Eq. (1)}$$

where Δp is static pressure jump across the fans [Pa], V_n is local normal velocity [m/s]. The rest of the unit was empty, filled only with moist air. The swirling jets of air blown from the fans to the chamber where visualized and measured. Air jets took the shapes of divergent cones. The angle of divergence was in range 80°÷90° and the inclination angle of velocity vector to the circumference of the fans was about 15°÷20°. On the basis of these parameters the radial and tangential components of velocity were defined by means of UDFs. The other solid parts of the cooling unit were excluded from the domain of solution.
Moist air was modelled as a mixture of oxygen, nitrogen and water vapour described by the species transport model without chemical reactions. The air was regarded as an ideal incompressible gas with physical properties modelled as the fourth-degree polynomial functions of temperature with coefficients taken from ANSYS Fluent library.

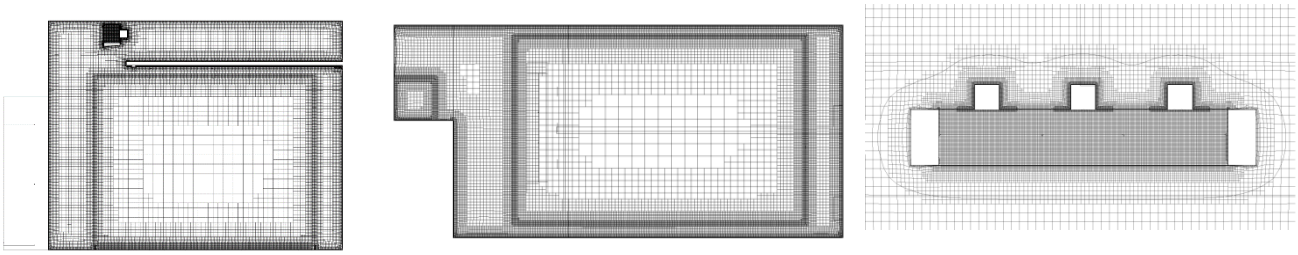

Figure 3: View of the mesh of the chamber: side view (left), top view (middle) and air-cooler (right)

The governing equations for the airflow in the cold storage chamber are the continuity equation for the moist air, the Navier-Stokes momentum equation, two energy equations for fluid and solid zones of porous medium, and two species transport equations for oxygen and water vapour. The mass fraction of nitrogen was calculated as a supplement to unity. The Reynolds time-averaging procedure was applied to transform Navier-Stokes equations into RANS equations, closed by the turbulence model. ANSYS Mesher with cut cell method was used to obtain the computational grid of 19.2 million control volumes (see Fig. 3). Calculations were carried out with SIMPLE (Semi-Implicit Method for Pressure Linked Equations) algorithm due to its lower memory requirements.

3. RESULTS AND DISCUSSION

View of the investigated experimental storage chamber seen from the cooler side is presented in Fig. 1. During the post-harvest storage in the investigated cold room an experimental study was conducted in order to get environmental information (velocity, temperature and relative humidity of air) required to examine the computational model. Velocity and relative humidity of air measurements were carried out in the mid-plane (for X=0.99 m) of the chamber at grid points

locations presented in Fig. 2 at four level above the load (marked as V1÷V4) and on one level (V5) near the side wall (for X=0.25 m) using mobile measuring system presented in Fig.1. Velocity was measured at levels: V1 - 5 cm below the ceiling, V2 – 20 cm below the ceiling, V3 - 40cm from the ceiling, V4 - just above the bed, 63 cm from the ceiling. Measurement level V5 was located 52 cm below the ceiling (z = 2.41 m). Relative humidity was measured at RH level. Velocity and humidity sensors travelled along the horizontal linear guide carried by a slide moving automatically between points of the measuring grid shown in Fig. 2. The data were collected at 8 verticals during 10 min of rest at each position with frequency of 1 Hz. Air temperature measurements in the bulk of cabbages were also performed at 7 points marked in Fig. 2 as yellow points.

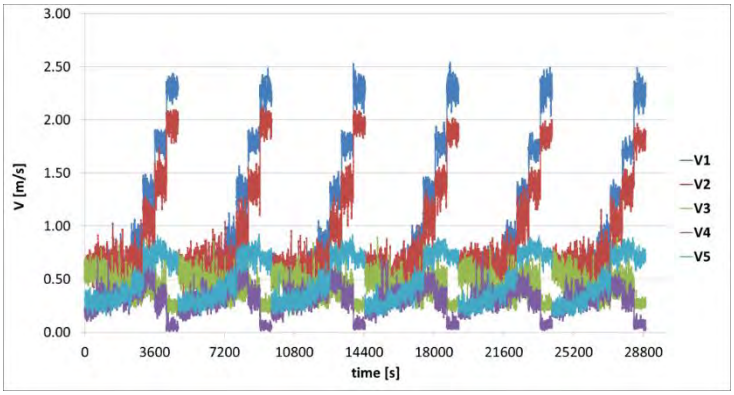

Figure 4: Velocities measured by the data acquisition system

Omni-directional transducers Delta Ohm HD103t were applied to measure the magnitude of velocity vector with air speed accuracy of ±0.04 m/s in the range of 0 ÷ 0.99 m/s and ±0.2 m/s in the range of 1 ÷ 5 m/s. Relative humidity was measured with an EE Elektronik sensor of J type with accuracy of 2.7% in the range above 90% relative humidity and 1.5% below 90% of relative humidity. Air temperature in the bulk of cabbage was measured with T-type thermocouples Czaki (precision ±0.2 K), at points marked in Fig. 2 as Tp points.

Thermal conditions in the cold store were changed constantly, mostly because of the requirements as to defrost cycle (2 times a day) of the cooler executed by the electric heaters accompanied by stopping of the fans, but there were some periods of time when conditions in the chamber were more stable. In Fig. 4 presents the velocities at levels V1÷V5 measured by the data acquisition system during 6 runs of the measurement line movement along the guide axis. Data collected at this time were selected after averaging for comparisons with the steady state simulations results.

A series of test calculations with the following models of turbulence for RANS equations were carried out: the standard model k-ε, RNG k-ε and realizable k-ε (with enhanced wall treatment), and with the model SST k-ω. The results of calculations obtained for different turbulence models are shown in the following figures.

Table 1. Comparison of experimental and calculated results of RH

Relative humidity at RH level [%]								
	1	2	3	4	5	6	7	8
RH exp.	88.40	88.20	88.00	87.90	87.20	89.10	89.70	88.80
RH *sst k-ω*	93.20	93.20	93.20	93.19	93.20	93.22	93.22	93.19
RH *k-ε*	93.16	93.45	93.82	94.15	94.38	94.10	94.45	91.87
RH *realizable k-ε*	91.96	92.60	93.27	93.77	94.29	94.93	94.66	95.06
RH *RNG k-ε*	97.18	97.52	98.23	98.66	98.82	98.98	98.31	98.86
Relative difference of measured and computed RH [%]								
δ_{RH}^{sst} [%]	5.43	5.67	**5.91**	**6.02**	**6.88**	**4.62**	**3.92**	4.94
$\delta_{RH}^{k-\varepsilon}$ [%]	**5.38**	5.96	6.61	7.11	8.23	5.61	5.29	**3.46**
$\delta_{RH}^{real.}$ [%]	4.02	**4.99**	5.99	6.68	8.13	6.55	5.53	7.05
δ_{RH}^{rng} [%]	9.93	10.56	11.63	12.24	13.33	11.09	9.60	11.33

Table 2. Comparison of experimental and calculated results of the temperature

Air temperature in the bulk [K]							
	1	2	3	4	5	6	7
T exp.	274.36	274.36	274.13	273.93	273.93	274.00	273.94
T sst k-ω	274.33	274.32	274.31	274.32	274.28	274.15	274.19
T k-ε	274.34	274.33	274.32	274.32	274.28	274.22	274.18
T realizable k-ε	274.20	274.33	274.32	274.33	274.30	274.22	274.20
T RNG k-ε	274.34	274.33	274.32	274.33	274.30	274.23	274.21
Relative difference of measured and computed temperature in the bulk [%]							
δ_t^{sst}	0.011	0.016	**0.066**	**0.142**	**0.127**	**0.055**	0.091
$\delta_t^{k-\varepsilon}$	**0.008**	0.011	0.069	0.144	0.129	0.080	**0.088**
$\delta_t^{real.}$	0.060	**0.010**	0.070	0.144	0.136	0.082	0.094
δ_t^{rng}	0.008	**0.010**	0.070	0.144	0.137	0.086	0.100

The comparison of experimental data and calculated relative humidity of air is presented in Table 1. Relative difference of measured and computed relative humidity vary between 4 and 13%. Turbulence model SST from k-ω gives calculated values the closest to the experimental ones. The smallest values of relative differences are bolded. On the other hand, RNG k-ε predicts relative humidity with the highest error. The comparison of experimental and calculated temperature in the bulk is presented in Table 2. The highest difference is 0.40 K regardless of the turbulence model was obtained at a point Tp4, that is in the middle of the bulk. Again, the smallest relative differences are bolded.

Figures 5 - 9 show the calculated and measured velocities magnitudes. In these figures the average experimental velocities, and also, the lowest and the highest velocities readings at each of the grid point are shown. It is seen that for different measurement levels the velocity distributions are predicted with different accuracy, regardless of turbulence model. The computed data extend beyond this range in many locations, especially at V3 level. However, for each level it is possible to find several points at which the calculated velocity is consistent with the experimental data with high or lower accuracy.

For example, RNG k-ε model gives very good accuracy for level 2 and level 4, but it fails for level 1 and 3. It is worth to note that the measurement level V2 is approximately at the same distance from the ceiling as the axis of the fans. The shape of the air jet strongly affects the results at V1 and V3 levels. Velocity magnitude at V3 level depends also on the disturbances caused by the guide of the measuring system. Also, the figures show that for level V1-V4 (see Fig. 5-8), models overpredicts the velocity with few exceptions. Velocity at level 2 is predicted the most accurately, and only few points lie beyond the measured minimum or maximum values. On the other hand, the largest differences are observed for level 1 and level 4. For level 5 (see Fig. 9) at the side wall of the chamber all tested models underpredicts the velocity but behind the bed of vegetables the velocity is overpredicted.

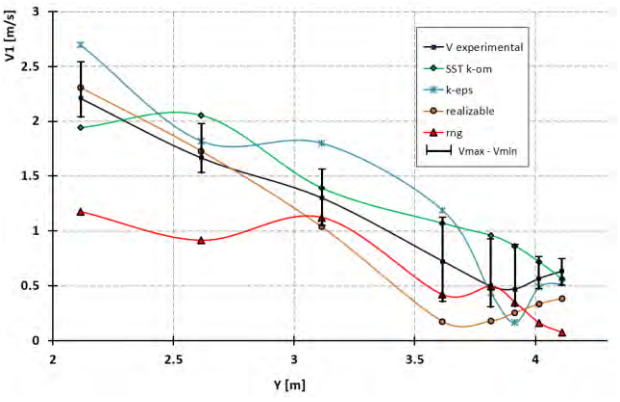

Figure 5: Comparison of experimental and calculated velocities at level V1

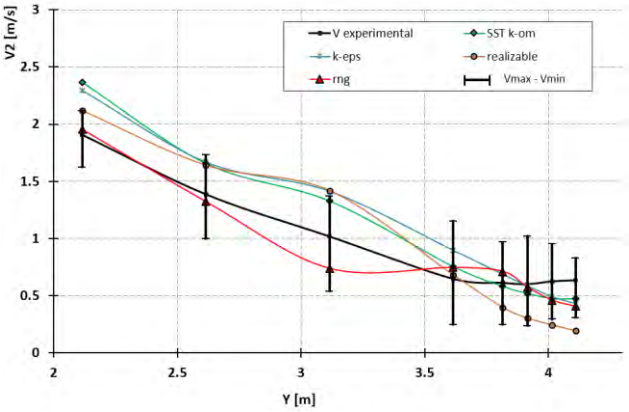

Figure 6: Comparison of experimental and calculated velocities at level V2

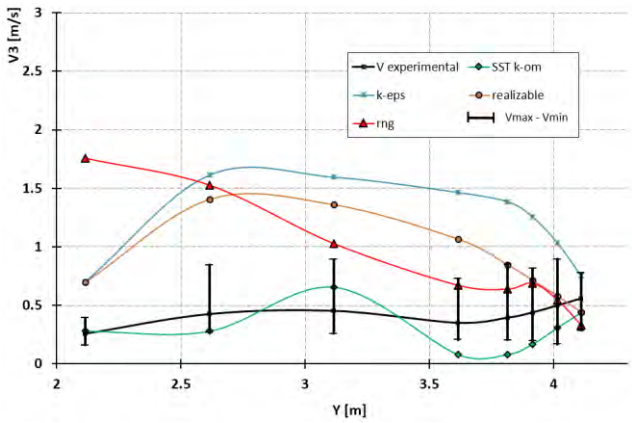

Figure 7: Comparison of experimental and calculated velocities at level V3

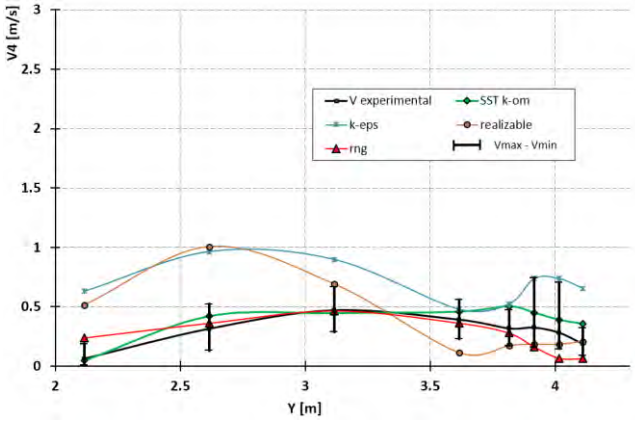

Figure 8: Comparison of experimental and calculated velocities at level V4

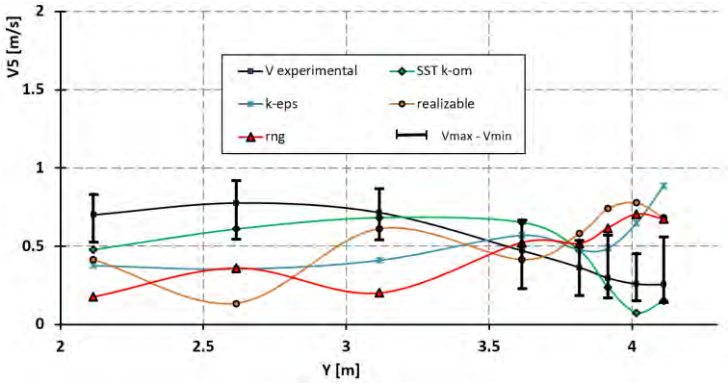

Figure 9: Comparison of the experimental and calculated velocities at level V5

It is clearly seen from Fig. 8-9 that the range of velocity readings taken at the same positions are fairly wide, so the airflow in the jet blown out by the fans is highly turbulent and unstable. Three swirling jets interfere with each other, with ceiling of the room, walls, rough and changing in time top surface of the bed and with supports of the measurement system. Thus, the stationary process assumed there may be only a quite rough approximation of a real flow that occurs in such a complex system.

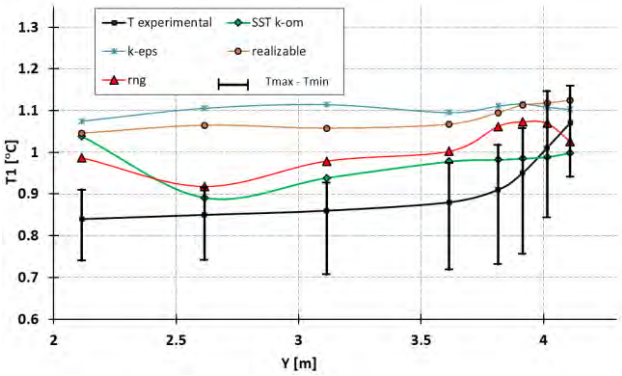

Figure 10: Comparison of experimental and calculated temperatures at level V1

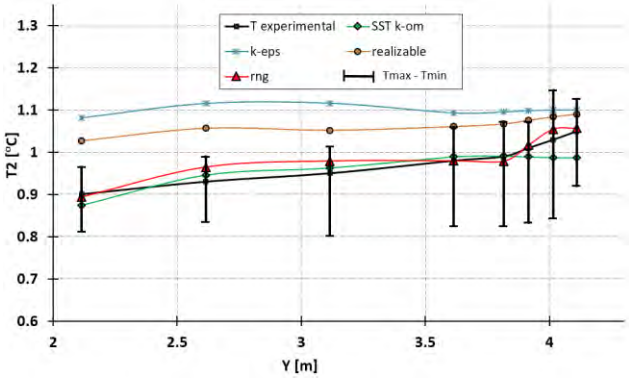

Figure 11: Comparison of experimental and calculated temperatures at level V2

Figures 10 - 14 shows the temperature distributions at each locations of the measurement sensors. The experiments showed that the lowest air temperature above the stored products was measured at the level 1 (5 cm below the ceiling). Temperature at level 2 is approx. 0.5 K higher than at level 1.

At level 3 and level 4 an influence of the swirl can be observed. In the middle of the measurement line the temperature sensor is inside the cold air stream and temperature is slightly decreasing. At this point cold air blown from the cooler starts to penetrate the products. It can be seen that the tested turbulence models in most of the cases overpredict temperature of the circulating air. The opposite trend at level 4 is observed. This might be an effect of not sufficient data inserted to numerical model dealing with respiration of the cabbage. In general, temperature lines obtained from the tested models are almost flat which means that these models give almost constant temperature along the measurement lines. In addition, temperature obtained from k-ε model among all tested models differs most significantly from the experimental data. Similarly, to velocity, temperature at level 2 is predicted with the highest accuracy. The most accurate temperatures were obtained from simulation with SST k-ω and RNG k-ε models.

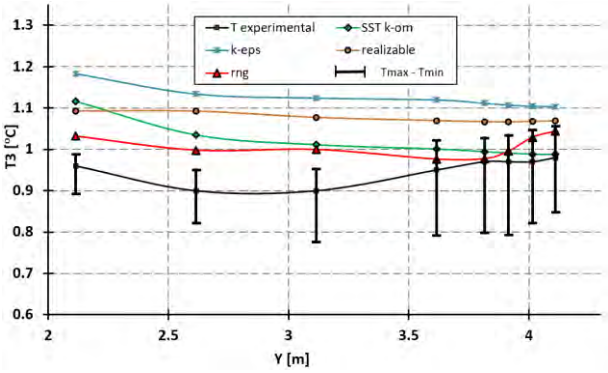

Figure 12: Comparison of experimental and calculated temperatures at level V3

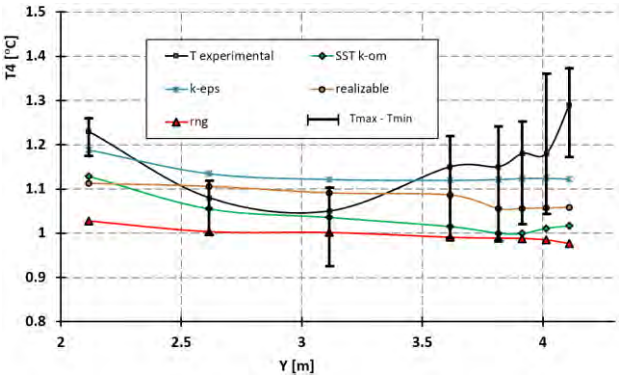

Figure 13: Comparison of experimental and calculated temperatures at level V4

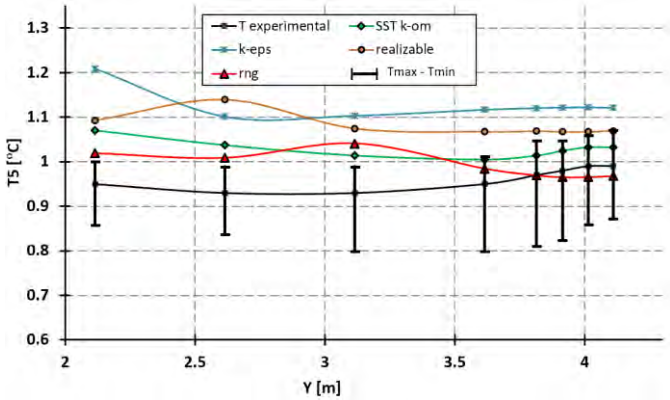

Figure 14: Comparison of the experimental and calculated temperatures at level V5.

4. CONCLUSIONS

Cooling units are equipped with fans mounted either at the inlet to the cooler or at the outflow to the chamber. The second ones create important problems in simulation due to difficulties in modelling the details of the jets blown from the fans, their shapes and their swirls. These are the first important factors that affect the flow pattern above the vegetables bed. The other one is the model of turbulence that have an impact on the way the air jets interact with each other and with the surroundings. In the present paper popular RANS turbulence models were tested. Velocity, relative humidity and air temperature were compared with experimental data. From all of the tested models, the realizable k-ε and SST k-ω models were the most promising. The realizable k-ε model was slightly better in prediction of the velocity distribution at the level V1 and V2 than the SST model, but it was not able to reproduce the velocity profile at V3, V4 and V5 levels. The SST k-ω model was the only one which managed to form air stream outflow wide enough to get close to the experimental data obtained at V5 level. Temperature distributions obtain from different models were in most cases overpredicted. However, the SST k-ω model gives the most accurate values. Air temperature in the bulk and relative humidity are well predicted by SST k-ω turbulence model. Relative difference of measured and computed relative humidity is below 7%.

The SST k-ω model of turbulence proved to be the better one from all of the RANS models tested, because of its better ability to represent the airflow above the bed, although slightly short of our expectations. Hence, the other time dependent models should be taken into account in future research. The comparison shows that further work has to be undertaken in modelling of air jets blown from the air cooler.

ACKNOWLEDGEMENTS

The research was carried out as part of research work no. S/WM/1/2018 at the Bialystok University of Technology and financed from a subsidy provided by the Minister of Science and Higher Education

REFERENCES

Chourasia, M.K., Goswami, T.K., 2007. Steady state CFD modeling of airflow, heat transfer and moisture loss in a commercial potato cold store, Int. J. Refrig., 30, 672-689.

Delele, M.A., Schenk, A., Tijskens, E., Ramon, H., Nicolai, B.M., Verboven, P., 2009a. Optimization of the humidification of cold stores by pressurized water atomizers based on a multiscale CFD model, J. Food Eng., 91, 228-239.

Delele, M.A., Schenk, A., Ramon, H., Nicolai, B.M., Verboven, P., 2009b. Evaluation of a chicory root cold store humidification system using computational fluid dynamics, J. Food Eng., 94, 110-121.

Hoang, H.-M., Duret, S., Flick, D., Laguerre, O., 2015. Preliminary study of airflow and heat transfer in a cold room filled with apple pallets: Comparison between two modelling approaches and experimental results, Appl. Therm. Eng. 76, 367-381

Hoang, M.L., Verboven, P., De Baerdemaeker, J., Nicolai, B.M., 2000. Analysis of the air flow in a cold store by means of computational fluid dynamics, Int. J. Refrig., 23, 127-140.

Kołodziejczyk M., Butrymowicz D., Gagan J., Śmierciew K., Investigations of Chinese cabbage cold storage chamber operation, 16th International Refrigeration and Air Conditioning Conference at Purdue, West Lafayette, July 11-14, 2016

Mirade, P.-S., Rougier, T., Daudin, J.-D., Picque, D., Corrieu, G, 2006. Effect of design of blowing duct on ventilation homogeneity around cheeses in a ripening chamber, J. Food Eng. 75, 59-70.

Moureh, J., Menia, N., Flick, D., 2002. Numerical and experimental study of airflow in a typical refrigerated truck configuration loaded with pallets, Comput. Electron. Agric. 34, 25-42.

Moureh, J., Tapsoba, M., Flick, D., 2009a. Airflow in a slot-ventilated enclosure partially filled with porous boxes: Part I – measurements and simulations in the clear region, Comput. Fluids, 38, 194-205

Moureh, J., Tapsoba, S., Flick, D., 2009b, Airflow in a slot-ventilated enclosure partially filled with porous boxes: Part II - measurements and simulations within porous boxes, Comput. Fluids, 38, 206-220

Nahor, H.B., Hoang, M.L., Verboven, P., Baelmans, M., Nicolai, B.M., 2005. CFD model of the airflow, heat and mass transfer in cool stores, Int. J. Refrig., 28, pp. 368-380.

Śmierciew, K., Kolodziejczyk, M., Gagan, J., Butrymowicz, D., Numerical modelling of fin heat exchanger in application to cold storage, 9th International Conference on Computational Heat and Mass Transfer : ICCHMT 2016, Cracow, May 23-26, 2016.

Tapsoba, M., Moureh, J., Flick, D., 2006. Airflow patterns in an enclosure loaded with slotted pallets, Int. J. Refrig., 29, 899-910.

Manuscript ID: 574
DOI: 10.18462/iir.icr.2019.0574

Influence of thermal properties of brown seaweeds (Saccharina Latissima) on atmospheric freeze-drying process in fluidized bed

Ignat TOLSTOREBROV [(a)], Trygve M. EIKEVIK [(a)], Maren Sæther [(b)]

[(a)] Norwegian University of Science and Technology, Department of Energy and Process Engineering, Trondheim, 7491, Norway, ignat.tolstorebrov@ntnu.no
[b)] Seaweed Energy Solutions AS, Trondheim, 7018, Norway, sather@seaweedenergysolutions.com

ABSTRACT

Study explains the influence of thermal properties on the atmospheric freeze-drying process of brown seaweeds in fluidized bed, especially on fluidization, that is important for efficient and rapid drying. Two different types of raw materials (washed and raw) were investigated using differential scanning calorimetry technique. Raw seaweeds contained high amount of salts and water soluble fraction on the surface, that influences significantly the amount of unfrozen water at low temperatures (up to 11.6 % w.b. at -25.0 °C), while washed seaweeds showed almost complete freezing without significant depressing of freezing point. The diagram that shows the amount of ice with respect to temperature and total moisture content was obtained. The efficient drying process can be obtained using washed seaweeds, which do not contain water-soluble elements on the surface, while raw seaweeds showed agglomeration of particles during drying, due to significant depression of freezing point.
Keywords: Seaweeds, Ice Content, Atmospheric Freeze-Drying, Unfreezable Water, Glass Transition.

1. INRODUCTION

Most of the seaweeds, which are used for food purpose in Norway belong to aquaculture products, when hatching, growth and harvesting is controlled continuously. The harvesting season occupies approximately 2 weeks in a year to provide the best quality of the seaweed's blades. The processing technology requires immediate treatment of raw seaweeds to ensure production of sustainable and high quality product. Due to high quantities of raw seaweeds during harvesting, immediate freezing is applied to prevent deterioration. However, drying is a common way to preserve food products like seaweed and most of the seaweeds are sold in a dried form (Forster and Radulovich, 2015). Solar and natural drying of seaweeds is a cost-effective method. At the same time climate conditions can result in a high final moisture content in the dried product (Phang et al., 2015) due to high moisture absorption ability (Lemus et al., 2008), also, the process is quite long and lasts between 5 and 7 days (Fudholi et al., 2011).

Due to this, the producers of Saccharina Latissima are considering an atmospheric freeze-drying process in fluidized bed as the most reliable for the given processing condition in Norway. However, first drying tests showed the agglomeration of particles that created significant difficulties, when drying even at -10.0 °C. The particle stick together and form bulks, which cannot be penetrated by air flow. This increases the drying time significantly and leads to quality degradation. Thus, design of equipment and adjustment of the processing parameters is complicated without knowledge of thermal phase transitions at freezing temperatures. The study discusses the thermal properties of seaweeds (raw and washed) and seaweed's mucus and their influence on the atmospheric freeze-drying process in fluidized bed.

2. MATERIALS AND METHODS

2.1. Description of Experiments

The brown algae *Saccharina latissimi* that is commonly referred as kelp (Sugar kelp or kombu) was used for the experiments. The seaweeds was cultivated for one year in an aquaculture farm, which is situated in Sør-Trøndelag (Norway). Harvesting season was 15 days in May 2017 to maintain the best quality of the seaweeds and avoid high amount of biofouling. The seaweed was harvested into nets (75-150 kg). The nets were buffered in the seawater at the farm where they were kept in refrigerated seawater (-1.0 °C) for 1 week before freezing. Then the seaweed was weighed out and packed inside vacuum bags with high barrier properties (2.0 kg each). Freezing was done at –46.0 °C until temperature in the center of the bag reached -18.0 °C. After freezing the bags were packed in cardboard boxes, put on pallets and placed in freeze storage at -18.0 °C. The kelp was delivered in a frozen state by the supplier (June 2017). The seaweeds were defrosted at +4.0 °C (15.0 hours). Three types of samples were investigated during this study using differential scanning calorimetry methods:

- Raw seaweeds (seaweed blades) without pre-processing;
- Mucilage from seaweed surface (mucus), as soon as, this substance covers surface of seaweed particles;
- Washed seaweed, when the mucilage is removed from the surface by preprocessing.

Washing of seaweeds took place in a boiling water (100.0 ºC) for 1.0 min. The blanched seaweeds were immediately cooled in water (5.0 °C).

2.2. Chemical Content Determination

Chemical composition of *Saccharina latissima* at harvesting season (analysis performed by accredited analytical laboratory Kystlab preBIO, Frøya, Norway).

2.3. DSC Analysis

The DSC analysis was done with a DSC Q 2000 (TA instruments, USA) equipped with a Liquid Nitrogen Cooling System. The heat capacity was calibrated with a sapphire in the range between –150.0 and 180.0 °C. Helium was chosen as a purge gas at 25 mL/min, according to TA's instrument recommendations. The reference sample was an empty hermetically sealed aluminum pan.
The samples with masses between 13.0 mg and 20.0 mg were placed into aluminum pans with hermetic lids. The pans were sealed with a Tzero® DSC Sample Encapsulation Press (TA Instruments, USA). The pans were placed by an autosampler into the DSC cell. Samples were cooled and equilibrated for 5 minutes at –150.0 °C; the cooling rate was 10.0 °C min^{-1}. The annealing procedure was applied at –50.0 °C. This was done to avoid cold crystallization during scanning. Then the samples were heated up to 50.0 °C (application of higher temperatures was not effective due to evaporation of moisture) with the heating rate of 10.0 °C min^{-1}.

2.4. Determination of Glass Transition

The glass transition was determined with TA Universal Analysis 2000 version 4.5A software (TA instruments, USA). The glass transition is characterized with the following parameters: the onset, end and inflection points. It should be noted, that the glass transition in seaweeds with high moisture content is relatively weak. Thus, the inflection point was determined as a negative peak of the derived heat flow curve (Tolstorebrov et al., 2014).

2.5. Determination of the end of Freezing and Initial Freezing Point

The onset of ice melting (or the end of freezing point), was determined by analyzing the DSC heating curve. The freezing point was estimated as a minimum value of the derivation of ice melting endothermic peak on the DSC heat flow curve.

2.6. Determination of Ice Fraction and Unfreezable Water

The amount of unfreezable water and ice fraction was detected by the DSC melting curve analysis. The DSC melting peaks were integrated with the sigmoidal tangent baseline function from the onset

of ice melting point. The ice fraction was determined as a ratio of melting energy to latent heat of fusion of pure ice. As soon as melting energy of ice is a function of temperature, the empirical equation suggested by Riedel (1978).
The amount of unfreezable water was obtained as the difference between the total water fraction in the product and the ice fraction.

2.7. Statistical Analysis

The analysis of variance (ANOVA: single test and two-factor test with replication) was applied to analyze the obtained data. The difference was considered significant at $p<0.05$. All the experimental points were done in six parallels.

3. RESULTS AND DISCUSSION

3.1. Chemical Composition of *Saccharina latissima*

Water content of the washed seaweeds was at 94.6 (0.9) % w.b. Chemical composition of the aquaculture seaweeds is given in the Table 1.

Table 1. Chemical composition of *Saccharina latissima*

Chemical composition	%, d.b.	Minerals , $mg \cdot kg^{-1}$ d.w.	
Proteins	11.2	Potassium	84000
Fats	2.9	Sodium	52000
Carbohydrates	55.3	Calcium	10000
Incl. Dietary fiber	46.6	Magnesium	7500
Ash	37.9	Sulfur	7300
Incl. Salt (NaCl)	14.6	Iodine	3670
Water	900.0	Phosphrus	1700

Protein content of the seaweeds was determined at 11.2 % d.b., which was in a common range for brown seaweeds between 3.0 and 15.0 % (Fleurence, 1999). The aquaculture seaweeds form Damariscotta bay (USA) had a protein content of 6.87 % d.b. (Sappati et al., 2017), which was in the range (between 9.9 and 7.6 % d.b.) of the previously obtained results for wild sugar kelp form Scotland, Isle of Seil (Schiener et al., 2015).
Salt (NaCL) content was very high in the Norwegian cultivated seaweeds due to washing process in seawater before freezing at factory. It is important to note that age of Saccharina's biomass was not determined in the mentioned above studies. Carbohydrate and ash content of Norwegian sugar kelp was almost the same as for aquaculture kelp from USA (53.36 % and 37.79 % d.b. respectively) but different, when compared with wild sugar kelp form Scotland (63.1 % and 31.7 %). The carbohydrates in Saccharina latissima are presented by alginate, mannitol, cellulose and laminarin. The available research for cultivated Norwegian sugar kelp reports mannitol and laminarin content in the ranges between 3.0-7.0 % d.b. and 0.2-0.9 % d.b. respectively (Tønder, 2014). Such deviation was explained by difference in the depth of cultivation of seaweeds. These compounds belong to storage carbohydrates since they are utilized as energy source during winter for new tissue growing (Schiener et al., 2015).

3.2. Glass Transition Phenomena in Raw Seaweeds, Seaweed Mucus and Washed Seaweeds

Three types of the samples were investigated: raw seaweeds (seaweed blades), seaweed's mucus and washed seaweeds. The DSC investigation revealed two glass transitions at the ultra-low temperature region at -81.4(2.6) and -62.14(0.46) °C for seaweed's blades and at -76.41(2.15) and -55.02(0.48) °C for mucus (Fig. 1).

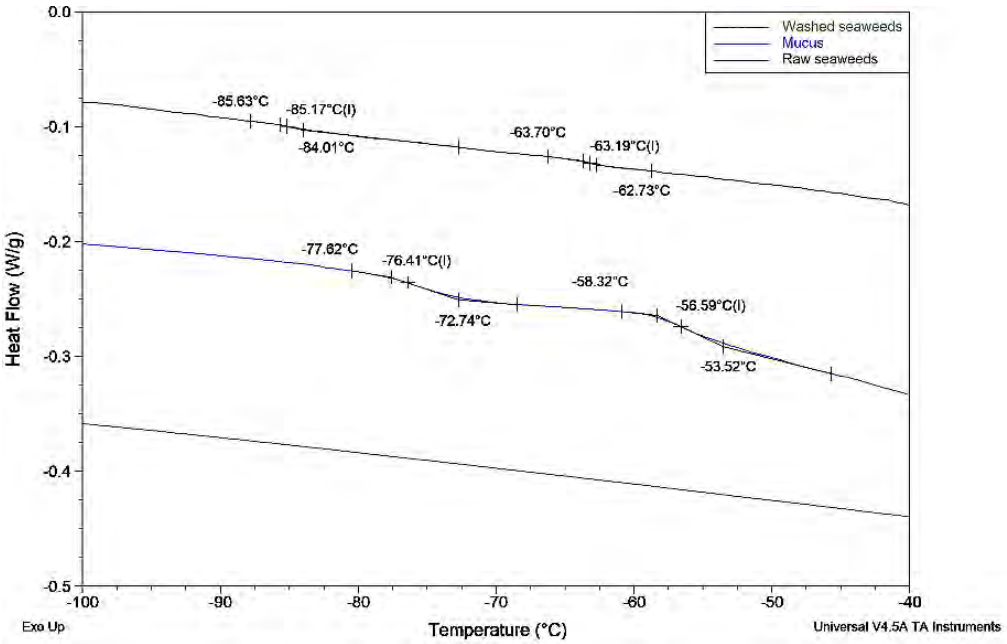

Figure 1: Example of glass transition of raw seaweeds, seaweed mucus and washed seaweeds

It should be noted, that the glass transition phenomena was weak due to the high amount of water fraction in the product, however, the negative peak was clearly observed on the derived heat flow curve. In previous study of Sappati et al. (2017) only one glass transition event was determined. The occurrence of two glass transitions refers to the different fractions of unfreezable water, which independently form different maximal freeze concentrated solutions. Each of the solutions has a unique point of glass transition. The presence of more than one glass transitions for low-moisture foods, which contain carbohydrates and proteins, was reported before (Figueroa et al., 2016). It is explained by the transitions of blends and thermal history of the sample. Also, immiscible compounds, which forms individual maximal-freeze concentrations solutions, can cause several glass transitions. However, it is not a strict rule (Gaikwad et al., 2008). The washed seaweed did not show the glass transition event at low and ultra-low temperature ranges. As a conclusion, one can state that the second order phase transition will not influence the atmospheric freeze drying process (temperature range between -5.0 and -10.0 ºC), while ice is presented in the product.

3.3. End of Freezing and Melting Peaks of Raw Seaweeds and Seaweed Mucus

A so-called “end of freezing” is an equivalent of the incipient point of ice melting on DSC heat flow curve (considering equilibrium freezing process). This point can be found on the heat flow curve derived by temperature (or time). The detailed information of the method available in Tolstorebrov et al. (2014).

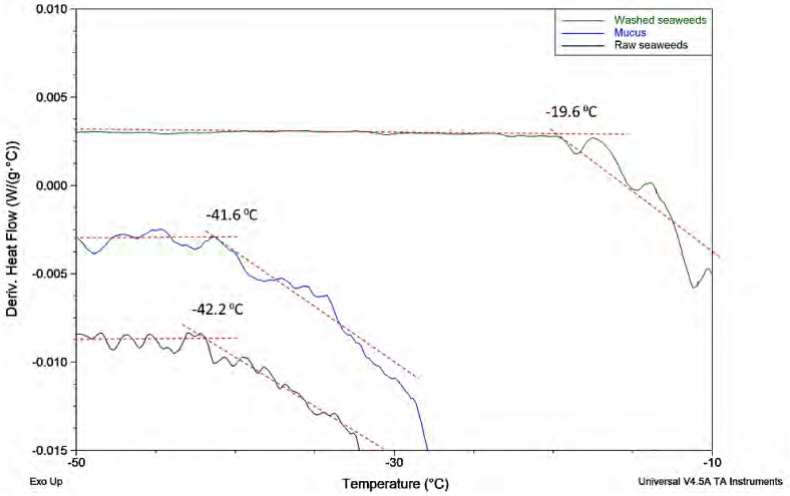

Figure 2: End point of freezing (onset of ice melting) for raw seaweeds, mucus and washed seaweeds on derived heat flow curve

Seaweeds blades and mucus showed the same values of the end of freezing point -42.2(1.6) and -42.1(1.7) °C ($p<0.05$). At the same time, washed seaweeds had incipient point of ice melting at -20.0 (1.2) °C, Fig. 2. This data was used for the derivation of melting peak for obtaining melting energy.

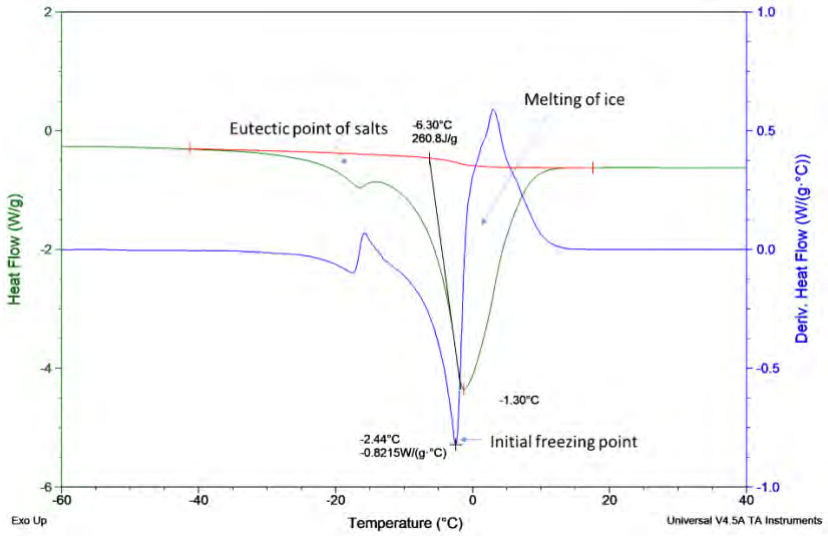

Figure 3: Melting peaks, initial freezing point of raw seaweeds

The melting endotherm consisted of two peaks for both raw seaweeds and mucus, Fig.3. The low temperature melting peak reflected eutectic point of salts (mostly *NaCL*), the high temperature melting peak shows the crystallization (melting) of water. Initial freezing point was determined as an extremum of the derivate line of ice melting peak at -2.4(0.2), -2.5(0.2) and -0.2(0.05) °C for seaweed blades, mucus and washed seaweeds respectively.

Analysis of the melting peak revealed that a significant part of moisture was in a crystalline form at freezing temperatures. The value of melting energy was found at 267.4(5.1), 259.4(1.0) and 307.2 (4.8) kJ kg^{-1} for raw seaweeds, mucus and washed seaweeds respectively. It is remarkable, that a high amount of ice was formed in the raw seaweeds ($p<0.05$) while the mucus had a higher moisture content 92.6(0.4) vs. 88.8(0.6) % w.b. ($p<0.05$). Relatively low freezing point and low ice content in the temperature range between -5.0 and -10.0 ºC, created difficulties for atmospheric freeze-drying process. The summing up of thermal events, which occurred in raw seaweeds and seaweeds mucus, are introduced of Fig. 4. The transitions of washed seaweeds were limited by Stage 1 and Stage 2 only.

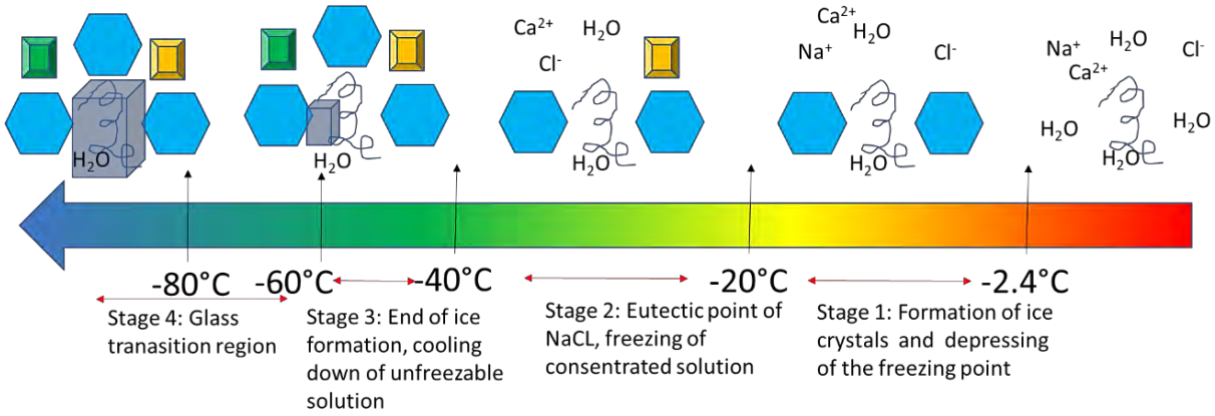

Figure 4: Simplified diagram of phase transitions in raw seaweeds and seaweed mucus

3.4. Ice Content and Unfreezable Water in Seaweed's Blades and Mucus with Respect to Temperature

Raw seaweeds showed 5.4(1.4)% w.b. of unfreezable water, while the value of 11.4(1.1) % w.b. was determined for mucus. Washed seaweeds had the lowest content of unfreezable water 2.2 (1.0)% w.b., which is at the sensitivity border of applied method. The value of unfreezable water in mucus

was relatively high when compared with other foods. This will result in a low content of solids in the maximal freeze concentration solution that was formed during the transition of water into ice. At the end point of freezing, the freeze concentration was at 66.4(11.5) and 39.2 (3.05) of solids % w.b. for seaweed's blades and mucus respectively.
All the types of samples showed a significant increasing of ice content in the vicinity of initial freezing point, Fig. 5, which is typical for seafood products of a high moisture content.

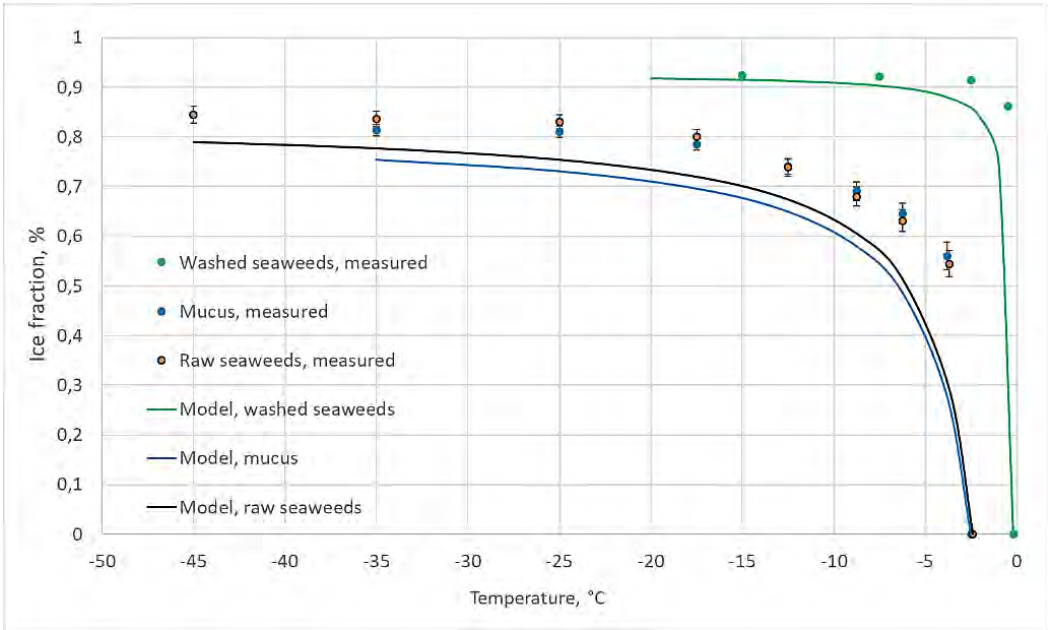

Figure 5: Ice fraction in raw seaweeds, mucus and washed seaweeds: measurements and model

The concentration of ice reached 70.0, 70.5 and 92.2 % w.b. at -10.0 °C and 60.0 (0.42) and 60.4 (0.9) % w.b. at -5.0 °C for raw seaweeds, mucus and washed seaweeds respectively. This temperature range was considered to be the most common for atmospheric freeze-drying process application (Claussen et al., 2007). The model of Schwartzberg (Schwartzberg, 1976) was used to predict the ice fraction, $x_{ice,T}$, %, at different temperatures (Eq. (1)):

$$x_{ice,T} = \left(1 - \frac{T_{i.ice}}{T}\right)\left(x_{water} - x_{ufreezable.water}\right) * 100\% \qquad \text{Eq. (1)}$$

where, $T_{i.ice}$ – initial freezing point, ºC; x_{water} – total water content, kg kg^{-1}; $x_{ufreezable.water}$- unfreezable water content, kg·kg^{-1}.
The model accuracy were weak for all the samples. This occurred due to the high salt content in raw seaweeds and in mucus (formation of hydrates of salts and crystallization of salt during freezing), while, washed seaweeds behaved rather similar to wet cotton than to a food material.
One can notice that the values of ice content are not so different in the raw seaweeds and mucus (for the same temperature intervals). At the same time, the concentration of solids (kg·kg^{-1}, w.b.) was different, which influenced on the ice development during the atmospheric freeze-drying process.

3.5. Development of Ice Content During Drying

The ice content in a product is in equilibrium with freeze concentrated solution and temperature: decreasing of the temperature results in the increasing of ice content, while increasing of solids in a freeze concentrated solution provoke the ice melting. Classical explanation of atmospheric freeze-drying process includes sublimation of ice and formation of dry front in the product. However, this situation would not occur in the case of seaweeds, as soon as ice crystals will be covered by the layer of unfrozen brine, which include dissolved salt ions, carbohydrates (mannitol) and proteins. Obviously, evaporation of unfrozen brine will be predominant. This will increase the concentration of solids in the concentrated solution and the ice crystals will melt (Fig. 5).

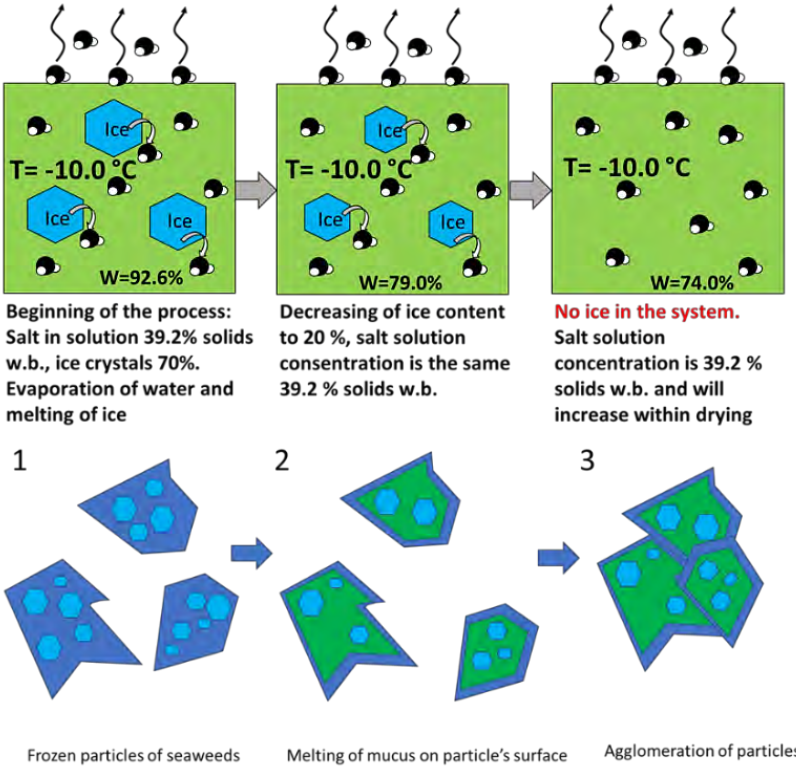

Figure 5: Example of atmospheric freeze drying of raw seaweeds, surface of seaweeds

Fig. 6 introduces the decreasing of ice content with respect to the total moisture content. Ice melting occurred much more rapidly for mucus (blue lines on Fig. 6). Thus, the surface of the product will show the different drying behavior when compared with the whole blades. The application of temperatures below the initial freezing point is suitable only at a high moisture content of the product. When the moisture content (kg·kg^{-1}, w.b.) decreases, for example, to 73.0 % for seaweeds and to 82.0 % for mucus at -5.0 °C, the application of freezing temperatures is not required, as soon as all the ice will melt.

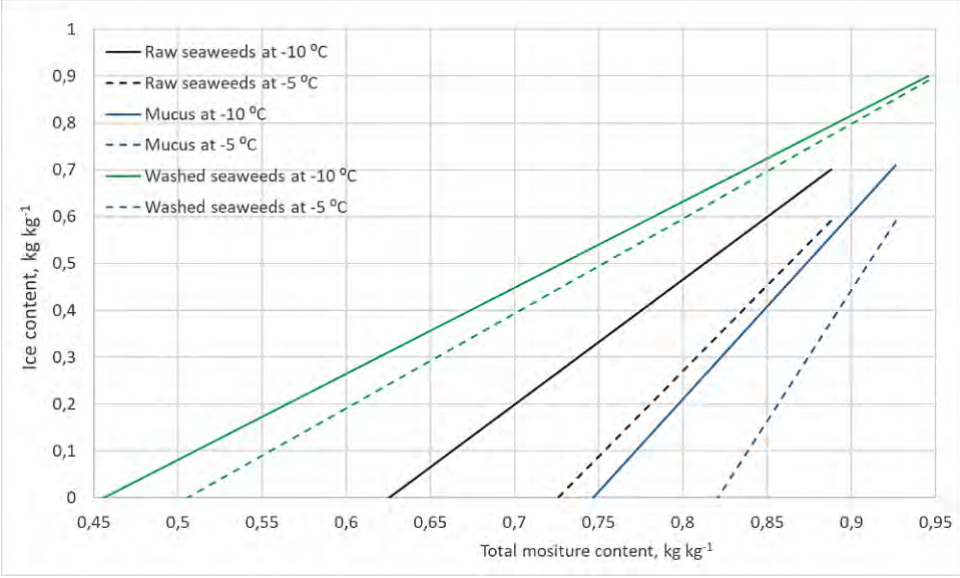

Figure 6. Equilibrium ice fraction in seaweeds (left) and mucus (right) for different atmospheric-freeze drying temperatures (with respect to total water content)

Diagram on the Fig. 6 can be used for the determination of desired freeze-drying temperatures. However, the specific properties of seaweed mucus limit the application of atmospheric freeze drying process in fluidized bed, due to active ice melting when decreasing the moisture content. The

washed seaweeds showed the best properties for atmospheric freeze-drying in fluidized bed due to maintenance of high ice content even at low total moisture content. This was achieved due to low concentrations of solutes in the tissues and on the surface of the washed seaweeds.

4. CONCLUSIONS

The two glass transition phenomena was detected at the ultra-low temperature region at -84.77(1.35) and -62.14(0.46)°C for seaweed's blades and at -74.44(2.15) and -55.02(0.48) for mucus. Seaweeds blades and mucus showed different values of the end of freezing point: -52.23(1.61) and -42.1(0.65) °C. The unfreezable water content in seaweed blades was 5.4(1.4)% w.b., while the value of 11.4(1.1) % w.b. was determined for mucus. Due to this, the maximal freeze concentration was at 66.4(11.5) and 39.2 (3.05) of solids % w.b. for seaweed's blades and mucus respectively. The application of atmospheric freeze-drying process is limited by full ice melting when the total moisture content is still high (during drying process). This leads to agglomeration of particles and decreasing of drying efficiency. Washed seaweeds, in contrast, showed better properties for atmospheric freeze-drying in fluidized bed.

REFERENCES

Claussen, I.C., Ustad, T.S., Strømmen, I., Walde, P.M., 2007. Atmospheric Freeze Drying—A Review. Drying Technology 25, 947-957.

Figueroa, Y., Guevara, M., Perez, A., Cova, A., Sandoval, A.J., Muller, A.J., 2016. Effect of sugar addition on glass transition temperatures of cassava starch with low to intermediate moisture contents. Carbohydr Polym 146, 231-237.

Fleurence, J., 1999. Seaweed proteins. Trends in Food Science & Technology 10, 25-28.

Forster, J., Radulovich, R., 2015. Chapter 11 - Seaweed and food security A2 - Tiwari, Brijesh K, in: Troy, D.J. (Ed.), Seaweed Sustainability. Academic Press, San Diego, pp. 289-313.

Fudholi, A., Othman, M.Y., Ruslan, M.H., Yahya, M., Zaharim, A., Sopian, K., 2011. Design and testing of solar dryer for drying kinetics of seaweed in Malaysia, Proceedings of the 4th WSEAS international conference on Energy and development - environment - biomedicine. World Scientific and Engineering Academy and Society (WSEAS), Corfu Island, Greece, pp. 119-124.

Gaikwad, A.N., Wood, E.R., Ngai, T., Lodge, T.P., 2008. Two Calorimetric Glass Transitions in Miscible Blends Containing Poly(ethylene oxide). Macromolecules 41, 2502-2508.

Lemus, R.A., Pérez, M., Andrés, A., Roco, T., Tello, C.M., Vega, A., 2008. Kinetic study of dehydration and desorption isotherms of red alga Gracilaria. LWT - Food Science and Technology 41, 1592-1599.

Phang, H.-K., Chu, C.-M., Kumaresan, S., Rahman, M.M., Yasir, S.M., 2015. Preliminary study of seaweed drying under a shade and in a natural draft solar dryer. International Journal of Science and Engineering 8, 10-14.

Sappati, P.K., Nayak, B., van Walsum, G.P., 2017. Effect of glass transition on the shrinkage of sugar kelp (Saccharina latissima) during hot air convective drying. Journal of Food Engineering 210, 50-61.

Schiener, P., Black, K.D., Stanley, M.S., Green, D.H., 2015. The seasonal variation in the chemical composition of the kelp species Laminaria digitata, Laminaria hyperborea, Saccharina latissima and Alaria esculenta. Journal of Applied Phycology 27, 363-373.

Schwartzberg, H.G., 1976. Effective heat capacities for the freezing and thawing of food. J. Food Sci. 41, 152-156.

Tolstorebrov, I., Eikevik, T.M., Bantle, M., 2014. Thermal Phase Transitions and Mechanical Characterization of Atlantic Cod Muscles at Low and Ultra-low Temperatures. J. Food Eng. 128, 111-118.

Tønder, T., 2014. A Study of the Seasonal Variation in Biochemical Composition of Saccharina latissima, Institutt for biologi. Norwegian University of Science and Technology, NTNU, p. 62.

Manuscript ID: 575
DOI: 10.18462/iir.irc.2019.0575

The use of nanoencapsulated essential oils embedded in the ice has an antimicrobial effect and extends the shelf life of refrigerated fresh sea bream with ice toping

Antonio LÓPEZ-GÓMEZ[(a,b)], Laura NAVARRO-SEGURA[(a)], María ROS-CHUMILLAS[(a)]

[(a)] Food Engineering and Agricultural Equipment Department, Universidad Politécnica de Cartagena, Paseo Alfonso XIII 48, E30203 Cartagena, Spain, e-mail: antonio.lopez@upct.es
[(b)] Instituto de Biotecnología Vegetal, Universidad Politécnica de Cartagena, Edificio I+D+I, Campus Muralla del Mar E30202 Cartagena, Spain, e-mail: antonio.lopez@upct.es

ABSTRACT

Sea bream (*Sparus aurata*) is one of the most important fish species farmed in Mediterranean countries. Its demand has increased during the past decade. However, it's a perishable product and ice toping is widely used in order to extend its shelf life. Essential oils (EOs) have antimicrobial and antioxidant properties. EOs have been used in ice to improve fish preservation. Although, EOs affect sensory properties in fresh fish. To avoid that effect EOs can be encapsulated in beta-cyclodextrin (β-CD). The aim of this study was to evaluate the antimicrobial effect and the shelf life of refrigerated fresh sea bream stored at 2 ºC in polystyrene boxes with nanoencapsulated EOs in β-CD embedded in the ice toping (as antimicrobial ice). The results demonstrated that nanoencapsulated essential oils embedded in the ice reduce microbial growth and improve shelf life. Furthermore, the sensory attributes of refrigerated sea bream with nanoencapsulated antimicrobial ice were better evaluated.
Keywords: antimicrobial ice, quality, fresh fish.

1. INTRODUCTION

The sea bream (*Sparus aurata*) is one of the most important fish species farmed in several Mediterranean countries as Greece, Turkey, and Spain. Furthermore, its demand has increased significantly during the last decade due to consumers demand fresh fish because of its quality and healthy characteristics (Goulas and Kontominas, 2007; FEAP, 2016). However fresh sea bream is extremely perishable. It is highly susceptible to spoilage during ice storage due to enzymatic and chemical reactions, and microbial activity that is responsible for the obvious spoilage and its short shelf life of 14-15 days (Carrascosa et al, 2015). Ice storage is widely used to preserve fresh fish but other methods have been studied in order to extend shelf life and avoid undesirable spoilage. It is known that the essential oils (EOs) have preservative properties. In fact, essential oils have antimicrobial properties with the potential to extend the shelf life of foods. Methods as icing with various antimicrobial and antioxidants, including EOs, have been reported. However, EOs usually have a strong flavor that can affect negatively to fish sensory properties (Burt, 2004). In order to avoid this negative effect, we used Cyclodextrins (CDs) in this work. CDs are cyclic oligomers of α-D-glucopyranose. The β-cyclodextrin (β-CD) molecule is made up of 7 D-glucose monomers linked by α (1,4) bonds, exhibiting the shape of a truncated hollow cone. The cavities of β-CD are hydrophobic, whereas the external faces are hydrophilic. These qualities allow that β-CD is a good option for essential oils encapsulation to increase water solubility and avoid undesirables flavor in the food. Hence, β-CD has been utilized in food mainly for molecular encapsulation of EOs forming the EOs+β-CD complex (Szente and Azejtli, 2004; Ayala-Zavala et al., 2008).
Within a great variety of EOs, bergamot, and grapefruit essential oils are very interesting to be used in fish preservation. Bergamot is the common name of the fruit *Citrus bergamia Risso* (family *Rutaceae*), which is a rich source of flavonoids (such as naringin, neoeriocitrin, neohesperidin, rutin, neodesmin, rhoifolin, and poncirin) and has a fresh and elegant aroma. The major compounds of bergamot EOs are limonene, linalyl acetate, linalool, γ-terpinene, and β-pinene. Grapefruit essential

oil is one of the most popular fragrances in body care products because it adds a refreshing quality. These essential oils are a mixture of volatile compounds like terpenes and oxygenated derivatives such as aldehydes (citral), alcohols and esters, their main component being D-limonene. Bergamot and grapefruit extracts have been studied to inhibit the oxidation of fish lipid with successful results and were the most preferred citrus in terms of sensory analyses (Yerlikaya et al, 2016).
By other hand, oregano EOs are one of the most used antimicrobial and antioxidant agents in fish and seafood products (Hassoun and Çoban, 2017). The major compounds of oregano EOs are carvacrol and thymol (phenols) which have antioxidant and antimicrobial activity (Juliano et al, 2000). Carvacrol is reported to be the main compound responsible for the antimicrobial and antioxidant activity of oregano essential oils (Rodríguez-García et al, 2016).
To increase the shelf life of the fresh sea bream stored in ice, in this work a combination of EOs encapsulated in β-CD were included in the ice, and this antimicrobial ice was applied as top icing on the fresh sea bream packaged in polystyrene packages.

2. MATERIAL AND METHODS

Carvacrol, Bergamot (*Citrus bergamia*), and grapefruit essential oils were obtained from Lluch Essence Company (Barcelona, Spain). β-Cyclodextrin (β-CD) was supplied by Roquette Freres (Lestrem, France). The EOs+β-CD inclusion complex powder was prepared following the kneading method (Marques, 2010), and the crushed ice including EOs+β-CD embedded in the ice crystals was manufactured by adding and dissolving the EOs+β-CD powder in the feeding water to the ice machine (Scotsman, Milan, Italy). The EOs+β-CD concentration in ice is expressed in mg of EOs/kg of ice. A combination of Carvacrol and two essential oils (Bergamot and Grapefruit), in a ratio of 3:1:1 (w/w/w), respectively, were used to obtain this antimicrobial ice.
The fresh fish (650 ± 50 g body mass, bm) were obtained from a fish farm of the Spanish company "Servicios Atuneros del Mediterráneo SL" (San Pedro del Pinatar, Murcia, Spain) located in South-eastern Spain. Fish was caught and slaughtered by hypothermia using seawater and ice in a ratio of 1:1 (w/w). Then, after 2 hours from killing the whole fish was packaged in polystyrene boxes and covered with two kinds of crushed ice: (i) ice without antimicrobial (control), and (ii) the cited antimicrobial ice. The ice/fish ratio (1:3, w/w) was held constant throughout the refrigerated storage experiments. The polystyrene boxes were provided with holes for water drainage. The fish packaged in these boxes was stored in a cold room at 2 ± 0.5 ºC for 19 days. Samples were taken on day 0, 7, 13, 15 and 19 of storage to perform the different analyses. Two fish pieces were used for physicochemical and microbiological analyses and another one for the sensory analysis.
In order to perform the microbiological counts, 25 g of fish muscle sample was added to 225 mL of sterile peptone water (Scharlau Chemie) and homogenized with a stomacher (Colwort Stomacher 400 Lab, Seward Medical, London, UK). From this dilution, other decimal dilutions were prepared and plated on the appropriate media. Plate Count Agar (Scharlau Chemie) was used for enumeration of mesophilic and psychrophilic aerobic bacteria, and plates were incubated for 48 h at 30 ºC and 7 days at 4 ºC respectively. *Pseudomonas sp*. were determined on Cetrimide Agar (Scharlau Chemie) after incubation at 37 ºC for 48 h. *Enterobacteriaceae spp*. were counted on violet red bile glucose agar (Scharlau Chemie) incubated at 37 ºC for 24 h. All plates were performed in triplicate and the results were expressed as logarithms of the number of colony-forming units per gram (log CFU/g).
The pH was measured with a pH meter (pH-meter Basic 20, Crison). Fish muscle (5 g) was homogenized thoroughly with 10 mL of distilled water and the homogenate was used for pH determination.
Trimethylamine nitrogen (TMA-N) was determined using the Picric Acid Method (AOAC, 1998) and measured by spectrophotometer at 410 nm. TMA content was expressed as mg N/ 100 g fish muscle.
The Water-holding capacity (WHC) analysis was based on the method described by Grau and Hamm (1953). WHC was expressed in percentage.
The sensory evaluation of samples was performed by a sensory panel of seven people (24–50 years) trained for sensory quality analyses. The evaluations were done in a sensory room according to international standards (ASTM STP 9133, ASTM, 1986). Sensory evaluation was conducted in individual booths under controlled conditions of light, temperature and relative humidity.

3. RESULTS

The changes in the microbial flora of fresh sea bream under the two different ice toping packaging techniques, and during the ice storage, are shown in Fig. 1, 2 and 3.

The initial *Pseudomonas* count at the beginning of ice storage was very low. By day 15 of storage at 2 ºC, *Pseudomonas* count in sea bream packaged with the control ice and with antimicrobial ice (EOs+β-CD) was similar. However, at the end of refrigerated storage time (19 days), sea bream packaged with the control ice reached a count of 4.91 log CFU/g while sea bream stored with antimicrobial ice reached the value of 4.15 log CFU/g (Fig. 1).

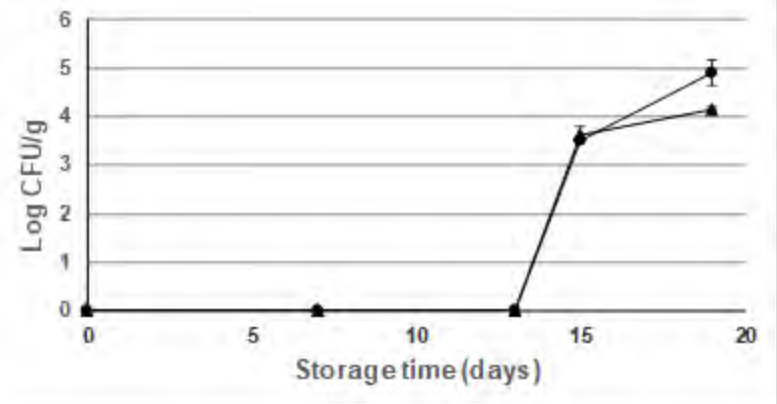

Figure 1: Changes in the counts of *Pseudomonas* of whole sea bream along with ice storage at 2 ºC with different top icing conditions: with control ice (●) and with antimicrobial ice including EOs+β-CD (▲)

During storage time, mesophilic aerobic bacteria counts of sea bream packaged with control ice increased and exceeded the value of 7 log CFU/g considered as the maximum level for acceptability for sea fish (ICMS, 2002) by day 19 of ice storage. However, at the end of the storage period (day 19), results showed a significant effect of antimicrobial ice on mesophilic counts (Fig. 2). It can be observed that sea bream ice stored with antimicrobial ice has a lower final count on mesophilic aerobic bacteria.

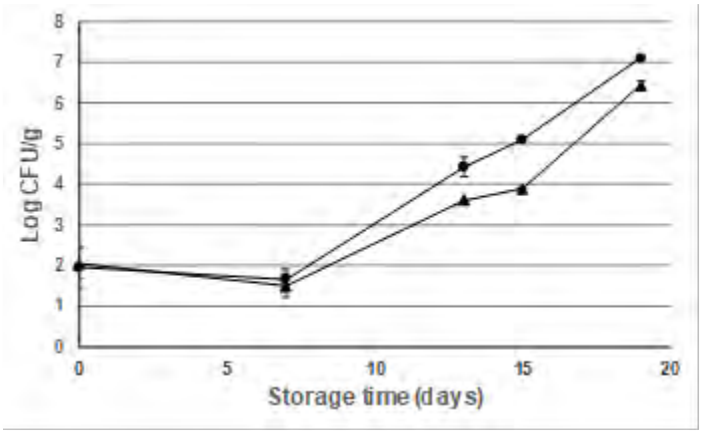

Figure 2: Changes in the counts of mesophilic aerobic bacteria of sea bream along with ice storage at 2 ºC with different top icing conditions: with control ice (●) and with antimicrobial ice including EOs+β-CD (▲).

The low initial psychrophilic bacteria counts indicate good fish quality. Psychrophilic bacteria counts exceeded the value of 6 log CFU/g, considered as the upper acceptability limit for marine species (Carrascosa et al., 2015), on 19 storage day at 2 ºC in both conditions. However, sea bream packaged with antimicrobial ice presents a lower psychrophilic bacteria counts as compared with control sea bream (Fig. 3).

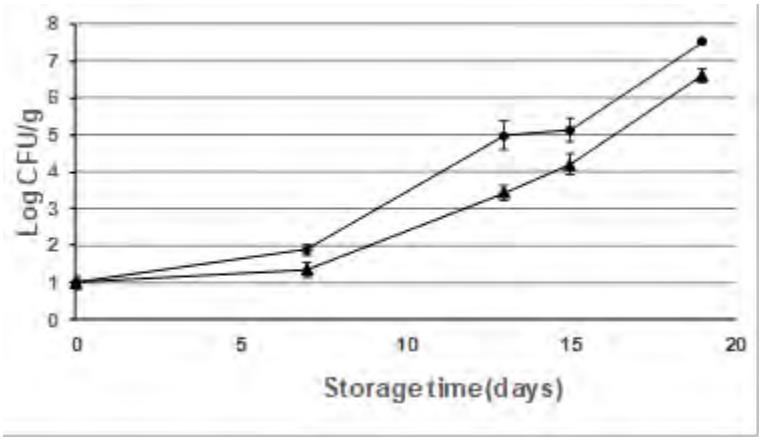

Figure 3: Changes in the counts of psychrophilic bacteria of sea bream along with ice storage at 2 ºC with different package icing conditions: control ice (●) and ice including EOs+β-CD (▲)

The ICMSF has established a mesophilic aerobic bacteria count limit of 7 log CFU/g on fish for human consumption. This value was reached on day 16 of ice storage in sea bream packaged with control ice if we use a regression analysis (obtaining the shelf life equation) to obtain the shelf life.

$$Log\ CFU = 1.7666 + 0.3207\ days$$

Based on this procedure, sea bream ice stored with antimicrobial ice will have the shelf life equation, obtained by regression analysis, for obtaining the microbial counts as a function on storage time

$$Log\ CFU = 1.4538 + 0.2921\ day$$

Then, the mesophilic aerobic bacteria count limit would be reached on day 18 of ice storage using antimicrobial ice. Hence, sea bream stored with antimicrobial ice increased the shelf life in 2 days if comparing to control ice storage.

TMA-N is used as a quality indicator for fish. In fresh fish, TMA-N value is less than 1 mg/100 g while in spoiled fish it is above 8 mg/100 g (FAO, 1986). TMA-N values increased along storage time in both conditions. However, at the end of storage TMA-N values in sea bream in control ice was higher than TMA-N values of sea bream ice stored with antimicrobial ice (Table 1).

Table 1. TMA-N values of sea bream during ice storage at 2 ºC (mg TMA-N/100 g)

	Days of storage				
	1	7	13	15	19
Control	0.19±0.35	0.33±0.11	0.49±0.12	0.57±0.06	0.63±0.11
EOs+β-CD	0.20±0.06	0.17±0.05	0.31±0.05	0.40±0.03	0.40±0.01

The initial pH of sea bream was between 6.06 and 6.10 and these values increased during ice storage at 2 ºC (Table 2). The pH values increased throughout the storage time and no significant differences were found across all treatment groups. The increase of pH values along ice storage time is due to the accumulation of basic compound, such as ammonia compounds and TMA (Goulas and Kontominas, 2007).

Table 2. pH changes of sea bream during ice storage at 2 ºC

	Days of storage				
	1	7	13	15	19
Control	6.06±0.00	6.26±0.06	6.42±0.14	6.37±0.02	6.41±0.14
EOs+β-CD	6.11±0.06	6.27±0.05	6.34±0.01	6.26±0.01	6.39±0.11

The WHC values ranged from 71 to 82 %, which is considered typical values for fresh fish. Control and antimicrobial ice decrease WHC values throughout the ice storage time. However, sea bream stored with antimicrobial ice has always higher WHC values than sea bream in control ice.

Table 3. Changes in WHC of sea bream along with ice storage at 2 ºC

	Days of storage				
	1	7	13	15	19
Control	77.47±0.35	77.42±0.80	76.08±6.66	72.19±2.42	71.87±4.72
EOs+β-CD	82.17±1.93	78.76±1.22	78.29±0.71	75.12±2.46	75.06±5.34

Sensory panellists did not detect EOs odor during storage. At the beginning of ice storage time there were no significant differences in sensory characteristic, although, at the end of storage time, sea bream ice stored in control ice showed worse attributes scores than sea bream stored with antimicrobial ice.

4. CONCLUSIONS

Fresh sea bream packaged in antimicrobial ice (including a combination of carvacrol, bergamot, and grapefruit essential oils nanopencasulated in β-CD, and embedded in the ice crystals) showed lower microbiological counts due to the antimicrobial effect of the EOs vapors released from the EOs+β-CD inclusion complex when ice melting. In this manner, the EOs vapors act as surface decontamination agents on the whole fish stored in ice. Pseudomonas, Mesophilic aerobic bacteria and psychrophilic counts were reduced by more than 0.5 log CFU/g after 19 storage days. Using antimicrobial ice extended the shelf life of fresh sea bream 2 days if comparing to fresh sea bream stored in control ice, and considering the mesophilic aerobic bacteria count limit as shelf life criterium. Concerning to TMA-N values, sea bream stored with antimicrobial ice showed lower values than sea bream stored in control ice, indicating better conservation of the freshness.
When using the EOs nanoencapsulated in β-CD, and embedded in the ice crystals of the crushed ice, in ice storage of fish the odor of the ice is pleasant and the odor of the fresh fish is fresher. This observation is related to better conservation of the fish freshness along with storage.
In conclusion, the use of EOs+β-CD inclusion complex embedded in ice crystals could be applied to ice storage of fish to significantly extend shelf life, with a sustainable cost and using more natural preservatives.

ACKNOWLEDGEMENTS

This work was funded by Pescados de Acuicultura de Murcia SL Company (San Pedro del Pinatar, Murcia, Spain) and CDTI (Madrid, Spain) (Project Number IDI-20150100), and co-financed by the European Regional Development Fund (ERDF) through the Pluriregional Operational Programme for Intelligent Growth.

REFERENCES

Ayala-Zavala, J.F., Soto-Valdez, H., González-León, A., Álvarez-Parrilla, E., Martín-Belloso, O., & González-Aguilar., G.A., 2008. Microencapsulation of cinnamon leaf (*Cinnamomum zeylanicum*) and garlic (*Allium sativum*) oils in β-cyclodextrin. J. Incl. Phenom. Macrocycl Chem. 60, 359–368.

Burt, S., 2004. Essential oils: their antibacterial properties and potential applications in foods-a review in press. Int. J. Food Microbiol. 94 (3), 223–253.

Carrascosa, C., Millán, R., Saavedra, P., Jaber, J. R., Raposo, A., Pérez, E., ... & Sanjuán, E. 2015. Microbiological evolution of gilthead seabream (Sparus aurata) in Canary Islands during ice storage. J. Food Sci. Technol. 52(3), 1586-1593.

FAO, 1986. FAO food and nutrition paper manuals of food quality control food analysis: Quality, adulteration, and tests of identity. Rome: Food and Agriculture Organization

FEAP, 2016. European aquaculture production report 2007-2015. Available from http://www.feap.info/

Goulas A.E., Kontominas M.G., 2007. The combined effect of light salting, modified atmosphere packaging and oregano essential oil on the shelf-life of sea bream (Sparus aurata): Biochemical and sensory attributes. Food Chem. 100, 287-296.

Grau, R., Hamm, R., 1953. Eine einfache methode zur bestimmung der wasser bindung im muskes. Naturwissenschaften 6, 29–30

Hassoun, A., & Çoban, Ö. E. 2017. Essential oils for antimicrobial and antioxidant applications in fish and other seafood products. Trends Food Sci. Technol., 68, 26-36.

ICMSF International Commission on Microbiological Specifications for Foods. 2002. Microorganisms in Foods 7, Microbiological Testing in Foods Safety Management. Kluwer Academic/Plenum Publishers. Springer, Londres.

Juliano, C., Mattana, A., & Usai, M. 2000. Composition and in vitro antimicrobial activity of the essential oil of Thymus herba-herbona Loisel growing wild in Sardinia. J. Essential Oil Res. 12, 516–522.

Marques, H.M.C., 2010. A review on cyclodextrin encapsulation of essential oils and volatiles. Flavour Fragr. J. 25, 313–326.

Rodriguez-García, I., Silva-Espinoza, B. A., Ortega-Ramirez, L. A., Leyva, J. M., Siddiqui, M. W., Cruz-Valenzuela, M. R., ... & Ayala-Zavala, J. F. 2016. Oregano essential oil as an antimicrobial and antioxidant additive in food products. Critical Rev. Food Sci. Nutrition 56(10), 1717-1727.

Szente, L., Szejtli, J., 2004. Cyclodextrins as food ingredients. Trends Food Sci. Technol. 15, 137–142.

Yerlikaya, P., Gokoglu, N., Topuz, O. K., Gumus, B., & Aydan Yatmaz, H. 2016. Antioxidant Activities of Citrus Albedo and Flavedo Fragments Against Fish Lipid Oxidation. J. Aquatic Food Product Technol. 25(8), 1339-1347.

Manuscript ID: 576
DOI: 10.18462/iir.irc.2019.0576

The treatment with vapors of essential oils in the vacuum cooling has a significant effect on surface microbial decontamination of fresh vegetables

Antonio LÓPEZ-GÓMEZ[(a,b)], María ROS-CHUMILLAS[(a)], Sonia SOTO-JOVER[(a)], Laura NAVARRO-SEGURA[(a)], Laura BUENDÍA-MORENO[(a)], Vera ANTOLINOS-LOPEZ[(a)], María J. SANCHEZ-MARTINEZ[(a)]

[(a)] Food Engineering and Agricultural Equipment Department, Universidad Politécnica de Cartagena, Paseo Alfonso XIII 48, E30203 Cartagena, Spain, email: antonio.lopez@upct.es

[(b)] Instituto de Biotecnología Vegetal, Universidad Politécnica de Cartagena, Edificio I+D+I, Campus Muralla del Mar, E30202 Cartagena, Spain, email: antonio.lopez@upct.es

ABSTRACT

Fresh vegetables are vulnerable to microbial contamination. Washing treatments with synthetic disinfectants are generally used in fresh vegetables. However, consumers demand natural antimicrobial substances. Many reports have demonstrated that the application of essential oils (EOs) in the vapor phase can decrease the dose to inactive surface microbial contamination. Vacuum cooling has been reported as a good method of fast cooling of many types of vegetables. Also, another characteristic of this cooling method is that vacuum level at the end of the cooling is generally of 5-6 hPa. In these conditions, the application of vapor of EOs can be more effective than at atmospheric pressure. This work has highlighted that treatment with vapors of EOs at the end of the vacuum cooling reduces the surface microbial contamination in 4 Log CFU and increases the shelf life of the produces. Moreover, sensory analysis of vegetables treated with vapors of EOs at vacuum was better during shelf life.

1. INTRODUCTION

In the last few years, the demand of fresh vegetables and healthy products together with the changes in costumer life style, and the advancement of retail marketing, have led to an explosively increase of the market for fresh fruit and vegetables (F&V) (Betts, 2014; Caleb et al., 2013; Rabobank, 2011; WHO, 2010). Nevertheless, the number of outbreaks of foodborne illnesses caused by the consumption of contaminated minimally processed F&V has also increased (Callejon et al., 2015; Castro-Ibañez et al., 2017). Chlorine is the disinfectant more extended in the food industry (Gil et al., 2009). However, harmful compounds for human health and the environment are produced as a consequence of the continuous replenishment of chlorine into wash water highly charged with organic matter (Luo et al., 2012; Yang et al., 2012). Alternative technologies have been studied including different physical and chemical postharvest treatments such as antimicrobial solutions in water (peroxyacetic acid, chlorine dioxide, hydrogen peroxide, organic acids, calcium), electrolyzed water, hot water treatment, ultraviolet radiation, ultrasounds, high pressure processing, hydrogen peroxide, ozone, super-atmospheric oxygen (in combination with MAP) and MAP enriched with inert gases (Ar, He, Xe) or N_2O. However, most of them have only been studied at laboratory scale, showing similar o less effect than chlorine on microbial populations in different fresh cut vegetables (Ali et al., 2017; Gil et al., 2015; Issa- Zacharia et al., 2011).

Plant essential oils (EOs) and their components, generally recognized as safe (GRAS) by the American Food and Drug Administration (FDA, USA), have shown a wide antimicrobial activity due to their composition which includes terpenes and terpenoids, and aromatic and aliphatic

compounds of low molecular weight. Because of this, these compounds have been investigated as natural sanitizer alternatives for controlling spoilage bacteria and naturally occurring pathogens associated with minimally processed vegetables (Belletti et al., 2008; Siroli et al., 2015).

Application of essential oils in the vapor phase can get decrease the necessary dose of EOs to inactivate microorganisms (Seo et al., 2015) avoiding sensorial alteration of the products. Different studies have tested the direct application of vapors of essential oils on minimally processed cut fruit and vegetables (Fhiser and Philips, 2006; Fisher et al., 2009; Inouye, 2003; López-Gómez et al., 2018; Tyagi and Malik, 2012). However, there has never been presented equipment allowing the industrial application of these vapors for solid food decontamination with evaporation periods enough short to be implemented in Vacuum cooler. Vacuum cooling, a technique based on the principle of the evaporative cooling, is able to rapid decrease temperature of porous products that have free water. At the end of this cooling, consequence of the vacuum level (approx. 5-6 hPa), is it possible the industrial application of EOs vapors through a rapid vaporization phase obtaining a homogeneous distribution of the disinfectant vapors that can be more effective than EOs application at atmospheric pressure.

Among RTE vegetables, fresh-cut aromatic herbs (FCAHs) market has recently shown a growing trend at world trade level because of their intense flavor, convenience and nutritional benefits. (Curutchet et al., 2014; Santos et al., 2014). On the other hand, garlic is a food ingredient widely used in gastronomy, which possesses many high organo-sulfur compounds content (Augusti & Mathew, 1974) responsible of the wide biological properties of this product (Lanzotti, 2006). Specifically, it has been reported that garlic exhibit different medical effects including prevention of cardiovascular disease and antimicrobial, antioxidant, anticarcinogenic, antimutagenic, antiasthmatic, immunomodulatory and prebiotic activities (Corzo-Martínez at al., 2007). As a consequence, garlic, as much in feeding as in therapeutic, is a vegetable with a huge projection, especially when is peeled and offered to consumers as a fresh ready-to-eat (RTE) vegetable. However, due to the cultivate techniques and handling post-harvest (products minimally processed, storage, distribution, sale and/or use), these products are exposed to a wide range of microbial contamination (McKee, 1995).

In this research work, the antimicrobial effect of vapors of different combinations of EOs and/or their components was studied "*in vitro*" in order to select those with the higher antibacterial activity. Subsequently, the surface microbial decontamination caused by the vapor phase of the selected EOs combinations was studied in garlic and FCAHs, under vacuum conditions at industrial scale using decontamination technology as was previously described in the work of López-Gómez et al (2018).

2. MATERIALS AND METHODS

2.1. Natural Antimicrobial Compounds and Vegetal Material

Oregano and peppermint essential oils, carvacrol and linalool were obtained from Lluch Company (Spain). Citral was supplied by Sigma-Aldrich (Germany). The combinations of EOs studied were obtained by mixing carvacrol:oregano (CO), carvacrol:peppermint (CP) and Linalool:oregano (LO) 80:20 % (v/v). Besides, carvacrol (C) and citral (Ci) were tested as single compounds.

Peeled garlic cloves and fresh curly and flat parsley, dill, coriander, rosemary, thyme and peppermint were kindly provided by local suppliers. Until use, garlic and FCAHs, were stored at 2 ºC.

2.2. *In Vitro* Study of the Antimicrobial Effect of EOs Vapor

To study the antimicrobial effect of EOs vapors at "*in vitro*" scale a vapor test was performed. To this end, solidified agar medium (Rose Bengal agar, Scharlau Chemie, Barcelona, Spain) was inoculated with 100 µL of buffered peptone water containing 10^2, 10^3 and 10^4 log CFU/mL of molds isolated from FCAHs. Then, the antimicrobial agent (EO or specific compound) was added (300 mg/m^2) to a 3.5 cm sterile blank filter and placed on the medium-free cover of the plate. The Petri plate was then sealed using sterile adhesive tape (Deltalab, Rubi, Spain). Controls samples were performed by introducing paper discs without EOs addition. The combinations of EOs studied were: CO, CP and LO 80:20 % (v/v). C and Ci were tested as single compounds.

Plates were incubated face down to ensure the absence of contact between paper discs and agar, at 25 ºC during 5-7 days.
All plates were performed in triplicate and the microbial counts were expressed as logarithms of the number of colony-forming units per mL (Log CFU/mL). The inhibitory effect of EOs and/or their components were expressed as the difference of Log CFU/mL observed between control samples and treated samples.
Target molds used in this study were isolated from fresh curly and flat parsley, dill, coriander, rosemary, thyme and peppermint. To this end, FCAHs were submerged separately in buffered peptone during 1 h, at refrigeration temperature and constant shaking (150 rpm). After the contact period, 0.1 mL of the liquid was spread in triplicate in Rose Bengal plates and incubated at 25 ºC during 5-7 days. Obtained colonies were selected following morphologic criteria and inoculated in Potato Dextrose broth tubes which were subsequently incubated at 25 ºC during 5-7 days and finally stored at 4 ºC until use.

2.3. Industrial Application of EOs Vapor

Industrial application of EOs vapors for surface disinfection was performed using vacuum cooling technology as was previously described (López-Gómez and López-Cánovas, 2018) (Fig. 1). To this end, two local companies adapted their vacuum cooling systems and performed trials in duplicated in which EOs vapors were applied at 8 µL/L concentration. Peeled garlic cloves and fresh FCAHs (curly parsley, dill and peppermint) samples were exposed to CO and CP 80:20 % (v/v) vapors, respectively.

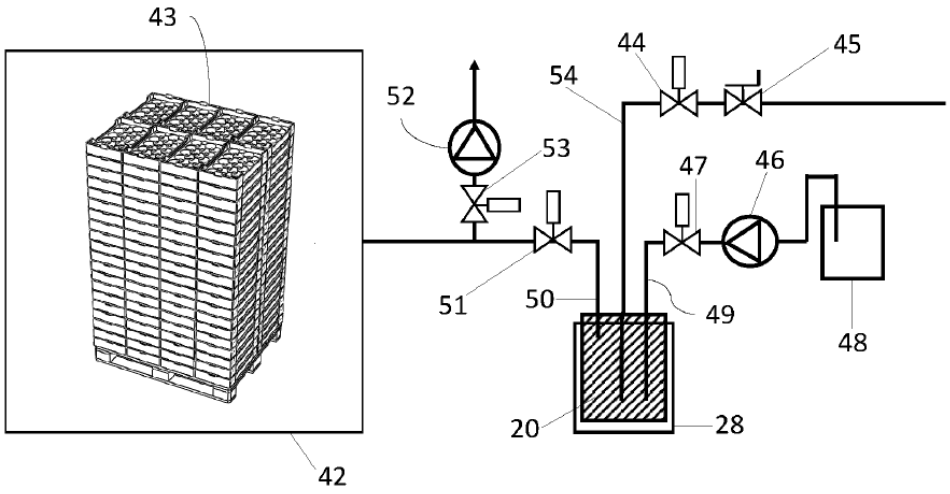

Figure 1: Industrial installation of an EOs vaporization device in a vacuum cooling. Description: Vacuum evaporation of EOs is performed in a vessel (20) which is heated by a jacket (28). Vacuum application of EO vapors is performed within vacuum cooling chamber (42) (right after applying the step of vacuum cooling) for the microbial surface decontamination of fresh plant products packaged in crates (43) made of plastic material. 49, 50 y 54 are connection tubes and 52 is a vacuum pump. 44, 45, 47, 51 y 53 are valves. Liquid EOs are dosed with a metering pump (46) taking the essential oil from a storage vessel (48).

To assess the effect of the antimicrobial treatment on vegetables, 25 g of sample were added to 225 mL of sterile peptone water (Scharlau Chemie, Barcelona, Spain) and homogenized with a stomacher (Colwort Stomacher 400 Lab, Seward Medical, London, UK). From this dilution, other decimal dilutions were prepared and plated on the appropriate media. Plate Count Agar (Scharlau Chemie, Barcelona, Spain) was used for enumeration of mesophilic and psychrotrophic aerobic bacteria, and plates were incubated at 30 ºC for 48 h and at 4 ºC for 7 days, respectively. Bacteria from the Enterobacteriaceae family were counted on violet red bile glucose agar (Scharlau Chemie, Barcelona, Spain) and incubated at 37 ºC for 24 h. Lactic acid bacteria were grown in De Man, Rogosa and Sharpe agar and incubated at 31 ºC during 48 h in a microaerophilic atmosphere. Finally, molds were counted in Rose Bengal agar and incubated at 25 ºC during 5-7 days. All plates were performed in triplicate and the results were expressed as logarithms of the number of colony-forming units per gram (Log FU/g).

3. RESULTS AND DISCUSSION

Molds are the main responsible for FCAHs spoilage. In this scenario, different studies have been performed to assess the surface antimicrobial effect of different EOs and their combinations against saprophyte molds isolated from fresh FCAHs.

When the target molds were exposed to 300 mg/m2 of EOs vapors at *in vitro* scale, different surface antimicrobial effects were observed and results were expressed as a reduction of Log CFU/g (Table 1). It was shown that growth inhibition depends on the vegetal material treated. Specifically, CO was the most effective condition against molds isolated from coriander, obtaining a reduction of 3 log CFU/g. CO condition also produced the major growth decrease on curly parsley, thyme and peppermint fungi. However, other conditions tested displays the same inhibition growth on these vegetal products. Carvacrol (C) was the more effective compound against molds from flat parsley, with reduction major than 4 Log CFU/g. The condition CP was shown to be the most effective against molds from dill and rosemary. Notably, the growth of this later was inhibited similarly when was exposed to carvacrol.

Table 1. Reduction of Log CFU/g observed in molds isolated from FCAHs after exposition in the plate to vapor of different combinations of EOs and its components, at a concentration of 300 mg/m^2

	Antimicrobial treatment				
	CO	CP	C	LO	Ci
Coriander	3.203	2.890	2.890	0	1.574
Dill	2.190	3.253	1.134	0	2.190
Peppermint	2.416	1.998	1.650	0.205	1.738
Curly parsley	2.260	0.024	0.577	2.260	2.260
Flat parsley	2.530	2.291	4.291	0	2.530
Rosemary	1.440	2.425	2.425	1.440	1.440
Thyme	2.229	1.123	1.198	0.056	2.229

Based on the fact that the antimicrobial effect of EOs vapors depends on the vegetal material treated, CO combination was selected as the most effective against the molds isolated from dill, peppermint and curly parsley. However, oregano EOs cause sensorial disturbances in the product due to its intense aroma. Because of this, it was considered inappropriate for FCAHs decontamination at industrial scale. Conversely, CP combination did not affect sensorial attributes of the fresh aromatic herbs studied. This fact, together with the result observed at *in vitro* scale, leads to the selection of CP mix for industrial trials.

Industrial studies were performed in curly parsley, dill and peppermint treated with CP combination at 8 µL/L dose. Surface antimicrobial effect was assessed through microbiological studies in which bacteria from the Enterobacteriaceae family, molds and mesophilic and psychrotrophic aerobic bacteria were measured. Results obtained are represented in Fig. 2, 3 and 4.

When curly parsley was studied it was observed that the count of bacteria from the Enterobacteriaceae family was reduced 2 log CFU/mL after EOs treatment in comparison to the control sample (Fig. 2).

When peppermint samples were treated with EOs vapors it was observed a slight decrease in the surface load of bacteria from the Enterobacteriaceae family compared to the control condition. However, no significant differences were observed in the rest of the studied microorganisms (Fig. 3). Finally, industrial treatment of fresh dill showed a slight reduction of mesophilic aerobic bacteria.

In parallel, the effect of EOs vapors applied using adapted industrial vacuum technology was also studied in peeled garlic cloves. CO was selected as antimicrobial treatment based on *in vitro* studies. The intense aroma of garlic allowed the use of oregano EO because sensorial attributes were not affected. Counts of lactic acid bacteria, bacteria from the Enterobacteriaceae family, mesophilic aerobic bacteria, molds and yeast were studied before and after CO treatment (8 µL/L) (Table 2).

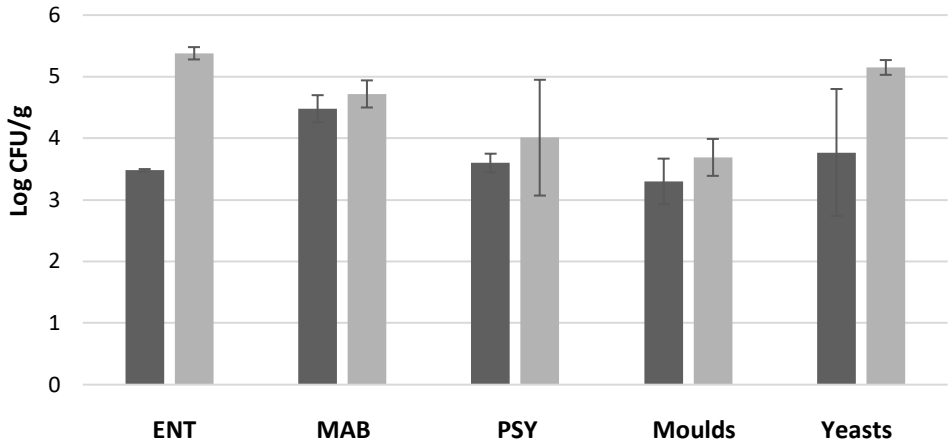

Figure 2. Microbial counts observed after industrial treatment of fresh curly parsley with CP vapors. Black: samples treated with 8 µL/L of CP; Grey: control samples. ENT: bacteria from the Enterobacteriaceae family, MAB: mesophilic aerobic bacteria, PSY: psychrotrophic aerobic bacteria

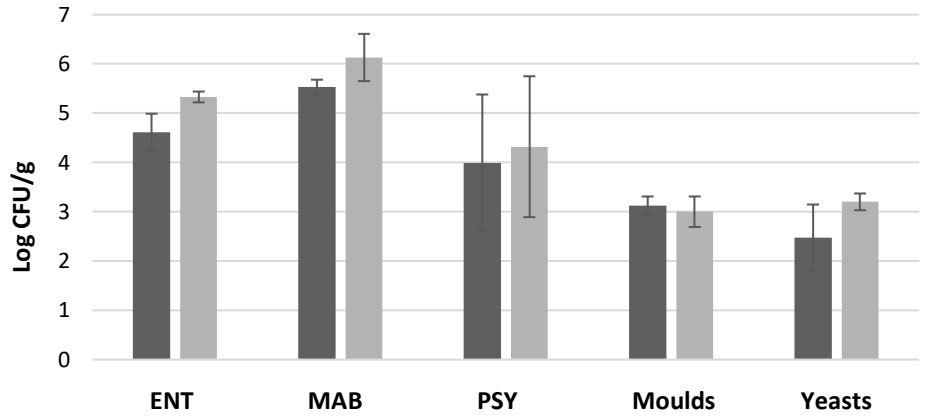

Figure 3. Microbial counts observed after industrial treatment of fresh peppermint with CP vapors. Black: samples treated with 8 µL/L of CP; Grey: control samples. ENT: bacteria from the Enterobacteriaceae family, MAB: mesophilic aerobic bacteria, PSY: psychrotrophic aerobic bacteria

Results showed that all the microorganisms studied were affected by the antimicrobial effect of CO vapors (Table 2). Specifically, lactic acid bacteria and mesophilic aerobic bacteria decrease after EOs treatment more than 3.8 and 3.3 Log CFU/g, respectively. Likewise, counts of bacteria from the Enterobacteriaceae family were reduced 2.81 Log CFU/g. Molds and yeast were the microbial populations less affected by CO vapors (with a reduction of 0.77 Log CFU/g).

Results obtained are in accordance with those reported by Mohammad et al (2009). They observed that the antimicrobial effect of allyl isothiocyanate, cinnamaldehyde and carvacrol applied as vapor phase had a variable antimicrobial effect, depending on the vegetable material studied, lettuce or spinach leaves. Besides, they observed that these compounds inactivated 4 log of *E. coli* O157:H7. Lopez et al. (2007) studied the vapor-phase antimicrobial activities of cinnamon, thyme and oregano EO against Gram-positive and negative bacteria and molds. Results showed that the oregano EO displayed the major antimicrobial activity, especially against Gram-negative. Likewise, the antimicrobial effect of peppermint EOs vapors have been tested against fungi (Sellamuthu et al., 2013) and partial inhibition of the growth was observed. In the present work, carvacrol combined with peppermint or oregano EO has shown the major antimicrobial effect against molds isolated from FCAHs.

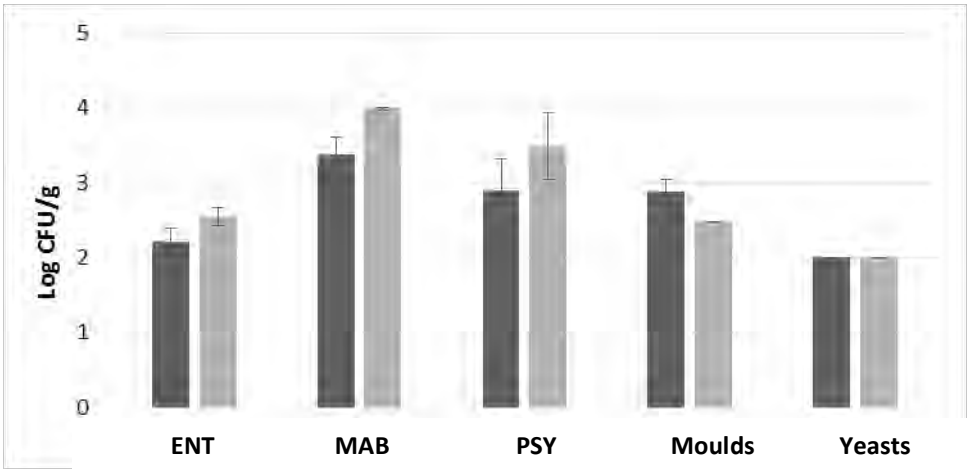

Figure 4. Microbial counts observed after industrial treatment of fresh dill with CP vapors. Black: samples treated with 8 µL/L of CP; Grey: control samples. ENT: bacteria from the Enterobacteriaceae family, MAB: mesophilic aerobic bacteria, PSY: psychrotrophic aerobic bacteria

Table 2. Microbial counts obtained in peeled garlic cloves before and after industrial application of CO vapors

Microorganism	Before treatment (Log CFU/g)	After treatment (Log CFU/g)
Lactic acid bacteria	4.845	1.000
Bacteria from the Enterobacteriaceae family	5.477	2.662
Mesophilic aerobic bacteria	7.278	3.886
Molds and yeast	2.079	1.301

On the other hand, vapors of linalool and citral have clearly shown that reduce the microbial load of Gram-positive bacteria on cabbage leaf (Fisher and Phillips, 2006). Our results have shown that LO combination was the condition with less antimicrobial effect on fungi growth. Finally, we observed that citral and carvacrol vapors applied separately displayed an intermediate surface antimicrobial effect.

4. CONCLUSIONS

EOs vapors applied at *in vitro* scale possess antimicrobial activity against mold populations isolated from FCAHs. Growth inhibition degree depends on EOs combinations applied and FCAHs treated. CO and CP treatments displayed the major antimicrobial activity.

CO vapors applied at vacuum cooling industrial scale reduce the surface microbial population of peeled garlic cloves increasing the shelf life of this product without affecting sensorial attributes.

Treatment with vapors of EOs at the end of the vacuum cooling reduces the surface microbial populations increasing fresh vegetable shelf life.

ACKNOWLEDGMENTS

This work was funded by CDTI (Madrid, Spain), Project Numbers: IDI-20150926 and IDI-20170712, and co-financed by the European Regional Development Fund (ERDF) through the Pluriregional Operational Programme for Intelligent Growth.

REFERENCES

Ali, A., Yeoh, W.K., Forney, C. and Siddiqui, M.W. 2017. Advances in postharvest technologies to extend the storage life of minimally processed fruits and vegetables. Critical Rev. Food Sci. Nutrition DOI: 10.1080/10408398.2017.1339180.

Augusti, K. T., & Mathew, P. T. 1974. Lipid-lowering effect of allicin (diallyl disulfide oxide) on long-term feeding in normal rats. Experientia 30, 468-470.

Belletti N., Lanciotti R., Patrignani F., and Gardini F. 2008. Antimicrobial efficacy of citron essential oil on spoilage and pathogenic microorganisms in fruit-based salads. J. Food Sci. 73:M331–M338.

Betts, R. 2014. Microbial update: Fruit and salad. Int. Food Hygiene, 25, 9-12.

Caleb, O. J., Mahajan, P.V., Al-Said, F. A. and Opara, U.L. 2013. Modified Atmosphere Packaging Technology of Fresh and Fresh-cut Produce and the Microbial Consequences—A Review. Food Bioprocess Technol, 6, 303–329.

Callejón, R. M., Rodríguez-Naranjo, M. I., Úbeda, C., Hornedo-Ortega, R., García-Parrilla, M. C., & Troncoso, A. M. 2015. Reported foodborne outbreaks due to fresh produce in the United States and European Union: Trends and causes. Foodborne pathogens and disease, 12, 32-38.

Castro-Ibañez, I., Gil, M.I. and Allende, A. 2017. Ready-to-eat vegetables: Current problems and potential solutions to reduce microbial risk in the production chain. LWT - Food Sci. Technol. 85, 284-292.

Curutchet, A., Dellacassa, E., Ringuelet, J. A., Chaves, A. R., & Viña, S. Z. 2014. Nutritional and sensory quality during refrigerated storage of fresh-cut mints (Mentha piperita and M. spicata). Food Chem. 143(0), 231e238.

Gil, M. I., Selma, M. V., Lopez-Galvez, F. and Allende, A. 2009. Fresh-cut product sanitation and wash water disinfection: problems and solutions. Int. J. Food Microbiol. 134:37–45.

Gil, M. I., Selma, M. V., Suslow, T., Jacxsens, L., Uyttendaele, M., & Allende, A. 2015. Pre- and postharvest preventive measures and intervention strategies to control microbial food safety hazards of fresh leafy vegetables. Critical Rev. Food Sci. Nutrition 55, 453-468.

Inouye, S. (2003). Laboratory of evaluation of gaseous essential oils (Part 1). Int. J. Aromatherapy, 13, 95–107.

Issa-Zacharia A., Kamitani, Y., Miwa, N., Muhimbula, H., Iwasaki, K. 2011. Application of slightly acidic electrolyzed water as a potential non-thermal food sanitizer for decontamination of fresh ready-to-eat vegetables and sprouts. Food Control, 22, 601-607.

FAO (Food and Agriculture Organization of the United Nations). 2010. Processing of fresh-cut tropical fruits and vegetables: A technical guide Accessed 13 June 16 http://www.fao.org/docrep/014/i1909e/i1909e00.htm.

Fisher, K. & Phillips, C. 2006. The effect of lemon, orange and bergamot essential oils and their components on the survival of *Campylobacter jejuni*, *Escherichia coli* 0157, *Listeria monocytogenes, Bacillus cereus* and *Staphylococcus aureus in vitro* and in food systems. J. Applied Microbiology 101, 1232-1240.

Fisher, K., Phillips, C. and McWatt, L. 2009. The use of an antimicrobial citrus vapor to reduce *Enterococcus* sp. on salad products. Int. J. Food Sci. Technol. 44, 1748–1754.

Lanzotti, V. 2006. The analysis of onion and garlic. J. Chromatography A, 1112, 3-22.

Lopez, P., Sanchez,C., Batlle, R. and Nerin, C. (2007). Vapor-Phase Activities of Cinnamon, Thyme, and Oregano Essential Oils and Key Constituents against Foodborne Microorganisms. J. Agric. Food Chem. 55, 4348−4356.

López-Gómez, A. and López-Cánovas, D.A. 2018. Method for the surface decontamination of packaged solid food. US Patent Nº US 2018/0064146 A1.

López-Gómez A., Soto-Jover S., Ros-Chumillas M. 2018. New technology for enhancement the food safety of minimally processed fruits and vegetables. Acta Horticulturae 1194 (2), 545-551.

Luo, Y, McEvoy, J.L., Wachtel. M.R, Kim, J.G. and Huang, Y. 2004. Package atmosphere affects postharvest biology and quality of fresh-cut cilantro leaves. HortScience 39(3), 567-570.

Marta Corzo-Martinez, Nieves Corzo and Mar Villamiel. 2007. Biological properties of onions and garlic. Trends Food Sci. Technol. 18 (2007) 609e625

McKee, L.H. 1995. Microbial contamination of spices and herbs: a review. Lebensm. Wiss. Technol. 28, 1–11

Obaidat, M.M. and Frank, J.F. 2009. Inactivation of Salmonella and Escherichia coli O157:H7 on Sliced and Whole Tomatoes by Allyl Isothiocyanate, Carvacrol, and Cinnamaldehyde in Vapor Phase. J. Food Protection, 72 (2), 315–324

Rabobank International, 2011. Retrieved from: <http://www. freshconveniencecongress.com/resources/documents/1308561709cindyvanrijswick.pdf

Santos, J., Herrero, M., Mendiola, J.A., Oliva-Teles, M.T., Ibañez, E., Delerue-Matos, C. and Oliveira, M.B.P.P. 2014. Fresh-cut aromatic herbs: Nutritional quality stability during shelf-life. LWT - Food Sci. Technol. 59, 101-107.

Sellamuthu, P.S., Sivakumar, D. and Soundy, P. 2013. Antifungal activity and chemical composition of thyme, peppermint and citronella oils in vapor phase against avocado and peach postharvest pathogens. J. Food Safety 33(1), 86-93.

Seo, H. S., Beuchat, L. R., Kim, H., and Ryu, J.H. 2015. Development of an experimental apparatus and protocol for determining antimicrobial activities of gaseous plant essential oils. Int. J. Food Microbiol. 215, 95-100.

Siroli, L., Patrignani, F., Serrazanetti, D. I., Tappi, S., Rocculi, P., Gardini, F., and Lanciotti, R. 2015. Natural antimicrobials to prolong the shelf-life of minimally processed lamb's lettuce. Postharvest Biol. Technol. 103, 35-44.

Tyagi, A. K., and Malik, A. 2012. Bactericidal action of lemon grass oil vapors and negative air ions. Innov. Food Sci. Emerging Technol. 13, 169-177.

Yang, Y., Luo, Y., Millner, P., Shelton, D. and Nou, X. 2012. Enhanced chlorine efficacy against bacterial pathogens in wash solution with high organic loads. J. Food Process. Preserve. 36:560–566.

Manuscript ID: 650
DOI: 10.18462/iir.icr.2019.0650

The impact of storage temperature on postharvest quality and chilling injury of 'Okubao' peaches

LiJun SUN[(a,b)], Qi ZHANG[(a,b)], Sheng LIU[(a,b*)], JinHua ZUO[(b)], ZhongYang FAN[(b)], Yan LI[(a,b)], JunYan WANG[(b)], YuFu ZHONG[(a,b)], XiaoMing DUAN[(b)]

[(a)] Shanghai Ocean University
Shanghai, 201306, P. R. China, 380469845@qq.com

[(b)] Beijing Vegetable Research Center, Beijing Academy of Agriculture and Forestry Sciences, National Engineering Research Center for Vegetables, Beijing Key Laboratory of Fruits and Vegetable Storage and Processing, Key Laboratory of Vegetable Postharvest Processing, Ministry of Agriculture
Beijing, 100097, P. R. China, liusheng@nercv.org

ABSTRACT

Peach is a popular fruit worldwide with its great coloration, high sweetness, desirable flavour and nutritional value. In order to evaluate the effects of different temperatures on postharvest quality and chilling injury (CI) of peach, four different temperatures (0, 2, 5 and 8°C) were chosen and the quality parameters and CI incidence were analysed simultaneously. CI was characterized mainly by the appearance of flesh browning. The results showed that the browning index was 6.2%, 17.6%, 28.8% respectively at 0, 2 and 5°C for 28 days. Sensory evaluation of peach stored was 6.5, 6.2, 6.8 and 6.4 respectively at 0, 2, 5 and 8°C for 28d, 14d, 7d and 7d. The peaches had the lowest decay index, the lightest CI, the highest nutritional content and the best sensory evaluation at 0°C for 28d.
Keywords: Peach, Cold Storage, Browning, Firmness

1. INTRODUCTION

Peach (*Prunus persica* L.) is an economically important fruit crop in global commerce that may have originated in China where it has been cultivated for 3000 years (Font i Forcada et al., 2013). Peaches are sought by consumers for their good taste and high nutritional value around the world (Yu et al., 2017). However, peach fruit normally suffer rapid softening, decay after harvest and is cold-sensitive and vulnerable to chilling injury (CI) during cold storage, which leads to undesirable quality and reduced commercial value (Gao et al., 2016). In recent years, many preservation methods which included modified atmosphere, 1-MCP and Ultraviolet B irradiation had showed effective functions of inhibiting the degradation of peach quality (Akbudak and Eris, 2004; Huan et al., 2018; Wang et al., 2018).

Fresh peaches are perishable and cold storage remains the main method to slow the product deterioration in terms of consumer perception and nutritional value (Tsantili et al., 2010). Unfortunately, sub-tropical and tropical fruits such as pomegranate, banana and orange are often susceptible to CI at these low temperatures and represent a major factor limiting their storage life (Kashash et al., 2019; Koushesh Saba and Moradi, 2017; Liu et al., 2019; Rasouli et al., 2019). Several technologies, such as treatment with nano-ZnO-packaging, glycine betaine, and oxalic acid, have been reported to alleviate CI in peaches during cold storage (Jin et al., 2014; Li et al., 2017;

Shan et al., 2016).

Temperature represents one of the most important external factors affecting plant apoptosis. Suitable storage temperature that reduces the overall fruit metabolism and transpiration rate is fundamental for keeping peach quality as long as possible to supply the market chain with high quality fruit (Saquet, 2019). In order to evaluate the effects of different temperatures on postharvest fruit quality and CI of peach, four different temperatures (0, 2, 5 and 8°C) were chosen and the quality parameters and CI incidence were analyzed simultaneously.

2. MATERIALS AND METHODS

2.1. Raw Materials and Treatments

Peach fruits (*P. persica* L. Batsch cv. *'*Okubao*'*) were harvested at commercial maturity from a commercial orchard in Beijing, China, and immediately transported to the laboratory where sorted for uniformity of size, color and lack of defects. Peaches were packed in standard foldable plastic boxes (600×400×235 mm). After forced-air precooled to 8℃ , peaches were divided into four homogeneous groups of 120 fruits and stored at 0, 2, 5, and 8℃ for 28 days. Analyses were carried out initially and at 7 days interval for physicochemical measurements and sensory evaluation.

2.2. Sensory Evaluation

Sensory quality of peaches in terms of changes in visual appearance, browning, color, decay were evaluated on a 1-9 scales, where excellent, freshly=9; very good=7; good, limit of marketability=5; fair, limit of usability=3 and poor, unusable=1, where 6 is considered the minimum for salability (Cantwell and Thangaiah, 2012). A score of 6.0 indicated minimum commercial acceptability. The sensory analysis was performed by a trained panel of three members.

2.3. Browning Index

CI was characterized mainly by the appearance of flesh browning. CI index was evaluated visually based on the internal browning of peach flesh. Peaches were cut along the fruit suture and the browning scale (B) was divided into four degrees according to the percentage of browning area of flesh; 0: no browning; 1: B ≤ 25%; 2: 25% < B ≤ 50%; 3: 50%< B < 75%; 4:>75%. The browning index was calculated based on the following formula:

$$\text{Browning index } (\%) = \frac{\sum(\text{browning scale} \times \text{the amount of this peaches at this scale})}{\text{total peach number} \times 4} \qquad \text{Eq. (1)}$$

2.4. Decay, Weight Loss, and Colour

Percentage of decayed fruit was calculated from the number of fruit that shown signs of decay over the initial number of fruit. The weight of individual peach was recorded before and after storage and the weight loss was expressed on a wet weight basis (%). External color was measure along the equatorial axes each fruit using CR-400 colorimeter, which provided L^*, a^* and b^* coordinates.

2.5. Firmness , Soluble Solids Content, Titratable Acidity and Vitamin C

Fruit firmness was determined with a penetrometer (TR-FT 327, Italy) fitted with a 5 mm diameter

plunger. Measurements were taken at two equatorial positions on each fruit after removal of a thick slice of skin and results expressed as Newton (N).

Soluble solids content (SSC) was determined with a digital refractometer (Atago Co.Ltd., Tokyo, Japan), and results were expressed as %. Titratable acidity (TA) was determined by titrating 5mL juice with 0.1mol·L^{-1} NaOH to pH 8.2 and was expressed as % citric acid. Vitamin C content was determined by molybdenum blue colorimetric method (Li, 2000).

2.6. Relative Electrolyte Leakage and Malondialdehyde (MDA) content

Electrolyte leakage was measured using the methodology according to Chen et al. (2008), with slight modifications. MDA was measured according to the method of Shah et al. (2001) and expressed as micromoles per gram of fresh weight.

2.7. Polyphenol oxidase (PPO) and peroxidase (POD) enzyme activities

1g of tissue was taken from 6 different fruits and homogenized in 5mL of phosphate buffer. After centrifugation at 12,000g for 20 min at 4℃ , 2 mL supernatant was collected as enzyme extract. POD and PPO activities were assayed following the method of Cao et al., (2013).

2.8. Statistical Analysis

Experiments were performed in triplicate and the average values were reported in the analysis. Analysis of variance *(p<0.05)* was done. Differences at $P < 0.05$ were considered as significant.

3. RESULTS AND DISCUSSION

3.1. Sensory Evaluation, Decay, Weight Loss and Chilling Injury

It can be seen from Fig.1a that the longer the storage time, the lower the sensory score. Peach stored at 0℃ had the best sensory quality and the sensory score was 6.5 after 28 days. When stored at 2°C for 14 days, the sensory score was 6.2, indicating that the peach was acceptable within two weeks. When stored at 5 and 8°C for 14 days, the sensory score was 5.2 and 5, respectively, which means that there is no commercial.

Fig.1b shows that the peach at 0°C did not decay within 7 days, and the peach decay rate did not differ much at 0 and 2°C when stored 14 days. However, after 14 days storage, only peach fruits at 5 and 8℃ showed the rotting higher than 5% and was widespread when stored for 28 days and the decay rate reached 15.3%, 28.3% respectively.

Fig.1c shows that the weight loss rate of peach is less than 3% in two weeks at four temperatures. Compared to the other three temperatures, the weight loss rate of peach at 5°C is always high. By 28 days, overall weight losses were 6.4%, 7.6%, 8.4% and 8.8% at 0, 2, 5 and 8°C, respectively.

As illustrated by Fig.1d, the degrees of browning were statistically different at different temperature and increased substantially as storage progressed (P<0.05). Peaches hold at 0 and 2 °C did not develop CI within 14 days, but those exposed to 5°C began exhibiting CI and the index increased thereafter. The browning index of peach stored 28 days were 6.2%, 17.65%, 28.78%, 0.5%, respectively at 0, 2, 5, and 8°C. Although the peach stored at 8°C did not show CI during the whole storage period, the fruit quickly matured and softened. In summary, peaches should be stored for less than 14 days at 5°C compared to 21 days at 0°C to avoid development of CI.

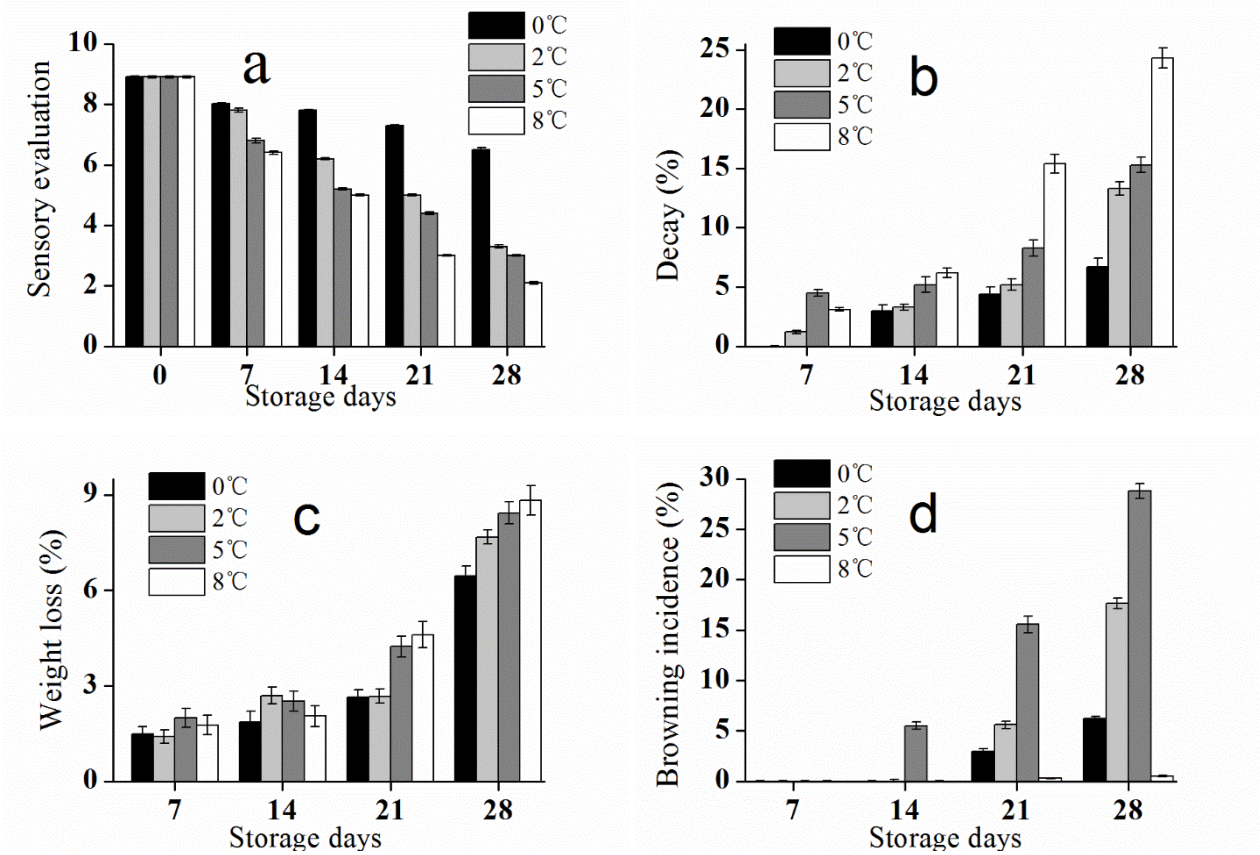

Figure 1: Sensory evaluation (a), decay (b), weight loss (c) and chilling injury (d) of peach during cold storage at different temperatures

3.2. Colour

Fig.2 shows that with respect to color, lightness (L* value), redness (h° value) and intensity of color (C* value), fruit stored at 0 and 2ºC were greater than that of fruit stored at 5 or 8℃ . After stored for 28 days, the L* values of peaches refrigerated at 0, 2, 5, and 8°C were 47.6, 43.7, 40.2, 42.0 (fig. 2a), and the h° values were 33.1, 30.9, 28.5, 29.8 (fig.2b), and C* values are 34.9, 34.8, 30.3, 31.1 (fig.2c), respectively. L* and h° values decreased more rapidly at 5℃ or 8℃ than at 0℃ as the fruit turned darker red, which is undesirable to consumers. After 28 days storage, fruit stored at 5℃ showed the typical browning associated with internal breakdown. This alteration was reflected by h° lower than those from fruit stored at 0℃ .

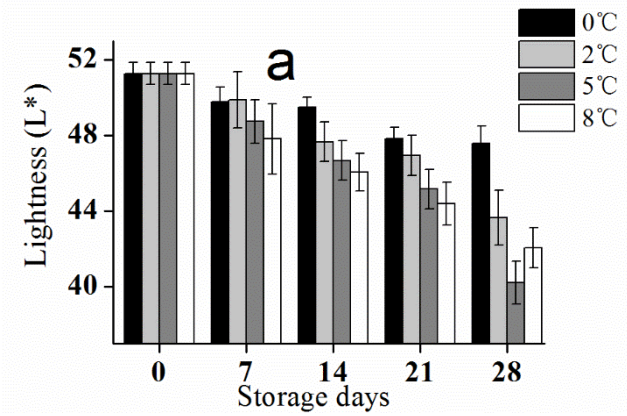

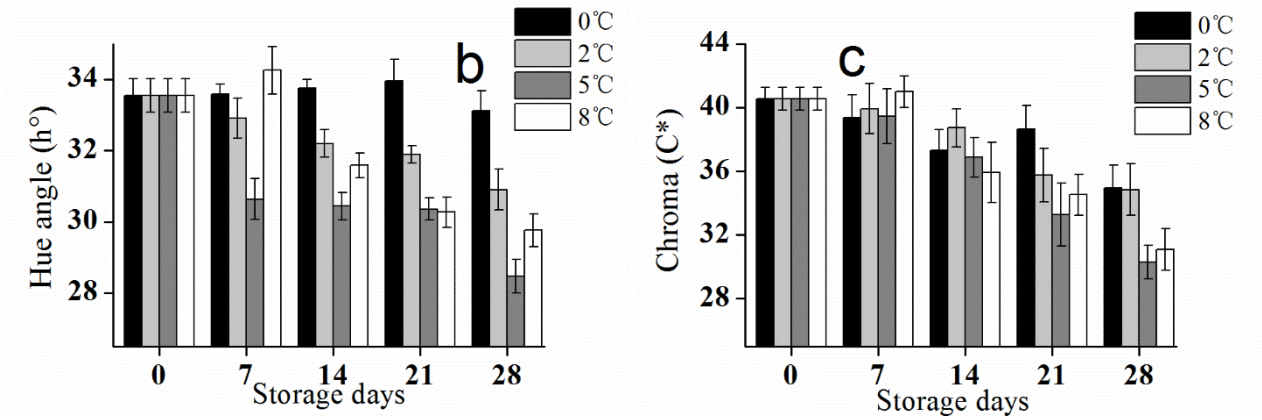

Figure 2: Lightness (L*), hue angle (h°) and chroma (C*) values of peach during cold storage at different temperatures

3.3. Relative Electrolyte Leakage and MDA Content

As shown in Fig.4, the relative electrical leakage of peaches refrigerated at 0, 2, 5, and 8°C were 41.3%, 73.3%, 89.3%, and 88.8%, respectively, and the MDA contents were 0.0019, 0.0027, 0.0037, 0.003 μmol·g^{-1}, respectively, after storage for 28 days. Therefore, peach at 0°C can limit the rise in electrolyte leakage and MDA content effectively, suggesting better membrane integrity. The damage to the cell membrane maybe initiate ethylene production, increased respiration, and disruption of cellular and subcellular structures.

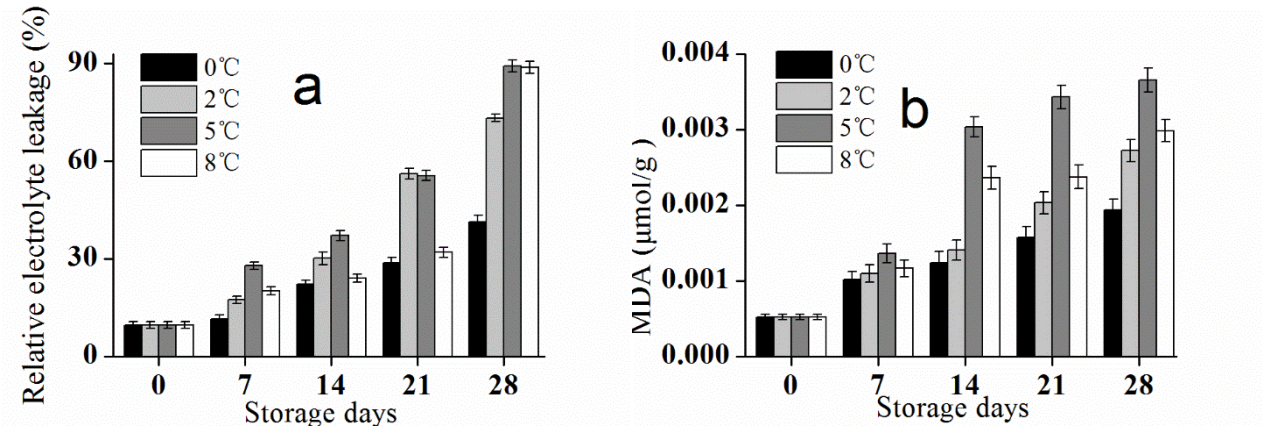

Figure 3: Relative electrolyte leakage (a) and MDA content (b) of peach during cold storage at different temperatures

3.4. Firmness, SSC, TA and Vitamin C

The firmness loss was significantly different among temperatures in Table.1. The hardness of peach fruit refrigerated at 0, 2, 5, and 8℃ decreased sharply during the whole storage period, the retention rate of that was 85%, 43.4%, 15.2%, 16.5% respectively after storage for 28 days. The hardness of peach fruit at 0°C has been maintained at a high level compared with other temperatures.

The nutrient content of peach fruit was obviously maintained at 0°C. After storage for 28 days, the contents of SSC, TA and Vitamin C of the peach stored at 0, 5 and 8°C retained at 113.8%, 47.1%, 37.5%, 91.5%, 44.2%, 33.3% and 92.9%, 38.8%, 27.9%, respectively. The content of SSC of the peach increased at 0°C. The peach were soften and decayed at 8°C.

Table 1. Changes in firmness, SSC, TA and Vitamin C of peach during cold storage at different temperatures

Quality parameters	Temperature (°C)	0d	14d	21d	28d
Firmness (N)	0	39.08±1.53	40.36±1.96	38.03±3.50	33.20±3.08
	2		28.17±3.30	21.87±4.04	17.00±5.93
	5		17.22±3.77	14.63±3.54	10.43±4.01
	8		14.28±1.92	13.52±4.32	6.43±0.64
Total soluble solids (%)	0	9.40±0.30	10.60±0.15	10.23±0.27	10.07±0.28
	2		10.30±0.18	9.23±0.03	9.03±0.17
	5		10.13±0.03	8.97±0.15	8.60±0.26
	8		9.47±0.27	9.00±0.12	8.73±0.47
Titratable acidity (%)	0	0.312±0.005	0.259±0.012	0.177±0.012	0.147±0.008
	2		0.252±0.011	0.145±0.002	0.135±0.005
	5		0.178±0.005	0.146±0.013	0.138±0.005
	8		0.145±0.011	0.141±0.009	0.121±0.009
Vitamin C ($mg \cdot g^{-1}$)	0	0.563±0.003	0.451±0.003	0.347±0.003	0.211±0.016
	2		0.434±0.005	0.299±0.004	0.132±0.021
	5		0.402±0.005	0.269±0.001	0.188±0.003
	8		0.404±0.002	0.278±0.002	0.157±0.006

3.5. POD and PPO Activities

As illustrated by Fig.5, POD and PPO activities increased gradually during storage. 0℃ significantly ($p < 0.05$) inhibited the activities of both enzymes during the whole storage. The activities of PPO and POD of peach stored at 0℃ were 66.3% and 20.4% lower than those showed by fruit held at 5℃ on the 28th day, respectively. The activity of PPO of peach at 5℃ was significantly higher than other temperatures ($p < 0.01$), and the browning index of peach fruit was positively correlated with PPO activity. PPO and POD activities were 8.7 and 0.3 $\mu g^{-1} \cdot min^{-1}$, respectively. Since both PPO and POD are associated with decay development in peaches, it is possible that 0℃ might have inhibited and delayed decay of flesh tissue through the inhibition of PPO and POD activities.

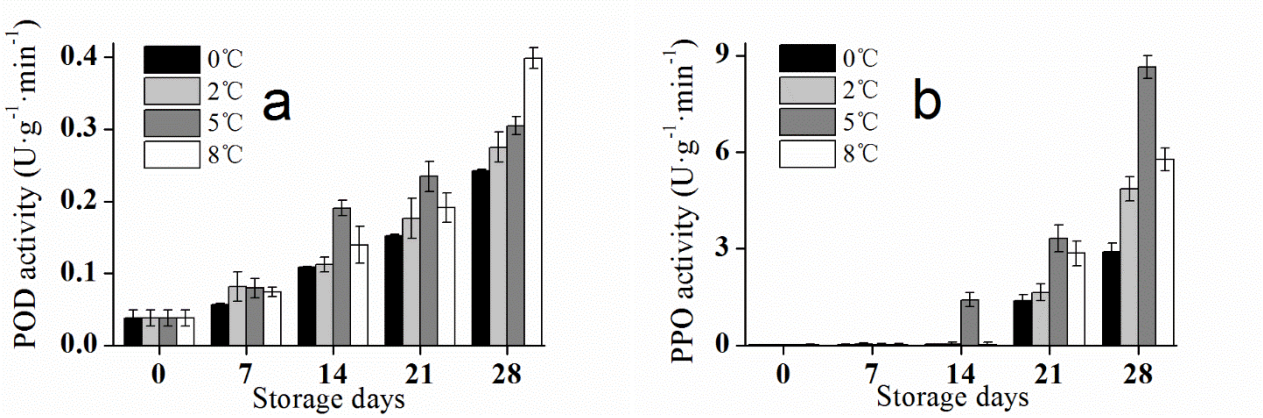

Figure 4: POD (a) and PPO (b) activities of peach during cold storage at different temperatures

4. CONCLUSIONS

The peach stored at 0℃ has best sensory quality, bright color, crisp texture, good flavor and slight browning of flesh, even PPO and POD activities are significantly reduced, and the relative electrolyte leakage and MDA content are reduced. The results showed that ‘Okubao’ peach is prone to CI when stored at 5°C. There is almost no CI at 8°C, but the fruit seriously rotted. In comparison, the symptoms of CI at 0 and 2°C are lighter. Our results may provide a reference for chilling treatment to extend shelf life of peach fruit. We can conclude that the peach should be controlled at 8°C in cold chain within one week, and it has energy saving effect compared other temperatures. The nutritional content and sensory evaluation of peach stored at 0℃ are the highest and best. It's best to choose cold chain method at 0°C for long-distance transportation or export.

ACKNOWLEDGEMENTS

The research was financed by the National Science and Technology Support Program (No. 2018YFD0401305) and Science and Technology Innovation Special Construction Funded Program of Beijing Academy of Agriculture and Forestry Sciences (No.KJCX20170206).

REFERENCES

Akbudak, B., Eris, A., 2004. Physical and chemical changes in peaches and nectarines during the modified atmosphere storage. Food Control 15, 307-313.

Cantwell, M.I., Thangaiah, A., 2012. Acceptable cooling delays for selected warm season vegetables and melons. Acta Horticulturae 934, 77-84.

Chen, J., He, L., Jiang, Y., Wang, Y., Joyce, D.C., Ji, Z., Lu, W., 2008. Role of phenylalanine ammonia-lyase in heat pretreatment-induced chilling tolerance in banana fruit. Physiol. Plant. 132 (3), 318–328.

J. K. Cao, W. B. Jiang, Y. M. Zhao, et al., 2013. Experimental Guidance of Postharvest Physiology and Biochemistry of Fruits and Vegetables, 3rd ed. China Light Industry Press: Beijing, China.101-107.

Font i Forcada, C., Gogorcena, Y., Moreno, M.A., 2013. Fruit sugar profile and antioxidants of peach and nectarine cultivars on almond×peach hybrid rootstocks. Scientia Horticulturae 164, 563-572.

Gao, H., Zhang, Z., Lv, X., Cheng, N., Peng, B., Cao, W., 2016. Effect of 24-epibrassinolide on chilling injury of peach fruit in relation to phenolic and proline metabolisms. Postharvest Biol. Technol 111, 390-397.

Huan, C., An, X., Yu, M., Jiang, L., Ma, R., Tu, M., Yu, Z., 2018. Effect of combined heat and 1-MCP treatment on the quality and antioxidant level of peach fruit during storage. Postharvest Biol. Technol 145, 193-202.

Jin, P., Zhu, H., Wang, L., Shan, T., Zheng, Y., 2014. Oxalic acid alleviates chilling injury in peach fruit by regulating energy metabolism and fatty acid contents. Food Chem. 161, 87-93.

Kashash, Y., Doron-Faigenboim, A., Holland, D., Porat, R., 2019. Effects of harvest time on chilling tolerance and the transcriptome of 'Wonderful' pomegranate fruit. Postharvest Biol. Technol. 147, 10-19.

Koushesh Saba, M., Moradi, S., 2017. Sodium nitroprusside (SNP) spray to maintain fruit quality and alleviate postharvest chilling injury of peach fruit. Sci Hort. 216, 193-199.

Li, D., Li, L., Luo, Z., Lu, H., Yue, Y., 2017. Effect of nano-ZnO-packaging on chilling tolerance and

pectin metabolism of peaches during cold storage. Sci. Hort. 225, 128-133.
Liu, J., Li, F., Li, T., Yun, Z., Duan, X., Jiang, Y., 2019. Fibroin treatment inhibits chilling injury of banana fruit via energy regulation. Sci. Hort. 248, 8-13.
Rasouli, M., Koushesh Saba, M., Ramezanian, A., 2019. Inhibitory effect of salicylic acid and Aloe vera gel edible coating on microbial load and chilling injury of orange fruit. Sci. Hort. 247, 27-34.
Saquet, A.A., 2019. Storage of pears. Sci. Hort. 246, 1009-1016.
Shan, T., Jin, P., Zhang, Y., Huang, Y., Wang, X., Zheng, Y., 2016. Exogenous glycine betaine treatment enhances chilling tolerance of peach fruit during cold storage. Postharvest Biol. Technol.114, 104-110.
Shah, K., Kumar, R.G., Verma, S., Dubey, R., 2001. Effect of cadmium on lipid peroxidation, superoxide anion generation and activities of antioxidant enzymes in growing rice seedlings. Plant Sci. 161, 1135–1144.
Tsantili, E., Shin, Y., Nock, J.F., Watkins, C.B., 2010. Antioxidant concentrations during chilling injury development in peaches. Postharvest Biol. Technol. 57, 27-34.
Wang, X., Fu, X., Chen, M., Huan, L., Liu, W., Qi, Y., Gao, Y., Xiao, W., Chen, X., Li, L., Gao, D., 2018. Ultraviolet B irradiation influences the fruit quality and sucrose metabolism of peach (*Prunus persica* L.). Environ Exp. Bot. 153, 286-301.
Yu, L., Shao, X., Wei, Y., Xu, F., Wang, H., 2017. Sucrose degradation is regulated by 1-methycyclopropene treatment and is related to chilling tolerance in two peach cultivars. Postharvest Biol. Technol. 124, 25-34.
Zhao, M.X., Yan, S.J., Xiao, L.X., 2005. Infrared CO_2 analyzer to determine the fruit respiration intensity parameter. Now the instrument. 2, 30-32.

Manuscript ID: 813
DOI: 10.18462/iir.icr.2019.0813

Food thermal distribution-based control of industrial freezers

Cyril TOUBLANC[(a)], Lionel BOILLEREAUX[(a)]

(a) ONIRIS, GEPEA, CNRS, Université de Nantes
Nantes, Rue de la Géraudière – CS 822251, France, cyril.toublanc@oniris-nantes.fr

ABSTRACT

There is a growing need for advanced solutions of freezer control based on multi-criteria decisions (energy and quality). One of the challenges is to propose a reliable non-intrusive method to measure temperature and ice distribution of food at the freezer exit. In this paper is proposed an innovative approach permitting to evaluate the ice distribution from superficial temperature measurements. It involves submitting the frozen food, immediately at the freezer exit, to a sudden pulse of heat flux and to record its superficial thermal response. From this response, the temperature distribution-and consequently its corresponding ice distribution- of the frozen food at the exit can be estimated thanks a minimization procedure. Beyond controlling final product quality, such an approach could provide in the near future valuable information on freezer operation. The relevancy of this approach requires a preliminary model-based numerical assessment which is the subject of this work.
Keywords: Refrigeration, Quick-Freezing, Freezing Equipment, Process Control, Energy Efficiency.

1. INTRODUCTION

According to IIF-IIR (2015), frozen food products are highly demanded and the annual consumption is constantly increasing. However, according to this same organization, refrigeration sector consumes about 17% of the overall electricity used worldwide and forecasts shows that the refrigeration sector will grow in coming decades. Indeed, the lack of a cold chain is responsible of up to almost 20% of the global food losses. However, the benefit of refrigeration for the reduction of food losses must be assessed in relation to its impact on the environment, especially CO2 emissions. For freezing, which consists in lowering the temperature of a food product below its initial freezing point, it is important to have an efficient refrigeration plant. However, it is equally important to design the freezing equipment properly in order to limit the fan energy consumption. Kristófersson et al. (2018) showed that substantial energy savings could be obtained, up to 68 %, by optimizing the airflow through a freezing tunnel.

Beyond the interest of freezing to limit food losses, energy consumption and quality are the keystones of the competitiveness of the refrigeration sector. Concerning quality after a freezing/ defrosting cycle, it has been shown that freezing rate is a parameter of utmost importance, and depends of the freezing system technology and food's characteristics as size/geometry, structure and composition (Sun, 2011). In summary, a high freezing rate permits first to limit physical, biochemical and microbiological changes. More, it prevents from undesirable too large and potentially disruptive ice crystals, which damage cells and consequently induce excessive drip losses during thawing. For this reason, quick-freezing or deep-freezing concept was proposed in the 70s, in opposition to a conventionally freezing process for which no specific freezing rate is expected and where a loosely bound storage temperature of -12°C is preconized. In the absence of international standard definition, most of regional directives and national regulations refer to the Codex Alimentarius standards, which recommend practices for the processing and handling of quick frozen foods (CRC/RCP 8) which are also included in the European "Directive" regulation 89/108/EEC. In these definitions of quick-freezing, a concept ''as quickly as possible'' is open to greater interpretation and the target temperature -18°C have no physical significance.

To avoid any troubles with sanitary authorities, industrials tend to over-freeze with the energy consequent effects. As a consequence, the parameters of the freezers (speed of belt conveyer, speed of fan, air temperature) are chosen with safety factors and in the best scenario adapted by human intervention to the characteristics of the products.

Based on the IIR definition of a frozen product given by (Borgh-Sorensen, 2006), which mentions that a product is considered as a frozen one either if its temperature is -10°C or colder or if a high proportion (usually more than 80% of the water content) of its freezable water is converted into ice, Le Bail et al. (2008) proposed a relevant but time-consuming (about 12 minutes) procedure to evaluate this criterion. More recently, Pandey et al. (2018), showed the capability of a millimeter wave sensor for monitoring food frozenness.
In this paper, we propose a new approach permitting to evaluate the temperature and ice distribution in a frozen product, in a sufficiently short time making possible to envisage a real-time control of the freezers. This methodology is presented hereafter then carried out and proven in simulation.

2. DESIGN OF THE FREEZER CONTROL METHODOLOGY

2.1. Schematic, description and principle

This paper proposes a thermal methodology to estimate the ice content distribution of the frozen product at the exit of the freezer, represented in Figure 1 (a). The characterisation method, illustrated on Figure 1 (b), is based on the analysis of the thermal response following a thermal excitation (φ_{rad} in W/m^2) applied at the top surface of the product during a period (t_{flash} in seconds).

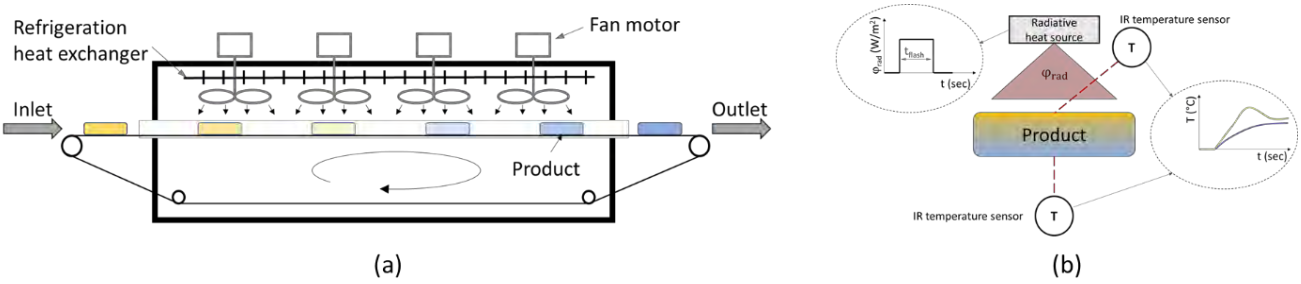

Figure 1: Sketches of a freezing tunnel (a) and based-thermal flash characterisation method (b)

The methodology can be summarized as follows: the pulse of heat flux applied at the top surface of the frozen product induces a thermal response of the product, which is registered at the top and bottom surfaces. A heat transfer model permitting to describe the temperature evolution inside the product is used and the simulated top and bottom temperatures evolutions are extracted. A nonlinear least squares approach is then used to estimate the optimal initial temperature distribution (which is the temperature of the product at the exit of the freezer) permitting to minimize the RSS (residual sum of squares) between simulated and measured superficial temperatures.

2.2. Heat transfer model and product properties

As mentioned in the previous section, the methodology requires the development of a heat transfer model. In this study, we will consider a 1D model meaning that heat exchange only occurs in the direction of product's depth:

$$\frac{\partial}{\partial t}\theta(z,t) = \alpha \frac{\partial^2}{\partial z^2}\theta(z,t) \qquad \text{Eq. (1)}$$

With the thermal diffusivity coefficient $\alpha = \frac{\lambda}{\rho \cdot c_p}$ (in m^2.s^{-1})

There are two variables, z and t, which are two independent variables. Such parabolic equation is usually solved after reduction to lumped parameters system, using finite elements, finite differences, and orthogonal collocation. These methods consists in considering the temperature evolution in a finite number of spatial points usually called nodes.

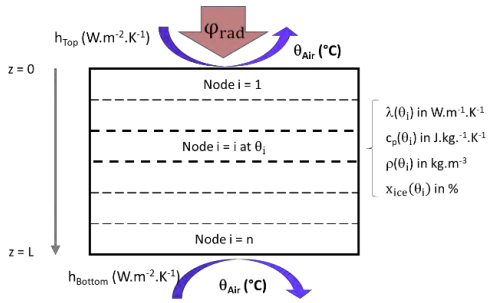

Figure 2: Food model description with boundary conditions

During the flash procedure at the exit of the freezer, the following boundary and initial conditions are considered, radiative heat source (φ_{rad}) at the top surface.

$$-\lambda \left.\frac{\partial \theta}{\partial z}\right|_{z=0} = h_{Top}\,(\theta_{z=0} - \theta_{air}) - \varphi_{rad} \qquad \text{Eq. (2)}$$

$$-\lambda \left.\frac{\partial \theta}{\partial z}\right|_{z=L} = h_{Bottom}\,(\theta_{air} - \theta_{z=L}) \qquad \text{Eq. (3)}$$

$$\theta_{t=0,z} = \theta_{exit}(z) \qquad \text{Eq. (4)}$$

Where h_{Top} and h_{Bottom} are the convective heat exchange coefficients (W.m^{-2}K^{-1}), φ_{rad} the radiative coefficient induced by the flash, and $\theta_{exit}(z)$ the temperature distribution inside the food at the freezer's exit.

The quantity of ice (x_{ice}) is assumed to be dependent on the temperature and on the free water content. This variable is estimated by using a simplified semi-empirical (equation 5) proposed by Rouaud and Pham (2012). This function is applicable on all the temperature range of freezability, from the initial freezing point (θ_{IFP}) to the final freezing point (θ_{FFP}).

$$x_{ice}(\theta) = (x_{WC} - x_{UFW})\left(1 - \frac{\theta_{IFP}}{\theta} \cdot \left(\frac{\theta_{IFP} - \theta_{FFP}}{\theta - \theta_{FFP}}\right)^n\right) \qquad \text{Eq. (5)}$$

Knowing the ice content, it is possible to determine the remaining liquid phase:

$$x_W(\theta) = x_{WC} - x_{UFW} - x_{ice}(\theta) \qquad \text{Eq. (6)}$$

Derivatives of ice and liquid free water equations with respect to θ are as following:

$$\frac{dx_{ice}}{d\theta} = -\frac{dx_w}{d\theta} = (x_{WC} - x_{UFW}) \cdot \frac{-\theta_{IFP}}{(\theta_{IFP} - \theta_{FFP})^n} \cdot \frac{n \cdot \theta \cdot (\theta - \theta_{FFP})^{n-1} - (\theta - \theta_{FFP})^n}{\theta^2} \qquad \text{Eq. (7)}$$

In this work, the food product studied is mashed potatoes because of its easy production for further experiments. It requires knowledge of mass fractions and properties of each constituent according to temperature dependent equations. All the equations, used in the model, are given by the Ashrae Handbook (2014). Composition and freezing properties of mashed potatoes are reported in Table 1. Notice that without value from literature or experimental data, we arbitrarily considered that all the freezable water is frozen at -25 °C.

Table 1: Composition and freezing properties of mashed potatoes (Ashrae, 2014)

Water content	Unfreezable water	Fat	Proteins	Carbohydrates and fibers	Simple sugars	Ash
x_{WC}	x_{UFW}	x_f	x_p	x_c	x_{ss}	x_a
78.96 %	0.4 x_p	0.1 %	2.07 %	17.98 %	0 %	0.89 %
Initial freezing point	θ_{IFP}	-0.6 °C	Final freezing point	θ_{FFP}	-25°C	

The density of food (ρ in kg.m^{-3}) and the thermal conductivity (λ in W.m^{-1}.K^{-1}) are calculated by using the two following equations:

$$\rho(\theta) = \frac{1}{\sum_i \left(\frac{x_i(\theta)}{\rho_i(\theta)}\right)} \quad \text{Eq. (8)}$$

$$\lambda(\theta) = \rho(\theta) \cdot \sum_i \left(\frac{x_i(\theta) \cdot \lambda_i(\theta)}{\rho_i(\theta)}\right) \quad \text{Eq. (9)}$$

The specific heat of a food (c_p in J.kg^{-1}.K^{-1}), at temperatures above its initial freezing point ($\theta > \theta_{IFP}$), is obtained from the mass average of the specific heats of the food components. The specific heat of an unfrozen food determined by the following expression does not included an excess specific heat term to compensate for specific heat of bound or unfrozen water and the interaction of the components.

$$c_p(\theta) = \sum_i \left(\frac{x_i(\theta)}{\rho_i(\theta)}\right) \quad \text{Eq. (10)}$$

Below the initial freezing point($\theta \leq \theta_{IFP}$), the specific heat of a frozen food is determined as follows:

$$c_p(\theta) = \sum_i \left(\frac{x_i(\theta)}{\rho_i(\theta)}\right) - L_{ls} \cdot \frac{dx_{ice}}{d\theta} \quad \text{Eq. (11)}$$

With the specific latent heat of fusion of ice (L_{ls}) equal to 334 kJ.kg^{-1}.

2.3. Description of flash methodology

As mentioned previously, the objective is to evaluate the ice content distribution inside the food at the exit of the freezer. By applying a sudden exciting pulse of heat flux immediately at the exit of the freezer, a thermal response with sufficient variations can be obtained at the top surface of food. It may even have effect on the bottom surface temperature thanks to the thermal diffusivity provided that the thickness is sufficiently small. It can be assumed that different initial temperature distributions produce different superficial temperatures evolution to allow distinguishing these initial conditions.
One important mathematical condition must be verified to warrant that initial conditions can be distinguished and estimated with the only measurement of superficial temperatures: the observability. Using finite difference scheme for heat equation as presented above usually leads to a tri-diagonal system (Martín-Vaquero and Sajavicius, 2019), that is, in the case of our flash system

$$\frac{d\theta(z_k)}{dt} = f\left(\theta(z_{k-1},), \theta(z_k), \theta(z_{k+1})\right) \ \forall\ k \epsilon [2, p-1] \quad \text{Eq. (12)}$$

and for the boundary temperatures,

$$\frac{d\theta(z_1)}{dt} = f\left(\theta(z_1), \theta(z_2)\right) + g\left(h_{top}, \theta_{air}, \varphi_{rad}\right) \quad \text{Eq. (13)}$$

$$\frac{d\theta(z_p)}{dt} = f\left(\theta(z_{p-1}), \theta(z_p)\right) + g(h_{bottom}, \theta_{air}) \quad \text{Eq. (14)}$$

Functions f and g are nonlinear when the thermal and physical properties are temperature dependent. z_k ($k \epsilon [1, p]$) represents the kth node with $z_1 = 0$ and $z_p = L$.
If one of the boundary temperatures is measured, such a system belongs to the class of single-output control affine systems. Consequently, if the top temperature is measured, uniform observability is verified if the system is upper-triangular with strict bonds [a, b, c] (Gauthier and Kupka, 1994; Gauthier and Bornard, 1981; Akkari at al., 2006). It means that the upper diagonal does not contain any null element. On the contrary; if the bottom temperature is measured, uniform observability is verified if the system is lower-triangular with strict bonds. A tri-diagonal system verifies both conditions, and the observability is thus guaranteed whatever is the chosen surface measurement. It means that from a theoretical point of view, the initial conditions could be estimated

either from top or bottom temperatures. In practice, the uncertainty of the estimation values is directly linked to the thickness of the product and to its thermal diffusivity. To limit this uncertainty, combining both measurements brings more guarantee.
In this approach, we choose to represent the initial temperature distribution using polynomial:

$$\theta_{exit}(t=0,z)=\sum_{i=0}^{n}\alpha_i z^i \quad \text{Eq. (15)}$$

Let us denote $\theta_{top}(t)$ and $\theta_{bottom}(t)$ the evolution of the superficial temperatures during the flash procedure. These temperatures are measured at sampling times t_i. Let us now denote $\hat{\theta}_{top}(t)$ and $\hat{\theta}_{bottom}(t)$ the same temperatures issued from the model. The methodology consists in estimating the required n+1 polynomial coefficients α_i which minimize the following cost function:

$$(\alpha_i)_{optimal}=\text{argmin}\sum_{i=0}^{N-1}\left(\hat{\theta}_{top}(t_i)-\theta_{top}(t_i)\right)^2+\sum_{i=0}^{N-1}\left(\hat{\theta}_{bottom}(t_i)-\theta_{bottom}(t_i)\right)^2 \quad \text{Eq. (16)}$$

Where the simulated temperatures are obtained with the following initial conditions:

$$\hat{\theta}_{exit}(z_k,t_0)=\sum_{i=0}^{n}\alpha_i z_k^i \quad \text{Eq. (17)}$$

$(\alpha_i)_{optimal}$ can be obtained using nonlinear least square routine implemented in Matlab©.
Because $\theta_{exit}(t=0,z=0)$ are $\theta_{exit}(t=0,z=L)$ correspond to the measurements of superficial temperatures during the flash procedure at initial time, two roots of the polynomial can be fixed, and the set of parameters to evaluate is reduced to $\alpha_2,\ldots,\alpha_n$. Indeed:

$$\alpha_0=\theta_{top}(t=0) \quad \text{Eq. (18)}$$

$$\alpha_1=\theta_{bottom}(t=0)-\theta_{top}(t=0)-\sum_{i=2}^{n}\alpha_i L^i \quad \text{Eq. (19)}$$

3. ASSESSMENT OF THE FREEZER CONTROL APPROACH IN SIMULATION

In order to evaluate the relevance of such a methodology, both experimental freezing and flash stages have been replaced by simulators, which permit easily to evaluate different cases:

3.1. Freezing stage

The objective is to obtain different exit temperature distributions. For this, a heat transfer model as described in section 2.2 was used but by considering the temperature in the freezer as θ_{air}, an homogeneous initial condition and a top boundary condition with $\varphi_{rad}=0$. The chosen parameters are common for spiral or tunnel industrial freezers. Indeed, a slab initially at 20 °C, is put on a mesh conveyor and goes inside the freezer at -30 °C. The heat transfer coefficients at the top and the bottom of food product are assumed to be equal to 35 and 25 W.m^{-2}.K^{-1} respectively. To produce simulations as accurate as possible, a large number of spatial nodes (301) was considered on the thickness of product.
Given the energy savings potential claimed in previous sections, three different freezer outlet conditions are studied here: (i) the product temperature has reached -18°C at the thermal center, (ii) the product temperature has reached -10°C at the thermal center and (iii) 80% of the water content has been converted into ice.
Figure 3 (left) represents time-temperature curves from simulations at different location of the product in depth. It points out that large fan energy savings are possible with case 2 (-10 °C) and case 3 (80 %) strategies because food products last 8.5 % and 26.5 % less time than with reference case 1 (-18 °C) respectively. The lower the outlet target temperature, the higher the standard deviation of temperature profiles
Figure 3 (right) represents simulated time-ice rate curves and gives quite the same information as temperature's figure.

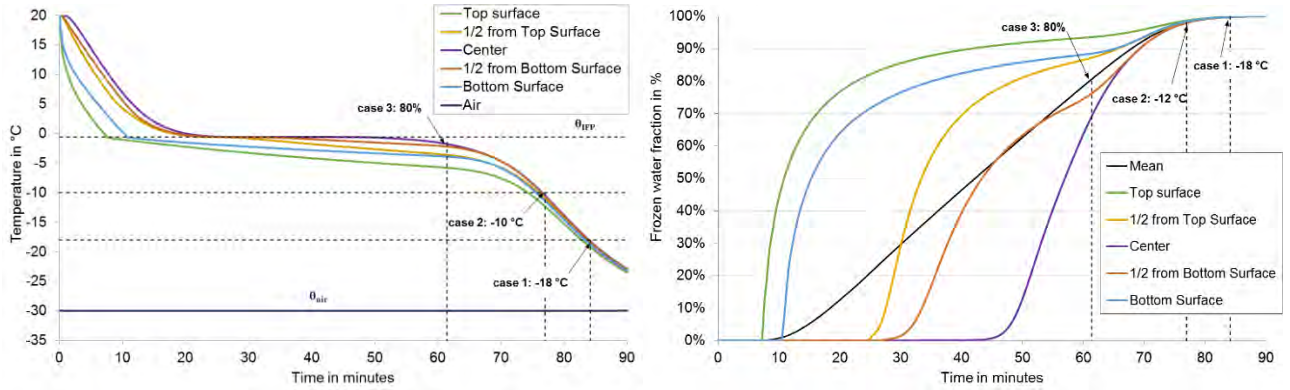

Figure 3: Temperature (left) and ice rate (right) curves during freezing process.

Figure 4 represents the distribution of temperature (solid) and ice (dashed) in the thickness of the product when the product leaves the freezer. In both cases 1 and 2, ice content gradient is very weak and mean value is higher than 95%. On the other hand, case 3 is completely different because inner temperature-distribution is more heterogeneous: surface temperatures are -5.8 °C at the top and -4.3 °C at the bottom whereas the hot spot is at -1.6 °C (17 mm depth). In this temperature range, the corresponding ice-distribution gradient is very large too: ice content is about 90-93 % at both ends of the product against 65 % at the thermal center.

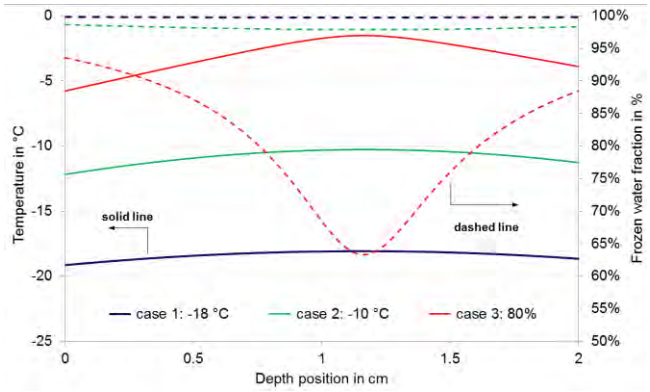

Figure 4: Temperature (θ_{exit}) and ice distribution in the thickness of the product

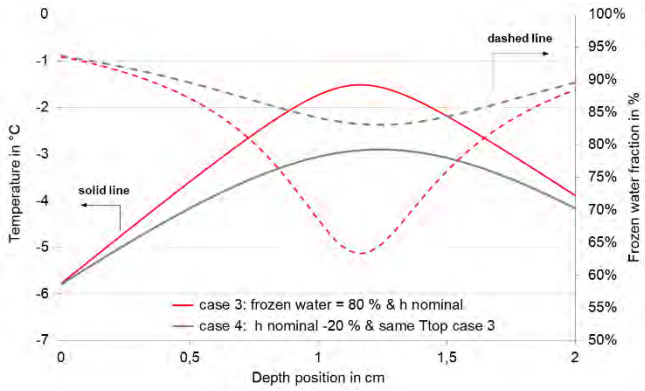

Figure 5: Impact of heat transfer coefficients on temperature (θ_{exit}) and ice distribution

By studying Figure 4, we could imagine to control the state of products at the freezer exit by a simple measurement of the top surface temperature (depth position = 0 cm), which seems to be discriminant enough. However, Figure 5 proves that each freezing process, conducted with its own parameters like conveyor speed, fan speed and air temperature, exhibits a unique temperature distribution inside the product. To illustrate that, let us start from a practical industrial case, which correspond to frost formation at the freezer heat exchangers surface. In such this regular situation, the overall thermal efficiency of refrigeration heat exchangers decreases as well as the airflow. In order to maintain the top surface temperature while overcoming the reduction of convective transfer coefficients, the product's residence time in the equipment has to be extend. Such a situation has been simulated (case 4) with some results drawn on Fig. 6. The corresponding freezing parameters are those already used previously and reported in Table 2 with the exception of heat transfer coefficients which are reduced by 20 %, i.e.: $28\,\mathrm{W.m^{-2}.K^{-1}}$ and $20\,\mathrm{W.m^{-2}.K^{-1}}$. We notice that the thermal center temperature is lower than in case 3. Consequently, the mean ice content is higher with a value equal to 86% against the initial target of 80 % (case 3). We also note that the ice content curve is more flat meaning that the inner-gradient is less important.
This case perfectly demonstrates the need for a special characterization method such as the one proposed in this study.

3.2. Flash test

A second simulator similar to the previous one was used, with 301 nodes too, by considering the initial conditions $\hat{\theta}_{exit}(t=0,z)$ recovered from the exit of the freezer in cases 3 and 4 aforementioned. For the top boundary condition, different combinations of heat flux and time pairs have been investigated: $\varphi_{rad} = 500 \text{ or } 1000 \text{ W.m}^{-2}$ t_{flash} = 5, 10 or 20 seconds. Each time, the thermal response was registered during 2 minutes by considering $h_{Top} = h_{Bottom} = 5$ W.m^{-2}.K^{-1}, θ_{air} = 5°C.

Figure 7 reports both top and bottom temperature histories resulting from a flash stage for case 3 only. It shows that thermal pulses have no effect on the bottom surface temperature. Indeed, whatever the intensity and duration of the thermal excitation, all the bottom temperature curves are superimposed. This temperature increases due to heat exchange by convection with surrounding air. On the other hand, the top surface temperature evolution depends on flash parameters. Those studied are satisfactory because they give sufficient amplitude of variation in temperature to be measurable on an industrial production line. In the article, we haven't sought to optimize these two parameters.

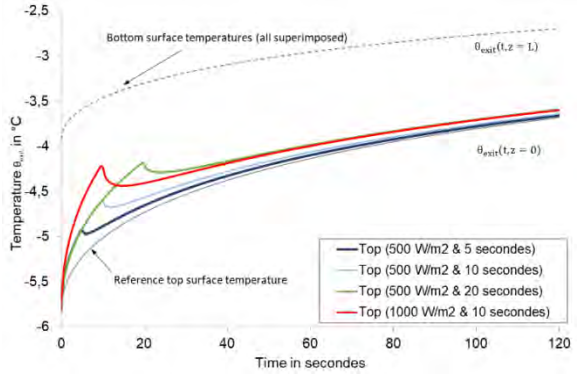

Figure 7: Top and bottom temperature history during and following a thermal flash in case 3

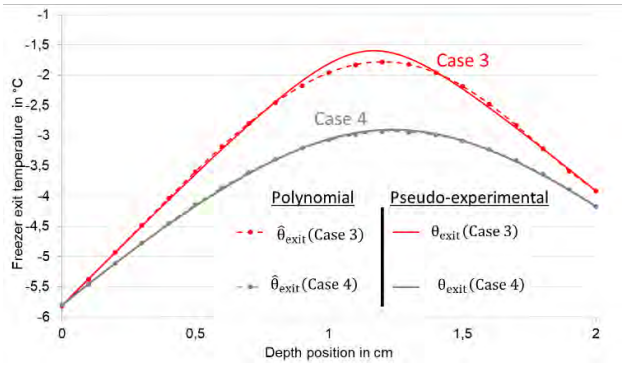

Figure 8: Polynomial and pseudo-experimental temperature distributions (cases 3-4)

3.3. Reconstruction of inner temperature field at the freezer outlet

The initial condition $\hat{\theta}_{exit}(t=0,z)$ is the function which needs to be estimated, because representing the unknown temperature distribution at the exit of the freezer. However, because top and bottom superficial temperatures are measured during the flash procedure, $\theta_{exit}(t=0,z=0)$ and $\theta_{exit}(t=0,z=L)$ are known.

For the least squares procedure, this one was carried out with polynomials from order 2, that is with only one coefficient to estimate. The procedure was repeated by increasing the degree of polynomial while the AIC criterion (Akaike 1974) decreased significantly. Here results are satisfactory from a 4th degree polynomial.

Figure 8 depicts real inner temperature distribution in depth (θ_{exit}) with the one deduced from a 5th degree polynomial $(\hat{\theta}_{exit})$. Here, the real temperatures are actually pseudo-experimental temperatures since they result from the freezing stage model applied to cases 3 and 4 explained before. The figure shows a good agreement between $\hat{\theta}_{exit}$ and θ_{exit}. The higher the inner temperature gradient the lower the prediction. Indeed accuracy is better with case 3 than with case 4. However, the maximum deviation is always lower than 0.5 K. Once temperatures converted into ice contents by using equation 5, it is possible to predict the mean ice content to within 1 % (case 3: $\hat{x}_{ice} = 80.7$ % against $x_{ice} = 80$ % and case 4: $\hat{x}_{ice} = 86.2$ % against $x_{ice} = 86$ %).

4. CONCLUSIONS AND PERSPECTIVES

A thermal methodology has been investigated to estimate the ice content distribution in a frozen product at the exit of the freezer. It is based on the comparison of modeled and experimental superficial temperatures following a thermal excitation. Simulations show that it is possible to rebuilt the inner temperature field and then to deduce the ice content distribution. This tool could lead to

important energy savings in freezing process. Indeed, the product could leave the tunnel at a higher temperature than usual and finish its freezing in the storage chamber, which is less energy intensive. However, such strategy can induce high ice content gradients within the product at the tunnel exit. It means that thereafter, during the finishing freezing process in a storage room, the mobile unfrozen water could promote the formation of larger disruptive ice crystals. Therefore, energy savings must be evaluated regarding a product's quality assessment.
It remains now to validate the solution with a first prototype in order to replace the pseudo-experimental temperature by real ones. This step will be also essential to determinate bias due to metrology and thermophysical property models. Once all these steps satisfied, we can develop a reliable and cost effective flash device for the industry.

REFERENCES

Akaike, H., 1974, A new look at the statistical model identification, IEEE Transactions on Automatic Control, 19(6), 716 - 723

Akkari, E., Chevallier, S., Boillereaux, L., 2006, Observer-based monitoring of thermal runaway in microwaves defrosting, Journal of Process Control, 16, 993-1001

ASHRAE, 2014, ASHRAE Handbook refrigeration, 926 pages

Borgh-Sorensen, L., 2006, Recommendations for the processing and handling of frozen foods, 4th Ed. Technical guide, IIF-IIR publisher, Paris, 176 pages.

Evans J., 2012, Carbon emissions from chilled and frozen cold chains for a typical UK Sunday roast chicken meal, RD&T report, 64 pages

FAO, 1976, codex alimentarius (CAC/RCP 8-1976)

Gauthier, J.P., Bornard, G., 1981, Observability for u(t) of a class ofnonlinear systems, IEEE Transactions on Automatic Control, 26, 922–926

Gauthier, J.P., Kupka, P., 1994, Observability and observers for non-linear systems, SIAM Journal of Control Optimization, 32, 975–994.

IIF-IIR, 2015, The role of refrigeration in the global economy: 29th informatory note on refrigeration technologies by the International Institute of Refrigeration, 16 pages

Kristófersson, J., Reinholdt, L., Kramer, K., Bork, A.R.L., Reinholdt, N.P., 2018, Energy optimization of batch freezing tunnel for meat, Proceedings of the 13th IIR Gustav Lorentzen Conference, Valencia, Spain, 8 pages

Le-Bail A., Chapleau N., Anton-De Lamballerie M., Vignolle M., 2008, Evaluation of the mean ice ratio as a function of temperature in a heterogeneous food: Application to the determination of the target temperature at the end of freezing. Int. J. Refrigeration 31, 816 – 821.

Martín-Vaquero, J., Sajavičius, S., 2019, The two-level finite difference schemes for the heat equation with nonlocal initial condition, Applied Mathematics and Computation, 342, 166-177

Pandey, G., Vandermeiren, W., Dimiccoli, L., Stiens, J., 2018, Contactless monitoring of food drying and freezing processes with millimeter waves, Journal of Food Engineering, 226, 1-8

Rouaud, O., Pham Q.T. 2012, Heat transfer modelling during freezing of foodstuffs, Proc. Comsol Conference, Milano

Sun, D.W., 2011, Handbook of Frozen Food Processing and Packaging: 2nd Edition, CRC press, 936 pages

Manuscript ID: 827
DOI: 10.18462/iir.icr.2019.0827

Study of convective heat transfer and chilling kinetics of Atlantic salmon in refrigerated sea water: experiments and modelling

Ignat TOLSTOREBROV [(a)], Trygve M. EIKEVIK [(a)], Kristina N. WIDELL [(b)], Tom Ståle NORDTVEDT [(b)]

[(a)] Norwegian University of Science and Technology, Department of Energy and Process Engineering, 7491 Trondheim, Norway, ignat.tolstorebrov@ntnu.no
([b)] SINTEF Ocean, Trondheim, Norway

ABSTRACT

The study is devoted to the investigation of heat transfer phenomena of Atlantic salmon in refrigerated sea water with the aim to clarify strategies of large scale industrial chilling of big-size fishes. Experiments were conducted using polyurethane copies of real fishes (3.5 and 6.0 kg), which were equipped with temperature sensors at different points. Convective heat transfer coefficient was determined with a numerical model. Tests were verified using real slaughtered salmon. A simplified solution for transient problem was suggested. Convective heat transfer coefficient varied between 16.0 and 300 W m^{-2} K^{-1} with respect to chilling mode. High values of convective heat transfer coefficient (over 200 W m^{-2} K^{-1}) requires high flow of cooling agent even for laboratory scale chilling tank. Experiments at industrial slaughter house revealed convective heat transfer coefficient in the range between 112.0 and 139.0 W m^{-2} K^{-1}. Simulation showed that the target temperature of 2.0 °C in the fish centre is difficult to achieve, when strict time limits are applied at factory, especially for fishes over 5.0 kg weight.
Keywords: Atlantic Salmon, RSW, Chilling, Heat Transfer, Modelling.

1. INTRODUCTION

The rapid and effective chilling process is the most important step during the production. The temperature of fish should be lowered down to the range between 0.0 and -2.0 °C at a high rate after slaughtering. (FAO/WHO, 2003). Slow and insufficient chilling of fish results in a significant decrease of quality: gaping, decreasing of shelf-life, decreasing of fillet yield, increasing of extracellular ice in frozen fish etc. (Einen et al., 2002; Flesland and Magnussen, 1990).
Three different methods of chilling are used in industry for quality preservation after slaughtering: chilling in refrigerated sea water (RSW), chilling in ice, chilling in binary mixtures (ice-water, ice-RSW, slurry ice etc.) (Erikson et al., 2011; Skjervold et al., 2002). The chilling process of salmon takes in practice significant amount of time. Large scale industrial chilling of salmon requires the estimation of chilling time for salmon of different sizes (Widell et al., 2018).
The determination of convective heat transfer coefficient during chilling of salmon for industrial cases is complicated. Most of models can give approximate values as soon as flow of RSW is far from ideal for large systems, also, most of the equations are developed for high Reynolds numbers (Kreith et al., 2011), that is not achievable for chilling tanks of a big volume (100 m^3). Reported data concerning convective heat transfer coefficient for immersion chilling relates to small fishes like sprat or trout and lays in the range between 200.0 and 300.0 W m^{-2} K^{-1} (Fikiin, 1992). The convective heat transfer coefficient was determined by the heat balance method. Flesland and Magnussen (1990) determined the convective heat transfer coefficient for salmon chilled in RSW in the range between 150.0 and 200.0 W $m^{-2}{\cdot}K^{-1}$. Resent investigations of Bantle and all (Bantle et al., 2015) revealed the heat transfer coefficient in the range between 50.0 and 100.0 W $m^{-2}{\cdot}K^{-1}$, when chilling salmon in laboratory tanks. The infinite cylinder model was used in all the investigations. The high internal thermal resistance of Atlantic salmon will created such a high deviation in results, when using such an approach.

This paper investigates the chilling kinetics of Atlantic salmon with respect to the real geometry, weight and convective heat transfer coefficient in a chilling tank. The created model for salmon chilling is based on the results of laboratory and industrial tests

2. MATERIALS AND METHODS

2.1. Description of Experiment

Experiments included the following measures:

- Polyurethane model of Atlantic salmon (PU-fish) chilled in RSW laboratory tanks (1m^3 each), when fish position and brine flow were varied;
- PU-fish chilling in a box with cooling agent;
- PU-fish chilling in industrial tanks, constant flow and unknown fish position in tanks.
- Atlantic salmon chilling in RSW laboratory tanks (verification of numerical model and analytical solution);
- Atlantic salmon chilling in industrial tanks.

Atlantic salmon was replaced by PU-fish in most of the experiments due to high rate of spoilage and variation in geometry, which will decrease the accuracy of measurements especially when the temperature difference between fish and cooling media was low. At the same time, the thermal diffusivity, which is the key parameter for transient thermal processes, of PU-fish was $1.16*10^{-7}$ $m^{-2}s^{-1}$ while Atlantic salmon showed it in the range between $1.3\text{-}1.4*10^{-7}$ m^{-2} s^{-1}.
The measurements were used for the determination of convective heat transfer coefficient with respect to chilling mode and for the verification of numerical model for fish chilling.

2.2. Fish Chilling in RSW Laboratory Tanks

A laboratory chilling system consisted of two tanks, dimensions: 1.0x1.4x0.8 m and CO_2 refrigeration system, Fig. 1. Brine came from the refrigeration system to the first tank (Tank1) at the bottom via pipe (diameter 0.15 m). The level of RSW in the first tank was always 0.7±0.02 m, the direction of RSW flow was chaotic and unpredictable. The brine flowed free to another tank (Tank 2) through the upper part of the back wall of Tank 1; Tank 2 was 0.10 m lower. Brine level in the second tank was in the range between 0.20 and 0.25 m with respect to the flow of RSW. The direction of RSW flow from one wall to another was observed for this tank as soon as the brine was drained at the opposite side of Tank 2. Brine concentration was at 3.1 (0.1) % of NaCl. Brine circulation was organized in such a way that the water flow was set up at 9.0, 18.0 and 36.0 m^3 h^{-1}, accuracy ±0.01 m^3 h^{-1}. Inlet and outlet brine temperature was measured, accuracy ±0.3 °C. The RSW flow was equivalent to RSW exchange rate that occurs in spiral tank chambers during industrial chilling of salmon.

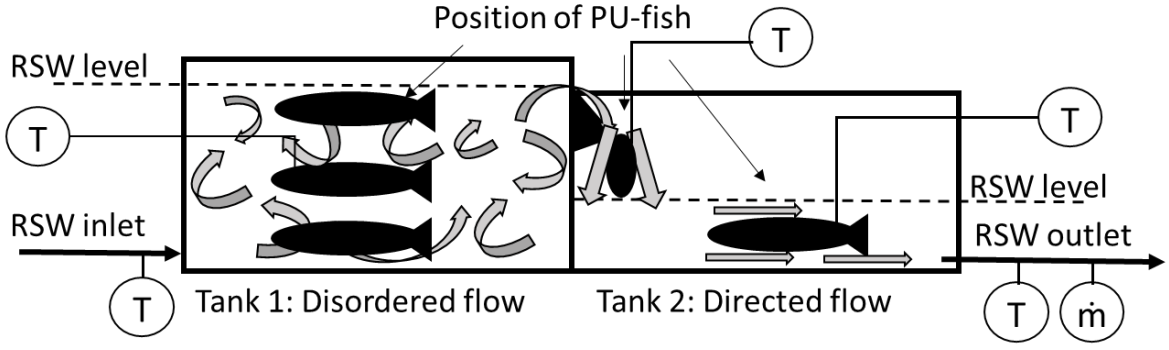

Figure1: Position of PU-fish in laboratory RSW chilling tanks

PU-fishes were equilibrated in the climate chamber KMF 115 (Binder, Germany) at 20.0 ±1 °C for 15±0.2 hours. A PU fish was connected to a frame that was immersed into laboratory RSW tank for chilling. The experiments are introduced in Table 1.

Table 1. Experiment design

Tank	Volume of brine, m3	Fish position	Flow, m3 h-1
1	1.0	Bottom, middle, under surface	0.0; 9.0; 18.0; 24.6
2	0.25	Backbone, guts, nose and tail to flow direction	9.0; 18.0; 36.0
Free falling flow of brine	-	Between tank 1 and 2 Backbone to flow	9.0, 18.0

2.3. Fish Chilling in Box with Cooling Agent

Two types of cooling media was used:
Flake ice (particle size of 1.0 cm): PU-fish was placed with ice into an insulated box with the ratio of fish to ice 3:1;
Mixture of flake ice and water 1:1 by weight: PU-fish examination in an insulated box with the mixture of fish to ice 3:1.

2.4. Fish Chilling in Industrial Tank

The chilling tank consisted of a semi-cylindrical vessel with a perforated screw, Fig. 2. The vessel was filled 60% (approx.); thus, the screw created isolated chambers along the vessel. Fish feeding was made by belt conveyor, equipped by tank filling degree control unit that allowed feeding any chamber of the tank by moving the controlling device or having stationary position in the case of crew rotation. At the same time, unloading occurred through the end of the chilling tank (unloading port) by screw rotation. RSW flow organized along the tank from unloading port (end) to the beginning through the openings on the screw and between the screw and the tank wall. Experiments were conducted for two different sizes of tanks. All the tanks had a volume of 100 m^3 (diameter 4.2-4.5 m, length 11.0-12.0 m). The volume of chambers was 6.6 and 7.0 m^3 respectively.
PU-fish was placed in different chambers of the spiral tank. The following parameters were registered during chilling test: time of chilling, temperature of fish vs. time, RSW temperature inlet and outlet, fish density in chilling chambers.

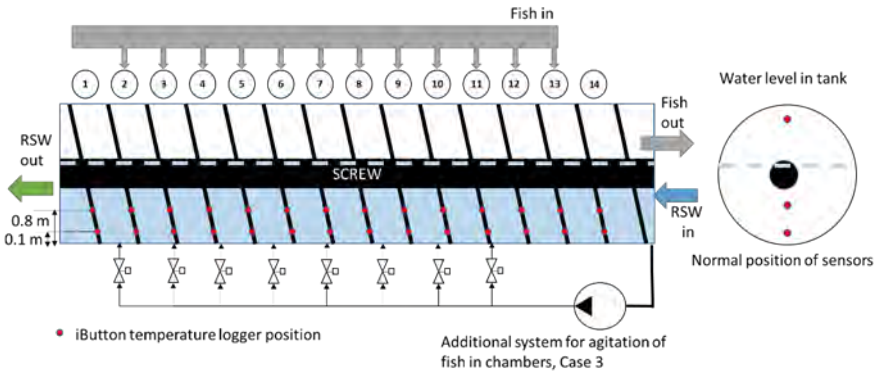

Figure 2: Simple sketch of spiral tank for industrial chilling of Atlantic salmon

2.5. Determination of Thermal Properties

Thermal properties of polyurethane and fish tissues were measured by two different techniques: DSC (TA instruments, USA) and Transient Plane Source (ISO 22007-2:2015). DSC technique was used to measure precise heat capacity of the samples. Analysis was done on DSC Q 2000 (TA instruments, USA) equipped with liquid nitrogen cooler. The heat capacity for different types of fish tissues were in a good agreement with calculation methods based on chemical composition of material, which are introduced in ASHRAE (2014). The thermal conductivity for salmon was measured in the range between 0.37(0.01) and 0.50 (0.01) W m^{-2} K^{-1}. Rahman (Rahman, 2009) reported values of 0.47 W m^{-2} K^{-1} for pink salmon of 72.5 % water content. Thermal conductivity of polyurethane was 2 times less, when compared to the thermal conductivity of fish muscles. This

will reduce the sensitivity of PU-fish models, when measuring the convective heat transfer coefficient, to 300-350 W m^{-2} K^{-1}, due to high internal thermal resistance.

Table 1. Thermal properties of Atlantic salmon and PU-fish

Type	Heat capacity, $J \cdot kg^{-1} \cdot K^{-1}$	Thermal conductivity (at 20.6 °C), $W \cdot m^{-1} \cdot K^{-1}$	Density, (at 20.6 °C), $kg \cdot m^{-3}$
Polyurethane	1692	0.24 (0.005)	1222.0 (1.0)
Fish muscle, 66.0 (0.2)%	3400.0 (20.0)	0.50 (0.007)	1050.0 (5.0)
Fatty tissues,56.96 (0.2)%	3199.0 (35.0)	0.38 (0.01)	1020.0 (5.0)
Fish skin, 34.9 (1.0) %	2906 (50.0)	0.37 (0.01)	1050 (5.0)

2.6. Polyurethane fish and Atlantic salmon: temperature measurements

Polyurethane fish (PU-fish) (GM 951-1 A/B (Ebalta, Germany)) replicated the shape of real salmons of 3.0 kg and 5.0 kg weight. Total weight of the models was 3.5 kg, and 6.0 kg. The PU-fish was equipped with T-thermocouples connected to data loggers. Data was logged by FLUKE universal input module (FLUKE Corp., USA) for laboratory tests and by 8-channels iLog Data logger (Versalog, USA). Accuracy of the measurements were ±0.2 and ±0.5 °C respectively. Thermocouples were calibrated at 0.0 °C (in ice) and 20.0 °C (thermostat) before experiments. Temperature was logged each 60.0 sec. The position of thermocouple is introduced on Fig. 2 (left).

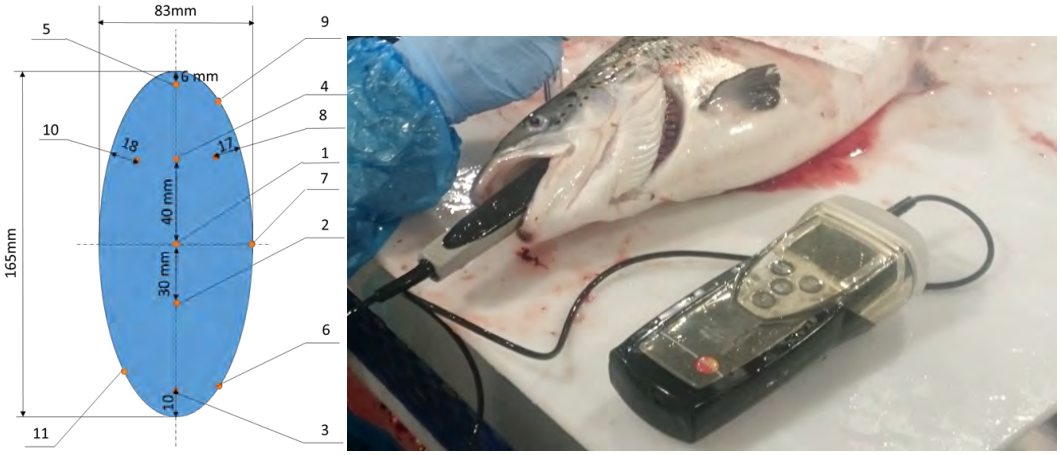

Figure 2: Position of thermocouples for PU-fish 5.5 kg (left) and measurement of temperature of Atlantic salmon (right)

A Testo temperature measuring instrument (Testo, 2017) with a 23 cm long probe, was used for measuring temperatures inside the fish, both before and after chilling. Accuracy: ± 0.2 °C. The sensor was placed at the center of the fish in its thickest part, Fig. 2 (right)

2.7. Description of a Numerical Model

The models of Salmon and PU-fish were created in PDE Tool work package in Matlab R2017a. The geometries, which were used, represented the exact dimensions of PU-fishes for heat transfer determination, and the average dimensions of salmons of 3.0±0.3, 5.0±0.3 and 8.0±0.5 kg. Totally 25 fishes of each weigh group were measured. Standard deviation of the dimensions form average values did not exceed 8.0 %. The fish was split into 2-D slices, that reflects the dimensions of the PU-fish or a real fish. The model of real fish included guts, fatty tissues, skin and muscles with the related thermal properties, Fig. 3.

The Neumann boundary conditions were applied, since the surface temperature is varying over the time. Initial condition were set at $T_o=T(\tau_o)$. Initial temperature T_o was decided to be uniformly distributed in the fish. Heat transfer coefficient and ambient temperature were specified, Eq. (1):

$$\vec{n} \cdot (k \nabla T) = h_c (T - T_{amb}) \qquad \text{Eq. (1)}$$

where $\vec{n}$ - the outward unit normal; $\vec{n}\cdot(k\nabla T)$ – is the heat flux, W m^{-1}; h_c – the convective heat transfer coefficient W m^{-2} K^{-1} , k – the thermal conductivity, W m^{-2} K^{-1};T – the temperature of object, K; T_{amb} – the temperature of cooling media, K.
The transient heat transfer problems were solved by parabolic PDE equations, which use a time-dependent algorithm, assuming the absence of heat source inside the fish and zero heat flow from the sides of fish slices, Eq. (2):

$$\rho C_p \frac{\partial T}{\partial \tau} - \nabla \cdot (k \nabla T) = 0 \qquad \text{Eq. (2)}$$

where T – is the transient two-dimensional temperature distribution, K; ρ – the density, kg m^{-3}; C_p – the specific heat capacity, J kg^{-1} K^{-1}; τ – the time, sec.
Solution vectors were produced from the mesh, the boundary conditions, and the equation coefficients. The solution was introduced as a two-dimensional temperature distribution on the nodes of the mesh. As soon as the position of each node was known, the average temperature for each node triangle was determined. This simple method gave an opportunity to determine the temperature of any segment of the slice or bulk temperature of the whole slice. The segments, which introduced the positions of temperature sensors in PU-fish, were determined. The simulation of real Atlantic Salmon included segment area, which refers to the temperature probe position (Fig. 2, right), when measuring fish temperature before and after chilling, Fig. 3.

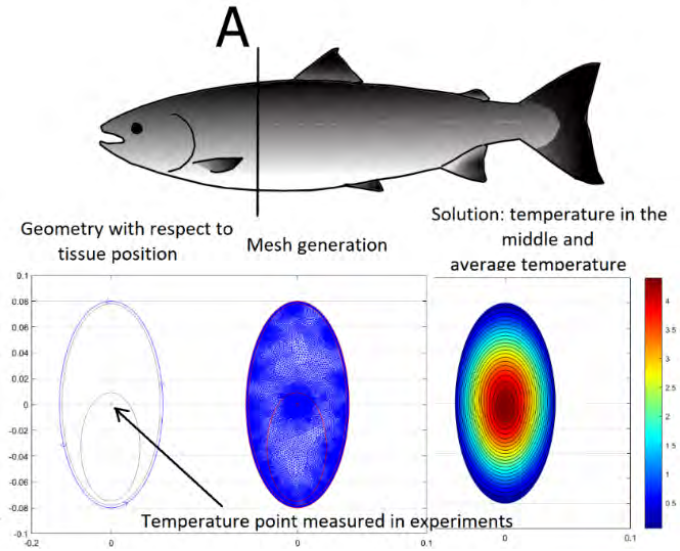

Figure 3: Example of presentation Atlantic salmon geometry in Matlab 2017a Pde-tool

2.8. Determination of Convective Heat Transfer Coefficient

Convective heat transfer coefficient for PU-fish was determined using the numerical model by adjusting convective heat transfer coefficient in numerical simulation until the sum of mean square errors between the measured and modelled temperature values reached the minimum value. The temperature values were taken from the beginning until the end of chilling process.
The verification of the convective heat transfer was done by the chilling of Atlantic salmon at the same conditions as PU-fish. Geometries of the fishes were determined for each test. Two temperature values were taken for analysis: initial temperature and final temperature (with respect to chilling time).

2.9. Simplification Approach for Chilling Problem

The use of MatLab script consumes significant amount of resources due to its complicity. The model was simplified by use of one type of tissues – muscle tissues and by the determination of equivalent radius of fish that allows to apply a simple analytical solution for an infinite cylinder.
A special case for the analytical solution of transient heat transfer problem, applied to the chilling of Atlantic salmon can be introduced by the following equation, Eq.(3):

$$\theta_{center} \sum_{n=1}^{n\to\infty} \frac{2J_1(\mu_n)}{\mu_n[J_0^2(\mu_n)+J_1^2(\mu_n)]} exp\,(-\mu_n^2 Fo) \qquad \text{Eq. (3)}$$

where μ - is the root of parametric equation, J – the Bessel function, Fo – the Fourier number, Bi- the Boit number; θ –the dimensionless temperature.
The geometry was simplified by the application of an equivalent radius that was found empirically using experiments and numerical simulation (standard error between numerical simulation and analytical solution did not exceed 0.7%), Eq. (4):

$$r_{equivalent} = 0{,}929045 * (b/2)^{0{,}722475} * (a/2)^{0{,}226227} \quad \text{Eq. (4)}$$

where b – is the thickness of fish at the thickest part, m; a – the height of fish at the thickest part, m.

2.10. Statistical Analysis

The thermal property tests were done in 5 parallels. Each experimental test point was done in 3 parallels. The quality of the model was checked by residual analysis: adjusted R^2, F-significance and p-value. Standard deviation is introduced in brackets. The variation of some parameters are marked with "±" symbol.

3. RESULTS AND DISCUSSION

3.1. Convective Heat Transfer Coefficient for Natural and Forced Convection at Laboratory Tank

Table 2 introduces the influence of chilling modes on the convective heat transfer coefficient. Flake ice showed the lowest values and it cannot be accepted for rapid and efficient chilling of Atlantic salmon, especially, when the weight of fish is over 3.0 kg. Chilling of PU-fish in Tank 1, was much slower, when compared with chilling in Tank 2. This occurred due to high volume of brine in Tank 1, which reduced the velocity of brine. Also, the velocity of brine was not uniform in the volume of the tank and the highest values of convective heat transfer coefficient were obtained on the bottom where the brine flow entering the tank ($p<0.05$). The increasing of the brine flow to 24.6 m^3 h^{-1} resulted in the increasing of convective heat transfer coefficient up to 300 W m^{-2} K^{-1}, that is the boundary sensitivity of PU-fish.
The brine flow, which had a direction form one wall of the Tank 2 to the other, showed higher values of convective heat transfer coefficient when compared with those obtained for Tank 1. This, obviously, occurred due to smaller volume of brine in the tank and higher average velocities. The position of fish in Tank 1 did not have a statistically significant difference on convective heat transfer ($p>0.05$). Free falling of brine did not show any influence of flow on the convective heat transfer coefficient for PU-fish ($p>0.05$).
It is important to note that the high brine flows (>18.0 m^3 h-1) were required for obtaining convective heat transfer coefficient over 200 W m^{-2} K^{-1} for laboratory chilling tank of 1 m^3 volume. This value will be even more difficult to achieve for large-scale units.
The chilling of Atlantic salmon in the laboratory tank of 5.0 ±0.5 kg weight revealed a good agreement between simulation and measurements. The temperature difference (after chilling) between the simulation and measurement temperatures was in the range between -2.5 and 2.2 %. The temperature, which was measured by probe, referred to geometric center of the fish in its thickest part.

Table 2. Convective heat transfer coefficient determined for different modes of PU-fish chilling

Experiment	Brine flow ($m^3 \cdot h^{-1}$)	Convective heat transfer coefficient ($W \cdot m^{-2} \cdot K^{-1}$)	Brine velocity ($m \cdot s^{-1}$)
Tank 1 (unpredicted flow)	0.0	102.0 (5.0)	0.0
	9.0	117.0-141.0 (9.0)	N/A
	18.0	155.0-219.0 (10.0)	N/A
	24.6	240.0-300.0 (11.0)	N/A
Tank 2 (flow form one side to the other)	9.0	171.0 (8.0)	0.01
	18.0	247.0 (9.0)	0.02
	36.0	300.0 (12.0)	0.04
Free-falling of brine	9.0	151.0 (9.0)	N/A
	18.0		N/A

Flake ice, 0.01 m	N/A	16.0 (2.0)	N/A
Flake ice/water	N/A	115.0 (5.0)	N&A

3.2. Convective Heat Transfer Coefficient for Industrial Spiral Tank

Field tests at the industrial slaughter house were conducted with PU-fishes of 5.5 kg. The RSW flow was organized along the chilling tank (from one side to another). It is remarkable, that increasing of RSW flow did not cause the same effect on the convective heat transfer coefficient as for laboratory tests, even for high exchange rate, Table 3.

Table 3. Convective heat transfer coefficient determined by PU-fish in industrial tank 100 m^3

RSW flow ($m^3 \cdot h^{-1}$)	Convective heat transfer ($W \cdot m^{-2} \cdot K^{-1}$)	Fish density in chambers (%)	RSW exchange rate in chamber (h^{-1})
PU fish			
200.0	121.0(5.0)	33.0-38.9	30.3
65.0	122.0(5.0)	43.7	9.28
	134.0(8.0)	42.0	
	139.0(8.0)	41.6	
	117.0(8.0)	N/A	
Real salmon			
65.0	112.0(7.0)	7.6	9.28; 0.0025 ($m \cdot s^{-1}$)

The convective heat transfer coefficient was determined in the range between 117 and 139 $W \cdot m^{-2} \cdot K^{-1}$. It looks like the fishes formed a stack, which influenced the flow distribution inside the chilling chambers. Due to this, some variations of convective heat transfer occurred even for the same flows of RSW (65.0 $m^3 \cdot h^{-1}$).
In addition, the temperature sensor, which was measuring RSW temperature in vicinity of the fish surface, detected a significant temperature alteration during the chilling process, when the detected temperature exceeded the RSW outlet temperature by 1.5-2.0 °C, Fig. 4 (grey and red lines). The density of fish in the chambers reached 43.07 % for some experiments.

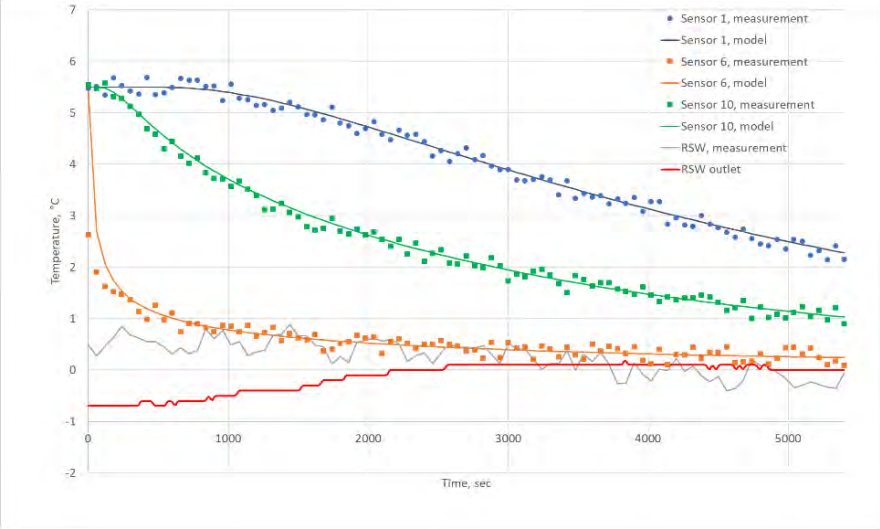

Figure 4: Example of temperature alteration in PU-fish with respect to RSW temperature at the surface (RSW, measurement) and RSW temperature at an outlet of the chilling tank

Thus, the direct determination of convective heat transfer coefficients for Atlantic salmons in the chilling tank was false, due to the absence of information on the exact temperature at the fish surface. However, one experiment set was successful due to low density of fish in one chamber, when the temperature of RSW over the fish surface was predictable (in the range of 0.5 °C). The convective heat transfer coefficient was 112.0 (7.0) W m^{-2} K^{-1}, which is in agreement with the average low velocity of RSW in the chamber. Seems to be that large scale chilling units cannot provide a sufficient flow of RSW for reaching high values of convective heat transfer coefficient. At the same time, the importance of convective heat transfer coefficient for chilling process is

decreasing, when reaching the value of 250 W m^{-2} K^{-1} and over due to high internal heat resistance.

3.3. Chilling Kinetics of Atlantic Salmon

The chilling process of Atlantic salmon takes between 90 and 120 min for big industrial slaughterhouses. Fig. 5 is based on the simplified analytical solution of the transient problem for salmon chilling (Eq. (3)). It indicates that the aim of 2.0 °C at the fish center is hardly achievable for fishes with weight over 5.0 kg. The dimensionless temperature can be calculated by Eq. (5):

$$\theta = \frac{T_\tau - T_{RSW}}{T_0 - T_{RSW}} \qquad \text{Eq.(5)}$$

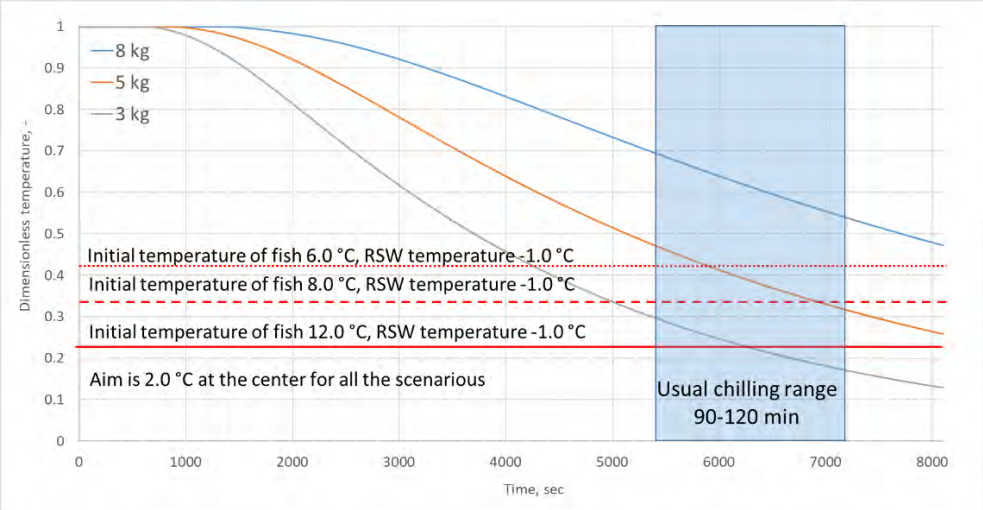

Figure 4: Temperature in the center of Atlantic salmon with respect to weight, initial temperature of fish and RSW temperature, convective heat transfer coefficient 150.0 W m^{-2} K^{-1}

Additional challenges occur during summer and autumn harvesting when the sea temperature increases up to 15.0 °C. The temperature of Salmon will be at the same temperature in such a case. Thus, the pre-chilling of big-size salmon to +6.0 °C before slaughtering (or two stage chilling) is required for slaughterhouses with limited chilling capacities.

4. CONCLUSIONS

The convective heat transfer coefficient up to 300 W·m^{-2}·K^{-1} can be achieved for chilling of Atlantic salmon at a laboratory chilling tank. However, a high flow of cooling media is required. Due to this, the convective heat transfer coefficient at large-scale industrial chilling units was determined in the range between 112.0 and 139.0 W·m^{-2}·K^{-1}. Another important issue was the high density of fish in the chamber of the industrial chilling tanks that caused insufficient RSW flow distribution. The higher values were not achieved as a result. The temperature at the fish surface was higher when compared to RSW outlet temperature. The simulation model showed that Atlantic salmon of big sizes could not be effectively chilled within time intervals, which are common for processing factories.

ACKNOWLEDGEMENTS

The authors gratefully acknowledge the Research Council of Norway for the financial support for carrying out the present research [NFR project No. 269175].

REFERENCES

Bantle, M., Stavset, O., Nordtvedt, T.S., Gullsvåg, P.E., Eikevik, T.M., Tolstorebrov, I., 2015. Chilling of salmon in refrigerated sea water, Proceedings of the 24th International Congress of Refrigeration. International Institute of Refrigeration.
Einen, O., Guerin, T., Fjæra, S.O., Skjervold, P.O., 2002. Freezing of pre-rigor fillets of Atlantic salmon. Aquaculture 212, 129-140.
Erikson, U., Misimi, E., Gallart-Jornet, L., 2011. Superchilling of rested Atlantic salmon: Different chilling strategies and effects on fish and fillet quality. Food Chem. 127, 1427-1437.
FAO/WHO, 2003. Code of practice for fish and fishery products, in: FAO/WHO (Ed.), CAC-RCP 52-2003, p. 125.
Fikiin, A.G., 1992. New method and fluidized water system for intensive chilling and freezing of fish. Food Control 3, 153-160.
Flesland, O., Magnussen, O.M., 1990. Chilling of farmed fish, International congress of refrigeration. IIF, Aberdeen, UK, pp. 185-191.
Kreith, F., Manglik, R.M., Bohn, M.S., Tiwari, S., 2011. Principles of heat transfer, 7th ed., SI. ed. Cengage Learning, Stamford, Conn.
Rahman, S., 2009. Food properties handbook, 2nd ed. ed. CRC Press, Boca Raton, Fla.
Skjervold, P.O., Fjæra, S.O., Snipen, L., 2002. Predicting live-chilling dynamics of Atlantic salmon (Salmo salar). Aquaculture 209, 185-195.
Testo, 2017. Temperature measurement / Thermometer.
Widell, K.N., Nordtvedt, T.S., Tolstorebrov, I., Fossen, I., 2018. Experimental investigation of chilling tank for Atlantic salmon, 5th IIR Conference on Sustainability and the Cold Chain : proceedings. International Institute of Refrigeration, pp. 331-339.

Manuscript ID: 830
DOI: 10.18462/iir.icr.2019.0830

Challenges of effective chilling of Atlantic salmon in refrigerated sea water: field tests

Ignat TOLSTOREBROV [a], Kristina N. WIDELL[b], Tom Ståle NORDTVEDT[b], Trygve M. EIKEVIK[a]

[a] Norwegian University of Science and Technology, Department of Energy and Process Engineering
Trondheim, 7491, Norway, ignat.tolstorebrov@ntnu.no
[b] SINTEF Ocean
Trondheim, 7465, Norway kristina.widell@sintef.no

ABSTRACT

This papers is summing up main challenges which occur at large-scale industrial slaughter houses when chilling Atlantic salmon by refrigerated sea water (RSW). The study includes strategies of efficient chilling in 100 m^3 spiral tanks based on the field tests. Analysis showed high density of fish in a chilling tank and low refrigerated sea water flow lead to non-uniform temperature distribution in the tank. Temperature at the surface of the fish can exceed values of RSW outlet temperature, which increases the chilling time, reduces efficiency of the process and limits capacity of equipment. The chilling index can vary from 66 to 108% for the same type of chilling tank with respect to operation parameters. Agitation of fish in the chilling tank increases chilling efficiency up to 87.9 %. The limited time of fish holding in the chilling tank (75-100 min) was not sufficient for achieving temperature of 2.0 °C for any scenario, when initial temperature of fish was higher than 11.0 °C.
Keywords: Atlantic Salmon, RSW, industrial chilling, heat transfer, modelling, chilling index

1. INTRODUCTION

Atlantic salmon aquaculture is a sector of industry that shows high growth through the recent years. Norwegian salmon production reached the value of 1.236 million tons in 2017 (StatisticsNorway, 2018). The following requirements are applied for chilling of Atlantic salmon at big slaughter houses. A rapid and effective chilling process is the important step during the production for high product quality and sustainable shelf-life. The final temperature of fish should be in the range between 0 and -2.0 °C as fast as it possible after slaughtering (FAO/WHO, 2003; Venugopal, 2006). A slow and insufficient chilling of fish results in a significant decreasing of quality: gaping, reduced shelf-life, decreasing of fillet yield, increasing of extracellular ice in frozen fish etc. (Einen et al., 2002; Erikson et al., 2011; Magnussen and Hardarson, 1987).
Previous research revealed high variations of fish and RSW temperatures in an industrial chilling tank (Widell et al., 2018), which created difficulties for evaluation and comparison of different chilling processes for further optimization. Laboratory chilling tests determined high influence of geometry on chilling time and relatively high deviation of convective heat transfer coefficient in the range between 75.0 and 150.0 W m^{-2} K^{-1} (Bantle et al., 2015).
This study is devoted to the analysis of chilling of Atlantic salmon in spiral tanks. This type of equipment is characterized by high capacity and large volume. A modelling part was supported by experimental results from three industrial field visits, when the major influencing factors were varied.

2. MATERIAL AND METHODS

2.1. Experimental campaign description

The experiments were conducted during 3 visits to salmon processing plants. Each chilling test had the following measurement procedure:

- Measurement of initial and final fish temperature in the center, geometry (height and width) and weight;

- Logging of chilling time, amount of fish in the chambers of chilling tank – data provided by factory logging system;
- Logging of RSW inlet and outlet temperature and flow;
- Measuring of RSW temperature at vicinity of fish (flexible temperature sensor connected to polyurethane fish, distance 0.05-0.1 m from the surface of fish);
- Logging of RSW temperature between chambers of the chilling tank.

iButton temperature sensors (Maxim Integrated, 2017) were used to log RSW temperatures between the chambers inside the tank. The sensors were attached to the screw with a plastic holder, at the distances of 0.1 (bottom) and 0.8 m (middle) from the edge of the screw. Temperature was measured each minute, an accuracy ± 0.5 °C.

A Testo temperature measuring instrument (Testo, USA) with a 0.23 m long probe, was used for measuring temperatures in thermal center of the fish, an accuracy: ± 0.2 °C.

2.2. Description of spiral tank operation

The chilling tank consists of half-cylinder with a perforated screw. The tank was filled 60% (approx.); thus, the screw creates isolated chambers along the tank, Fig.1. Fish filling of the tank was made by a belt conveyor, which allowed to fill any chamber by moving the controlling device or to have stationary position in the case of crew rotation. At the same time, the unloading occurs through the end of the chilling tank (unloading port) by screw rotation. RSW flow direction was along the tank from the fish unloading port to the beginning through the openings on the screw and between the screw and a tank wall. All the tanks had a volume of 100 m^3 (diameter 4.2-4.5 m, length 11.0-12.0 m).

The processing plants had either two or three of these tanks in parallel to provide chilling capacity. The tanks were working in a semi-continuous mode. The example of a battery, which consists of two units is given below:

- Filling both tanks with RSW;
- Filling chambers of tank 1 with fish at the beginning of working shift (40-90 min), the screw is not moving;
- Fish held in the tank 1 (40-60 min), screw is not moving. Simultaneous filling of tank 2;
- Unloading of tank 1 (20-30 min), rotation of the screw. Simultaneous filling of tank 2, the screw is not moving;
- Simultaneous unloading and filling of tank 1 (20-30 min), the screw is moving. Fish held in tank 2;
- Unloading of tank 2, rotation of the screw. Filling of tank 1 (20-30 min), the screw is not moving.

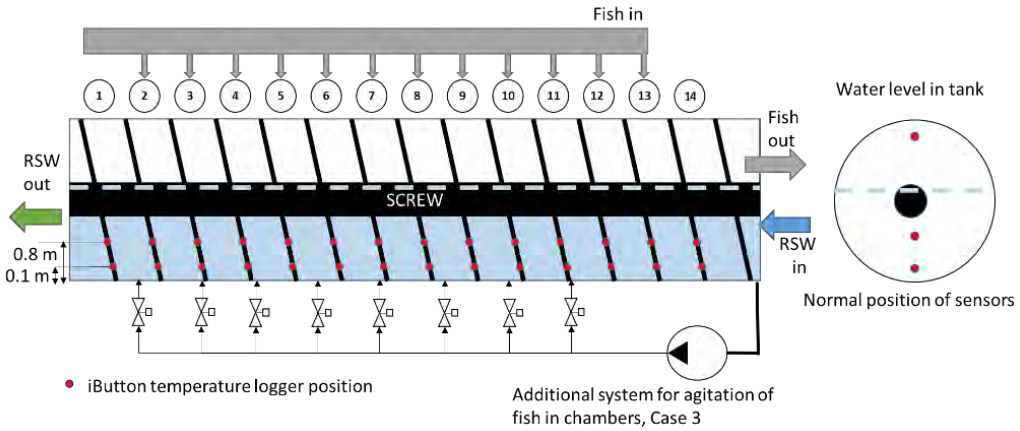

Figure 1: Simple sketch of spiral tank for industrial chilling of Atlantic Salmon

2.3. Experimental cases

Three industrial field trips were conducted at summer, autumn and winter. One chilling tank was used for tests in each experimental case. The parameters of the chilling tanks are introduced in Table 1. Case 1 had a battery of 3 tanks. The system was characterized by high RSW flow, relatively low amount of fish in the chambers (fish density, %) and low heat flow from the fish, but fresh water of 10.0 °C was added at the RSW outlet from the tank. RSW inlet temperature was unstable, thus, only one test was considered to be representative.

Table 1. Parameters of spiral chilling tanks

Case	RSW flow, $m^3\ h^{-1}$	Fish in chambers*, % (volume)	Average weight of fish*, kg	Fish initial temperature, °C	RSW inlet, °C	Chilling sets	Additional agitation devices
1	200.0 (10)	33.3÷38.9	4.6÷5.4	5.0÷7.0	0.4 (0.1)	2	NO
2	50-65(10)	40.1÷43.7	4.7÷5.1	5.0÷7.0	-1.6 (0.1)	5	NO
3	65.0 (10)	33.5÷45.6	3.9÷5.4	11.0÷12.0	-1.4 (0.1)	4	YES
* Range of average values per a test							

Case 2 and 3 had similar parameters such as a battery of 2 tanks, low RSW flow. At the same time, Case 3 included additional agitation device installed in the tank, which consisted of RSW pump and 8 valves and nozzles. The nozzles operated consequently in 5 min intervals followed by 5 min pause. The fish initial temperature for Case 3 was significantly higher, when compared with Case 2 and 1.

2.4. Chilling index

The chilling experiment has unique parameters, which can vary significantly: the initial (T_0, ºC) and final (T_τ, ºC) temperatures of fish; the geometry of fish; RSW temperature (T_{RSW}, ºC); the chilling time in spiral tank, τ; the flow of RSW in tank chambers etc. These factors make direct comparison of chilling modes (or systems) complicated.

First assumption, for simplification of the evaluation, is using the dimensionless temperature (θ, -) for all the experiments. This will allow to compare temperature variation in the center of the fish as a relative value to compare different initial conditions which related to different temperature profiles of RSW and fish, Eq.(1):

$$\theta = \frac{T_\tau - T_{RSW}}{T_0 - T_{RSW}} \quad \text{Eq. (1)}$$

where T_τ – the fish temperature at the center at time τ, °C; T_0 – the fish temperature before chilling, °C; T_{RSW} – the refrigerated sea water temperature, °C.

All the tests are characterized by different fish size and quantities of fish in the chambers of chilling tank. This influences on the flow distribution inside the chambers, temperature variation and appearances of stagnations areas. In this case, the following reference boundary conditions, which introduces the ideal case for comparison, can be applied.

- Predominance of internal thermal resistance over external thermal resistance, when Biot number if higher than 100 (convective heat transfer coefficient is over 1000 $W\ m^{-2}\ K^{-1}$). This measure is important as soon as RSW flow is not uniform in the tank and the areas of high velocity and flow stagnation are common. High internal thermal resistance limits the influence of convective heat transfer on transient processes (Flesland and Magnussen, 1990);
- Optimized (reference) temperature of RSW, which reflects the weighted arithmetic mean of RSW temperature at outlet of the tank during the chilling process.

The efficiency of chilling can be introduced via following equation of chilling index (*Ch.I, %*), Eq. (2) and/or Eq.(3):

$$Ch.I = \frac{T_0 - T_{fish,measured}}{T_0 - T_{fish,model}} * 100\% \quad \text{Eq. (2)}$$

$$Ch.I = \frac{1 - \theta_{fish,mearured}}{1 - \theta_{fish,model}} * 100\% \quad \text{Eq. (3)}$$

Chilling index is just a comparison between the obtained temperature of fish (in the center) and modelled ideal temperature of fish, which can be obtained for the same process but at reference condition, which is introduced in %. The chilling index below 100 % introduces weak chilling process, when RSW flow is weak, convective heat transfer coefficient is low and RSW temperature at the surface of fish is higher when compared with reference RSW temperature. The value of 100% and higher means that the system operates at high efficiency, which is very close to ideal conditions: high convective heat transfer coefficient and low temperature at the surface of the fish.

The use of half-cooling time principle and comparison with dimensionless temperature, when chilling at reference conditions, is necessary for calculation of real RSW temperatures at the fish surface. This can show the gradient of RSW temperatures for dense package of fish inside chilling chambers, when the flow of RSW is blocked by fish. It can be used as indication of flow stagnation in the chambers during the chilling process, Eq. (4):

$$T_{RSW,real} = \frac{T_0\theta_{fish,model} - T_{fish,measured}}{1-\theta_{fish,model}}$$ Eq. (4)

2.5. Modelling of fish temperature

The geometric models of Atlantic salmons were created in PDE Tool work package in Matlab R2017a. Fish was introduced as the series of 2D-slices with a known area, thickness and weight. The Neumann boundary conditions were applied, since the surface temperature is varying over the time. Initial condition were set at $T_o=T(\tau_o)$. The model utilized thermal properties of fresh Atlantic salmon, which were determined for this study. Transient heat transfer problems were solved by parabolic PDE equations, which use time-dependent algorithm.
A special case for the analytical solution of transient heat transfer problem, which was based on numerical simulation, was used for the chilling of Atlantic salmon, the temperature in center of fish, Eq.5, the average temperature, Eq.6:

$$\theta_{center} = \sum_{n=1}^{n\to\infty} \frac{2J_1(\mu_n)}{\mu_n[J_0^2(\mu_n)+J_1^2(\mu_n)]} exp(-\mu_n^2 Fo)$$ Eq. (5)

$$\bar{\theta} = \sum_{n=1}^{n\to\infty} \frac{4Bi^2}{\mu_n^2(\mu_n^2+Bi^2)} exp(-\mu_n^2 Fo)$$ Eq. (6)

where μ - the root of parametric equation, J – the Bessel function, Fo – the Fourier number, Bi- the Boit number; θ – the dimensionless temperature, -.
The geometry was simplified by the application of equivalent radius, which was found empirically using experiments and numerical simulation (standard error between numerical simulation and analytical solution did not exceed 0.4%), Eq.7:

$$r_{equivalent} = 0{,}929045 * (b/2)^{0{,}722475} * (a/2)^{0{,}226227}$$ Eq. (7)

where b – the thickness of fish at thicker part, m; a - the height of fish at thicker part, m.
This approach can be applied at a factory as soon as calculation algorithm is simple and can be easily utilized without special software like Matlab.

2.6. Determination of thermal properties

Thermal properties of fish tissues were measured by two different techniques: DSC (TA instruments, USA) and Transient Plane Source ISO 22007-2:2015(ISO, 2015). The average thermal properties were used for modelling the fish temperature and chilling index. This approach was tested in previous experiments and gave good agreement between modelling and experimental results (Statistical error 3.5 %). Thermal conductivity was determined at 0.52 W m^{-1} K^{-1}, overall heat capacity - 3600 J kg^{-1} K^{-1}, density - 1050 kg m^{-3}. The main parameter, which was used for calculations of chilling time (Eq.5 and Eq. 6), is thermal diffusivity, and it varied in the range ±7.0 % from average value with respect to fat content in fish.

2.7. Statistical analysis

Thermal property tests were done in 5 parallels. Each experimental test, when determining the thermal properties, was done in 3 parallels. Fish temperature, weight and geometry was determined for 30-150 pieces for test. The quality on the models were checked by the residual analysis: adjusted R^2, F-significance, and p-value. Standard deviation is introduced in brackets.

3. RESULTS AND DISCUSSION

3.1. Temperature in chilling tank at vicinity of fish surface

Fig. 2 shows an example of temperature at the vicinity of fish, which was measured for Case 2, test 3 experimental campaign. The temperature at the surface of fish was significantly different ($p<0.05$) between the chambers. In most cases, the temperature had higher values when compared with RSW outlet temperature. Rotation of the screw influenced on alteration of the temperature due to mechanical agitation. This measure can have a negative effect on fish when transferring fish from “cold” to “warm” area in a chamber as it happened with the fish in chamber 12 on Fig. 2 (black line). The formation of long-term warm areas may occur for low flow of RSW (Case 2 and 3).

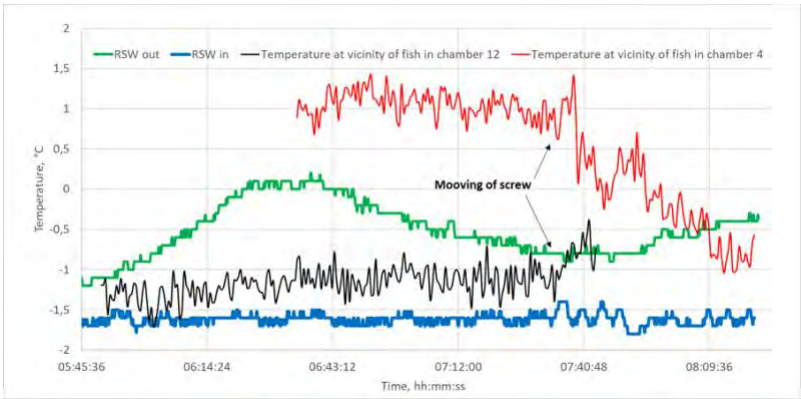

Figure 2: Example of RSW temperature at inlet/outlet of chilling tank and RSW temperature at vicinity of fish, Case 2, test 3, chambers 4 and 12.

3.2. Temperature field in chambers

The high flow of RSW (200 m^3 h^{-1}) and low density of fish in the chambers (38.9 %), Case 1, resulted in a slight and short-term increasing of RSW temperature after loading the chambers, Fig. 3A, yellow and red lines. The observed temperatures varied in the range between RSW inlet and RSW outlet temperature values. The same trend was observed for all other chambers for Case 1.

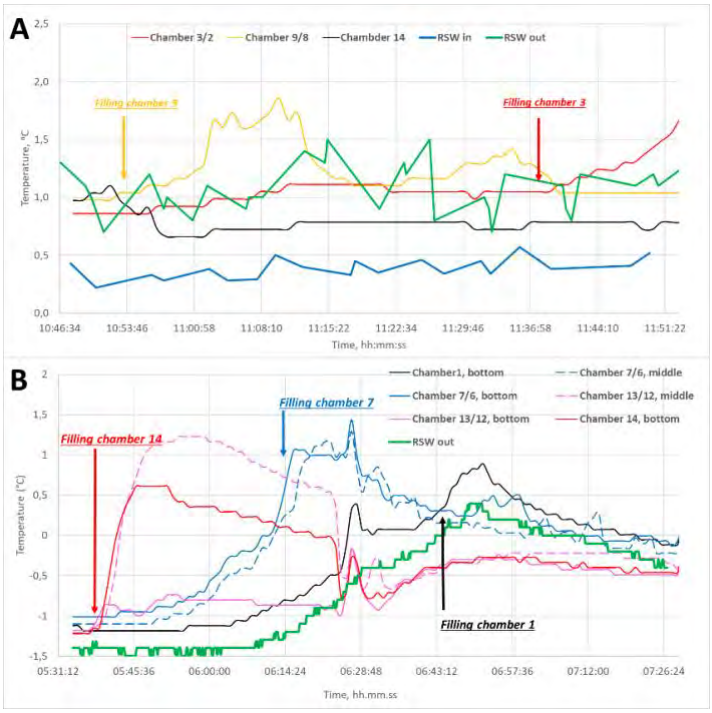

Figure 3: Comparison of RSW temperatures at inlet/outlet of chilling tank and between chambers for different RSW flows; Case 1, test1 (A), 200 m^3 h^{-1}; Case 2, test1 (B),65.0 m^3 h^{-1}.

Case 2 and 3 were characterized by low RSW flow (65.0 m^3 h^{-1}), while density of fish varied significantly for Case 3. The filling of fish in the chambers resulted in a significant, rapid and long-term ($p<0.05$) increasing of the temperature, which was measured by iButton loggers, Fig. 3B (red, pink, blue and black lines). This was observed during all the experiments in cases 2 and 3 for all the chambers. The temperature curves on Fig. 3B (right) shows a few peaks which are attributed with slight movements of screw, when the logger position was changed.

Temperature values, which were measured at the bottom and at the middle points between the chambers, were non-uniform and varied significantly during the tests. Temperature increasing were also detected in the upstream empty chambers during filling: some warm water was pushed out from filled chambers (counter flow).

The system in Case 3 was equipped with an additional fish agitation system. However, it did not influence the trend of temperature alteration between the chambers. RSW outlet temperature (green line on Fig. 3B) increased consequently with some time delay due to large scale of the tank, when it

requires time for warm RSW to reach the outlet temperature sensor. It takes approximately half of an hour for RSW of 65.0 m^{-3} h^{-1} to pass through the chilling tank of 100 m^3.

3.3. Chilling index

The temperature of fish after chilling process varied significantly during one test ($p<0.05$), that was expected due to the difference in geometry, chilling time (the screw rotation was not constant during loading and unloading), and the variations of RSW outlet temperature. Chilling index was calculated based on RSW outlet temperature using data delivered by logging system from the factory. The statistical distribution was characterized by low kurtosis values (thin tails of distribution) and skewness between -0.3 and 0.58, which means that fish was chilled in random order, Fig. 4 A.
The chilling index reached the average value of 108.0% in Case 1, that means that the average temperature at the surface of fish was below the RSW outlet value (1.3 °C), Fig. 4B (blue dots). This occurred due to low density of fish 38.9 % and high RSW flow of 200 m^3 h^{-1}.
The decreasing of RSW flow to 65.0 m^3 h^{-1} and increasing of fish density in chambers up to 43.7 % resulted in the reduction of the chilling index to 76.8 % in Case 2 test 1 (average values), Fig. 4B (orange dots). The chilling index varied between 71.1 and 76.8 % for Case 2.
The highest value of chilling index for Cases 2 and 3 was observed for experiment when filling empty tank the lowest value occurred when the RSW flow decreased to 50 m^3 h^{-1}. Empty tank had higher chilling capacity, when compared with the tank in operation, due to higher amount of “fresh” RSW.

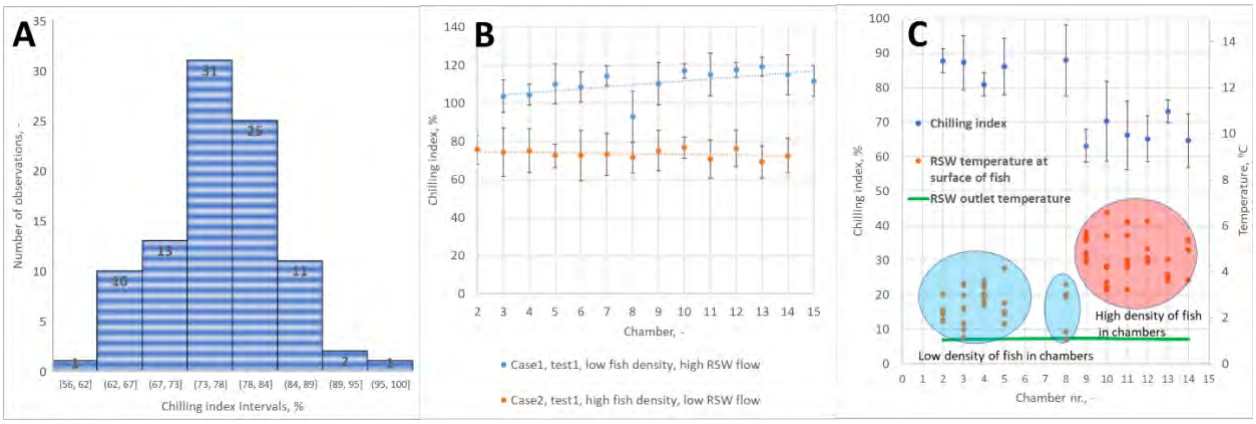

Figure 4: Example of statistical distribution of chilling index values in experiment, Case 2, test1 (A); Influence of RSW flow and fish density on chilling index (B); Chilling index and temperature at vicinity of fish with respect to fish density in chambers (C).

The calculated chilling index for Case 3 was in the range between 66.0 and 88.0 % with respect to the density of fish in the chambers. The experiments with high density of fish (between 41.3 and 42.2 %) showed the chilling index similar to the values obtained in Case 2 (in the range between 75.1 and 78.1 %), while the initial temperature of the fish was significantly higher. Thus, an additional agitation device can compensate the additive heat flow from the warmer fish.
Fig. 4C introduces test 3 (Case3), when the fish size varied during processing. Chambers 14-8 were filled with the fishes of high weight (5.4 kg), while chambers 5-1 were filled with the fishes of 4.0 kg average weight. Chamber 8 had six times less fishes when compared with chambers 14-9. High density of fish created a significant temperature alteration in chambers 14-9, when compared with chambers 5-1 or 8, 4.6 °C vs 2.4 and 2.6 °C respectively (blue and red circles, Fig. 4C). Seems to be, that the increasing of fish density in the chambers created fish agglomeration, which could not be penetrated by RSW flow of 65.0 m^3 h^{-1}. The RSW flow was distributed non-uniformly in the volume of a chamber. The major part of the flow would follow the route of minimum resistance along the wall of the chilling tank. At the same time, RSW at flow of 65 m^3 h^{-1} is sufficient for transferring heat from fish, as soon as, the chilling for Case 3 was of the same efficiency as for Case2.

3.4. Factors influencing chilling index

The influence of a chamber number on the chilling index was unclear during this study. It had some fluctuations within the experiments, but an average trend was the constant chilling index in chambers, when the density of fish in the chambers was the same. A direct comparison of factors influencing on the chilling index between these 3 cases was complicated due to high variation of experimental parameters: the difference between RSW and initial fish, the density of fish in

chambers, the flow of RSW and the presence fish agitation in chambers, a time-line of production process etc. The comparison of chilling index vs volumetric heat load form fish, which is calculated as an average value of energy (kWh) by chamber volume (m^3), is preferable in such a case. This value will reflect the cumulative influence of fish density in a chamber and the difference between RSW and initial temperatures of fish (heat flow form fish).
The increasing of RSW flow from 65.0 to 200.0 m^3 h^{-1} results in significant increasing of the chilling index (orange and black points on Fig. 5); the high RSW flow provides better temperature distribution and higher average convective heat transfer coefficient. The additional agitation device (blue points) can increase the efficiency of chilling (chilling index) by 10.0-12.0 % when compared with non-modified system (orange points), even for a high heat flow from fish.

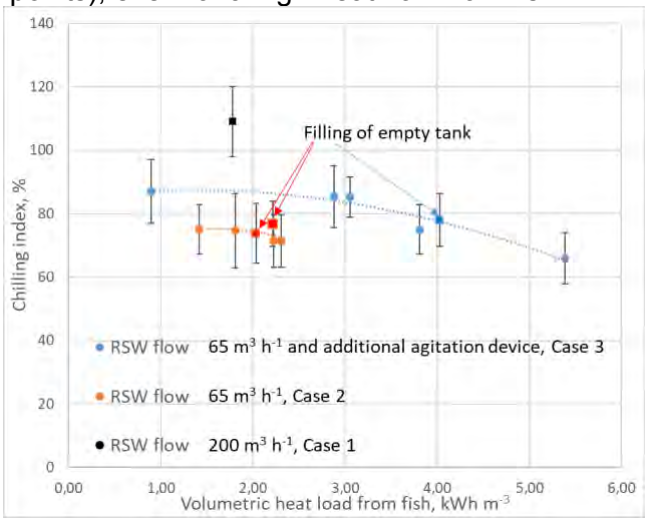

Figure 5: Chilling index vs volumetric heat load from fish with respect to RSW flow

The decreasing of the heat load below 1 kWh m^{-3}, which refers to chamber 8 (Case 3, test3), resulted in a slight increase of the chilling index from 85.3 to 87.9 % which does not have statistical significance ($p>0.05$). The approach, which was used for determination of the chilling index utilizes the high convective heat transfer coefficient of 1000 W m^{-2} K^{-1} as a reference parameter. At the same time, the RSW flow of 65.0 m^3 h^{-1} was not able to provide such a high heat transfer coefficient and uniform flow distribution even with the help of periodic agitation, thus, the process approaches to the maximum limit of chilling efficiency. Possibly, the flow of 65 m^3 h^{-1} cannot provide sufficient dynamic pressure for such a large cross-section (8.0-7.0 m^3).

Table 2. Summary table of experimental results and modelling

Test	Chilling index, %/ Density of fish, %	Time, τ, min	Load, kWh/m^3 of tank	Chilling capacity, ton/hour	RSW temperature, ºC at vicinity of fish (average values)	Fish temperature after chilling	
						$T_τ$, ºC	θ, -
Case 1, RSW flow 200.0 m^3 h^{-1}							
1	108.0(11)/38.9	95	1.78	13.0	0.9(0.5)	2.4(0.6)	0.30 (0.07)
2	91.0(12)/33.3	100	1.35	11.0	3.6(0.5)	4.3(0.6)	0.28 (0.07)
Case2, RSW flow 65.0 m^3 h^{-1}; 50.0 m^3 h^{-1} for test 5							
1	76.8(7.1)/43.7	105	2.21	19	1.3(0.6)	3.1(0.5)	0.49(0.07)
2	74.7(11.7)/42.0	85	1.81	21	1.4(0.7)	3.4(0.5)	0.55(0.08)
3	73.8(7.8)/41.6	130	2.03	15	1.3(0.6)	2.4(0.5)	0.42(0.08)
4	75.1(7.8)/41.8	120	1.42	16	1.3(0.6)	2.7(0.5)	0.45(0.05)
5	71.1(8.3)/40.1	125	2.31	22	1.4(0.4)	2.5(0.5)	0.42(0.08)
Case 3, RSW flow 65.0 m^3 h^{-1}							
1	78.1(8.3)/42.2	100	4.03	21	3.53(1.0)	6.9(1.0)	0.50(0.09)
2	75.1(7.8)/41.3	95	4.56	20	4.3(0.9)	7.1(1.0)	0.50(0.09)
3a	66.7(8.1)/45.6	95	5.39	21	4.6(0.9)	7.6(0.7)	0.61(0.06)
3b	87.9(10.2)/7.6	95	0.90	-	2.6(0.7)	6.1(1.0)	0.47(0.11)
3c	85.3(6.4)/33.5	95	3.05	16	2.4(1.0)	5.3(0.8)	0.40(0.08)

4	85.34(9.8)/34.3	75	2.88	18	2.5(1.1)	6.6(1.1)	0.51(0.10)

Thus, maximum fish density in chambers should not exceed 3.0 kWh m^{-3} or 33.5 % for chilling tank of 100 m^3. At the same time, the chilling capacity of the system will fall down to 16.0 tons h^{-1}. The summary of results and modelling is introduced in Table 2. It should be noted, that the chilling time does not influence the chilling index as soon as chilling index is calculated with respect to the real time holding of fish in the chilling tank. Time of chilling influences the final temperature of fish: the increasing of the chilling time will decrease the final temperature of fish. The chilling index introduces the efficiency of chilling related to the existing processing parameters in dimensionless form, while final temperature of fish is time-dependent value and it can be calculated via Eq.(5) and/or Eq.(6). However, increasing of the chilling time will decreases the chilling capacity of a tank significantly (Case 2, test 3 and 4).

Chilling time is, usually, limited by a factory schedule. Case 3 showed that the allotted time (between 75 and 100 min) was not sufficient for reaching the desired maximum temperature of 2.0 °C in fish center. Setting up the ideal conditions of chilling (RSW temperature of -1.6 °C and Biot number of 100) can decrease the final temperature by 2.0 K, that will be insufficient for any scenario expect of twofold increasing of the chilling time.

4. CONCLUSIONS

A significant temperature increase of temperature in the chambers was detected during chilling of Atlantic salmon, when RSW flow was at 65.0 m^3 h^{-1}, while 200 m^3 h^{-1} showed the best chilling. Additional periodic agitation of fish in the chambers could compensate the increased heat flow from fish, however, the chilling index did not exceed the value of 87.9%. The optimal volumetric heat load was below 3.0 kWh m^{-3}.

Effective chilling for 100 m^3 spiral tanks was possible when decreasing density of fish in the chambers to 33% and below and increasing of RSW flow up to 200 m^3 h^{-1}. However, such limitations, which are applied on a factory to the chilling time make the desired temperature of 2.0 °C in fish center unachievable.

ACKNOWLEDGEMENTS

The authors gratefully acknowledge the Research Council of Norway for the financial support for carrying out the present research [NFR project No. 269175].

REFERENCES

Bantle, M., Stavset, O., Nordtvedt, T.S., Gullsvåg, P.E., Eikevik, T.M., Tolstorebrov, I., 2015. Chilling of salmon in refrigerated sea water, Proceedings of the 24th International Congress of Refrigeration. International Institute of Refrigeration.

Einen, O., Guerin, T., Fjæra, S.O., Skjervold, P.O., 2002. Freezing of pre-rigor fillets of Atlantic salmon. Aquaculture 212, 129-140.

Erikson, U., Misimi, E., Gallart-Jornet, L., 2011. Superchilling of rested Atlantic salmon: Different chilling strategies and effects on fish and fillet quality. Food Chem. 127, 1427-1437.

FAO/WHO, 2003. Code of practice for fish and fishery products, in: FAO/WHO (Ed.), CAC-RCP 52-2003, p. 125.

Flesland, O.S.R.E., Trondheim (Norway)), Magnussen, O.M., 1990. Chilling of farmed fish.

ISO, 2015. Plastics, Determination of thermal conductivity and thermal diffusivity Transient plane heat source (hot disc) method. ISO, p. 20.

Magnussen, O.M., Hardarson, V., 1987. The influence of storage, freezing and thawing on fillet yield of fish, XVIIth International Congress of Refrigeration, Wien, pp. 382-388.

StatisticsNorway, 2018. Aquaculture. Statistics Norway.

Venugopal, V., 2006. Bulk Handling and Chilling, in: Venugopal, V. (Ed.), Seafood processing adding value through quick freezing, retortable packaging, cook-chilling

Ringgold Inc, Portland, pp. 61-94.

Widell, K.N., Nordtvedt, T.S., Tolstorebrov, I., Fossen, I., 2018. Experimental investigation of chilling tank for Atlantic salmon, 5th IIR Conference on Sustainability and the Cold Chain : proceedings. International Institute of Refrigeration, pp. 331-339.

Manuscript ID: 847
DOI: 10.18462/iir.icr.2019.0847

Crushed ice including nanoencapsulated clove essential oil improves animal welfare in farmed European sea bass during stunning and slaughtering

Antonio LOPEZ-GOMEZ[(a)], Amanda E. LOPEZ-CANOVAS[(a)], María ROS-CHUMILLAS[(a)], Isabel CABAS[(b)], Alfonsa GARCÍA-AYALA[(b)]

[(a)] Food Engineering and Agricultural Equipment Department, Universidad Politécnica de Cartagena, Paseo Alfonso XIII 48, E30203 Cartagena, Spain, email: antonio.lopez@upct.es

[(b)] Department of Cell Biology and Histology, Faculty of Biology, Universidad de Murcia, Campus de Espinardo, E30100 Murcia, Spain, email: amandaesperanza.lopez@um.es

ABSTRACT

The traditional procedure for stunning and slaughtering of farmed sea bass involves the use of crushed ice mixed with seawater. This system causes enough stress on the fish, as the agony to death by hypothermia takes longer than 10 minutes. Pre-slaughtering stress involving increased physical activity before death leads to biochemical processes impacting negatively on the quality and accelerate the loss of fish freshness. Therefore, they are investigating new methods to achieve the aforementioned decrease in stress and increase animal welfare. In this work, a new technology for stunning and slaughtering of farmed sea bass using crushed ice including nanoencapsulated clove essential oil is studied. When this technology is applied on farmed sea bass times of stunning lower than 60 seconds are achieved, resulting in lower levels of stress (measured by means of glucose and other blood parameters) and better quality and shelf life of the fresh fish.
Keywords: fish, ice, nanotechnology, quality.

1. INTRODUCTION

In aquaculture, fish reared under farm conditions are exposed to various high intensity/short duration stressors (Wendelaar-Bonga, 1999), such as stunning and slaughtering methods. Those methods could have a strong negative effect on fish welfare, affecting the stress response (Wendelaar-

Bonga, 1999; Olsen et al., 2006; Ashley, 2007). The majority of farmed fish from the Mediterranean Sea is asphyxiated by immersing in a slurry mixture of ice and seawater or packaged live in ice flakes or crushed ice. This treatment can create unnecessary stress to the fish (Lerfall et al., 2015), which involves metabolism-related changes, such as increases in glucose level, hydromineral balance, cardiovascular, respiratory and immune functions (Pankhurst and Dedual 1994; Barton, 2002). Previous studies showed, from a comparison of commercial and experimental killing methods in the European sea bass (*Dicentrarchus labrax*), asphyxia was confirmed to be the most stressful killing method, showing either the most prolonged period prior to death or a remarkable physical activity and affecting the final quality (EFSA, 2012). This way, those wide ranges of stressors by aquaculture procedures are also affecting fillet quality (Sigholt et al., 1997; Martinez et al., 2011; Lerfall et al., 2015). Jeyasekaran et al. (2006) identified that *Pseudomonas* spp plays a considerable role as an indicator of fish quality as a spoilage organism. Further, the total viable *Enterobacteriaceae* counts strongly suggest the urgent need to improve the fish quality control systems (Yagoub, 2009). Along these lines, *Pseudomonas* spp and *Enterobacteriaceae* spp could suggest additional knowledge to enhance the proper control of the fresh fish storage life, and fish product quality in our study.

Pre-slaughter methods should offer a rapid loss in sensibility and consciousness in terms of fish welfare (Zhang et al., 2017), as there is a broad scientific consensus that fish are sentient and have the capacity to suffer (Brown, 2015). Stress response could be alleviated with an anesthetic (Le et al., 2019). There are several anesthetics for fish treatment (Hoseini et al., 2018a), but the most common is eugenol/clove oil (Taheri Mirghaed et al., 2018a). Clove essential oil (CEO) is an effective, local, and natural anesthetic, which may be appropriate for use in commercial aquaculture situations (Javahery et al., 2012). One of the possible disadvantages of the CEO is that it has an intense aromatic odor and flavor, which can drastically change the sensory properties of the food fish (Hill et al., 2013). The β-cyclodextrin (βCD) inclusion complex with CEO does not only mask the flavor of CEO to be used as a stunning agent but also protect against oxidation, and allowing CEO increases water solubility, bioavailability, and effectivity as an anesthetic agent (López-Cánovas et al., 2019).

We decided to study with specimens of European sea bass (*Dicentrarchus labrax*) because is a species of high importance in aquaculture (FEAP, 2016) and one of the most important fish species in the Mediterranean aquaculture (Sahu and Lambris, 2001). European sea bass is also known to be susceptible to husbandry stressors (Fanouraki et al., 2008). The aim of this work was to achieve the minimum concentration of CEO-βCD inclusion complex, included in the ice crystals of the crushed ice used with seawater at slaughtering, to minimize the stress at slaughtering time, and to see the effects of this stunning method on quality and shelf life in farmed European sea bass.

2. MATERIAL AND METHODS

Fresh sea bass (*Dicentrarchus labrax*) was obtained from the aquaculture farm of Servicios Atuneros del Mediterráneo Company (San Pedro del Pinatar, Murcia, Spain). Fish were slaughtered in the following conditions: (i) Control group: Crushed ice with seawater at - 0.2 ºC (ratio ice:seawater of 1:1, w/w); and (ii) Treated groups: crushed ice with seawater at - 0.2 ºC (ratio ice:seawater of 1:1, w/w), and with CEO (15 and 30 mg/kg ice) encapsulated in βCD (CEO-βCD). Blood samples were taken using lithium heparin anticoagulant, 2 hours after stunning and slaughtering, and the serum was obtained by centrifugation. In all the serum samples, the levels of glucose (ng/ml) and lactate (mmol/L) were analyzed by an i-STAT Portable Clinical Analyzer (i-STAT, Abbot, Unit City, CA), using i-STAT CG4+ disposable cartridge. Then, fish was transported to the laboratory and cold room (at 2 ºC) within 1 h in foamed polystyrene boxes with top icing. The average weight of the whole fresh fish was 600±50 g. For microbiological analyses, 25 g of sample was diluted with 225 mL of sterile buffered peptone water (Scharlau Chemie) in a sterile stomacher bag (Model 400 Bags 6141, London, UK) and homogenized for 1 min using a masticator (Colwort Stomacher 400 Lab, Seward Medical, London, UK). Serial dilutions of each suspension were made in sterile peptone water (Scharlau Chemie), and analyzed for microbial counts. Appropriate aliquots (0.1 or 1 mL) were spread on agar plates. Plate Count Agar (Scharlau Chemie) was used for enumeration of mesophilic and psychrotrophic bacteria, and plates were incubated for 48 h at 30 ºC and 7 days at 4 ºC respectively. *Pseudomonas* sp. were determined on Cetrimide Agar (Scharlau Chemie) after incubation at 37 ºC for 48 h. Lactic acid bacteria were counted on Man Rogosa and Sharpe Agar (Scharlau Chemie) incubated at 31 ºC for 48 h. Enterobacteriaceaes pp. were counted on violet red bile glucose agar (Scharlau Chemie) incubated at 37 ºC for 24 h. All plates were performed in duplicate and the results were expressed as logarithms of the number of colony-forming units per gram (Log CFU/g).
Data were analyzed by one-way ANOVA and a post hoc Bonferroni multiple comparison test to determine differences between groups. All statistical analyses were carried out using the IBM SPSS Statistic 23 program.

3. RESULTS

Glucose and lactate levels in the plasma of European Seabass showed some differences between the different treatments applied. Glucose levels decreased when CEO-βCD (15 and 30 mg/kg) was included, embedded in the ice crystals, in the crushed ice (Fig. 1A) used at slaughtering, however, lactate up regulated at higher concentration (Fig. 1B).
By day 15 of storage at 4 ºC, *Enterobacteria* count in sea bass stunned and slaughtered with CEO-βCD at 15 and 30 mg/kg ice was lower than the control condition (the sea bass slaughtered without anesthesia). The use of this stunning technology allows extending the shelf life of sea bass. At the end of

refrigerated storage time (15 days) with ice toping, sea bass stunned and slaughtered with CEO-βCD did not exceed the value of 1 Log CFU/g while sea bass slaughtered without stunning with CEO-βCDs reached a count of 2.32 Log CFU/g (Fig. 2A). Thus, Enterobacteria count was reduced by 1.3 Log CFU/g after 15 storage days. *Pseudomonas* has been reported to be the specific spoilage bacteria in fresh Mediterranean fish stored in ice. By day 15 of storage at 4 ºC, *Pseudomonas* count of sea bass slaughtered in control ice, without anesthesia was higher (2.78log UFC/g) than sea bass stunned and slaughtered with crushed ice including CEO-βCD at 15 and 30 mg/kg ice (2.08 and 2.12 respectively) (Fig. 2B).

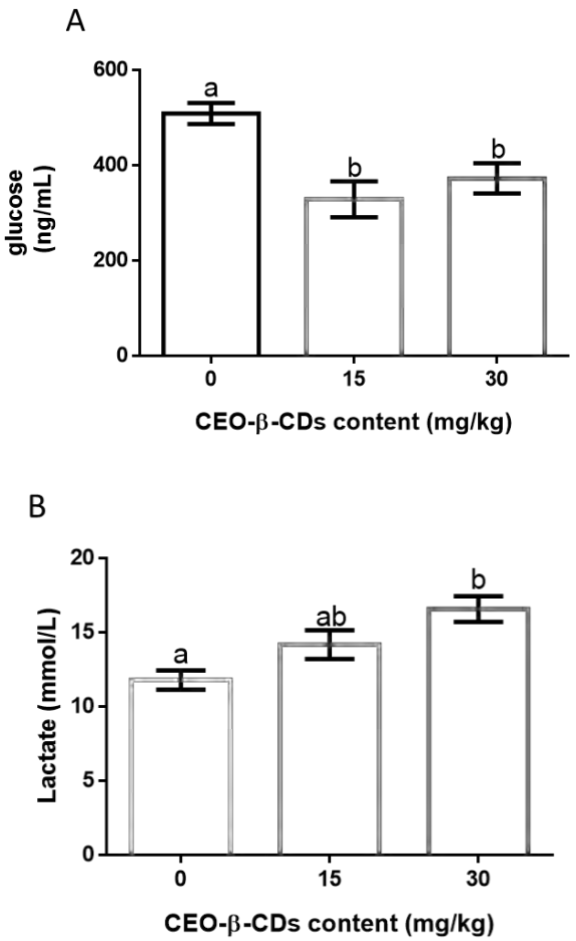

Figure 1. Plasma glucose (A) and lactate (B) levels of slaughtered European Sea bass in open sea farm conditions, including CEO-βCD at 0, 15 and 30 mg/kg of crushed ice used with seawater at slaughtering. Each value represents the mean ± S.E.M. of n=4–12 fish per group in each sampling condition. The letters indicate statistically significant differences between groups compared to control group (letter a) and according to one-way ANOVA and Bonferroni test (P≤.05).

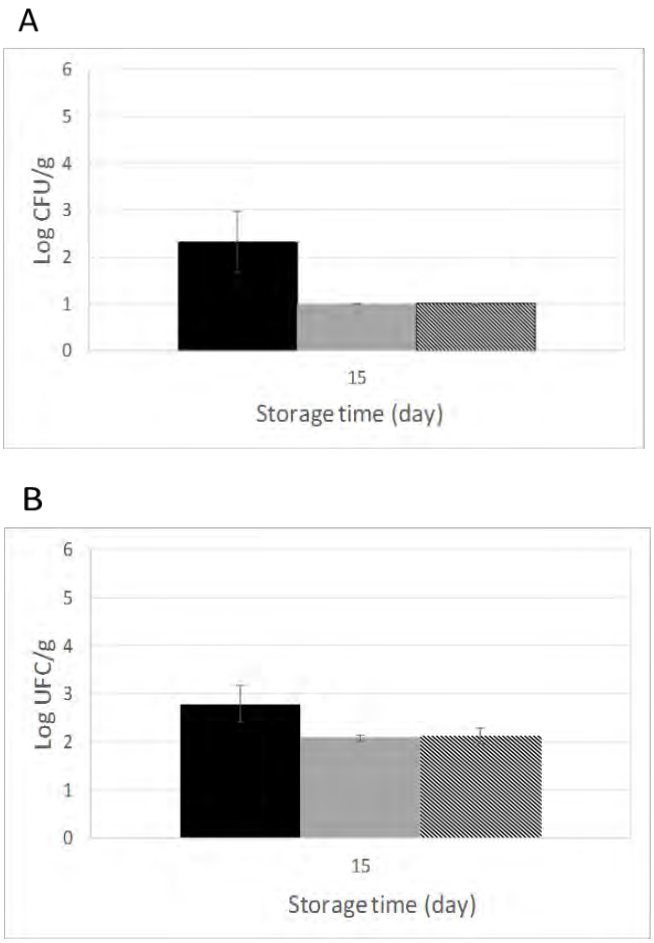

Figure 2. Counts (Log CFU/g) of *Enterobacteria* (A) and *Pseudomonas* (B) of sea bass at the end of storage time at 4 ºC (day 15). Conditions of slaughtering: control slaughtering without anesthesia (black bar); slaughtering using stunning/anesthesia with crushed ice including CEO-β-CDs at 15 mg/kg ice (grey bar) and at 30 mg/kg ice (striped bar). The error bars represent the standard error of three replicates (n=3).

4. CONCLUSIONS

A wide range of methods is used for fish stunning and killing. Few of which would be considered acceptable for other vertebrates, due to the agony times that could very long. Different parameters have been analyzed such as *rigor mortis*, glucose, and cortisol levels to measure the stress suffered by the fish at slaughtering. CEO-βCD included as an anesthetic agent in the crushed ice used at fish slaughtering improve the stress conditions of European Seabass at slaughtering by considering the decrease in the glucose levels in

comparison to those levels of fish stunned without CEO-βCD. This decrease is higher when the concentration of the CEO used is low as 15 mg/kg.
Fresh European sea bass stunned and slaughtered with CEO-βCD showed lower microbiological values due to the demonstrated antimicrobial properties of the clove essential oils. *Enterobacteria* and *Pseudomonas* counts were reduced by 1-1.3 Log CFU/g after 15 days of ice storage. β-CD has been utilized in the food industry for molecular encapsulation of essential oils. When this technology is applied on farmed sea bass times of stunning/slaughtering lower than 60 seconds are achieved, resulting in lower levels of stress (measured by means of glucose and other blood parameters), and better quality and shelf life of the fresh fish. Therefore, this new stunning technology using CEO-βCD included in the crushed ice for the slaughtering of farmed fish can be used to significantly decrease the fish stress and extend the shelf life of fresh farmed fish.

ACKNOWLEDGEMENTS

This work was funded by CUBI-PLAYA SL Company (San Pedro del Pinatar, Murcia, Spain), and the European H2020-SME-Instrument phase 2 Program (ICE2LAST Project, Grant agreement ID: 804493, funded under H2020-EU.3.2.5, H2020-EU.3.2.3, and H2020-EU.2.3.1 programmes).

4. REFERENCES

Ashley, P.J., 2007. Fish welfare: current issues in aquaculture. Applied Animal Behaviour Science 104(3-4), 199–235.

FEAP., 2016. European Aquaculture Production Report 2007–2015. Federation of European Aquaculture Producers.

Fanouraki, E., Papandroulakis, N., Ellis, T., Mylonas, C.C., Scott, A.P. and Pavlidis, M., 2008. Water cortisol is a reliable indicator of stress in European sea bass, *Dicentrarchus labrax*. Behaviour, 1267-1281.

Hill, E.L., Gomes, C and Taylor, M.T., 2013. Characterization of beta-cyclodextrin inclusion complexes containing essential oils (trans-cinnamaldehyde, eugenol, cinnamon bark, and clove bud extracts) for antimicrobial delivery applications. LWT-Food Sci. Technol. 51(1), 86-93.

Hoseini, S.M., Taheri Mirghaed, A and Yousefi, M., 2018. Application of herbal anesthetics in aquaculture. Rev Aquaculture doi:10.1111/raq.12245.

Javahery, S., Nekoubin, H and Moradlu, A.H., 2012. Effect ofanesthesia with clove oil in fish (review). Fish Physiology Biochem. 38(6), 1545-1552.

Jeyasekaran, G., Ganesan, P., Anandaraj, R., Jeya-Shakila, R., Sukumar, D., 2006. Quantitative and qualitative studies on the bacteriological quality of Indian white shrimp (*Penaeus indicus*) stored in dry ice. J. Food Microbiol. 23(6), 526-533.

Lerfall, J., Roth, B., FlønesSkare, E., Henriksen, A., Betten, T., Dziatkowiak-Stefaniak, M.A., and Rotabakk, B.T., 2015. Pre-mortem stress and the subsequent effect on flesh quality of prerigor filleted Atlantic salmon (*Salmo salar* L.) during ice storage. Food Chem. 175,157–165.

Le, Q., Hu, J., Cao, X., Kuang, S., Zhang, M., Yu, N., Zheng, H., Wang, Y., Liu, H., Yan, X., 2019. Transcriptomic and cortisol analysis reveals differences in stress alleviation by different methods of anesthesia in Crucian carp (*Carassius auratus*). Fish & Shellfish Immunology 84, 1170-1179.

Martinez, I., Wang, P.A., Slizyté, R., Jorge, A., Dahle, S.W., Cañas, B., Yamashita, M., Olsen, R.L., and Erikson, U., 2011. Protein expression and enzymatic activities in normal and soft textured Atlantic salmon (*Salmo salar*) muscle. Food Chem. 126(1), 140–148.

Olsen, S.H., Sorensen, N.K., Stormo, S.K., and Elvevoll, E.O., 2006. Effect of slaughter methods on blood spotting and residual blood in fillets of Atlantic salmon *(Salmo salar*). Aquaculture 258(1-4), 462–469.

Pankhurst, N.W. and van der Kraak, G., 1997. Effects of stress on reproduction and growth of fish. Pages 73-93 in G. K. Iwama, A. D. Pickering, J. I? Sumpter, and C. B. Schreck, editors. Fish stress and health in aquaculture. Society for Experimental Biology Seminar Series 62. Cambridge University Press, Cambridge, England.

Yagoub, S.O., 2009. Isolation of Enterobacteriaceae and Pseudomonas spp. from raw fish sold in fish market in Khartoum state. J. Bacteriology Res. 1(7), 85-88.

Sahu, A., and Lambris, J.D., 2001. Structure and biology of complement protein C3, a connecting link between innate and acquired immunity. Immunological Rev. 180(1), 35-48.

Sigholt, T., Erikson, U., Rustad, T., Johansen, S., Nordtvedt, T. S., and Seland, A., 1997. Handling stress and storage temperature affect meat quality of farmed-raised Atlantic salmon (*Salmo salar*). J. Food Sci. 62(4), 898–905.

Taheri Mirghaed, A., Ghelichpour, M., Zargari, A., Yousefi, M., 2018. Anesthetic efficacy and biochemical effects of 1,8-cineole in

rainbow trout (*Oncorhynchus mykiss*, Walbaum, 1792) Aquaculture Res. 49 (6), 2156-2165.

Wendelaar-Bonga, S.E., 1999. The stress response in fish Physiol. Rev., 77 (1997), pp. 591-625.

Manuscript ID: 866
DOI: 10.18462/iir.icr.2019.0866

Experimental study of the consequences of controlled atmosphere conservation environment on cherry characteristics

Luís P. ANDRADE[a,b,c], José NUNES[a], Maria P. SIMÕES[a,b], Diogo MORAIS[d,e], Cristina CANNAVARRO[a,b], Christophe ESPÍRITO SANTO[c], Pedro D. GASPAR[d,e], Pedro D. SILVA[d,e], Mafalda RESENDE[c], Catarina CASEIRO[c], Helena BEATO[c], Yuran BELANE[a,c], Dora FERREIRA[a]

[a] Agriculture School, Polytechnic Institute of Castelo Branco, Quinta da Senhora de Mercoles, 6001-909 Castelo Branco, Portugal
[b] CERNAS – Research Center for Natural Resources, Environment and Society, Polytechnic Institute of Castelo Branco, Av. Pedro Álvares Cabral, 12, 6000-084 Castelo Branco, Portugal
[c] CATAA - Agrofood Technology Center, Centro de Apoio Tecnológico Agro-Alimentar, Castelo Branco, Portugal
[d] University of Beira Interior, Rua Marquês d'Ávila e Bolama, 6201-001, Covilhã, Portugal
[e] C-MAST - Centre for Mechanical and Aerospace Science and Technologies, Covilhã, Portugal

ABSTRACT

Cherry is a highly perishable fruit widely appreciated that is only commercialized during a short period. The post-harvest control and monitoring of this fruit is central and essential for optimal consumption in its highest state of quality. The conservation process aimed to inhibit the microbial propagation is usually accomplished by low temperatures and/or variable atmosphere composition. This paper describes experimental tests conducted in different refrigeration chambers located in industrial and laboratorial facilities. The latter one includes modified atmosphere and controlled atmosphere chambers. The tests were performed with four different concentration of O_2 and CO_2 in the controlled atmosphere chamber. Fruit samples extracted from each chamber were analyzed at specific residence times and several organoleptic characteristics were analyzed. The results show that the modified and controlled atmosphere maintain the fruit quality in terms of size, color, appearance and firmness, thus increasing their shelf life and food safety.
Keywords: Cherry Experimental test, Cold Storage, Modified atmosphere. Shelf life

1. INTRODUCTION

Food waste is a persistent problem for modern worldwide societies, causing both ethical and economic impacts. According to the Food and Agriculture Organization of the United Nations (FAO), one-third of the total food produced for human consumption is lost or wasted, approximately to 1.3 billion of tons and annual costs of over 750 billion dollars (Gustavsson *et al.*, 2011). Moreover, 821 million people suffer from malnutrition around the world (FAO et al. 2018), therefore food waste should be eradicated. Lastly, natural resources (water and soil) and energy are also wasted, and biodiversity conservation and air quality are affected (Gustavsson *et al.*, 2011). Thus, conservation of high-quality food products by increasing its shelf-life is a major priority for producers, distributors and consumers. Vegetables and fruits play an important role in human nutrition, mainly as a source of vitamins (C, A and B6), minerals and dietary fiber. In the post-harvest process, losses of nutritional quality may be significant, particularly in vitamin C, and these losses are associated with physical damage, prolonged storage, high storage temperatures, low humidity and cold damage (Kader 2013).

Cova da Beira (between *Fundão, Covilhã* and *Belmonte*) is one of the most important fruit and vegetable producer regions in the Centre of Portugal. Unique soil and climate conditions allow fruits

with high sugar content and a balanced acidity. Cherry trees are an important revenue for the region, with more that 30% of the total land (Instituto Nacional de Estatísticas 2018). More than 8500 tons are produced in the Centre of Portugal and more than 90% are produced in the Cova da Beira.
Cherries are a highly perishable food product, due to their high water and nutrient content, that allows microorganisms to easily grow. Hence, special conservation conditions are essential to maintain cherry freshness and quality (Shellie et al., 2001; Palma *et al.*, 2012; Wang and Vestrheim, 2002; Mattheis *et al.*, 1997; Wang and Vestrheim, 2003; Tian *et al.*, 2004; Gross *et al.*, 2016). Cherries lose their quality by water loss, surface punctures, stem darkening and rotting (Dugan and Roberts, 1997; Tian *et al.*, 2004). Cherry is a non-climacteric fruit, and its respiration rate decreases over time after harvest. Given its characteristics, it needs a pre-cooling at the time after the harvest. The pre-cooling serves to maintain the intrinsic and extrinsic characteristics that make it appealing to the consumer, such as color and taste. By reducing the surface temperature and increasing the water content in the air (increase of the RH), cherries do not to lose volume nor the characteristic red color (Gross *et al.*, 2016). If on the one hand cooling favors the extension of cherry life time, on the other hand, when applied in the wrong way, it favors the development of lesions. A correct parameterization of the cameras is one of the ways to guard against such events. Several studies were carried out to determine the cherry conservation parameters that considered the extension of the shelf life and the development of chilling damages, as shown in Table 1.

Table 1. Temperature, relative humidity and controlled atmosphere for cherry conservation conditions

Temperature [°C]	Relative humidity [%]	Conservation time	Controlled Atmosphere [%]		Reference
			CO_2	O_2	
0 to 4	90 – 95	14 days	-	-	Baptista (2007)
-0.5 to 0.5	90 – 95	-	-	-	Mitcham *et al.* (2009)
-1 to -0.5	90 – 95	-	20 to 25	0.5 to 2	Silva (2002)
-1 to 0	>95%	2 to 4 weeks	-	-	Gross *et al.* (2016)
-	-	-	5 to 20	1 to 5	Gross *et al.* (2016)
≈1	≈95%	27 days	10	8	Palma *et al.* (2012)
0 to 2	>95%	up to 3 weeks	>15	<10	Wang and Vestrheim (2002)
≈1	≈95%	60 days	10	5	Tian *et al.* (2004)
0 to 5	-	28 to 35 days	10 to 15	3 to 10	Ben-Yehoshua *et al.* (2005)
≈1	-	6 weeks	15 or 20	5	Mattheis *et al.* (1997)

Recently, controlled atmospheres in conjunction with low temperatures have been explored to increase shelf-life, avoiding waste and loss of economic value. This consists in using a chamber under a certain temperature and atmosphere to conserve cherries. Controlled atmospheres are constantly monitoring, renewing and adjusting air gases composition: nitrogen, oxygen and carbon dioxide. This offers a solution to increase cherry shelf-life without using non-natural chemicals, between harvest and market distribution.
Controlled atmosphere act on fruit respiration by lowering the rate, just by reducing oxygen concentration. Additionally, carbon dioxide can be increased to reduce surface microbes and rotting (Chavez-Franco and Kader, 1993; Dugan and Roberts, 1997; Tian et al., 2004; Tian et al., 2001; Vries-Paterson et al., 1991). Problems that occur by the usage of this technique normally occur at consumption stage. This may include, irregular maturation, potentiate undesirable odours and flavours, physiological alterations or increase susceptibility to rotting (after controlled atmosphere conservation). The potential benefit of this technology depends on the fruit, cultivar, physiological age, temperature and duration (Beaudry, 2000).
Oxygen level is crucial to control under controlled atmosphere conservation. Very low oxygen

concentrations can lead to anaerobic fermentation, altering organoleptic characteristics of the fruit or vegetable (Beaudry, 2000). High concentrations can also be harmful to fruit and vegetable quality, by accelerating rot or by oxidizing the product (Wszelaki et al., 1999).
Carbon dioxide also influences quality during controlled atmosphere conservation. Increasing the concentration helps reduce fruit and vegetable decay due to its fungistatic action. However, not all fruits tolerate high carbon dioxide concentrations. This can trigger or aggravate physiological problems, irregular maturation, off flavours and odours, or even increase fruit decay susceptibility after conservation (Kader, 1995; Wszelaki et al., 1999). In this case, cherries are able to tolerate carbon dioxide by up to 40% concentration during conservation (Tian et al., 2004; Vries-Paterson et al., 1991). Nevertheless, oxygen concentrations cannot be lower than 1%, otherwise anaerobic fermentation occurs (Beaudry, 2000).
There are many studies on cherries conserved by controlled atmospheres (Table 1), and the principal focus is to determine oxygen and carbon dioxide gas proportions for best conservation results. The recommended atmosphere should have 10 to 15% carbon dioxide and 3 to 10% oxygen (Ben-Yehoshua et al., 2005; Tian et al., 2004; Kupferman and Sanderson, 2001) under a temperature of 0 to 5ºC (Ben-Yehoshua et al., 2005).
Here, we show a conservation study under controlled atmosphere of Cherries cv Satins using industrial size refrigeration chambers. The main objective is to increase cherries shelf-life by using controlled atmosphere conservation. Results from the study will aid on the application of this technology to cherries produced at Cova da Beira region.

2. MATERIALS AND METHODS

Cherries cultivar Satin used for controlled atmosphere studies were selected and hydrocooled at the producer CERFUNDÃO (Portugal). The start of the study was on the 26th June 2018 and ended on the 14th August 2018. Samples were taken after 3, 7, 14, 21 and 35 after the start of the study for normal atmosphere conditions; and 7, 21, 35, 42 and 49 days for controlled atmospheres.
Satin cv. cherries were stored and conserved in six different setups: at the farmer's organization refrigeration chamber under normal atmosphere; and at the research centre CATAA under normal atmosphere and 4 different controlled atmospheres: A (3% O_2 | 10% CO_2); B (3% O_2 | 15% CO_2); C (10% O_2 | 10% CO_2), and D (10% O_2 | 15% CO_2).
Farmer's refrigeration chamber was monitored for temperature and relative humidity using 2 data loggers "EL-USB-2-LCD+" from LASCAR ELETRONIC. One of the data loggers was positioned in the packages at the top of the pallet, while the other was placed in the lower packages, the measurement interval was done every 60 seconds.
CATAA cold chambers (≈ 26 m^3) with a refrigeration unit Zanotti model C16 are equipped with a controlled atmosphere unit GAC 5000 (Fruitcontrol, Italy) that is able to monitor and modify atmospheres of individual pallets. Fruits trays (50x30 cm) are inserted on a euro-size pallet (size: 121x81.5 cm), a LDPE plastic is used to cover the fruits, and the plastic is sealed by a metal platform between the pallet and fruit trays. The atmosphere control unit is connected to the plastic chamber by 2 gas taps. Gases used to control atmospheres was carbon dioxide (Linde, Portugal) and nitrogen (Sysadvance, Portugal), oxygen increments were obtained using an air compressor (Hyundai HYAC24-2).
Cherries were conserved under temperature and relative humidity of 1.5 ºC and 92 - 96%, respectively. These values were obtained using a datalogger installed at the refrigeration chamber centre.
Samples of 50 cherries were inserted in the middle of a 5 kg cherry tray (± 4500 cherries), from these 50 cherries, 20 were individually numbered.
Cherries were individually weighted using a digital scale (Sartorius model TE1502S, Germany), before and after the conservation study.
Colour evaluation in both sides of the fruit was measured using a tristimulus colorimeter (Konica Minolta model CR-400 Chroma Meter, USA and illuminant D65, using CIE system L* (lightness) a* (green to red) b* (blue to yellow) and Colour Data CM-S100w software) having a 8 millimetre viewing area.
Texture was determined on the fruit cheek area as a skin mechanical resistance, with the help of a texture analyser (Stable Micro systems model TA-XTplus, United Kingdom), with a P75 compression

probe (75mm ø). The results are obtained by the software Exponent and expressed in Newton (N).
According to NP EN 12143 (1999), soluble solids content (SSC) expressed as ºBrix using Atago model PR-32 alpha refractometer (Bellevue, WA, USA).
Titratable acidity, expressed as mEq/100 g, was obtained by potentiometric titration to pH 8.1 by a 0.1M NaOH solution using an automatic titrator (Crison, model Titromatic 2S+3B and TiCom software, Spain).
Statistical analisys was performed using SPSS 24 (IBM, 2016). Data assumptions of variance normality and homogeneity were verified using, respectively, the Kolmogorov–Smirnov test and the Levene Statistic (Maroco, 2011). Despite data normal distribution was not observed, sample was large enough to allow the use of a parametric test (Maroco, 2011).
One-Way ANOVA analysis was used to find significant statistical differences between time, for all modalities. After analysis, Scheffe test was applied for multiple comparisons.

3. RESULTS

3.1. Temperature and Humidity Conditions

The temperature and humidity values monitored at the producer facility are shown in Fig. 1. Values presented are based on 4 measurements performed every 7 days. By the analysis of Fig. 1(A) it is possible to verify that the air temperature ranges between -0.5 ºC and +0.5 ºC that most of the time. Isolated temperature peaks are observed.

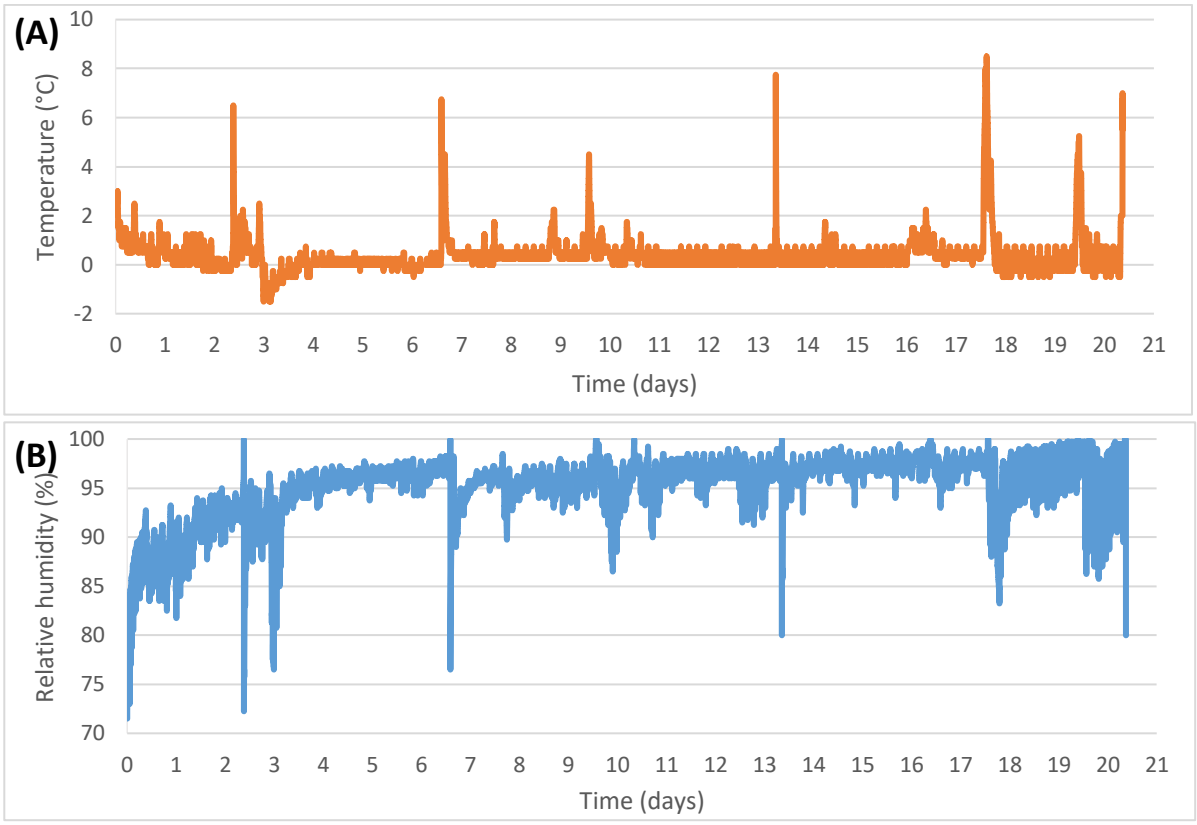

Figure 1: Evaluation of conservation parameters in the producer conservation chamber (A) Temperature, (B) Relative humidity

The peaks values arise from several factors, such as the increase of the thermal load of the chamber, opening of doors for logistics, thawing of the refrigeration system. These considerations are verified by the analysis of the relative humidity plot, Figure 1 (B), where the inverse relative humidity peaks correspond to the temperature peaks. This behaviour comes from the pallet movement inside the chamber during the test period, as a consequence of the producer's logistics. There were times

where different products, at different temperatures, were inside the chamber. This fact also led to the need to remove the pallet from the refrigerated chamber to collect data from the data loggers, due to the limited space available for moving inside the chamber. One of the most recurring phenomena that affects the conservation environment is the opening of doors, with approximately 17 openings of short duration.

3.2. Fruit Quality Assessment

Initial cherry weight was, in average, 8.58 g ± 0.99 g, with a SSC of 17.78 % ± 1.73 % and 12.54 mEq./100 g ±1.24 mEq./100 g acidity.
Under normal atmosphere at the producer chamber, weight loss was decrease during conservation time, reaching -3.5 % after 21 days. Acidity also decreases but only statistically difference at 21 days conservation. No difference was observed for texture measurements (Table 2).

Table 2. Cherry quality evolution under normal atmosphere at farmer's organization chamber

Time	**Weight loss** [%]	**SSC** [°Brix]	**Texture** [N]	**Acidity** [mEq./100 g]
0 (harvest)		17.78 ±1.73	2.02 ±0.45	12.54 ±1.24
3	-1.37 a	16.77 b	2.12	13.98 a
7	-2.00 a	17.34 ab	2.07	13.63 a
14	-2.73 b	17.60 a	2.29	13.10 a
21	-3.51 c	18.03 a	2.16	11.25 b

Different letters mean significant differences between values in the same columns (p-value<0,05).

At the research facility (CATAA) the normal atmosphere modality which temperature and relative humidity conditions are described above (section 2.1), show a higher weight decrease overtime compared with the producer's chambers (Table 3), probably related to temperature difference between the two conditions. After 21 days weight loss was -6.6 %, and -9.3% after 35 days conservation time. Similarly, to producers' conditions acidity decreases, however, three statistical different groups were observed. Texture is maintained until 21 days conservation and lowers at 35 days conservation. If considering only the 21 days period, texture maintains similarly between the two normal atmosphere conditions (farmers organization and CATAA) (Table 3).

Table 3. Cherry quality evolution under normal atmosphere at CATAA chamber conditions

Time	**Weight loss** [%]	**SSC** [°Brix]	**Texture** [N]	**Acidity** [mEq./100 g]
0 (harvest)		17.78 ±1.73	2.02 ±0.45	12.54 ±1.24
3	-2.21 a	18.08 ab	1.65 a	14.03 a
7	-2.78 a	17.70 b	1.56 a	12.65 ab
14	-4.67 b	18.53 ab	1.59 a	12.71 ab
21	-6.65 c	18.59 ab	1.49 a	11.37 bc
35	-9.39 d	19.11 a	1.21 b	10.83 c

Different letters mean significant differences between values in the same columns (p-value<0.05).

Under controlled atmosphere conditions that reached 49 days (14 days longer than normal atmosphere), we observe a decrease of weight and acidity over conservation time for all modalities (Table 4). Weight loss reached a maximum of -3.73 % (Table 4), which is correspondent to one third of the observed average at 35 days under normal atmosphere (table 3). On the other hand this value is similar compared to the farmer's organization condition at end of conservation period (21 days, Table 2). Texture is maintained for modalities B and C, decreases for A and D. SSC varies only for modality A, and not consistently.

Considering acidity, all modalities decrease however, modalities B and C show less decrease not reaching under 10 mEq/100g. For modality A, acidity was 9.02 mEq/100 g and D was 8.69 mEq/100 g both at 49 days.

Table 4. Cherry quality evolution under controlled atmosphere at CATAA refrigeration chambers.

Modality	Time	Weight loss [%]	SSC [°Brix]	Texture [N]	Acidity [mEq./100 g]
A	**7**	-1.75 a	17.04 ab	1.95 ab	11.93 a
	21	-2.54 b	17.57 a	2.20 a	10.79 b
3%O_2-10%CO_2	**35**	-3.35 c	16.76 ab	2.11 ab	10.36 b
	42	--2.51 b	16.19 b	1.57 c	9.70 c
	49	-3.02 c	17.02 ab	1.88 b	9.02 d
B	**7**	-1.60 a	18.15	1.90	12.86 a
	21	-2.14 b	17.62	1.86	10.31 b
3%O_2-15%CO_2	**35**	-2.31 b	18.11	1.81	10.73 b
	42	-3.00 c	17.98	1.83	10.02 b
	49	-3.73 d	17.84	1.86	10.16 b
C	**7**	-2.29 a	18.02	2.05	13.09 a
	21	-2.66 a	17.75	2.01	11.04 b
10%O_2-10%CO_2	**35**	-2.62 a	18.07	2.09	11.06 b
	42	-3.18 b	17.76	1.97	10.73 b
	49	-2.64 a	17.57	2.01	10.19 b
D	**7**	-2.43 a	17.75	2.10 a	12.28 a
	21	-3.01 ab	17.79	1.70 bc	11.12 ab
10%O_2-15%CO_2	**35**	-3.20 b	17.55	1.74 bc	10.40 bc
	42	-3.27 b	17.49	1.57 c	9.29 dc
	49	-3.17 b	17.49	1.88 ab	8.69 d

Different letters mean significant differences between values in the same columns (p-value<0.05).

Table 5 show Pearson's correlation coefficient (r), between variables (weight loss, SSC, texture and acidity) and time. Modalities B and C are the conditions were cherry quality is maintained for a longer period of time. No significant correlation between time and both, SSC and texture were observed. Although significant correlation, modality C shows the lowest Pearson's correlation coefficient compared with other modalities. Table 5 results underline results presented in table 4.
Taking into account all results presented here, modality C conditions are indicative to be the most appropriate to extend cherry cv. Satin shelf-life.

Table 5: Pearson's coefficient correlation between variables (weight loss, SSC, texture and acidity) and time under different conservation conditions

Modality	Weight loss [%]	SSC [°Brix]	Texture [N]	Acidity [mEq./100 g]
Farmer's	-0.49 **	0.24 **	ns	-0.86**
CATAA	-0.80 **	0.20 **	-0.38**	-0.86**
A (3%O_2-10%CO_2)	-0.31 **	-0.12 *	-0.19**	-0.97**
B (3%O_2-15%CO_2)	-0.68 **	ns	ns	-0.67**
C (10%O_2-10%CO_2)	-0.21 **	ns	ns	-0.31**
D (10%O_2-15%CO_2)	-0.21 **	ns	-0.24**	-0.94**

Pearson's Correlation Coefficient (r) significant correlated (** p-value<0.01; * p-value<0.05; ns: p-value>=0.05)

4. CONCLUSIONS

The present work shows that Satin cherry quality was maintained for 21 days in farmer's organization conditions, where temperature and relative humidity were mainly between 0ºC - 1ºC and 95%, respectively. Hence, these conditions are according to usual conservation recommendation.
Controlled atmospheres results indicate that Satin cherries could be conserved until 49 days. Also

suggests that modality C (10% O_2 and 10% CO_2) maintains initial cherry quality for longer time, thus, extending cherry cv. Satin shelf-life.

ACKNOWLEDGEMENTS

This study is within the activities of Project "PrunusPÓS - Optimization of processes for the storage, cold conservation, active and/or intelligent packaging and food quality traceability in post-harvested fruit products", project n.º PDR2020-101-031695, Partnership n.º 87, initiative n.º 175, promoted by PDR 2020 and co-funded by FEADER within Portugal 2020.
We thank CERFUNDAO farmers' organization for cherries supply and participation.

REFERENCES

Baptista, Paulo. 2007. *Sistemas de Segurança Alimentar Na Cadeia de Transporte e Distribuição de Produtos Alimentares*. Guimarães: Forvisão.

Beaudry, Randolph M. 2000. "Responses of Horticultural Commodities to Low Oxygen : Modified Atmosphere Packaging." *HortTechnology* 10 (September): 491–500. https://doi.org/http://horttech.ashspublications.org/content/10/3/491.abstract.

Ben-Yehoshua, Shimshon, Randolph M. Beaudry, Svetlana Fishman, Sastry Jayanty, and Nazir Mir. 2005. "Modified Atmosphere Packaging and Controlled Atmosphere Storage." In *Environmentally Friendly Technologies for Agricultural Produce Quality*, 61–112. CRC Press. https://doi.org/10.1201/9780203500361.ch4.

Chavez-Franco, Sergio H., and Adel A. Kader. 1993. "Effects of CO2 on Ethylene Biosynthesis in 'Bartlett' Pears." *Postharvest Biology and Technology* 3 (3): 183–90. https://doi.org/10.1016/0925-5214(93)90054-7.

Dugan, F. M., and R. G. Roberts. 1997. "Pre-Harvest Fungal Colonization Affects Storage Life of Bing Cherry Fruit." *Journal of Phytopathology* 145 (5–6): 225–30. https://doi.org/10.1111/j.1439-0434.1997.tb00390.x.

FAO, IFAD, UNICEF, WFP, and WHO. 2018. "The State of Food Security And Nutrition in the World 2018. Building Climate Resilience for Food Security and Nutrition." Rome: FAO. http://www.fao.org/state-of-food-security-nutrition/en/.

Gross, Kenneth C., Chien Yi Wang, and Mikal Saltveit, eds. 2016. *The Commercial Storage of Fruits, Vegetables, and Florist and Nursery Stocks*. *Agricultural Research Service USDA*. Boston, MA: Springer US. https://doi.org/10.1007/978-1-4613-1127-0.

Gustavsson, Jenny, Christel Cederberg, Ulf Sonesson, Robert van Otterdijk, and Alexandre Meybeck. 2011. "Global Food Losses and Food Waste – Extent, Causes and Prevention. Rome." In . Düsseldorf: FAO. https://doi.org/10.1098/rstb.2010.0126.

IBM. 2016. "IBM SPSS Statistics for Windows." Armonk, NY: IBM Corp.

Instituto Nacional de Estatísticas. 2018. *Estatísticas Agrícolas - 2017*. Lisboa: INE. https://doi.org/0079-4139.

Kader, Adel A. 1995. "REGULATION OF FRUIT PHYSIOLOGY BY CONTROLLED/MODIFIED ATMOSPHERES." *Acta Horticulturae*, no. 398 (March): 59–70. https://doi.org/10.17660/ActaHortic.1995.398.6.

———. 2013. "Postharvest Technology of Horticultural Crops - An Overview from Farm to Fork." *Ethiop .J. Appl. Sci. Technol.*, no. 1: 1–8.

Kupferman, Eugene, and Peter Sanderson. 2001. "Temperature Management and Modified Atmosphere Packaging to Preserve Sweet Cherry Quality." *POSTHARVEST INFORMATION NETWORK*, 1–9.

Maroco, J. 2011. *Statistical Analysis with SPSS Statistics (in Portuguese).* 5th ed. Pero Pinheiro: Report Number.

Mattheis, J. P., D. a. Buchanan, and J. K. Fellman. 1997. "Volatile Constituents of Bing Sweet Cherry Fruit Following Controlled Atmosphere Storage." *Journal of Agricultural and Food Chemistry* 45 (1): 212–16. https://doi.org/10.1021/jf960234v.

Mitcham, Elizabeth J, Carlos H Crisosto, and Adel A Kader. 2009. "Sweet Cherry." UC Davis.

Palma, V., A.C. Agulheiro-Santos, G. Machado, A.E. Rato, M.J. Cabrita, M. Lozano, and D. Gónzález. 2012. "Effect of Different Storage Conditions on Nutritional and Quality Parameters

of ‘ Sweetheart ’ Cherry.” In *Proc. XXVIIIth IHC – IS on Postharvest Technology in the Global Market*, edited by M.I. Cantwell and D.P.F. Almeida, 1027–32. Acta Hort. 934, ISHS 2012.

Shellie, K. C., L. G. Neven, and S. R. Drake. 2001. “Assessing ‘Bing’ Sweet Cherry Tolerance to a Heated Controlled Atmosphere for Insect Pest Control.” *HortTechnology* 11 (2): 308–11.

Tian, Shi Ping, Ai Li Jiang, Yong Xu, and You Sheng Wang. 2004. “Responses of Physiology and Quality of Sweet Cherry Fruit to Different Atmospheres in Storage.” *Food Chemistry* 87 (1): 43–49. https://doi.org/10.1016/j.foodchem.2003.10.014.

Tian, Shiping, Qing Fan, Yong Xu, Yi Wang, and Aili Jiang. 2001. “Evaluation of the Use of High CO2 Concentrations and Cold Storage to Control Monilinia Fructicola on Sweet Cherries.” *Postharvest Biology and Technology* 22: 53–60. https://doi.org/10.1016/S0925-5214(00)00177-0.

Vries-Paterson, R. M. De;, A. L.; Jones, and A.C. Cameron. 1991. “Fungistatic Effects of Carbon Dioxide in a Package Environment on the Decay of Michigan Sweet Cherries by Monilinia Fructicola.” *Plant Disease* 75 (9): 943. https://doi.org/10.1094/PD-75-0943.

Wang, L., and S. Vestrheim. 2002. “Controlled Atmosphere Storage of Sweet Cherries (Prunus Avium L.).” *Acta Agriculturae Scandinavica, Section B — Soil & Plant Science* 52 (4): 136–42. https://doi.org/10.1080/090647103100004825.

Wang, L, and S Vestrheim. 2003. “Controlled Atmosphere Storage of Sweet Cherries (Prunus Avium L.).” *Acta Agriculturae Scandinavica, Section B - Soil & Plant Science* 52 (4): 136–42. https://doi.org/10.1080/090647103100004825.

Wszelaki, Annette, Shimshon Ben Yehoshua, and Beth Mitcham. 1999. “Do High Oxygen Atmospheres Control Postharvest Decay of Fruits and Vegetables ?” *Perishables Handling Quarterly*, no. 99: 22–25.

Manuscript ID: 950
DOI: 10.18462/iir.icr.2019.0950

Industrial storage of root vegetables: Energy and quality aspects of existing cold-storages.

Erlend INDERGAARD[(a)], Mette THOMSEN[(b)], Pia HELTOFT[(b)], Belachew ASALF[(c)], Berit NORDSKOG[(c)], Kristina N. WIDELL[(a)], Tom S. NORDTVEDT[(a)], Torgeir TAJET[(d)] Hanne LARSEN[(e)].

[(a)] SINTEF Ocean AS
Trondheim, 7465, Norway, erlend.indergard@sintef.no
[(b)] NIBIO, Division of food production and Society
Kapp, 2849, Norway, mette.thomsen@nibio.no
[(c)] NIBIO, Division of Biotechnology and Plant Health
Ås, 1433, Norway, belachew.asalf.tadesse@nibio.no
[(d)] NLR, Norwegian Agriculture Advisory Service, Stokke, 3160, Norway, torgeir.tajet@nlr.no
[(e)] Nofima, Norwegian Institute of Food, Fisheries and Aquaculture Research, Ås, 1433, Norway, hanne.larsen@nofima.no

ABSTRACT

After harvesting, the Norwegian root vegetables are normally stored at refrigerated temperatures for 5 to 7 months. During this period, up to 30% of the products are lost. The goal is to reduce the diseases, the product loss and energy consumption, in addition to increase shelf-life and storage period. Twenty-eight commercial root vegetable cold-stores were instrumented to measure air temperature, relative humidity and product temperature. The study was done over two years. The cold-stores were located in four different regions of Norway. The three focus-products carrot, swede and celeriac were harvested from one field in each region in open wire nets. The nets were placed in the various cold-stores in the respective regions and put in the wooden bins together with the producer's own products. The quality and yield of the products were determined and correlated to the storage condition. The various storage condition negatively affects the respiration and quality of the root vegetables, storage-life, and influence on the cooling capacity of the refrigeration systems.

Keywords: industrial cold-store, refrigeration, yield, storage-life, carrot, swede, celeriac, post-harvest

1. INTRODUCTION

Long-time storage of vegetables in Norway is necessary but challenging, with an estimated loss of 20-30% mostly due to weight loss and diseases. In 2017, Norwegians consumed 50,200 tons (10.7 kg per capita) of carrot, swede and celeriac (SSB, 2017), and 10-15,000 tons are expected lost before consumption. It is important to reduce the loss of root vegetables during storage, considering global climatic aspects, and economical aspects for the producers who has invested time and cost to grow, harvest and store products.

Many traditional refrigerants have high Global Warming Potential (GWP), and in line with the Kyoto- and Montreal-agreements, these refrigerants are beeing and will be fased out from the market the next years (Regjeringen, 2014). Already, it is not allowed to refill media like R401a and R22 into refrigeration systems due to Ozone-damage effects. To address the coming challenge to phase out synthetical refrigerants with high GWP, the existing refrigeration systems were mapped in this study. Challenges with refrigerants with high GWP are notified from all around the world, regarding the restrictions according to the EU Reg. No. 517/2014 (i.e. Cardoso et al., 2017, Zhao et al., 2018).

Several hundred vegetable stores in Norway alone, needs to be optimized to maintain the quality of the products. Newer, more stable, energy efficient and environmentally friendly cold-stores are preferred, but it is realistic to assume that it will take decades to renew all the existing stores. A study of 38 food cold stores in Europe showed a potential to reduce the energy consumption by 8-72% for all the storages (Evans et al., 2014). Research on new environmentally friendly refrigeration systems show that it is possible with energy-saving rates of 55% to 65% by using CO_2 heat pumps (Liu et al., 2016). Systems with hydrocarbons like propane and butane is also suited (Kauffeld and Gund, 2019), with high coefficient of performance (COP) for refrigeration purposes. A more general consideration to reduce energy for systems with a short period with high cooling demand, is use of thermal energy storage (TES). Any improvements in thermal energy management practices can significantly benefit the producers (Alva et al., 2018). An intention to reduce loss of products and go green, with focus on a sustainable food chain are taken all around the world (Wu and Huang, 2018, Halloran, 2014).

If stored in conditions with misfit relative humidity and higher temperatures, it is known that many vegetables will lose weight and get more diseases. This in interaction with series of biological factors (Baugerød et al., 1986). The temperature should be 0-1°C and relative humidity 95-99%. Studies have shown that storage conditions may play a significant role in creating conditions suitable for latent infections to develop and spread within the bins and packing houses (Thomsen et al., 2018). To reduce the loss of vegetables in Norway is a small but important contribution to the predicted statement that we must increase global food production by 70% before 2050 (Mc Carthy et al., 2018).

In the project Optirot (2016-2019), the goal is to reduce the product loss of root vegetables during storage by 10%, in addition to increase shelf-life and storage period by two months by linking biology and technology closely together. The work includes i) studies of various fertilisers (balanced micro- and macronutrients) during growing to make the harvested products 'prepared' for storage, ii) studies of optimal wound healing periods before stable storage, iii) optimization of existing vegetable cold-houses, presented in this paper, iv) designs for future cold-stores, and v) optimization of plastic layers inside the wooden bins.

2. MEASUREMENTS AND METHODS

2.1 Survey areas and location of cold-stores

Norway is a long country far up north, where the golf stream gives mild and moist winters by the cost, but cold and dry climate inland. A study to see how the climate variations affect the storage air in cold-stores was performed in four different regions in Norway: i) Mid – Middle part of Norway, north of Trondheim, ii) Rog – Southwest, south of Stavanger, iii) Osl – Southeast, both sides of the Oslo-fjord, and iv) Inn – East, Inland around Lillehammer. Weather data like air temperature and relative humidity for the regions were collected for the periods of two season (Sept to April) from MET (The Norwegian Meteorological Institute).

2.2 Storage of root vegetables, product temperature and weight lose measurement

Carrot, swede and celeriac were harvested from one field in each region in 10-20 kg (100 carrot or 25 swede/celeriac roots) open wire nets. The nets were placed in the twenty-eight various cold-stores in the respective regions and dug down in four wooden bins at each store together with the producer's own products. The weight of the root vegetables was measured before and after the two storage seasons. The temperature and relative humidity were measured in the circulation air and inside the product in the wooden bins placed randomly together with the other bins. Signatrol SL51T ibuttons and EasyLog USB-2-LCD+ dataloggers were used.

2.3 Calculation of cooling demand

A new, more tailored excel-based calculation program has been developed (NLR, SINTEF), and linked to MET data for outdoor air- and ground (product) temperatures for the various regions. The respiration energy as function of temperature were included (Hoftun, 1980). The daily rate of stocking was defined by total storage capacity and expected harvesting period. Removing heat from the products were linked to the empirical data on measured cooling rate of the root vegetables. Other factors included were heat through buildings, condensation of moist on evaporators due to respiration, and air change (to prevent CO_2 accumulation).

3. RESULTS AND DISCUSSION

3.1 Calculation of cooling demand

The respiration energy as function of temperature were included (Fig. 1a). There was not found any verified data for respiration loss for celeriac (Fig 1b), but the temperature dependent loss is assumed to be close to the ones for carrot and swede (Fig.1a). Removing the respiration heat is the most significant factor regarding cooling demand during stocking, closely followed by the cooling demand to lower the product temperature. The calculated worst-case scenarios resulted in a designed cooling capacity 20% lower for some regions in Norway, compared with the general worst-case scenarios used by refrigeration suppliers. The average cooling demand mid-term was around 10% compared to the stocking period.

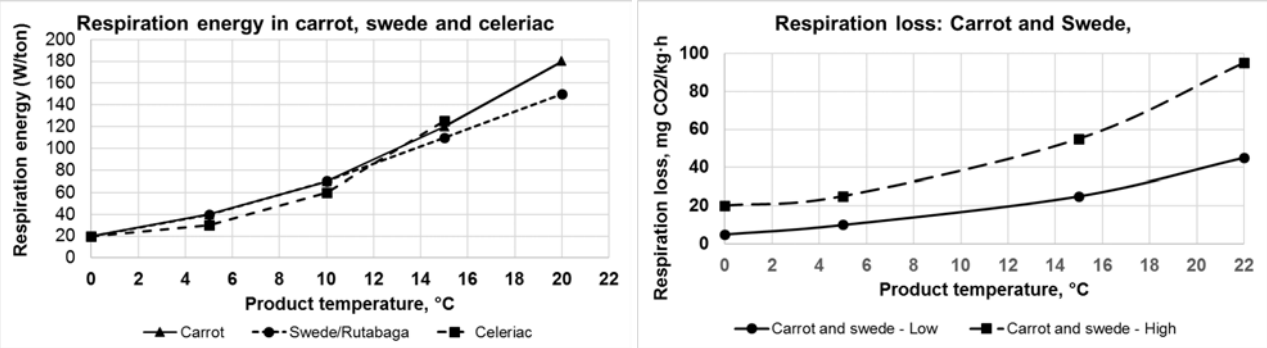

Figure 1: Respiration energy (1a, left) and respiration loss (1b, right) for carrot, swede, celeriac

3.2 Principles for air distribution in cold-stores

Between the twenty-eight cold-stores, there were seven different strategies to distribute the air through and between the bins. The four most used principles are shown in Fig. 2.

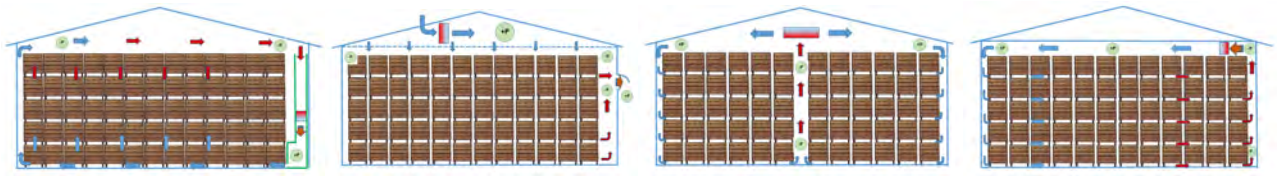

Figure 2: Four most common principles for air distribution in the cold-stores. From left: a) Findus, b) Grae, c) Trad. air circulation – mid-evaporator and d) Trad. air circulation – rear-evaporator.

The seven different strategies to circulate the air: a) Chimney heat rise (Findus), b) Ceiling suction (Grae), c) Traditional air circulation, evaporator placed in the ceiling in the mid-part of storage and distribute air to both sides, d) Traditional air circulation, evaporator placed in the ceiling in the rear of storage, e) Traditional air circulation, evaporator near floor in the rare of storage and air distributed by ventilation pipes up and forward, f) Concrete basement of farmhouse, no mechanical air distribution, g) Suction wall system, fans sucks air through channels in back wall.

Ten cold-stores have installed humidifiers. The two main types installed were high pressure nozzles (Noz. - atomise small water droplets), and mechanically sprayed evaporator (Evap.- water vaporized and brought to the circulated air).

3.3 Mapping of existing cold-stores

An overview of the twenty-eight cold-stores are presented in Table 1. From Table 1, the necessary cooling demand can be found empirically. Enough cooling capacity was judged by the ability to maintain the circulated air temperature close to set-point during the storage period (Fig. 5-6). It seems that cold-stores with a cooling capacity less than 0.12 kW/tonnes did not have enough capacity(-). Between 0.13 and 0.20, it seemed ok(+), and over 0.20 it was more than needed(++). One exeption was a larger, new system (Inn3/Inn7) with 0.09 which had ok(+) cooling capacity.

Table 1: Operating and mechanical parameters for the twenty-eight cold-stores.

Producer code	Product	Plastic liner in bin	Storage capacity, tonnes	Air circ. System *1)	Humidifier	Fresh air	capacity, kW *2)	Ratio (EER)	tonne product	10°C	Installed kW/tonne	capacity *3)	Installed kW per 100 tonnes	Refrigeration media	DX evap., DX
Mid1	Carrot	yes	250	a)	Noz.	Fan	114*	3.00	0.46	38	0.15	++	15.2	R410a	No
Mid2	Carrot	yes	1200	c)	No	Fan	170	4.05	0.14	42	0.04	+	3.5	410a	no
Mid3	Swede	no	350	e)	Noz.	Slot	62	3.44	0.18	18	0.05	+	5.1	R1234z	yes
Mid4	Swede	no	520	a)	No	-	123*	3.00	0.24	41	0.08	++	7.9	410a	no
Mid5	Carrot	yes	1100	c)	No	-	133*	3.00	0.12	44.4	0.04	-	4.0	R22	no
Mid5b	Carrot	yes	345	c)	yes	-	165	3.37	0.48	49	0.14	++	14.2	R134a	yes
Rog1	Carrot	yes	400	d)	No	-	86	3.31	0.22	26	0.07	?	6.5	R22	yes
Rog2	Carrot	yes	350	e)	Noz.	Slot	62	3.44	0.18	18	0.05	+	5.1	R1234z	yes
Rog3	Carrot	yes	1800	d)	no	Fan	166	3.29	0.09	50.4	0.03	-	2.8	CO2	yes
Rog4	Swede	yes	330	d)	no	-	32	2.42	0.10	13.2	0.04	?	4.0	507a	yes
Rog5	Swede	no	360	d)	no	-	90	2.81	0.25	32	0.09	++	8.9	401a	yes
Inn1	Carrot	no	500	a)	no	Slot	57	2.71	0.11	21	0.04	-	4.2	R407c	no
Inn2	Carrot	yes	800	d)	Noz.	-	243*	3.00	0.30	81	0.10	++	10.1	R134a	yes
Inn3	Carrot	yes	3050	c)	Noz.	Slot	265	4.05	0.09	65.5	0.02	+	2.1	R1270	no
Inn4	Swede	no	80	f)	no	Gate	Air	-	-	-	0.00		0.0		
Inn5	Swede	no	180	a)	no	Fan	Air	- .	- .	-	0.00		0.0		
Inn6	Swede	no	300	b)	Evap.	Fan	20	3.64	0.07	5.5	0.02	-	1.8	R404a	yes
Inn7*	Swede	no	3050	c)	Noz.	Slot	265	4.05	0.09	65.5	0.02	+	2.1	R1270	no
Inn8	Swede	no	200	d)	Noz.	-	30*	3.00	0.15	12.6	0.06	+		R22	yes
Osl1	Carrot	yes	2700	c)	no	Fan	474*	3.00	0.18	158	0.06	+	5.9	R507a	no
Osl2	Carrot	yes	110	c)	no	-	66*	3.00	0.60	22	0.20	?	20.0	R22	yes
Osl3	Carrot	yes	350	d)	no	-	50*	3.00	0.14	16.5	0.05	+	4.7	R22	yes
Osl4	Swede	no	700	c)	no	-	200	2.82	0.29	71	0.10	++	10.1	R134a	no
Osl5	Swede	no	400	a)	no	Slot	126*	3.00	0.32	42	0.11	++	10.5	R407a	no
Osl6	Swede	no	220	d)	no	-	50	3.33	0.23	15	0.07	?	6.8	CO_2	yes
Osl7	Celeriac	no	300	g)	Evap.	Slot	60*	3.00	0.20	20	0.07	+	6.7	134a	yes
Osl8	Celeriac	no	360	a)	no	-	114*	3.00	0.32	38	0.11	?	10.6	R410a	no
Osl9	Celeriac	no	225	d)	no	Slot	77*	3.00	0.34	25.6	0.11	++	11.4	R404a	yes
Osl10	Celeriac	no	50	b)	Evap.	Fan	8,4*	3.00	0.17	2.8	0.06	? .	5.6	134a	yes

*1) Air circulation system refers to the listed air distribution principles in 3.2. *2) The cooling capacities marked with * are unknown, but calculated by an energy efficiency ratio (EFR) of 3.0. *3) Sufficient cooling capacity was judged by the ability to maintain the circulation air temperature close to set-point during the stocking period, (-) Not enough, (+) ok, and (++) more than enough. Inn7* - same refrigeration system as Inn3, but different room/cooling cell.

As mentioned, many synthetic refrigerants have high global warming potential, and the GWP values in Table 2 refered to kg CO_2-eqv. per kg gas (over 100 years). Only 5 of the 26 cold-stores with refrigeration systems contain refrigerants suited for the future. It could be risky to postpone a change to climate friendly refrigeration units, and hope there is no leakage. During season 1, eleven cold-stores and in season 2, seven cold-stores had a breake-down influencing the product

temperature. It will be necesseary for the industry to plan a significant reinvestment in new environmental friendly systems in the years to come.

Table 2. Refrigeraion media in the mapped cold-stores

Producer	Refrig. media	GWP	Year of phase-out (EU)
Rog4, Osl1	R507a	3985	2020
Inn6, Osl9	R404a	3922	2020
Mid1, Mid2, Mid4, Osl8	R410a	2088	2022
Inn1, Osl5	R407a	2107	2022
Mid5b, Inn2, Osl4, Osl7, Osl10	R134a	1430	2025
Rog5	R401a	1182	Not allowed, O_3
Mid5, Rog1, Inn8, Osl2, Osl3	R22	1810	Not allowed, O_3
Mid3, Rog2	R1234ze	7	
Inn3 = Inn7	R1270	2	
Rog3, Osl6	CO_2/R744	1	

3.4 Outdoor climate correlated with cold-store air

The storage air parameters (temperature and relative humidity) in cold-stores with no humidifiers are presented in Fig. 3 and correlated with average outdoor air for the regions Mid, Osl, Inn and Rog. The weather varies among the regions, and the ambient air influences the indoor storage air parameters negatively for the stores without humidifiers. The indoor air tended to have parameters closer to the ambient air. It is most essential to manipulate the storage air by adding moist mechanically in regions with higher winter temperatures (coastal regions in Norway). This was opposite of what might be expected regarding the facts that the relative humidity in the ambient air increases when entering the cold-store (Fig. 4b). The higher ambient temperature increased the time for the refrigeration system to run, and more water from the air condensate on the evaporators.

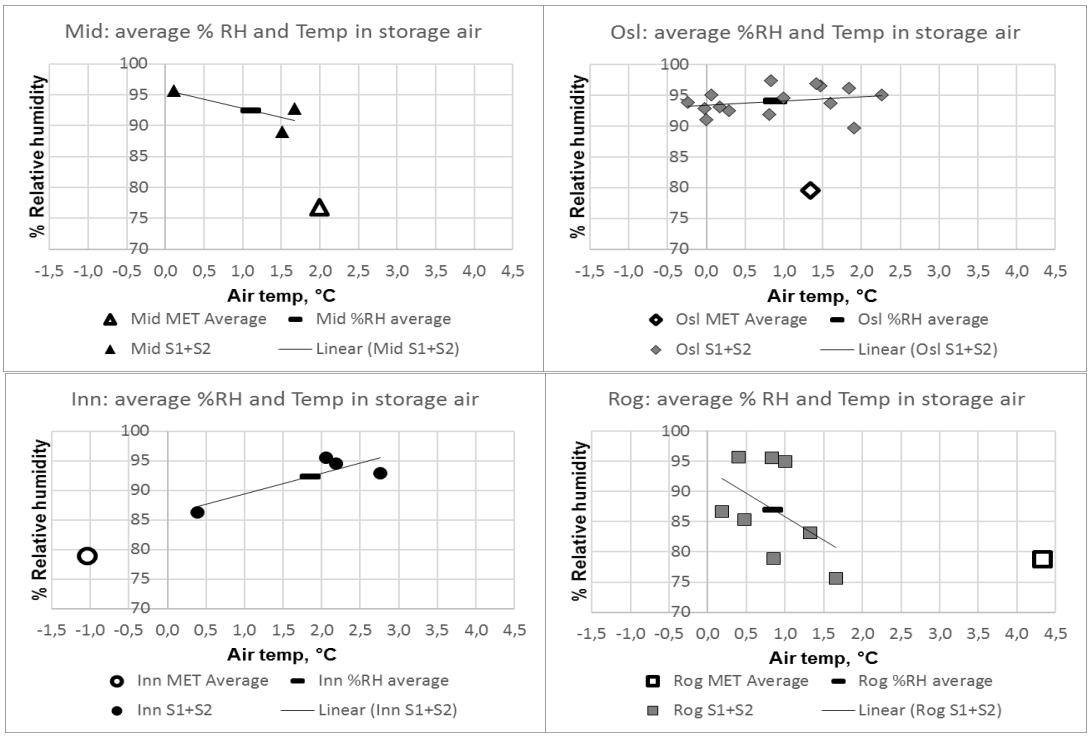

Figure 3: Air temperature and relative humidity in cold-store without humidifiers, correlated to ambient air. Each dot in the figure represents one store, and S1 and S2 refers to season one and two.

Fig. 4a shows that the ten cold-stores with humidifiers had significant higher relative humidity than most of the cold-stores without humidifiers. Swede and celeriac are normally stored without plastic liners inside the wooden bins and are more exposed for dehydration. Carrot is mostly stored with plastic liners with small holes and is not affected much by lower humidity in the air.

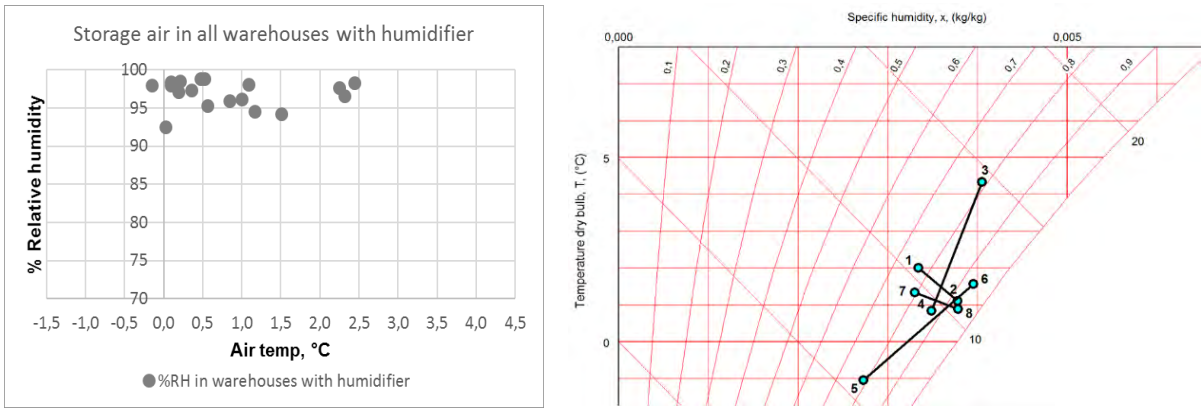

Figure 4: Relative humidity in cold-stores with humidifiers is higher and more stable than without (Fig. 4a-left). Refrigerated air in correlation with ambient air in Mollier diagram (Fig. 4b-right).

3.5 Mapping of cold-store air temperature and relative humidity

The circulation cold-store air and the product temperature (inside the bins) were measured during two storage seasons. The weekly average temperatures are shown in Fig. 5-12.

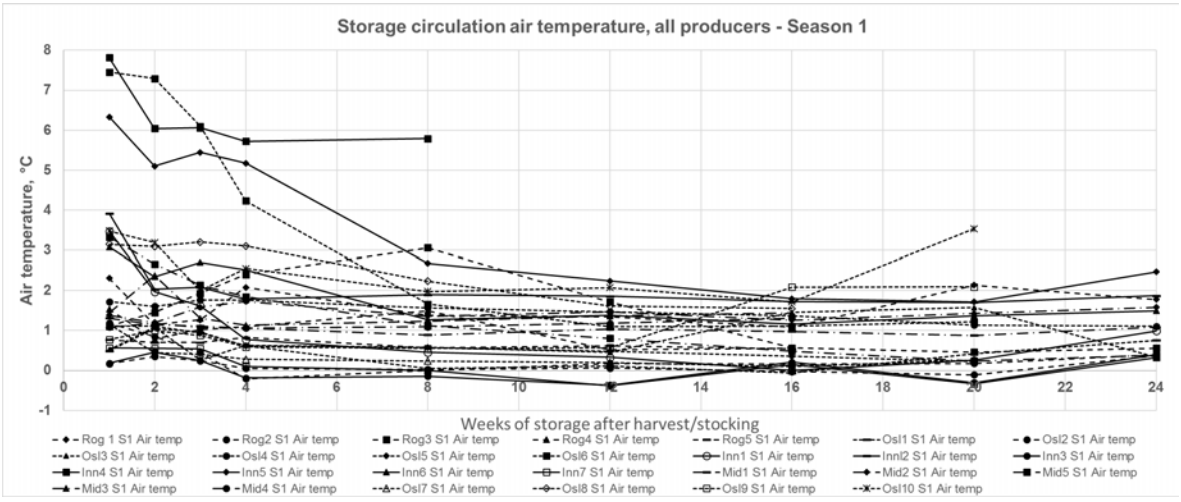

Figure 5: Air temperature during storage in 28 cold-stores season 1, all producers

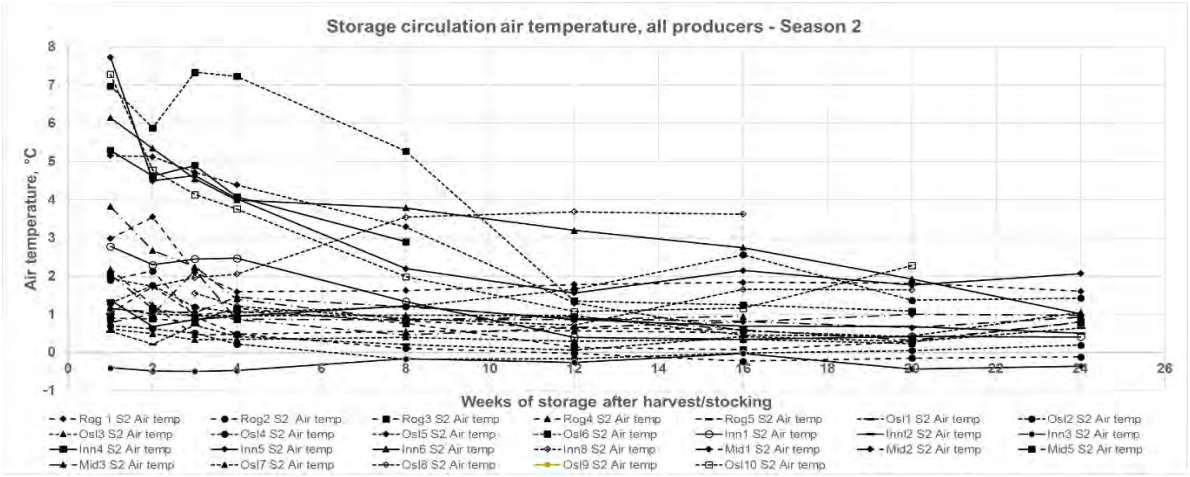

Figure 6: Air temperature during storage in 28 cold-stores season 2, all producers

3.6 Mapping of product temperature during storage

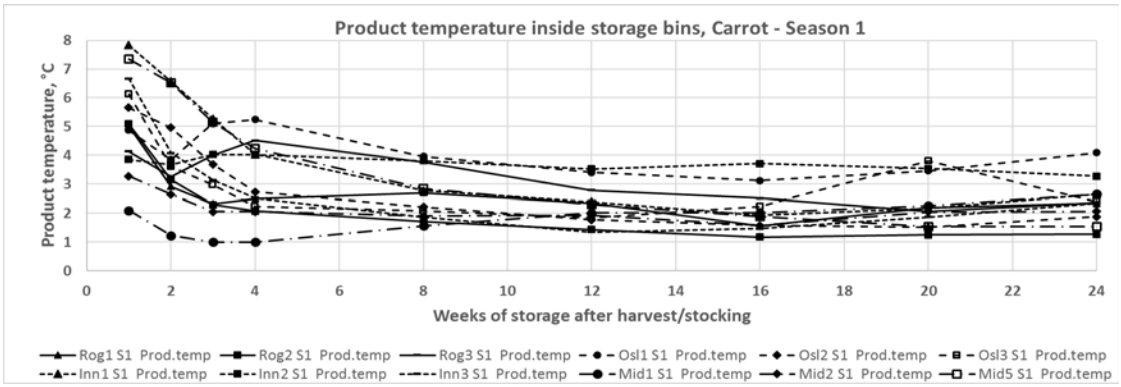

Figure 7: Carrot, season 1: Product temperature (inside bins) during storage

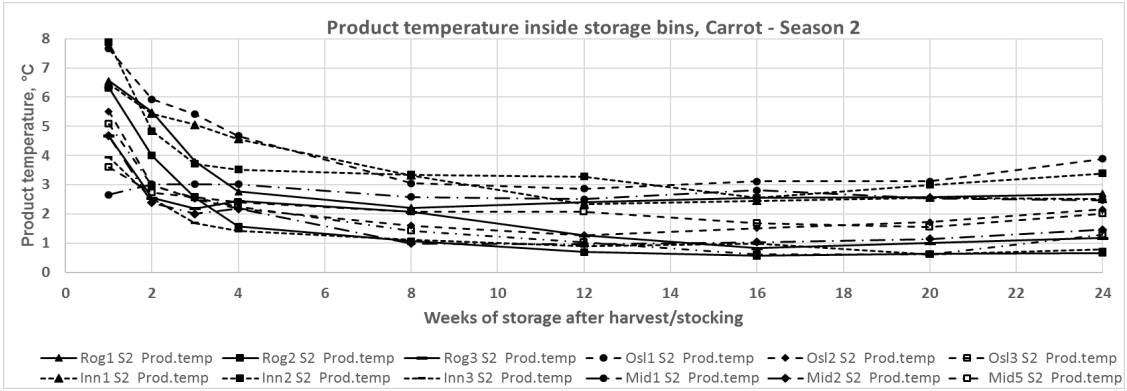

Figure 8: Carrot, season 2: Product temperature (inside bins) during storage.

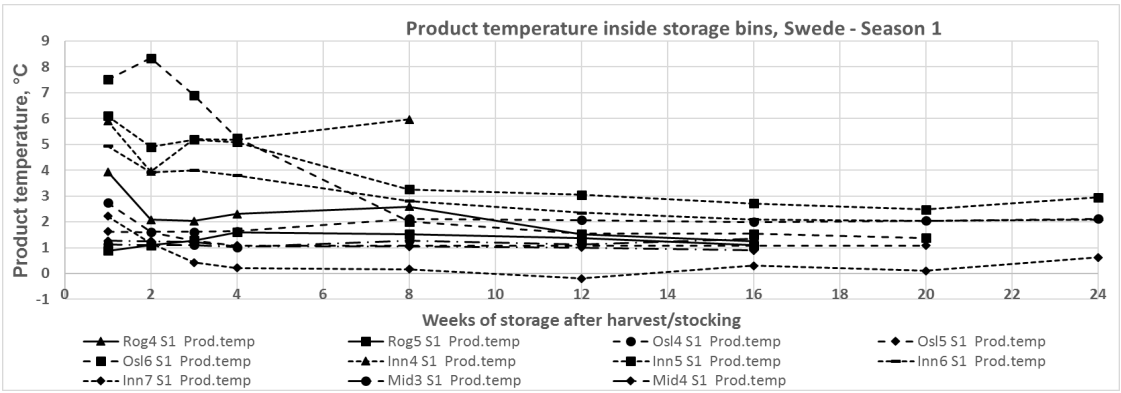

Figure 9: Swede, season 1: Product temperature (inside bins) during storage.

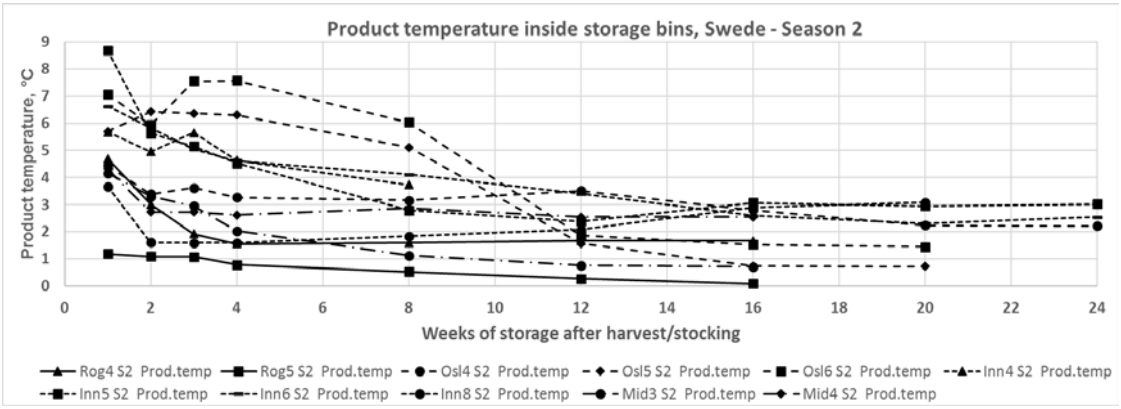

Figure 10: Swede, season 2: Product temperature (inside bins) during storage.

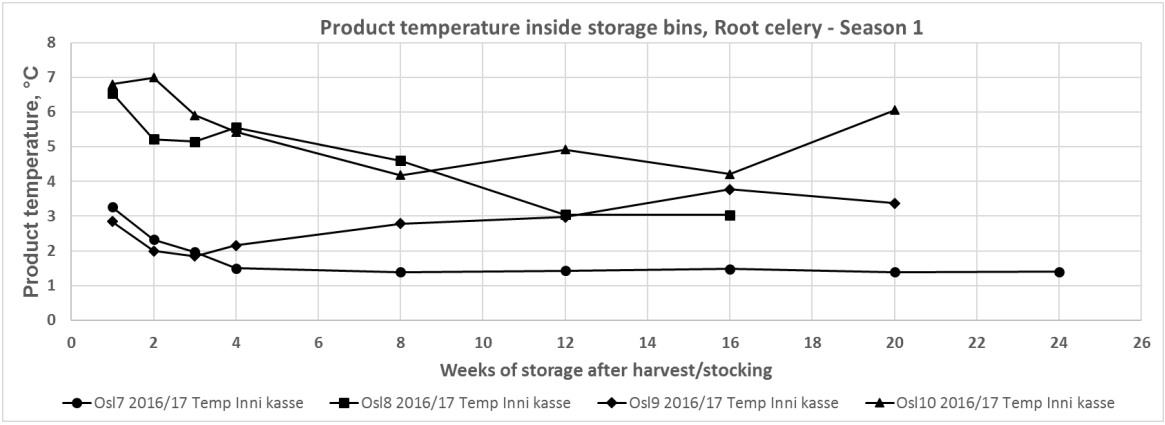

Figure 11: Celeriac, season 1: Product temperature (inside bins) during storage.

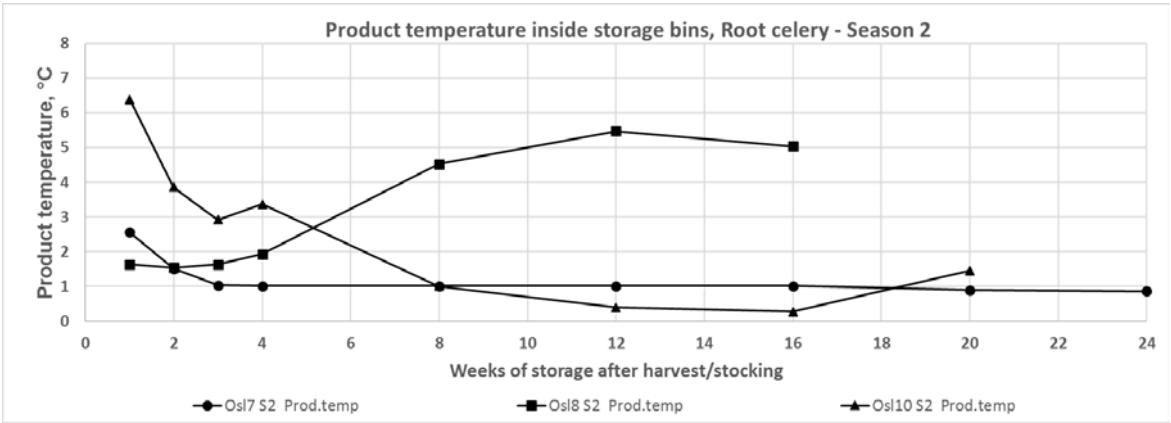

Figure 12: Celeriac, season 2: Product temperature (inside bins) during storage.

As seen in Fig. 1b, the respiration loss due to conversion of sugar and O_2 to CO_2 and H_2O was very dependent on the product temperature. The influence of temperature over time is essential because the storage-life will dramatically reduce when the loss of weight from respiration is between 20-25 g per kg product (Hoftun, 1980). The products accumulated day-degree (average product temperature per day over x days) is presented in Fig. 13, together with the limits where the expected loss of 20-25g/kg occurs. There was an increase in storage-life from 15 to 30 weeks if the average product temperature was 1°C instead of 6°C. The average day-degree (red curve) for all products showed an expected storage-life of 18.5-24 weeks. If the cold-stores with the 50% highest product temperature lower their product temperature equal to the 50% with the lowest temperature (green curve), it is expected that the storage-life will increases to 21-27 weeks. The development of disease in the various cold-stores related to the storage parameters will be presented in a separate article.

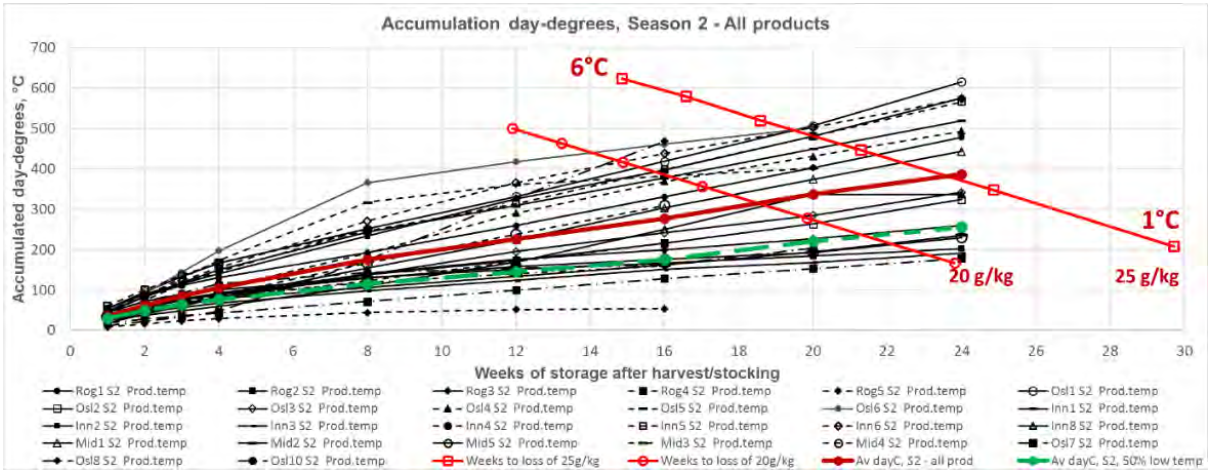

Figure 13: Accumulated day-degrees influenced the expected shelf-life of the products.

3.6 Weight loss related to temperature and relative humidity.

It was expected that the weight loss would increase when the relative humidity was low in the cold-stores, but as seen from Fig. 14, this was not detected. The reason for this could be that the nets were placed in the core of the bins where the relative humidity was close to 100% during the whole storage period.

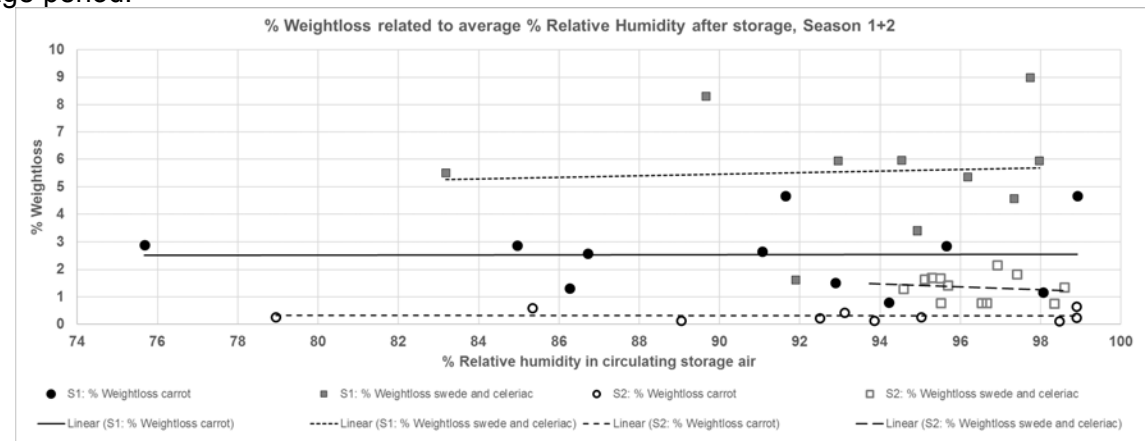

Figure 14: Weight loss of product related to relative humidity in the cold-store during storage.

There was a difference in the weight loss for the three products between the two seasons. It was not possible to conclude the reason for this, other than that the climate was different between these two seasons.

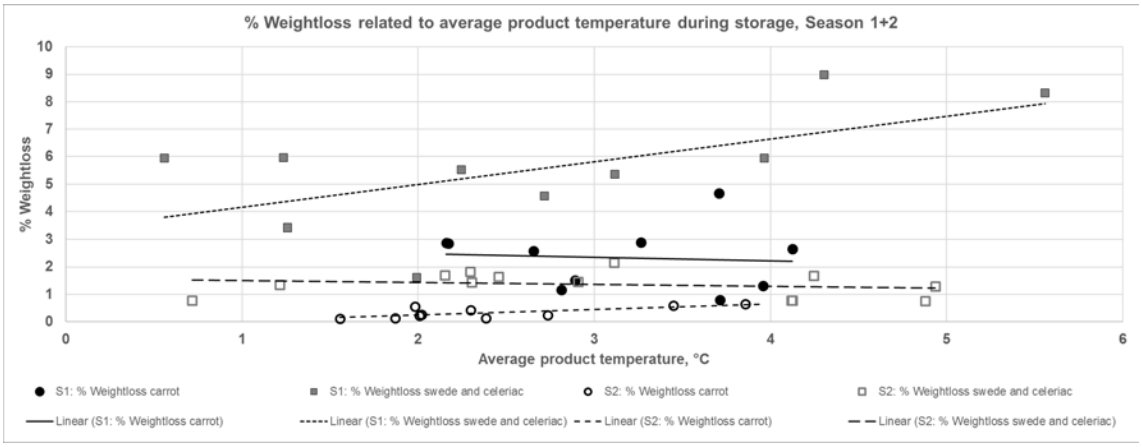

Figure 15: Weight loss of product related to product temperature during storage.

When the weight loss was correlated with average product temperature, there was a tendency that the weight loss increased when the temperature increased at least in season1 for Swede and Celeriac (Fig. 15). As mentioned, the analysed nets were placed inside the bins, so the circulating air did not have much influence. The increased weight loss was therefor likely due to increased respiration loss caused by increased temperature. As mentioned, studies have shown that storage conditions may play a significant role in creating conditions suitable for latent infections to develop and spread within the bins and packing houses.

4. CONCLUSION

Twenty-eight different commercial cold-stores for carrot, swede and celeriac located in four regions in Norway were studied regarding energy and quality aspects. The climate variation between the regions affected the indoor refrigerated air in cold-stores without humidifiers. Unsuitable storage condition negatively affects the respiration and quality of the root vegetables and storage-life, and influenced on the cooling capacity of the refrigeration systems. Quality of the products reflects on the storage parameters but is mostly related to disease brought into the storage with the products from the fields.

There was no difference in product temperature between the seven different principle of air distribution in the cold-stores, except for the Chimney heat rise (Findus) stored with carrot. A very limited amount of circulated air in this system affect the ability to remove the respiration heat. The Grae-principle is only suited in areas with very cold climate, because the storage air is sucked out to maintain negative pressure in the storage room.

The level of optimization and energy reduction of the existing refrigeration systems must affect the fact that there is a huge variation in age, cooling capacity and services between the systems. The cooling demand is highly variable during the season, and many systems do not have good regulation. Optimization must be done individually with various initiatives for each producer. A general way to improve the systems is to reduce the cooling capacity by energy storage. Respiration is the most significant factor regarding cooling demand, close to lowering the product temperature. The calculated worst-case scenarios resulted in a designed cooling capacity 20% lower for some regions in Norway, compared with the general worst-case scenarios used by refrigeration suppliers.

ACKNOWLEDGEMENT

This work has been financed by The Norwegian Research Council under the project 256847 Optirot. The project partners include 28 producers/stores of root vegetables, The Norwegian Research Institutes: SINTEF Ocean, NIBIO, Nofima and NMBU in cooperation with Norwegian Agriculture Advisory Service (NLR), two refrigeration technology suppliers, a developer of sensor technology and a packing supplier. Since several institutions and producers are involved in the project it is not possible to mention the name of all here, so we would like to thank all the

producers, owners of cold storages, extention agents and technicians from each institution for their contribution in the project.

REFERENCES

Alva, G., Lin, Y., Fang, G., 2018, An overview of thermal energy storage systems, Energy, Volume 144, p. 341-378

Baugerød, H., Willumsen, K. (1986) Air humidity with wet cooling (Norwegian), Inst for Hagebruk, NLH

Cardoso B.J., Lamas, F.B., Gaspar, A.R., Ribeiro, J.B., 2017, Refrigerants used in the Portuguese food industry: Current status, International journal of refrigeration 83, p. 60–74

Evans, J.A., Hammond, E.C., Gigiel, A.J., Fostera, A.M., Reinholdt, L., Fikiin, K., Silio, C., 2014, Assessment of methods to reduce the energy consumption of food cold stores, Applied Thermal Engineering 62, p.697-705.

Halloran, A., Clement, J., Kornum, N., Bucatariu, C., Magid, J., 2014, Addressing food waste reduction in Denmark, Food Policy 49, p.294–301

Hoftun, H., 1980, Climatic requirement for storage of vegetables (In Norwegian), NLH (NMBU), Institute for vegetable cultivation, J.nr.13/80

Kauffeld, M., Gund, S., 2019, Ice slurry – History, current technologies and future developments, International Journal of Refrigeration, Volume 99, p. 264-271

Liu, Y., Groll, E.A., Yazawa, K., Kurtulus, O., 2016, Theoretical analysis of energy-saving performance and economics of CO2 and NH3 heat pumps with simultaneous cooling and heating applications in food processing, International journal of refrigeration 65, p. 129–141

Mc Carthy, U., Uysal, I., Badia, R. M., Mercier, S., O'Donnell, C., Ktenioudaki, A., 2018, Global food security – Issues, challenges and technological solutions, Trends in Food Science & Technology 77, p.11–20

Regjeringen (The Norwegian Government), 2018,
https://www.regjeringen.no/no/sub/eos-notatbasen/notatene/2014/juni/revidert-f-gassforordning-/id2434380/

SSB - Statistics Norway, 2017,
https://www.frukt.no/globalassets/materiell/totaloversikten/totaloversikten2017-hyperlenker-korr2.pdf

Thomsen, M., Indergård, E., Tadesse, B. A., Heltoft, P., Wold, A., Nordskog, B., Dyste, J., & Larsen, H., 2018: Optimization of produce quality and storage conditions to reduce loss during long-term storage of root vegetables in Norway, ISHS International Conference 17-20 October 2017, Madrid

Wu, P., Huang, P., 2018, Business analytics for systematically investigating sustainable food, Journal of Cleaner Production 203, p.968-976

Zhao, H., Liu, S., Tian, C. Yan, G. Wand, D., 2018, An overview of current status of cold chain in China, International Journal of Refrigeration 88, p.483–495

Manuscript ID: 962
DOI: 10.18462/iir.icr.2019.0962

The effect of supercooling-freezing on inhibition of ice recrystallization during storage

Yasuho ISHIKAWA[(a)], Manabu WATANABE[(a)], Toru SUZUKI[(a)]

[(a)] Graduate School of Tokyo University of Marine Science and Technology
Tokyo, 108-8477, Japan, m182004@kaiyodai.ac.jp

ABSTRACT

In this paper, the effect of supercooling-freezing (freezing via supercooling) on ice crystal recrystallization in tofu (soybean curd) during frozen storage was investigated. The ice crystal growth rate by recrystallization depends on the storage temperature; however, there is an assumption that the size of ice crystals influences the ice crystal growth rate, and the assumption was investigated. Using a conventional freezing method, the ice crystal size of surface and center of food tends to be different. In contrast, supercooling-freezing is known to form minute and nearly uniform ice crystals in food. Each sample was frozen by rapid freezing(R), supercooling-rapid freezing (SR), and supercooling-slow freezing (SS) to observe the difference of ice crystals growth. The samples were preserved for up to 1 month at several temperatures. From the X-ray CT images, characteristics of ice crystals were observed, and the growth rate of ice crystal was calculated for each freezing method.
Keywords: Frozen Storage, Frozen Food, Freezing, Ice Crystal, Recrystallization, Supercooling.

1. INTRODUCTION

Frozen storage is especially important technology for preserving food that only the technology can preserve raw food as it is for a long time. However, even during frozen storage ice crystals continue to grow, damage the tissues and degrade food quality. In the growth process of this ice crystal, a lot of small ice crystals particles migrate to few numbers of large ice crystals particles and are assimilated, and the number of larger ice crystals particles increase, which is called recrystallization (Hagiwara, 2018). Recrystallization of ice crystals in food progresses gradually over time. Therefore, it is one of the main problems in the storage process and distribution process of frozen food where temperature change is likely to occur (Hagiwara, 2010). Although recrystallization can be delayed by lowering the temperature, it is concerned that lowering of the temperature raises operational cost of the refrigerator, waste of energy, environmental issues. From these facts, recrystallization has been regarded as one of the difficult problems to solve. In frozen storage, it is considered that passing rapidly through the zone of maximum ice crystal formation temperature is effective for maintaining the quality of food, so rapid freezing has been used in various situations. However, since the object was frozen from the surface by rapid freezing, the size of ice crystals generated in the object differs between the center and the surface, which causes recrystallization. Supercooling freezing is a new freezing method which has been studied in recent years and it is reported that fine ice crystals of uniform size are generated simultaneously in the whole of the object after releasing the supercooled state (Kobayashi et al. 2014). Additionally, it is considered that there is little effect on ice crystals by changing freezing rate after supercooling is released. According to the result of preserving tofu stored at -30 ° C after supercooling-freezing for a maximum of 28 days, it has been experimentally shown that the influence of recrystallization is smaller than that of tofu kept for the same day after rapid freezing (Kobayashi et al, 2018). From these previous studies, it is predicted that supercooled frozen foods are slower to grow ice crystals than rapidly frozen foods and foods can be stored for a long time at a higher temperature and it is studied in this paper. For the experimental sample, tofu (soy bean curd) was used, which is made of protein, has a large moisture content of 89.4% (Makiuchi et al, 2014), due to easy to confirm the difference in structure frozen by supercooling freezing. Since tofu has no cell structure, the tissue structure is less complicated than other foods (vegetables, fish and meat), and various enzymes are inactivated by heat, and there is no influence of the enzyme. In this study, for the purpose of verification of recrystallization after supercooling freezing, it was observed the ice crystals by the X-ray CT image after storage of tofu subjected to supercooling freezing and rapid freezing, and the growth rate of ice crystals was

calculated. In addition, it was examined that whether the freezing method after supercooling affects the structure of ice crystals.

2. MATERIAL AND METHOD

2.1. Sample Preparation

A commercial tofu (“Kinugoshi-tofu”, MORINAGA MILK INDUSTRY Co., Ltd., Japan) was cut into a cylinder (diameter 2cm, height 2cm) by a cork borer. The moisture on the surface of tofu was wiped off with a paper towel and wrapped with a polyethylene film to prevent drying. Then, a T type thermocouple of 0.254 mm diameter was inserted into the surface and center of the sample for temperature measurement. Temperature was measured with a data logger (HIOKI LR8431 MEMORY HILOGGER, HIOKI Co., Ltd., Japan).

2.2 . Freezing Method

The sample was placed in a stocker (VT-78, NIHON FREEZER Co., Ltd., Japan) at an ambient temperature of -80 ° C and frozen. After the sample was reached at -50 ° C, it was moved and stored. This frozen sample was taken as a rapid freezing (R) sample. The supercooling-rapid freezing (SR) sample was placed in an incubator (FMU-0541, FUKUSHIMA INDUSTRY Co., Ltd., Japan) at an ambient temperature of -10 ° C, and after supercooling state was released, it was placed in the stocker of -80 ° C until the temperature of sample was reached at -50° C. Then, the sample was moved and stored. The supercooling-slow freezing (SS) sample was placed in an incubator at an ambient temperature of -10 ° C, and after supercooling state was released, it was placed in deep freezer (SC-DF25, Twinbird Electrical Appliance Co., Ltd., Japan) with -10° C. After the sample temperature was reached at -5° C, the sample was moved to the stocker of -80 ° C and placed until the temperature reached at -50° C. Then, the sample was stored. The freezing curve of samples was shown in Fig. 1. The degree of supercooling for (SR) and (SS) samples were controlled to be always identical about -6° C. The storage time was divided into 3 categories of one week, two weeks, and one month. The storage temperatures were 3 categories of -10° C, -20° C, and -30° C.

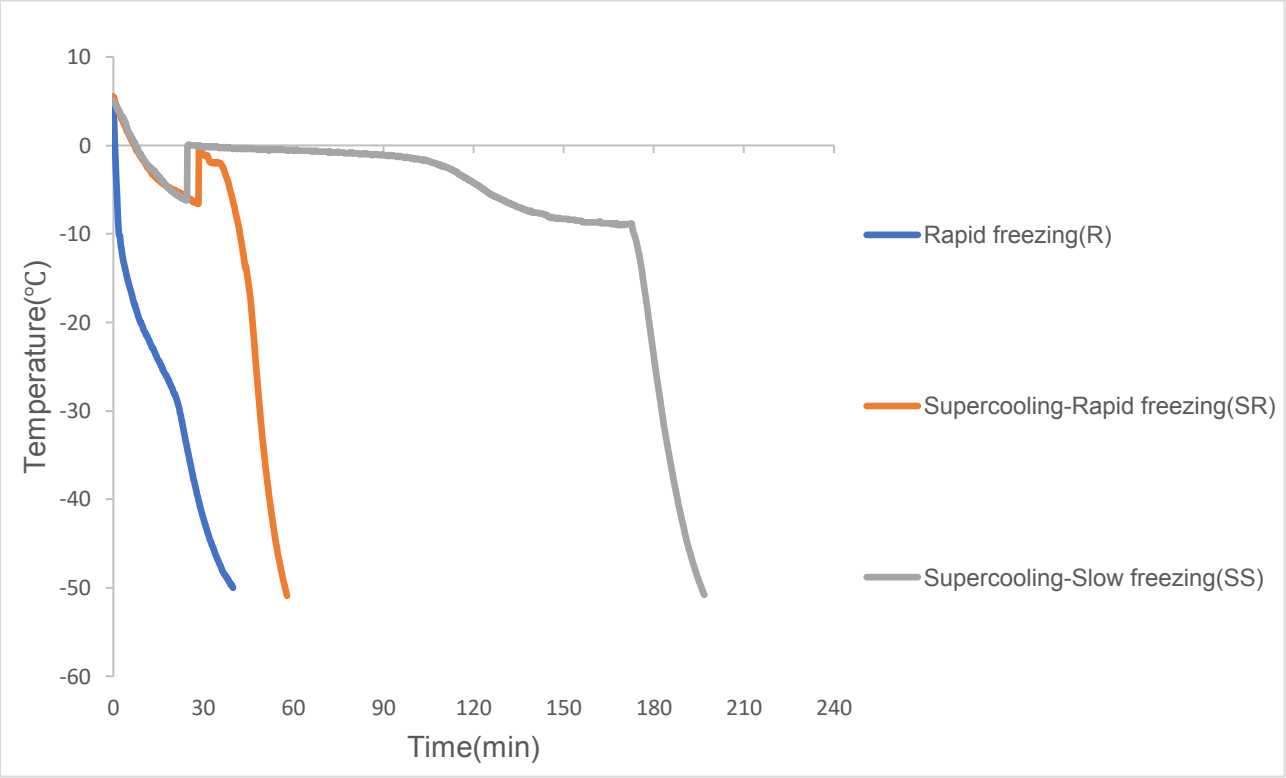

Figure 1: Freezing curve of samples by various freezing method

2.3. Freeze-Dried Sample Preparation

In freeze-drying, moisture sublimes in the place where ice crystals existed, and only the tissue remains, therefore it is suitable for observation of ice crystals growth (Okawa et al., 2017). The sample after storage was cut in a cuboid with an electric saw. The cuboid sample was placed on a stainless steel tray at -40 ° C to stabilize the tissue structure of samples, and then freeze-dried by using a freeze dryer (RLE-52, Kyowa Vacuum Technology Co., Ltd., Japan).

2.4. Observation and Evaluation of ice crystals using X-ray CT

The size of ice crystals was evaluated by using X-ray CT. The sample after freeze-dried was taken CT image with 3.5 μm/pixels using an X-ray micro CT scanner (SkyScan1172-MS, BRUKER MICROCT). The X-ray source was 60 kV, 100 μA, scanning step 0.4°, 180° rotation. After taking CT images, reconstruction of the images was performed using a software (NRecon, BRUKER MICROCT Corp., USA), then image was analysed using a software (CTAn, BRUKER MICROCT Corp. USA) and growth of ice crystals was observed. The morphology of ice crystals is complex and difficult to quantify; thus, structure separation was used. Structure separation shows the thickness of the spaces of the CT image, so that it shows the thickness of the ice crystal of the sample. The thickness of the structure is measured from the distance until it touches with the structure by spreading the concentric spheres from each voxel constituting the pore structure. Using this structure separation value, the growth of ice crystals was analysed.

3. RESULT AND DISCUSSION

The CT images of tofu frozen by different freezing method were shown in Fig. 2. From Fig. 2, it was shown that the shape of ice crystals formed by each freezing method was clearly different. It is shown that (R) had columnar ice crystal, (SR) had fine spherical ice crystal, and (SS) had large spherical ice crystals. Additionally, the ice crystals generated in (SR) seem to be the smallest from the CT image. Due to the shapes of ice crystals were different by freezing method, the graph of distribution of percent volume in structure separation (Fig. 3) was made to compare the size of ice crystal generated in samples. In Fig. 3, It was shown that the distribution of structure separation of (SS) was broader than other freezing method and the shape of peak was different from the others. From this result, it was considered that the ice crystal generated in (SS) samples grew by slow freezing after supercooling state was released. Distribution of percent volume in structure separation of -10 °C sample frozen by different freezing methods was shown in Fig. 4. From this graph, it was shown that the peak of structure separation distribution moved with storage time. As shown in Fig. 4, since the distribution was changed, the change rate of ice distribution was calculated.

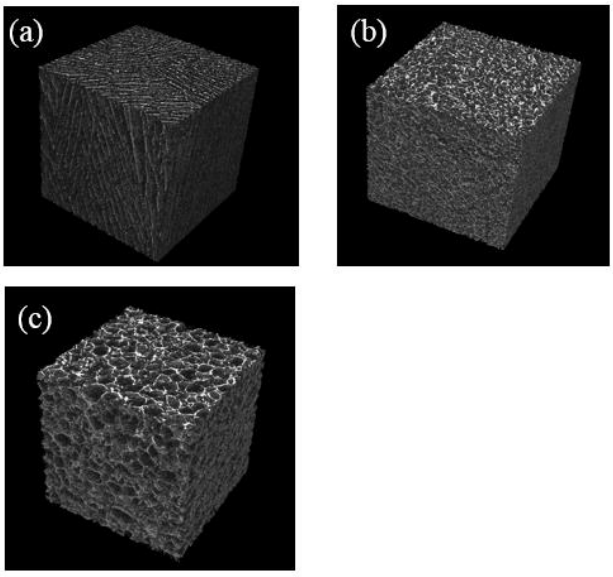

Figure 2: The 3D images of structure of tofu (2.5×2.5×2.5mm) by (a) Rapid freezing; (b)Supercooling-Rapid freezing; (c) Supercooling-Slow freezing

(a)

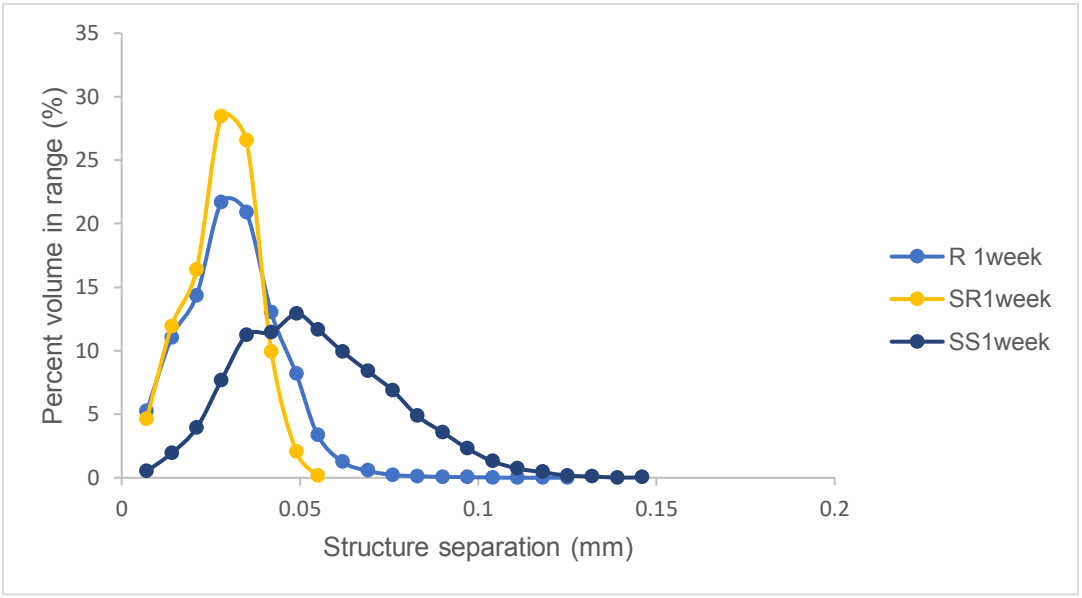

(b)

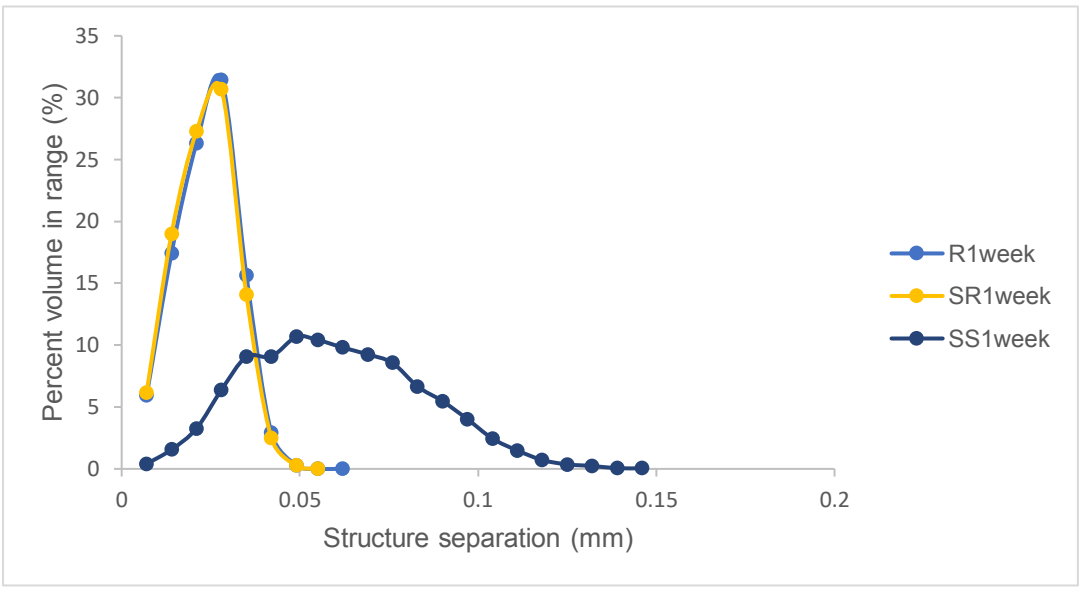

(c)

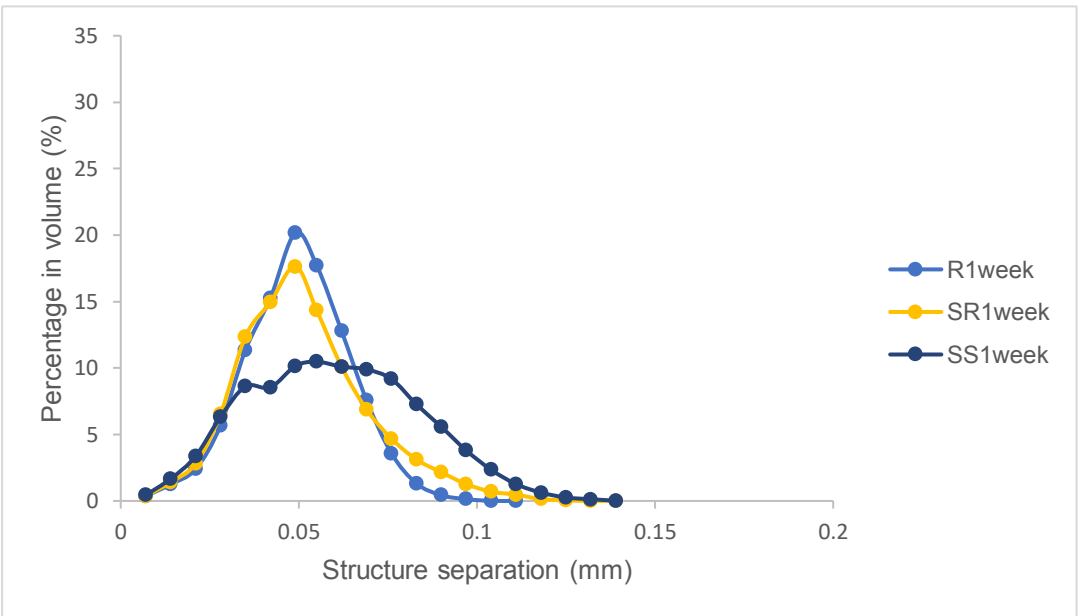

Figure 3: Distribution of percent volume in structure thickness of 1week stored sample at (a)-10°C; (b) -20°C; (c) -30°C

(a)

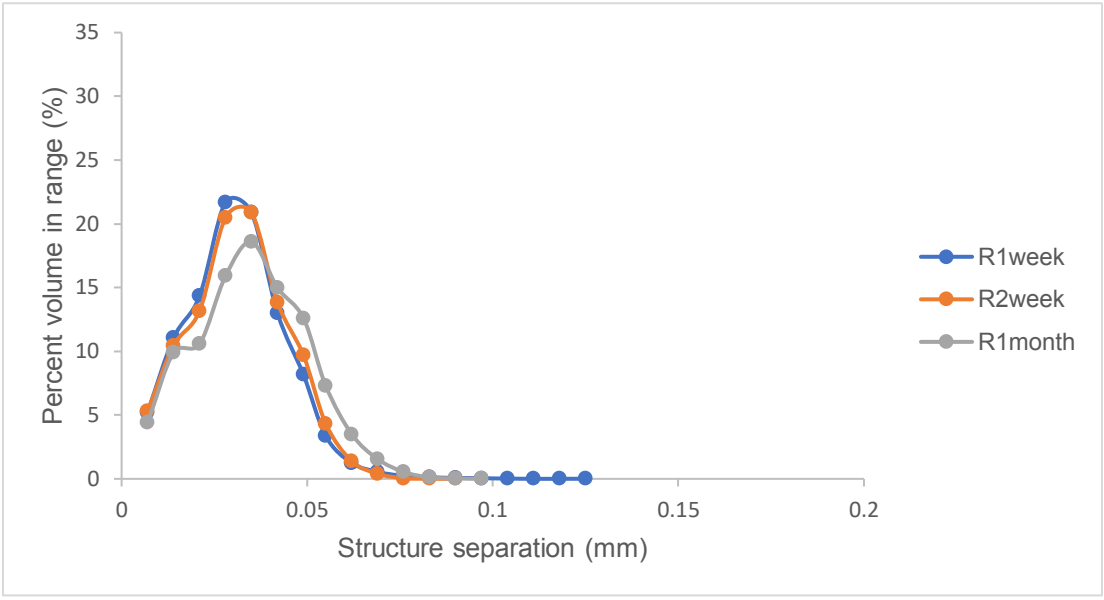

(b)

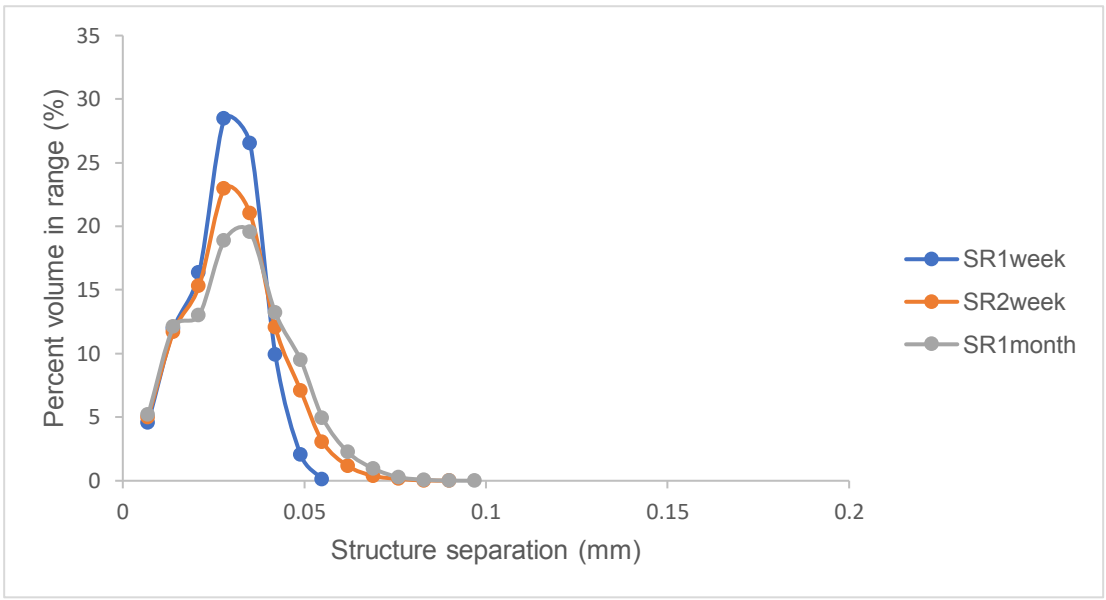

(c)

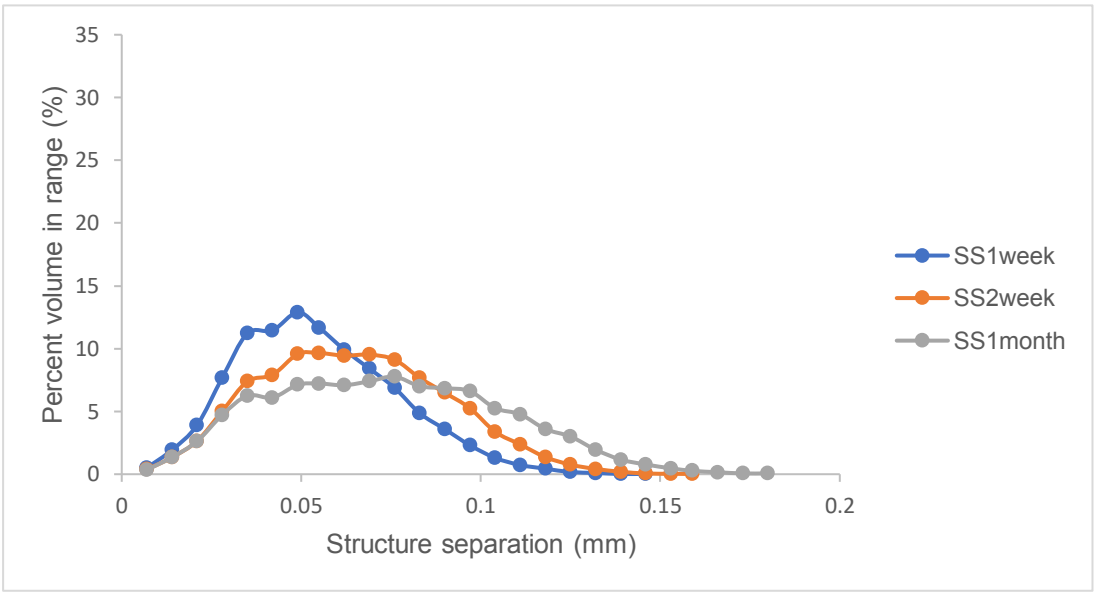

Figure 4: Distribution of percent volume in structure thickness of -10°C sample frozen by (a) Rapid freezing; (b) Supercooling - Rapid freezing; (c) Supercooling-Slow freezing

In order to calculate the change rate of distribution, it is necessary to express the distribution of the structure separation by one value. To express it by one value, the weighted arithmetic mean of structure separation was calculated as its index. The result of this calculation is shown in Fig. 5. Each point in this figure shows the value representing the distribution, and the change over time (week) for each freezing method is shown. From this figure, it is found that each value is increased for each elapsed time. When an approximate straight line is drawn about these values, the gradient of line represents the rate of change. The gradient of approximation straight line of the weighted average graph was taken as the change rate and was considered the rate of ice crystal growth due to recrystallization. The value obtained for various conditions of freezing method and storage temperature were shown by a bar graph as seen in Fig. 6. From Fig. 6, it was shown that the growth rate of (R) and (SR) has similar trend. Since the tendency of ice crystal growth at -20 ° C sample was not good compared with other samples, it must be verified again. Additionally, it was shown that the ice crystal growth rate of (SS) was twice or more as compared with the others. Therefore, it was assumed that the freezing rate after supercooling state released affects the growth of ice crystals.

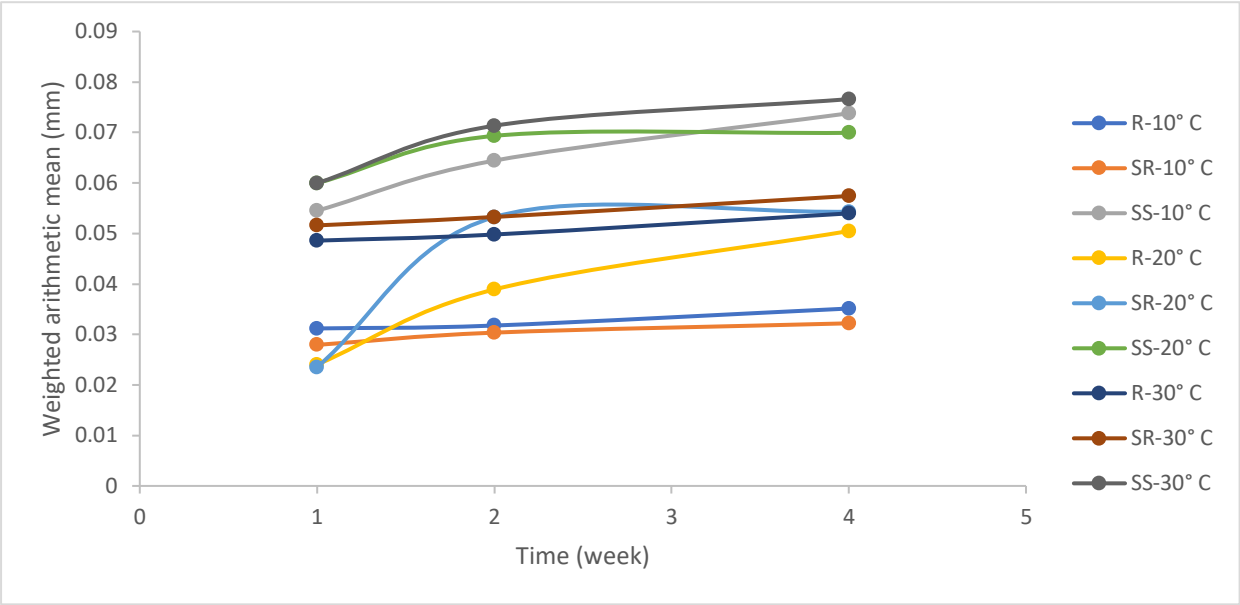

Figure 5: The change of weighted arithmetic mean of structure separation for -10 °C, -20 °C, and -30°C sample

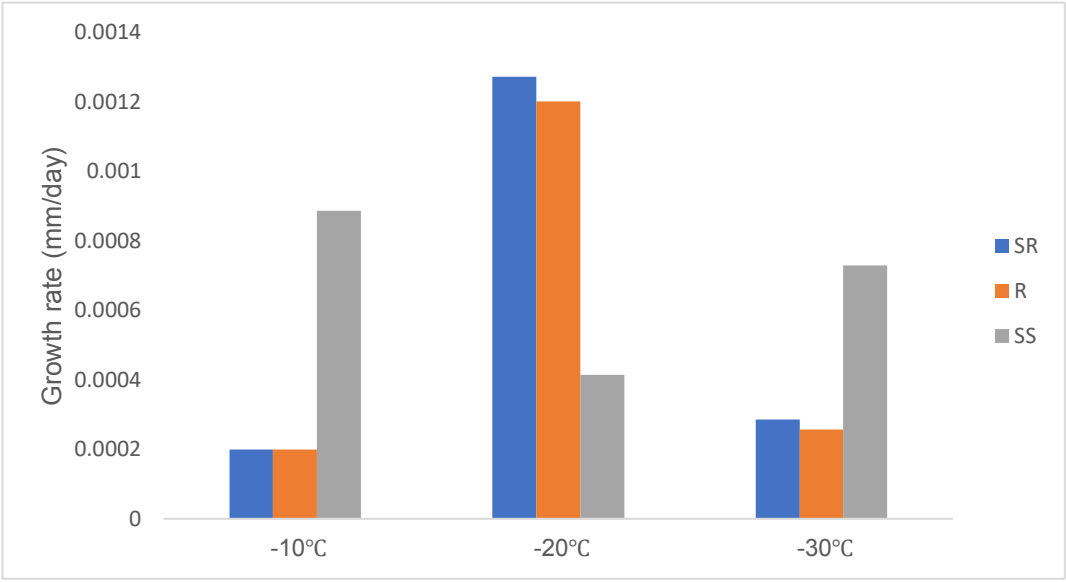

Figure 6: The change rate of ice crystals frozen by different method

4. CONCLUSION

The size and shape of ice crystal generated in tofu is depending on the freezing method. However, the shape of ice crystal in samples that once supercooled kept spherical shape after releasing supercooling state. It was also found that the size and structure separation distribution of ice crystals produced by (SR) and (SS) were completely different even though the sample was supercooled the same degree of supercooling. The shape of ice crystals generated by (R) and (SR) were different. However, the volume percent distribution of structural separation for (R) and (SR) samples shows similar trend. Therefore, new indicator is needed to evaluate the difference between the shape of (R) and (SR) ice crystals. In addition, since the growth rates of ice crystal between (R) and (SR) samples was about the same value at one month's storage at -30 ° C, longer storage samples need to be analysed.

REFERENCES

Hagiwara, T., 2010. Recrystallization of ice crystals in frozen foods. Japan journal of food engineering 11 (4), 169-175.

Hagiwara, T., 2018. Prediction and control of ice crystal growth in frozen foods. Japan Journal of Food Engineering 19 (1), 79-88.

Kobayashi, R., Kanesaka, N., Watanabe, M., Suzuki, T., 2014. Effect of the breaking temperature of supercooling on ice characteristics and drip loss of foods in supercooled freezing method. Japan Society of Refrigerating and Air Conditioning Engineers 31 (3), 297-303.

Kobayashi, R., Kimizuka, N., Watanabe, M., Takenaga, F., Suzuki, T., 2018. Property Changes Frozen Storage in Frozen Soy Bean Curds Prepared by Freezing Accompanied with Supercooling. Japan Society of Refrigerating and Air Conditioning Engineers 35 (3), 269-276.

Makiuchi, T., Osanai, T., Mori, Y., Okawa, S., Hozumi, T., 2014. Food freezing by making use of supercooling influence of breaking of supercooling on the food structure. Japan Society of Refrigerating and Air Conditioning Engineers D121-1-4.

Okawa, S., Mori, Y., Osanai, T., Hozumi, T., 2017. Suppression of expansion of ice crystal size while food freezing using supercooling. Japan Society of Refrigerating and Air Conditioning Engineers 34 (1), 25-34.

Manuscript ID: 1022
DOI: 10.18462/iir.icr.2019.1022

Fractal Structure Evolution of Moisture-containing Porous Media under the Weak Potential Difference in Cases of Garlic Stems

Lin CHAI[(a)], Bin LIU[(a)], Yu MENG[(a)], Aiqiang CHEN[(a)], Georges EL ACHKAR[(a)], Rachid BENNACER[(a)]

[(a)] Tianjin Key Laboratory of Refrigeration Technology, Tianjin University of Commerce, Tianjin, 300134, P. R. China, lbtjcu@tjcu.edu.cn

ABSTRACT

In cases of garlic stems, during ice-temperature storage (0 °C) with precooling air velocities of 1.0 m/s, 1.5 m/s and 2 m/s, the variations of fractal parameters such as pore fractal dimension, porosity, tortuosity and tortuous fractal dimension were studied. The results showed that the selection of precooling air speed plays a major role in maintaining the moisture contained in garlic stems after harvest. Compared with precooling air velocities of 1.5 m/s and 2.0 m/s, the precooling air velocity of 1.0 m/s has more significant impact on the porosity, the tortuosity and the tortuous fractal dimension in the cells microstructure. Cells at the epidermis were more affected than cells at the 1/2 radius and the center. Meanwhile, there is a significant two-dimensional linear correlation among the average tortuosity, porosity and tortuous fractal dimension in the three conditions during ice-temperature storage. The two-dimensional correlation coefficients under the precooling treatment of 1.0 m/s is the largest among the three air velocities.
Keywords: Precooling, Bioproduct tissue, Microstructure, Fractal analysis.

1. INTRODUCTION

The daily intake of fresh fruits and vegetables has been used by the World Health Organization (WHO) as an important indicator to measure the health of people in a certain area. The porous media composed of the solid skeleton and the fluid is the material basis of the earth biosphere and the form of microstructure of fruits and vegetables. Currently, research methods for controlling water loss in fruits and vegetables mainly focus on the application, such as light irradiation, vacuum packaging and drug application. These are mainly based on the application level research, and there is the absence of research on the mechanism of water loss and the effect of water migration on the structure of the porous microstructure system. In addition, there are few research results in the field of plant microstructural changes in the process of adapting to change the environment. And the water content in fruit and vegetables is an important element in determining its quality. Currently, various new refrigeration technologies play a major role in preserving fresh water through the action of the water, to study the evolution of porous microstructure, the change of material specific gravity and the transformation of life characteristics in the microstructural system of fruits and vegetables during storage. This research expands the knowledge of fruits and vegetables preservation technologies, and has significant practical guidance for the application of rich fractal theory and its methods in the field of bioproducts preservation.

2. MATERIALS AND METHODS

This experiment used differential pressure precooling and ice temperature storage, whilst the fractal theory was used to determine the evolution of porous microstructure of fruits and vegetables, and the correlation analysis method was combined to explore the relationship between four parameters of microstructure, and summarizes the influence of different cold air speeds on porous microstructure under weak pressure difference. The garlic stalks in the experiment were collected from the Henan Zhongmu (Henan province) and transported to the Tianjin University of Commerce Engineering Center for differential pressure precooling within 24 hours after purchase. The garlic stems stalks

were selected with a moderate maturity, no pests and diseases, no mechanical damage, uniform thickness of the stalks and a length of 35 cm or more.
In contrast to the different precooling air speeds, the test pressure of precooling speeds of the Testo 425 (Testo AG Co., Ltd) was set to 1.0 m/s, 1.5 m/s and 2.0 m/s, respectively. The garlic stalk was precooled to 4 °C. The garlic stalks were positioned in an air-conditioned fresh-keeping bag and placed in an ice temperature store (Daqing Industry Co., Ltd). The relative humidity of the ice temperature library was 85%, and the temperature was 0 °C. The entire experimental storage period was 135 days. Garlic samples were obtained from the MX100 data collector (Yokogawa Electric Corporation) every 15 days before and after precooling and storage for microscopic image observation and pore fractal dimension, porosity, average tortuosity and tortuous fractal dimension determination. The microscopic images obtained in this experiment were converted into binary images thanks to Adobe Photoshop and Matlab software (Fig. 1) and used for structural parameter calculations.

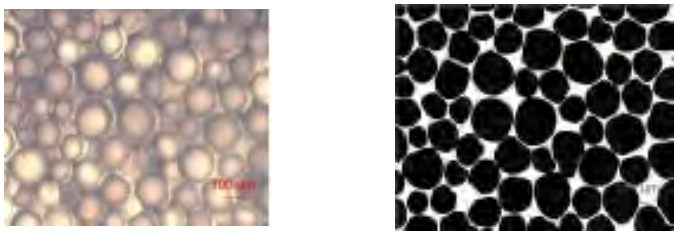

(a) Microscopic image (b) Binary image

Figure 1: Conversion of microscopic image (a) into binary image (b)

2.1. Changes in garlic stalks with precooling time under different precooling air speeds

The precooling supply air temperature is determined according to the storage temperature of fruits and vegetables. To reflect the actual effect of precooling and to exclude the influence of different cold air temperatures on the precooling time of different fruits and vegetables, this paper used 4/5 cooling time to measure the cooling effect, and its mathematical expression is shown in Eq. (1):

$$\frac{T-T_f}{T_0-T_f}=\frac{1}{5} \qquad \textbf{Eq. (1)}$$

Where *T* is the temperature of fruits and vegetables in °C, T_f is cold air temperature in °C and T_0 is the initial temperature of fruits and vegetables in °C. In this test, the average initial temperature of garlic stalks was 22 °C, and the average temperature of cold air was 2 °C. Therefore, the 4/5 cooling time of garlic stalks was the time corresponding to the temperature of garlic stalks reduced to 6 °C. For each air speed, the average value of 36 measuring points at the same time (i) is taken as the temperature value T_i (i = 0, 5, 10, ..., 130) at that time in the working condition, and the temperature is different under different precooling air speeds. Fig. 2 shows the relationship among temperature change with precooling time under different precooling air speeds. It also shows that at three different air speeds, the temperature cooling rate of garlic stalks decreases as the cooling time increases (the heat transfer process of differential pressure precooling includes heat conduction and convection, where convection plays a leading role). As the air supply speed increases, the cooling rate increases (the air supply speed increases, the turbulence effect of the cold air is strengthened, and the convection effect is enhanced, and the temperature drop rate is increased), from 1.5 m/s to 2.0 m/s. The cooling rate is significantly improved, but the cooling rate is not significantly improved from 1.0 m/s to 1.5 m/s. The cooling time is a function of air speed. Indeed, when the air speed is not too low, the increase of air speed has a greater impact on the cooling time of garlic. Therefore, combined with the cooling time and the energy consumption of the fan, the garlic tunnel type differential pressure precooling can preferentially select the air supply speed of about 2.0 m/s.

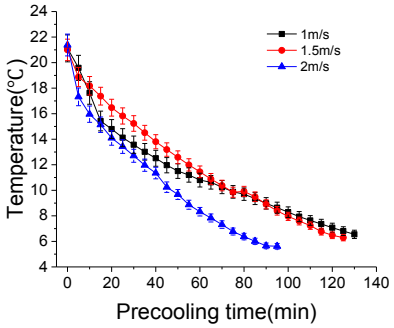

Figure 2: Evolution of garlic temperature as a function of precooling time under different precooling air speeds

2.2. Calculation Methods of Parameters

2.2.1. Pore fractal dimension

In the self-similar range, based on the fractal capillary beam and using the box-counting dimension method, the pore fractal dimension is expressed as follows:

$$D_f = \lim_{\lambda/\lambda_{\max}\to 0} \frac{\ln N(\geq \lambda)}{\ln \frac{1}{\lambda / \lambda_{\max}}} \quad \textbf{Eq. (2)}$$

Where D_f is the pore fractal dimension; $\mathrm{N}(\geq \lambda)$ is the cumulative number of porosity greater than $\lambda(\mu\mathrm{m})$; λ_{max} is the maximum void fraction size in $\mu\mathrm{m}$.

2.2.2. Porosity

Using the surface porosity as the porosity of the image, the porosity is expressed as follows:

$$\varepsilon = \frac{A_1}{A_0} \quad \textbf{Eq. (3)}$$

Where ε is the porosity; A_1 is the total area of the voids in the image in $\mu\mathrm{m}^2$; A_0 is the total area of the image in $\mu\mathrm{m}^2$.

2.2.3. Tortuosity

The ratio of the length of the fluid flow line to the length of the medium characteristic is defined as the degree of tortuosity τ, in the fractal capillary beam model the average tortuosity is expressed as follows:

$$\tau_{av} = \frac{1}{2}\left[1 + \frac{1}{2}\sqrt{1-\varepsilon} + \sqrt{1-\varepsilon}\,\frac{\sqrt{\left(\frac{1}{\sqrt{1-\varepsilon}} - 1\right)^2 + \frac{1}{4}}}{1-\sqrt{1-\varepsilon}}\right] \quad \textbf{Eq. (4)}$$

Where τ_{av} is the average tortuosity.

2.2.4. Tortuous fractal dimension

In the fractal capillary beam model, considering the relationship between the average pore diameter λ_{av} $(\mu\mathrm{m})$ and the maximum pore diameter λ_{max} $(\mu\mathrm{m})$, and combining with the characteristic length L_0 $(\mu\mathrm{m})$ of the medium. Therefore, the tortuous fractal dimension is expressed as follows:

$$D_T = 1 + \frac{4\ln\tau_{av}}{\ln\dfrac{\pi^2(4-\mathrm{D}_f)\mathrm{D}_f(1-\varepsilon)^2}{16(2-\mathrm{D}_f)^2\varepsilon^2}} \qquad \textbf{Eq. (5)}$$

Where D_T is a distorted fractal dimension.

3. RESULTS AND DISCUSSION

3.1. Pore Fractal Dimension

Fig. 3 shows the variations of pore fractal dimension with storage time for three precooling air speeds. At different radius positions for the same air speed, the pore fractal dimension presents an overall trend for the extension of storage time: in the early and the late stages, the fractal dimension develops gently, but in the middle stage, the fractal dimension first rises and then falls. However, pore fractal dimension values in the epidermis were slightly different under different air speeds. Meanwhile, the numerical difference during the whole storage period is significantly larger than the other two air speeds under the condition of precooling air speed of 1.0 m/s. When the precooling air speed is 1.5 m/s and 2 m/s, there is no significant difference in the variation trend of pore fractal dimension between the 1/2 radius and the central radius. Under the condition of precooling air speed of 1.0 m/s, the pore fractal dimension of the 1/2 radius and the central radius in the end of storage is always significantly lower than the other two conditions. It can be seen that under the three different precooling air speeds, the cell gap distribution at the 1/2 radius and the central radius is similar in complexity, which indirectly reflects the similar complexity of the individual cell distribution, and under the 1.0 m/s precooling air speed, the complexity of the skin is significantly higher than the other two precooling air speeds.

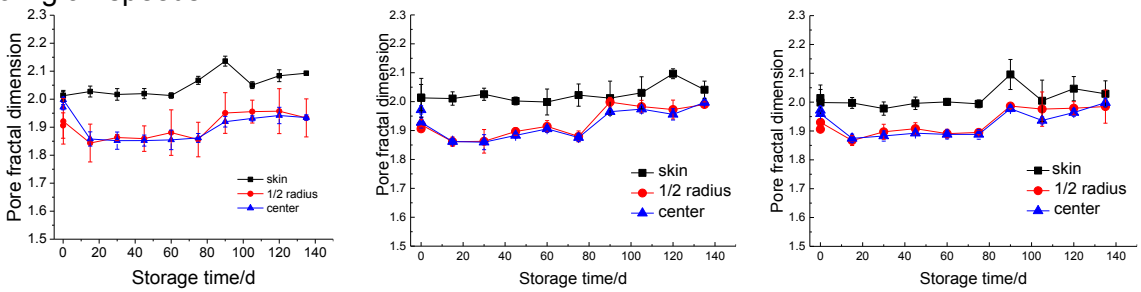

(a) Precooling air speed of 1.0 m/s (b) Precooling air speed of 1.5 m/s (c) Precooling air speed of 2.0 m/s

Figure 3: Variations of pore fractal dimension with storage time for three precooling air speeds

3.2. Porosity

Fig. 4 shows the variations of the porosity with storage time for three precooling air speeds. It can be observed that the porosity changes with storage time under the same air speed at different radial positions are similar. With the extension of storage time, the porosity generally decreases in the early stage, the slight fluctuation in the medium stage and the slow rise in the late stage. When the precooling air speed is 1.5 m/s and 2.0 m/s, the overall value of porosity is the largest at the center radius, the second largest at the 1/2 radius, and the smallest at the skin. But when the precooling air speed is 1.0 m/s, the overall value of porosity is the largest at the epidermis, the second at the center, and the smallest at the 1/2 radius. According to the experimental results, it is speculated that the different precooling air speeds lead to different precooling time, which causes the difference in the numerical values of the porosity under the corresponding air speeds. In other words, the precooling time has a great influence on the internal volume ratio of the intercellular space inside the garlic stalks, but the precooling time has little effect on the overall change trend during storage.

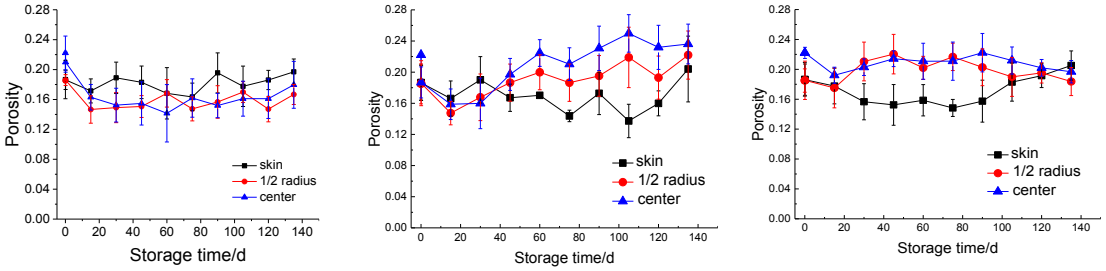

(a) Precooling air speed of 1.0 m/s (b) Precooling air speed of 1.5 m/s (c) Precooling air speed of 2.0 m/s

Figure 4: Variations of porosity with storage time for three precooling air speeds

3.3. Tortuosity

Fig. 5 shows the variations of the average tortuosity changes with storage time for three precooling air speeds. At different radial positions under the same air speed, the average tortuosity presented as a whole with the extension of storage time: the trend of obvious increase in the early stage, gentle fluctuation in the middle stage and slow increase in the late stage, when the precooling air speed is 1.5 m/s and 2.0 m/s. The average tortuosity value of the epidermis is significantly higher than the 1/2 radius and the central radius during the whole storage period ($P<0.05$). And to the end of storage, there is no significant difference between the three precooling air speeds; and at the precooling air speed of 1.0 m/s, the average tortuosity value at the end of storage is always significantly lower than the value at 1/2 radius and central radius. It can be observed that the variation of the degree of curvature of the intercellular space at different positions inside the garlic stems stalk precooled by 1.5 m/s or 2.0 m/s air speed is similar to the direct storage treatment. In other words, the two air speeds are less affected, and precooling treatment of 1.0 m/s air speed has a significant influence on the variation of the internal bending degree of the garlic stems.

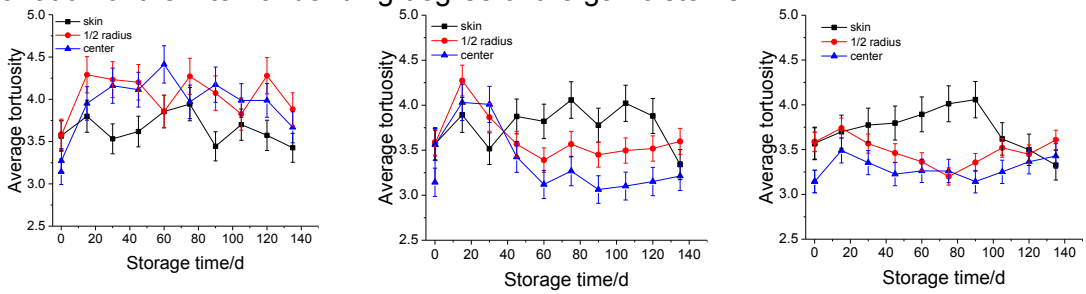

(a) Precooling air speed of 1.0 m/s (b) Precooling air speed of 1.5 m/s (c) Precooling air speed of 2.0 m/s

Figure 5: Variations of average tortuosity with storage time for three precooling air speeds

3.4. Tortuous Fractal Dimension

Fig. 6 shows the variation of the tortuous fractal dimension with storage time. From the Fig. 5, it can be found that the overall change trend of tortuous fractal dimension is consistent with the extension of storage time at different radii under the same working condition: it increases rapidly in the early stage, develops gently in the middle stage, and decreases slowly in the late stage. When the precooling air speed is 1.5 m/s and 2 m/s, there is no significant difference between the 1/2 radius and the central radius in the middle of storage. But there is a significant difference between the two in the late stage due to the difference in the rate of decline, to the end of storage, and both are smaller than the value of the epidermis. However, when the precooling air speed is 1.0 m/s, the values at the 1/2 radius are not significantly different during the entire storage period, and the values are basically the same at the three different radii in the end of storage. It can be seen that different from the precooling air speed of 1.0 m/s, the complexity of water migration channels formed by intercellular space at different positions in the garlic bolts treated with other two air speeds changes similarly.

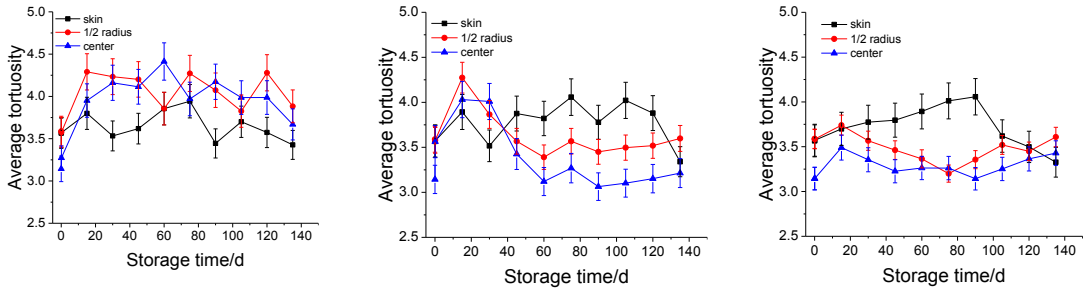

(a) Precooling air speed of 1.0 m/s (b) Precooling air speed of 1.5 m/s (c) Precooling air speed of 2.0 m/s

Figure 6: Variations of tortuous fractal dimension with storage time for three precooling air speeds

3.5. Parameter Correlations

The Pearson correlation coefficient R is used to identify the linear correlation degree and related direction between each structural parameter and the fractal parameter. The measured values are given in Table 2, 3 and 4. There was a major negative correlation between the average tortuosity and its corresponding porosity under three conditions during ice-temperature storage. It shows that when other microstructural parameters are constant, the porosity is larger, and the corresponding degree of bending of the internal fluid passage of the corresponding garlic stems itself is smaller, among them the change of porosity under the condition of precooling air speed of 1.0 m/s has the greatest influence on average tortuosity values. At the same time, the tortuous fractal dimension of the distortion is also significantly negatively correlated with its corresponding porosity, which shows that the greater the porosity during ice-temperature storage, the smaller the complexity of the internal fluid flow line bending of the corresponding garlic stems itself, and among them the change of porosity under the precooling air speed of 1.0 m/s has the greatest influence on the value of the tortuous fractal dimension. It can be observed that the average tortuosity during ice-temperature storage is consistent with the variation of the tortuous fractal dimension of the distortion. At the same time, Table 2, 3 and 4 also show that there is a significant positive correlation between the tortuous fractal dimension and its corresponding average tortuous under the three conditions, and among them, the average tortuosity variation under the precooling air speed of 1.0 m/s has the greatest influence on the value of the tortuous fractal dimension, which qualitatively illustrates the consistency of the two. When the precooling air speed is 1.5 m/s and 2 m/s during ice-temperature storage, there is a significant negative correlation between tortuous fractal dimension of the warp and its corresponding pore fractal dimension. But when the precooling air speed is 1.0 m/s, the correlation between the two phenomena is not significant. Pore fractal dimension was negatively and positively correlated with average tortuosity and porosity, respectively, and the relationship was significant under 1.5 m/s precooling air speed. This could be because the precooling treatment of 1.0 m/s air speed has obvious influence on the change of the complexity of water migration channel and the pore fractal dimension values at the epidermis were at the highest level as a whole when the precooling air speed was 1.0 m/s during the whole storage period.

Table 2. Correlation between structural parameters and fractal parameters for a precooling air speed of 1.0m/s

Margin Position	Pore fractal dimension	Porosity	Average tortuosity	Tortuous fractal dimension
Pore fractal dimension	1	0.502	-0.502	-0.509
Porosity	0.502	1	-0.998**	-0.894**
Average tortuosity	-0.502	-0.998**	1	0.896**
Tortuous fractal dimension	-0.509	-0.894**	0.896**	1

**. There was a significant correlation at the 0.01 level (bilateral); *. There was a significant correlation at the 0.05 level (bilateral).

Table 3. Correlation between structural parameters and fractal parameters for a precooling air speed of 1.5m/s

Margin Position	Pore fractal dimension	Porosity	Average tortuosity	Tortuous fractal dimension
Pore fractal dimension	1	0.834**	-0.711*	-0.796**
Porosity	0.834**	1	-0.922**	-0.889**
Average tortuosity	-0.711*	-0.922**	1	0.816**
Tortuous fractal dimension	-0.796**	-0.889**	0.816**	1

**. There was a significant correlation at the 0.01 level (bilateral); *. There was a significant correlation at the 0.05 level (bilateral).

Table 4. Correlation between structural parameters and fractal parameters for a precooling air speed of 2.0m/s

Margin Position	Pore fractal dimension	Porosity	Average tortuosity	Tortuous fractal dimension
Pore fractal dimension	1	0.601	-0.559	-0.757**
Porosity	0.601	1	-0.942**	-0.634*
Average tortuosity	-0.559	-0.942**	1	0.710*
Tortuous fractal dimension	-0.757**	-0.634*	0.710*	1

**. There was a significant correlation at the 0.01 level (bilateral); *. There was a significant correlation at the 0.05 level (bilateral).

4. CONCLUSIONS

Through the experimental study on garlic stems structure under weak potential difference, the variation of fractal dimension, porosity, average tortuosity and tortuous fractal dimension of garlic stems in three different precooling air speeds was explored, and the following conclusions can be drawn: it is found that the selection of precooling air speed plays an important role in maintaining the quality of post-harvest garlic stems life through experimental research. Because the suitable precooling air speed can maintain the life quality of the harvesting vegetables and reduce the loss during storage. Compared with the precooling air speed of 1.5 m/s and 2.0 m/s, the changes of pore fractal dimension, porosity, average tortuosity and tortuous fractal dimension at different radii of plant microstructure were significantly affected by the precooling air speed of 1.0 m/s, and cells at the epidermis were more affected than cells at the 1/2 radius and the center radius. There is a significant linear correlation between porosity, average tortuosity and tortuous fractal dimension, respectively. The correlation between the two is the largest when the precooling air speed is 1.0 m/s.

NOMENCLATURE

A_0	total area of the image (μm^2)	A_1	total area of the voids in the image (μm^2)
T	temperature of fruit and vegetables (℃)	T_f	cold air temperature (℃)
T_0	initial temperature of fruit and vegetables (℃)	λ_{max}	maximum void fraction size (μm)

REFERENCES

Bear, J., 1972. Dynamics of fluids in porous media. Engineering Geology, 7(2), 174-175.

Cai, J.C., Hu, X.Y., 2015. Fractal Theory in Porous Media and Its Application. Science Press, Beijing, 208 p.

Feng, A.B., Yang, G., He, L., Wang, D.D., Li, Q., Yang, B., Wang, K.H., 2018. Study on the Migration of Bamboo Shoots with Different Storage Conditions by Low-field Magnetic Resonance Spectroscopy. Food & Fermentation Sciences & Technology, 54(1), 18-23.

Guo, Z.L., Chen, X.N., Xu, L., Yang, X.F., Zhang, Q., Cheng, J.L., 2016. Research progress of preservation technology and mechanism of leaf vegetables under map. Chin Agric Bull, 32(21), 161-165.

Guo, X.Q., Feng, A.G., Xia, G.H., Li, X.D., 2017. Effect of Precooling Treatment on Quality of Frozen Tilapia Fillets. Food Science, 38(13), 257-262.

Liu, Y.Z., Chen, S.Q., Sun, H., 2004. Characterizing pores in freeze-dried materials by fractal models and fractal dimensions. Transactions of the Chinese Society of Agricultural Engineering, 20(6), 41-45.

Li, X.H., Guo, X.L., Li, W.X., Xing, Y.G., Xu, Q.L., Liu, X., Pan, Y.F., Bi, X.F., 2018. Research Process on the Effectiveness of Keeping Fresh and Preparation of Chitosan-Based Composite Coating of Keeping Fresh Materials for Fruits and Vegetables. Journal of Xihua University, 37(3), 1-19.

Mainvil, L.A., Horwath, C.C., Mckenzie, J.E., Lawson, R., 2011. Validation of brief instruments to measure adult fruit and vegetables consumption. Appetite, 56(1), 111-117.

Nicolas, V., Salagnac, P., Glouannec, P., Ploteau, J.P., Jury, V., Boillereaux, L.., 2014. Modelling heat and mass transfer in deformable porous media: Application to bread baking. Journal of Food Engineering, 130(3), 23-35.

Ousegui, A., Moresoli, C., Dostie, M., Marcos, B., 2010. Porous multiphase approach for baking process – Explicit formulation of evaporation rate. Journal of Food Engineering, 100(3), 535-544.

Sun, H.J., Zhao, L.H., 2005. Creation and Application of the Fractal Theory. Journal of Liaoning Institute of Technology, 25(2), 113-117.

Temple, N.J., Gladwin, K.K., 2003. Fruit, vegetables, and the prevention of cancer: research challenges. Nutrition, 19(5), 467-470.

Wang, S.F., Yu, B.M., Zheng, Q. , Duan, Y.G., Fang, Q.T., 2011. A fractal model for the starting pressure gradient for Bingham fluids in porous media embedded with randomly distributed fractal-like tree networks. Advances in Water Resources, 34(12), 1-1580.

Xu, L., Jia, F., Luo, C.Y., Zhao, H.F., Gao, F., Liu, Y., Dai, R.T., Li, X.M., 2017. Using LF-NMR to study the changes of moisture content of egg white under carbon dioxide modified atmosphere storage. Science & Technology of Food Industry, 38(2), 313-318.

Xu, P., Yu, B.M., 2008. Developing a new form of permeability and Kozeny–Carman constant for homogeneous porous media by means of fractal geometry. Advances in Water Resources, 31(1), 74-81.

Yu, N., Deng, H.H., Li, Q.M., Mi, Q.H., Han, B., Ai, X.Z., 2015. Effects of Red and Blue Light Quality on the Metabolites and Key Enzyme Activities of Carbon-Nitrogen Metabolism in Celery. J Plant Physiol, 51(1), 112-118.

Yan, D.M., 2017. The application of phase change in food cold chain logistics. Refrigeration and Air-Conditioning, 17(11), 1-5.

Zhao, F., Jing, H.P., Wu, X.L., Guan, W.Q., Liu, B., Zhang, D.Q., 2015. Effect of Modified Atmosphere Packaging in Combination with Ice-Temperature on Quality of Mutton during Storage. Food Science, 45(9), 3772-3778.

Zhang, R.Y., 2003. Packaging Technology for Fresh fruit and vegetables and Its Research Progress in Modern Logistics. Packaging Engineering, 24(1), 71-73.

Manuscript ID: 1058
DOI: 10.18462/iir.icr.2019.1058

Experimental error in large scale cooling operations

Jamal R. OLATUNJI[(a)], Young-Min SHIM[(b)], Andrew R. EAST[(b)]

[(a)] Massey University, Auckland, 0632, New Zealand, j.olatunji@massey.ac.nz
[(b)] Massey University, Palmerston North, 4474, New Zealand, a.r.east@massey.ac.nz

ABSTRACT

Pre-cooling is a vital process for the horticultural cool chain, reducing produce to storage temperature quickly and efficiently. Capturing the 'true' temporal and spatial cooling rates in pre-coolers is prohibitively expensive in terms of time and resources due to their large size, resulting in a worrying trend where small sample sizes are taken as representative of the entire process; and no experimental repetitions eliminates information on the bounds of experimental uncertainty. This study starts to address these concerns by repeating a large scale experimental pre-cooling set up five times – pallets of polylined Hayward kiwifruit (*Actinidia deliciosa*) cooled in laboratory conditions, with a large number of temperature probes. Variability between trials for an entire pallet was ±16%, and variability of observed HCT on an individual box scale was ±21%. A substantial portion of this variability (7%) could be attributed solely to a ±0.5 °C error in thermocouple accuracy.
Keywords: Chilling, Fruit, Modelling, Packaging.

1. INTRODUCTION

A vital component to the horticultural cool-chain is pre-cooling, a dedicated process designed to quickly and efficiently reduce the temperature of fruits and vegetables from their field to storage temperature (Boyette et al., 1989). The most common horticultural pre-cooling process is forced-air cooling, where large batches of produce are palletised and fans are used to pull refrigerated air through the pallet structure (Opara and Zou, 2007). Recently there has considerable focus on improving pre-cooling performance (e.g. Ferrua and Singh, 2009a; Defraeye et al., 2013; O'Sullivan et al., 2016; Berry et al., 2017), as it represents a concentration of capital and operational expenses when viewing the cool-chain as a whole. Small improvements in pre-cooling performance have a disproportionately large flow-on effect to the cool-chain: reductions in cooling time mean higher overall throughout, and reductions in fan-power and refrigeration energy usage translate into large savings in operational expenses, as pre-cooling is the most energy intensive stage of the cool-chain (James and James, 2010).

Measuring the performance of a pre-cooler, or determining the performance impact of an innovation or intervention to a current operation, can be challenging and prohibitively expensive due to the large scale and positional complexity of these systems. This can result in limitations to experimental practice, where for example, a few temperature probes are used to collect data that is interpreted as representing the entire pallet system (e.g. Mercier et al., 2019) or a single temperature probe is used to represent the cooling rate of a box (e.g. Wu et al., 2018; Mukama et al. 2019). Likewise, true replicate measurements of the same system are very rarely performed, with a recent exception being Mukama et al. (2019) who performed three replicates of a large scale cooling trial for pomegranates.

Low sample sizes and a lack of replication threatens the validity and confidence of important innovations in the pre-cooling field. For example, take a hypothetical pre-cooling operation, Operation A. After the cooling performance of Operation A is measured, an intervention is applied, such as a new package design, pallet orientation or refrigeration system, creating a new pre-cooling process, Operation B. After one measurement, Operation B is found to

outperform Operation A by 5%. Reporting these results verbatim conveys a scenario like Figure 1a. However, this is may not be the reality of the situation. If, for example, after performing replicates of both Operation A and Operation B, an experimental error of 10% is observed, the differences between the operations should instead be viewed as Figure 1b. While Operation B may be an improvement over Operation A on average, the advantage is less pronounced than previously implied when taking into consideration the known variability. In this hypothetical situation, declaring Operation B an improvement risks a Type I statistical error (Shuttleworth and Wilson, 2008).

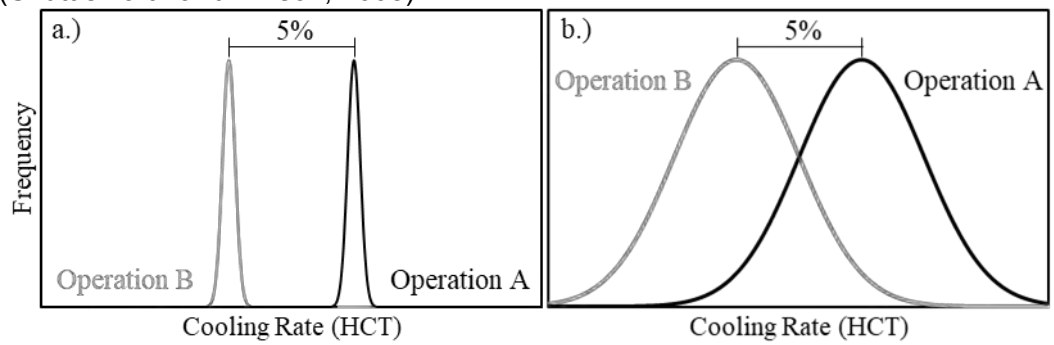

Figure 1: A hypothetical example of how cooling trial results are often presented (a) versus how they should be presented, with statistical uncertainty included (b)

An alternative to experimental systems is to use mathematical models to study pre-cooling (e.g. Ferrua and Singh, 2009a; Defraeye et al., 2013; Han et al., 2017). If a model can be developed and validated, then changes to a pre-cooling operation can be investigated in a digital environment, where materials costs are free and many different iterations can be explored simultaneously. While modelling is increasingly becoming a vital design tool, without information pertaining to uncertainty levels on the data which is used to validate a model, model-derived innovations also risk being Type I statistical errors if the percentage improvement is below the level of uncertainty.

The problem of the lack of definition of experimental error in pre-cooling trials begins to be addressed in this paper. A large scale pre-cooling operation with a high temperature probe sample size was repeated a number of times so that experimental error could be quantified. Five pallets of kiwifruit were assembled and pre-cooled in a laboratory environment, with care to replicate the initial conditions and cooling conditions as much as possible. The results provide guidelines to other researchers as to the levels of experimental error and variability between repeated measures that can be expected in similar large scale pre-cooling processes.

2. METHODS AND MATERIALS

2.1 Experimental

This paper repeats previously published experimental work (O'Sullivan et al., 2016; Olatunji et al., 2017) to determine the bounds of experimental variability, which was previously unmeasured. For clarity, key details of the experimental set up are repeated below; while full details can be found in O'Sullivan et al. (2016) and Olatunji et al. (2017).

The industrial forced-air pre-cooling process widely used by the New Zealand kiwifruit industry was replicated at a smaller scale in a laboratory setting through the construction of a wind-tunnel inside of a refrigerated room with tight temperature and humidity controls, situated at Massey University, Palmerston North, New Zealand. Hayward kiwifruit (*Actinidia deliciosa*) was supplied by Zespri International Ltd. and stacked into pallets weighing roughly 500 kg each – approximately half the size of the pallets used in industry. Type-T thermocouples were inserted into the centre of 16 kiwifruit per selected box (red fruit, Figure 2a) and connected to 64-channel data loggers (1000 Series Squirrel Meter/Logger, Eltek Ltd. Cambridge, UK) to record the fruit temperature every minute for the duration of each repetition. Fourteen (14)

boxes were instrumented: 7 in row B (red, Figure 2b) and 7 in row D (green, Figure 2b) to give a wide spatial sample of 224 temperature positions throughout the pallet. Fresh packaging and fruit was used for each repetition. Each repetition was cooled for 24 h.

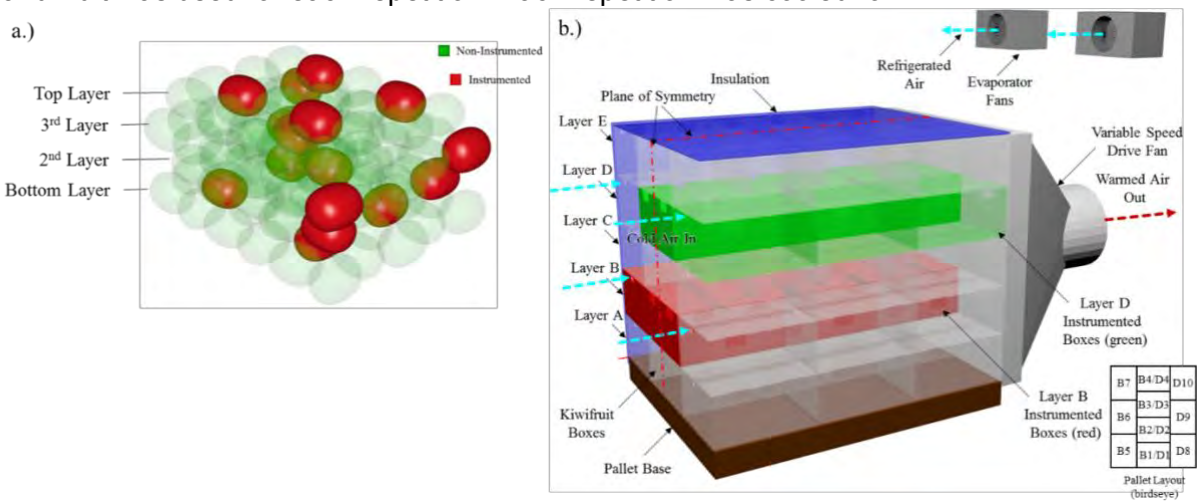

Figure 2: The wind-tunnel constructed to replicate the forced-air cooling process used widely by the New Zealand kiwifruit industry: a.) Ordered stacking pattern of kiwifruit with instrumented fruit highlighted in red; b.) Laboratory forced-air cooling tunnel set-up: 50 boxes of kiwifruit stacked into a pallet, connected to a VSD fan. 14 boxes were instrumented: 7 in layer B (red) and 7 in layer D (green). Images based on Olatunji et al., 2017 with permission from original authors

To minimise differences between replicates, the following steps were taken. Kiwifruit were stacked into 4 ordered rows (Figure 2a) to reduce the impact that random stacking patterns between boxes and experimental replicates might have on the cooling rate. All pallets of fruit were equilibrated at 20 °C for 48 h prior to cooling to ensure a uniform starting temperature across repetitions. The refrigerated air temperature was set to 0 °C and relative humidity to 80% across all repetitions. The variable speed drive fan (AP0502AA5/16, Fantech, Wellington, New Zealand; Figure 2b) was tuned at the beginning of each cooling trial to give a volumetric flow rate of 0.38 $m^3 s^{-1}$ (0.76 L s^{-1} kg $product^{-1}$).
In addition to the first cooling experiment detailed in O'Sullivan et al., 2016 and Olatunji et al., 2017, four additional repetitions were completed over a two-year period (2014-2016) to give a total of 5 replicates of the same precooling system.
Cooling performance was reported as the half-cooling time (HCT) at two levels of detail: pallet scale and box scale. The pallet average HCT was calculated as the average of all thermocouple readings in the pallet, when the Fractional Unaccomplished Temperature Change (FUTC), Y_P, reached 0.5 (Eq. (1); Brosnan and Sun, 2001):

$$Y_{P,t} = \frac{T_{P,t} - T_a}{T_{P,i} - T_a} \qquad \text{Eq. (1)}$$

Where Y is the FUTC (-), T is the temperature (°C), T_a is the refrigerated air temperature (°C); subscript P is the pallet replicate (replicate 1, replicate 2, etc), t is time (hours) and i is initial (t = 0).

At the box scale, symmetry dictates that there are 7 individual box cooling profiles per pallet (Figure 2b). The box average HCT is therefore calculated as the average of all thermocouple readings in that box over both layers B and D, when the FUTC reaches 0.5 (Eq. (2));

$$Y_{B,P,t} = \frac{T_{B,P,t} - T_a}{T_{B,P,i} - T_a} \qquad \text{Eq. (2)}$$

Where subscript B is the specific box (boxes in the centre of the pallet are grouped according to B1/D1, B2/D2, etc.; while boxes on the sides are grouped according to B5/D8, B6/D9 etc.). Average performance is reported as the mean, μ, of HCTs with the unit hours (h). Experimental uncertainty is reported as the standard deviation, σ, in HCTs with the unit hours (h). The coefficient of variability, θ, is also reported, which is the standard deviation divided by the mean, $\theta = \sigma/\mu$, and is dimensionless (-).

2.2 Mathematical Modelling

A computational fluid dynamics (CFD) model of a pallet scale pre-cooling operation for kiwifruit published previously (O'Sullivan et al., 2016) is used in this paper to compare with the experimental work. The intention of this comparison is to provide a more robust validation of the model. The new comparison provides guidelines for the degree to which innovations and interventions derived from a modelling approach must be an improvement on the status quo without undue risk of a Type I statistical error. For instance, in O'Sullivan (2016), the validated CFD model is used to investigate the cooling performance of a new package design with additional ventilation, which in the digital environment was observed to decrease the pallet average HCT by 4.6%. If the experimental uncertainty is larger than 4.6%, then the superiority of this new package design may be minimal in comparison to the random variability that exists. Details of the model are found in O'Sullivan et al. (2016).

3. RESULTS AND DISCUSSION

3.1 Experimental Uncertainty

The average pallet HCT across all 5 replicates was μ = 4.7 h, with a standard deviation σ = 0.76 h, and a coefficient of variability $\theta = \sigma/\mu$ = 0.16, or 16%. The variability between replicates is distributed throughout the pallet in different ways.

Figure 3a shows the box average HCT across the 5 replicates as well as the predicted cooling rates of the pallet scale CFD model (O'Sullivan et al., 2016).

Figure 3b is a more direct comparison between CFD and experimental results, with the average HCT across the 5 replicates, with error bars as the 95% confidence interval.

Figure 4a shows the standard deviation compared to the mean HCT of each box, and

Figure 4b the relative error compared to the mean HCT of each box.

Error at an individual box level was high – for example, box B7/D10 has a HCT of 8.8 h in replicate 2, but 4.6 h in replicate 5. The error in individual boxes appears to increase when the cooling rate is slower: for example, box B1/D1, which is the fastest cooling box as it is nearest to the inlet of refrigerated airflow, had a standard deviation of just 0.65 h; whereas box D4/B4, the slowest cooling box as it is the furthest away from the inlet of refrigerated airflow, had a standard deviation of 1.47 h – over twice the level of uncertainty.

Figure 4a elucidates the general upward trend between the standard deviation and the cooling rate. There does not seem to be much relative increase in error, however: the coefficient of variability stays fairly constant (Fig.

Figure 4b).

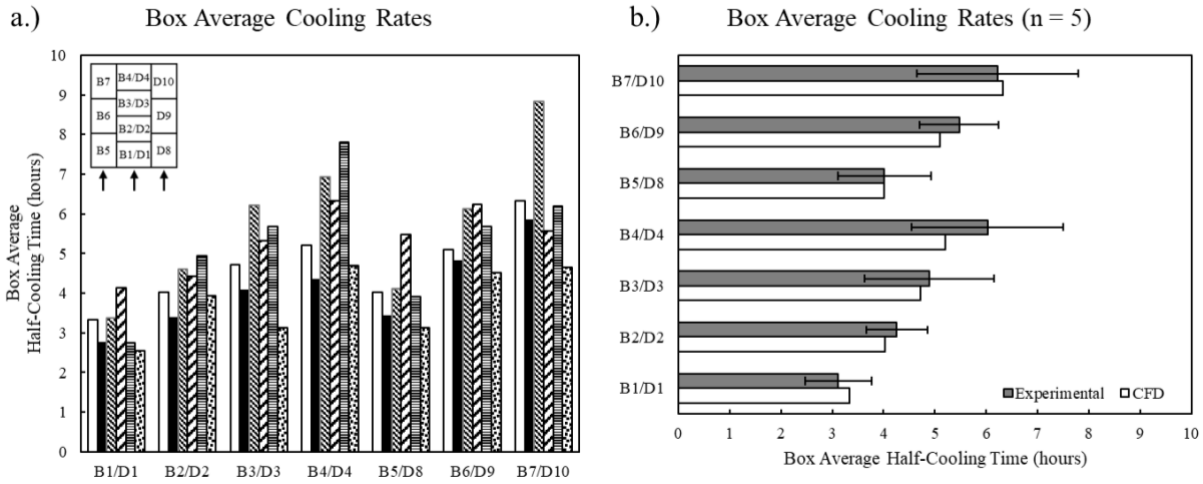

Figure 3: Overall experimental uncertainty. a.) HCT of each Box, experimental vs. CFD model (O'Sullivan et al., 2016); b.) Average HCT of each box, experimental vs. CFD model (O'Sullivan et al., 2016; error bars 95% C.I.)

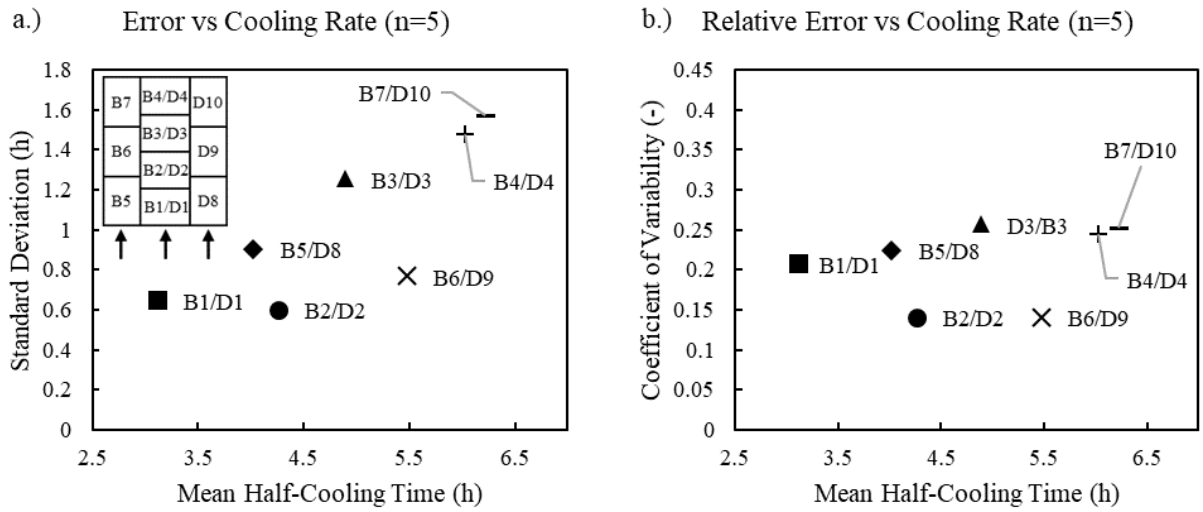

Figure 4: Error in different positions of the pallet: a.) Absolute error (standard deviation) compared with the mean cooling rate per box; b.) Relative error (coefficient of variability) compared with the mean cooling rate per box

These results (Fig. 3) further validate the CFD model developed in O'Sullivan et al. (2016). While the CFD model tends to slightly under predict the HCT at a per box level, it was still well within the bounds of experimental uncertainty across all 7 comparisons. With an overall level of error of ±16%, this is potentially problematic for model use as a design tool. In order to confidently avoid a Type I error, the model must produce a new package design that is at least a 16% improvement over the status quo.

Viewed from another perspective, these results (Fig. 3b) could strengthen model use as a design tool in this field, as the CFD model predicted the average results very closely. This could be interpreted as the model removing many of the random errors of cooling that are present experimentally that result in adding substantially more variability to the system. Variability is introduced through different fruit sizes (Wu et al., 2018), different fruit thermal properties, variable initial and air delivery temperatures and variable pressure drops across the system (Shim et al., 2016). Without these random errors in a modelling environment, there are only systematic errors associated with how the model is constructed. If these are managed correctly, then modelling remains an important tool for driving innovation in this area. For example, despite the high level of error in overall HCT prediction, the model of O'Sullivan et al. (2016) remains useful in showing that boxes furthest away from the inlet of refrigerated

airflow had the slowest cooling rates. Therefore a model based design that redirects fresh airflow to boxes at the rear of the pallet will be a superior design. In other words, a validated model can be useful in showing *where* improvements to an operation need to be made.
From these results, new guidelines can be developed. When reporting pallet average HCT, in the absence of a measured experimental uncertainty range, it is recommended that a ±16% margin of error is used. Assuming that
Figure 4b shows an insignificant correlation between θ and μ, the average θ for the 7 boxes across 5 replicates can serve as the new benchmark for experimental uncertainty at the individual box level; the average coefficient of variability being 0.21, or 21%. It is therefore recommended that (in the absence of a measured experimental uncertainty range) measured box average HCTs use a ±21% margin of error.

3.2 Thermocouple Error

While there are many potential contributors to the random error observed in the results, one potential source is the temperature measurement equipment, which may also explain the increase in error when the cooling rate is slower (

Figure 4 4a). In this section the error introduced purely from the thermocouple equipment is quantified.

The Type-T thermocouples used during experimentation have a ±0.5 °C margin of error according to the manufacturer (1000 Series Squirrel Meter/Logger, Eltek Ltd. Cambridge, UK). This error is defined as ε. The implication of this is that boxes that are cooling slower will have intractably larger variance when reporting cooling rates in terms of the HCT, as ε becomes more meaningful. To demonstrate, imagine a hypothetical box that is cooling in a perfectly exponential fashion from T_i = 20 °C to T_a = 0 °C:

$$Y = e^{\left(\frac{\ln(0.5)}{HCT}\right)\cdot t} \qquad \text{Eq. (3)}$$

Where the proportionality constant $\ln(0.5)/HCT$ reflects that the FUTC will halve every period of HCT. The HCT is defined as the time when the thermocouple reads Y = 0.5:

$$t = \frac{HCT}{\ln(0.5)} \cdot \ln(Y) \qquad \text{Eq. (4)}$$

First, it is assumed that the box has a HCT of 2 h, and there is no thermocouple error (ε = 0 °C). The measured HCT will be:

$$t = \frac{2}{\ln(0.5)} \cdot \ln(0.5) = 2 \qquad \text{Eq. (5)}$$

However introducing ε = 0.5 °C means the temperature reading when the box reaches 10 °C (the HCT) could be 10.5 °C or 9.5 °C. This corresponds to FUTC values of 0.525 and 4.75, respectively:

$$t = \frac{2}{\ln(0.5)} \cdot \ln(0.525) = 1.86 \qquad \text{Eq. (6)}$$

$$t = \frac{2}{\ln(0.5)} \cdot \ln(0.475) = 2.15 \qquad \text{Eq. (7)}$$

So that ε = 0.5 °C translates into a ±0.15 h error in HCT measurement. Continuing the exercise, applying Eq. (4) to a box with a HCT of 4 h, ε = 0.5 °C now translates into a ±0.30 h error in HCT measurement. This trend continues so that the absolute error in HCT doubles with every doubling of the HCT. As the relationship is linear, the coefficient of variability (θ) is

constant: $\theta_{thermocouple}$ can therefore be derived by Eq. (8) as a function of the starting temperature, T_i, the refrigeration temperature, T_a, and the thermocouple error, ε:

$$\theta_{thermocouple} = \frac{\left[1 - \frac{\ln(Y_{+\varepsilon})}{\ln(0.5)}\right] + \left[\frac{\ln(Y_{-\varepsilon})}{\ln(0.5)} - 1\right]}{2} \quad \text{Eq. (8)}$$

Where:

$$Y_{+\varepsilon} = 0.5 + \frac{\varepsilon}{T_i - T_a} \quad \text{Eq. (9)}$$

$$Y_{-\varepsilon} = 0.5 - \frac{\varepsilon}{T_i - T_a} \quad \text{Eq. (10)}$$

For T_i = 20 °C to T_a = 0 °C and ε = 0.5 °C, $\theta_{thermocouple}$ = 0.072, or 7.2%. Remembering that total variance per box was 21%, this shows that thermocouple error can potentially represent a large portion of total error in HCT measurement and is the most likely culprit for the increase in error as the HCT increases (
Figure 4a).
The implications of this analysis are that setting a starting temperature of T_i = 30 °C reduces relative error to $\theta_{thermocouple}$ = 4.8%; and if thermocouples can be purchased with ε = 0.1 °C, relative error reduces to just $\theta_{thermocouple}$ = 1.4%.

4. CONCLUSIONS

In this study, the level of experimental error in large scale pre-cooling operations was determined by repeating a popular forced-air cooling process for kiwifruit 5 times and observing the differences between trials. It was found that the level of relative error on a pallet average HCT basis was ±16%; and from a box average perspective, the relative error was ±21%. It is recommended that these levels of experimental error are adopted by other researchers in the absence of a measured experimental uncertainty range. This study also suggests that mathematical modelling can be an accurate method of predicting the average cooling rates of individual boxes, and can be a good tool to assess how the physics of a system combines to produce a measured cooling rate. However, model-derived designs that show improvements of less than 16% should be viewed with scepticism until the ability to measure large-scale cooling operations is improved. We predict up to 7.2% of the relative error is a result of the ±0.5 °C uncertainty associated with the Type-T thermocouples used in these experiments, for the commonly used cooling change of 20 °C to 0 °C.

ACKNOWLEDGEMENTS

The authors gratefully acknowledge the New Zealand Ministry of Business, Innovation and Employment for funding this work (Fibreboard Packaging Design Project, MAUX1302). We also acknowledge the help of Dr. Justin O'Sullivan for planning and assisting in the original experimental work; and students Alicia Tan, Lyall McDonald, Julia Zhou, Angela Yang and Tim Cook for their help collecting experimental data.

REFERENCES

Berry, T. M., Fadiji, T. S., Defraeye, T., Opara, U. L., 2017. The role of horticultural carton vent hole design on cooling efficiency and compression strength: A multi-parameter approach. Postharvest Biol. Technol., 124, 62-74.

Boyette, M.D., Wilson, L.G., Estes. E.A., 1989. Forced-air cooling. North Carolina Agricultural Extension Service.

Brosnan, T., Sun, D.W., 2001. Precooling techniques and applications for horticultural products — a review. Int. J. Refrigeration 24(2), 154-170.

Defraeye, T., Lambrecht, R., Tsige, A.A., Delele, M.A., Opara, U. L., Cronjé, P., Verboven, P., Nicolai, B., 2013. Forced-convective cooling of citrus fruit: Package design. J. Food Eng. 118(1), 8-18.

Ferrua, M.J., Singh, R.P., 2009a. Modeling the forced-air cooling process of fresh strawberry packages, Part I: Numerical model. Int. J. Refrigeration 32(2), 335-348.

Ferrua, M.J., Singh, R.P., 2009b. Modeling the forced-air cooling process of fresh strawberry packages, Part III: Experimental validation of the energy model. Int. J. Refrigeration 32(2), 359-368.

Han, J.W., Qian, J.P., Zhao, C.J., Yang, X.T., Fan, B.L., 2017. Mathematical modelling of cooling efficiency of ventilated packaging: Integral performance evaluation. Int. J. Heat and Mass Transfer 111(Supplement C), 386-397.

James, S.J., James, C., 2010. The food cold-chain and climate change. Food Res. Int. 43(7), 1944-1956.

Mercier, S., Brecht, J. K., Uysal, I., 2019. Commercial forced-air precooling of strawberries: A temperature distribution and correlation study. J. Food Eng. 242, 47-54.

Mukama, M., Ambaw, A., Berry, T. M., Opara, U. L., 2019. Analysing the dynamics of quality loss during precooling and ambient storage of pomegranate fruit. J. Food Eng. 245,166-173.

O'Sullivan, J., 2016. Significant factors affecting the forced-air cooling process of polylined horticultural produce (PhD thesis). Massey University, Palmerston North, New Zealand.

O'Sullivan, J., Ferrua, M. J., Love, R., Verboven, P., Nicolaï, B., East, A.R., 2016. Modelling the forced-air cooling mechanisms and performance of polylined horticultural produce. Postharvest Biol. Technol. 120, 23-35.

Olatunji, J., Love, R., Shim, Y., Ferrua, M., East, A., 2017. Quantifying and visualising variation in batch operations: A new heterogeneity index. J. Food Eng. 196, 81-93.

Opara, L.U., Zou, Q., 2007. Sensitivity analysis of a CFD modelling system for airflow and heat transfer of fresh food packaging: inlet air flow velocity and inside package configurations. Int. J. Food Eng. 3 (5). Article 16.

Shim, Y.M., Olatunji, J.R., Zhou, J., Love, R.J., Ferrua, M.J., East, A.R., 2016. Industry survey on the pressure drop across palletised horticulture produce during precooling. 4th International Institute of Refrigeration International Conference on Sustainability and the Cold Chain, Auckland, New Zealand, 7-9 April 2016.

Shuttleworth, M., Wilson, L.T., 2008. Type I Error and Type II Error. Retrieved from Explorable.com: https://explorable.com/type-i-error.

Wu, W., Häller, P., Cronjé, P., Defraeye, T., 2018. Full-scale experiments in forced-air precoolers for citrus fruit: Impact of packaging design and fruit size on cooling rate and heterogeneity. Biosystems Eng. 169, 115-125.

Manuscript ID: 1084
DOI: 10.18462/iir.icr.2019.1084

Experimental measurements of the pressure drop loss coefficient for vent configurations of packaging designed for air cooling of horticultural products

Nicolas I. TAPIA[(a)], Richard J. LOVE[(a)], Emilia NOWAK[(b)], Andrew R. EAST[(a)].

[(a)] Massey University, Palmerston North, 4442, New Zealand, a.r.east@massey.ac.nz
[(b)] Massey University, Auckland, 0745, New Zealand.

ABSTRACT

In fresh produce precooling applications, an important feature of packaging design are the vents that allow airflow within, between and through stacked packages. The pressure drop through an orifice (i.e. a vent) can be characterised in terms of a loss coefficient and numerous correlations exist to predict this in literature, which theoretically can be used to predict the airflow distribution for a given packaging system. However, many such correlations were developed for orifices with much larger total open area (TOA) than are typically encountered in packaging vents (2 - 8%) and do not account for apparently significant vent design parameters such as number of vents, and location on the packaging face. In this work, the pressure loss coefficient for different vent designs were measured and compared with literature sourced coefficients. In addition to vent size, results presented consider and describe the influence of number and location of vents on the package.
Keywords: Pressure Drop, Loss Coefficient, Vent Size, Vent Location, Vent Number, TOA.

1. INTRODUCTION

The horticulture industry is able to trade globally due to the cool chain. One mechanism to extend shelf life is through abrupt reduction of the produce temperature to storage temperature, slowing the metabolic processes of the fruit (Brosnan and Sun, 2001). For many horticultural products, the forced draft cooling method is used for the initial temperature reduction. This method consists of pulling refrigerated air through a stack of palletised boxes filled with produce by using fans to create a pressure differential across the packaging system. The resulting airflow pathway through the boxes allows direct convective heat transfer between the cold air and the warm produce.

A key area of research that influences forced draft cooling effectiveness is the design of the vents of the packaging. Well designed venting allows the air to reach every fruit in the box effectively, reducing cooling time and heterogeneity (Olatunji et al., 2017). Additionally, appropriate vent design can result in reduced pressure differential requirements through the stack of produce (for a given flowrate), thus potentially reducing the fan energy requirements of the cooling operation.

Modelling the momentum and energy balances during forced draft cooling have been largely done by using direct numerical simulations (Defraeye et al., 2013; Dehghannya et al., 2011; Ferrua and Singh, 2009; O'Sullivan et al., 2016) or as porous media (Alvarez et al., 2003; Delele et al., 2013; Gruyters et al., 2018; Verboven et al., 2006), implemented in complex software packages (Dehghannya et al., 2010). Such approaches can be robust but the model preparation, solving time, and computational power make these approaches incompatible for combination with optimisation routines such as generic algorithms or Monte Carlo simulations (Martinez-Hermosilla et al., 2018), where thousands of similar scenarios would be simulated. In particular, the complex internal geometry of fruit within boxes can be very difficult to model via these methods without simplification (O'Sullivan et al., 2016).

An alternative approach that has the potential to both be accurate and fast in predicting airflow pathways through a system is the resistance network airflow model (Smale et al., 2006). For the scenario of forced draft cooling of palletised fruit, vents on the package become a major resistance in the system that requires quantification to enable prediction. In the kiwifruit modular bulk packaging

(MBP) system (O'Sullivan et al., 2016; Olatunji et al., 2017), as a polylined system, headspace flow becomes highly relevant, as this acts as the heat transfer surface where refrigerated air flows through the palletised boxes, similar to a network of pipes connected by orifice plates. Should the airflow pathways resistances be predicted, a robust, fast approach to optimise box design could potentially be developed. This airflow resistance approach has been applied previously for refrigerated shipping systems (Smale, 2004) and refrigerated display cabinets (Ben-abdallah et al., 2018; Love and Cleland, 2007).

A mechanical energy balance can be applied to determine the pressure differential through one or more boxes. Darcy's relationship (Darcy, 1857) describes this phenomena when air passes through a physical barrier, in this case, a vent hole, as this relationship describes pressure drop due to orifices and other accessories in a pipe system. Physical barriers are represented by a loss coefficient (k), in this case, the impact of the vent hole geometry on the total pressure loss through a box. In most cases, loss coefficients and friction factors are tabulated for specific pipe features ultimately based on empirical data. Idelchik (1994), developed a formula to calculate a loss coefficient based on an orifice plate size with some distinction between different ranges of Reynolds number. While this approach is well-understood in pipeline design, there is no certainty that this approach will accurately account for the features present in palletised boxes including the number of vents, vent size, and vent location. Literature recommends a TOA of 14% for optimising cooling performance (de Castro et al., 2005), while the internal TOA between the headspaces of adjacent boxes is much greater (≈50%; Fig. 1b). Previously, Vigneault et al. (2004) showed that for 1, 5 and 80 (slit) orifices there was a difference in pressure drop at 25% TOA. What happens when the number of vents varies between 1 and 5 is still uncertain. The aim of this research is to investigate the effect of vent hole size, location and number on the loss coefficient and to evaluate the accuracy of the approaches found in the literature for the calculation of this coefficient.

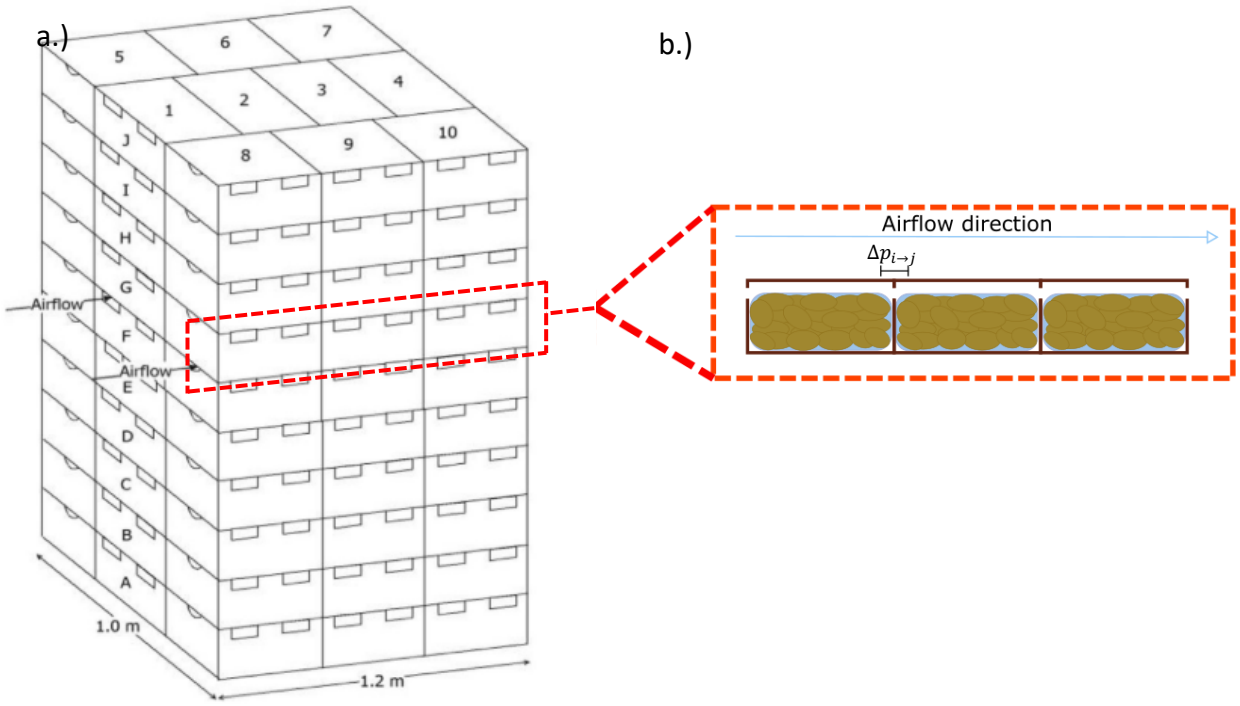

Figure 1: Diagram of airflow direction during forced-air cooling of a.) Pallet of produce (adapted from O'Sullivan et al. (2016)), and b.) Airflow pathway between boxes, where $\Delta p_{i \to j}$ is the pressure drop in the vent between two boxes

2. METHODOLOGY

2.1. Experimental Design

This experiment was conducted in a temperature controlled wind tunnel (Fig. 2) set at 25°C, with a variable speed drive fan for wind speed control. Uniform airflow is achieved with a flow straightener and a mesh grid. The wind tunnel has a square cross section with sides of 27.8 cm.
Test plates were made of medium density fibre (MDF) of 5 mm thickness, cut with a laser cutter (Fusion M2 Epilog Laser, Epilog, USA) to mimic potential box faces used in the horticultural industry. Fig. 3 shows the designs.
To monitor pressure drop, a differential pressure sensor (SSCSNBN002NDAA5, Honeywell, Morris Plains, USA) with a range of 498 Pa and an accuracy of ±2% was used, placing each pressure probe at 7.5 mm distance from the plate in both directions at the top of the tunnel. Pressure data was logged every second for 150 seconds using a data logging system (Picolog1216, Pico Technologies, UK). A hot wire anemometer (9545 Velocicalc Air velocity meter, TSI, USA) with an accuracy of ±3% was used to measure point velocity at the centre of the tunnel 50 cm upstream of the plate. From the point velocity the mean tunnel superficial velocity was determined from a calibration curve previously created (data not shown). Each plate was measured at 10 different wind speeds, in triplicate.

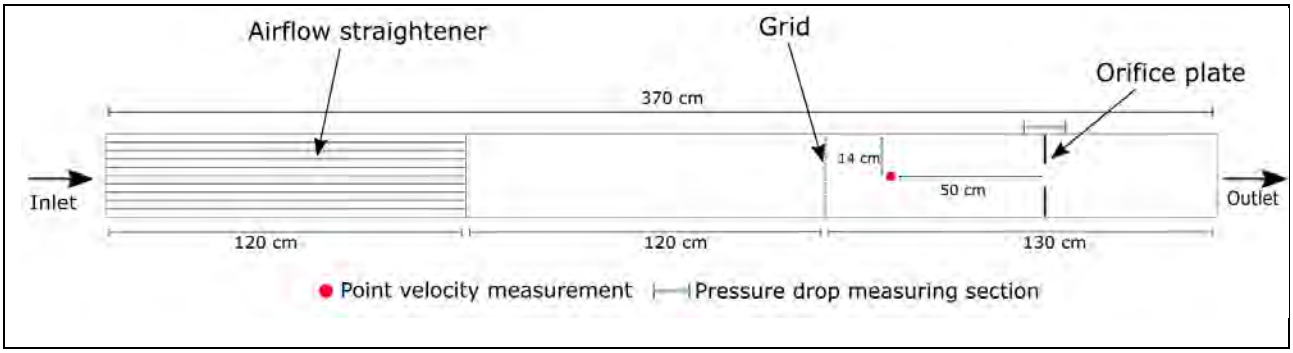

Figure 2: Longitudinal drawing of a variable speed fan wind tunnel and test section

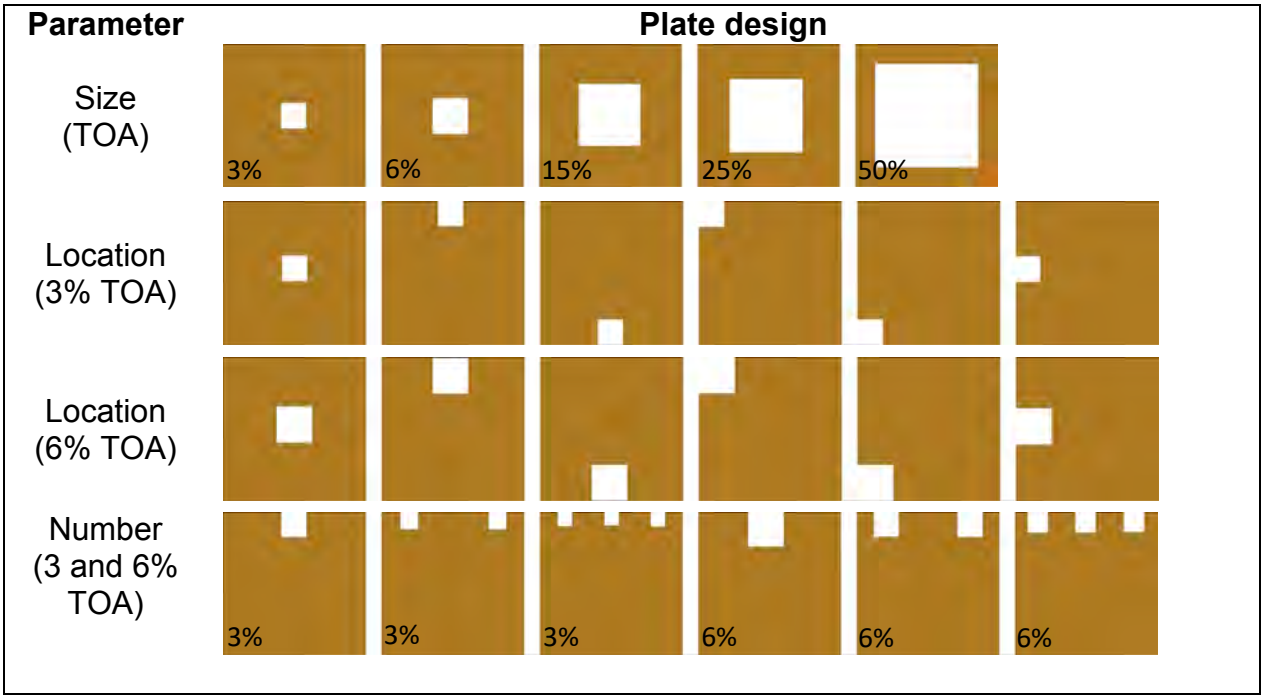

Figure 3: Experimental plate design classified by each design parameter tested. Each plate has a 27.8 cm hydraulic diameter

2.2. Data Analysis

The measured data was compared to Darcy's relationship of pressure loss due to an orifice plate (Eq. 1) using Idelchik's relationships to calculate the loss coefficient k (Idelchik, 1994).

$$\Delta p = k\rho\frac{v^2}{2} \quad \text{Eq. (1)}$$

$Re \geq 10^5$

$$k = \left(1 + 0.707\sqrt{1 - \frac{A_0}{A_1}} - \frac{A_0}{A_1}\right)^2 \left(\frac{A_1}{A_0}\right)^2 \quad \text{Eq. (2)}$$

$Re < 10^5$

$$k = \left[k_\varphi + \zeta_0{}^{-Re}\left(1 + 0.707\sqrt{1 - \frac{A_0}{A_1}} - \frac{A_0}{A_1}\right)^2\right]\left(\frac{A_1}{A_0}\right)^2 \quad \text{Eq. (3)}$$

Where Δp is the pressure drop across the orifice (Pa), v is the superficial velocity (m/s), ρ is the air density at 25°C, k is the pressure loss coefficient (-), A_1 is the cross sectional upstream area of the tunnel (i.e. the box face) (m^2), and A_0 is the total open cross sectional area of the vents (m^2). Values of $\zeta_0{}^{-Re}$ and k_φ are coefficients of the jet section of the flow dependant on Reynolds number and the TOA. These coefficients are tabulated and can be found in detail in Idelchik (1994).

3. RESULTS

3.1. Effect of Vent Size on the Loss Coefficient

Fig. 4 shows the effect of vent size on the pressure loss for 5 different TOAs. As expected, as the vent TOA increases, the pressure drop decreases for a given superficial velocity. Idelchik's formula for an orifice plate of TOA between 3 and 15% appears to model the results well. For 25 and 50% TOA, the calculated loss coefficient under predicts the data. This was unexpected as the formula of Idelchik were developed for larger vents, commonly found in pipe network systems.

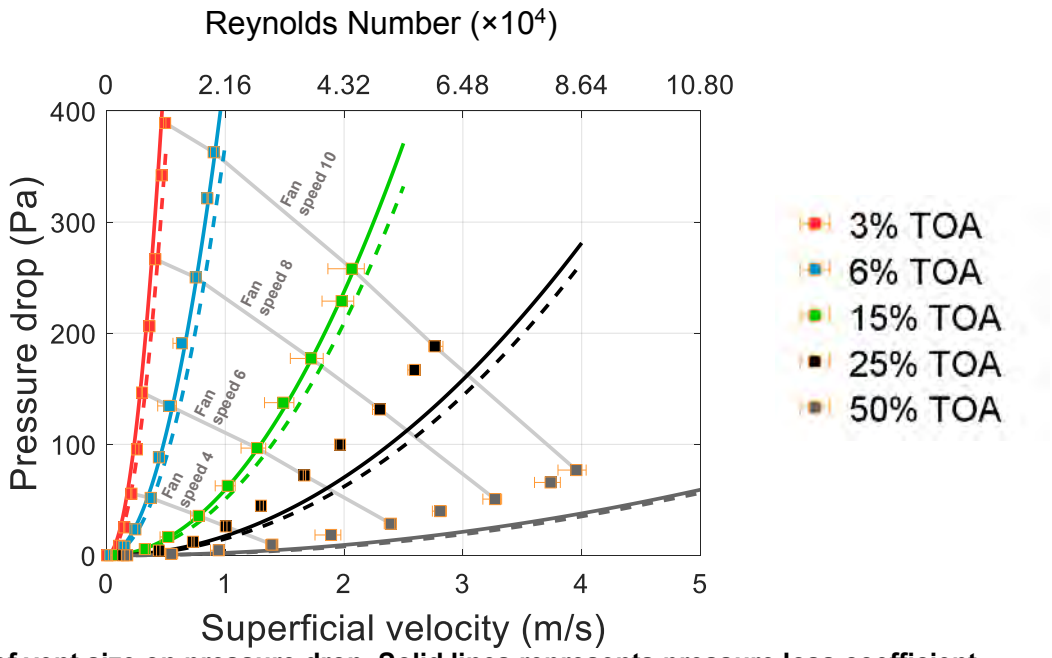

Figure 4: Effect of vent size on pressure drop. Solid lines represents pressure loss coefficient calculated by Eq. (2), and dashed lines represents pressure loss coefficient calculated by Eq. (3). Error bars represent the range of measured superficial velocity data. Grey lines represent corresponding fan speed for each TOA

When comparing 6% TOA to 3% TOA, the differences in pressure drop at each fan speed are not substantial, with a maximum difference of 6.7% at the highest fan speed, while the superficial velocity is almost double for 6% TOA compared to 3% TOA. This is an important insight when considering the size of vent holes of a package of low TOA, as relatively similar pressure drops are obtained with an important increase in the superficial velocity and hence potentially faster cooling.
For this case, the use of either Eq. (2) or (3) did not make a significant difference, despite Eq. (2) strictly being intended for a higher Reynold's number regimes than these experimental conditions. This may be an advantage as Eq. (2) does not depend on Reynolds number and hence can be applied to calculate the k coefficient independent of air flowrate. This means that a procedure to predict air flowrate from pressure drop may not need to be iterative even at low flow conditions.

3.2. Effect of Vent Location on the Loss Coefficient

Vent location had little effect on the loss coefficient and, hence on the pressure drop for 3 and 6% TOA (Figs. 5 and 6). Difference between superficial velocity between centre vent and top vent (Figs. 5b and 5e is 13.8%, while differences on pressure drop for the same vents is only 2.14%. Eq. (2) or (3) can both be used to estimate the loss coefficient with similar accuracy. This is an important finding as vent location is a key design parameter and it is valuable that the loss coefficient can be predicted for variable locations using a single existing relationship. Of course, this does not account for the effect of potential vent obstructions. In practice, vents not located at the top of the box will possibly have fruit immediately in the airflow path. This will also be the case in box configurations with minimal headspaces, where in case of an obstruction, this may affect the loss coefficient of the vent and the obstruction itself (Ai and Mak, 2013).

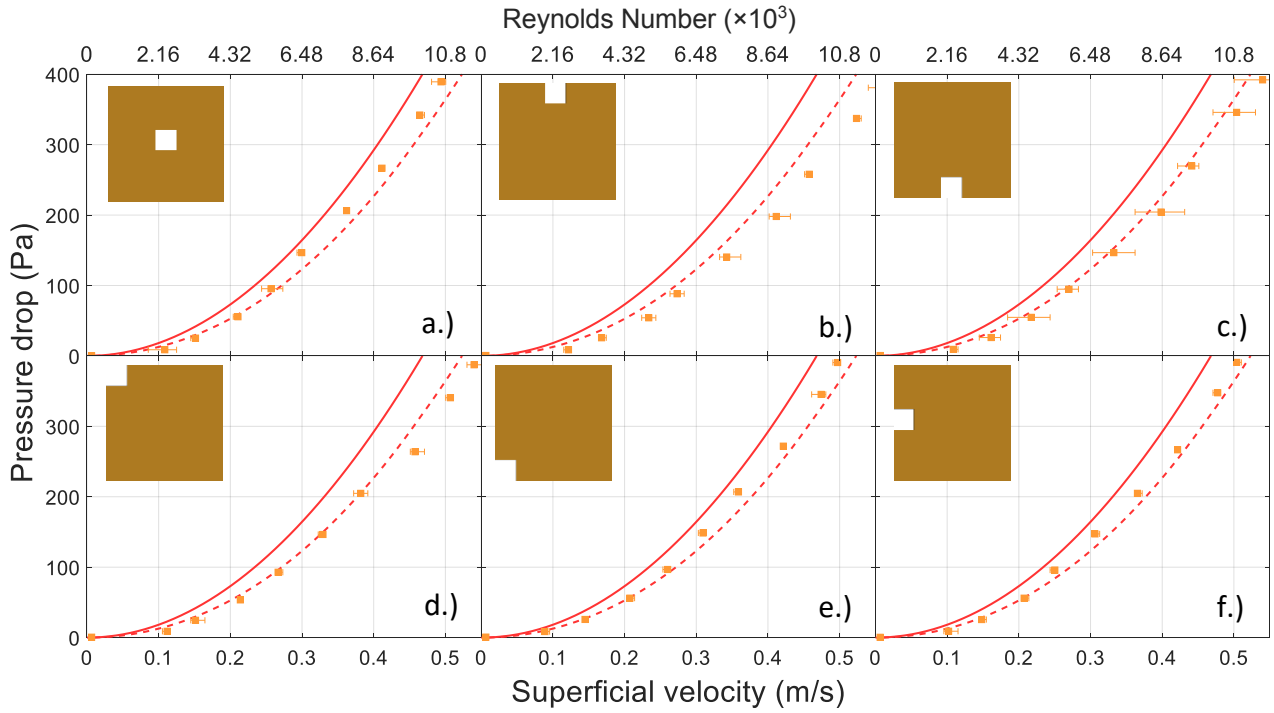

Figure 5: Effect of vent location on the pressure drop for a 3% TOA. Solid lines represents pressure loss coefficient calculated by Eq. (2), and dashed lines represents pressure loss coefficient calculated by Eq. (3). Error bars represent the range of measured superficial velocity data

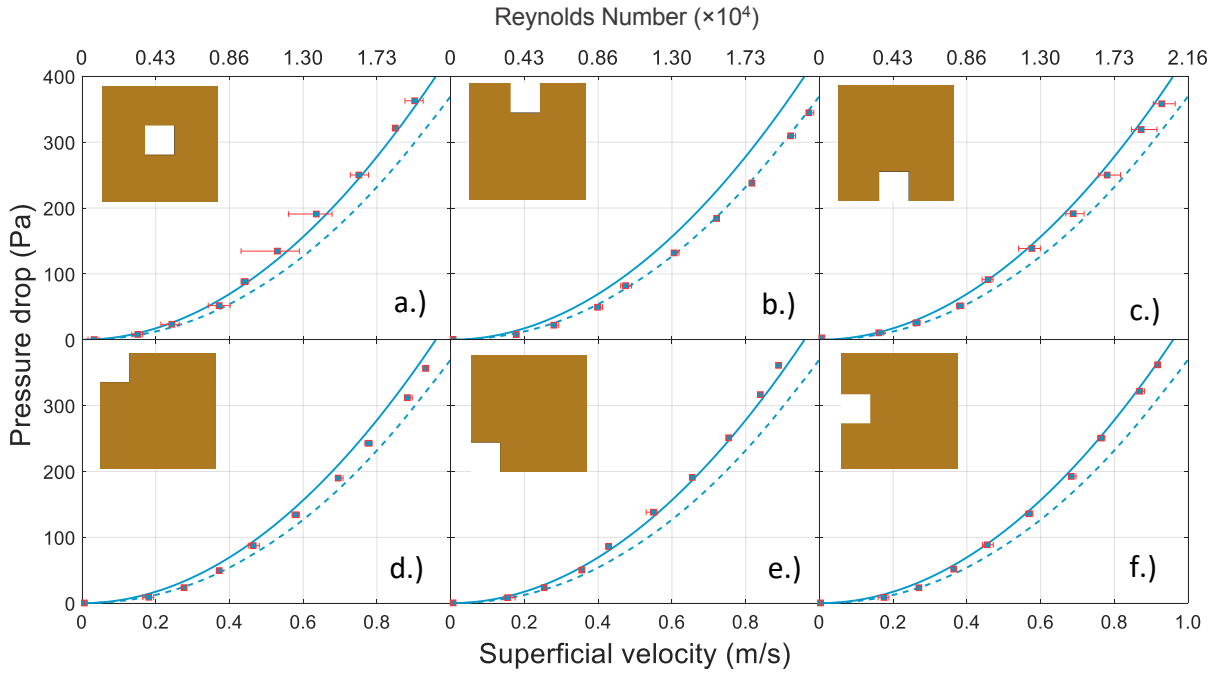

Figure 6: Effect of vent location on the pressure drop for a 6% TOA. Solid lines represents pressure loss coefficient calculated by Eq. (2), and dashed lines represents pressure loss coefficient calculated by Eq. (3). Error bars represent the range of measured superficial velocity data

3.3. Effect on Vent Number on the Loss Coefficient

For the measured cases of up to 3 vents located at the top of the plate, there was no significant differences between the pressure drop recorded for the same TOA distributed over 1, 2 or 3 vents shown in Fig. 7 and Fig. 8. Vigneault et al. (2004) previously found differences in pressure drop imparted by vent number at 25% TOA plates. Those results suggest that pressure drop should increase with vent number, but that study was conducted with the TOA distributed over larger number of vent holes (up to 80). Thus, there may be a point at which the number of vents that the TOA is distributed over becomes significant regarding to pressure drop, but this number may be greater to the typically observed on horticultural packaging.

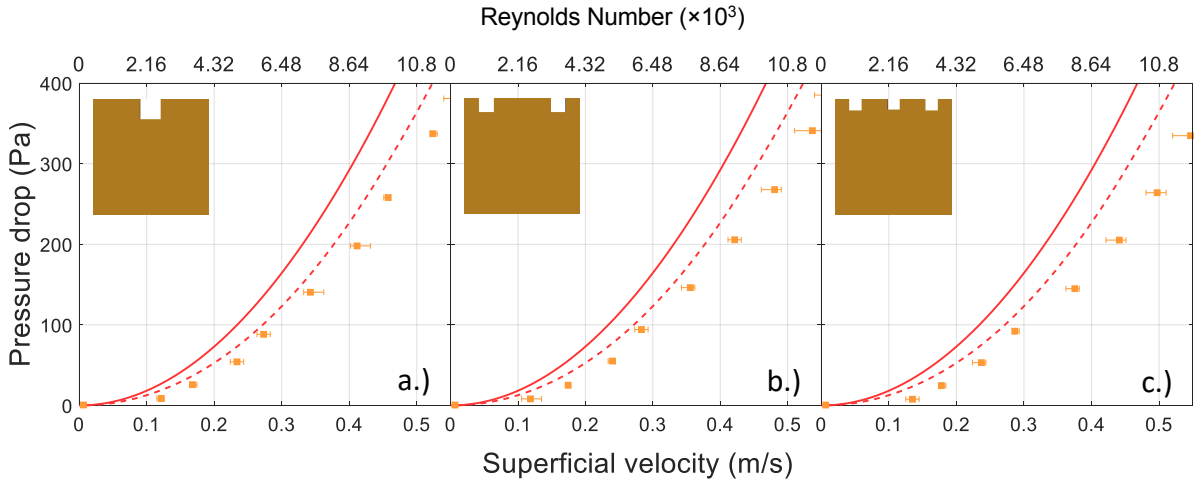

Figure 7: Effect of vent number on the pressure drop for 3%. Solid lines represents pressure loss coefficient calculated by Eq. (2), and dashed lines represents pressure loss coefficient calculated by Eq. (3). Error bars represent the range of measured superficial velocity data

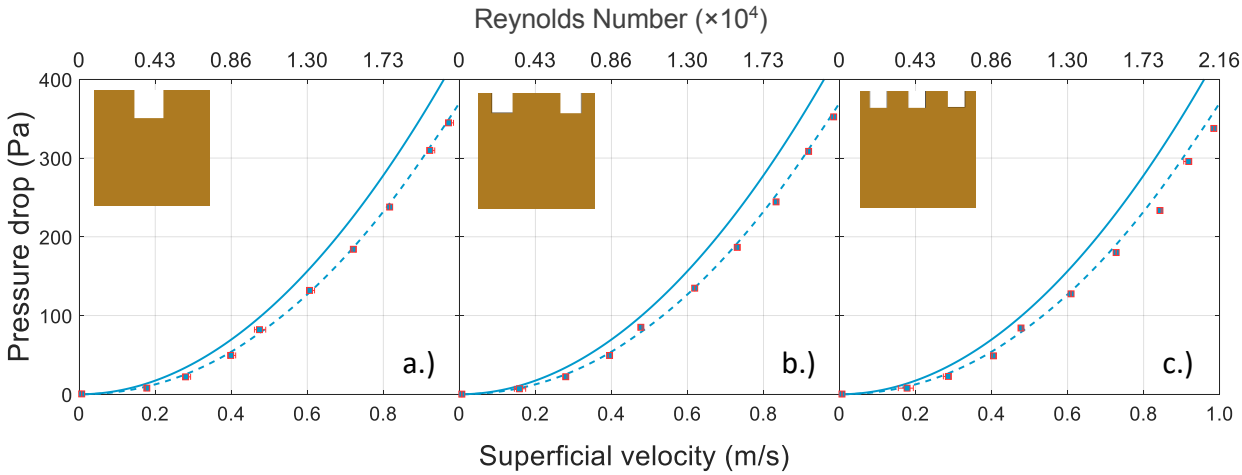

Figure 8: Effect of vent number on the pressure drop for 6% TOA. Solid lines represents pressure loss coefficient calculated by Eq. (2), and dashed lines represents pressure loss coefficient calculated by Eq. (3). Error bars represent the range of measured superficial velocity data

4. CONCLUSIONS

Vent size effects on pressure drop were investigated empirically and theoretically. An increase in the vent size results in a decrease in the pressure drop. For 3, 6 and 15% TOA, empirical data fits the loss coefficients that are predicted by Darcy and Idelchik equations (Eq. (1) to Eq. (3)). Interestingly, a comparison between 3 and 6% TOA showed that this increase on the TOA increase the superficial velocity without significant decay on the pressure drop. Vent location and the number of vents for 3 and 6% TOA had no significant effect on the pressure drop for up to 3 vents at constant TOA. The results show that prediction of the loss coefficient for a high Reynolds number ($Re \geq 10^5$; Eq. (2)) can be applied accurately to lower Reynold's number conditions, for the studied vent designs. This is an advantage as the high Reynold's number equation is simpler and thus easier to incorporate into a rapid computational scheme for modelling airflow distribution.

ACKNOWLEDGEMENTS

This work is part of the Fibreboard Packaging Design project funded by the Ministry of Business, Innovation and Employment of New Zealand (MAUX1302).

REFERENCES

Ai, Z.T., Mak, C.M., 2013. Pressure losses across multiple fittings in ventilation ducts. Sci. World J. 2013, 11.

Alvarez, G., Bournet, P.-E., Flick, D., 2003. Two-dimensional simulation of turbulent flow and transfer through stacked spheres. Int. J. Heat Mass Trans. 46, 2459-2469.

Ben-abdallah, R., Leducq, D., Hoang, H.M., Pateau, O., Ballot-Miguet, B., Delahaye, A., Fournaison, L., 2018. Modelling and experimental investigation for load temperature prediction at transient conditions of open refrigerated display cabinet using Modelica Environment. Int. J. Refrigeration 94, 102-110.

Brosnan, T., Sun, D.-W., 2001. Precooling techniques and applications for horticultural products — a review. Int. J. Refrigeration 24, 154-170.

Darcy, H., 1857. Recherches expérimentales relatives au mouvement de l'eau dans les tuyaux. Mallet-Bachelier, Paris, 769 p.

de Castro, L.R., Vigneault, C., Cortez, L.A.B., 2005. Cooling performance of horticultural produce in containers with peripheral openings. Postharvest Biol. Technol. 38, 254-261.

Defraeye, T., Lambrecht, R., Tsige, A.A., Delele, M.A., Opara, U.L., Cronjé, P., Verboven, P., Nicolai, B., 2013. Forced-convective cooling of citrus fruit: package design. J. Food Eng. 118, 8-18.

Dehghannya, J., Ngadi, M., Vigneault, C., 2010. Mathematical modeling procedures for airflow, heat and mass transfer during forced convection cooling of produce: A review. Food Eng. Rev. 2, 227-243.

Dehghannya, J., Ngadi, M., Vigneault, C., 2011. Mathematical modeling of airflow and heat transfer during forced convection cooling of produce considering various package vent areas. Food Control 22, 1393-1399.

Delele, M.A., Ngcobo, M.E.K., Getahun, S.T., Chen, L., Mellmann, J., Opara, U.L., 2013. Studying airflow and heat transfer characteristics of a horticultural produce packaging system using a 3-D CFD model. Part II: Effect of package design. Postharvest Biol. Technol. 86, 546-555.

Ferrua, M.J., Singh, R.P., 2009. Modeling the forced-air cooling process of fresh strawberry packages, Part I: Numerical model. Int. J. Refrigeration 32, 335-348.

Gruyters, W., Verboven, P., Diels, E., Rogge, S., Smeets, B., Ramon, H., Defraeye, T., Nicolaï, B.M., 2018. Modelling cooling of packaged fruit using 3D shape models. Food Bioprocess Tech. 11, 2008-2020.

Idelchik, I.E., 1994. Handbook of Hydraulic Resistance, 3rd ed. CrC Press, Boca Raton, FL. 790 p.

Love, R.J., Cleland, D.J., 2007. A model for self-contained solid door refrigerated display cabinets. ASHRAE Trans. 113, 253-262.

Martinez-Hermosilla, G.A., Kueh, C., Dahm, K., Bronlund, J.E., 2018. Combined modelling methodology for optimisation of box design based on hybrid genetic algorithm. Packaging Technol. Sci. 31, 709-722.

O'Sullivan, J., Ferrua, M.J., Love, R., Verboven, P., Nicolai, B., East, A., 2016. Modelling the forced-air cooling mechanisms and performance of polylined horticultural produce. Postharvest Biol. Technol. 120, 23-35.

Olatunji, J.R., Love, R.J., Shim, Y.M., Ferrua, M.J., East, A.R., 2017. Quantifying and visualising variation in batch operations: A new heterogeneity index. J. Food Eng. 196, 81-93.

Smale, N.J., 2004. Mathematical modelling of airflow in shipping systems: model development and testing: PhD thesis. Massey University, Palmerston North, New Zealand. 2004. 278 p.

Smale, N.J., Moureh, J., Cortella, G., 2006. A review of numerical models of airflow in refrigerated food applications. Int. J. Refrigeration 29, 911-930.

Verboven, P., Flick, D., Nicolaï, B.M., Alvarez, G., 2006. Modelling transport phenomena in refrigerated food bulks, packages and stacks: basics and advances. Int. J. Refrigeration 29, 985-997.

Vigneault, C., Markarian, N. R., da Silva, A., Goyette, B., 2004. Pressure drop during forced-air ventilation of various horticultural produce in containers with different opening configurations. ASAE Trans 47, 807-814.

Manuscript ID: 1090
DOI: 10.18462/iir.icr.2019.1090

Effects of continuous cooling on physiological and biochemical indexes of the blue mussels

Zejin WANG[(a,b)], Dechao RAO[(a,b)], Ying HUANG[(a,b)], Zhenshan LIN[(a,b)], Jinhua TONG[(a,b)]

[(a)] College of food science, Fujian Agriculture and Forestry University, Fuzhou, 350002, PR China, wangzejin863@126.com
[(b)] Fujian agricultural and sideline products preservation technology development base, Fuzhou, 350002, PR China, bxjd863w@126.com.

ABSTRACT

The blue mussels (*Mytilus edulis*) were used to investigate the physiological and biochemical indexes during the continuous cooling process (from 18 ℃ to 1 ℃). When temperature of the samples reached the corresponding temperature (18 ℃, 12 ℃, 7 ℃, 5 ℃, 3 ℃ and 1 ℃), the body fluid were subjected to the assessments. Results showed that the respiratory and excretion level of the samples decreased as the temperature decreased. There were no obvious changes of content of glutamic-oxaloacetic transaminase, glutamate-pyruvic transaminase and creatinine between the original and the final temperature point ($p > 0.05$). And the concentration of glucose, triglyceride, and cholesterol of the samples first went up and then reduced as the decrease of temperature. While the uric acid concentration increased overall. Results would be helpful to illustrate the dormant mechanism of the blue mussels induced by continuous cooling.
Key words: Blue Mussels, Continuous Cooling, Physiological Index, Biochemical Index.

INTRODUCTION

The blue mussel (Mytilus edulis) which is edible marine bivalve mollusc, belongs to Mollusca, Bivalvia, Ostreoida, Mytilidae, *Mytilus*. Since the blue mussels are delicious and nutritious, they have received the general consumers' affection. In China, they are mainly distributed in Fujian, Shandong, Zhejiang and other coastal provinces. Limited by current keeping-alive technology, only local consumers can get access to some fresh blue mussels, but most of the blue mussels are still sold as processed or frozen products. And there are numerous studies about the drying technology or frozen preservation technology of the mussels (Qiu, 2004; Lv et al., 2015). Currently, the keeping-alive technology has received more and more attention due to growing demands for the fresh shellfish by consumers. The key of this technology is the induction of the mussels to become dormant at low temperature. So far, continuous cooling has been regarded as good method for shellfish (Ni & Shen, 2013). However, few studies focused on the blue mussels which become dormant status through continuous cooling. Comprehensive effects of continuous cooling on the blue mussels were unclear, and the cryogenic dormant mechanism has not been fully discovered.

In this study, the blue mussels were subjected to the continuous cooling process from 18 ℃ to 1 ℃, and investigated effects of temperature changing on physiological and biochemical indexes. Results would be helpful to illustrate the cryogenic dormant mechanism of shellfish seafoods including the blue mussels.

2. MATERIALS AND METHODS

2.1. Samples Collection

The blue mussel samples were obtained from the breeding base which is located in Jiangyin town, Fuqing city, Fujian province, China. The samples were transported to the lab within 4 hours. They were selected and the criterion was about (40 ± 1) g. Then their surface were rinsed by precooled,

man-made sea water (18 ℃).

2.2 Continuous Cooling Process

A total of 120 selected blue mussels were divided into three groups and put into the three different aquariums filled with 6 L man-made sea water (18 ℃). Two aquariums were placed in the cold room at -2℃ in order to achieve the continuous slow cooling. As control group, the third aquarium was placed in the cold room at 18℃.

2.3 Determination of the Oxygen Consumption Rate and the Ammonia Excretion Rate

When reaching the temperature (18 ℃, 12 ℃, 7 ℃, 5 ℃, 3 ℃ and 1 ℃), three blue mussels were taken out from one aquarium and put into one plastic box filled with 600 mL precooled water. Then the boxes were placed in the cold room with the corresponding temperature. After 3 hours, the samples were subjected to the tests for the oxygen consumption rate and the ammonia excretion rate. Meanwhile, the blue mussels of the control group were taken out for the same assessments at each time point.
Winkle method was used to measure the oxygen consumption rate (Xu et al., 2010). The ammonia excretion rate was determined according to the method described by Harding et al. (2004).

2.4 Biochemical Index Tests

When reaching the temperature (18 ℃, 12 ℃, 7 ℃, 5 ℃, 3 ℃ and 1 ℃), three blue mussels were taken out from another aquarium. 1 mL of the body fluid was collected from each mussel, and centrifuged at 12000 rpm for 20 min at 4℃. The equal volume of the supernatant of three mussels were mixed as one samples and stored at -80℃ before using. Meanwhile, the blue mussels of the control group were taken out for the same assessment at each time point. All biochemical indexes of the samples were measured using the biochemical analysis equipment (Beckman Coulter, USA), including glutamic-oxalacetic transaminase (GOT), glutamate-pyruvic transaminase (GPT), creatinine (CREA), urine nitrogen (UN), glucose, triglyceride (TG), cholesterol (CHOL), total protein (TP), albumin, and uric acid (UA).

2.5 Statistical Analysis

Data processing and statistical analyses were conducted using SPSS V21.0. The adopted level of extreme significance and significance were 1% ($p < 0.01$) and 5% ($p < 0.05$)

3. RESULTS AND DISCUSSION

3.1 The Changes of the Oxygen Consumption Rate and the Ammonia Excretion Rate

Respiration and excretion are important physiological activities of shellfish. In the test group, it took about 7 hours for the blue muscle samples to decrease the temperature from 18℃ to 1℃. The oxygen consumption rate of the blue muscles gradually went down as the decrease of the temperature, and the dropping trend between the temperature range of 7℃～1℃ was more steep than other range (Fig.1). When the temperature reached 1℃, the oxygen consumption rate was 0.01mgO_2/g.h, which suggested that the respiration of the blue mussels nearly stopped and they entered the dormant stage. Results suggested that temperature had significant effects on the oxygen consumption rate of the blue mussel samples ($p < 0.01$). Similar results were also reported in oyster (Jiao et al., 2017) and clam (Xu et al., 2015). Within the same period, the samples in the control group, which was placed at 18℃, showed no obvious change in the oxygen consumption rate ($p > 0.05$). So did other assessments for the control group.

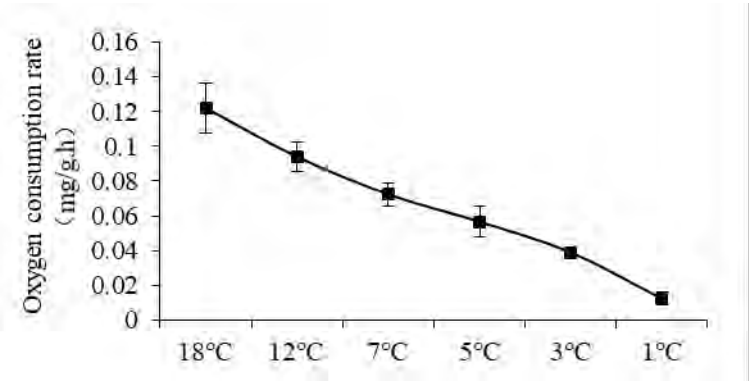

Figure 1: Changes of the oxygen consumption rate of the blue mussel samples during the cooling process

The excrements of bivalve shellfish mainly consist of ammonia, urea, uric acid, amino acid, and so on. And the proportion of ammonia is much higher than other excrements, accounting for at least 70% of the total excrements. As shown in Fig. 2, the ammonia excretion rate of the blue mussels showed the similar changing trend as the oxygen consumption rate. Similar results were also reported in clam (Feng et al., 2004; Xiao et al., 2006). When temperature dropped from 18 ℃ to 1 ℃, the ammonia excretion rate gradually became smaller. Results suggested that temperature had significant effects on the ammonia excretion rate of the blue muscles samples ($p < 0.01$). Moreover, the blue muscles nearly became dormant.

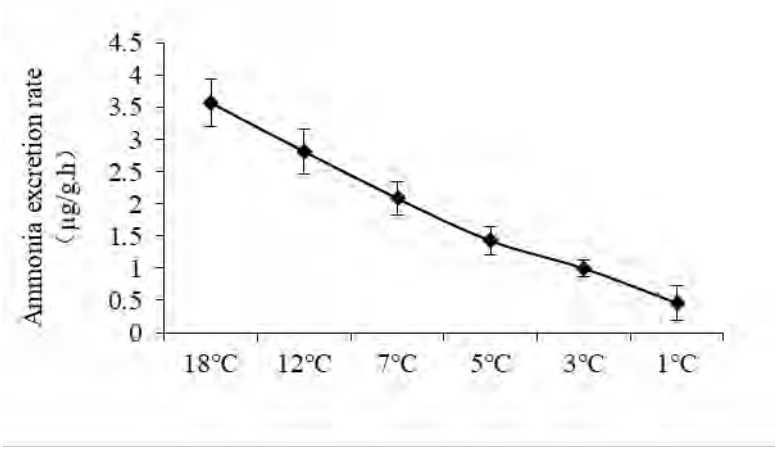

Figure 2: Changes of the ammonia excretion rate of the blue mussel samples during the cooling process

3.2 The changes of the GOT and GPT concentration

Usually GOT concentration is used to indicate the healthy status of the heart muscle. As can be seen from Fig. 3, GOT concentration in the blue mussel samples presented a small fluctuating change during the continuous cooling process. When the temperature decrease from 18 ℃ to 12 ℃, the GOT concentration fell to 59 U/L; As the temperature continued to reduce, conversely, the GOT concentration reached the highest value (66.67 U/L). However, there was no significant difference of GOT concentration between the beginning and the final temperature point. Results suggested that the continuous cooling process had little traumatic effect on myocardial function in the blue mussel samples. Moreover, the samples had already adapted to low temperature after being subjected to the induction by continuous cooling process.

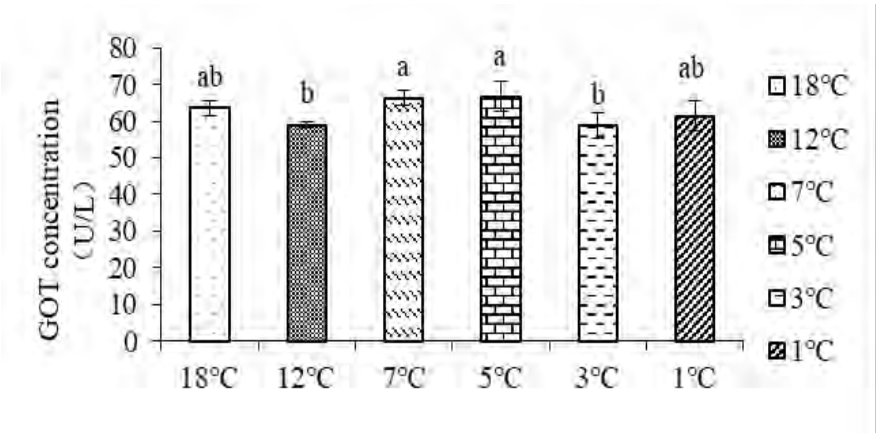

Figure 3: Changes of the GOT concentration of the blue mussel samples during the cooling process

During the continuous cooling process, the GPT concentration showed similar changing trend as GOT concentration (Fig. 4). The GPT concentration had the highest value of 14.67 U/L at 5 ℃. And the concentration at 1 ℃ had no significant difference from that of the original level. Results suggested that the samples had already adapted to low temperature and there was little damage to the liver.

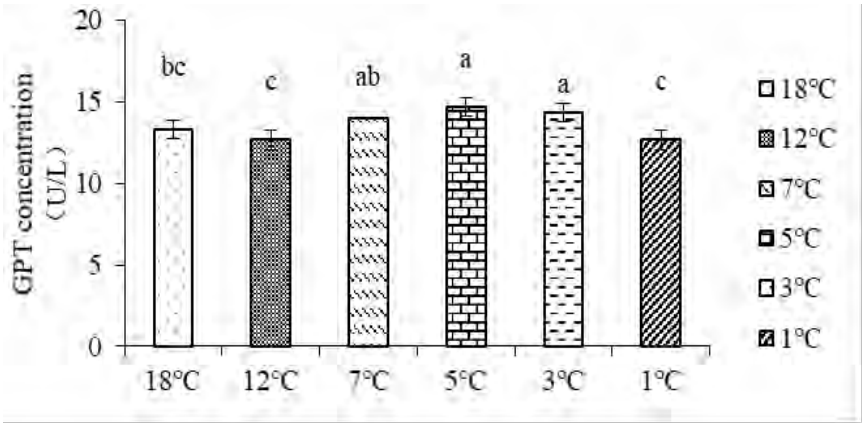

Figure 4: Changes of the GPT concentration of the blue mussel samples during the cooling process

3.3. The Changes of CREA and UN Content

Creatine slowly generates CREA through irreversible non-enzymatic dehydration reaction, and then CREA is discharged through glomerular filtration. The CREA level is usually related to the kidney function. As shown in Fig. 5, when the temperature deceased from 18 ℃ to 3 ℃, the CREA level of the blue mussel samples dropped to the lowest level (1.35 μmol·L^{-1}), which was significantly different from the initial level ($p < 0.05$). However, there was no obvious change of the CREA level between the samples at the beginning and the samples at the end of cooling process ($p > 0.05$). Similar results was reported by Chen et al. (2012). Therefore, it was suggested that the creatine metabolism of the blue mussel was normal during the continuous cooling process, and the low temperature induction did not cause damage to the kidney tissue of the blue mussel.

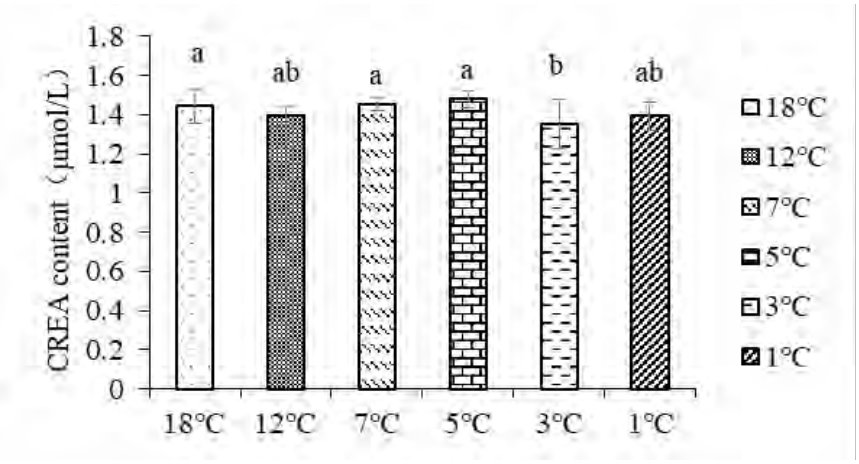

Figure 5: Changes of the CREA content of the blue mussel samples during the cooling process

UN is another indicator which is commonly used in the clinical examination of kidney function. The increase of UN could indicate either too much proteins in daily dietary or kidney dysfunction. As shown in Fig. 6, within the first period of the temperature dropping from 18 ℃ to 7 ℃, the UN content slightly increased, but there was no obvious change (p> 0.05). After 7 ℃, the overall trend of UN content was downward. When the temperature dropped to 3 ℃, the UN content decreased to the lowest value (0.16 μmol·L^{-1}), which was significantly different from those of higher temperature points (p<0.05) but not significantly different from that of 1℃ (p > 0.05). Such downward trend of UN content could be due to the inhibition of amino acid deaminase, transaminase and uricase at low temperature (Weihrauch et al., 2009). Consisting with CREA result, the UN result also suggested this continuous cooling process did not cause damage to the kidney.

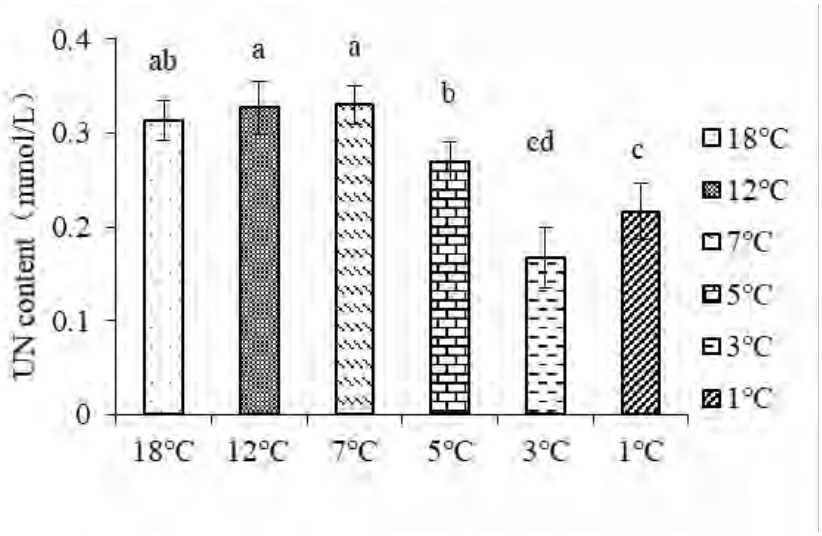

Figure 6. Changes of the UN content of the blue mussel samples during the cooling process

3.4. The changes of glucose concentration

Glucose is an important energy substance in the organism body, the concentration of which commonly maintains a dynamic balance. During the cooling process from 18 ℃ to 1 ℃, the glucose concentration of the blue mussel samples presented approximate bell-curve shape overall (Fig. 7). The glucose reached the highest concentration of 1.69 mmol·L^{-1} at 7 ℃, which was significantly different from those of other temperature point (p < 0.05). The temporary rising of glucose concentration was possibly because of the stress reaction against the cold temperature, involving the gluconeogenesis or the breakdown of glycogen (Ji, 2014; Shao et al., 2017). However, there was no significant difference of glucose concentration between the first and last temperature points (p > 0.05), which suggested that the samples had adapted to the cold temperature.

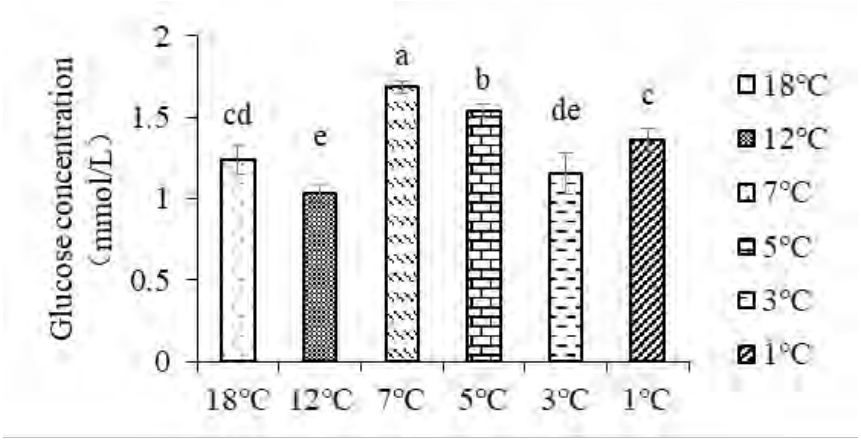

Figure 7: Changes of the glucose concentration of the blue mussel samples during the cooling process

3.5 The Changes of TG and CHOL Content

The Fig. 8 shows that as the temperature was reduced, TG levels of the blue mussel went down after rising first. When the temperature decreased from 18 ℃ to 5 ℃, the TG content went up and reached the highest level (1.49 mmol·L^{-1}), which suggested that this increasing TG level possibly could enhance the cold resistance of the mussel during the earlier stage. When the temperature decreased to 1℃, the TG level went down to the lowest value (0.88 mmol·L^{-1}), which was significantly different from the initial level ($p < 0.05$). The later stage of decreasing trend of TG content may be due to the inhibition of TG synthesis after entering into the dormancy status.

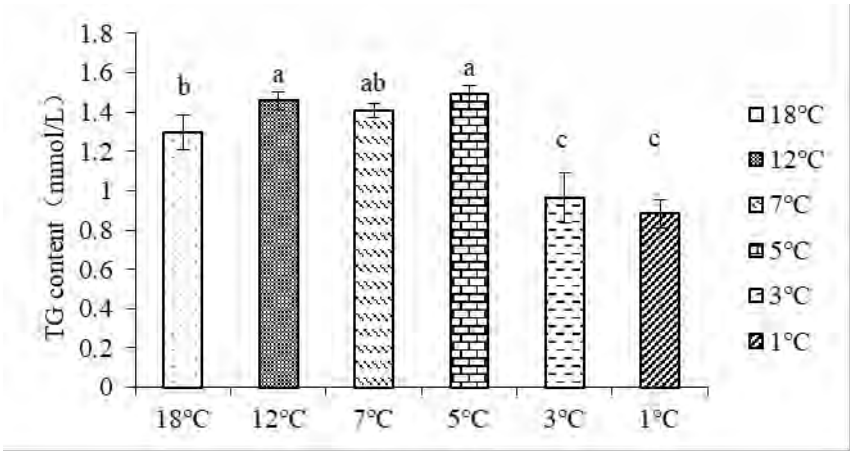

Figure 8 Changes of the TG content of the blue mussel samples during the cooling process

As for another kind of lipid, similar trend was also present in CHOL content during the continuous process. As shown in Fig. 9, the CHOL level went up to the highest value (5.93 mmol·L^{-1}) at 5 ℃and then down to the lowest value (2.89 mmol·L^{-1}) at 1℃, both of which were significantly different from the initial level ($p < 0.05$). The later decreasing of CHOL content may be due to the inhibition of CHOL synthesis.

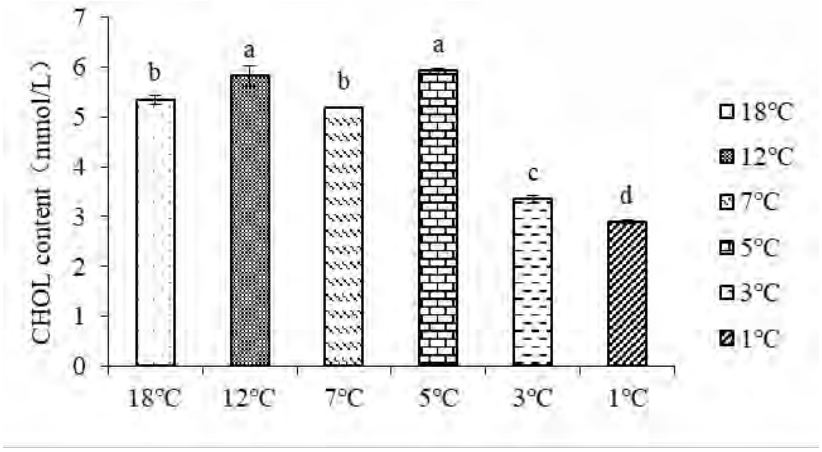

Figure 9: Changes of the CHOL content of the blue mussel samples during the cooling process

3.6 The changes of TP and albumin content

The changes of TP content in body fluid of samples during the continuous cooling process were shown in Fig. 10. As the decrease of temperature, the TP content increased first and then decreased. The TP contents at the temperature between 7℃and 3℃ were significantly from that of the beginning stage ($p < 0.05$). When the temperature went down to 1℃, the TP content of the blue mussel samples dropped down to the level which was not significantly from the initial level ($p > 0.05$).

As for the albumin content in the blue mussel samples, it showed the similar changing trend as the TP content during this cooling process (Fig. 11). The albumin content increased first and reached 22 $g \cdot L^{-1}$at 3℃, which was significantly higher than that of the beginning level (17.33 $g \cdot L^{-1}$) ($p < 0.05$). Then the albumin content return to level which was not significantly from the initial one ($p > 0.05$). Moreover, the increasing trend of both TP and albumin content at the first stage may be due to the higher expression of stress protein against cold temperature (Ji, 2014). When the blue mussel gradually adapted to the cold temperature and became dormant, these protein content returned to the original level.

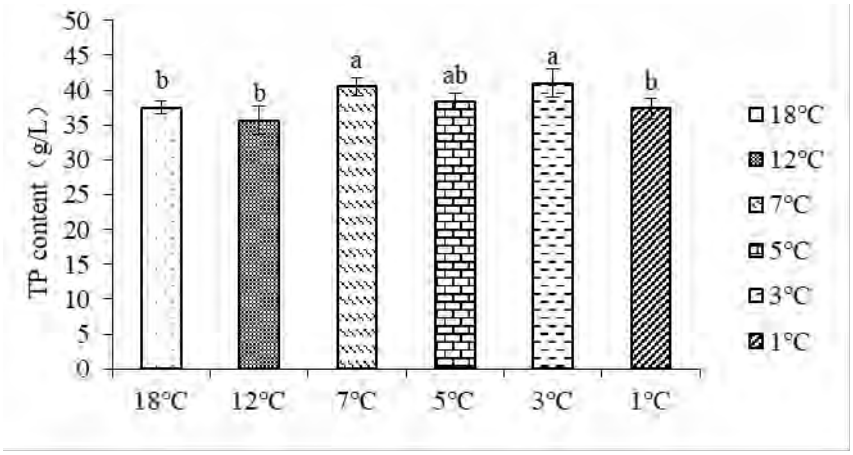

Figure 10: Changes of the TP content of the blue mussel samples during the cooling process

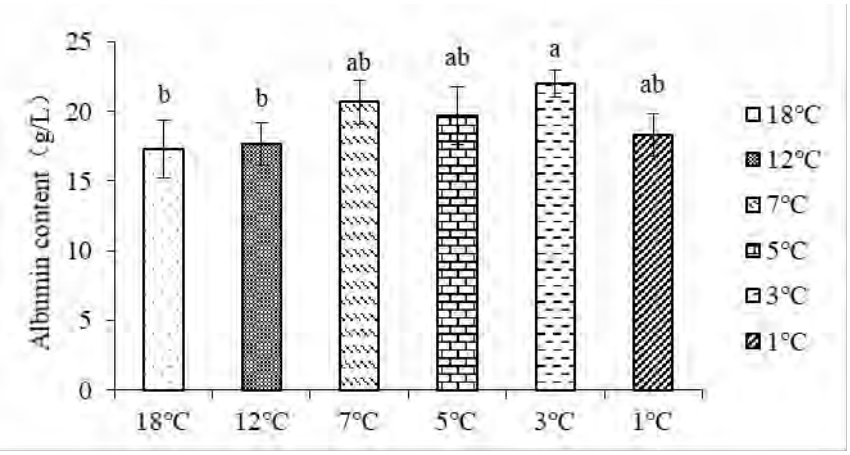

Figure 11: Changes of the albumin content of the blue mussel samples during the cooling process

3.7 The Changes of UA Content

UA is the catabolic product of purine nucleotides. Overall, the UA content of the blue mussel samples showed a rising trend as the temperature reduce (Fig. 12). Compared with the initial level, UA content of the samples rose to 188 mol·L^{-1} at 1℃, increasing by 29.38%. This possibly because more stress proteins were needed to be synthesized at low temperature, correspondingly more nucleic acid metabolism could occur (Jiang et al., 2017). Moreover, UA content of the samples at 5 ℃ was significantly higher than that of 7 ℃, but significantly lower than that of 3 ℃ (p < 0.05).

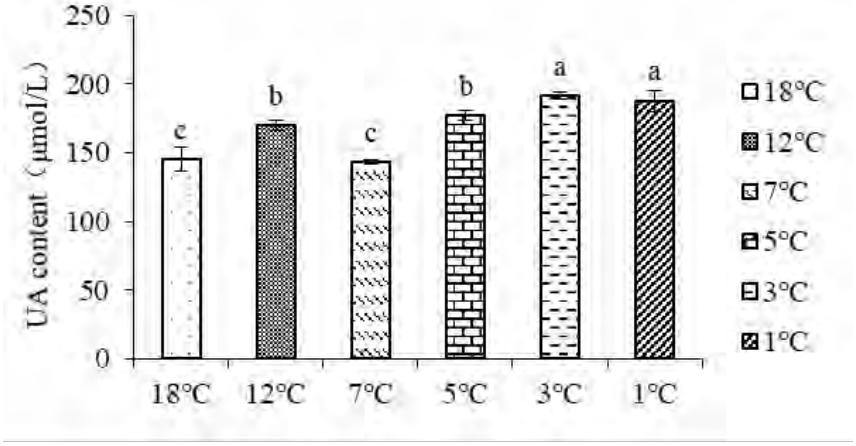

Figure 12: Changes of the UA content of the blue mussel samples during the cooling process

4. CONCLUSION

Results above suggested that the continuous cooling process could be helpful for the blue mussels to enter the dormancy status. Moreover, 1 ℃ was suitable temperature point for the blue mussels to become dormant and keep alive.

REFERENCES

Chen, C., Shi, Z., Xue, B. et al., 2012. Influence of low-temperature stress on serum biochemical parameters in juvenile *Epinephelus septemfasciatus*. J. Fish. China 36(8), 1249-1255.

Feng, J., Wang, M., Chen, H., et al., 2004. Effects of temperature and body size on oxygen consumption rate of Meretrix meretrix. J. Shanghai Fish. Univ. 13(2), 126-129.

Harding, J.M., Couturier, C., Parsons, G.J., et al., 2004. Evaluation of the neutral red assay as a stress response indicator in cultivated mussels (*Mytilus* spp.) in relation to post-harvest processing activities and storage conditions. Aquaculture 231(1-4), 315-326.

Ji, L., 2014. Effect of continuous cooling on serum physiological, biochemical indexes and molecular mechanism of adult *Scophthalmus maximus*. Doctor Dissertation Ocean Univ. China

Jiang, W., Jiang, Z., Du, M., et al. 2017. Physiological and biochemical responses of *Zhikong scallop*, *Chlamys farreri*, to different thermal stressors. Aquac. Res. 48(2), 83-97.

Jiao, H., Zheng, D., Yan, Q. et al., 2017. Effects of water temperature and salinity on oxygen consumption rate and ammonia excretion rate of *Saccostrea cucullata*. Acta Ecologica Sinic 37(2), 692-699.

Lv, F., Shen, J. & Ding, Y. 2015. Changes in mussel quality during heat-pump drying. Mod. Food Sci. Technol. 31(6), 142-149.

Ni, J., & Shen, J., 2013. Use of refrigerated-seawater spray in Keeping *Haliotis discus hannai* alive at ecological ice temperature. Mod. Food Sci. Technol. (5), 953-956.

Qiu, C., 2004. Research on storage biochemical properties, preserving and enzymatic hydrolysis of Mussel (*Mytilus* sp.). Doctor Dissertation Ocean Univ. China

Shao, Y., Chen, C., Li, Y., et al., 2017. Effects of Low Temperature Stress on Serum Biochemical Indices of the Juvenile Hybrid of Epinephelus moara♀ × Epinephelus lanceolatus♂. Prog. Fish. Sci. 38(2), 70-76.

Weihrauch, D., Wilkie, M.P., & Walsh, P.J., 2009. Ammonia and urea transporters in gills of fish and aquatic crustaceans. J Exp Biol 212(Pt 11), 16-30.

Xiao, G., Zhang, J. ,Cai, X., et al., 2006. Sutdies on the filtration feeding, respiration and excretion of *Ruditapes philippinarum* juvenile. J. Appl. Oceanography (1), 33-38.

Xu, D., Zhang, J., Wang, W., et al., 2010. Effects of temperature elevation on oxygen consumption rate and ammonia excretion rate of *Patinopecten yessoensis*. J. Fish. Sci. China 17(5), 1101-1106.

Xu, X., Yang, F., Zhu, H., et al., 2015. Effects of low temperature on oxygen consumption rate, ammonia excretion rate of juvenile Manila clam *Ruditapes philipinarum* with three color shells. J. Dalian Ocean Univ. 30(6), 627-633.

Manuscript ID: 1096
DOI: 10.18462/iir.icr.2019.1096

X-ray CT-based CFD study to investigate the cooling process of packed pear fruit

Willem GRUYTERS[(a)], Zi WANG[(a)], Pieter VERBOVEN[(a*)], Bart NICOLAÏ[(a,b)]

[(a)] BIOSYST-MeBioS, Katholieke Universiteit Leuven, Willem de Croylaan 42, B-3001 Leuven, Belgium. pieter.verboven@kuleuven.be
[(b)] Flanders Centre of Postharvest Technology, Willem de Croylaan 42, B-3001 Leuven, Belgium.

ABSTRACT

Proper temperature management is needed to maintain the quality of fresh fruit such as pears. Understanding the cooling process is crucial and possible with numerical modelling techniques such as computational fluid dynamics (CFD). In this work, X-ray computed tomography (CT) based CFD modelling was validated with experimentally obtained cooling profiles. First, CT images of pear fruit of different cultivars randomly stacked in boxes were obtained. Next, horizontal forced-air cooling experiments with the different packings were conducted. After CT image reconstruction, CFD simulations with the realistic pear stacking were performed. Experiments agreed well with simulation results. Cooling time of individual pears differed up to 4 hours and large differences in cooling time between the pear cultivars were observed. Individual fruit shapes clearly influence cooling behaviour. Eventually, these parameters can be effectively taken into account in numerical models using fruit shape models and Discrete Element Modelling, avoiding the need of CT imaging.
Keywords: Computational Fluid Dynamics, Pear Fruit, Biological Variability, X-Ray CT Imaging, Forced-Air Cooling.

1. INTRODUCTION

From the moment fresh fruit are harvested, they solely rely on their internal reserves to fuel their respiration metabolism (Jackson, 2003). By lowering fruit temperature, the respiration rate is slowed down and thus, the speed of senescence and deterioration processes (Prusky, 2011). Understanding the cooling process is crucial and possible with numerical modelling techniques such as computational fluid dynamics (CFD). In the explicit CFD modelling approach, the complex features of the package material and produce are taken into account. However, validation of such models requires one-to-one comparison of predicted and measured temperature profiles in specific fruit stacks. Previous research often approximated the fruit stacks with simplified regular geometries such as spheres (Ambaw et al., 2017; Defraeye et al., 2013; Delele et al., 2013). For spherically-shaped produce such as oranges or apples, the average cooling process can be predicted fairly well (Defraeye et al., 2013; Wu et al., 2018), although the local cooling behaviour within the fruit package is underestimated with this assumption (Gruyters et al., 2018). However, studying the cooling behaviour of non-spherical fruit such as pears is more complex: because of their shape, their stacking pattern is much different from that of spherical fruit and likely affects the local airflow and heat transfer considerably. Their actual shape thus needs to be incorporated in the CFD model.
In this study, CT images of randomly stacked pear fruit of three different cultivars (cv. 'Doyenné', cv. 'Conference' and cv. 'Durondeau') in a corrugated package were used to reconstruct a 3D geometrical model of the actual filling pattern inside the package. These geometries were incorporated in a CFD model of a horizontal FAC process and the simulations were validated with temperature measurements inside different fruit inside the package during cooling. Experiments were executed in a precooling setup with a controlled airflow.

2. MATERIALS AND METHODS

2.1. Pear Fruit

Fruit from three pear cultivars (*Pyrus communis*, cv. 'Durondeau', cv. 'Conference' and cv. 'Doyenné') were collected on September 25th 2017 from a commercial grower (Van Der Velpen; Bierbeek, Belgium). The pears were picked late August 2017 at Bierbeek, Belgium. The pears were stored at –0.5 °C for 25 days under ambient atmosphere. All pears were free of visual defects.

2.2. Fruit Box

In this study, a telescopic, single layer corrugated fibreboard cardboard (CFC) box design (LC Packaging, Sint-Katelijne-Waver, Belgium) with outer dimensions of 50 cm × 33 cm × 31 cm and a 0.3 cm wall thickness was used. The short side has one large horizontally oriented, rectangular vent hole (i.e. the handle) on the top middle region resulting in a total open area of 2.45 %. No vent holes were present on the other sides of the box. One box per cultivar was randomly filled with pears, resulting in an average weight of $25.55\ \text{kg} \pm 0.28\ \text{kg}$ per box. The total number of pear fruit was 114, 122 and 104 for 'Durondeau', 'Conference' and 'Doyenné' respectively. Figure 1 shows the dimensions of the box and the three randomised pear-filling patterns.

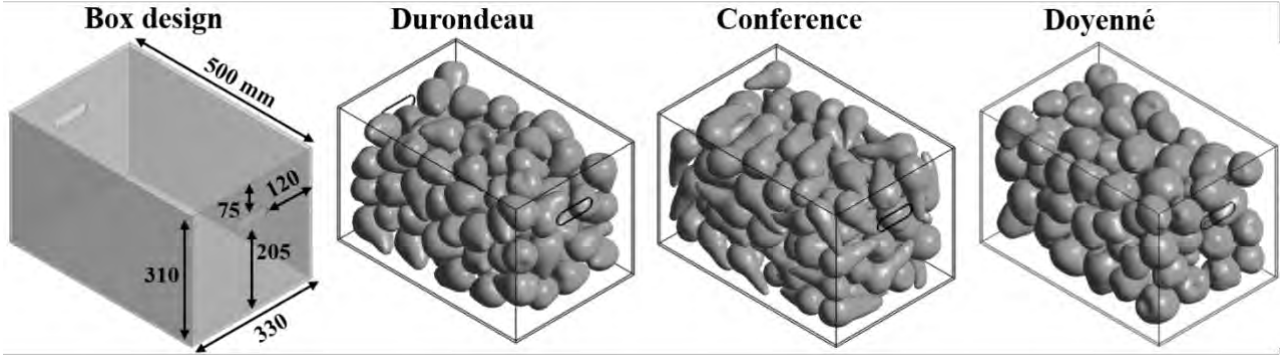

Figure 1: Geometrical representation of the box design and corresponding stack fillings based on CT images of packaged fruit of three pear cultivars

2.3. Reconstruction of the CT images

Cross-sectional slices of three boxes filled with pears and thermocouples placed in selected 'sample fruit' were obtained with X-ray CT imaging on October 3rd 2017. The X-ray CT scans were made with a Siemens Somatom (KU Leuven, Gasthuisberg, Belgium), operating at a tube setting of 500 mA and 140 kV to capture the projection images. After obtaining the X-ray CT scans, image analysis was done with Avizo 9.5 (FEI, Bordeaux, France). Due to the distinctive greyscale intensity of the box, all pixels marking the box were manually removed from the volume, prior to segmentation of the pears and thermocouple wires. By selecting proper greyscale values, images were segmented in pear objects and thermocouple wiring. Subsequently, all segmented pear objects were separated from each other by subjecting them to a watershed segmentation. In a final step, a surface mesh of the individual pears was exported to ANSYS SpaceClaim (ANSYS, Canonsburg, PA, USA) where small artefacts and protrusions on the surface mesh were manually removed to create a smooth assembly of 3D solid pear bodies (see Fig. 1).

2.4. Forced-air cooling experiments

All forced-air cooling (FAC) experiments were conducted at the Flanders Centre of Postharvest Technology (VCBT, Belgium) on October 3rd and 4th 2017. First, the three fruit boxes were equilibrated to a temperature of about 16.4 °C. Next, the short side of the box was placed in front of a FAC system, located inside a coolstore. The FAC airflow was regulated to obtain an AFR that was within range of what is commonly used in the precooling industry (Brosnan and Sun, 2001). The airflow rate was measured in a single point at the end of the circular airshaft with an anemometer (TSI VelociCalc 9545, Kritech & Co PGmbH, Belgium; accuracy of ± 0.015 m s-1). The temperature and relative humidity of the cool stores were kept at –0.46 ± 0.17 °C and 87.00 % ± 1.00 %, respectively, for all experiments. The FAC system employed a centrifugal fan (G2E140AI2801, EBM-

Papst, Benelux B.V.) that drew the refrigerated air through the box. The pressure drop over the box was measured with a differential pressure sensor (GEMS Sensors, Hampshire, UK; accuracy of ± 1 Pa). Fruit pulp temperatures of several pears at distinct positions in the filling ('sample fruit') were monitored every 15 s with T-type thermocouples (OMEGA Engineering, USA; accuracy of ± 0.025 °C). The positions of the thermocouples inside the fruit are illustrated in Fig. 2.

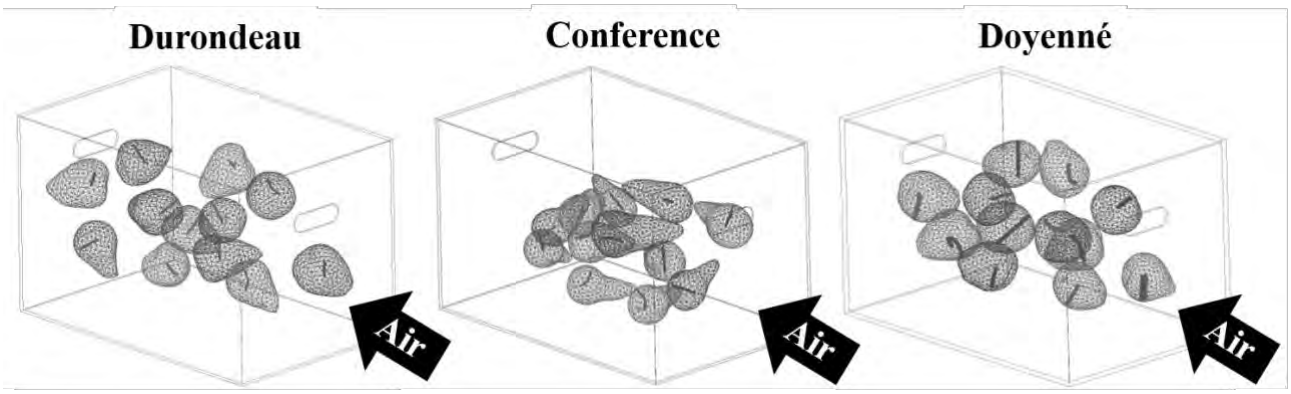

Figure 2: The relative position of the 12 sample fruit in the filling and the corresponding location of the thermocouples inside the fruit for the three pear cultivars. In all three boxes, six fruit were located in both the bottom and top region and were evenly distributed on each side along the depth direction to distinguish a front, middle and back region in the box

2.5. CFD model

Explicit CFD models of the three fruit boxes were constructed. The free-stream air was modelled as a fluid domain while both fruit and box design were modelled as solid domains. The thermophysical model parameters of the box, the fruit and the air were assumed temperature independent due to the relatively small temperature range (Ferrua and Singh, 2009), and are presented in Table 1.

Table 1: Model parameters of the air, the pear fruit and the single box

	Density (kg m^{-3})	Thermal conductivity (W m^{-1} K^{-1})	Specific heat capacity (J kg^{-1} K^{-1})	Reference
Air	1.185	0.024	1004	(ASHRAE, 2013)
Pear	1000	0.52	3800	(Nahor et al., 2005)
Box	145	0.064	1338	(Ho et al., 2010)

Fig. 3 presents the computational domain with the implemented boundary conditions (BCs), simulating a horizontal FAC process of a single box. At the inlet of the fluid domain, an ambient atmospheric pressure condition and medium turbulence (5 %) were imposed. At the air domain outlet, a negative pressure was imposed to simulate the operation of the centrifugal fan in the FAC system (see Table 2). All other sides of the air domain were modelled as a symmetry BC. The box was modelled as no-slip walls with zero roughness with a fixed temperature BC on the outer box walls (~0 °C). The Reynolds-averaged Navier-Stokes (RANS) equations combined with the shear stress transport $k-\omega$ turbulence model (SST $k-\omega$ model) and wall functions were solved. This turbulence model was validated previously for a very similar computational setup (Defraeye et al., 2013; Delele et al., 2008; Han et al., 2015; Wu et al., 2018). Transient heat transfer simulations similar to the experimental conditions were performed. This allowed the evaluation of the cooling performance by calculating and monitoring the fruit temperatures at the same location as the thermocouples used in the experiment. The inlet cooling air temperature and initial fruit temperature were taken the same as the average value measured in the experiment (see Table 2).

Table 2: The experimental conditions that were implemented in the CFD model

-	Durondeau	Conference	Doyenné
$T_{initial}$(°C)	16.6	16.3	16.8
T_{inlet} (°C)	-0.7	-0.2	-0.2
ΔP (Pa)	- 465	- 463	- 460
v_{inlet} (m s^{-1})	0.2	0.2	0.2

* Measured as the area average value at the inlet of the air domain

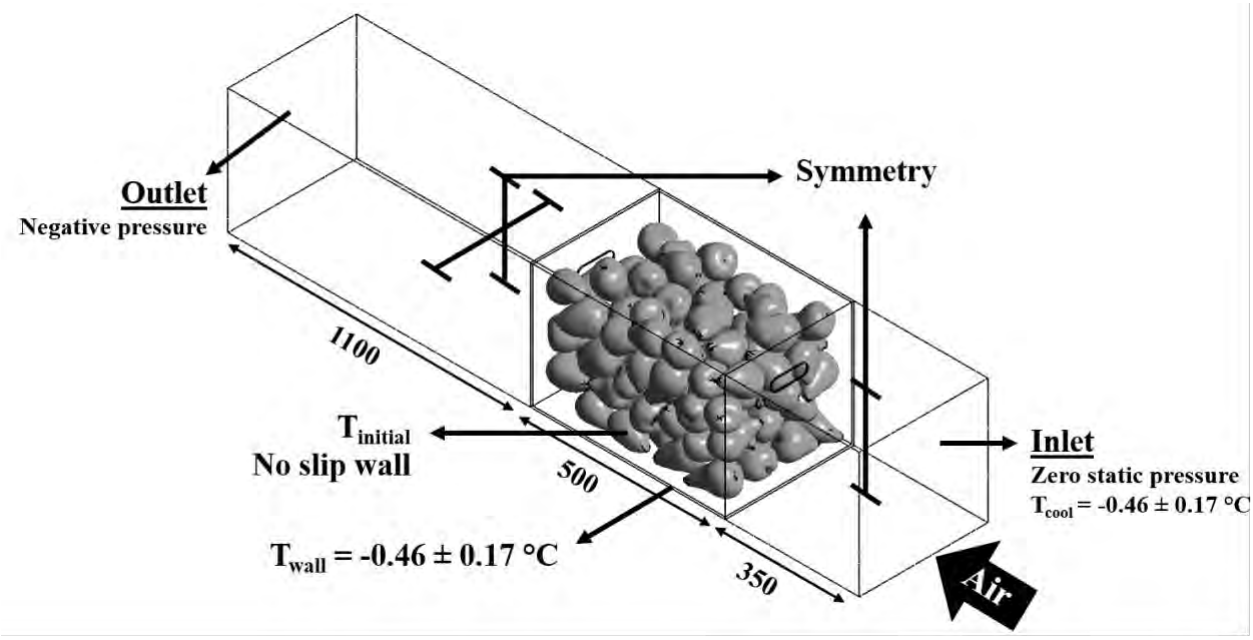

Figure 3: Graphical representation of the implemented boundary conditions in the CFD model. The implemented boundary conditions were the same for all pear geometries. The air enters the computational domain from the right hand side. The dimensions are expressed in mm

All domains were discretised with tetrahedral and hexahedral mesh cells. In total, the 'Durondeau', 'Conference' and 'Doyenné' models had 4.28 × 10^6, 4.58 × 10^6, and 4.29 × 10^6 mesh cells. A grid sensitivity analysis with Richardson extrapolation was performed to calculate the spatial discretization error (Celik et al., 2008; Franke et al., 2007; Roache, 1994). For the pressure drop over the box and the surface-averaged heat transfer coefficients of the fruit, the spatial discretisation error was maximally 3 % for all computational models. All calculations were performed on a 64-bit Intel® Xeon® CPU E5-2630, 2.30 GHz, 128 GB RAM, Windows 7 PC. All transient simulations (for a period of 24 h after cooling) took more than 56 h to complete.

3. RESULTS

3.1. Fruit Cooling behaviour

Table 3 shows the experimental and numerical results of the minimum, average and maximum values of the cooling time for the three pear boxes. There is a good agreement between the predicted and experimentally measured cooling times. Between the different boxes, large differences are noticed with a maximum difference up to 4 h in cooling time between individual pear fruit. Compared to the other two fruit fillings, the 'Conference' filling cooled more heterogeneous. 'Conference' pears are typically more elongated than 'Durondeau' or 'Doyenné' of which the shape is rather spherical.

Table Error! No text of specified style in document.**: The minimum, average and maximum value of the cooling time (min) of the sample fruit measured in the experiment (Exp.) and calculated with the CFD model (CFD)**

-	Durondeau			Conference			Doyenné	
	Exp.	CFD		Exp.	CFD		Exp.	CFD
Min	173	161		100	109		131	120
Avg*	259±63	258±57		244±83	238±83		209±50	214±59
Max	367	345		379	378		304	311

* Standard deviation calculated from the 12 sample fruit

To gain a better insight in the cooling behaviour, the spatial distribution of temperatures inside the fruit and convective heat transfer coefficients on the fruit surfaces are discussed next. The convective heat transfer coefficient, h (W m^{-2} K^{-1}) relates the heat flux normal to the fruit surface to the difference between the fruit surface and a reference temperature (in this case the incoming air temperature). Fig. 4 shows the spatial temperature distribution inside the three pear boxes with temperature contour plots in the right vertical plane of the pear box after 0.5 h of cooling. Clearly, large temperature differences exist between the top and bottom region of the box. Furthermore, most pears located in the front cooled faster than in the back region of the box. However, this was not the case for 'Conference', where the top pear in the front seemed to cool slower. Further analysis of the numerical results revealed that the incoming air was deflected by adjacent pears located in front of the vent hole. Therefore, this particular pear was shielded from direct exposure to the cold air and thus, cooled slower.

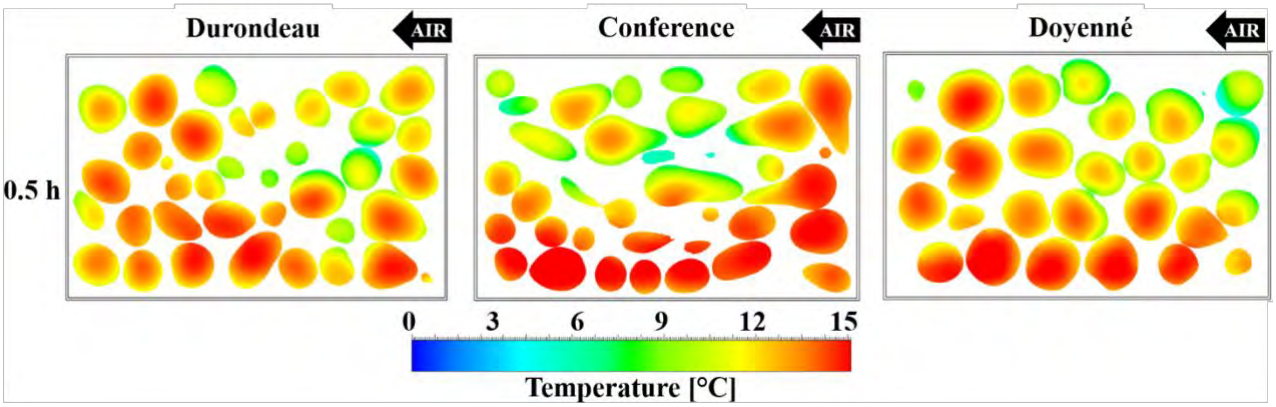

Figure 4: Temperature contour plots in the right vertical plain of the pear boxes after 0.5 h of cooling. The air enters the computational domain from the right hand side

Fig. 5 illustrates a contour plot of local convective heat transfer coefficients calculated on the surface of individual pear fruit. In general, a slow cooling rate is associated with low values of the heat transfer coefficient. In addition, the degree in which these coefficients differ throughout the fruit filling pattern can be used as a measure of local cooling heterogeneity within the fruit stacks (Gruyters et al., 2018). For each pear box, a large variability in heat transfer coefficients is observed with high values in front of the vent hole and low values in the bottom region of the box. This corresponds well with the observed temperature differences shown in Fig. 4.

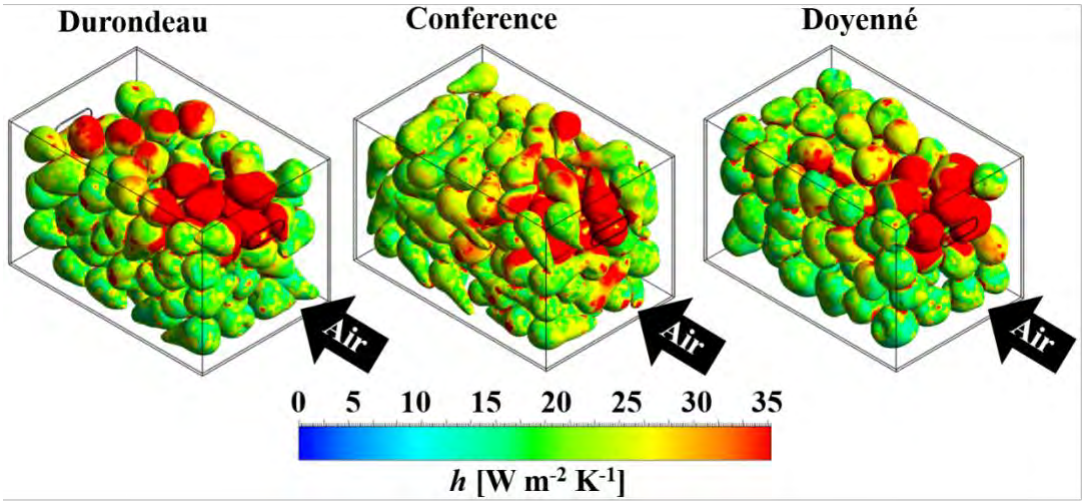

Figure 5: Contour plot of the convective heat transfer distribution on the fruit surface for the three boxes filled with pears. The air enters the computational domain from the right hand side

4. CONCLUSIONS

In this study, a novel methodology for constructing a geometrical model of the actual fruit filling pattern inside corrugated boxes from CT images was successfully demonstrated. An individual corrugated box was filled with three different pear cultivars (cv. 'Durondeau', 'Conference' and 'Doyenné') after which horizontal forced-air cooling experiments were performed to validate the CFD models. There was a very good agreement between the numerical simulation and experimental results. Large local differences in cooling behaviour between the three boxes were observed. A more pronounced temperature heterogeneity was observed for the 'Conference' filling. Clearly, the cooling behaviour is affected by fruit shape in particular stacking patterns.

ACKNOWLEDGEMENTS

This work was supported by Flanders Innovation & Entrepreneurship (project VLAIO 120745).

REFERENCES

Ambaw, A., Mukama, M., Opara, U.L., 2017. Analysis of the effects of package design on the rate and uniformity of cooling of stacked pomegranates: Numerical and experimental studies. Comput. Electron. Agric. 136, 13–24. doi:10.1016/j.compag.2017.02.015

ASHRAE, 2013. ASHRAE: Handbook - Fundamentals.

Brosnan, T., Sun, D.W., 2001. Precooling techniques and applications for horticultural products - a review. Int. J. Refrig. 24, 154–170.

Celik, I.B., Ghia, U., Roache, P.J., Freitas, C.J., 2008. Procedure for estimation and reporting of uncertainty due to discretization in CFD applications. J. Fluids Eng. 130, 4. doi:10.1115/1.2960953

Defraeye, T., Lambrecht, R., Tsige, A.A., Delele, M.A., Opara, U.L., Cronjé, P., Verboven, P., Nicolai, B., 2013. Forced-convective cooling of citrus fruit: Package design. J. Food Eng. 118, 8–18. doi:10.1016/j.jfoodeng.2013.03.026

Delele, M.A., Ngcobo, M.E.K., Getahun, S.T., Chen, L., Mellmann, J., Opara, U.L., 2013. Studying airflow and heat transfer characteristics of a horticultural produce packaging system using a 3-D CFD model. Part I: Model development and validation. Postharvest Biol. Technol. 86, 536–545. doi:10.1016/j.postharvbio.2013.08.014

Delele, M.A., Tijskens, E., Atalay, Y.T., Ho, Q.T., Ramon, H., Nicolai, B.M., Verboven, P., 2008. Combined discrete element and CFD modelling of airflow through random stacking of horticultural products in vented boxes. J. Food Eng. 89, 33–41. doi:10.1016/j.jfoodeng.2008.03.026

Ferrua, M.J., Singh, R.P., 2009. Modeling the forced-air cooling process of fresh strawberry packages, Part I: Numerical model. Int. J. Refrig. 32, 335–348. doi:10.1016/j.ijrefrig.2008.04.010

Franke, J., Hellsten, A., Schlünzen, H., Carissimo, B., 2007. Best practice guidelines for the CFD simulation of flows in the urban environment. COST Action 732 Qual. Assur. Improv. microscale Meteorol. Model. Hamburg, Ger.

Gruyters, W., Verboven, P., Diels, E., Rogge, S., Smeets, B., Ramon, H., Defraeye, T., Nicolai, B.M., 2018. Modelling cooling of packaged fruit using 3D shape models. Food Bioprocess Technol. 11, 2008–2020. doi:https://doi.org/10.1007/s11947-018-2163-9

Han, J.W., Zhao, C.J., Yang, X.T., Qian, J.P., Fan, B.L., 2015. Computational modeling of airflow and heat transfer in a vented box during cooling: Optimal package design. Appl. Therm. Eng. 91, 883–893. doi:10.1016/j.applthermaleng.2015.08.060

Ho, S.H., Rahman, M.M., Sunol, A.K., 2010. Modelling of the thermal response of a multi-tray food self-heating unit 68, 123–134. doi:10.2495/HT100111

Jackson, J.E., 2003. The biology of apples and pears - Biology of horticultural crops. Cambridge University Press, Cambridge, United Kingdom.

Nahor, H.B., Hoang, M.L., Verboven, P., Baelmans, M., Nicolaï, B.M., 2005. CFD model of the airflow, heat and mass transfer in cool stores. Int. J. Refrig. 28, 368–380. doi:10.1016/j.ijrefrig.2004.08.014

Prusky, D., 2011. Reduction of the incidence of postharvest quality losses, and future prospects. Food Secur. 3, 463–474. doi:10.1007/s12571-011-0147-y

Roache, P.J., 1994. Perspective: a method for uniform reporting of grid refinement studies. J. Fluids Eng. 116, 405–413.

Wu, W., Cronjé, P., Nicolai, B., Verboven, P., Opara, U.L., Defraeye, T., 2018. Virtual cold chain to model the postharvest temperature history and quality evolution of fresh fruit – A case study for citrus fruit packed in a single carton. Comput. Electron. Agric. 144, 199–208. doi:10.1016/j.compag.2017.11.034

Manuscript ID: 1110
DOI: 10.18462/iir.icr.2019.1110

Effect of dynamic storage temperatures on microstructure of frozen carrot imaged by X-ray Computed Tomography

Victor VICENT[a, b], Fatou T. NDOYE[a], Pieter VERBOVEN[b], Bart NICOLAÏ[b], Graciela ALVAREZ[a]

[a] IRSTEA, Refrigeration Processes Engineering Research Unit, Antony, France
[b] BIOSYST-MeBioS, KU Leuven, Leuven, Belgium
fatou-toutie.ndoye@irstea.fr

ABSTRACT

Temperature abuses are often encountered during cold storage and distribution chain of food products such as frozen vegetables. The subsequent ice recrystallization results in microstructural changes, which is closely linked to the final vegetable quality. In this work, X-ray µCT was used to visualize and quantify 3D ice crystal changes in carrot over a period of two months of frozen storage with dynamic change of temperatures. The results obtained revealed a significant increase in ice crystal size during the storage period, simultaneous to a significant reduction in ice crystal count number. The 3D data on ice crystals acquired within this work provide a better insight for the description of microstructure evolution, and for a better control of cold storage sector of frozen vegetable.
Keywords: frozen vegetables, ice recrystallization, X-ray µCT, 3D microstructure.

1. INTRODUCTION

One of the greatest challenges for the frozen food industry is to preserve the quality of food materials during extended storage for consumer's convenience. Food-processing operations, including freezing and frozen storage, may change the tissue structure significantly (Aguilera and Stanley, 1999; Ullah et al., 2014). During freezing of plant-based materials such as carrots (*Daucus carota* L.), ice crystals are formed throughout the cellular structure. The formation of ice crystals and subsequent ice recrystallization that occurs during storage, can modify the tissue microstructure of plant-based materials (Mousavi et al., 2007; Ullah et al., 2014; Ndoye and Alvarez, 2015; Vicent et al., 2017; Guo et al., 2018; Mo et al., 2018). Indeed, ice recrystallization involves ice crystals resizing and redistribution because of the growth of large ice crystals at the expense of the small crystals (Donhowe and Hartel, 1996; Hartel, 1998; Pronk et al., 2005; Hagiwara et al., 2006). Pronk et al. (2005) commented that in food materials, Ostwald ripening is the main mechanism for ice recrystallization. Recrystallization is more likely to occur if frozen food undergoes temperature abuse, such as dynamic temperatures during frozen storage and within the distribution chain (Zaritzky, 2000). Ice crystal growth is strongly linked to food microstructural changes that often affect the stability and quality of frozen foods. These changes include alteration in texture, sensory quality and nutritional values (Zaritzky, 2000; Ho et al., 2013). Vicent et al. (2018) recently showed changes of quality such as drip loss in frozen apple tissue as a result of ice recrystallization during storage with temperature fluctuations. Therefore, investigating the microstructural changes could help to elucidate the quality and stability changes occurring in vegetables. Most studies explore the microstructure of frozen food materials in 2D images (Donhowe and Hartel, 1996; Aguilera and Stanley, 1999). 2D information depends on the section plane of visualization and does not provide perfect quantitative morphology of volumetric elements such as cells, airspaces and ice crystals in frozen plant-based materials. Evaluation of the food microstructure in 3D has been proposed more relevant (Ho et al., 2013). The potential of X-ray micro-computed tomography (X-ray µCT) as a 3D imaging technique to visualize and quantify the internal microstructure features of frozen vegetables has been demonstrated (Mousavi et al., 2007; Voda et al., 2012; Ullah et al., 2014; Zhao and Takhar, 2017). Mousavi et al. (2007) used X-ray µCT to investigate the 3D ice crystals during freezing of different food products, including carrots, and stated that ice crystals varied in sizes according to the freezing rates applied. Ullah et al. (2014) applied X-ray µCT to visualize ice recrystallization in

frozen potatoes during storage with temperature fluctuations, and reported the ice crystals increased in size with the increase in amplitude of temperature fluctuations. Zhao and Takhar (2017) also used X-ray µCT to study ice recrystallization phenomena in frozen potatoes subjected to different temperature fluctuations during storage. However, all these works were carried out on frozen foods after a freeze-drying process to lyophilize frozen water. Authors assumed that the void structures formed in the freeze-dried products represented the ice crystal morphology. In fact, the freeze-drying process may have change frozen-food structures investigated through shrinkage (Voda et al., 2012), leading to inconclusive results. To circumvent this issue, Vicent et al. (2017) developed and validated an X-ray µCT imaging procedure directly on frozen samples to investigate the 3D microstructure of ice crystals in apple tissue at a low temperature (-18 °C). The method employed prior knowledge by incorporating X-ray attenuation coefficients of reference samples into the image analysis. The method remains to be tested to determine whether it is suitable for investigating the relationship between the 3D microstructure of the ice crystals and the storage temperature without requiring a freeze-drying step.
The objective of this study was to quantify 3D ice crystal growth in frozen carrots stored over a period of two months at dynamically changing temperature. X-ray µCT was used to visualize ice crystal propagation due to ice recrystallization. Image analysis was performed using the X-ray attenuation coefficients of reference model samples.

2. MATERIALS AND METHODS

2.1. Carrot sample preparation and freezing

Prior to freezing, cylindrical carrot (Daucus carota L., cv. Nantesa) samples with a height of 14 mm were excised from carrot tissue using a cork bore with an inner diameter of 6 mm. Subsequently, each excised sample was placed in a straw to facilitate the mounting of samples onto the cooling stage for image acquisition using X-ray µCT. Next, five replicate carrot samples were numbered and packed in two plastic bags.
The prepared samples were frozen in an air blast freezer set at a temperature of -33 °C. For sample temperature records, a calibrated thermocouple (type T; 0.2 mm) was inserted into a sample core of the representative bag. The air freezer temperature was recorded as well. Freezing was completed when the sample core temperature reached -18 °C. An overall freezing rate of approximately 9.1 °C per min was achieved.

2.2. Dynamic change of storage temperatures

Two freezers were used to achieve dynamically changing temperature conditions storage of frozen samples. Carrots samples were held for 23 h in the first freezer set at a temperature of -23 °C and then moved for 1 h to the second freezer set at a temperature of -5 °C, as shown in Fig. 1.

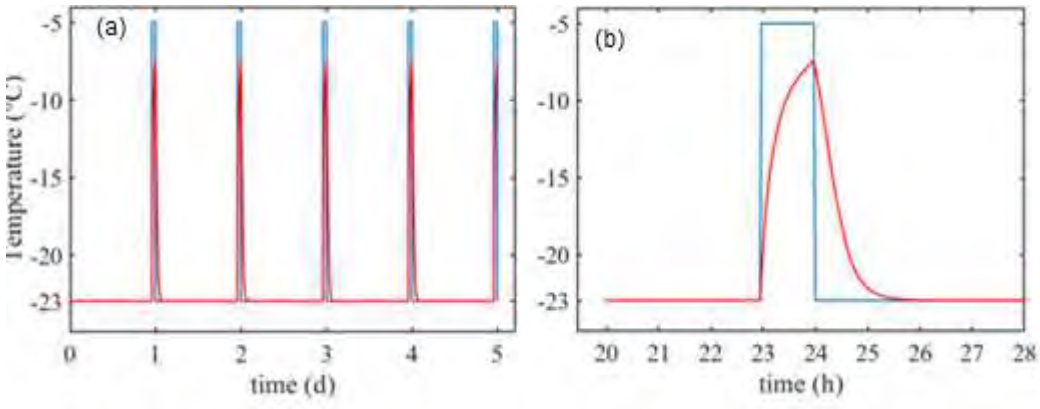

Figure 1: Air (blue line) and product (red line) temperatures records under dynamic storage: (a) 5 days record; (b) 1 day record

The dynamic temperature cycle was performed daily over a period of two months, with the exception of weekends. This storage scenario made it possible to study the effects of the poor practice in terms of temperature dynamic conditions that could occur during frozen storage. The

glass transition temperature of carrot was measured to be approximately -32 °C (Reid et al. 2003; Gonçalves et al. 2007). This indicates that no amorphous solid phase in the frozen carrot tissue was formed during freezing and dynamic storage experiments.

2.3. X-ray µCT imaging

3D images of frozen carrot samples were acquired using a high-resolution X-ray µCT apparatus (DeskTom RX 130, Chavanod, France). The frozen sample at -21 °C was gently placed into a cooling stage cylinder made of phase change material (PCM) designed to maintain the sample temperature during the entire scanning protocol. PCM consisted of NaCl (25 % w/w) and commercial blend gum (5 % w/w) (Germantown Premium IC Blend, Danisco) was used. The cooling stage was surrounded by and covered with polystyrene foam in order to isolate both the samples and PCM from the environment. Image acquisition was carried out with an X-ray tube power setting of 60 kV and 133 µA. A voxel resolution of 8.9 µm was applied. 896 projection images were recorded over a 360 degrees rotation with a step size of 0.4 degrees. The exposure time was of 0.2 s per projection resulting a total scanning time of 11 min per sample. After each scan, the sample was placed back in the freezer set at a temperature of -23 °C for sequential storage. This enabled us to follow the microstructural changes for the same carrot sample throughout the storage experiment.
3D images were reconstructed from a series of X-ray radiograph projections using XAct 2 software (RX Solution, Annecy, France). Noise filtering and phase contrast correction were applied to improve image quality. The scanning and reconstruction procedures outlined above were utilized to acquire CT images of frozen carrot at each time point during storage.
Fresh carrot scans were acquired using a SkyScan 1172 high-resolution desktop X-ray µCT (Bruker micro CT, Kontich, Belgium) at a voxel resolution of 2.9 µm. For comparison purposes to the frozen samples, five replicates of the fresh carrot tissue were imaged using the optimized scanning and reconstruction workflows detailed by Vicent et al. (2017).

2.4. Image processing

The procedure of image analysis was implemented using Avizo 9.2.0 software (FEI VSG, Bordeaux, France). A representative elementary volume (REV) analysis was carried out prior to image processing based on the method proposed by Mendoza et al. (2007). A REV of 340 × 340 × 340 voxels equivalent to a volume of 27.71 mm3, showed no appreciable difference in the standard deviation with the largest sample volume and was selected as the best for each set of images for further quantitative analysis to provide representation of the macroscopic properties of the frozen carrot.
Ice crystals in carrot samples were segmented using the methodology developed by Vicent at al. (2017) based on X-ray attenuation coefficients of reference model samples (frozen distilled water and concentrated carrot juice to identify X-ray attenuation coefficients of pure ice crystals and of the unfrozen-matrix respectively in frozen carrot tissue). Intensity densities ranging from 0 to 255 greyscales across the frozen carrot image was found according to the components (Fig. 2). The greyscale range between 0 and 20 was assumed to represent airspace, ice was found to have greyscale values between 10 and 130, while concentrated carrot juice resulted in greyscale levels between 100 and 220. The greyscale histogram of frozen carrot overlapped with that of the two reference samples, as it comprises both the frozen and unfrozen voxels. A preliminary test suggested that the majority of ice voxels had greyscale values between 20 and 120. Subsequently, these threshold values of 20 and 120 (shown by arrows in Fig. 2) were applied to each REV of frozen carrot to segment the ice fraction from the unfrozen matrix and air.
The spatial resolution at which the objects with small density deviations can be identified was determined according to a statistical method suggested by Hsieh (2009). A resolution of two voxels (18 µm) was found to be the smallest resolution for which the greyscale level was still significantly different between frozen water and concentrated juice.

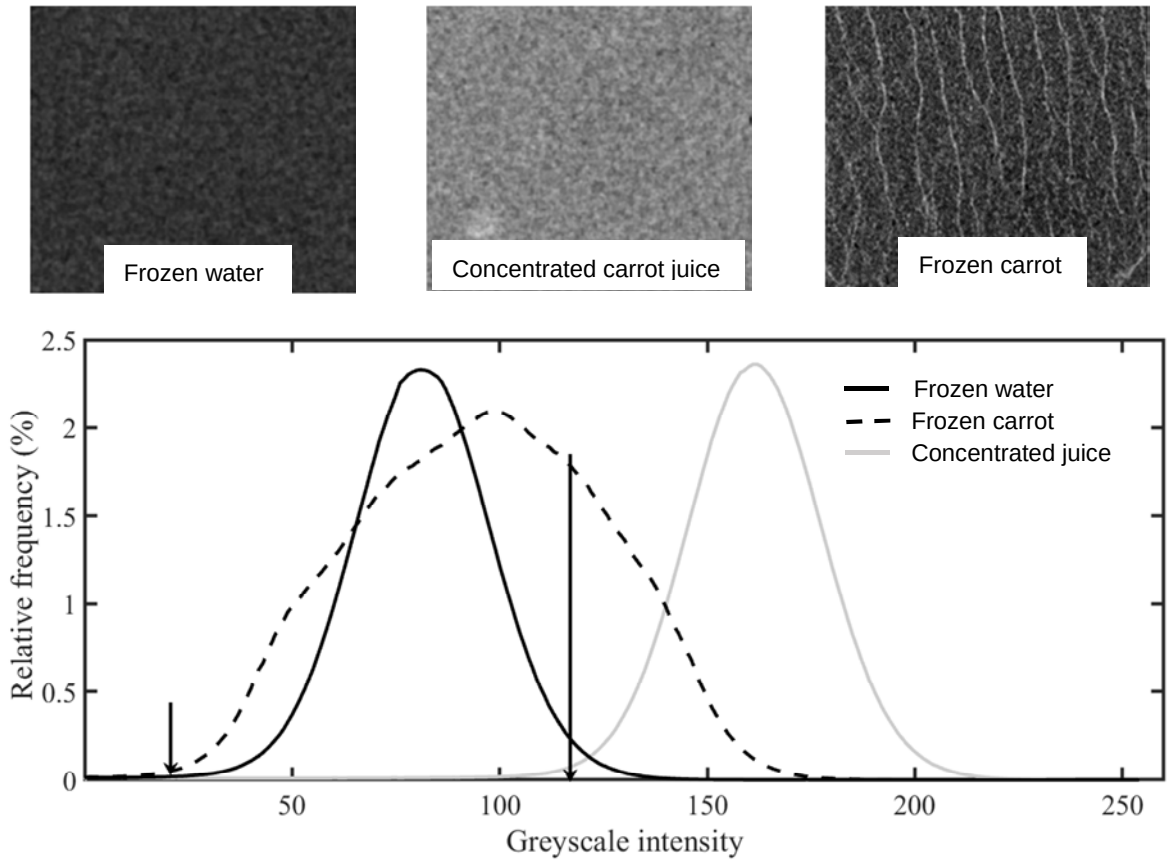

Figure 2: **CT cross-section slices of reference samples and corresponding greyscale intensity histogram.**

For subsequent quantitative analysis, a watershed separation procedure (Fig. 3) was applied to the region of interest (ROI) binary images of the frozen phase to separate the connected ice crystals. The separated ice crystals (Fig. 3b) were superimposed to the original CT image (Fig. 4) to elucidate how well the ice crystals were separated from each other. The separated ice crystals were then labelled individually as shown in Fig. 3c. To facilitate quantitative analysis, the ice crystals intersecting the borders of the REV may generate improper structure information that needs to be excluded by using a border kill module. The separated ice crystal dataset produced by Avizo Platform were imported into Matlab (R2015a, Mathworks Inc., Natick, MA, U.S.A), where their ice size distributions were analysed in five replicates. Lastly, a two-sample Kolmogorov-Smirnov test ($p < 0.05$) was carried out for statistical comparison of the data.

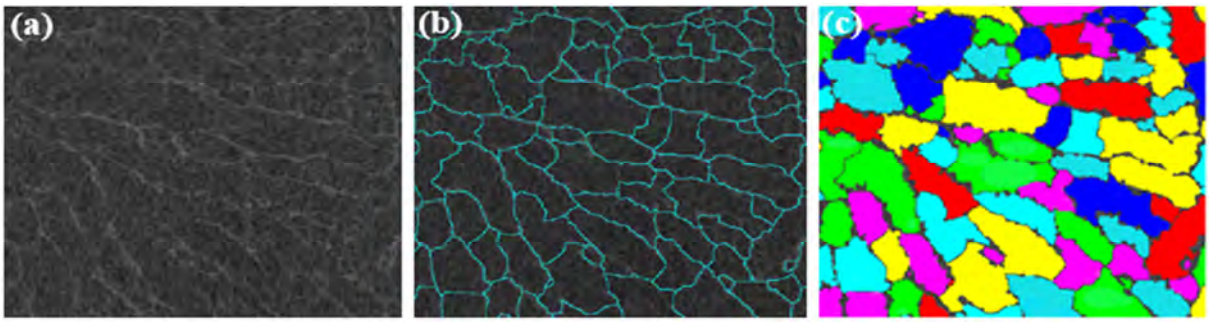

Figure 3: **Image processing procedure: (a) binary image of ROI; (b) separated ice crystals using watershed method; (c) labelled separated ice crystals**

3. RESULTS AND DISCUSSION

3.1. Microstructural changes

Fig. 4 illustrates the effect of the dynamically change of storage temperature on the microstructure of cylindrical carrot samples. Fig. 4a shows a µCT slice scan of fresh carrot tissue obtained at a voxel resolution of 2.9 µm. The dark spots represent airspaces, and the grey regions show the cellular matrix. Fig. 4b-f shows µCT cross-section slices of the same frozen carrot sample acquired at different time points (7, 14, 30 and 60 days) during a two-month storage period. The intermediate grey regions probably correspond to the frozen phase in frozen carrot tissue. The bright voxels correspond to the unfrozen-matrix (insoluble tissue materials and unfrozen water) which has a higher density than water and lights up in brighter interconnected lines. The µCT images clearly show a patchwork of oblong ice crystals with liquid concentrated juice in between. µCT images show clearly an increase in ice crystals size with increasing storage time (Fig. 4b-f). This can plausibly be explained by ice recrystallization occurring often during storage when temperatures fluctuate. When the frozen carrot undergoes temperature variations during frozen storage, the small ice crystals are subjected to melting-diffusion-refreezing cycles leading to crystal growth (Ndoye and Alvarez, 2015; Guo et al., 2018; Mo et al., 2018). This was shown to lead to microstructural changes in different frozen-food materials (Mousavi et al., 2007; Ullah et al., 2014; Zhao and Takhar 2017).
The qualitative information in the µCT images of the frozen carrot visibly prompted us to quantitatively analyse them to obtain a comprehensive insight into 3D ice crystal morphology (size, number and spatial distribution).

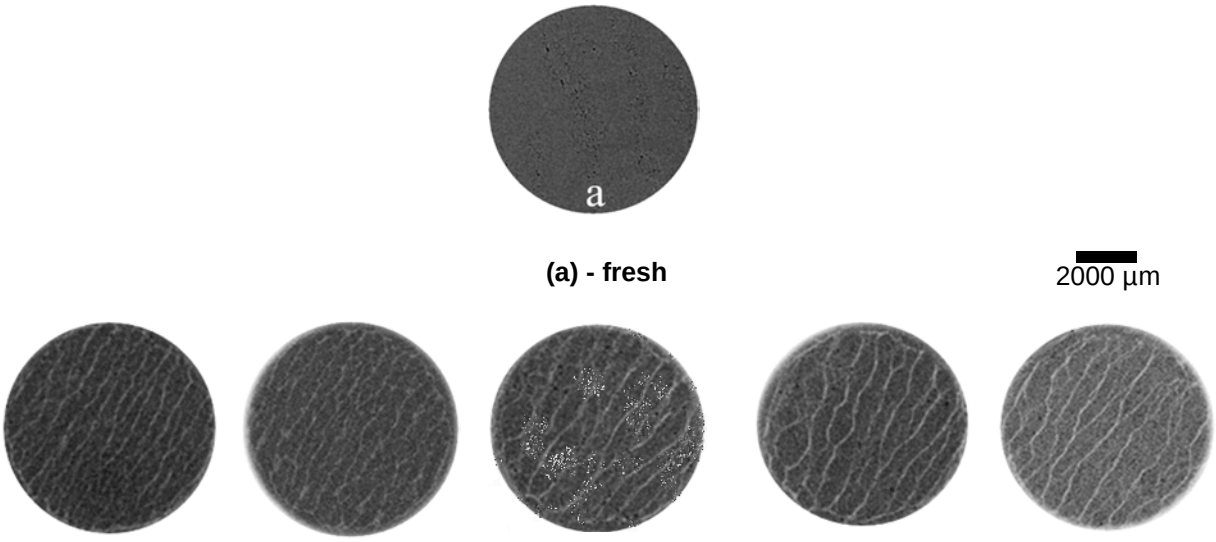

Figure 4: Effect of frozen storage under dynamically changing temperature on microstructure of carrots: µCT cross-section slices of the same frozen carrot sample at different storage time

3.2. Quantitative analysis of ice crystals

Fig. 5 shows ice crystal size distributions obtained from five replicates carrot samples for each time point. The distributions were found to be significantly different ($p < 0.05$). The size distribution became broader with increasing storage time. Just after freezing, initial ice crystal size distribution in the carrot samples ranged from 20 to about 590 µm. During storage, a gradual widening of the size distributions was observed up to size ranging from 20 to over 1120 µm after 60 days of storage. By comparing the size distributions, it can be seen that at 0 day, only 5% of ice crystals was larger than 400 µm. This value reached 12%, 20% 32% and 38% after 7 d, 14 d, 30 d and 60 d of storage, respectively.

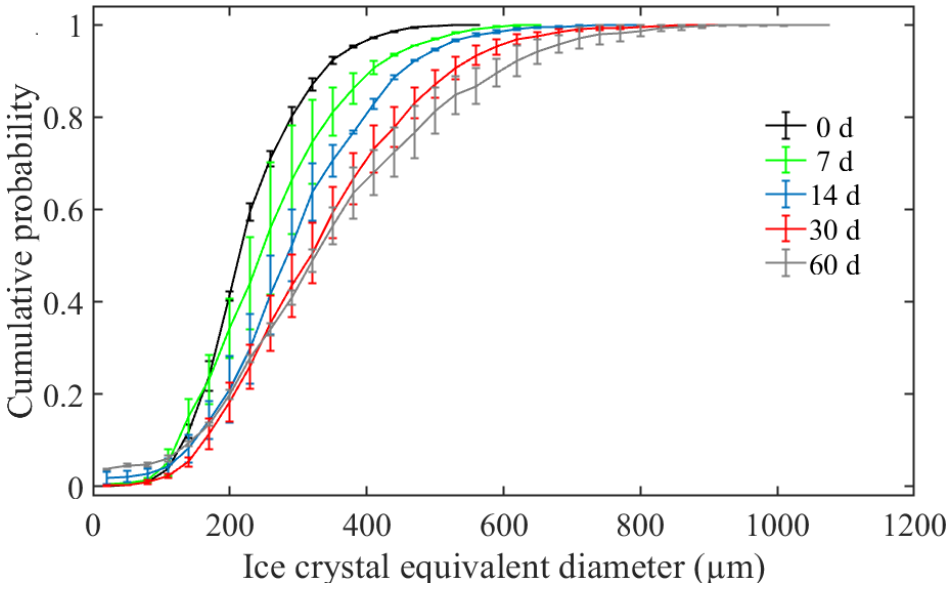

Figure 5: Cumulative ice crystal size distribution in frozen carrot samples stored under dynamically changed temperature during two month

The mean equivalent diameter of ice crystals in frozen stored carrots also increased with storage time accordingly to ice crystal size distribution broadening. Mean sizes of 240 ± 27, 270 ± 17, 308 ± 22, 362 ± 17 and 438 ± 28 were found at 0 d, 7 d, 14 d, 30 d and 60 d storage time, respectively. While ice crystal sizes increased, their total count number significantly decreased with storage time as shown in Table 1. At 0 d a large number (N = 2301 ± 175) of small crystals were found with a mean equivalent diameter equal to 240 ± 27 µm (Table 1). During further storage the mean equivalent diameter and number of ice crystals continued to gradually increase and decrease, respectively, until 60 d. At the end of the two-month storage period, the total number of ice crystals was reduced to 870 ± 45 whereas the mean equivalent crystal diameter reached a larger size of 438 ± 28 µm.

Table 1. Page margins for manuscripts submitted to the Nth IIR Conference

Storage time (d)	Ice crystal size range (µm)	Mean equivalent diameter (µm)	Median equivalent diameter (µm)	Mean number of crystals
0	20 - 590	240 ± 27	245 ± 22	2300 ± 175
7	20 - 680	270 ± 17	257 ± 11	1630 ± 144
14	20 - 810	308 ± 22	309 ± 15	1510 ± 130
30	20 - 990	362 ± 17	345 ± 60	1050 ± 60
60	20 - 1120	438 ± 28	390 ± 60	870 ± 45

The initial ice crystal size found in this study at day 0 (246 ± 16 µm) concurs well with those reported in the literature. Voda et al. (2012) investigated the freezing of carrot tissue at -28°C and reported ice crystal size of 239 µm. A similar value (241 µm) was found by van der Sman et al. (2013) for carrot tissue frozen at -28°C too. The subsequent ice crystal growth during storage found in this study, as the reduction in the total number of ice crystals was also stated in other studies, especially in a context of temperature abuse Ullah et al. (2014) and Zhao and Takhar (2017). Ullah et al. (2014) stored frozen potatoes under fluctuating temperatures during 30 days and reported a mean equivalent ice crystal diameter increasing from of 284 µm at day 0 to 605 µm after 30 days of storage under stepwise increasing temperature fluctuations: from -17°C to -16°C

for 10 days, from -17°C to -11°C for the next 10 days and from -17°C to -7°C during the last 10 days of storage. Comparable findings were published by Zhao and Takhar (2017) who used also stepwise increasing temperature fluctuations for frozen potatoe samples. Ice crystals grew from 113 µm to 833 µm during 42 storage days at -17°C to -16°C for 14 days, at -17°C to -11°C for the following 14 days and finally at -17°C to -7°C for the last 14 days. Ndoye and Alvarez (2015) showed a similar trend of ice crystal growth in ice cream stored under temperature fluctuations during a six month period. All these authors suggested that ice crystal growth is due to ice recrystallization phenomena such as Ostwald ripening mechanism where the smaller crystals merged with large ice crystals, and this process was as important as the amplitude of temperature fluctuations increased.

In the current study, the enlargement of ice crystals in carrot sample is likely due to ice recrystallization by Ostwald ripening mechanism. The decrease in ice crystals number could be explained by the melting of small crystals whose water molecules will refreeze on large crystals, implying the increase of mean ice crystal size. The alternating rise and lowering of storage temperature between -23°C and -5°C influenced the detachment of water molecules from small crystals where they are more weakly bound than in large crystals and their mobility through the matrix to bind to large crystals that become larger (Hartel, 1998; Hagiwara et al., 2006). As a result, both the ice crystal size distribution as well as their spatial distribution changed during storage (Hartel, 1998; Zaritzky, 2000; Hagiwara et al., 2006; Ndoye and Alvarez, 2015).

4. CONCLUSIONS

3D ice crystal size distributions and count in frozen carrot tissue were investigated using X-ray µCT under dynamically changing temperature in order to evaluate ice recrystallization phenomenon. A broadening of ice crystal size distributions was found for each time point involving an increase in the size of ice crystals. In addition, the total number of ice crystals was found to reduce in carrot during the two-month storage period. 3D imaging of ice crystals provided quantitative data sets that are useful for modelling purposes at the microscopic level such as population balance model, which can help to predict ice recrystallization. Such a modelling work can also help to acquire a better understanding of the relationship between microstructural changes and quality changes induced at the macroscopic scale in plant-based food materials during frozen storage under temperature abuse conditions. It can also be concluded that X-ray µCT provides a huge potential to image the 3D microstructure of ice crystals without significant preparation of the sample, and can thus be used for quality-control processes of frozen vegetables in the cold storage and distribution sector.

ACKNOWLEDGEMENTS

The authors wish to thank DIM ASTREA (as proposed by the Regional Council of Ile-de-France, France) for financial support under Award No. Ast 140054, 2014. They also acknowledge financial support from the KU Leuven (project C16/16/002, KA/16/057) and VLAIO (IWT 140992).

REFERENCES

Aguilera, J.M., Stanley, D.W., 1999. Food structuring. In: Aguilera, J.M., Stanley, W.D. (Eds.), Microstructural Principles of Food Processing and Engineering, 2nd ed. Aspen Publishers, Inc, Gaithersburg, Maryland, pp. 238-244.

Donhowe, D.P., Hartel, R.W., 1996. Recrystallization of ice during bulk storage of ice cream. International Dairy Journal, 6(11-12), 1209-1221.

Gonçalves, E.M., Lopes, C., Pinheiro, J., Lourenco, J.A.A., Abreu, M., Brandão, T. R.S., Silva, C.L.M., 2007. Differential scanning calorimetry as a tool for optimizing vegetables freezing and storage conditions. In EFFost/EHEDG Joint National Conference, Lisbon, Portugal, 14-16 November, 2007.

Guo, E., Kazantsev, D., Mo, J., Bent, J., Van Dalen, G., Schuetz, P., Rockett, P., StJohn, D., Lee, P.D., 2018. Revealing the microstructural stability of a three-phase soft solid (ice cream) by 4D synchrotron X-ray tomography. Journal of Food Engineering, 237, 204-214.

Hagiwara, T., Hartel, R.W., Matsukawa, S., 2006. Relationship between Recrystallization Rate of Ice Crystals in Sugar Solutions and Water Mobility in Freeze-Concentrated Matrix. Food Biophysics, 1(2), 74-82.

Hartel, R.W., 1998. Mechanisms and kinetics of recrystallization in ice cream. In: Reid, D.S. (Ed.), The Properties of Water in Foods. Springer US, Boston, MA, pp. 287-319.

Ho, Q.T., Carmeliet, J., Datta, A.K., Defraeye, T., Delele, M.A., Herremans, E., Opara, L., Ramon, H., Tijskens, E., van der Sman, R., Van Liedekerke, P., Verboven, P., Nicola ï, B.M., 2013. Multiscale modeling in food engineering. Journal of Food Engineering, 114(3), 279-291.

Hsieh, J., 2009. Computed Tomography: Principles, Design, Artifacts, and Recent Advances, 2nd ed. SPIE Press, Bellingham, Washington, USA, pp. 158-159.

Mendoza, F., Verboven, P., Mebatsion, H.K., Kerckhofs, G., Wevers, M., Nicolaï, B., 2007. Three-dimensional pore space quantification of apple tissue using X-ray computed microtomography. Planta, 226(3), 559-570.

Mo, J., Guo, E., McCartney, D., Eastwood, D., Bent, J., Van Dalen, G., Schuetz, P., Rockett, P., Lee, P., 2018. Time-Resolved Tomographic Quantification of the Microstructural Evolution of Ice Cream. Materials, 11(10), 2031.

Mousavi, R., Miri, T., Cox, P.W., Fryer, P.J., 2007. Imaging food freezing using X-ray microtomography. International Journal of Food Science and Technology, 42(6), 714-727.

Ndoye, F.T., Alvarez, G., 2015. Characterization of ice recrystallization in ice cream during storage using the focused beam reflectance measurement. Journal of Food Engineering, 148, 24-34.

Pronk, P., Infante Ferreira, C.A., Witkamp, G.J., 2005. A dynamic model of Ostwald ripening in ice suspensions. Journal of Crystal Growth, 275(1-2), 1355-1361.

Reid, D.S., Kotte, K., Kilmartin, P., Young, M., 2003. A new method for accelerated shelf-life prediction for frozen foods. Journal of the Science of Food and Agriculture, 83(10), 1018-1021.

Russ, J.C., 2016. 3D Visualization. In: The Image Processing Handbook. 6th ed. CRC press, Boca Raton, FL, pp. 707-763.

Sutton, R.L., Lips, A., Piccirillo, G., Sztehlo, A., 1996. Kinetics of Ice Recrystallization in Aqueous Fructose Solutions. Journal of Food Science, 61(4), 741-745.

Ullah, J., Takhar, P.S., Sablani, S.S., 2014. Effect of temperature fluctuations on ice-crystal growth in frozen potatoes during storage. LWT - Food Science and Technology, 59(2), 1186-1190.

van der Sman, R.G.M., Voda, A., van Dalen, G., Duijster, A., 2013. Ice crystal interspacing in frozen foods. Journal of Food Engineering, 116(2), 622-626.

Vicent, V., Ndoye, F.T., Verboven, P., Nicolaï, B., Alvarez, G., 2018. Quality changes kinetics of apple tissue during frozen storage with temperature fluctuations. International Journal of Refrigeration, 92, 165-175.

Vicent, V., Verboven, P., Ndoye, F.T., Alvarez, G., Nicolaï, B., 2017. A new method developed to characterize the 3D microstructure of frozen apple using X-ray micro-CT. Journal of Food Engineering, 212, 154-164.

Voda, A., Homan, N., Witek, M., Duijster, A., van Dalen, G., van der Sman, R., Nijsse, J., van Vliet, L., Van As, H., van Duynhoven, J., 2012. The impact of freeze-drying on microstructure and rehydration properties of carrot. Food Research International, 49(2), 687-693.

Zaritzky, N.E., 2000. Factors affecting the stability of frozen foods. In: Kennedy, C.J. (Ed.), Managing Frozen Foods. Woodhead Publishing, pp. 111-135.

Zhao, Y., Takhar, P.S., 2017. Micro X-ray computed tomography and image analysis of frozen potatoes subjected to freeze-thaw cycles. LWT - Food Science and Technology, 79, 278-286.

Manuscript ID: 1168
DOI: 10.18462/iir.icr.2019.1168

Cold thermal energy storage with low-temperature plate freezing of fish on offshore vessels

Espen H. VERPE[(a)(b)], Ignat TOLSTOREBROV[(b)], Alexis SEVAULT[(a)], Armin HAFNER[(b)], Yves LADAM[(c)]

(a) SINTEF Energy P.O. Box 4761 Torgården, NO-7465 Trondheim, Norway, espenhv@gmail.com
(b) Norwegian University of Science and Technology, Department of Energy and Process Engineering, Trondheim, Norway
(c) Kuldeteknisk AS, Tromsø, 9010, Norway

ABSTRACT

This paper presents the results of a numerical and experimental study of freezing time for fish in plate freezers, and the potential for improvement by altering fish block thickness and lowering evaporation temperature. Furthermore, the benefits of implementing cold thermal energy storage (CTES) in the system are presented.
The numerical freezing model relied on the apparent heat capacity method and was validated experimentally with an industrial plate freezer.
The freezing model demonstrated good agreement with experiments. Results suggested an increase in fish production capacity by 66 % when using -50 °C systems compared to -30 °C. Another 13 % increase in production capacity is possible if 50-mm thick fish blocks are used instead of 100-mm. Implementing CTES suggested a reduction in freezing time of 3.2 %, by maintaining constant plate temperatures during freezing.
Reduced evaporating temperature, thinner fish blocks and implementation of CTES proved to be beneficial for freezing processes on offshore vessels.
Keywords: CTES, Plate Freezing, R744, Freezing Model, Energy Efficiency.

1. INTRODUCTION

In the last decade, there has been an increase in natural refrigerants used in refrigeration systems (Oña, 2017). On offshore vessels, most systems use either R717 (ammonia) or R744 (CO_2), which can evaporate at temperatures as low as -50 ºC. Though operating at lower temperatures reduces freezing times, it also lowers the system efficiency and requires a higher installed compressor capacity.
This study focuses on plate freezing of fish onboard small fishing vessels, where compact equipment and high production capacity (kg frozen fish per day) is essential. Plate freezers are compact and uses plates, inside which the refrigerant evaporates, in direct contact with the fish to ensure fast freezing. On smaller vessels, whole, ungutted, fish are distributed between the plates and frozen to fish blocks with core temperature of at least -20 °C (Karlsen, 2018). Prediction of freezing times is an important parameter when designing freezing systems.
A new CO_2 system installed on a fishing vessel displayed significantly longer freezing time than expected (Karlsen, 2018). This is likely due to the heat load from the product side is highly varying during the freezing process, while the compressors are dimensioned for the average heat load to avoid over dimensioning the system. This results in insufficient compressor capacity during peak heat load, leading to elevated temperature in the low-pressure receiver and evaporator, causing prolonged freezing times.

1.1 Aim of the study

This study investigates the possibility to optimize the freezing process and equipment on board fishing vessels, by installing a cold thermal energy storage (CTES) system. The CTES system stores energy when the compressor capacity is larger than the heat load, and releases energy when needed, typically in the beginning of the freezing process. The effect on the freezing time and necessary equipment will be investigated.

To reach this aim, the following activities were done:

1) Development of a numerical model for the fish freezing process
2) Development of a numerical model for the temperature development in the low-pressure receiver
3) Model validation by freezing experiments and data from low-pressure receiver from freezing facility
4) Suggestion of CTES system and effects on key performance indicators of freezing system

This paper is based on the first author's master thesis (Verpe, 2018), where more details and results can be found.

2. METHODS AND MATERIALS

2.1 Description of Offshore CO_2 Freezing System

This study is based on an offshore, two-stage, sea-water cooled, flooded evaporator, R744 freezing system. A simplified model description is illustrated in Figure 1. The plate freezer has 24 stations and approximately 1250 kg fish capacity.

A model to estimate the system COP (Coefficient of Performance) was established with refrigerant data fromfree software RnLib. Reasonable assumptions included: isentropic compressor efficiency of 0.7, sea water temperature of 8 °C, temperature difference of 5 K in condenser and pressure drop in evaporator and condenser estimated by methods from Sardeshpandea et al. (2015), which encompass acceleration loss, friction loss and height difference.

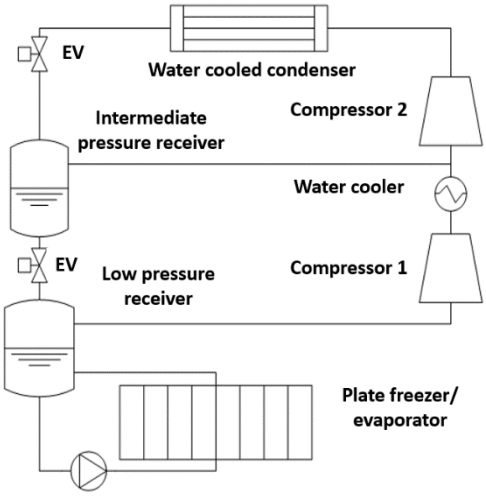

Figure 1: Simplified model description of a two-stage freezing system

2.2 Numerical Description

2.2.1 Freezing model

To be able to predict freezing times for various evaporating temperatures and fish block thicknesses, a numerical freezing model was written in MATLAB. The numerical domain contained the cross section for the fish block while the selected numerical method was to solve the two-dimensional heat diffusion equation, see Eq. 1, by an implicit finite difference scheme, described in Tannehill et al. (1997)

$$\frac{\partial}{\partial t}(\rho(T)c_a(T)\cdot T) = \vec{\nabla}\cdot\left(k(T)\cdot\vec{\nabla}T\right) \quad (1)$$

Eq. 1 uses apparent heat capacity, c_a, which includes both latent and sensible energy, described by Schwartzberg (1976). Other temperature-dependent thermodynamic properties were calculated using methods described in ASHRAE (2010). Note that the conductivity for porous media was used, to compensate for larger air voids between the packed fish, resulting in more realistic thermal conductivity values than for a homogenous material.

At first, the boundaries of the numerical domain, simulating contact with the freezer plates, were set to constant values (Dirichlet boundary condition). The required heat load, Q, to maintain boundary at constant temperature was calculated, and it was recognized such heat loads are not practically possible due to limited installed compressor capacity. Transient freezer plate temperature was therefore implemented, as described in Section 2.2.2.

2.2.2 Pressure receiver model

Limited compressor capacity results in insufficient refrigerant gas removal from the low-pressure receiver, see Figure 1**.** Increased pressure in the receiver elevates evaporating temperature in the freezer, which in turn, prolongs freezing time. Therefore, a model was made attempting to simulate the evaporating temperature during freezing of fish by assuming constant compressor capacity and calculating heat load from freezing fish. A gas mass balance was set around the receiver, enabling the possibility to calculate specific volume, v, for the tank, see more details in Verpe (2018). The simulated transient liquid temperature in the low-pressure receiver was used as transient boundary conditions in the freezing model, described in Section 2.2.1.

2.2.3 Energy Storage Tank Model and Description

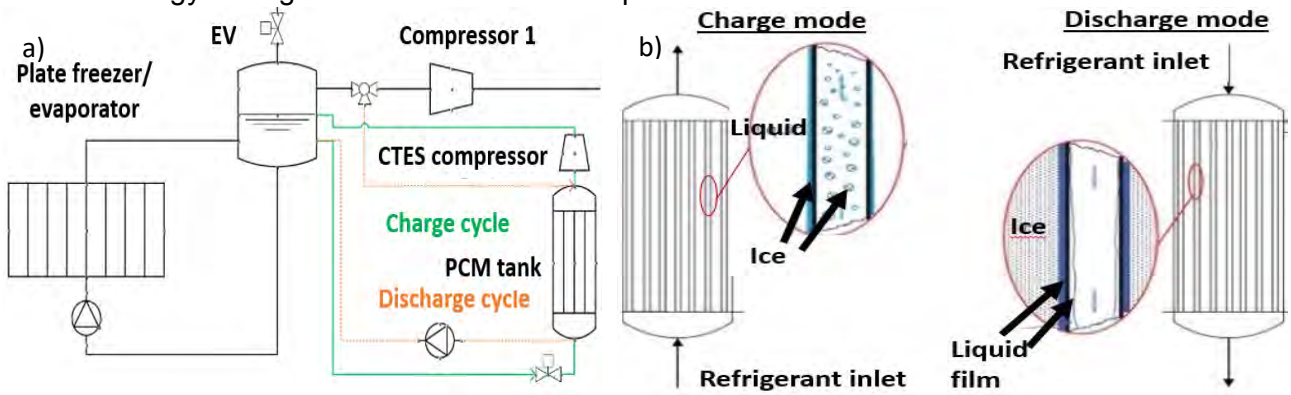

Figure 2: Charge/discharge of the CTES system (a) and a close-up on the PCM tank (b), adapted from Hafner et al. (2011)

An increase in the evaporating temperature, and therefore freezing time, due to insufficient compressor capacity could in theory be eliminated by implementing a CTES system. In this study, a theoretical shell-and-tube heat exchanger containing PCM (Phase Change Material) on the shell side was used to store energy, as suggested by Agyenim et al (2010). Charging, or freezing, of PCM is done when surplus energy is available, in other words when the compressor capacity is larger than the heat load from the product. Energy is released from the PCM tank (discharging) during the first minutes of freezing, when the heat load is largest. This essentially helps the compressor to remove gas, by condensing refrigerant in the storage tank and melting the PCM, see Figure 2.
The PCM was also chosen to be CO_2 due to matching phase changing temperatures and relatively high thermal conductivity, which is a key factor to improve the heat transfer rates. To store energy around -50 °C, the charging temperature of refrigerant in the tubes must be below the triple point, indicating solid dry ice particles to be formed. In charge mode, the liquid refrigerant from the receiver is expanded, generating solid ice to be sublimated in the tubes, while PCM is freezing on the shell side. During discharge, refrigerant gas is removed from the receiver, helping the compressor to maintain low pressure and temperature. The refrigerant gas is condensed when in contact with the colder PCM, which is melted and releases the stored energy. Dimensioning of equipment is fundamental, therefore PCM melting and freezing was modelled, based on the two-dimensional illustration in Figure 3.

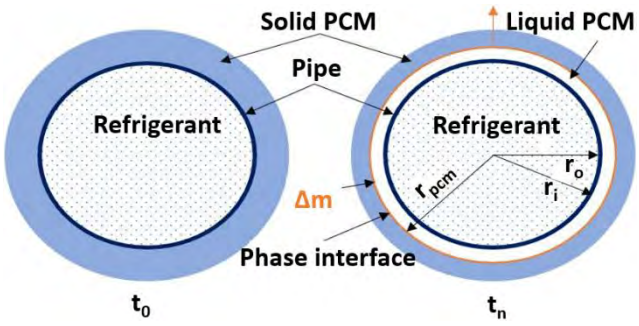

Figure 3: Close-up on pipe in PCM tank during discharge

Table 1: Suggested pressure and temperature levels in CTES tank

	Tube side		Shell side
	Charge	Discharge	PCM
Temperature	-65 °C	-49 °C	-57 °C
Pressure	3 bar	7 bar	8 bar

Assuming heat is transferred from phase changing refrigerant, through metal pipes, liquid PCM and to the interface of phase changing PCM, an expression for the overall heat transfer coefficient is described by Eq. 4 (Bergman et al. 2013).

$$UA = \frac{2\pi L}{\frac{1}{r_i h_{conv}} + \frac{ln(r_o/r_i)}{k_{pipe}} + \frac{ln(r_{pcm}/r_o)}{k_{pcm}}} \quad (4)$$

Eq. 4 is valid for liquid PCM at rest. However, buoyancy effects lead to heat transport by natural convection, resulting in higher heat transfer in the liquid layer. Nusselt number, *Nu*, which relates heat transfer in convective fluids to pure conduction in fluids at rest, is defined in Eq. 5.

$$Nu = \frac{h}{k} d \quad (5)$$

Heat flow to the melting PCM can be expressed by:

$$\dot{Q} = UA \cdot \Delta T = \frac{\Delta m \Delta H}{\Delta t} \quad (6)$$

Inserting Equation 4 into equation 6, by use of Equation 5 and expressing Δm by known quantities, yields:

$$\Delta r_{pcm}^{n+1} = \frac{1}{\frac{1}{r_i h_{condens}} + \frac{ln(r_o/r_i)}{k_{pipe}} + \frac{ln(r_{pcm}^n/r_o)}{k_{pcm} Nu_d}} \cdot \frac{\Delta T \Delta t}{\Delta H \rho_{pcm} r_{pcm}^n} \quad (7)$$

Equation (7) describes and incremental change in the PCM radius, Δr, for time steps n and n+1, and will be used to evaluate the required amount of PCM, and size of the tank. Pressures and temperatures assumed for the PCM tank are described in Table 1. Condensing heat transfer, $h_{condens}$, inside the tubes is hard to predict correctly. Therefore, values between 1700 and 4000 W/(m^2·K), considered to be high and low boundaries by *Zang et al. (2012)*, were implemented for sensitivity analysis. Results concluded that they had a limited impact on PCM development, because the overall heat transfer is dominated by the low conductivity of the PCM. Aluminium pipe diameter was assumed to be 10 mm with 3-mm thick wall. The Nusselt number could not be determined precisely due to the complexity of the dynamics at play. Therefore, "most probable" Nusselt numbers between 1 and 4 were assumed.

2.3 Validation of models

To validate the numerical freezing model, a test material consisting of agar-gel, was selected due to good contact with plates, no internal circulation during freezing, high density of nucleation sites and convenience to monitor temperature. Thermal conductivity of the gel was measured using HotDisk TPS (Transient Plane Source) method. The test material was frozen in an industrial plate freezer, while measuring core temperature with a TC (Temperature Couple) monitor. Evaporating temperature was measured to be -49 ºC during the whole experiment, due to almost empty freezer, giving optimal conditions for a constant plate temperature assumption.
Validation of the pressure receiver model was done by comparing model results with data, gathered from another land-based freezing facility with similar freezing system.

3. RESULT AND DISCUSSION

3.1 Validating Models

To validate the models, different strategies were chosen. The numerical freezing model was validated by comparing results with experiments in an industrial plate freezer, carried out by the authors.

3.1.1 Freezing time

In Figure 4, the experimentally measured core temperature is compared to the numerical freezing model. To achieve a core temperature of -20 ºC, there was only a difference of 2.9 % in freezing time.
Results from the numerical model were in good agreement with the experimental data. One can therefore assume reasonable agreement also to frozen fish, provided correct model inputs.

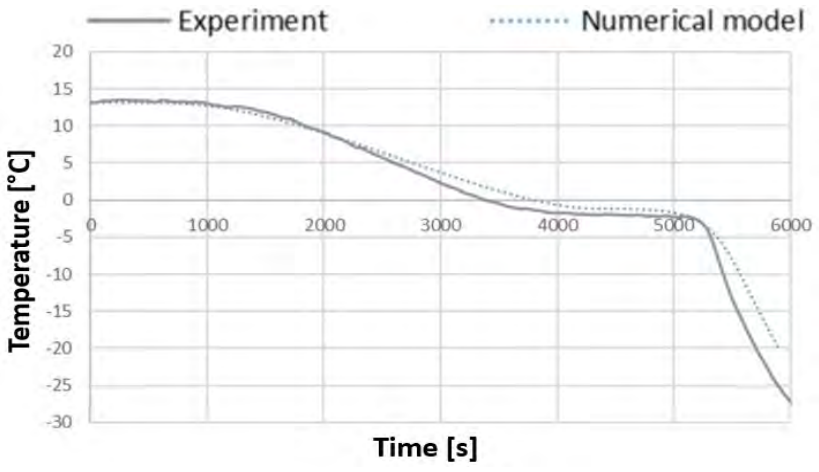

3.1.2 Temperature in receiver

In Figure 5, the theoretical temperature is compared to measured temperatures in the low-pressure receiver. The theoretical model overestimates the elevation of peak temperature, by 4 to 7 K. In addition, the temperature peak seems sharper than in the experiments, which may be explained by different compressor control strategies.

Modelling pressure in a receiver is a complex task since it is influenced by a number of parameters, e.g., control of compressor, heat loss, liquid level, gas and liquid in non-equilibrium and other factors difficult to implement in numerical models. However, numerical results seem to be in acceptable agreement with experimental data.

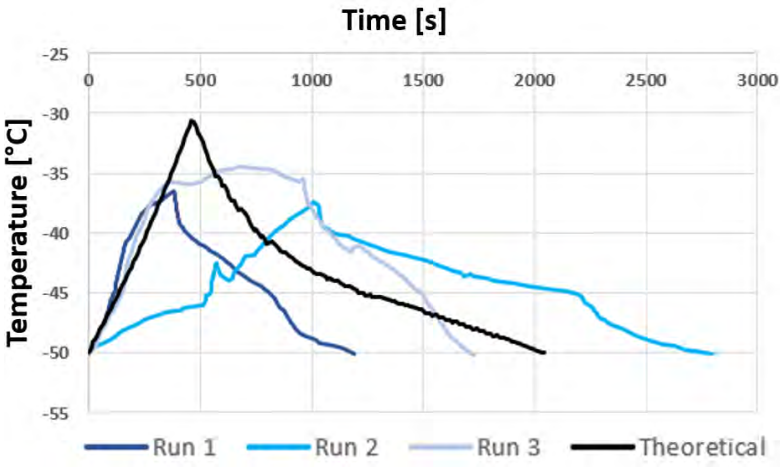

Figure 5: Model prediction and measured data on temperature in the low-pressure receiver during freezing

3.2 Results from numerical models

3.2.1 COP of system

The efficiency of the freezing system illustrated in Figure 1 was estimated by simple steady state models. The COP was calculated to be 1.75 and 3.0 for evaporation temperatures between -50 °C and -30 °C, which is just below 50 % of the theoretical Carnot efficiency for the respective temperature levels.

3.2.2 Freezing time, energy use and production capacity

Based on the calculations of the freezing times and the system COP, the key performance indicators could be determined, as shown in Table 2. A freezer with 25 plates was assumed.

Table 2: KPIs for a R744 plate freezer. Reference values: freezing time: 301 min, energy use: 43.2 kWh/ton, production capacity: 233 kg/h

		Freezing time [min]			Energy use [kWh/ton]			Production capacity [kg/h]		
Evaporating temperature		-50°C	-40°C	-30°C	-50°C	-40°C	-30°C	-50°C	-40°C	-30°C
Block thickness [mm]	50	19 %	23 %	31 %	149 %	108 %	81 %	188 %	161 %	126 %
	75	36 %	45 %	61 %	156 %	122 %	90 %	177 %	146 %	111 %
	100	58 %	73 %	100 %	172 %	133 %	100 %	166 %	134 %	100 %

Energy use is calculated using COPs for the CO_2 system, and a heat loss from the freezer is included. Production capacity calculations are made assuming a reset time (defrost, unloading/ loading of product) of 20 minutes between the freezing cycles.

The increase in the energy use by lower evaporation temperature can be explained by a decreasing COP and increasing heat loss, even though the freezing time is reduced. In addition, the energy use is lower for thinner blocks. This can be explained by the freezing times, which seem to be dependent on thickness squared, while the mass is linearly dependent on thickness. The same argument is also valid when examining production capacity. Therefore, production capacity can be greatly increased, both with reduction in evaporating temperature and plate thickness. In practice, too thin fish blocks will reduce surface contact and increase air void fraction, which in turn prolongs the freezing time.

3.3 Cold thermal energy storage

Figure 6 illustrates when and how much energy can be stored in the PCM tank, for a 1250-kg capacity freezer. Charging of the tank is done when the compressor capacity is larger than the heat load. The same energy can be released in the beginning of the next freezing cycle.

In practice, the pressure in the receiver determines whether the compressor capacity is higher than the heat load since this cannot be directly measured. Lower pressure than designed indicates surplus energy available and should signal the expansion valve to open and start the CTES compressor, see Figure 2.

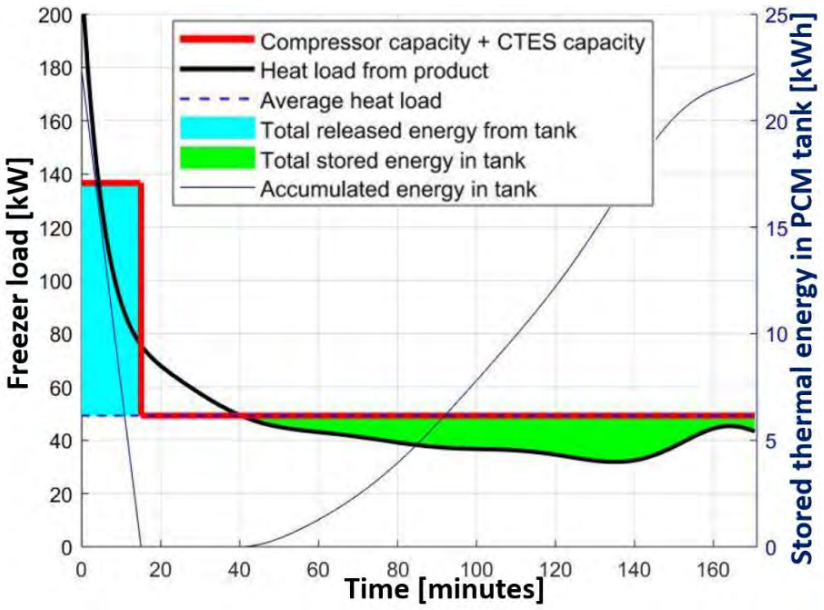

Figure 6: Heat load, compressor capacity and discharged/accumulated thermal energy during freezing

The *effective* compressor capacity, compressor + CTES freezing capacity, matches the heat load far better. This nearly eliminates the temperature elevation in the low-pressure receiver, which is clearly present if the installed compressor capacity alone does not cover the maximum heat load in the beginning of the freezing process.

3.3.1 Ice melting and sizing of the PCM system

To determine the number of tubes and the size of the storage tank, the melting (discharge) of PCM had to be modelled. It is likely that discharging of the tank would be the dimensioning criteria due to the short time and the resulting high heat transfer rates. The development of the melting layer was modelled for different Nusselt numbers, as shown in Figure 7.

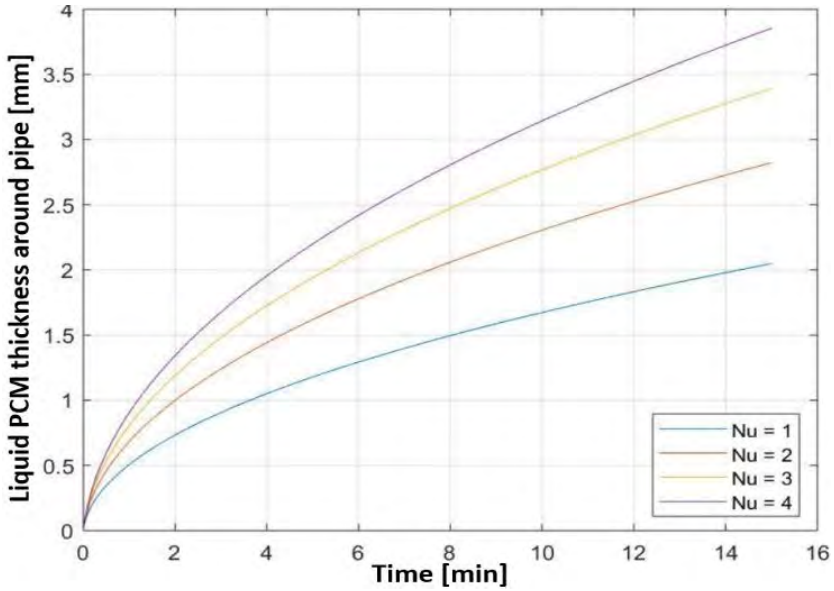

Figure 7: Evolution of the liquid PCM thickness for various Nusselt numbers

The total amount of PCM required for each 1-m long tube can then be calculated by knowing the amount of storable surplus energy, found from Figure 6. One can also determine the number of tubes, average heat transfer rates and total PCM tank volume, see Table 3.

Table 3: Dimensioning properties of CTES

	Nusselt number			
	1	2	3	4
Melted PCM thickness [mm]	2.02	2.74	3.34	3.64
No. of 1m tubes required	1377	979	805	702
Total volume of tank [L]	614	501	451	422
Mean heat transfer, U [W/m^{2}K]	264	372	452	518

The number of tubes and the total volume of the tank are especially interesting since they influence the capital investment cost and the space requirement, respectively. A 500 L tank occupies valuable space onboard fishing vessels.
Methods of heat transfer enhancements *(Agyenim et al. 2012),* may be needed to achieve the heat transfer rates, calculated in Table 3. The enhancement might also reduce the number of tubes and size, however, investment cost is likely to increase.

3.3.2 Effect on freezing system

Now, it is possible to calculate new freezing times when a CTES systems is enforcing constant plate temperature, since higher effective freezing capacity is installed. The potential benefits of installing a CTES system are also investigated.

Table 4: Potential benefits of installing a CTES system

	With CTES	Without CTES	Difference [%]
Freezing time [min]	168	174	-3.17
Specific energy use [kWh/ton]	80.2	74.3	7.94
Production capacity [kg/h]	399	388	2.92

Note the increase in energy use, due to the added CTES compressor. Freezing time is decreased by over 3 %, due to lower average plate temperature during the whole freezing process, which in turn results in 2.9 % production capacity increase. Capacity and freezing time are not directly correlated due to the assumed 20-min reset time, for defrost, unloading and loading of product between each freezer batch.

4. CONCLUSION

The numerical freezing model was validated by freezing a test material with good contact and constant plate temperature. The prediction of the temperature in the low-receiver, and therefore the freezer plate temperature, demonstrated good agreement with the experimental data, though the receiver temperature is erratic and varies from cycle to cycle.
Both decrease in block thickness and lower evaporating temperature, enabled by R744 systems, result in increased production capacity for the freezer, which is more influential than the increased energy consumption. The freezing station is the bottleneck of the production line, making the short-term storage on the boat (often refrigerated sea water, RSW-tanks) to be filled up while there is still fish to be harvested. Vessels with installed R744 systems, having fast freezing rates, can therefore spend less time at sea, which in turn reduces operational costs and fuel consumption.
Implementing a CTES system with a low-temperature R744 system, using CO_2 as PCM and storing energy when the compressor capacity is larger than the product heat load, was estimated to increase the production capacity by 2.9 %. The storage tank practically eliminates the temperature increase in the low-pressure receiver, by condensing the refrigerant gas that the compressor is unable remove. The PCM tank size was determined to be between 600 and 400 litres, depending on the achievable internal heat transfer rates. The tank required between 1400 and 700 tubes to be able to release the stored energy within 15 minutes.

ACKNOWLEDGEMENTS

This publication has been partly funded by HighEFF - Centre for an Energy Efficient and Competitive Industry for the Future, an 8-year Research Centre under the FME-scheme (Centre for Environment-

friendly Energy Research, 257632/E20). The authors gratefully acknowledge the financial support from the Research Council of Norway and partners of HighEFF. Furthermore, the study was partly carried out through the research project PCM-Eff - Novel phase change material solutions for efficient thermal energy storage - supported by SINTEF Energy Research and the Research Council of Norway.

NOMENCLATURE

ρ	Density [kg/m^3]	$\dot{m}$	Mass flow [kg/s]	r	Radius [m]	Q	Heat [W]
c_a	Apparent heat capacity [kJ/(kg·K)]	υ	Specific volume [m^3/kg]	L	Length [m]	U	Overall heat transfer coefficient [W/(m^2·K)]
T	Temperature [K]	$\dot{V}$	Volume flow [m^3/s]	h	Convective heat transfer [W/(m^2·K)]]	A	Area [m^2]
k	Thermal conductivity [W/(m·K)]	x	Vapour fraction	t	Time [s]	H	Heat of fusion [kJ/kg]

REFERENCES

Agyenim, F. et al., 2010. A review of materials, heat transfer and phase change problem formulation for latent heat thermal energy storage systems (LHTESS). Renewable and Sustainable Energy Reviews, 615-628

American Society of Heating, Refrigeration and Air-conditioning, 2010. ASHRAE handbook: Refrigeration. ASHRAE inc, Atlanta, 749 p.

Hafner, A. et al., 2011. Energy saving potential in freezing applications by applying cold thermal energy storage with solid carbon dioxide. 11th International Congress on Engineering and Food (ICEF11), 448 – 454

Bergman, T.L, et al., 2013. Principles of Heat and Mass Transfer (7 ed.). John Wiley & Sons Inc, Hoboken NJ, 1050 p.

Karlsen, S. R., 2018. Captain of fish freezing vessel. Verbal communication.

Sardeshpandea, M.V., et al., 2014. Two phase flow boiling pressure drop insmall channels. International Journal of Heat and Fluid Flow, 61(Part B), 636-649.

Schwartzberg, H.G., 1976. Effective heat capacities for the freezing and thawing of food. Journal of Food Science, 41(1):152-156.

Tannehill, J.C., et al., 1997. Computational Fluid Mechanics and Heat Transfer (2nd ed.). Taylor & Francis, Washington DC, 783 p.

Verpe, E.H. , 2018. Low temperature plate freezing of fish on boats using R744 as refrigerant and cold thermal energy storage. Master thesis at Norwegian University of Science and Technology.

Zang, Z. et al., 2012. CO2 condensation heat transfer coefficient and pressure drop in a mini-channel space condenser. Experimental Thermal and Fluid Science, 356–363

Manuscript ID: 1192
DOI: 10.18462/iir.icr.2019. 1192

Differential Scanning Calorimetry as a Tool to Monitor Polysaccharide Transformations

Antonio Diego MOLINA-GARCIA, Eva GOMEZ-ORDOÑEZ, Pilar RUPEREZ

Institute of Food Science and Technology and Nutrition (ICTAN-CSIC)
Madrid, 28040, Spain, antoniom@ictan.csic.es

ABSTRACT

Many industrial/natural processes involve transformations of the ubiquitous polysaccharides. These macromolecules are major components of plant foods, responsible for most of their energy (starch) and structural features (cellulose). Their industrially designed transformations or even those naturally occurring, driven by bio-catalysers, are difficult to monitor, due to their restricted interactions with other molecules.
Low-temperature differential scanning calorimetry (cryo-DSC) is a widespread technique, which can inform of the evolution of these macromolecules. Their influence on the ice dynamics and glass transition behaviour of water can provide information related to their alterations. Examples of processes involving starch and cellulose-based systems will be shown, indicating how the different glass transition and ice parameters yielded by DSC (glass transition temperature, different freezing and melting temperatures, enthalpy) can be a rich information source.
Keywords: low-temperature calorimetry, cellulose, glass transition, ice, starch

1. INTRODUCTION

Polysaccharides and carbohydrates in general are ubiquitous molecules of singular importance in every aspect of the Natural Sciences, and most significantly in Food Science and Technology. Not only the biological realm is concerned, as many technical and industrial applications and processes, from clothing fibres to paper, are based on these or related molecules.
Characterization of molecules, especially of macromolecules, where proteins are the main example and model, can be performed by many different ways. The highly active character of proteins, with many different states and prone to interact with many other small and large molecules, facilitates different methods of analysis and characterization. However, polysaccharides are less active, more inert molecules, especially in many cases of interest, such as those molecules that form part of structural elements in Nature and their role is, precisely, to keep a constant and stable structure.
Differential scanning calorimetry (DSC), a technique frequently used in biophysical studies on Food and bio-products as well as in the polymer and plastic world (e.g., Biliaderis, 1983; Höhne et al., 2013), can be used to obtain interesting information about these substances, for example, on structural changes derived from processing or about specific structure requirements for specific uses. Examples of small carbohydrates, oligo and polysaccharides, and thermally (starch) and pressure (cellulose-rich plant by-product) driven processes are shown.

2. MATERIALS AND METHODS

2.1. Materials

Artichoke by-product was obtained from a local manufacturer, lyophilized, milled and stored dry until use. It approximately contains (dry weight) 60 % total fiber (50 % insoluble, 10 % soluble), 20 % protein, 8 % ash, 7 % soluble sugars, 3 % lipids, 2 % inulin (determined by HPLC). Corn starch and laboratory purified rice starch were generous gifts from Roquette Laisa S.A. (Benifaió, Spain) and M. Raisa (UN Entre Ríos, Argentina), respectively. Avicel® PH-101 (microcrystalline cellulose, 50 µm particle size) and methylcellulose (Methocel MC 400 cP, viscosity of 2% water solution 350-550 mPa-s) were from Sigma (St. Louis, MI, USA). D(+)-trehalose dihydrate was a product of

Prolabo (Paris, France). Inulin (raftiline) was from Orafti-Beneo (Oreye, Belgium). Water was Milli-Q filtered, Millipore (Burlington, MA, USA).

2.2. Methods

Differential scanning calorimetry was carried out with a TA Instrument (Newcastle, DE, USA) TA 1000 equipment. The calorimeter allowed working at low temperature (until -150 ºC). It was conveniently calibrated with indium and zinc pure samples and the 0 ºC point was additionally checked with pure water. Samples were sealed in hermetic 40 µl aluminium pans. The scan rate was always 10 ºC/min and nitrogen was used as an ambient gas. Pans contained approximately 10 mg of dry or wet sample. Dry weight was determined after 24 hour low- pressure 110ºC heating. This allowed the determination of sample water content. Downwards processes are endothermic in the representation chosen for thermograms.
Electron scanning microscopy was carried out using a Hitachi microscope (Tokyo, Japan) model SU8000. Images were taken using secondary electrons.
Artichoke by-product was suspended in milli-Q water (10%) and treated by high pressure using a Stansted Fluid Power Food Processor (Stansted, UK). Treatments were performed at 50 ºC and lasted 30 min. Pressure levels were 200, 400 and 600 MPa.

3. A FEW THINGS THAT DSC CAN TELL US ABOUT CARBOHYDRATES AND POLYSACCHARIDES

A large number of review and research articles have dealt with DSC applications to food and specially carbohydrate systems (e.g., Biliaderis & Maurice, 1980; Borde et al., 2002; Roos & Karel, 1990, 91). Although some polysaccharides exhibit particular behaviours that makes them more sensitive to study, for example, the strongly energetic and variable starch gelatinization process, others, such as cellulose, are more stable and impervious. Fig.1 shows the effect of different intensity high hydrostatic pressure treatments on artichoke by-product. It is, basically, cellulose fibre still containing rests of the structural elements of the plant, with some other compounds, such as lipids, proteins and fragments of cellulose, such as cellulose-derived oligosaccharides.

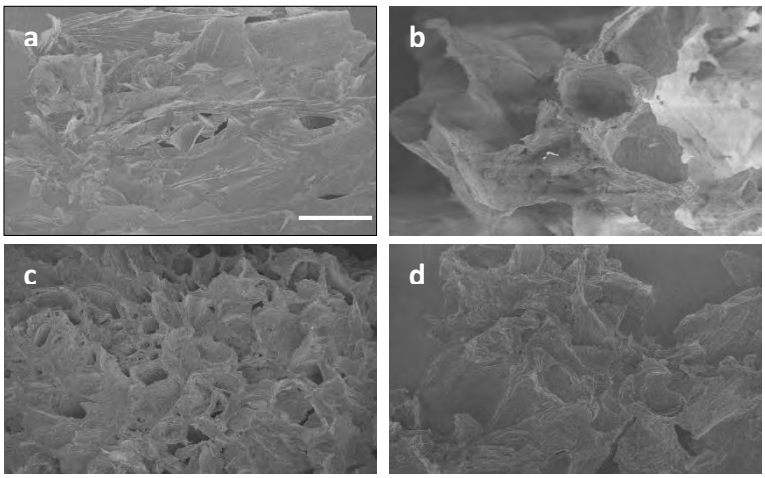

Figure 1: Typical electron scanning microscopy (SEM) images of artichoke by-product: a) untreated, and high hydrostatic pressure treated for 30 min at 50 ºC at b) 200 MPa, c) 400 MPa, d) 600 MPa. Bar = 25 µm.

The scanning electron micrographs are showing little differences among the untreated samples (a) and those submitted to high pressure (b, c, d). An increasing degradation degree and, perhaps, a more inflated or hydrated structure might be observed in the high pressure-treated samples.

3.1. High temperature DSC analysis

Differential scanning calorimetry (DSC) can be used to obtain information from these polysaccharide systems by performing heating scans. Different compounds can show a distinctive

high temperature decomposition or combustion. However, these conditions often could be considered too far from those of usual work with the analysed sample, and not always are so relevant to the sought structural and functional polysaccharide properties.
Thermograms can show exo- or endothermic events, reversible or irreversible, originated by particular structural interactions, or simply changes in the crystalline state. Crystallinity can be a way to distinguish different processing procedures and can be related to the particular activity of the sample (e.g., Schick, 2009; Sundaramurthi & Suryanarayanan, 2010). However, these properties are mostly lost when the substance of interest is hydrated.
Fig. 2. shows heating thermograms of dry methylcellulose and inulin, the fructose polymer energy reserve of some plants. Methylcellulose shows no event at all in this temperature interval, a typical behaviour for many polysaccharides. Meanwhile inulin shows a small endothermic transition that could mean a crystallinity lost, as it disappears upon heating, a second scan not showing it.

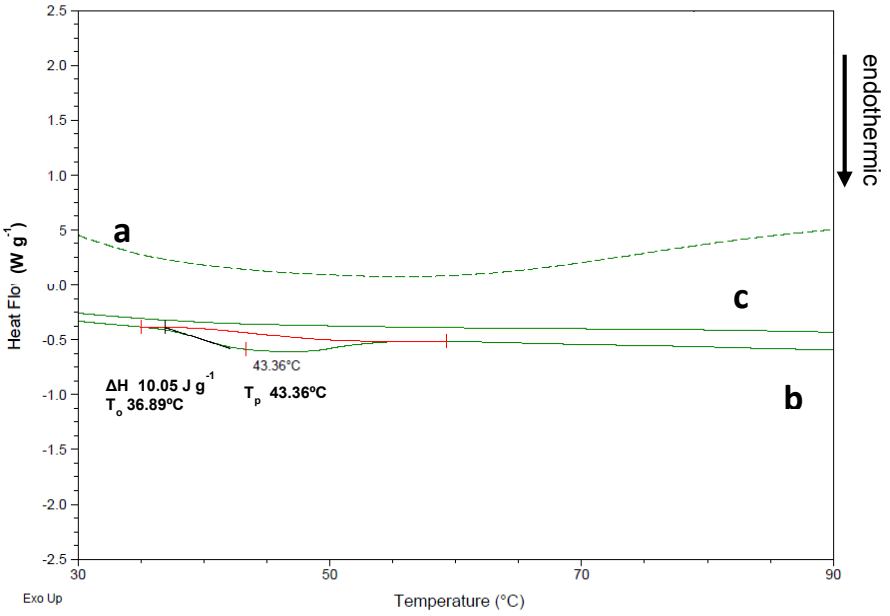

Figure 2: High temperature differential scanning calorimetry (DSC) thermograms of: a) dry methylcellulose, b) dry inulin and c) a second scan on the same inulin sample. Frequently carbohydrates show no appreciable thermal events (below decomposition temperatures), or the heat involved is small. Thermal parameters onset (T_o) and peak (T_p) temperatures and specific enthalpy corresponding to a non-reversible event observed for inulin are noted in the diagram, together with is specific enthalpy (ΔH).

The calorimetric study of the same samples of Fig. 1 shows what could be possible ascribed to a glass transition (after the heat capacity base line decrease and the diagnostic of the calorimeter program analysis) and an exothermic enthalpic peak at higher temperatures (Fig. 3). Glass transitions are often related to mobility and reactivity differences, but they are very sensitive to the fluidizing agent concentration increase, water in this case. In the wet state of the artichoke by-products, which is the state higher interest for this sample, a glass transition detected for dry state at 50-60 ºC would be expected to quickly decrease to very low (negative) temperatures with relatively low water amounts (data not shown). Alternative interpretations can be considered in this complex sample: an exothermic process (between 50-60 ºC) or an exothermic wider transition (between 60-70 ºC). Further experiments should be performed to decide among these possibilities. The dependence of these events with hydrostatic pressure treatments is still under study.

3.2. Low temperature DSC analysis

DSC can be used to indirectly obtain interesting information from polysaccharide systems, by studying their effect on water freezing behaviour (e.g., Nakamura et al., 1981; Goff et al., 1993). Fig. 4 shows how pure water freezing and thawing behaviour (a) is altered by the presence of the otherwise rather inert Avicel® and methylcellulose. The sharp exothermic freezing peaks reflects the brisk freezing of the metastable supercooled water at a nucleation temperature (T_n) which is, on one hand highly variable, as resulting from stochastic water molecules movements, and on the

other, sensitive to both nucleation by particles in suspension and, in the opposite sense, by viscosity increases. In this case, the presence of polysaccharides causes a strong increase in T_n, which could be related to the facilitation of ice nucleation sites by the polysaccharide itself.
The warming scans after ice formation show the corresponding endothermic ice thawing event, which is usually characterized by their initial, onset, temperature corresponding to the equilibrium

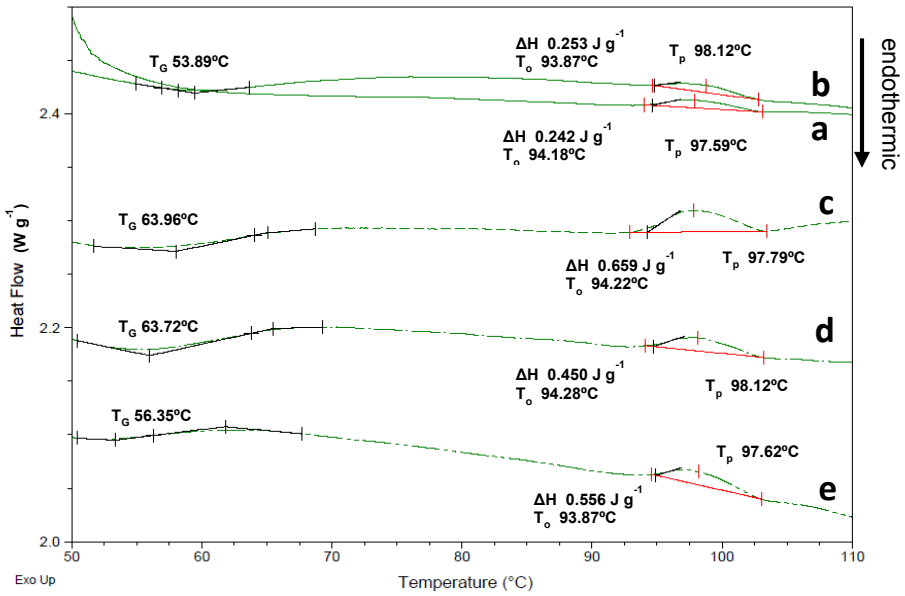

Figure 3: Typical high temperature DSC thermograms of dry (<10% water) artichoke by-product: a) and b) untreated (two consecutive scans), and high hydrostatic pressure treated for 30 min at 50 ºC and c) 200 MPa, d) 400 MPa, e) 600 MPa. The relative positions of baselines in the ordinate axis are arbitrary. At the left side of the thermogram, an event has been analysed as a glass transition: glass transition temperatures (T_G), the midpoint of the event, are included in the diagram. For alternative interpretations, see text. On the right side, an exothermic enthalpic event (of unknown origin) has been identified and (T_o), (T_p), and (ΔH) are shown.

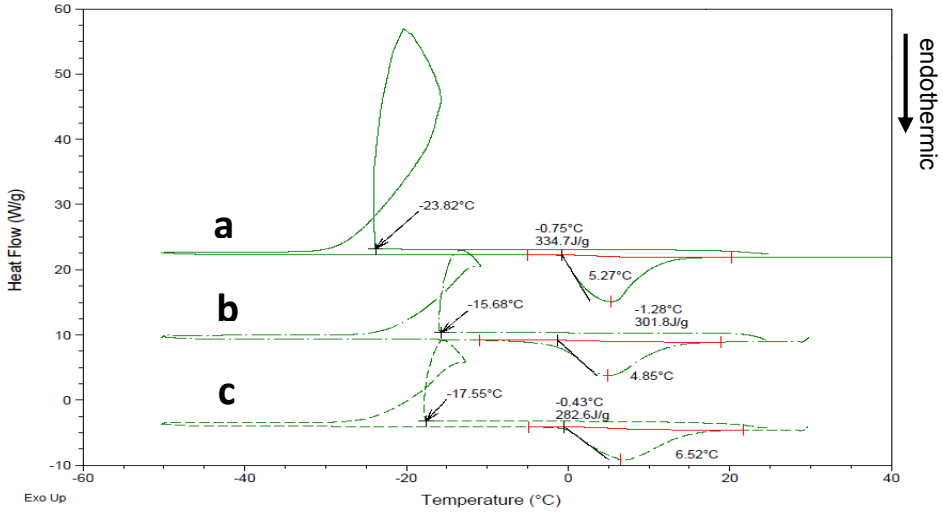

Figure 4: Low temperature DSC thermograms of: a) water, b) 9%wt methylcellulose and c) 9.6%wt Avicel® aqueous suspensions. Each sample was submitted to a cooling scan from room temperature to -50 ºC, followed by a warming scan back to room temperature. Nucleation temperatures (T_n) of exothermic freezing events in the cooling scans are noted in the diagram. Also, thermal data of ice melting endothermic events observed in warming scans are shown: T_f, T_p and ΔH (for water). The effect of polysaccharides is shown in these parameters.

freezing temperature (T_f), and other temperatures describing the progress of the thawing process. Such are peak temperature (T_p), the effective midpoint of the transition and end (endset)

temperature (T_e). T_f, which is decreased by the solute concentration, as described by Raoult's Law, should not be too affected by large polymers (being the number of molecules small). Here we see some effect on this temperature which may be related to salts present in the used product.
Additionally, the area between the heat capacity curve and the extrapolated baseline is proportional to the enthalpy involved in the process (ΔH). When it is compared with the weight difference-measured water content and the 334 J/g thawing enthalpy of pure water, the fraction of water actually frozen is obtained. The concept of bound water that used to be derived from this

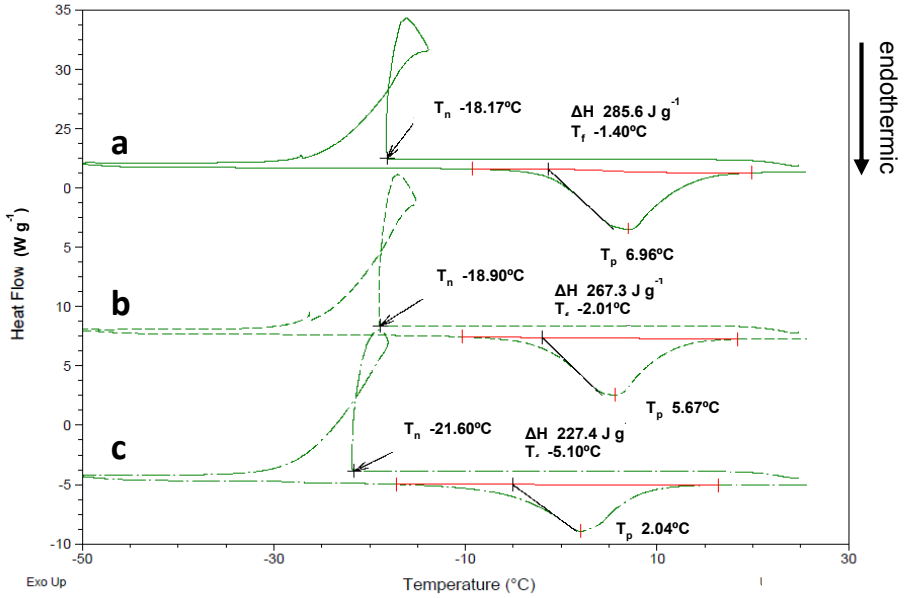

Figure 5: Low temperature DSC thermograms of aqueous solutions of trehalose of increasing concentrations: a) 3.7 %wt, b) 8.5 %wt and c) 21.6 %wt. Each sample was submitted to a cooling scan from room temperature to -50 ºC, followed by a warming scan back to room temperature. T_n of the exothermic freezing events taking place in the cooling scans have been noted in the diagram. Also, the thermal data of the ice melting endothermic events observed in the warming scans are shown: T_f, T_p and ΔH (for water). The effect of the increasing solute concentration is shown as a decrease of nucleation and melting temperatures and the amount of water frozen.

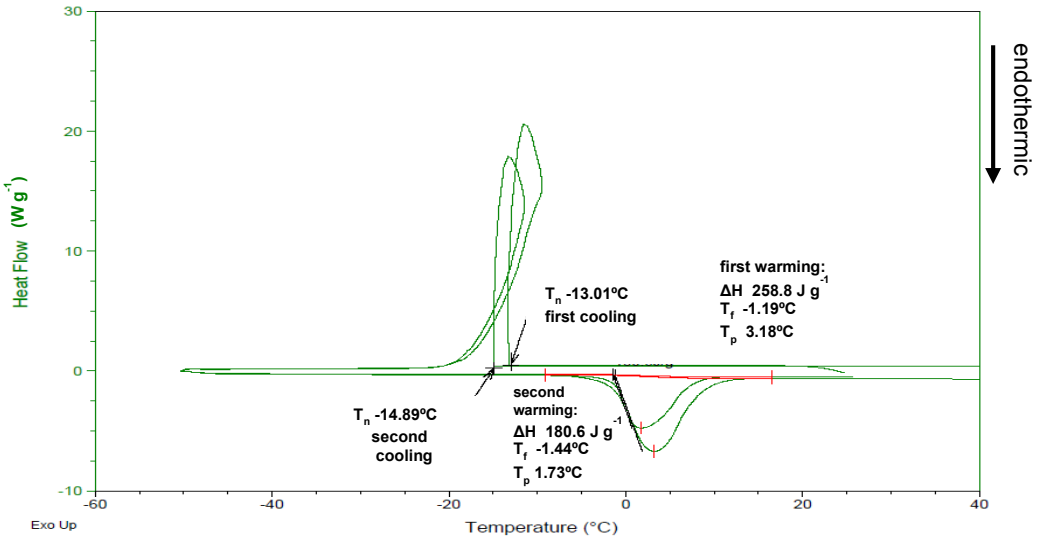

Figure 6: Low temperature DSC of a 15%wt aqueous suspension of native rice starch. Four consecutive scans performed with the same sample are shown. First, the sample was taken from room temperature to -50 ºC. Then it was warmed to 100 ºC. Afterwards, it was cooled down again to -50 ºC. And, lastly, warmed to room temperature. In the two cooling steps, ice freezing exothermic events can be observed and T_n have been noted in the diagram. In the two warming steps, the ice melting endothermic events are shown and their T_f, T_p and ΔH (for water) are noted in the diagram. The difference between the first and second scan pairs is the (not shown) gelatinization of starch, taking place when it was heated to 100 ºC. The differences observed in freezing parameters are justified by the change of state of starch.

fraction has been strongly criticised (Franks, 1983a, 1986). Actually, the supposedly bound water population has been shown to have relatively high mobility (Franks, 1983b; Li et al., 1998). In this work, the term “not frozen water” is consequently employed.
The frozen water ratio can be calculated here as 90% for methylcellulose (9.0%wt) and 86% for Avicel® (9.6%wt). This parameter can be also taken as a proof of the interaction degree of the polymer with the solvent, which can be of interests to predict behaviours (i.e. reactivity, degradation rate).
Fig. 5 shows how smaller molecules, such as the disaccharide trehalose (strongly related to cold stability of proteins and cells) acts on these three parameters, nucleation and freezing temperatures and thawing (i.e., freezing) enthalpy. T_n is decreasing with the increase of trehalose concentration, which is also causing the viscosity of the system to grow. T_f also decreases by the mentioned “cryoscopic decrease”. Although this effect can analytically yield solute concentrations, this is not possible for many real systems, such as those highly concentrated (not ideal) as those employed here, or with several solutes and suspended substances coexisting. However, it is a good estimation of the degree of carbohydrate-water interaction. ΔH, as in the previous case, decreases with the solute concentration and so does the calculated frozen water percentage:86%for the solutions at 3.7%wt, 80% for trehalose at 8.5%wt and 68% for solutions at 21.6%wt.
Starch is a particular case among polysaccharides presenting a well characterized endothermic transition associated to its gelatinization process, where a mayor intra- and intermolecular reorganization takes place with strong changes in their interactions with water. This transition is not considered here, as it has been the subject of many studies before (for example, Teixeira et al, 2018). However, it can be used to illustrate the potential of DSC to elucidate the differences in the interaction of polysaccharides with the surrounding water. In Fig. 6, a suspension of rice starch is first frozen, then thawed and heated over its gelatinization temperature, to be finally frozen and thawed again. The comparison of the freezing behaviour of water with native starch granules, showing little interaction with water, and the strongly interacting gelatinized sample, are evident. T_n decreases due to the viscosity increment, T_f is also decreasing and ΔH has a strong decrease (from 77 to 54 %, in terms of frozen water).
Fig. 7. shows the same phenomenon for corn starch at different (high) concentrations and how frozen water can decrease to values as low as 20% and ice nucleation is migrating nearly out of the experimental conditions in the highly viscous system (see Figure text).

4. SOME PROBLEMS AND PRECISSIONS

DSC yields a useful set of parameters to characterize the state and interactions of polysaccharides and carbohydrates in general. However, the information provided is not always easy to transform to quantitative terms. As it has been mentioned, at concentrations relatively high, mixtures of solutes and suspended particles often preclude analytical calculations.
It must be mentioned that ΔH should be ideally corrected to the equilibrium water freezing temperature conditions (see Teixeira et al., 2013). This correction can be of some relevance, especially if the degree of the amount of frozen water is important.
Fig. 8 shows the curious nature of the nucleation process itself. While to have separated water droplets in the DSC pan yield a unique thawing event, the nucleation events can be different. This is due partly to the stochastic nature of T_n and the nucleation process, and also reflecting the lower nucleation probability on smaller water masses. Consequently, the effects observed on T_n must be taken prudently, as their value is highly variable. Again, its area is not a sufficiently accurate source for ΔH and the corresponding frozen water ratio.

5. CONCLUSIONS

DSC, either at high or low temperatures, particularly taking advantage of their effect on water freezing behaviour, is a useful probe for the structural and interactive characteristics of molecules apparently inert, such as many polysaccharides. Workers in this field would profit of the use of this easy and widespread technique.

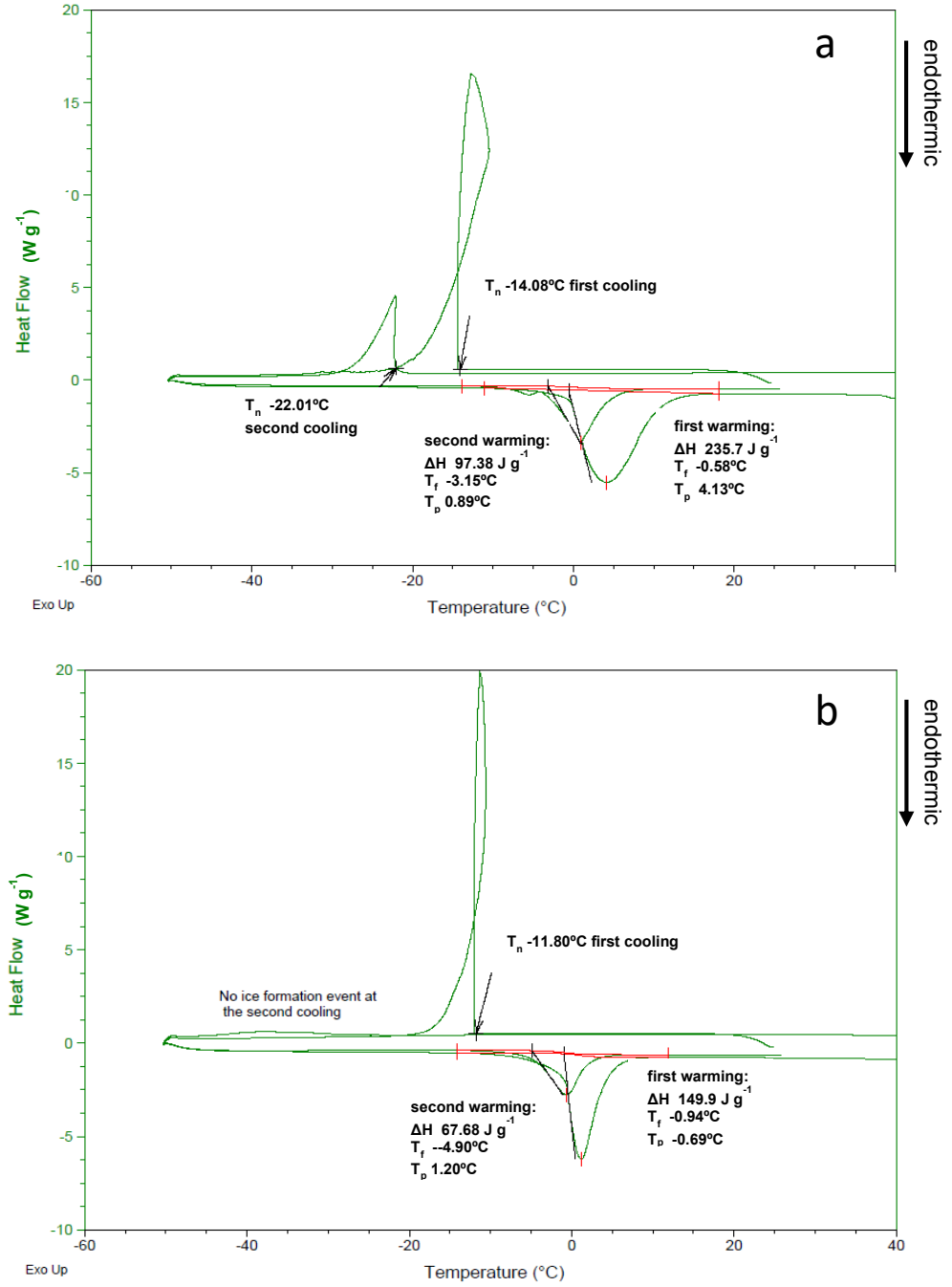

Figure 7: Low temperature DSC thermograms of a 36%wt (a) and 55%wt (b) aqueous suspension of native corn starch. The experiments were performed as explained for Figure 6. The second cooling scan on the very viscous 55%wt starch sample is not showing, but, as it can be appreciated in the later warming scan water melting, it presumably took place during the one minute waiting time separating cooling and subsequent warming scans.

ACKNOWLEDGEMENTS

This work has been carried out thanks to project “APHENZ” (AGL2016-77056-R) of the Spanish Ministry of Economy and Competitiveness (co-financed by EU FEDER fund). The technical help of S. Chamorro and R. Domínguez (DSC) and D. Gómez (SEM), and the starch gift of M. Raisa are acknowledged.

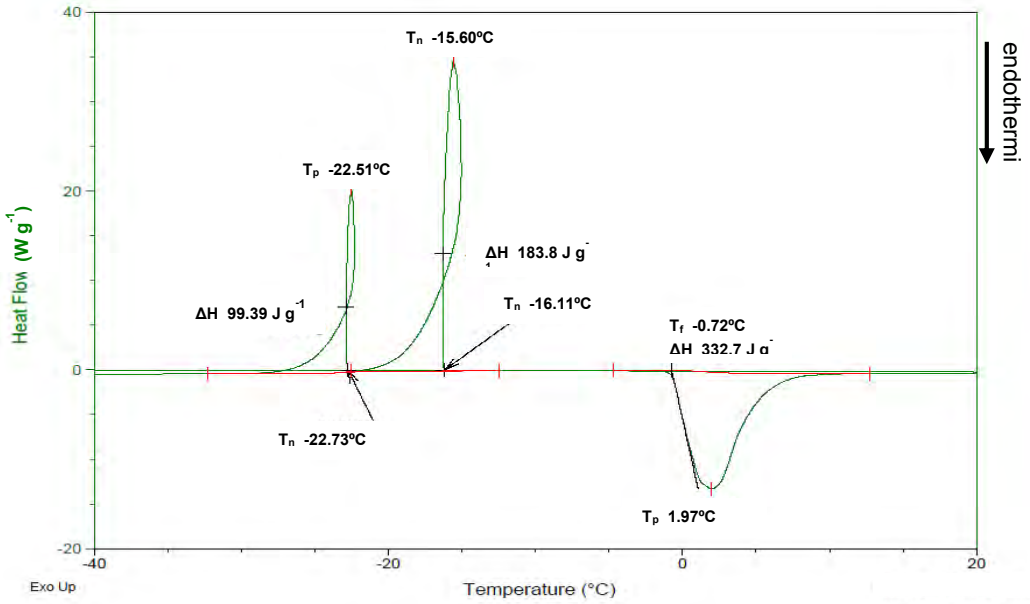

Figure 8: Pure water low temperature DSC thermograms. Water was carefully placed in the DSC pan as two unequal size droplets. It was cooled (room temperature to -50 °C) and warmed back to room temperature. T_n of exothermic freezing events and thermal data of ice melting endothermic event in the warming scan are shown: T_f, T_p and ΔH (for water). Water in each droplet freezes separately but thaws in a single event.

REFERENCES

Biliaderis, C.G., 1983. Differential scanning calorimetry in food research-a review. *Food Chem. 10*(4), 239-265.

Biliaderis, C.G., Maurice, T.J., Vose, J.R., 1980. Starch gelatinization phenomena studied by differential scanning calorimetry. J.Food Sci. *45*(6), 1669-1674.

Borde, B., Bizot, H., Vigier, G., Buleon, A., 2002. Calorimetric analysis of the structural relaxation in partially hydrated amorphous polysaccharides. I. Glass transition and fragility. *Carbohydrate Polym.*, *48*(1), 83-96.

Franks, F. 1983. Bound water: fact and fiction. Cryo-Lett. 4, 73-74.

Franks, F., 1983. Solute-water interactions: Do polyhydroxy compounds alter the properties of water? Cryobiology 20, 335-345.

Franks, F, 1986. Unfrozen Water, Yes; Unfreezable Water, Hardly; Bound Water Certainly No. Cryo.Lett. 7, 207.

Goff, H.D., Caldwell, K.B., Stanley, D.W., Maurice, T.J., 1993. The influence of polysaccharides on the glass transition in frozen sucrose solutions and ice cream. J. Dairy Sci., *76*(5), 1268-1277.

Höhne, G., Hemminger, W.F., Flammersheim, H.J., 2013. *Differential scanning calorimetry*. Springer Science & Business Media.

Li, S., Dickinson, L.C, Chinachoti, P., 1998. Mobility of “Unfreezable” and “Freezable” Water in Waxy Corn Starch by 2H and 1H NMR. J. Agric. Food Chem.46, 62−71.

Nakamura, K., Hatakeyama, T., Hatakeyama, H., 1981. Studies on bound water of cellulose by differential scanning calorimetry. Textile Res. Stu., *51*(9), 607-613.

Roos, Y., Karel, M., 1990. Differential scanning calorimetry study of phase transitions affecting the quality of dehydrated materials. Biotechnol. Progr*., 6*(2), 159-163.

Roos, Y., Karel, M., 1991. Phase transitions of mixtures of amorphous polysaccharides and sugars. Biotechnol. Progr., *7*(1), 49-53.

Schick, C., 2009. Differential scanning calorimetry (DSC) of semicrystalline polymers. Anal. Bioanal. Chem., *395*(6), 1589.

Sundaramurthi, P., Suryanarayanan, R., 2010. Trehalose Crystallization During Freeze-Drying: Implications On Lyoprotection. J. Phys. Chem. Lett. 1(2), 510–514.

Teixeira, A.S., Deladino, L.… Molina-García, A.D., 2018. Microstructure analysis of high pressure induced gelatinization of maize starch in the presence of hydrocolloids. Food Bioprod. Proces. 112, 119-130.

Teixeira, A.S., González-Benito, M.E., Molina-García, A.D., 2013. Glassy state and cryopreservation of mint shoot tips. Biotechnol. Progr. 29(3), 707-717.

Manuscript ID: 1194
DOI: 10.18462/iir.icr.2019.1194

Connected Indexes for food product temperature and quality monitoring

X. ALBETS-CHICO[(a)], P. MORENO[(a)], I. MUÑOZ[(b)], J.COMAPOSADA[(b)], S. BOVER [(b)], A. JOFRE [(b)], R. ROVIRA[(a)]

[(a)] AKO Group
St. Pere de Ribes, 08812, Spain, xalbets@ako.com
[(b)] IRTA-Food Technology
Monells, 17121, Spain, israel.munoz@irta.cat

ABSTRACT

Related to food retail and food services in general, two clear market tendencies can be distinguished nowadays: *i)* food retail is shifting towards smaller, specialized quality-based proximity and convenience stores and *ii)* delivery-based food retail and catering services are substantially growing. Both tendencies require even greater degrees of food product control temperature, quality standards and food microbiology risk analysis, either for stored or transported foods. The aim of this paper is to present two different indexes related to *a)* storage quality regarding drying conditions and *b)* product shelf-life evolution based on storage temperature. Both indexes are part of a greater connected data facility, using new cellular wireless technologies and internet of things (*IoT*) concepts, such that the indexes are able to provide full traceability in real time, therefore demonstrating and quantifying whether the food storage or transport conditions have abided optimal quality standards and if microbiology hazards are under control.
Keywords: Air-Transport, Drying, Food Industry, Microbiological Quality, Quality.

1. INTRODUCTION

Food retail stores and catering services are nowadays addressing their quality standards only on temperature monitoring, without any quantification of the impact of temperature-time and/or air relative humidity on the food products. Moreover, it is often found that the food retail industry presents an important lack of knowledge related to optimal refrigeration/storage conditions for specific products, while air relative humidity is generally neglected. The lack of knowledge related to the effects of variations with respect to the optimal conditions is seen in to directions:

- Effects of the storage temperature and air relative humidity (when different from optimal) on the drying/weight loss rate of fresh products, therefore, on its water content and related organoleptic and visual features, i.e. sensory characteristics.
- Effects of the storage temperature and time on the growth of microorganisms in perishable products, therefore, on its microbiological quality, safety and general sensory characteristics.

Beyond the effects on both drying/weight loss and microbiological aspects of the perishable products, another point of interest is the traceability of the cold chain and the compliance of HACCP (Hazardous Analysis of Critical Control Points). Indeed, despite big efforts made by the industry in the recent years, it is still not yet a common practice to consistently monitor and register storage conditions all along the cold chain from the farm to the table. One of the most important barriers related to this aspect is the still technical complexity of data management and connectivity, often related to complex wired sensors networks, local databases and lack of accessible engineered front-ends where all the information can be gathered and analysed (or when these current technical solutions are still cost prohibitive for many applications). The still incipient *IoT* (Internet of Things) technologies and practices can clearly provide interesting functionalities for this field, as the independent internet connection of devices through cellular telecommunication networks allow a comprehensive and flexible data management at reasonable cost. And most importantly, *IoT* allows a monitoring that is feasible along the time and space that food product remains in the cold chain:

including production, processing, transport and food-retail or food-service. Hence, the current paper is presenting the indexes for food quality monitoring all along the cold chain, thanks to their embodiment in connected *IoT* battery-operated wireless devices.
The indexes, under patent (Albets-Chico et al., 2019*)*, quantify the impact of the cold chain on the weight loss, organoleptic and microbiological quality of the food. Such information can be useful for the cold-chain stakeholders to assess, improve and manage nominal cold-chain conditions (set-points for temperature and air relative humidity); but also to react accordingly in front of incidences concerning the cold chain conditions (deviations in time from both storage temperature and air relative humidity conditions). The indexes, in their *IoT* embodiment, consequently represent a tool for comprehensively improving both the design and HACCP (Hazardous Analysis of Critical Control Points) processes for all the segments of the cold-chain.
The paper is organized as follows: Section 2 presents the definition of the indexes related to quality, preservation and microbial growth of food products. Section 3 details the calculation methodology for the indexes. Section 4 briefly explains *IoT* connectivity through Narrow Band technology. Section 5 presents some quantitative experiments and real case analyses using the presented indexes and, finally, Section 6 summarizes the concluding remarks of this work.

2. INDEXES: DEFINITION

Two different indexes are presented. The first one, the so-called ***drying index*** DI is concerned to food storage quality regarding drying conditions (effects of the temperature and air relative humidity with respect to optimal conditions for a specific food product). The second index, the so-called ***shelf-life index*** SLI, is related to the potential impact of microbial growth on the durability (shelf-life) of the food product. As the reader may guess, both indexes quantify the relationship between the actual/recorded storage conditions of the food products with respect their optimal or desired storage conditions, which are associated with specific food categories.

2.1. Drying index

The absolute evaporation (water mass transfer) from the food product towards the surrounding air depends on the ambient temperature, ambient relative humidity and air velocity to which the food is exposed. The drying index is defined as the actual evaporation rate (computed as evaporated water in kg / m^2 s) at the surface of the food product, with respect to the optimal evaporation rate; being the optimal evaporation rate defined as the one at optimal temperature and air relative humidity conditions, optimal temperature and relative humidity being in their turn tabulated in Handbooks, for example (Thompson et al., 1996) for different kinds of food product.
Being the actual evaporation rate (mass transfer) defined as mt_a, and the optimal evaporation rate (mass transfer) as mt_o, the drying index (*DI*) is defined by Eq. (1):

$$DI = \frac{mt_o}{mt_a} \cdot 100 \qquad \text{Eq. (1)}$$

The values for the DI range from 100 (when the actual rate is equal or lower than the optimal one, as DI is limited to 100 points) and tends to 0, for an extreme evaporation rate, i.e. extreme drying conditions; hence 100 points representing optimal conditions and 0 extremely drying conditions. Additionally, in case the actual evaporation rate is much lower than that at optimal conditions (1/2 log smaller or less), index is also corrected as non-quantifiable “condensation risk”, since the evaporation is too low and the food product is not able to transpire.

It must be noted that the DI index is a real-time index, hence with a single value for each monitoring sample. Details about the computation of the mass transfer rate are given in section 3.1. A second form of the index is the inverse of the DI, which represents the relative drying rate at the actual conditions with respect to the optimal conditions, i.e. defines the acceleration rate of evaporation mass transfer due to actual storage temperature and air relative humidity values. The drying acceleration index (DA) is defined by Eq. (2).

$$DA = \frac{mt_a}{mt_o} \cdot 1 \qquad \text{Eq. (2)}$$

The values for the DA range from *1 x times* (when the actual rate is equal or lower than the optimal one) and tends to *infinity x times*, for extremely adverse drying conditions; hence when the DA takes values greater than *1 x times*, the indicator can be used as the multiplier of the actual storage time to compute the effective drying time of the food product, had the food product been stored at optimal drying conditions. For example, an apple stored 2 days with a DA = 4*x* will suffer the same weight loss as an apple during 8 days at optimal conditions.

2.2. Shelf-life Index

The shelf-life index of a food product depends on the temperature and the time that the product is stored at such temperature. It can be modelled by an exponential equation, which is detailed in section 3. The shelf-life reduction due to microbial growth depends on the foods and it is described in several scientific publications, Food Safety Standards and Handbooks (Doyle, 1989; Food Code, 2013).

Being the elapsed shelf-life at a desired storage (set-point) temperature esl_{sp} and the elapsed shelf-life at a given temperature esl_T (which considers the respective shef-life reduction in case temperature T had been higher than the desired T_{sp}), the shelf-life index (SLI) is defined by Eq. (3):

$$SLI = \frac{esl_{sp}}{esl_T} \cdot 100 \qquad \text{Eq. (3)}$$

The values for the SLI, as they did for the drying index DI, range from 100 (when the elapsed shelf-life is equal or shorter than the reference one, as SI is limited to 100 points) and tends to 0, for extremely adverse storage conditions; hence 100 points representing reference conditions and 0 extremely aging conditions, i.e. indicating instantaneous food product deterioration. It is important to mention that this index, as the previous DI is a real-time index, hence the elapsed time concept here refers to a short period of time, of the order of minutes, typical sampling frequency of monitoring systems. As already said, details about the computation of the shelf-life reduction and elapsed shelf-life are given in section 3.2. A second form of the index is the inverse of the SLI, which represents the relative aging velocity at the actual conditions with respect to the desired conditions, i.e. defines the acceleration rate of microbiological growth due to actual conservation storage. The shelf-life deterioration/acceleration SLA is defined by Eq. (4).

$$SLA = \frac{esl_T}{esl_{sp}} \cdot 1 \qquad \text{Eq. (4)}$$

The values for the SLA range from *1 x times* (when the actual conditions are at temperature T_{sp} or lower) and tends to *infinity x times*, for an extremely adverse aging/microbial growth conditions; hence when the SLA takes values greater than *1 x times*, the indicator can be used as the multiplier of the actual storage time to compute the effective (shelf-life based) storage time of the food product, had the food product been stored at desired temperature conditions. For example, a pork-loin stored 3 days with a SLA = 3*x* will suffer the same microbial growth, and consequently the same shelf-life reduction, as the same pork-loin during 9 days at reference temperature conditions.

In summary, both indexes can be expressed in two different forms: (*i*) a real-time percentile indicating proximity to the optimal (in case of dehydration effects) or desired (in case of microbial growth) conditions; and (*ii)* an acceleration term that represents a storage-time multiplier for the food product in terms of weight loss or microbiological proliferation, respectively. While the percentile expression helps identifying how far the current conserving conditions are from the reference/optimal ones (in real-time), the acceleration indexes allow computing the effective storage time for the specific food product for a given storage time. As the reader may guess, the same time and temperature might produce different kind of results in the indexes depending on the food product. Hence, a specific

temperature excursion for chicken might be critical, while the same temperature excursion might be moderate for beef or pork, for example.

3. COMPUTATIONAL METHODOLOGY

3.1. Computational methodology for the food – ambient water mass transfer

Evaporation mass transfer at both actual and optimal conditions must be calculated for determination of DI and DA indexes. For both conditions, water mass transfer from food to bulk ambient is computed in the same way and under the following assumptions: *a*) during refrigeration cycles air is circulating half of the storage time (50% ON, 50% OFF) therefore evaporation takes place under both forced and natural convection conditions; and *b*) typical air velocity is approximately 0.5 m/s for the forced convection conditions. It must be pointed out that these specific conditions have a very moderate effect on the drying indexes DI and DA, as the index is relative to the optimal conditions, where the same assumptions concerning forced convection time and air speed are made, therefore index DI and DA capture only effects of temperature and relative humidity with respect to optimal conditions. Water mass transfer (*mt)* is then computed as defined by Eq. (6), capturing both natural and forced convection situations:

$$mt = \left(0.5 \cdot mt_{natural} + 0.5 \cdot mt_{forced}\right) \quad \text{Eq. (6)}$$

Both $mt_{natural}$ and mt_{forced} are computed using Eq. (7), following methodology described in (Lienhard, 2008):

$$mt = h_m \cdot 1/\rho_{iface}^{air} \cdot (Y_1 - Y_2) \quad \text{Eq. (7)}$$

Being h_m the mass transfer coefficient obtained by correlations as further down detailed, ρ_{iface} the density of air at the interface food-ambient temperature, Y_1 the water content in the bulk air and Y_2 the water content of the food product, computed directly from its water activity (assumed generally at 0.99, typical for fresh products) and the partial vapour pressure at the food product temperature (water content of the food not detailed here for brevity). In its turn h_m is obtained from the dimensionless Sherwood number Sh, the characteristic length L (inversely proportional to that typical of a food product of *l*X*l*, i.e. a flat plate of *l*x*l*, being *l*=10 cm assumed by this work) and δ_{iface} the water diffusivity of air at the interface food-ambient temperature. Hence h_m is generally computed following Eq. (8) (Lienhard, 2008):

$$h_m = (Sh \cdot \delta_{iface}^{air})/L \quad \text{Eq. (8)}$$

The dimensionless Sherwood number Sh for the food product depends on the Rayleigh (Ra) or Reynolds (Re) numbers, under natural (Eq. 9) or forced convection cases (Eq. 10) when computing $mt_{natural}$ and mt_{forced}, respectively. For a flat plate in both cases:

$$Sh = 0.27 \cdot (Ra)^{1/4} \quad \text{Eq. (9)}$$

$$Sh = 0.664 \cdot (\mathrm{Re})^{1/2} \cdot (S_c)^{1/3} \quad \text{Eq. (10)}$$

Being S_c the *Schmidt* number not defined here for brevity. For closure, the Rayleigh and Reynolds numbers are computed using Eq. (11) and Eq. (12), considering a flate plate (Lienhard, 2008):

$$Ra = 9.81 \cdot \left(\rho_{bulk}^{air} - \rho_{iface}^{air}\right)^{1/2} \cdot (L)^3 / (\mu\delta)_{iface}^{air} \quad \text{Eq. (11)}$$

$$\mathrm{Re} = (D \cdot v \cdot \rho_{iface}^{air})/(\mu)_{iface}^{air} \quad \text{Eq. (12)}$$

Where v is the velocity, of approximately 0.5 m/s, as previously explained; μ_{iface} the viscosity, δ_{iface} the water diffusivity and ρ_{iface} the density of air, all of them at the interface food-ambient temperature; while ρ_{bulk} is the density of the bulk air, this is, at storage temperature.
Finally, the calculation of the food product temperature (which must be slightly lower with respect to the bulk air temperature, as per latent heat effects of the evaporation) and the interface food-ambient temperature (assumed as an average between the food and the bulk air temperatures) are computed assuming a thermal equilibrium at the interface food- bulk ambient temperature. Precisely, latent heat effects of the evaporation on the food product are balanced with the air sensible heat at the air/product interface. Details about this calculation are here dismissed for brevity.

3.2. Computational methodology for the reduced and elapsed shelf-life time of the food products

For the calculation of the SLI and SLA indexes in Eq. (3) and (4), elapsed shelf-life (esl) at both actual and desired conditions are needed. As previously stated, several scientific publications and Handbooks describe the evolution of the shelf-life for food products following simple kinetic reaction approaches of the first order, typical for vitamin loss, oxidative colour loss or microbial growth, among others (Villota and Hawkes, 1992). Such first-order quality functions are *log* or *ln* based; as microbial growth rate increases exponentially with increasing storage temperature, reduction of the relative shelf-life (*rsl)* at desired temperature T_{sp} when actual temperature conditions are defined by T can be generally quantified as per Eq. (13) (Spencer and Baianes, 1964; Olley and Ratkowsky, 1973):

$$rsl = \left(a \cdot (T - T_{sp}) + 1\right)^{b} \quad \text{Eq. (13)}$$

Where T is the actual storage temperature and T_{sp} the desired storage temperature. Hence, Eq. (13) allows to quantify the relative effect of a temperature excursion, when actual conditions match (or are below) desired conditions rsl equals 1, i.e. no reduction of shelf-life takes place with respect to reference storage conditions, being the function limited to values equal or greater than 1. Once the reduction of the relative shelf-life (rsl) is computed for a given a & b coefficients (which depend on the specific food product) the elapsed shelf-life (esl) is computed as per Eq. (14):

$$esl = time_{sample} \cdot rsl \quad \text{Eq. (14)}$$

Where $time_{sample}$ is the typical monitoring time (i.e of the order of minutes). Then, esl_{sp} will always equals $time_{sample}$ as rsl =1. The value for rsl is equivalent to the SLA index defined by Eq. (4), although for monitoring and averaging purposes, it is deliberately defined in such a way (being able to integrate different sampling times with different thermal conditions over extended time periods).

4. *NB-IOT* CONNECTIVITY AT A GLANCE

NB-IoT is based on the concept of Low-power WAN (LPWAN), i.e. a wireless wide area network technology that interconnects low-bandwidth, battery-powered devices with low bit rates over long ranges. The aim of narrowband *IoT* (NB-*IoT*) is to provide cost-effective connectivity to billions of *IoT* devices, supporting low power consumption, the use of low-cost devices, and provision of excellent coverage – all rolled out as software on top of existing LTE, this is to say, existing telecommunication infrastructures. Consequently, NB-*IoT* technology presents very important features for the application in consideration (food quality monitoring), most importantly: its wide area with ubiquitous coverage and related low power consumption (up to 5-10 year battery life). Both assets allow to use battery-powered devices, therefore being able to be placed next to the food products moving together all along the cold chain. More information about this connectivity technology can be found at (NB-IoT White Paper, 2019), for instance.

5. ILLUSTRATIVE EXAMPLES. APPLICATION OF INDEXES

Two different illustrative examples are presented. Section 5.1 shows the application of the DI and DA indexes related to storage of apples and their related weight loss. Section 5.2 presents the potential aging effects of a supermarket poultry display.

5.1. DI & DA indexes application for apple storage

An application of the drying indexes is carried out by an apple storage test. 20 apples were purchased from a food retailer, avoiding samples at store display, the apples were taken directly from the food retailer cold rooms. Apples were put into two groups of 10 apples each: refrigerated and unrefrigerated. The unrefrigerated group was kept at room temperature/air relative humidity for 17 days, while the refrigerated group was kept inside a cold-room under controlled temperature and air relative humidity for the same exact period of time. A wireless NB-*IoT* connected device was used to monitor both %RH and temperature, as seen in Fig. 1 (a) for the unrefrigerated group.



(a) (b) (c) (d)

Figure 1: a) Monitoring device for the unrefrigerated apples group; b) Refrigerated apple sample at day 16; c) Unrefrigerated apple sample at day 16; d) Monitoring device for chicken display at supermarket

Fig.2 presents temperature and %RH for both groups. As seen, despite the refrigerated group could not always reach desired relative humidity set-point, as apples optimal conditions are between 0 – 2ºC, 90- 98% RH. (Thompson et al., 1996), both temperature and humidity were much closer to optimal conditions with respect the unrefrigerated group. The unrefrigerated group suffered low and very low relative humidity values (ranging from 20% to 50%).

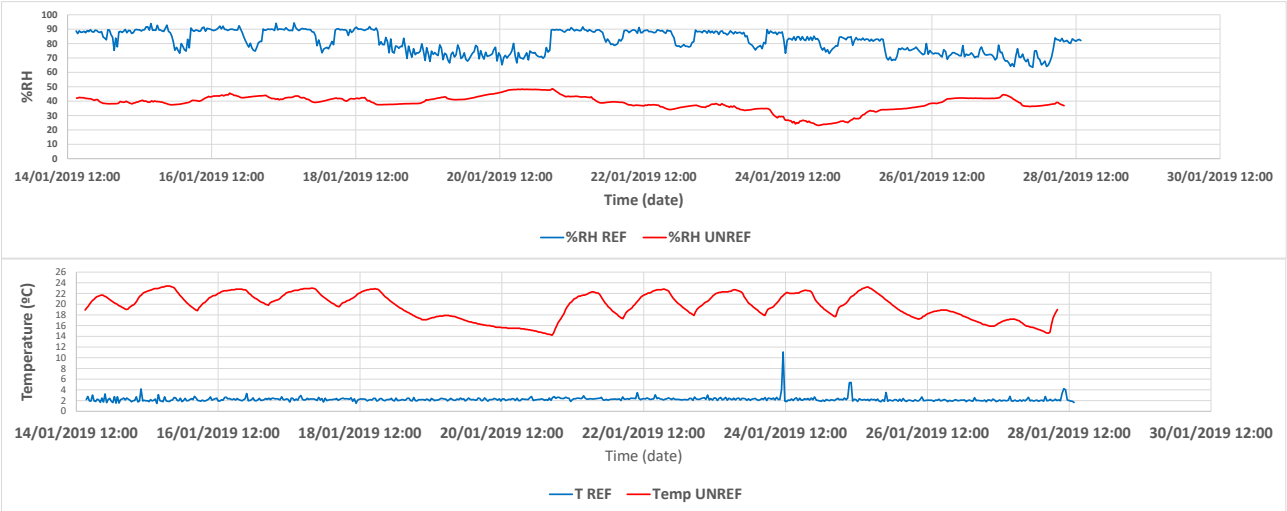

Figure 2: Storage conditions for the storage apple test. %RH (above) and Temperature (below)

Fig. 3 shows the corresponding DI indexes for both groups. As expected, the refrigerated group, despite not reaching 100% during all time, is related to a much higher DI index. It is interesting to see how, during weekends and nights (as the humidifier was not working) the DI index dropped from values around 90-100 to values around 40-50 due to inappropriate %RH. Indeed, Table 1 displays

the average (during 2 weeks) numbers for DI and DA indexes, as well as the weight loss for the two groups, also seen in Fig. 4.

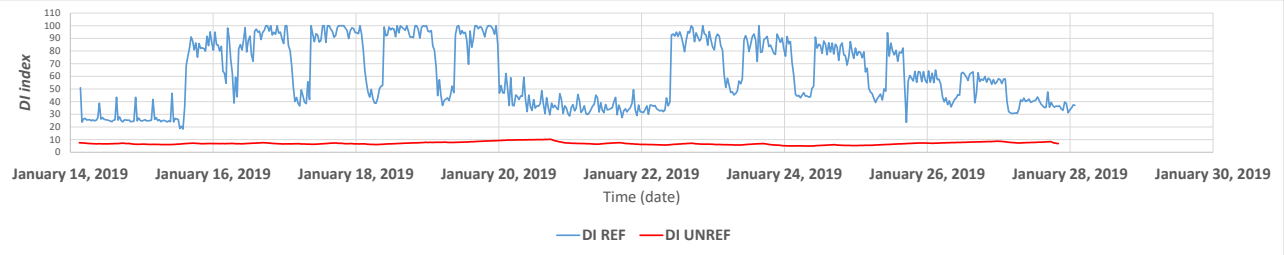

Figure 3: Drying Indexes (DI) for the refrigerated and unrefrigerated groups of apples.

Table 1. Relationship between DA indexes and apple weight loss

Apples	DI (%)	DA(x times)	Day 2 avg. weight (g)	Day 16 avg. weight (g)	Weight loss (%)	DA_{UNREF} / DA_{REF}	(Weight-loss)$_{UNREF}$/ (Weight-loss) $_{REF}$
REF	58.62	1.71	255.3	253.1	0.5%	8.37	8.31
UNREF	6.99	14.31	255.4	246.4	4.2%		

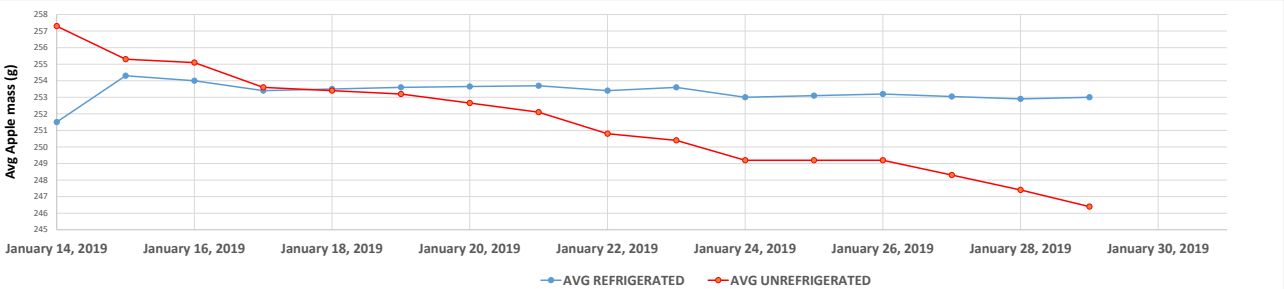

Figure 4: Weight loss due to drying effects for both refrigerated and unrefrigerated apple groups.

Table 1 shows a remarkable weight loss for the unrefrigerated set of apples, losing 4.2% of mass in two weeks (from day 2 to day 16). On the other hand, the refrigerated group of apples only loses 0.5% of the total mass at day 16. Hence, the unrefrigerated group has lost, in the same period of time, around 8.31 times the relative mass lost by the refrigerated one. It must be underlined that the relationship between DA indexes (8.37) perfectly agrees with this experimental number, showing how the DA index is capable of measuring the acceleration of mass transfer due to storage conditions. Equivalently, the ratio between indexes indicates the relative weight loss between the two groups during the same storage time. The visual appearance of two samples after 16 days of test can be seen in Fig. 1 (b, c). Finally, it has to be pointed out that the reference weight for this analysis was the mass recorded at the second day, as the refrigerated group increased its mass due to an unexpected rehydration process once stored under controlled %RH. The ability of the apples to capture and retain more water once stored in adequate air relative humidity conditions, even after being purchased, also demonstrates how commercial refrigeration retailers generally neglect %RH aspects along the cold chain.

5.2. SLI & SLA indexes application for chicken storage

An application of the SLI and SLA indexes for microbial growth analysis is presented in this section. A NB-*IoT* connected monitor was installed in a refrigerated display cabinet for poultry in a supermarket in Seville (Spain), as shown in Fig. 1(d). Temperature and SLI are displayed by Fig. 5 (a). The food retailer expected the refrigerated cabinet to be at 4ºC, expecting at least 3 days of shelf-life in the supermarket. This is consistent with an expected 5 days shelf-life for chicken at 4 ºC (Stoecker, 1998), assuming the product has lost some shelf-life in previous steps of the cold chain. Until day 13th the average SLI was 95%, so a slight 1.05 acceleration aging took place. As seen, on July 13th the refrigerated display had a technical problem (defrost did not disconnect) around 9:30 AM, rapidly rising its temperature. From inspection of the elapsed effective time after the incident (esl) = SLA x registered time – displayed in Fig. 5(b) - it is seen that around 11:00 AM the aging of

the product reached 2 effective storage days since the incident, while at 12:00PM it reached the maximum allowed by the food retailer (3 days at 4ºC). Due to alarms triggered by the connected monitoring device, the supermarket was rapidly notified about the cold chain break and the SLA index provided valuable information for the decision-making, considering the potential risk signalled and quantified by the system.

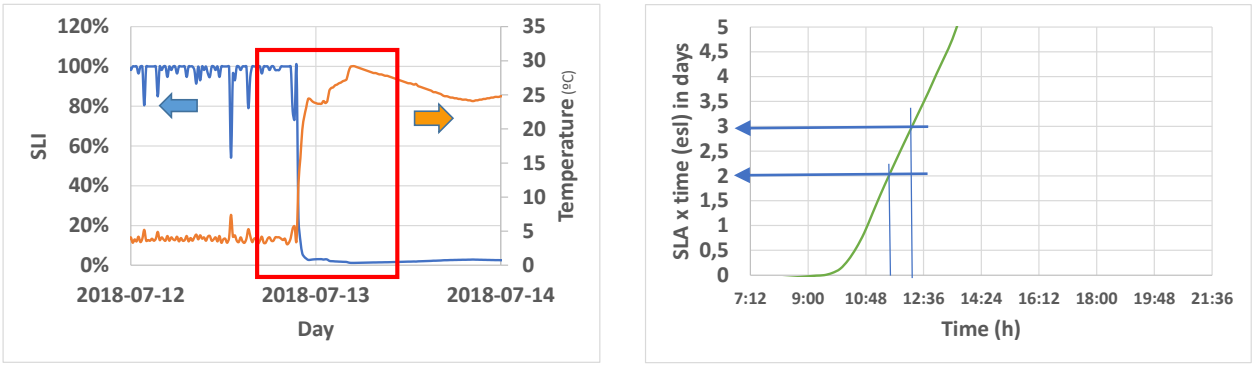

(a) **(b)**

Figure 5. a) *SLI* and Temperature at the chicken refrigerated display; b) elapsed time since the incident (*SLA* x registered time).

6. CONCLUSIONS

Two quality indexes (under patent Albets-Chico *et al.*, 2019) concerning food storage have been presented. The indexes quantify the effects of temperature and air relative humidity on the food products. The drying index DI is able to quantify the drying/weight loss impact of the storage conditions on the products, while the shelf-life index SLI is a support tool to evaluate effects of time-temperature on microbial growth. Both indexes are delivered as a part of a monitoring wireless NB-*IoT* connected device, which allows the proposed food quality monitoring to be integrated all along the cold chain with affordable costs for the industry.

REFERENCES

Albets-Chico, X. *et al.,* 2019. Indexes for food product temperature and quality monitoring. PATENT WO/2019/XXXXXX.

Lienhard J.H., 2008. Heat Transfer Texbook. Third Edition. Phlogiston Press. Cambridge Massachusets, USA.

Spencer, R. and Baianes, C.R., 1964. The effect of temperature on the spoilage of wet white fish. I. Storage at constant temperatures between -1ºC and -25ºC. Food Technology, (18), 769.

Olley, J.; Ratkowsky D.A., 1973. Temperature Function Integration and Its importance in the storage and distribution of flesh foods above the freezing point. J. of Food Tech. in Australia 25(2):66-73.

Thompson, J., A. Kader, and K. Sylva, 1996. Compatibility chart for fruits and vegetables in short-term transport or storage. Oakland: Univ. Calif. Div. Ag. & Nat. Res. Publ. 21560

Doyle, J.P., 1989. Seafood shelf life as a function of temperature. Alaska Sea Gram No. 30. Marine Advisory Program, University of Alaska, Fairbanks.

Food Code 2013 : https://www.fda.gov/Food/GuidanceRegulation/RetailFoodProtection/FoodCode/ucm374275.htm

W. F. Stoecker, 1998. Industrial Refrigeration Handbook. Chapter 17: THE REFRIGERATION AND FREEZING OF FOOD, McGraw-Hill Professional, 17-1, 17-59.

NB-IoT White Paper, 2019: https://www.huawei.com/minisite/iot/img/nb_iot_whitepaper_en.pdf

Manuscript ID: 1206
DOI: 10.18462/iir.icr.2019.1206

Airflow design in refrigerated retail display cabinets and its impact on food quality

Ana C. MARQUES[(a)], David VAGG[(b)], Edward C. HAMMOND[(a)], Shaun PITCHERS[(c)]

[(a)] London South Bank University, Department of Engineering
London, SE1 0AA, United Kingdom, catarina.marques@lsbu.ac.uk
[(b)] Assured Quality solutions Limited
Peterborough, PE7 8GX, United Kingdom
[(c)] Applied Design and Engineering Limited
Lowestoft, NR33 7NL, United Kingdom

ABSTRACT

This paper investigates how refrigerated display cabinet airflow design can enhance temperature distribution and potentially reduce food waste. Conventional refrigerated retail cabinets have a single column of cold air from the top to the bottom of the merchandising envelope. By contrast separating the retail space into individual cells, each with its own shorter air-curtain reduces infiltration and improves temperature control.
The quality and safety of bagged salad over an extended display period was evaluated in a conventional and multiple short air-curtain cabinet. At the end of the test period there was a visible difference in cabinet temperature and relative humidity, which had a direct impact on the salad organoleptic quality and microbiological safety. The temperature band was 11.2ºC and 5.4ºC in the conventional and multiple air curtain cabinets respectively, resulting in a higher degree of salad wilting and shrivelling and an increase on total yeast counts on the conventional cabinet.
Keywords: Refrigeration, Food Quality, Retail Display Cabinet, Air Curtain, Temperature stability

1. INTRODUCTION

Food waste has a considerable environmental and economic impact. According to a study commissioned by the Food and Agriculture Organization of the United Nations about one third of food produced worldwide is wasted, accounting for a total 1.3 billion tonnes (FAO, 2013). It is estimated that the UK retail sector is responsible for 0.25 Mt of food waste every year (WRAP, 2015). An effective cold chain is fundamental to maintain both food safety and quality as refrigeration significantly reduces the rate of growth of pathogens and spoilage organisms and slows down physiological (e.g. ripening), biochemical (e.g. pigmentation) and physical processes (moisture loss) within food products (Gwanpua et al., 2015).
Fresh vegetables are living tissues that undergo respiration and transpiration processes, which dramatically affect product quality and the rate of these processes is greatly affected by temperature. During respiration oxygen is consumed and sugar is converted into CO_2, water and heat energy. The heat of respiration increases with temperature resulting in metabolic changes in composition, texture and colour. Loss of moisture due to transpiration where there is loss of water vapour from the living tissues results in wilting and shriveling, two obvious signs of lost freshness (ASHRAE, 2006). Leafy vegetables such as iceberg and romaine lettuce, baby leaf lettuce and spinach are particularly sensitive to temperature abuse. It is recommended that fresh leafy vegetables are kept below 5°C at all times throughout the cold chain to ensure food safety. The recommended shelf life for lettuce (iceberg and romaine, chopped, shredded and whole leaf) and spinach (whole and cut leaves) is 6 days (when packaged in air) (FAO/WHO 2008).
A European survey on open refrigerated display cabinets showed that cabinet temperatures range from -2.2 to 12.2°C (EFSA, 2007). Evans et al. (2007) further reported that the majority of high temperature abuse (97%) was located at the front of the open-refrigerated display cases (closest to the aisle) and that refrigeration systems and designs of retail displays were not sufficient to keep

temperature or humidity within recommended ranges. Furthermore, temperature profiles in commercial retail displays showed large variation depending on location of the products in the displays (Nunes et al. 2009). Kou et al. (2014) studied the refrigerators temperature profile and its impact on the product quality of baby spinach. They showed that many of the food-products in an open display cabinet are cooled below freezing. This can cause ice-crystal formation and freeze damage of the products. The average temperature differential within the refrigerator was found to be 7.3ºC and many of the products located at the front of the cabinet were not cooled sufficiently.

A common way to distribute cool air in a multi deck display cabinet is through perforated plates in the rear of the cabinet, and in the front of the cabinet is an air curtain. Air is blown out of the back panel between the shelves to cool the load and stabilise the air curtain and enable a lower discharge velocity to be used for the air curtain. Typically the air velocity between the shelves will be 0.05 to 0.4 $m.s^{-1}$, 3 to 5 times less than that of the air curtain (Axell et al., 1999). Significant research has been carried out to determine the ratio of back panel flow to air curtain flow. Gray et al. (2008) claims that 70% of the air circulated should be used to supply the curtain and 30% of the flow should be discharged through the back panel for the best results. More recently Wu et al. (2013) conducted similar investigations using Computational Fluid Dynamics and experimental techniques, they found that the optimal split was still approximately 70/30.

The air curtain of an open display refrigerator is a turbulent plane jet of air that seals the refrigerated retail space from the ambient air. The momentum created by the air curtain provides a non-physical barrier against heat and moisture, while facilitating easy access for customers. The amount of heat and mass transfer across the air-curtain is directly affected by the initial velocity, turbulence intensity and the length of air-curtain and width of the jet (Pitchers et al., 2018). The best performing air-curtain will be one with the minimum required velocity to completely seal the product space. An air-curtain with an initial velocity that is too slow will not have sufficient momentum to seal against the ambient air and will allow excessive heat and moisture to infiltrate into the cabinet. An air-curtain that has an initial velocity that is much higher than required will experience an increased amount of viscous mixing between the still ambient air and the fast turbulent jet of air; this process of viscous mixing is referred to as entrainment.

Shorter air-curtains will require less minimum velocity to seal against the ambient air and will thus entrain much less heat and moisture into the cabinet resulting in a reduction in the refrigerated energy consumption. If short air curtains were to be utilized, a stable air curtain can be created using a slow velocity and so the problematic back panel flow can be eliminated. The elimination of back panel flow will then enable better temperature control independently of cabinet loading (Hammond et al. 2016).

Short air curtain technology works by dividing the refrigerated display area into separate airflow managed cells with short, stable air columns. Each cell has its own air curtain, which is more efficient than the full height air curtain on a conventional retail display refrigerator. The net result is less pressure on the air curtain of each cell, reduced entrainment rates, and a substantial reduction in cold air spillage from the cabinet (Wood, 2013). As a result, energy efficiency and product temperature control is improved.

This paper investigates how cabinet airflow design can enhance temperature distribution and potentially reduce food waste. In order to achieve this, the quality and safety of bagged salad over an extended display period was evaluated in both a conventional refrigerated retail cabinet and cabinet with multiple short air-curtains.

2. MATERIALS AND METHODS

The cabinet tests described in this paper were carried out at Adande's test facility in Lowestoft. All Adande test chambers comply with the ISO 23953:2015 specifications. Ambient and product temperatures were recorded using PT100 temperature probes with an accuracy of ±0.2ºC, readings were recorded every 15s. Relative humidity was recorded using humidity sensors with an accuracy of ±3%, readings were recorded every 60s.

The ambient conditions in the test rooms were controlled to climate class 3 (25°C, 60% relative humidity) and measured in front of each cabinet following the ISO 23953-2:2015. Cabinet A (multiple air curtain technology) was set up in test room 1 and cabinet B (conventional single air curtain) was set up in test room 3.

Each cabinet was loaded with bagged salad in the following locations: top shelf left (6 bags), middle shelf centre (6 bags), bottom shelf right (6 bags). The salad bowls were placed in the following locations: top shelf right (6 bowls), middle shelf centre (6 bowls), bottom shelf left (6 bowls). The intermediate shelves had 7 bags/bowls for microbiological samples (one replicate per day). The remaining space was filled with test packages. Measurement packages were placed in the top, middle and bottom shelves at the front and back of each shelf to give an indication of product temperature. The m-packs and test packs have the same thermal properties as lean beef.
Dataloggers were placed on the centre of top, middle and bottom shelves to record cabinet air temperature and relative humidity over the 7-day display period.
Figs. 1 and 2 show the multiple air curtain technology (cabinet A) and conventional cabinet (cabinet B) loading respectively.



Figure 1: Cabinet A



Figure 2: Cabinet B

The baby leaf salad bags and house salad bowls displayed in both cabinets were photographed at the beginning of the trial (day 0) and days 5 and 7 to monitor product appearance.
The baby leaf salad bags contained baby iceberg lettuce; baby spinach and red Batavia, whilst the house salad bowls contained a mix of crisp iceberg and romaine lettuce, cherry tomatoes, cucumber, red onion and radish. An organoleptic assessment of the salad bags/bowls was carried out on day 7 following the food scoring system illustrated in Fig. 3.

	Not Acceptable Quality	Significant Difference	Marginal	Slight Difference	**Equal to TARGET**	Slight Difference	Marginal	Significant Difference	Not Acceptable Quality
Sensory Score	1	2	3	4	5	6	7	8	9
%QI	0%	25%	60%	85%	100%	85%	60%	25%	0%

Figure 3: Nine-point bipolar food scoring system

3. RESULTS

3.1. Temperature Stability

Table 1 shows a comparison of the air temperature and relative humidity in both cabinets.

Table 1: Average air temperature and relative humidity in cabinets A and B

Probe location	Air Temperature (ºC)		Relative Humidity (%)	
	Cabinet A	Cabinet B	Cabinet A	Cabinet B
Top Shelf Centre	4.02	5.06	79.76	80.90
Middle Shelf Centre	2.60	7.98	89.06	70.61
Bottom Shelf Right	3.71	11.52	87.99	68.69

The air temperature in the multiple air curtain cabinet (cabinet A) was on average 1 to 7.5°C cooler than the conventional cabinet (cabinet B) and the relative humidity was 9% higher in cabinet A. Figs. 4 and 5 show the measurement packs temperature during the test in cabinets A and B respectively.

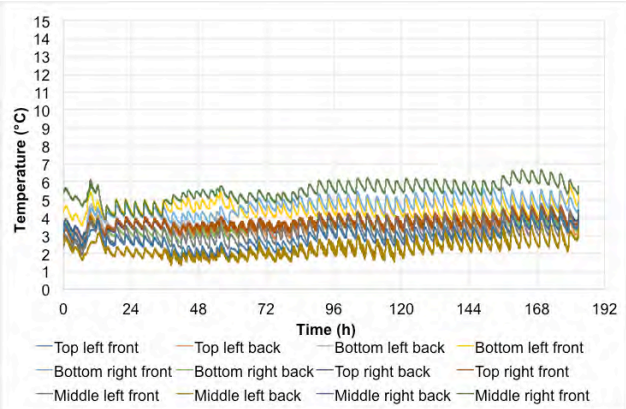

Figure 4: Temperature stability in cabinet A

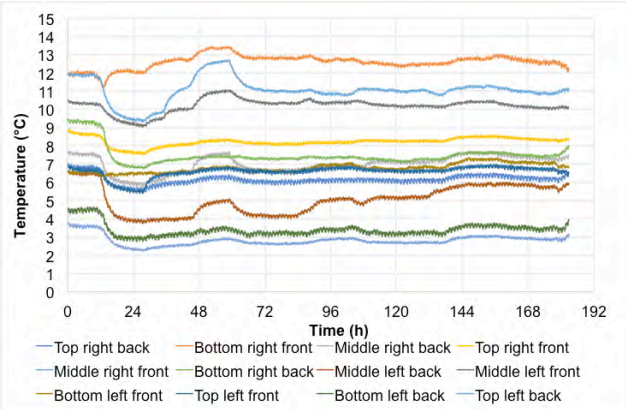

Figure 5: Temperature stability in cabinet B

As can be seen in Fig. 4 the product temperature in the cabinet A was controlled within a tight band throughout the trial period and the average packs temperature was 3.71°C. The temperature in the conventional cabinet B was considerably wider compared to cabinet A with temperatures between 2.23°C and 13.46°C. The average packs temperature was 7.28°C in cabinet B.

3.2. Baby Leaf Salad Bags Quality

The baby leaf salad quality on day, the last day of the use by date is shown in Figs. 6 and 7.



Figure 6: Day 5 – Baby leaf salad

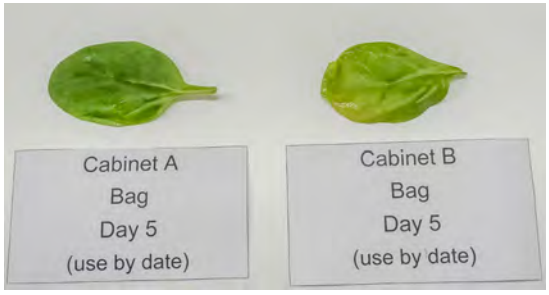

Figure 7: Spinach from cabinets A and B

There was a higher degree of shrivelling in the baby leaf salad displayed in the conventional cabinet compared to the multiple air curtain cabinet on day 5. The spinach displayed in the conventional cabinet had turned yellow and there was moisture at the surface of the leaf, the spinach displayed in th cabinet A was still green on the last day of its use by date.
The baby leaf salad on day 7, two days after the use by date is shown in Figs. 8 and 9.



Figure 8: Day 7 – Baby leaf salad in bags

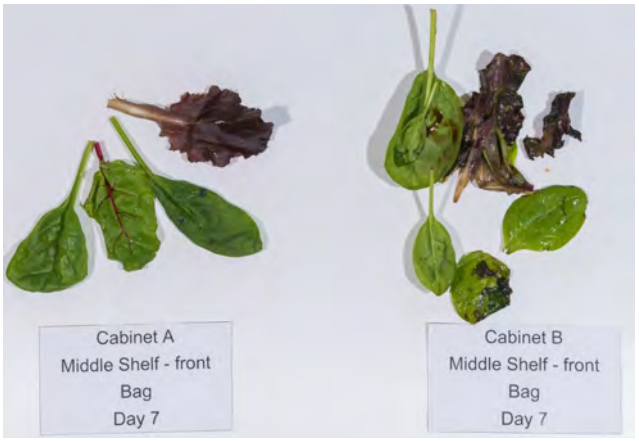

Figure 9: Day 7 – Baby leaf salad leaves

On day 7 there was visible cellular breakdown on the red Batavia stored in the conventional cabinet demonstrated by the red tinged water accumulated in the bag (see Figure 8).

3.3. House Salad Bowls Quality

The house salad on day 5, one day after the use by date is shown in Figs. 10 and 11.



Figure 10: Day 5 – House salad



Figure 11: Radish from cabinets A and B

The house salad in cabinet B was very wet, lacked body and the radish was dry. Figs. 12 and 13 show the salad on day 7.



Figure 12: Day 7 – House salad



Figure 13: Radish, cucumber and tomato

There was significantly more volume on the house salad displayed in the cabinet A compared to the salad displayed in the conventional cabinet B after 7 days. Cabinet A had crip lettuce and cucumber, firm tomatoes and a clean aroma, whilst the conventional cabinet had limp lettuce, soft slimy cucumber, soft tomatoes and a musty green earthy aroma.

3.4. Organoleptic Assessment

Figs. 14 and 15 show the baby leaf salad overall finished quality score after a day 7 display period in cabinets A and B respectively. The back diamonds indicate the m-package temperature in each

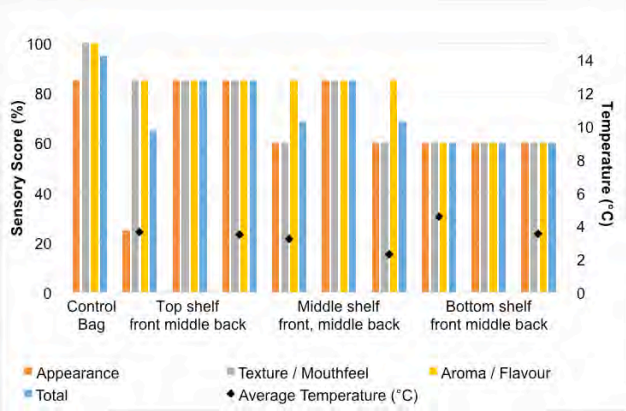

Figure 14: Organoleptic assessment: cabinet A

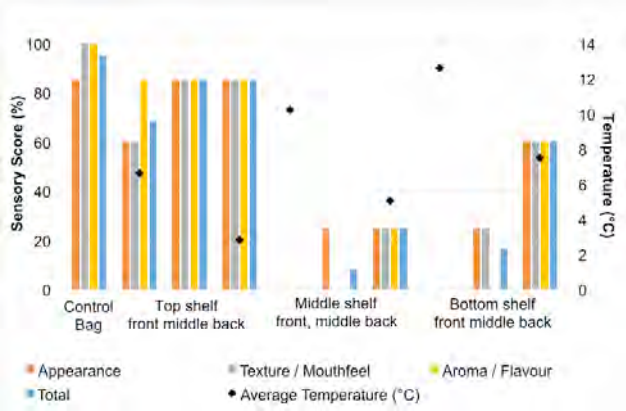

Figure 15: Organoleptic assessment: cabinet B

The total quality score (appearance, texture and flavour/aroma) of the baby leaf salad in cabinet A was equal to or above 60%, which indicates a marginal difference from target. The only case where the appearance was rated low (25%) was on the top front shelf bag, which was the warmest point in the cabinet.

As can be seen in Figure 15 the baby leaf salad overall quality in the conventional cabinet was rated above 60% in the top shelf which had an average air temperature of 5.06°C. However, the middle and bottom shelves show a considerable deterioration in quality on day 7 with a score of 25% in some positions within the selves, which indicates a significant difference from target. The average air temperature in the middle and bottom shelves was 7.98°C and 11.52°C respectively. Similar results were obtained for the house bowls salads: overall quality score for the salad displayed in cabinet A was 68% compared to 44% on cabinet B.

3.5. Microbiological Tests

Figs. 16 and 17 show the total viable counts (incubated at 30°C for 48 h) and the yeast growth in the samples of baby leaf salad displayed in both cabinets.

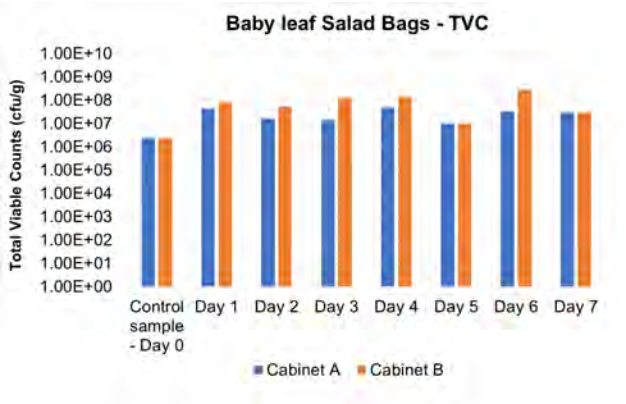

Figure 16: Total viable counts in baby leaf salad



Figure 17: Yeast count in baby leaf salad

As can be seen in Fig. 16 the total viable counts (TVC) were consistently higher in the baby leaf salad bags stored in the conventional cabinet compared to the multiple air curtain cabinet. The highest TVC in cabinet A was 5.0 x 10^7 cfu/g compared to 2.8 x 10^8 cfu/g in cabinet B.

Fig. 17 shows a substantial difference on the total yeast count between the multiple air curtain and conventional cabinet. By day 5 (use by date) there was 1.6 x 10^4 cfu/g in cabinet A compared to 3.0 x 10^5 cfu/g in cabinet B (the yeast count was 18.8 times higher in cabinet B). Figs. 18 and 19 show the total viable counts and the yeast growth in the samples of the House salad displayed in cabinets A and B.

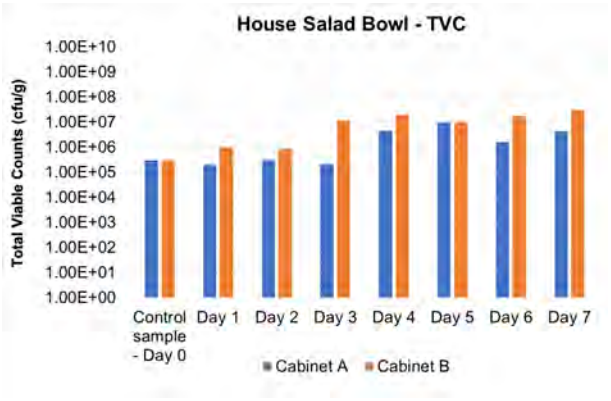

Figure 18: Total viable counts in House salad

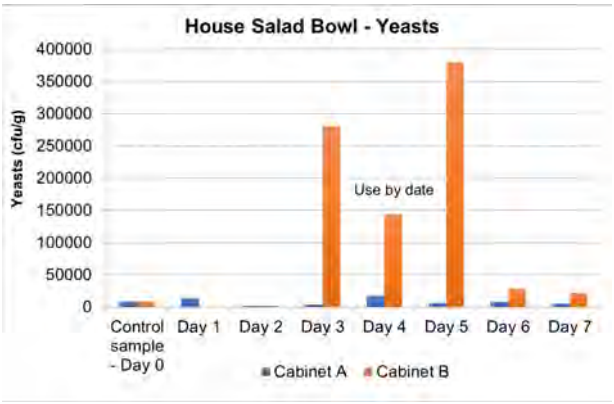

Figure 19: Yeast count in House salad

Again, the total viable counts in the house salad bowls were consistently higher in cabinet B compared to cabinet A. By day 3 (one day before the use by date) the total yeast on the salad displayed in the conventional cabinet was 70 times higher than on cabinet A, 2.8 x 10^5 cfu/g and 4.0 x 10^3 cfu/g respectively.

4. CONCLUSIONS

The multiple air curtain technology showed a significant improvement on temperature stability compared to a conventional single air curtain cabinet with temperature spans of 5.4ºC and 11.2ºC respectively. The relative humidity was also 9% higher on the multiple air curtain cabinet.

There was a significant difference in salad quality at the end of the display period in both cabinets. By day 5, which was the use by date for the baby leaf salad there was a higher degree of wilting and shrivelling in the lettuce and spinach displayed in the conventional cabinet compared to the multiple air curtain cabinet. The spinach in the conventional cabinet was yellow and moisture pooled at its surface indicating a clear loss in freshness. The house salad displayed for 5 days in the conventional cabinet was very wet and was lacking body compared to the one displayed in the multiple air curtain cabinet, which only showed slight leaf damage.

By day 7, two days after the use by date for the baby leaf salad and three days for the house salad there was a more pronounced difference in quality between vegetables displayed on both cabinets. Cellular breakdown on the red Batavia lettuce tinged the water red on the bags stored in the conventional cabinet, which did not occur on the multiple air curtain cabinet. The baby leaf salad displayed in the middle and bottom shelves of the conventional cabinet scored below 25% in the organoleptic assessment showing a clear deterioration in quality, which is directly correlated to the higher average storage temperature of 7.98ºC and 11.52ºC respectively. The baby leaf salad in the multiple air curtain cabinet was rated equal or above 60% in all shelves.

The house salad displayed on the multiple air curtain cabinet generally had more volume and less leaf damage compared to the conventional cabinet. The overall house salad quality was rated at 68% in the cabinet A and 44% in cabinet B.

The total viable counts in the baby leaf and house salad were consistently higher in the conventional cabinet. The total yeast count was 70 times higher on the house salad displayed in the conventional cabinet one day before its use by date.

Overall the test results show a clear difference on salad quality and microbiological safety between the multiple air curtain and conventional cabinet, which can be correlated to the storage

temperature within each cabinet. Additional testing is required to determine if the multiple air curtain technology can increase the shelf life of leafy vegetables by one extra day.

REFERENCES

Food and Agriculture Organisation of the United Nations (FAO), International Fund for Agricultural Development (IFAD), United Nations World Food Programme (WFP), 2013. The State of Food Insecurity in the World 2013 - The multiple dimensions of food security. Available at: http://www.fao.org/docrep/018/i3434e/i3434e00.htm

Waste and Resources Action Programme (WRAP), 2015. Estimates of Food and Packaging Waste in the UK Grocery Retail and Hospitality Supply Chains. Available at: http://www.wrap.org.uk/sites/files/wrap/UK%20Estimates%20October%2015%20%28FINAL%29_0.pdf

Gwanpua S.G., Verboven P., Leducq D., Brown T., Verlinden B.E., Bekele E., Aregawi W., Evans J., Foster A., Duret S., Hoang H.M., Van der Sluis S., Wissink E., Hendriksen L.J.A.M., Taoukis P., Gogou E., Stahl V., El Jabri M., Le Page J.F., Claussen I., Indergård E., Nicolai B.M., Alvarez G., A.H. Geeraerd., 2015. The FRISBEE tool, a software for optimising the trade-off between food quality, energy use, and global warming impact of cold chains. Journal of Food Engineering 148, 2–12.

ASHRAE, 2006.Vegetables. In: ASHRAE (ed.) Refrigeration Handbook.

Food and Agriculture Organisation of the United Nations / World Health Organization (FAO/WHO), 2008. Microbiological hazards in fresh leafy vegetables and herbs. Available at: http://www.fao.org/3/a-i0452e.pdf

European Food Safety Authority (EFSA), 2007. Request for updating the former SCVPH opinion on Listeria Monocytogenes risk related ready-to-eat foods and scientific advice on different levels of Listeria Monocytogenes in ready-to-eat foods and the related risk for human illness. Available at: https://efsa.onlinelibrary.wiley.com/doi/epdf/10.2903/j.efsa.2008.599

Evans, J., Scarcelli, S., Swain, M. V. L., 2007. Temperature and energy performance of refrigerated retail display and commercial catering cabinets under test conditions. International Journal of Refrigeration 30(3), 398-408.

Nunes, M., Emond, J. P., Rauth, M., Dea, S., Chau, K. V., 2009. Environmental conditions encountered during typical consumer retail display affect fruit and vegetable quality and waste. Postharvest Biology and Technology 51(2), 232-241.

Kou, L., Luo, Y., Ingram, D. T., Yan, S., Jurick, W. M., 2014. Open-refrigerated retail display case temperature profile and its impact on product quality and microbiota of stored baby spinach. Food Control Journal 47, 686-692.

Axell, M., Fahlen, P., Tuovinen, H., 1999. Influence of air distribution and load arrangements in display cabinets, 20th International Congress of Refrigeration, Sydney, Australia.

Gray, I., Luscombe, P., Mclean, L., Sarathy, P., Sheahen, P., & Srinivasan, K., 2008. Improvement of Air Distribution in Refrigerated Vertical Open Front Remote Supermarket Display Cases. International Journal of Refrigeration 31(5), 902 – 910.

Wu, X., Chang, Z.,Yuan, P., Lu, Y., Ma, Q.,Yin, X., 2013. The optimization and effect of back panel structure on the performance of refrigerated display cabinet. Food Control Journal 40, 278-285.

Pitchers, S., Marques C., Rees R., Cooper R., 2018. Performance comparison between shorter and conventional air curtains in retail display refrigerators. 5th IIR International Conference on Sustainability and the Cold Chain, Beijing, China.

Hammond E., Marques C., Ketteringham L., 2016. Application of short air curtains in retail display refrigerators, 4th IIR International Conference on Sustainability and the Cold Chain, Auckland, New Zealand.

Wood, I., 2013. Energy efficient retail refrigeration, which doesn't cost the earth. The Grocery Trader. Available at: https://grocerytrader.co.uk/energy-efficient-retail-refrigeration-which-doesnt-cost-the-earth/

Manuscript ID: 1215
DOI: 10.18462/iir.icr.2019.1215

Characterization of sorbet microstructure by using X-Ray Microtomography

Véronique MASSELOT [a, b], Véronique BOSC [a], Hayat BENKHELIFA [a, b*]

[a] Ingénierie Procédés Aliments, AgroParisTech, INRA, Université Paris-Saclay, 91300, Massy, France
[b] Irstea, UR GPAN, Refrigeration Process Engineering Research Unit, 1 rue Pierre-Gilles de Gennes, F-92761 Antony, France

*hayat.benkhelifa@agroparistech.fr

ABSTRACT

Sorbet is a complex multiphasic system composed of a dispersion of ice crystals and air bubbles inside a concentrated liquid matrix. The functional properties and quality attributes of the finished product are mainly related to ice crystal and bubble size distributions. These latter are strongly dependent on operating conditions and also on the formulation. The use of a non-destructive 3D imaging technique is a real advantage for a better visualization and understanding of the frozen microstructure.
In this study, X-Ray microtomography coupled with a cooling stage was used to visualize and quantify at negative temperature the sorbet microstructure after freezing. An image analysis protocol was developed to segment frozen phase from unfrozen matrix. The resulting images allow the determination of ice and bubbles size distribution and show the influence of the formulation on the sorbet microstructure.
Keywords: Freezing, Sorbet, Microstructure, Microtomography.

1. INTRODUCTION

Sorbet is a frozen fruit juice with high sugar content stabilized by gum stabilizers (Marshall et al., 2003). The mixture consists of air bubbles and ice crystals dispersed in a matrix with high concentrations of sugars and stabilizers.
Before freezing, the mixture of ingredients (called ‘mix’) contains an average of 70%wt of water, almost 30%wt of sugar (sugars contained in fruit juices and added sugars) and up to 0.5%wt of stabilizers (Arbuckle, 1986; Marshall and Arbuckle, 1996; Stogo, 1998; Clarke, 2004). Industrial processing of sorbets comprises three stages: preparation of the mix (mixing of ingredients, pasteurization and ageing), freezing and hardening. The freezing step takes place in a scraped surface heat exchanger (SSHE) or freezer, and is the core of the manufacturing process. The mix enters the freezer at approximately 4 °C and is converted into sorbet by simultaneous aerating, freezing and mixing to generate ice crystals and air bubbles while the matrix is continuously concentrated into sugars and stabilizers and becomes increasingly more viscous (Clarke, 2004). At the outlet of the exchanger, the sorbet contains an average of 40%wt of ice while the concentration of sugars and stabilizers in the unfrozen matrix is almost double that in the original mix. Its final temperature is between -5 °C and -6 °C (Marshall et al., 2003).
The stabilizers usually used in sorbets are natural polysaccharides (Thombare et al., 2016). The first purpose for using them is to increase mix viscosity and to produce smooth texture. The presence of stabilizers also facilitates the incorporation of air and the pumping and filling of the molds after the freezing step. During conservation and storage, stabilizers slow down the melting and growth of ice crystals. They also slow down the migration of water and stabilize the formed foam (Arbuckle, 1986; Marshall et al., 2003; Clarke, 2004).

The influence of the formulation and especially of stabilizers on crystallization during the freezing step (initial size of the ice crystals and the amount of frozen water) is still the subject of debate in the literature and depends on the type of polymer or the type of freezing process applied.
Most of the studies published about this subject were performed using microscopic techniques: LT-SEM (Low Temperature Scanning Electron Microscopy) or optical microscopy. These techniques are useful to image the microstructure but present several drawbacks: some are invasive and require denaturing the product (for example by replacing the ice crystals with a resin or after a freeze-drying step) and all allow only a two-dimensional visualization of the sample.
Using these techniques, several authors have shown an effect of the stabilizers on the size of ice crystals formed during the freezing of a mix (Fernandez et al., 2007, Thiebaud et al., 2002, Goff et al., 1993, Park et al., 2006). Other studies conclude that stabilizers have no effect on the size of the crystals of frozen products. (Buyong and Fennema, 1988; Flores and Goff, 1999; Bolliger et al., 2000; Yuennan et al., 2014).
A small number of studies deal with the analysis of frozen desserts (ice cream or sorbet) using 3-D imaging techniques, such as X-ray micro-computed tomography (X-ray micro-CT). This technique generates a series of X-ray radiograph shadows of the material acquired from different angles that depend on material properties such as density and thickness. 3D images are then reconstructed from these radiographies. This technique can be non-invasive and non-destructive when no substantial sample preparation is used. In the case of frozen foods, this means that the sample is observed at frozen state without any prior preparation. As far as we know, the influence of stabilizers on the size and morphology of ice crystals has not yet been studied using X-ray micro-CT. Pinzer et al. (2012) observed the effect of a change in temperature on the size of ice crystals and air bubbles in ice cream by using X-ray tomography with the help of a contrast agent. More recently, Guo et al. (2017 and 2018) described the influence of temperature cycles on the size and morphology of ice crystals and air bubbles in ice cream using synchrotron X-ray tomography technique.
The objective of the present study was to visualize, characterize and quantify 3D ice crystals and air bubbles in a frozen sorbet using a high-resolution X-ray micro-computed tomography. Sorbet mixes containing respectively only water and sucrose, and water, sucrose and one hydrocolloid as stabilizer (hydroxypropylmethylcellulose) were formulated and frozen in a batch SSHE. Frozen samples were analyzed by X-ray micro-CT technique directly at frozen state by using a cooling stage. Ice crystal size distributions and air bubbles size were obtained for the different formulations.

2. MATERIALS AND METHODS

2.1. Products

Hydroxypropylmethylcellulose (HPMC) was purchased from Dow®. Its viscosity was evaluated at about 4000 cP (2% in water at 20 °C). It contained between 19 and 24% of methoxy groups and between 7 and 12% of hydroxypropoxy groups. Sucrose was purchased from Béghin Say®. Solutions were prepared with deionized water (conductivity 17 µS.m-1) to ensure constant quality of water.

2.2. Preparation and Freezing of the Mixes

In order to simplify the composition of the mixes and to study specifically the effect of the stabilizer, only sucrose was used as sugar. The initial concentrations of sugar and stabilizer were close to that usually found in commercial solutions: the mix contained 25%wt of sucrose and 0.315%wt of HPMC. A control sample without stabilizer was also formulated.
Mixes were prepared by dispersing sucrose and HPMC in water at ambient temperature under strong stirring. The solution was then cooled at 4 °C for at least 12 hours before freezing. This ageing step allowed the complete solubilization, hydration and expansion of polymer molecules in the solvent (Clarke, 2004). The mixes (800 ml) were frozen in a batch domestic scraped surface heat exchanger (Magimix® Gelato Expert). Frozen samples were placed in a plastic straw (6 mm of diameter, 2.3 cm long) and put in a freezer at -20 °C for 24 hours. Three straws were prepared per condition.

2.3. X-ray Microtomography Analyses

For the two mixes studied (the control mix and the stabilized mix), the three frozen samples were analyzed by X-ray micro-CT (RX Solution DeskTom 130®, Chavanod, France). The straws were previously placed in a cooling stage consisting in a cylindrical double jacket box containing a frozen phase change material, in order to maintain the sample temperature at -20 °C during the scanning time. The cylindrical box was surrounded by polystyrene foam (1 cm of thickness) for isolation.
Samples were positioned in the micro-CT so that their middle part is analyzed with a voxel resolution of 8.89 µm. 896 projection images were captured over a 360 ° rotation with a step size of 0.4 °. The system was operating at a X-ray tube voltage of 50 kV and a current intensity of 160 µA. The total scanning time per sample was 13 min.
XAct 2® software (RX Solution, Chavanod, France) was used to reconstruct 3D volume from raw images using the filtered back-projection algorithm and applying ring artifact filter and phase contrast correction for better image quality. From this volume reconstruction, more than 1100 slices were provided in 16-bits resolution.

2.4. Image Processing

After micro-CT acquisition and 3D volume reconstruction, data were loaded on Avizo 9.1.1® software (FEI VSG, Bordeaux, France) for image analysis. As the whole volume image also includes the wall of the plastic straw and elements that are not part of the sample, a cubic sub-volume (32.8 mm^3) was cropped at the center of the reconstructed 3D volume.
In the selected sub-volume, images of frozen samples revealed three main materials from low to high density: air bubbles (dark), ice fraction (intermediate gray) and unfrozen matrix which consists of the remaining unfrozen liquid water containing sugars and stabilizers (light gray). Images were segmented thanks to the level of attenuation of these three materials.
Once the image has been segmented, only the ice phase or the air phase was kept for further image processing. Objects in contact were separated using a watershed algorithm. For the data analysis, crystals or bubbles in contact with the sub-volume walls were suppressed. At the end of the image processing, a three dimensional view of the phase of interest was obtained. Data were then exported to Excel® to analyze ice crystals or air bubbles size distribution and volume fraction of these two phases.

3. RESULTS

3.1. Image Analysis

The raw images obtained in X-ray microtomography (images (a) of figs. 1 and 2) show, as explained in section 2.4, that the three constituent phases of the sorbet have different attenuation levels. They therefore appear in different gray levels: the air is in black, the ice phase in dark gray and the cryoconcentrated matrix containing sugars and stabilizers appears in light gray. As a result, phase separation is possible and a range of gray levels is assigned to them.
Once the three phases are characterized by their gray levels, it is possible to select only one of them for further processing; this corresponds to the segmentation step as shown on Figs. 1b and 2b. During this step, the selected phase is visible in blue and the sum of the two other phases appears in black. For example, in the case of Fig. 2b, the frozen phase appears in blue while the air and the unfrozen matrix appear in black, it is then no longer possible to distinguish them one from the other. As this first step of the image processing does not allow to separate each crystal or air bubble from its neighbor, a step of watershed is then applied. The result of this step is shown on Figs 1c and 2c. Then, the elements that are in contact with the edges of the selected sub-volume are removed thanks to an algorithm called Borderkill.
Finally, ice crystals and air bubbles data were exported to Excel® to analyze their size distribution.

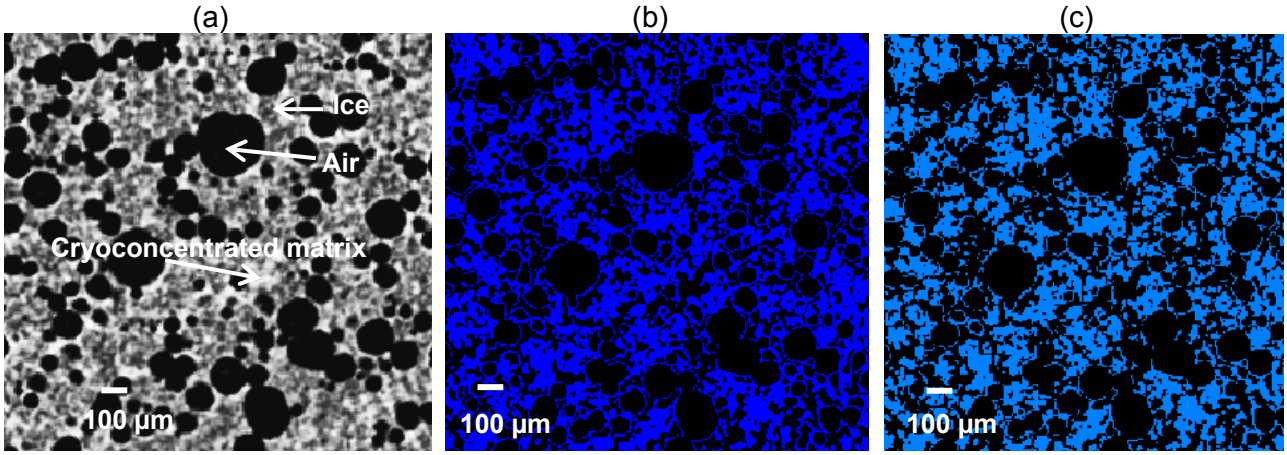

Figure 1: Image processing of the ice phase on one slice of the HMPC sample:
(a) Raw micro-CT image
(b) Segmented binary image: ice phase appears in blue
(c) Image obtained after applying watershed algorithm

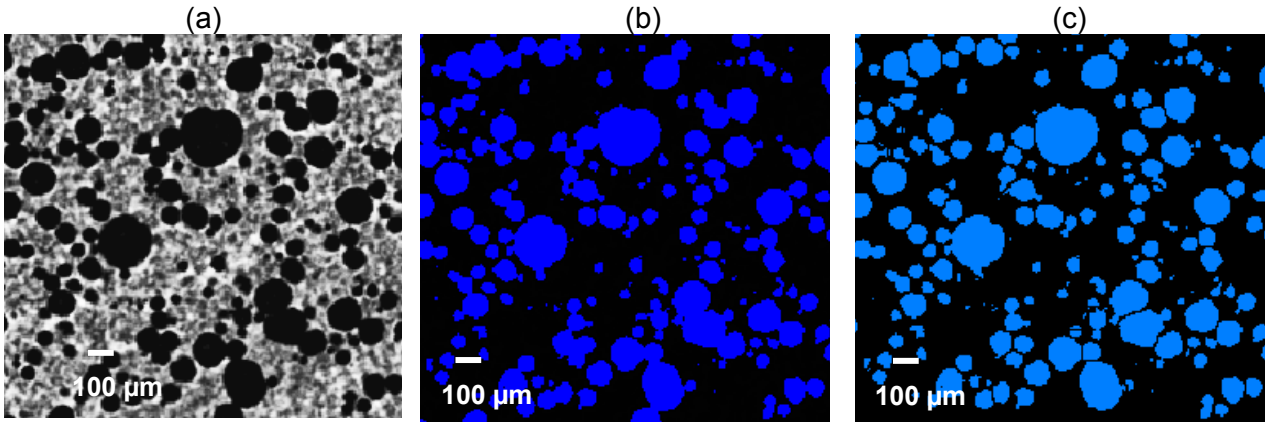

Figure 2: Image processing of the air phase on one slice of the HMPC sample:
(a) Raw micro-CT image
(b) Segmented binary image: air phase appears in blue
(c) Image obtained after applying watershed algorithm

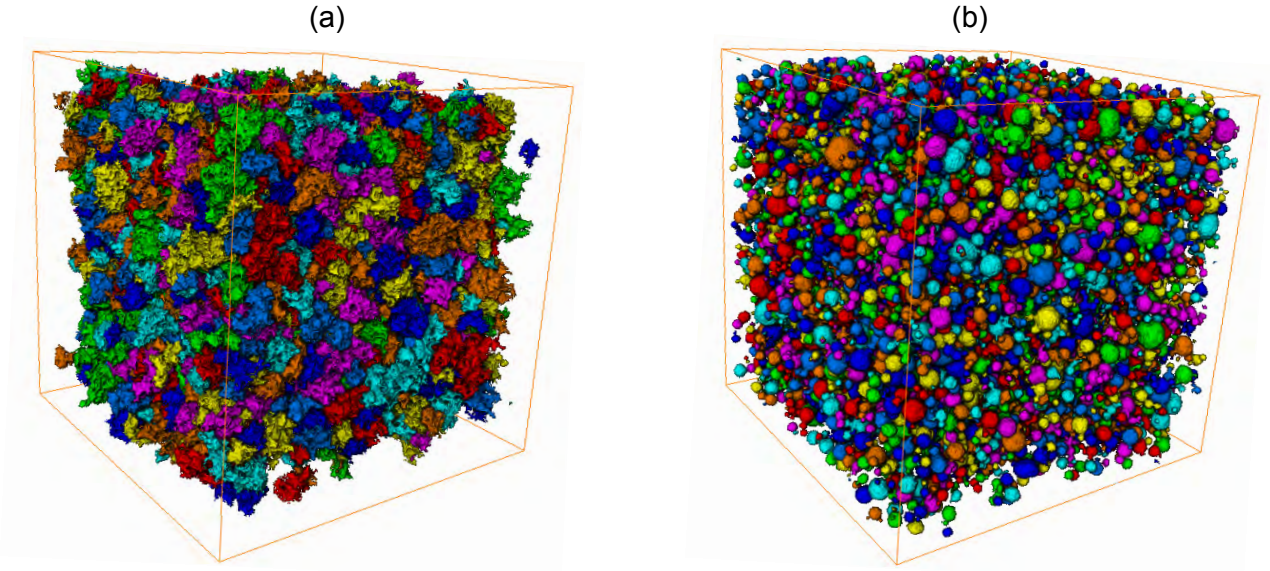

Figure 3: 3D representations of ice crystals (a) and air bubbles (b) in the stabilized sample (HPMC). The volume of the cube is equal to 32.8 mm^3

Fig. 3 represents the 3D visualization of the ice crystals (fig. 3 (a)) and of the air bubbles (fig. 3 (b)) in the case of HPMC sample. Each element is represented with a different color from the neighboring particles. This visualization mode makes it easy to visualize the spatial distribution of ice crystals and bubbles. The ice crystals seem to be uniformly distributed in size and number and their shape seems to be ovoid (Fig. 3(a)). In the case of the sample stabilized by the HPMC, there is a very large number of air bubbles whose size and space distribution seems relatively homogeneous. This result is not surprising; the HPMC is a stabilizer with surfactant properties: the molecules are attached to the interfaces between the air and other phases and stabilize the bubbles. Finally, the air bubbles seem to be smaller than the crystals and seem to be located between the crystals. Further analysis of the data extracted from the image processing will confirm these observations (section 3.2).

3.2. Data analysis

The processing of the images section allowed to individualize the elements of a segmented phase. Several parameters concerning each element can then be obtained: volume, equivalent diameter, sphericity etc. In the context of this study, it was therefore possible to collect and process data concerning ice crystals and air bubbles.
Fig. 4 shows the cumulative distribution of ice crystal sizes in control and HPMC stabilized samples. The equivalent diameter is defined as the diameter of a sphere with the same volume as the particle of interest (crystal). For each system studied, two distributions are shown to illustrate the repeatability. In both cases, the superposition of the curves is satisfactory, so the analysis technique employed seems particularly repeatable. Regarding the differences between the two mixes, it seems that the ice crystals are slightly smaller in the case of the stabilized mix than in the case of the control mix. The crystals ice size is distributed between 50 and 350 µm.

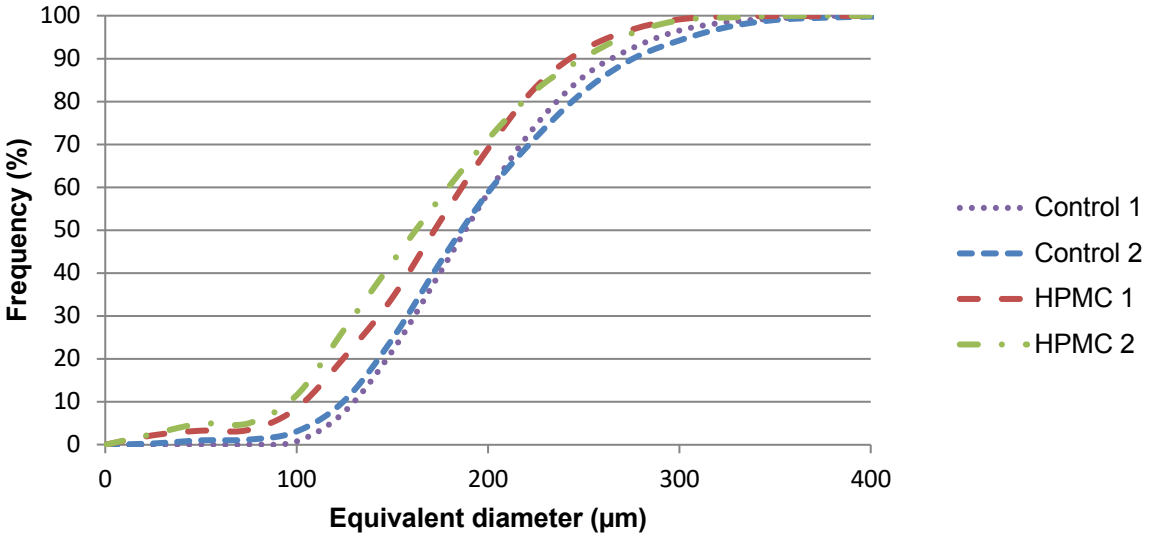

Figure 4: Cumulative distributions of equivalent diameters of ice crystals in the two samples. For each composition (control or HPMC), two replicates are shown

The mean and median equivalent diameters and the volume fractions of the ice crystals and air bubbles were calculated. The values are given in Table 1 for ice crystals and in Table 2 for air bubbles. Regarding ice crystals (table 1), for both formula, the mean diameter is quite large (>150µm) compared to the diameters of ice crystals generally encountered in industrial ice creams (< 50 µm). This can be explained by the batch domestic freezing process used that does not allow fast freezing rates and then promotes larger crystals. Moreover, ice crystals appear to be smaller in the case of the stabilized sample. The mean diameter is reduced by nearly 13% when using HPMC in the formula, meaning that the macromolecules may limit crystal growth during freezing. For each sample, the mean and median values are quite close, which means that the population of ice crystals is quite homogeneous in both cases. The ice volume fraction is higher in the control sample than in the sample containing HPMC. This result is due to the presumed presence of a larger amount of air in the stabilized sample. This will be verified with the air data (Table 2). Indeed, density of HPMC

sample will be lower than the one of the control sample, then ice mass fraction of both samples will be closer than ice volume fraction.

Table 1. Ice crystals

	Control sample	HPMC sample
Mean size (µm)	193.4 ± 0.2	168.4 ± 4.7
Median size (µm)	187.8 ± 0.1	167.4 ± 7.1
Volume fraction of the total phase (%)	34.3 ± 1.1	23.1 ± 1.3

Table 2 shows that the air volume fraction was much larger in the case of the sample containing HPMC. This is in agreement with the 3D observations of the sample (fig.3) and this is not surprising considering the surfactant properties of this stabilizer. In both cases, air volume fraction is low compared to those encountered in commercial ice creams. Indeed, it is known that in sorbets, overrun is generally lower than 50% (corresponding to nearly 25% of air volume fraction) (Marshall et al., 2003). In our case, this low air volume fraction can also be explained by the use of a batch freezer with no control of air incorporation. Furthermore, on Table 2, air bubbles are significantly smaller in the case of the control sample. However, the median size is significantly smaller in this case, which means that the population of air bubbles is not homogeneous in this control sample. On the contrary, in the case of the stabilized sorbet, the mean and the median size of air bubbles are close, meaning a relative homogeneity of the air bubbles in this case. The surfactant properties of HPMC lead to a higher air volume incorporation with a homogeneous distribution within the complex matrix.

Table 2. Air bubbles

	Control sample	HPMC sample
Mean size (µm)	49.0 ± 4.4	97.1 ± 0.6
Median size (µm)	26.3 ± 0.5	98.6 ± 3.4
Volume fraction of the total phase (%)	4.4 ± 0.5	23.2 ± 0.9

4. CONCLUSIONS AND PERSPECTIVES

A sorbet mix containing sucrose and a stabilizer was frozen and analyzed by X-ray microtomography at frozen state. The protocol used for this study allowed a repeatable and nondestructive analysis of a complex and triphasic frozen product. The images were processed and an effective separation of the 2 phases of interest (ice crystals and air bubbles) was carried out. The data collected gave the desired information about the frozen phase and the air phase (volume faction, size distribution and spatial distribution thanks to the 3-dimensional visualization). As a result, X-ray microtomography seems to be a particularly interesting technique for the analysis of frozen products.

The first results seem to show an effect of the formulation on the microstructure of the sorbet: the ice crystals seem smaller in the case of the stabilized mix and it contains much more air than the control sample. These results will have to be confirmed. The main perspective of this work is to extend the use of this technique to the study of different compositions of mixes (other stabilizers such as galactomannans, xanthan gum, or mixtures of several stabilizers) in order to conclude about the effect of stabilizers on the crystallization of sorbets.

NOMENCLATURE

HPMC	Hydroxypropylmethylcellulose	SSHE	Scraped Surface Heat Exchanger
LT-SEM	Low Temperature Scanning Electron Microscopy		

REFERENCES

Arbuckle, W. S., 1986. Ice Cream. Springer, New York, 483.

Bolliger, S., Wildmoser, H., Goff, H. D. and Tharp, B. W., 2000. Relationships between ice cream mix viscoelasticity and ice crystal growth in ice cream. Int. Dairy J. 10(11), 791-797.

Buyong, N. and Fennema, O., 1988. Amount and size of ice crystals in frozen samples as influenced by hydrocolloids. J. Dairy Sci. 71(10), 2630-2639.

Clarke, C., 2004. The science of ice cream. The Royal Society of Chemistry, Cambridge, 187.

Fernandez, P. P., Martino, M. N., Zaritzky, N. E., Guignon, B. and Sanz, P. D., 2007. Effects of locust bean, xanthan and guar gums on the ice crystals of a sucrose solution frozen at high pressure. Food Hydrocolloid 21(4), 507-515.

Flores, A. A. and Goff, H. D., 1999. Ice crystal size distributions in dynamically frozen model solutions and ice cream as affected by stabilizers. J. Dairy Sci. 82 1399-1407.

Goff, H. D., Caldwell, K. B., Stanley, D. W. and Maurice, T. J., 1993. The influence of polysaccharides on the glass-transition in frozen sucrose solutions and ice-cream. J. Dairy Sci. 76(5), 1268-1277.

Guo, E., Kazantsev, D., Mo, J., Bent, J., Van Dalen, G., Schuetz, P., Rockett, P., StJohn, D. and Lee, P. D., 2018. Revealing the microstructural stability of a three-phase soft solid (ice cream) by 4D synchrotron X-ray tomography. J. Food Eng. 237 204-214.

Guo, E., Zeng, G., Kazantsev, D., Rockett, P., Bent, J., Kirkland, M., Van Dalen, G., Eastwood, D. S., StJohn, D. and Lee, P. D., 2017. Synchrotron X-ray tomographic quantification of microstructural evolution in ice cream-a multi-phase soft solid. RSC Adv. 7(25), 15561-15573.

Marshall, R. T. and Arbuckle, W. S., 1996. Ice cream. Chapman & Hall, New York, 349.

Marshall, R. T., Goff, H. D. and Hartel, R. W., 2003. Ice cream. Springer, New York, 371.

Park, S.-H., Hong, G.-P., Kim, J.-Y., Choi, M.-J. and Min, S.-G., 2006. The influence of food hydrocolloids on changes in the physical properties of ice cream. Food Sci. Biotechnol. 15(5), 721-727.

Pinzer, B. R., Medebach, A., Limbach, H. J., Dubois, C., Stampanoni, M. and Schneebeli, M., 2012. 3D-characterization of three-phase systems using X-ray tomography: tracking the microstructural evolution in ice cream. Soft Matter 8(17), 4584-4594.

Stogo, M., 1998. Ice cream and frozen desserts: a commercial guide to production and marketing. John Wiley & Sons, Hoboken, 541.

Thiebaud, M., Dumay, E. M. and Cheftel, J. C., 2002. Pressure-shift freezing of o/w emulsions: influence of fructose and sodium alginate on undercooling, nucleation, freezing kinetics and ice crystal size distribution. Food Hydrocolloid 16(6), 527-545.

Thombare, N., Jha, U., Mishra, S. and Siddiqui, M. Z., 2016. Guar gum as a promising starting material for diverse applications: A review. Int. J. Biol. Macromol. 88 361-372.

Yuennan, P., Sajjaanantakul, T. and Goff, H. D., 2014. Effect of Okra cell wall and polysaccharide on physical properties and stability of ice cream. J. Food. Sci. 79(8), 1522-1527.

Manuscript ID: 1272
DOI: 10.18462/iir.icr.2019.1272

Influence of 2.45 GHz microwave radiation supplied with or without intermittency on the size of ice crystals during an innovative freezing process

Olivier ROUAUD[(a)], Mathieu SADOT[(a)], Sylvie CHEVALLIER[(a)], Sébastien CURET[(a)], Alain LE-BAIL[(a)], Michel HAVET[(a)]

[(a)] ONIRIS – GEPEA (UMR CNRS 6144)
Nantes, CS 82225, 44322, France, olivier.rouaud@oniris-nantes.fr

ABSTRACT

The objective of this study was to evaluate the ice crystals sizes during a microwave assisted freezing. The process consisted in freezing (with Nitrogen at -45°C) a piece of methylcellulose gel in a rectangular waveguide. 2.45 GHz microwave radiation was supplied in the waveguide according to several duty cycles (0/0.167/0.33/0.5/1). By varying the microwave power, the energy delivered to the product was maintained constant for each experiment.
A methodology was developed to evaluate the size of ice crystals by 3D imaging analysis and X-ray micro-tomography. The control freezing condition (no microwave) resulted in the highest mean diameters of ice crystals whereas microwave assisted freezing was able to reduce the size of ice crystals whatever the duty ratio. The ice crystals size could be reduced up to 28% and results tended to show that the reduction was not due to thermal oscillations (duty ratio < 1).
Keywords: Freezing, Ice Crystal Sizes, Microwave, Innovative Process.

1. INTRODUCTION

Freezing is a convenient method to reduce the chemical reaction rates (Lim et al., 2004) and control the microbial activity (Bremer and Ridley, 2004) in food products. Freezing process, thus preserving the organoleptic and nutritive food qualities, is very often used in food industry. Usually, the quality of frozen food is related to the size of ice crystals, small ice crystals giving rise to better quality. Indeed, freeze detrimental modifications are usually lower for smaller crystals (Delgado and Sun, 2001) because large ice crystals can damage cell membranes. The water expansion during phase change exerts a larger pressure on cell membranes, which can crack and cause loss of mass during thawing (Bevilacqua et al., 1979; Delgado and Sun, 2001).
It is recognized that faster freezing improves the quality of frozen food while forming smaller ice crystals (Devine et al., 1996). Unfortunately, these processes are energy-demanding because they imply the use of very cold environments such as cryogenics (Dempsey and Bansal, 2012). Therefore, innovative processes have to be developed to control ice nucleation without increasing the energy consumption. Mechanical agitation, pressure shift, ultrasound, magnetic fields or AC/DC electric fields were studied to help the control of ice nucleation (Jha et al., 2017, Dalvi-isfahan et al., 2017; Le Bail et al., 2002; Woo and Mujumdar, 2010;). Among the freezing processes investigated, experimental studies have shown that smaller ice crystals could be obtained if the product was submitted to microwave during freezing. Ice crystals with smaller dimensions and better ultrastructural preservation were found by Hanyu et al. (1992) in squid retina frozen at 83 K with microwave assistance (frequency at 2.45 GHz). For these authors, the rotations of water molecules due to microwave interfere in h-bond network establishment between water molecules. The network could be a crystalline structure precursor and this phenomenon could explain ice formation inhibition. More recently, smaller ice crystals were detected by Xanthakis et al. (2014) during the freezing of pork meat assisted by pulsed microwave (2.45 GHz). Temperature oscillations were observed during freezing due microwaves pulses and the authors proposed that the partial melting due to these temperature oscillations could induce a secondary nucleation and consequently more crystals with smaller volume.

So currently, the influence of microwave on crystallisation is not clear and it is difficult to know if the expected improvement is due to electrical or thermal effect. Recently an innovative pulsed microwave assisted freezing process was modelled (Sadot et al., 2017). Numerical simulations quantified the temperature oscillations due to microwave pulses during the freezing of methylcellulose gel. Results have particularly shown the influence of microwave on the freezing front. Hot and cold spots displacements were observed and explained by the change in dielectric properties during phase change. Based on the first numerical study, experiments have to be carried out to check if the influence of microwave on freezing is sufficient to control ice nucleation. So the objective of this work was to perform experiments of freezing with microwave and to measure the size of ice crystals.

2. MATERIALS AND METHODS

To determine the impact of freezing process on the food quality, it was first necessary to build an apparatus dedicated to the freezing experiments, combining microwave and cold environment. Secondly a specific methodology had to be developed to observe crystal size distribution in frozen food.

2.1. Experimental Device

An experimental device was developed to study the microwave assisted freezing of methylcellulose gel in controlled conditions. As shown in Fig. 1 which presents the experimental set-up, a liquid nitrogen tank (2) is put under pressure by a nitrogen gas bottle (1). The liquid nitrogen is pushed into the steel pipe where it vaporises. The gas temperature of -45°C at the inlet of the applicator (4) is controlled by a heating part at the end of the pipe (3). The applicator is a part of a rectangular waveguide WR 340 (section 86 mm x 43 mm). The dimensions of the waveguide are such that they ensure the propagation of the fundamental single-mode TE_{10} at a frequency of 2450 MHz: the electric field is perpendicular to the wave propagation direction with a zero value at the small walls and a maximum value at the centre of the long walls. Two splits of 10 mm height located on the small sides of the waveguide and perpendicular to the microwaves propagation direction allow the inlet and the outlet of the nitrogen gas.
To perfectly control the power emitted, a solid state generator (GMS200, SAIREM, France) was used rather than the magnetron technology (5). Microwave pulses were generated thanks to a switch (6) that sends alternatively microwave to a matched load (7) and to an antenna (8) placed at the inlet of the waveguide. This one is also equipped with two powermeters (9) (HX2462A, TechniWave, France) able to measure the incident and reflected powers. A water load (10) at the bottom of the waveguide absorbs the residual microwave to avoid any reflection.
The experimental set-up was used to freeze samples of methylcellulose gel according to several external conditions presented in Table 1. The product was thus frozen by its top surface with nitrogen gas and microwave penetrates the food also from the upper surface.

Table 1. Experimental conditions during microwave assisted freezing

Incident microwave power (W)	0	6	3	2	1
Duty ratio	0	0.167	0.333	0.5	1
Microwave energy (J) for 30 s	0	30	30	30	30
Mean Nitrogen temperature (°C)	-47 ± 3	-47 ± 3	-47 ± 3	-47 ± 3	-47 ± 3

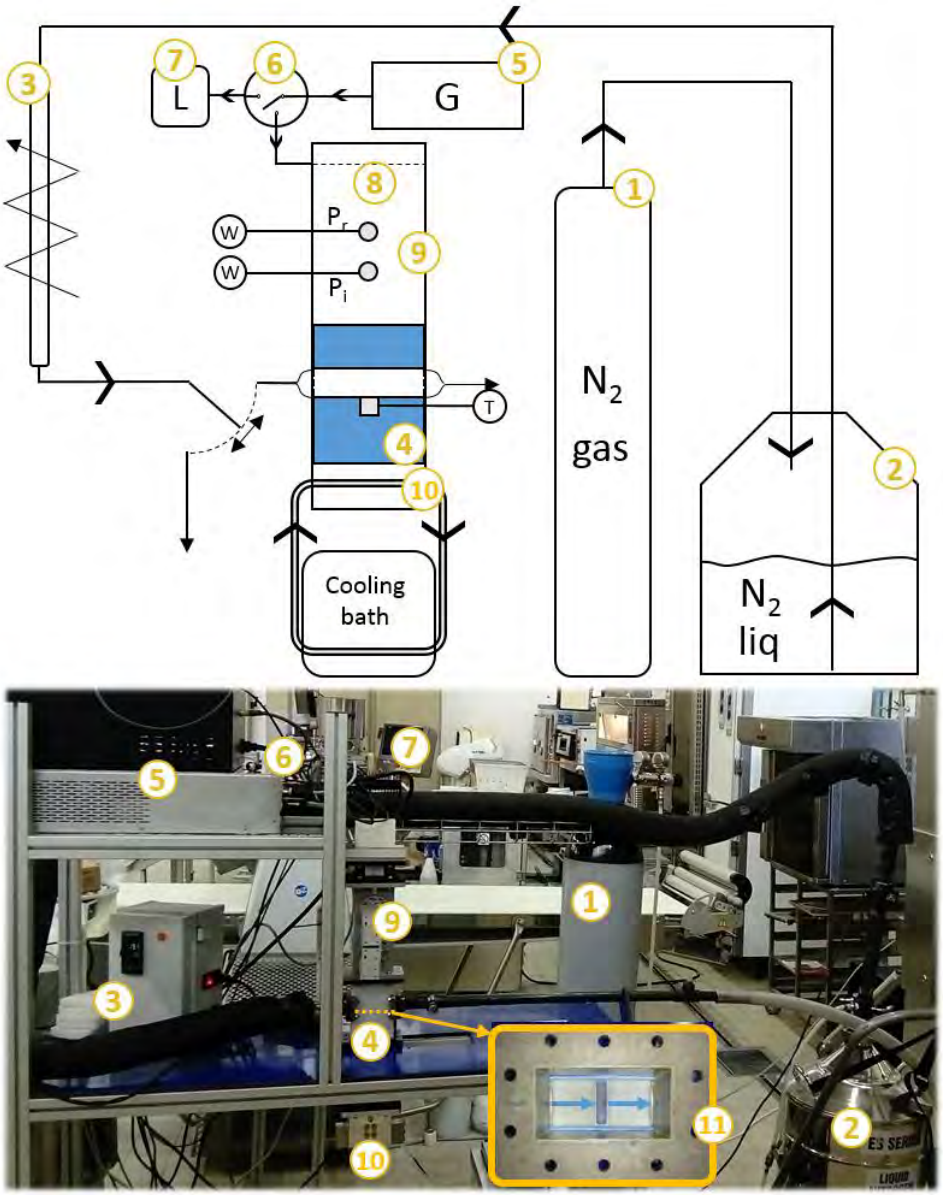

Figure 1: Experimental set-up

To evaluate the methodology used for determining the crystals size, freezing of 25 mm high samples were first performed without microwave. The height of samples was different when the influence of microwaves was studied. Indeed, to limit the effect of the sample dimension on the size of the ice crystals, thin pieces of methylcellulose gel (3 mm) were frozen. Moreover, the sample was centred in the applicator in such a way that it was subjected to the maximum of the microwave energy (11: the blue arrows indicate the nitrogen flow direction).

2.2. X-ray Micro-Tomography

The Skyscan 1174 (Brucker micro-CT, Kontich, Belgium) was used to characterize the structure of the methylcellulose gel by X-ray micro-tomography. Just after freezing, the sample was removed and directly placed in a freeze-dryer (Flexi-dry, FTS Systems, USA). All the ice was sublimated after 24 h (at - 85 ℃ and around 50 mTorr) and ice crystals were replaced by cavities (ghosts of ice crystals). The sample was cut and the resulting parallelepiped was inserted in plastic tube of 8 mm diameter. As shown in Fig. 2, no shrinkage was observed after freeze-drying. The sample was rotated during measurement while the detector and the source were fixed. The acquisition and reconstruction parameters are reported in Table 2.

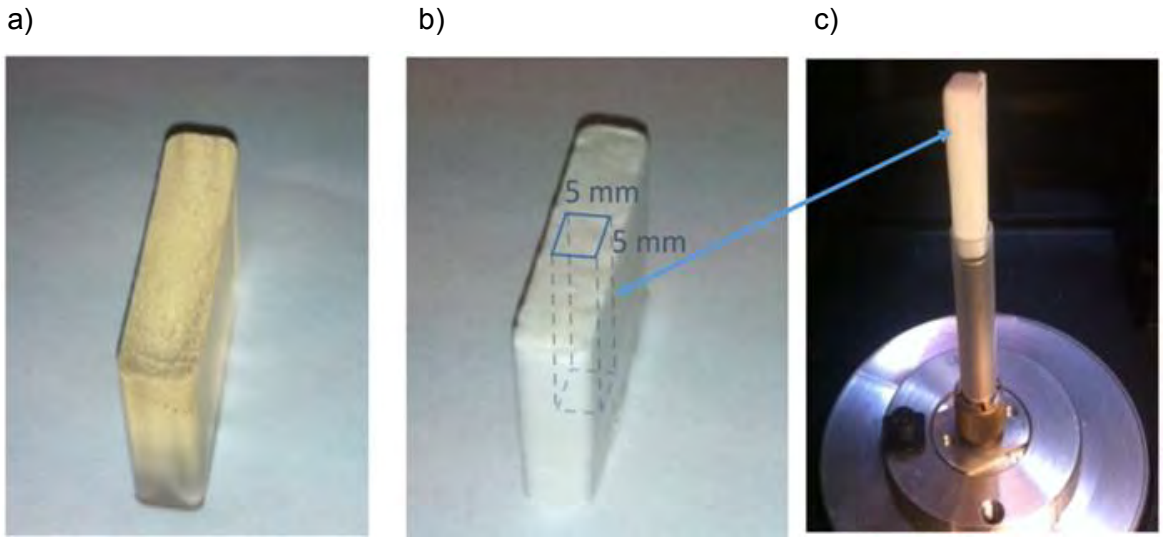

Figure 2: a) Fresh sample, b) freeze-dried sample, c) sample used in the X-ray tomography equipment

Table 2. Micro-tomography parameters used for acquisition and reconstruction

Acquisition parameters	Value	Reconstruction parameters	Value
Image size (pixels)	1024 × 1304	Image size (pixels)	924 × 824
Exposition time (ms)	1600	Number of sections	119 to 2383
Pixel size (µm)	6.46	Smoothing	0
Rotational step (°)	0.1	Ring artefact reduction	20
Frame averaging	2		

An automatic thresholding (Otsu's method) is performed to get binary images of reconstructed sections. The ice crystals are then measured from the size of the gas cells which correspond to the ghosts of the crystals. A 3D image is finally acquired and crystal size distributions can be calculated in several volumes of interest.

3. RESULTS

3.1. Assessment of the Measurement Methodology for Ice Crystals Sizes

It was first necessary to evaluate the methodology chosen for measuring the ice crystal sizes distribution. For this, a sample of methylcellulose gel was frozen on its upper surface by nitrogen at -40°C with a heat transfer coefficient close to 100 $W.m^{-2}.K^{-1}$. 8 volumes of interest were defined at different depths and the 3D calculation on the volumes displayed significant differences. As shown in Fig. 3 the ice crystal sizes distributions evolve along the depth of the sample. Except for the first and the last volume, where there is an influence of the boundaries on the calculation methodology, the ice crystals diameters increase linearly with the depth. The ice crystal size is thus smaller close to the surface exposed to the gas nitrogen and the results are consistent with previous studies (Woinet et al., 1998). The experimental results have been associated with numerical simulations carried out for the same conditions. It was possible with simulations to calculate the local characteristic freezing time, which was defined as the time necessary for a point to go from -1°C to -7°C; over such interval, more than 80% of the freezable water was frozen, corresponding to the maximal crystallisation temperature interval. The experimental results of the ice crystal sizes have thus been plotted against this freezing time in Figure 4. Except for the first volume, a linear correlation between ice crystal sizes and characteristic freezing times can be observed. There is also a correlation between the diameters and the displacement of the freezing front (not shown here).

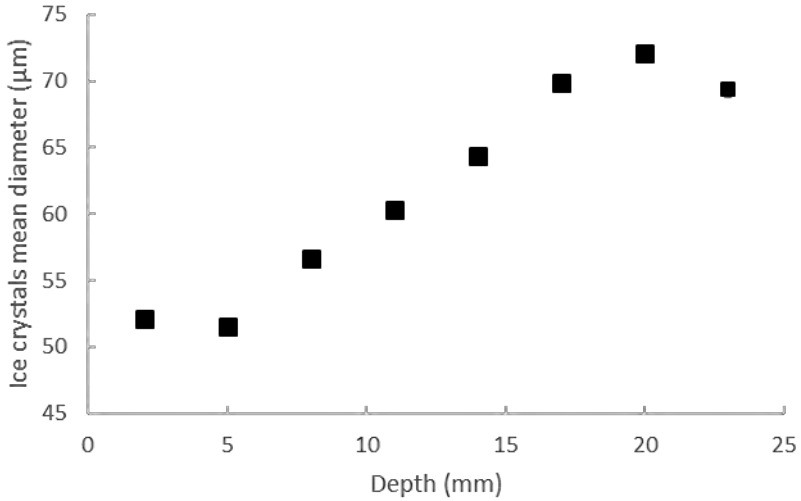

Figure 3: Influence of the depth on the ice crystal sizes for a freezing from the top surface

According to the classical nucleation theory, the crystal size is influenced by two kinetics: the nucleation rate and the crystal growth rate. The former is higher if the temperature decreases and the second increases with the number of liquid water molecules in contact to crystal surface. So the faster the temperature decreases – the lower the freezing time - the larger the number of crystals and the smaller the ice crystal size.

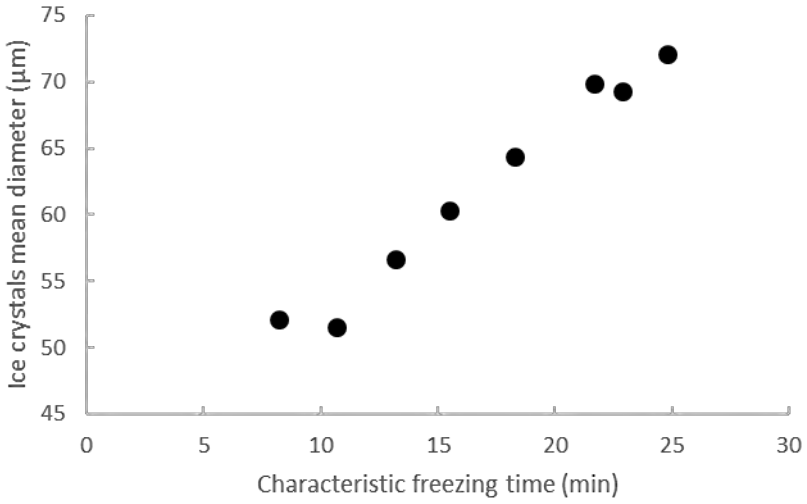

Figure 4: Influence of the freezing time on the ice crystal sizes

In conclusion, the results have shown that the X-ray micro-tomography can be viewed as a relevant methodology for the evaluation of the mean size of the ice crystals after freezing of methylcellulose gel. It gives access to the 3D structure of a freeze-dried sample from which the size distributions of the ice crystals ghosts can be deduced.

3.2. Influence of microwave on crystal sizes after microwave assisted freezing

The previous analyses have shown the influence of the sample depth on the ice crystal sizes so it was decided to perform microwave assisted freezing on thin samples (3 mm thick) and analyse the whole product. The choice was also motivated by the fact that the electric field is more uniformly distributed in thin samples than in the thick ones.
The freezing time is also an important parameter that influences the dimension of the ice crystals. To exclude this influence, freezing with the same emitted microwave energy was performed.

Thereby, the freezing time was expected to be the same for each experiment and only the time during which the samples were submitted to microwaves could influence the ice formation. The ice crystals mean diameters measured by X-ray tomography is thus displayed in Fig. 5 according to duty cycles defined in Table 1. Several experiments were carried out for each duty ratio to make it possible the evaluation of measurement uncertainties.

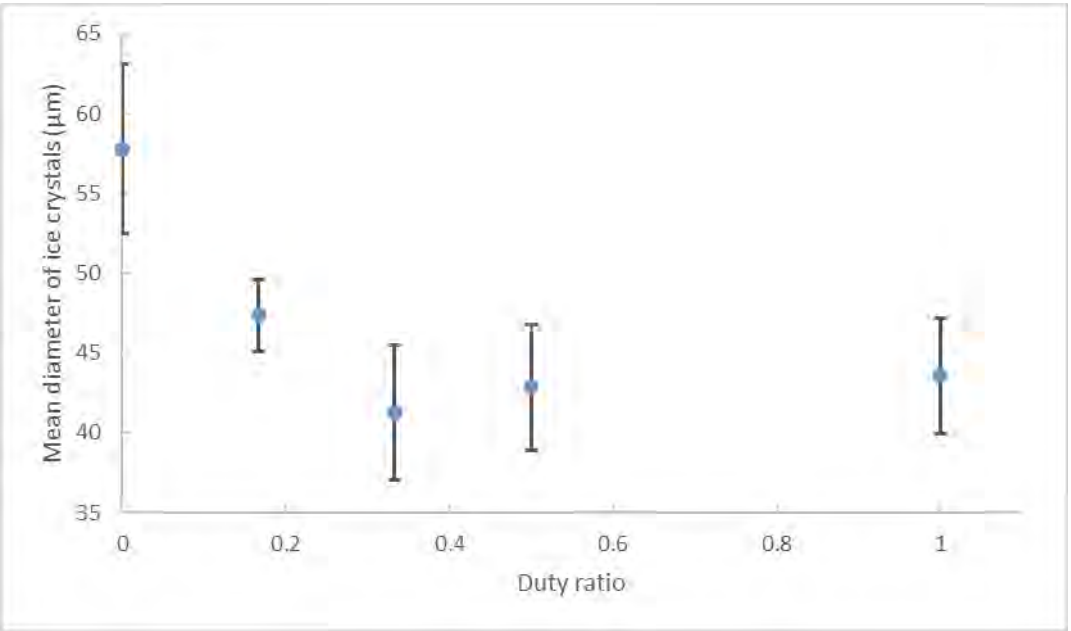

Figure 5: Ice crystals mean diameters for constant incident microwave energy

The influence of microwaves is clear from Fig. 5. The addition of electromagnetic waves such as microwaves during freezing induces a reduction of the ice crystal mean diameter. The values decrease from 57.8 µm for the control freezing without microwaves to 41.3 for microwave assisted freezing with a duty ratio of 0.333. It corresponds to a reduction of 28.6%. The reduction obtained with a low duty ratio of 0.167 is less than the one resulting from higher duty cycles. From a duty ratio of 0.333, there seems to be no significant difference between the experiments. Results obtained for the duty ratio of 0.167 could be explained by a too short exposure duration to microwaves or by a too long duration without microwave. Indeed, for the lower duty ratio, the resting time between two microwave exposures is 25 s and during this period, a part of the sample could rapidly freeze without the influence of electromagnetic waves and consequently without the ice formation being disrupted. The fact that there is a reduction of the ice crystal sizes for continuous applied microwaves tends to confirm an electromagnetic effect on nucleation. It should be mentioned however that other experiments performed in the laboratory on apple, seems to indicate that the thermal effect may also be effective, temperature oscillations resulting in a favoured secondary nucleation in the case of pulsed microwave emission (Jha, 2018).

4. CONCLUSION

Microwave assisted freezing process was investigated in this work. A methodology to determine the size of ice crystals was first considered and X-ray micro-tomography has proven to be a powerful tool in characterizing the microstructure of freeze-dried samples. Freezing was then performed with and without microwaves thanks to a convenient experimental apparatus developed in our lab. The electromagnetic waves were supplied according to several duty cycles; from 0.167 to 1 for which the microwaves were continuously applied. The results have shown that the ice crystals sizes could be reduced with microwaves for each conditions of our experiments. More research is still needed to clearly identify the role of microwave energy and the optimal duty ratio to be used according to food products, especially if we want to reduce this additional energy.

ACKNOWLEDGEMENTS

The work received financial support from the French National Research Agency (ANR) under the FREEZEWAVE project (ERANET call “SUSFOOD”, grant number ANR-14-SUSF-0001). The authors would also like to thank Christophe COUËDEL for developing the experimental set-up.

REFERENCES

Bevilacqua, A., Zaritzky, N.E., Calvelo, A., 1979. Histological measurements of ice in frozen beef. J. Food Technol. 14, 237–251.

Bremer, P.J., Ridley, S.C., 2004. Safety of Frozen Foods, in: Hui, Y.H., Cornillon, P., Guerrero Legaretta, I., Lim, M.H., Murrell, K.D., Nip, W.-K. (Eds.), Handbook of Frozen Foods. New York, 595–618.

Dalvi-isfahan, M., Hamdami, N., Xanthakis, E., Le-bail, A., 2017. Review on the control of ice nucleation by ultrasound waves, electric and magnetic fields. J. Food Eng. 195, 222–234.

Delgado, A.E., Sun, D.-W., 2001. Heat and mass transfer models for predicting freezing processes – a review. J. Food Eng. 47, 157–174.

Dempsey, P., Bansal, P., 2012. The art of air blast freezing: Design and efficiency considerations. Appl. Therm. Eng. 41, 71–83.

Devine, C.E., Bell, R.G., Lovatt, S., Chrystall, B.B., 1996. Red Meat, in: Jeremiah, L.E. (Ed.), Freezing Effects on Food Quality. New York, 51–83.

Hanyu, Y., Ichikawa, M., Matsumoto, G., 1992. An Improved Cryofixation Method - Cryoquenching Of Small Tissue Blocks During Microwave Irradiation. J. Microsc. 165, 255–271.

Jackson, T.H., Ungan, A., Critser, J.K., Gao, D., 1997. Novel microwave technology for cryopreservation of biomaterials by suppression of apparent ice formation. Cryobiology 34, 363–72.

Jha, P.K., Sadot, M., Vino, S.A., Jury, V., Curet-Ploquin, S., Rouaud, O., Havet, M., Le-Bail, A., 2018. A review on effect of DC voltage on crystallization process in food systems, Innov. Food Sci. Emerg. Technol. 42, 204-219.

Jha, P.K., 2018. Study on the effect of electromagnetic radiations during freezing on ice structure and quality of fruit and vegetable tissues, PhD thesis, ONIRIS and Université de Nantes, 176 p.

Lim, M.H., McFetridge, J.E., Liesebach, J., 2004. Frozen Food Components and Chemical Reactions, in: Hui, Y.H., Cornillon, P., Guerrero Legaretta, I., Lim, M.H., Murrell, K.D., Nip, W.-K. (Eds.)

Sadot, M, Curet, S., Rouaud, O., Le-Bail, A., Havet, M., 2017. Numerical Modelling of an Innovative Microwave Assisted Freezing Process. Int. J. Refrigeration 80, 66-76.

Woinet, B., Andrieu, J., Laurent, M., Min, S.G., 1998. Experimental and theoretical study of model food freezing. Part II. Characterization and modelling of the ice crystal size. J. Food Eng. 35, 395–407.

Woo, M., Mujumdar, A., 2010. Effects of Electric and Magnetic Field on Freezing and Possible Relevance in Freeze Drying. Dry. Technol. 28, 433–443.

Xanthakis, E., Le-Bail, A., Ramaswamy, H., 2014. Development of an innovative microwave assisted food freezing process. Innov. Food Sci. Emerg. Technol. 26, 176–181.

Manuscript ID: 1288
DOI: 10.18462/iir.icr.2019.1288

Physics of freezing under electromagnetic conditions; a review

Alain LE-BAIL[(a)], Piyush Kumar JHA[(a)], Epameinondas XANTHAKIS[(b)], Michel HAVET[(a)]

[(a)] Oniris, UMR 6144 GEPEA, BP 82225, 44322 Nantes Cedex 3 France
Email: alain.lebail@oniris-nantes.fr
[(b)] RISE- Agrifood and Bioscience, 41276 Gothenburg, Sweden
epameinondas.xanthakis@ri.se

ABSTRACT

Phase change in biological tissues may be affected by electric field, magnetic field and electromagnetic waves. This presentation proposes a review based on existing literature as well as some very recent results on freezing under static electric field and microwave conditions. The fundamentals of thermodynamics associated to freezing will be reminded. The interaction between water, water crystallization and electro-magnetic disturbances will be highlighted and different assumptions will be proposed. A review of existing results showed that for example the supercooling was decreased with increasing electromagnetic waves power level whereas the theory predicts the opposite. Besides, the theory supporting water freezing under static electric field matches well with the experimental results. A controversy exists about the possible impact of magnetic field (static and oscillating); this point will be tackled and discussed based on electromagnetism theory.
Some parts of this paper have been published recently in the ICCC conference proceedings (IIR- Beijing 2018).
Keywords: Freezing, Freeze Damage, Electric Field, Magnetic Field Microwaves, RF.

1. INTRODUCTION

Crystals are well-organized structures made of atoms or molecule through precipitating from a solution and/or molten mass, freezing or deposition from a gas (i.e. frost). Crystallisation is used to form solids or soft condenses materials and is linked to mass transfer of a solute from the liquid solution to a pure solid crystalline phase. Two families of crystals can be considered, ionic crystals made of cation and anion bound together by their electrostatic attraction (i.e. NaCl), and those made of uncharged species which are often observed in biological substances. Crystallisation corresponds to a drop in enthalpy and entropy of the system to step from a randomized organization to a well-organized packing. During crystallisation, the 2 phases A and B (i.e. Solid and Liquid) have the same chemical potential. Crystallisation process is usually initiated by change in temperature or concentration; it occurs in general under a given supercooling (ΔT_{SC}), which is defined as the temperature difference between the effective temperature and the initial phase change temperature; in the case of an aqueous solution of a given solute, reducing the temperature at a given concentration may reach in a supersaturated state that is needed to trigger crystallisation of water or of the solute. Temperature and concentration are the main drivers of crystallisation. Pressure can also be considered to initiate crystallization (Le-Bail et al., 2002). The use of seeding (introduction of small crystals acting as seeds to produce larger crystals) is the preferred solution to control the onset of crystallisation (i.e. used in the sugar & dairy industries).

2. STATIC ELECTRIC AND MAGNETIC FIELD; IMPACT ON FREEZING

2.1. Interaction between Atoms, Molecules and Static Electric Field

Pruppacher et al. (1968) and Fletcher (1970) explained that a semi-liquid layer develops around an ice crystal under formation during the freezing of an aqueous solution containing a solute. Within this semi-liquid layer, solute ions are moving towards the mother solution, whereas H_3O^+ and OH^- ions are travelling towards the pure ice crystal. A voltage difference of up to 10 V generating a tiny current in the range of 10^{-7} A has been proposed by Fletcher (Fletcher, 1970) (Figure 1). Applying an external electric field may interfere with these charge motion. Since SEF is directional, it is likely that crystals growth may be rather favoured in selected facets of the crystals under formation.

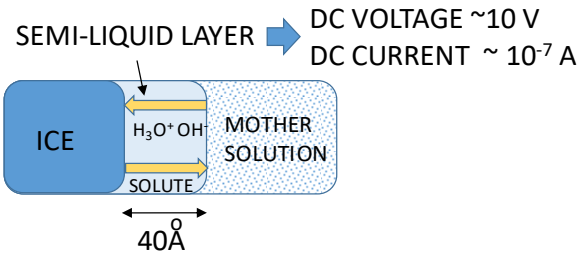

Figure 1: Scheme of the semi-liquid layer surrounding ice crystals under formation within an aqueous solution (Fletcher, 1970). A tiny voltage difference is present within this layer and is linked to mass diffusion of chemical species (solute) and ions travelling within this layer. Imposing an external voltage and static charges may affect ice crystallisation and as a global approach any crystallisation process (Fletcher, 1970)

An Electric Field (EF**)** is specified by both a direction and a magnitude (or strength) and is represented by a vector field that associates to each point in space the Coulomb force that would be experienced per unit of electric charge, by an infinitesimal test charge at that point. Interactions between EF, and atoms or molecules can be classified into LOW and HIGH fields. For LOW FIELDS (E< 0.1 V/Å or 10^8V/m) atoms and molecules only get polarized with a change in energy equal to P.E (P=polarizability). For example, considering an ion at position r of charge q, the gain in potential energy will be q.E(r)·r. For HIGH FIELDS (E> 0.1 V/Å or 10^8 V/m), which are of the order of electrostatic fields inside atoms, will affect the level structure of atoms and thus alter their chemical characteristics making and breaking new bonds in molecules. EF are created by electric charges and can be induced by time-varying magnetic fields. The electric field combines with the magnetic field to form the electromagnetic field. A DC-SEF (DC Static Electric Field) can be obtained by applying a DC voltage between two electrodes. The value of the electric field E (V/m) is given by the ratio between the voltage and the distance between the two electrodes; however, the effective local electric field depends on the dielectric relative permittivity of the matrices located between the electrodes. Computation of the effective EF in a complex system can be done knowing the permittivity's of the different materials in presence. Such modelling has been done in several configuration used in experimental studies with Comsol Multiphysics® are as shown in Figure 2 (Havet et al., 2009).

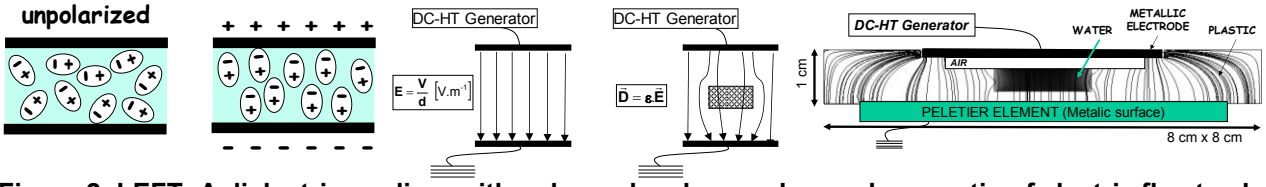

Figure 2: LEFT: A dielectric medium with polar molecules can have a lower ratio of electric flux to charge (more permittivity) than empty space. Molecules will lock to the field for given DC-SEF. CENTER: the permittivity of the medium exposed to a DC-SEF has to be considered to determine the effective displacement field. RIGHT: modelling done at ONIRIS-GEPEA for a SEF crystallisation prototype; the sample was water as a model food undergoing freezing

In the presence of a DC-SEF (E), the expression of the variation of free energy is modified resulting in an increase of the volume term of the variation of free energy. Eqs. 1 and 2 by a term proportional to the E (Marand et al., 1988). In these equations, V_C is the volume of the system subjected to the electric field, P the polarizability (C.m^{-2}). The resulting impact on the free energy variation function is shown in Figure 3, yielding in a reduction of the critical radius; smaller crystals are therefore expected.

$$G = U - TS + pV - [V_C.E.(\varepsilon_0.\varepsilon_r.E + P)] \quad \text{Eq. (1)}$$

$$\Delta G = 4\pi r^2\sigma - \frac{4}{3}\pi r^3\left(\Delta G_p + PE\right) \quad \text{Eq. (2)}$$

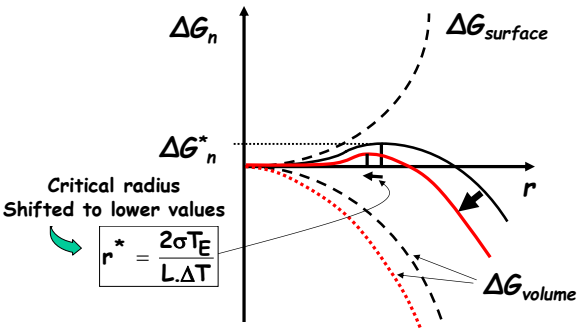

Figure 3: Impact of DC-SEF on crystallisation. A reduction of the critical radius is observed thanks to the increase of the volumetric term of the free Energy variation function (equation 2). The maximum of this function defines the critical radius of ice crystal; in the case of DC-SEF, the critical radius is shifted to lower values resulting in a better stability of smaller ice crystals and also to a higher nucleation rate. This theory has been established by (Marand et al., 1988) and applies to freezing but also to any material exposed to DC-SEF

In practice, DC-SEF in the range of 0.1×10^{10} V/m seems sufficient to obtain good results for electro-crystallisation. Svishchev and Kusalik (1996) studied ice formation with DC-SEF of 0.05 to 0.1×10^{10} V/m. Cubic ice formation is triggered by applying DC-SEF and amorphous ice may be obtained but seem to be unstable. Critical DC-SEF to lock water molecule to EF is ~3×10^{10} V/m (Sutmann, 1998). For DC-SEF of 10^5 to 10^6 V/m, hydrogen bonds are weakened. Higher DC-SEF permits to reduce supercooling and to trigger ice formation (Hozumi et al., 2005, 2003; Orlowska et al., 2009; Wei et al., 2008). For DC-SEF above 0.25×10^{10} V/m, water dissociation may occur (Cassone et al., 2014). For DC-SEF of 0.5×10^{10} V/m freezing is inhibited due to water molecules reorientation in ice (Shevkunov and Vegiri, 2002). The figure (Figure 4) below shows the impact of DC-SEF on the size of ice crystals in the case of pork loin.

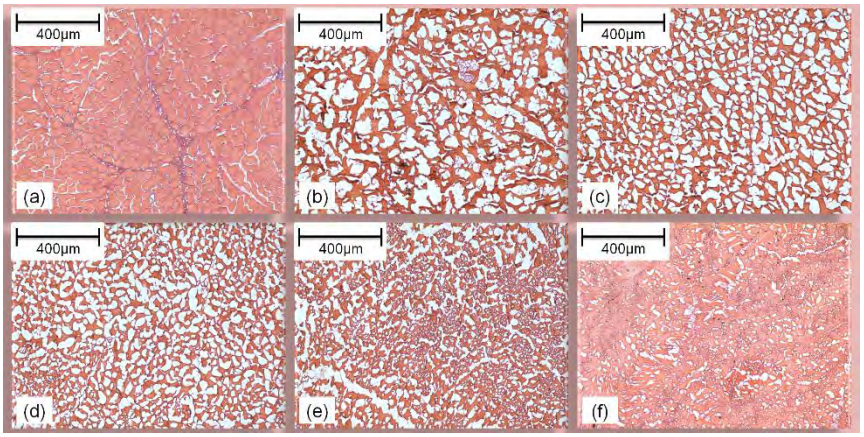

Figure 4: Impact of increasing SEF on the size of ice crystals in pork meat (tenderloin). a) non-frozen, b) frozen without SEF and c, d, e, f with increasing SEF of 3, 6, 9, 12 kV respectively. 12 kV corresponded to ca. 6×10^6 V/m (Orlowska et al., 2009). The refinement of the ice crystals is clearly visible (Xanthakis et al., 2013)

2.2. Interaction between Atoms, Molecules and Magnetic Field

A Magnetic Field (MF) is also represented by a vector field. MF is used for two distinct but closely related fields denoted by the symbols B (in teslas - symbol T) and H (in Ampere/meter or $A.m^{-1}$), where H is measured in units of amperes per meter (symbol: $A \cdot m^{-1}$ or A/m) in the SI. B is measured in teslas (symbol: T) and newtons per meter per ampere (symbol: $N \cdot m^{-1} \cdot A^{-1}$ or $N/(m \cdot A)$). B is most commonly defined in terms of the Lorentz force it exerts on moving electric charges. S-MF defines a Static MF stable with time and O-MF defines a fluctuating MF. The interaction between MF and molecules or atoms undergoing phase change such as crystallisation is still under debate in the literature. The MF on earth is 0.5 Gauss (5×10^{-5} T).

Former studies on this topic revealed that specific properties of water such as surface tension force and viscosity, optical property (changes in optical feature of water including infrared, Raman, visible, ultraviolet lights and X-ray spectra), electromagnetic property (refractive index, dielectric constant and electrical conductivity), thermodynamic property (enthalpy of vaporization), dynamic property (self-diffusion coefficient) and molecular structure of water (hydrogen bond structure) change upon the application of S-MF (Cai et al., 2009; Chang and Weng, 2006; Deng and Pang, 2007; Hosoda et al., 2004; Martiniano and Galamba, 2013; Pang and Bo, 2008b, 2008a; Toledo et al., 2008; Wang et al., 2013; Zhao et al., 2015; Zhou et al., 2000). However, the exact mechanisms on how S-MF affects water properties are unclear. Most of the theory concluded that S-MF application modifies the hydrogen-bond networks, but there is no agreement on how they are affected. Some have reported that S-MF application can weaken the hydrogen bonds and consequently decrease the average hydrogen bonding number between the water molecules (Wang et al., 2013; Zhou et al., 2000). On the contrary, some researchers claim that S-MF makes the bonding among the water

molecules more robust (Chang and Weng, 2006). The modification of hydrogen bonds structure (either weakening or strengthening) is expected to profoundly affect the properties of water governing the kinetics of processes such as freezing or other related processes.

The use of O-MF has also proven to affect the freezing behaviour of water and other aqueous solutions. Semikhina and Kiselev (1988) reported that water (bi-distilled water) subjected to a weak O-MF (B = 0.025 μT to 0.88 mT and frequencies between 10^{-2} and 200 Hz) for 5 h had a larger supercooling compared to the untreated sample. It was also found that the degree of supercooling was dependent on the strength and frequency of applied O-MF. Moreover, when a particular strength of O-MF was used, the maximum degree of supercooling was obtained at a specific MF frequency. For instance, Niino et al. (2012) studied the relationship between the frequency of O-MF (50 Hz to 200 kHz) and the degree of supercooling in physiological saline solutions at a fixed strength of O-MFs (0.12 ± 0.02 mT). Among all the frequencies been studied, the highest degree of supercooling ($\approx 18\ ^{\circ}\mathrm{C}$) was observed for the sample which was treated by O-MF of 2 kHz frequency. James et al. (2014) noticed that the O-MF application during the freezing of garlic bulbs using CAS technology (Cell Alive System marketed by ABI Company – Japan) (MF of 0.1–0.4 mT at frequencies ≤ 50 Hz) had minor additional effect on the degree of supercooling when compared to similar freezing conditions in the absence of O-MF (garlic freezing).

Few research papers have claimed that MF application can also influence the shape and size of ice crystals. Mok et al. (2015) observed that the ice crystals formed under the influence of S-MF were more irregular shaped than those obtained without MF. The pattern of ice crystals formed depended on the type of the applied external S-MF (attractive or repulsive). For instance, 'parting' pattern of ice crystals was obtained under attractive S-MF, while repulsive S-MF yielded a unique pattern of ice crystals. Iwasaka et al. (2011) reported that the freezing of aqueous solution under pulsed-train magnetic fields up to 325 T/s at 6.5 mT produced larger and more uniform ice crystals vs. ice crystals obtained without MF.

Some studies such as Watanabe et al. (2011) demonstrated that there was no impact, both from a theoretical and experimental point of view using food systems exposed to freezing with horizontal S-MF 5 to 100 Gauss (G) and also high frequency field O-MF) used in NMR with a vertical high-frequency magnetic field of (1 MHz / 1.2 G). Similar to Watanabe et al. (2011), Otero et al. (2018) and Naito et al. (2012) reported no effect of S-MF (attractive S-MF = 107 to 359 mT and repulsive S-MF = 0 to 241 mT) and O-MF (0.5 mT at 30 Hz) on freezing parameters (such as induction time, degrees of supercooling and the phase transition and total freezing times) of saline and distilled water. At this point in time, many doubts exist about real effects of magnetic fields on freezing and the science behind the potential mechanisms involved. Thus, extensive research is required in this domain to reach a decisive conclusion on the efficacy of MF vs quality of frozen products.

3. MICROWAVE and RADIO FREQUENCY ASSISTED FREEZING

Some experimental studies have shown that it is possible to obtain smaller ice crystals by using electromagnetic waves assisted freezing: Hanyu et al. (1992) reported that MW irradiation (for 50 ms) followed by freezing produced smaller ice crystals in the frozen samples (squid retina, rat liver, and heart muscle) with a good repeatability. Chaplin (2015) has proposed that depending on the frequency, water can be affected by different means; for microwaves (2.45 GHz), and enhancement of water mobility is foreseen, in the GHz domain, the free water is mainly concerned, whereas in the MHz domain both free and bound water are concerned and in the KHz domain only ice is concerned.

Focusing on MW, the zone of good freezing extended to a greater depth into the microwaves irradiated sample than compared to the control sample. The zone of freezing can be referred as the area where there is no sign of detectable ice-crystal damage. In other words, MW irradiated sample had a larger ice-free (vitrified) region compared to the untreated sample. Hanuy et al. (1992) have shown a clear reduction of ice crystals size in living tissue (Squid Retina) exposed to freezing under microwave. The explanation proposed is that MW (2.45 GHz) are disrupting water pentamers (5 water molecules making ca 85% of liquid water) in monomers, resulting in a higher supercooling and higher nucleation rate. Jackson et al. (1997) reported that the continuous application of MW (2.45 GHz and 1000 W) during attempted vitrification of ethylene glycol solution (cryo-protectant) caused a significant reduction in ice formation.

A more recent studies made by Anese et al. (2012) and Xanthakis et al. (2014) showed a clear reduction of ice crystals size in port loin exposed to RF waves and MW respectively as shown in Figure 5 and Figure **6**. Anese et al. (2012) used a pilot-scale RF equipment was used while liquid nitrogen was flowing in a chamber in order to provide cryogenic freezing conditions to their samples. Although no data were presented on ice crystal size, the histological micrographs seemed to indicate that the ice crystal size decreased as shown in Figure 5. Further investigations are being carried out by ONIRIS (France), RISE (Sweden), TTZ (Germany) and SAIREM (France – SME on MW) to better optimize the freezing assisted by microwaves. Indeed, MW represents some energy dissipation and optimization

must be carried out to reduce MW energy while improving efficiently the microstructure of frozen tissues.

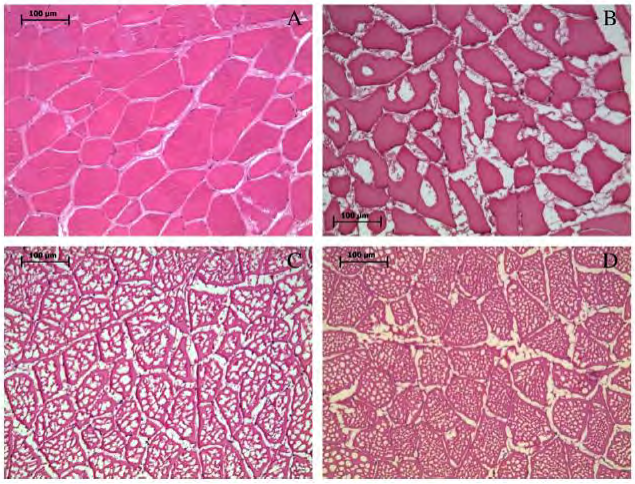

Figure 5: Reduction of the size of ice crystals in pork loin exposed to RF waves (27.12 MHz) during freezing (Anese et al., 2012). A (Fresh), B (air blast freezing), C (cryogenic freezing), D (Cryogenic freezing + RF)

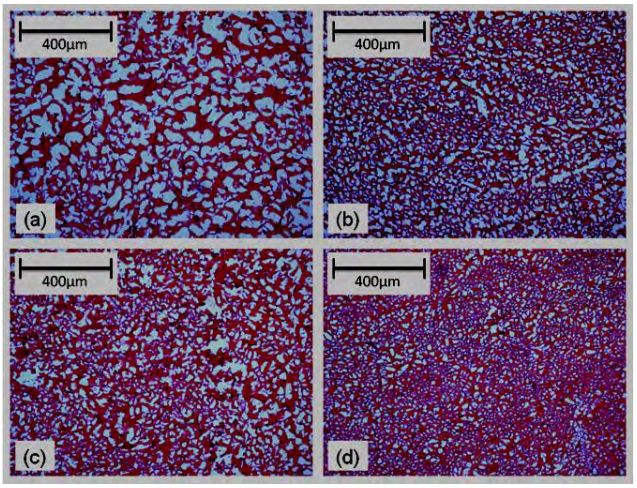

Figure 6: Reduction of the size of ice crystals in pork loin exposed to MW (2.45 GHz) during freezing (Xanthakis et al., 2014). a) Static freezing (control condition), b), c), d) increasing MW power irradiation

Two concepts are proposed to explain the observed ice crystal size reduction in frozen systems by using microwaves. The "NITOM" concept (Nucleation Induced by Temperature Oscillation caused by Microwaves) is based on the fact that under specific duty ratio, the temperature of the sample undergoing freezing will oscillate (Xanthakis et al., 2014). The fluctuating temperature is expected to favour secondary nucleation which in turn suppress the crystal growth. This concept is illustrated in figures 7 & 8 below.

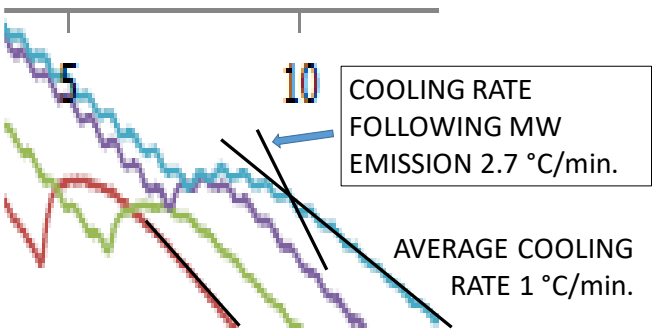

Figure 7: Zoom on cooling rates during the tests done by Xanthakis et al (2014). A much faster cooling was observed during temperature drop following MW emission

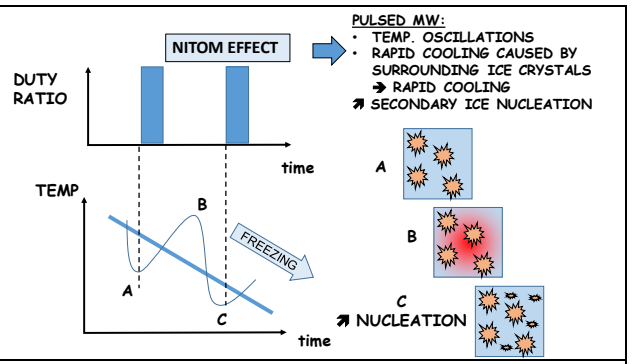

Figure 8: Scheme presenting the "NITOM" effect; Following MW emission, a faster cooling promotes the apparition of new ice nuclei, resulting in a refined ice crystals population

The second concept is called "NIMIW" (Nucleation Induced by constant or pulsed MIcroWaves power) and it is based on constant or pulsed (short time) emission. NIMIW can be explained by the impact of MW on the hydrogen bonds between water molecules, which may affect the water cluster structures during freezing. It is expected that MWs could exert a torque and displace the water molecules from their equilibrium relationships in the ice cluster resulting in fragmentation of existing ice crystals when ice crystals are in the form of nuclei. The fragmented ice crystals nuclei may act as new nucleation sites and promote the secondary nucleation, thus, causing ice crystal size reduction (Hanyu et al., 1992; Jackson et al., 1997; Anese et al., 2012; Xanthakis et al., 2014; Dalvi-Isfahan et al., 2016; Cheng et al., 2017). Another possibility could be that the electrical disturbances caused by MWs application would alter the mass diffusion in the quasi-liquid layer surrounding the ice crystals under formation (Fletcher, 1970). The delayed growth of ice crystals would, in turn, yield a higher nucleation rate resulting in a refinement of the size of ice crystals in the product (Hanyu et al., 1992; Jackson et al., 1997; Anese et al., 2012; Dalvi-Isfahan et al., 2016, Hafezparast-Moadab et al. 2018). These two hypotheses, NITOM and NIMIW may thus be considered to explain the observed reduction of ice crystals size in samples under electromagnetic waves assisted freezing.

ACKNOWLEDGEMENTS

Financial support from ONIRIS and for FREEZEWAVE project by ERANET – European project FREEZEWAVE is appreciated ad well as financial support of the Région Pays de Loire. Special thanks are addressed to C. COUEDEL, L.GUIHARD and A.OGE (ONIRIS) who developed the different experimental set-up used.

NOMENCLATURE

CAEMF = Crystallisation Assisted by Electric and or Magnetic Fields DC-SEF=DC Static Electric Field, AEF or AC-EFor OEF: Alternating Current EF, S-MF = static magnetic field, O-MF = oscillating MF

REFERENCES

Anese, M., Manzocco, L., Panozzo, A., Beraldo, P., Foschia, M., Nicoli, M.C., 2012. Effect of radiofrequency assisted freezing on meat microstructure and quality. Food Res. International 46, 50–54.

Cai, R., Yang, H., He, J., Zhu, W., 2009. The effects of magnetic fields on water molecular hydrogen bonds. J. Mol. Structure 938, 15–19.

Cassone, G., Giaquinta, P. V, Saija, F., Saitta, a M., 2014. Proton conduction in water ices under an electric field. J. Phys. Chem. B 118, 4419–24.

Chang, K., Weng, C., 2006. The effect of an external magnetic field on the structure of liquid water using molecular dynamics simulation. J. Appl. Physics 100, 43917–43922.

Deng, B., Pang, X., 2007. Variations of optic properties of water under action of static magnetic field. Chinese Sci. Bulletin 52, 3179–3182.

Fletcher, N.H., 1970. The chemical physics of ice. Cambridge University Press, Cambridge.

Hanyu, Y., Ichikawa, M., Matsumoto, G., 1992. An improved cryofixation method: cryoquenching of small tissue blocks during microwave irradiation. J. Microscopy 165, 255–271.

Havet, M., Orlowska, M., Le-Bail, A., 2009. Effects of an electrostatic field on ice nucleation. Proceedings of the International Conference on Bio and Food Electrotechnologies, Compiègne, France, Université de technologie de Compiègne, 22-23.

Hosoda, H., Mori, H., Sogoshi, N., Nagasawa, A., Nakabayashi, S., 2004. Refractive indices of water and aqueous electrolyte solutions under high magnetic fields. J. Phys. Chem. A 108, 1461–1464.

Hozumi, T., Saito, A., Okawa, S., Eshita, Y., 2005. Effects of shapes of electrodes on freezing of supercooled water in electric freeze control. Int. J. Refrigeration 28, 389–395.

Hozumi, T., Saito, A., Okawa, S., Kazuharu, W., 2003. Effects of electrode materials on freezing of supercooled water in electric freeze control. Int. J. Refrigeration 26, 537–542.

Iwasaka, M., Onishi, M., Kurita, S., Owada, N., 2011. Effects of pulsed magnetic fields on the light scattering property of the freezing process of aqueous solutions. J. Appl. Physics 109, 1–4.

Jackson, T.H., Ungan, A., Critser, J.K., Gao, D., 1997. Novel microwave technology for cryopreservation of biomaterials by suppression of apparent ice formation. Cryobiology 34, 363–72.

James, C., Reitz, B., James, S.J., 2014. The Freezing Characteristics of Garlic Bulbs (Allium sativum L.) Frozen Conventionally or with the Assistance of an Oscillating Weak Magnetic Field. Food Bioprocess Technology 8, 702–708.

LeBail, A., Chevalier, D., Mussa, D.M., Ghoul, M., 2002. High pressure freezing and thawing of foods: A review. Int. J. Refrigeration 25, 504–513.

Marand, H.L., Stein, R.S., Stack, G.M., 1988. Isothermal crystallization of poly(vinylidene fluoride) in the presence of high static electric fields. I. Primary nucleation phenomenon. J. Polym. Sci. Part B Polym. Physics 26, 1361–1383.

Martiniano, H.F.M.C., Galamba, N., 2013. Insights on Hydrogen-Bond Lifetimes in Liquid and Supercooled Water. J. Phys. Chem. B 117, 16188–16195.

Mok, J.H., Choi, W., Park, S.H., Lee, S.H., Jun, S., 2015. Emerging pulsed electric field (PEF) and static magnetic field (SMF) combination technology for food freezing. Int. J. Refrigeration 50, 137–145.

Naito, M., Hirai, S., Mihara, M., Terayama, H., Hatayama, N., Hayashi, S., Matsushita, M., Itoh, M., 2012. Effect of a Magnetic Field on Drosophila under Supercooled Conditions. PLoS One 7,1–4.

Niino, T., Nakagawa, T., Noguchi, S., Sato, I., Kawai, T., Yamashita, H., Masamune, K., Dohi, T., Mihara, M., 2012. Whole Ovary Cryopreservation Applying Supercooling under Magnetic Field. Mech. Eng. Cryopreserv. Reprod. Technique 5, 14–20.

Orlowska, M., Havet, M., Le-Bail, A., 2009. Controlled ice nucleation under high voltage DC electrostatic field conditions. Food Res. International 42, 879–884.

Otero, L., Rodríguez, A.C., Sanz, P.D., 2018. Effects of static magnetic fields on supercooling and freezing kinetics of pure water and 0.9% NaCl solutions. J. Food Engineering 217, 34–42.

Pang, X.F., Bo, D., 2008b. The changes of macroscopic features and microscopic structures of water under influence of magnetic field. Phys. B Condens. Matter 403, 3571–3577.

Pang, X.F., Bo, D., 2008a. Investigation of changes in properties of water under the action of a magnetic field. Sci. China Ser. G Physics, Mech. Astronomy 51, 1621–1632.

Pruppacher, H.R., Steinberger, E.H., Wang, T.L., 1968. On the Electrical Effects that Accompany the Spontaneous Growth of Ice in Supercooled Aqueous Solutions. J. Geophys. Research 73, 571–584.

Semikhina, L.P., Kiselev, V.F., 1988. Effect of weak magnetic fields on the properties of water and ice. Sov. Phys. Journal 31, 351–354.

Shevkunov, S. V., Vegiri, A., 2002. Electric field induced transitions in water clusters. J. Mol. Struct. THEOCHEM 593, 19–32.

Sutmann, G., 1998. Structure formation and dynamics of water in strong external electric fields. J. Electroanal. Chemistry 450, 289–302.

Svishchev, I.M., Kusalik, P.G., 1996. Electrofreezing of Liquid Water: A Microscopic Perspective. J. Am. Chem. Society 118, 649–654.

Toledo, E.J.L., Ramalho, T.C., Magriotis, Z.M., 2008. Influence of magnetic field on physical – chemical properties of the liquid water : Insights from experimental and theoretical models. J. Mol. Structure 888, 409–415.

Wang, Y., Zhang, B., Gong, Z., Gao, K., Ou, Y., Zhang, J., 2013. The effect of a static magnetic field on the hydrogen bonding in water using frictional experiments. J. Mol. Structure 1052, 102–104.

Watanabe, M., Kanesaka, N., Masuda, K., Suzuki, T., 2011. Effect of Oscillating Magnetic Field on Supercooling in food freezing. Proceedings of the 23rd IIR International Congress of Refrigeration on Refrigeration for Sustainable Development, Praha, Czech Republic, IIR, 21-26.

Wei, S., Xiaobin, X., Hong, Z., Chuanxiang, X., 2008. Effects of dipole polarization of water molecules on ice formation under an electrostatic field. Cryobiology 56, 93–99.

Xanthakis, E., Le-Bail, A., Ramaswamy, H., 2014. Development of an innovative microwave assisted food freezing process. Innov. Food Sci. Emerg. Technologies 26, 176–181.

Xanthakis, E., Havet, M., Chevallier, S., Abadie, J., Le-Bail, A., 2013. Effect of static electric field on ice crystal size reduction during freezing of pork meat. Innov. Food Sci. Emerg. Technologies 20, 115–120.

Zhao, L., Ma, K., Yang, Z., 2015. Changes of Water Hydrogen Bond Network with Different Externalities. Int. J. Mol. Sciences 16, 8454–8489.

Zhou, K.X., Lu, G.W., Zhou, Q.C., Song, J.H., Jiang, S.T., Xia, H.R., 2000. Monte Carlo simulation of liquid water in a magnetic field. J. Appl. Physics 88, 1802–1805.

Manuscript ID: 1294
DOI: 10.18462/iir.icr.2019.1294

Current status and future trends of monitoring technologies for food products traceability

Diogo MORAIS[(a)], Pedro D. GASPAR[(a,b)], Pedro D. SILVA[(a,b)], Luís P. ANDRADE[(c,d,e)], José NUNES[(c)]

[(a)] University of Beira Interior, Rua Marquês d'Ávila e Bolama, 6201-001, Covilhã, Portugal
[(b)] C-MAST - Centre for Mechanical and Aerospace Science and Technologies, Covilhã, Portugal
[(c)] Agriculture School, Polytechnic Institute of Castelo Branco, Quinta da Senhora de Mercoles, 6001-909 Castelo Branco, Portugal
[(d)] CATAA - Food Technology Support Center, Centro de Apoio Tecnológico Agro Alimentar, Castelo Branco, Portugal
[(e)] CERNAS – Centro de Estudos em Recursos Naturais, Ambiente e Sociedade

ABSTRACT

This paper presents the current status and future trends of sensor technologies for food products traceability, specifically for systems devoted to be applied in the cold storage and refrigerated transport of horticultural products. The available monitoring technologies such as dataloggers, TTI, WSN, RFID, and combined approaches are evaluated and compared in terms of dimensions, sensor parameter (temperature, relative humidity, water vapor, ethylene and other gases released during the biological processes of fruit), robustness, reliability, energy autonomy, bandwidth (if applicable), connection, among others. The aim of the study consists in evaluating how these technologies can be successfully applied for traceability of horticultural products and are what the future trends in terms of technical and technological specifications that will guide the development of these systems. It is expected that the increasing use of these systems for food traceability increases food quality and safety, reducing food waste.
Keywords: Current status; Future trends; Monitoring technologies; Food traceability; Sensors.

1. INTRODUCTION

Distribution chains still have challenges to overcome, such as the lack of a monitoring system that allows monitoring the product at all stages and evaluating the remaining time of validity.
This fact is reflected in the amount of food products that are wasted before reaching the final consumer, approximately one-third of the total production. In horticultural products this waste reaches 45% (Gustavsson *et al.*, 2017). Food waste arises from factors associated with distribution chains, such as inadequate transport conditions and non-compliance with storage temperatures. Another relevant point of the distribution chain where this food conservation break exists is in places of merchandise transition, namely airports and sea ports, where the containers with the perishable products are sometimes placed under high solar exposure and subjected an undesirable thermal amplitude (Badia-Melis *et al.*, 2018). As distribution has become a worldwide system it is usual that not all countries have the same regulation for the cold chain, proving to be another factor that affects food quality. Figure 1 shows the large problems faced by the distribution chains and that lead to food waste.

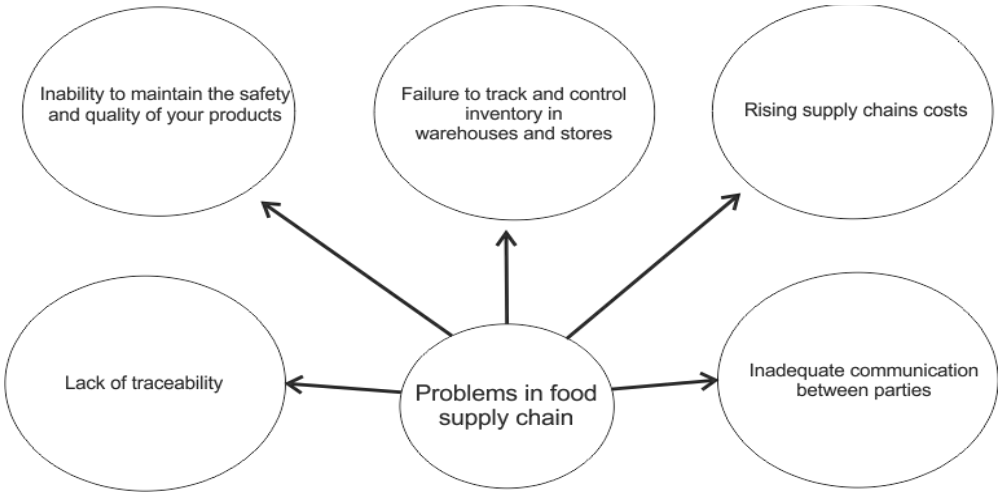

Figure 1: The main problems in the food supply chain.

Due to the different characteristics of the food products, there is no solution that solves efficiently all problems in the distribution chain. On the other hand, over time, monitoring systems, forecasting methods, computational fluid simulations, and other solutions have been developed with the purpose of monitoring and evaluating the product. Fruit and vegetable products, being of biological origin and therefore subject to senescence processes, require a more demanding control regarding storage conditions. Ruiz-Garcia *et al.* (2010) evaluated the storage conditions inside a refrigerated truck. It was concluded that the temperature was above the set point programmed 98% of the time. The location of the pallet during this period is also relevant, as proved by Margeirsson *et al.* (2012), Moureh *et al.* (2002) and Laguerre *et al.* (2002).

But, why is food preservation necessary? The globalization of trade routes causes many products to be transported over long distances but reaching the final destination with quality and safety. As mentioned by Rediers *et al.* (2009), conservation is, first and foremost, essential to maintain optimum product quality, as it reduces several physiological processes, such as perspiration and respiration. This can be accomplished by the reduction of temperature that decreases the growth rate of microorganisms. Solving these issues involves the implementation of monitoring systems that allow the producer to analyze the conservation environment to which the product is subject. The real-time knowledge of this data facilitates the decision making, leading to optimized distribution chain. In this context, Internet of Things (IoT) is one of the solutions that can be implemented. The connectivity of the devices with the Internet allows the establishment of wireless sensor networks (WSN) and, in this way, permanent monitoring is possible. This study presents the relevant publications in food monitoring, as well as the technological trends in communication and sensing that have been tested and implemented in the market.

2. CURRENT STATE

In the cold chain, any perturbation in the temperature, regardless of duration or severity and the stage at which it occurs, may compromise the whole chain and all the efforts made up to that point (Mahajan *et al.*, 2014). The study carried out by Ruiz-Garcia *et al.* (2009) shows that the temperature oscillations inside a conservation chamber caused by the on-off cycles leads to variations between 3 and 6ºC. Other parameters such as the temporary opening of the doors of both the truck and the camera and the loading of the products also influence the temperature variation (Carneiro *et al.*, 2017; Göransson *et al.*, 2018). The environmental temperature is another factor that determines the time necessary for the total cooling of the product, as evaluated in Redier *et al.* (2009), who also demonstrated small temperature variations during the transport of endive.

The implementation of traceability systems has long attracted the attention of traders, and over time practical and accessible solutions have been developed that allow a rapid assessment of the state of conservation. In recent years, several projects have focused on the development of hardware required for traceability, predictive validity models, QTT (Quality oriented Tracking and Tracing) and FEFO systems such as Chill-On, PASTEUR, FRISBEE, DANAHMAT and Intelligent container. The following table shows the duration and focus of these projects.

Table 1: Similar projects in traceability systems for food supply chain.

Project & Reference	Duration	Focus
Chill-On (Olafsdottir *et al*., 2010)	2006-2010	TTI with chemical detection and RFID interface
PASTEUR (Hoofman, 2013)	2009-2012	RFID tag with multiple sensors (temperature, humidity and gas detection)
Intelligent container (Jedermann *et al*., 2014)	2010-2013	Prototype container for QTT and FEFO
FRISBEE (Gwanpua *et al*., 2015)	2010-2014	Simulation and creation of database for temperature mapping and models of life time
DANAHMAT (Jevinger *et al*., 2014)	2013-2016	Concepts for dynamic labeling capable of determining validity

Despite efforts, these systems have not been implemented on a large scale. But, in contrast, devices such as Time-Temperature Integrators or Indicators (TTIs) and data loggers are used. Although they do not provide real-time monitoring, allow to record the temperature history throughout the chain and the subsequent analysis of the results.
The origin of the IoT remote to the year 1999, with the creation of a network of objects interconnected using Radio Frequency IDentification (RFID). But IoT offers much more possibilities of sensing and acting with the use of low power microcontrollers. In addition to this class of cyber-physical systems, also communication protocols that allow the sending of data must pointed out (Nukala *et al.*, 2016).

3. TIME-TEMPERATURE INTEGRATORS/INDICATORS (TTI)

Temperature indicators as a function of time are devices that allow, in a simple way, food control by the trader and the consumer through changes observable to the naked eye, such as a change in color or shape. These devices can record the total or partial temperature history of a product from the producer to the consumer. There is a high diversity of these indicators that resort to a variety of physical-chemical properties (Selman, 1995). The rate of change is temperature, light or humidity dependent, i.e. the parameter accumulation influences a variable such as the deterioration reactions responsible for deteriorating product quality (Pavelková, 2012). The indicators can be classified according to their operating principle.



Figure 2: TTIs classification relatively to working principle.

When active, the state change is irreversible. Its activation may be presented as a deformation, a change of color or change in the intensity of the coloration. The rate of visibility change depends on the temperature and its variation (Biega, 2017). These indicators can also be grouped into three categories.

- **Critical Temperature Indicator (ITC)** indicates exposure above or below a reference temperature. The denaturation of an important protein above a critical temperature or the development of pathogenic organisms are situations in which these indicators prove usefulness.
- **Temperature / Critical Time Indicator (TTIC)** are useful for indicating abnormalities in a distribution chain and in products, important in quality or safety, and are initiated when temperatures above the critical temperature are being measured. Examples are the increase in reactions in microorganisms or the enzymatic activity that is triggered at a certain temperature.
- **Temperature Time Indicators (ITT)** provides a continuous indication of temperature variation. For example, raising the temperature will darken the alert color.

These devices are a simple and affordable way of specifying when the product was exposed to an unsuitable environment and thus helping to optimize transportation, being one of the requirements of the current smart packaging.

4. WIRELESS SENSOR NETWORK (WSN)

Wireless Sensor Networks are the most used systems for monitoring and traceability, with a market share of 78% (Kassal *et al.*, 2018). Despite their great market representation, they show a disadvantage related to the impossibility of ensuring continuous monitoring of the distribution chain and, consequently, of estimating the remaining validity of the products. Figure 3 shows the evolution of scientific publications related to the different communication protocols with application in traceability systems from 2007 to 2016.

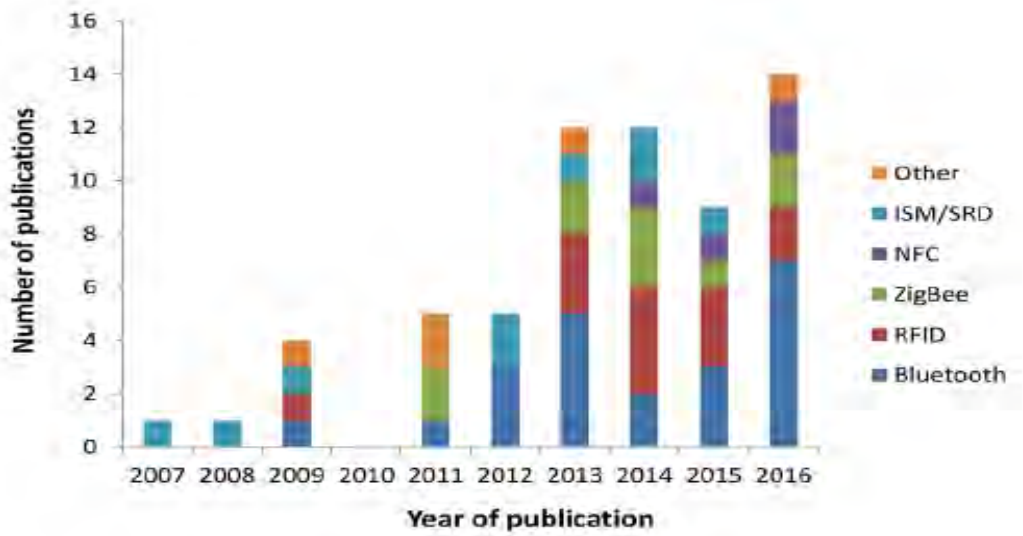

Figure 3: Incidence of different communication protocols presented in scientific publications between 2007 and 2016 (Kassal *et al.*, 2018).

Another disadvantage of WSN is the waveband used. Microwave, 2.4GHz, which is used for communication, is interfered by the resonant frequency of water. Communication flaws can occur since monitoring is required in refrigerated products, where the surrounding environment has a high-water content, i.e., relative humidity (Badia-Melis *et al.*, 2018). Monitoring during maritime transport is also affected by this phenomenon, with the crash of ships' hulls on the waves. There are several WSN systems for food monitoring. Examples are those presented by Xiangsheng, 2014; Wang *et al.*, 2015) and Maigler *et al.* (2013), who use communication protocols such as Bluetooth, ZigBee, LORA and NFC for the development of systems capable of monitoring the environment in which products are found. Fig. 4 summarize the most relevant protocols within WSN systems currently Their characteristics are presented in Table 2.

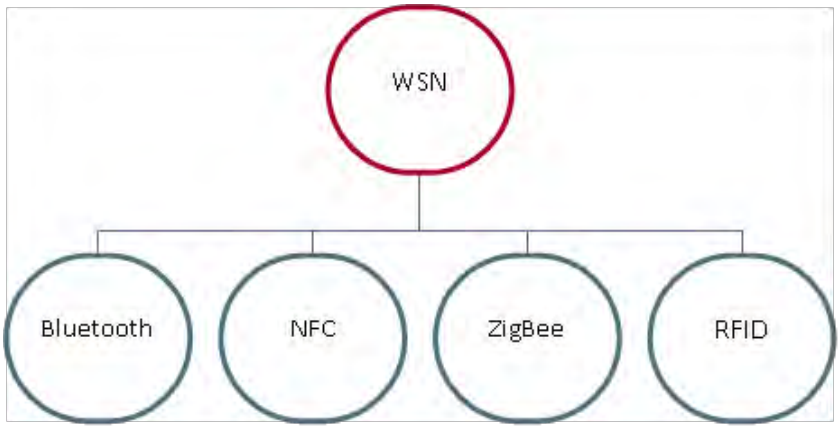

Figure 4: The most used communications protocols in WSN systems.

Table 2: Different communication protocols and their principal characteristics.

Protocol	Radio Band	Data rate	Range	Features
Bluetooth	2.4 GHz	1 Mbps	10 – 100 m	Good for real time data transfer, Smartphone compatible, Good indoor range
NFC	13.56 MHz	<424 kbps	< 5 cm	Ultra-low power, good for secure file swaps, contactless only
RFID	128-135 kHz, 13.56MHz, 860 – 960 MHz	<100 kbps	<15 m (frequency dependent)	Ultra-low power, short range or contactless, very low data rate, good for e labels and small file transfers
Wi-Fi (802.11)	2.4, 3.6, 5 GHz 60 GHz	6-780 Mbps 6.75 Gbps at 60 GHz	100 m (range can be affected by building materials)	Has a standardized protocol for all countries, devices can be added without any cost, Standards development is continuous, with incremental improvements

2.1. Bluetooth

Bluetooth is a short-range, low-power wireless communication protocol proposed in 1994 (Chadha *et al.*, 2013). Operating in the range 2400-2483.5 GHz in the ISM standard, it allows different devices to connect. With the emergence of IoT, Bluetooth was one of the existing options able to meet the communication needs due to popularity and simplicity. But with these factors, an issue arises, the security. As an open system, one of the current concerns is data loss and intrusion prevention in networks, with the level of security being defined by hardware and software manufacturers. The way a Bluetooth connection works is relatively simple. Initially, when feeding the device, it starts searching for the Master, if it is not already paired. When the Master device responds to the Slave's request, a connection is established if the Slave continues to listen on the network. After the formalities, it is performed the synchronization between devices (Master and Slave), using FHSS (Frequency hopping spread spectrum) to data is sent. One of the communication topologies used is Piconet allowing at most 8 devices to connect (1 Master, 7 Slaves), resembling an adhoc network. Because communication is never done simultaneously, signal interference is not a problem. Although Bluetooth communication only allows 8 devices to communicate simultaneously, the maximum number of connections is 255, that is, it allows 255 devices to pair in the network. There are several predefined connection topologies, each with a different combination of error protection mechanisms.

- **Point-to-point**
  It is aimed at the interaction between 2 devices, namely for streaming music, also working with loudspeakers, hands free and headsets. It can also be used for file transfer, using the Bluetooth mode Low energy.
- **Broadcast**
  This typology allows establishing the connection between several devices (one-to-many). It is optimized for location sharing, traceability and point-to-interest. This typology is present in devices such as beacons, which consists in the diffusion of data to the network actors.
- **Mesh**
  With a typology like Broadcast, it allows the connection between several devices (many-to-many). This variant allows, for example, to establish a network of sensors in a limited environment.

2.2. RFID

The appearance of the RFID technology occurred during World War II (1939-1945) for the identification of military aircraft Friend or Foe (IFF), based on wireless communication between a tag and a reader with radio frequency. RFID was then seen as one of the most promising technologies for identifying products compared to other technologies already in use, such as bar codes. Due to the possibilities offered by this technology, there was a growing interest among several economic sectors, such as logistics, identification, tolls and traceability of products, pallets and animals, where more than 3000 applications are known (Bibi *et al.*, 2017). To add value to this technology, several

sensors have been developed to be implemented in tags for the monitoring of various environmental parameters in the transportation of perishable products. This combination of systems offers the possibility of creating a database accessible to traders and consumers through the unique identification code. Several sensors have been developed, such as, for example, gas (Vergara *et al.*, 2007; Steinberg & Steinberg, 2009; Bhadra *et al.*, 2011; Potyrailo & Surman, 2013; Steinberg *et al.*, 2014), moisture (Abad *et al.*, 2009; Martinez-Olmos *et al.*, 2013) to be implemented in smart packaging. For the correct functioning, several components are needed, such as an RFID antenna for communication, a chip for identification and storage of data, a reader and a computer. Tags can also be divided into three groups, depending on your power source:

- **Passive RFID tags:** They do not have battery, being fed by the reader. The different mechanisms allow the exchange of energy and data. The energy rate that is transferred varies between 10 μW and 1 mW.
- **Semi-Passive RFID tags:** They incorporate a battery to keep the memory in the tag or to feed the different electronic devices that make it possible to modulate the electromagnetic waves emitted by the reader.
- **Active RFID tags:** They are powered by an internal battery that is used to run the circuit of the microchip, thus being more expensive than passive tags.

Despite the many possibilities that RFID presents in food monitoring, there are still some disadvantages that systems such as Bluetooth can easily overcome, such as reading distance. To read a tag, the reference distance is 10 cm. For readings at higher distances, an antenna with higher power is required, which consequently causes the system to use more power. RFID is a promising technology with high development in the last years, since it allows the encoding of several types of radio frequencies and sensors in the tags, making this system have a high potential (Bibi *et al.*, 2017).

5. SENSORS

For monitoring purposes it is necessary to convert an environmental parameter into an understandable signal, thereby using a sensor. In addition to monitoring air temperature and air humidity, there are other parameters that must be monitored to ensure the quality of the food product, such as ethylene or oxygen/carbon dioxide gases. In fruit and vegetables, the ethylene release rate is related to the maturational state. In an advanced state, the ethylene release is substantially higher. In the meat industry, it's the development of microorganisms. It is in this field that electrochemical sensors, biosensors and gas sensors can convert a stimulus into an interpretable signal. The difference between an electrochemical sensor and a biosensor is in the recognition layer, i.e. in a chemical sensor, the receptor is a chemical component whereas in a biosensor, the layer is composed of biological materials such as enzymes and antibodies (Ghaani *et al.*, 2016). In recent years, different types of electrochemical sensors have been developed for the food industry. Examples are shown by Gao *et al.* (2015); Goulart *et al.* (2016); Liu *et al.* (2015); Nasirizadeh *et al.* (2015) and Pacheco *et al.* (2015). An ideal sensor, according to Hanrahan *et al.* (2004), should have the following characteristics: specificity for each product, sensitivity to changes of concentrations in the product, rapid response time to variation, durability and reduced dimensions, with possibility of low production cost.

6. FUTURE TRENDS

Perishable product monitoring is a sensitive area and as such, the systems to be implemented need to comply with hygiene and safety standards so as not to compromise the assets to be monitored. In addition, they must ensure continuous monitoring with real-time data transmission in a secure manner. WSN simplified the development of sensor-based applications to monitor hazardous environments or remote areas, resulting in a reduction in the complexity and cost of maintenance (Wang *et al.*, 2006). IoT-related technologies can be applied to food transport and conservation, with a variety of objectives, such as optimization of post-harvest processes, monitoring of conservation conditions, conservation treatments and data for decision-making; as well such as the optimization of the distribution chain, the development of autonomous lorries and boats or swarms of drones for delivery (Tzounis *et al.*, 2017). The technologies described in this paper present themselves as systems capable of being implemented in the distribution chains for traceability, demonstrating that they can enhance the food industry. However, they have disadvantages that do not go unnoticed, such as the high cost of implementation (Badia-Melis *et al.*, 2018). With monitoring systems, the

concepts of smart and/or active packaging emerge. Smart packaging is called when there are sensors that evaluate the environment, able to send the data through a communication protocol, and this information is accessible at any time. An active packaging incorporates materials in its construction that allow the maintenance and prolongation of the shelf life of the product it transports (Mane *et al.*, 2016).

7. CONCLUSIONS

Despite the diversity of existing solutions in the market, there is no one that can meet all the requirements demanded by the industry, making it more complicated to implement them. But the optimization of distribution chains with emphasis on reducing food waste also involves a change in the mentality of FIFO (First in First Out) for FEFO (First expires- First out). It is expected that with the development of these technologies, the gaps will be corrected making these systems more feasible and reliable to implement. Using traceability systems goes in line with three main objectives: improve supply management; facilitate traceback for food safety and quality; and differentiate and market foods with subtle or undetectable quality attributes. In relation to packaging, a global goal is the elimination of plastics, therefore it is necessary to develop a packaging that is recyclable and non-polluting, capable of interacts with the product, which will drive the implementation of a monitoring system in response to demand (Han *et al.,* 2018).

ACKNOWLEDGEMENTS

This study is within the activities of Project “PrunusPós - Optimization of processes for the storage, cold conservation, active and/or intelligent packaging and food quality traceability in post-harvested fruit products”, project n.º PDR2020-101-031695, Partnership n.º 87, initiative n.º 175, promoted by PDR 2020 and co-funded by FEADER within Portugal 2020.

REFERENCES

Badia-melis, R., Carthy, U.M., Ruiz-Garcia, L., Garcia-Hierro, J., & Villalba, J.I.R. (2018). New trends in cold chain monitoring applications - A review. *Food Control*, *86*, 170–182.

Bhadra, S., Bridges, G. E., Thomson, D. J., & Freund, M. S. (2011). Electrode potential-based coupled coil sensor for remote pH monitoring. *IEEE Sensors Journal*, *11*(11), 2813–2819.

Carneiro, R., Gaspar, P.D., & Silva, P.D. (2017). 3D and transient numerical modelling of door opening and closing processes and its influence on thermal performance of cold rooms. *Applied Thermal Engineering, 113*, 585-600.

Steinberg, M.D., Kassal, P., Tkalčec, B. & Steinberg, I.M. (2014). Miniaturised wireless smart tag for optical chemical analysis applications. *Talanta. 118*, 375-81.

Abad, E., Palacio, F., Nuin,M., Zárate, A.G., Juarros, A., Gómez, J.M., & Marco, S. (2009). RFID smart tag for traceability and cold chain monitoring of foods: Demonstration in an intercontinental fresh fish logistic chain. *Journal of Food Engineering, 93*, 394-399.

Gao, F., Zheng, D., Tanaka, H., Zhan, F., Yuan, X., Gao, F., et al. (2015). An electrochemical sensor for gallic acid based on Fe2O3/electro-reduced graphene oxide composite: estimation for the antioxidant capacity index of wines. *Materials Science and Engineering: C*, *57*, 279 – 287.

Ghaani, M., Cozzolino, C.A., Castelli, G., & Farris, S. (2016). An overview of the intelligent packaging technologies in the food sector. *Trends in Food Science and Technology*, *51*, 1–11.

Göransson, M., Nilsson, F., Jevinger, Å., 2018. Temperature preformance and food shelf-life accuracy in cold food supply chains – Insights from multiple field studies. *Food Control*, *86*, 332–341.

Goulart, L. A., Cruz de Moraes, F., & Mascaro, L. H. (2016). Influence of the diferente carbon nanotubes on the development of electrochemical sensors for bisfenol A. *Materials Science and Engineering:* C, 58, 768 - 773.

Gustavsson, J., Cederberg, C., Sonesson, U., van Otterdijk, R., & Meybeck, A. (2011). Global Food Losses and Food Waste – Extent, causes and prevention. Study conducted for the International Congress SAVE FOOD! at Interpack2011, Düsseldorf, Germany. *Food and Agriculture Organization of the United Nations* (FAO), Rome, Italy.

Guðrún Ólafsdóttir, Tómas Hafliðason, Sigurður G. Bogason (2010). CHILL-ON Field Trials Summary Report Deliverable 5.10. University of Iceland, *Applied supply chain systems research group*, December 2010.

Han, J.W., Ruiz-Garcia, L., Qian, J.P., & Yang, X.T. (2018). Food Packaging: A Comprehensive Review and Future Trends. *Comprehensive Reviews in Food Science and Food Safety*, *17*(4), 860-877.

Hanrahan. G., & Wang, J. (2004). Electrochemical sensors for environmental monitoring: design, development and applications. *Journal of Environmental Monitoring, 6*(8), 657-664.

Jedermann, R., Poetsch, T., & Lang, W. (2014). Smart Sensors for the Intelligent Container. Smart SysTech 2014*; European Conference on Smart Objects, Systems and Technologies*, 2–3.

Jevinger, Å., Göransson, M., & Båth, K. (2014). A Field Test Study on a Dynamic Shelf Life Service for Perishables. Paper presented at the *26th Conference of the Nordic Logistics Research Network* (NOFOMA), Copenhagen, Denmark.

Wang, J., Wang, H., He, J., Li, L., Shen, M., *et al.* (2015). Wireless sensor network for real-time perishable food supply chain management, *Computers and Electronics in Agriculture, 110*, 196-207.

Liu, B., Xiao, B., Cui, L., & Wang, M. (2015). Molecularly imprinted electrochemical sensor for the highly selective and sensitive determination of melamine. *Materials Science and Engineering*: C, *55*, 457-461.

Mahajan, P. V., Caleb, O. J., Singh, Z., Watkins, C. B., & Geyer, M. (2014). *Postharvest treatments of fresh produce. Philosophical Transactions of the Royal Society A: Mathematical, Physical and Engineering Sciences, 372*.

Margeirsson, B., Lauzon, H.L., Pálsson, H., Popov, V., Radovan, G., Jonsson, M.P., *et al.* (2012). Temperature fluctuations and quality deterioration of chilled cod (*Gadus morhua*) fillets packaged in different boxes stored on pallets under dynamic temperature conditions. *International Journal of Refrigeration, 35*(1), 187-201.

Mane, K.A. (2016). A review on active packaging: An innovation in food packaging. International Journal of Environment, *Agriculture and Biotechnology*, *3*(1), 544-549.

Maigler, M.V., Alcalá, J.V., Berrueco, J.P., & Alcaide, T.R. (2013). Wireless Sensor Network Solution for Sustainable Food Production. *Seminario Anual de Automática, Electrónica Industrial e Instrumentación*,5.

Moureh, J., Laguerre, O., Flick, D., & Commere, B. (2002). Analysis of use of insulating pallet covers for shipping heat-sensitive foodstuffs in ambient conditions. *Computers and Electronics in Agriculture*, *34*(1–3), 89–109.

Nasirizadeh, N., Hajihosseini, S., Shekari, Z., & Ghaani, M. (2015). A novel electrochemical biosensor based on a modified gold electrode for hydrogen peroxide determination in different beverage samples. *Food Analytical Methods*, *8*, 1546 - 1555.

Pacheco, J. G., Castro, M., Machado, S., Barroso, M. F., Nouws, H. P. A., *et al*., (2015). Molecularly imprinted electrochemical sensor for ochratoxin a detection in food samples. *Sensors and Actuators B: Chemical*, *215*, 107 - 112.

Potyrailo, R.A., & Surman, C. (2013). A passive radio-frequency identification (RFID) gas sensor with self-correction against fluctuations of ambient temperature. *Sensors and Actuators, B: Chemical*, *185*, 587–593.

Rediers, H., Claes, M., Peeters, L., & Willems, K.A. (2009). Evaluation of the cold chain of fresh-cut endive from farmer to plate, *Postharvest Biology and Technology*, *51*, 257–262.

Ruiz-Garcia, L., Barreiro, P., Robla, J. I., & Lunadei, L. (2010). Testing ZigBee motes for monitoring refrigerated vegetable transportation under real conditions. *Sensors*, *10*(5), 4968–4982.

Ruiz-Garcia, L., Lunadei, L., Barreiro, P., & Robla, J. I. (2009). A review of wireless sensor technologies and applications in agriculture and food industry: State of the art and current trends. *Sensors*, *9*(6), 4728–4750.

Selman J.D. (1995) Time-temperature indicators. In: Rooney M.L. (eds) *Active Food Packaging*. *Springer*, Boston, MA.

Steinberg, I.M., & Steinberg, M.D. (2009). Radio-frequency tag with optoelectronic interface for distributed wireless chemical and biological sensor applications. *Sensors and Actuators, B: Chemical, 138*(1), 120–125.

Tzounis, A., Katsoulas, N., Bartzanas, T., & Kittas, C. (2017). Internet of Things in agriculture, recent advances and future challenges. *Biosystems Engineering, 164*, 31–48.

Vergara, A., Llobet, E., Ramírez, J. L., Ivanov, P., Fonseca, L., *et al.* (2007). An RFID reader with onboard sensing capability for monitoring fruit quality. *Sensors and Actuators, B: Chemical, 127*(1), 143–149.

Wang, N., Zhang, N., & Wang, M. (2006). Wireless sensors in agriculture and food industry - Recent development and future perspective. *Computers and Electronics in Agriculture, 50*(1), 1-14.

Wei, Y. B. (2014). Design and Implementation of Intelligent Community Information System Based on WSN Technology. *Applied Mechanics and Materials, 686*(11), 407–411.

Manuscript ID: 1308
DOI: 10.18462/iir.icr.2019.1308

Development of fruit simulators for postharvest cold chain optimization

Huijian HUANG[a,b], Mark C. TUNNICLIFFE[c], Young-Min SHIM[b] , and John E. BRONLUND[a]

[a] Department of Chemical and Bioprocess Engineering, Massey University
Palmerston North, 4474, New Zealand, J.E.Bronlund@massey.ac.nz
[b] Massey AgriTech Partnership, Massey University
Palmerston North, 4474, New Zealand.
[c] Department of Operations and Engineering Innovation, Massey University
Palmerston North, 4474, New Zealand

ABSTRACT

Due to the high cost and variable nature of fruit, it is not easy to conduct commercial scale experiments for research. Replacing fruit with simulators/analogues could solve these issues. To mimic fruit, a simulator must contain the same important properties so that the simulation is representative of the fruit cooling condition (e.g. the heat transfer mechanisms involved in precooling and storage).
This study describes how a time-scaled heat transfer approach can be applied to fruit simulator design. The time-scaled approach hypothesis is that, if an object mimics the shape and thermal conductivity of the product, the cooling profile of the object can represent the product with scaled adjustment by the ratio of volumetric specific heat capacity. Experiments have been conducted. and the results confirm the feasibility of the approach. This implies that experimental results can be obtained with a significant reduction in experimental time, if the time-scaled approach simulator is used.
Keywords: Refrigeration, Precooling, Fruit Simulator, Optimization Tool.

1. INTRODUCTION

Food exportation is one of the major economic contributor for New Zealand (Carson and East, 2017). In 2017, New Zealand exported more than NZD$5 Billion worth of horticultural products, being 10.3% of the total merchandise exports (FreshFacts, 2017). In order to maintain or increase the export markets, businesses have to be innovative. Optimization of the chilling process is an important part of improving the supply chain to ensure delivery of high quality fruit (Carson and East, 2017), as a slight delay in fruit precooling can decrease the marketability. Chilling optimization is generally done via experiments or mathematical modelling (Redding et al., 2016). Optimization via experiment requires extensive collection of data, which is labour intensive, logistically difficult, expensive (Redding et al., 2016), and can have low replicability. Fruit cooling experimentation is generally difficult to reproduce, due to the natural variation and degradation of the fruit if it is used repeatedly (Redding et al., 2016; Vigneault and Castro, 2005). Optimization via mathematical modelling, on the other hand, tends to suffer from computational limitations, modelling uncertainties and the need for validation. In general, the computational time of mathematical models is longer than the prediction time (

Table 1).
A simulator is a physical substitute of the real fruit in an experiment, which can provide controllable and stable properties, increasing the replicability of the experiment (Vigneault and Castro, 2005). Utilizing a fruit simulator can eliminate the seasonal availability problem and reduce the material cost (as it can be reused without degradation of properties).

Table 1.Review of modelling computational time

	Prediction time (h)	Computational time (h)
Ferrua and Singh (2009)	2	>2
Delele et al. (2009)	20	20
Tutar et al. (2009)	2	16
Defraeye et al. (2014)	12	40
Delele et al. (2013b)	16	9-28
Delele et al. (2013a)	27	22
Defraeye et al. (2016)	20	48
O'Sullivan et al. (2016)	14	24
Berry et al. (2016)	12	96
Han et al. (2018)	20	30

Redding et al. (2016) used a one dimensional analytical model to demonstrate the linear relationship between the volumetric specific heat capacity and the cooling rate, proposing the concept of chilling time scaling (Eq. (1)). This concept can be generalized. The temperature profile of a given fruit can be predicted based on the Fourier Equation (Eq. (2)) with appropriate boundary conditions (Eq. (3)). Theoretically, the volumetric specific heat capacity, ρc, should have linear relationship with the rate of temperature change, $\partial T/\partial t$, if the boundary condition and all other properties remain consistent. Therefore, the required chilling time for a given temperature change should be time-scalable based on the volumetric specific heat capacity.

$$\frac{t_1}{t_2} = \frac{\rho_1 c_1}{\rho_2 c_2} \quad \text{Eq. (1)}$$

$$\frac{\partial T}{\partial t} = -\frac{\lambda}{\rho c} \nabla T \quad \text{Eq. (2)}$$

$$-\lambda \frac{\partial T}{\partial x_i} = f\,(T, t, x_i) \quad \text{Eq. (3)}$$

$$-\lambda \frac{\partial T}{\partial x_i} = hA(T_{amb} - T_s) \quad \text{Eq. (4)}$$

$$Bi = \frac{hL}{\lambda} \quad \text{Eq. (5)}$$

In order to maintain consistency of the boundary condition, the thermal conductivity of the simulator needs to be matched with the targeted fruit (Eq. (3)-Eq. (5)). In a third type of boundary condition (convective heat transfer boundary Eq. (4)), such as the demonstrated model in the Redding et al. (2016) study, matching the shape of the fruit could simulate the heat transfer behaviour (the Biot number would be the same; Eq. (5)). However, in a complex system (packaged fruit), the fruit boundary condition could be one of or, a combination of multiple heat transfer modes (Eq. (3)), such as radiation, evaporation and condensation. It was uncertain if only matching the thermal conductivity and shape of the fruit would be enough for a time-scaled simulator. Therefore, this study was to a) validate the time-scale concept and b) testify the feasibility of a time-scaled simulator in a precooling experiment, where the simulator only matches those two properties. If the time-scaled concept is valid in a complex system, the simple boundary condition system descripted by Redding et al. (2016) would also be valid.

A polylined packaged system (kiwifruit were used in this study) was used to test the concept, as the fruit in this system have a more complex boundary condition than a non-polylined package system,

such as an apple box (Tanner et al., 2002). Fruit inside a polyliner package have little exposure to the air flow and this significantly reduces the magnitude of the convective heat transfer and increases the magnitude of other potential heat transfer modes, such as radiation and conduction. In contrast, a non-polylined package, allows air movement within the stack of the fruit making convective heat transfer the dominant heat transfer mechanism. In this case, the fruit boundary condition will become similar to a third type boundary condition (Redding et al., 2016).

2. METHOD AND MATERIAL

2.1. Fruit Simulator and Kiwifruit

Rapid prototype fruit simulators were developed (Figure 1). The simulator was made of a casting resin with metal filler. Ten kiwifruit (count size 36, class A) were used as master specimens for making ten silicone moulds (Mould Star 15, Smooth-On, USA). One hundred kiwifruit simulators were made from the ten silicone moulds. The length, width and thickness of the simulators were 61.7±2.1, 51.8±0.5, and 48.3±0.8 mm, respectively. The volume fraction of the metal filler was adjusted to match the thermal conductivity of the kiwifruit (Table 2). The density of the simulator was measured by Archimedes' method (McGlone et al., 2002), the specific heat capacity was measured by differential scanning calorimetry method (Q2000, TA Instruments, USA) and the thermal conductivity was measured by the line source method (Jasim and Mohammad Shafiur, 2009). The thermal properties of kiwifruit were given by O'Sullivan et al. (2016). Based on the available data, it was expected that the simulator should cool 2.5 ± 0.2 times faster (time scale factor) than real kiwifruit (Eq. 1).

Table 2.Thermal properties of the kiwifruit and simulator

	Density (kg/m^3)	Specific heat Capacity (J/kg.K)	Thermal conductivity (W/m.K)
Kiwifruit	1066±3	3710±140	0.56±0.04
Simulator	1537±16	1050±20	0.51±0.04

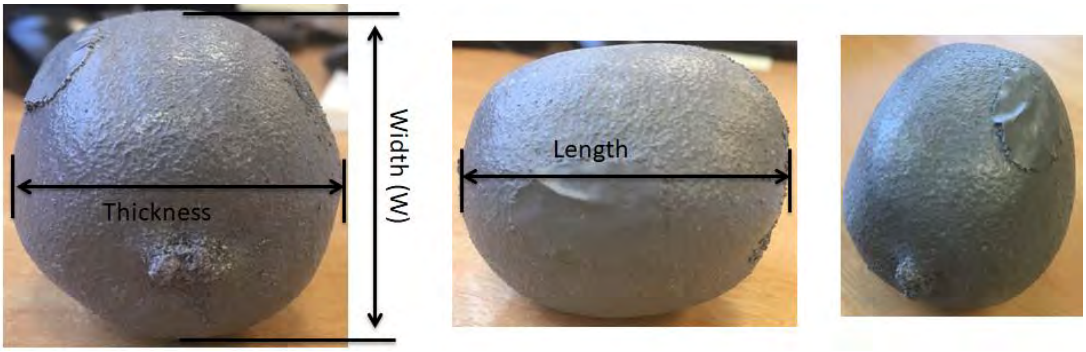

Figure 1: Example images of fruit simulators

2.2. Experimental Setup

A standard modular bulk (MB) package of kiwifruit was cooled in a wind tunnel (0.4 by 0.6 by 1m) inside a refrigerated room (0 °C and 95% RH), where the MB package consists of a corrugated fireboard box (0.3x0.4x0.2 m; WLH), polyliner (10 µm thick; HDPE) and 100 kiwifruit (size 36, class A kiwifruit). The detail of the MB package and the wind tunnel can be found in O'Sullivan (2016). The superficial air velocity of the wind tunnel was measured to be 4.2 m±1.4 m/s (95% CI) by a hot wire anemometer (TSI 9545 VelociCalc, USA), from the average of nine measurement positions across the inlet of the wind tunnel (Figure 2, left). The MB box was placed on a mesh (0.1x0.4x0.3m) to allow refrigerated air movement on all package surfaces.

There were two trials conducted; one using only real kiwifruit and one using only fruit simulators made as described above in 2.1.1. In sixteen positions (Figure 2, right) inside the MB box the kiwifruit

or the simulator were instrumented with thermocouples (type T, 3mm diameters) at the centre of the kiwifruit/simulator. Temperature was recorded by data logger (S2020, Grant, UK) every minute until the end of the experiment. Each trial consisted of three replicates, each with two cooling cycles. The MB box was initially equilibrated to approximately 20 °C, and then placed inside the wind tunnel for cooling. After the first cycle, the MB box was equilibrated to approximately 20 °C again without any modification. This equilibrated MB box was cooled the second time inside the wind tunnel. The cooling time for the kiwifruit MB box was approximately 20 hours and for the simulator MB box it was approximately 6 hours (about 3 times less than the real kiwifruit).

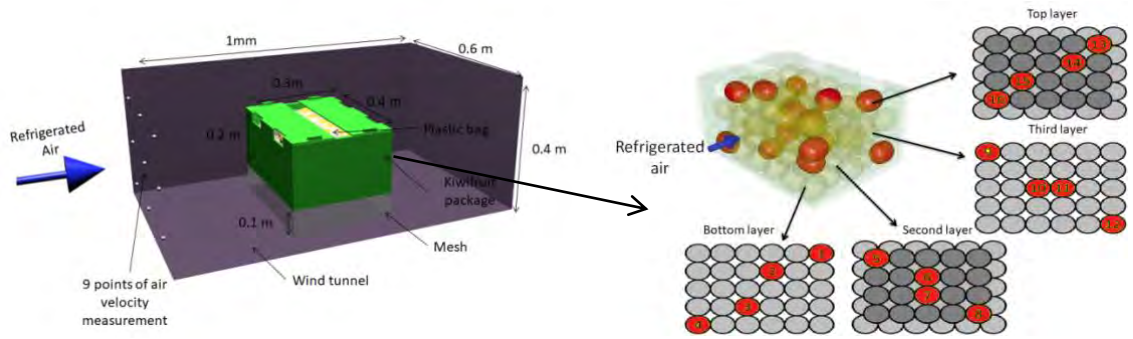

Figure 2: Experimental set up, tunnel set up (left) and instrument set up (right)

2.3. Data Analysis

The recorded temperature was normalized as the fraction of unaccomplished temperature change, Y (Eq. 6). As mentioned, the kiwifruit simulator experiment was time scaled and, therefore, the Fourier number, Fo (Eq. 7) is used to normalize the time scaling effect. Since the kiwifruit simulator has a similar shape the kiwifruit (as a direct copy), the characteristic length (L) of the kiwifruit and simulator should be the same, and it is arbitrary defined as the average of the length, width and thickness of the simulator at 54.0 mm. Although the thermal conductivity of kiwifruit and kiwifruit simulator contain a range of variation, the value is fixed as $0.54\ \mathrm{Wm^{-1}K^{-1}}$ (the average between simulated and real fruit) for the Fo calculation, as the time scaling is only based on the volumetric specific heat capacity.

$$Y = \frac{T - T_{amb}}{T_{int} - T_{amb}} \qquad \text{Eq.(6)}$$

$$Fo = \frac{\lambda\, t}{\rho c\, L^2} \qquad \text{Eq.(7)}$$

The derived cooling profiles for each trial are shown in Fig. 3. The Y difference of kiwifruit and simulator was calculated using Eq. (8), where $\bar{Y}_{kiwi}$ and $\bar{Y}_{sim}$ are the average Y value of kiwifruit and simulator respectively. A positive Y_{diff} means the kiwifruit cooled slower and negative means the kiwifruit was cooled faster than the simulator. The maximum absolute difference (*MAD*) between two Y values throughout the cooling was calculated using Eq. (9). Ideally for a good fruit simulator *MAD* should be close to zero.

$$Y_{diff} = \bar{Y}_{kiwi} - \bar{Y}_{sim} \qquad \text{Eq.(8)}$$

$$MAD = \max\left|Y_{dff}(t)\right| \qquad \text{Eq.(9)}$$

The half cooling time at real time scale (HCT_t) is often used to describe cooling experiments (Brosnan and Sun, 2001) and is defined as the time required for the temperature at a key reference point to reach Y = 0.5. Similarly, the half cooling time at Fo scale (HCT_{Fo}) can be obtained by find the corresponding Fo value when Y = 0.5. The observed time scale factor (Eq. 10) and theoretical time scale factor (Eq. (1)) were calculated to validate the time scaling concept.

To determine the validity of assuming that the time-scaled approach can be used a two-way ANOVA was performed (using Minitab 17) to determine the p-value of kiwifruit vs simulator, where the

response variable is HCT_{Fo}, the factors were the kiwifruit or simulator and the fruit position. The results of this analysis are discussed in section 3.

$$observed\ \ time\ scale\ factor = \frac{HCT_{t\ kiwi}}{HCT_{t\ sim}} \qquad \text{Eq.(10)}$$

3. RESULT AND DISCUSSION

In comparing the derived cooling profiles (Fig. 3) it can be seen that the simulator (using the Fo time frame) has similar cooling profiles as the real kiwifruit (Figure 3, left axis), where the profiles are overlapping, and the shape of the profiles are similar. Graph 11 and 13 are enlarged (Figure 4), where Fruit 11 is near the centre of the package and Fruit 13 is at a top corner package, which is slowest and fasting position, respectively. The range of profiles has been plotted by considering experimental variation and thermal property uncertainties. Three replicates trials were carried out for both real and simulated fruit, each with two cooling cycles, giving a total of six experimental cycles. Because there is uncertainty in the volumetric heat capacity, the upper and lower values were used for the calculation of Fo. This results in a total of 12 cooling profiles for each fruit on Figs. 3 and 4. Note that the real fruit at position 11 had slight temperature increase at the beginning, but simulator did not. This might be due to the heat production from fruit respiration. However, this slight temperature increase is very small (less than 0.5 °C). Position 13 exhibits the most variation for real fruit. This is sensible, as this is the fastest cooling position, which would be more sensitive to the slight condition changes in the experimental work (Mercier et al., 2017).

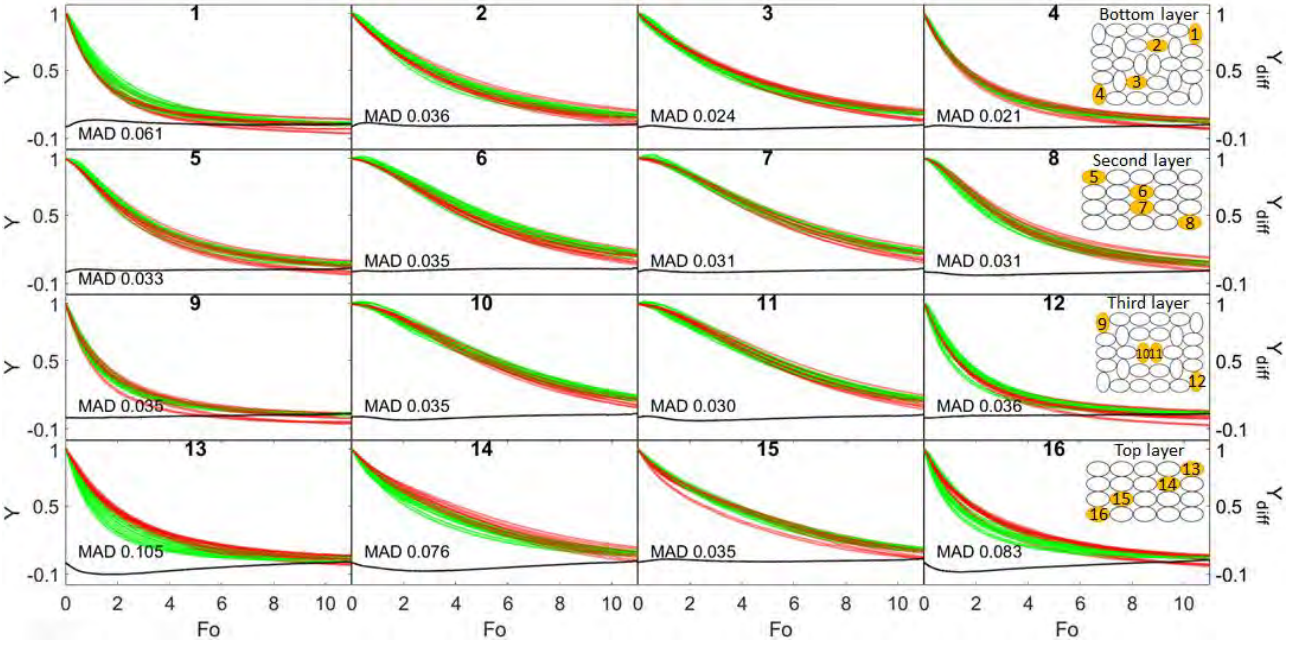

Figure 3: Cooling profile of the kiwifruit (—), simulator (—) and the Y_{diff} (—)

The twelve profiles were averaged, and the Y_{diff} was calculated (Figure 3, right axis). The average *MAD* throughout the sixteen fruit was 0.044. This is equivalent to 0.88 °C difference (between the kiwifruit and simulator), assuming the initial fruit temperature was 20 °C and ambient temperature was 0 °C. This 0.88 °C difference is well within the measurement error of type T thermocouples (Tong, 2001). The top layer fruit generally have larger *MAD* than other layers within the package, and fruit 13 has the largest MAD (0.105), which is equivalent to a 2 °C difference. This 2 °C difference can be explained by the experimental variation and uncertainties, as the fruit in the top layer generally have a wider cooling profile range. This large variation could be attributed to the flapping of the polyliner during the cooling (movement could be generated by the air flow). The offset of fruit position could be another attribute, the fruit stacking could be slightly different each time and the accumulated offset of the top layer fruit could be significant. Overall, the cooling profile suggests the simulator

behaved similarly to the real kiwifruit in all locations. This indicates the validity of the time-scaled concept.

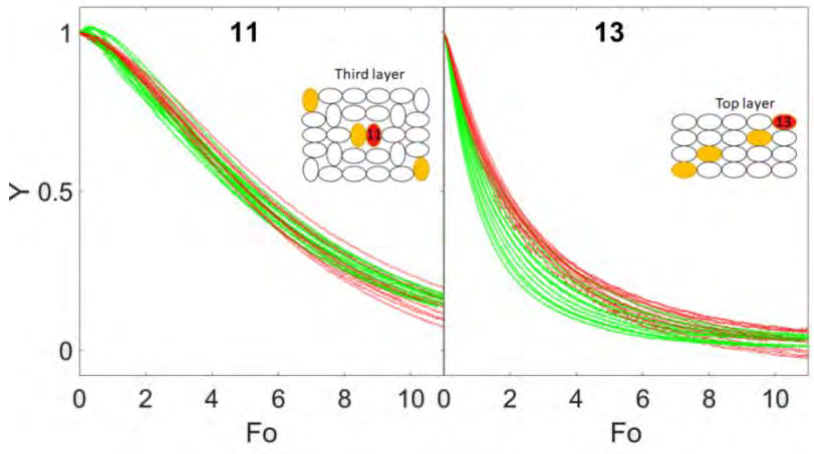

Figure 4: Enlargement of fruit 11 and 13 from Figure 3

The HCT_{Fo} of kiwifruit and simulator were compared (Figure 5a), where HCT_{Fo} of each fruit were obtained from $\bar{Y}_{sim}$ and $\bar{Y}_{kiwi}$ (n=12 for Fo scale). The comparison shows that there are no significant between them, where the HCT_{Fo} difference is fluctuated around the zero (Figure 5a, right). This observation is agreed with the two ways ANONVA that no statistical significant different between kiwifruit and simulator HCT_{Fo} (p-value = 0.246). Comparing the HCT of the simulator and the kiwifruit (Figure 5b), the simulator cooled 2.36 ± 0.14 times faster than real kiwifruit (Figure 5b, right axis) and this is in approximate agreement with the theoretical time scale factor 2.46 ± 0.18 based on the thermal properties (Table 2; Eq. 1). This further validates the time-scaled concept and confirms the feasibility of time-scaled simulator.

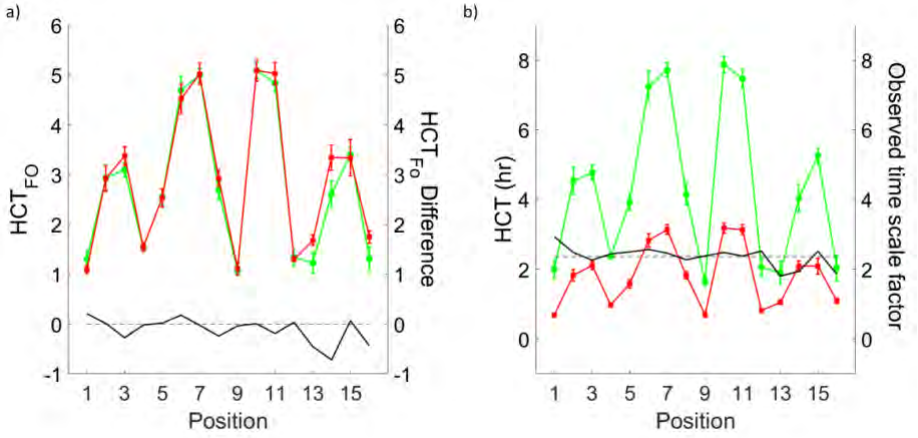

Figure 5: HCT_{Fo}(a; left axis) and HCT (b; left axis) vs fruit position for kiwifruit (—) and simulator (—), HCT_{Fo}difference between the kiwifruit and simulator (a; right axis), and the observed time scaled factor (b; right axis)

It is interesting to note that the simulator is commonly believed to introduce less experimental variation than real fruit, due to their stable and consistent properties (Vigneault and Castro, 2005). On average, Figure 5b, shows that the standard error of the simulator (8.3%) appear to be smaller than the real kiwifruit (9.9%), however the two way ANOVA suggests that the experimental variation from real fruit experiments is not significantly different from the simulator experiments (p-value = 0.322).

The simulator was validated in a complex system where boundary conditions of the simulator during the cooling could involve internal radiation, convection, evaporation and condensation. This suggests that the time scaling effect can be generalized to complex systems.

The experiment also showed that by matching the thermal conductivity and the shape of the fruit, a time-scaled simulator could be developed, and it can be a powerful tool for cool chain optimization. Instead of a long experimental time, this simulator can reduce the time requirements significantly. The generality of the equations show that the time-scaled simulation is not limited to a third type boundary, but could be even larger if an appropriate material is used and the thermal conductivity is still matched. Also, instead of limiting the number of experiments due to the availability of the product, out of season experiments are possible using the simulator.

4. CONCLUSIONS

A time-scaled simulator was developed and validated, in which the simulator only needs to match the thermal conductivity and shape of the fruit. The validation of the simulator also confirms the concept of the time-scaling approach. While the idea of time scaling can be shown simply for individual fruit undergoing convective cooling, in this paper, the concept was demonstrated in a complex system where other modes of heat transfer and conduction from fruit to fruit are also important. Because of the advantages of long term stability and shorter experimental times, the use of fruit simulators could provide a useful alternative to real fruit in cooling and storage system optimisation.

5. ACKNOWLEDGEMENTS

We gratefully acknowledge the New Zealand Ministry of Business, Innovation and Employment for funding this work (Fibreboard package Design project – MAUX1302).

6. NOMENCLATURE

ρ	Density (kg/m^3)	c	Specific heat capacity (J/kg.K)
T	Temperature of the product (°C)	t	Time (s)
λ	Thermal conductivity (W/m.K)	x_i	Cartesian coordinates (m) in i direction
L	Characteristic length (m)	Fo	Fourier's number
T_{amb}	Ambient temperature (°C)	T_{int}	Initial temperature of the product (°C)
Y	Unaccomplished temperature change	$\bar{Y}_{sim}$	Average Y value of simulator
$\bar{Y}_{kiwi}$	Average Y value of kiwifruit	HCT_t	Half cooling time in real time scale (s)
HCT_{Fo}	Half cooling time in Fo scale	h	Heat transfer coefficient (W/m^{2}K)

7. REFERENCES

Berry, T.M., Defraeye, T., Nicolai, B., Opara, U.L., 2016. Multiparameter Analysis of Cooling Efficiency of Ventilated Fruit Cartons using CFD: Impact of Vent Hole Design and Internal Packaging. Food Bioprocess Tech 9, 1481-1493.

Brosnan, T., Sun, D.-W., 2001. Precooling techniques and applications for horticultural products — a review. Int. J. Refrigeration 24, 154-170.

Carson, J.K., East, A.R., 2017. The cold chain in New Zealand – A review. Int. J. Refrigeration.

Defraeye, T., Lambrecht, R., Delele, M.A., Tsige, A.A., Opara, U.L., Cronjé, P., Verboven, P., Nicolai, B., 2014. Forced-convective cooling of citrus fruit: Cooling conditions and energy consumption in relation to package design. J. Food Eng. 121, 118-127.

Defraeye, T., Nicolai, B., Kirkman, W., Moore, S., Niekerk, S., Verboven, P., Cronjé, P., 2016. Integral performance evaluation of the fresh-produce cold chain: A case study for ambient loading of citrus in refrigerated containers. Postharvest Biol. Technol. 112, 1-13.

Delele, M.A., Ngcobo, K., Opara, U.L., Meyer, C.J., 2013a. Investigating the Effects of Table Grape Package Components and Stacking on Airflow, Heat and Mass Transfer Using 3-D CFD Modelling. Food Bioprocess Tech 6, 2571-2585.

Delele, M.A., Ngcobo, M.E.K., Getahun, S.T., Chen, L., Mellmann, J., Opara, U.L., 2013b. Studying airflow and heat transfer characteristics of a horticultural produce packaging system using a 3-D CFD model. Part I: Model development and validation. Postharvest Biol. Technol. 86, 536-545.

Delele, M.A., Schenk, A., Tijskens, E., Ramon, H., Nicolaï, B.M., Verboven, P., 2009. Optimization of the humidification of cold stores by pressurized water atomizers based on a multiscale CFD model. J. Food Eng. 91, 228-239.

Ferrua, M.J., Singh, R.P., 2009. Modeling the forced-air cooling process of fresh strawberry packages, Part I: Numerical model. Int. J. Refrigeration 32, 335-348.

FreshFacts, 2017. New Zealand Horticulture. jusFreshFacts, New Zealand.

Han, J., Zhao, C., Qian, J., Ruiz-Garcia, L., Zhang, X., 2018. Numerical modeling of forced-air cooling of palletized apple: Integral evaluation of cooling efficiency. Int. J. Refrigeration 89, 131-141.

Jasim, A., Mohammad Shafiur, R., 2009. Thermal Conductivity Measurement of Foods, Food Properties Handbook, Second Edition. CRC Press.

McGlone, V.A., Jordan, R.B., Seelye, R., Martinsen, P.J., 2002. Comparing density and NIR methods for measurement of Kiwifruit dry matter and soluble solids content. Postharvest Biol. Technol. 26, 191-198.

Mercier, S., Marcos, B., Uysal, I., 2017. Identification of the best temperature measurement position inside a food pallet for the prediction of its temperature distribution. Int. J. Refrigeration 76, 147-159.

O'Sullivan, J.L., 2016. Significant factors affecting the forced-air cooling process of polylined horticultural produce:. Massey University.

O'Sullivan, J.L., Ferrua, M.J., Love, R., Verboven, P., Nicolai, B., East, A., 2016. Modelling the forced-air cooling mechanisms and performance of polylined horticultural produce. Postharvest Biol. Technol. 120, 23-35.

Redding, G.P., Yang, A., Shim, Y.M., Olatunji, J., East, A., 2016. A review of the use and design of produce simulators for horticultural forced-air cooling studies. J. Food Eng. 190, 80-93.

Tanner, D.J., Cleland, A.C., Opara, L.U., Robertson, T.R., 2002. A generalised mathematical modelling methodology for design of horticultural food packages exposed to refrigerated conditions: part 1, formulation. Int. J. Refrigeration 25, 33-42.

Tong, A., 2001. Improving the accuracy of temperature measurements. Sensor Review 21, 193-198.

Tutar, M., Erdogdu, F., Toka, B., 2009. Computational modeling of airflow patterns and heat transfer prediction through stacked layers' products in a vented box during cooling. Int. J. Refrigeration 32, 295-306.

Vigneault, C., Castro, L.R., 2005. Produce-simulator property evaluation for indirect airflow distribution measurement through horticultural crop package. Journal of Food, Agriculture and Environment 3, 67-72.

Manuscript ID: 1333
DOI: 10.18462/iir.icr.2019.1333

Design of a CO_2 heat pump drier with dynamic modelling tools

Michael JOKIEL[(a)], Michael BANTLE[(a)], Christian KOPP[(a)], Ingrid C. CLAUSSEN[(a)], Ignat TOLSTOREBROV[(b)]

(a) Department of Energy Processes, SINTEF Energy Research, NO-7465 Trondheim, Norway, Michael.Jokiel@Sintef.no
(b) Norwegian University of Science and Technology, Department of Energy and Process Technology, 7465 Trondheim, Norway

ABSTRACT

Drying is an energy and time intensive process which thermal energy demand is mostly provided by fossil resources. Especially in the food processing industry it is important to increase the energy efficiency of drying processes in terms of organic products and sustainability. The potential of using a heat pump with R744 (CO_2) as a working media to provide the thermal energy was investigated for typical food drying temperature of 50 °C at a relative humidity of 20 %. A dynamic heat pump-assisted dryer model has been developed and validated. The model was created with respect to heat transfer, pressure loss and flow requirements. The simulated results showed that a closed-loop heat pump assisted drying process has the potential to reduce the energy demand by around 80 % compared to conventional open-loop drying processes with fossil resources as energy source. Furthermore, the implementation of a bypass in the air cycle was examined to further enhance the energy efficiency of the system.

Keywords: Heat pump, Modelica, simulation, convective drying, CO_2, food drying

1 INTRODUCTION

The process of drying is widely-used in all kind of industries and is a very energy consuming process. It is estimated that about 12 % of the total energy used in industries is used by drying processes (Strumillo et al. 2014), whereas the major amounts are demanded by the food and paper industries.

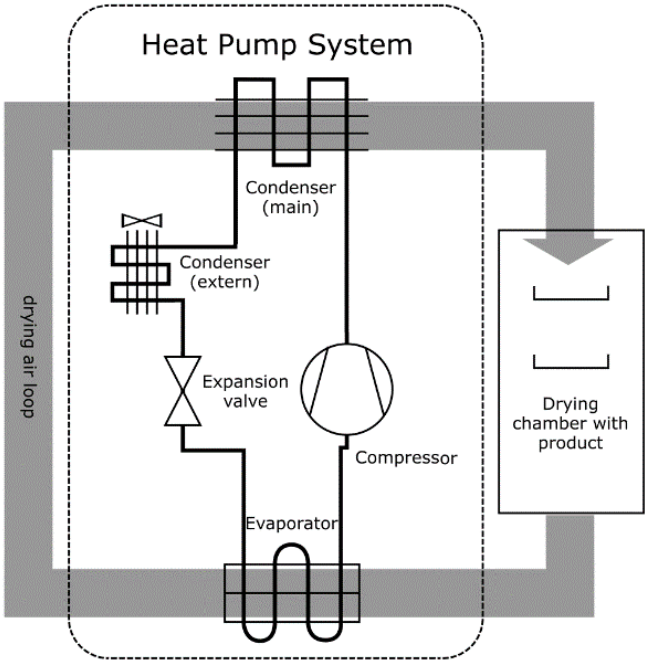

Figure 1: Scheme of a heat pump driven convective drying process

In addition, convective drying based on air as drying agent is the most common used drying technology with around 85 % (Atuonwu et al. 2011). With this big percentage in energy demand, it is not surprising that the process of drying has been, and still is a very important field of research in terms of energy efficiency and product quality. In this study, a heat pump driven model of a convective food drier was developed as shown in the scheme in Figure 1. The energy efficiency of the heat pump driven dryer was then compared with other conventional methods. The basic advantages of heat pump driven convective drying results from the ability to recover energy from the used drying air and reuse it in the process. This results in one of the highest specific moisture extraction ratio (SMER), often between 1 to 4 since the heat can be recovered from the moist air (Chou et al. 2006). This can result in a drying efficiency of up to 95 % compared to 30 - 40 % for other hot air drying methods (Perera & Rahman, 1997). Industrial heat pumps with a heat sink of up to 100 °C using natural refrigerants (R717, R718 and R744) are already conventionally established which makes heat pumps very suitable for drying of food which is usually performed at temperature levels up to 70 °C.

2 MAIN SECTION

The present study investigates different system designs for closed-loop drying processes that have been enhanced with a heat pump, using R744 as refrigerant. To evaluate the potential increase of energy efficiency, an open loop drying process with a fossil fuel-based burner serves as a benchmark. The validation was conducted with measurement data from an actual drying system.

2.1 Modelling the drying chamber

The drying chamber model has been implemented in Modelica using already existing model libraries, TIL and TIL Media (Gräber et al. 2010). TIL is a model library for thermal components and systems, while TIL Media contains a model library including thermophysical properties for the utilized fluids

The newly derived model consists of a volume cell representing the drying chamber, where the drying product is exposed to the moist air. The model focusses on the heat and mass transfer between the incoming moist air, the product that is to be heated and dried, and the outgoing moist air.

The model for the drying chamber is connected to the rest of the system via two gas ports for in- and outgoing moist air. Heat and mass transfer quantities are calculated with the help of the corresponding coefficients: The heat transfer coefficient α is calculated based on convective heat transfer (Baehr 2003) according the following equations:

$$Nu_{m,turb} = \frac{0{,}037 Re^{0,8} Pr}{1 + 2{,}443 Re^{-0,1}(Pr^{2/3} - 1)} \quad \text{Eq. (1)}$$

$$Nu_{m,lam} = \frac{\sqrt{\pi}}{2} Re^{1/2} * \frac{Pr^{1/2}}{(1 + 2{,}55 Pr^{1/4} + 48{,}66 Pr)^{1/6}} \quad \text{Eq. (2)}$$

utilizing the dimensionless flow quantities of the Reynolds number Re and Prandtl number Pr. Since flow conditions in the range between laminar and turbulent flow are existing, the Nusselt number is averaged by equation (3)

$$Nu_m = \sqrt{Nu_{m,lam}^2 + Nu_{m,turb}^2} \quad \text{Eq. (3)}$$

Finally, the heat transfer coefficient is calculated by equation (4)

$$\alpha = \frac{Nu_m * \lambda}{L} \quad \text{Eq. (4)}$$

The mass transfer coefficient β is essentially based on the same principles, combined with the film theory for mass transfer, taken from (Baehr 2003):

$$\beta = \frac{\alpha * Le}{\rho * c_p} \quad \text{Eq. (5)}$$

with considering the empiric Lewis-factor Le. Furthermore, properties of the drying product needs to be provided as input parameters. Property data like heat capacity for liquid water is provided by a temperature and pressure dependent object class. However, for the moist air two of these object classes are utilized to consider the special conditions in the drying chamber: One pressure and enthalpy dependent moist air object that represents the incoming dry and hot air and one pressure and temperature dependent air object that calculates the property data of the moist air directly at the surface of the drying product. It is assumed that the air on the product surface features the same temperature as the product and is considered as saturated air with a relative humidity of 100 %.

Combining the quantities outlined above, the mass flow rate for the water that is being removed of the product over the time can be calculated, based on film theory for mass transfer (H.D. & K., 2003):

$$\dot{m} = \frac{\widetilde{M}_{water}}{\widetilde{M}_{air}} * \frac{p}{(T * R_B)} * \beta * A * a * (x_{i,sat} - x_{i,inlet}) \quad \text{Eq. (6)}$$

with $\widetilde{M}$ as the molar mass of water and air, R_B as the specific gas constant, xi as the mass fraction and a as the activity coefficient, which considers the decelerated mass transfer at the end of a drying process when the capillary forces are limiting the water release from the product (Deans, 2001). The activity factor is characteristic for each type of product and needs to be measured.

For the drying chamber model, the usual energy and mass balances are augmented with equation (7), which considers the progress of the drying:

$$\frac{dm_w}{dt} = -\dot{m} \quad \text{Eq. (7)}$$

The modelling of the dryer cell was conducted in an object-oriented way with the potential to theoretically investigate various different drying products. That way, the standalone cell can be universally implemented in both open-loop or closed-loop drying processes.

2.2 Validation of the model

The model for the drying chamber is validated against measurement data which was provided by Innotech GmbH, a German manufacturer of drying systems. The validation is conducted with two types of measurement data sets, which differ in the general scaling of the drying processes.

The model was provided with measured input parameters for the inlet relative humidity, the air velocity in the drying chamber and the inlet temperature of the moist air according Table 1.

Table 1: Measurement data for apple drying, provided by Innotech GmbH

Mass of product	**3 kg**	**100 kg**
Drying temperature	55 °C	70 °C
Inlet relative humidity	16 %	10 %
Outlet relative humidity	40 %	-
Moist air volume flow	0.07 m³/h	5500 m³/h
Moist air velocity	1.3 m/s	-
Drying time	8 h	8 h
Removed water	-	15-20 kgH20/h

Figure 2 (left) shows the successful simulation of the drying curve for the small-scaled system, with a maximum deviation of 10 % between the measurement and the model. For the large-scaled

measurement of 100kg apples in figure 2 (right), it is measured that five hours after the drying process has started, 70kg of water has been removed from the product, which has been correctly estimated by the model. Therefore, the model reproduces the system behaviour for both measurement data sets in an accurate way and can be thus considered successfully validated.

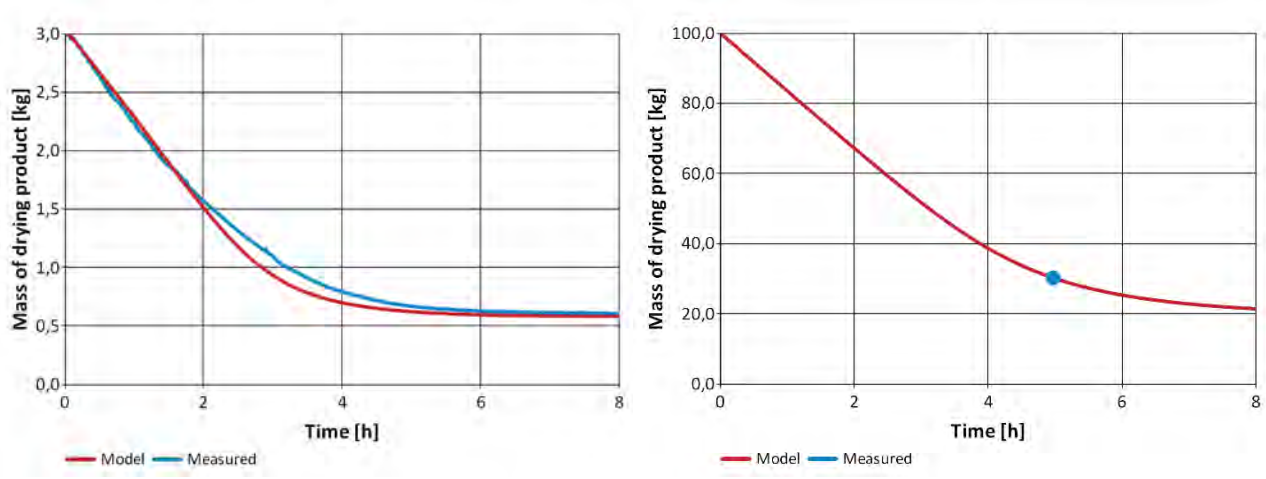

Figure 2: Drying of initially 3kg (left) and 100kg (right) of apples, measurement Innotech GmbH vs Modelica model

2.3 Implementation of a heat pump

The final aim of this study is to utilize the validated model of the drying chamber to evaluate heat pump-assisted drying systems. To be able to make more precise statements on the energetic efficiency of a drying process, various system setups are investigated in this section: A benchmark open-loop system without heat pumps, a simple heat pump system with two gas coolers and a more elaborated heat pump system with two evaporators. Furthermore, the effect of direct recirculation of moist air by usage of a bypass will be examined.

The simplest system for a drying process is an open-loop process, where ambient air is heated via a fossil fuel burner and being released to the environment after passing the drying chamber, as depicted in figure 3 (left). The general requirements to the system regarding components or control schemes are low. As for the model, ambient air of 25 °C is sucked in and heated up with approximately 80 kW to keep the inlet temperature at 70 °C.

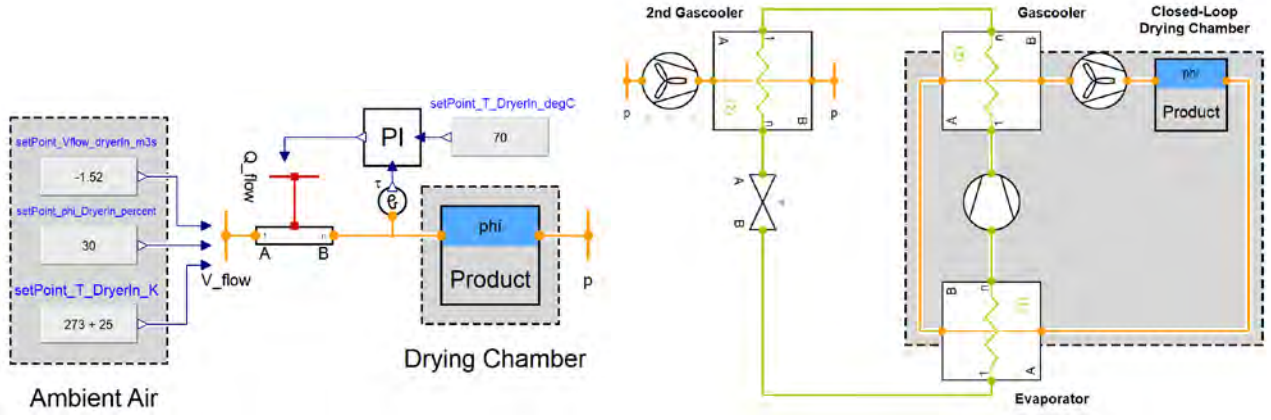

Figure 3: Main components of the simulated open-loop benchmark setup (left) and the simulated heat pump drying process with R744 (right)

However, to increase the energy efficiency of any drying process, a closed-loop system for the moist air is a promising setup to lower energy consumption. The amount of heating load that is required to provide a specific drying temperature can be decreased by re-utilization of the still hot air from the drying chamber outlet. Therefore, a heat pump with CO_2 (R744) as refrigerant is used, as shown in figure 3 (right). To drain the absorbed water, the moist air needs to be conditioned to a lower

temperature. First, the air is cooled down in the evaporator to enforce condensation and remove moisture. Afterwards, it is reheated again by the gas cooler to provide relatively dry hot air to the drying chamber.

In the CO2-cycle a second gas cooler is required. On one hand to ensure an efficient CO2-cycle with crossing the critical point before the following expansion in the valve, on the other hand to dispose excess heat: surplus heat is introduced into the heat pump system via the compressor load, and since drying is an isenthalpic process and since the moist air cycle is a closed-loop system, an additional heat sink is needed. Figure 4 shows a CO2 heat pump cycle in a temperature-entropy diagram, with the corresponding cooling and re-heating of the moist air for humidity removal in the evaporator.

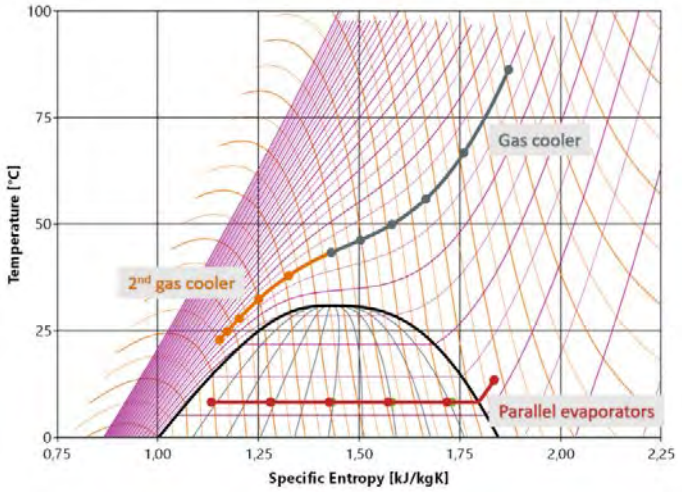

Figure 4: Heat pump assisted drier with R744 for a drying temperature of 50 °C

Furthermore, an assessment of the control variables for the system in figure 3 (right) shows that a second evaporator might be beneficial: The load of the second gas cooler is controlled by the speed of the fan to control the inlet temperature to the valve. The valve position is controlling the high pressure and the compressor speed is used to control the inlet temperature to the drying chamber. The moist air fan is providing a constant volume flow. Therefore, there is a lack of a control variable to control the low pressure of the CO_2-cycle and thus the evaporator load. This leads to the introduction of a second evaporator arranged in a parallel setup, as shown in figure 5 (left).

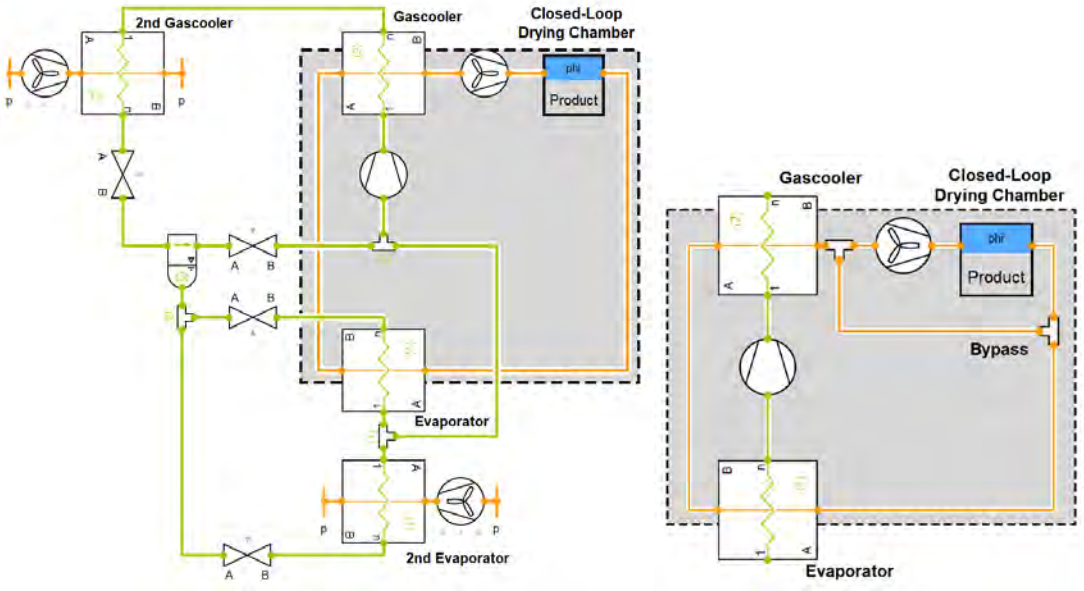

Figure 5: Enhanced components of the simulated heat pump drying process (left) and exemplary scheme for a heat pump drying process with a bypass on air side, with cut-off heat pump (right)

The last system setup that is evaluated in the next section features the implementation of a moist air bypass within the closed-loop cycle. A direct recirculation of 20 % and 50 % of the overall moist air volume flow will be examined. The percentage of recirculation is adjusted by choosing appropriate pressure drop values for the tubes in the bypass and evaporator circuit. By reducing the volume flow in both the evaporator and gas cooler, less energy consumption is expected due to a reduced compressor load. Any of the previously introduced systems could be equipped with a bypass on the air side. A simplified scheme of the system layout is illustrated in figure 5 (right), for reasons of clarity with a cut-off heat pump.

2.4 Simulation results and outlook

Three different system setups for a heat pump assisted dryer are investigated regarding their quantity of energy savings in comparison towards an open-loop benchmark setup. The heat pump system with two parallel evaporators (figure 5 (left)) will in the following be referred to as "No Bypass". Furthermore, this system will be upgraded with a bypass, which enables a 20 % and 50 % direct recirculation of the overall moist air flow. Therefore, four system designs are compared in figures 6-8.

The investigated systems are based on a dryer capacity which provides the removal of up to 7 kg water per hour at the considered drying conditions. The inlet temperature for the drying chamber has been controlled to 50 °C for all four systems. For the open-loop system, the moist air is just being released to the environment. For the three heat pump-assisted systems, the moist air is cooled down in the evaporator to 30 – 35 °C, depending on the amount of bypassed air, as seen in figure 6 (left):

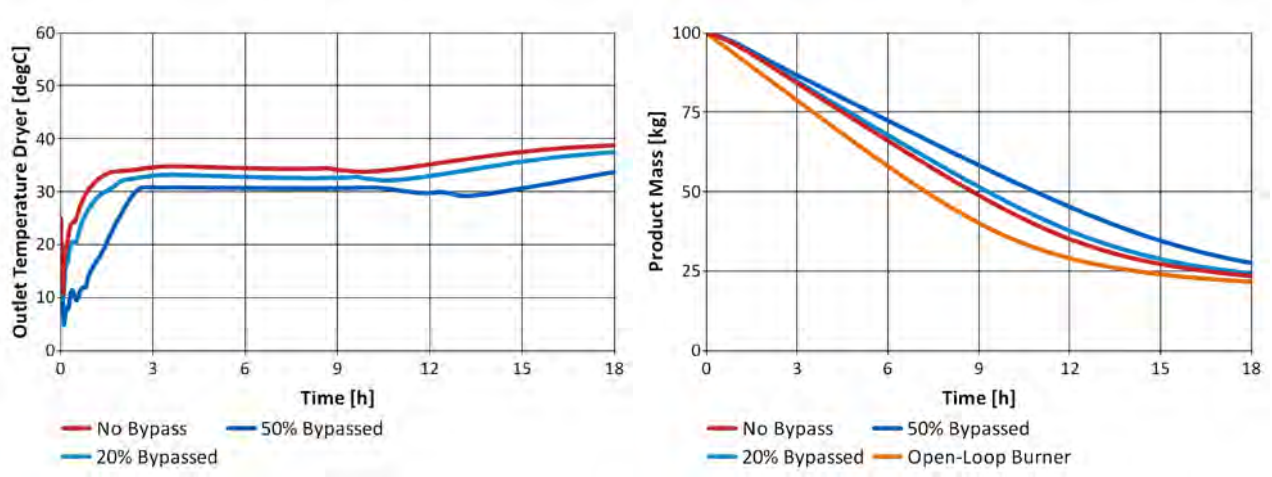

Figure 6: Simulation results for four investigated systems, dryer outlet temperature (left) and product mass (right)

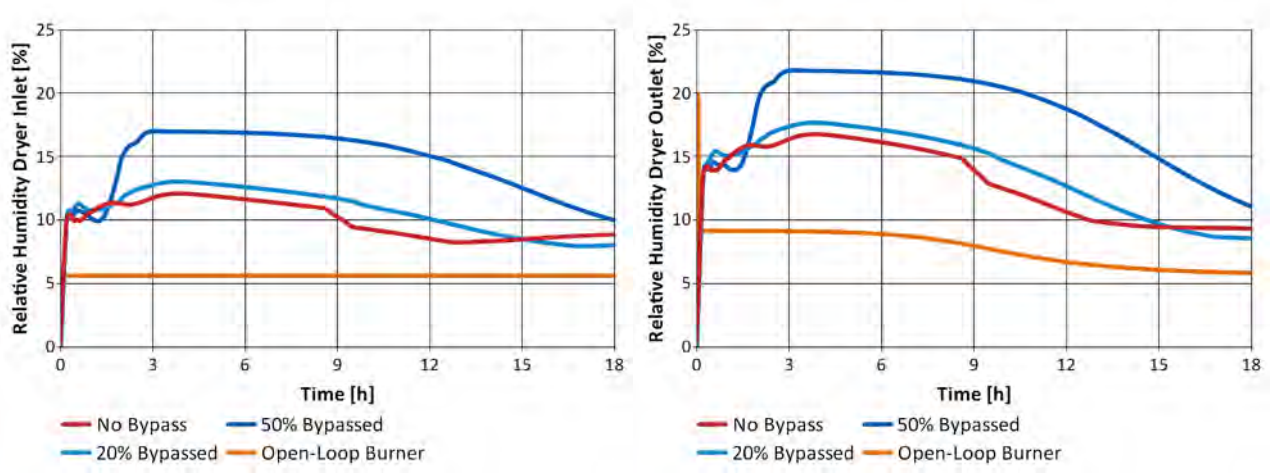

Figure 7: Simulation results for four investigated systems, relative humidity for the dryer inlet (left) and outlet (right)

If the end of the drying process is defined with 70 kg of water that has been evaporated from the initial 100 kg of apples, then the following times are needed to finish the drying: "Open-loop Benchmark" 11.7 h, "No Bypass" 13.6 h, "20 % Bypass" 14.5 h and "50 % Bypass" 16.8 h, as illustrated by figure 6 (right) The required drying time is the shortest for the open-loop benchmark system, as relatively dry air is heated and fed to the drying chamber. The circulation of air within a closed-loop setup leads to a higher relative humidity and thus extended drying times (figure 7). Relatively, the utilization of heat pumps leads to an increase in time by 13 – 43 % regarding the setup.

The COP for all three heat pump-assisted systems is approximately 3.2, with a gas cooler to compressor load ratio of $\frac{\dot{Q}}{P_{compr}}$ [kW/kW] = 29/9 for "No Bypass", 25/8 for "20 % Bypass" and 18.5/6 for "50 % Bypass". The heat supply of the "Open-Loop Burner" was 56 kW.

The process efficiency was evaluated through the specific moisture evaporation rate (SMER) for the drying process, which states how much water can be removed from the product with the utilization of 1 kWh. The SMER is defined by

$$SMER = \frac{amount\ of\ evaporated\ water\ (kg)}{energy\ used\ (kWh)} \qquad \text{Eq. (8)}$$

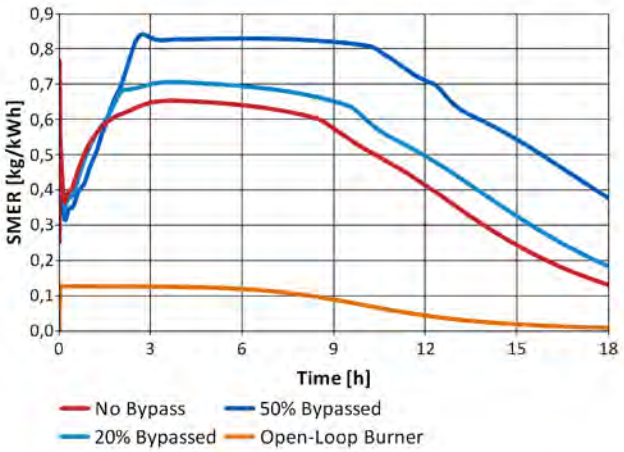

Figure 8: Simulation results for four investigated systems, comparison of the specific moisture evaporation rate (SMER)

In the examined temperature range, the latent heat of water evaporation is 0.63 kWh (2250 kJ). This amount of energy is required to evaporate 1 kg of water, leading to a reciprocal value of 1.6 kg/kWh. Therefore, figure 8 shows that the SMER for the open-loop benchmark system is quite low in comparison to typical values for the SMER than can be found in literature (Chou et al. 2006). This indicates rather inefficient drying conditions and a product that is difficult to dry (in this case apples, with an initial moisture content of approximately 80 %).

The implementation of a heat pump has the potential for energy related savings of 80 % in comparison to the examined benchmark process, which can be even increased with the usage of a bypass. Since the open-loop benchmark system was operated without a bypass, the evaluation of the bypass cycles should be referred to the "No Bypass"-system, to highlight the impact of the bypass utilization towards the same general system setup. Therefore, in comparison to the "No Bypass"-system, the "50 % Bypass"-system offers a decrease in energy consumption by 28 %, but also an increase of the drying time by 24 %.

It should be noted that the investigated bypass systems were not optimally controlled in this study, leading to a constant recirculation of moist air and thus, to a non-optimal utilization of the bypass. An adequate control strategy to address the varying heat demand during a typical drying process provides potential for further energy and time savings.

The loss of heating load in the second gas cooler was not considered in the calculations for energy consumption. To further improve the SMER of the heat pump-assisted drying, the heat losses to the environment through the second gas cooler could be cut by applying an on/off regulation in case the drying temperature is getting to high due to the surplus heat from the compression work.

Generally, the heat transfer properties between CO_2 and moist air are a limitation towards the overall system efficiency. The application of intermediate water or glycol sub-cycles between the heat pump and the drying loop could enhance the overall heat transfer and provide more control in adjusting the dryer inlet temperature, with the utilization of water tanks to store heat and cold, respectively.

3 CONCLUSION

A dynamic model for the drying chamber was developed in Modelica to demonstrate the potential energy saving for drying processes at common food drying temperatures. The model allows better understanding of the drying characteristics of the heat pump assisted drying system and enables more sophisticated dimensioning and design of future drying systems. The simulation results were successfully validated towards measurement data.

The simulations show that the desired drying conditions can be reached with the suggested R744 heat pump system. It has been shown that the utilization of a heat pump to provide heating and cooling for a drying process can increase the energetic efficiency by up to 80 % but results in an increased drying time by 13 – 43 %. Furthermore, a variation of the heat pump system design holds further improvements in efficiency. A bypass for direct recirculation of moist air was investigated to decrease the loads in gas cooler and evaporator, providing energy savings of 28 % but demanding a drying time increase by 24 %. A second evaporator was introduced to control the low pressure and thus the evaporator load and water drain.

Further studies are especially required in the overall control of the heat pump system. As indicated, a more sophisticated dynamic control for the bypass mass flow offers great potential for further optimizations during the different phases of the drying process, especially regarding the energy consumption.

ACKNOWLEDGEMENTS

The work was supported by the Research Council of Norway, grant 286127 – Core Organic Cofund: SusOrgPlus project as part of the ERA-NET action CORE Organic Plus. The authors acknowledge the financial support for this project provided by transnational funding bodies, being partners of the H2020 ERA-net project, CORE Organic Cofund, and the cofund from the European Commission.

REFERENCES

Atuonwu, J. C., Jin, X., van Straten, G., Deventer Antonius, H. C. v., & van Boxtel, J. B. (2011). "Reducing energy consumption in food drying: Opportunities in desiccant adsorption and other dehumidification strategies", Procedia Food Science, 1, 1799-1805. doi:https://doi.org/10.1016/j.profoo.2011.09.264

Baehr, H.D., K. Stephan (2003). "Wärme- und Stoffübertragung", 7. Auflage, Springer Verlag

Chou, S.K., C. Kian Kiang, and Jon, 47 Heat Pump Drying Systems. 2006.

Deans, J. (2000). "The modelling of a domestic tumbler dryer" Applied Thermal Engineering 21 (2001), 977-990

Gräber, M., K. Kosowski, C. C. Richter and W. Tegethoff (2009). "Modelling of heat pumps with an object-oriented model library for thermodynamic systems " Proceedings Mathmod 2009, Vienna, Austria: 1396-1404.

Perera, C. O., & Rahman, M. S. (1997). Heat pump dehumidifier drying of food. Trends in Food Science & Technology, 8(3), 75-79. doi:https://doi.org/10.1016/S0924-2244(97)01013-3

Strumillo, C., P.L. Jones, and R. Żyłła, Energy Aspects in Drying. 2014. 1075-1101.

Manuscript ID: 1399
DOI: 10.18462/iir.icr.2019.1399

Suppression of damage on frozen fish by the post-harvest treatment using ice slurry

Kensuke NISHI [(a)], Manabu WATANABE* [(a)], Toru SUZUKI [(a)]

[(a)] Department of Food Science and Technology
Tokyo University of Marine Science and Technology, 4-5-7 Konan, Minato-ku, Tokyo, 108-8477, Japan, mwat@edu.kaiyodai.ac.jp

ABSTRACT

The frozen storage of fish has already been practically used all over the world, but if the quality is further improved, there is a possibility that the fish can be frozen preserved with the quality that can be used for sushi. To that end, improvement of post-harvest treatments is effective. The treatments currently used are slow killing in ice water or individual quick killing, both are followed by immersion cooling in ice water. However, individual quick killing is not practical for massively caught fish and ice water has a problem such that the temperature distribution may not be uniform. To solve this problem, ice slurry is thought to be effective. In this study, we used living horse mackerel. Some were killed and cooled by using ice slurry while others were treated with conventional method. The difference in their quality was quantitatively verified.
Keywords: Fish, Frozen Food, Ice Slurry, Postharvest Treatment.

1. INTRODUCTION

Currently, fishery produces are put in ice water which is made of crushed ice and sea water onboard after fishing, and are kept until returning to the port. However, in this storage method, crushed ice tends to damage the fish body, the temperature distribution of ice water is not uniform, and there is a problem that the temperature of the fish body cannot be uniformly controlled at low temperature. According to Kominami et al.(2014), It is obvious that the cold storage period before freezing affects the formation of ice crystals and it is possible to suppress freezing damage by suppressing the degradation of fish after death. By improving postharvest treatment, it can be expected to suppress the postmortem change of fish and improve the quality of frozen fish. Therefore, it is possible to increase the value of frozen fishery products by improving postharvest treatment. In recent years, ice slurry has begun to be used in the fishing port. Ice slurry is a solid-liquid two-phase mixture of fine ice and water and has both ice and water properties. It has features such as high cooling capacity, fluidity, uniform temperature distribution, less damage to fish body, etc. It is known that ice slurry is effective for postharvest treatment of fishery produces. However, existing researches that investigated the effect of ice slurry treatment on fish qualities has little scientific basis. In this study, the effectiveness of postharvest treatment using ice slurry is verified by scientific manner.

2. MATERIAL AND METHODS

Ice slurry was prepared by mixing flake ice and salt water of 0 ° C in temperature by using a mixer. The properties of ice slurry used in this experiments were temperature = -30° C, IPF (Ice Packing Factor) = 30%, salt content = 3.0%. Ice water (IPF=30%) was prepared with tap water and crushed ice. Live horse mackerel (*Scomber japonicus*) of 441±50 g in weight, 31.0±1.5 cm in body length was used as experimental sample. We purchased fish in living state that reached us by live fish transportation vehicle. In this study we used three killing methods those were; ice slurry killing, ice water killing, struggle killing that was realized by putting live fish into empty Styrofoam box and tightened the lid and left untouched. After the death, all samples were placed in ice water for 30 minutes and then froze with air blast freezer at -40° C. It was stored at -80 ° C so as not to change the state after freezing, and analysis was carried out within 3 months at the latest. Thawing was carried out by two methods: ice water thawing (rapid thawing) and low temperature air thawing (slow thawing). In addition, the frozen fish was cut to 1 cm width, 6.5-7cm height, 5.5-6cm length, and thawed. K value, pH, impedance and drip were measured at the timing as shown in Fig. 1.

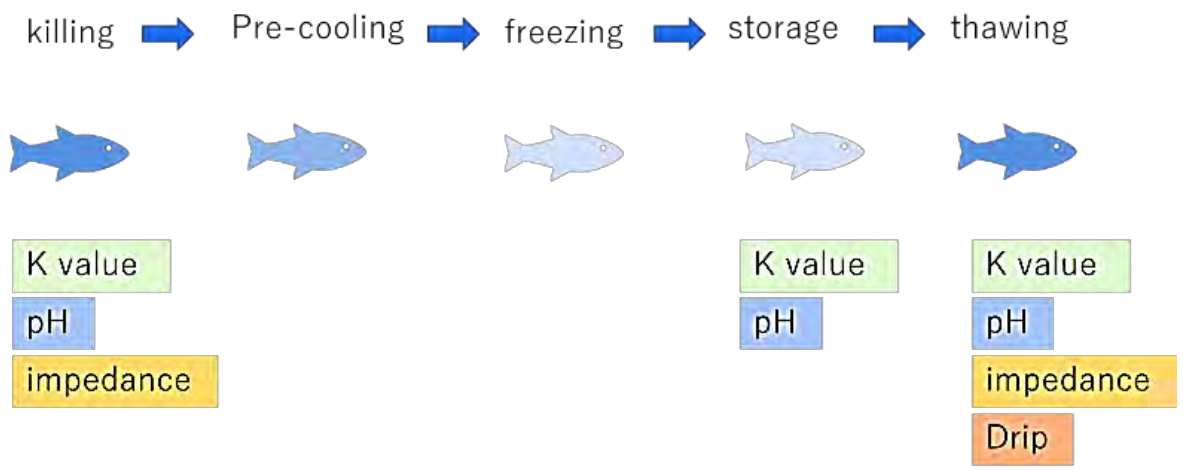

Figure 1: Experimental method

3. RESULT AND DISCUSSION

3.1 K value

Extraction of ATP related compound was performed at an arbitrary timing. The sample solution was extracted according to the method of Ehira et al.(1970) 1 g of fish meat on the dorsal side was taken, 4 mL of 10% PCA, 4 mL of 5% PCA, 4 mL of ion exchanged water was added and ground. After centrifugation(20000g,10min,4° C), the supernatant was adjusted to pH 6.8-7.0 and further centrifuged(2000g,10min,4° C) to a volume of 20 mL. Thereafter, the filtered solution was used as a sample solution. Analysis was performed by HPLC(LC-10A:SHIMADZU co.) equipped with a reversed phase column(silica C18M 4D:Shodex). The analysis conditions are shown in Table 1.

Table1. HPLC analysis conditions

Column	**Silica C18M 4D: Shodex**
Column temperature	**35°C**
Mobile phase	**0.13M phosphoric acid,0.13M trimethylamine, 0.26M Acetonitrile mixture (pH6.8)**
Flow rate	**0.8 mL·min^{-1}**
Detector	**UV260 nm**

Since the K value is 3% or less under all conditions, the result is omitted. The proportion of ATP related compound is shown in Fig. 2.

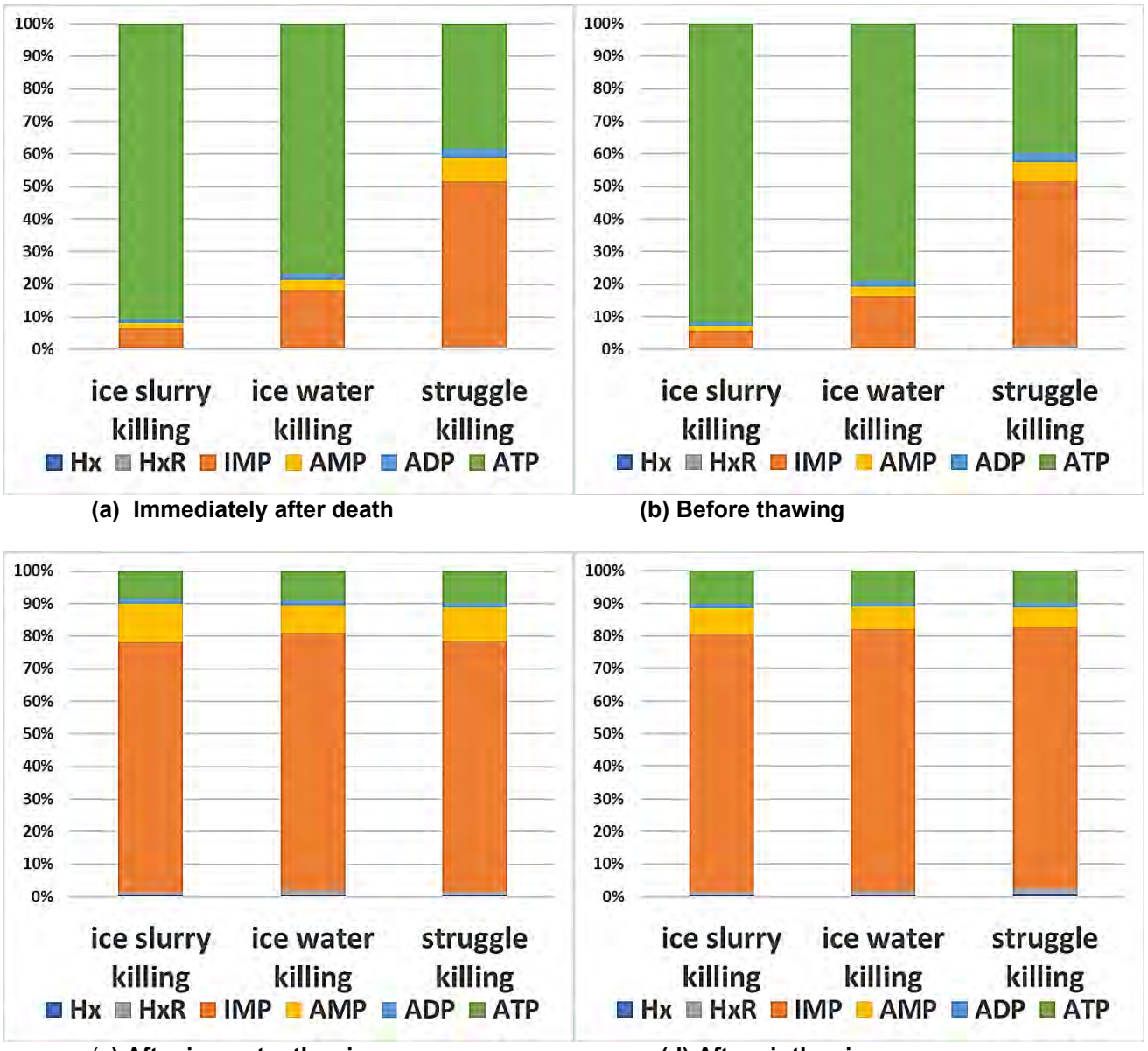

(a) Immediately after death (b) Before thawing

(c) After ice water thawing (d) After air thawing

Figure 2: Result of ATP related compound measurement

From the ratio of ATP related substances after death, it was found that by using ice slurry, it dies almost without consuming ATP. In addition, proportion of ATP related substances have hardly changed from death to freezing. However, the ratio of ATP related substances after thawing showed the same tendency in spite of the different thawing conditions. Since we had expected thawing condition affected the fish quality after thawing, current result was against our expectation. The fact that the proportion of ATP related substances showed almost no change during storage under – 80 °C even after three months.

3.2 pH

The pH was measured at an arbitrary timing. The pH was measured according to the method of Bito et al.(1980)10 mL of 0.02 M sodium iodoacetate solution was added to 1 g of fish meat and homogenized, and measured with a pH meter. Results are shown in Table 2.

Table 2. Result of pH measurement

	Immediately after death	before thawing	Ice water thawing	air thawing
Ice slurry killing	6.58	6.14	6.11	5.84
Ice water killing	6.05	6.08	5.89	5.80
Struggle killing	5.96	5.99	6.00	5.87

It is not statistically reliable because the number of samples is not enough, but it turned out that the pH tends to rise when using ice slurry. In addition, when thawing with ice water, pH tended to be higher than air thawing.

3.3 Impedance

Complex impedance measurement was performed in the frequency range of 50 Hz to 3 MHz. The impedance measurement conditions are shown in the Table 3.

Table 3. Impedance analysis conditions

Equipment	LCR meter (HIOKI, 3532-50, LCR Hi-TESTER)
Electrode (material, interval)	Platinum wire(ϕ 0.3mm×5mm)
	30mm
Frequency	50~3M [Hz]
Sample size	10mm×10mm×10mm

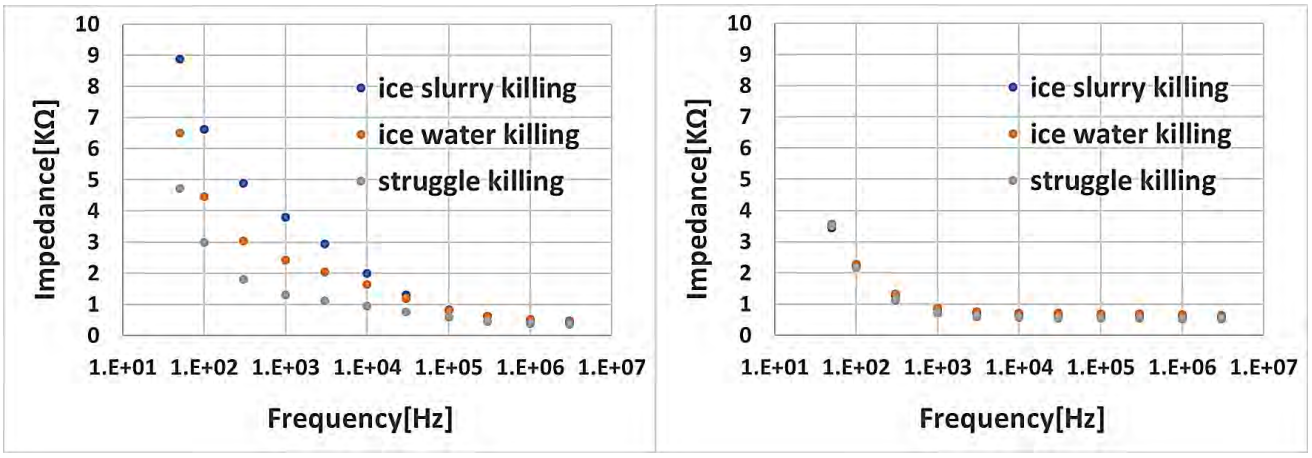

(a) immediately after death

(b) After ice water thawing

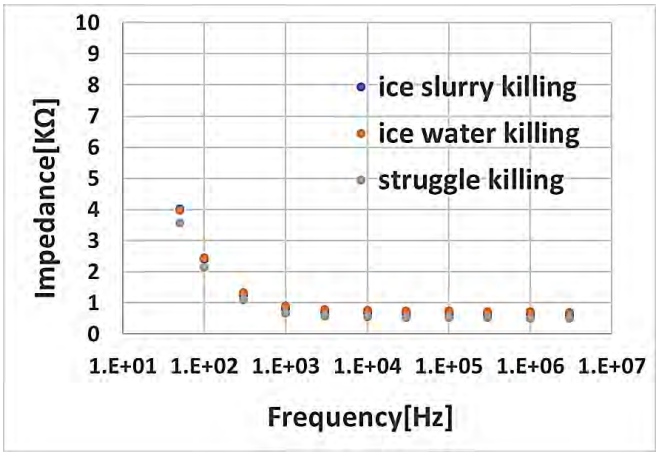

(c) After air thawing

Figure 3: Result of Impedance measurement

In Fig. 3a, the impedance was kept higher in the order of ice slurry, ice water, struggle killing. That is, it is considered that damage of cells is small when ice slurry is used. However, after thawing, there was no change in impedance, regardless of thawing method. In Fig. 3c, the impedance of struggle killing was lower than that of ice water killing. This seemed reasonable trend but when we compare Figs. 3b and 3c, we found unreasonable trend that the impedance of ice water killing sample was higher in air thawing than in ice water thawing. This trend should be examined again.

3.4 Drip Loss

The weight before thawing and the weight after wiping off the drip after thawing were measured, and the drip loss was calculated from the following equation.

$$\boldsymbol{drip\ loss}[\%] = \frac{\boldsymbol{W_f - W_t}}{\boldsymbol{W_f}} \times \mathbf{100}$$

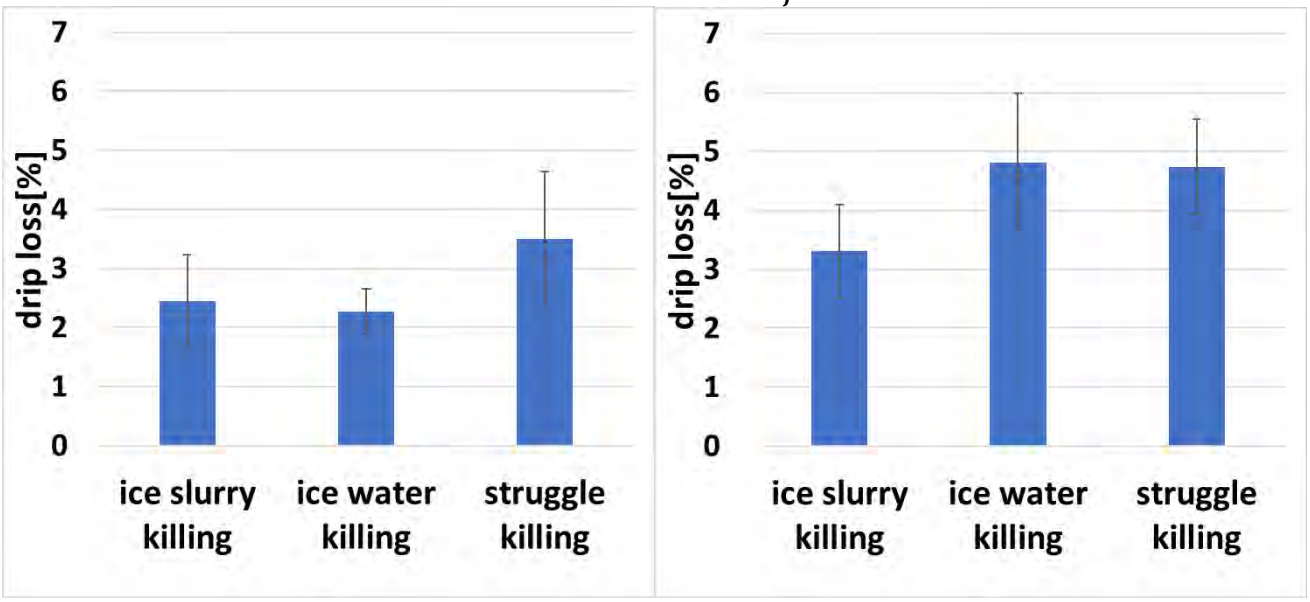

(a) After ice water thawing **(b) After air thawing**

Figure 4: Result of drip loss measurement

It was shown that the ice water thawing tended to lessen drip loss than air thawing. Also, in both thawing methods, there was a tendency that the drip amount increased in the case of struggle killing. However, the measured value of drip loss for ice water killing sample did not show reasonable trend.

4. CONCLUSION

From the current experimental results, it is indicated that using ice slurry in postharvest treatment was mostly effective to improve the fish quality. In detail, however, the data on fish killed with ice water indicated some unreasonable trend. It was no doubt the ice slurry instant killing was significantly better than the agony of death. Also, it was interesting that there was no change in ATP related compounds in storage (- 80° C) for 3 months. In our future plan, more variations of thawing method, e.g. thawing by running water and thawing by ice slurry, should be examined.

REFERENCES

Kominami, Y., 2014. Effects of Storage Time before Freezing on the Ice Crystal Morphology in the Frozen Fish Muscle Tissue, Trans. of Japan Society of Refrigerating and Air Conditioning Engineers 31(2), 47-56

Ehira, E., Uchiyama, H., Uda, F., Matsumiya, H., 1970. A Rapid for Determination of the Acid-soluble Nucleotides in Fish Muscle by Concave Gradient Elution, Bulletin of the Japanese Society of Scientific Fisheries 36(5), 491-496

Bito, M., 1980. Effect of Degradation of NAD and ATP in Frozen-Stored Sardine Meat on the Changes

of pH and Amount of Drip in the Thawed Meat, Bulletin of Tokai Regional Fisheries Research Laboratory 103,65-72

Okano, T., 2015, Utilization and Prospect of Slurry Ice for Marine Products, Bulletin pf Japanese Association of Refrigeration 90(1050), 33-37

Ohnishi, S., 2004, Effect of freezing on electrical and rheological properties of food materials, Food Science and Technology 10(4), 453-459

Abe, S., 2009, The effect of thawing condition for frozen fish meats -The thawing speed dependence on fish muscle protein denaturation and drip amount-, Trans. Of the Japan Society of Refrigerating and Air Conditioning Engineers 26(2), 149-158

Takeuchi, M., 2017, Effects of handling after fishing, freezing method, and storage temperature on quality of frozen Mackerel, Report of Aomori Prefectural Industrial Technology Research Center Food Research Institute 7-8, 42-47

Manuscript ID: 1442
DOI: 10.18462/iir.icr.2019.1442

Study of intelligent antibacterial and antioxidant poly(vinyl) alcohol film on the fresh-keeping effect and quality dynamic monitoring of *Pseudosciaena crocea*

Zhi-peng TANG[(a)], Chen-wei CHEN[(a,b,d)], Jing XIE[(a,b,c,d)*], Jian-rong LI[(e)]

[(a)]Shanghai Ocean University College of Food Science and Technology, Shanghai 201306, China, jxie@shou.edu.cn
[(b)]Shanghai Aquatic Products Processing and Storage Engineering Technology Research Center, Shanghai 201306, China,jxie@shou.edu.cn
[(c)]Shanghai Professional Technology Service Platform on Cold Chain Equipment Performance and Energy Saving Evaluation, Shanghai 201306, China,jxie@shou.edu.cn
[(d)]National Experimental Teaching Demonstration Center for Food Science and Engineering (Shanghai Ocean University), Shanghai 201306, China, jxie@shou.edu.cn
[(e)]College of Food Science and Engineering, Bohai University, Jinzhou, Liaoning, 121013, China, jxie@shou.edu.cn

ABSTRACT

In this study, 1% nano-TiO_2 and 3% anthocyanin were incorporated into poly(vinyl) alcohol, and the intelligent poly(vinyl) alcohol packaging film was prepared by solution casting method. In order to study the effect of the packaging film on the storage quality of *Pseudosciaena crocea*, the indexes of TBA, total bacteria and pH were used to evaluate the freshness of *Pseudosciaena crocea* during refrigerated storage. The visible dynamic color changes of the film due to the change of pH value of *Pseudosciaena crocea* fish meat was also studied to discuss the freshness preservation and quality dynamic monitoring ability of intelligent poly(vinyl) alcohol packaging film. The results showed that the TBA, total bacteria and pH values of the PVA-nano-TiO_2-anthocyanin film packaged group were better than those of the unpackaged and pure PVA film packaged groups. The total number of bacteria at the 16th day of storage reached 7.11 lg cfu/g for PVA-nano-TiO_2-anthocyanin film packaged group, compared with 7.14 lg cfu/g and 7.03 lg cfu/g on the 12th day of storage in other experimental groups, the shelf life was extended 4 days. During the 20 days storage period, the poly(vinyl) alcohol-nano-TiO_2-anthocyanin film can well responded with the changes of pH values of *Pseudosciaena crocea* fish meat by visible color changes. Therefore, the intelligent poly(vinyl) alcohol packaging film prepared in this study can not only have beneficial effects on the preservation of foods, but also can serve as a color indicator to achieve intelligent monitoring in the food storage process.

Key words: Poly(vinyl) Alcohol, Nano-TiO_2, Anthocyanin, Intelligent Monitoring, Preservation Quality.

1. INTRODUCTION

Pseudosciaena crocea (large yellow croaker) is a warm-water offshore cluster of migratory fish. And it is deeply loved by consumers because of its delicate meat, delicious taste and rich in nutrition. However, the high moisture content, pH and nutrient content of fresh large yellow croaker made it become one of the products that are prone to spoilage during transportation and storage. Spoilage during the preservation of large yellow croaker was usually caused by lipid infiltration and microbial growth, and resulting in lipid oxidation and protein degradation, the shelf life of the fish was greatly shorten (Ojagh et al., 2010). At present, biological preservatives (Liu et al., 2015), ice preservation method (Wang *et al*., 2009) and ozone treatment (Yuan et al., 2010) was used to effectively extend the shelf life of large yellow croaker for domestic and foreign researchers. However, the intelligent antibacterial and anti-oxidation packaging film based on poly(vinyl)alcohol has not been involved in the preservation of large yellow croaker.

Based on previous studies on the physicochemical properties of PVA-nano-TiO_2 active films and PVA-nano-TiO_2-anthocyanin active films, suitable active substance addition ratios were screened. In this study, the antibacterial property of nano-TiO_2 and the antioxidant property of anthocyanins were

combined. The PVA-nano-TiO_2-anthocyanin film was used to package large yellow croaker. The sensory quality changes, lipid peroxidation (TBA), total bacterial count (TVC), volatile base nitrogen (TVB-N), pH value of large yellow croaker fish were studied during packaging storage. And the dynamic color difference of the film caused by the change of the pH value of the large yellow croaker fish was also studied. In this way, the preservation effect and quality dynamic monitoring ability of this intelligent antibacterial anti-oxidation packaging film are discussed, which provides a reference for the development of smart packaging film in the future.

2. MATERIALS AND METHODS

2.1. Preparation of Packaging Film

2.1.1. Preparation of PVA glue, PVA-nano-TiO_2 blending solution and ANT solution

Refer to the solution casting method of Chen et al (Chen *et al*., 2017). 22 g of PVA resin pellets and 200 mL of distilled water were placed in a beaker, heated solution at 95 °C and continuously stirred until completely swollen, 1 mL of glycerol was added as a plasticizer and stirred for 30 min, and finally obtain a PVA glue.

Nano-TiO_2 (relative to 1% w/w of PVA dry mass) was mixed into the PVA glue, continued stirring for 2 h until the nano-TiO_2 was uniformly dispersed in the solution, finally a PVA-nano-TiO_2 blending solution was prepared.

The purple potato anthocyanins (ANT) (3% w/w relative to the dry mass of PVA) were dissolved in 50 mL HCL (pH = 3) in a 100 mL Erlenmeyer flask and magnetically stirred for 2 h at room temperature. The ANT solution was finally prepared, and the conical flask was wrapped in aluminum foil and stored in a cool place.

2.1.2. Preparation of Pure PVA Film and ANT-PVA-TiO_2 Film

The PVA glue was poured onto a glass plate of a thermostat heater, and the temperature of the glass plate was adjusted to 60 °C. The glue was uniformly coated on the glass plate by the tie rods with the same gap height. After pre-experiment, the film drying time was 50 min. The prepared pure PVA film was packaged in a high-resistance aluminum foil bag for use.

The PVA-nano TiO_2 blending solution was mixed with the ANT solution, magnetically stirred at 40 ° C for 20 min, and then the ANT-PVA-TiO_2 blending glue was placed in a vacuum oven at 23 ± 1 °C for 1 d to remove air bubbles. The prepared blended glue was poured on a glass plate of a thermostat heater, and the temperature of the glass plate was adjusted to 60 °C. The glue is uniformly coated on the glass plate by the tie rods with the same gap height. After pre-experiment, the film drying time was 40 min. The prepared PVA packaging film was packaged in a high-resistance aluminum foil bag for use, which marked ANT-PVA-TiO_2.

2.2. Raw Material Sample Pre-treatment and Packaging Preservation

The fresh large yellow croakers were brought back to the laboratory. After killing the fish by placing in ice cubes, quickly cut a back muscle of a large yellow croaker (200±5 g), and then took 80±5 g of fish into a 4°C refrigerator for storage and preservation, which used in comparison. The packaged fresh-keeping group was packaged with the prepared ANT-PVA-TiO_2 film and pure PVA film, and placed in a refrigerator at 4 ° C. The control group was directly placed in a refrigerator at 4 ° C without any packaged treatment. The fresh-keeping indicators were sampled after 0, 4, 8, 12, 16 and 20 d, and each index was made into three groups of parallel.

2.3. Determination of Lipid Peroxidation (TBA)

Referr to the TBA determination method of Wu et al. (2017).

2.4. Determination of the Total Number of Bacteria (TVC)

The total number of colonies referred to the plate counting method in GB 4789.2-2016 National Food Safety Standard, which named Determination of the total number of colonies in food microbiology

test (GB 4789.2., 2016).

2.5. Determination of pH and Dynamic Colour Difference

The pH value was determined by reference to the pH-acidity method (GB/T 5009.45., 2003) in the analytical method for aquatic product hygiene standards. The pH was measured at 0, 4, 8, 12, 16 and 20 d, respectively.

The color difference meter was used to measure the dynamic color difference of the ANT-PVA-TiO_2 film due to the change in the pH of the fish sample, and photographed by using a smart camera. The white standard plate was tested as a background in triplicate, where in the measured color parameter L* value was brightness (black-white), a* value was red (green-red), and b* value was yellow (blue-yellow). The color difference (ΔE) represents the following equation:

$$\Delta E = ((\Delta L^*)^2 + (\Delta a^*)^2 + (\Delta b^*)^2)^{0.5} \quad \text{Eq.(1)}$$

where $\Delta L^*=L^*-L_0^*$, $\Delta a^*=a^*-a_0^*$, $\Delta b^*=b^*-b_0^*$.

2.6. Statistical Analysis

The experimental data was analyzed by SPSS 19.0 software. The results were expressed as mean ± standard deviation, and the data curves were drawn using Origin Pro V8.5 software.

3. RESULTS AND DISCUSSION

3.1. Changes of Lipid Peroxidation during the Preservation of Large Yellow Croaker

Fig. 1 shows the effect of different packaging treatments on the TBA value of large yellow croaker during storage at 4 °C. It can be seen from the figure1 that with the increase of storage time, the TBA values of large yellow croakers in different treatments are increasing. The rise of TBA in the untreated group was the fastest, the pure PVA film packaging treatment group was followed, and the increase in the ANT-PVA-TiO_2 film packaging treatment group was the slowest. This was mainly because the fat in the untreated group of fish was constantly in contact with oxygen. With the storage time increased, the degree of oxidative rancidity became more and more serious, resulting in a rapid increasing in TBA value. Fish meat packaged in pure PVA film can hinder the contact between fish and oxygen to a certain extent, and slowed a slower oxidation rate of fish lipids. On the one hand, ANT-PVA-TiO_2 film has good antioxidant capacity by combining anthocyanins. On the another hand, the addition of nano-TiO_2 can impart excellent oxygen barrier properties to the film, the study by Alateyah et al. (2013) also showed that the incorporation of nano-TiO_2 into the film can effectively block oxygen from one side of the film to the other. Under the action of these two factors, the TBA of the ANT-PVA-TiO_2 film packaging treatment group was significantly lower than that of the other treatment groups. So, during the storage of the active film packaging, the ANT-PVA-TiO_2 film continuously released anthocyanins. The surface of the fish removes oxygen free radicals, and the other side blocks the contact of the fish with the outside oxygen, which greatly reduces the rate of lipid peroxidation of the fish, thereby effectively extending the shelf life of the large yellow croaker. Shen et al. (2011) used fresh cellulose and proanthocyanidin film to package fresh lard. The results showed that anthocyanin was slowly released from the film into lard and had excellent antioxidant properties, which could effectively extend the shelf life of food.

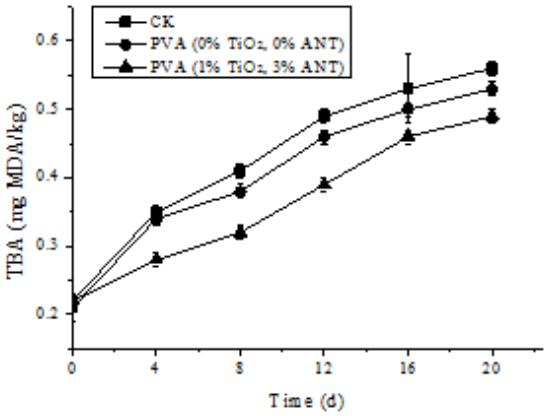

Figure1: Changes in TBA values of Pseudosciaena crocea during 4℃ storage.

3.2. Changes in the Total Number of Bacteria during the Preservation of Large Yellow Croaker

Fig. 2 showed the changes in the total bacterial count of large yellow croaker under different treatments during storage at 4 °C. With the increase of storage time, the total number of bacteria in the three groups of different treatments showed an upward trend. The total number of bacteria on the 12th day of the untreated group and the pure PVA film packaging treatment group reached 7.14 lg cfu/g and 7.03 lg cfu/g, respectively, which exceeded the international standard. The upper limit of the total number of acceptable bacteria in fresh fish was 7 lg cfu. /g (ICMSF) (1986), the results showed that the shelf life of large yellow croaker in these two treatments was 12 days, mainly because the bacteria in the fish grow and multiply as the storage time increases, which directly led to the spoilage of fish. The total number of bacteria on the 12th day of the large yellow croaker treated with ANT-PVA-TiO_2 film reached 6.37 lg cfu/g, which was still within the acceptable range. The total number of bacteria on the 16th day rose to 7.11 lg cfu/ g. On the one hand, nano-TiO_2 was released from the active film to the surface of the fish, and its excellent antibacterial property inhibited the growth of bacteria in the fish, Lian et al (Liu *et al*., 2016) bind the nano-TiO_2 into the PVA/chitosan film. It was also proved by the inhibition zone experiment that the antibacterial activity of the film increased with the increase of the concentration of nano-TiO_2, and the simulation showed that the nano-TiO_2 could be slowly released from the film. On the other hand, ANT-PVA-TiO_2 film had excellent oxygen barrier properties and greatly inhibits the growth of aerobic bacteria. Therefore, packaging large yellow croaker with ANT-PVA-TiO_2 film can effectively extend the shelf life of large yellow croaker.

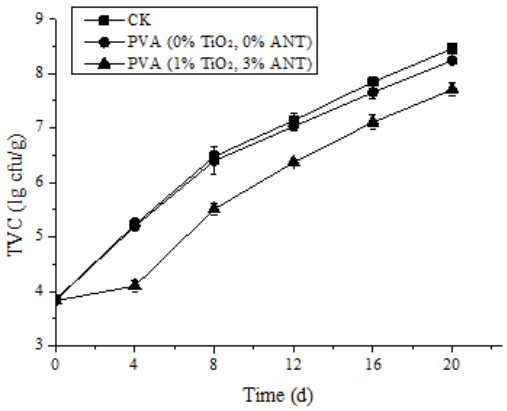

Figure 2: Changes in total viable counts (TVC) of Pseudosciaena crocea during 4℃ storage.

3.3. Changes of Dynamic Color Difference in Packaging Film and pH during the Preservation of Large Yellow Croaker

Fig. 3a reflected the change in pH of large yellow croaker in three treatments during storage at 4 °C. The initial pH of fresh large yellow croaker was 6.65-6.66. In the early stage of storage, sugar was

produced in the fish. The original decomposition into pyruvate, and then decomposed into lactic acid, which led to a decrease in the pH of the fish (Qiu et al., 2014), from the middle to the end of the storage period, due to microbial growth, a large amount of protein and other nutrients were decomposed and some basic products were produced, which made the pH of the fish gradually increase (Xu et al., 2014). The pH values of the untreated group and the pure PVA film packaging treatment group on the 4th day were 6.64 and 6.59, respectively, which were slightly lower than the initial value, because the large yellow croaker treated in these two ways was in the middle of storage on the 4th day. The formation of lactic acid in fish meat has ended, and nutrients such as protein have begun to decompose to produce alkaline substances, and the pH value in fish meat was gradually rising. The pH value of large yellow croaker treated by ANT-PVA-TiO_2 film was reduced to 6.37 on the 4th day, which was significantly different from that of the untreated group and the pure PVA film packaging treatment group. This was because the ANT-PVA-TiO_2 film packaging treatment group was still in the pre-storage period on the 4th day, and the lactic acid in the fish meat was continuously formed, resulting in a significant decrease in pH. At the storage time of 4-20 days, the pH value of the yellow croaker under the three treatment methods showed an increasing trend, but the upward trend of the ANT-PVA-TiO_2 film packaging treatment group was significantly lower than that of the untreated group and the pure PVA film. This was mainly because ANT-PVA-TiO_2 film continuously releases anthocyanins and nano-TiO_2 to the surface of fish during the process of storing large yellow croaker, which effectively blocking the contact between fish and oxygen, and played an important role in preservation. The results showed that the treatment of large yellow croaker with ANT-PVA-TiO_2 film can prolong the lactic acid formation time during storage and effectively extend the shelf life of large yellow croaker.

The color changes of ANT-PVA-TiO_2 film during storage of large yellow croaker at 4 °C were shown in Fig. 3b. The film was grayish brown (0 d), reddish brown during storage. (4 d), light reddish brown (8 d), flesh color (12 d), gray (16 d) and dark gray (20 d), which in turn responded to changes in fish pH during storage of large yellow croaker for 20 days. According to Table 1, the brightness (L*) of the film decreased first and then increased, the redness (a*) increased first and then decreased, and the yellowness (b*) increased first, then decreased and then increased. Because the large yellow croaker was packaged on the 0th day, the starting color of the film remained as the original grayish brown. During the storage period of 0-4 d, the pH value of the fish meat gradually decreased due to the formation of lactic acid in the fish meat of the large yellow croaker. The anthocyanin in the ANT-PVA-TiO_2 film responded to the change of the environmental pH, and the dynamic color difference of the film occurred. The a* value and the b* value increased significantly, the L* value decreased significantly, and the film exhibited a reddish brown color, and its color difference (ΔE) with respect to 0 d also increased significantly. During the storage period of 4-16 d, the nutrients such as protein in the fish gradually decomposed into alkaline substances, the pH value of the fish gradually increased, and the film began to change to the original film color (gray brown), so the film performance at 8th day was light reddish brown. On the 12th day, the film showed flesh color and the 16th day film showed gray color. The a* value and b* value decreased significantly, the L* value increased significantly, and the film ΔE value gradually decreased with respect to 0 d. During the storage period of 16-20 days, the pH value of the fish of the large yellow croaker has exceeded 7, and the film turned dark gray. The a* value and L* value gradually decreased, while the b* value and ΔE value increased significantly. The results showed that the ANT-PVA-TiO_2 film can truly reflect the change of the pH value of the large yellow croaker fish meat during the storage process of 20 d.

Table 1. Color parameters (the values of L *, a*, b* and ΔE) of active packaging film during 4℃ refrigerated storage

Time (d)	L*	a*	b*	ΔE
0	81.90±0.09^{a}	3.81±0.18^{c}	12.45±0.14^{e}	16.94±0.15^{e}
4	76.48±1.06^{c}	6.13±0.70^{a}	15.57±0.35^{b}	24.25±0.82^{a}
8	78.27±0.59^{b}	5.10±0.46^{b}	14.45±0.11^{c}	21.25±0.60^{b}
12	78.38±1.51^{b}	4.80±0.44^{b}	14.11±0.65^{cd}	20.14±0.78^{bc}
16	80.40±0.66^{a}	4.37±0.27^{bc}	13.58±0.27^{d}	19.03±1.02^{c}
20	77.37±0.65b^{c}	3.59±0.44^{c}	18.04±0.47^{a}	23.28±0.66^{a}

Data as average ± standard deviation ($p < 0.05$).

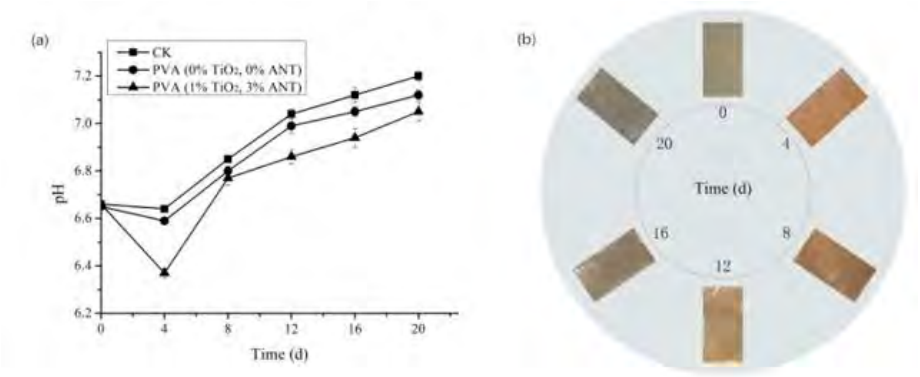

Figure 3: Changes in pH values of Pseudosciaena crocea during 4℃ storage (a), the corresponding dynamic color changes of the active packaging film during 4℃ storage (b).

4. CONCLUSION

During storage at 4 °C, the treatment of large yellow croaker with ANT-PVA-TiO_2 film can effectively inhibit the growth and reproduction of bacteria in fish, fat oxidation and amino acid decomposition, and extend the shelf life by 4 days compared with blank. During the storage period of 0-20 days, ANT-PVA-TiO_2 film can respond well to the color changes of pH value in the fish of large yellow croaker by visible color change, which was characterized by grayish brown (0 d), reddish brown (4 d) and light. Reddish brown (8 d), flesh (12 d), gray (16 d) and dark grey (20 d). Compared with other conventional fresh-keeping large yellow croaker technology, this study has the advantages of not only effectively extended the shelf life of large yellow croaker, but also visually understood the quality changes of large yellow croaker during the storage process through visible film color changes. Excellent performance in monitoring and active packaging. On the one hand, the film-forming process of this study was relatively manual, so if it was to be put into production, it will be necessary to improve the film-making process and improve the efficiency; on the other hand, for the active substance in the ANT-PVA-TiO_2 film from the film to the large yellow croaker. The release mechanism of the surface needs further study.

ACKNOWLEDGMENTS

This study has been financed by the National Key Research and Development Program (2016YFD0400106), Shanghai Professional Technology Service Platform on Cold Chain Equipment Performance and Energy Saving Evaluation (17DZ2293400), Shanghai Municipal Science and technology project to enhance the capabilities of the platform (16DZ2280300), Special foundation for science and technology development of Shanghai Ocean University (A2-0203-00-100218)and the project Shanghai Science and Technology Committee Engineering Research Center Construction: Shanghai Engineering Research Center of Aquatic-Product Processing& Preservation(16DZ2280300).

REFERENCES

Ojagh, S. M., Rezaei, M., Razavi, S. H., Hosseini, S. M. H. 2010. Effect of chitosan coatings enriched with cinnamon oil on the quality of refrigerated rainbow trout. Food Chemistry 120(1), 193-198.

Liu, N. N., Zhao, Y., Ren, Z. Z., Wang, Y. B., Fu, L. L. 2015. Effect of extracellular products produced by bacillus coagulans for large yellow croaker during storage. Food Science & Technology 4, 199-204.

Wang, Z. Z., Dong, S. Y., Liu, Z. Y., Zhang, W. T., Niu, B. W. 2009. Effects of Vacuum Packaging on Freshness of Large Yellow Croaker Psedosciaena crocea under Ice-temperature Condition. Fisheries Science 28(8), 431-434.

Yuan, Y. J. 2010. Effect of ozone treatment and low temperature storage on yellow croaker preservation. Journal of Nuclear Agricultural Sciences 24(5), 987-990.

Chen, C. W., Xie, J., Yang, F. X., Zhang, H. L. 2017.Development of moisture absorbing and antioxidant active packaging film based on poly(vinyl alcohol) incorporated with green tea extract and its effect on the quality of dried eel. Journal of Food Processing & Preservation 42, e13374.

Wu, T., Wu, C., Fang, Z., Ma, X., Chen, S., & Hu, Y.2017. Effect of chitosan microcapsules loaded with nisin on the preservation of small yellow croaker. Food Control 79, 317-324.

GB 4789.2-2016. National Food Safety Standards.

GB/T 5009.45-2003. Analytical method for aquatic product hygiene standards.

Alateyah, A. I., Dhakal, H. N., Zhang, Z. Y. 2013. Processing, properties, and applications of polymer nanocomposites based on layer silicates: a review. Advances in Polymer Technology 32(4), 5153-5162.

Shen, J., Wang, J. J., Liu, X. X., Fan, C. Y. 2011. The Research on the structures and antioxidantion properties of procyanidins/cellulose acetate packaging membrane. Journal of Zhejiang Sci-Tech University 24(1), 2694-2699.

ICMSF. 1986. Sampling plans for fish and shellfish. In International commission on microbiological specifications for foods, microorganisms in foods. Sampling for microbiological analysis: Principles and scientific applications (2nd ed.). Canada: University of Toronto Press 2, 181-196.

Lian, Z., Zhang, Y., Zhao, Y. 2016.Nano-TiO_2 particles and high hydrostatic pressure treatment for improving functionality of poly(vinyl) alcohol and chitosan composite films and nano-TiO2 migration from film matrix in food simulants. Innovative Food Science & Emerging Technologies 33, 145-153.

Qiu, X., Chen, S., Liu, G., Yang, Q. 2014. Quality enhancement in the Japanese sea bass (Lateolabrax japonicas) fillets stored at 4°C by chitosan coating incorporated with citric acid or licorice extract. Food Chemistry 162(162), 156.

Xu, G., Tang, X., Tang, S., You, H., Shi, H., & Gu, R. 2014. Combined effect of electrolyzed oxidizing water and chitosan on the microbiological, physicochemical, and sensory attributes of American shad (Alosa sapidissima) during refrigerated storage. Food Control 46, 397-402.

Liu, B., Xu, H., Zhao, H., Liu, W., Zhao, L., Li, Y. 2017. Preparation and characterization of intelligent starch/PVA films for simultaneous colorimetric indication and antimicrobial activity for food packaging applications. Carbohydrate Polymers 157, 842-849.

Manuscript ID: 1446
DOI: 10.18462/iir.icr.2019.1446

Effects of nozzle structures of air impinging freezer on heat transfer characteristics on steel strip

Yuyan LIU[b, d], Jinfeng WANG[a, b, c, d], Jing XIE[a, b, c, d]

[a]Shanghai Engineering Research Center of Aquatic Product Processing and Preservation, Shanghai 201306, China
[b]Shanghai Professional Technology Service Platform on Cold Chain Equipment Performance and Energy Saving Evaluation, Shanghai 201306, China
[c] National Experimental Teaching Demonstration Center for Food Science and Engineering (Shanghai Ocean University), Shanghai 201306, China
[d] College of Food Science and Technology, Shanghai Ocean University, Shanghai 201306, China, jxie@shou.edu.cn

ABSTRACT

Due to the low efficiency and high energy consumption in air impinging freezer, two kinds of nozzle structures were compared with the aim of finding the best structure and improving the Nusselt number and heat transfer uniformity. The results showed that when the H/D_E was in the range of 2-12, the average Nusselt number on the steel strip surface under the circular funnel nozzle was higher than that under the circular orifice nozzle, which was higher with about 5.41% to 15.10%. The change of the average Nusselt number on the steel strip surface under both two kinds of nozzle structures were greatly influenced by the H/D_E and was less affected by the cross flow. The heat transfer uniformity index η on the steel strip surface under the circular funnel nozzle was lower than that under the circular orifice nozzle with 7.06%-34.52% lower. As the H/D_E increasing, the η different between the two kinds of nozzle structures was gradually decreased. The circular funnel nozzle was recommended to reduce the freezing time.
Keywords: Jet Impact, Freezer, Nozzle, Nusselt Number, Heat Transfer Uniformity.

1. INTRODUCTION

In recent years, because the growing demand of the quick-frozen food, quick-frozen food industry has developed rapidly (Huan et al., 2003). However, high energy consumption and low efficiency are the main problems in quick-freezer. Therefore, how to improve the performance of quick-freezer has been attracted much attention (Shaikh and Prabhu, 2007). In the case of the same mass flow rate at the cooling air inlet, changing the air outlet system is a more economical and effective way to improve the efficiency of air impinging quick-freezer (Yang et al. (2017) and Lee et al. (2015) found that the cross flow and the heat transfer intensity on the target surface were influenced by circular nozzle number, diameter, spacing distance, and nozzle-to-surface distance. Shan et al. (2015) found that as the ratio of the nozzle-to-surface distance to the circular nozzle diameter (H/D_E) increased, the peak of local Nusselt number on the target surface was shifted toward the region near the pressure outlet. Most of the above literature focused on the Nusselt number on the target surface. But few literature paid attention to heat transfer uniformity on the target surface. Heat transfer uniformity is an important index for measuring the heat transfer characteristics for quick-freezers (Yu et al., 2017). Quality of quick-frozen foods is directly influenced by heat transfer uniformity (Li et al., 2018).

In this paper, two kinds of nozzle structures of impinging quick-freezing experimental table were taken as the research object. When the mass flow rate at the cooling air inlet was same, the influence of the nozzle-to-surface distance on the heat transfer characteristics under the circular orifice nozzle and circular funnel nozzle was compared. In order to provide theoretical basis for the optimization in air impinging quick-freezer, the optimum nozzle structure was found from the point of view of average Nusselt number and heat transfer uniformity on the steel strip surface.

2. EXPERIMENTAL MODEL AND SETUP

2.1. Experimental Model

Fig. 1a was shown the model of the impinging quick-freezing experimental table. The cooling air was driven by the centrifugal fan into the static pressure chamber of the impinging quick-freezing experimental table. It was directly sprayed through the orifice plate to steel strip surface and flowed in the confined rectangular channel.

Compared with the measured data of the impingement tunnel quick-freezer in Nantong Square Cold Chain Equipment Company, the change of internal flow field in the impinging quick-freezing experimental table and the impingement tunnel quick-freezer was same when the size of static pressure chamber was 300 mm × 300 mm × 500 mm and the orifice plate was 300 mm × 300 mm × 2 mm in the impinging quick-freezing experimental table. Figs. 1b, 1c and 1d were shown the model of circular orifice nozzle and circular funnel nozzle. And the outlet area of two kinds of nozzle structures was the same. In order to rationally distribute the nozzles, the size of static pressure chamber and orifice plate was increased in equal proportion, which were 600 mm x 600 mm x 500 mm and 600 mm x 600 mm x 2 mm respectively (Wen, 2011). This model was symmetrical, so only 1/2 model was used for simulation. Under this size of model, two kinds of nozzle structures parameters were shown in Table 1.

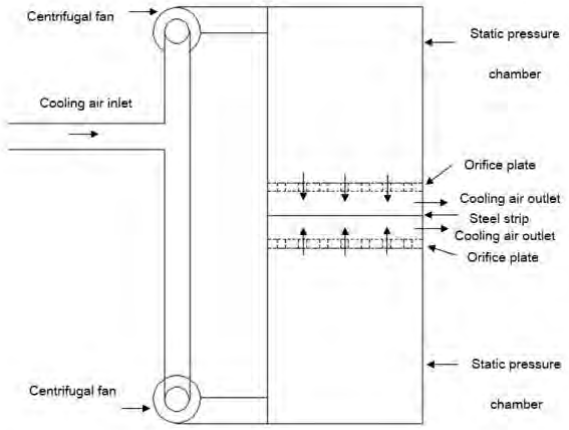

a: Model of impacting freezing test bench

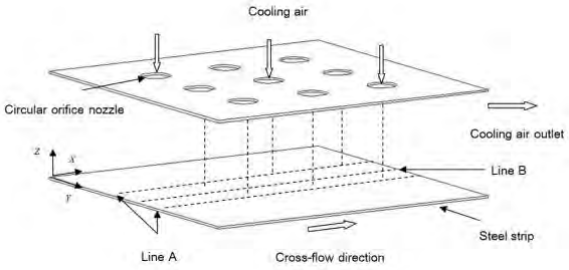

b: Model of circular orifice nozzle

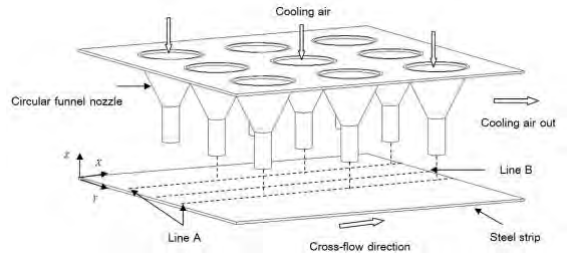

c:Model of circular funnel nozzle

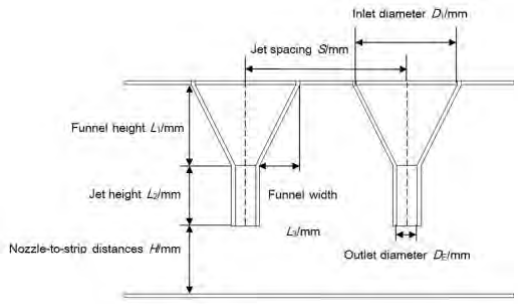

d: Circular funnel nozzle structure

Figure 1: Physical models of impacting freezing test bench and two kinds of nozzle structures.

Table 1. Nozzle structure parameters

Items	Circular orifice nozzle	Circular funnel nozzle
Inlet diameter D_1 (mm)	-	50
Outlet diameter D_E (mm)	10	10
Funnel height L_1 (mm)	-	40
Jet height L_2 (mm)	-	30
Funnel width L_3 (mm)	-	20
Nozzle spacing (S.mm^{-1})	80	80
Nozzle Number (N)	7×7	7×7

2.2. Numerical Simulation

2.2.1. Mesh Division

The physical model was discretized by ANSYS15.0 and the mesh around the nozzle was densified appropriately, as shown in Figure 2 (Xu *et al*., 2017). For circular orifice nozzle, the minimum size of the densified mesh was 0.517 mm. The number of nodes in the whole computing domain was 634363 and the number of mesh was 224215.

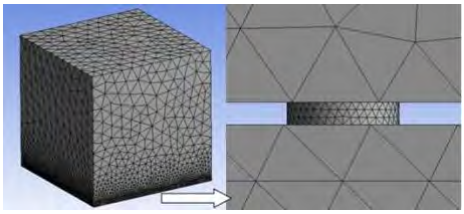

Figure 2: Mesh division.

2.2.2. Setting of Simulation Condition

The flow medium was air, and the simulation process assumes: (1) The wall of static pressure chamber was adiabatic (Zhu et al., 2017). (2) Air was an incompressible, homogeneous viscous fluid (Li *et al*., 2018).(3) During the normal operation, the internal flow field of the model was regarded as steady state (Chen et al., 2017).

The model was involved the conservation of flow and thermal mass, so it was necessary to be combined with the three-dimensional continuity equation, the momentum equation, the energy equation, the k equation and the ε equation (Hou *et al*., 2018). Referring to the test method of Wang et al. (2017), the inlet pressure P_{in} was 250 Pa and the outlet pressure P_{out} was 0 Pa. The inlet and outlet temperature of cooling air in frozen area were 230 K and 235 K. The mass flow rate at the inlet of the cooling air was 0.0644kg·s^{-1}. The target surface was the steel strip. It was selected as wall and with a thermal conductivity of 16.3 W·(m·℃)$^{-1}$.

2.2.3. Experimented Verification

Due to the limitations of the test conditions, only the original model size could be test verification（the size of static pressure chamber was 300mm × 300mm × 500mm, the orifice plate size was 300 mm×300 mm×2 mm, the outlet diameter of circular orifice nozzle was 10 mm, the nozzle spacing was 34 mm, the nozzle number was 8×8, the ratio between nozzle-to-strip distances and outlet diameters was 2）.By adjusting the fan frequency of the impinging quick-freezing experimental table, the differential pressure on TESTO-510 air differential pressure instrument was kept at 250Pa. Then the velocity in the vertical steel strip surface direction (*Z* direction) at the nozzle outlet was measured by TESTO-425 hot wire anemometer. The data were recorded once every 10 seconds, and the average values of three groups were measured in parallel. The results of the test were compared with those of the numerical simulation, as shown in Table 3.The errors of them were within 2.83%-4.95%. It was concluded that the numerical simulation of the impinging quick-freezing experimental table was reliable (Chen et al., 2014).

Table 2. Test instrument technical parameters

Instrument	Factory	Model	Range	Resolution ratio
TESTO-510 air differential pressure instrument	Testo AG	TESTO-510	0～10^4Pa	1Pa
TESTO-425 hot wire anemometer	Testo AG	TESTO-425	0～ +20m.s^{-1}	0.01 m.s^{-1}

Table 3. Velocity of each circular orifice nozzle outlet in Zdirection

Number of nozzle rows	Simulation value (m·s^{-1})	Test value (m·s^{-1})	Error (%)
1	11.95	12.10	1.24
2	12.39	12.70	2.44
3	13.25	12.80	3.51
4	14.05	13.39	4.93
5	14.70	13.75	6.90
6	15.62	14.97	4.34
7	15.83	15.36	3.06
8	16.04	15.69	2.23

2.2.4. Parameter Definition

Referring to the method of Attalla et al. (2017), the heat transfer characteristics of each position on the steel strip surface were analyzed by selecting line A and line B. Line A was corresponded to the center of each row of nozzles which was 7, detailed in Fig. 1b and 1c.Line B was corresponded to the center of each row of nozzle spacing which was 6, detailed in Fig. 1b and 1c.The average Nusselt number on line A and line B was:

$$\overline{Nu_A} = \frac{Nu_{A1}+Nu_{A2}+\cdots+Nu_{A7}}{7} \quad \text{Eq. (1)}$$

$$\overline{Nu_B} = \frac{Nu_{B1}+Nu_{B2}+\cdots+Nu_{B6}}{6} \quad \text{Eq. (2)}$$

The heat transfer uniformity index (η) on the steel strip surface is defined as the ratio of the standard deviation of local Nusselt number (σ_{Nu}) to the average Nusselt number ($\overline{Nu}$) on the steel strip surface (Wen et al., 2018). The η represents the difference of Nusselt numbers at each position on the steel strip surface. The smaller the η, the more uniform the heat transfer on the steel strip surface is (Ma *et al*., 2016). The formula is as follows:

$$\eta = \frac{\sigma_{Nu}}{\overline{Nu}} \qquad \text{Eq. (3)}$$

3. RESULTS AND DISCUSSIONS

3.1. Heat Transfer Characteristics And Uniformity On The Steel Strip Surface

Fig. 3 was shown the local Nusselt number distribution on line A and B under different H/D_E.For line A, when H/D_E = 2 and 6, the difference between the maximum and minimum of the local Nusselt numberunder the circular funnel nozzlewas 27.01% lower than that under the circular orifice nozzle. When H/D_E = 8 and 12, the difference between the maximum and minimum of the local Nusselt number under the two kinds of nozzle structureswas not significant. For line B, when H/D_E=2, 6, 8, and 12, the local Nusselt number under the circular funnel nozzle was higher than that under the circular orifice nozzle.

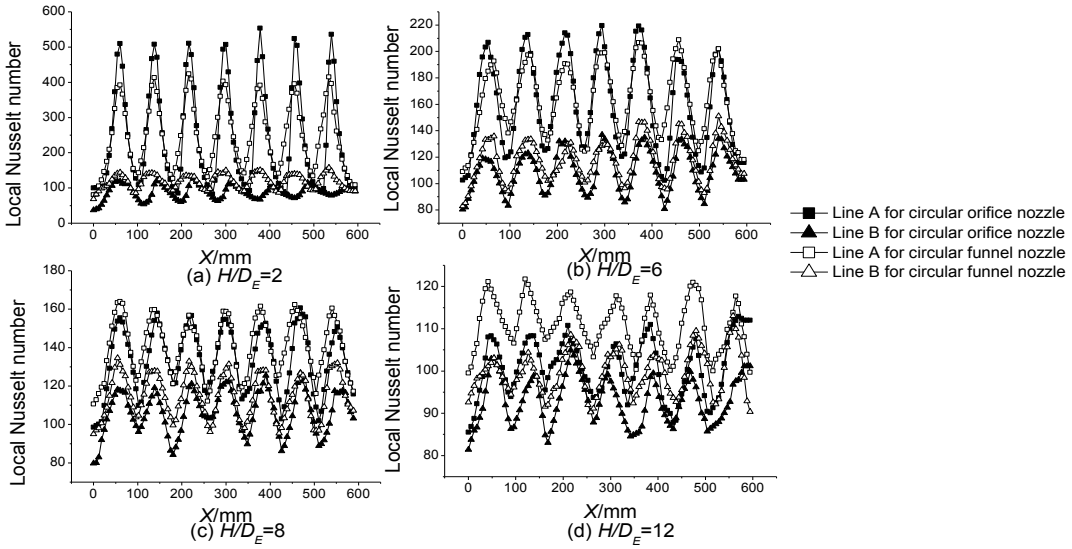

Figure3: The local Nusselt number distribution on Line A and B under different H/D_E.

The average Nusselt number on line A and B under different H/D_E were shown in Fig. 4. When H/D_E were increased from 2 to 12, for line A and line B, the average Nusselt number of the two kinds of nozzle structures were decreased gradually. The average Nusselt number on line A and B under the circular funnel nozzle were 1.83%-13.99% and 9.05%-11.64% higher than those under the circular orifice nozzle respectively. Similar researchhas shown that with the increasing of the nozzle-to-surface distance, the average Nusselt number on the center of the nozzle and the nozzle spacingwas decreased (Attalla et al., 2017).

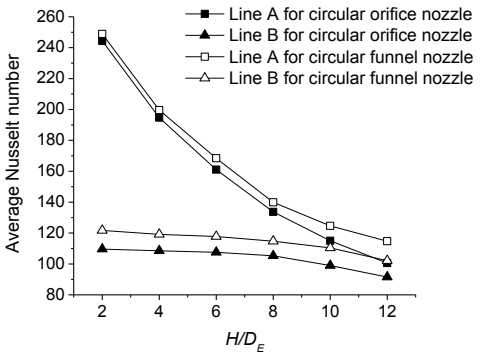

Figure4: Average Nusselt number on line A and B.

The average Nusselt number on steel strip under different H/D_E was shown in Fig. 5. When H/D_E were increased from 2 to 12, the average Nusselt number on steel strip surface under the circular funnel nozzle was always higher than that under the circular orifice nozzle, which was about 5.41% to 15.10% higher. Meena et al. (2016) and Vinze et al. (2016) also found that the heat transfer intensity on the target surface was decreased with the increasing of the nozzle-to-surface distance.

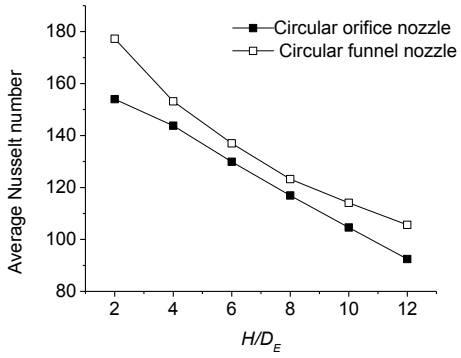

Figure5: Average Nusselt number on steel strip.

Fig.6 was shownthe heat transfer uniformity index on steel strip under different H/D_E. When H/D_E were increased from 2 to 12, the heat transfer uniformity indexes of the two kinds of nozzle structureswere decreased gradually, which was 86.20% and 90.28% respectively. The heat transfer uniformity index undercircular funnel nozzle was always lower than that under circular orifice nozzle, which was 7.06% to 34.52% lower. Similar researches have shown that the heat transfer on the target surface was more uniformly when the nozzle-to-surface distance was increased (Wen et al., 2018; Ma et al., 2016).

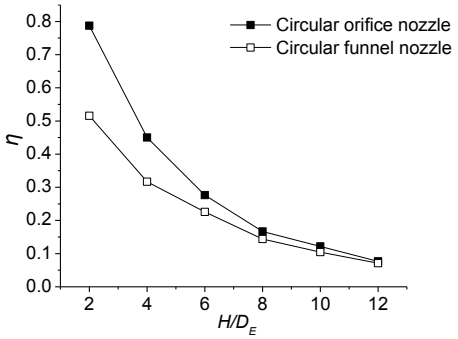

Figure6:The heat transfer uniformity index on steel strip under different H/D_E.

3.2. Analysis

One of the important factors affecting the heat transfer characteristics of impinging jet is cross flow. Cross flow is defined as the fluid flow in the direction perpendicular to the impinging jet. It can be formed by external flow or accumulating spent flow. The cross flow has an adverse effect on the heat transfer on the impinging surface. The cross flow effect must be minimized in order to achieve effective heat transfer (Nuntadusit et al., 2012 and Katti and Prabhu et al., 2009).For example, taking frozen food as the shrimp, the cross flow velocity at 10 mm above the steel strip surface was used to simulate the crossflow velocity of shrimp during freezing, as shown in Fig. 7 (Wang et al., 2017).When $H/D_E$was increased from 2 to 12, the crossflow velocity at 10 mm above the steel strip under the circular orifice nozzle and circular funnel nozzle was decreased, which was 63.20% and 61.39% respectively. Although the crossflow velocity of the two kinds of nozzle structureswas decreased with the increasing ofH/D_E, it can be seen from Fig. 5 that the average Nusselt number on the steel strip of the two kinds of nozzle structures was decreased. The reason wasthat the velocity in Z direction at 10 mm above line A under the two kinds of nozzle structureswas decreased

gradually. Katti et al.(2009) also found that the heat transfer effect on the target surface was decreased with the increasing of the nozzle-to-surface distance. The resultsshowed that the average Nusselt number on the steel strip surface under the two kinds of nozzle structures was greatly influenced by H/D_E and less by cross flow.

Fig.8 was shown the velocity in Z direction at 10 mm above line A and line B of the two kinds of nozzle structures. WhenH/D_E was in the range of 2-12, the velocity in Z direction at 10 mm above line B of the circular funnel nozzle was higher, so theaverage Nusselt number on the line B was higher andthe heat transfer uniformity index was lower, which was theheat transfer on the steel strip surfacewas more uniformly.

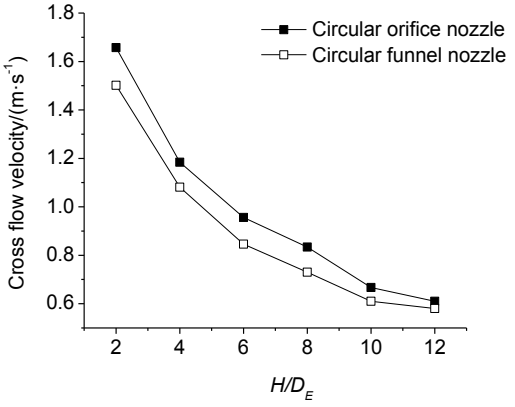

Figure7: Cross flow velocity distribution at 10 mm above the steel strip surface.

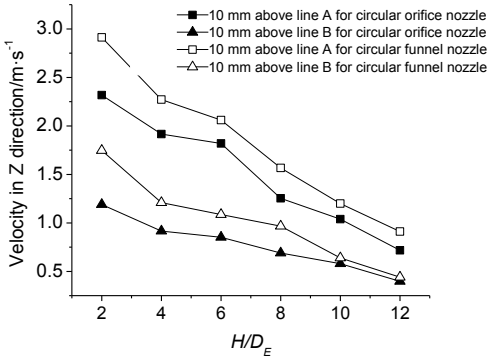

Figure 8:The velocity in Z direction at 10 mm above line A and line B.

Flow vector diagram of nozzle outlet was shown in Fig. 9. For circular funnel nozzle, the "convex" shaped area formed between the two kinds of nozzle structures was a cross flow buffer zone.On the one hand, the velocity of the cross flow in the channel was reduced. Therefore, the average Nusselt number under the circular funnel nozzle was more significant. On the other hand, the velocity in Z direction above line B was enhanced by the large vortex formed on the left of the circular funnel nozzle.So the average Nusselt number on the line B was increased and the heat transfer uniformity index was decreased.

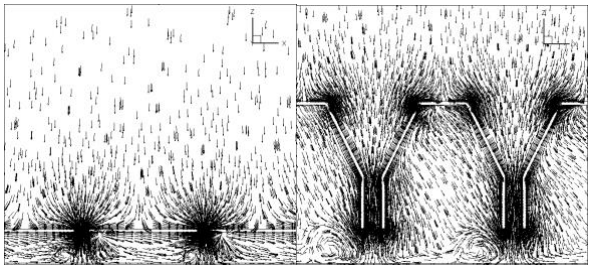

a: Circular orifice nozzle b: Circular funnel nozzle

Figure 9. Flow vector diagram of nozzle outlet.

4. CONCLUSIONS

In this paper, two kindsof nozzle structures of impinging quick-freezing experimental table were taken as the research object.When the mass flow rate at the cooling air inlet was same,the influence of the nozzle-to-surface distance on the heat transfer characteristics under the circular orifice nozzle and circular funnel nozzle was compared. The main findings were shown as flollows:

(1) When the H/D_E was in the range of 2 to 12, the average Nusselt number under the circular funnel nozzle was 5.41%-15.10% higher than that under the circular orifice nozzle. And the heat transfer uniformity index undercircular funnel nozzle was 7.06%-34.52% lower than that under circular orifice nozzle. As the H/D_E increasing, the η different between the two kinds of nozzle structures was gradually decreased.The circular funnel nozzle was recommended to reduce the freezing time.

(2) When the H/D_E was in the range of 2 to 12, the average Nusselt number on the steel strip surface under the two kinds of nozzle structures was greatly influenced by H/D_E and less affected by cross flow.

ACKNOWLEDGEMENTS

This work was supported by the Special Fund for Development of Science and Technology of Shanghai Ocean University (No. A2-0203-17-100207), National Key R&D Program of China (No. 2016YFD0400303), Shanghai Science and Technology Commission Platform Capacity Building Project (No. 16DZ2280300), Shanghai Municipal Science and Technology Commission Public Service Platform Building Project (No. 17DZ2293400), Young Teachers Training Funding Scheme of Shanghai University (No. ZZSHOU16013), Doctoral Research Fund of Shanghai Ocean University (No. A2-0203-17-100317).

REFERENCES

Huan, Z., Ma, Y., He, S.,2003. Airflow blockage and guide technology on energy saving for spiral quick-freezer. International Journal of Refrigeration 26(6), 644-651.

Shaikh, N I., Prabhu, V.,2007. Mathematical modeling and simulation of cryogenic tunnel freezers. Journal of Food Engineering 80(2), 701-710.

Yang, B., Chang, S., Wu, H., et al.,2017. Experimental and numerical investigation of heat transfer in an array of impingement jets on a concave surface. Applied Thermal Engineering 127(25), 473-483.

Lee, J., Ren, Z., Ligrani, P., et al., 2015. Crossflows from jet array impingement cooling: Hole spacing, target plate distance, Reynolds number effects. International Journal of Thermal Sciences 88, 7-18.

Shan, Y., Zhang, J, Z., Xie, G, N. 2015. Convective heat transfer for multiple rows of impinging air jets with small jet-to-jet spacing in a semi-confined channel. International Journal of Heat & Mass Transfer 86, 832-842.

Yu, P., Zhu, K., Sun, T., et al.,2017. Heat transfer rate and uniformity of mist flow jet impingement for glass tempering. International Journal of Heat and Mass Transfer 115, 368-378.

Li, D., Zhu, Z., Sun, D, W.,2018. Effects of freezing on cell structure of fresh cellular food materials: A review. Trends in Food Science and Technology, 75, 46-55.

Wen, J, L. 2011. Fundamentals of Fluid Mechanics. Bei Jing: China MachinePress,55-65.

Xu, L,. Jin, L,. Ma Y, et al., 2017. Numerical study on heat transfer by swirling impinging jets issuing from a screw-thread nozzle. International Journal of Heat and Mass Transfer 115, 232-237.

Zhu, X, W., Zhu, L., Zhao, J, Q. 2017. An in-depth analysis of conjugate heat transfer process of impingement jet. International Journal of Heat and Mass Transfer 104, 1259-1267.

Li, Y., Li, B., Qi, F., et al., 2018. Flow and heat transfer of parallel multiple jets obliquely impinging on a flat surface. Applied Thermal Engineering 133(25), 588-603.

Chen, L., Brakmann, R, G, A., Weigand, B., et al., 2017. Experimental and numerical heat transfer investigation of an impingement jet array with V-ribs on the target plate and on the impingement plate. International Journal of Heat and Fluid Flow 68,126-138.

Hou, Y., Tao, Y., Huai, X., et al., 2018. Numerical simulation of multi-nozzle spray cooling heat transfer. International Journal of Thermal Sciences 125, 81-88.

Wang, J, F., Li, W, J., Xie J., et al., 2017. Influence of two ddifferent nnozzle fforms on the flow field and heat transferring characteristics. Food and Machinery 33(12), 80-85+90.

Chen, L, Q., Zhang, D., Chen, W., 2014. Numerical simulation and test on two-phase flow inside shell of transfer case based on fluid-structure interaction. Transactions of the Chinese Society of Agricultural Engineering (Transactions of the CSAE) 30(4), 54-61.

Attalla, M., Maghrabie, H, M., Qayyum, A., et al., 2017. Influence of the nozzle shape on heat transfer uniformity for in-line array of impinging air jets. Applied Thermal Engineering 120(25), 160-169.

Wen, Z, X., He, Y, L., Ma, Z.,2018. Effects of nozzle arrangement on uniformity of multiple impinging jets heat transfer in a fast cooling simulation device. Computers and Fluids 164(15), 83-93.

Ma, C., Yan, C., Cao, X, W., et al., 2016. Numerical Study on Array Air jet heat transfer uniformity. Journal of Engineering Thermophysics, 37(11): 2378-2384.

Meena, H, C., Reodikar, S, A., Vinze, R., et al., 2016. Influence of the shape of the orifice on the local heat transfer distribution between smooth flat surface and impinging incompressible air jet. Experimental Thermal & Fluid Science 70: 292-306.

Vinze, R., Chandel, S., Limaye, M, D., et al., 2016. Effect of compressibility and nozzle configuration on heat transfer by impinging air jet over a smooth plate. Applied Thermal Engineering 101: 293-307.

Nuntadusit, C., Wae-Hayee, M., Tekasakul, P., et al., 2012. Local heat transfer characteristics of array impinging jets from elongated orifices. International Communications in Heat and Mass Transfer 39(8): 1154-1164.

Katti, V., Prabhu, S, V., 2009. Influence of streamwise pitch on local heat transfer distribution for in-line arrays of circular jets with spent air flow in two opposite directions. Experimental Heat Transfer 22(4): 228-256.

Manuscript ID: 1463
DOI: 10.18462/iir.icr.2019.1463

Modelling freezing of food products at ice crystal scales

Violette MULOT[(a,b,c)], Christophe DOURSAT[(b)], Hayat BENKHELIFA[(a,b)], Fatou-Toutie NDOYE[(a)], Didier PATHIER[(c)], Denis FLICK[(b)]

[(a)]IRSTEA, UR GPAN, Refrigeration Process Engineering Research Unit, Antony, F-92160, France, violette.mulot@irstea.fr
[(b)]UMR Ingénierie Procédés Aliments, AgroParisTech, INRA, Université Paris-Saclay, Massy, F-91300, France
[(c)]Air Liquide, Paris-Innovation Campus, Jouy-en-Josas, F-78350, France

ABSTRACT

During food freezing, controlling the crystallization is a key factor in quality. Most often, modelling of freezing is carried out assuming local thermodynamic equilibrium, considering the food product as an equivalent monophasic material and solving numerically the problem with cells much larger than the ice crystals. In the present work, a numerical model was developed at the scale of the ice crystals with cells of some micrometers. This way, the solute/water mutual diffusion and the conduction of latent heat released in the vicinity of each crystal is directly taken into account. The model was implemented with MatLab® on a 2D mesh by considering in each cell the temperature (energy equation) and the volume fraction of water, ice and solutes (phase change and diffusion equations). The model allows analyzing and explaining the influence of heterogeneous nucleation sites and surrounding temperature on the evolution of ice fraction and crystals size distribution.
Keywords: Modelling, Ice Crystals, Crystallization, Food Solution.

1. INTRODUCTION

Freezing allows preserving food and extending shelf life by reducing the product temperature and thanks to water crystallization. The crystallization process is divided into two mechanisms: nucleation and crystal growth.
First, nucleation is the precipitation of water molecule due to a sub-cooling under the equilibrium fusion temperature: the system will evolve to reach the thermodynamic equilibrium by nucleation (Kashchiev et al., 2003). Only nuclei reaching a sufficient size defined as the critical radius can grow and form ice crystals. Secondly, crystal growth is led by three main mechanisms: the incorporation of water molecules to the crystal, the water diffusion from the liquid phase to the crystal surface and the dissipation of the latent heat of water solidification by conduction (Hartel, 2001; Kiani et al., 2011). Thus, nucleation and crystal growth rates control the final number and sizes of ice crystals. These rates are function of the freezing rate (temperature decrease versus time): an increase of the freezing rate leads to more numerous and smaller ice crystals as demonstrated in various food products: bakery dough (Mousavi et al., 2005, Ban et al., 2016), fish (Kaale et al., 2013, Kobayashi et al., 2015) and meat (Mousavi et al., 2007). For food and biological products, ice crystal characteristics (size, shape and location) have a direct impact on the microstructure because crystals may provide irreversible cell and tissue damages resulting on quality losses (Alizadeh et al., 2007, Boonsumrej et al., 2007).
Some models were developed to predict crystallization in solutions from nucleation and crystal growth rate expressions (Hartel, 2001; Kiani et al., 2011; Leiter et al., 2016) according to the deviation of the system from the thermodynamic equilibrium (Bald, 1991). Based on these assumptions, the population balance method (Randolph et al., 1988) was able to predict, in a representative elementary volume, the crystal size distribution. This method is expressed as a non-linear differential equation describing the

number of crystal incoming and outgoing in a certain range of size due to crystal growth and nucleation. To our knowledge, only one model was developed for freezing, considering energy and mass transfer at ice crystal scale for each phase of a sucrose solution (van der Sman, 2016). A phase field method was used for the numerical solving at the interface between the liquid and the solid phase.
The aim of the present work is to develop a crystallization model at ice crystal scale in a solution during freezing. This 2D model solves the energy and mass transfer in each phase (liquid and solid) of the solution during freezing, using an original level-set finite volume method. With this model, the temperature and the volume fraction of water, ice and solute are estimated in each cell. Some simulations were performed to predict the crystallization characteristics in a sucrose solution according to the freezing conditions (mechanical and cryogenic).

2. MATERIALS AND METHODS

2.1. Main Assumptions of Modelling

The model aims to predict crystallization in 2D for a motionless solution during freezing. For this article, the model was applied to a sucrose solution, so two components were considered: water (or ice) and sucrose, and two phases: liquid (water/sucrose) and solid (ice). Expansion due to freezing and density variation with temperature or solute concentration were neglected. The model considers a rectangular slice (width=200 µm, height=10 mm) of plate-like product from the symmetry plane to the surface which is cooled down by cold air or nitrogen. The stochastic secondary nucleation is assumed: nucleation sites are randomly located with a given nuclei density. Nucleation on such a site begins if a sufficient super-cooling is reached (Eq. (1)):

$$T < T_{eq}(C_s) - \Delta T_s \qquad \text{Eq. (1)}$$

where $T_{eq}(C_s)$ is the equilibrium freezing temperature which depends on the solute fraction in the liquid phase (C_s) and ΔT_s is a random super-cooling. Here a uniform distribution law between 2 and 5°C was assumed for ΔT_s.

2.2. Transfer Phenomena

Energy and mass transfer equations are separately written for each phase.
There is no solute in the solid phase, only heat conduction is considered throughout crystals. The energy conservation equation coupled with Fourier's law gives Eq. (2) (Second Fourier's law):

$$\rho C_{pi} \frac{\partial T}{\partial t} = \vec{\nabla}.\left(\lambda_i \vec{\nabla} T\right) \qquad \text{Eq. (2)}$$

where ρ is the density, Cp_i is the mass specific heat capacity of ice, T is the temperature, t is the time and λ_i is the ice thermal conductivity.
In the liquid phase, mutual sucrose/water diffusion has to be taken into account. Indeed, when an ice crystal grows, liquid water concentration decreases near its surface but solute remains in the liquid phase where its concentration increases. Thus, sucrose concentration gradients appear. Coupling the mass conservation equation and Fick's law leads to Eq. (3) (Second Fick's law):

$$\frac{\partial S}{\partial t} = \vec{\nabla}.\left(D \vec{\nabla} C_S\right) \qquad \text{Eq. (3)}$$

where S is the sucrose volume fraction in the product and D is the sucrose diffusivity in water.
As for the solid phase, heat conduction is considered throughout the liquid phase (Eq. (4)):

$$\rho C p_l \frac{\partial T}{\partial t} = \vec{\nabla}.\left(\lambda_l \vec{\nabla} T\right) \qquad \text{Eq. (4)}$$

where Cp_l is the mass specific heat capacity of the liquid phase (water and solute) and λ_l its thermal conductivity.

2.3. Interface and Boundary Conditions

At the interface between the liquid and the solid phase, crystal growth happens. The growth rate (G_i in m s^{-1}) is calculated thanks to Eq. (5):

$$G_i = \alpha\left(T_{eq}(C_s) - T\right) \quad \text{Eq. (5)}$$

where α is the crystalline growth coefficient which here only takes into account the resistance of incorporation for the water molecules in ice crystal structure.
As explained above, crystals are formed as pure ice, the solute remains in the solution and tends to move away from the crystal surface. So, the sum of the diffusive flux in the liquid phase (l) and convective flux is null at the interface (Eq. (6)):

$$\left(-D\vec{\nabla}C_s.\vec{n}\right)|_l + G_i S = 0 \quad \text{Eq. (6)}$$

$\vec{n}$ is the unit normal vector to the interface oriented from the solid phase to the liquid phase.
The heat flux continuity is expressed with Eq. (7) considering the heat conduction in the solid (i), the heat released by the water solidification and the heat conduction in the liquid phase (l):

$$\left(-\lambda_i\vec{\nabla}T.\vec{n}\right)|_i + \rho G_i L_f = \left(-\lambda_l\vec{\nabla}T.\vec{n}\right)|_l \quad \text{Eq. (7)}$$

where L_f is the latent heat of water fusion.
There is no heat flux at the lateral faces and at the symmetry plane. At the product surface, the conductive heat flux is released to the surrounding cold air by convection (Eq. (8)):

$$-\lambda\vec{\nabla}T.\vec{n} = h(T - T_{\text{ext}}) \quad \text{Eq. (8)}$$

where h is the convective heat transfer coefficient, T_{ext} is the temperature of the surroundings.
At all boundaries, there is no solute flux.

2.4. Numerical Solution

Different numerical techniques can be employed to solve such a numerical problem considering moving interfaces. First, a moving mesh can be used so that each cell still contains only one phase (either solid or liquid). Secondly, a phase field approach can be applied as done by van der Sman (2016). Here an original level-set approach was implemented where a cell can contain both phases if an interface crosses the cell.
For the space discretization in 2D, a finite volume method with a fixed mesh of squares (of size Δx) was used. Each cell is characterized by the temperature (T), and the volume fraction of ice (I), of liquid water (W) and of solute (S). Most of the cells are only composed of one phase: liquid (I=0 C_s=S/(S+W)) or solid (I=1, W=S=0). When an interface belongs to a cell, it contains both phases. The position of the interface is not precisely determined, but the volume fraction of each phase in the cell is known: the volume fraction of the solid corresponds to I and the volume fraction of the liquid phase to S+W. In all the case, the solute fraction in the liquid is C_s=S/(S+W).
The numerical solving is divided into three steps in the following order: crystallization, solute diffusion and heat conduction.

2.4.1 Crystallization

The ice crystallization is solved with an explicit scheme.
A nucleus in a cell is activated if the local temperature is low enough according to Eq. (1) that takes into account the equilibrium temperature and the super-cooling. In cells where a nucleus was activated, the ice volume fraction is set to a small value ε and crystal growth can begin.
For example, if the problem of crystallization is considered in 1D and we suppose a cell (1) containing only ice, an adjacent cell (2) containing ice and liquid solution (water and solute) and a last cell (3) filled

only with liquid. During the time step (Δt), there is no modification for cell (1), it is still full of ice. For cell (2), the volume fraction of ice increases by ΔI which is calculated by Eq. (9):

$$\Delta I = G_i \frac{\Delta t}{\Delta x} \quad \text{Eq. (9)}$$

So, the new volume fraction of water in cell (2) is decreased by ΔI. In this cell, if the ice volume fraction increase ΔI is higher than the remaining water volume fraction ($\Delta I > W$), ice overflows in the next cell (cell (3)) and cell (2) is full of ice. In cell (3), the new volume fractions are also updated. Ice growth only occurs in cells containing solid/liquid interface.

2.4.2 Solute diffusion

The solute diffusion is solved with an ADI scheme (Alternative Direction Implicit) to improve the numerical stability.
The solute diffusion in the liquid phase is taken into account by Fick's law as shown by Eq. (3). One of the key parameter of this model is the diffusivity of the solute in water. This diffusivity strongly depends on the viscosity and the temperature of the solution. A reference value for the diffusivity of sucrose in water (D_0) was taken as 0.52×10^{-9} m² s^{-1} (dilute solution at T_0=25°C) (Bimbenet *et al.* 2002). Then, from this reference, Stokes-Einstein law was used to link the diffusivity to the temperature and to the dynamic viscosity of the solution (Eq. (10)):

$$D = \frac{k(T + 273.15)}{6\pi r \mu} \Rightarrow D = D_0 \frac{T + 273.15}{T_0 + 273.15} \frac{\mu_0}{\mu} \quad \text{Eq. (10)}$$

μ_0 is the dynamic viscosity of pure water at 25°C and μ is the viscosity of the sucrose solution estimated as a function of the temperature and the solute fraction in the solution with Génotelle equation (1978) (Bubník *et al.* 1996) (Eq. (11)):

$$\mu = 10^{-3} 10^{22.46N - 0.114 + M\left(1.1 + 43.1N^{1.25}\right)} \quad \text{Eq. (11)}$$

$$\text{with } N = \frac{100C_s}{1900 - 1800C_s} \text{ and } \mathrm{M} = \frac{30 - \mathrm{T}}{91 + \mathrm{T}}$$

2.4.3 Heat conduction

The conduction is also solved with an ADI scheme including the heat released by water crystallization in cells containing phase interfaces: $L_f \Delta I$.
The model was implemented with MatLab® for a cell size of 2.5 µm. The time step was chosen so that the maximal value of ice fraction increase ΔI remains lower than 5%. This way, it was possible to calculate at each time step and for each cell of the mesh, the corresponding temperature and the volume fractions of water, ice and sucrose.

3. RESULTS AND DISCUSSIONS

A sucrose solution of 20% w/w with an initial temperature of 0°C was considered. Simulation were run for a mechanical freezing condition (T_{ext}=-30°C, h=55 W m^{-2} K^{-1}) and a cryogenic freezing condition (T_{ext}=-100°C, h=67 W m^{-2} K^{-1}) until the product core temperature reaches -18°C.

3.1. Freezing monitoring at microscopic scale

Data estimated by the model were used to monitor the various variables during the freezing process.

Results of temperature, ice volume fraction and solute volume fraction in the solution were visualized near the product surface (from 0 to 400 µm depth) for three different times: at the beginning of freezing

(t=50 s), at about mid-time (t=800 s) and at the end (t=1320 s) for T_{ext}=-30°C (Fig. 1).
After 50 s of freezing (Fig. 1), the surface temperature is close to -5°C. The super-coiling is low enough to activate some nucleation sites where crystal growth starts. The solute fraction is zero inside the

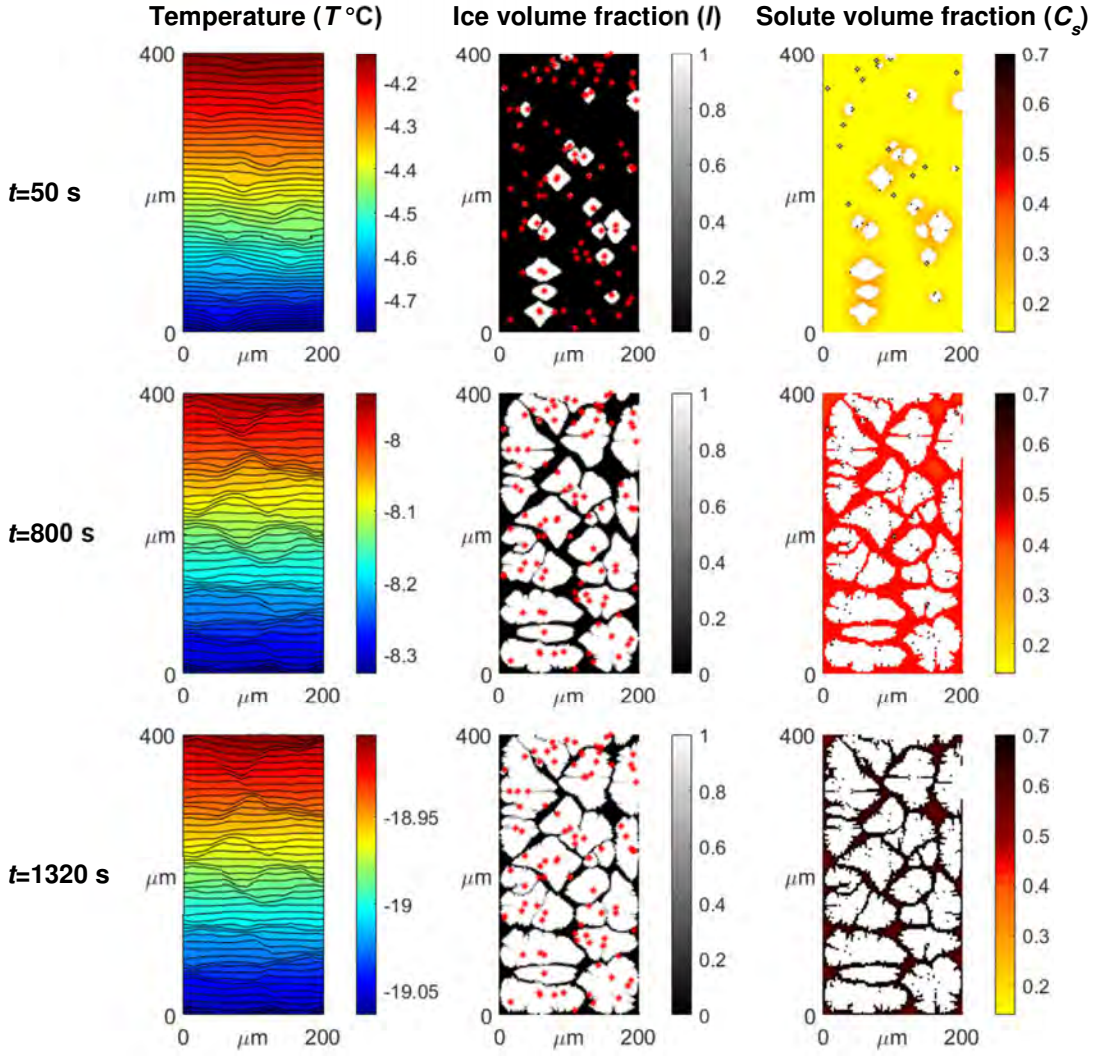

Figure 1: Temperature, volume fraction of ice and solute volume fraction in the solution near the product surface during freezing (t=50 s, t=800 s and t=1320 s). Black lines on temperature diagrams represent temperature isotherms. Red points on diagrams of ice volume fraction are the positions of nucleation sites

crystals and solute is repealed from the crystal surface, increasing the solute fraction in the solution in their vicinity.
During freezing, the heat is conducted throughout the product from its core to its surface where it is released. Thermal conductivity is about 4 times higher for ice than for the unfrozen solution. So, the temperature gradients are lower in the ice crystals than in the unfrozen solution. This phenomenon is revealed by temperature isotherms on Fig. 1.
Considering the ice volume fraction, during freezing, the cooling allows activating deeper and more numerous nucleation sites leading to crystal growth.
Finally, crystals keep growing until the end of freezing, repealing the solute which volume fraction increases in the remaining unfrozen solution.
Temperature versus time is plotted on Fig. 2 for the product surface, its core and for 3 points A, B and C. For all the points, three main freezing periods are observed: pre-cooling, freezing step and sub-cooling. Moreover, the phenomenon of super-cooling is noticeable between the pre-cooling and the

freezing step. This super-cooling is needed for nucleation, once nucleation sites are activated the nuclei grow rapidly and a large amount of latent heat of solidification is released. This is why temperatures suddenly increase after super-cooling. This super-cooling is lower for the mechanical condition (surface reaches -5°C before freezing) than for the cryogenic one (surface reaches -10°C before freezing) which means that less nuclei would grow as crystals. Furthermore, for both conditions, the super-cooling is high at the product surface and becomes lower when going deeper in the product.

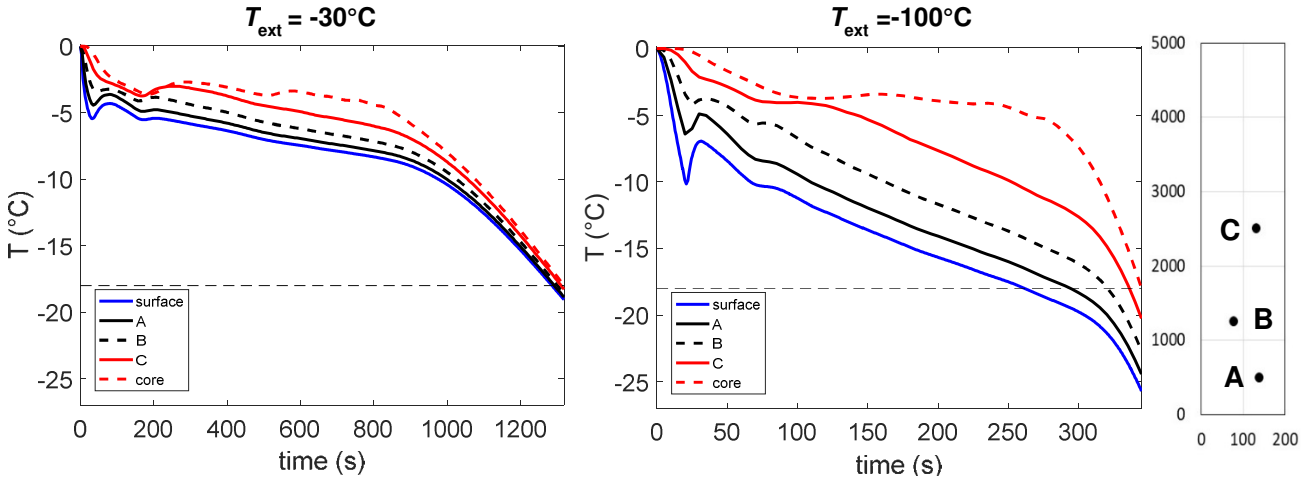

Figure 2: Temperature at the surface, core and at position A, B and C of the product according to the freezing time. The diagram on the right shows the location of A, B and C

3.2. Final results on ice crystals

Fig. 3 presents the ice crystals from the product surface to a 2500-µm-depth for both freezing temperatures at the end of freezing (when core temperature reaches -18°C). From these results, a graph showing each crystal equivalent diameter according to its depth in the product is deducted (the equivalent diameter is the diameter of a circle having the same surface as the crystal).
Crystals are smaller for T_{ext}=-100°C (about 18 µm) than for T_{ext}=-30°C (50-100 µm). Moreover, crystals are smaller near the surface and larger at the product core: averagely the crystal size increases from 50 to 100 µm for T_{ext}= -30°C. Indeed, as shown on Fig. 2, going closer to the product core decreases the freezing rate and nucleation. However, for the fast freezing (-100°C), this effect is less visible: crystal size increases from 15 to 18 µm. When the freezing rate is high (Fig. 2), nucleation is almost simultaneous in the whole product and many small ice crystals are formed throughout the product.
Finally, equivalent diameters were estimated from final results for each crystal in the whole sample. Fig. 4 presents the corresponding cumulative crystal size distributions. Results given by the developed model evolves in the same way as what can be found with experiments. Indeed, crystals are about twice smaller for the freezing at -100°C (median=36.7 µm) than for the freezing at -30°C (median=70.8 µm). Moreover, the distribution is narrower for -100°C (range: 16 to 90 µm) than for -30°C (range 16 µm to 190 µm) as can also be seen on Fig. 3. These results point out the positive effect of the freezing rate on ice crystal characteristics.

4. CONCLUSIONS

The model developed at ice crystal scale is able to predict ice crystal growth throughout the product considering ice crystallization, solute diffusion and heat transfer at microscopic scale. Moreover, various freezing conditions can be compared with this model. First, a qualitative comparison can be easily done by visualization of all the crystals at different times and different positions. Secondly, quantitative results about the crystal size distributions can be obtained. Results highlight the effect of the freezing rate on crystal size distributions and numbers (much smaller and numerous crystals for cryogenic conditions) and also of the position in the product (smaller crystals near the product surface).

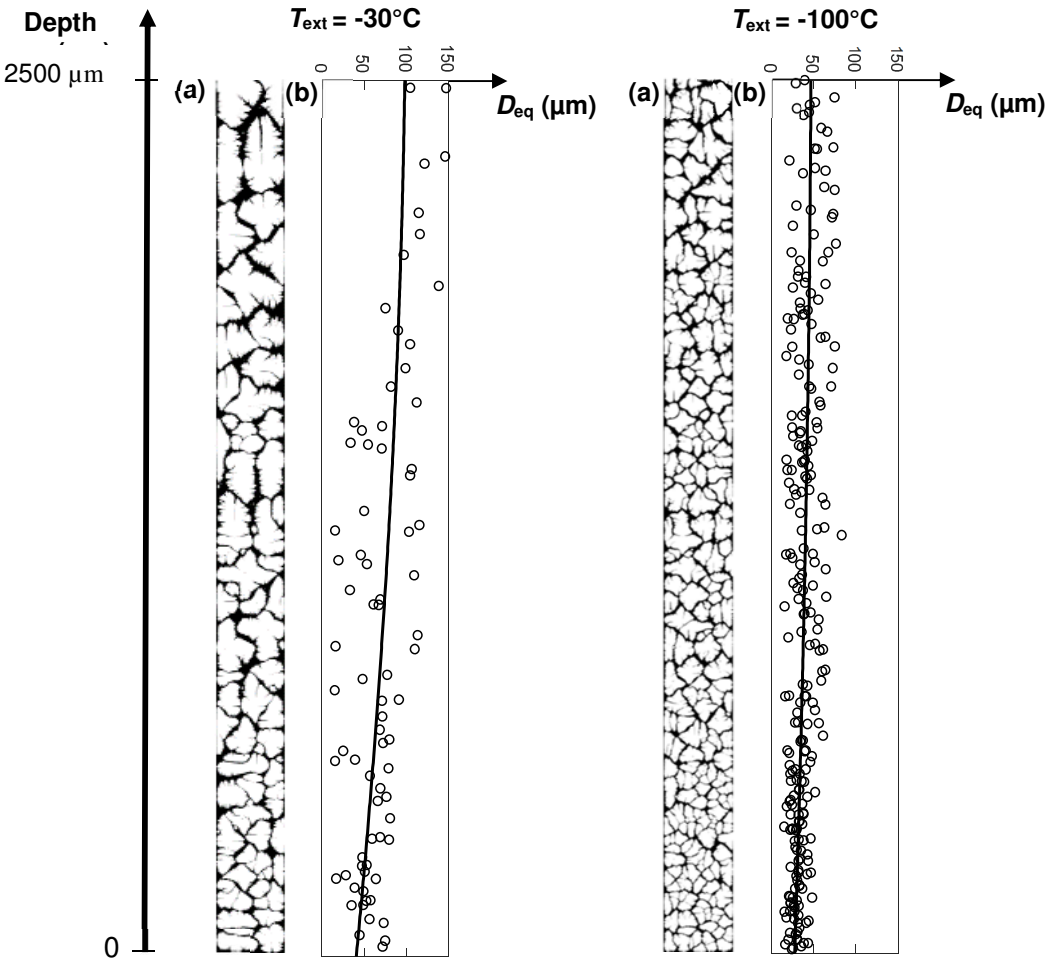

Figure 3 : Ice crystals at the end of freezing from the product surface to a 2500-µm-depth for a freezing at -30°C and at -100°C. Ice crystal visualizations (a) and ice crystal equivalent diameter according to the product depth (b)

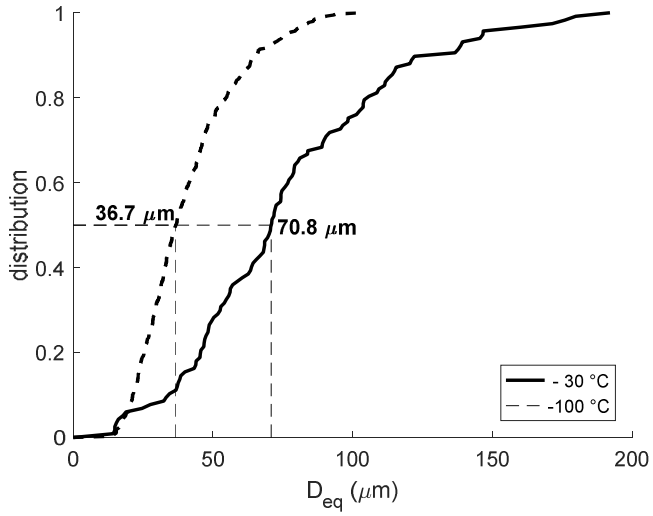

Figure 4: Predicted distributions of equivalent diameter of ice crystals for a freezing at -30°C (h=55 W m^{-2} K^{-1}) and -100°C (h=67 W m^{-2} K^{-1})

ACKNOWLEDGEMENTS

The authors gratefully acknowledge the financial support granted by the CIFRE department (Conventions Industrielles de Formation par la Recherche) from the French ANRT (Association Nationale Recherche et Technologie).

REFERENCES

Alizadeh, E., Chapleau, N., de Lamballerie, M. and Le-Bail, A., 2007. Effect of different freezing processes on the microstructure of Atlantic salmon (Salmo salar) fillets, Innovative Food Science & Emerging Technologies 8(4), 493-499.

Bald, W. B., 1991. Food freezing, Today and Tomorrow.

Ban, C., Yoon, S., Han, J., Kim, S. O., Han, J. S., Lim, S. and Choi, Y. J., 2016. Effects of freezing rate and terminal freezing temperature on frozen croissant dough quality, Lwt-Food Science and Technology 73, 219-225.

Bimbenet, J. J., Duquenoy, A. and Trystram, G., 2002. Génie des procédés alimentaires-Des bases aux applications, Dunold.

Boonsumrej, S., Chaiwanichsiri, S., Tantratian, S., Suzuki, T. and Takai, R., 2007. Effects of freezing and thawing on the quality changes of tiger shrimp (Penaeus monodon) frozen by air-blast and cryogenic freezing, Journal of Food Engineering 80(1), 292-299.

Bubník, Z. and Kadlec, P., 1996. Formulas for calculation of properties of sugar solutions and sucrose crystals.

Hartel, R. W., 2001. Crystallization in Foods. Gaithersburg, Maryland, Aspen Puublishers,Inc.

Kaale, L. D. and Eikevik, T. M., 2013. A study of the ice crystal sizes of red muscle of pre-rigor Atlantic salmon (Salmo salar) fillets during superchilled storage, Journal of Food Engineering 119(3), 544-551.

Kashchiev, D. and van Rosmalen, G. M., 2003. Review: Nucleation in solutions revisited, Crystal Research and Technology 38(7-8), 555-574.

Kiani, H. and Sun, D.-W., 2011. Water crystallization and its importance to freezing of foods: A review, Trends in Food Science & Technology 22(8), 407-426.

Kobayashi, R., Kimizuka, N., Watanabe, M. and Suzuki, T., 2015. The effect of supercooling on ice structure in tuna meat observed by using X-ray computed tomography, International Journal of Refrigeration-Revue Internationale Du Froid 60, 270-277.

Leiter, A. and Gaukel, V., 2016. Food Freezing: Crystal Structure and Size. Reference Module in Food Science, Elsevier.

Mousavi, R., Miri, T., Cox, P. W. and Fryer, P. J., 2005. A novel technique for ice crystal visualization in frozen solids using X-ray micro-computed tomography, Journal of Food Science 70(7), E437-E442.

Mousavi, R., Miri, T., Cox, P. W. and Fryer, P. J., 2007. Imaging food freezing using X-ray microtomography, International Journal of Food Science and Technology 42(6), 714-727.

Randolph, A. D. and Larson, M. A., 1988. Theory of Particulate Processes - Analysis and Techniques of Continuous Crystallization, Academic Press

van der Sman, R. G. M., 2016. Phase field simulations of ice crystal growth in sugar solutions, International Journal of Heat and Mass Transfer 95, 153-161.

Manuscript ID: 1478
DOI: 10.18462/iir.icr.2019.1478

Forced-air cooling of dairy product in pallets: influence of process parameters on energy and quality

Michel HAVET[(a)], Victor GRIVIER[(a)], Fabien BATICLE[(a)], Luc GUIHARD[(a)], Edith PATISSIER[(b)], Benoit GARDES[(b)], David HUFFSCHMIDT [(b)]

[(a)] Oniris, GEPEA, CNRS
44322 Nantes, France, michel.havet@oniris-nantes.fr
[(b)] Clauger
69530 Brignais, France, dhuffschmidt@clauger.fr

ABSTRACT

Forced-air cooling of food products in pallets is a common refrigeration process. It is applied to quickly lower the temperature of dairy product from their fermentation temperature to their storage temperature. It leads to high energy consumption due to pressure drop and to heterogeneity of temperature due to the complex airflow pattern. To reduce this heterogeneity we designed a new apparatus where air is blown through the pallet alternatively by two sides. To improve energy efficiency, air velocity is adapted to pressure drop with EC fans. Experiments were conducted to evaluate the cooling rate, the heterogeneity and the energy consumption for various process parameters (fan velocity, alternation time). With the experimental design methodology, we show that short alternation time should be favored for optimal results with a drastic reduction of the heterogeneity index. Then, we propose a model and a strategy to control the cooling rate according to production constraints and energy aspects.
Keywords: Refrigeration, Food, Pallet, Cooling, Transient heat transfer, Energy Efficiency.

1. INTRODUCTION

Forced air convection is widely used to cool fresh products and some thermally treated products. Temperature control of these products stored on pallets and cooled through ventilated packaging is essential to preserve quality. Alvarez and Flick (1999a, 1999b) were among the first who pointed out preferential airflow pathways through bins. They also explained heterogeneity of cooling by the increase in air temperature when passing around products, but also by the variation of heat transfer coefficient with position. Since this pioneering work, there were numerous studies concerning cooling heterogeneity especially in the case of fruits. As the temperature-time history of fruits can be directly related to produce quality loss, non-uniform cooling induces heterogeneities in quality evolution of individual fruit. Recent works aim to quantify heterogeneities like experiments performed by Wu et al. (2018) on citrus. Numerical modelling is more and more performed to study the complex phenomena in these systems. The review done by Zhao et al. (2016) confirmed that CFD is an efficient tool for simulating different cooling processes in the fresh-produce industry. Wu and Defraye (2018) performed simulation that combined temperature-time history with quality evolution for each individual fruit. To provide retailers and customers with a uniform product quality, reducing cooling heterogeneity is imperative. An important factor affecting cooling heterogeneity is the ventilated package design and their stacking pattern on the pallet. If most of studies concern the postharvest supply chains, similar problems also arise for other products. With a modelling approach Mercier et al. (2017b) mapped the temperature inside a pallet of fish fillets from a limited amount of temperature measurements inside the pallet.
In their review, Mercier at al. (2017b) pointed out that precooling is critical for removing heat from perishable food after harvesting or production. They identified 3 specific subjects as being

critical to investigate in future research on the cold chain: efficient precooling, accurate forecasts of the impacts of management systems based on time–temperature measurement, the cold chain in developing countries.
For dairy products like yoghurts and cheese, these conclusions are very relevant. In Middle East countries, refrigeration is generally carried out in conventional cooling chambers. This treatment is then rather long, leads also to thermal heterogeneity inside the pallet and to inhomogeneous qualities of products. To improve product qualities and to reduce cooling time, specific equipments are required. In their conclusion, Alvarez and Flick (199b), indicated that alternating the airflow direction though the product would homogenise not only the air temperature but also the local intensity of heat transfer. It is on this principle that was designed the bi-way cell. In this work, we analysed the time-history temperature of yoghurt during cooling in this system and characterised heterogeneity and energy consumption according to process parameters.

2. EXPERIMENTAL DESIGN

2.1. The 'Bi-Way' Cell

As the refrigeration of yoghurts is generally carried out in conventional cooling chambers, the treatment is long and heterogeneous. To overcome these phenomena, a specific device 'the bi-way cell' was designed to allow the ventilation of the products with alternating airflows so that they can benefit from similar exposure period on both sides. At the rear of the cell, a blower (EC fan) is positioned to suck the air from the cooling chamber. When a pallet is introduced in the cell, cold air enters in this latter by one side and flows across the pallet during a chosen time. A system of flaps permits to modify the direction of the flow and to alternate airflows until the desired treatment is reached. Experiments were performed on this device equipped with airbags to adapt to the size of the pallet and to limit air leakages. Fig. 1 presents a sketch of the cell and depicts the possible arrangements of airflows. In all experiments, the initial arrangement is with air coming from the left (b). The alternation time is defined as the duration of a cycle.

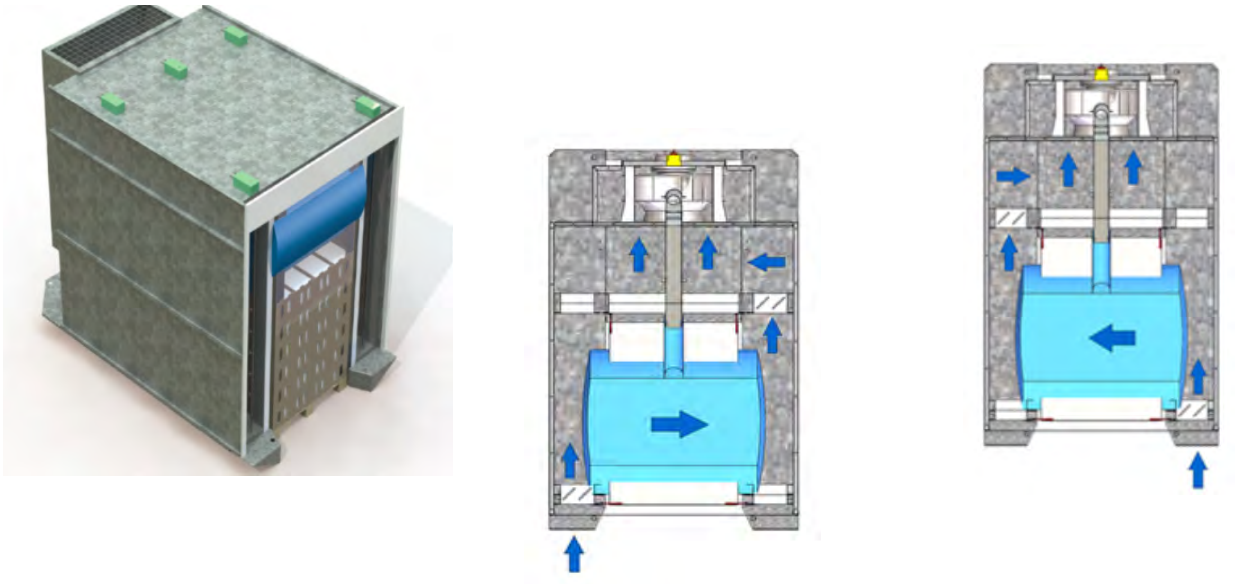

(a) (b) (c)

Figure 1: Biway cell (a), top view with two airflow conditions: from the left (b), from the right (c)

2.2. Experimental Procedure

As the objective of this study is to evaluate the real benefit of alternating airflows by considering a multi-criteria approach, experiments were conducted on a pallet of yoghurts in ventilated package (Fig. 2). Each package contains 16 yoghurts on two stages. Thermocouples are inserted in the geometrical centre of 34 yoghurts located in the second layer of packages when starting from the top. Their locations are chosen to get information on the heterogeneities on transverse and longitudinal directions. Some thermocouples are also located at other layers and in the air. Air temperatures on both sides of the cell are also recorded. Energy measurements are performed using an energy counter connected to the electrical input of the blower. All data are recorded on a data logger (SA70, AOIP).

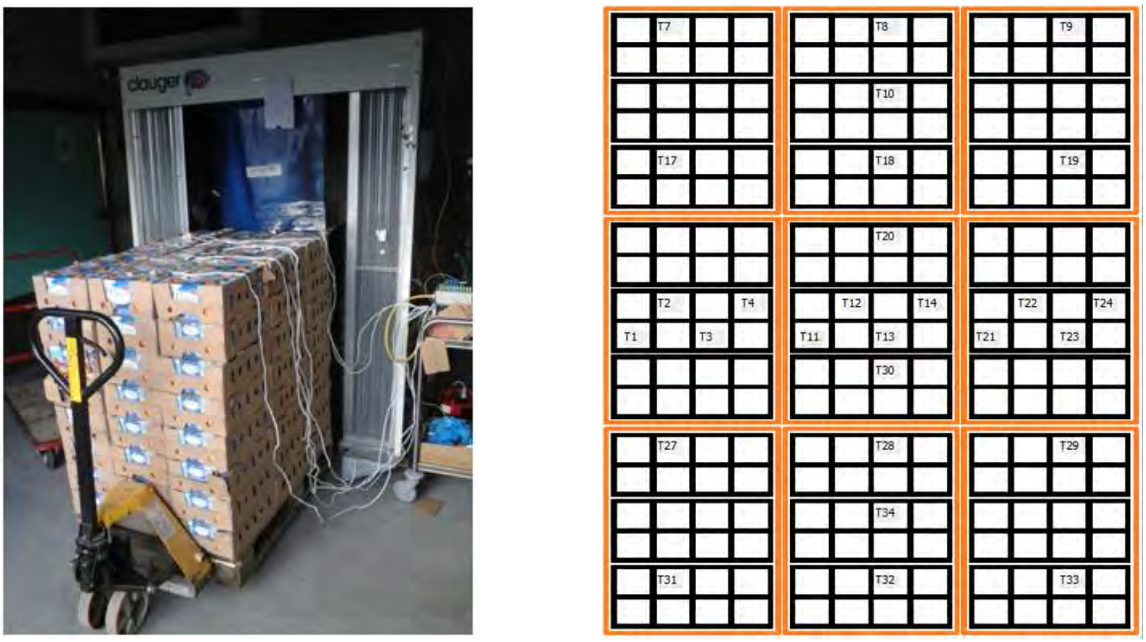

(a) (b)

Figure 2: Pallet of yoghurts (a) and scheme of yoghurts with thermocouples (b, top view)

All experiments are performed on yoghurts that were stored over night at 50°C with thermocouples previously installed. They are palletized and introduced in the cell located in a cold chamber where temperature is controlled at 8°C. Experiments are running until the temperature of all yoghurts is less than 12.5°C.
For the experimental design, two parameters are considered: the flow rate and the duration of each alternating cycle. The maximum flow rate is fixed at 13000 m^3/h. The maximum duration of a cycle is 30 minutes. From these considerations, a central composite design is performed with parameters given on table 1, leading to 10 experiments.

Table 1. Central composite design

-	-α	-1	0	1	α
Flow rate (%)	15	31	57	83	100
Alternation time (min)	0	6,07	15	23.93	30

The response variables are the half cooling time (HCT), the energy consumption and the heterogeneity of cooling by looking at the maximum variance of products temperature and the maximum value of reheating.
As it is quite difficult to have always similar initial constant temperature of products and to keep always the same ambient temperature in the cooling chamber, we treat the data to get dimensionless temperature. Like recommended by Olatunji et al. (2015) on kiwis, we used the Fractional Unaccomplished Temperature Change, or FUTC defined by Eq. (1). *T(t,n)* corresponds to the temperature of the nth yoghurt at the time *t*, *Ta* is the mean air temperature and *Tmax* is the maximum temperature reached by the nth yoghurt. Defraye et al. (2017) also employed this concept on apples. In our cell, the maximum temperature is not always the initial one due to the alternation of the flow. In fact we may observe some reheating at some location due to the alternating air flow system. In order to compare different experiments, a dimensionless time is also considered using the Average Fractional Unaccomplished Temperature Change described by Eq. (2). It describes the proportion of cooling yet to be achieved. *m* represents the total number of yoghurts. As indicated by Olatunji et al. (2015), the difference between these two concepts permits to determine the temperature variability (Eq.3). The heterogeneity index over time can be plot to offer a visual tool to compare the heterogeneity of two systems across the entire cooling process.

$$FUTC(t,n) = \frac{T(t,n)-T_a}{Tmax(n)-T_a} \quad \text{Eq. (1)}$$

$$AFUTC(t) = \frac{\sum_{n=1}^{m} FUTC(t,n)}{m} \quad \text{Eq. (2)}$$

$$HI(t) = FUTC(t,n) - AFUTC(t) \quad \text{Eq. (3)}$$

In our experiments, it is not possible to reach AFUT=0. This condition would require an infinite experimental cooling time. We decide to set a final value AFUT=0.3. It means that we consider a cooling time on 70% of the total temperature range, *ie* a final mean value of 12.6°C. The half cooling time is considered as an important response as it is generally the constraint fixed in the dairy industry. A powermeter installed on the blower registers the electric power on a period of 5 s. Values are then integrated to get the energy required to cool the pallet. Variance analysis (Anova) is performed using Stagraphics.

3. EXPERIMENTAL RESULTS

Typical temperature evolutions of yoghurts according to the process parameters are depicted on Fig. 3 for two experiments. Fig. 3a concerns the cooling with the maximum flow rate and an alternation period of 15 min whereas Fig. 3b concerns a lower flow rate (30%) and a higher alternation period (24 min). Time temperature history is given for thermocouples T1, T13 and T23 according to location in Fig. 2b. One can notice firstly the strong influence of the flow rate. As expected, reducing the ventilation considerably increases the cooling time. Secondly, the effect of reversing the flow has a great impact on temperature, especially for the yoghurt face

to the airflow entering in the pallet (T1). When the flow is reversed, this yoghurt is then colder than air coming from the other side because it was reheated by other yoghurts. Yoghurt in the centre of the pallet is less influenced by the alternation. From all measurements in the pallet, we calculate the AFUT and the Heterogeneity Index for each experiment. Fig. 4 presents the heterogeneity plot for same experiments as Fig. 3. These plots are qualitative tool for visually comparing the heterogeneity for different conditions. From these measurements, we calculate the maximum variance on temperature.

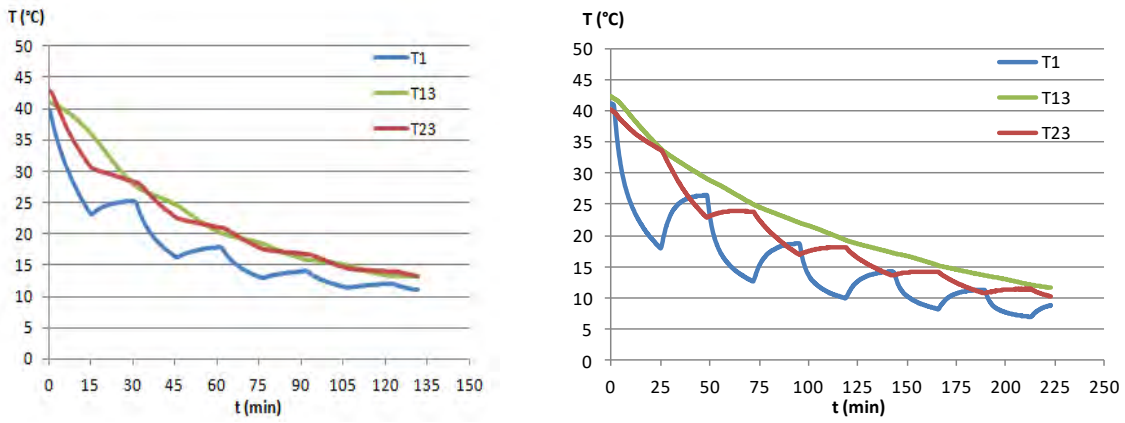

(a) (b)

Figure 3: Time temperature history in 3 yoghurts for 2 conditions of flow rate and alternating time: 100%, 15 min. (a) and 30%, 24 min. (b)

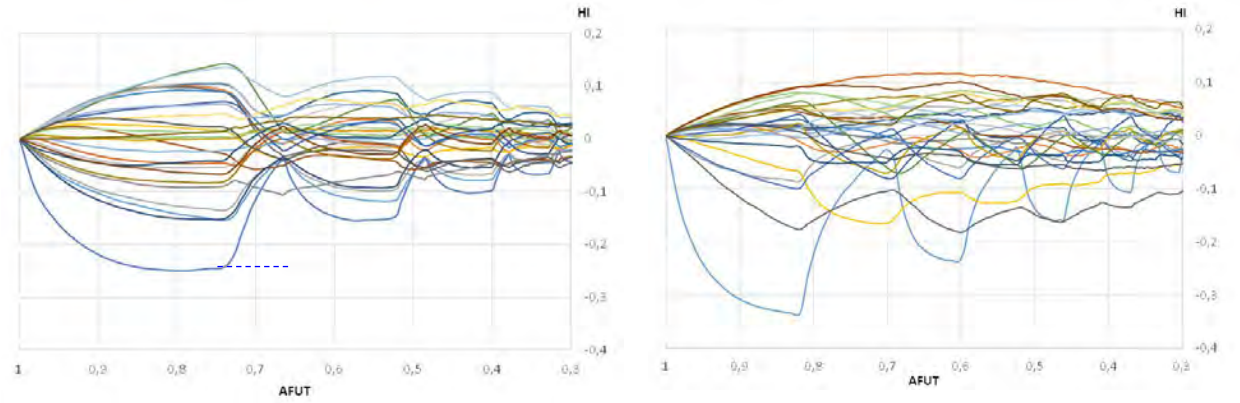

(a) (b)

Figure 4: Heterogeneity plot for 2 conditions of flow rate at and alternating time: 100%, 15 min. (a) and 30%, 24 min. (b)

Table 3 provides the different responses according to the two process parameters. Using Statgraphics a variance analysis (ANOVA) is performed as it is useful for response surface methodology. We present in this paper some selected results to emphasize on specific aspects.

Table 3. Results of the experimental design

Factor: Flow rate (%)	Factor: Alternating time (min)	Response: Half cooling time (min)	Response: Energy consumption (Wh)	Response: Heterogeneity (maximum variance)	Response: Maximum reheating (°C)
29%	6	76.6	403.2	0.0038	3.4
86%	6	33.1	3498.3	0.0060	4.8
29%	24	76.5	496.2	0.0080	14.4
86%	24	29.1	4265.2	0.0118	7.7
14%	15	249.0	249.0	0.0100	10.1
100%	15	39.1	6982.5	0.0092	13.0
57%	3	53.5	1728.0	0.0048	6.2
57%	30	63.9	2183.2	0.0123	7.7

Concerning the half-cooling time and the energy, Fig. 5 clearly indicates that the flow rate has the main effect on these responses. Decreasing the flow rate induces very high cooling time and lower energy consumption. We can also remark that the alternation has a small effect.
Concerning the heterogeneity, we can conclude from figure 6 that reducing the alternating time is very effective to reduce heterogeneity. Additional experiments, not discussed in this paper, confirmed that without any alternation heterogeneity is always greater.
We can also notice the slight effect of the flow rate. Working with a medium air velocity may reduce heterogenity. Another response about the reheating of yoghurts due to alternation was analysed but is not discussed as variance analysis was not satisfactory. It could just be mentioned that influence of flow rate is low when alternating time is short. Short alternation time permits to minimize reheating of products.

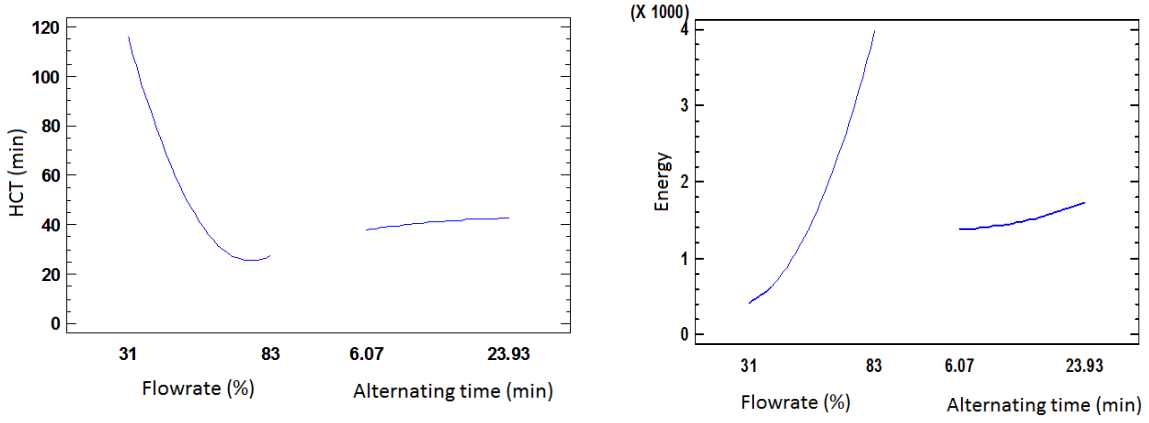

(a) (b)

Figure 5: Influence of flow rate and alternating time on Half Cooling Time (a) and Energy (b)

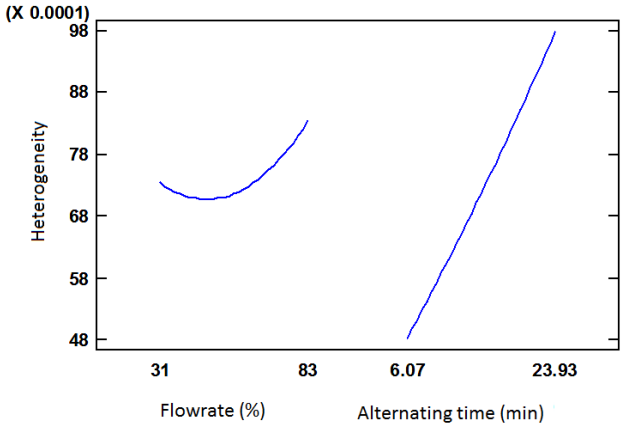

Figure 6: Influence of flow rate and alternating time on Heterogeneity Index

From the variance analysis, we plot the cartography of responses (Fig. 7). It is another way to visualize the effects of factors. According to the flow rate and alternation time, we see for example that energy (black lines) increases with flow rate, HCT decreases with increasing flow rate and heterogeneity (red lines) increases with increasing alternating time. It is then possible to determine optimum values of parameters according to the objectives. If the main objective is to respect a desired cooling time, the flow rate should be higher than 80% but if energy consumption is taken into account, it is not recommended to use the maximum flow rate. To minimize heterogeneity, an alternation time of 6 minutes seems appropriate. Results indicate that with these parameters, energy consumption is reduced from 6980 Wh to 3040 Wh (more than 50% reduction). It corresponds to a reduction from 58 kJ/kg to 25 kJ/kg of product with a better temperature homogeneity but with an increase of the half cooling time from 39 to 46 minutes.

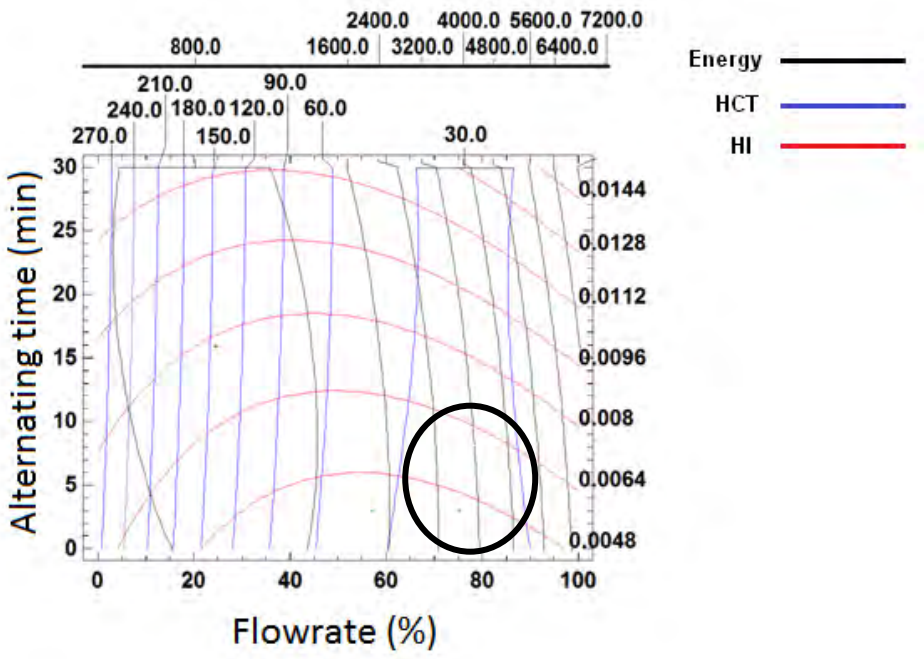

Figure 7: Response cartography (The circle corresponds to an optimal zone)

4. CONCLUSIONS

Several extensive cooling experiments were performed on yoghurts in the bi-way cell. This work permits to quantify the influence of the alternation on the airflow on the thermal

homogeneity of yoghurts. Using the concept of Fractional Unaccomplished Temperature Change (FUTC), the Heterogeneity Index that was calculated clearly demonstrates that heterogeneity can be halved with alternation cycle of 6 minutes. Moreover, the impact on energy consumption and half cooling time is negligible.
Results obtained from the experimental design also permits to propose optimal strategies according to multi-objective criteria. We quantify a 50% of energy reduction when reducing the flow rate from 100% to 80% of the nominal value. The impact on the half cooling time was also quantified. These results were obtained in a specific configuration of yoghurts for a given package. For other cases, optimum would be different. This work demonstrates that the bi-way cell is a flexible equipment that offer several cooling strategies. It allows adapting to industrial constraints of production with control of the qualitative and energetic criteria.

NOMENCLATURE

T	temperature (K)	FUTC	Fractional Unaccomplished Temperature Changed
Ta	air temperature (K)	AFUTC	Average Fractional Unaccomplished Temperature Change
Tmax	maximum temperature (K)	m	number of yoghurts
t	time (s)		

REFERENCES

Alvarez, G., Flick, D., 1999a. Analysis of heterogeneous cooling of agricultural products inside bins part I: aerodynamic study. Journal of Food Engineering, 39, 227-237

Alvarez, G., Flick, D., 1999b. Analysis of heterogeneous cooling of agricultural products inside bins part II: thermal study. Journal of Food Engineering, 39, 239-245

Defraeye, T., Wu, W., Prawiranto, K., Fortunato, G., Nicolai, B., 2017. Artificial fruit for monitoring the thermal history of horticultural produce in the cold chain. Journal of Food Engineering 215, 51-60

Mercier, S., Marcos, B., Uysal, I., 2017a. Identification of the best temperature measurement position inside a food pallet for the prediction of its temperature distribution. Int. J. Refrigeration, 76, 147–15

Mercier S., Villeneuve S., Mondor, M., Uysal, I., 2017b. Time–Temperature Management Along the Food Cold Chain: A Review of Recent Developments. Comprehensive Reviews in Food Science and Food Safety 16, 647-667.

Olatunji, J. R., Shim, Y. M., Love, R J., Ferrua, M. J., East, A. R., 2015. Exploring a new heterogeneity index to quantify the variation of cooling rates within systems that undergo the forced air cooling process. Proceedings of the IIR Conference ICR 2015, IIF/IIR, Yokohama, Japan.

Wu, W., Defraeye, T., 2018. Identifying heterogeneities in cooling and quality evolution for a pallet of packed fresh fruit by using virtual cold chains. Applied Thermal Engineering, 133, 407-417.

Zhao, C.-J., Han, J.W., Yang, X.-T., Qian, J.P., Fan, B.-L., 2016. A review of computational fluid dynamics for forced-air cooling process. Applied Energy 168, 314-331.

Manuscript ID: 1639
DOI: 10.18462/iir.icr.2019.1639

Effects of on-board bleeding methods and superchilling on quality of cod and saithe

Sæmundur ELIASSON[(a,c)], Sigurjon ARASON[(b,c)], Bjorn MARGEIRSSON[(a,d)], Arnljotur B. BERGSSON[(c)], Olafur P. PALSSON[(a)]

[(a)]University of Iceland, Faculty of Industrial Engineering, Mechanical Engineering and Computer Science, Hjardarhagi 2-6, IS-107, Reykjavik, Iceland, saemundur@matis.is
[(b)]University of Iceland, Faculty of Food Science and Nutrition, Eiriksgata 29, IS-101, Reykjavik, Iceland
[(c)]Matis (Icelandic Food and Biotech R&D institute), Vinlandsleid 12, IS-113 Reykjavik, Iceland
RPC Saeplast, Gunnarsbraut 20, IS-620 Dalvik, Iceland.

ABSTRACT

An overview of studies for technological developments in the first stages of the value chain of groundfish in Iceland is introduced. It presents the results of recent research performed on board fresh fish trawlers and is aimed to evaluate the process performance in terms of product quality and shelf-life for fresh cod and saithe. This includes studies on time and temperature control, different bleeding conditions, superchilling methods and storage. The main objectives of the research are to provide design parameters to the processing deck redesign and to evaluate the impact of new on-board processes from catch to post-processing storage. The results of the studies indicate that storage methods have a greater impact on fish quality than the specific method of cooling. Also, the results indicate which parameters should be adjusted during the bleeding process to achieve the most effective drainage of blood from the fish.
Keywords: Superchilling, Bleeding, Fresh-fish, Colour, Shelf-Life.

1. INTRODUCTION

This study is related to developments in the Icelandic fishing industry where a large proportion of the fish processing companies have switched from frozen to fresh products and many main companies have or are starting to build new vessels. The aim of this research is to provide some design parameters and prerequisites to the redesign process of fresh fish trawlers processing. The goal of the development is to produce uniform and high-quality raw material for fish processing but also to provide better working conditions and more economic fishing and processing. High quality fresh products, like loins and fillets from cod (*Gadus morhua*) and saithe (*Pollachius virens*), require the raw material to be chilled, well drained of blood and uniform in colour. Low temperature slows microbial growth in the fish muscle and effective removal of blood also contributes to extended product shelf life (Huss, 1995; Olafsdottir et al., 2006). The research focus in this study is on on-board processing, a part of the fresh fish value chain where technical developments in the last decades has been less than in land-based processing. Land-based processing has seen a dramatic increase in automation and quality control and the aim is to implement that methodology in the on-board processing. A part of this development is also to improve data gathering in this sector, where data flow from fishing and on-board processing further along the value chain is often insufficient. This study is important to evaluate the impact of new industrial technology in the groundfish value chain. The innovation of processing on board is aimed to improve automation, sustainability and process control and the benefits of the new solutions need to be analysed for verification and for further technological development. Also, the results can set a benchmark for fresh fish producers in Iceland regarding shelf-life and quality indicators of fresh fish products. Prior to being taken aboard a trawler the fish has been battling against the trawl net, up the ramp and into the reception hold. Olsen et al. (2013) showed the negative effects of large haul sizes and long haul duration on the fish quality. They also had better results in terms of exsanguination with two-step bleeding/gutting (throat cut, bleeding for 30 minutes, gutting and washing) compared the commercial method of direct gutting (one-step procedure as described by Botta et al., 1986). Exsanguination of fish can be influenced by many factors. Insufficient bleeding can affect the shelf life of products through product taste, odour,

visual appearance and residual blood can also promote lipid hydration, provide good nourishment for bacteria and cause increased enzymatic activity (Richard and Hutlin, 2002). In a study by Digre et al. (2011a), the drainage of blood from a stressed cod was indicated to be worse than for unstressed cod. Botta et al. (1986) demonstrated in his research that the bleeding of the fish is an important factor for improving the colour of the flesh. Studies by Botta et al. (1986) and Olsen et al. (2014) implied that the most important factor is to process the fish as soon as possible at the bleeding stage. Olsen et al. (2014) indicated that bleeding and exsanguination should take place within 30 minutes after the catch has been hauled on board. Karlsdottir et al. (2014) researched the effect of different bleeding methods and temperature of the bleeding medium on the quality and storage life of cod and saithe products. Their main results indicated that washing the cod in slurry ice rather than unchilled seawater resulted in better product quality. However saithe showed the opposite reaction to chilled seawater compared to the cod, as saithe showed better end-quality bled in non-chilled seawater. There are debates as to the best methods of cutting or bleeding fish. The main three methods are a gill cut, cutting of the throat and direct gutting. The most important aspect of the procedure of bleeding, was noted in the studies of Botta et al. (1986) and Olsen (2014). They indicated that the time-factor was more important than the method itself. In the study by Olsen (2014), it was noted that the fish needed to start bleeding within 30 minutes after arrival to the processing deck, to produce the best exsanguination of the blood from the muscles. Another study by Roth (2009) observed that the washing of the fish for minimum of 12 minutes in a constant supply of clean seawater streaming into a washing bin/tub, could result in improving the exsanguination of the blood from the muscles. Superchilling is a method involving partial freezing of water in food (e.g. cod muscle), in which commonly the food is cooled 1-2 °C below the initial freezing point (T_f) resulting in 5-30% of water inside the product forming ice crystals (Aune, 2003; Kaale et al., 2011). For whitefish the initial freezing point is close to -1 °C (Margeirsson et al. (2012) modelled it -0.92 °C for cod) and ice crystal formation increases rapidly at lower temperatures. This study refers to this as “superchilling”, however the method of superchilling food is also known as partial freezing (Duun and Rustad, 2007), deep chilling (Wu et al., 2014) or a more recent industry term “sub-chilling” (Skaginn 3X, 2018). According to Magnussen et al. (2008), the method can extend shelf life of fresh cod by 2-3 days, compared to traditionally iced cod with shelf-life of 9-13 days (Lauzon et al., 2010). This is in accordance with Digre et al. (2011b) whose results showed lower microbiologial activity and better quality for superchilled cod at day 14 compared to cod stored in ice. According to Olafsdottir et al. (2006) it was concluded that controlling and keeping the correct temperature during storage is an important factor in preserving the quality of the fish, since a high product temperature can influence the growth of bacteria. Studies by Lauzon et al. (2010) and Olafsdottir et al. (2006) indicated that lowering the temperature from 0-0.5 °C to -1.5 °C prolonged shelf-life of fresh fish. As the temperature is one of the key factors in the onset of rigor mortis stage by cooling down the fish to around 0 °C, the onset of rigor mortis can be delayed and thus the subtractions of the muscles will be less powerful and extreme when the fish goes through rigor mortis at higher temperatures, resulting in gaping in the flesh (Huss, 1995). A study by Eliasson et al. (2019) showed that while shelf-life effects of on-board superchilling of whole gutted fish are minimal compared to ice cooling it can reduce the growth of spoilage bacteria. The bleeding and cooling processes in the new ships are time and temperature controlled, first in-first out systems. There has been developed equipment for automatic transport of the fish tubs down to the cargo hold, which helps to standardize the quality of the catch. Also, there is no ice in the tubs that presses into the fish, which is stored at around -1 °C. Next expected steps are developments of bleeding robots to speed up the on-board processing time, as described by Toldnes et al. (2014).

2. METHODS

The experiments were performed on-board four fresh fish trawlers fishing saithe and cod around Iceland during the period 2014-2017. Fig.1 shows a flow chart of the on-board processing research topics; I) Bleeding, II) Chilling and III) Storage/shelf-life. The bleeding process includes methods of cut and gutting with regard to possible automation, temperature of the bleeding medium and waterflow conditions for effective bleeding. The newer trawlers studied are equipped with different methods of superchilling aimed to bring the core temperature of the fish down to -1 °C before on-board storage. Some of the systems are using chilled seawater (around -1.5 °C) and other use brine with temperature down to -4 °C. The chilling process involves whole gutted fish and the effects of the chilling method and on-board storage on shelf-life and quality were evaluated. For experimental design, comparison samples were always taken from the same haul in order to limit variation. Haul

sizes of samples ranged from 3 to 6 tonnes with hauling times 80 to 160 minutes. The samples were generally taken at the start of processing so they represent the best possible quality from the haul. During experiment for waiting time in the reception hold, samples were gutted after different waiting time (0, 60 and 120 minutes for saithe and 0, 30, 60 and 90 minutes for cod) and put in the same bleeding and chilling process before being iced in tubs. Samples bled at different temperatures were bled for 20 minutes in medium at different temperatures and then put through the same superchilling process before being packed without ice in a superchilled storage at -1 °C. Saithe samples with different bleeding times were bled for 5, 12, 18 and 30 minutes before being packed with ice in tubs. When evaluating different gutting methods samples were bled and chilled in a controlled system, a first-in first-out screw conveyor (SUB-CHILLING™ – Onboard, 2018). They were either directly gutted from the reception hold and into bleeding tanks or a two-step bleeding/gutting process as described by Botta et al. (1986), where the fish is bled by cutting the ventral aorta, bled for 15 minutes in seawater and then gutted, washed and chilled. Another sample from this group was directly gutted into an older uncontrolled trawler system for comparison (the uncontrolled system was made of three separate tanks with elevator conveyor belts transporting the catch through).

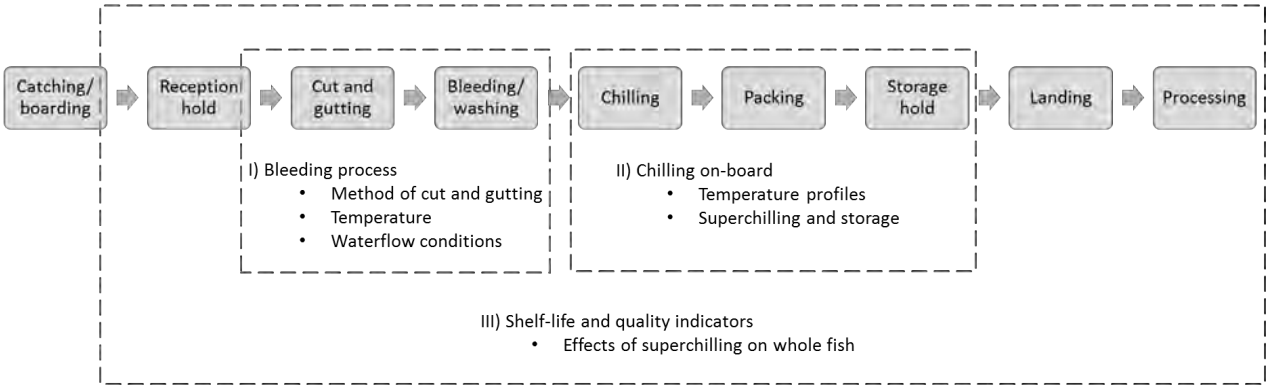

Figure 1: Overview of research topics relating to on-board trawler processing

Temperature monitoring was done with loggers placed both inside the flesh (centre of the loin for core temperature of the whole gutted fish) and one outside the fish to monitor the ambient temperature throughout bleeding, cooling and storage. Temperature logging and shelf-life evaluation were performed as described in Eliasson et al. (2019). Temperature loggers used were iButton (Micro-T DS1922L) from Maxim Integrated Products distributed by NexSens Technology (Dayton, OH, USA). Sensory evaluation and fillet quality was evaluated by standards as described by Martinsdottir et al. (2001). Fillets colour was evaluated by trained experts, Fig.2 shows the scale for fillet colour evaluation, developed by Icelandic Ltd (2012) for cod and also adjusted for saithe in this study. One Way ANOVA was used for statistical analysis of fillet colour measurements (with XLSTAT version 2018.5), the significance level was set at 5% ($p<0.05$).

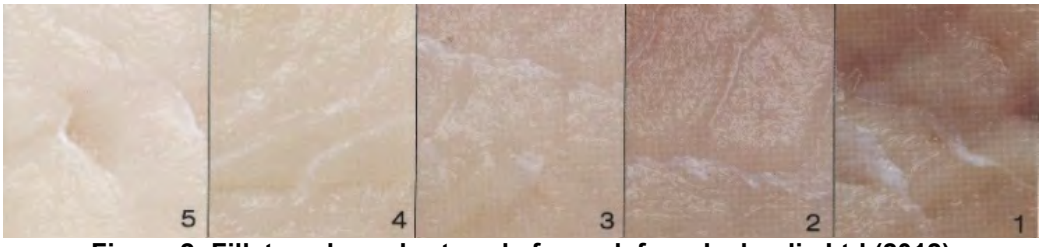

Figure 2: Fillets colour chart scale for cod, from Icelandic Ltd (2012)

3. RESULTS AND DISCUSSION

Fig.3 shows results of experiments where different waiting time in the trawler reception hold is evaluated from fillet colour after processing. The results in Fig.3a) for saithe show a significant reduction in fillet colour comparing saithe bled straight from the reception hold after catch to saithe that was bled 60 minutes and 120 minutes later. Results for different waiting time for cod show a significant difference for cod bled straight after catch and again after 30 and 60 minutes, Fig.3b). There was no significant difference found in fillet colour between cod that waited for 60 and 90 minutes. The results indicate that the fish must be bled within 30 minutes from catch to maintain a light fillet colour. This is in accordance with results by Botta et al. (1986) and Olsen et al. (2014)

which both concluded that the time from catch to bleeding was a deciding factor influencing exsanguination of cod. The fisheries companies involved in this study have now set a reference limit on the acceptable size of hauls, to minimize the load to the catch but mainly to reduce the waiting time in the reception hold, underlining the importance of fillet quality.

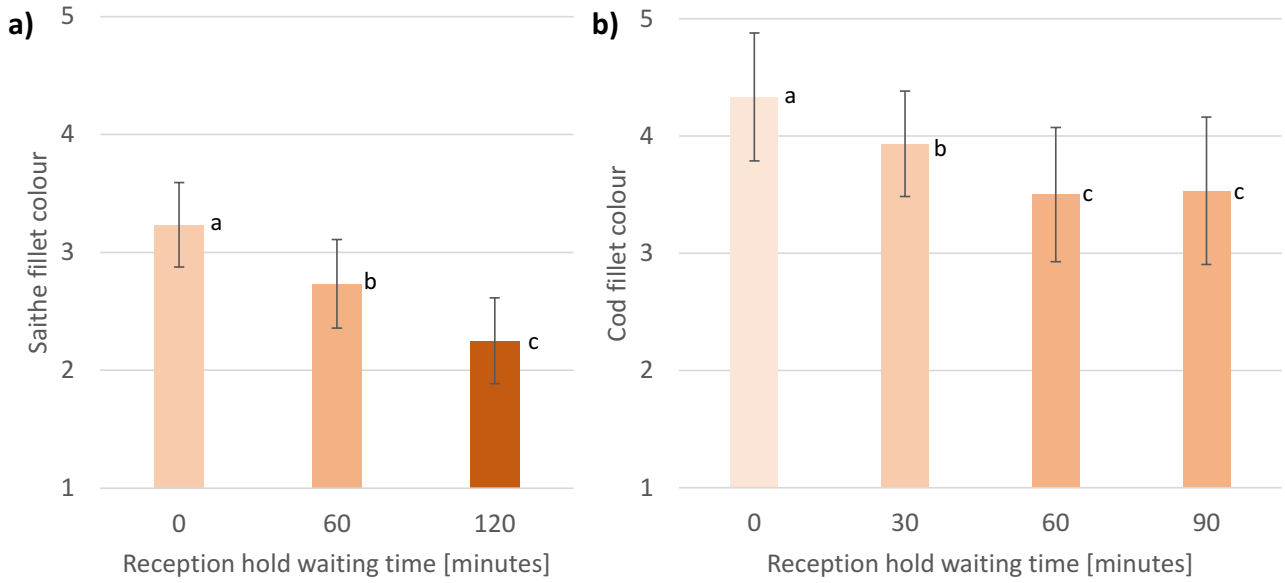

Figure 3: Colour of a) saithe and b) cod fillets for different waiting times in a trawler reception hold (n=30 fillets). Significant difference between groups is represented by different letters a, b, c ($p<0.05$). Error bars show standard deviation from mean values ($\bar{\mu} \pm \sigma$)

Fig.4 shows cod fillets bled for 20 minutes at three different temperatures; -1 °C, 2 °C and 6 °C. Fillets bled in unchilled seawater (6 °C) showed the best results in terms of uniform colour. When bled at lower temperatures blood was more apparent in the fillets, especially in the belly flap area. Karlsdottir et al. (2014) showed the same results for saithe, however for cod they had better exsanguination at lower temperatures.



Figure 4: Cod fillets bled in seawater for 20 minutes at three different temperatures; -1 °C, 2 °C and 6 °C. Photo taken after filleting, four days after catching

Fig.5 shows fillets colour for saithe after 5, 12, 18 and 30 minutes bleeding process before tub packing. Comparing the fillets colour after filleting (4 days after catch) did not show significant difference but after further storage of fillets (9 days from catch) there were significant difference ($p<0.05$). Groups bled 5 and 12 minutes showed darker colour compared to lighter colour for groups bled 18 and 30 minutes. The results after 9 days from catch indicate that the bleeding time for saithe should exceed 12 minutes and that the effects of insufficient bleeding are not necessarily apparent immediately after filleting. The fillet storage between day 4 and 9 was simulating sea transport of fresh fish at -1 °C so day 9 from catch is approximately the timing of delivery to buyers in Europe.

The results for 9-day fillets support that bleeding time should exceed 12 minutes, for system design however that is depended on the waterflow and circulation in the bleeding medium. Results of on-board bleeding systems have also shown that circulation or active movement of the fish in bleeding medium is a more deciding factor than the rate of water replacement.

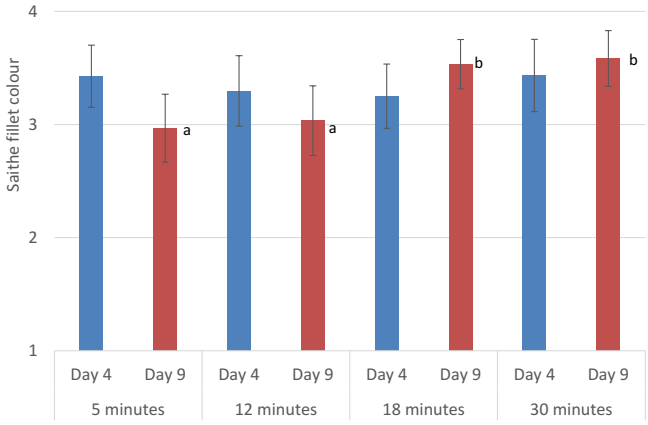

Figure 5: Saithe fillet colour after 5, 12, 18 and 30 minutes bleeding in seawater. Blue columns represent fillet colour after fillet processing (Day 4 from catch) and red columns fillet colour on day 9 from catch. Error bars show standard deviation from mean values ($\overline{\mu} \pm \sigma$)

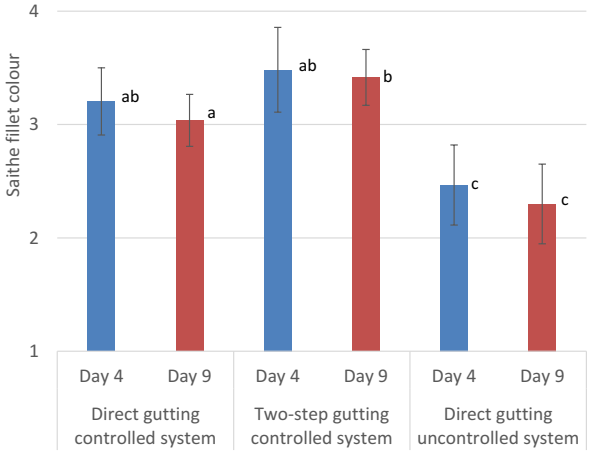

Figure 6: Fillet colour of saithe for different gutting methods and on-board processing systems. Significant difference between groups is represented by letters a, b, c ($p<0.05$). Error bars show standard deviation from mean values ($\overline{\mu} \pm \sigma$)

Results of an experiment comparing direct gutting of saithe to bleeding (15 minutes) and gutting in a two-step procedure are shown in Fig.6. The groups were time controlled first-in first-out systems and were also compared to a group using an uncontrolled trawler system (as described in methods). Similar to results by Olsen et al. (2014) the method of bleeding and gutting in a two-step procedure resulted in slightly better colour, significantly apparent after simulated storage, 9 days from catch. The difference of using a controlled first-in first-out system however was more decisive factor than the method of gutting. Temperature profiles of the uncontrolled system are shown in Fig.7.

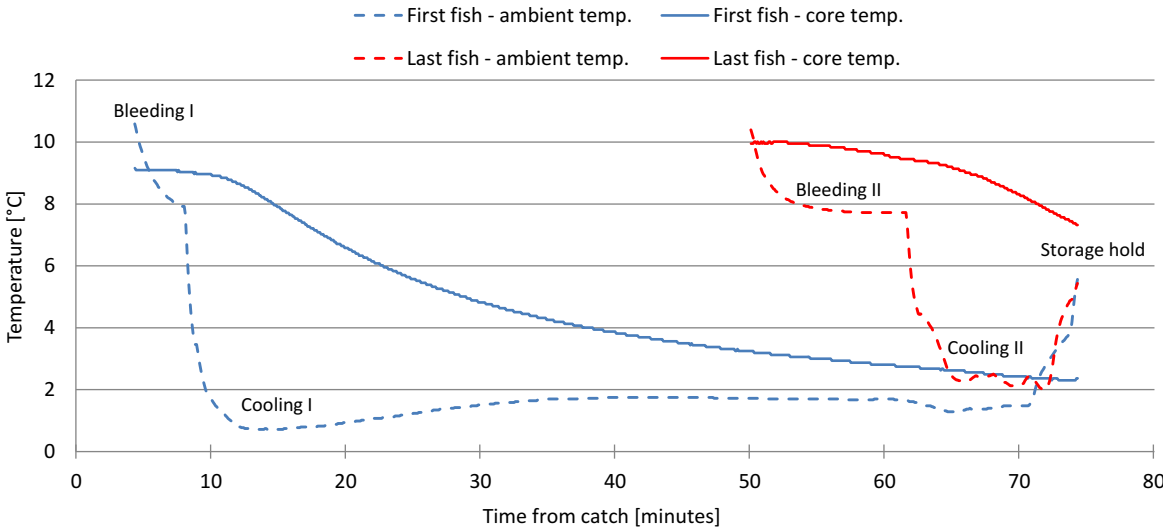

Figure 7: Temperature profiles for the first and last fish (3 kg) in an uncontrolled bleeding/cooling system

The example shows profiles of measured fish, the first and last fish to be processed in a saithe haul. The dotted lines represent the ambient temperature around the fish in the system and the solid line the flesh temperature in the core of the fish. The first fish (blue line) is gutted after 5 minutes from catch and only stays in the bleeding tank for 4 minutes, after which it tumbles in the cooling tanks for over 60 minutes and therefore gets sufficient cooling time. The last fish (red line) to be gutted gets 15 minutes in the bleeding tank but only stays in the cooling tanks for a few minutes before being transferred down to the storage hold. The initial temperature of the fish was 9 °C but the last fish is at 10 °C into the system because of the waiting time in the reception hold. The temperature profiles

show the inconsistency of an uncontrolled system with variable bleeding time and the final temperature of the first fish at 2 °C while the last fish is packed at 7 °C in the storage hold. Fig.8 shows fish temperature profile in a first-in first-out superchill system compared to traditional flake ice cooling as a reference. In the superchill system the core temperature of the fish can reach -1 °C within 1 hour, after which it is packed in a tub and stored in the storage hold at -1 °C ambient temperature without any ice. After landing the superchilled fish is kept in a storage at -1 °C before fillet processing.

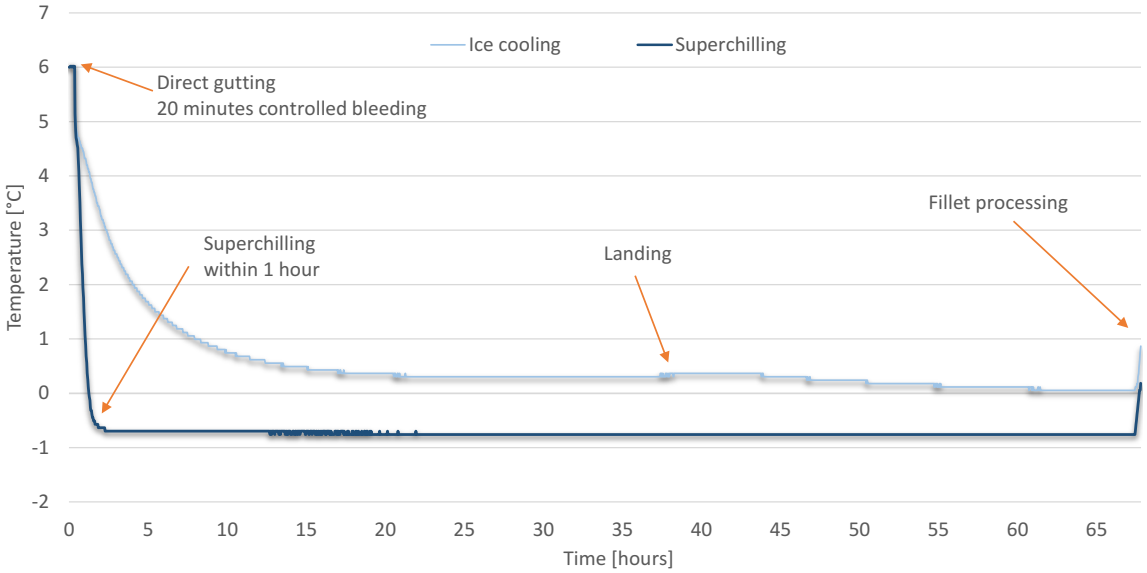

Figure 8: Controlled super-chilling system compared to traditional flake ice cooling. 3 kg fish core temperature from catch to fillet processing

Samples from the temperature profiles shown in Fig.8 were evaluated at different storage temperature simulating the whole value chain in at study by Eliasson et al. (2019). The results for different storage temperatures at +1 °C and -1 °C showed (Fig.9) that the main deciding factor in the fresh fish chill chain is the temperature of the fillets after processing. However, the superchilling of whole gutted fish on-board results in less bacterial growth and slows down some spoilage factors.

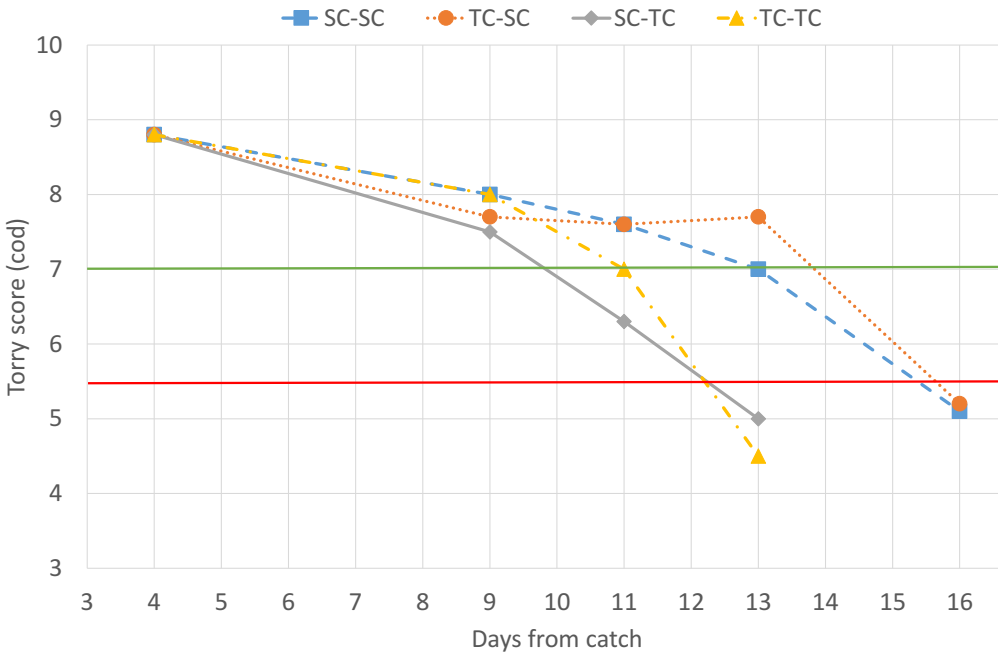

Figure 9: Mean Torry freshness scores for cooked cod samples on days 4, 9, 11, 13 from catch. Groups are labelled by different on-board chilling methods (SC-super-chilled, TC-traditional ice cooling) and different fillet storage temperature (SC stored at -1 °C and TC stored at +1 °C). The green line indicates loss of freshness (Torry score = 7) and the red line indicates end of shelf life (Torry score = 5.5). Figure adapted from Eliasson et al. (2019)

4. CONCLUSIONS

The results of the bleeding experiments indicate that the fish should be bled within 30 minutes after catch to maintain quality in terms of fillet colour. The bleeding process should exceed 12 minutes and be carried out in un-chilled seawater ensuring movement and refresh rate of the bleeding medium. Evaluation of the older uncontrolled systems showed that they are unreliable both in terms of bleeding and cooling. As for the method of bleeding and gutting saithe, the two-step process of bleeding and gutting showed slightly better results in terms of fillet colour, compared to direct gutting. The two-step method is suitable for automation of the bleeding process on-board trawlers to shorten the waiting time in the reception hold, which was found to be the main deciding factor influencing fillet colour. The on-board super-chilling of whole fish reduces some spoilage factors but did not considerably extend shelf-life. However, the simulation of a super-chilled value chain to the market indicates that the freshness period and shelf-life can be extended by up to four days, compared to traditional ice cooling and +1 °C storage.

ACKNOWLEDGEMENTS

This research was conducted as part of the research project “Redesign of demersal wetfish trawler processing decks” supported by the Technology Development Fund (grant number 142667-0611) and the AVS R&D Fund of Ministry of Fisheries and Agriculture in Iceland (grant number R 15 068-14). Thanks to the crew on board the trawlers for cooperation with experiments and to the staff of HB Grandi, Samherji and FISK Seafood for helping with processing the samples. Thanks also to Matis staff participating in sample storage and chemical measurements.

REFERENCES

Aune, E.J., 2003. Superchilling of foodstuff, a review. In Proceedings of the 21st International Congress of Refrigeration, International Institute of Refrigeration, Washington, DC, USA.

Botta, J. R., Squires, B.E., Johnson, J., 1986. Effect of bleeding/gutting procedures on the sensory quality of fresh raw Atlantic cod (Gadus morhua). Canadian Institute of Food Science and Technology 19(4), 186-190.

Digre, H., Erikson, U., Mismi, E., Standal, I, Gallart-Jornet, L., Riebroy, S., Rustad, T., 2011a. Bleeding of farmed Atlantic cod: residual blood, color, and quality attributes of pre- and postrigor fillets as affected by perimortem stress and different bleeding methods. Journal of Aquatic Food Product Technology 20, 391-411.

Digre, H., Erikson, U., Aursand, I., Gallart-Jornet, L., Misimi, E., Rustad, T., 2011b. Rested and stressed farmed Atlantic cod (Gadus morhua) chilled in ice or slurry and effects on quality. Journal of Food Science 76, 89-100.

Duun, A.S., Rustad T., 2007. Quality changes during superchilled storage of cod (Gadus morhua) fillets. Food Chemistry 105(3), 1067-1075.

Eliasson, S., Arason, S., Margeirsson, B., Bergsson, A.B., Palsson, O.P., 2019. The effects of superchilling on shelf-life and quality indicators of whole Atlantic cod and fillets. LWT – Food Science and Technology 100 (1), 426-434.

Huss, H. H., 1995. Quality and changes in fresh fish. FAO Fisheries Technical Paper, No.348. Rome.

Icelandic Ltd, 2012. Fillet color chart. Issued by Icelandic Services LTD in March 2012. www.icelandic.is

Kaale, L.D., Eikevik, T.M., Rustad, T., Kolsaker, K., 2011. Superchilling of food: a review. Journal of Food Engineering,107(2), 141-146.

Karlsdottir, M. G., Minh, N.V., Arason, S., Olafsdottir, A., Romotowska, P.E., Bergsson, A.B., Bjornsson, S., 2014. Effects of bleeding methods on quality and storage life of cod and saithe products. Matís Report 07-14, Icelandic Food and Biotech R&D. Reykjavik, Iceland.

Lauzon, H. L., Margeirsson, B., Sveinsdottir, K., Gudjonsdottir, M., Karlsdottir, M.G., Martinsdottir, E., 2010. Overview on fish quality research - Impact of fish handling, processing, storage and logistics on fish quality deterioration. Matis report 39-10. Reykjavik, Iceland.

Magnussen, O.M., Haugland, A., Hemmingsen, A.K.T., Johansen, S., Nordtvedt, T.S., 2008. Advances in superchilling of food - Process characteristics and product quality. Trends Food Science & Technology 19(8), 418-424.

Margeirsson, B., Palsson, H., Popov, V., Gospavic, R., Arason, S., Sveinsdottir, K., Jonsson, M., 2012. Numerical modelling of temperature fluctuations in superchilled fish loins packaged in expanded polystyrene and stored at dynamic temperature conditions. International Journal of Refrigeration 35(5), 1318-1326.

Martinsdottir, E., Sveinsdottir, K., Luten, J., Schelvis-Smith, R., Hyldig, G., 2001.

Sensory Evaluation of Fish Freshness. Reference Manual for the Fish Sector. Available at: http://www.qim-eurofish.com/.

Olafsdottir, G., Lauzon, H.L., Martinsdottir, E., Oehlenschlauger, J., Kristbergsson, K., 2006. Evaluation of Shelf Life of Superchilled Cod (Gadus morhua) fillets and the influence of temperature fluctuations during storage on microbial and chemical quality indicators. Journal of Food Science 71(2), 97-109.

Olsen, S.H., Tobiassen, T., Akse, L., Evensen, T.H., Midling, K.Ø., 2013. Capture induced stress and live storage of Atlantic cod (Gadus morhua) caught by trawl: Consequences for the flesh quality. Fisheries Research 147, 446-453.

Olsen, S.H., Joensen, S., Tobiassen, T., Heia, K., Akse, L., Nilsen, H., 2014. Quality consequences of bleeding fish after capture. Fisheries Research, 153, 103-107.

Roth, B., Obach, A., Hunter, D., Nortvedt, R., Oyarzun, F., 2009. Factors affecting residual blood and subsequent effect on bloodspotting in smoked Atlantic salmon fillets. Aquaculture 297, 163-168.

Skaginn 3X, 2018. SUB-CHILLING™ – Onboard. Technical equipment description from Skaginn. Available at http://skaginn3x.com/products/sub-chilling-onboard [accessed July 26th 2018].

Toldnes, B., Erikson, U. G., Salomonsen, C., Eilertsen, A., Mathiassen, Bartle J.R., Westavik, H., Grimsmo, L., 2014. Automatisk bløgging av villfisk. SINTEF Fiskeri og havbruk; A26238, Research report. ISBN 978-82-14-05758-4.

Wu, C. H., Yuan, C. H., Ye, X. Q., Hu, Y. Q., Chen, S. G., Liu, D. H., 2014. A critical review on superchilling preservation technology in aquatic product. Journal of Integrative Agriculture 13(12), 2788–2806.

Duide Manuscript ID: 1674
DOI: 10.18462/iir.icr.2019.1674

Influence of Different Nozzle Forms on Heat Transfer Characteristics of Quick Freezer

Jinfeng WANG[a,d], Yingyu PENG[a], Jin XIE[a,b], Jiahao HUANG[a], Dazhang YANG[a,c]

[a] Shanghai Ocean University, Shanghai, 1
Shanghai, 201306, People's Republic of China,jfwang@shou.edu.cn
[b]Shanghai Engineering Research Center of Aquatic Product Processing & Preservation, 2
Shanghai, 201306, People's Republic of China, jxie@shou.edu.cn
[c] Shanghai Professional Technology Service Platform on Cold Chain Equipment Performance and Energy Saving Evaluation, 3
Shanghai, 201306, People's Republic of China,dzyang@shou.edu.cn
[d]Quality Supervision, Inspection and Testing Center for Cold Storage and Refrigeration Equipment,4
Shanghai, 201306, People's Republic of China, 15000159007@163.com

ABSTRACT

In this paper, the V-type slit nozzle in an impact type quick freezer is selected as the research object. The effects of five different nozzle structures on the heat transfer characteristics and non-uniformity of steel band surface in the direction of quick-freezing width in the quick-freezing machine are compared. The results shows that: compared with other nozzle structures, V-type slit nozzle can make the surface of steel band have larger heat transfer coefficient and surface uniformity; the existence of V-type diversion groove and nozzle outlet have an important influence on the heat transfer intensity of steel band surface. In summary, choosing the appropriate nozzle structure will effectively improve the heat transfer characteristics of steel band surface.The research provides the theoretical basis for the optimization design of the flow field of the impact freezer.

Keywords: Quick Freezer, V-Type Slit Nozzle, Heat Transfer Intensity, Nussle Number.

1. INTRODUCTION

In the field of heat and mass transfer, the impact cooling has higher local heat transfer coefficient.The average heat transfer coefficient of heat transfer surface can be obtained by changing the impinging conditions and structural parameters. In recent years, a large number of studies have been conducted on the heat transfer characteristics between the impinging jet and the object (JiaHong, 2002). It has been found that impinging jet has high heat and mass transfer rates and can be used in the fields of electronic equipment cooling and food quick-freezing. The impinging quick-freezer equipment has gradually been taken seriously.

This kind of equipment usually combines multiple nozzles in a certain arrangement, so as to achieve uniform heat transfer coefficient on the impinging surface in a wide range (Makatar and Perapong, 2014).However, in the actual working process, there is a great difference in the heat transfer intensity of the target plate surface, which is mainly affected by the arrangement of nozzles and the structural parameters of nozzle inlet and outlet. According to the characteristics of internal flow field of impact quick-freezing equipment, Zhang et al (2008) use computational fluid technology to simulate the influence of orifice opening rate on the heat transfer characteristics of internal flow field. The results show that with the increase of orifice opening rate from 2% to 15%, the wind speed in the static pressure box decreases continuously. In the area between orifice plate and baffle, the pressure distribution is gradually uniform, and the stress concentration is also reduced. Among them, the optimum perforation rate of orifice plate is 5%.Hukam Chand Meena et al (2016) utilize the infrared thermal imaging technique to estimate the local heat transfer characteristics among various nozzle shapes (circular, square, triangular, elliptical, etc.).The results show that, due to the change of angle and velocity attenuation characteristics of different

nozzle shapes, the heat transfer of circular nozzle is the largest, while elliptical nozzle, square nozzle and triangle nozzle is smaller. Bai et al. (2011) use the standard model of $k-\varepsilon$ to simulate the pressure and velocity fields near the wall of V-type slit nozzle. The results show that the velocity distribution near the wall is affected by the height of the nozzle and the width of the slit nozzle. Wang et al. (2018) take the V-type slit nozzle of the impinging quick-freezer as the research object, and study the influence of changing the ratio of distance between the steel strip and the nozzle outlet and the width of the slot to the surface heat transfer characteristics of the frozen area under different cutting ratios. The results show that under different cutting ratio, the surface heat transfer intensity of the steel strip of the quick-freezer machine is obviously different. Ran et al. (2018) use the turbulence model to simulate the 3D numerical simulation of the nozzle outlet with and without straight section, and study the effect of two nozzles with or without straight section on the heat transfer, pressure characteristics and velocity distribution of the jet flow. The results show that the velocity of the nozzle outlet is uniformly distributed in the straight section, and the velocity near the jet center is higher than that of the nozzle without straight section, so the heat transfer effect is better. The pressure near the outlet of the nozzle with straight section is lower than that of the nozzle without straight section. The latter has obvious pressure drop, which increases the energy loss. Under the same initial and boundary conditions, Liu et al. (2007) use FLUENT software to simulate and analyze the length-diameter ratio and outlet diameter of conical nozzle with cylindrical outlet. It is found that the velocity in the core section of the jet increases with the decrease of the outlet diameter of the nozzle. When the length-diameter ratio of the cylindrical section at the nozzle outlet is about 3 and the contraction angle of the conical section is about 13 degrees, the velocity in the core section of the jet is the largest. Yu et al. (2009) discuss the influence of four main structural parameters (contraction angle, transition shape of inlet and outlet, length and outlet diameter) on the outlet velocity and dynamic pressure of the nozzle. The results show that the contraction angle of the nozzle has the greatest influence on the flow field of the nozzle among the four parameters, and the flow field characteristics of the nozzle with contraction section and horizontal transition section at the outlet are better and the axial velocity is greater. Lee et al. (2004) set a uniform heat flux boundary by using gold film Interrex and investigate the effect of nozzle diameter on heat transfer and fluid flow for a round turbulent jet impinging on a flat plate surface. The results show that the local Nussle numbers increase with the increasing nozzle diameter in the stagnation point region corresponding to $0 \le r/d \le 0.5$. Katti et al. (2013) study the heat transfer characteristics of jet arrays impinging on the surface of an object when the nozzles are linearly arranged. The results show that when the distance between nozzles is S=4D (in which D is the diameter of nozzle),the heat conduction rate in the extended direction of jet flow is higher than that in the distance between nozzles S=2D and S=6D.In summary, the structural parameters of nozzle inlet and outlet will affect the heat transfer intensity of the target surface, but most of the literature focus on the study of Nussle number on the target surface, ignoring the heat transfer uniformity of the target surface. In the freezer, heat transfer uniformity is one of the important factors affecting the quality of frozen food (Li et al., 2018 and Li et al., 2018), so it cannot be ignored in the study of heat transfer characteristics in the freezer(Ianiro et al., 2012 and Yu et al., 2017).

In this paper, the V-type slit nozzle of impinging quick-freezer machine is taken as an object to solve the problem of uniformity of heat transfer coefficient on the surface of steel strip along the width direction of quick-freezing machine. By changing the structural parameters of V-type slit nozzle in the quick-freezing machine, the uniformity of heat transfer coefficient on the surface of steel strip is improved, and the temperature of frozen products tends to be the same when the quick-freezing food is processed to reach the outlet.

2. NUMERICAL SIMULATION

2.1 Establishment of Numerical Model

The structure of v-type slit nozzle is shown in Fig.1, and the nozzle structure parameters are shown in table1. In this paper, the heat transfer uniformity of steel band surface along the width direction of quick-freezing during quick-freezing process is simulated under five conditions: traditional V-type slit nozzle and changing nozzle structure parameters (with or without exit section, with or without V groove, changing nozzle width and nozzle length). Fig. 2a is a 3D structural model for optimizing v-type slit nozzle.

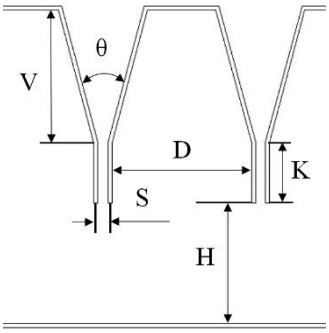

Figure 1: V type slit nozzle structure

Table 1. Nozzle structure parameters

Structure parameters	D	K	X_L	Y_W	S	V	θ
V-type slit nozzle	73mm	30mm	750mm	600mm	5mm	66mm	30°

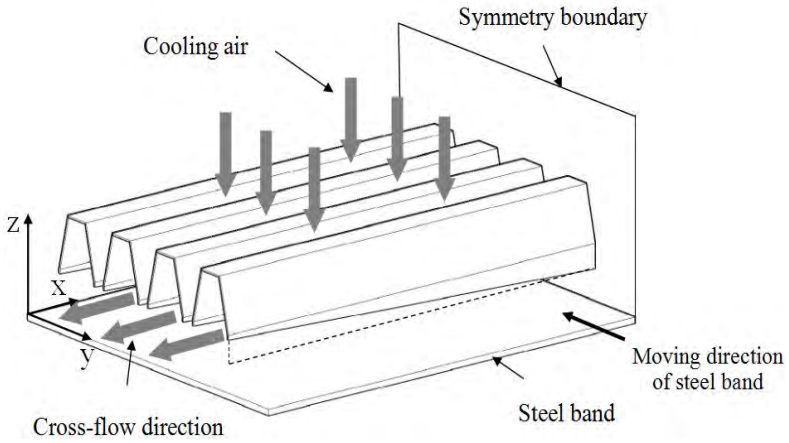

Figure2: Schematic diagram of V-type slit nozzle structure optimization

2.2 Numerical Model Conditioning

The flow medium is air, and the simulation process assumed:
(1)Air is an incompressible, homogeneous viscous fluid.
(2)The wall of the nozzle is considered as no slip wall, that is, the air velocity at the wall is U=0.
(3)The wall of nozzle is adiabatic, that is, heat flux q=0 W/m^2.
Continuity equation, momentum equation and energy equation are used to solve the numerical simulation process.

- Continuity equation:

$$\frac{\partial u}{\partial x}+\frac{\partial v}{\partial y}+\frac{\partial w}{\partial z}=0 \qquad \text{Eq. (1)}$$

- Momentum equation:

$$\frac{\partial(\rho u^2)}{\partial x}+\frac{\partial(\rho uv)}{\partial y}+\frac{\partial(\rho uw)}{\partial z}=-\frac{\partial p}{\partial x}+\frac{\partial}{\partial x}\left(\lambda\nabla\cdot V+2\mu\frac{\partial u}{\partial x}\right)+\frac{\partial}{\partial y}\left[\mu\left(\frac{\partial v}{\partial x}+\frac{\partial u}{\partial y}\right)\right]+\frac{\partial}{\partial z}\left[\mu\left(\frac{\partial u}{\partial z}+\frac{\partial w}{\partial x}\right)\right]+\rho f_x \qquad \text{Eq. (2)}$$

$$\frac{\partial(\rho uv)}{\partial x}+\frac{\partial(\rho v^2)}{\partial y}+\frac{\partial(\rho uw)}{\partial z}=-\frac{\partial p}{\partial x}+\frac{\partial}{\partial x}\left[\mu\left(\frac{\partial v}{\partial x}+\frac{\partial u}{\partial y}\right)\right]+\frac{\partial}{\partial y}\left(\lambda\nabla\cdot V+2\mu\frac{\partial v}{\partial y}\right)+\frac{\partial}{\partial z}\left[\mu\left(\frac{\partial w}{\partial y}+\frac{\partial v}{\partial z}\right)\right]+\rho f_y \qquad \text{Eq. (3)}$$

$$\frac{\partial(\rho uw)}{\partial x}+\frac{\partial(\rho vw)}{\partial y}+\frac{\partial(\rho w^2)}{\partial z}=-\frac{\partial p}{\partial z}+\frac{\partial}{\partial x}\left[\mu\left(\frac{\partial u}{\partial z}+\frac{\partial w}{\partial x}\right)\right]+\frac{\partial}{\partial y}\left[\mu\left(\frac{\partial w}{\partial y}+\frac{\partial v}{\partial z}\right)\right]+\frac{\partial}{\partial z}\left(\lambda\nabla\cdot V+2\mu\frac{\partial w}{\partial z}\right)+\rho f_z \quad \text{Eq. (4)}$$

- Energy equation:

$$\frac{\partial(\rho uT)}{\partial x}+\frac{\partial(\rho vT)}{\partial y}+\frac{\partial(\rho wT)}{\partial z}=\frac{k}{c_p}\left(\frac{\partial^2 T}{\partial x^2}+\frac{\partial^2 T}{\partial y^2}+\frac{\partial^2 T}{\partial z^2}\right) \quad \text{Eq. (5)}$$

- k equation:

$$\frac{\partial}{\partial t}(\rho k)+\frac{\partial}{\partial x_i}(\rho k U_i)=\frac{\partial}{\partial x_j}[(\mu+\frac{\mu_t}{\sigma_k})\frac{\partial k}{\partial x_j}]+G_k-\rho\varepsilon \quad \text{Eq. (6)}$$

Where, turbulent viscosity:

$$\mu_t=\rho C_\mu\frac{k^2}{\varepsilon} \quad \text{Eq. (7)}$$

- ε equation:

$$\frac{\partial}{\partial t}(\rho\varepsilon)+\frac{\partial}{\partial x_i}(\rho\varepsilon U_i)=\frac{\partial}{\partial x_j}[(\mu+\frac{\mu_t}{\sigma_\varepsilon})\frac{\partial\varepsilon}{\partial x_j}]+C_{1\varepsilon}G_k\frac{\varepsilon}{k}-C_{2\varepsilon}\rho\frac{\varepsilon^2}{k} \quad \text{Eq. (8)}$$

Among, G_k is the turbulent energy caused by the average velocity gradient. In this equation, the constants of $C_{1\varepsilon}$, $C_{2\varepsilon}$, σ_k, σ_ε, C_μ are 1.44,1.92,1.0,1.3,0.09 respectively。
The calculation model is set as follows:
(4)Pressure inlet is used as the entry boundary condition, Pressure outlet as the exit boundary condition, and Pin = 250 Pa, temperature Tin = 228 K, Pout = 0 Pa, Tout = 233 K.
(5)The calculation model and the whole adjacent part of the freezer are used to set the mirror boundary, i.e. Symmetry 1 and Symmetry 2, as shown in Fig. 3.
(6)A solution method is based on k-ε turbulence model, the SIMPLE algorithm with second order upwind (Vikas et al., 2012) for all spatial discretization.

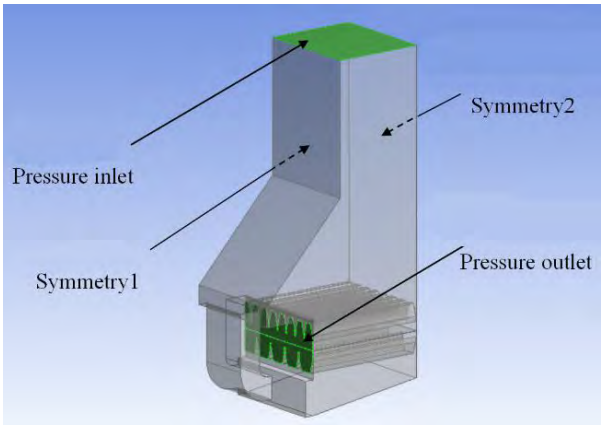

Figure 3: Numerical model and boundary condition setting

2.3 Five Nozzle Structures

In this paper, the effects of five different nozzle structures on the heat transfer characteristics and non-uniformity of steel band surface in the direction of quick-freezing width in the quick-freezing machine are compared, as shown in Fig. 4. Fig. 4a is the traditional V-type slit nozzle, Fig. 4b is the V-type nozzle without exit section, Fig.4c is the V-type nozzle without V groove, Fig. 4d is the V-type nozzle which has longer nozzle length. Fig. 4e is the V-type nozzle which has wider nozzle width. The five nozzle structure parameters are shown in Table 2.

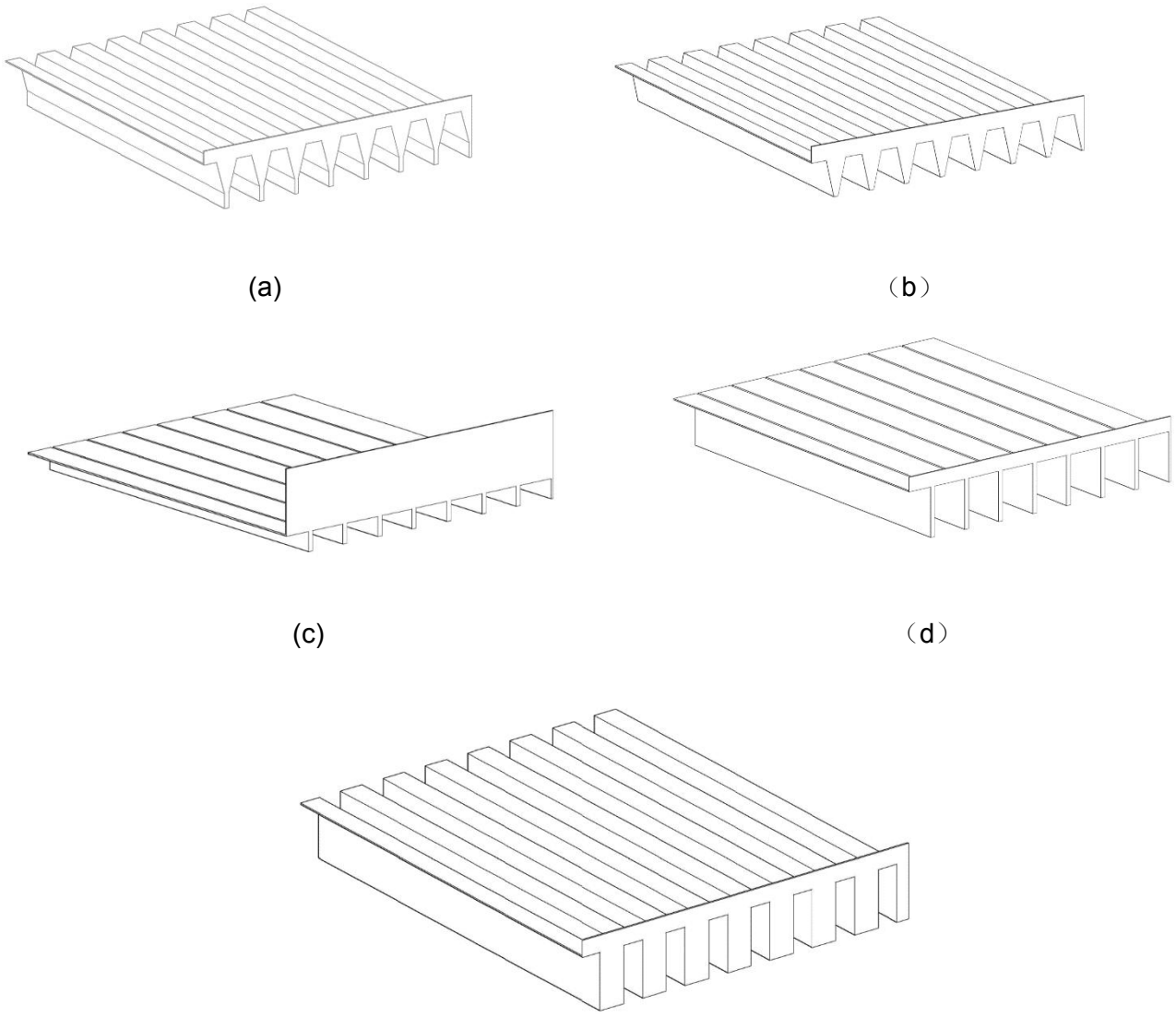

Figure 4: Five different nozzle structures

Table 2. Five nozzle structure parameters

Number	D	K	X_L	Y_W	S	V	θ
a	73 mm	30 mm	750 mm	600 mm	5 mm	66 mm	30°
b	73 mm	0 mm	750 mm	600 mm	5 mm	66 mm	30°
c	73 mm	30 mm	750 mm	600 mm	5 mm	0 mm	0°
d	73 mm	0 mm	750 mm	600 mm	5 mm	66 mm	0°
e	73 mm	30 mm	750 mm	600 mm	39 mm	66 mm	0°

3. CONCLUSIONS

3.1 Effect of Nozzle Structure on Heat Transfer Characteristics of Steel band Surface

As shown in Fig. 5, along the longitudinal direction of the band (X direction), the heat transfer intensity on the surface of the strip is quite different, that is, the Nu number on the surface of the strip downstream of the cross flow is obviously higher than that on the upstream of the cross flow. When the nozzle structure changes, the heat transfer intensity on the steel band surface is inconsistent. Compared with Fig. 5a and 5b, the heat transfer intensity along the transverse

direction (Y direction) of the band increases without the nozzle exit section, but overall, the surface Nu of the band along the longitudinal direction (X direction) decreases. Compared with Fig. 5a and Fig. 5c, the heat transfer coefficient of steel band surface shows a significant downward trend when there is no V-type diversion groove at the nozzle inlet. Compared with Fig. 5c and Fig. 5d, as the nozzle height increases, the heat transfer intensity along the longitudinal direction of the band decreases and the Nu along the transverse direction of the band becomes more uniform. Compared with Fig. 5d and Fig. 5e, when the nozzle width increases, the heat transfer coefficient of steel band surface decreases greatly, and the heat transfer effect is poor.

The reasons for the above phenomena are as follows: when the nozzle has outlet section, the outlet velocity distribution is uniform, and the flow velocity near the jet centre is higher than that of the nozzle without outlet section; the existence of V-type diversion groove can obviously increase the outlet velocity of the nozzle, which can improve the jet density and thus improve the heat transfer coefficient of the steel band surface. In the freezer, with the increase of the length and width of the nozzle, the jet density decreases gradually, and the heat transfer intensity on the steel band surface decreases gradually. In summary, when the nozzle structure of quick freezer changes, choosing the appropriate nozzle structure will effectively improve the heat transfer characteristics of steel band surface.

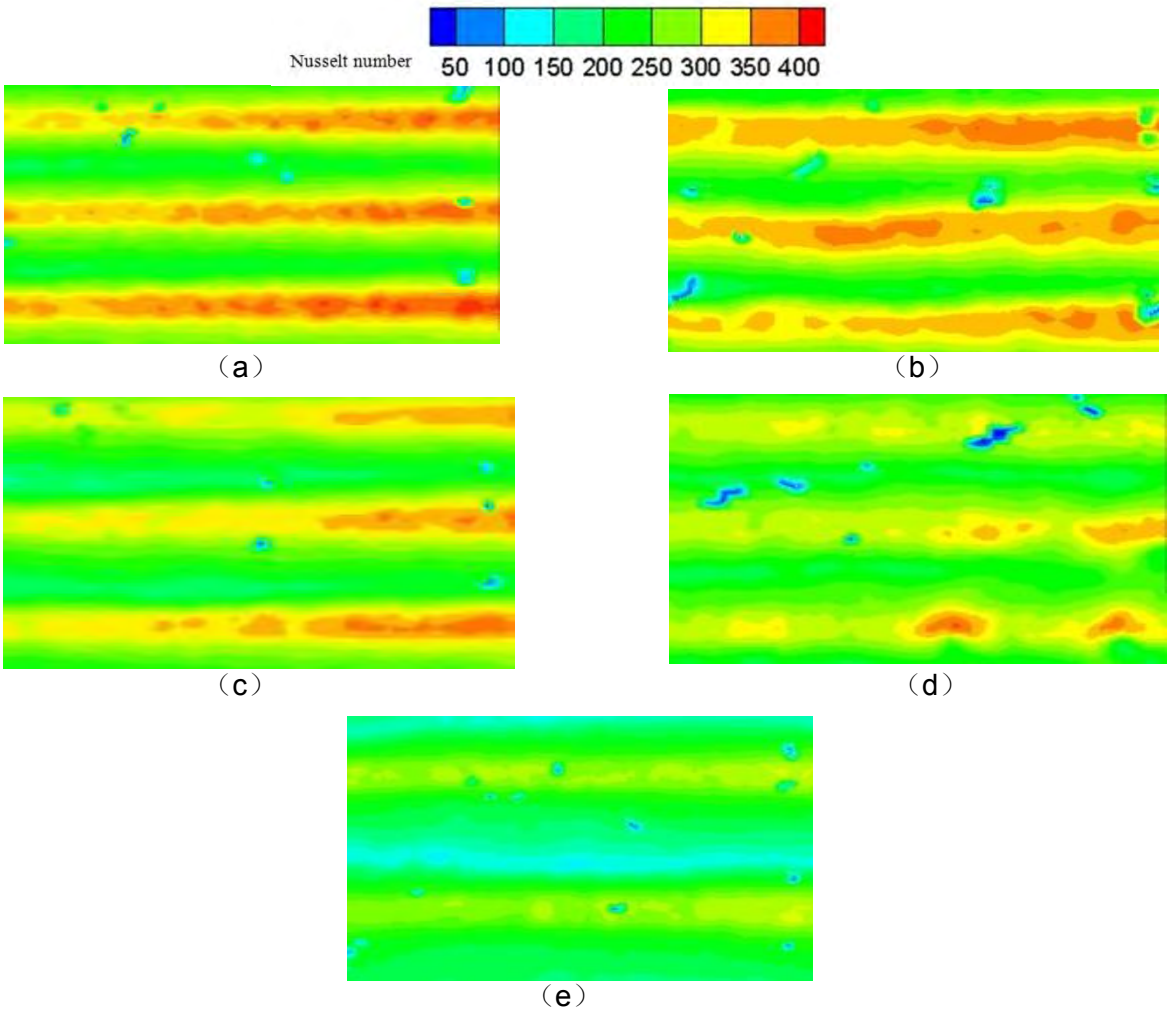

Figure 5: Nussle Number Distribution on Steel band Surface under different nozzle structures

3.2 Effect of Nozzle Structure on Heat Transfer Uniformity of Steel Band Surface

The heat transfer uniformity index η on the surface of the steel band is defined as the ratio (Subasi et al., 2016) between the standard deviation of the local Nussle number σ_{Nu} on the surface of the steel band and the average Nussle number Nu_{ave} on the surface of the steel band. The value η represents the difference of Nu number at each position on the surface of the steel band. The smaller the value η is, the more uniform the heat transfer is on the surface of the steel band. The calculation formula is as follows:

$$\eta = \frac{\sigma_{Nu}}{Nu_{ave}} \quad \text{Eq. (9)}$$

The average Nussle number of steel band surface under five structures can be obtained by FLUENT. Through comparison, it can be seen that the Nu_{ave} of V-type slit nozzle in Fig.4 (a) is the largest, and the vertical value of the surface uniformity index of steel band reaches the minimum, that is, the surface heat transfer uniformity of steel band is the best. In Fig.4 (e), the average Nussle number Nu_{ave} of the steel band under the nozzle structure is the lowest, and the vertical value of the surface uniformity index of the steel band reaches the maximum, that is, the surface heat transfer uniformity of the steel band is the worst. The average Nussle number of the other three structures is between them. When the vertical value reaches the minimum value, the surface heat transfer intensity of the steel band is the strongest at this time, so the food freezing time is the least. When the total production of the quick freezing machine is constant, the quick freezing machine has the highest efficiency and the lowest energy consumption. To sum up, when v-type slit nozzles are used, the average Nussle number Nu_{ave} on the surface of steel band is the largest, and the vertical value of uniform heat transfer index is the smallest, which is the optimal nozzle structure.

ACKNOWLEDGEMENTS

This research was financially supported by the National Key R & D Program of China (2016YFD0400303).

NOMENCLATURE

u	Partial velocity in X direction(m/s)	v	Partial velocity in Y direction(m/s)
w	Partial velocity in Z direction(m/s)	ρ	Density(kg/m^3)
p	Pressure (kPa)	T	temperature (K)
μ	Dynamic viscosity(kg/（m·s^{-1}）)	k	Heat transfer coefficient(W/ (m2·K))
C_p	Specific heat at constant pressure(J/ (kg· K))		

REFERENCES

DaeHee, L., Jeonghoon, S., et al. 2004.The effects of nozzle diameter on impinging jet heat transfer and fluid flow [J]. J.Heat Transfer. 126 (4):554-557

Hong, Y., TingKan, L., et al.2009. Numerical simulation study on structure design and parameters optimization of high pressure water jet cutting nozzle [J]. Machine Tool＆Hydraulics. (11):90-92.

Hukam,C. M. , Reodikar, S.A., et al . 2016. Influence of the shape of the orifice on the local heat transfer distribution between smooth flat at surface and impinging incompressible air jet [J].Experimental Thermal and Fluid Science. (70):292-306.

Jiahong, C. 2002.Freezing becomes a breeze [J]. FMC Food Technology. 9(1):32-34.

JinFeng, W., WenJun, L., et al. 2018.Influence of V type slit nozzle cutting ratio on belt surface heat transfer characteristics of quick freezer [J]. FOOD＆MACHINERY.(4):94-98.

Katti V., Prabhu, S.V. 2008. Influence of spanwise pitch on local heat transfer distribution for in-line arrays of circular jets with spent air flow in two opposite directions [J]. Experimental Thermal and Fluid Science,33(1): 84-95.

Li, D., Zhu, Z., et al.2018. Effects of freezing on cell structure of fresh cellular food materials: A review [J]. Trends in Food Science and Technology.75:46-55.

Laniro, A., Cardone, G.2012.Heat transfer rate and uniformity in multichannel swirling impinging jets [J]. Applied Thermal Engineering. 49 (1): 89-98.

Li, Y., Li, F., et al. 2018.Radio frequency tempering uniformity investigation of frozen beef with various shapes and sizes [J]. Innovative Food Science and Emerging Technologies. 48:42-55.

LuGuang, R., YunLiang, Z., et al.2018.Effect of straight section of nozzle outlet on flow field of jet pump. Seminar on Development Strategy of Hydraulic Machinery.34:79-83.

Makatar, W.H., Perapong, T., et al. 2014.Effect of cross-flow velocity on flow and heat transfer characteristics of impinging jet with low jet-to-plate distance[J]. J.Mechanical Science and Technology.28(7): 2909-2917.

Ping, L., DongSu, Z., et al.2007. Computational study on the effect of nozzle geometric parameters on the performance of jet flow field [J]. J. Machine Design. (11):50-52.

Subasi, A., Sahin, B., et al. 2016, Multi-objective optimization of a honeycomb heat sink using response surface method [J]. International Journal of Heat & Mass Transfer.101:295-302.

Vikas, K, Ai, P., W., et al. 2012. 3-D Computational Fluid Dynamics Model for Forced Air Cooling of Eggs Placed in Trays [J].Int. J. Food Engineering.108 (3):480-492.

WenHua, B., NengSheng, B., et al. 2011.Numerical simulation of V-shaped slot nozzle impinging jet of printing and coating oven[J].Packaging Engineering. 54(3):28-32.

Yu, P. P., Zhu, K., Q., et al. 2017. Heat transfer rate and uniformity of mist flow jet impingement for glass tempering [J]. Int. J.Heat and Mass Transfer.115:368-378.

Zhen, Z., Jin, X., 2008. Numerical simulation and verification on the velocity field of impingement freezer [J]. Cryogenics, (6):45-50.

Manuscript ID: 1765
DOI: 10.18462/iir.icr.2019.1765

Effect of various freezing rate on freeze-drying process of water diagnosed by ultrasonic technology

Chin-Chi CHENG[(a)], Yen-Hsiang TSENG[(b)], Hong-Ping CHENG[(a)]

[(a)] National Taipei University of Technology, Taipei, Taiwan
1, Sec. 3, Zhongxiao E. Rd., Taipei 10608 Taiwan, newmanch@ntut.edu.tw, hpcheng@ntut.edu.tw
[(b)] Tai Yiaeh Enterprise Co., Ltd., New Taipei City, Taiwan
8, Ln. 283, Zhongzheng 3rd Rd., Yingge Dist., New Taipei City 239, Taiwan, yhtntut@gmail.com

ABSTRACT

In this paper, an ultrasonic transducer (UT) is integrated onto the bottom of a specially designed frozen bottle for the purpose of monitoring the freeze-drying process of water under various freezing rate. The temperature and visual observation made with a camera are then compared with the corresponding ultrasonic signature. In order to evaluate the various freezing rate, two kinds of freeze-drying processes are designed. The temperature and ultrasonic signals indicated the phase change of cooling and freezing periods. These two periods are shorter when the shelf temperature is set at a lower value. However, only ultrasonic signals indicate the phase change of drying period. The visual observation indicates that the lower shelf temperature setting results in the smaller ice crystal nuclei. This study demonstrates an innovative frozen bottle with an integrated ultrasonic sensor used to measure the freeze-drying process of water under the various freezing rates.
Keywords: Freeze-Drying Process Diagnosis, Freezing/Drying Point, Ultrasonic Transducer (UT), Cooling/Freezing/Drying Periods.

1. INTRODUCTION

Freeze-drying process is one of the drying methods, and it is utilized in reservation of food, drug, and biopharmaceutical products (Toshniwal and Karal, 2013). The freeze-drying process includes a freezing, primary drying and secondary drying step (Ratti, 2001) in order to withdraw the water from a product. These three steps affect the phase change of water into ice, and the exhaust of ice from the products. Therefore, the accuracy of measurement and perform of each step will influence the final product quality significantly (Rahman, 2007). The normal measuring tools in freeze-drying process include on-line and off-line tools. The off-line tools compose cryo-microscope (Nail et al., 1994), differential scanning calorimetry (DSC), thermo-mechanical analysis (TMA), and dynamic mechanical thermal analysis (DMTA) (Roos et al., 1996). All these tools are expensive and need skilful technicians. The on-line tools contain temperature, pressure and visual recording instruments. These tools may cause pollution of products and be limited to transparent container. In this paper, a novel frozen container with an ultrasonic sensor is provided as the solution of above problems. The phase change and three periods of freeze-drying process are indicated through the measured results. This study demonstrates a frozen bottle with an integrated ultrasonic sensor used to measure the freeze-drying process of water under the various freezing rates.

2. EXPERIMENTS

In this study, a freeze-drying machine, equipped with vacuum chamber, shelf, cold trap, refrigeration unit and vacuum pump, is utilized for carrying out all experiments. A designed frozen bottle, equipped with a transparent tube and a steel plate, can contain the sample and pass through the freeze-drying process, as shown in Figure 1. The ultrasonic transducer (UT) is integrated on the plate by the sol-gel fabrication technology. The transmitted energy of ultrasound is less than 50 μJ. A camera is utilized for recording all the physical variation of the sample. A thermocouple is installed in the middle of the frozen bottle. The temperature, chamber pressure, visual records, and ultrasonic signals will be compared for verifying the phase change and process phenomena.

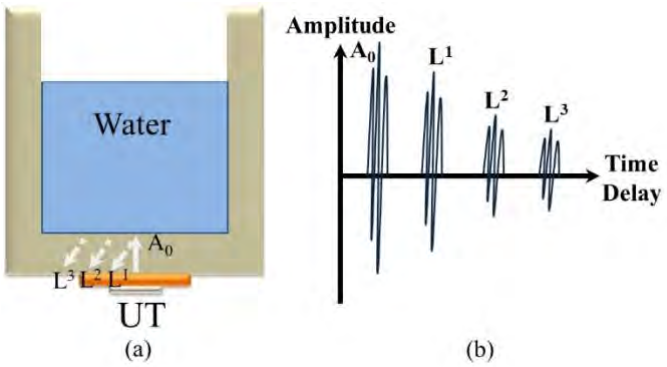

Figure 1: (a) Designed frozen bottle with ultrasonic transducer, (b) Ultrasonic signal with respective to time-delay.

For evaluating the effect of various freezing rates, two types of freeze-drying processes are designed for freeze-drying the water in the level of 15 mm, as shown in Table 1. The water is utilized to evaluate the performance of diagnosing sensors, and most of the pharmacy use water as the solution. For the 1st process, shelf temperature and freezing period were set at -30°C and 120 min, respectively, to freeze water. After sufficient cooling and freezing, the chamber pressure was decreased from 760 to 0.17 Torr within several seconds. During the following primary and secondary drying processes, the shelf temperature was continuously raised from -30 to 10°C at heating. The difference between 1st and 2nd procedure is the setting of shelf temperature. For 2nd procedure, the shelf temperature was continuously raised from -20 to 20°C. The various freezing rate is achieved by setting the different shelf temperature.

Table 1. Two procedures used for the freeze-drying process

No.	Shelf temp. (°C)	Freezing period (min)	Chamber pressure (Torr)	Drying temp. (°C)	Heating period (min)
1	-30	120	760→0.17	-20→ -10→ 0→ 10	60
2	-20	120	760→0.17	-10→ 0→ 10→ 20	60

3. RESULTS AND DISCUSSIONS

3.1. Diagnosed by temperature during freezing process

Two containers, which were filled with water in the height of 15 mm, passed through the freeze-drying process under the shelf temperature settings of -20 and -30°C, respectively. The experimental results of water temperature during the freezing stage are shown in Figure 2. Figures 2 (a) to (b) are the temperature variation of water under the shelf temperature settings of -30 and -20°C, respectively, during the freezing stage. The timings of supercooling and phase change end indicated by temperature are 19.2, 38.5 and 46.7, 74.1 minute-mark for the water under the shelf temperature settings of -30 and -20°C, respectively. The cooling ($\triangle P_{CT}$) and freezing ($\triangle P_{FT}$) periods determined by sample temperature are shown in Figures 2 (a) to (b). The cooling/freezing periods under the shelf temperature of -30°C are shorter than those of -20°C, due to faster freezing rate.

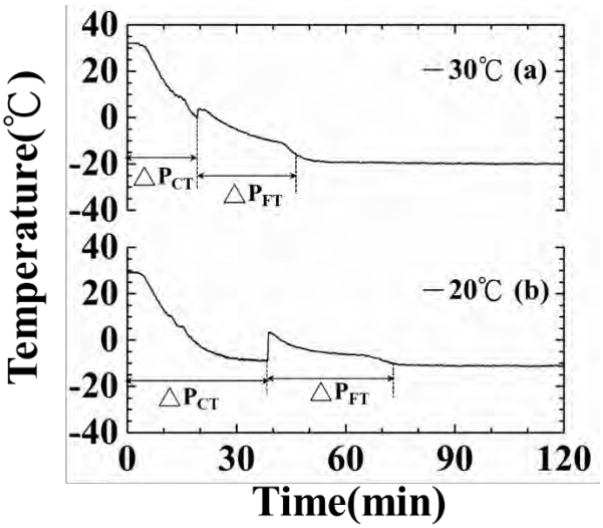

Figure 2: Temperature variations with respect to various shelf temperatures at freezing stage. Shelf temperature: (a) -30 and (b) -20°C.

3.2. Diagnosed by ultrasonic amplitude during freeze-drying process

The experimental results of amplitude of ultrasonic L^3 echo during the freezing stage are shown in Figure 3. Figures 3 (a) to (b) are the amplitude variations of ultrasonic L^3 echo in water at the height of 15 mm during the freezing stage under the shelf temperature settings of -30 and -20°C, respectively. The timings of freezing point and phase change end indicated by ultrasonic L^3 echo are 19.5, 37.9 and 45.8, 74.7 minute-mark for the water under the shelf temperature settings of -30 and -20°C, respectively. The cooling/freezing periods under the shelf temperature settings of -30 and -20°C are defined and indicated in Figures 3 (a) to (b). The corresponding timings of water-in, freezing point and phase change end indicated by temperature and ultrasonic L^3 echo are illustrated in Table 2. The cooling/freezing periods indicated by ultrasonic L^3 echo are similar with those indicated by temperature in Figure 2 (a) and (b). In order to compare the cooling/freezing periods indicated by temperature and ultrasonic L^3 echo, the calculated cooling/freezing periods from Figures 2 and 3 are shown in Figure 4. In Figure 4, the cooling/freezing periods indicated by ultrasonic L^3 echo are illustrated with □ and ∆, respectively. Those period indicated by temperature are illustrated with ○ and ◊, respectively. The cooling/freezing periods indicated by temperature and ultrasonic L^3 echo could be expressed in the following equations:

$$\Delta P_{CT} = 22.29 + 0.25 \times T \quad \text{Eq. (1)}$$

$$\Delta P_{CUT} = 22.32 + 0.25 \times T \quad \text{Eq. (2)}$$

$$\Delta P_{FT} = 67.73 + 1.39 \times T \quad \text{Eq. (3)}$$

$$\Delta P_{FUT} = 71.23 + 1.57 \times T \quad \text{Eq. (4)}$$

where T is the shelf temperature setting. Therefore, the temperature and ultrasonic L^3 echo are capable to distinguish the various cooling/freezing rate.

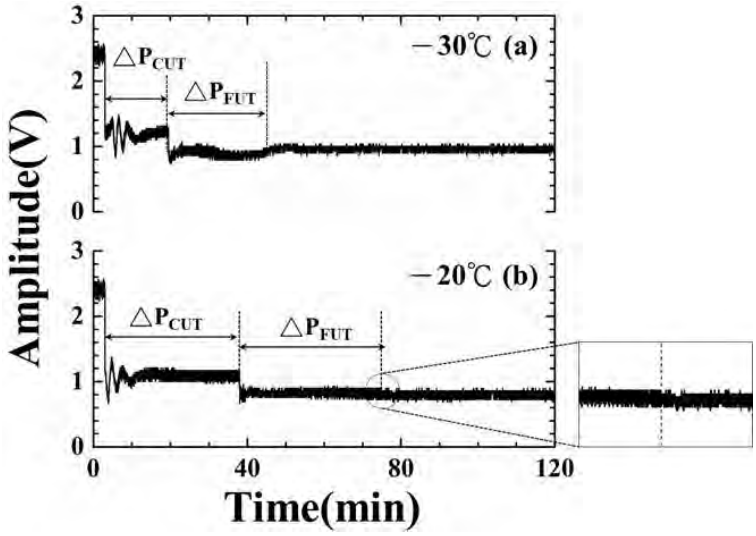

Figure 3: Amplitude variations of ultrasonic L^3 echo at freezing stage with respect to various shelf temperatures of (a) -30 and (b) -20 °C, respectively.

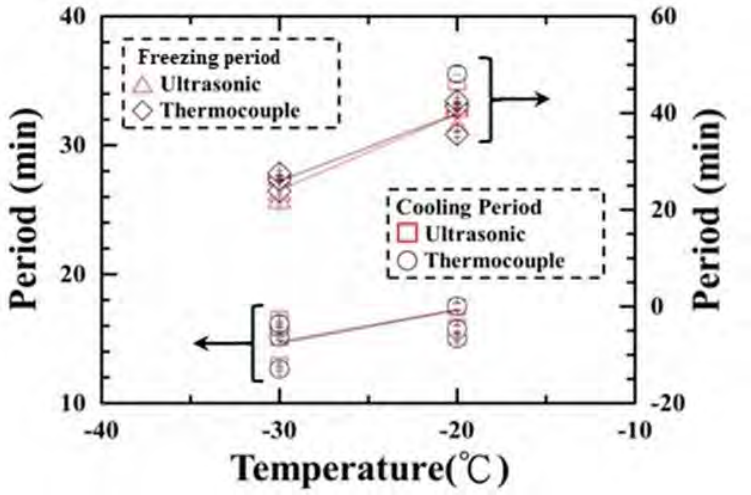

Figure 4: Cooling/freezing periods determined by ultrasonic or temperature signals with respect to various shelf temperatures.

Table 2. Timings and temperatures of water in, freezing point, phase change end and drying point indicated by temperature and ultrasonic L^3 echo for water level of 15 mm.

Shelf temperature (°C)	Items	Water in	Freezing point	Phase change end	Drying point
−30	$Time_{Temp}$ (min)	3.0	19.2	46.7	N/A
	$Time_{UT}$ (min)	3.0	19.5	45.8	838.0
	Temperature (°C)	32.1	−0.4 (Supercooling)	−16.5	N/A
−20	$Time_{Temp}$ (min)	3.0	38.5	74.1	N/A
	$Time_{UT}$ (min)	3.0	37.9	74.73	835.9
	Temperature (°C)	28.8	−8.5 (Supercooling)	−10.5	N/A

Figures 5 (a) to (c) are the amplitude variations of ultrasonic L^3 echo in water at the height of 15 mm during the drying stage under the shelf temperature settings of -30 and -20°C, respectively. The amplitudes of ultrasonic L^3 echo rise from the bottom value at 350.4 and 297.8 minute-mark for the water under the shelf temperature settings of -30 and -20°C, respectively, when the primary drying stage ends. This is due to the sublimation of ice and less contact of ice with bottle surface. In Table 1, the drying temperature settings of procedure 2 are higher than those of procedure 1. This causes the ending time difference of the primary drying stage under the shelf temperature settings of -30 and -20°C. After the end of primary drying stage, the amplitudes of ultrasonic L^3 echo drop/rise at a stable level at 838.0 and 835.9 minute-mark for the water under the shelf temperature settings of -30 and -20°C, respectively, when the second drying stage ends. This is due to the desorption of ice and less contact of residual with bottle surface. These phenomena will be further evidenced in the following sections. The drying periods of various water levels are also indicated. The corresponding timings of drying end indicated by ultrasonic L^3 echo are illustrated in Table 2. It seems that the various cooling/freezing speeds won't affect the timings of drying end under the same water level.

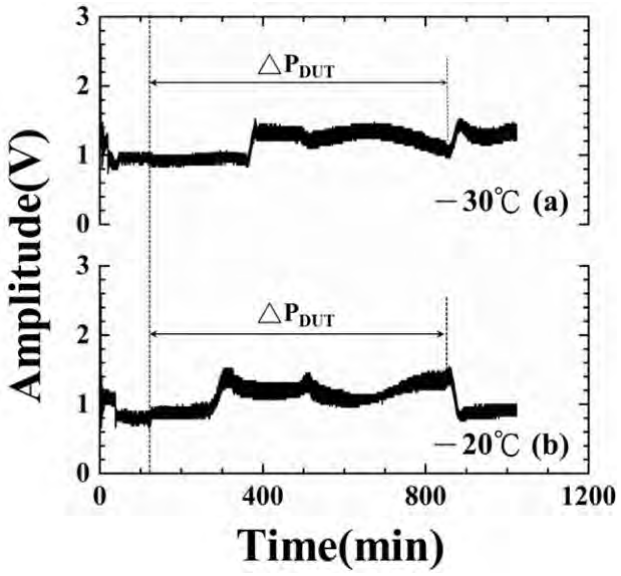

Figure 5: Amplitude variations of ultrasonic L^3 echo at drying stage with respect to various shelf temperatures of (a) -30 and (b) -20 °C, respectively.

3.3. Diagnosed by visual observation under the various cooling speeds

Various cooling speed in water would show different physical property and dynamic phenomena that can be observed in the container through visual records during the freeze-drying process at great length. These phenomena could also be the evidence of other measured parameters. Figures 6 (a) ~ (b) are the photographs of the container with ice during the drying process. One can see that the ice crystal nuclei in Figure 6 (b) are larger than those in Figure 6 (a), due to that the faster cooling speed during freezing stage will cause smaller ice crystal nuclei. The various size of ice crystal nuclei could be evaluated during the freezing stage by ultrasonic signals and temperature real-time.

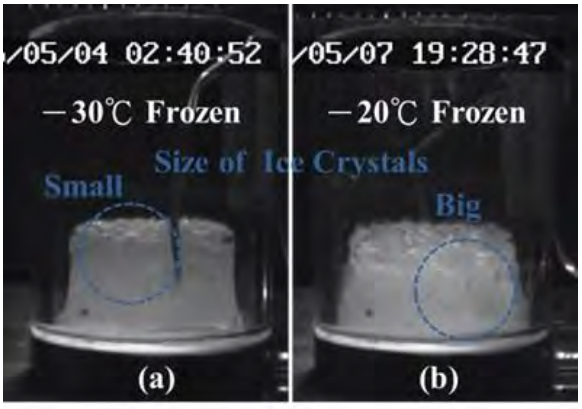

Figure 6: Photographs of ice in frozen bottle at freezing stage with respect to shelf temperature of (a) -30 and (b) -20 °C, respectively.

4. CONCLUSIONS

In this paper, an ultrasonic transducer (UT) is integrated onto the bottom of a specially designed frozen bottle for the purpose of monitoring the freeze-drying process of water. The temperature and visual observation made with a camera are then compared with the corresponding ultrasonic signature. In order to evaluate the various freezing rates, two kinds of freeze-drying processes are designed. The temperature and ultrasonic signals indicated the phase change of cooling and freezing periods. These two periods are shorter when the shelf temperature is set at a lower value. However, only ultrasonic signals indicate the phase change of drying period. The visual observation indicates that the lower shelf temperature setting results in the smaller ice crystal nuclei. This study demonstrates an innovative frozen bottle with an integrated ultrasonic sensor used to measure the freeze-drying process of water under the various freezing rates.

ACKNOWLEDGEMENTS

This work is funded by Ministry of Science and Technology of Taiwan, ROC under Contracts No: MOST 104-2221-E-027-121, MOST-105-2221-E-027-103 and MOST 107-3113-E-008-003.

NOMENCLATURE

UT	ultrasonic transducer	$\triangle P_{CT}$	cooling period determined by sample temperature
$\triangle P_{FT}$	freezing period determined by sample temperature	L^3	3rd ultrasonic reflecting echo
$\triangle P_{CUT}$	cooling period determined by ultrasonic echo	$\triangle P_{FUT}$	freezing period determined by ultrasonic echo
$\triangle P_{DUT}$	dryling period determined by ultrasonic echo		

REFERENCES

Nail, S.L., Her, L., Proffitt, C.P.B., Nail, L.L., 1994. An improved microscope stage for direct observation of freezing and freeze drying. Pharm. Res. 11, 1098–1100.

Rahman, M.S., 2007. Handbook of Food Preservation. 2nd ed., CRC Press, Boca Raton, FL, 125 p.

Ratti, C., 2001. Hot air and freeze-drying of high-value foods: A review. J. Food Eng. 49, 311–319.

Roos, Y.H., Karel, M., Kokini, J.L., 1996. Glass transitions in low moisture and frozen foods: effects on shelf life and quality. Food Technol. 50, 95–108.

Toshniwal, U., Karal, S., 2013. A review paper on Solar Dryer. Int. J. Eng. Res. Appl. 3, 896–902.

Manuscript ID: 55
DOI: 10.18462/iir.icr.2019.0055

Optimal control of thermal energy storage for a solar energy driven refrigeration plant to cool a fruit storage facility

Leo J.S. LUKASSE, Edo B. WISSINK
Wageningen UR Food & Biobased Research
6700 AA Wageningen, The Netherlands, leo.lukasse@wur.nl

ABSTRACT

There is a growing need to adjust electricity consumption to electricity generation due to the rising share of electricity generation from solar and wind energy. Refrigerated storage can support this by thermal energy storage in *e.g.* an ice buffer.
Aim of this study is to investigate how optimal control can help to optimize the exploitation of an ice buffer.
In this study the controlled system has a number of cold rooms for fruit storage, a refrigeration plant, and an ice buffer, connected by a network of pipes in which a brine circulates. Electric energy is supplied from local PV panels, supported by the power grid. It is shown how the formation and melting of ice is adjusted to forecasted electricity tariffs.
The results demonstrate how an optimally controlled ice buffer can help to shape the electric energy consumption, while maintaining temperatures in the storage rooms.
Keywords: control (automatic), energy storage, solar energy, storage.

1. INTRODUCTION

Electric energy supply grids come from an era where demand was dictated by electricity users, and network managers controlled the energy supply. Controlling energy supply was not difficult as the electric power supply by coal and gas fired power plants is easily adjustable. With the growing share of electricity generated from sustainable sources, like wind and solar energy, the power supply becomes ever less controllable. Therefore power grid operators explore ways to control power demand in smart grids, amongst others by using price mechanisms.
One option to control the electricity demand from networks is to shift running times of refrigeration plants (see *e.g.* Almenta *et al.*, 2016) using ice buffers as thermal batteries. Also IPCC (2018) sees the potential of smart controls when it “considers Artificial Intelligence, Internet-of-Things and nanotechnologies as valuable general purpose technologies for smart lighting and air conditioning”.
Fruit storage facilities typically have multiple cold rooms connected to one refrigeration plant. The refrigeration plant has enough capacity to rapidly cool down the fruit in the days after harvest. Consequentially there is a large overcapacity in the rest of the storage season. Ice buffers are effective batteries for thermal energy, due to the large latent heat of melting of water. The combination of refrigeration overcapacity together with large thermal capacity gives opportunities to shift the operation times of the refrigeration plant over time.
This paper presents a case study on the use of optimal control theory to manipulate the operation of refrigeration plants with the purpose to shift electric energy consumption, while using an ice buffer to store thermal energy. The concept may help to shape power demand in smart grids.

2. DESCRIPTION OF CONTROLLED SYSTEM

The controlled system is drawn in Fig. 1, and briefly explained here with reference to that figure. It’s an indirect refrigeration system. A compressor compresses the primary refrigerant, which condenses in an air-cooled condenser, then passes through a subcooler where the subcooling can be increased, expands in an electronic expansion valve (EEV), then evaporates in an evaporator where it extracts heat from a secondary refrigerant, and then is drawn into the compressor again. The secondary refrigerant is a brine, typically maintained at a temperature between approximately -3 and -15 °C. From the brine buffer three pumps extract brine. Pump 1 circulates brine over the evaporator to extract heat from the brine. Pump 2 circulates brine over the N air-to-liquid heat

exchangers Hex i (i = 1, …, N), installed in the connected cooling chambers in which temperature needs to be maintained. The ice buffer is nothing but an insulated water vessel, in which two separate pipe bundles are installed. The ice buffer can be charged by running pump 3. When pump 3 runs it circulates the main brine through the first pipe bundle, and ice grows on the pipes while extracting heat from the buffer. The ice buffer can be discharged by running pump 4. When pump 4 runs brine circulates in a second separate brine circuit. It extracts heat from the subcooler, and conveys that heat to the ice buffer. The increased subcooling of the primary refrigerant condensate yields extra refrigeration capacity in the evaporator and is an efficient way to make the stored latent heat of ice available as sensible heat at the desired evaporation temperature level. The next section presents the mathematical model of this system used to solve the optimal control problem.

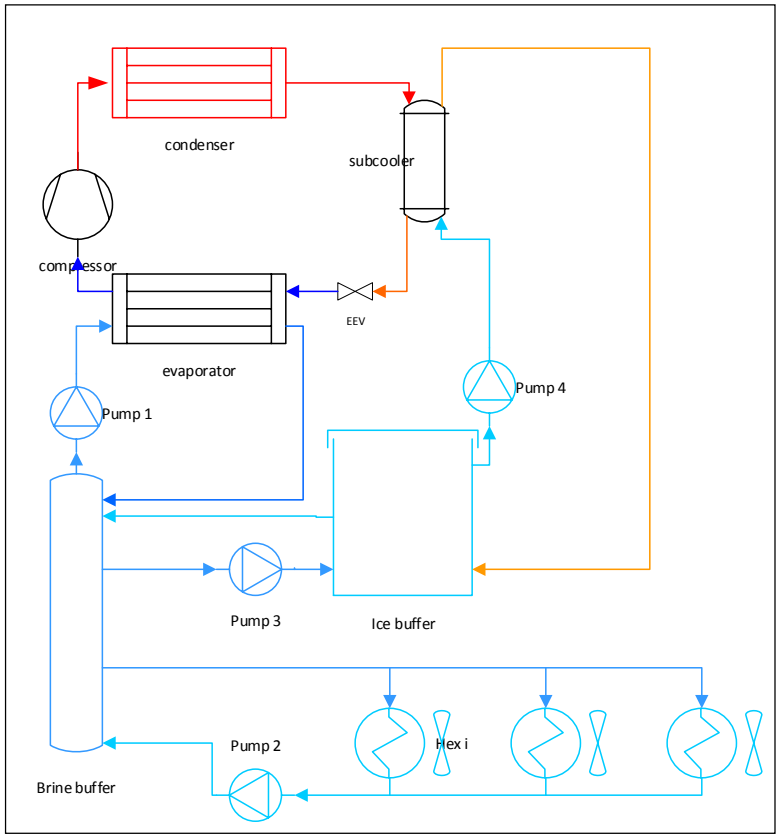

Fig. 1, schematic overview of the controlled refrigeration plant.

3. MODEL

The state vector for the complete model is the conjunction of two types of states:

$$\mathbf{x}(t) = \begin{bmatrix} \mathbf{x^m}(t) \\ \mathbf{x^L}(t) \end{bmatrix} \tag{1}$$

With

$\mathbf{x^m}$ = model states to describe the dynamic energy balances of the system depicted in Fig. 1.

$\mathbf{x^L}$ = objective functional states used in formulating the optimal control problem.

The following subsections will define both types of states.

3.1 Modelling the heat balances of the controlled system

The faster system dynamics are assumed to be in steady state. Also the chamber temperatures are left out of consideration, because local controllers will keep them constant. The complete model state $\mathbf{x^m}(t) \in \mathbb{R}^2$ is then given by

$$\mathbf{x^m}(t) = \left[x^m_{T,b}(t),\ x^m_{H,ib}(t)\right]^T \tag{2}$$

With

$x^m_{T,b}(t)$ = temperature of the brine in the brine buffer [°C]

$x^m_{H,ib}(t)$ = enthalpy-content of the water/ice-content of the ice buffer [kJ]

The brine temperature dynamics are modelled according to

$$\frac{dx^m_{T,b}}{dt} = \frac{3600}{m_b c_{p,b}} * \left(Q_{hex}(t) + Q_{ib,charge}(t) - P_{th,comp}(t) - Q_{ib,discharge}(t)\right) \quad [°C.h^{-1}] \tag{3}$$

The dynamic enthalpy balance of the ice buffer is given by

$$\frac{dx_{H,ib}^{m}}{dt} = 3600 * (\frac{UA_{ib,amb}(d_{Tamb}(t) - T_{ib}(t))}{1000} - Q_{ib,charge}(t) + Q_{ib,discharge}(t)) \quad [\text{kJ.h}^{-1}] \quad (4)$$

Where the enthalpy content of the water/ice in the ice buffer is a sum of sensible and latent heat:

$$x_{H,ib}^{m}(t) = m_{ice}(t) * c_{p,ice} * T_{ib}(t) - h_{melt} m_{ice}(t) + m_{water}(t) * c_{p,water} * T_{ib}(t) \quad [\text{kJ}] \quad (5)$$

$x_{H,ib}^{m}(t)$ = 0 kJ when all mass is 0 °C water, *i.e.* when $m_{ice}(t)$ = 0 kg en $T_{ib}(t)$ =0 °C.
In the above equation the three quantities $m_{ice}(t)$, $m_{water}(t)$, $T_{ib}(t)$ vary over time. They relate to model state $x_{H,ib}^{m}(t)$ according to algebraic equations.
In eqn. 4 the term $UA_{ib,amb}(d_{Tamb}(t) - T_{ib}(t))/1000$ [kW] accounts for the ingress of ambient heat into the buffer through the walls, $Q_{ib,charge}(t)$ represents the withdrawal of heat from the ice buffer by the main brine buffer, $Q_{ib,discharge}(t)$ represents the supply of heat to the ice buffer from the subcooler. For calculation of these three terms it is necessary to know $T_{ib}(t)$. It follows algebraically from $x_{H,ib}^{m}(t)$. After that $Q_{ib,charge}(t)$ in eqn. 4 can be calculated from

$$Q_{ib,charge}(t) = UA_{ib,charge}(t) * u_{charge}(t) * (T_{ib}(t) - x_{T,b}^{m}(t))/1000 \quad [\text{kW}] \quad (6)$$

Where $x_{T,b}^{m}(t)$ is the brine buffer temperature. The only unknown in eqn. 6 is the heat transfer coefficient $UA_{ib,charge}(t)$. For the time being it is chosen to use a black box model. In analogy with Jekel *et al.* (1993) a more complete physical description is possible, but it would probably add little in view of the existing parameter uncertainty.
The subcooler brine temperature is assumed to be uniform, and its dynamics are assumed to be infinitely fast. The brine's heat rejected to the ice buffer then equals the heat absorbed in the subcooler, and the heat transfer resistances from ice water to subcooler brine, and from subcooler brine to condensed refrigerant are a series connection, modelled as one lumped parameter:

$$Q_{ib,discharge}(t) = u_{discharge}(t) * UA_{ib,discharge}(t) * \left(T_c(t) - T_{ib}(t)\right)/1000 \quad [\text{kW}] \quad (7)$$

The only unknown in eqn. 7 is $UA_{ib,discharge}(t)$. It is treated like $UA_{ib,charge}(t)$.

3.1.1 Model of primary refrigeration circuit

The dynamics of the primary refrigeration circuit are much faster than the ice buffer dynamics, and therefore assumed to be infinitely fast.
The refrigeration capacity generated by the compressors is

$$P_{th,comp}(t) = u_{comp}(t) * P_{th,comp,max}(t) \quad [\text{kW th.}] \quad (8)$$

The maximum refrigeration capacity is the nominal max. refrigeration capacity $P_{th,comp,max,nom}(t)$, specified at nominal condensation and evaporation temperatures $T_{c,nom}$ and $T_{0,nom}$, increased with 2% per 1 °C decrease of T_c - T_0, but always positive:

$$P_{th,comp,max}(t) = max\left(0;\ P_{th,comp,max,nom} * \left(1 + 0.02 * \left(\left(T_{c,nom} - T_{0,nom}\right) - \left(T_c(t) - T_0(t)\right)\right)\right)\right) \quad [\text{kW th}$$

With condensation temperature

$$T_c(t) = \begin{cases} 22 & if \quad d_{Tamb}(t) \leq 10 \\ d_{Tamb}(t) + 12 & if \quad d_{Tamb}(t) > 10 \end{cases} \quad [\text{°C}] \quad (10)$$

And evaporation temperature $T_0(t)$ is the set evaporation temperature of -7 °C.
The supplied refrigeration capacity equals the sum of thermal compressor capacity and the heat absorbed from the subcooler:

$$P_{th,supply}(t) = P_{th,comp}(t) + Q_{ib,discharge}(t) \quad [\text{kW th.}] \quad (11)$$

Due to EEV limitations $Q_{ib,discharge}(t)$ can never be more than ± 10% of $P_{th,comp}(t)$. This knowledge is brought in the simplified model by adding a constraint:

$$Q_{ib,discharge}(t) - 0.1 * P_{th,comp}(t) \leq 0 \quad [\text{kW}] \quad (12)$$

Substitute eqn. 7 and 8 in the equation above to get

$$u_{discharge}(t) * UA_{ib,discharge}(t) * \big(T_c(t) - T_{ib}(t)\big)/1000 - 0.1 * u_{comp}(t) * P_{th,comp,max}(t) \leq 0 \quad \text{[kW]}$$

3.1.2 Electric power uptake

Thermal compressor capacity demands an electric power uptake of

$$P_{el,comp}(t) = P_{th,comp}(t)/COP(T_c(t), T_0(t)) \quad \text{[kW el.]} \quad (14)$$

Where Coefficient Of Performance (COP) depends on $T_c(t)$ and $T_0(t)$ according to a fixed compressor efficiency η_{comp} multiplied by the theoretical Carnot efficiency:

$$COP = \eta_{comp} * \frac{(T_0+273.15)}{T_c(d_{Tamb}(t))-T_0} \quad \text{[(kW th.).(kW el.)}^{-1}\text{]} \quad (15)$$

Brine pumps for charging and discharging the ice buffer use 1 kW electricity when running at maximum speed. In the refrigeration system there are many other users of electric energy, think of brine pumps, air circulation fans and electric defrost actions. Their electric power uptake $P_{el,others}(t)$ is considered constant.

The electric power supplied to the plant from the grid follows from

$$P_{el,AC}(t) = P_{el,comp}(t) + 1 * (u_{charge} + u_{dis,charge}) + P_{el,others} - P_{el,PV}(t) \quad \text{[kW]} \quad (16)$$

In this project $P_{el,PV}(t)$ is treated as an external disturbance input.

3.2 Objective functional states (x^L)

The objective functional consists of multiple cost terms. First of all there is the electricity costs:

$$\frac{dx_{el}^L}{dt} = \begin{cases} d_{e,consumption}(t) * P_{el,AC}(t) & if \quad P_{el,AC}(t) \geq 0 \\ -d_{e,production}(t) * P_{el,AC}(t) & if \quad P_{el,AC}(t) < 0 \end{cases} \quad \text{[€.h}^{-1}\text{]} \quad (17)$$

A hard constraint is that at any time $-55 < P_{el,AC}(t) < 55$ kW, because 55 kW is the low voltage connection capacity above which the main circuit breaker will trip. As explained in *e.g.* Pierre (1969) and van Henten (1994) a convenient way to deal with state constraints is to implement it as a soft constraint:

$$\frac{dx_{el,AC,max}^L}{dt} = \big(\big|P_{el,AC}(t)\big| > (p_{P,AC,max}^d - 1)\big) * \big(\big|P_{el,AC}(t)\big| - (p_{P,AC,max}^d - 1)\big)^{p_j(5)} \quad \text{[kW}^{pj(5)}\text{]} \quad (18)$$

with $p_{P,AC,max}^d$ = 55 kW.

In a similar way the upper constraint on $Q_{ib,discharge}(t)$ is treated (eqn. 13):

$$\frac{dx_{Qib,discharge,max}^L}{dt} = \Big(\Big(Q_{ib,discharge}(t) - 0.1 * P_{th,comp}(t)\Big) > -1\Big) * \big(Q_{ib,discharge}(t) - 0.1 * P_{th,comp}(t) + 1\big)^{p_j(6)} \quad \text{[kW}^{pj(6}$$

In the same way the optimization routine is forced to always keep the brine buffer temperature below the set evaporation temperature + 4 °C:

$$\frac{dx_{T,b}^L}{dt} = \big((x_{T,b}^m(t) - T_{0,ref} - 4) > -1\big) * \big(x_{T,b}^m(t) - T_{0,ref} - 4 + 1\big)^{p_j(7)} \quad \text{[kW}^{pj(7)}\text{]} \quad (20)$$

All $\mathbf{x^L}$-terms together form the vector

$$\mathbf{x^L} = \big[x_{el}^L, x_{el,AC,max}^L, x_{Qib,discharge,max}^L, x_{T,b}^L\big]^T \quad (21)$$

where

x_{el}^L = electricity costs [€]

$x_{el,AC,max}^L$ = penalty on power uptake outside the range $[-p_{P,AC,max}^d, p_{P,AC,max}^d]$ [kW$^{pj(5)}$h].

$x_{Qib,discharge,max}^L$ = penalty on $Q_{ib,discharge}(t) > 0.1 * P_{th,comp}(t)$ [kW$^{pj(6)}$h].

$x_{T,b}^L$ = penalty on brine temperatuur > set evaporation temperature + 4 °C [kW$^{pj(7)}$h].

3.3 Control inputs, disturbance inputs and initial conditions

The model has 3 control inputs, which need to be optimized:

$$u(t) = [u_{comp}(t),\ u_{charge}(t),\ u_{discharge}(t)]^{\mathrm{T}} \quad \in \mathbb{R}^3 \tag{22}$$

where

$u_{comp}(t)$ = activated fraction of installed refrigeration capacity [-], $0 \le u_{comp}(t) \le 1$
$u_{charge}(t)$ = activated fraction of ice buffer charging capacity [-], $0 \le u_{charge}(t) \le 1$
$u_{discharge}(t)$ = activated fraction of ice buffer discharging [-], $0 \le u_{discharge}(t) \le 1$

The model has four disturbance inputs, *i.e.* uncontrolled non-constant external inputs:

$$\mathbf{d}(t) = [d_{Tamb}(t),\ d_{Pel,PV}(t),\ d_{e,consumption}(t),\ d_{e,production}(t)]^{\mathrm{T}} \quad \in \mathbb{R}^4 \tag{23}$$

where

$d_{Tamb}(t)$ = ambient air temperature [°C]
$d_{Pel,PV}(t)$ = electric power generated by PV solar panels. [kW]
$d_{e,consumption}(t)$ = price paid for electricity drawn from the power grid [€.kWh^{-1}]
$d_{e,production}(t)$ = price received for electricity supplied to the power grid [€.kWh^{-1}]

In every call to the optimization routine the following initial conditions $\mathbf{x^m}(t_0)$ are used:

$$\mathbf{x^m}(t_0) = \left[\hat{x}^m_{T,b}(t_0),\ \hat{x}^{\mathrm{m}}_{\mathrm{H,ib}}(t_0)\right]^T \tag{24}$$

$$\mathbf{x^L}(t_0) = \mathbf{0} \quad \text{with} \quad \dim(\mathbf{x^L}(t_0)) = 4 \times 1 \tag{25}$$

Where

$\hat{x}^m_{H,ib}(t_0)$ = estimated current enthalpy content of the ice buffer, which is an algebraic function of the actual water level and temperature measurement [kJ].

3.4 Optimal control (OC) problem

The dynamic optimization problem is

$$\min_{\mathbf{u}} J(u_{comp}, u_{charge}, u_{discharge}) = p_j(1) * x^L_{el}(t+H) + p_j(2) * x^L_{el,AC,max}(t+H) + p_j(3) * x^L_{Qib,discharge,max}(t+H) + p_j(4) * x^L_{T,b}(t+H) \quad [€] \tag{26}$$

Subject to the modelled system dynamics (eqns. 1 - 25) and hard constraints

$$\mathbf{0} \le [u_{comp}(t) \quad u_{charge}(t) \quad u_{discharge}(t)] \le \mathbf{1} \tag{27}$$

In eqn. 26 H the prediction horizon [h]. The parameter vector p_j is a vector of tuning parameters.

4. SIMULATED CASES

In the MATLAB® simulation environment the above OC problem was combined with a self-programmed gradient-based search algorithm to solve the OC problem. For more details on the algorithm see Lukasse *et al.* (2009).
In simulation a number of optimal control cases has been solved, to test and illustrate the functioning of the optimal controller. Following cases are presented here:

1. Constant electricity price: $d_{Tamb}(t)$ = 10 °C, $d_{Pel,PV}(t)$ = 0 kW, $d_{e,consumption}(t) = d_{e,production}(t) = 4 * 10^{-2}$ €.kWh^{-1}.
2. Day-night electricity tariff: $d_{Tamb}(t)$ = 10 °C, $d_{Pel,PV}(t)$ = 0 kW, $d_{e,consumption}(t) = d_{e,production}(t) = 7 * 10^{-2}$ €.kWh^{-1} if $7 < t < 23$ h, else $1 * 10^{-2}$ €.kWh^{-1}.

3. One hour with large solar energy production, during which the reward for supply to the grid is zero: $d_{Tamb}(t)$ = 10 °C, $d_{Pel,PV}(t)$ = 25 kW if 12 < t < 13 h else 0 kW, $d_{e,consumption}(t)$ = 4 * 10^{-2} €.kWh^{-1}, $d_{e,production}(t)$ = 0 €.kWh^{-1}.
4. One hour with large solar energy production, during which the price for supply to the grid is high: $d_{Tamb}(t)$ = 10 °C, $d_{Pel,PV}(t)$ = 25 kW if 12 < t < 13 h else 0 kW, $d_{e,consumption}(t)$ = 4 * 10^{-2} €.kWh^{-1}, $d_{e,production}(t)$ = 8 * 10^{-2} €.kWh^{-1}.

The next section presents the simulation results.

5. RESULTS

In simulation the optimal solution was first computed for case 1, in which all disturbance inputs are constant over time. The resulting optimal control inputs $\mathbf{u}^*$ are virtually constant (not shown for brevity). Case 2 differs from case 1 only in terms of electricity tariff. The higher tariff between 7 and 23 h is an incentive to shift compressor activity $u_{comp}(t)$ to outside that time window. This is exactly what happens. See Fig. 2 and Fig. 3. In the period 0 < t < 7 h te ice bank is charged. In the interval 6 < t < 7 h $u_{comp}(t)$ gradually increases resulting in decreasing $x_{T,b}^{m}(t)$. In exchange for that $u_{comp}(t)$ is reduced in the interval 7 < t < 8 h, and the ice bank is discharged in the period 7 < t < 23 h. In the period 23 < t < 24 h the reverse happens, though less clear because it interferes with the terminal effect, like in case 1.

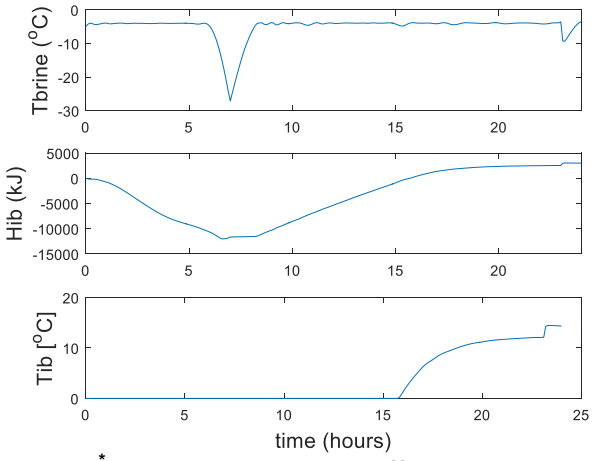

Fig. 2, $\mathbf{x}^*$ (case 2, day-night tariff).

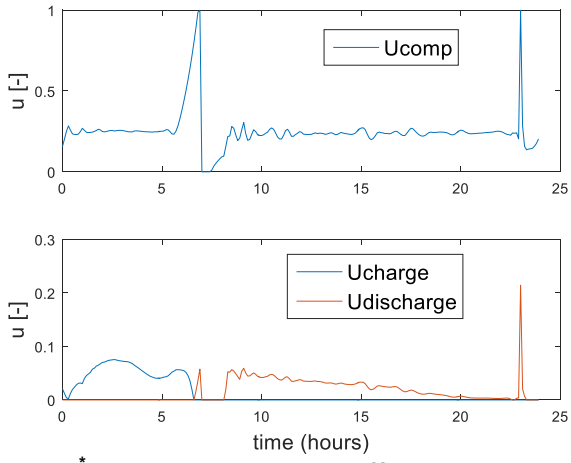

Fig. 3, $\mathbf{u}^*$ (case 2, day-night tariff).

In both case 3 (Fig. 4 and Fig. 6) and 4 (Fig. 5 and Fig. 7) there is 25 kW solar electricity $P_{el,PV}$ available between 12 and 13 h. In case 3 the price $d_{e,production}(t)$ for supplying this electricity to the grid is = 0 €.kWh^{-1}, *i.e.* an incentive to use it locally. In case 4 the price $d_{e,production}(t)$ for supplying this electricity to the grid is = 8 €.kWh^{-1}, *i.e.* an incentive to supply it to the grid. As a consequence in case 4 the optimizer chooses to run the compressors u_{comp} less than average in that time period (Fig. 7), with some compensation effects in the hours before and after that period. In case 3 the irregularity around 12 < t < 13 h is exactly the other way round (Fig. 6) because the price incentive works the other way round. Apparently neither in case 3 nor in case 4 does the algorithm see an advantage in charging the ice bank around the time window 12 < t < 13 h.

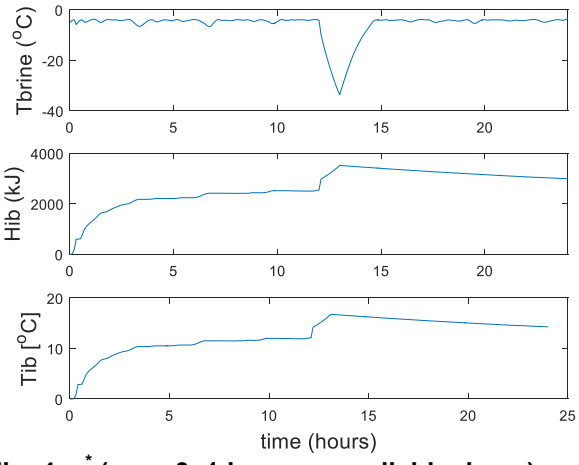

Fig. 4, x^* (case 3, 1 hour non-sellable $d_{Pel,PV}$).

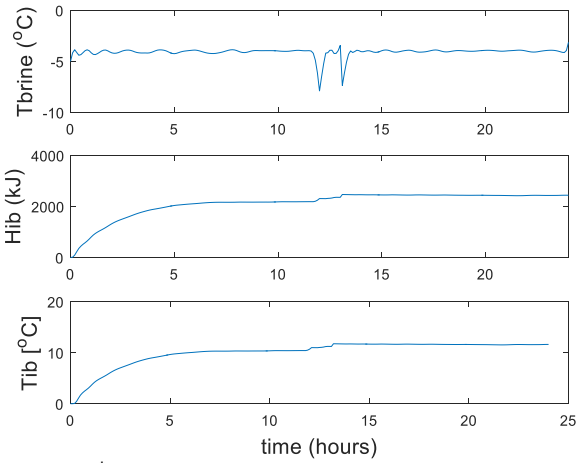

Fig. 5, x^* (case 4, 1 hour $d_{Pel,PV}$ sellable at high price).

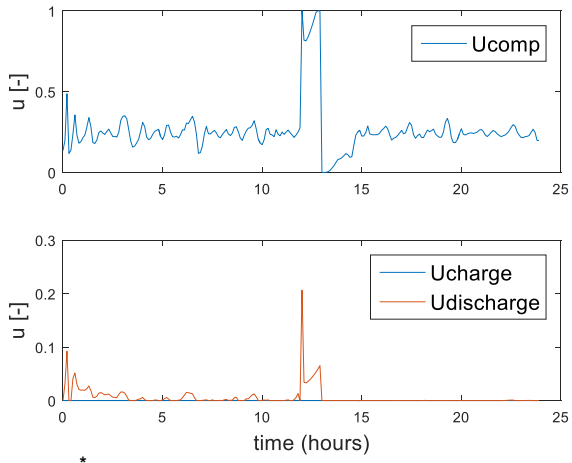

Fig. 6, u^* (case 3, 1 hour non-sellable $d_{Pel,PV}$).

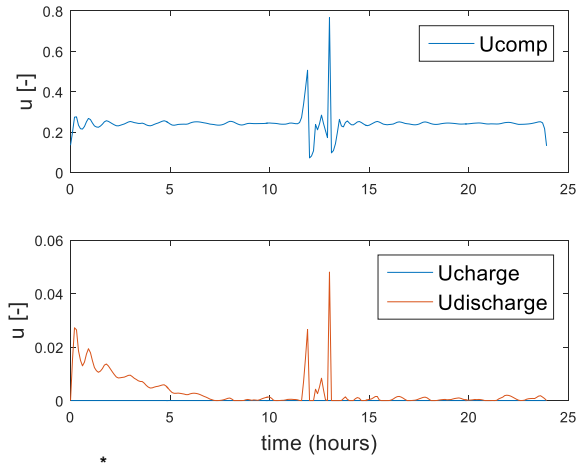

Fig. 7, u^* (case 4, 1 hour $d_{Pel,PV}$ sellable at high price).

6. DISCUSSION

The numerical optimization algorithm is a gradient-based search algorithm. This is computationally powerful, provided the optimization problem is well-shaped. Well-shaped first of all means that the controls must be continuous, and the derivatives $dJ/du_i(t)$ must be continuous. Numerical challenges easily arise. In the process of obtaining the simulation results presented here multiple issues had to be solved. In this case for example the upper constraint on $Q_{ib,discharge}(t)$ in eqn. 19 seems a reasonable way to impose $Q_{ib,discharge}(t) \leq 0.1*P_{th,comp}(t)$ at any time. But if $u_{comp}(t) = 0$ then $P_{th,comp}(t) = 0$ and $Q_{ib,discharge}(t)$ can only be at the edge of violating the constraint. Then numerical errors in the computation of $dJ/du_{discharge}(t)$ tend to dominate the calculated gradients and the optimization may get stuck in a local minimum induced by numerical errors, instead of the true local minimum.

Although the results show promising opportunities, more is needed before this concept can be implemented. A first hurdle is tuning the parameter values. *E.g.* what is the brine-to-water heat transfer coefficient $UA_{ib,charge}(t)$ in the ice buffer, and how does it change when ice accumulates? The domain of recursive parameter estimation offers tools to add self-learning features to the concept (*e.g.* Ljung & Söderström, 1983).

Another hurdle is how to make this optimal control algorithm cooperate with all the existing local controllers currently used to control the system. For example the optimal controller calculates compressor control $u_{comp}(t)$, but in practices local controllers control the compressors. These local controllers often include very useful safety and stability characteristics. Therefore ways need to be found that make the local controllers imitate the optimal behaviour.

The optimal controller needs a model of the controlled system. When an installation company wants to install this kind of controllers on new systems, it needs to program the model in the controller. A generic concept is desirable to limit the amount of effort needed. Also bug fixing after the initial installation becomes a lot more complex, as the controller's degree of complexity largely increases.

7. CONCLUSIONS

A cold store with a refrigeration plant coupled to a thermal buffer can help to shape electric power demand from the power grid.
Optimal control theory can help to make the refrigeration plant's control system anticipate forecasted future disturbance inputs in an optimal way.
The network operator can in principle use flexible price incentives to automatically shape the cold store's electric power uptake, because the optimal controller is responsive to price incentives.

ACKNOWLEDGEMENTS

This work is part of the ZoCool project, a cooperative project of Wageningen UR Food & Biobased Research, Van Kempen koudetechniek, Direct Current BV, Solar Comfort, DNV-GL and Fruitpakt. The project was financed by Foundation TKI Energy (the Dutch Ministry of Economic Affairs) (project number 6230075106, TKI number TEZGL 113003).

REFERENCES

Almenta M.M., Morrow D.J., Best R.J., Fox B., Foley A.M. (2016). Domestic fridge-freezer load aggregation to support ancillary services. Renewable Energy 87, 954-964. DOI 10.1016/j.renene.2015.08.033.

Henten, E.J. van (1994). Greenhouse climate management: an optimal control approach. PhD-thesis.

IPCC (2018). Special report on Global Warming of 1.5°C (SR15) - an IPCC special report on the impacts of global warming of 1.5 °C above pre-industrial levels and related global greenhouse gas emission pathways, in the context of strengthening the global response to the threat of climate change, sustainable development, and efforts to eradicate poverty.

Jekel T.B., Mitchell J.W., Klein S.A. (1993). Modelling of ice-storage tanks. ASHRAE transactions 99(1), 1016-1024.

Lewis, F.L. (1995). Optimal Control. 2nd edition, Wiley-Interscience Publications.

Ljung L., Söderström T. (1983). Theory and Practice of Recursive Identification. MIT Press, Cambridge, Massachusetts.

Lukasse Leo, Jan van Maldegem, Enrico Dierkes, Aart-Jan van der Voort, Janneke de Kramer-Cuppen, Gerrit van der Kolk (2009). Optimal control of indoor climate in agricultural storage facilities for potatoes and onions. Control Engineering Practice, DOI: 10.1016/j.conengprac.2009.04.001.

Pierre, D.A. (1969). Optimization theory with applications. Wiley, New York.

Manuscript ID: 68
DOI: 10.18462/iir.icr.2019.0068

Influence of Coil Geometrical Parameters on the Solidification Process in an Ice on Coil Cold Storage System

Seyed Soheil Mousavi Ajarostaghi [(a)], Sébastien Poncet [(b)], Kurosh Sedighi [(a)], Mojtaba Aghajani Delavar [(a)]

(a) Babol Noshirvani University of Technology, Shariati Av., 47148-71167, Babol, Iran, s.s.mousavi@stu.nit.ac.ir, ksedighi@nit.ac.ir, m.a.delavar@nit.ac.ir
(b) Université de Sherbrooke, 2500, boulevard de l'Université, Sherbrooke (QC) J1K 2R1, Canada, Sebastien.Poncet@USherbrooke.ca

Abstract

Growing energy demand from economic output and improved standards of living will likely put added pressure on energy supplies. Storing energy allows researchers to balance the supply and demand of energy. There are three types of thermal storage energy systems including sensible heat storage, latent heat storage and thermo-chemical storage. Ice storage system is a latent cold storage which uses ice for cold energy storage. Cold energy storage helps cooling capacity overnight for later usage during peak hours. The most common form of cold storage air conditioning technology is the ice-on-coil energy storage. In this study, the solidification process in an ice-on-coil cold storage system is numerically investigated. The porosity-enthalpy method is used to simulate the solidification process. Once carefully validated, the model is extended to quantify the effects of different geometrical parameters including helix pitch of coil, coil diameter and length on charging process.
Keywords: Cold Energy System, Ice Storage, Solidification, Phase Change Material (PCM), Numerical Simulation, Porosity-Enthalpy Method

1. INTRODUCTION

Thermal energy storage (TES) is the most common method to store energy and shift the electricity peak load. TES systems have as main advantages to reduce installation and maintenance costs and to lower possible environmental impacts over chemical based technologies. Energy storage allows extra thermal energy to be used for future consumption. For example, energy demand can be balanced between day and night or heat can be stored in summer then used in winter or vice versa. Generally, thermal energy storage can be applied in two different ways: sensible heat and latent heat. The energy density is much higher for energy storage by latent heat and the efficiency of such systems is generally higher too. The interesting reader can refer to the recent and comprehensive review of Sarbu and Sebarchievici (2018) on TES.

Conventional central air-conditioning systems of commercial building represent about 50% of the electrical demand, leading to high electricity costs. Air-conditioning using TES is currently seen as a way to solve this problem. Cooling load demand during the warmest hours of summer days leads to an increase in electrical energy request, intensifying the peak load. Thus, to reduce electrical energy consumption during peak hours, cold energy storage systems are used. One of the most common adopted methods is the ice on coil energy storage system. Based on this fact that the electrical rates in the night time is low, so by designing the system to operate at night, the costs decrease. This system has flexibility to control the peak of electrical rates. It should be noted that daytime energy costs are six times more than night time energy costs.

In air-conditioner and refrigeration application, ice storage system is the efficient type of thermal energy storage (Jang, 2000). Ice storage systems are divided to two different types including static type and dynamic type. External melt ice-on-coil type, internal melt ice-on-coil type and encapsulated ice type are belonging to Static types. Dynamic type includes ice slurry type and ice harvesting type. In the HVAC systems, currently internal melt types are utilized widely.

In both types of internal and external melt ice-on-coil systems, heat transfer fluid (usually glycol solution) flows through coils in charging mode to create ice around the coils. Charging and discharging modes are belonging to solidification and melting processes, respectively which analysis these processes plays an important role in design of HVAC cold storage system.

There were many published research studies which analyzed the thermal characteristics of ice-on-coil cold storage systems. However, most of them analyzed the ice-on-coil cold storage systems thermodynamically and experimentally. A few number analyzed the ice-on-coil tanks numerically in both charging and discharging modes.

Some of the studies related to the experimental analysis of the ice-on-coil cold storage system are noted following. Jannesari and Abdollahi (2017) analysed the thermal performance of an internal melt ice-on-coil ice storage system experimentally and numerically. Two different heat transfer enhancement methods including thin rings and annular fins around tubes were utilized to increase the ice formation and melting and accordingly increase the performance of the cold storage system. Results indicate that tube with annular fins has the best performance.

A novel paraffin-based cold storage system was investigated experimentally by Torregrosa-Jaime et al. (2013). The results showed that in the melting process, the natural convection within phase change material is the dominant mechanism in heat transfer. At the lowest supply temperatures and mass flow rates, better efficiency was achieved. Lopez-Navarro et al. (2013) performed an experimental analyse with an internal melt-ice-on-coil system. The solidification process (charging) has been investigated for different inlet temperatures and mass flow rates of the heat transfer fluid. Fastest charging tests showed the lowest energy consumption.

A comprehensive study has been presented about both solidification and melting process in internal melt ice-on-coil cold storage system experimentally by Ezan et al. (2011). A shell and tube type latent cold storage system was considered which water is in the shell and ethylene glycol as heat transfer fluid (HTF) flowed in the tube. Experimental results showed that, for both solidification and melting processes, natural convection was the dominant heat transfer mechanism after a short heat conduction dominated period.

Besides the experimental studies, there are some articles which analyse the charging or discharging process of the ice storage system by numerical modelling. As noted above, the Jannesari and Abdollahi (2017) performed numerical simulations beside the experimental study to show the process of the water solidification. Zheng et al. (2011) simulated the charging and discharging processes of an internal melt ice-on-coil thermal storage system using Simulink. Their basic model provided qualitative results about the heat transfer. The results indicated that by increasing the coil diameter, the heat transfer and accordingly the thermal efficiency. However, the heat resistance increases simultaneously. Xie and Yuan (2014) performed numerical simulations to study the material, thickness and arrangement of thin layer ring in ice storage system which was utilized to enhance the heat transfer. The results indicated that material and arrangement of thin layer ring have the most significant effect on the ice formation.

Although significant works have been published on ice-on-coil storage tanks, the literature on shell and coil tube ice storage systems is more scarce. Moreover, the influence of the geometry of the HTF (Heat Transfer Fluid) channel may be more important in horizontal ice storage systems. Seddegh et al. (2016) studied numerically using the enthalpy method, the heat transfer in a horizontal and vertical shell and tube energy storage system including phase change materials (PCM). Their results indicated that the horizontal position of the PCM storage provides a significantly higher performance compared to the vertical position.

The present study is then an attempt to quantify in details the effects of the main geometrical parameters on the solidification process (charging) in a horizontal shell and coil tube ice storage system. A 2D numerical flow solver has been developed then validated against three sets of experimental data. The influences of the coil geometrical parameters including coil pitch, diameter and height are presented and discussed in details. To the best of the authors' knowledge, such an extensive parametric study with three well validated flow solver has never been done so far for the solidification process in a shell and coil tube ice storage system.

2. MATHEMATICAL MODELING

The governing equations of the solidification process of the ice in a shell and coil tube ice storage are solved for laminar, unsteady and three dimensional flow configurations using the enthalpy-porosity method (Brent et al., 1988). For problems including natural convection, the variations of density with temperature are generally accounted by considering the Boussinesq assumption, which improves besides the convergence rate (Faghri and Zhang, 2006). The viscous dissipation term is considered as negligible (Brent et al., 1988). The enthalpy-porosity method has proven to be an efficient method to simulate the melting and solidifications of PCMs (like ice) (Mousavi Ajarostaghi et al. 2017, Zheng et al. 2011, Seddegh et al. 2016, Jannesari and Abdollahi 2017). The continuity, momentum, and thermal energy equations can be then expressed as follows, respectively:

$$\partial_t(\rho) + \partial_i(\rho u_i) = 0 \quad \text{Eq. (1)}$$

$$\partial_t(\rho u_i) + \partial_j(\rho u_i u_j) = \mu \partial_{jj} u_i - \partial_i p + \rho g_i + S_i \quad \text{Eq. (2)}$$

$$\partial_t(\rho h) + \partial_t(\rho \Delta H) + \partial_i(\rho u_i h) = \partial_i(k\, \partial_i T) \quad \text{Eq. (3)}$$

where u_i are the fluid velocity components, ρ is the density of phase change material (water) obtained through the Boussinesq approximation, μ its dynamic viscosity, k its thermal conductivity, p is the pressure, g is the gravity acceleration, and h is the sensible enthalpy which is defined as follows:

$$h = h_{ref} + \int_{T_{ref}}^{T} C_p dT \quad \text{Eq. (4)}$$

The enthalpy can be defined as:

$$H = h + \Delta H \quad \text{Eq. (5)}$$

where h_{ref} is the reference enthalpy at the reference temperature T_{ref}, C_P is the specific heat, ΔH is the latent heat content of ice that may vary between zero (solid) and 1 (liquid). Therefore, the liquid fraction β, can be written as follows:

$$\beta = \Delta H / L = \begin{cases} 0 & if \quad T < T_{solidus} \\ 1 & if \quad T > T_{liquidus} \\ (T - T_{solidus}) / (T_{liquidus} - T_{solidus}) & if \quad T_{liquidus} < T < T_{solidus} \end{cases} \quad \text{Eq. (6)}$$

Liquidus temperature of the ice is 273.15 K. Temperature difference between liquidus and solidus, in a mushy zone is 0.1 K (Sugawara and Beer, 2009; Shih and Chou, 2005). The Darcy's law damping terms S_i are added as source terms to Equation (2) and include the phase change effect on convection. They are defined by:

$$S_i = (C(1-\beta^2)/\beta^3)u_i \quad \text{Eq. (7)}$$

The coefficient C is a mushy zone constant in which the liquid fraction changes between 0 and 1. In the present study, this constant is fixed at 10^5 kg/m^{3}s as proposed by Brent et al. (1988).

The total energy of the system for a given time can be defined as the integration of specific energies for each control volume, over the whole domain. The total rejected energy can be calculated as follows:

$$E(t) = E_{Sensible}(t) + E_{Latent}(t) \quad \text{Eq. (8)}$$

Sensible and latent components can be defined for the melting process as:

$$E_{Sensible}(t) = \begin{cases} C_{Water} T & : \ Liquid\ Phase \\ C_{Ice} T & : \ Solid\ Phase \end{cases} \quad \text{Eq. (9)}$$

$$E_{Latent}(t) = \rho_{Ice} \times f(t) \times L \quad \text{Eq. (10)}$$

where L is the latent heat and f (t) is the fraction of ice volume in each control volume.

3. VALIDATION OF THE FLUID FLOW AND PHASE CHANGE SOLVER

Generally, two different cases are considered for validation purpose. For the first case, the heat transfer process in a shell and coil tube heat exchanger is investigated numerically and the obtained results are compared with the experimental results of the Jamshidi et al. (2013). The

second case includes three different 2D solidification processes which are validated with experimental results. All CFD simulations are performed in a commercial CFD software, ANSYS Fluent 18.2 and the phase change is modelled by using the Enthalpy-Porosity model.

3.1. Heat Transfer Process in a Shell and Coil Tube Heat Exchanger

In order to model the solidification process in the shell and coil tube PCM storage, the heat transfer process in a shell and coil tube heat exchanger should be modelled and validated first. The experimental results of Jamshidi et al. (2013) are then used for comparison purpose with the predictions of the present flow solver. The hot and cold fluids flow in the tube and shell respectively. Both flows (Water) are considered as steady-state, incompressible and in single-phase. A tetrahedral unstructured mesh grid is applied for the simulation. The outer wall of the shell is adiabatic. Fig. 1a displays the variations of the averaged Nusselt number within the inner side coil tube (hot side) with the Dean number of inner coil tube. As it can be clearly seen, the present results compare fairly well with the measurements of Jamshidi et al. (2013) (maximum error: 4.76% at De_i=700). The streamline of the flow in the coil tube with temperature contour is illustrated in Fig. 1b.

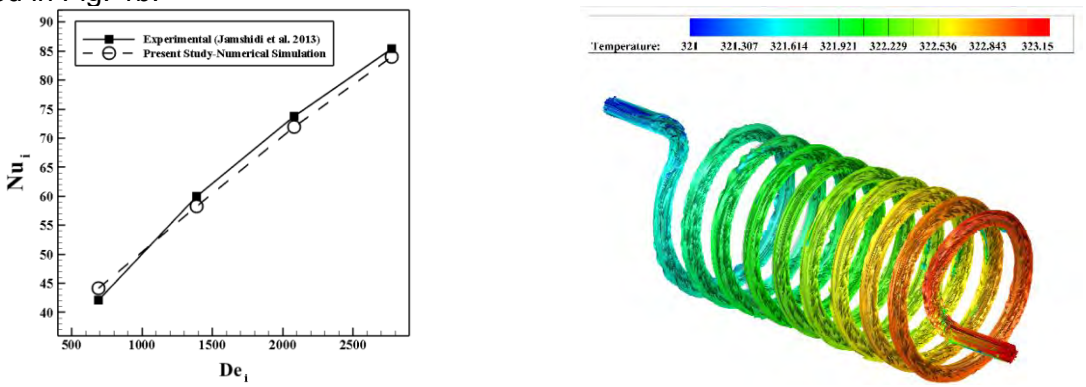

(a) (b)

Figure 1: (a) Comparison in terms of the averaged Nusselt number versus the Dean number between the present study and the experimental data of Jamshidi et al. (2013). (b) The streamline of the flow in the coil tube with temperature contour.

3.2. 2D Validation of Ice Solidification Modelling

For the 2D validation of ice solidification process, three different cases are modelled and the results are presented. For all models, the thermo-physical properties of water, ice and ethylene glycol (Xie and Yuan, 2014) are listed in Table 1 which are constant but the values are different for the solid and liquid phases. The buoyancy effect is modelled by using the Boussinesq approximation.

Table 1: Thermo-physical properties of water, ice and ethylene glycol (Xie and Yuan, 2014)

Parameter	Symbol	Value
Density of Fluid [kg/m^3]	ρ_f	999.833
Specific Heat of the Fluid [J/ (kg.K)]	C_l	4180
Specific Heat of the Solid [J/ (kg.K)]	C_S	2217
Thermal conductivity of liquid water [W/ (m·K)]	K_S	1.918
Thermal conductivity of ice [W/ (m·K)]	K_l	0.578
Viscosity of the fluid [kg/ (m.s)]	μ_f	0.00162
Latent Heat of Phase Change [J/kg]	L	334000
Melting Temperature [K]	T_f	273.15
Thermal Expansion Coefficient [K^{-1}]	β	-6.733353×10^{-5}

3.3. Water Freezing in a Differentially Heated Cubic Cavity

The first case concerns the modelling of water freezing in a differentially heated cubic cavity of a height L. We consider freezing of water after the thermal boundary condition is abruptly changed from T_c = 273K to T_c = 263K at the cold wall. Two vertical walls are isothermal, kept at

temperatures T_H, T_C. All remaining walls are assumed to be adiabatic. The temperature difference between the vertical walls, $T_H - T_C$ is 10K. The initial temperature of the fluid is set at T_0 = 278K. In the present case, the 144400 cells (380×380 nodes) is utilized. Dimension of the cavity L is 38mm. The configuration of the present case is illustrated in Fig. 2a. The validation curves of present study in comparison with the Michalek and Koawlewski (2003) results are shown in Figs. 2b and 2c. Accordingly, there is a good agreement between present results and reference study.

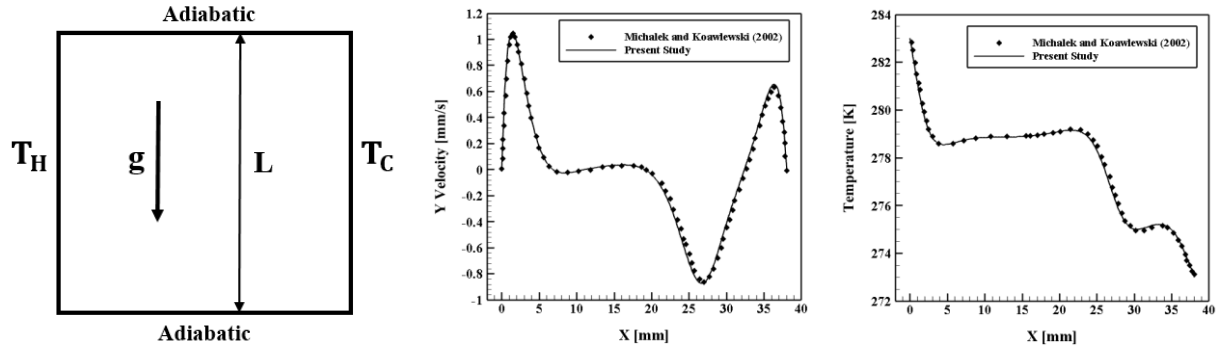

(a) (b) (c)

Figure 2: (a) The 2D configuration of first case for ice formation validation (b) and (c) Validation curves of present study in comparison with the Michalek and Koawlewski (2003) results

3.4. Water Freezing around a Single and Two Vertically Spaced Cylinders in a Rectangular Cavity

In this cases, two different 2D domain including single and two vertically spaced cylinders in a rectangular cavity are considered to model the ice formation. The obtained results of the present simulations are compared with the experimental results of the Sasaguchi et al (1997). The geometries of the single and two vertically spaced cylinders in a rectangular cavity filled with water are shown in Fig. 3a. The physical system consists of a rectangular cavity which contains two horizontal, vertically spaced cylinders with diameter d, and all the walls (left, right, top and bottom walls) are assumed to be insulated. In this study d is set at 0.0254 m. The initial temperature of the domain and the wall temperature of the cylinders are kept constant 4℃ and -10℃, respectively. The timewise variations of the solid volume ratio, A_S/A_C, which is defined as the ratio of the solidified area to the total cross-sectional area of the cylinder(s), is used to draw the validation curves. The validation curves with good agreement of both models from the present simulations in comparison with the experimental results are shown in Figs. 3b and 3c.

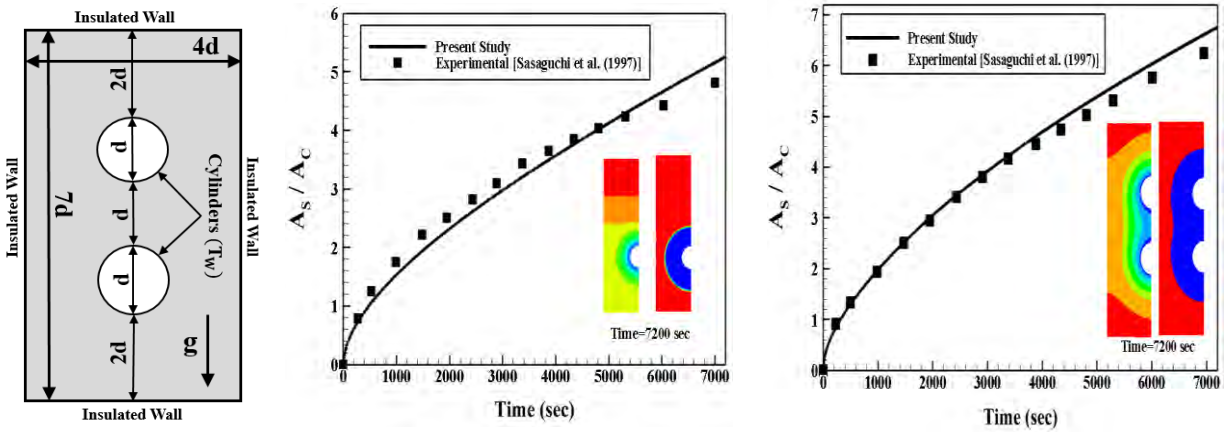

(a) (b) (c)

Figure 3: (a) The geometries of the single and two vertically spaced cylinders in a rectangular cavity which is full of water in solidification point (b) Comparison between the present numerical results and the experimental results of Sasaguchi et al (1997) study for single cylinder (c) two vertical spaced cylinder

3.5. Water Freezing around Four Tube in a Rectangular Tank

In this section, solidification around the four cylindrical tubes immersed in a water rectangular cavity is simulated. The geometrical dimensions are shown in Figs.4a and 4b. symmetry condition at left and right boundaries. adiabatic and no-slip conditions at the top and the bottom walls. experimental results demonstrate that the variation of temperature versus time from the start of the ice formation till the end of the process is around 1 K for each tube. Therefore, temperature boundary condition for each tube is set to the average temperature value during ice formation including 270.15 K, 270.65 K 271.15 K and 273 K, for the first tube to the forth tube, respectively. The timewise variations of the solid volume ratio, A_S/A_C, is used to draw the validation curve in the Fig. 4c. It can be seen that good agreement is achieved between present study and experimental results.

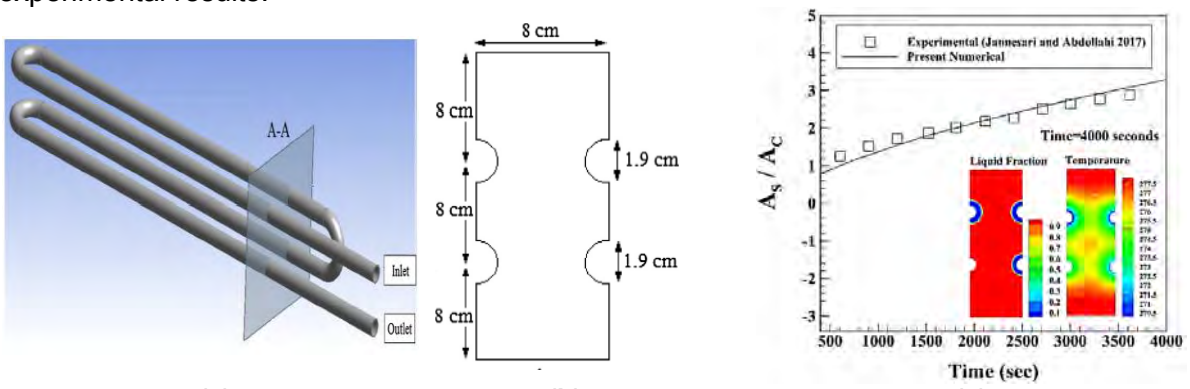

(a) (b) (c)

Figure 4: (a) General view of tubes in cool storage tank and (b) Solution domain for simulation Geometrical dimensions in the simulation (c) Compare the solid volume ration, A_S/A_C, of present numerical results with the results of Sasaguchi et al. (Experimental) for four cylinders

4. RESULTS AND DISCUSSION

The geometry considered now is a shell and coil tube ice storage tank as displayed in Fig. 5 with the main relevant parameters. The length of the tank, coil tube diameter and pitch are 400, 10 and 80 mm, respectively. Ethylene glycol is used as HTF fluid within the coil tube. Four different mesh grids have been considered for mesh independent. Finally, grid with 584300 cells is used for all simulations. The mesh is unstructured and based on tetrahedral elements with 10 prismatic layers near coil wall. The shell is full of ice at the initial condition. The inlet mass flowrate and temperature of the heat transfer fluid (ethylene glycol) are 2 l/min and -10℃, respectively.

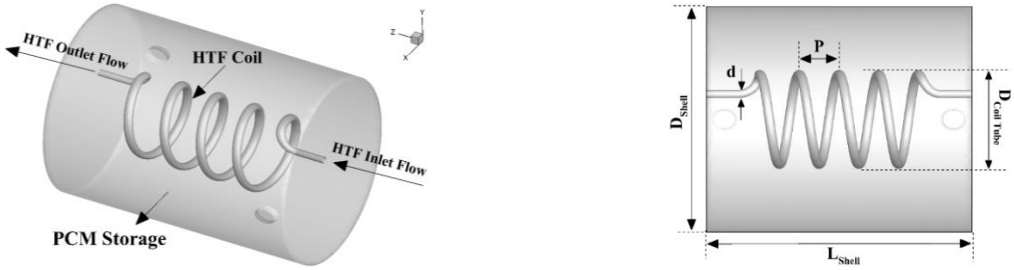

Figure 5: Schematic of the shell and coil tube PCM storage with relevant geometrical parameters.

In this study, the effects of geometrical parameters including coil pitch (P), coil diameter (d) and coil height (H_c) are investigated numerically on the solidification of water in a horizontal shell and tube type of ice on coil cold storage system. It should be noted that in order to compare logically the cases, in the cases which should be compared with together (A with B, C with D and E with F), the heat transfer area that is the lateral area of the coil, is kept constant. Accordingly, one of the geometrical parameters is considered free parameters (helix diameter (D_C)). The coil geometrical parameters for all investigated models are listed in Table 2. Liquid fraction of the all simulations are illustrated in Fig. 6. The cases A with B (Fig. 6a), C with D (Fig. 6b) and E with F (Fig. 6c) are compared. For instance, the liquid fraction contours of 4 cases at two different time

(after 2 and 6 hour) are illustrated in Fig. 7. Results show that by increasing coil pitch (A to B) and height of spiral coil (E to F), liquid fraction decrease 6.35 and 4.1%, respectively after 6 hours. By increasing the coil diameter (C to D), liquid fraction increases 10.28% after 6 hours.

Table 2: The coil geometrical parameters of the investigated models.

Models		Height of spiral coil	Coil pitch	Helix diameter	Spiral coil length	Coil diameter	Heat Transfer Area
		H_C (m)	P (m)	D_C (m)	L (m)	d (m)	A (m^2)
Effect of P	Case A	0.36	0.04	0.17	4.83	0.016	9.7×10^{-4}
	Case B	0.36	0.12	0.48	4.55	0.016	9.7×10^{-4}
Effect of d	Case C	0.36	0.09	0.48	6.05	0.016	1.2×10^{-3}
	Case D	0.36	0.09	0.25	3.17	0.022	1.2×10^{-3}
Effect of H_C	Case E	0.24	0.04	0.43	8.13	0.016	1.6×10^{-3}
	Case F	0.42	0.04	0.25	8.27	0.016	1.6×10^{-3}

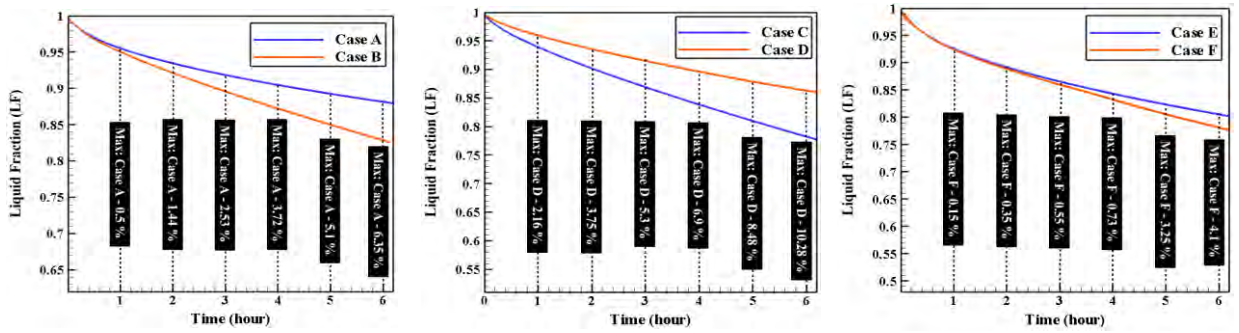

(a) (b) (c)

Figure 6: Curves of liquid fraction for different cases (A-F) after six hours (a) Compare case A with B (b) Compare case C with D (C) Compare case E with F

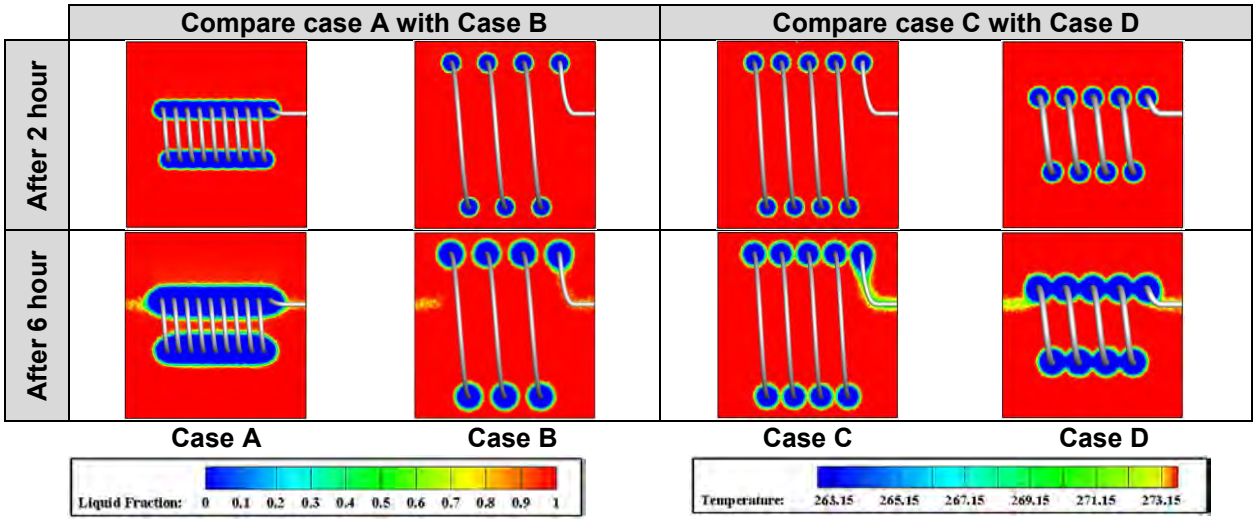

Figure 7: Contours of liquid fraction for cases A, B, C and D at two different time (after 2 and 6 hours)

5. CONCLUSIONS

In the present paper, the solidification process of ice in a horizontal shell-and-tube ice storage system has been numerically investigated using the enthalpy-porosity method in ANSYS Fluent 18.2 software. The flow solver has been first carefully validated against two sets of experimental data, one considering the heat transfer process in a horizontal shell and coil tube heat exchanger and one considering the ice solidification process (three different 2D validation). By investigating the effects of coil geometrical parameters, obtained results show that by increasing coil pitch (case A to case B) and height of spiral coil (case E to case F), liquid fraction decrease 6.35 and 4.1%, respectively after 6 hours. By increasing the coil diameter (case C to case D), liquid fraction increases 10.28%.

NOMENCLATURE

C_P	specific heat ($J.kg^{-1}.K^{-1}$)	Nu	Nusselt number ($Nu=h\times d\times k^{-1}$)
g	gravitational acceleration ($m^2.s^{-1}$)	De	Dean number ($De = Re \times (d \times D_c{}^{-1})^{0.5}$)
h	sensible enthalpy ($J.kg^{-1}$)	Re	Reynolds number ($Re=4 \times \dot{m} \times \pi^{-1} \times d^{-1} \times \mu^{-1}$)
H	enthalpy ($J.kg^{-1}$)	μ	dynamic viscosity of the fluid ($kg.m^{-1}.s^{-1}$)
k	thermal conductivity ($W.m^{-1}.K^{-1}$)	ρ	density ($kg.m^{-3}$)
L	latent heat fusion ($J.kg^{-1}$)	v	kinematic viscosity ($m.s^{-2}$)
T	temperature (K)	β	liquid fraction

REFERENCES

Brent, A.D., Voller, V.R., and Reid, K.T.J., 1988. Enthalpy-Porosity technique for modeling convection-diffusion phase change: Application to the melting of a pure metal. Numerical Heat Transfer, Part A Applications, vol. 13, no 3, pp. 297-318.

Ezan, M.A., Ozdogan, M., and Erek, A., 2011. Experimental study on charging and discharging periods of water in a latent heat storage unit. International Journal of Thermal Sciences, vol. 50, no 11, pp. 2205-2219.

Faghri, A., and Zhang, Y., 2006. Transport phenomena in multiphase systems. Academic Press. Jamshidi, N., Farhadi, M., Ganji, D.D. and Sedighi, K., 2013. Experimental analysis of heat transfer enhancement in shell and helical tube heat exchangers. Applied Thermal Engineering, vol. 51, pp. 644-652.

Jang, M.C., 2000. Characteristics of electric power demand and promotion of the distribution of ice storage cooling system, in: Proceedings of the SAREK 2000 Summer Annual Conference (I), Pyeongchang, pp. 795–804.

Jannesari, H., and Abdollahi, N., 2017. Experimental and numerical study of thin ring and annular fin effects on improving the ice formation in ice-on-coil thermal storage systems. Applied Energy, vol. 189, pp. 369-384.

López-Navarro, A., Biosca-Taronger, J., Torregrosa-Jaime, B., Corberán, J. M., Bote-García, J. L., and Payá, J., 2013. Experimental investigations on the influence of ice floating in an internal melt ice-on-coil tank. Energy and Buildings, vol. 57, pp. 20-25.

Michalek, T., and Kowalewski, T. A., 2003. Simulations of the water freezing process–numerical benchmarks. Task Quarterly, 7(3), 389-408.

Mousavi Ajarostaghi, S.S., Aghajani Delavar, M. and Dolati, A., 2017. Numerical investigation of melting process in phase change material (PCM) cylindrical storage considering different geometries. Heat Transfer Research, vol. 48, no 16, pp. 1515-1529.

Sasaguchi, K., Kusano, K., and Viskanta, R., 1997. A numerical analysis of solid-liquid phase change heat transfer around a single and two horizontal, vertically spaced cylinders in a rectangular cavity. International Journal of Heat and Mass Transfer, 40(6), 1343-1354.

Sarbu, I. and Sebarchievici, C., 2018. A Comprehensive Review of Thermal Energy Storage, Sustainability, vol. 10, no 191, pp. 1-32.

Seddegh, S., Wang, X. and Henderson, A.D., 2016. A comparative study of thermal behaviour of a horizontal and vertical shell-and-tube energy storage using phase change materials. Applied Thermal Engineering, vol. 93, pp. 348-358.

Shih, Y.C. and Chou H., 2005, Numerical study of solidification around staggered cylinders in a fixed space. Numerical Heat Transfer, Part A: Applications, vol. 48, no 3, pp. 239-260.

Sugawara, M. and Beer, H., 2009. Numerical analysis for freezing/melting around vertically arranged four cylinders. Heat and Mass Transfer, vol. 45, no 9, pp. 1223-1231.

Torregrosa-Jaime, B., López-Navarro, A., Corberán, J. M., Esteban-Matías, J. C., Klinkner, L., and Payá, J., 2013. Experimental analysis of a paraffin-based cold storage tank. International Journal of Refrigeration, vol. 36, no 6, pp. 1632-1640.

Xie, J., and Yuan C., 2014. Numerical study of thin layer ring on improving the ice formation of building thermal storage system. Applied Thermal Engineering, vol. 69, pp. 46–54.

Zheng, Z.H., Chao, J., and Wei-Xiao, W., 2011. Numerical simulation of internal melt ice-on-coil thermal storage system. Energy Procedia, vol. 12, pp. 1042-1048.

Manuscript ID: 124
DOI: 10.18462/iir.icr.2019.0124

Reducing energy demand using cooling efficiently (REDUCE)

Jolyon P. AXELROD[(a)], Graeme G. MAIDMENT[(b)]

[(a)] FJB Systems LLP
Weybridge, KT13 9UH, UK, ja@fjb.co.uk
[(b)] London South Bank University
London, SE1 0AA, UK, maidmegg@lsbu.ac.uk

ABSTRACT

UK peak electrical demand and energy prices are rising. Concurrently, there is greater use of intermittent renewable energy and increased requirements for energy storage.
Refrigerated storage facilities (RSF) provide opportunities to store heat energy with potential to help balance energy demand with supply; reduce peak demand; facilitate more efficient operation; and reduce both costs and environmental impact.
REDUCE field studies investigated impact of load-shedding in RSF on food products; energy consumption and costs; and carbon emissions. Product temperatures met safety and legal limits. Peak tariff cost savings averaged >70% and carbon emission reductions were >10%.
REDUCE supports industry confidence in load-shedding which offers financial paybacks to users and reduces environmental impact. REDUCE highlights practical issues and areas for discussion and future research for successful implementation and monitoring of load-shedding.
Keywords: Refrigeration, Load-Shedding, Product Safety, Energy Efficiency, Environmental Impact.

1. INTRODUCTION

This paper describes our study into Reducing Energy Demand by Using Cooling Efficiently (REDUCE). Despite investigations into load shedding in RSF since the 1970s in the United States of America (USA) (Ashby et al., 1979), in the United Kingdom (UK) the take up of load shedding is limited, with concerns over product safety being a significant concern. There is potential for significant savings of energy, carbon emissions and financial costs, but the extent of such savings and issues involved in refrigeration load shedding in the UK require further investigation. Pressure on the electrical grid and constraints in demand, coupled with global environmental concerns have led to discussion about the potential of load shedding in RSF, but possible benefits are not fully known or understood.
Four linked field studies were conducted in chilled or frozen RSF to investigate issues around load shedding, yielding quantitative data collected from various monitors and probes and allowing product temperatures, energy use and costs to be analysed, estimated and compared. Observations of facilities were made throughout the studies provided further relevant evidence. This resulted in estimations of benefits of load shedding and highlighted some barriers to using it. Although industry experts believe that some RSF practice load shedding, there are no published UK details regarding this and neither the effects on product temperatures nor implications for costs and savings, nor any guidance for the industry have so far been published.
This paper describes the REDUCE study. Section 2 provides the general background to the subject, Section 3 describes the investigation and the results and discussion are covered in Section 4 and 5. Conclusions and areas of further work are described in Section 6.

2. BACKGROUND

2.1 UK Energy and Refrigeration

Reviewing government data, increases of circa 2% can be seen in air-conditioning consumption over the past 6 years. Total electricity consumed by the Refrigeration, Air Conditioning and Heat Pump (RACHP) industry is 17.8% of total electricity supplied to the UK (DBEIS, 2016). For the UK to meet

2050 targets, 60% more energy from renewables will be required, with 50% increase in distributed generation and investment into energy, including energy storage balancing. Electrical vehicles could drive large increases in peak demand, along with decarbonising heat, with technology such as air source heat pumps. The National Grid made 4 predictions for future energy demand: Two Degrees; Slow Progression; Steady State; and Consumer Power (National Grid, 2017a). All show peak electricity increases and incentives are needed to optimally reduce this peak demand (Fig. 1). These initiatives have already begun with incentives to consumers to use energy more dynamically. Peak UK electrical demand makes up around 21% of total peak energy demand. Heat demand in buildings and industry (supplied by gas) currently makes up 75% of peak heat demand (Connolly, 2017).

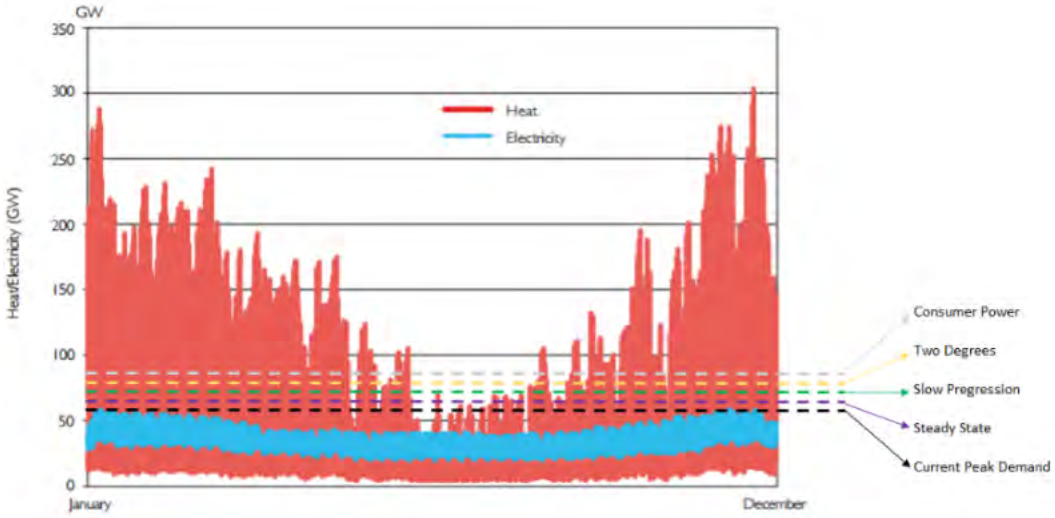

Figure 1. Indicative comparison of UK peak heat and electricity demand variability across a year – (National Grid, 2017a; Department of Energy and Climate Change, 2012).

2.2 UK Commercial and Industrial Electrical Energy Costs and Billing

Larger consumers of electricity pay certain additional charges on top of their actual electricity consumption, which are separated, and itemised on their bill. Two of these charges could be either partly, or fully avoided. Triad charges fall under Transmission of Network use of System (TNUoS) charges and the 'Triad season' runs from 1st November to the end of February. Charges comprise the total amount of electrical energy consumed within the three-half hourly (HH) periods multiplied by the tariff charge. The average current charge is £48.08 per kW used while in the HH Triad period, but is dependent on location. An average increase of circa 34% to 2022/23 is predicted (National Grid, 2017b). All previous Triad periods were in the zone ending between 17:30 and 18:30. Distribution Use of System (DUoS) charges are in place to recover the costs of installing and maintaining the local networks. For consumers on HH data meters, these DUoS charges vary with time of day, split into bands of red, amber and green. For example, UK Power Network (Eastern Power Network) are as follows (Table 1).

Table 1. DUoS time period and example costs

Time Period	Red Time Band	Amber Time Band	Green Time Band
Monday to Friday (including Bank Holidays) - All year	16:00 – 19:00	07:00 – 16:00 19:00 – 23:00	00:00 – 07:00 23:00 – 24:00
Saturday and Sunday - All year	-	-	00:00 – 24:00
LV HH Metered Tariff Unit Charge ($p \cdot kWh^{-1}$)	10.911	0.078	0.014
HV HH Metered Tariff Unit Charge ($p \cdot kWh^{-1}$)	6.384	0.020	0.004

2.3 Legal Control and Temperatures for Food Storage

UK food legislation at present is harmonised with European Union (EU) regulations. EU Regulations require that official controls are in place to check food operators, with the onus on food operators to conduct their own hazard analysis and critical control point (HACCP) assessments. Regulation EC 853/2004 sets standards for foods of animal origin defining minimum storage temperatures of some meat products. UK temperature control requirements do not apply to foodstuffs already covered by the EU. To all other chilled foodstuffs that are 'likely to support the growth of pathogenic micro-organisms', 'a temperature above 8°C commits an offence' (HM Government, 2013). Quick-frozen foodstuffs (QFF) are required to be maintained at -18°C throughout the product. The British Frozen Food Federation (BFFF) provides product temperature regulations (not air temperature) (BFFF, 2012), and suggest -18°C is selected for food quality issues rather than food safety issues, e.g. ice cream at -15°C becomes soft and its appearance may be affected by crystallisation (BFFF, 2009).
Evans reports that temperatures in many instances '(especially in frozen stores) are kept lower than necessary to provide a safety margin in case of plant failure' (Evans, 2009). 'At chilled temperatures the growth of micro-organisms occurs only slowly', ensuring food quality can be maintained for extended periods. In the large majority of foods 'microbial growth will be inhibited at temperatures below -12°C'. In the main, 'food will spoil about four times as fast at 10°C and twice as fast at 5°C, as at 0°C'. 'Spoilage micro-organisms do not grow below -10°C to -12°C and pathogens below -1°C' (Motarjemi and Lelieveld, 2014). Two studies on fluctuations in frozen storage found fluctuations should be kept to a minimum or not more than ±3°C (Phimolsiripol, et al., 2007; Ashby et al., 1979).

2.4 Load Shifting and Shedding

Load shifting involves moving energy demand (load) to a different time period. The idea is that while net load remains constant, consumption and cost may be lower due to increased efficiency of plant, or more economical energy rates. An interesting study, conducted on shifting load in wet appliances, space heating cooling and electric vehicles, found load shifting proved invaluable for demand side management (DSM), and that peaks could be reduced, enabling more efficient use of renewable energy because of less constraints of the energy source (Wimmler et al., 2016). Many studies conducted since the late 1970s, reviewed by Ashby et al. (1979), showed how load shedding is controlled in buildings, leading to three distinct areas of research for refrigerated storage facilities using Building Thermal Mass (BTM), Thermal Energy Store (TES) or Phase Change Material (PCM) strategies. In the UK, it is widely accepted that load shedding takes place, but no UK research has emerged for RSF. Load shedding offers clear wins for consumers (more efficient plant; less maintenance and lower consumption costs); the environment; and the grid; (peaks are reduced, putting less demand on the already struggling electrical grid).

3. INVESTIGATION

The four linked REDUCE field studies were set in chilled or frozen RSF, yielding quantitative data from various monitors and probes, showing product temperatures, energy use and costs for analysis, estimation and comparison, resulting in estimations of benefits of load shedding. Observations of facilities, made throughout, provided additional evidence and highlighted some barriers to use.

3.1 Site Selection, Installation and Review



Figure 2. Facility 3 marshalling and storage area

Qualitative observational data was collected and considered in conjunction with quantitative results. All facilities' refrigerated chambers were constructed using insulated composite panels. The three facilities physical area/volume of refrigerated space varied considerably. Plant was controlled via a supervisory control and data acquisition (SCADA) system. The refrigeration systems main components were individually metered with power sub meters (with displays). Defrosting was via hot gas or off cycle, which had to be disabled during the REDUCE field studies, in order to avoid higher temperatures while load shedding. RSF operated normally throughout all field studies (Fig. 2).

3.2 Field Studies

Evans found it was common for operators to switch off refrigeration during peak demand periods when energy is more expensive, stating the room temperature is allowed to rise slowly and only reduced once the cost of energy is lower, but with no data on the impact to space/product temperature (Evans, 2009). REDUCE field studies measured product temperature, chamber temperature and electrical energy consumption while load shedding. Refrigeration systems were shut down to match both the DUoS and TNUoS charge periods. Sequenced shut down began at 15:45 and was turned back on from 19:00. Sequencing is important, as fully loading the refrigeration plant can cause issues with electrical load.

Table 2. Product data logged for investigation

RSF	Chamber	Product 1	Product 2	Product 3
1	1	1 Yogurt (500g pack (125g/yogurt))	1 Salad Bag (100g Pack)	Salmon (225g 2 fillet package)
	2	1 Orange	1 Cauliflower	-
2	1	N/A	N/A	N/A
	2	Ice Cream (8 pack, 500g each - Surface Temperature)	Pizza (350g Boxed - Surface Temperature)	Pizza (350g Boxed - Internal Box Temperature)
	3	Ice Cream (8 pack, 500g each - Surface Temperature)	Pizza (350g Boxed - Surface Temperature)	Pizza (350g Boxed - Internal Box Temperature)
	4	Ice Cream (8 pack, 500g each - Surface Temperature)	Pizza (350g Boxed - Surface Temperature)	Pizza (350g Boxed - Internal Box Temperature)
3	1	Whole Chicken (1,250g)	Chicken Breast (600g)	1 Sausage (from packaged 150g 4 pack)
	2	1 Orange	1 Pomegranate	-
	3	Vine Tomato's (250g pack)	1 Butternut Squash	-
	Marshalling	Whole Chicken (1,250g)	Chicken Breast (600g)	1 Sausage (from packaged 150g 4 pack)

Some frozen product was pre-selected (RSF 2), for comparison to previous temperature fluctuation studies (Phimolsiripol et al., 2007; Schalbart et al., 2014): such as a dough-based product (pizza); and ice cream. All other product was selected to get a good range of stored product and was data logged and recorded for each facility (Table 2). All product was removed from pallets and stored independently, perceived to be 'worst case' as product within pallets offers much higher thermal mass. Chamber 1 (of 4) in Facility 2 remained operational throughout the study. It became apparent in Facility 1 that chill facilities were susceptible to health and safety issues due to condensation forming on the concrete slab while the refrigeration system was isolated (reported by maintenance team, close to the dock doors, during major refrigeration failure). In chilled facilities 1 and 3, Gemini's Tinytag data loggers were used, using needle probes, inserted into the core of the product. Chamber air temperature was recorded on the air inlet to the evaporator. Floor slab temperature was recorded via a needle probe with the surface extended with tin foil, and insulation and a heavy weight placed over the probe, to ensure good slab contact. Facility 2 frozen product temperature was logged at the surface only, to avoid product damage. Product absorbs heat outside-in, so, core temperature would be lower. For pizza, both box and inner product were plastic wrapped, so probe was inserted into the wrap. Facilities 1 and 2 energy meters were logged every 10 minutes for power in kW used. Facility 3 had a calibrated energy system on site, recording site energy data at 10-minute intervals.

3.3 Data and Analysis

Temperature increase by product and electrical energy consumption (Table 3), showed Facility 1, Chamber 1, temperatures increased as expected during load shedding but fell to between 0.8°C and 2.8°C following it. Facility 2, Chamber 2 ice cream increased 2.45°C, to -17.56°C, the only ice cream to increase past -18°C for approximately 3 hours (manufacture recommends storage of at least -18°C). Ice cream core temperatures would be lower as product will absorb heat from the outside in. All chilled product remained below 4°C, the required minimum storage temperatures. Facility 3 is 16 m high, and stratification of air is believed to have been an issue. Altwies and Reindl, (2001), suggested evaporator fans operate for short periods of time during load shedding to avoid this.

Table 3. Load shedding temperatures

RSF	Chamber	Item	Temperature at 15:00 (°C)	Max Temperature During Load Shedding (°C)	Temperature Increase (°C)
Facility 1	1	Chamber Air Temperature 1 (a)	2.87	5.31	2.44
		Chamber Air Temperature 1 (b)	2.74	5.14	2.40
		Salad Bag	4.30	5.02	0.72
		Yogurt	3.24	3.88	0.64
		Salmon	2.31	3.79	1.48
	2	Chamber Air Temperature 2 (a)	6.11	8.44	2.33
		Chamber Air Temperature 2 (b)	6.78	8.60	1.82
		Orange	7.11	7.49	0.38
		Cauliflower	7.06	7.51	0.45
Facility 2	2	Chamber 2 - Air	-19.31	-15.17	4.14
		Chamber 2 - Ice Cream	-20.01	-17.56	2.45
		Chamber 2 - Pizza (Surface)	-20.42	-16.06	4.36
		Chamber 2 - Pizza (Internal)	-20.47	-16.86	3.61
	3	Chamber 3 - Air	-19.96	-16.71	3.25
		Chamber 3 - Ice Cream	-20.03	-18.34	1.69
		Chamber 3 - Pizza (Surface)	-20.19	-17.13	3.06
		Chamber 3 - Pizza (Internal)	-20.28	-17.68	2.60
	4	Chamber 4 - Air	-19.98	-17.05	2.93

		Chamber 4 - Ice Cream	-20.37	-19.04	1.33
		Chamber 4 - Pizza (Surface)	-20.63	-18.30	2.33
		Chamber 4 - Pizza (Internal)	-20.63	-18.45	2.18
Facility 3	Marsha-lling	Marshalling Air Temperature	4.37	6.97	2.60
		Chicken Breast	2.75	3.22	0.47
		Whole Chicken	2.84	3.14	0.30
		Sausage	2.78	3.39	0.61
	1	Chamber 1 Air Temperature	0.81	2.06	1.25
		Chicken Breast	1.03	1.26	0.23
		Whole Chicken	1.00	1.23	0.23
		Sausage	1.29	1.66	0.37
	2	Chamber 2 Air Temperature	4.34	4.80	0.46
		Orange	3.85	4.23	0.38
		Pomegranate	3.70	3.97	0.27
	3	Chamber 3 Air Temperature	9.95	10.44	0.49
		Tomato	8.85	8.80	-0.05
		Butternut Squash	8.83	8.76	-0.07

Condensation occurs when the surface temperature of a material is colder than the dew point temperature of the air. Fig. 3 shows floor condensation analysis carried out during the investigation. Dew point temperature does encroach upon the slab temperature at one point during the trial in Facility 3, so it is believed both external ambient conditions and floor slab construction would need to be considered. No condensation was noted during the study.

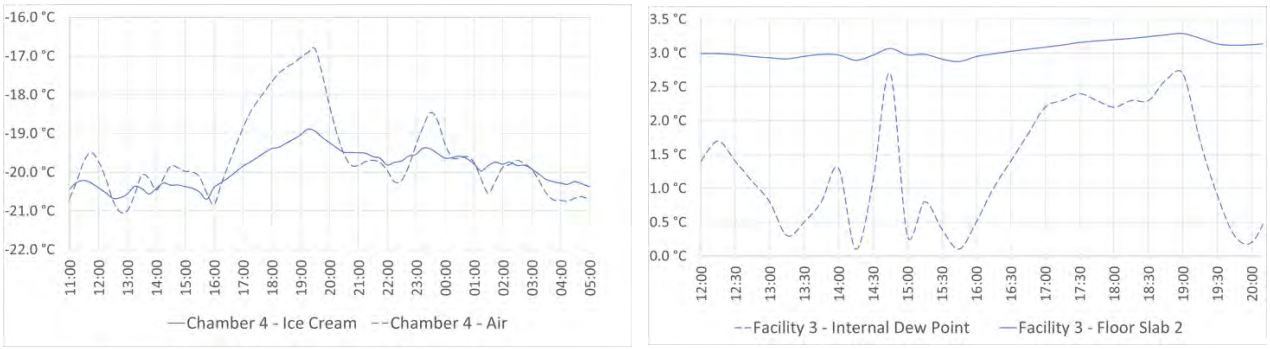

Figure 3. Example product temperature data and floor condensation assessment

Fig. 4 shows an example of refrigeration electrical energy, with kW readings from each power meter recorded over each 10-minute period. With data split into total compressor, condenser and individual chamber consumption. Data included the total consumption 3 hours before, energy during and energy 3 hours after load shedding. Initially it was expected that there would be no net gain or loss in energy due to load shedding as energy is being shifted from one period to another.

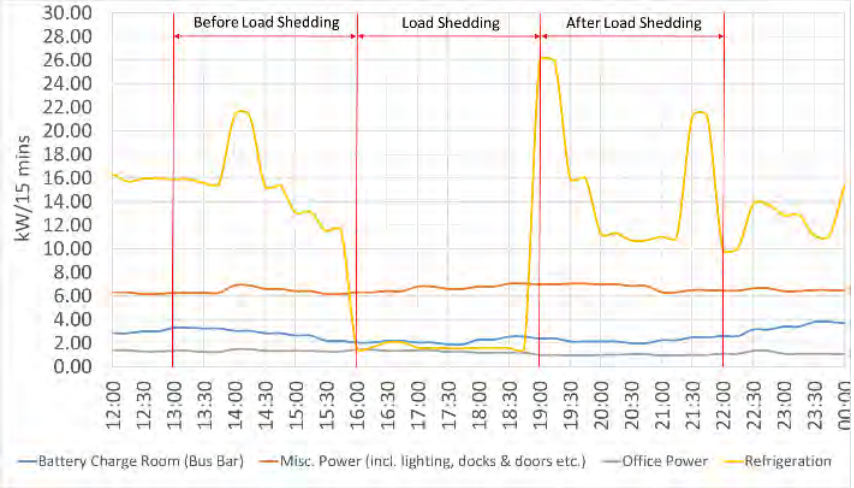

Figure 4. Facility 3 refrigeration electrical energy consumption

Table 4 shows the energy consumed before, during and after the load shedding period. While evaporators were isolated during load shedding, the plant continued to maintain the ammonia temperature in the surge vessel. Facility 1 (a) was the only result to show a net increase in energy. It was noted that isolating battery charging could be an easy win for consumers. Less energy consumption following load shedding can only occur due to a number of variables: efficiency of the refrigeration plant; lower ambient temperatures, higher operating efficiency; higher operating efficiency at full load and less heat load on the chamber; less product; less heat gains.

Table 4. Facility refrigeration load shedding energy analysis

RSF	Before Load Shedding (kWh)	During Load Shedding (kWh)	After Load Shedding (kWh)
Facility 1 a	465.2	101.3	885.7
Facility 1 b	335.6	9	547.5
Facility 2	3,706	2,341	3,854
Facility 3	185.4	20.1	192.2

Facility 1 raised questions over the control and operation, as both product and air temperatures were reduced to lower than their start point following load shedding. Following a second trial it was found that Facility 1, was controlled with a floating suction set-point, as the temperature of the chamber increased the suction temperature decreased. This was set to a maximum of 0°C, then decreasing (or increasing) 0.2°C every 5 minute. During trial B, compressor set point was manually set to 0°C. Over the 3-hour load shedding period the temperature decreased to -7.2°C, and effects of this are seen in both chamber temperatures and energy increases.

4.0 RESULTS

Data analysis showed load shedding is possible without risk to product, peak tariffs can be reduced by up to 95% and carbon reductions can be up to 11%. Using average half hourly consumption, the Triad charge with no load shedding can be calculated. DUoS ‘red band’, cost savings can be calculated using the calculated amount of energy that was load shed during the period between 16:00 and 19:00. Carbon savings can be calculated using the data from Table 4. RSF 1 figures would improve if the system control was adapted, RSF 2 if all chambers were isolated during loading shedding. Shedding could be carried out during November to February (Triad season) or the entire year. Table 5 shows the results of each RSF load shed.

Table 5. Cost and carbon savings

	RSF 1 a	RSF 1 b	RSF 2	RSF 3
Triad Charge (£/kWh)	51.87	51.87	51.87	49.2
Average HH (no load shed) (kWh)	77.5	55.5	617.7	30.9
Average HH (with load shed) (kWh)	16.88	3	390.2	6.7
Total Triad Saving with Load Shed (£)	9,433	8,170	35,401	3,572
Total Energy Shed (kWh)	363.9	326.6	1,365	165.3
*DUoS saving per day (£)	23.23	20.85	87.14	10.55
*DUoS saving if in 'Triad Season' (£)	2,788	2,502	10,457	1,266
*DUoS saving if conducted all year (£)	8,456	7,610	31,719	3,851
Total tariff reduction during 'Triad Season' (%)	78	95	37	78
Net Energy Change due to load shed (kWh)	+56.6	-115	-1,217	-158.5
Carbon Emission Change per day ($kgCO_2e$)	+19.90	-40	-427.85	-55.72
Carbon Emission Change per Triad Season ($kgCO_2e$)	+2,388	-4,839	-51,342	-6,686
Carbon Emission Change per year ($kgC0_2e$)	+7,244	-14,718	-155,737	-20,282
Total carbon change due to load shedding (%)	+4	-11	-11	-26

* DUoS 'Red Band' Charge £0.06384. Carbon Factor for Electricity 0.35156 $kgCO_2e$

5. DISCUSSION

REDUCE shows load shedding has promising financial and environmental paybacks, with potential to reduce peak period electrical load on the grid. Whilst REDUCE findings are restricted to three RSF of differing sizes and temperatures, it offers scalability. Load shedding offers a simple solution to financial and environmental challenges, making it of great interest. Little UK research exists on the effects of daily load shedding on very short-term product temperature fluctuations. Future research must consider potential of RSF for excess energy storage from the grid (such as renewables). Rather than shedding energy, and making constraint payments, using constrained electrical energy to over-cool during high generation periods, can reduce peak load requirements.

Observations from REDUCE show more investigation is needed on how PCMs and TES could improve storage of energy in large facilities. Clear guidelines and regulatory documentation for RSF operators, explaining acceptable fluctuations in temperature for specific products, duration and frequency are needed. Control adaptations to reduce temperatures prior to a load shed, or, as in Facility 3 addition of a maximum air temperature override, reduces risk to product in chambers. Better controlled sequencing of evaporator fans could avoid stratification of air. Implications include advanced sequencing to avoid defrosting during load shedding and the following hour (for example). Operators must consider timing of product deliveries during load shedding periods to ensure maintenance of correct temperature. Overall design of refrigeration plant and of entire operational management systems is extremely important for successful load shedding with consideration for liquid refrigerant storage, and availability of the necessary vessel size. Load shedding must take place at peak times and any resulting operating issues could be costly as these often occur on start-up of the refrigeration plant, which for many contractors is out of hours and charged at a higher rate.

6. CONCLUSIONS

REDUCE contributes to understanding the effects of load shedding on energy consumption, product temperature and carbon emissions in RSF and to industry confidence in load shedding. It is important,

because there is no relevant, published UK data, despite various bodies acknowledging load shedding takes place. Scaled up savings show huge reductions in peak electrical tariffs, reductions in carbon emissions and reduced peak demand on the electrical grid. Incorporating load shedding can help balance the grid, but with little evidence on effectiveness, benefits, savings and pitfalls. REDUCE' results show load shedding has great potential for RSF operators, reducing financial operating costs to consumers, as well as overall energy and carbon consumption. Product temperatures in all facilities remained within their defined tolerances. While the concept of load shedding is relatively simple there are many pitfalls. The REDUCE project has found many areas of discussion and practical issues associated with load shedding. Expert consideration of overall management of individual variations in facilities is needed. For example, in our field study we found that floor condensation is an issue to be considered in chill stores. Further work is urgently required to better understand the amount of current RSF in the UK; the total energy consumption of RSF; and to verify the DBEIS estimated consumption data. A load shedding regulatory document for operators would be extremely beneficial and could help enormously with UK uptake of load shedding. Expertise in load shedding in RSF can contribute to global energy solutions.

REFERENCES

Altwies, J., Reindl, D., 2001. Passive Thermal Energy Storage in Refrigerated Warehouses. Int. Journal of Refrigeration 24, 149-157.

Ashby, B., Bennett, A., Bailey, W., Moleeratanond, W., Kramer, A., 1979. Energy Savings and Quality Deterioration from Holding Frozen Foods at Two Daily Temperature Levels. Transactions of the ASAE 22 (4), 938-943.

Connolly, D., 2017. Heat Roadmap Europe: Quantitative Comparison between the Electricity, Heating and Cooling Sectors for Different European Countries. Energy 139, 580-593.

Department for Business, Energy and Industrial Strategy (DBEIS), 2016. Energy Consumption in the UK 2016 - User Guide. (https://www.gov.uk/government/uploads/. Accessed online 16th November 2017)

Department of Energy and Climate Change (DECC), 2012. The Future of Heating: A Strategic Framework for Low Carbon Heat in the UK. (https://www.gov.uk/government/uploads/system/uploads/attachment_data/file/48574/4805-future-heating-strategic-framework.pdf. Accessed online 15th November 2017).

Evans, J., 2009. Food Chilling and Freezing Technologies: Potential for Energy Saving. Food Refrigeration and Process Engineering Research Centre (FRPERC). (http://www.design-technology.info/alphaindex/manufacturing-foodchillfreeze.pdf. Accessed online 11th November 2017).

HM Government, 2013. The Food Safety and Hygiene (England) Regulations. The Stationery Office Limited, UK.

Motarjemi, Y., Lelieveld, H., 2014. Food Safety Management - A Practical Guide for the Food Industry. Academic Press.

National Grid, 2017a. Future Energy Scenarios. (http://fes.nationalgrid.com/ media/1253/final-fes-2017-updated-interactive-pdf-44-amended.pdf. Accessed online 13th November 2017).

National Grid, 2017b. Forecast TNUoS Tariffs for 2018/19. (https://www.nationalgrid.com /sites/default/files/documents/October%20Forecast%20TNUoS% 20Tariffs%20for%20201819%20Report.pdf. Accessed online (25th November 2017).

Phimolsiripol, Y., Siripatrawan, U., Tulyathan, V., Cleland, D., 2007. Effects of Freezing and Temperature Fluctuations During Frozen Storage on Frozen Dough and Bread Quality. Journal of Food Engineering 84, 48-56.

Schalbart, P., Leducq, D., Alvarez, G., 2014. Ice-cream Storage Energy Efficiency with Model Predictive Control of a Refrigeration System Coupled to a PCM Tank. International Journal of Refrigeration 52 140-150.

The British Frozen Food Federation, 2009. Improving the Energy Efficiency of the Cold Chain. Accessed online (8th December 2017): http://bfff.co.uk/wp-content/uploads/2013/06/Energy-Efficiency-Report.pdf.

The British Frozen Food Federation, 2012. Guide to the Storage and Handling of Frozen Foods. UK: The British Frozen Food Federation.

Wimmler, C., Hejazi, G., Fernandes, E., Moreira, C., Conners, S., 2016. Impacts of Load Shifting on Renewable Energy Integration. Energy Procedia 107, 248-252.

Manuscript ID: 190
DOI: 10.18462/iir.icr.2019.0190

Experiences with selecting natural refrigerant solutions for small capacity industrial food production and temperature controlled storage applications

Robert LAMB[1]

[1]Star Refrigeration Ltd
Derby, DE56 0GX, United Kingdom rlamb@star-ref.co.uk

ABSTRACT

Synthetic refrigerants have been widely used in small industrial refrigeration applications. The phase down of high global warming potential refrigerants is underway across the world as part of the agreement to tackle climate change. This provides an opportunity for the use of natural refrigerants such as ammonia and carbon dioxide.
This paper looks at the use of both ammonia and carbon dioxide for small industrial refrigeration applications. It discusses refrigerant and system selection and key criteria including safety, energy efficiency, cooling capacity and capital cost. Two examples are provided for spiral freezing and temperature controlled storage applications. Small capacity applications are defined as ranging from 60kW up to 300kW and temperatures from -40°C to +12°C. The use of ammonia and carbon dioxide in cascade is also discussed.
Keywords: Refrigeration, Carbon Dioxide, Ammonia, Cascade, Efficiency, Temperature Controlled Storage, Spiral Freezer.

1. INTRODUCTION

The f-gas Regulation (EU) 517/2014 is part of Europe's commitment to reducing greenhouse gas emissions. The 2014 update to Regulation (EU) 842/2006 sets out a phase down timetable for the placing of global warming hydrofluorocarbon (HFC) refrigerants onto the market. Fig. 1 shows how this phase down is measured based on tonnes of carbon dioxide (CO_2) equivalent compared to 2009 to 2012 average consumption.

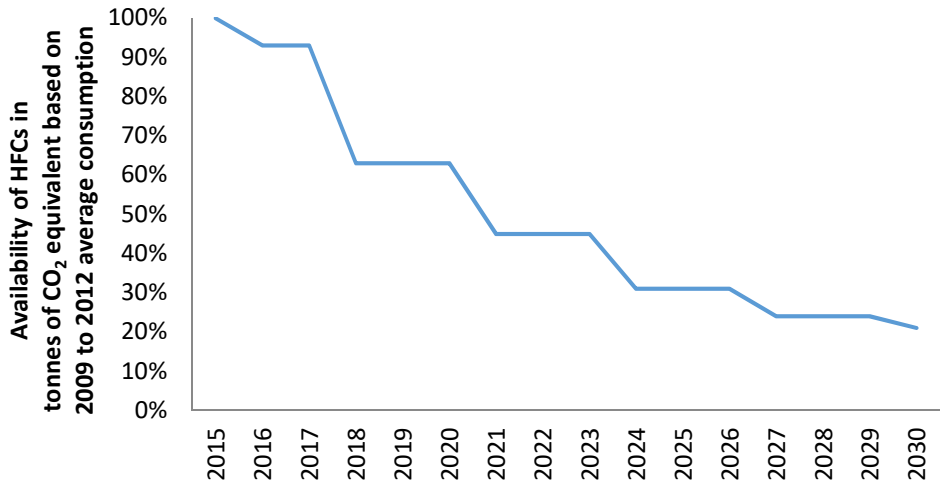

Figure 1. Phase down timetable for availability of global warming refrigerants

The phase down began in 2016 with a 7% reduction in consumption and was followed by a further 30% cut in 2018. There is also a ban on the use of new refrigerant with a global warming potential (GWP) greater than 2,500 for servicing equipment from 1st January 2020.

A consequence of this phase down timetable has been a steep rise in the cost of high global warming refrigerants including R404A and R507. Typical increases in the market prices of several popular gases between 2016 and 2017 are shown in Table 1.

Table 1. Refrigerant Price Increases

Refrigerant	GWP	Average supplier price increase February 2016 – December 2017
R134a	1430	320%
R422D	2729	532%
R404A	3922	1146%

In addition to the increase in refrigerant prices, there has been concerns over availability, with manufactures indicating the end of production of some high GWP gases and limiting production of others. Lower GWP synthetic alternatives are available in response to the HFC phase down as can be seen from Table 2. An array of fluids are also under development and subject to field trials by the refrigerant manufacturers.

Table 2. Lower GWP Refrigerants

Refrigerant	Components	Composition % by weight	Safety Class	GWP
R448A	R32/R125/R134a/R1234ze /R1234yf	26/26/21/7/20	A1	1387
R449A	R32/R125/R1234yf/R134a	24.3/24.7/25.3/25.7	A1	1397
R-450A	R134a/R1234ze	42/58	A1	547
R-452A	R32/R125/R1234yf	11/59/30	A1	2141
R-454A	R32/R1234yf	35/65	A2L	239
R454B	R32/R1234yf	69.9/31.1	A2L	466
R-454C	R32/R1234yf	21.5/78.5	A2L	148
R-455A	R32/R1234yf/R744	75.5/21.5/3	A2L	145
R513A	R1234yf/R134a	56/44	A1	631

Many of these are blends of HFC and hydrofluoro-olefin (HFO) fluids and their development has been a compromise between GWP and flammability in order to achieve similar operating pressures and temperatures to the refrigerants they are replacing (Lamb, 2016). The majority of non-flammable synthetic refrigerants have a GWP greater than 1,000 and are intermediate refrigerants rather than long-term solutions. Those with GWPs lower than 1,000 typically fall into the ISO817:2014 Safety Classification of 2L, lower flammability. This is the same category as ammonia and requires additional safety measures to be implemented relating to gas detection and ventilation.

2. NATURAL FLUIDS FOR SMALL CAPACITY INDUSTRIAL APPLICATIONS

The use of ammonia in large capacity industrial refrigeration applications has been common for more than 100 years. In the past 20 years, there has been a growth in the use of carbon dioxide across Europe for retail applications. Large industrial applications for temperature controlled storage (Pearson and Cable, 2003) and food freezing (Blackhurst, 2002) have used both fluids in cascade.

For smaller capacity industrial applications up to 300 kW, the choice of refrigerant for new installations is less clear, particularly for medium to low temperatures. Following the phase out of ozone depleting refrigerants under the Montreal Protocol, HFCs such as R404A have been widely used, with ammonia viewed as being too expensive. However, the f-gas phase down means that

high GWP synthetic fluids are no longer a viable solution for those wanting to invest in equipment for 15 to 20 years. This has seen increased interest in carbon dioxide as it uses similar components and materials to HFCs, albeit at higher operating pressures. The use of ammonia for smaller applications has also become more widespread, helped by a reduction in refrigerant charge and price per kilowatt through the introduction of low charge, packaged systems. Both fluids provide long-term certainty, as they are not subject to phase down. This has resulted in the use of both fluids in applications where HFCs would previously have been used, despite there being an increase in capital cost.

3. CARBON DIOXIDE FOR SPIRAL FREEZING

A UK pizza manufacture had a 202 kW cooling requirement for a new spiral freezer installation. Historically, they would have selected an HFC refrigerant for this capacity but were aware of the phase down and wanted to invest in a solution with 20 years' life expectancy. The operator also had concerns over the use of ammonia inside the factory space due to its toxicity and flammability.

3.1 Two-Stage, Transcritical Carbon Dioxide Freezer System

An alternative two-stage carbon dioxide solution shown in Fig. 2 has semi-hermetic reciprocating compressors for the subcritical and transcritical stages. Limitations in swept volume mean that three are required for both stages to achieve the 202 kW cooling capacity. The gas cooler is designed to achieve a 3 K approach between the ambient air and vapour outlet temperature during transcritical operation. The gas is then reduced to an intermediate pressure before entering an interstage vessel. Intermediate pressure liquid flows from this vessel to the tube side of a shell and tube heat exchanger that forms part of the low pressure receiver (LPR) vessel. Here it exchanges heat with low pressure liquid on the shell side and is subcooled before expansion and entering the spiral freezer evaporator. The majority of liquid boils but a small amount (around 5% by weight) remains at the evaporator outlet and separates in the LPR vessel. Any liquid overfeed evaporates through heat transfer with the intermediate pressure liquid in the sub cooler and the vapour flows to the low stage compressors (LS COMP). A suction to liquid heat exchanger (SUC/LIQ HX) superheats the vapour before it enters the compressor using heat from the intermediate pressure liquid. A coil inside the interstage vessel cools discharge gas from the low stage compressor before it mixes with the 'flash gas' from the same vessel and enters the high stage compressors (HS COMP).

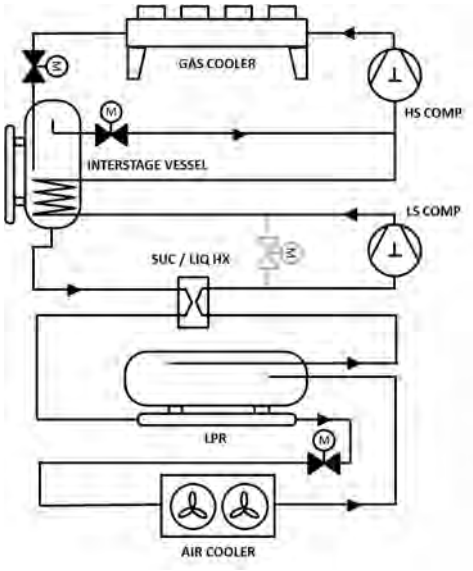

Figure 2. Simplified Schematic of Two-Stage CO_2 Refrigeration Plant

This low pressure receiver principle was developed using R502 for cold storage systems before being adapted for R22 and ammonia (Pearson, 1996). It delivers flooded evaporator performance

without the need for a recirculation pump, reducing the refrigerant charge by around 80%. It eliminates the need for superheat at the evaporator outlet (required in direct expansion systems) and this enables a closer temperature approach, typically 6 K. For CO_2 applications, the LPR vessel provides a useful storage and expansion space, avoiding the need for a separate refrigeration system to maintain system pressure during stand still conditions.

Although the system is designed to operate at freezer conditions, it has the flexibility to run at higher air temperatures for chilled product. A bypass valve diverts vapour from the LPR around the low stage compressors and directly into the high stage compressors. This operation is also used during pull down at the start of production.

The compressors, pressure vessels, electrical panel and control valves are mounted, wired and insulated on a factory built package, reducing site installation time. The package can be installed in a plant room or outside in a weatherproof housing. The gas cooler can be mounted on the package or located remotely depending space availability. Connections are also included for the addition of a CO_2 to water heat exchanger at the outlet of the gas cooler. This can extract waste heat to generate hot water for use in the production facility.

3.2 Comparison of Compressor Performance for R407F, Ammonia and Carbon Dioxide

Design conditions for the spiral freezer application were 202 kW at a -40ºC saturated compressor suction and ambient dry bulb air temperature of +32ºC. Table 3 shows compressor coefficient of performance (COP) at this condition and an average ambient temperature of +10ºC. It assumes an intermediate temperature of -5ºC for the two-stage CO_2 system. This is compared with an air cooled, direct expansion R407F system and a low charge, air cooled ammonia package solution using low pressure receiver technology with low evaporator overfeed. Both the R407F and ammonia systems assume the use of single stage, economised screw compressors.

Table 3. Comparison on Compressor Performance for R407F, Carbon Dioxide and Ammonia

Refrigerant	Carbon Dioxide		R407F		Ammonia	
Cooling Capacity (kW)	202					
Ambient Temperature (ºC)	32	10	32	10	32	10
Condensing Temperature (ºC)	35*	19.5	46.6	24.5	44	22.1
Absorbed Power (kW)	192	120	262	111	180	111
Coefficient of Performance (COP)	1.05	1.69	0.77	1.82	1.12	1.82
Annual Compressor Energy Cost (£)	76,800	48,000	104,800	44,400	72,000	44,400

*Gas cooler off temperature during trans-critical operation

At the design condition, the two-stage CO_2 solution has a 6.3% lower efficiency than ammonia but is 36% higher than R407F. It is assumed that all three systems are designed to float condensing pressure with changes in ambient conditions and that none will operate at the design condition for the majority of the year. The data in Table 3 assumes that the systems will maximise use of available condenser surface area to minimise condensing pressure and optimise system performance. At an average ambient condition of +10ºC the carbon dioxide system operates subcritical with a condensing pressure of 19.5ºC. The lower ambient temperature improves performance across all three systems and results in identical theoretical compressor performance for R407F and ammonia. In reality, direct expansion will operate at a lower evaporating temperature of between 2 K and 5 K to ensure the necessary superheat at the evaporator outlet. This will reduce compressor performance by around 4% and 10% based on a 2% reduction in COP per 1 K fall in evaporating temperature. Carbon dioxide requires 8.1% more compressor energy for the same suction condition as ammonia when using the low pressure receiver design.

The refrigeration plant is to operate for around 4,000 hours per year and an estimate for the compressor electrical cost at both the design and average ambient condition is shown in Table 3. This assumes an energy cost of £0.10 $kWhr^{-1}$. Compressor performance for ammonia at the design

conditions indicates a £3,600 benefit in running costs compared to CO_2. It is expected that CO_2 will deliver a small energy improvement over R407F when accounting for the lower evaporating temperature necessary to achieve the evaporator outlet superheat required for the direct expansion systems.

The increase in capital cost for ammonia for this project was estimated to be around £100,000 compared to both carbon dioxide and R407F. This results in a 28 years payback that, along with the company's health and safety concern, was not acceptable. Concerns over the medium term availability and cost of R407F led the company to rule out this option.

Unlike ammonia and many of the recently developed A2L synthetic refrigerants, carbon dioxide is classified as an A1 refrigerant. It is both non-toxic and non-flammable, reducing the health and safety risk when used in a production environment. This was a significant factor in its selection for this project and several others. In all cases, gas detection and ventilation to the plant room and spiral freezer is design in line with the EN378 to avoid the risk of asphyxiation in the event of a leak.

The two-stage, transcritical CO_2 package was installed in 2018 and has been in operation for more than 12 months. It is located in a dedicated plant room inside the factory and within 10 m of the spiral freezer. This has helped lower refrigerant charge and reduce suction pressure drop to 1 K, benefiting efficiency by around 2%. The gas cooler is remote to the packaged unit and located externally at ground level.

4. AMMONIA AND CARBON DIOXIDE FOR TEMPERATURE CONTROLLED STORAGE

A UK retailer wanted to retrofit refrigeration into an existing warehouse that required 1170 kW and 60 kW of cooling for the chill and freezer areas, respectively. The preference was to use natural refrigerants and previous facilities had used pumped recirculation ammonia systems to both chill and freezer chambers. Recent health and safety concerns relating to large ammonia charges and leaks at some facilities led to the consideration of an alternative option based on ammonia with secondary glycol for the chill and CO_2 for the freezer.

An initial lease period on the facility of only five years meant that capital cost was of particular importance and the company wanted to invest in a solution that could be reused elsewhere in the future if possible. The proposal was to use packaged ammonia chillers to cool a secondary glycol and circulate this to the chill areas, satisfying the need for low ammonia charge. The resulting 300kg total charge (0.26 kg kW^{-1}) for the entire warehouse is less than 15% of what would be required for a pumped recirculation system of the same capacity. The packaged chiller design also means that they could be easily relocated elsewhere within the operator's estate at the end of the lease period.

A simplified schematic of the chiller circuit is shown in Fig. 3 and includes two reciprocating compressors with variable speed drive motors, an air cooled condenser with EC fans and flooded plate and shell evaporator with integrated separation space to avoid the need for a surge vessel. Lamb (2016) describes how this chiller design delivers improvements in European Seasonal Energy Efficiency Ratio (ESEER) of 36% when compared to a previous generation of chiller using fixed speed screw compressor technology.

A recent study (Evans et al., 2013) looking at the energy performance of temperature controlled warehouses included surveys of more than 300 stores and data from a further 500 facilities. Fig. 4 shows how energy consumption varies with store volume for chill, frozen and mixed temperature facilities based on lines of best fit for all the data collected. It is not clear in many cases as to whether data relates to just the refrigeration plant or the entire site but it is generally accepted that refrigeration typically represents around 70% of a site's total energy consumption. Variation in data from the study suggests that there is likely to be little variation in the specific energy consumption curves based on the power meter location. An additional data line is also shown based on a UK study carried out by the Energy Technical Support Unit in 1994 (ETSU, 1994). Both studies show that specific energy consumption can vary between 30 kWhr m^{-3} yr^{-1} and 64 kWhr m^{-3} yr^{-1} depending on the application and store volume.

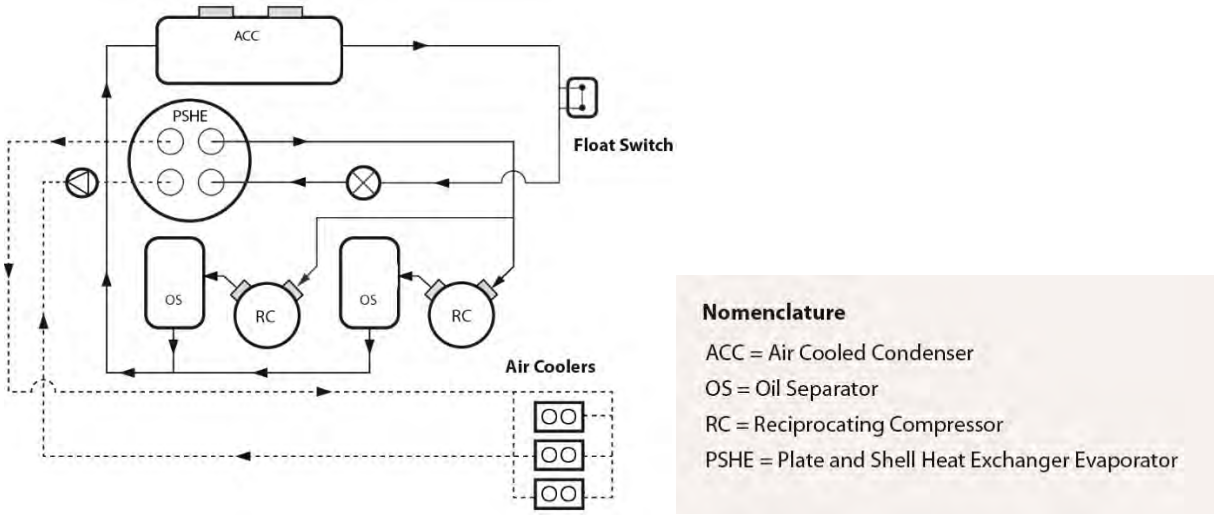

Figure 3. Schematic of Air Cooled Package Chiller

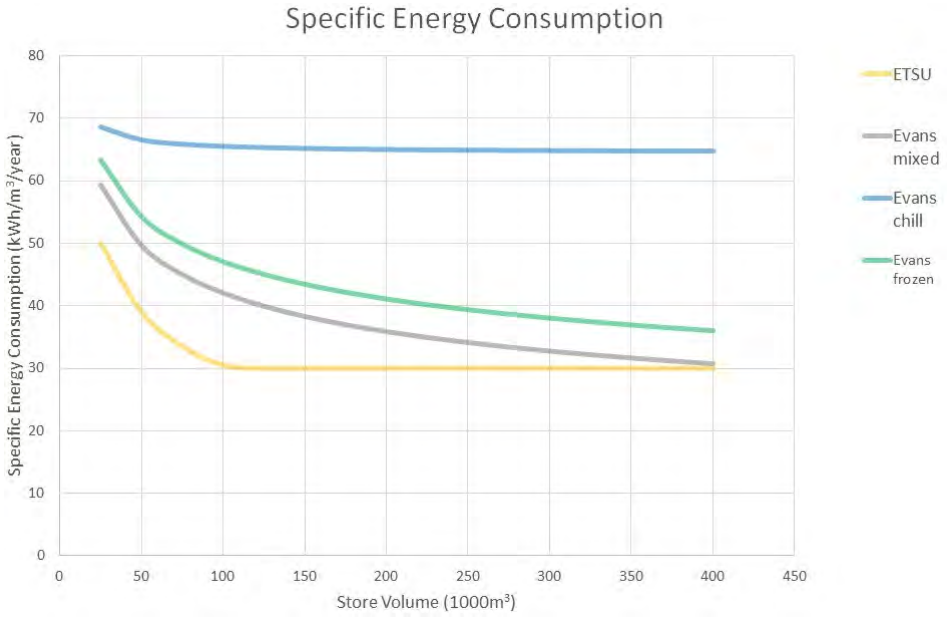

Figure 4. Specific Energy Consumption Curves for Temperature Controlled Warehouses

Energy data taken from two recent facilities using the low charge packaged chillers described above have indicated specific energy consumption of between 10 kWhr m^{-3} yr^{-1} and 15 kWhr m^{-3} yr^{-1}. The chamber volume for these projects was 58,500 m^{-3} and 224,666 m^{-3}, respectively. Both sites are operating significantly below the curves in Fig. 6, with energy consumption running between 25% and 50% of the European average. This demonstrates the chiller's efficient design and operation.

4.1 Subcritical Carbon Dioxide Cold Store Refrigeration Package

The cold store operates at -23°C and is designed with a subcritical carbon dioxide package. Fig. 5 shows a simple schematic of the system, including its integration with the chill store glycol cooling circuit for heat rejection. It uses the same low pressure receiver technology described earlier and has two, single stage reciprocating compressors to satisfy the 60kW cooling requirement. Two CO_2 to glycol condensers ensure cooling to the freezer is maintained in the event that one condenser is out of operation. There are two evaporators in the freezer chamber, each with electric defrost.
This design provides flexibility in terms of its physical location as it can be connected into any part of the glycol circuit. This is of particular benefit in facilities where one or more cold stores are located

across the facility. It also avoids long runs of pipework and electrical cabling from the plant room to the evaporators and helps minimise refrigerant charge.

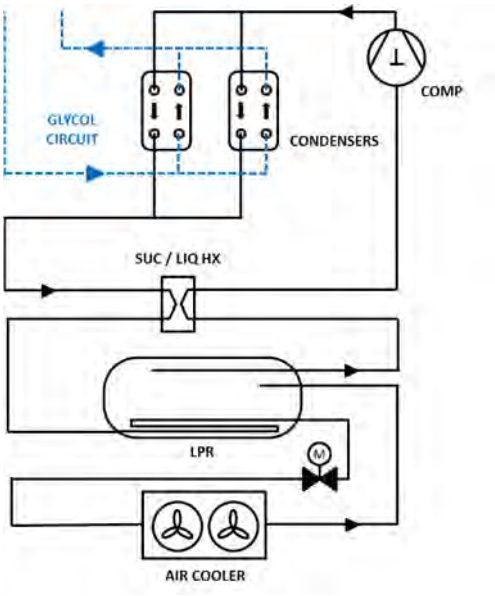

Figure 5. Subcritical Carbon Dioxide Cold Store Refrigeration Package

4.2 Comparison of Subcritical Carbon Dioxide with Single and Two-Stage Transcritical

Table 5 details a comparison of performance of this subcritical CO_2 design with single and two-stage transcritical systems. The additional glycol pumping power needed to reject heat from the subcritical unit to the chiller is assumed negligible and omitted from all calculations. Total package power consumption inclusive of gas cooler fans is included, along with performance data for the packaged ammonia chillers. The additional chiller capacity required to remove the subcritical systems heat of reaction is excluded from the total system COP calculation as it is non-useful cooling but the electrical energy is included. Estimations of energy consumption are made for the +32°C design condition and an average ambient temperature of +10°C. To account for seasonal variations in cooling load, it is assumed that the freezer and chill cooling capacities are 50% of design at the +10°C ambient condition. The chiller design glycol flow and return temperatures are -7°C and -2°C, respectively and the CO_2 subcritical unit's condensing temperature remains constant at +0.5°C. Floating heat pressure control and optimum use of the available condenser surface area are assumed in all cases. The subcritical CO_2 system coefficient of performance (COP) is higher than both transcritical systems at the design and average ambient conditions. However, when accounting for the additional chiller energy necessary to reject its heat to atmosphere, the total system COP (CO_2 and ammonia) of all three systems are within 2.2% of each other for the design ambient condition. The two-stage transcritical solution consumes the lowest energy at 433.8 kW compared to 437.5 kW and 444 kW for the subcritical and single stage systems, respectively.

Calculations at the average ambient condition indicate almost identical total system COPs for the subcritical and single stage systems and a 2% improvement with the two-stage solution. Despite the transcritical systems having similar COPs, their energy consumption is 1.5 kW to 3.2 kW higher, respectively resulting in long term energy savings when using the subcritical solution.

There are also capital savings for the subcritical system of between £10,000 and £20,000 compared to single and two-stage packages, respectively, which further strengthen the case for its use.

Table 5. Comparison on Subcritical and Transcritical Freezer Carbon Dioxide Solutions

Carbon Dioxide Solution	Subcritical		Single Stage T/C		Two Stage T/C	
Freezer Cooling Load (kW)	60	30	60	30	60	30
Ambient Temperature (°C)	+32	+10	+32	+10	+32	+10
CO_2 Condensing Temperature (°C)	+0.5	+0.5	+34.0	+13.3	+34.0	+14.8
Absorbed Power (kW)	14.3	6.2	53.2	14.2	43.0	12.5
Coefficient of Performance	4.21	4.81	1.13	2.11	1.40	2.40
Chill Cooling Load (kW)	1119	560	1119	560	1119	560
Total Chiller Cooling Load (kW)	1193	596	1119	560	1119	560
Chiller Condensing Temperature (°C)	+42.7	+19.6	+42.0	+19.0	+42.0	+19.0
Total Chiller Consumption (kW)	423.2	83.7	390.8	78.9	390.8	78.9
Ammonia Chiller COP	2.83	7.12	2.86	7.09	2.86	7.09
Total System COP	2.70	6.32	2.66	6.33	2.72	6.45

5. CONCLUSIONS

The phase down of HFC refrigerants under the f-gas regulation in Europe is resulting in operators moving to natural solutions using ammonia and carbon dioxide for small industrial applications.

Carbon dioxide systems using single and two-stage compression can provide cost effective, long term alternatives to HFCs for medium to low temperature applications. Energy efficiency is typically greater than HFCs at design conditions and similar at average ambient conditions for the UK. Ammonia delivers the highest efficiency but concerns over toxicity, flammability and cost mean that it is not suitable for some operators and applications.

Low pressure receiver technology previously developed for R502, R22 and ammonia has been successfully adapted for use with CO_2 in spiral freezing and cold storage applications. This can be either as an independent system or in cascade with glycol and ammonia chillers. The resulting solution has no detriment to operating efficiency and can be located local to the point of cooling.

ACKNOWLEDGEMENTS

The author would like to thank the directors of Star Refrigeration for permission to publish this paper. Thanks are also due to my colleagues who provided the supporting information.

REFERENCES

Lamb, R., 2016, Refrigerant choices for the future – Small Industrial Refrigeration Applications, Institute of Refrigeration Technical Paper, Institute of Refrigeration, 1-11

Pearson, A., Cable, P., 2003, Distribution warehouse with CO_2 as refrigerant, International Congress of Refrigeration 2003, Washington, D.C., IIF/IIR, B2-7, 26-30

Blackhurst, D.R., 2002, CO_2 vs NH_3 A comparison of two systems, Proc. Inst. R. Session 2002-03, Institute of Refrigeration, 2 1-11

Pearson, S.F., 1996, Ammonia low pressure receivers, Proc. Inst. R. Session 1995-96, Institute of Refrigeration, 4 1-8

Lamb, R., 2016, Modern, Low Charge Ammonia Systems for the Cold Chain, 4th IIR Conference on Sustainability & the Cold Chain, Auckland, IIF/IIR, 217-224

Evans, J.A., Huet, J-M., Reinholdt, L., Fikiin, K., Zilio, C. Houska, M. Landfeld, A. Bond, C. Scheurs, M. van Sambeeck, T.W.M., 2013. Cold Store Energy Performance, Proceedings of the 2nd IIR Conference on the Cold Chain and Sustainability, Paris, IIF/IIR, 310-317

ETSU, 1994, Energy Consumption Guide 37: Cold Storage Section. Energy Efficiency Office, Department for the Environment, Harwell, United Kingdom

Manuscript ID: 233
DOI: 10.18462/iir.icr.2019.0233

Performance of domestic refrigerators in laboratory and home environments

Alessandro BIGLIA [a], Andrew GEMMELL [b], Helen FOSTER [b], Judith EVANS [c,d,]
[a] DI.S.A.F.A. – Universitá degli Studi di Torino, 2 Largo Paolo Braccini, 10095 Grugliasco (TO), Italy, alessandro.biglia@unito.it
[b] BRE – Bucknalls Lane, Garston, Watford, Hertfordshire WD25 9XX, United Kingdom, Andrew.Gemmell@bregroup.com, Helen.Foster@bre.co.uk
[c] School of Engineering – London South Bank University, Churchill Building, Langford, Bristol BS40 5DU, United Kingdom, j.a.evans@lsbu.ac.uk
[d] RD&T – Churchill Building, Langford, Bristol BS40 5DU, United Kingdom, j.a.evans@rdandt.co.uk

ABSTRACT

Data was collected on temperature control and energy consumption of domestic refrigerators in the home. Data from the survey was extracted to compare the performance of the refrigerators in the home with performance in a test environment.
Due to differences in internal and external appliance temperatures between laboratory and home data, the energy measured in the home was normalised to enable direct comparison between laboratory and home energy consumption. Overall without normalisation 61% of appliances consumed more energy in the home than the laboratory. After normalisation this value was increased to 85%. The rank order of energy use was also assessed and found to vary considerably between the laboratory and the home (irrespective of whether energy consumption was normalised for temperature effects). The reasons for the differences in energy use are discussed and suggestions made to provide consumers with a more transparent method to assess performance of refrigerated appliances in their homes.

Key words: Survey, Domestic refrigerators, Domestic freezers, Energy consumption, Laboratory testing

1 INTRODUCTION

Worldwide there are around 1.4 billion domestic refrigerators and freezers each of which are claimed to consume on average 453 kWh of energy per year (Barthel and Götz, 2012). This amounts to a total worldwide energy use of 649 TWh annually which according to the IEA equates to almost 4% of global electricity (IIR, 2015). The worldwide market for appliances is expected to increase. Barthel and Götz (2012) state that worldwide a 27% increase in cold appliances is expected by 2020 and that this will increase to 62% by 2030.
Improving the energy efficiency of refrigerators and freezers has a significant impact on future electricity consumption. A number of countries and areas have applied methods to reduce energy consumed by refrigerated appliances through the application of energy labelling and/or MEPS (minimum energy performance standards). The EU applied MEPS and energy labelling in 1993 and since that time the MEPS have been reduced. When labels were first introduced no appliances were labelled better than A. By 2011 all appliances were better than A rated and some had reached A+++ (Waide, 2011).
There is substantial information on energy used by domestic refrigerators under test conditions as all domestic refrigerators in Europe are energy labelled. In Europe most testing in laboratories is carried out to EN 62552:2013 (Household refrigerating appliances - Characteristics and test methods) and this standard is used for energy labelling of appliances. A more recent test standard; IEC 62552:2015 (Household refrigerating appliances - Characteristics and test methods) exists which is likely to be used in the future for energy labelling. Both tests require appliances to be tested in a specific test room with controlled ambient temperature and air flow. In the EN

62552:2013 the freezer and chiller section of appliances is loaded with a simulated load consisting of 'tylose' test packs. The food storage section (refrigerated section that operates between 0 and 8°C is not loaded and temperatures are measured at 3 positions in the vertical centre of the compartment using temperature sensors that are 'damped' by insertion into brass blocks. In the IEC 62552:2015 standard test for energy consumption none of the compartments are loaded and all temperature measurements is carried out using temperature sensors inserted into brass blocks or 500 g blocks of simulated food. None of the energy tests simulates usage of the appliance as appliance doors remain closed during the tests and the appliances are not loaded or used as they would be in the home. These tests therefore do not replicate real usage. Ideally testing should provide the consumer with some indication of how much energy an appliance should use in the home.

Although there is substantial information on performance of domestic appliances in test laboratories there is minimal information on whether tests carried out in a test room reflect performance of refrigerators in the home. Authors such as Bansal (2003) consider that a more lifelike test should be carried out but evidence also suggests that the test regime is a good estimate of usage in the home (MTP, 2007; Sidler et al., 1998). Real operating conditions of appliances are difficult to test in the laboratory since the behaviour of householders is quite varied. For example little information is available on the number of times appliance doors are opened, the types and temperature of the food placed in the appliance and the ambient temperature where the appliance is installed which does not remain constant over time. Several research activities have been carried out in order to evaluate the effects of operating conditions on the energy consumption of domestic refrigerated appliances. Meier (1995) found that the energy used by similar refrigerators varied widely in consumers' homes and that this was primarily due to ambient temperature and door openings whereas ambient humidity had a relatively minor impact on energy consumed.

As consumer usage of appliances is known to be extremely variable it is probably unrealistic to expect a test to be able to perfectly predict accurately usage in the home. However, it would be reasonable to expect that the best performing appliance in a test should also be the best performing in the home. This then means that if a consumer purchases a product with claimed low energy consumption (in a laboratory test) it should also have low energy when used in the home.

The aim of this work was to determine whether a laboratory test provides a reasonable assessment of usage in the home. Information on appliances was collected from a recent large scale survey in the UK (Gemmell et al, 2017; Biglia et al, 2018). The survey involved around 1,000 domestic refrigerators and freezer appliances. During the survey the following data were monitored: (1) ambient temperature of the room where the appliance was installed, (2) internal compartment temperature in the appliance compartments and (3) power consumption. Householders were also questioned about the management of their appliance in respect of door openings, quantity of food loaded in the appliance and shopping habits. Appliance models were also recorded in order to obtain information on storage volume and the energy label for the appliance. Results of the work are analysed to assess the relationship between performance in a test facility and the home.

2 METHOD

2.1 Trial design

A large-scale survey was conducted across England in which 998 cold appliances were monitored in 766 properties (Biglia et al, 2018). Data was collected over a period of 9 months, from March to November 2015. Simultaneous measurements of the temperature inside and outside of the cold appliances, as well as the electricity consumption were taken over a period of seven days. The cold appliances monitored in the work survey included: (1) Fridge-freezers; (2) Refrigerators with an ice-box; (3) Larder fridges; (4) Chest freezers and (5) Upright freezers.

Data and information on appliances were collected by interviewers. On the first visit to each property the interviewers installed the monitoring equipment and obtained information about each appliance. One week later they returned to remove the equipment and data was downloaded ready

for analysis. The appliances were monitored for seven days to ensure the data reflected the performance of the cold appliances as accurately as possible.
The temperatures both inside and outside the appliance were monitored using TinyTag Transit 2 data loggers with a monitoring range of -40°C to 70°C, a reading resolution of 0.01°C and a reading accuracy of <0.8°C between -40-0°C, and <0.4°C between 0-50°C. One data logger was placed on the middle shelf of each appliance compartment in a plastic bag and one was attached to the outside of the door of the appliance.
The electricity consumption data of each cold appliance was collected using a Watts Up PRO monitor and data logger with an accuracy of +/- 1.5%. Each appliance was connected to the data logger, which itself was plugged into the wall socket. The electric power in Watts was monitored every 30 seconds for the period the appliance was plugged in.
Only complete data sets where appliance volume and information on the manufacturers claimed energy use could be used in the analysis to compare real life versus laboratory performance. This reduced the data set to 124 appliances (around 12.4% of the total data set). Table 1 presents the numbers of each type of cold appliance with valid monitoring data.

Table 1: Numbers of cold appliances in the survey

Appliance type	Total number in survey	Number available for analysis
Fridge-freezer	524	79
Larder refrigerator	145	18
Upright freezer	186	18
Chest freezer	86	7
Refrigerator with ice-box freezer	57	2
TOTAL	**998**	**124**

2.2 Analysis of data

Data were analysed to determine whether there was any relationship between energy used in the survey and the energy usage claimed by manufacturers (measured in a test laboratory).
A direct comparison between energy used in a laboratory and in the home is not necessarily fair. In particular the temperature performance of the appliance may vary when assessed in the laboratory and the home. In the laboratory (using EN 62552:2013) the energy consumption is assessed in an ambient of 25°C and at an average internal temperature of 4°C for the fresh food compartment and ≤-18°C in the freezer. A temperature normalisation was carried out to enable direct comparison between appliances. Fresh food compartments were normalised to 4°C, freezer compartments to -18°C and ambient temperature was normalised to 25°C using Eq. (1)

$$E_{\mathrm{n}} = E \cdot f_{\mathrm{n}} \qquad \text{(Eq 1)}$$

where E_{n} is the normalised energy (kWh per year), E is the monitored energy (kWh per year) and f_{n} is the normalisation factor, which in case of fridge-freezers and refrigerators with an ice-box was defined as

$$f_{\mathrm{n}} = \frac{\left(\frac{T_{\mathrm{rf,std}} - T_{\mathrm{a}}}{T_{\mathrm{rf}} - T_{\mathrm{a}}}\right) + \left(\frac{T_{\mathrm{fz,std}} - T_{\mathrm{a}}}{T_{\mathrm{fz}} - T_{\mathrm{a}}}\right)}{2} \qquad \text{(Eq 2)}$$

while for larder fridges, chest and upright freezers it was defined as

$$f_{\mathrm{n}} = \left(\frac{T_{\mathrm{rf,std}} - T_{\mathrm{a}}}{T_{\mathrm{rf}} - T_{\mathrm{a}}}\right) \quad \text{or} \quad f_{\mathrm{n}} = \left(\frac{T_{\mathrm{fz,std}} - T_{\mathrm{a}}}{T_{\mathrm{fz}} - T_{\mathrm{a}}}\right) \qquad \text{(Eq 3)}$$

where $T_{\mathrm{rf,std}}$ is the fresh food standard and recommended internal temperature (4°C), $T_{\mathrm{fz,std}}$ is the freezer standard and recommended internal temperature (-18°C), and T_{a} is the test laboratory ambient temperature (25°C), T_{rf} is the monitored mean refrigerator internal temperature and T_{fz} is the monitored mean freezer internal temperature. Based on an analysis of the models examined

an assumption was made that the compartments in fridge-freezers were of approximately similar volume.

3 RESULTS

3.1 Energy used in the home versus energy used in the laboratory before normalisation

The annual energy claimed by the manufacturers in a test laboratory versus the annual energy used in the home is compared in Figure 1. It can be seen that there was considerable variation between the energy used in the laboratory and the home. In terms of the percentage differences between what was claimed by the manufacturers and what was measured in the home; 60.6% of appliances used more energy in the home than they did in the laboratory.

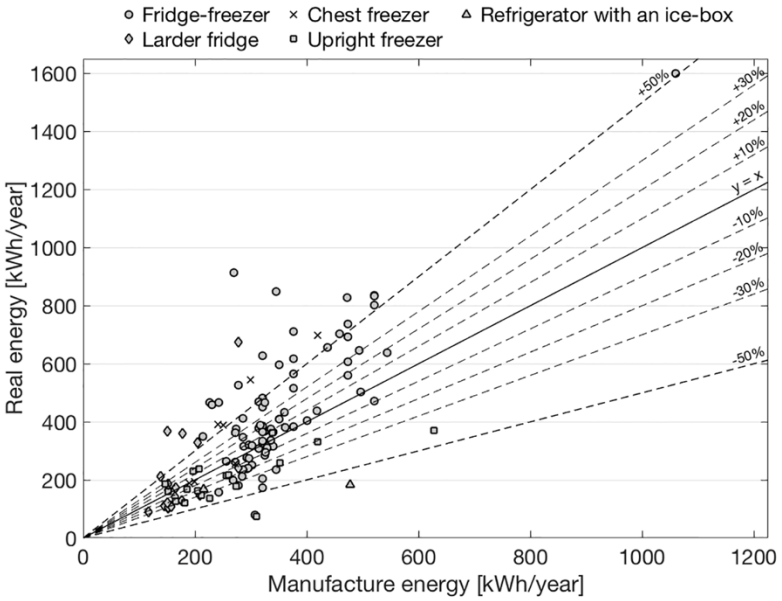

Figure 1: Energy claimed by manufacturers versus energy used in the home (non-normalised data)

If differences between energy measured in the home and in the laboratory occur this would be less significant if the rank order of energy consumed did not change. The consumer would then only be misled on the actual energy the appliance used but the best appliance in the laboratory would also be the best performing appliance in the home. Figure 2 shows the rank order for each appliance type in the laboratory and in the home. It can be seen that considerable differences occurred between the rank order in each situation.

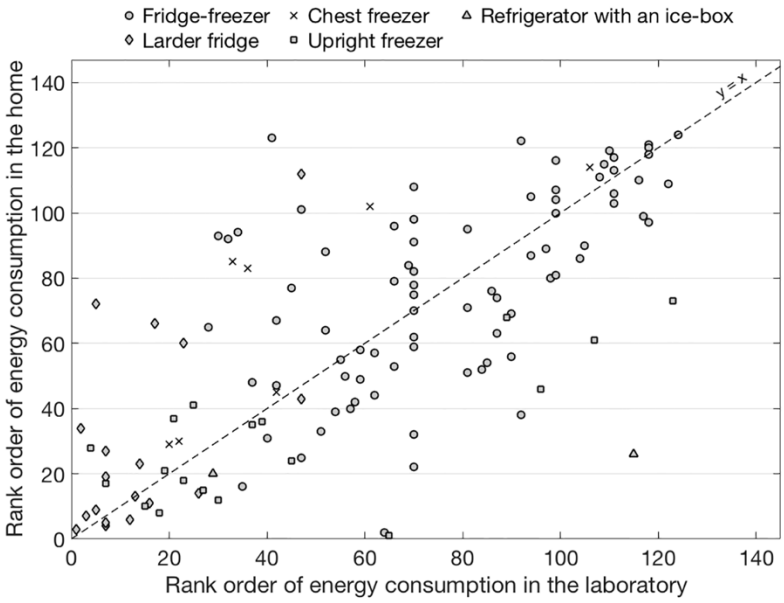

Figure 2: Rank order of energy used by appliances in the laboratory and the home (non-normalised)

3.2 Energy used in the home versus energy used in the laboratory after normalisation

When the energy measured in the home was normalised to the same internal and ambient temperatures as in the laboratory this had a significant effect on results with the main effect being to increase energy consumed in the home. This was primarily due to the ambient temperatures in the survey being in most cases less than the temperature in the laboratory test (25°C). The mean ambient temperature in the survey for the appliances analysed was 18.9 ± 2.6°C (Biglia et al, 2018). Some differences in energy use after normalisation were also due to internal appliance temperatures. However, these had less impact as before normalisation mean refrigerator temperatures were 4.6 ± 2.3°C and mean freezer temperatures were -20.4 ± 4.4°C (Biglia et al, 2018).

Figure 3 shows the comparison between energy used in the laboratory versus that measured in the home after the data was normalised for temperature differences. Overall 85% of appliances used more energy in the home than in the laboratory.

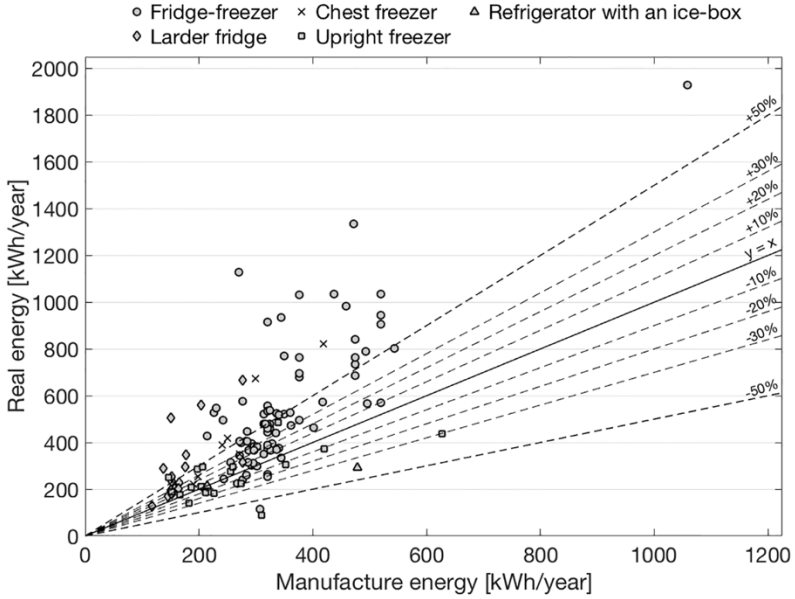

Figure 3: After normalisation for temperature: energy claimed by manufacturers versus energy used in the home

The impact of the normalisation on rank order of the energy used by the appliances is shown in Figure 4. Normalisation marginally improved the correlation between rank order in the laboratory with rank order in the home.

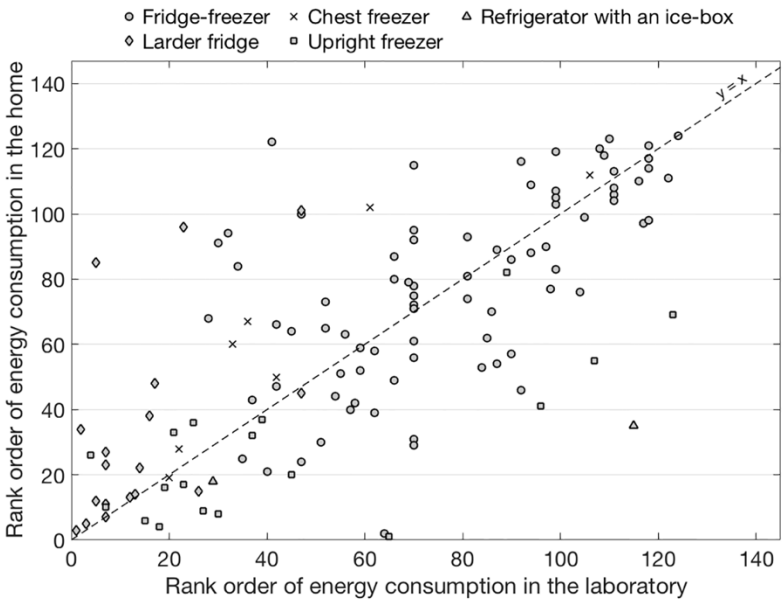

Figure 4: Rank order of energy used by appliances in the laboratory and the home (normalised)

3.3 Energy used by similar appliance models

Within the survey population there were a limited number of replicate appliance models. The normalised energy consumed by these appliances was compared to assess the impact of the same appliance operating in different households. Figure 5 shows the results from 40 appliances divided across 9 appliance models. In almost all cases the appliances used more energy in the home than had been measured in the laboratory. The results indicate that on occasions the energy used by an appliance in different homes was quite similar. Conversely differences in the energy consumed by the same appliance model could also vary widely, by often as much at ±100%. This indicates that usage in the home has a significant impact on energy consumption.

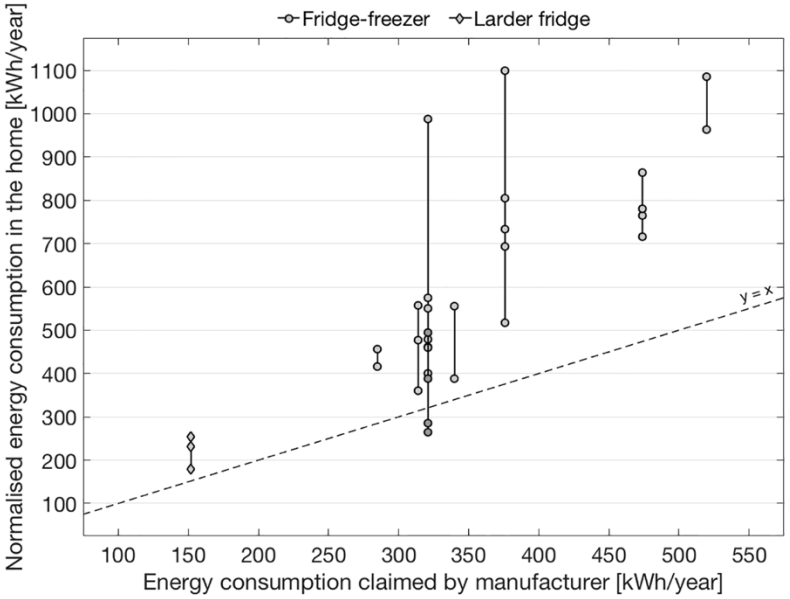

Figure 5: Energy used by the same appliance model in different households

4 DISCUSSION AND CONCLUSIONS

Reducing energy consumption is a major policy driver for many governments. To be able to accurately identify the best performing domestic refrigerated appliances is an important aspect of developing policy and encouraging consumers to purchase the most efficient appliances. This work indicates that although there has been an increased uptake of 'A' rated and better appliances since 2000 this may not necessarily be reducing energy consumption as much as policy makers anticipate.

It is not surprising that the energy consumed by domestic appliances can vary. However, it seems reasonable to expect that any laboratory test should provide a reasonable average indicator of energy used in the home. This was shown not to be the case as on average energy used in the home was on average 19% higher in the home than the laboratory.

The difference between laboratory and home energy consumption would be less of an issue if the rank order of the energy used by appliances was similar in both environments. Although consumers would not have an accurate indication on how much energy an appliance uses they would be able to identify the lowest energy consuming option. An analysis of the rank order of appliances in laboratory and home use demonstrated that the rank order was extremely variable.

Even when the same appliance model was compared across several households there were often differences in energy use of over 100%. This would indicate that although the laboratory test tends to under estimate the energy consumed in the home that it would be challenging to develop a comprehensive laboratory test that reflected the range in real life usage accurately. Further work is required to better understand how consumer usage of appliances affects energy use. This could lead to more realistic laboratory tests that provide more accurate information on performance of appliances to householders. This should ideally provide a means to ensure that appliances identified as being energy efficient in the laboratory are also efficient when used in the home. It is suggested that such a test for energy consumption should include some form of usage such as door openings or food temperature reduction that better mimics the way consumers use refrigerated appliances in the home.

ACKNOWLEDGEMENTS

The authors would like to acknowledge the funding from the UK Department of Energy and Climate Change (now Department for Business, Energy & Industrial Strategy) for the work reported in this publication.

REFERENCES

Bansal PK. Developing new test procedures for domestic refrigerators: harmonisation issues and future R&D needs—a review. Int J Refrig 2003;26: 735-48. https://doi.org/10.1016/S0140-7007(03)00045-8.

Barthel C, Götz T. The overall worldwide saving potential from domestic refrigerators and freezers. bigEE, Germany, Wuppertal Institute for Climate, Environment and Energy. 2012.

Biglia A, Gemmell AJ, Foster HJ, Evans JA. Temperature and energy performance of domestic cold appliances in households in England. Int J Ref 2018;87:172-84. https://doi.org/10.1016/j.ijrefrig.2017.10.022.

Gemmell AJ, Foster HJ, Busola S, Evans JA. Study of Over-Consuming Household Cold Appliances. Field trial report. BRE, 2017.

International Institute of Refrigeration (IIR). The Role of Refrigeration in the Global Economy. France. 2015.

Meier A. Refrigerator energy use in the laboratory and in the field. Energy Buildings 1995;22:233-43. https://doi.org/10.1016/0378-7788(95)00925-N.

MTP. BNC11: Domestic refrigerator test standard vs real-use energy consumption. 2007. http://www.mtprog.com/ApprovedBriefingNotes/PDF/MTP_BNC11_2007May2.pdf

Sidler O, Waide P, Lebot B. An experimental investigation of cooking, refrigeration and drying end uses in 100 households. 1998.

Waide P. Overview and Update of the ERP Directive, Energy Labelling Directive and Eco-label in the European Union. Guilin, China, Asia Energy Efficiency Standards and Labelling Forum and 2011 2nd BRESL. 2011.

Manuscript ID: 280
DOI: 10.18462/iir.icr.2019.0280

The impact of retrofitting doors on performance of a retail display cabinet

Tim BROWN, Alan FOSTER and Judith EVANS

London South Bank University, Churchill Building, North Somerset, Langford, BS40 5DU, UK

tim.brown@lsbu.ac.uk.

ABSTRACT

Open fronted retail display cabinets for chilled food are prone to infiltration of warm and moist ambient air. This increases the heat loads on the cabinets, reducing energy efficiency and ability to maintain temperature control. Air curtains are employed to form a barrier to infiltration but are typically limited in their effectiveness. Adding doors can curtail a considerable proportion of the infiltration depending on door opening frequency.

This paper describes ISO23953 test room measurement of the impact of retrofitting doors to a typical open fronted display cabinet. The open fronted cabinet was found to maintain test pack temperatures between 7.4 and -1.0°C (M2 classification with rounding applied) and consume 46.9 kWh/m^2. Fitting doors to the same cabinet reduced the temperature span to between 3.6 and -1.0°C (M0 classification) and energy consumption to only 51.5% of that used by the open cabinet. Further adjustments were made to raise the maximum pack temperature to a value similar to the open cabinet and the resultant temperature span was between 7.2 and 3.4°C (M2 classification with rounding applied) and energy consumption only 39.4% of that used by the open cabinet.

Key words: Retail display, temperature control, energy consumption, doors, retrofitting

1 INTRODUCTION

Supermarket energy consumption is widely reported as being comparatively high, with typical energy intensities being almost double those of other buildings (Mukhopadhyay and Haberl, 2014). Published energy consumption indices for supermarkets vary depending on factors such as location and store size. Foster et al (2018) reported a mean specific energy consumption (SEC) of 566 kWh.m^2.year^{-1} based on electrical energy consumption and sales floor area, for one UK retailer. This rose to 759 kWh.m^2.year^{-1} when gas was included. From other studies (van der Sluis et al., 2015, Tassou et al., 2011) the SEC varied from 407 to 1700 kWh.m^2.year^{-1} based on electrical energy consumption.

The vector for most of this energy is electricity, and consequently supermarkets are the most electricity-intensive type of commercial building. Energy efficiency is therefore increasingly of concern to supermarket owners and facility managers (Lindberg 2014).

A large proportion of the energy is used for storage and display of refrigerated food, for which refrigeration typically accounts for between 40 and 60% of the total electricity used in supermarkets (e.g. Axell and Lindberg, 2005 and Evans, 2014), with the remainder being split between Heating Ventilation and Air Conditioning (HVAC), food preparation and lighting. As the different systems interact with each other, it is not always easy to calculate and separate the impact of individual factors. Nevertheless, measures which reduce the energy used by the refrigeration system are likely to have the greatest impact on total supermarket energy consumption.

Prepared food and groceries such as meat, dairy, fruit and vegetables make up a large part of the sales of refrigerated food in supermarkets. Such products must be stored and displayed at chilled temperatures as they are perishable and sensitive to temperature abuse. The refrigerated cabinets used for display are often open-fronted, with no physical barrier between the customer and the food. While perceived to be good for customer accessibility and hence sales, open-fronted cabinets allow a large proportion of the refrigerated air to continually spill out and be exchanged with warm store ambient air (Foster and Quarini, 2001). This imposes high heat loads on the supermarket refrigeration systems, increasing their energy consumption.

The exchange of air also has other detrimental effects. Spillage of cold air into the supermarket aisles reduces ambient temperatures in the aisles and can affect customer behaviour, tending to reduce the time they spend in the relatively cold aisles. To counteract this, additional heating is often required, resulting in further increases in energy consumption of the store. Warm moist air entering the cabinets not only imposes heat loads, but also increases the need for defrosting. Temperature control in the cabinets is more difficult, and large temperature differences between different positions in the cabinets are common, as are differences over time resulting from the impact of defrosts. The temperatures of food on display are consequently unstable and often warmer than they should be. In the extreme, food quality and safety can suffer.

Open-fronted cabinets rely on fan-driven air curtains to form a barrier to the exchange of air but not to customers, but they vary in their effectiveness and typically still allow considerable infiltration. A far more effective means of reducing air exchange is to close the front of the cabinets using doors. With adequate seals and correct fitting, doors can eliminate exchange completely, but of course only while they are closed. During loading periods and access by customers, the doors will be opened with varying frequency and for varying durations. The type of doors (sliding versus hinged) also affect air exchange and effectiveness (Orlandi, 2013).

This paper reports the results of ‘before and after’ testing of an open fronted cabinet to which doors were retrofitted by the manufacturer.

2 METHOD

A production model of an open fronted 2.5 m long chilled retail display cabinet was obtained from its manufacturer. It was installed in an ISO 23953:2015 test room and connected to a remote refrigeration plant running on R448A refrigerant. It was then loaded and tested at Climate Class 3 (25°C and 60% RH) according to the ISO 23953:2015 test standard (see Figure 1). The cabinet was tested such that it did not control on set point from a temperature controller, but instead the cabinet received refrigerant all the time and temperature was controlled by setting an appropriate evaporating temperature of refrigerant. As the cabinet was not off-cycling due to thermostatic control, the defrost (off cycle) was set to every hour to avoid icing of the evaporator.

The evaporating temperature was set to achieve the M2 temperature classification. It was not possible to achieve a lower temperature classification, e.g. M1, due to the wide temperature range of test packs in the cabinet during the test.



Figure 1. Open fronted cabinet

On completion of the open fronted testing, the manufacturer installed double skinned plastic doors which are typical of the manufacturer's current type of retrofitted doors being installed in supermarkets (see Figure 2). A door opening mechanism was attached to the cabinet in the test room. Prior to the start of the 12 hour period of door opening, each of the four doors was opened once consecutively for 3 min. During the 12 hour door opening period, each of the four doors was opened consecutively at 6 minute intervals for 15 seconds.

Initial results with doors identified that the defrost termination temperature for the open cabinet was excessive once doors had been fitted. Being an off-cycle defrost it was found that termination did not occur based on temperature once the doors had been fitted, which meant that the defrost terminated instead on the maximum defrost time setting. This was therefore reduced from 45 minutes to 14 minutes to match the off-cycle duration observed during the open fronted cabinet defrosts.



Figure 2. Cabinet with retrofitted doors

A first test of the doored cabinet found that the coldest packs reduced to less than -1.0ºC. As this was outside of the M2 classification and below the freezing temperature of the packs, the evaporating temperature was increased by 0.4ºC such that the coldest packs were at the same temperature for both open and closed door tests. As the maximum pack temperature had reduced considerably there was scope to achieve further energy savings, by increasing the evaporating temperature further. A second test was therefore conducted with adjustment of the evaporator saturation temperature to raise the maximum pack temperature to a value similar to that achieved in the open tests, with the aim of maximising the energy savings.

A summary of the settings for the tests is shown below in Table 1.

Test	Set point	Defrost interval	Maximum defrost time	Mean value of the saturated evaporator temperature during Φ_{run} (θ_{mrun})		
	°C	h	mins	Dew (°C)	Bubble (°C)	Average (°C)
Open	0.8	1	45	-0.6	-6.5	-3.5
Open	0.8	1	45	-1.0	-6.9	-3.9
Doored	0.7	1	14	-0.6	-6.5	-3.5
Doored	0.7	1	14	3.4	-2.4	0.5

Table 1. Control settings used in the tests

3 RESULTS

3.1 Temperature performance

The maximum and minimum temperatures achieved during the tests are shown in Table 2 below.

Test	M-pack temperature		Classification
	Max (°C)	Min (°C)	
Open	7.49	-0.7	M2 *
Open	7.4	-1.0	M2 *
Doored	3.6	-1.0	M0
Doored	7.15	3.39	M2 *
			* with rounding

Table 2. Temperatures during the tests

The open fronted cabinet narrowly achieved the temperature classification M2 with rounding to the nearest integer (highest pack 7°C and lowest -1°C), as shown in Figure 3. With doors the cabinet was able to achieve an M0 classification (highest pack 4°C and lowest -1°C) as shown in Figure 4. When the maximum temperature was raised back up to that measured in the open cabinet to allow further energy savings, the cabinet achieved M2 classification with a far smaller temperature span between maximum and minimum temperature (see Figure 5).

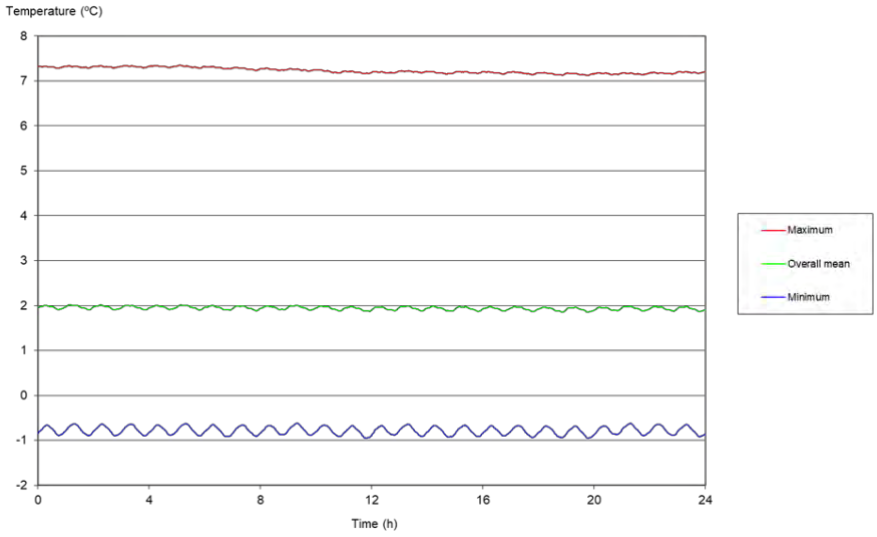

Figure 3. Temperatures achieved during open fronted operation

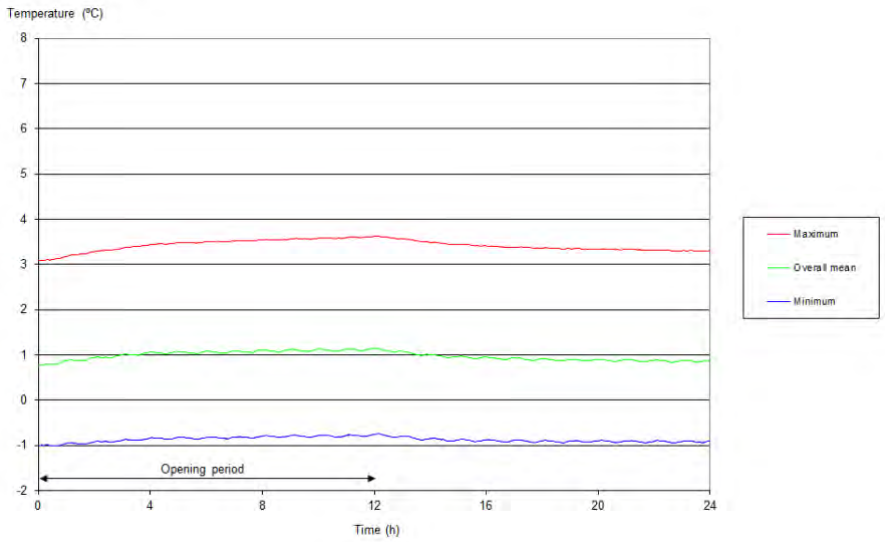

Figure 4. Temperatures achieved with doors added

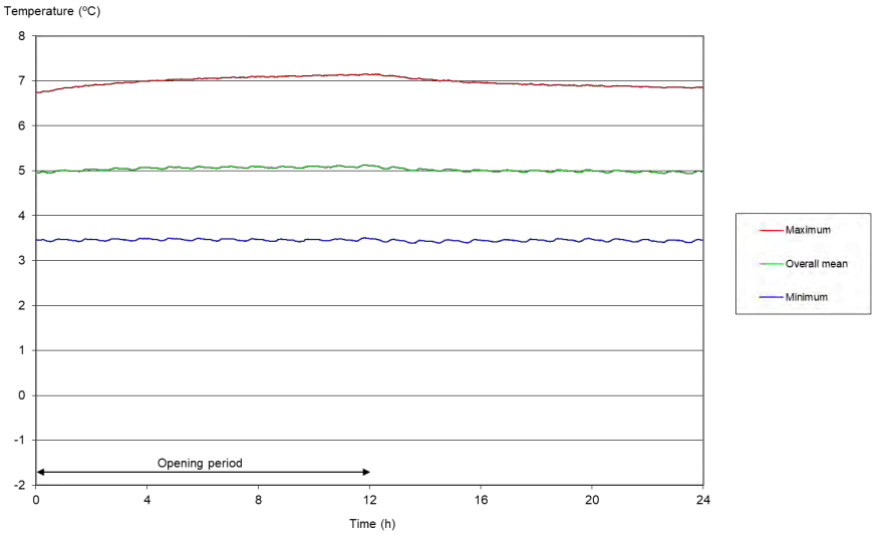

Figure 5. Temperatures achieved with doors after adjustment of maximum temperature

3.2 Energy consumption

The energy consumed by the remote refrigeration system and the cabinet during the tests is shown in Table 3 below.

Test	Refrigeration electrical energy consumption (REC)	Direct electrical energy consumption (DEC)	Total energy consumption (TEC)	Total Display Area (TDA)	TEC/TDA	Percentage relative to highest open energy consumption
	kWh/24h	kWh/24h	kWh/24h	m^2	kWh/24h/m^2	%
Open	44.59	2.18	46.78	4.39	10.66	99.7
Open	44.75	2.17	46.92	4.39	10.69	100.0
Doored	22.25	2.17	24.42	4.43	5.51	51.5
Doored	16.47	2.20	18.67	4.43	4.22	39.4

Table 3. Energy consumption during the tests

Fitting doors reduced the daily energy consumption to 51.5% of the open cabinet consumption while achieving the same minimum pack temperature (-1.0°C) and a greatly reduced maximum temperature. When the maximum temperature was then raised to be close to that of the open cabinet (7.2°C) the daily energy consumption reduced further to 39.4% of the open consumption.

3.3 Comparison with other test laboratory studies

For cabinets with well-fitted effective doors, the extent to which infiltration is reduced will depend mainly on the door opening frequency and duration. The door opening regime used in the testing was that defined in the EN23953:2015 test standard for the purposes of evaluating cabinet performance, but this can differ markedly from real-life opening patterns. For the purposes of a more direct comparison with the current results, the following test laboratory studies are therefore more appropriate than results based on in-store trials.

Faramarzi et al, 2002 reported that in laboratory tests, retrofitted glass doors reduced the total cooling load of a display case by 68%, and reduced the refrigerant mass flow by 71% with consequent reduction of compressor power demand by 87%. These tests were however done under slightly different conditions – the standard followed was ANSI/ASHRAE 72-183 with a slightly different climate class (75°F and 55%RH) and a door opening regime of each door opening every 12 minutes for 16 seconds during the whole 24 hour test period. For the door tests, an additional fan was placed such that air was blown into the open doorways to simulate shopper traffic – this would of course reduce the impact of the doors.

Lindberg et al, 2010 compared the performance of cabinets with and without doors in a test laboratory. An open fronted cabinet was initially tested according to the then current ISO standard test method for measurement of performance (EN ISO 23953:2005) in a test room operating at 22°C and 65% RH (Climate Class 2). The cabinet was refrigerated using an indirect propylene glycol system and was operated with night blinds down during a 12 hour night period. Hinged glass doors were then fitted and the cabinet was re-tested under 2 door opening regimes (the standard 10 or increased shopper simulation of 30 openings per hour of 6 seconds duration for 12 hours). Both the standard and increased opening frequency differ from that in ISO 23953: 2015 as used in the current tests. When tested with doors, additional lighting was added to the cabinet (3x 28W). To maintain the same temperature classification for the cabinet it was possible to increase the inlet heat exchanger temperature by 10 K when doors were fitted. Adding the doors reduced heat extraction by between 61 and 66% during the day and by between 46 and 53% at night.

In another laboratory study, Atilio de Frias et al, 2015 reported comparison of a cabinet holding packaged baby spinach, first open and then closed with retrofitted doors. Ambient conditions were 21°C +/-3°C and 60–70% relative humidity. Closed cabinet product temperatures were greater than 5°C for only 1% of the four-day test period, compared with 24% for the open cabinet. The range between maximum and minimum temperatures was also reduced by up to 6 K, and at the same time daily energy consumption was 69% lower. Interestingly it was reported that energy consumption was the same for the doored cabinet when the doors were kept closed as it was when they were opened according to ASHRAE standard 72-2014, with each door being opened sequentially and fully opened 6 times per hour for 6 s for a period of 8 h.

4 DISCUSSION AND CONCLUSIONS

The reported series of tests confirmed the findings of previous studies that adding doors to open fronted retail display cabinets is an effective way to improve temperature control and at the same time reduce energy consumption. Doors can be added at the production stage or retrofitted in most existing retail installations which currently have open cabinets. The findings help to reinforce initiatives adopted by some but not all retail operators.

The temperature results suggest that in practice there may be different operating strategies when retrofitting doors. Lower and more uniform temperatures can be achieved to improve food safety and quality retention and possibly lead to less food waste, at the same time as reasonable

reductions in energy consumption. Alternatively, similar (but more uniform) maximum temperatures can be achieved with even greater reductions in energy consumption.

The average evaporator temperature increased to above 0ºC in the doored test at the higher temperature. This provides an opportunity to run the cabinet without the need for defrosts. In this test the refrigerant had 5.9ºC glide, therefore, even though the average temperature was 0.5ºC, the entrance to the evaporator would have been at -2.4ºC (bubble point). If a refrigerant without glide was used, it may have been possible to run the cabinet without the need for defrosts.

5 ACKNOWLEDGEMENTS

This work was carried out as part of the EPSRC i-STUTE EUED energy centre and End Use Energy Demand Centres Collaborative Projects (EP/P006779/1).

6 REFERENCES

Axell, M. and U. Lindberg (2005) Field Measurements in supermarkets, IIF/IIR, Italy.

de Frias J.A., Luo Y., Kou L., Zhou B. and Wang Q. (2015). Improving spinach quality and reducing energy costs by retrofitting retail open refrigerated cases with doors, Postharvest Biology and Technology 110, 114–120.

Energimyndigheten (2010) Energianvändning i handelslokaler Förbättrad statistik för lokaler, *STIL2*. 2010.

ENOVA (2015) Enovas Byggstatistik, 48pages.

Evans J.A. (2014) Are doors on fridges the best environmental solution for the retail sector? Proc. Inst. R. 2014-15, 5-1.

Faramarzi, R.T., Coburn, B.A. and Sarhadian, R. (2002) Performance and energy impact of installing glass doors on an open vertical deli/dairy display case. ASHRAE Trans.108 (Part 1), 673–679.

Foster, A., Evans, J., Maidment, G. Benchmarking of supermarket energy consumption. 5th IIR Conference on Sustainability and the Cold Chain, Beijing, China, 2018.

Foster A.M. and Quarini, G.L. (2001) Using advanced modelling techniques to reduce the cold spillage from retail display cabinets into supermarket stores to maintain customer comfort. Proceedings of the Institution of Mechanical Engineers, Part E: Journal of Process Mechanical Engineering, 215(1): p. 29-38

ISO 23953-2:2015(E) Refrigerated display cabinets - Part 2: Classification, requirements and test conditions.

Lindberg U., Axell M. and Fahlén P. (2010) Vertical display cabinets with doors - Influence of the door-opening frequency on storage temperature and cooling demand. Sustainable Refrigeration and Heat Pump Technology Conference. Stockholm, Sweden.

Mukhopadhyay J. and Haberl J.P.P.E. (2014) Reducing Energy Consumption in Grocery Stores: Evaluation of Energy Efficiency Measures. ASHRAE Transactions. 120: p. 416-436.

Orlandi M., Visconi F.M. and Zampini S. (2013). CFD assisted design of closed display cabinets. 2nd IIR International Conference on the Cold Chain and Sustainability Paris.

Tassou S.A., Ge Y., Hadawey A. and Marriott D. (2011) Energy consumption and conservation in food retailing, Applied Thermal Engineering, 31(2-3): p. 147-156.

van der Sluis, S.M., Lindberg U.L. and Lane A.-L., J. Arias (2015) Performance indicators for energy efficient supermarket buildings, in Proceedings of ICR 2015, August 16 - 22 - Yokohama, Japan12th IEA Heat Pump Conference, Rotterdam, p. 9.

Manuscript ID: 285
DOI: 10.18462/iir.icr.2019.0285

Defrosting performance and control strategy with hot gas bypass for a medical refrigerator

Lifen YUAN, Suxin QIAN*, Jianlin YU, Gang YAN

Department of Refrigeration and Cryogenic Engineering, School of Energy and Power Engineering, Xi'an Jiaotong University
Xi'an, 710049, China, qiansuxin@xjtu.edu.cn

ABSTRACT

Frosting is a common phenomenon in refrigeration and frozen equipment, which degrades heat transfer performance and leads to more energy consumption. This paper investigates the application of hot gas bypass defrosting as an alternative to the electric heater defrosting method. The hot gas from the discharge port enters the evaporator to melt the frost layer on the surface of the evaporator. Experimental data indicate that more than 80% defrosting efficiency can be achieved. The defrosting efficiency increases with thicker frost layer and larger bypassed flow rate. In the end, a defrosting control strategy dedicated to medical refrigerator application is proposed.
Keywords: Medical Refrigerator, Hot Gas Bypass, Defrost, Defrost Efficiency.

1. INTRODUCTION

Frosts are inevitable in any vapor compression system with evaporating temperature less than the freezing point of water. Many studies have shown that the heat transfer performance of the evaporator degrades with frost accumulation (Seker et al., 2004). Therefore, it is essential to equip defrosting devices. According to the latest Good Supply Practice (GSP) regulation in China, refrigerating temperature should be maintained between 2~10°C, and the relative humidity should be maintained between 35~75%. These simultaneous requirements for temperature and humidity control brings more challenges for the defrosting device of such a medical refrigerator. To date, most of the frost-free refrigerators use either internal air circulation defrosting or electrical resistance heater defrosting. Among them, most of the heat from electrical resistance heater is absorbed by metals of the evaporator and air, and only a minor portion is utilized to melt frost (Knabben et al., 2010). In fact, only 30.3% of heat is effectively absorbed by the frost, while the energy consumption of the refrigerator increases by 17.7% to compensate for the dissipated heat (Bansal et al., 2010). Another study was carried out for a frost-free refrigerator with aluminium distributed heater, and a similar 32% defrosting efficiency was achieved (Özkan et al., 2012). Therefore, increasing the defrosting efficiency of electric heater is a key topic in domestic refrigeration sector. By depositing the frost layer more uniformly, the defrosting efficiency was improved by 29.8% (Li et al., 2017). Electric heater imposed by pulse current offers another way to improve the efficiency by 15% (Yoon et al., 2018).

To maintain the temperature and humidity requirements according to GSP regulations, high efficiency defrosting is necessary to reduce the defrosting duration and reduce the associated temperature rise. In this paper, the applicability of the hot gas bypass defrosting method is investigated for a medical refrigerator. The defrosting efficiency benefit is revealed, while the impacts of frost layer thickness and bypass flow rate are discussed, before concluding with a proposed control strategy for engineering application.

2. EXPERIMENTAL SETUP

2.1. Principle

The schematic of the refrigeration system used in a medical refrigerator with hot gas bypass defrosting loop is plotted in Fig. 1. The refrigerated volume is 360 liters. The ball valve is used to

switch open or close of the hot gas bypass loop. The micro-metering valve (needle valve) adjusts the bypassing flow rate, while the check valve prevents backflow of liquid refrigerant during the normal operation process. When the system shifts to defrosting mode, the ball valve is switched to open, while the evaporator fan is switched off. Meanwhile, most of the hot refrigerant from the discharge port of compressor enters the evaporator and melts the frost layer through the bypassing loop. When the defrosting process terminates, the system shifts back into normal refrigeration mode. T-type thermocouples are used to measure the wall temperatures with uncertainties of ±0.5°C. Pressures are monitored by pressure transducers. The temperature and relative humidity of the refrigerated cabinet are monitored by three temperature and humidity data loggers (model: RCW-800WIFI), which are located at the top, middle and bottom inside the cabinet, according to the national industrial standard YY/T0086-2007. Averaged temperature and relative humidity are used. Uncertainties are ±0.5°C and ±5%RH for temperature and relative humidity, respectively.

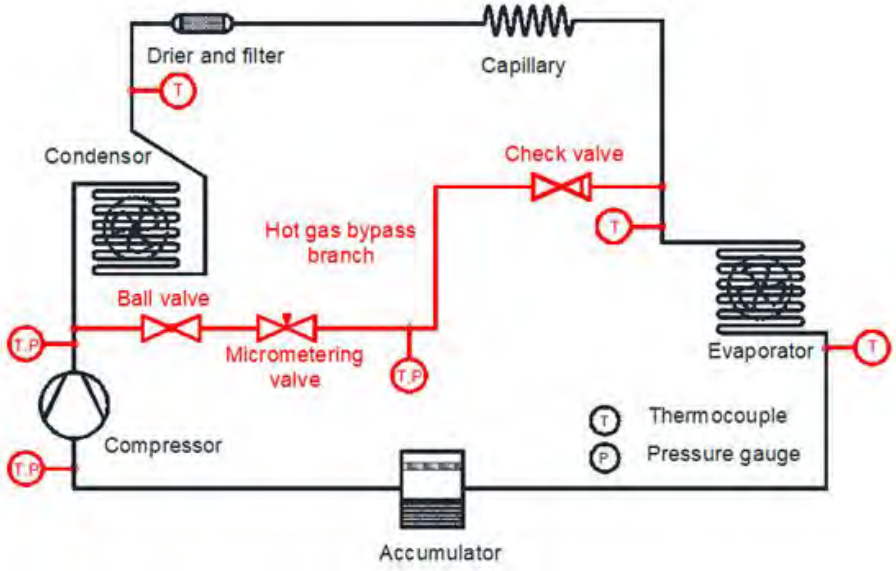

Figure 1: Schematic of the hot gas bypass defrosting system

2.2. Frosting and Defrosting

The tests are carried out in an environmental chamber dedicated for assessments of refrigerator and freezer. The specifications of temperature and humidity of the chamber follow the national standard GB/T 8095. These test conditions and other important parameters used for the defrost tests are listed in Table 1. To expedite the frosting process, the chamber is operated under 25°C and 90% relative humidity condition. During the simulated frosting process, the refrigerator door is opened for 30 seconds in every 10 minutes. All the tests are conducted when the system reaches a cyclic steady state condition, i.e. temperature and humidity of the storage cabinet are steady. The bypass loop is switched open during the compressor "on" period to start the defrosting test. The defrosting test is continued until no liquid droplet can be observed from the draining pipe. The melted frost mass is evaluated by measuring the mass difference of the draining receiver before and after the defrosting process. It should be noted that the moisture entering the cabinet could condense onto the draining pan rather than frost on evaporator surface during opening the refrigerator door. Therefore, this part of condensate on the draining pan is measured before defrosting and is subtracted from the measured melted water after defrosting.

Table 1. Relevant testing conditions and parameters

Experimental condition	Parameters
Dry Bulb temperature (°C)	25±0.2
Wet Bulb temperature (°C)	23.7±0.2
Voltage (V)	220
Frequency (Hz)	50
Storage temperature (°C)	4~6
Storage relative humidity (%)	45~65
Compressor control mode	ON/OFF
Refrigerant	R290

Evaporation temperature (°C)	-12
Frequency of open the door (seconds per 10 min)	30

2.3. Data Reduction

In this study, the defrosting efficiency is used to evaluate the hot gas bypass defrosting method. The defrosting efficiency is shown in Eq. (1), which is defined as the ratio between the heat absorbed by the frost and the heat released from the compressor. The heat absorbed by the frost is given by Eq. (2), which consists of melting latent heat and sensible heat of frost. The heat released from the compressor is estimated based on the accumulated input power, as shown in Eq. (3), neglecting the heat loss to the ambient.

$$\eta = {Q_{melt}}/{Q_{com}} \quad \text{Eq. (1)}$$

$$Q_{melt} = h_{sl} m_{melt} + c_{p,f} m_{melt} (T_{melt} - T_{eva}) \quad \text{Eq. (2)}$$

$$Q_{com} = \int \dot{W}_{com} dt \quad \text{Eq. (3)}$$

In the above equations, the melting latent heat is assumed to be 3.35×10^5 J·kg^{-1}. The specific heat of frost is 2.1×10^3 J·kg^{-1}·K^{-1}. T_{melt} is the melting point of 0°C. T_{eva} is the wall temperature of the evaporator when the defrosting process starts. The defrosting efficiency has a measurement error based on the error propagation procedure specified in Eq. (4).

$$\Delta\eta = \sqrt{\left(\frac{\partial \eta}{\partial m_{mlet}}\left(U_{m_{melt}} + \sigma_{m_{melt}}\right)\right)^2 + \left(\frac{\partial \eta}{\partial T_w} U_{T_{eva}}\right)^2 + \left(\frac{\partial \eta}{\partial W_{com}}\left(U_{W_{com}} + \sigma_{W_{com}}\right)\right)^2} \quad \text{Eq. (4)}$$

In Eq. (4), the parameter U stands for the instrument uncertainty, in which U_{melt} and U_{Tw} are ±2 g and ±0.5°C, respectively. The compressor power is measured by the built-in voltage and current sensor of the chamber, which has a 1% full-scale uncertainty. Since the compressor power is a transient signal, the time variation standard deviation σ_{Wcom} is also included. Each test is repeated two times, and the average melted mass is used. The standard deviation of repeatability is considered by the σ_{melt} term in Eq. (4).

3. RESULTS

3.1. Transient Characteristics

After 16 hours of regularly opening the refrigerator door for 30 seconds in every 10 minutes, the frost layer on the evaporator surface is fully developed. The defrosting process starts at 5.5 minutes in Fig. 2, and the temperature variations of the evaporator are plotted. Before the defrosting process, due to severe frosting, the evaporating temperature reaches -25°C, which is 13°C lower than the evaporating temperature of the normal no-frost condition, to maintain a 4~6°C cabinet temperature. When the bypassing loop is switched open, the evaporator's temperature increases rapidly to 5~6°C in 4 minutes, and maintains at 5~6°C for another 15 minutes. During this latent heat period, the frost layer absorbs heat and gradually melts. After the latent heat period, the evaporator's temperature reaches 15°C in 4 minutes. Meanwhile, no frost can be observed on the evaporator's surface. When the defrosting process ends, 1056 grams of melted water are collected. Note that 78 grams of condensate are collected before defrosting. Therefore, the 978 grams of melted water are used to calculate defrosting efficiency after excluding the condensate. The average compressor power is 332 W during the 22-minute period. Consequently, the defrosting efficiency is 86.7% in this case, according to Eqs. (1-3). This efficiency is much higher than the those reported using an electric heater, which are 30~45% (Bansal et al., 2010; Özkan et al., 2012). Therefore, it is beneficial to use the hot gas bypass to defrost in the medical refrigerator.

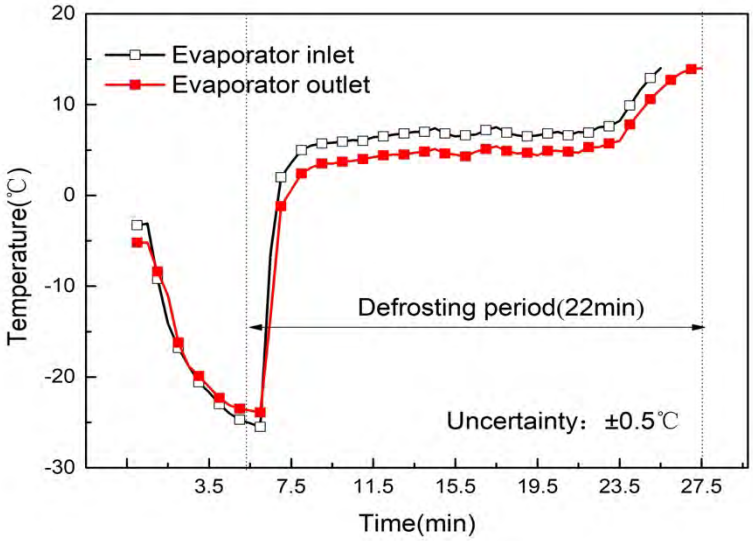

Figure 2: Temperature variation of the evaporator during defrosting

In addition, after the 16 hours to the fully develop the frost layer, the variations of temperature and relative humidity are plotted in Fig. 3. As the frost layer melts, both temperature and relative humidity inside the cabinet increases. The temperature reaches 10°C at the end of defrosting, while the relative humidity reaches 75%. These values do not violate the regulations of GSP. After the defrosting process, the system is back into normal cyclic operation. The cabinet temperature and relative humidity reach steady state in 15 minutes. On the contrary, the conventional defrosting using electric heater usually leads to excessive cabinet temperature and requires the system to precool the evaporator, which means more energy consumption and less efficient defrosting performance.

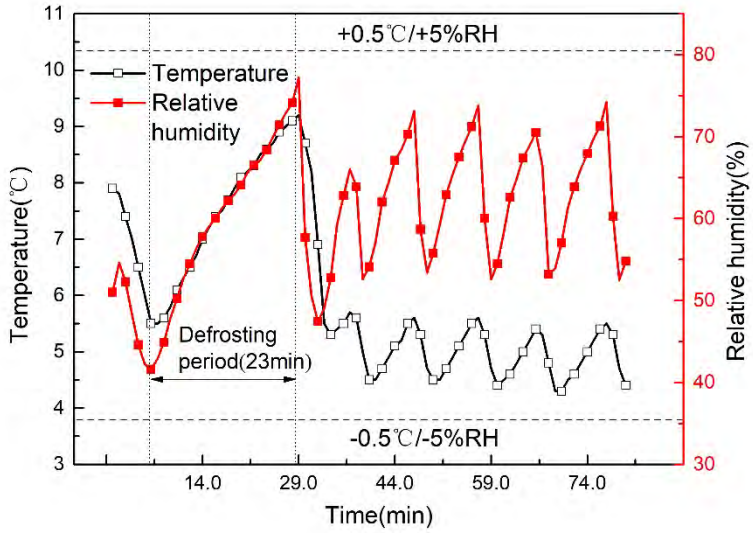

Figure 3: Temperature and relative humidity variations in the cabinet during defrosting process

3.2. Impacts of Frost Layer Thickness and Flow Rate

To best illustrate the optimum conditions of hot gas bypass defrosting, this study investigates the impacts of frost layer thickness and bypassing flow rate on the defrosting efficiency. By varying the frosting duration and layer thickness, Table 2 lists the measured defrosting duration, melted mass (excluding the condensate on the draining pan), defrosting efficiency and the average temperature of the evaporator ($T_{eva,d}$). The tests are repeated twice and their average is used. One observation is that the defrosting time (t_d) and melted mass increase almost linearly with frosting duration, while the defrosting efficiency decreases monotonically. The decreasing of efficiency is due to increased compressor power. Furthermore, some of the released heat from hot gas could dissipate to fins and air where there is a thinner frost. This means defrosting efficiency of the hot gas bypass method

favors thicker frost layer. However, during normal operation, thicker frost means lower evaporating temperature and worse heat transfer performance. Under severe conditions, we observed frosting on the suction line, which indicates liquid refrigerant is carried over from the accumulator since the evaporator becomes ultra-inefficient. Therefore, considering the normal operation and defrosting efficiency, when the accumulated door open time reaches 24~36 minutes, it is recommended to start the defrosting sequence, and defrosting should be terminated once the evaporator surface reaches 15°C.

Table 2. Variation of defrosting performance for different frosting duration and thickness

Frosting duration (hour)	16	12	8	4
Door open time (min)	48	36	24	12
t_d (min)	23	16	10	6
m_{melt} (kg)	1.003	0.701	0.412	0.242
Q_{melt} ($\times 10^5$J)	3.88	2.40	1.38	0.84
W_{com} (W)	332	332	356	361
η (%)	86.5 ± 5.0	75.3 ± 5.2	65.0 ± 5.6	64.9 ± 6.9
$T_{eva,d}$ (°C)	15.0 ± 0.5	11.4 ± 0.5	17.5 ± 0.5	16 ± 0.5

When the valve opening varies, the defrosting time, melted mass, defrosting efficiency and other parameters are listed in Table 3. Based on the pressure difference (ΔP_{valve}), the flow rate of hot gas reduces when the valve opening reduces. This leads to longer defrosting duration, if the frosting duration and frost thickness are maintained constant. Furthermore, the compressor power increases significantly when the valve opening reduces, due to the higher pressure ratio of the compressor is required to overcome the throttling of the needle valve. The discharge temperature increases when the valve opening reduces, however, the overall released heat from the hot gas reduces due to reduced flow rate. Based on the implemented needle valve and the tested range, larger valve opening is preferred for a better defrosting efficiency. Future studies will be carried out to investigate the optimum bypass flow rate.

Table 3. Variation of defrosting performance for different valve opening and flow rate

Frosting duration (hour)	8			4		
Opening of micro-metering valve (laps)	6	4	2	6	4	2
t_d [min]	10	10	14.5	6	7	7
m_{melt} [kg]	0.412	0.394	0.448	0.242	0.249	0.254
Q_{melt} [$\times 10^5$J]	1.38	1.39	1.50	0.84	0.87	0.89
W_{com} [W]	356	369	385	361	381	385
η [%]	65.0±5.6	62.6±3.7	44.8±.2.0	64.9±6.9	54.1±3.1	54.9±2.2
$T_{eva,d}$ [°C]	17.5±0.5	14.8±0.5	10.0±0.5	16±0.5	14.7±0.5	9.1±0.5
T_{dis} [°C]	24.4±0.5	25.8±0.5	31.1±0.5	24.6±0.5	29.3±0.5	31.3±0.5
ΔP_{valve} [kPa]	157±11	193±17	346±12	161±10	201±15	347±6

4. CONTROL STRATEGY

Based on the analysis in section 3, we propose to determine the start of the defrosting process based on the accumulated opening time of the refrigerator's door. The end of defrosting process is determined based on the evaporator's surface temperature. These prestored values are used as references, which can be adjusted based on ambient temperature and humidity. According to the proposed control process diagram in Fig. 4, the hot gas bypass defrosting starts when the accumulated door opening time t_0 is greater than the reference time $t_{0,r}$. The bypass loop is opened and the evaporator fan is turned off. If there is damper in the duct, it should be switched to close. The evaporator's surface temperature and defrosting time are monitored during the defrosting process. When the evaporator's surface temperature T_{eva} reaches the reference temperature $T_{eva,r}$, or if the defrosting duration exceeds reference time $t_{d,r}$, the defrosting process is terminated. The evaporator's fan and damper can hold for 30 seconds before entering normal operation as a precooling process. Details regarding the optimum delayed time will be studied in the future.

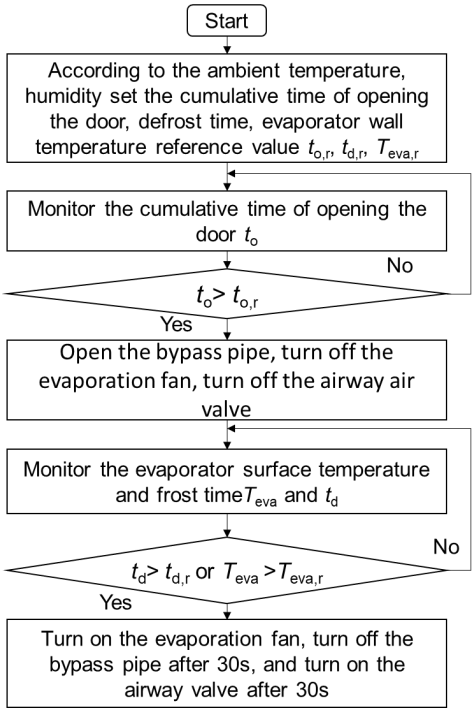

Figure 4: The diagram of the defrosting control strategy using hot gas bypass method

5. CONCLUSIONS

This study investigates the hot gas bypass defrosting method for a medical refrigerator. Hot gas bypass can reach defrosting efficiency over 80%, which doubles the efficiency of conventional electric heater defrosting method. In addition, experimental data indicate that defrosting efficiency favors longer frosting duration or thicker frost, but thicker frost layer leads to degradation of system performance. Furthermore, increasing the bypass flow rate improves the defrosting efficiency. Based on these observations, a defrosting control strategy is proposed for a medical refrigerator operated in humid and mild or tropical climate. The defrosting starts at an accumulated door opening time of 24~36 minutes, while the defrosting should be terminated when the evaporator's temperature reaches 15°C.

NOMENCLATURE

$c_{p,f}$	frost specific heat ($J \cdot kg^{-1} \cdot K^{-1}$)	T_{dis}	discharge temperature (°C)
$h_{s,l}$	melting latent heat of frost ($J \cdot kg^{-1}$)	T_{eva}	evaporator wall temperature (°C)
m_{melt}	melted mass (kg)	U	uncertainty
Q	heat (J)	$\dot{W}$	instant power (W)
t	time (sec)	Δp	pressure difference (kPa)
t_0	accumulated door opening time (sec)	η	efficiency
t_d	accumulated defrosting time (sec)	σ	standard deviation
Subscript			
r	reference	com	compressor

REFERENCES

Bansal, P., Fothergill, D., Fernandes, R., 2010. Thermal analysis of the defrost cycle in a domestic freezer. Int. J. Refrig. 33, 589–599. doi:https://doi.org/10.1016/j.ijrefrig.2009.11.012

Knabben, F., Hermes, C., Melo, C., 2010. Numerical assessment of frosting and defrosting of 'no-frost'' evaporators,' in: International Refrigeration and Air Conditioning Conference. p. 1014.

Li, Z., Zhao, D., Ding, G., Ren, T., Miao, S., Han, X., Noda, T., 2017. Improving defrosting performance by controlling frost distribution to match defrosting heat distribution in frost-free

household refrigerators. Int. J. Refrig. 77, 136–148. doi:https://doi.org/10.1016/j.ijrefrig.2017.03.003
Özkan, D., Özil, E., İnan, C., 2012. Experimental Investigation of the Defrosting Process on Domestic Refrigerator Finned Tube Evaporators. Heat Transf. Eng. 33, 548–557. doi:10.1080/01457632.2012.624867
Seker, D., Karatas, H., Egrican, P.D.N., 2004. Frost formation on fin- and- tube heat exchangers. Part II—Experimental investigation of frost formation on fin- and- tube heat exchangers. Int. J. Refrig. 27, 375–377. doi:https://doi.org/10.1016/j.ijrefrig.2003.12.004
Yoon, Y., Jeong, H., Lee, K.-S., 2018. Adaptive defrost methods for improving defrosting efficiency of household refrigerator. Energy Convers. Manag. 157, 511–516. doi:https://doi.org/10.1016/j.enconman.2017.12.039

Manuscript ID: 307
DOI: 10.18462/iir.icr.2019.0307

Modelling and development of high-pressure-lift ejector for low temperature evaporators in R744 refrigeration systems for supermarkets

Krzysztof BANASIAK[(a)], Ángel Á. PARDIÑAS[(b)], Ekaterini KRIEZI[(c)]

[(a)] SINTEF Energi AS, Kolbjørn Hejes vei 1B,
Trondheim, 7034, Norway, krzysztof.banasiak@sintef.no
[(b)] Department of Energy and Process Engineering, NTNU,
Trondheim, 7491, Norway, angel.a.pardinas@ntnu.no
[(c)] Danfoss A/S Nordborgvej 81,
Nordborg, 6430, Denmark, ekk@danfoss.com

ABSTRACT

Decreasing the complexity of R744 commercial refrigeration systems for supermarkets could substantially reduce their cost, promoting worldwide spreading.
Typically, the share of the low-temperature (LT) load in the total load for supermarkets is low. Nevertheless, significant investments must be made to cover this demand, including dedicated compressors, inverter, desuperheater, oil management equipment, etc.
The objective of this paper is to describe and numerically validate a new concept based on high-pressure-lift ejector to support LT evaporators. This solution reduces the cost of the system by replacing the whole LT compressor section with a fixed geometry ejector. In addition, elimination of the compressor(s) allows overfeeding operation of LT evaporators.
The paper explores application range of this concept, using a 0-dimensional model of the refrigeration system.
Keywords: Commercial refrigeration, R744, Ejector, Parallel compression

1. INTRODUCTION

As broadly concluded (e.g., Gullo et al., 2018), efficient R744 refrigeration systems are currently able to outperform HFC-based units for supermarkets across Europe, thanks to the implementation of different technologies improving energy performance, such as overfed evaporators, vapour ejectors for unloading the medium-temperature (MT) compressors or AC production (Pardiñas et al., 2018), as well as mechanical subcooling (Karampour and Sawalha, 2018), among others. Still, that continuous adoption of more and more sophisticated technical solutions for boosting of energy performance made the system layouts and control strategies more complex, elevating the investment costs for 'all-in-one' R744 solutions above the level of typical HFC units (Gullo et al., 2018). Therefore, researchers and manufacturers need to find the compromise between the system efficiency, complexity, and capital costs in order to maintain the increase in number of installed transcritical CO_2 refrigeration units that has been occurring during the current decade.
While a lot of research attention was dedicated to the system optimization for the MT load, AC load or Heat Reclaim (HR) (Pardiñas et al., 2018, Gullo et al., 2018), relatively moderate efforts were put into the investigation of upgrading of the low-temperature (LT) section, where improvement might mean both lower energy consumption or/and lower investment costs. Some researchers (Gullo et al., 2017) concluded that by applying flooded LT evaporators with elevated evaporation temperature (supported by internal heat exchanger and suction accumulator in the LT suction line for compressor protection) one can decrease the annual energy consumption even by ca. 25%, for the refrigeration capacity ratio (called also load factor and defined as ratio of MT refrigeration load to LT refrigeration load) equal to 4.8. Another study (Karampour and Sawalha, 2018) claimed to

have effectively elevated the LT evaporation temperature from -32 °C to -29 °C by using flooded mode, which resulted in less frosting in addition to energy savings. However, apart from this relatively obvious trend to eliminate superheating also in the LT cabinets, no direct use of more advanced techniques, like for example vapour ejectors for refrigerant circulation in the LT cabinets, has been reported so far for supermarkets.

The concept of ejector-supported freezers has been previously widely studied for domestic refrigerators, specifically for isobutane (Liu et al., 2010, Wang et al., 2014). Various layouts for two-evaporation-level systems for household refrigerator-freezers were evaluated, finding the improvement in COP compared to a baseline cycle (without ejector) up 10% (Jeon et al., 2018). Moreover, a modified dual-temperature CO_2 transcritical refrigeration cycle, in which two cascade ejectors were applied to enhance the performance of a refrigerator-freezer, eliminating the LT compressor entirely, was proposed (Bai et al., 2017). Compared to a basic dual-evaporator cycle without ejectors, the authors claimed to have obtained up to 25% improvement in energy and exergy efficiency, for evaporation temperatures typical for the supermarket applications and load factor equal to 1.

The potential for ejector implementation to invoking circulation in the LT cabinets in a transcritical R744 system will be always determined by load factor (Bai et al., 2017). This is particularly true for booster configuration for supermarkets, where the pressure difference applied in individual expansion devices in cabinets is in practice fixed, independently of the ambient conditions, fixing thus pressure lift of the LT ejector. Typical load factors for supermarkets of different size around Europe range between 2 and 8 (Gullo et al., 2017), for evaporating temperatures ranging from -10 °C to -2 °C for the MT section and from -35 °C to -25 °C for the LT section (Gullo et al., 2018). An interesting feature of the LT cabinets is that, due to the relatively low product temperature, they are usually equipped with doors, which results in an almost constant load profile throughout the year and the day. This, along with the substantially fluctuating MT or AC loads, entails typically fluctuating load factor conditions, which imposes more demanding off-design operational regime for a potential LT ejector.

On the other hand, refrigerant circulation in the LT section supported purely by ejectors (no LT compressors) enables elevation of the evaporation temperature and running in flooded mode, which reduces pressure lift of the LT ejector.

State-of-the-art "all CO_2" refrigeration systems encompass a separate group of dedicated LT compressors, at least one of them usually equipped with a variable speed drive (VSD) for managing the potential changes in load, oil-feeding systems, safety systems, etc. Replacement of all those components with a single ejector (or battery of several ejectors in parallel) supporting the LT cabinets could reduce the investment costs. Therefore, the objective of this paper is to describe and numerically validate a new concept based on high-pressure-lift ejector to support LT evaporators and reduce the complexity and cost of transcritical CO_2 refrigeration systems.

The paper explores application range of this concept, using a 0-dimensional model of the refrigeration system.

2. CONCEPTS INVESTIGATED

Several ejector-supported LT section concepts have been evaluated numerically to compare the energy performance of the pack. This section describes (i) the state-of-the-art booster unit supported by parallel compression, treated as a reference layout (Fig. 1, left side), (ii) an upgrade that allows overfed MT evaporators (Fig. 1, right side), and two novel configurations with the (iii) upstream-gas cooler split and (iv) downstream-gas cooler split LT ejector replacing the dedicated LT compressors (Fig. 2, left and right side, correspondingly).

Fig. 1 left illustrates the state-of-the-art booster unit supported by parallel compression. Two groups of compressors, MT and LT compressors, are devoted to keeping the evaporation temperature at the cooling and freezing cabinets or rooms, respectively. Both groups of evaporators are supplied by liquid refrigerant from the bottom of the liquid receiver, and it is usual that each evaporator has an individual expansion device that adjusts the flow of refrigerant depending on the demand. State-of-the-art systems try to regulate the flow so that there is a certain degree of superheat at the outlet of the evaporators and to guarantee that only vapour (superheated) reaches the suction of the compressors.

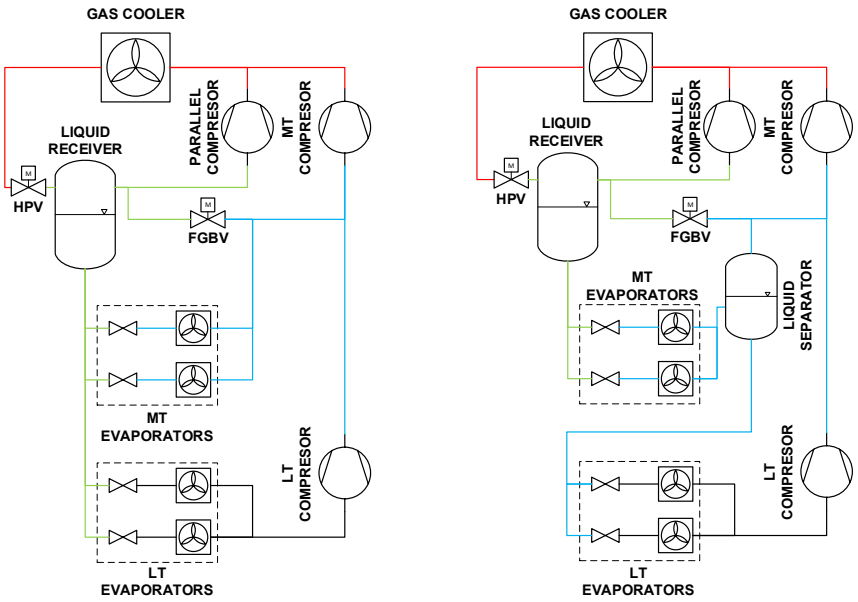

Figure 1: CO_2 refrigeration systems for commercial refrigeration with cooling (MT evaporators) and freezing (LT evaporators) cabinets. Left, traditional booster system supported by parallel compressors. Right, upgrade of the traditional booster system with overfed MT evaporators and active control of the liquid separator level

The third group of compressors, the so-called parallel compressors, regulate the intermediate pressure level at the liquid receiver by removing the flash gas. In case the amount of flash gas is low, which usually happens when heat is rejected at the gas coolers at low ambient temperature, it is the flash-gas bypass valve (FGBV in Fig. 1) that solely controls this pressure, by throttling vapour to the suction of the MT compressors. Heat is rejected to the ambient in the gas cooler, and the high pressure is regulated by means of the high pressure valve (HPV in Fig. 1).

The second configuration represented in Fig. 1 right is based on the previous layout with an auxiliary liquid separator downstream of the MT evaporators and two completely independent liquid lines added. This allows flooded operation of the MT evaporators, which reduces power consumption of the system, keeping the operational safety of the MT compressors uncompromised. The liquid level at the liquid separator is normally controlled by a pump or a liquid ejector, which returns liquid from the separator to the receiver. An alternative was proposed by EPTA (Mastrapasqua, 2017), which provides an additional liquid line from the separator to the LT evaporators. Thus, LT evaporators are fed from the separator if there is liquid in it, and from the receiver if the separator is empty.

The concept proposed in this study is a development of EPTA's solution, where the LT evaporators are always independently fed with liquid refrigerant from the liquid separator. This involves active control of the liquid level, by coordinated opening of the expansion valves at all the MT evaporators, which in addition leads to their flooded (and thus more efficient) operation.

Fig. 2 left shows the first ejector-supported LT section considered in this study. It is based on hot-gas-driven ejector(s) entraining the outlet stream leaving the LT evaporators, both vapour and small amounts of non-evaporated liquid. LT ejector discharges to the liquid separator, covering pressure lift in the range of 13 bar to 19 bar. The usual source of the driving stream would be the gas cooler outlet side, thus refrigerant at high pressure and relatively low temperature. However, first evaluation of this solution indicated that substantial amounts of liquid leaving the LT ejector and entering the MT accumulator would flood the liquid separator and in the end require a separate liquid return, e.g., dedicated liquid ejectors or pumps. Relatively high pressure lift that is requested entails very low entrainment ratio, i.e. relatively large motive mass flow rate is needed to entrain the vapour at low pressure. Consequently, motive flow from the discharge of MT and parallel compressors, upstream of the gas cooler (high pressure and high temperature and thus high expansion potential, reducing the requested motive nozzle mass flow rate), was considered as the suitable option for this LT ejector system.

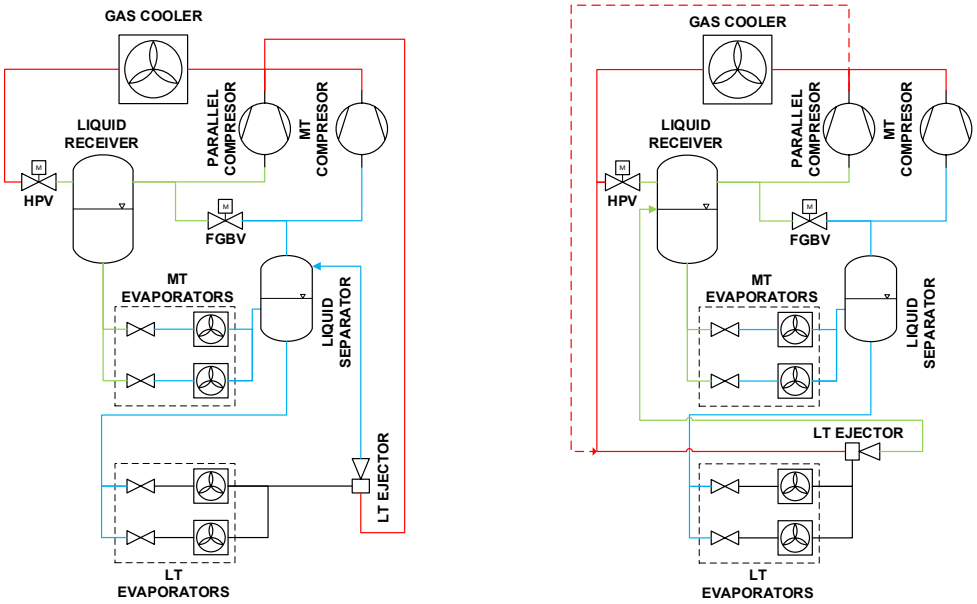

Figure 2: CO_2 booster system with LT ejector discharging to the liquid separator (left) or to the liquid receiver (right)

Another solution with LT ejector was proposed in this work, Fig. 2 right. The discharge port of the ejector is connected to the liquid receiver at intermediate pressure, involving even higher pressure lift (close to 25 bar). This discharge of the LT ejectors imposes no actual danger of flooding the liquid separator, so a standard source of driving stream could be used, i.e., gas cooler outlet. However, it was anticipated that this mass flow would be insufficient in practice, particularly as the gas cooler outlet temperature decreases and expansion work potential for the LT ejector motive nozzles diminishes. Consequently, an auxiliary line from the discharge of compressors (dashed in Fig. 2 right) should be implemented to support the motive flow if necessary, i.e., the overall mass flow rate flowing out of the gas cooler would not be enough to support the required LT capacity.

3. SIMULATION MODEL AND CONDITIONS

The four systems described in the previous section were modelled using Modelica object-oriented programming language in Dymola 2018 environment (Dassault Systems, Vélizy-Villacoublay, France). The models developed are based on TIL 3.5 library, and R744 properties are provided by the TILMedia 3.5 library, both from TLK-Thermo GmbH (Braunschweig, Germany). The effects of oil and of the oil management system were neglected.

Refrigeration capacities for cooling (MT evaporators) and freezing (LT evaporators) were selected in order to reflect typical size of a European supermarket (Gullo et al., 2017, Karampour and Sawalha, 2018). The design MT capacity was set at 100 kW (evaporation temperature -10 °C and superheating degree 8 K), while the LT capacity was assumed constant at 20 kW (evaporation temperature -32 °C and superheating degree 8 K). The design point at the outlet of the gas cooler was assumed at 40 °C, and the liquid receiver pressure at 40 bar (controlled by the parallel compressors). For these conditions, performance maps for real compressors by Bitzer were applied, as indicated in Table 1 (nominal frequency 50 Hz). The machines indicated in white cells were used as base design, the ones marked with grey background account for the extra capacity that was needed when the system used LT ejectors (and thus no LT compressors). Namely, a fifth MT compressor was needed for the system with LT ejector discharging to the liquid separator, meanwhile a third parallel compressor was added to cover the need for capacity with LT ejector discharging to the liquid receiver.

Table 1. Compressors selected for the model, and their displacements

MT Compressors	4MTC-10K (VSD)	4MTC-10K	4HTC-20K	4FTC-30K	4DTC-25K
Displacement [m^3/h]	6.5 (30 – 70 Hz)	6.5	12	17.8	21.2
PAR Compressors	4JTC-15K (VSD)	4JTC-15K	4FTC-30K		
Displacement [m^3/h]	9.2 (30 – 70 Hz)	9.2	17.8		
LT Compressors	2HME-4K (VSD)	2GME-4K			
Displacement [m^3/h]	4.34 (30 – 70 Hz)	5.05			

The compressor efficiencies were modelled with correlations dependent on the suction and discharge conditions, the rotational speed for VSD (variable speed drive) compressors. These correlations are based on published data from the manufacturer (Bitzer Software https://www.bitzer.de/websoftware/).

The gas cooler was modelled as a fin-and-tube heat exchanger, with a regulation of the volumetric flow of air so that the temperature at the outlet of the gas cooler ($T_{gc,out}$) could be adjusted for each simulation. High pressure was adjusted according to the optimum performance curve, i.e., setpoint was selected as a function of $T_{gc,out}$ and of the region of operation - subcritical, transcritical or transition. For subcritical operation ($T_{gc,out}$ equal to or below 25 °C), a subcooling degree equal to 3 K was set. Transcritical operation corresponded to $T_{gc,out}$ higher than or equal to 30 °C, where the pressure depended linearly on $T_{gc,out}$. The relation between both parameters is defined by the pair of points (30 °C,76.4 bar(a)) and (40 °C,102.4 bar(a)).

MT and LT evaporators were modelled also as fin-and-tube heat exchangers, where the volumetric flow of air was controlled to adjust the load for each simulation at each evaporator. For the state-of-the-art booster, with direct expansion (DX) evaporators both at the MT and LT, the aim for the regulation was achieving a superheating degree at the evaporators equal to 8 K. The booster system with overfed evaporators and liquid line from the liquid separators to the LT cabinets adjusted the opening of the MT evaporator expansion valve to keep the liquid separator level at half its capacity (LT evaporators running DX with setpoint for the superheat equal to 8 K). In both configuration with LT ejector, the control of MT evaporator expansion valve was as in the previous case (constant liquid level at separator). The LT evaporators ran overfed, which was modelled by adjusting the mass flow to attain quality at the outlet of the evaporator of 0.95.

Concerning the LT ejector model, for the sake of simplicity of the simulations, ability to continuous modulation of the opening degree (cross-section area of the flow-restricting channel, i.e., throat of the motive nozzle) was assumed for all the cases modelled. In practice a battery of several parallel ejector geometries could be used (stepwise control) or single geometry with modulated cross section area of the motive nozzle (continuous control with a regulating needle). Ejector of constant efficiency (defined as in Elbel and Hrnjak, 2008), equal to 25%, was assumed and applied in all the simulation cases.

Table 2 summarizes the main conditions and setpoints for the simulations for each of the four configurations presented. The MT evaporation temperature was considered 5 K higher for configurations with overfed evaporators than for those with DX evaporators. Similarly, the LT evaporation temperature was up to 7 K higher for the configurations with LT ejector (where overfed operation is possible) than for those with LT compressors. Simulations were performed with different load factors (defined in section one as the ratio of the MT refrigeration load to LT refrigeration load), kept always constant the LT load at 20 kW.

Table 2. Conditions and setpoints for the parametric study and for the different configurations tested: SAB (state-of-the-art booster), BOLS (booster with overfed MT evaporators due the liquid line at the liquid separator), LTEj_LS (LT ejector discharging to the liquid separator) and LTEj_LR (LT ejector discharging to the liquid receiver).

Configurations	SAB	BOLS	LTEj_LS	LTEj_LR
$T_{gc,out}$ [ºC]	10 – 40 (5 ºC intervals)			
$T_{evap,MT}$ [ºC]	-10	-5		
$T_{evap,LT}$ [ºC]	-32		-28 & -25	-25
MT Load [kW]	60, 80 & 100			
LT Load [kW]	20			
p_{LR} [bar(a)]	40			

4. RESULTS

Fig. 3 illustrates the main results of this study, which compare the different configurations proposed, grouped per load factor (5, 4 and 3 from top to bottom, respectively). The height of bars represents the ratio of the pack power consumption of a certain configuration to the pack power consumption of the reference configuration (state-of-the-art booster), at the same gas cooler outlet temperature.

It is clear in all cases that the pack power consumption decreases with the booster configuration with overfed MT evaporator and independent liquid line to the liquid separator (BOLS in Table 2) compared to the reference case, i.e. the ratio is always lower than 1 (in general between 15% and 5% lower). This effect was expected, as the evaporation temperature can be raised due to the enhanced operation of the evaporator.

Concerning the systems with LT ejector, in most cases the ratios were above the unity. Thus, the pack power consumption increases compared to the reference system when LT compressors are replaced by the LT ejector, even when LT ejector configurations account for the benefit of operating with flooded LT and MT evaporators. A separate analysis of the two configurations with LT ejector shows differences between them.

The first system with the LT ejector that uses hot gas as motive flow and discharging to the liquid separator (LTEj_LS in Table 2) always entails a significant increase of power consumption compared to the reference. The reason is the increased capacity at the MT compressors to supply the hot gas at the ejector, even if the entrainment ratio of the LT ejector with this hot gas is relatively high (from 0.17 to 0.53). The extra power consumption, in ratio, is higher if the load factor decreases.

The second option, with the motive of the LT ejector using as much flow from downstream of the gas cooler as possible and discharging to the liquid receiver (LTEj_LR in Table 2), shows different trends. With high gas cooler outlet temperature, and particularly with load factor equal to 5, the reference unit is outperformed by this solution of LT ejector. This good result is a combination of the increased evaporation temperatures and the reduced or inexistent utilization of hot gas to support the gas cooler pressure at the setpoint. However, and increased flow of hot gas from the compressors' discharge is requested as the gas cooler outlet temperature and load factor decrease, deteriorating the performance of the solution.

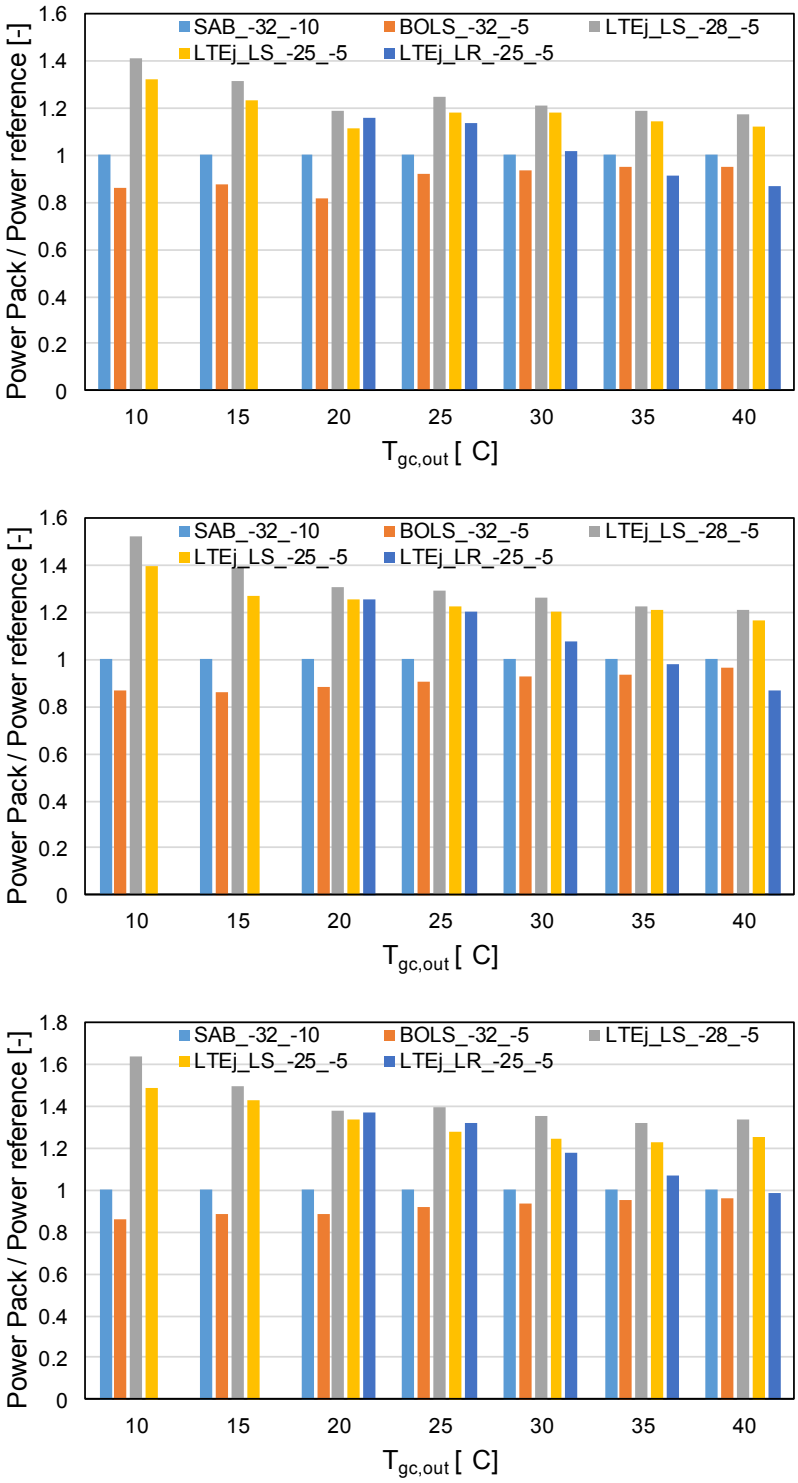

Figure 3: Ratio of the pack power consumption of a given configuration to the pack power consumption of the reference configuration (state-of-the-art booster) for the same gas cooler outlet temperature. The uppermost graph corresponds to load factor equal to 5, the middle graph to 4 and the bottom graph to 3. Abbreviation according to Table 2. The numbers indicated in the legend denote the LT and MT evaporation temperatures in degrees Celsius for each run of simulations

5. CONCLUSIONS

This study delved in different solutions to reduce the complexity of CO_2 booster systems for commercial refrigeration by replacing the LT compressors with auxiliary systems by dedicated high-pressure lift ejector(s). In general, such simplified layouts involve a deterioration of the system energy performance due to the pressure lift to be overcome and the use of hot gas as motive flow for the ejector. This deterioration is higher with low load fractions, i.e. with low ratio of MT refrigeration load to the LT refrigeration load.

A practical difficulty to be handled is proper design of a dedicated LT ejector geometry, enabling efficient energy performance (ejector efficiency not lower than 25%) at relatively high pressure lift, namely from 14 bar to 18 bar for the LTEj_LS configuration and 23-24 bar for the LTEj_LR configuration. Another challenge imposed on constant-geometry ejectors will be given by greatly changeable boundary conditions for the motive nozzle, from 50 bar/40 °C to 102 bar/115 °C, and from 60 bar/23 °C to 102 bar/45 °C for the LTEj_LS and LTEj_LR layouts, correspondingly.

ACKNOWLEDGEMENTS

The authors gratefully acknowledge the support received from the Research Council of Norway and user partners through HighEFF - Centre for an Energy Efficient and Competitive Industry for the Future, an 8-year Research Centre under the FME-scheme (Centre for Environment-friendly Energy Research, 257632/E20).

REFERENCES

Bai, T., Yan, G., Yu, J., 2017. Performance evolution on a dual-temperature CO_2 transcritical refrigeration cycle with two cascade ejectors. Appl. Therm. Eng. 120, 26-35.

Elbel, S., Hrnjak, P., 2008. Experimental validation of a prototype ejector designed to reduce throttling losses encountered in transcritical R744 system operation. Int. J. Refrigeration 31, 411-422.

Gullo, P., Hafner, A., Cortella, G., 2017. Multi-ejector R744 booster refrigerating plant and air conditioning system integration – A theoretical evaluation of energy benefits for supermarket application. Int. J. Refrigeration 75, 164-176.

Gullo, P., Hafner, A., Banasiak, K. 2018. Transcritical R744 refrigeration systems for supermarkets applications: Current status and future perspectives. Int. J. Refrigeration 93, 269-310.

Jeon, Y., Kim, D., Jung, J., Jang, DS, Kim, Y., 2018. Comparative performance evaluation of conventional and condenser outlet split ejector-based domestic refrigerator-freezers using R600a. Energy 161, 1085-1095.

Karampour, M., Sawalha, S., 2018. State-of-the-art integrated CO_2 refrigeration system for supermarkets: A comparative analysis. Int. J. Refrigeration 86, 239-257.

Liu, Y., Xin, T., Cao, L., Wan, Ch., Zhang, M., 2010. Compression-injection hybrid refrigeration cycles in household refrigerators. Appl. Therm. Eng. 30, 2442-2447.

Mastrapasqua, F., 2017. EPTA Natural Refrigeration Systems, CO_2 transcritical FTE System. Full Transcritical Efficiency, ATMOsphere Asia/ Bangkok/

Pardiñas, Á.Á., Hafner, A., Banasiak, K., 2018. Novel integrated CO_2 vapour compression racks for supermarkets. Thermodynamic analysis of possible system configurations and influence of operational conditions. Appl. Therm. Eng. 131, 1008-1025.

Wang, X., Yu, J., Zhou, M., 2014. Comparative studies of ejector-expansion vapor compression refrigeration cycles for applications in domestic refrigerator-freezers. Energy 70, 635-642.

Manuscript ID: 351
DOI: 10.18462/iir.icr.2019.0351

Permanent magnet synchronous motors for commercial refrigeration

Bryan R. BECKER[(a)], Brian A. FRICKE[(b)]

[(a)] University of Missouri – Kansas City
Kansas City, MO, 64110, USA, beckerb@umkc.edu
[(b)] Oak Ridge National Laboratory[1]
Oak Ridge, TN, 37831, USA, frickeba@ornl.gov

ABSTRACT

Various evaporator fan motor technologies used in commercial refrigeration are discussed. Data from a DOE-sponsored evaporator fan motor laboratory and field demonstration project are presented. Historically, shaded-pole, permanent split capacitor (PSC), and electronically commutated (EC) motors have been used as evaporator fan motors in commercial refrigeration equipment. A permanent magnet synchronous (PMS) AC motor that can directly use grid-supplied AC current without the need to rectify to DC has recently been commercialized. It was found that PMS motors consume 79% less power and draw 82% less current than shaded pole motors, and 34% less power and 49% less current than EC motors. PMS motors exhibit a power factor of 0.82, which is 40% greater than that of existing evaporator fan motors. The measured data is extrapolated to project the economic and environmental benefits from upgrading the installed base of commercial refrigeration evaporator fan motors to PMS motors.
Keywords: Display Cabinet, Evaporator, Fan, Moteur Electrique, Refrigerateur Commercial

1. INTRODUCTION

The US Department of Energy Building Technologies Office (DOE BTO) estimates that the commercial sector uses approximately 18% of all primary energy consumed in the United States, or 18.3 EJ (NCI, 2013). Of that 18.3 EJ of primary energy, DOE BTO estimates that the primary energy consumption of electric motor-driven systems in the commercial sector is 5.14 EJ and that the motors in central commercial refrigeration, walk-in coolers/freezers and beverage vending machines account for 0.34 EJ, 0.29 EJ and 0.19 EJ of that 5.14 EJ respectively (NCI, 2013). Thus, although the evaporator fan motors used in these types of commercial refrigeration systems are only fractional horsepower in size, due to their wide proliferation and nearly constant operation, they are a significant consumer of electrical energy in the US. Moreover, DOE BTO reports that since compressor motors are usually high efficiency, greater energy savings can be realized by upgrading evaporator and condenser fan motors rather than compressor motors (NCI, 2013).

Although higher-efficiency motors have been increasingly used in central commercial refrigeration and beverage vending machines, the installed base of smaller 6–12 W evaporator fan motors continues to be dominated by lower-efficiency shaded-pole (SP) motors. This is also true of the installed base of 38–50 W motors used in walk-in coolers and freezers, which is dominated by lower-efficiency permanent split capacitor (PSC) motors. Over the past 10 to 15 years, the higher-efficiency electronically commutated (EC) motor has begun to penetrate the market. While EC motors are significantly more efficient than shaded pole and PSC motors, newly available permanent magnet synchronous (PMS) motors offer even greater efficiency at a comparable first cost. In addition to transforming electrical energy into mechanical energy more efficiently than EC motors, PMS motors have much higher power factors, meaning that they accept energy from the grid much more

[1] Notice: This manuscript has been authored by UT-Battelle, LLC, under Contract No. DE-AC05-00OR22725 with the U.S. Department of Energy. The United States Government retains and the publisher, by accepting the article for publication, acknowledges that the United States Government retains a non-exclusive, paid-up, irrevocable, world-wide license to publish or reproduce the published form of this manuscript, or allow others to do so, for United States Government purposes.

efficiently. The resulting reduced current draw means that the electric utility can reduce the amount of energy that it needs to supply to the grid.
This paper provides background information on various fractional-horsepower electric motor technologies used for evaporator fan applications in commercial refrigeration and summarizes data from a DOE-sponsored evaporator fan motor laboratory and field demonstration project. This paper also projects the potential economic and environmental benefits resulting from upgrading the current installed base of commercial refrigeration evaporator fan motors to PMS motors.

2. EVAPORATOR FAN MOTOR TECHNOLOGIES

Evaporator fan motors are fractional horsepower in size, responsible for moving air across the evaporator coil, and typically run at one speed. The manufacturer will match the motor size and blade to the evaporator coil to meet the expected load under most conditions. Higher-efficiency evaporator fan motors reduce energy consumption by requiring less electrical power to generate the same motor shaft output power (NCI/PNNL, 2011).
Historically, shaded-pole induction motors have been the most commonly used evaporator fan motors in commercial refrigeration equipment. These are the simplest and least expensive type of fractional-horsepower motor, with an efficiency of approximately 20%. Given that motor efficiency losses are released as heat, this inefficiency also increases the refrigeration load, further increasing the refrigeration system energy consumption (Fricke and Becker, 2015).
Electronically commutated (EC) permanent magnet motors, also known as brushless DC motors, were initially commercialized in the late 1980s, and their use in commercial refrigeration applications has increased within the last 10 to 15 years because of economic incentives and regulatory requirements. State-of-the-art EC motors are approximately 66% efficient. Another induction motor type, the permanent split capacitor (PSC) motor, offers a mid-point between shaded-pole and EC motor price and efficiency levels. PSC motors are typically about 29% efficient.
A permanent magnet synchronous (PMS) AC motor that can directly use grid-supplied AC current without the need to rectify to DC has recently been commercialized. This new motor exhibits a peak efficiency of 75% and has the potential to significantly reduce the energy consumption of evaporator fan motors in commercial refrigeration equipment.
Synchronous motors are so named because the rotation of the motor's shaft is synchronized with the frequency of the supplied current. Previously, synchronous motors have been prohibitively expensive for commercial refrigeration evaporator fan applications because of the high cost of the electronic control circuit that is required to bring the synchronous motor up to synchronous speed. However, the PMS motor makes use of a new patented controller that is simpler and lower in cost than previous synchronous motor controllers or EC motor controllers, making the PMS motor a cost-effective alternative in the commercial refrigeration market (Flynn and Tracy, 2016).
Moreover, because they can use AC power directly from the grid, PMS motors have much higher power factors than EC motors. While the higher power factor does not mean that the PMS motor uses less power on site, it does mean that the utility is able to supply less power to the grid per unit of output power of the motor.

3. LABORATORY EVALUATION OF FAN MOTOR TECHNOLOGIES

Laboratory evaluation of evaporator fan motor technologies was performed to quantify and compare the performance of shaded-pole, PSC, EC, and PMS evaporator fan motors in a controlled environment, so as to minimize the influence of external factors and anomalies.
The laboratory evaluation included dynamometer testing of the fan motors and airflow testing of the motor/fan assemblies (Fricke and Becker, 2019). A photograph of the dynamometer test set-up showing a display case evaporator fan motor mounted in the motor stand and coupled to the hysteresis brake dynamometer is given in Fig. 1. Measured quantities in the dynamometer testing of fan motors included torque, rotational speed (RPM), and mechanical power output of the motor under test as well as voltage, current, power input and power factor of the electrical power provided to the subject motor. Fan motor efficiency was then calculated from the measured data.



Figure 1: Photograph of dynamometer test set-up showing a display case evaporator fan motor coupled to the hysteresis brake dynamometer

Fig. 2 shows the fan motor efficiency and power factor for a 6–12 W PMS motor. This 6–12 W PMS motor exhibits a peak efficiency of 75% with a power factor of approximately 0.9 at a power output of 11 W.

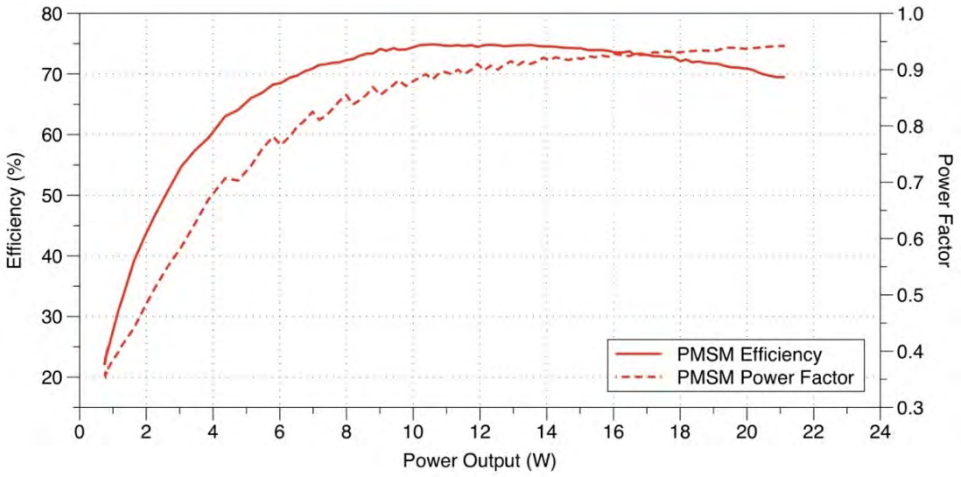

Figure 2: Fan motor efficiency and power factor for a 6–12 W PMS motor

Fig. 3 shows the fan motor efficiency and power factor for a 38–50 W PMS motor. This 38–50 W PMS motor exhibits a peak efficiency of 82% with a power factor of approximately 0.9 at a power output of 35 W.

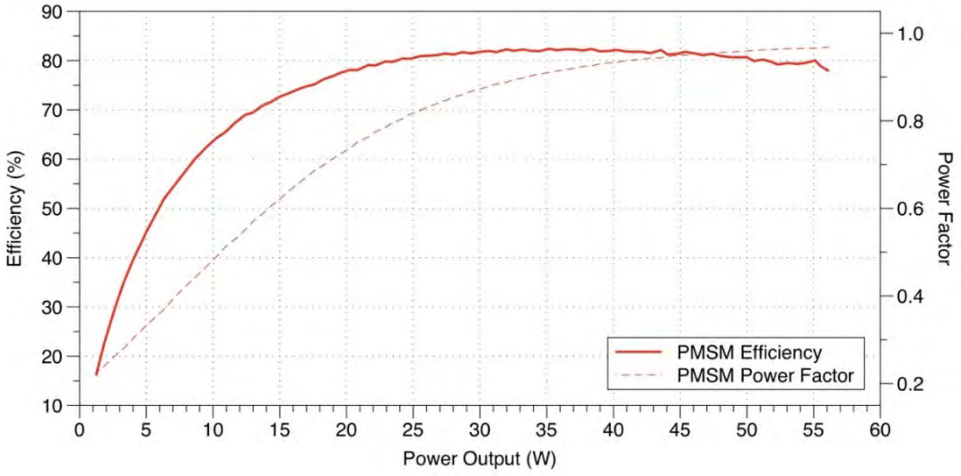

Figure 3: Fan motor efficiency and power factor for a 38–50 W PMS motor.

A summary of measured evaporator fan motor efficiency and power factor determined from the dynamometer testing is given in Table 1.

Table 1. Summary of measured evaporator fan motor efficiency and power factor

Evaporator fan motor type	Efficiency (%)	Power factor
6–12 W fan motors		
SP	26	0.64
EC	63	0.61
PMS	75	0.91
38–50 W fan motors		
SP	24	0.61
PSC	50	0.97
EC	69	0.61
PMS	82	0.92

Airflow testing of SP, PSC, EC, and PMS motor/fan assemblies was performed using an ANSI/AMCA Standard 210-16/ASHRAE Standard 51-16 airflow test chamber to measure the performance of the subject motor/fan assembly and to determine the incumbent display case system impedance (AMCA, 2016; Fricke and Becker, 2019). Fig. 4 shows a photograph of the airflow test set-up with an evaporator motor/fan assembly mounted at the inlet to the test chamber. Also visible are the static pressure gauge display, differential pressure gauge display, variable power supply, power analyzer, optical sensor, panel tachometer, and variable frequency drive used to control the auxiliary fan. Measured quantities in the airflow testing included airflow rate, static pressure at the front of the airflow test chamber, differential pressure across the orifice plate of the airflow test chamber, laboratory air temperature and humidity, as well as voltage, current, and electrical power input provided to the motor/fan assembly and rotational speed (RPM) of the motor/fan assembly.

A family of fan curves (static pressure vs airflow rate and electrical power input vs airflow rate) was generated for the 6–12 W PMS motor/fan assemblies with 20 cm fan blades and for the 38–50 W motors paired with 25 and 30 cm blades. Various incumbent motor/fan assemblies were also tested in the laboratory airflow test chamber and their fan curves were generated.

Fig. 5 shows static pressure and input power versus airflow rate for a 6–12 W PMS evaporator fan motor with 17° to 24° pitched blades. At a static pressure of 75 Pa, the airflow rate was 30 L/s and the input power was 11.2 W for a 17° blade, while the airflow rate was 52 L/s and the input power was 16.3 W for a 24° blade. At a static pressure of 0.0 Pa, the airflow rate was 102 L/s and the input power was 6.0 W for a 17° blade, while the airflow rate was 144 L/s and the input power was 9.5 W for a 24° blade. The 6–12 W motors in display case applications typically operate at a static pressure between 25 and 50 Pa.

4. FIELD EVALUATION OF FAN MOTOR TECHNOLOGIES

4.1. Display Case Evaporator Fan Motors

Field evaluation of refrigerated display case evaporator fan motors was accomplished by performing side-by-side comparisons of 6–12 W PMS motors to 6–12 W SP and EC fan motors, in a total of six test sites, shown in Table 2 (Fricke and Becker, 2019). Since refrigeration effect depends upon airflow rate, an effort was made to match the airflow rate of the incumbent motor/fan assembly during the installation of PMS fan motors at each test site, by using appropriately pitched fan blades on the PMS motors. This is a significant issue when evaluating energy savings, because the energy usage of a fan motor depends upon how much air it is moving.

Different fan motor rotational speeds have implications for airflow rate. PMS motors are designed to run at 1800 RPM on a 60 Hz AC power supply. Typically, the incumbent evaporator fan motors were found to operate at approximately 1550 RPM. Given the faster rotational speed of the PMS motor, the use of a slightly lower pitched blade on the PMS motor, operating at 1800 RPM, gives a comparable airflow rate to that of the incumbent motor/fan assembly operating at 1550 RPM.

It was found that, on average, a PMS motor consumes 79% less power and draws 82% less current than a shaded pole motor, and on average, 34% less power and 49% less current than an EC motor. In addition, the PMS motor exhibits an average power factor of approximately 0.82, which is on average 40% greater than that of existing evaporator fan motors.



Figure 4: Photograph of the airflow test set-up showing a display case evaporator motor/fan assembly mounted at the inlet to the airflow test chamber

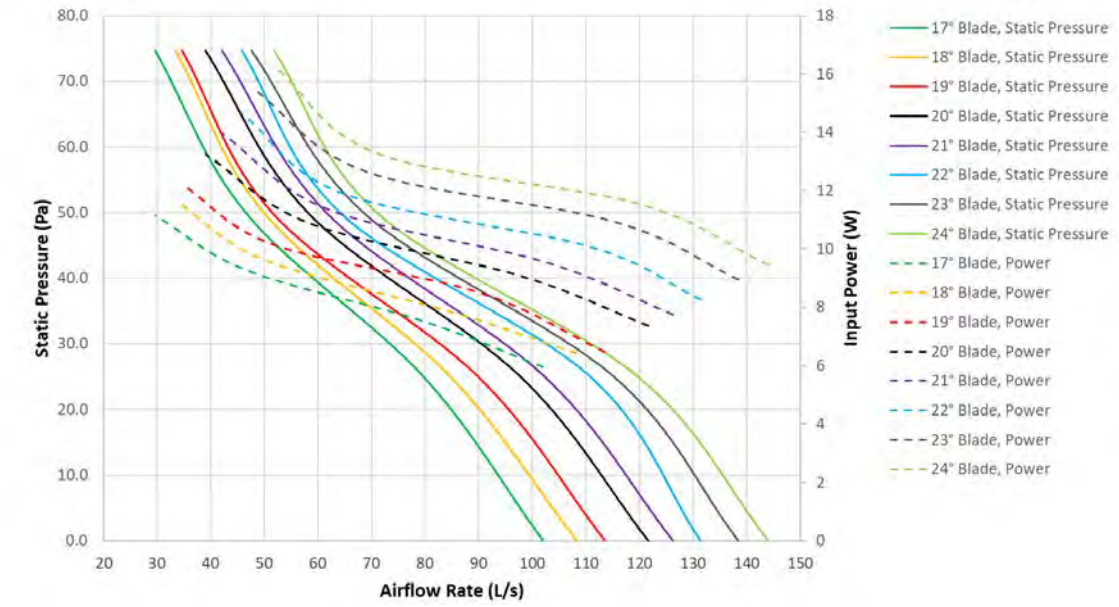

Figure 5: Static pressure and input power versus airflow rate for a 6–12 W PMS evaporator fan motor with 20 cm fan blades pitched from 17° to 24°

Table 2. Summary of field test sites for side-by-side comparison of evaporator fan motors in medium-temperature refrigerated display cases

Number and type of fan motor		Display case type	Data collection duration	Location
Electrical circuit A	Electrical circuit B			
Two shaded-pole	Two PMS	One 4.9 m open multi-deck	14 months	Kansas City, MO Site #1
Four EC, type A	Four PMS	Two 3.7 m open multi-deck	Five months	Kansas City, MO Site #2
Two EC, type B	Two PMS	Two 2.4 m open multi-deck	17 months	Lee's Summit, MO
One EC, type B	One PMS	One 2.4 m open multi-deck	Six months	San Diego, CA
Three EC, type C	Three PMS	Two 3.7 m open multi-deck, retrofit with doors	Five months	San Antonio, TX Site #1
Two EC, type C	Two PMS	One 3.7 m open multi-deck, retrofit with doors	Five months	San Antonio, TX Site #2

4.2. Walk-in Cooler/Freezer Evaporator Fan Motors

Two field test sites were selected to evaluate the performance of the larger 38 to 50 W PMS evaporator fan motors in walk-in cooler/freezer applications (Fricke and Becker, 2019). At each supermarket, two walk-in units were selected for investigation: one walk-in dairy cooler and one walk-in freezer. A summary of the number of evaporators and evaporator fan motors used in the walk-in cooler/freezer evaporator fan motor evaluation is provided in Table 3.

Table 3. Summary of walk-in coolers/freezer evaporators and evaporator fans

Supermarket location	Walk-in type	Number of evaporators	Number of fans per evaporator	Total number of evaporator fans
South Burlington, VT	Dairy Cooler	4	3	12
	Freezer	2	4	8
Colchester, VT	Dairy Cooler	3	4	12
	Freezer	2	5	10

A 61% decrease in fan motor power was measured when retrofitting existing evaporator fan motors with PMS motors in the walk-in cooler. In addition, a 48% decrease in fan motor power was measured when retrofitting existing evaporator fan motors with PMS motors in the walk-in freezer.

4.3. Whole Store Evaporator Fan Motor Retrofit

The culmination of the field evaluation of fan motor technologies was a whole-store retrofit conducted at a supermarket (Fricke and Becker, 2019). Pre- and post-retrofit measurement of evaporator fan motor power in medium- and low-temperature refrigerated display cases and walk-in coolers/freezers was performed.

Each display case line-up or walk-in cooler/freezer had a dedicated electrical circuit breaker that supplied electrical power to the evaporator fans in that display case line-up or walk-in. The evaporator fan motor electric power measurements were made at the circuit breaker level. Thus, the electrical power measurements represent the motor power, voltage, current, and power factor for all the fans operating on a given circuit. A total of 22 display case evaporator fan circuits, representing 185 fan motors, and 20 walk-in evaporator fan circuits, representing a total of 77 motors, were monitored and recorded. By motor type, 103 EC motors and 82 shaded pole motors were replaced in the monitored refrigerated display cases, and 73 PSC motors and 4 EC motors were replaced in the monitored walk-ins. During the installation of PMS evaporator fan motors, since refrigeration effect depends upon airflow rate, care was taken to meet or exceed the airflow rate of the incumbent fans by using appropriately pitched fan blades on the PMS motors. Measured quantities for each electrical circuit included fan motor power, voltage, current, and power factor, and these quantities were measured every 30 seconds and then averaged and recorded every two minutes.

Table 4 shows the average reduction in power and current draw as well as the improvement in power factor for the PMS evaporator fan motors, compared to the incumbent motors, as determined from the whole-store fan motor retrofit.

Table 4. Performance comparison of 6–12 W and 38–50 W incumbent and PMS evaporator fan motors from whole-store fan motor retrofit

Incumbent evaporator fan motor type and output power	Equivalent PMS evaporator fan motor performance comparison		
	Power reduction	Current draw reduction	Power factor improvement
SP, 6–12 W	50%	60%	30%
EC, 6–12 W	38%	54%	33%
PSC, 38–50 W	49%	43%	-10%
EC, 38–50 W	47%	43%	-6%

Overall for the whole-store retrofit, the current supplied to all monitored evaporator fan motors was reduced by 52%, the real power was reduced by 46% and the apparent power was reduced by 51% following the retrofit of the 262 evaporator fan motors that were monitored.

5. POTENTIAL ENERGY SAVINGS

Based on the results of the laboratory and field evaluations of evaporator fan motors, the potential site and source energy savings associated with retrofitting the existing installed base of 6–12 W and 38–50 W commercial refrigeration evaporator fan motors with PMS fan motors can be estimated.

For purposes of comparison, it was estimated that there are approximately 15.8×10^6 6–12 W evaporator fan motors installed in commercial refrigeration equipment and beverage vending machines and approximately 14.4×10^6 38–50 W evaporator fan motors installed in walk-in coolers and freezers (Progressive Grocer, 2015; NACS, 2015; NRA, 2015; IBIS World, 2015; Statistic Brain, 2015).

For the baseline case, it was estimated that 15.1×10^9 kWh per year of site electricity is consumed by the existing installed base of 6–12 W and 38–50 W evaporator fan motors. Assuming the cost of electricity is 10.58 cents per kilowatt-hour (EIA, 2015), this translates into nearly $1.6 billion. Also, assuming carbon dioxide equivalent emissions of 0.76 kg of CO_2 per kilowatt-hour of electricity delivered (Deru and Torcellini, 2007), the CO_2 emissions associated with the currently installed base of evaporator fan motors is estimated to be 11.4×10^9 kg.

If all 30.2×10^6 currently installed 6–12 W and 38–50 W evaporator fan motors were retrofitted with PMS fan motors, the total site electricity consumption was estimated to be 8.0×10^9 kWh per year. Thus, the total retrofit of all evaporator fan motors represents a site energy savings of approximately 7.1×10^9 kWh/year or 47%, resulting in an annual cost savings of $748 million compared with the base case. Furthermore, PMS motors are estimated to reduce the annual CO_2 equivalent emissions by approximately 5.35×10^9 kg compared with the baseline.

Based on the site energy analysis presented, the potential source energy savings associated with retrofitting existing 6–12 W and 38–50 W commercial refrigeration evaporator fan motors with PMS fan motors can be estimated. Recall that “source energy” refers to the sum of the energy consumed at the site (site energy) plus the energy required to extract, convert, and transmit that energy to the site, whereas “site energy” refers to the energy directly consumed at the site (Deru and Torcellini, 2007). Furthermore, DOE estimates that the conversion from site to source electric energy is 3.16 units of source energy per unit of site energy (DOE, 2011). Therefore, if all currently installed 6–12 W and 38–50 W evaporator fan motors were replaced with PMS fan motors, the total source or primary energy attributed to all electric motors in central commercial refrigeration and beverage vending machines could be reduced by 0.080 EJ/year resulting in a source energy consumption of 0.44 EJ/year, representing a savings of 16%.

6. CONCLUSIONS

This paper discussed various fractional-horsepower electric motor technologies used for evaporator fan applications in commercial refrigeration, summarized data from a DOE-sponsored evaporator fan motor laboratory and field demonstration project, and projected the potential economic and environmental benefits resulting from upgrading the current installed base of commercial refrigeration evaporator fan motors to PMS motors. The laboratory evaluation included dynamometer testing of fan motors and airflow testing of motor/fan assemblies. Side-by-side comparisons of 6–12 W display case evaporator fan motors was performed at six field test sites. Two field test sites were selected to evaluate the 38–50 W PMS evaporator fan motors in walk-in cooler/freezer applications. Finally, a whole-store retrofit was conducted at a supermarket.

Overall for the whole-store retrofit, the current supplied to all monitored evaporator fan motors was reduced by 52%, the real power was reduced by 46% and the apparent power was reduced by 51% following the retrofit of the 262 evaporator fan motors that were monitored. It was estimated that if all currently installed 6–12 W and 38–50 W evaporator fan motors were replaced with PMS fan motors, the total source or primary energy attributed to all electric motors in central commercial refrigeration and beverage vending machines could be reduced by 0.080 EJ/year resulting in a source energy consumption of 0.44 EJ/year, representing a savings of 16%.

ACKNOWLEDGEMENTS

This material is based upon work supported by the Department of Energy's Office of Energy Efficiency and Renewable Energy, Building Technologies Office, under Award Number DE-EE0006741. This report and the work described were sponsored by the Commercial Buildings Integration program within the Building Technologies Office of the US Department of Energy Office of Energy Efficiency and Renewable Energy. The authors wish to acknowledge the contributions of Amy Jiron and Charles Llenza in guiding this work.

REFERENCES

AMCA, 2016. ANSI/AMCA Standard 210-16/ASHRAE Standard 51-16, Laboratory Methods of Testing Fans for Certified Aerodynamic Performance. Air Movement and Control Association (AMCA) International Inc., Arlington Heights, Illinois.

Deru, M., Torcellini, P., 2007. Source Energy and Emission Factors for Energy Use in Buildings. NREL/TP-550-38617, National Renewable Energy Laboratory, Golden, Colorado.

DOE, 2011. 2010 Buildings Energy Data Book. Office of Energy Efficiency and Renewable Energy, US Department of Energy (DOE), Washington, D.C.

EIA, 2015. Electric Power Monthly with Data for March 2015. Energy Information Administration (EIA), US Department of Energy, Washington, D.C.

Flynn, C. J., Tracy, C.N., 2016. Divided Phase AC Synchronous Motor Controller. US Patent No. 9,300,237 B2, March 29.

Fricke, B. A., Becker, B.R., 2015. Q-Sync Motors in Commercial Refrigeration: Preliminary Test Results and Projected Benefits. ORNL/TM-2015/466, Oak Ridge National Laboratory, Oak Ridge, Tennessee.

Fricke, B. A., Becker, B.R., 2019. Permanent Magnet Synchronous Motors for Commercial Refrigeration: Final Report. ORNL/TM-2018/971, Oak Ridge National Laboratory, Oak Ridge, Tennessee.

IBIS World. 2015. Bars and Nightclubs in the US: Market Research Report. IBIS World, New York. Accessed July 15, 2015. http://www.ibisworld.com/industry/default.aspx?indid=1685.

NACS, 2015. U.S. Convenience Store Count. Association for Convenience and Fuel Retailing (NACS), Alexandria, Virginia. Accessed July 15, 2015. http://www.nacsonline.com/research/factsheets/scopeofindustry/pages/industrystorecount.aspx.

NCI (Navigant Consulting Inc.) and PNNL (Pacific Northwest National Laboratory). 2011. Preliminary Technical Support Document (TSD): Energy Conservation Program for Certain Commercial and Industrial Equipment: Commercial Refrigeration Equipment. Appliances and Commercial Equipment Standards, Building Technologies Program, Office of Energy Efficiency and Renewable Energy, US Department of Energy, Washington, D.C.

NCI (Navigant Consulting Inc.), 2013. *Energy Savings Potential and Opportunities for High-Efficiency Electric Motors in Residential and Commercial Equipment*. Building Technologies Program, Office of Energy Efficient and Renewable Energy, US Department of Energy, Washington, D.C.

NRA, 2015. Facts at a Glance. National Restaurant Association, Washington, D.C. Accessed July 15, 2015. http://www.restaurant.org/News-Research/Research/Facts-at-a-Glance.

Progressive Grocer, 2015. 82nd Annual Report of the Grocery Industry. Progressive Grocer, Chicago, Illinois.

Statistic Brain Research Institute, 2015. “Vending Machine Industry Statistics. Statistic Brain Research Institute, Los Angeles, California. Accessed July 15, 2015. http://www.statisticbrain.com/vending-machine-industry-statistics/.

Manuscript ID: 395
DOI: 10.18462/iir.icr.2019.0395

Thermophysical Properties of Water-based Carbon Nanotubes Nanofluid as Cold Storage Media

Meibo Xing, Ruixiang Wang

Beijing Engineering Research Centre of Sustainable Energy and Buildings, School of environment and energy engineering, Beijing University of Civil Engineering and Architecture, Beijing, 100044, P. R. China, xingmeibo@bucea.edu.cn

ABSTRACT

In this paper, the thermophysical properties of water-based single-walled carbon nanotube nanofluids (SWCNTs-nanofluids) as cold storage media were experimentally studied. The detailed measurements on the thermal conductivity, viscosity and density of SWCNTs-nanofluids with SWCNTs concentration ranging from 0.1 to 1wt% were carried out in a temperature range of 10-60°C. Thermal conductivity enhancement for SWCNTs-nanofluid is observed under the experimental conditions, which increases with an increase in the concentration and temperature. In addition, the viscosity of SWCNTs-nanofluid increases as increasing SWCNTs concentration but decreases with increasing temperature. The maximum thermal conductivity enhancement of SWCNTs-nanofluid is found to be 16.2% for the concentration of 1wt% at 60°C. Correspondingly, the viscosity will be increased by the maximum value of 35.9%. SWCNTs-Nanofluids with the higher thermal conductivity show great potential in the cold storage application.
Keywords: Cold storage; Carbon nanotube; Nanofluid; Thermal conductivity.

1. INTRODUCTION

Phase change cold storage is an effective method to realize peak load shifting and valley filling in power grid. Existing cold storage materials have large supercooling degree. In order to achieve nucleation and crystallization of cold storage materials, it is necessary to reduce the evaporation temperature of refrigerators, which results in large energy consumption. Therefore, reducing the supercooling of phase change materials has always been the goal of researchers. Supercooling suppression induced by nucleating agents is an important solution. Nanofluids as a new cold storage material for nucleating agent of nanoparticles have been proposed and investigated in the recent [1-3].

Nanoparticles, nanosheets, nanofibers, nanotubes, nanowires, nanorods or droplets have also been evaluated for the improvement of the thermal conductivity of phase change materials. He et al. [4] studied the TiO_2 nanoparticles in the aqueous solution of saturated $BaCl_2$, indicating that thermal conductivity increases nearly linearly with the volume fraction of the nanoparticles. An increment of 16% in thermal conductivity was observed at room temperature. Liu et al. reported 15% increment in the thermal conductivity for $BaCl_2$ aqueous phase change solution with 1.13 wt% of TiO_2, with a decrement in the storage time of the ice storage from 541 to 421 min and the total melting time from 269 to 160 min due to the high thermal conductivity of the nanoparticle additives [5]. Wu et al. numerically investigated the fusion process of the paraffin doped with copper nanoparticles [6]. After the addition of 1 wt% copper particles in the paraffin, the melting time reduced by 13%, showing that the addition of the nanoparticles is an effective way to improve the heat transfer in LHTES systems. Nazir et al. [7] summarizes the research carried out over the past 10 years on different additives in PCMs and the thermal properties obtained. It is evident from the Table that alumina is the most commonly used additive, but the thermal conductivity has been improved by 250% using carbon nanotubes, while thermal conductivity increased by 52.1% with the combination of silica and alumina as additives. On the other hand, both the latent heat and degree of supercooling were reduced with the use of nanoparticle additives.

In recent years, carbon nanotubes (CNTs) with high thermal conductivity have attracted particularly close attention from researchers, which have also been used to realize nanofluids. CNTs with a very high aspect ratio have unusual heat transfer properties. Along the length direction, they show an excellent heat transfer performance. Besides, they possess a remarkable thermal property with

ultra-high thermal conductivity (2000-6000) which is much higher than those of the metallic (hundreds times) or their oxide nanomaterial used in nanofluids (tens times). Ding et al. [8] found that thermal conductivity of CNT based aqueous nanofluid increases significantly with the temperature by 15% at 20°C, 30% at 25°C and by 79% at 40°C for the same volume fraction. Khoshmehr et al. [9] investigated MWCNT-water with four different concentrations heat transfer in boiling phenomenon. Moreover, Lotfi et al. [10] discovered heat transfer enhances in the presence of multi-walled nanotubes in comparison with the pure water. From the recent researches, it is demonstrated there is a substantial increase in the heat transfer performance of different CNTs-nanofluids in comparison to their base fluids. In general, CNTs-nanofluids research has blossomed in many different directions, and has attracted a great deal of attention to researchers. Further research on various thermal features of CNTs-nanofluids is clearly essential to advance their potential applications in industrial and civil fields.

In this study, the Single Walled Carbon Nanotubes (SWCNTs) with remarkable thermal conductivity properties are used to prepare the phase change cold storage materials. Further, the thermal physical properties of the nanofluid, including thermal conductivity, viscosity and density, are investigated experimentally. The aim of this study is to provide a guide for selecting the SWCNTs-nanofluid as a potential cold storage media.

2. PROCEDURES AND APPARATUS

The SWCNTs with long cylindrical tubular shape was applied in this work. The CNTs were synthesized by catalytic decomposition of methane with cobalt catalyst, and then oxidized in air to remove the activated carbon. The detailed properties of SWCNTs product are given in Table 1. The morphological characterization was obtained using transmission electron microscopy (TEM), which is shown in Fig. 1. In order to obtain the even dispersion solution, the surfactant of Hexadecyltrimethylammonium bromide (CTAB) was selected as an additive, which was provided by Sinopharm chemical Reagent Co., Ltd, China.

Table 1 Properties of SWCNTs

Properties	value
Outer diameter (nm)	1-2
Inner diameter (nm)	0.8-1.6
Length (um)	5-30
Aspect ratio	2500-30000
Special surface area (m2/g)	>380
Thermal conductivity (W/m K)	~4000
Pure density (g/cm3)	2.1
Purity	>90%

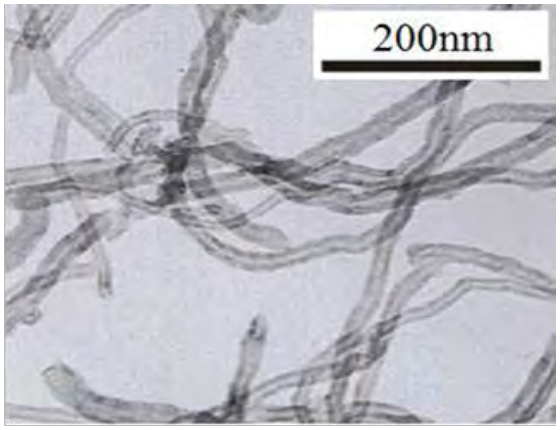

Fig. 1 The TEM image of SWCNTs

For preparation of SWCNTs-nanofluid with good dispersion stability, both the physical and chemical methods were used in the present study. After dispersing the SWCNTs and surfactant in

the based fluid, the mechanical mill and ultrasonication as physical methods were taken to ensure the excellent dispersion stability of those SWCNTs suspensions, respectively. The NETZSCH laboratory sand mill with MINICER 993.0490, provided by SIEMENS Co., Ltd., was employed for grinding the SWCNTs-nanofluid. Ultrasonic vibration on the prepared nanofluid was undertaken at the settling time of 60 min using a KQ2200DB numerical control ultrasonic oscillator after grinding the nanofluid in grinding miller for 120 min.

The SWCNTs-nanofluids at mass fraction of 0.1-1wt% were prepared by the above mentioned method. In order to verify the long stability of sample SWCNTs-nanofluids, the stability with time was examined using a common observation method. Fig. 2 shows the photo of the samples of SWCNTs-nanofluid taken by using a digital camera, where they correspond to the new preparation samples and sedimentation samples after two months. After sedimentation, the SWCNTs-nanofluid without surfactant of CTAB displays severe agglomeration and sedimentation as shown in Fig. 2 (b). However, the SWCNTs-nanofluid samples with added CTAB have lesser variations in color and precipitation of solution over a substantially long period of time. There is no layered phenomenon and less sedimentation in each sample can be found from the photo. Hence, the prepared SWCNTs-nanofluid with CTAB samples could meet application needs for next tests.



Fig. 2 The photo of SWCNTs-nanofluids: (a) fresh samples; (b) after two months

The transient hot-wire method was used to measure the thermal conductivities of the SWCNTs-nanofluid. The experimental apparatus TC3010L was provided by XIATECH Co. Ltd.. The measurement accuracy is within ±2%, repeatability is ±2% and the measurement range is 0.001-5.0 . Applying voltage to a hot wire causes a temperature rise of sample fluid surrounding the hot wire and the variation value depends on the thermal conductivity of fluid. A Wheatstone bridge is used to measure the resistance variation of the hot wire, which is determined by the measured the voltage across the bridge and the temperature of the hot wire.

The dynamic viscosity and density are measured with a vibrating wire viscometer & densimeter. The viscosity and density can be detected simultaneously using vibrating wire method. The experimental apparatus VS3000 was provided by XIATECH Co. Ltd.. For the viscosity, measurement accuracy is within ±2%, repeatability is ±2% and the measurement range is 0.1~15 . Accordingly, measurement accuracy is within ±0.5%, repeatability is ±0.2% and the measurement range is 500-2000 for the density measurement.

3. RESULTS AND DISCUSSION

3.1. Thermal conductivity

Thermal conductivities of SWCNTs-nanofluid with various mass concentrations at different temperatures are shown in Fig. 3. As can be seen from the figure, SWCNTs-nanofluids can obtain higher thermal conductivity values than that of the base fluid. Furthermore, the thermal conductivity increases with an increase in the mass fraction of SWCNTs and temperature. The increment of thermal conductivity from 0.6032 to 0.7055 was obtained at 0.1wt% mass concentration, and the increment from 0.6268 to 0.7602 was obtained at 1wt% mass concentration in the temperature range of 10 °C to 60°C. The enhancement is caused by the Brownian motion of the particles. The

results show that comparing to the pure water, the maximum thermal conductivity enhancement ratio of SWCNTs-nanofluid obtained for 1wt% SWCNTs at 60°C were found to be 16.2%. Consequently, the SWCNTs-nanofluid shows great potential to be used as advanced heat transfer fluid.

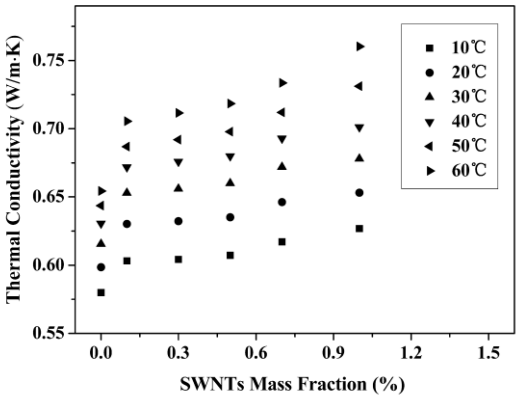

Fig. 3 Experimental thermal conductivity of SWCNTs-nanofluid

Fig. 4 displays a comparison of thermal conductivity ratio between experimental results and predictive models, which is defined as the ratio of thermal conductivity of nanofluid ( ) to the thermal conductivity of base liquid ( ). From the experimental results, higher thermal conductivity ratio can be observed with increasing SWCNTs loading in DIW and the temperature of nanofluid. When the temperature is varied from 10 to 60°C, the thermal conductivity ratios predicted by Hamilton-Crosser model are almost identical at the same percentage of mass concentration. Thus, this model is inappropriate to predict the thermal conductivity of the SWCNTs-nanofluid because the predicted values are lower than the experimental results. In fact, Hamilton-Crosser model only considers the effect of temperature on the base fluid thermal conductivity while varying the temperature. It is not enough to reflect the effect of temperature on the thermal conductivity of nanofluid. This indicates that the important role of other factors has been neglected in this model. Further modified model need to be developed by considering the effect of the motion of nanoparticles in the fluid.

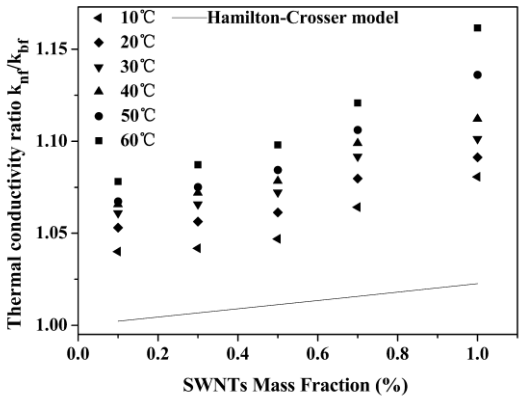

Fig. 4 Experimental thermal conductivity ratio in comparison with the Hamilton-Crosser model

3.2. Viscosity

When applying nanoparticles into fluid to improve the thermal conductivity, another important transport property of viscosity is also changed, and thus that affects the thermal performance of heat transfer devices. Fig. 5 shows the viscosity of SWCNTs-nanofluid along with various mass fractions at different temperatures. It is observed that the viscosity of the SWCNTs-nanofluid

increases with an increase in the nanoparticles concentration and decreases with the increasing temperature. The viscosity for concentration of 0.1wt% is increased from 6.88% to 8.30% compared to DIW in the temperature range of 10°C to 60°C. Similarly, for the SWCNTs-nanofluid of 1wt% concentration, the viscosity is enhanced from 26.53% to 35.90% compared to DIW as the temperature varied from 10 °C to 60 °C.

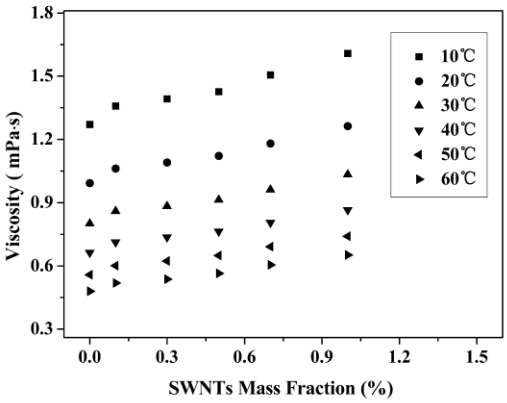

Fig. 5 Experimental viscosity of SWCNTs-nanofluid

3.3. Density

Fig. 6 shows the density of SWCNTs-nanofluids at different temperatures in the concentration range of 0-1wt%. It can be clearly seen that the density of DIW and the SWCNTs-nanofluids decreases with the increase in temperature at the same concentration. When the temperature increases from 10°C to 60°C, the density of DIW decreases from 999.61 to 984.12 . Typically, the density of the 0.1 wt% SWCNTs-nanofluid decreases from 1000.13 to 984.65 and the density of the 1 wt% SWCNTs-nanofluid decreases from 1004.88 to 989.46 as the temperature increases from 10°C to 60°C. Furthermore, it is indicated that the density of SWCNTs-nanofluids increases with the increase in the mass fraction of SWCNTs. The variation of density is 0.52-0.54% at the mass concentration of 1wt% for the different temperatures of SWCNTs-nanofluid. Consequently， the addition of SWCNTs has a slight influence on the density of the base fluid.

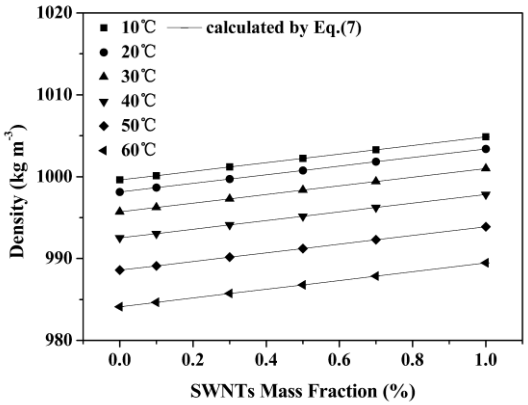

Fig. 6 Experimental density of SWCNTs-nanofluid

4. CONCLUSIONS

In this study, the SWCNTs nanofluids were prepared with highly dispersion stability as the cold storage media. The thermophysical properties of SWCNTs-nanofluids including thermal conductivity, viscosity and density were measured and discussed with the mass fraction of 0.1-1wt% in the temperature range of 10-60°C. Thermal conductivity enhancement of SWCNTs nanofluid is observed under the experimental condition and further increases with an increase in the

concentration and temperature. The viscosity of SWCNTs-nanofluid increases as increasing SWCNTs concentration and decreases with the increasing temperature. The maximum thermal conductivity enhancement of SWCNTs-nanofluid is found to be 16.2% for concentration of 1wt% at 60°C. Correspondingly, the viscosity will be increased by the maximum value of 35.9%. Consequently, the thermal conductivity of nanofluid cannot be considered alone as a criterion for nanofluid selection.

ACKNOWLEDGEMENTS

This study is financially supported by the Science and Technology Project of Beijing Education Commission under the Grant KM201910016010. The authors would like to thank for the sponsorship.

REFERENCES

[1] Nor Azwadi Che Sidik, Tung Hao Kean, Hoong Kee Chow, et al., 2018. Performance enhancement of cold thermal energy storage system using nanofluid phase change materials: A review. Int. Commun. Heat Mass Transfer 94, 85-95.

[2] X.J. Wang, X.F. Li, Y.H. Xu, et al., 2014. Thermal energy storage characteristics of Cu–H2O nanofluids. Energy 78, 212-217.

[3] Jia Yin Sze, Chenzhong Mu, Fadhel Ayachi, et al., 2018. Highly efficient nanofiller based on carboxylated graphene oxide in phase change materials for cold thermal energy storage. Energ. Procedia 152, 198-203.

[4] Q. He, S. Wang, M. Tong, et al., 2012. Experimental study on thermophysical properties of nanofluids as phase-change material (PCM) in low temperature cool storage. Energ. Convers. Manageme. 64, 199–205.

[5] Y. Liu, Y.G. Zhou, M. Tong, et al., 2009. Experimental study of thermal conductivity and phase change performance of nanofluids PCMs. Microfluid Nanofluid 7, 579–584.

[6] S. Wu, H. Wang, S. Xiao, et al., 2012. Numerical simulation on thermal energy storage behavior of Cu/paraffin nanofluids PCMs. Procedia Engineering 31, 240–244.

[7] Hassan Nazir, Mariah Batool, Francisco J. Bolivar Osorio, et al., 2019. Recent developments in phase change materials for energy storage applications: A review. Int. J. Heat Mass Tran 129, 491–523.

[8] Y. Ding, H. Alias, D. Wen, et al., 2006. Heat transfer of aqueous suspensions of carbon nanotubes (CNT nanofluids). Int. J. Heat Mass Tran 49, 240–250.

[9] H.H. Khoshmehr, A. Saboonchi, M.B. Shafii, 2014. The quenching of silver rod in boiling carbon nano tube-water nanofluid. Int. J. Therm. Sci 75, 95-104.

[10] R. Lotfi, A.M. Rashidi, A. Amrollahi, 2012. Experimental study on the heat transfer enhancement of MWNT-water nanofluid in a shell and tube heat exchanger. Int. Commun. Heat Mass 39, 108–111.

Manuscript ID: 412
DOI: 10.18462/iir.icr.2019.0412

Application of demand response in cold room: evaluation of energy performance using different modelling approaches

M. Akerma[(a)], H. M. Hoang[(a)], R. Ben Abdallah[(a)], A.Le Montagner[(a)], D. Leducq[(a)], N.Mellouli-Nauwycnk[(b)], A. Delahaye[(a)]

[(a)] Irstea, UR GPAN, Refrigeration Processes Engineering Research Unit,
1 rue Pierre-Gilles de Gennes, F-92761 Antony, France
mahdjouba.akerma@irstea.fr

[(b)] Institut universitaire de technologie de Montreuil,Université Paris 8
40 Rue de la Nouvelle France, 93100 Montreuil,France

ABSTRACT

The few technologies actually used to store electricity need to be improved while new solutions to overcome the intermittency of the renewable energy need to be developed. Demand response (DR) is one of the levers that can help to balance the electricity grid. Warehouses and cold rooms by their high thermal inertia are promising candidates for applying DR. However, the DR impacts (temperature rise and energy impact) can present a challenge to the DR deployment. These impacts were evaluated in the present work using two approaches for the modelling of a cold room and its refrigeration system:"white box" (based on energy balance) and "black box" (machine learning). An experimental pilot to measure DR effects in a loaded cold room was also developed. The comparison between these two approaches and the experimental results were performed to select a suitable method to be implemented. Several DR scenarios were tested in order to choose the right condition for DR application.

Keywords: demand response (DR); refrigerated warehouse; modeling; thermal behavior; energy consumption

1. INTRODUCTION

Many countries around the world, in particular in Europe are interested in reducing electricity consumption by using the strategy of Electrical Demand Response (DR). DR consists in changing the electricity used by end-users from their usual energy consumption patterns for a period in response to monetary incentives. So it can mean non-consumption of electricity (power cutting-off), or the shift in consumption in order to better match the power demand with the electricity supply. With a potential estimated at 10% of the available power, DR is one of the levers allowing a better management and balancing between the energy production and energy consumption. The refrigerated storage industry represents a substantial electrical load with a total number of 1.7 million of cold stores in Europe, accounting for 60–70 million m^3 of storage volume and high energy consumption (specific energy consumption (SEC) between 4 and 250 kWh m^{-3} $year^{-1}$, Evans et al. (2014)). More specifically the average SEC of the refrigeration system used for frozen products is 66.2 kWh m^{-3} $year^{-1}$.

Cold stores have a high potential for DR, thanks to the thermal inertia of stored products. However, the control of the refrigeration food quality requires that the air temperature in the room must not exceed a given maximum temperature, except for short term fluctuation (Brooks, Green, Cleland, & Senior, 1999). In order to choose the best way to implement DR, it is necessary to predict the system behavior during and after the DR application.

Recent studies have focused on the importance of the prediction of energy consumption (Amasyalia & El-Goharyb, 2016; S. Karatasou, Santamouris, & Geros, 2006) and air temperature inside a building (H.U Frausto, J. G. Pieters, & J. M.Deltour, 2003; H.U. Frausto & J.G. Pieters, 2004; Mustafaraj, Lowry, & Chen, 2011). Many approaches seem to be adapted to predict thermal

behavior and evaluation of energy performance of a cold store. Generally, three types of modeling approaches: data driven, physics based and grey box have been used for similar systems. Modeling methods are reviewed in (Afram & Janabi-Sharifi, 2014).
Nevertheless, the prediction of the system behavior in terms of temperature rise and energy impact can present a challenge to the DR deployment in cold storage (refrigeration warehouse and cold room). Few studies are devoted to evaluate the impacts of DR. (Brooks et al., 1999) have investigated experimentally the potential use of the thermal inertia of frozen products to shift the electricity consumption, the air and product temperature rise was less than 4°C when the refrigerated supply was cut off for 8 hours, while still leaving the fan on to ensure uniformed storage conditions.
The present paper focuses on the comparison between black box and while box models to predict the system behavior during and after DR period. Literature reviews related to these two approaches are presented in the following paragraphs. Developed models are validated by experimental data.

1.1. Data driven models (Black-box)

In this case, the physical constitution of the system is ignored. This approach is often favored by the energy management/DR operators to predict the behavior of HVAC systems. The modeling is essentially constructed by mathematical relations linking the inputs and the outputs of the system. These models have the particularity that its relations are parametric equations (algebraic, differential, or recurrent) and its parameters can be obtained by having little knowledge about the studied system and its processes. The black-box depends entirely on the experimental data (temperature, energy…). So, it can only be developed if these data are available. This approach is described by a simple schema (Fig.1).
Several categories of data driven models can be distinguished. Black-box models can be differentiated mainly into two groups: linear parametric and non-linear models (Afram & Janabi-Sharifi, 2014; Kramer, van Schijndel, & Schellen, 2012). As cold storage is a dynamic system with time variation, the non-linear model is chosen to predict the system behavior in terms of temperature fluctuation and energy consumption.
A wide variety of data mining and machine learning algorithms, such as artificial neural networks ANNs is applied in behavior system predictions (Mustafaraj et al., 2011). (X. Qiu, L. Zhang, G. Amaratunga, & P. N. Suganthan, 2014) have used different methods of deep learning, among which Deep Belief Networks (DBN), Vector Regression (SVR), Recurrent Neural Networks (RNN), and Feedforward back-propagation Neural Network (FNN), for regression time series based on electrical load demand data. As the obtained results are promising, these methods can be adapted to the prediction of time series.
In our case we choose the methods of deep learning, one of derived technologies of machine learning and artificial intelligence such as convolutional neural network, long short term memory.
Several data driven models, adapted to the implementation of DR strategies, are tested.

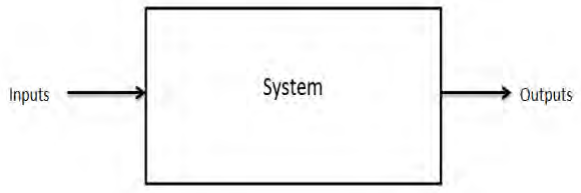

Figure 1: Simplified representation of the data driven approach

1.2. Physics based models (white box)

Physical knowledge of the system is used to develop the models and their mutual interaction. It is based on equations describing the physical phenomena that occur in the system, such as the heat balance on the building taking into account the given cooling capacity. These models are obtained based on the conservation equations for energy and mass balance. Many simulation programs, such as EnergyPlus (D. B. Crawley et al., 2004), ESP-r (Anonymous, 2002; Ben-Nakhi &

Mahmoud, 2004), TRNSYS (T. Berthou, Stabat, Salvazet, & Marchio, 2012; Thomas. Berthou, Stabat, Salvazet, & Marchio, 2014), DeST (Li, Meng, Cai, Yoshino, & Mochida, 2009), as well as others tools use physical models(Drury B. Crawley, Hand, Kummert, & Griffith, 2008). This approach requires detailed knowledge of heat loads in the storage, refrigeration machine behavior and other detailed information on the characteristics of the system.
Cold storage environment is a very complex system and depends on the conception of the refrigerated stores and of the weather, climate conditions (H.U Frausto et al., 2003). Although studies (X. Qiu et al., 2014; Xue, Wang, Yan, & Cui, 2015) have been carried out in the very broad framework of DR, no such method seems to have been applied to electrical erasure in the cold field. Given the energy importance of this area, this leaves a panel of important possibilities, which could make it possible to demonstrate or invalidate the use of DR in cold rooms and cold stores.

2. MATERIALS AND METHODS

2.1. Experimental setup

The cold room used in this study is about 2.4m long x 2.4m width x 2m high. For wall insulation, a 10cm layer of polyurethane with λ=0.023W/m.K is used. A global heat transfer coefficient Uc=0.29W/m^{2}K is obtained by measurement. The room temperature is controlled using an on/off strategy and is kept at -16.3 °C (within a limited range (set-point) between -15.5°C and -19°C). The refrigerated unit consists of a single evaporator with single speed fan. The measured coefficient of performance (COP) is 1.4 at -16°C. The cold room is installed inside an external cell equipped with an air conditioning unit to simulate the meteorological conditions (summer, spring…). To limit the infiltration load, the doorway is kept closed during measurements. In order to measure the air and product temperature, thermocouple sensors are used (Fig. 2). These thermocouples are distributed as follows:

- 3 for cold blowing air (T_s) and 3 for return air (T_r)
- 14 for air temperature inside the cold room (T_{int}): 6 in the middle of each wall, 1 near the door, 1 at one wall surface (sample inside cold room), 6 at the corners (2 other corners are not accessible by thermocouples)
- 5 for air temperature in the external cell (T_{ext}) on the surface of each wall

Two wattmeters are used to measure the instantaneous electricity consumption of the refrigeration system (compressor and auxiliary).

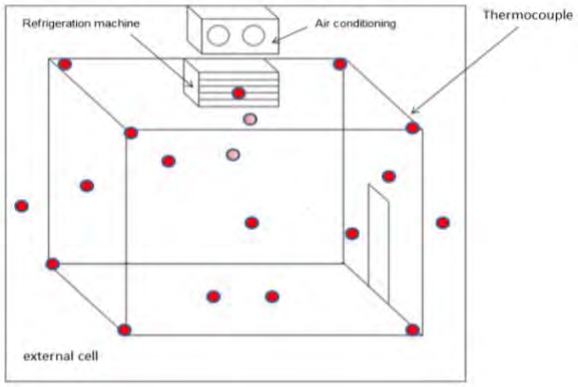

Figure 2 : the configuration of the cold room (red dots representing thermocouple positions)

2.2. Model development

2.2.1. Data driven model

Among the existing nonlinear models, Stacked LSTM (Stacked Long Short Term Memory) was chosen in this study. This model consists of a stack of several layers of LSTM. The LSTM is a recurrent neural network, which has been used to solve many time sequence problems; the LSTM provides good forecasting results because it permits to keep short-term information (recent changes and current data trends) and long-term information (periodicity, recurring or non-recurring

events) (Ping-Huan & Chiou-Jye, 2018). In some prediction problems, it is indeed very advantageous to increase the depth of a network to obtain much better results.
Two phases are needed to identify the model: training period (blue line in Fig.3) and test period (red line in Fig.3), which are represented as time series data. The training phase allows the identification of the constants of the chosen mathematical model and the test phase makes it possible to check the relevance of the model based on known past events (recent observations). It is important to choose a training period long enough to contain a representative panel of modes of excitation of the system to be modeled and a time step small enough to take into account fast dynamics. For this study we have two series of data.

2.2.2. Time series data

A. Time series data 1 is obtained with an empty room: the training period is fixed at 3.5 days (60% of the total data), the test period is fixed at 0.5 days (40% of the total data) and the simulation time step is fixed at 20 seconds. The DR has 1 hour of duration (bigger peaks in Fig.3) and it is applied with an automatic period (3h between 2 DR). In addition, we manage that the defrosting periods (10 minutes, smaller peaks in Fig.3) do not occur during a DR event (Fig.3).

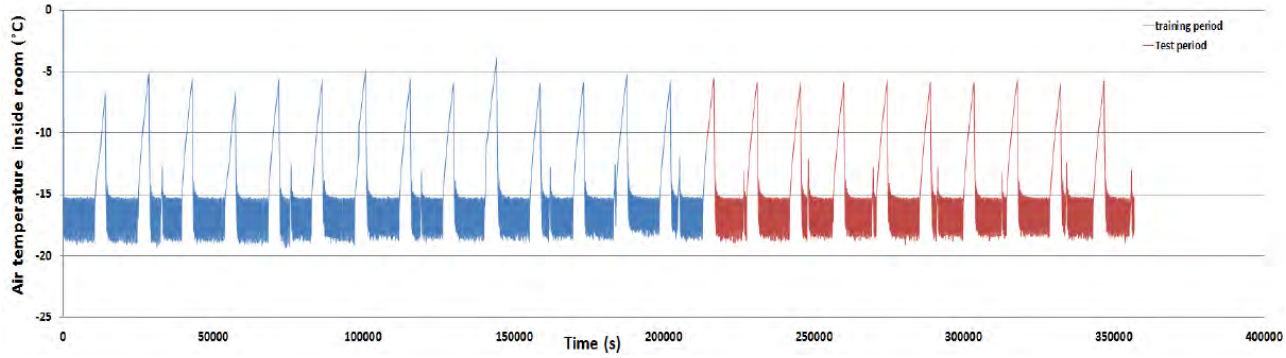

Figure 3 : Measured air temperature inside room (training and testing period) series 1

B. Time series data 2 is also obtained with an empty room: data is recorded during two weeks, the repartition between training and testing periods is also 60% and 40% of the total data. The simulation time step is fixed at 5 second. 3 different durations (30 minutes, 1 hour and 2 hours) were applied for DR. These periods are spread over several days with one DR at fixed times per day for five days. For this series, the defrost periods are not controlled, so the defrost and DR periods can overlap as shown in figure 4 at 5890 second (the defrosting of the fan is not complete because it is interrupted by DR).

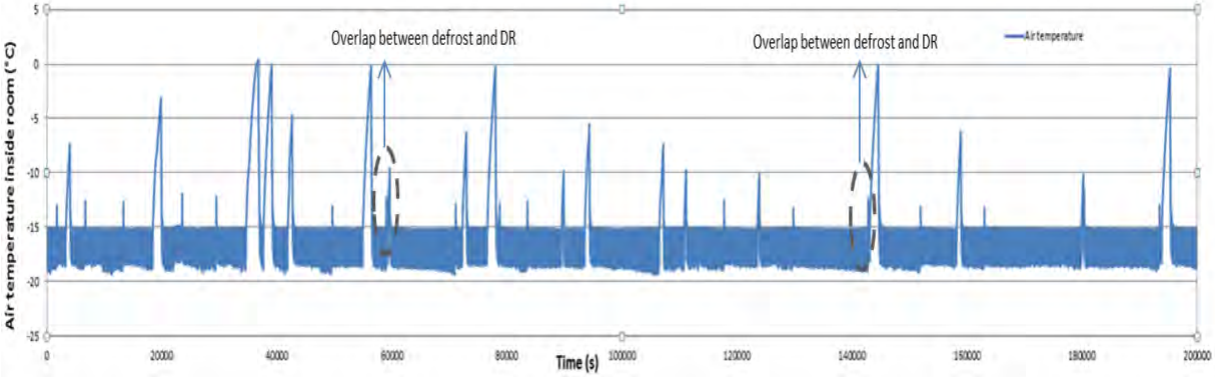

Figure 4 : Measured air temperature inside room series 2

C. Input and output data

For the two data series, the average of the set temperature is -16.3°C and the outside temperature is 20°C for the first data set and 17°C for the second data set. The inputs and outputs of the model are the same for the two time series 1 and 2. The data for this study are obtained by experimental measurements and additional features have been added in order to obtain better results:

- Dr [0, 1] - DR periods, binary data to indicate if at a time step t, the system is in a DR period (1) or not (0), including both the phase when the cooling system is turned off and the rebound phase of cooling (cooling system works to restore the set temperature).
- Def [0,1] – Defrosting periods, binary data, to indicate if at a time step t, the system is in a defrosting period (1) or not (0).
- Comp [0,1] - Compressor on/ off periods, which happen very regularly and in some punctual ways, also a binary data.
- Time Dr, the elapsed time since the last DR, allows the model to predict better the behavior of the cold room in the moments following the DR, while the state is not yet stabilized.
- Time def, the elapsed time since the last defrost, also allows predicting better the behavior of the cold room in the moments following the defrost step.

Input and output of the system are summarized in Table 1

Table 1. Inputs and the outputs of the data-driven model

	Name	Description
Output	Tr (°C)	air return temperature inside room
	P (W)	Electric power consumed
Input	Text (°C)	Outside temperature
	Def [0,1]	Defrost period
	Dr [0,1]	Demand response period
	Time def	The elapsed time since the last erasure
	Time Dr	The elapsed time since the last defrost
	Comp [0,1]	On/ off compressor

2.2.3. Physics based model

The model is developed in python and is used to simulate the dynamic air temperature inside the room and energy consumption by the compressor.
This model is based on equations describing the physical phenomena that occur in the system, such as energy and mass balance equations and the heat transfer phenomena in the building taking into account the given cooling capacity.
The model is chosen for its capacity to represent the main physical phenomena of the different type of cold storage (cold room and refrigeration warehouse). It is a compromise between simplicity (thus generic and easily identifiable) and precision (better taking into account the dynamics of the system).

3. RESULTS AND DISCUSSION

The two models (data driven model and physic based model) are compared with the experimental data on their capacity to predict the air temperature inside the room.
These figures present a zoom on a period where the evolution of air temperature and energy consumption before, during and after DR can be observed.

3.1. Data driven model

Fig.5 presents the comparison between the return air temperature (T_r) obtained by the data driven model (stacked_LSTM, blue curves) and experimental data (red curves) in the test period. In these two cases (series 1 and series 2) the duration of DR is 1 hour. In Fig.5a, the air temperature obtained by the stacked LSTM model predicts well the dynamics of the system. The presence of the small disturbance is due to external noise. Fig.5b presents the temperature evolution obtained with the time series 2. The model also shows a good prediction of the air temperature rise during DR, although DRs are fewer and more spaced than in the time series 1 (Fig.5a).

A slight difference between experimental data and model is observed. Data obtained by two measurement time steps (20 s - Fig.5a and 5 s - Fig.5b) were tested and the model is more sensible to noise with data obtained with smaller time steps. These preliminary results will be the source of improvement in future works by integration of signal analysis, for example the Fast Fourier Transform (FFT), which identifies the nature of the signals.

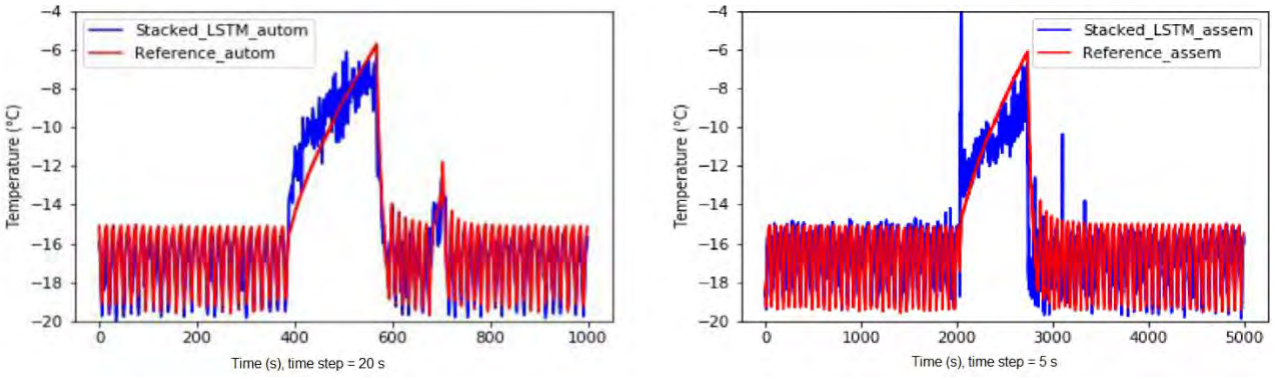

(a) Inside air temperature with series 1 (b) Inside air temperature with series 2

Figure 5: Comparison between the result of data driven model and experimental data for inside air temperature with 1 hour of demand response (DR)

Fig.6 presents the comparison between the energy consumption obtained by the data driven model (stacked_LSTM, blue curves) and experimental data (red curves) in the test period**.** For Fig.6a, we observe that energy consumption obtained by the stacked LSTM model follows the energy consumption obtained by experimental data with the presence of the small difference in the period of demand response; this can be due to the short period of training. For Fig.6b, a good prediction is obtained by the stacked LSTM model. These results are very promising for the prediction of energy consumption by neural networks models.

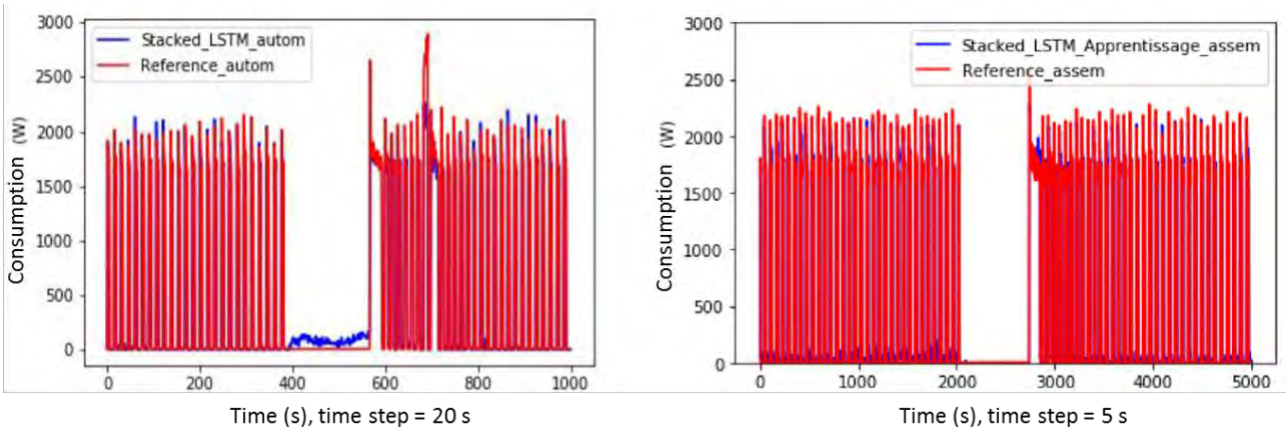

(a) Energy consumption with series 1 (b) Energy consumption with series 2

Figure 6 : Comparison between the result of data driven model and experimental data for energy consumption by compressor with 1 hour of demand response (DR)

3.2. Physics based model

Fig.7 presents the comparison between the results of physics based model (red curves) and experimental data (blue curves). In Fig.7 (a and b), the air temperature obtained by the physics model does not really follow the dynamics of the system. This model is very simplified (based on calculated heat loads); it is not designed to predict the system behavior in short terms of fluctuation of temperature. However the model predicts the same temperature range as experimental data.

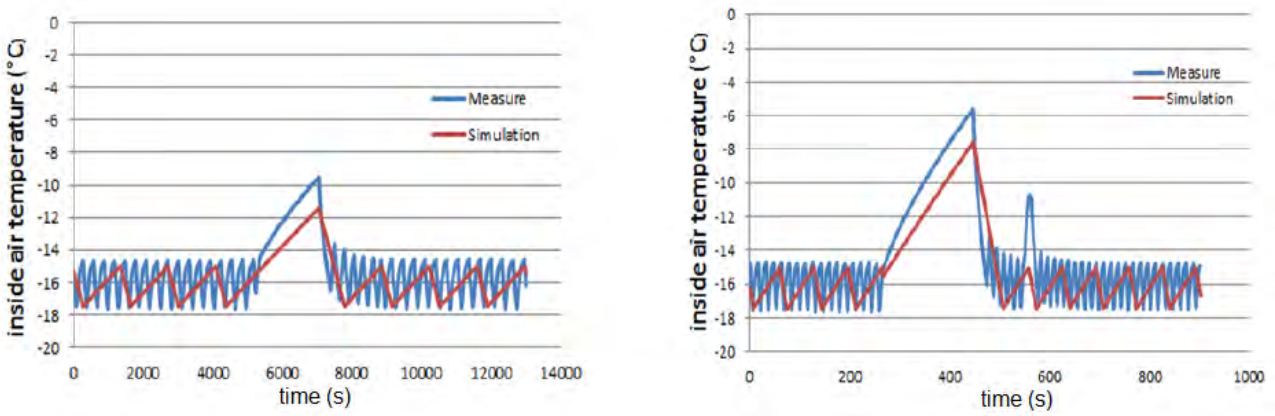

a) Inside air temperature with 30 min of DR

(b) Inside air temperature with 1hour of DR

Figure 7 : Comparison between the result of physics model and experimental data for inside air temperature

4. CONCLUSIONS

In this study, the two approaches of modelling (data driven and physics based) were developed. An experimental device has been set up to validate these models. This device is also used to collect the data (inputs and outputs) for the development of both approaches. The obtained results show that the neural network succeeds in predicting the system behaviour. They appear to be promising for their use in prediction of Demand response impacts.

As perspectives:

- Data driven model: the results will be improved and more data will be applied for the model.
- Physics based model: will be improved by including more short term dynamics and adapted to our case.
- Experimental device: the room will be loaded with products (the previous tests were performed with an empty room) and different scenarios of DR will be tested (duration, percentage of the load, season …) and more data will be collected and will be tested with modelling.

ACKNOWLEDGEMENTS

This work was funded by the agency for the Environment and Energy Management (ADEME) [Project Flexifroid, 2016 - 2019].

REFERENCES

Afram, A., & Janabi-Sharifi, F. (2014). Review of modeling methods for HVAC systems. Applied Thermal Engineering, 67(1–2), 507-519.

Amasyalia, K., & El-Goharyb, N. (2016). Building Lighting Energy Consumption Prediction.

Anonymous. (2002). The ESP-r System for Building Energy Simulation, User Guide Version 10 Series. University of Strathclyde, Energy Systems Research Unit. Retrieved from http://www.esru.strath.ac.uk/Documents/ESP-r_userguide.pdf, accessed on 02/07/2019.

Ben-Nakhi, A. E., & Mahmoud, M. A. (2004). Cooling load prediction for buildings using general regression neural networks. Energy Conversion and Management, 45(13–14), 2127-2141.

Berthou, T., Stabat, P., Salvazet, R., & Marchio, D. (2012). Comparaison de modèles linéaires inverses pour la mise en place de stratégies d'effacement. Paper presented at the XXXe Rencontres AUGC-IBPSA, Chambéry, Savoie, 6.

Berthou, T., Stabat, P., Salvazet, R., & Marchio, D. (2014). Development and validation of a gray box model to predict thermal behavior of occupied office buildings. Energy and Buildings, 74(Supplement C), 91-100.

Brooks, R. W., Green, R. H., Cleland, A. J., & Senior, P. (1999). The potential of refrigerated stored for electricity load managment Paper presented at the 20th International Congress of Refrigeration, Sydney,September 1999, Vol. IV, p. 1289-1296 (paper 231).

Crawley, D. B., Hand, J. W., Kummert, M., & Griffith, B. T. (2008). Contrasting the capabilities of building energy performance simulation programs. Building and Environment, 43(4), 661-673.

Crawley, D. B., Lawrie, L. K., Pedersen, C. O., Winkelmann, F. C., Witte, M. J., Strand, R. K., . . . Gu, L. (2004). EnergyPlus. Retrieved from https://www.researchgate.net/publication/268390898_EnergyPlus_An_Update, accessed on 02/07/2019.

Evans, J. A., Foster, A. M., Huet, J. M., Reinholdt, L., Fikiin, K., Zilio, C., . . . van Sambeeck, T. W. M. (2014). Specific energy consumption values for various refrigerated food cold stores. Energy and Buildings, 74(0), 141-151.

H.U Frausto, J. G. Pieters, & J. M.Deltour. (2003). Modelling Greenhouse Temperature by means of Auto Regressive Models. Biosystems Engineering, 84(2), 147-157.

H.U. Frausto, & J.G. Pieters. (2004). Modelling greenhouse temperature using system identification by means of neural networks. Neurocomputing, 56, 423-428.

Kramer, R., van Schijndel, J., & Schellen, H. (2012). Simplified thermal and hygric building models: A literature review. Frontiers of Architectural Research, 1(4), 318-325.

Li, Q., Meng, Q., Cai, J., Yoshino, H., & Mochida, A. (2009). Applying support vector machine to predict hourly cooling load in the building. Applied Energy, 86(10), 2249-2256.

Mustafaraj, G., Lowry, G., & Chen, J. (2011). Prediction of room temperature and relative humidity by autoregressive linear and nonlinear neural network models for an open office. Energy and Buildings, 43(6), 1452-1460.

Ping-Huan, K., & Chiou-Jye, H. (2018). A High Precision Artificial Neural Networks Model for Short-Term Energy Load Forecasting. Retrieved from https://www.researchgate.net/publication/322547645_A_High_Precision_Artificial_Neural_Networks_Model_for_Short-Term_Energy_Load_Forecasting, accessed on 02/07/2019.

S. Karatasou, Santamouris, M., & Geros, V. (2006). Prediction of energy consumption in buildings with artificial intelligent techniques and Chaos time series analysis. Paper presented at the International Workshop on Energy Performance and Environmental,Quality of Buildings, Milos island, Greece.

X. Qiu, L. Zhang, G. Amaratunga, & P. N. Suganthan. (2014). Ensemble Deep Learning for Regression and Time Series Forecasting. Paper presented at the IEEE Symposium on Computational Intelligence in Ensemble Learning (CIEL).

Xue, X., Wang, S., Yan, C., & Cui, B. (2015). A fast chiller power demand response control strategy for buildings connected to smart grid. Applied Energy, 137, 77-87.

Manuscript ID: 448
DOI: 10.18462/iir.icr.2019.0448

A2L Refrigerants Leak and Ignition Testing for a Walk-in Cooler System

Xudong WANG

Air-Conditioning, Heating, and Refrigeration Institute
Arlington, VA 22201, USA, xwang@ahrinet.org

ABSTRACT

Environmental concerns have triggered a series of activities globally to curtail the use of high GWP hydrofluorocarbons (HFCs). Many of these alternative refrigerants are mildly flammable (A2L safety classification per ASHRAE 34).
To properly address A2L refrigerants in safety standards, the Air-Conditioning, Heating, and Refrigeration Technology Institute (AHRTI) undertook a research project to investigate A2L refrigerants, specifically to carry-out leak and ignition testing under whole room scale conditions.
This paper summarizes the results of A2L refrigerants R-455A and R-457A leak and ignition tests for a walk-in cooler system. A 12x14x8ft walk-in system was built with a ceiling mounted unit cooler installed inside the walk-in box. The testing simulated refrigerant leaks from the evaporator with ignition sources present. The results showed that the leak location (coil face vs. return bend) influenced the ignition results. The maximum temperatures observed inside the walk-in box were in the range of 1500~1700F in ignition events.
Keywords: Refrigerant, Flammability, Walk-in cooler.

1. INTRODUCTION

The air conditioning and refrigeration industry is undergoing a transition from high GWP refrigerants to lower GWP refrigerants. The AHRI Low-GWP Alternative Refrigerants Evaluation Program (Wang et al, 2014 and 2016) has shown that many promising alternatives are classified as A2L (mildly flammable, such as HFOs) or A3 (flammable, such as hydrocarbons) according to ASHRAE Standard 34 (ASHRAE, 2016).
To allow flammable refrigerants to be practically used in the field, relevant safety standards and building codes must be changed to adopt the use of these refrigerants. In order to support code and standard activities related to the use of flammable refrigerants, AHRI surveyed committees and working groups working on flammable refrigerants related standards for existing knowledge gaps of using flammable refrigerants. Among the survey responses, the top priority research needs were identified below:

- Whole room or real life leaks, with ignition sources present, are needed to validate or recalibrate current AHRI and OEM risk assessments.
- The HVAC industry needs to understand the risk/consequence after refrigerant ignition, in order to establish quantified risk tolerance limits for severity of event rather than just probability of ignition.
- The HVAC industry needs to assess the ability of 2L refrigerants to sustain an ignition (with % oil included), and possibly cause a secondary combustion event compared to current refrigerant/lubricant systems which are proven in use.

To address these identified needs, AHRTI launched a research project to conduct whole room scale testing. The testing was conducted by UL at its test facility in Northbrook, IL. The objective of the project was to conduct refrigerant leak and ignition testing under whole room conditions to understand the potential ignition associated with the use of A2L refrigerants as opposed to the A1 refrigerants currently in use while considering ambient conditions (temperature and humidity) and refrigerant lubricants (Gandhi et al, 2017).
The entire project included parametric testing to investigate how variables (ambient, refrigerant amount etc.) influence the ignition and scenario testing to investigate the refrigerant flammability under whole room scale. Whole room scale testing consisted of scenarios that represented

refrigeration and air conditioning applications. The refrigeration applications included a convenience store with reach-in cooler and a walk-in cooler inside a commercial kitchen. Air conditioning scenarios included (i) motel room with PTAC unit; (ii) residential basement with split air conditioning unit; and (iii) commercial kitchen with a rooftop unit. The residential scenarios considered the impact of refrigerant leak at the A-coil into the hallway and servicing error. Data were also developed on fire hazards from the failure of hermetic electrical pass-through component of a residential air-conditioning unit.
The parametric testing and results of residential air-conditioner and reach-in cooler tests were previously presented (Wang et al, 2018). This paper is only a high level summary of the walk-in cooler tests done by UL, More detailed information is contained in the project final report (Gandhi et al, 2017).

2. TEST SETUP AND PROCEDURES

Two A2L refrigerants were tested for the walk-in cooler. Their information is listed in Table 1. They have different burning velocity within the 2L category. R455A has a much lower laminar burning velocity and higher Lower Flammability Limit (LFL) than R457A.

Table 1. Test refrigerants properties

Parameter	R-455A	R-457A
Lower Flammability Limit (LFL, % volume)	11.8	6.0
(LFL, kg/m³)Sea Level	0.423	0.215
(LFL, kg/m³) 200 m (650 feet)	0.415	0.211
Upper Flammability Limit (UFL, % volume)	12.9	18
Laminar Burning Velocity (cm/s)	<1.5	6.3
Composition (% mass)	R1234yf/R32/R744 (75.5/21.5/3)	R1234yf/R32/R152a (70/18/12)

During the test, the refrigerant in liquid phase was released into the walk-in box with variety of viable ignition sources present. The refrigerant release system is illustrated in Fig. 1. Its two main components are a pressurizer tank and a release tank that are equipped with accessories such as control valves and temperature and pressure measurement. Both tanks contained the same refrigerant and were submerged in heated water tanks to achieve desired pressure and temperature conditions. The pressurizer tank ensures the release tank to release liquid refrigerant to the test room at a constant rate. The refrigerant release rate was controlled by a control valve that continuously adjusts its opening according to the feedback from the mass flow meter. The release system can perform tests including lubricating oil with injecting lubricants to the refrigerant stream using a gear pump; however the walk-in cooler tests only used pure refrigerant without lubricant.
The ignition sources used in the scenario tests included electric arc ignition sources and open flame sources consisting of tea candles (38.1 mm (1.5 inch) in diameter). The tea candles were lit manually prior to start of tests. The electric arcs were created by a step-up gas tube transformer. The electric arc transformer was continuously energized for several minutes during the tests. A full scale walk-in cooler was built to simulate real application. The plain view of the test setup is shown in Fig. 2. The walk-in box dimensions were 3.7x4.3x2.4 m (12x14x8 ft). Objects representing shelves were located in the walk-in box. A ceiling-mount unit cooler was installed toward one end of the room opposite to the walk-in door. The locations of the instrumentation, and ignition sources were located in clusters at locations A, B, C and D shown in Fig. 2. A total of 24 Type K thermocouples were used to measure the temperature at different locations and heights within the walk-in box. The thermocouple response time was approximately 3 seconds. The leaked refrigerant gas concentration in the test room was measured by total hydrocarbon analyzers calibrated for the specific refrigerant of interest. High definition video cameras installed at different angles to document the test events. The location of thermocouples, electric arc igniters and refrigerant concentration sensors are shown in Fig. 2.

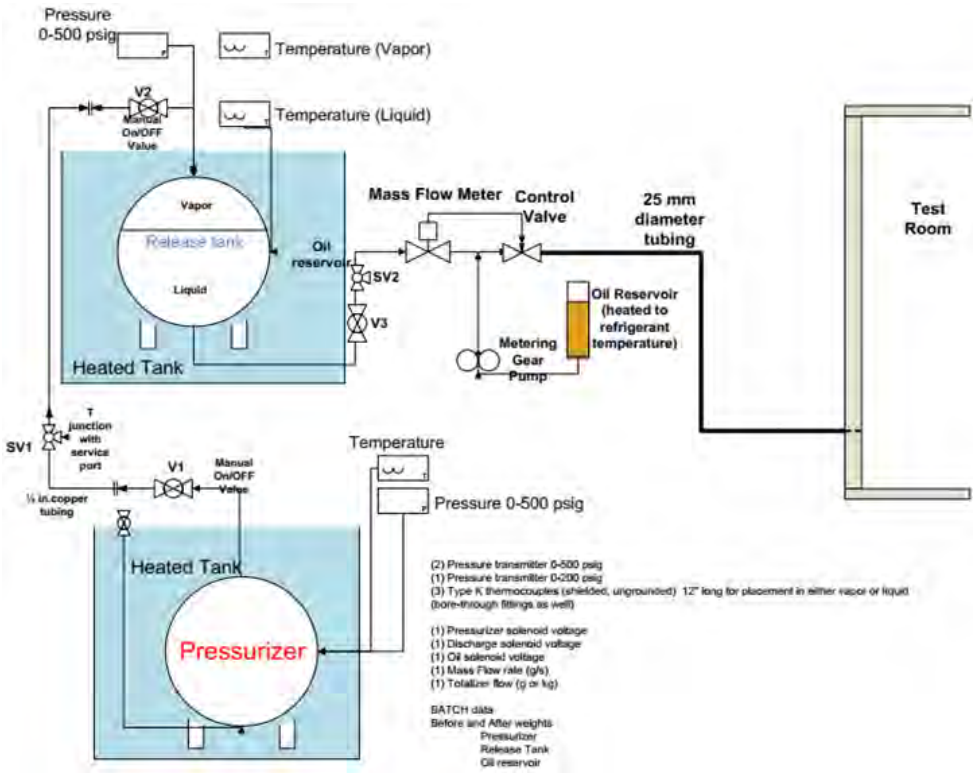

Figure 1: Schematic of the refrigerant release mechanism setup (Gandhi et al, 2017)

The general procedure for testing was to get the refrigerant release system ready, light the candles, turn on electric arcs, and initiate the data acquisition system 60 seconds prior to release of the refrigerant. When the target quantity of refrigerant was released with the target flow rate, refrigerant sampling through the refrigerant sensors was discontinued. The data were collected until all flaming had ceased for at least 2 minutes. At the end of a test sequence, the test room was exhausted through a smoke abatement system and replenished with fresh air. After each test, the test facility was exhausted through UL's smoke abatement system, and the conditions in the facility were monitored with open path gas FT-IR.

The test matrix is shown in Table 2. The tests simulated a ceiling mounted commercial refrigeration unit with the refrigerant leak in the evaporator section. The leak occurred at either the coil face or a return band inside casing when the door of the walk-in box was either open or closed. The refrigerant release quantities were based on the proposed charge limit per a draft version of IEC Standard 60335-2-89. The draft was developed by IEC Subcommittee 61C, Safety of Refrigeration Appliances for Household and Commercial Use, Working Group 4 Commercial Refrigerating Appliances using more than 150 g of Flammable Refrigerant. The draft standard required that the flammable refrigerant charge limit was 13 times LFL of a particular refrigerant (13 m^3×LFL kg/m^3). For this reason the release amount for R-455A and R-457A was calculated to be 5.4kg and 2.7kg respectively. The release in all cases was set to 50 g/s through a 3/8 inch diameter copper tube.

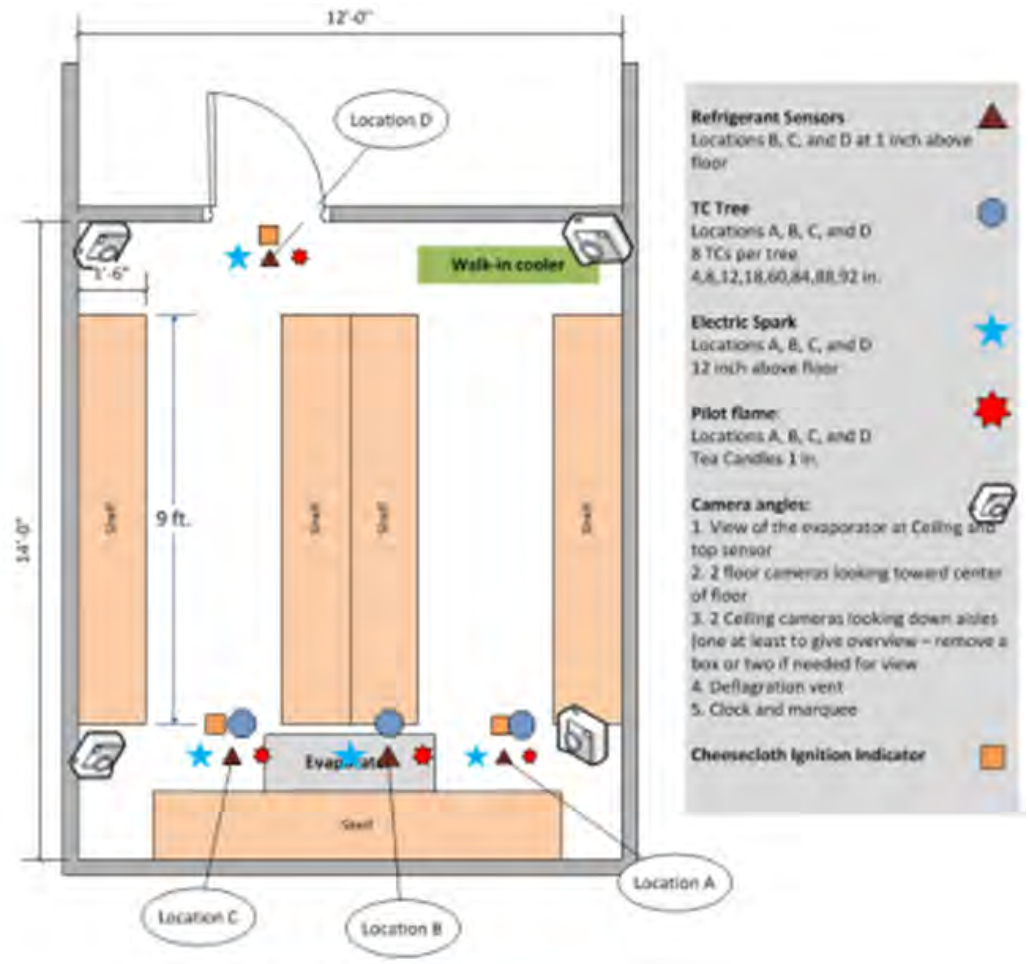

Figure 2: Schematic of the walk-in cooler test setup (Gandhi et al, 2017)

Table 2. Walk-in cooler test matrix

Refrigerant	Test Number	Door Condition	Leak Location	Planned Discharge (kg)	Discharge Rate ($g.s^{-1}$)
R-455A	Walkin08	Closed	Return Bend	5.4	50
R-457A	Walkin09	Closed	Return Bend	2.7	50
R-457A	Walkin10	Open	Return Bend	2.7	50
R-455A	Walkin11	Open	Return Bend	5.4	50
R-455A	Walkin12	Closed	Coil Face	5.4	50
R-457A	Walkin13	Closed	Coil Face	2.7	50
R-455A	Walkin14	Open	Coil Face	5.4	50

3. TEST RESULTS

For walk-in cooler tests, the first two tests were for R455A and R457A at a target charge level with the walk-in door closed. The leak was created at the coil return band. This would be the worst case scenario when leaked refrigerants were trapped inside the walk-in box. Ignition occurred for both tests, however, R457A showed a localized ignition only. Higher temperatures were observed for R455A. Then, the tests were repeated with the walk-in door open to see if the refrigerants ignition may be mitigated due to the fact that they can dissipated outside the walk-in box. The remaining three tests were conducted for the leaks occurring at the coil face. The ignition was observed for

R455A at the 5.4kg charge level but with a less severity than the leak at return band. No ignition was observed for R457A.
The location of the discharge influenced ignition results. Tests with the discharge at the return bend forced the refrigerant to leave the unit cooler through the condensate drain and drop to the floor because the refrigerant momentum was significantly reduced in this process. This direct path to floor level and less mixing with air resulted in flammable refrigerant mixtures. In contrast, the discharge through the coil face resulted in turbulent mixing of the refrigerant with air before the cooled mixture dropped to the floor. This indirect path to floor level resulted in less flammable mixtures. The position of the door, open or closed, appeared to have little impact on ignition results. Fig. 3 shows a bar chart of maximum temperature for the seven experiments based on the three factors of: Refrigerant type (R-455A or R-457A), Discharge Location (Coil Face or Return Bend), and Door Position (Closed or Open). The chart shows that ignition of the R-455A discharge lead to the highest temperatures, but only from the return bend. There was no ignition for either refrigerant when discharged from the coil face. There was a small effect on maximum temperature depending on whether the walk-in door was open or closed. Tests showed that ignition occurred only at locations A, B, or C in Fig. 2. No ignition occurred at location D (near the walk-in door).

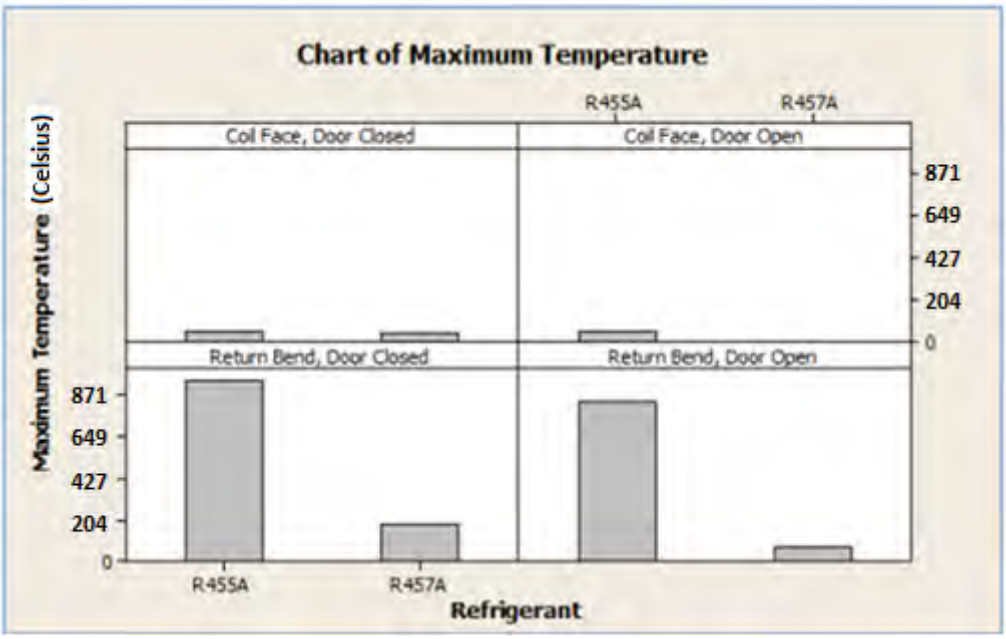

Figure 3: Maximum temperature versus discharge location and door position (Gandhi et al, 2017)

4. DISCUSSION

Due to the limited resources, only typical equipment and setup were tested. Care must be exercised when attempting to make broad conclusions because small statistical sample sizes were used for most tests. It must also be stressed that the testing was more focused on understanding the ignition event severity, rather than the probability of the refrigerant ignition event. Some tested ignition events represented the scenarios with low probability of occurrence. For instance, ignition sources used in the testing had sufficient energy (i.e., much greater than the minimum ignition energy) to cause ignition of a flammable mixture. In addition, ignition sources were located where combustible mixtures were most likely to occur. Therefore, some relatively low probability events were forced to occur. The intention was to establish the worst case scenario using the most conservative way so that relevant standard working groups and manufacturers can build upon them with additional requirements and design features to mitigate potential risks.
In the testing, thermocouples were used to measure temperatures; however, their readings do not reflect actual flame temperatures. The instantaneous temperatures of the flames are higher than what the thermocouples recorded because thermocouples have response time delay, and the flames have fast movements. This may create a difficult time when the measured temperatures are used to validate modeling simulations; however, the relative values and trends among different scenarios do reflect the different severity levels for tested scenarios.

5. SUMMARY

The testing provided the following key learnings:
The location of the discharge had a significant effect on ignition results. When the refrigerant release occurred at the return bend of the evaporator in the unit cooler, the refrigerant was forced to leave the unit cooler through the condensate drain and drop to the floor. This direct path to floor level (approximately 7 ft., 2.1m) resulted in flammable refrigerant mixtures. In contrast, the discharge through the coil face resulted in turbulent mixing of the refrigerant with air before the cooled mixture dropped to floor. This indirect path to floor level resulted in greater mixing of the refrigerant with room air. There was no ignition of the refrigerant when the discharge was from the coil face due to turbulent mixing before the mixture dropped to the floor. The position of the test room door, open or closed, appeared to have little impact on ignition results.
The testing was more focused on understanding the ignition event severity, rather than the probability of the refrigerant ignition event. The future work should include characterization of refrigerant leak scenarios with actual equipment in “on” and “off” states, and real world ignition sources in terms of ignition energy, quantity, spatial location throughout the room, and activation frequency.

ACKNOWLEDGEMENTS

The project was strongly desired and supported by the HVACR industry. A group of industry experts provide technical guidance and products for testing. AHRI is grateful to all of them for contributing their expertise and resources to the project.

REFERENCES

ASHRAE, 2016, ASHRAE Standard 34: Designation and Safety Classification of Refrigerants.

Gandhi, P, Hunter, G., Haseman, R. and Rodgers, B., 2017. Benchmarking Risk by Whole Room Scale Leaks and Ignitions Testing of A2L Refrigerants, AHRTI Project 9007 Final Report.

IEC, 2018, International Electrotechnical Commission (IEC), 60335-2-89, Household and similar electrical appliances – Safety – Part 2-89: Particular requirements for commercial refrigerating appliances with an incorporated or remote refrigerant unit or compressor.

Wang, X., Amrane, K., 2014, AHRI Low Global Warming Potential Alternative Refrigerants Evaluation Program (Low-GWP AREP)-Summary of Phase I Testing Results, 15th International Refrigeration and Air Conditioning Conference at Purdue.

Wang, X., Amrane, K., 2016, AHRI Low Global Warming Potential Alternative Refrigerants Evaluation Program (Low-GWP AREP)-Summary of Phase II Testing Results, 16th International Refrigeration and Air Conditioning Conference at Purdue.

Wang, X., Gandhi, P, 2018, A2L Refrigerants Leaks and Ignitions Testing under Whole Room Scale, 17th International Refrigeration and Air Conditioning Conference at Purdue.

Manuscript ID: 466
DOI: 10.18462/iir.icr.2019.0466

Real energy efficiency of DX NH_3 versus HFC

Stefan S. JENSEN
Scantec Refrigeration Technologies Pty. Ltd. Murarrie, QLD 4172, Australia,
ssjensen@scantec.com.au

ABSTRACT

The paper details the decommissioning of several existing HFC based, air-cooled refrigeration plants servicing a refrigerated warehouse and replacement of these with a central, low charge, dry expansion, NH_3 based refrigeration plant.

Comparisons are shown between the recorded energy performances of the new DX, NH_3 system and those of the previous HFC based systems. The basis of this comparison are the supply authority records of the electrical energy consumed by the HFC plant and the consumption records generated using the SCADA system of the new ammonia plant.

The geographic location of the plant is Mackay, North Queensland, Australia. High ambient dry bulb/wet bulb temperatures characterize this region.

The paper discusses the technical and economic viability of NH_3 DX based solutions for the small to medium capacity range such as this. Technical details and images of the former HFC plant as well as the replacement DX type, central NH_3 installation are also provided.

1. INTRODUCTION

Around one third of all signatories to the Kigali Amendment have now ratified it. The Kigali Amendment to the Montreal Protocol commits the signatories to a gradual phase-down of the consumption of hydrofluorocarbon (HFC) refrigerants. In many non-Article 5 countries, the HFC phase-down commenced January 2019. In other jurisdictions, the HFC phase-down has been a reality for much longer. In 2007 Denmark was the first country in the world to ban HFC's in all systems with refrigerant inventories <0.15 kg and >10 kg; the European Union started the phase-down of HFC's in January 2015.

The official commencement of the HFC phase-down in Australia was January 1, 2018. Between 2019 and end of 2036, HFC importation into Australia is scheduled to reduce gradually from 8,000 tons CO_2e to < 2,000 tons CO_2e.

In January 2019, fifteen of the hottest locations in the World were in Australia with the highest night-time temperature of 35.9°C recorded at Noona in central New South Wales. The year 2018 was the third warmest year ever recorded for the Australian continent. Three years ago, Australia started using the 55°C isotherm on the weather maps. Many refrigerated warehouses in the major urban centres of Australia are now being designed to accommodate ambient dry bulb temperatures >45°C for three consecutive days with a peak of up to 48°C within that three day period.

Leapfrogging low global warming potential, synthetic refrigerant blends in new RACHP installations raises special challenges in Australia. Not only is this because of the high ambient temperatures. It is also due to the generally low level of awareness of natural refrigerant-based solutions and a relatively low level of preparedness for the imminent proliferation of flammable working fluids.

Several solution providers in Australia offer imported transcritical CO_2 based packaged systems for retail and refrigerated warehouse applications. In jurisdictions with high ambient temperatures, these solutions do not deliver energy efficiencies significantly better than the HFC solutions they replace,

if at all. In the interest of compliance with the Paris Climate Treaty, Australia must therefore seek to implement RACHP solutions that not only eliminate the dependence upon HFC refrigerants, but also reduce energy consumption (reduce indirect emissions) at the same time. One such solution are low charge, central type, NH_3 based refrigeration systems with dry expansion (DX) refrigerant feed.

2. THE REFRIGERATED WAREHOUSE

The plant that is the subject of this paper is a relative small dual stage, ammonia refrigeration system servicing a refrigerated storage/distribution facility owned and operated by a food service company. Fig. 1 shows a plan view of the facility with design temperatures. Dimensions are as indicated in millimetres. Strictly speaking, the plan is incorrect. Following preparation of the layout, a decision was taken to remove the wall between the two freezer rooms and relocate the air coolers to the wall along the top of Fig. 1. Prior to this decision, air circulation between the two freezer rooms by mechanical means was envisaged. With the removal of the wall, this became unnecessary. Secondly, the dividing wall between the two segments of the Chiller was also removed following preparation of this layout. This was in order to limit the number of air coolers required in this area to one. The prefabricated dual stage, central ammonia plant room is not shown, but it is located along the exterior wall along the top of Fig. 1 immediately adjacent to the wall that the freezer evaporators were relocated to. This keeps NH_3 pipelines relatively short.

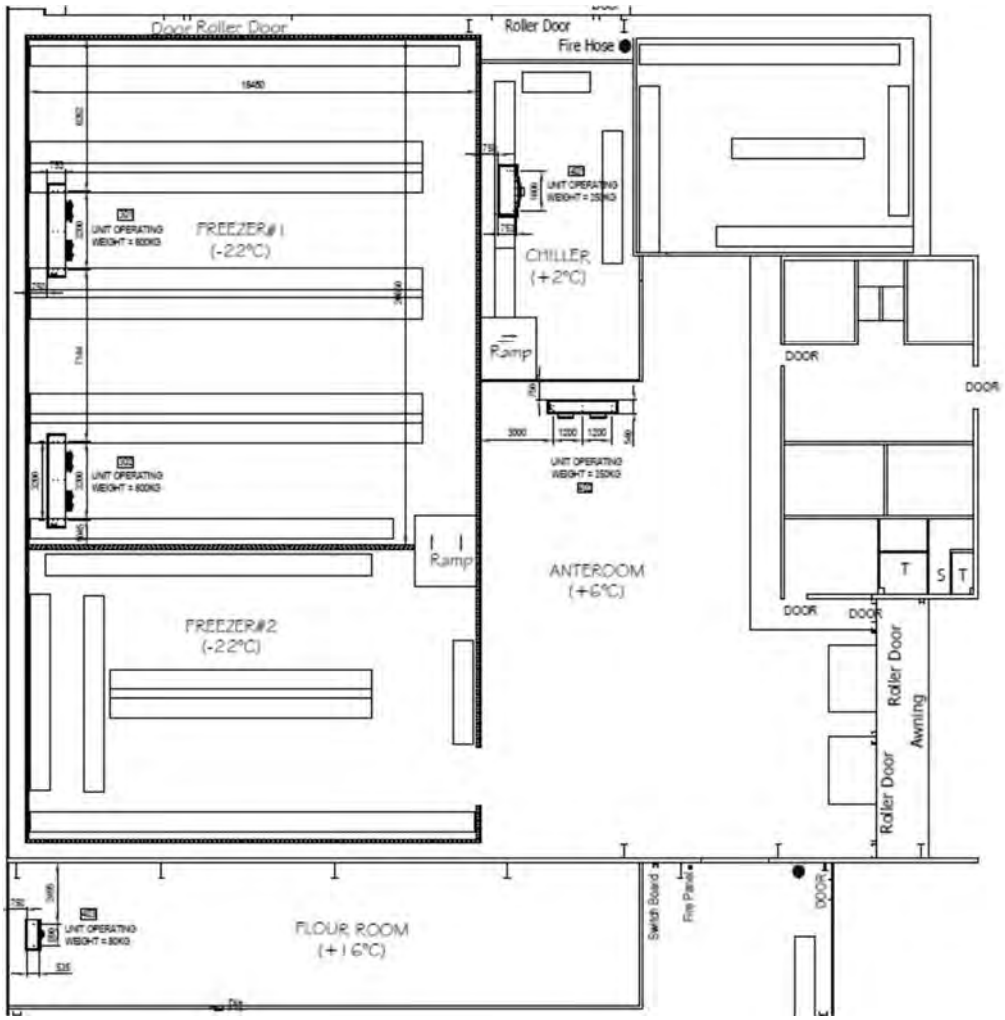

Figure 1. Plan layout of the refrigerated storage facility.

The warehouse is situated at Mackay, Queensland, Australia. The local design conditions for air conditioning plant at the Mackay Post Office is 33.5°C dry bulb temperature, 26.7°C wet bulb temperature, standard deviation 0.9°C, sample size 40 years (K. Bremhorst et al, 2006). The highest

recorded dry bulb temperature for the region is 36.9°C. Mean rainfall and temperatures for Mackay are shown in Fig. 2 (Meat & Livestock Australia, https://www.mla.com.au).



Figure 2. Mean rainfall and temperatures for Mackay, Queensland, Australia.

The estimated design heat loads for the warehouse are shown in Table 1. The temperature at each room reference represents the temperature used for the heat load estimation.

Table 1. Design heat loads in kW

DESIGN HEAT LOADS:	Low temperature	Medium Temperature	Propylene Glycol
Refrigerant temperature, °C →	-32	-11	-7
Freezer, -24°C	45.2		
Chiller, 0°C			17.6
Flour Room, 16°C			11.0
Ante Room, 6°C			20.2
TOTAL, kW	**45.2**		**48.8**

3. THE PREVIOUS HFC BASED REFRIGERATION SYSTEM

The HFC based refrigeration plant servicing the facility described above ceased operations in 2015 coinciding with a commercial decision to relocate the food service activities temporarily to other premises. Discussions regarding replacement of the existing HFC based systems with a new; more energy efficient central refrigeration system commenced fourth quarter of 2017 resulting in completion of the new installation August 2018.

The previous system comprised a number of low temperature Bitzer 4NC-12.2-LCS2-LS condensing units suitable for outdoor installation and one medium temperature condensing unit of unknown make, but believed to be Lovelock with a Copeland semi-hermetic compressor. These were connected to ten matching commercial evaporators with the low temperature units being arranged for electric defrost. The refrigerant was R404A in the low temperature segment. The refrigerant used in the medium temperature segment is unknown. The medium temperature refrigerant previously used is believed to be R22, but this could have been replaced with a drop-in refrigerant. The importation of HCFC 22 into Australia ceased in 2015.

The subfloor heating system used under the freezer floors is electrically powered. It comprises two independent resistance heating circuits for redundancy. The subfloor temperature is thermostatically controlled by switching the power supply on/off. The subfloor heating system was tested prior to the plant modifications commencing. It was found to be functioning and was therefore retained. More energy efficient heating options exist and are indeed used in new installations, but replacement of the subfloor heating system was considered too disruptive and too capital intensive in this case. Fig.

3 shows the HFC based refrigeration plants. The total peak power consumption of this plant excluding the power absorbed by the subfloor heating system and the drain/door heaters was 118 kW with all defrost heaters operational.



Figure 3. Previous HFC based, air cooled refrigeration systems

4. THE REPLACEMENT LOW CHARGE NH_3 REFRIGERATION SYSTEM

The replacement refrigeration system is a central type, dual stage, low NH_3 inventory refrigeration plant with dry expansion refrigerant feed for the low temperature freezer evaporators and a propylene glycol loop for the medium temperature services. The total NH_3 inventory is approximately 200 kg. The glycol/NH_3 plate heat exchanger for the secondary refrigerant loop is gravity flooded using the intercooler as surge vessel. The plant employs three open industrial reciprocating compressors all fitted with variable frequency drives. One compressor is a dedicated booster, one compressor is a dedicated second compression stage machine and the third compressor is connected for dual duty capability. Two compressors can service the estimated heat loads whereas the third is for redundancy. There are no ammonia pumps. A closed circuit water cooling segment incorporated within the evaporative condenser services the compressor top and side cooling. This closed loop includes a duty and a standby cooling water circulation pump. The freezer evaporators are controlled using the combined superheat/quality control principle. Overall, the plant follows the same general design principles as the sixteen other commercially operating low charge NH_3 plants (Jensen, 2015, Fig. 2; Jensen, 2017). The entire engine room including base frame, weatherproof enclosure, electrical control system, motor control centre, ventilation systems, pressure vessels, oil management system, glycol pump and NH_3/glycol heat exchanger was manufactured off site. All interconnecting NH_3 pipelines are 304SS for durability and low friction. The anticipated technical life of the plant is identical to what can be anticipated for larger industrial ammonia refrigeration systems i.e. 30-40 years. Images of plant room exterior and interior are shown in Fig. 4 and Fig. 5.

The design details of each of the two dry expansion freezer evaporators are detailed in Table 2. Fig. 6 shows the two NH_3 evaporators installed.

Table 2. Freezer evaporator design details

Fin thickness, mm	0.35
Vertical and horizontal tube pitches, mm	50/50
Tube outside/inside diameters, mm	16.0/13.6
Tube pattern	Square
Finned length x height x depth, mm	3200x1200x300
Refrigerant distributor	Gravity type
Fin spacing, mm	10.0
Face velocity at full fan speed, rpm	2.7
Evaporating temperature, °C	-31.0
Internal/external fouling resistances, m²K/W	0.0004/0.0035

Air on/off, °C	-24.0/-25.8
Relative humidity on/off, %	80/89
Air flow at full fan speed, m³/s	10.4
Total/sensible capacity, kW	26.9/26.1
Surface area, m²	227.0
Fans; no./diameter/speed/capacity, -/mm/rpm/kW	2/800/850/1.44



Figure 4. Plant room exterior, evaporative condenser in the background



Figure 5. Plant room interior, pressure vessels in the background



Figure 6. Freezer evaporators

5 ENERGY CONSUMPTION

The energy consumption details per month for the facility were obtained from the energy retailer, Ergon Energy for December 2009 to January 2015 inclusive. When the HFC-based plants serviced the warehouse, the daily average energy consumption was recorded at 2,020 kWh. Fig. 7 shows a graphical representation of these energy consumption details. A slightly rising trend in monthly energy consumption is evident over the period analysed.

Several building modifications were incorporated coinciding with the installation of the new ammonia refrigeration plant. As mentioned previously, the two Freezer Rooms were combined into one room, as were the two Chiller Rooms. The previous installation did not incorporate a refrigerated Ante Room – the Freezer and Chiller Rooms opened into an area covered by a weather roof and

surrounded by uninsulated walls. The modified facility has had a refrigerated Ante Room added. The previous facility also did not include a Flour Room. The modified facility has had a Flour Room added within the existing non-refrigerated Dry Store as shown in Fig. 1. Finally, a rapid roller door was included between the new Ante Room and the Dry Store to facilitate access/product movement between Ante Room and Dry Store/Flour Room. The refrigerated area/volume prior to the building modifications were 792/3,169 m²/m³. Following the modifications, these had increased to 1,263/5,245 m²/m³ or by 37/40% respectively.

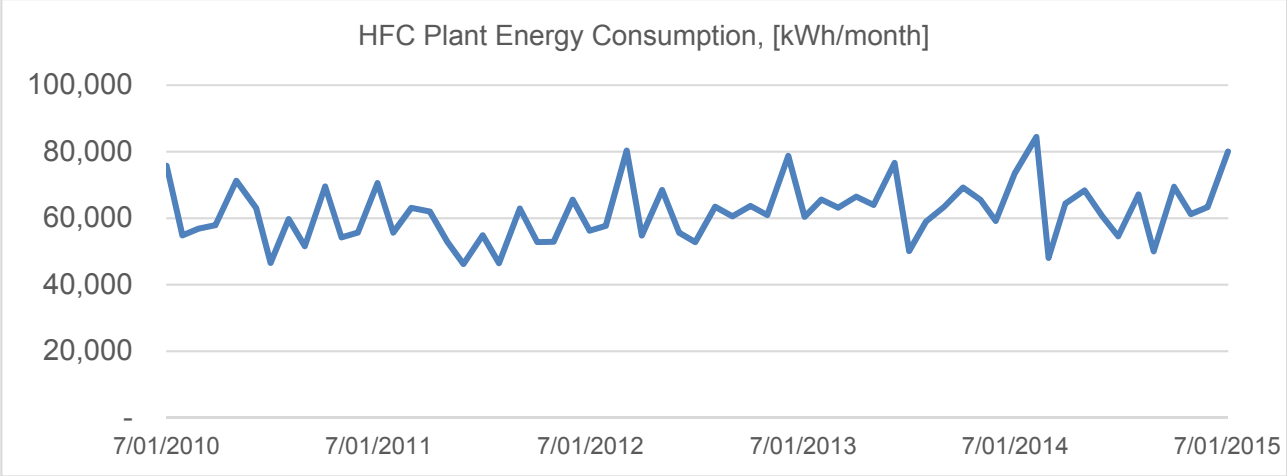

Figure 7. Monthly facility energy consumption with HFC based refrigeration systems

As with most other similar plant upgrades in the commercial world, building modifications are usually included as part of the refrigeration plant replacement/upgrades. This makes a straight forward "before/after" energy consumption comparison difficult and this case is no different.

The kWh-meter readings for the low charge NH_3 refrigeration plant are:

Start date:	3 October, 2018	Reading:	5,107 kWh
End date:	18 January, 2019	Reading:	141,303 kWh.

This represents an average consumption of approximately 1260 kWh/day or a specific annual energy consumption (SEC) based on refrigerated volume of 88 kWh/m³*a. This is on the higher side of expectations and there are several reasons for this. Firstly, the freezer had only been operational for approximately two months when recording started. The subsoil temperature had therefore not reached steady state. Secondly, the subsoil heating system temperature set point was excessive at 24°C. This was adjusted down to 5°C in January 2019. Thirdly, there were insulated panel imperfections (air leaks) that were subject to repairs during the recording period. Fourth, significant infiltration loads were observed from the Dry Store to the Ante Room during the recording period. The recording period falls within the Australian summer. The energy consumption for the same summer period during the years 2013/14 was recorded at an average of 2,243 kWh/day or 258 kWh/m³*a.

For the NH_3 system, the energy consumption was recorded via the supervisory control and data acquisition (SCADA) system. It therefore represents the energy consumption of the refrigeration plant only. This is not the case for the HFC plant records. The records for that plant includes auxiliary consumers such as general light and power, office air conditioning and forklift charging. Empirically, these services represent approximately 20% of the total energy consumed within refrigerated facilities owned and operated by this particular user (Jensen, 2017). The corrected SEC for the HFC plants to make it comparable with the NH_3 performance records is therefore 258*0.8=206 kWh/m³*a. This recorded SEC reduction of (1-88/206)*100=57% by replacing industry standard HFC based systems with a central, low charge NH_3 plant as described herein is within expectations. Similar values have been recorded and documented elsewhere (Jensen, 2017).

6 ECONOMICS

In the commercial world, decisions are generally based on economic rationalism unless the decision making process is affected by split incentives, Government policy or emotion. The popular saying "large corporations will not go green unless it is profitable" does have a significant element of truth to it. Where legislation encourages a user/owner to replace existing, aging HFC-based systems, there are several competing replacement options available. Not all relevant replacement options may be presented to the user, the options presented may not always include all the information required for the user/owner to make a fully informed purchasing decision or the information presented may indeed be incorrect and/or commercially biased.

The system replacement options considered are summarized in Table 3. The capital costs shown in per cent use the low charge NH_3 system as the base; the capital cost of this is therefore 100%. The capital cost ratios summarized in Table 3 are not transferable to other applications.

Table 3. Refrigeration plant replacement options

Refrigeration Plant Concept	Capital Cost, [%]
Central, low NH_3 inventory, dual stage refrigeration system with hot gas defrost, evaporative condenser and secondary refrigerant medium temperature loop	100
Transcritical CO_2 based dry expansion system with warm glycol defrost, adiabatically assisted gas cooler and SCADA system	71
Transcritical CO_2 based dry expansion system with electric defrost, adiabatically assisted gas cooler and SCADA system	62
Replacement plant comprising industry standard HFC based air cooled condensing units, electric defrost and no SCADA system.	45

A significant element of those factors influencing purchasing decisions is energy consumption costs. As Fig. 8 shows, the specific energy consumption (SEC) in kWh/m³*a for refrigerated warehouses varies greatly (Jensen, 2018). Importantly, the relatively poor energy performance of a transcritical CO_2 system in the jurisdiction of Melbourne, Australia may influence purchasing decisions towards a replacement concept that is <u>not</u> CO_2-based if indeed this is brought to the attention of the buyer.

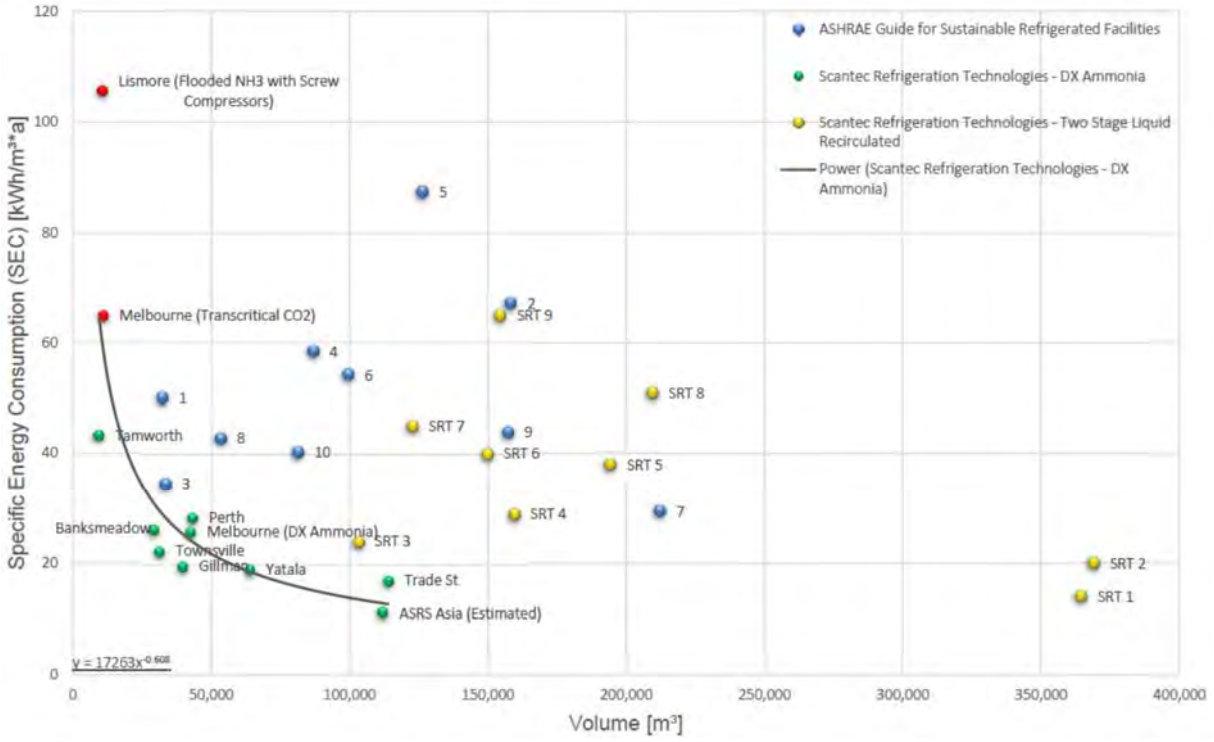

Figure 8. SEC for various plant types as a function of refrigerated volume

The HFC-based replacement option was not considered. Based on Fig. 8, the facility operator considered the additional energy consumption associated with the low capital cost CO_2 option to be at risk of being around 40% greater than the low charge NH_3 concept. This would have translated into an annual energy consumption of approximately 800 MWh/a, which is only approximately 15-25% less than a replacement HFC-based solution would likely have been. The difference between 800 MWh/a and the recorded NH_3 system energy consumption of around 460 MWh/a represents around AUD 65,000-70,000 at current local unit electricity costs. This would deliver a simple payback of four years for the differential investment between the low inventory NH_3 option and the electric defrost transcritical CO_2 option in Table 3. Other similar economic considerations carried out for other similar applications in jurisdictions with similar climates have delivered very similar results.

7 DISCUSSION

In 2016, global agreement was reached in relation to two major treaties that will trigger widespread technology transformation within the global RACHP industries. The agreements referred to are of course the Kigali Amendment to the Montreal Protocol and the Paris Treaty seeking to limit the maximum global temperature anomaly to 2K by year 2100. In transitioning away from HFC refrigerants towards lower global warming potential refrigerant alternatives, it is important not only to consider the elimination of direct emissions, but also the minimization of indirect emissions. These are the CO_2 emissions associated with electricity generation by means of combusting fossil fuels.

The eagerness with which direct emissions pertaining to HFC refrigerants are sought eliminated by refrigerant replacements, often drown out the significantly more important minimization of indirect emissions. Procurement of replacement systems with low global warming potential (GWP) working fluids and basing these buying decisions on capital cost minimization is often the result. The owner (and the environment) may then be stuck with a replacement system that has failed to fully explore the maximum energy conservation potential during the replacement process. Excessively high indirect emissions for the life of the plant are therefore a real possibility in this scenario. Aside from increasing the energy consumption costs to the plant owner unnecessarily, this also violates the intent of the Paris Treaty.

This paper has described a solution that not only seeks to eliminate direct emissions, but also seeks to minimize indirect emissions from the new plant in the tropical jurisdiction where it is installed. Practical energy performance comparisons between central, low NH_3 inventory refrigeration systems of the capacity range described here and equivalent transcritical CO_2 systems for tropical jurisdictions are very rare in the literature. Such comparisons are nevertheless important to enable fully informed procurement decisions to be taken. They are also important to prevent the HFC phase-down from literally transferring us from the ashes into the fire.

REFERENCES

Peterson E, Williams N, Gilbert D, Bremhorst K., 2006. New air-conditioning design temperatures for Queensland, Australia. AIRAH publication Ecolibrium 5(1), 26-36.

Jensen S.S., 2015. Operating Experiences with NH_3 Dry Expansion Systems Servicing Refrigerated Distribution Centres. Proceedings IIAR Ammonia Refrigeration Conference and Exhibition, San Diego, California.

Jensen S.S., 2017. Energy Performance of Low Charge, Central Type, Dual Stage NH_3 Refrigeration Systems in Practice. Proceedings IIAR Ammonia Refrigeration Conference and Exhibition, San Antonio, Texas.

Jensen S.S., 2018. Zentrale NH_3 Kälteanlagen mit Trockenexpansion. Proceedings Deutscher Kälte- und Klimatechnischer Verein (DKV) Tagung, Aachen, Germany.

Manuscript ID: 537
DOI: 10.18462/iir.icr.2019.0537

Applicability of numerical code for simulation of ice-slurry flows in heat exchangers

Shaimaa HEFNY, Thomas TANNERT, Ullrich HESSE

Technical University Dresden,
Institute of Power Engineering,
Bitzer Chair of Refrigeration, Cryogenics and Compressor Technology,
01062 Dresden, Germany,
Shaimaa.Hefny@tu-dresden.de, Thomas.Tannert@tu-dresden.de, Ullrich.Hesse@tu-dresden.de

ABSTRACT

The applicability of available computational fluid dynamic codes (CFD) for the calculation of ice-slurry flow comes more in focus of current research. Therefore this paper intends to give the results of a literature review about the numerical modelling and available data for the validation.
An Overview of previous publications referring to governing equations, modelling approaches is presented. The simulation of isothermal ice-slurry flow is performed as two phase flow in horizontal pipelines for ice mass fractions (0%-50%) and flow velocities (2-5 m/s).
The review reveals multiphase models provided by the CFD codes. The validated simulation results show the influence of particles size, volume fraction, phase interactions and granular properties on the radial distribution of concentration profiles.
In conclusion, it can be stated, CFD codes are capable to predict satisfactorily the behavior of ice slurry flows in different cases.
Keywords: CFD, –Ice Slurry, Simulation, Two-Phase Flow.

1. INTRODUCTION

Ice slurry plays an important role as a secondary refrigerant in various cooling processes. Ice slurry is usually a mixture of small ice particles that are typically rangeing from 0.1 to 1 mm in diameter) and a carrier fluid, which is a binary solution of water and an additive such as salt (calcium or sodium chloride, potassium acetate or potassium formiat), glycol, alcohol or ammonia for decreasing the freezing temperatur below 0 °C.
There are four typical flow patterns as shown in Fig. 1 and 2. It depends on the characteristics of the slurry, which varies as a function of numerous parameters. The complexity of these solid–liquid flows is reflected in the large number of independent variables to describe these flow patterns. Generally, this causes the flow behavior of these systems to vary over a tremendous range. The geometry of a pipeline (diameter, length, roughness, fittings), the properties of the solids (size and size distribution, shape, density, strength) and of the liquid (density, rheology), and the operating conditions (mixture flowrate, solids concentration) all influence the nature of the flow and the pressure gradient. As ice slurry is based on phase change material (PCM) it is also called as a phase change slurry (PCS), which change phase at the melting temperature of the dispersed phase (Kauffeld et al., 2005). The important properties of ice slurries can be derived from the individual propertied of the aqueous solution and of ice by combining the respective properties in the correct ratio. The ice fraction or concentration is the crucial parameter. Nevertheless also the viscosity, thermal conductivity and enthalpy of the ice slurry have to be determined accurately (Ake Melinder et al., 2005). The operation of ice slurry systems aimed at the transfer of mass and heat between system components, depends on the governing principles of fluid dynamics. The derivation of a macroscopic theory for ice slurry flows leads to very complex multi-phase mass, momentum and energy conservation equations (Kauffeld et al., 2005).

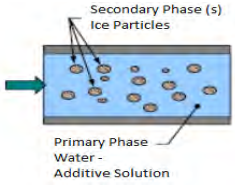

Figure 1: Simple schematic of ice slurry flow

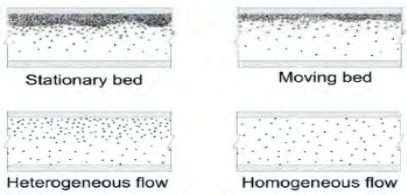

Figure 2: Simple schematic of Flow Patterns

Computational Fluid Dynamics (CFD) seems nowadays a remarkable and an influential tool to acquire abundant accuracy details and information of multi-phase flows, especially when the deep details of ice slurry flow are expected to be analysed. Such details include: pressure drops, velocity and concentrations distributions, phase interactions between ice slurry particles and wall, granular properties of ice slurry particles, the time behaviour for growing/melting on ice slurry particles, blocking and turbulence regions in heat exchangers with different geometries. There are various CFD software packages for simulating phase change material (PCM) process and multiphase flows with different model approaches such as COMSOL Multiphysics, ANSYS (CFX, Fluent), OpenFoam and Star CMM+.

Previous publications reveal the general applicability of CFD tools. A turbulent dispersion is modelled by carrying out a time average of the interphase drag term in an eulerian multi phase flow model, and is expressing it in terms of Favre averaged variables. The Favre Averaged Drag (FAD) model has been processed in the commercial CFD package CFX-5, and it has been tested against a range of dispersed multiphase flows (e.g. bubbly flows, liquid-solid) (Burns et al., 2004). Al-abidi et al., (2013) presents previous studies on the numerical modelling of PCM flow through CFD software and concludes that using CFD software is an effective way to save money and time. He also found, that the software Fluent has a specific model that can simulate a range of different melting and solidification problems in engineering, including casting, melting, crystal growth, and solidification (Al-abidi et al., 2013). The possibility to simulat ice slurry flow is based on the known CFD procedures for both Bingham fluids and multiphase flow models (the mixture and Eulerian models). It gives a correct description of the momentum transfer in the investigated laminar region. A good agreement between the simulations and measurement results was found with the accuracy better than 10 % (Niezgoda-Żelasko and Zalewski 2006). The numerically predicted steady state, laminar hydrodynamics and thermal fields of an ice slurry (water with 15 % ethanol and 12.26 % ice particles) and a homogeneous binary, single phase mixture (water with 17.1 % ethanol) were modelled by using a commercial CFD code (Fluent) which employs a control volume method and SIMPLE algorithm (Trabelsi et al., 2010). An Euler-Euler model based on the kinetic theory of granular flow using CFD code Fluent was applied to investigate the isothermal flow of ice slurry in various pipes to solve the distributions of ice slurry flow, the ice particle concentration and the pressure drop. The relative errors of the numerical computation are within 15 % with respect to measurements (Wang et al., 2013). A mixture CFD model which is based on the different rheological behaviour describes the heterogeneous ice slurry flow and was applied and validated by experiments. The relative errors of numerical computation are almost within ±15 % (Wang, et al., 2013). A numerical simulation of ice slurry in ice cooling was investigated to investigate factors which influence transportation security: ice packing fractions, ice particle size, additive concentrations and pipe size. The results and proposed guidelines are of significance for predicting the critical velocity for safe transportation and guiding the safety, design and operation of ice cooling systems (Tian et al., 2014). Numerical Simulation of ice slurry heat transfer characteristics in a straight horizontal tube were applied by using of CFD software. The VOF model in FLUENT was used. Laminar and turbulent flow regimes with various ice concentration were studied and used as a design tool and to analyse ice slurry flow in different operating conditions. The relative errors between simulations and experimental results for calculating nusselt number were within 15 % (Li et al., 2016). Numerical simulation for CFD analysis of the melting of particles slurry flow between parallel plates were presented. The motion of the solid particles was determined by using a Lagrangian approach, while hydrodynamics and heat transfer throughout the fluid were determined by using a finite volume scheme (Shabgard et al., 2016). A 3D - CFD model was applied for studying the characteristics of propylene glycol ice slurry isothermal flow as a Newtonian fluid with effective properties depending on the local ice fraction and includes the shear induced migration. It has been validated for laminar and turbulent conditions (Onokoko et al., 2018). Pipeline slurry flow of mono-dispersed fine particles at several of high concentration is numerically simulated using Mixture and Eulerian two-phase models in the CFD software package FLUENT. The results from Eulerian Model are more accurately than the results from mixture model. Also the concentration distributions obtained using Eulerian model found to be in good agreement except for few experimental data from the same author (Kaushal, et al. 2005, Kaushal et al., 2012).

2. MULTIPHASE MODELS

2.1 General Approach

In multiphase flow a phase can be defined as an identifiable class of material that has a particular inertial response to and interaction with the flow and the potential field in which it is immersed. Different multiphase flow regimes are described. To solve a problem the regime needs to be determined, which represents the flow best. Furtheron the degree of interphase coupling for flows involving bubbles, droplets, or particles, and the appropriate model for different amounts of couplings need to be determined. For example: Ice slurry (liquid and solid particles) is classified as slurry flow or hydrotransport, sedimentation and fluidized beds as shown in Fig. 5. The fundamental behaviour of liquid-solid flows varies with the properties of the solid particles relative to those of the liquid.

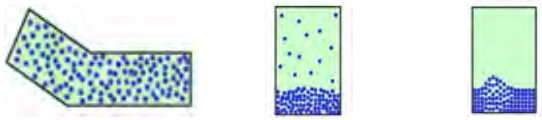

Figure 3: Flow regimes, (a) slurry flow or Hydro transport, (b) sedimentation, (c) fluidized bed

The use of a specific multiphase approaches to charactrize momentum transfer depends on the volume fractions of ice particles (Versteeg et al. 1995) , (ANSYS Fluent User's Guide 18) , (ANSYS Fluent Theory Guide 18). There are two approaches for the numerical calculation of multiphase flow as following: 1) Euler-Lagrange Approach, and 2) Euler-Euler Approach.

2.2 The Euler-Lagrange Approach

The Euler-Lagrange approach is called the Lagrangian discrete phase model in ANSYS Fluent. The fluid phase is treated as a continuum by solving the governing equations, while the dispersed phase is solved by tracking a large number of particles through the calculated flow field. The dispersed phase can exchange momentum, mass, and energy with the fluid phase. This requires that the dispersed second phase occupies a low volume fraction.

2.3 The Euler-Euler Approach

In the Euler-Euler approach the different phases are treated mathematically as interpenetrating continua. Since the volume of a phase cannot be occupied by the other phases, the concept of phasic volume fraction is introduced. Conservation equations for each phase are derived to obtain a set of equations, which have similar structure for all phases. In ANSYS Fluent, there are three different Euler-Euler multiphase models are available as following: a) The volume of fluid (VOF) model, b) The mixture model, c) The Eulerian model. The appropriate model for each kind of flow regimes can be selected based on the following guidelines: For slug flows and for stratified/free-surface flows the VOF model shall be used. For fluidized beds the Eulerian model shall be used. For granular flow, for slurry flows and for hydrotransport the mixture or Eulerian model shall be used, For sedimentation the Eulerian model shall be used. Thus the numerical simulation of ice slurry can be analysed by using the Mixture model and the Eulerian model. But the previous literature suggests that the results from Eulerian Model are the best agreement with the experimental results.

2.1.1. The Eulerian Model

The Eulerian model is the most complex of the multiphase models in Fluent, It solves a set of momentum and continuity equations for each phase. The Eulerian model assumed that the slurry flow consists of solid "s" and fluid "f" phases, which are separeted, yet they form interpenetrating continua, so that $\alpha_f + \alpha_s = 1.0$ where α_f and α_s are volumetric concentrations of fluids and solid phase, respectively. Coupling is achieved through the pressure and interphase exchange coefficients. The manner in which this coupling is handled depends upon the type of phases involved. Granular (fluid-solid) flows are handled differently than non-granular (fluid-fluid) flows.

2.1.2. Granular Properties

The granular properties for ice slurry flow are believed to be of importance because granular model includes models, which are taking friction and collisions between particles into account as shown in

Fig. 4. The non-granular model lack the possibilities to set a maximum packing limit which makes it less suitable for the modelling of flows with particulate as secondary phase. The simulation results with non-granular model do not show good agreement with experimental results.Since the concentration of particles is an important factor in the calculation of the effective viscosity for the mixture, the collisional $\mu_{s,col}$ and kinetic $\mu_{s,kin}$ parts, and the optional frictional $\mu_{s,fr}$ part, are added to give the solids shear viscosity μ_s:

$$\mu_s = \mu_{s,col} + \mu_{s,kin} + \mu_{s,fr} \quad \text{Eq. (1)}$$

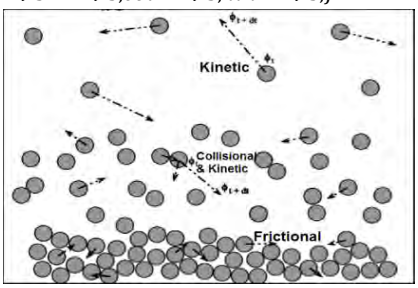

Figure 4: Pictorial explanation of $\mu_{s,col}$, $\mu_{s,kin}$ and $\mu_{s,fr}$ (Kaushal et al., 2012)

2.1.3. Phase Interactions

The Phase Interactions allow imporatant parameters define the interaction between phases in Eularian Model as following:

(a) Virtual Mass: includes the virtual mass force $F_{\upsilon m}$ that is present when a secondary phase accelerates relative to the primary phase. This item appears only for the Eulerian model.

$$F_{\upsilon m} = C_{\upsilon m}\alpha_s\rho_f\left(\overrightarrow{U_f}\mathrm{g}\nabla\overrightarrow{U_f} - \overrightarrow{U_s}\mathrm{g}\nabla\overrightarrow{U_s}\right) \quad \text{Eq. (2)}$$

where: $C_{\upsilon m}$ is the coefficient of virtual mass force, α_s is the volume fraction of solid particles, ρ_f is the desity of fluid, v_s and v_f are velocity of solid and fluid phase, respectively.

(b) Drag: displays the Drag Coefficient inputs. Drag Coefficient specifies the drag function for each pair of phases. Drag force caused by the velocity differences between two phases, $K_{sf}\left(\overrightarrow{U_f} - \overrightarrow{U_s}\right)$, where: K_{sf} is the inter-phase drag coefficient.

(c) Lift: displays the Lift Coefficient inputs. Lift Coefficient specifies the lift function for each pair of phases.

$$F_L = C_L\alpha_s\rho_f\left(\overrightarrow{U_f} - \overrightarrow{U_s}\right)\times\left(\nabla\times\overrightarrow{U_f}\right) \quad \text{Eq. (3)}$$

where: C_L is the coefficient of Lift force.

(d) Viscous force includes ζ_f and ζ_s are the stress tensors for fluid and solid.

2.4 Solidification and Melting Model

There is a wide range of solidification/melting problems, including melting, freezing, crystal growth, and continuous casting in ANSYS-Fuent.

2.5 Eulerian Wall Films

A thin liquid film forms as liquid drops impinge on a solid surface in the domain. The thin film assumption is one usually made in both Eulerian and Lagrangian film modeling approaches, specifically that the thickness of the film is small compared to the radius of curvature of the surface so that the properties do not vary across the thickness of the film and that films formed are thin enough so that the liquid flow in the film can be considered parallel to the wall.

2.6 Turbulence Model

The choosing of the turbulence model will depend on considerations such as the physics encompassed in the flow. The important turbulence models for solid-fluid are *(k-ε)* and *(k-ω)*, gradual change from the *(k-ω)* model in the inner region of the boundary layer to a high-Reynolds-number version of the *(k-ε)* model in the outer part of the boundary layer. The most general multiphase turbulence model solves a set of *k* and ε or ω transport equations for each phase. This turbulence model is the appropriate choice when the turbulence transfer among the phases plays a dominant role.

3. GOVERNING EQUATIONS

Governing Equations for Eulerian Model are as following:

3.1. Continuity Equations

$$\nabla g\left(\alpha_t \rho_t \overrightarrow{U_t}\right) = 0 \qquad \text{Eq. (4)}$$

3.2. Momentum Equations

Momentum equations set up for both fluid phase and solid phase.
For fluid phase:

$$\nabla g\left(\alpha_f \rho_f \overrightarrow{U_f}\overrightarrow{U_f}\right) = -\alpha_f \nabla P + \nabla g\overline{\zeta_f} + \alpha_f \rho_f \overline{g} + K_{sf}\left(\overrightarrow{U_s} - \overrightarrow{U_f}\right)$$
$$+C_{Um}\alpha_f \rho_f\left(\overrightarrow{U_s} g \nabla \overrightarrow{U_s}\right) + C_L \alpha_s \rho_f\left(\overrightarrow{U_f} - \overrightarrow{U_s}\right)\times\left(\nabla\times\overrightarrow{U_f}\right) \qquad \text{Eq. (5)}$$

For solid phase:

$$\nabla g\left(\alpha_s \rho_s \overrightarrow{U_s}\overrightarrow{U_s}\right) = -\alpha_s \nabla P + \nabla g\overline{\zeta_s} + \alpha_s \rho_s \overline{g} + K_{sf}\left(\overrightarrow{U_f} - \overrightarrow{U_s}\right)$$
$$+C_{Um}\alpha_s \rho_f\left(\overrightarrow{U_f} g \nabla \overrightarrow{U_f} - \overrightarrow{U_s} g \nabla \overrightarrow{U_s}\right) + C_L \alpha_s \rho_f\left(\overrightarrow{U_s} - \overrightarrow{U_f}\right)\times\left(\nabla\times\overrightarrow{U_f}\right) \qquad \text{Eq. (6)}$$

4. NUMERICAL CFD-MODEL AND VALIDATION

4.1 CFD model description

With a view to solve the above governing equations with the specific boundary conditions the commerical CFD code ANSYS-Fluent has been used. The discretization of conversation equations was solved by using the finite volume method. The governing equations are integrated over all control volumes of cells which are divided by the finite volume method. The second-order upwind schemes and SIMPLE algorithm are used in the solver method in Fluent software. To solve all problems in these present paper, it is recommended to optimize the initial operating conditions 3D-steady state solution and pressure-based coupling algorithm. The numerical computation should be considered converged when the residual is less than 10^{-6}. The Euler-Euler CFD model certainly employs various amount of approximations with good efficiency and flexibility of the CFD method. In this present study, there are three different cases with corresponding experimental data to validate CFD numerical results. The first two cases are for liquid-solid slurry pipeline flow with two different sizes of particles (fine particles 125 μm and croase particles 400 μm) (Kaushal, Sato et al. 2005, Kaushal, Thinglas et al. 2012) and the last case is ice slurry flow in horizontal pipe with different sizes of ice particles(Wang, Wang et al. 2013). The flow information about velocity, concentation profiles with non-granular and granular properties are computed to compare with the actual flow.

4.2 Geometry and Boundary Conditions

The geometry of the first two cases is 0.5 m long and 54.9 mm diameter, and for the last case is 0.5 m long and 103 mm diameter in horizontal pipe as shown in Fig. 5. The boundary conditions for mixture phase (2-phases liquid-solid) are defined, mass flow rate/velocity is at inlet, and for outlet, pressure outlet is specified. For isothermal ice slurry, the wall is specified as adiabatic and no slip shear condition. CFD Numerical results validated with experimental measurements of volume fraction distribution as shown in Fig. 6.

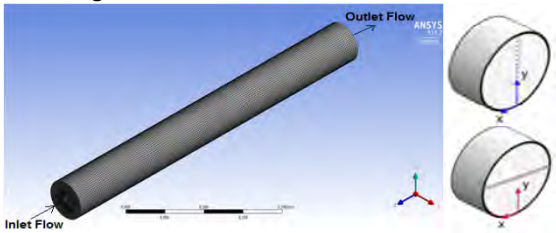

Figure 5: Schematic geometry of horizontal pipe for CFD model

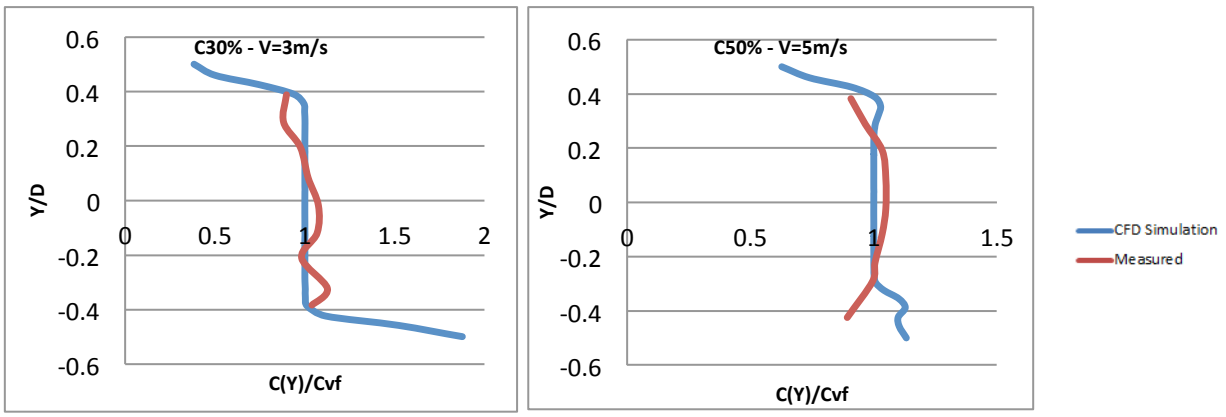

Figure 6: Validation of Volume Fraction Distribution values along vertical diameter for d_s=125 µm

5. RESULTS AND DISCUSSION

The distributions of volume fraction of solids in solid–liquid flows would be reduced gradually in the upper parts of the pipeline, and they would be increased in the lower parts, and in fully developed turbulent flow region, these distributions are kept as constants in the middle of center pipe as shown in Fig. 7 and 8. But with granular properties, at higher concentration and velocity, in addition to the above dissipation form, grains can collide shortly, this gives rise to further dissipation and stress, named collisional, at very high concentration (50 % in volume) and velocity, grains start to endure long, sliding and rubbing contacts, which gives rise to a totally different from of dissipation and stress, named frictional as shown in Fig. 7 and 8. This effect appears significatly at coarse particle size (400 µm) as shown in Fig. 8 (b). It is also shown by the volume fraction profile in Figure 9. For ice slurry, The concentration profile is divided into three regions which are high-concentration region near the top wall, uniform concentration region in the center of pipe cross section and low-concentration region near the bottom of the pipe. It is observed that the ice particle size and velocity effect on the flow regimes in pipeline to be heterogeneous and homogeneuos as shown in Fig. 9 (b) (Kaushal, Sato et al. 2005, Kaushal, Thinglas et al. 2012, Wang, Wang et al. 2013).

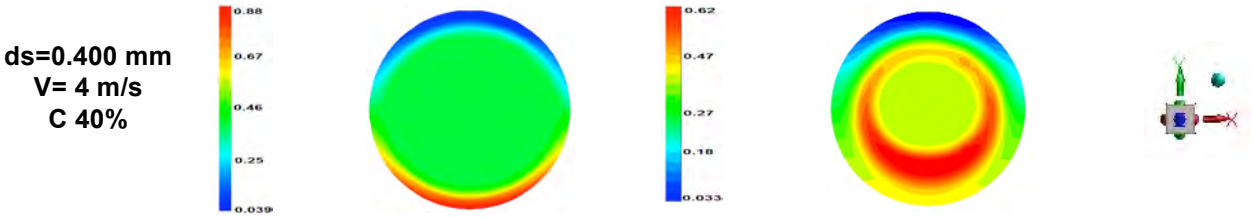

(a) Non-granular model **(b) Granular model**

Figure 7: Comparison profiles of solid volume fractions

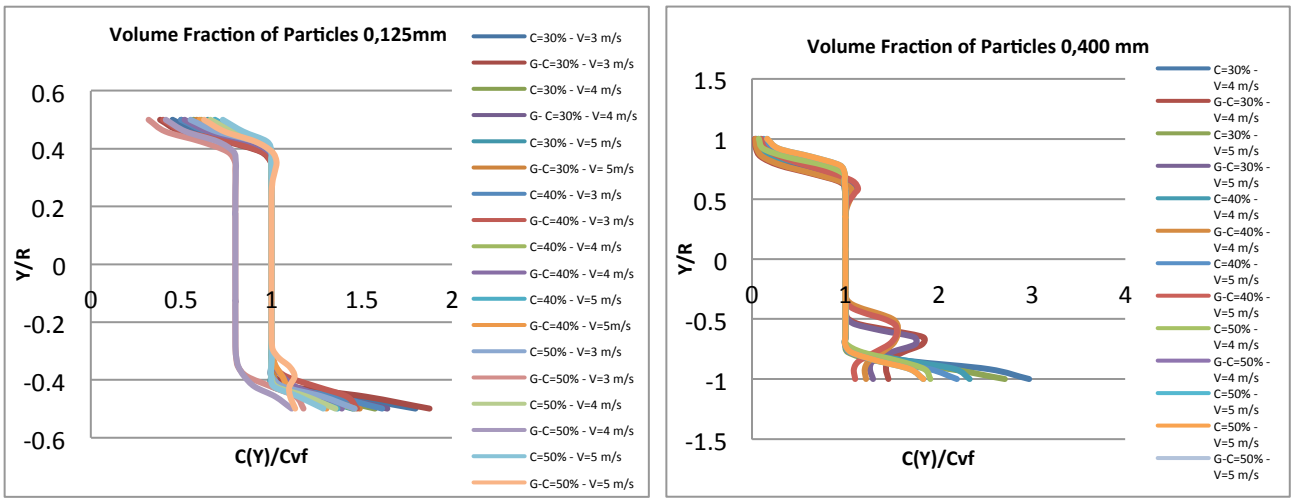

Figure 8: Volume Fraction Distribution values along vertical diameter without granular properties and with granular properties ds=0.125mm, ds=0.400mm.

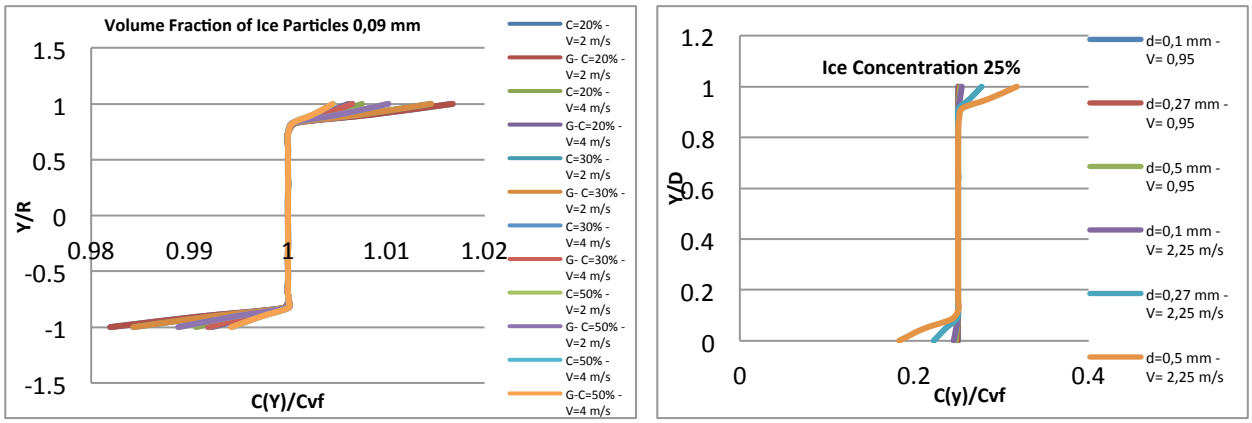

Figure 9: Volume Fraction Distribution of Ice slurry along vertical diameter for different parameters

6. FUTURE INVESTIGATIONS

There are many potential applications for ice slurry, but the use of ice slurry in a broad field of applications to utilize the described advantages is hindered by the lack of suitable and at the same time cost-effective heat exchangers. The next investigations are focussed to improve the modelling of flow and heat transport processes when using ice slurry and to optimize the designs of heat exchangers in general. From studies of heat exchangers, it is found that plate heat exchangers would be a good choise to enhance the efficiency of a system and to come to simple and compact heat exchangers. First Simulation results of a single plate heat exchanger channel are shown in Figs. 10 and 11 but it is not validated. This simulation was two phase ice/fluid of adiabatic case of ice slurry flow for particle diameter 90 µm, velocity 2 m/s and ice concentration 10 % by using Eulerian model in ANSYS-Fluent. 3D steady state solution was applied.

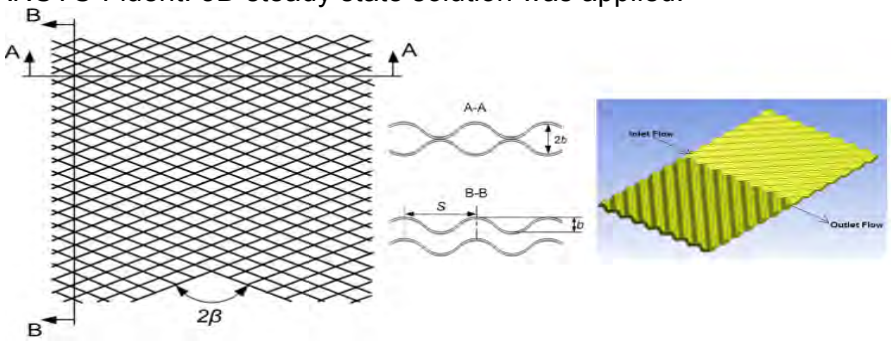

Figure 10: Schematic geometry of cross section for the sinusoidal form of PHE's plate for CFD model



(a) **(b)**

Figure 11: Cross-section for Distribution profiles of (a) Velocity , (b) Volume Fraction

7. CONCLUSIONS

In this paper, the summery of definitions different models of CFD code such as Euler models, turbulence models, solidification and melting, Eulerian model can be applied to get significatly of different accuracy CFD parameters to improve the efficiency of flow and heat transfer of slurry flow. Granular properties and phase interactions parameters include various factors which are affecting on particles and are close to practicle results. those factors are very important for taking into consideration to prevent unstable and blocking systems and then for optimizing new designs. The effect of these factors appeared at high concentation and large particle size for solid-fluid flow and ice-fluid flow.The Euler-Euler CFD model is valideted and used to investigate future technologies to improve the efficiency of refrigerent systems. The numerical simulation of plate heat exchanger is already done but it is not valideted. There are predications to optimize new designs for ice slurry.

ACKNOWLEDGEMENTS

The research is funded by the Bundesministerium für Wirtschaft und Energie - Project 03ET1476B.

NOMENCLATURE

C	Concentration of solid particles (%)	V	Velocity (m/s)
's'	Radius of pipeline (m)	*'f'*	fluid

REFERENCES

Al-abidi, A., Sohif Bin Mat, K. Sopian, M.Y. Sulaiman, Abdulrahman Th. Mohamed , K.Sopian, Abdulrahman Th., 2013. CFD applications for latent heat thermal energy storage: a review. Renewable and Sustainable Energy Reviews 20: 353-363.

ANSYS Fluent Theory Guide (18), 2018.

ANSYS Fluent User's Guide (18), 2018.

Burns, D.B., Frank, T., Hamill, I., Shi J-M., 2004. The Favre Averaged Drag Model for Turbulent Dispersion in Eulerian. 5th International Conference on Multiphase Flow, 392.

Kauffeld, M., Kawaji, M., W.Egolf, P., 2005. Handbook on Ice Slurries.

Kaushal, D. R., Sato, K., Toyota, T., Funatsu, K., Tomita, Y., 2005. Effect of particle size distribution on pressure drop and concentration profile in pipeline flow of highly concentrated slurry. International Journal of Multiphase Flow 31(7): 809-823.

Kaushal, D. R., Thinglas, T., Tomita, Y., Kuchii, S., Tsukamoto, H., 2012. CFD modeling for pipeline flow of fine particles at high concentration. International Journal of Multiphase Flow 43: 85-100.

Li, Y., Wang, S., Wang, J., Zhang, T., 2016. CFD Study of Ice Slurry Heat Transfer Characteristics in a Straight Horizontal Tube. Procedia Engineering 146: 504-512.

Ake Melinder, 2005. PhD- Doctoral thesis Thermophysical Properties of aquous solutions.

Niezgoda-Żelasko, B., Zalewski, W., 2006. Momentum transfer of ice slurry flows in tubes, modeling. International Journal of Refrigeration 29(3): 429-436.

Onokoko, L., Poirier, M., Galanis, N., Poncet, S., 2018. Experimental and numerical investigation of isothermal ice slurry flow. International Journal of Thermal Sciences 126: 82-95.

Shabgard, H., Hu, H., Boettcher, P., McCarthy, M., Sun, Y., 2016. Heat transfer analysis of PCM slurry flow between parallel plates. International Journal of Heat and Mass Transfer 99: 895-903.

Tian, Q., He, G., Wang, H., Cai, D., 2014. Simulation on transportation safety of ice slurry in ice cooling system of buildings. Energy and Buildings 72: 262-270.

Trabelsi, H., Galanis, N., Orfi, J., 2010. Simulation of forced convection ice slurry flow in a heated tube. Proceedings of the 14 th International Heat Transfer Conference.

Versteeg, H. K., Malalasekera, W., 1995. Introduction to CFD - Finite Volume Method.

Wang, J., Wang, S., Zhang, T., Liang, Y., 2013. Numerical investigation of ice slurry isothermal flow in various pipes. International Journal of Refrigeration 36(1).

Wang, J., Zhang, T., Wang, S., 2013. Heterogeneous ice slurry flow and concentration distribution in horizontal pipes. International Journal of Heat and Fluid Flow 44.

Manuscript ID: 548
DOI: 10.18462/iir.icr.2019.0548

Operation Costs for Heat Recovery from Supermarkets to District Heating Grids

Christian HEERUP
Danish Technological Institute
Gregersensvej 2, 2630 Taastrup, Denmark, chp@dti.dk

ABSTRACT

The rebuilding of three Danish supermarket CO_2 booster refrigeration plants with heat recovery heat exchangers is in the planning phase. The systems are situated in buildings heated by local district heating grids. The heating and cooling load characteristics have been analysed for one of the installations and control schemes have been suggested based on the cost profiles for power and heating, including distribution costs and taxes. The sale of excess heat to the grids has been evaluated as well as the value of using auxiliary cooling load for maximising the heat produced in heat pump operation mode. The experience from operation of plants with an earlier design has been integrated and the payback time for the investments has been estimated. The results are analysed considering the state of the heating systems in the building and the local cost structures. The estimated direct payback period varies between three to ten years.

Keywords: Refrigeration, Carbon Dioxide, COP, Energy Efficiency, CO2, district heating, heat recovery.

1. INTRODUCTION

To conserve energy and save costs as well as reduce carbon footprint at the same time, heating and cooling needs can be addressed by integrating systems. Furthermore, individual systems can be integrated across building perimeters in areas covered by a district heating grid.
The optimum way to achieve high efficiencies, when recovering heat from a CO_2 refrigeration system, is to use at least two temperature levels as supply temperature for the heating system, e.g. floor heating and radiators (Funder, 2017 and Mazyar, 2018). However, heating systems in existing buildings supplied from a district heating network are designed for a relatively high supply temperature. In a district heating grid, the supply temperature is often within range of 60 to 75 °C with a return temperature of 30 to 35 °C. However, it is the experience that heating systems in supermarket buildings often return higher temperatures, and the lower range of temperatures is returned by residence housing. See Fig. 1 for the supply and return temperatures as well as the heat demand for one of the investigated supermarkets. In winter, the supply temperature is increased to

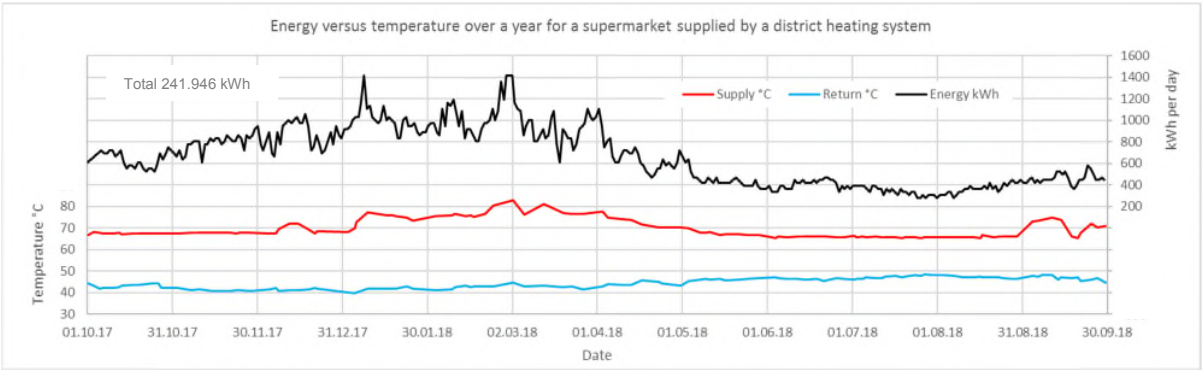

Figure 1. District heating demand and supply and return temperatures for a supermarket building.

enable the individual heating systems to cover the local heating loads. This enables the supermarket heating system to return a relatively low temperature. Vice versa occurs during the summer where only hot tap water preparation is needed, i.e. the supply temperature is relatively low, and the return

temperature is high. This indicates that there is some room for improvement of the control settings, which might result in slightly lower return temperatures during the summer. Thus, the operating modes will have to be calculated for the higher return temperatures to evaluate the business case. Furthermore, the refurbishment with the heat recovery option is often required to have the shortest possible payback time. This means that the investment will not cover a major rebuilding of the heating system, but only the piping and the controls for the heat recovery heat exchanger (HRX). In this paper, the economy of a planned installation is investigated based on information available prior to the refurbishment with an HRX.

2. DESIGN OF INSTALLATION

Fig. 2 shows a simple PI diagram together with the operating modes. The layout on the water side of the system is represented by the simplest possible configuration. When the amount of recovered heat is higher than the needed amount of heat in the building, the surplus of heat can be supplied to the district heating grid instead. On the other hand, if the recovered heat is lower than needed, the grid will make up for the difference. The meters for consumed and produced heat are not shown. Usually, there will be three meters: The first meter is for the heat supplied from the grid, the second for the heat supplied to the grid, and the third meter measures the amount of heat recovered. A fourth meter measuring the power consumed by the MT compressor set will often be needed as well. This is the case in Denmark due to tax issues. The pump is speed controlled to maintain a given setpoint of the water leaving the HXR. Thus, if the leaving temperature is below the setpoint, the pump speed is reduced - and vice versa. The pump will have to overcome the supply pressure on the district heating system as well as the pressure drop in the HXR and the associated components. The control range for the pump will have to be very large to meet all the operating conditions. If the minimum flow does not match the low load conditions of the refrigerating system, the leaving temperature will be too low to meet the requirements of the heating system or the grid. If the water flow is too low at high loads on the refrigeration system, the heating capacity will not meet the potential at the given condition, even if the leaving temperature increases. In most cases, the low load condition is most critical as this will prevail during the winter, where the heat demand is highest when the refrigeration load simultaneously is at its lowest.

Out of the first nine installations for HR to district heating, three installations have failed due to fractures caused by thermal stress. These problems are known to the manufacturers of plate heat exchangers, and they can be mitigated by three main measures (Alfa Laval, 2017): The first measure is to stop both the primary and the secondary flow at compressor stop or when heating is no longer needed. This will prevent a high temperature difference over the full plate length at start-up. The increase of the lifetime is theoretically estimated to 120 times compared to the stop of the water flow first and 16 times compared to stop of the CO_2 flow first.

The second measure is to use long plates in the heat exchanger, which in practice means the use of multi-pass HXR or two or more heat exchangers mounted in series. This will also minimise the temperature difference and in addition increase the performance. By using a manufacturer calculation tool (SWEP, 2019) for the investigated case, calculations show that the efficiency was increased by 5 to 10 % on both the heating COP and the capacity for a given set of temperatures by a three-pass configuration compared to a one-pass configuration, both with the same heat exchange surface and price. The HXR is shown with a three-pass configuration in Fig. 2 with the plates in horizontal position. This is intentionally done, even though it differs from the normal upright position with vertical plates used for evaporators and condensers. These use one-pass configuration, where the plates work with the refrigerant in the two-phase region whereas the HXR with CO_2 works in one-phase only. The horizontal position of the plates will still facilitate oil transport and drain of CO_2 liquid, if any, in sub-critical conditions. On the water side, it will help bleed air out of the heat exchanger when commissioning the system.

The third measure is to avoid load on the connections due to both thermal expansion of piping and other mechanical loads. A substantial load reduction on the connections is achieved by mounting the heat exchanger on fixtures, which incorporate an elastic material such as rubber instead of a hard mount directly on the compressor rack.

The CO_2 piping shown in Fig. 2 represents a booster system with the MT and LT compressor groups and evaporators. Compared to a standard system, components for heat recovery (HR) are added; motorised on-off three-way control valves for isolating the HXR and the gas cooler, and the valves A, B, and C for controlling the gas cooler as an auxiliary load.

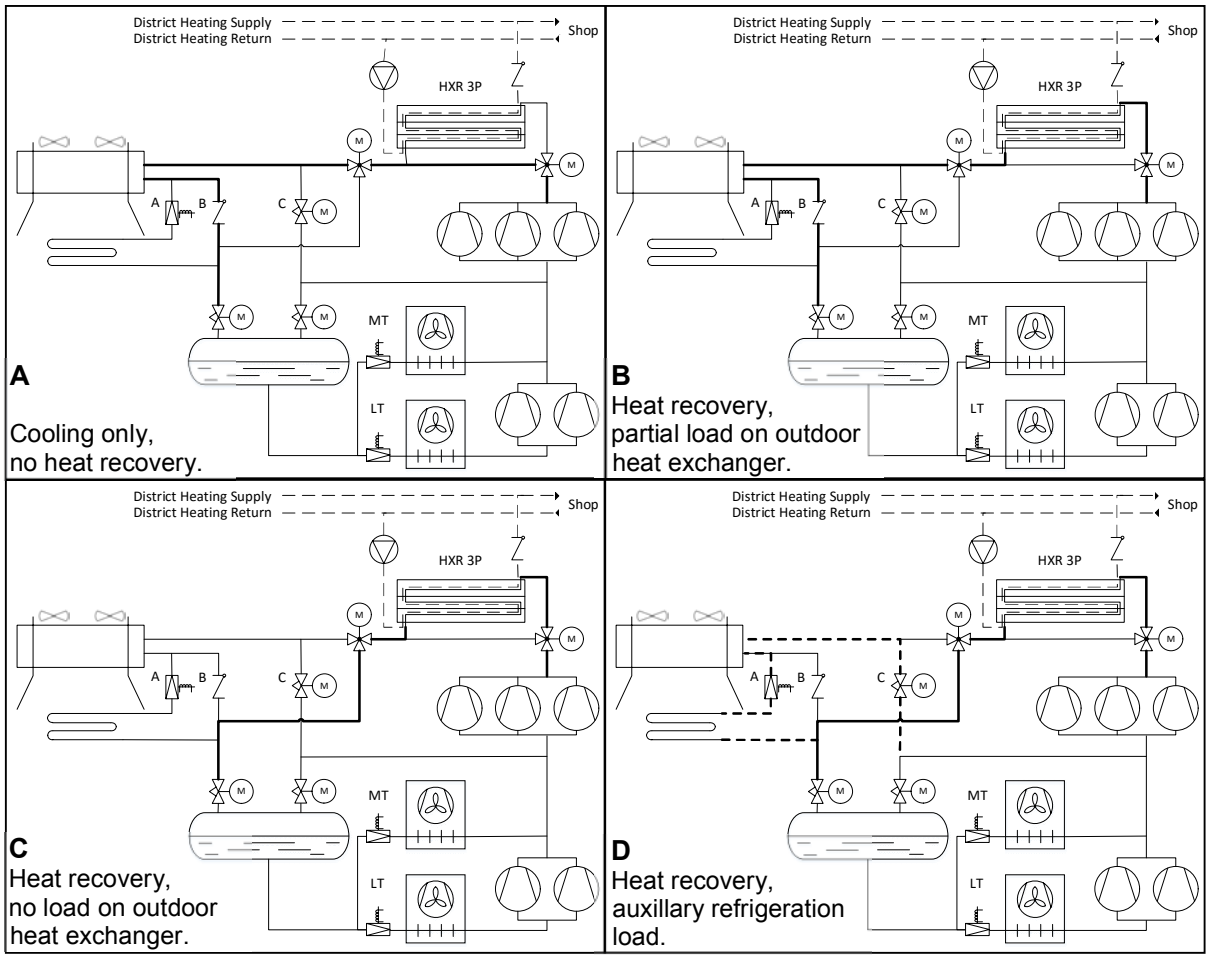

Figure 2. The four basic operating modes for the refrigeration system with heat recovery.

The operating modes A, B, and C correspond to no HR, partial HR, and full HR, respectively. Operation mode D uses spare compressor capacity for heating as an air to water heat pump. The auxiliary load via the outdoor air and the gas cooler could be replaced by other heat sources like a bore hole or sea water, but the configuration is suggested as a cheap solution using the components already at hand to minimise the investment.

The transition from mode C to D is as follows: Valve C opens and meters CO_2 gas to the suction line, which increases the load enabling the compressor pack to meet the required heat production. The pressure in the gas cooler drops, which lowers the saturated temperature to a few degrees below the outdoor temperature. To maintain the pressure and to ensure a sufficient flow of gas, the expansion valve A opens to feed liquid to the heat exchanger, while being controlled by the super heat measured on the suction line (the discharge line in normal operation). The configuration is bottom feed to ensure dry gas at the outlet. Standard fan operation will result in counter flow, but this could be mediated by reversing the fan during heat pump mode. This would also facilitate the discharge of water drops at the fin edge after defrosting. The pipe feeding the expansion valve A has a serpentine like loop distributed on the surface under the gas cooler. This will prevent the build-up of ice at ambient temperatures below zero after defrosting, and it ensures that the water can drain away. Defrosting will be necessary at regular intervals at prolonged operation. It is estimated that defrosting will be needed four to eight times a day. It is expected that the energy needed for

defrosting will reduce the supplied heat by 20%. Defrosting is initiated by a timer, and it takes place by reverting to operation mode B. It is stopped by a defrosting sensor (not shown). Calculations of the coil geometry show that enough capacity would be achieved at a temperature difference across the heat exchanger in the range of 2 to 3 K, maybe slightly higher depending on the stability of the super heat signal. With saturated suction temperatures on the MT compressors in the range of -8 to -10 °C, it will only be very few hours during the winter that the heat pump mode will require a lower evaporation temperature, or that the pump must be stopped. According to the Danish Design Reference Year (DRY), there are only 280 hours a year where the temperature is lower than -5 °C. However, the question remains if the heat pump mode will pay off in combination with a district heating grid. This is investigated in the following section, but first the achievable efficiencies are looked at.

In Fig. 3 to 7, the operating modes are represented in h,T diagrams and for reference also in h,logP diagrams. In the h,T diagrams, the water temperature through a HXR is represented as a solid straight blue line and the CO_2 temperature as a solid red line coinciding with an isobaric line (any pressure drop is ignored). Thus, the temperature differential in an HXR is visualised. All graphs are calculated with both the approach and the pinch point differential equal to 1 K, which is economically feasible to achieve in a plate heat exchanger. In all cases, the total load on MT and LT cabinets is 100 kW with evaporation temperatures of -10 °C and -35 °C, respectively. Fig. 3 is the winter reference situation as the plant will operate at the minimum condensing temperature most of the time. It is possible to recover heat without extra energy consumption, but only a very limited amount.

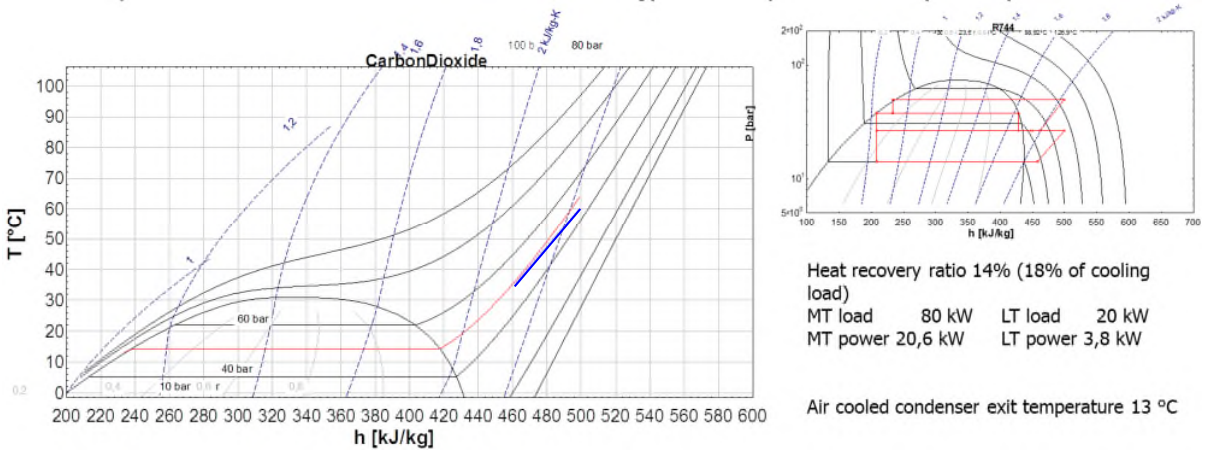

Figure 3. Operating mode B. Floating or minimum head pressure. In this case 50 bar (t_{sat} = 15 °C).

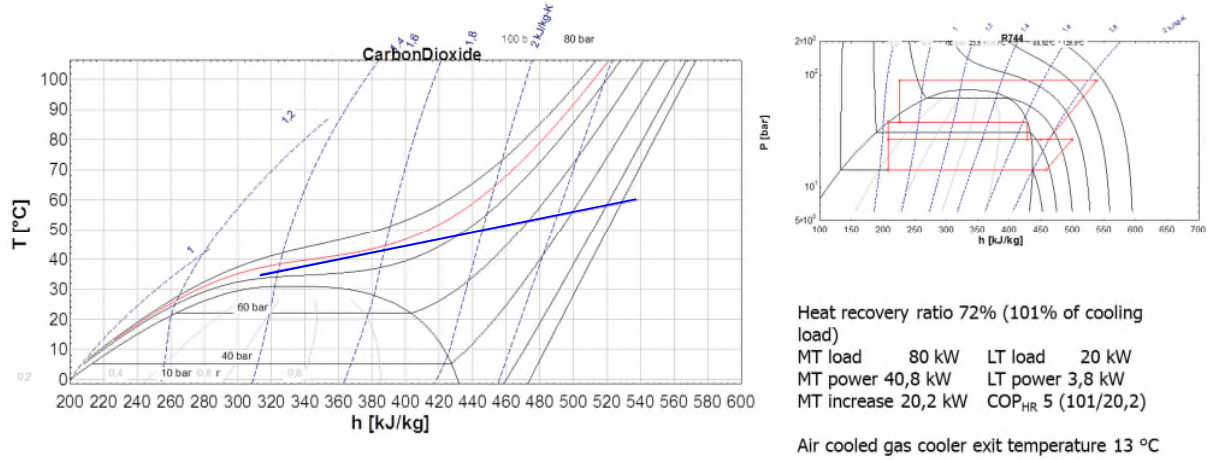

Figure 4. Operating mode B. Increased head pressure 90 bar. Water temperature 35/ 60 °C.

By increasing the pressure, it is possible to recover more heat, but at the expense of a higher energy consumption. Every time higher temperatures or a higher heating capacity are achieved compared to the reference state, the corresponding COP_{HR} is reduced.

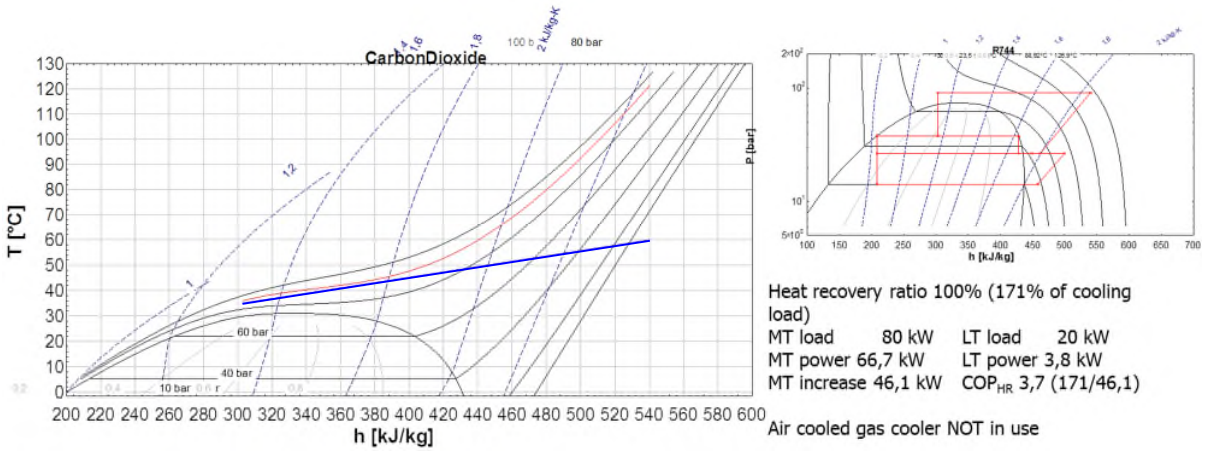

Figure 5. Operating mode C. Increased head pressure 91,4 bar. Water temperature 35/ 60 °C.

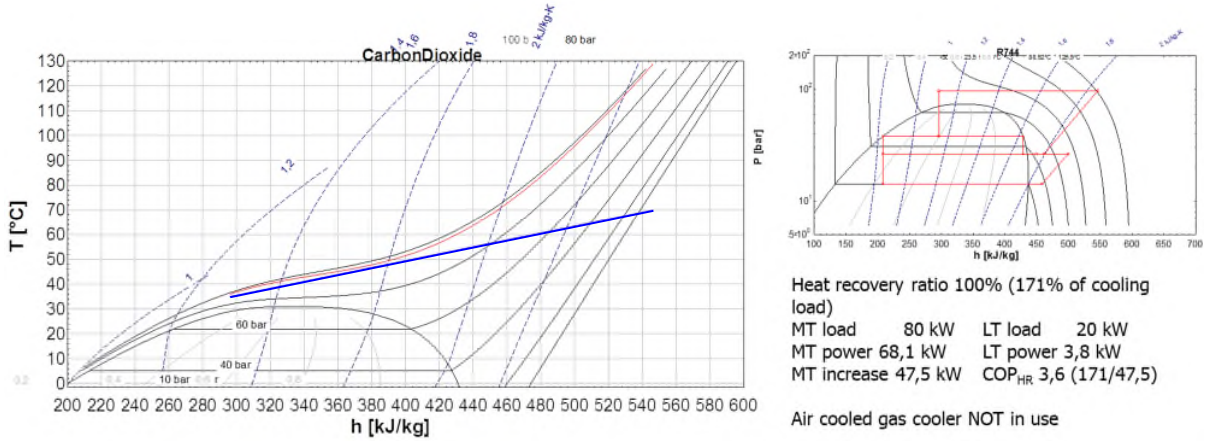

Figure 6. Operating mode C. Increased head pressure, 97,3 bar. Water temperature 35/ 70 °C.

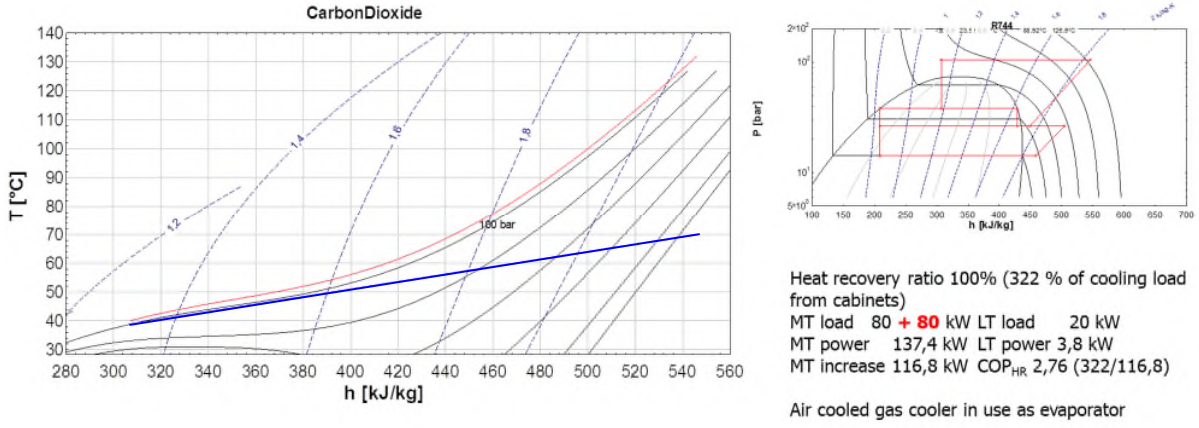

Figure 7. Operating mode D. Increased head pressure, 105 bar. Water temperature 39/ 70 °C.

The ultimate limit for the heating capacity is the installed compressor capacity when an auxiliary load is employed as well.

Note that the optimum pressure for a given condition might be higher than the optimal pressure without heat recovery due to the constraints given by the temperature profiles as exemplified in Fig. 6 (Christensen, R., 2018).
As can be seen from Fig. 1, the supply and retur temperatures for the investigated case are higher than these examples. The cost of the produced heat will be estimated accordingly in the following.

3. THE LOAD PROFILE

Fig. 8 shows the measured heat load profile for the day in 2018 with the highest heating demand. The spikes are not an exact representation of the changes in the heating load, but rather a consequense of the meter supplying the data in (large) kWh increments. The demand covers both space heating and hot tap water. For most of the vinter period, the ambient temperature is low so that refrigeration systems without HR operate at their minimum condensing temperature. For the actual plant, this corresponds to a mean engaged capacity of 21% out of 100% installed compressor swept volume based on data from December 2018 and January 2019. This corresponds to a 41 kW mean refrigeration load on the MT compressors. The heating capacity for this refrigeration load at operating mode C at 105 bar and water temperature 40/ 70 °C is 69 kW. The variation is small from day to day varying between +/- 1%, whereas the variation from day to night is larger. Both night and day are seen from 0% to 40% engaged capacity with more frequent stops at night. The mean day load in swept volume from 4:00 am to 20:59 pm is up to 25% and at night from 21:00 pm to 3:59 am it is down to 13%. The HR potential based on this cooling load and these temperatures is represented by the dashed line in Fig. 8.

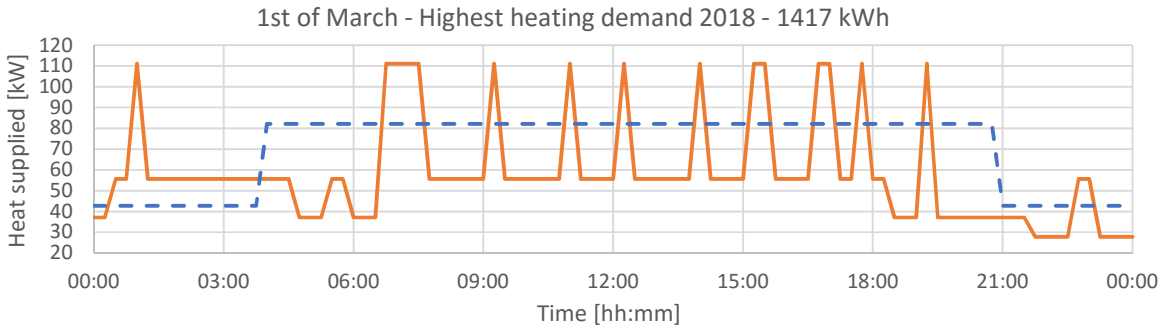

Figure 8. Heating load and HR profile for the day in 2018 with the highest demand.

Note that the load profiles are not based on data from the same day, and they probably represent an extreme case. Even so, the heating spikes, which are not covered, represent only 5% of the heat load. For the winter as a whole, it is only 4% (8200 kWh) that cannot be covered by operating mode B and C, and all heating needs are covered with HR in the summer with floating head pressure. This means that the investments needed to enable operating mode D cannot be justified unless there is a business case for selling heat to the district heating grid.

As a large part of the load stems from door openings and insulation losses from room and cabinets, a significant part of this load adds to the load of the heating system. A guestimate is 80% corresponding to 787 kWh (41x24x0.8). This is more than half of the heating load on the day with the highest heating demand. The remaining 20% is covered by internal electric loads in the cabinets from lights, fans, and defrost heaters (no data in this study presently available).

In Table 1, the number of hours and the heating demand correspond to those shown in Fig. 8. The heat recovered (HR) and the consumed power (Ptot) are calculated based on the supply and return temperatures close to the measured values in Fig. 1. The condition is operation mode B with only a limited subcooling in the gas cooler achieved by reducing the speed of the gas cooler fans. This is necessary to respect the application limits from the compressor manufacturer and at the same time use as much as possible of the HR potential.

Pref is the power, which the plant would have consumed in cooling mode only. Pnet is the difference between Ptot and Pref, and thus the extra power used to enable heat recovery. COP_{HR} is the ratio between HR and Pnet. When the pressure and the absorbed power are increased to enable HR, the compressor(s) is considered as a heat pump, and the tax has to be paid based on Ptot. The cost of power includes mandatory tax, distribution, and production costs. Note that the power price on the Danish spot market has increased from 0.224 DKK/kWh as a mean value in 2017 to 0.376 DKK/kWh, which is the mean value from January 2019 used in this calculation. Specific cost HR is the price paid per kWh and Cost is the total price in the interval. DH cost is the price if the same amount of

heat should have been supplied from the district heating grid. The saving for the specific day would have been increased from 104.69 DKK to 207.29 DKK if the temperatures for the supply and the return are lowered to 75 °C and 35 °C, respectively. For the summer condition, the calculation is more favourable as the heat needed for hot tap water preparation can be supplied without increasing the pressure or the temperature as the cooling load is higher and the price for the district heating is also higher (0.47 DKK/kWh) due to the tarif structure in this specific case.

Table 1. Calculation of cost and efficiencies for the 1st of March

		Winter worst case Supply - Return 85 °C - 45 °C							
	Unit	Night				Day			Totals
Number of hours	h	1.75	1.25	3.75	0.25	3.75	9.75	3.5	24
Cooling demand	kW	25	25	25	25	49	49	49	
Heating demand	kW	28	37	56	111	37	56	111	(1417)
HR	kW	28	37	45	45	37	56	111	
Ptot	kW	13.8	17.7	23	23	20.9	27.1	56.6	
Pref	kW	5.4	5.4	5.4	5.4	10.4	10.4	10.4	
Pnet	kW	8.4	12.3	17.6	17.6	10.5	16.7	46.2	
COP_{HR}		3.3	3.0	2.6	2.6	3.5	3.4	2.4	
Tax 0.15 DKK/kWh	DKK/h	2.07	2.66	3.45	3.45	3.14	4.07	8.49	
Power 0.63 DKK/kWh	DKK/h	5.29	7.75	11.09	11.09	6.62	10.52	29.11	
Total Cost	DKK/h	7.36	10.40	14.54	14.54	9.75	14.59	37.60	
Specific cost HR	DKK/kWh	0.26	0.28	0.32	0.32	0.26	0.26	0.34	
Energy Recovered	kWh	49	46	169	11	139	546	389	1349
Cost	DKK	12.88	13.01	54.52	3.63	36.56	142.21	131.59	394.40
DH cost 0.37 DKK/kWh	DKK	18.13	17.11	62.58	4.17	51.34	202.02	143.75	499.09
Savings day total	DKK								104.69

However, the surplus heat, which can be sold to the district heating company in the summer, is very limited, and the price paid by the grid owner is in this case only 0.15 DKK/kWh, and the slightly higher payment available in the pay back period (0.20 DKK/kWh) cannot justify increased expences. The total revenue is calculated to 51896 DKK (winter 16330 DKK, summer 32938 DKK, and sale of surplus heat 2628 DKK). These calculations are based on winter and summer mean conditions, respectively. As the variations in the summer load is higher and not yet measured, it is expected to be a conservative estimate, which means that the amount of surplus heat could be higher.

If the heating system can be optimised to accept a lower supply temperature at 70 °C and reduce the return temperature to 35 °C as well, then the revenue can be increased to around 70000 DKK. The present high price of power is in part due to the low amount of water in the resevoirs for water power in Norway and Sweden and less wind for Danish wind turbines. In round figures, the revenue will increase by further 10000 DKK, if these conditions change and consequently the power price drop to the level of 2017.

4. DISCUSSION

Due to the differentiation in price for heat supplied versus heat delivered in the presented case, the most favourable operation implies that the cost is displaced from the grid to the operating of the refrigeration system rather than selling energy to the district heating grid. The result is that most of the load from the supermarket building is lifted from the grid. The analysis shows that it will make no sense to supply the grid by boosting the amount of energy produced with the auxiliary load, e.g. the gas cooler in operation mode D, except when the variable price of the power is negative. However, if the supermarket building is not connected to the grid, it would make perfect sense as the heat could be produced to practically the same price as supplied from the district heating company.

The prices reported for refurbishing existing refrigeration systems with the heat recovery option is in the range of 200000 to 300000 DKK. In this case, this will give a direct payback time between three to six years. For smaller supermarkets, the payback time will probably be longer unless the solution

is supplied as integrated in a new installation. As the revenue is limited, it is very important that the refrigeration system owner is not imposed to extra cost due to maintenance and repairs. Thus, the design and operation of the system should ensure the longest possible lifetime of the system.

The characteristic fluctuations usually seen in connection with the loading and unloading of the compressor pack are not favourable for optimal control of a heat recovery system. The dynamics imposed on the HXR increase the thermal stress and make it difficult to meet the desired set point for the leaving water temperature. Today, the fluctuations are inherent in most supermarket control systems as they are commissioned, and a considerable effort is necessary to identify optimal operating parameters and set points to achieve a more stable control regime. This will reduce the thermal stresses of the HXR, and thus increase the lifetime of the installation. Furthermore, it will improve the efficiency of the heat recovery and possibly also the refrigeration system.

A secondary control issue is the fluctuating prices on the power market. When the maxima of heat load and the spot prices coincide, the cost of HR is higher than that of district heating. A simple solution is to limit the HR in the times of the day where the prices are often the highest. However, a price signal from the power company is also a possibility, either for a day ahead or hour by hour, depending on the available services. In addition, care should be taken not to produce hot tap water in critical periods. Therefore, another simple measure is a storage tank for hot water sufficiently sized to enable hot water production at night where the other heat loads as well as the power price are often lower.

5. CONCLUSIONS

It is shown that fair efficiencies are possible when heat recovery is applied on refrigeration systems with CO_2, even if the conditions often are unfavourable as they are defined by the design of the existing heating system in terms of the required high supply temperatures and the achieved equally high return temperatures.

Despite the required relatively high investments, a moderate payback time between three to six years is achieved for both supermarket buildings connected to a district heating grid as well as remote locations where the heat recovered can replace oil and gas burners and improve both operation costs and carbon footprint.

However, preceding cases of heat recovery installations show that there is room for improvement in terms of establishing good practice when installing critical components such as heat exchangers and developing sound control regimes as well as commissioning guidelines to ensure a long service life and high efficiencies.

ACKNOWLEDGEMENTS

This paper is a contribution in the project Super Supermarkets supported by the Danish Energy Agency under the EUDP program. One of the project goals is the making of a book of guidelines to facilitate good and reliable heat recovery installations in supermarkets with CO_2 refrigeration systems.

REFERENCES

Funder-Kristensen, T., Larsen, L.F.S., Thorsen, J.E., 2017. Integration of the hidden refrigeration capacity as heat pump in smart energy systems. 12th IEA Heat Pump Conference 2017, Rotterdam, The Netherlands, IEA ID 87.

Karampour, M., Sawalha, S., 2018. State-of-the-art integrated CO2 refrigeration system for supermarkets: A comparative analysis. Int. J. Refrigeration 86, 239-257.

Alfa Laval, 2017, Installation Guideline, AXP Heat Exchangers in CO_2 systems.

SWEP, Calculation software SSPG8, 2019.

Manuscript ID: 690
DOI: 10.18462/iir.icr.2019.0690

Load peak shifting using phase change materials in open display cabinets: an experimental investigation

Ronia BEN-ABDALLAH[a,b], Denis LEDUCQ[a], Hoang-Minh HOANG[a], Olivier PATEAU[b], Bénédicte BALLOT-MIGUET[b], Elyamin DAHMANA[a], Laurence FOURNAISON[a], Anthony DELAHAYE [a]

[a]IRSTEA, UR GPAN, Refrigeration Process Engineering Research Unit, Antony, F-92160, France, violette.mulot@irstea.fr
[b]EDF –R&D, EDF Lab les renardières, Avenue des Renardières, 77250 Écuelles

ABSTRACT

Display cabinets are widely used in supermarkets and represent an important part of their energy consumption. The present study is focused on the performance of the display cabinet with integrated phase change material (PCM). To enhance the heat transfer and facilitate the PCM melting and freezing, PCM is placed into a heat exchanger. The experimental results show an important potential of PCM to preserve the temperature during a compressor stop. In addition, adding PCM to the refrigerated display cabinet is considered as an interesting lever for electricity. PCM heat exchanger integration inside the rear duct may also affect the airflow.

Keywords: Phase Change Materials, Display cabinet, refrigeration, thermal behavior

1. INTRODUCTION

The refrigeration is one of the most energy consuming applications in the food supply chain. About 35% of this electricity consumption is used by the food sector (Evans et al., 2014). Today, commercial refrigeration becomes an important segment of the economy and shows a constant increase. It represents around 4% of the annual electricity consumption in industrialized countries (Gullo, Hafner, & Banasiak, 2018; Tassou, Ge, Hadawey, & Marriott, 2011) and 35-50% of this total electricity is consumed by the refrigeration (Sawalha, 2014). In fact, display cabinet is the most widely used and energy intensive equipment in food retail (Evans, Scarcelli, & Swain, 2007; Tahir & Bansal, 2005). In this context, the integration of energy storage devices using Phase Change Materials (PCM) in the display cabinet can present opportunities for reducing peak demand and supermarket energy cost. Indeed, PCM inside display cabinet increase the flexibility of the device. In fact, flexibility is the key to the energy transition success. PCMs allow reducing the demand at critical moment (peak consumer demand) by attenuating peaks in demand and deferring a part of the power consumption at another time (peak shaving). PCMs can defer the energy demand at the optimal time for electricity supplier (curtailment), and consequently avoid building new power plants or using priced electricity [12]. Moreover, PCMs can be a solution to the intermittency of renewable energy sources and encourage supermarkets to self-consumption via solar energy or wind energy. It should be noted that many governments offer incentive to encourage such use.

Many studies have focused on the application of phase change materials for energy storage in refrigeration equipment such as for example refrigerator(Belman-Flores, Barroso-Maldonado, Rodríguez-Muñoz, & Camacho-Vázquez, 2015). Azzouz and al. (Azzouz, Leducq, & Gobin, 2008) placed PCM sheets on the back side of a refrigerator evaporator. The heat transfer between the liquid and solid PCM was shown to be significantly higher than the heat transfer generated by natural

convection in the compartment area of the refrigerator without PCM. The result was a higher evaporation pressure, an increased refrigeration capacity and a significant performance enhancement.

PCM has received a considerable interest for its use in refrigerated trucks. A PCM thermal storage unit can even be a substitute to a conventional refrigeration system (Liu, Saman, & Bruno, 2012). In this case, the PCM storage unit is charged by a refrigeration unit located off the vehicle. This concept has been proved as feasible for mobile transport. In addition, the system has been found to consume less energy and to produce much lower greenhouse gas emissions. So far, only few studies concerning the application of PCMs in display cabinets have been published. Lu et al.(Lu et al., 2010) in their work have integrated heat pipes and PCM within shelves to improve heat transfer and reduce temperature heterogeneity. The results showed that the new shelf with heat pipe leads to lower food temperature (3 to 5 °C) and improves the uniformity of temperature distribution. Sevault et al. focused on a novel PCM accumulator for a refrigerated display cabinet (A. Sevault, 2018). The PCM accumulator used is composed of three fluids: PCM (pure water), air to be cooled and CO2 as refrigerant. Their work consists to optimize the PCM accumulator design. They observed the influence of the distance between CO2 coils and air ducts on the charge and discharge of PCM. Alzuwaid et al. (F. A. Alzuwaid, Ge, Tassou, & Sun, 2016; F. Alzuwaid, Ge, Tassou, Raeisi, & Gowreesunker, 2015) used PCM charged into two single panel radiators, in the back flow channel of an open vertical display cabinet. The tests results showed energy savings, lower cabinet temperatures and a significant stabilization of product temperatures during defrost.

The purpose of this work is to study experimentally the PCM integration on an open display cabinet. Important quantity of the PCM is investigated (7kg), the container is a heat exchanger and the PCM is pure water without additives. The work's originality is the characterization of the PCM heat exchanger and its effect on the thermal performance of the display cabinet. Moreover, the comparison of the air and product temperature rise obtained with a normal display cabinet (without PCM) and a modified display cabinet (with PCM) during a compressor stop (curtailment) is discussed.

2. MATERIALS AND METHODS

2.1. Display cabinet description

The display cabinet used in the present study is shown in Figure 1. It has five shelves (from 1st for top to 5th for bottom). It is loaded with packages of test product.

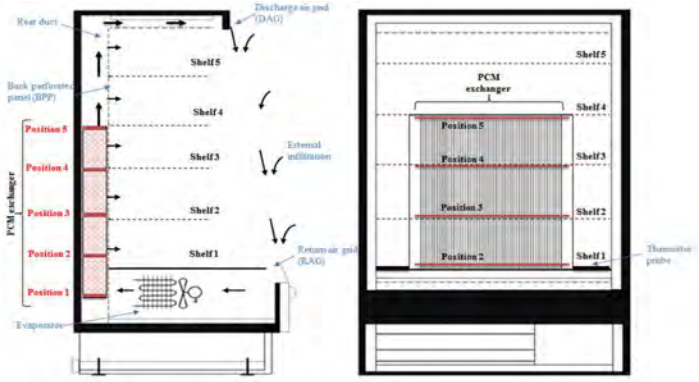

Figure 1: Integration of PCM heat exchanger inside the display cabinet

Cold air from the outlet of the evaporator circulates vertically through the PCM heat exchanger placed in the rear duct (up to the 3rd shelf) to the discharge air grid (DAG), then flows down into the return air grid (RAG). Along the rear duct and even along the PCM heat exchanger, a part of this air flows

horizontally through the back perforated panel (BPP) and provides cooling directly to products. A part of the ambient air is infiltrated and mixed to the top-down flow (Figure. 1).

2.2. PCM heat exchanger description

Water is chosen as the PCM used in this application due to.its properties: high latent heat (334 kJ.kg-1) and specific heat (4184 J.kg-1.K−1), easily available, safe, cheap, non–toxic, non–flammable. Water can be considered as one of the best suited PCM for food application. To integrate PCM inside the display cabinet, many positions were suggested. However, the suitable position depends on some important criteria. First of all, the PCM freezing and melting temperature: indeed, the air temperature is different from one position to another inside the display cabinet. That's why a temperature test is carried out to determine the temperature range in different areas of the display cabinet (rear duct, discharge air grid, return air grid, under shelves…) for different ambient conditions (T=15, 20 and 25°C). Results showed that the rear duct is the best zone to introduce PCM, due to its temperature range. More details can be found in previous works [23] [22]. The second criterion is the important PCM quantity needed to ensure at least 1h of compressor stop without a large product temperature rise (less than 4°C). In our case, PCM is introduced inside a heat exchanger. This configuration is selected not only because heat exchanger contributes to enhance total heat exchange surface is S_exch=25 m^2 (manufacturer's data), but also because the evaporator is located at the bottom of the display cabinet, giving enough free room in the rear duct to install a heat exchanger. Moreover, the ease of installing of the PCM is also taken into account. Finally, the position in the rear duct just after the evaporator (Figure.1) is also interesting since the air velocity is here at its maximum value, resulting in a local convection heat transfer around 20$W.m^{-2}.K^{-1}$. The heat exchanger is filled with 7kg of PCM. This quantity is related to the display cabinet power (600 W) and the targeted duration of curtailment of 1h. PCM volume occupies 70% of the total volume of the heat exchanger to take into account the water volume expansion during the phase change.

2.3. Instrumentation

T-type thermocouples (TMC) were used for measurement of: Temperature of products at the surface and at the core (blue dot) and air temperature: at the air curtain, air supply (DAG) and return grill (RAG), in the back duct and room temperature (green cross). The positions of these thermocouples are shown in Figure.2. The PCM heat exchanger is also instrumented with T-type thermocouples (black cross) according to the schema (Figure.3) in 5 levels related to different charging ratio. At each level, two positions are instrumented: at the middle and at the right side. All thermocouples were calibrated and have a precision of 0.3°C.

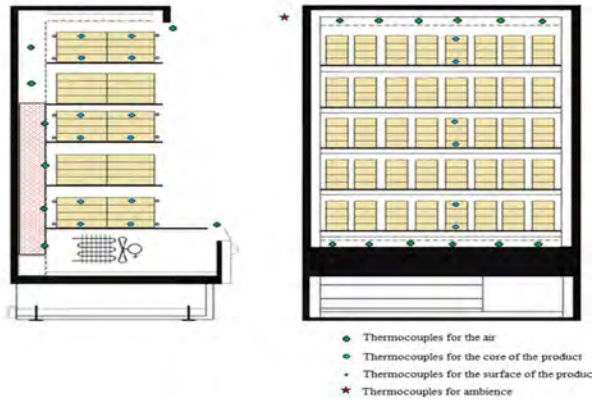

Figure 2: Modified display cabinet instrumentation

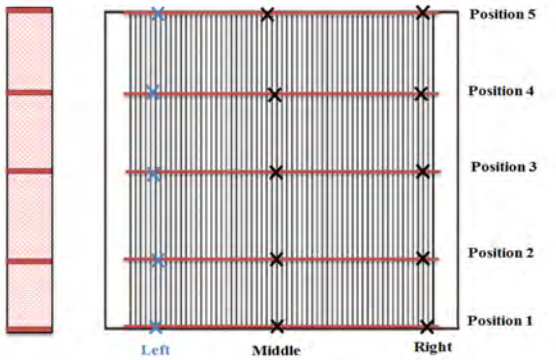

Figure 3: PCM heat exchanger instrumentation

2.4. Test conditions

Temperature inside the display cabinet is controlled by a thermistor probe located at the bottom of the display cabinet, at the right side of the rear duct and at the level of the first shelf. For all experiments, the settings parameters of the electronic controller are fixed as follows: the compressor is turned off when the temperature measured by the thermistor probe reaches the set point temperature -5°C with a differential temperature (+2°C compared to the set point temperature). The defrost starts periodically each 8 hours. Defrosting is done by stopping the compressor. Defrost period ends when the temperature sensor of the display cabinet reaches 11°C. The display cabinet is located in a test room in which the ambient temperature is fixed at 16°C.

2.5. Charging and discharging Ratio

In order to characterize the PCM behavior during phase change processes and the heat exchanger performance, charging ratio is defined according to the temperature of PCM at 4 positions inside the heat exchanger. These positions (Figure.3) correspond to the charging ratios of 0% (position1), 25% (position 2), 50% (position 3), 75% (position 4) and 100% (position 5). During the charging process, the phase change is complete when the temperature at one position is lower than 0°C (freezing temperature of PCM) and begins to decrease (point C in Figure.4); the PCM is then considered to be fully solid. Conversely, during discharging process, the PCM is considered to be fully liquid when the temperature begins to increase after the phase change stage (Point F in Figure.4).

3. RESULTS AND DISCUSSIONS

3.1. PCM heat exchanger characterization

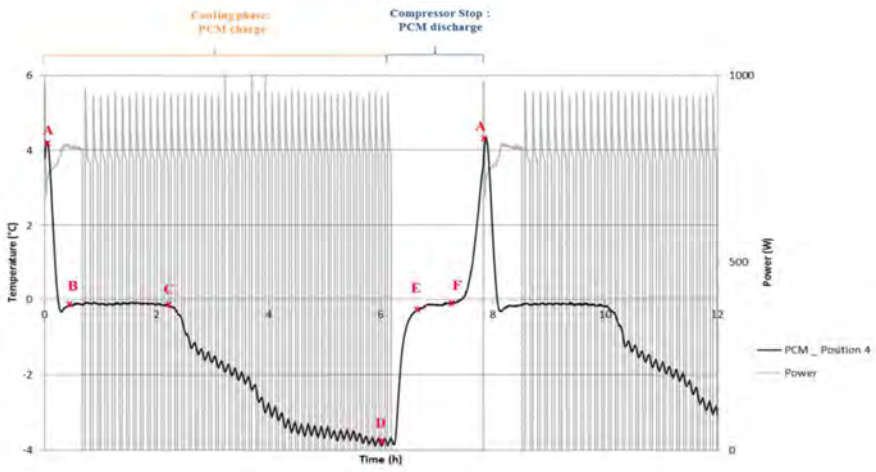

Figure 4: Temperature evolution of the PCM inside the position 4

The Figure 4 illustrates the PCM behavior during a cycle of charge and discharge processes at the position 12 of the PCM heat exchanger. In this cycle, 6 phases can be defined:

-A-B: Cooling phase 1 - PCM in liquid state: the PCM temperature decreases to the phase change level (near 0°C)

-B-C: Cooling phase 2 - liquid to solid phase change: during this period, a temperature plateau around 0°C is observed, latent heat is stored by PCM. At the end of this phase, the PCM is completely solid.

-C-D: Cooling phase 3 - PCM in solid state: PCM temperature continues to decrease,

-D-E: Compressor stop phase 1- PCM in solid state: during this phase, the compressor is stopped due to defrost. The PCM temperature increases until it attains the phase change level around 0°C

-E-F: Compressor stop phase 2 - solid to liquid phase change: while the PCM temperature stays around 0°C

-F-A: Compressor stop phase 3 - PCM in liquid state, PCM temperature increases

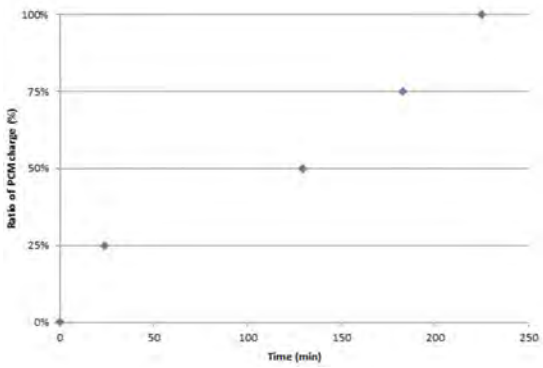

Figure 5: PCM ratio of charge during time

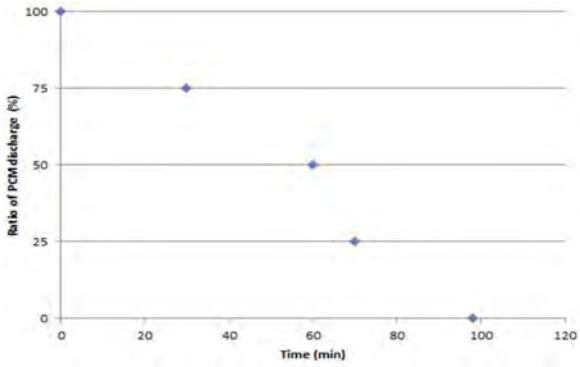

Figure 6: PCM ratio of discharge during time

Figure 5 and 6 show the time evolution of the PCM ratio of charge and discharge. The time necessary to totally charge the heat exchanger (i.e. the PCM becomes completely solid) is 220 min (3h40 min). However, it takes only 100 min (1h 40min) to melt the PCM: the discharging time is 3 times faster than the charging time. This result can be explained by the larger temperature difference between the air and the PCM during discharge.

		Left	Middle	Right
0 min	Position 5	9	10	9
	Position 4	9,5	9,7	9,5
	Position 3	9,6	10,2	9,6
	Position 2	10,8	11,3	10,8
	Position 1	10,7	11,3	10,8
		Left	Middle	Right
50 min	Position 5	-0,1	-0,1	-0,1
	Position 4	-0,1	-0,1	-0,1
	Position 3	-0,1	-0,2	-0,1
	Position 2	-3,3	-4,0	-3,3
	Position 1	-3,3	-4,4	-3,3
		Left	Middle	Right
125 min	Position 5	-0,1	-0,1	-0,1
	Position 4	-0,1	-0,4	-0,1
	Position 3	-0,4	-3,4	-0,4
	Position 2	-5,0	-5,6	-5,0
	Position 1	-3,6	-4,6	-4,6
		Left	Middle	Right
185 min	Position 5	-0,1	-0,2	-0,1
	Position 4	-0,3	-3,1	-0,3
	Position 3	-2,6	-3,3	-2,5
	Position 2	-3,6	-3,5	-3,6
	Position 1	-2,5	-2,7	-2,5
		Left	Middle	Right
225 min	Position 5	-0,1	-2,7	-0,1
	Position 4	-1,6	-3,9	-1,6
	Position 3	-3,0	-3,3	-3,0
	Position 2	-4,2	-4,0	-4,2
	Position 1	-3,1	-3,2	-3,1
		Left	Middle	Right
250 min	Position 5	-0,7	-3,5	-0,7
	Position 4	-2,8	-3,5	-2,8
	Position 3	-3,6	-3,6	-3,6
	Position 2	-4,2	-4,2	-4,2
	Position 1	-3,3	-3,3	-3,3

Table 1: PCM temperature during

		Left	Middle	Right
0 min	Position 5	-3	-4	-3
	Position 4	-2.9	-3.7	-2.9
	Position 3	-3.4	-3.7	-3.4
	Position 2	-5.6	-5.9	-5.6
	Position 1	-4.2	-5.4	-4.2
		Left	Middle	Right
50 min	Position 5	-0.1	-0.1	-0.1
	Position 4	-0.1	-0.1	-0,1
	Position 3	-0.1	0.7	-0.1
	Position 2	7.1	7,3	7.1
	Position 1	7.7	7.4	7.7
		Left	Middle	Right
75 min	Position 5	-0.1	-0.2	-0,1
	Position 4	0.9	0.9	0.9
	Position 3	5.3	7.9	5.6
	Position 2	8.3	8.4	8.3
	Position 1	8.9	8.5	8.9
		Left	Middle	Right
100 min	Position 5	0.2	0.5	0.2
	Position 4	6.9	8.5	6.1
	Position 3	8.6	9.3	8.6
	Position 2	9.4	9.4	9.4
	Position 1	10.2	9.7	10.2
		Left	Middle	Right
125 min	Position 5	10.6	10.8	10.6
	Position 4	10.9	10.9	10.9
	Position 3	9.6	9.9	9.6
	Position 2	10.3	10.4	10.3
	Position 1	10.8	10.4	10.8

Table 2: PCM temperature during discharge

In order to understand the progress of the charging process, table 1 illustrates the evolution of the

temperature in different positions in the heat exchanger at several moments. Initially (0 min), the PCM temperature was positive (red cases). After 50 min, positions 1 and 2 situated near the evaporator were the first to change phase. Then, at 125 min later, position 3 starts to freeze in the middle, followed by the two others (position 4 at 185 min and position 5 at 225 min). From these results, it can be concluded that the PCM charge is progressive and the middle is more sensible to temperature variation than the tube extremities. This phenomenon is due to the position of the fan and the airflow pattern inside the display cabinet. The same behavior is observed for the discharge process (table 2): the discharge is also progressive and starts from the middle of the tube to the extremities. (*t*=50 s), at about mid-time (*t*=800 s) and at the end (*t*=1320 s).

3.2. PCM effect on the air temperature inside the rear duct

Figure.7 presents the air temperature evolution during a compressor stop for a modified display cabinet. Dashed curves represent air temperature measured at the heat exchanger level and continuous line curves represent air temperature after the PCM heat exchanger in the rear duct. The dynamic behavior of the 2 types is different. For the first category, the air temperature decreases more at each level. This is due to the PCM melting that cools the air though the PCM heat exchanger. The air temperature evolutions after the PCM exchanger ($T_{air\ 4}$ and $T_{air\ 5}$) are influenced by the PCM melting. It reaches only 6.5°C after 1h40 min of a compressor stop.

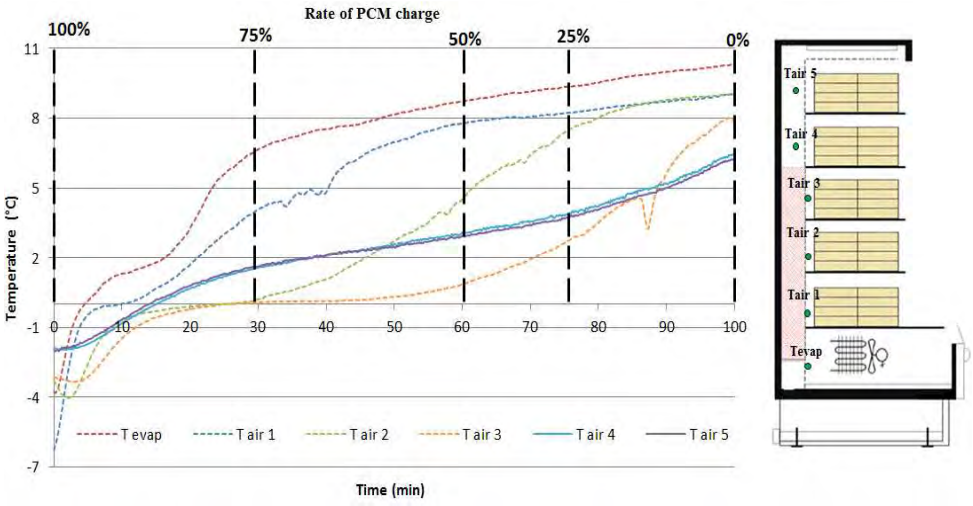

Figure 7: Air temperature in the rear duct during a compressor stop

3.3. Comparison between a modified and unmodified display cabinet during a compressor stop

Figure.8 shows a comparison between temperature rise ΔT ($\Delta T = T_t - T_{ini}$, temperature gap between the temperature at every instant and the temperature at the beginning of the compressor stop) of packages for a modified and an unmodified display cabinet during a compressor stop. Globally, PCM heat exchanger is able to provide cooling for the packages during a compressor stop: ΔT is much less important for modified display cabinet. For the 1st shelf, ΔT for the back product is around 0°C. This can be explained by the PCM heat exchanger location and the control set temperature for the experiment.

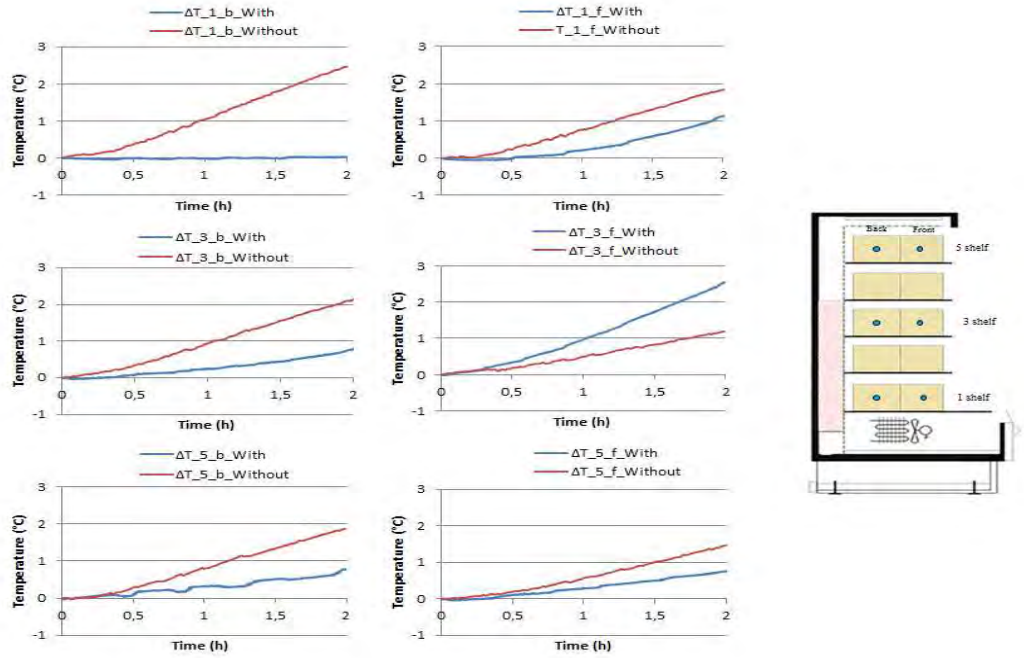

Figure 8: Comparison between the packages temperature for a modified and an unmodified display cabinet during a compressor stop

Figure.9 represents the comparison between the dimensionless air temperature ($\Theta = (T_t - T_{ini})/(T_{amb} - T_{ini})$) in the rear duct with and without PCM exchanger during a compressor stop. It is interesting to observe the slope change with the PCM exchanger: the temperature rise is damped by the PCM melting. These two results confirm the potential of applying curtailment with the display cabinet with PCM.

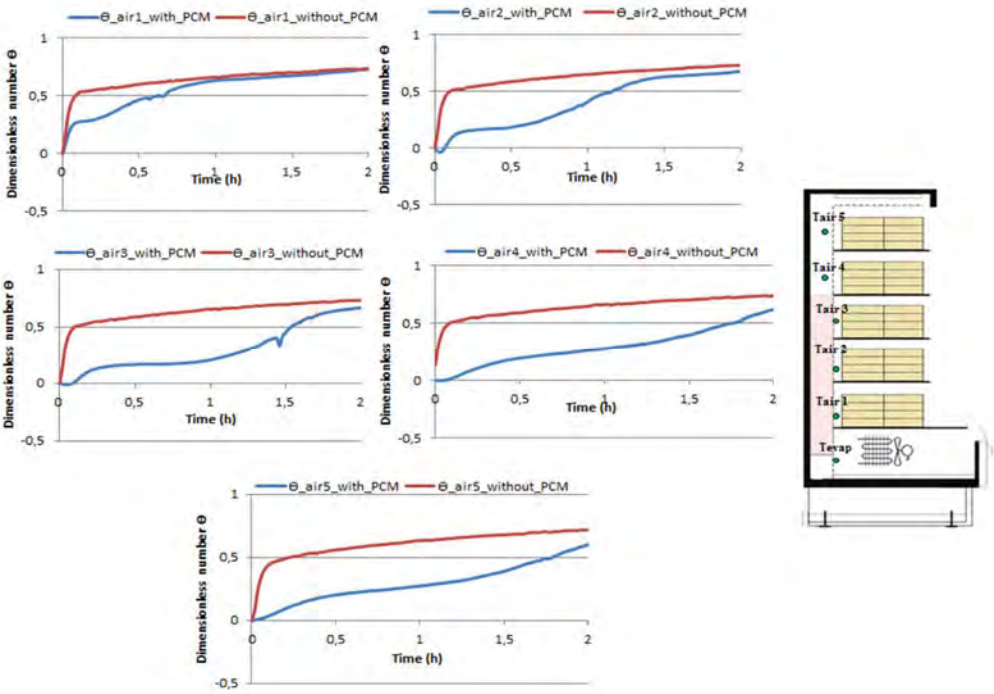

Figure 9: Comparison between the air temperature in the rear duct for a modified and an unmodified display cabinet

4. CONCLUSIONS

The experiment study of the modified display cabinet show interesting results. In fact, despite the presence of the PCM exchanger in the rear duct, the display cabinet is able to cool and conserve the temperature product and in the same time store cool in PCM. During the compressor stop, PCM provide cool and the temperature rise for air and product is damped. This work proves the PCM integration feasibility and confirms the PCM potential inside display cabinet.

ACKNOWLEDGEMENTS

The authors gratefully acknowledge the financial support granted by the CIFRE department (Conventions Industrielles de Formation par la Recherche) from the French ANRT (Association Nationale Recherche et Technologie).

REFERENCES

A. Sevault, K.Banasiak, J. Bakken, A. Hafner. (2018). *A novel PCM accumulator for refrigerated display cabinet: design and CFD simulations*. Paper presented at the 12th IIR Conference on Phase-Change Materials and Slurries for Refrigeration and Air Conditioning Orford (Québec), Canada.

Alzuwaid, F. A., Ge, Y. T., Tassou, S. A., & Sun, J. (2016). The novel use of phase change materials in an open type refrigerated display cabinet: A theoretical investigation. *Applied Energy, 180*, 76-85. doi:

Alzuwaid, F., Ge, Y. T., Tassou, S. A., Raeisi, A., & Gowreesunker, L. (2015). The novel use of phase change materials in a refrigerated display cabinet: An experimental investigation. *Applied Thermal Engineering, 75*, 770-778.

Azzouz, K., Leducq, D., & Gobin, D. (2008). Performance enhancement of a household refrigerator by addition of latent heat storage. *International Journal of Refrigeration, 31*(5), 892-901. doi: https://doi.org/10.1016/j.ijrefrig.2007.09.007

Belman-Flores, J. M., Barroso-Maldonado, J. M., Rodríguez-Muñoz, A. P., & Camacho-Vázquez, G. (2015). Enhancements in domestic refrigeration, approaching a sustainable refrigerator – A review. *Renewable and Sustainable Energy Reviews, 51*, 955-968.

Evans, J. A., Foster, A. M., Huet, J. M., Reinholdt, L., Fikiin, K., Zilio, C., . . . van Sambeeck, T. W. M. (2014). Specific energy consumption values for various refrigerated food cold stores. *Energy and Buildings, 74*, 141-151.

Evans, J. A., Scarcelli, S., & Swain, M. V. L. (2007). Temperature and energy performance of refrigerated retail display and commercial catering cabinets under test conditions. *International Journal of Refrigeration, 30*(3), 398-408.

Gullo, Paride, Hafner, Armin, & Banasiak, Krzysztof. (2018). Transcritical R744 refrigeration systems for supermarket applications: Current status and future perspectives. *International Journal of Refrigeration, 93*, 269-310. doi: https://doi.org/10.1016/j.ijrefrig.2018.07.001

Liu, Ming, Saman, Wasim, & Bruno, Frank. (2012). Development of a novel refrigeration system for refrigerated trucks incorporating phase change material. *Applied Energy, 92*, 336-342.

Lu, Y. L., Zhang, W. H., Yuan, P., Xue, M. D., Qu, Z. G., & Tao, W. Q. (2010). Experimental study of heat transfer intensification by using a novel combined shelf in food refrigerated display cabinets (Experimental study of a novel cabinets). *Applied Thermal Engineering, 30*(2–3), 85-91.

Sawalha, Mazyar karampour and Samer. (2014). Supermarket refrigeration and heat recovery using CO2 as refrigerant.

Tahir, A., & Bansal, P. K. (2005). MEPR versus EEPR valves in open supermarket refrigerated display cabinets. *Applied Thermal Engineering, 25*(2–3), 191-203.

Manuscript ID: 771
DOI: 10.18462/iir.icr.2019.0771

Combined refrigeration, heating and air conditioning systems in supermarkets: seeking energy efficient solutions

Paola D'AGARO, Michele A. COPPOLA, Giovanni CORTELLA
DPIA – University of Udine
Udine, 33100, Italy
giovanni.cortella@uniud.it

ABSTRACT

A deep synergy between the refrigeration and the HVAC plants is a viable solution to reduce the energy use of supermarkets. Not only heat recovery can be performed from the refrigerating plant in favour of space heating and hot water production, but also provision of AC capacity.
A model based on TRNSYS and in-house types, validated with field data gathered from a fully instrumented plant in an active supermarket, allows to seek the optimal coupled solution. The model has been used to predict its feasibility and energy use at different climate conditions, for a reference supermarket. An energy saving of about 9% was predicted, regardless of the climate conditions, if the energy performance quality of the building envelope is kept constant.
The integration of the refrigeration and HVAC systems shows to be effective in terms of energy use. Significant reductions can also be obtained in the investment costs, space occupied by the plants and amount of refrigerant charge.
Keywords: Carbon dioxide, Commercial building, Commercial refrigeration, Heat recovery, Modelling, Supermarket

1. INTRODUCTION

The efficiency of CO_2 plants in supermarkets is a critical issue at warm climate conditions, when yearly energy consumption can be higher than that of conventional HFCs plant, thus contrasting the efforts to reduce the greenhouse gas emission. This drawback is partially overcome by employing one or more improved system configurations, such as parallel compression, overfed evaporators, compression work recovery (Gullo et al, 2016). A key role in making CO_2 systems attractive can be played by heat recovery, which can take advantage of the high discharge temperature and properties of the transcritical carbon dioxide and turn the use of this natural refrigerant into an advantage (Polzot et al 2016, 2017a, Sawalha 2013, D'Agaro et al 2018). In the view of reducing substantially the investment cost and increasing the compactness of the system, the integration between the refrigerating and the HVAC systems can be extended also to the air conditioning function, which can be assigned to the commercial refrigerating unit. Different solutions have been investigated, with similar or even slightly lower energy use (Karampour and Sawalha 2017, 2018; D'Agaro et al. 2019; Pardiñas et al, 2018). Modelling the whole system is the main tool when looking for the best solution, possibly with validation by comparison from field data (Minetto et al. 2014; Karampour and Sawalha 2017; Cortella et al. 2018).
A small supermarket (1200 m^2 selling area) located in Modena (Italy) has been considered as case study for this work. It was recently refurbished in the framework of the FP7 European Project CommONEnergy, involving several aspects such as plants, envelope, solutions for both artificial and natural lighting and the refrigeration system, which is fully integrated with the HVAC one. A comprehensive model has been setup in the Trnsys environment, and validated with field data. With such model the performance of the integrated system is estimated at various climate conditions, to help identifying a design rule when replicating this installation in other sites.

2. REFRIGERATION AND HVAC COUPLING

The commercial refrigeration system considered supplies cooling capacity to 14 m of new refrigerated display cabinets for the low temperature level (LT) and 40 m of closed cabinets and 23 m of serve-over or open ones for the medium temperature level (MT). The commercial refrigeration unit coupled with the

HVAC plant is sketched in Fig. 1. It is a transcritical CO_2 booster system with receiver at the intermediate pressure p_{INT} and parallel compression for the flash gas, which is expanded to MT pressure in subcritical operation or is compressed to the high stage (HS) pressure p_{HS} in transcritical operation. The evaporating temperature is -35 °C and -10 °C for the MT and LT application respectively. The system performs waste heat recovery at two temperature levels at the exit of HS compressors: heat exchanger HR1 recovers heat for DHW production (70 - 55 °C) and heat exchanger HR2 supplies lower temperature water for space heating purposes (50 - 40 °C). In order to increase the amount of heat recoverable in wintertime, the refrigeration system is forced to operate in transcritical regime, at a p_{HS} value higher than the subcritical one which would be driven by the outdoor temperature.
An evaporator at p_{INT} pressure (AC supply) may be used to provide cooling capacity for air conditioning system. Both compressor racks, LS and HS, are composed of two compressors, distinguished as master and slave compressor. The master is controlled by an inverter and the slave is an ON/OFF type.

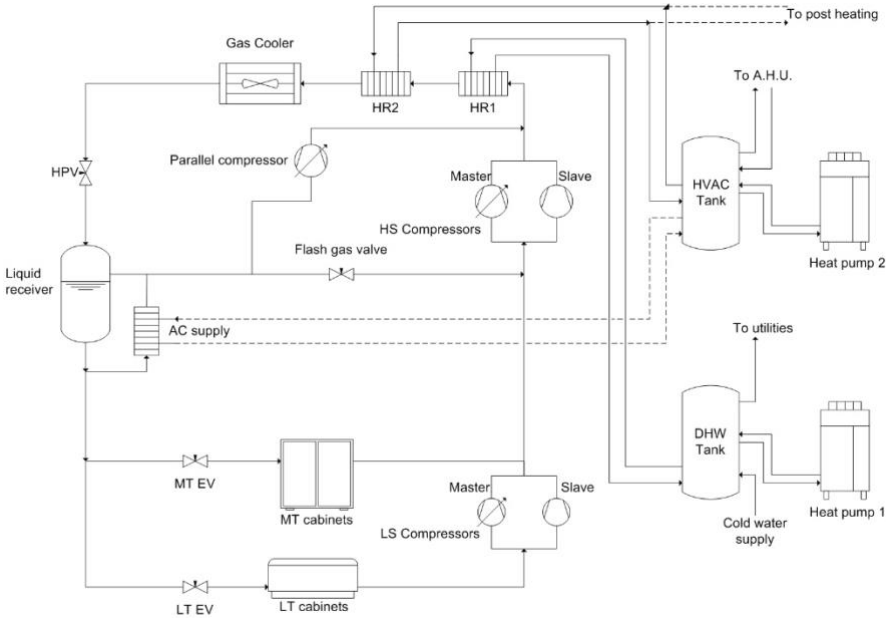

Figure 1: Schematic of the CO_2 refrigeration system with heat recovery and evaporator for AC supply

The comprehensive model of the entire refrigeration system, which includes the operation of the display cabinets, cold rooms and of the refrigerating unit has been implemented in the TRNSYS environment, developing in-house routines for each component. In particular, the sub-hourly cooling load profiles at the two evaporating levels are predicted by adjusting the cooling capacity at rated condition of each display cabinet in accordance with time-dependent operating conditions in the supermarket as described in detail in Polzot 2017b. Regarding the refrigerating unit, the thermodynamic and thermophysical properties of the refrigerant are calculated by linking our in-house routines in the TRNSYS environment to the CoolProp libraries (Bell et al., 2014). The compressors are described through correlations provided by the manufacturer in accordance with the Standard EN12900:2013.
The values of the main design parameters are reported in Table 1.
The control rules implemented in the model are described in D'Agaro et al (2019). If there is no heating demand from the HVAC system in the supermarket ($q_{HEA} = 0$), the high stage pressure p_{HS} is driven by the outdoor temperature as in Polzot 2017b; otherwise, when there is heating demand ($q_{HEA} \neq 0$), the refrigerating unit is switched to transcritical mode at 78 bar.

$$\begin{cases} \text{if } q_{HEA}=0 \Rightarrow \begin{cases} \text{in transcritical operation: } p_{HS} = \max(75;1.75t_{GC\_out} + 22.13) \text{ [bar]} \\ \text{in subcritical operation: } p_{HS} = \max\left(p_{sat}(t_{cond,\min}); p_{sat}(t_{GC\_out} - \Delta t_{sc})\right) \text{ [bar]} \end{cases} \\ \text{if } q_{HEA} \neq 0 \Rightarrow p_{HS} = 78 \text{ [bar]} \end{cases} \quad \text{Eq. (1)}$$

In the integrated system, the heat recovery in heat exchanger for both DHW and heating is active whenever the outlet water temperature (t_{w,HR_out}) is higher than the temperature in the corresponding tank

(t_{tank}). Whenever the temperature in the tank drops below the minimum value ($t_{tank,min}$), the corresponding heat pump HP (Fig.1) is activated to bring the set point value ($t_{tank,set}$) back.

$$\begin{cases} \text{if } t_{w,HR\_out} > t_{tank} \text{ and } t_{tank} < t_{tank,set} \Rightarrow \text{HR active} \\ \text{if } t_{tank} < t_{tank,\min} \Rightarrow \text{HP active} \end{cases} \quad \text{Eq. (2)}$$

The COP profiles for the two heat pumps used to fulfil DHW/Heating demands are shown in Fig. 2 as a function of the outdoor temperature.

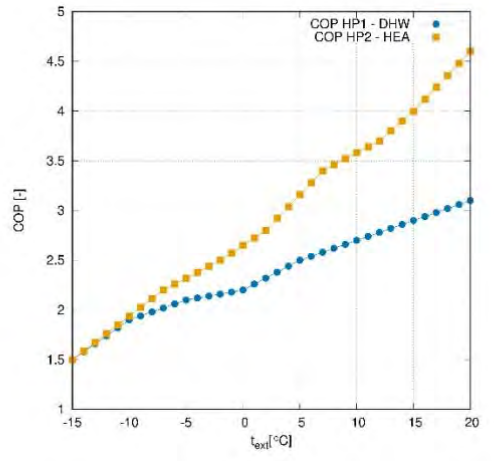

Figure 2: Coefficient of Performance of the heat pumps for DHW and heating

As regards the AC capacity, the evaporator at p_{INT} pressure (AC supply) supplies cooling capacity up to a limiting value imposed by the maximum compressor displacement, aiming at reaching the setpoint value. Whenever the temperature in the tank raises above the maximum value, the corresponding unit (HP2 in Figure1) is activated to bring the set point value back. The EER of this chiller unit is given by:

$$EER = 5.629 - 0.0886\ t_{ext} \quad \text{Eq. (3)}$$

The set point and minimum/maximum temperature values are reported in Table 1.
The model has been validated with data from a whole year of monitoring (D'Agaro et al, 2019).

Table 1. Main design parameters for the commercial refrigeration unit

Parameter	Unit	Value
Nominal cooling capacity at MT	kW	70.5
Nominal cooling capacity at LT	kW	10.8
MT evaporating temperature	°C	-10
LT evaporating temperature	°C	-35
Minimum condensing temperature $t_{cond,min}$	°C	6
Liquid receiver pressure p_{INT}	bar	35
Degree of subcooling at subcritical conditions ΔT_{sc}	K	3
Gas Cooler/Condenser approach ΔT	K	4
Superheat at LS/HS suction	K	30/20
DHW tank setpoint temperature / min temperature	°C	70/55
HVAC tank setpoint temperature / min temperature (heating use)	°C	45/35
HVAC tank setpoint temperature / max temperature (AC use)	°C	7/12

3. SUPERMARKET BUILDING AND HVAC DEMANDS

The supermarket, which was a democase in the EU CommONEnergy project, has a selling area of 1200 m^2. It is rectangular in plan and occupies the ground floor of a building. The north-east façade of the building is visible in the picture of Fig. 2 (marked 1 in the plan sketch of the supermarket in the right). The supermarket is in the lower glazed part, shaded by a porch and it is just 3.16 meters high; the upper floor is entirely occupied by a gym and a warehouse area is located in the underground. The other external façade (marked 2) is mainly opaque, as just 2% of its surface is glazed. A gallery runs along the two other façades. The thermal transmittance of the opaque elements as well as the thermal and the solar energy transmittance of the transparent elements of the envelope are provided in Table 2.

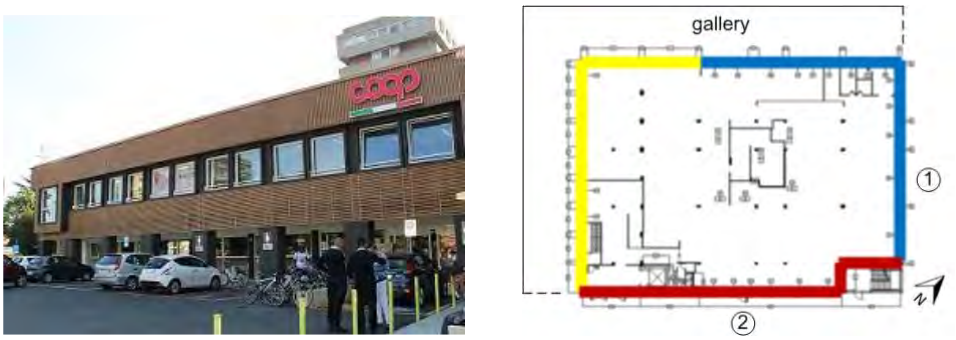

Figure 2: Case study supermarket: main façade after retrofit (left) and sketch of the plan (right)

The model for the building energy simulation, which was realized using multi-zone building Type 56, derives from the outcomes of the EU CommONEnergy project. Antolin et al. (2016) report the full data set for the simulation model, in Table 2 just the main values of building loads and the heating and cooling temperature set point values are summarized. The building was subject to a deep renovation, which included the wall insulation and new glazed façade, Load from lighting have been substantially reduced by massively using LED lamps and solar light tubes. It should be underlined that the sensible and latent contributions from the display refrigerated cabinets to the HVAC system are dynamically calculated: the heat and mass transfer between the refrigerated volumes and the indoor environment are assessed, for each cold room and display cabinet typology, as a function of the indoor air temperature and humidity.

Table 2. Main input data for the simulation model of the building for the actual building (climate 4)

Building envelope	U ($W\ m^{-2}\ K^{-1}$)	g
Exterior wall (marked in yellow in Fig.2)	0.275	-
Exterior wall (marked in red in Fig.2)	0.290	-
Ceiling/interior floors	0.930	-
Ground floor	1.73	-
Exterior glazed façade (marked in blue in Fig.2)	1.80	0.6
Building loads and set points		
Lighting (W/m^2)	12	
Appliances (W/m^2)	10	
Occupancy in the selling area ($persons/m^2$)	0.2	
Heating set point temperature (°C)	22	
Cooling set point temperature (°C)	26	

In this study, 5 locations representative of different Italian climate conditions are considered. The weather files for the simulation of both the commercial refrigeration unit and the building are the Typical Meteorological Year (TMY) which derive from the Meteonorm database (Meteonorm, 2017). In order to perform a fair comparison among the loads on the HVAC system at different climate conditions, the energy performance quality of the building, with reference to the winter performance, has been keep constant. The thermal characteristics of the building envelope at each location have

been corrected to attain approximately the same ratio as the actual building at climate 4:

$$\frac{EP_{H,nd}}{EP_{H,nd,\lim}} = 0.35 \qquad \text{Eq. (4)}$$

between the annual heating energy need per unit area $EP_{H,nd}$ (EN ISO 13790) and its benchmark value $EP_{h,nd,lim}$ calculated, as indicated by the Italian National Decree of June 26th, 2015, assuming the prescribed thermal transmittances values for the elements of the building envelope.

4. SIMULATION RESULTS

Table 3 reports the locations, identified with an increasing number from the warmest (1) to the coldest (5) one, the value of Heating Degree Days and Cooling Degree Days (estimated from the weather data for 18 °C indoor temperature and outdoor temperature lower than 15 °C for HDD according to EUROSTAT; for 21°C indoor temperature and outdoor temperature higher than 24 °C for CDD according to JRC/MARS), the climate zone classification according to Italian regulation, the annual energy need for heating $EP_{H,nd}$ and for cooling $EP_{C,nd}$, both per unit area.

Table 3. Reference Italian cities, climatic region, annual energy need per unit volume for heating $EP_{H,nd}$ and for cooling $EP_{C,nd}$

Climate	HDD	CDD	Climate zone	$EP_{H,nd}$ [kWh m^{-2}y^{-1}]	$EP_{C,nd}$ [kWh m^{-2}y^{-1}]
1	606	380	A/B	20.61	22.66
2	1112	237	C	31.65	13.50
3	1600	248	D	51.39	13.08
4	1837	395	E	55.19	16.66
5	2438	65	E	76.08	5.60

The simulations performed on the building at the various climate zones gave rise to different distributions of heating and cooling loads, which are summarized in terms of monthly energy values in Fig. 3. The heating load for DHW has been assumed constant for all climates, given the commercial use of the building. Also the LT and MT cooling loads at the display cabinets have been assumed not to be affected by outdoor conditions, and their monthly values are shown in Fig. 4.

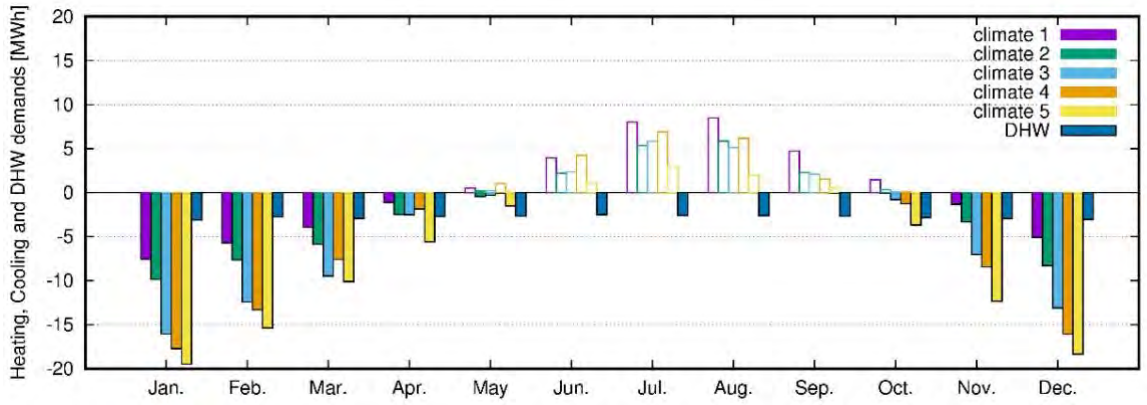

Figure 3: Heating, cooling and DHW demands

Although the building envelope has been adapted to face the various climates, the great influence of outdoor conditions on both the heating and cooling demands appears clearly.

A slight oversizing of the commercial refrigeration unit, especially of its parallel compressor, with the control rules described above allows the load coverages reported in Figure 5. Coverage of the heating demand by heat recovery is from 70 to 76% depending on the climate. Hot water production is guaranteed up to 97 %. Similarly, air conditioning is fully covered at the coldest climate, and almost fully covered at all climates with the exception of climate 4 (coverage: 94%), which is not the warmest.

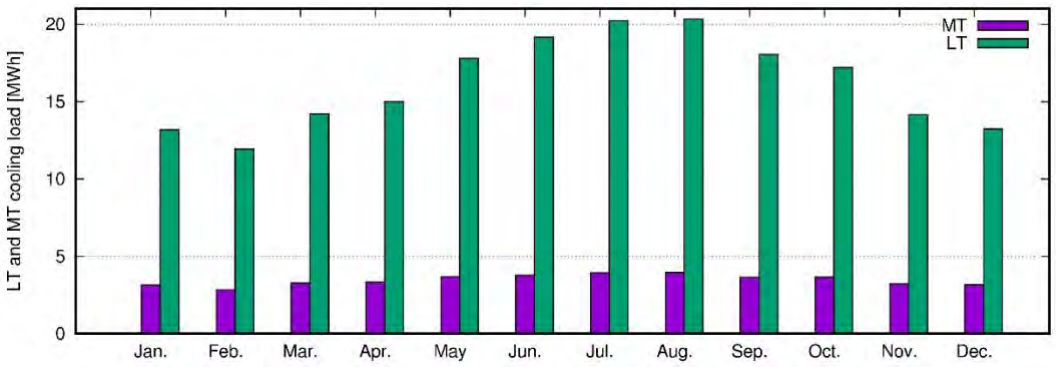

Figure 4: LT and MT cooling load of the display cabinets

This is due to the distribution of outdoor temperature values (and consequently cooling load) which is characterized by higher temperature values for shorter periods in climate 4 when compared to climate 1, typical of Mediterranean seaside location. This can also be seen in Fig. 6, where the number of hours of operation of the parallel compressor is given as a function of its fractional capacity for climates 1 and 4. For climate 4 the parallel compressor works at its nominal capacity for a larger number of hours.

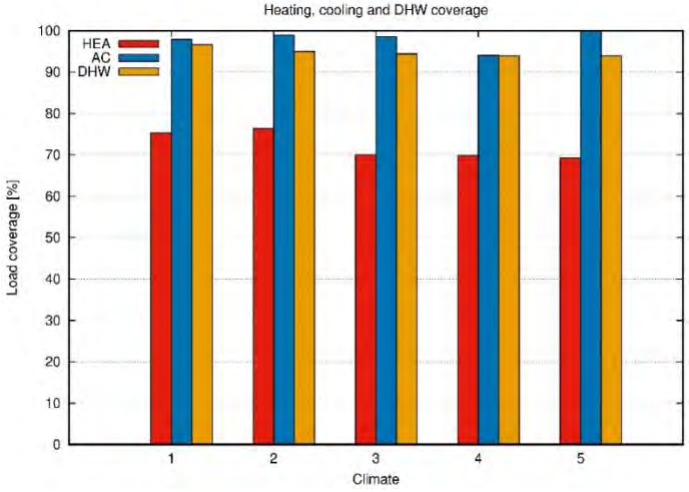

Figure 5: Load coverage of the energy need for space heating (HEA) and cooling (AC) and of the energy demand for DHW production

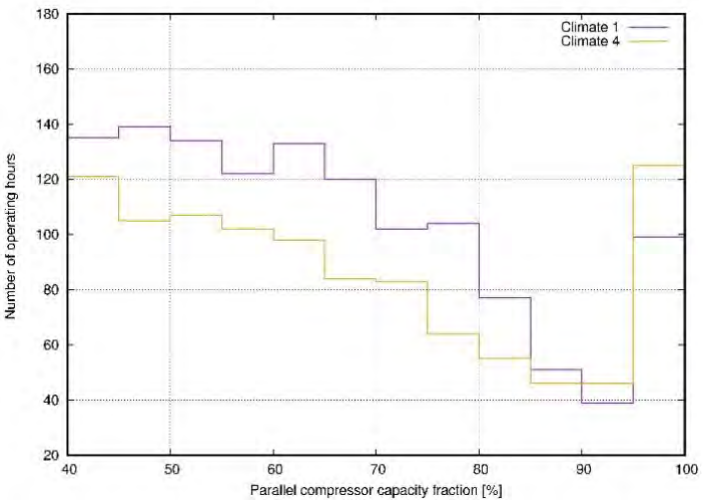

Figure 6: Number of operating hours of the parallel compressor in each capacity fraction range

The annual energy use has been evaluated for all the climates, and compared to the solution with separate refrigerating, heating, cooling and how water production systems (Table 4). In the integrated system the residual portion of loads not covered by the CRU relies on heat pumps. In all cases the integrated system leads to an energy saving around 9 %, with the highest value at the coldest climate, where heat recovery can be effectively exploited. Uniformity in energy saving values could be due to the high quality of the envelope, which damps the influence of outdoor conditions, and to some oversizing of the CRU, which limits the operation of the auxiliary heat pumps.

Table 4. CRU and Heat Pumps yearly electrical energy demand for the integrated system

Climate	CRU [kWh y^{-1}]	HEA HP [kWh y^{-1}]	DHW HP [kWh y^{-1}]	AC HP [kWh y^{-1}]	TOT [kWh y^{-1}]	Savings [%]
1	141813	1682	403	202	144101	8.8%
2	136005	2679	633	60	139378	8.9%
3	135848	5854	733	85	142520	9.5%
4	139597	6669	807	458	147531	9.7%
5	129117	9442	832	0	139391	10.8%

5. CONCLUSIONS

Simulations have been performed with a validated model, to find a design rule for replicating integrated refrigerating systems in supermarkets at various locations with different climate conditions. A recently refurbished supermarket was chosen as reference. The thermal characteristics of the building envelope at each location have been corrected to attain approximately the same energy performance quality as the actual reference building. At such conditions, it was found that using an integrated system for commercial refrigeration, hot water production, space heating and air conditioning in replacement of separate systems with heat pumps can give an energy saving around 9 %, at every climate condition considered. Such uniformity in energy saving figures is due to the high quality of the envelope, which damps the influence of outdoor conditions, and to some oversizing of the CRU, which limits the operation of the auxiliary heat pumps. At such conditions the plants design can be easily extended to new facilities in the occasion of refurbishment, since the integration of the refrigeration and HVAC systems shows to be effective in terms of overall energy efficiency. Significant reductions can be obtained in the investment and running costs, space occupied by the plants and amount of refrigerant charge. It has to be underlined that the reference building is quite small and with limited heating and especially cooling loads. The next step in this work is to extend the investigation to other buildings with different ratios between the refrigerating, heating and cooling loads, and to evaluate the feasibility of “all-in-one” plants at such conditions.

ACKNOWLEDGEMENTS

The research leading to these results has received funding from the MIUR of Italy within the framework of PRIN2015 project «Clean Heating and Cooling Technologies for an Energy Efficient Smart Grid». EPTA Refrigeration is gratefully acknowledged for their continuous and precious assistance in gathering data, and for the fruitful discussions.

NOMENCLATURE

AC	Air Conditioning	HR	Heat recovery
CDD	Cooling Degree Days	HS	High Stage
COP	Coefficient Of Performance	HVAC	Heating, Ventilation, Air Conditioning
CRU	Commercial Refrigeration Unit	GC	Gas Cooler
DHW	Domestic Hot Water	LS	Low Stage
$EP_{H,nd}$	annual heating energy need [kWh m^{-2} y^{-1}]	LT	Low Temperature
$EP_{C,nd}$	annual cooling energy need [kWh m^{-2} y^{-1}]	MT	Medium Temperature
HDD	Heating Degree Days	p_{INT}	Intermediate pressure [bar]
HEA	Space Heating	RDC	Refrigerated Display Cabinets
HP	Heat Pump	t	Temperature [°C]

REFERENCES

Antolín J., Macía A., Samaniego J, Bujedo L. Á., Barchi G., Belleri A., Dipasquale C., Haase M., 2016. Deliverable WP6_D6.4. Energy saving results. CommONEnergy. http://www.commonenergyproject.eu [accessed 27.01.2019].

Bell, I.H, Wronski, J., Quoilin, S., Lemort, V., 2014. Pure and Pseudo-pure Fluid Thermophysical Property Evaluation and the Open-Source Thermophysical Property Library CoolProp. Ind. Eng. Chem. Res. 53(6), 2498-2508.

Cortella G., D'Agaro P., Coppola M.A., 2018. Simulations and field tests of a CO_2 refrigerating plant for commercial refrigeration, Proc. 13th IIR Gustav Lorentzen Conference, Valencia, 2018.

D'Agaro P., Cortella G., Polzot A., 2018. R744 booster integrated system for full heating supply to supermarkets, Int. J. Refrig., 96, 191-200.

D'Agaro P., Coppola M.A., Cortella G., 2019. Field Tests, Model Validation and Performance of a CO_2 Commercial Refrigeration Plant Integrated with HVAC System. Int. J. Refrig., in press, https://doi.org/10.1016/j.ijrefrig.2019.01.030.

Gullo P., Cortella G., Minetto S., Polzot A., 2016. Overfed Evaporators and Parallel Compression in Commercial R744 Booster Refrigeration Systems– an Assessment of Energy benefits, 12th Gustav Lorentzen Natural Working Fluids Conference, Edinburgh, (UK).

EN ISO 13790:2008, Energy performance of buildings -- Calculation of energy use for space heating and cooling. International Organization for Standardization, 2008.

EUROSTAT, http://ec.europa.eu/eurostat/web/energy/data/database

JRC/MARS, http://agri4cast.jrc.ec.europa.eu/DataPortal/Index.aspx

Karampour M., Sawalha S., 2017. Energy efficiency evaluation of integrated CO_2 trans-critical system in supermarkets: field measurements and modelling analysis. Int. J. Refrig. 82, 470-486.

Karampour M., Sawalha S., 2018. State-of-the-art integrated CO_2 refrigeration system for supermarkets: a comparative analysis. Int. J. Refrig. 86, 239-257.

Meteonorm - Irradiation data for every place on Earth, 2017. URL: www.meteonorm.com

Minetto S., Girotto S., Salvatore M., Rossetti A., Marinetti S., 2014. Recent installations of CO_2 supermarket refrigeration system for warm climates: Data from the field. In: 3rd IIR International Conference on Sustainability and Cold Chain, London (UK).

Pardiñas A.A., Hafner A., Banasiak K., 2018. Novel integrated CO_2 vapour compression racks for supermarkets. Thermodynamic analysis of possible system configurations and influence of operational conditions. Appl. Therm. Eng. 131, 1008-1025.

Polzot A., Gullo P., D'Agaro P., Cortella G., 2016. Performance Evaluation of a R744 Booster System for Supermarket Refrigeration, Heating and DHW, 12th Gustav Lorentzen Natural Working Fluids Conference, 21-24 August 2016, Edinburgh, (UK), paper 1022.

Polzot A., D'Agaro P., Cortella G., 2017a, Energy analysis of a transcritical CO_2 supermarket refrigeration system with heat recovery. Energy Proced, 111:648-657, 2017.

Polzot A., 2017b. Energy benefit assessment of various refrigeration systems integrated with HVAC units in shopping malls. PhD Thesis, Università degli Studi di Udine, Italy. https://air.uniud.it/handle/11390/1132161#.W8htjGgzZaQ [accessed 27.01.2019]

Sawalha S., 2013. Investigation of heat recovery in CO_2 trans-critical solution in supermarket refrigeration, Int. J. Refrig., 36, 145-156.

Manuscript ID: 776
DOI: 10.18462/iir.icr.2019.0776

Dynamic modelling of a refrigerated cabinet with integrated phase change material thermal storage

Michael JOKIEL[(a)], Krzysztof BANASIAK[(a)], Hanne KAUKO[(a)], Alexis SEVAULT[(a)]

[(a)] SINTEF Energy Research, Postboks 4761 Torgarden, 7465 Trondheim, Norway, Michael.Jokiel@Sintef.no

ABSTRACT

Thermal storage can help to maintain constant temperature in a refrigerated cabinet during defrost cycles or power outage. This contributes to reduced loss in product quality and hence less food being wasted. Dynamic modelling was applied to study the benefits of integrating phase change material (PCM) thermal storage in a refrigerated cabinet. The PCM was integrated in a CO_2 evaporator, coupled in series with a regular evaporator. This system was compared to a reference case with no PCM.
The results show that the maximum cabinet temperature during defrost is reduced by up to 10 K when a PCM-enhanced evaporator is utilized. The goods temperature is constantly kept low, prolonging shelf life and product quality. The demand for refrigerant is reduced and furthermore, compressor capacity and evaporator size can be decreased due to reduced maximum cooling capacities, leading to overall lower energy use. During power outages, PCM-equipped systems still provide cooling for several hours.

Keywords: Refrigeration, Carbon Dioxide, Thermal Storage, Phase Change Material, Evaporator Defrosting, Supermarket, Cooling Cabinet.

1. INTRODUCTION

Thermal energy storage (TES) can be applied whenever a temporal mismatch occurs between production and demand of thermal energy. In most cases, thermal energy is stored in the form of sensible or latent heat (Fleischer, 2015). In a sensible heat storage, heat is stored by heating a medium with high specific heat capacity, while in the case of latent heat storage, the latent heat of melting or solidification is utilized to store and release heat.
An advantage of latent heat storage is its high energy density in comparison to sensible heat storage, resulting in smaller storage volumes. For a given temperature range, the high latent heat of fusion enables PCMs to store 5–14 times more heat per unit volume than common sensible storage materials such as water or rock (Sharma et al. 2009).
Utilization of PCMs has been reported for various low-temperature latent heat storage applications, such as for protection of food and beverages (Oró et al., 2012), air conditioning (Al-Abidi et al., 2012) or industrial refrigeration (Li et al., 2013; Veerakumar and Sreekumar, 2016). Especially for low-temperature application, water is the most used PCM when the desired process or product temperature is close to 0 °C. Furthermore, water provides beneficial thermal properties as well as low cost, long stability and lack of toxicity.
Refrigerating cabinets and freezers are among the most energy-demanding devices in supermarkets due to their continuous operation (Elarem et al., 2017). Therefore, even small performance enhancements provide great potential for energy saving. In general, the energy efficiency of a refrigerator depends upon several factors, such as components efficiency, ambient temperature, door openings or refrigerant type. Performance enhancement of refrigeration systems covers a vast research area since each part of the system exhibits its own complexity. Significant increase in efficiency of refrigeration systems can be achieved through the following measures: development of efficient compressors, enhancement of thermal insulation and heat transfer enhancement in the heat exchangers.
The cooling of refrigerated cabinets is switched off several times a day to avoid the building of ice on the evaporators, which are needed to cool down the circulating air. These periods without cooling are called defrost cycles. In order to minimize heat gain or cabinet temperature fluctuations caused by defrost cycles and evaporator outage, the number of defrost cycles should be kept to a minimum. For most applications, two to four defrost cycles per day should be adequate. In this study, it is assumed that a defrosting cycle occurs every 5.5 h and lasts 30 min, until the evaporator is free of ice again.
PCMs can be utilized to mitigate the effect of defrost cycles and power outages on the goods temperature and to generally dampen temperature fluctuations (Lu et al., 2010). Due to their high latent heat, the integration of PCMs in the evaporator could reduce the compressor load and reduce the

amplitude of the temperature fluctuations of the food products over time.
The aim of this work is to investigate the integration of a PCM evaporator to improve the thermal performance during defrost cycles, door openings and electrical power failure. Regular and extreme scenarios were studied for various amounts of PCM and their corresponding overall energy use was evaluated.
To integrate the PCM into the cabinet, a second evaporator that was enhanced with PCM was built in series after the normal evaporator, along the air circulation path in the lower part of the refrigerated display cabinet. In this PCM-enhanced evaporator, heat is exchanged between three media: the refrigerant CO_2, the recirculating cabinet air and the PCM. Water is chosen as the PCM, as the heat absorption and release take places at a constant temperature of 0 °C, which is beneficial for providing chilled air in a temperature range of 2-4 °C.
The PCM-unit would store cold energy during low demand periods and can provide free cooling when the general cooling system goes through defrost cycles or power breakdowns. Free cooling can also be provided during night time, when the doors of the display cabinet remain closed for several hours.
Previous results (Sevault 2018) showed that a variation of a few millimeters in the distance between the air ducts and CO_2 coils for a given PCM accumulator dimension yields considerably different charging and discharging times. The calculated integrated heat flux from all air ducts provided a useful indication to select the configuration giving the best match for a given application, e.g. covering defrost cycles or night-time cooling. For this study, it was decided to use reasonable values to describe the heat transfer properties of both evaporators, without altering them between different system setups.

2. MAIN SECTION

2.1. Numerical Model

The modeling work was carried out with the dynamic simulation software Dymola (Dassault 2018), using the object-oriented language Modelica (Modelica 2018) with already existing model libraries, TIL and TIL Media (Gräber et al., 2009). TIL is a model library for thermal components and systems, while TIL Media contains a model library including thermophysical properties for the utilized fluids. A detailed model for both the PCM-evaporator and the refrigerated cabinet was provided by TLK-Thermo GmbH (TLK-Thermo 2018). With this approach, all the created components represent real physical parts in the system and can be re-used for different settings. Utilizing a dynamic simulation program implies that the simulated variables are obtained as a function of time for each component. Fig. 1a shows a schematic of a refrigerated cabinet with PCM thermal storage and Fig. 1b the corresponding simplified model structure.

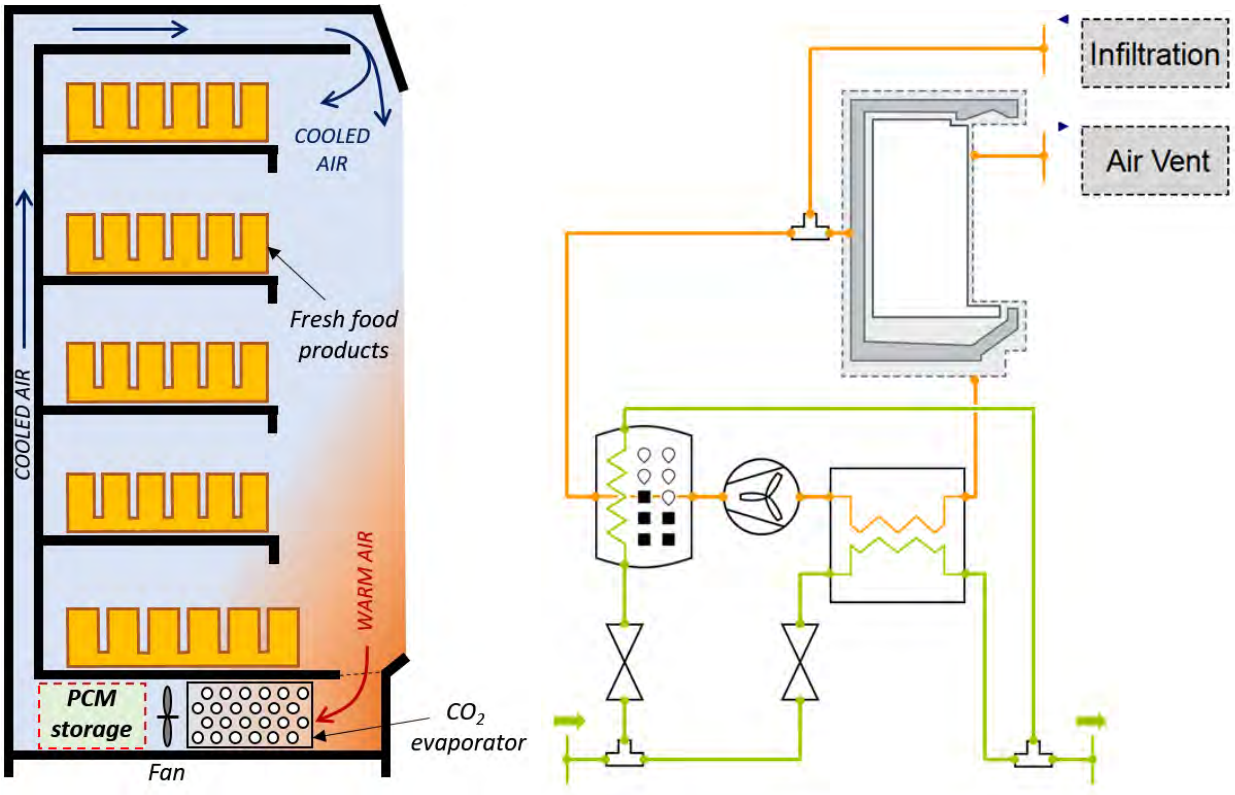

Figure 1: Schematic layout for (a) the refrigerated cabinet and (b) simplified system model

2.1.1. Cabinet model

The cabinet model has a compartment air volume of 8.5 m^3 and contains 1000 kg of goods, which need to be cooled to 2 °C. The fan controls the cabinet outlet temperature to 2 °C, resulting in a volume flow of approximately 1 m^3/s in steady-state operation and 1.5 m^3/s as maximum volume flow. The cabinet is equipped with doors, resulting in rather low infiltration volume flows, assumed to ca. 10 % of the steady state value (i.e., a constant infiltration flow of 0.1 m^3/s). The infiltration accounts for the effect of warm ambient air mixing into the chilled air within the cabinet, due to general leakages or door openings by customers. The evaporator was dimensioned to provide the required cooling load in the described boundary conditions for the system without PCM. An identical evaporator was used in the systems with PCM-evaporators, resulting in a slightly oversized evaporator for these cases.
The cabinet model considers a temperature gradient between the cabinet interior space and the ambient room temperature of 25 °C, as well as the heat transfer from and through the glass doors. This results in a heat flow to the cabinet air of approximately 2.6 kW during steady-state operation. The model considers various temperature levels: the highest temperatures (25 °C) are represented by the room temperature and the outside surface temperature of the cabinet. The lowest temperatures (ca. 2 °C) are the goods temperature, and several intermediate temperature levels are represented by glass doors or inner walls.
The chilled goods are exposed to heat transfer rates by conduction and radiation, due to the high temperature gradient towards the room and due to illumination units, resulting in a required cooling capacity of approximately 2.6 kW in steady-state operation.

2.1.2. The PCM evaporator

The PCM-enhanced evaporator model consists of tubes for the refrigerant and tubes for the air, surrounded by the PCM and arranged in a cross-flow design. The model calculates the particular heat transfer rates from the refrigerant through the tube wall to the PCM, as well as the heat transfer from the PCM through the tube wall to the air.
To estimate the required amount of PCM, the required cooling capacity during a defrost cycle was calculated. During the 30 min of defrosting, the infiltrated air needs to be cooled down from ambient conditions (25 °C) to 2 °C at the cabinet inlet, which takes ca. 2.75 kW of cooling for a mass flow rate of 0.1 kg/s. Additionally, 2.6 kW of cooling load needs to be provided due to further heat sources in the cabinet: Therefore, 5.4 kW of cooling capacity is needed. During a typical defrost cycle of 30 min, this yields a total cooling energy of 2.7 kWh (9720 kJ).
With the specific latent heat of fusion for water (334 kJ/kg) and under the assumption of perfect heat transfer conditions, approximately 30 kg of ice would be sufficient to cover the cooling load during a typical defrost cycle of 30 min. However, since the PCM is integrated in an evaporator, the cooling effect from the CO_2 circulating at reduced rate will also contribute to the cooling, as well as the effect of the ice melting on the original evaporator during defrost. Furthermore, the PCM is subcooled during steady-state operation, resulting in an additional cooling capacity due to sensible heat. It was hence decided to investigate two systems: (1) with a small PCM mass (8 kg, 25 % of the calculated required mass) and (2) with a large PCM mass (235 kg, 800 %).

2.1.3. Control strategy

The main goal of the cooling system is to keep the outlet air temperature at 2 °C and the goods temperature between 1-4 °C. Therefore, the fan is controlled to keep the air temperature on the outlet of the cabinet at 2 °C. The inlet air temperature should be below 2 °C, but above 0 °C to prevent freezing of the goods. Directly at the inlet of the cabinet, the impact of warm air infiltration on the recirculated air is considered. To obtain an air inlet temperature of 0-2 °C after the mixing with 25 °C, the air temperature between the evaporator outlet and cabinet inlet must be below zero. Hence, the PCM will always be subcooled and charged by the air during steady-state operation, and some of the cooling load from the evaporator will be used to chill the PCM.
The valves controlling the flow of CO_2 through the evaporators (with and without PCM) were both set to maintain 5 K superheating. Since the PCM is already charged via the air, the CO_2 mass flow through the PCM-evaporator is only 20 % of the overall CO_2 mass flow, while 80 % flows through the normal evaporator (steady-state operation).

2.2. Results and Discussion

Simulations were conducted for three different cases: A reference system without PCM is compared to two systems with PCM-enhanced evaporators, with 8 kg and 235 kg mass of PCM, respectively. The simulations were performed over 48 hours. The initial condition for the PCM is -2 °C and thus, completely charged and frozen. The conventional scenario considers a constant infiltration flow rate of 0.1 m3/s, as

discussed above.

2.2.1. Conventional scenarios

Figs. 2-4 show the results of a two-day analysis. The air temperature is successfully controlled to a constant value of 2 °C after each defrosting cycle for each system (Fig. 2a). The goods temperature generally increases (Fig. 3a), since it would normally converge towards 2.2 °C, because an inlet temperature of 2 °C is not sufficient to keep the goods temperature at exactly 2 °C. A slight decrease in inlet temperature would be needed for that but increases the risk of sub-zero temperature infiltration. Fig. 3a shows that the goods temperature can be generally reduced by nearly 1 K by using a PCM-system. However, it should be noted that the goods were considered as a lump in the available cabinet model, resulting only in a bulk estimate of the goods temperature.
Fig. 2b illustrates a typical defrost cycle of 30 min, starting at 12 h and ending at 12.5 h. During the 30 min of defrosting, the cabinet air temperature cannot be kept at 2 °C and rises to 16.5 °C (no PCM), 9.3 °C (8 kg PCM) or 6.8 °C (235 kg PCM). Because of these high temperatures, the goods temperature increases more during 30min of defrost than it is reduced during 5.5 h of normal steady-state operation due to the comparatively small temperature difference towards the 2 °C inlet air temperature.

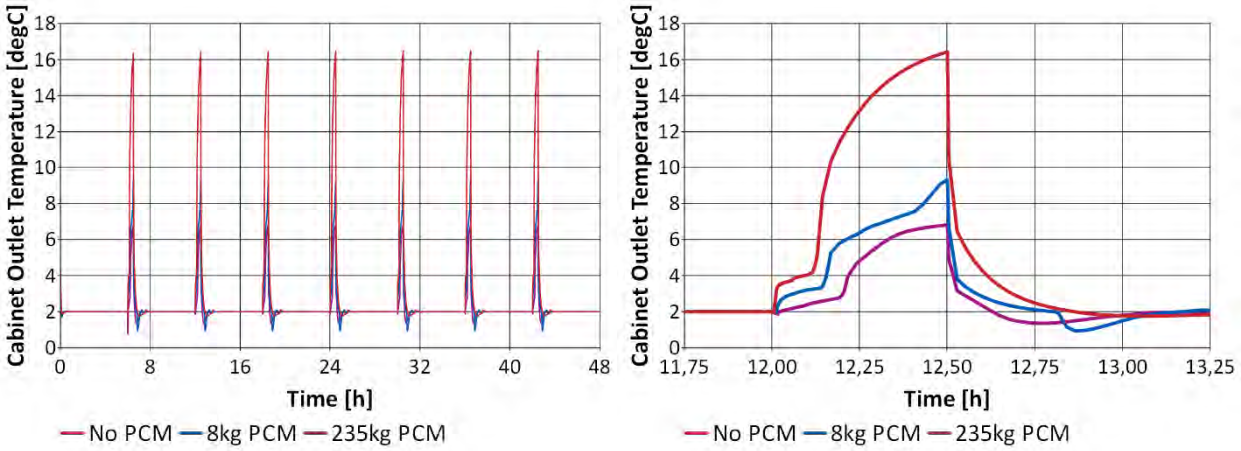

Figure 2: Simulation results for the conventional scenario: cabinet outlet temperature for air, (a) for 48 hours, (b) zoomed in for one exemplary defrost cycle

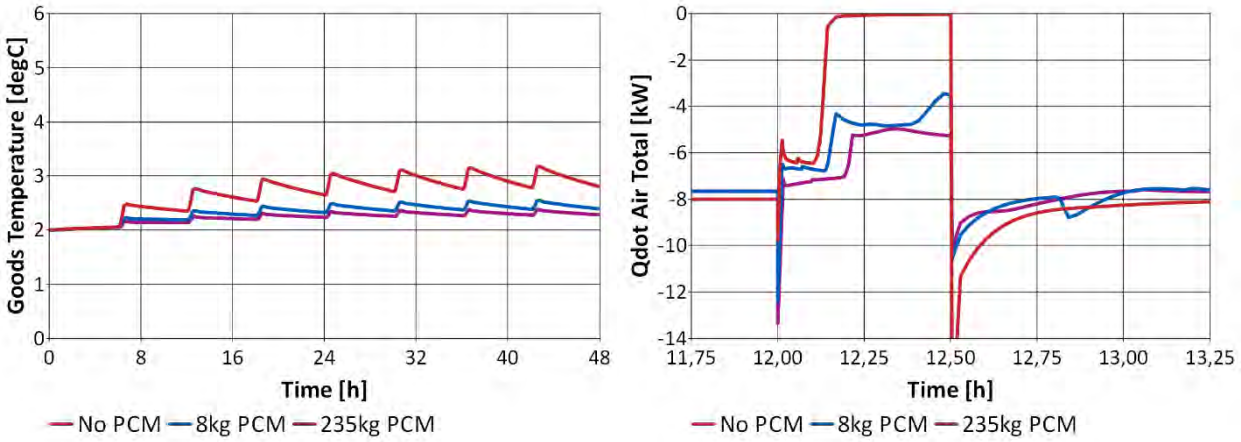

Figure 3: Simulation results for the conventional scenario: (a) goods temperature for 48 hours, (b) cooling load of the air (zoomed in for one exemplary defrost cycle)

Fig. 3b illustrates the heat flow towards the air, which is negative since the air is cooled down. In steady-state operation, the total required cooling capacity for the air (sum of effect of PCM evaporator and ordinary evaporator) is almost the same for all investigated systems (ca. 8 kW). A deviation occurs because the systems with PCM utilize a slightly lower air volume flow (1.05 m^3/s with "No PCM", and ca. 0.7 m^3/s for the PCM-systems). This is due to (1) an increased overall heat transfer area when utilizing a second evaporator and (2) an increased subcooling of the air before the mixing with ambient infiltration air occurs.
As soon as the defrost cycle begins, the cooling load drops for all systems to a slightly lower value (implying an increase of the negatively defined heat transfer rate in Fig. 3b). In this short period in the beginning of the defrosting, the ice in the main evaporator melts and provides extra latent heat, in addition to the actual PCM-evaporator.
Afterwards, the cooling load drops to zero for the system without PCM (Fig. 3b). The cooling load in

PCM systems remains on a relatively high level of approximately 5 kW. As soon as the defrost cycle ends, the cooling capacity for the "No PCM" system increases drastically to 18 kW due to the high temperature difference, while the maximum capacity for the PCM systems is 10 kW. The utilization of PCM in the second evaporator enables a more uniform supply of cooling to the system with decreased peaks. This enables the potential for downsizing the ordinary evaporator or compressor.

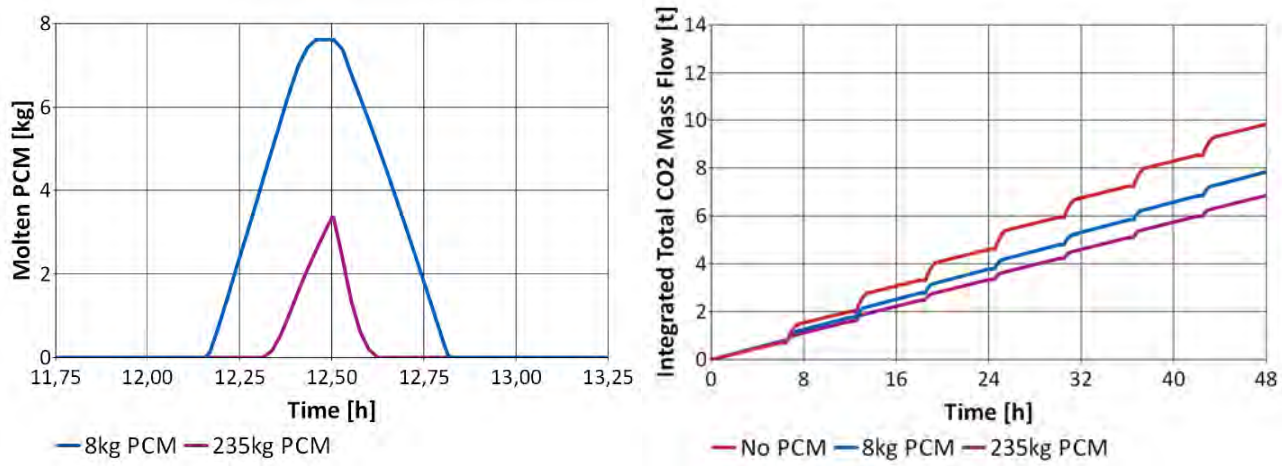

Figure 4: Simulation results for the conventional scenario: (a) mass of melted PCM (zoomed in for one exemplary defrost cycle), (b) integrated mass flow rate of CO2 for 48 hours

Fig. 4a compares the 8 kg- and the 235 kg PCM evaporator regarding the melted PCM mass. In the 8 kg PCM system, all PCM is melted at the end of the defrost cycle. The 235 kg PCM melts by just 3.3 kg, implying that the main cooling load results from the increased amount of sensible heat, which can be recognized in the late start of melting. For the 235 kg PCM, melting starts 20 min after the beginning of the defrost cycle (meaning, 2/3 of the defrost time has already passed), while the 8 kg PCM already starts melting after 10 min.

For the sake of completion it should be noted, that the subcooling of the 235 kg PCM (-5.5 °C vs. -4.7 for the 8 kg PCM) is almost 1 K lower due to the larger mass of available frozen PCM. During the defrost cycle, after the PCM has completely melted, a superheating of 5 K occurs for the 8 kg PCM system.

Furthermore it should be noticed, that the difference in cooling load between the 8 kg- and 235 kg PCM systems are rather small (see figure 3b, only 1 kW lower). This is due to the late utilization of the actual melting of PCM, since additional cooling is already provided by three other sources: the ice melting from the first evaporator, the sensible heat of subcooled PCM, and the basic cooling load of the second evaporator due to the CO_2 mass flow.

Finally, Fig. 4b shows the potential of reducing the compressor capacity (and thus the energy consumption) when PCM-systems are utilized. The mass flow rates through both evaporators are summed up and integrated over time. During steady-state operation, the CO_2 mass flow for all three systems is roughly the same, which can be identified by the same gradients for each graph, especially in the first 6 h until the first defrost cycle starts. The largest difference between the three systems is the boost in CO_2 demand directly after each end of defrost, when the system without PCM requires a strong increase in CO_2 to cool down the air to 2 °C again. This particular increase directly after the defrost can be reduced by over 50 % when the system is enhanced with a PCM evaporator. Therefore, the overall demand for refrigerant is reduced for PCM-systems, since the same overall cooling load is achieved with a decreased air volume flow, as discussed before. The lower overall demand for CO_2 results in lowered compressor power and therefore significantly lower energy use over time thanks to the proposed implementation of PCM.

2.2.2. Extreme scenarios

As shown in the previous section, even more potential of the PCM-enhanced system could be retrieved, since only partial melting of PCM occurred and since the goods temperature could be reduced by just 1 K (see Fig. 3a) in comparison to the "No PCM"-system. This section focuses on abnormal boundary conditions such as increased infiltration flows or power outages, to further illustrate the advantages of PCM-enhanced systems compared to ordinary systems.

When more customers are opening the cabinet doors on busy days or when employees are stocking the shelves, an increased amount of warm ambient air is putting strain on the refrigeration as the cooling capacity needs to be increased. In figure 5 and 6, the infiltration rate was doubled from 0.1 to 0.2 $m^3 \cdot s^{-1}$.

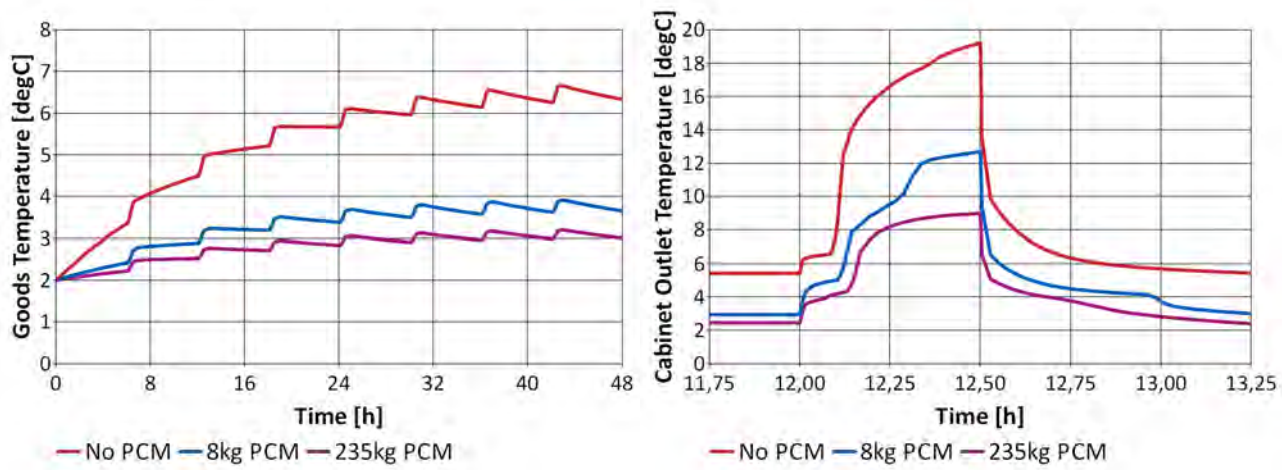

Figure 5: Simulation results for the scenario with increased infiltration: (a) goods temperature for 48 hours, (b) cabinet outlet temperature for air (zoomed in for one exemplary defrost cycle)

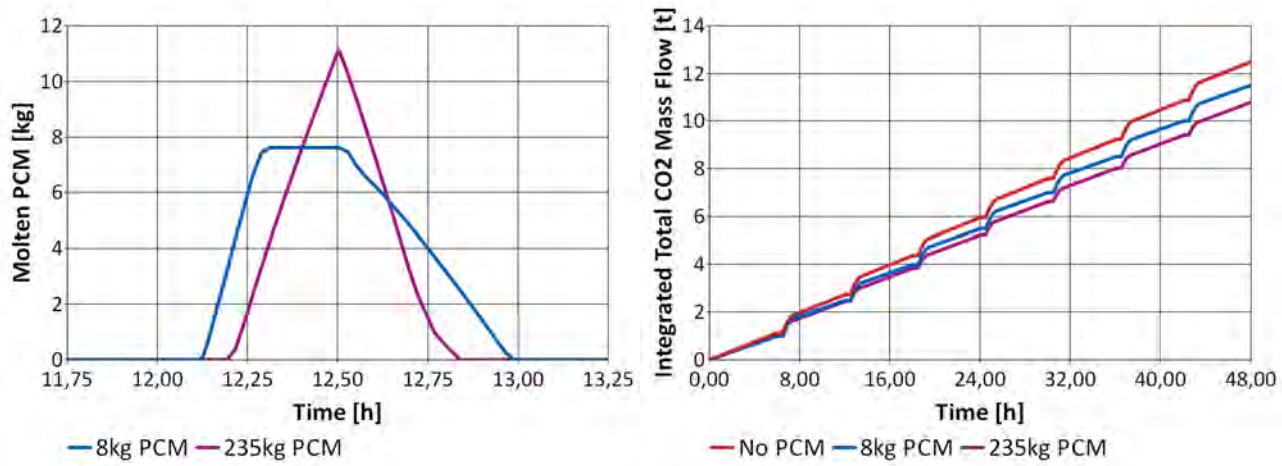

Figure 6: Simulation results for the scenario with increased infiltration: (a) mass of melted PCM (zoomed in for one exemplary defrost cycle), (b) integrated mass flow rate of CO_2 for 48 hours

The previously discussed differences between the systems are more evident. The amount of melted PCM is 11 kg for the 235 kg PCM system, still indicating the significant effect of the sensible heat coming from the subcooled ice, as illustrated in Fig. 6 (a). Fig. 5 (b) shows, the inlet temperature for the air in the cabinet raises for all three systems, even in steady-state: since the same design parameters for the evaporators and the fan are applied, the evaporator is now reaching its maximum cooling rate. As seen in Fig. 5b, only the 235 kg PCM system is capable to keep the inlet temperature to roughly 2 °C, while both the 8 kg system (3 °C) and the PCM-free system (5.5 °C) provide higher inlet temperatures in steady state operation. Consequently, the temperatures during the defrost are increased as well: 19.5 for the PCM-free system, and 12.7 and 9 °C for the 8 kg and 235 kg PCM system. Therefore, the PCM systems are once again capable of reducing the peak air temperature by over 10 K, even under abnormal boundary conditions. That way, the negative impact on the goods can be clearly reduced, as the goods temperature increases to only 3-4 °C for the PCM-systems (Fig. 5 (a)). For the PCM-free system, the goods temperature reaches 6-7 °C which puts the shelf life of the product at risk.

Finally, analogous to the previous case, Fig. 6b shows once again the potential of lowering the energy use over time with implementing PCMs, as overall demand for CO_2 is reduced.

Another threat for the shelf life is power outage, resulting in a cut off for the compressor and thus, refrigerant flow. It should be noted that the fan is usually equipped with backup batteries to still provide air flow in case of outages. In that case, the PCM needs to fully compensate the evaporator failure and provide enough cooling to sustain shelf life as long as possible.

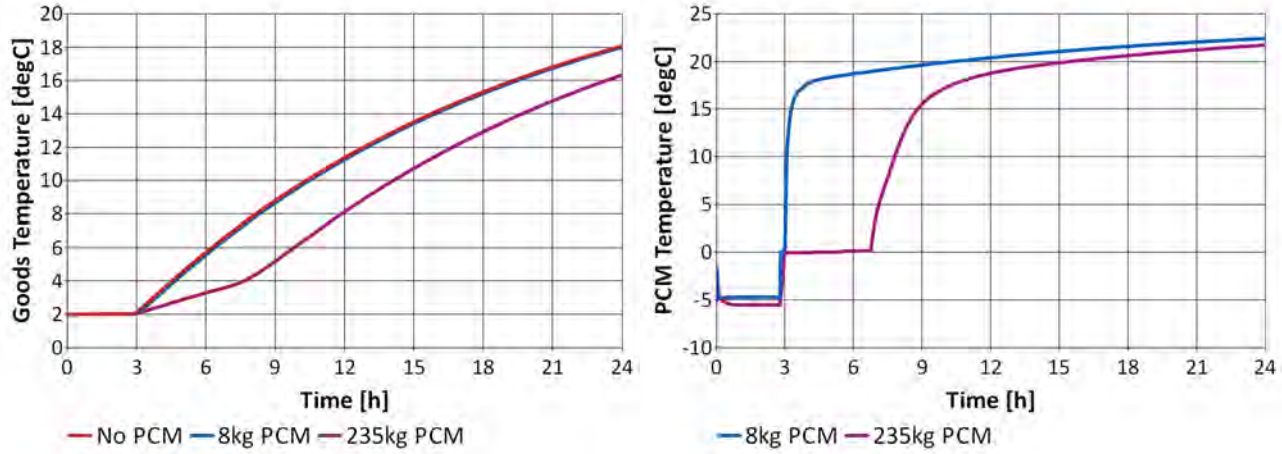

Figure 7: Simulation results for the scenario with power outage at 10,000s: (a) goods temperature, (b) temperature of PCM

In Fig. 7a, the power outage is initiated shortly before 3 h. The 8 kg PCM system features insufficient cooling capacity as the latent heat is immediately consumed, resulting in a trend very similar to the PCM-free system.
As illustrated in Fig. 7b, it takes 4 h until the 235 kg PCM is fully melted. Therefore, for over 4 h after the power outage occurs, a cooling capacity through latent heat can be provided to keep the goods temperature under 4 °C. This time frame might be sufficient to gain enough time until the power is restored again. For the PCM-free system, the goods temperature would be over 7 °C about 4 h after the outage (Fig. 7a), resulting in endangered shelf life for the products.

3. CONCLUSIONS

The implementation of PCM in refrigerated cabinets shows a significant potential for performance improvement compared to conventional systems. PCM-enhanced evaporators have been studied to counter the temperature increase in the cabinet during defrost cycles or power outages. It has been shown that the increase of air temperature is reduced by up to 10 K when PCMs are used to provide cooling in case of evaporator malfunctions. A more uniform supply of cooling to the system despite the periodic defrost cycles enables the potential for downsizing the ordinary evaporator and the compressor, as maximum cooling peaks are decreased. It has been shown that PCM-systems provide the same cooling capacity with a reduced air volume flow and with a decreased utilization of CO_2, leading to potentially lower overall energy use.
Especially for abnormal operating conditions such as increased infiltration rates or power outages, the full potential of PCM-enhanced evaporator-systems can be utilized, when PCM is contributing to keep goods temperature low despite the increased demand for cooling. It has been clearly shown that PCM-enhanced systems are capable of securing shelf life of supermarket goods in all investigated cases, preventing loss in product quality and hence less food being wasted.
Future work includes the development of alternative control strategies for the two evaporators, as well as experimental validation.

ACKNOWLEDGEMENTS

The current study was carried out through the research competence-building project PCM-Eff supported by SINTEF Energy Research and the Research Council of Norway. The project aims at investigating novel phase change material solutions for efficient thermal energy storage at low and medium-high temperature.

REFERENCES

Al-Abidi, A. A., Bin Mat, S. , Sopian, K., Sulaiman, M. Y., Lim, C. H., Mohammed, A. Th., 2012. "Review of thermal energy storage for air conditioning systems." Renewable and Sustainable Energy Reviews 16(8): 5802-5819.

Dassault Systèmes, DYMOLA Systems Engineering, 2018. URL, https://www.3ds.com/products-services/catia/products/dymola/

Elarem, R., Mellouli, S., Elmchaouri, A., Jemni, A., 2017. Performance analysis of a household

refrigerator integrating a PCM heat exchanger, Applied Thermal Engineering 125, 1010-1016.

Fleischer, A.S., 2015. Thermal energy storage using phase change materials: fundamentals and applications, Springer.

Gräber, M., Kosowski, K., Richter, C. C. , Tegethoff, W., 2009. Modelling of heat pumps with an object-oriented model library for thermodynamic systems, Proceedings Mathmod, Vienna, Austria, 1396-1404.

Li, G., Hwang, Y., Radermacher, R., Chun, H.H., 2013. Review of cold storage materials for subzero applications. Energy 51,1-17.

Lu, Y. L., Zhang, W. H., Yuan, P., Xue, M. D., Qu, Z. G., Tao, W. Q., 2010. Experimental study of heat transfer intensification by using a novel combined shelf in food refrigerated display cabinets. Applied Thermal Engineering 30(2–3), 85-91.

Modelica, Modelica and the Modelica Association, 2018. URL, https://modelica.org/

Oró, E., de Gracia, A., Castell, A., Farid, M. M., Cabeza, L. F., 2012. Review on phase change materials for cold thermal energy storage applications. Applied Energy 99, 513-533.

Sevault A., Banasiak, K., Bakken, J., Hafner, A., 2018. A novel PCM accumulator for refrigerated display cabinet: design and CFD simulations, Science et Technique du Froid, Proceedings of 12th IIR Conference on Phase Change Materials and Slurries for Refrigeration and Air Conditioning, 43-49.

Sharma, A., Tyagi, V.V., Chen, C.R., Buddhi, D., 2009. Review on thermal energy storage with phase change materials and applications, Renewable and Sustainable Energy Reviews 13, 318-345.

TLK-Thermo GmbH, TIL Suite Thermal Systems, 2018. URL,https://www.tlk-thermo.com/index.php/en/software-products/til-suite.

Veerakumar, C., Sreekumar, A., 2016. Phase change material based cold thermal energy storage: Materials, techniques and applications – A review. International Journal of Refrigeration 67, 271-289.

Manuscript ID: 784
DOI: 10.18462/iir.icr.2019.0784

Subcooling with AC and adiabatic gas cooling for energy efficiency improvement: field tests and modelling of CO_2 booster systems

Giovanni CORTELLA, Michele A. COPPOLA, Paola D'AGARO

DPIA – University of Udine
Udine, 33100, Italy
giovanni.cortella@uniud.it

ABSTRACT

In the last decade several plant configurations and components have been proposed to increase the efficiency of CO_2 refrigeration systems. Among these, subcooling is considered a simple but effective solution, together with the employment of adiabatic cooling systems at the gas cooler.
In this work, a fully instrumented CO_2 booster plant installed in a supermarket is considered, to compare parallel compression, subcooling and adiabatic cooling. Subcooling is performed taking advantage of chilled water available from the HVAC system. The experimental data are used to validate a model for the comparison on a yearly basis.
Parallel compression and subcooling show to be almost equivalent in terms of yearly energy use, while the adiabatic cooling system gives the best performance.
Comparisons reveal that the subcooler cooling capacity should be chosen carefully to avoid oversizing, while the influence of the EER for the chiller appears quite small. Subcooling performed at the expense of an HVAC plant shows to be an interesting solution, while a great benefit was experienced with the employment of an adiabatic gas cooler.
Keywords: Carbon Dioxide, Commercial refrigeration, Energy saving, Modelling, Monitoring, Subcooling, Supermarket

1. INTRODUCTION

In order to extend the convenience of use of CO_2 in warm climates, several technologies and alternative plant schemes have been studied and analyzed, showing that improvements of the performance of trans-critical CO_2 refrigeration plants can be achieved. Among the available solutions, the improvements associated with subcooling are being recently investigated by many researchers (Llopis et al., 2018). If we focus on booster systems in transcritical conditions, it permits to reduce the amount of flash gas at the liquid receiver, and allows to decrease the optimal rejection pressure providing additional advantage (Llopis et al, 2015). The subcooling function can also be performed by means of a secondary fluid for other purposes, like air conditioning chillers, or taking advantage of water storage systems (Polzot et al., 2015, Polzot et al., 2016). Several investigations are available in the literature about the performance of CO_2 systems with subcooling at laboratory conditions (e.g. Bush et al., 2017, Nebot-Andrés et al., 2018), but very few information is available on the behavior of an actual plant. In this paper, a fully instrumented CO_2 booster plant installed in an actual supermarket is monitored (Cortella et al., 2018), to compare its performance with parallel compression, subcooling and adiabatic cooling. Subcooling is performed taking advantage of chilled water from the HVAC system. The experimental data are used to validate a comprehensive model, which includes display cabinets and the building, for the comparison of the various solutions on a yearly basis.

2. THE REFRIGERATION SYSTEM AND ITS MODEL

The Commercial Refrigerating Unit (CRU) analyzed in this work is a transcritical CO_2 booster system with parallel compression and subcooling provided by chilled water from a HVAC plant. Such plant is part of a test system installed in a small supermarket (1200 m^2 selling area) which has been refurbished in the framework of the FP7 European Project *CommONEnergy* (Commonenergy 2017). The nominal cooling capacity is 70.5 kW at -35 °C and 10.8 kW at -10 °C respectively for the MT and LT applications. The intermediate pressure at the liquid receiver is 35 bar. Both compressor racks, LS and HS, are composed of two compressors, distinguished as master and slave compressor. The master is controlled by an inverter and the slave is an ON/OFF type.

The gas cooler is equipped with an Adiabatic Cooling System (ACS) made of evaporative pads positioned on the long sides of the gas cooler, so that only a fraction of the air flow rate undergoes adiabatic saturation. Pads are fed with water when the outdoor temperature exceeds a set point value. A mixing ratio ε of the overall process, that takes into account both the position and the efficiency of the panels themselves, is defined based on the wet and dry bulb (T_{wb} and T_{db}) outdoor air temperature, so that the temperature of air at the inlet of the heat exchanger is

$$T_{in,air,GC} = T_{wb}\varepsilon + T_{db}(1-\varepsilon) \quad \text{Eq. (1)}$$

The mixing ratio is estimated at ε = 0.6, value that has been proven empirically to be adequate and well chosen. In this way, the temperature at the outlet of the gas cooler is then evaluated as:

$$T_{out,GC} = T_{in,air,GC} + \Delta T_{app,GC} \quad \text{Eq. (2)}$$

The adiabatic saturation of air is described in the model using the CoolProp libraries (Bell et al., 2014) for humid air. The control rule for setting the optimal HS pressure is based on the CO_2 temperature at the gas cooler outlet, based on a correlation optimized for this specific design without (Eq. 3) and with (Eq. 4) parallel compressor with constant intermediate pressure (Polzot et al., 2016, D'Agaro et al., 2019):

$$p_{GC,out} = \max\left(75;\ 2.56\,T_{GC,out} - 1.247\right) \quad \text{Eq. (3)}$$

$$p_{GC,out} = \max\left(75;\ 1.75\,T_{GC,out} + 22.13\right) \quad \text{Eq. (4)}$$

Due to this control rule, the adoption of the ACS allows a reduction of the pressure ratio at the HS compressors, with benefits in terms of energy consumption.

As an alternative to ACS, a heat exchanger can be activated in order to perform subcooling at the exit of the gas cooler/condenser. The beneficial effects of subcooling in a transcritical booster system are well known (Llopis et al., 2018), and make the use of CO_2 plants attractive also at warm climate conditions. In this system, subcooling is made at the expense of chilled water from the HVAC system. This solution has been chosen thanks to its low investment cost, given that the water chiller was already available and adequately sized, and to the simplicity of regulation when compared to a traditional dedicated mechanical subcooler. Chilled water is supplied at 7 to 9 °C to the heat exchanger which is designed for a maximum heat exchange of 18 kW. The investigated plant enables several configurations, and is also designed to allow waste heat recovery at two temperature levels for space heating and hot water production, and cooling capacity for air conditioning. Such features are not considered in this paper, but a detailed analysis is described in D'Agaro et al. (2018), D'Agaro et al. (2019).

Fig. 1 shows a schematic drawing of the refrigerating system, where also the additional heat exchangers for heat and cooling recovery are depicted, as well as the main measurement points.

Mathematical models of the refrigeration system, display cabinets and cold rooms have been developed in the TRNSYS environment, including mutual interactions with the building and its HVAC system, at given climate conditions. A sub-hourly cooling load profile is thus predicted based on the realistic and time-dependent working conditions in the supermarket, as well as on the interactions between the cabinets and the indoor climate (Polzot et al., 2016). The thermodynamic and thermophysical properties of the refrigerants are calculated by linking our in-house routines in the TRNSYS environment to the CoolProp libraries (Bell et al., 2014). The compressors are described through correlations provided by the manufacturer in accordance with the Standard EN12900:2013.

The values of the main design parameters are reported in Table 1.

Table 1. Main design parameters for the commercial refrigeration unit

Parameter	Unit	Value
LT evaporating temperature	°C	-35
MT evaporating temperature	°C	-10
Minimum condensing temperature	°C	6
Liquid receiver pressure	bar	35
Degree of subcooling at subcritical conditions	K	3
Gas Cooler/Condenser ΔT_{app}	K	4
Subcooler heat exchanger ΔT_{app}	K	7
Superheat at LS/HS suction	K	30/20

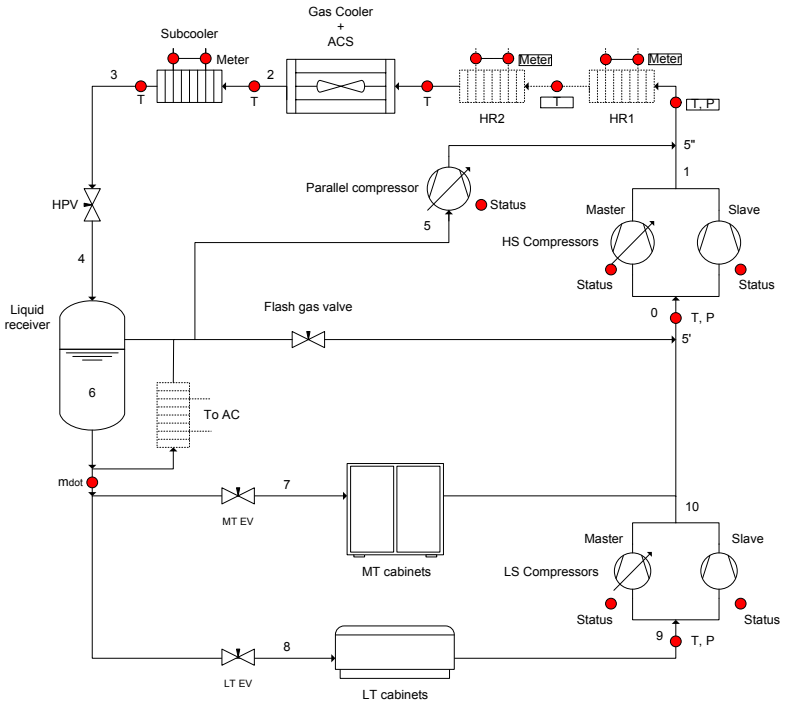

Figure 1: Schematic drawing of the CO_2 refrigeration system. The approximate position of the probes is indicated by the red flags. T: temperature probe, P: pressure gauge, Meter: energy meter, mdot: mass flow meter, Status: compressor status sensor

3. FIELD TESTS AND MODEL VALIDATION

With the aim of validating the model at warm climate conditions and checking the efficacy of subcooling compared to the use of ACS, the system has been operated during summer 2018. The outcomes of the data acquisition have been used for comparison with the model prediction, thus allowing the identification of the pros and cons of each solution. Five weeks have been selected as representative of three different operating conditions:

Adiabatic Cooling System	(ACS)	week 1 (1-7 June, 2018) and 2 (15-21 June, 2018);
Subcooling	(SC)	week 3 (7- 13 Sept, 2018) and 4 (14-20 Sept, 2018);
Both systems	(ACS + SC)	week 5 (27 July to 2 August, 2018).

3.1. Adiabatic Cooling System (ACS)

The employment of the ACS system showed to be quite effective in reducing the gas cooler outlet temperature, and consequently the gas cooler pressure. Fig. 2 shows an example of the difference between the gas-cooler pressure predicted in dry gas-cooling conditions and the one measured with ACS, for weeks 1 and 2.

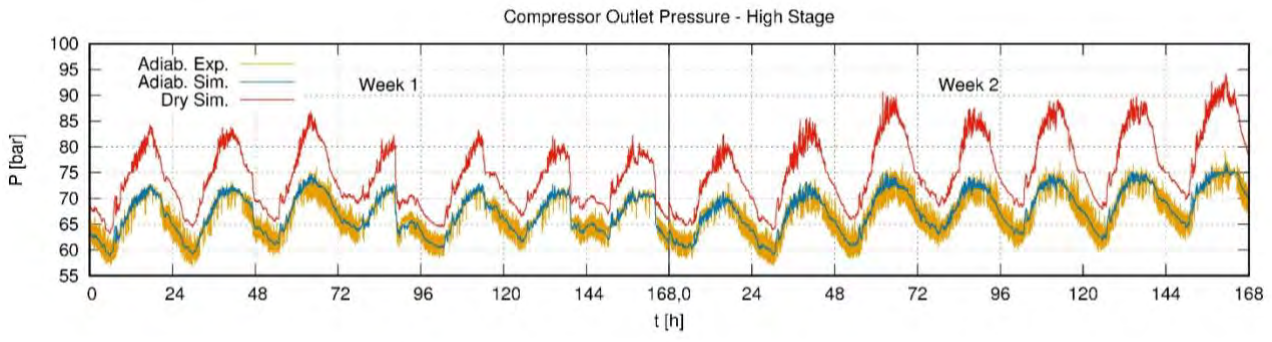

Figure 2: HS pressure: comparison between dry and adiabatic cooling, and between experimental and simulated results in weeks 1 and 2

An average reduction of 4K in the gas cooler outlet temperature can be achieved by using ACS, corresponding to a reduction of approximately 10 bar in the HS pressure. Also the computed values of the HS pressure with ACS are plotted, to witness the good ability of the model to reproduce the actual operation of the gas cooler and of the ACS for a rather wide range of outdoor conditions typical of the summer season. Validation of the model for the "dry cooling" operation had already been done successfully (D'Agaro et al, 2019). The outdoor temperature and relative humidity are inputs for this model, and are taken from the monitored data.

3.2. Subcooling (SC)

Subcooling is based on the use of a heat exchanger at the exit of the gas-cooler/condenser and prior to the high pressure valve. The mass flow rate of chilled water supplied by the HVAC system is regulated depending on the outlet temperature at the gas cooler. Full opening is reached with 23 °C gas cooler outlet temperature, corresponding at about 19 °C outdoor air temperature. Fig. 3 depicts the temperature profiles of CO_2 inlet and outlet and of water inlet together with the water mass flow rate at the subcooler heat exchanger during week 3. Inoperative periods are characterized by null water flow.

It can be observed that chilled water that enters the subcooler exchanger is on average around 8-9 °C when the system is activated. Moreover, an important parameter that can be inferred from such data is the approach point of the subcooler which is around 7 K, parameter that allows modelling the exchanger with a method based on this number and on the maximum heat flow available, which depends on the size of the heat exchanger and is around 18 kW in this plant.

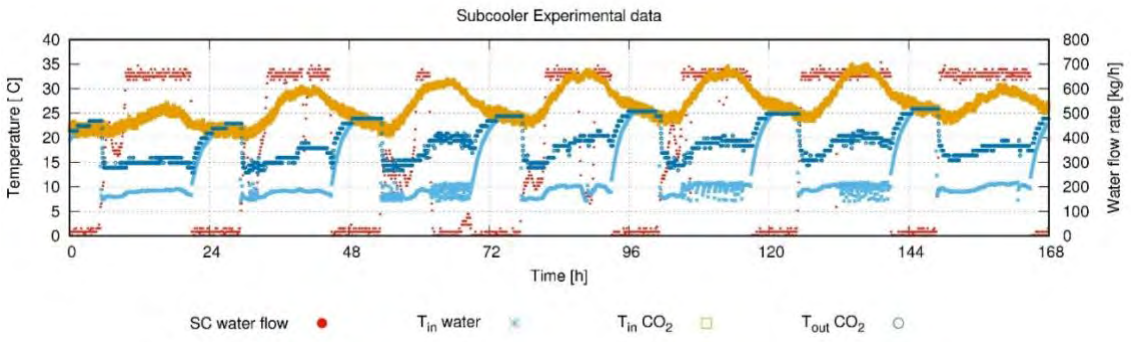

Figure 3: Temperature values at the subcooler and water flow rate in week 3

The subcooling degree ranges between 10 and 15 K, a value close to the optimum for single stage CO_2 systems at 25-30 °C outdoor temperature (Nebot-Andrés et al, 2017). When subcooling is performed, the HS pressure should be optimized in order to achieve the best efficiency of the system. Llopis et al (2015) showed that a significant reduction in the HS pressure would be suggested by optimization, and this would allow an increase in the COP around 2 % at the operating conditions here considered. However, given the complexity due to the interaction between the HVAC and the refrigerating plants, in the system considered the HS pressure was not optimized during SC operation.

The model seemed sufficiently reliable to reproduce the operation of the actual plant, even if a degree of uncertainty in the estimation of the subcooler operation was encountered, due to frequent and significant fluctuations in the inlet water temperature. A further analysis for a week with both the systems active has been carried out. The validation process also applied for this week, confirming the affordability of the model.

The model showed finally to be reliable enough in the prediction of the electric energy use, which is underestimated around 2.6 % due to the above mentioned temperature fluctuations in the actual plant.

4. YEARLY PERFORMANCE SIMULATIONS

The entire model that describes the CRU, the refrigerated cabinets and the heat recovery potential of the system had been already validated under different operating conditions (D'Agaro et al, 2019). With the analysis carried out in this work, further features have been added and validated with the

result of obtaining a CRU model usable to simulate different system layouts among which the subcooling (SC) and the Adiabatic Cooling System (ACS) and compare them in an annual timespan, with realistic cooling capacity profiles and actual outdoor conditions.
The results of this simulation apply to a mild weather typical of Northern Italy where the supermarket under exam is located. Simulations are carried out for a whole year with 15 minutes time step. The indoor conditions of the supermarket come from a thorough transient simulation of the thermal behavior of the building. Thus, the comprehensive model of the building developed in the framework of CommONEnergy (Dipasquale et al, 2016) has been integrated in the TRNSYS environment with the in-house routines of the display cabinets and CRU. The cases analyzed in this work are:

- REF: (reference case), CO_2 booster system;

with such features added to the reference case:

- PC: Parallel Compression
- ACS: Adiabatic Cooling System
- PC + ACS: Parallel Compression and Adiabatic Cooling System
- SC: Subcooler
- SC + ACS: Subcooler and Adiabatic Cooling System

ACS is activated when the outdoor temperature is equal or greater to 19°C, which is the lower limit of the transition zone between subcritical and trans-critical conditions (Polzot et al., 2016). Filippini et al. (2018) defined an activation rule of the ACS at 17 °C, which resulted from an economic optimization. In order to obtain a fair comparison, the same control rule is adopted for the SC, which is activated when the outdoor temperature exceeds 19 °C. The minimum subcooler outlet temperature for CO_2 is set at 15°C and the maximum heat extraction rate is 18 KW as it is in the real plant. The EER for the water chiller supplying subcooling is set in accordance with actual values of units available in the market and literature. For 2 °C evaporating temperature, the EER is

$$EER_{water\ chiller} = 5.629 - 0.0886\ T_{out} \qquad \text{Eq. (5)}$$

Chilled water at the inlet of the sub cooler is set at 8°C.
For the above mentioned reasons, no gas cooler pressure optimization is considered during SC operation. No heat recovery or AC supply to HVAC is considered.
As regards the cooling capacity, LT and MT loads are obtained from the simulation of the display cabinets and cold rooms. The integration between the refrigeration system and the building allows capturing the demand variation over the day and over the year because of the different set point values for the indoor temperature in the opening hours.
The electrical energy utilization of the CRU and of the entire system for a whole year, in the analyzed cases, is reported in Table 2.

Table 2. Annual electrical energy demand

Annual Electrical Energy Demand [MWh]					
	CRU	Subcooler	Total	Energy use vs REF [%]	Energy use vs PC [%]
REF	132.5	-	132.5	0.0	-
PC	126.1	-	126.1	-4.8	0.0
ACS	119.3	-	119.3	-10.0	-5.4
PC + ACS	117.2	-	117.2	-11.5	-7.1
SC	119.9	7.9	127.8	-3.5	1.4
SC + ACS	114.6	4.2	118.8	-10.3	-5.7

The results, in terms of energy, are also presented on a monthly basis in the histogram of Fig. 4.
Fig. 4 clearly shows that the performance enhancement methods yield benefits in the warm and hot months, when the system suffers trans-critical operation.
The parallel compression scheme with ACS offers the highest energy savings in this example of real CO_2 trans-critical booster system. But it can be observed that the key role is played by the ACS

rather than the parallel compressor. All cases where ACS is active yield total energy saving that are equal or higher than 10%. This is also due to the reduction in the HS pressure consequent to the lower temperature of CO_2 at the gas cooler outlet.
Another important aspect that should be examined regarding ACS is the activation temperature. The lower the activation temperature the higher are the energy savings on a yearly basis, due to a longer activation time. However, the advantages of the system decrease with low outdoor temperature, therefore this issue should be further investigated with an economical optimization approach.
Subcooling (SC) appears to be an energy saving solution and an effective alternative to parallel compression although the energy savings compared to PC show to be around 1% lower. The employment of chilled water from the HVAC plant implies a limit in the effectiveness of the subcooling system, given that a secondary fluid (water) is used and consequently the evaporating temperature is much lower with respect to a dedicated direct expansion subcooler. However, a significant saving in investment and maintenance costs makes this solution appealing. Reduction of the HS pressure through its optimization could lead to slightly higher benefit.

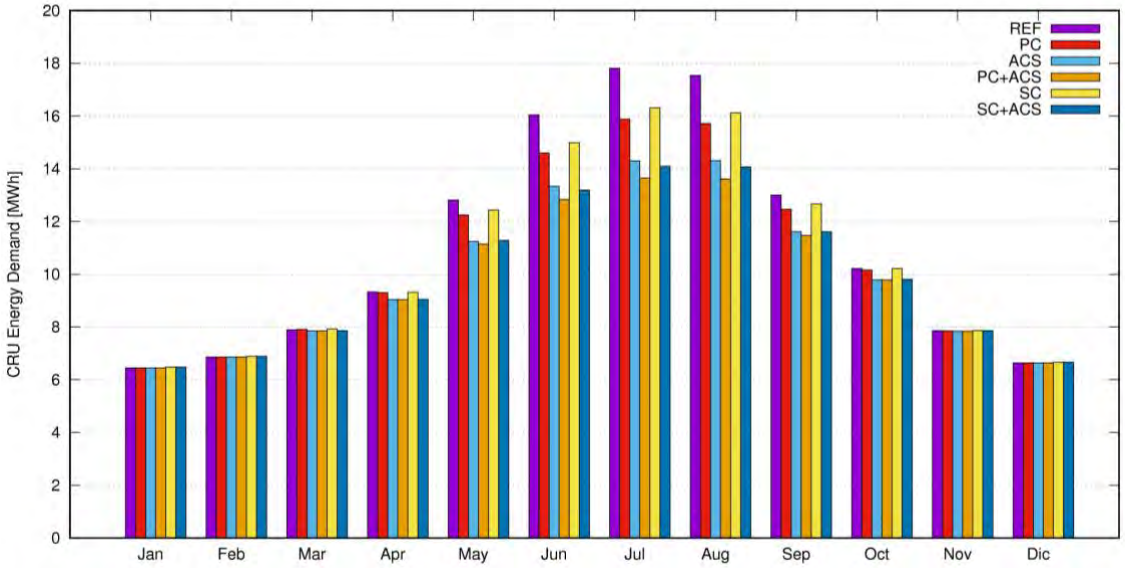

Figure 4. Monthly electrical energy demand.

The effect of the EER of the water chiller on the total energy consumption of the system has been investigated. Values 10 % and 20 % higher than those given by Eq. (4) have been considered for the cases SC and SC + ACS. The results are shown in Fig. 5, and demonstrate just a small reduction in the total energy consumption, which doesn't affect the considerations on the results.

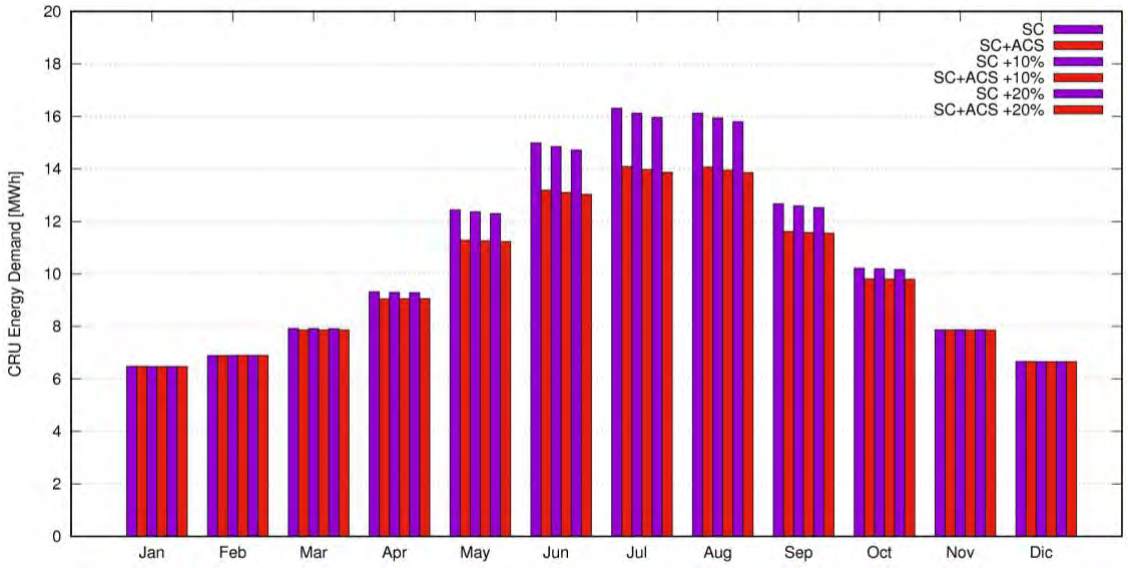

Figure 5: Monthly electrical energy demand, with increased EER values of the water chiller.

Finally, the effect of the maximum cooling capacity of the subcooler has been investigated, considering a couple of values below and above the chosen one for the simulations. The results (Table 3) show that the total value is almost constant, with a slightly lower value at 18 kW. Subcooling solution allows energy savings pretty close to the ones gained with the adoption of parallel compression.

Table 3. Influence of the SC cooling capacity

		Annual Electrical Energy Demand [MWh]				
SC cooling capacity		CRU	Subcooler	Total	Energy use vs REF [%]	Energy use vs PC [%]
	REF	132.5	-	132.5	0.0	-
8 kW	SC	124.0	5.4	129.4	-2.3	2.7
12 kW	SC	121.5	6.9	128.4	-3.0	1.9
18 kW	SC	119.9	7.9	127.8	-3.5	1.4

Fig. 6 represents both the experimental and simulated profiles of the CO_2 outlet temperature and of the heat flow at the subcooler for weeks 3 and 4. It appears that the maximum cooling capacity of the subcooler (18 kW in this case) is often exploited, without reaching the minimum CO_2 outlet temperature (15 °C). Therefore, the choice of the best subcooler capacity is a matter of balance between energy (and thus emissions) and cost benefits.

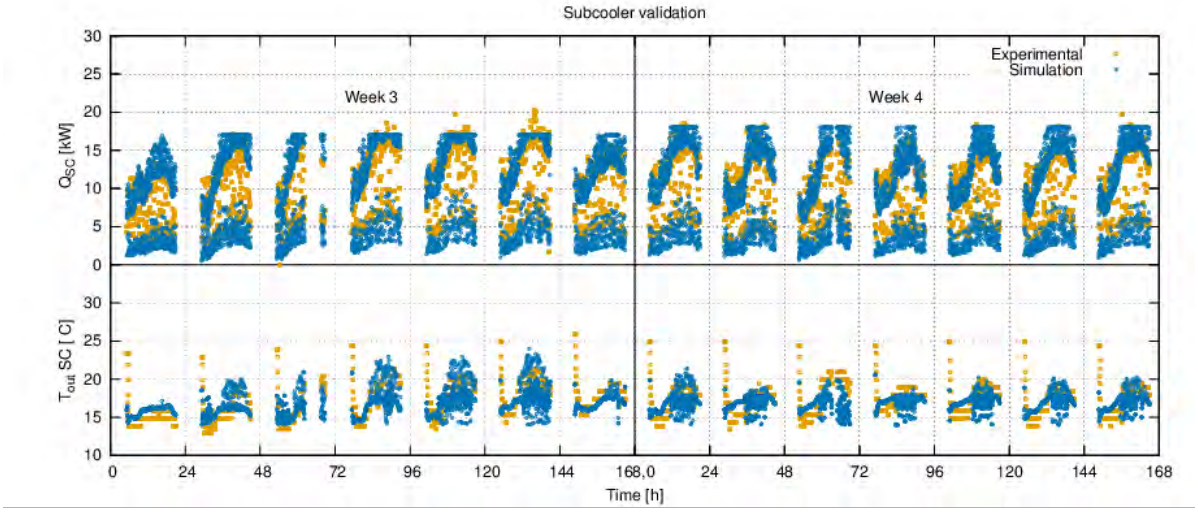

Figure 6: CO_2 outlet temperature and heat flow at the subcooler, weeks 3 and 4

5. CONCLUSIONS

Solutions to improve the efficiency of a CO_2 booster system for commercial refrigeration have been investigated, among parallel compression, subcooling and adiabatic cooling at the gas cooler. Subcooling was performed taking advantage of chilled water available at 7 °C from the HVAC system. For the system considered, and at its climate conditions, parallel compression and subcooling showed to be almost equivalent in terms of yearly energy use, while the adiabatic cooling system gave the best performance. This last solution in combination with parallel compression or subcooling can lead to about 10% energy saving compared to a basic booster cycle, while it allows reducing energy use by 7% compared to parallel compression alone. Comparisons revealed that the subcooler cooling capacity should be chosen carefully to avoid oversizing, while the influence of the EER for the chiller appeared quite small. Subcooling performed at the expense of an HVAC plant showed to be an interesting solution, great advantage was experienced with the employment of an adiabatic gas cooler.

ACKNOWLEDGEMENTS

The research leading to these results has received funding from the MIUR of Italy within the framework of PRIN2015 project «Clean Heating and Cooling Technologies for an Energy Efficient Smart Grid». EPTA Refrigeration is gratefully acknowledged for their continuous and precious assistance in gathering data, and for the fruitful discussions.

NOMENCLATURE

AC	Air Conditioning	HVAC	Heating, Ventilation, Air Conditioning
ACS	Adiabatic Cooling System	LS	Low Stage
app	Approach	LT	Low Temperature
CRU	Commercial Refrigeration Unit	MT	Medium Temperature
DHW	Domestic Hot Water	PC	Parallel Compression
EER	Energy Efficiency Ratio	*T*	Temperature (°C)
GC	Gas Cooler	RDC	Refrigerated Display Cabinets
HPV	High Pressure Valve	SC	Subcooling
HS	High Stage		

REFERENCES

Bell, I.H, Wronski, J., Quoilin, S., Lemort, V., 2014. Pure and Pseudo-pure Fluid Thermophysical Property Evaluation and the Open-Source Thermophysical Property Library CoolProp. Ind. Eng. Chem. Res. 53(6), 2498-2508.

Bush, J., Beshr, M., Aute, V. & Radermacher, R. 2017, "Experimental evaluation of transcritical CO_2 refrigeration with mechanical subcooling", Science and Technology for the Built Environment, vol. 23, no. 6, pp. 1013-1025.

Cortella G., D'Agaro P., Coppola M.A., 2018. Simulations and field tests of a CO_2 refrigerating plant for commercial refrigeration, Proc. 13th IIR Gustav Lorentzen Conference, Valencia, 2018

D'Agaro, P., Cortella, G., Polzot, A. 2018, R744 booster integrated system for full heating supply to supermarkets, Int. J. Refrig., 96, 191-200.

D'Agaro P., Coppola M.A., Cortella G., 2019. Field Tests, Model Validation and Performance of a CO_2 Commercial Refrigeration Plant Integrated with HVAC System. Int. J. Refrig., 100, 380-391

Dipasquale C., Belleri A., Lollini R., 2016. Integrative Modelling Environment, D 4.1 CommONEnergy. http://www.commonenergyproject.eu/uploads/deliverable/file/15/WP4_D4_1_20161124_P01_Integrative_Modelling_Environment_FINAL_v9.pdf [accessed 27.01/2018]

Filippini, S., Mariani, G., Perrotta, L., Merlo, U., 2018. New CO_2 Gas Cooler for Dry and Wet Operation. 13th IIR Gustav Lorentzen Conference on Natural Refrigerants, Valencia (E).

Llopis, R., Cabello, R., Sánchez, D., Torrella, E., 2015. Energy improvement of CO_2 transcritical refrigeration cycles using dedicated mechanical subcooling. Int. J. Refrig. 55, 129–141.

Llopis R., Nebot-Andrés L., Sánchez D., Catalán-Gil J., Cabello R., 2018. Subcooling methods for CO_2 refrigeration cycles. A Review. Int. J. Refrig., 93, 85-107.

Nebot-Andrés, L., Llopis, R., Sánchez, D., Catalán-Gil, J., Cabello, R. 2017, CO_2 with mechanical subcooling vs. CO_2 cascade cycles for medium temperature commercial refrigeration applications thermodynamic analysis, Applied Sciences (Switzerland), 7(9) 955.

Nebot-Andrés, L., Llopis, R., Catalán-Gil, J., Sánchez, D., Cabello, R. 2018, "Energy evaluation of the mechanical subcooling impact on a CO_2 DX-system in a commercial MT cabinet", 13th IIR Gustav Lorentzen Conference, Valencia (E).

Polzot, A., D'Agaro, P., Gullo, P., Cortella, G., 2015. Water storage to improve the efficiency of CO_2 commercial refrigeration systems, 24th IIR International Congress of Refrigeration, Yokohama (JP), 2765-2772.

Polzot, A., D'Agaro, P., Gullo, P., Cortella, G. 2016, Modelling commercial refrigeration systems coupled with water storage to improve energy efficiency and perform heat recovery, Int. J Refrig., 69, 313-323.

Manuscript ID: 787
DOI: 10.18462/iir.icr.2019.0787

Experimental Evaluation of a Multi-Ejector Trans-critical CO_2 System for Supermarkets

Simarpreet SINGH[(a)], Armin HAFNER[(b)], Krzysztof BANASIAK[(c)], Prakash M. MAIYA[(a)], Petter NEKSA[(c)]

[(a)]Indian Institute of Technology Madras, 600036, India, simarleo89@gmail.com
[(b)]Norwegian University of Science and Technology, 7491 Trondheim, Norway
[(c)]SINTEF Energy Research Trondheim, 7034 Trondheim, Norway

ABSTRACT

In the present experimental study, the performance of a multi-ejector based trans-critical CO_2 cooling system is tested at high ambient temperature up to 46°C for a supermarket application with and without internal heat exchanger (IHX) and evaporative cooling. The experimental results indicate that the evaporative cooler capacity reaches a maximum at 10 cm pad thickness. However, a very marginal improvement is observed in terms of COP and PIR (Power Input Ratio) for 15 cm pad thickness. Maximum improvement in COP with IHX and evaporative cooler are 11% and 40% respectively. On the other hand, maximum reduction in the system PIR with IHX and evaporative cooler are 8.5% and 26% respectively. However, marginal enhancement in COP and PIR of 4% and 6% are observed respectively with 15 cm cooling pad thickness. From the study, it is evident that the evaporative cooling for the gas cooler of the CO_2 system seems a potential solution to its application at high ambient temperature.

Keywords: Evaporative cooling, COP.

1. INTRODUCTION

CO_2 was proposed as a feasible working fluid for various applications such as automobile air conditioning, residential heating and water heating (Lorentzen, 1994). It is also popular among residential heating applications in cold climates (Richter et al., 2003). However, the implementation of the CO_2 system is not comparable with that of similar systems using synthetic refrigerants in the context of high ambient temperatures due to the unavoidable/inevitable disadvantage of large throttling losses. Potential modifications of the basic vapor compression system to suit tropical ambient temperatures (its operation in cold climates has been proven) to enhance the overall efficiency of the CO_2 system have been reported earlier in the literature. Various modifications suggested to enhance the overall performance of the system for different operating conditions include, two-phase multi-ejectors (Banasiak and Hafner, 2013), internal heat exchanger (IHX) (Se et al., 2017), work recovery expander (Shariatzadeh et al., 2016; Singh and Dasgupta, 2016). Among the various options available and tested, two-phase ejector is considered as a most appropriate option than the latter due to lack of moving parts in the system (Taylor et al., 2007). The pressure lift gained through the ejector results in the reduction of the total workload of the system compressors (Minetto et al., 2013).

Evaporative cooling is one of the most popular technology used in HVAC&R in the last five decades. It is also successfully adopted in numerous applications to improve the heat transfer process. Ball and Visser (2015) used normative evaporative cooling condenser to improve the heat rejection from the gas cooler of a CO_2 refrigeration system. The single and double pass condenser were evaluated. The overall performance of the CO_2 cooling system improves with condensers / gas coolers operating near sub-critical conditions. However, the study was not extended to high ambient temperatures beyond 38°C. The objective of the present experimental study is to evaluate the performance of a multi-ejector based CO_2 cooling system with IHX for varying pad thickness for evaporative cooling of gas cooler at high ambient temperatures up to 46°C for supermarket applications.

2. CO_2 SUPERMARKET TEST-FACILITY LOCATION AND PRESENT AMBIENT CONDITIONS

Fig. 1 shows the location of CO_2 supermarket test-facility/system and ambient conditions during the test. It is installed in southern Asia where the average ambient temperature conditions are high as shown. The location was selected to evaluate the performance of the system for the extreme ambient temperature conditions.

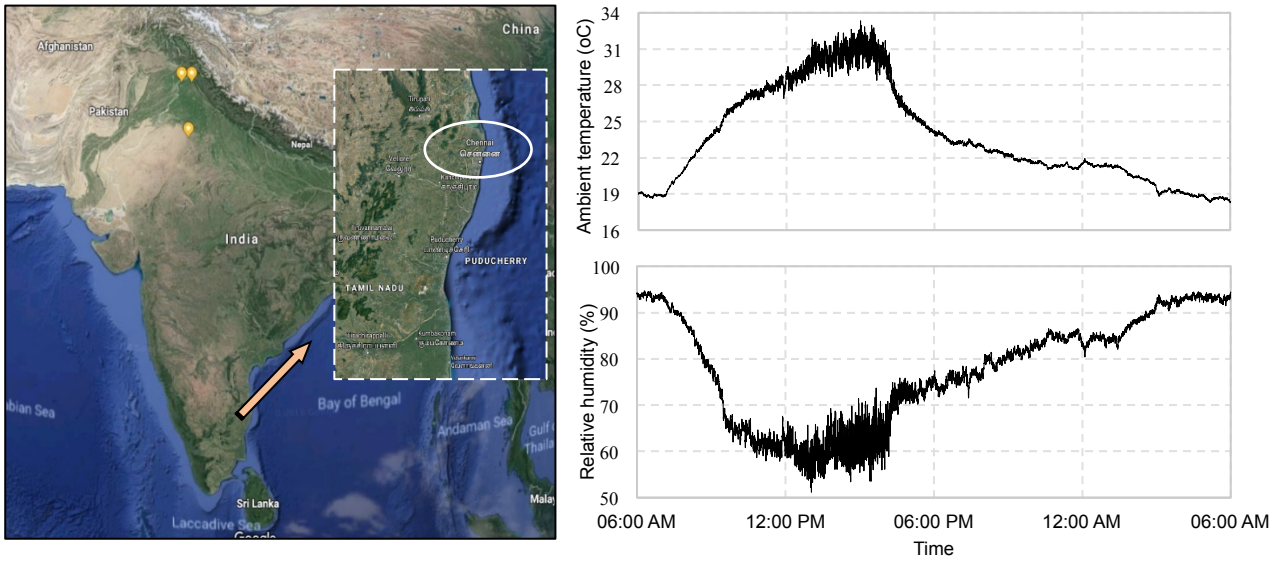

Figure 1: The location of CO_2 supermarket test facility and ambient conditions during the test

3. CO_2 TEST-FACILITY WITH EVAPORATIVE COOLER: A SYSTEM DESCRIPTION

A fully instrumented multi-ejector based CO_2 cooling system test facility for supermarkets is developed and installed at Indian Institute of Technology Madras, India, as shown in Figure 2. It has a total cooling capacity of 33 kW and is designed for supermarket applications, to maintain three different evaporation temperature levels: +6°C (20 kW) for comfort air conditioning (AC), -6°C (10 kW), and -28°C (3 kW) for freezing / food preserving (LT) and for low temperature refrigeration (MT). The test facility is also equipped with a heat recovery system at high temperature with a glycol solution loop to be able to simulate the heat conditions to the evaporators.

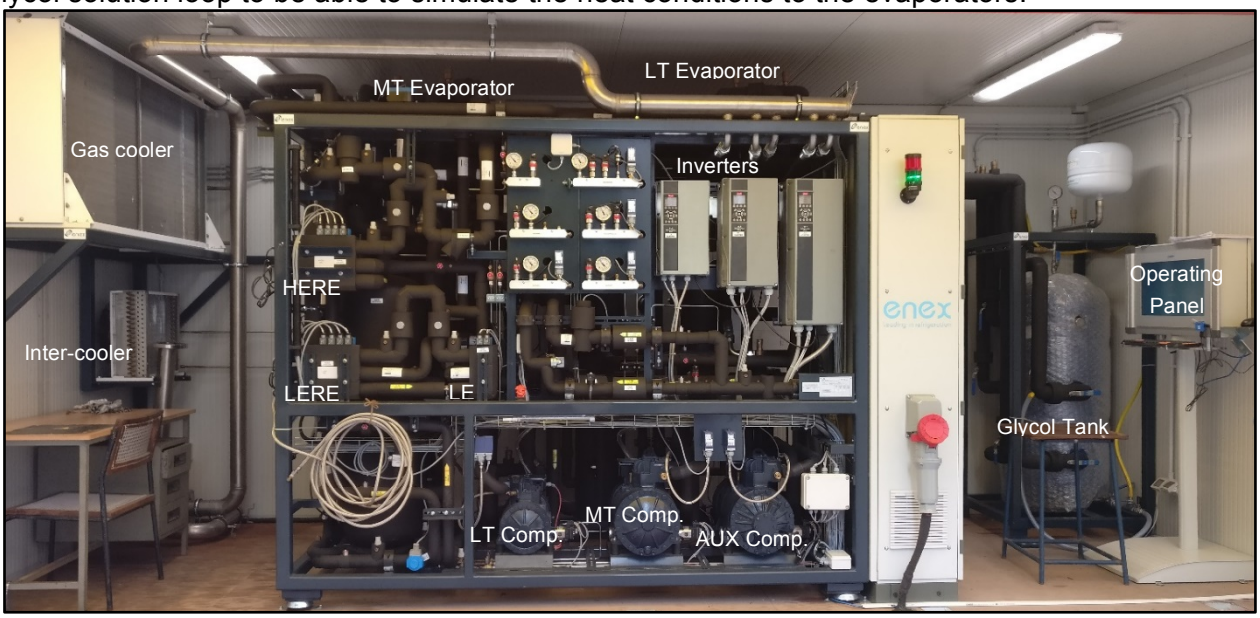

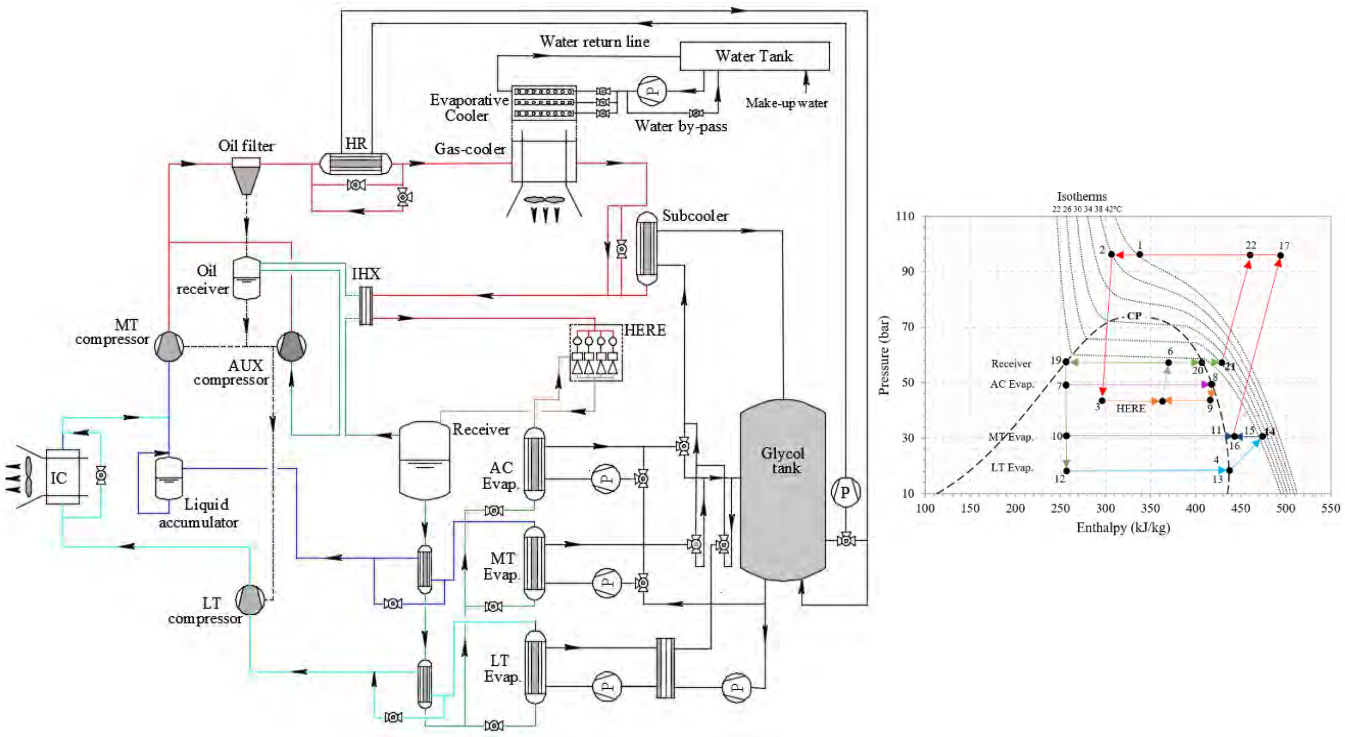

Figure 2: Ejector based CO_2 cooling system test-facility for supermarkets

The two glycol circuits are arranged with different glycol concentrations. LT loop is charged with 55% glycol concentration and the rest of the system which is connected with the glycol tank is charged with 45% glycol concentration in the water. The evaporation temperatures are controlled by suction of the compressors. LT and MT compressors work in tandem with an additional auxiliary (*AUX*) compressor to handle high amounts of flash gas from the receiver. This operates in parallel to the MT compressor, hence the name “parallel compression”. One liquid suction accumulator is also installed to enable the secure separation of liquid and vapor upstream of the compressors to allow a liquid overfeed operation of the evaporators throughout the year. Two ejectors are installed: one with low ejection ratio and a second unit with a high ejection ratio. Multi-ejector with six cartilages with different capacities is used in the test-facility.

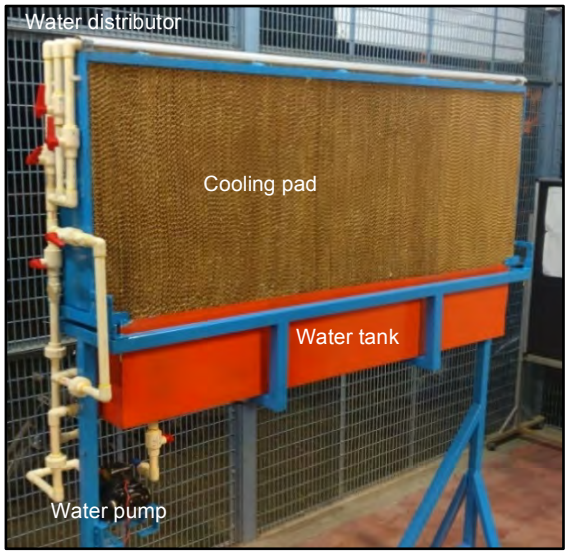

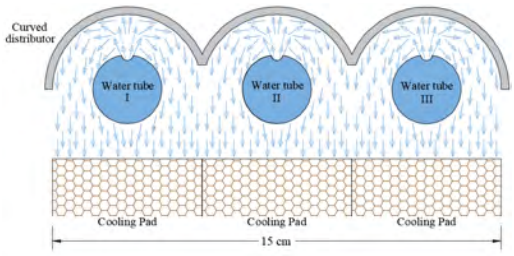

Table 1. Cooling pad details

Details	Units	Value
Face area	m^2	1.157
Cooling pad thickness	cm	5,10,15
Cooling pad design	---	Honeycomb
Water pump capacity	Liters hr^{-1}	1300
Water distribution circuits	---	3

Figure 3: Evaporative cooler with honeycomb cooling pad and water distribution circuit

The operation of switching on/off is taken care by the high pressure (HP) expansion valve opening. The capacity regulation is carried out by on/off switching of the multi-parallel slot ejector cartages. The six cartages with different loads are designed to operate with an individual solenoid valve to

handle different loads. Pressure lifters are also provided in the suction flow entrance to the ejector cartages. The system controllers facilitate both manual and automatic optimization of the gas cooler pressure level with respect to the gas cooler outlet temperature. The facility also has a manual fan controller to vary the airflow rate through the gas cooler to adjust the exit refrigerant temperature. An evaporative cooler with provision to insert up to three honeycomb pads of 5 cm each is positioned in front of the gas cooler. The same fan is made to draw air through this evaporative cooler and the gas cooler as shown in Fig. 2. The evaporative cooling system with three pipes one each to a pad with top holes for even water distribution is shown in Figure 3 and the details are tabulated in Table 1.

4. SUPERMARKET OPERATION

The high pressure CO_2 gas from the gas cooler discharge (state 2) is the motive fluid to the HERE (Fig. 2) and vapour exiting the AC evaporator (state 8) is drawn as the suction fluid to the HERE. HERE lifts CO_2 gas from the low pressure stream (state 8) to higher pressure at the ejector exit (state 6) utilizing high pressure stream (state 2). The receiver separates the two vapour-liquid mixture (state 6). The vapour (state 21) is further compressed in the AUX compressor (state 22) and liquid (state 19) is fed to AC (state 7), MT (state 10) and LT (state 12) evaporators after throttling to the corresponding pressures. The vapor at LT evaporator exit (state 13) is compressed separately up to the suction pressure of the MT compressor (state 14). The LT part of the cycle is not connected with the ejector cycles, which means that the compression takes place from LT evaporator pressure level with no additional boosted pressure lift unlike the other evaporators. Pure vapor (state 11) from the MT evaporator is then mixed with the discharge high pressure vapour of the LT compressor (state 14) and the mixed fluid (state 16) is further compressed by the MT compressor up to the gas cooler pressure (state 17).

4.1. Experimental procedure

The CO_2 circuit side parameters such as temperature of evaporators (AC, LT and MT) receiver pressure (RP), gas cooler outlet temperature, etc. are determined in the test-facility service tool. The gas cooler pressure is automatically optimized according to the gas cooler outlet temperature with the controlling sensor. After directing the system with CO_2 side parameters, the system is turned ON from the main controller (manually). After 15 minutes, the loads of the three evaporators are maintained constant by the secondary water/glycol loop. The loads on the evaporators are controlled by the changing mass flow rate of the glycol solution in the secondary loop. The CO_2 system requires approximately two hours to reach steady state. System performance is evaluated for all steady state conditions using the hourly data and averaged for a single operational temperature. Properties of CO_2 and glycol solution are obtained from REFPROP software and the various operating parameters used for the performance evaluation are tabulated in Table 2. Evaporative cooling system introduced in the CO_2 system is tested for the above 40°C system operating temperature. During the procedure, CO_2 system is set to operate at constant gas cooler outlet temperature by adjusting the gas cooler fan speed manually and keeping it constant. After recording the performance of the system for the set operating temperature, the cooling pad thickness is increased to 5, 10 and 15 cm, one by one allowing the gas cooler outlet temperature to drop at the fixed gas cooler fan speed. The fan speed needs to be reduced manually to achieve the higher gas cooler outlet temperature.

Table 2: CO_2 system operating parameters.

Operating Parameter	Units	Value/Range
Operating temperature	°C	36 to 46
Gas cooler pressure	Bar	80 to 120
Receiver pressure	bar	45
AC Evaporator temperature	°C	+6
LT Evaporator temperature	°C	-28
MT Evaporator temperature	°C	-6

4.2. Performance evaluation

Performance of the ejector based CO_2 cooling system for supermarket applications at high ambient temperature is computed using the following equations.
Efficiency of the evaporative cooler (η_{ec}) is computed by:

$$\eta_{ec} = \frac{T_{inlet\_ec} - T_{outlet\_ec}}{T_{inlet\_ec} - T_{wb}} \quad \text{Eq. (1)}$$

COP of the CO_2 cooling system is computed by,

$$COP = \frac{Q_{AC} + Q_{LT} + Q_{MT}}{P_{AUX} + P_{LT} + P_{MT}} \quad \text{Eq. (2)}$$

Where, load on the three evaporators AC, LT and MT of the system is computed from the glycol side by:

$$\dot{Q}_{AC} = \dot{m}_{AC} * c_p * (T_{AC\_outlet} - T_{AC\_inlet}) \quad \text{Eq. (3)}$$

$$\dot{Q}_{LT} = \dot{m}_{LT} * c_p * (T_{LT\_outlet} - T_{LT\_inlet}) \quad \text{Eq. (4)}$$

$$\dot{Q}_{MT} = \dot{m}_{MT} * c_p * (T_{MT\_outlet} - T_{MT\_inlet}) \quad \text{Eq. (5)}$$

The utility temperatures (T_{UT}) of the three evaporators AC, LT and MT are 22°C, -18°C and 4°C, respectively.

- Power Input Ratio (*PIR*) of the CO_2 cooling system is computed by,

$$PIR = \frac{P_{AUX} + P_{LT} + P_{MT}}{P_{AUX,Carnot} + P_{LT,Carnot} + P_{MT,Carnot}} \quad \text{Eq. (6)}$$

where Carnot power consumption of the three compressors AUX, LT and MT is computed by,

$$P_{AUX,Carnot} = \frac{\dot{Q}_{AC}}{T_{UT\_AC}} * (T_{amb} - T_{UT\_AC}) \quad \text{Eq. (7)}$$

$$P_{LT,Carnot} = \frac{\dot{Q}_{LT}}{T_{UT\_LT}} * (T_{amb} - T_{UT\_LT}) \quad \text{Eq. (8)}$$

$$P_{MT,Carnot} = \frac{\dot{Q}_{MT}}{T_{UT\_MT}} * (T_{amb} - T_{UT\_MT}) \quad \text{Eq. (9)}$$

5. RESULTS AND DISCUSSION

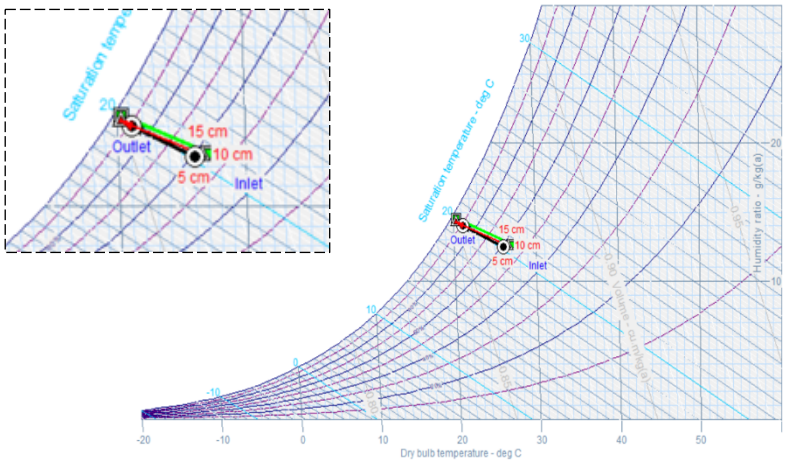

Figure 4: Conditions of air at the inlet and outlet of evaporative cooler on the psychometric chart for 5, 10 and 15 cm thick cooling pad

Fig. 4 shows the conditions of air at the inlet and outlet of evaporative cooler on the psychometric chart for 5, 10 and 15 cm thick cooling pad. The inlet air condition is more or less the same for all the three pad thicknesses as required to compare their performance. It is observed that as the cooling pad thickness increases, relative humidity (RH) increases and dry bulb temperature (DBT) decreases due to increase in the contact surface area between water and cooling pad. However, the law of diminishing returns applies here and the benefit approaches zero when thickness is increased beyond 10 cm.

Fig. 5 shows the evaporative cooler efficiency and evaporative cooler capacity with different cooling pad thickness at various system operating temperatures. It is observed that the efficiency of the evaporative cooler increases with pad thickness at the set gas cooler exit temperature. This is ascribed to the increasing contact surface area between water and air. However, the increment in the evaporative cooler efficiency is only marginal beyond 10 cm cooling pad thickness and the maximum evaporative cooler efficiency observed as 95%. The fan speed had to be set at lower level to achieve higher gas cooler outlet temperature. The resulting lower air velocity increases the residence time and thereby the efficiency increase as the gas cooler exit temperature is set to higher temperatures. Also, pad thickness of 10 cm is observed to be optimum yielding maximum cooler capacity. The pad thickness has two opposing influences; to decrease the face velocity of air due to increase in pressure drop and thereby to increase the cooler efficiency. Hence the same optimum thickness irrespective of the gas cooler exit temperature (set for without evaporative cooling). Within the range of study, the air velocity is the dominant factor governing cooler capacity. Therefore, as the figure indicates, cooler capacity decreases with increase in the set gas cooler temperature where the fan had to be set at lower speeds. Drop in the evaporator cooler capacity is ascribed to the reducing air velocity with respect to the increasing cooling pad thickness beyond 10 cm, which is overall affecting the cooler efficiency. However, as the system operating temperature increases, the evaporator cooler capacity observed decreasing. The maximum capacity observed is 13 kW at 10 cm cooling pad thickness.

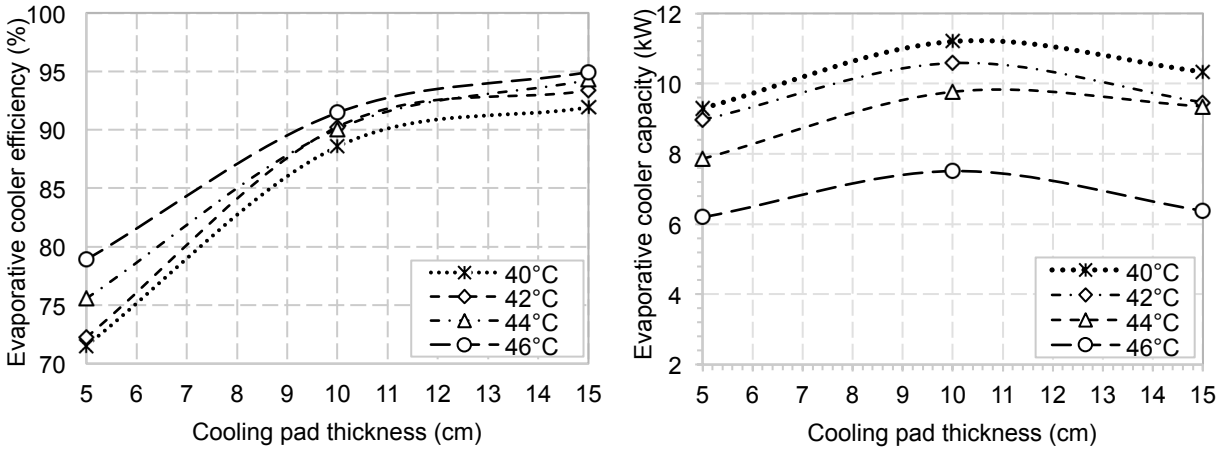

Figure 5: Evaporative cooler efficiency and evaporative cooler capacity with different cooling pad thickness at various system operating temperatures.

Fig. 6 shows the gas cooler outlet temperature and gas cooler capacity with cooling pad thickness at various system operating temperatures. It is observed that as the cooling pad thickness increases, the temperature drop in the gas cooler increases, ascribed to the reduced DBT of air at the inlet of the gas cooler due to the evaporative cooler. As the cooling pad thickness increases, the contact surface area between water and air also increase. Therefore, a progressive reduction in the temperature is observed with respect to increasing cooling pad thickness. However, the gas cooler temperature drop at outlet is marginal beyond 10 cm cooling pad thickness. As the gas cooler outlet temperature decrease, the gas cooler capacity also decreases. Hence, a reduction in cooler capacity is observed as the cooling pad thickness increase. Furthermore, as the system operating temperature increases, the gas cooler capacity also increases. Maximum drop in temperature at gas cooler outlet is ~7K. Also, the maximum gas cooler capacity observed is 34 kW with 5 cm cooling pad thickness at 46°C system operating temperature.

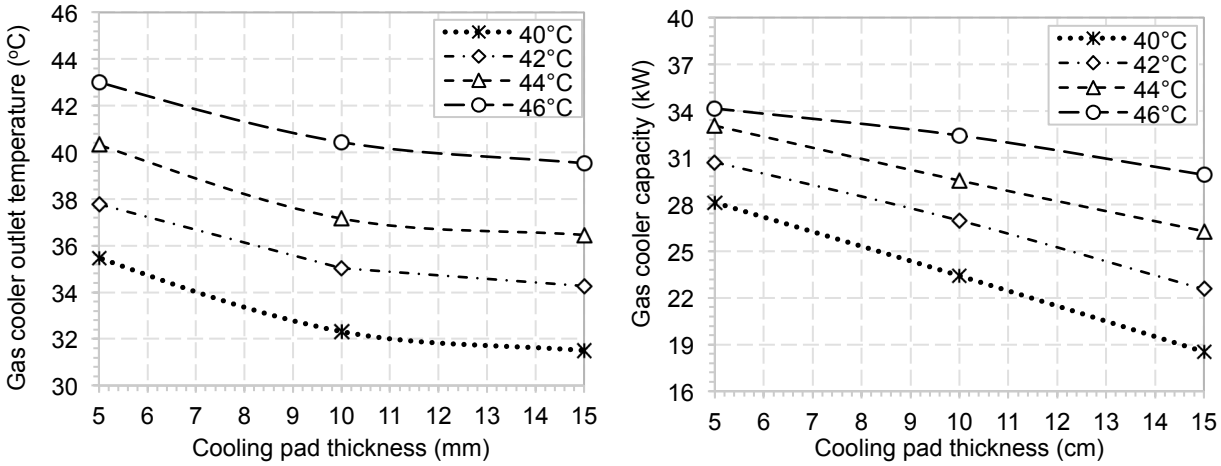

Figure 6: Gas cooler outlet temperature and gas cooler capacity with cooling pad thickness at various system operating temperatures.

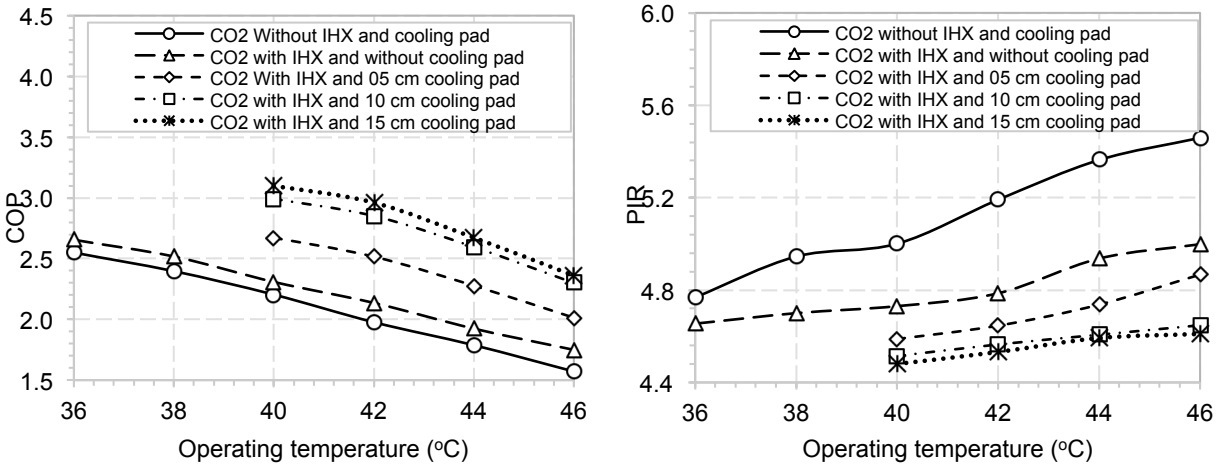

Figure 7: COP and PIR with operating temperatures for CO_2 cooling system with/ without IHX.

Fig. 7 shows the COP and PIR with system operating temperatures for CO_2 cooling system with/ without IHX. It is observed that as the system operating temperature increase, COP of the system decreases and PIR increases. This is due to the increasing system operating gas cooler temperature and pressure at higher operating temperature, which requires more work input to the system. Also, it is observed that, with the use of IHX in the CO_2 system configuration, COP of the CO_2 cooling system improves and PIR reduces. Moreover, with the use of evaporative cooling pad in the system above 40°C, further improvement in the overall performance of the CO_2 cooling system is observed due to reduction in DBT of the air at the gas cooler inlet after crossing the evaporative cooler. From the experimental results, it is also evident that with the increasing cooling pad thickness, the system performance improves further, however, marginal improvement in the overall system performance with the cooling pad thickness beyond 10 cm is observed.

Fig. 8 shows the improvement in COP and reduction in PIR with system operating temperatures. From the experimental results, it is evident that a noteworthy improvement in the overall performance of the CO_2 cooling system is observed with IHX and evaporative cooling in the system configuration. It is observed that, with the support of IHX, maximum COP improvement and PIR reduction are 11% and 8.5% respectively. Moreover, high improvement is observed with the evaporative cooling in CO_2 gas cooler with varying cooling pad thickness. A noteworthy 40% improvement in COP and 26% reduction in system PIR is observed with 15 cm cooling pad thickness. However, a marginal increment in COP and reduction in PIR are 4% and 6% are observed above 10 cm cooling pad thickness.

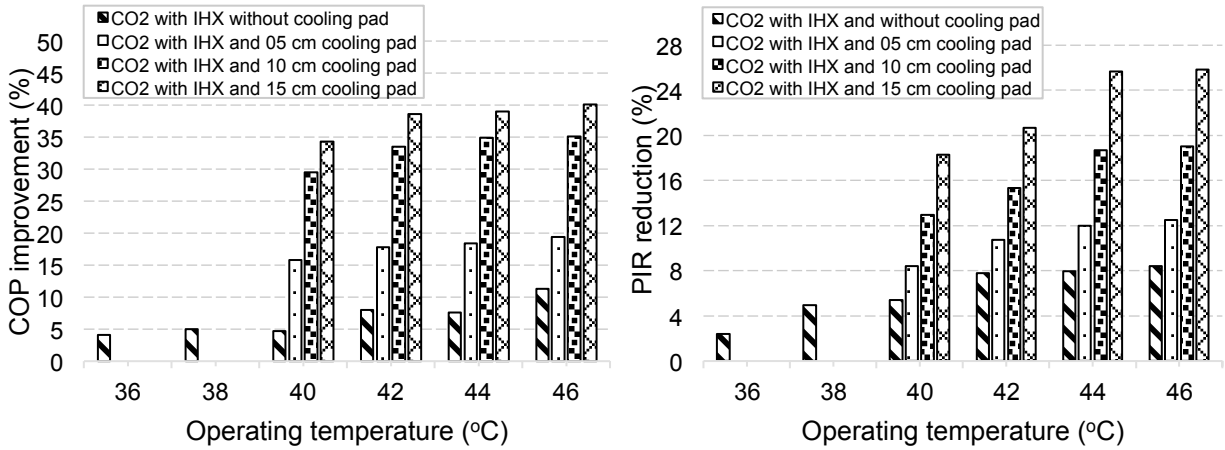

Figure 8: Improvement in COP and reduction in PIR with system operating temperatures

6. CONCLUSIONS

In this experimental study, performance evaluation of a multi-ejector based CO_2 cooling system with/without IHX and evaporative cooling is carried out at high ambient temperature conditions up to 46°C for a supermarket application with different cooling pad thickness. The evaporative cooler is designed, fabricated and tested in the CO_2 cooling system for supermarket application above 40°C with the influence of cooling pad thickness 5, 10 and 15 cm to reduce the gas cooler working pressure in order to improve the overall performance. Evaporative cooling in the CO_2 system configuration appeared as an efficient method to improve the overall performance of the system at high ambient temperature conditions. Experimental results project the maximum evaporative cooler capacity at 10 cm pad thickness, however, very marginal improvement is observed in terms of COP and PIR for 15 cm pad thickness. The maximum improvement in COP with the support of IHX and evaporative cooler are 11% and 40% respectively. On the other hand, the maximum reduction in the system PIR with the support of IHX and evaporative cooler are 8.5% and 26% respectively. Marginal enhancement in COP and PIR observed are 4% and 6% respectively above 10 cm cooling pad thickness. From the present experimental study, it is therefore concluded that, adoption of evaporative cooling in the CO_2 system configuration is a suitable option for supermarket applications for high ambient temperature conditions.

ACKNOWLEDGEMENTS

The research work presented is part of an ongoing Indo-Norwegian project funded by the Ministry of Foreign Affairs, Government of Norway, coordinated by SINTEF, Norway. The Indian authors would like to gratefully acknowledge the additional support received from the Department of Science and Technology (DST) under project: PDF/2017/000083.

REFERENCES

Ball, J., Visser, K., 2015. Applying Evaporative Condensers to Subcritical CO2 Condensing and Transcritical CO2 Gas Cooling, in: Industrial Refrigeration Conference & Exhibition San Diego, California. pp. 1–48.

Banasiak, K., Hafner, A., 2013. Mathematical modelling of supersonic two-phase R744 flows through converging-diverging nozzles: The effects of phase transition models. Appl. Therm. Eng. 51, 635–643.

Lorentzen, G., 1994. Revival of carbon dioxide as a refrigerant. Int. J. Refrig. 17, 292–301.

Minetto, S., Brignoli, R., Banasiak, K., Hafner, A., Zilio, C., 2013. Performance assessment of an off-the-shelf R744 heat pump equipped with an ejector. Appl. Therm. Eng. 59, 568–575.

Richter, M.R., Song, S.M., Yin, J.M., Kim, M.H., Bullard, C.W., Hrnjak, P.S., 2003. Experimental results of transcritical CO2heat pump for residential application. Energy 28, 1005–1019.

Se, M., Hoon, D., Soo, M., Kim, M., 2017. Investigation on the optimal control of gas cooler pressure for a CO 2 refrigeration system with an internal heat exchanger. Int. J. Refrig. 77, 48–59.

Shariatzadeh, O.J., Abolhassani, S.S., Rahmani, M., Nejad, M.Z., 2016. Comparison of transcritical CO2 refrigeration cycle with expander and throttling valve including/excluding internal heat exchanger : Exergy and energy points of view. Appl. Therm. Eng. 93, 779–787.

Singh, S., Dasgupta, M.S., 2016. Evaluation of research on CO2 trans-critical work recovery expander using multi attribute decision making methods. Renew. Sustain. Energy Rev. 59, 119–129.

Taylor, P., House, M., Street, M., Wt, L., Groll, E.A., Kim, J., 2007. Review of Recent Advances toward Transcritical CO2 Cycle Technology. HVAC&R Res. 13, 499–520.

Manuscript ID: 860
DOI: 10.18462/iir.icr.2019.0860

Flow characteristics of silica hard-shell microcapsule slurries treated with additives

Hiroshi SUZUKI[(a),(b)], Sohei USA[(a)], Ruri HIDEMA[(a),(b)]

[(a)] Department of Chemical Science and Engineering, Kobe University
Kobe, 657-8501, Japan, hero@kobe-u.ac.jp
[(b)] Complex Fluid and Thermal Engineering Research Center, Kobe University
Kobe, 657-8501, Japan, hero@kobe-u.ac.jp

ABSTRACT

The sedimentation and flow characteristics of micro-encapsulated phase change materials have been investigated. As a phase change material, trimethylolethane clathrate hydrate having 218 $kJ \cdot kg^{-1}$ of latent heat was used and encapsulated in silica hard-shell microcapsules with 17 μm of the diameter. A cationic surfactant, oleylbishydroxyethylmethylammonium chloride with a counter-ion, sodium salicylate was used as drag reducing additives and poly vinyl alcohol was used as a stabilizer. From the results, it was found that the combination additive prevents effectively the microcapsule sedimentation. The drag reduction was also observed to occur in the high Reynolds number region. Thus, the present additive was concluded to be promising for the latent heat transportation by use of silica hard-shell microcapsules containing phase change materials.

Keywords: Phase Change Material, Latent Heat Transportation, Microcapsule, Drag Reduction

1. INTRODUCTION

The thermal-energy consumption in residential and commercial areas in Japan is 1.9×10^{18} J per year ($1.9\ EJ \cdot y^{-1}$). This amount can be more than 50% of the total energy consumption in these areas. On the other hand, unused thermal energy exhausted from industries, power plants, etc comes up to $2.5\ EJ \cdot y^{-1}$ (Kasagi *et al*., 2013). If those unused thermal energies could be used for residential and commercial areas, thermal-energy consumption could be drastically reduced. However, there is a spatial thermal gap between demand and supply. To utilize the thermal energy from industries for residential energy consumption, a heat transportation technology is required.

A latent heat transportation system containing fine phase change particles in water has higher density of heat than a water sensitive heat transportation system as phase change materials have high latent heat (Kato *et al*., 2016). Thus, the flow rate of transportation can be reduced, and then the pumping power can be effectively saved. Additionally, the heat media have temperature sustainability. Thus, the heat transfer characteristics can be expected to be high.

Many researchers developed latent heat transportation systems, such as systems using ice (Fukusako *et al*., 2000, Inaba *et al*., 2005, Egolf and Kauffeld, 2005, Suzuki *et al*., 2010b), clathlate hydrate (Darbouret *et al*., 2005, Indartono *et al*., 2006, Suzuki *et al*., 2006, Linet *et al*., 2008, Komoda *et al*., 2010, Suzuki *et al*., 2010, Kumano *et al*., 2012, Ma and Zhang, 2013), emulsion (Delgado *et al*., 2000, Fumoto *et al*. 2013, Morita *et al*., 2013) and inorgnic hydrate (Suzuki *et al*., 2010, 2012, 2013, Toyoda *et al*., 2014a). However, the particle growth and agglomeration of phase change materials dispersed in heat media causes pipe blockage. Thus, these systems are not widely used for thermal energy transportation.

To solve this problem, Toyoda *et al.* (2014b) fabricated a technique for microencapsulation of the phase change materials with a hard shell. Tamaru *et al*. (2017) have succeeded in the encapsulation of non-flammable inorganic phase change materials using disodium hydrogen phosphate 12 hydrates with a silica hard shell. They also reported that the microencapsulation of phase change materials depresses the super-cooling of the materials.

However, the density of microcapsules is higher than water, because of high density of silica; 2,100 kg・m^{-3}. This might cause significant sedimentation in a tank and in a pipe for the latent-heat transportation system. In this study, the sedimentation characteristics of the hard-shell microcapsules containing the trimethylolethane clathrate hydrate as phase change material were investigated. Hidema *et al*. (2014) suggested to use a combination system of drag-reducing surfactants and of poly (vinyl alcohol) (PVA) for preventing the particle sedimentation and for improving the fluidity of the ammonium alum hydrates. It is expected that this combination system can prevent the sedimentation of the microcapsules. In this study, sedimentation and flow characteristics of microcapsules containing phase change materials with combination additives will be experimentally investigated.

2. EXPERIMENTAL METHODS

2.1. Materials

As phase change materials, a clathrate hydrate, trimethylolethane・trihydrate (TME・3H_2O) was used. It has 218 kJ・kg^{-1} of latent heat. The phase change temperature is changed with the concentration and the phase separation on this material occurs at higher concentration than 60 wt% (Yamazaki et al., 2002). Then, in this study, the concentration was set at 25 wt% in water as that in the previous study (Toyoda *et al*. 2014b). At this concentration, the phase change temperature and latent heat were 15ºC and 87.5 kJ・kg^{-1}. The hard-shell microcapsules containing this phase change material were prepared following the methods reported in the previous studies (Toyoda *et al*., 2014b, Tamaru *et al*., 2017). Figure 1 shows the SEM photos of microcapsules containing the TME 25% solutions. The mean diameter was 17μm and the void fraction of the microcapsules was set at 74 % with the method reported by Watanabe *et al*. (2018). The densities of TME 25% solution and of the outer shell of SiO_2 were 1,044 kg・m^{-3} and 2,100 kg・m^{-3}, respectively. Thus, the mean density of the microcapsules with this micro-encapsulated material are 1,319 kg・m^{-3}.

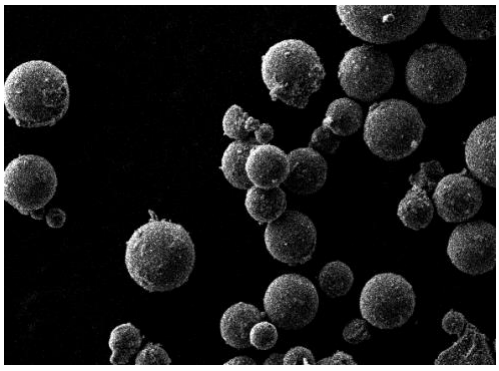

Figure 1: Microcapsules containing phase change materials

As drag-reducing surfactants, a cationic surfactant of oleylbishydroxyethylmethylammonium chloride was used with a counter-ion supplier of sodium salicylate at the molar ratio of 1.5 to surfactants (Suzuki *et al*., 2004, 2012). The surfactant concentration was fixed at 6,000 ppm in this study. As a stabilizer, polyvinyl alcohol (PVA) of full saponification and of 500 polymerization was used. Hidema *et al*. (2018) reported this stabilizer and the surfactant combination forms very large network structure in water. The concentration of PVA was also fixed at 2,000 ppm. The solution was allowed to equilibrate for at least one day prior to any experiments. The surfactants react with unreacted sodium silicate as reported in the previous study (Suzuki *et al*., 2018). This reaction reduces the concentration of surfactants. In order to prevent this reaction, the microcapsules were washed by the surfactants prior to the present experiments.

2.2. Rheological and Flow Characteristic Measurements

The apparent viscosities of the mixture solutions and of the slurries with microcapsules were measured by a stress-control rheometer. The parallel plates with 50 mm diameter were used in the rheometer.

The friction coefficients of the solutions and of the slurries with a once-through flow system, as shown in Fig. 2, were measured as used in the previous study (Suzuki *et al*. 2006). The samples were pressurized in the reservoir tank. When the valve mounted in the downstream of the test section was opened, the flow entered the test section. The pressure in the tank decreased gradually, and then the flow velocity gradually decreases. Thus, the flow decelerated in a pseudo-steady state. From this, the friction coefficients were obtained in a wide range of velocities when the flow passed once through a pipe.

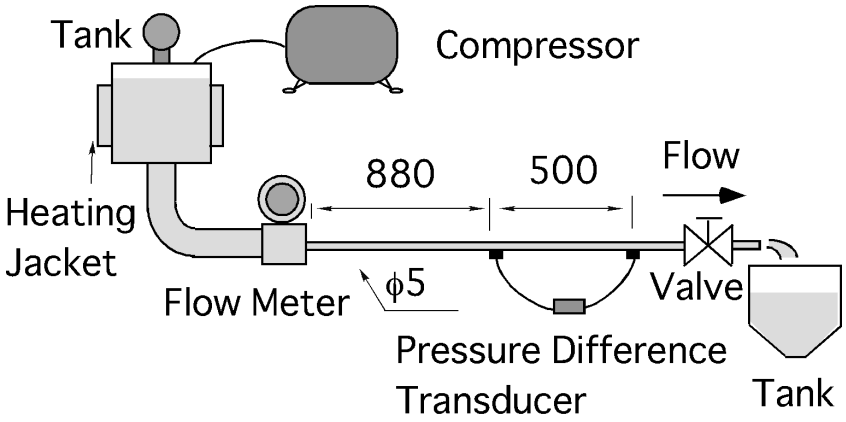

Figure 2: Once-through system for measuring the friction coefficients

In these experiments on the rheological characteristics and the flow characteristics, the concentration of microcapsules was set at 10 wt%. The temperature was kept constant at 10°C

2.3. Sedimentation Characteristics Measurements

The schematic view of sedimentation measurements is shown in Fig. 3. The sedimentation experiments were performed in test tubes with a diameter of 16 mm. Each slurry of 25 mL was poured into a tube in a constant-temperature bath where the temperature was set at 10°C. The concentration of the microcapsules with phase change materials was also set at 10 wt% in this experiment. The apparent volume fraction was defined as the sedimentation length, L_s[m], divided by the slurry length, L[m], as shown in Fig. 3. The sedimentation characteristic in each dispersion solution was observed for 72 h. In the sedimentation experiments, each dispersion solution was named as tabulated in Table 1.

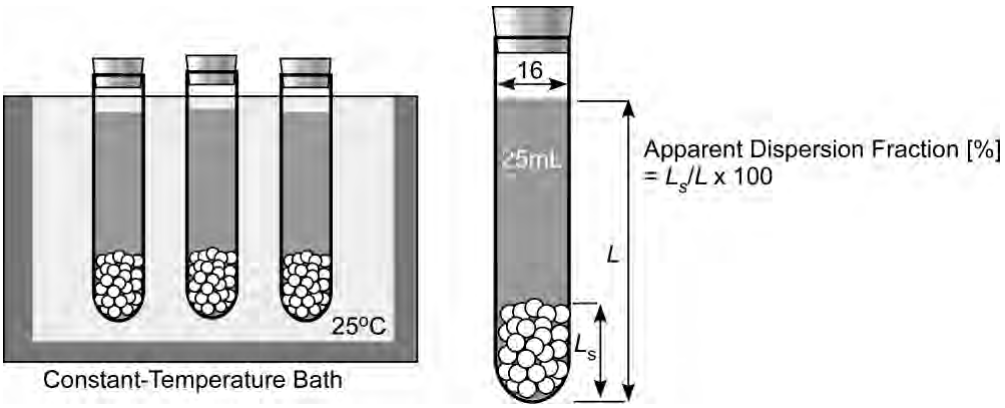

Figure 3: Sedimentation experiments

Table 1: Samples for sedimentation experiments

Sample	A	B	C	D
Surfactant Conc.	0 ppm	6,000 ppm	0 ppm	6,000 ppm
PVA Conc.	0 ppm	0 ppm	2,000 ppm	2,000 ppm

3. RESULTS AND DISCUSSIONS

3.1. Viscosity Characteristics

Figures 4(a) and (b) show the apparent viscosities in the cases without and with microcapsules, respectively. In the cases of water with microcapsules, the viscosity is low and constant as taking almost the same values in the case without microcapsules. The volume fraction of the microcapsule slurry is only 7.9 vol% in the present cases. Then, the addition of microcapsules does not affect the viscosity. In the case only with PVA addition, the viscosity takes almost the same values as those of water. Thus, it is found that the effect of PVA addition is very small at the concentration of 2,000 ppm. On the other hand, the surfactant addition significantly increases the viscosities in both cases with and without microcapsules. The present surfactant system shows high viscoelasticity. Then, the apparent viscosity of the system takes high values in the low range of shear rate and shows shear-thinning tendency as reported by Usui *et al.* (1998) and Suzuki *et al*. (2004). It is also found in the figures that the effects of PVA addition on the viscosities are very small. This indicates that PVA addition does not disturb the viscoelastic structure of the surfactants.

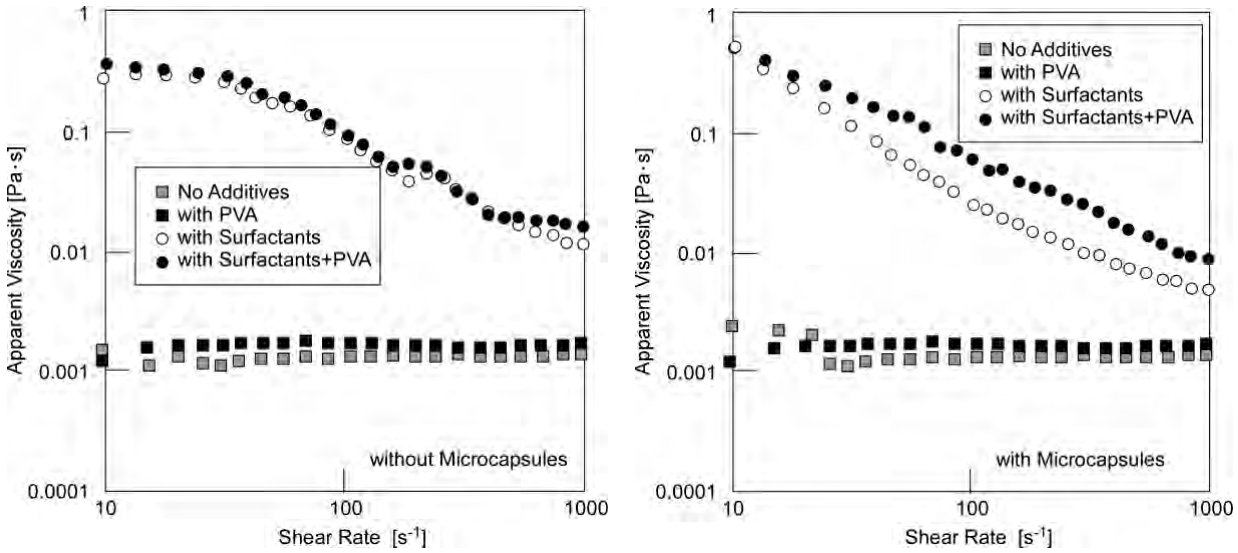

(a) without microcapsules (b) with microcapsules

Figure 4: Apparent viscosities of solutions and of microcapsule slurries

3.2. Sedimentation Characteristics

Figure 5 shows the photos of sedimentation experiments at 0, 1 and 72 hours from the beginning of the experiments. A to D in the figure correspond the conditions tabulated in Table 1.

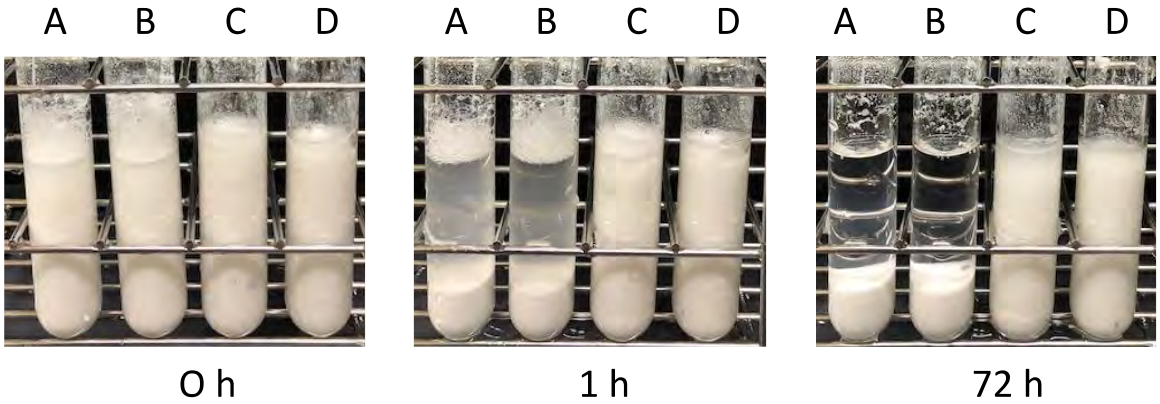

Figure 5: Photos of sedimentation experiments

From this figure, it is found that the sedimentation of microcapsules occurs immediately in the cases without additives and only with PVA. On the other hand, the dispersion states in the cases of surfactant addition with PVA and without PVA are well kept until 72 hours.

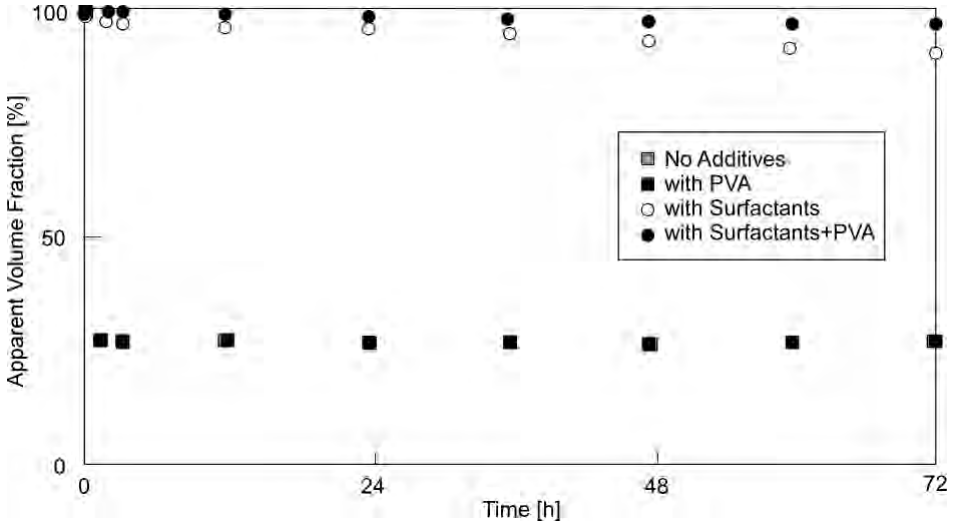

Figure 6: Apparent volume fraction

Figure 6 shows the apparent volume fraction defined above. From this, it is found that microcapsules completely sediment until 1 hour in the cases of water and PVA solution. In the cases with surfactant, the apparent volume fractions show high values until 72 hours. In the case of combination system of surfactant and PVA, the apparent volume is 96.6%.

The sedimentation velocity, V [m] can be estimated by the following Stokes' equation.

$$V = \frac{d^2\left(r_p - r\right)}{18h} \qquad \text{Eq. (1)}$$

Here, d [m], ρ_p [kg・m^3], ρ [kg・m^3] and η [Pa・s] are microcapsule diameter, densities of the microcapsule and fluid viscosity. From this, the sedimentation velocity in the case of water is estimated as 3.88x10^{-6} m・s^{-1}. However, it means it should take 2.5 h for the complete sedimentation, though it occurred within 1 h. Then, it is considered that the agglomeration of microcapsules occurs in water and also in PVA solution and then the sedimentation is accelerated. In the case with surfactants, the sedimentation velocity can be estimated to be 1.61x10^{-8} m・s^{-1} when the viscosity at the shear rate of 1 s^{-1} was used. From the figure, it is found that the mean sedimentation velocity is measured as 1.64x10^{-8} m・s^{-1}. This well agrees with the estimation by Stokes' equation. This indicates that the sedimentation delay occurs due to the high viscosity in the case with surfactants. On the other hand, the mean sedimentation velocity in the case of combination additives is experimentally obtained to be 6.50 x10^{-9} m・s^{-1}, which is lower than the Stokes' estimation of 1.44 x10^{-8} m・s^{-1}. Hidema *et al*. (2018) in the previous study revealed the present surfactant stretches PVA and forms a very large structure and they form a network in the solution. Thus, this sedimentation delay is considered to occur due to such a network structure formation.

3.3. Flow Characteristics

Figures 7(a) and (b) show the friction coefficients in the cases without and with microcapsules, respectively. In the figures, the theoretical values on laminar flows and the turbulent ones of Balsius' equation are plotted in solid lines. The friction coefficient, f [-] and solvent Reynolds number defined with water viscosity, Re [-] are as follows

$$f = \frac{t_w}{\frac{1}{2} r U_m} \quad \text{Eq. (2)}$$

$$Re = \frac{r U_m D}{m} \quad \text{Eq. (3)}$$

Here, τ_w[Pa], U_m[m·s^{-1}], D[m] and μ[Pa·s] are the wall shear stress, the mean velocity, the pipe diameter and the water viscosity, respectively.

The friction coefficients in the case of water well agrees with the theoretical values of laminar flow and also with the Blasius' equation in the higher region than *Re* = 3,000 on both cases without and with microcapsules. Thus, the existence of microcapsules does not significantly affect the flow characteristics when the concentration of microcapsules is set at 10 wt%. On the other hand, the friction coefficients in the cases with surfactants and with combination additives take high values in the region less than *Re* = 15,000. This causes due to the high viscosity. However, in high Reynolds number region more than 15,000, the friction coefficients take lower values than those of Blasius' equation for both cases without and with microcapsules. Thus, drag reduction occurs in the turbulent region for both cases without and with microcapsules. From the figure, it is also found that the PVA addition does not significantly affect the flow characteristics.

Thus, it is concluded that the present combination additives of surfactant and PVA effectively cause not only the sedimentation depression but also the drag reduction of microcapsules containing phase change materials.

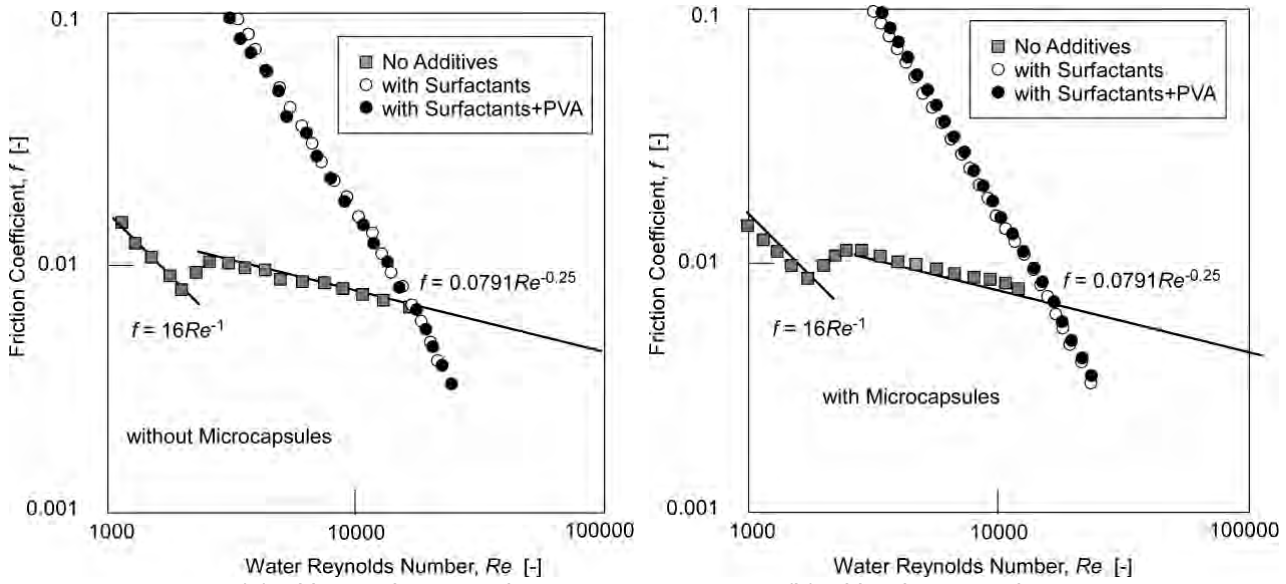

(a) without microcapsules (b) with microcapsules

Figure 7: Friction coefficients

4. CONCLUSINOS

In this study, the sedimentation and flow characteristics of the slurries of microcapsules containing 25 wt% solution of trimethylolethane as phase change materials. In order to improve those characteristics, surfactants as drag reducers and PVA as stabilizers were added into the slurries with the microcapsules at 10 wt% at the concentrations of 6,000ppm and of 2,000ppm. From the results, it was found that the sedimentation depression occurs by surfactant additive and by the combination additive of surfactants and of PVA. In the case only with surfactant, the sedimentation depression occurred due to the high viscosity. On the other hand, the combination additive formed

a network structure, which caused the more effective sedimentation depression. The surfactants caused the effective drag reduction in the range larger than 15,000 of water Reynolds number and PVA addition did not disturb the drag reduction effects. Thus, the present combination additives are concluded to be promising for improving the sedimentation and the fluidity of the slurries of microcapsules.

On the other hand, the friction coefficient took high values in low Reynolds number region. This occurred due to high viscosity. In the present study, the concentrations of additives were fixed. In order to improve this, the optimum concentration of additives should be investigated. The concentration of microcapsules was also fixed in this study. In order to transport more thermal energy, the concentration of microcapsules should be increased. Near future, they will be discussed.

ACKNOWLEDGEMENTS

This study was partially supported by NEDO (New Energy and Industrial Technology Development Organization) project: “Incubation Research on Innovative Technologies in the Thermal Energy Storage Materials/Research and Development Project for Innovative Thermal Management Materials and Technologies” and partially by JST-Mirai-project grant number, JPMJMI17EK, Japan.

NOMENCLATURE

D	test pipe diameter (m)	d	microcapsule diameter (m)
f	friction coefficient (-)	L	slurry length (m)
L_s	sedimentation length (m)	Re	Reynolds number (-)
U_m	mean velocity in the test pipe (m・s-1)	V	sedimentation velocity (m・s-1)
η	fluid viscosity (Pa・s)	μ	water viscosity (Pa・s)
ρ	fluid density (kg・m^3)	ρ_p	microcapsule density (kg・m^3)
τ_w	wall shear stress (Pa)		

REFERENCES

Darbouret, M., Cournil, M., Herri, J.-M., 2005, Rheological Study of TBAB Hydrate Slurries as Secondary Two-Phase Refrigerants, *Int. J. Refrigeration*, 28: 663-671.

Delgado, M., Lazaro, A., Mazo, J., Zabla, B., 2012, Review on Phase Change Material Emulsions and Microencapsulated Phase Change Material Slurries: Materials, Heat Transfer Studies and Applications, *Renewable and Sustainable Energy Reviews*, 16: 253-273.

Fukusako, S., Kozawa, Y., Yamada, M., Tanino, M., 2000, Fundamental Researches and Developments on Fine Crystalline Ice Slurries in Japan, *Trans. JSRAE*, 17: 413-437.

Fumoto, K, Sato N, Kawaji, M., Kawanami, T., Inamura, T., 2014, Phase Change Characteristics of Nanoemulsion as a Latent Heat Storage Material, *Int. J. Thermophysics*, 35: 1922-1932.

Egolf, P. W. and Kauffeld, M., 2005, From Physical Properties of Ice Slurries to Industrial Ice Slurry Applications, *Int. J. Refrigeration*, 28: 4-12.

Hidema, R, Tano, T, Suzuki, H, Fujii, M, Komoda, Y, Toyoda, T., 2014, Phase Separation Characteristics of Ammonium Alum Hydrates with Poly Vinyl Alcohol, *J. Chem. Eng. Jpn*. 47(2): 169-174.

Hidema, R, Tano, T, Sato, H., Komoda, Y., Suzuki, H, 2018, Ammonium Alum Hydrate Slurries with Surfactants and Polyvinyl Alcohol as a Latent Heat Transportation Material for High Temperature, *Int. J. Heat Mass Transfer*, 124: 1334-1346.

Inaba, H., Inada, T., Horibe, A., Suzuki. H., Usui, H., 2005, Preventing Agglomeration and Growth of Ice Particles in Water with Suitable Additives, *Int. J. Refrigeration*, 28: 20-26.

Indartono, Y. S., Usui, H., Suzuki, H., Komoda, Y., Nakayama, K., 2006, Hydrodynamics and Heat Transfer Characteristics of Drag-Reducing Trimethylolethane Solution and Suspension by Cationic Surfactant, *J. Chem. Eng. Japan*, 39: 623-632.

Kasagi, N., Shikazono, N., Suzuki, I., Sekine, Y., Nakamura, R., 2013, *Technology Survey on Advanced Utilization Medium to Low Temperature Heat*, *JST Research Rep*., Japan Science and Technology Agency, Tokyo.

Kato, Y., Suzuki, H., Shikazono, N., 2016, Heat Storage, Transportation and Transfer, *Energy Technology Roadmaps of Japan-Future Energy Systems Based on Feasible Technologies Beyond 2030* (ed. Kato Y. Kato, Koyama, M., Fukushima, Y., Nakagaki, T.), Springer Japan, Tokyo.

Komoda, Y., Yamaguchi, H., Kanki, T., Suzuki, H., Usui, H., 2010, Agglomeration of Hydrate Particles in Aqueous Surfactant Solution with Counter Ion, *J. Chem. Eng. Japan*, 43: 1: 23-28.

Kumano, H., Hirata, T., Mitsuishi, K., Ueno, K., 2012, Experimental Study on Effect of Electric Field on Hydrate Nucleation in Supercooled Tetra-n-Butyl Ammonium Bromide Aqueous Solution," *Int. J. Refrigeration*, 35: 1266-1274.

Linet, W., Delahaye, A., Fournaison, L., 2008, Phase Equilibrium and Dissociation Enthalpy for Semi-Clathrate Hydrate of CO_2 + TBAB, *Fluid Phase Equilibria*, 264: 220-227.

Ma, Z.W. and Zhang, P., 2013, Influence of Crystal Layer on the Flow and Heat Transfer Characteristics during TBAB CHS Generation in a Double-Tube Heat Exchanger", *Int. J. Thermal Sciences*, 68: 173-180.

Morita, S., Hayamizu, Y., Horibe, A., Haruki, N., Inaba, H., 2013, Experimental Study on Latent Heat Storage Characteristics of W/O Emulsion -Supercooling Rate of Dispersed Water srops by Direct Contact Heat Exchange-", *Int. J. Thermal Science*, 22: 145-151.

Suzuki, H., Fuller, G.G., Nakayama, T., Usui, H., 2004, Development Characteristics of Drag-reducing Surfactant Solution Flow in a Duct, *Rheol. Acta*, 43: 232-239.

Suzuki, H., Higuchi, H., Watanabe, H., Komoda, Y., Ozawa, S., Nishimura, T., Takenaka, N., 2012, Relaxation Behavior of a Drag-Reducing Cationic Surfactant Solution, *Nihon Reoroji Gakkaishi*. 40: 85-90.

Suzuki, H., Itotagawa, T., Indartono, Y.S., Usui, H, Wada, N., 2006, Rheological Characteristics of Trimethylolethane Hydrate Slurry Treated with Drag-Reducing Surfactants, *Rheol. Acta*. 46: 287–295.

Suzuki, H., Kishimoto T., Komoda Y., Usui H., 2010a, Investigation of Thermal Properties of Na_2HPO_4 Hydrate Slurries for Evaluating Their Use as a Coolant in Absorption Chillers, *J. Chem. Eng. Japan*, 43: 34-39.

Suzuki, H., Konaka, T., Komoda, Y., 2010b, Particle Size Depression and Drag Reduction of Ice Slurry Treated with Combination Additives of Surfactants and Poly (vinyl alcohol), *J. Chem. Eng. Japan*, 43: 23-28.

Suzuki, H., Konaka, T., Komoda, Y., Ishigami, T., 2013, Flow and Heat Transfer Characteristics of Ammonium Alum Hydrate Slurry, *Int. J. Refrigeration*, 36: 81-87.

Suzuki, H., Konaka, T., Komoda, Y., Ishigami, T., Fudaba, T., 2012, Flow and Heat Transfer Characteristics of Ammonium Alum Hydrate Slurry Treated with Surfactants, *J. Chem. Eng. Japan*, 45: 136-141.

Suzuki, H., Tateishi, S., Komoda, Y., 2010c, Effect of Molar Ratio of Counter-ions to Cationic Surfactants on Drag Reduction Characteristics of Trimethylolethane Hydrate Slurries, *Int. J. Refrigeration*, 33: 1632-1638.

Suzuki, H., Watanabe, I., Hidema, R., Komoda, Y., Horie, T., Ohmura, N., Asano, H., 2018, Dispersion and Flow Characteristics of Hard-Shell Microcapsules with Phase Change Materials, *Proc. 12th IIR Conf. on Phase Change Materials and Slurries for Refrigeration and Air-Conditioning*, #0023, Orford.

Tamaru, M., Suzuki, H., Hidema, R., Komoda, Y., Suzuki, K., 2017, Fabrication of Hard-Shell Microcapsules Containing Inorganic Materials, *Int. J. Refrigeration*, 82: 97-105.

Toyoda, T., Hidema, R., Suzuki, H., Komoda, Y., 2014a, Crystal Growth and Viscosity Behaviors of Ammonium Alum Hydrate Solution with PVA in Shear Flow, *Nihon Reoroji Gakkaishi*, 42: 219-226.

Toyoda, T., Narisada, R., Suzuki, H., Hidema, R., Komoda, Y., 2014b, Fabrication Process of Silica Hard-shell Microcapsule (HSMC) Containing Phase-change Materials, *Chem. Lett*., 43(6): 820-821.

Usui, H., Itoh, T., Saeki, T., 1998, On Pipe Diameter Effects in Surfactant Drag-Reducing Pipe Flows, *Rehol. Acta*, 37: 122-128.

Watanabe, I., Furukawa, N., Kuroda, N., Hidema, R., Suzuki, H., Komoda, Y., Horie, T., Asano, H., Ohmura, N., 2018, Effects of Fabrication Conditions on Silica Hard-Shell Microcapsules

Containing Phase Change Materials, *Int. Heat Trans. Conf. 16*, DOI: 10.1615/IHTC16.ecs.022594, Begell House, USA.
Yamazaki, M., Sasaki, C., Kakiuchi, H., Osano, Y.T., Suga, H., 2002, Thermal and Structural Characterization of Trimethylolethan Trihydrate, *Thermochim. Acta*, 387:39-45.

Manuscript ID: 861
DOI 10.18462/iir.icr.2019.0861

Numerical and experimental evaluation of the aerodynamic drag of the air curtain in Vertical Open Refrigerated Display Cases

Samuel M. NASCIMENTO[(a,b)], Gustavo G. HEIDINGER[(a,b)], Pedro D. GASPAR[(b,c)], Pedro D. SILVA[(b,c)]

[(a)] Eletrofrio Refrigeração Ltda, rua João Chede 1599, 81170-220, Curitiba - PR, Brazil
e-mail: samuel@eletrofrio.com.br, web: http://www.eletrofrio.com.br
[(b)] University of Beira Interior, rua Marquês d'Ávila e Bolama, 6201-001, Covilhã, Portugal
[(c)] C-MAST - Centre for Mechanical and Aerospace Science and Technologies, Covilhã, Portugal
e-mail: dinis@ubi.pt, dinho@ubi.pt, web: http://www.ubi.pt

ABSTRACT

This paper presents the experimental and numerical results of a set of air curtain evaluations in a Vertical Open Refrigerated Display Cases (VORDC) when subjected to external disturbances due to the transfer of people in front of the air curtain. Previous experimental studies identified that the stability of the air curtain depends on the climatic conditions and ambient air movement inside the stores. The ambient air and VORDC air curtain can be disturbed during the movement of people in front of the VORDC, causing a certain amount of cold air to flow out of the VORDC and consequently hot and humid air entering. It is not possible to quantify exclusively the increase in energy consumption due to the transfer of people in the real case, due to the other variables involved in the process. Thus, a robot (Automated Mannequin for Interference Reproduction in the Air Curtain - MARIA) was mounted on a rail placed around the VORDC, in a climate chamber with controlled environment according to climatic class (n. º 3: T=25°C; ϕ=60%). MARIA performed clockwise and counterclockwise movements around the VORDC, with velocities of 0.2 $m{\cdot}s^{-1}$ at 0.8 $m{\cdot}s^{-1}$, with a pitch of 0.2 $m{\cdot}s^{-1}$. For the numerical evaluation, a 3D CFD model was developed to predict and analyze the air flow and heat transfer in the air curtain and outside both ways, refrigerated space and ambient air due to transfer of a body parallel to the air curtain.
Keywords: Air curtain, Experimental, Robot, VORDC, CFD.

1. INTRODUCTION

Since ancient times, man has the need and the will of obtaining cooling ways that make the temperature of foods products to reach a value below the environmental temperature in order to preserve them for longer periods of time. The perishable food products, from production to the final consumer, are preserved and channeled through the system named as cold chain. According to Rigot (1991), the cold chain can be described by five main links: Cold in the production stage; Cold during storage, Refrigerated transportation; Cold in the distribution stage; and Home cooling. The fourth link in the cold chain, which is the subject of this paper, is commonly referred as commercial refrigeration by being placed at the trade level. ASHRAE (2010) indicates that the percentage of energy consumed in a typical supermarket due to the refrigeration systems reaches 50%. According to Faramarzi (1999), ASHRAE (2010) and Gaspar et al. (2011), the thermal load due to ambient air infiltration to VORDC corresponds respectively from 67% to 81% of the total thermal load, depending on the ambient air conditions. Hayes and Stoecker (1969) developed a correlation that describes the ability of the air curtain to provide a proper separation between environments. The correlation is given by a dimensionless parameter named as deflection modulus, D_m, which is the ratio between the air curtain momentum and the modulus of the transverse forces caused by temperature difference between the contiguous environments. Faramarzi (1999) determined the relative weight of the total cooling load components for VORDC, composed by thermal loads from infiltration, radiation, conduction, product pull-down cooling, devices (lights and fans), defrost and anti-sweat

heaters, and product respiration. Chen et al. (2005, 2009, 2011) developed studies using Computational Fluid Dynamics (CFD) codes to evaluate the thermo-physical parameters of the air curtain in VORDC. The performance of air curtain was evaluated by the following dimensionless numbers/parameters: Reynolds number, Grashof number, Richardson number and dimensionless temperature. Navaz et al. (2005) developed further studies using Digital Particle Image Velocimetry (DPIV), focusing mainly in studying the effectiveness of the air curtain and maintaining the temperature of food products to a predetermined value. The results indicate that the Reynolds number has direct effect on the ambient air entrainment into the refrigerated equipment due to its role in the turbulence development. Yu et al. (2009) developed the TEF equation. The correlation is given by eq. (1) to eq. (2) including the dimensionless temperature given by eq. (3).

$$TEF = (1-\beta)X_j - \beta X_j X_{PBP} \quad \text{Eq. (1)}$$

$$\beta = \frac{\dot{m}_{PBP}}{\dot{m}_{PBP} + \dot{m}_{DAG}} \quad \text{Eq. (2)}$$

$$X_{PBP} = \frac{T_{PBP} - T_{DAG}}{T_{Amb} - T_{DAG}} \quad \text{Eq. (3)}$$

The results obtained by Yu et al. (2009) show a good approximation for TEF and temperature value at the return air grille (RAG) with deviations of 0.9% and 0.1 °C respectively. Gaspar *et al.* (2009, 2010, 2011) evaluated the stability of the air curtain for climatic classes n.º 1, n.º 2 and n.º 3 according to EN-ISO 23953 (2005) and other classes beyond the standard. The evaluation was made by experimental testing and numerically using CFD models. The results showed that the ORDC performance strongly depends on the ambient air conditions such as temperature, humidity, velocity and direction of ambient air flow in relation to the VORDC's frontal opening. Laguerre *et al.* (2012) developed a simplified analytical model based on heat transfer equations to determine the values of air and product temperatures at various locations of a VORDC. Cao et al. (2010, 2011) developed a new strategy for conception and optimization in the air curtains design for vertical VORDC. The strategy is based on the heat transfer model between two fluids (two-fluid of cooling loss - CLTF) developed based on a Support Vector Machine (SVM) algorithm. Mousset and Libsig (2011) developed the correlation described by eq. (9) that quantifies, for any ambient air condition, the cooling load increment relatively to the cooling load in the climate class n.º 3 (T_a = 25°C; ϕ_a = 60%) of ISO23953 (2005).

$$\Phi_{24\,(CLASS_x)} = \Phi_{24\,(CLASS_3)} \frac{Enthalpy_{(CLASS_x)}}{Enthalpy_{(CLASS_3)}} \quad \text{Eq. (4)}$$

Where, $\Phi_{24\,(CLASS_x)}$ [W] is the heat extraction rate in the ISO climate class *x* while the $\Phi_{24\,(CLASS_3)}$ [W] is the heat Extraction Rate in the ISO climate class n.º 3. Similarly, *Enthalpy*$_{(CLASS\ x)}$ [kJ/kg] is the enthalpy of the humid air calculated with the temperature and humidity of the class *x* and *Enthalpy*$_{(CLASS\ 3)}$ [kJ/kg] is the enthalpy of the humid air calculated with the temperature (25°C) and humidity (60%RH) of the climate class n.º 3. In the field of numerical simulation, computational codes have been widely used by several researchers and product developers. For studies involving air flow with heat and mass transfer, one of the best known and accepted computational tools among users is Computational Fluid Dynamics (CFD). The evolution of models and capacities of computational resources, have increased the precision of the numerical results. Some relevant examples of CFD models develop to study the air flow and heat transfer in VORDC and it air curtain can be highlighted: George and Buttsworth (2000), Ge and Tassou (2001), Gaspar et al. (2002), Axell (2003), Cui & Wang (2004), D'Agaro et al. (2006), Gaspar et al. (2007c), Yu et al. (2007), Gaspar et al. (2008) Gaspar et al. (2009), Traboulsi (2009), Gaspar et al. (2010a, 2010b), Ge (2010). Barve (2011), Wu et al. (2014), Carneiro et al. (2015, 2017). These studies were based in 2D or 3D CFD models developed to characterize air curtain efficiency and to investigate the influence of range of parameters such as: jet height, width and velocity on (discharge air grille) DAG output, turbulence models, distance of the air curtain to boundary conditions, external obstructions, orientations regarding airflow in the room, ratio of flow rates between DAG and perforated back panel (PBP), porosity distribution on PBP, door opening, among others. As seen, no studies have been developed to evaluate the influence of consumers on the air curtain performance.

2. EXPERIMENTAL PROCEDURE

Experimental tests were conducted in an environmental test chamber constructed according to ISO 23953 (2015). There is an air treatment to keep the air temperature and humidity surrounding the display cases at the climatic class n.° 3 (T_a = 25°C; ϕ_a = 60%). The test room is a thermally insulated parallelepiped shaped space in which two of the opposing sidewalls are designed to provide a uniform horizontal airflow (v_a = 0.1 to 0.2 m·s^{-1}) through the room. The vertical ORDC provided by Eletrofrio Refrigeration LTDA - Brazil has 2.5x1.1x2.1 m^3. As shown in Fig. 1, it comprises: (1) an insulating body (IB) surrounding all the equipment; (2) tube and fins heat exchanger (HX); (3) discharge air grille (DAG); (4) return air grille (RAG); (5) perforated back panel (PBP) and; (6) shelves (SH).

The temperature of the refrigerated compartment is provided by the cold air mass flow that exits DAG and PBP and returns to RAG to be cooled again in the HX. The air flow exiting DAG forms an air curtain which protects the inner refrigerated compartment. Note that this equipment has a primary air curtain (PAC) and a secondary air curtain (SAC) in order to promote a more effective aerothermodynamics sealing.

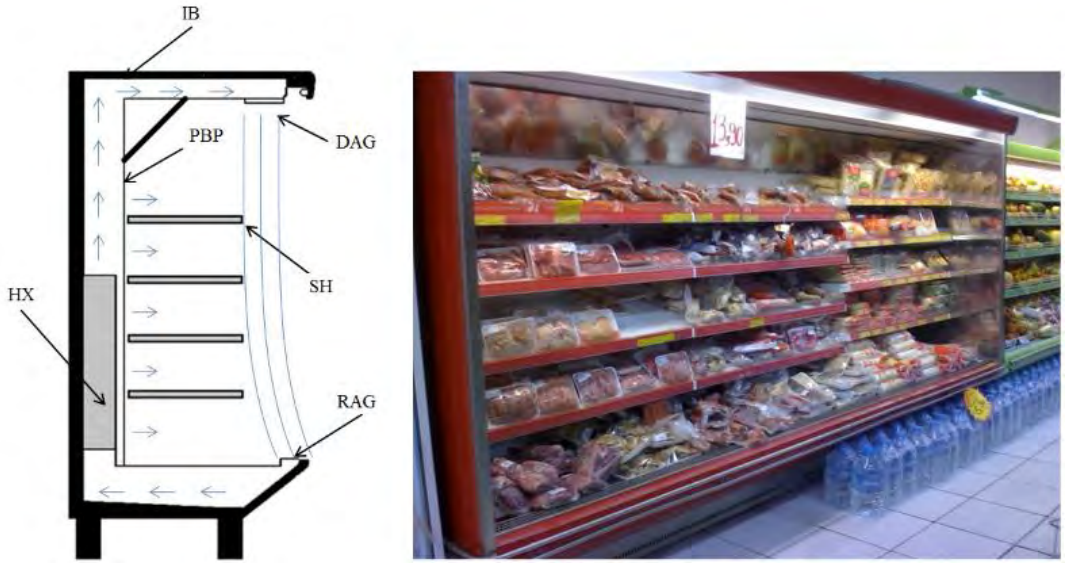

Figure 1: Vertical open refrigerated display cabinet.

The device has four fans with 53 W each to supply a flow rate of 0.4 m^3·s^{-1} to DAG and PBP. The air, before reaching the DAG, passes through an evaporator with dimensions 2.20x0.13x0.35 m^3 constituted by 222 fins and three rows of tubes in the air flow direction and 8 rows of tubes perpendicular to it. The DAG has a total width, b, of 140 mm, which is equally distributed to form the PAC (b_{PAC} = 70 mm) and SAC (b_{SAC} = 70 mm). This equipment is used to display products with temperature class M1 (-1 °C to +5 °C). It was installed a remote mechanical system with a compressor Octagon 2DC-3.2 and water condenser. The measuring instruments were selected in order to obtain reliable measurements of the relevant physical properties' variation collected every minute during the experimental test.

2.1. Robotic Mannequin

A robot, MARIA (Mannequin for Automatic Replication of the Interference in the Air), was designed and constructed for the experimental study. The robot was programmed to move in front of display case during 24h with a time period of 5 min, with a translation velocity of 0.6 m·s^{-1}. This velocity value was obtained with field analysis and corresponds to the average velocity of people transferring inside a supermarket when they are in front of VORDC in the butchery sector. Experimental tests were performed with and without the translation movement of MARIA in order to obtain experimental data that allow the comparison of the display case performance with and without interference of the air curtain due to the systematic transfer of MARIA. Fig. 2 shows the layout of the experimental testing procedure. Tests were performed under the same climate condition and air velocity in the test room.



Figure 2: MARIA in front of the VORDC

2.2. Numerical Model

In addition to the experimental evaluations, a 3D CAD model was developed with the use of SolidWorks 2016 CAD software for geometry, Mesh Ansys 2016 was used for the mesh generation and Fluent Ansys 2016 for case modeling through the finite volume technique. To develop and process each numerical model, a Z280 Workstation with Intel(R) Xeon(R) CPU E5-2640 v2 @ 2.00GHz CPU with 32 GB of RAM was used.

3. ANALYSIS AND DISCUSSION OF RESULTS

3.1. Experimental results

The experimental results of both case studies (with and without interference) were analyzed and compared based on 24h data of the difference of air temperature and relative humidity between the DAG and RAG. Additionally, the thermal load obtained in both case studies was also compared. Fig. 3a and Fig. 3b shown respectively the 24h data of difference of air temperature and (absolute) humidity between the DAG and RAG for the experimental testing without and with (against the direction of air flow from the test room) MARIA movement around the VORDC.

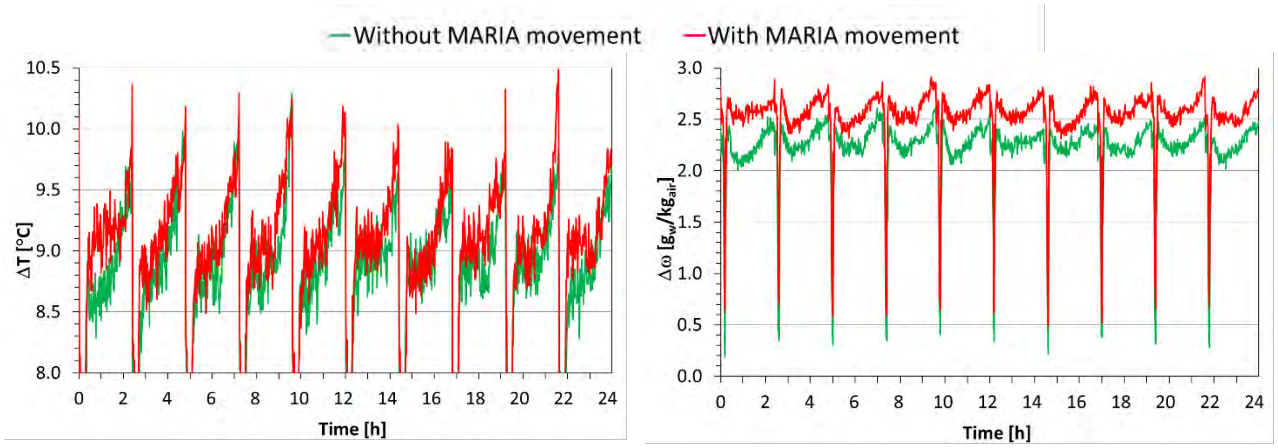

(a) Temperature difference: $\Delta T = T_{RAG}-T_{DAG}$ [ºC]. (b) Humidity difference: $\Delta \omega = \omega_{RAG}-\omega_{DAG}$ [g_w/kg_{air}].

Figure 3: Air temperature and humidity differences between RAG and DAG

Fig. 3 allows to detect the effect of defrost period on the air temperature and humidity. Since the evaporator defrost system is a heating coil placed inside the evaporator fins, when the system operates (set to 2h30m intervals), the air temperature and humidity at DAG increase in large amount. After the defrost system stop, the refrigeration system starts up and takes approximately 30 minutes to return air temperature and humidity to the proper values for the products conservation. MARIA moves around the VORDC during all testing period (refrigeration and defrost cycles). The objective of the experimental testing is to evaluate the increase of air temperature and humidity at DAG, RAG and conservation zone after 24 hours. During this period, the refrigerant flow and the enthalpies difference were measured/calculated. Thus, the influence on thermal performance of the parallel movement in front of the VORDC and consequent interference of the air curtain can be quantified. The values of air temperature and humidity at RAG show a small increase at end of the test period due to the translational movement of MARIA. The values of air temperature and humidity at DAG maintained approximately constant during the test period because the heat exchanger absorbs the heat gain of the air curtain due to external interferences. The thermal load was measured based on the refrigerant flow and enthalpies difference. The enthalpy difference increases from 5317 [W] to 5328 [W] (4.6%) due to perturbations, disturbances or interference with the air curtain of VORDC.

3.2. Numerical results

The numerical solution for evaluating the movement of MARIA at a constant velocity was developed in a single model with different movement and stopping times. The motion starts at t = 1sec after the start of the simulation for the movement opposite to the air flow in the climatic room (see Fig. 4 and Fig. 5). After reaching the other side the block stops for t = 1 sec and resumes the movement, now in the same direction of the room air flow. For each translation speed, a numerical model was developed, configured with the same dynamics described previously. This method presented some advantages, such as: (1) a single model corresponds to two Experimental Test; (2) reduction of the computational cost for the evaluation of the movement. In addition, the stopping time of t = 1 sec before the start of the movement, allows stabilization of the flow in steady state. Fig. 6 shows the displacements of MARIA in front of the VORDC, identified from 1 to 10. Fig. 6 describe the prediction of the evolution of temperature and thermal load along the RAG for the velocities of 0 $m{\cdot}s^{-1}$ to 0.8 $m{\cdot}s^{-1}$, with 0.2 $m{\cdot}s^{-1}$ steps. The time is divided by two as the velocity increases.

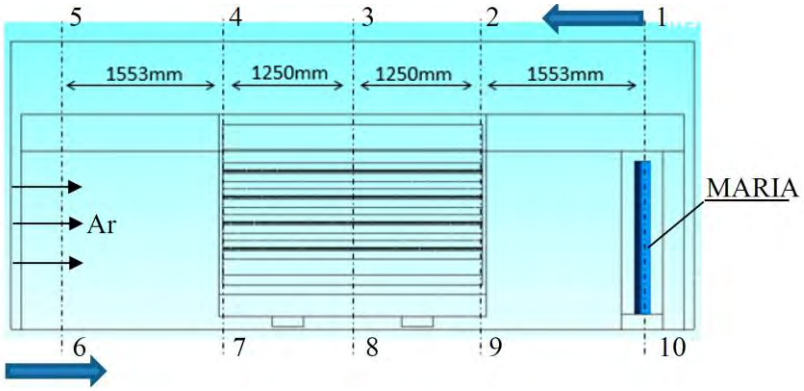

Figure 4: Displacements of MARIA in front of the VORDC

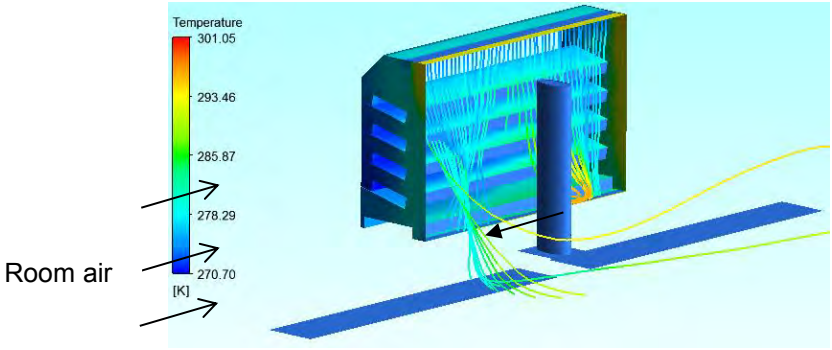

Figure 5: Streamline from the CAP to (t = 6.67s).

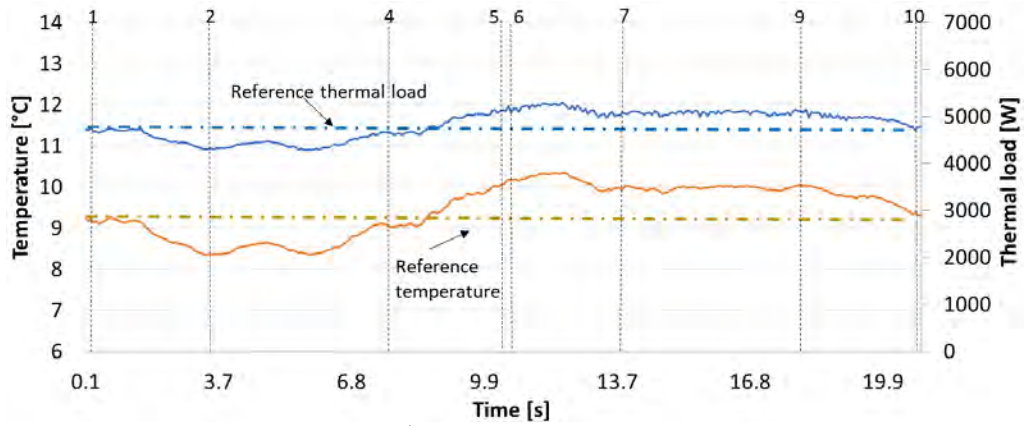

(a) MARIA at 0.0 m·s^{-1} (No movement in front of the VORDC).

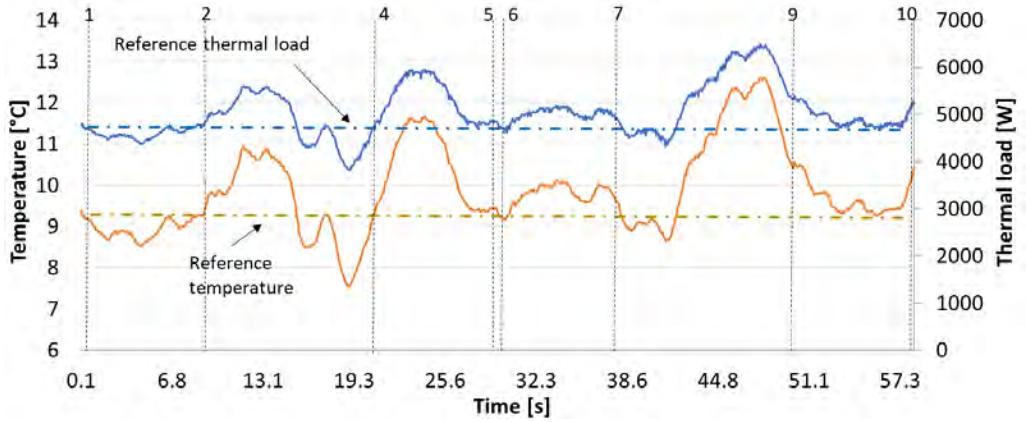

(b) MARIA at 0.2 m·s^{-1}.

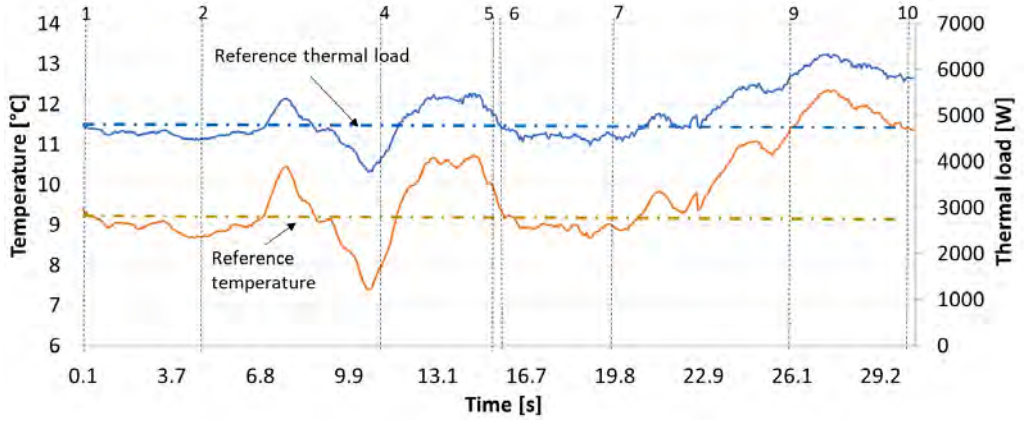

(c) MARIA at 0.4 m·s^{-1} (1/2 of total time).

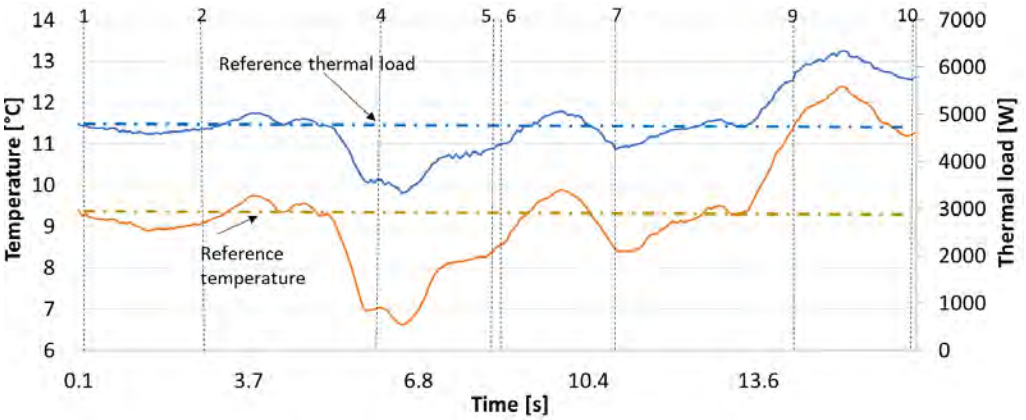

(d) MARIA at 0.8 m·s^{-1} (1/4 of total time).

Figure 6: Average temperature and thermal load at RAG

In all test cases of Fig. 6 it is possible to see that in the displacement of MARIA against flow, when it is close to point 4, the averages of temperatures and energy consumption tend to reduce in relation to the reference value, because at that point the solid body ends up blocking the air flow of the room and thereby reducing the effect of the external ambient air on the VORDC air curtain. Just after passing from point 4 to point 5, the room airflow again reaches the VORDC air curtain, generating an increase in temperature and energy consumption. The same effect occurs in the return of MARIA with a displacement in the same direction of the room airflow (points 7 to 9). In this case the arrival of the body at point 7 forms a barrier to the airflow of the room. As it approaches point 9, it leaves the air curtain subject to room airflow. In addition, the movement of the body causes drag and provides a large instability to the air curtain. In the same way, it is possible to observe that, with the increase of the transfer velocity, the reduction of the average temperature in the RAG is more acute, as the peaks of temperatures close to point 9 do not present large differences for the different velocities, being around 13.5°C. At that moment, the air curtain is in contact with the air flow of the room and not with MARIA. Fig. 7 shows the results of smoke injection technique to qualitatively evaluate the effect of the actual movement on the air curtain, providing an idea how the airflow is affected by the human transfer in front to VORDC.



Figure 7: Drag due to human displacement

4. CONCLUSIONS

This paper describes the performance results of a VORDC when subjected to external disturbances on the air curtain. With the robotic mannequin developed for this purpose, MARIA (Mannequin for Automatic Replication of the Interference in the Air curtain), it was possible to simulate systematically the movement of customers inside the store and quantify the increase of air temperature and thermal load due to this disturbance. It has been observed experimentally that the air temperature and humidity at RAG have a slight increase, approximately 0.2 °C and 0.4 $g_{water}/kg_{dry\ air}$. Thus, the air enthalpy is higher than in the case study without MARIA moving around the VORDC.

At supermarkets, there are several models of display cases, and all are subject to external interference due to customers transfer. This study allows to quantify for this condition, a thermal load increase of approximately 4.6%, which is for the model in study represents an increase of 210 [kcal/h]. In the numerical evaluation, it was possible to observe in more detail the effect of the MARIA movement for a single pass in front of the VORDC in different directions and velocities, showing that in the MARIA's movement opposite to the room airflow tends to contribute to the performance of the air curtain when it is close to point 4. The same occurs with the opposite direction movement. Instabilities were measured and predicted when MARIA approaches point 9, since the VORDC's air curtain is subject only to the room's airflow. Additionally, the turbulence generated by the drag due to the movement of MARIA also generates instability in the air curtain. Despite these instabilities in the air curtain, the temperature peak in the RAG reaches a value close to 13.5 °C for the 4 simulated velocities.

ACKNOWLEDGEMENTS

This work was fully supported by Eletrofrio Refrigeração. Authors thank Mr. Paulatti and Mr. Eng. Chueire for their continuous support and encouragement.

REFERENCES

ASHRAE. 2010. ASHRAE Handbook: Refrigeration. ASHRAE, Inc.

Cao, Z., Gu, B. Mills, G., Han, H., 2010. A novel strategy for predicting the performance of apen vertical refrigerated display cabinets based on the MTF model and ASVM algorithm, Int. J. of Refrigeration, 33(7), 1413-1424.

Cao, Z., Gu, B. Mills, G., Han, H., 2010. Application of an effective strategy for optimizing the design of air curtains for open vertical refrigerated display case, Int. J. Therm. Sci., 49(6), 976-983.

Cao, Z., Gu, G., Han, H., 2011. A novel optimization strategy for the design of air curtains for open vertical refrigerated display cases, Applied Thermal Engineering, 31(16), pp. 3098–3105.

Chen, Y., Yuan, X.-L., 2005. Simulation of a cavity insulated by a vertical single band cold air curtain, Energy Conversion and Management, 46(11-12), 1745-1756.

Chen, Y., 2009. Parametric evaluation of refrigerated air curtains for thermal insulation, International Journal of Thermal Sciences, 48(10), 1988-1996.

Chen, Y., Xia, D.H., 2011. The flow characteristics analyses of refrigerated air curtains in multi-deck display cabinets, International Congress of Refrigeration), 23rd ed., Pargue, Czech Republic.

Faramarzi, R., 1999. Efficient display case refrigeration, ASHRAE Journal, 41(11), 46–52.

Foster, A.M., Madge, M., Evans, J.A., 2005. The use of CFD to improve the performance of a chilled multi-deck retail display cabinet, International Journal of Refrigeration, 28(5), 698–705.

Gaspar, P.D., Gonçalves, L.C.C., Vogeli, A., 2009. Dependency of air curtain performance on discharge air velocity (grille and back panel) in open refrigerated display cabinets, ASME Int. Mechanical Engineering Congress and Exposition, Lake Buena Vista, Florida, U.S.A.

Gaspar, P.D., Gonçalves, L.C.C., Ge, X., 2010. CFD parametric study of ambient air velocity magnitude influence in thermal behaviour of open refrigerated display cabinets, European Conference on Computational Fluid Dynamics, 5rd ed., Lisbon, Portugal.

Gaspar, P.D., Gonçalves, L.C.C., Ge, X., 2010. Influence of ambient air velocity orientation in thermal behaviour of open refrigerated display cabinets, ASME 2010 10th Biennial Conference on Engineering Systems Desing and Analysis, Istanbul, Turkey, July.

Gaspar, P.D., Gonçalves, L.C.C., Pitarma, R.A., 2011. Experimental analysis of the thermal entrainment factor of air curtains in vertical open display cabinets for different ambient air conditions, Applied Thermal Engineering, 31(5), 961–969.

Gaspar, P.D., Gonçalves, L.C.C., Pitarma, R.A., 2011. Análise Experimental da estabilidade de cortinas de ar de equipamentos de refrigeração para diferentes condições do ar ambiente, International Conference on Engineering UBI2011, 28-30 Nov 2011, UBI, Covilhã, Portugal.

Hayes, F.C., Stoecker, W.F., 1969. Design data for air curtains, ASHRAE Trans., 75(2), 68-180.

Laguerre, O., Hoang, M.H., Flick, D., 2012. Heat transfer modelling in a refrigerated display cabinet: the influence of operating conditions, Journal of Food Engineering, 108(2), 353-364.

Navaz, H.K., Henderson, B.S., Faramarzi, R., Pourmovahed, A., Taugwalder F., 2005. Jet entrainment rate in air curtain of open refrigerated display cases, Int. J. Refrig, 28(2), 267–275.

Rigot, G. 1991, Meubles et Vitrines Frigorifiques, PYC DITION, París, France, 340p.

Yu, K., Ding, G., Chen, T., 2009. A correlation model of thermal entrainment factor for air curtain in a vertical open display cabinet, Applied Thermal Engineering, 29(14-15), 2904–2913.

Ge, Y.T and Tassou, S.A., 2001. Simulation of the performance of single jet air curtain for vertical display cabinets', Applied Thermal Engineering, 21, 201-219.

Wu, X., Chang, Z., Yuan, P., Lu, Y., Ma, Q., Yin, X., 2014. The optimization and effect of back panel structure on the performance of refrigerated display cabinet. Food Control, 40, 278-285.

Manuscript ID: 869
DOI:10.18462/iir.icr.2019.0869

Energy savings in supermarket using control theory

Min-Lun CHAI, Yen-Tin SHIEN, Wen-Der HSIEH
Green Energy and Environment Research Laboratories, Industrial Technology Research Institute Hsinchu, 31057, Taiwan, R.O.C., mlchai@itri.org.tw

ABSTRACT

The refrigeration and air conditioning (AC) systems in a typical supermarket account for 70% and 10% of total energy consumption of store, respectively. Generally, it is difficult to find the optimal store temperature for minimizing the total energy consumption of both systems and customers' comfortableness. This paper attempts to find the optimal set point through a developed control device installed in a typical supermarket. From the data acquisition system, the preliminary results show that the total energy consumption of both systems under coordinated control method is lower than that of 25℃ store temperature by 14%, and total energy consumption of store can be saved at least 5%. Since the store temperature cannot be decreased unlimitedly for consideration of customers' comfortableness. The future work has been conducting to find the optimal set point in the supermarket by using our developed control device.
Keywords: Energy savings, Energy consumption, Temperature, Supermarket, Display cases

1. INTRODUCTION

Refrigerated display cases are commonly used to keep chilled food at a lower temperature in a supermarket in Taiwan. Due to the high population density, the open display cases have been chosen instead of the closed type because there is no restriction between customers and goods. Despite the convenience of open display cases, the ambient infiltration would lead to high energy consumption because of the humid subtropical climate. According to the measurement data, the refrigeration and air conditioning systems in a supermarket accounts for approximately 70% and 10% of its total energy consumption. In order to lower the energy waste, the energy saving strategies should be carried out. Many studies have investigated the relation between indoor humidity and the energy consumption of refrigerated display cases. Howell and Adams (1991) studied the effects of indoor space conditions on refrigerated display case performance. Howell (1993) evaluated the effects of relative humidity in typical food retail store and the result showed that for a 5% reduction in store relative humidity, the display case refrigeration load is reduced by 9.25%. Orphelin (1999) et al. discussed a novel method in typical French supermarkets. They estimated the impacts of temperature and humidity set points on the total energy balance. The result showed that the acceptable set point in terms of energy consumption and customer comfort would be calculated by the well-known performance of air-conditioning and refrigeration systems. Latuerre et al. (2012) studied the effects of temperature changes inside the display cases with increasing room temperature, which was controlled at 20°C, 25°C and 30°C. The results showed that higher room temperature led to the higher product and air temperatures in a display case, which means that the heterogeneity would be influenced by the manufacturing design and the ambient condition. Chen et al. (2005) studied the relationship between ambient temperature and the temperature inside the refrigerated display cases. The results showed that increasing ambient temperature would not only increase the temperature of the cases but also cause the rising of supplied and returned air temperature. Yoshida et al. (2018) analyzed the heat load in the supermarket by CFD. The results showed that when reducing the set temperature from 28°C to 19°C, the heat load of display cases and the total heat load of display cases and air conditioning would decrease 21% and 11%, respectively. Previous studies showed that the lowering room condition would increase the energy consumption of air

conditioning, but reduce the heat load of the refrigeration system in some specific field. However, because each store has a unique layout and ambient condition, it is difficult to find a general temperature set point. Therefore, a coordinated control device which can be utilized in any supermarket was constructed.

2. EXPEMENTAL METHOD

The energy consumption of the refrigeration system is directly related to the refrigeration load, which consists mainly of air infiltration through the open front of the case, heat conduction through case panels and walls and thermal radiation from the ambient to the display case.[7] Fig. 1 showed that the air infiltration is the most significant part of heat load in the open display case, which is resulted by the temperature difference between room temperature and the temperature inside the refrigeration display cases.

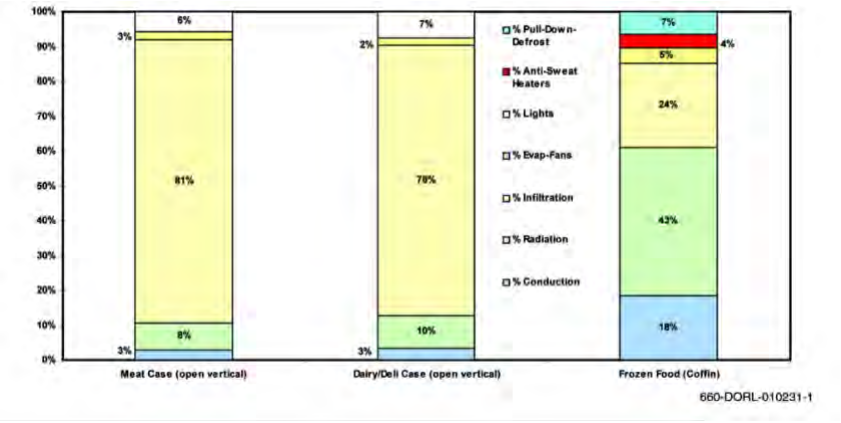

Figure 1: Refrigeration load percentage breakdown for meat, dairy and frozen food display cases (Walker et al., 2004)

In order to simulate the interaction of display cases and room conditions, several assumptions were proposed. First, we assumed that there was a steady-state and isolated 270 m^3 room, which would not transfer the heat by the convection, radiation, and conduction from the room to the ambient. Second, in order to simulate the ambient air infiltration from outdoor, an air change rate (ACH) of 20 had been chosen. The heat load caused by the air change was calculated by the equation 1.

$$q_{air\ change} = V \times \rho \times C_{p,air} \times (T_{ambient} - T_{room}) \quad \text{eq. (1)}$$

Third, the refrigeration load of each display cases was 2 kW at 26°C and would vary by the heat transfer formula in Table 1. All the coefficients of heat transfer were calculated by the refrigeration load percentage, display case temperature, and room temperature. The last assumption is that the refrigeration leakage from the display cases to the room was assumed as 80% of the refrigeration load. And the full refrigeration load of a single display case at different room temperature was shown in Fig. 2.

Table 1. Heat transfer formula

Refrigeration Load	Percentage (ORNL)	Heat Transfer Formula	
Convection	80 %	Newton's law	$q_{cov} = h\,(T_{room} - T_{case})$
Radiation	10 %	Stefan–Boltzmann law	$q_{rad} = \sigma\epsilon\left({T_{room}}^4 - {T_{case}}^4\right)$
Conduction	3 %	Fourier's law	$q_{con} = k\frac{(T_{room} - T_{case})}{x}$
Heat loss from electricity equipment	7 %	-	$q_{equip} = q_{fan} + q_{light} + \cdots$

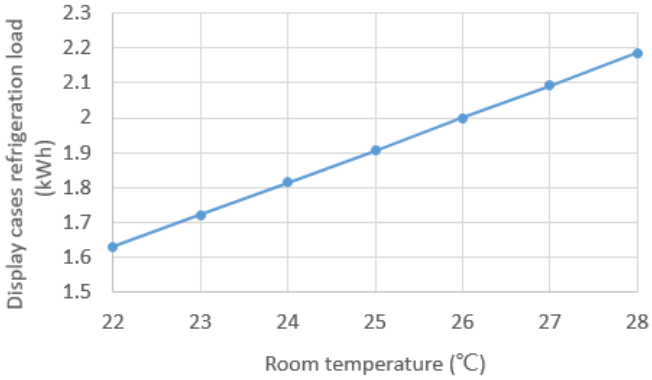

Figure 2: Refrigeration load of display case at different room temperature

Two simple cases with 5 and 10 open display cases were considered to verify the effects on energy savings. Outdoor temperature was range from 26°C to 34°C and the room temperature, which was controlled by air conditioning temperature setpoint, was range from 22°C to 28°C. As we all know, the heat load is proportional to the temperature difference and when the ambient temperature increases, the heat load increases as well. For example, if the room temperature was fixed at 22°C when the ambient temperature increased from 26°C to 34°C, the heat load would significantly rise from 8 kWh to 24 kWh.

Table 2. Refrigeration load (kWh) of the 270 m³ room with 20ACH

T_{room} \ $T_{ambient}$	26	28	30	32	34
22	8.01	12.02	16.02	20.03	24.03
23	6.01	10.01	14.02	18.02	22.03
24	4.01	8.01	12.02	16.02	20.03
25	2.00	6.01	10.01	14.02	18.02
26	-	4.01	8.01	12.02	16.02
27	-	2.00	6.01	10.01	14.02
28	-	-	4.01	8.01	12.02

Considered the spillage of the cold air from the open display cases, part of the cooling demand was shared by the open display cases. In other words, the refrigeration contribution of air conditioning became lower. In several conditions, because the refrigeration leakage was more than the refrigeration demand, the air conditioning would not need to operate. The refrigeration load of air conditioning in each condition was shown in Table 3.

Table 3. Refrigeration load (kWh) of air conditioning with 5 display cases (Case 1)

T_{room} \ $T_{ambient}$	26	28	30	32	34
22	1.49	5.49	9.50	13.50	17.51
23	0.00	3.12	7.13	11.13	15.14
24	0.00	0.75	4.76	8.76	12.77
25	0.00	0.00	2.39	6.39	10.40
26	-	0.00	0.01	4.02	8.02
27	-	0.00	0.00	1.65	5.65
28	-	-	0.00	0.00	3.28

To calculate the total energy consumption, the COP of air conditioning and display cases were assumed as 3.6 and 1.6, respectively. Table 4 showed the total energy consumption in case 1 and Table 5 showed the result in case 2. In case 1, the best room temperature set point was 24°C when the ambient temperature was at 28°C, but in case 2, the optimal set point was 22°C at the same outdoor temperature which was resulted from the different amount of refrigeration leakage. As we can see, every ambient temperature would have its own energy conservation set point and the energy would waste at most 34% if the temperature was controlled at the wrong condition.

Table 4. Total energy consumption (kWh) in Case 1 (5 display cases)

T_{room} \ $T_{ambient}$	26	28	30	32	34
22	5.51	6.62	7.73	8.85	9.96
23	5.38	6.25	7.36	8.47	9.59
24	5.67	5.88	6.99	8.10	9.22
25	5.96	5.96	6.62	7.73	8.85
26	6.25	6.25	6.25	7.36	8.48
27	6.54	6.54	6.54	6.99	8.11
28	6.83	6.83	6.83	6.83	7.74

Table 5. Total energy consumption (kWh) in Case 2 (10 display cases)

T_{room} \ $T_{ambient}$	26	28	30	32	34
22	10.19	9.90	11.02	12.13	13.24
23	10.76	10.76	10.83	11.94	13.06
24	11.34	11.34	11.34	11.76	12.87
25	11.92	11.92	11.92	11.57	12.69
26	12.49	12.49	12.49	12.49	12.50
27	13.07	13.07	13.07	13.07	13.07
28	13.65	13.65	13.65	13.65	13.65

According to the results of the simulation, it is impossible to have an optimal temperature set points without enough information of the store layout, devices performance and the outdoor temperature. In order to deal with the difficulty, a coordinate control method had been investigated.

3. COORDINATE CONTROL PROCESS

The basic process was proposed to minimize the total energy consumption of refrigeration and air conditioning by measuring the outdoor temperature and power consumption.

1. Measure the ambient temperature and the total power consumption of the air conditioner and the display cases in time interval A. (such as 10 minutes)
2. If the ambient temperature difference is smaller than the temperature setting interval dT, air conditioning operates the cooling operation. And if the ambient temperature difference is greater than the temperature setting interval dT, the operation would be decided by the previous data and the ambient temperature.
3. Calculate the total power consumption of the air conditioner and the display cases in time interval B.
4. If the sum of the power consumption in time interval B is smaller than the power consumption in time interval A, which means the cooling operation can save some energy and the cooling operation will be continued.
5. If the sum of the power consumption in time interval B is greater than the power consumption

in time interval A, which means the cooling operation wastes more energy and the cooling operation will be replaced by the heating operation.

6. Repeatedly run the upper cycle to make the total power consumption minimize.

4. RESULTS and DISCUSSION

First, a coordinated control device consists of at least two wattmeters were constructed to verify the coordinate control hypothesis could be utilized in a real field, a food retail store with 5 open display cases and 3 independently controlled 5RT air conditioner was chosen. The results in Fig. 3 showed that when setting the air conditioning temperature at 25 °C, the total power consumption was around 65 kWh. But when reducing 1°C of the set temperature, the total power consumption was 54kWh, which had a 17% reduction of energy usage. This short-term test had proved that decreasing the setting temperature would have a positive effect on energy saving in a store with open display cases.

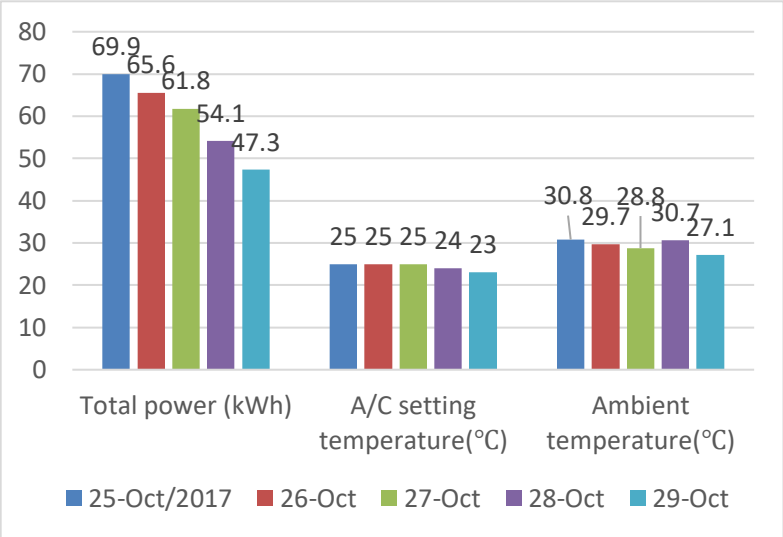

Figure 3: Total energy consumption data and temperature in a food retail store

After the small store test, a supermarket which contains 12 open display cases were selected to be the test field. The layout of the supermarket was displayed in Fig. 4. The entrance and exit were at the bottom side and the open display cases were marked in yellow at the right-hand side in the figure. Because the arrangement of the display cases was in the same area, the coordinate control device only controlled the air conditioners near the display cases. Figure 5 showed the total power consumption from July 14 to July 31 and Table 6 showed the outdoor conditions and power consumption. The coordinated control device operated 5 days and then turned off to compare the energy saving rate. When using coordinated control method, the air conditioner temperature setpoint automatically controlled at 22°C to 27°C and the average total power consumption was 811.8 kWh/day. When using the normal control method at 25°C, the operation time of the air conditioner decreased as well as the air conditioner power consumption. However, the average energy consumption of the refrigeration increased from 691 to 854 kWh/day and the total energy consumption increased about 14%, which means the coordinate control device worked well and had a 14% energy saving potential.

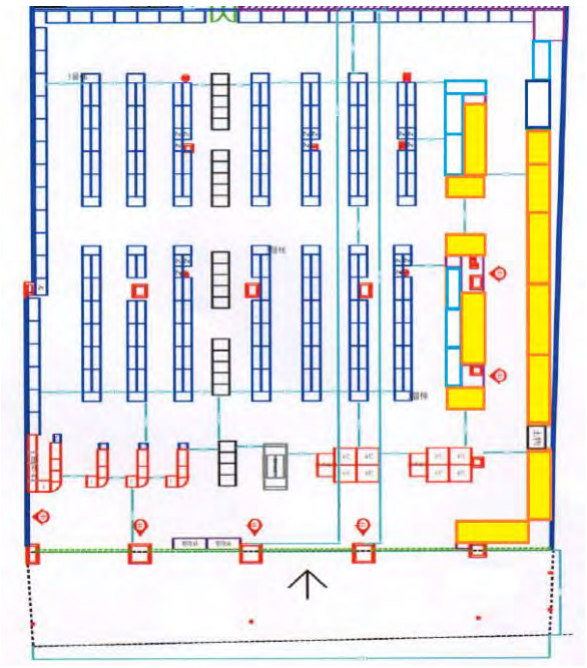

Figure 4: Layout of the supermarket

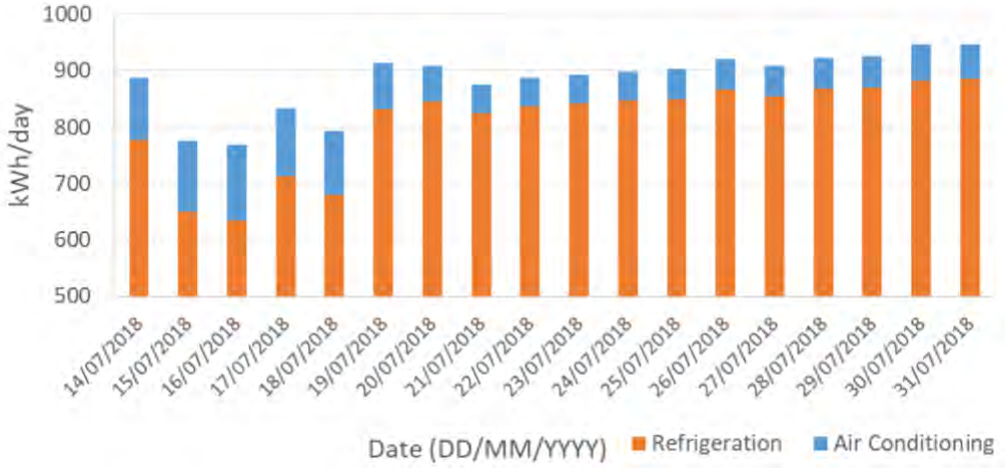

Figure 5: Energy consumption of the supermarket measuring data

Table 6. Outdoor conditions and power consumption

Date	Avg. Outdoor Condition		Power Consumption(kWh)			Using Controller
	Temperature (℃)	Humidity (%RH)	Air Conditioning	Refrigeration	Total	
14/07/2018	28.5	73	111	777	888	YES
15/07/2018	28.2	73	124	651	775	YES
16/07/2018	29	70	134	635	769	YES
17/07/2018	30	69	121	713	834	YES
18/07/2018	29.9	67	114	679	793	YES
19/07/2018	30.2	66	82	831	913	NO
20/07/2018	29	69	62	846	908	NO
21/07/2018	26.8	80	51	825	876	NO
22/07/2018	26.9	82	50	837	887	NO
23/07/2018	27.6	79	50	842	892	NO

5. CONCLUSIONS

Every store had a unique layout and ambient condition, so it was difficult to find a general optimal temperature. The coordinate control devices were invented to solve the problem and were conducted to verify the energy performance of the proposed energy saving in the supermarket. The simulation and the field test verified the hypothesis of the coordinate control method. And the results above showed that the coordinate control device was reliable and was able to lead to energy saving up to 14% by automatically control the air conditioner temperature set point. To sum up, the coordinate control device would be one of the energy-saving methods to improve energy usage in supermarkets.

ACKNOWLEDGEMENTS

The authors would like to thank the Bureau of Energy of the Ministry of Economic Affairs of Taiwan for sponsoring this research work.

NOMENCLATURE

q	Heat flux (kW)	ρ	Air density($kg \cdot m^{-3}$)
C_p	Specific Heat Capacity ($kJ \cdot kg^{-1} \cdot K^{-1}$)	V	Volume (m^3)
T	Temperature (℃)	h	Heat transfer coefficient ($W \cdot m^{-2} \cdot K^{-1}$)
σ	Stefan–Boltzmann constant (5.67×10^{-8} $W \cdot m^{-2} \cdot K^{-4}$)	ϵ	emissivity
k	Thermal conductivity ($W \cdot m^{-1} \cdot K^{-1}$)	x	Material thickness (m)

REFERENCES

Howell, R.H., Adams, P.A., 1991. Effects of indoor space conditions on refrigerated display case performance. Final report, ASHRAE-596 RP.

Howell, R.H., 1993. Effects of store relative humidity on refrigerated display case performance. ASHRAE Trans 1993;99(1):667–78.

Orphelin, M., Marchio, D., D'Alanzo, S.L.,1999. Are there optimum temperature and humidity set points for supermarkets? ASHRAE Trans 1999;105(1):497–507.

Laguerre, O., Hoang, M. H., Flick, D., 2012. Heat transfer modelling in a refrigerated display cabinet: the influence of operating conditions. Journal of Food Engineering, 108(2), 353-364.

Chen, Y.G, Yuan, X.L., 2005. Experimental study of the performance of single-band air curtains for a multi-deck refrigerated display cabinet. Journal of Food Engineering, 69(3), 261-267.

Yoshida, K., Fujita, Chen, W., M., Narumi, D., 2018. Energy saving of cold air leakage in showcases by CFD analysis. Research Report of the Kanto Branch Department of the Architectural Institute of Japan in 2017. (transfer from Japanese)

Walker, D.H., Faramarzi, R.T., Baxter, V.D., 2004. Investigation of Energy-Efficient Supermarket Display Cases. ORNL/TM-2004/292.

Manuscript ID: 983
DOI: 10.18462/iir.icr.2019.0983

Characterization of refrigeration systems in the Portuguese food processing industry

Diogo MORAIS[(a)], Pedro D. GASPAR[(a,b)], Pedro D. SILVA[(a,b)], Luís C. PIRES[(a)], Luís P. ANDRADE[(c,d,e)], José NUNES[(c)]

[(a)] University of Beira Interior, Rua Marquês d'Ávila e Bolama, 6201-001, Covilhã, Portugal, dinho@ubi.pt
[(b)] C-MAST - Centre for Mechanical and Aerospace Science and Technologies, Covilhã, Portugal, dinis@ubi.pt
[(c)] Agriculture School, Polytechnic Institute of Castelo Branco, Quinta da Senhora de Mercoles, 6001-909 Castelo Branco, Portugal, jnunes@ipcb.pt
[(d)] CATAA - Food Technology Support Center, Centro de Apoio Tecnológico Agro Alimentar, Castelo Branco, Portugal, luispa@ipcb.pt
[(e)] CERNAS – Centro de Estudos em Recursos Naturais, Ambiente e Sociedade, Castelo Branco, Portugal, luispa@ipcb.pt

ABSTRACT

This paper presents the results of audits performed in 60 companies of the food processing industry, specifically of meat, dairy, horticultural and bread products. The refrigeration volume, type of refrigeration system, refrigerant, building and insulation materials of infrastructure and refrigeration chambers, average air temperature and humidity, and the energy consumption are presented, compared and discussed per sector. The analysis allows to provide several measures and best practices aimed for the improvement of the thermal performance and energy efficiency of the food processing industry. The implementation of simple and very cost-effective transversal electricity savings measures such as awareness and/or training of operators, proper maintenance and monitoring tasks can benefit the sector. Tailored energy efficiency measures by sector, which may offer savings on several levels, are discussed. These best practices may increase productivity and competitiveness and reduce the environmental impact, and thus improve the global sustainability of the Portuguese food sector.
Keywords: Food Processing Industry, Characterization, Refrigeration System, Audit, Best Practices.

1. INTRODUCTION

The world's population is increasing, and with it also increases the need to produce more food. According to forecasts of the Food and Agriculture Organization of the United Nations (FAO), the global food production will increase by 70 percent to sustain the world population expected to reach 9 billion by the year 2050 (Morais et al., 2018). Currently, the food industry still faces many losses during the food chain, in part due to the unproper conservation conditions to which products are subjected. It is estimated that one-third of all food produced is lost during the steps preceding the final consumption (Gustavsson et al., 2011). For companies in the agro-food sector, these losses are sometimes crucial for their continuity in the market. In the case of Portugal, the manufacturing industry is made up mostly of small and medium-sized enterprises (SMEs), representing, in 2016, 11% of the country's economic activity. Given its economic characteristics, it is essential for SMEs to minimize the ratio between the produced and lost product.
Another factor that also has a high weight in the continuity of a company is the energy bill. The equipment used in the agro-industry requires more energy to operate due to its characteristics, and without the correct utilization, the energy consumption will be greater. For example, one of the main reasons for the high energy consumption in the conservation chambers is the considerable thermal load caused by infiltration of the surrounding air while the doors are open (Gil-Lopez et al.,

2013). In order to reduce this expense, it is necessary to adopt measures that aim at operational efficiency. Energy efficiency measures can go from simple and costless measures to measures that require an initial investment, but which translate into a surprising reduction of long-term energy expenditure. One way to assess the energy efficiency of an industry is through energy indicators, which aim to gain an understanding of the major techno-economic influences in industry's final energy consumption, and in individual sub-industries or industries (Morais et al., 2018). Food quality control is necessary, both to protect the consumer against disease and to maximize the efficiency of the food industry (Ghaani et al., 2016). However, as in case of food storage in controlled environment chambers, the energy consumption could result very high especially when these devices are not optimally designed.This article characterizes the refrigeration systems of the food processing industry in Portugal, based on an audit conducted to 60 companies under the project +AGRO (www.maisagro.pt).

2. ENERGY EFFICIENCY

The term "efficiency" describes, according to Hordeski (2005), the capacity of equipment that operate in cycles or processes, to produce the expected results. In a physical view, the concept of "efficiency" would be limited to processes in which there is energy conversion and in which the initial and final forms are visible or perceptible - kinetic, potential and electric energy. In a simpler way, energy efficiency can be defined as the ratio between the amount of final energy used and a produced good or service performed. The technologies around energy efficiency are a way to reduce the energy consumption without change services or consumer's behavior (Pradella *et al.,* 2017). There are two sets of energy efficiency measures that can be applied, being classified as transversal measures and specific measures, oriented to each type of industry. The transverse measures translate four groups of technological performance: Electric Motors, Heat and Cold Production, Lighting, Industrial Process Efficiency and Other Measures not specified. (Evans & Gigiel, 2007, Evans & Gigiel, 2010, Evans *et al*., 2014). Surveys demonstrated that energy savings of about 30-40% were achievable by optimizing usage of stores, repairing current equipment and retrofitting of energy efficient equipment (Evans *et al*., 2014b).
For practical use of these indicators it is necessary to simplify the presentation by constructing the corresponding aggregates for most structural effects. Structural changes, the effects of international trade and permanent changes in energy consumption are mainly driven by improvements in efficiency. These improvements can be explained mainly by various technological changes, as well as influenced by other factors:

- Changes in technical efficiency;
- Replacement of technological processes;
- Changes in the manufacturing process used, (e.g., dry-path wet-making ceramics or vice-versa) that reduces the process energy consumption.

3. METHODOLOGY

The present study is a summary of the main results of an activity of project +AGRO: Organizational, Energy and Occupational Health and Safety Qualifications in the AgriFood Industry (Project 04 / SIAC / 2015 – SIAC 16159) (www.maisagro.pt) (Gaspar et al., 2018). The Project +AGRO aims to qualify SMEs in the agri-food sector, namely in the product subsectors of Meat, Horticultural, Dairy and Bread/Bakery products. The project focused in three topics of upmost important for the competitiveness of the agri-food processing industries: Occupational Safety and Health (OSH): Energy efficiency; and Organizational management of the productive processes. The project activities included the characterization of these topics in each subsector. The results of audits conducted to characterize the subsectors were used to develop a set of computational tools based on ICT as well as to develop specific good practices tools to reduce the inefficiencies.
Companies were contacted to explain the objectives of the study and what was intended with their participation. After the first contact, it was necessary to visit all the facilities to present the project in a more dynamic and interactive way, allowing to know the dynamics of the company.
To carry out the initial information collection, a data collection model was developed that reflected the current characteristics of the company / industry.

Objectives: To carry out a general characterization and an energetic characterization of the companies under study.
Sample: The data collection model was applied to 60 agri-food companies from 4 different subsectors: Meat, Horticultural, Dairy and Bread/Bakery products.
Variables: The following variables were analyzed: Chamber volume, material used for thermal insulation and flooring, air temperature and humidity and energy consumption.
Method of Collection: Personally, through meetings marked with the companies surveyed, and using appropriate equipment.
In order to maintain the privacy of the companies, a numerical codification was adopted and assigned to each company according to the sector of operation and the region.
In the energy characterization component of each company, it was necessary the installation of energy analyzers in the electric boards, which allowed the acquisition of the necessary data for the elaboration of the study. For refrigeration and freezing equipment, the data collected concern the temperature and humidity inside the chambers. To obtain the data, the following equipment was used: Individual Protective Equipments; Clamp meter; Multimeter; Power analyzers; Multicontacts; Infrared Distance Meter; Camera; Thermographic camera; Other general tools. Data were also required from companies, such as:

- Energy consumption (electricity, heating oil, natural gas, propane gas, firewood, naphtha, pellets, others);
- Characteristics of tariffs and consumption of electricity;
- Infrastructures (plant location);
- Features with heat generators;
- Disaggregation of the consumption of electric energy;
- Characteristics of cold rooms;
- Specification of cooling systems.

4. RESULTS

Based on the audits results, it was possible to characterize the refrigeration systems used in the Portuguese food processing industry. The sectors with the highest volume in the conservation chambers, as shown in Fig. 1, are the meats and dairy sectors, with an approximate average of 80 m^3, followed by the bakery sector (20 m^3) and the horticultural sector (8 m^3).

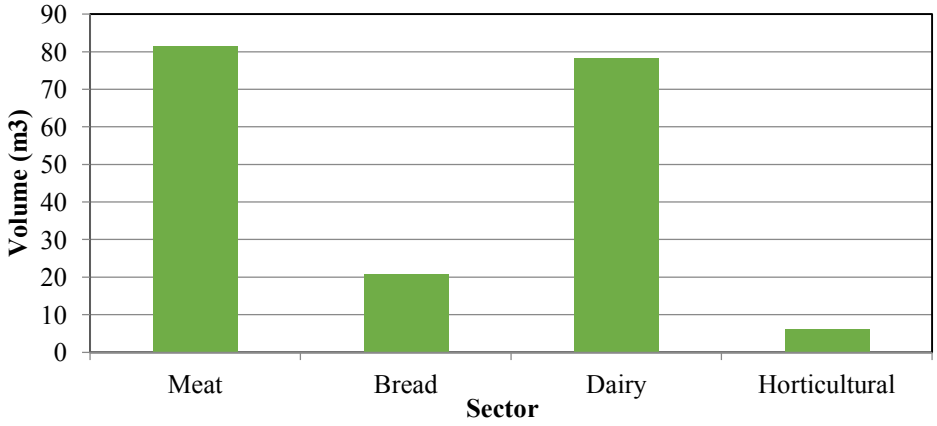

Figure 1: Average volume of chambers by sector

80% of the conservation chambers use thermal insulation panels, as shown in Fig. 2. A correct choice of materials used in the construction of the chambers is the first step to increase energy efficiency. Inherent in this choice are factors such as the method of manufacture and the necessary investment that sometimes prove to be obstacles to business.

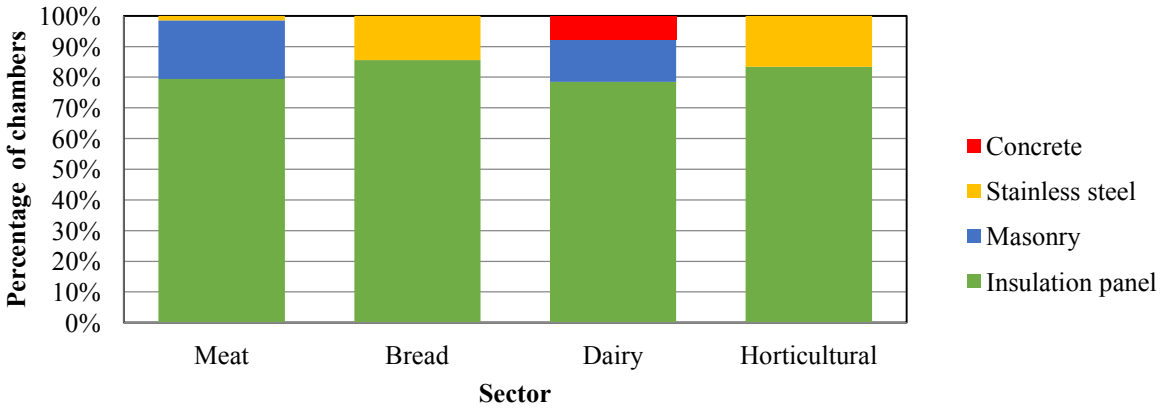

Figure 2: Material used in the construction of chambers of refrigeration and freezing

For the coating of the chambers, the choice fell to the concrete with 75% of use. From Fig. 3, it is still possible to verify that the horticultural sector is the one that presents a greater use of thermal insulation panels for the coating of the chambers.

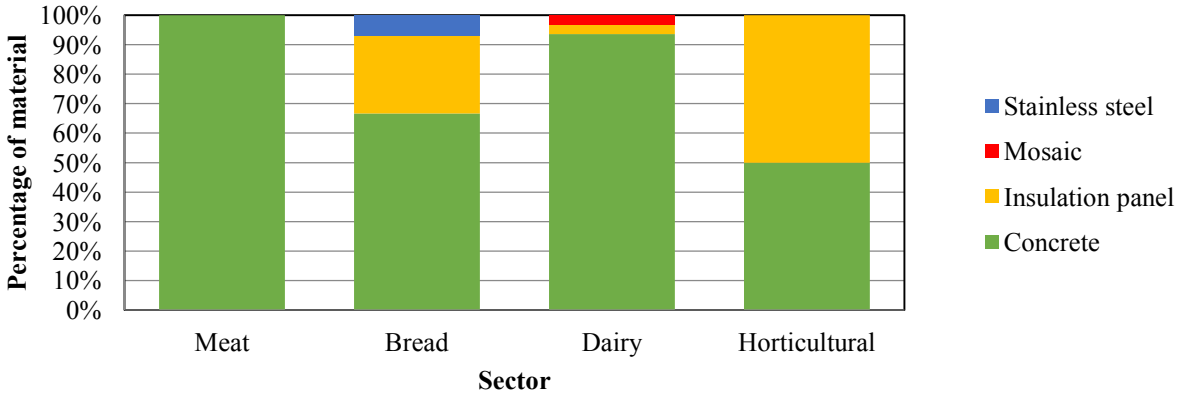

Figure 3: Material chosen for the coating of chambers

The thermal insulation materials employed, with approximately 85% use of the polyurethane, is shown in Fig. 4. In the sectors of the bakery and horticultural is the insulation of choice. On the other hand, about 20% of the companies surveyed in the dairy sector do not have any thermal insulation inside the chambers. In this situation it will be expected a higher thermal load and, consequently, a greater difficulty of the refrigeration equipment to maintain the temperature inside the chamber.

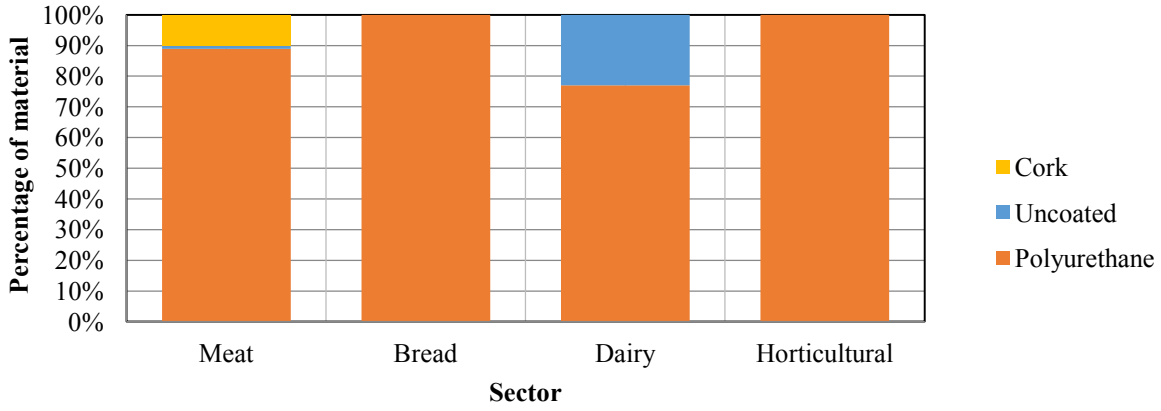

Figure 4: Thermal insulation materials used in chambers

The type of refrigerant used in refrigeration systems was also evaluated. It can be seen from Fig. 5 that industries still resort to fluids that have been banned, such as R22 (6%). There is also a great use of R404A (75%), which according to the Food & Drink Federation, will be banned from the Market in early 2020 because of its GWP (Global Warming Potential) value. Thus, this is a very important insight in the characterization, because the Portuguese agri-food industry must start to retrofit their cooling systems to adopt alternative refrigerants.

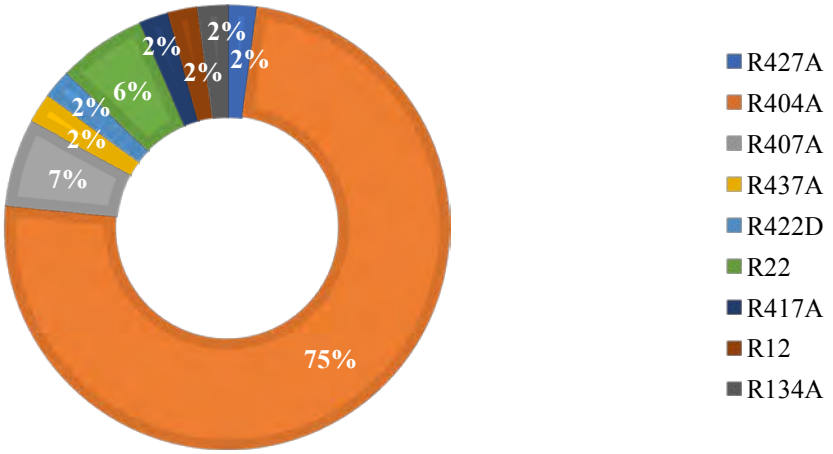

Figure 5: Breakdown of the type of Refrigerant (%)

Regarding the environment inside the chambers, as shown in Fig. 6, there is a high variation between the minimum and maximum values of air temperature, especially in the meat and bakery sectors. This air temperature range force the refrigeration equipment to work almost continuously resulting in higher values of energy consumption. Fig. 7 shows the average measured values of air relative humidity.

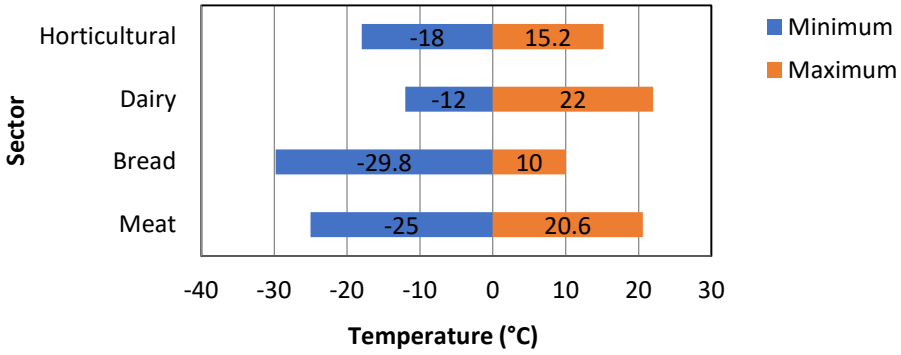

Figure 6: Range of temperature values inside the chambers, per sector

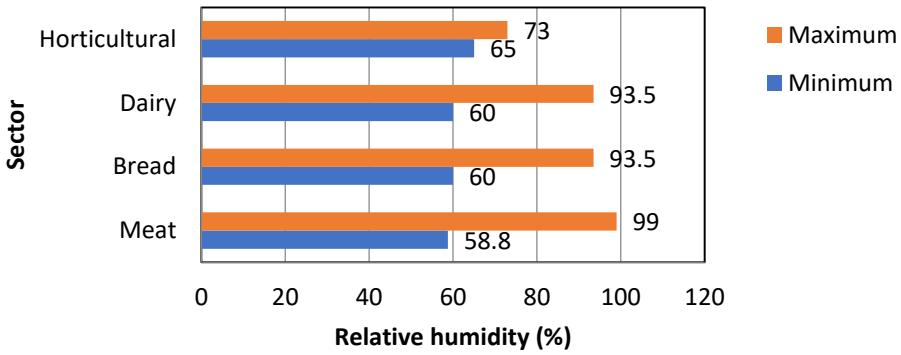

Figure 7: Range of relative humidity values inside the chambers, per sector

Depending on the needs of each sector, different refrigeration systems are adopted. Approximately 50% of the systems used in the different sectors are of the “individual” type, being the choice of all companies in the horticultural sector, as shown in Fig. 8. This individuals’ systems are constituted by a compressor, a condenser, an expansion valve and an evaporator.

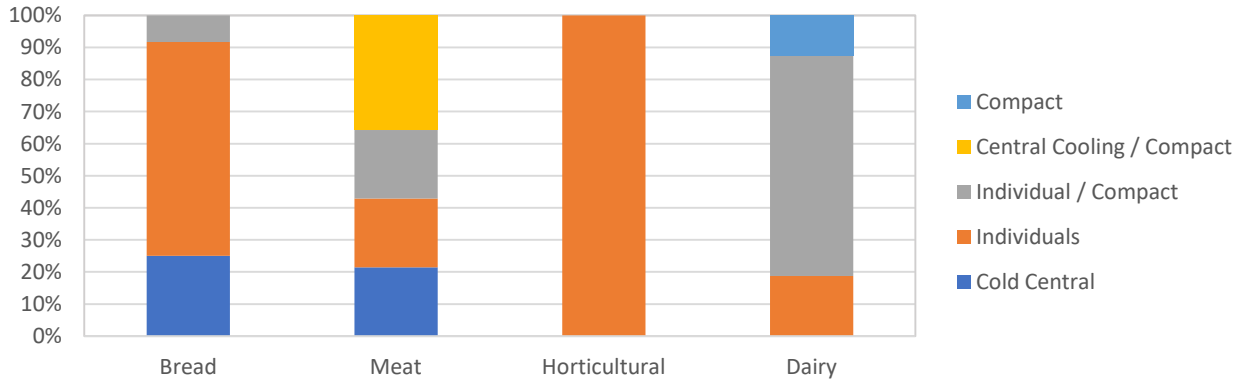

Figure 8: Types of Refrigeration systems, per sector [%].

Due to the chambers characteristics, it’s necessary to have artificial light to provide the necessary work conditions to operators, so, illumination is another important factor when it comes to efficiency in industries (Sudhir, 2016). The most used lighting systems is the fluorescent type, as you can see in Figure 9, whose efficiency is very poor when compared with LED

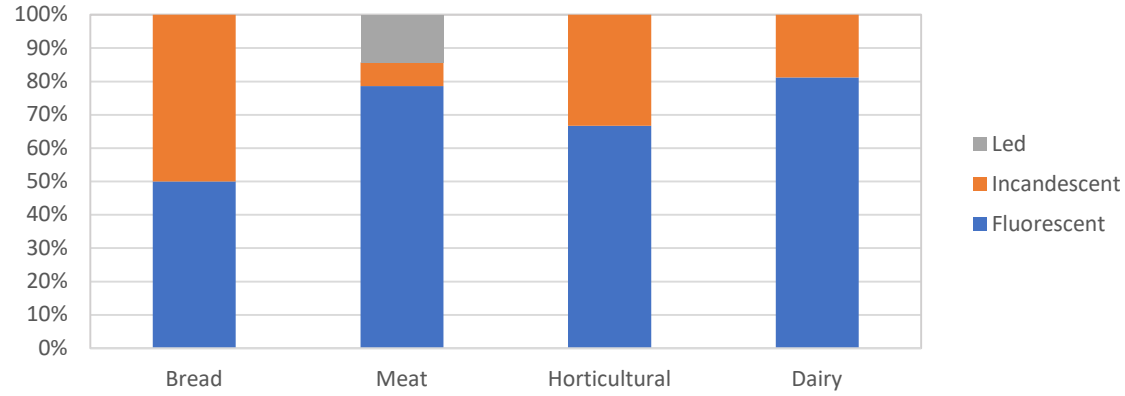

Figure 9: Illumination used inside the refrigeration chambers, per sector (%)

The examination of Fig. 10, where the energy expenses by energy source is presented, shows that the preference for renewable sources is not yet part of the choices of the sectors under analysis, perhaps justified by the higher investment required by new equipment acquisition. However, between January and July 2018, 58% of the electricity produced in Portugal came from renewable sources (APREN, 2018).

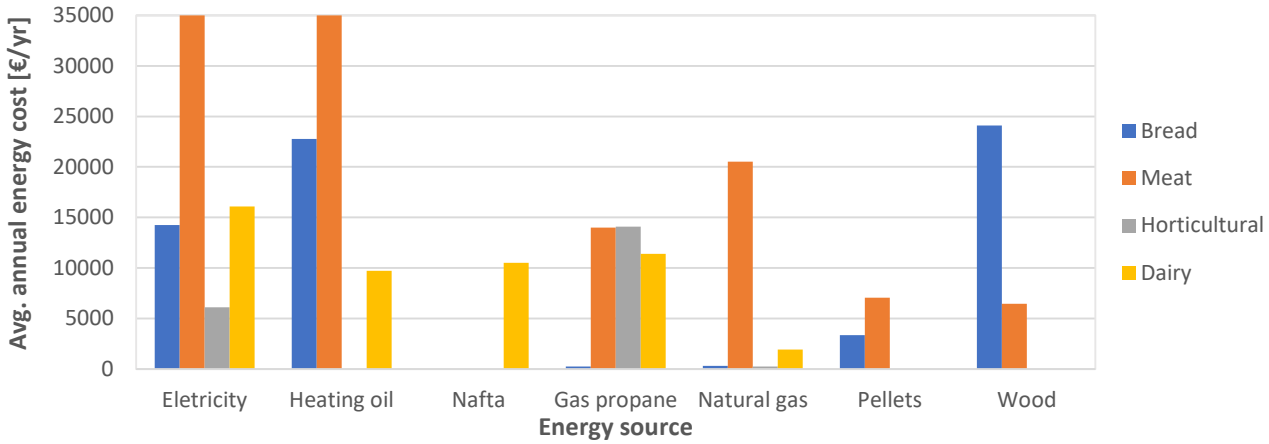

Figure 10: Average annual energy cost per energy source (€/year)

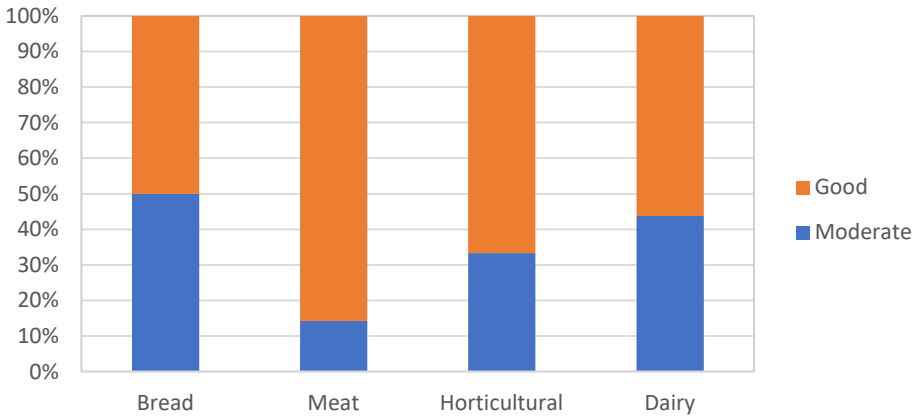

Figure 11: Storage conditions of cold rooms, by sector

Based on the results obtained, the storage conditions in the Portuguese food processing industries can be classified as good, in Fig. 11. The bakery sector has a lower classification compared to the meat, horticulture or dairy sectors.

5. CONCLUSIONS

The present study aims to characterize the refrigeration systems used in the different food sectors in Portugal, based on efficiency. Similar studies were carried out by Bastos et al. (2013), Gaspar et al. (2013), Nunes et al., (2014, 2015) and Morais et al., (2018), . It turns out that obtaining electricity for the operation of the equipment still comes from most fossil sources, which contributes to the increase of carbon dioxide emissions to the atmosphere. With the increase in the demand for food, it is necessary to maximize the conservation processes, namely the refrigeration chambers and the first step is through the analysis of the energy consumptions and the conditions of construction. Approximately 80% of the industries use insulation panels and a good thermal insulation for the construction of the chambers, showing concern for the chambers construction and structure as well as its insulation properties. Regarding the material used for coating, many companies opt for the concrete.

The measured temperatures present a large amplitude, indicating thermal losses. These losses can be caused not only by the incorrect sizing of the chamber and the refrigeration system for the product to be conserved, but also by the logistics processes, such as the opening of doors. The use of LED lighting is also not yet a 100% adopted by industries, as shown in Figure 9, which contributes to the decrease in the efficiency of the chambers. Concerning the refrigeration systems, some of the refrigerating fluids used have already been banned from circulation and others will be banned in the next 2 years. Changing fluids sometimes involves retrofitting or replacing the equipment, which is associated with a cost that is not always tolerable for SMEs, but which is mandatory for those seeking to maximize manufacturing processes. Secondly, some freezing/refrigeration equipment is not always sized for the effect in question, having implications in the thermal load to which they will be subject and therefore, the amount of energy that they use. From Figure 10 it can be concluded that the meat industry is the one that spends most on energy, with approximately 100 000 €/year (average per plant), and is due in part to the nominal power that the equipment has to ensure freezing temperatures.

The state in which the chambers of refrigeration of the different sectors are in general, can be evaluated like good.

ACKNOWLEDGEMENTS

This study is within the activities of project Project +Agro: Organizational, Energy and Occupational Health and Safety qualifications in the AgriFood Industry (Project 04 / SIAC / 2015 – SIAC 16159) promoted by COMPETE2020 and co-financed by FEDER under the Portugal 2020 initiative.

REFERENCES

APREN. 2018. Boletim Energias Renováveis – Boletim Mensal julho de 2018. - Associação de Energias Renováveis.

Ayres, R. U., Turton, H., & Casten, T. 2007. Energy efficiency, sustainability and economic growth. Energy, 32(5), 634–648.

Bastos, E., Cruz, A., Silva, P.D., Gaspar, P.D. 2013. Caracterização dos consumos de energia eléctrica dos sistemas de refrigeração de empresas no setor agroindustrial - Beira Interior Norte. Int. Conference on Engineering ICEUBI 2013, Covilhã, Portugal.

Brito, P., Lopes, P., Reis, P., & Alves, O. 2014. Simulation and optimization of energy consumption in cold storage chambers from the horticultural industry. Int. J. Energy Environ Eng 5(88).

Gaspar, P. D., & da Silva, P. D. 2015. Handbook of Research on Advances and Applications in Refrigeration Systems and Technologies. IGI Global, Hershey.

Ghaani, M., Cozzolino, C. A., Castelli, G., & Farris, S. 2016. An overview of the intelligent packaging technologies in the food sector. Trends in Food Science and Technology 51, 1-11.

Gil-Lopez, T., Castejon-Navas, J., Galvez-Huerta, M. A., & O'Donohoe, P. G. 2014. Energetic, environmental and economic analysis of climatic separation by means of air curtains in cold storage rooms. Energy and Buildings 74, 8-16.

Morais, D., Gaspar, P. D., Silva, P. D., Andrade, L. P., Nunes, J. 2018. Energy consumption and energy efficiency measures in the Portuguese food processing industry. International Congress on Organizational Management, Energy Efficiency and Occupational Health and Safety in Agrifood Industry (+AGRO 2018), Castelo Branco, Portugal.

Morais, D., Gaspar, P. D., Silva, P. D., Andrade, L. P., Nunes, J. 2018. Assessment of the energy consumption and technologies in the bakery and pastry sector – The Portuguese case study. 2nd International Conference on Sustainable Energy and Resource Use in Food Chains, ICSEF 2018, Paphos, Cyprus.

Nunes, J., Silva, D., Andrade, P., & Gaspar, D. 2015. Avaliação energética das centrais de fruta da Região da Beira Interior. Int. Conference on Engineering – Engineering for Economic Development ICEUBI 2015, Covilhã, Portugal.

Nunes, J., Silva, P. D., Domingues, L., Andrade, L. P., & Gaspar, P. D. 2014. Energy evaluation of refrigeration systems in Portuguese fruit and vegetable industry. 3rd Int. Conference on Sustainability and the Cold Chain, Twickenham, London, 397-404.

Nunes, J., Silva, P. D., Andrade, L. P., & Gaspar, P. D. 2014. Characterization of the specific energy consumption of electricity in the Portuguese sausage industry. WIT Transactions on Ecology and the Environment, 186, 763-774.

Nunes, J., da Silva, P. D., Andrade, L. P., Domingues, L., & Gaspar, P. D. 2016. Energy assessment of the Portuguese meat industry. Energy Efficiency, 9(5), 1163-1178.

J. Nunes, Pedro D. Silva, L.P. Andrade, Pedro D. Gaspar. Key points on the energy sustainable development of the food industry – Case study of the Portuguese sausages industry. Renewable and Sustainable Energy Reviews (57), 393-411.

Pradella, A. M., Costa, S. E. G., Lima, E. P. De, & Silva, W. V. 2017. Energy efficiency indicators in the food industry: a systematic review. 24th Int. Conference on Production Research ICPR 2017, 685-690.

Silva, P.D., Gaspar, P.D., Andrade, L.P., Nunes, J., & Domingues, C. 2016. Best practices in refrigeration applications to promote energy efficiency – The Portuguese case study, Ch. 3, in D. Cunningham (Ed.), Food Industry: Assessment, Trends and Current Issues, Series Food and Beverage Consumption and Health, Nova Publishers, USA.

Sudhir, L. S., 2016. Led Illumination: A Case Study on Energy Conservation. Int. J. Engineering Research and General Science. 4(2), 283-289.

Manuscript ID: 1006
DOI: 10.18462/iir.icr.2019.1006

Extending the autonomy time of an icelined solar powered vaccine cooler

Jonas K. JENSEN [(a)], Christoffer BUSK [(a)], Claus CORDING [(c)], Per Henrik PEDERSEN[(b)], Wiebke B. MARKUSSEN[(a)]

[(a)] Department of Mechanical Engineering, Technical University of Denmark
Kgs. Lyngby, 2800, Denmark, jkjje@me.dtu.dk
[(b)] Danish Technological Institute
Taastrup, 2630, Denmark, prp@mek.dtu.dk
[(c)] Vestfrost Solutions A/S
Esbjerg, 6705, Denmark, info@vestfrostsolutions.com

ABSTRACT

The autonomy time of an icelined solar powered vaccine cooler expresses the amount of hours the cooler is able to keep vaccines within an acceptable temperature range during low solar radiation conditions, i.e. when the compressor of the cooling system is idle. This study investigates how different parameters related to the cooler cabinet and ice storage affect the autonomy time. A dynamic model of the vaccine cooler cabinet including the ice storage was used for the investigation. The model was calibrated using measurements from three different experimental setups, and the calibrated model showed a good agreement with the measurements. The results show that the mass of ice in the storage was the most promising parameter to consider for prolonging the autonomy time. Furthermore, it was shown that reduction of the thermal bridges in the cabinet also is of great importance.
Keywords: Icelined Refrigerator, Autonomy Time, Solar Powered Refrigeration, Vaccine Cooler, WHO.

1. INTRODUCTION

In many developing countries, the electrical grid is either unreliable or not existing, especially in the rural regions and small villages. A study by Adair-Rohani (2013) showed that 25 % of health facilities in Sub-Saharan Africa did not have access to any kind of electricity. Furthermore, 1/3 of hospitals in the area experienced unreliable grid connections. This leads to limited use of electrical applications, such as cooling systems for of medical supplies and products.
Medical supplies such as vaccines are critical in the developing countries. According to the World Health Organization (WHO), the global immunization coverage, i.e. the amount of people with effective vaccines in their blood, has stalled at around 85 % (WHO, 2018) and only very limited progress was attained over the last years. It is stated that 1.5 million lives could be saved if the global immunization coverage improves.
One reason for the fading progress is that vaccines need to be stored cold, in order to avoid spoilage and loss of potency. According to WHO (2015) vaccines should be kept at a storage temperature between 2 °C and 8 °C at all times from manufacturing to administration, in order to ensure the quality of the vaccines. Keeping vaccines cold in rural regions of developing countries is complicated, due to the lack of reliable electricity, as well as challenging ambient conditions in terms of both temperature and humidity.
To solve this issue several commercial coolers exists, which are able to operate without a grid connection. These coolers typically use photovoltaic (PV) modules for power supply and either a battery or an ice bank for energy storage.

1.1. Literature Review

Fatemulla (2011), investigated a refrigeration system using PV modules and a battery for energy storage. The study focused on comparing the costs of using PV, rather than conventional grid

electricity. They found that a payback period of around 7 years was expected from the PV modules. Since this was shorter than the expected lifetime, the authors deemed PV a viable investment.
Several studies have investigated the use of thermoelectric coolers for off-grid cooling purposes (Hans et al., 2016, Wang et al. 2011). Hans et al. (2016) investigated a thermoelectric cooler driven by a PV and with a battery for storage. Through experimental testing, they found that the cooler was able to keep the cold room temperature within the defined boundaries of 10-15 °C, while operating with a coefficient of performance (COP) of 0.34.
Aktacir (2011) also considers a refrigerator powered by a PV / battery combination. The system performance on a daily, as well as a seasonal level was investigated for one of the warmest regions of Turkey. It is found that the PV solution was able to deliver the required amount of energy needed to operate the refrigerator at desired conditions.
As stated in Pedersen et at. (2019) experience has shown that the use of batteries in vaccine coolers often is related to increased costs, since the life-time of the batteries is suffering from the high ambient temperatures and the frequent deep discharging. This encouraged the development of direct drive solar powered vaccine coolers with ice storage. Since PV modules generate direct current (DC), it is often advantageous to use a DC compressor for the refrigeration system. In this way the compressor may be connected directly to the PV panels, as a so-called direct drive compressor.
In a study by Ekren (2013), such a DC compressor was investigated, to see if the energy usage could be reduced by use of a variable speed controller, rather than an on/off controller. It was found that the use of variable speed control leads to an increase in COP as well as exergetic efficiency, particularly at high rotation speeds.
In Jensen et al. (2019) three different compressor control strategies were investigated for two different direct drive compressors. Through numerical modelling it was found that by selecting an appropriate compressor control strategy the amount of PV panels needed to operate a vaccine cooler could be halved if the compressor start power could be supplied by e.g. a capacitor or a smart start algorithm.
Pilatte (1984) investigated a refrigerator powered by PV cells, which had the ability to produce ice and use this for energy storage. The cooler was relatively large, with a vaccine storage chamber of 70 litres, and an additional storage room of 70 litres, with a temperature of about 10 °C. The ice-storage of 14 litres was able to produce 2 kg of ice within 24 hours. Performing several tests revealed that the cooler was able to deliver the requirements set by the WHO for vaccine coolers in tropical regions. During operation, the cooler had an average energy consumption of 370 Wh within 24 hours and by using a high level of thermal insulation COPs as high as 1.6 were measured.
Walker (2007) investigated how to design a low-cost vaccine cooler, focusing on a heat transfer regulating device, whose purpose is to control the temperature within the vaccine storage chamber. This cooler also utilized an ice storage. Through modelling of the system, the temperature response of the vaccine chamber due to openings of the cooler lid was investigated. It was found that even though only one vial is present, and the entire cooler is filled with air at 45 °C, the single vial still remained within the boundary of the acceptable temperature range.

1.2. Scope

Autonomy time of a vaccine cooler, as defined by WHO, is the number of hours the vaccine cooler can keep the vaccines within the acceptable temperature range during low solar radiation conditions, i.e. lower than what is required for the compressor to run, but low-consumption equipment such as fans or electronics might be operating. A measurement of the autonomy time starts when the compressors shuts off and ends once a single temperature measurement of the vaccines reaches a temperature of 8 °C. In the present study we focus on extending the autonomy time of vaccine coolers using ice storage. By use of numerical analysis, we investigate how different parameters of the ice storage and cabinet affect the autonomy time of the vaccine cooler.

2. METHODS

In order to investigate the autonomy time of a vaccine cooler a dynamic model of the cabinet including the ice storage was created. The model was implemented in Engineering Equation Solver (Klein, 2018).

2.1. Cabinet Model

Fig. 1 (left) shows a sketch of the considered vaccine cooler layout. The sketch is a cut through the middle of the vaccine cooler and it should be noted that the ice-storage surrounds the four side walls of the vaccine compartment. Furthermore, the evaporator is a spiral-shaped pipe, wrapped around the ice-storage. The condenser is also a long pipe, but placed on one side of the unit, similarly to a household refrigerator. The ice-storage itself is placed in the top part of the side wall and separated of the vaccine chamber by the frame with a thin layer of plastic material between the frame and the ice-storage. All walls are insulated with PU foam as well as a vacuum insulation panel on the outside of the insulation. The vaccine cooler also contains a lid, which is insulated by PU foam.
For the modelling the condenser and evaporator tubes were disregarded, since the refrigeration system is idle during autonomy time. The vaccine cooler was divided into eight control volumes as seen in Fig. 1 (right). The arrows indicate how a given control volume interacts with the neighbouring control volumes. Red arrows indicate heat transfer by convection, calculated by multiplying a convective heat transfer coefficient with the heat transferring area and the temperature difference between the surface and the ambient or cabinet inside air temperature.

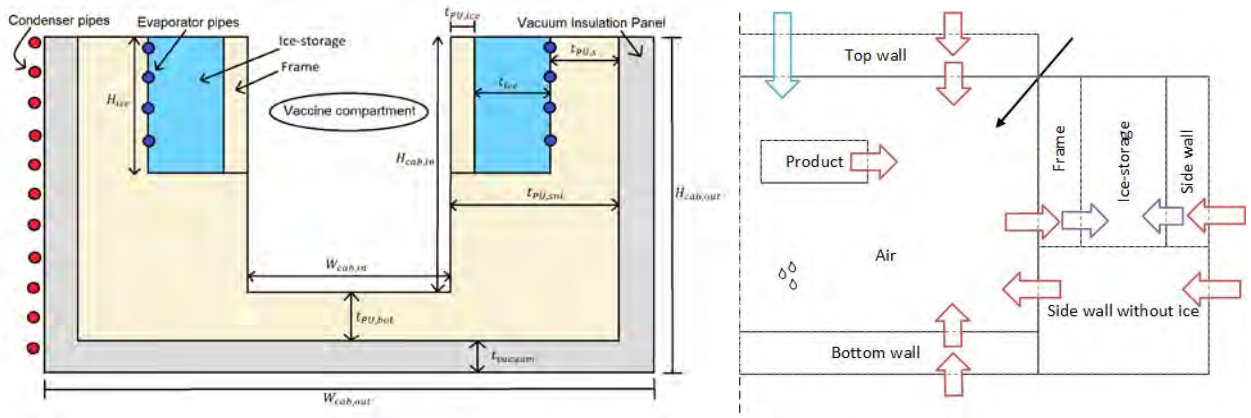

Figure 1: (Left) Sketch of the vaccine cooler cabinet with ice storage. (Right) Sketch of the modelled control volumes and their interactions

The two purple arrows indicate heat transfer by conduction. The blue arrow indicates heat transfer through thermal bridges. This was modelled by fixing a UA-value for the thermal bridges and multiplying this with the temperature difference between the ambient air and the air inside the vaccine compartment. Air infiltration, indicated by the solid black arrow in Fig. 1, was taken into account in the energy balance of the air control volume as well as possible condensation of moist air, as indicated by the water droplets in the figure.
Dynamic mass and energy balances were formulated for all control volumes. For the air, product and ice-storage control volumes a lumped capacitance approach was chosen, while transient conduction through a composite wall was applied for the wall and frame insulation control volumes. The walls consisted of an outer layer of steel, a vacuum insulation panel, a layer of insulation material (PU-foam) and another layer of steel on the inside. The walls were discretised such that a calculation node was placed at each material interface and additionally 10 nodes were placed inside the layer of PU foam.
The frame consisted of an aluminium layer, a thin layer of insulation material and another aluminium layer. Since the insulation material only a thin layer only 3 nodes were added in this layer. Furthermore, a contact resistance of 500 W $m^{-2}K^{-1}$ between the ice and the aluminium layer was defined.
The product consisted of a number of vials. Each vial was assumed to have a cylindrical shape. The density and heat capacity of the vials was assumed to be similar to liquid water.

2.2. Ice Bank Storage

The ice bank storage was able to interact with the frame and the side wall. The model was built such that both freezing and thawing of the ice could be simulated. Since the water is placed in a closed and stable container some degree of subcooling of the liquid is experienced prior to freezing and the water will be at a metastable state until it reaches the freezing point. For the simulations the freezing

point temperature was a user input, based on experiences from experimental tests. The properties of the subcooled water were considered similar to non-sub-cooled liquid water. When reaching the

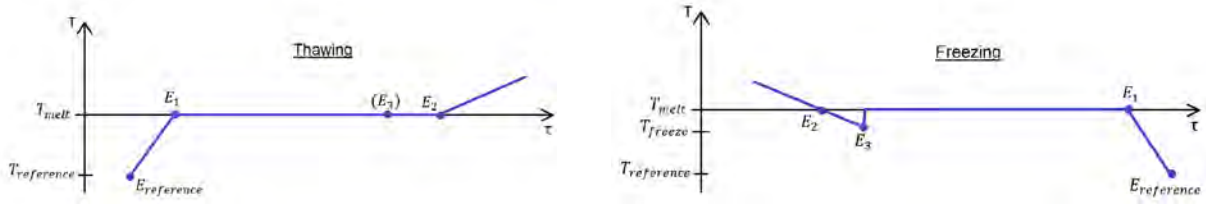

Figure 2: Temperatures and energy levels in the ice-storage during freezing and thawing

freezing point temperature, part of the ice would freeze rapidly and the temperature would instantly increase to 0 °C. Figure 2 sketches the assumed temperature course during freezing and thawing. A reference temperature was defined at -15 °C. This reference temperature was used for calculating reference levels of internal energy of the ice:

$$E_{\text{reference}} = M_{\text{ice}} \cdot u(T_{\text{reference}}, p) \quad \text{Eq. (1)}$$

$$E_1 = E_{\text{reference}} + M_{\text{ice}} \cdot c_{\text{ice}} \cdot (T_{\text{melt}} - T_{\text{reference}}) \quad \text{Eq. (2)}$$

$$E_2 = E_1 + M_{\text{ice}} \cdot \Delta h_{fs} \quad \text{Eq. (3)}$$

$$E_3 = E_2 - M_{\text{ice}} \cdot c_{\text{water}} \cdot (T_{\text{melt}} - T_{\text{freeze}}) \quad \text{Eq. (4)}$$

By comparing the changes in internal energy of the ice calculated from the dynamic energy balance to the energy levels, E_1, E_2 and E_3 the current temperature and ice fraction was calculated. The melting point temperature, T_{melt}, was set to 0 °C, while the freezing point temperature, T_{freeze}, was set to -6 °C.

2.3. Calibration

As a first step a calibration of the model was carried out. The parameters fixed in the calibration were:

- The UA-value representing the losses through thermal bridges in the cabinet
- The convective heat transfer coefficient on the inside of and outside of the cabinet

It was assumed that the heat transfer coefficient on the outside of the cabinet was equal to the heat transfer coefficient on the inside of the cabinet, and also the heat transfer coefficient between the product and the air was assumed equal to the heat transfer coefficient between the inside wall and the air. For the calibration the simulated results were compared to test results from autonomy time measurements of three different test setups using the considered vaccine cooler cabinet. Apart from the autonomy time also the steady state temperature was used as a target parameter. The steady state temperature denotes the temperature of the air, when the entire system is in a steady state condition during phase change in the ice-storage.

One of the tests was carried out according to the WHO performance quality and safety (PQS) standard at hot zone conditions, i.e. an ambient temperature, T_{amb} = 43 °C (WHO, 2010). According to the test standard, 1/5 of the nominal cabinet volume should be filled with water packages, each package containing 0.4 kg of water, which corresponded to 4.4 kg for the considered cabinet. For the simulations a single volume of water was assumed. The second test was carried out by the Danish Technological Institute (DTI), at temperate zone conditions i.e. T_{amb} = 32 °C. In this test the hold-over time was measured instead of the autonomy time. This meant that the measurement was carried out until the vaccines reached a temperature of 12 °C in stead of 8 °C, which was the case for the two other tests. The product inside the cooler cabinet was one test package Tylose gel of 0.5 kg. The last test was carried out at DTU. In this test the ambient conditions were not controlled, and the average ambient temperature in the lab during measurements was 22.1 °C. In this test the cabinet was empty during measurements and the time was stopped when the air inside the cabinet reached 8 °C.

2.4. Simulated Cases

A baseline model was established using geometrical data from the considered vaccine cooler cabinet and values of the convective heat transfer coefficient and UA-value representing the thermal bridges obtained from the calibration procedure. Taking this baseline model as a reference, the following parameters were varied in order to investigate their impact on the autonomy time and steady state temperature:

- The height of the ice bank. In this case the mass of ice was kept constant, while the thickness of the ice bank was changed as a function of the height.
- The mass of the ice. The thickness of the ice storage was held constant while the height was changed to give room for extra mass.
- The thickness of the PU insulation. For this case the inner dimensions of the cabinet were held constant while extra insulation was added on all walls.
- The UA-value of the thermal bridges.

3. RESULTS

3.1. Model Calibration

By running the model with different combinations of the convective heat transfer coefficient and the overall heat transfer coefficient representing the thermal bridges, the best combination of parameter values was found using the values stated in Table 1.

Table 1. Values of calibrated parameters

Convective heat transfer coefficient, W m^{-2} K^{-1}	7
UA-value of thermal bridges, W K^{-1}	0.26

Using the baseline model including the values presented in Table 1 and input parameters for ambient conditions corresponding to the three different measurement environments, simulated autonomy times were found as seen in Table 2. The simulated autonomy times corresponded well with the measurements, showing discrepancies of less than 3 %. Apart from the autonomy time also the steady state temperatures are shown in Table 2. As seen the steady state temperature during simulations corresponded very well with the measured temperatures.

Table 2. Comparison of autonomy time and steady state temperature of the air for measurements and simulations with the calibrated model

	Measured h	Simulated h	Deviation h	Deviation %
WHO	72.4	74.5	2.1	2.9
DTI	111.3	111.6	0.3	0.3
DTU	156.4	154.3	2.7	1.7
	Measured °C	Simulated °C	Deviation °C	
WHO	5.8	5.8	0.0	n/a
DTI	4.3	4.2	0.1	n/a
DTU	3.0	2.9	0.1	n/a

3.2. Extending Autonomy Time

In Fig. 3 (left) the autonomy time and steady state temperature of the air inside the cabinet is shown as a function of the ice bank height for two different ambient temperatures. The mass of ice was kept constant in this case, which meant that the ice bank thickness was decreasing with added height. As seen the autonomy time decreases slightly with increasing height for both 32 °C and 43 °C ambient temperature. At the same time the steady state temperature was found to decrease. By increasing the ice bank height also the area between air and frame is increased, which results in an increased convective heat transfer from this surface, and the air temperature thus decreases. The lower air temperature inside the cabinet then results in larger heat losses through the outer walls which causes the decrease in autonomy time. At an ambient temperature of 32 °C the steady state temperature of the air got below the lower limit 2 °C when increasing the ice bank height by 18 cm. Fig. 3 (right) shows the autonomy time and steady state temperature as a function of the ice bank mass. In this case the height of the ice bank was also increased while the thickness was kept constant. In this

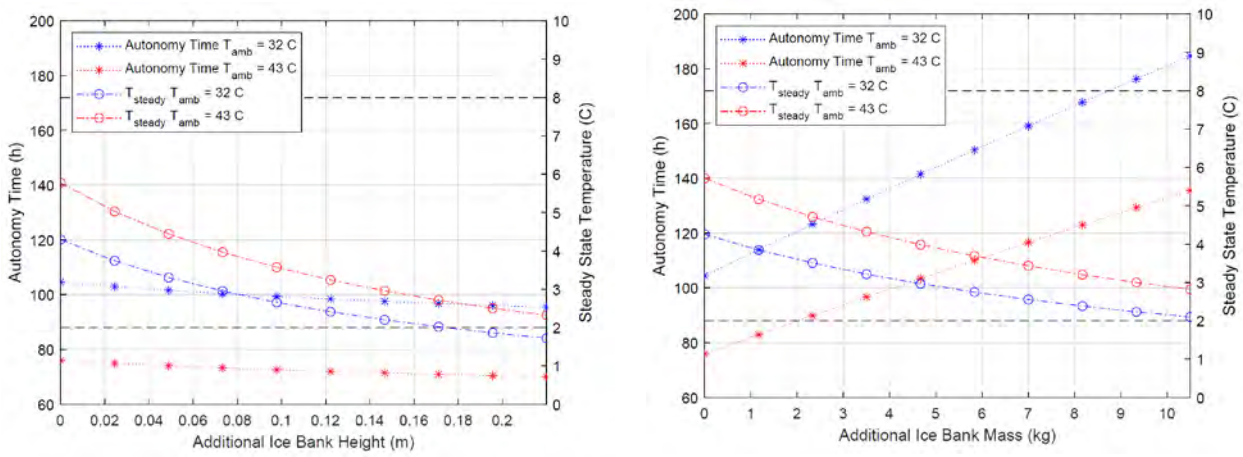

Figure 3: Autonomy time and steady state temperature as a function of additional ice bank height (left) and additional ice bank mass (right) compared to the baseline model

case the autonomy time increases significantly with added mass of the ice. This trend was expected as added mass in the ice bank means a larger storage capacity. Adding 10 kg of ice to the storage of the reference model resulted in around 80 % increase in autonomy time for both ambient temperatures. The steady state temperatures show a similar decrease as for the case where height is increased with constant the ice bank mass, however, staying within the limits, above 2 °C.
Fig. 4 (left) shows the autonomy time and steady state temperature as a function of added PU-insulation in all outer cabinet walls. As seen the autonomy time increases slightly with increasing

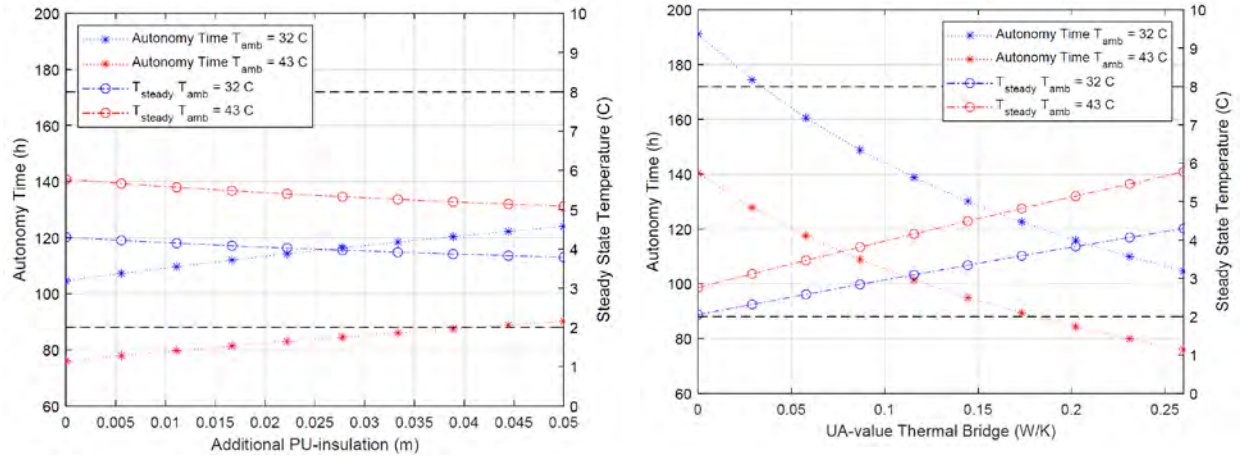

Figure 4: Autonomy time and steady state temperature as a function of additional PU-insulation in the cabinet walls (left) compared to the baseline model and as a function of the UA-value of the thermal bridges (right)

insulation thickness. Increasing the insulation thickness of the outer walls reduces the convective heat loss through the walls, which leads the increase in autonomy time. Adding extra 5 cm to the insulation of the outer walls increases the autonomy time by 10 to 20 % depending on the ambient temperature. The steady state temperature is mainly governed by the insulation thickness between the ice storage and the vaccine chamber, and therefore only changing less than 1 °C, when adding 5 cm to the insulation thickness of the outer walls.
In Fig. 4 (right) the UA-value of the thermal bridges was varied between 0 WK^{-1}, meaning no losses due to thermal bridges, up to 0.26 WK^{-1}, which was the value found from the calibration of the baseline model. For a cabinet without thermal bridges autonomy times of 190 h and 140 h were obtained for ambient temperatures of 32 °C and 43 °C, respectively. Removing all thermal bridges thus has almost the same impact on the autonomy time as adding 10 kg of ice to the ice to the ice storage. Also the steady state temperatures are significantly influenced by the thermal bridges. At an ambient temperature of 43 °C the steady state temperature decreases from 5.8 °C to 2.9 °C when removing the thermal bridges, and at an ambient temperature of 32 °C the steady state temperature decreases from 4.2 °C to 2.0 °C, which is at the limit of the acceptable air temperature inside the cabinet.
For the solar powered vaccine cooler a longer autonomy time means a less vulnerable system in periods with low solar radiation. For extending the autonomy time, the results presented in Figure 3 and Fig. 4 suggest that focus is put on increasing the mass of the ice storage and reducing the thermal bridges of the cabinet.

4. DISCUSSION

The model showed good agreement with measured values of the autonomy time, when using the calibrated values of the heat transfer coefficient and UA-value of the thermal bridges. Considering the UA-value of the thermal bridges the results showed that both the autonomy time and the steady state temperature were quite sensitive to the chosen value. A more thorough analysis of the thermal bridges therefore seems relevant for future work. Considering the convective heat transfer coefficient, the same value was used for calculating the heat transfer on the inside wall, the outside wall and between the product and the air. Due to different geometries, air flow conditions and different temperature levels it is expected that the heat transfer coefficients would not be equal in reality. A refinement of the convective heat transfer coefficients could possibly lead to a more realistic model, however this would also increase the number of parameters to be calibrated.
For the air, ice and product control volumes it was assumed that the lumped capacitance method could be applied. In reality temperature gradients are expected in all three control volumes. A sensitivity analysis calculating the Biot number for different combinations of convective heat transfer coefficients and ice storage thicknesses relevant in this study, showed that the Biot numbers were close to 0.1, which is usually seen the limit of the validity of the lumped capacitance method. Furthermore, as soon as the ice starts to melt and the ice storage is filled with an increasing amount of liquid water natural convection will occur inside the ice storage, which is not accounted for in the current model. Natural convection on the water side will decrease the resistance and might thus decrease the expected autonomy time.

5. CONCLUSIONS

A dynamic model of an ice-lined vaccine cooler cabinet was used to investigate the autonomy time and the steady state temperature of the air during phase change of the ice. A baseline model representing an existing cabinet was calibrated against experimental results from three different measurement setups. The calibrated baseline model showed a good agreement with the measurements. It was investigated how different parameters related to the cooler cabinet and ice storage affected the autonomy time, while making sure that the steady state temperature stayed in an the acceptable range between 2 °C and 8°C. The results showed that the mass of ice in the storage was the most promising parameter to consider for prolonging the autonomy time. Furthermore, it was shown that a reduction of the thermal bridges in the cabinet also is of great importance.

ACKNOWLEDGEMENTS

This research project is financially funded by EUDP (Energy Technology Development and Demonstration). Project title: "Second Generation Solar Direct Drive Refrigerators", project number: 64017-0556

NOMENCLATURE

c	Specific heat (J kg^{-1} K^{-1})	p	pressure (kPa)
E	Internal energy level (J)	T	temperature (K)
M	mass (kg)	u	Specific internal energy (J/kg)

REFERENCES

Adair-Rohani, H., Zukor, K., Bonjour, S., Wilburn, S., Kuesel, A.C., Hebert, R., Fletcher, E.R., 2013. Limited electricity access in health facilities of sub-Saharan Africa: a systematic review of data on electricity access, sources, and reliability. Global Health: Science and Practice 1 (2) 249-261.

Aktacir, M.A., 2011. Experimental study of a multi-purpose PV-refrigerator system. International Journal of Physical Sciences 6(4):746-757.

Ekren, O., Celik, S., Noble, B., Krauss, R., 2013. Performance evaluation of a variable speed dc compressor. International Journal of Refrigeration 36(3),745-757.

Fatehmulla, A., Al-Shammari, A.S., Al-Dhafiri, A.M., and Al-Bassam A.A., 2011. Design of energy efficient low power PV refrigeration system. In Electronics, Communications and Photonics Conference (SIECPC), 2011 Saudi International, pages 1-5. IEEE.

Hans R., Kaushik S.C., Manikandan, S., 2016. Experimental study and analysis on novel thermo-electric cooler driven by solar photovoltaic system. Applied Solar Energy 52 (3) ,205-210.

Jensen, J.K., Moeller, H., Katic, I., Pedersen, P.H., Markussen, W.B., 2019. Comparison of compressor control strategies for solar direct drive refrigerators. In Proceedings of the 25th IIR International Congress of Refrigeration, August 24-30, Montreal, Canada

Klein, S.A., 2018. Engineering equation solver academic professional v10.478.

Pedersen, P.H., Katic, I., Markussen, W.B., Jensen, J.K., Cording, C., Moeller, H., 2019. Direct drive solar coolers. In Proceedings of the 25th IIR International Congress of Refrigeration, August 24-30, Montreal, Canada

Pilatte, A., 1984. A photovoltaic refrigerator for storage of vaccines and icemaking. In Energy for Rural and Island Communities. In Proceedings of the Third International Conference Held at Inverness, Scotland, pages 229-237. Elsevier.

Walker, C.D., 2007. Design and manufacture of low cost vaccine cooler. PhD thesis, Massachusetts Institute of Technology, 2007.

Wang F.J., Chang J.C., Lin K.C., Yau, Y.H., 2011. Performance testing of a thermoelectric cooler for medical application. In Advanced Materials Research 255,1537-1540.

WHO, 2010, Refrigerator or combined refrigerator and water-pack freezer: compression-cycle. Solar direct drive without battery storage, PQS Independent type-testing protocol, E003/RF05-VP.2

World Health Organization, 2015. Immunization in practice: a practical guide for health staff, 2015 update. World Health Organization. http://www.who.int/iris/handle/10665/193412

World Health Organization, 2018. Immunization coverage. http://www.who.int/mediacentre/factsheets/fs378/en/, last visited January 31, 2019.

Manuscript ID: 1024
DOI: 10.18462/iir.icr.2019.1024

DIRECT DRIVE SOLAR COOLERS

Per Henrik Pedersen[(a)], Ivan Katic[(a)], Jonas Kjær Jensen[(b)], Wiebke Brix Markussen[(b)], Hendrik Moeller[(c)], Claus Cording[(d)]

[(a)]Danish Technological Institute
Gregersensvej 2, DK-2630 Taastrup, Denmark,
prp@teknologisk.dk
[(b)]Technical University of Denmark, Department of Mechanical Engineering
Nils Koppels Allé, Building 403,
2800 Kgs. Lyngby, jkjje@mek.dtu.dk
[(c)]Nidec Global Appliance Germany GmbH
Mads-Clausen-Str. 7, 24939 Flensburg, Germany
hendrik.moeller@mail.nidec.com
[(d)]Vestfrost Solutions
Falkevej 12, DK-6705 Esbjerg Ø,
CLC@vestfrostsolutions.com

ABSTRACT

For many years, photovoltaic power has been used in areas without grid electricity for vaccine refrigerators with a lead-acid battery to store electric energy and to provide the start current for the compressor. The problem with this technology is that the lifetime of the battery is short due to deep discharging of the battery during periods with low irradiance and high ambient temperature.
The development of solar “direct drive” refrigerators started in 1999 at Danish Technological Institute (DTI).
It was demonstrated that the energy density of ice produced by a compressor is at the same magnitude as the lead-acid battery. As of to date (January 2019), 40 direct drive vaccine coolers from eight different manufacturers are listed on the website of the World Health Organization (WHO), with the technology being one of the fastest growing technologies in the vaccine cold chain.
This paper describes the status and new development and discusses how the technology can be used for other purposes in the future. The paper also discuss how remote monitoring can help to prevent destruction of vaccines by early warning and automatic call for service.

Keywords: Photovoltaic, Direct drive, Vaccine coolers, Natural refrigerant, Isobutane, Remote monitoring.

1. INTRODUCTION

Health organizations have developed a cold chain system with health centres in regions without grid electricity, and correct storage of vaccines has been a challenge for them. Many vaccines must be kept at temperatures between +2 °C and +8 °C. Some deviations in the upper end can be allowed but freezing would immediately destroy the vaccines resulting in the loss of potency.
The vaccines used in immunization programmes are stored in a dedicated special vaccine cooler approved and prequalified by the World Health Organization (WHO) and listed in the “Performance, Quality and Safety” (PQS). New and traditional vaccines used in country immunization programmes are expensive and often much more expensive than the refrigerators themselves in the long run.
Since the early 1980s, photovoltaic power has been used for such refrigerators with a lead-acid battery to store power and provide start and operating current to the compressor. The problems

with this solution are the relatively high cost and the limited lifetime of the battery due to high ambient temperatures and deep discharging of the battery during periods with little sun as well as the lack of timely planning for the replacement of the batteries.
Therefore (and because of lower investment costs), gas and kerosene powered absorption refrigerators have been standard in the remote setting health facilities until recently. Absorption refrigerators need a constant fuel supply, and they are, therefore, expensive to run over its lifetime. Moreover, the temperature control is often poor, which results in expensive vaccines being destroyed.
The above challenges formed the background for developing and testing solar "direct drive" (DD) refrigerators, where the energy is stored in ice instead of a battery and thereby eliminating the practical and financial difficulties with battery replacement.
The development of solar "direct drive" refrigeration started in 1999 at Danish Technological Institute (DTI). Here, a prototype was produced with funding from the Danish Energy Agency. A normal DC compressor (with high start current) was used and a big capacitor helped to start the compressor. It was demonstrated that the energy content in ice produced by this compressor was higher than the energy content in a lead-acid battery, in terms of both volume and weight. (Pedersen and Katic, 2016).
Contact was established to international organizations, and after a meeting in Frankfurt the "SolarChill Partnership" was established with United Nations International Children's Emergency Fund (UNICEF), WHO, United Nation Environmental Program (UNEP), Deutcshe gesellschaft für Internationale Zusammenarbeit (GIZ), Program for Appropriate Technology in Health (PATH), Greenpeace International and the Danish Technological Institute (DTI) as partners. The goal was to develop and implement PV-powered vaccine refrigerators without batteries but using natural refrigerants. (Pedersen and Maté, 2007).
At the same time, a compressor manufacturer developed a DC-compressor for R600a and with "soft start", which made it possible to wire the compressor directly to the PV-panels (DD – direct drive). In 2004, with additional field tests carried out in three countries (Indonesia, Senegal and Cuba), the results were so promising that the partners chose to continue the further development of the solar direct drive refrigerator to pre-qualify the product for WHO PQS standards for safe storage of vaccines. (Pedersen and Maté, 2010).

2. CURRENT STATUS

This section describes the current status for vaccine coolers for health stations in rural areas in developing countries.

2.1. Ice storage versus batteries

Relief organizations want to avoid lead batteries as the main source of energy to keep the vaccines cold during night-time and periods with little solar power. Previous experience has shown that additional costs are related to the batteries in that high ambient temperatures and frequent deep discharging result in a fast degradation and short life cycle of the batteries. This by itself is one key reason why the solar battery powered refrigerators have often been more expensive than kerosene or LPG-powered absorption refrigerators.
In the SolarChill project, ice bank "batteries" have been developed as an alternative source of energy storage. In (Pedersen and Katic, 2016) there is an analysis and comparison between the energy storage in a typical lead battery and in ice.
The conclusion is that the cooling energy capacity of ice storage is in the same order of magnitude as that of a traditional lead battery on volumetric and mass basis. The cooling energy capacity of ice storage is approx. 123 % higher (for the ice storage) on weight basis and approx. 21 % higher on volume basis.
Commercialization of long-life lithium based batteries with high energy density might change the role of battery storage in solar refrigeration. However, the ice storage in SolarChill is the simplest and most cost-efficient solution so far. A disadvantage when using ice storage is that the ice has to be stored inside the insulation of the cabinet. Thus, the net volume inside the refrigerator will be smaller.

2.2. Compressor for “Direct-Drive” (DD)

There are only very few PV direct drive compressors available on the market today. The most common model is the BD-35K. The compressor manufacturer also developed a new integrated electronic control for the compressor, which ensures that the photovoltaic panels can be connected directly to the compressor without external control. The electronic control also ensures a “soft start”, which is important when no battery is used.
The electronic control is equipped with an adaptive speed control (Adaptive Energy Optimizer – AEO). By using this control, the compressor will stepwise speed up from low speed to maximum speed in steps of approx. 12.5 RPM/min. If the photovoltaic panels cannot provide enough power, the compressor will stop and after a short while it will try to start again. The compressor will try to start every minute, and once the power from the panels is enough, the compressor will start at a lower speed. The first start in the morning is at approx. 2500 RPM. After a thermostat cut-out, the compressor will start up at the latest speed minus 400 RPM. The speed range is from 2000 to 3500 RPM.
The controller accepts a voltage between 10 and 45 V. The voltage from photovoltaic panels can vary, and a wide voltage range is an important and crucial feature for solar powered refrigerators and freezers. When using 12 V modules, the starting current of the compressor is less than 3 A; typically, there will be enough power a few hours after sunrise. The compressor runs continuously at about 3 A at lower speed. Using a standard compressor control, the start current would be much higher, which requires much bigger PV-panels or the use of a big capacitor to help start the compressor.
In the prototypes (chest and upright), the expansion device is a capillary tube with a heat exchange to the suction line. In the chest type cabinets, integrated skin condensers are used as in most chest freezers.
The evaporator in the vaccine chest refrigerator is a wire-on-tube-type placed in the ice storage as shown in figure 1a. The evaporator in the upright-type is a box-type roll bond-aluminium evaporator as known from old refrigerators with a small freezer compartment.

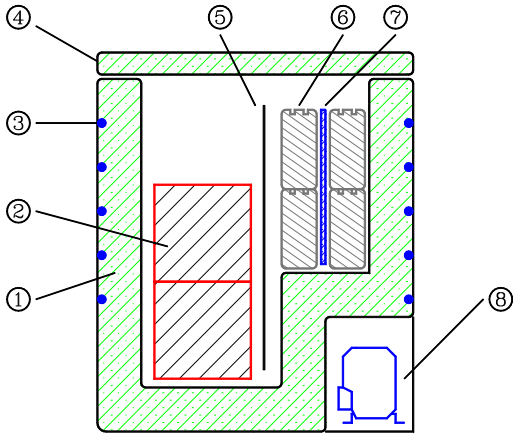



1 – Cabinet
2 – Vaccine compartment
3 – Skin condenser
4 – Lid
5 – Internal wall, insulated
6 – Ice storage (26 „ice packs“, 600 ml)
7 – Evaporator, wire on tube
8 – Compressor.

Figure 1a: Figure with basic principles for the first prototype vaccine cooler.

Figure 1b: Photo of a DD solar compressor. The integrated solar electronic control is placed on the left-hand side of the compressor.

2.3. Field test experience and commercialization

DTI has been running an extensive field test program, where the performance of the first series of solar DD appliances was documented in terms of practical use in health clinics.
Pedersen and Maté (2007) explain how the field test of this vaccine cooler took place in Indonesia, Senegal and Cuba using 180 W photovoltaic panels (3*60 W peak). Moreover, the tests show the hold-over time of about five days without any energy available. The field test lasted about one year and the ice banks were never completely melted, except when the connections to the PV-panels were disconnected intentionally. However, the vaccine temperature was not always within the preferable range of 2-8 °C in connection with this early prototype.
Vaccine specialists have developed new criteria for DD vaccine coolers. This work was done in cooperation with the partners of the SolarChill partnership and other technical experts.
The first generation of the WHO PQS (Performance Quality Safety) criteria for DD vaccine refrigerators was introduced in 2010, and the first test for WHO approval was conducted at DTI in 2010.
The WHO PQS prequalification is a condition in most tenders for the procurement of cold chain equipment for organizations that procure cold chain equipment used for storage of vaccines. This ensures the quality of vaccines stored in these products as safe for use in immunization programmes.
Currently there is a new field test going on with a selection of WHO approved DD vaccine coolers in a GEF (Global Environmental Facility) project.

2.4. Two main types of DD vaccine refrigerators

The WHO website holds an increasing number of approved DD vaccine coolers. In January 2019, it contained 40 units from eight different manufacturers. 37 of the units use the natural refrigerant isobutane (R600a). Three of the units use a HFC-refrigerant (R134a).
Today, there are two main types of DD vaccine coolers on the market.
The first type is the ice-pack type, where the ice storage (and/or PCM-materials) is built into the walls of the cabinet or in a special compartment close to the evaporator. This type of DD vaccine cooler is often based on a chest type cabinet. Such types of cabinets are relatively cheap to manufacture, but precise temperature control may be a challenge.
This (or a very similar) technology is applied in 34 of the 40 DD vaccine coolers on the WHO list in January 2019.



Figure 2: Ice pack type of DD vaccine cooler.

The other main type of vaccine refrigerator is the tank type using a mixture of ice and water surrounding the vaccine chamber. Water has the highest density at about +4 ˚C and with a top-

mounted ice storage. This ensures that water in the bottom of the tank and in thermal contact with the vaccine storage is about +4 ˚C, which is ideal for storage of vaccines, and it eliminates the risk of freezing.
The DD vaccine refrigerators using this technology ensure a very stable temperature and a long hold-over time, but they can be more expensive to manufacture if the special tank is manufactured in smaller quantities.
This technology is applied in six of the 40 DD vaccine coolers on the WHO list in January 2019.



Figure 3: Tank type DD vaccine cooler.

3. FUTURE PERSPECTIVES

The existing refrigeration technology in solar direct drive vaccine coolers is about 17 years old. Therefore, a new R&D project has been started involving the Technical University of Denmark, a compressor manufacturer, a manufacturer of vaccine coolers and Danish Technological Institute, who is the project manager. The Danish Energy Agency is funding the project.

The project started in 2017 and the aim is to develop:
- Concept for a new compressor
- Concept for a new cabinet, new ice storage and remote monitoring.

The compressor will be more energy efficient compared to the present DD compressors. The results from the first prototype, named BDS5.0K tested in lab, primo 2019 shows to fulfil this goal. In addition to this, the variable speed compressor is supposed to have higher cooling capacity and a broader span in capacity. This will give possibilities to use this compressor for bigger cabinets and for new applications in addition to the present use of this type of compressor.
Furthermore, efforts are made to develop a more efficient control strategy (Jensen, Moeller, Katic, Pedersen and Markussen, 2019).
DTI hosted a meeting with the WHO PQS working group in November 2018. In a discussion about future generation of direct drive compressors for vaccine coolers it was the impression that the group wants to avoid dependence on batteries for energy storage – also in the future.
The future cabinet is supposed to have a longer “hold-over time”, which can be met by using bigger ice storage and/or better insulation. The future vaccine coolers are supposed to be remote monitored to ensure safe storage of vaccines and early warning if something goes wrong.
According to the WHO PQS working group, high relative humidity and even presence of water inside the vaccine compartment is a problem. In some coolers creation of mould has taken place. Thus, the next generation of vaccine coolers are supposed to solve this problem.

3.1. Remote monitoring

Refrigerators used for vaccine storage need to be extremely robust and must be able to keep the temperature withing the limits specified by WHO. A spoiled load of vaccine costs thousands of dollars, and manufacturers and users are therefore looking for methods to send early warnings in case of malfunction. In the past, monitoring had to be based on manual readings and download of data, but today IoT technologies are available from many providers of monitoring systems and are already used by some appliance manufacturers. DTI has investigated a range of systems using GSM mobile network for data transmission in connection with a large field test project (SolarChill) for solar direct drive refrigerators.
Ideally, the data acquisition system should have the following characteristics:

- Robust and reliable automatic data acquisition not relying on grid connection or internet
- Easy download of data, preferably automatic transmission
- Not too expensive and simple to install and operate.

In the SolarChill project, the following values are being monitored:

Table 1: List of data monitored by the advanced datalogger and the simple datalogger in the ongoing SolarChill project.

Advanced data logger	Basic data logger
Solar irradiance in plane of array	
Ambient temperature	Ambient temperature
Internal temperatures (4)	Internal temperatures (4)
Relative humidity	
Current	
Voltage	
Open/close events	

Both data loggers are uploading data with a user defined frequency to the manufacturer's server. The user can see and download data from a web portal, and alarms can be sent automatically by email.
Because the project is about solar powered refrigeration in remote areas, there is no grid power nor regular internet connection available at the installation sites. Therefore, mobile network or satellite communication are the only options for daily long distance access to the measurement systems.
For short distance, there are several other wireless technologies available, they may be used for internal communication between sensors and a GSM base station, also called Remote Terminal Unit (RTU) or cellular gateway.

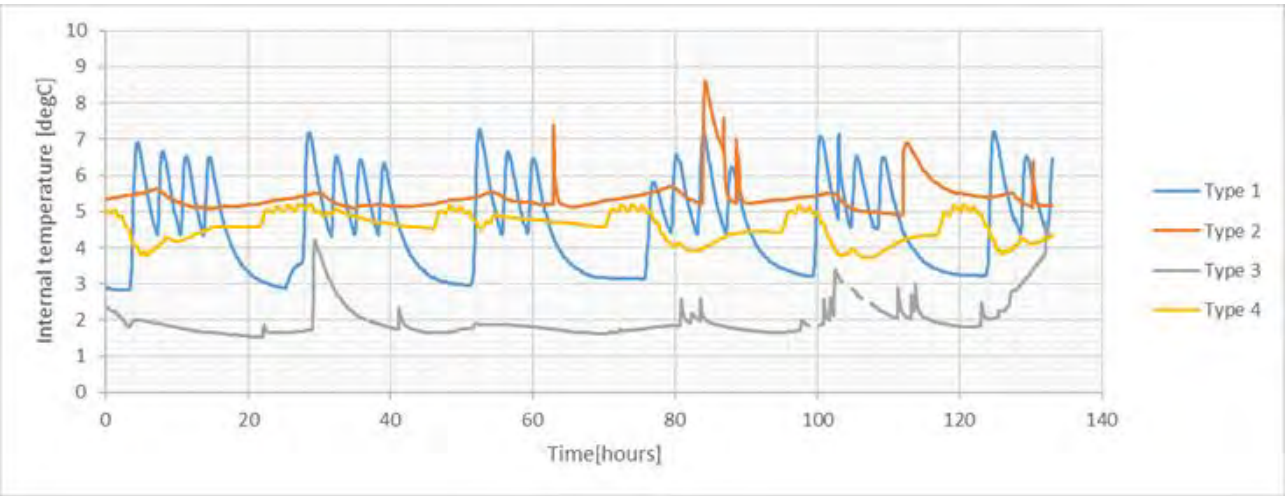

Figure 4: Example of field test data (from four different sites). This figure represents four different models of vaccine coolers in the ongoing SolarChill project. Every type of refrigerator has its own temperature "fingerprint" that may be useful in preventive maintenance.

There are several remote monitoring systems in the market that can be used for temperature monitoring alone. These are either single channel devices (some disposable) or multichannel with replaceable battery power supply. For collection of other data, like solar irradiance and voltage, there are not as many options. These systems are mostly configured with a central GSM gateway or base station that can be connected with or without wire to a range of different sensors. The gateways usually have a considerably higher energy consumption than the integrated sensor systems and needs external power supply for long term operation (Option for PV panel). Some are always connected to the GSM network for near-Realtime monitoring, others are only calling and updating hourly or daily.
Internal power supply of the DAQ system may be provided by either:

- Dry cell batteries (single use)
- Rechargeable batteries (To be occasionally charged from grid or a vehicle)
- PV power from the systems under measurement (Parasitic power)
- Separate PV supply.

The software for cloud based data collection and monitoring is mostly offered as a subscription service per month or per year for each connected device. It could therefore add up to a considerable amount. Most software is proprietary and can only be used with the company's own data loggers.
There is also software paid with a onetime license per user/PC and this could be a cheaper solution in the long term.

3.2. Vaccine coolers - future perspectives

Since the first solar DD refrigerator project in 1999, the cost of PV modules have dropped from about 4 USD/W to 0.4 USD/W or a factor of 10. In the same period, the unit size of a typical panel has increased from less than 100 W to about 300 W nominal power. This means that the same SolarChill refrigerator can now be run with a single PV panel instead of 2-3 panels, translating to simpler mechanical support and circuitry with the invention of plug and play MC connectors. In comparative terms, the retail cost of a single panel of 150 W, which provides enough energy for these products in most tropical climates, would typically be 500 USD, which is about the same cost as a set of high quality batteries. With even cheaper PV modules foreseeable in the future, new refrigerators will not have to focus that much on energy efficiency, but rather on the overall system costs and performance.
The interaction between the PV panel and the compressor can be further improved. Instead of the current "trial and error" method for adjustment of the compressor speed, it would be better if a maximum power point tracker could continuously adjust the compressor speed.

3.3. Other applications - DD coolers for food and drinks

Besides the need for vaccine storage refrigerators, there is a huge need for cooling of food and drinks in regions without a grid. There are only few battery-free coolers available on the market so far, and it is difficult to bring the costs down to a level that is comparable with the conventional household appliances. The power demand for such appliances is much higher than for vaccine refrigerators, and the current DD compressors are not always sufficient. It would be interesting if new and bigger devices could be developed for this market. As an alternative solution, the current models may be used in parallel-configuration.
On an even larger scale, there is a growing interest to use the solar DD technology for commercial cooling demands such as milk cooling, ice production for the fishing industry, cold stores etc. For such applications, it might be better to include a (small) battery bank, so that the PV power can be used for light and other secondary power needs as well.

4. CONCLUSIONS

The SolarChill field test has shown that DD solar cooling is indeed a robust and reliable technology that is particularly suited for cooling in the most remote areas of the world where there are no access to electricity. The uptake of this concept by more and more manufacturers confirms that the idea of directly driven cooling is viable within the medical healthcare market, where reliability is essential. The WHO PQS web-site contains 40 different products of DD vaccine coolers, whereof 36 products are using natural refrigerant (R600a).

For other markets there are still some way to go, mainly because there are only very few DD compressors available, and they are too small for many generic cooling applications.
The future of the DD technology depends on the will of the manufacturer to develop cost-effective and more powerful compressors as well as further optimization of the electronic controller. If they succeed in this, a new range of applications in the commercial and household sector could open up.

ACKNOWLEDGEMENTS

The authors would like to thank the partners of the SolarChill Partnership.
The authors would also like to thank the Danish Energy Agency for financial support to develop this new technology.

REFERENCES

Pedersen P. H., Katic I. Direct Drive Solar Coolers, 12th IIR International Gustav Lorentzen natural working Fluids Conference, Edinburgh, 2016.

SolarChill Partnership: www.solarchill.org.

WHO PQS website:
http://apps.who.int/immunization_standards/vaccine_quality/pqs_catalogue/categorypage.aspx?id_cat=17

Pedersen P. H. , Maté J. “SolarChill Vaccine Cooler and Refrigerator: A Breakthrough Technology”, Industria Informatione, special international issue on refrigeration and air conditioning, UNEP, ATF and Centro Studi Galileo, 2007.

Pedersen P.H., Maté J. SolarChill technology, Solar powered direct drive refrigerators with hydrocarbon refrigerants. 9th IIR Gustav Lorentzen Natural Working Fluids Conference, Sydney, 2010.

Jensen, J.K., Moeller H., Katic I., Pedersen P.H., Markussen W.B. Comparison of compressor control strategies for solar direct drive refrigerators. The 25th IIR International Congress of refrigeration, August 2019, Montreal, Canada.

Manuscript ID: 1044
DOI: 10.18462/iir.icr.2019.1044

CO_2 commercial refrigeration system in Jordan

Nour ABDIN [(a)], Armin HAFNER [(b)], Sergio GIROTTO [(c)], Franziska MENTEN [(d)], Yannick PRUSS [(b)], Riccardo SAVIGLIANO [(d)]

[(a)] Abdin Industrial Est., Bayader Wadi El-Sier – Amman 11814, JORDAN: headoffice@abdin.com.jo
[(b)] Norwegian University of Science and Technology, NORWAY
[(c)] Enex srl, ITALY
[(d)] United Nations Industrial Development Organization (UNIDO), AUSTRIA

ABSTRACT

According to IPCC/TEAP the annual refrigerant leaks from commercial refrigeration units related to the total charge are between 15 and 20 % in Europe and ~30 % outside Europe. Phasing out the current H(C)FC systems in the near future with energy efficient systems applying natural working fluids would result in a significant reduction of the environmental impact of commercial refrigeration. Currently the main barrier for introducing low-GWP alternatives, especially carbon dioxide (CO_2 / R744) in the supermarket sector outside of Europe, is the lack of knowledge and experience that these systems actually can perform even better than state of the art HFC technology. Another barrier is the limited availability of equipment in these regions.
Through a CCAC-funded project, implemented by UNIDO, the first transcritical CO_2 unit is implemented in so-called HAT (high ambient temperature) country. The supermarket is located in the capital city of Jordan, Amman. Commissioning of the unit took place in early 2018. The unit is equipped with a data acquisition system.
The work will briefly describe the different parts of the CO_2 unit and the display cabinets. Initial measurement results and performance analysis indicate a significant improvement of the energy efficiency, compared to the previous R22 units.
Keywords: CO_2 Transcritical, Ejector, HAT, Commercial Refrigeration.

1. INTRODUCTION

In 1850 carbon dioxide (CO_2, R744) was first described in a patent registration as a potential refrigerant from Alexander C. Twining. Until 1940, CO_2 and Ammonia (NH_3, R717) have been the only refrigerants applied in industrial refrigeration systems. By that time, the CO_2 systems faced challenges related to leakages and a shift of compressor technology. In addition, there was an offensive marketing from the chemical industry for their newly developed, synthetic CFC refrigerants (e.g. R12) in the 1930's. CO_2 refrigeration technology disappeared from the market. In the 1980's, CO_2 was rediscovered as a potential working fluid by the team of Gustav Lorentzen in Norway. Their initial development focused on mobile AC-systems for the automotive industry (Lorentzen & Pettersen, 1993), as these sector has high refrigerant leakage rates and hot water heat pumps, as CO_2 is exceptional energy efficient when applied in high temperature lift heat pumps.
The EU F-gas regulation (Commission, 2014) is in favour for modern CO_2 refrigerant technology as an viable alternative to replace refrigerants with a high Global Warming Potential (GWP). The European phasedown and the global effort as a result of the Kigali amendment of the Montreal Protocol aims for a significant reduction of the carbon dioxide equivalent emission from the refrigeration sector. This forces the market to replace the refrigerants with high GWP i.e. HFC-404A in Europe and HCFC-22 on global perspective. The annual leakage rate within the European Supermarket sector is estimated to be between 15% and 20% for HFC-404A units and around 30% for HCFC-22 units elsewhere (Hafner et al., 2014).
Carbon dioxide as a refrigerant (R744) is a safe, non-toxic, non-flammable, inexpensive working fluid. It is globally available and offers advantageous thermo-physical properties (Kim, Pettersen, & Bullard, 2004). This encouraged food retailers and industrial end- users all over the world to explore different solutions with this ultra-low GWP refrigerant permanently replacing HFC- based systems.

A common trend within the retail sector is to apply all CO_2 solutions whenever local contractors are able to provide the installation and service.
Transcritical CO_2 refrigeration systems have become a standard solution in northern parts of Europe. Related to energy demand and environmental impact, a conventional CO_2 booster system outperforms solutions based on “man-made” refrigerants at outdoor temperatures up to about 25 °C (Sawalha et al., 2017) and (Finckh et al., 2011). However, the low critical temperature of CO_2 (31.1 °C) the system layout has to be adapted to enable an energy efficient operation in all seasons in high ambient temperature (HAT) countries. Just to apply a north European CO_2 booster system would result in lower energy efficiencies compared to HFC- based units (Sawalha, 2008). This resulted in the creation of the concept of the “CO_2 equator” (Matthiesen et al., 2010). It refers to an imaginary geographical limit splitting Europe into the Northern region, where basic transcritical R744 booster refrigeration systems are more energy efficient on an annual comparison towards traditional HFC units. Moving or eliminating this ‘equator’ is possible with innovative CO_2 supermarket refrigeration systems as described in this work. As an example, when implementing parallel compression, “CO_2 only” units were finally able to perform similarly or slightly more energy efficient than HFC-based systems (Gullo and Cortella, 2016; Gullo et al., 2016; Purohit et al., 2017). To push the “CO_2 equator further south, the multi-ejector concept was introduced” (Hafner et al., 2014). This concept development utilises the two-phase ejector for expansion work recovery and enables a permanent non-superheat operation of the evaporators. With all technologies combined (parallel compression, expansion work recovery through two phase ejectors and evaporator operation without superheat) in one unit, energy savings of 23 % compared to a conventional “CO_2 only” unit in the South of Italy, could be achieved (Minetto et al., 2014).
Demonstration of the ejector supported parallel compression CO_2 booster systems in new regions in the world is essential to achieve the global climate targets. These units are the ambassadors for modern refrigeration technology and can act as active training sites to enable knowledge and technology transfer.

2. SYSTEM DESCRIPTION

The Supermarket is located in the capital city of Jordan, Amman. It is the Middle East’s first transcritical CO_2 system in the food retail sector, commissioned in January 2018 at the Al-Salam military supermarket. The refrigeration system is an ejector supported CO_2 booster system with parallel compression and direct expanding (DX) refrigerant at both temperature levels (medium temperature [MT] = chilled food and low temperature [LT] = frozen food). To achieve a high energy efficiency even at hot ambient temperatures in Amman, the system is equipped with state-of-the-art features such as: parallel compressors (AUX, total installed suction volume flow rate: 7.73 m^3/h), flash gas by-pass valve, multi-ejector, de-superheater downstream of the low stage compressors (LT; total installed suction volume flow rate: 16.59 $m^3 \cdot h^{-1}$), non-superheated evaporators (MT and LT). The MT compressors do have a total installed suction volume flow rate of: 25.88 $m^3 \cdot h^{-1}$. Fig. 1 shows a simplified system circuit.
The following part describes the main components and their functions, starting from the lower right hand side of Fig. 1. After heat rejection to the ambient, via the de-superheater, the discharge gas from the LT compressors merges with the vapour from the medium temperature liquid separator. When reducing the temperature of the LT refrigerant part in this way the superheat of the merged suction gas towards the three MT compressors is within an acceptable range. Elevated superheat values could result in extreme discharge temperatures of the high pressure stage reducing the live time of the parts exposed to these temperatures at corresponding high pressure values. Heat recovery is a very attractive option for CO_2 units, therefore, the high temperature heat of the system is utilised downstream of the high pressure compressors for heating up domestic hot water. Due to heat rejection with gliding temperatures in a transcritical mode, water can be heating up to 90 °C. However, a gascooler rejects the remaining heat to the ambient air.
For transcritical CO_2 systems, it is essential to achieve a low temperature difference at the outlet of the gascooler (temperature approach), in this case after the heat rejection towards the ambient air. The energy efficiency and performance of the CO_2 system highly depends on the control of the pressure level on the high side and the temperature approach. Stene (2005) and Kauf (1999) visualized the importance of an optimum high pressure, since the coefficient of performance (COP)

is directly influenced by the high pressure. A further reduction of the CO_2 temperature upstream the expansion device is achieved by an internal heat exchanger, transferring heat from the high side pressure part towards the suction flow of the parallel compressors, thus securing the required super heat.

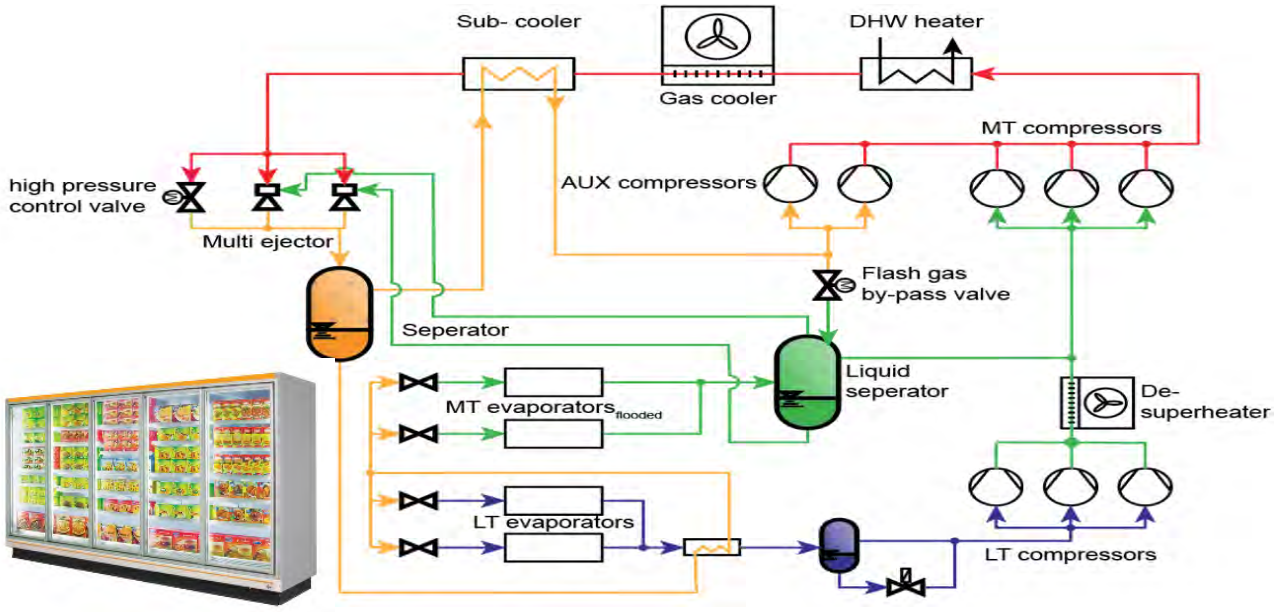

Figure 1: Circuit of CO_2 booster system operating in Amman, Jordan and picture of the applied display cabinets

After the heat rejection, the multi-ejectors throttle the gas into the separator at intermediate pressure level, while the traditional high pressure control valve is in stand-by mode for redundancy reasons. The multi-ejectors recover parts of the expansion work, by pumping refrigerant from the MT liquid separator to the intermediate pressure separator. Thereby, the high pressure refrigerant flow gets accelerated in a motive nozzle, thus the static pressure at its outlet drops below the medium pressure level and the refrigerant from the liquid separator is entrained and merged into the flow towards the separator, as described by Elbel and Hrnjak (2008). This means that the MT compressors are partly unloaded, i.e. load is moved from MT to the parallel compressors. The two-phase refrigerant separates after throttling in the separator. Only the liquid refrigerant is further subcooled utilizing the temperature difference between the liquid line and the exit of the LT evaporators. The subcooled liquid is supplied directly towards all MT and LT evaporators. The higher the ambient temperature the higher the amount of flash gas increases which occurs in the separator. The parallel compressor suction group controls the pressure level in the separator. As long as there is enough vapour, as it is the case at high ambient temperatures and when the ejectors are actively unload the MT compressors, the parallel compressors are in operation. At lower ambient temperatures, the flash gas bypass valves controls the pressure level by flashing the vapour towards the suction group of the MT compressors. The advantages of directly compressing the flash gas is on one hand avoiding throttling losses and “re- compression” with the MT compressors on the other hand the direct compression is more energy efficient, since the pressure ratio of the parallel compressors is lower compared the ratio of the MT-compressors. The largest share of the energy efficiency improvement relates to the non-superheated operation of the evaporators. The separators downstream of the evaporators protects the compressors from liquid slugs. If liquid passes through the evaporators, either it is returned by the ejector in case of the MT part or it is utilised to sub-cool the liquid towards the evaporators. The refrigerant feeding of the evaporators is not a function of the superheat rather a function of the air temperature inside the cabinets. This enables to utilise the entire surfaces of the evaporators for cooling the air rather than to provide superheat. This results in saturation temperatures of -2 °C (MT) and -25 °C (LT) in the presented CO_2 unit in Amman, compared to temperature levels of -10 °C and -35 °C in traditional units.

The refrigerated food is displayed in refrigeration cabinets of the type Shobak, designed and manufactured by Abdin in two different versions, each optimized for their use to guarantee optimum

performance and high energy savings. Equipped with double glass doors (MT version) and triple glass doors (LT version) with self-closing mechanism and the effective LED light. This kind of display cabinets, as shown on the left hand side in Fig. 1 provide a high product visibility and simultaneously reduce energy costs. Shobak is a full glass door refrigerated display cabinet for fresh pre-packed and frozen food as well as suitable for ice. The internal base is made of one PVC skin platted galvanized steel piece to prevent dirt tapping and is also inclined for easier cleaning and water disposing. PVC transparent ticket holder allow fully adjusting the PVC coated shelves. CFC free polyurethane foam insulates the body with of a thickness of 60 mm and a density of 38- 42 kg/m^3. The EC fan assisted cooling system, with electronic temperature & defrost control, and electronic expansion valves (AKV) secures the even distribution of the temperature within the cabinet. The cabinets can be multiplexed and are suitable for working temperatures of 2-4 °C (MT) and -18 to -20 °C (LT).

3. MEASURMENT AND EVALUATION METHODES

The CO_2 refrigeration unit is equipped with a certain number of pressure transducers, temperature sensors and energy meters.

3.1. Pressure and Temperature Measurements

A pressure and temperature measurement is necessary to obtain the thermodynamic properties of the refrigerant. In the described CO_2 refrigeration system, one pressure sensor for each pressure level is installed. To evaluate the performance of the different components (compressor, evaporators, gas cooler, etc.) the temperatures before and after the component is measured. Thus, the thermodynamic change of state can be documented. The data acquisition system records the ambient temperature value directly and stores an hourly average value. Allowing a more precise analysis of the system performance, the time steps for the ambient temperature values were changed to a ten minutes average value from the 7.11.2018 on. If values between the hourly average are required, a linear interpolation was applied.

3.2. Electrical Power Consumption Measurement

The ideal electrical power consumption measurement would determine the power consumption for every compressor suction group of the system separately on different measurement channels. With the power consumption in each compressor unit, the mass flow of the refrigerant, which is needed for the calculation of the cooling capacity and COP, can be estimated. Other components such as cabinets, fans, pumps, etc. should be measured separately. Unfortunately, during the initial operation period the separate electrical power consumption measurements for the supermarket in Amman where not in operation. Therefore, only the total power consumption of the entire supermarket was recorded in 2018. Since these separate energy meters are in operation now further studies will utilise and disseminate these results.

3.3. Data Acquisition

For data acquisition during the project, a web-based software is used. The supermarket transfer the data towards *powerfocus* provided by Danfoss as data acquisition software. Powerfocus stores measurement data in a database (cloud) accessible via web access at any time. The required data sets can simply be downloaded and exported into spreadsheet programs. The data stored within the powerfocus system are having a 10 minutes average time step.

4. SYSTEM PERFORMANCE ANALYSIS

In order to evaluate the systems performance, the key performance indicators of the system are compared in Fig. 2 and Fig. 3. The key performance indicators are: pressure levels versus ambient temperature (A), air- and evaporation temperature in the MT (B) and LT (D) cabinets and the corresponding MT (C) and LT (E) compressor operation (running) capacity. The investigated period is one day. Fig. 2 shows the performance of a hot summer day, while Fig. 3 shows a medium to low temperature day in winter.

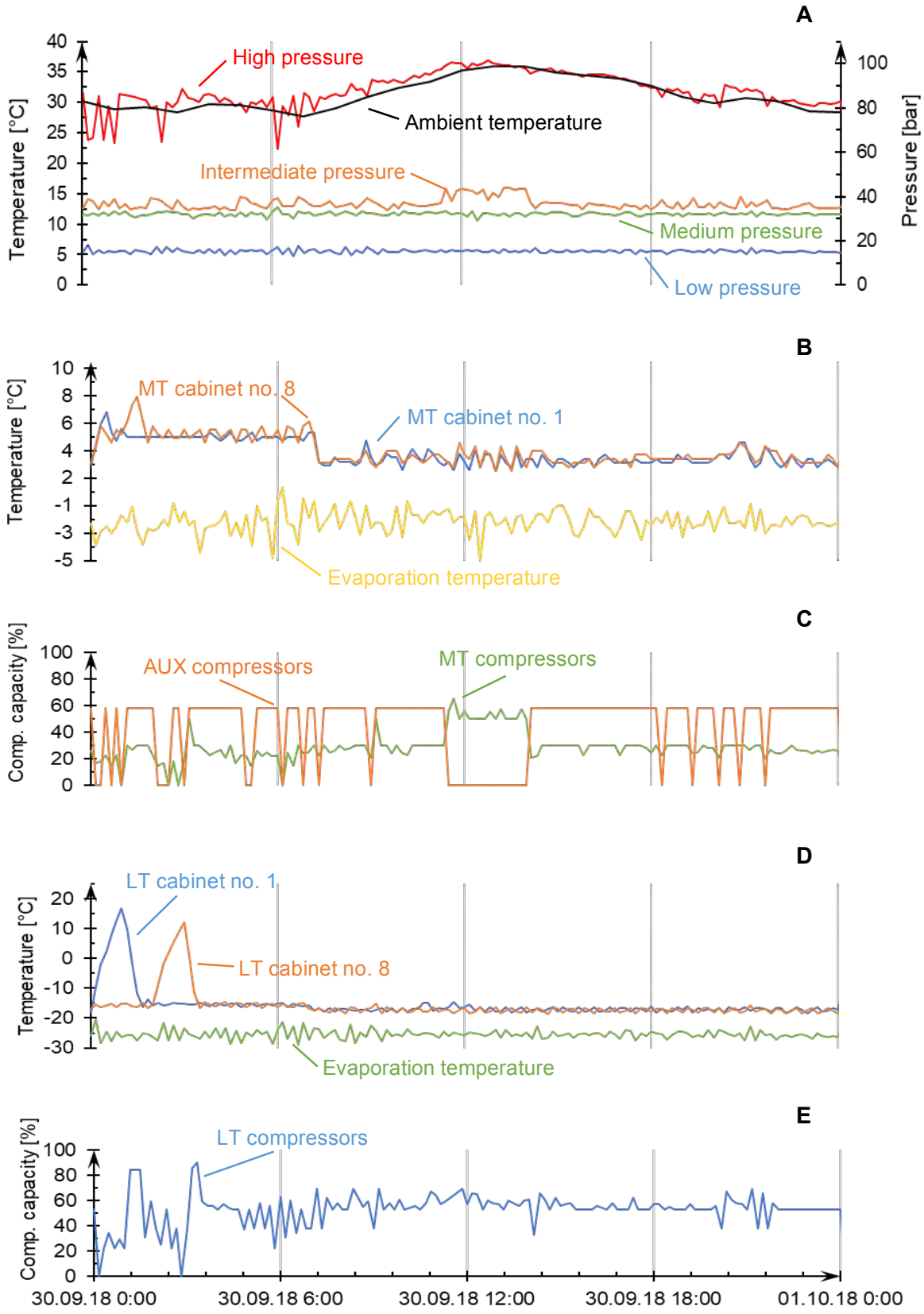

Figure 2: Key performance indicator overview of the 30.09.2018

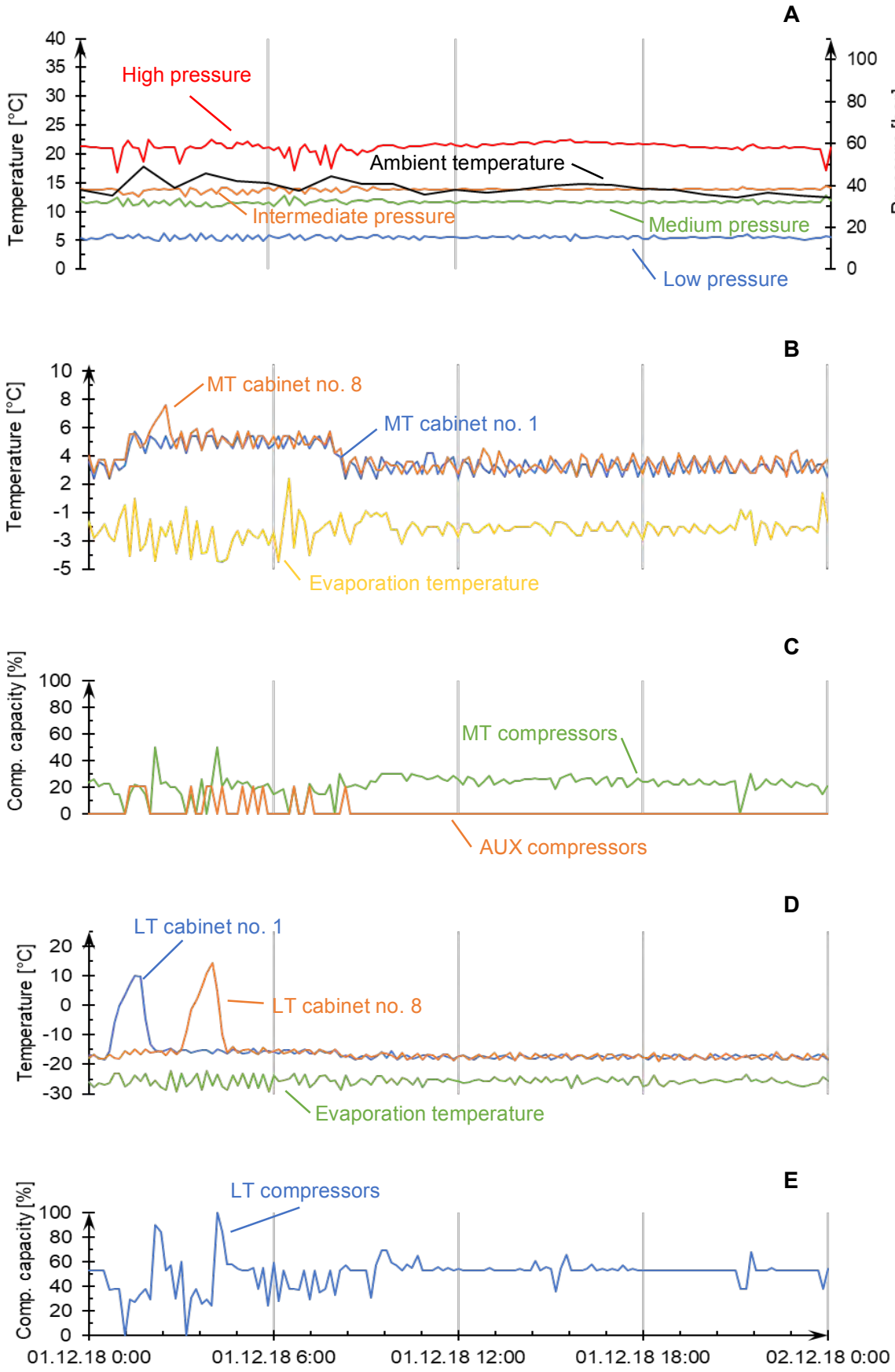

Figure 3: Key performance indicator overview of the 01.12.2018

The main difference between the operation at high ambient temperatures in summer and the low ambient temperatures in winter is the high pressure level and the demand for parallel compression. When comparing Fig. 2A with Fig. 3A, one can see that in summer the system operates in a so-called transcritical mode, since the high side pressure is above the critical pressure of CO_2 ($p > 73.8$ bar, $t > 31.1$ °C). During operation in the cold season the pressure level on the high side is at sub-critical pressure (around 60 bar) as a traditional refrigeration system with a condenser.
The high pressure correlates with rising ambient temperatures in summer to achieve a low temperature approach downstream of the gas cooler, while the other pressure levels remain at constant pressures all year to realize the required temperatures inside the evaporators / cabinets. With higher ambient temperatures and thus, higher gas cooler pressures levels, the amount of flash gas increases after the expansion from the high pressure side (via the multi-ejector) to the intermediate pressure. Therefore, the capacity of the parallel compressors is increasing to compress the flash gas and the vapour transferred by the ejectors from the MT pressure level, toward the high side pressure. Part (C) of Figure 2&3 shows the parallel compressor capacity together with the MT compressor capacity. The shutdown of the parallel compressors at 30 Nov2018 12:00 shows the operation with an active flash gas by- pass valve controlling the pressure level in the separator. It resulted in slightly higher intermediate pressure, since the pressure is regulated either by the flash gas by- pass valve or by the parallel compressors. At the same time the required MT compressor capacity rises, due to the expansion of the flash gas, i.e. the MT compressors transfers the entire refrigerant flow rate to the high side pressure level, as in a traditional CO_2 booster system.
The system achieves the desired temperatures in the cabinets at a steady state air temperature of 3 °C for MT and -17,5 °C for LT, both in summer Fig. 2 (B and D) and during the cold season, Fig. 3 (B and D). Since the LT and MT evaporator operates at temperatures below 0°C the evaporators require some defrost. The defrost period is scheduled and executed once a day between 00:00 and 04:00. During the defrost period, the reduction of cooling demand results in a partly on/off operation of the compressors.
In general, the capacity of the MT compressors allows for a further increase of the number of cabinets in the future. Even at hot summer days, the system requests only 60 % of the compressor running capacity, even when the parallel compressor is off. With the parallel compressors turned on, the MT compressor capacity revolves around 20 to 30%. The MT compressor operation capacity is not affected by the ambient temperature, due to more or less constant cooling demand, as can be seen in part (C) of the Figs. 2 and 3. Excluding the defrost period, the LT compressors operate between 40 and 60% of the installed capacity. The individual defrost periods of the cabinets will be adapted for the next investigation period; to investigate if continues operation of the compressors is possible with the current number of cabinets.

5. SUMMARY AND CONCLUSION

The first transcritical CO_2 booster system with ejector supported parallel compression installed in a high ambient temperature country is in operation since January 2018.
The feedback from the end-user:

- First year operation without extraordinary maintenance visits, i.e. no failure in the system nor the cabinets
- Zero food wastage due to stable temperature levels in the display cabinets
- Reduction of energy demand related to the refrigeration unit by more than 30% compared to similar new HFC installations in the region

As shown in this example, training and knowledge transfer is the key for a successful and fast phase in of CO_2 refrigeration units globally. Relative high first costs to install integrated CO_2 refrigeration systems are still the main barrier to a fast phase in of this technology on a global scale, especially when none of the local vendors has delivered such units before. The initial support by CCAC/UNIDO/Jordan Ministry of Environment to enable the first CO_2 based supermarket installation in that region shows that such a technology transfer is possible regardless of the previous conditions. Therefore, to continue this success, multilateral funds should support global education, training and certification. It is very beneficial if these funds are able to establish programs covering additional first costs with affordable loans (no interest rate), so that the end-users can return the loan during the

operational phase, as the new energy efficient CO_2 refrigeration system gives the end-users a significant energy/cost saving.

ACKNOWLEDGEMENTS

The project “Demonstration of non-HFC alternatives to HCFC-22 in retail installations in countries with high ambient temperatures” leading to these results received funding from the Climate and Clean Air Coalition (CCAC - http://ccacoalition.org/en). Activities were implemented by UNIDO and supported by the Ministry of Environment of Jordan.

The project showcases the feasibility of non-hydrofluorocarbon-based technology in high-ambient temperature environments, in the context of the international environmental agreement (the Montreal Protocol) to phase out hydrochlorofluorocarbons (HCFCs), subsequently extended to a phase-down of HFCs by the Kigali Amendment.

REFERENCES

Commission, E., 2014. *Regulation (EU) No 517/2014 of the European Parliament and of the Council of 16th April 2014 on fluorinated greenhouse gases and repealing Regulation (EC)*.

Finckh, O., Schrey, R., Wozny, M., & Refrigeration, I. I. o., 2011. Energy and efficiency comparison between standardized HFC and CO2 transcritical systems for supermarket applications. Proceedings of the 23rd International Congress of Refrigeration; Prague, Czech Republic.

Gullo, P., & Cortella, G., 2016. Comparative Exergoeconomic Analysis of Various Transcritical R744 Commercial Refrigeration Systems.

Gullo, P., Elmegaard, B., & Cortella, G., 2016. Energy and environmental performance assessment of R744 booster supermarket refrigeration systems operating in warm climates. *International Journal of Refrigeration-Revue Internationale Du Froid, 64*, 61-79. doi:10.1016/j.ijrefrig.2015.12.016

Hafner, A., Forsterling, S., & Banasiak, K., 2014. Multi-ejector concept for R-744 supermarket refrigeration. *International Journal of Refrigeration-Revue Internationale Du Froid, 43*, 1-13. doi:10.1016/j.ijrefrig.2013.10.015

Kauf, F. (1999). Determination of the optimum high pressure for transcritical CO 2-refrigeration cycles. *International Journal of Thermal Sciences, 38*(4), 325-330. doi:10.1016/S1290-0729(99)80098-2

Kim, M. H., Pettersen, J., & Bullard, C. W. (2004). Fundamental process and system design issues in CO2 vapor compression systems. *Progress in Energy and Combustion Science, 30*(2), 119-174. doi:10.1016/j.pecs.2003.09.002

Lorentzen, G., & Pettersen, J. (1993). A New, Efficient and Environmentally Benign System for Car Air-Conditioning. *International Journal of Refrigeration-Revue Internationale Du Froid, 16*(1), 4-12. doi:Doi 10.1016/0140-7007(93)90014-Y

Matthiesen, O., Madsen , K., & Mikhailov, A. (2010). Evolution of CO2 systems design based on practical experiences from supermarket installations in Northern Europe. *In: Proceedings of the 9th IIR Gustav Lorentzen Conference on Natural Working Fluids; 12th – 14th April; Sydney, Australia*.

Minetto, S., Girotto, S., Salvatore, M., Rossetti, A., & Marinetti, S. (2014). *Recent installations of CO2 supermarket refrigeration system for warm climates: data from field*. Paper presented at the Proceedings of the 3rd IIR International Conference on Sustainability and Cold Chain London, UK.

Purohit, N., Gullo, P., & Dasgupta, M. S. (2017). Comparative assessment of low-GWP based refrigerating plants operating in hot climates. *International Conference on Recent Advancement in Air Conditioning and Refrigeration, Raar 2016, 109*, 138-145. doi:10.1016/j.egypro.2017.03.079

Sawalha, S. (2008). Theoretical evaluation of trans-critical CO2 systems in supermarket refrigeration. Part II: System modifications and comparisons of different solutions. *International Journal of Refrigeration-Revue Internationale Du Froid, 31*(3), 525-534. doi:10.1016/j.ijrefrig.2007.05.018

Sawalha, S., Piscopiello, S., Karampour, M., Manickam, L., & Rogstam, J. (2017). Field measurements of supermarket refrigeration systems. Part II: Analysis of HFC refrigeration systems and comparison to CO2 trans-critical. *Applied Thermal Engineering, 111*, 170-182. doi:10.1016/j.applthermaleng.2016.09.073

Stene, J. (2005). Residential CO 2 heat pump system for combined space heating and hot water heating. *International Journal of Refrigeration, 28*(8), 1259-1265. doi:10.1016/j.ijrefrig.2005.07.006

Manuscript ID: 1047
DOI: 10.18462/iir.icr.2019.1047

First field test results of a solar thermal off-grid refrigerator for vaccines

Roland KÜHN[(a)], Kilian MÄHNE[(a)], Karsten DÜWEL[(a)], Christoph GÖLLER[(a)], Julia RÖMER[(a)]

[(a)] Coolar UG (haftungsbeschränkt)
Berlin, 13187, Germany, roland@coolar.co

ABSTRACT

This paper presents the first results from field-testing a novel solar heat driven off-grid medical refrigerator. The refrigerator is cooled by a miniature adsorption cycle, designed to run without any electricity. It is powered by hot water heated by a standard solar thermal collector, in contrast to other solar off-grid adsorption refrigerators. Water is used as the refrigerant.
Firstly, the configuration of the Coolar adsorption refrigerator is introduced and then results from the first autonomous test are discussed, followed by an outlook on future steps.
The refrigerator compartment temperature needs to stay within 2 to 8 °C at ambient temperatures of up to 32°C to satisfy the World Health Organization's (WHO) requirements for off-grid vaccine refrigerators in temperate climates. This goal has not been fully achieved. However, easy to implement measures for improvement were identified and will be conducted to ensure sufficient performance of new prototypes ahead of the subsequent field tests.
Keywords: Adsorption Cooling, Vaccine Storage, Global South, Solar Thermal, Off-Grid.

1. INTRODUCTION

Close to one billion people worldwide have no access to electricity (IEA, 2018) and many more have no reliable access. For many of these people a sufficient medical care is not guaranteed since many medicines require cooling and this is largely realized with electricity driven refrigerators. The case of vaccines is especially severe because they mostly have to be stored between 2 and 8°C and they are highly needed for the immunization of children. According to Ozawa et al. (2016), every dollar invested in effective child vaccination in a low- or middle-income country yields $16 of economic benefit through prevention of diseases. The impact even reaches up to $44, if the increased productivity and the generally improved state of health are considered (Ozawa et al., 2016). However, in 2014 98% of the off-grid utilities in developing regions had either out-dated (23%), improper (41%), non-functioning (14%) or not any (20%) refrigeration solutions (WHO/UNICEF, 2016). As a result, vaccines are exposed to the risk of inadequate or excessive cooling in 78% of all cases (WHO/UNICEF, 2016). With insufficient cooling, the vaccines slowly lose effectiveness, while freezing immediately spoils the vaccines. Therefore, big investments are done by NGOs and ministries of health (McCarney et al., 2013) to reliably cool vaccines at between 2 and 8 °C in the affected regions in the Global South.
The most common off-grid cooling systems include electric refrigerators powered by photovoltaic or diesel generators and direct-fired absorption refrigerators (McCarney et al., 2013). In the latter systems, fuel procurement is often a challenge, while photovoltaic systems struggle with short battery life-time (WHO/UNICEF, 2017) and decreasing conversion efficiency at high ambient temperatures or diffusive solar radiation. Today, the WHO recommends using vaccine refrigerators without electrical storage and without the need for fuel (WHO/UNICEF, 2017). As a result, the current primary solution, so-called SDD ("solar direct drive") refrigerators, are sold. These use ice storages in the refrigerator to store the cold instead of storing electrical energy in batteries. A problem with this more robust technology is that the compressors are connected directly to the photovoltaic system and therefore are not regulated. Cold is provided as long as sufficient solar irradiation is present. This often results in ice storages becoming either significantly too cold so that the vaccines freeze (WHO/UNICEF, 2017) or the storage space inside the refrigerator not getting cold enough so that no ice is produced (WHO, 2018) and then the desired temperatures cannot be

maintained overnight. In this context, the complex dimensioning of the photovoltaic system plays a crucial role (WHO/UNICEF, 2017).
A completely different alternative are solar thermally driven adsorption refrigerators.

2. SYSTEM DESIGN

The concepts of small solar adsorption cooling units of the previous state of the art as well as their shortcomings will be briefly presented below. Afterwards the system structure of the novel Coolar off-grid vaccine refrigerator, which is also based on adsorption cooling, will be described.

2.1. State of the Art

There were some previous attempts to realize cooling via solar thermally driven adsorption refrigeration units in the last 30 years. In these approaches the utilisation of solar thermal energy and the actual refrigeration are separate phases of the overall process. Thus, cooling can be provided even though the sun is not shining, and the cooling can take place over a much longer period of time than solar irradiation is available (Anyanwu and Ezekwe, 2003). This represents a clear difference to photovoltaic refrigerators (WHO, 2018).
Most of the concepts developed over the last 30 years produce either cold water or ice at night. There is no temperature control and methanol is used as the refrigerant (N'Tsoukpoe et al., 2014). They use solar thermal collectors that are filled with the sorption medium (N'Tsoukpoe et al., 2014; Boubakri, 2000/1992). These have to be connected to the cooling unit in a vacuum-tight manner, which greatly limits the flexibility to place the refrigerator according to user's needs and makes the system very prone to failure from leakages. Sufficient ice production for cooling has so far only been achieved at ambient temperatures well below 30 °C (Anyanwu and Ezekwe, 2003; Boubakri, 2000,1992). Fig. 1 shows the typical structure of solar thermal adsorption refrigeration units according to the prior art. At the highest point of the system is a solar collector that is filled with an adsorbent, and therefore also serves as the adsorber (Anyanwu and Ogueke, 2007). Below are a condenser, a condensate collector, an evaporator and the cooling compartment. The whole system works under vacuum.

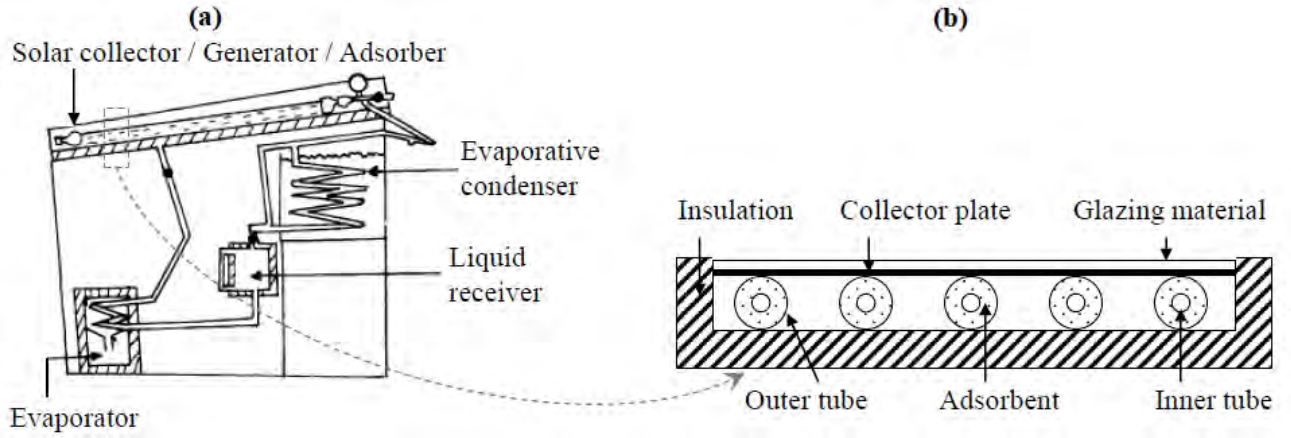

Figure 1: State of the art for solar adsorption refrigerators (Anyanwu and Ogueke, 2007)

At night, the solar collector and the adsorbent that it contains cool down. Thus, the pressure in the entire system decreases and the refrigerant in the evaporator starts to evaporate. The vapour is soaked up by the adsorbent, more refrigerant evaporates and the evaporator cools down. During daytime the solar irradiation heats up the solar collector and the adsorbent therein, the adsorbed refrigerant evaporates and ideally condenses completely in the condenser. The condensate flows into the condensate collector and then into the evaporator within the cooling compartment. If no valve is arranged in front of the evaporator, the evaporator is heated significantly during the day by the warm water or by incompletely condensed vapour from the condenser (Boubakri, 1992; Anyanwu and Ezekwe, 2003). Thus, the intervention of the user is always required, as they have to manually transfer either the stored goods or the ice (Boubakri, 1992/2000) into a separate cool box.

2.2. Setup of the Adsorption Cycle of the Coolar Prototype

Fig. 2 shows a schematic of the setup of the Coolar refrigerator in a side and rear view. Like other adsorption refrigeration units, the Coolar refrigerator also consists of an evaporator, a condenser and an adsorber. During refrigeration, the refrigerant water evaporates in the evaporator, flows through a pipe and a valve and is adsorbed in the adsorber. If the adsorbent is saturated, it must be regenerated. For this purpose, pipes are provided inside the adsorber. Hot water flows through them during the regeneration phase and supplies heat to the adsorber. The refrigerant evaporates from the adsorbent and flows through a pipe and a valve into the condenser where it is condensed. The condenser and evaporator are directly coupled through a U-tube. Thus, small amounts of refrigerant are returned to the evaporator during the entire regeneration. Simultaneously, the U-tube acts as a throttle, so that the refrigerant flows into the evaporator with evaporator temperature (Kühn et al., 2018a) and not with condenser temperature as in the state of the art (see above) (Boubakri, 1992). As a result, the temperature stability inside the refrigerator compartment is significantly increased, which is very important for vaccine cooling.

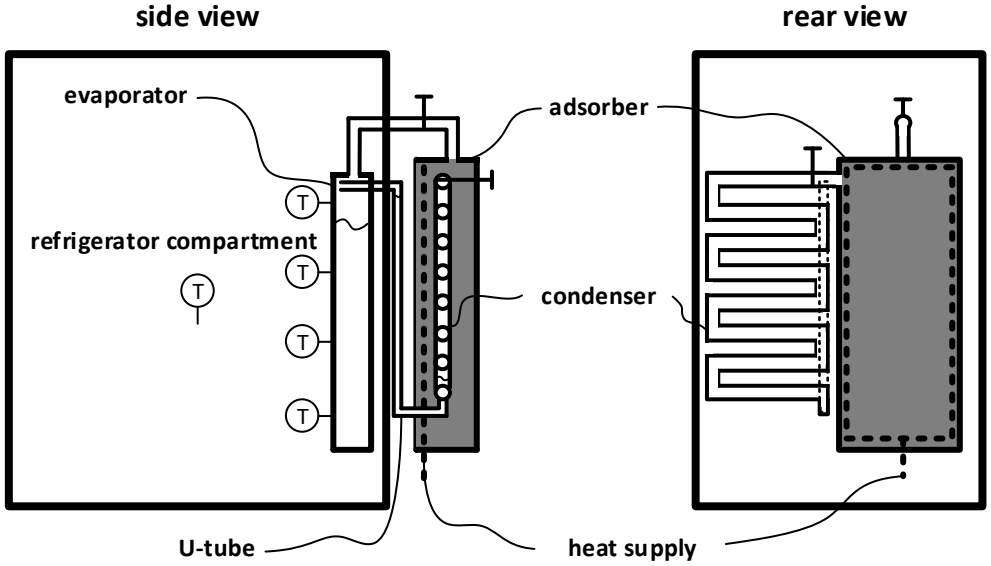

Figure 2: schematic of the prototype setup according to Kühn et al. (2018a)

The valves for the separation of evaporator and adsorber and accordingly adsorber and condenser are in-house developed automatic check valves which respond to pressure differences of less than 1 mbar. Since the presented concept is a single-chamber system, no cooling of the refrigerator compartment takes place during the regeneration phase.

2.3. The External Circuits

Like the Coolar refrigerator, most adsorption cooling machines do not require electrical power internally. In order to enable off-grid operation completely without power, the external circuits have to operate without electrical power, too. The evaporator developed for the vaccine refrigerator enables cooling over all side walls and over the entire height of the refrigerator compartment. In addition to this, even complete freezing of the refrigerant water does no damage to the evaporator. When ice is formed the cooling process is strongly limited, so that the evaporator is preserved at 0 °C to prevent freezing of vaccines inside of the storage area. Thus, the large evaporator area is necessary to ensure the required refrigerator compartment temperature of 2 to 8 °C even at such small cold side temperature differences. The condenser is passively cooled with ambient air.
Heat has to be supplied to the adsorber during regeneration and has to be removed from the adsorber during cold production. The heat is supplied by a solar thermal hot water system. For this purpose, pipes are present within the adsorber in such a manner that allows a natural circulation of the hot water through the adsorber and solar thermal collector (solid red arrows, Fig. 3). In order to ensure the natural circulation, the upper end of the solar thermal collector must be located lower than the top end of the adsorber. A possible setup with the prototype investigated here can be seen in Fig. 3.

During adsorption, the pipes in the adsorber are used for recooling. A passive recooler is situated above the adsorber to allow a natural circulation of the cooling water (dashed green arrows, Fig. 3). Thus, the process cycle is controlled over the day night cycle of the sun. When the solar thermal collector heats the water it flows into the adsorber and drives the regeneration. If the solar thermal collector cools down the natural circulation through the collector comes to a standstill and the cooling of the adsorber with the natural flow through the recooler starts and refrigeration is enabled. Thus, the cooling is done as long as no sun shines and typically over a longer period than the regeneration takes place. This long cooling phase particularly distinguishes the adsorption driven from the photovoltaic powered SDD refrigerators. Additionally, the adsorbent as solar energy storage makes the adsorption refrigerators less prone to irregularities from unsuitable weather conditions while also being directly driven with solar energy.



Figure 3: Prototype with 2 m² solar thermal flat plate collector

3. MEASUREMENTS AND RESULTS

In this chapter, the results from the measurement of the prototype of the off-grid vaccine refrigerator are presented and discussed. The off-grid autonomous operation test was carried out in September 2018 in Berlin with two vacuum tube solar thermal collectors supplied by Augusta Solar.
The WHO (2018) issues precise specifications for the approval of vaccine refrigerators for off-grid use:

- compliance with 2 to 8 °C in the refrigerator compartment (short-time between 0-2 °C permissible)
- at constant ambient temperatures: 27 °C(moderate), 32 °C (temperate), 43 °C (hot)
- refrigerator compartment temperatures below 10 °C for up to 3 days in unpowered state (holdover time)
- placement in a locked room

With the prototype presented here, the conditions for a temperate climate with a holdover time of one day are addressed.

3.1. System Balancing

For measuring and balancing the refrigerator prototype, several digital temperature sensors of the type Dallas DS18B20 are used. The measurement uncertainty is 0.5 K.
To determine the cooling capacity, the heat capacity of the refrigerator compartment and the heat infiltration rate into the refrigerator cabinet have to be known. The heat capacity of the refrigerator compartment results from the masses and heat capacities of the internals and fluids. The heat infiltration rate is determined by a heating test. The refrigerator compartment is heated with a pre-determined electrical load P_e until a stationary point is reached. The heat infiltration rate UA can

then be calculated via Eq. (1) and includes both the heat transfer through the refrigerator housing and the air circulation through seals. The heat capacity of the refrigerator compartment without water (C_{W}) is $C_{\mathrm{RC}} = 2.6\ \mathrm{kJ \cdot K^{-1}}$ and the heat infiltration rate $UA = 0.8\ \mathrm{W \cdot K^{-1}}$. In addition to this, there is water as refrigerant in the evaporator and during some measurements in the refrigerator compartment as vaccine equivalent or as cold storage around the evaporator. The cooling capacity $\dot{Q}_0$ can then be calculated via Eq. (2). Here, the temperature difference between the individual refrigerator compartment components as well as their different rate of temperature change is neglected.

$$UA = \frac{P_{\mathrm{e}}}{T_{\mathrm{RC}} - T_{\mathrm{A}}} \qquad \text{Eq. (1)}$$

$$\dot{Q}_0 = \frac{1}{t_2 - t_1} \int_{t_1}^{t_2} [UA \cdot (T_{\mathrm{RC}}(t) - T_{\mathrm{A}})]\ \mathrm{d}t + (C_{\mathrm{RC}} + C_{\mathrm{W}}) \frac{T_{\mathrm{RC}}(t_2) - T_{\mathrm{RC}}(t_1)}{t_2 - t_1} \qquad \text{Eq. (2)}$$

The hot water supply, as well as the recooler cannot be balanced on the prototype since the volume flows in the solar circuit and in the recooler, as well as the volume flow of ambient air at the condenser are unknown.

3.2. Cool-Down and Holdover Test

In the laboratory experiments, the prototype is housed in an enclosure that allows heating of the immediate refrigerator environment to ensure stable ambient temperature conditions throughout testing. The hot water is generated by an electric hot water boiler, whose temperature is limited to 85 °C. The refrigerator contains about 5 litres of water as a vaccine equivalent. The cooling curve of the refrigerator compartment was determined at two different ambient temperature levels. The adsorber is regenerated for 6 hours with hot water temperature at 84 °C. Then the hot water is turned off.

Cool-down curves of the refrigerator compartment and the evaporator for one test at 24 °C and one test at 32 °C ambient temperature are shown in Fig. 4. The evaporator temperature is determined with four temperature sensors, which are attached to the outer evaporator surface at different heights. Fig. 4 shows the arithmetic mean evaporator temperature. The starting point (00:00) is the moment when the hot water supply is switched off. After switching off the heat supply, it takes about 60 minutes at 24 °C ambient temperature until the passive re-cooler has cooled down the heating circuit and the adsorber to the point where adsorption starts. At 32 °C it takes about 80 minutes. In both cases, the lowest refrigerator compartment temperature is reached approx. 9 hours after adsorption begun.

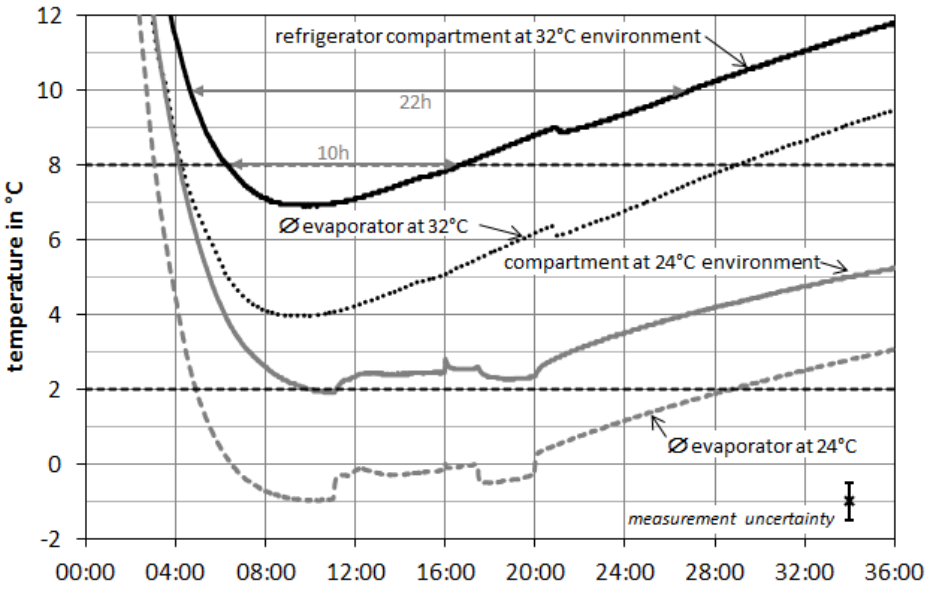

Figure 4: Cool-down and holdover test at laboratory conditions

At 24 °C ambient temperature the minimum refrigerator compartment temperature is 1.7 °C and at 32 °C just 7 °C. At 24 °C ambient temperature, a large part of the water inside the evaporator is initially undercooled until it freezes at about 11 hours after the start of the experiment. At that point,

the temperature in the evaporator and refrigerator compartment rises suddenly. The cold storage, formed by the ice, keeps the refrigerator compartment temperature relatively constant for about 9 hours. The temperature remains below 8 °C for significantly longer than one day.
At 32 °C ambient temperature, the temperature profile is qualitatively similar to the 24 °C test, but the minimum evaporator temperature reached was only 1.8 °C and the mean evaporator temperature 4 °C. Thus, no ice is formed and the low temperature does not remain for a long period. Even though the refrigerator compartment temperature just falls to 7 °C it still remains below the required 8 °C for about 10 hours. When determining the holdover time, where up to 10 °C inside the refrigerator compartment are permitted, a period of about 22 hours was achieved.

3.3. Cooling Capacity in Cool-Down Test

For the cool-down experiments described above, the cooling capacity was determined. Fig. 5 shows the cooling capacity, which is the moving average over one hour. Additionally, the cooling capacity required to compensate the heat infiltration is displayed (dotted lines). If the provided cooling capacity is greater than this minimum cooling capacity for maintaining the refrigerator compartment temperature, the compartment cools down; when the cooling capacity is smaller, the compartment heats up, if no latent heat storage such as ice is present inside.

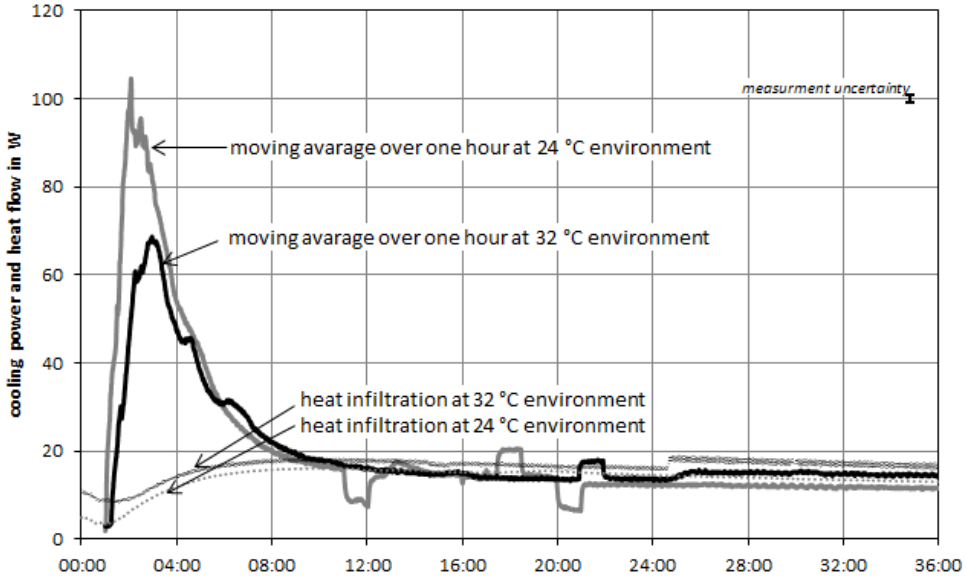

Figure 5: Cooling capacity in the laboratory tests

As is typical for adsorption chillers, the cooling capacity is greatest at the beginning and reaches about 100 W at 24 °C and nearly 70 W at 32 °C ambient temperature. The steep peak of the cooling capacity curve in Fig. 5 is due to the averaging over one hour with zero cooling capacity in the beginning. After a few hours the cooling capacity drops significantly. At 32 °C ambient temperature, the cooling capacity provided by the system falls below the necessary cooling capacity for temperature maintenance after about 10 hours, resulting in the heat-up of the refrigerator compartment and the evaporator seen in Fig. 4. The cooling capacity then stabilizes at about 15 W at 32 °C and slightly less at 24 °C ambient temperatures. This results from the slow increase in the refrigerator temperature over time, which results in an increase in vapour pressure in the evaporator, which also increases the adsorption capacity of the adsorbent that triggers further water vapour adsorption. At the lower ambient temperature of 24 °C, the heat infiltration is less, resulting in a slightly lower cooling capacity in the end. The steps in the cooling capacity are equivalent to the temperature steps in Fig. 4. The last step after 24 hours in the 32 °C curve, results from a spontaneous increase in ambient temperature during the test.

3.4. Autonomous Operation with Solar Thermal Hot Water System

From the beginning of September till mid October 2018, an autonomous operating test was carried out with the grid-independent refrigerator prototype in Berlin. A simple solar thermal system with two direct-flow vacuum tube collectors with an aperture area of almost 2 m² was used. To keep the refrigerator in an environment of approximately 32 °C, it was placed in a separate room, which was

heated by a fan heater. The actual prototype is designed for driving temperatures below 100 °C, to reduce complexity during manufacturing. Therefore, the recooler of the adsorber was coupled to the solar circuit via a thermal valve, so that the maximum driving temperature could not exceed 95 °C. During this test, the refrigerator compartment was furthermore equipped with an additional cold storage of 30 litres of water around the evaporator to improve temperature stability.
Fig. 6 shows the process temperatures and the global solar irradiation (HTW Berlin, 2018) over three cooling cycles of the prototype at the end of September 2018 in Berlin. To illustrate the difference between the solar irradiation in September and the optimal summer irradiation for Berlin, Fig. 6 also shows the irradiation curve of the 7th of June 2018 (HTW Berlin, 2018). It can be seen, that it takes more than one hour after sunrise to provide sufficient hot water to drive the regeneration process due to the heat capacity of the water in the solar circuit. The minimum refrigerator compartment temperature of a day is reached at this time, because the adsorber stops adsorption at this point. During regeneration the refrigerator compartment temperature increases at an almost constant rate. After the regeneration phase, the cooling starts again, as soon as the solar thermal system is cooled down below 50 °C. Similar to the heat incursion during daytime, the cool-down over night occurs at a close to constant rate as well. The ambient temperature varies between 29 and 34 °C due to the on/off control of the fan heater. The increase above 32 °C during the day occurs due to the waste heat during regeneration and the position of the ambient temperature sensor close to the refrigerator.
The hot water temperature on the 20th of September was relatively stable above 90 °C, although the solar irradiation varies significantly. Only with even stronger fluctuations in solar irradiation on the 21st of September a reduction in driving temperature as well as in regeneration time occurs. Nevertheless, the target temperature of below 8 °C in the refrigerator compartment is temporarily reached in the subsequent night. As the single-chamber system cannot supply any cooling during regeneration, the temperature inside the refrigerator compartment increases by up to 6 K during the day, even though a cold storage is installed. The cold storage's capacity could be significantly bigger, if ice was formed instead of only cold water as in the test. . Nevertheless, temperature fluctuations were significantly reduced in comparison to the cyclic laboratory tests without cold storage (Kühn et al., 2018b), where it has been 13 K over the day. Hence, a refrigerator compartment temperature of 2 °C would have to be reached while cooling is applied to remain within the set limit of 2 to 8 °C during daytime, if the refrigerator cabinet is not changed. However, as shown in chapter 3.2, by reaching 2 °C refrigerator compartment temperature it can be considered as certain, that ice is formed within the cold storage close to the evaporator. In that case the refrigerator compartment temperature will be stabilized significantly as shown in Fig. 4 at 24 °C.

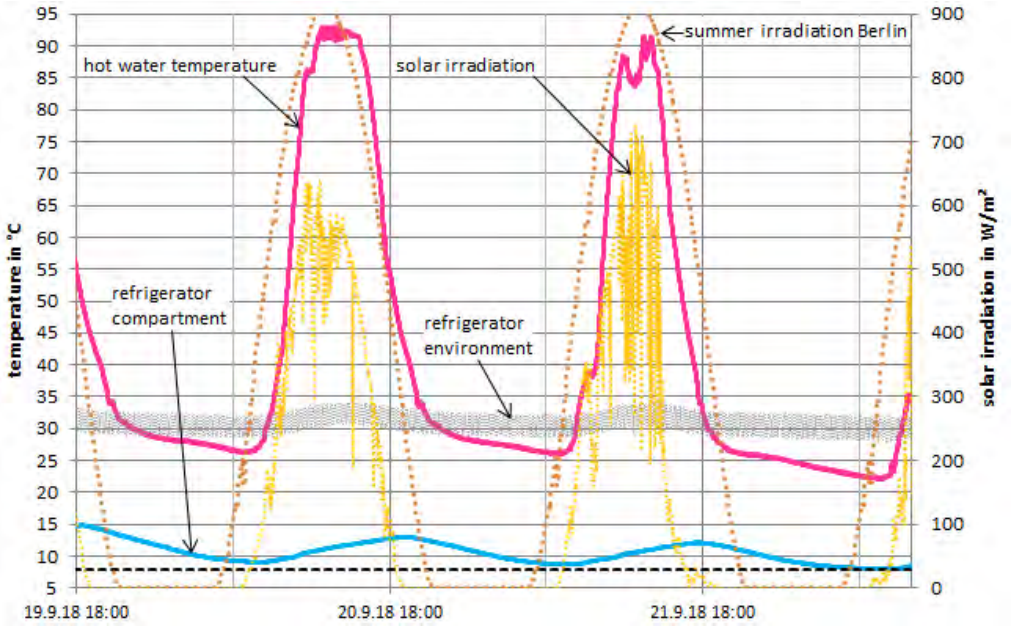

Figure 6: temperature profiles and solar irradiation (HTW Berlin, 2018) in autonomous operation test

To achieve the goal of stable temperatures between 2 and 8 °C inside of the refrigerator, two measures can be undertaken. In particular a refrigerator cabinet with better insulation can be used,

which enables both a lower minimum refrigerator compartment temperature and lower temperature fluctuations. Reducing the heat infiltration by at least 20% is easily possible with refrigerator cabinets already tested by Coolar and would reduce the required cooling capacity accordingly. On the other hand, the cooling capacity can be increased by scaling-up the adsorber. Besides, the regeneration cycle could be extended by up to 4 hours under optimal irradiation conditions during the summer months, as shown in Fig. 6, which also leads to an increase in cooling capacity. The solar energy supply in the target regions is even higher than in Berlin, although the days in closer to the equator locations in the Global South are shorter than in Berlin in the summer. In a field test that was conducted with the very same prototype in Tenerife until April 2019 ice was produced and remained during daytime even with maximum ambient temperatures of 36 °C. This was achieved even though a low-cost and less efficient flat-plate solar collector as shown in Fig. 3 was used.

4. CONCLUSIONS AND OUTLOOK

In the paper at hand, the design of an off-grid solar adsorption refrigerator for vaccine cooling in the Global South was presented. A first prototype for 32 °C constant ambient temperature was built. The target was to provide temperatures between 2 and 8 °C inside the refrigerator compartment and to assure a holdover time without operation below 10 °C for 24 hours. The prototype's performance was measured in the laboratory and in an autonomous operation test in Berlin in September.

The determined cooling capacity of the prototype is between 100 W and 15 W. The refrigerator compartment can be cooled down within 10 hours from ambient temperature to its minimum temperature. Both in the laboratory and in the autonomous test, a refrigerator compartment temperature of less than 8 °C was achieved. However, the refrigerator temperature was within 2 and 8 °C just for 10 hours per day at 32 °C constant ambient temperature and, thus, not permanently within the target temperature range. During the laboratory tests at 24 °C ambient temperature ice is formed inside of the evaporator, which allows an almost constant refrigerator compartment temperature of 2 °C over a period of 9 hours. Thus, a holdover time of several days is achieved at 24 °C ambient temperature, but just 22 hours at 32 °C ambient temperature. A subsequent field test with the very same prototype that was conducted up until April 2019 in Tenerife revealed that the performance improves under the local weather conditions, even though a low cost and less efficient flat-plate solar collector is used.

The work on a new prototype for 32 °C ambient temperatures has already begun. To maintain the refrigerator temperature between 2 and 8 °C, it makes use of a refrigerator cabinet with better insulation to reduce both the necessary cooling capacity and the temperature fluctuations in the daily cycle. In addition to this, the adsorber is up-scaled to increase the cooling capacity and the cold storage is improved. The new prototype will be deployed for field testing with a partner in the summer of 2019.

ACKNOWLEDGEMENTS

We thank the EIT Climate-KIC for its support in 2015/16, as well as the Dubai Expo 2020 Expo Live Program for support in the current field test. We also thank our partner Arctiko. Our thanks also go to the many students, journalists, members of NGOs and people from the development cooperation community, as well as private persons, whose interest in and enthusiasm for our activities keeps motivating us to move forward and develop the best solutions possible and to pursue their wide dissemination.

NOMENCLATURE

C	heat capacity ($J \times K^{-1}$)	*A*	ambiance
P_e	electrical power input (W)	*RC*	refrigerator compartment
$\dot{Q}_0$	cooling capacity (W)	*W*	water
t	time (s)		
T	temperature (K)		
UA	heat infiltration rate ($W \times K^{-1}$)		

REFERENCES

Anyanwu, E.E., Ezekwe, C.I., 2003. Design, construction and test run of a solid adsorption solar refrigerator using activated carbon/methanol, as adsorbent/adsorbate pair. Energy Conversion and Management 44(18), 2879-2892.

Anyanwu, E.E., Ogueke, N.V., 2007. Transient analysis and performance prediction of a solid adsorption solar refrigerator. Applied Thermal Engineering 27(14-15), 2514-2523.

Boubakri, A., Guilleminot, J.J., Meunier, F., 2000. Adsorptive solar powered ice maker: experiments and model. Solar Energy 69(3), 249-263.

Boubakri, A., Arsalane, M., Yous, B., Ali-Moussa, L., Pons, M., Meunier, F., Guilleminot, J.J., 1992. Experimental study of adsorptive solar-powered ice makers in Agadir (Morocco) - 1. Performance in actual site. Renewable Energy 2(1), 7-13.

HTW Berlin, 2018. Weather data of HTW Berlin. http://wetter.htw-berlin.de/SolarCalendar.

IEA - International Energy Agency, 2018. World Energy Outlook 2018. OECD/IEA.

Kühn, R., Mähne, K., Römer, J., 2018a. Sorptionskältevorrichtung - Patent EP 3351873A1, EPA.

Kühn, R., Mähne, K., Düwel, K., Göller, C, Römer, J., Zimmermann, A., 2018b. Vorstellung eines neuartigen Adsorptionskühlschranks für die Impfstoffkühlung in netzfernen Regionen: Systemaufbau und erste Ergebnisse, Proceedings DKV Tagung, Aachen.

McCarney, S., Robertson, J., Arnaud, J., Lorenson, K., Lloyd, J., 2013. Using solar-powered refrigeration for vaccine storage where other sources of reliable electricity are inadequate or costly, Vaccine 31(51), 6050-6057.

N'Tsoukpoe, K.E., Yamegueu, D., Bassole, J., 2014. Solar sorption refrigeration in Africa, Renewable and Sustainable Energy Reviews 35, 318-335.

Ozawa, S., Clark, S., Portnoy, A., Grewal, S., Brenzel, L., Walker, D.G., 2016. Return on investment from childhood immunizations in low- and middle-income countries 2011-20. Health Affairs (Millwood) 35(2), 199-207.

WHO, 2018. PQS devices catalogue. WHO website.

WHO/UNICEF, 2016. Achieving immunization targets with the comprehensive effective vaccine management (EVM) framework. WHO/UNICEF Joint statement.

WHO/UNICEF, 2017. Solar direct-drive vaccine refrigerators and freezers: evidence brief. WHO website.

Manuscript ID: 1091
DOI: 10.18462/iir.icr.2019.1091

Energy efficiency in cold store refrigeration systems

Anna LAURI[(a)], Alessia ARTECONI[(a)], Lino CASALENA[(b)], Fabio POLONARA[(a,c)]

[(a)]Università Politecnica delle Marche, Dipartimento di Ingegneria Industriale e Scienze Matematiche, Via Brecce Bianche 12, Ancona (AN), 60131, Italy, a.arteconi@univpm.it, a.lauri@pm.univpm.it, f.polonara@univpm.it

[(b)]Frigo Tecnica Internazionale, Via Valtesino km 4500, 63065, Ripatransone (AP), Italy, l.casalena@frigotecnica.com

[(c)]Consiglio Nazionale delle Ricerche, Istituto per le Tecnologie della Costruzione, Viale Lombardia 49, San Giuliano Milanese (MI), 20098, Italy

ABSTRACT

Refrigerated warehouses for chilled and frozen foods represent a large portion of the energy demand in the refrigeration sector. This paper analyses the influence of different configurations and technologies in industrial refrigeration systems. Furthermore, given the absence of a clear methodology to assess the energy performance of commercial and industrial refrigeration systems and a reference baseline to quantify the effect of actions to improve such performance, this study wants to contribute to increase the awareness towards the role of certain design features on the overall behavior of the system. A survey among Italian companies in this specific sector together with simulation analysis are used to present the state of the art in industrial refrigeration systems and to quantify the effect of potential technological improvements.
Keywords: Energy Efficiency; Industrial Refrigeration; Cold Store; Compressor.

1. INTRODUCTION

Refrigerated warehouses generally store food at cold temperature (typically between 0 °C and -10 °C), frozen temperature (typically until -42 °C) and storage temperature (typically until -35 °C). While in the first two cases a transformation of the product from the entry to the exit of the cell is expected, in the last case the cold stores provide only the food stocking.

In 2012, in Europe there were approximately 1.6 million cold stores, of which 67% were small stores with a volume of less than 400 m^3 (Mudgal et al., 2011). The cold chain is believed to be responsible for approximately 2.5% of global greenhouse gas emissions through direct and indirect energy consumption effects (Guilpart et al., 2008). In cold storage facilities, 60-70% of the electrical energy is used for refrigeration, therefore there is a high interest in reducing such energy consumption (Evans et al., 2014). In their project ICE-E, Evans et al. (2014) identified different actions to increase the energy efficiency in this sector by means of a survey among cold storages in Europe. These actions consist of optimizing usage of stores, repairing current equipment and retrofitting energy efficient equipment. Most energy saving options were only selected and installed after a case had been made for a relatively short payback period. This often required a level of knowledge not possessed by most of the cold store operators. It was therefore difficult for cold store operators to obtain a clear and unbiased view on whether energy saving options would be worthwhile in terms of carbon and financial savings.

In 2002, the International Institute of Refrigeration (IIR) estimated that cold stores use between 30 and 50 kWh/m^3/year (Duiven et al., 2002). The minimum value from this study was similar to values from a study carried out in the Netherlands by Bosma (1995), who found the average energy consumption of cold stores to be 35 kWh/m^3/year. Previous detailed energy audits carried out by other researchers (Evans and Gigiel, 2007; Evans and Gigiel, 2010) on a small number of cold stores have shown that energy consumption can dramatically exceed the values reported above, reaching values 30-40% higher.

This paper presents a collection of data from 4 refrigerated warehouses. The performance of 4 cold stores were examined to determine the initiatives that could be implemented to save energy.

2. CASE STUDY

The purpose of this survey is to identify the areas with the most common problems and where most of electrical energy can be saved. These actions are intended to encourage owners of cold stores to undertake energy efficiency initiatives, such as installation of new technologies and equipment. To this end, a questionnaire similar to the one used in the ICE-E project (Foster et al., 2016) on energy efficiency was proposed to Italian companies operating in the cold chain. Since the main interest of the present work was to establish a baseline of cold-chain plant configurations in Italy and their corresponding degrees of improvement, some questions of the original questionnaire have been modified accordingly.

The audit started in July 2018 and was developed using a Google Modules web application. The data were saved in a Google database. The survey allowed participants, owners of cold stores, to initially register their details and then to enter data about as many refrigeration systems as they wished. This audit was set up to collect information per single refrigeration system that might supply one of the several cold stores. The survey was designed to be user-friendly, so that a cold-store operator should take only a few minutes to complete it. The link to the survey was sent by e-mail. After this first contact with the companies, additional in-depth worksheets were sent them. The audits were selected to cover different locations, sizes, types and uses. The data from these audits were used as inputs to specific simulation models, in order to highlight where improvements could be achieved. To date, only 4 companies have joined the project by answering the survey. In order to maintain the anonymity of sensitive data, the companies have been identified with codes (A, B, C and D for the present study). Table 1 provides the main information of the companies under study.

Table 1. Main data of the companies under study

Parameter	A	B	C	D
Electrical power supplied by the electricity company (kWe)	900	900		310
Electrical power of the refrigeration system (kWe)	1800	200	850	240
Electrical power of the compressors (kWe)	1480	500	600	220
Electrical energy of the refrigeration system (kWh·year^{-1})	2780601	1500000	2800000	500000
Handling input of food and finished raw materials (t· year^{-1} at room temperature)	4300	700		
Handling input of food and finished raw materials (t· year^{-1}of chilled food: 0/+4 °C)	1250	100	800	
Handling input of food and finished raw materials (t· year^{-1}of frozen food: -18 °C)	6300	100	5000	9000
Plant production temperature (°C)	15	25	15	25
Plant storage temperature (°C)	-18	-18	-25	-25
Plant production volume (m^3)	25872	21000		0
Plant storage volume (m^3)	20076	9000		13000
Refrigeration cycle	Single stage economized	Single stage economized	Single stage economized	Single stage
Compressor type	Open screw cooled with liquid injection	Open screw cooled with liquid injection	Open screw cooled with liquid injection	Screw semi-hermetic
Primary refrigerant	Ammonia	HFC (R404A)	Ammonia	HFC (R404A)

For all the 4 companies, the annual turnover is less than 50 million euros. The age of the plants is more than 20 years for the companies A and C, and between 10 and 20 years for the companies B and D. The companies A, B and C are characterized by the same kind of food storage. In particular, they have:

- storage cells where the handling of incoming loads is the same as for outgoing loads;
- transformation of the chilled products;
- transformation of the frozen products.

However, due to the inaccuracy of the data provided, it was not possible to estimate the exact amount of loads divided between frozen, chilled and food storage, and therefore efficiency in the three cases. The company D, instead, deals with food storage only.

3. SYSTEM MODELING

The refrigeration systems installed in the considered companies were modelled with BITZER Software (BITZER, 2018) and EES (Engineering Equation Solver) (EES, 2019). Fig. 1 depicts the data flow of the system modelling. Based on the data provided by the survey, the refrigeration system cooling power and the evaporating/condensing temperatures were used as inputs of BITZER Software. As concerns the evaporating temperature, for the simulation under study a value of -35 °C was considered for the cases A, B and C. This value, in fact, allowed to determine the refrigeration system COP necessary for freezing, which represents the worst-case condition. For case D, instead, an evaporating temperature of -40 °C was selected in order to take into account an approach of 5 °C in the evaporators. For all the cases, the condensing temperature was considered to be equal to 35 °C in summertime and equal to 25 °C in wintertime. These temperatures were considered to be adequate for the outdoor conditions of the sites under study.

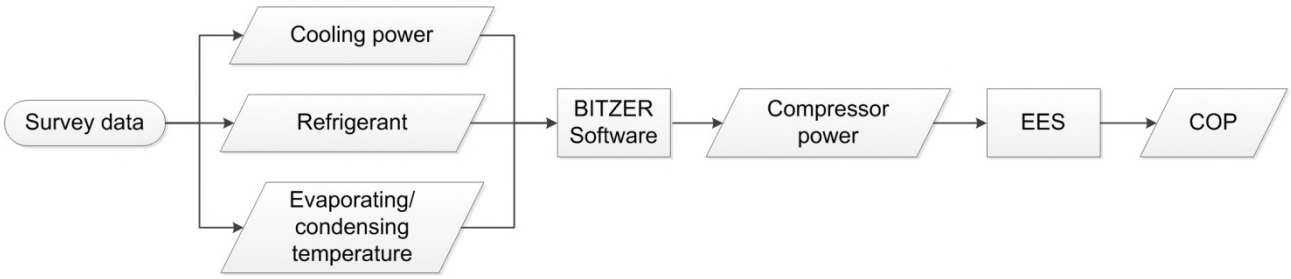

Figure 1: Dataflow of the system modelling

Using the refrigeration system cooling power and the evaporating/condensing temperatures defined as above, BITZER Software allowed to check the compressor size and determine the correct compressor power to use for the simulation. For the case A and C, it has been verified that the compressor suitable for the economized system and ammonia is the model OSNA8591-K. For the cases B and D, instead, the results of the survey did not specify the actual refrigerant used, but only its type (HFC). For this reason, in both cases it was assumed R404A as refrigerant. Specifically, the compressor selected by BITZER Software was OSNA8571-K for case B and HSN7451-60-40P for case D.

The compressor power estimated by BITZER Software was therefore used as an input of an EES model that simulates the refrigeration systems under study. Two refrigeration cycles were considered: a single-stage vapour-compression cycle that is representative of the plant schemes considered, and a two-stage vapour-compression cycle that was considered as an improvement of the first system. Both the schemes realize subcooling of the refrigerant (1 °C) by means of an economizer. A superheating of 1 °C was also considered in order to avoid suction of liquid refrigerant at the compressor stage. Fig. 2 shows the schematics of the refrigeration cycles simulated with EES.

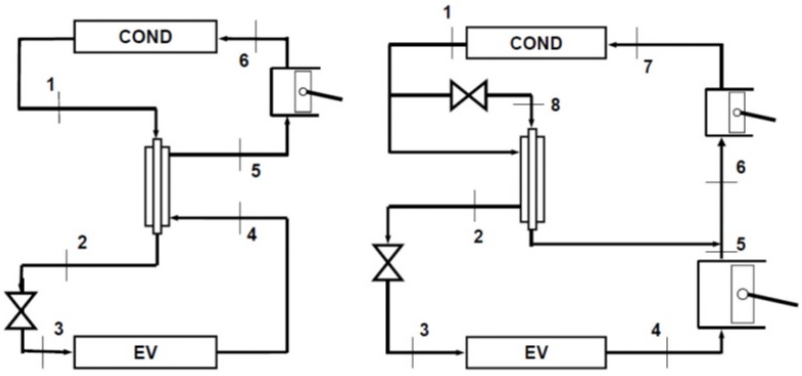

Figure 2: Schematics of the refrigeration cycles: single-stage (left) and two-stage (right)

4. RESULTS

Based on the inputs provided by the survey and by BITZER Software, the COP determined by EES for the case A was equal to 1.63 and 2.30 for the summertime and the wintertime conditions, respectively. For instance, Fig. 3 shows the thermodynamic inverse cycle associated to the single-stage system during the summer period.

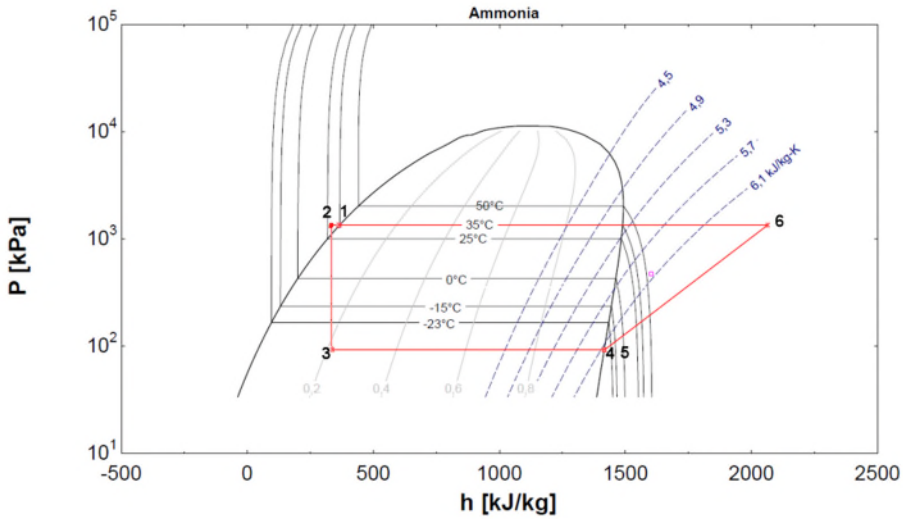

Figure 3: Thermodynamic cycle of the single-stage system for case A-C in summertime

The yearly average COP, determined by the summer/winter values considered above, is equal to 1.97. This COP, however, does not take into account the losses associated to liquid injection and the internal and external cycle irreversibility. In order to account for these losses, a penalization of -30% was considered (Cavallini and Mattarolo, 1992). In this way, the real yearly average COP for the case A is 1.38. This COP is also valid for case C as the refrigeration system associated to this case has the same input values of case A.

As regards case B, the COP calculated by EES for the summer condition is equal to 1.57 while the COP obtained for the winter condition is 2.05. Fig. 4 shows the thermodynamic cycle corresponding to the summer condition. In a same fashion of case A, the yearly average COP was determined to be 1.81. Additionally, considering again a penalization of -30% that accounts for the irreversibilities of the real thermodynamic cycle, the real COP for case B is determined to be 1.27.

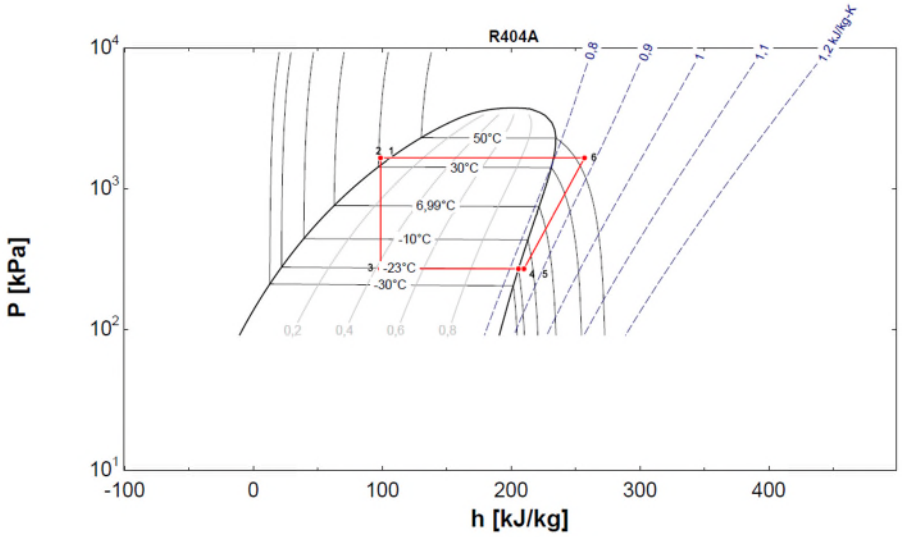

Figure 4: Thermodynamic cycle of the single-stage system for case B in summertime

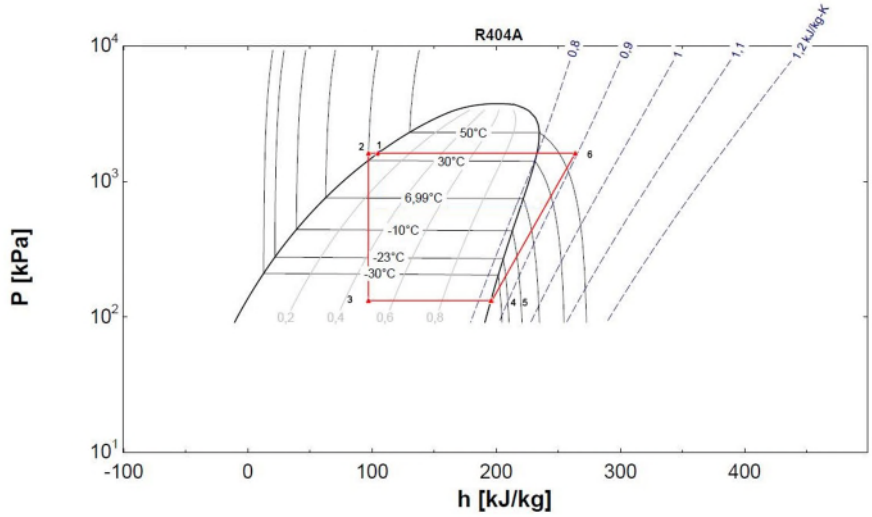

Figure 5: Thermodynamic cycle of the single-stage system for case D in summertime

The COP determined by EES for case D is equal to 1.43 in summertime and equal to 1.85 in wintertime. The thermodynamic cycle associated to the summer condition is depicted in Fig. 5. The yearly average COP for case D is therefore 1.64 and, taking into account a -30% inefficiency, the corresponding real COP is 1.15.

A possible solution to improve the efficiency of the considered cases consists of modifying the reference refrigeration system from a single-stage to a two-stage cycle. Considering case A (which is equal to case C, as seen above), the COP of the two-stage vapour-compression cycle during the summer period was determined through EES to be 1.60, while the COP for the winter condition was determined to be equal to 1.97. Fig. 6 depicts the two-stage thermodynamic cycle for the summer condition. The annual average COP is therefore equal to 1.79. The penalization associated to the two-stage cycle does not account for the loss associated to liquid injection, therefore in this case it is possible to consider an inefficiency of -15%. Thus, the real yearly COP for the cases A/C based on a two-stage cycle is equal to 1.52. Respect to the single-stage system, the COP is about 10% higher.

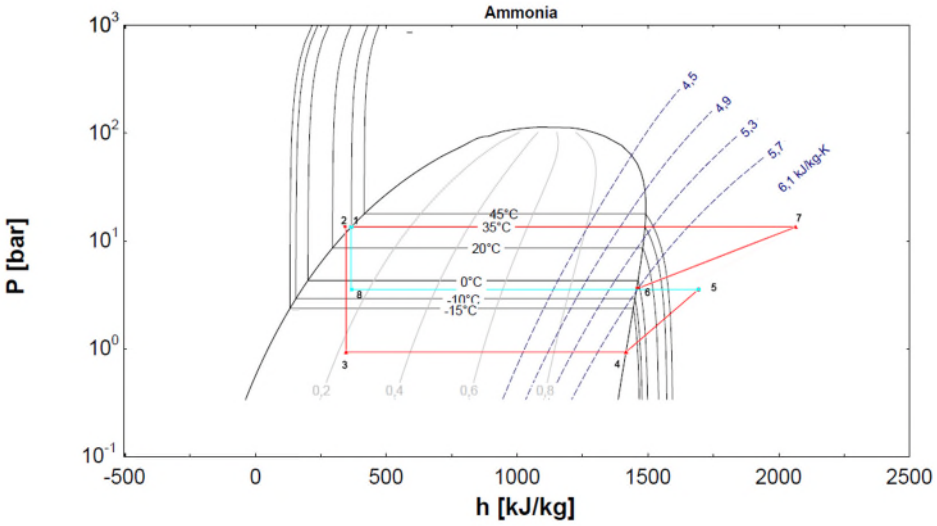

Figure 6: Thermodynamic cycle of the two-stage system for case A-C in summertime

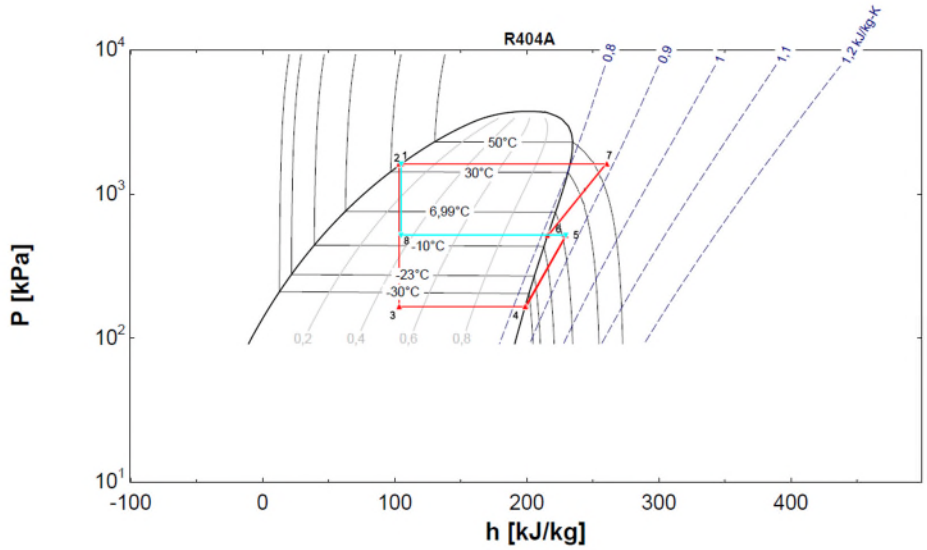

Figure 7: Thermodynamic cycle of the two-stage system for case B in summertime

As concerns the case B, the COP associated to the two-stage vapour compression cycle is equal to 1.56 during the summer period and to 2.05 in the winter period. Fig. 7 shows the thermodynamic cycle referring to the summer condition. Considering these two values, the yearly average COP of the cycle is 1.80. Again, taking into account an inefficiency of -15%, the real annual COP is equal to 1.53, value that is around 20% higher than the corresponding single-stage system.

Finally, the two-stage COP for case D is equal to 1.43 for the summer period and 1.85 for the winter period. The thermodynamic cycle corresponding to the summer period is shown in Fig. 8. The yearly average COP is 1.64; when accounting for a penalization of -15%, the real COP is determined to be 1.39. This COP is about 21% higher than the corresponding single-stage value.

Table 2 summarizes the COP obtained for the different 4 cases.

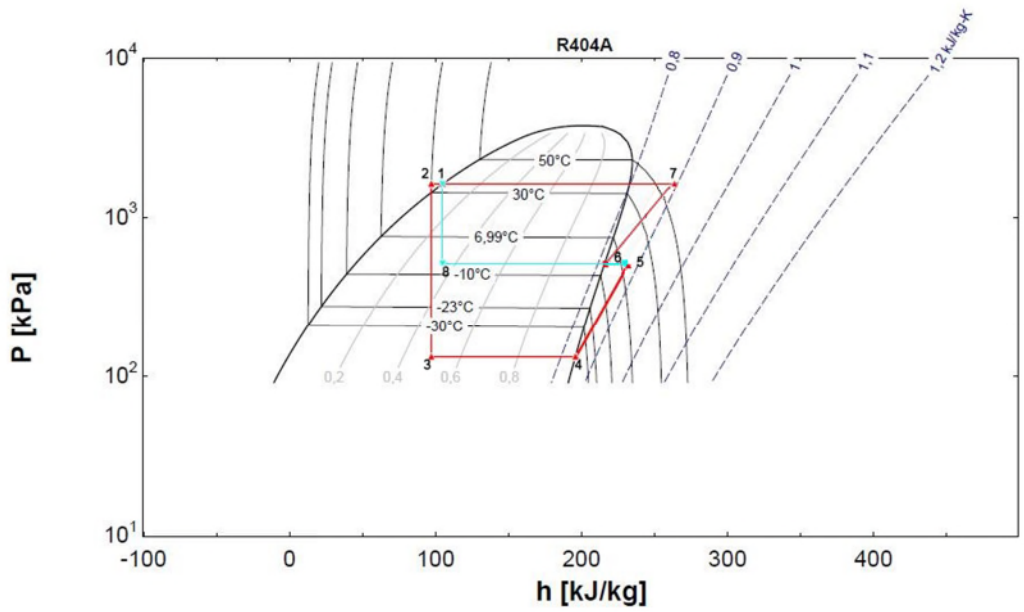

Figure 8: Thermodynamic cycle of the two-stage system for case D in summertime

Table 2. COP of the considered cases (single-stage and two-stage compression)

-	COPr (single-stage)	COPr (two-stage)
A	1.38	1.52
B	1.27	1.53
C	1.38	1.52
D	1.15	1.39

5. CONCLUSIONS

In spite of the few data available, this study tried to shed light on the Italian panorama of refrigerated warehouses. In particular, it estimates which COP can be expected by real refrigeration systems installed in companies operating in the refrigeration sector. The data of 4 companies (A, B, C, D), obtained from a technical survey, were used as inputs of mathematical models developed with BITZER Software and EES. The following COP were found for the refrigeration systems of the 4 companies: 1.38, 1.27, 1.38 and 1.15. All these COP refer to a vapour-compression cycle operating according to a single-stage system. The study also demonstrates that it is possible to achieve higher efficiencies in terms of COP by adopting a two-stage system. In this case, the 4 refrigeration systems show COP of 1.52, 1.53, 1.52 and 1.39, values that are more than 10% higher than the corresponding single-stage COP.

ACKNOWLEDGEMENTS

This work has been supported by MIUR of Italy in the framework of PRIN2015 project: “Clean heating and cooling technologies for an energy efficient smart grid”, Prot. 2015M8S2PA.

REFERENCES

BITZER, 2018. BITZER Software 6.9.1.2074. URL: https://www.bitzer.de/websoftware

Bosma, J., 1995. Inventory study of the energy conservation potential in cold storage insulations in

the Netherlands. 19th International Congress of Refrigeration, Vol. II, 382-391.

Cavallini, A. and Mattarolo, L., 1992. Termodinamica applicata. Cleup.

Duiven, J. E. and Binard, P., 2002. Refrigerated Storage: New Developments. Bulletin of the IIR, Vol. 2002-2.

EES, 2019. Engineering Equation Solver. URL: www.fchart.com/ees

Evans, J. A. and Gigiel, A. J., 2007. Reducing the energy consumption in cold stores. 22nd IIR International Congress of Refrigeration, Beijing, China.

Evans, J. A. and Gigiel, A. J., 2010. Reducing energy consumption in cold storage rooms. IIR ICCC, Cambridge.

Evans, J. A., Hammonda, E. C., Gigiel, A. J., Fostera, A. M., Reinholdt, L., Fikiin, K., Zilio, C., 2014. Assessment of methods to reduce the energy consumption of food cold stores. Appl. Therm. Eng. 62, 697-705.

Foster, A. M., Reinholdt, L. O., Brown, T., Hammond, E. C., Evans, J. A., 2016. Reducing energy consumption in cold stores using a freely available mathematical model. Sust. Cities and Soc. 21, 26-34.

Guilpart, J., 2008. Froid et alimentation: Sécurité, sûreté ou proceed. Conférence Centenaire du froid, Paris, France.

Mudgal, S., Tinetti, B., Bain, J., Cervantes, R., de Prado Trigo, A., 2011. Preparatory study for Eco-design requirements for EuPs Lot 1. Task 2: Economic and market analysis, Paris, France.

Manuscript ID: 1103
DOI: 10.18462/iir.icr.2019.1103

Global market and policy trends for CO_2 in refrigeration

Klara ZOLCER SKAČANOVÁ[(a)]
[(a)] shecco
Brussels, 1000, Belgium, klara.skacanova@shecco.com

ABSTRACT

This article outlines the main market, technology and policy trends for CO_2-based systems primarily in commercial and industrial refrigeration. In commercial refrigeration, CO_2 transcritical is quickly becoming the mainstream technology for new stores, with close to 20,000 stores using this technology globally today. In Europe, CO_2-based supermarkets account for 14% of total food retail stores (over 400m^2) and the projections indicate the number of stores could grow to 65,000 – 85,000 by 2030.
In Japan, CO_2 condensing units are a well-established technology with more than 8,500 units running in the market by the end of 2017. Manufacturers in other parts of the world are making progress in commercialisation of CO_2 condensing units and mini boosters, which is expected to have an impact on cost reduction.
The article combines quantitative data from primary research - collected among leading industry players – with theoretical research.
Keywords: CO_2, Transcritical, Commercial Refrigeration, Industrial Refrigeration, Ice Rinks.

1. INTRODUCTION

Cooling is essential to preserve food, medicine, data and ensure comfort. With the growing demand in developing countries and the booming middle class the demand for cooling is expected to rise exponentially over the next decades. Today, most refrigeration and air conditioning technologies rely on man-made fluorinated refrigerants, hydrochlorofluorocarbons (HCFCs) and hydrofluorocarbons (HFCs). Left unchecked, HFCs could account for nearly 20% of global greenhouse gas emissions by 2050.
The Paris Agreement reached among nearly 200 countries at the 21st Conference of the Parties (COP21) to the UNFCCC aims to keep the global temperature rise below two degree Celsius, while pursuing efforts to limit it to 1.5°C (compared to preindustrial levels) by 2100.
In October 2016, world's nations adopted the Kigali Amendment to the Montreal Protocol, a historic accord committing the economies worldwide to significantly reduce consumption and production of HFCs. It is estimated the Kigali Amendment will prevent 80 billion tonnes CO_2e by 2050 under a business as usual scenario, avoiding almost 0.5°C warming by the end of the century. The Kigali Amendment will enter into force on 1 January 2019 and it will affect countries around the world. It is therefore essential to look at future-proof solutions already today.
Driven by the legislative action, increased focus on safety, and proactivity of some technology end-users there has been an increased use of advanced natural refrigerant-based systems in commercial and industrial refrigeration using CO_2. The competition between natural refrigerant solutions is growing as CO_2 is adopted for use in industrial refrigeration, traditionally dominated by ammonia.

2. KEY POLICY DEVELOPMENTS

The legislative pressure on fluorinated refrigerants is intensifying and with the Kigali Amendment to the Montreal Protocol coming in force as of 2019 the opportunities for natural refrigerants, such as CO_2 will become more important. Developed economies will take the lead in the global HFC phase-down with the first cut of 10% in 2019 and a much bigger reduction of 40% in HFCs that will enter in force in 2024 (compared to 2011-2013 levels).

Developing countries are split into two groups under the Kigali Amendment. The first one – which includes China and African nations – will freeze consumption of HFCs by 2024, with their first reduction steps starting in 2029. A second group including India, Iran, Iraq, Pakistan and the Gulf countries will meet a later deadline, freezing their use of these gases in 2028 and reducing consumption from 2032.

The legislative action on HFCs varies across different countries and regions in terms of pace and type of measures to limit the refrigerant emissions. The EU F-Gas Regulation is currently the most advanced piece of legislation. It aims to reduce HFC emissions by 79% by 2030 (compared to average 2009-2012 levels). There are currently signals that the market is moving faster than anticipated. According to research conducted in 2016 (Skačanová, 2016), first-movers who had invested in future-proof HFC-free solutions ahead of the EU-wide regulatory changes were able to reap the benefits of their competitive advantage before the Regulation came into effect. In the survey carried out by shecco among 230 industry representatives, 73% of respondents declared they had taken action before the F-Gas Regulation came into force.

The HFC phase-down already triggered a 5-times increase in HFC prices in 2017 and 20-times increase is expected in 2018 as a result of the 37% cut in HFC quotas and the inclusion of HFCs contained in pre-charged equipment under the phase down (Toby, 2017). This will help build the business case for natural refrigerants even faster. The Regulation will be revised in the future, which might bring about further restrictions on HFCs.

In the U.S., the pressure to move away from HFCs is not so strong yet as in the EU. However, California regulators are moving ahead with ambitious legislation, which would introduce a combination of measures. With the objective to reduce HFC emissions by 40% by 2030, the policy-makers are in the process of designing legislation that would include prohibitions on new equipment using HFCs with GWP over 150 in non-residential refrigeration as of 2021, among other measures.

The state of California is the leader when it comes to environmental legislation in North America. For the past fifty years the California Air Resources Board (CARB) has helped put California among the first US states to adopt clean air regulations for many different polluting sectors, and experience shows that the state's environmental legislation is eventually adopted nationally for the entire US. Already now a growing number of U.S. states are joining efforts to reduce emissions of HFCs with concrete commitments.

In Japan, the shift to CO_2 in refrigeration has been accelerated especially through a subsidy scheme run by the Ministry of the Environment, in addition to regulatory action. In 2017, the Japanese Environment Ministry announced a new 5-year subsidy project (2018 - 2022), helps end-users reduce the capital cost of natural refrigerant technologies in food retail, food manufacturing and cold stores (McLaughlin, 2017). In the financial year 2018, the scheme operated with a budget of ¥6.4 billion (€47 million) and the amount confirmed for the next year is ¥7.4 billion (€58 million) (Yoshimoto, 2018a). In addition to incentivising the end-users to adopt natural refrigerants, the High Pressure Safety Institute of Japan re-classified CO_2 under Japan's High Pressure Gas Safety Act, alleviating the barrier for CO_2 adoption in larger commercial and industrial refrigeration applications (McLaughlin, 2017).

The aforementioned changes in the policy world, together with country-specific initiatives to reduce HFCs, indicate that opportunities are arising for natural refrigerants to penetrate the market more.

3. MARKET TRENDS – FROM NICHE TO MAINSTREAM

The key drivers of the uptake of natural refrigerants in the market are on-going legislative pressure, strong retail groups asking for these solutions, decreasing costs of systems, and increasing efficiency. On the other hand, a lack of trained technicians on HFC alternatives has been seen as a major barrier to the deployment of such technology - a situation, which is slowly improving in maturing markets, such as Europe.

3.1 CO_2 in Supermarket Refrigeration

Commercial refrigeration has been the most dynamic sector in terms of shift to natural refrigerants in recent years across different world regions. CO_2 has become one of the most interesting technologies for new systems and major refurbishments for a number of major retailers who are leading this trend.

Findings indicate that Europe is by far the most advanced region in the level of adoption of CO_2 applications for commercial and industrial refrigeration – mainly as a result of the EU F-Gas Regulation and ambitious legislation in some of the European countries. The strict legislation has pushed companies to innovate and invest in future-proof technology. In the process, leading European companies reported that they had gained a competitive advantage in the global market, which will become even more important as other regions look to reduce their reliance on HFCs. Europe's leading position in CO_2 technology for refrigeration was made possible through the important research of major scientists in this field. Norwegian scientist Gustav Lorentzen, a professor at the University of Trondheim, rediscovered how CO_2 could be used as a refrigerant in heating and cooling applications in the 1980s. Lorentzen developed the modern thermodynamic transcritical CO_2 cycle in 1988-1991, heralding a crucial breakthrough that has led supermarkets to opt for transcritical CO_2 systems in Europe.

It should be noted that there are other natural refrigerant-based technologies used in commercial refrigeration, and the future might see growing competition between CO_2 and hydrocarbons especially in small and medium-sized stores and warmer climates. Overall, regions differ in terms of technology focus, store formats and retailer commitments (Skačanová et al, 2018).

CO_2 is quickly becoming the preferred option in new supermarkets as storeowners are looking to future-proof the refrigeration equipment. With the implementation of the EU F-Gas Regulation, the shift towards CO_2 is expected to intensify in the next few years. On the technology side, CO_2 refrigeration systems are moving towards more compact, easy-to-install and service-friendly design. The growing commercial availability by a large number of suppliers and standardisation of CO_2 boosters have pushed the price of the technology down in the last few years. The cost of CO_2 compressors is now lower than the cost of equivalent HFC compressors. Depending on the market and the technology, the total installation price is currently on par with conventional HFC-based systems or in the range of 5-10% higher. Although the technology for warmer ambient climates using parallel compression or ejectors is currently higher in terms of initial cost, this is expected to go down as technology becomes more widespread (as has been proven for the standard CO_2 booster system). Industry experts estimate that with ejector technology and parallel compression, the price of a system is a maximum 10% higher than traditional booster.

The last three years have seen impressive growth of CO_2 transcritical (TC) systems worldwide, particularly in North America, and the APAC region. The data collected from equipment manufacturers and suppliers, shown in Fig. 1, indicate that Europe experienced the largest growth in absolute numbers, reaching approximately 16,000 stores by late 2018. This represents about 14% of the food retail market (food retail stores in the EU, Norway and Switzerland bigger than 400 m^2).

The U.S. has experienced the largest relative growth in the last three years. Canada also boasts a significant number of CO_2 stores, with more than 80 belonging to Sobeys, the most proactive retailer in the country in terms of adoption of CO_2 systems. The transition in Canada was accelerated in Quebec by subsidies provided by the province's 'EcoPerformance' programme. Accelerated by a subsidy scheme run by the Japanese Ministry of the Environment, Japan is the second largest market for CO_2 stores globally, boasting more than 3,530 stores by late 2018. In contrast to other regions, the technology in Japan has been adopted pre-dominantly in small store formats. With the revised High Pressure Gas Safety Act, CO_2 is starting to pick up quickly in larger supermarkets as well.

Australia and New Zealand are following the global trend with the number of stores currently at 20+ and 40+ respectively. Even though the market is still insignificant in China, it is expected to grow soon with international supermarkets, such as Carrefour and Metro AG, looking to increase penetration of CO_2 technologies in China. The first CO_2 transcritical system in China has been installed at a Metro Beijing Lishuiqiao store (Yoshimoto, 2018b). The installation includes two indoor racks, both with parallel compression, two-stage gas cooling and heat

reclaim. Refrigerating capacities are 55.97 kW medium temperatures and 93.5 kW low temperature. The high-temperature rack has a cooling capacity of 184.04 kW. In 2019, China will see a number of additional CO_2 transcritical installations in supermarkets. Tab. 1 shows the number of CO_2 stores globally and their growth rate from 2015 to 2018, based on primary research among leading market players.

Table 1. Growth of CO_2 stores between 2015 and 2018 in selected regions

Regions	2015	2018	Growth rate
USA	52	370+	612%
Canada	139	245+	76%
Europe	5,500	16,000+	190%
New Zealand	9	40+	344%
Australia	4	20+	400%
Japan	1,500	3,530+	135%

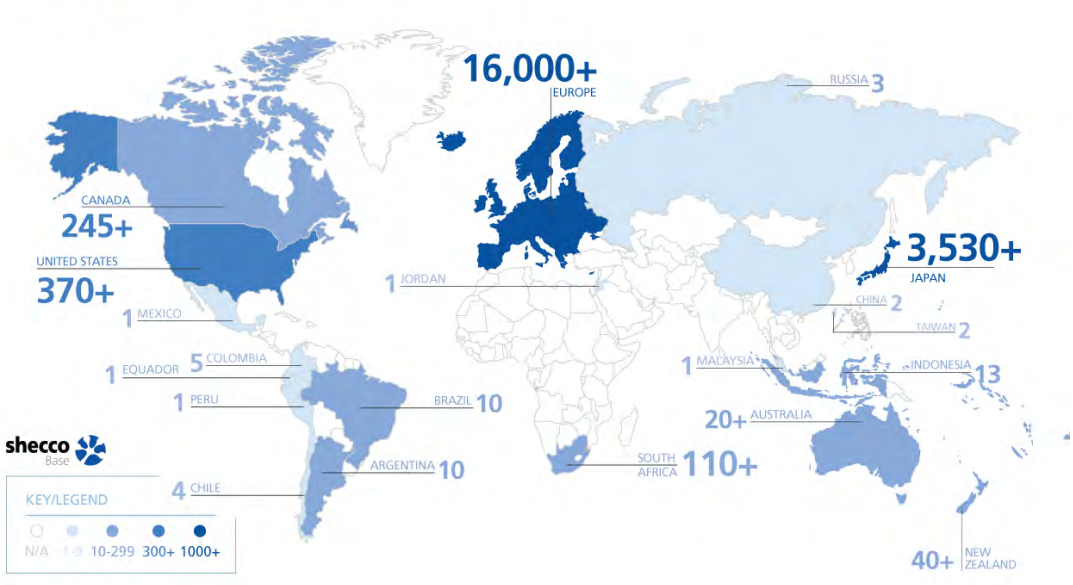

Figure 1: CO_2 transcritical stores in global perspective (status by October 2018).

The overall increase in installations of CO_2 transcritical refrigeration systems in Europe is remarkable and is only expected to translate into continued exponential growth in the future. According to research and estimates for the European market by shecco, sustained growth is expected to continue in the future (Fig. 2). The graph illustrates two scenarios of CO_2 store growth by 2030. The projections are based on increasingly stringent regulations, technological advancements in warmer climates, and the growing acknowledgement and acceptance of the technology and its energy-efficient properties. The conservative scenario assumes that the growth will be a bit slower, mainly due to competition with other low-GWP refrigerant technologies. According to the prognosis there will be between 4,000 – 6,000 new CO_2 stores annually between 2020 and 2030, with a total of 65,000 – 85,000 stores using such technology in Europe by 2030.

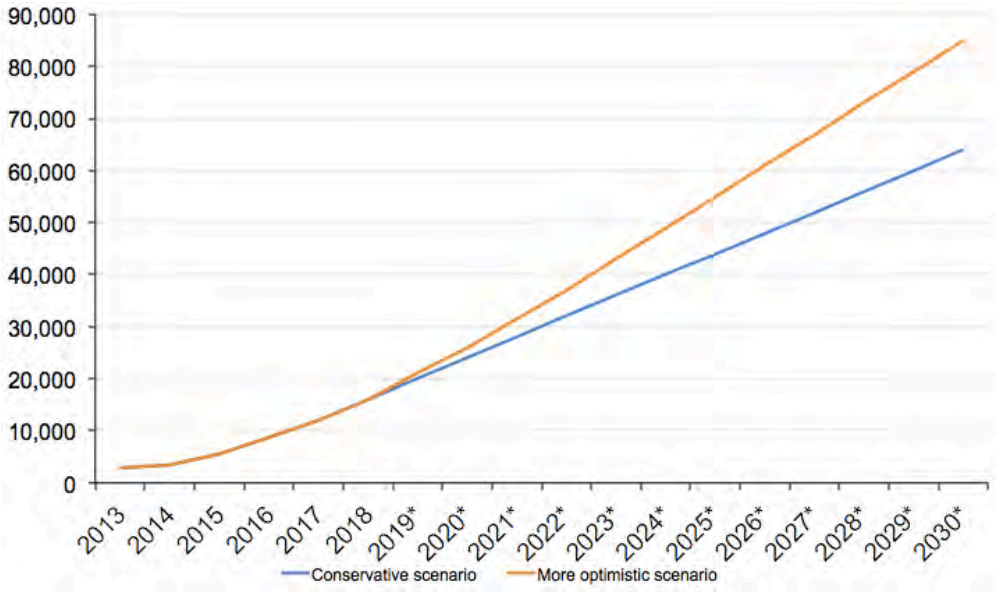

Figure 2: Projected number of CO_2 transcritical stores by 2030 in Europe.

3.2 Technologies to Enhance Energy Efficiency of CO_2 in Warmer Climates

Innovations such as parallel compressor, ejectors, mechanical sub-cooling, and adiabatic/evaporative coolers, CO_2 transcritical technology is now suitable for climates up to 45°C (Danfoss, 2016).

Adding an adiabatic gas cooler to a CO_2 transcritical system in warmer climates offers additional annual energy savings of 8-12%. Parallel compression delivers 6-8 per cent savings, and in combination with gas ejectors, savings can reach 8-10% compared to a transcritical system not using these enhancements (Schönenberger et al, 2014). Some experts in the field believe that ejector technology is the solution to remove the CO_2 equator – a geographical line below which CO_2 systems were believed to be less energy efficient than their HFC counterparts.

CO_2 systems using ejectors have been reported to offer up to 40% energy savings compared to HFC systems without ejectors (shecco, EIA, 2018). With parallel compression and ejectors the CO_2 transcritical technology is suitable for warmer climates up to 45°C. A study, supported by the Swiss Federal Office of Energy (SFOE) and published in December 2017 by the German magazine Kälte Klima Aktuell, reports that, “according to estimates, several hundred [CO_2] ejector systems are currently in use, the majority of which are in Europe”. Migros, the largest retailer in Switzerland, last year counted 60 stores fitted with CO_2 refrigeration technology using ejectors and said it planned to add 30 more every year (Vogel, 2017).

Although the advanced CO_2 technology is now more expensive than HFC-based systems in terms of initial cost, this is expected to go down as technology becomes more widespread (as has been proven for the standard CO_2 booster system) (Pisano, 2017). Industry experts estimate that with ejector technology and parallel compression, the price of a system is a maximum 10% higher.

3.3 CO_2 Technologies for Small Stores

The condensing unit market is largely dominated by high-GWP HFCs, primarily supplied by Asian manufacturers.

CO_2 is the most environmentally friendly alternative for condensing units, applied already in a large number of convenience stores. An estimated 6,000+ stores use CO_2 condensing units and mini boosters globally, with a growing number of suppliers offering such equipment. In Japan, CO_2 condensing units have been a well-established technology since many years with more than 8,500 units running in the market by the end of 2017. One of the major suppliers of

the technology recently presented findings on tests conducted with its new 20HP CO_2 condensing unit featuring heat reclaim. The system, which has an evaporating temperature of -15°C, also has the ability to supply 8.5 liters of hot water per minute at 70.4°C (Yoshimoto, 2018c).
In Europe and other parts of the world, retailers that have gained experience with CO_2 in supermarket refrigeration push the manufacturers to commercialise and decrease the cost of CO_2 condensing units and mini boosters. The result of this is a growing offer of commercially available CO_2-based products to fulfil the cooling needs in small stores.
Besides CO_2, hydrocarbons are also making headway in the condensing unit sector. Although the offer is currently limited, the potential for the technology is significant and may become a more serious competitor to CO_2 provided the safety standards allow higher charges of the flammable refrigerant in a single refrigeration circuit.

3.4 Growing Market for CO_2 in Industrial Applications

After becoming well established in commercial refrigeration market, manufacturers are focusing on developing transcritical CO_2 systems for larger applications in industrial refrigeration. Numerous examples from Europe indicate that CO_2 is becoming increasingly competitive as a solution for this segment too, with existing systems up to 2-3MW – an area that until recently was exclusively dominated by ammonia. shecco estimates there are more than 200 known installations with CO_2 transcritical in industrial refrigeration, with more than 25 known suppliers offering such technology.
New technological developments, particularly for compressors, have allowed CO_2 trancritical systems to reach higher capacities and capture a part of the industrial refrigeration market. This market is moving toward CO_2-only systems, partly due to the safety and technical challenges of using ammonia. According to expert engineers, CO_2 compressors can have an equally long life as the ammonia ones without the need for special and more expensive components.
As the technology progresses, the distinction between commercial and industrial refrigeration is becoming less clear, and competition between different natural refrigerant solutions is increasing.

3.5 CO_2 Ice Rinks on the Rise

The market for CO_2 in ice rinks is relatively new, with about 60 installations done to date mostly in Europe and North America (Garry, 2018). Technology manufacturers believe that the running costs of CO_2 transcritical systems in ice rinks whether direct or using a secondary brine/glycol, are lower as compared to fluorinated refrigerants and ammonia, especially in mild and cold climates. This is mainly due to the possibility to use heat reclaim and the fact that CO_2 performs efficiently in such climates (Garry, 2018).

In terms of installation cost, a transcritical CO_2 direct ice rink system can run higher than systems using synthetic refrigerants or ammonia, mostly due to the stainless-steel piping required under the rink.
As a direct system, CO_2 is believed to produce better quality ice than a secondary glycol system, because CO_2 changes from liquid to gas under the rink, cooling the rink at a constant temperature throughout, in contrast with glycol, which produces slightly different temperatures across the rink.

4. CONCLUSIONS

The legislative pressure on HFCs and HCFCs, propelled by the Kigali Amendment to the Montreal Protocol, creates new market opportunities for technologies that do not rely on these refrigerants. CO_2 has already gained market presence in commercial refrigeration in certain parts of the world. With the growing number of suppliers, the focus is now on improving energy efficiency of systems especially in warmer climates, reducing the cost, as well as integrating the refrigeration system with air-conditioning and heating (space and water). The speed of technology adoption will also be determined by the availability of technicians able to safely install and maintain the equipment. This will especially be a challenge in developing countries where the infrastructure is not yet well developed.
The development of large compressors and other key system components make it possible to deliver CO_2-based systems for different sizes of industrial refrigeration installations, with cooling capacities of up to 2-3MW. As CO_2 is entering into areas where it was previously not used, the technologies will see a growing competition with other natural refrigerant-based systems as well as those using lower GWP HFCs.

NOMENCLATURE

HFC	hydrofluorocarbons	CO_2	carbon dioxide
HCFC	hydrochlorofluorocarbons	EU	European Union
F-Gas	Fluorinated greenhouse gases	HVAC&R	heating, ventilation, air-conditioning and refrigeration
HFO	hydrofluoroolefins	GWP	global warming potential

REFERENCES

Danfoss, 2016. Making the case for CO_2 refrigeration in warm climate. Danfoss.com, Service and Support, Case studies.

Garry, M., 2018. Ice rinks: Which refrigerant is best? Accelerate America 40. 35-43 p.

McLaughlin, C., 2017. Key Japan CO_2 regulation lifted. R744.com.

Pisano, G., 2017. The use of ejectors in CO_2 technology: How to boost efficiency in warm climates – A real example from Italy. Atmo.org, ATMOsphere America 2017.

Schönenberger, J., Hafner, A., Banasiak, K., Girotto, S., 2014. Experience with ejectors implemented in a R744 booster system operating in a supermarket. Proceedings of the 11th IIR Gustav Lorentzen Conference on Natural refrigerants, IIR/IIF, Hangzhou, China.

Skačanová, K., Gkizelis A., 2018. Technical report on energy efficiency in HFC-free supermarket refrigeration for the project Global Corporate and Policy Measures to Incentivise Highly Efficient HFC-Free Cooling. 53 p.

Skačanová, K., Chasserot M., Masson N., Boccabella E., Tamasiunaite J., 2017, Guide to Natural Refrigerants Training in Europe, shecco, 102 p.

Skačanová, K., 2016. F-Gas Regulation Shaking UpThe HVAC&R Industry, shecco, The Greens / European Free Alliance in the European Parliament. 55 p.

Toby, P., 2017. Retail refrigeration: Making the transition to clean cold, Birmingham Energy Institute, University of Birmingham, 16125, 8 p.

Vogel, B., 2017. Ejector cooling system conquers the market, Swiss Federal Office of Energy Swiss Federal Office of Energy (SFOE).

Yoshimoto, D., 2018a. €58 million in Japan NatRef subsidies confirmed for FY2019, R744.com.

Yoshimoto, D., 2018b. China's first transcritical CO_2 store opens, R744.com.

Yoshimoto, D., 2018c, Panasonic developing CO_2 CDU with heat reclaim, R744.com.

Manuscript ID: 1154
DOI: 10.18462/iir.icr.2019.1154

Monitoring of a CO_2 commercial refrigeration system serving a supermarket in Southern Europe

Simone DUGARIA[(a)], Marco AZZOLIN[(a)], Livio CALABRESE[(b)], Silvia MINETTO[(c)], Davide DEL COL[(a)]

[(a)] University of Padova, Department of Industrial Engineering
Padova, 35131, Italy, e-mail: davide.delcol@unipd.it
[(b)] Frascold SpA, Rescaldina (MI), 20027, Italy, e-mail: livio.calabrese@frascold.it
[(c)] National Research Council of Italy (CNR), Construction Technologies Institute (ITC),
Padova, 35127, Italy, e-mail: silvia.minetto@itc.cnr.it

ABSTRACT

In the present paper, a CO_2 commercial refrigeration unit serving a 1500 m^2 supermarket located in Southern Europe is presented.
The unit consists of a booster compressor rack with parallel compression, with ten compressors arranged to provide around 20 kW cooling capacity at low temperature and 90 kW cooling capacity at medium temperature. The system, in addition to the cooling load, provides all the thermal functions in one unit: it integrates a heat exchanger for the air conditioning (130 kW) and two stages heat recovery, for sanitary hot water production (20 kW) and for space heating (100 kW).
The refrigeration unit is fully equipped with pressure and temperature sensors, flow meters, power consumption and capacities analysers.
The monitoring data are useful to understand how the considered system operates under different boundary conditions across a year. The focus of this paper is on the performance of the system during the winter period when some heat is recovered from the cycle for space heating purposes.
Keywords: Refrigeration, Carbon Dioxide, Compressor, Heat Recovery

1. INTRODUCTION

Under the restrictions on the use of high GWP refrigerants imposed by the European F-Gas Regulation (No 517/2014) and the global agreement to phase down HFCs - the Kigali Amendment to the Montreal Protocol (UNEP, 2016), the use of carbon dioxide as environmentally friendly refrigerant is one of the most promising and long-lasting solution in food retail sector. CO_2 booster systems have been initially adopted in supermarkets in the northern European Countries since their performance at ambient temperature lower than about 25°C are comparable with conventional HFC systems. Although the efficient use of CO_2 in transcritical booster system presents some difficulties at higher ambient temperature, it offers the opportunity of heat recovery and air conditioning integration that should be considered to evaluate the application of this system in temperate and warm climates.
Despite the installation of CO_2 refrigeration systems for supermarket has rapidly increased all over Europe, only few publications on field measurements of CO_2 system with integrated heat recovery and air conditioning system has been presented. Tambovtsev et al. (2011) investigated a heat recovery strategy involving gas cooler bypass by monitoring a supermarket located in Germany. Their results show that the adoption of the gas cooler bypass can increase the total COP of the system up to 20%. In the work of Funder-Kristensen et al. (2013), a CO_2 refrigeration system integrating heat recovery for a supermarket in Denmark has been studied. The heat recovery unit replaced a conventional gas heating system providing the entire heating demands of the supermarket saving 20% of running cost. A field measurements analysis of a supermarket CO_2 refrigeration system with heat recovery installed in Sweden was presented by Abdi et al. (2014). The monitoring of the working conditions shows that only 30–70% of the heat theoretically available for recovery was utilized, while the rest was rejected outdoor. In 2015, Sawalha et al. (2015) presented field measurements of three different CO_2 transcritical solutions operating in five supermarkets

located in Sweden installed between 2007 and 2010. The study showed that gas removal from the flash tank, increase in the evaporating temperature and in the compressor global efficiency are the main factors for the performance improvement comparing the new and the old systems. Hafner et al. (2016) presented the integration of heat recovery and air conditioning units in a CO_2 refrigeration system for a supermarket in Italy. The performance of the refrigeration and air conditioning system with and without a multi-ejector unit has been compared. This study showed that the configuration with the multi-ejector unit can provide a total energy saving between 15% and 30%. Karampour and Sawalha (2017) monitored the performance of an integrated CO_2 transcritical booster system including space and water heating, air conditioning, and parallel compression installed in a supermarket in Sweden. Their results showed that the system was capable to provide the entire air conditioning demands and recover a great fraction of the available heat, with high COP values. Measured data of a CO_2 transcritical system integrating all the thermal functions of a supermarket in Northern Italy, has been presented by Cortella et al. (2018). A numerical model has been validated against experimental data but the measured performance of the system was not presented.
In the present study, the performance of a transcritical CO_2 commercial refrigeration system capable to satisfy both the cooling and heating demands of a supermarket is investigated. The studied refrigeration unit is located in Northern Italy and it is fully instrumented with pressure and temperature sensors, flow meters, power consumption and capacities analysers. The objective of this study is to investigate the working conditions and performance of the system while providing refrigeration and heating.

2. SYSTEM DESCRIPTION

The considered CO_2 commercial refrigeration unit is a transcritical booster system with parallel compression serving a 1500 m^2 supermarket located in Monticello Brianza (45°43′ N - 9°19′ E), near Milan in Italy, and has been in operation since August 2017. The schematic of the CO_2 system is shown in Fig. 1.
The system is a booster compressor rack with parallel compression, with ten compressors arranged to provide around 20 kW cooling capacity at low temperature (LT) and 90 kW cooling capacity at medium temperature (MT). In addition to the cooling capacity, it provides all the thermal needs: it integrates a two stages heat recovery system on the high pressure line and a heat exchanger for the air conditioning at the intermediate pressure. The recovered heat is used to satisfy the demands for sanitary hot water and space heating of the supermarket.
The LT compressors rack (CLT) consists of three compressors A1.5-3SK3 (Frascold, 2017a), while three compressors S20-12TK (Frascold, 2017b) compose the MT compressors rack (CMT). In both compressors racks, one compressor is equipped with a speed regulator to fill the capacity gaps given by on/off compressors. Four additional compressors are installed as a parallel compression unit (CAUX): three of four compressors S20-12TK are operating in on/off mode while the last compressor is a S15-10TK (Frascold, 2017b) equipped with a speed regulator. The lubricant is a fully miscible POE85 oil. The lubricating oil is collected in a separator installed downstream the discharge line of the MT and auxiliary compressors. An electronic regulator of the oil level is installed on each compressor and the oil is distributed from the separator to each compressor on demand.
The superheated vapour exiting the LT evaporators is compressed by the CLT rack and directed to the suction line of the CMT where it mixes with the vapour coming from the evaporators working at medium pressure. After being compressed to the high pressure, the hot gas discharged from the CMT and CAUX passes through the two stages heat recovery system. A gas cooler (GC) installed on the roof of the supermarket is used to reject the remaining heat to the outdoor ambient. The CO_2 exiting the GC enters an internal heat exchanger (SCHE) where it is cooled by the cold vapour stream flowing in the suction line of the auxiliary compressors. Although the subcooling effect has been found to be very small, the presence of this internal heat exchanger ensures that only vapour is present at the suction line of the auxiliary compressors. The subcooled liquid is throttled by the high pressure regulating valve (HPRV) to the intermediate pressure. Here, depending on the demand of the air conditioning system, the two-phase CO_2 can flow through the air conditioning heat exchanger (ACHE) or it can enter directly an internal heat exchanger (IHE) where it is partially condensed by the cold vapour stream coming from the intermediate pressure regulating valve (IPRV). The ACHE cools the water taken from a cold water storage tank, from 12°C to 5°C while partially evaporating CO_2 at the intermediate pressure. Connected to the outlet of the internal heat exchanger (IHE), the intermediate pressure receiver (IPREC) separates vapour and liquid. The liquid

is used to feed the MT and LT evaporators, while the vapour stream can be alternatively directed to the IPRV (through the IHE) or to the suction line of the CAUX (through the SCHE). This choice depends on the amount of the vapour in the IPREC, which strongly depends on the GC outlet temperature of the CO_2, and the minimum mass flow rate that can be processed by the smallest auxiliary compressor.

In the first heat recovery stage, a brazed plate heat exchanger (SHWHE) is placed at the discharge section of the CMT and CAUX used to heat water from 60°C to 65°C. The heated water is then pumped back to an external heat exchanger where it heats up the sanitary water stored in a tank. The CO_2 outlet temperature is sufficiently high to allow a second stage heat recovery dedicated to space heating. A brazed plate heat exchanger (SHHE) is connected to a second storage tank with water at 55°C in and 50°C out temperatures. This second tank directly feeds the hydronic circuit for space heating. Fixed speed pumps keep constant water flows in the circuits connected to the SHWHE and SHHE, while two independent three-way valves are used to completely bypass these heat exchangers when no space heating nor hot water are requested. When the heat absorbed by the cabinets (MT evaporators) and freezers (LT evaporators) cannot satisfy the thermal demands of the heating system, an additional evaporator (EXTEV) is used to evaporate the excess of liquid. This is an air-cooled heat exchanger, equipped with a dedicated expansion valve, where the liquid CO_2 coming from the flash tank receiver evaporates at the medium pressure. The EXTEV is placed in the same framework of the gas cooler (GC) and served by the same fans. The superheated vapour exiting the EXTEV is sent to the suction line of the MT compressors.

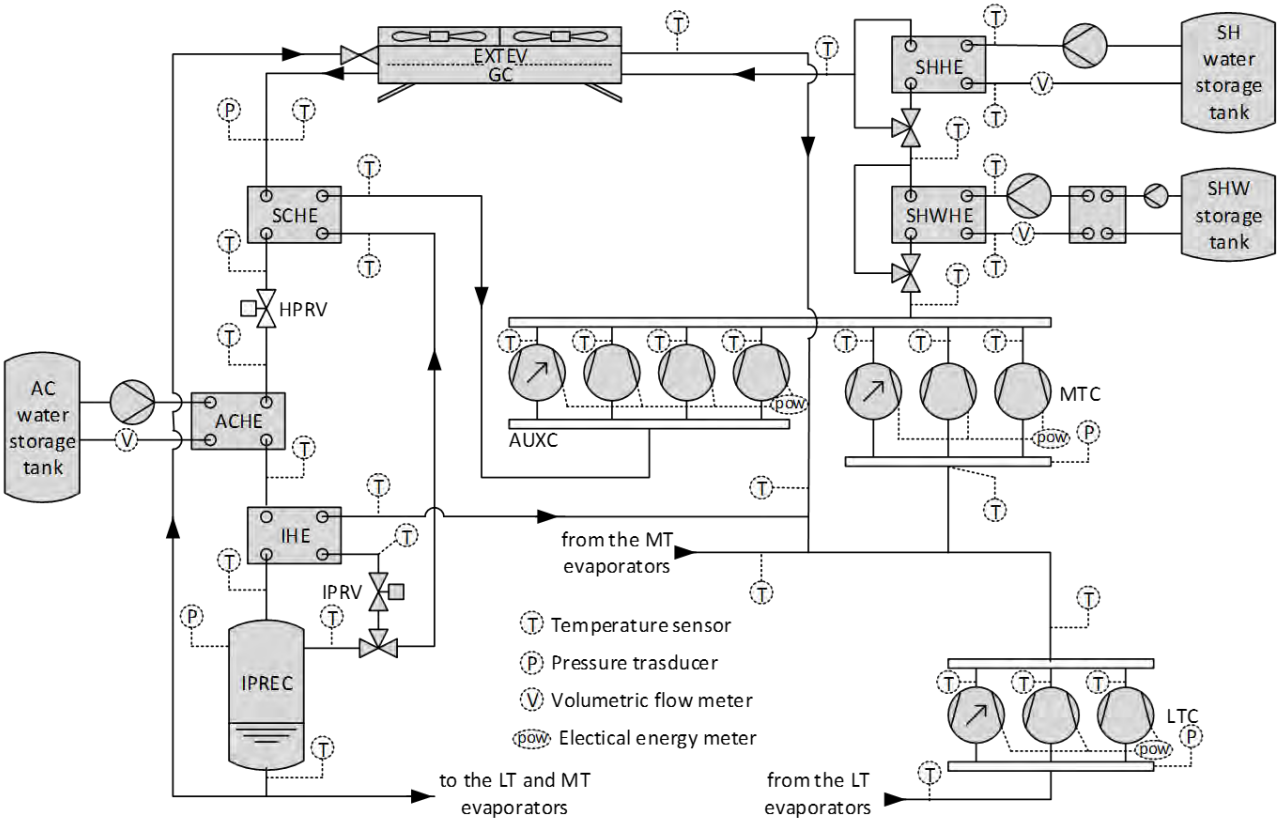

Figure 1: Schematic of the booster system with parallel compression, two stages heat recovery and air conditioning system

3. MEASUREMENTS AND EVALUATION OF NON-MEASURED PARAMETERS

The monitored parameters on this unit are temperatures and pressures in different points of the system, activation status and percentage capacity of the valves and compressors and electrical power consumptions. Moreover, magnetic flow meters are installed on the return water lines of the heat exchangers for heat recovery and air conditioning. The instant values of the monitored parameters are measured and stored in an online database with different time intervals. Some parameters which were not directly measured, such as the CO_2 mass flow rates and the thermal loads, were determined from a steady-state model of the refrigeration CO_2 cycle.

3.1. Temperature and Pressure Measurements

As shown in Fig. 1, temperature NTC sensors are installed at the inlet and outlet of the main components. Supply and return water temperatures at the heat exchangers dedicated to heat recovery and air conditioning are measured too. The external ambient temperature, which affects the regulation of the high pressure and the heat rejection to the external ambient, is measured at the inlet and outlet of the gas cooler.
Relative pressure transducers are installed in the CO_2 circuit at each pressure level. The low and medium pressures are measured at the suction line of the CLT and CMT, respectively. The intermediate pressure is measured in the upper side of the IPREC. The high pressure is measured in two positions: at the discharge line of the CMT and CAUX and at the outlet of the gas cooler. An additional pressure transducer is installed after the expansion valve of the external air-cooled evaporator.

3.2. Electrical Consumption

In this system, the electrical consumptions are measured for each compressor rack. When the total rack power consumption needs to be divided among the working compressors, the method adopted here is based on the power and mass flow rate polynomial expressions for the compressor series SK3 and TK given by the manufacturer of the compressor. In these expressions, the mass flow rate and the power absorbed by the compressor are given as a function of the evaporating temperature at the suction and discharge pressure, at the nominal frequency of 50 Hz and 10 K superheating. The coefficients of the polynomial expressions are obtained from laboratory tests according to the European Standard EN 12900 (2013) and verified through field measurements. Corrections to account for different superheating and frequency are applied as specified by the manufacturer. The electrical power consumption of the fixed speed compressors can be calculated knowing the suction pressure and temperature of each compressor and its activation status. The activation status of the compressors is monitored and it can be verified by measuring the temperature of the CO_2 at the discharge lines of the compressors.
Once the power consumptions of the fixed speed compressors are calculated, the actual electrical power consumptions of the variable speed compressors can be estimated.
The electrical consumption of the fans on the GC is determined by subtracting the estimated electrical power consumptions of compressors and auxiliary devices (mainly pumps, evaporators, fans and control system) from the total electrical consumption of the unit. The electrical power consumption of the auxiliary devices is evaluated as the difference between the total and the compressors electrical power consumption when the fans of the GC are off.

3.3. CO_2 Mass Flow Rate Evaluation

No flow rate sensors are installed in the CO_2 circuit. The total mass flow rate of the CO_2 flowing in the line between the CMT, CAUX discharge collector and the IPREC inlet can be obtained by applying energy balances at the external heat exchangers ACHE, SHWHE and SHHE.
The absence of CO_2 mass flow meters requires an indirect method to evaluate the distribution of the total mass flow rate in the different lines of the system. When the external temperature is lower than 25°C the CAUXs are usually not working, and the vapour mass flow separated in the IPREC is entirely processed by the CMT. From the power consumptions of the fixed speed compressors, by means of the power and mass flow rate polynomial expressions of the compressors given by the manufacturer, the frequencies of the inverters can be estimated. Once the running frequencies and the suction conditions of the compressors are known, it is possible to determine the mass flow rate elaborated by the compressors. The measurements of the discharge temperatures are then used to verify the estimated parameters. The vapour flow rate is easily determined since the vapour quality at the IPREC inlet is known by assuming an isenthalpic expansion at the HPRV. The remaining of the mass flow rate elaborated by the CMT comes from the CLT and the MT cabinets when the valve of the EXTEV is closed. The mass flow rate flowing to the LT freezers is entirely elaborated by the CLT. From the analysis of the data points acquired with a closed valve of the EXTEV, a relationship between the actual number of running CMT, the frequency of the inverter serving the MT compressor and the mass flow rate to the MT evaporators can be obtained. Under the assumption that the MT cooling load is not influenced by the heat demand, this relationship may be used to determine the CO_2 flow rate at to the EXTEV accounting also for the measured opening degree of its valve.

3.4. Cooling and Heating Loads

The heating loads in the heat recovery and air conditioning heat exchangers are calculated by knowing the mass flow rates and the enthalpy differences at the water side. The enthalpies of the water are obtained from the measurements of the pressure and the inlet and outlet temperatures at these heat exchangers.

The cooling loads of the systems are determined by estimating the CO_2 mass flow rate and the inlet and outlet enthalpies of the LT and MT lines. These enthalpies are calculated by measuring temperature and pressure at the outlet of the IPREC and by evaluating the outlet conditions of the evaporators. The evaporators outlet temperatures are difficult to measure due to a high number of cabinets and freezers present in the supermarket. Hence, a number of cabinets and freezer is selected and the outlet temperature for each device is measured. This approach was also adopted by Sawalha et al. (2015). The analysis of the selected evaporators shows average superheating for the LT freezers slightly higher than 11 K and close to 12 K for the MT cabinets. These average values are taken as reference for all LT and MT evaporators. The CO_2 flowing in the lines from the evaporators to the compressors exchanges heat with the environment; this heat does not contribute to the cooling capacity and usually has a negative effect on the performance of the system, because it increases the suction temperature at the compressors. The return lines of the evaporators merge in different points and their length may vary considerably, and therefore it is complicated to account for the contribution of each line to the non-useful cooling. Hence, the total non-useful superheating is evaluated by subtracting the estimated evaporators outlet temperatures from the temperatures at the suction collectors of the CMT and CLT. The external evaporator does not give any contribution to the cooling effect of the unit: the heat exchanged here and in the return line to the CMT is properly accounted for.

4. RESULTS AND DISCUSSION

A first monitoring activity of the transcritical booster unit has been conducted from October 2017 to September 2018, with a sampling time of 5 minutes. In this period, the measurements of the water mass flow rates and electrical power consumption were not available. The data acquired in this period were used to understand how the system works under variable boundary conditions and variable loads.

Fig. 2a reports the outlet pressure at the gas cooler as a function of the external air ambient temperature. When no heat recovery is required the gas cooler pressure is regulated as a function of the external temperature. During the winter period, to increase the amount of heat available for heat recovery, the pressure is increased over its critical value at around 8.5 MPa, forcing the system to work in transcritical mode.

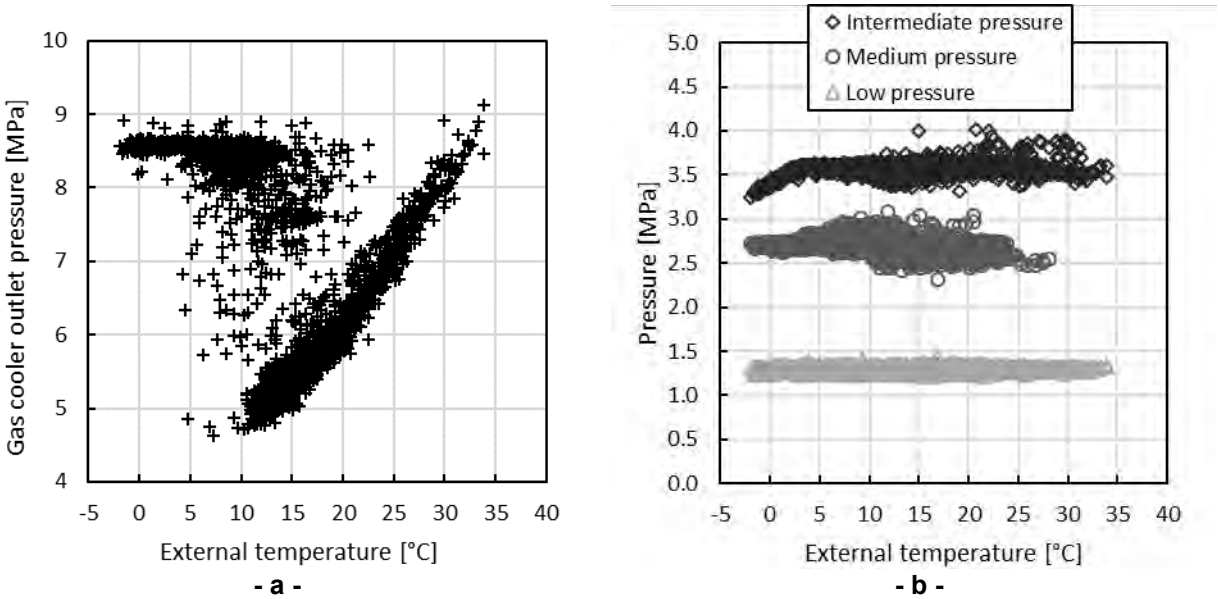

- a - **- b -**

Figure 2: Monitored gas cooler outlet (a) and intermediate, medium and low pressures (b) as a function of the external ambient temperature. The points were acquired with a time step of 5 minutes between October 2017 and September 2018

Fig. 2b shows the pressures at LT and MT evaporators and flash tank receiver as a function of the external temperature. The LT evaporators pressure is around 1.3 MPa (average value), which corresponds to a saturation temperature around -33°C. The average pressure at the MT evaporators is 2.7 MPa (corresponding to a saturation temperature around -9°C). The IPREC works at an average pressure of 3.6 MPa and only at external temperature lower than about 2.5°C, the intermediate pressure is reduced to avoid the presence of subcooled liquid entering the IPREC. The control algorithms operate on compressors and valves to keep the pressure variations within 0.05 MPa. Greater fluctuations are due to the variation of the boundary conditions of the system.
The temperature approach point at the gas cooler is given by the temperature difference between the CO_2 at the outlet and the external temperature. For ambient temperatures lower than 5°C, the measured gas cooler outlet temperature is very close to the external one and the average approach temperature difference is less than 1 K. In subcritical conditions, the fans speed is regulated to obtain a constant subcooling in the liquid at the gas cooler outlet. The average value of the subcooling results close to 3 K.
To evaluate the performance of the system in winter conditions, a second monitoring campaign was conducted. The measurements of the water mass flow rates and electrical power consumptions were available. The results presented in this work refer to the monitoring period between 19 December 2018 and 19 January 2019. In this monitoring period, the sampling time has been reduced to 30 seconds and the monitored data were averaged every 5 minutes. The data collected in stable conditions are filtered and used to evaluate the cooling (Fig. 3) and heating loads (Fig. 4), the electrical consumptions (Fig. 5) and the COP (Fig. 6). The values of the COP for each data point are calculated as follows:

$$COP_{ref} = \frac{Q_{MT} + Q_{LT}}{P_{CMT} + P_{CLT}} \quad \text{Eq. (1)}$$

$$COP_{tot} = \frac{(Q_{MT} + Q_{LT}) + Q_{SH}}{P_{CMT} + P_{CLT}} \quad \text{Eq. (2)}$$

where, Q_{MT} and Q_{LT} are respectively the cooling capacities at the MT and LT evaporators, Q_{SH} is the space heating load and P_{CMT} and P_{CLT} are the electrical power consumptions of the CMT and CLT, respectively.

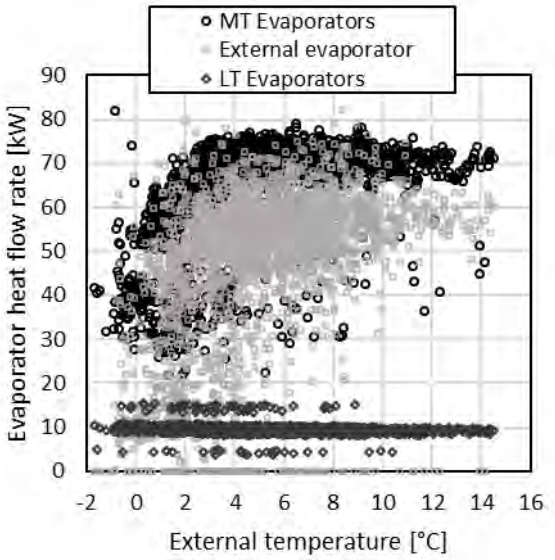

Figure 3: Cooling loads at the LT, MT and external evaporators vs. external temperature (winter month)

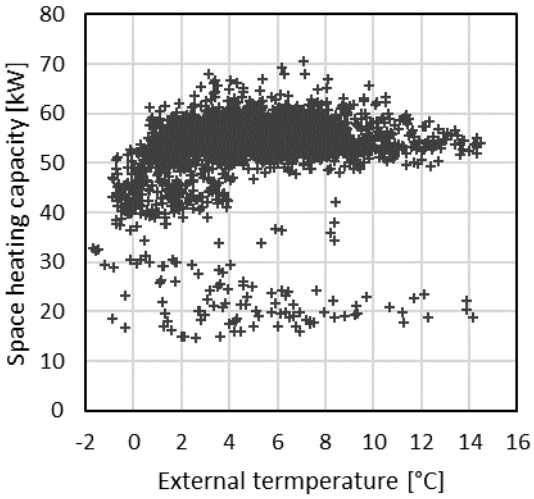

Figure 4: Space heating load vs. external temperature (winter month)

The influence of the external temperature on the LT and MT cooling loads (Fig. 3) and the heat absorbed at EXTEV is limited. The cooling load at the LT evaporators shows a typical trend mainly affected by the number of active compressors. Most of the data points were collected when two of three compressors were working and the measured cooling load results close to its average value (10 kW). Only few points refer to the conditions in which one or three compressors are running, with a cooling load of 4 kW and 14 kW, respectively. The significant decrease in the heat absorbed in the

MT evaporators and EXTEV that can be observed for external temperature lower than about 3°C is caused by the reducing in the demand for space heating (Fig. 4) and required cooling capacity at the MT cabinets that occurs during night-time. For temperature lower than 0°C the heat absorbed by the MT and LT evaporators is sufficient to satisfy the space heating demand and the use of the EXTEV is limited. The data points displaying a heat flow rate at the EXTEV equal to zero were acquired when the valve at the EXTEV was closed

In Fig. 5 it can be observed that the two main electrical power consumptions of the system are those of the CMT and the fans of the GC. In particular, the variation of electrical power consumption of the CMT when a fixed speed compressor is switched on can be clearly recognised. Most of the time, at low ambient temperature, the fans are regulated in order to provide a sufficient air flow rate to evaporate the excess of liquid present in the IPREC through the EXTEV.

The total number of data points have been grouped considering external temperature intervals of 1 K (bin). For each bin, the average values of the refrigeration COP and total COP are calculated and plotted in Fig. 6. The number of collected data points (external temperature frequency) at each temperature range (bin) is also reported in the same figure. All the points reported in Fig. 6 refers to operating conditions where the transcritical regime was forced. In these conditions, the cooling performance of the system results strongly penalized. The average value of the refrigeration COP is 2.1. However, the benefit of working in transcritical regime can be appreciated accounting for the heat recovery for space heating. The total COP presents an average value of 3.6. The average COP values account for variable load and the same external temperature, which means variable heating capacity and variable heat flow rates at the LT, MT and external evaporators. The refrigeration and total COP increase with the external temperature, due to the decrease of the ratio between the heating and the refrigeration loads.

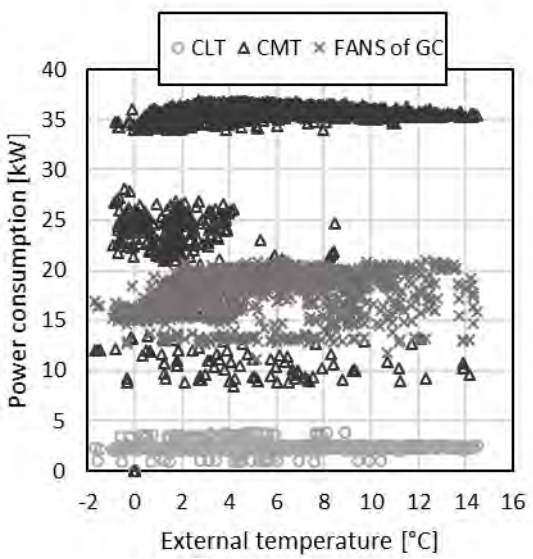

Figure 5. Electrical power consumption of CLT, CMT and fans of the GC vs. external temperature (winter month)

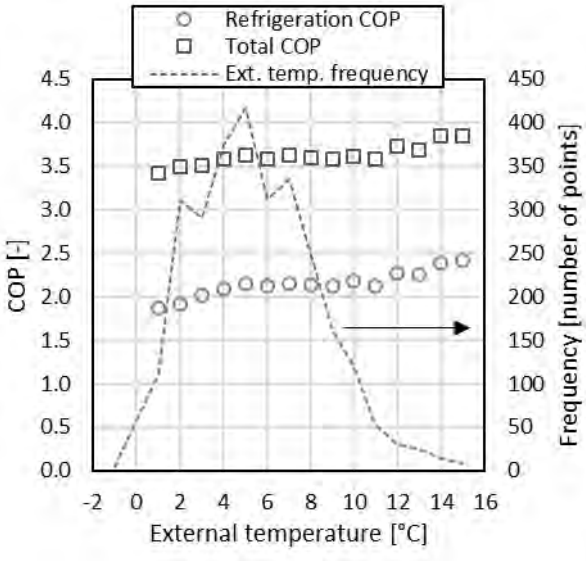

Figure 6. Refrigeration COP, total COP and external temperature frequency vs. external temperature (winter month)

5. CONCLUSIONS

The results of the monitoring activities of a CO_2 refrigeration unit capable to satisfy both the cooling and heating demands of a supermarket located in Southern Europe have been presented.

A first monitoring activity of the transcritical booster unit was conducted from October 2017 to September 2018. A second monitoring activity was carried out between December 2018 and January 2019. The data collected under stable conditions allow to evaluate the performance of the system working in transcritical operation while providing refrigeration and heating.

The average values of the refrigeration COP and total COP calculated at each temperature interval increase with the external temperature. Their average values are equal to 2.1 and 3.6 for the refrigeration COP and the total COP, respectively. During daytime, the cooling and heating loads present small variations around their average values. The cooling capacity at the MT cabinets and

the space heating load decrease in the night-time. The two main electrical power consumptions of the system are those of the MT compressors and the fans of the gas cooler. Data show that the effect of the outdoor temperature on the performance of the unit is limited because during the winter month the system is forced to work in transcritical conditions to provide space heating to the supermarket.

REFERENCES

Abdi, A., Sawalha, S., Karampour, M., 2014. Heat recovery investigation of a supermarket refrigeration system using carbon dioxide as refrigerant. Proceedings of the 11th IIR Gustav Lorentzen Conf. on Nat. Refrig., Hangzhou, China.

CEN/TC113. EN 12900:2013 Refrigerant compressors - Rating conditions, tolerances and presentation of manufacturer's performance data.

Cortella, G., D'Agaro, P., Coppola, M. A., 2018. Simulations and field tests of a CO_2 refrigerating plant for commercial refrigeration. Proceedings of the 13th IIR Gustav Lorentzen Conf. on Nat. Refrig., Valencia, Spain.

Frascold, 2017a. Semi-hermetic reciprocating compressors for CO_2subcritical applications. Product selection catalog Version 50Hz. FCAT140.2.

Frascold, 2017b. Cooling solutions CO_2 Transcritical semi-hermetic reciprocating compressors. Technical documentation FCAT150_02_EN.

Funder-Kristensen, T., Fösel, G., Bjerg, P., 2013. Supermarket refrigeration with heat recovery using CO_2 as refrigerant. Proceedings of the 5th International Conference on Cryogenics and Refrigeration (ICCR), Hangzhou, China.

Hafner, A., Banasiak, K., Herdlitschka, T., Fredslund, K., Girotto, S., Haida, M., et al., 2016. R744 ejector system, case: Italian supermarket, Spiazzo. 12th IIR Gustav Lorentzen Conf. on Nat. Refrig., Edinburgh, Scotland.

Karampour, M., Sawalha, S., 2017. Energy efficiency of integrated CO_2 trans-critical system in supermarkets: A field measurements and modelling analysis. Int. J. of Ref. 82, 470-486.

Karampour, M., Sawalha, S., 2018. State-of-the-art integrated CO_2 refrigeration system for supermarkets: A comparative analysis. Int. J. of Ref., 86, 239–257.

Sawalha, S., Karampour, M., Jorgen Rogstam, 2015. Field measurements of supermarket refrigeration systems. Part I: Analysis of CO_2 trans-critical refrigeration systems. Appl. Therm. Eng. 87, 633-647

Tambovtsev, A., Olsommer, B., Finckh, O., 2011. Integrated heat recovery for CO_2 refrigeration systems. Proceedings of the 23rd IIR International Congress of Refrigeration, Prague, Czech Republic.

UNEP, United Nations Environment Programme, 2016. Report UNEP/OzL.Pro.28/12. Twenty-Eighth Meeting of the Parties to the Montreal Protocol on Substances that Deplete the Ozone Layer, Kigali, 10–15 October.

Manuscript ID: 1266
DOI: 10.18462/iir.icr.2019.1266

Not-in-kind approach to remote monitoring in CO_2 refrigeration systems

Silvia MINETTO[(a)], Giacomo TOSATO[(a)], Antonio ROSSETTI[(a)], Sergio MARINETTI[(a)], Sergio GIROTTO[(b)], Krzysztof BANASIAK[(c)]

[(a)] National Research Council, Construction Technology Institute
Corso Stati Uniti 4, 35127 Padova, Italy
[(b)] ENEX Srl,
Via Veneto 12, 31038 Padernello di Paese, Italy
[(c)] SINTEF Energy Research
Kolbjørn Hejes vei 1D, 7465 Trondheim, Norway

ABSTRACT

The complexity of CO_2 layouts for commercial refrigeration installed in warm climates, integrating also air conditioning and heating, with different load ratios, poses challenges in evaluating and comparing energy performances. Both analysis based on first or second law of thermodynamics requires the measurement of refrigerant mass flow rate to straight forward evaluate useful effects. A low-cost, reliable and low intrusive option to measure CO_2 volume flow will be illustrated, demonstrating the use of not-in-kind sensors in commercial refrigeration systems. Signals coming from the field might be used to evaluate the system performance, i.e. Coefficient of Performance and exergetic efficiency, and potentially to promptly identify anomalous working conditions leading to inefficient operations or failure. Field data will validate the possibility of identifying the system performance and its health status using a limited amount of signals and filtering them through proper figures.
Keywords: Refrigeration, Carbon Dioxide, Compressors, COP, Evaporators, Energy Efficiency.

1. INTRODUCTION

Commercial refrigeration with CO_2 has rapidly and widely spread in the last years, reaching near 14.000 installation in Europe in early 2018, according to Shecco, 2018. Different layouts have been developed, to provide the market with suitable solutions, according to the climate or utililsation. In particular, integrated solutions providing refrigeration, air conditioning and heating are currently required from the market, due to their cost and performance competitiveness, as demonstrated by Karampour and Sawalha(2018).
Although detailed and reliable simulation models are developed by many research groups and companies, there is an increasing demand for performance data collected in the field. Field Data can assure the market about feasibility, reliability, energy efficiency of CO_2 integrated systems (Multipack, 2019) and promote fast transition to low environmental impact solutions in the food retail sector by awareness raising (SuperSmart, 2019).
Monitoring Systems and Monitoring Solutions are commonly used to refer to a wide range of different systems, with different characteristics and features. Based on their capabilities and scopes, three different categories can be identified, i.e.Monitoring Systems, Remote Control and Planning Systems and Integrated and Optimized Control Systems. Monitoring systems centralize the data, make non conformal or fault data available to head quarters, which can identify the right procedure to fix the problem. Control systems allow remote operation reducing the need for on-site service; remote control can be used as planning tool and set-ups can be changed or reset autonomously by the system under given conditions. Integrated control systems can handle more complex planned operations and they can take advantage of sub-system interactions.

Monitoring systems are powerful tools for management, providing a centralized database and representing an effective tool to improve food quality (continuous temperature monitoring and recording) and reduce food waste (prompt identification of non-conformal system behaviours).
Control systems include all the functionalities of monitoring systems, they allow to act on the system parameters in the local controllers and permit to define a virtual control room accessible form multiple platform (PC, Tablet…). Access to this environment can be granted to specialized technicians, consultants, suppliers, thus reducing service time and improving the overall system performance. Control systems represent the simplest type of Smart Systems and their natural development is represented by integrated and optimized control systems; they can positively impact on different aspects such as energy saving, food quality, system reliability, nevertheless they require high integration and high overall complexity.
Monitoring & Control Systems are themselves subsystem that need maintenance and constant attentions as all the other subsystems. They can provide significant improvements, but only if used and interpreted by trained and professional personnel with expertise in data analysis and HVAC&R systems.
The huge amount of data coming from the field can actually represent an obstacle to the obtainment of the benefits deriving from remote monitoring and control, if data are not properly filtered and processed by experienced people.
In addition, the increasing complexity of CO_2 system layouts calls for even higher expertise level and by the wide range of designs offered by the market.
According to the past gained experience, it seems relevant to try to provide commercial refrigeration with reliable and sustainable monitoring systems and to offer an insight into some parameters that could offer a future sharable way of interpreting and comparing system performances, as well as highlighting operations that might not follow design requirements.

2. CASE STUDY

For the present study a supermarket included in the Multipack project has been selected. MulitPACK [2019] is an EU project demonstrating and building up confidence for standardised integrated cooling & heating packages installed in high energy demanding buildings. The overall aim of MultiPACK is devoted to demonstrate performances of the integrated CO_2 vapour compression packs at a commercial level through full-scale applications at the end-users in Southern Europe. Namely, the concept of multifunctional Heating, Ventilation, Air Conditioning and Domestic Hot Water (HVAC & DHW) units are demonstrated for a group of various commercial and public high-energy-consumption buildings throughout Southern Europe, while refrigeration prioritized packs for supermarkets are proven in three medium size shops located in Portugal and Italy. The supermarket which is considered in this paper is located in central Italy.

2.1. System Layout

The system overall layout is presented in Fig. 1. The unit is based on a booster concept with parallel compression and expansion work recovery by means of ejectors for both vapour pre-compression (10) and liquid recirculation (9).
Semi-hermetic compressors are installed, three each rack of compression level: Medium Temperature MT(1), Low Temperature LT(3), Auxiliary (2). For each rack, one out of the three compressors are inverter driven to allow a smoother capacity modulation.
The unit also satisfies the heating and the cooling loads of the supermarket by means of an Air Handling Unit AHU (11), in which CO_2 directly flows in to heating and cooling coils. In winter time, a three way valve (12) deviates CO_2 to the AHU coil if requested by the building temperature control, consequently high pressure is increased. If the heating demand exceeds the heat recovered from the refrigeration system, the heat pump mode is activated, i.e.the external evaporator (6) is fed with liquid from the receiver (7). The heat pump mode, supported by dedicated auxiliary compressor, can work independently from those removing flash gas, thanks to the solenoid valve (16) In summertime, the AHU cooling coil is fed with two-phase refrigerant expanded through the electronic expansion valve (17), which is thermostatically controlled. Post –heating is also provided by CO_2 in summertime.
A liquid receiver (7) is located after the expansion valve, able to manage charge variations in the circuit and to provide sufficient liquid head to circulate CO_2 into the two refrigeration lines. In case of

liquid flow back from MT evaporators, due to the adopted Electronic Expansion Valve EEV control, the liquid accumulated in the suction liquid receiver (13) is pumped back to the receiver (7) by liquid ejectors.

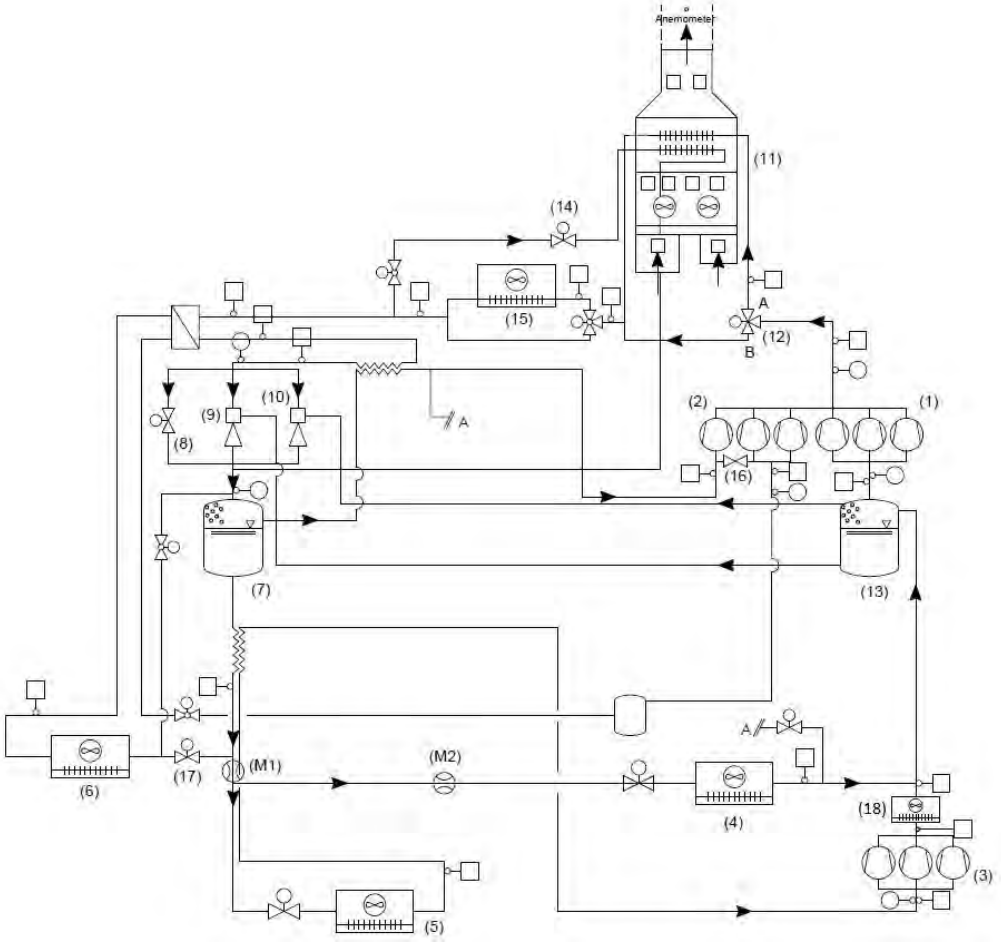

Figure 1: System lay-out

2.2. Measuring Devices

Following the requirements from the MultiPACK project, the system is fully equipped with measuring instruments, for pressure, temperature, refrigerant mass flow and compressor input power measurements. The location of the instruments is referenced in Figure 1, where temperature probes are indicated with a square and pressure sensor with a circle.

There are 18 commercial type NTC 10 kΩ ±1% at 25 °C Beta 3435 sensors, whose manufacturer's declared precision is ±0.5°C at 25°C and ±1.0°C in the range -40°C to +90°C. Pressure is measured with six commercial type piezoresistive pressure transmitters (circle in Figure 1), with accuracy ranging from ± 1%FS to ± 4 %FS, depending on temperature level pressure sensors have FS 60 10^5 Pa, except those on high pressure side (150 10^5 Pa).

In order to evaluate the total electric power input, three-phase electric power meters are located before each compressors rack to measure the power input to Low Temperature (P_{LT}), Medium Temperature (P_{MT}), and Auxiliary (P_{AUX}) compressors. Their accuracy is ± 0.5 % FS (FS is 24 kW for LT compressor rack and 120 kW for MT and AUX compressor racks). The status of every single compressor and the inverter frequency are also acquired. The total power input to the system, including auxiliaries (fans, pumps, valve motors,..) is monitored.

Two Coriolis mass flow meters (M) are placed on the liquid lines, the first (M1) one measures both MT and LT CO_2 mass flow, the second one (M2) is dedicated to MT flow. Their accuracy is 0.1% of the actual flow. On the AHU side, eight temperature and relative humidity sensors are installed to measure enthalpy differences before and after the coils, together with building return air and external air temperature and humidity. A hot wire anemometer (accuracy ± 0.2 m/s+3% of measured value) is installed on the main air duct, to measure air velocity of the whole air volume flow, so it is possible to calculate the total cooling and heating power provided by the unit. The accuracy of the RH probes

is ± 3% and of the reading (temperature range 0 -40°C, RH up to 90%) and ± 0.5 °C for temperature from+10°C to+30 °C.

3. PERFORMANCE EVALUATION

The variety of technical solutions offered by manufacturers as an alternative to F-gases banned from 2020 (like R-404A) and the availability of very new integrated solutions for refrigeration and air conditioning based on CO_2 require a comparison of systems in terms of energy efficiency, rather than energy consumption. It claims for experimental methodologies, as consolidated and validated models for those systems are not yet available or affordable or, if available, they are not easily applicable to different systems, as they are typically tailored and validated on a specific site.
To this extent, the performance evaluation is based on measured values of power input and cooling capacity and remote monitoring and subsequent data processing play a major role.
Both first and second law of thermodynamics efficiencies are presented, in order to evaluate the best approach.
The second law approach in commercial refrigeration systems analysis, which compares the actual power input to the ideal one, i.e. the Carnot one, to provide the same useful effect, has been explicitly proposed by the EU project SuperSmart.
To the Authors' knowledge, it has been first applied, based on experimental data from the field, by Blust et al, 2018.
When considering the MT cycle, the first law Coefficient of Performance COP follows the definition of equation (1), taking into consideration all useful effects with respect to the power input to get it. With reference only to refrigeration, COP has been defined for the MT cycle, considering also the heat rejected to the MT circuit from the LT one, i.e. $\dot{Q}_{LT} + P_{LT} - \dot{Q}_{ds}$, being $\dot{Q}_{ds}$ the heat rejected to the desuperheater (18).

$$COP_{MT} = \frac{\dot{Q}_{MT}+(\dot{Q}_{LT}+P_{LT}-\dot{Q}_{ds})}{P_{MT}+P_{Aux}} \quad \text{Eq. (1)}$$

The above definition is not valid when there is cooling at AHU ($\dot{Q}_{AC}$).In heating season, if ($\dot{Q}_H > 0 \wedge P_{Aux}>0$), Eq (1) is not applicable; however, if the status of the auxiliary compressors removing vapour from the flash tank (7) is off, Eq (1) can be used imposing $P_{Aux}=0$ because auxiliary compressors are only working for heating purposes.
For the LT cycle, only the power input to the LT compressors has been considered, thus defining the COP of the low stage cycle:

$$COP_{LT} = \frac{\dot{Q}_{LT}}{P_{LT}} \quad \text{Eq. (2)}$$

Finally, a total COP_{tot}, considering useful effects at every temperature level follows the equation:

$$COP_{tot} = \frac{\dot{Q}_{MT}+\dot{Q}_{LT}+\dot{Q}_{AC}+\dot{Q}_H}{P_{MT}+P_{LT}+P_{Aux}} \quad \text{Eq. (3)}$$

On the other hand, secondo law efficiency relates the actual power input to the ideal minimum value to get the same useful effect, i.e. the Carnot Power, which results in taking care of the temperature level of each heat sink and source.
Equation (3) might then be reformulated as:

$$\eta_{tot} = \frac{P_{C,MT}+P_{C,LT}+P_{C,AC}+P_{C,H}}{P_{MT}+P_{LT}+P_{Aux}} = \frac{\dot{Q}_{MT}\left(\frac{T_{amb}}{T_{MT,ref}}-1\right)+\dot{Q}_{LT}\left(\frac{T_{amb}}{T_{LT,ref}}-1\right)+\dot{Q}_{AC}\left(\frac{T_{amb}}{T_{AC,ref}}-1\right)+\dot{Q}_H\left(1-\frac{T_{amb}}{T_{H,ref}}\right)}{P_{MT}+P_{LT}+P_{Aux}} \quad \text{Eq. (4)}$$

Where the reference temperatures $T_{MT,ref}$, $T_{LT,ref}$, $T_{AC,ref}$, $T_{H,ref}$ for MT, LT, AC and space Heating might be respectively 273.15 K, 251.15 K, 299.15 K, and for heat recovery 294.15 K, considering the standard prescriptions of 26°C and 21°C air temperature during cooling and heating seasons, respectively.

In general terms, while the second law approach mitigates the effect of outdoor temperature with respect to COP approach, which shows huge variations of the same system performance at equal Load Ratio ($LR = \dot{Q}_{MT}/\dot{Q}_{LT}$) when changing outdoor temperature, it completely reverses the effect of load ratio variations at the same operating conditions. This means that, while the COP decreases when decreasing the load ratio, the exergetic efficiency might have a different trend depending on MT and LT performances. Similar considerations can be applied also to AC and heating loads, in the case of heating pump mode.
The parametric analysis of the impact of boundary conditions, including load ratio, on the first and second law efficiencies dares a dedicated effort; this manuscript just aims at presenting the alternative approaches, to be eventually implemented in remote monitoring, and at showing the calculated values of the reference system.
The thermal loads to be used equally in equations 1, 2, 3 and 4, are calculated, using measured values of total refrigerant mass flow rates to the MT, LT and AC sections, taken at the inlet of each distribution line and the enthalpy of the refrigerant before and after the MT, LT and AC evaporators. Power inputs are also measured at compressor racks.

3.1. Performance Measurements in the Field

The field test started in December 2018, thus providing us, so far, with winter operations, i.e. subcritical conditions or transcritical with heat recovery or heat pump mode.
The main peculiarities of the registered working conditions are the high MT evaporation temperature (-5°C), together with the quite low load ratio $LR = \dot{Q}_{MT}/\dot{Q}_{LT}$, with respect to similar installations in Italy (D'Agaro et al., 2019, Dugaria et al., 2019).
Fig. 2 reports the trend of thermal loads during a 24hours period, clearly showing that, during the nightime the AHU is switched off. Although the data acquisition time step was set to 1 min, due to connection issues, some acquisitions were not stored; nevertheless, the presented data are obtaining by moving average over a 60 min. period.

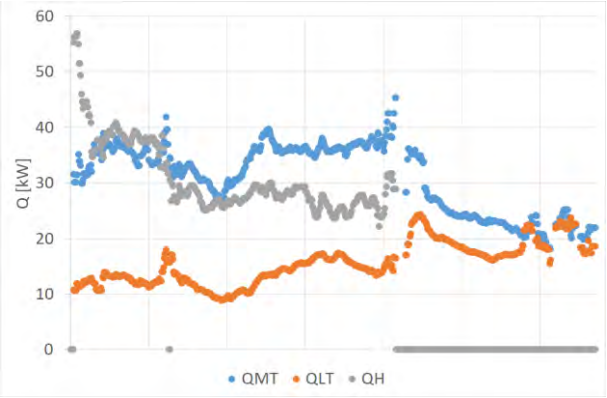

Figure 2: Cooling and heating loads during a 24h period

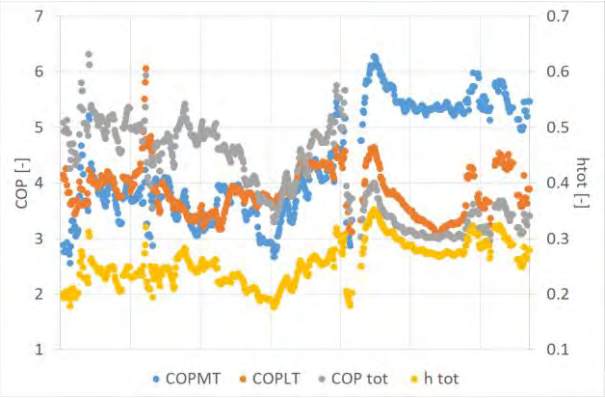

Figure 3: COP and η_{tot} during a 24h period

First law COPs, as defined in equations (1-3) are reported in Fig. 3, together with total efficiency (equation 4).
Table 1 shows the average values of the working conditions and measured performance (useful effect) values for data illustrated in Figs. 3 and 4, over the all stable period; COP and efficiency is calculated considering the total energy values over the stable period.
It is worth observing how the COP_{tot} and η_{tot} can provide different information when considering the proposed boundary conditions. While the first law approach is commonly used, the second law one requires more use to get acquainted to it.
It is worth reminding that both first and second law approaches require the values of refrigerant mass flow rates in the involved lines. As pointed out by Minetto et al.(2018), the evaluation of refrigerant mass flow rates with compressor curves, despite sufficiently accurate in the case of simple systems, might not be easily applicable in complex layouts, such as those involving ejectors.

Table 1. Measured values of boundary conditions and performances during winter operations

-	-	22/12/2018	22-23/12/2018	12/12/2018	12-13/12/2018
T_{amb}	(°C)	14.5	14.2	10.6	9.9
T_{evMT}	(°C)	-4.6	-5.0	-4.9	-5.1
T_{evLT}	(°C)	-31.3	-30.2	-30.4	-30.9
T_{evaux}	(°C)	2.6	-	-0.8	-
p_{gc}	(10^5 Pa)	70.3	55.8	77.3	53.7
Q_{MT}	(kW)	35.0	24.2	31.4	22.4
Q_{LT}	(kW)	13.4	19.4	16.9	14.5
Q_H	(kW)	30.9	-	49.3	-
LR	(-)	2.6	1.2	1.9	1.5
COP_{MT}	(-)	2.7	5.3	3.2	6.3
COP_{LT}	(-)	3.8	3.7	4.0	4.1
COP_{tot}	(-)	3.6	3.3	4.4	4.0
η_{tot}	(-)	0.20	0.29	0.23	0.27

4. FLOW METER: A PROPOSAL

As it emerges from the previous sections, the measurement of refrigerant mass flow is crucial to define the useful effects of the system and classify it according to first or second law approach.
Installing flow meters in commercial refrigeration systems is not common practice; therefore, there have been no specific developments for providing the market with reliable, sufficiently accurate, small and low cost sensors, to be finally included in remote monitoring systems.
Flow meters for fluids based on the hot wire anemometer principle are available on the market; however their size and their cost does not make them suitable for large scale application, especially when many sensors are required in the same system, as in the case of complex layouts as the one of Fig. 1.
In the following section, the theoretical analysis of an in-house flow meter dedicated to the application is presented.

4.1. Schematic Description

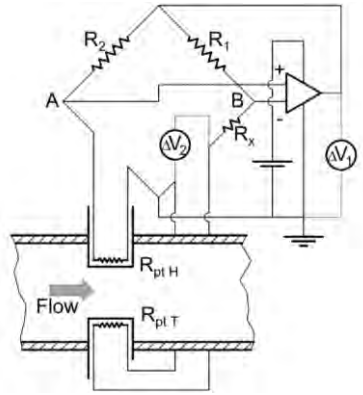

Figure 4: System sketch

Table 2. Circuit sizing

Resistor	Nominal Resistance
R_1	500 Ω
R_2	50 Ω
R_x	15 Ω
R_{ptH}	100 Ω
R_{ptT}	1000 Ω

The proposed sketch in Fig. 4 presents the sensor electrical circuit, which is based on the constant temperature hot wire anemometer principle. The anemometer is composed of two sensors: The first is the velocity probe ($R_{pt\,H}$ in Figure 4) and the second is the temperature compensation sensor ($R_{pt\,T}$ in Figure 5). In the proposed set-up both sensors are platinum resistors. Due to the high pressures and possible mechanical stress given by oil droplets or pressure fluctuations, both the probes are assumed to be enclosed at the top of cylindrical stainless steel housing.
The Voltage signal ΔV_1 represents the velocity signal. The second output Voltage channel ΔV_2 is used to obtain a reading on the temperature compensation probe, which expected to be more precise than the temperature measures available on the field, being inside the fluid flow.

4.2. Expected performance

In order to correctly design the Wheatstone bridge, and to assess the overall precision of this sensor, numerical simulation were run. The system is resolved imposing the energy equilibrium of the probes heating element (Equations 5 and 6) and the Wheatstone bridge equilibrium between points A and B (Equation 7):

$$i_H^2 R_{ptH} = \left(\frac{\Delta V_1}{R_2+R_{ptH}}\right)^2 R_{ptH} = \alpha A\left(T_{ptH} - T_{CO_2}\right) \quad \text{Eq.(5)}$$

$$i_T^2 R_{ptT} = \left(\frac{\Delta V_1}{R_1+R_x+R_{ptT}}\right)^2 R_{ptT} = \alpha A\left(T_{ptT} - T_{CO_2}\right) \quad \text{Eq.(6)}$$

$$i_H R_2 = \frac{\Delta V_1 R_2}{R_2+R_{ptH}} = \frac{\Delta V_1 R_1}{R_1+R_x+R_{ptT}} = i_T R_1 \quad \text{Eq.(7)}$$

Equations 5-7 allow to solve the three unknown ΔV_1, T_{ptT} and T_{ptH}, once the dependency on temperature of the resistors R_{ptT} and R_{ptH}, and the convection coefficient α are defined. The Callendar–Van Dusen equation was used to describe the Pt sensor sensitivity to the temperature. Convective heat exchange coefficient was computed applying the flat-plate correlation, using the probe diameter as reference length.

The output signal was then computed, assuming four different installation points: the MT line (subcooled liquid), the LT return line (superheated vapour), the compressors rack outlet line (GL_{in} and GC_{in} ^{sup}) and the gas cooler return line (GL_{out} and GC_{out} ^{sup}). As the refrigeration unit can work in both super critical and subcritical cycle, a total of six reference conditions has been studied.

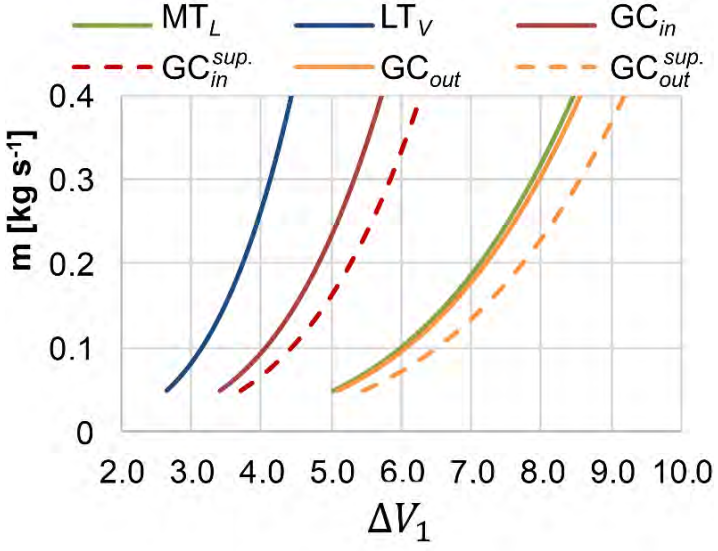

Figure 5: Expected output voltage difference ΔV_1 for in different measuring points in the system

Table 3. Reference conditions and equilibrium sensors temperatures

MT_L $p = 38.0$ bar		LT_V $p = 13.8$ bar	
T_{CO_2}	-2.3 °C	T_{CO_2}	3.2 °C
T_{ptT}	-1.8 °C	T_{ptT}	3.6 °C
T_{ptH}	2.0 °C	T_{ptH}	7.4 °C
GC_{in} $p = 64.8$ bar		GC_{out} $p = 64.8$ bar	
T_{CO_2}	69.4 °C	T_{CO_2}	16.5 °C
T_{ptT}	69.9 °C	T_{ptT}	16.9 °C
T_{ptH}	73.8 °C	T_{ptH}	20.8 °C
GC_{in} sup. crit. $p = 100.0$ bar		GC_{out} sup. crit. $p = 100.0$ bar	
T_{CO_2}	120.0 °C	T_{CO_2}	40.0 °C
T_{ptT}	120.4 °C	T_{ptT}	40.4 °C
T_{ptH}	124.4 °C	T_{ptH}	44.3 °C

The expected output signals ΔV_1 are presented in Fig. 5, while in Table 3 reports used reference conditions, as well as the equilibrium temperature for the sensors. The highest signals can be obtained in the liquid lines (or the dense vapour when supercritical condition is considered), thanks to the higher heat exchange coefficient. The Value of resistance Rx in the Wheatstone bridge defines the temperature difference between the sensors. The use of a 15 Ω resistor results in a temperature difference $T_{ptH} - T_{ptT} \cong 4$ K, while the difference between the temperature sensor and the actual flow temperature is $T_{ptT} - T_{CO_2} \cong 0.4$ K. In order to avoid phase change in the high temperature sensor, the difference $T_{ptH} - T_{CO_2}$ (approximatively 4.4 K) should be lower than the subcooling of the liquid, while no restriction is present when the vapour or the supercritical condition are considered.

As result of the sensitivity study in Figure 6, the proposed sensor seems a feasible alternative to the much expensive flow meter M1 and M2 (Figure 1), when sufficient subcooling is present The

measurement taken in the supercritical region ($GC_{in\ sup.}$) might pose some challenges for the determination of Q_H.

5. CONCLUSIONS

In this manuscript, data collected from remote monitoring of a fully instrumented Integrated Refrigeration unit based on CO_2 have been processed to evaluate energy performance both on a first and second law of thermodynamics approach. The second law approach can offer the opportunity of weighting the different useful effects, based on their temperature level and on load ratios. The two methodologies can propose a different insight and dare a further detailed sensitivity analysis. Refrigerant mass flow measurement is the straightforward way to evaluation of cooling and heating loads and should be included in remote monitoring. However, reliable, small and low-cost sensor for large scale implementation is a key issue. A new sensor based on the hot wire anemometry, potentially small and low cost, is presented and its performances theoretically evaluated according to the actual location it might have in the real plant. According to the proposed arrangement, location in the liquid line to MT and LT cabinets offers encouraging results.

AKNOWLEDGEMENTS

The integrated refrigeration unit presented in the paper was built and fully instrumented under the Project MultiPACK.
MultiPACK is a European project funded under the Horizon 2020 Research and Innovation Programme, project number 723137.

REFERENCES

Blust S., Singh S., Hafner A., Krzysztof Banasiak K., Nekså P., 2018. Environment-friendly refrigeration packs for indian supermarkets: experimental investigation of energy performance of a multiejector-driven R744 integrated compressor rack. 13th IIR-Gustav Lorentzen Conference on Natural Refrigerants, Valencia-Spain.

D'Agaro P., Coppola M.A., Cortella G., 2019. Field tests, model validation and performance of a CO_2 commercial refrigeration plant integrated with HVAC system, International Journal of Refrigeration Elsevier, International Journal of Refrigeration, Volume 100, April 2019, Pages 380-391.

Dugaria S., Azzolin M., Calabrese L, Minetto S., Del Col D., 2019, Monitoring of a CO_2 commercial refrigeration system serving a supermarket in Southern Europe, submitted to the 25th IIR International Congress of Refrigeration, Montreal, Canada.

Karampour M, Sawalha S., 2018. State-of-the-art integrated CO_2 refrigeration system for supermarkets: A comparative analysis, International Journal of Refrigeration 86: 239–257

Minetto S. Girotto S., Rossetti A., Marinetti S., Tosato G., 2018. A new approach to performance data harvesting and processing in commercial refrigeration systems, 13th IIR-Gustav Lorentzen Conference on Natural Refrigerants, Valencia-Spain, 2018.

Multipack, Horizon 2020 Research and Innovation Programme, project number 723137. https://www.ntnu.edu/multipack (last retrieved 1st February 2019)

Shecco, 2018. Accelerate Australia and New Zeland, Autumn issue.

SuperSmart H2020 Innovation Framework Programme, project number 696076. http://www.supersmart-supermarket.info (last retrieved 1st February 2019).

Manuscript ID: 1296
DOI 10.18462/iir.icr.2019.1296

Comparing open and closed vertical refrigerated display cabinets at mild and tropical external environments

Gustavo G. HEIDINGER[(a,b)], Samuel M. NASCIMENTO[(a,b)], Pedro D. GASPAR[(b,c)], Pedro D. SILVA[(b,c)]

[(a)] Eletrofrio Refrigeração Ltda, rua João Chede 1599, 81170-220, Curitiba - PR, Brazil
e-mail: gustavo@eletrofrio.com.br, web: http://www.eletrofrio.com.br
[(b)] University of Beira Interior, rua Marquês d'Ávila e Bolama, 6201-001, Covilhã, Portugal
[(c)] C-MAST - Centre for Mechanical and Aerospace Science and Technologies, Covilhã, Portugal
e-mail: dinis@ubi.pt, dinho@ubi.pt, web: http://www.ubi.pt

ABSTRACT

This paper reports the results of experimental tests performed according to ISO 23953 in vertical open and closed refrigerated display cabinets (VORDC vs. VCRDC). Tests were performed at a mild climate class (n. º 3: T=25°C; ϕ=60%) and a tropical one (n. º 6: T=27°C; ϕ=70%). The direct energy consumption is 46% higher at VCRDC due to the heated glass doors frame and defrost heaters. The product simulator temperature is higher and more stable at VORDC. The highest product simulator temperature is lower (-1.4°C) at the VCRDC and less stable (+2.7°C variation) due to the opening doors period. The total mass of condensed water at the evaporator is reduced 87% and the total heat load is 77% lower at the VCRDC. Thus, the estimated total energy consumption is reduced 42%. Given the current concerns with energy consumption and sustainability of the heat exchange processes, the VCRDC provide the best solution.
Keywords: Air Curtain, Climatic Chamber, Closed Cabinet, Experimentation, Open Cabinet.

1. INTRODUCTION

In general, refrigerated displays cases are designed and certified to operate in supermarkets that have ambient air conditioning, the European industry considers the mild climatic condition of dry bulb temperature and humidity of T_a = 25°C and ϕ_a = 60% (climate class n.°3 - ISO 2395, 2015) as standard for approval pattern of this type of equipment (critical summer condition). In practice, there are stores located at semi-tropical or tropical climate regions without ambient air conditioning, therefore, more adverse conditions of air temperature and humidity are regularly found. To meet this demand, the ambient air condition of T_a = 27°C and ϕ_a = 70% (climate class n.° 6 - ISO 23953, 2015) was defined as the climatic class of tropical climates for conducting the experimental tests.
Refrigerated display cases are usually classified on vertical, semi-vertical, horizontal and combined; which can be closed or opened to the store environment; for self-service or not. Open refrigerated displays cases are those whose products access occurs without the need to open doors or lids and closed refrigerated displays cases are the opposite (ISO 23953, 2015). Vertical open refrigerated displays cases (VORDC) are the most susceptible classification to problems due to ambient temperature oscillation and local air humidity. Since the external air infiltration is the most relevant aspect of the refrigeration load which is between 67 and 81% (Faramarzi, 1999, Gaspar et al., 2011 and Chieffo et al., 2018), therefore, the surrounding ambient influence on the performance and energy consumption of this type of equipment should be analyzed carefully in order to minimize the thermal exchange between the external (environmental) and internal (refrigerated space) air, therefore, optimize the overall operation of the VORDC (Gaspar et al., 2010, Chen et al., 2011, Cao et al., 2011, Laguerre et al., 2012, Nascimento et al., 2015 and Nascimento et al., 2016). Nowadays the VORDC are being replaced or retrofitted by the vertical closed refrigerated display case (VCRDC), i.e., with glass doors to reduce the energy consumption. Orlandi et al. (2013) quantify by computational fluid dynamics simulations the

VCRDC heat load components. Evans (2014) compiled a series of studies related to the installation and/or retrofit using VCRDC that can reduce the refrigeration load by 25 to 86%. The insertion of a physical barrier between the consumer and the exposed products is the main negative impact provided by the door glass that may reduce the product sales. Nevertheless, Frickie and Becker (2010) concluded that the installation of VCRDC do not have effect on product sales, but may improve the food safety and eliminate the cold aisle effect.
Comparing the VORDC and the VCRDC performance based on experimental results, the present work aims to assists the refrigerated display cases design and operation mainly in countries that have a high thermal amplitude from region to region and in stores that do not have equipment to control the temperature and the humidity of the ambient air. The results of experimental tests, performed according to ISO 23953 in VORDC and VCRDC at climate classes n.º 3 (T_a = 25°C; ϕ_a = 60%) and n.º 6 (T_a = 27°C; ϕ_a = 70%), evaluate the influence of double glass doors in the direct energy consumption, product simulator temperature, evaporator total condensed water mass, total heat load and total energy consumption.

2. EXPERIMENTAL PROCEDURE

Experimental tests were conducted in an environmental test chamber constructed according to ISO 23953 (2015) shown in Fig. 1. There is an air treatment to keep the air temperature and humidity surrounding the display cases at the climatic class n.° 3 (T_a = 25°C; ϕ_a = 60%) or at the climatic class n.°6 (T_a = 27°C; ϕ_a = 70%). The air treatment steps are cooling, heating and humidification, which are carried out respectively by an evaporating coil, heating devices and water vapor mixed to the airflow on the ducts. The test room is a thermally insulated parallelepiped shaped space in which two of the opposing sidewalls are designed to provide a uniform horizontal airflow (v_a = 0.1 to 0.2 m·s^{-1}) through the room.

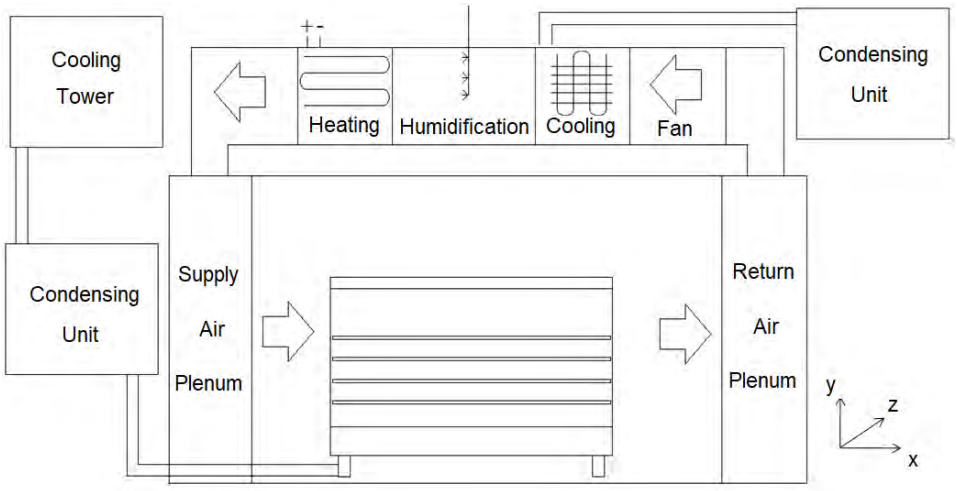

Figure 1: Environmental test chamber

The refrigerated display cases manufacturer recommends an evaporation temperature of -10±1 °C, when the VORDC and VCRDC are used for displaying fresh meat products, which temperature should be maintained between -1°C and +5°C (ISO 23953 class M1). The tested VORDC has 2.62m×2.12m×1.10m with a dual air curtain and 4 shelves as shown in Fig. 2a. The tested VCRDC has 3.82×2.10m×0.92m with six doors and four shelves as shown in Fig. 2b. The VORDC has 2.50 meters and the VCRDC has 3.75 meters of useful length (x). This industry field develop the display cases to be modular. In this case, the equipment lengths could be multiples of 1.25m, and the fans, lighting and heaters are proportionally disposed. Thus, the condensed water mass comparisons will be made per unit of length. One of the main functions of refrigerated cases is display as many products as possible into the smallest available display area, so the energy consumption comparisons will be based on the Total Display Area (TDA) of the equipment.

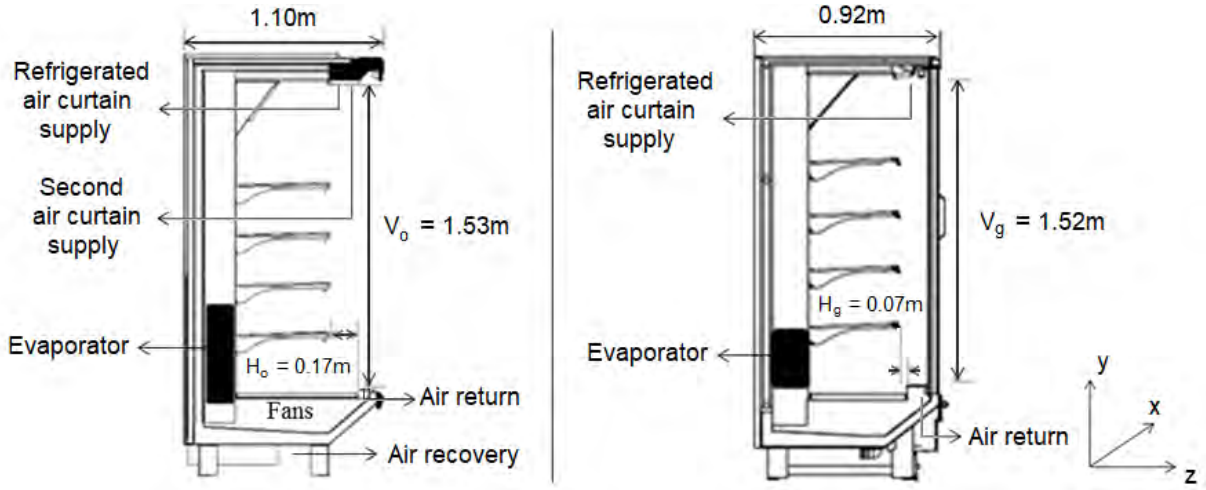

(a) (b)

Figure 2: Tested refrigerated display cases: (a) VORDC and (b) VCRDC

The VCRDC needs a special device to open doors automatically, each door must open once every ten minutes. The total duration of each door opening should be 6 seconds. Opening to an angle greater than 60° should last 1 second, 4 seconds of open door (> 60°) and 1 second for closing. The door opening test period should be 12 hours per day (ISO 23953, 2015).

Each test period lasted 24 hours and was repeated three times. The mass of water condensed during defrost was manually collected and measured in each test period. The temperature and pressure were collected on the suction and liquid lines to measure the R22 refrigerant enthalpies, and a Coriolis flowmeter was used to measure the outlet mass flow of the liquid coolant, $\dot{m}_r$, that passed through the evaporator during each operating period. The warmest product simulator temperature is collected to classify the refrigerated display cases as function of the displayed required product temperatures.

The remote refrigeration system is composed by a cooling tower and a hydraulic pump that drives the water used to draw heat from the cooling system in the condenser. A control valve, which keeps the condensing temperature approximately constant (39±1 °C), controls the water flow. The compressor pack was maintained in the same operating condition (evaporation pressure) by an inverter and there is no controller to stop the compressor work, i.e., there is no solenoid valve or set-point control at the refrigerant liquid line, thus the display cases are at the maximum possible refrigeration capacity during all the tests period. The compressor is only turned off when the defrosting process begins.

ISO 23953 (2015) defines the equations to calculate the TDA and the energy consumption indicators: *Direct daily electrical Energy Consumption*, DEC ($kWh{\cdot}24h^{-1}$); *Refrigeration daily electrical Energy Consumption*, REC ($kWh{\cdot}24h^{-1}$); *Total daily electrical Energy Consumption*, TEC ($kWh.24h^{-1}$); and *Specific daily electrical Energy Consumption*, SEC = TEC/TDA ($kWh{\cdot}24h^{-1}{\cdot}m^{-2}$).

The TDA is based on the display case length and on the horizontal (open – H_o and glazed - H_g) and vertical (open – V_o and glazed - V_g) projections dimensions (Fig. 2), i.e., the parameter that allows the comparison between product visualization and energy consumption, even between different types and lengths (x axis, open or glazed) of refrigerated display cases. The DEC includes the energy consumption of fans, heaters and lighting and is evaluated from its electrical power and respective operation times. The REC is calculated based on the total heat load to estimate the compressor energy consumption on a standard operational compressor condition. In its turn, the total heat load is calculated from the mass flow of the refrigerant fluid that passes across the evaporator during each operation period and the corresponding enthalpy change. The TEC is the sum of DEC and REC. In order to compare the VORDC and the VCRDC performance, as they have different lengths, the specific energy consumption indicators were used based on the total display area.

Table 1 shows the experimental tests (ET) conditions. The comparisons between experiments are based on the electrical nominal data, warmest product simulator temperature, total mass of

condensed water on the evaporator fins, total heat load and energy consumption (direct, refrigeration, total).

Table 1. Experimental tests

ET	Display case	Climate class
01	VORDC	3 (25°C/60%)
02	VORDC	6 (27°C/70%)
03	VCRDC	3 (25°C/60%)
04	VCRDC	6 (27°C/70%)

3. ANALYSIS AND DISCUSSION OF RESULTS

3.1 Operational and Direct Energy Consumption Data

The constructive and operational differences between the VORDC and VCRDC are presented in Table 2.

Table 2. Constructive and operational data of VORDC and VCRDC

Constructive and operational data	VORDC	VCRDC
Evaporation mean temperature (°C)	-10	-10
Number of daily defrosts	10	2
Defrost duration (min)	12	25
Defrost type	Natural	Electrical
Fans power (W)	318	159
Anti-sweat heaters power (W)	0	472
Lighting power (W)	32	48
Defrost heaters power (W)	0	2200
Total electrical power (W)	350	2879
Direct energy consumption- DEC ($kWh \cdot 24h^{-1}$)	8.02	17.56
Total display area – TDA (m^2)	4.24	5.63
Specific direct energy consumption SDEC ($kWh \cdot 24h^{-1} \cdot m^{-2}$)	1.89	3.12

The number of daily defrosts has been reduced from 10 to 2, because the doors are a much more efficient barrier than just the air curtain to the external air infiltration, which also explains the reduction in fans power. The LED lighting used in the tests was proportional based on the display case length. The refrigerated display cases are designed to operate in tropical climates, so there are anti-sweat heaters to prevent the water condensation on the frames of the double glass doors. During night and closed-door defrost periods, there is less ambient air infiltration and, consequently, a difficulty defrost without heating the air, so defrost heaters are used in the VCRDC evaporators. Thus, the total installed electrical power of the VCRDC is 8 times higher than the electrical power installed in the VORDC. However, it must be pointed out that defrost heaters are turned on only for 50 minutes per day.

3.2 Product Simulator Temperature

The VORDC show higher and more uniform product storage temperature values because the infiltration of external air into the refrigerated space is constant throughout the operation period under the test conditions. The VCRDC test show lower temperature values of the product simulators and with considerably variation due to the periods with and without door opening (Fig. 3). During the door opening period, product temperatures range up to 2.7°C due to the external air infiltration into the refrigerated space. The warmest product simulator is the most representative temperature to classify the refrigerated display cases as function of the displayed required product temperatures. Thus, comparing the ETs in climatic class n.° 3 (ET01 and ET03), the maximum temperature of the warmest product simulator is 1.4°C lower in VCRDC tests. In the

climatic class n.° 6 experimental tests (ET02 and ET04), the maximum temperature of the warmest product simulator is 1.0°C lower in the VCRDC tests. Thus, the two displays meet the standard temperatures (class M1, from -1.0°C to +5.0°C), but the VCRDC presents lower product conservation temperatures.

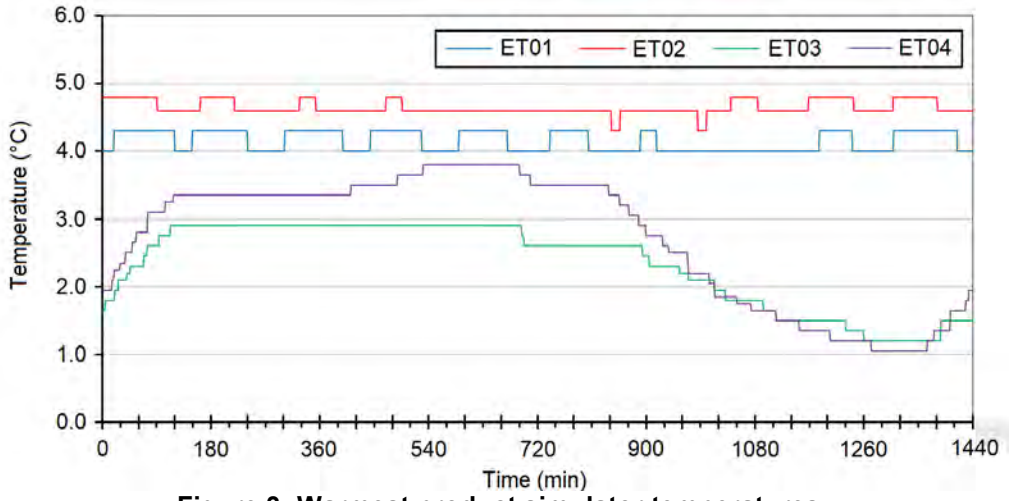

Figure 3: Warmest product simulator temperatures

3.3 Condensed defrost water

As much for VORDC as for VCRDC, when the climactic class changes from n.° 3 to n.° 6 (ET01 *vs.* ET02; ET03 *vs.* ET04) occurs an increase of approximately 46 % in the evaporator condensed water mass. However, the absolute quantity is quite different as shown by the same environmental condition tests (ET01 *vs.* ET03; ET02 *vs.* ET04), the water and ice formation in the VCRDC evaporator is reduced by 87% (Fig. 4). Therefore, the drastic reduction in the amount of defrost water due to the doors use is fundamental to increase the efficiency of refrigerated display cases once the air infiltration is decreased. This situation also allows to reduce the stops required to defrost the evaporator, and, consequently, reduces the temperature pull-down energy consumption.

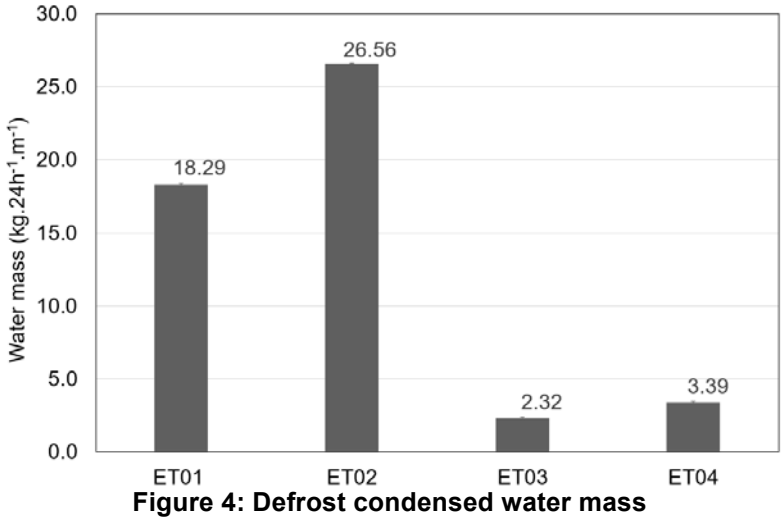

Figure 4: Defrost condensed water mass

3.4 Refrigeration Energy Consumption

The VCRDC total heat load is substantially reduced due to the increased protection provided by the doors use. The air infiltration reduction reduces mainly due to the latent heat load decrease as less moisture exists at the refrigerated space. Fig. 5 shows the SREC in each of the ETs.
The $SREC_{VORDC}$ increases 25% when the climatic class changes from n.° 3 to n.° 6 (ET01 *vs.* ET02) while the $SREC_{VCRDC}$ increases 12% (ET03 *vs.* ET04). Thus, the increase on the ambient air

enthalpy affects more intensely the VORDC than the VCRDC due to the doors that protect the refrigerated space from the warm and humid air infiltration. Comparing the ETs in climatic class n.° 3 (ET01 and ET03), the SREC of the VCRDC is 72% lower than in the VORDC. At the climatic class n.°6 (ET02 and ET04), the SREC in the VCRDC is 75% lower than in the VORDC. Therefore, the compressor energy consumption is significantly lower when the vertical refrigerated displays cases have doors and the main benefit is the impact on the heat load. The hotter and humid the environment is, the more important is the doors use because the VORDC energy consumption is very dependent on the climate conditions.

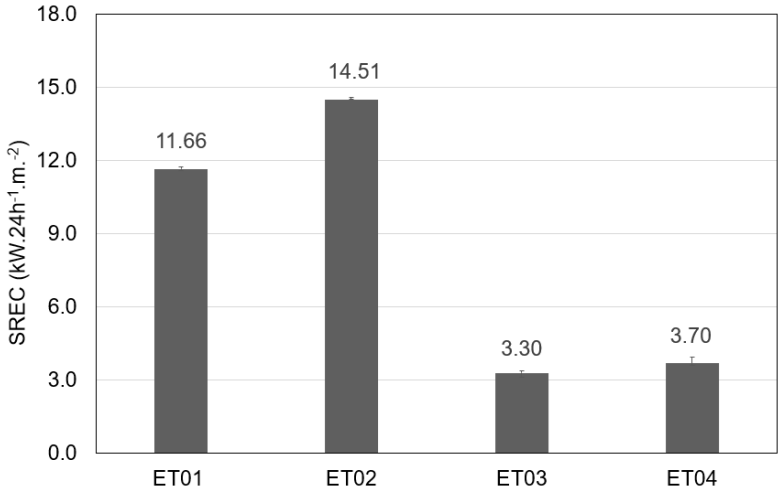

Figure 5: Specific refrigeration consumption

3.5 Total Energy Consumption

Considering the energy consumption of the fans, lighting and heaters, SDEC, added to the estimated compressor energy consumption, SREC, i.e., the total energy consumption of the refrigerated display cases per unit of display area, SEC, represents the absolute difference between the energy performance of VORDC and VCRDC. Fig. 6 shows the SEC values for the ET's.

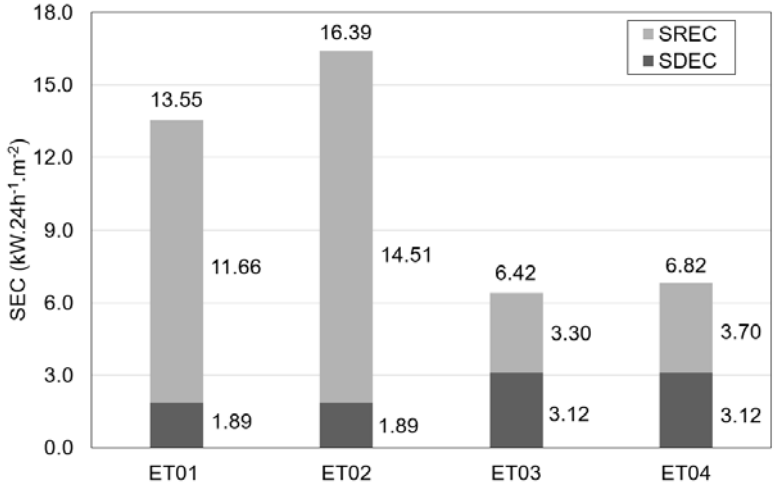

Figure 6: Specific total energy consumption

The operation of the defrost and anti-sweat heaters on VCRDC will cause an increment of 65% in the SEC value. When the environmental condition changes from climate class n.° 3 to the climate class n.° 6 the SEC_{VORDC} increases 21% while the SEC_{VCRDC} increases 6%. At climate class n.° 3 the VCRDC uses 52% less energy than the VORDC and in climatic class n.° 6 the reduction increases to 58%. Thus, the VCRDC needs more DEC (+65%) but the REC is reduced (up to -75%) which is much more significant to these display cases energy efficiency performance.

4. CONCLUSIONS

The significant increase in the electrical energy cost motivates and accelerates the use of more efficient refrigerated display cases. The maximum product temperatures on VCRDC are about 1.4°C lower than the VORDC, however, more temperature oscillation occurs due to the door opening period. The use of glass doors propitiates a latent heat load reduction up to 87% and a total saving on energy consumption up to 58% (-9.57 $kWh{\cdot}24h^{-1}{\cdot}m^{-2}$), being these factors of extreme relevance when choosing the right equipment even if the VCRDC initial investment cost is shown to be superior. The defrost and anti-sweat heaters impact on a higher specific direct energy consumption in the VCRDC than in the VORDC (up to 65%, +1.23 $kWh{\cdot}24h^{-1}{\cdot}m^{-2}$ in this case). Other benefit to the commercial establishment of food retailing lie in the reduced index of spoiled products as a function of a lower storage product temperature at the VCRDC (- 1.4°C).
The use of the doors is highly recommended when the equipment will operate in tropical climates and, due to its acceptable acquisition cost (+28%), many commercial establishments invest in the retrofit of their equipment, that is, they install the doors on equipment that are originally open. Thus, it is verified that the use of refrigeration equipment closed to ambient air is increasingly seen as the definitive solution, given the current concerns with the energy consumption and sustainability of the heat exchange and food preservation processes. In this perspective, the design of vertical refrigerated display cases under tropical climates could use the 4 experimental tests results presented in this paper to consider the specific refrigeration energy consumption data and the water condensation rates tendency to design the heat exchanger area for climatic conditions that exceed the limit defined worldwide as standard for homologation of open and closed refrigerated displays cabinets.

ACKNOWLEDGEMENTS

This work was fully supported by Eletrofrio Refrigeração. Authors thank Mr. Paulatti and Mr. Eng. Chueire for their continuous support and encouragement.

NOMENCLATURE

ET	Experimental test	(–)
DEC	Direct energy consumption	($kW{\cdot}24h^{-1}$)
H	Horizontal projection	(m)
REC	Refrigeration energy consumption	($kW{\cdot}24h^{-1}$)
SDEC	Specific direct energy consumption	($kW{\cdot}24h^{-1}{\cdot}m^{-2}$)
SEC	Specific total energy consumption	($kW{\cdot}24h^{-1}{\cdot}m^{-2}$)
SREC	Specific refrigeration energy consumption	($kW{\cdot}24h^{-1}{\cdot}m^{-2}$)
T	Temperature	(°C)
TDA	Total display area	(m^2)
TEC	Total energy consumption	($kW{\cdot}24h^{-1}$)
v	Velocity	($m{\cdot}s^{-1}$)
V	Vertical projection	(m)
VCRDC	Vertical closed refrigerated display case	(–)
VORDC	Vertical open refrigerated display case	(–)
ϕ	Relative humidity	(%)

Subscript

a	Air
o	Open
g	Glazed

REFERENCES

ASHRAE 72, 2014. Method of testing open and closed commercial refrigerator and freezers. American Society of Heating, Refrigeration and Air-Conditioning Engineers (ASHRAE).

Cao, Z., Gu, G. & Han, H., 2011. A novel optimization strategy for the design of air curtains for open vertical refrigerated display cases. Applied Thermal Engineering 31(16), 3098–3105.

Chen, Y.G. & Xia, D.H., 2011. The flow characteristics analyses of refrigerated air curtains in multi-deck display cabinets. 23rd International Congress of Refrigeration, Prague, Czech Republic.

Chieffo, M., Heirlmeier, B.R. & Roberts, C., 2018. Retail food store refrigeration and equipment. In Owen, M.S. & Kennedy, H.F. (Eds). ASHRAE Handbook: Refrigeration (15.1- 15.30). Atlanta,USA: Edition: ASHRAE.

Evans, J., 2014. Are doors on fridges the best environmental solutions for the retail sector? London Chamber of Commerce and Industry, London, England.

Faramarzi, R., 1999. Efficient display case refrigeration. Ashrae Journal 41(11), 46–52.

Frickie, B. & Becker, B., 2010. Doored display cases. ASHRAE Journal 52(9), 18-26.

GAS Research Institute, 2000. Investigation of relative humidity impacts on the performance and energy use of refrigerated display cases. Final Report.

Gaspar, P.D., Gonçalves, L.C.C. & Vogeli, A., 2009. Dependency of air curtain performence on discharge air velocity (grille and back panel) in open refrigerated display cabines. ASME International Mechanical Engineering Congress and Exposition, Lake Buena Vista, Florida, U.S.A.

Gaspar, P.D., Gonçalves, L.C.C. & Pitarma, R.A., 2010. Experimental analysis of the thermal entrainment factor of air curtains in vertical open display cabinets for different ambient air conditions. Applied Thermal Engineering 31(5), 961–969.

Gaspar, P.D., Gonçalves, L.C.C. & Pitarma, R.A., 2011. Análise Experimental da estabilidade de cortinas de ar de equipamentos de refrigeração para diferentes condições do ar ambiente. International Conference on Engineering, Universidade of Beira Interior, Covilhã, Portugal.

Heidinger, G.G., Nascimento, S.M. & Gaspar, P.D., 2013. Impact of environmental conditions on the performance of open multideck display case evaporators. 2nd IIR International Sustainability and the Cold Chain Conference, Paris, France.

Heidinger, G.G., Nascimento, S.M., Gaspar, P.D. & Silva, P.D., 2016. Relevant parameters on the energy efficiency of closed refrigerated multideck display cases. WIT Transactions on Ecology and the Environment 205, 71-81.

ISO 23953. 2015. Refrigerated display cabinets, International Organization for Standardization (ISO).

Laguerre, O., Hoang, M.H. & Flick, D., 2012. Heat transfer modelling in a refrigerated display cabinet: the influence of operating conditions. Journal of Food Engineering 108(2), 353-364.

Mousset, S. & Libsig, M., 2011. Energy consumptions of display cabinets in supermarket. 23rd International Congress of Refrigeration, Prague, Czech Republic.

Nascimento, S.M., Heidinger, G.H., Gaspar, P.D. & Silva, P.D., 2015. Experimental analysis to optimize the performance of air curtains and heat exchangers: application to refrigerated display cases. In Gaspar, P.D. & Silva, P.D. (Eds.), Handbook of research on advances and applications in refrigeration systems and technologies (590-640). Edition IGI Global.

Nascimento, S.M., Heidinger, G.G., Gaspar, P.D. & Silva, P.D., 2016. Numerical quantitative evaluation of the thermal performance of refrigerated display cabinets with variation of air curtain thickness and porosity of the back panel. Purdue International Refrigeration and Air Conditioning Conference, West Lafayette-IN, USA.

Orlandi, M., Visconti, F. & Zampini, S., 2013. CFD assisted design of closed display cabinets. 2nd IIR International Sustainability and the Cold Chain Conference, Paris, France.

Tassou, S.A. & Datta, D., 1999. Influence of supermarket environmental parameters on the the frosting and defrosting of vertical multideck display cabinets. Ashrae Transactions 105(1), 91-496.

Manuscript ID: 1571
DOI: 10.18462/iir.icr.2019.1571

Snowmelt modelling and solutions for outdoor snow storage

Marianne HEIMDAL[a], Trygve M. EIKEVIK[a], Ignat TOLSTOREBROV[a],

[a] Norwegian University of Science and Technology, Department of Energy and Process Engineering
Trondheim, 7491, Norway, heimdalmarianne@gmail.com

ABSTRACT

As a result of the increasing global temperatures, shorter periods of natural snow and warmer winter temperatures are threatening winter sports facilities close to the cities. Different solutions for outdoor snow storage in Granåsen was studied with the intention to reduce the melting loss. 24 000 m^3 snow covered by sawdust will be stored from the beginning of April to the end of September. A snowmelt model was developed for calculation of the snowmelt due to heat from the ground, precipitation, the surrounding air and solar radiation. The snowmelt during the season was found to be 20 %, and the heat from the surrounding air and solar radiation constitute more than 80 % of the total melt. Increasing the thickness of the sawdust layer proves to be the solution which reduces the snowmelt the most. However, a thicker layer of insulation increases the costs.
Keywords: Outdoor environment, Snow storage, Storage conditions

1. INTRODUCTION

A worrying trend is developing with shorter winter seasons and milder winter temperatures. The increasing global temperatures reduce the periods of natural snow, which is threatening winter sports facilities. The climate changes are making it more difficult and complicated to provide skiing conditions close to the cities. In order to face the climate changes and still being able to provide good skiing facilities, snow storage might be a solution to prolong the winter season. Storing snow for the next season gives a certain predictability and a guarantee for skiing arenas, users and winter games arrangers. It also reduces the economic risk of not having enough snow. Snow storage can make it possible to provide skiing facilities at temperatures too warm for traditional snowmaking equipment. This article describes snowmelt calculations for outdoor ground storage of a thermal insulated snow pile in Granåsen.

When a snow pile is being stored outside it requires thermal insulation to shelter the snow and reduce the snowmelt. Today both natural wooden materials, such as sawdust and wood chips, and fabricated materials, such as plastic sheets and geotextile, are used for outdoor snow storage applications. Important parameters for the performance of the cover materials are radiative properties, thermal conductivity, permeability, tensile strength, surface roughness and thickness of the insulation material (Olefs and Fischer, 2008). These characteristics affect the components of the energy balance for the sheltered snow. The guideline published by the Norwegian Ministry of Culture, recommends a thickness of 0.3-0.5 cm sawdust for a snow pile stored outside (Gjerland and Olsen, 2014).

2. METHODS

2.1 Heat and Mass Transfer for an Insulated Snow Pile

Snow being stored during the summer will suffer from heat leakage and snowmelt due to air temperatures above freezing and stronger solar radiation. Heat from precipitation, wind, radiation and humidity, together with the thermal properties of the insulating material, will affect the convective heat and mass transfer through the insulation.

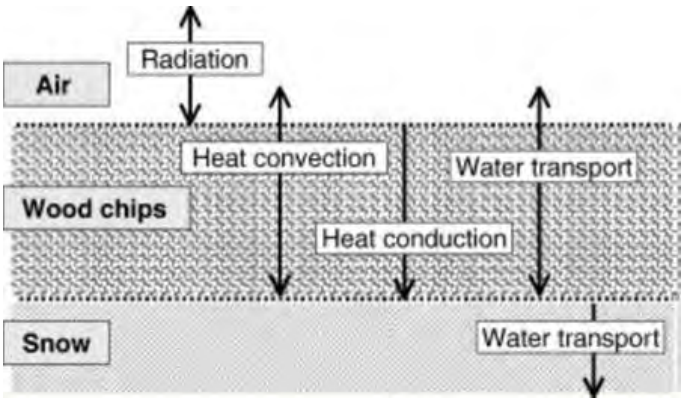

Figure 1: Heat and mass transfer for an insulating layer for snow storage (Skogsberg and Lundberg, 2005).

Fig. 1 illustrates the principle of heat and mass transfer through an insulting layer covering snow (Skogsberg and Lundberg, 2005). Water will be transported downwards through the snow, but because of capillary forces and evaporation, a fraction of the water will be transported upwards through the insulation layer (Lintzén, 2016). Energy is necessary for the evaporation to happen, and the insulating layer will therefore be cooled, and the melting rate will decrease. Heat from both short-wave radiation and long-wave radiation will be exchanged at the surface of the insulation. Depending on the albedo of the insulation material, some radiation will be reflected.

2.2 Snowmelt

When a snowpile is stored outside, snowmelt will occur in form of ground melt, rain melt and surface melt (Nordell and Skogsberg, 2007). Heat transfer causes the ground melt from the ground beneath the storage, while heat transfer from the ambient air and radiation causes the surface melt. The rain melt occurs due to precipitation. This section describes the snowmelt model including the equations, which simplifies the snowmelt to heat from the ground, heat from rain and heat from the surroundings. The total volume of melted snow during the storage period will then be the sum of the contribution from each heat source, Eq.(1):

$$V_{total} = V_{ground} + V_{rain} + V_{surroundings} \quad \text{Eq.(1)}$$

The heat transfer between the pile and the ground area covered by the snow pile, Eq. (2):

$$q_g = k_g A_g \frac{\Delta T_g}{l} \quad \text{Eq.(2)}$$

where q_g - heat transfer between ground and snow pile, W; k_g - thermal conductivity of ground material, W m^{-1} K^{-1}; A_g - ground area covered by snow pile, m^2; ΔT_g - temperature difference, °C between the snow pile and the temperature at a distance l , m, down in the ground (Lintzén, 2016). The volume flow of melted snow due to heat from the ground is then, Eq(3):

$$v_g = \frac{q_g}{h_{lf}\rho_{snow}} \quad \text{Eq.(3)}$$

where v_g - volume flow of melted snow due to heat from ground, m^3 s^{-1}; h_{lf} - latent heat of fusion for ice, J kg^{-1}; ρ_{snow} - density of snow, kg m^{-3}. The volume of snowmelt caused by ground heat. Eq.(4):

$$V_{ground} = v_g t \quad \text{Eq.(4)}$$

where t - duration of storage period [s].
For a period with P measured precipitation, m, the volume of melted snow due to the rain, Eq.(5):

$$V_{rain} = \frac{P A_s \rho_{water} c_{p,water} T_{sa}}{h_{lf}\rho_{snow}} \quad \text{Eq.(5)}$$

where A_s - surface area of snow pile,m^2; ρ_{water} - density of water, kg m^{-3}; $c_{p,water}$ - heat capacity of water, J kg^{-1}K^{-1}; T_{sa} - temperature of surrounding air, °C (Lintzén, 2016).

The surface melt is caused by the heat transfer from the surrounding air and solar radiation, to the snow pile. The solar radiation absorbed by a surface, Eq.(6):

$$q''_{abs} = q''_{GHI} a = q''_{GHI}(1 - r) \quad \text{Eq.(6)}$$

where q''_{abs} - absorbed radiation, W m^{-2}, q''_{GHI} - measured global horizontal irradiation, W m^{-2}; a - absorptivity of surface; r - reflectivity/albedo of surface.
Since the sides of the snow pile will have different tilts and orientations relative to the sun, the solar radiation must be decomposed for each side. The solar radiation on a surface with a given tilt and orientation, Eq.(7):

$$q_{surface} = q_{abs} A_s [\cos(\alpha) \sin(\theta) \cos(\psi - \varphi) + \sin(\alpha) \cos(\theta)] \quad \text{Eq.(7)}$$

where $q_{surface}$ - solar radiation on decomposed side; A_s - surface area of decomposed side, m^2; α - elevation angle of the sun, °; θ - tilt angle of surface, °; φ - solar azimuth angle, °; ψ = azimuth angle that the surface faces (clockwise from north), ° (PV Education, 2017).
The exterior surfaces of the insulated snow pile will be affected by the outdoor air temperature as well as the solar radiation. Depending on the properties of the covering material and the orientation of each surface relative to the sun, a certain amount of the radiation will be absorbed on the surface of the insulation. This will result in an insulation surface temperature which is higher than the temperature of the surrounding air. The surface temperature can be found from the following equation, Eq.(8):

$$T_s = T_o + \frac{q''_{surface}}{h_o} \quad \text{Eq.(8)}$$

where T_s - surface temperature, °C; T_o - outdoor air temperature, °C; h_o - outside surface conductance, W m^{-2}K^{-1} (Spitler, 2010). Since the snow pile will be exposed to wind, h_o can be set to 6 W m^{-2}K^{-1} (ASHRAE, 2010). The heat transfer between the insulated pile and its surroundings, Eq.(9):

$$q_{sur} = k_{avg} A_s \frac{T_s - T_{snow}}{\Delta z} \quad \text{Eq.(9)}$$

where q_{sur} - heat transfer between insulated pile and surroundings, k_{avg} - average value of the thermal conductivity for water and the insulation material, W m^{-1} K^{-1}; T_{snow} - temperature of the snow, °C; Δz - layer thickness of insulation material, m (Lintzén, 2016). k_{avg} takes into account that the insulating material will have a varying thermal conductivity depending on its moisture content (Skogsberg and Lundberg, 2005). The volume flow and the total volume of melted snow can then be determined from the Eq. (10) and Eq. (11):

$$v_{sur} = \frac{q_{sur}}{h_{lf} \rho_{snow}} \quad \text{Eq.(10)}$$

$$V_{surroundings} = v_{sur} t \quad \text{Eq.(11)}$$

2.3 Outdoor Snow Storage in Granåsen

Table 1 summarizes the specifications for the stored snow pile. The snow pile was assumed to have the shape of an isosceles trapezoid prism.

Table 1. Snow storage specifications.

Period of storage	April1-Sept30	Insulation material	Sawdust
Volume of stored snow	24090 m^3	Δz	0.4 m
Ground area, A_g	4400 m^2	Conductivity of water, k_{water}	0.58 W m^{-1}K^{-1}
Length, a	20 m	Conductivity average, k_{avg}	0.33 W m^{-1}K^{-1}
Length, b	40 m	Ratio, r (dry/wet)	0.3/0.15
Height, h	7.3 m	Ground material	
Length, L	110 m	Conductivity of ground, k_g	0.7 W m^{-1} K^{-1}
Tilt angel of surface, Θ	36º	Density of water, ρ_{water}	1000 kg m^3
Snow temperature	0 ºC	Heat of ice melting, h_{lj}	334 kJ kg^{-1}
Snow density, ρ	600 kg m^3	Heat capacity of water, $c_{p,water}$	4.18 kJ kg^{-1} K^{-1}

Some assumptions and approaches for the snowmelt calculations are listed below.

- Weather statistics for Granåsen was obtained for eight years, 2009-2016, which includes measured values for air temperature, relative humidity, cloud cover, precipitation and global horizontal irradiance for every hour during the storage period.
- When it was raining, or it had been raining during the last 12 hours, the albedo was set to 0.15. If no precipitation was registered the last 12 hours, the albedo was set to 0.30. These values were taken from another study regarding snow storage done by Ødegård (2013).
- For calculation of snowmelt due to the surroundings, the five outer surfaces of the pile was treated separately.
- The horizon of the snow pile in Granåsen was projected for every 15° using a topographic map.
- From the latitude, longitude and time zone for the location of the storage, the snowmelt model calculates the solar elevation angle and the solar azimuth angle for every hour. By comparing the solar elevation angle to the horizon of the pile, it was possible to know when the snow storage would be exposed to solar radiation for each day. Fig. 2 shows the solar elevation angle for three different days plotted against the horizon of the snow storage (yellow curve). The figure illustrates the variations in hours with solar radiation during the season. The blue curve and the dark green curve show the solar elevation for the first and last day respectively. The light green curve illustrates the solar elevation for the day when the sun reaches its highest point in the sky.

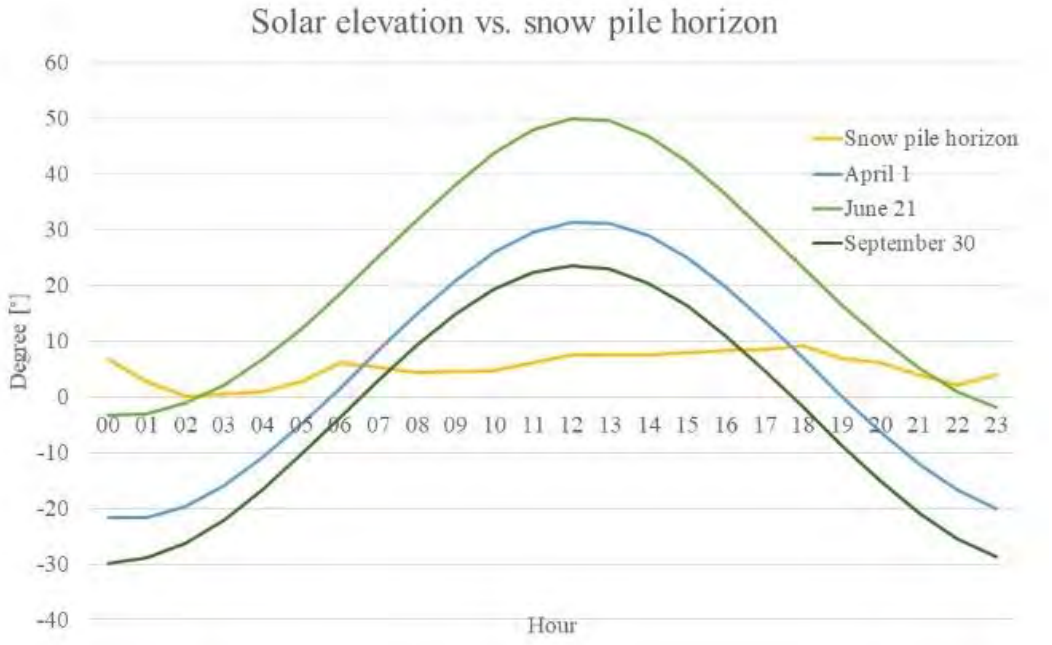

Figure 2: The solar elevation for three different days plotted against the horizon of the snow storage.

3. RESULTS

Table 2 presents the theoretical melting losses for each year obtained from the snowmelt model. The last column states the average values. The amount of measured precipitation during each season is included in brackets.

Table2. Theoretical snowmelt losses.

Source of melting	2009	2010	2011	2012	2013	2014	2015	2016	Average
Ground [m^3]	243	243	243	243	243	243	243	243	243
Rain [m^3]	643	457	900	480	490	509	610	557	581
Precipitation [mm]	617.3	470.9	787.4	555.3	459.7	482.2	608.5	526.2	563.4
Surroundings [m^3]	4 210	3 755	4 111	3 552	4 044	4 469	3 777	3 978	3 987

Total melting loss [m^3]	5 096	4 455	5 253	4 276	4 777	5 221	4 630	4 778	4 811
Volume last day [m^3]	18 994	19 635	18 837	19 814	19 313	18 869	19 460	19 312	19 279
Loss in %	21	18	22	18	20	22	19	20	20

The percentage snowmelt contribution related to each heat source is shown in Table 3. The average values are included in the last column.

Table3. Snowmelt contribution from each heat source.

Source of melting	**2009**	**2010**	**2011**	**2012**	**2013**	**2014**	**2015**	**2016**	**Average**
Ground [%]	5	5	5	6	5	5	5	5	5
Rain [%]	13	10	17	11	10	10	13	12	12
Surrounding [%]	83	84	78	83	85	86	82	83	83

The results presented in Table 2 and Table 3 indicate that the surroundings (solar radiation and surrounding air temperature) have a remarkable impact on the snowmelt and constitute more than 80 % of the total snowmelt. By comparing the results to other practical examples of outdoor ground storage in Scandinavia (Lintzén, 2016), 20 % melting loss during the season can be assumed to be a reasonable result.

Considering Table 2 one can see that the seasons in 2011 and 2014 have the largest melting losses. The season of 2014 also has the highest amount of melting caused by the surroundings, which constitutes 86 % of the total melt. The highest amount of measured precipitation was in 2011, which results in a considerable part of melting due to heat from the rain. The storage seasons in 2010 and 2012 have the smallest losses. These seasons also had rain melt below average. The ground melt was the same for each year as the temperature in the ground and the temperature of the snow pile are both assumed to be constant during the entire storage season. This is a reasonable assumption as the contribution from the ground heat was much smaller than the heat from rain and surroundings, as stated in Table 3.

To evaluate different solutions to reduce the snowmelt for the outdoor snow storage in Granåsen, the weather statistics for 2016 was used. Considering Table 2 and Table 3 the storage season of 2016 was a good representation of the average values. This section studied the effect of three solutions; solar shading, thicker layer of insulation and changes in snow pile geometry.

The top surface and the side facing south of the snow pile were highly exposed to the radiation from the sun 17.4 and 13.9 W m^{-2} (50 and 40 % from total) respectively. A wall for solar shading could be placed in front of the side facing south to reduce the impact of the solar radiation. A 4 m high “model” wall, which was placed 3 m from the side facing south, was therefore included to the horizon in the snowmelt model. The effect of a solar shading wall is shown in Table 4.

Table4. Snowmelt with and without solar shading wall.

Source of melting	**No wall**	**Wall**
Ground [m^3]	243	243
Rain [m^3]	557	562
Surroundings [m^3]	3 978	3 734
Total melting loss [m^3]	4 778	4 539
Volume last day [m^3]	19 312	19 551
Loss in %	20	19

From Table 4 one can see that the snowmelt has been slightly reduced, and that the rain melt is a bit higher for the case with the solar shading wall. The reason for that is probably related to the lowered snow-melting rate, leading to a larger surface area being exposed to the rain. However, a solar shading wall did not reduce the conductive heat transfer between the surrounding air and the snow pile, thus the total snowmelt reduction was small. It may provide shelter from the wind, but effects from wind was not taken into consideration for the calculations.

Eq. (9) states that the heat transfer between the snow pile and the surroundings is inversely proportional to the thickness on the insulation material. This means that an increase in the thickness

of the insulation layer will reduce the heat transfer. By changing the insulation thickness in the snowmelt model, the effect of this factor can be studied. The results are shown in Table 5. From Table 5 one can easily observed the remarkable impact of a thicker layer of insulation, and that the snowmelt due to the surroundings was decreasing with increasing Δz. As for the case with the solar shading wall, the rain melt increases for higher values of Δz. The same explanation applies here: a larger surface area of the snow pile was exposed to the rain.

Table 5. Snowmelt result for different insulation thicknesses.

Source of melting	**Δz = 0.3 m**	**Δz = 0.4 m**	**Δz = 0.5 m**	**Δz = 0.6 m**	**Δz = 0.7 m**	**Δz = 0.8 m**
Ground [m^3]	243	243	243	243	243	243
Rain [m^3]	536	557	570	579	585	590
Surroundings [m^3]	5 150	3 978	3 239	2 732	2 362	2 080
Total melting loss [m^3]	5 929	4 778	4 052	3 553	3 190	2 913
Volume last day [m^3]	18 161	19 312	20 038	20 537	20 900	21 177
Loss in %	25	20	17	15	13	12
Total cost [NOK]	152 033	159 565	175 597	196 189	219 461	244 473

Having a thicker layer of insulation was an option that requires more space. The sawdust must be stored and dried when it is not used. A cost estimate was therefore done to compare whether it is cheaper to have a thicker layer of sawdust, or a thinner layer and compensate for the snow loss by buying the corresponding amount of snow. Choosing Δz = 0.8 m as reference case, it implies that 21 177 m^3 snow was needed at the end of each storage season. The price for sawdust and snow was set to 57 NOK m^{-3} and 20 NOK m^{-3} respectively (Ødegård, 2013; Berg et al., 2016). The estimated cost is shown in the last row of Table 5 and states that the needed amount of sawdust was the major cost. This supports the recommended insulation thickness of 0.3-0.5 m, given by the Norwegian Ministry of Culture.

The top surface is exposed to the highest amount of solar radiation per square meter. Different geometries were implemented in the snowmelt model. The geometries must still satisfy the volume requirement of 24 000 m^3 and a ground area limitation of 112 m x 51 m. The calculated snowmelt losses are presented in Table 6.

Table 6. Snowmelt result for different snow pile geometries.

	Isosceles trapezoid prism			**Rectangular pyramid**	**Rectangular prism**
Properties	**a = 20 m; b = 40 m**	**a = 15 m; b = 45 m**	**a = 10 m; b = 50 m**	**b = 50 m**	**a = b = 30 m**
Top surface area [m^2]	2 200	1 650	1 100	-	3 300
Ground surface area [m^2]	4 400	4 950	5 500	5 500	3 300
Total surface area [m^2]	5 362	5 758	6 222	6 266	5 344
SA:V [m^{-1}]	0.223	0.239	0.258	0.260	0.222
Source of melting					
Ground [m^3]	243	273	304	304	182
Rain [m^3]	557	595	638	647	551
Surroundings [m^3]	3 978	4 110	4 287	4 146	4 240
Total melting loss [m^3]	4 778	4 978	5 229	5 096	4 973
Volume last day [m^3]	19 312	19 112	18 861	18 999	19 117
Loss in %	19.83	20.66	21.71	21.15	20.64

A snow pile with the form of a triangular prism was of the ideal geometry to minimize the top surface area parallel to the ground. However, Table 6 shows that this geometry will have a larger total surface area, and the total snowmelt was larger than for two of the trapezoid prisms and the rectangular prism. The surface area of the snow pile should be as small as possible to reduce the exposure to

solar radiation and surrounding air. The surface-area-to-volume ratio (SA:V) for the different geometries are included in Table 6. The lowest value for SA:V was found for the rectangular prism. However, the total melting loss for the rectangular prism was slightly larger than for the first of the three trapezoid prisms. These two shapes have the same cross-sectional area, but the top surface area for the rectangular prism is larger. As previous stated, the top surface of the snow pile is the side which is exposed to the highest amount of solar radiation. This may explain why the rectangular prism did not have the smallest melting loss, despite its SA:V.
Reducing the surface area would also reduce the amount of sawdust needed to cover the snow pile, as well as the costs related to the insulation. However, there will be challenging to form the snow pile into any desired shape as the snow storage is being produced. Limitation in maximum height, time, available vehicles and whether the areas around the storage is accessible by vehicles, are factors that have impact on the production and shape of the outdoor snow storage.

4. DISCUSSION

The developed snowmelt model gave reasonable snowmelt results for an outdoor snow storage, as the calculated results match the snowmelt from other practical snow storage examples. The results also verify that the surface melt, due to solar radiation and surrounding air, constitutes the largest part of the total melt, as found by Skogsberg (2005). The model can be used for other snow storage facilities, as long as the latitude, longitude and horizon for the location is known, and weather statistics is available.

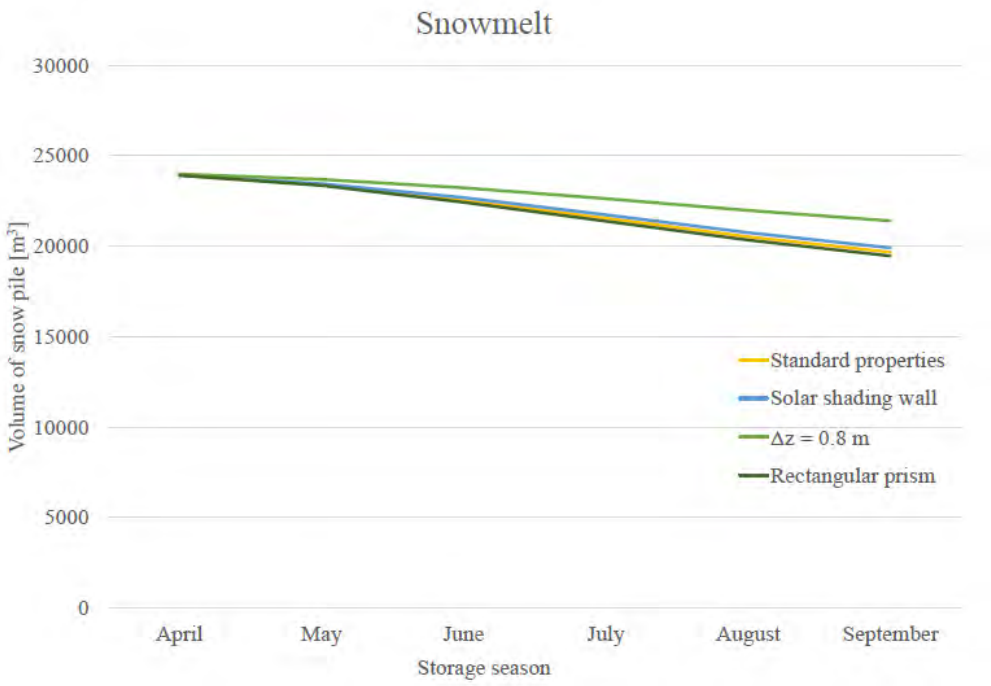

Figure 3: Decreasing of snow pile volume during the period of storage.

Fig. 3 shows the decreasing snow pile volume during the season in 2016 for four different cases. The yellow curve illustrates the melting rate for the snow pile with the specifications given in Table 1. Each one of the three other curves shows an investigated solution for snowmelt reduction. Only the increase in insulation thickness has a considerable reduction in melting rate, as can be seen from the light green curve in Fig. 3. The same effect of insulation thickness was found in a laboratory experiment by Skogsberg and Lundberg (2005).
The cost estimation regrading insulation thickness has demonstrated that a thickness of 0.3-0.5 m sawdust can be recommended, with respect to total snowmelt and insulation material costs. A solar shading wall cannot be regarded as a useful solution, as the reduction in snowmelt is minimal. Furthermore, the wall would permanently occupy space on the parking lot in Granåsen, when no snow is being stored. The results obtained by changing snow pile geometry, demonstrate only small

variations in total snowmelt. The difference between the best and worst case of melting is only 451 m^3, which constitutes less than 2 % of the initial snow pile volume. This indicates that the shaping of the snow pile when the snow storage is being produced, can be given less focus, as long as the snow pile is kept compact. The main priority should therefore be given to efficient drying and maintenance of the insulation material.

5. CONCLUSION

When 24000 m^3 snow is stored outdoor in Granåsen, it can be assumed that approximately 20 % of the insulated snow pile will melt during the season. The snowmelt calculations have demonstrated that heat from the surroundings (solar radiation and surrounding air) will have the greatest impact on the snowmelt. The contribution from the surroundings is found to be 78-86 % of the total snowmelt. Increasing the thickness of the insulation layer is further found to be the best solution to reduce the melting rate. Changing the insulation thickness from 0.4 m to 0.8 m reduces the snowmelt from 20 % to 12 %. However, increasing the insulation thickness gives higher expenses. Thus, a thickness of 0.3-0.5 m can be recommended. Changing the snow pile geometry or use of a solar shading wall does not lead to any significant melt reduction. For that reason, it can be concluded that maintenance of the sawdust is the most important measure to reduce the snowmelt. This includes necessary drying to maintain the quality and the low thermal conductivity of the sawdust, which will reduce the cost related to buying new sawdust. Drying methods for sawdust has not been studied in this article, and should therefore be suggested as further work. Snow storage is a good alternative to guarantee for skiing facilities in Granåsen from the beginning of October. This makes it possible to provide skiing trails even if no natural snow has fallen, or the temperature is too high for traditional snowmakers. However, there is a chance that the distributed snow will melt fast due to high temperatures in October. A short skiing trail located to areas with less sunlight should be considered as an alternative in October.

REFERENCES

ASHRAE, 2010. Refrigeration. ASHRAE, Atlanta, GA.

Berg, O. E. H., Hagen, T. B., Haugen, A. and Sagmoen, S., 2016. Lagring og utlegging av kunstsnø. Technical report.

Clulow, M. G., 2006. Indoor snowmaking. ASHRAE Journal 48(7),18.

Gjerland, M. and Olsen, G., 2014. Snøproduksjon og snøpreparering. Kulturdepartementet (ed.), 201 p.

Lintzén, N., 2016. Properties of snow with applications related to climate change and skiing. PhD thesis, Luleå tekniska universitet.

Nordell, B. and Skogsberg, K., 2007. The Sundsvall snow storage – six years of operation. In Thermal Energy Storage for Sustainable Energy consumption. Springer, 349-366

Olef, M. and Fischer, A., 2008. Comparative study of technical measures to reduce snow and ice ablation in alpine glacier ski resorts. Cold regions science and technology, 52(3), pp. 371-384.

PV Education, 2017. Arbitrary orientation and tilt. http://www.pveducation.org/pvcdrom/
arbitrary-orientation-and-tilt. Accessed December 7, 2017

Skogsberg, K., 2005. Seasonal snow storage for space and process cooling. PhD thesis, Luleå tekniska universitet.

Skogsberg, K. and Lundberg, A., 2005. Wood chips as thermal insulation of snow. Cold regions science and technology, 43(3), 207-218.

Spitler, J. D., 2010. Load calculation applications manual. Second edition. American Society of Heating, Refrigeration and Air-Conditioning Engineers, 340 p.

Ødegård, R. S., 2013. Optimalisering av snølagring om sommeren i et subalpint klima i Sør-Norge (versjon 2.5.14).

Manuscript ID: 1663
DOI: 10.18462/iir.icr.2019.1663

Sizing of thermal energy storage with phase change materials for a battery-free solar-powered refrigerator

Adriana COCA-ORTEGON[(a)], Juan PRIETO[(a)], Alberto CORONAS [(a)]

[(a)] Universitat Rovira i Virgili, Mechanical Engineering Department, CREVER,
Av. Països Catalans 26, 43007, Tarragona, Spain, adriana.coca@urv.cat

ABSTRACT

Solar-powered refrigerators are useful for preserving food in isolated regions where there is no electricity supply or there are frequent power outages. Currently, these systems use electrical batteries for storing energy; however, other technologies, with less environmental impact and maintenance requirements, can be applied. One option is to store cold with phase-change materials. This study evaluates the energy autonomy of a solar-powered refrigerator which has a PCM slab in contact with the evaporator wall. The objective is to size the PCM slab for a battery-free system for two tropical locations.
A validated dynamic model was developed and simulations were carried out with several values of PCM slab thickness, insulation thickness, and air-change rate.
Results are better for longer compressor cycle time, which can be increased when both the PCM slab and insulation thickness are higher. In addition, the control strategy was defined to improve the use of the solar resource.

Keywords: Cold storage, phase-change materials, solar energy, refrigerator, photovoltaic.

1. INTRODUCTION

Solar-powered refrigerators are a useful solution for food preservation and manage the cold chain in isolated regions where there is no electricity supply, or there are frequent power outages (as is the case in some developing countries) (Katic et al., 2010). Although data from the World Bank shows that there has been a considerable improvement in access to electricity over the last 25 years (WB and ESMAP, 2017), 12.6% of the world population still do not have access.
The countries with the least access to electricity are located mainly in Sub-Saharan Africa, the Caribbean, Southeast Asia and the Pacific, and in numerous small islands worldwide. However, one important advantage of these regions that solar energy is readily available, so solar refrigerators can be more feasible.
There are two main types of solar-powered refrigerators: refrigerators activated by photovoltaic (PV) panels, and refrigerators activated for solar thermal collectors (Kim and Infante Ferreira, 2008). Nowadays, only the first type is commercially available; this type is usually activated by vapor compression refrigerators with a direct current (DC) compressor.
PV systems usually store energy by using conventional electrical lead-acid batteries. The main advantage of this technology is its lower cost. However, they have a short lifespan, some models require more maintenance, and they usually have a toxic electrolyte, which is potentially dangerous to the environment (Sørensen, 2015). One alternative for solar-powered refrigerators is to store cold using phase change materials (PCM) integrated into refrigerators.
The most common PCMs are based on paraffin or hydrated salts, which are neither toxic to humans nor pollute the environment (Dincer and Rosen, 2011; Zalba et al., 2003). In addition, PCMs can support a high number of thermal cycles, about 10,000 for paraffin and 3,000 for hydrated salts, while conventional electrical lead-acid batteries support an average of 500 cycles. Only the most advanced nickel and lithium electrical batteries can support more than 1,000 cycles (Sørensen, 2015).
Most of the previous studies, in relation to the use of PCMs in conventional on-grid refrigerators, have analyzed PCM slabs in contact with the evaporator surface (Azzouz et al., 2008; Marques et al., 2014; Yusufoglu et al., 2015), and PCM cylinders around condenser tubes (Cheng et al., 2017;

Mastani Joybari et al., 2015; Oró et al., 2012). Some of the effects reported in these studies are the increased compressor cycle time, the improvement in the temperature stability of the product, and the fewer compressor starts, which sometimes means that single speed compressors consume less electricity. Some solar-powered refrigerators on the market have use PCM for cold storage, but very few studies have shown how to improve the integration between the thermal energy storage and the PV system.

Because conventional DC vapor compression refrigerators are more common at the commercial level, in this study we analyzed a DC vapor compression refrigerator, activated by a PV system with a passive thermal cold storage slab with encapsulated phase change materials (PCM). However, this energy storage option can be applied not only to DC vapor compression refrigerators but to all types of solar-powered refrigerators.

The main purpose of this study is to size the PCM slab in order to increase the autonomy of the refrigerator without using conventional electrical batteries. To do so, a validated dynamic model was developed, and simulations were carried out for a product preservation temperature of 11°C, under different ambient temperatures, several values of PCM thickness, insulation thickness, and air change rates. In addition, a control strategy was defined to improve the use of solar energy, and it was verified for two typical tropical locations in Kenya and Cuba.

2. METHODOLOGY

2.1 System Description

The system studied (Fig.1) consists of a horizontal refrigerator, which has a useful capacity of 350 l, and a direct current compressor driven by photovoltaic panels. Passive cold storage, with a PCM slab, is installed inside the refrigerator, in contact with the evaporator wall.

As is usual in domestic and commercial refrigerators, the equipment uses a simple mechanical compression vapor cycle. The evaporator is made of copper tube, embedded in the refrigerator walls; the condenser is of the “wire on tube type”, natural air-cooled, and the expansion device is a capillary tube also made of copper. The DC compressor is hermetic (Danfoss-Secop, 35BD), working with refrigerant R134a.

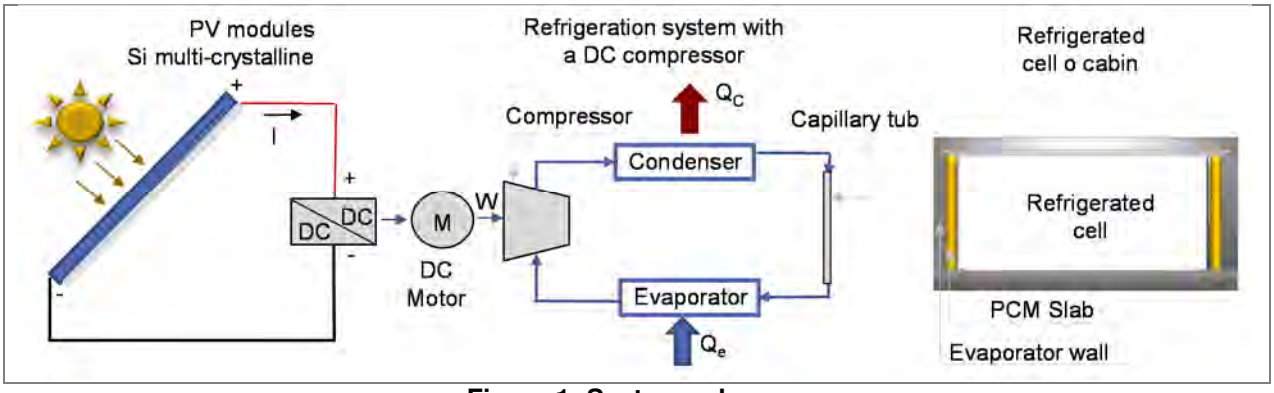

Figure 1: System scheme

The photovoltaic system consists of multi-crystalline silicon modules and a DC/DC converter, which adapts the voltage output of PV-modules to the requirements of the compressor control unit. This control unit makes it possible to vary the final voltage that activates the motor-compressor and regulates the speed according to the power available. In addition, the refrigerator’s refrigeration capacity and electricity consumption are regulated by the compressor speed.

The refrigerator was adapted to store 16 kg of product, which is simulated using water, distributed in a total of 40 polyethylene packages, arranged in aluminum shelves. In addition, two fans are installed inside a refrigeration cell to cool the stored product by forced convection heat transfer.

Passive cold storage has encapsulated phase change material (PCM) in polyethylene-aluminum bags, arranged on steel sheets. They are placed around the internal refrigerator walls in contact with the evaporator. The purpose of this system is to activate the compressor only during the daylight hours, so that the PCM slab can be charged while there is solar radiation. Later, during the night, the thermal energy stored in the PCM slab is used to handle the system’s refrigeration demand. The

more solar radiation there is, the faster the compressor works. In any case, the product must be stored in the required temperature range (11+/-2°C in this case).
The system was modeled with well-known methods for PV and refrigeration systems. However, the charge and discharge of the PCM slab need a validation procedure. So, the experimental setup presented in Fig. 2 was implemented.
The refrigerator was tested under constant ambient temperature inside a climatic room, according to the European Norm EN 62552. The electricity required by the DC compressor was produced by a DC source, which was connected to a standard AC electrical panel. In total, 30 thermocouples were installed in different elements (refrigerator wall, PCM slab, and product store). In addition, the voltage and the electrical current required by the DC compressor were measured.
The PCM used during the experiments was a paraffin mixture, with a phase change temperature between 5 and 6°C, manufactured by Rubitherm, product reference RT5HC. Other details of this experimental setup have been reported in a previous study (Coca-Ortegón et al., 2017).

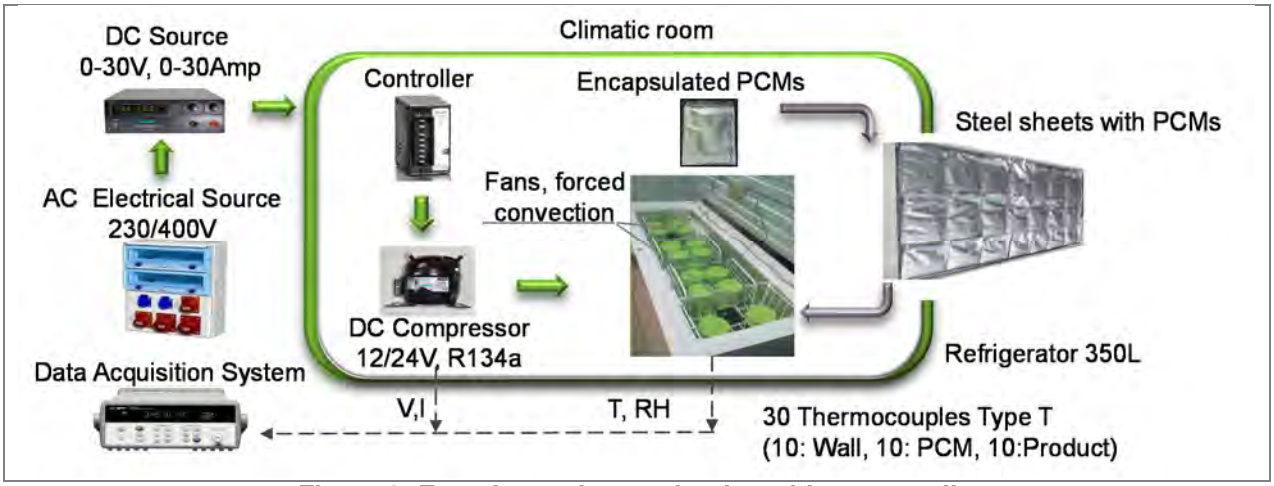

Figure 2: Experimental setup for the refrigerator cell

2.2 PCM Selection

The first basic characteristic considered for selecting the phase change material (PCM) was the melting temperature. For the system analyzed, this temperature must be an intermediate value between the evaporator temperature and the preservation temperature of the stored product. The purpose of this temperature is to guarantee the complete solidification of the PCM during the charging process and take advantage of the latent thermal storage.

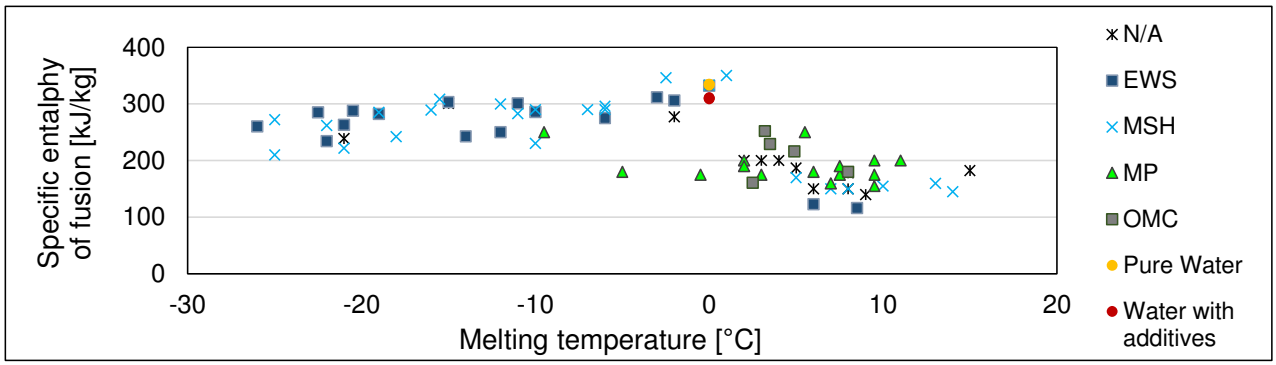

EWS: Euectic Water Solution, MSH: Hydrated Salts Mixtures, MP: Paraffin Mixtures, OMC: Organic Multi-Component.

Figure 3: Specific enthalpy of fusion Vs melting temperature for commercial PCMs

The second characteristic considered was the specific enthalpy of fusion, which should be as high as possible, to increase the energy density of the PCM slab. Fig. 3 shows these characteristics for commercially PCMs from eight international manufacturers. This Figure was prepared by consulting some reviews of PCM for refrigeration applications (Cabeza et al., 2011; Li et al., 2013; Oró et al., 2012; Zalba et al., 2003) and by an additional consultation on the websites of the manufacturers. Specifically, in the temperature range analyzed, the most common PCMs available are made of

paraffin mixtures (MP) and hydrated salt mixtures (MSH). In comparison to the hydrated salts, the advantage of paraffin is its greater long-term stability and lower sub-cooling. On the other hand, they have a lower thermal conductivity, and flammability if the maximum temperature is exceeded.
On the basis of the above information, we selected an organic PCM, type MP (paraffin mixture), with a melting temperature between 7 and 10°C and a heat storage capacity of 130 kJ.kg^{-1} between 4 and 13°C. The main characteristics of this PCM are presented in Table 1.

Table 1. Main characteristics of PCMs used in the study

Characteristic	Units	Value
Manufacturer / reference	-	Rubitherm / RT9
Type	-	Organic - Paraffin mixture
Phase change temperature	[°C]	7 to 10
Heat storage capacity (0 to 17°C)	[kJ kg^{-1}]	175
Specific heat capacity (solid) / (liquid	[kJ kg^{-1} K^{-1}]	2.0 / 2.0
Density (solid) / (liquid)	[kg m^{-3}]	880 / 760
Thermal conductivity (solid) / (liquid)	[W m^{-1} K^{-1}]	0.2 /0.2

2.3 Modeling and Simulation

The model has four main parts: the refrigerated cell, the PCM slab with encapsulated phase change materials (PCM slab), the refrigeration sub-system, and the photovoltaic sub-system. The simulation was implemented in Matlab, and the dynamic simulation software, TRNSYS, was used as a complementary tool to simulate the photovoltaic sub-system. The general considerations and the procedure applied in the model developed is described below.
The average temperature inside the refrigerated cell was calculated by the energy balance equation (Eq. (1)), which includes the thermal load components, and the heat transfer rate between the PCM slab and the air inside the refrigeration cell ($q_{PMC\text{-}air}$). The thermal load components were calculated using the ASHRAE standards. These components include the transmission heat gains or losses through the refrigerator enclosures (q_{los}), the product thermal load (q_{Pr}), the heat gains due to internal equipment (q_{Int}), and the infiltration heat gains (q_{Inf}) (ASHRAE, 2010).

$$q_{PCM-air} = q_{los} + q_{pr} + q_{Int} + q_{Inf} \quad \text{Eq. (1)}$$

The heat transfer in the PCM slab was modeled with a one-dimensional conduction heat transfer model. In this case, the convection heat transfer inside the PCM was neglected. This procedure has also been applied, with accurate results, in other studies on PCM slabs in contact with evaporators in household refrigerators (Azzouz et al., 2008; Cheng et al., 2017; Marques et al., 2014).

$$\frac{\partial}{\partial x} k_{PCM}.\frac{\partial T_{PCM}}{\partial x} = \rho_{PCM}.\frac{\partial h_{PCM}}{\partial t} \quad \text{Eq. (2)}$$

The heat transfer inside the PCM is governed by Eq. (2), in which the PCM temperature (T_{PCM}) and the PCM specific enthalpy (h_{PCM}) vary in space (x) and time (t). PCM thermal conductivity (k_{PCM}) and density (p_{PCM}) are constant in the liquid phase and in the solid phase, while in the phase-change region these properties are calculated by interpolation (Özisik, 1993). This equation was solved by applying the finite difference method and explicit solution procedure (Özisik, 1993), in which the PCM slab is divided into a finite number of elements. In addition, the boundary conditions had to be defined in the external nodes of the PCM slab, one of which was in contact with the evaporator and the other in contact with the air inside the refrigerated cell.
The refrigeration sub-system model uses a simple mechanical compression refrigeration cycle, with a DC compressor and R134a as a refrigerant. The simulation of this sub-system was based on the performance curves of the Danfoss-Secop BD35F compressor, provided by the manufacturer, in accordance with the European Norm EN-12900. In this standard, the compressor performance is characterized by cubic regression curves, according to Eq. (3), where the dependent variable "X" represents the cooling capacity (q_{com}) or electrical power consumption (W_{com}). The explanatory variables are the evaporation (T_e) and condensation temperature (T_c). The corresponding coefficients of these equation, were taken from the manufacturer's web page (Danfoss, 2019).

$$X = C_1 + C_2.T_e + C_3.T_c + C_4.T_e^2 + C_5.T_e.T_c + C_6.T_c^2 + C_7.T_e^3 + C_8.T_e^2T_c + C_9.T_eT_c^2 + C_{10}.T_c^3 \quad \text{Eq. (3)}$$

In order to carry out the simulations, the evaporation and condensation temperatures were estimated 11°C below set product temperature and 10°C above ambient temperature, respectively, and the minimal condensation temperature was 35°C.
The power produced by the PV sub-system was simulated using the “five-parameter model” (De Soto et al., 2006), in which the relation between the voltage (V) and the current intensity (I) produced by a PV module or PV array is described by Eq. (4).

$$I = I_L - I_D.\left(e^{\frac{V+I.R_S}{a}} - 1\right) - \frac{V + I.R_S}{R_P} \qquad \text{Eq. (4)}$$

The five parameters of this model are the light current (I_L) produced by a current source, the inverse saturation current of a diode (I_D) connected in parallel with the current source, the series resistance (R_S), the parallel resistance (R_P), and the "a" parameter.
These parameters are calculated at reference conditions using the technical information from the manufacturer's datasheet. In this study, the simulations were made with multi-crystalline PV modules, with a peak power of 80, 100 and 150W STC (Standard Test Conditions), “SolarWorld” brand, models SW80, SW100, and SW150 (Sunfields Europe, 2018).
TRNSYS 16 was used as a simulation tool. In particular, type 194 was used to simulate PV production. The efficiency considered for the DC-DC conversion in the PV-system was 98%.
The control strategy is based on two main variables. First, the solar radiation available: the compressor is ON only when there a minimal value of PV power production, and the compressor speed is adapted according to the ambient temperature, product temperatures and the PV power available. This speed is based on the compressor performance curves mentioned in Eq. (3).
The second variable is the set temperature of the stored product, which is controlled by a thermostat consisting of an ON-OFF control with hysteresis. At the beginning of each day, this ON-OFF control is restarted to avoid possible delays in the use of the solar resource.

3. RESULTS AND DISCUSSION

3.1 Parametric Analysis of Compressor Cycle Time and System Performance Indicators

For better integration of the PCM slab and the photovoltaic system, the number of daily compressor cycles should be reduced nearly to one. In this way, the electricity produced by the PV system can be used during the day to cool the product and to charge the PCM slab. Later, the stored thermal energy can be used when solar radiation is low or during the night.
Hence, the present study first analyses how such variables as PCM slab thickness, insulation thickness, and air change rate affect the compressor cycle time. The thicker the PCM slab is, the longer the compressor cycle. For a cycle time of about 18 hours, the PCM slab needs to be more than 10 mm and 12 mm thick for an ambient temperature of 25 and 30°C, respectively. In this regard, Fig. 4 (a) shows the results for an insulation thickness of 80 mm and 0.25 air changes per hour.

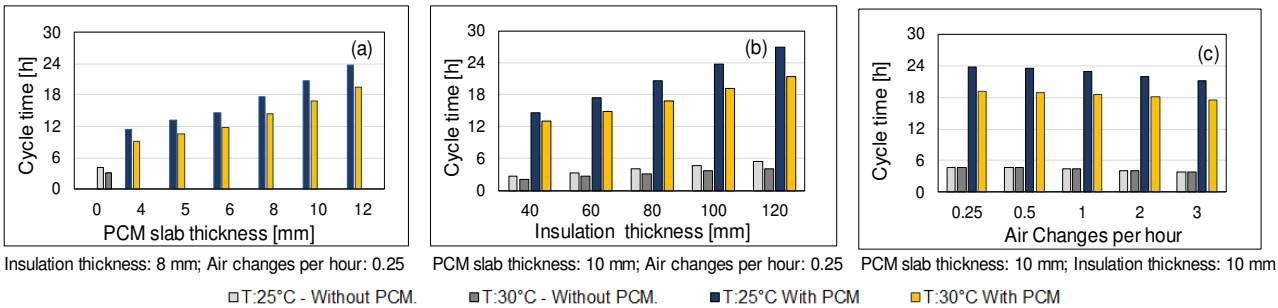

Figure 4: Influence of variables on maintenance refrigeration cycle time

Likewise, a greater insulation thickness increases the compressor cycle time, as Fig. 4 (b) illustrates. In tropical locations, refrigerators usually have insulation materials with thermal conductivities above 0.5 $Wm^{-1}K^{-1}$ and thicknesses of 100 mm. Therefore, to complete our selection of the design parameters, we will consider the minimum insulation thicknesses of 100 mm.
Finally, Fig. 4 (c) presents the incidence of constant air-change rates for the two ambient temperatures (25 and 30°C) and an external relative humidity of 60%. As expected, the higher the air-change rate, the shorter the compressor cycle is.

Table 2. Simulation results for the maintenance cycle under ambient temperature 30°C

PCM slab thickness [mm]	Insulation thickness [mm]	Air changes per hour	Cycle time [h]	Time ON [h]	Time OFF [h]	Q_{load} [kJ/ Cycle]	E_{load} [kJ/ Cycle]	COP_{sys} [-]	Daily electricity consumption [kJ/day]
0	80	0.25	3.2	0.6	2.6	326	136	2.4	1,031
4	80	0.25	9.2	2.0	7.2	1,224	483	2.5	1,256
8	80	0.25	14.4	3.1	11.2	1,921	757	2.5	1,266
10	80	0.25	16.9	3.7	13.2	2,264	894	2.5	1,270
12	80	0.25	19.5	4.3	15.2	2,619	1,035	2.5	1,276
10	60	0.25	14.8	4.1	10.7	2,494	986	2.5	1,601
10	80	0.25	16.9	3.7	13.2	2,264	894	2.5	1,270
10	100	0.25	19.1	3.5	15.7	2,131	841	2.5	1,055
10	120	0.25	21.5	3.3	18.1	2,044	809	2.5	905
10	100	0.25	19.1	3.5	15.6	2,131	841	2.5	1,055
10	100	0.50	19.0	3.5	15.4	2,153	853	2.5	1,081
10	100	1.00	18.6	3.6	15.0	2,195	870	2.5	1,121
10	100	2.00	18.0	3.7	14.3	2,284	902	2.5	1,200

The main details of how the system performs – cycle time, compressor time ON, compressor time OFF, refrigeration load (Q_{load}) electricity consumption (E_{load}), the coefficient of performance of the system (COP_{sys}) and daily electricity consumption – for maintenance cycles are presented in Table 2 for an ambient temperature of 30°C. In general, the COP is very little affected by the PCM slab. However, the daily electricity consumption increases up to 23.76%, when the insulation thickness is 80 mm according to the specific simulated conditions.

3.2 Sizing of the PCM Slab for Two Tropical Locations

The thermal storage slab was sized for two typical tropical locations: one in an African country (Nyanza, Kenya, latitude 0.08°N, longitude 35.06°E) and the other in the Caribbean (Guantanamo, Cuba, latitude 20.14°N, longitude 75.95°W). Specifically, we analyzed a complete week for a critical month, in which ambient temperature is high and solar radiation is lower than similar months. Table 3 shows the main weather characteristics for each case.

Table 3. Main weather and load characteristics for studied cases

Location	Month	Solar irradiation [$kJ.m^{-2}$/day]	Ambient temperature [°C]	RH [%]
1. Kenya	November	19.5	23.2	68.7
2. Cuba	June	21.6	28.1	72.5

The insulation thickness selected for the two analyzed locations was 100 mm, according to the analysis presented in section 3.1. To achieve compressor cycle times of about 18 hours, the initial thickness selected for the PCM slab was 8 mm and 10 mm for Kenya and Cuba, respectively. Under these conditions, Table 4 presents the daily refrigeration load (Q_{load}), the daily electricity consumption (E_{load}), the Time ON of the compressor in each cycle, and the average power load (W_{load}) required for the two cases analyzed.

Table 4. Main weather and load characteristics for the cases studied

Location	PCM slab thickness [mm]	Insulation thickness [mm]	Q_{Load} [kJ/day]	E_{Load} [kJ/day]	COP_{sys}	Time ON [h]	W_{Load} [W]
1. Kenya	8	10	1,996.6	735.9	2.71	2.69	76
2. Cuba	10	10	2,491.7	976.2	2.55	3.43	79

The initial peak power considered for the multi-crystalline PV module was 80 Wp, this value was chosen taking into account the average power load (W_{Load}) calculated. Fig. 5 shows the PV power production, the load power, and the product temperature, for the simulations carried out for a complete week (168 hours). The final size of the PV modules for the cases analyzed was 100Wp for Kenya and 150Wp for Cuba, which allows the refrigerator to be operated without an electrical battery.

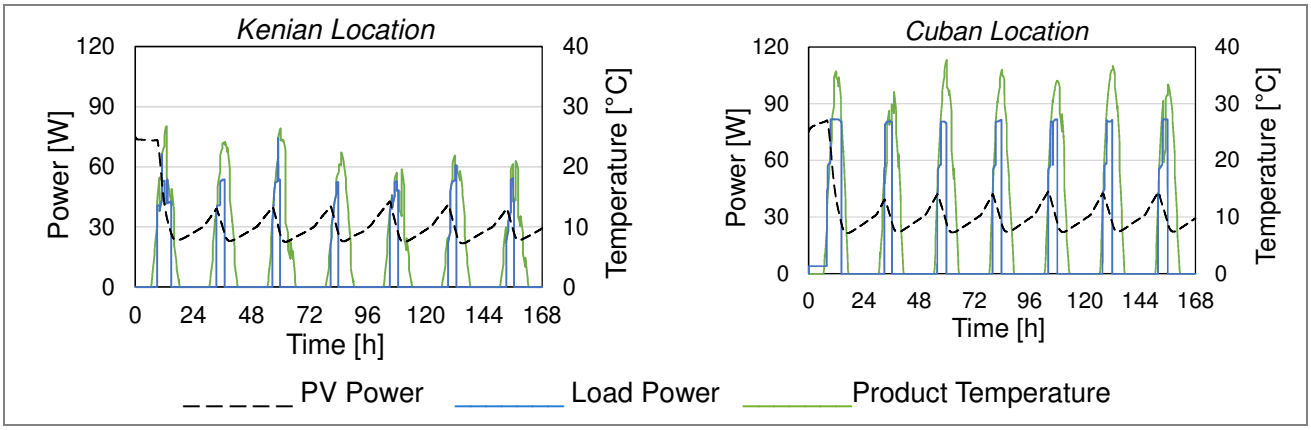

Figure 5: Dynamic simulation of a free battery solar-powered refrigerator for 2 tropical locations

Table 5 shows the thermal storage capacity for various PCM slab thicknesses for a total area of evaporator wall of 2,143 m^2, a specific heat capacity storage of 130 kJ kg^{-1}, for a PCM working temperature between 4 and 13°C, and the PCM density value in the liquid state (760 kg m^{-3}). With this information, the ratio between the theoretical storage of the PCM slab and the daily refrigeration demand was calculated as 0.84 and 0.85 for the Cuban and Kenyan locations, respectively.

Table 5 Thermal storage capacity for different slab thickness

PCM slab thickness	[mm]	4	6	8	10	12
Heat storage capacity 4 to 13°C	[kJ]	846.9	1,270.4	1,693.8	2,117.3	2,540.7

4. CONCLUSIONS

A dynamic model was implemented to simulate a solar-powered refrigerator driven by a PV without electrical battery and equipped with a passive thermal energy storage slab with phase change materials. This slab is placed on the internal wall of the refrigerator, in contact with the evaporator.
The system was analyzed for a preservation temperature of 11°C and the phase-change material (PCM), selected was a paraffin mixture with a melting temperature between 7 and 10°C.
This type of refrigerator is useful for preserving food in countries or developing areas where there is no electricity supply. To this end, the thermal storage slab was studied and sized for two typical tropical locations: Kenya, in Africa, and Cuba, in the Caribbean.
For the initial sizing of the PCM slab, a parametric analysis was carried out under stable ambient conditions, including ambient temperatures of 25 and 30°C. In this analysis, the compressor cycle time was evaluated at different values of such major variables as the PCM slab thickness, insulation thickness, and air-change rate.
For better integration of the PCM slab and the photovoltaic system, the compressor cycle time should be close to 18 hours a day. This is the cycle time obtained when the PCM slab is above 8 mm and 10 mm for external temperatures of 25°C and 30°C, respectively, with an insulation thickness of 100 mm, and 0.25 air changes per hour. The more air changes there are, the shorter the cycle compressor is and the thicker the PCM slab needs to be.
For the two locations analyzed, the system was sized for 1.0 air change per hour and an insulation thickness of 100mm. Finally, the autonomy of the system without an electrical battery was determined with a PCM slab thickness of 80mm and 100mm, and with multi-crystalline PV modules of 100Wp and 150Wp for Kenya and Cuba, respectively, which allows the solar-powered refrigerator to be operated without an electrical battery.

ACKNOWLEDGMENTS

The authors are grateful to the AGAUR program, FI-DGR 2018, co-financed by the EU Social Funds.

NOMENCLATURE

h	Specific enthalpy ($kJ.kg^{-1}$)		Subscripts
q	Heat flow rate (W)	*air*	Air
Q	Thermal energy (kJ)	*com*	Compressor
T	temperature (K)	*c*	Condenser
W	Electrical power (W)	*e*	Evaporator
E	Electrical energy (kJ)	*Int*	Internal equipment
V	Voltage (V)	*Inf*	Infiltration
I	Electrical current (A)	*los*	Losses
R	Resistance (Ohm)	*pr*	Product
x	Spatial dimension (m)	*Load*	Load
t	Time (s)	*Sys*	System
k	Thermal conductivity ($Wm^{-1}K^{-1}$)	*S*	Series
ρ	Density (kg/m^3)	*P*	Parallel
C	Coefficients compressor curves	*D*	Diode
COP	Coefficient of operation (-)		

REFERENCES

ASHRAE, 2010. Handbook of Refrigeration. American Society of Heating, Refrigerating and Air-Conditioning Engineers (ASHRAE), Atlanta (US).

Azzouz, K., Leducq, D., Gobin, D., 2008. Performance enhancement of a household refrigerator by addition of latent heat storage. Int. J. Refrig. 31, 892–901.

Cabeza, L.F., Castell, A., Barreneche, C., De Gracia, A., Fernández, A.I., 2011. Materials used as PCM in thermal energy storage in buildings: A review. Ren. Sustain. Ene. Rev. 15, 1675–1695.

Cheng, W. long, Ding, M., Yuan, X. dong, Han, B.C., 2017. Analysis of energy saving performance for refrigerator with thermal storage of condenser and evaporator. Ene Conv.Man.132,180–188.

Coca-Ortegón, A., Torres-Toledo, V., Müller, J., Coronas, A., 2017. Assessment of a Solar Powered Refrigerator Equipped with Thermal Storage for a Dairy Application, in: Solar World Congress 2017. ISES, Abu Dhabi, UAE. doi:Paper ID 10796

Danfoss, 2019. Coolselector®2.http://coolselectoronline.danfoss.com/ (accessed 2.6.19).

De Soto, W., Klein, S.A., Beckman, W.A., 2006. Improvement and validation of a model for PV array performance. Sol. Energy 80, 78–88.

Dincer, I., Rosen, M.A., 2011. Thermal energy storage. Systems and applications, 2nd ed. Wiley. A John Wiley and Sons, Ltd., UK.

Katic, I., Pedersen, H., Jacobsen, E., 2010. Standalone cool/freeze cluster driven by solar PV energy. EUDP Project, Contract No. EFP07-II No. 33033-0297. Copenhague (Denmark).

Kim, D.S., Infante Ferreira, C. a., 2008. Solar refrigeration options - a state-of-the-art review. Int. J. Refrig. 31, 3–15.

Li, G., Hwang, Y., Radermacher, R., Chun, H.H., 2013. Review of cold storage materials for subzero applications. Energy 51, 1–17.

Marques, A.C., Davies, G.F., Maidment, G.G., Evans, J. a., Wood, I.D., 2014. Novel design and performance enhancement of refrigerators with thermal storage. Appl. Ther. Eng. 63, 511–519.

Mastani Joybari, M., Haghighat, F., Moffat, J., Sra, P., 2015. Heat and cold storage using PCMs in domestic refrigeration systems: The state-of-the-art review. Energy Build. 106, 111–124.

Oró, E., De Gracia, A., Castell, A., Farid, M.M., Cabeza, L.F., 2012. Review on phase change materials (PCMs) for cold thermal energy storage applications. Appl. Energy 99, 513–533.

Özisik, M.N., 1993. Heat Conduction, 2nd ed. John Wiley & Sons, Inc., New York (US).

Sørensen, B., 2015. Solar Energy Storage, 1st ed, Solar Energy Storage. Elsevier Ltd., London (UK).

Sunfields Europe, 2018. PV Modules SolarWorld. https://www.sfe-solar.com/paneles-solares/solarworld/ (accessed 4.15.18).

WB, ESMAP, 2017. State of Electricity Access Rep ort (SEAR). World Bank (WB).

Yusufoglu, Y., Apaydin, T., Yilmaz, S., Paksoy, H.O., 2015. Improving performance of household refrigerators by incorporating phase change materials. Int. J. Refrig. 57, 173–185.

Zalba, B., Marín, J.M., Cabeza, L.F., Mehling, H., 2003. Review on thermal energy storage with phase change: materials, heat transfer analysis and applications. Appl.Ther. Eng. 23, 251–283.

Manuscript ID: 1790
DOI: 10.18462/iir.icr.2019.1790

Energy mapping of large refrigerated warehouses co-located with renewable energy sources across Europe

Kostadin FIKIIN [(a)], Paola MAZZUCCHELLI [(b)], Alan FOSTER [(c)], Judith EVANS [(c)], Stepan AKTERIAN [(d)], Graciela ALVAREZ [(e)], Denis LEDUCQ [(e)], Mihn HOANG [(e)], Gabriel GARCIA [(f)], Liz VARGA [(g)], Ian TRUCKELL [(g)], Tim BROWN [(c)], Ina COLOMBO [(h)]

[(a)] Technical University of Sofia, 8 Kliment Ohridski Blvd., BG-1756 Sofia, Bulgaria, k.fikiin@tu-sofia.bg

[(b)] Association of European Renewable Energy Centres (EUREC), Place du Champ de Mars 2, B-1050 Brussels, Belgium

[(c)] London South Bank University, London South Bank University, Langford BS40 5DU, UK

[(d)] University of Food Technologies, 26 Maritza Blvd., BG-4002 Plovdiv, Bulgaria

[(e)] National Research Institute of Science and Technology for Environment and Agriculture (IRSTEA), 1 rue Pierre Gilles de Gennes, CS 10030, F -2761 Antony Cedex, France

[(f)] National Renewable Energy Centre (CENER), Av. Ciudad de la Innovacion 7, 31621 Sarriguren, Navarra, Spain

[(g)] Cranfield University, Bedford MK43 0AL, UK

[(h)] International Institute of Refrigeration, 177 Boulevard Malesherbes, F-75017 Paris, France

ABSTRACT

Powering refrigerated warehouses by renewable energy sources (RES) turns from an extravagancy to a routine. RES intermittency requires suitable energy storage for both off-grid and on-grid applications. Cryogenic energy storage, integrated synergistically with RES and large refrigerated warehouses, is a promising environmentally friendly technology (addressed by the EU CryoHub project). Hence, studies were carried out to identify where large energy-intensive refrigerated warehouses are situated across Europe and how much power they consume. By employing diverse instruments and data sources, some 1049 warehouses were established, while 503 energy intensive ones were mapped and further co-located with 3200 solar PV and 11700 onshore wind parks to discover the best areas for RES integration across EU28. As compared with similar international surveys, the CryoHub statistics covers simultaneously warehouse capacity, geographical location and energy data, which permit a comprehensive analysis and strategic planning in both food refrigeration and energy sectors.

Keywords: Refrigeration, Food, Refrigerated Storage, Warehousing, Renewable Energy, Energy Storage, Mapping, European Union

1. INTRODUCTION

Low- or zero-carbon cold chain economy is only achievable by intensive utilisation of renewables and building associated energy storage infrastructure to compensate for their intermittent nature and to balance the electrical grids (Fikiin and Stankov, 2015). The EU CryoHub project investigates and develops the potential of cryogenic energy storage (CES) at refrigerated food warehouses. The innovative CES technology is based on storing renewable energy as a cryogenic liquid (being liquid air in this project), which is then boiled at low temperatures to generate electricity for on-site or grid use. Unlike the stand-alone CES installations, CryoHub co-generates both power and refrigeration supply to the warehouse, with a number resulting benefits (Fikiin *et al.,* 2017).

The need for energy mapping, reported in this contribution, was a logical consequence of the three important prerequisites needed to implement CryoHub-like liquid air energy storage (LAES) Europe-wide: (i) existence of large refrigerated food warehouses; (ii) presence of RES, and (iii) reasonable geographical proximity between the warehouses and RES, possibilities for mutual integration, along with potential benefits from the technology uptake.

2. REFRIGERATED FACILITY MAPPING SURVEY

2.1. Data collection methodology

Studies were carried out by the CryoHub project consortium to identify where large scale refrigerated warehouses and food factories are situated across Europe (Fig. 1). In addition, their power usage was mapped. The first step towards achieving this goal was the development of an on-line version of the CryoHub energy mapping survey with a detailed questionnaire of 14 queries published in the English language (CryoHub, 2017a). Translated questionnaires were also prepared and published on-line in 5 EU national languages (German, French, Bulgarian, Spanish and Italian).

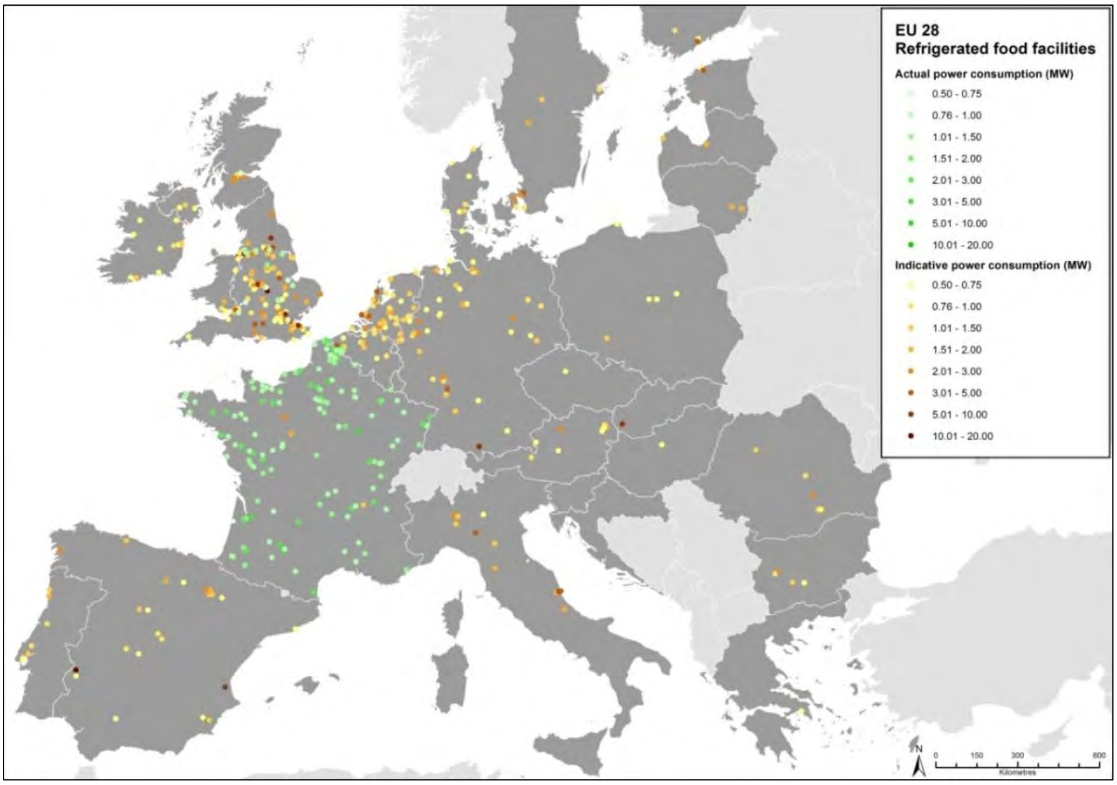

Figure 1: Mapping large refrigerated food warehouses (over 0.5 MW) across EU28.

To maximise the response to the CryoHub mapping survey, a stimulating award system was designed and applied by ranking the project-assisting organisations as *'Bronze', 'Silver'* and *'Gold'* CryoHub Champions, depending on whether they contributed data to the survey, offered an on-site case study or accepted to host the CryoHub demonstration plant. Certificates of merit were rewarded to champion companies whose professional achievements were then publicised by all available means.

The CryoHub survey was then actively promoted via the established channels of governmental and non-governmental professional organisations, editorial boards and sectorial networks. For instance, the following stakeholders' organisations were approached and provided with information about the survey:

- ☑ ECSLA (*European Cold Storage and Logistics Association*) and relevant national associations, GCCA (*Global Cold Chain Alliance*), IAR (*International Academy of Refrigeration*), GCI (Green Cooling Initiative), IIAR (*International Institute of Ammonia Refrigeration*), ASHRAE (*American Society of Heating, Refrigerating and Air-Conditioning Engineers*), AFF (*Association Française du Froid*), EHPA (*European Heat Pump Association*), EPEE (*European Partnership for Energy and the Environment*), AREA (*Air Conditioning and Refrigeration European Association*), Euroheat & Power, Eurocommerce, Eurovent, Eurammon, etc.
- ☑ FoodDrink Europe, EFFoST (*European Federation of Food Science and Technology*), ETPs (*European Technology Platforms*) *'Food for Life',* and *'Renewable Heating and Cooling',* EHEDG (*European Hygienic Engineering & Design Group*).

- ☑ FSDS (*Food Storage and Distribution Federation*), FDF (*Food and Drink Federation*), CFA (*Chilled Food Association*), BFFF (*British Frozen Food Federation*), IOR (*Institute of Refrigeration*) in the UK.

As a result of the above-mentioned endeavours, survey-related articles and the relevant Call for CryoHub Champions were published worldwide by various international organisations and networks, specialised periodicals, professional magazines and mass media (CryoHub, 2017a). Furthermore, the energy mapping survey and Call for Champions were presented at several international fora (Fikiin, 2016a, 2016b), including many IIR's sponsored and co-sponsored conferences around the globe, alongside the IIR newsletters, web-publications, social media and e-mailings to IIR members of different categories – a network of over 6000 professional subscribers.

2.2. Correlating capacity and energy data

As the on-line survey received a rather modest public response (because of the conservatism in the sector, reluctance of warehouse operators to share their energy data and the need for a much longer period of data collection), another approach was therefore employed, based on warehouse capacity data. This required determining the warehouse size (in m^2, m^3 or tonnes) and then using its specific energy consumption to estimate the energy spent. A data collection spreadsheet, summarising statistics for all warehouses found out in every country of EU28, provided input data to a calculation methodology correlating warehouse capacity and energy usage via specific energy consumption values established in a previous study (Evans *et al.,* 2014). The special focus was on large warehouses consuming over 500 kW of electrical power on average.

When capacity information was not available, the warehouse volume was estimated by using Satellite Imaging and Google Maps to find the refrigerated facility and then using the Google measurement tool to ascertain the floor area. By means of a custom-made methodology, Google Streetview was also used to ascertain height by comparing the height of the store with items of known height (or by resorting to a fixed nominal height of 10.3 m in the exclusive case when no actual value can be determined), as detailed in CryoHub (2017a) and illustrated in Fig. 2.



Figure 2: Satellite imaging of large refrigerated food warehouses to correlate their capcity (in m^2, m^3 or tonnes) with the energy use.

Different databases for warehouse locations and capacities (in terms of m^2, m^3, tonnes or pallet number) were employed, for example:

- Printed editions of the GCCA International Cold Chain Directory, GCCA Directory of Refrigerated Warehouse and Distribution Centres, ECSLA Directory of European Cold Stores, etc.
- On-line Global Cold Chain Directory of GCCA.
- Euro-pages on the Internet (Business Directory).

- Data of UK Environment Agency (through the freedom of information act).
- Database of French Ministry of Environment (containing both capacity and energy consumption figures).
- DG SANTE website linked to the sites of national food safety authorities, providing information for refrigerated warehouses and food factories permitted to operate at an EU level.
- National cold chain associations.

2.3. Mapping results

While a total of 1049 refrigerated food warehouses throughout the EU were reported (consuming together some 933 MW on average), some 503 of them had an estimated average power consumption exceeding 500 kW and spend approx. 780 MW in total (CryoHub, 2017a). These highly energy intensive warehouses are widely distributed on the European map, but the highest concentration of such large refrigeration facilities exists in Benelux, Southern England, Northern France and Northern Germany, which coincides very logically with the highest population density in Europe approximately in the same regions (Fig. 1). This study covered comprehensively EU28, with a little exception for Croatia, Malta, Luxemburg, where less attention was paid and no facilities were taken into account. While the first of these countries is the newest EU member, no indications were found for existence of large refrigerated warehouses in the second two states.

A number of EU countries' groups have been identified and classified (based on their geographical location; climatic similarities; traditions; economic, administrative and cultural interlinks), as follows: (i) Benelux (Belgium, the Netherlands and Luxemburg); (ii) Central and Eastern Europe (Bulgaria, Croatia, Czech Republic, Hungary, Poland, Romania, Slovakia and Slovenia); (iii) Germany and Austria; (iv) Mediterranean countries (Cyprus, France, Greece, Italy, Malta, Spain and Portugal); (v) Nordic and Baltic countries (Denmark, Estonia, Finland, Latvia, Lithuania and Sweden), and (vi) UK and Ireland. Energy consumption maps were elaborated for the large warehouses in each one of these groups of countries, where the situation was analysed in more details (CryoHub, 2017a). Along with the overall map of EU28, individual maps for each explored country were featured as well.

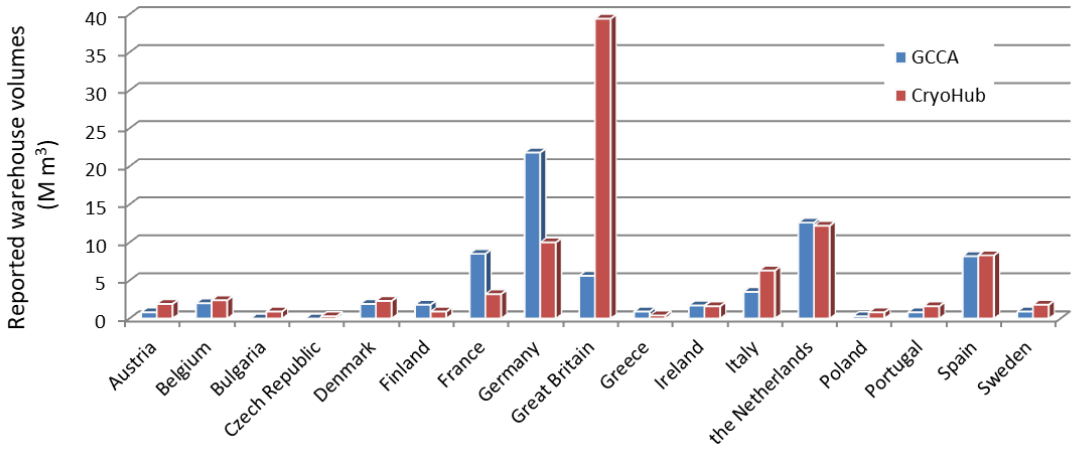

Figure 3: Refrigerated storage warehouse space (in millions of cubic meters) for 17 representative EU countries – comparison between the CryoHub and GCCA surveys.

2.4. Comparison with other warehouse surveys

To ascertain whether the CryoHub mapping survey adequately represents the amount of cold storage capacities and resulting energy expenditure in Europe, a comparison was made of the CryoHub results with those of the 2010 IARW Global Cold Storage Capacity Report (by Victoria Salin, Texas A&M University), using information collected from international offices of GCCA (Global Cold Chain Alliance). Newer versions named 2016/2018 GCCA Global Cold Storage Capacity Report (GCCA, 2018) are also available, along with the associated web-based GCCA Global Cold Chain Directory (CryoHub, 2017a). CryoHub found out more warehouse space than GCCA for 12 out of 17 representative countries (Fig. 3), with a total difference of approx. 23 M m^3. For two of these countries CryoHub afforded data for the first time.

The CryoHub database can further be improved by paying more attention to key countries, such as France and Germany, which are expected to have more cold storage capacities than were actually identified by the CryoHub data gathering exercise. Another important data survey, which can serve as a reference source to compare with, is ICE-E (2012). The main features and capabilities of the three datasets considered are summarised in brief in Table 1.

Table 1. Functionality of different international surveys of refrigerated warehouses.

Survey	Capacity Data	Location Data	Energy data	Mapping
GCCA	YES	YES	NO	NO
ICE-E	YES	PARTLY	YES (mostly actual)	NO
CryoHub	YES	YES	YES (mostly indicative)	YES

Obviously, CryoHub represents a substantial advancement, as compared with GCCA and ICE-E, because this is the only international survey of refrigerated food warehouses which brings together capacity, geographical and energy information, including Europe-wide mapping suitable for further analysis and strategy planning in the food refrigeration sector. It is, however, important to note that GCCA affords a global survey, which does not focus specifically on Europe.

3. MAPPING OF RENEWABLE ENERGY RESOURCES

This task focused on finding information about existing installations of wind and solar PV in EU28. Additional installations have been also identified in non-EU countries, such as Switzerland, Norway and Turkey. After some search, data from La Tene Maps (latenemaps.com) with proven reliability were acquired, being previously collected in cooperation with the major European renewable energy associations. In particular, datasets containing the following information (available in June 2016) were used:

- **Major Solar PV installations:** location of 3200 built Solar PV installations in Europe over 1 MW.
- **Major Onshore wind farms installations:** location of 11700 onshore installations in Europe. Offshore wind farms installations were not considered relevant for our analysis since they are not located close to refrigerated warehouses and food factories.

By using ArcGis software, characteristic maps of wind and PV installations were produced for EUE28 (Fig. 4) and for the same groups of countries, formerly addressed by the warehouse study (see Section 2.3). The results of the mapping revealed a concentration of renewable energy (PV and wind) sites in Germany, Benelux, Ireland and UK, as well as in the Mediterranean areas, in particular, Spain. Solar PV installations tend to be more concentrated in Spain, Germany, South of France, Italy, Bulgaria, Greece, and the UK. Simultaneously, wind installations are more geographically concentrated in Germany, Benelux, Spain, Portugal, UK, Ireland, France and Sweden (CryoHub 2017b).

The total power output of renewable energy installations, considered by the RES mapping exercise, amounts to 154,758 GW, representing about 70% of the solar and wind energy installed capacity in EU28 (CryoHub 2017b). This is a good approximation of the existing installed capacity for wind and solar in EU28, given that only installations with a power output over 1 MW were included. A number of suitable wind and solar PV installations were found across EU, which are located in close proximity of, or directly in the territory of refrigerated warehouses, thereby permitting an easier renewable integration and CES application.

Data on the PV and wind penetration in the EU28 were also gathered (as detailed in CryoHub, 2017b), e.g.:

- ☑ **The PV and wind share in the electricity mix**, as a proxy of countries where the introduction of cryogenic storage to balance the transmission grid could be more promising, given the high penetration of PV and wind.
- ☑ **Wind and PV share in the renewable electricity mix** to give an order of magnitude of the importance of wind and PV, respectively, in the electricity mix, as a proxy to check the completeness of the available data on installations.

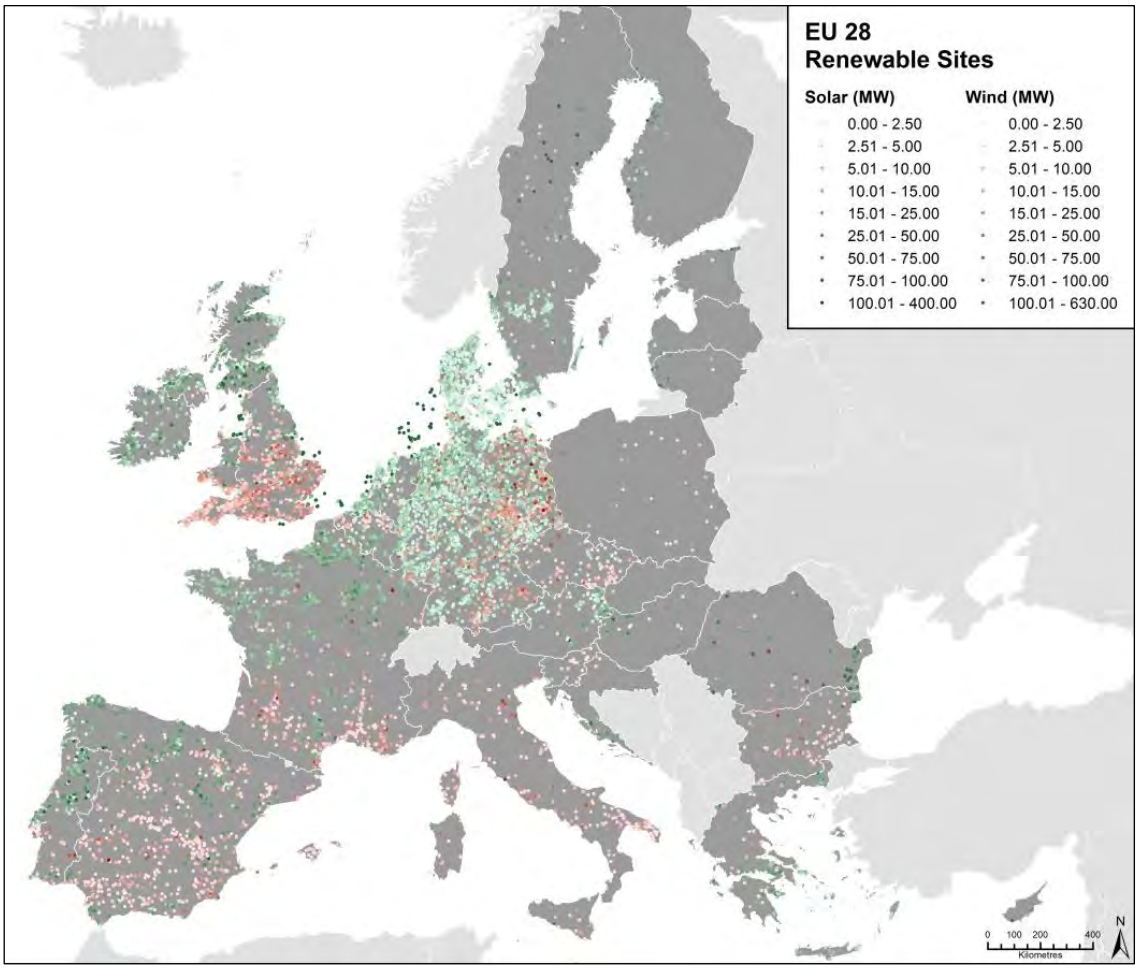

Figure 4: Mapping RES (both wind and PV) across EU28.

It was found out that renewable energy installations are widely spread across the EU28. Solar PV installations are spread all over Europe, but with an important presence in Spain, Germany, South of France, Italy, Bulgaria, Greece, and the UK. Wind installations are more concentrated in Germany, Benelux, Spain, Portugal, UK, Ireland, France, and Sweden. Countries with an important share (over 50%) of variable renewable energies, where the CES and LAES can potentially find place, are Belgium, Denmark, Germany, Greece, Ireland, Spain and the UK (CryoHub, 2017b). Small countries, such as Malta and Cyprus, even if they have a substantial share of variable renewable energy, does not possess sufficient RES and warehouse capacities to benefit from large scale energy storage. The share of wind and solar energy in the electricity generation is projected to grow from 6% in 2010 to 36% in 2050 (CryoHub, 2017b). This opens up promising opportunities for the introduction of energy storage technologies to ensure that variable renewable energies can be used at any time. A number of other countries thus become interesting as potential hosts of the novel technology, given their quickly increasing share of variable renewable energy (e.g. Estonia, Lithuania, the Netherlands, etc.).

4. LOCATIONS SUITABLE FOR CES-BASED TECHNOLOGIES

Mapping of energy used by refrigerated warehouse sites and comparing this to renewable energy availability permits to identify the EU regions and areas which are most promising for renewable energy projects in industrial food refrigeration. However, in some countries the smaller size of food storage installations might limit the suitability of such applications. The results of this work provide an on-going tool for determining the potential of CryoHub as an emerging sustainability-enhancing technology in both energy and food preservation sectors.

Fig. 5 depicts the sites of large refrigerated food facilities across EU28, which are located in close proximity (within 1 km) to reliable renewable energy sources, as described in more details in CryoHub (2017b, 2017c).

The mapping studies were the first stages in assessing how the technology can be adopted in industry. Some of the mapping survey findings can be outlined as follows:

- ***Lack of very substantial variance of energy use across seasonal differences*** - even though energy use is generally higher in the summer and lower in the winter, there are significant peaks between November and January, possibly due to the additional demand of Christmas and New Year shoppings.
- ***Clear correlation between warehouse capacity, renewable energy availability and population of site locations***. Such localities of large refrigerated warehouses (consuming on average over 500 kW of power) are closely related to the need to process and preserve perishable food commodities.
- ***Climate*** is influential with higher need for refrigeration capacities in the warmer regions, while the largest refrigerated facilities are still located in Northern Europe.

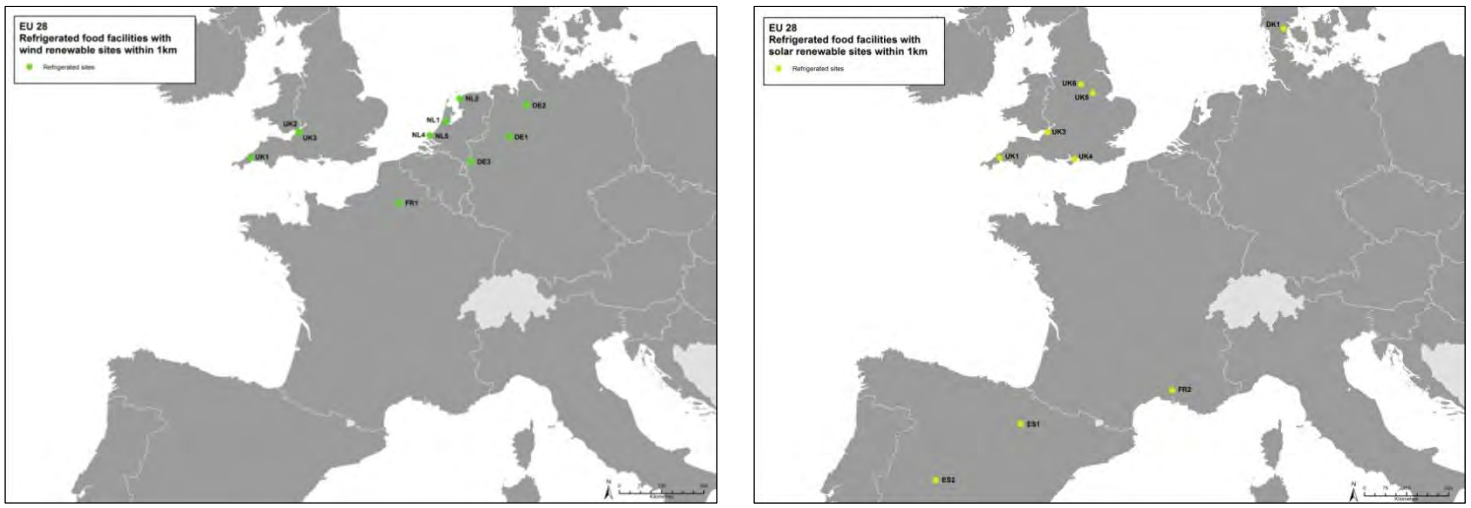

Figure 5: Mapping refrigerated food warehouses (over 500 kW) located closely (within 1 km) to wind energy parks (*left*) and solar PV installations (*right*).

As a result of the CryoHub mapping survey, the refrigerated warehouse of Frigologix in the city of Lommel, Belgium (a company not qualifying to be mapped on Fig. 5 prior to 2017) was selected as a *"Gold CryoHub Champion"* to host the CryoHub Demonstrator (currently under construction). A detailed business case was developed to estimate the potential benefits from exploiting the project results.

5. CONCLUDING REMARKS

The information gathered by this survey ensures a science-based approach to the RES integration in refrigerated warehousing. The-first-of-its-kind Europe-wide mapping of the energy expenditure by the sector, co-located with the RES availability, permits to identify the EU regions and areas which are most promising for renewable energy projects in the area of industrial food refrigeration.

The concentration of large refrigerated warehouses in Europe clearly depends on the population density and the production capacities for perishable food commodities. Although the importance of climate, the potential for using CES and particularly LAES at refrigerated food facilities depends on the overall technology level and the economic development in a country or region, rather than just on the demand for food storage. Factors, such as population growth, migration and urbanisation processes, dietary habits (e.g. increase use of ready-to-eat and chilled foods), etc., also have a strong impact on economies and sustainability, thereby warranting further investigations.

It appears that, to date the reported CryoHub exercise is the only international survey of refrigerated food warehouses which brings together capacity, geographical and energy information, made readily available for strategic planning in the food refrigeration sector.

ACKNOWLEDGEMENTS

The CryoHub Innovation Action receives funding from the European Union's Horizon 2020 Research and Innovation Programme under Grant Agreement No. 691761.

ACRONYMS

CES	Cryogenic Energy Storage	IARW	International Association of Refrigerated Warehouses
DG SANTE	Directorate-General for Health and Food Safety	LAES	Liquid Air Energy Storage
EU	European Union	PV	PhotoVoltaic
IIR	International Institute of Refrigeration	RES	Renewable Energy Source

REFERENCES

CryoHub, 2016. EU Horizon 2020 Project GA No. 691761 *"Developing Cryogenic Energy Storage at Refrigerated Warehouses as an Interactive Hub to Integrate Renewable Energy in Industrial Food Refrigeration and to Enhance Power Grid Sustainability – CryoHub",* cryohub.eu

CryoHub, 2017a. Report on refrigerated food facility mapping. Deliverable 2.1, EU H2020 Project GA No. 691761, lnkd.in/dDE6CRZ

CryoHub, 2017b. Report on RES mapping, EU H2020 Project GA No. 691761, Deliverable 2.2, lnkd.in/dsxfX3m

CryoHub, 2017c. Report on potential opportunities for CryoHub in Europe, EU H2020 Project GA No. 691761, Deliverable 2.3, lnkd.in/dR_4iRM

Evans J.A., Foster A.M., Huet J.-M., Reinholdt L., Fikiin K., Zilio C., Houska M., Landfeld A., Bond C., Scheurs M. and van Sambeeck T.W.M., 2014. Specific energy consumption values for various refrigerated food cold stores. *Energy and Buildings,* 74, 141-151, doi: 0.1016/j.enbuild. 2013.11.075

Fikiin K.A., 2016a. CRYOHUB – Cryogenic energy storage at refrigerated food warehouses to enhance the sustainability of cold chain and power supply. *Publications of the 6th International Conference of Cold Chain Management & Temperature Controlled Logistics,* University of Bonn, Germany, lnkd.in/d6QP3Fq

Fikiin K.A., 2016b. Cryogenic energy storage for renewable food refrigeration and power supply (Keynote Presentation). *30th EFFoST International Conference,* Vienna, Austria, bit.do/effost-30

Fikiin K.A., Stankov B.N., 2015. Integration of renewable energy in refrigerated warehouses. Chapter 22, In: Gaspar P.D., Da Silva P.D, *Handbook of Research on Advances and Applications in Refrigeration Systems and Technologies,* 1st edition, Engineering Books, IGI Global, Pennsylvania, USA, pp. 803-853.

Fikiin, K., Stankov, B., Evans, J., Maidment, G., Foster, A., Brown, T., Radcliffe, J., Youbi-Idrissi , M., Alford, A., Varga, L., Alvarez, G., Ivanov, I. E., Bond, C., Colombo, I., Garcia-Naveda, G., Ivanov, I., Hattori, K., Umeki, D., Bojkov, Ts., Kaloyanov, N., 2017. Refrigerated warehouses as intelligent hubs to integrate renewable energy in industrial food refrigeration and to enhance power grid sustainability. *Trends in Food Science & Technology,* 60, 96-103, doi: 10.1016/j.tifs.2016.11.011.

GCCA, 2018. GCCA Global Cold Storage Capacity Report. Global Cold Chain Alliance, Arlington, Virginia, USA, 25 p., bit.do/GCCA

ICE-E, 2012. EU Intelligent Energy for Europe Project No. IEE/09/849/SI2.558301 *"Improving Cold Storage Equipment in Europe (ICE-E)",* bit.do/icee-eu

Manuscript ID: 1794
DOI: 10.18462/iir.icr.2019.1794

Dynamic energy model of a refrigerated warehouse operating synergistically with a cryogenic energy storage system

Borislav STANKOV[(a)], Kostadin FIKIIN[(a)], Gabriel GARCIA[(b)], Alicia KALMS[(b)], Marionel ESTEVEZ[(b)], Raquel GARDE[(b)]

[(a)] Technical University of Sofia, Kliment Ohridski Blvd.,
BG-1756 Sofia, Bulgaria, bstankov@tu-sofia.bg, k.fikiin@tu-sofia.bg
[(b)] National Renewable Energy Centre (CENER), Av. Ciudad de la Innovacion 7,
31621 Sarriguren (Navarra), Spain,

ABSTRACT

This contribution focuses on a dynamic energy model of a refrigerated warehouse, which is used in conjunction with a counterpart model of a liquid-air energy storage (LAES) system. These coupled models represent a newly designed LAES pilot plant, which is to be integrated with an existing refrigerated warehouse in Belgium. The designed pilot plant stores excess renewable energy in periods of high availability and generates electricity in periods of high demand. Evaporating liquid air employed for power generation is also utilized to directly refrigerate the warehouse. Along with the usual energy storage benefits, the additional effect is reduced refrigeration demand of the warehouse and improved round-trip efficiency of the LAES system. The developed model serves to predict the temperature of the refrigerating air in the warehouse, as an important control variable for the integrated LAES-warehouse system.
Keywords: Food Storage, Refrigerated Warehousing, Energy Storage, LAES, Energy Management

1. INTRODUCTION

Energy storage plays a key role in the transition to a more sustainable electricity system (European Commission, 2017). It can help accommodate the increasing share of renewables in the energy supply mix by compensating for the mismatch between the periods when the availability of renewable energy is high and the periods of high energy demand in the power grid. LAES is a recently proposed and tested technology for large-scale renewable energy storage (Morgan *et al*., 2015). It offers the potential benefit of efficient integration with important industrial processes, such as refrigerated warehousing of food and pharmaceuticals (Fikiin *et al.*, 2017). A LAES system stores energy by liquefying air (charge stage). When the demand is high, the system returns power to the grid by boiling the stored cryogen (liquid air) at very low temperature and expanding it through a series of turbines (discharge stage). The cooling effect of the cryogen evaporation process can be employed to refrigerate on-site industrial facilities, thereby reducing their energy demand and improving the round-trip efficiency of the LAES system.

The capability of synergistic operation of LAES with refrigerated warehouses and food factories is investigated and developed by the EU-funded CryoHub project (CryoHub, 2016). One of the research and development activities of CryoHub is a LAES pilot demonstrator, which is planned to be assembled at the premises of the Frigologix company, located at the Maatheide industrial area in Lommel, Belgium. The company has several refrigerated warehouses on site, one of which is to be integrated with the LAES system. The warehouse consists of two refrigerated spaces – a large frozen storage room and a loading dock (Fig. 1).

A combined dynamic energy model of the complete LAES system (including the refrigerated warehouse) was developed prior to installation of the pilot plant. A MATLAB-based model was used to explore different high-level control strategies and to identify optimal energy management scenarios. The contribution focuses on the refrigerated warehouse model, which is used to simulate its dynamic temperature response under variable load, plant's refrigeration capacity and climatic conditions. Notably, it accounts for the high thermal inertia of the refrigerated products and its effect on the thermal behaviour of the warehouse via a simple lumped-capacitance model. The model of the warehouse is presented, along with a brief discussion of its interaction with the model of the LAES system and the results of the performed simulations for different scenarios.

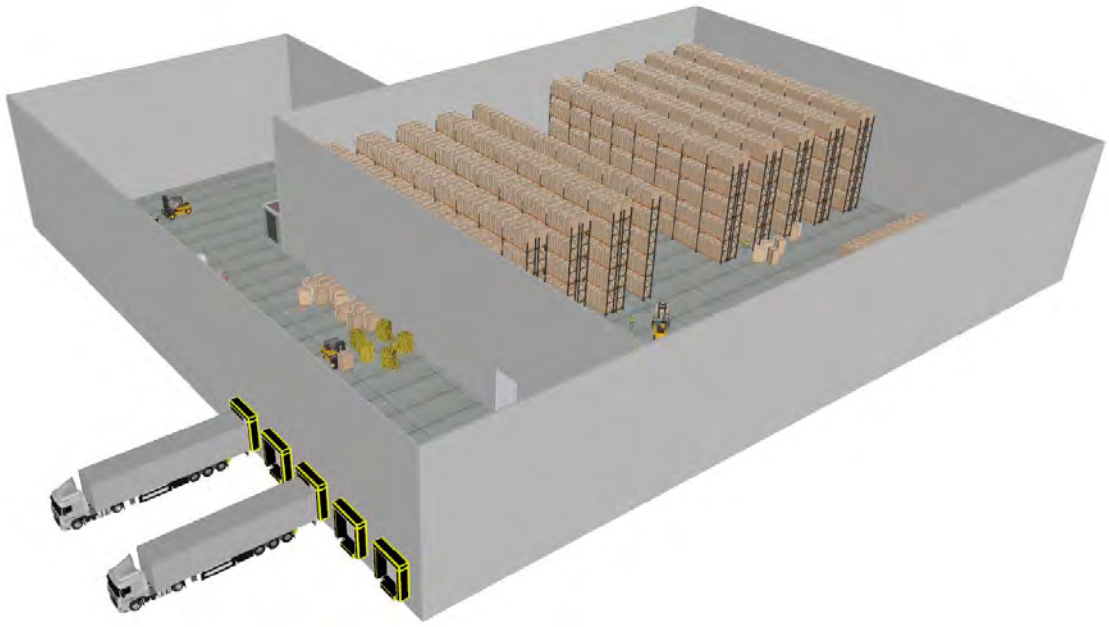

Figure 1: Sketch of the modelled cold store.

2. ENERGY MODEL OF THE REFRGERATED WAREHOUSE

The simplified warehouse model is designed to provide a reasonable approximation of the rate of the refrigerating air temperature change during the simulation time step. The temperatures of the refrigerated air in the frozen storage room and loading dock are important control variables for the pilot plant as they determine the refrigeration capacity that has to be provided by either the LAES system during discharging or the conventional vapour-compression refrigeration system available on site. The calculations are based on the balance between the total refrigeration load and the refrigeration capacity provided. The difference between them equals the amount of thermal energy stored or released in the refrigerated space. The input and output variables of the model are summarized in Fig. 2.

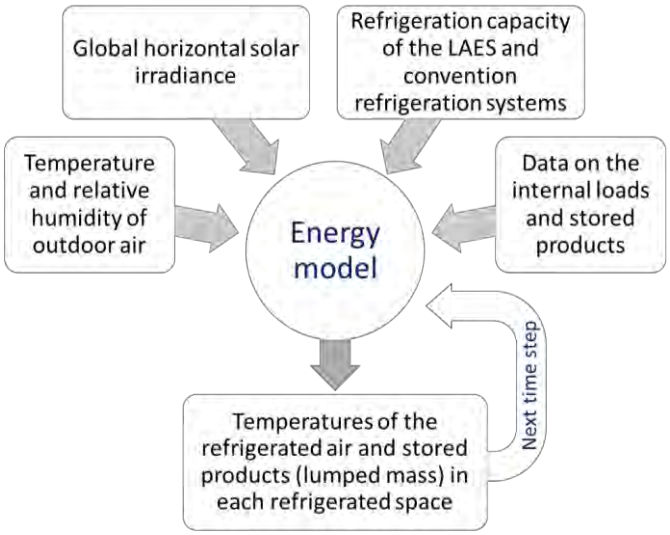

Figure 2: Inputs and outputs of the model.

Since the total heat capacity of the refrigerating air and the building envelope is very small, in comparison with that of the stored products, the thermal inertia of the frozen storage room is to a large degree determined by the heat capacity of the products.

2.1. Refrigeration loads

Calculations of the refrigeration loads are based on the methodology presented in ASHRAE (2018). Since the general load calculation procedures are well known, the description below focuses on the transient aspects of the model.

2.1.1. Transmission

The transmission heat gain through each element of the building envelope is calculated as the product of: its overall heat transfer coefficient, the surface area, and the temperature difference between the external environment and the refrigerating air. For the roof and the external walls, the temperature difference is adjusted to compensate for the solar radiation absorbed at the external surface. The walls and the roof of the warehouse are made of 22-cm-thick PIR panels, whereas the floor of the frozen storage room is provided with a frost heave protection system, which is assumed to maintain the temperature below the floor insulation at 4 °C. While the overall heat transfer coefficients and areas are constants in the model, the outdoor temperature, the temperatures of the refrigerating air in each of the two refrigerated spaces and the temperature allowance for solar effect are variable. Based on the heat balance of the external surfaces of the roof and the walls, the temperature allowance for solar effect is calculated as:

$$\Delta T_{se} = \alpha I / h_e \qquad \text{Eq. (1)}$$

The global horizontal solar irradiance (i.e., the solar irradiance incident on the roof of the warehouse) is an input obtained from hourly weather data, along with the outdoor air temperature. As a simplification, the solar irradiance on all vertical surfaces (the external walls of the warehouse) is calculated by multiplying the global horizontal solar irradiance by an adjustment factor. Although this is a crude simplification, the resultant heat gain is not very sensitive to the exact value of the solar irradiance within the expected range of error. Meanwhile, this approximation reduces the computational time and eliminates the need for additional inputs to the model.
Values for the adjustment factor were obtained via simulations, using hourly solar radiation data for Brussels (about 75 km from the site of the warehouse). The diffuse radiation model of Perez *et al.* (1988) was used for calculating the solar irradiance on all external surfaces for each hour of the year. The adjustment factors for the external walls of the frozen storage room (0.67) and the loading dock (0.51) were calculated by dividing the annual area-weighted average solar irradiance on the external walls by the global horizontal irradiance.

2.1.2. Infiltration

The heat flow due to infiltration of air through each doorway is calculated according to the equation of Gosney and Olama (ASHRAE, 2018). The density and enthalpy of moist air are calculated from the temperature, relative humidity and barometric pressure, using the appropriate psychrometric equations. The relative humidity of the refrigerating air is assumed to remain constant at 90% in the frozen storage room and 80% in the loading dock. The relative humidity of the outdoor air is obtained from the hourly weather data.
There is one door between the storage room and the loading dock with an estimated average time of door openings per day of 5400 s (doorway open-time factor of 0.0625). The door is equipped with a plastic strip curtain with an estimated effectiveness of 0.9. The loading dock has six external doors with an estimated average time of door openings per day of 1.8 hours (doorway open-time factor of 0.075). When a truck is loading or unloading, infiltration occurs around the crack between the truck and the door, which has an estimated effective leakage area of 10% of the total door area. Infiltration is assumed to occur through the whole unobstructed door area during 10% of the opening time, and around the crack between the loading/unloading truck and the door – during the rest of the time. Thus, on average infiltration occurs through 19% of the total door area, which is equivalent to a protective device effectiveness of 0.81.

2.1.3. Internal loads

The internal heat gains from people were calculated as a function of the temperature in the refrigerated space (ASHRAE, 2018). The internal heat gains from equipment operating in the refrigerated space (such as lighting, forklifts, packaging equipment, etc.) is calculated as a sum of the heat gains from each piece of equipment, which are taken at their average daily values. These, along with the number of people present, are assumed constant for each refrigerated space.

The operation of the refrigeration equipment also contributes to the refrigeration load, primarily due to heat gains form fan motors and coil defrosting. The heat gains associated with refrigeration equipment operation were roughly estimated as a fraction of the refrigeration capacity (which is an input to the model). This fraction is estimated at 15% for the frozen storage room and 5% for the loading dock (the former requires substantial amount of defrosting).

2.2. Passive thermal storage.

2.2.1. Heat transfer between the refrigerating air and the stored products

The transient behaviour of the warehouse is determined by the presence of internal heat capacity in each refrigerated space. In a cold store the total heat capacity of the building envelope and the refrigerating air is very small compared to that of the stored products. Thermal storage in the products is thus a major factor determining the thermal inertia of the system. As a simplification, it is assumed that, during loading and unloading operations, the products leaving and entering the frozen storage room have the same amount. Furthermore, products brought into the frozen storage room are supposed to have the same temperature as the products already there (without a need for heat removal to bring the products to storage temperature). It is therefore, assumed that most products remain in long-term storage, while a relatively small percentage of the total amount is loaded/unloaded during a day. The products entering storage are also sufficiently pre-cooled and only a small amount of heat is gained during transportation.
The products are thus represented as a fixed heat capacity with uniform temperature. As the model is intended to provide only an estimate of the thermal inertia of the refrigerated space and not the actual temperature distribution in the products, the products are modelled as a simple lumped capacitance system. The heat stored in them is represented by a single volume-average temperature. The heat transfer between the products and the refrigerating air (either increasing or decreasing the load) is calculated as the difference between the average temperatures of the products and the air, divided by the total thermal resistance. Considering that the conduction thermal resistance of the products is not negligible and is of the same order of magnitude as the surface thermal resistance, an adaptation of the lumped capacitance model was used, where a combined thermal resistance accounts, to a first approximation, for both the external (surface) and internal (conduction) resistances of the lumped capacitance system (Lienhard and Glicksman, 2016):

$$R_s = [1/h_s + (V_s/A_s)/k_s](1/A_s) \qquad \text{Eq. (2)}$$

All pallets in the frozen storage room were assumed as loaded with frozen food, packaged in boxes or reusable plastic containers, which are stacked on standard Euro-pallets. Each pallet holds 56 packages with 23 kg of frozen food. The pallets are loaded on nineteen 30-metre-long mobile racks with five rows each. Each row holds a total of 32 stacked pallets. Thereby a total of 3040 pallets are stored in the frozen storage room. All assumptions and parameters, which refer to the products in the frozen storage room, are summarized in Table 1.

Table 1. Assumptions and parameters related to the products in the frozen storage room.

Products	Thermal conductivity [W/(m K)]	1.3
	Specific heat capacity [J/(kg K)]	2100
	Net product mass per package [kg]	23
Palletization and racking	Number of packages per pallet	56
	Number of pallets per rack	160
	Number of racks	19
	Total number of pallets	3040
Overall	Volume of product stack on pallet [m^3]	1.6128
	Surface area of product stack on pallet [m^2]	8.64
	Surface heat transfer coefficient [W/(m^2 K)]	10
	Total mass of products in the room [kg]	3 915 520
	Total heat capacity of the stored products [J/K]	8 222 592 000

Only the heat capacity of the frozen food was considered, whereas the presence of packaging material was not deemed essential for the calculations. It was also assumed that the whole surface area of the product stack on each pallet is exposed to the refrigerating air and uniformly exchanges heat with it. The thermal conductivity and specific heat capacity of the internal thermal mass were assumed equal to those of the packaged frozen food. The frozen products passing through the loading dock absorb some heat from the warmer refrigerating air in the dock. However, if the logistical operations are performed efficiently and the product turnaround is relatively small, the magnitude of this heat transfer is negligible as compared with the total refrigeration load. Hence, this effect was not considered in the model. Finally, heat transfer between the products and the refrigerating air was considered for the frozen storage room only, where its effect is significant.

2.2.2. Additional heat capacity

The use of a zone capacitance multiplier is a simple approach to account for the presence of additional heat capacity in the refrigerated space, except that of the stored products. Considering the concrete slab of the floor above the floor insulation as the only significant additional heat capacity for both rooms, the capacitance multiplier was used to add the total heat capacity of the floor slab to that of the indoor air. This simplification was made with the understanding that the temperature gradient of the floor construction occurs in the insulation below the slab and the average slab temperature is close to the air temperature. The capacitance multiplier for both spaces was calculated as approximately equal to three. The calculations showed that the heat capacities of the air and the floor slab in each refrigerated space are of the same order of magnitude, whereas in the frozen storage room the heat capacity of the products is about two orders of magnitude larger.

2.2.3. Rate of temperature change

The rate of temperature change of the refrigerating air and the stored products, which are both modelled as lumped capacitances, was determined by a system of two ordinary differential equations (ODE) with respect to time (the index *k* applies to each calculated heat flow influencing the temperature of the refrigerating air):

$$dT_i/dt = \sum_k \dot{Q}_k/C_i \qquad \text{Eq. (3)}$$

$$dT_s/dt = -\dot{Q}_s/C_s \qquad \text{Eq. (4)}$$

The heat flows involved in the differential equations are functions of the two temperatures. For each time step of the simulation (defined as a time-span vector), the equations were solved in MATLAB using one of the built-in ODE solvers (MathWorks, 2018).

2.3. Temperature response of the refrigerated warehouse

There is a substantial difference between the temperature response of the frozen storage room and that of the loading dock. The substantial heat capacity present in the frozen storage room makes it much more thermally inert. Thus, the temperature of the refrigerating air in it changes more gradually, which permits greater flexibility in the operation of the refrigeration system. The products in the warehouse serve for passive thermal storage and can be used for load shifting. This permits some time lag for the provision of refrigeration. For instance, the refrigeration load can be shifted to periods when the LAES system is discharging, thereby saving energy from the operation of the vapour-compression refrigeration system. The efficiency and feasibility of such a strategy have previously been investigated by the Night Wind project (Van der Sluis, 2008).
The thermal inertia of the frozen storage room is illustrated in Fig. 3, which shows the temperature response within one hour when the initial temperatures of the refrigerating air and the products are −21 °C. Three scenarios are shown: (i) no refrigeration capacity is provided to offset the refrigeration load (left); (ii) the refrigeration capacity approximately balances the load (middle); and (iii) refrigeration capacity significantly exceeds the load (right). Fig. 4 shows the temperature response of the refrigerating air in the same scenario as the one shown on the left side of Fig. 3, as compared with another scenario where no products are stored in the room.

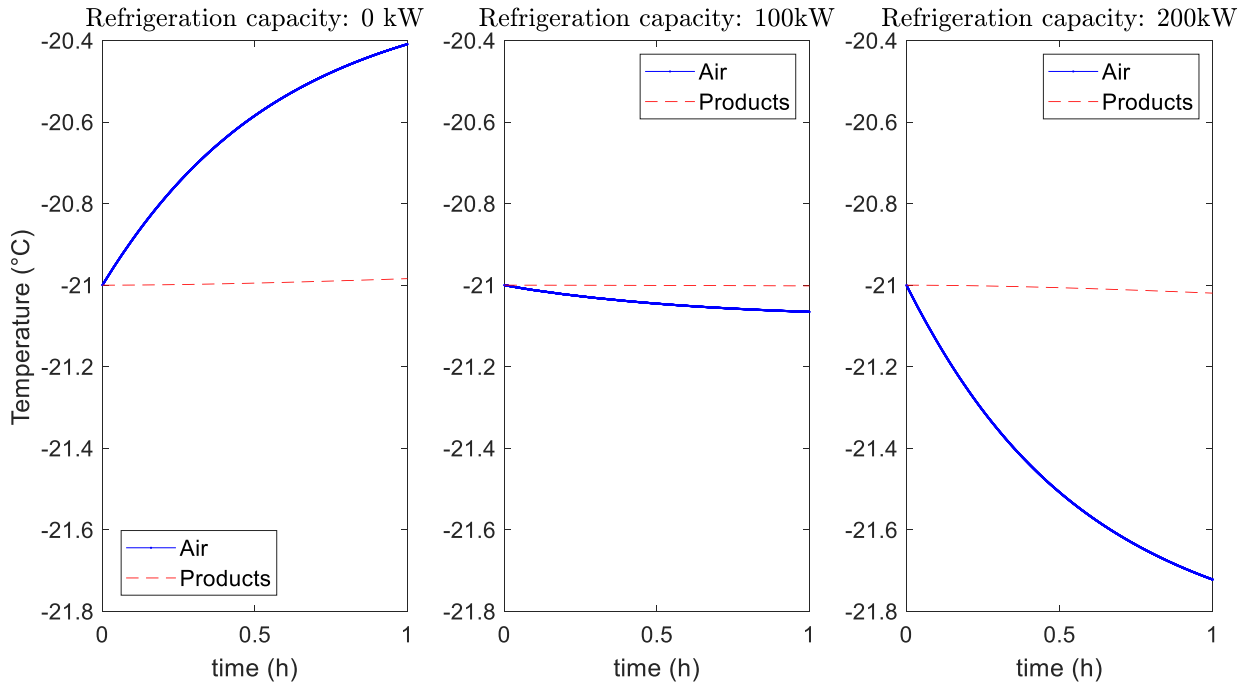

Figure 3: Temperature response of the frozen storage room in three scenarios – no cooling (left); refrigeration capacity balancing the load (middle); refrigeration capacity exceeding the load (right).

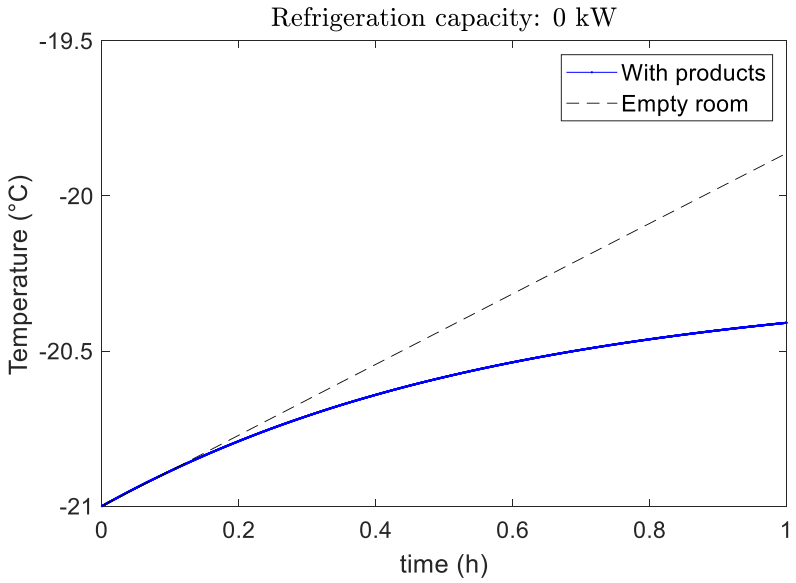

Figure 4: Comparison of the temperature response of the refrigerating air in the frozen storage room in the scenario of Figure 3 (left) with the case of a complete absence of stored products

The figures above demonstrate the significant influence of the passive thermal storage in the frozen food on the thermal inertia of the refrigerating air in the room.

3. INTERACTION WITH THE LAES SYSTEM

3.1. Control strategies and energy performance metric

The complete energy model of the integrated pilot demonstrator (including cryogen liquefaction and storage, a photovoltaic array as a renewable energy source, power generation turbines, and a food warehouse refrigerated by both a conventional vapour-compression system and a LAES-enabled one) was simulated to explore different high-level control strategies.

Regarding the existing vapour-compression refrigeration equipment of the warehouse, there are 6 compressors available, which are switched on/off in pairs, resulting in 3 possible operation steps with a maximum refrigeration capacity of 270 kW_{th}. The thresholds for activation of the compressors are between −20 ºC and −21 ºC during peak-tariff periods, and between −22 ºC and −23 ºC during low-demand valley-tariff periods.
The primary performance metric used for the LAES system is the round-trip efficiency, which is the ratio between the energy recovered by the system during the discharge stage and the total energy input. The recovered energy consists of the electricity produced by the turbines and the electricity saved by cooling the warehouse by means of the LAES system. The latter is equivalent to the power consumption of the conventional vapour-compression refrigeration system which should have been necessary to meet the same refrigeration load and can be calculated via the coefficient of performance (COP) of the conventional system. The temperatures of the refrigerating air in the frozen storage room and the loading dock (determined via the energy model of the warehouse) are used to control and alternate the refrigeration supply from the LAES and conventional refrigeration systems. Three different high-level control strategies for the LAES system (with increasing level of complexity) have been investigated:

- **Strategy 1:** The LAES system is charged whenever surplus renewable energy is available;
- **Strategy 2:** In addition to the former, the system could be charged from the power grid, taking advantage of low-tariff periods;
- **Strategy 3:** Same as above with the inclusion of a weather forecast service, which considers the expected renewable generation in the following hours.

3.2. Simulation outcomes

The energy performance of the system under the three control strategies has been simulated for a reference week with varying external conditions (including days with high and low solar radiation). The results of the simulations are summarized in Table 2.

Table 2. Energy performance of the LAES system for the reference week

Parameter	Strategy 1	Strategy 2	Strategy 3	Unit
Electricity consumption for liquefaction	3503.9	5690.2	8246.9	kWh
Electricity generated by the turbines	502.5	857.6	1326.0	kWh
Electricity saved through refrigeration	419.3	666.9	934.6	kWh
Round-trip-efficiency	26.3	26.8	27.4	%

In all simulated scenarios, the electricity saved through LAES-assisted refrigeration of the warehouse has a substantial effect – almost doubling the round-trip efficiency of the LAES system.

4. CONCLUSIONS

The elaborated model employs a rather simplified approach for representing the transient thermal behaviour of the refrigerated warehouse. However, it is computationally efficient and suitable for the purpose of estimating the rate of temperature change in the given context. Notably, it is applied in a situation where the allowed temperature variations are quite small. In the simulations the temperature of the refrigerating air varied in the range of about 1 K, while the temperature change of the products was negligible. In situations with prolonged periods of substantial mismatch between the refrigeration load and refrigeration capacity of the system (e.g., if using the products for passive thermal storage), the model response is quite sensitive to the assumptions made regarding the product parameters. The model is designed to work in the given circumstances and should be applied with caution in any other context.
The energy performance simulations, carried out for each of the three investigated control strategies, showed a substantial improvement in the round-trip efficiency of the LAES system, due to the utilization of evaporating cryogen for on-site refrigeration. The results indicate the importance of synergistic operation of LAES systems and on-site refrigerated facilities, in order to make this energy storage technology economically viable in a near future. The simulations could be validated when the pilot plant becomes operational and enough data on its performance is made available.

ACKNOWLEDGEMENT

This contribution is prepared as part of the EU's CryoHub Project. The CryoHub Innovation Action receives funding from the European Union's Horizon 2020 Research and Innovation Programme under Grant Agreement No. 691761.

NOMENCLATURE

A	exposed surface area (m^2)	R	total thermal resistance ($K.W^{-1}$)
C	total heat capacity ($J.K^{-1}$)	T	temperature (K)
h	heat transfer coefficient ($W.m^{-2}\times K^{-1}$)	t	time (s)
I	solar irradiance ($W.m^{-2}$)	V	volume (m^3)
k	thermal conductivity ($W.m^{-1}\times K^{-1}$)	α	solar absorptivity
$\dot{Q}$	heat flow (W)	ΔT	temperature difference

Subscripts

e	external (outdoor air)	s	*stored products*
i	internal (refrigerating air)	se	*allowance for solar effect*

REFERENCES

ASHRAE, 2018. Chapter 24 - Refrigerated-facility loads. In: ASHRAE Handbook – Refrigeration, ASHRAE, Atlanta, GA.

CryoHub, 2016. EU Horizon 2020 Project GA No. 691761 "Developing Cryogenic Energy Storage at Refrigerated Warehouses as an Interactive Hub to Integrate Renewable Energy in Industrial Food Refrigeration and to Enhance Power Grid Sustainability – CryoHub", [Online]. cryohub.eu

European Commission, 2017. Energy storage – the role of electricity. [Online]. bit.do/eu-store

Fikiin, K., Stankov, B., Evans, J., Maidment, G., Foster, A., Brown, T., Radcliffe, J., Youbi-Idrissi , M., Alford, A., Varga, L., Alvarez, G., Ivanov, I. E., Bond, C., Colombo, I., Garcia-Naveda, G., Ivanov, I., Hattori, K., Umeki, D., Bojkov, Ts., Kaloyanov, N., 2017. Refrigerated warehouses as intelligent hubs to integrate renewable energy in industrial food refrigeration and to enhance power grid sustainability. Trends in Food Science & Technology, 60, 96-103. http://dx.doi.org/10.1016/j.tifs.2016.11.011.

Lienhard, J., Glicksman, L., 2016. Modeling and approximation in heat transfer. Cambridge University Press, New York, NY.

MathWorks, 2018. MATLAB R2018a Documentation. [Online]. bit.do/ode15s

Morgan R., Nelmes S., Gibson E., Brett G, 2015. Liquid air energy storage – Analysis and first results from a pilot scale demonstration plant. Applied Energy 137, 845-853.

Perez, R., Stewart, R., Seals, R., Guertin, T., 1988. The development and verification of the Perez diffuse radiation model. Sandia National Laboratories, Albuquerque, NM.

Van der Sluis, S., 2008. Cold storage of wind energy – Night Wind. Paper presented at the Fourth International Congress for South-Eastern Europe 'Energy Efficiency and Renewable Energy Sources', Sofia, Bulgaria.

Manuscript ID: 1861
DOI: 10.18462/iir.icr.2019.1861

Experimental investigation on the integration of cold energy storage into a R744 refrigeration system

Raluca I. MANESCU[(a)], Yosr ALLOUCHE[(a)], Ana Larrañaga Janeiro[(b)], Armin HAFNER[(a)]

[(a)]Norwegian University of Science and Technology, NTNU
Department of Energy and Process Engineering
Kolbjørn Hejes vei 1D, 7491 Trondheim, Norway
raluca.i.manescu@ntnu.no

[(b)]University of Vigo, Faculty of Mining and Energy Engineering, Vigo, Spain

ABSTRACT

In this paper, an experimental study on the efficient integration of cold storage (CTES) unit into a R744 refrigeration system for food storage in supermarket cabinets is presented. The main idea is to make use of the free space located at the top of the cabinet to place the cold storage. For this purpose, the cold discharging process is a zero energy consumer and only operates using the CO_2 thermosiphon effect. In this work, the CTES is a tube-in-tank storage unit where water is used as a latent storage medium. It is connected from one side to the CO_2 transcritical facility to ensure the cold charging process, and from the other side to a glycol loop through a double-pipe heat exchanger to simulate the supermarket cabinets' load during the cold discharging process. The optimal operating conditions that ensures the thermosiphon process were identified as being a wider pressure range, and a higher heat load applied to the evaporator.
Keywords: Cold Thermal Energy Storage, Carbon Dioxide, Thermosiphon, Commercial Refrigeration, Supermarkets, Transcritical Refrigeration System.

1. INTRODUCTION

Nowadays, the main challenge faced by the supermarket industry is to meet both efficiency and the environmental sustainability criterion in order to reduce the share of the refrigeration energy consumption, limit the greenhouse gas emission and provide a good food quality to the customers. Compared to synthetic refrigerants, R744 represents a very attractive alternative. It presents no Ozone Depleting Potential and a negligible Global Warming Potential. In addition, it is neither toxic nor flammable. R744 is widely available and its utilization is one of the main tasks set by the new environmental policies when it comes to the CO_2 capture, storage and utilization (CCSU). Nevertheless, the high-pressure operation of R744 transcritical systems leads to higher initial costs (D'Agaro et al., 2018). The need for thermal energy storage (TES) in the supermarket industry is increasing steadily in order to tackle both the high power consumption and the initial costs. Although the performance of R744 transcritical systems was thoroughly investigated in the last decade (Gullo et al., 2018), the application of cold thermal energy storage integrated with a display cabinet is barely studied (Fidorra et al., 2016). According to the authors knowledge a similar technology does not exist at an industrial scale. Thermal energy storage is considered to have a double benefit. First, it allows for the rationalization of the energy supply capacity by supplying the extra energy demand during peak hours. Second, it improves the cost effectiveness when there is a time shift between energy supply and demand.

In this paper, experimental investigations on the efficient integration of thermal cold storage (TCS) into a CO_2 transcritical system were carried out. The main idea is to take advantage of the free space located at the top of the display cabinet and integrate the storage. The cold discharging process is zero energy consumer and only operates using the CO_2 thermosiphon effect. The experimental setup consists of a coil-in-tank storage unit connected to the CO_2 transcritical system. The tank is filled with water as the phase change medium (ice storage) and the refrigerant (CO_2) is flowing into a

helically coiled tube heat exchanger immersed in the water. The CTES is connected from one side to SuperSmart_Rack transcritical R744 facility (Pardiñas et al., 2018) to ensure the cold charging process. It is connected from the other side to a glycol loop through a double-pipe heat exchanger to simulate the supermarket cabinets' load during the cold discharging process. This paper aims to identify the main operating conditions that ensures the thermosiphon effect to take place.

2. EXPERIMENTAL SETUP AND TEST PROTOCOL

The test rig is built in order to simulate a supermarket display cabinet with an integrated TCS. The main challenge encountered with the design of this new generation of display cabinets is related to an optimized integration of the storage taking into account the small free space available in the supermarkets. The use of the free space at the top of the cabinets is then of big interest. Nevertheless, a special consideration to the cabinet structure should be attributed to take into account the extra volume weight of the storage and the eventual water leakage. The evaporator is located at the bottom of the cabinet in order to ensure the thermosiphon working conditions.

The experimental setup is represented in Fig.1. The cold storage is connected to the R744 transcritical system through a helically coiled tube heat exchanger (HEX) in order to ensure the charging process. In this configuration, the cold storage acts as an evaporator. For the discharging process, the cold storage is connected to a glycol loop which simulates the cooling load. In this case, the cold storage will act as a condenser. Both cycles are related through a tube-in-tube heat. PT-100 temperature sensors are located at the CO_2 inlet (PT-1) and the CO_2 outlet (PT-2) of the charging cycle. The inlet and outlet glycol temperature to the tube-in-tube HEX are measured using (PT-3) and (PT-4), respectively. The cold storage is connected to the Super_Smart Rack CO_2 refrigeration unit through the valves (V-900) and (V-905), respectively. The differential (DP1) and absolute (AP) pressures are used to measure the pressure drop in the helically coiled tube HEX and the pressure at the CO_2 outlet, respectively. A pump (P-1) is mounted in the glycol cycle to circulate the glycol through the HEX. Heat is applied to the glycol through an electrical heater (H-1) in order to simulate the supermarket display cabinet's load.

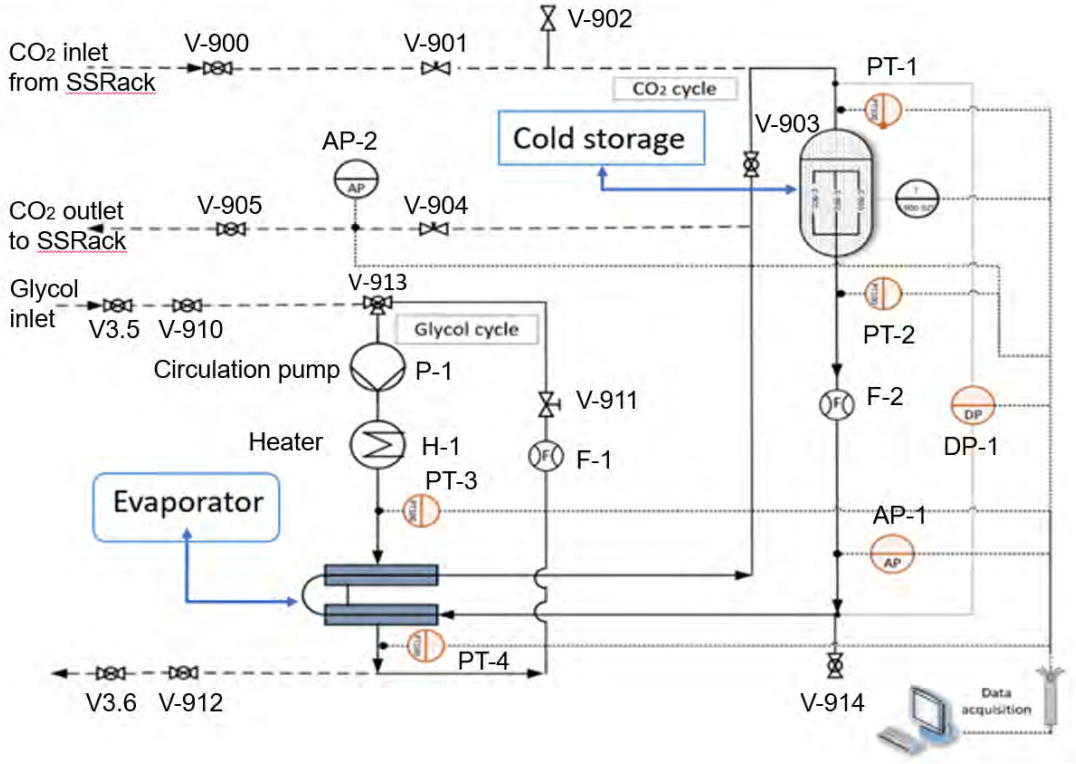

Figure 1: PID diagram of the experimental setup

The CO_2-glycol loop (Fig. 2b) is located at the ground level and the cold storage (Fig. 2a) is situated at an upper level in order to guarantee the thermosiphon height conditions. The tube-in-tube HEX

will act as an evaporator during the discharging process. Insulation material is applied to the cold storage in order to reduce the heat losses to the environment.

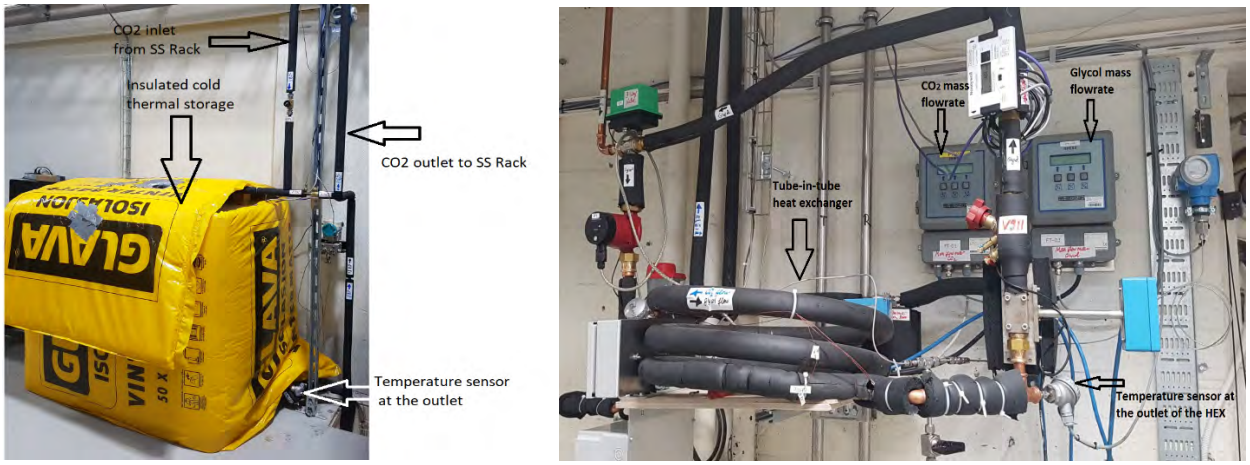

(a) Cold storage (b) Evaporator

Figure 2: Actual experimental setup at the NTNU laboratory

2.2. Ice Storage Design

The ice storage consists of a tank with a total volume of 1m^3. A three concentric helically coiled tubes HEX is immersed in the tank. CO_2 is flowing through the HEX to remove heat from the storage medium and ensure the charging process. Fig. 3a represents the front view of the solidworks HEX model. Fig. 3b shows the real arrangement from the experimental setup. The tubes are made of copper, and have the same length, in order to ensure a similar pressure drop at the outlet of the cold storage and enable the thermosiphon effect. Every coil is composed of 6 turns. Different diameters have been applied for each coil in order to enhance the heat transfer. The applied diameters are 540 mm, 360mm and 225mm, 180mm and 115mm. The thermal dilatation was considered in the design of the heat exchanger. The cyclically loading (charging and discharging) of the ice storage was not taken into consideration in the mechanical design and service life.

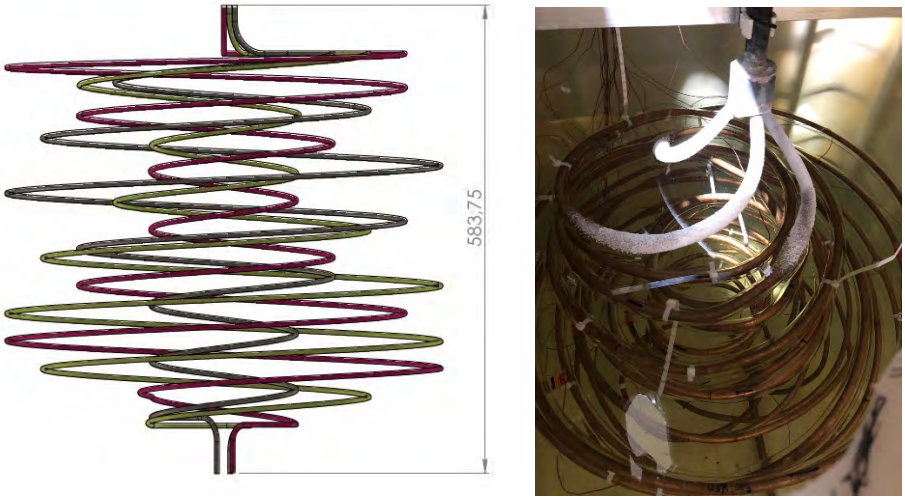

(a) 3D CAD model (b) actual arrangement in the lab

Figure 3: Coil tubes distribution inside the CTES

During charging process, the CO_2 refrigerant comes from the Super_Smart Rack, through the expansion valve V-900 (see Fig.1) at a pressure of 27 bar. Heat transfer occurs inside the cold storage between the liquid CO_2 at boiling point, and the water. The temperature of the water at the beginning of the experiments is around 12℃. Fig. 4 shows the position of both temperature sensors for the CO_2 refrigerants at the inlet and outlet of the cold storage. At the exit of the cold storage, the

CO_2 flows through the glycol heat exchanger, and goes back to the refrigeration system through valve V-905 (see Fig.1). The mass flowrate of the CO_2 is regulated by the valve V-901(see Fig.1).



(a) inlet of CTES (b) outlet of CTEs

Figure 4: Temperature sensors located at the inlet and outlet of the CTES

During discharging, both inlet and outlet valves to the main CO_2 refrigeration system are closed. Valve V-903 will be opened, to ensure the circulation of the CO_2 in a closed loop. The refrigerant will travel from the cold storage to the glycol heat exchanger via the thermosiphon working principle of the evaporator.

2.3 Thermosiphon Heat Exchanger

During the discharging process the CO_2 stream enters the tube-in-tube HEX. The glycol flows through the outer tube, while the CO_2 flows through the inner tube (see Fig.2b). The glycol loop is used to simulate the cabinet temperature, thus one of the aims of the experiments is to keep the glycol outlet temperature constant at 4℃. The working principle of the thermosiphon effect is depicted in Fig. 5. The cold storage is represented by the condenser, while the cabinets evaporator is represented by the reboiler. The thermosiphon working principle is based on natural convection. Natural convection works based on the density difference between the two CO_2 phases. The blue line represents the CO_2 liquid phase, that leaves the cold storage and will go the evaporator. The red line represents the CO_2 vapour, that goes from the evaporator to the cold storage, through natural convection. At the outlet of the cold storage, the CO_2 liquid phase should be at boiling point. At the inlet of the cold storage, the CO_2 vapour phase should be at the dew point. For 27 bar pressure, the CO_2 saturation temperature is -9.3℃. The force that drives the thermosiphon, is the pressure difference between the vapour and the liquid streams. The pressure difference is influenced by the densities of the CO_2, but also by the height between the cold storage and the evaporator. The height between the condenser and the reboiler in the test facility is 2.05m. The normal height of a display cabinet for a supermarket is around 2.1m.

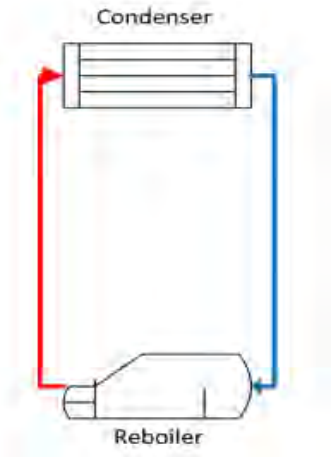

Figure 5: The thermosiphon effect

2.4 Test Conditions

The focus of this paper is to carry out experiments only on the discharging process in order to have a better understanding of the cold storage performance. For this purpose, two objectives were set: achieving a constant and stable outlet glycol temperature around 4℃, and identifying the parameters that influence the thermosiphon working principle. Table 1 presents the parameters that were kept constant during discharging, for different set of experiments.

Table 1. Discharging mode parameters

Parameters	Experiment 1	Experiment 2	Experiment 3
Cold storage capacity, kJ	5540	6187	5800
Heater load, W	0	150	460

Time of discharging, h	6	6	6

3. RESULTS AND DISCUSSIONS

3.1 Thermosiphon Working Conditions

The pressure drop is the main key factor of a successful thermosiphon process. For this purpose, the influence of the CO_2 flowrate on the pressure drop was firstly studied. Fig. 6 shows the variation of the refrigerant mass flowrate with the pressure drop during the discharging mode. At the beginning of the discharging process, there is an increased pressure drop in the first 15 minutes, for the last two experiments, where different heat loads were applied to the glycol system. The increased pressure drop was due to a larger temperature difference between the refrigerant and the glycol, inside the evaporator. The glycol temperature and heat transfer rates are represented in Fig. 7. In the first experiment, it can be noted that in the beginning of the discharging, the inlet temperature of the glycol flow was 10℃ (see Fig. 7a). After 3 hours, the temperature decreased to 3.8℃, and it remained constant for the rest of the experiment. The outlet glycol temperature remained constant at 3.2℃ after the first 3 hours until the end of the experiment. No heat transfer occurred due to an insignificant pressure drop, which is the driving force for the thermosiphon (see Fig. 6). In the second experiment, the discharging started with a glycol inlet temperature of 17℃ (see Fig. 7b), it reached a peak at 28℃, and decreased to 11℃ by the end of the experiment. The glycol outlet temperature reached a temperature of 8.4℃ by the end of the discharging process. There was insignificant pressure drop, and no mass flowrate for the refrigerant (see Fig. 6). In the third experiment, the heat load applied to the glycol loop was increased to 460W, which led to a slightly higher pressure difference in the thermosiphon evaporator, on the CO_2 side (see Fig. 6). The discharging process started with an inlet glycol temperature of 19℃, reached a peak at 40℃, and decreased to 13℃ after 3 hours, where it remained constant for the rest of the experiment (see Fig. 7c). The outlet temperature of the glycol, remained constant after 3 hours at 7.6℃.

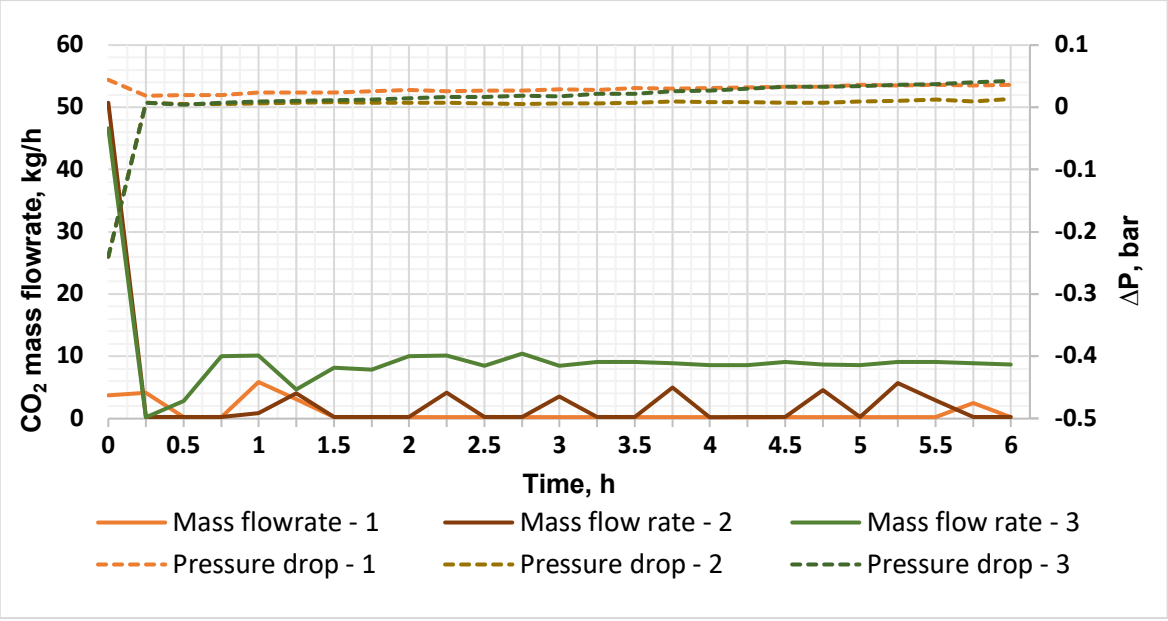

Figure 6: CO_2 mass flowrate and pressure drop variation during discharging for: 0W (1), 150W (2), and 460W (3) heat load

The glycol mass flowrate was kept constant throughout the experiment at 1.4 kg/min. The heat transfer rate inside the evaporator can be observed in Fig. 7. A similar behavior for the heat transfer rate was observed in the experiments. A larger temperature different between the inlet and the outlet temperatures of the glycol lead to a better heat transfer rate. In the first experiment (Fig. 7a) the heat

transfer inside the evaporator is very low, due to a lower glycol temperature difference (ΔT_{glycol}). In the second experiment (Fig. 7b), the temperature difference increases, giving a better heat transfer within the heat exchanger. However, the thermosiphon HEX was not able to decrease the glycol temperature to 4℃, since the pressure drop on the CO_2 side, which drives the thermosiphon, was still low. The third experiment (Fig. 7c) showed the best results in terms of heat transfer rate (average value of 0.3 kJ/s compared to no heat transfer rate in the first experiment, and 0.1 kJ/s for the second experiment). The ΔT_{glycol} remained constant at 5℃ after the first two hours, with a constant outlet glycol temperature of 8℃. The reason the evaporator was not able to fulfill the 4℃ requirement at the outlet of the glycol loop, was that after the first 2 hours, the system's driving force, the Δp, was too low to get the thermosiphon work.

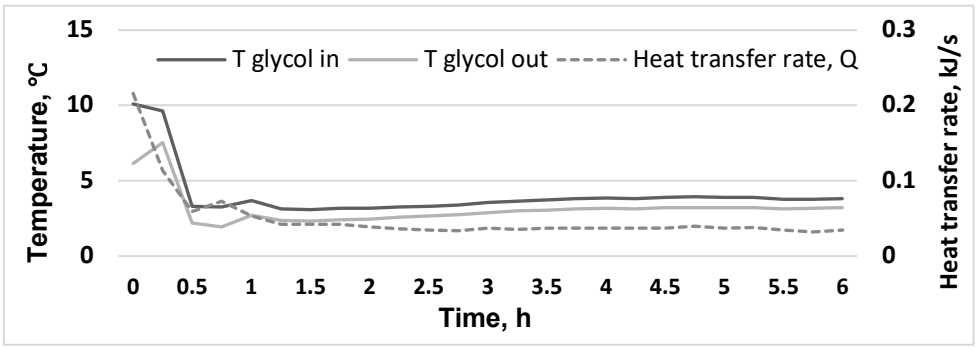

(a) 0W heat load

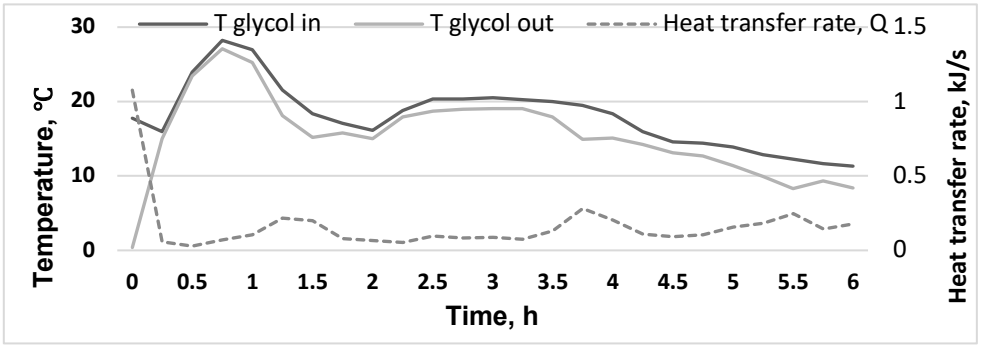

(b) 150W heat load

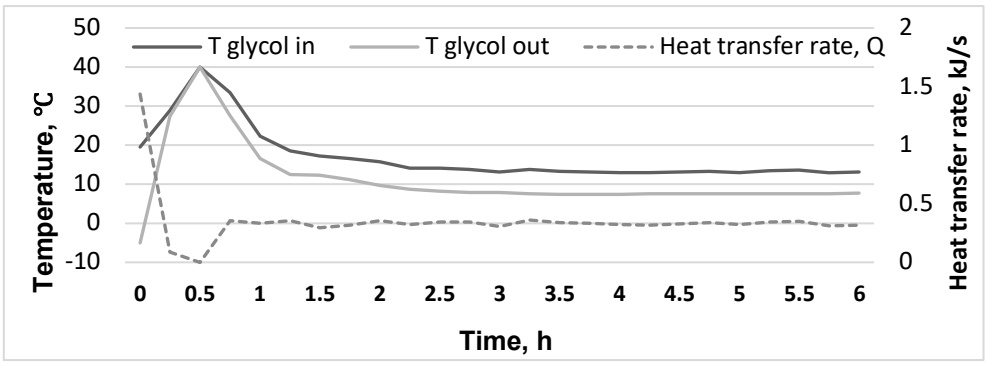

(c) 460W heat load

Figure 7: Glycol temperature and heat transfer rate distribution during discharging

3.2 Ice Storage Temperature Profile

The temperature profile for different locations inside the cold storage was analyzed for a better understanding of the discharging process. Fig. 8 shows the vertical distribution of the water temperature for the entire discharging process. In Fig. 8, TC16, TC11 and TC22 refer to the thermocouple readings located at the top, middle and the bottom of the HEX. A similar behavior has been observed in the three experiments. A sensible heat storage occurs during the first 15 minutes, rising the ice temperature to 0℃. Then, the phase change "plateau" is clearly observed until the phase change is completed, and the water temperature increases again. The first two sets of experiments (Fig. 8a, and Fig. 8b), have a similar temperature profile. The temperature readings at the bottom of the storage (TC22) show that there is no latent heat transfer occurring (only sensible heat). In the third experiment (Fig. 8c), the higher heat input (460W) to the evaporator leads to a shorter phase change time. The higher temperature values for water show that the storage is not able to cool the CO_2 bellow 4℃. This implies that the glycol temperature at the outlet of the evaporator will not be able to meet the requirements from the supermarket (See Fig. 7c).

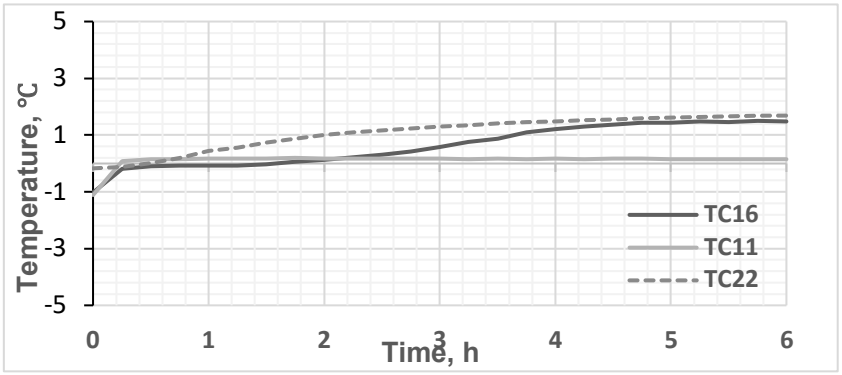

(a) 0W heat load

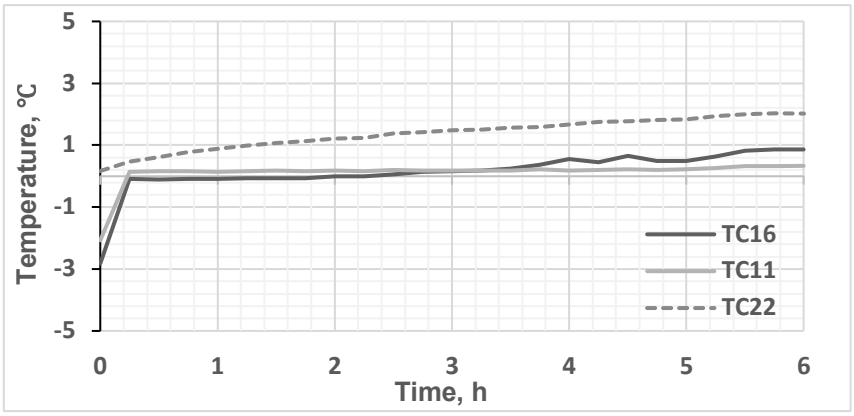

(b) 150W heat load

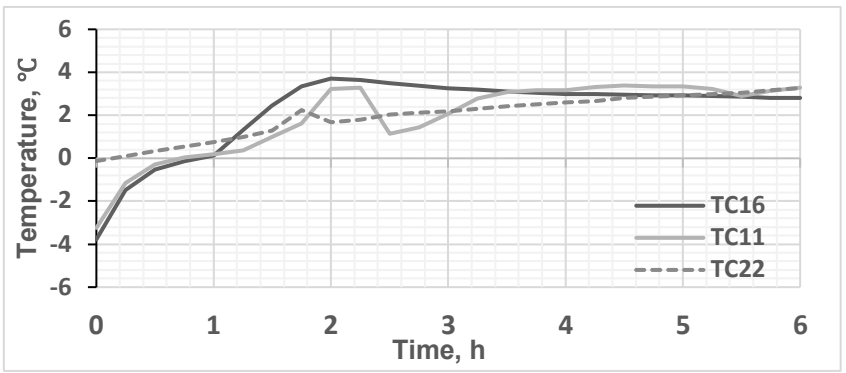

(c) 460W heat load

Figure 8: Ice temperature vertical distribution inside the cold storage during discharging

4. CONCLUSION AND FURTHER WORK

This paper presents the first set of experiments for the discharging process carried out on a CTES connected to a transcritical R744 refrigeration system. The thermosiphon effect took place for the high refrigerant operating pressures, ranging from 27 to 40 bar. In order to keep the CO_2 flow circulating through the thermosiphon HEX, a higher heat load applied to the glycol loop was needed in the evaporator. Due to the extra heat load, the temperature difference inside the evaporator increased, which enabled a better heat transfer rate (0.03 kJ/s). The maximum heat load applied to the system during the experiments, was 460W. A real display cabinet, in a supermarket, has a cooling capacity of 2000W (Alzuwaid et al., 2015). With a 460W heat load, the thermosiphon evaporator was able to cool the glycol temperature from 20℃ to 8℃, in the first 2 hours, and kept it constant throughout the discharging process. The cold storage (charging) process will be further investigated and the results will help to analyze the stationary and the dynamic behavior of the cold storage. A numerical model using the Modelica and Dymola computer programs is actually being performed to simulate the entire system, for various ambient and boundary conditions. The model will be validated using the available experimental data.

NOMENCLATURE

CCSU	Carbon dioxide capture, storage and utilization
CTES	Cold thermal energy storage
HEX	Heat exchanger
PCM	Phase change material
PID	Process and instrumentation diagram
TES, TCS	Thermal energy storage, Thermal cold storage
TC	Thermocouple
$\dot{Q}$	Heat transfer rate, kW

REFERENCES

Alzuwaid F., Ge Y.T., Tassou S., Raeisi A., Gowreesunker L., 2015, The novel use of phase change materials in a refrigerated display cabinet: An experimental investigation, Applied Thermal Engineering 75, 770-778.

D'Agaro P., Cortella, G., Polzot, A., 2018, R744 booster integrated system for full heating supply to supermarkets, Int. J. of Refrigeration 96, 191-200.

Fidorra, N., Minetto, S., Hafner, A., Banasiak, K., Köhler, J., 2016, Analysis of cold thermal energy storage concepts in CO2 refrigeration systems, 12th IIR Gustav Lorentzen Natural Working Fluids Conference, Edinburgh, UK.

Gullo, P., Hafner, A., Banasiak, K., 2018, Transcritical R744 refrigeration systems for supermarket applications: Current status and future perspectives, Int. J. of Refrigeration 93, 269-310.

Manescu, R., Hafner, A., Fidorra, N., Försterling, S., Köhler, J., 2017, A new approach for cold thermal energy storages in supermarket refrigeration systems, 7th IIR Ammonia and CO2 Refrigeration Technologies Conference, Ohrid, Republic of Macedonia.

Pardiñas, Á., Hafner, A., Banasiak, K., 2018, Integrated R744 ejector supported parallel compression racks for supermarkets. Experimental results, 13th IIR Gustav Lorentzen Natural Working Fluids Conference, Valencia, Spain.

United Nations Environment Programme, 2016: Further Amendment of the Montreal Protocol [Press release]. Retrieved from http://web.unep.org/kigali-amendment-montreal-protocol-another-global-commitment-stop-climate-change.

Manuscript ID: 43
DOI: 10.18462/iir.icr.2019.0043

Numerical modelling of heat and mass transfer in a refrigerated truck trailer

Sergio CROQUER, Alla Eddine BENCHIKH LEHOCINE, Sébastien PONCET

Mechanical engineering department, Université de Sherbrooke
Sherbrooke, J1K 2R1, Canada, Sebastien.Poncet@USherbrooke.ca

ABSTRACT

The present work reports the numerical modeling of the heat and mass transfer inside a refrigerated truck trailer. The numerical model solves the conjugated heat and mass transfer inside the trailer under unsteady conditions. The conservation equations of mass, momentum and energy are solved in 3D and closed using the k-ω SST model. It has been first validated against the numerical and experimental data of Lafaye de Micheaux et al. (2015). The results are then extended to a refrigeration system based on eutectic plates and placed in a refrigerated truck trailer used to transport frozen products. An innovative way to represent fans is also proposed. The inter-plate distance and the direction of the fans are optimized.
Keywords: Truck Trailer, Refrigeration System, Computational Fluid Dynamics, Turbulence Modeling.

1. INTRODUCTION

Food transport, including motive power and refrigeration, is estimated to be responsible for around 2% of total greenhouse gas emissions in developed countries (Tassou et al., 2007). Road transport refrigeration equipments need to operate reliably in harsher environments compared to stationary equipments. Legislations exist and provide common standards for temperature-controlled transport vehicles and tests to be done on such equipments for certification purposes (UN Economic commission for Europe, 2003). As an example, milk for industrial processing and ice cream should be transported at 6°C and -25°C, respectively. Apart from these operating conditions required to preserve the cold chain, constraints due to available space, noise and weight make them less efficient than stationary systems.

For road transport vehicles, different types of refrigeration units exist depending mainly on the size of the vehicle and its load: vapour compression systems with a vehicle or an auxiliary alternator unit, a direct belt drive or an auxiliary diesel unit. The majority of medium to large vehicles use refrigeration units that include a self-contained diesel engine. Running at full capacity to guarantee -20°C within the trailer, the fuel consumption of this unit is up to 5 liters per hour. To overcome that, eutectic systems have been developed and used in prototype vehicles. They consist of tubes, beams or plates filled with a phase change material to store energy and produce a cooling effect. They are charged at night and they operate silently during the day for a specific duration of time. Such systems may be suitable for short distance deliveries. However, the heat losses though frequent door openings can be a major concern in humid climates, inducing condensation and the formation of ice along the plates, which blocks the heat transfer with the surrounding air.

The heat and mass transfers inside a refrigerated chamber exhibit some similarities with the truck trailer configuration and have received much more attention (Azzouz et al., 1993; Hoang et al., 2000; Foster et al., 2003). To the best of our knowledge, only Tso et al. (2002), and more recently Lafaye de Micheaux et al. (2015), investigated the velocity and temperature distributions in a truck trailer with different door openings. These last authors provided a combined experimental and numerical investigation, which will serve to validate the present solver. However, compared to the present case, they did not consider any refrigeration system. The main objective of the present study is then to develop an efficient and accurate numerical model able to determine the flow field

and temperature distribution inside a truck container refrigerated with eutectic plates for the transportation of frozen goods.

2. NUMERICAL MODELING

Two configurations have been simulated in the following sections: the test bench developed by Lafaye de Micheaux et al. (2015) has been first modeled for validation purposes, before considering a new configuration including eutectic plates.

2.1. Geometrical Modeling

Fig. 1 shows the system configuration assessed in this study and the characteristic dimensions. At the back of the truck trailer, three vertical plates containing the frozen eutectic mixture act as the cooling source. During normal operation, the fusion inside the plates keeps their surface at a constant temperature equal to 244 K during about 8 hours. They are separated from the rest of the trailer by a vertical wall letting an opening denoted (d) at the bottom of the plates. The interplate spacing (f=h=g) will be varied to optimize the flow between the plates. All dimensions, which are based on commercially available plates and truck container, are given in Table 1.
A set of four fans mounted above the plates maintains the air circulation between the plates and within the container. Two directions for the air flow are considered: blowing and suction. Fans are modeled by adding a source term ($\rho_{air}U_{fan}$) in the momentum equations with a characteristic value U_{fan}=8.4 m.s^{-1} to match the existing fans.

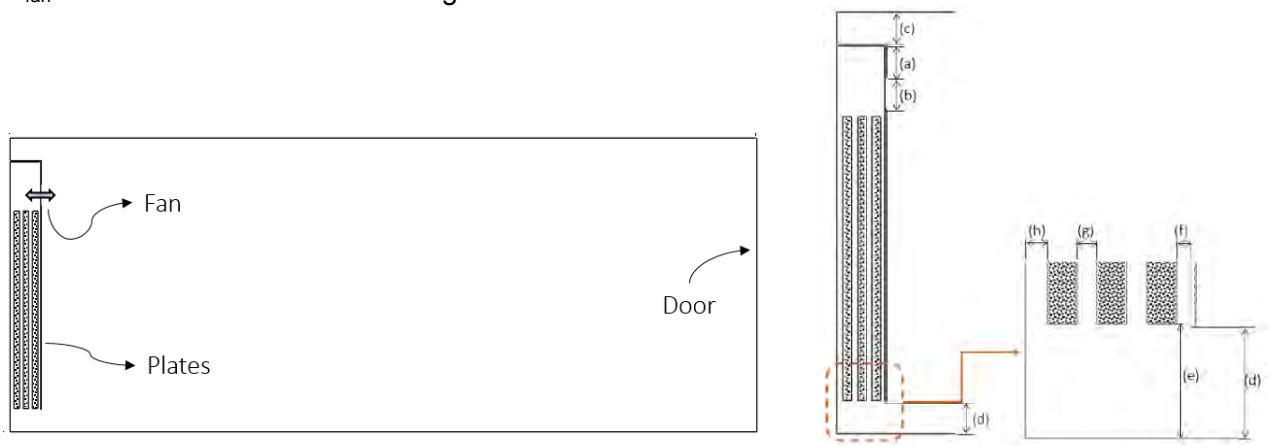

Figure 1: 2D view of the truck trailer with eutectic plates (left) and zoom on the eutectic plates (right) with relevant notations

Table 1. Container and eutectic plate dimensions (in m)

Container	
Length	7.33
Height	2.616
Plates	
Thickness	0.054
Height	1.76
Longitudinal spacings	
f=g=h	0.036, 0.06 or 0.1
Vertical spacings	
a, b, c, d, e	0.05, 0.2, 0.346, 0.2, 0.206

2.2. Numerical Method

All calculations are performed using the finite-volume software CFX ANSYS v16.1. The flow and heat transfer are modeled by solving the Unsteady Favre Averaged Navier-Stokes equations (UFANS) as well as the conservation of mass and total energy. Buoyancy driven flows with temperature differences over 20 K are expected. Therefore, dry air is supposed to be an ideal gas with variable density but constant transport properties. Turbulence effects are accounted for using the Shear Stress Transport k-ω model (k-ω SST) with production terms representing buoyancy contributions to the turbulent field. Second-order upwind and centered schemes are chosen respectively for the spatial discretization of the advective and diffusive terms, while a second-order Backward-Euler scheme with implicit time-stepping is used for the temporal discretization. A Rhie-Chow fourth-order algorithm is applied to overcome the pressure-velocity coupling.

2.3. Numerical Parameters

Unstructured meshes composed of triangular elements are generated using Centaur for the spatial discretization of the 2D domain (Fig. 2). 12 prismatic layers are added close to all solid boundaries including the plates with a refinement rate set to 1.1. Local refinements are also imposed in the door interface region and at the location of the fans. The mesh grid composed of 903 084 cells provides grid-independent solutions. The first element is located at around 1 mm of solid walls.

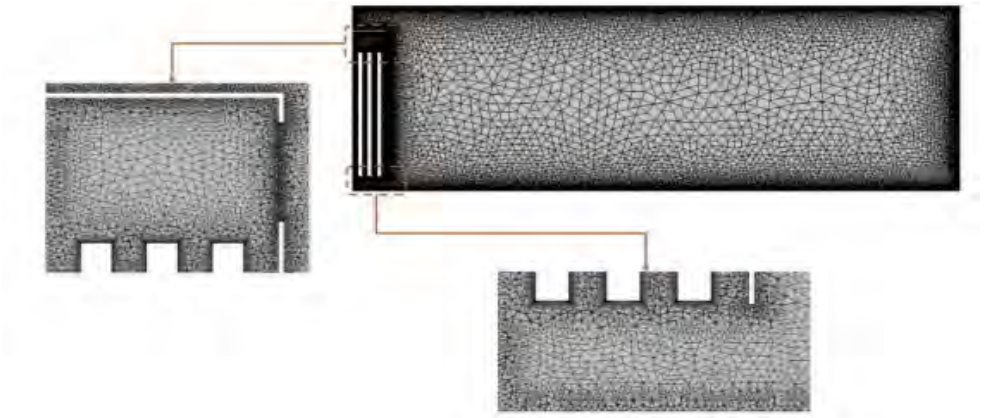

Figure 2: Details of the 2D mesh used for the container with eutectic plates

An adaptive time-step approach is adopted to ensure a smooth time convergence. Generally, the time step remains around 5×10^{-3} s. At each time step, the discretized UFANS equations are solved using an inner-loop with convergence criteria for mass, momentum and energy residuals RMS under 10^{-5}. Simulations are performed using 20 CPU nodes with 12 AMD Opteron 6172 cores 32 GB RAM per node (supercomputer Mammouth-MP2, Université de Sherbrooke). For close configurations, steady-state results converge after about 3 hours.
All trailer walls are supposed to be adiabatic. A general-connection interface is set at the opening doorway, through which the air may flow freely in any direction. All calculations are initialized with constant pressure (101 325 Pa), a zero velocity field and temperatures for each sub-domain depending on the assessed case.

3. RESULTS AND DISCUSSION

3.1. Validation of the Flow Solver

The numerical model has been first validated against the experimental and numerical results of Lafaye de Micheaux et al. (2015) for a similar configuration but without eutectic plates and fans. The truck container is completely empty and has inner dimensions equal to 2.35×2.5×5.51 m³ (Height × Width × Length). It is placed midway in a tunnel (5.43×5.5×31 m³) at a distance of 0.35 cm from the floor. In the baseline experiment, the container and wind tunnel initial temperatures are respectively fixed to 253 K and 293 K. At t=0 s, the container doorway is fully open and data inside the container and at the door (comprising velocity and temperature) are registered for about 60 s.

The model is the one described in Section 2 except the following numerical details. All wind tunnel walls are supposed to be adiabatic, whereas the container walls are either adiabatic or allow for heat conduction with a thermal equivalent resistance of 1.84 $W.m^{-2}.K^{-1}$, which is based on typical refrigerated container insulation layers. An opening boundary condition is imposed at the wind tunnel rightmost surface, allowing an air flow in any direction (inlet air having a temperature of 293 K). A symmetry condition is imposed at the mid-plane of the 3D case to reduce the computational cost. For the 2D and 3D cases the mesh grids are composed of 146 000 and 13 400 000 elements respectively, leading to a wall coordinate at the container walls close to 5.

At 10 s

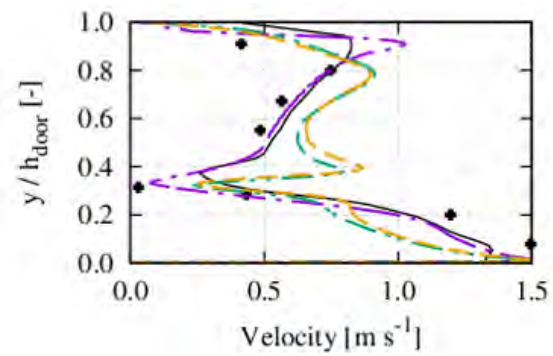

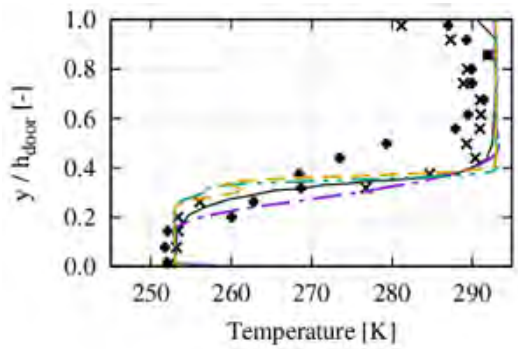

At 20 s

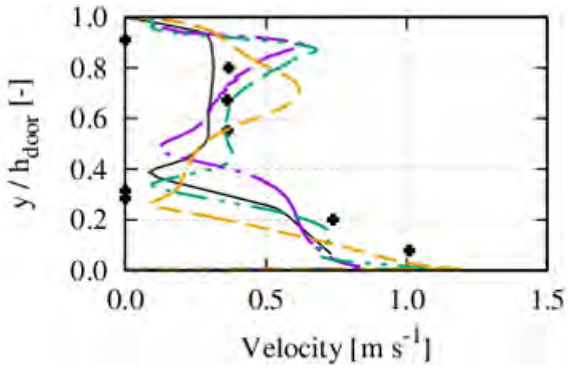

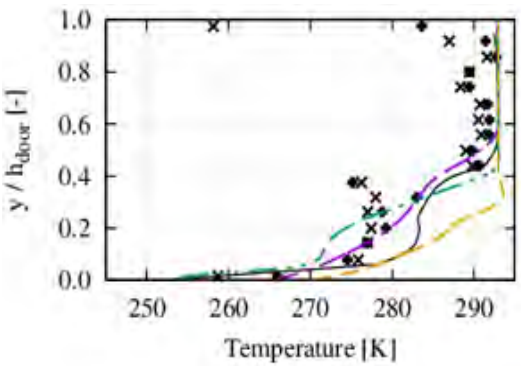

At 40 s

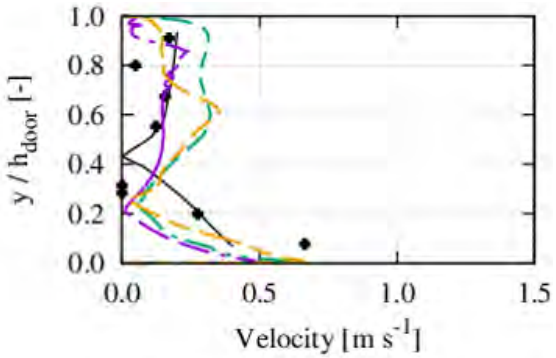

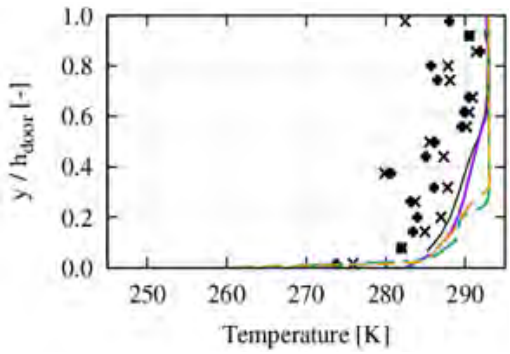

At 60 s

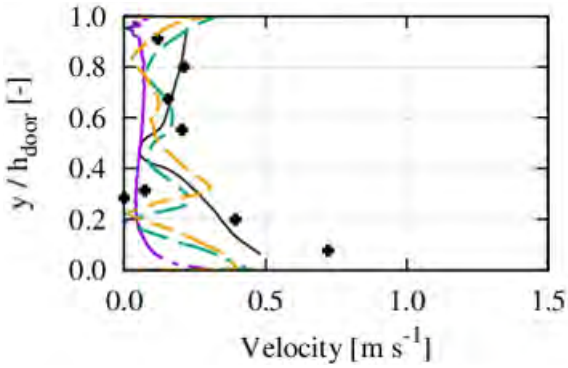

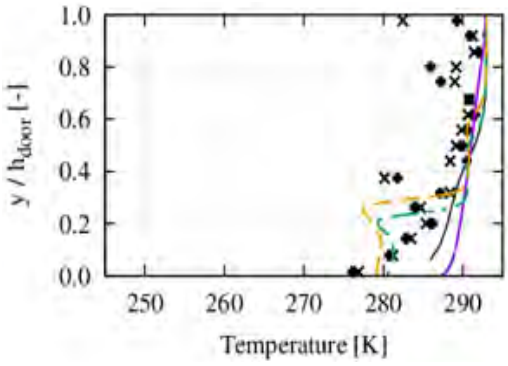

Figure 3: Axial distributions of the streamwise mean velocity (left) and temperature (right) at four different times. Comparisons between the experimental (symbols) and numerical (–) data of Lafaye de Micheaux et al. (2015) and the present simulations: (– -) 3D /adiabatic walls, (– -) 2D / adiabatic walls and (– -) 2d / heat losses

For the benchmark study, a baseline case with container and wind tunnel initial temperatures of respectively 253 K and 293 K is modeled using three numerical configurations: (i) 3D domain without heat losses through the container walls, (ii) 2D domain with conducting container walls and (iii) 2D domain with adiabatic walls. At t=0 s, the back door is fully (and instantaneously) open.
The axial distributions of the mean velocity and temperature at the door opening are displayed in Fig. 3 for t=10 s, 20 s, 40 s and 60 s. The present numerical results are compared with the experimental and numerical data of Lafaye de Micheaux et al. (2015). These authors used a 2D unsteady realizable k-ε model. A good general agreement is observed whatever the numerical assumptions. The 3D numerical setup seems to better fit the experimental data, in particular at t=10 s and t=40 s. Both 2D approaches show good accuracy and even a better capture of the velocity profile at t = 60 s. Due to the measure uncertainty reported by these authors, no definitive conclusion can be drawn from these profiles.
Regarding the temperature distributions, at t = 10 s, the air flow is yet in an early stage not far from the initial step profile, with a constant temperature close to 293 K for $y/h_{door}>0.4$ and a large temperature gradient along the trailer bottom. No distinguishable differences are seen between all the numerical setups. As the time passes, the profile evolves into a curved shape with a maximum temperature of about 289 K. All numerical approaches seem to overpredict its maximum by about 1 K. At instants t=20 s and t=40 s, both 2D solvers fail to fully replicate the experimental profiles for $y/h_{door}\leq0.2$, which is particularly noticeable for the 2D case with adiabatic walls at t=20 s. Nonetheless, the differences are of the same range as the dispersion of the experimental data. Important deviations are also observed in the near-wall regions, particularly for $y/h_{door}\rightarrow1$, where the numerical models predict a constant wall temperature of 293K whereas the experimental data reveals an important temperature gradient. The temperature gradient at the bottom is well captured, specially by the 2D models.

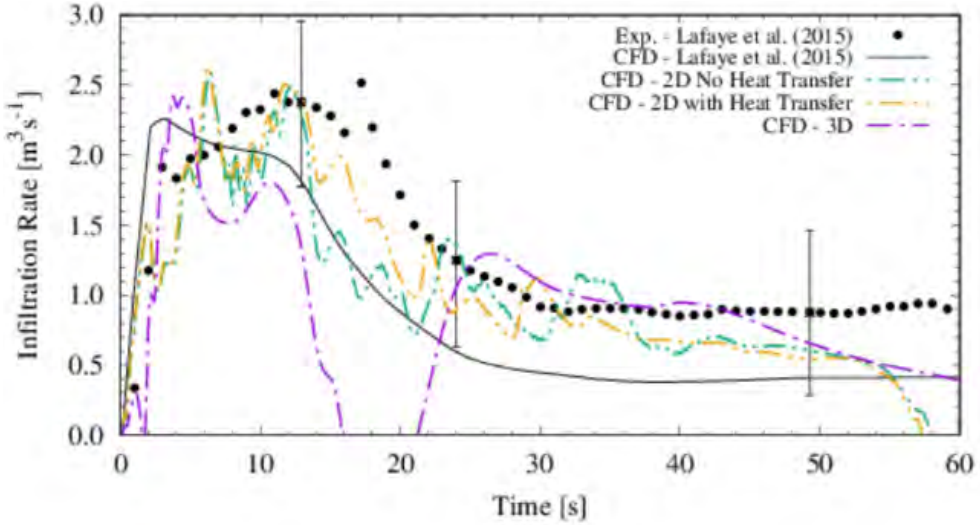

Figure 4: Temporal evolution of the infiltration rate through the door. Same legend as Figure 3

Fig. 4 displays the temporal evolution of the infiltration rate, i.e. the time dependent volume flow rate across the doorway. It accounts for the external humidity level from the surroundings. The determination of this infiltration rate is fully detailed in Lafaye de Micheaux et al. (2015). It is noteworthy first that the experimental uncertainty on this quantity is huge as reported on the figure. The three numerical setups are able to properly capture the main features of the experimental results, in particular the initial flow acceleration and the time needed for reaching a steady state (after approximately 32 s). The greatest difference is attained by the 3D model for the period between 11 s and 22 s, which coincides with the passing of a large eddy across the doorway, implying recirculation and thus negative infiltration values for a short period. It is besides unclear if the experimental procedure properly reports these structures as the reported values are averaged

over the door centerline, whereas the 3D results comprise a full integration over the door surface. This would also explain the better fit of both 2D models.
As a conclusion, although the 3D approach shows a better overall agreement with the experimental data, both in terms of velocity and temperature profiles across the door, it does not bring a significant improvement over the results obtained with the 2D models. The same can be concluded with regards to the inclusion of heat conduction across the container walls. Therefore, given its better compromise in terms of complexity versus accuracy, the 2D setup with adiabatic walls has been chosen for modeling the refrigerated container with eutectic plates.

3.2. Heat and Mass Transfer within the Trailer Equipped with Eutectic Plates

The truck trailer equipped with 3 eutectic plates and fans, as described in Section 2.1, is now considered in 2D with adiabatic walls. Fig. 5 reports 2D maps of the temperature and velocity fields for a closed trailer with an interplate spacing g=0.1 m. Fans suck air from the trailer to the plate region. As shown in Fig. 4, the transient period is usually short such that if the doorway is not open, the steady-state regime is attained after less than 1 min. The temperature is well homogenized in the trailer, around -24ºC, except close to the separation wall and between the plates. The most important point is that temperature is not uniform when comparing it between plates 1 and 2 and plates 2 and 3. It is mainly due to the geometrical configuration, where air is constrained to flow between plates 2 and 3. On the contrary, air between plates 1 and 2 is almost at rest. In the trailer, fans impose a large recirculation with a thin boundary layer along the bottom wall.

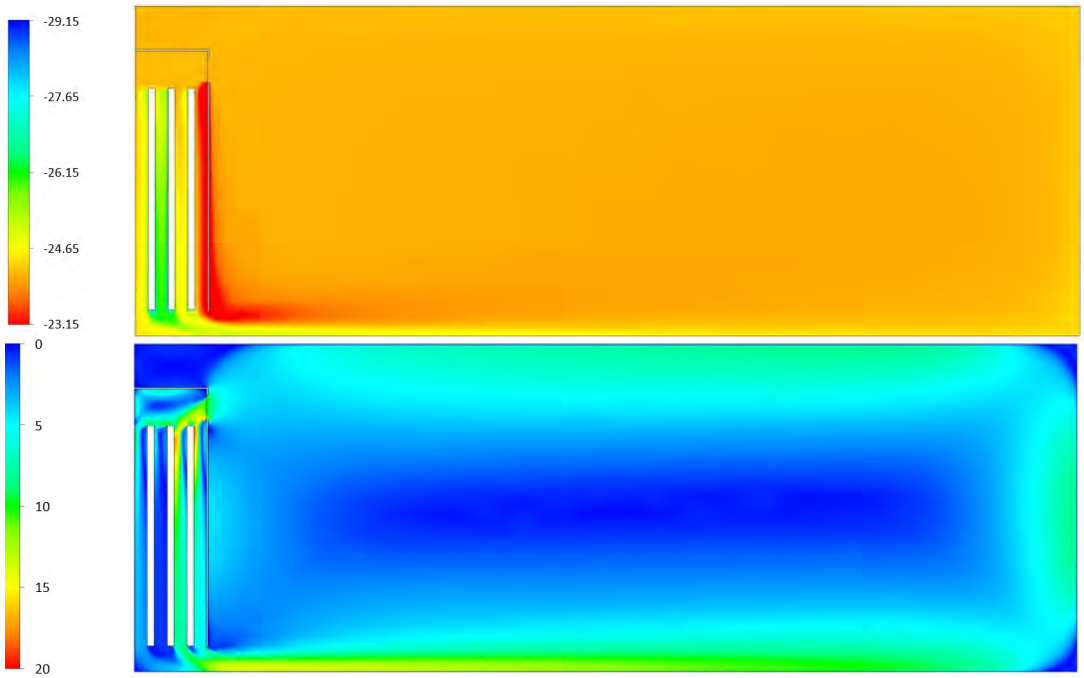

Figure 5: 2D maps of temperature (top, in ºC) and velocity (bottom, in m.s^{-1}) for the case with an interplate spacing g=0.1 m and a suction effect induced by the fans

To better distribute air between all plates, the influence of the interplate spacing g has been quantified. The results are summarized in Table 2 for three interplate spacings and the blowing and suction modes. They are reported in terms of the average air temperature and velocity. There is no real influence of g on these two quantities. The blowing mode provides the lowest average temperature whatever the value of g. The case with g=0.06 cm induces the lowest temperature in the loading region and has been chosen in the following.

Table 2. Influence of the interpolate spacing g (=f=h) on the average air temperature and velocity in the loading and plate regions of the trailer

g (cm)	Average temperature (□C)				Average air velocity (m.s^{-1})			
	Loading region		Plate region		Loading region		Plate region	
	blowing	suction	blowing	suction	blowing	suction	blowing	suction
0.036	-22.88	-21.03	-22.31	-21.69	3.42	3.85	11.51	11.62
0.06	-24.06	-22.63	-23.53	-22.84	3.09	3.64	7.07	7.24
0.10	-23.52	-21.52	-23.37	-22.29	2.94	3.74	5.16	4.60

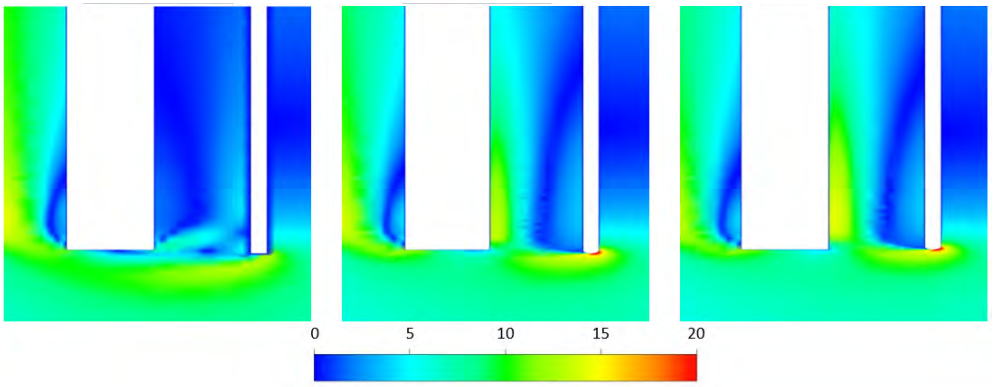

Figure 6: 2D maps of the velocity magnitude (m.s^{-1}) for the case with an interplate spacing g=0.06 m and a blowing effect induced by the fans. Zooms along the bottom wall between the separation wall and the first plate. From left to right: base case, rounded separation wall, rounded separation wall with d=e

Fig. 6 displays 2D maps of the velocity field for the most favorable case (g=0.06 m and blowing mode) at the bottom of the spacing between plate 3 and the separation wall. It is noticeable that contrary to the case g = 0.1 m, air flows easily between plates 2 and 3 but remains almost at rest between plate 3 and the separation wall. To improve the air distribution, two small geometrical modifications have been introduced: the bottom of the separation wall has been rounded (middle, Fig. 6) and then the separation wall has been aligned vertically with plate 3 (d=e). Rounding the bottom of the separation wall improves the air passing between this wall and plate 3. It is even more improved when aligning the plate and the wall. A geometrical optimization is however still required to prevent from the formation of the recirculation zone observed at the back of plate 3 in these 3 cases (Fig. 6).

4. CONCLUSIONS

A numerical model has been developed and carefully validated to predict the turbulent flow and heat transfer inside a refrigerated truck trailer equipped with an innovative refrigeration system based on three eutectic plates. The model has been first validated against the experimental and numerical data of Lafaye de Micheaux et al. (2015). 3D effects are preponderant regarding the infiltration flowrate when the doorway is open. On the contrary, including heat losses by conduction and 3D effects does not influence significantly the velocity and temperature distributions at the midplane of the doorway. The k-ω SST silghtly improves the predictions of the realizable k-ε model of Lafaye de Micheaux et al. (2015).
Future developments should include a multiphase model to account for both the humidity of air and the phase change of the eutectic mixture. The major concern is besides the formation of ice along the plates, which blocks the heat transfer with the surrounding air. Large Eddy Simulations could also be performed to better predict the 3D coherent structures appearing when the doorway is open and which may be responsible for the mixing of the humid hot air from the surrounding with the dry cold air from the trailer.

ACKNOWLEDGEMENTS

The authors would like to thank the NSERC chair on industrial energy efficiency established at Université de Sherbrooke in 2014 and supported by Hydro-Québec, Natural Resources Canada (CanmetEnergy in Varennes) and Rio Tinto Alcan. The project has been initiated by a NSERC engage grant with FrygyCube. Calculations have been performed using the supercomputer Mammouth Parallèle 2 of Compute Canada's network, which is also gratefully acknowledged.

NOMENCLATURE

Acronyms

CFD	Computational Fluid Dynamics
UFANS	Unsteady Favre Average Navier Stokes

Greek letter

ρ_{air}	Air density (kg·m$^{-)}$

Symbols

g	Interplate spacing (m)
h_{door}	Height of the doorway/trailer (m)
U_{fan}	Heat flux (m·s^{-1})
t	Times (s)
y	Vertical distance (m)

REFERENCES

Azzouz, A., Gossé, J., Duminil, M., 1993. Détermination expérimentale des pertes de froid occasionnées par l'ouverture d'une porte de chambre froide industrielle, Revue Internationale du Froid 16 (1), 57-66.

Foster, A.M., Swain, M.J., Barrett, R., James, S.J., 2003. Experimental verification of analytical and CFD predictions of infiltration through cold store entrances, Int. J. Refrigeration 26, 918-925.

Hoang, M.L., Verboven, P., De Baerdemaeker, J., Nicolaï, B.M., 2000. Analysis of the air flow in a cold store by means of computational fluid dynamics, Int. J. Refrigeration 23, 127-140.

Lafaye de Micheaux, T., Ducoulombier, M., Moureh, J., Sartre, V., Bonjour, J., 2015. Experimental and numerical investigation of the infiltration heat load during the opening of a refrigerated truck body, Int. J. Refrigeration 54, 170-189.

Tassou, S.A., De-Lille, G., Lewis J., 2007. Food transport refrigeration, Report from Brunel University.

Tso, C.P., Yu, S.C.M., Poh, H.J., Jolly, P.G., 2002. Experimental study on the heat and mass transfer characteristics in a refrigerated truck, Int. J. Refrigeration 25, 340-350.

UN Economic commission for Europe – Inland Transport Committee, 2003. ATP as amended on 7 November 2003 – Agreement on the International Carriage of Perishable Foodstuff and on the Special Equipment to be used for such Carriage.

Manuscript ID: 54
DOI: 10.18462/iir.icr.2019.0054

An airflow enhancing floor cover to improve temperature uniformity in maritime refrigerated containers

Leo J.S. LUKASSE, Marcel G. STAAL, Edo B. WISSINK
Wageningen UR Food & Biobased Research
6700 AA Wageningen, The Netherlands, leo.lukasse@wur.nl

ABSTRACT

In maritime refrigerated containers air is drawn from just below the ceiling into the refrigeration unit, where it is cooled to the desired temperature and then supplied into 60 mm high longitudinal T-bars, which make up the container floor. Cargo temperatures at the door-end are usually 2 °C higher than the supply air temperature. A better air flow distribution could improve the temperature uniformity. In earlier work four different air flow enhancing floor cover shapes were tested in a climate chamber.
The aim of this study is to assess the effectiveness of the best of those four air flow enhancing floor covers in a field experiment with commercial container shipments from South Africa to The Netherlands. Three test containers contained that air flow enhancing floor cover, three reference containers did not. All other parameters were, to the extent possible, the same for all containers.
Based on the test results it is concluded that the tested air flow enhancing floor cover reduces the difference between the warmest and the coldest cargo temperature in shipments of precooled grapes by approximately 30%.
Keywords: air distribution, air flow, duct, refrigerated container, temperature difference.

1. INTRODUCTION

In maritime refrigerated containers air is drawn from just below the ceiling into the refrigeration unit, where it is cooled to the desired temperature and then supplied into 60 mm high longitudinal T-bars, which make up the container floor. Door-end temperatures are usually up to 2 °C higher than supply air temperature.
In earlier work Lukasse & Staal (2018) found that air flow enhancing T-bar floor covers (hereinafter referred to as 'air flow enhancers') can help to guide more air towards the door-end and hence create more uniform temperatures. The subject of this study is a large scale field experiment to assess the effectiveness of the best air flow enhancer found by Lukasse & Staal (2018).
The aim is to experimentally assess the effect of that air flow enhancer on temperature gradients during real reefer container transport of grapes.

2. THEORY

2.1 Air flow distribution in reefer containers

As already explained in Lukasse & Staal (2018) for climate control in contained spaces conditioned air needs to be guided to the place where it is needed. This is typically done by air ducts. For example virtually every office building has these air ducts, usually hidden behind the ceilings. In the design of air ducts the diameter of the ducts is tuned to air flow rates: wide ducts close to the air conditioning unit, and small ducts delivering the air to the most distant office space. The relatively high air flow resistance of the air duct outlets, as compared to the resistance inside the ducts, helps to achieve a relatively even air distribution throughout the office building.

Reefer containers have a T-floor. The T-floor exists of 35 longitudinal T-bars extending over the complete length of the container's cargo space (see Fig. 1). T-bars are the air ducts of reefer containers, but their design is rudimentary: the cross section is the same over the complete length, and the air flow resistance of the air outlet at the top of the T-bars is very low. Hence most air escapes from the ducts before reaching the container door-end if no further measures are taken. Therefore dedicated air flow enhancers or cargo stowage patterns, closing off the right areas of the T-bar top openings, are a means to guide air to where it is needed and thus improve temperature management. That's why the use of fillers, also known as dunnage is recommended (see e.g. anonymous, no year; de Haan, no year; Montsma et al., 2011). Also covering parts of the floor has been reported (Cronje et al., 2015; Defraeye et al., 2016; Elíasson et al., 2013). Lawton (1995; 1999) presents an L-shaped board placed against / on top of the door-end pallets with the aim to exploit the fact that air in side T-bars warms more than in centre T-bars. The test results reported in Lawton (1999) concern a hand-stowed cargo, while there is no mentioning of palletized cargo. The system is especially meant for tight stows. For loads of trays, specifically facilitating horizontal air flow, even more complex air guidance systems have been proposed (Dodd & Worthington-Smith, 2006).
Lukasse & Staal (2018) were the first to propose a trapezoid shape air flow enhancer, covering the major part of the floor. They report a nearly 50% reduction of cargo temperature differences, measured in climate chamber tests. The subject of this study is to assess the effectiveness of that air flow enhancer in real transports.

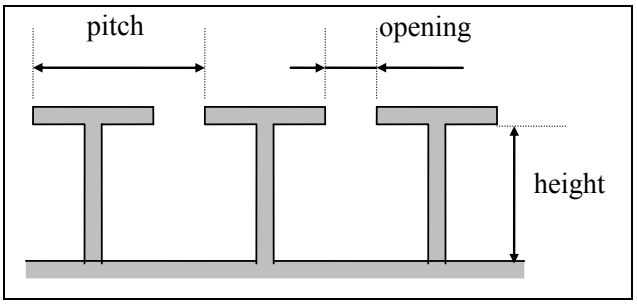

Fig. 1, schematic cross section of a T-bar floor section. Standard dimensions in 40ft HC reefers: height = 60 mm, pitch = 63.5 mm, opening = 35 mm.

2.2 Key performance indicators

In an experimental study on temperature distribution in reefer containers lots of temperature measurements need to be evaluated, and somehow condensed to one or a few simple measures. In climate chamber tests one would typically create a pure steady state. That is not possible in field experiments. Therefore a practical approach needs to be taken.
Table 1 lists the key performance indicators used to evaluate the data collected by the experiment's 31 loggers per container, which are more or less evenly distributed throughout the container load. The KPIs will be explained in the following paragraphs.

Table 1, key performance indicators (KPIs) used to evaluate the results

Name	Description
$\overline{T}$	average over all loggers and all sampling instants
std(*T*)	standard deviation over all loggers and all sampling instants
$(warmest\text{-}coldest)_{all\_trip}$	Warmest time-averaged sensor minus coldest time-averaged sensor in a container. The time-average is taken over the whole trip.
$(warmest\text{-}coldest)_{hot\_ambient}$	Warmest time-averaged sensor minus coldest time-averaged sensor in a container. The time-average is taken over the 48 hours period where ambient temperature was highest.
$(coldest\ sensor\ ID)_{hot\_ambient}$	Location of the sensor which recorded the coldest time-averaged temperature during the 48 hours period where ambient temperature was lowest.
$(warmest\ sensor\ ID)_{hot\_ambient}$	Location of the sensor which recorded the warmest time-averaged temperature during the 48 hours period where ambient temperature was highest.

$\overline{T}$ is just one number, being the average over the temperatures recorded by all loggers over all sampling instants from stuffing till unstuffing:

$$\overline{T} = \frac{\sum_{ti=1}^{Ni}\sum_{s=1}^{Si} T(s,ti)}{Ni*Si} \quad [°C] \quad (1)$$

with

T(*s,ti*) = the temperature recorded by logger *s* on time instant *ti.*

Si = total number of loggers per container (= 31).

Ni = total number of sampling instants from stuffing till unstuffing.

Reefer containers set at -0.5 °C control the supply air temperature measured by the unit's supply air temperature sensor to set point. A low mean temperature is therefore indicative of more uniform temperatures. However the unit's supply air temperature sensor is not perfect. A sensor offset of e.g. +0.1 °C reduces the temperature at all locations in the container by 0.1 °C, thus reducing the mean temperature, without affecting temperature uniformity. Hence solely analysing mean temperature is not good enough.

Standard deviation does not suffer the above described weakness. The standard deviation *std*(*T*) of the temperature readings recorded by all loggers over all sampling instants from stuffing till unstuffing:

$$std(T) = \sqrt{\frac{1}{Ni*Si-1}\sum_{ti=1}^{Ni}\sum_{s=1}^{Si}(T(s,ti) - mean\ temp.)^2} \quad [°C] \quad (2)$$

In general, a low standard deviation indicates that the data points tend to be close to the mean value of the data set. Assuming normally distributed temperature readings, 68% of the readings are within the range $\overline{T}$ ± *std*(*T*). Hence, the lower *std*(*T*) the more uniform the temperatures within the container. Another criterion, insensitive to possible unit sensor faults, is the difference between the warmest and the coldest logger. $(warmest\text{-}coldest)_{all\_trip}$ is the warmest time-averaged logger minus coldest time-averaged logger in a container, where the time-average is taken over the whole trip:

$$(warmest - coldest)_{all\_trip} = \max_s\left(\frac{\sum_{ti=1}^{Ni}T(s,ti)}{Ni}\right) - \min_s\left(\frac{\sum_{ti=1}^{Ni}T(s,ti)}{Ni}\right) \quad [°C] \quad (3)$$

When ambient temperature is highest the temperature gradients inside the container tend to be biggest. Therefore it is informative to analyse the difference between the warmest and the coldest logger specifically during the period where ambient temperature was highest, this is done in $(warmest\text{-}coldest)_{hot\_ambient}$:

$$(warmest - coldest)_{hot\_ambient} = \max_s\left(\frac{\sum_{ti=ths}^{the}T(s,ti)}{the-ths+1}\right) - \min_s\left(\frac{\sum_{ti=ths}^{the}T(s,ti)}{the-ths+1}\right) \quad [°C] \quad (4)$$

where

ths = time instant defining the start of the period of hot ambient.

the = time instant defining the end of the period of hot ambient.

Finally, it is informative to know the locations of the coldest and the warmest spots. These are given in $(coldest\ sensor\ ID)_{hot\_ambient}$ and $(warmest\ sensor\ ID)_{hot\_ambient}$:

$$(coldest\ sensor\ ID)_{hot\_ambient} = \operatorname{argmin}_s\left(\frac{\sum_{ti=ths}^{the}T(s,ti)}{the-ths+1}\right) \quad [-] \quad (5)$$

$$(warmest\ sensor\ ID)_{hot\_ambient} = \operatorname{argmax}_s\left(\frac{\sum_{ti=ths}^{the}T(s,ti)}{the-ths+1}\right) \quad [-] \quad (6)$$

Apart from the KPIs described in Table 1 temperature contour plots for cross sections of the containers will be made to visualize temperature gradients throughout the containers at some moments during the trip.

3. MATERIALS AND METHODS

A field experiment was done in a commercial shipment of six standard 40 ft. HC reefer containers travelling at the same time in the same corridor. The three test containers contained an air flow enhancer, the three reference containers did not contain the air flow enhancer. All other parameters were as much as possible identical: all containers are 40 ft. HC reefers with Carrier PrimeLine refrigeration units, set point -0.5 °C, fresh air exchange closed. Manufacturing date is 2015 for five containers, and 2009 for one container. All containers are positioned on deck on tier 1, none of them at the outer bay. Hence all of them are shaded from direct sunlight and experience approx. the same ambient temperature. See Table 2 for detailed specifications of the journey. Just before unstuffing the data recordings from the refrigeration units' controllers were retrieved.

Table 2, trip details.

Characteristic	Value
date of stuffing	21-01-2017
place of stuffing	Gouda, South Africa
date of loading on vessel	26-01-2017
date of unloading from vessel	13-02-2017
date of unstuffing	14-02-2017
place of unstuffing	Barendrecht, The Netherlands
port of loading	Cape Town, South Africa
port of unloading	Rotterdam, The Netherlands

3.1 Packaging and stowage

Each container was stowed with 21 pallets according to the floorplan sketched in Fig. 3. Pallet 19 is a europallet (80 x 120 cm), all other pallets are standard pallets (100 x 120 cm). All grapes are cultivar Thompson Seedless, class 1, of regular berry size.
A standard pallet carries 5 stacks of 25 trays. The height of the pallets stacked with trays is 2.40m. Trays are made of corrugated cardboard, and measure L x W x H = 60 x 40 x 9 cm. The bottom of the trays contains four vent openings of ø25mm. The trays have an open top. In the upper end of the long sides the trays have an opening of 33 x 220 mm, allowing for some horizontal air flow.
When filling a tray first one LDPE liner is placed. 11 Punnets with grapes are placed inside the liner. One SO_2 pad is placed on top of the punnets, then the liner is folded over the punnets and SO_2 pad, and non-hermetically closed with three small adhesive tapes. The liners contain 52 vent openings of ø6mm, evenly distributed over the sides, and the outer areas of top and bottom area folded around the 11 punnets.
The space for vertical air flow through a pallet load is very limited, because vent openings in the bottom of trays are limited in size and number and effectively blocked by the liner inside the tray. The space for horizontal air flow through a pallet load is also limited. The short sides of trays have no vent openings. The long sides of trays have a vent opening, but most of this area is obstructed by punnets folded in the liner. Moreover, the bottom of the next tray ± rests on top of the punnets in a tray. Possibly only the three stacks next to each other, with connected vent openings in the long tray sides, allow for some horizontal air flow through the pallet load. See Getahun et al. (2017) for possible consequences on temperature gradients.

3.2 Air flow enhancing T-bar floor cover

The field trial's airflow enhancers were provided by www.otflow.com. The company manufactures air flow enhancers based on the shape of the best air flow enhancer found by Lukasse & Staal (2018). For ease of manufacturing the dimensions deviate a little from those of the best floor cover reported in Lukasse & Staal (2018). See Fig. 2 for a sketch of the air flow enhancer used in this trial, including its dimensions.
Thanks to the trapezoid shape first the wall-side T-bars open up. The further from the unit-end the more side T-bars open up. This favourably stimulates air, leaving the T-bars before the door-end, to flow between the cargo and the wall, where heat enters the container. The air in the centre T-bars can only leave the T-bars near the door-end, and is used for removing heat from the door-end.

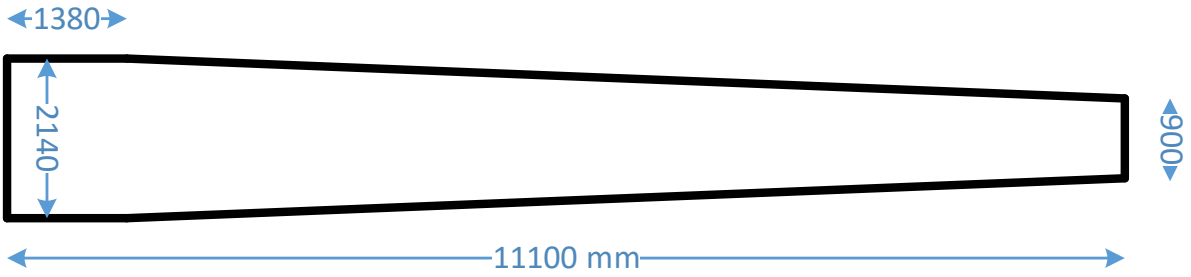

Fig. 2, sketch of air flow enhancer used in the experiment (dimensions in mm). The narrow end is placed at the door-end 580 mm from the end of the T-bar. As a result the 2140 mm wide section at the unit-end covers 1050 mm of T-bar and approx. 330 mm of baffle plate.

3.3 Measurements and instrumentation

In each container the temperatures were recorded with LogTag trix8 temperature loggers in 31 locations. All loggers are placed inside grape cartons. See Fig. 3 for the exact positions. The loggers

have a 0.1 °C resolution. Temperatures were logged at 10 min. intervals. Loggers were pre- and post-calibrated at 0 °C and 30 °C. The maximum observed deviation from reference is 0.3 °C @ 30 °C, and only 0.1 °C @ 0 °C.

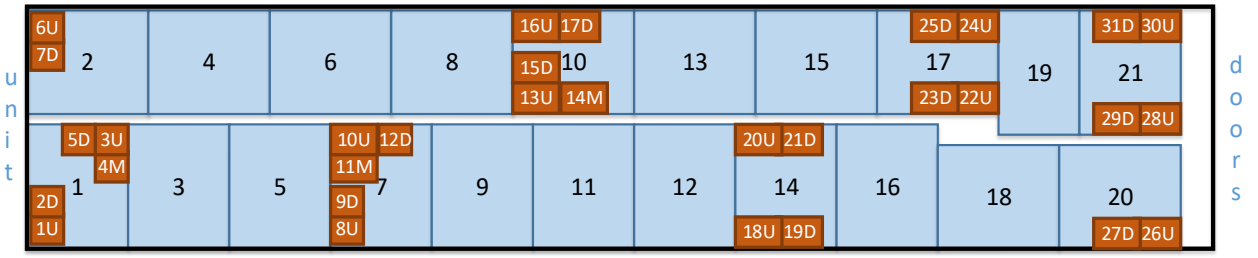

Fig. 3, placement of temperature recorders in all trial containers (top view). Red squares indicate positions of temperature logger numbers, U = Up (top layer), D = Down (bottom layer), M = Middle (layer 12). All Upper loggers are drawn in the right position. D- and M- loggers are positioned right underneath the U-loggers. It's just for ease of drawing in the 2D plane that they're drawn beside each other.

4. RESULTS

The data recordings retrieved from the refrigeration units' controllers (not shown) confirm that all units operated normally. The unit datalogs also recorded ambient temperature. The warmest ambient temperatures are recorded between 31-01-2017 and 02-02-2017, day 10 till 12 of the trial. In that period all six units record very similar ambient temperatures, fluctuating between 26 and 35 °C.

4.1 Temperatures recorded by experiment's loggers

Two of the 186 loggers went missing, all others recorded flawlessly. Table 3 lists the values for the KPIs defined in section 2.2. Columns 2 till 7 present the values for the six trial containers.

Table 3, key performance indicators per container (A till C are containers with air flow enhancer, and D till F without).

KPI	A	B	C	D	E	F
$\bar{T}$	0.1	0.2	0.2	0.4	0.1	0.4
$std(T)$	0.6	0.6	0.5	0.8	0.7	0.7
$(warmest\text{-}coldest)_{all\_trip}$	1.6	2.0	1.6	2.4	2.3	2.9
$(warmest\text{-}coldest)_{hot\_ambient}$	2.2	2.6	1.9	2.9	3.2	3.6
$(coldest\ sensor\ ID)_{hot\_ambient}$	7	4	7	4	7	4
$(warmest\ sensor\ ID)_{hot\_ambient}$	30	18	27	18	26	28

In Table 3 the mean temperature in container E is distinctly lower than in containers D and F. The cause is unclear, but may *e.g.* be due to an offset of the unit's supply air temperature sensor. The other criteria are less ambiguous.

The three lowest standard deviations $std(T)$ are observed in the three containers with air flow enhancer, showing that the air flow enhancer helps to reduce temperature gradients. The criteria $(warmest\text{-}coldest)_{all\_trip}$ and $(warmest\text{-}coldest)_{hot\_ambient}$ show the same: the smallest temperature differences are found in the containers with air flow enhancer.

Compare $(warmest\text{-}coldest)_{all\_trip}$ for container (A, B, C) to container (D, E, F) to see that the air flow enhancer reduces the average difference between warmest and coldest temperature by approx. 30%. The same holds during the hottest part of the trip (see '(warmest-coldest), hot ambient' in Table 3).

The air flow enhancer has no clear effect on the location of the coldest spot: $(coldest\ sensor\ ID)_{hot\_ambient}$ is 4 in container B, D and F, and 7 in container A, C, and E. As illustrated in Fig. 3 both are located in the lower half of the two unit-end pallets.

The air flow enhancer has no clear effect on the location of the warmest spot: $(warmest\ sensor\ ID)_{hot\_ambient}$ is different in nearly every container, but all locations are in the door-end half of the container, mostly near the doors and against the ceiling. See Fig. 3 for illustration of sensor locations.

Another informative, though more qualitative, way of analysing temperatures is by looking at contour plots. Fig. 4 present the contour plots of temperatures for a side view of the containers at moment of the trip where ambient temperature was highest. The position of sensors in the 3D container is defined by (length, width, height). Fig. 4 plots in the 2D surface spanned by (length, height), using all 31 sensors per container. When at a specific (length, height)-combination multiple sensors are present, the figures present the average of those sensors. For example the temperature at (length, height) = (0, 0) is the average of the readings from sensors 2 and 7, while the temperature at (length, height) = (1.0 m., 0) is the reading of sensor 5 (see Fig. 3).

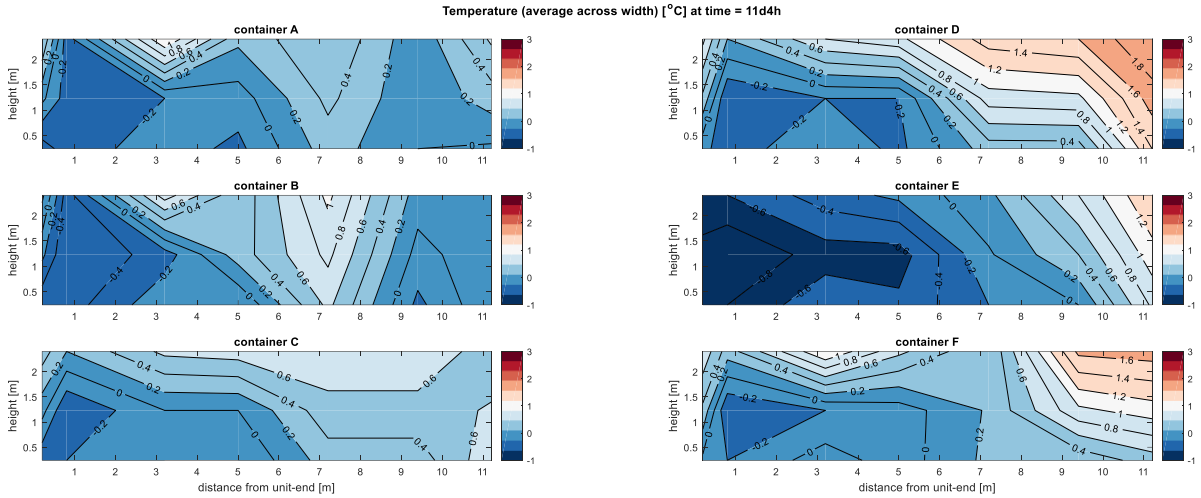

Fig. 4, contour plot of temperatures (side view) when ambient temperature is highest (30 ~ 35 °C).

Fig. 4 nicely visualizes the effectiveness of the air flow enhancer in suppressing high door-end temperatures during hot ambient conditions.

5. DISCUSSION

A priori a concern was whether the air flow enhancer would limit the air flow in the lower parts of pallets 1 till approx. 7 too much, resulting in hot spots due to autonomous heat production in that zone. None of that was observed. Apparently, in this low respiring fruit, the air flow enhancer allows for sufficient airflow in the lower regions of the pallets at the unit-end.

The trial containers were carried on deck. Many reefer containers are carried in holds below deck. In the holds ambient temperatures are usually higher than on deck. Hence it is to be expected that in many shipments air flow enhancers will have a bigger effect than observed in this trial.

The air flow enhancer has a positive effect on temperature uniformity. How to appreciate that? In many cases the temperature effect may be too small to observe an effect on quality. Then the use of the air flow enhancer may be pointless. On the other hand the air flow enhancer has a positive effect on temperature, and therefore mitigates the risk of temperature-related quality issues.

How will the air flow enhancer perform in transport of different products? This trial proves the positive temperature effect of this air flow enhancer for a load of properly precooled grapes. Of course the results apply to a wider range of commodities. The same effect is to be expected in any load of properly precooled low-respiring product.

Where to use the air flow enhancer in practice is a commercial decision: it's a trade-off between extra costs, extra work and extra waste against a reduced risk of temperature-related quality issues. A shipment reaching the receiver with temperature-related quality issues concentrated at the door-end would have benefited from the air flow enhancer. It is probably not useful to apply the air flow enhancer in every grape transport. The use of the air flow enhancer is first of all recommended in transports of weak batches of temperature-sensitive products, travelling in trade lanes with long transit times and hot ambient conditions.

Another potentially interesting application domain of the air flow enhancer is in cold treatment shipments. Cold treatment shipments are shipments during which a cold treatment is applied to the fruit. Cold treatments are treatments meant to control specific pests associated with the shipments of fruit. Many quarantine authorities of fruit importing countries have their own authorized cold treatment schedules. All of them are based on the principle that a given pest insect, *e.g.*

Mediterranean fruit fly, cannot survive a temperature colder than *treatment limit* °C for *duration* days. In cold treatment shipments three temperature recorders have to be inserted in the fruit in prescribed locations. At least one of those locations is in a pallet near the doors. Failing to maintain the three recorded temperatures below the *treatment limit* °C for *duration* days can have large commercial impacts. An air flow enhancer increases temperature uniformity and hence increases the chance of complying with the protocol. For more details on cold treatment see *e.g.* Anonymous (2016).
It remains to be seen how this air flow enhancer performs in commodities which are not properly precooled or have a high autonomous heat production. In the (large volume) banana trade it is standard practice to stuff without precooling the fruit. Moreover bananas have a relatively high autonomous heat production. Therefore a test on a load of palletized bananas would be informative. Most informative would be a long shipment through hot climates, *e.g.* Ecuador to Europe in containers placed below deck.
During stuffing it turned out that the air flow enhancer could not stand the weight of the forklift. The cover tore in many places. In the experiment the tears were repaired with duct tape. This has been reason for Otflow to revisit the design of the air flow enhancer after the experiment. In the new design it is installed in parts such that the forklifts don't need to drive on it during stuffing.

6. CONCLUSIONS

This trial's air flow enhancing floor cover reduces the temperature difference between warmest and coldest measurement location in shipments of precooled grapes by approx. 30%.

ACKNOWLEDGEMENTS

This work is part of the GreenCHAINge Vegetables & Fruits project work package 1, which was jointly commissioned by Bakker Barendrecht, VEZET, Albert Heijn and Maersk Line. The commissioning companies jointly financed the research, with financial support by Foundation TKI Horticulture (the Dutch Ministry of Economic Affairs) (project number 623 909 0301, TKI number 1406-031). We acknowledge all of them for their contribution.
Scientific field experiments like this are only possible if all parties involved, give their full cooperation. That happened. We are therefore very grateful for the excellent support received from the trial partners Maersk Line (represented by Steen Aunstrup and Johann Bosman), Bakker Barendrecht (represented by René Geelhoed), Horizon Fruits (represented by Cobus van der Merwe) and Otflow (represented by Otto de Groot).

REFERENCES

Anonymous (no year). Hamburg Süd reefer guide.

Anonymous (2016). USDA treatment manual. By U.S. Department of Agriculture, Animal and Plant Health Inspection Services (USDA,APHIS). Available from www.aphis.usda.gov/import_export/plants/manuals/ports/downloads/treatment.pdf

Cronje P., Aunstrup S., Bosman J., Norrefeldt V., Sibiya G. (2015). Ambient loading of citrus fruit to cold sterilization markets – 2015 experiments.

Defraeye T., Nicolai B., Kirkman W., Moore S., Niekerk S. Van, Verboven P., Cronje P. (2016). Integral performance evaluation of the fresh-produce cold chain: A case study for ambient loading of citrus in refrigerated containers. Postharvest Biology and Technology. 112, pp. 1-13. Doi 10.1016.

Dodd M.C., Worthington-Smith P. (2006). Managing airflow in reefer containers benefits fruit quality. IIR-IRHACE, Auckland.

Elíasson S., Margeirsson B., Arason S. (2013). Improved reefer container for fresh fish. Matís - Icelandic Food and Biotech R&D report no. 01-13. ISSN1670-7192.

Getahun S., Ambaw A., Delele M., Meyer C.J., Opara U.L. (2017). Analysis of airflow and heat transfer inside fruit packed refrigerated shipping container: part II – evaluation of apple packaging design and vertical flow resistance. Journal of Food Engineering, pp. 1-12, DOI 10.1016/j.jfoodeng.2017.02.011.

Haan H. De (no year). De Beer's consolidated manual on the transportation of perishable cargo in reefer containers.

Lawton A.R. (1995). Controlling the temperature of cargo in a container. UK patent GB 2282873.

Lawton A.R. (1999). The splitter board system for improving temperature distribution in ISO containers. Vol. IV (paper 446) in proc. of ICR1999, Sydney, Australia.

Lukasse L.J.S., Staal M.G. (2018). Optimizing air flow distribution in maritime refrigerated containers. Acta Hortic. 1194. ISHS 2018. DOI 10.17660/ActaHortic.2018.1194.195. Proc. VIII International Postharvest Symposium: Enhancing Supply Chain and Consumer Benefits – Ethical and Technological Issues. Eds.: F. Artés-Hernández et al.

Montsma M., Staal M., Lukasse L.J.S. (2011). Optimizing shipment of lily bulbs in 40ft reefer containers. Wageningen UR Food & Biobased Research report no. 1246.

APPENDIX 1, TEST LOG

Date [dd-mm-yyyy]	Description of activities
14-12-2016	pre-calibration of temperature loggers
20-01-2017	preparation and labelling of experimental pallets
21-01-2017	stuffing of all six trial containers
13-02-2017	Retrieval of refrigeration units' data records in port of destination
14-02-2017	unstuffing of trial containers
15-02-2017	post-calibration of temperature loggers

Manuscript ID: 131
DOI: 10.18462/iir.icr.2019.0131

A Strategy for improved temperature control in the supply and processing stages of Surimi cold chain in India

Mani Sankar DASGUPTA[a], Srikanta ROUTROY[a], Kristina N. WIDELL[b], Souvik BHATTACHARYYA[a], Maitri THAKUR[b]

[(a)]BITS Pilani, Pilani Campus, Rajasthan 333031, India, dasgupta@pilani.bits-pilani.ac.in, srikanta@ pilani.bits-pilani.ac.in, souvik@pilani.bits-pilani.ac.in
[(b)]SINTEF Ocean, NO-7465, Trondheim, Norway, Kristina.Widell@sintef.no, Maitri.Thakur@sintef.no

ABSTRACT

Supply of raw material (fish) to the land-based Surimi processing plants in India involves harvesting of various fish species by motorized boats, mainly from the Arabian Sea. The catch is stored in compartments with ice for an average trip duration of 10 days. The raw material changes hand at the dock. The fish is washed with fresh water, manually unloaded, weighed and re-packed in iced crates. It is then transported in insulated trucks, either as whole fish or after it is manually headed and gutted (by pre-processors). Once inside the plant, the Surimi processing is essentially automated employing standard machinery. Ammonia based vapour compression systems are mostly used for supplying ice, for chilling of fresh water required during processing and deep freezing of Surimi slabs for storage. This paper explores improvement strategies for temperature control during the non-standard cold chain and also for meeting the in-plant cooling demand to improve product quality and energy efficiency.

Keywords: Surimi Supply Chain; Surimi Processing, Cold chain, Refrigeration, Energy efficiency

1. INTRODUCTION

Fishing and allied activities is a prominent provider of job and sustenance for a large population along the 7500 km long coastline of India. Apart from the catch from open sea, a larger share of fish for both domestic consumption and export comes from various inland rivers, ponds and water bodies under culture. It is estimated that about 60% of the domestic population consumes fish (Salim, 2016) but the annual per capita consumption of fish among fish eating population is only 8-9 kg, which is well below the global average. The domestic consumption also has regional bias towards fresh catch from sweet water sources such as river and farm fish. For India, the total earnings from sea food export was $7.08 billion during the financial year 2017-18 (Nambudri, 2018), of which 44% was generated from export of just one single species – white leg shrimp (Litopenaeus Vannamei). Whole frozen fish is the second largest export product and contributed to 25.6% in terms of quantity and 10.4% in terms of earning. Overall there was healthy growth of sea food export from India in recent years.

Among the processed seafood exported from India, Surimi is an important product, which had a value share of 2.5% of total export earnings. Surimi is minced and processed fish, exported in the form of frozen blocks, often made from inexpensive whitefish. Surimi is used as raw material for various processed food. Japan is by far the largest importer of Indian Surimi. Considering the large Surimi demand in USA, Japan, China and various European countries, there is potential to grow export from India. Market potential of Surimi derived ready-to-eat food made in India also may be explored.

A 2008 study (Raghuram and Asopa, 2008) pointed out the absence of requisite cold chain infrastructure in the supply side for the Indian Surimi industry as one of the main barriers for growth. Our survey also finds this as one of the major challenges. The current study named

ReValue (supported by Inno-Indigo) is a horizontal ERA-Net project with India, which focuses on improving the surimi value chain, by for example improving the cold chain. As part of this multi-lateral research initiative, several visits have been made to various fish landing docks, Surimi manufacturing units and Rest Raw Material (RRM) processing units for observation and measurements. In addition, two international workshops and group meetings were conducted to connect with both international research partners and industry stakeholders (Thakur, 2018).

2. THEORY AND METHODS

2.1. Temperature measurement

Low temperature storage is one of the most important factors to preserve fish quality and extend shelf life. The decay rate of both fish (raw material) as well as Surimi (product) are temperature dependent. Measurement and control of temperature of fish from the point of harvest until the processed fish reaches cold storage, needs constant vigilance to ascertain suitable temperature throughout handling and storage. Hand held digital thermometer (as seen in Fig. 1c) with an accuracy of ±0.5 °C is recommended by FAO for measuring temperature of wet fish (Smith, w/o year). The document also stressed that for large fish, there may be substantial difference between the surface temperature and core temperature, especially during freezing and thawing processes. Therefore, it is recommended that major part of the thermometer probe is inserted into the fish while measurement is taken and that the tip of the probe is near the centre of the largest cross sectional dimension of the fish (thermal centre of the fish). Since the fish sizes are small for Surimi (less than 20 mm in thickness), only the surface temperature were measured in this study, using quick response digital thermometer.

Fish harvested for Surimi is stored within layers of crushed ice. Melting ice with adequate water drainage facility ensures storage at 0 °C. When exposed to ambient temperatures (typically can go up to 35 ^{o}C), the small fishes for Surimi heats up relatively quickly owing to much greater surface area per unit volume helping in the heat transfer process.

Processed fish as Surimi can be stored long term (more than a year) in frozen condition. Various aspects of freezing of fish and fish products for long term storage and quality issues have been well studied (Johnston, et al. 1994, Gelman, et al. 2001, Burgaard, 2010, Dawson, et al. 2018). Burgaard (2010) experimentally investigated degradation effects on fish muscle over long-term storage within the range of −20 °C to −80 °C. It is established that lower the temperature, longer fish can be preserved.

2.2. Quality assessment

Freshness of iced whole fish depend upon the species and ambient temperature; for example, one of the shortest is for Cod (7 day) and one of the longest is for Red fish (14 days) (Hélène et al., 2010). The average duration of fishing excursions for a boat during this survey was found to be 10 days. No scientific study has been found in the open literature for Indian Surimi fish varieties in iced condition. Sensory evaluation of freshness is a standard and scientific practice for fish quality assessment, which uses standard tables and charts to interpret characteristics of fish as perceived by senses of smell, touch, colour, odour, texture, taste etc. European Union (EU) freshness grading scheme and Quality index method (QIM) are commonly accepted sensory assessment techniques that have been standardized for various fish species. QIM was developed by the European fisheries research institutes, in close cooperation with the seafood industry; sensory assessment is achieved in a safe and systematic process employing an objective quality assessment method. There are many studies (Howgate, 2015, Cheng et al., 2015) that reported experiments conducted over specific fish species such as evaluation of un-gutted European sea bass for storage in melting ice based on sensory assessment using EU scheme for a range of days of storage. While for up to 3 days of storage, the fish was found to be in the highest grade of E as per the EU Scheme, the fish quality was observed to deteriorate nonlinearly with passing days and beyond 17 days it was rendered *unfit for consumption* and the degradation process could be assessed using sensory assessment. In general, the QIM method is considered more objective and accurate compared to the EU Scheme to determine fish freshness. It is based on

characteristic changes that occur in raw fish related to the attributes of its outer appearance of the eye, skin, gill and odour etc. over a 0 to 3 scale and a cumulative score on all the evaluative are used for final assessment. QIM method suggests skin stiffness outcome to be segregated as following: Stiff, *in rigor mortis* – 0 (fresh); Firm elastic – 1; Soft – 2; Very soft – 3 (stale).

3. DESCRIPTION OF SURIMI SUPPLY CHAIN – RESULTS AND OBSERVATIONS

Surimi produced in India is essentially for the export market as domestic consumption of Surimi is almost non-existent. There are not many Surimi producers in India and majority of them are located along the west coast and sources raw material from the Arabian Sea. The raw material is mostly small size lean fish dominated by Pink Perch of 20-30 gm weight category (Fig. 1c), which otherwise do not fetch good price in the local market. The industry also faces a major challenge in terms of a seasonally variable and non-uniform supply of raw material.

Surimi is exported as frozen 10 kg slabs with a thickness of 55 to 60 mm. The price of Surimi in the international market varies according to colour, consistency and gel strength, apart from assurance of food safety. Surimi export market is quality conscious and good quality white Surimi having the right consistency fetches higher price and have greater demand. Freshness of fish arriving at processing plant plays a major role in deciding the output quality.

3.1. Handling of catch after haul

Shelf life of the whole fish is limited by enzymatic and microbial spoilage that sets in as soon as fish is harvested. The degradation rate is accelerated by warm and humid climate and this factor is especially relevant to weather condition at Indian sea coasts. Preservation of the catch after the haul, until it is unloaded at landing centres, is therefore important for fishermen.

It was observed during this survey that use of purse seines gear is predominantly the method for fish harvesting in western India. It is also a standard practice for fishing boats to carry crushed ice in some of the wooden/fibre compartments that are built into the boat deck. Fresh catch, after washing and sorting, are stored between layers of ice in such compartments. It may be noted that a catch is a mix of many varieties of fish species, which personnel on board separates and the suitable ones is stored separately in different compartments and the rest is discarded. In order of preference, the fish for Surimi is generally lower down the list of choice for the fishermen due to the price difference. For iced storage, fishermen use a thumb rule of 3:2 to 1:1 by volume of fish to ice in storage compartments. The quantity of ice appears to be sufficient for 10 to 15 days for storage in melting ice as per sample calculation provided (Huss, 1995, Thanu Agritech portal, 2014). However, it was observed that some fishing boats arrive with their iced compartments flooded with no solid ice left. In one case, fish surface temperature was measured as high as 9 °C on unloading, while ambient temperature was 25 °C. However, in majority of the cases, fish arrives well lumped with crushed ice inside the compartments.

Fish quality may also be affected due to inappropriate handling methods and storage or stacking condition which can lead to physical, chemical, biological and microbial changes in fish and may also lead to contamination. Time interval between hauling and actual storage is also important, during which fish post-mortem remain exposed to sun on the deck. It is prescribed (Reilly, 2000) that the wash water and ice used should be free of contamination. During the survey, we did not find any quality assurance measure in place for the supplied ice and water to the boats. Literature also cites benefits of use of 10 PPM chlorinated water for both ice and wash water towards abatement of bacterial contamination and slime formation on fishing gear and boat deck (Burns, 1985).

3.2. Fish handling at landing centres

The general practice we found is that unloading from boat is sequential with compartments containing fish for Surimi unloaded last. Sometimes a boat needs to dock at multiple landing centres to unload different variety of catch. Landing at multiple sites also extends the time from catch to processing, which can affect the quality of the Surimi. Simultaneous unloading was

observed at Mirkarwada Dock in Ratnagiri where many boats were found to predominantly cater to Surimi plant and this helps in reducing the time span from catch to processing.



Figure 1. Practice and processes at a fish landing centre

Water at varying ambient temperature is pumped to the containers in boat to remove ice from fish before unloading. De-icing is necessary at landing point to weigh the catch, as the raw material changes hand from fishermen to intermediate consolidators at this point. The unloading process is observed to be rather slow and clumsy, during which porters wearing rubber boots and gloves are observed to stand inside containers directly over iced fish and scoop out fish using small containers for transfer from boat to land. Fig. 1 a, exhibit the boat unloading practice and process at landing centres. Some limited spillage of small fish during handling was also observed. A study reported 10% damage of whole fish resulting from large heaping at hold and workers directly treading over fish while handling (Thanu Agritech portal, 2014). Fish is also subjected to sampling for limited sensory evaluation to ascertain its quality upon landing, which decides pricing. During this study, we essentially found finger press test to be conducted on fish samples to assess freshness. After weighing, the fish is placed in standard HDPE plastic crates between layers of crushed ice. The iced crates are then loaded into insulated trucks and are either sent directly to Surimi manufacturing plants or to one of the various heading and gutting centres. Near the landing site, there are a number of heading and gutting centres where the process is entirely manual. These centres also serve to a manual prawn de-shelling process, which as a business volume is perceivably much larger. These centres may also serve as intermediate holds for fish, before being sent to Surimi plants. However, we find this intermediate unchilling, storage and temperature abuse a matter of serious concern and avoidable with appropriate logistics planning.

3.3. Fish handling at Surimi processing plant

Fish for Surimi production, filled in standard plastic crates and mixed with ice, may arrive round the clock at the processing plant. Depending upon availability, the fish is either taken up immediately for processing or kept in a refrigerated room for up to 2 days at 4 °C. This is necessary for the processing plant as supply is not at regular interval. In most cases, the input raw material comes as de-headed and de-gutted, while the plant also maintains a small sorting and heading-gutting facility equipped with metal lined tables and manned by contract labour. Incoming raw material is washed to remove dirt and ice and weighed again before being fed to conveyer-cum-washing drum. The surface temperature of fish at this point ranges from 4 °C to 10 °C. The process hereafter is fairly standardised and automated with minimal human intervention. Throughout the processing stage, the temperature is maintained near 10 °C, essentially utilising cold water for the various wash cycles. From loading on the conveyor to final outgoing of Surimi slabs, fish meat spends about 2 hours inside the factory. The Surimi blocks are immediately after production wrapped in food grade plastic and then frozen in plate freezers. The evaporator temperature of the plate freezers is −40 °C and the Surimi slabs are frozen for about 2 hours. This reduces the core temperature of the Surimi slab to below −18 °C. The Surimi is then packed in cardboard boxes and transferred to a cold storage maintained at −18 °C. It is stored there before being dispatched in refrigerated trucks for export.

4. SUGGESTIONS FOR IMPROVEMENTS

4.1. Handling of catch after haul

Every care must be taken on the deck to shorten the time interval between catch and storing in crushed ice and also to avoid mechanical damage to fish and exposure to sunlight – the processes which can hasten fish degradation. This is important because once the freshness and nutritional value of fish is lost, it cannot be recovered in the processing stages. Immediate bleeding of fish after catch and/or gutting before chilling can help in preserving freshness but considering the small size of fish for Surimi and the large numbers in which they are caught, on-board manual gutting process is impracticable. Valuable RRM is also lost in this process. Discrete fishing site choice for specific varieties and use of appropriate mesh size of fishing net can potentially reduce the variety and size mix in a catch and thereby shorten on-deck sorting activities and delay in storage.

Ice and water used in the boat are loaded at the start of the trip and there is much needed quality assurance measure on the same in order to avoid bacterial and chemical contamination of fish. Fishing boats with on-board refrigeration facility is a common practice elsewhere in the world and can contribute in a big way towards enhancing fishing duration as well as fish quality. On-board refrigeration also opens up potential to explore use of RSW (Refrigerated Sea Water). For example, in Norway, pelagic fish (e.g. herring, mackerel, blue whiting) is stored in RSW tanks of capacity up to 300 m^3 (Widell et al., 2016). Deep sea water is considered to have sound biological property as organic material concentrations are nearly constant (Wiesenburg and Little, 1987) and have much lower concentration of dissolved as well as particulate organic carbon compared to sea surface or near shore. It contain about 3% salt thereby its phase change temperature is about −2 °C. Further heat capacity of sea ice is 2900 J kg^{-1} k^{-1} while that of fresh water ice is 2108 J kg^{-1} k^{-1}; this favourable thermophysical property of sea ice could be very helpful in fish preservation for a longer duration.

There is scope of use of better insulation material like EPS lining etc. inside the compartments in boat and on the compartment lead for preservation of temperature for a longer duration as suggested (Shawyer, et al. 2003). Alternately the complete storage compartments can be re-designed with suitable material along with provision for drainage of water, which at this point is missing.

4.2. Fish handling at landing centres

Manual boat unloading process at dock needs technology intervention which will reduce delay, decay, potential contamination and pilferage of fish. There is scope of redesigning containers for

holding fish, as mentioned earlier, which are detachable from boat and this can hasten the unloading process and also avoid physical damage to fish and loss. The container design also should aid weighing of fish and sampling process. A vertically integrated cold chain solution, where in each member of the supply chain like fishermen, consolidator etc. are owned or managed by the Surimi manufacturing company combined with appropriate tagging of containers can eliminate the need of weighing at the intermediate stage.

Maximum time that various Indian fish varieties used for Surimi can hold without ice in a fish processing line, i.e. the critical time, needs to be determined. It was also observed that he discards from the heading and gutting centres and Surimi plant are sent to RRM (rest raw material) processing centres located at considerable distance. The pricing level do not permit use of refrigerated truck or iced containers for such transport. Viability study and development of smaller RRM processing plants within short distance from the fish processing centres needs to be explored.

Appropriate scientific basis for accurate sensory assessment of Indian fish varieties for iced storage needs to be developed for improvement in food safety assessment.

4.3. Fish handling at Surimi processing plant

With a cycle time of only two hours in Surimi processing, the working temperature 4 to 10 °C maintained inside the plant is not crucial except for the waiting time of up to 2 days for some consignments. Ensuring regular supply through vendor development or vertical integration of supply chain is, therefore, important for maintaining input quality.

Both Surimi price and demand in International market are seasonally variable. This is another reason why Surimi manufacturers invest in large cold storages. It is also well known that Surimi gel strength, depending upon variety, deteriorate under long term storage even at frozen state as discussed in 2.1. The rate of degradation is lower with dip in cold storage temperature but at the same time, the operating cost of refrigeration will increase substantially. For example to maintain Surimi slabs at -23 °C in place of current practice of -18 °C, there will be about 20% hike in energy consumption cost. Hence there is a complex time – temperature – economic trinity of Surimi storage, which needs specific localized optimum solution. A Surimi manufacturer in India would like to know the optimum holding time and temperature combination to maximize profit in export market. There is scope of detailed thermoeconomic analysis and optimization of energy systems specific to Surimi storage.

The Surimi making process demands large amount of treated chilled water for multiple wash cycles. The water requirement is roughly 4 times the weight of raw fish input or 10 times the weight of Surimi produced (Pond, 1977). All the cooling demands during Surimi processing is met using an ammonia based vapour compression refrigeration unit. Since the refrigeration system was not designed specifically to meet the multiple cooling demands at various temperature, we observed generous retrofitting and changes done to the original setup, evidently the refrigeration system is not operating at its design or optimum condition. Further, there is a potential of utilizing the warm side of the refrigeration system for water heating (Singh and Dasgupta, 2017), which can be gainfully utilised for cleaning of premises and food equipment. Use of CO_2 – Ammonia cascade system for refrigeration should also be explored, which has potential to reduce energy consumption and also decrease ammonia charge and thereby improving safety.

Large amount of wash water is discarded as it contains biological material (fish fat and water soluble proteins) and is not suitable for re-circulation, but the temperature is still below ambient. There is potential of ingenious use of the same for pre-chilling of incoming fresh water.

5. CONCLUSIONS

Indian Surimi industry has a good growth potential both in terms of market volume and market spread. However, low technology penetration in fishing and handling practices as well as limitations in cold chain infrastructure in the supply side of the Indian Surimi industry are the main barriers for growth. Technology intervention accompanied by awareness and training programmes

for the people working at various stages of raw material procurement, processing and storage can enhance quality and assure necessary food safety.

Fish is one of the most perishable food items and adequate measures of temperature control along the entire post-harvest supply chain needs to be ensured to reduce quality degradation. Reduction of the many manual touch points along the supply chain can be a target for improving the Surimi supply chain. This study has also shown that the present process in place provides sustenance to a large number of semi-skilled and unskilled labour force in coastal area.

With the world population set to approach an estimated 9 billion by 2050, against a background of finite natural resources, we need renewable biological resources for securing healthy food and animal feed to meet the nutritional requirements of the growing population. Surimi, derived from low value fish, is a valuable source of protein. The wash water and the rest raw material from this industry could be used for making nutrition rich food additives; they together can address food security issues for a large and populous country such as India.

This study has also shown that the present process in place for fish handling provide sustenance to a large number of semi-skilled and unskilled labour force in coastal area. Any sustainable solution for improvement cannot overlook the socio-economic and political challenges involved in implementation.

ACKNOWLEDGEMENTS

This work is supported under grant from DBT India, ref. BT/IN/INNO-Indigo/12/NK/2017-18 and NFR Norway project number 281262.

REFERENCES

Burden, M., Gilbert, G., Sylvia, 2004. Optimal storage temperature design for frozen seafood inventories: application to pacific whiting surimi, IIFET 2004 Japan Proceedings, Jan.

Burgaard, M. G., 2010. Effect of frozen storage temperature on quality-related changes in fish muscle: Changes in physical, chemical and biochemical quality indicators during short- and long-term storage. Kgs. Lyngby, Denmark: Technical University of Denmark (DTU)

Burns, F. D., 1985. Tuna handling and refrigeration on Purse seiners, NOAA Technical Memorandum, US Deptt. of Commerce, August.

Cheng, J. H., Sun, D. W., Zeng, X. A., Liu, D., 2015. Recent Advances in Methods and Techniques for Freshness Quality Determination and Evaluation of Fish and Fish Fillets: A Review, Critical Reviews in Food Science and Nutrition, 55:7, 1012-1225.

Dawson, P., Al-Jeddawi, W., Remington, N., 2018. Effect of Freezing on the Shelf Life of Salmon, Int. J. of Food Science, vol. 2018, Article ID 1686121, 12 pages,

Gelman, A., Glatman, L., Drabkin, V., Harpaz, S., 2001. Effects of storage temperature and preservative treatment on shelf life of the pond-raised freshwater fish, silver perch (Bidyanus bidyanus), J Food Prot. Oct. 64(10):1584-91.

Hélène L. Lauzon, Björn Margeirsson, Kolbrún Sveinsdóttir, María Guðjónsdóttir, Magnea G. Karlsdóttir and Emilía Martinsdóttir, 2010. Overview on fish quality research. Impact of fish handling, processing, storage and logistics on fish quality deterioration, Icelandic Food and Biotech R&D, Matís Report 39-10,

Howgate, P., 2015. A History of the Development of Sensory Methods for the Evaluation of Freshness of Fish, Journal of Aquatic Food Product Technology, 24:5, 516-532.

Huss, H. H., 1995. Quality and quality changes in fresh fish, FAO fisheries technical paper- 348, Rome, FAO.

Johnston, W. A., Nicholson, F. J.; Roger, A., Stroud, G. D., 1994. Freezing and refrigerated storage in fisheries, FAO Fisheries Technical Paper. No. 340. Rome, FAO. 143p

Nambudri, S., 2018. India's seafood exports cross $7 billion, TNN July 2 2018, available at https://timesofindia.indiatimes.com/business/india-business/indias-seafood-exports-cross-7-billion/articleshow/64830505.cms

Pond, G. R., 1977. Water supplies for Fish Processing Plants, Fisheries and Environment, Technical Report Series, Canada – Undated, available at http://www.dfo-mpo.gc.ca/Library/59329.pdf

Raghuram, G., Asopa, V. N., 2008. Issues in Infrastructure for Export of Marine Products from India, IIM Ahmadabad Working Paper No. 2008-07-04 July

Reilly A., 2000. Discussion paper on the use of chlorinated water, WHO, Ålesund, Norway, 5-9 June.

Salim, S., 2016. Fish consumption pattern in India, experts - Overview, Food & Beverage News, August 1-15.

Shawyer, M., Avilio F. Medina Pizzali, A. F. M., 2003. The use of ice on small fishing vessels, FAO Fisheries Technical Paper. No. 436. Rome, FAO. 2003. 108 pp

Singh, S., Dasgupta, M. S., 2017. CO2 heat pump for waste heat recovery and utilization in dairy industry with ammonia based refrigeration Int. J. of Refrigeration 78, 108-120.

Smith, J. G. M., (w/o year) Temperature measurement in the fish industry, Torry Advisory Note No. 94 available at http://www.fao.org/wairdocs/tan/x5992e/X5992e01.htm

Thakur, M., 2018. ReValue: Innovative technologies for improving resource utilization in the Indo-European fish value chains, available at https://www.sintef.no/prosjekter/revalue/

Thanu Agritech portal, 2014. Central Institute of Fisheries Technology, Cochin available at http://agritech.tnau.ac.in/fishery/fish_fishingtech_onboard.html

Widell, K. N., Nordtvedt, T. S., Eikevik, T. M., 2016. Natural refrigerants in refrigerated seawater systems on fishing vessels, 1156: 12th IIR Gustav Lorentzen Natural Working Fluids Conference, Edinburgh.

Wiesenburg A. D., Little J. Brenda, 1987. A synopsis of the Chemical / Physical properties of Sea water, Ocean Physics and Engineering, 12 (3&4), 127-165

Manuscript ID: 149
DOI: 10.18462/iir.icr.2019.0149

Surimi value chain in India: A strategy for improved resource utilization

Srikanta ROUTROY[(a)], Manisankar DASGUPTA[(a)], Maitri THAKUR[(b)], Souvik BHATTACHARYYA[(a)], Kristina N. WIDELL[(b)]

[(a)]BITS Pilani, Pilani Campus, Rajasthan, 333031, India, srikanta@pilani.bits-pilani.ac.in, dasgupta@pilani.bits-pilani.ac.in, souvik@pilani.bits-pilani.ac.in
[(b)]SINTEF Ocean, NO-7465, Trondheim, Norway, Maitri.Thakur@sintef.no, Kristina.Widell@sintef.no

ABSTRACT

In India, the supply stage of surimi value chain starts with fish harvested in sea by small boats and is completed when either whole or headed-and-gutted fish reaches the surimi processing plant. The identified critical factors which play a crucial role in maintaining fish and rest raw material quality are fragmented ownerships, fishing area identification, fishing boat and its capacity, old boat unloading practice, real time information sharing, visual inspections of fish quality at various stages, non-standard cold chain, temperature measurement system, manual touch points and location of operations. There is a need to map the existing system along with these critical factors considering cold chain logistics, activity time, technology adoption, innovative practice(s)/system(s) implementation, feasibility and economic challenges to make the process both efficient and agile. The use of techniques such as value stream mapping and 5S practice is explored to develop a strategy for improved resource utilization.
Keywords: Surimi Supply Chain, Resource Utilization, Value Stream Mapping, 5S Practice

1. INTRODUCTION

Surimi is an intermediate material for manufacturing various seafood products (Kim and Park, 2007); it is made from a variety of fish species in India, US and Europe. The variety of seafood products from surimi includes both traditional Japanese fish cakes and imitation seafood products (e.g. 'crab sticks') which is the most common form in the US and Europe (Mansfield, 2003). Surimi supply chain includes all the activities from "Sea" to "Plate" such as inbound logistics, warehousing practices, process sequence, rest material management and finally the outbound logistics of surimi paste and various surimi products.

The current study focuses on the supply side of surimi supply chain in India that includes all the processes related to fish harvesting (i.e. sea operations), transporting, sorting, and other handling until the fish reaches the surimi processing plant (Fig. 1-4). Although a surimi supply chain comprises stages starting from fishing boat to consumer, this article only considers the *supply side* of surimi supply chain. During the processing of fish for surimi production, the head, guts and skin portion of the fish, termed as *rest raw material* (RRM), are discarded which are processed by certain secondary industries to value-added products. The by-products generated from seafood processing can be classified into four major groups, such as plant fertilizers, livestock feeds, value-added foods, and specialty ingredients. The value addition is minimum in plant fertilizers and maximum in case of value-added foods and specialty ingredients (Torres et al., 2007). During the processing, the quality of fish plays a vital role for the quality of surimi, which depends on the complex interactions between natural inputs and their environments,

production techniques and technologies, and foods and their uses (Mansfield, 2003). In India, marginal fishermen carry out a significant portion of fishing for surimi production with skills often passed down by generations and more often, they remain unaware of various innovative technologies.
Most of the processes in the surimi supply chain are not organized including logistics activities of fish raw material and RRM and cold chain management and this has a negative impact on various aspects such as fish quality, cost, profitability and quality of the value-added products. Hence, the various losses, causes and potential value-addition solutions in the Indian seafood sector need to be analyzed and the factors such as the lack of consumer awareness and education, scattered nature of the sector, inappropriate cold chain management and lack of unified protocols for quality assurance must be overcome (Ravishankar, 2018). In the process, the sustainable management of available resources will be possible to create an ecosystem for waste reduction and develop value-added products from RRM. High-income countries such as USA, Japan, Spain and France have well developed surimi supply chain practices and a well-developed market. Their practices are also different from Indian practices because of differences in fish availability, harvesting practices, marginal internal market and environmental conditions. Surimi supply chain in India is not well developed in general. In the current study, the various aspects of the surimi supply chain in Indian ecosystem and its supply chain capabilities in terms of agility and responsiveness are examined.



Figure 1: Boat used for fishing



Figure 2: Fish unloading



Figure 3: Fish in crate at dock



Figure 4: De-heading at aggregator

The structure of the remainder of this paper is as follows: Section 2 provides an overview of surimi supply chain in India; and Section 2.1 elaborates the importance of factors that play a crucial role in maintaining fish and RRM quality. Section 3 presents an analysis on the strategy for surimi supply chain in India using the concept of Cost-Responsiveness Efficient Frontier (CREF) (discussed in Section 3.1) and strategic fit (discussed in Section 3.2) in order to study the existing and required status of it in terms of responsiveness and agility. Section 4 concludes the article with a direction for future scope of research.

2. OVERVIEW OF SURIMI VALUE CHAIN IN INDIA

In India, there are around 15 surimi processing plants such as Gadre Marine Export, Kaiko Surimi, Ratna Surimi, Han Kishan Surimi and Kan Victual, located mainly in the western coastal area, in the state of Gujarat and Maharashtra. Surimi is mainly produced from Ribbon Fish, Rani Fish and Lizard Fish (weight of the catch ranging from 20 to 100 g). It is produced through various sequential processes including de-heading, gutting, filleting, deboning, washing, dewatering, mixing with cryo-protectants and freezing. Surimi supply chain is a cold chain in which temperature control after harvesting is very important to maintain the protein, quality of meat and its gel forming capabilities. The Indian surimi supply chain consists of independent groups of fishermen, aggregator, surimi processing plant, RRM plant and export market (Fig. 5) and many logistic activities are carried out between successive stages. The arrows in Fig. 2 show the flow of fish (i.e. marginal fisherman-aggregator-surimi processing plant), RRM (aggregator-RRM plant; and surimi plant-RRM plant), surimi (surimi processing plant-export/Indian market) and value added products (RRM plant-both Indian and export market). The surimi supply chain starts with harvesting of various fish varieties such as Pink Perch (major variety), Big eye, Ribbon fish, Lizard fish, Croaker fish, Barracuda, Reef cod, Bronze croaker, Sardine and Mamakari from the Arabian sea within 10-20 km from the Mumbai seashore. The supply process (i.e. fisherman and aggregator) provides raw material (i.e. fish) to surimi processing plant and is completed when either whole or headed, and gutted fish reaches the processing plant. The wholesaler aggregates the whole fish from marginal fishermen and de-heading is carried out to separate mainly the head from whole fish and the head proportion is sent to RRM plant where it is processed into value-added products such as feed, oil or both.

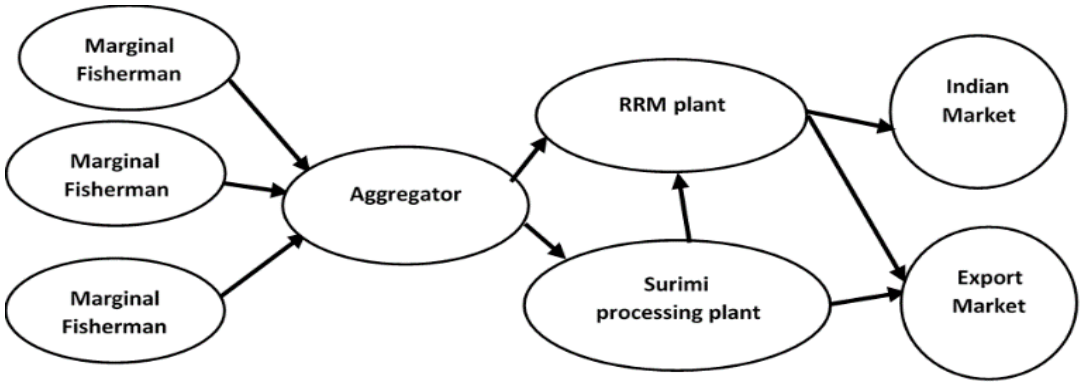

Figure 5: Surimi supply chain in India

2.1 Factors Influencing the Fish and RRM Quality

The factors playing a crucial role for maintaining fish and RRM quality are: fragmented ownership, fishing area identification, fishing boat and its capacity, boat unloading practice, real time information sharing, visual inspections of fish quality at various stages, non-standard cold chain, temperature measurement system, manual touch points and location of operations. These factors are elaborated below.

Fragmented ownership: Most of the surimi processing plants procure fish from the marginal fishermen having one to five boats. However, a few big players such as *Gadre Marine Export* have exclusive contracts with selected fishermen who must sell all the fish related to surimi to only Gadre Marine Export. This satisfies the significant proportion of the demand and the remaining is purchased through usual route. Mostly, fishermen sell whole fish at the dockyard to a third party who supplies de-headed fish to the surimi processing plant. De-heading is carried out either in the processing center near the dockyard or in the processing plant depending upon the demand and workforce availability. The price is decided

based on the supply and demand situation and fishermen generally sell their fish to different surimi processing plants at different points of time. The ownership of supply chain is fragmented and it operates independently without coordination. The total catch of a boat also includes other fish varieties that the boat unloads and is sold at different nearby dockyards. This unloading often happens earlier than the fish identified for surimi.

Fishing area identification: The current method of fishing area identification depends upon mere experience and personnel acumen. To attract the fish population that generally comprises a single variety of fish, fishermen adopt age old techniques such as lighting of lamps to attract fishes in the sea and observe sea water coloration that is affected by population of Phytoplankton and Zooplankton (fish food) in an area.

Fishing boat and its capacity: Most of the marginal fishermen use boats having 12-20 in-built compartments each having a capacity of about 600 kg content (fish with ice). Fresh catch is stored with multiple layers of crushed ice stuffed in these compartments, which remains frozen for approximately 15 days. Basic sorting of fish is carried out on the boat itself immediately after the catch. Wireless communication devices are used to communicate among boats in sea or with land-based boat owner but no information related to fish quality is recorded or shared with surimi processing plant.

Boat unloading practice: Age-old practice of bucket by bucket unloading of fish from boat is adopted at dock. This is a slow and inefficient process. Unloaded fish is weighed in standard plastic crates and then transferred and packed in other plastic crates sandwiched between layers of crushed ice for transport. The entire process has many manual touch points.

Real time information sharing: The real time information related to various parameters of fish and RRM (such as point of time, temperature log, quantity, quality etc.) along various locations of surimi supply chain are not captured, documented and shared on real time basis which has a negative impact for achieving coordinated sea logistics.

Manual inspections: The manual inspections such as thumb impression test (the impression remains when fish is not fresh while it recovers in case of fresh fish exhibiting good elasticity) and visual inspections (i.e. color of eyes, skin color and texture, bulging of eye etc.) are made to check quality for both fish and RRM (mostly head part) at different stages of the surimi supply chain.

Non-standard cold chain: No temperature measurement system is in place for the entire chain between fishing and surimi processing plant delivery. Desired temperature maintenance using crushed ice layers (generally three layers i.e. bottom, middle and top in a plastic crate) at various stages of surimi supply chain for fish and RRM (mostly head part) is practiced based on experience and observations by personnel to maintain and control quality.

Temperature measurement system: Temperature measurement is essential at various points and stages of the surimi supply chain to maintain and control the temperature as per the requirement so that both fish and RRM quality is maintained deploying optimum refrigeration level. However, as noted above, no temperature monitoring is present along the surimi supply chain to address this criticality including features such as identification of temperature sensing points and their appropriate temperature levels, refrigeration level, technology adoption, feasibility, economics etc.

Manual touch points: Number of manual touch points is quite high starting from fish unloading from boat to fish loading on truck at dockyard to fish de-heading centers / surimi processing plant. These touch points have direct impact on quality of fish and RRM. It also contributes to waste generation due to exposure to ambient temperature, pilferage and damage. Therefore, the current study aspires to focus on manual touch point reduction leading to enhanced quality and increased productivity while reducing related wastes.

Location of the operations: The basic sorting of fish variety is carried out in the sea in the existing system. The possibility of carrying out the de-heading process in the sea should be explored. This will enable RRM (mostly head part) to transport from boat to RRM processing plant. This will eliminate few operations on land and enhance the quality collection of RRM along with speed and efficiency.

3. DEVELOPMENT OF SUPPLY CHAIN STRATEGY

Supply chain strategy is defined as the process of managing organizational resources in a way that best fits its supply chain capability and meets its competitive strategy (i.e. the set of customer needs that the organization wants to fulfill) by exploiting the right balance between efficiency and responsiveness (Khorramshahgol, 2018). Manufacturing firms should formulate, adopt and implement its supply chain strategy in such a way that it can help firms to increase their competitiveness in today's dynamic, uncertain, and risky business environments (Roh et al., 2014). Although supply chain strategy in Indian manufacturing and service sector is well understood and implemented, but it is not the case for surimi supply chain in India in particular. Hence, the supply chain strategy (i.e. supply chain capability) of surimi supplies chain in India merits exploration (Section 3.1 and Fig. 6) and development in terms of right level of responsiveness (agility) and efficiency (cost) (Section 3.2 and Fig. 7).

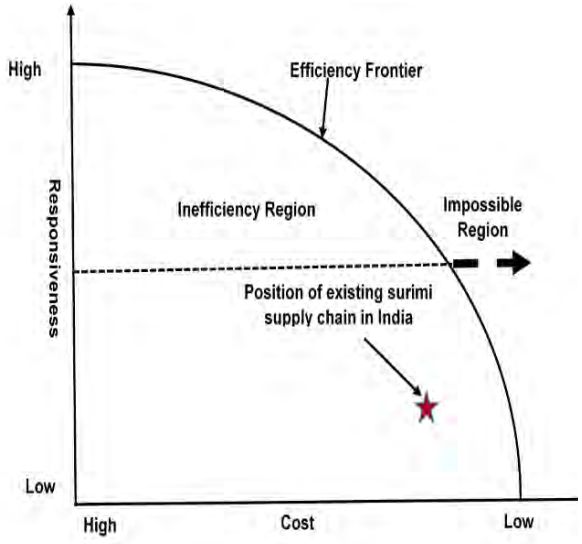

Figure 6: REF of surimi supply chain

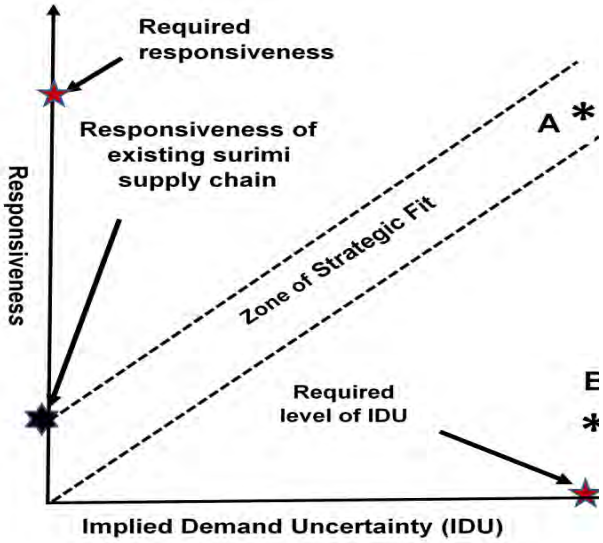

Figure 7: Strategic fit of surimi supply chain

3.1. Development of Cost-Responsiveness Efficient Frontier for Surimi Supply Chain in India

The Cost-Responsiveness Efficient Frontier (CREF) helps organizations to find the right balance between responsiveness and efficiency, and hence achieve a strategic fit between organizational strategy and supply chain capabilities (Al Husain and Khorramshahgol, 2018). The Cost-Responsiveness Efficient Frontier (CREF) was drawn for the surimi supply chain in order to understand the degree of inefficiencies in terms of responsiveness and efficiency. The CREF curve denotes the lowest possible cost incurred in the supply chain/system for developing the required level of responsiveness based on the existing technology (Chopra et al., 2016). While developing CREF in a specific environment, one has to estimate qualitatively the cost involved (taken in X-axis with highest value at origin and then cost value decreases) and maximum level responsiveness involved (taken in Y-axis with highest value when X is at origin) that can be developed in that environment. Therefore, the zone below CREF is an inefficient zone, the zone above CREF is impossible and all the points on the CREF are efficient points. The CREF was developed for surimi supply chain (Fig. 6) based on a few industrial visits and discussions held with various stakeholders. It was found that the existing position of surimi supply chain in India is in the inefficient zone (Fig. 6) and needs to move from present position to reach the CREF by enhancing both responsiveness and efficiency. Hence, there is an immediate need to enhance the existing level of responsiveness/agility of surimi supply chain in India looking at its existing *Implied Demand Uncertainty* (IDU) and perishable nature of the raw material (fish harvested for

surimi and RRM). However, the optimum use (change or modify) of the existing technology/practices in the existing supply chain configuration will not able to provide the required level of agility and competitive efficiency. This is because of fragmented supply chain ownership and large distance between supply chain stages (for example between dock and RRM or surimi processing center) which increases the cold chain logistics cost significantly along the supply chain.

3.2. Development of Strategic Fit for Surimi Supply Chain in India

Strategic fit refers to a consistency between the needs for supply requirements and supply chain capabilities to achieve strategic fit along the surimi supply chain in India to gain competitive advantage. The three steps for developing right supply chain strategy are i) evaluation of IDU, ii) understanding the Supply Chain Capabilities (SCC) in terms of responsiveness, and iii) matching of IDU and SCC (Fisher, 1997). In the current study, IDU is evaluated based on the level of uncertainty imposed on the surimi supply chain while satisfying its supply requirements. It was observed and captured in Indian environment through industrial visits and formal and informal discussions with various supply chain members including key persons such as company owner and plant manager at two surimi and a RRM processing plant, fish aggregator, fishermen at fishing dock etc. The various factors such as fishing duration, distance travelled from dock to first fishing point, quantity and quality of fish in a catch distance travelled between two catches, distance between boats at different point of time, weather condition, and logistics infrastructure make the IDU value quite high due to their inherent uncertainty behavior (i.e. first of strategic fit). It was also concluded that the existing supply chain configurations and practices have high cost of operations and low agility creating the supply chain inefficient. The level of responsiveness achieved in the existing surimi supply chain in India was also estimated (i.e. the second aspect of strategic fit). The strategic fit was drawn considering level of IDU and required level of responsiveness. It is shown in Fig. 7 and the exact location in the zone of strategic fit is at point “A”. The level of IDU and present agility when mapped in the same graph, the exact location (i.e. in point B) which is not in the zone of strategic fit and found much below point “A”. This indicates that the improvement is needed in both dimensions (i.e. cost and responsiveness). The offshore surimi processing plant (i.e. surimi processing in the sea) is well developed and implemented in developed countries that have the capability to enhance both agility and cost significantly. However, it may not be feasible to adopt the same in India as it has many obvious impediments such as high initial investments and low utilization, adoption and technology risk in Indian environment, eliminating the employability of the marginal fishermen etc. However, the existing practices have to be both efficient and agile with adoption of optimum scheduling/use of resources such as fishing boats, adoption of technology for real time information visibility and developing Surimi/ RRM processing centers in proximity creating an ecosystem of deep localization.

4. SUGGESTED APPROACHES FOR ACHIEVING STRATEGIC FIT

In order to achieve the strategic fit as mentioned and discussed in Section 3.1 and Section 3.2, the various approaches such as 5S practices, logistics optimization and value stream mapping need to be adopted in the supply chain. Many manufacturers have adopted 5S practices for maintaining an orderly workplace to achieve significant organizational benefits such as productivity, quality enhancement, cost optimization, waste elimination, eliminating unplanned downtime, improving the workplace, eliminate searching time of items at workplace, eliminating difficulties in using and returning of items and exercising enhanced inventory management, employee empowerment and delivery adherence (Bayo-Moriones et al., 2010 and Randhawa and Ahuja, 2017). It is made from five Japanese words starting with letter S: Seiri (sort), Seiton (set in order), Seiso (shine), Seiketsu (standardize), and Shitsuke (sustain) and is essential for total quality environment (Osada, 1991). The surimi supply chain stores fish and RRM at various stages such as in boat and aggregator and the storage activities are not well managed. Therefore, 5S practices should be applied for improved resource utilization and better

housekeeping. The significant proportion of activities carried out in the surimi supply chain consist of logistics activities i.e. transportation and storage in both at fisherman and aggregator stage. It was observed that logistics (mostly transportation) is not carried out optimally and logistics optimization should be applied for managing the logistics. Similarly, the present surimi supply chain should be studied using value stream mapping in detail to identify the inefficiencies/wastes and develop an efficient and agile system considering cold chain logistics, activity time, technology adoption, innovative practice(s) / system(s) implementation, feasibility and economic challenges.

5. CONCLUSIONS

The various operational aspects of surimi supply chain in India are examined in the current study. The surimi supply chain in India was analyzed based on agility and responsiveness using Cost-Responsiveness Efficient Frontier (CREF) and strategic fit considering experts' judgment and experience. There may be minor variations in the exact position or accuracy of different values considered along different dimensions. However, it gives an overall picture of the existing status of the surimi supply chain in India and shows directions of the improvement areas where the focus and effort should be in order to make it both efficient and responsive. It was suggested that use of optimization techniques in logistics operations, deep localization of supply side operations such as RRM processing for value added products, and use of 5S techniques for better housekeeping in both fishing boats and consolidator side should be adopted to have improved resource utilization, better business sustainability and enhanced profit. The implementation of the proposed strategies need a deep analysis on various factors such as technology adoption, cost involved employability, training requirement etc. The way forward is to evaluate few operations in sea (offshore) such as de-heading in Indian condition for its global business sustainability and growth.

ACKNOWLEDGEMENTS

This work is supported by the ReValue project funded through the INNO-Indigo programme under a DBT India grant (BT/IN/INNO-Indigo/12/NK/2017-18 dt. 21/02/18) and the Research Council of Norway project number 281262.

REFERENCES

AlHusain, R., Khorramshahgol, R., 2018. A multi-objective approach to design strategic supply chains and develop responsiveness- efficiency frontiers. Int. J. Logistics Management 29(1), 365-386.

Bayo-Moriones, A., Bello-Pintado, A., Merino-Díaz de Cerio, J., 2010. 5S use in manufacturing plants: contextual factors and impact on operating performance. Int. J. Quality & Reliability Management 27(2) 217-230.

Chopra, S., Meindl, P., Kalra, D.V., 2016. Supply chain management. Strategy, planning and operation. Pearson Education. Delhi, 32-34.

Fisher, M.L., 1997. What is the right supply chain for your product? Harvard Business Review. 75(1), 105-117.

Kim, J.S., Park, J.W., 2007. Mince from seafood processing by-product and Surimi as food ingredients. In Maximising the value of marine by-products Woodhead Publishing, 196-228.

Mansfield, B., 2003. Fish, factory trawlers, and imitation crab: the nature of quality in the seafood industry. J. Rural Studies 19(1), 9-21.

Osada, T., 1991. The 5S's: five keys to a total quality environment. Tokyo: Asian Productivity Organization.

Randhawa, J.S., Ahuja, I.S., 2017. 5S implementation methodologies: literature review and directions. Int. J. Productivity and Quality Management 20(1), 48-74.

Ravishankar, C.N., 2018. Losses in the Indian seafood sector: Causes and potential value addition solutions. Sustainable technologies for food processing and preservation. 1st RE-Food Symposium Goa, India, 12-13.

Roh, J., Hong, P., Min, H., 2014. Implementation of a responsive supply chain strategy in global complexity: The case of manufacturing firms. Int. J. Production Economics 147(1), 198-210.

Torres, J.A., Chen, Y.C., Rodrigo-Garcia, J., Jaczynski, J., 2007. Recovery of by-products from seafood processing streams. In Maximising the value of marine by-products. Woodhead Publishing, 65-90.

Manuscript ID: 163
DOI: 10.18462/iir.icr.2019.0163

Combination of vacuum insulation panels and phase change materials in temperature-controlled containers

Abbes KACIMI, Gilles LABRANQUE
SOFRIGAM, 1 rue de l'Union, Rueil Malmaison, CS 20137, 92565 Cedex, France
E-mail: abbes.kacimi@sofrigam.com

ABSTRACT

Insulated containers equipped with phase change materials (PCMs) are used to transport health products. The performance of these solutions can be improved by increasing the insulation or the thermal capacity storage of the PCM.
Aqueous eutectics are not suitable for above-zero temperatures. The performance of conventional insulations is not sufficient for long transport durations (> 72 hrs) and for extreme temperatures. Vacuum insulation panels (VIPs) offer the best heat transfer coefficient. The suitable PCM provides the thermal storage in the required range. The combination of both allows to develop high performance containers with single configuration. Temperature-controlled solutions with single operating procedure are optimised and validated to transport health products in stringent temperature ranges for up to 168 hours, under hot and cold profiles.
Keywords: Vacuum insulation panels, Phase change materials, Temperature-controlled container, insulated box, health products, cold chain.

1. INTRODUCTION

The market of temperature-sensitive health products (vaccines, medicines, blood derivatives, cells, biopsies...) is fast growing. The strict regulation and the variable logistics constraints require high performance temperature-controlled containers. The solution should maintain products in stringent temperature ranges (+2/+8 °C, +15/+25 °C) for more than 72 hours, under hot and cold temperature profiles and using a single preparation all year round. To meet these requirements, the solution should be improved by increasing the quality of the insulation or the thermal capacity storage of the PCM in the required temperature range.
Kacimi and Labranque (2011) provide a comparison between the performance of polyurethane boxes and VIP boxes. The same authors (2014) provide results for the use of PCMs in insulated boxes with seasonal preparation. This study focuses on the combination of vacuum insulation panels (VIPs) and phase change materials (PCMs) to develop high performance temperature-controlled containers, with single validated preparation all year round. These solutions are used to ship health products in strict temperature ranges: vaccines, medicines, biological samples, advanced therapy medicinal products...

2. VIPs AND PCMs IN TEMPERTAURE-CONTROLLED CONTAINERS

The temperature-controlled solution is the combination of an insulated box equipped with thermal accumulators (PCM or eutectic plates) to maintain the temperature range inside the box. Conventional insulating materials (such as polyurethane and polystyrene) and vacuum insulation panels are used to make insulated boxes. Aqueous eutectic solutions and other phase change materials (organic and inorganic PCMs) are used for the thermal storage. The solution is designed according to a heat balance.

2.1. Vacuum insulation panels

A vacuum insulated panel (VIP) are made by sealing a core material (silica, fibreglass...) wrapped in a barrier film under vacuum. VIPs are used in insulated boxes to improve their thermal performance or to reduce the wall thickness. The vacuum level of VIPs is about 0.1 to 1 mbar for

silica core material, and 0.01 to 0.001 mbar for fibreglass. The density of fibreglass is about 180 to 220 kg.m^{-3}, while silica is about 150 to 180 kg.m^{-3}. VIPs with both materials can achieve a thermal conductivity between 0.003 and 0.004 W.m^{-1}·K^{-1}. These values do not correspond to the overall coefficients of heat transfer of insulated containers, because of various thermal bridges and the edge effect of the barrier film. The thermal conductivity of VIPs is 4 to 6 times that of the polyurethane and 6 to 9 times that of the polystyrene. Kacimi and Labranque (2011) provide a comparison between the performance of polyurethane boxes and VIP boxes.
The exchanged heat Q, across the surface S, during a duration t, for a difference of temperature ΔT between the inside of the *container* and the ambient surrounding is given in eq. (1).

$$Q = K\ S\ \Delta T\ t \qquad \text{Eq. (1)}$$

2.2. Energy storage

Energy is stored by the phase change materials (PCMs) by solid or liquid sensible form and by latent form (solid/liquid or liquid/solid phase change). Both sensible heat and melting latent heat are successively used within the required temperature range. The energy Q [J] stored is given by equation 2.

$$Q = m[cs(Tf - T1) + Lf + cl(T2 - Tf)] \qquad \text{Eq. (2)}$$

Where m is mass of the material in kg, cs is specific heat of the material in solid state in J.kg^{-1}K^{-1}, cl is specific heat of the material in liquid state in J.kg^{-1}K^{-1}, Lf is melting latent heat in J.kg^{-1}, T1 is initial temperature of the PCM in K, T2 is final temperature of the PCM in K, and Tf is melting temperature of the PCM in K.
The phase change solidification/melting of aqueous eutectic solutions is performed at constant temperature and the most part of the thermal storage capacity is at the melting temperature. The solidification/melting and the thermal storage capacity of other PCMs is performed over a temperature range. The exchanged heat Q between the inside of the container and the ambient surrounding, given by Eq. (1), must equal the quantity absorbed by the PCM, given by Eq. (2).

2.3. PCMs used in insulated boxes

The phase change materials PCMs used in temperature-controlled boxes are chosen according to several criteria. The melting point of the PCM should be in the desired range with a high thermal storage capacity. The supercooling and the hysteresis are undesirable phenomena. The price and the impact on the environment are also important factors to choose the suitable PCM. Kacimi and Labranque (2014) provide results for the use of PCMs in insulated boxes, by using them in liquid state for cold profiles (winter) and in solid state for hot profiles (summer).
Aqueous solutions are non-toxic, abundant, cheap and with high latent heat, but their melting temperatures are below or equal to 0 °C. They can be used to maintain products between +2 °C and +8 °C under hot ambient profiles, but they are not adapted to cold temperature profiles.
PCMs with above-zero melting temperatures are used to maintain products within different strict temperature ranges, such as +2/+8 °C and +15/+25 °C, under hot and cold ambient temperature profiles. By choosing the melting temperature within the required temperature range, both melting and solidification of the PCM can be used. Organic PCMs (paraffins and fatty acids) are more expensive and lighter than inorganic PCMs (Salt hydrates). The phase change of these PCMs (solidification/melting) is performed over a temperature range. The thermal storage distribution of melting and solidification can be different. When the phase change range is reduced, the thermal storage of the PCM is concentrated and its performance in insulated boxes is better.
PCMs with melting temperature at about +5 °C are used to maintain products between +2 °C and +8 °C. The part of the thermal storage capacity actually used in this application is between +2 °C and +8 °C and better concentrated between +4 °C and +6 °C. Rubitherm (2018) gives in their technical Sheets the thermal storage capacities of different PCMs.
Fig. 1(a) shows the distribution of the thermal storage capacity of an organic PCM with a melting temperature at about +5 °C: 250 kJ.kg^{-1} for melting and 243 kJ.kg^{-1} for solidification, between -2 °C and +13 °C, about 88% of which between +2 °C and +8 °C and 80% between +4 °C and +6 °C. It is a high thermal storage capacity with the suitable distribution, compared to other +5 °C PCMs.

Fig. 1(b) shows the thermal storage capacities of two organic PCMs with a melting temperature at about +5 °C. The values of these capacities are given in Table 1.

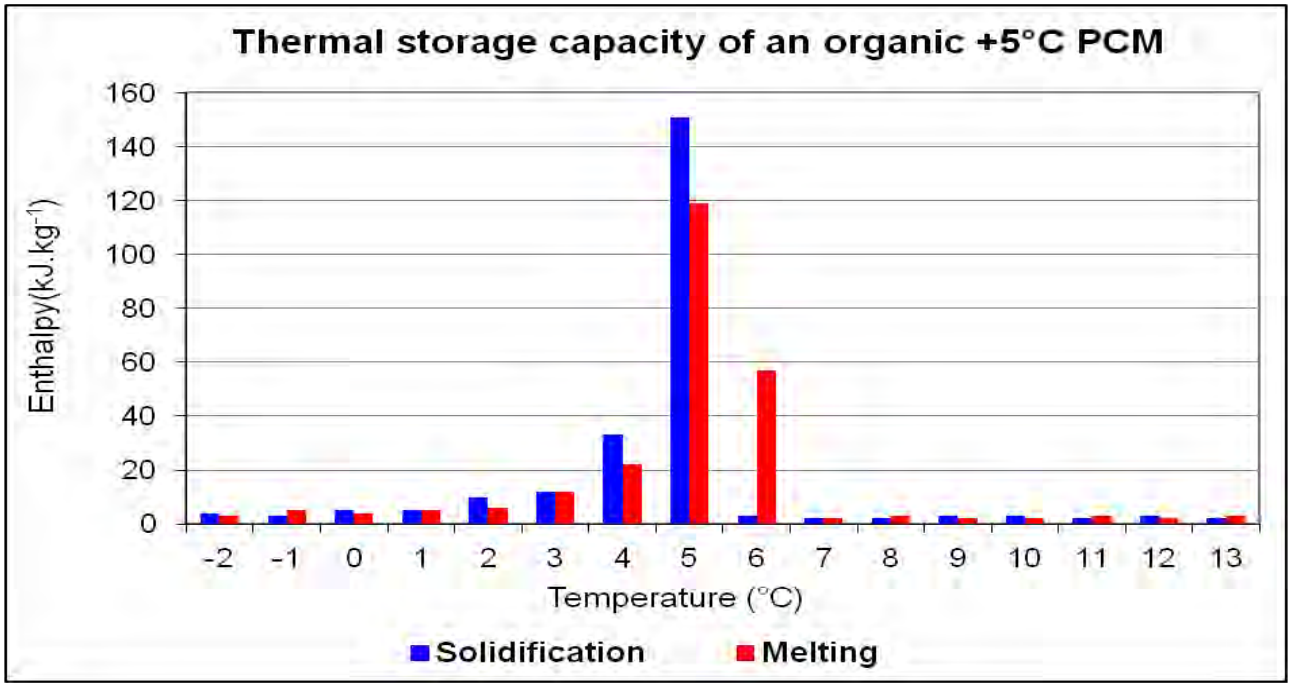

Figure 1(a). Thermal storage capacity of an organic +5 °C PCM between -2 °C and +13°C

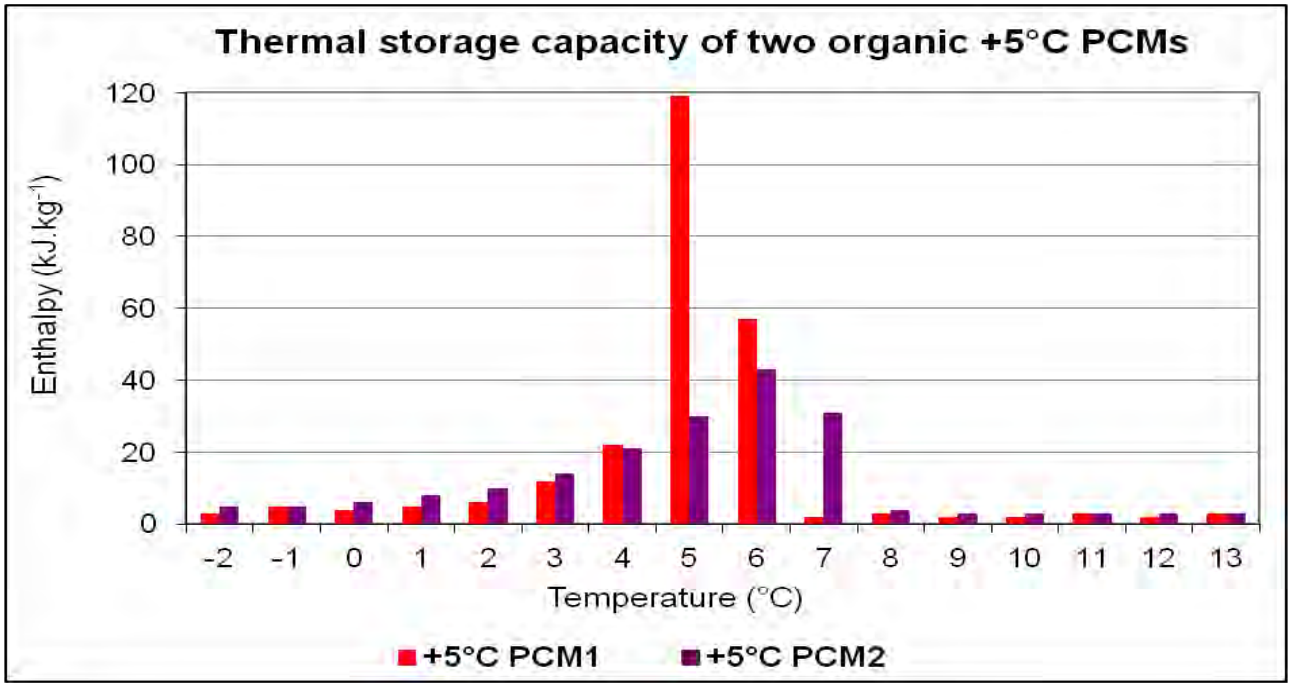

Figure 1(b). Thermal storage capacities of two +5 °C PCMs between -2 °C and +13°C

Table 1. Values of the thermal storage capacities of two +5 °C PCMs

	Thermal storage capacity (kJ.kg^{-1})	
Temperature range	+5°C PCM 1	+5°C PCM 2
Between -2 °C and +13 °C	250	192
Between +2 °C and +8 °C	221	153
Between +4 °C and +6 °C	198	94

The +5 °C PCM 1 offers 30% more capacity than the +5 °C PCM 2 between -2 °C and +13°C, 45% between +2 °C and +8 °C and 111% (more than twice) between +4 °C and +6 °C. The PCM 1 is about 2 times high performance in insulated boxes than PCM 2, but more expensive.
PCMs with melting temperature at about +21 °C are used in insulated boxes to maintain products between +15 °C and +25 °C. The part of the thermal storage capacity actually used in this application is between +15 °C and +25 °C and better concentrated between +19 °C and +23 °C.
Fig. 2(a) shows the distribution of the thermal storage capacity of an organic PCM with a melting temperature at about +21 °C: 199 kJ.kg^{-1} for melting and 195 kJ.kg^{-1} for solidification between +13 and +28 °C, about 91% of which between +15 °C and +25 °C and 74% between +19 and +23 °C. It is a high thermal storage capacity with the suitable distribution, compared to other +21 °C PCMs.
Fig. 2(b) shows the thermal storage capacities of two organic PCMs with a melting temperature at about +21 °C and the values of these capacities are given in Table 2.

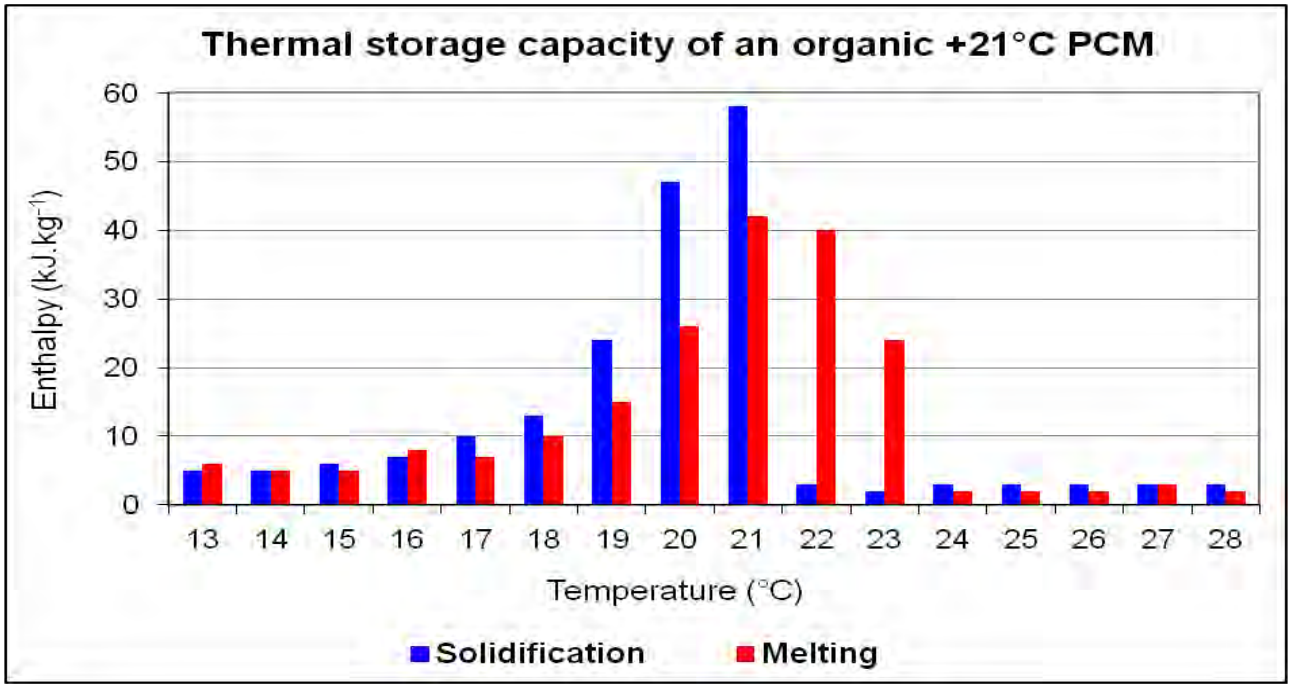

Figure 2(a). Thermal storage capacity of an organic +21 °C PCM between +13 and +28 °C

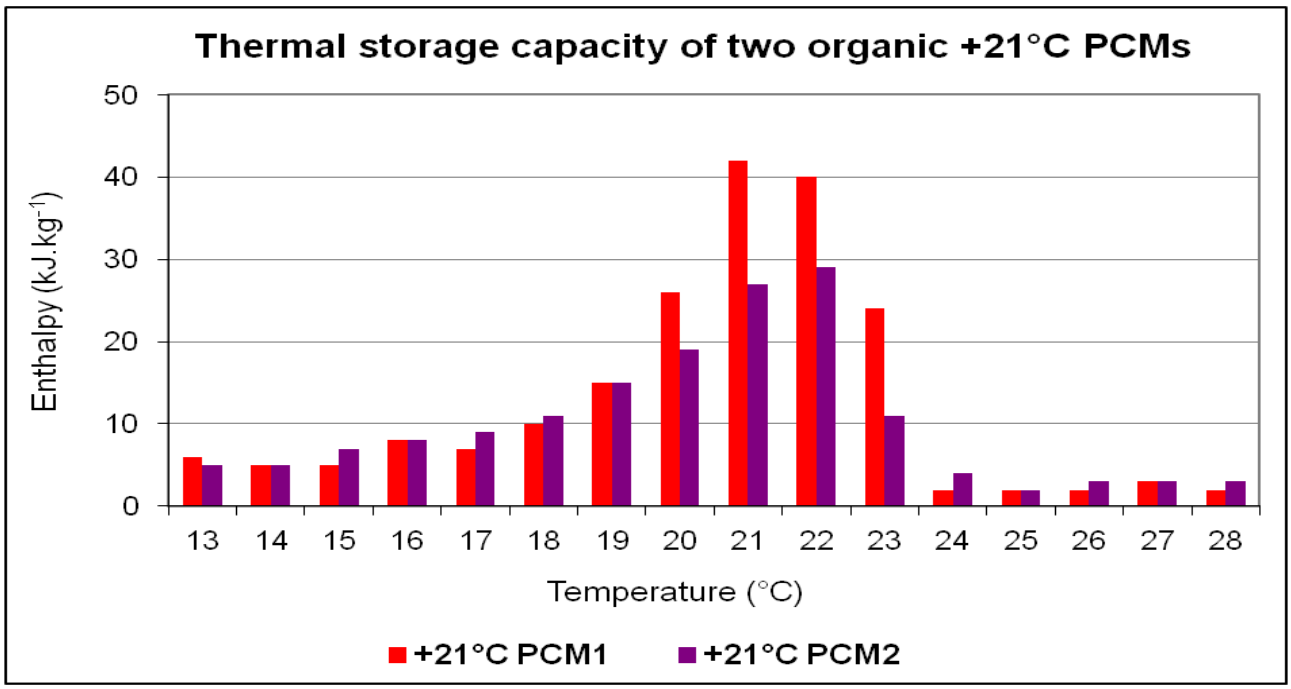

Figure 2 (b). Thermal storage capacities of two +21 °C PCMs between +13 and +28 °C

Table 2. Values of the thermal storage capacities of two +21 °C PCMs

	Thermal storage capacity (kJ.kg^{-1})	
Temperature range	**+21°C PCM 1**	**+21°C PCM 2**
Between +13 °C and +28 °C	199	161
Between +15 °C and +25 °C	181	142
Between +19 °C and +23 °C	147	101

The +21 °C PCM 1 offers 24% more capacity than the +21 °C PCM 2 between +13 °C and +28°C, 27% between +15 °C and +25 °C and 46% between +19 °C and +23 °C. The performance of insulated boxes with the PCM 1 is higher than the PCM 2, but more expensive.

3. UNIVERSAL SINGLE CONFIGURATION

3.1. VIP boxes insulated boxes

Several reusable insulated boxes with internal volumes from 15 litres to 64 litres made of VIPs and equipped with PCM packs are tested. Two types of VIP boxes are made:

- The first is made of 25 mm thick VIPs using silica core material and white polymer film. The assembled VIP box is inserted in a polypropylene external packaging and protected by an internal polypropylene box.
- The second is made of 20 mm thick VIPs using fibreglass core material and aluminium film and protected by with 5 mm polyurethane layer injected around the VIP on sides and edges. Both sides of polyurethane protection are covered an external aluminium facing. The total VIP/PU thickness is 30 mm. The assembled VIP+PU box is inserted in a polypropylene external packaging without additional internal protection.

The same insulated boxes are equipped with +5 °C PCM for the temperature range +2/+8 °C and with +21 °C PCM packs for +15/+25 °C. A single operating procedure all year round is defined for hot and cold external temperature profiles. The PCM packs are inserted at the beginning of the melting to maintain the required internal temperature range under hot and cold external profiles. The PCM can be the cold source or the heat source, depending on the external temperature.

3.2. Single configuration of VIP boxes with +5 °C PCM packs

VIP boxes are used with +5 °C organic PCM packs to maintain health products between +2 °C and +8 °C. The PCM packs are completely frozen (solidified) at -20 °C and then left in the cold room for 4 hours or at room temperature for 30 minutes. They are inserted in the box around products on the six faces. Using this universal operating method, the PCM packs are inserted at the beginning of the melting (at +5 °C) to absorb heat for hot external profiles and absorb cold for cold external profiles. The preparation time after freezing is determined according to the temperature of the room (cold room or room temperature) and quantity, the mass and the thickness of the PCM packs.

3.3. Single configuration of VIP boxes with +21 °C PCM packs

VIP boxes are used with +21 °C inorganic PCM packs to maintain health products between +15 °C and +25 °C. The PCM packs are stabilised at +20 °C and inserted directly in the box on four faces (at the bottom, on 2 opposite sides and on the top). Using this universal operating method, the PCM packs are inserted at the beginning of the melting (at +20 °C) to absorb heat for hot external profiles and absorb cold for cold external profiles.

4. TEST RESULTS AND DISCUSSION

Thermal performance tests are conducted by “Ater Métrologie” Laboratory (2016 to 2018). These tests are performed with empty vaccine vials representing the lowest thermal inertia (the worst case) and also with water bags representing the highest thermal inertia (the best case). For both temperature ranges, the boxes are tested under the hottest and the coldest temperature profiles described in ISTA 7D standard (summer and winter). The cyclic ISTA 7D summer profile varies between +22 °C and +35 °C with an average temperature of +30.3 °C. The cyclic ISTA 7D winter profile varies between -10 °C and +18 °C with an average temperature of +4.7 °C. This paper presents test results for both temperature ranges (+2/+8 °C and +15/+25 °C).

4.1. Tests with +5 °C PCM packs to maintain products between +2 °C and +8 °C

Insulated boxes are tested with universal single configuration using +5 °C PCM packs to maintain products between +2 °C and +8 °C.

4.1.1. Type 1 of VIP boxes

Four boxes made of 25 mm VIPs using silica core material and white polymer film are assembled and inserted in polypropylene external packaging and protected by internal polypropylene boxes. They are equipped with 35 mm thick rigid packs containing +5 °C organic PCM. The internal volumes of these boxes are 15 litres, 27 litres, 41 litres and 64 litres. They are tested with empty vaccine vials and with water bags, according the single configuration described in 3.2. Fig. 3 and Fig. 4 show the test results of the 27L VIP box equipped with rigid packs containing 8 kg of +5 °C PCM and tested with empty vaccine vials, under ISTA 7D hot and cold profiles.

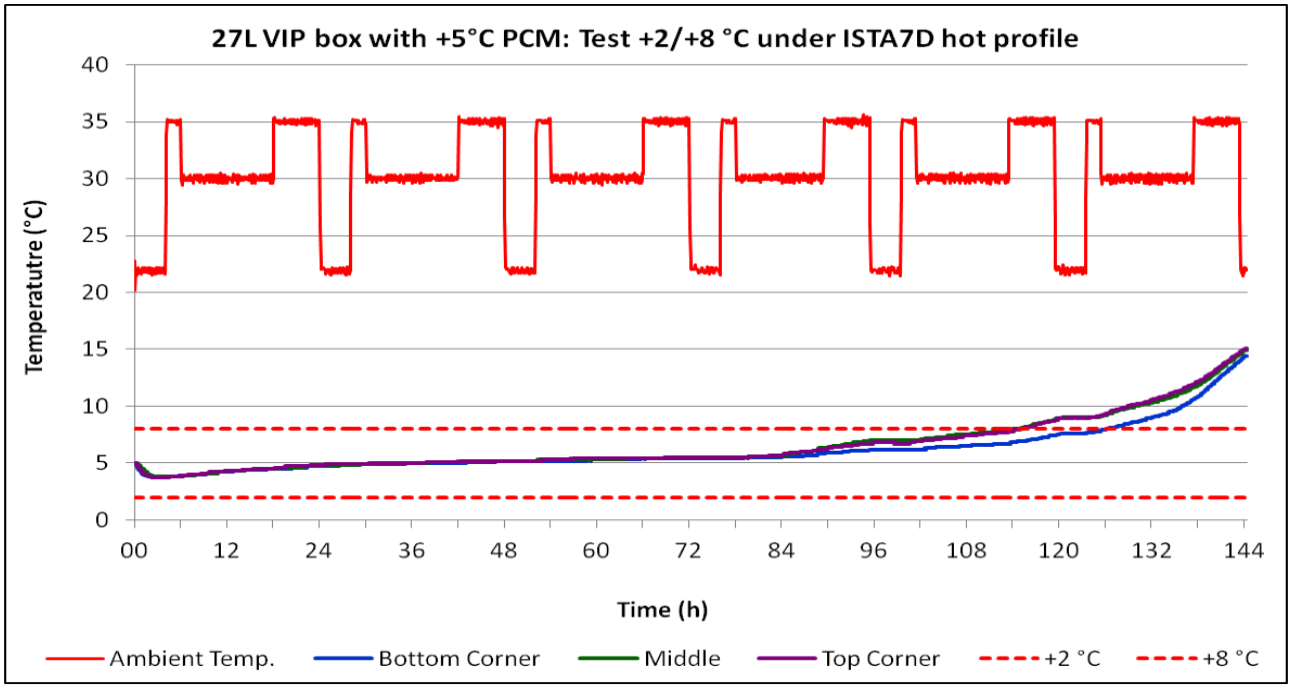

Figure 3. VIP box 27L with empty vaccine vials: 115 hours under ISTA 7D hot profile

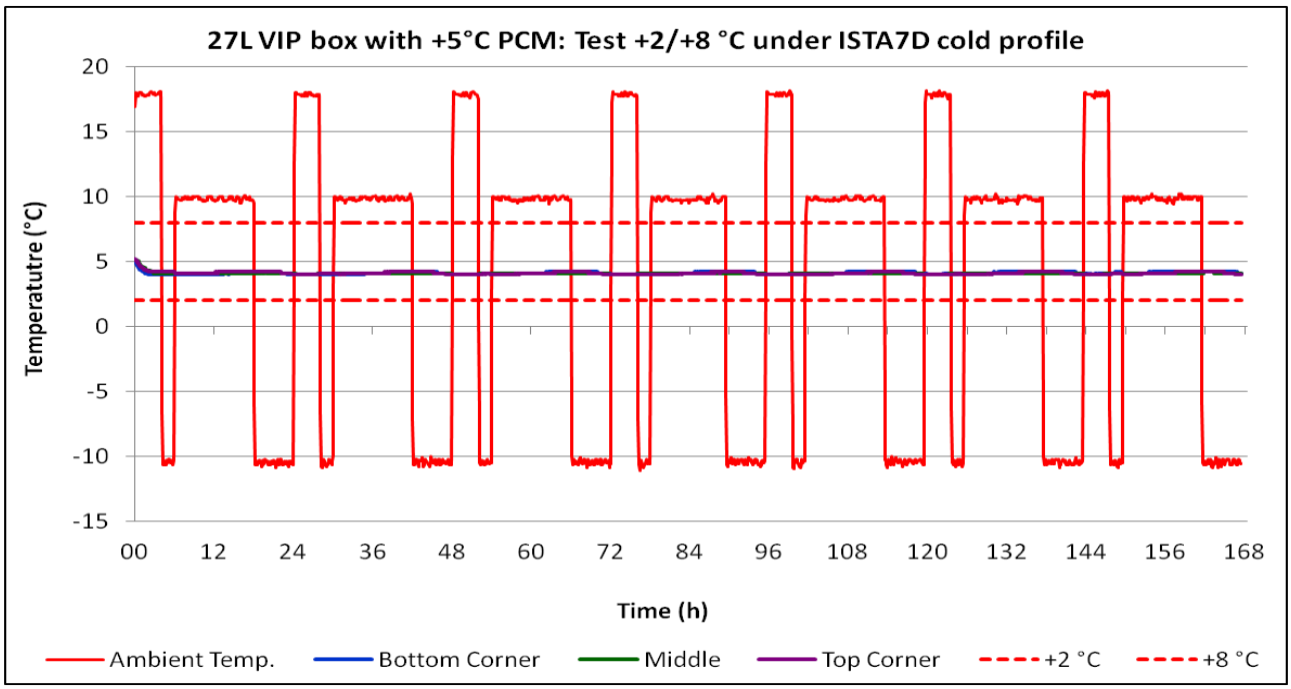

Figure 4. VIP box 27L with empty vaccine vials: At least 168 h under ISTA 7D cold profile

The VIP box 27L maintains products between +2 +C and +8 °C for 115 hours under the ISTA 7D hot standard profile and for at least 168 hours under the ISTA 7D cold standard profile. The results of the four boxes with empty vaccine vials and with water bags are given in Table 3.

Table 3. Test results of VIP boxes with +5 °C organic PCM for +2/+8 +C

		Thermal performance : Duration (hours)			
		15L	27L	40L	64L
With empty vaccine vials	ISTA 7D hot	106 h	115 h	116 h	107 h
	ISTA 7D cold	> 168 h	> 168 h	> 168 h	> 168 h
With water bags	ISTA 7D hot	95 h	131 h	160 h	114 h
	ISTA 7D cold	> 168 h	> 168 h	> 168 h	> 168 h

All the VIP boxes maintain empty vaccine vials and water bags for more than 168 hours under the cold profile. The results under ISTA 7D cold profile are better becasue this profile is comprised of alternate hot segments (+18 °C and +10 °C) and cold segments (-10 °C). They are better with water bags thanks to its high thermal inertia, compared to empty vials. In this range, the performance of medium volumes are better than the smalest and the largest.

4.1.2. Type 2 of VIP boxes

This type is made of 20 mm thick VIPs using fibreglass core material and aluminium film, and protected with 5 mm polyurethane layer. The polyurethane layer is injected around the VIP on sides and edges, and covered by an aluminium facing. The 30 mm VIP/PU box is assembled and inserted in a polypropylene external packaging. The tested box with an internal volume of 24 litres is equipped with 22 mm thick rigid packs containing 6 kg of +5 °C organic PCM. It tested with empty vaccine vials and with water bags, according the previous single configuration. The VIP+PU box maintains empty vaccine vials for more than 120 hours under ISTA 7D cold profile and for 93 hours under ISTA 7 D hot profile. It maintains water bags for more than 120 hours under ISTA 7D cold profile and for 105 hours under ISTA 7 D hot profile. The results under ISTA 7D cold profile are better becasue this profile is comprised of alternate hot segments (+18 °C and +10 °C) and cold segments (-10 °C). The results are better with water bags thanks to its high thermal inertia. Fig. 5 and Fig. 6 show the test result with empty vaccine vials.

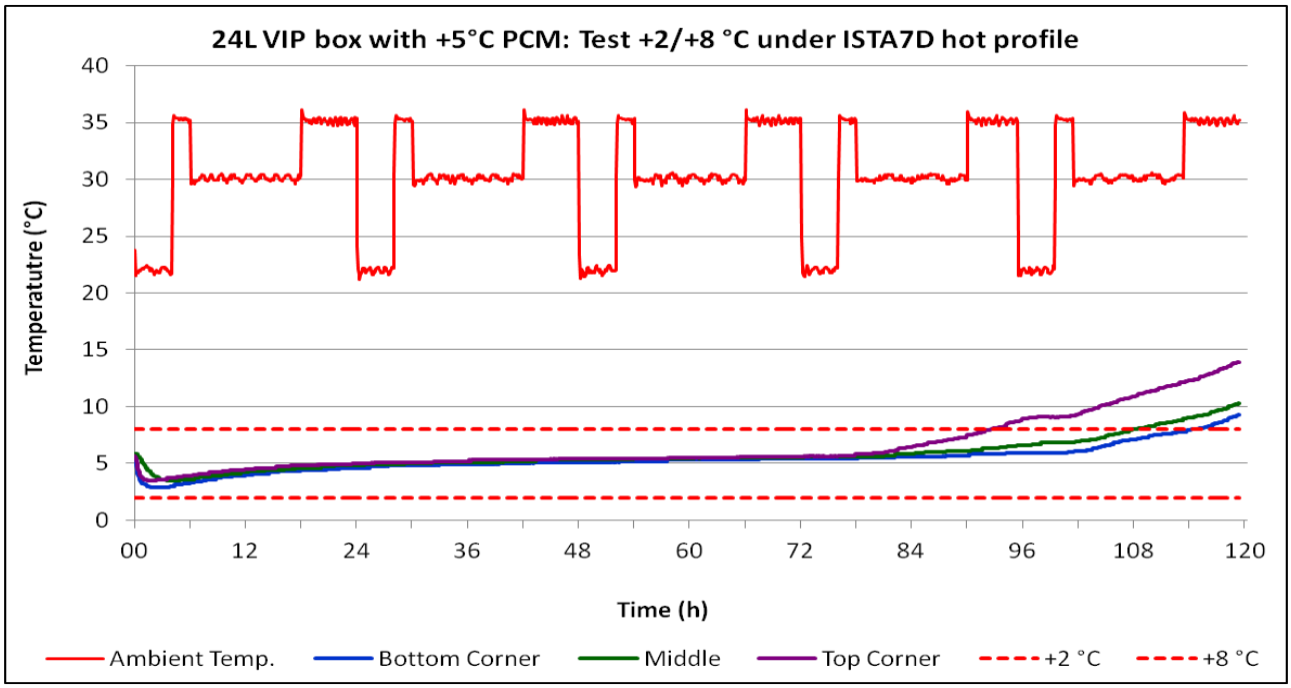

Figure 5. VIP/PU box 24L with empty vaccine vials: 93 hours under ISTA 7D hot profile

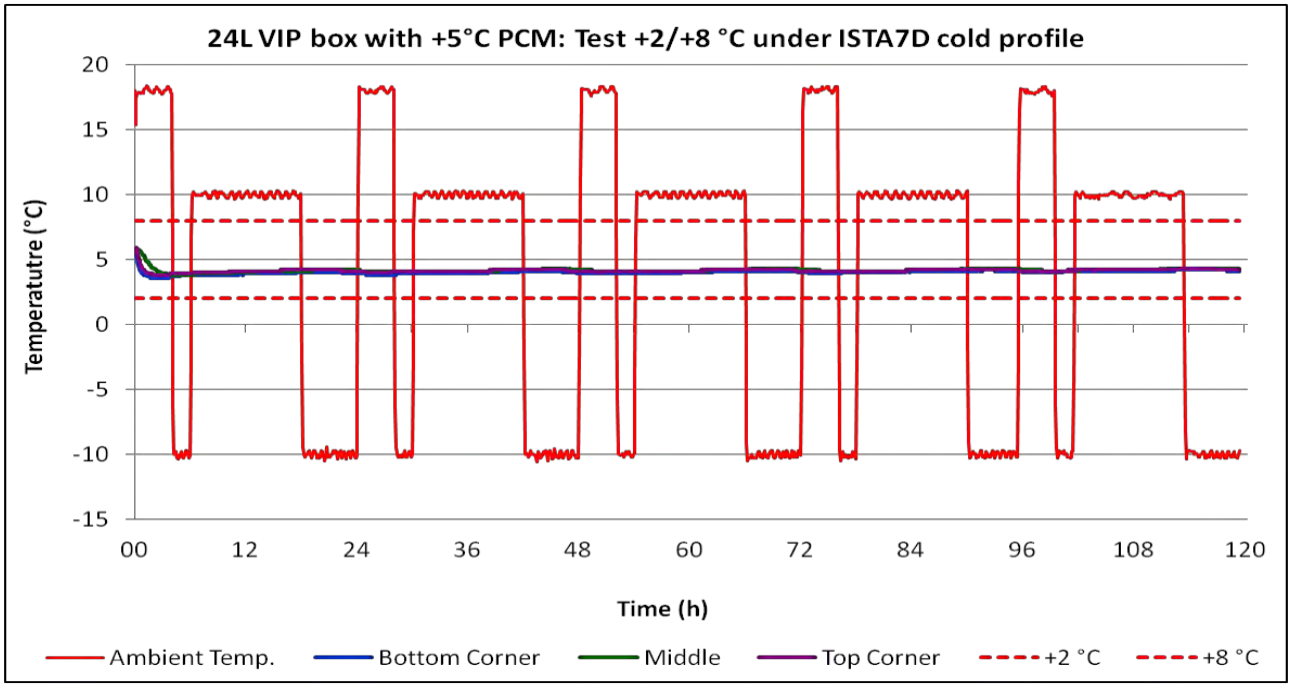

Figure 6. VIP/PU box 24L with empty vaccine vials: At least 120 h under ISTA 7D cold profile

4.2. Tests with +21 °C PCM packs to maintain products between +15 °C and +25 °C

The same VIP boxes are tested with universal single configuration using +21 °C inorganic PCM packs to maintain products between +15 °C and +25 °C. They are tested with empty vaccine vials, according the single configuration described in 3.3. The test results are given in Table 4.

Table 4. Test results of VIP boxes with +5 °C inorganic PCM for +15/+25 +C

		Thermal performance : Duration (hours)			
		15L	**27L**	**40L**	**64L**
With empty vaccine vials	ISTA 7D hot	> 168 h	> 168 h	> 168 h	> 168 h
	ISTA 7D cold	93 h	140 h	168 h	139 h

Fig. 7 and Fig. 8 show the test results of the 27L box equipped with rigid packs containing 12 kg of +21 °C inorganic PCM and, under ISTA 7D hot and cold profiles.

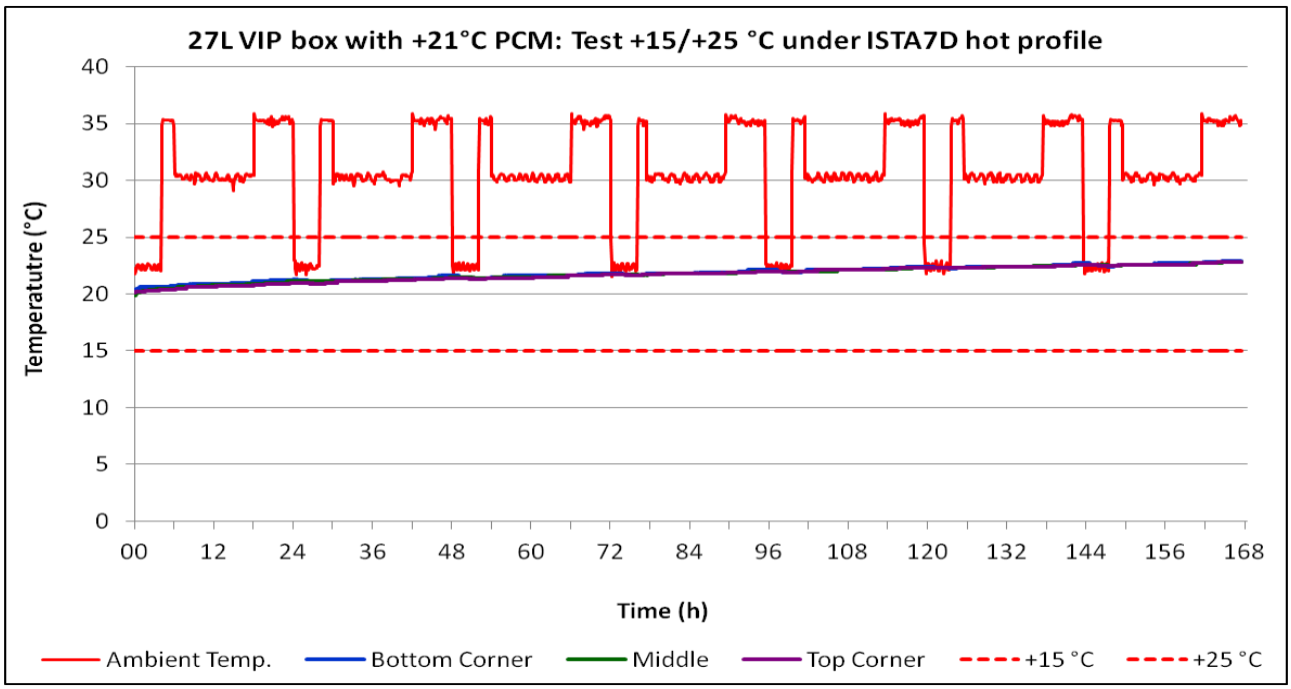

Figure 7. VIP box 27L with empty vaccine vials: At least 168 hours under ISTA 7D hot profile

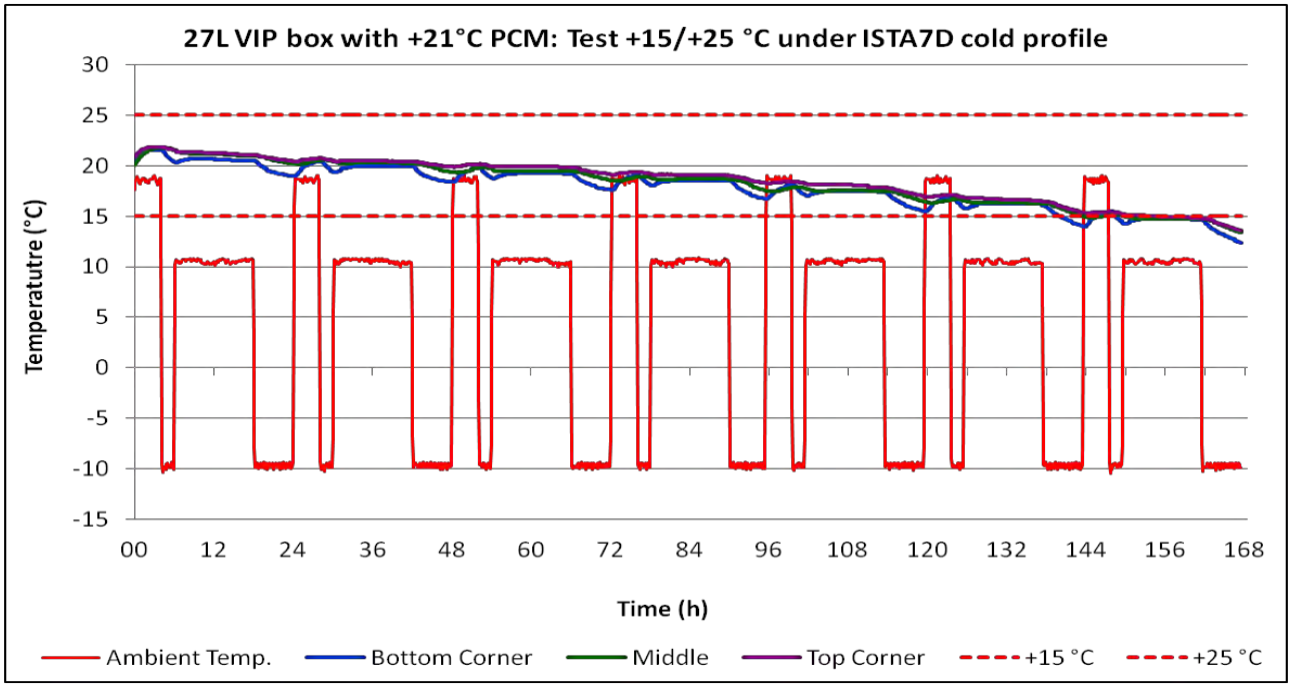

Figure 8. VIP box 27L with empty vaccine vials: 140 hours under ISTA 7D cold profile

The four VIP boxes maintain products betaween +15 °C and +25 °C for more than 168 hours under the hot profile because it is less binding this temperature range. The performance of medium volumes are better than the smalest and slightly better the the largest.

5. CONCLUSIONS

The combination of vacuum insulation panels (VIPs) and phase change materials (PCMs) with melting temperatures above 0 °C allows to develop temperature-controlled containers with single configuration. These solutions are optimised and validated to maintain health products for up to 168 hours, under hot and cold temperature profiles, using the same preparation method all year round. VIP boxes are used with +5 °C organic PCMs to maintain products between +2 °C and +8 °C. The PCM packs are completely frozen at -20 °C and then left in the cold room for 4 hours or at room temperature for 30 minutes before inserting them in the box. The same boxes are used with +21 °C PCM packs to maintain products between +15 °C and +25 °C. The PCM packs are stabilised at +20 °C and inserted directly in the box. Using this universal single operating method, the PCM packs are inserted at the beginning of the melting to absorb heat for hot external profiles and absorb cold for cold external profiles. These solutions are reusable to reduce the total logistic cost and the impact on the environment.

REFERENCES

Kacimi, A., Labranque, G., 2014. Phase Change Materials (PCM) in Temperature-controlled Containers. 3rd IIR International Conference on the Cold Chain & Sustainability, London, UK, 3-8.

Kacimi, A., Labranque, G., 2011. Vacuum Insulated panels (VIP) in insulated packaging. 23rd IIR International Congress of Refrigeration held in Prague, Czech Republic, 4-8.

Ater Métrologie Laboratory, 2016 to 2018. Thermal performance tests of VIP insulated boxes with PCMs.

International Institute of Refrigeration IIR, 2007. International Dictionary of Refrigeration, IIF/IIR Paris.

Rubitherm Technologies GmbH, 2018. Technical Sheets of PCMs.

Manuscript ID: 179
DOI: 10.18462/iir.icr.2019.0179

Experimental characterization and modelling of refrigeration of pork carcasses during transport in field conditions

Mouna MERAI[a,c], Steven DURET[a], Evelyne DERENS[a], Alain LEROUX[b], Denis FLICK[c], Onrawee LAGUERRE[a]

[a]Irstea, UR GPAN, Refrigeration Process Engineering Research Unit, 1 rue Pierre-Gilles de Gennes, 92761 Antony, France, onrawee.laguerre @irstea.fr

[b]IFIP, Institut du Porc, La Motte au Vicomte B.P. 35104, 35651 Le Rheu Cedex, France, alain.leroux@ifip.asso.fr

[c]UMR Ingénierie Procédés Aliments, AgroParisTech, INRA, Université Paris-Saclay, 91300 Massy, France, denis.flick@agroparistech.fr

ABSTRACT

Measurements of air and product temperatures were conducted at different positions in a semitrailer loaded by 480 warm half carcasses of pork (core temperature ~ 14°C, surface temperature ~ 7°C). The refrigerating curves of 8 instrumented half carcasses during the transport shows that the core temperature decreases significantly reaching the recommended value of 7°C almost everywhere after 9h whereas the product surface temperature decreases slightly (~ 5°C after 9h). A simplified model base on an analytical solution was proposed to predict the surface, core and average temperature changes during transport. The convective heat transfer coefficient of 7.7 $W.m^{-2}.K^{-1}$ was used in the modelling. This value represents the average value of the measurement in a reduced scale of refrigerated vehicle loaded by reduced scale of carcasses model. The refrigerating capacity was estimated for different loading ratios of warm carcasses in semitrailer. It was shown that the studied semitrailer has enough capacity to evacuate the heat whatever the percentage of warm carcasses.
Keywords: Transport, Warm Carcass, Temperature Prediction, Refrigerating Capacity

1. INTRODUCTION

To prevent quality loss, since 1964 in the European Union, pork carcasses must be chilled immediately after the post-mortem inspection and kept at a constant core temperature below 7°C until consumption. Because of the improvement in hygiene in the meat sector, slaughterhouses are now requesting derogations in order to be allowed to load warm carcasses (core temperature of 15°C) into refrigerated trucks under the condition that the surface temperature is below 7°C. This work was carried out with the following objectives:

- To present field data on the transport of pork carcasses in a refrigerated vehicle.
- To evaluate the heat load of the warm carcasses, thus, the capacity of the refrigerating system.

Transport of a food product in a refrigerated trailer is a specific process because of the high heterogeneity of air temperature and velocity (Merai et al 2018; Merai et al, 2019). Non-uniform air distribution inside the trailer was identified as the main problem in refrigerated transport (James, 1996). Lower product temperature is often observed at the front of the vehicle, while higher temperatures are observed at the rear close to the doors (Moureh and Flick, 2005). The potential position of high temperature can be influenced by the trailer design, the carcass arrangement and the loading density. Thus, knowledge of the airflow and the heat transfer at different positions is essential in order to enable the identification warm zones (areas of low air velocities and low convective heat transfer coefficients). During transport, conduction occurs within the carcass, while convection and water evaporation take place at the air-product interface. These phenomena, which vary with time, depend on the air characteristics (temperature, velocity and humidity). Several studies

have been undertaken in order to characterize the airflow distribution inside chilled rooms by experimental and modelling approaches (Mirade and Picgirard, 2001; Mirade 2007). These studies have made it possible to develop solutions enabling control of the chilling parameters and to minimize product weight loss. However, experimental studies in field are rare because of the difficulty of implementation.

2. EXPERIMENTAL CONDITIONS

2.1. Loaded semi-trailer

The studied refrigerated vehicle was a semi-trailer (length x width x height = 13.30 x 2.46 x 2.50 m), with an airflow rate at the discharge air outlet of 5000 $m^3.h^{-1}$ and a refrigerating capacity of 13 kW. According to the measured air temperature change with time, it was observed that the duration of compressor “on”/”off” cycles was 4 h, then, a defrosting duration of 20 min was undertaken during which the compressor was “off”.
This semitrailer was equipped with 5 rails for product hanging, but only 4 rails were used in our study (rail 3 in the center was empty), as shown in Fig. 1a. There were 120 pork half-carcasses on each rail (total of 480 half-carcasses in the semi-trailer), with an average weight of 30.7 kg per half-carcass. Cold air was discharged at the top front area of the semi-trailer via an 11-metre long air distribution duct made of plastic with fine holes (Fig. 1b). Part of the cold air flows through the “porous” zones constituted by the half carcasses and exchanges heat with them, then, the air becomes warmer. The other part of air flows above the carcasses until it reaches the rear of the semi-trailer. The warm air then returns to the front to be cooled down by the refrigeration system.

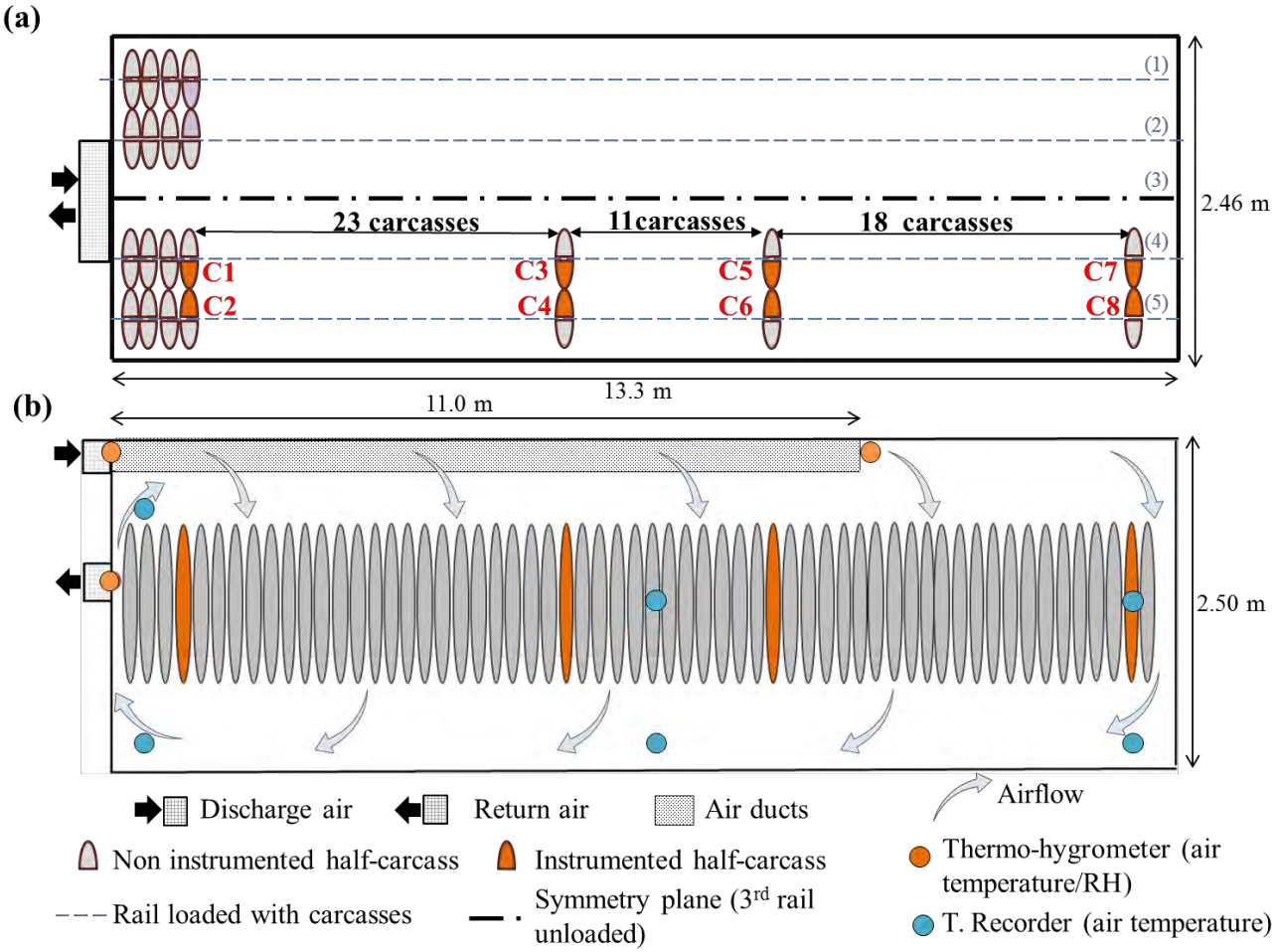

Figure 1: Positions of measurements in a semi-trailer loaded with pork carcasses (a) - Top view; (b) - Side view

2.2. Instrumentation

Considering a symmetry plan in the semitrailer, a half of the semi-trailer was instrumented and the other half was not instrumented (Figure 1a). Eight half-carcasses located at 4 distances from the cold air discharge outlet were instrumented. The average weight of the instrumented carcasses is 30.6 ± 1.7 kg and the thermo-physical properties of pork are shown in Table 1. On each instrumented carcass, rigid thermocouples (Testo 171-4, T-type, precision ± 0.2°C) were inserted to a depth of 12 cm under the ham surface and 6 cm under the shoulder surface. To measure the product surface temperature, temperature recorders (trade name thermo-buttons Progesplus, 22L type, precision ± 0.5°C) were pasted on the ham and shoulder surfaces. To measure the air temperature and relative humidity near the product, thermo-hygrometers (Testo 174H, ± 0.5°C, precision ± 3% RH) were located at about 5 cm from the ham and the shoulder surfaces.
Data were recorded every minute over 9 h (total transport duration). The water content in the air (kg water/kg dry air) was calculated using a humid air diagram (Beysens, 1995).

Table 1. Thermophysical properties of pork

Property	Value	Reference
Equivalent radius, R_{eq} (m)	0.1	$R_{eq} = 0.005(12.93 + 0.24W)$ W = Weight of half-carcass (kg) Daudin and Kuitche, 1996
Density, ρ ($kg.m^{-3}$)	1072	Harkouss et al., 2018
Thermal conductivity, k ($W.m^{-1}K^{-1}$)	0.45	Kondjoyan et al., 2013
Thermal capacity, Cp ($J.kg^{-1}.K^{-1}$)	3200	Kondjoyan et al., 2013
Thermal diffusivity, $\alpha = \frac{k}{\rho C_p}$ ($m^2.s^{-1}$)	1.31×10^{-7}	

3. EXPERIMENTAL RESULTS OF TEMPERATURE CHANGES DURING TRANSPORT

The temperatures of the half-carcasses and air near the carcasses (5 cm from the product surface) decreased gradually during transport. The example of the half-carcass located at the center of the semi-trailer (C3) is presented in Fig. 2a. During transport, the core temperature decreased by about 6.5°C both for ham and shoulder (from 13.8°C to 7.4°C for ham and 13.4°C to 6.8°C for shoulder). The surface temperature decreased by about 2.9°C both for ham and shoulder (from 6.8°C to 4.0°C for ham and 8.4°C to 5.4°C for shoulder). The air temperature decreased by 1.3°C near the ham (5.0°C to 3.7°C), whereas it decreased by 4.1°C near the shoulder (from 7.7°C to 3.6°C). The air temperature near the shoulder was much higher than that near the ham at the beginning of the transport because at this position (bottom), the air was previously warmed up when flowing around the carcasses while the air surrounding the ham (top), was blown from the discharge air (Fig. 1b).
The surface and core temperatures of ham and shoulder of the eight instrumented carcasses at the beginning (t = 0 h) and at the end of transport (t = 9 h) are shown in Fig. 2b and 2c respectively. The surface temperatures of certain carcass cannot be presented because the temperature recorders were removed from the surface during the transport. At the beginning (t = 0 h), the surface temperature ranged from 5.0°C (C4) to 8.0°C (C6), the core temperature ranged from 8.8°C (C7) to 14.0°C (C5) The lower core temperature of the carcasses C7 compared with those at other positions can be explained by several reasons: (1) this carcass may have spent a longer period in the cold room of slaughterhouse (2) the carcass was thinner than the other carcasses and (3) the position of the probe was not exactly in the core. At the end of transport (t = 9 h), the surface temperatures were in all parts of the vehicle lower than 7°C, which complies with the recommended value. The core temperatures ranged from 4.7 to 8.0°C, even if some core temperatures were still above 7°C after 9h of transport, it still complies with the derogation which concerns the surface temperature.

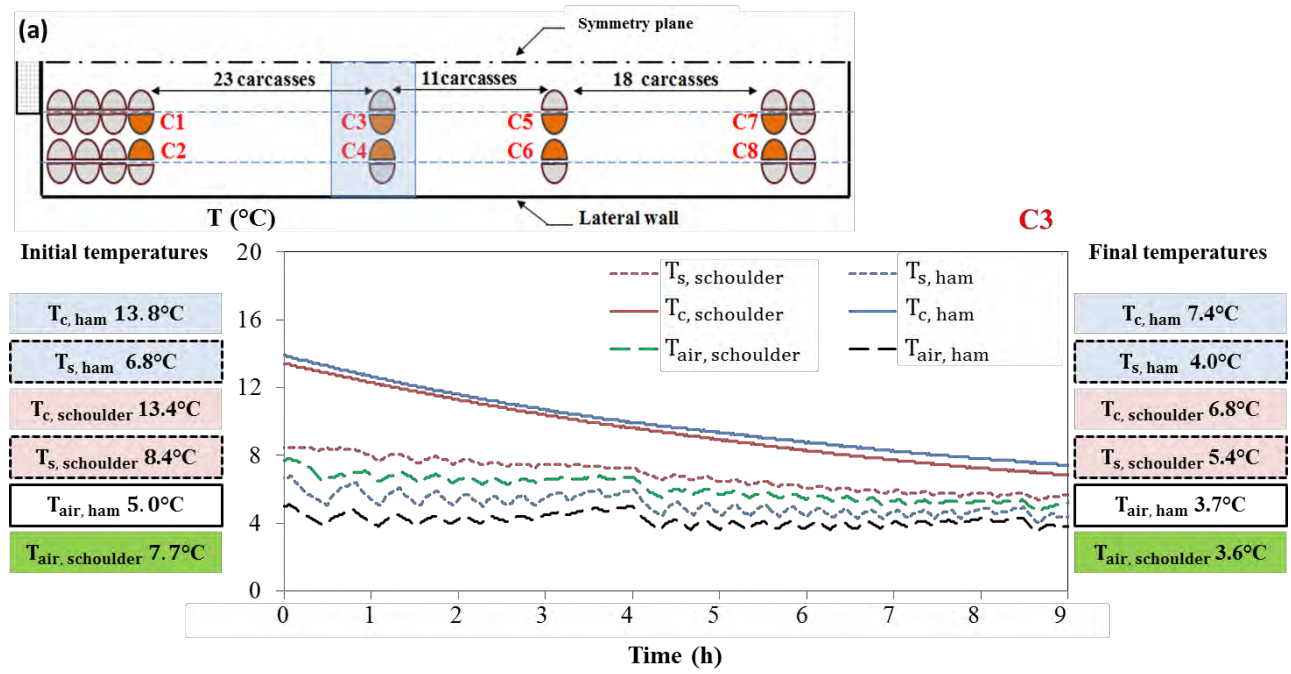

(b)

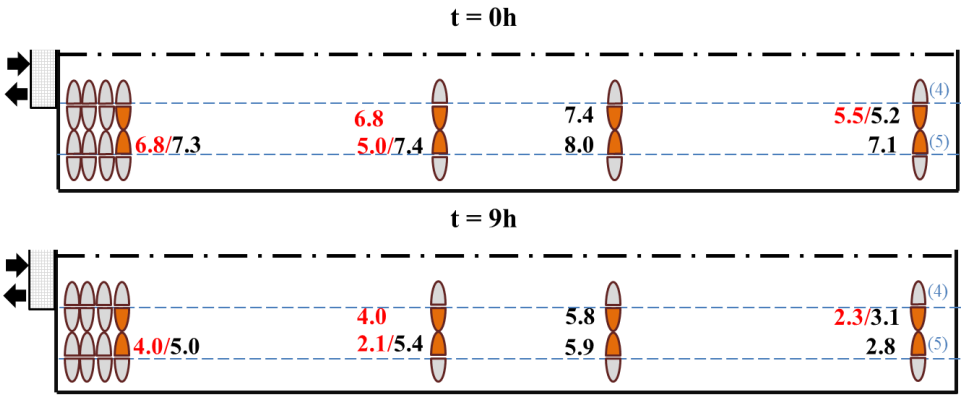

Red value → ham surface temperature

Black value → shoulder surface temperature

(c)

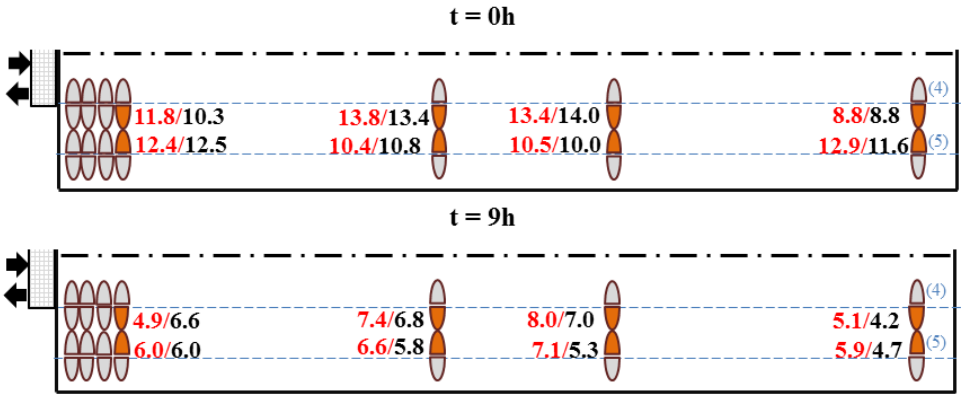

Red value → ham core temperature

Black value → shoulder core temperature

Figure 2: (a) - Product and air temperature changes during transport (9 h) of the carcass C3; (b) - Product surface temperature (c) - Product core temperature at the beginning (t=0) and at the end (t=9h) of transport

4. ESTIMATION OF HEAT LOAD OF WARM CARCASSES

Considering a carcass as a semi-infinite cylinder, the average temperature change can be represented as follows (Carslow and Jaeger, 1959):

$$T^*_{av} = 4Bi \sum_{n=1}^{\infty} e^{-\beta_n^2 Fo} \frac{J_1(\beta_n)}{\beta_n(\beta_n^2 + Bi^2)J_0(\beta_n)} \quad \text{Eq.(1)}$$

For simplification purposes, only the first term is considered:

$$T^*_{av} \cong 4Bi.\, e^{-\beta_1^2 Fo} \frac{J_1(\beta_1)}{\beta_1(\beta_1^2 + Bi^2)J_0(\beta_1)} \text{ with } Fo = \frac{\alpha t}{R_{eq}^2} \quad \text{Eq.(2)}$$

Equation 2 was used to calculate the average carcass temperature changes in the cold room of a slaughterhouse and in the semi-trailer in the following manner.

Semitrailer can be loaded with both warm (T_c=15°C and T_s=7°C according to the derogation) and cold (T_c=7°C and T_s=7°C according to the regulation) carcasses. In both cases, it is assumed that after slaughtering, the carcasses (initial temperature T_0 = 40°C) are cooled down in the cold room of a slaughterhouse and in the semi-trailer with the same air temperature T_a of 2.5°C and with the same heat transfer coefficient h of 7.7 $W.m^{-2}.K^{-1}$ (average value measured in a reduced scale semitrailer loaded by reduced scale carcass model, Merai et al. (2019). Carcasses benefiting a derogation leave the cold room of the slaughterhouse after the duration t_D at which the core temperature reaches $T_{c,D}$ = 15°C while the carcasses under regulation stay in the cold room for a duration t_R corresponding to a core temperature $T_{c,R}$ of 7°C (Fig. 3a).

Both types of carcasses are then loaded at the same time into a semi-trailer. The evolution of the core and average temperatures of warm and cold carcasses during transport in a semi-trailer with are shown in Fig. 3b.

The rate of heat flow to be evacuated from the carcass ($\dot{Q}$) can be estimated as follows:

$$\dot{Q} = -Cp\left(m_{tot.R}\frac{dT_{av.R}}{dt} + m_{tot.D}\frac{dT_{av.D}}{dt}\right) = Cp(T_o - T_a)\left(m_{tot.R}\frac{dT^*_{av.R}}{dt} + m_{tot.D}\frac{dT^*_{av.D}}{dt}\right)$$

$$= Cp(T_o - T_a)4Bi\frac{J_1(\beta_1)\beta_1^2\alpha/R_{eq}^2}{\beta_1(\beta_1^2 + Bi^2)J_0(\beta_1)}\left(m_{tot.R}.e^{-\frac{\beta_1^2\alpha(t+t_R)}{R_{eq}^2}} + m_{tot.D}.e^{-\frac{\beta_1^2\alpha(t+t_R)}{R_{eq}^2}}\right)$$

This heat flow is maximal at the beginning of transport (t = 0 h) and can be estimated as follows:

$$\dot{Q} = Cp(T_o - T_a)4Bi\frac{J_1(\beta_1)\beta_1^2\alpha/R_{eq}^2}{\beta_1(\beta_1^2 + Bi^2)J_0(\beta_1)}\left(m_{tot.R}.e^{-\frac{\beta_1^2\alpha t_R}{R_{eq}^2}} + m_{tot.D}.e^{-\frac{\beta_1^2\alpha t_D}{R_{eq}^2}}\right) \quad \text{Eq.(3)}$$

The terms in Eq. 3 involving t_R ($e^{-\frac{\beta_1^2\alpha t_R}{R_{eq}^2}}$) and t_D ($e^{-\frac{\beta_1^2\alpha t_D}{R_{eq}^2}}$) can be obtained by using eq. 4 and 5 since the values of $T_{c,R}$, $T_{c,D}$, T_0 and T_a are known:

$$T^*_{c,R}(t_R) = \frac{T_{c,R} - T_a}{T_0 - T_a} = 2Bi\frac{1}{(\beta_1^2 + Bi^2)J_0(\beta_1)}e^{-\frac{\beta_1^2\alpha t_R}{R_{eq}^2}} \quad \text{Eq.(4)}$$

$$T^*_{c,D}(t_D) = \frac{T_{c,D} - T_a}{T_0 - T_a} = 2Bi\frac{1}{(\beta_1^2 + Bi^2)J_0(\beta_1)}e^{-\frac{\beta_1^2\alpha t_D}{R_{eq}^2}} \quad \text{Eq.(5)}$$

Considering that a semi-trailer (with an air temperature Ta = 2.5°C) is loaded with different percentages of half-carcasses benefiting from a derogation (core temperature $T_{c,D}$ = 15°C) and regulated carcasses (core temperature $T_{c,R}$ = 7°C). For a total number of half-carcasses of 480 (35 kg/carcass, the mass of half-carcasses generally observed in practice), the heat flow to be evacuated ($\dot{Q}$) at the beginning of the transport (t = 0) should be less than the refrigerating capacity of the semi-trailer required to cool down all of the half-carcasses is presented in Table 2. When all the half-

carcasses benefiting from derogation are loaded into the semi-trailer (100%), the refrigerating capacity should be about 10 kW.

Table 2. Estimated refrigerating capacity ($\dot{Q}$) of the semi-trailer (ambient temperature T_a = 2.5°C) required to cool down 480 half-carcasses (35 kg/carcass) at the time of loading (t = 0h) with different ratios of half-carcasses benefiting from a derogation (core temperature Tc = 15°C) and regulated half-carcasses (core temperature Tc = 7°C).

Percentage of half-carcasses benefiting from a derogation	Weight of half-carcasses benefiting from a derogation (kg)	Weight of regulated half-carcasses (kg)	$\dot{Q}$ (W)
0	0	16.800	3.544
20	3360	13.440	4.804
40	6720	10,080	6.064
60	10.080	6.720	7.324
80	13.440	3.360	8.584
100	16.800	0	9.844

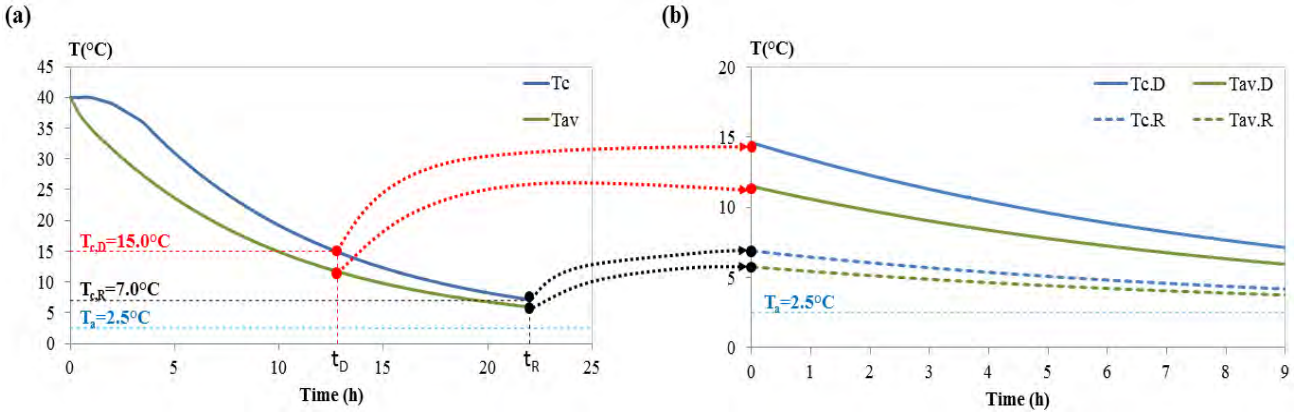

Figure 3: Carcass core and average temperature changes during refrigeration: (a)-in a cold room of a slaughterhouse; and (b)-in a semi-trailer (Dotted lines show the corresponding temperatures of carcasses transferred from a cold room to a semitrailer)

It should be borne in mind that heat loss also occurs through the walls of the semi-trailer, and these losses are higher in summer (when the external ambient temperature is 30°C) than in winter (when the external ambient temperature is 5°C). Considering a heat transmission K = 0.44 $Wm^{-2}K^{-1}$ (average value of 97 semi-trailers tested by Cemafroid, personal communication), the estimation of the heat losses in summer through the walls is as follows:

$$\dot{Q} = K.A\,(T_{ext} - T_{int}) = 0.44 \text{ x } 144.3 \text{ x}(30 - 2.5) = 1745 \text{ W} \qquad \text{Eq.(6)}$$

A = surface area of the semi-trailer = 144.3 m^2 (length x width x height =13.3 x 2.46 x 2.5 m)

The total required refrigerating capacity of a semi-trailer loaded with warm carcasses and taking into account heat loss through the semi-trailer walls can therefore reach about 12 kW.

The refrigerating capacity of the studied semi-trailer was 13 kW, and thus it can be considered that the cooling capacity of the semi-trailer was sufficiently high to cool a load of up to 100% of half-carcasses benefiting from derogation. According to the information of semitrailer refrigerating system, the refrigerating capacity can vary from 12.0 to 18.5 kW (Carrier, https://www.carrier.com/truck-trailer/fr/fr/products/eu-truck-trailer/trailer/).

5. CONCLUSIONS

This study was carried out in order to acquire knowledge of the transport of pork carcasses under real conditions, and was designed to complement our previous studies on heat transfer and airflow on a laboratory scale under well-controlled conditions. This study demonstrated the heterogeneity of the surface and core temperatures of carcasses located at different positions in a semi-trailer. The experimental results (transport of half carcasses of average weight of 30.5 kg) demonstrated that the studied semi-trailer allowed product cooling during the transport of warm carcasses: the product surface temperature was lower than 7°C (recommended temperature) in all locations at the end of a transport period of 9 h. The average convective heat transfer coefficient identified from the experimental cooling curves of carcasses during transport (7.7 Wm-2K-1) is close to that measured in a laboratory. The numerical study on the transport of different ratios of warm and cold carcasses in the studied semi-trailer showed that the refrigerating capacity of the refrigeration system was sufficient to remove the heat from the carcasses. The results of this study can be used by industry and public authorities to support decision making related to the carcass initial temperatures during transportation.

ACKNOWLEDGEMENTS

This research work was carried out within the framework of a DIM ASTREA grant by the Regional Council of Ile-de-France, France. The authors would like to thank “IFIP” for the contact with the meat industry and Cemafroid (Private Organism of refrigerating vehicles test) for providing statistical data on the insulation of refrigerated vehicles in use.

NOMENCLATURE

A	Exchange surface area (m^2)	K	Coefficient of heat transmission of the semi-trailer ($W.m^{-2}.K^{-1}$)
Bi	Biot number $= \frac{hR_{eq}}{k}$	m	Product mass (kg)
Cp	Thermal capacity of pork ($J.kg^{-1}.K^{-1}$)	R_{eq}	Equivalent radius of carcass (m)
F_o	Fourier number $= \frac{\alpha t}{R_{eq}^2}$	T	Temperature (°C)
$\dot{Q}$	Rate of heat flow to be evacuated from the carcass (W)	T*	Dimensionless temperature $= \frac{T(t)-T_a}{T_0-T_a}$
h	Convective heat transfer coefficient ($W.m^{-2}.K^{-1}$)	t	Time (s)

Greek symbols

ρ	Density ($kg.m^{-3}$)	α	Thermal diffusivity ($m^2.s^{-1}$)

Subscript

a	Air	ext	External
av	Average	int	Internal
c	Core	0	Initial
D	Derogation	R	Regulation
		s	Surface

REFERENCES

Beysens, D., 1995. The formation of dew. Atmos. Res. 39, 215-237.

Daudin J.D., Kuitche A., 1996. Modelling of temperature and weight loss kinetics during meat chilling for time variable conditions using an analytical based method - III. Calculations versus measurements on pork carcass hindquarters. J. Food Engineering 29(1), 39-62.

Harkouss, R., Chevarin C., Daudin J.D., Sicard J., Mirade P.S., 2018. Development of a multi-physical finite element-based model that predicts water and salt transfers, proteolysis and water activity during the salting and post-salting stages of the dry-cured ham process. J. Food Engineering 218, 69-79.

James, S., 1996. The chill chain “from carcass to consumer”. Meat Science 43(1), 203-216.

Mirade, P.S., Picgirard, L., 2001. Assessment of airflow patterns inside six industrial beef carcass chillers. Int. J. Food Sci. Technol. 36, 463-475.

Kondjoyan, A., S. Oillic, S. Portanguen, J.B. Gros, 2013. Combined heat transfer and kinetic models to predict cooking loss during heat treatment of beef meat. Meat Science 95(2), 336-344.

Merai M., Flick D., Guillier L., Duret S., Laguerre O., 2018. Experimental characterization of airflow inside a refrigerated trailer loaded with carcasses. Int. J. Refrigeration 88, 337-34.

Merai M., Flick D., Guillier L., Duret S., Laguerre O., 2019. Experimental characterization of heat transfer inside a refrigerated trailer loaded with carcasses. Int. J. Refrigeration 99, 194-203.

Mirade, P.S., 2007. CFD modelling of indoor atmosphere and water exchange during the cheese ripening process. Da-Wen Sun (Ed.), Computational fluid dynamic in food processing, CRC Press, 697-726.

Moureh, J., Flick, D., 2005. Airflow characteristics within a slot-ventilated enclosure. Int. J. Heat and Fluid Flow 26, 12-24

Manuscript ID: 306
DOI: 10.18462/iir.icr.2019.0306

Design and application of a novel cold chain pallet using a phase change material

Guanghai LIU[(a)], Junzhang WU[(a)], Ruhe XIE[(a)], Judith EVANS[(b)], Alan FOSTER[(b)]

[(a)] Management School, Guangzhou University, Guangzhou 510006, China
broadsea@gzhu.edu.cn
[(b)] School of Engineering, London South Bank University,
Bristol, BS40 5DU, UK, alan.foster@lsbu.ac.uk

ABSTRACT

Transport vehicles have low utilisation rates in developing countries. This is due to the initial cost of the refrigerated transport vehicles and the high operating costs consisting of energy consumption and manual labour. A novel cold chain pallet incorporating water as a phase change material (PCM) has been designed. When in use, the PCM pallet is put into a cold store and the water is frozen. In transportation, the foods are stored in an insulated vehicle along with PCM pallets. The latent heat of water is used to maintain the temperature inside the vehicle. Air temperature inside the carriage was measured for different PCM mass (100, 200, 300 kg), different time (24, 48, 72h), with and without forced convection. The experimental results show that the time the air temperature was <10ºC was 66.3%, 92.1% and 94.7% of the duration without forced convection and 92.5%, 97.3% and 98.6% with forced convection, when the PCM mass was 100, 200 and 300 kg respectively. Because no special refrigeration system is needed and the number of PCM pallets can be selected according to the required cooling capacity, the initial investment and operating costs of PCM pallets is much lower than existing refrigerated trucks.
Keywords: Refrigerated Transport, Phase Change Material, Energy Consumption, Temperature Distribution.

1. INTRODUCTION

With improvements in living standards and the demand for perishable food increasing, the use of refrigerated transport equipment has grown rapidly in developing countries. China Federation of Logistics & Purchasing (2018) shows that the number of refrigerated transport vehicles increased from 41,000 to 134,000 in China in the past 5 years. The average annual growth rate in this sector is expected to be more than 10% over the next 5-10 years. Despite rapid growth, there is a significant difference in the number of refrigerated vehicles per capita between China and developed countries (for example, 1/10,000 in China and 14/10,000 in the UK) (Rai and Tassou, 2017).

China's perishable food transportation capacity was more than 300 million tons in 2017. Non-refrigerated transport vehicles (insulated or uninsulated) are often used in transportation of fresh fruits and vegetables. These issues result in the food waste associated with food logistics being more than 30% (China Federation of Logistics & Purchasing, 2018). In 2016 annual food loss was valued at RMB 100 billion (Chinese Association of Refrigeration, 2016).

In China, less than 20% of goods are transported by pallets (Ministry of Commerce of China, 2017). Although reducing the initial investment in logistics, it is inefficient, time-consuming and costly. According to China Federation of Logistics & Purchasing (2017), energy consumption and labour cost account for more than 80% of the total cost in China's cold chain logistics operation. Therefore the transporter must balance the quality of the food and the cost of transportation. To ensure food is of high quality and to reduce the cost of transporting food it is necessary to reduce the energy consumption of refrigerated transportation and improve mechanization.

Phase change material (PCM) based refrigerated vehicles have been used for many years in many countries to reduce costs (Chinese Association of Refrigeration, 2016). PCMs have the following advantages compared with mechanical refrigerated transport compartments. They make rational use of power resources, allowing charging of the PCM at night, when electricity is cheap and

using/discharging the PCM during the day. They can replace fossil energy (diesel fuel) with electrical energy. This has the potential to reduce greenhouse gas emissions (as grid energy becomes decarbonised), air pollution and heat island effects in the city (as combustion is moved from away from the city) (Li et al., 2018).
Countries, such as the United States, Britain and Italy, have developed PCM refrigerated trucks, and the related technologies and performance have been rapidly improved (Li, et al., 2018). Liu et al. (2012) simulated a mobile refrigeration system incorporating PCM and used this in refrigerated trucks in Australia. The simulation showed that the PCM could maintain the refrigerated space at -18ºC for 10 hours using 250 kg PCM without opening the door. Darzi et al. (2016), Zarma et al. (2017) and Xie et al. (2017) analysed the PCM heat transfer structure, heat transfer performance and layout respectively. Zhan et al. (2008) analysed the effect of the PCM at different positions in the refrigerated vehicle. Zhang et al. (2013) simulated the temperature field of the PCM refrigerated vehicle by different cargo stacking methods. The above research provides a reference for the improvement and optimization of the cold storage transportation equipment.
In this paper, a novel PCM pallet was designed to aid cold chain logistics and improve operational efficiency for developing countries. The PCM was frozen using off peak night electricity in a cold store and moved through the cold chain with the perishable product. The PCM can be used in insulated and unrefrigerated vehicles. The paper presents information on temperature within the transport vehicle and the effect of air distribution in the vehicle.

2. METHOD

2.1. The Size and Structure of the PCM Pallet

The pallet's structure and physical drawings are shown in Fig. 1 and Fig. 2.

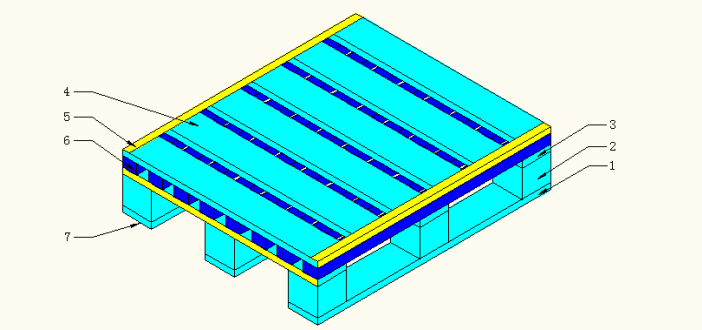

Figure 1: The schematic diagram of PCM pallet.



Figure 2: Photograph of PCM pallet.

The pallet was composed of bottom deck boards, top deck boards, load-bearing blocks, stringer boards and cold storage tubes. The cold storage tubes were made of food grade No.304 hollow rectangular stainless steel pipes (wall thickness, 1.5mm) with the PCM sealed in them. Eight cold storage tubes were evenly placed below the top deck boards with dimensions of 100 (W) × 50 (H) × 1200 (L) mm. Each cold storage tube could contain up to 5 kg of the PCM, therefore, each pallet could carry up to 40 kg of PCM. The bottom deck boards, top deck boards, load-bearing blocks and stringer boards were made of wood and angle steel was used to protect the cold storage tubes. The bottom of the pallet was provided with an antiskid shim to avoid the pallet sliding on water or ice. The above components were connected by fastening bolts so that any damaged parts could be replaced separately according to actual needs during use. On the basis of considering the convenience of circulation between companies, the size of the cold chain pallet used in this study was standardised to 1.0 × 1.2 m.

2.2. The Selection of the PCM

In China, frozen trucks which are used to transport meat and fish account for more than 90% of the cold-chain trucks. Fruits and vegetables are often transported without temperature control causing the loss of vitamins and other nutrients (Chinese Association of Refrigeration, 2016). Due to the lack of refrigerated transport for fruit and vegetables the focus of this study was chilled transportation.

The PCM therefore needed to control temperature between 0 and 10ºC, have a large latent heat phase change, stable chemical composition, be non-toxic and have a low price. Water, was selected for this study for the following reasons. Firstly the phase transition temperature of water is 0ºC, which meets the transportation needs of most chilled products. Secondly, the chemical properties of water are stable and non-toxic, even if the pallet is damaged during use, it will not contaminate the food. In addition, the latent heat of fusion of water is high (334 kJ/kg), and the price is almost negligible.

2.3. Design of Test Platform

In order to investigate the effect of the PCM pallets, a test was carried out using an insulated truck, as shown in Fig. 3.

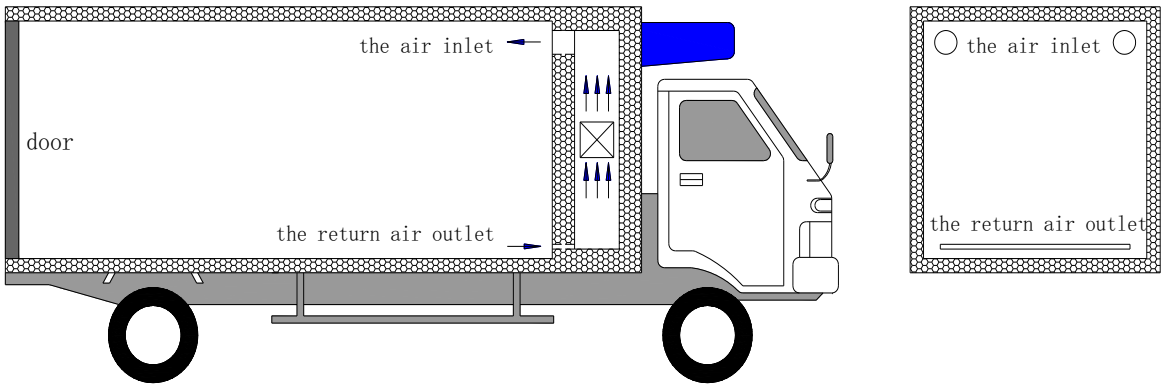

Figure 3: The insulated truck for testing.

(1) The outside and inside dimensions of the containers (in m) were 5.80×2.28×2.24 and 4.98×2.04×2.00 (length×width×height) respectively. The walls of the container and inner partition between the fan section and container were all polyurethane insulation board, and the inner and outer skin used fibre reinforced polymer/plastic (FRP) composite. The thickness of the walls of the carriage were 0.12 m and the floor was pattern aluminum plate.
(2) The truck had a forced convection air system which was located at the front end of the vehicle and was connected with the vehicle through the air inlet and the return air outlet. The air inlet was located on both sides of the front end of the vehicle, which was 0.05 m and 0.10 m from the roof and side walls, respectively. The inlet hole was circular, 0.25 m in diameter. The return air inlet was located near the floor at the front of the carriage. The rectangular structure was 1.7 × 0.04 m (length × height). The air circulation was controlled by the fan in the forced convection system.
(3) In order to investigate the temperature stability of the PCM pallet, the system was tested to conform with refrigerated transportation equipment standards, such as ISO 1496-2, GB/T 7392, GB 29753, etc.
When the temperature field was tested, the refrigerated carriage and PCM pallets remained empty of product. Eleven temperature sensors were arranged 0.10 m from the outer surface of the carriage, (Figure 4a). Fifteen temperature sensors were arranged 0.10 m from the inside of the carriage (Figure 4b). The semi-conducter temperature sensors (TZ-Tag06B, Tzone Digital Technology Co. Ltd.), had an accuracy of ± 0.3K over the range -40ºC to +125ºC.

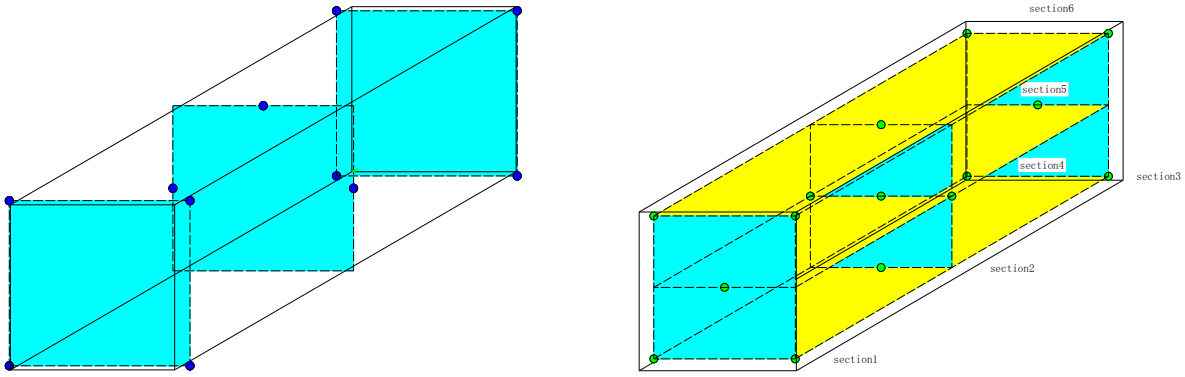

a) Temperature sensor layout outside the carriage b) Temperature sensor layout inside the carriage

Figure 4: Temperature sensor layout of the carriage.

2.4. Experiment Design

The concept of the PCM pallet was different from the traditional cold storage vehicle in its application. Firstly, the PCM pallet was put into a cold store and the PCM was frozen by the refrigeration system in the cold store (for freezing quickly, the air temperature of cold store should be below -18ºC). When fruits and vegetables are picked, they are packed in boxes and crates, then transported to cold store and placed on PCM pallets. When they need to be transported, the fruits/vegetables and PCM pallets are transported together in a thermal insulated vehicle (no refrigeration). The latent heat of the PCM was used to maintain the temperature inside the vehicle during its delivery.

A stationary prototype thermally insulated vehicle was constructed and tested. The insulated carriage of corresponding sizes and construction were manufactured following strict criterions designed by Guangzhou Baier Cold-Chain Polyurethane Technology Co.,Ltd (www.pvc123.com/b-gzbaier/). The use of thermally insulated materials and polyurethane foaming technology is the most stable and safe practice within the insulated truck industry. The heat leakage rate of the carriage was measured as 24 W/K by previous experiments. All test behavior were monitored in Guangzhou, the largest city in the south of China. Although the ambient temperature may have been different during the testing, it was still well controlled in which the ambient conditions were at approximately 31ºC in the day and at approximately 25ºC at night.

The following two problems should be solved when designing the PCM pallet.

(1) The calculation of cold storage capacity

The PCM relies mainly on the latent heat of phase change at 0°C rather than the sensible heat to maintain the temperature in the vehicle. To test the effect of the cold chain pallet, the researchers tested 100, 200 and 300 kg of PCM in a vehicle (pallets of 12.5, 25 and 37.5 kg, respectively) over 24, 48 and 72 h, respectively. The timescales selected from the trials were based on transportation temperatures in China for most fruits and vegetables being no more than 10ºC (based on GB 22918/T, China's Recommended National Standards) and the transportation times being less than 3 days. The PCM pallets were cooled for 10 hours in the cold store (using low tariff electricity price from 10 pm to 8 am). Previous experiments using a temperature sensor in the PCM showed that the temperature dropped below freezing temperature in this time. During cooling the air temperature in cold store was -18ºC. The pallets were then transferred to an insulated vehicle and laid evenly in the base of the vehicle. The vehicle door was closed and the temperature changes in the carriage were recorded.

(2) The distribution of temperature in the carriage

The PCM pallet was located at the base of the vehicle, to reduce the center of mass and increase the available storage space. However, due to buoyancy, temperatures would likely stratify without forced convection. So, the same group of pallets with the same weight were tested twice, with and without forced convection.

3. RESULTS

3.1. Influence of Different PCM Mass and Forced Convection on Temperature Control

Fig. 5 shows the effect of cold storage capacity and convection on vehicle temperature control. When the PCM was 100, 200 and 300 kg in the vehicle.

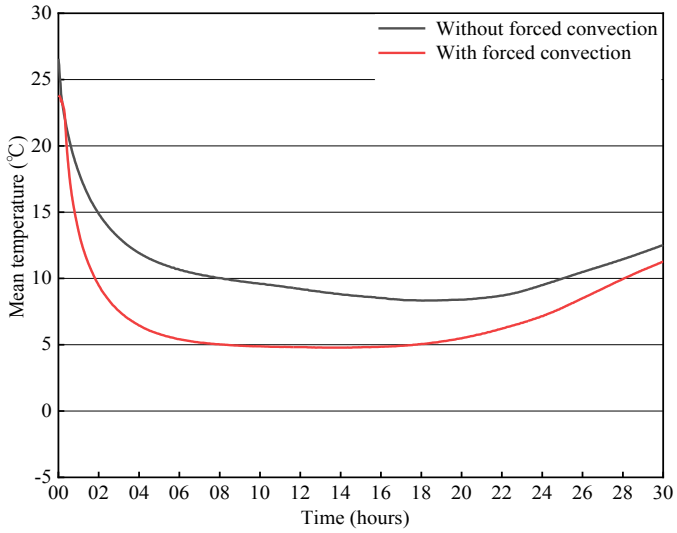

a) A total of 100 kg of PCM

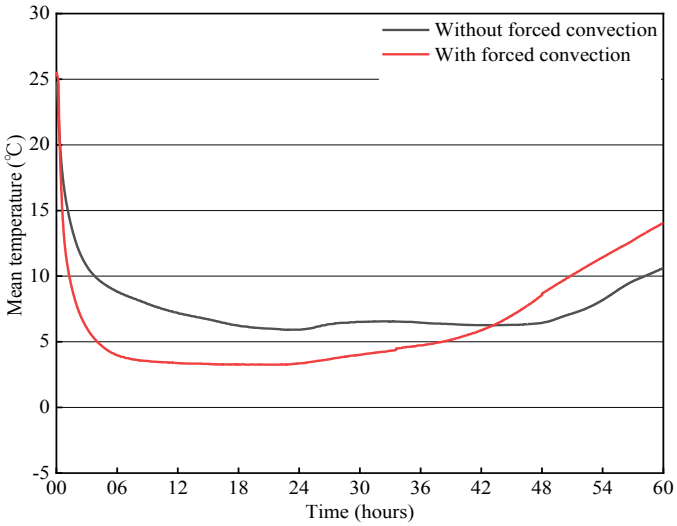

b) A total of 200 kg of PCM

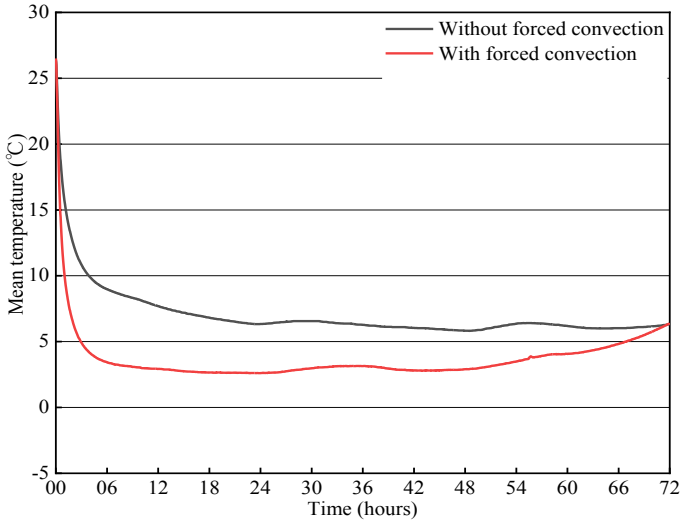

c) A total of 300 kg of PCM

Figure 5: Average temperatures measured in the carriage with or without forced convection.

Table 1 shows the variation of mean temperature and temperature <10ºC in the truck under different PCM weights and with or without forced convection. So, transporters can therefore choose the number of PCM pallets needed according to the transportation time, avoiding the shortcomings of traditional PCM trucks which have fixed PCM weight. Measurements also shows a significant difference in cooling time (from ambient temperature to 10 ºC) with and without forced convection. Without forced convection, as the PCM pallets are located at the bottom of the carriage, they do not drive natural convection and the convection heat transfer between the cold chain pallets and the air in the vehicle is slow, thus the time to cool the vehicle is long.

Figs. 6 and 7 show the distribution of air temperature in each group of experiments without and with forced convection. It can be seen that when there is no forced convection in the vehicle, the vertical stratification of temperature in the carriage is significant, and the difference in temperature between the section 4 and section 6 is approximately 3 K. When forced convection is applied in the carriage, temperature stratification is reduced. The temperature fluctuation range between section 1 to section 6 is less than 0.7 K.

Table 1. The temperature in the carriage under different condition

PCM mass (kg)	Forced convection condition	Mean temperature (ºC)	Percentage of temperature < 10ºC in the test period
100	No	10.4	66.3
	Yes	6.2	92.5
200	No	7.3	92.1
	Yes	4.6	97.3
300	No	7.0	94.7
	Yes	3.7	98.6

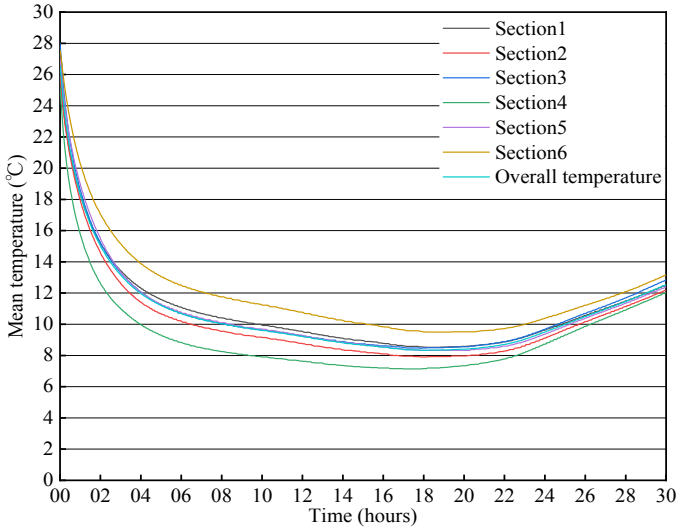

（a）

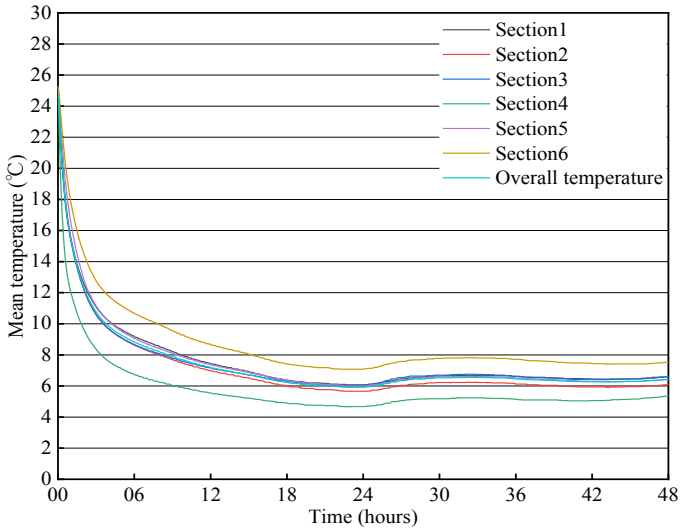

（b）

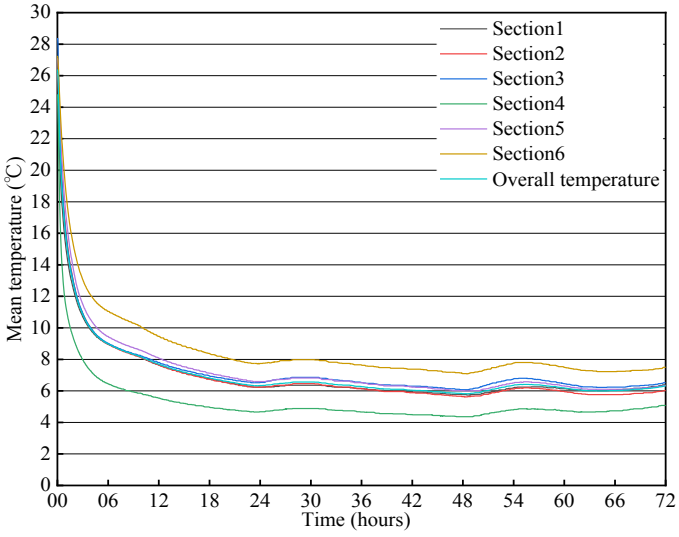

（c）

Figure 6: Average temperature history of each section of carriage without forced convection: (a) 100 kg of PCM, (b) 200 kg of PCM, and (c) 300 kg of PCM.

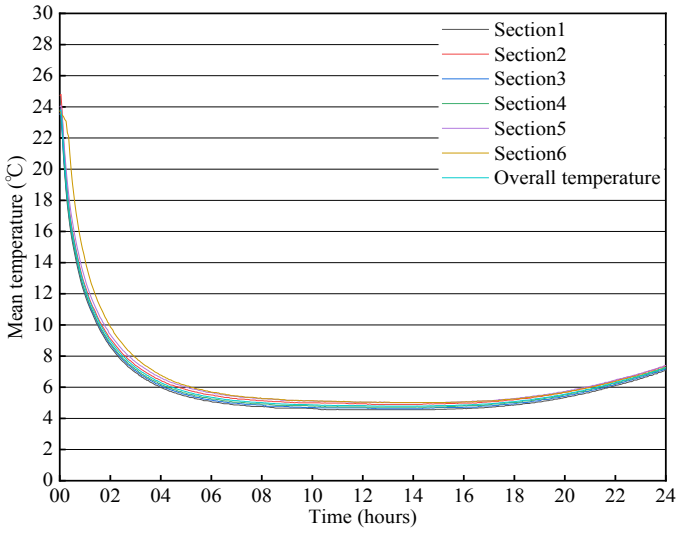

（a）

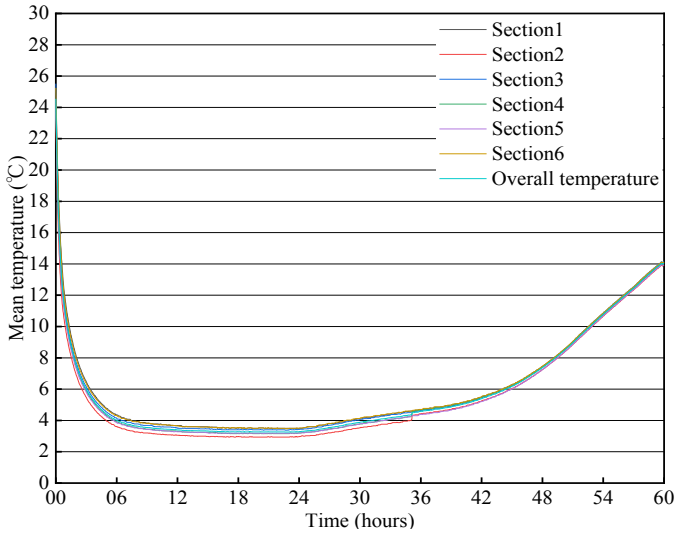

（b）

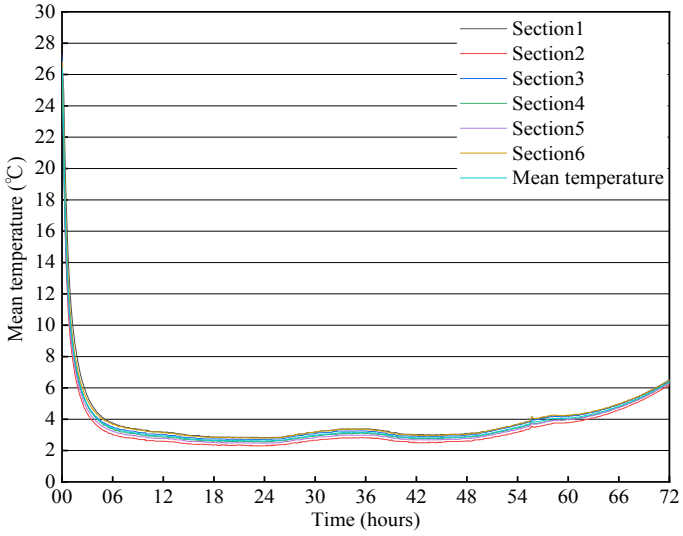

（c）

Figure 7: Average temperature history of each section of carriage with forced convection: (a) 100 kg of PCM, (b) 200 kg of PCM, and (c) 300 kg of PCM.

4. CONCLUSIONS

A novel PCM pallet has been designed. The PCM pallet enables the use of cheap electricity at night to store energy, instead of using diesel fuel from a refrigerated vehicle. When in use, the PCM in the pallet can be frozen by the refrigeration system of a cold store. In transportation and distribution, foods are stored on the PCM pallet in a thermal insulation vehicle (no refrigeration). The weight of PCM can be selected according to the transportation time when using the PCM pallets. When forced convection is applied, the temperature distribution in the carriage is uniform. Because no special refrigeration system is needed, the initial investment and operating costs of PCM pallets are much lower than most existing refrigerated trucks. It can effectively reduce the transportation cost while guaranteeing the quality and safety of goods, and provides the potential for the application of the PCM refrigerated truck in developing countries. Further work will consider the effects of food loading, environmental temperature, PCM material and humidity.

ACKNOWLEDGEMENTS

This work was done collaboratively between Guangzhou University and London South Bank University. The authors would like to thank the financial support from Department of Science and Technology of Guangdong Province (No.2017B020206006) and Department of Commerce of Guangdong Province in China.

REFERENCES

China Federation of Logistics & Purchasing, 2018. The current situation and trend of cold chain logistics in China. China Fortune Press, Beijing, 31-36.

China Federation of Logistics & Purchasing, 2017. The current situation and trend of cold chain logistics in China. China Fortune Press, Beijing, 16-29.

Chinese Association of Refrigeration, 2016. Research Report on the strategic development of China's refrigeration industry. China Architecture & Building Press, Beijing, 256-269.

Darzi, A.A.R., Jourabian, M., Farhadi, M., 2016. Melting and solidification of PCM enhanced by radial conductive fins and nanoparticles in cylindrical annulus. Energy Conversion and Management, 118, 253-263.

Chinese Automobile Standardization Technical Committee, 2014. Safety requirements and test methods for refrigerating van for transporting food and biological products on road: GB 29753, China Standards Publishing House, Beijing, 1-15.

Chinese Refrigeration Standardization Technical Committee, 2008. Technical requirements for temperature-controlled transportation of perishable food: GB/T 22918, China Standards Publishing House, Beijing, 1-23.

Chinese Freight Containers Standardization Technical Committee, 2008. Series 1 thermal containers--Specification and testing: GB/T 7392. China Standards Publishing House, Beijing, 1-46.

Li, J., Xie, R., Liu, G., Foster, A., 2018. Development of New Low Temperature Phase Change Storage Material and Equipment Used in Refrigerated Transportation. Journal of refrigeration 39(4), 32-37.

Liu, M., Saman, W., Bruno, F., 2012. Development of a novel refrigeration system for refrigerated trucks incorporating phase change material. Applied Energy 92, 336-342.

Ministry of Commerce of China, 2017. Monitoring and analysis report on China's pallet standardization development in 2016. Beijing.

Rai, A., Tassou, S.A. 2017. Energy demand and environmental impacts of alternative food transport refrigeration systems. Energy Procedia 123, 113-120.

The Freight Containers Technical Committee of International Organization for Standardization, 2008. Series 1 freight containers-Specification and testing - Part2: Thermal containers: ISO 1496-2-2008. International Organization for Standardization, Geneva. 1-20.

Xie, R., Tang, H., Tao, W., Liu, G., Liu, K., Wu J., 2017. Optimization of cold-plate location inrefrigerated vehicles based on simulation and test of no-load temperature field. Transactions of the Chinese Society of Agricultural Engineering 33(24), 290-298.

Zarma, I.H., Hassan, H., Ookawara, S., Ahmed, M., 2017. Thermal energy storage in Phase Change Materials: - applications, advantages and disadvantages. 1st International Cnferecne of Chemical, Energy and Environmental Engineering, Egypt, 1-11.

Zhang, Z., Gu, Y., Tian, J., Li, M., 2013. Numericalsimulationand experiment of temperature fielddistribution in box of coldplate refrigerated truck. Transactions of the Chinese Society of Agricultural Engineering 29(25), 18-24.

Zhan, Y., Dong, Q., Wang, S., 2008. Simulation on inner temperature field of railroad cold-plate refrigerator car with cold plates laid on side. Cryogenics (3), 61-64.

Manuscript ID: 352
DOI: 10.18462/iir.icr.2019.0352

Design and performance evaluation of an R744 multi-temperature refrigerated container

Neal LAWRENCE [(a)], Stefan ELBEL [(a, b)], Pega HRNJAK [(a, b)]

[(a)] Creative Thermal Solutions, Inc.
2209 N. Willow Rd., Urbana, IL 61802, USA
neal.lawrence@creativethermalsolutions.com
[(b)] Air-Conditioning and Refrigeration Center
Department of Mechanical Science and Engineering
University of Illinois at Urbana-Champaign
1206 W. Green St. Urbana, IL 61801, USA

ABSTRACT

This paper describes the design and experimental validation of a multi-temperature refrigerated container unit using transcritical R744 as the refrigerant. The unit is required to maintain refrigerated and frozen compartment temperatures of 3.3°C and -20.6°C at an ambient temperature of 57°C. The paper discusses the unique design challenges presented by a small-capacity (around 7 kW) R744 system operating at these extreme temperature conditions. A number of system improvements are implemented in order to meet the capacity requirements at the design condition, namely the addition of an internal heat exchanger (IHX) and an ejector for expansion work recovery to the cycle as well as the use of microchannel heat exchangers for gas coolers. The details of the design of the system and components to address the unique challenges of this application are discussed. Initial experimental results investigating the operating range of the compressor are presented.
Keywords: Transcritical carbon dioxide; refrigerated container; booster cycle; system design; energy efficiency

1. INTRODUCTION

CO_2 (R744) refrigeration systems have gained interest in recent years due to its reputation as an environmentally friendly refrigerant and its good performance in refrigeration systems in low to moderate ambient temperatures. Of particular interest have been stationary refrigeration systems including supermarkets (where the use of CO_2 booster systems is spreading rapidly) and light commercial refrigeration such as glass door merchandisers (though CO_2 use has declined in the past few years in this application). CO_2 would be equally suitable for mobile refrigeration applications, such as refrigerated containers, rail cars, or trucks and trailers, through these applications have gained less attention so far, possibly because they are smaller industries compared to commercial refrigeration. This paper focuses on the design of a CO_2 refrigeration unit for a refrigerated container with a focus on improving unit operating range and energy efficiency.

While refrigerated containers have been in use for many years, conversion to a CO_2 refrigeration unit has only been attempted very recently. Refrigerated containers with CO_2 refrigeration units are currently available on the market for single-temperature containers; these systems use a two-stage compressor with intercooling and vapor injection at intermediate pressure to improve performance (Carrier, 2015). Lawrence *et al.* (2018) showed through numerical simulation that a baseline CO_2 container system with multi-stage compression but no IHX or ejector could achieve a COP of 0.57 at an ambient temperature of 57°C. Addition of an IHX could improve COP by 35 %, while addition of an ejector (without IHX) could improve COP by 27 %; combining an ejector and an IHX into the same system yielded a COP of up to 0.96, an improvement of 69 %. Barta *et al.* (2018a) also investigated a multi-temperature CO_2 container unit numerically and focused on controls optimization

for a system with an expander instead of an ejector. Barta et al. (2018b) reported that a COP of up to 1.28 could be achieved for an ambient temperature of 57°C with an expander efficiency of 70 %. Poolman *et al.* (2018) presented experimental results for a commercially available ejector installed in the single-temperature CO_2 refrigerated container on the market described above; they observed that the ejector could reduce annual energy consumption by 1 % on its own and by up to 6 % when combined with an internal heat exchanger (IHX).

The objective of this paper is to discuss details of the design of a 20 ft. (6 m) ISO multi-temperature refrigerated container using CO_2 as the refrigerant. Design and implementation of a container unit with reasonable energy efficiency is challenging in this application because of the very high design ambient temperature of 57°C and because the small size and capacity of the system limits the equipment that can be included to help improve efficiency. The solutions being implemented to help improve efficiency, including compressor selection, heat exchanger design and selection, and expansion work recovery, are presented and discussed. Initial experimental results investigating the operating range of a compressor of interest are also investigated.

2. CO_2 REFRIGERATION UNIT DESIGN

2.1 Design Requirements

The container is being designed specifically for military applications, which requires that 1/4 of the container be kept at low temperature (-20.6°C) for frozen food and the other 3/4 of the container be kept at medium temperature (3.3°C) for fresh food, as shown in Fig. 1(a). It was estimated that at the design ambient temperature of 57.2°C, 2.5 kW of cooling capacity is required for the LT portion of the container, and 3.2 kW of cooling capacity is required for the MT portion of the container. Fig. 1(b) shows the currently used unit, which uses R404A as the refrigerant; comparison to the baseline unit is not part of the current study, as the baseline unit cannot meet the capacity requirement at high ambient temperature. The performance targets of the unit include allowing for 30 % reserve capacity at the design condition, with a COP of at least 1.0. The refrigeration unit, which is mounted to an extension on the end of the container, is also limited to a 1.8 m (W) x 0.6 m (D) x 0.6 m (H) space and a weight of 540 kg.

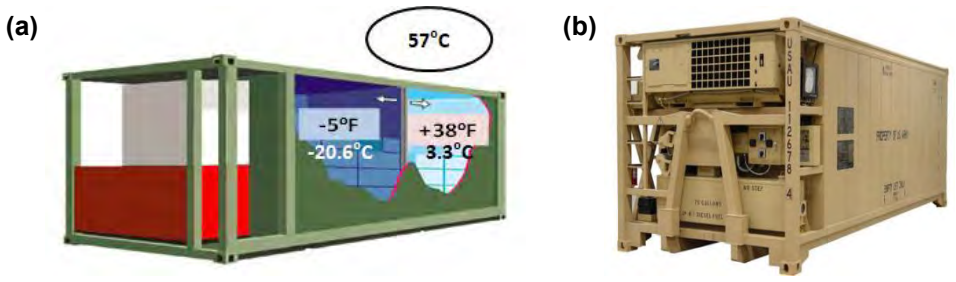

Fig. 1: Refrigerated container for military applications: (a) design conditions of container and (b) baseline R404A unit

2.2 Compressor Selection

Compression between LT evaporator pressure (approximately 14 bar) and high-side pressure (130 bar) cannot be accomplished in a single or possibly even two stages of compression. To help reduce the pressure ratio, compression from LT pressure to MT pressure is commonly accomplished with a subcritical booster compressor. Most CO_2 refrigeration compressors are designed for supermarkets or other stationary industries where size and weight are less of a concern than in mobile applications. As a result, the majority of CO_2 compressors are semi-hermetic reciprocating compressors, which are generally high in weight in order to safely accommodate high pressures. Hermetic scroll compressors are advantageous because of their much lower weight compared to semi-hermetic reciprocating compressors, though the scroll design is limited in pressure and often cannot operate above 50 bar. The majority of subcritical CO_2 compressors are reciprocating type, though there is one line of subcritical scrolls currently on the market. The subcritical scroll selected for this system has a nominal displacement of 2.6 m^3 hr^{-1} (yielding a predicted capacity of 2.6 kW at full speed), an

operating pressure range down to 7 bar (-50°C saturation temperature) on the suction side and up to 40 bar (5°C) on the discharge side, and a weight of 22 kg (compared to close to 50 kg for comparable subcritical reciprocating compressor options) and is pictured in Fig. 2(a).

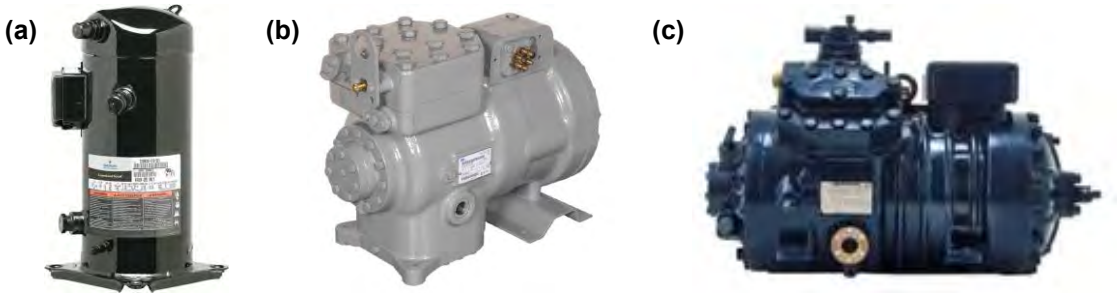

Fig. 2: (a) subcritical scroll compressor, (b) two-stage transcritical compressor for MT refrigeration and (c) two-stage transcritical compressor for LT refrigeration

No scroll compressor options were available for a transcritical applications due to the pressure limitation of scroll compressors. Several options for transcritical rotary CO_2 compressors are available but only in lower capacity ranges than needed in this system. Thus, the only option for the transcritical compressor is a reciprocating compressor. As will be shown in the experimental results presented below, it is difficult for a single-stage compressor to yield reasonable COP for a refrigeration system even at 40°C ambient, meaning that in order to reach the design ambient temperature of 57°C, it is likely that two-stage compressor will be necessary. Two-stage compression will improve the COP of the cycle (reduced compressor power) as well as expand the operating range of the cycle due to the reduction in compressor discharge temperature and ability to operate at higher discharge pressures. The options for two-stage transcritical CO_2 reciprocating compressors are currently limited, as only two different suitable product lines could be identified, one of which was intended for LT refrigeration (very low suction pressures) only and the other intended for MT refrigeration (more in line with suction pressures to be used in this system). The two-stage compressor for MT refrigeration, shown in Fig. 2(b), was selected for use in this system; it has a nominal displacement of 5.8 $m^3\ hr^{-1}$ (allowing for a capacity of close to 10 kW at its maximum speed) and an operating range of suction pressure down to 29 bar (-5°C saturation temperature) and discharge pressure up to 125 bar.

2.3 Heat Exchanger Design

In order to achieve as high of COP as possible at the design condition, it will be critical to achieve as small of gas cooler approach temperature (refrigerant outlet less ambient) as possible because of the very high ambient condition, making gas cooler design important to achieving the desired system efficiency. Because of their superior air-side performance and the fact that they were made with light-weight, low-cost aluminum, microchannel gas coolers were selected for this system. Multiple microchannel slabs were chosen to ensure sufficient gas cooler area for the system. The microchannel slabs have different face area but the same tube and fin geometry, and each slab was 4 rows deep. The major and minor diameter of the microchannel tubes were 7.9 mm and 1.4 mm, respectively, and each tube had 4 microchannel ports of around 0.9 mm hydraulic diameter. The fin pitch was approximately 1.5 mm. An example of one of the slabs used is shown in Fig. 3(a). The combined air-side area of the microchannel slabs is 20.2 m^2. As will be shown in the experimental results section, these gas coolers would be expected to achieve an approach temperature less than 2 K, which is generally considered to be good gas cooler performance. Additionally, the use a two-stage compressor allows for the addition of an intercooler to the system; the intercooler had the same tube and fin dimensions as the gas cooler slabs, with a total air-side area of 2.8 m^2.

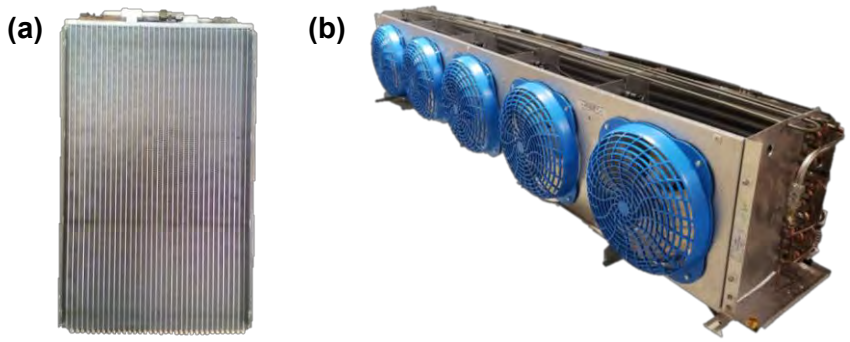

Fig. 3: Heat exchangers to be used in system: (a) microchannel gas cooler slab and (b) round-tube evaporator (same for both LT and MT)

On the other hand, a microchannel heat exchanger, while used as evaporators in automotive applications, are generally not suitable for refrigeration applications due to their difficulty in handling condensate and frost as well as the issue of refrigerant maldistribution when a two-phase flow enters the header. Instead, conventional round-tube evaporators are still used even transcritical CO_2 systems, with the particular unit used as both MT and LT evaporators shown in Fig. 3(b). The evaporator coils have 3 rows of 14 tubes each (9.5 mm tube diameter), arranged in three refrigerant circuits for optimized mass flux. The overall finned height, width and depth of the coil are 370 mm, 2030 mm, and 66 mm, respectively, and the fin pitch was 4.2 mm. These dimensions yield a total air-side area of approximately 24 m^2 per evaporator, which is oversized for the desired capacity but should help improve system efficiency; the face velocity is about 2 m s^{-1}.
Evaporator performance was simulated using the software package Evap-Cond (NIST, 2016). It was found that with 10K refrigerant-to-air temperature difference in the evaporator and 5 K of superheat under LT conditions, the evaporator would allow for up to 6.7 kW of capacity, which is about double what would be needed for MT conditions. Thus, the system should easily be able to operate at design condition with less than 10 K temperature difference in the evaporators. Nonetheless, this larger evaporator area will be beneficial during pulldown operation when larger capacity is desired.

2.4 Internal Heat Exchanger and Expansion Work Recovery

One simple way to significantly boost the capacity and COP of a CO_2 cycle is to include an internal heat exchanger (IHX), which further cools the high-pressure fluid after the gas cooler using the lower-temperature fluid from the evaporator. This is most easily accomplished with a small brazed plate heat exchanger capable of withstanding the CO_2 pressures. In this system, the CO_2 IHX had a heat transfer area of 0.33 m2, overall dimensions of 191 mm (length) x 77 mm (width) x 43 mm (height), and a weight of 2.4 kg.
Another very effective method for improving the performance of transcritical CO_2 cycles is expansion work recovery, as commonly accomplished with an ejector or an expander, with much recent research opting for the ejector due to its simplicity in construction and implementation. In a multi-temperature refrigeration system, the ejector is most commonly used to lift the pressure of the fluid exiting the MT evaporators. In supermarket systems, multiple ejector in parallel are used to pump liquid and vapor separately, with the vapor being sent to a set of parallel compressors. However, in this smaller-scale application, it is not reasonable to include multiple ejectors or parallel compressors, meaning the ejector simply lifts the pressure of the MT evaporator flow before the MT compressor. Sample experimental results demonstrating the potential of an ejector in this system are presented in the following section. An ejector was designed and built in-house, shown in Fig. 4, based on extensive previous experience with CO_2 ejectors. The ejector uses a stepper motor to control the position of a needle in the motive nozzle which is used to control and optimize high-side pressure of the system.

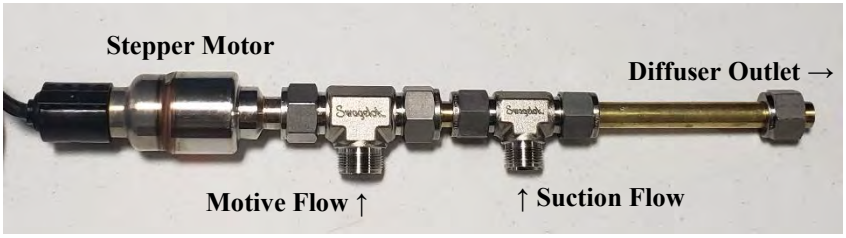

Fig. 4: In-house, modular, adjustable ejector

3. EXPERIMENTAL RESULTS

3.1 Ejector Results

Experimental results for the performance of the in-house ejector described above were obtained on an ejector component testing rig; the results for ejector pressure lift (outlet pressure less suction pressure) and work recovery efficiency (actual power to compress suction stream divided by theoretical maximum power available from expansion of motive stream) are presented in Fig. 5. Ejector suction pressure and quality were around 30 bar and 0.9, which is on the high end in terms of pressure of what the ejector would be expected to see in the container system though still fairly reasonable. Several different ambient conditions were simulated, with ejector motive temperature shown on the chart; given the large temperature difference in the IHX, it can be assumed that the gas cooler outlet temperature would be around 15 K higher than the motive inlet temperature. In this case, the two points at highest motive temperature would then be representative of the design condition of the container system.

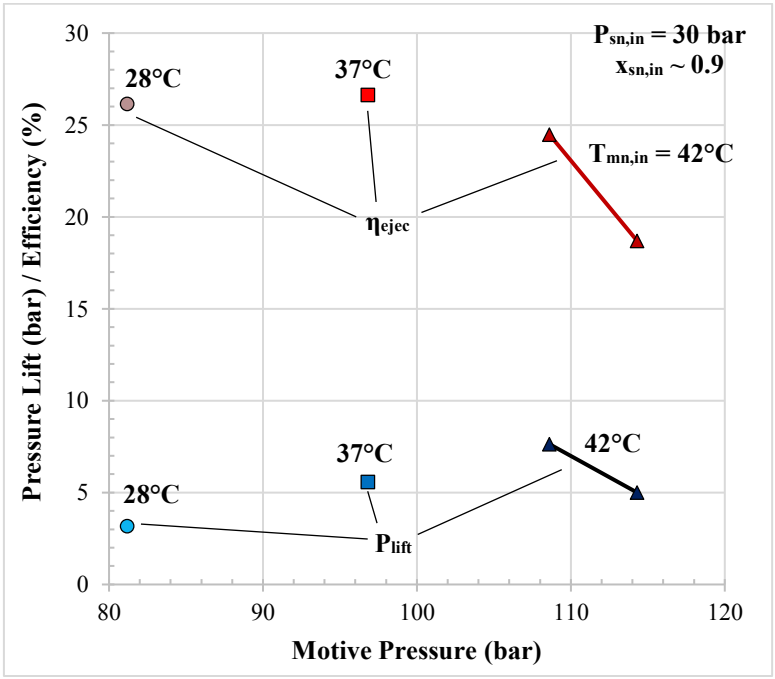

Fig. 5: Sample performance results from in-house ejector shows opportunity for significant pressure lift (up to 8 bar) at container design condition

It can be seen from Fig. 5 that significant ejector pressure lift (maximum observed up to 7.6 bar) is achievable at conditions representing the design condition of the container, meaning a direct increase of 7.6 bar in MT compressor suction pressure and a considerable improvement in energy efficiency. The ejector work recovery efficiency was only 24 % in this case; slightly higher efficiency was achieved at conditions of lower motive pressure and temperature. This demonstrates that with further ejector geometry optimization, a few percent higher ejector efficiency could possibly achieved, yielding still higher ejector pressure lift.

3.2 Baseline System-level Results

Initial experimental results have been obtained on a breadboard test facility with similar components that will be used in the container unit described above. A transcritical CO_2 system with a single-stage compressor and a single evaporator was assembled in environmental chambers to control refrigerated (indoor) and outdoor conditions. Open loop wind tunnels were used to control air flow rate and temperature to the gas cooler and evaporator. A single-stage compressor was used; the compressor speed was maintained at 40 Hz, yielding a displacement rate of 5.0 $m^3\ hr^{-1}$ at this speed. The refrigerated air temperature was set to 3°C (dry), while the outdoor temperature was varied between 20 and 40°C. The gas coolers described above were used for these tests. The evaporator was a round tube heat exchanger but was different than the evaporator coils described above being installed in the container unit. Other components, such as the IHX, expansion valve, and intermediate pressure receiver, are the same or very similar to what will be used in the container.

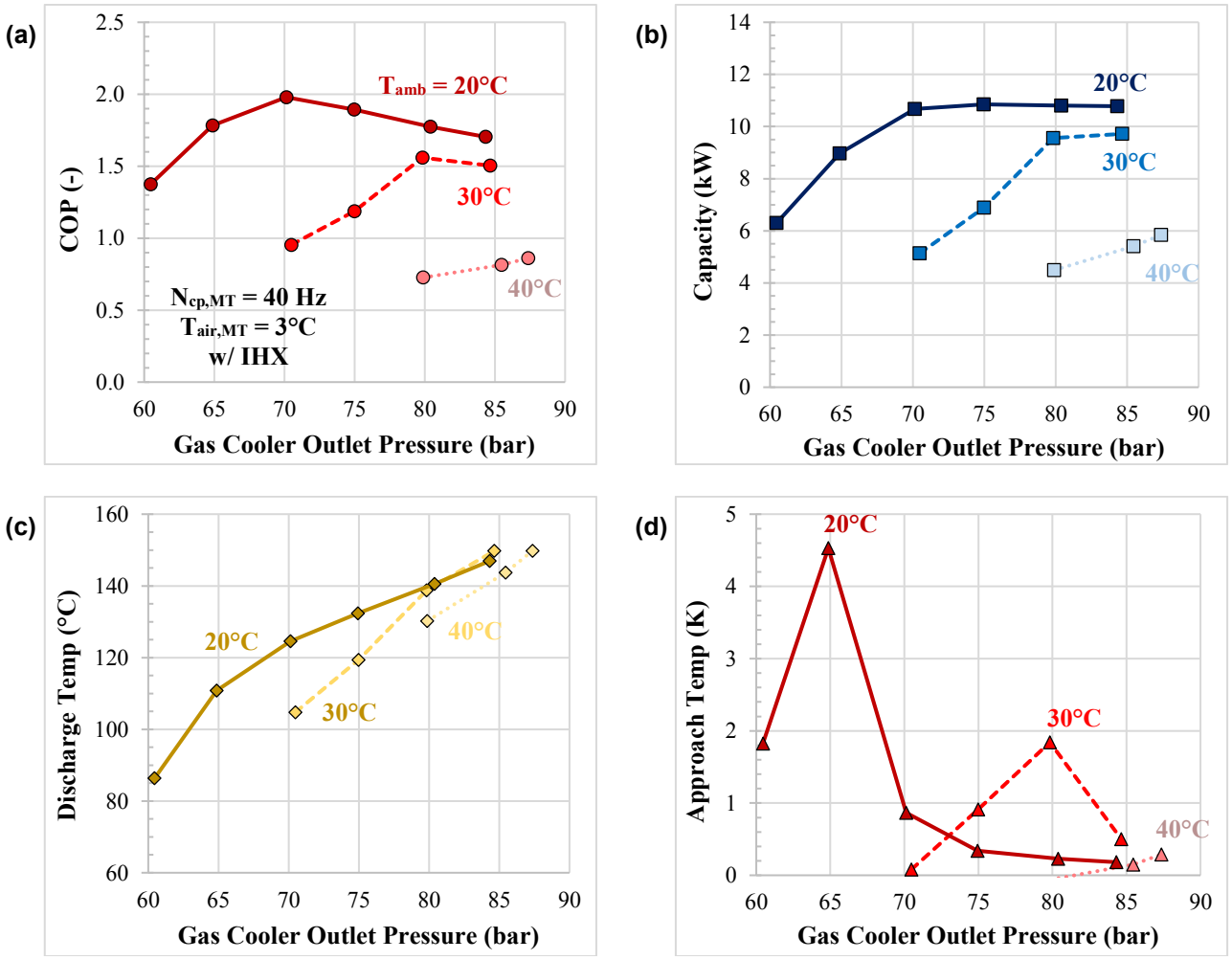

Fig. 6: Performance of single-stage compression refrigeration cycle: (a) COP, (b) MT cooling capacity, (c) compressor discharge temperature, and (d) gas cooler approach temperature

The experimental results for system-level performance are shown in Fig. 6. It can be seen from Fig. 6(a) that the COP of the cycle, when optimized, can reach up to 2.0 at 20°C ambient temperature. However, the COP cannot reach even 1.0, as the high-side pressure was limited by a compressor discharge temperature of 150°C, as shown in Fig. 6(c); thus the system with the single-stage compressor seems to be limited to ambient temperature up to 40°C. Fig. 6(b) shows the MT capacity, which would demonstrate the total capacity if a two-temperature system were used. A capacity of about 6 kW is needed at the design condition, and it can be seen from the Fig. that greater compressor displacement (higher speed) would be needed to meet the capacity requirement at higher ambient temperature. Evaporation pressure was generally in the range of 25 – 30 bar

depending on the high-side pressure and thus demanded capacity; this is about the range of pressures that the MT evaporator would be expected to operate at in the container unit. IHX effectiveness varied between 80 % and 95 % over the range of conditions, though most points were close to 90 %, which indicates that the IHX is sufficiently large. Fig. 6(d) shows the approach temperature of the gas cooler. It can be seen that for the points where optimum COP is observed, the gas cooler approach temperature is in the range of 1 – 2 K, indicating good gas cooler performance with the selected gas cooler slabs. Fig.s 7 and 8 compare the system performance with and without IHX. The system without an IHX has lower compressor suction superheat, meaning it can operate at higher discharge pressure before meeting the discharge pressure limit. For a given high-side pressure, the system with an IHX is always better. For the case of 30°C ambient temperature, for which the optimum high-side pressure is reached, the system with an IHX achieves higher COP and capacity. However, for the case of 40°C ambient temperature, the system with an IHX can actually achieve slightly higher COP and capacity because of its extended range of high-side pressure. This effect will need to be investigated further when being used with a two-stage compressor.

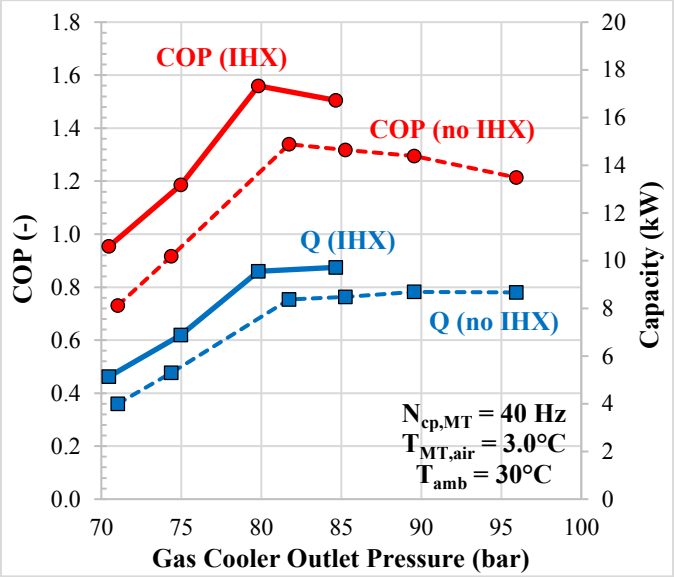

Fig. 7: Comparison of system performance with and without IHX at 30°C ambient

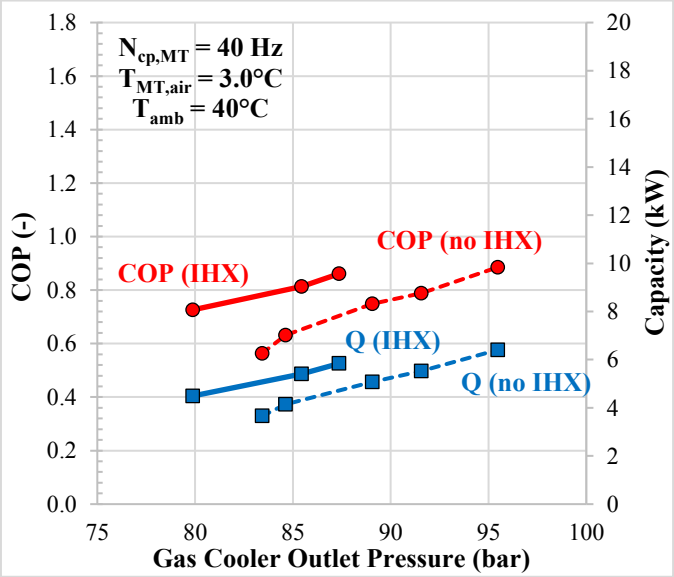

Fig. 8: Comparison of system performance with and without IHX at 40°C ambient

4. SUMMARY

This paper has discussed the design and initial experimental results of a multi-temperature CO_2 refrigerated container. The system is being designed for a very high ambient temperature of 57°C. In order to achieve reasonable performance at this condition, a system architecture involving multi-stage compression and expansion work recovery with an ejector is being implemented. The experimental results for an ejector have shown that very promising ejector performance (work recovery efficiency in the range of 25 – 30 % and pressure lift upwards of 8 bar at the design condition). System level experimental and model results have shown that the heat exchangers (evaporators, gas cooler, and IHX) all achieve good performance. It was also seen that a single-stage transcritical compressor will not be able to meet the requirements of the system, and a two-stage compressor will be necessary to achieve the desired operating range and energy efficiency.

ACKNOWLEDGEMENTS

The research presented in this paper was funded through the U.S. Army Natick Soldier Research, Development, and Engineering Center (NSRDEC). Any opinions, findings, and conclusions or recommendations expressed in this material are those of the authors and do not necessarily reflect the views of the U.S. Army NSRDEC.

NOMENCLATURE

Symbols and Abbreviations

COP	Coefficient of Performance (-)	P	pressure (bar)
IHX	internal heat exchanger	T	temperature (°C)
LT	low temperature	x	vapor mass fraction (-)
MT	medium temperature	η_{ejec}	ejector efficiency (-)

Subscripts

air	air-side of heat exchanger	lift	increase provided by ejector
amb	ambient	mn	motive nozzle of ejector
cp	compressor	sn	suction nozzle of ejector

REFERENCES

Barta, R.B., Groll, E.A., Hugenroth, J.J., 2018a. Modeling and control strategy of a transcritical carbon dioxide cycle for application in multi-temperature refrigerated container systems. 13th IIR Gustav Lorentzen Conference, Valencia, Spain, Paper 1116.

Barta, R.B., Groll, E.A., Hugenroth, J.J., 2018b. Modeling of S-RAM energy recovery compressor integration in a transcritical carbon dioxide cycle for application in multi-temperature refrigerated container systems. 13th IIR Gustav Lorentzen Conference, Valencia, Spain, Paper 1117.

Carrier, 2015. NaturaLINE Product Brochure. Document 62-11866.

Lawrence, N., Elbel, S., Hrnjak, P., 2018. Design and validation of a transcritical CO_2 mobile refrigerated container system for military applications. 13th IIR Gustav Lorentzen Conference, Valencia, Spain, Paper 1301.

National Institute of Standards and Technology (NIST), 2016. EVAP-COND v4.0 (b). Gaithersburg, MD, USA.

Poolman, C., Verma, P., Lee, K., 2018. Modulating two phase ejectors in transport refrigeration. 13th IIR Gustav Lorentzen Conference, Valencia, Spain, Paper 1396.

Manuscript ID: 422
DOI: 10.18462/iir.icr.2019.0422

Live transport of Norway lobster with mobile RSW system for an international market

Robert WOLFF, Guro Møen TVEIT, Kristina N. WIDELL*, Ulf ERIKSON, Erlend INDERGÅRD, Tom Ståle NORDTVEDT

SINTEF Ocean, Trondheim, Norway
* kristina.widell@sintef.no

ABSTRACT

There is a large potential in increased export of seafood from Norway and one of the categories that yet is little explored is live crustaceans. Transport of living animals requires extra precautions regarding the health and well-being of the animal. In this study, Norway lobster (*Nephrops norvegicus*) were chilled with refrigerated sea water, while transported in a truck. A mobile RSW system with CO_2 as refrigerant was used to provide chilled water below 5 °C. The temperatures in the chilling water were stable during the entire transport and the water had good oxygen saturation and stable pH-values, which is important for the welfare and survival rate of the lobsters. The survival rate of the crustaceans was good after transportation, and overall, the study showed that there is a potential for increased transportation of live lobster, without limiting the welfare of the animals.

Keywords: CO_2, live transportation, seafood, Norway lobster, RSW

1 INTRODUCTION

The market for live seafood is of great interest globally, and Norwegian seafood like the crustacean Norway lobster (*Nephrops norvegicus*) is no exception. In 2016 the total value from crustacean fishery was 1.9 billion NOK, a growth by 21 % from 2015 (Statistics Norway, 2018). High demand by international byers, suggest that this growth will continue. The lobster is sensitive to variations in environmental conditions, especially to temperature. Due to this and its potentially high commercial value, Norway lobster was selected as the model organism in this trial. It is of particular interest to study how industrial handling procedures can be optimized to enhance animal welfare and reduce stress and mortality in the value chain. Norway lobster has been extensively studied in terms of its physiology, and as to how both natural and anthropogenic stressors will affect this species.

A typical value chain Norway lobster consists of the following steps from capture to market (where it is sold alive):

1. caught in lobster pots by small fishing vessels (< 10 m) in coastal areas
2. transfer of individuals to lobster cells ("tube tray matrix") onboard the fishing vessel
3. transport to a commercial handling facility (< 2 h)
4. at the handling facility the lobsters are fasted for at least two days in tanks with running sea water
5. before packing, the lobsters are chilled in a mixture of crushed ice and sea water (about 1.5 °C) to make the animals torpid for easy handling prior to packaging in EPS boxes containing moist cloths and gel ice packs
6. transport to market by vehicle and/or plane

To avoid mortalities and to maintain a high-quality product, the industry states that the current transport method is suitable for no more than 2 - 3 days, depending on season. Stress related to capture and subsequent handling is more severe in late summer/early autumn than in winter (Lund et al, 2009), due to elevated temperature and directly sun exposure. The limitations to the transporting time can be a logistical challenge, since landing facilities often are located at outskirts

along the Norwegian coast. Further, the growing industry is interested in increasing production and to find new and more distant markets for their high-value products.

Today, transportation of live lobster is mostly done in EPS-boxes, where they are stored side-by-side in the box. Dry transportation exposes the animal to air and cause severe changes in haemolymph chemistry (Ridgeway et al. 2006), (Fotedar and Evans, 2011), which is a well-established stress parameter. In the absence of water, gills are greatly impaired, leading to respiratory acidosis (drop in pH), accumulation of CO_2 (hypercapnia) and ammonia in the haemolymph (Schmitt and Uglow, 1997). To minimize these metabolic processes, maintaining a low holding temperature is essential (Bernasconi and Uglow, 2008). Typically, temperatures of around 4-5°C are maintained during transport. In addition to negative influence from air exposure, the animals are often transported side by side, which can result in injuries where active lobsters can cut off each other's legs and claws.

Preliminary tests with dry transportation for up to 3 days has showed negative impact on stress and survival and emphasized the importance of wet transportation of lobsters, which can ensure better animal welfare as well as supplying the European market with live lobster of good quality (Read more under 2.6 preliminary tests). New innovative transportation solutions are therefore searched for by the industry. Transportation in sea water might be a solution to this.

In the current industrial trial, a transportation system including a truck dedicated for transport of live salmon smolts were tested. Due to the seasonal variation's alternative application for these kind of truck trailers are searched for. Transportation of live seafood such as crustaceans, is a potential new marked area for transportation companies. Salmon smolts are normally not that sensitive to rise in temperature during transportation, and due to this the trucks are not equipped with an RSW-system (Refrigerated Sea Water) to retain chilled temperature. Other spices, such as Norway lobster, are more sensitive to high temperatures, and require chilled sea water during transportation.

RSW-systems are widely used in the seafood industry for cooling of fish on board fishing vessels as well as in well boats, and for chilling in land-based fish processing plants. The RSW system used in this trial, is based on CO_2 as refrigerant and are designed to manage and control a stable or varying temperature during transportation. For this purpose, SINTEF's mobile RSW pilot unit were mounted on the truck.

Introducing transport of live lobster in refrigerated sea water as a feasible option to traditional dry transportation, is an innovation worth exploring. New business models must be developed, and alternative technology like specially designed transportation units, must be tested and developed. Wet transportation will reduce the matter of necessity of manually handling the animal more than necessary. Immersion of the animals in water is necessary for survival, and a common practice both on the boat immediate post-harvest (Neil 2012) and after transport to the market (in order to let them recover from the physiological disturbances associated with prolonged air exposure). However, this has not been common during transportation. An obvious advantage of transporting animals in water is that it is possible to avoid the gradual weakening (or death) of the animals due to anaerobic respiration. To succeed it is however important that the water quality is adequate and that temperatures are kept at a minimum within the species optimum temperature range.

2. MEASUREMENTS AND METHODS

2.1 Study Area

The trial was carried out in between the 4th and 5th of August 2018 on board one of Malo Transport's special built Volvo truck trailers. The transportation started off from Gjemnes (NO) 05:30 pm at the north-west coast of Norway, via ferry boat from Kristiansand (NO) to Hirtshals (DK). The total duration of transport was 18 hours and 45 minutes.

2.2 Trailer and Transportation

The trailer used for transportation of the lobsters was equipped with 12 closed tanks in total, each with a volume of 2 cubic meter (width 215 cm, length 100 cm, height 90 cm) and a hatch measuring 70x60 cm (Fig. 1) The truck itself was equipped with five closed tanks (T1, T2, T3, T4 and T5). In addition, the vehicle could tow a trailer, which was equipped with an additional seven closed tanks

(T6-T12). The tanks were all filled with fresh sea water from approximately 80 meters of depth. Container T1 to T5 were all connected through an internal manifold were each tank could be filled with sea water (the same is valid for T6-T12 on the trailer). In addition, a piping system for recirculation of sea water were mounted. In this study, trails were carried out by evaluating tank 2 (T2) and 5 (T5) on the truck. During the trial the other tanks were used for transportation of other crustaceans. Each tank was equipped with sensors measuring temperature (ºC), pH and oxygen saturation (DO).



Figure 1: Top - Trucks used for transportation of live lobsters. Bottom – tanks used for transportation of the lobsters, equipped with RSW circulation and sensors measuring temperature (ºC), pH and oxygen saturation (DO)

2.3 RSW System

In this trial a mobile RSW-unit was tested. The main purpose was to consider if RSW is a suitable system to maintain an optimal temperature below 5°C for live transportation of Norway lobster from Norway to Denmark. The RSW-unit was mounted outside the truck as shown in Fig. 2. Preliminary testing of the settings used for the trial showed that the custom made mobile RSW-unit could produce water with temperature of 0.5°C ± 0.2°C. The refrigeration unit was operated with a transcritical semi-hermetic CO_2 compressor (Dorin CD380H, Max operating current 9.4 A at 400V, 50Hz). The cooling capacity was measured to be 10-12 kW, resulting in a COP of 2.7-3.2. The sea water chiller (with pump capacity 320 l/min) was a MIT produced titanium pipe heat exchanger with flow-switch. The condenser heat was removed by running tap water in a Kaori condenser/gas-cooler, in addition to a parallel external air condenser. An internal Kaori heat-exchanger regulated the gas temperature into the compressor.

2.4 Norway Lobsters

A total of 291 kg live Norway lobsters were collected from Gjemnes (6475 Gjemnes, Norway). Typical weight of Norway lobster varies from 150 to 450g. The lobster is distinguished by weight. In T2 smaller lobster were stored, typically 150 – 250 g, and in T5 lobster sized above 300 g were stored. The lobsters were starved before transportation to ensure better water quality (less defecation in the water). Prior to being loaded onto the vehicle the lobsters were packaged and stored in special designed tube tray matrix system used by the processors for storage at their facilities (Fig. 3). Boxes of the tube tray systems were placed in tank T2 (135 kg) and T5 (156 kg) on the truck. Individual storage of lobsters in trays are important to ensure that the lobsters don't attack each other. Additionally, the trays enabled a larger number of animals to be stored in each tank.

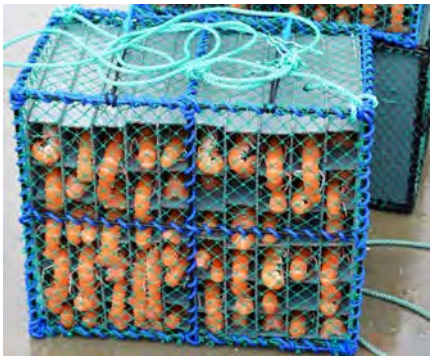

Figure 2: Typical tube tray matrix for individual handling of lobsters

2.5 Survival and Vitality

Vitality of Norway lobsters are normally determined using an establishes score board (range 1-5) where high values (score 5 or 4) indicate the lobsters of high vitality suitable for transportation, and low values indicate lobsters unsuitable for transportation that are dead, moribund or weak (score 3-1). However, since this trial was a proof-of concept for RSW as a feasible technology to control sea water temperature during transportation of live crustaceans the observations of vitality were done the traditional way by subjective evaluation by the operators before and after transportation.



Figure 3: Vitality score index ranges between 1 to 5 for Norway lobsters. Left picture shows lobsters with low score (typical 2), right picture lobsters with high vitality, typical score of 5.

2.6 Preliminary Tests

During the spring of 2018 a preliminary test were conducted to evaluate how different treatment methods and temperatures affected survival, stress and recovery of Norway lobster during traditional dry transportation for up to 3 days. Prior to the test, the lobsters were starved for 5 days placed in the tube tray matrix in plastic tubs with running sea water (5.6 °C). The lobsters were subjected to three different temperature treatments before packaging by the traditional methods in EPS-boxes. Results showed that pre-treatment with RSW (chilled to 1°C) gave mortality rates of 3 %, 4 % and 0 % on day 1, 2 and 3 respectively. For comparison, packaging of lobsters that had been stored in sea water at 5.6 °C prior to packaging and transportation had mortality rates of 15 %, 6 % and 11 %. Results from the measurements showed a clear decrease of vitality for each day of transportation. Regardless of pre-treatment methods, dry transportation had a negative effect on the animals. Some lobsters had experienced loss of arms or claws loss during the transportation. The lobsters also showed anaerobe respiration with reduced pH in haemolymph, high lactate values, and low white muscle pH indicating that the animals had some muscle activity during the test. Air exposure during the traditional dry transportation impairs the gills, which in turn lead to respiratory acidosis or

suffocation. The results from the preliminary tests emphasized the importance of how wet transportation of lobsters can ensure much better animal welfare, as well as supplying the European market with live lobsters of good quality.

3. RESULTS AND DISCUSSION

The results and data described in this section were extracted from sensors mounted on the truck. Sea water quality in the closed tanks was determined by logging dissolved oxygen (DO), pH (CO_2) and temperature (ºC) continuously during the entire transport of our study.

3.1 Temperature during transport

The water temperature profiles during the entire transport are shown in Fig. 4. The present study covers typical Norwegian sea water temperatures during late summer conditions (10-12 ºC). The sea water temperature in two tanks (T2 and T5) were measured and started at approx. 10 ºC and were subsequently reduced to the desired transportation temperature of 4 ºC within 3 hours. This corresponds to a decrease in temperature of 2.1 ºC/h. After reaching the desired setpoint, the temperature was maintained at 4 ºC throughout the trial. This is within the reported optimal temperature range for Norway lobster, which is 4-10 ºC. Also, if the water gets to colder (below 0 ºC) or higher (above 19 ºC) the mortality rate of the lobster increases significantly (Barrento, 2009). Lobster activity and its demand for oxygen increases with temperature, but at higher temperatures, sea water holds less oxygen. Due to the link between temperature and dissolved oxygen it is essential to ensure enough waterflow and oxygenation to provide adequate oxygen for the lobsters (Beard and McGregor, 2004).

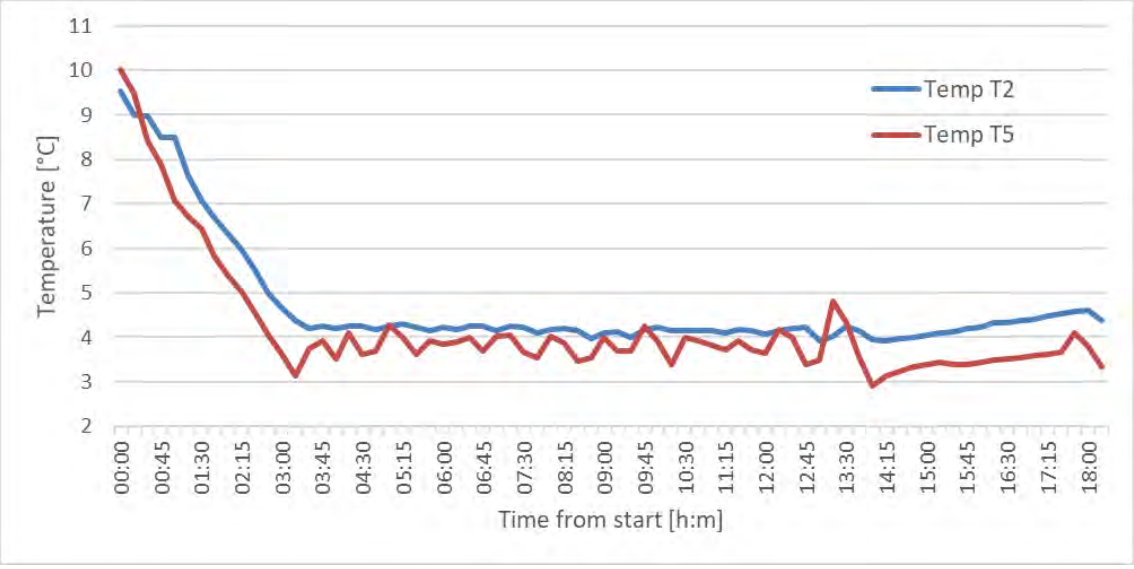

Figure 4: Temperature measured in tank 2 and 5 during transportation of Norway lobster

3.2 pH and Oxygen Saturation

In both tanks, the dissolved oxygen levels varied around the set point of 100 % saturation (Fig. 5), which is known as the maximum solubility at normal atmospheric pressure. Lobsters have been reported to tolerate low oxygen levels (e.g. 50%), however the aim should be to keep the water well oxygenated at all times (above 70%) (Barrento, 2009). Compared to the traditional use of the RSW tanks, the biomass oxygen demand, were much lower for crustaceans than for fish. Hence, the oxygenation system had no problem with supplying the animals with more than the adequate oxygen levels. Moreover, due to the low temperature, the lobsters also required less oxygen to survive. As shown in the figure, the DO (especially tank 5) peaked just after DO in tank was measured below the setpoint (DO = 100 %). Probably, the regulator responded and opened the inlet valve for oxygen, resulting a DO peak.

The oxygenation system mounted on current transportation system, seems to be oversized for transportation of lobsters. The transportation system was originally designed for transporting live

salmon smolt and wrasse in the aquaculture industry. Further studies regarding correct oxygenation level during live transportation of lobsters, must be conducted.

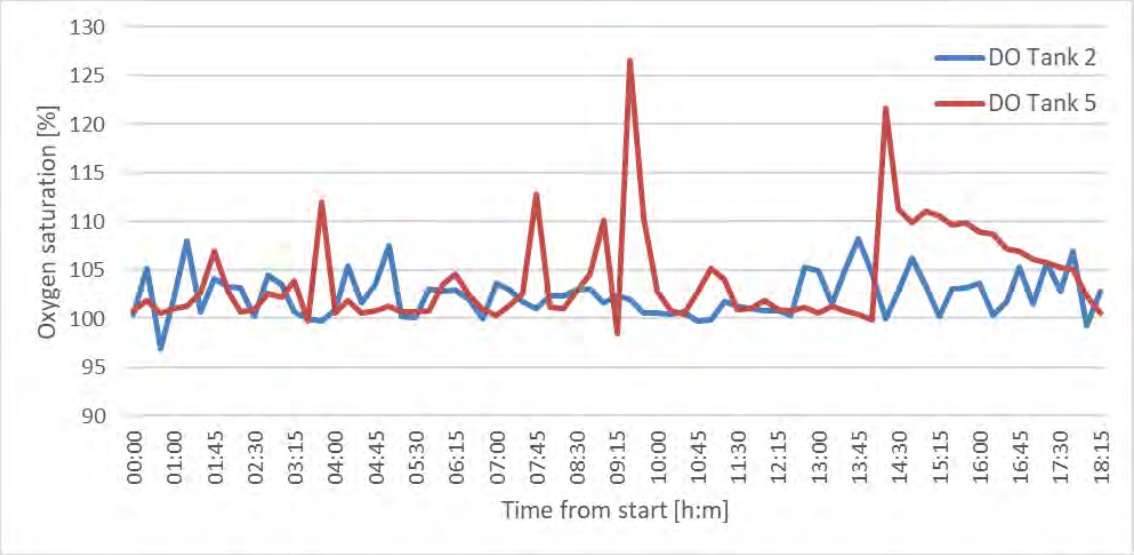

Figure 5: Oxygen saturation (DO) in sea water during transportation. Fluctuations around the set-point of 100 % is shown

The sea water pH showed stable values throughout transport with values around 7.2 and 7.4 (Fig. 6). Normal pH in sea water ranges between 7.5 and 8.4 (Chester and Jickells, 2012), and the optimum conditions for the lobsters are reported to be within the range of 7.8 and 8.2 (Barrento, 2009). Considering the low biomass, and thereby a low production of CO_2, as well as the large capacity of the system (when crustaceans are considered), pH in the system seems a little low. A dramatic drop of pH was basically not observed except for the slight drop observed in Tank 2 by the end of the transport. However, lethal pH values for lobsters are reported as lower than 5 or higher than 9 (Barrento, 2009). Nevertheless, it should be noted that the sea water pH-levels in the tanks are somewhat low already at beginning of the trial. We are unable to pinpoint the reason for the consistently low values, but one explanation could be that the electrodes were out of sync. According to information from the transportation company, the pH-electrodes are calibrated every third month according to established procedures. The electrodes were not calibrated prior to this trial. Another possibility could be that the water used to fill the tanks were of low quality with low pH due to contaminants from waste water released into the sea water from nearby industry, or that the water was filled on the tanks a while before trial start. However, it should be stated that the somewhat low pH values probably had no negative affect on the live transportation of the crustaceans.

In further experiments there is a need to sample and analyse water from the transportation tanks before and after transportation to get a clearer picture of the water chemistry.

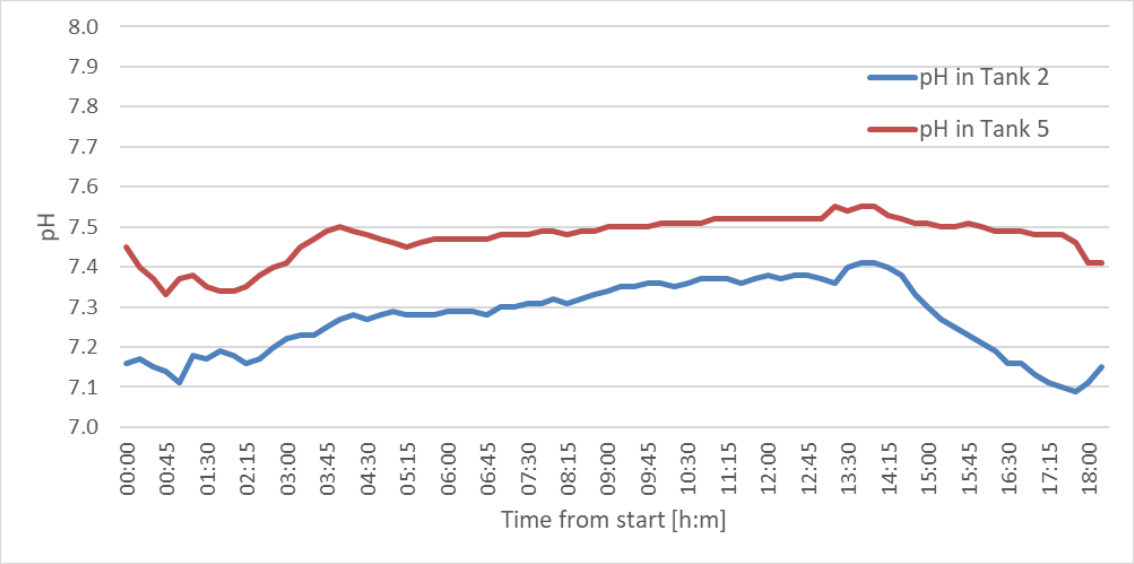

Figure 6: pH in chilling water during live transportation of lobster. pH was stable during the complete transport

3.3 Condition of the Lobster after Transport

Upon arrival at the receiving facility in Hirtshals (DK), after almost 19 hours of transportation in tanks on the trucks, the lobsters were filmed while they were released into storage tanks. The lobsters were reported exhibiting high vitality and low mortality (approx. 3 % mortality) according to the staff at the receiving facility. Figures of mortality by dry transportation during the same period, late summer condition, are reported from the industry to vary a lot, but numbers from 10 to 30 % are mentioned. The animals were reported to show higher vitality compared to what is normal for lobsters from dry transport in EPS-boxes. Traditional dry transportation in EPS-boxes are limited up to two days. Additionally, recovery time from dry transportation is reported to be higher than for the lobsters that had been transported by truck in RSW. Recovery time was not measured during this study but will be one objective of further work. It would be useful for both the storage facilities and transportation vehicles to keep records on all mortalities to build a picture of what is regarded as a "normal" level of mortalities. It is important to extinguish between the immediate post-transportation deaths and the day-to day mortalities that that can be expected also in the best systems. By regularly observing the stored lobsters the staff will soon develop an awareness of what is normal or abnormal behaviour, and be able to detect abnormal behaviour patterns early, which can give a valuable early warning of deteriorating conditions in for example water conditions.

During the preliminary test conducted during the spring of 2018 (see 3.6) we saw loss of claws or walking legs. This could be a sign of stressed animals, as lobsters are known to shed their claws or legs by autonomy if they are exposed to severe stress (Barrento, 2009). This can often be linked to excessive handling or drastic changes in environmental conditions like for example to high or low temperature (Barrento, S., 2009). During the present study the influence of ΔT on the welfare of lobsters was not studied. However, this would be an interesting topic for future studies.

Transportation of lobsters in refrigerated sea water results in less management and treatment of the animal throughout the value chain. As a consequence, this allow the lobsters to be packed directly into the specially designed tube tray matrix system during harvesting. This will reduce the need for intermediate handling (e.g. sedation step and packing), and also reduce dramatically the use of EPS-boxes.

4. CONCLUSIONS AND FURTHER WORK

With testing of this mobile pilot RSW-unit, it has been showed that wet transportation of live Norway lobster (*Nephrops norvegicus*) in chilled sea water can be an alternative compared to established and traditional dry transportation. Wet transportation result in less handling, can increase travel time and ability to survive over longer distance, hence improve quality. The RSW system unit tested in this trial provided the lobsters with sea water at constant low temperature throughout the transportation. The measurements results show that temperature can be reduced gradually and maintained at a desired level during the transport. Norway lobster can now be offered to a greater seafood markets, especially the growing high-end marked in southern Europe.

The transportation system used in current trial, provided the lobsters with ample access of oxygen at all time. The oxygenation system was designed for transportation of fish with a higher oxygen demand, and hence oversized for this use, considered the reduced need for oxygen of lobsters stored at low temperature. This should be adjusted and will be part of further studies.

The measured pH values were low but stable throughout the entire transportation with values between 7.2 and 7.4. In further experiments there is a need to sample and analyse water from the transportation tanks before and after transportation to get a clearer picture of the water chemistry to prevent the value of sinking below the optimum range.

The current industrial trial shows that wet transportation might be an innovative solution for live transportation of lobster in special and live seafood in general. The trial reviled some interesting topics which include development of alternative and special designed storing tubes. Further studies regarding special designed logistic system, as well as recovery time after transportation and destination, must be studied further.

ACKNOWLEDGEMENTS

The authors greatly acknowledge the Norwegian Research Council for the financial support through the FORREGION program for carrying out the present research. Also, thanks to Malo Transport AS for close collaboration.

REFERENCES

Barrento, S., 2009. European guideline for quality of live crustaceans in retail and HORECA segments. Technical Report supported by Project No. 030421, FP6 – SME CrustaSea, Sep 1, 2006

Beard, T.B., McGregor, D., 2004. Storage and care of live lobsters. The Centre for Environment, Fisheries & Aquaculture Science (CEFAS). Laboratory Leaflet Number 66 (Revised). Lowestoft, 2004.

Bernasconi CJ, Uglow RF 2008. Effects of emersion-induced hypoxia on some haemolymph constituents of Nephrops norvegicus. Dis Aqu Org 82, 135-143.

Chester, R., Jickells, T., 2012. Marine Geochemistry, 3rd Edition, Blackwell Publishing. ISBN 978-1-118-34907-6

Lund HS et.al., 2009. Recovery by the Norway lobster Neophrops norvegicus (L.) from physiological stresses of trawling: Influence of season and live-storage position. J Exp Mar Biol Ecol, 373(2), 124-132

Neil DM 2012. Minireview: Ensuring crustacean product quality in the post-harvest phase. J of Inv Pat 110, 267-275

Ridgeway ID et.al. 2006. Morbidity and mortality in Norway lobsters, Neophrops norvegicus: physiological, immunological and pathological effects of aerial exposure. J Exp Mar Biol Ecol 328, 251-264.

Schmitt ASC, Uglow RF. 1997. Haemolymph constituent levels and ammonia efflux rates of Nephrops norvegicus during emersion. Mar Biol 127, 403-410

Statistics Norway (2018), retrieved september 2018 from https://www.ssb.no/statbank/table/05278/

Manuscript ID: 555
DOI: 10.18462/iir.icr.2019.0555

Experimental assessment of the difference between new refrigerated trucks and their corresponding prototypes

Claudia CAPO [a, b, c], Frantz LATCHAN [a], Thomas SUQUET [a], Jean-Marc PETIT [c], Rémi REVELLIN [b], Jocelyn BONJOUR [b], Gérald CAVALIER [a]

[a] Cemafroid, 5 Avenue des Prés - Fresnes cedex - France
[b] Univ Lyon, CNRS, INSA-Lyon, Université Claude Bernard Lyon 1, CETHIL UMR5008, F-69621, Villeurbanne, France
[c] Univ Lyon, CNRS, INSA-Lyon, Université Claude Bernard Lyon 1, LIRIS UMR5205, F-69621, Villeurbanne, France
gerald.cavalier@cemafroid.fr

ABSTRACT

The ageing process is a common problem in refrigerated transport. This phenomenon has always been studied from the comparison of the *K* value of the in-service vehicles at nine or twelve years of use with the *K* value of their prototypes. This is a method that stems from the current regulation for the international transport of perishable foodstuff which allows certifying a new refrigerated vehicle produced in series on the basis of its prototype. The vehicle produced in a series may have a different *K* coefficient compared to its prototype due to reasons intrinsic to the production process or to discrepancies on the body itself. The estimation of this difference is necessary for the study of ageing. It is also an important issue for new refrigerated trucks certification. A previous paper highlighted the comparison of the *K* coefficient of fourteen newly manufactured semi-trailers and their prototypes. In this paper, the same experimental assessment is proposed for a representative number of refrigerated trucks. A comparison with previous results is also presented.

Keywords: Ageing Phenomena, Thermal Insulation, *K* coefficient, Refrigerated Transport, Refrigerated Vehicles, Prototypes, In-service Vehicles.

1. INTRODUCTION

The performance of insulated enclosures for refrigerated vehicles is usually characterized by their overall insulation coefficient ("*K* coefficient") which usually increases with time because of the ageing of the enclosure. This increase with the time may lead to excessive temperature ranges in the cargo space and faster warming in the absence of refrigeration (Lawton and Marshall, 2008). The oversizing of the cooling power of the refrigeration unit counteracts the excessive temperature ranges due to the increasingly aging but results in greater energy consumption and environmental pollution through GHG emissions. Considering that the refrigerated road transport fleet amounts to some 4 million pieces of equipment in service worldwide (Cavalier and Tassou, 2011), the effect of refrigerated transportation on the environment is not negligible. It is thus important to understand which kind of changes and interventions could be made on the vehicle to gain in terms of insulating performance and to reduce the ageing phenomena. According to the rule for renewal defined in the current regulation for the international transport of perishable foodstuff (named ATP Agreement), the evaluation of ageing may be made by comparing the *K* coefficient value of the in-service vehicle at the n-th year, K_n to the initial *K* value of the prototype equipment, K_p, being, usually, the only one available at the initial time. The ageing at twelve years of the in-service vehicle is thus defined as:

$$A_{12} = \frac{K_{12}}{K_p} \qquad \text{Eq. (1)}$$

This definition includes some biases in that sense that the real vehicle produced in the series with the same design of the prototype, may vary in terms of surface and number of accessories, with the tolerance allowed by the previously mentioned regulation. Their internal surface, for example, may vary by ±20 % compared to the prototype, and the real equipment could present less accessories or openings. Furthermore, there are also some intrinsic reasons to the production process that could alter the real *K* coefficient value: for instance, among others, the curing of the insulant foam before manufacturing may be quite different from one case to another.
The reference prototype may have small differences in size and geometry, and hence a different initial *K* value compared to the initial *K* value of the vehicle realized in the series. This circumstance may affect the assessment of the real ageing. This aspect was previously analysed by Capo et al. (2018) owing to the measurement of the K coefficient of fourteen newly manufactured semi-trailers. All the measured *K* values of the new semi-trailers were found to be greater than the measured *K* values of their reference prototypes. For five of them, the insulation class as granted on the basis of the prototype vehicle was even found to be wrong. Considering the *K* value of the prototype (K_p) as the reference measurement is not only the cause of an erratic evaluation of the ageing: it may thus also result in a wrong insulation class for some of the bodies realized in the series.
The estimation of the difference between the real value of the *K* coefficient and that of the reference prototype is proposed in this study for fourteen newly manufactured trucks. The *K* coefficients of these trucks were measured in the Cemafroid test chamber and compared to the *K* coefficients of their reference prototypes.

2. ATP TEST PROCEDURE FOR EVALUATING THE PERFORMANCE OF INSULATED BODIES

The overall insulation coefficient is calculated as:

$$K = \frac{Q}{S.\Delta T} \qquad \text{Eq. (2)}$$

Where *Q* is the heating power or the cooling capacity, as the case may be, required to maintain a constant absolute temperature difference ΔT between the mean internal temperature T_{int} and the mean external temperature T_{ext}, during continuous operation, when the mean outside temperature T_{ext} is constant for a body of mean surface area *S.* The mean surface area of the body is represented by the geometric mean of the internal surface area S_{int} and the external surface area S_{ext} of the body:

$$S = \sqrt{S_{int}.S_{ext}} \qquad \text{Eq. (3)}$$

For refrigerated trucks included in this study *K* was measured by following the ATP test procedure, based on “the inner heating method”. This method is the same as that used in Capo et al. (2018). It includes the measurement of twenty-four temperatures owing to as many probes, twelve of which are placed inside the vehicle and twelve on the outside. The test typically takes more than twelve hours of stabilization. The refrigerated vehicle was placed in the Cemafroid test chamber that is accredited by COFRAC, the French accreditation body, for tests and calibrations according to ISO 17025 and that it is able to control the temperature of the chamber with an accuracy of ±0.5 K. Fig. 1 schematically shows the main conditions of the ATP test procedure, which requires a mean outside temperature, T_{ext} of 7°C± 0.5 K and air flow velocity ranging from 1 to 2 m. s^{-1}.

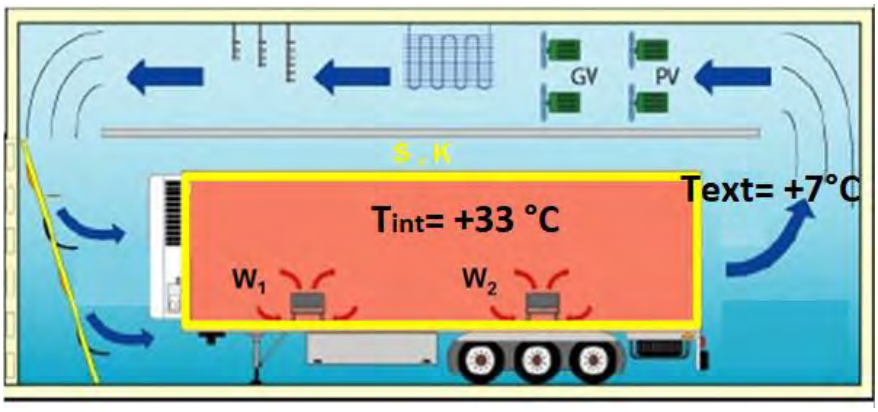

Figure 1: Measurement principle of the *K* coefficient.

The measurements are made when steady state is reached with a mean inside temperature around the value of 33°C ± 0.5 K. The presence of some ventilated electric heaters is needed to reach a temperature difference between the inside of the body and the test chamber equal to 25 K ± 2 K. Furthermore, the walls of the body have to be maintained at an average temperature of +20°C ± 0.5 K. For the heat balance to be satisfied, the total required cooling power, *Q,* which is used in Eq.(2), is the sum of the total heating power W_1 and ventilating power W_2 of the devices placed inside the body. Depending on the value of the K coefficient, insulating vehicles and bodies are classified in:

- Normal Insulated Equipment (IN) when $0.40 < K \leq 0.70$ $W.m^{-2}.K^{-1}$;
- Reinforced Insulated Equipment (IR) if $K \leq 0.40$ $W.m^{-2}.K^{-1}$.

The uncertainty of each measurement is calculated, taking into account several sources of uncertainty: the heating power, Q, the temperature difference ΔT between the mean internal temperature Ti_{nt} and the mean external temperature T_{ext}, and the surface area of the body. The combined uncertainty for K coefficient measurement was evaluated as following:

$$u^2(K) = \left(\frac{1}{S.\Delta T}\right)^2 u^2(W) + \left(\frac{W.\Delta T}{(S.\Delta T)^2}\right)^2 u^2(S) + \left(\frac{W.S}{(S.\Delta T)^2}\right)^2 u^2(\Delta T) \quad \text{Eq. (4)}$$

3. COMPARAISON BETWEEN THE K VALUE OF A NEWLY MANUFACTURED TRUCK AND ITS REFERENCE PROTOTYPE

In order to confirm the deviation of the real vehicle from its prototype at the initial time, already studied by Capo et al. (2018), fourteen newly manufactured trucks were tested and comparisons were made with the *K* coefficient of their prototype but also with theoretical values. For such refrigerated trucks, Capo et al. (2018) suggested that for such refrigeration trucks, a first estimate of the theoretical *K* value can be calculated as:

$$K_{th} = \lambda \frac{\sum S_i/\delta_i}{\sum S_i} \quad \text{Eq. (5)}$$

Where, λ is the initial thermal conductivity of the foam, while S_i and δ_i are respectively, the mean surface and the thickness of the *i*-th wall of the insulated body. Eq. (5) assumes that the thermal resistance of the whole body is related only to the insulating foam and gives an ideal reference value that neglects the thermal bridges due to geometric singularities. Previous studies concluded on a statistical basis that this contribution can reach up to 30-35% of the theoretical value as defined by Eq. (5) (Boldrin et al., 1990). When the K_{th} values of the prototype and the real vehicle are nearly the same, one can thus suppose that the geometry does not affect the variation between the measured *K* values. Fig. 2 shows the measured *K* values for each truck and its

reference prototype. The white bars with the defined contours represent the measured *K* values for the prototypes, K_p whereas the filled bars represent the measured *K* values at initial time for the real in-service trucks, K_0.

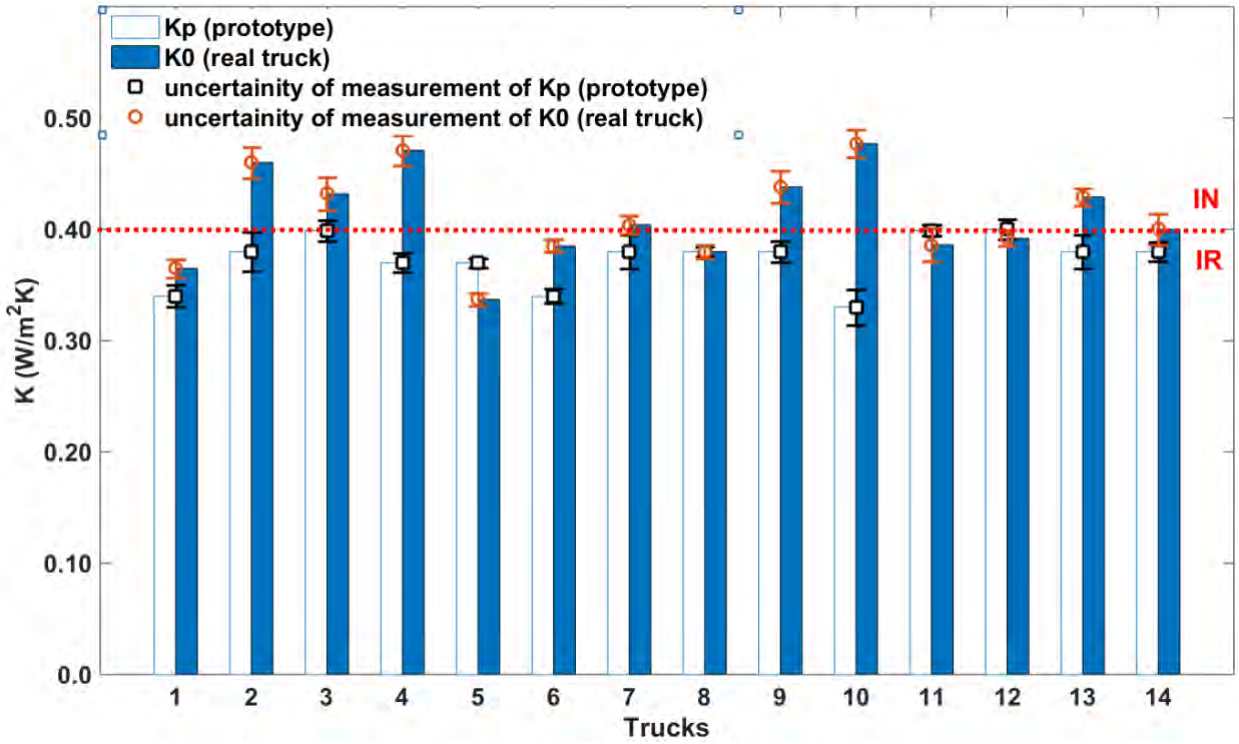

Figure 2: measured K values of fourteen newly manufactured trucks, compared to the respective prototypes values. Red dot line represents the ATP threshold between reinforced insulation, IR, and normal insulation, IN.

Excluding trucks 5, 8, 11, 12 which have been conceived better than the reference prototypes, the others measured K_0 values of the new trucks are greater than the measured values of the prototypes, K_p. Also, trucks 2, 3, 4, 9, 10 and 13 results show to what extend the difference between K_0 and K_p can have an impact on the real performance of the vehicles actually circulating on the road. Taking as reference their K_0, which are greater than 0.40 $W.m^{-2}K^{-1}$, these trucks would have obtained a different insulation class (IN) compared to that obtained based on the corresponding K_p (IR). This difference between K_0 and K_p which, in relative terms (i. e. $(K_0-K_p)/K_p$), reaches a mean value around 11% and a maximum of 45%, has an impact on the evaluation of the real ageing of the vehicles. The maximum value of this difference is greater than the maximum value obtained by Capo et al. (2018) for the semi-trailers, i.e. 26%. The uncertainty of K coefficient measurement for both the prototype and the real truck are shown in Fig.2 (respectively round markers and square markers). In both cases these uncertainties vary from 1.2 % to 3.8 %.
Figure 2 allows concluding that K_p is not a good reference for the assessment of ageing.
Fig. 3 shows the theoretical *K* values calculated using eq. 5, based on the geometry of the system and on an initial thermal conductivity of 0.025 $W.m^{-1}.K^{-1}$ for the foam (as declared by manufacturers).The white bars with the defined contours represent the theoretical *K* values for the prototypes ($K_{p\text{-}th}$) whereas the filled bars represent the theoretical *K* values for the real in-service trucks ($K_{0\text{-}th}$). All trucks have nearly the same theoretical values meaning that the difference existing in the measured values does not depend on the geometry and is probably due to all the changes carried out on the new trucks, including the assembling of the refrigeration unit on them. For truck number ten the theoretical *K* value of the prototype was not calculated due to a lack of data on the dimensions of the vehicle.
These results are consistent with those for semi-trailers previously presented by Capo et al. (2018).

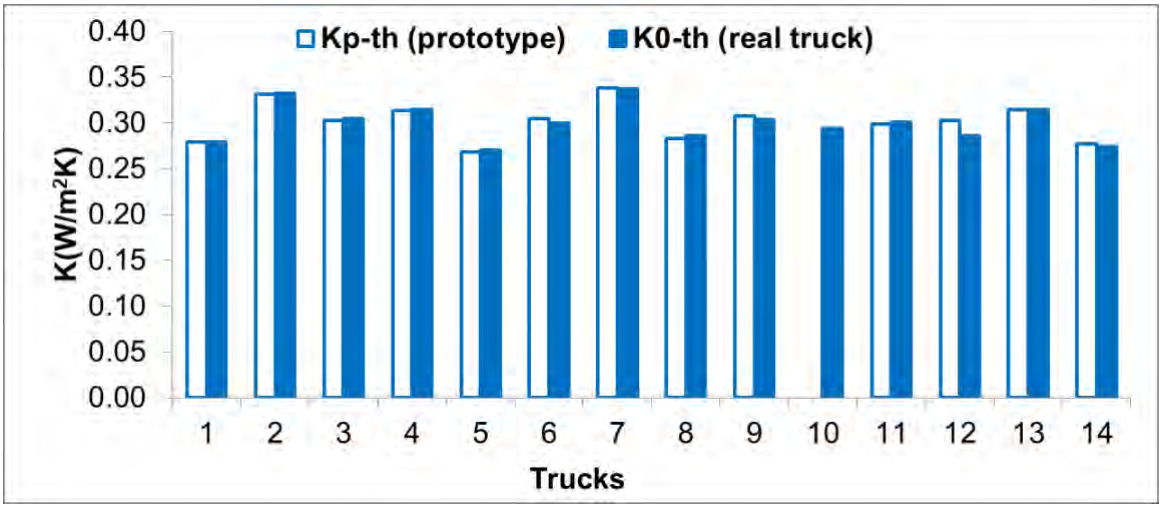

Figure 3: theoretical *K* values of fourteen newly manufactured trucks, compared to the respective theoretical prototypes values.

The theoretical values of *K* ($K_{0,th}$ and $K_{p,th}$) displayed on Fig. 3 were obtained assuming an ideal situation where the refrigerated enclosures of the trucks are made only of polyurethane foam. However, in order to resist to cracking, crumbling, shifting, and packing from the shock, vibration, and flexing of the body structure, but also in order to prevent from breakdown at extreme temperatures, the real vehicles are not made only of polyurethane foam but include a solid matrix. Using the values of K_0 *of* twenty-eight real vehicles (of which fourteen real trucks presented in this study and fourteen real semi-trailers previously presented by Capo et al. (2018), it is possible to define an apparent thermal conductivity (λ_{app}) which takes into account the presence of the solid matrix as:

$$\lambda_{app} = K_0 \delta_{average} \quad \text{Eq. (6)}$$

Where $\delta_{average}$ is the average thickness of the vehicle, calculated as:

$$\lambda_{app} = K_0 \delta_{average} = K_0 \frac{\sum \delta_i s_i}{\sum s_i} \quad \text{Eq. (7)}$$

The relationship for all the dataset between K_0 and $1/\delta_{average}$ is shown on Fig. 4. In this figure, the triangle-shaped markers represent the results for semi-trailers whereas the square-shaped markers refer to trucks. A linear regression was performed separately for the semi-trailers as well as for the trucks in order to identify the apparent conductivity that is the slope of the line. The continuous line in Fig. 4 represents the trend for trucks whereas the dotted line refers to semi-trailers. One reaches:

$$K_{0,calculated\ for\ trucks} = 0.0313 \left(\frac{1}{\delta_{average}}\right) \quad \text{with } R^2 = 0.136 \quad \text{Eq. (8)}$$

i.e. λ_{app} = 0.0313 W.m^{-1}.K^{-1},
and

$$K_{0,calculated\ for\ semi\ trailers} = 0.0294 \left(\frac{1}{\delta_{average}}\right) \quad \text{with } R^2 = 0.517 \quad \text{Eq. (9)}$$

Gathering together the trucks and the semi-trailers as a unique series of vehicles, the same kind of linear was performed to identify the average apparent conductivity:

$$K_{0,calculated\ for\ all\ vehicles} = 0.030 \left(\frac{1}{\delta_{average}}\right) \quad \text{with } R^2 = 0.1067 \quad \text{Eq. (10)}$$

i.e. the apparent thermal conductivity (0.030 W.m^{-1}.K^{-1}) is greater than the thermal conductivity of polyurethane foam (0.025 W.m^{-1}.K^{-1}) by 20%.

Another way to apprehend the quality of the regression consists in plotting the values of K_0 as calculated by Eq. (10) against the measured values (Fig. 5). Note that 80% of the available data points fall within a ±10% error band. For a statistical analysis, the mean percentage error (*MPE)* and the mean average percentage error (*MAPE)* are considered. They are defined as:

$$MPE = \frac{1}{n}\sum_{i=1}^{n}\frac{K_{0,measured}-K_{0,calculated}}{K_{0,measured}} \quad \text{Eq. (11)}$$

$$MAPE = \frac{1}{n}\sum_{i=1}^{n}\left|\frac{K_{0,measured}-K_{0,calculated}}{K_{0,measured}}\right| \quad \text{Eq. (12)}$$

where n is the sample size (equal to twenty-eight in this study), $K_{0,measured}$ corresponds to the experimental K_0 obtained for the real in-service vehicles at initial instant of life, and $K_{0,calculated}$ the predicted values obtained using Eq. (10). *MPE* and *MAPE* obtained for the present data are respectively of -0.3% and 7.0%.

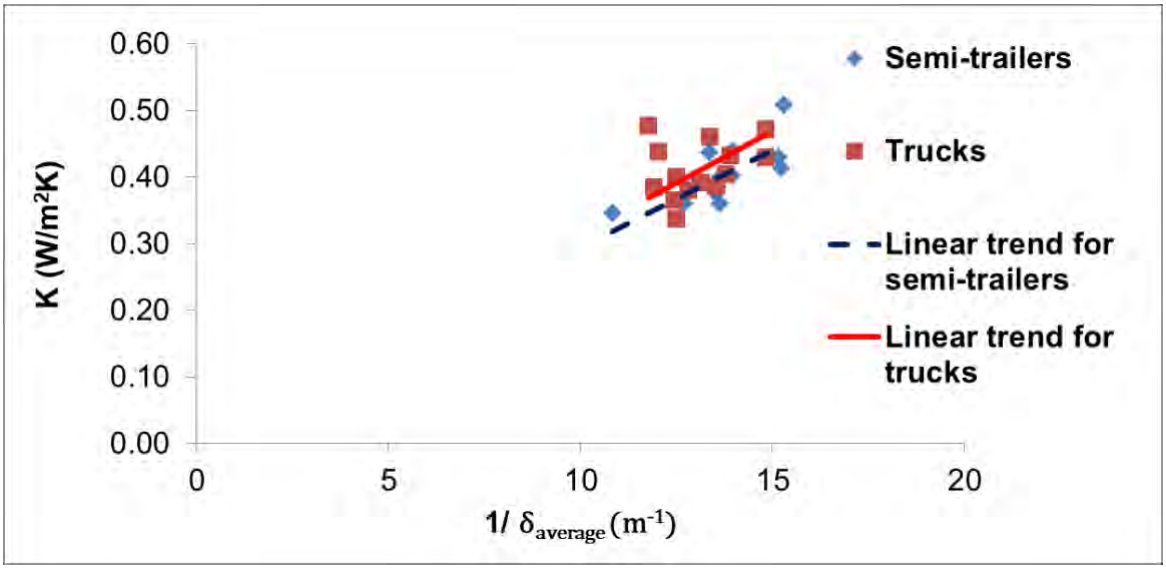

Figure 4: measured K values of fourteen newly manufactured trucks and fourteen newly manufactured semi-trailers as a function of $1/\delta_{average}$.

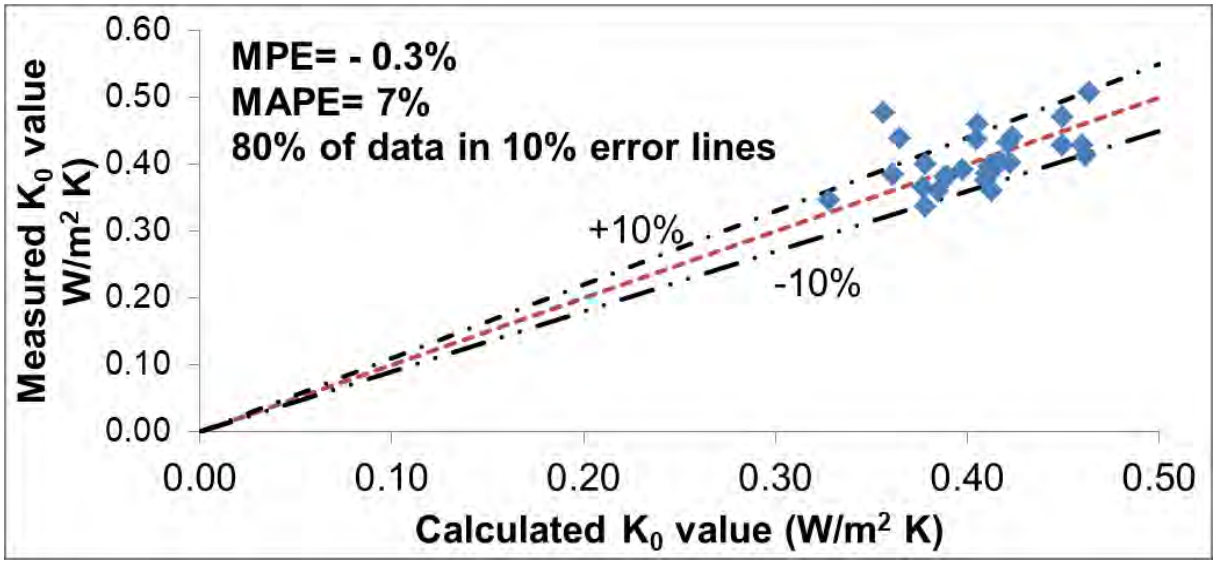

Figure 5: Comparison of measured K_0 values with calculated K_0 values using Eq. 9.

4. IMPACT OF THE REFRIGERATING UNIT

At the beginning of its life, the refrigerated vehicle may undergo various interventions which could differently impact on the *K* coefficient (Capo et al., 2018). This may be the case, for example, of the mounting on the vehicle of the refrigerating unit. With the aim of assessing the impact of this intervention on the insulation performance of the vehicle, four refrigerated newly manufactured semi-trailers, having a mean surface area equal to 158 m^2, were tested under two different conditions, i.e. in presence or absence of the refrigeration unit. When the refrigeration unit was absent from the semi-trailer, a shutter buffer was taking its place. Results of this experimental assessment are shown in Fig. 6. The non–colored parts of the bars having defined contours represent the measured K_0 values in absence of refrigerating unit. When the refrigerating unit is mounted, the K_0 values increase by an amount that depends from case to case. This amount is highlighted by the colored parts of the bars. For these fours semi-trailers, the mean value of the difference between *K* measured in these two conditions, i.e. in presence or absence of the refrigerating unit, is equal to 0.019 $W.m^{-2}.K^{-1}$.

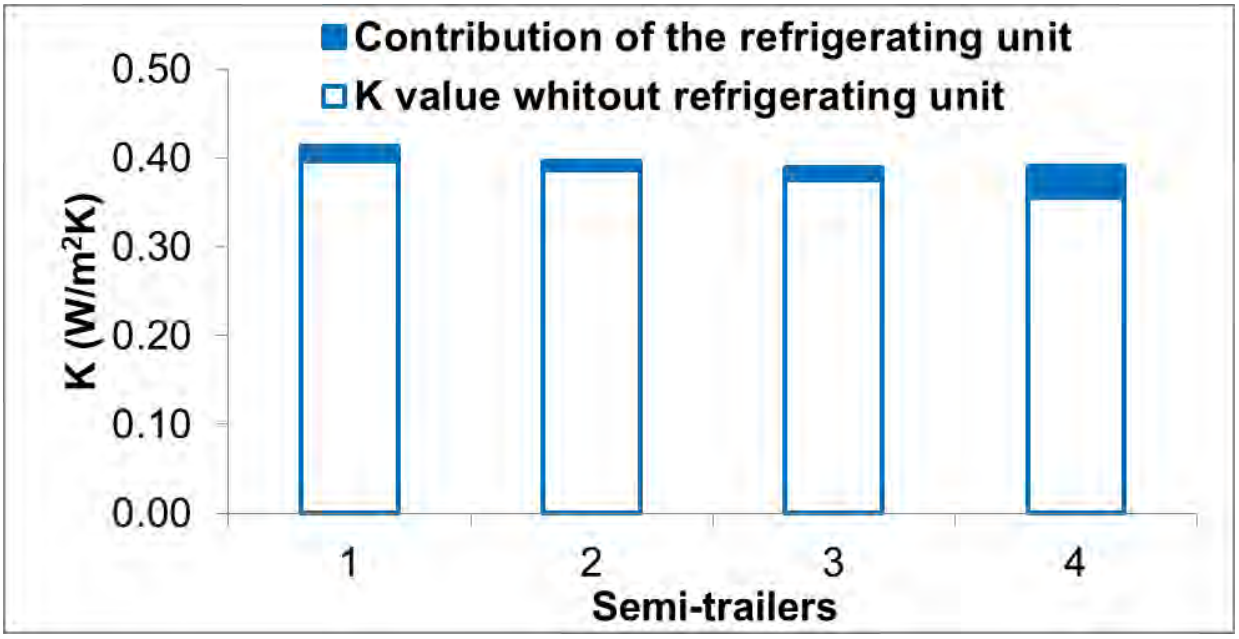

Figure 6: measured *K* values for four semi-trailers in presence and absence of the refrigeration unit.

5. CONCLUSIONS

This communication mainly reports experimental results of *K* coefficient tests for fourteen different newly manufactured trucks. These results are consistent with those previously presented by Capo et al. (2018) for fourteen newly manufactured semi-trailers and confirm that K_p is not a good indicator for the evaluation of ageing. Owing to experimental data for the trucks presented in this paper, it was demonstrated that even in the case where geometry has a negligible effect on the variation of the *K* value, there are significant differences (up to 45 %) between the measured *K* coefficients of the new trucks and the values of their reference prototypes. This difference is greater than that obtained for semi-trailers (up to 26%). Except for

four trucks, all the measured K values of the new vehicles were found to be greater than those of their reference prototype. Moreover, considering the K value of the prototype (K_p) as the reference measurement, some of the trucks realized in the series, would have received a wrong insulation class according to the ATP Agreement.

Combining the results of this paper with those previously presented by Capo et al. (2018), an apparent thermal conductivity (λ_{app}) was calculated and found to be equal to 0.030 $W.m^{-1}.K^{-1}$. This parameter takes into account the presence of the solid matrix that improves the mechanical robustness to the structure of the vehicle. This value is greater than that of the polyurethane foam (0.025 $W.m^{-1}.K^{-1}$) by 20%, i.e. the matrix does not drastically affect the insulation performance of the enclosure.

Another important result of this paper is that mounting of the refrigerating unit on the refrigerated enclosure of the vehicle has a noticeable impact on the insulating performance of the vehicle. As a matter of fact, four semi-trailers were tested under two different conditions, i.e. in presence or absence of the refrigerating unit, and the mean value of the difference between K measured in these two conditions was found to be equal to 0.019 $W.m^{-2}.K^{1}$. Improving the mounting technique and the insulation of the refrigerating unit thus appear to be two useful tracks to enhance the insulation performance of the vehicles realized on the series.

NOMENCLATURE

		Subscripts	
A_{12}	ageing	*ext*	external
Q	power (W)	*int*	internal
S	Area (m^2)	*p*	prototype
K	overall insulation coefficient ($W.m^{-2}.K^{-1}$)	*0*	initial
T	temperature (K)	*n*	n-th year
λ	thermal conductivity ($W.m^{-1}.K^{-1}$)	*i*	i-th
δ	thickness (mm)	*th*	theoretical
t	*time (s)*	*app*	apparent
R^2	coefficient of determination		
MPE	*mean percentage error (%)*		
MAPE	mean average percentage error (%)		

REFERENCES

Boldrin, B., Minotto G., Panozzo, G., Toniolo, B., Varotto, G., 1990. Ageing of insulated vehicles: statistical elaboration of test result. Proc. of Commissions B2, C2, D1, D2/3, Dresden, Germany, IIF/IIR, 839-845.

Capo, C., Latchan, F., Michineau, T., Petit, J.M., Revellin, R., Bonjour, J., Cavalier, G., 2018. Factors affecting the ageing of refrigerated transport equipment. Proc. 5th IIR Conference on Sustainability and the Cold Chain, Beijing, China.

Cavalier, G., Tassou, S. A., 2011. Sustainable refrigerated road transport. 21st Informatory Note on Refrigerating Technologies, International Institute of Refrigeration.

Lawton, A. R., Marshall, R. E., 2007. Developments in refrigerated transport insulation since the phase out of the CFC and HCFC refrigerants. Proc. 22nd Int. Congr. Refrig., Beijing, China, ICR07-D2-848.

Manuscript ID: 713
DOI: 10.18462/iir.icr.2019.0713

Towards a Comprehensive Modelling Framework for Flammable Refrigerant Leaks in Transport Containers

Hugh O'REILLY[(a,b,*)], Dermott CROMBIE[(a)], Rory F.D. MONAGHAN[(b,c,d)], Padraig MOLLOY[(b)]

[(a)] Ingersoll Rand – Thermo King, Monivea Road, Mervue, Galway, Ireland.
[(b)] School of Engineering, National University of Ireland Galway, University Road, Galway, Ireland.
[(c)] Ryan Institute, Galway, Ireland.
[(d)] MaREI Research Centre of Marine and Renewable Energy, Galway, Ireland.
*hugh.oreilly@irco.com

ABSTRACT

Recent research has identified the importance of understanding computational fluid dynamics (CFD) in the analysis of flammable refrigerant leaks. Limited work has been documented on the use of CFD in refrigerated transport applications. This paper describes progress towards a CFD-based simulation framework to assess the risks of flammable refrigerant leaks in a marine refrigerated container. The paper details a range of tests of refrigerant leaks and quantitative validation of a CFD model setup for leaks that occur when evaporator fans in the refrigeration unit are powered on. Experimental and simulated results are presented for distributions of gas concentration within the container, along with temperature data. Results of a model performance study using the fractional bias, normalised mean square error, geometric mean bias and geometric variance of the datasets are also presented. In this study, all performance metrics fall within the acceptance criteria and therefore, the modelling methodology is deemed robust and accurate.

Keywords: CFD, computational fluid dynamics, flammability, low GWP, refrigerant, refrigerated transport

1. INTRODUCTION

Many important factors differentiate the transport refrigeration sector from the high-profile commercial and residential heating, ventilation, air-conditioning and refrigeration (HVACR) sector in terms of refrigerant technology. These include equipment size restrictions, weight restrictions and operating profiles. Furthermore, a refrigerated transport container will mostly likely operate in, a number of geographical regions over its lifespan and therefore it may need to comply with multiple codes and regulations. This highlights the need for a comprehensive understanding of using low global warming potential (GWP) flammable refrigerants in refrigerated transport containers.

One of the fundamental concerns regarding the transition to flammable refrigerants is refrigerant leakages and associated risks. Such concerns are particularly relevant to transport refrigeration, due to the sealed and confined space within the refrigerated container. Current literature relating to flammable refrigerant leakages in transport refrigeration focuses primarily on R290 (Colbourne *et al.*, 2016; Konig *et al.*, 2016; Poolman *et al.,* 2016). In all of these studies, concentrations greater than the lower flammability limit (LFL) of R290 are evident in a significant number of cases, even when a reduction in charge size has been applied.

The LFL is the minimum concentration of gas required for flame propagation to occur in air, which is 0.038 kg/m^3 for R290. It is thus classified as flammability Class 3 by ANSI/ASHRAE Standard 34 (ANSI/ASHRAE, 2016) and ISO 817 (ISO, 2014). This low value is problematic in applications requiring larger charge sizes, such as transport refrigeration units. Class 2/2L refrigerants have an LFL greater than 0.10 kg/m^3 by definition and therefore higher concentrations are needed for flammable conditions to form. This reduces the risk associated with leakage events and allows larger

charge size to be used in the equipment. Hence, they are currently being investigated as a lower GWP alternative refrigerant for transport refrigeration.

There are limited published studies on the dispersion and fluid flow physics of a point-source release of a gas in a sealed and un-ventilated environment, such as a refrigerated transport container. The authors of this paper have previously presented work on an experimentally-validated computational fluid dynamics (CFD) model for the prediction of gas dispersion and distribution due to a leak in a refrigerated transport container, where forced convection mixing has taken place due to the evaporator fans being in operation (O'Reilly *et al.,* 2018). In that study, a qualitative cross-comparison between CFD and experimental data was carried out, which demonstrated that the CFD could predict the steady-state uniformly mixed concentration of released gas to within ±5% of experimentally observed data.

However, as with all numerical modelling, rigorous verification and validation is required and it is desirable to quantitatively measure agreement between model predictions and experimental measurements. There are many tools available for this purpose, such as classical ANOVA (Analysis of Variance), pattern comparison tests and weighted average fractional bias plots (Meroney *et al.,* 2016). Hanna (1993) performed extensive work on dispersion model validation and Chang and Hanna (2004) proposed a model performance methodology based on the fractional bias, the geometric mean bias, the normalised mean square error and the geometric variance. Further detail is given on these metrics in Section 2 below. These measures have been adopted across a number of gas dispersion modelling studies, using both buoyant and heavy gases (Giannissi *et al*., 2015; Schleder and Martins, 2016; Dong *et al*., 2017).

The objective of this paper is to evaluate the performance of the numerical model using typical statistical performance metrics as described above. The next section gives an overview of the model used in this study and the experimental set-up used for data measurement. The model performance metrics, which are used to quantify the accuracy of the model, are also described. Section 3 presents the results of the study. Finally, Section 4 presents the conclusions we draw from this work and describes the next steps in the development of this modelling framework.

2. METHODS AND MATERIALS

2.1. Simulation Framework

The overall focus of this work is to develop a comprehensive CFD-based simulation framework to assess the risks of flammable refrigerant leakages in refrigerated transport containers. The use of flammable refrigerants in the scale of experiments required by this work poses many challenges, including health and safety risks, environmental concerns and high equipment cost. So, a refrigerant surrogate gas is used for the experimental aspect of this work. CO_2 was selected as the surrogate gas for this work, as it is an inert heavy gas which is readily sensible. Once fully validated using the experimental data from CO_2 releases, the model will be modified to allow for flammable refrigerant leakages to be studied. The work will also further extend to modelling and simulation of natural convection mixing (i.e. when evaporator fans are powered off) when a leak occurs, which is more difficult to predict due to the stochastic nature of natural convection turbulence.

2.2. Data Acquisition

The authors have previously presented work illustrating the modelling set-up and detailing the experimental equipment (O'Reilly *et al.,* 2018). However, a brief overview is given here for continuity. A series of leak tests were conducted, which were designed to simulate multiple possible refrigerant leakages into a 6-m (20-ft) refrigerated container, fitted with a Thermo King MagnumPlus refrigeration unit. Twelve experimental tests were carried out to develop a library of experimental results for comparison with CFD simulations. A total of 36 CO_2 sensors were installed in a regular pattern in the container, as shown in Figure 1. The sensors used non-dispersive infra-red (NDIR)

detection and were accurate to ±5% of reading for a range of 0-20% v/v, with a sensing frequency of 20 Hz. Temperature at these locations was also recorded, using NiCr-Ni Type K thermocouples.

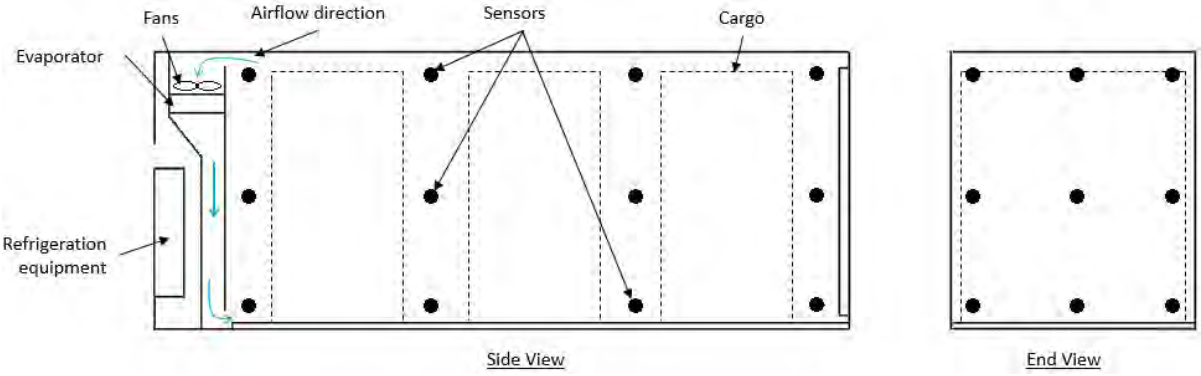

Figure 1. Refrigerated container layout

This particular refrigeration unit contained a charge of 4 kg R134a, which is the typical charge size for this type of unit. This equates to 1.7 kg CO_2 on a molar basis. This mass of CO_2 was injected via an auxiliary hose, placed through a drainage hole in the bulkhead of the container. The leak flow rates were based on a leak duration, which were selected to represent leakages due to a range of causes, such as corrosion, fatigue fracture or impact fracture of components. Both low (0.55 m^3/s) and high (1.12 m^3/s) speed settings on the evaporator fans were utilised to determine if the fan flow rate had any effect on the dispersion of released gas, while both empty and partially loaded container configurations were also studied. A cargo load was represented by plastic boxes, the outline of which is illustrated by the dashed line in Figure 1. The boxes were sealed and air-tight per manufacturers specification. Therefore, CO_2 absorption by the load was deemed negligible. Due to installation of the sensors, the volume occupied by cargo was limited to 38% of total internal volume. The fresh-air exchange mechanism was not used for this work and any possible air-leakge points were sealed for this testing, except the door seals which were accounted for in the model. Table 1 gives a summary of each test and the experimental variables used.

Table 1: Experimental variables

#	Leak time (min)	Flow rate (g/s)	Fan speed (m^3/s)	Cargo (%)
1	4	7.08	0.55	0
2	15	1.89	0.55	0
3	60	0.47	0.55	0
4	4	7.08	1.12	0
5	15	1.89	1.12	0
6	60	0.47	1.12	0

#	Leak time (min)	Flow rate (g/s)	Fan speed (m^3/s)	Cargo (%)
7	4	7.08	0.55	38
8	15	1.89	0.55	38
9	60	0.47	0.55	38
10	4	7.08	1.12	38
11	15	1.89	1.12	38
12	60	0.47	1.12	38

The 3D CFD domain comprised one half of the container, by using symmetry about the central vertical plane along the container's length, as shown (Figure 2). A mass flow rate boundary condition at the inlet, based on the CO_2 flow rates, was applied and an atmospheric pressure outlet to replicate the rear door seals was used. The mesh was composed of unstructured tetrahedral cells and grid independence was achieved with 215,021 elements for simulations with an empty container and 206,896 elements for simulations with cargo. Also visible in Figure 2(a) are the symmetry plane and the monitor points which were located at the same position as the sensors as used in experimental work are illustrated in Figure 2(b). The heat flux through the walls to be imposed in the CFD simulation was determined by using a transient thermal resistance-capacitance lumped model comprising the internal air mass, evaporator, rear-plate, T-bar floor, internal aluminium wall, intermediate polyurethane insulation layer and external steel wall. The fan power input at high speed

was 751 W and 184 W at low speed. Each sensor dissipated 1.8 W, or 64.8 W in total. This gave the mean heat flux out of the CFD domain at the walls of 3.3 W/m^2 for low fan speed and 10.5 W/m^2 for high fan speed. The difference in values was largely due the higher energy consumption of the fans while running at the higher speed, while each individual case varied slightly due to the ambient temperature at which the corresponding experiment was carried out.

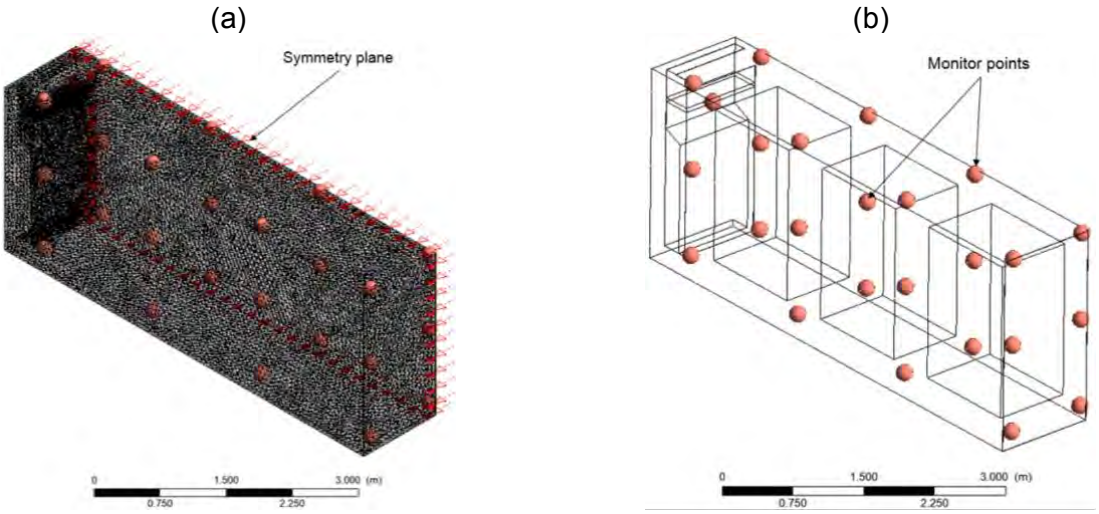

Figure 2. Computational domain of the container for (a) the empty container with mesh shown and (b) the container with cargo and no mesh shown for clarity

The commercial CFD code, ANSYS CFX 19.1 (ANSYS, 2018) was used to carry out the simulations, along with the RANS *k-ε* turbulence model (Launder and Spalding, 1974). The second-order backward Euler scheme was used to approximate all transient terms and the high resolution scheme approximated the spatial derivatives. The ideal gas law was used to calculate the gas densities and a variable composition binary mixture composed of air and CO_2 was used, with air as the constraint component. The Reynolds-averaged transport equation was then solved for CO_2.

2.3. Model Performance Metrics

In order to quantitatively assess the model performance, a number of statistical performance measures were considered, as mentioned above. Such metrics are typically used in pairs, with one parameter used to indicate concentration under- or over-prediction and the other to indicate the level of scatter (Giannissi *et al.*, 2015). Chang and Hanna (2004) recommend the fractional bias (FB), the geometric mean bias (MG), the normalised mean square error (NMSE) and the geometric variance (VG), which are defined as follows:

$$FB = \frac{\left(\overline{C_{exp}} - \overline{C_{CFD}}\right)}{0.5\left(\overline{C_{exp}} + \overline{C_{CFD}}\right)} \quad \text{Eq. (1)}$$

$$NMSE = \frac{\overline{\left(C_{exp} - C_{CFD}\right)^2}}{\overline{C_{exp}}\,\overline{C_{CFD}}} \quad \text{Eq. (2)}$$

$$MG = exp\left[\overline{\ln\left(\frac{C_{exp}}{C_{CFD}}\right)}\right] \quad \text{Eq. (3)}$$

$$VG = exp\left[\overline{\ln\left(\frac{C_{exp}}{C_{CFD}}\right)^2}\right] \quad \text{Eq. (4)}$$

The FB (Equation 1) represents the residual error of the experimentally measured (C_{exp}) and modelled gas concentrations (C_{CFD}). The bias is normalised by the mean concentration of the data-

set. FB indicates if the model under- or over-predicts concentration. Positive values mean that the model under-predicts, while negative values indicate over-prediction and the ideal value is 0. The FB should be accompanied by NMSE (Equation 2), which indicates the scatter of the entire data-set. It is the variance of FB and estimates the overall deviation between the observed and the predicted values. Good model performance is indicated by small values of NMSE, with the ideal value equal to 0. The second pair of statistical metrics used in this work are MG (Equation 3) and VG (Equation 4). MG is the exponent of the logarithm of the ratio of experimental measurement to modelled value. By taking the logarithim of the ratio, the influence of extreme ratios is reduced. It is a measure of the relative mean bias and is less influenced by extreme ratios. Similarly, VG measures the relative scatter. Both of these metrics have ideal values of 1.

Chang and Hanna (2004) further define an acceptable model as one where the random scatter is about two or three of the mean, i.e. VG < 4 or NMSE < 9, and the relative mean bias is within ±30% (0.7 < MG < 1.3 or |FB| < 0.3). A summary of the metrics, along with their ideal values and acceptance criteria, is given in Table 2 below. These values are typically used for natural convection dispersion work. The work presented here is of the forced convection type, however these values are widely accepted and provide a suitable baseline for comparison.

Table 2. Model performance metrics summary

	Ideal value	Acceptance criterion
FB	0	±30%
NMSE	0	< 9
MG	1	±30%
VG	1	< 4

Furthermore, gas dispersion studies are typically limited to recording the maximum concentration in a given set of experiments, for which the performance metrics are evaluated from. The maximum concentration is ususally the paramteter of interest, so this is deemed acceptable. However, in this work, the experimental and modelled results are both spatially and temporally directly comparable. This is due to the identical positioning of monitoring points (i.e. sensors in experiment) in both the physical simulations and the CFD model and the ability of the sensors to take readings at frequencies up to 20 Hz.

3. RESULTS AND DISCUSSION

3.1. Comparison between experiment and CFD

A typical time evolution of spatially-averaged temperature within the container is shown for Test 3 in Figure 3(a) and for Test 12 in Figure 3(b). The experimental temperature data (T_{exp}) is shown by dashed line and the solid line shows the CFD results (T_{CFD}). Per Table 1, these tests were carried out at the same gas leak rate with different fan speed and different cargo load.

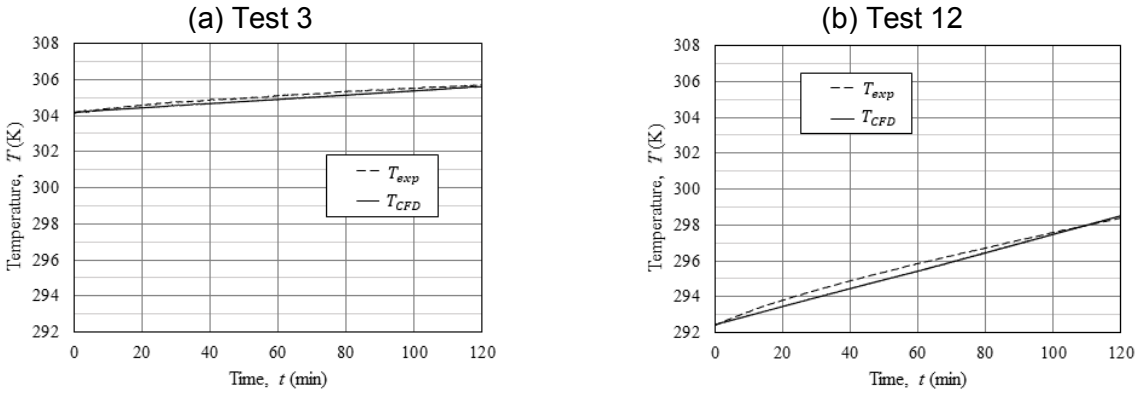

Figure 3. Temperature plots for experiment and CFD for (a) Test 3 (60min leak, low fan speed, empty container) and (b) Test 12 (60min leak, high fan speed, 38% loaded container)

Ambient temperature was also different, as represented by different temperatures at the start of the tests (t = 0). The temperature rise in the container during the test can be attributed to the energy input from both the evaporater fans and CO_2 sensors. The results show that the experimentally recorded values and CFD predicted values demonstrate satisfactory agreement, with a larger temperature increase obtained in the test where the fans were operated at high speed, as expected. These results indicate that the thermal boundary conditions are correctly established in the model. Similar plots were produced for the other test cases and the same trends were apparent.

The time evolution of mean CO_2 concentration for Test 5 is illustrated in Figure 4(a) and for Test 8 in Figure 4(b). The dashed line shows the spatially-averaged CO_2 readings from experiment (C_{exp}), while the solid line shows CO_2 predictions from the CFD model (C_{CFD}). The tests show linear CO_2 concentration increase due to constant leak flow rate with higher steady-state concentration evident in Test 8 due to the presence of cargo. Concentration values for all test cases were plotted and similar trends were obtained.

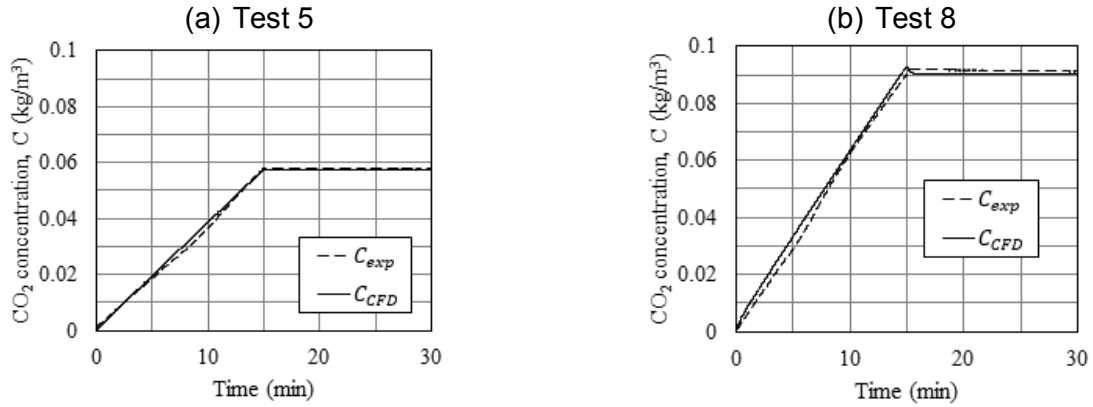

Figure 4. CO_2 concentration plots from experiment and CFD for (a) Test 5 (15min leak, high fan speed, empty container) and (b) Test 8 (15min leak, low fan speed, 38% loaded container)

3.2. Model Performance Evaluation

Table 3 displays the statistical measures for the concentration for the entire duration of the tests at all monitoring points. The values are very close to ideal values for all metrics, with all values inside acceptance criteria given in Table 2 which indicates satisfactory overall agreement.

Table 3. Statistical measures for each test

Test No.	Leak time (min)	Flow rate (g/s)	Fan speed (m^3/s)	Cargo (%)	FB	NMSE	MG	VG
Ideal value:					0	0	1	1
1	4	7.08	0.55	0	0.0078	0.0018	0.9808	1.0291
2	15	1.89	0.55	0	-0.0077	0.0026	1.0286	1.0164
3	60	0.47	0.55	0	0.0550	0.0025	1.0346	1.0141
4	4	7.08	1.12	0	-0.0404	0.0017	0.9761	1.0260
5	15	1.89	1.12	0	-0.0186	0.0005	1.0068	1.0202
6	60	0.47	1.12	0	-0.0457	0.0019	1.0139	1.0105
7	4	7.08	0.55	38	-0.0228	0.0041	0.8942	1.0760
8	15	1.89	0.55	38	-0.0557	0.0009	0.9527	1.0166
9	60	0.47	0.55	38	-0.1338	0.0007	0.9848	1.0082
10	4	7.08	1.12	38	-0.0117	0.0020	0.9305	1.0360
11	15	1.89	1.12	38	0.0111	0.0033	1.0195	1.0068
12	60	0.47	1.12	38	-0.0652	0.0035	1.0361	1.0062

According to FB, the model over-estimates the concentration for all tests except Tests 1, 3 and 11, as indicated by positive values. In contrast, MG shows over-prediction for all tests with a leak time of four minutes in addition to Tests 8 and 9. Due to the formulation of FB (see Equation 1), it is highly influenced by infrequent large under- or over-predictions in the dataset, which is likely to affect results. MG shows more consistencey in this case, with exception of Tests 8 and 9, which warrants further investigation.

Furthermore, all four minute leak tests have highest scatter according to VG, with sixty minute leak tests consistently having lowest scatter. Compared to NMSE, the trend in VG is more consistent, which is similar to FB and MG comparison. If the model shows a mean bias but no random scatter, the data point would be on the curve shown in Figure 5 ($ln(MG)^2 = ln(VG)$), which represents the minimum possible value of VG corresponding to a particular MG (Kisa and Jelemensky, 2009). As such, all points must lie above the curve. In addition, Figure 5 shows that all MG values are very close to the ideal value of unity, with the worst performing model being for Test 7. However, all values are well within acceptance criteria detailed in Table 2.

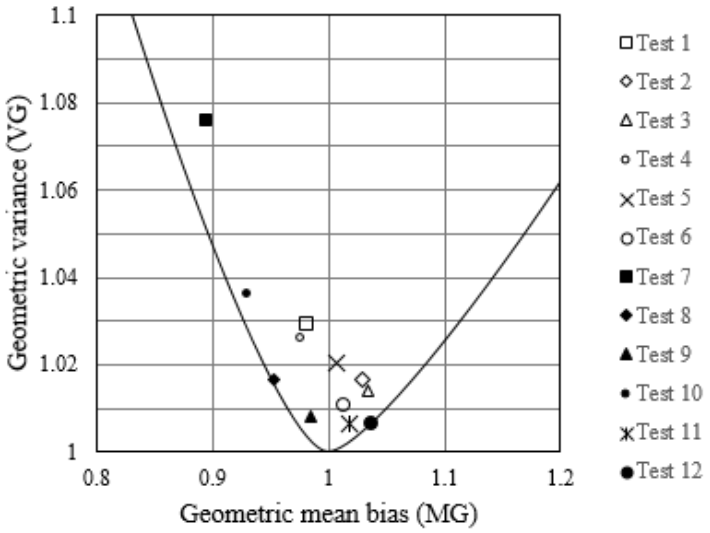

Figure 5. Geometric mean bias (MG) and geometric variance (VG) for all tests presented in Table 1

4. CONCLUSIONS

Regulations and legislation are forcing the phase-down of conventional high GWP refrigerants. Next generation refrigerants, with sufficiently low GWP to satisfy these new laws and protocols have some degree of flammability. For the transport refrigeration industry, this represents a challenge due to the potential for flammable refrigerant leakages into the refrigerated compartment of the container, where build up of flammable gas may result in hazardous cloud formation. This work sets out to develop a methodology for creating an experimentally validated CFD model to allow simulation of refrigerant leakages into a refrigerated transport container.

This paper advances the authors' previous work on CFD model validation and verification by utilising a series of model performance metrics, which have been widely used in the literature in gas dispersion studies. These include fractional bias, normalised mean square error, geometric mean bias and geometric variance. These metrics have the ability to quantify the accuracy of the model and define model under- or over-prediction of gas concentration, along with scatter in the data. The model performace study also allows the use of a pre-defined acceptance criteria to ensure a rigourous model validation procedure.

Overall, the results presented here show that the CFD model correlates satisfactorily with experimental data for the dispersion of a released gas in the container with evaporator fans in operation. The results of this study are within the acceptance criteria for all test cases that have been considered. This indicates that the model configuration is robust and accurate. In addition, the use

of temperature data to further verify the model serves to show reliability in the modelling approach. Thus, further modelling predictions can be used with a high degree of confidence.This approach will be particularly beneficial for the next phase of this work, which entails modelling the dispersion of the released gas for buoyancy driven and natural convection flows, when the evaporator fans are powered off. This will be a much more challenging task given the difficulties expected to be encountered in modelling natural convection.

ACKNOWLEDGEMENTS

The authors acknowledge financial support from the Irish Research Council under the Employment Based Postgraduate Programme (grant number EBPPG/2015/216).

REFERENCES

ANSI/ASHRAE Standard 34-2016, Designation and Safety Classification of Refrigerants. American Society of Heating, Refrigerating and Air-Conditioning Engineers, Inc., Atlanta, GA 30329.

ANSYS, 2018. ANSYS CFX-Pre User's Guide, Release 19.1. Canonsburg, PA 15317.

Chang, J.C., & Hanna, S.R., 2004. Air quality model performance evaluation. Meteorology and Atmospheric Physics, 87(1–3), 167–196.

Colbourne, D., Solomon, P., Wilson, R., de Swardt, L., Schuster, M., Oppelt, D., Gloel, J., 2016. Development of R290 Transport Refrigeration System. Proceedings of the 12th IIR Gustav Lorentzen Natural Working Fluids Conference, Edinburgh.

Dong, L., Zuo, H., Hu, L., Yang, B., Li, L., Wu, L., 2017. Simulation of heavy gas dispersion in a large indoor space using CFD model. Journal of Loss Prevention in the Process Industries, 46, 1–12.

Giannissi, S.G., Shentsov, V., Melideo, D., Cariteau, B., Baraldi, D., Venetsanos, A.G., Molkov, V., 2015. CFD benchmark on hydrogen release and dispersion in confined, naturally ventilated space with one vent. International Journal of Hydrogen Energy, 40(5), 2415–2429.

Hanna, S.R., 1993. Uncertainties in air quality model predictions. Boundary-Layer Meteorology, 62(1–4), 3–20.

ISO 817:2014. Refrigerants - Designation and Safety Classification. International Standards Organization, Geneva.

Kiša, M., Jelemenský, L., 2009. CFD dispersion modelling for emergency preparadnes. Journal of Loss Prevention in the Process Industries, 22(1), 97–104.

Konig, H., Bararu, M., Holtappels, K., 2016. Practical Tests with R290 Used In Container Container Refrigeration Leakage Testing. Proceedings of the 12th IIR Gustav Lorentzen Natural Working Fluids Conference, Edinburgh.

Lauder, B.E., Spalding, D.B., 1974. Numerical Computation of Turbulent Flows, Computer Methods in Applied Mathematics and Engineering, 3, 269-289.

Meroney, R., Ohba, R., Leitl, B., Kondo, H., Grawe, D., Tominaga, Y., 2016. Review of CFD Guidelines for Dispersion Modeling. Fluids, 1(2), 1–16.

O'Reilly, H., Kohoutek, T., Crombie, D., Monaghan, R.F.D., Molloy, P., 2018. An Experimental and Numerical Study of Refrigerant Leaks in Refrigerated Transport Containers. Proceedings of the 1st IIR International Conference on the Application of HFO Refrigerants, Birmingham.

Poolman, C., Papas, P., Rusignuolo, G., Eddy, R., 2016. Low GWP Refrigerants in Transport Refrigeration: Risk and Benefit Assessment of Flammable and Mildly Flammable Alternatives. Proceedings of the 12th IIR Gustav Lorentzen Natural Working Fluids Conference, Edinburgh.

Schleder, A.M., Martins, M.R., 2016. Experimental data and CFD performance for cloud dispersion analysis. Journal of Loss Prevention in the Process Industries, 43, 688–699.

Manuscript ID: 754
DOI: 10.18462/iir.icr.2019.0754

Comparison of novel environmental control systems in aircrafts based on a vapor compression cycle

Steffen GOLLE, Ullrich HESSE

Technische Universität Dresden, Institut für Energietechnik,
Bitzer-Professur für Kälte-, Kryo- und Kompressorentechnik,
Münchner Platz 3, 01062 Dresden, Germany
Steffen.Golle@tu-dresden.de
Ullrich.Hesse@tu-dresden.de

ABSTRACT

The environmental control systems (ECS) of commercial aircrafts are currently based on a pneumatically driven air cycle. The achievable COP is significantly lower compared to a vapor compression cycle. Furthermore, the usage of bleed air is critical due to new engines with high bypass ratios and potential health risks to the passengers.
Therefore new approaches for ECS with a vapor compression cycle are investigated. The different technology paths comprise pneumatically and electrically driven systems, as well as the utilization of cabin exhaust air.
Seven novel ECS are compared to a reference system in respect of energy efficiency and total additional fuel consumption. This investigation includes the design process and the calculation models of the new ECS with detailed heat exchanger and turbo-machine models.
The results show a significant reduction in fuel consumption of the ECS to a minimum of 20% in ground cases and 40% in flight cases compared to the reference system. The overall fuel consumption of the aircraft can be decreased up to 1.8%.
Keywords: aircraft, environmental control system, vapor cycle, pneumatically driven, electrically driven

1. INTRODUCTION

In most commercial aircrafts an open, 2-stage air cycle is utilized as environmental control system (Conceição et al., 2007; Rossow et al., 2014). The basic process with the main components is shown in figure 1.

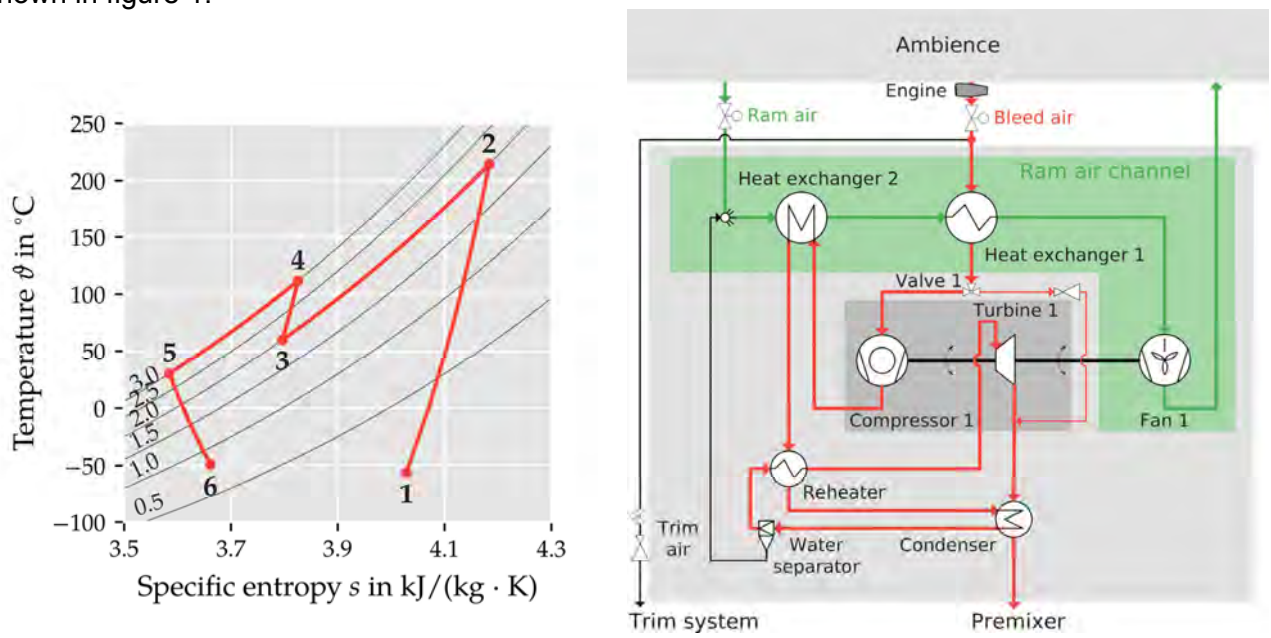

(a) Temperature-entropy diagram **(b) Circuit diagram**

Figure 1: Basic 3-wheel air cycle machine (bootstrap)

The bleed air is compressed in the engine (states 1-2), then cooled in the first air to air heat exchanger (states 2-3) and compressed further in the air compressor (states 3-4). Then the air passes the second heat exchanger (states 4-5) and the water separation cycle, which is neglected in the temperature-entropy diagram. The ram air is used to dissipate the heat from the ECS to the environment. Before the bleed air exits the air cycle machine to the mixing unit it is expanded in the air turbine to cabin pressure (states 5-6). Compressor, turbine and fan are located on the same shaft in an integrated machine set inside the environmental control system. The changes of state in the heat exchangers are almost isobaric with a certain pressure drop. The state changes in the compressor and turbine are polytropic with certain isentropic efficiencies. However the air cycle cannot achieve the same energy efficiency as the vapor compression cycle for the given boundary conditions because the cooling and heating of the air is not isothermal. Additionally the fresh air supply to the cabin must be provided by the bleed air, which has a defined temperature and pressure in the associated operating case. Thus the possible control mechanisms are limited. Excess power is usually handled by throttling the bleed air pressure. Furthermore new researches show that the application of bleed air as fresh air supply to the cabin could cause health issues for the passengers (Harrison and Ross, 2016). For this reason new concepts of environmental control systems for future aircrafts based on a vapor compression cycle are investigated with the main goal to increase the energy efficiency and hence decrease the fuel consumption caused by the ECS. The resulting seven systems are simulated with a detailed process model. Turbo-machines are integrated based on performance maps with all wheels on one shaft at the same rotation speed. Heat exchangers are modelled on the basis of their geometry with division in different cells for the evaporators and condensers. Finally the new systems are compared with the reference system from figure 1. The boundary conditions with the operating map for the reference aircraft Airbus A320 are shown in a previous paper (Golle et al., 2015). The main operating cases are defined on ground (1: ISA+23, 2: ISA-38, 9: ISA), in cruise (3: ISA+23 failure case, 8: ISA+23, 12: ISA-38, 13: ISA-38 failure case, 25: ISA) and during climb (11: ISA+38).

2. NEW CONCEPTS AND SYSTEMS

The main concept of this work is the application of the more efficient vapor cycle to partially or completely replace the air cycle. Additionally the replacement of bleed air in an electrically driven system can provide further benefits because of the better possibilities to control the turbo-machines and mass flow of all main airflows. No throttling of air is necessary which results in less energy dissipation. Finally the utilization of cabin exhaust air with an expansion turbine can generate additional power for the environmental control system and hence reduce the power input from the aircraft. In the next subsections the new systems are described for one pack. The ECS usually consists of two identical machines in order to cover possible failure cases.

2.1. Application of a vapor compression cycle

In pneumatically driven systems only one stage of the air cycle can be replaced because bleed air is expanded in a turbine to generate the necessary power for the ECS. Therefore a vapor cycle is used instead of a second bleed air compressor. In the evaporator the air can be cooled below the ambient temperature, so that the cabin entrance conditions are identical to the reference system. Furthermore the excess power of the system is used to drive an ambient air compressor, so that the bleed air mass flow can be reduced, but the fresh air supply is equal. This results in an overall decreased power and fuel consumption. In figure 2a the pneumatically driven environmental control system with a vapor cycle (PN1) is shown. This system can be used in current commercial aircrafts as retrofit. In electrically driven systems bleed air is completely replaced with ambient air as fresh air supply. The system is driven by electric motors. The pressure level in the ECS can be controlled precisely for every operating case. In ground cases excess water in the air needs to be separated, thus a higher pressure than ambient conditions is preferred. In flight the pressure level can be adjusted to cabin pressure, which offers additional reductions in power input. The electrically driven vapor cycle machine with a 1-stage compression (EL1) is shown in figure 2b. There is also a version with 2-stage compression (EL2). The two versions are calculated to investigate the influence of the ambient conditions at different operating cases and the performance maps of the ambient compressor. Earlier calculations indicate that the huge pressure difference from ground to flight cases may not be covered with only one compressor. However the final results demonstrate the possibility to use one compressor with variable inlet guide vanes.

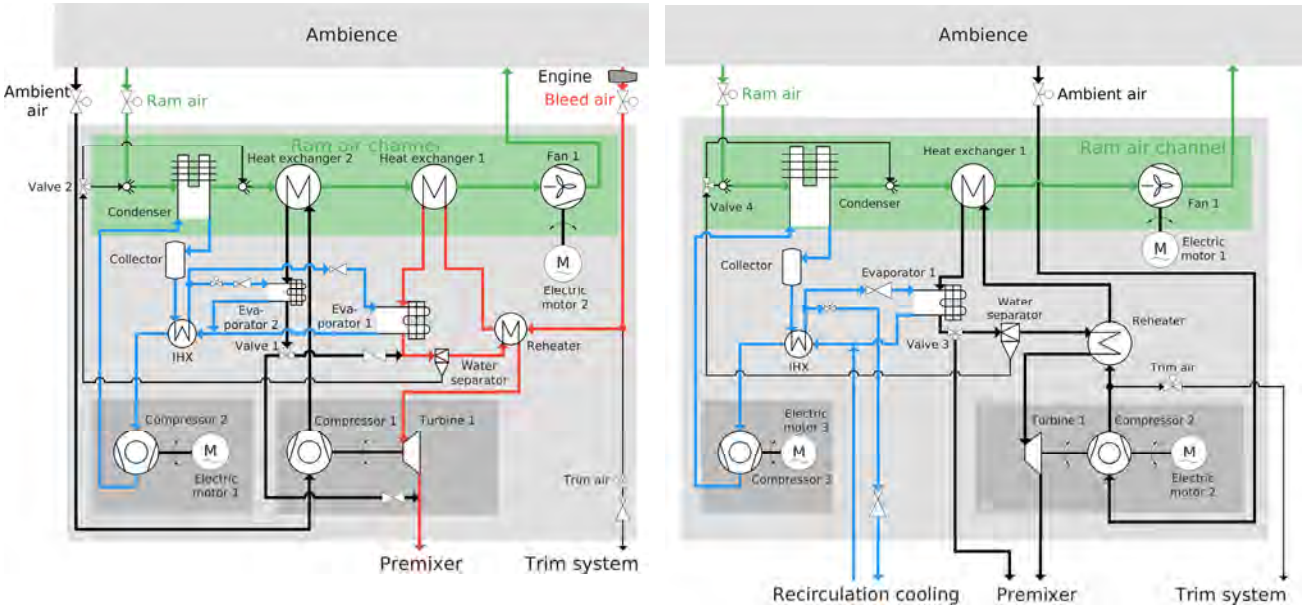

(a) Pneumatically driven (PN1) **(b) Electrically driven (EL1)**

Figure 2: Environmental control systems based on a vapor cycle

2.2. Utilization of cabin exhaust air

The same amount of air like the fresh air mass flow to the cabin also needs to be discharged in order to comply with the mass balance of the cabin. In cruise and flight cases the exhaust air has a higher pressure level than the ambience. In current aircrafts the air exits at the cabin discharge valve, which controls the cabin pressure. However the pressure difference can be used to generate additional power in the ECS before leaving the aircraft. The pneumatically and electrically driven systems with utilization of cabin exhaust air (PNK1, ELK1) are shown in figure 3. The pneumatically driven vapor cycle machines are split in three versions (PNK1 – PNK3). The first version only uses bleed air as fresh air supply to the cabin, version 2 uses bleed air on ground and ambient air in flight cases and version 3 only uses ambient air. The pneumatically driven systems are quite complex with many turbo-machines in order to separate the different airflows and pressure levels. The electrically driven system realizes a reduced power input in flight cases especially for compressing the ambient air. Compared to the vapor cycle machine without utilization of cabin exhaust air the electric motors can be designed smaller and lighter with less power output.

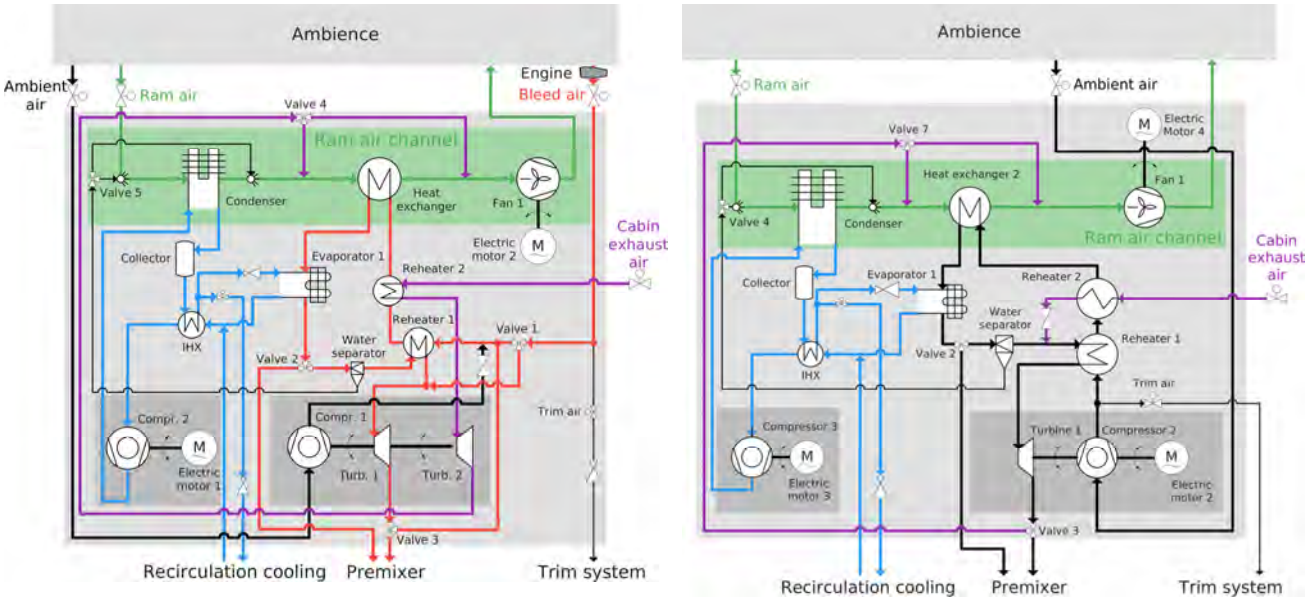

(a) Pneumatically driven (PNK1) **(b) Electrically driven (ELK1)**

Figure 3: Environmental control systems based on a vapor cycle with utilization of cabin exhaust air

3. PROCESS, TURBO-MACHINE AND HEAT EXCHANGER MODELS

The development of the new systems consists of two major steps: design and recalculation. The design calculations are aimed at the determination of the mass flow of e. g. the bleed, ambient, ram and trim air with defined $k \cdot A$ values for the air to air heat exchangers, temperature profiles for evaporators and condensers as well as fixed efficiencies and pressure ratios for all turbo-machines. During the recalculation the mass flows are fixed and the turbo-machines are implemented as performance maps and the heat exchangers as a geometry-based model. The recalculation offers a detailed representation of the process. The operating cases of the turbo-machines are determined with a performance map and the rotation speed is matched for all machines on a shaft. The heat exchangers take different inlet conditions into consideration with the help of a cell based model. The occurring heat exchange and pressure drop mechanisms are calculated with varying correlations.
The process simulation is conducted with an own process model implemented in the programming language Python. At first the environmental control systems are discretized to a finite number of reference points, which is shown exemplary in figure 4 for system ELK1. Afterwards the stationary thermodynamic states are calculated at the reference points in an iterative way.

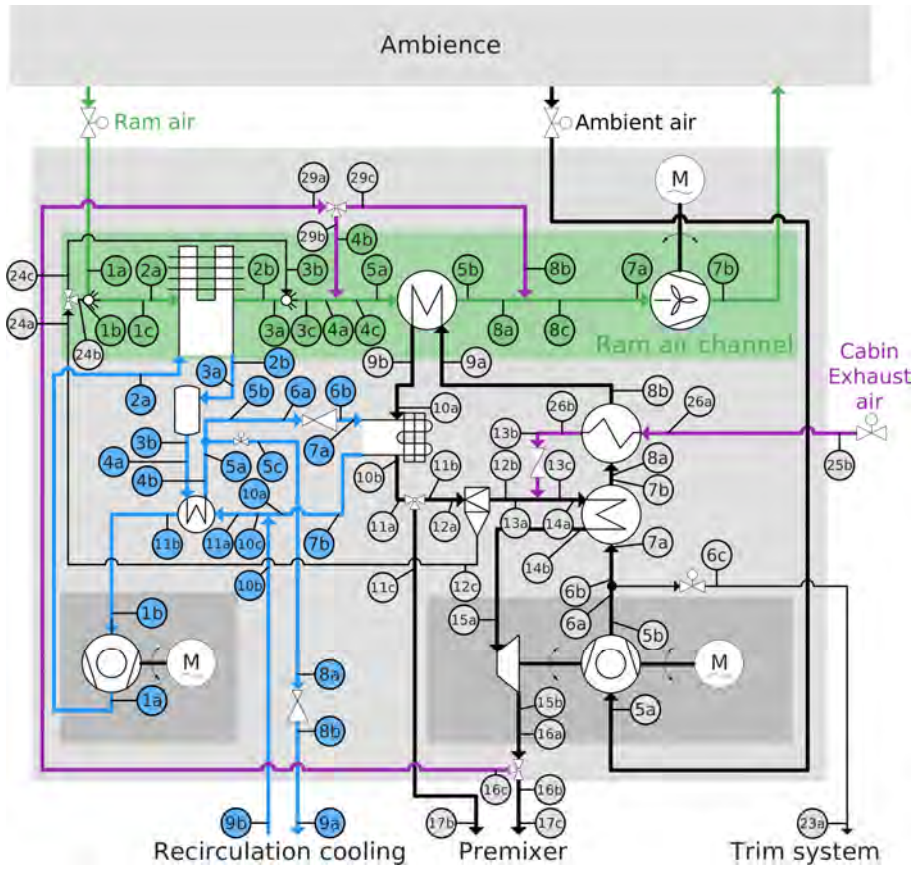

Figure 4: Reference points of the electrically driven system with utilization of cabin exhaust air (ELK1)

The operating points of the turbo-machines in the performance maps highly depend on the entrance conditions. Especially the ambient air compressor must cover the different pressure levels on ground and in flight. Therefor the process simulation must include the determination of the operating points of the turbo-machines with the help of performance maps. Otherwise it is possible that in certain operating cases the desired exit state cannot be reached. Preferably the design of the turbo-machines and the process simulation should be combined in order to reduce the needed design iterations. The descriptions of the map generation and interpolation as well as rotation speed matching are shown in a previous paper (Golle et al., 2017). The example of a compressor map for the system ELK1 with all operating points is shown in figure 5. The operating cases on ground 1, 2 and 9 can be covered by an additional variable inlet guide vane (VIGV).

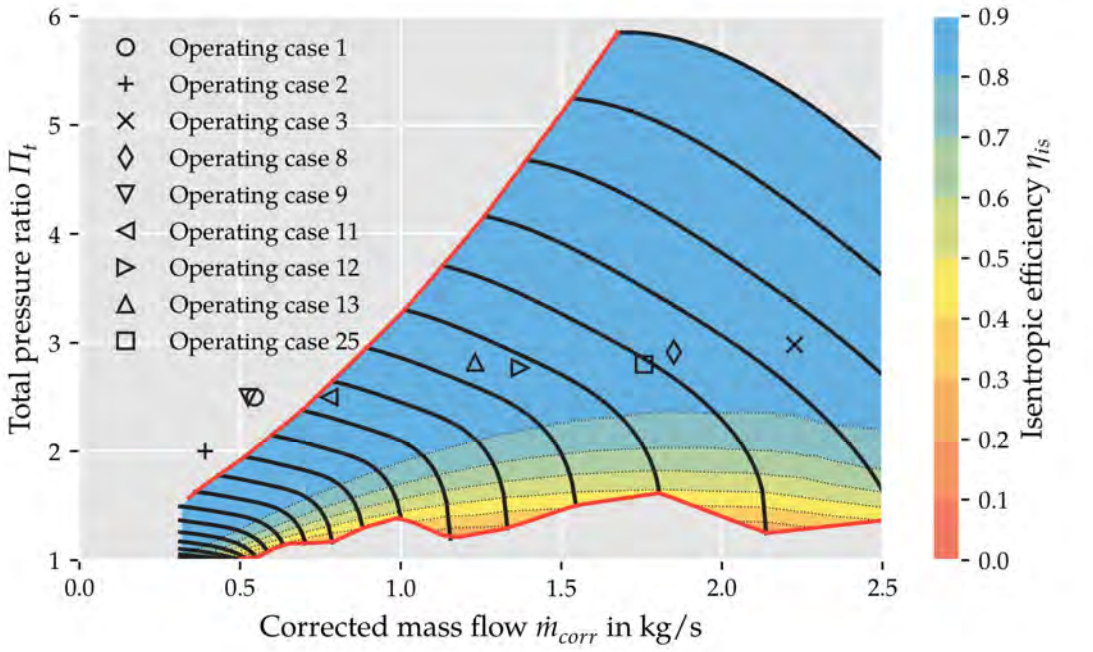

Figure 5: Turbo-machine performance maps of compressor 2 in system ELK1

The detailed heat exchanger model is implemented in a modular way in Python. The model is divided in two main parts: linking and discretizing of the network, solver. It can be used for various heat exchanger types. In this work the following types are used: plate, fin-and-tube and plate-fin heat exchanger. At first the heat exchanger is divided in cells, which are connected in a defined way (linking and discretizing). This results in a network or directed graph. Every cell in the graph can then be calculated with the solver. This also yields the outlet conditions. In each cell the heat, mass and momentum balance must be applied. The heat flow between the two fluids is given by:

$$\dot{Q} = k \cdot A(T_2 - T_1) \qquad \text{Eq. (1)}$$

where T_1 and T_2 are the fluid temperatures of the fluids in K, A the heat transfer area in m² and k the heat transmission coefficient in W/(m²K). The coefficient k depends on the heat transfer coefficients of both fluids α_1 and α_2 as well as the thermal conductivity λ and the geometry of the dividing wall. These coefficients are calculated with empirical or semi-empirical correlations by different authors that are summarized in table 1.

Table 1. Heat transfer and pressure drop correlations

Transport mechanism	Heat transfer correlation	Pressure drop correlation
One phase inside tube	VDI, 2013	Glück, 1988 (with Prandtl and Colebrook)
Two phase inside tube (evaporation)	Shah, 2017	Friedel, 1979
Two phase inside tube (condensation)	Shah, 2016	Friedel, 1979
One phase outside louvered fins	Park and Jacobi 2009	Park and Jacobi 2009
One phase inside plate heat exchanger with chevron corrugation patterns	Martin, 1996	Martin, 1996
One phase inside plate-fin heat exchanger with rectangular offset strip fins	Manglik and Bergles, 1995	Manglik and Bergles, 1995

4. COMPARISON

The comparison of all ECS is challenging because of the different factors that influence the efficiency or rather fuel consumption. The main factors are bleed air mass flow, electrical power input, ram and ambient air mass flow as well as the weight of the system. Bleed air and electrical power consumption have a direct impact on the fuel consumption of the engines because they are taken from respectively generated in the engine. The electric generator is attached to a shaft in the engine. Ram and ambient airflow influence the drag coefficient of the aircraft and hence increase the needed thrust the engines must provide. Similarly the weight of the ECS raises the required aerodynamic lift and therefor also the thrust. In summary all factors can be reduced to additional fuel consumption due to additional thrust. The weight of the ECS and secondary influences such as the weight of bleed air pipes from the engine to the ECS, which are not needed in electrically driven systems, cannot be covered in this work due to missing information from the aircraft (e. g. the lift coefficient). Thus only the first three factors are calculated and used for the comparison of the systems. The equations for calculating the additional fuel consumption are given in Scholz et al., 2013 and Scholz, 2017. In figure 6 the absolute additional fuel consumption, which is caused by the entire ECS, is shown. The values range from about 0.005 to 0.04 kg/s over the different operating cases and systems. The electrically driven systems achieve the lowest fuel consumption in every operating case. In the flight cases 3, 8, 11, 12, 13 and 25 the utilization of cabin exhaust air yields a significant reduction of required power input. The pneumatically driven systems with cabin exhaust air from PNK1 to PNK3 show an increase of fuel consumption according to the amount of ambient air compression. System PNK3 only uses ambient air as fresh air supply. However the system requires the most power input. In every operating cases the novel environmental control systems offer a significant reduction of fuel consumption except systems PNK1-PNK3 in operating case 11 (climb, ISA+23). Figure 7 represent the relative additional fuel consumption of the new systems compared to the reference ECS of current commercial aircrafts. The values range from 20 to 80% except in operating case 11 for the pneumatically driven systems with utilization of cabin exhaust air. Regarding all operating cases the electrically driven systems reach the lowest fuel consumption, with system ELK1 as the best environmental control system. With an exemplary flight profile the reference system needs about 2.6 to 3.2% of the overall fuel consumption of the aircraft. The pneumatically driven systems range from about 1.7 to 2.6%, and the electrically driven systems from 0.8 to 1.6% (Scholz et al., 2013; Slingerland and Zandstra, 2007). This results in a considerable reduction of up to 1.8% of the entire fuel consumption of the aircraft. For the A320 this means a decrease of up to 200kg of kerosene for a three hour flight.

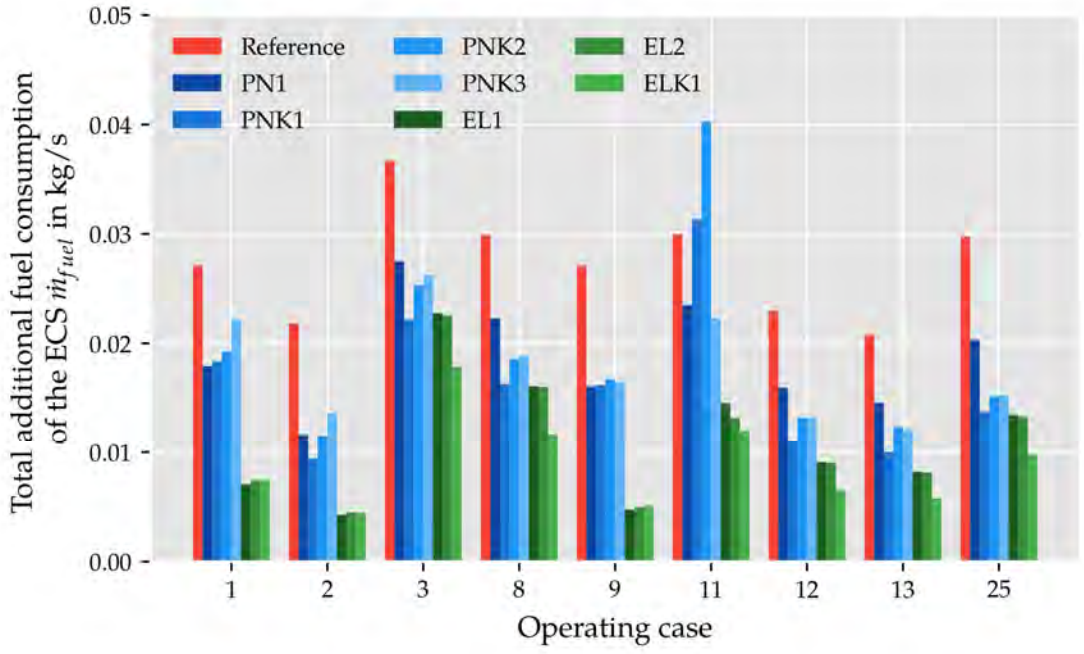

Figure 6: Absolute additional fuel consumption caused by the ECS

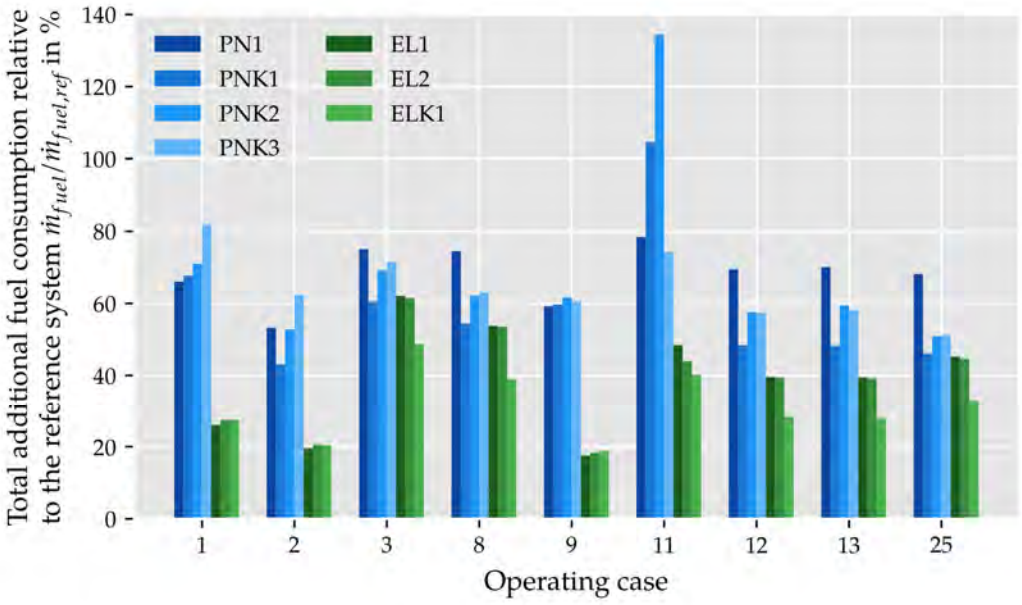

Figure 7: Relative additional fuel consumption caused by the ECS compared to the reference system

5. CONCLUSIONS

In this work two major concepts of new environmental control systems are discussed: application of a vapor cycle machine and utilization of cabin exhaust air. A total of seven novel systems are developed and calculated with a detailed process simulation. The comparison with the reference system of current commercial aircrafts shows a significant reduction of the additional fuel consumption caused by the environmental control system. The values range from 20% to 80% fuel consumption compared to the reference system. This results in a decrease of up to 1.8% of the overall fuel consumption of the aircraft for the electrically driven system with utilization of cabin exhaust air (ELK1). System ELK1 reaches the highest efficiencies of all investigated ECS. The weight of the new systems are not examined and neglected for the comparison. The application of a vapor cycle machine in aircraft environmental control systems, either pneumatically or electrically driven, offers a significant increase of the overall efficiency and hence a reduction of fuel consumption. Especially the electrically driven systems show great benefits and could replace the current ECS in future more electric aircrafts.

NOMENCLATURE

A	heat transfer area (m²)	k	heat transmission coefficient (W×m^{-2}×K^{-1})
$\dot{m}_{fuel}$	fuel mass flow (kg×s^{-1})	$\dot{m}_{corr}$	corrected mass flow (kg×s^{-1})
$\dot{Q}$	heat flow (W)	s	specific entropy (J×kg^{-1}×K^{-1})
T	temperature (K)		
α	heat transfer coefficient (W×m^{-2}×K^{-1})	η_{is}	isentropic efficiency (-)
λ	thermal conductivity (W×m^{-1}×K^{-1})	Π_t	total pressure ratio (-)
ϑ	temperature (°C)		

REFERENCES

Conceição, S.T., Zaparoli, E.L., Turcio, W.H.L., 2007. Thermodynamic Study of Aircraft Air Conditioning Air Cycle Machine: 3-wheel × 4-wheel. Proceedings of the XVI SAE Brasil International Congress and Exposition, São Paulo, Brazil.

Friedel, L., 1979. Improved Friction Pressure Drop Correlations for Horizontal and Vertical Two-Phase Pipe Flow. Proceedings of the European Two-Phase Flow Group Meeting, Ispra, Italy, 485-491.

Glück, B., 1988. Hydrodynamische und gasdynamische Rohrströmung: Druckverluste. VEB Verlag für Bauwesen, Berlin, 488 p.

Golle, S., Hesse, U., Klimpel, F., 2015. New Approaches for the Environmental Control System in Aircrafts with the Application of a Vapor Compression Cycle. Proceedings of the 24th IIR International Congress of Refrigeration, Yokohama, Japan.

Golle, S., Klausner, E., Hesse, U., 2017. Multiparameteroptimierung von Turbomaschinen mit Hilfe von evolutionären Algorithmen und Integration in eine Prozessberechnung. Proceedings of the 44th „Deutsche Kälte- und Klima-Tagung“, Bremen, Germany.

Harrison, V., Ross, S.J.M., 2016. An emerging concern: Toxic fumes in airplane cabins. Cortex 74, 297-302.

Manglik, R.M., Bergles, A.E., 1995. Heat transfer and pressure drop correlations for the rectangular offset strip fin compact heat exchanger. Experimental Thermal and Fluid Science 10(2), 171-180.

Martin, H., 1996. A theoretical approach to predict the performance of chevron-type plate heat exchangers. Chemical Engineering and Processing: Process Intensification 35(4), 301-310.

Park, Y.-G., Jacobi, A.M., 2009. Air-Side Heat Transfer and Friction Correlations for Flat-Tube Louver-Fin Heat Exchangers. Journal of Heat Transfer 131.

Rossow, C.-C., Wolf, K., Horst, P. (Ed.), 2014. Handbuch der Luftfahrzeugtechnik. Carl Hanser Verlag GmbH Co KG, München, 837 p.

Scholz, D., Seresinhe, R., Staack, I., Lawson, C., 2013. Fuel Consumption due to Shaft Power Off-Takes from the Engine. Proceedings of the 4th Workshop on Aircraft System Technologies, Hamburg, Germany.

Scholz, D., 2017. Fuel Costs due to Aircraft Systems. Retrieved from http://www.fzt.haw-hamburg.de/pers/Scholz/Aero/Aero_M_FuelCostsDueToAircraftSystems_07-12-11.pdf.

Slingerland, R., Zandstra, S., 2007. Bleed Air versus Electric Power Off-takes from a Turbofan Gas Turbine over the Flight Cycle. Proceedings of the 7th AIAA Aviation Technology, Integration and Operations Conference, Belfast, United Kingdom.

Shah, M.M., 2016. A correlation for heat transfer during condensation in horizontal mini/micro channels. International Journal of Refrigeration 64, 187-202.

Shah, M.M., 2017. Unified correlation for heat transfer during boiling in plain mini/micro and conventional channels. International Journal of Refrigeration 74, 606-626.

Verein Deutscher Ingenieure, 2013. VDI-Wärmeatlas. VDI E.V., Berlin, 1445 p.

Manuscript ID: 805
DOI: 10.18462/iir.icr.2019.0805

Laboratory determination of hazardous R40 concentration in HFC-134a systems, application to intermodal container refrigeration and pacification technique

A. R. LAWTON [(a)], P. CLARKE [(b)]

[(a)] Cambridge Refrigeration Technology, 140 Newmarket Road, Cambridge, CB5 8HE
crt@crtech.co.uk
[(b)] A P Moller Maersk, Esplanaden 50, 1908 Copenhagen K, Denmark.

ABSTRACT

Results of extensive testing of HFC-134a and R40 (chloromethane) mixtures and their reaction with aluminium are presented. The interaction of R40 with aluminium is of particular interest as it can cause the formation of trimethyl aluminium, a pyrophoric chemical which can place service technicians at risk.
Investigation of the chemical processes is provided along with a pacification process of a system that has reacted after being contaminated with R40.
The reaction mechanism in in-service refrigeration systems is explored and the application of laboratory observations is provided.
Results have shown that the reaction is difficult to trigger and it is likely that likely that 35% of a standard charge size substituted by chloromethane is needed to consume all of the oil and, in the absence of moisture, allow a pyrophoric reaction to take place. Pacification is achieved using isopropyl alcohol which allows the system to be safely decommissioned by technicians.
Keywords: Contamination, Container, R134a, R40.

1. INTRODUCTION

On the 27th April 2011, five people were seriously injured, two fatally, when the refrigeration unit of an empty shipping container inexplicably exploded at the terminal in Cat Lai, Vietnam. The following day a, second container exploded. This explosion luckily caused no injuries. Both containers had been serviced some weeks before and then put on the stack, at the time of the explosions they had been brought down to be set up and sent out for cargo.
Around the end of July 2011, a container was under repair in Oakland, US when spontaneous ignition of the refrigerant gas was noticed during a release of the gas to the atmosphere. The compressor was allowed to cool and the container isolated from the electrical supply. Again the gas was released and observed to ignite, indicating an organometallic compound.
Another compressor later exploded in Brazil in October 2011. At the time of the explosion, the container was being serviced by an experienced technician on the third tier of a service area; he was fatally injured. The explosion completely destroyed the crankcase of the compressor, forcing it upwards and breaking the condenser coil in half. Debris was scattered around the front of the container and actually inside the container as the bulkhead was ruptured. A further explosion occurred in China, this container was again a 40' refrigerated container. The compressor exploded during a PTI again in October 2011 in Qingdao Great Asia depot.
The common thread was that all these refrigerated containers at passed through Cat Lai at around the same time as the explosions occurred there. As the container in Oakland had

shown evidence of a pyrophoric compound, it was deduced that a counterfeit refrigerant had been charged into the refrigeration units of the containers, probably methyl chloride (R40) which reacted with aluminium to form trimethyl aluminium (TMA).
From the Oakland refrigerated container that had not exploded a sample was taken and analysed by gas chromatography / mass spectrometry (GCMS). The gas samples were found to contain was in addition to HFC-134a, methyl chloride, various hydrocarbons and traces of tetramethylsilane.
An oil sample was also taken and shipped to the UK and tested using nuclear magnetic resonance, (NMR) where TMA and other longer chained variants were was identified as shown below.

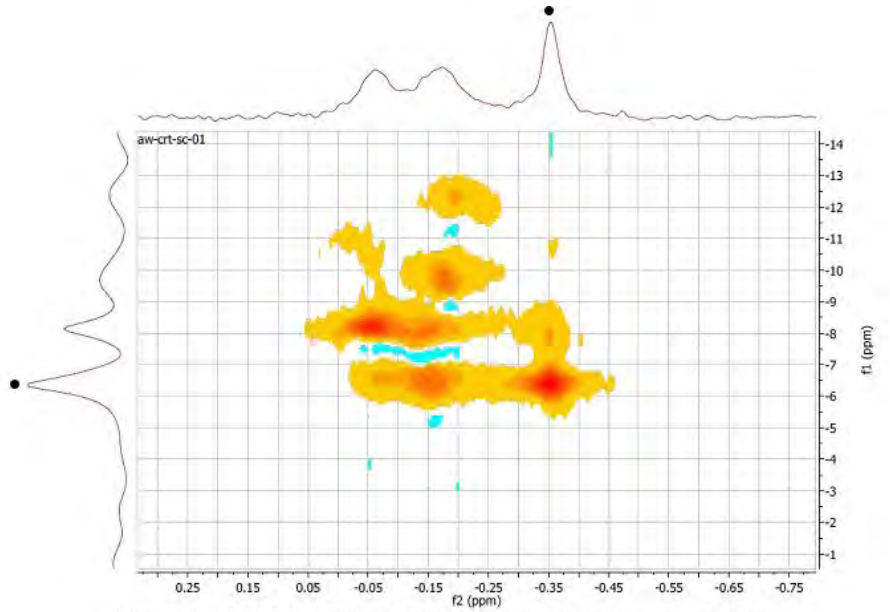

Figure 6 HSQC NMR spectrum of industrial aliquot 1, revealing at least three types of $AlCH_n$ ($n = 1, 3$) unit, including TMA (•). The analysis of a second industrial sample revealed essentially identical results

Figure 1: NMR spectrum identifying TMA

2. METHYL CHLORIDE (R-40)

Methyl chloride, or “chloromethane”, ASHRAE classification R-40 is a clear, colourless gas, formula CH_3Cl. Methyl chloride is a chemical compound of the group of organic compounds called haloalkanes. It has a faint, sweet odour that is noticeable only at levels that may be toxic. It is heavier than air and extremely flammable. It is stored and shipped under pressure.

Clear, colourless gas
Flammable
Formula CH3Cl
Density 0.75g/ml
Vapour pressure 3800 torr at 22°C
Similar to HFC-134a
Ionisation 11.4 EV

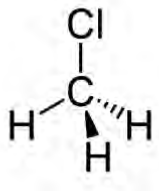

Figure 2: **Methyl Chloride properties**

Methyl chloride was frequently used as a refrigerant up until around 30 years ago but no longer, at least in the western world, due to its toxicity and flammability. It is, however, still used in many other applications such as the production of silicone rubber and is widely

available for purchase. If the temperature and pressure chart is studied it can be seen that it could easily be used as a substitute refrigerant for HFC-134a.

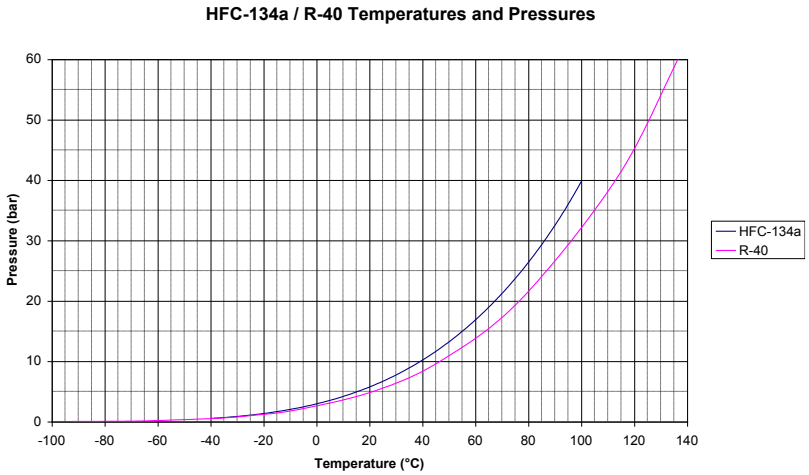

Figure 3: **Pressure temperature relationship**

If R-40 were to be used in a system containing aluminium, as modern refrigeration compressors do, then it is possible that the aluminium would react with the R-40 to produce an alkyl-aluminiums such as TMA. This reaction was reported by Walker and Wilson (1937).

3. TRIMETHYL ALUMINIUM

TMA exists as a dimer molecule with the formula $Al_2(CH_3)_6$ as the dative covalent bonds formed are energetically favourable than an arrangement with two separate molecules.
Below are some plausible stoichiometric reactions and products formed in the refrigeration system when methyl chloride is present.

$6CH_3Cl$	+	$4Al$	→	$Al_2(CH_3)_6$	+	$2AlCl_3$
(R-40)		aluminium		trimethyl aluminium		aluminium chloride

Trimethyl aluminium is a powerful reducing agent and reacts violently with the following: oxidisers, alcohols, amines, amides, inorganic hydroxides, carbon dioxide, carbon tetrachloride, halon, halogens and halogenated hydrocarbons, oxides of nitrogen or sulphur, phenols, triethylborane, and many other substances.

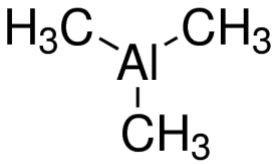

Figure 4: Trimethyl aluminium properties

Trimethyl aluminium is a liquid at room temperature, melting at 15°C. It is a dimer and is pyrophoric, combusting spontaneously with contact with air. The probable reaction is as follows:

$Al_2(CH_3)_6$	+	$24O_2$	→	AL_2O_3	+	$6CO_2$	+	$9H_20$
trimethyl aluminium		air		aluminium oxide		carbon dioxide		water

The product of combustion in air is alumina, which is a white powder. Other reactions are possible, as detailed above, notably the reaction with halogenated hydrocarbons, which are, in fact, refrigerants such as HFC-134a.

3. PRESENCE OF METHYL CHLORIDE IN CONTAINER REFRIGERATION SYSTEMS

Around 1000 refrigerated containers were tested for the presence of R40 using a flame halide test and gas chromatography. The findings, where the intended refrigerant was HFC 134a, approximate to the following:

Table 1. Contamination percentages

Failed Flame Test:	31%	Min R-40 Found:	0.02%
Passed Flame Test:	69%	Containing R-40:	15%
Containing > 99.5% HFC-134a:	71%	Containing > 0.5% R-40:	7%
Max R-40 Found:	59%		

The point of interest was that many containers were contaminated with R40, some with substantial concentrations and yet only a few reacted to form TMA. Because of this puzzling anomaly an investigation as to the reaction dynamics was investigated to find out why this should be.

4. LABORATORY INVESTIGATION

Test rigs (four) were constructed as shown below so as to determine what conditions are required to enable the reaction of methyl chloride and aluminium to proceed. The test rig set up is shown along with one rig with a piston to be inserted.



Figure 5: Test rig and setup

For each test, the test rig as shown was carefully cleaned and then a refrigeration machine aluminium piston and conrod was placed inside. The rig was leak tested then evacuated and charged with the particular gas/oil/chemical mixture as indicated. The test rig was then placed on a hotplate in most instances at a steady 50°C within an insulated enclosure and left to react in each case for 10 days. During that period the pressure and temperature was monitored. At the end of the ten day period gas was sampled and analysed then the test rig was carefully opened and any reactant products noted

5. RESULTS

In total 75 tests were carried out. Preliminary tests were carried out using aluminium wire further tests used aluminium refrigeration compressor pistons. Tests were carried out with the reactants listed, the balance gas was HFC134a and the typical total refrigerant charge was 200g on a hot plate at 50°C. The pertinent results are shown in the table 2 below:

Table 2. Test results

Test ID	R40	Catalyst	Dried in oven	Filter drier	Oil	Water / HCl	Metal	Comment
B	100%	-	-	-	-	-	Al Rods	No reaction
C	50%	-	-	-	1ml	-	Al Rods	No reaction
H	50%	AlCl3 0.25g	-	-	1ml	1ml Water	Al Rods	No reaction
1	100%	Iodine 0.25g	-	-	Trace	-	Al Rods	White smoke
2	100%	Iodine 0.25g	-	-	Trace	-	NT40 Piston	TMA/Combustion
7	10%	Iodine 0.25g	-	-	Trace	-	NT40 Piston	Foam/ slow burn
11	10%	Iodine 0.25g	-	-	2ml	-	NT40 Piston	No reaction
14	51%	Iodine 0.25g	-	-	2ml	-	NT40 Piston	Reaction
21	20%	Iodine 0.25g	-	-	1ml	HCl 0.5ml	NT40 Piston	No reaction
22	20%	Iodine 0.25g	-	-	1ml	Water 0.5ml	NT40 Piston	No reaction
23	100%	Iodine 0.25g	-	-	1ml	Water 0.5ml	NT40 Piston	No reaction
24	49%	Iodine 0.25g	-	-	1ml	Water 0.5ml	NT40 Piston	No reaction
25	40%	Iodine 0.25g	-	-	1ml	Water 0.5ml	NT40 Piston	No reaction
26	29%	Iodine 0.25g	-	-	1ml	Water 0.5ml	NT40 Piston	No reaction
27	100%	Iodine 0.25g	-	-	1ml	HCl 0.5ml	NT40 Piston	No reaction
29	50%	Iodine 0.25g	-	-	1ml	HCl 0.5ml	NT40 Piston	No reaction
31	100%	Iodine 0.25g	-	-	-	-	NT40 Piston	Strong reaction
32	100%	Iodine 0.25g	-	-	-	-	NT40 Piston	No reaction
36	100%	-	Yes	12g	-	-	NT40 Piston	Reaction
37	100%	AlCl3 0.25g	Yes	11g	-	-	NT40 Piston	Reaction

38	50%	Iodine 0.25g	Yes	12g	-	-	NT40 Piston	Reaction
49	5%	-	Yes	12g	-	-	MCI Al Piston	Reaction
50	10%	Iodine 0.25g	Yes	12g	1ml	-	NT40 Piston	Reaction
52	50%	-	Yes	12g	1ml	1ml methanol	NT40 Piston	Reaction
54	50%	Iodine 0.25g	Yes	12g	1ml	10ml methanol	NT40 Piston	Reaction
55	10%	Iodine 0.25g	Yes	12g	50ml	-	NT40 Piston	Reaction
61	50%	Iodine 0.25g	Yes	12g	200ml	-	NT40 Piston	Foam
63	70%	Iodine 0.25g	Yes	12g	200ml	-	NT40 Piston	Reaction/foam
65	20%	Iodine 0.25g	Yes	10g	200ml	-	NT40 Piston	Foam
67	35%	Iodine 0.25g	Yes	11g	200ml	-	NT40 Piston	Reaction/ foam

6. TYPICAL REACTIONS

Typical reactions were, no reaction, reaction forming a foam of polymerised oil, flames and profuse white smoke.







Figure 6: Exemplar reactions

It was found the Iodine aided reaction as it probably attacks the oxide layer making the aluminium more reactive but was not essential as the reaction was found to be able to proceed without it. When only methyl chloride was present, the pressure in the test rig decreased as it was consumed.
For the reaction to occur the absence of water is perquisite, the presence of oil was found to have a pacifying effect and is polymerised to foam. When all the oil is reacted free TMA is formed which reacts pyrophorically when exposed to air.

6. PACIFICATION

Neutralisation of TMA is difficult as any exposure to air causes a pyrophoric reaction similarly the reaction with water is energetic. In the laboratory TMA is typically pacified by mixing with Hexane, though this chemical is considered unsuitable for relatively large scale use.
An alternative is to use isopropyl alcohol; this compound is relatively inexpensive and reacts slowly enough with TMA to avoid a fire though it is in its self a flammable compound therefore considerable care is required. The reaction evolves methane:

$Al_2(CH_3)_6$ (TMA) + 6 C_3H_8O (IPA) → 2 $Al(C_3H_7O)_3$ + 6 CH_4 (Methane)

Injection of isopropyl alcohol was tested in the field on heavily contaminated units and was successful in making them safe without any significant pyrophoric reaction, though again care has to be taken to avoid any excessive pressures developing due to the evolution of considerable quantities of methane. In some circumstance sodium bicarbonate was also used as a blanketing reagent principally to neutralise the TMA formed in some of the laboratory trials.

$Al_2(CH_3)_6$ (0.95 litres TMA) + 6 C_3H_8O (2.27 litres IPA) → 2 $Al(C_3H_7O)_3$ + 6 CH_4 (727.27 litres Methane)

During the pacification process white smoke was also observed which could be reaction with air producing aluminium oxide and also the isopropyl alcohol is not entirely pure and contains traces of water which may also be contributory.

7. CONCLUSION

Refrigerated container compressor explosions have previously been identified as a result of refrigerant contaminated with methyl chloride. This paper has described how the reaction between aluminium and methyl chloride was investigated and the subsequent reaction with the oil.

In the field it has been found that some containers have substantial concentrations of methyl chloride yet reaction rarely occurs. It was determined by laboratory testing that for the reaction to proceed, there has to be an absence of water. Once the reaction starts it appears to proceed until all the methyl chloride has been consumed. The formed TMA then goes on to react with the lubricating oil and it was found that the oil can consume approximately 30% of the equivalent refrigerant charge before free TMA forms in the compressor crankcase.

For heavily contaminated units that have reacted and have free TMA in the crankcase, a method of pacification using isopropyl alcohol was tested in the field and found to be effective and relatively safe provided sufficient care taken.

REFERENCES

Andrew Wheatley Dr. Phil Harford PhD, 2012, Report No.2 Investigation of the composition and reactivity of counterfeit refrigerant (Private correspondence); Chemistry Department Cambridge University

Walter O Walker and Karl S Wilson, August 1937, The Action of Methyl Chloride on Aluminium, Research Department, Ansul Chemical Company Murinette, Wise

Wiley's Guide to Chemical Incompatibilities, 2009, Trimethylalane or Trimethylaluminum (75-24-1) (Ch3)

Maersk Line, 16th December 2011, Technical Bulletin, Halide Torch Information.

Lawton and Cavalier, 2012, Risk Inherent in the Use of Counterfeit Refrigerants, 23rd Informatory Note on Refrigeration Technologies, IIR, November 2012.

A.R Lawton, N Marshall and P Clarke Counterfeit Refrigerant in Food Transportation Sea Containers ICCC 2013

E. Hamilton Examination of the Reaction of R40 with Refrigeration System Materials: R134a, POE Oil, Al1100, Al380, and Fe, Cu, Zeolite

Silicate and Alumina Metal Catalysts (1665-RP) ASHRAE Research Project Report 1665-RP

Manuscript ID: 814
DOI: 10.18462/iir.icr.2019.0814

Influence of temperature sensors on temperature control of marine reefers

Santiago MARTINEZ, Miguel A. FERRER

Thermo King
Barcelona, 08980, Spain, santiago.ballester@irco.com

ABSTRACT

Temperature control in marine container application is very important, especially in chilled mode and for sensitive cargo like banana. Therefore, cargo owners specify tight temperature control requirements for the reefers. The paper analyzes the temperature control of a reefer working in different operating modes paying special attention to the differences in the temperature control depending how it is measured, mainly number and technology of the sensors used. The results also show the value that the cargo owner would see in the unit logs. The lack of a standard specifying the methodology to measure the temperature, as there are in other applications, increases the uncertainty when comparing test results among different laboratories. The results show that differences can be very large depending on the instrumentation used, affecting not only to the temperature control but also to the energy consumption and compressor cycles.

Keywords: Reefer, Temperature Control, Energy Consumption, Standards.

1. INTRODUCTION

Reefers are used for Marine container transportation where the cargo has to be shipped under a certain controlled condition. These containers are specially designed for this kind of transportation and at the end of the container (Fig. 1) a unit is installed to provide both cooling and heating. The cooling is provided by means of a vapor compression system, and the heating mainly by electric heaters, although some manufacturers also produce heat by using hot gas. During last years, solutions have been developed even for controlling the CO_2 and O_2 inside the container in order to extend the life of the product by e.g. delaying the ripening of the cargo.

The variety of cargo is enormous: meat, fish, vegetables, fruit and even flower bulbs. Regarding temperature control, the cargo is basically classified in two kinds; frozen and chilled. Frozen usually corresponds to meat or fish which is frozen below -10 °C, commonly at -21 °C, while chilled cargo is usually vegetables and fruits, which are stored above -10 °C. The temperature to be specified in chilled cargo depends completely on the product. The chilled cargo is usually quite sensitive to the temperature and special attention has to be paid at the temperature distribution inside the container to avoid cargo injuries and therefore expensive claims.

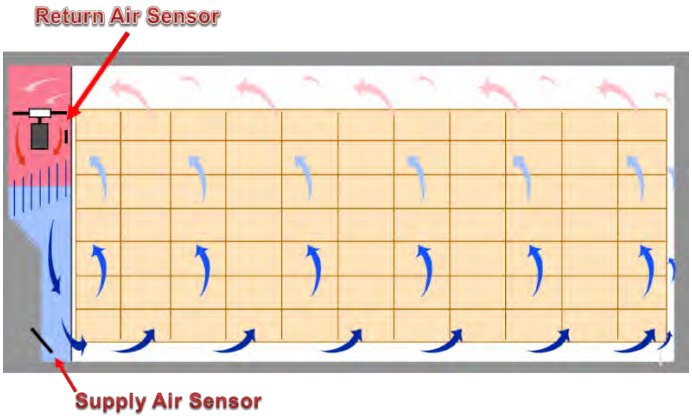

Figure 1: Air flow path within container and unit

The correct temperature control means both uniform distribution and correct value, and if the cargo is correctly loaded into the container, this is done by the reefer unit. To do so, is very important the correct pallet stacking and location, while respecting the max. load indication to allow the air flow through the boxes and returning to the unit. Fig. 1 shows the path that the air follows, how the air is supplied to the special floor with channels (T-floor) which distributes the air along the container returning by the top of the unit.

The reefer unit can only work with two variables to control the temperature and its distribution within the container; temperature and air flow. During chilled mode, the unit is controlled to deliver the supply air at the set point temperature, within a certain temperature control band. Most of customers request to the manufacturers that this control band is ±0.25 K. Another way to monitor the cargo temperature is by using USDA sensors configuration (USDA, 2019), which emphasizes more in the cargo temperature. However these sensors are only for logging, since unit will not control based on them.

The fresh cargo is quite sensitive to the temperature variation, and the reason to control based on supply air (Fig. 1) is to prevent the cargo close to the air supply suffers of chilling or freezing injury. The temperature thresholds and the injury produced by either a temperature below or above the objective value are well known and documented in the literature (ASHRAE, 2016; Strauch, 2008). In order to minimize the existence of hot points within the container, the fans are usually running at high speed for chilled cargo. There are commodities, e.g. banana, very sensitive to temperature variation and probably ±0.25K variation is close to the limit that they can withstand, however there are others than can withstand larger temperature variations without any injury.

Nowadays CO_2 emissions and energy consumption are very important factors, and minimization of them can be done by optimizing the temperature control. If energy savings can be achieved by penalizing the accuracy of the temperature control, it could be used in cargo which is currently over serviced because is not so sensitive to temperature variations. This is the idea behind the different optimization software implemented by the different manufacturers (Lukasse et al., 2011; Thogersen et al., 2013)

In summary, temperature control in marine containers is a key parameter, and the cargo owner's requests are quite demanding. The current standard 1496 part 2, which gives the basic specifications and testing requirements for ISO series 1 thermal containers (ISO 1496-2, 2015), specifies tests for evaluation of the performance of the unit. However there is no requirement on measuring and reporting the temperature control variation during the performance tests. In the author's point of view, many technicians and inspectors analyze only the temperature logs, but most of the units among manufacturers uses different temperature sensors technologies, like thermistor or resistance temperature detectors (RTDs), with really have different time constants and will impact on the temperature excursion shown in the temperature logs. So, the authors think that measuring and reporting a parameter so important for the cargo should be required by the standards. Currently the ISO

1496-2 only specifies certain temperature variation restrictions for the heat leakage characterization (UA of the container) test.

However, it is also important how temperature is measured when small temperature variations are measured in a fluctuating flow. The temperature variations specified in ISO 1496-2 restrictions are for the variations in the average of internal and external temperature sensors. The requirement is only on the value not in the sensor technology or installation in the container. Some requirements restricts temperature differences to 3 K, which is a relatively low. The current 1496-2 standard specifies accurately the number and place of the sensors, but not the technology or installation as other standards do when dealing with similar problems. ISO 15502, which establishes the testing conditions of household refrigerators, specifies how the temperature sensors have to be installed. In fact specifies that the temperature sensor is installed into a copper or brass cylinder, with a weight of 25 g ±5% and a diameter of 15.2 mm. AHRI Standard 210/240 (2017) which is about Performance Rating of Unitary Air-conditioning & Air-source Heat Pump Equipment, also specifies the temperature sensor technology for some air flow measurements.

The main aim of the present paper is to show how the design of a unit and its performance change depending on the maximum temperature excursion allowed in the set-point by using different sensor technologies. The paper does not focusses in what is the right temperature variation for protecting the cargo but how the conclusions can be different based on the temperature sensors, suggesting that current standards should specify the sensors installation when testing such an important parameter. The paper also tries to show that how each tenth of temperature degree in the control has impact in energy consumption and how can be reduced if this temperature control is not really required.

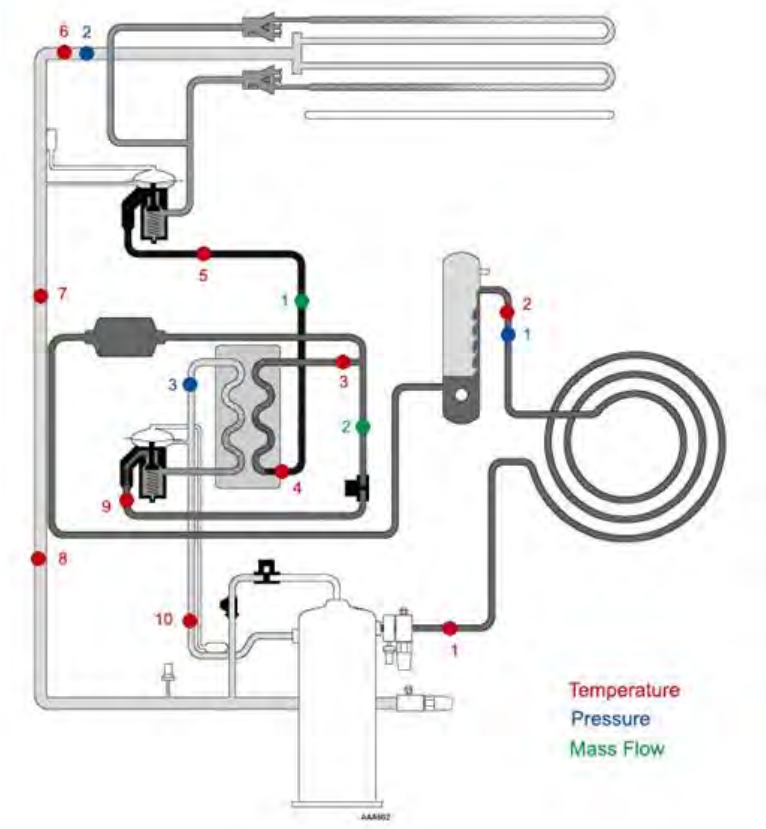

Figure 2: Refrigeration system and instrumentation

2. EXPERIMENTAL TEST BENCH

The unit used to evaluate the impact of the temperature control is a commercial one; Magnum + model (Thermo King, 2019). The refrigeration system consists of a two-stage vapor compression cycle with vapor injection and economizer. Fig. 2 shows the schematics. Both condenser and evaporator are fin and tube coils, the economizer is a brazed plate heat exchanger, and both expansion valves are thermostatic. The compressor is scroll technology and to meet the tight temperature control demand, the capacity control is made by means of pulse width modulating (PWM) the compressor load, which allows a huge capacity unloading with compressor loaded a few seconds.

The current unit controller modifies the capacity loading as a function on the conditions and how close the controlled temperature is to the set point. When the set point is reached, the compressor keeps running continuously with a uniform duty cycle and unloading ratio. Part of the scope of work is to analyze situations with difference temperature control hysteresis, so for convenience a new control, just for the purpose of this work, based on an on/off compressor state was used. So by cycling on/off at same frequency and duty cycle as the current unit does, we can achieve same temperature hysteresis. To do so, a temperature controller Omron E5AJ was used, which allows to set the temperature hysteresis as an adjustable factor. This controller also accepts different temperature sensor technologies.

All the tests analyzed in this work are in chilled conditions, specifically at 13 °C box temperature with 30 °C ambient temperature. During chilled mode, the commercial unit controls the temperature by means of a RTD (PT1000) located at the supply air channel, as shown in Fig. 3, whose readings can be logged by the unit controller. The PT1000 sheath is 60 mm length with a diameter of 6 mm. Two different sensor technologies were used to control; a T-type thermocouple and an RTD (PT100) with a sheath of 100 mm length and 3 mm diameter, having a priori a smaller time constant than the original PT1000 sensor. These sensors were all mounted at the same location as the original PT1000 sensor.

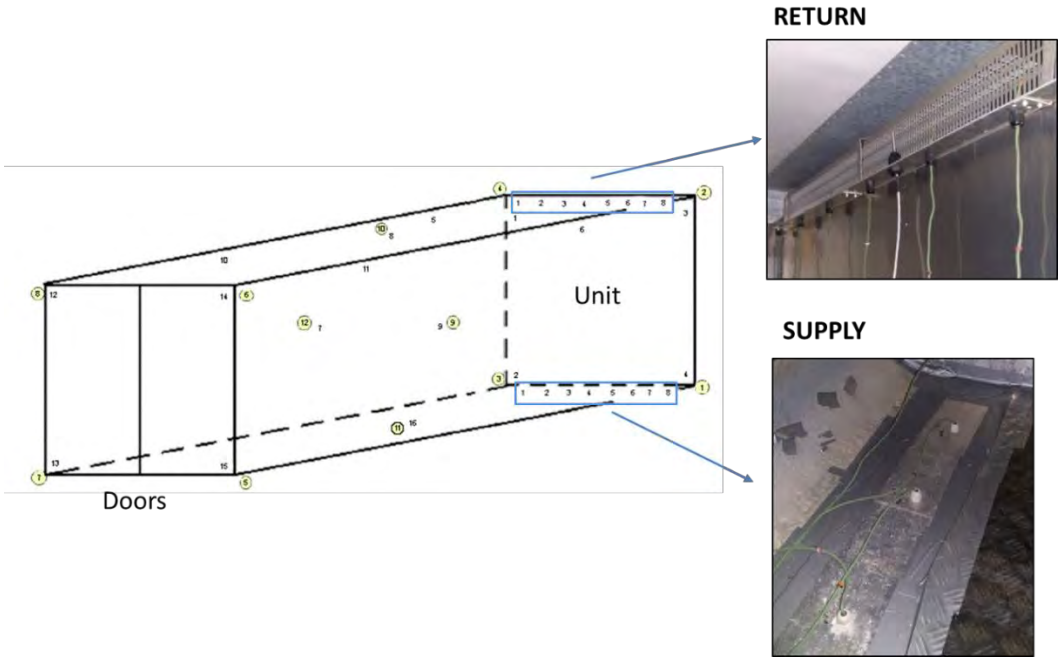

Figure 3: Position of temperature sensors within and outside the container (as per ISO 1496-2) and additional thermocouples installed at supply and return of the unit

In the refrigerant loop, the pressure at condenser, evaporator and economizer outlets are measured with pressure transducers. The temperature at inlet and outlet of each component is measured within the tube, in direct contact with the refrigerant, with PT100. The sensors locations are shown in Fig. 2. The current of all electrical components (valves, fans, compressor…), power of the whole unit and electric power of the heater placed inside the container are measured.

3. RESULTS

Fig. 4 shows the temperature readings during the test controlled by the TC with a control hysteresis of ±0.2 K. The figure shows the readings of the evaporator air outlet temperature (EAOT) measured with the control thermocouple ($EAOT_{TC}$) and with the PT100 used by the experimental controller ($EAOT_{PT100}$), which in this plot is not being used by the controller. It is also reported the average temperature of all the 8 TCs ($EAOT_{avg}$) positioned at the supply as described in Fig. 3. The figure also includes the unit power, which clearly shows when the compressor switches on and off.

The comparison between the different sensors shows the largest temperature variation in $EAOT_{avg}$. This variation is much larger than in the rest of sensors. The lowest variation corresponds to the $EAOT_{PT100}$. It is important to take into account that when compressor is off, evaporator and condenser fans are still running continuously.

It is interesting to realize the large temperature undershoot in the control. The undershot has a really negative impact, since it is pushing the control to make the compressor work with much shorter periods compared to what really would be required. The temperature undershoot can be seen how is opposite to the thermal inertia of each sensor.

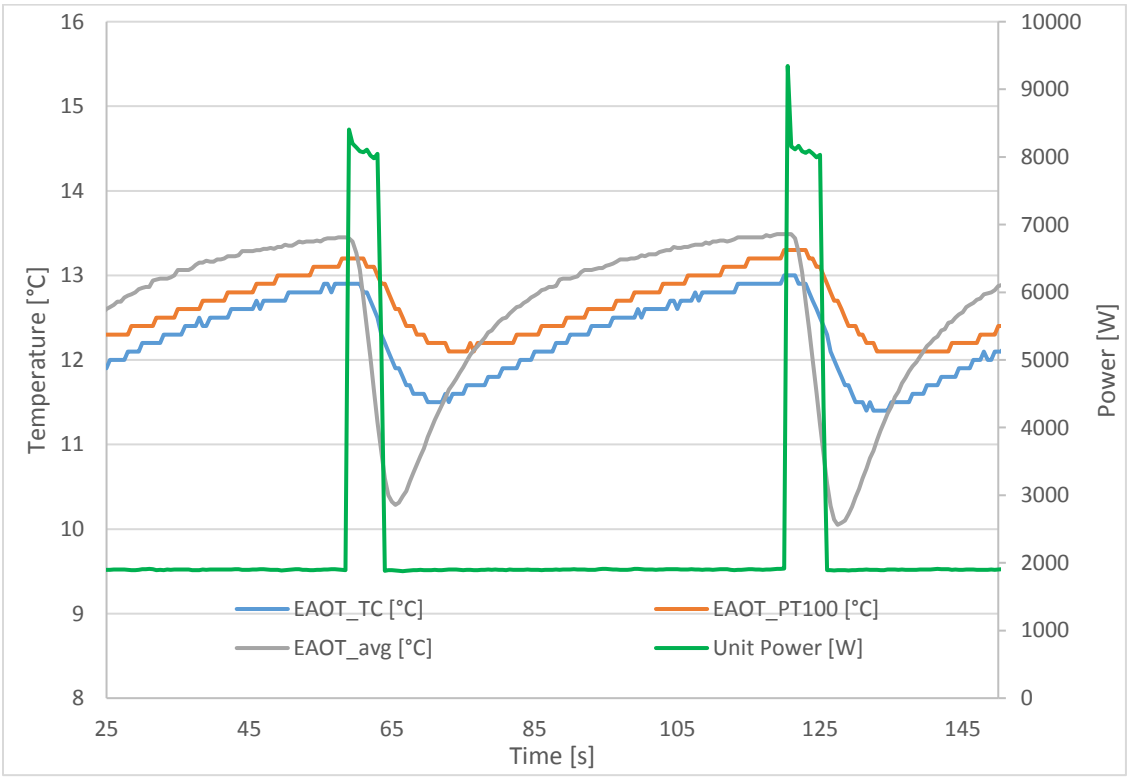

Fig 4 shows the temperature measurements for a tests which was controlled by the TC with ±0.2K hysteresis

Table 1 summarizes the results for both TC and PT100 as control sensors, controlling with both hysteresis ±0.2 K and ±0.1 K. The row showing the ∆T in controller (PT1000) corresponds to the temperature variation logged in the controller data, seen by the cargo owner and used to control the temperature in the commercial unit.

All the measurements are showing more temperature variation than the baseline, but all of them, excepting the PT100 with ±0.2 K hysteresis, are fulfilling the temperature control requirements of the product, i.e. ±0.25K measured by the PT1000 of the unit.

Table 1. Temperature variations and cycling parameters with the tested control options

	Baseline control (PWM)	TC (±0.2K)	TC (±0.1K)	PT100 (±0.2K)	PT100 (±0.1K)
Sensor location	Supply	Supply	Supply	Supply	Supply
∆T in $EAOT_{avg}$ [K]	±0.25	±1.6	±1.3	±2.2	±1.8
∆T in controller (PT1000) [K]	±0	±0.2	±0.1	±0.35	±0.25
Cycling frequency [1/hour]	-	53	77	60	59
Compressor ON time [s]	-	6	3	7	5.5

If we now select those closer to the control requirement, we focus in the TC and PT100 with hysteresis of ±0.2 K and ±0.1 K respectively. Therefore the PT100 needs half the hysteresis used by the TC to produce the same temperature control for the unit logs. These two options clearly shows how important is to modify the temperature control settings based on the technology sensor. Differences in temperature are really small, but note that the cargo owner is requesting maximum variation of ±0.25K.

At the bottom of the table is also reported the compressor cycling frequency and the time that the compressor is on. It is observed how sensitive the on time is to the hysteresis, in fact in case of the TC increasing it just by ±0.1K, the on time increases to twice. Therefore it is noticeable that each tenth of degree in the temperature control requirement could have strong impact in the compressor reliability because of the higher number of cycles and much less on time. Special attention has to be paid to avoid over servicing the temperature variation requirements.

4. CONCLUSIONS

Temperature control in marine reefers is a very important parameter for the cargo owners. Temperature control requirements are very ambitious requesting usually maximum temperature excursion in the control temperature of ±0.25 K. This requirement is usually checked with the unit logs.
The aim of the work is to show how the measurement of the temperature excursion is strongly affected by the sensor technology, due to differences in their time constant. Main outcomes of the paper are:

- The temperature variation that controller logs provide is lower than the measured by other common sensor technologies used in laboratories.
- The temperature variation when measured with thermocouples is larger than when measured with RTDs
- If same temperature control hysteresis is used regardless the temperature sensor technology, it would impact negatively the temperature control or the compressor reliability because of cycling more frequently unnecessarily

Given the importance of the temperature control for protecting the cargo, the authors strongly suggest that the current standard 1496-2 should address how to measure this parameter requesting a specific tests and clearly specify the sensors technology and installation as other similar cited standards do.

NOMECLATURE

RTD	Resistance temperature detector	*Subscripts*	
UA	Container global conductance (W K^{-1})	avg	Average of 8 TCs
PWM	Pulse width modulation	TC	Measured with TC
TC	Thermocouple	PT100	Measured with PT100
EAOT	Evaporator outlet temperature (C)		

REFERENCES

ANSI/AHRI Standard 210/240, 2017. Performance Rating of Unitary Air-Conditioning and Air-Source Heat Pump Equipment. Air-Conditioning, Heating, and Refrigeration Inst., Arlington, VA

ASHRAE, 2006. ASHRAE Handbook: Refrigeration (SI)

ISO 15502:2005, 2005. ISO 15502:2005. Household refrigerating appliances – Characteristics and test methods.

Lukasse L.J.S., Baerentz M.B., Kramer-Cuppen J.E. DE, 2011. Quest II: Reduction of CO_2 Emissions of Reefer Containers. 23rd IIR International Congress of Refrigeration, Czech Republic.

Strauch, AG W., 2008. Container Handbook. Gesamtverband der Deutschen Versicherungswirtschaft e.V. (GDV)

Thermo King, 2019. Refrigeration units. Retrieved from https://marine.thermoking.com/

Thogersen, O., Dyrmose, A., Steffensen, D.V., 2013. Controlling chilled state of a cargo. United States Patent No. US 8607582 B2

USDA - United States Department of Agriculture, 2019. Treatment Manual. Retrieved from https://www.aphis.usda.gov/aphis/ourfocus/planthealth/import-information/sa_quarantine_treatments/ct_quarantine-treatment

Manuscript ID: 1089
DOI: 10.18462/iir.icr.2019.1089

Intelligent fault detection for refrigerated reefer containers

Jorrit WRONSKI[(a)], Ragnar I. JONSSON[(a)]

[(a)] IPU
Lyngby, 2800, Denmark, {jowr, rij}@ipu.dk

ABSTRACT

Traditionally, the shipping industry spends a considerable amount of money on pre-trip inspections (PTIs) of refrigerated reefer containers. The objective of this work is to cut these expenses and to improve the fault detection performance using online system monitoring. The presented approach is based on advanced statistical methods and creates fingerprints for each container to determine normal and faulty operation. The novelty is that a refrigeration unit simulation code has been integrated tightly with the detection algorithm using one generalized model for all container types running with either R134a or R404A as refrigerant. Measurements and simulation results are eventually combined to assess the units' performance and to trigger or to postpone maintenance and repair actions. After 5 years of operation and millions of analyzed trips, the efficiency of the reefer maintenance operations could be improved by over 40%.
Keywords: Automatic Operation, Container Ship, Modelling, R134a, R404a, Refrigerated Container, Remote Monitoring, Ship.

1. INTRODUCTION

In the globalized economy, seaborne trade is directly related to economic growth. According to (Hoffmann, et al. 2018), global seaborne trade volumes reached 10.7 billion tons in 2017 and the past annual growth of approximately 4% is expected to continue for the next couple of years. Containerized trade accounts for 17.1% of the total trade volume and exhibits a growth rate of over 6% per annum. Furthermore, container ships are estimated to carry about 75% of the value of maritime transport (Svensson 2014). The fleet of refrigerated reefer containers is also growing and global reefer sales are estimated to over 120,000 units per year. The total fleet of operational reefer units is assumed to count over 1 million containers causing annual CO_2 equivalent emissions of over 4 million tons (Lukasse, Baerentz and Kramer-Cuppen 2011). Besides the increasing environmental concerns and energy efficiency measures described earlier by (Fitzgerald, et al. 2011), there is also a monetary incentive to improve reefer maintenance and repair scheduling.
Considering the whole lifetime of a reefer container, the procurement cost is small when compared to the costs associated with inspections, repairs and energy use (Sørensen 2015). Traditionally, every reefer undergoes a pre-trip inspection (PTI) before it is booked for a journey to minimize the risk of malfunctions while it is carrying temperature sensitive cargo. Data-driven fault detection can replace these PTIs and improve the energy efficiency as well as the Quality of Service (QoS) through early detection of faults and through failure mitigation, respectively. An automated assessment of the reefer state also limits the impact of the varying quality of PTIs caused by weather influences and variations in equipment quality and personnel qualifications around the world. On top of that, the time that the unit has to stay onshore is reduced, which leads to a higher utilization rate throughout the reefer fleet.

This work presents an approach that employs statistical methods to create fingerprints for each container. Building upon a classical fault detection approach, the algorithm performance is improved by coupling the data analysis with a simplified model of the refrigeration system. The savings potential for an average reefer fleet is expected to be in the range of 60% to 70%.

2. METHODOLOGY

2.1. Reefer Container Hardware

A typical reefer container operates in the cargo temperature range from -30 °C to 30 °C and runs with R134a or R404A. To maintain a certain temperature and to control the humidity levels, a reefer consumes approximately 4 kW of electricity in chilled operation and more for frozen cargo (Svensson 2014). The actual power consumption is not only governed by the cooling load, but is also a function of the currently active heat rejection mode. Depending on the location of the container, the condenser of the refrigeration unit can be cooled with air using a fan or with cooling water. A standard reefer container typically costs less than US$ 20,000 and can be of either the 20 ft or 40 ft type. During their lifetime of approximately to 15 years, a reefer completes 3 to 4 journeys per year (Churchill 2015) resulting in a total of over 50 trips. Lately, specialized units that use R744 or R513A as well as units that can provide cooling at -75 °C have received more and more attention, but standard designs described above still account for the vast majority of the reefer fleet in 2018.

This work describes a centralized fault detection solution that utilizes operational data to assess the condition of the machinery. One of the first challenges for the container operators when implementing a data-based fault detection system is to provide data recording and transmission equipment. Retrofit solutions that can tap into the existing sensor infrastructure have to be developed for all reefers in the fleet consisting of units from several manufacturers and a multitude of container models. Modifications of the refrigeration unit itself should be avoided to reduce the risk of introducing new sources of malfunctions and to maintain flexibility with regard to service personnel and spare parts.

Furthermore, a communication strategy has to be designed and rolled out allowing all operating units to report to a central database regardless of whether the container is located on a truck, at a port or onboard a vessel. The sampling frequency used in the implemented system and the tests presented below is limited to one reading per hour. This reduces the amount of data traffic and allows the shipping company to implement caching measures related to satellite communication and centralized data processing. Having a working monitoring system in place does not only enable the fault detection system, but also comes with other benefits such as improved possibilities for cargo monitoring and documentation of cold chain requirements.

2.2. Refrigeration System Model

The calculation of reefer performance is carried out by means of a generalized model that can be adapted to match the configurations of the different container models. Figure 1 shows a sketch of the generalized model with highlighted state points for operation without hot gas bypass. Starting at point 1 in the suction line, the refrigerant is compressed in the low pressure stage before it is mixed with a bypass stream coming from point 19 yielding state point 3, which is located in the admission pipe for the high pressure compressor. After the compression, the refrigerant passes the condenser from state point 4 to state point 5 before it enters the receiver with the liquid outlet at point 6. As the flow approaches the economizer that is located between point 7 and 8, it gets split and stream 17 passes a valve before it runs through the economizer in a counter flow arrangement from 18 to 19. After point 8, the liquid injection stream leaves the main refrigerant line and passes a valve from point 15 to 16 before it is fed into the low pressure suction line between point 14 and point 1. The main flow proceeds to state point 9 and runs through the internal heat exchanger reaching point 10 before the pressure drops at the expansion valve yielding state 11. The refrigerant runs through the evaporator that cools air circulated inside the reefer unit and additional heat is added in the internal heat exchanger from state 12 to state 13. A suction pressure valve is located between state 13 and 14 where the liquid injection line meets the main refrigerant flow.

The internal heat exchanger and the economizer are modelled using a temperature-based counterflow efficiency model

$$T_{\mathrm{A,out}} = T_{\mathrm{A,in}} - \epsilon_{\mathrm{HX}} \cdot (T_{\mathrm{A,in}} - T_{\mathrm{B,in}}) \qquad \text{Eq. (1)}$$

that assumes that there is no phase change and that stream A has the lowest heat capacity flow rate. An energy balance equation is used to determine the outlet temperature for stream B

$$\Delta H_{\mathrm{HX}} = \dot{m}_{\mathrm{A}} \cdot c_{p,\mathrm{A}} \cdot \left(T_{\mathrm{A,in}} - T_{\mathrm{A,out}}\right) = m_{\mathrm{B}} \cdot c_{p,\mathrm{B}} \cdot (T_{\mathrm{B,out}} - T_{\mathrm{B,in}}). \qquad \text{Eq. (2)}$$

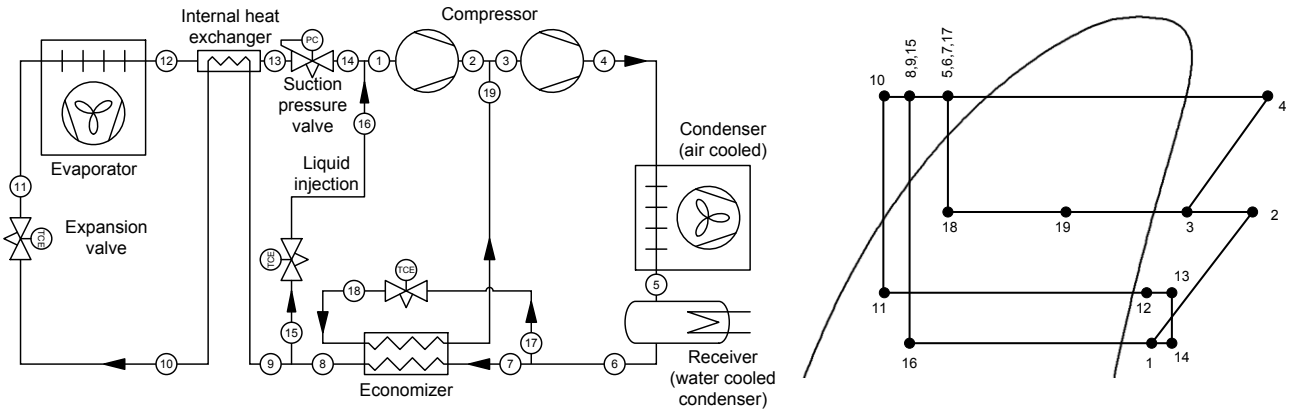

Figure 1: Cycle sketch of the generalized refrigeration unit model

The evaporator calculation assumes constant nominal heat transfer coefficients for the air side $\alpha_{\text{air,nom}}$ and for the refrigerant side $\alpha_{\text{ref,nom}}$ that are scaled using a moisture condensation enhancement factor and the compressor capacity ratio r_{comp}, respectively. These figures are then used to calculate the heat transfer using the number of transfer units (NTU) approach as follows

$$UA_{\text{evap}} = ((\alpha_{\text{air}} \cdot A_{\text{air}} \cdot \eta_{\text{fin}})^{-1} + (\alpha_{\text{ref}} \cdot A_{\text{ref}})^{-1})^{-1} \quad \text{Eq. (3)}$$

$$\text{NTU} = UA_{\text{evap}} \cdot (\dot{m}_{\text{air}} \cdot c_{\text{air}})^{-1} \quad \text{Eq. (4)}$$

$$\epsilon_{\text{evap}} = \left(1 - \text{e}^{-\text{NTU}}\right) \quad \text{Eq. (5)}$$

$$\dot{Q}_{\text{evap}} = \epsilon_{\text{evap}} \cdot \dot{m}_{\text{air}} \cdot c_{\text{air}} \cdot (T_{\text{air}} - T_{\text{evap}}) \quad \text{Eq. (6)}$$

with a fixed fin efficiency of η_{fin} of 85%. Another assumption used in Eq. (4) is that the air mass flow rate can be estimated from

$$\dot{m}_{\text{air}} = \dot{\text{V}}_{\text{air}} \cdot \rho_{\text{air}} \cdot (1 + w_{\text{air}})^{-1} \quad \text{Eq. (7)}$$

using the volumetric flow rate of air calculated from the evaporator fan speed. The condenser is not modelled in detail, but a capacity ratio r_{cond} is determined based on the nominal *UA*-value

$$UA_{\text{cond}} = \dot{Q}_{\text{cycle}} \cdot (T_{\text{cond}} - T_{\text{amb}}) \quad \text{Eq. (8)}$$

$$r_{\text{cond}} = UA_{\text{cond}} \,/\, UA_{\text{cond,nom}} \quad \text{Eq. (9)}$$

to make sure that the condenser does not leave its specified operating regime. The compressors are modelled using a fixed nominal isentropic efficiency for each container type and a scaling function based on the pressure ratio, the compressor type and the refrigerant as shown in Figure 2.

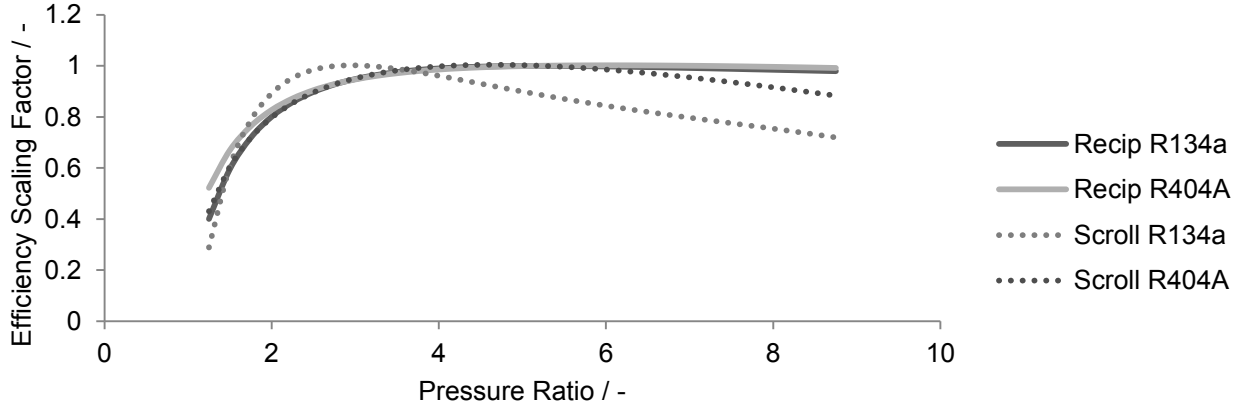

Figure 2: General compressor efficiency correction functions

Pipes are regarded as ideal components without pressure drop or heat transfer and all mixing processes are assumed to occur instantly and without any entropy generation. Valves are also calculated as isenthalpic throttling devices without entropy generation.
The fluid properties for R134a and R404A are obtained from custom functions that were fitted to reference data generated with REFPROP (Lemmon, Huber and McLinden 2010) based on the work of (Tillner-Roth and Baehr 1994) and (E. Lemmon 2003), respectively. Explicit functions are available for $v(T,p)$ and $h(T,p)$ and $s(T,p)$ as well as for the corresponding saturation routines. Explicit backwards formulation for $T(h,p)$ and $T(s,p)$ have also been generated to speed up the calculations and to avoid the use of solvers to obtain fluid properties.
The calculation procedure starts by estimating the cargo temperature and the operating mode based on previous measurements. For cooled cargo with a setpoint temperature above 5 °C, the air-side outlet temperature of the evaporator is assumed to be equal to the setpoint temperature, to avoid too low temperatures inside the reefer. For lower setpoint temperatures, the controller is assumed to keep the air-side inlet temperature of the evaporator at the setpoint. At each analyzed data point, the calculation model is called using the existing temperature measurements on the air side of the evaporator and the condenser as well as the outdoor temperature as inputs. Mass and energy balance equations are solved using Powell's hybrid method (Powell 1970) to find a solution that yields the compressor capacity, condensation temperature and evaporator cooling load.

2.3. Fault Detection Algorithm

Classical fault detection is based on the creation of residuals that express a deviation from an expected behavior (Blanke, et al. 2003). Residual generation exploits known relations between two or more input variables. Due to the low number of existing sensors and the limited sampling frequency, the simulation model described above was introduced to add more relations and to increase the number of detection input variables. As also described in the patents (Jónsson, Skovrup, et al. 2015) and (Jónsson, Granlund, et al. 2016), the output of the refrigeration model allows the algorithm to exploit additional direct relations like the one of saturation temperature and pressure, but also more complex cases like the interdependency of pressure ratio, compressor efficiency and discharge temperature.
The actual fault detection can be summarized using the flow chart in Figure 3. The three upper boxes with the darker background represent the hardware of the refrigerated container. The input values like the temperature setpoint and the latest sensor readings are processed by the reefer controller that generates the control signals for the refrigeration unit and other auxiliary equipment. Based on these inputs, the plant provides cooling while the sensors provide data for the next update of the control signals. Each of the functional units can be prone to malfunctions.
The arrows on Figure 3 illustrate the flow of information and the dashed lines indicate that not all sensor data and controller signals are fed to the simulation model, while controller and simulation share all general inputs like the setpoints for temperature and air exchange. The output of the simulation model is processed together with the sensor readings to generate the residuals x. In many cases, the residuals are calculated based on differences between modeled and measured performance figures. Afterwards, these values are processed by a change detection block that uses reference data for normal operation and reference values for known malfunctions as additional inputs. The statistical model focusses on the distribution of the residual values employing an estimated probability density function L for normal and faulty operation. The logarithm of the likelihood ratio is then accumulated over a certain period of time from t_1 to t_2 to obtain a fault indicator called the decision function

$$D = \sum_{i=t_1}^{t_2} \ln \frac{L_{\text{fault}}(x(i))}{L_{\text{normal}}(x(i))} \qquad \text{Eq. (10)}$$

for each of the defined residual functions indicating a change in the mean values. The decision function values are eventually compared to threshold values for fault detection to trigger alarms or warnings. If possible, a final fault isolation and identification step is carried out to provide more meaningful alarm messages.

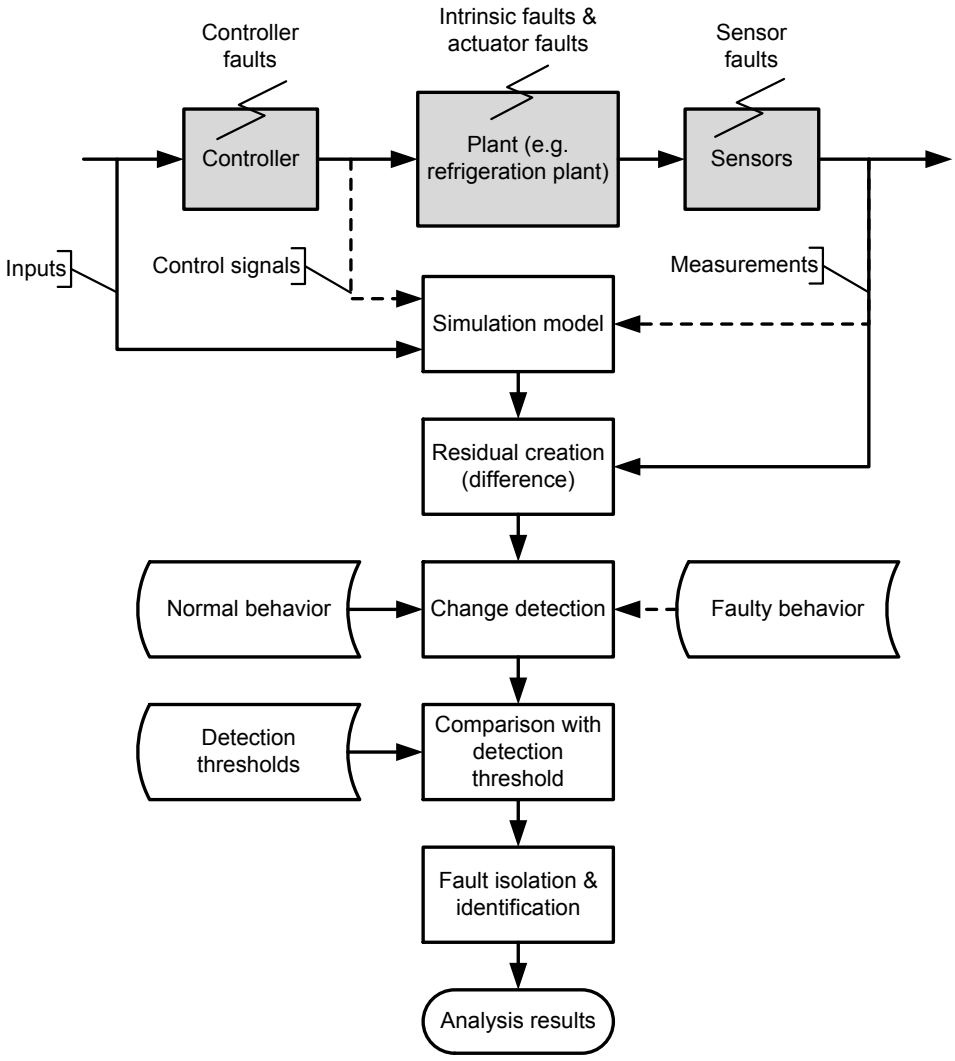

Figure 3: Fault detection algorithm structure

2.4. Tests and Fault Example

The fault detection and simulation performance has been tested with a selection of reference cases. For all cases, the reefer ran for a certain amount of time with a fixed setpoint before malfunctions were introduced in a controlled and reproducible manner. The data presented in this work were recorded in January 2012 in Denmark using a Carrier T-340 PrimeLine reefer in normal operation from the 25th 12:45 to the 27th 07:15 and with reduced air flow thorugh the evaporator from the 27th 08:45 to the 30th 11:15. The average outdoor temperature was approximately 0 °C and a heat source running with an average output of 1 kW was placed inside the reefer to simulate the heat load resulting from 25 °C ambient temperature. A similar approach was used at the condenser, where an insulated room was built around the controller and the heat rejection unit to maintain a temperature of 25 °C. The setpoint temperature for the refrigeration unit was 2 °C. The residual functions presented below are defined based on the air-side temperature difference at the evaporator and the discharge pressure, respectively:

$$x_{\mathrm{evap}} = \left(T_{\mathrm{meas,in}} - T_{\mathrm{meas,out}}\right) - \left(T_{\mathrm{simu,in}} - T_{\mathrm{simu,out}}\right) \quad \text{Eq. (11)}$$

$$x_{\mathrm{disc}} = p_{\mathrm{meas,disc}} - p_{\mathrm{simu,disc}} \quad \text{Eq. (12)}$$

3. RESULTS AND DISCUSSION

The measurements presented in Figure 4 show the discharge pressure and the suction pressure from the reefer as solid lines and the modelling results as dotted lines. The measured data change in as soon as the fault is introduced and both the discharge pressure and the suction pressure are affected. The reduced heat exchanger performance causes a slight decrease in suction pressure and an increase in discharge pressure. The modelled data is very stable throughout the whole tests and no change can be seen after the fault was introduced. However, Figure 4 also documents that there is a difference between the modelled pressures and the measurements. The performance of the heat exchangers is overestimated on the cold and on the warm side of the refrigeration unit. The simulated evaporator pressure and evaporation temperature are approximately 1.5 bar higher than the recorded test data and the discharge pressure and the condensation temperature are about 0.5 bar lower for the simulation results compared to the measured data.

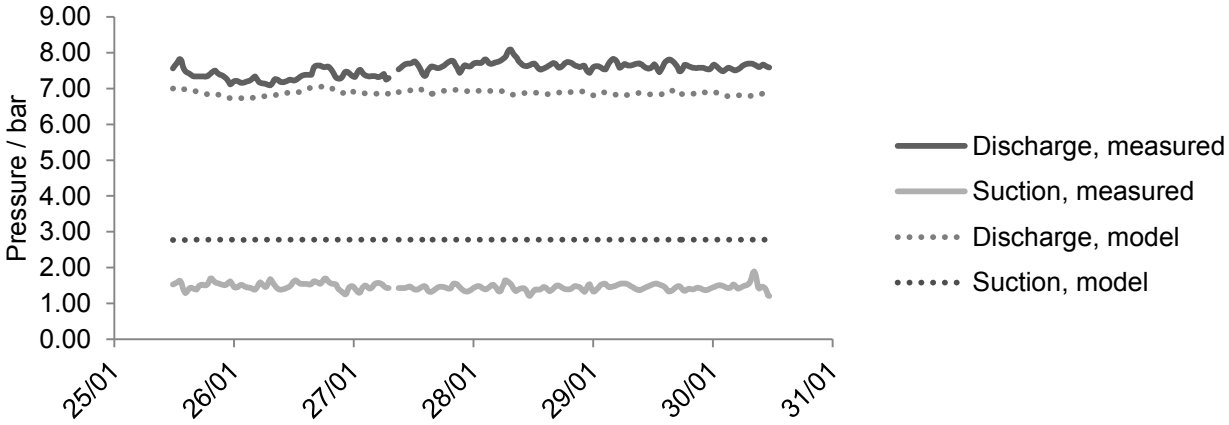

Figure 4: Pressure history for normal and faulty operation

In accordance with Figure 3, the measured air temperatures and pressures are converted to residual functions employing Eq. (11) and Eq. (12) provided above. Both residuals are included in Figure 5 and it shall be noted that are shown in arbitrary units (a.u.). Both residual functions increase after the fault has been introduced and the change in the evaporator residual value is more pronounced than in the discharge pressure residual. The mean value of the evaporator residual increases by 0.6 from -1.1 to -0.5 when the evaporator malfunction commences while the mean discharge pressure residual only increases by 0.3 from 0.5 to 0.8.

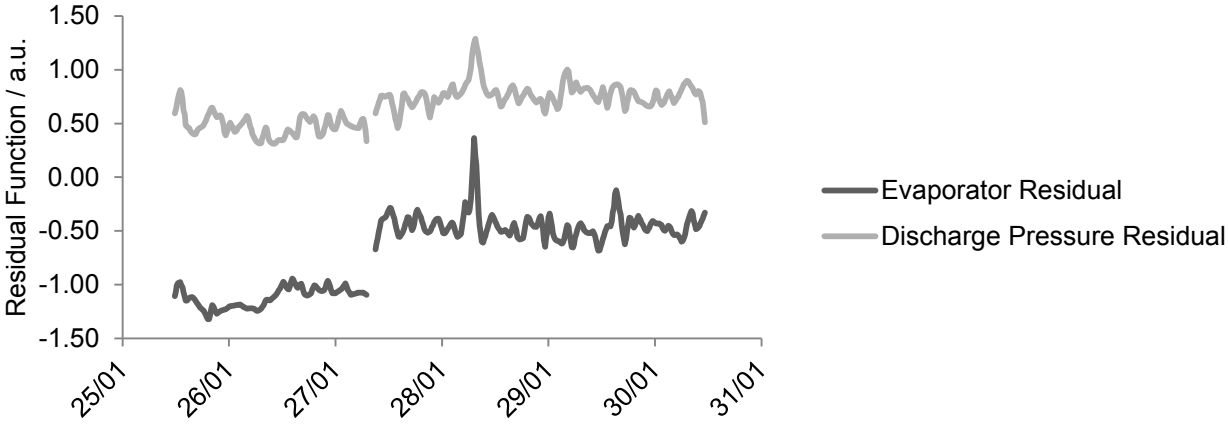

Figure 5: Calculated residual function for evaporator and discharge pressure

The reference distributions used for the evaporator and the discharge pressure residual functions are shown as line graphs in Figure 6 with the solid line representing the fit for normal operation and the dashed line indicating the fit for faulty operation. The bar graphs in Figure 6 indicate the normalized observation frequency for the period of normal operation and for the data recorded with reduced evaporator air flow. The bar graphs are normalized based on the total number of observations for each of the test series and are also shown in arbitrary units “a.u.“.

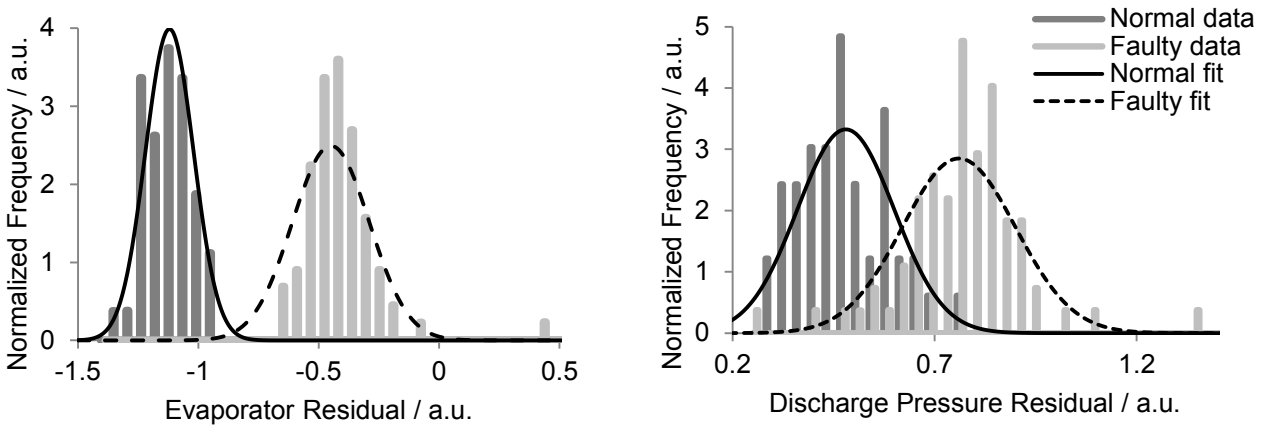

Figure 6: Distribution of residual function values

The next data processing step uses the distributions presented above to calculate the logarithmic likelihood ratio with Eq. (10). Starting at a zero value, the decision function evolves as the calculation results for each data point are added resulting in the data series shown in Figure 7.

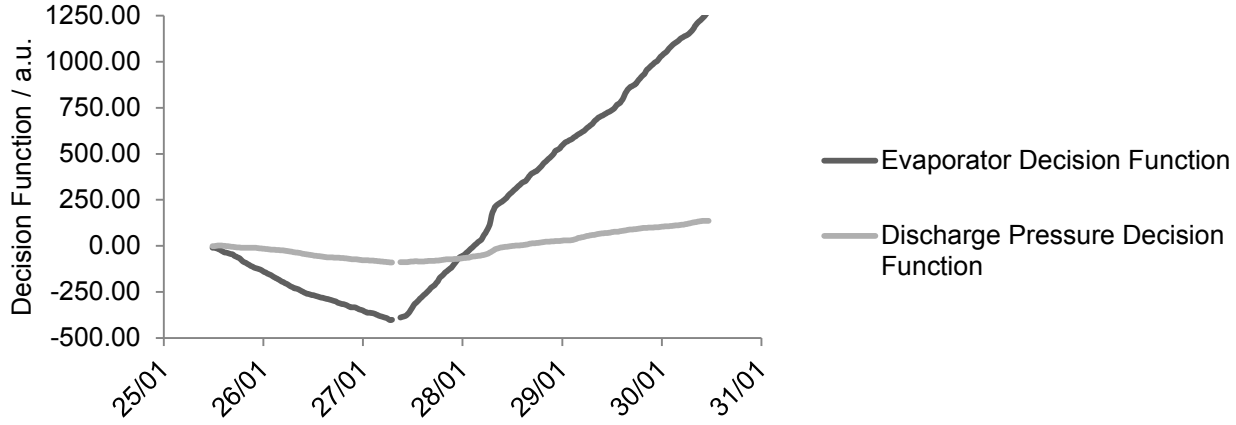

Figure 7: Decision function calculated based on residual data

For residuals that are more likely to belong to the fit for the normal operation, the ratio becomes less than unity yielding a negative value for the logarithm causing a decent of the decision function. If the likelihood ratio is reversed and the residuals at the point of investigation are more likely to belong to the fitted distribution of the faulty operation, the decision function value increases as values that are larger than zero are added continuously.
For the final implementation of the detection system, threshold values are used to trigger alarms and warnings based on the values of the decision functions. In many cases the decision function is limited to values larger or equal to zero.

4. CONCLUSIONS

After over 5 years of operation and millions of analyzed trips, it can be documented that a system built upon the principles introduced above is able to detect malfunctions reliably increasing the efficiency of the reefer maintenance operations by over 40%. The presented approach was able to detect reefer faults using residual functions based on measured data and simulation results. Introducing reference distributions expressing normal and faulty operation made it possible to employ simplified component models by removing the need for accurately modelling results. However, the creation of reference distributions requires experimental data for faulty operation, which could be considered a weakness of the methodology.

ACKNOWLEDGEMENTS

The authors would like to thank Maersk Line for the possibility to work on this interesting topic and the valuable input regarding reefer design and operation. Furthermore, the help received from Kristian Fredslund, Morten Skovrup and Rasmus Eriksen regarding the experimental campaign, the model development and the algorithm design is highly appreciated.

NOMENCLATURE

A	area (m^2)	T	temperature (K)
c	specific heat capacity (J kg^{-1} K^{-1})	t	time (s)
D	decision function (-)	U	total heat transfer (J m^{-2} K^{-1})
H	enthalpy (J)	v	specific volume (m^3 kg^{-1})
h	specific enthalpy (J kg^{-1})	$\dot{V}$	volumetric flow rate (m^3 s^{-1})
L	likelihood value (-)	w	humidity ratio (kg_{H2O} kg_{air}^{-1})
m	mass (kg)	x	residual value (a.u.)
$\dot{m}$	mass flow rate (kg s^{-1})	α	heat transfer coefficient (J m^{-2} K^{-1})
p	pressure (Pa)	ϵ	heat exchanger efficiency (-)
$\dot{Q}$	heat flow rate (W)	η	compressor or fin efficiency (-)
r	ratio (-)	ρ	density (kg m^{-3})
s	specific entropy (J kg^{-1} K^{-1})		

REFERENCES

Blanke, Mogens, Michek Kinnaert, Jan Lunze, and Marcel Staroswiecki. *Diagnosis and Fault-Tolerant Control.* Berlin, Heidelberg, New York: Springer, 2003.

Churchill, John. “Smart containers listen & talk.” *Maersk Group Annual Magazine*, 2015: 20-23.

Fitzgerald, Warren B., Oliver J. A. Howitt, Inga J. Smith, and Anthony Hume. “Energy use of integral refrigerated containers in maritime transportation.” *Energy Policy*, no. 39 (2011): 1885-1896.

Hoffmann, Jan, et al. *Review of Maritime Transport.* Geneva, Switzerland: United Nations Conference on Trade and Development, 2018.

Jónsson, Ragnar Ingi, Morten Juel Skovrup, Rabia Line Bonding Granlund, Thierry Seurin, Rasmus Solmer Eriksen, and Morten Rene Baerentz. A computer-implemented method of monitoring the operation of a cargo shipping reefer container. Worldwide Patent WO2015028072A1. 05. 03. 2015.

Jónsson, Ragnar Ingi, Rabia Line Bonding Granlund, Rasmus Solmer Eriksen, Thierry Seurin, and Morten Rene Baerentz. Method and system for reefer container evaluation. Worldwide Patent WO2016139364A1. 09. 09. 2016.

Lemmon, E. W., M. L. Huber, and M. O. McLinden. “NIST Standard Reference Database 23: Reference Fluid Thermodynamic and Transport Properties-REFPROP.” National Institute of Standards and Technology, 2010.

Lemmon, E.W. “Pseudo Pure-Fluid Equations of State for the Refrigerant Blends R-410A, R-404A, R-507A, and R-407C.” *International Journal of Thermophysics* 24, no. 4 (2003): 991-1006.

Lukasse, Leo J. S., Morten R. Baerentz, and Janneke E. de Kramer-Cuppen. “QUEST II: Reduction of CO2 Emissions of Reefer Containers.” *Proceedings of the 23rd IIR International Congress of Refrigeration.* Prague, Czech Republic, 2011. ID: 459.

Powell, M. J. D. “A hybrid method for nonlinear equations.” In *Numerical methods for nonlinear algebraic equations*, by Philip Rabinowitz (ed), 87-114. New York: Gordon and Breach Science Publishers, 1970.

Sørensen, Kresten Kjær. *Model Based Control of Reefer Container Systems.* PhD Thesis, Aalborg University, 2015.

Svensson, Robert. *Improving refrigerated marine container management with pervasive connectivity.* Emerson Climate Technologies - Transportation Solutions, 2014.

Tillner-Roth, R., and H.D Baehr. “An International Standard Formulation of the Thermodynamic Properties of 1,1,1,2-Tetrafluoroethane (HFC-134a) for Temperatures from 170 K to 455 K at Pressures up to 70 MPa.” *Journal of Physical and Chemical Reference Data* 23 (1994): 657-729.

Manuscript ID: 1200
DOI: 10.18462/iir.icr.2019.1200

Numerical transient simulation of the insulating performance of a refrigerated truck body

Paolo ARTUSO [b], Antonio ROSSETTI [a], Silvia MINETTO [a], Sergio MARINETTI [a], Davide DEL COL [b]

[a] National Research Council, Construction Technology Institute
Corso Stati Uniti 4, 35127 Padova, Italy
[b] Università degli Studi di Padova, Industrial Engineering Department,
via Venezia 1, 35131 Padova, Italy

ABSTRACT

The thermal load of a refrigerated truck is affected by both the external environment and the operating conditions. In order to predict the effects of the loads on the trend of the cooling demand, the insulated box thermal capacity has to be included into the model, in addition to its average conductivity. The paper uses a validated unsteady numerical simulation of a refrigerated truck insulated body to simulate a short distance delivery missions under different reference climates. The results allow to critically discuss the impact of the cooling unit sizing on the overall performance in terms of food security and energetic efficiency.
Keywords: Refrigeration, Road Transport, Dynamic Simulation, COP, Energy Consumption, Energy Efficiency.

1. INTRODUCTION

Lifestyle changes over the past decades led to increasing consumption of fresh and frozen foods, which are easier and quicker to prepare than the traditional types of food. In order to ensure product quality and safety, refrigeration systems are widely used in modern society to transfer thermal energy from one physical location to another. The refrigeration system of a refrigerated truck is one example. As an essential link in the cold chain, refrigerated transport has widely developed and strongly contributed to the cold chain supply in the last 70 years. In 2010, an estimation of around 4 million refrigerated vehicles in service worldwide, including vans (40%), trucks (30%), semi-trailers or trailers (30%) was reported, forecasting by 2030 a growth by 2.5% a year of global road freight transport (UNEP, 2010). A more recent document by Eurostat in 2017 reported that the total number of refrigerated vehicles in Europe was superior to 4 million at the end of 2016, with an increase of 1.6% respect to the previous year.

In a typical refrigerated transport system operation, the refrigeration unit interacts with the truck cargo space and regulates its temperature to a certain set-point, depending on the type of transported goods. By far, the most common temperature control in the refrigerated transport having a cooling unit based on a vapor compression cycle is a simple on-off feedback controller with hysteresis (James et al., 2006), where the compressor on or off control action is driven by the difference between measured cargo space temperature and set-point temperature.

After all, the maintenance of an optimal product temperature should be assured from production to consumption. The postproduction handling chain (perishable freights distribution and delivery) is one of the weakest links in the cold chain, especially in short or medium distance delivery runs where the chilled or frozen products can be subjected to many doors opening, with relevant heat loads directly related to infiltration air (James et al., 2006; Pereira et al., 2010). Frequent door openings can also lead to increased evaporator frosting, resulting in a reduction of the evaporator's performance and an increase in the need for defrosts, particularly in humid weather conditions (Estrada-Flores et al., 2006).

The performance of the small refrigeration units can be significantly reduced by the absence of a proper control of the cooling capacity, which is often driven by the power available at the vehicle engine. This is the case of the refrigeration units of small trucks, where the compressor is powered

by the vehicle's internal combustion engine. As a result, there are substantial difficulties in maintaining the optimal temperature of refrigerated products and proper cycling, especially when multi-drop deliveries to retail stores and caterers are considered (James et al., 2006). In this case, in fact, the cooling demand presents strong fluctuations due to the repetition of pull-down periods, associated to the door openings, and the driving time.
The present paper discusses the performance of a simple compression refrigeration cycle, when coupled to a small refrigerated truck employed in a daily delivery mission. A dynamic numerical model of the refrigerated box is coupled with the performance maps of the refrigeration unit and an ON-OFF control system.
Simulations are carried out for two different climates (Athens and Strasbourg), representative of European mild and hot areas, and for different sizing of the cooling unit. Results allowed highlighting the limits of the fixed capacity units.

2. NUMERICAL MODEL DESCRIPTION

2.1. Refrigerated Cargo Space Model

In the present study, the insulated body of a refrigerated van with an internal air volume of 9.75 m^3 is considered, built according to current technology. The walls of the insulated body consist of a polyurethane foam sandwiched between two thin fiberglass-based layers, reinforced with wooden and metallic structural components in order to obtain the desired sturdiness. The floor includes an additional layer of plywood plate, necessary to meet the requested mechanical resistance. The main external dimensions of the insulated body are reported in Table 1.

Table 1- External dimensions of the insulated body of the refrigerated van

Height [m]	2.00
Length [m]	3.00
Width [m]	2.00
Surface [m^2]	32.0

A lumped capacitance zero dimensions transient method is used to model the insulated box, solving the node temperature as a function of time. The full description and validation of the model has been extensively presented in Artuso et al., 2018. Thus, for sake of brevity, this section reports only the main features of the models.

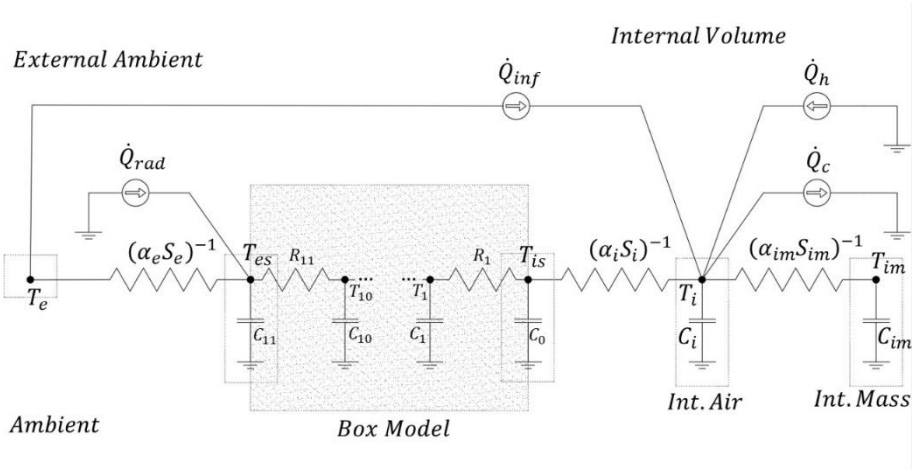

Figure 1: Numerical model of the refrigerated vehicle

The system composed by the insulated body walls, internal air, perishable goods inside of the box, was modelled as a 0-D model defined by a series of resistances and capacities, as reported in Fig. 1.

$$C_i \frac{dT_i}{dt} = -\dot{Q}_c + \dot{Q}_h + \alpha_i S_i (T_{is} - T_i) + \alpha_{im} S_{im} (T_{im} - T_i) + \dot{Q}_{inf} \quad \text{Eq. (1)}$$

$$C_j \frac{dT_j}{dt} = \frac{1}{R_{j+1}} \left(T_{j+1} - T_j\right) + \frac{1}{R_j} \left(T_{j-1} - T_j\right) \ , \ j = 1 \ldots 10; \text{ with } T_0 = T_{is} \text{ and } T_{11} = T_{es} \quad \text{Eq. (2)}$$

$$C_{es} \frac{dT_{es}}{dt} = \frac{1}{R_{11}} (T_{es} - T_{10}) + \alpha_e S_e (T_{amb} - T_{es}) + \dot{Q}_{rad} \quad \text{Eq. (3)}$$

$$C_{im} \frac{dT_{im}}{dt} = \alpha_{im} S_{im} (T_i - T_{im}) \quad \text{Eq. (4)}$$

Eq.s (1-4) describe the transient heat balance of the numerical model of the insulated body which provide the mean temperature of the system's components. The internal air temperature is obtained by the transient thermal balance in eq. (1), composed by the algebraic sum of heat flow provided by the cooling unit, $\dot{Q}_c$, convective heat flow between the internal air and the internal walls, $\alpha_i S_i (T_{is} - T_i)$, convective heat flow between the internal air and the perishable goods located inside the cargo space during the mission and infiltration heat flux, $\dot{Q}_{inf}$, given by the leakage of outside air into the insulated body during the opening of the vehicle's doors or due to the imperfect seal of the doors during operation.
Preliminary studies, demonstrated that the use of 12 capacities (C_0,…,C_{11}) and 11 resistances (R_1,….,R_{10}) were enough to reproduce the experimental response of the box. Eq. (2) describes the insulated box walls model as T_0 and T_{11} represent the internal and external mean surface temperature. Eq. (3) instead, express the unsteady heat balance at the external surface of the refrigerated van, given by the conductive heat flux, $(T_{es} - T_{10})/R_{11}$, the convective heat flow, $\alpha_e S_e (T_{amb} - T_{es})$ and the net solar radiation insisting on the external surface, $\dot{Q}_{rad}$. In eq. (4), the heat balance of the perishable cargo inside the insulated body is provided.
The values of the thermal capacities C_i and thermal resistances R_w have been defined by best fit of experimental data.

2.2. Refrigeration System Model

The cooling unit is modelled after a basic R-134a vapour compression system with a nominal cooling power of 2000 W, at the reference condition of $T_i = 0$ and $T_{amb} = 30°C$, modulating the cooling capacity provided to the cargo space $\dot{Q}_c$ by turning ON and OFF the compressor. The ON/OFF controller is implemented by means of a simple thermostat with 2°C hysteresis.

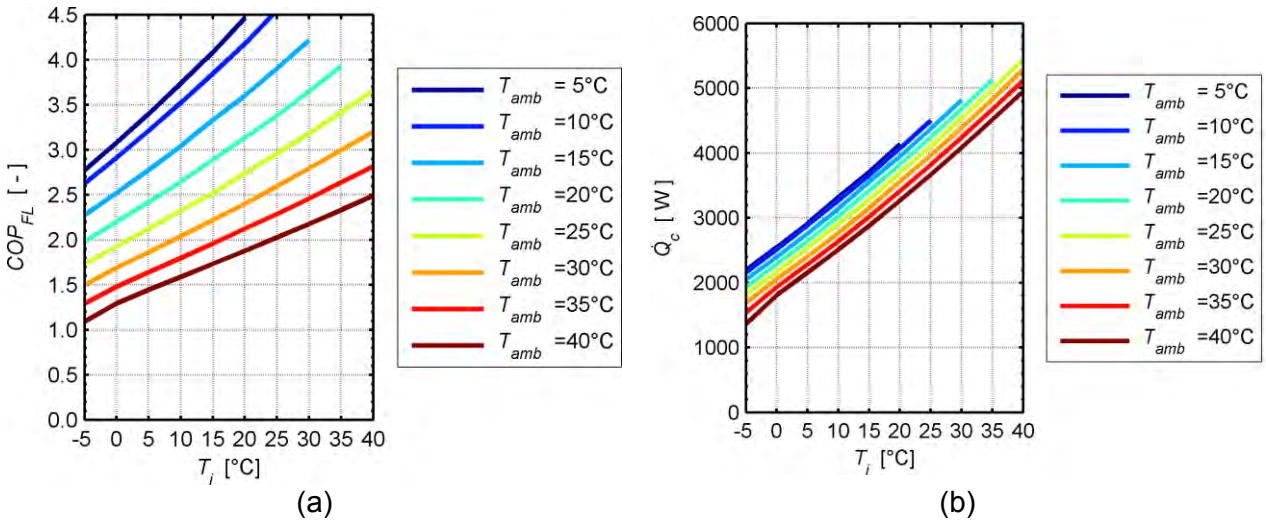

Figure 2: Cooling unit performance: (a) full load COP; (b) cooling capacity

The refrigeration unit performances were obtained using an in-house developed simulation tool (Artuso, 2019). The performance maps, reported in Fig. 2, were then implemented in the truck model by means of interpolation tables. Interpolation was based on the internal air mean temperature T_i

and the external environment temperature T_{amb} resulting in the refrigerating capacity $\dot{Q}_c$ and the full load coefficient of performance $COP_{.FL}$.
In order to account for the reduction of the performance associated with ON/OFF cycles, a degradation factor was included in the model. The degradation factor C_d is assumed equal to 0.25, in accordance with UNI-EN-14825[2012], while the capacity ratio C_R is assumed equal to the mean duty cycle during operation. The resulting coefficient of performance at partial load is then obtained as:

$$COP_{PL} = COP_{FL}\left(1 - C_d \cdot (1 - C_R)\right) \quad \text{Eq. (5)}$$

2.3. Delivery Mission

This paper studies the simulation of a local distribution activity. The mission starts with the pre-cooling activity of the insulated body, as common practice in the industry, when the cooling unit is kept on with the doors closed and the internal air is pulled down to the set-point temperature, reaching a steady state condition while the refrigerated vehicle is kept still under the fluctuating ambient conditions. After two-hours of pull down, the cooling unit is switched off and the loading operation takes place: the perishable cargo is loaded inside the insulated body, while the refrigerated cargo with the doors completely open is kept in contact with a controlled environment at $T_{amb} = T_i^{set} = 4°C$ and the perishable cargo is already at the set-point temperature when is loaded.
Standard profiles ECE and EUDC are then used to construct the delivery mission profile. Five EUDC cycle, corresponding to a 30 km drive, are used to simulate the rural drive condition between the logistic facilities to the city. Then the urban drive condition is defined as 5 ECE cycle, corresponding to 5 km in 15 minutes with frequent stops. The urban drive is repeated 6 times before a new rural cycle is performed. Between each urban cycle, a stop of 5 min is considered, where the doors are opened to the ambient for 4 minutes, and part of the refrigerated cargo is unloaded. This mission in then repeated during the afternoon.
In this delivery mission, a total of 400 kg of meat products are distributed evenly during the 12 deliveries.
The mission stages are reported in Table 2.

Table 2 Mission structure

Start Time (h.mm)	Duration (h.mm)	Activity	Travel distance (km)
6.00 AM	2.00	Pull Down	-
8.00 AM	1.00	Loading	
9.00 AM	0.30	Rural Drive	30
9.30 AM	2.00	6 Delivery Cycles:	
	0.17	- Urban Drive	5
	0.01	- Stop	-
	0.04	- Delivery	-
11.30 AM	0.15	Urban Drive	5
11.45 AM	0.30	Rural Drive	30
12.15 PM	1.45	Stop	-
2.00 PM	0.30	Rural Drive	30
2.30 PM	2.00	6 Delivery Cycles:	
	0.17	- Urban Drive	5
	0.01	- Stop	-
	0.04	- Delivery	-
4.30 PM	0.15	Urban Drive	5
4.45 PM	0.30	Rural Drive	30
5.15 PM	-	Stop	-
TOTAL:	11.15		190

3. NUMERICAL RESULTS

The numerical model was run to evaluate the average performance of the cooling unit, assuming different climates and different refrigeration unit size. Athens and Strasburg were identified as reference for hot and temperate climate, so to assess the impact of the ambient data on the results. First the response of the vehicle to the mission, in terms of temperature and loads using the expected capacity of the group $\dot{Q}_c = 2000$ W. Then, the refrigeration unit size is be discussed in terms of daily consumption and overall performance.

3.1. Mission Results

The internal average temperature for each part of the delivery mission is reported in Fig. 3, as well as the goods temperature and the ambient temperature. Ambient data are referred to the 15th of August of the standard year (EnergyPlus).

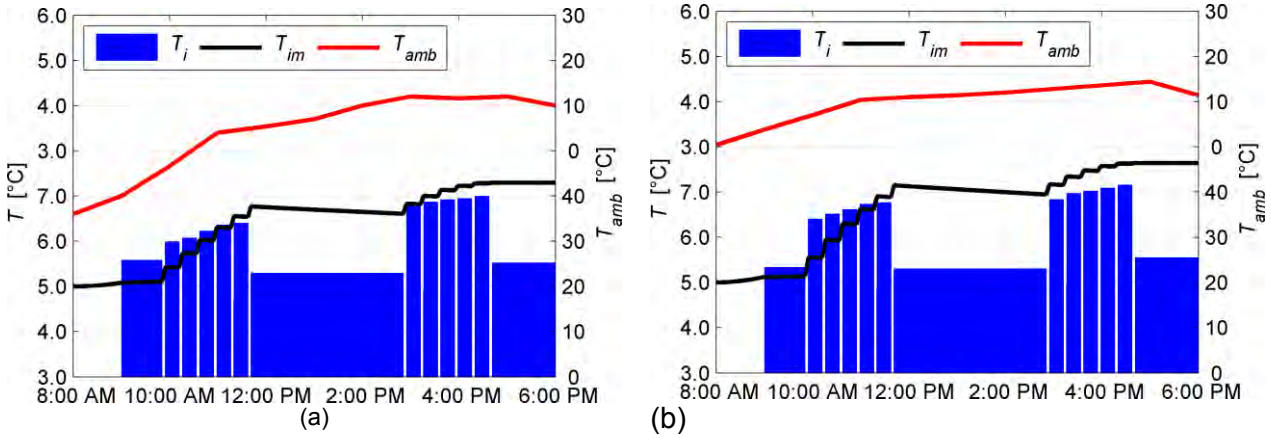

Figure 3: Temperature trend for the month of August: a) Strasburg; b) Athens

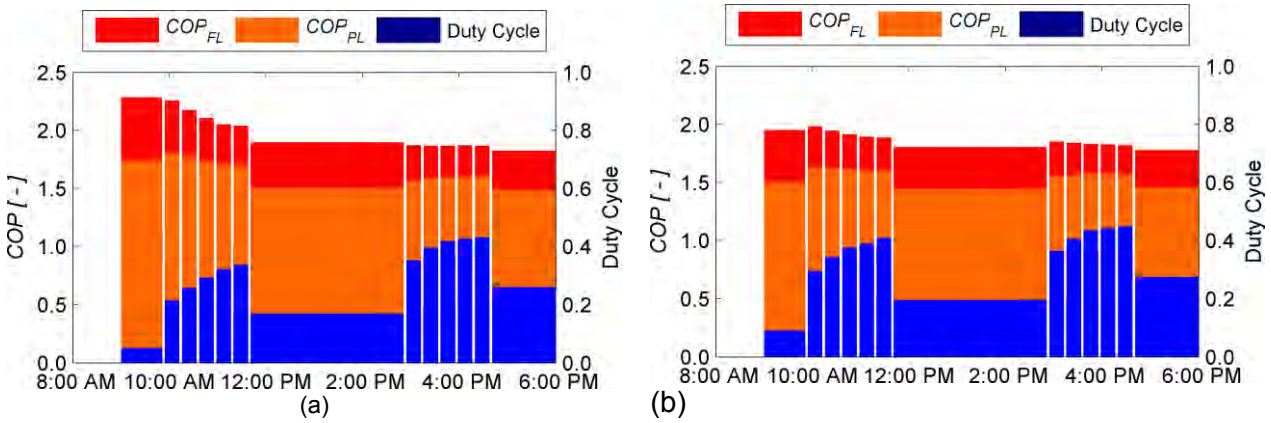

Figure 4: Coefficient of performance and duty cycle: a) Strasburg; b) Athens

As expected, the average internal temperature is close to set point of 4°C during transport and the long stop at noon, when the doors are kept closed. On the contrary, during the delivery phase the average internal temperature increases, as the result of the hot ambient air entering the refrigerated box during the door opening. The increase after each stop does not represent in this case a cumulative effect, as the cooling unit can efficiently remove the heat from the air, but is caused by the increase in temperature of the infiltrating air, which reach its maximum in the late afternoon.
On the contrary, the transported goods show a clear cumulative effect associated to the doors opening. The goods temperature increases steeply during each door opening, due to the high temperature difference with the infiltrating air, which promote the exchange. On the contrary, due to the relatively small temperature difference $T_{im} - T_i$, the removal of the infiltrated heat from the goods is slow, as clearly shown by the small gradient of T_{im} between 12:00 PM and 13:00 AM, when the doors are kept closed.

Figure 4 reports the refrigeration unit performances for each part of the missions. Each graph reports the duty cycle, the full load and partial load coefficient of performance COP_{FL} and COP_{PL} respectively. When the full load performances are compared, the temperate climate in Strasburg allows obtaining significant higher COP_{FL} than in Athens. However, when the performance degradation ascribed to cycling is considered (eq. 5); the Strasburg data series present a marginal improvement only in the first hours of the morning. In fact, the lower cooling demand in Strasburg directly reduces the unit Duty Cycle, which is furthermore reduced by the increase of the capacity lead by the lower external ambient temperature.

3.2. Comparison between Cooling Capacities

As results of these observations, the ideal size of the refrigeration unit to complete the chosen mission is subject to antithetical requests. On one side, the unit capacity should be large enough to pull-down promptly the box temperature when the doors are closed, to reduce the temperature increase of the transported goods. On the other side, high capacities lead to small duty cycles thus reducing the actual energy performance.
In order to discuss the optimum cooling capacity, the ATP limit capacity $\dot{Q}_{c\,min}$ is considered, where:

$$\dot{Q}_{c\,min} = 1.75 * K_{nom} S\, \Delta T_{nom} \qquad \text{Eq. (6)}$$

with $K_{nom} = 0.7$ for refrigerated goods, S the average box surface and $\Delta T_{nom} = 30$ K. This value was then used as the reference to define the capacity ratio $r = \dot{Q}_c / \dot{Q}_{c\,min}$. For the considered test case, $\dot{Q}_{c\,min} = 1100$ W.
Simulation were then run with $r \in [0.6\,..\,5.1]$, for the 15th of March, the 15th of June and the 15th of August, for both the reference locations. Fig. 5 report the daily average of COP_{PL} against the time for which $T_i > T_{set}^{+}$.
As expected, the increase of the group capacity decreases both the average efficiency and the exposure of the goods to high temperature. The sensitivity to the capacity ratio increase as the average temperature increases. The exposure time of the goods to high temperature decreases by increasing of the capacity ratio, but it can't be reduced to zero, as it is bounded by the opening time (a total of 48 minutes in this mission) and the ambient condition which rules the air infiltration when doors are open.
The data presented in Fig. 5 justify the choice of installing a 2000 W capacity unit ($r = 1.8$) for the considered case, as an acceptable compromise between food safety and energy consumption. Further increase in the cooling capacity, in fact, has a marginal impact on the exposure time while decreasing the actual coefficient of performance.
In order to fulfil the two objective (quick pull-down and high efficiency), simulation were run assuming a step modulating unit, with a minimum capacity equal to $\dot{Q}_{c\,min}$, and a maximum capacity equal to $r\,\dot{Q}_{c\,min}$. A simple logic was implemented on the ON/OFF unit controller, using the highest capacity during the pull-down phases and the lowest when the temperature is inside the thermostat limits:

$$\dot{Q}_c = r\,\dot{Q}_{c\,min} \text{ when } T_i > T_{set}^{+} \qquad \text{Eq. (7)}$$

$$\dot{Q}_c = \dot{Q}_{c\,min} \text{ when } T_i \in [T_{set}^{-},\ T_{set}^{+}] \qquad \text{Eq. (8)}$$

Results of this different control logic can be observed in Fig. 6. The use of lower capacity when the temperature is between the thermostat hysteresis bounds allows increasing the average Duty Cycle during the mission, thus reducing the performance degradation due to partial loads (eq. 5). Implementing this step control reduces the sensitivity of the average COP_{PL} to the capacity, when compared to the results in Fig. 5.

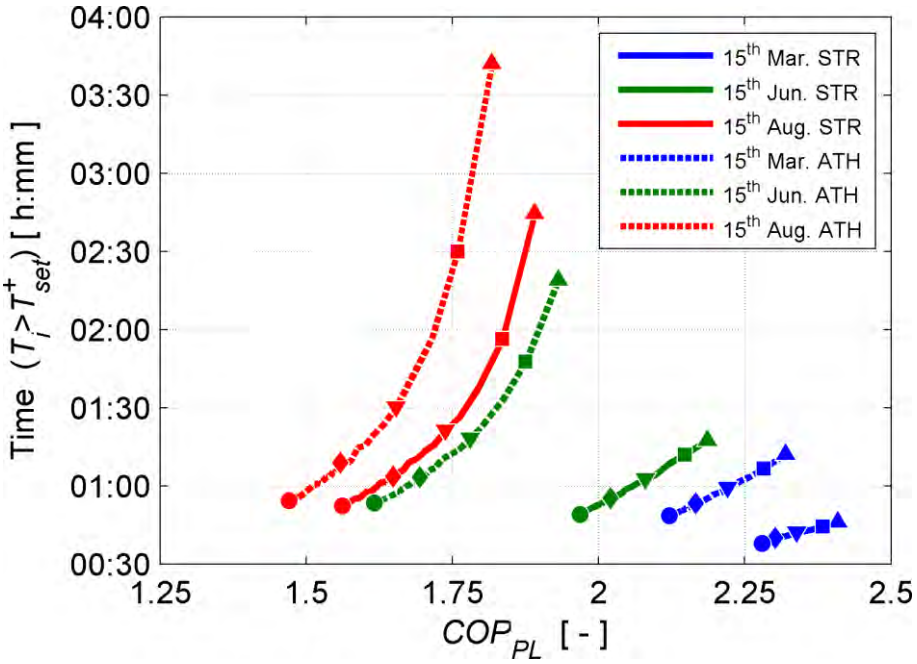

Figure 5: Performance comparison between capacities ratios: ▲ $r = 0.6$; ■ $r = 0.7$;▼ $r = 1.0$;♦ $r = 1.8$;● $r = 5.1$

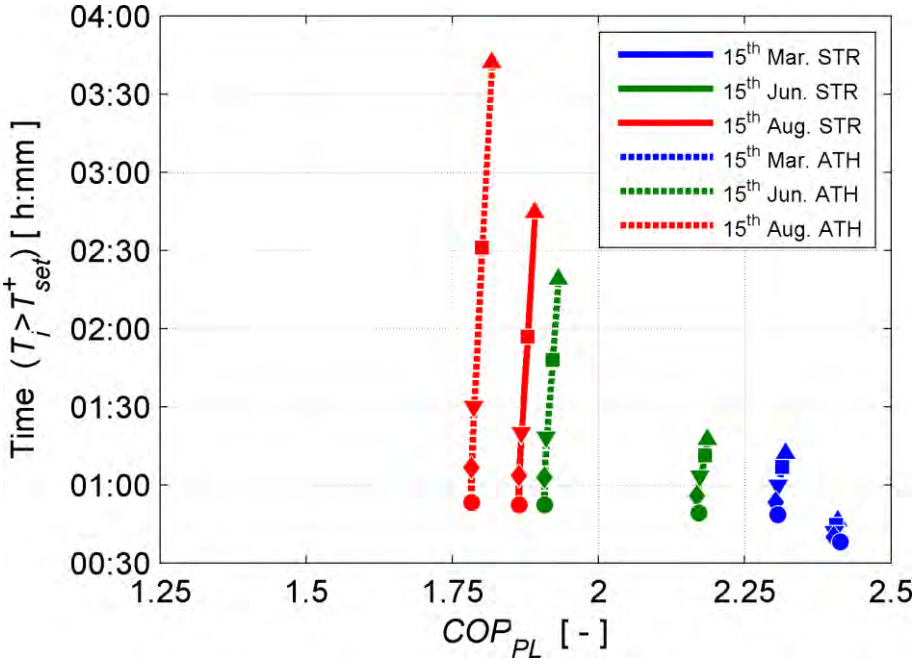

Figure 6: Performance comparison between capacities ratios: ▲ $r = 0.6$; ■ $r = 0.7$;▼ $r = 1.0$;♦ $r = 1.8$;● $r = 5.1$

4. CONCLUSIONS

This paper presents the numerical simulation of a refrigerated truck insulated body during a short distance delivery mission. Simulations are conducted for different climates and cooling capacities. Despite the simplicity of the model employed, results allow to discuss the impact of the cooling unit sizing on the overall performance, in terms of food security and energetic efficiency. While high capacities are needed to effectively pull down the temperature after each door opening, the low duty cycle of these units during the driving time can significantly reduce the overall performance of the system. The use of a step modulation of the unit capacity can positively affect the overall performance of the system, reducing the performance degradation at partial load.

In order to obtain more precise data further development of this research will be oriented to couple the refrigerated box dynamic model with a detailed dynamic model of the refrigeration unit.

NOMENCLATURE

α	Convective heat transfer coefficient [$Wm^{-2}K^{-1}$]	r	Refrigerating capacity ratio [-]
C	Lumped thermal capacity [J kg^{-1} K^{-1}]	S	Surface [m^2]
C_d	Degradiation factor [-]	ΔS	Average box surface [m^2]
C_R	Capacity ratio [-]	T	Temperature [°C]
COP	Coefficient of performance [-]	T_{set}^{+}	Upper bound set point temperature [°C]
$\dot{Q}$	Heat flux [W]	T_{set}^{-}	Lower bound set point temperature [°C]
R	Thermal resistance [K W^{-1}]		

SUBSCRIPT

amb	Ambient	is	Internal surface
c	Cooling	inf	Infiltration
e	external	im	Internal mass
es	External surface	min	Minimum
FL	Full load	nom	Nominal
h	Heating	PL	Partial load
i	Internal	set	Set point

REFERENCES

Artuso, P., Rossetti, A., Minetto, S., Marinetti, S., Del Col, D. 2019 Numerical investigation on the thermal performance of a new cooling unit for refrigerated transport application using CO2 as working fluid. Ammonia and CO2 Refrigeration Technologies, April 11-13, Ohrid, Republic of Macedonia.

Artuso, P., Rossetti, A., Minetto, S., Marinetti, S., Del Col, D., 2019. Dynamic modeling and thermal performance of a refrigerated truck body during operation. Int.J.Ref, 99: 288-299.

Cavalier, G., Tassou, S., 2011. Sustainable Refrigerated Road Transport. 21st Informatory Note on Refrigerating Technologies, International Institute for Refrigeration.

Estrada-Flores S., Eddy A., 2006. Thermal performance indicators for refrigerated road vehicles. Int. J. Refrigeration, 29: 889-898.

EnergyPlus - https://energyplus.net/ Last visit 01/2019

James S.J., James C., Evans J.A., 2006. Modelling of food transport system- a review. Int.J.Refrigeration, 29: 947-957.

Pereira V.F., Doria E.C., Carvalho jr B.C., Neves jr L.C., Silveira jr V., 2010. Evaluation of temperatures ina refrigerated container for chilled and frozen food transport. Ciencia e Tecnologia de alimentos, campinas, 30(1), 158-165.

UNEP. Report of the Refrigeration, Air conditioning and Heat Pumps Technical Options Committee, 2010.

Manuscript ID: 1205
DOI: 10.18462/iir.icr.2019.1205

Innovative layout for electric powered refrigeration for insulated trucks: the integration of photovoltaic generator

Antonio ROSSETTI [(a)], Paolo ARTUSO [(b)], Silvia MINETTO [(a)], Sergio MARINETTI [(a)], Dario ZENNARO [(c)]

[(a)] National Research Council, Construction Technology Institute
Corso Stati Uniti 4, 35127 Padova, Italy
[(b)] Università degli Studi di Padova, Industrial Engineering Department,
via Venezia 1, 35131 Padova, Italy
[(c)] ISOKIT Srl,
Via Terza Strada, 10, 35026 Conselve PD, Italy

ABSTRACT

Small insulated truck refrigeration units are usually powered by the internal combustion engine used for the vehicle traction, as the system size does not require the use of a dedicated prime engine.
The paper presents an innovative layout where an electrically driven compressor is connected to a battery pack, which is powered by a photovoltaic generator placed on the roof of the insulated box. The battery packs are also connected to the vehicle alternator, which is used as a backup source.
A fully functional prototype of the system is presented and characterized.
Numerical simulations are then used to forecast the impact of the solar contribution to the system performances under different ambient conditions. Numerical simulation results demonstrate the proposed system can sustain itself for most of the considered cases, resulting in a significant reduction of the annual consumption for the vehicle.
Keywords: Refrigeration, Carbon Dioxide, Compressors, COP, Evaporators, Energy Efficiency.

1. INTRODUCTION

The refrigerated transport has widely developed and strongly contributed to the cold chain supply in the last 70 years. In 2010, an estimation of around 4 million refrigerated vehicles in service worldwide, including vans (40%), trucks (30%), semi-trailers or trailers (30%) was reported, forecasting by 2030 a growth by 2.5% a year of global road freight transport (UNEP, 2010).
The contemporary achievement of perishable goods safety and sustainability are the challenges that refrigerated transport equipment designers and manufacturers are facing. Today's refrigerated vehicles, on the other side, can be improved in many aspects: the enhancement of the insulation capabilities; the optimization of the external aerodynamics of the boxes, and the optimization of the refrigeration units and its control (Cavalier, 2011).
One of the most problematic point in small applications is the dependency of the refrigeration unit on the traction engine. While in long-haul refrigerated trailers a dedicated diesel engine powers up the refrigerated unit, on short-distance refrigerated vehicles, the traction diesel engine runs also the refrigerated unit's compressor. This negatively impacts both the preservation of the cold chain, due to the reduction of the cooling capacity at low speed or stops, and the environmental impact, as the required power can be drawn from the engine when it is conversion efficiency is very low. The uncoupling between the diesel engine and the compressor can be achieved by using an electric generator connected to engine powering an electric hermetic compressor (Cavalier, 2011) limiting the above mentioned problems.
The use of electric powered compressor opens to the integration of renewables in the system. Solar photovoltaic driven/aided refrigeration represents a technology useful to reduce CO2 emissions and dependency from oil, as well as a market opportunity. Literature on the topic is limited and dated. Bahaj (1998, 2000) reports the results obtained replacing the diesel generator of conventional trailers with a photovoltaic system. Such a systems can also avoid noise limitations, generally occurring in nighttime in city centres. The absence of a backup power unit to supply energy once the battery are

fully discharged was highlighted as a major critical point, as the user has to be aware of the battery status to avoid cold chain interruptions.
In the same years, the Sandia National Laboratories conducted an extensive feasibility study for chilled and refrigerated long distance transport (Bergeron, 2001). It demonstrated the technological feasibility of these systems and a moderate economic justification.
Elliston B. et al. carried out a second study on the feasibility of PV-assisted refrigerated transport of goods frozen in Australia in 2009 following the results of Bahaj's papers. The thermal load was evaluated by a simple 0D thermodynamic model, in which the thermal load applied to the inner contents is the sum of the conductive heat load through the walls for average daily temperature data (by month) in Canberra and the refrigerator thermal power. The sizing of the components is conducted by the estimation of the PV production. The economic analysis proved that the system was unattractive, but authors highlighted this was caused by the low pricing of the diesel fuel in Australia at that time.
This paper presents the feasibility study of a vapour compression cycle aided by electrical energy provided by photovoltaic panels. The main object is to revise early researches on the basis of up-to-date technology, changing the case study from the long-haul chilled transport to short-distance refrigerated delivery truck.
First, preliminary experimental results will be showed to verify the coherence of the component design, then, an accurate 3D numerical analysis will be presented to assess the impact of photovoltaic generators on the energy consumption of a small size refrigerated truck.

2. CASE STUDY

For the present study, a small refrigerated truck is considered as test case. The external dimension of the refrigerated body are reported in Table 1. The overall internal volume was 9.75 m^3, with a double door covering the whole rear face and a smaller side door.
The walls and the ceiling are made of polyurethane foam covered on all the exposed sides with two thin fiberglass-based layers. The floor is reinforced by means of a plywood plate and wood beams. Due to the reduced size of the box, no wooden reinforcement was necessary on the walls and the ceiling. Metallic structural palates are also included in the design as necessary, to couple the bolts connecting the body to the frame of the truck, the hinges of the doors and the evaporator.

Table 1. Main external dimensions of the insulated box.

Height [m]	2.00
Length [m]	3.00
Width [m]	2.00
Surface [m2]	32.0

2.1. System Layout

The proposed system overall layout is presented in Fig. 1. Photovoltaic generators (a) are connected to a charge controller (b)that transforms the panel voltage to 24 V DC, which is a standard for light truck applications. This controller optimizes the photovoltaic panel voltage to maximize the conversion efficiency and limit the power when the battery pack (e) reaches the maximum charge.
The refrigeration unit considered in this study is simple and representative of the standard for this application. An ON/OFF controller is implemented by means of a simple thermostat (c) with 3°C of hysteresis.
In order to guarantee the system functionalities, the batteries can be connected to the truck electrical system (f) as needed, thus allowing the refrigeration unit to function as a standard electrical unit powered by the vehicle alternator.

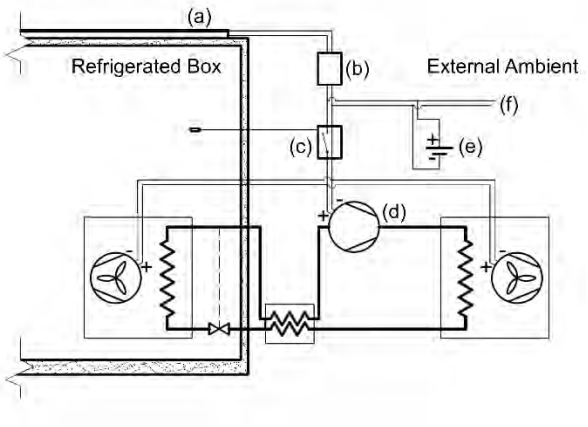

Figure 1: System sketch

Table 1. System main parameters

PV generators	
Tot. Area	5.5 m^2
Nom. Efficiency	21%
Nom. Power	940 W
Battery pack	
Capacity	8 640 kJ
Refrigeration Unit (at T_{amb}= 30°C T_i = 0°C)	
Capacity	2.00 kW
Total electrical consumption	1.30 kW

The global heat transfer coefficient of the insulated box was expected to be lower than 0.4 $Wm^{-2}K^{-1}$. Given the box dimension this correspond to a reference thermal load of approximatively 380 W at the reference condition of external ambient temperature T_{amb}= 30°C, and an internal temperature T_i = 0°C. The refrigerant unit was sized according to technical practice, which suggests installing a cooling capacity from 5 to 10 times the expected steady load. This is necessary to overcome the sudden increases of the cooling demand given by the doors opening and the pull down of the refrigerated box after a period of inactivity, resulting in a design nominal capacity of 2.00 kW at reference condition.
The solar panels were sized to use the available roof surface, accordingly to the sizes available into the market. The built prototype uses 6 modules of 1375 mm X 665 mm, for an overall nominal power of 940 W. Table 1 reports the main components specifications.

3. PRELIMINARY EXPERIMENTAL DATA

The refrigerated box and a first prototype of the solar aided refrigeration system was tested at the ATP test station, located at the Construction Technology Institute of the National Research Council in Padua (Italy). Experimental activities were carried out to verify the consistency of the system components and to provide experimental data for the numerical model validation.
As a first step, the insulated box was characterized in terms of global insulation capabilities. These measurements, following the criteria presented in the Annex 1 of the ATP guidelines, will be used to validate the numerical model of the box. The global heat transfer coefficient was also necessary to estimate the steady condition cooling demand of the refrigerated box.
Functional tests were then conducted maintaining the insulated box in the controlled environment of the ATP test facilities (Fig. 2), while the solar generators were placed horizontally outdoor (Figure 3). The test was aimed at demonstrating the capabilities of the solar system to satisfy a significant part of the cooling unit consumption under steady conditions. The tunnel was set to maintain a constant ambient temperature of 30°C while the cooling unit ON condition was set to +2°C with 3°C hysteresis, obtaining an average internal temperature of +0.4°C during the test. Solar generator were kept under the full light during the whole test that was performed the 26th of February. The test started at 11:10 AM and ended at 4:30 PM. At the beginning of the test battery were fully charged.
Figure 4 reports the power consumption of the refrigeration unit and the power provided by the photovoltaic panels. Figure 5 reports the nominal battery charge in percent, obtained comparing the net energy extracted from the battery to its nominal capacity.
Despite the refrigerated box was subject to a summer condition and the solar panel were instead exposed to a winter radiation, with a maximum altitude of 36°, the solar generators provided all the energy required to run the refrigeration unit for the most of the test (from 11:00 AM to 3:00 PM). The sudden decrease in the solar power after 3:00 PM was caused by the presence of light clouds and the decrease of the sun altitude over the horizon. Under these conditions, the system was able to run on batteries for one and a half hours, using 40% of the battery nominal capacity.



Figure 2: Tunnel experimental set-up



Figure 3: Solar generator set-up

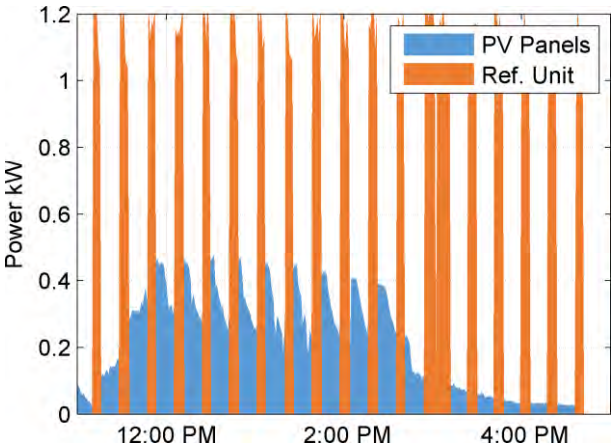

Figure 4: Power flows during the preliminary test

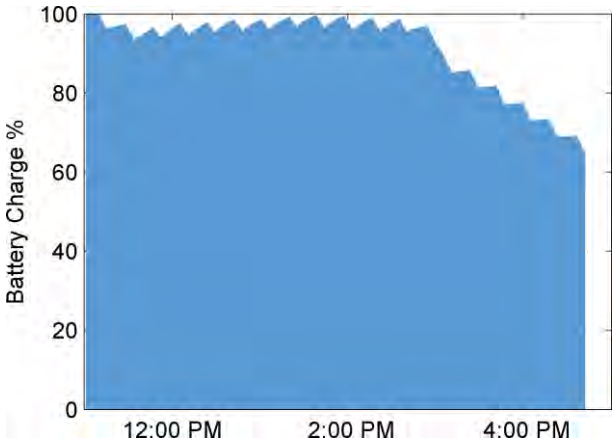

Figure 5: Nominal battery charge level

4. NUMERICAL MODEL

As the preliminary test demonstrated an interesting potential of the solar system in supporting the cooling unit, numerical simulations were conducted to forecast the system performance during a delivery mission in hot climate.

Numerical simulation were carried out using COMSOL Multiphysics (v5.4). The 3D model is presented in Figure 6. The model was develop to reproduce all the geometrical features of the tested box, including the wooden layer and beams to reinforce the floor; the structural iron plates anchoring the hinges and the gaskets on the doors contours. As the model was intended to address the global energy balance of the system, a CFD model of the internal air was unjustified when comparing the improvement on the accuracy and the computational cost. For this reason, the internal air was modelled using a 0D capacitive model represented by its average temperatureT_i, which was solved by means of its energy balance.

Unstructured tetrahedral grid was used for the main volumes of the model. Thin elements were discretized using local extrusion resulting in prism elements, to maintain a high grid quality.

Grid sizing was assessed during preliminary study. The experimental global heat transfer coefficient $K = 0.36$ W m^{-2} K^{-1} was used to validate the model, as well as the sensitivity of the numerical results to the grid size. The global values (average heat flux, and K parameter) demonstrated a sensitivity smaller than 1% on the grid size in the range between 300k to 1.5M nodes, with an absolute error on the K value lower than the experimental uncertainty. The grid used for the simulation was then selected to have 700k nodes.

4.1. Equations and Boundary Conditions

The model was set to resolve the heat transfer set of equations under unsteady boundary conditions. The solar radiation was applied on the external surfaces of the model, accounting for the direct, the

diffuse and the reflected solar radiation. The external surfaces were furthermore subject to radiative and convective heat transfer. For the radiative flux, the sky and the ambient temperature were used to quantify this exchange based on the surfaces normal of the horizontal surfaces, assuming for vertical surfaces that both the sky and the ambient temperature contribute with the same weight. External convection was set between the model external surface temperature and the ambient temperature. Heat transfer convective coefficient was assumed as the maximum between the forced convection coefficient (dominant when the vehicle is in motion) and the natural convection coefficient (dominant during low speed and stops).
On the internal side of the 3D model convection was set between the surface and the internal air. The average air temperature was regulated by an ODE imposing the air energy balance (where C_i is the internal air thermal capacity):

$$C_i \frac{dT_i}{dt} = \dot{Q}_{conv} - \dot{Q}_{ev} + \dot{Q}_{inf} \qquad \text{Eq. (1)}$$

This equation accounted for three different heat sources: the convection heat flux removed from the internal walls $\dot{Q}_{conv}$, the heat removed by the evaporator $\dot{Q}_{ev}$ and a last terms accounting for air infiltration $\dot{Q}_{inf}$ (further detail on this will be presented in section 4.3).
The actual cooling unit ON/OFF control system was reproduced by mean of a discrete state variable, with the same set point and hysteresis of the prototype, i.e. an ON set-point at T_i = +2°C and OFF set-point at T_i = -1°C

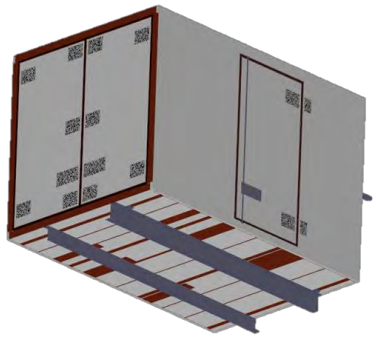

Figure 6: 3D BOX Model

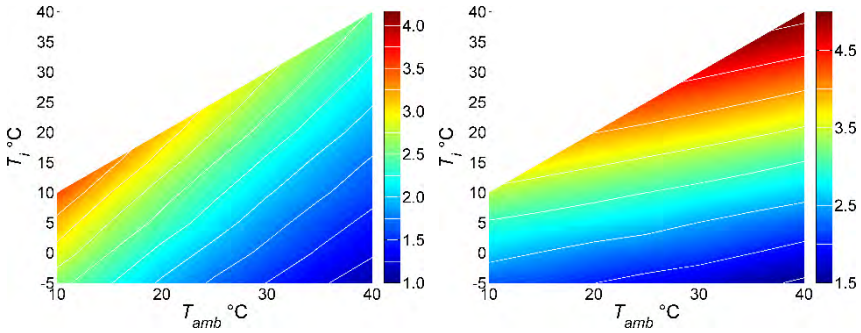

(a) (b)

Figure 7: Cooling unit capacity (a) and COP (b) as function of the internal and the ambient temperature

4.2. Solar Generators and Refrigeration Unit

Solar generators were assumed to be built-in the roof of the insulated box. This assumption has the effect of increasing slightly the cooling need of the refrigerated box in two ways. Firstly, by reducing the insulation thickness of the roof, secondly, by increasing both the surface emissivity and the short-wave absorptance with respect to the white fiberglass composite used for the rest of the external surface (from 0.7 and 0.15 to 0.8 and 0.9 respectively).
The panel's efficiency at standard conditions $\eta_{pv,std}$ and temperature coefficient β_{pv} are given by the product data sheet and are equal to 0.21 and 0.0046 °K^{-1} respectively. The actual efficiency was then evaluated as $\eta_{pv} = \eta_{pv,std}\left[1 - \beta_{pv}(T_{es} - 298\ \mathrm{K})\right]$ where T_{es} is the panel temperature. The electrical converted power was then computed as: $P_{pv} = \eta_{pv} A\left[G_{dh} - \bar{n} \cdot \overline{G_f}\right]$; where G_{dh} is the diffuse horizontal irradiance, $\bar{n} \cdot \overline{G_f}$ is the scalar product between the surface normal and the direct normal irradiance vector and A is the total area of the panels.
The refrigeration unit performances were obtained using an in-house developed simulation tool (Artuso, 2019). An R-134a simple compression cycle with thermostatic valve was considered and the unit components were selected to represent a unit available in the market. Simulation results were then compared against available homologation data sheet in order to check the consistency of the model with the actual performances of commercial units. The refrigeration unit numerical model was then used to map the cooling capacity $\dot{Q}_{ev}$ and the COP for different combinations of T_i and T_{amb} (Fig. 7). The first was used in Eq. 1; the second will be relevant in post process when the unit electrical consumption will be discussed. The evaporator and condenser fans electrical consumption

was also taken into account, which was set to 290W, on the base of commercial units homologation data sheet.

4.3. Mission Profile and Ambient Data

The mission profile was defined to describe a local distribution activity. The standard profiles ECE and EUDC, used for testing of emissions and fuel consumption from light duty vehicles [EEC Directive 90/C81/01], were used to construct the mission profile. Five EUDC cycle, corresponding to a 30 km drive, were used to simulate the rural drive condition between the logistic facilities to the city. Then the urban drive condition was defined as 5 ECE cycles, corresponding to 5 km in 15 minutes. The urban drive was repeated 6 times before a new rural cycle is performed to return to logistic centre. Between each urban cycle, a stop of 5 min was considered.
As the air infiltration is an important load in refrigerated transport, the air infiltration through the doors has to be addressed. Despite the absence of a detailed CFD description of the internal air prevent a full description of the phenomenon, the external air infiltration was included as a source term in the internal air energy equation, according to the model reported by T Lafaye de Micheaux *et al* [2015]. Door opening was then set to happen after every urban cycle, lasting 3 of the 5 minutes of the stop. The morning sequence is reported in Figure 7, starting at 9.00 AM and finishing at 12.15 AM. The same sequence was repeated between 2.00 PM and 5.15 PM.
Refrigeration unit was supposed to be started one hour before the vehicle departure (8.00 AM), to cool down the refrigerated box structure to the transportation temperature.

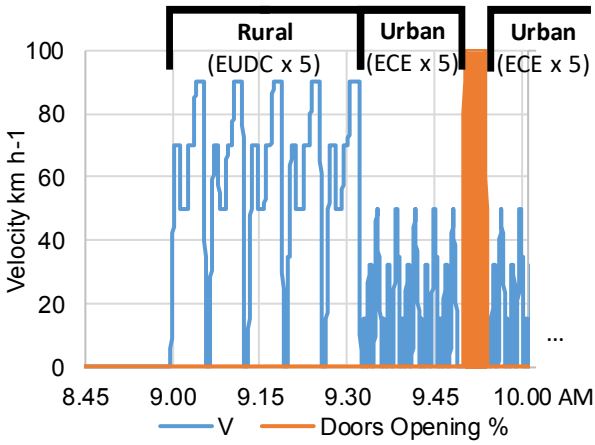

Figure 8: Rural and Urban driving profiles

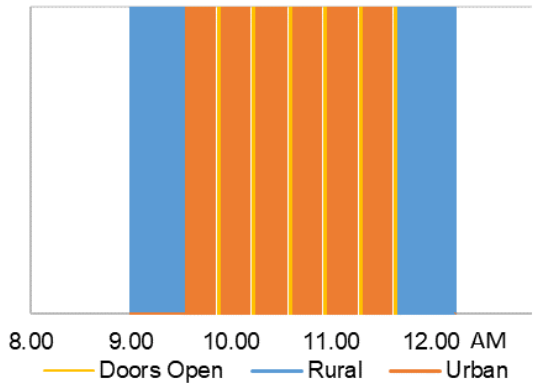

Figure 9: Morning sequence

Simulations were carried out for the same daily mission for different times of the year using as reference climate Athens so to test the system in hot climates. The standard year of Athens was used as reference for the ambient data (Energyplus). Instead of using a precise day to represent each considered month, the algebraic average of the daily trend over the whole month was preferred. Otherwise, results would be affected not only by the seasonal trend, but also by the day chosen for the simulation, as consecutive days can have strong differences in temperatures and sky cover.

5. NUMERICAL RESULTS

The numerical model was solved setting a maximum time-step of 3 seconds. Initialization was obtained in two steps. A stationary run was solved using the ambient data at 5.00 PM. This solution was then used to start a transient initialization run, to clear for the influence of the initial conditions, simulating the refrigerated box during the night before the mission starts, from 5.00 PM to 7.00 AM. Finally, this result set was used to start the actual mission run from 7.00 AM to 6.00 PM.
Results will be presented in the following two sections. First, results obtained for August average day ambient data will be presented. Secondly, the other months will be discussed to assess the impact of the photovoltaic panel on a yearly base.

5.1. Mission Result in August

August was chosen as reference as the most severe month in the year for the refrigerating system in Athens due to its highest average temperature. The ambient temperature and the internal temperature during the mission are reported in Fig. 10, as well as the average air temperature over every mission section (rural road, urban road, stops, and delivery)

Despite the oversizing of the refrigeration unit, the pull down after every door opening is slow enough to cause appreciable variation in the internal temperature. A step increase of the average internal temperature in respect of the driving condition is visible after the first opening (from 0.7° to 1.7°C), and a continuous drift between the stops toward higher temperatures (up to 3.2°C between the 4th and the 5th opening). This oscillation would be reduce if the thermal inertia of the goods were implemented in the model. However, the overall energy balance, thus the time required for the refrigeration unit to remove the infiltrating heat would remain the same. For these reason a larger unit should be considered to safety operate with frequent doors opening under hot climate environmental condition.

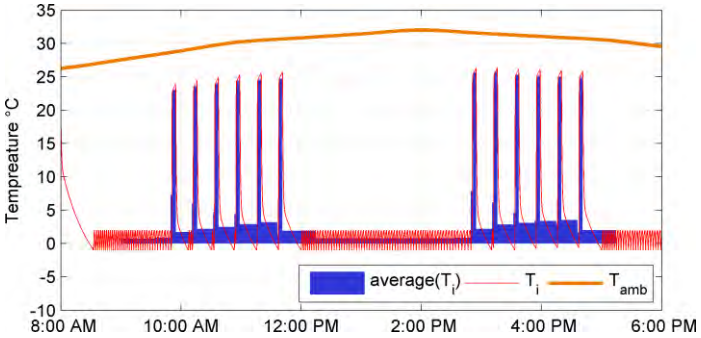

Figure 10: Temperature trend for the month of August

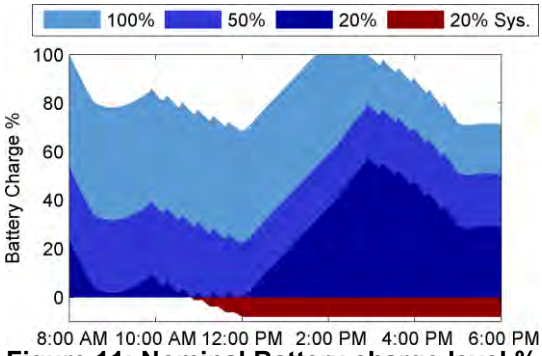

Figure 11: Nominal Battery charge level %

The battery charge status during the mission is reported in Fig.11, for three different initial charge level: 100%, 50% and 20%. Photovoltaic panels produce more energy than the one consumed by the refrigeration unit during long travel periods and the long stop between the two delivery missions. On the contrary, the pulling-down period, where the refrigeration unit is in continuous operation, and the frequent door opening during the delivery phase cause the energy consumption to exceed the production, leading to the partial battery discharge.

The produced energy is greater than the required when the cumulative daily balance is considered. On the other side, the finite dimension of the battery limits this balance, as when the battery is fully charged the energy production had to be limited to the instantaneous consumption of the load. On the other side, when the battery is fully discharged, the system needs to draw the necessary energy from the vehicle generator. The actual daily energy balance depends then on the starting condition of the battery. The battery net energy balance is slightly positive (+0.5%) for a starting charge of 50% and negative (-28.9%) when the battery is fully charged at the start of the mission. For a starting charge of 20%, the high energy request during the morning, causes the full discharge of the battery pack. The refrigeration unit runs then on the vehicle electrical system, for a total equivalent energy of 8.1% of the battery nominal capacity.

Table 2. System main parameters

Month	Energy Consumption kJ	Ideal Energy Production kJ	Battery off-balance %		
			100%	50%	20%
February	1 330	3 184	-0.3	49.6	77.3
April	2 594	5 370	0.0	50.0	80.0
June	5 326	7 088	-4.4	45.6	73.6
August	6 353	6 363	-28.9	0.5	8.6 (-8.1)
October	3 597	3 753	-26.9	6.6	6.6
December	1 448	2 073	-10.7	26.1	26.1

5.2. Yearly results

The same mission described in section 4.3, was run considering the average ambient data of six months over the year. The daily energy consumption, energy production as well as the battery off-balance between the start and the end of the mission are reported in Table 2.
June is the month with the highest production of energy, while august has the highest consumption. The energy production results to be greater than the requested energy by the refrigeration unit for all the considered cases, but the difference is not significant for August to October. For all the considered cases, the battery was capable of sustaining the group, with the exception of August for a low starting charge.

6. CONCLUSIONS

The paper presents the layout of an electric powered refrigeration for insulated trucks aided by photovoltaic generators. Experimental preliminary results demonstrated the feasibility of the system and the advantage given by the solar energy despite the test was performed under unfavourable conditions (summer load on the refrigerated box and winter radiation on the photovoltaic panels).
Numerical simulations were then carried out in order to assess the expected annual impact of the renewable energy on the energy consumption used to power the refrigeration systems. Simulation were carried out assuming a hot climate (Athens) and a short distance delivery mission with frequent stops and door openings. The model results demonstrated that the electrical energy produced by the photovoltaic panels is at least 25% greater than the energy required by the cooling unit during the mission, suggesting that the system can sustain itself without drawing energy from the vehicle alternator.
These results, while remaining encouraging should be interpreted as an optimistic forecast, as in the current model no shading effect was considered, while in actual urban environment building will often stops the direct radiation. More simulations will be carried out neglecting the direct radiation, considering the diffuse radiation only, in order to compare the current result with the worst-case scenario.
Further development of this research will focus on the design of a fully functional prototype including an autonomous control system and the systematic acquisition of data from the field.

REFERENCES

Artuso, P., Rossetti, A., Minetto, A., Marinetti, S., Del Col, D., 2019. Numerical investigation on the thermal performance of a new cooling unit for refrigerated transport application using CO2 as working fluid. Ammonia and CO2 Refrigeration Technologies, April 11-13, Ohrid, Republic of Macedonia.

Bahaj, A.S., 1998. World's First solar Powered Transport Refrigeration System. Renewable Energy, vol 15, 572-6

Bahaj, A.S., 2000. Photovoltaic power for refrigeration of transported perishable goods. Conference Record of the Twenty-Eighth IEEE Photovoltaic Specialists Conference, 15-22 Sept. 2000, Anchorage, AK, USA.

Cavalier, G., Tassou, S., 2011. Sustainable Refrigerated Road Transport. 21st Informatory Note on Refrigerating Technologies, International Institute for Refrigeration.

Bergeron, D., 2001. Solar Powered Refrigeration for Transport Application -- A Feasibility Study. SANDIA REPORT, SAND2001-3753.

Elliston D, Dennis M., 2009. Feasibility of Solar-Assisted Refrigerated Transport in Australia. Solar09, the 47th ANZSES Annual Conference 29 Sept.–2 Oct. , Townsville, Queensland, Australia

EnergyPlus - https://energyplus.net/ Last visit 01/2019

UNEP, 2010. Report of the Refrigeration, Air conditioning and Heat Pumps Technical Options Committee.

Manuscript ID: 1312
DOI: 10.18462/iir.icr.2019.1312

Factors affecting energy consumptions and carbon footprint in refrigerated road transport: a brief review of recent advances in technology, materials and methods

Rita MASTRULLO [(a)], Alfonso W. MAURO [(a) (*)], Girolamo PANOZZO [(b) (*)]
[(a)]
[(b)] Federico II University of Naples, Dept. of Industrial Engineering
P.leTecchio 80 Napoli, 80125, Italy, email: wmauro@unina.it[(*)]
[(c)] Past researcher of the ITC CNR Padova, Italy, email: gialui95@gmail.com

ABSTRACT

In this paper some research related to the thermal insulation of the body, the energy consumption and the environmental impact of the cooling units are presented. The use of new materials such as the aerogels (both at ambient pressure and under vacuum conditions) is considered as an option and discussed in terms of performance, reliability and costs. Concerning usual solutions for the insulating walls based on polyurethane foams, the actual thermophysical properties of the blowing agents used in insulating walls are discussed in the view of the new regulations for the use of F-GAS refrigerants. The methods to calculate the air infiltration rate and radiative properties of the walls are commented. The ageing of the material used for the insulation body is discussed with the relative issues related to the appropriate prediction of the life of in-service units. Concerning the energy consumptions and environmental impact results from works related to the classic option of vapor compression cycles is compared to new ones such as cryogenic units in terms of total environmental impact, running costs and feasibility. Finally, works discussing new alternatives for refrigerants in vapor compression systems are presented.
Keywords: Refrigerated Transport, Carbon Footprint, Refrigerants, VIP, Ageing.

1. INTRODUCTION

Roughly one-third of the edible parts of food produced for human consumption get wasted globally and around 360 million tons of perishable foods are lost each year due to an insufficient use of refrigeration (IIR, 2009). Some recent estimates indicate that about 795 million people in the world (around 10% of the whole population worldwide) were undernourished in 2014-16 (FAO 2015).
One technological step to reduce this trend is to widespread the use of refrigerated transport, especially in developing countries, and to have an appropriate performance to guarantee food preservation.
The terrestrial fleet of refrigerated transport equipment in the world amounts to 4 million of in-service vehicles including vans, trucks, semi-trailers and trailers, with 68% of the whole fleet concentrated in developed countries (Michineau et al., 2014).
In the European Union the refrigerated transport market is already mature and it is assessed to some 1.1 million of equipment of which 150 000 belong only to France (1 over 420 inhabitants), 120000 to Spain and 110000 to Italy; UK has almost 84000 vehicles. The situation is quite different in Asian countries: in India there are 9000 vehicles due to different methods for food preservation. In China there are 150 000 refrigerated vehicles, that means around one over 9500 inhabitants; this number is increasing quickly due to the increase of the refrigerating market (Capo et al., 2018). These numbers are changing consistently: a study by IIR (2009) pointed out that the road refrigerated transport should increase by 2.5% per year until 2030.

Refrigerated transport, as well as other type of refrigerating systems, is partially responsible for ozone depletion and global warming, because of the refrigerants used and the energy consumption of refrigerating equipment. The environmental impact is mainly due to the energy consumptions of the engine and of the cooling system, then to refrigerant leakages (Coulomb, 2008).
Nowadays different aspects are affecting the energy consumptions and carbon footprint like: the standards to comply with and materials available for the insulated vehicle, technologies for the cooling system, refrigerants available in the system. Some recent research trends are reported in the paper.

2. THERMAL LOAD

To guarantee appropriate performance of systems one step is the use of standards. The ATP, Agreement on the international carriage of perishable foodstuffs and on the special equipment to be used for such carriage (ATP, 1970), which has been in force since 1976, regulates the international transport of certain foods. The same parameters are present in the ISO standards for insulated containers (ISO 1496/II), in the Australian standards (AS 4982-2003), in the "Fiches Transfrigoroute" and in the new EU standards CEN.
ATP provides effective rules for the certification of the refrigerated vehicles used for land and rail transport of certain kind of foodstuffs, with the purpose of ensuring their safety.
ATP defines an overall coefficient of heat transfer (*K* coefficient), which represents the insulating capacity of the equipment, by the following formula:

$$K = W S^{-1} \Delta T^{-1} \qquad \text{Eq. (1)}$$

where W is the thermal capacity required in a body of mean surface area S to maintain the absolute difference ΔT between the mean inside temperature T_i and the mean outside temperature T_e, during continuous operation, when the mean outside temperature T_e is constant.
The factor K is influenced by thickness of the walls and thermal conductivities of the compound materials used for the wall, whose key part is made by an insulating material.
In some countries the width of vehicles is limited: for example in Europe ATP vehicles has a maximum width of 2.6 m. Since the refrigerated transport is palletized in Europe (combining pallets one can get 2.4 m), the effective thickness available for lateral walls is limited to 100 mm.
Some manufacturers, in order to reduce the K value, are increasing the thickness of the other walls (mainly the roof and the floor, as it is difficult to increase the front and rear wall thickness without affecting the ease of movement of the rear door and the correct positioning of the refrigerating unit on the front wall). (Panozzo, 2009)
Concerning the insulation materials, actually, the wall are mostly insulated by using foams expanded by blowing fluids with a high molecular weight. Over the years the limitations in the use of fluorinated gases have caused a reduction of the thermal conductivity of the expansion gases (see Fig. 1).
Limitations in the size of the walls and the thermophysical properties of refrigerants used for the expansion are pushing to search for new materials.
One option is the use of aerogel. The thermal conductivity of the monolithic aerogel is around 0.018 W/mK at ambient pressure (1.01 bar). When the sample is evacuated to pressures below 10 mbar (vacuum insulated panels, VIPs), the gaseous conductivity is 0.007 W/mK (Caps and Fricke, 2004). Hammond and Evans (2014) have presented a paper to study the viability of the use of vacuum insulating panels in the refrigeration sector. As reported in Fig. 2, the thermal conductivity of such a system is much less than the one of polyurethane or standard silica aerogel. In their study, they demonstrated that the economical convenience (based on the assumed prices for a non conventional technology) is possible, if the life of the component is long enough to recover the extra cost via the energy consumption reduction. In the case of refrigerated transport, the

mechanical stresses due to load and unload of the goods and the vibrations, is a factor which can compromise the vacuum causing damage to the sealing or contamination of the goods with aerogel which are toxic (Prakash et al., 2014). For the moment the most viable solution is the use of polyurethane foams. In the future some other solutions are possible: the use of rare gases (Kripton and Xenon, whose thermal conductivity is very close to that of R11: as example see Panozzo 2011) and the use of foams whose cells shall have nano-dimensions.

One important aspect related to the use of such insulation material is the deviation of the real performance from the ones of the baseline (prototype tested according to ATP) both at the starting of use and over the time. Deviations of the K value of the products from the original prototype can appear due to not perfectly repeatable production process or small differences in the real geometry allowed by the ATP agreement. This aspect has been studied by C. Capo et al. (2018), which have compared experimental data of the K values measured on insulated containers at few days after production and the reference value of the corresponding prototype. They have demonstrated that deviations of up to 10%-15% are possible in the K value between the prototype and the actual vehicle. Sometimes this deviation can give K values over the limits allowed by the ATP agreement, stressing the importance of an extension of the agreement application to all the vehicles since the first year. In the same paper, the authors compared the effective value of K with the one expected from the use of the insulating material without any thermal bridge or accessory. The influence of the thermal bridges due to load-bearing elements or to the insertion of the cooling system is detrimental to the K value up to 20% in the experiments they reported.

Nowadays new techniques could allow to define methods to detect thermal losses in some specific point, like using the thermography to map the heat flux at the wall (Bison et al., 2015). Also, a recent paper investigated on the detection of defects and thermal bridges in insulated truck box panels by active infrared thermography (Lei et al., 2017). They suggested the use of compressed air method, instead of classical heating method, for defects identification.

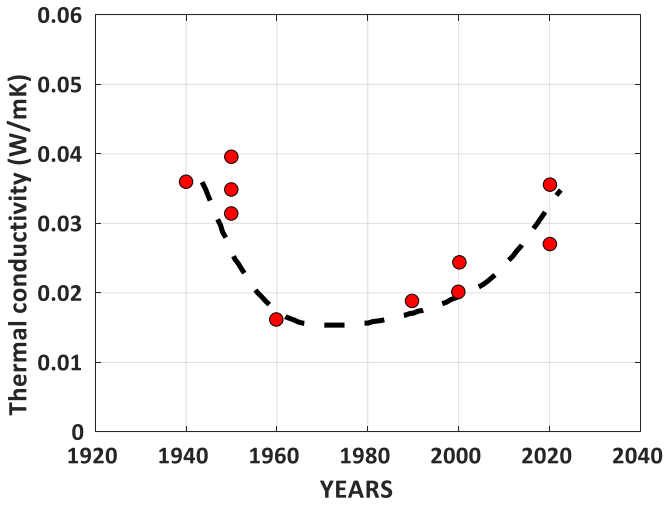

Figure 1: Trend of thermal conductivity of expansion gases used in foams for the road refrigerated transport

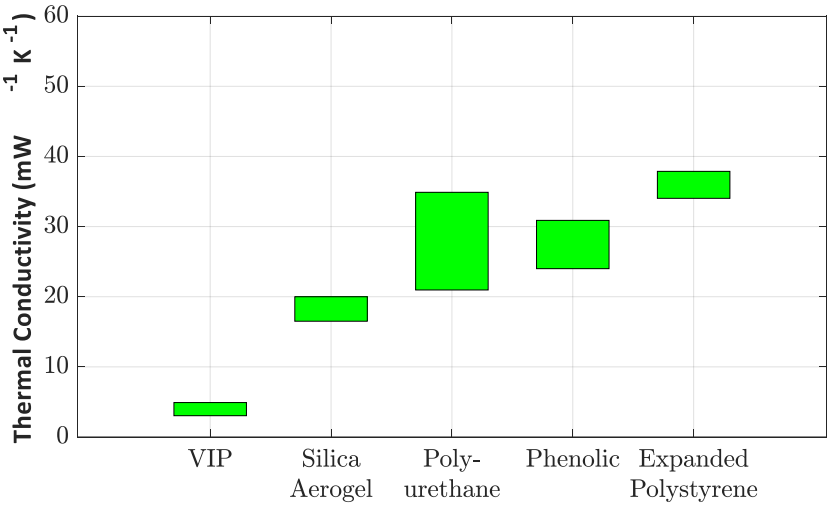

Figure 2: Comparison of thermal conductivities of insulating materials (Hammond and Evans, 2014)

Another important concern is the “ageing” of the insulation material: after the foaming the gas trapped into the foam cells tends to migrate due to concentration difference with the environment, mechanical vibration, damages and environmental effects. A parameter measuring the percentage variation of the K value over the time is defined as a possible measure of the ageing. In works by Boldrin et al. (1990, 1993) and Panozzo et al. (1995, 1999) the authors presented an amount of data statistically relevant related to the ageing of different categories of vehicles for the refrigerated transport working under different conditions (types of goods, working temperatures). The analysis of the data collected at the ITC-CNR of Padova allowed to isolate the causes of the ageing over the time. The main causes are related to: permeability of the foams to the gases (air and blowing agents), condensation of water into the foam cells, increasing of the percentage of the open broken cells (Klempner and Frisch, 1991).

Those data were discussed statistically in a work by Giuri (2006) and are reported in Fig. 3. In that Figure, the continuous line is representing the trend of the curve predicted by a model based on gas migration. The major effect was the migration of the air from the environment into the closed cells of the foam (the opposite migration of the blowing agent to the environment is too slow due to the larger dimensions of the blowing agents molecules in comparison with the molecules of the air, like O_2, N_2, CO_2, H_2O). It has been seen from the comparison with experimental results from Figure 3 that only few data are following the theoretical trend: those data are related to vehicles working with solid structures, which ageing behavior is less affected by mechanical stresses due to the usage.

The analysis of the correlation between the causes of the ageing and the relative effects has been deepen by Capo et al. (2018). The authors showed that one important aspect is the deviation of the real K value at the starting of the product with respect to the baseline value of the prototype, which is conventionally chosen to calculated the ageing parameter.

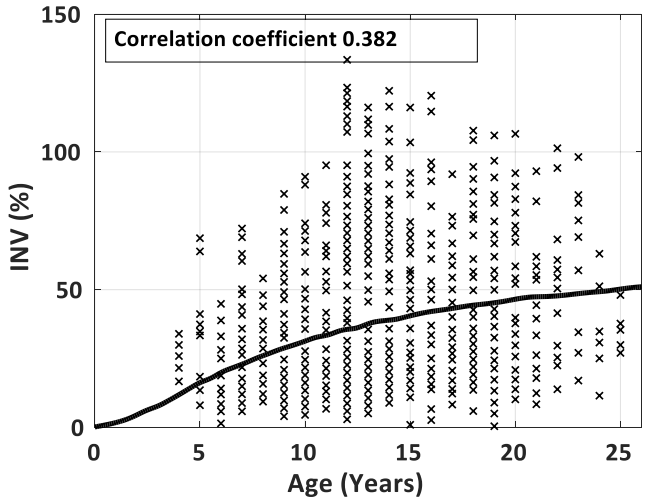

Figure 3: Percentage variation of the factor K over the time (INV%). Black, continuous line: theoretical curve based on diffusion of gases trapped in the cells under certain conditions typical for a class of refrigerated vehicles. Scattering of data based on realmeasurement on a corresponding class of vehicles (data collected at ITC-CNR of Padova)

Currently, new researches are ongoing to isolate the single effects of ageing and to have measurement of K values of prototype vehicles to avoid the errors in the ageing measurement. This would bring to new predictive tools which can improve the prediction of the K value over the time in order to estimate when the K value should go over the one allowed by standards, enabling the checks by certified institutions of the real value of the K factor with dynamic time interval and not the ones actually prescribed.

Other important contributions to the thermal load are the ones related to the radiation and the air infiltration, not directly accounted by the ATP regulations, whose estimation is of primary importance for the correct sizing of the system, the achieving of the desired thermal conditions (and indirectly for the extra energy consumptions related to ON-OFF cycling in direct expansion systems).

During the real operation (delivery or transport) it is important to consider radiation contribution only for slow speeds or for stopping. Concerning radiation contribution its evaluation is firstly related to the radiating conditions under real operation, which are often unknown. Once appropriate estimate of the climate data are available the second step is to know surface properties of the walls: surface optical properties of the surfaces can change due to dirty, but the estimation of the thermal load can be made on clean surface. About this topic the paper by Dragano et al. (2009) defined and experimentally validated a methodology to estimate the optical absorption coefficients of a sandwich panel used for the insulation of refrigerated vehicles. In particular, the optical absorption coefficient measurement is based on the measurement of temperature carried out both on the natural colored surface of the panel and in a zone painted on the purpose with a black varnish. The processing of the data under transient conditions allowed a data reduction to deduce the unknown surface property via a comparative method.

Concerning air infiltration its contribution to thermal load is particularly important, when the route includes frequent stops for the delivery of the goods. Several works have been made in the past to estimate the thermal losses due to air infiltration in refrigerated boxes. A recent study, specifically related to the refrigerated transport, has been proposed by Lafaye De Micheaux et al. (2015). The authors presented experiments carried out for different temperatures and different aperture ratios and found out two type of flows causing the infiltration: a buoyancy driven flow (density-driven flow which gives birth to an important heat load peak) and a boundary layer flow (quasi steady-state natural convection over the inner wall of the truck). They demonstrated the application of appropriate CFD models to predict the mass and momentum transfer; also proposed analytical

models for both the two kind of flows able to predict the heat flow rate with a good agreement with experiments.

3. ENERGY CONSUMPTIONS AND ENVIRONMENTAL IMPACT

The energy input to the cooling system depends on the useful energy required by the application (the thermal load multiplied by the number of hours of usage) and the coefficient of performance of the cooling unit itself. The thermal load have been discussed previously. Here a brief report of some recent researches on the factors affecting the energy consumption and the environmental impact is reported.

Raiet al. (2017) presented a paper about the approaches to reduce the energy consumption and the environmental impacts of road transport. In the paper they considered a diesel driven vapor compression system as the baseline for the cooling system and compared the results with a different option (cryogenic system). The use of a liquid cryogen (carbon dioxide or nitrogen) is considered as an option due to the reduced direct environmental impact of such fluids.

Both the production and operation emissions have been considered. The results showed a reduction up to 66% of the production emissions of the baseline solution with respect to the cryogenic system; this is mainly due to the energy required to produce the liquid refrigerants. Instead, when the total emissions are considered, all the solutions seem to be equivalent with small differences within the margin of error of the assumptions made. A drawback of the cryogenic systems is the volume required of liquid, which is between 5 and 40 times larger than the volume required for the diesel. Adding also considerations about the effective availability for the refilling of the tank, at the moment there are some barriers to make the cryogenic systems competitive for the road transport. The costs to run the two solutions are similar, even if the investment cost for the non-standard solution is higher at the moment.

The adoption of different solutions, like the cryogenic one, could become interesting depending on the evolution of the market of the refrigerant to be used in vapor compression system.

An interesting discussion about the comparison of three possible fluids (R404A, R410A and CO_2), as refrigerants for vapor compression systems used in refrigerated transport, have been compared in the paper by Wu et al. (2013). The analysis have considered a complex model to account for LCCP calculations under potentially real operating conditions (different climates, different type of vehicle, specific refrigerant leakages). They have found that often the R404A is not the best refrigerant in terms of LCCP; CO_2 is a good option when ambient temperature is low.

More recent regulations about the use of F-GASes have caused important changes in the refrigerant market with different option available (HFOs and HFC mixtures with intermediate values of GWP). Zilio et al (2015) considered the potential performance of three potential options for this field, even if other refrigerants appeared in the meanwhile and several questions about the technical reliability of compressors under the severe conditions of the refrigerated transport are still open.

An important consideration about the energy consumption is related to the strategy used to define the route. Even if the problem is well known for the optimization of the fleet usage, very few works have been conducted about the optimization of the environmental impact and/or of the energy consumption. A recent paper by Meneghetti et al. (2018) have posed the energy consumption minimization as target to define the optimal route for a refrigerated transport. In the conclusions of the study, the authors pointed out that while the minimum travel distance is usually the best solution due to the greater impact of travel requirements on total fuel consumption with respect to refrigeration ones, a preferred direction to run the circuit has been highlighted, depending on the different outdoor temperature of time slots triggered during distribution.

4. CONCLUSIONS

In this paper a brief resume of some recent papers concerning the methods, the technology and the research trends related to the thermal load containment, the energy consumption and the environmental impact is presented.
The aerogel based materials are an excellent option vs the polyurethane foams, but they actually suffers of a major cost, the difficulty to guarantee the vacuum once used in a mobile system (due to vibration) and the toxicity due to the risk of contamination of the good with the dust.
The use of sandwich panels is still the more common option: the thermal performance of such a system is downgrading due to the limitations in the use of HFC refrigerants with large molecular mass, which have lower values of the thermal conductivity. For a proper choice of the system sizing the thermal load of the air infiltration and of the radiative term to the thermal load have to be considered: recent papers proposed interesting method and models to do the calculations.
New models have been proposed in literature to refine the estimation of the carbon footprint under real conditions, and in particular the direct and indirect contributions. Based on one model predictions, the use of cryogenic systems with CO_2 should be equivalent in terms of total environmental impact to a vapor compression one operating with R404A. The vapor compression systems should be still the less impacting option when low GWP refrigerants will be used.
For future researches more accurate data of ageing should be collected to improve the models predictions of the ageing and of the energy consumptions under real conditions including, potentially, the ageing effect.
Also, the accuracy of the models which describe the energy performance of the refrigeration unit should be adequate to the level of accuracy expected for such a kind of studies.
Data of the energy consumptions under real conditions should be related to environmental and operational data to allow validation of models.

REFERENCES

Bison, P., Bortolin, A., Cadelano, G., Ferrarini, G., Lei, L., Maldague, X., Rossi, S., 2015. Mapping of the heat flux of an insulated small container by infrared thermography, 2929-2935, doi:10.18462/iir.icr.2015.0314.

Boldrin, B., Minotto G., Panozzo, G., Toniolo, B., Varotto, G., 1990. Ageing of insulated vehicles: statistical elaboration of test result. Proceedings of Commissions B2, C2, D1, D2/3, Dresden, Germany, IIF/IIR, 839-845.

Boldrin, B., Minotto., G., Panozzo, G., Toniolo, B., Lanza, W., Florio, G., Jacobini, A., Sallusti, L., 1993. New data about ageing of insulated vehicles in service: a statistical analysis. Proceedings of the Commissions B1, B2, D1, D2/3, Palmerston North, New Zealand, IIF/IIR, 555-564.

Capo, C., Bourez, D., Cavalier, G., 2018. Le parc d'engins de transport sous température dirigée en 2017. Les défis et les tendances. Revue Generale du Froid

Capo, C., Latchan, F., Michineau, T., Petit, J.M., Revellin, R., Bonjour, J., Cavalier, G., 2018. Factors affecting the ageing of refrigerated transport equipment. In: 5th IIR Conference on Sustainability and the Cold Chain, Beijin, China.

Caps, R., Fricke, J., 2004. Aerogels for Thermal Insulation. In: Aegerter M.A., Mennig M. (eds) Sol-Gel Technologies for Glass Producers and Users. Springer, Boston, MA.

Coulomb, D., 2008. Refrigeration and cold chain serving the global food industry and creating a better future: two key IIR challenges for improved health and environment. Trends in Food Science & Technology 19, 413-417.

Dragano, A., Rossi, S., Bison, P., Panozzo, G., 2009. Experimental evaluation of the optical absorption coefficient of a sandwich panel for insulated vehicles. Quant. InfraRed Therm. Journal 6 (2), 207-223.

Dupont, J.L., 2009. 5th IIR Informatory Note on Refrigeration and Food: The Role of Refrigeration in Worldwide Nutrition.

Giuri, S., 2006. Statistical analysis about the ageing velocity the thermal characteristics of insulated vehicles. Degree Thesis. University of Padova DFT. 10 March.

Hammond, E.C., Evans, J.A., 2014. Application of Vacuum Insulation Panels in the cold chain - Analysis of viability. Int. J. Refrigeration 47, 58-65.

Klempner, D., Frisch, K.C., 1991. Polimeric Foams. Hanser Publishers, p. 41.

Lafaye De Micheaux, T., Ducoulombier, M., Moureh, J., Sartre, V., Bonjour, J., 2015. Experimental and numerical investigation of the infiltration heat load during the opening of a refrigerated truck body. Int. J. Refrigeration 54, 170-189.

Lawton, A.R., Marshall, R.E., 2007. Developments in refrigerated transport insulation since the phase of CFC and HCFC refrigerants. In: Proc. 22nd ICR Conference, Beijin, China.

Lei, L., Bortolin, A., Bison, P., Maldague, X., 2017. Detection of insulation flaws and thermal bridges in insulated truck box panels. Quant. InfraRed Thermogr. Journal 14 (2), 275-284.

Meneghetti, A., Da Rold, G., Cortella, G., 2018. Sustainable refrigerated food transport: searching energy efficient routes. IFAC-PapersOnLine 51 (11), 618-623.

Michineau, T., Cavalier, G., Devin, E., 2014. Evaluation of French fleet of refrigerated equipment. Proceedings of the 3rd IIR International Conference on Sustainability and the Cold Chain, London, United Kingdom.

Panozzo, G., 1999. Parameters affecting the ageing of the insulated vehicles. In: XX International Congress of Refrigeration, Sydney, Australia.

Panozzo, G., 2009. Frozen Food Transport. Frozen Food Science and Technology, 276-302.

Panozzo, G., Boldrin B., Minotto, G., Toniolo, B., Biancardi, N., 1995. Ageing of insulated vehicles: theoretical model and experimental analysis. Proceeding of the 19th International Congress of Refrigeration, Den Hague, Netherlands, IIF/IIR, Volume II, 583-589.

Panozzo, G., Rossi, S., Cuogo, G., Cuccato, G., Franceschi, M., 2011. News solutions for insulated boxes. In: Proc. 23rd ICR Conference, Praha, Czech Republic.

Rai, A., Tassou, S.A., 2017. Environmental impacts of vapour compression and cryogenic transport refrigeration technologies for temperature controlled food distribution. En. Conv. Manag. 150, 914-923.

Thapliyal, P.C., Singh, K., 2014. Aerogels as Promising Thermal Insulating Materials: An Overview. Journal of Materials, Article ID 127049, 10 pages.

The State of Food Insecurity in the World. FAO 2015

United Nations Economic Commission for Europe, Inland Transport Committee, 1970. Agreement on the International Carriage of Perishable Foodstuffs and on the Special Equipment to be used for such Carriage. Geneva: United Nations. Including amendments thereto up to Sept 2003. p. 81.

Wu, X., Hu, S., Mo, S., 2013. Carbon footprint model for evaluating the global warming impact of food transport refrigeration systems. J. Cleaner Production 54, 115-124.

Zilio, C., Mancin, S., Brown, J.S., Longo, G.A., 2015. New refrigerant options for R404A replacement in truck refrigeration systems. In: ICR 2015, Yokohama, Japan.

Manuscript ID: 1407
DOI: 10.18462/iir.icr.2019.1407

Experimental investigation of a Multi-Temperature Insulation Box with phase change materials for cold Storage

Xu Xiaofeng[(a)] Zhang Xuelai[*(a)] Liu Sheng[(b)]

[(a)] Institute of Cool Thermal Storage Technology, Shanghai Maritime University, Shanghai, 201306, China; [(b)]Vegetable Research Center of Beijing Academy of Agriculture and Forestry Sciences, Beijing, 100097, China.

ABSTRACT

Cold chain transportation is an effective means for LTL shipping, specifically for perishable items over long distances. To improve the economy of logistics and ensure the quality of refrigerated transportation of fruits and vegetables, two multi-temperature zone insulation boxes with different phase change materials (PCM) were designed in this work for cold storage technology, which included 87% $C_8H_{16}O_2$ (n-octanoic acid) + 13% $C_{14}H_{28}O_2$ (myristic acid) as PCM1 and H_2O + 0.03 g/mL $C_6H_7KO_2$ (potassium sorbate) as PCM2. The experimental results showed that the phase transition temperatures of these phase change materials were 7.1 and -2.5 °C, the latent heats of phase change were 146.1 and 256.2 J/g, and the thermal conductivities were 0.2832 and 0.9427 W/(m•K), respectively. After 100 cycles, the cold storage materials exhibited good performance with no supercooling and a stable phase change platform. An insulation box temperature test system was established using good supply practice (GSP). The experimental results reveal that temperature zones 2 (medium zone) and 3 (low zone) of the insulation box can be kept cold at 7~9 °C for about 13 h and at -2~0 °C for about 14 h, respectively. The smaller warm temperature zone 1 of the insulation box maintained coolness at 7~8 °C for about 19 h, while warm zone 2 kept cold at 0 °C for 16 h. The research findings provide support for further design and optimization of insulation boxes for cold storage in cold chain logistics as well as the application of cold storage technology in the cold chain transportation of fruits and vegetables.

Keywords: cold chain; phase change cold storage; multi-temperature zone; vacuum insulation panel

1. INTRODUCTION

Perishable items, such as vegetables, fruits, meat products, seafood, vaccines, and other medicines, often travel long distances from the production to processing locations. For example, in winter, fruit from Hainan Province in Beijing, China, is transported more than 2,700 kilometers to various distributors. Such lengthy transportation is called “cold chain logistics,” in which a decrease in the quality and quantity of perishable foods and medicines is inevitable [1]. In China, the loss rate of fresh food during transportation is as high as 20-25%, far higher than the transport loss rate of 5% in developed countries [3-4]. However, China is the world's largest producer of perishable foods, and the cold chain industry has also brought enormous benefits to China's economic development over the past 15 years. Therefore, establishing an impeccable logistics system and accurately controlling the temperature during transportation is the key tois the key to prevent food and medicines from spoiling [5]. Cold chain transportation is divided into air

transportation and ground transportation. Air transportation is highly efficient and reliable, but requires high costs. Ground transportation is further divided into railway and road transportations. Comparatively, railway transportation faces difficult scheduling issues, while road transportation is the most used method because of its convenience, high flexibility, and low cost.

From 2010 to 2015, Chinese registered refrigerated transport trucks increased from 26,000 to 81,000 [6]. Several cooling methods are implemented into refrigerated trucks, which include: (a) mechanical compression refrigeration uses independent or independent cold storage units to provide refrigeration capacity; (b) cold plate implements phase change materials to store cold energy; (c) liquid nitrogen source or dry ice utilizes food liquid nitrogen source type or dry ice vaporization to cool food; and (d) LNG (liquefied natural gas), which is used as fuel to recover cold energy. At present, the main refrigerated truck transportation method in the market is mechanical compression refrigeration, yet it faces unit maintenance and refrigerant pollution problems [7]. Cold storage refrigerated transport, which incorporates a phase change material to cool food and medicine, is convenient and flexible, has precise temperature control, and does not require a refrigeration unit for transportation. Cool storage technology is based off a peak-to-valley electricity price difference to achieve economical purposes. Table 1 compares the performances of mechanical compression refrigeration, cold storage cold chain and dry ice cold chain transportation methods.

Table 1 performance comparison of different modes of cold chain transport

Refrigerated car type	Mechanical	Cool storage	Dry ice
Cooling capacity	The minimum temperature is about -20° C, the cooling capacity depends on the size of the car body, generally 1kw~12kw	The cooling temperature depends on the melting temperature of the phase change cold storage material.	Dry ice type can reach -20 °C
Temperature adjustment	The temperature controller can be adjusted from -20° C to 15 °C.	Use different phase change storage materials to change the temperature	No temperature control device
Carrying efficiency	Low load carrying efficiency	Carrying efficiency is higher than mechanical	The coolant occupies the bearing space, and the load carrying efficiency is lowered.
Pre-cooling time	Mechanical pre-cooling time as a benchmark for comparison	When the regenerator is frozen, it is pre-cooled at the same time. The freezing time is longer than the mechanical freezing time, but the nighttime operation is more, so the impact is less.	The coolant is unevenly mixed in the upper part and the lower part of the warehouse, the pre-cooling is incomplete, and the pre-cooling time is long.
Equipment cost	Usually the equipment costs are higher	Cheaper than mechanical	Equipment costs are cheaper
Usage fee	Higher fuel and repair costs	Use nighttime low valley power, lower usage fees	Higher cost of coolant (ice or dry ice)
Other	Noisier when used	No noise or low noise (when there is a fan)	No noise

Much research has focused on phase change materials to store large amounts of latent heat, which is

released during transportation [18-15]. The most used regenerative logistics transportation equipment is the cold storage insulation box due to its environmentally friendly sealing, flexible size, excellent thermal insulation performance, and flexible loading mode. Insulation boxes are also an effective tool for short-distance transportation and preservation of fruits and vegetables [16]. However, among the phase change materials currently developed, inorganic materials face supercooling and phase separation problems, while organic materials have low thermal conductivity [17]. Thus, several researches have studied how to avoid these shortcomings and rationally use phase change materials. For instance, Yoram Kozak developed transportation equipment that combines phase change materials with thermal insulation materials and analyzed its thermal properties to optimize its structure and size [18]. Three phase change materials were prepared by Yu-Chu M, and the influence of different melting points on food was investigated by cold chain transportation equipment [19]. Xu combined nano-phase change materials with the insulation technology of a vacuum insulation panel to develop cold chain logistics transportation equipment that can effectively maintain cold temperatures for 87 h [20]. In a previous study, we found that the new vacuum insulation panel technology can greatly reduce the thermal conductivity and increase cooling time, which is advantageous over traditional polyurethane insulation materials that have large thermal conductivity and detrimental pollution [21].

Another research direction of cold storage cold chain logistics transportation equipment is the multi-temperature co-matching mode. In the actual cold chain logistics transportation, there are many waste-free logistics resources, which that can greatly reduce the economy. In order to make up for the shortcomings of traditional cold chain logistics that cannot be “mixed”, multi-temperature zone transportation equipment has become a hot spot ofmajor research focus [22]. Liu Guanghai et al. [23] constructed a multi-temperature zone refrigerated truck model and analyzed the effect of seepage on the internal temperature field. Zhao Xiuhong et al. [24] designed a mechanical compression multi-temperature zone insulation box, and used FLUENT to simulate the temperature field.

According to different logistics distribution temperature zones, the independent research and development of cold storage materials and vacuum insulation panel technology was coupled to form a multi-temperature zone cold chain logistics transportation equipment. in this work. A three-dimensional unsteady model was established to analyze the temperature fields in different regions. The refrigerating equipment is equipped was supplied with a GPRS wireless remote temperature monitoring system, and which allows the user can to remotely and remotely know their cord temperature change changes of the transportation product through a mobile phone terminal. The incubator temperature test system was established by using the good supply practice (GSP) to verify the feasibility of the cold storage insulation box. The research results solve the problem of suggest that our proposed insulation system avoid less than load (LTL) logistics and multi-temperature co-coordination problems, reduce logistics cost and costs, allow precise temperature control, and ensure the quality of fruits and vegetables, further optimize and. The optimized design the insulation box of cold storage, and in-depth study and of the cold storage insulation box indicate its promising application of in cold storage technology in of fruit and vegetable for cold chain logistics for reference.

2. MATERIALS PREPARATION

The cold chain transportation equipment designed in this paperwork has three temperature zones. The temperature zone 1 is the normal temperature zone for transporting dry foods that do not need to be refrigerated. The temperature zone 2 is the medium temperature zone, and the refrigerating temperature is with temperatures between 7~10 °C. It can be used, which is best for refrigerating bitter gourd. Winter, winter melon, pumpkin, yam, and other vegetables; temperature. Temperature zone 3 is low temperature the medium zone, refrigerating temperature is that ranges from -3~- to -1 °C, can be used and is best for

refrigerating spinach, celery, apple, coconut, and other fruits and vegetables. The refrigerating equipment adopts self-developed phase change cold storage materials were adopted as the refrigerating equipment, and phase change materials of different temperature ranges were developed according to the requirements of the different temperature zones.

The chemicals used in the experiment, such as $C_8H_{16}O_2$ (n-octanoic acid), $C_{14}H_{28}O_2$ (myristic acid)), and $C_6H_7KO_2$ (potassium sorbate), are all produced bywere of pure analytical grade and obtained from Sinopharm Chemical Reagent Co., Ltd., and the purity is analytically pure. The latent heat value of the phase change was measured by differential scanning calorimeter (DSC (, 200F3 type, temperature accuracy < 0.1 °C, thermal enthalpy accuracy < 0.1%), and the thermal conductivity was measured by a Hot Disk (TPS2500 type, accuracy < 2%).

The modified low-temperature phase change material was subjected to 20, 50, and 100 cycles using a high-low temperature alternating box, and the. The temperature range of the high-low temperature alternating box was set to between -50 and 50 °C, and the cycle period was 50 min. The low temperature phase change material was subjected to a differential scanning calorimeter (DSC) was used to test its the melting temperature and latent heat value of the low-temperature phase change material.

2.1 PCM1：87%$C_8H_{16}O_2$ (n-Caprylic acid) + 13%$C_{14}H_{28}O_2$ (Myristic acid)

Both n-octanoic acid ($C_8H_{16}O_2$) and myristic acid ($C_{14}H_{28}O_2$) are saturated fatty acid phase change materials, which have good stability and no supercooling and good stability. After several experiments, it was determined that it was best to use 87% $C_8H_{16}O_2$ + 13% $C_{14}H_{28}O_2$ were used as the phase change cold storage materials. The phase change performance was measured by DSC, the cooling curve was measured by a low temperature bath, and the thermal conductivity was measured by a Hot disk. The Disk. From the experimental results are shown in Fig. 1 and Fig. 2. The data shows, it was determined that the phase transition temperature of the material was 7.1 °C, the latent heat of phase change was 146.1 J/g, the thermal conductivity is 0.2832 W/(m•K), no supercooling, occurred, and the phase change platform was stable, and the thermal conductivity is 0.2832 W/(m•K).After 100 freeze-thaw cycles, the phase transition temperature of the material was 7.5 °C, the latent heat of phase change was 145.1 J/g, and the phase transition temperature and latent heat of phase change remained the same.

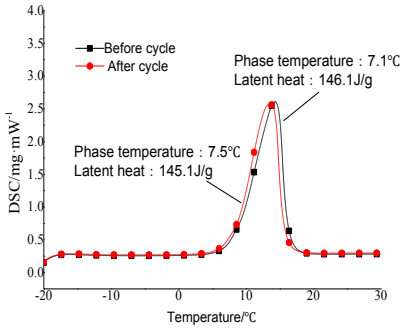

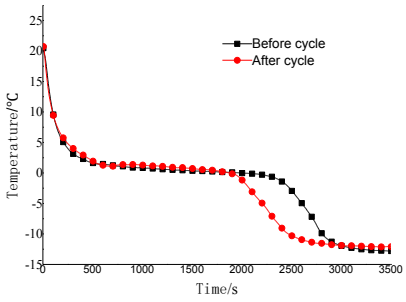

Figure 1: DSC of before and after PCM1 100 cycles **Figure 2: Cooling curve before and after PCM1 100 cycles**

2.2 PCM2：H_2O+0.03g/ml $C_6H_7KO_2$ (Potassium sorbate)

When pure water is used as a cold accumulating agent, there is a large degree of supercooling, which affects the cold storage effect. Potassium sorbate is often used in fruit and vegetable preservation since it is non-toxic and environmentally-friendly. Adding a certain concentration of potassium sorbate in water can eliminate the degree of supercooling and lower the phase transition temperature of water. In this

study, the phase change performance was measured by DSC, the cooling curve was measured by a low temperature bath, and the thermal conductivity was measured by a Hot Disk, and the experimental results are shown in Fig. 3 and Fig. 4. The phase transition temperature of 0.03 g/mL $C_6H_7KO_2$ + H_2O was measured to be -2.5 °C, the latent heat of phase change was 256.2 J/g, and thermal conductivity was 0.9427 W/(m•K). The platform demonstrated to be stable, and the heat storage and release process was good. After the melting and solidification cycle was performed 100 times, the phase transition temperature and phase change of latent heat fluctuation range of the material remained small, and the cycle stability was good.

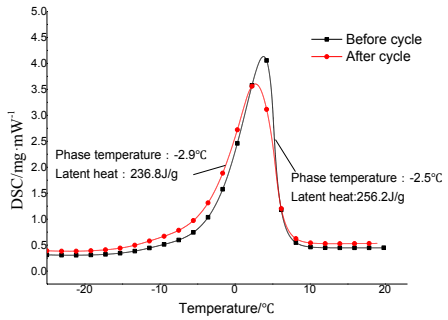

Figure 3: DSC of before and after PCM2 100 cycles

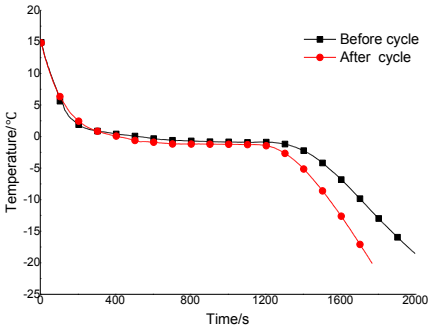

Figure 4: Cooling curve of before and after PCM2 100 cycles

3. THEORETICAL ARITHMETIC

3.1 System design

Considering that the quantity of goods varies depending on different transportations (or during transportation), different refrigerating equipment in temperature zone were designed in this work. Figure 5 displays an equipment structure diagram with an external dimension of 1560*860*760 mm^3, an internal dimension of 1450*750*650 mm^3, and a storage volume of 680 L. The thermal insulation materials of the maintenance structure are constructed of polyurethane and a vacuum insulation board, and the inside and outside surfaces are assembled with galvanized iron plate of 2.5-mm thickness. The three temperature zones, which are separated by the vacuum insulation plate of 30-mm thickness, and a roller is arranged between the vacuum insulation plate and the chute to allow size transformations of each temperature region. The grooves on both sides of the equipment facilitate manual transportation or machine hoisting.

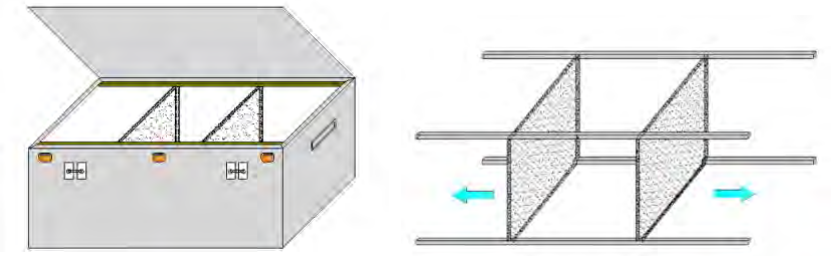

Figure 5 Equipment 1 structural diagram and insulation material

3.2 Heat leakage coefficient

The heat leakage coefficient of the storage heat preservation was obtained from the ratio of the box

structure to heat insulation property of the insulation box material. From this, the efficiency of the thermal storage box is maintained for a longer period, which can save energy and reduce emissions. An internal heating method was used to test the heat leakage coefficient. Because of the different types and complex physical properties of the products, it is difficult to implement unified parameters in the theoretical calculation model; thus, the heat absorbed by the product itself is not considered in the theoretical calculation.

The heat leakage coefficient of refrigerated equipment is expressed as U in W/K :

$$U = \frac{1}{n}\sum_{t=1}^{n} U_t (n \geq 17) \quad \text{Eq. (1)}$$

$$U_t = \frac{Q}{t_i - t_\theta} \quad \text{Eq. (2)}$$

where U is the total heat leakage coefficient in W/K, U_t is the heat leakage coefficient in W/K, Q is the sum of the total power consumed by the heater and fan in the heat preservation box in W; t_i is the average temperature in box in K, and t_θ is the temperature outside the box in K. t_i, t_θThe arithmetic average of the temperature measured at the end of each test record interval.The experimental results show that the heat leakage coefficient is 17.83 W/K.

The integral heat transfer coefficient of the heat preservation box can be calculated by the following formula:

$$k = \frac{U}{A} = \frac{\lambda}{\delta} \quad \text{Eq. (3)}$$

where K is the heat transfer coefficient of heat preservation box in W/(m^2·K), A is the box surface area in m^2,λ is the equivalent Thermal conductivity of Box tail structure in W/(m·K), and δ is the box enclosure structure thickness in m.The heat transfer coefficient of the whole and the equivalent thermal conductivity of the enclosure are obtained by the following equations:

$$K = 3.15 W/(m^2 K)$$

$$\lambda = 0.173 W/(mK)$$

3.3 Amount of cold storage agent

When applying the cold storage heat preservation box, the amount of cold storage agent filled in the cold plate is an important factor affecting the effective temperature range within the box. This filling quantity in the cold storage plate can be estimated by the following formula :

$$X = \frac{T \times K \times A \times (t_2 - t_1) \times n}{H} \quad \text{Eq. (4)}$$

where X is the quality of coolant in kg, H is the phase change latent Heat of Cold Storage Agent in kJ/kg, T is the cooling time in h, K is the coefficient of heat transfer in W/(m^2·K), Ai s the heat transfer area in m^2, t_2 is the outside temperature of incubator in K, t_1 is the heat preservation temperature in heat preservation box in K, and n is the number of open doors of the incubator, Don't open the door: n=1.

The ambient temperature is 25 °C, based on the calculation for the required effective cooling of 15 h. Each of the three temperature zones in the equipment has a size of 450*750*650 mm^3. Temperature zone 1 is the normal temperature zone with no phase change material. In temperature zone 2, n-octanoic acid-myristic acid composite phase change material was used, the phase transition temperature was 7.1 °C, and the latent heat of phase transition was 146.1 J/g. In temperature zone 3, the composite phase change material of potassium sorbate and water was used, the phase transition temperature was -2.5 °C, and the latent heat of phase transition was 256.2 J/g.

Table 2. Amount of cold storage agent

Temperature zone	Cooling time/h	Refrigerant quality/kg
Temperature zone two	15	13.8
Temperature zone three	15	12.1

4. EXPERIMENTAL

In order to verify the correctness of the simulation, an experimental system based on a temperature

monitoring device was built. As shown in Figure 6, the temperature monitoring device is a verification instrument host, containing a wireless temperature, humidity sensor, and a repeater from left to right. After the phase change material was prepared, it was placed in a polyethylene cold storage plate, and then stored in a cryostat for cold storage, in which the cooling temperature was set to -20 °C. The size of the equipment cold storage plate is 315*200*25 mm^3. The cold storage plate and box are bonded by waterproof male and female stickers, which can be flexibly disassembled for convenient secondary use. Cold storage plates were placed on the four sides and bottom of the second and third temperature zones of the equipment and also on top of the vacuum insulation board with a thickness of 2 cm to prevent loss of cooling capacity, as shown in Figure 7.



Figure 6: Temperature monitoring devices



Figure 7: Layout drawing of insulation box cold plate

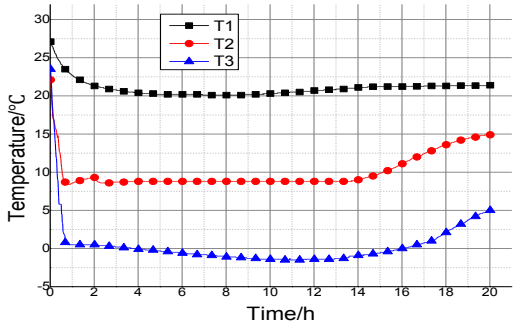

Figure 8: Equipment temperature monitoring curve

Figure 8 shows the temperature monitoring curve of the equipment, which was monitored for 20 h after the cold storage plates were placed in the box, and the ambient temperature was about 25 °C. The temperature in the normal temperature zone was lower than the ambient temperature by about 3~5 °C due to the influence of the temperature zone of the partition wall, but this does not affect the storage of products in T1. The phase transition temperature of the phase change material in T2 was 7.1 °C, and the time for releasing sensible heat was about 30 min, after which the phase change occurred in the material. The temperature of the phase change process box was between 7 and 9 °C, which was maintained for about 13 h, which is slightly smaller than the initial temperature. After 14 h, the temperature in T2 began to increase. The phase transition temperature of the phase change material in T3 was -2.5 °C, and the sensible heat release time was about 40 min. The temperature in the tank was maintained between -2~0 °C in the phase change process, and the maintenance time was 14 h, which is slightly higher than the temperature in T2 at the same time.

5. CONCLUSION

Combining the vacuum insulation board technology with cold storage technology, we propose the first design of a cold storage multi-temperature zone cold chain transportation equipment. Two different phase change materials suitable for cold chain transportation were prepared.The cold storage multi-temperature zone insulation box can be kept cold for about 15 h, which effectively guarantees the quality of food during transportation.In the actual situation, due to heat leakage and processing problems, the cooling time and temperature inside the box undergo certain changes, but within an acceptable range required for maintaining quality of perishable products. Our research findings on the designed cold storage multi-temperature zone insulation box are significant for solving problems associated with LTL logistics and can greatly improve the safety and economy of cold chain transportation. This work provides a new direction for the future development of more efficient cold storage cold chain transportation equipment.

ACKNOWLEDGMENTS

Thanks for this project funding: National key R & D Project(2018YFD0401300), Shanghai Municipal Science and technology project (16040501600), Doctoral innovation fund of Shanghai Maritime University (2016ycx081)

NOMENCLATURE

U	total heat leakage coefficient ($W \times K^{-1}$)	U_t	heat leakage coefficient ($W \times K^{-1}$)
Q	the sum of the total power consumed by the heater and fan in the heat preservation box (W)	k	heat transfer coefficient of heat preservation box ($W \times m^{-2} \times K^{-1}$)
t_θ	temperature outside the box (K)	t_i	average temperature in box (K)
A	box surface area (m^2)	λ	equivalent thermal conductivity of Box tail structure ($W \times m^{-1} \times K^{-1}$)
δ	box enclosure structure thickness (m)	X	quality of coolant (kg)
T	cooling time (h)	K	coefficient of heat transfer ($W \times m^{-2} \times K^{-1}$)
A	heat transfer area (m^2)	t_2	outside temperature of incubator (K)
H	phase change latent Heat of Cold Storage Agent ($kJ \times kg^{-1}$)	n	the number of open doors of the incubator, Don't open the door: n=1
t_1	heat preservation temperature in heat preservation box (K)		

REFERENCES

Balakrishnan, A., & Natarajan, H. P. (2014). Designing fee tables for retail delivery services by third-party logistics providers. IIE Transactions, 46(12), 1261–1278.

Blackburn, J., & Scudder, G. (2009). Supply chain strategies for perishable products: The case of fresh produce. Production and Operations Management, 18(2),129–137.

Cai, X., Chen, J., Xiao, Y., & Xu, X. (2010). Optimization and coordination of fresh product supply chains with freshness-keeping effort.Production and Operations Management, 19(3), 261–278.

Yunlong Yu, Tiaojun Xiao. Pricing and cold-chain service level decisions in a fresh agri-products supply chain with logistics outsourcing[J]. Computers & Industrial Engineering,111(2017):56-66.

Hongxia Zhao, Sheng Liu, Changqing Tian, et.al. An overview of current status of cold chain in China[J].International Journal of Refrigeration,2018,88:483-495.

Teng, Y., Chen, B. Seizing opportunities in China's cold chain logistics. China Business Review [online]. Available from: https://www.chinabusinessreview.com/ seizing- opportunities- in- chinas- cold-chain- logistics/. (Accessed 04.11.2017).

Zhu, L.R., 2017. A brief analysis of the current market situation and development direction of China's

refrigerated trucks. Machinery (in Chinese) 44 (3), 44–47.
Jose Pereira da Cunha, Philip Eames. Thermal energy storage for low and medium temperature applications using phase change materials – A review [J]. Applied Energy, 2016,177.
Manish K. Rathod, Jyotirmay Banerjee. Thermal stability of phase change materials used in latent heat energy storage systems: A review [J]. Renewable and Sustainable Energy Reviews, 2013, 18.
Zhang N, Yuan Y, Yuan Y, et al. Effect of carbon nanotubes on the thermal behavior of palmitic–stearic acid eutectic mixtures as phase change materials for energy storage [J]. Solar Energy, 2014, 110:64-70.
Yu Q, Tchuenbou-Magaia F, Al-Duri B, et al. Thermo-mechanical analysis of microcapsules containing phase change materials for cold storage[J]. Applied Energy, 2018, 211:1190-1202.
Xuejiao Jia, Xiaoqiang Zhai, Xiwen Cheng. Thermal performance analysis and optimization of a spherical PCM capsule with pin-fins for cold storage[J]. Applied Thermal Engineering,148 (2019) 929–938.
Tianrun Yang, Changjiang Wang, Qie Sun, et al. Study on the application of latent heat cold storage in a refrigerated warehouse[J]. Energy Procedia,2017,142:3546-3552.
M.A. Said, Hamdy Hassan. Parametric study on the effect of using cold thermal storage energy of phase change material on the performance of air-conditioning unit[J]. Applied Energy,2018,230:1380-1402.
Ting Zou, Wanwan Fu, Xianghui Liang, et al. Preparation and performance of modified calcium chloride hexahydrate composite phase change material for air-conditioning cold storage[J]. International Journal of Refrigeration,2018,95:175-181.
Wu Liyuan, SONG Wenji, GAO Rixin, et al. Experimental study of plate ice storage cold storage temperature based on the characteristics of cold[J]. Journal of Refrigeration, 2012(33): 66 - 69. (in Chinese with English abstract)
Zhang N, Yuan Y, Cao X, et al. Latent Heat Thermal Energy Storage Systems with Solid–Liquid Phase Change Materials: A Review[J]. Adv. Eng. Mater.2018, 1700753, DOI:10.1002/adem.201700753.
Yoram Kozak, Mohammed Farid, Gennady Ziskind. Experimental and comprehensive theoretical study of cold storage packages containing PCM[J]. Applied Thermal Engineering,115 (2017) 899–912.
Li Y C M, Chen Y H A. Assessing the thermal performance of three cold energy storage materials with low eutectic temperature for food cold chain[J]. Energy, 2016, 115:238-256.
Xiaofeng Xu, Xuelai Zhang, Sheng Liu. Experimental study on cold storage box with nanocomposite phase change material and vacuum insulation panel[J]. International Journal of Energy Research,2018,42(14):4429-4438.
Weiwen Xu, Xuelai Zhang. Preparation and Thermophysical Properties of Nanometer Copper Oxide/Octylic-myristic Acid as PCMs for Thermal Energy Storage[J]. Materials Review, 2016,30:60-64.
Zhao Yao, T ANG Gangzhi, ZHU Sunke. Research of air distribution characteristic for single evaporator multiple temperature zones refrigerated truck[J]. Food & Machinery, 2017,33(01):119-121.
Liu Guanghai, XIE Ruhe, ZOU Yifeng. Theoretical analysis and experiment of air tightness of multi-temperature refrigerated truck[J].Transactions of the Chinese Society for Agricultural Machinery，2017,48（01）：289-296.
Sun Yongcai. Analysis of Thermal performance of Refrigeration vehicle and Development of vacuum Insulation material [D]. Guangzhou: Guangzhou University, 2011.

Manuscript ID: 1688
DOI: 10.18462/iir.icr.2019.1688

Emission testing of a transport refrigeration unit

Richard LAWTON [(a)], Tobias MYNOTT [(b)], Nicholas MARSHALL[(c)] Florian WAGNER[(d)]

[(a, b, c)] Cambridge Refrigeration Technology,140 Newmarket Road,
Cambridge, CB5 8HE, UK
crt@crtech.co.uk
[(d)] Dearman Engine Company,
Dearman Technology Centre,
Unit 5 Stafford Cross Business Park, Stafford Road,
Croydon, CR0 4TU

ABSTRACT

Standards for exhaust emissions for road vehicles have enforced a significant reduction in particulates and NO_x for transport vehicles complying to those standards.
However, several larger UK conurbations have noticed that pollutants are not being reduced as much as had been hoped and that those measured at the roadside are from such sources as older vehicles, non-regulated engines, brakes and even tyres. One source is diesel engines powering nose-mounted refrigeration units, where it is common for the engine to be devoid of any emission controls.
Data is presented on testing carried out on a nose-mounted refrigeration unit at different temperature setpoints and conditions, with varying internal load: empty and with simulated cargo.
The data shows that these engines do contribute to both NO_x and particulates and that the current non-road mobile machinery regulation ("NRMM") will not significantly reduce those emissions.

Keywords: Emissions, NRMM

1. INTRODUCTION

There have been several studies recently investigating the environmental impact of temperature controlled transport in major UK cities and the potential for zero emissions alternatives. Outdoor air pollution contributes to around 40,000 deaths a year in the UK, according to the Royal Colleges of Physicians and of Paediatrics and Child Health.
In 2017, the UK government released a plan for tackling roadside Nitrogen Dioxide (NO_2) concentrations, this plan required local authorities to take action on reducing the annual average values to under 40µg/m^3, which is the statutory limit.
The major part of this plan was to look at emissions from road transport units as NO_2 is found in NOx (oxides of nitrogen), which is emitted from road transport units. In total there were 28 local authorities and London has been mandated to produce a plan to reduce air quality pollution, the first steps were the ultra-low emission zone (ULEZ) and toxicity charge in London.
Other cities like Leeds, Nottingham, Derby, Birmingham and Southampton have all begun to introduce a clean air zone (CAZ) which will give incentive for people with commercial vehicles, taxis and buses to use engines which are compliant to EURO VI whilst in CAZ zones.
The following study focuses on the emissions from a transport refrigeration unit (TRU); it focuses on larger nose mounted units that are seen on semi-trailers.

2. TEMPERATURE CONTROLLED TRANSPORT VEHICLE

The refrigeration unit that was selected for the trials is shown below in fig. 1; the trailer was built to ATP standards and was already in-service from November 2014.



Figure 1: Refrigeration unit and internal setup

The refrigeration unit used during the emissions trials was a Carrier Vector 1950MT; it had a refrigeration capacity of 18,200 Watts at 0°C and at -20°C a capacity of 9,800 Watt on high speed diesel; these both at 30°C ambient.
Emissions Analytics set up their portable emissions measurement system (PEMS); this measures the gases coming from refrigeration unit's exhaust pipe and was able to measure the following:

- Carbon monoxide (CO) and carbon dioxide (CO_2)
- Nitric oxide (NO) and nitrogen dioxide (NO_2)
- Oxides of nitrogen (NO_x=NO + NO_2)
- Total hydrocarbons (THCs)
- Particles
- Fuel economy (MPG) and fuel consumption (L/100km)

Fig. 2 below shows the emissions equipment installed in the test chamber, the equipment provided was a Sensors SEMTECH-LDV for gaseous emissions and a Pegasor Mi2 for particulates.

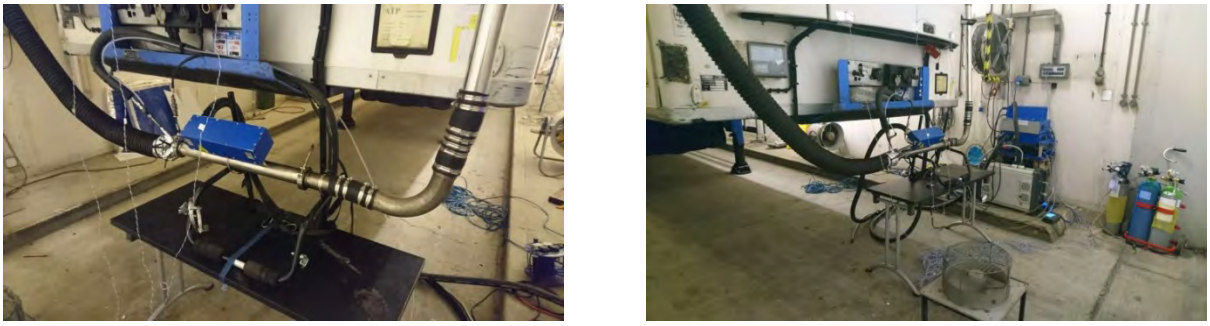

Figure 2: Emissions analytics' equipment

3. TEST METHODOLOGY

The test methodology used a modified version of EN16440 part 5.6.7 which is the measurement of energy consumption under rated conditions at part load. A copy of this is given below.

“5.6.7 Measurement of energy consumption under rated conditions at part load

After stable conditions have been achieved the test shall be carried out under thermostatic control with a fixed heat load P_{HL}.

All measurements shall be recorded at least every 10 s.

The measurements shall be carried out at +30/–20 °C and +30/0 °C both, on the road operation and, if fitted, standby operation. For cooling devices driven by the vehicle engine the measurement is carried out at the highest engine speed tested according to 5.6.6. At –20 °C the measurements are performed in start/stop operation and at 0 °C with the evaporator fan running continuously. If no start/stop operation is possible, the measurements are performed at both temperatures with the evaporator fan running continuously.

For cooling devices which are exclusively operated at 0°C and higher only measurements at +30/0 °C are carried out.

The cooling device is operated at +30/–20°C at part load of 35 % and at +30/0°C at a part load of 20 % of the measured cooling capacity Pc at full load according to 5.6.6. The maximum switching difference of the thermal control of the cooling device is 2 K.

All temperatures shall be measured over a period of 3 h and at least 20 cooling cycles. They shall be recorded. The measuring period starts with switching OFF the compressor and finishes with the first switching OFF of the compressor after 3 h and at least 20 cooling cycles of measurement. For each test the average value shall be indicated in the test report. The minimum and maximum values during testing shall also be indicated. The maximum deviation of the average air inlet temperature of the evaporator unit shall be ± 1 K of the reference value. The operating time t_O and standstill periods shall be recorded.

Continuously regulated systems shall be measured over a period of 3 h. The maximum deviation of the average inlet air temperature at the evaporator unit may be ± 1 K of the reference value.”

For the purpose of this test we reduced the stable conditions to 1 hour and also carried out tests at 10°C and 20°C ambient.

4. EMISSIONS FROM A DIESEL TRANSPORT REFRIGERATION UNIT (TRU)

Testing was carried out at Cambridge Refrigeration Technology (CRT) and an independent emissions monitoring company called Emissions Analytics. The unit tested was a nose-mounted refrigeration unit installed in a 13.6m semi-trailer. The test program that was conducted is shown below in table 1.

Table 1: Test Program

Test number	Type	Condition		Heat load (kW)
		Internal (°C)	External (°C)	
1	Pull down test	10 to 0	10	-
2	Part load test	0	10	3.0
3	Pull down test	0 to -20	10	-
4	Part load test	-20	10	3.0
5	Pull down test	20 to 0	20	-
6	Part load test	0	20	3.0
7	Pull down test	0 to -20	20	-
8	Part load test	-20	20	3.0
9	Pull down test	-20 to -25	20	-
10	Part load test	-25	20	3.0
11	Pull down test	30 to 0	30	-
12	Part load test	0	30	3.0
13	Pull down test	0 to -20	30	-
14	Part load test	-20	30	3.0

Tables 2, 3 and 4 shows the emissions data that was collected from each test conducted for CO_2, NO_X and $PM_{2.5}$. Fis. 3, 4 and 5 show the temperature data.

10°C ambient

Table 2 below shows the emissions data; the temperature graph of tests 3 and 4 is given in Fig. 3.

Table 2: 10°C emissions testing data

Test number	Type	Condition		CO_2 ($g \cdot s^{-1}$)	NO_X ($g \cdot s^{-1}$)	$PM_{2.5}$ ($g \cdot s^{-1}$)
		Internal (°C)	External (°C)			
1	Pull down test	10 to 0	10	3.8714	0.0268	0.0000337
2	Part load test	0	10	2.349	0.0184	0.0000312
3	Pull down test	0 to -20	10	3.6365	0.0241	0.0000346
4	Part load test	-20	10	2.8665	0.0188	0.0000306

The average CO_2 during the 10°C testing was 3.0088 (g/s), NO_X 0.0206 (g/s) and 0.0000319 (g/s) for $PM_{2.5}$.

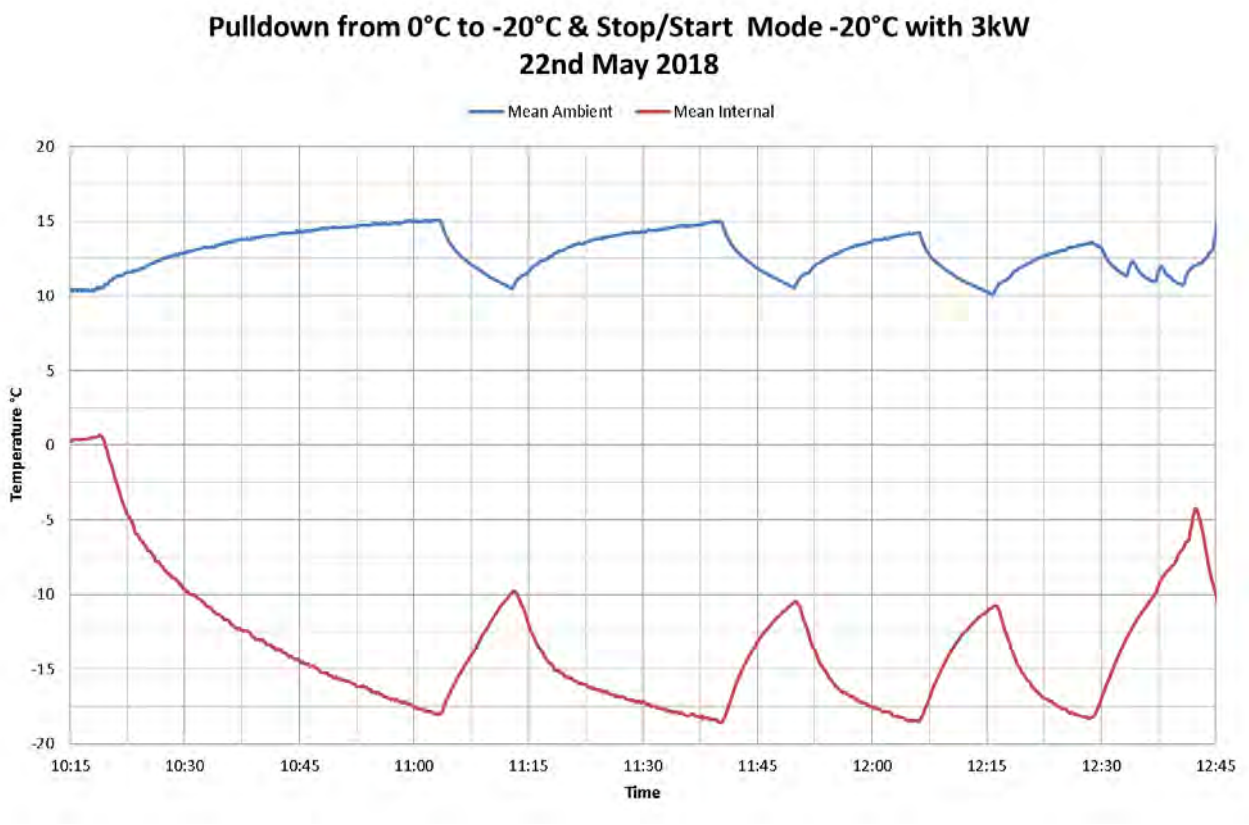

Figure 3: Temperature data 10°C ambient

20°C ambient

Table 3 below shows the emissions data; the temperature graph for test 8 is given in Fig 4.

Table 3: Emissions test results

Test Number	Type	Condition		CO_2 (g/s)	NO_X (g/s)	$PM_{2.5}$ (g/s)
		Internal °C	External °C			
5	Pull down test	20 to 0	20	2.7916	0.0199	0.0000322
6	Part load test	0	20	1.9237	0.0146	0.0000298
7	Pull down test	0 to -20	20	2.9495	0.0186	0.0000304
8	Part load test	-20	20	2.3741	0.0149	0.0000271
9	Pull down test	-20 to -25	20	2.0115	0.0128	0.0000214
10	Part load test	-25	20	1.883	0.0119	0.0000215

The average CO_2 during the 20°C testing was 2.1776 (g/s), NO_X 0.0142 (g/s) and 0.0000251 (g/s) for $PM_{2.5}$.

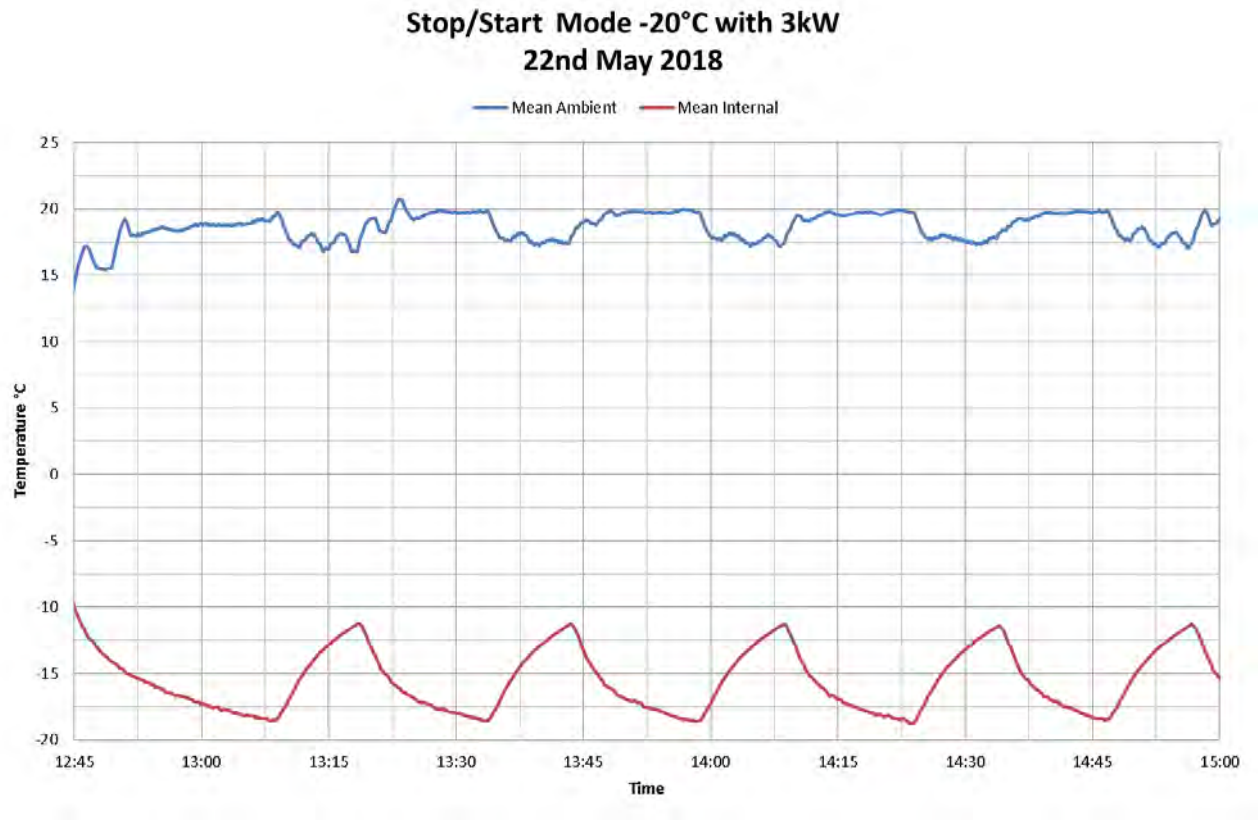

Figure 4: Temperature data 20°C ambient

30°C ambient

Table 4 below shows the emissions data; the temperature graph for test 11 is given in Fig. 5.

Table 4: Emissions test results

Test Number	Type	Condition		CO_2 (g/s)	NO_X (g/s)	$PM_{2.5}$ (g/s)
		Internal °C	External °C			
11	Pull down test	30 to 0	30	4.2007	0.0326	0.0000328
12	Part load test	0	30	2.47	0.0211	0.0000306
13	Pull down test	0 to -20	30	3.455	0.0238	0.0000330
14	Part load test	-20	30	2.1851	0.0148	0.0000228

The average CO_2 during the 30°C testing was 2.8506 (g/s), NO_X 0.0210 (g/s) and 0.0000286 (g/s) for $PM_{2.5}$.

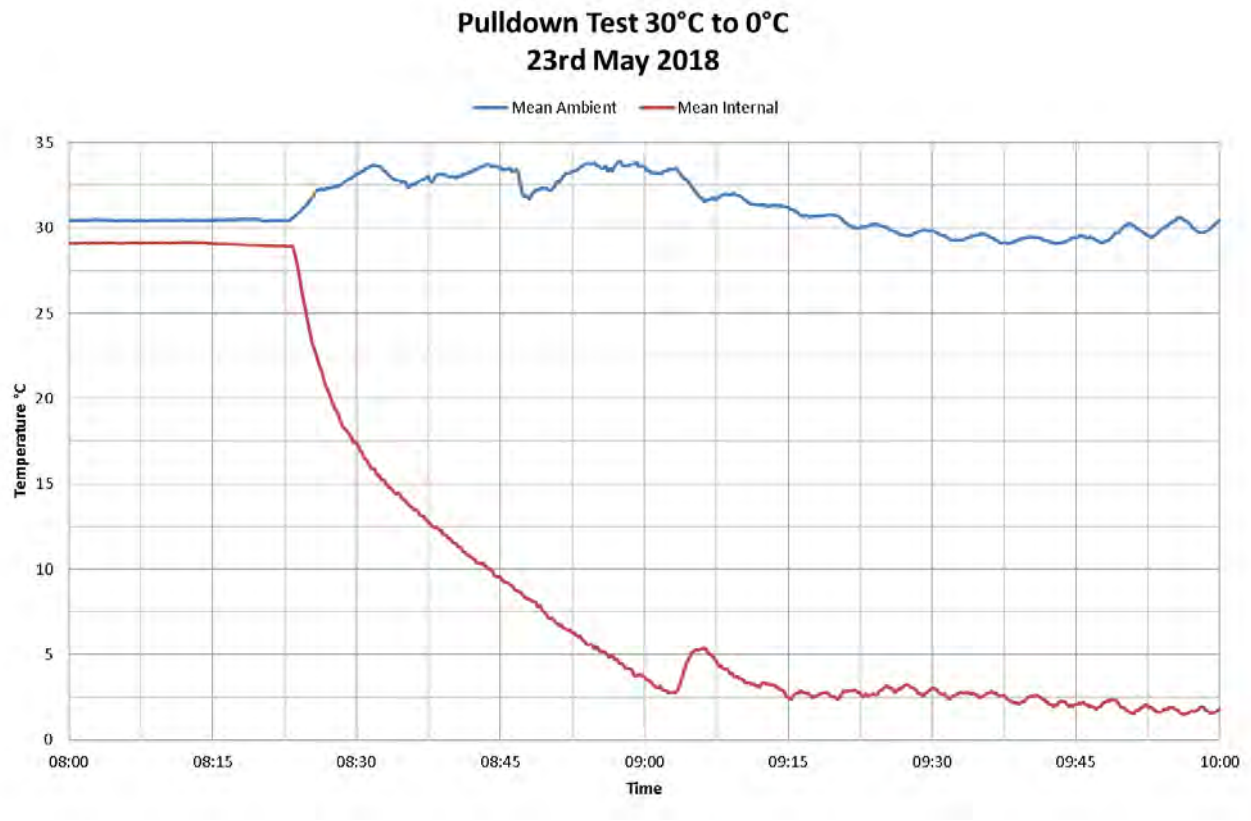

Figure 5: Temperature data 30°C ambient

Summary of emissions data

In order to compare the test results to the Euro VI emissions figure we first need to apply an emissions factor of 2.578 kg CO_2 / litre of diesel burnt to the CO_2 test results in tables 2, 3 and 4. This showed that, dependent on its operational state, the refrigeration unit emitted between 16 and 22 grams of NOx per litre of fuel consumed, and between 0.02 and 0.04g $PM_{2.5}$.

5. COMPARISON TO EURO VI AND NRMM STANDARDS

From the test results carried out at CRT we can compare the results with emissions data from three real world tests run by The Low Carbon Vehicle Partnership (LowCVP) in January 2017. This data and is shown below in Table 5 along with the final column showing the increase in emissions from the engine that was tested at CRT.

Table 5: Euro VI emissions

Vehicle	Duty Cycle (avg. speed kph)	gNO_x/km	gNO_x/litre	Euro VI times lower
44t Artic 320hp Euro VI	Urban delivery	0.20	0.41	39-54
	Regional delivery	0.13	0.35	46-62
	Long haul	0.11	0.34	48-66
44t Artic 460hp Euro VI	Urban delivery	0.33	0.65	25-34
	Regional delivery	0.22	0.50	32-44
	Long haul	0.22	0.54	30-41

Table 5 shows the comparison between gNO_X/litre of fuel burnt and when comparing the test data it shows that the auxiliary engine on test emitted between 25 – 66 times more NOx than a Euro VI truck engine, depending on the conditions.

NRMM (Non Road, Mobile Machinery) regulations

Whilst engine power was not recorded during the emission testing, the engine's runtime and speed were recorded. By cross-referencing engine speed against the manufacturer's performance curve of the engine, the kWh could be estimated. Further, because the compliance limits apply to combined NOx + HC, and HC was not measured by Emission Analytics, the split of NOx and HC was assumed to be 2/3rds NOx – in line with the NRMM stage V standards for engines over 56kW where NOx and HC do have individual compliance limits.
This analysis gave an indicative figure that the engine on test emitted between 4.1 and 5.0 g HC+NOx /kWh depending on its operating state. Although only indicative, this analysis suggests that this engine meets (and exceeds) the current NRMM Stage IIIA emission standard when in real-world operation and indeed may also meet the NRMM stage V emissions standard with a little modification. For the engine that was tested, this indicates that these types of equipment may not get cleaner on the introduction of NRMM Stage V as they are already within or close to compliance limits.

6. CONCLUSIONS

Emissions from temperature-controlled transport equipment are a growing concern as air quality rises up the political agenda; motive engines become cleaner and cities start to regulate against older, more polluting vehicles entering city boundaries. In this environment it is difficult to envisage a near future where restrictions are not placed on the types of TRUs permitted to enter cities.

NOMENCLATURE

NOx	Oxides of Nitrogen	$PM_{2.5}$	Particulate Matter
NO_2	Nitrogen Dioxide	CO_2	Carbon Dioxide
NO	Nitrogen Oxide		
HC	Hydrocarbon		

REFERENCES

Available via https://www.carrier.com/truck-trailer/en/eu/products/eu-truck-trailer/trailer/vector-1950-mt/

Cenex, Temperature Controlled Transport in Leeds, 2018

Manuscript ID: 1689
DOI: 10.18462/iir.icr.2019.1689

Ageing of in-service refrigerated transport vehicles: a statistical analysis

Claudia CAPO [a, b, c], Jean Marc PETIT [c], Rémi REVELLIN [b] Jocelyn BONJOUR [b], Gérald CAVALIER [a]

[a] Cemafroid, 5 Avenue des Prés - Fresnes cedex – France
[b] Univ Lyon, CNRS, INSA-Lyon, Université Claude Bernard Lyon 1, CETHIL UMR5008, F-69621, Villeurbanne, France
[c] Univ Lyon, CNRS, INSA-Lyon, Université Claude Bernard Lyon 1, LIRIS UMR5205, F-69621, Villeurbanne, France
gerald.cavalier@cemafroid.fr

ABSTRACT

The efficiency of the thermal insulation of bodies for refrigerated vehicles decreases with time, i.e. the body's overall insulation coefficient ("*K* coefficient") increases during ageing. Ageing is a twofold phenomenon involving both physio-chemical and mechanical factors: their estimation is very important for the design of better performing vehicles, but also for their smart use. Since 1953, Cemafroid has been determining, each year, the *K* coefficient for hundreds of in-service refrigerated vehicles at twelve years of life and more. This paper presents a statistical analysis of the data of some thousands of these vehicles. First results for a sample of refrigerated trucks highlight a greater ageing in the period 0-12 years (average variation of *K* up to 65%) than in the period 12-18 years (average variation of K equal to 5%). Furthermore, it turns out that the evolution of *K* in this 12-years window depends mainly on the type of vehicle, the type of insulation and the blowing agents, the quality of manufacturing, the type of refrigerating unit installed on the vehicle and the type of transported foodstuffs.
Keywords: Ageing Phenomena, Thermal Insulation, K Coefficient, Refrigerated Vehicles, Physio-Chemical Factors, Mechanical Factors, Statistical Analysis.

1. INTRODUCTION

Refrigerated transport vehicles have as main objective to supply consumers with good quality and safe perishable products. Today, a wide array of services to the cold chain is provided by using a diversified fleet that is continually evolving. In refrigerated transport, the thermal insulation of the body is one of the basic elements of the refrigerated equipment. The efficiency of this thermal insulation is quantified by the body's overall insulation coefficient ("*K* coefficient"), a parameter increasing during the time due to the ageing of the body's insulation. K coefficient may be controlled as required by the ATP (the International Agreement for the Transport of Perishable Foodstuff). The evolution of *K* with time can be very different from one vehicle to another due to many factors, whose analysis and modeling has been previously treated by several studies (Boldrin et al., 1990; Boldrin et al., 1993; Panozzo et al., 1995; Capo et al., 2018), highlighting various facets of this phenomenon. As stated by Panozzo et al. (1995), the ageing of an insulated enclosure for a refrigerated vehicle is mostly due to the permeability of the foam to the gases (air and blowing agent), to the condensation of water into the foam cells and to the increasing of the percentage of the open (broken) cells. These causes explain the ageing from a physio-chemical point of view and primarily concern the panels used to build the insulated enclosure and the insulation materials itself. Ageing of refrigerated vehicles also has a mechanical component due to the movements on the road, the routes covered and the payload. Capo et al. (2018) presented the factors playing a role in the aging process, classifying them into three different categories. The effects of some of these factors were analyzed in previous studies. A statistical analysis carried out by Panozzo et al. (1999) highlighted the influence in the ageing rate due to the rails and to the

refrigerating units. As pointed out by the authors, in presence of these accessories, the mechanical stresses are deeply increased. Capo et al. (2018) pointed out that, since the beginning of its life, the *K* value of the body has a deviation from the theoretical one (predicted by the heat conduction through its walls) due mainly to two contributions: the first one is due to the non-ideal foaming process, the thermal bridges and non-perfect sealing of the body; the second one is due to the presence of the refrigeration unit that causes further thermal losses. In order to discriminate others factors having an influence on the ageing process, this paper presents the statistical analysis of 1158 different refrigerated vehicles. The analysis was carried out on the basis of the following criteria:

i) type of equipment and materials,
ii) influence of the body manufacturer,
iii) influence of refrigerating units,
iv) usage of the vehicle.

2. EVALUATION OF PERFORMANCE OF INSULATED BODIES

The overall insulation coefficient is calculated through the formula:

$$K = \frac{Q}{\Delta T S} \qquad \text{Eq. (1)}$$

Where *Q* is the heating power or the cooling capacity, as the case may be, required to maintain a constant absolute temperature difference ΔT between the mean internal temperature T_{int} and the mean external temperature T_{ext}, during continuous operation, when the mean outside temperature T_{ext} is constant for a body of mean surface area *S*. The mean surface area of the body is represented by the geometric mean of the internal surface area S_{int} and the external surface area S_{ext} of the body:

$$S = \sqrt{S_{int}\, S_{ext}} \qquad \text{Eq. (2)}$$

For refrigerated vehicles included in this study *K* was measured by following the ATP test procedure, based on "the inner heating method". This method includes the measurement of twenty-four temperatures owing to as many probes, twelve of which are placed inside the vehicle and twelve on the outside. The test typically takes more than twelve hours of stabilization. The refrigerated vehicle was placed in the Cemafroid test chamber that is accredited by COFRAC, the French accreditation body, for tests and calibrations according to ISO 17025 and that it is able to control the temperature of the chamber with an accuracy of ±0.5 K. Fig. 1 schematically shows the main conditions of the ATP test procedure, which requires a mean outside temperature, T_{ext} of 7°C± 0.5 K and air flow speeding ranging from 1 to 2 $m.s^{-1}$.

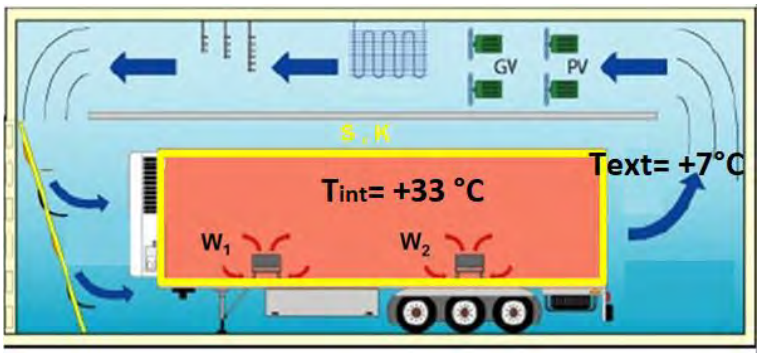

Figure 1: Measurement principle of the *K* coefficient

The measurements are made when steady state is reached with a mean inside temperature around the value of 33°C ± 0.5 K. The presence of some ventilated electric heaters is needed to reach a temperature difference between the inside of the body and the test chamber equal to 25°C ± 2 K. Furthermore, the walls of the body have to be maintained at an average temperature of +20° C ± 0.5 K, following strictly the conditions of ATP test both in terms of required temperature

(°C) and tolerance around the set point temperature (K). For the heat balance to be satisfied, the total required cooling power, *Q*, which is used in Eq. (1), is the sum of the total heating power W_1 and ventilating power W_2 of the devices placed inside the body.

2.1 Ageing Measurement

The ageing of a refrigerated vehicle used in the carriage of perishable foodstuffs is quantified through the evolution over the time of the *K* coefficient. The French Regulation requires that this coefficient is measured for all the in-service vehicles after twelve years from their owner whereas immediately after the manufacturing only the *K* coefficient of the prototype, K_p, is measured to certify the whole series. The *K* coefficient measurement at twelve years allows renewing the ATP certificate for other six years, after which the *K* coefficient test must be repeated for a renewal of a further six years. According to this rule for renewal, the ageing evaluation may be made by comparing the *K* coefficient value of the in-service vehicle at the twelfth year of life, K_{12} to the initial *K* value of the prototype equipment, K_p, through their ratio, A_{12}:

$$A_{12} = \frac{K_{12}}{K_p} \quad \text{Eq. (3)}$$

Another way to evaluate the ageing rate is through the average annual ageing coefficient introduced by Boldrin et al. (1994):

$$C.I.A = \frac{K_n - K_P}{K_P\ N} \quad \text{Eq. (4)}$$

Where K_n is the *K* coefficient value of the in-service vehicle at the *n-th* year (equal to K_{12} for data presented in this paper), *N* is the number of year of the vehicle's life (equal to twelve in this study).

3. FACTORS AFFECTING THE AGEING OF REFRIGERATED TRANSPORT EQUIPMENT

3.1 Dataset Description

At 31 December 2017, based on the Datafrig® data, the French fleet counted 109 122 refrigerated transport equipment having a valid ATP certificate (Capo et al. 2018). These equipments are divided into different categories, the main ones are: vans (vehicles with a total weight allowed in charge smaller than 3.5 tons), trucks (vehicles whose total weight allowed in charge varies from 3.5 to 29 tons) and semi-trailers (vehicles with total weight allowed in charge higher than 29 tons). The Datafrig® database is managed by Cemafroid and contains all the ATP in-service equipment in France. The Datafrig® data are first self-controlled by the body manufacturer, secondly automatically controlled and analysed by the Datafrig® software, then checked by a first technician and finally validated by a supervisor. During the audit of the manufacturing of the refrigerated vehicle an independent auditor verifies the quality of these data and compares them to the real equipment. These five steps quality control system give to these data high level of quality. At the end, a sample of 1158 highly curated data were extracted from the 109 122 refrigerated equipment registered in the Datafrig® database. These 1158 data represent different in-service vehicles of different firms, tested after twelve years in the laboratory of Cemafroid. For each of these vehicles more than 80 features are known. Ten of the most important features, from a domain expert point of view, were analysed including the K_{12}, the corresponding K_p, the type of vehicle, the body manufacturer, the nature of the refrigerated enclosures and their isolation, the use of the vehicles and the different types of transport to which they may be subjected. Our selection criteria for the sample of 1158 vehicles were based on data quality requirements applied on the ten selected attributes (or variables): no null values, no outliers, and no duplicates. The influence of these factors on the insulating performance of refrigerated transport equipment is presented below. It is worth noting that we rely on knowledge domain provided by experts to identify our ten features. Other approaches could be carried out based on statistical analysis, for instance with a correlation

coefficient between features to identify the 10 most uncorrelated features. This is out of the scope of this paper. The results of the statistical analysis are presented in this paper in terms of probability density function of A_{12} (see eq.3) through Kernel density estimation, a fundamental data smoothing method where inferences about the population are made, based on a finite data sample. From our dataset, the statistical analysis presented in this paper is based on the following observations. First, assume that A_{12} values have been divided into non-overlapping intervals of equal size. Then, each feature of our dataset can be grouped according to those intervals, leading to integer values (i.e. how many times values of each feature belong to a given interval). Each feature can now be represented with histograms with respect to A_{12} intervals. To better visualize and interpret those histograms, we have chosen to use probability density functions.

3.2 Type of Equipment and Materials

Depending on the category of the vehicle (i. e. vans, trucks and semi-trailers), the performance may vary. Fig. 2a shows the probability densities of A_{12} for three different samples of vehicles. These probability densities allow defining analytically the distribution of the variable A_{12} around the mean value, represented by the peak of the curve. The population covered by these curves are 227 vans, 470 trucks and 424 semi-trailers. The curve corresponding to the semi-trailers is located more to the right (i.e. to higher values of A_{12}) than the other curves. As a matter of fact, during their life, and because of their size, semi-trailers undergo further mechanical stress than trucks and vans. For this reason, after twelve years of life, semi-trailers generally have a K value diverging more from the initial K value of the prototype, than in the case of trucks and vans. However, the width of the curve corresponding to the semi-trailers is smaller than the widths of the other curves: the dispersion of the values of parameter A_{12} is less for semi-trailers due to the fact that they are realized in a more standardized way than trucks and vans. The standard deviation for semitrailers, $\sigma_{\text{semi-trailers}}$ which is equal to 0.18, is the lower one.

Refrigerated vehicles included in this study are made with “sandwich” panels in which the insulation is generally realized with polyurethane foam. The term rigid polyurethane represents a family of materials that in addition to the polyurethane (PUR) also includes polyisocyanurate (PIR). It is also possible to find solutions with expanded polyurethane (PSE). Independently of the nature of the foam, the insulated enclosure of the vehicle may be designed in two different ways: i) with integrated insulation or, ii) assembled on the vehicle platforms. The performance of the vehicle depends on the design of the refrigerated enclosure. Fig. 2b highlights this aspect.

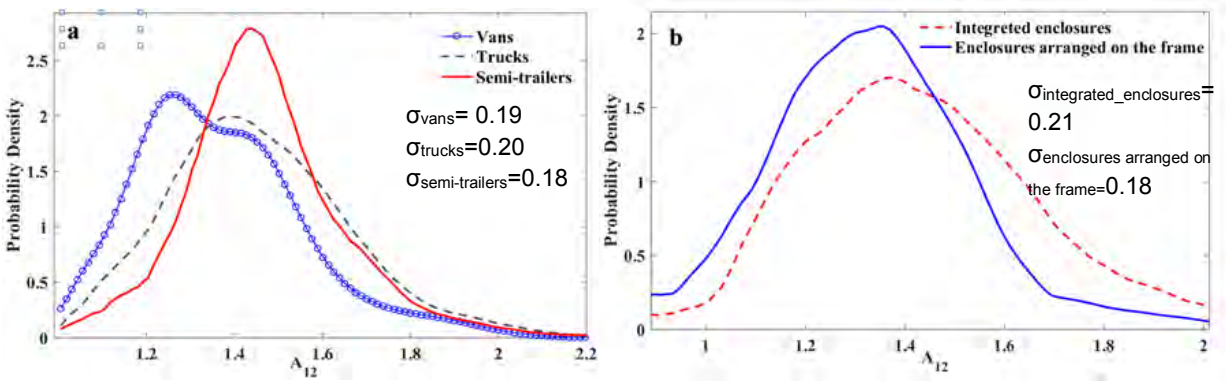

Figure 2: a) Probability densities of A_{12} for vans, trucks and semi-trailers; b) Probability densities of A_{12} for vehicles with integrated insulation and assembled on the vehicle platforms.

The curves of Fig. 2b represent the probability densities of the parameter A_{12} for 52 refrigerated enclosures with integrated insulation and 149 refrigerated enclosures assembled on the vehicle platforms. The vehicles which insulted enclosures are arranged on the vehicles platforms are represented by the curve which shape is more regular and centered around the mean value. The width of this curve, in fact, is smaller than the width of the curve which refers to integrated enclosures, highlighting that the dispersion of the values of A_{12} is less for vehicles with insulated enclosures assembled on the vehicle platforms than for vehicles with integrated insulation. As a

matter of fact the standard deviation, σ, is lower for the enclosures arranged on the frame than for the integrated ones (see Fig 2b). This is to be found in the different designs of the two types of insulated enclosures. Insulated enclosures assembled on the vehicle platforms are made in series through repeatable and mastered industrial process which allow more standardized performances than single and handicraft production of enclosures with integrated insulation.
Excellent insulation properties are obtained through the use of blowing agents. From the 1970s to the mid-1980s, polyurethane foams were expanded with chlorofluorocarbons (CFCs), such as R-11. These blowing agents had a good insulation capacity thanks to their low value of thermal conductivity. However, they had a strong impact on the environment due to their high ozone depletion potential value (ODP). Searching for new environmentally friendly fluids, to be used as working fluids in refrigeration systems and as blowing agents in insulating foams, became a matter of global concern after 1987, date of finalization of the Montreal Protocol. In 1995, manufacturers started realizing their insulated enclosure using the hydro chlorofluorocarbons (HCFCs) as blowing agents (R-141b and R-22). Hydro chlorofluorocarbons were less harmful to the environment than chlorofluorocarbons but they still had not a negligible impact on the ozone layer. In 2005, hydrocarbons (HCs) such as CO_2, cyclopentane and n-pentane and hydro fluorocarbons (HFCs) replaced HCFCs. Today, insulated enclosures are generally made with polyurethane foam expanded to cyclopentane. The insulation performance of the insulated enclosure varies depending on the used blowing agent. Three samples of semi-trailers, each one referring to a different blowing agent, are compared in Fig. 3, through the probability densities of A_{12}. Differently as expected, the curve which refers to the sample of 46 semi-trailers foamed with cyclopentane has a peak at smaller values of A_{12} than the one referred to a sample of 108 semi-trailers foamed with R-141 and the one referred to a sample of 47 foamed with R-11. Even if, cyclopentane is the blowing agent with the poorest initial thermal conductivity, it seems to be the one which allows a better long-term preservation of the insulating properties.

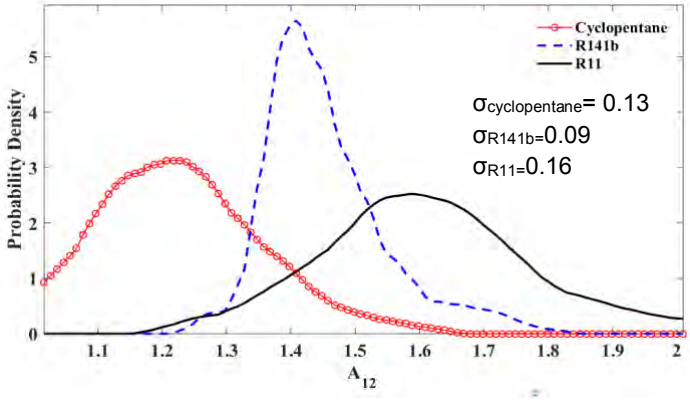

Figure 3: Probability densities of A_{12} for vehicles foamed with different blowing agents (cyclopentane, R141b and R11).

3.3 Influence of the Body Manufacturer

Manufacturing technology and assembly process vary from one body manufacturer to another and have an influence on the initial performance of the vehicle as well as on the long-term ageing. This aspect was already pointed out by Boldrin et al. (1990). The probability densities of A_{12} of different manufacturers of trucks are presented in Fig. 4. The number of vehicles considered here varies from 30 to 140 vehicles. The peaks of the curves are located at different values of A_{12}, highlighting the fact that each manufacturer has a different performance at the initial time as well as in the long term. The body manufacturer presenting the smaller dispersion of the values of A_{12} is the manufacturer number two. This manufacturer has a probability density represented by the curve having a more regular shape and with the smaller width. As a matter of fact it presents the lowest standard deviation (σ_{Manuf2}=0.15). Its manufacturing and assembly process appears to be more homogeneous than the others.

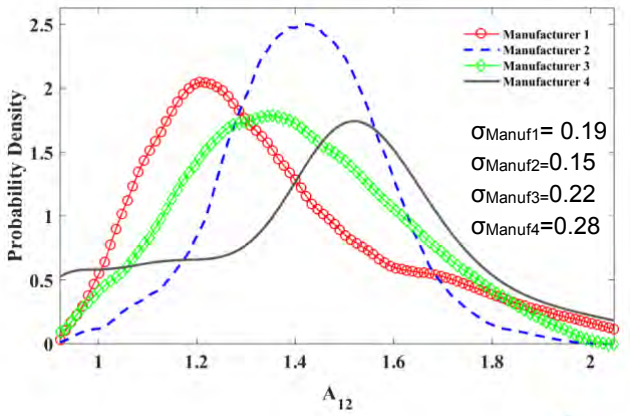

Figure 4: Probability densities of A_{12} for four different manufacturers of trucks.

3.4 Influence of Different Architectures of Refrigerating Units

Previous studies (Panozzo et al., 1999 and Capo et al., 2018) pointed out that the presence of the refrigerating unit causes further thermal losses and accelerates the ageing of the vehicle. In refrigerated transport it is possible to identify two different kind of refrigerating units' architectures: the monoblock architecture and the split one. The first one provides a cabinet which encloses the refrigeration circuit, the compressor and the fan. This cabinet is installed through a protrusion realized on the entire wall (front side of the vehicle). The wall due to this perforation has a reduced insulating performance. The second one, the split system, is characterized by an internal unit and an external one connected through the passage of two pipes in the wall. It requires only the realization of holes for the passage of the pipes. According to the different architectures, performances may vary. The probability densities of A_{12} for 533 vehicles equipped of monoblock mono-temperature units and 252 split mono-temperature units are presented in Fig. 5. The curve referring to monoblock units has a smaller width than the one referring to splits ones (i.e the standard deviation for monoblock units, $\sigma_{monoblock,units}$ is smaller than the standard deviation of split ones, $\sigma_{split\ units}$) . This is due to the fact that monoblock units are installed through a more repeatable and standardized process. As a matter of fact, the dispersion of the values of A_{12} is less for monoblock than for split units. Even if there is greater diversity in the installation on the vehicle of the split groups, this architecture has less influence on the long-term performance: the peak of the curve of split units is, for this reason, shifted to the right (i.e. at lower values of A_{12}).

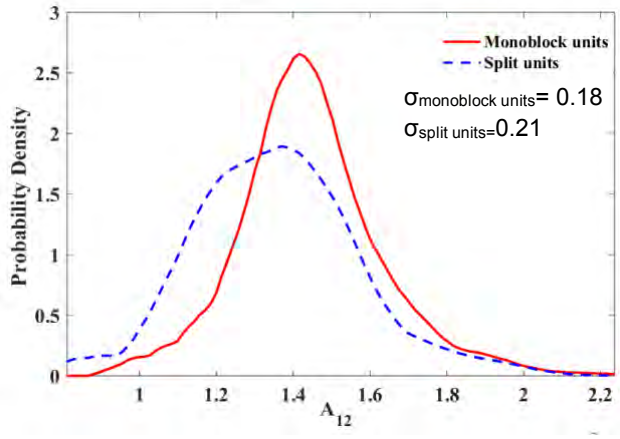

Figure 5: Probability densities of A_{12} for 533 vehicles equipped with monoblock units and 252 vehicles equipped with split units.

3.5 Usage of the Vehicle

The usage of the vehicle is one of the factors which allow a better understanding of the ageing phenomenon. Boldrin et al. (1993) highlighted this aspect. Different samples of vehicles dedicated to different kind of transport are presented in Fig. 6. In order to compare the ageing of these vehicles to the ageing of the vehicles presented by the cited studies, results of Fig. 6 are reported in terms of the annual ageing rate, through the *C.I.A.* parameter (see eq. 4). These results are

comparable to those presented by Boldrin et al. (1993) and confirm that the greater *C.I.A.* corresponds to vehicles dedicated to the transport of meat. In this type of transport the presence of the rails for suspending the carcasses on the roof may cause increased mechanical stresses for the body of the vehicle.

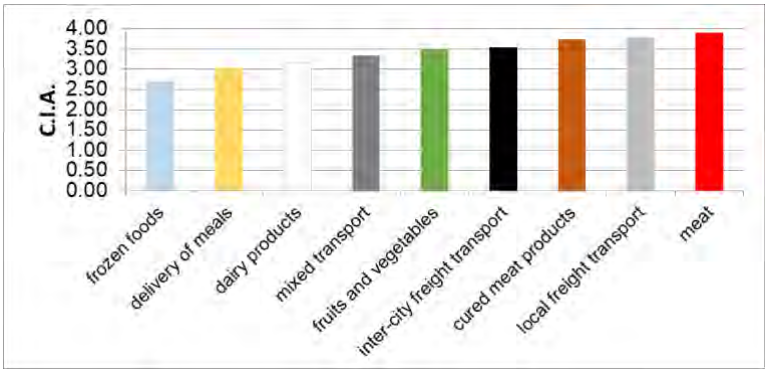

Figure 6: Average annual ageing coefficient (B. Boldrin et al. 1994) for samples of vehicles dedicated to different kind of transport.

4. COEFFICIENT F

In order to rank the importance of the factors having an influence on the ageing phenomena, presented in section three, a new weighting coefficient can be defined as follows:

$$F = \frac{MAX\ (average\ annual\ ageing\ coefficient)_i}{\min(\ average\ annual\ ageing\ coefficient)_i} \qquad \text{Eq. (5)}$$

Where the annual ageing coefficient is calculated using eq. 4 and the subscript i indicates the *i-th* factor. Note that F is a ratio of two quantities that are averaged over highly curated values, so as to limit any bias since no outliers exist. Fig. 7 shows the values of coefficient *F* calculated for each factor presented in section three showing their importance on the ageing process. Blowing agents and type of refrigerating units are the factors that more than all other factors have influence on the ageing of refrigerated transport equipment. The *F* coefficient allows ranking factors and thus provides a feature selection method. Such an approach is required to be able to predict K_{12} values using machine learning techniques. This is out of the scope of this paper.

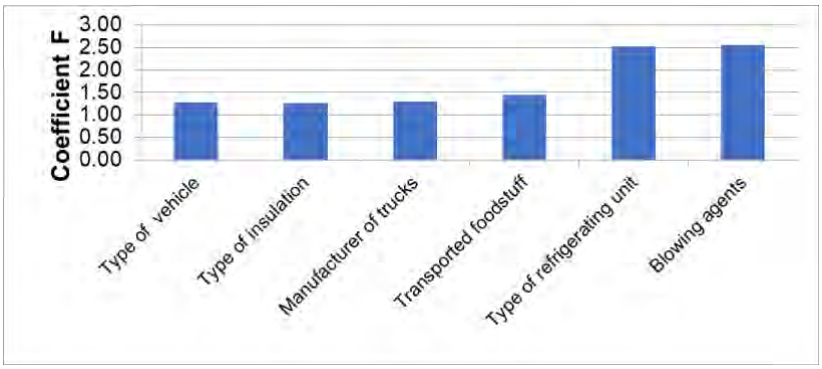

Figure 7: Coefficient F for factors affecting the ageing of refrigerated equipment

5. CONCLUSIONS

This paper reports the statistical analysis of the results of *K* coefficient tests realized in the

laboratory of Cemafroid for a sample of 1158 in-service refrigerated vehicles. This analysis allowed confirming the influence of factors already studied: the type of vehicle, the influence of manufacturer and the type of transport realized. Other important factors not yet considered before were analysed. Results highlighted that the performance in the long-term is higher for those refrigerated vehicles which insulated enclosures are assembled on their platforms than for vehicles with an integrated insulation. The influence of the refrigeration unit on the performance of the refrigerated vehicle was already treated in previous papers (Panozzo et al., 1999 and Capo et al., 2018).Through this statistical analysis it was possible to put in evidence the influence of the architecture of the refrigerating unit. Monoblock units are installed through a more homogeneous technology than splits ones but cause a greater reduction of the insulating performance due to the perforation that must be realized on the wall for their installation. Another important aspect, relevant for understanding the ageing phenomena, highlighted by the present study, concerns the influence of the blowing agent. Three samples of refrigerated semi-trailers foamed with different blowing agents were compared. This comparison showed that semi-trailers foamed with cyclopentane have better performance in the long period. It is important to point out that the analysis presented in this paper is made by comparing the insulation performance of refrigerated vehicles at twelve years of life to the initial performance of their reference prototypes. As stated by Capo et al. (2018) the K value of the reference prototype, K_p, is not the most correct indicator for the ageing evaluation due to the fact that reference prototype may have small differences in size and geometry, and hence a different initial K value compared to the initial K value of the vehicle realized in the series. Testing the vehicles realized in the series at the beginning of their life and following the evolution of their K coefficient during the whole life cycle is of primary importance for the study of the ageing phenomena.

NOMENCLATURE

A_{12}	ageing	t	time (s)
$C.I.A.$	average annual ageing coefficient	N	Number of years
Q	power (W)	ext	external
S	Area (m^2)	int	internal
K	overall insulation coefficient $(W.m^{-2}.K^{-1})$	p	prototype
T	Temperature (K)	n	n-th year
F	Weighting coefficient	i	i-th

REFERENCES

Boldrin, B., Minotto G., Panozzo, G., Toniolo, B., Varotto, G., 1990. Ageing of insulated vehicles: statistical elaboration of test result. Proc. of Commissions B2, C2, D1, D2/3, Dresden, Germany, IIF/IIR, 839-845.

Boldrin, B., Minotto., G., Panozzo, G., Toniolo, B., Lanza, W., Florio, G., Jacobini, A., Sallusti, L., 1993. New data about ageing of insulated vehicles in service: a statistical analysis. Proc. Commissions B1, B2, D1, D2/3, Palmerston North, New Zealand, IIF/IIR, 555-564.

Capo, C., Bourez, D., Cavalier, G., 2018. Le parc de transport des engins sous température dirigée en 2017. Revue générale et du conditionnement d'air, Vol. Mai/Juin 2018, 25-32.

Capo, C., Latchan, F., Michineau, T., Petit, J.M., Revellin, R., Bonjour, J., Cavalier, G., 2018. Factors affecting the ageing of refrigerated transport equipment. Proc. 5th IIR Conference on Sustainability and the Cold Chain, Beijing, China.

Panozzo, G., Alberti, O., Toniolo, B., Barizza, A., Boldrin, B., 1999. Parameters affecting the ageing of insulated vehicles. Proc. 20th International Congress of Refrigeration, IIR/IIF, Sydney, Vol. IV (Paper 472).

Panozzo, G., Boldrin B., Minotto, G., Toniolo, B., Biancardi, N., 1995. Ageing of insulated vehicles: theoretical model and experimental analysis. Proc. 19th Int. Congr. Refrig., Den Hague, Netherlands, Vol. II, 583-589.

Manuscript ID: 1691
DOI: 10.18462/iir.icr.2019.1691

Repair of Cables for Refrigerated Containers to Prevent Fires

Richard LAWTON[(a)], Christopher RHODES[(a)], Paul CLARKE[(b)]

[(a)] Cambridge Refrigeration Technology,140 Newmarket Road, Cambridge, CB5 8HE, United Kingdom, crt@crtech.co.uk

[(b)] A P Moller Maersk, Esplanaden 50, 1908 Copenhagen K, Denmark

ABSTRACT

This paper analyses the current issue of fires occurring in refrigerated containers during transportation deemed to have started in refrigeration machinery or cargo, the reasons behind such fires and recent developments in technology made with a view to reducing the frequency of such incidents and the safety implications. Initially an overview of the issues faced by operators of refrigeration machinery and the relevant codes of practice is presented. Details of current working methods and requirements of personal in a variety of departments are also considered. The principal causes are examined, discussion of methods to prevent failures on existing and future refrigeration systems and the operational issues surrounding any changes to work practices considered. The overwhelming majority of these hazardous refrigeration machinery fires are not as a result of the machinery itself or the cargo but rather damage to power cables and their subsequent sub-standard repair.
Keywords: Safety, Fire, Hazards, Cables.

1. INTRODUCTION

Whilst design of intermodal thermal containers (ITCs) is regulated by standards such as ISO-1496 the operation and use has to be by there very nature less clearly defined.
Refrigerated containers are moved by truck to customers, loaded and then transported to a terminal before being loaded onto a ship. It is not uncommon for containers to be discharged from one ship and then placed on another before reaching their final destination.
A further complication is that a container is not always handled by the shipping company that is operating it. They are also serviced by a network of independent companies, many in remote places, they are handled by third party terminals and are transported sometimes as “slot chartered”. As refrigerated containers are constantly on the move there is a temptation to carry out a quick repair, just to get it running as they know they are passing it on to the next operator in the chain and unlikely to come across it again.
On ships it has been determined that the overwhelming majority of these hazardous refrigeration machinery fires are not as a result of the machinery itself or the cargo but rather damage to power cables and their subsequent sub-standard repair.
One solution will be discussed by this paper is to provide in the repair kit a design of a stand-alone cable splice requiring little technical prowess that can be installed quickly and being virtually impossible to assemble incorrectly.

2. CONTAINER FIRES

There are 1.2 million refrigerated containers circulating around the world carrying refrigerated cargo, each container usually manages around four journeys and therefore is moved, plugged in and then unplugged several times during each journey.

Naturally with this number of refrigerated containers circulating and as they are electrically powered there are a number of fires. Fires are principally caused by three main issues, mis-declared cargo or dangerous cargo, defrost heaters and damaged power cables.
For defrost heater fires and other internal defects sensors will cause a refrigeration system to shut down in the event of continuous readings outside of the predicted regime that is expected when the system works as designed. Excessive heat emitted by motors or heaters can be inferred by increased current draw on one or more phases and various pre-trip inspection (PTI) procedures which can be carried out from the human-machine interface (HMI) will enable technicians to diagnose any such issues which may be encountered. The voltage of the power supply is measured by the control system and any irregularities will cause the controller to take corrective action or shut down the system. Poor connections at contactors are most likely to result in localised heating the will cause the conductor to fail before a fire starts. This will have the effect of triggering an alarm or a complete shutdown as the phase current will not be balanced. As ITCs have a four wire three phase supply it is required that each phase is evenly loaded to prevent damage to components.
However damage to cables cannot be detected by the control system and further ships electrical systems do not have an earth leakage detection system. Consequently cable fires on ships are an increasing problem. According to the largest shipping line (Ref, 2018) each year cable tray fires result in the total loss of around twenty containers of their containers, equating this to the overall market this means that around 100 containers are a total loss and an unspecified larger number are damaged.

3. CABLES AS A WEAK POINT

The power cables of ITCs experience more potentially-catastrophic events than any other part of the refrigeration system. Cables running from a power source either on a vessel or on land are exposed to possible damage from the cable being run over and crushed or snagged with insulation damage or stretching.
On vessels and in terminals it is not uncommon for containers to be accidentally discharged or moved whilst still connected to the ship's power supply. To avoid excessive damage cable cutters are incorporated into the design of the refrigeration system to avoid ripping out the control box. This results in a relatively clean break to the cable at the refrigeration system end.
The power cable according to ISO 1496-2 is defined as 20m long and therefore when damaged, repairs rather than replacement are encouraged by shipping companies, most allowing 2 or 3 repairs in its length with an approved cable splice.
In addition non-critical damage to cables have the potential to become critical with further wear and/or damage which is more likely to occur at the weakened section. As wires become stretched or individual cores or multi-core wire break the cross sectional area decreases. Due to the relationship between heat dissipated and cross sectional area there is a point where for a given current a wire will be too thin to safely carry the current required. Once this process starts it often snowballs due the effects on electrical resistance and heat capacity. It is not possible to see the effects of wire temperature until the insulating sheath around it starts to melt and even this may not be picked up on for a variety of reasons. Such defects often occur locally and a cable may be relatively cool to touch several meters away however cable lengths are around 20m and not always readily accessible even if time permitted regular inspections.

4. POORLY EXECUTED CABLE SPLICES

As a poorly executed cable splice experiences forces such as being coiled, uncoiled, pulled on, vibrations etcetera the connection will get worse and cross sectional area reduces leading to excessive heat. Although the heat flow to the surroundings of a wire varies predominantly with sheathing material, surface area and temperature difference the heat dissipated increases rapidly with decreasing cross-section. In normal conditions there is a cross-over point where the heat flow out of the wire is equal to the heat dissipated within the wire and the wire is at some temperature above its surroundings. Wire sheaths will start to

melt and eventually catch fire if the temperature in the wire becomes high enough. Often the materials used to wrap a cable splice will start to fail before the protective sheath.
Fig. 1 below shows several examples of cable splices found on in-service power cables



Figure 1: Examples of cable substandard splices

5. METHODS OF REPAIR

Ideally repair would be achieved by entirely replacing the cable, however this comes with a considerable cost and therefore most shipping companies allow several repairs as already indicated. Repair should be carried out by cutting out the entire portion of damaged cable and the outer sheathing removed enough to facilitate repair but not so much as to leave excess conductors unsheathed. Each of the four conductors should have their sheathing removed neatly and with no damage to the conductor before being tinned and cleaned. A Lineman splice, see Fig. 2, should be used as the joining method as this is the most reliable way to ensure good electrical conductivity without reducing cable cross section and at the same time provide sufficient mechanical strength to withstand significant tensile forces which may be applied during normal use. Lineman splices should be staggered on adjacent conductors to avoid a large build up. A suitable heat shrinkable sleeve providing sufficient electrical isolation should then be applied in accordance with the manufacturer's instructions around each conductor. The four spliced conductors should then be covered by an external sleeve shrunk around the outer sheathing of the original cable. Ideally sleeves should be UV resistant and water tight. Whilst not difficult to accomplish the process requires various tools, materials and significantly more time then is often spent by technicians repairing cable splices.



Figure 2: Lineman splice(NASA, 2011)

No internationally recognised standard exists with regards to making a cable splice to a minimum level of safety. Often repairs are conducted by technicians with a low level of skill, insufficient equipment and under time pressure. This results in inconsistent and often low quality repairs. It is not uncommon to find wires twisted together and wrapped in insulation tape without any soldering to ensure good connection. Further protection against moisture ingress is rarely applied and the resulting splice is can be significantly inferior with regards to electrical conductivity, mechanical strength and the chance of introducing foreign material increased. Other possibilities include using screw terminals to join wires and varied use of tape, heat shrink wrap and other similar materials. Screw terminals may not be available in the correct size - too small and cross sectional area of the conductor will be reduced and the fastener will not work as intended; too large and the conductor may not be securely held by the fastener.

Applying a suitable sleeve may also be problematic as open flames are not permitted on vessels or even many depots and terminals. Some exceptions known as “safe-areas” are available however to be of use on a vessel the cable would have to be removed from the main breaker requiring more time. On land the container could be positioned into a safe area however this requires time and logistical arrangement. Heat guns could be a solution to this however they provide practically no secondary value and require a single phase electrical supply.

In addition to low-skilled technicians there are also supply difficulties in some regions. Some service depots will not have suitable equipment and/or materials to enable them to carry out a cable splice to what would be considered a satisfactory level elsewhere. It is also a possibility that technicians simply will not know the dangers that may occur as a result of their work. It is considered unlikely that a technician would knowingly do a poor job with total disregard to the safety of others.

Time pressures are also a factor. Cable splicing should not, even when done to a very high standard, take a long time therefore it could be perceived as being of less importance and treated as such by technicians. Any solution to standardising splicing must consider this; it cannot take significantly longer to do then stripping the sheathing back, twisting the wires together and wrapping in tape otherwise it will not be used by technicians.

6. EVOLUTION OF CABLE SPLICE KIT

The first attempt at creating a stand-alone solution was made available as a consumable to vessels and depots in 2010. The kit comprised a four-gang cylindrical screw terminal connector, self-amalgamating tape, a tightening tool and a tool to strip the conductors and outer sheathing.

The correct procedure to install the kit was to cut out the damaged section of cable and strip the outer sheathing and conductors. The conductors were then inserted into the screw terminals and these tightened with an Allen key provided. Finally the self-amalgamating tape was installed to produce a water tight seal. The screw terminals were sized to take all cable sizes as this varies by manufacturer however variation is small due to similar power demands combined with the cost of cable leading to the smallest diameter whilst remaining safe with maximum current draw before the main circuit breaker trips. An example of the kit is shown below and correctly installed kit is seen in Fig. 4.



Figure 3 Fast splicing kit

Despite the cable splice kit becoming the only approved way to perform such maintenance on the fleet of one container owner and the apparent simplicity the problems persisted. Not only did splices continue to be found as seen in figure one a new problem of the cable splice kit being used incorrectly emerged. Examples were found where the screw terminals had not been sufficiently tightened resulting in poor connection and excessive heat buildup.
Improper use of the self-amalgamating tape occurred along with instances where it was disregarded altogether in favour of tape or no protection at all. The splice kit did not stand up to tugging, i.e. opposing forces applied either side of the join, and mechanical connections were compromised.



Figure 4: Initial solution installed correctly



Figure 5: Final solution installed correctly

Initially the connector block was redesigned with the intention of reducing the possibility of incorrect installation. Fasteners were designed with sheer heads were employed to this end. This contributed to reducing issues of not being tightened enough or even over-tightening which could damage the conductor. It remained possible to install the connector block with insufficient tightening.
Further difficulties in ensuring the self-amalgamating tape was installed correctly required the whole kit to be redesigned. The designers of the next iteration placed a higher priority on water tightness and mechanical strength as a result of how the product had been used. High strength plastic, silicon seals and careful design of the connector block achieved this. Compromise was made and the cable splice kit no longer included all the tools necessary. Wire cutting and sheathing removal would require tools that were not supplied with the kit.
Currently cables are spliced with the kit using the following technique. The damaged section of cable is cut out, external sheathing removed along with a small amount of sheathing from

the end of each conductor. Between three and six times the wire diameter should be stripped from the sheathing allowing good connections with no conductor being exposed outside of the connector block. Once the conductors are located in the screw terminals the sheer screws are tightened until the heads break off. It is then possible to cover the splice with the plastic protective casing. If the screws are not suitably tight the head(s) of the screw will prevent the outer cover passing over the connector block. Tightening the collars at each end compresses the silicone seals onto the cable forming a water tight seal. Once a good seal is made it is not possible to undo the collars however this also means that they will not loosen with time and allow moisture ingress.
Using a cable splice kit designed to make incorrect installation challenging is only a good solution where the kit is available. In less accessible terminals there will inevitably be a lack of uptake of such kits due to perceptions that they are surplus to requirements despite availability and mandatory use. There will also be times on vessels where technicians could run out of kits if they have numerous cable breakages during a voyage. Unfortunately the benefits of such solutions will go unrecognised by the technicians who carry out repairs such as seen in Figure 1 therefore it is possible in the near future that cable splices will either by of a high standard when completed using the kit or of a very low standard when the kit is either not available or not used.

7. CONCLUSION

Fires in cables due to poor practices are now an acknowledged problem within the refrigerated container shipping industry. Whilst defrost heaters and cargoes are reasonably well protected against the same cannot be said for cable defects. This paper describes a type of cable splice that if implemented worldwide would help to eliminate the problem.
It is proposed to initiate an ISO standard as an addition to ISO-1496 to clearly define the types and assemble methods for cable splices.

REFERENCES

Data from the Maersk Shipping company, (2018)

NASA, (2011). NASA-STD 8739.4 with Change 6, “Crimping, interconnecting cables, harnesses and wiring”, National Aeronautics and Space Administration, Washington DC.

Manuscript ID: 1692
DOI: 10.18462/iir.icr.2019.1692

Insulated bodies for refrigerated transport vehicles: past, present and future construction techniques

Claudia CAPO[(a)], Thomas SUQUET[(a)], Nicolas BOUDET[(a)], Gérald CAVALIER[(a)]

[(a)] Cemafroid, 5 Avenue des Prés - Fresnes cedex - France

gerald.cavalier@cemafroid.fr

ABSTRACT

Refrigerated vehicles used for cold chain are generally built today with «sandwich» panels in which the insulation is generally made of polyurethane foam. The term polyurethane stands for a family of insulating materials that in addition to the polyurethane (PUR) also includes polyisocyanurate foams (PIR). Sometimes vehicles are also realized with expanded polystyrene (PSE). Construction techniques vary from one country to another and the insulation properties are obtained by means of expanding gases. These gases have undergone a process of evolution since 1970, when chlorofluorocarbons (CFCs) were used for the construction of insulated vehicles. Design and technology continue to adapt to meet the regulatory requirements, improve the performance and reduce the environmental impact. This paper presents the evolution of construction techniques and materials used for the manufacture of insulated vehicles. Past, present and future trends in three key regions: Europe, Asia and North America.

Keywords: Refrigerated Vehicles, Sandwich Panels, Insulating Materials, Expanded Gases, Construction Techniques, Environmental Impact, Europe, Asia, North America.

1. INTRODUCTION

The demand for cold chain all over the world is growing (Cavalier and Tassou, 2011), but there is no cold chain without refrigerated transport and no refrigerated transport without insulated and refrigerated transport equipment. Since the first refrigerated transport by the French engineer Charles Tellier in 1876 (Tellier, 1910) the transport body insulation was a major issue. The goal of body manufacturers has always been to construct a lightweight body, having sufficient strength, in which the insulation could stay dry and maintain its original insulating value. First of all insulation protects perishable food from temperature excursions and then plays a role for food safety, especially when there is a break in production of cold in the refrigerated vehicle. However, in reducing the need of refrigeration, insulation has also an environmental impact contributing to save energy. An insulated body, in fact, when matched with suitable refrigeration system, should provide economical temperature control for the foodstuffs being transported or stored. The techniques developed by engineers and manufacturers changed all along the last 140 years to answer the evolution of transport from boat cold chambers, to rail insulated coaches since the beginning of the 20th century, to insulated trucks and trailers since 1940's and finally to insulated and refrigerated parcels for online sales recently. However insulation is also facing economic, environmental and legal constraints such as Kigali amendment or European F-Gas regulation on F-Gas mitigation, that have an important impact both on insulated materials and construction techniques. The agenda of environmental regulations oblige manufacturers to change some insulated materials within the next years. It is then important to analyse the different insulated materials currently used, the construction techniques used by insulated body manufacturers potential and finally to make an assessment of the potential alternatives for insulated body manufacturing in the near or mid-term future.

2. INSULATED BODY CONSTRUCTION TECHNIQUES

In refrigerated transport, the insulation of the body is one of the basic elements of the refrigerated equipment. The cooling power to be produced to obtain the desired temperature inside the cargo primarily depends on the insulation efficiency, characterized by the so-called *K* coefficient value. This coefficient is a parameter to be controlled as required by ATP (the International Agreement for the Transport of Perishables Goods) of the United Nations, after the manufacturing of the body and at different moments of the vehicle's life (after twelve years of life in France, but also after six and nine years of use in Italy).
The overall insulation coefficient is calculated through the formula:

$$K = \frac{Q}{S.\Delta T} \qquad \text{Eq. (1)}$$

Where *Q* is the heating power or the cooling capacity, as the case may be, required to maintain a constant absolute temperature difference ΔT between the mean internal temperature T_{int} and the mean external temperature T_{ext}, during continuous operation, when the mean outside temperature T_{ext} is constant for a body of mean surface area *S*. The mean surface area of the body is represented by the geometric mean of the internal surface area S_{int} and the external surface area S_{ext} of the body,

$S = \sqrt{S_{int}\ S_{ext}}$.

Depending on the value of the K coefficient, insulating vehicles and bodies are classified in:
- Normal Insulated Equipment (IN) when 0.40<K≤0.70
- Reinforced Insulated Equipment (IR) if K≤0.40.

2.1 The First Insulated Bodies

One of the first insulated body was built with a double panel system (see Fig.1) filled with the insulation material. For the insulation of this refrigerated ship, the "Frigorifique", Tellier built wood walls with wood panels of 12 mm covered with wax paper and assembled together with pine wood spacers of 10 cm for the external walls.

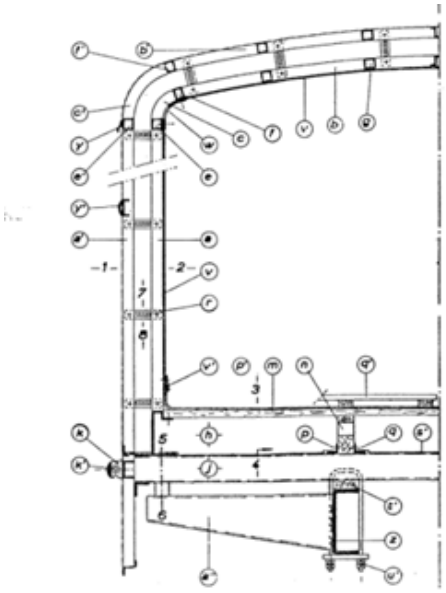

Figure 1: insulated enclosure built with a double panel system (Bogrow, 1982).

The space between insulation walls and the ship's hull was left open to manage air circulation, and collection of condensation. The internal wall separating cold chamber and machinery was thicker with 22 cm on insulating material. In both cases the volume between the wood panels were filled with either cork or straw when there was no more cork available. The internal face of the walls was covered with 1 mm plates of galvanised steel. This technique was adapted for the first insulated and

refrigerated rail coaches in the 1880s. This technique was improved but also used for the first insulated and refrigerated trucks from 1930s to 1960s. This double bodywork filled with insulating material remains of poor insulation performance. As stated by Bogrow (1982) in such a system, even with an insulating material with a thermal conductivity of 0.035 W. $m^{-1}.K^{-1}$, the overall insulation coefficient could not be lower than 2.25 $W.m^{-2}.K^{-1}$, a very high value compared with those of today.

2.2 Sandwich Panels: the European Race to *K* value

When the new insulating materials appeared in the 60s started, a new conception of the insulated bodies was developed in Europe. The technique of sandwich panels appeared. Slices of insulating foam are inserted in between still plates or polyester coverage reinforced with fiberglass. Where it was hardly possible to reach a *K* value of 0.50 $W.m^{-2}K^{-1}$ in the 50s with 150 to 180 mm of insulating material, it became possible to reach *K* values of 0.25 with only 80 to 100 mm of insulation: a tremendous progress in insulation performances. This technique took over the former double bodywork insulation and from nothing in 1952 reached 65% of the fleet in the 70s and 80s.
The ATP regulation, asking for high insulation performances with a maximum *K* value at 0.40 for frozen products, helps to switch from the old to the new technology. With regular test it also brings to good ageing performances of the equipment such as those presented by the truck shown in Fig. 2, tested at 30 years in Cemafroid with a *K* value of only 0.46 $W.m^{-2}.K^{-1}$.



Figure 2: Insulated enclosure built with a double panel system. 30 years old French refrigerated truck in Cemafroid ATP test laboratory in 2016.

European body manufacturers have also developed injection technologies. The insulating polyurethane foam is injected in between two skins in a mould. The skin may be made of steel or polyester. The full body may be made of injected panels or only some components most of the time doors and openings. Since 1970 all the European production is built with sandwich panels or injected panels either with polyester or metal skins. Sandwich panels allow very high thermal performances with a large variety of options and adaptations of the refrigerated transport body. The tests realised by Cemafroid in 2018 (Capo et al., 2018) underlined the quality of the production of this technology and its insulation performances even with thin panels down to 55 mm thickness.

2.3 The Race to Power in North America

While in Europe the construction technique with sandwich or injected panes was spreading, in the US and Canada another construction methodology was developed. The principle of double bodywork was also abandoned but the US bodybuilders choose a projection technique to insulate refrigerated transport equipment. In this kind of technique, a galvanised or stainless steel external or internal bodywork assures the mechanical structure of the body. It is made of vertical steel ribs on which a steel plate is riveted. On the other face, the polyurethane foam is projected on liquid phase and it is blowing on the panel. Then the panel is covered either with an aluminium, stainless still or polyester skin to finish the body. This technique also used in Australia and Asia is far cheaper but offer poorer insulation performances as shown by Estrada-Flores and Eddy (2006). Over some 100 insulated bodyworks they found only one with a *K* value lower than 0.40 $W.m^{-2}.K^{-1}$. As stated by Smith (2017) these insulated bodyworks are also far more sensitive to humidity. Smith (2017) related a two tonnes/vehicle water absorption by insulated bodyworks as “normal”, pointing out that their insulating performance may easily degrade within two or three years because of regular activities of pressure

washing. As far as the panels are not sealed they can absorb water which remains in the insulating material withdrawing its insulating performance and also introducing an important mass of water that have to be transported continuously. This additional mass of water also requires freezing if the payload, is deep frozen food. These inconveniences are balanced by installation of more powerful refrigeration units able to compensate thermal losses, but of course also result in more energy consumption. These insulated transport equipment are also facing a rapid and heavy aging, with their insulation performance decreasing rapidly (Fig. 3a and 3b).As a result these equipment have then much greater energy consumption per year due to higher thermal losses than optimally operating equipment. They can consume twice or three times more fuel per year. Their global environmental performance is very low compared to average European equipment.

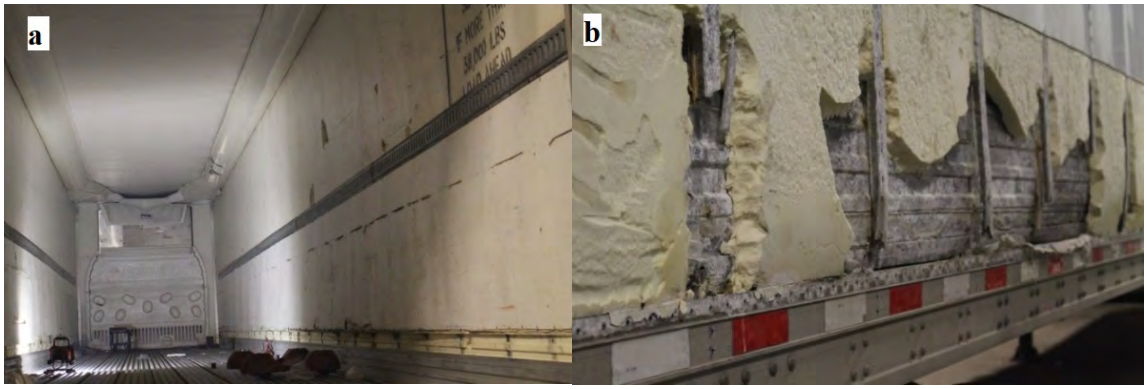

Figure 3: Two years old insulated Canadian semi-trailer: a) inside and b) after decoating.

3. INSULATED MATERIALS FOR REFRIGERATED TRANSPORT INSULATED BODIES

3.1 Natural Materials for Insulation of the First Refrigerated Transport Equipment

For the insulation of the cold room of the “Frigorifique”, Charles Tellier selected cork. Air would be the best insulating component after vacuum if it was possible to stop convection effects. It was necessary to find a way to encapsulate it in a material capable to store the largest amount of air. Tellier identified cork for its qualities, which at the time was not used as an insulating material. Cork has an important capacity of air storage, it is also waterproof which is an important quality for insulation in a boat and its thermal conductivity is around 0.040 $W.m^{-1}.K^{-1}$. Cork has been used for many years to insulate refrigerated boats. When the first insulated and refrigerated rail-coaches appeared in the 1880s cork was used as insulating material in between two wood panels. The first insulated trucks in the mid-thirties in United States and in the mid-forties in Europe also used cork encapsulated in between two wood panels. Cork is a very good natural insulation material, and harvested properly may be a renewable material; nevertheless its production is rare and not sufficient for the world insulation demand, neither in 1876 or nowadays. To insulate the “Frigorifique”, Tellier hardly found enough cork. To realize the full chamber insulation he was obliged to complete the insulating material by filling it with about 30 m^3 of chopped straw cut at 1 cm long. Chopped straw presented also good insulation properties but not so high than cork having a thermal conductivity around 0.070 $W.m^{-1}.K^{-1}$, which is nearly twice than the thermal conductivity of the cork. Chopped straw is also less waterproof. In the 50s, cork was abandoned for other insulating materials such as glass-wool and rock-wool (Bogrow, 1982). These materials have thermal conductivity around 0.045 $W.m^{-1}.K^{-1}$, comparable to that of cork but present also the important advantage of being far lighter and may be inserted in insulated transport bodies through the same technique used for cork. Nevertheless these materials have no mechanical resistance and are sensitive to humidity. They can absorb water in large quantity and totally lose their insulation performances.

3.2 The Impact of New Regulations on Refrigerated Transport between 1950 and 1970

The regulation on the refrigerated transport equipment with the French regulation of 1952 and the United Nations economic commission for Europe ATP agreement of 1970 impacted the construction

of transport equipment. The thickness of insulating material necessary to fulfil the requirements of these new regulations depends of its performance and the thermal conductivity. With the above solutions a minimum of 150 to 200 mm are necessary. These thicknesses reduce the useful transport volume and the payload of the truck or trailer. In the 60s the invention of new insulation materials on the market with the chemical foams was a very good opportunity for body manufacturers of insulated transport equipment. These foams offer a new characteristic with a rather good mechanical resistance offering new assembling possibilities. They are also far lighter than cork and not so sensitive to humidity than wools. First appeared Polyvinyl first appeared then polyurethane and polystyrene. Their thermal performance is far higher than cork, rock or glass wools. The excellent insulation properties of these materials are obtained through the use of blowing agents that have a low value of thermal conductivity. Depending on the blowing agent, the thermal conductivity of polyurethane foam is between 0.022 and 0.028 $W.m^{-1}.K^{-1}$, twice lower than those of cork and wools. Nevertheless, due to the presence of these blowing agents, these foams have as major inconvenience a strong direct environmental impact. The first blowing agents used to foam polyurethane were chlorofluorocarbons (CFC) such as R-11. Due to the high ozone depletion potential (ODP) of these agents, they were prohibited by Kyoto protocol. They were replaced in the 1990s by new blowing components mainly in the family of hydro chlorofluorocarbons (HCFC) such as R-141B. Then the HCFCs were also prohibited for their ozone depletion potential. In 2005 HCFCs were replaced by other blowing agents: cyclopentane, pentane and CO_2 were introduced to blow the polyurethane foams reducing strongly both ozone depleting potential and global warming potential (GWP). For polystyrene hydrofluorocarbons such as R-134a were introduced.

3.2 New Challenges for Chemical Insulation Foams

The insulation performance of the row foams have slowly decreased with these different changes of blowing agents. With European F-gas and Kigali amendments, HFCs will also soon be abandoned. HFCs have low ODP but they still have important GWP (1430 kg of CO_2/kg in the case of R134a). At the same time new blowing agents, including HFO's, have been tested. Manufacturers have also introduced new components in the foam mix such as carbon powder to improve their performance.

4. ALTERNATIVES FOR TRANSPORT INSULATED BODIES IN THE NEAR AND MID-TERM FUTURE

4.1 A Tremendous Potential of Improvement

In 2016, Cemafroid made a global assessment of the refrigerated transport fleet. Among the 4 million refrigerated trucks, trailers and semi-trailers in service in the world, 1 million are in Europe, 110 000 in China, 14 000 in South Africa and 10 000 In India. Considering the number of pieces of equipment in service worldwide, the effect of refrigerated transportation on the environment is not negligible. If the first regulation of refrigerated transport equipment were drawn only for food security and food safety, more recently regulations appeared to be also quite efficient for environmental issues mitigation as underlined by Cavalier (2016). The equipment rate is ten times more important in developed countries than in developing ones. On average there is one refrigerated vehicle for every 450 inhabitants in developed countries with respect to one vehicle for every 4 400 in developing ones (Cavalier, 2016). Although there is this disproportion among the different parts of the world, refrigerated transport is progressing and developing all over the world. This progress is needed to reduce the 360 million tons of perishable goods wasted every year in the world (Dupont, 2009) and it will be possible by the dissemination of the best refrigerated trucks manufacturing process but also by using new insulating materials and improved construction methodologies.

4.2 New Insulating Materials: Race to Thermal Conductivity

Facing the challenge of insulation performance and sustainability, insulating material manufacturers have developed new products. Polystyrene manufacturers must replace HFCs R134a as blowing agents in extruded polystyrene (PSE). They have proposed new PSE versions introducing graphite in the foam with a reduced quantity of R134a or without. They are replacing it with CO2 or hydrocarbons. This allows to keep the same insulating performances or to increase them while

reducing the environmental impact. Polyurethane manufacturers are producing HFCs free foam since 15 years, nevertheless they are trying to improve the insulation performances. They are testing new chemical mix for the foam but also new blowing agents such as hydrofluorooloeines (HFO). They are announcing higher thermal performances with thermal conductivity lower of ten percent.
Insulating material manufacturers have also introduced products such as vacuum insulated panels (VIP). VIP has higher performances but requires new assembling technologies. They can be introduced in sandwich panels but thermal bridges should not reduce the advantage of their insulation capacities. There are already commonly used for high performances insulated and refrigerated parcels, but still in test in refrigerated transport vehicles.
Aerogels, derived from silicate materials, present also very high insulation performances but with very low mechanical resistance alone. They represent a structural morphology (amorphous, open-celled nanofoams) rather than a particular chemical constituency.
They are already used in some insulated parcels for distribution of very high value products. They have been tested on reefer and tested by bodybuilders. They are among the most powerful insulation materials for the future since they offer several benefits over polyurethane foam and vacuum insulation panels. The principal benefits are superior insulation properties when compared to PU foams and a possibility of an absence of ageing that traditional materials exhibit. However, the use of such materials will prevent challenges as it does not have the structural strength that foam has especially when incorporated into a sandwich panel that many structures now rely on (Lawton and Marshall, 2007).

4.3 New Construction Scheme

Even with the best insulating material the global insulation performance may be low if the construction is not of good quality. The comparison between the overall insulation coefficient *K* measured according to ATP and the theoretical coefficient for a body only made with foam shows the potential of improvement for trucks and trailers insulation. Fig. 4 shows this comparison for fourteen prototypes of semi-trailers tested in Cemafroid test chamber following the methodology described by Capo et al. (2018). The white bars with the defined contours represent the theoretical *K* values for the prototypes, respectively $K_{p\text{-}th}$ and the filled bars represent the measured *K* values for these prototypes, K_p. The theoretical *K* value is always lower than the measured one. As pointed out by Capo et al. (2018) this is mainly due to the non-ideal foaming process, the thermal bridges and non-perfect sealing of the body. The theoretical *K* values were calculated by using the same formula introduced in Capo et al. (2018):

$$K_{th} = \lambda \frac{\sum \frac{S_i}{\delta_i}}{\sum_i^n S_i} \qquad \text{Eq. (2)}$$

Where, λ is the initial thermal conductivity of the foam, while S_i and δ_i are respectively, the mean surface and the thickness of the i-th wall of the insulated body. Eq. (2) gives an ideal reference value that neglects the thermal bridges and to geometric singularities. Most of these thermal bridges are due to wood or metal inserts necessary to clamp the body on the chassis, to fix the refrigeration unit on the body and moreover to install all the accessories inside the vehicle. New mechanical structures have been imagined such as carbon fiber bodywork directly insulated. This sandwich insulated carbon fiber body work would replace the assembled sandwich panels. Other structure modifications are also necessary to improve the connexion between refrigeration unit and bodywork. Evaporators and condensing unit are developed separately from the body while there are a lot of connexions and potential improvements with a strong reduction of thermal bridges. The tests of new ATP equipment conducted by Cemafroid in 2018 show an impact of the refrigeration unit installation of around 0.02 $W.m^{-2}.K^{-1}$ that is to say a deterioration of some 5 % of the *K* value of insulated bodywork even before its first utilization.

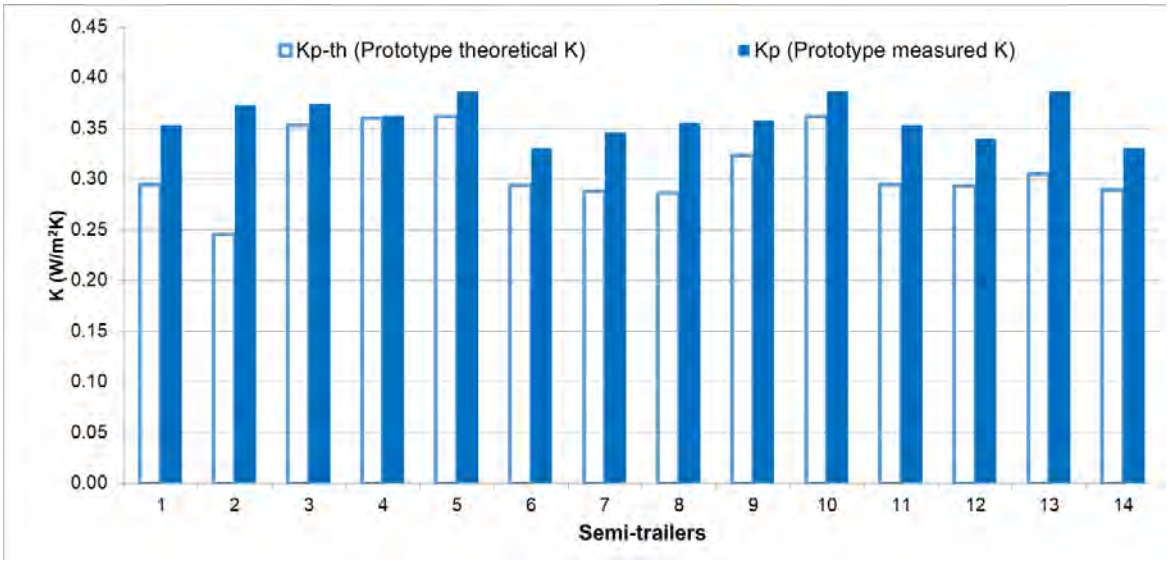

Figure 4: Comparison between theoretical and measured *K* values for 14 prototypes semi-trailers.

5. CONCLUSIONS

The 4 million fleet of refrigerated transport equipment may be classified in two major types: i) a high quality well insulated and quite well aging class built with sandwich panel technology mainly in Europe and, ii) a low cost, short living and poorly insulated class. Nevertheless, after eighty years of road refrigerated transport development in the world to face environmental and energy challenges both kind of refrigerated transport vehicles should change. Insulated bodies manufacturers should reduce direct impact on global warming banning the use of HFCs as blowing agents for insulating foams and the energy consumption by increasing the insulation performances. After 50 years of stability of the production it is certainly time to improve their performance and quality all over the world. It is the opportunity to strongly reduce the environmental impact of refrigerated transport.

NOMENCLATURE

Q	power (W)	*ext*	external
S	Area (m^2)	*int*	internal
K	overall insulation coefficient ($W.m^{-2}.K^{-1}$)	*i*	i-th
T	Temperature (K)	*p*	prototype
λ	thermal conductivity ($W.m^{-1}.K^{-1}$)		
δ	thickness (mm)		

REFERENCES

Bogrow, A. 1982. Evolution technique des véhicules à température dirigée. Génie Rural, Vol. Janvier-février, 21-27.

Bouchard, S., Smith, J. G., 2018. Chambres froides. Les remorques frigorifiques jouent un rôle crucial dans la chaîne du froid. Si vous croyez qu'elles n'ont pas évolué, vous vous trompez!. Transport routier, Vol. Janvier-février, 34-37.

Capo, C., Latchan, F., Michineau, T., Petit, J.M., Revellin, R., Bonjour, J., Cavalier, G., 2018. Factors affecting the ageing of refrigerated transport equipment. Proc. 5th IIR Conference on Sustainability and the Cold Chain, Beijing, China.

Cavalier, G. Sustainability in Transport Refrigeration Systems. Reference Module in Food Science, First Edition, 2016, Elsevier Inc. http://dx.doi.org/10.1016/B978-0-08-100596-5.03176-0.

Cavalier, G., Tassou, S. A., 2011. Sustainable refrigerated road transport. 21st Informatory Note on Refrigerating Technologies, International Institute of Refrigeration.

Dupont, J.L., 2009. 5th IIR Informatory Note on Refrigeration and Food: The Role of Refrigeration in

Worldwide Nutrition.

Estrada Flores, S., Eddy, A., 2006. Thermal performance indicators for refrigerated road vehicles. Int. J. Refrig. 29,889-898.

Lawton, A. R., Marshall, R. E., 2007. Developments in refrigerated transport insulation since the phase out of the CFC and HCFC refrigerants. Proc. 22nd Int. Congr. Refrig., Beijing, China, ICR07-D2-848.

Tellier, C., 1910. Histoire d'une invention moderne : le Frigorifique. In: Librairie Ch. De la Grave, Paris.

Manuscript ID: 1695
DOI: 10.18462/iir.icr.2019.1695

Ageing of Insulated Marine Containers

Richard LAWTON[(a)], Chris RHODES [(a)],Tobias MYNOTT [(a)]

[(a)] Cambridge Refrigeration Technology,
Cambridge, CB5 8HE, UK, crt@crtech.co.uk

ABSTRACT

Refrigerated marine containers are insulated with expanded polyurethanes foam. This foam has excellent structural and thermal insulation properties which is fundamental and key to the containers' design.
Due to environmental regulations, foam expanding agents such as CFC's HCFC's and now HFC's have been gradually and sequentially banned. Currently, the polyurethane foam expanding agent most commonly utilised is cyclopentane; like its predecessors it gradually leaks from the foam causing an increase in thermal conductivity known as "ageing".
Ageing data for containers insulated with polyurethane foam expanded with cyclopentane is presented over a number of years for both 40' and 20' containers. An estimate is made of the increased energy consumption commensurate with this increase over the lifetime of the container.
The results of this investigation has been incorporated into the latest version of standard ISO 1496-2 which now contains an informative annex describing this ageing.

Keywords: Blowing Agent, Foam, Insulated Container, Insulation, Intermodal Transport

1. INTRODUCTION

Insulated containers for carriage of temperature sensitive commodities come in many different designs depending upon the intended application. Such containers may be small with no auxiliary refrigeration system with an internal volume of less than $1m^3$ and up to $87m^3$ for road transport. Some regions permit larger vehicles than this however they are not approved for use in many countries and shall not be considered in this paper.
Common to many insulated containers is the use of expanded polyurethane foam and structural components. Increasingly energy efficiency regulations require improvements on existing coefficients of performance of refrigeration systems. Improving insulation is a very important part of reducing overall emissions as the heat flowing through the walls directly impacts upon the duty cycle of a refrigerating appliance. For small containers with no refrigeration system the impact of heat flow through the walls limits the duration that a commodity may be transported before product temperatures become unacceptably warm. The severity of such temperature excursions varies between minimal effect, such as a frozen cargo warming to a temperature still below -12°C, to cargo loss due to microbial/bacterial growth on raw meat. Reducing cargo loss is beneficial to society as a whole as the entire cold chain becomes more efficient.
Current regulation with regards to maximum heat leakage detailed in ISO 1496-2:2018 only mandates determination of overall heat transfer when a container is new and in good condition. Despite standards such as ISO 2440:1999 containing methodologies for ageing tests and previous papers by Wilkes et al (2002) and Cavalier et al (2016) with regards to increases in heat leakage over the lifetime of equipment the effects of ageing are often ignored from a regulatory compliance perspective and also calculations based upon the lifetime of a system. Insulated marine containers have an expected lifetime of 15 years and sometimes more therefore small changes in overall system (combined container and its refrigeration machinery) efficacy can greatly affect the energy consumption which has economic and environmental consequences as more power is required to maintain sufficient temperature control.
The ageing of polyurethane foam is only part of the deleterious effects of time and service as the structure of a container experiences wear and damage further contributing to increased thermal conduction to the cargo space.

2. MECHANISMS OF AGEING

Regardless of mechanical abuse that containers are subjected to throughout the cold chain chemical ageing will occur in the blown foam panels over time. Foam ageing is, in ideal conditions, the biggest contributor towards increased thermal transfer. Taking a typical refrigerated thermal container of sandwich panel construction with a 2mm Al external wall, a 50mm blown polyurethane foam interior and a 2mm Al internal wall and assuming a 40K temperature gradient we can calculate the influence of the foam on the total temperature change. The heat flux across each material interface must be equal due to conservation of energy therefore:

$$q = \left(\frac{\lambda \cdot \Delta T}{L}\right)_{foam} = \left(\frac{\lambda \cdot \Delta T}{L}\right)_{aluminium} \quad \text{Eq.(1)}$$

Thermal conductivity values of polyurethane foam and Al are 0.03 and 205W·m^{-1}·K^{-1} respectively. The total temperature difference is equal to:

$$T_{ext} - T_{int} = \Delta T_{foam} + 2\Delta T_{Al} = \Delta T \quad \text{Eq.(2)}$$

And by substitution:

$$\Delta T = \Delta T_{foam} \cdot \left(1 + 2 \cdot \frac{\lambda_{foam} \cdot L_{Al}}{\lambda_{Al} \cdot L_{foam}}\right) = 1.00001 \Delta T_{foam} \quad \text{Eq.(3)}$$

It is apparent that the heat transfer is mostly dependent upon the condition and quality of the insulating foam. Although the calculated value will change depending upon design and application of containers the heavy dependence upon the foam remains a valid assumption. During fabrication voids in the container are filled with foam and a blowing agent used to ensure homogeneity and to displace air and moisture.

Construction of containers has a structural bias as the integrity is of the utmost importance as failures could lead to serious injury or death in addition to cargo loss. The mechanical joints of marine thermal containers are rarely gas tight therefore the blowing agent will escape over time. In addition to this moisture and other contaminants will enter the foam further reducing its efficacy.

Mechanical damage to the protective Al skin from forklifts and/or pallet trucks inside and external impacts during ship-shore transfer can have an adverse effect on the encapsulated foam. Varying degrees of delamination occur which exposes the foam to the surrounding atmosphere. This is not accounted for with the testing conducted however moisture absorbed into foams is detrimental to insulating capacity. Impacts from movement apply stresses and strains to the mechanical joints which have to absorb the force which requires some flexibility in the structure which is not ideal for keeping the foam from exposure to contaminants.

The rate of increase in heat transmittance is greatest near the start of the container life cycle as air and other contaminants are absorbed into the foam. Once the foam has absorbed an unknown quantity of contaminants the blowing agent will, via diffusion, be displaced from the foam which will produce a slight rise in thermal transmittance but significantly less than the initial rises observed so far. It is theorised that the effect of contaminants initially entering the foam is of greater impact to the insulating properties than the displaced blowing agent.

At some point the insulating foam will lose all of its encapsulated blowing agent and reach a saturation point of contaminant absorption. Increases in thermal conductivity will plateau before the container reaches the end of its life as all of the blowing agent will have escaped and some maximum amount of foreign particles (eg moisture) will have been absorbed into the foam. It is not clear when this happens as continued testing over a four year period by the authors has not

produced a flat line with the thermal transmittance increasing each time at a relatively constant rate. Wilkes et al (2002) found that initially thermal conductivity rose quickly before slowing down.

3. CONSIDERATIONS FOR MARINE THERMAL CONTAINERS

Continued testing approximately every six months has been conducted on two 6.1m (20') marine containers. Testing has been performed in accordance with ISO 1496-2:1996 at two mean wall temperatures, 10°C and 20°C with both tests having a 20K temperature gradient from internal to external surfaces. Heat balance was used to maintain the temperature difference and a circulation fan employed to ensure minimal temperature spread through the conditioned volume. 24 thermocouples, 12 internal and 12 external, were used to record temperatures, these were located 140mm from the corners internally and externally along an axis extending through opposite corners via the centre of the volume. In addition thermocouples were placed 100mm parallel to the centre point of the four largest surfaces internally and externally. The results of testing were calculated over an eight hour period following a stability period. Over the course of eight hours the power fluctuations were below 3% and the average temperatures inside and out typically varying by <0.5K. Overall average figures were used to obtain thermal transmittance.
The 6.1 m containers arrived in Cambridge in mid-2015. One was stored internally and in use at around 25°C for 2 years before being repositioned to outside storage which averaged an ambient temperature of 10°C, the other remaining outside for the duration. Data is presented for both 10°C and 20°C mean wall temperature tests however showing relatively constant differences. Testing both mean wall temperatures show the same trend although the results are not directly comparable due to the refrigeration system properties. Thermal conductivity varies approximately linearly with temperature and Kay (1963) gives an equation for this:

$$\lambda = \lambda_0[1 + \beta \cdot (T - T_0)] \qquad \text{Eq.(4)}$$

The subscripts 0 refer to a standard reference point that the thermal conductivity is corrected from. For polyurethane foams the temperature coefficient is positive which sees thermal conductivity reduce with temperature whereas for most metals this is negative. The result of this is increased heat leakage through the machinery in colder ambient temperatures. Metal does not age as the foam does therefore any change in thermal transmittance of the container and machinery is entirely due to physical differences in the foam as it ages. Blowing agents are more temperature sensitive than foam and air so as it becomes displaced the curves for 10°C and 20°C transmittance values should converge to a degree which will give higher values at lower temperatures than would obviously be expected.

4. RESULTS OF TESTING

The results of testing can be seen in the graphs below. Thermal transmittance has been normalised to the manufacturer indicated value at 20°C. No value is given for 10°C therefore the results have been extrapolated to an age of zero and this value used for normalisation. Testing has been conducted on two 6.1m containers with the same refrigeration systems fitted and manufactured at the same time. One container has had light use and the refrigeration machinery changed several times before replacing the original system for thermal testing.
Combined standard uncertainty is shown for the measured thermal transmittance. Throughout testing the combined standard uncertainty has been between 3.5 and 4% with the average value, 3.7%, plotted.

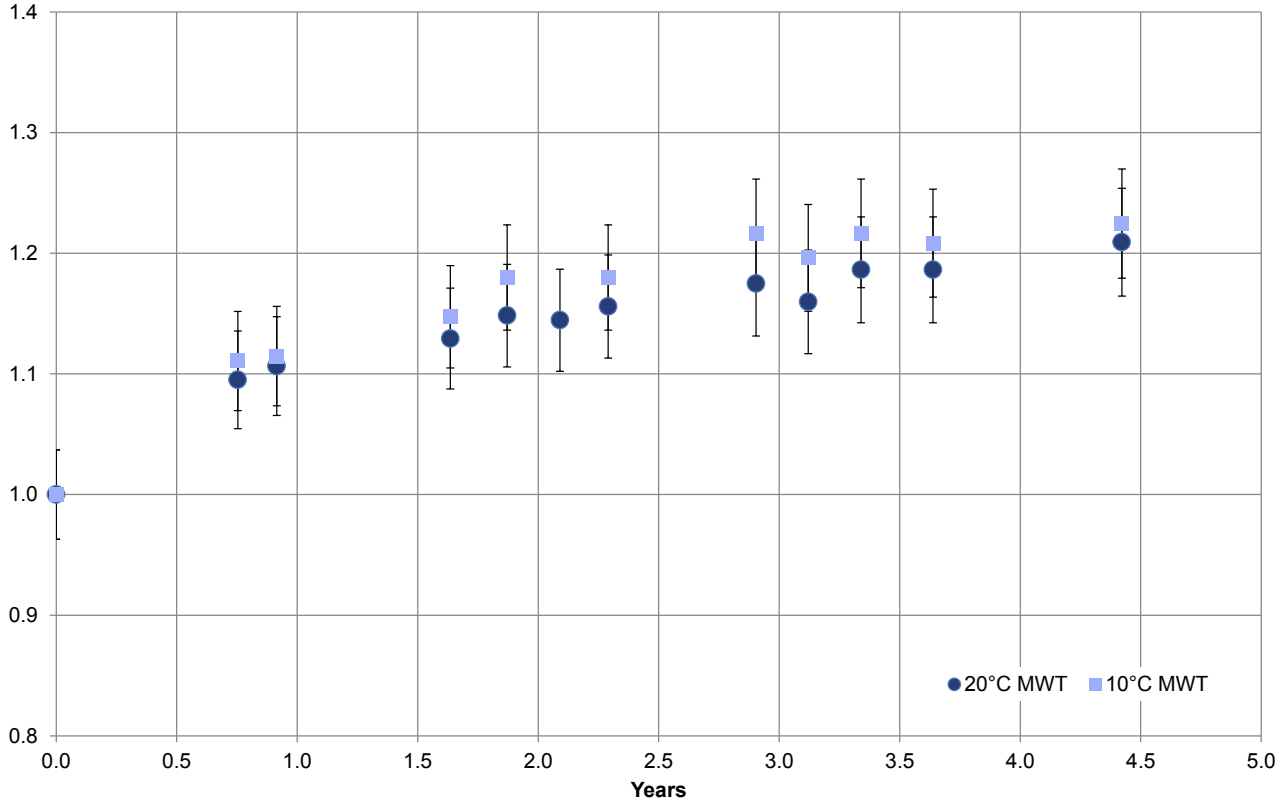

Figure 1: Thermal transmittance of a 6.1m container (machine changes)

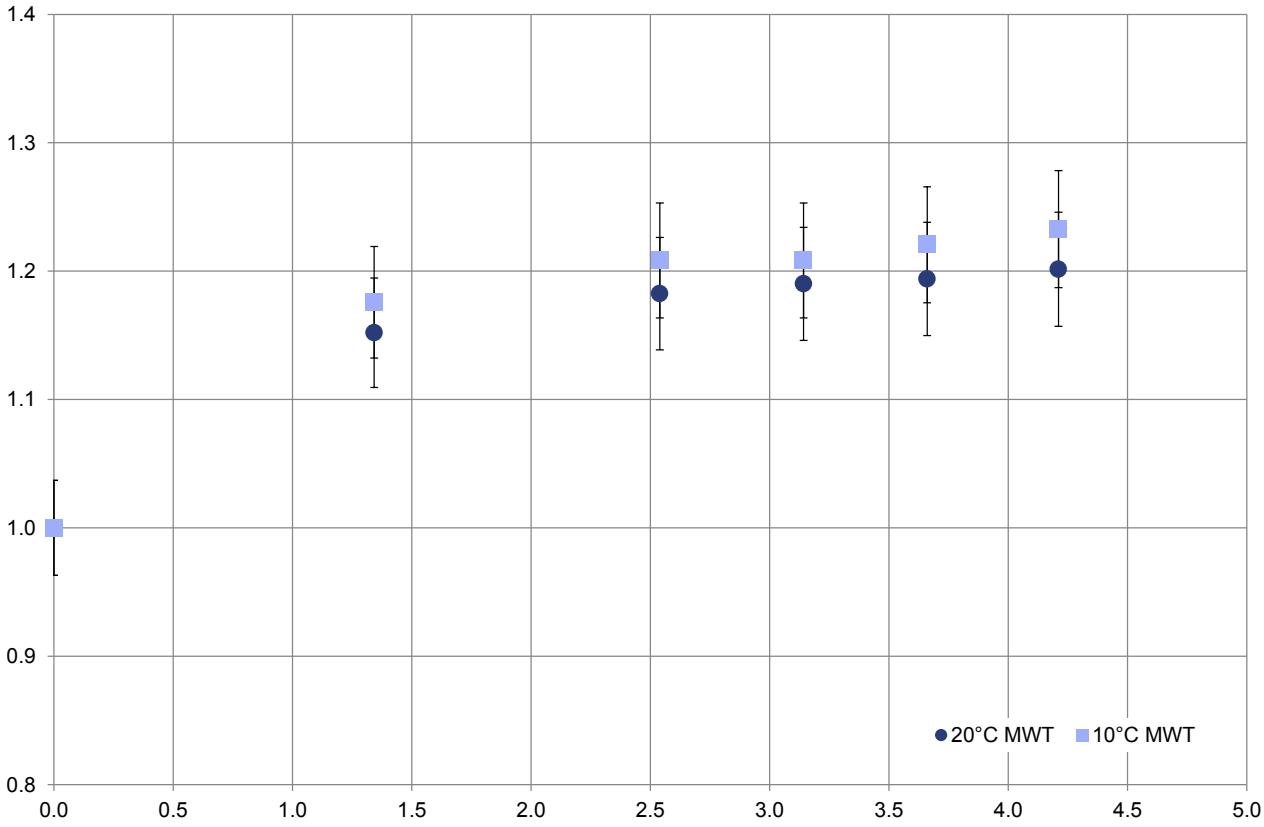

Figure 2: Thermal transmittance of 6.1m container (no changes)

5. DISCUSSION OF RESULTS

The relative increase in thermal transmittance measured during the 10°C tests is greater due to the contaminants being less temperature sensitive, i.e., having a lower temperature coefficient, than the blowing agent displaced therefore having less impact on the overall insulation. This was expected as mentioned in section three of this paper although the zero-day value is not known.
It is apparent that the thermal transmittance is plateauing and in keeping with one off tests on older containers performed by the authors for other testing purposes. Assuming that the rate of increases decreases to a negligible amount in the near future it will be shown that the majority of the ageing occurs in the first two and a half years with a significant amount occurring in the first year alone. For this reason it is considered that whilst manufacturer data is a useful comparative figure for potential customers to compare different options it is not a suitable figure to base economic calculations on. The power consumption of an intermodal container is many times more than the initial cost of the machinery therefore the actual heat leakage is of great relevance.
Data gathered throughout testing is on only one design of container and both made by the same manufacturer. It is not known if the rate at which other designs or manufacturers' builds is constant although given the similarities it is reasonable to assume that the ageing rate is at least comparable.
Further, the point at which the manufacturer-specified transmittance was obtained is unknown. Currently no standard exists to mandate testing within a given time period from a container coming off a production line. A blowing agent and its encapsulating foam undergo an exothermic reaction whilst they set. If a test is conducted in this window the internal heating method yields a lower value of transmittance as the chemical interaction is not accounted for. The magnitude that this may affect a result is also not known due to the impossibility of getting such a new specimen to a suitable independent environmental test chamber.
The trend shown by the graphs of thermal transmittance versus age is in keeping with work done by others (Wilkes, 2002) on smaller insulation samples however this is almost certainly a lower estimate of the increases in thermal transmittance of in-service containers. The specimens tested have only been lifted by a crane a handful of times and have been not been exposed to internal or external mechanical damage from general logistical operations as a container would in normal service. Frequent moving by cranes and fork lifts combined with vibration when undergoing road transport inflict mechanical wear to joint, seams and structurally integral components which will lead to higher rates of ageing then observed throughout testing.
Typical testing of insulating assemblies recorded in textbooks and academic papers are on smaller samples and often measure conductivity rather than transmittance. Given area and thickness conductivity can be used to calculate transmittance. Differing materials age at different rates however, as discussed in section three, only the foam will affect the overall transmittance. It is considered that once the blowing agent has entirely dissipated from the foam and the saturation point of contaminants has been reached ageing will no longer occur. Beyond this point the only noticeable effects on thermal transmittance will be mechanical damage inflicted (ie loss of material) which it is not really possible to account for and is not ageing as considered by this paper. Damage will of course increase thermal transmittance to values higher than that seen during testing.
It is not clear how the results translate to other forms of insulated boxes such as road transport or cold storage due to differing construction techniques and materials. It is thought that the blowing agent and foam part will age in a similar way to that seen in marine containers however the non-foam components of other structures may have more or less effect on the overall heat transmittance.

6. IMPACT ON ENERGY CONSUMPTION

Operational modes of marine thermal containers have been estimated by the authors using data downloads supplied to them – around 2.5×10^5 hours have contributed to the figures. The analysis does not include any periods of obvious malfunction however it is not known if the figures are representative of the global fleet of approximately 1.3×10^6 currently in service. The approximate split between frozen and chilled operation is 40% and 60% respectively although this will vary by container owners with regards to their respective industries.

Taking a global average annual temperature of 15°C and a nominal heat leakage rate of 42W·K^{-1} average heat leakage figures can be calculated to be 630W and 1386W for chilled and frozen cargos respectively. Data obtained by the author's shows that over four years around a 20% increase on the base figure of heat leakage occurs. This increases heat leakage values from 630W and 1386W to 756W and 1663W. Estimating three voyages of approximately six weeks per year the total time on power is around 3024 hours. During this time an extra 381kWh of energy flows through the walls at chilled setpoints compared to the maximum permissible heat leakage mandated by ISO1496-2. For frozen setpoints this increases to 838kWh annually. The ageing effects observed should begin to slow imminently if the containers behave as aged samples of foam sandwich panels have. Multiplying the extra power consumption by an expected lifespan of 15 years the total excess heat load placed on a refrigeration system is 3429kWh and 5029kWh for chilled and frozen setpoints respectively totalling 8459kWh over a 15 year time period.
Applying this to the fleet of reefers an extra 1.95x10^{9} kWh of heat per annum must be removed to maintain temperature control compared to when assuming a starting heat leak of 42W·K^{-1}. This is in addition to heat being removed if the heat leak were 42W·K^{-1} which accounts for around 80% of the heat ingress.

7. CONCLUSIONS

Given the clear trend of increasing heat leak with time it is in the industry's best interest to incorporate it is as factor for any economic calculations involving power consumption. Although the testing has been conducted on containers from the same manufacturer and from the same factory there is no reason to believe that any large deviation from the trend would be observed in a comparable specimen from a rival company.
Increases in energy consumption due to ageing are of both economic and environmental significance. Testing also shows that the degraded insulation allows more heat flow therefore reducing the time a container can be off-power during critical logistics therefore increasing the possibility of a cargo being rejected due to excessive temperature along with accompanying rise in food waste.
Results of laboratory testing by accelerating ageing of foams appear to yield results similar to those seen in containers however the initial increase in conductivity is slower in containers and most likely due to the foam ageing whilst the metallic superstructure does not.

NOMENCLATURE

q	heat flux (W×m^{-2})	λ	thermal conductivity (W×m^{-1}×K^{-1})
T	temperature (°C)	L	thickness (m)
β	temperature coefficient (K^{-1})		

REFERENCES

Cavalier, G., Devin, E., Suqet, T., Latchan, F., Boudet, N., (2016). "Ageing of Refrigerated Truck Insulation", 4th IIR Conference on Sustainability and the Cold Chain, Auckland.

Kay, J.M., (1963). "An Introduction to Fluid Mechanics & Heat Transfer", Cambridge University Press, Cambridge, p108.

Wilkes, K.E., Yarbrough, D.W., Nelson, G.E., (2002). "Aging of Polyurethane Foam Insulation in Simulated Refrigerator Panels – Four-Year Results with Third-Generation Blowing Agents", Journal of Cellular Plastics. 38. 10.1177/0021955X02038004142.

Manuscript ID: 1764
DOI: 10.18462/IIR.ICR.2019.1764

Food losses during refrigerated transport: a socio-economic analysis

Claudia CAPO [(a)], Gérald CAVALIER [(a)], M'hamed MERDJI [(b)]

[(a)] Cemafroid, 5 Avenue des Prés - Fresnes cedex - France

[(b)] Montpellier Business School, Départements d'Enseignements et de Recherche - Montpellier Cedex 4 – France

gerald.cavalier@cemafroid.fr

ABSTRACT

Food is lost or wasted worldwide throughout the supply chain, from initial agricultural production down to final household consumption. Thanks to the possibility of reducing bacterial growth in perishables goods through refrigeration, refrigerated transport represents a key element in the cold chain to reduce food losses and preserving its quality at all stages. International, European and French regulations impose obligations of means and results. During distribution of perishable goods, carriers must comply with the temperatures set by the regulations. These temperatures are fixed for the internal environment of the vehicle and the delivered products. This paper presents a socio-economic analysis of the losses during the refrigerated transport. With the aim of identifying the critical points encountered during transport, a wide population of carriers is called to respond to an ad-hoc created survey. This survey connects the problem of food losses to the maintaining of the correct temperature through the assessment of temperature excursions, their frequency and their costs. Results of this survey, already available for more than thirty carriers, are presented in this paper.
Keywords: Food Losses, Refrigerated Transport, Regulations, Socio-Economic Analysis, Survey, Carriers.

1. INTRODUCTION

Food is lost or wasted worldwide throughout the supply chain, from initial agricultural production down to final household consumption (FAO, 2011). This problem is to be solved to feed those 795 million people in the world that were undernourished in the period 2014–16 (FAO, 2015). Whether in industrialized countries the food wastage problem is due to an excess in food production, in developing countries the causes of food losses and food insecurity are to be found in poor and unhygienic handling and storage conditions and in the lack of infrastructure for transportation, storage, cooling and adequate temperature control. Thanks to the possibility of reducing bacterial growth in perishables goods through refrigeration, refrigerated transport represents a key element in the cold chain to reduce food losses and preserving its quality at all stages, from production to consumption (Capo et al., 2018). Nowadays refrigerated transport vehicles are able to maintain the appropriate temperature all along the transport. Nevertheless interfaces between transport and cold stores, cold rooms, supermarkets, shops or restaurants are still critical. Doors openings remain a weak point of cold chain. It is well known that in order to be efficient, application of cold has to be continuous, from harvest or processing, to the consumer's plate: the performance of the cold chain is equal to the performance of its weakest link. The development of the cold chain has to face a real challenge: to continue preserving food quality and safety and at the same time, to create the smallest possible carbon footprint (Guilpart, 2010).To guarantee the continuity of temperature all along the cold chain regulations and commercial contracts demand temperature traceability and controls and deliveries are rejected when the temperature of the load does not comply with those prescribed by actual regulations, such as the ATP (the International Agreement for the Transport of Perishables Goods) of the United Nations and the Regulation (EC) No 852/2004 of the European Parliament and of the Council. These rejections draw most of the time to the destruction of the products with an important economic, environmental and social impact but also deterioration of the professional and commercial relation between the transporter and his

customer. But the engagements are on the product temperature and most of the time only air temperature is measured and registered creating disagreement between the parties.
Willing to reduce these temperature conflicts with their customer, to avoid the losses of products and mitigate their impact on environment, and to save money refrigerated transport companies decided to search new ways to measure temperature during the transport and its interface or to analyse it. This will allow setting common rules between transporters and industries, and then reducing the conflicts. Before searching technical solutions, it was interesting to know and analyse the real social and economic impact of food losses due to temperature excursions during transport.
This article presents the study done among the French refrigerated transport companies to understand the importance of temperature problems, their origin and their impact. It was conducted by cold chain experts of Cemafroid and Montpellier Busines School. It first presents the methodology and the questionnaire and describes the companies who answered the questions, secondly it presents temperature problems and their economic impact and finally analyses the practices implemented by the companies.

2. METHODOLOGY AND QUESTIONNAIRE

2.1 Questions

A questionnaire was prepared including 47 questions gathered in five categories.
The first part was dedicated to the description of the companies with their turnover, staff, number of sites, their refrigerated transport fleet with the number of equipment, ownership and their mean age, the transport activity and the transported products.
The second part aimed at identifying the temperature problems during transport with the implementation of regulation, the registration of temperatures during delivery, and the problems faced during transport, their nature, their frequency, cost and importance, and the number of conflicts. The third part analysed the contracts between transporters and their customers.
The fourth one was dedicated to the temperatures controls done by the customers at the reception of the load, the procedures implemented, the training of the drivers, the methodology for temperature registration, equipment used, metrology, registration frequency.
The last part concerned the communication of the transport company with its customers and the information given on temperatures. Before its dissemination the questionnaire was tested by three refrigerated transport companies. These tests served to adapt and complete the questions. The questionnaire was proposed online to a restricted public composed of the management of refrigerated transport companies.

2.2 Sample of Transport Companies

A total of 20 companies representing the diversity of refrigerated transport business answered to the 47 questions. Most of them are small and medium companies (SMEs) as shown in Fig.1a and Fig. 1b. As represented by these figures they have, in fact, a turn over under 50 M€ and a staff under 250 people. 35% of the 20 companies have less than 100 employees, 25% between 101 and 300 and, 40% more than 300 (Fig.2). Only 20 % of these companies operate more than 5 sites and 40 % have only one or two and 89 % of them only operate from France while 11 % have sites in other countries in Europe.

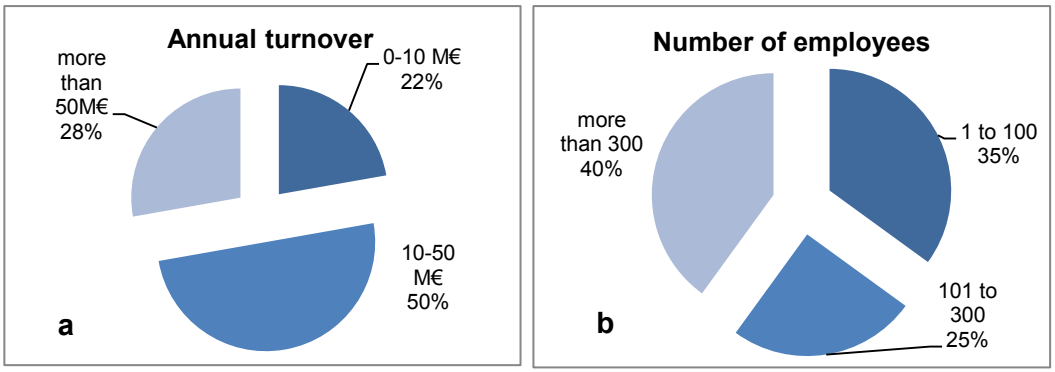

Figure 1: a) Annual turnover of the companies; b) Number of employees of the companies

3. THE REFRIGERATED TRANSPORT FLEETS

The size of the fleet varies a lot among the 20 companies as shown in Fig. 2a. Most of them, 40 % have between 51 and 200 refrigerated transport equipment, 35 % between 1 and 50 and 25 % more than 200. The average age of the fleet is detailed in Fig. 2b and half of the companies have a fleet with an average age of 4 to 6 years, 35% between 7 and 9 and 15 % lower than 3.

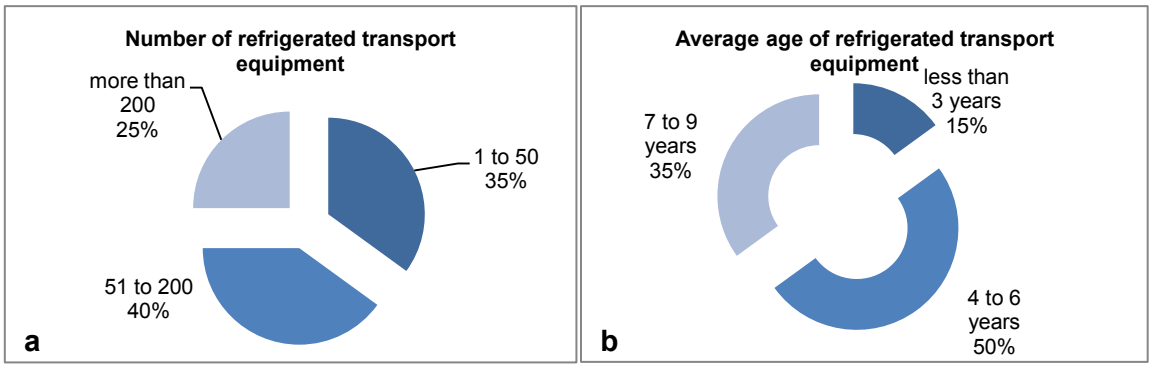

Figure 2: a) Refrigerated transport fleets; b) Average age of the fleets

The ownership of the fleet may also have an importance. 80 % of the companies own their fleet as detailed in Fig. 3a.

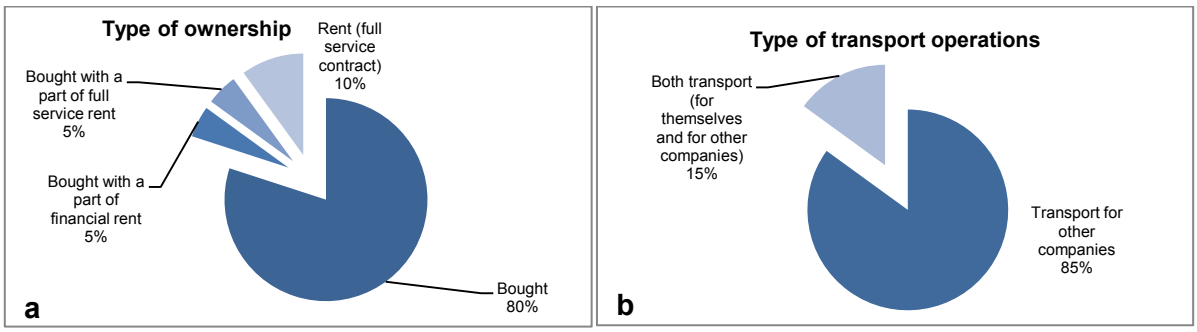

Figure 3: a) Type of ownership; b) Transport activities of the companies

Fig. 3b shows that most of the companies who answered the questionnaire are doing transport for other companies and the other 15 % are doing both transports for others and for themselves. The 60 % are doing long distance and distribution operations and 40 % only distribution. For years long distance refrigerated transport has strongly decreased in France.

4. TEMPERATURES ISSUES DURING REFRIGERATED TRANSPORT

4.1 Products Transported and Temperatures

The temperature issues depend first of all of the transported products which have all their own temperature limits. The products transported by the companies who answered represent the variety of perishable foodstuff transported under controlled temperature and their proportions are not too far from the percentages of consumption in France as shown in Fig. 4. Their transport temperatures are ruled by the European regulations, 178/2004, n°852 and 853/2004, also called “food law”.

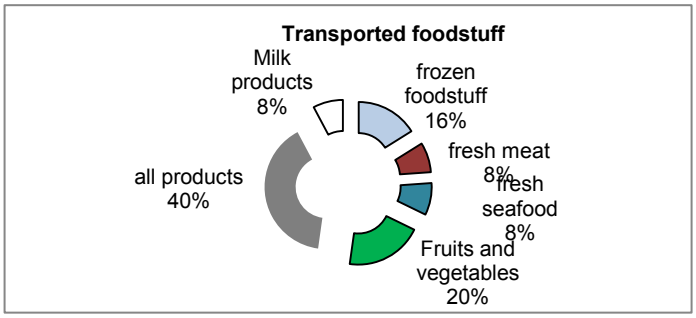

Figure 4: Transported foodstuff.

4.2 Temperature Measurement and Recording and Controls

Transports companies have been questioned on the temperature measurement and recording during transport. As shown in Fig. 5a, 60 % of them systematically record air temperature during transport operations, but 5 % never do this temperature relief.

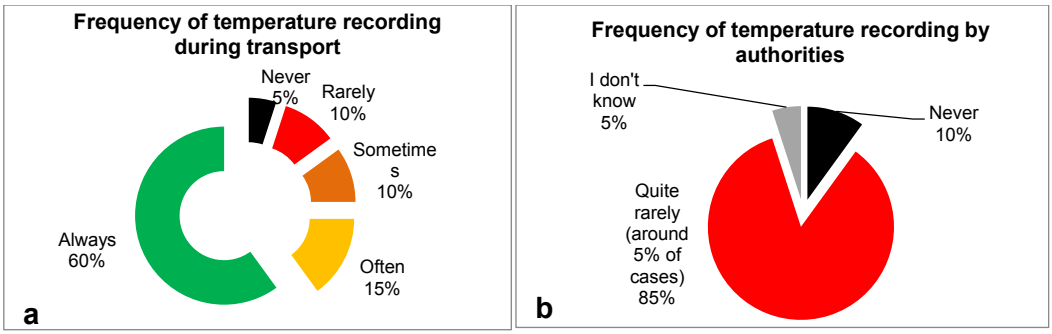

Figure 5: a) Recording policies; b) Frequency of temperature recording.

These temperatures may be controlled on the road by police, customs or veterinary services. Only 10 % of the companies said having never been controlled. For the others, controls are rare as presented in Fig.5b.

4.3 Type and Importance of Temperature Problems Encountered in Refrigerated Transport

The most commonly reported problem of temperature in refrigerated transport is the rejection of the delivery due to excursions of temperatures during transport operations. As shown in Fig.6a, only 10 % of the companies never met load rejection due to temperature excursions. And 30 % faced more than ten rejections during the last two years. Even if according to Fig. 6b, 88 % of them acknowledge the economic impact is less than 0.5 % of their turnover, 6 % declare it is between 1.1 and 2 %. With an average result of 1 % in 2012 according to Meyronneinc (2013), these rejections are at a great level and may impact the sustainability of these companies.

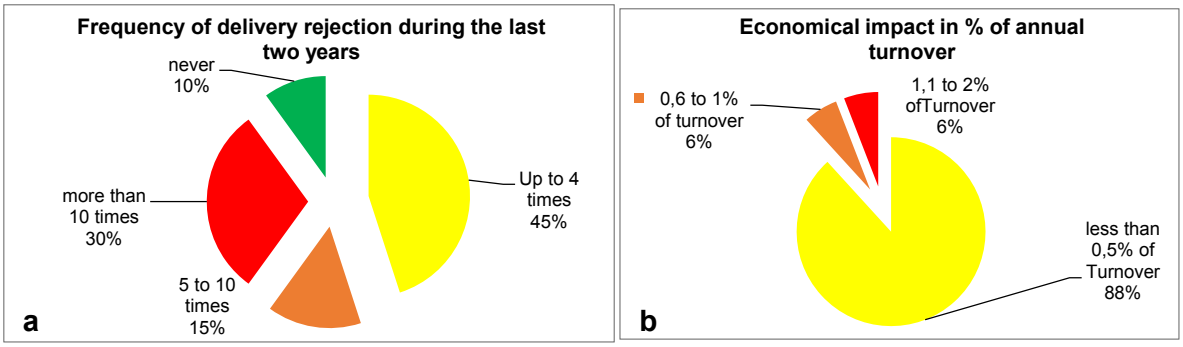

Figure 6: a) Delivery rejection due to temperature excursions during transport; b) Economic impact in % of turnover of load delivery rejection due to temperature excursions.

These problems may come from the initial temperature of the load. The study reveals in Fig. 7a that 80 % of the companies rarely refuse to load on products that are not at the right temperature, 5 % never and 15 % sometimes. Nevertheless the evaluation of these costs remains difficult to evaluate for25 % of the companies.

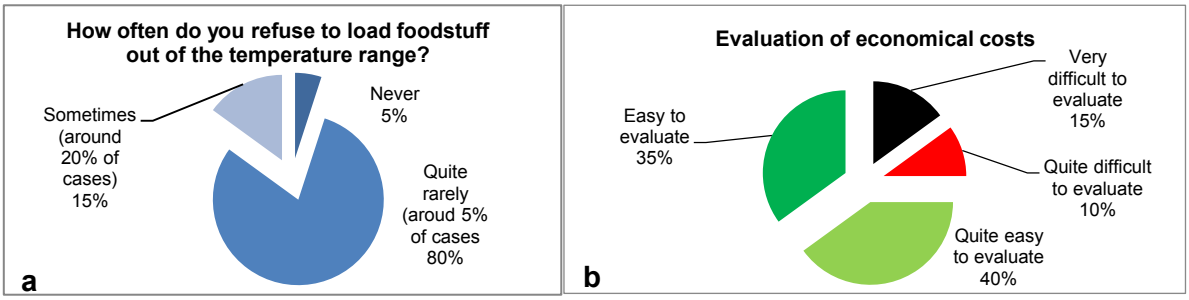

Figure 7: a) Delivery rejection due to temperature; b) Economic impact of delivery rejection.

Globally the companies consider they are well reimbursed by the insurances as shown in Fig 8a. The abusive rejections are rare for 65 % of the companies and occur sometimes for 30 % as shown in Fig.8b.

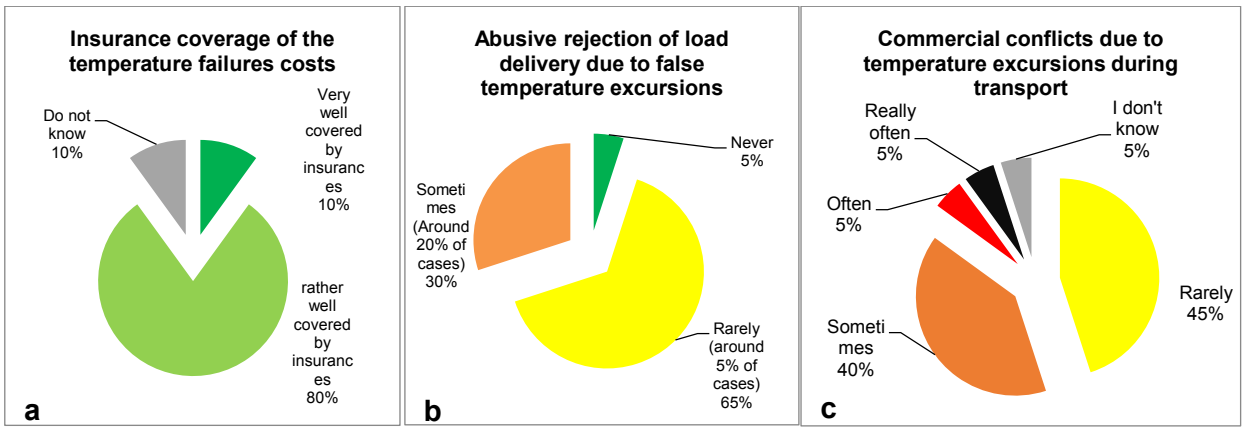

Figure 8: a) Reimbursement by the insurances of the temperature problems; b) Abusive rejection of load delivery due to false temperature excursions; c) Commercial conflicts due to temperature excursions during transport.

4.4 Contracts

Refrigerated transport unions developed a model of transport contract ruling the relation between the transport company and its client including the issues of temperature. It is surprising to see on Fig. 9a that only 55% use it systematically.

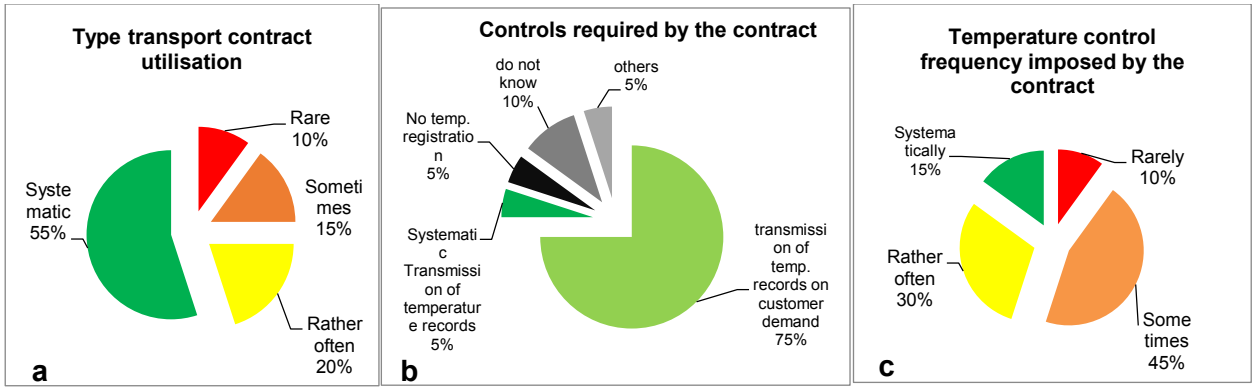

Figure 9: a) Utilisation of the type transport contract; b) Controls required by the contracts; c) Temperatures controls frequency.

Only 5 % of the clients require systematic transmission of temperatures recording as seen on Fig.8b.The transport companies themselves have different practices for temperature recording as shown by Fig.9c, and only 15 % do it systematically.

5. TEMPERATURE CONTROL AT RECEPTION AND DURING TRANSPORT: EQUIPMENT AND METHODS

5.1 Temperature Control at Reception

Most of the problems of temperatures came out of the reception control. These controls are contradictory between the driver and the receptionist in 75 % of the cases as shown by Fig 10a. Nevertheless Fig.10b reveals that in 57 % of the cases there is no clear methodology for these controls.

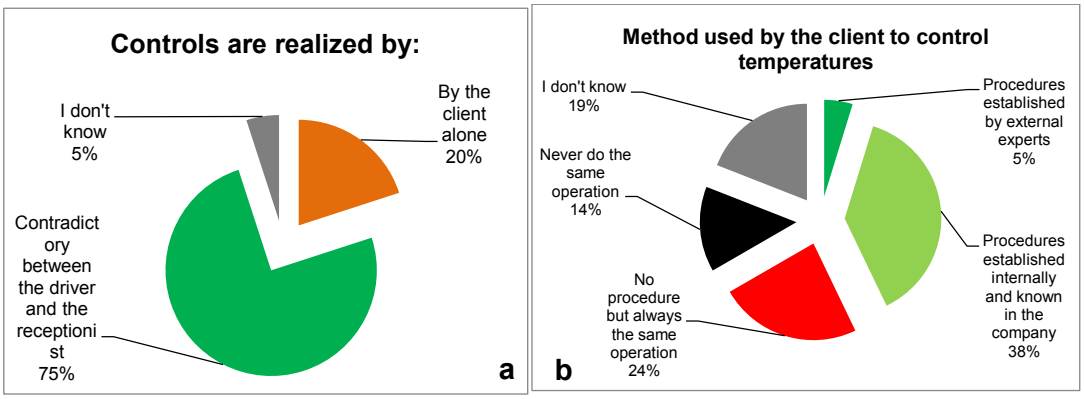

Figure 10: a) Who is realising the controls? ; b) Method used by the client to control temperatures.

Fig. 11a reveals that for the control of these temperatures in 54 % of the cases the equipment is not appropriate or not known. In 39 % of the cases infrared pyrometers are used. Another issue is underlined by Fig.11b with 15 % of the drivers which have not been trained and only 15 % who are trained regularly.

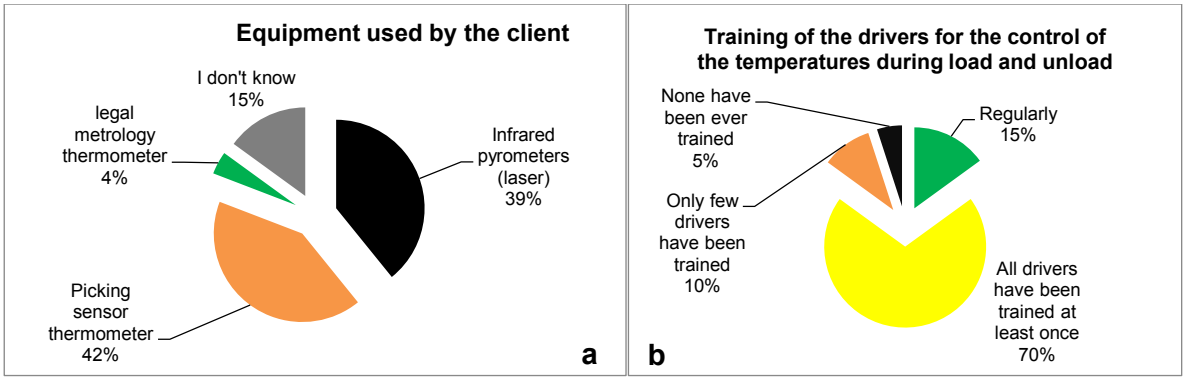

Figure 11: a) Equipment used by the client; b) Training of the drivers for the control of the temperatures during load and unload.

Nevertheless 85 % of them as shown in Fig.12a are equipped with a thermometer and 90 % of these thermometers have a picking sensor according to Fig. 12b. Unfortunately, even if they have appropriate equipment, and have been trained, only 65 % have a measurement procedure (see Fig. 12c.

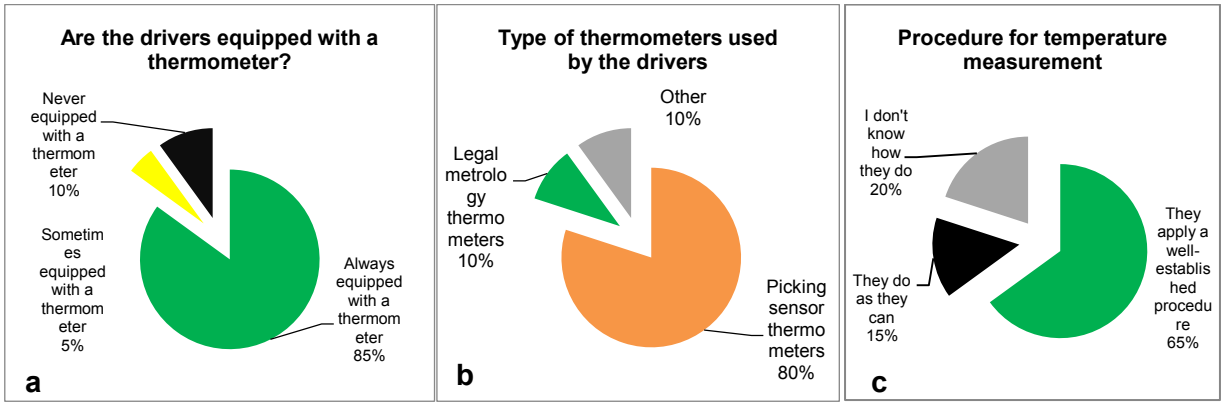

Figure 12: a) Equipment of the drivers; b) Type of thermometers; c) Procedure for temperature measurement.

5.2 Temperature recording during transport

During transport, 60 % of the companies record systematically the temperature even if according to European regulation 37/2005 it is only mandatory for frozen products transport as shown in Fig. 13a. Fig.13b details the recording frequencies used by the transport companies. More than 50 % record temperatures at least every 10 minutes.

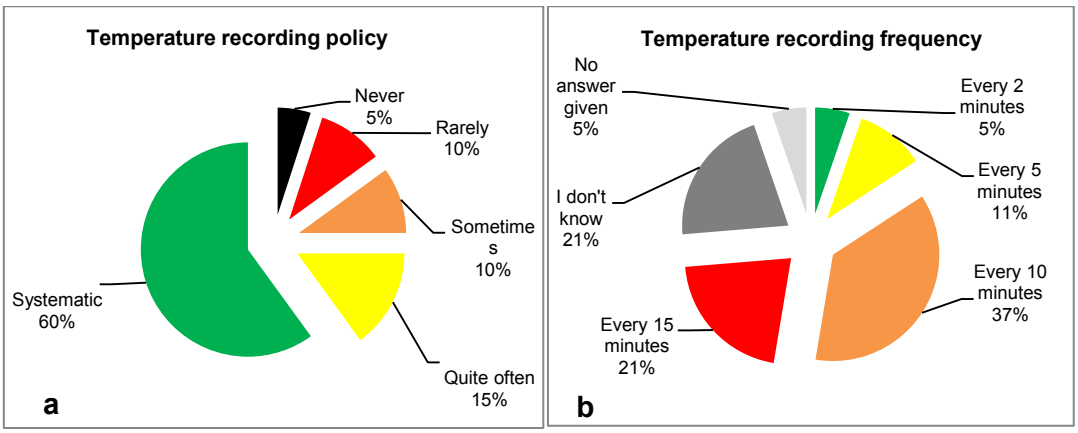

Figure 13: a) Temperature recording policy; b) Temperature recording frequency.

For this measurement and recording of temperature, most of the companies use temperature recorders with one sensor per compartment, conform to European standard EN 12 830 that has just been revised in 2018 and which is required by European regulation 37/2005 as shown in Fig. 14a and 14b.

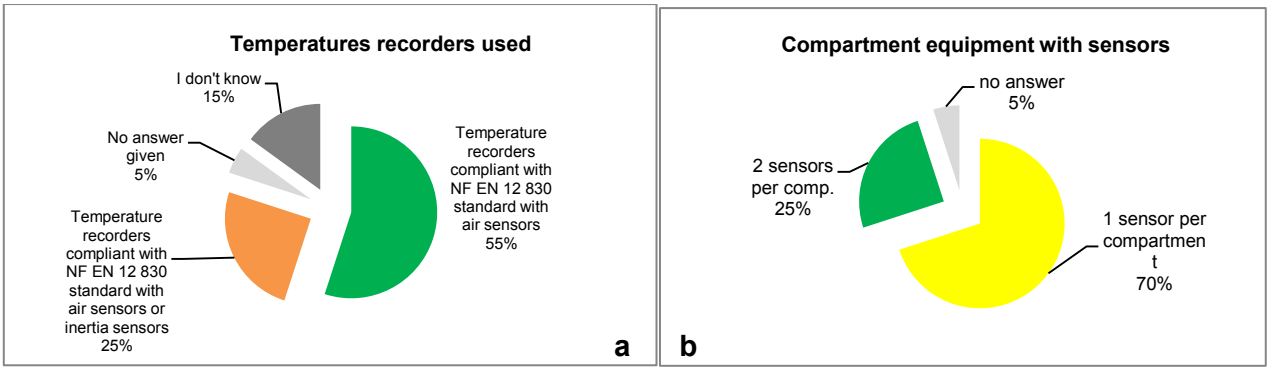

Figure 14: a) Temperature recorders; b) Sensors of the temperature recorders.

5.3 Other controls recorded during refrigerated transport

Refrigerated transport companies record more and more information useful for the traceability and security of the products and the performance of the transport operations. Half of the companies who answered the question record the doors openings (see Fig.15a) and half of them have between 6 and 10 doors opening by transport operation (see Fig. 15b). When they stop on refrigerated platform, a third of them stop between 30 minutes and half an hour (see Fig. 15c). When they download outside, doors opening time is shorter but for those who measure it, it is half of the time longer than 10 minutes (see Fig.16c).

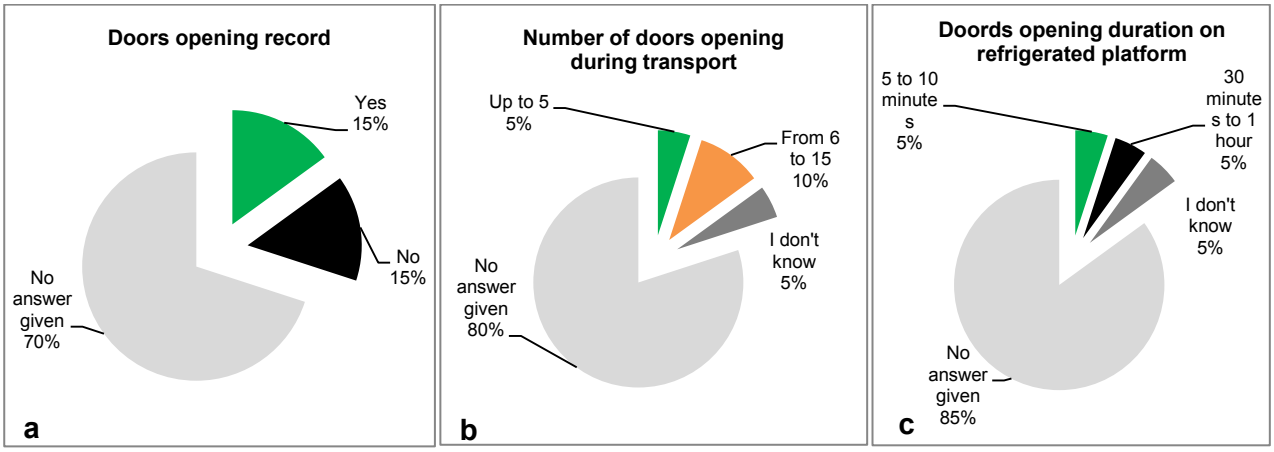

Figure 15: a) Doors opening record; b) Number of doors openings; c)Doors opening duration.

Other information is quite interesting such as the operation mode of the refrigeration unit. It is a good indicator of the best practices implementation by the drivers. But only 30 % register the on/off of the refrigeration unit (see Fig. 16a).

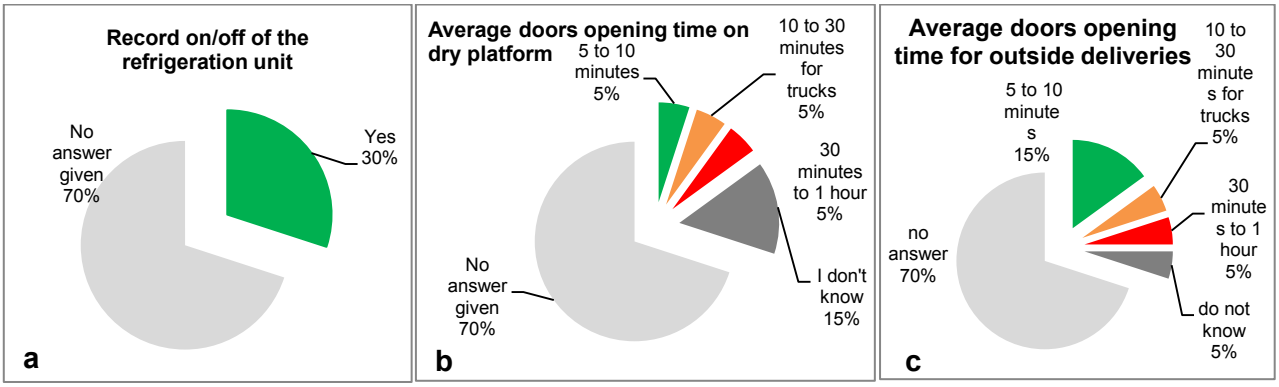

Figure 16:a) Recording of on/off mode of the refrigeration unit; b)Average doors opening time on dry platform; c) Average time opening for outside deliveries.

6. CONCLUSION

Thanks to the involvement of Transfrigoroute France this study met a rather good welcome by French refrigerated transport companies who seriously answered the forty-seven questions. With twenty answers from a broad panel of societies, we get a representative overview of the temperatures issues and the practices of the transporters.

The analysis of the results shows that even if the real cost of the temperature problems is generally lower than one per cent of the annual turnover of the company and well covered by the insurances, it represents an amount comparable to the net annual result in refrigerated transport. In this context it is surprising to see that only fifty-five percent of the companies systematically use the type contract for refrigerated transport. It is also surprising that if transport companies are facing deliveries rejection due to temperature excursions they rarely refuse to load foodstuff out of the scope of temperatures.

The study reveals that an increasing number of companies systematically record temperatures during transport and also record other information such as doors openings and refrigeration unit operation mode. Nevertheless it is surprising to see that a lot of them do not use the proper equipment to measure and record temperature either during transport either at the interface at reception. The lack of robust measurement procedures, of appropriate procedures and trained people do not help to avoid any doubt on the load temperature and the quality of the transport operation.

Even if refrigerated transport performance is rather good in France with few incidents this study shows that there are still margin of progress to reduce losses and increase confidence and food safety. The respect of best practices, the use of robust and approved procedures and the training of operators, are indispensable to guarantee the quality and the performances of refrigerated transport.

REFERENCES

Capo, C., Latchan, F., Michineau, T., Petit, J.M., Revellin, R., Bonjour, J., Cavalier, G., 2018. Factors affecting the ageing of refrigerated transport equipment. Proc. 5th IIR Conference on Sustainability and the Cold Chain, Beijing, China.

Guilpart, J.,2010. Recent research and progress in measuring and improving the performance of the cold chain. Proc. Ist IIR Conference on Sustainability and the Cold Chain, Cambridge,England.

FAO, 2011. Global food losses and food waste – Extent, causes and prevention. Roma, Italy.

FAO, IFAD and WFP, 2015. The State of Food Insecurity in the World 2015. Meeting the 2015 international hunger targets: taking stock of uneven progress. Roma, Italy.

Meyronneinc, J. P. « La santé financière du transport routier frigorifique en 2012 – Bilan »

Manuscript ID: 71
DOI: 10.18462/iir.icr.2019.0071

Evaluation of Photovoltaic Cooling Application to a Data Center

Adenilson C. BELIZÁRIO[a], José R. SIMÕES-MOREIRA[b]

SISEA – Alternative Energy Systems Lab., Mechanical Engineering Department
Escola Politécnica, University of São Paulo, Brazil
acbelizario@usp.br[a], jrsimoes@usp.br[b]

ABSTRACT

Nowadays, data processing is a fundamental operation for business such as banks, among others. However, computers dissipate heat and as the operating temperature increases and these machines cannot operate properly. Consequently, it is necessary to air conditioning systems to keep the proper temperature as well as the room temperature itself. Therefore, a data center air conditioning system drains electrical energy in the installation. Based on this, this paper evaluates a photovoltaic cooling to support the electric chiller system showing the energy saving. The case is analyzed in a Data Center located in São Paulo, Brazil. The electrical power density consumed by the computers is 0.5, 1.0, 2.0, 4.0 and 8.0 kW/m^2. Local solar irradiation indexes are based on the ASHRAE Data Bases temperature. The results represent a 22%, 12%, 13%, 5% and 3% of energy savings, respectively.
Keywords: Air conditioning, photovoltaic cooling system, data center, sustainability, solar cooling.

1. INTRODUCTION

In recent years, the expansion of critical environments, in special data centers, has adopted the use of air conditioning systems. In the controlled environment, temperature and humidity must be set by several parameters for servers and mainframes operational safety. In commercial buildings, the air-conditioning system is accountable for 40% of the electrical energy bill (Papadopoulos *et al.*, 2003). In continuous cooling applications, that figure goes up. In a data center, it is possible to achieve participation as much as 50% (Strutt et al., 2012). Evidently, each kilowatt-hour saved could be reinvested in new computers or to be used to increase and keep the building efficiency. In addition, in some places in the world, the electrical energy cost is higher at peak time, usually between 5 and 10 PM (ANEEL, 2015). It occurs because in this period of time, the public illumination is turned on and people arrive home. Besides the fact that some offices and factories keep an evening work shift. That peak demand does not justify itself new investments on the expansion of the electric power grid. In this context, the development of alternative air conditioning systems is a great solution and an opportunity for new businesses. In this case, chillers powered by solar energy would be a solution.

Solar systems can save part of the electrical energy consumption. However, there are some disadvantages in this case: The customer needs an area to install solar collectors and to build an energy storing system, such as a thermal accumulation tank (thermal storage) or a battery bank (electrical storage). Typically, the initial investment is higher than a simple and conventional electric chiller installation. Also, the solar system cannot be considered an air-conditioning redundancy system, because of the solar intermittency. Moreover, solar cooling technology can reduce the environmental impact raised by conventional air-conditioning systems. That is because refrigerants used in these systems are environmentally friendly, natural refrigerants and are CFC free. Therefore, these systems have zero ozone depleting as well as zero global warming potentials (Hassan and Mohamad, 2012).

The goal of this paper is the evaluation of a solar air conditioning system based on the photovoltaic cooling technology for a data center and the index of electrical energy provided by the net. In a previous paper (Belizário and Simões-Moreira, 2017) the authors analyzed the use of solar-powered absorption chiller.

2. PV SOLAR COOLING

A photovoltaic electric cooling system basically consists of a conventional electrical compression chiller powered by electricity produced in photovoltaic panels. In 2010, crystalline silicon photovoltaic cells accounted for around 93% of the total photovoltaic market(Ferreira and Kim, 2014; Fraunhofer Institute for Solar Energy Systems, 2018).

In this case, the total irradiation (direct + diffuse) is captured by the photovoltaic cells and transformed into electrical energy (A). For charge regulation, this system is provided with controllers (B). Therefore, it must be necessary to choose between two different methods. The first way would be necessary to connect inverters on the public electrical net (E), providing energy and capturing on the lack of periods. This procedure depends on local rules and regulation. The second way is to provide energy to battery load bank and unload this according to the previous schedule (C). To use this energy, frequency inverters were installed (D). They were responsible for regulating the frequency and transform DC voltage in AC voltage. Losses are associated with photovoltaic panel efficiency, transmission, inverter yields and battery banks(Baltus et *al.*, 1997). Panel efficiency is measured by the ratio between the available energy for photovoltaic cells and used energy in chillers.

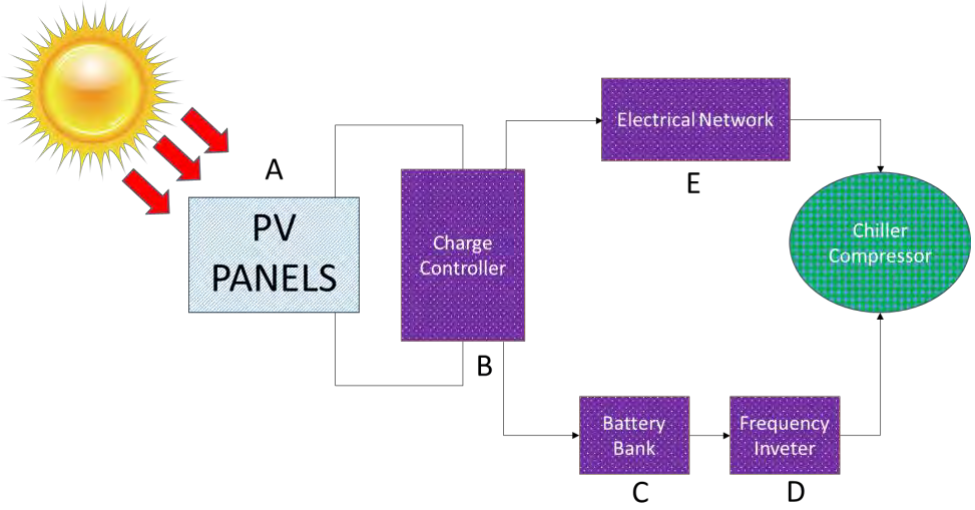

Figure 1 – Photovoltaic cooling procedure. (Belizário, 2018)

3. DATA CENTER CONDITIONING

For a data center, up to 100 kW power consumption can occur to feed the computers installed. A traditional system uses air conditioning system by indirect expansion precision air handling units (CRAH) to promote the heat transfer by cold water and conditioned environment, chillers to cool the water and cooling towers to heat transfer between the chiller and outdoor environment.

According to ASHRAE TC (ASHRAE, 2016b) computers should operate in the temperature range of 5° and 40° C and the humidity should be in the range of 10% and 90%. For a data center, the A1 condition presented in the psychrometric chart in Figure 4 is recommended. In A1 condition, the temperature must be between 15°C and 35°C and the relative humidity between 20% and 80%. However, in a recent revision ASHRAE, TC 9.9 (ASHRAE, 2016a), has extended the humidity to the range from 10% to 90%. Those operating zones are shown in Fig. 2.

The guidelines of Data Center conditioning recommend that a computer inlet of air is turned to air conditioning Insufflation and the outlet is turned to air handling return. When it is applied, this reduces investments and operational costs, increases data processing efficiency and reduces the maintenance stops(Strutt et al., 2012).

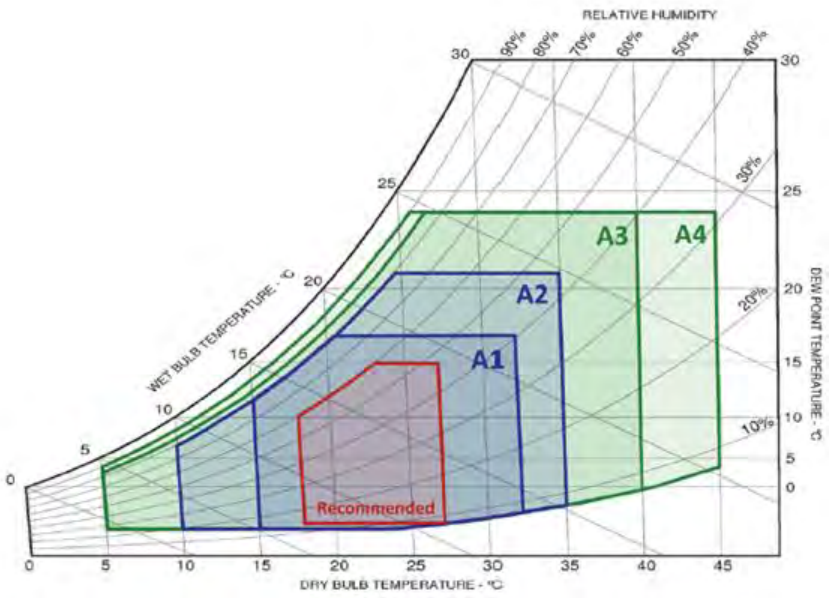

Figure 2: Data Center Temperature according to ASHRAE TC 9.9. (ASHRAE, 2016b)

4. ENVIRONMENTAL CONDITIONS

For this work, it was considered data obtained by ASHRAE fundamentals (ASHRAE, 2017) for the city of São Paulo, Brazil measured in 24 hours during 365 days in 2001. The collected data were dry bulb temperature, wet bulb temperature, solar irradiation, and beam irradiation.

To carry out the analysis it was adopted a typical data center plant considering and the associated facilities. The only area that is conditioned by this project is the data hall. For this building, it is reserved a 625 m² data hall area, and 2030 m² of total building area. The solar collectors are installed on the roof top of the total building area (2030 m²).

Racks dissipation density is 2 kW/m² at the data hall, computed from an average bank system (The Green Grid, 2012), resulting in a total dissipation of 1250 kW. This study has been analyzed other densities such as 0.5, 1, 4 and 8 kW/m². Other facilities areas (green square) are cold water room (chillers room – 280 m²), fire facilities (80 m²), electrical infrastructure room (255 m²), technical aisles (fan coils room – 200 m²), Circulation aisle (160 m²). The acclimatization of these areas (except data hall) must be conditioned according to comfort rules and should not be included in the air conditioning precision system related in this paper. Electrical generators area, cooling tower and primary cabinet of net energy must be outside the building. The computer room should conform to the following conditions: (1) the maximum water return temperature must be 34°C; (2) dissipated power by computers: 1250 kW; (3) density of illumination: 20 W/m²; (4) constant occupation: 2 people; (5) working schedule: 24 hours/ day.

The thermal load and chiller capacity was calculated according to the maximum temperature that has occurred in the last 20 years (ASHRAE, 2006). In this simulation, IT was considered that the energy peak occurs in January when the external temperature reaches 31°C and 40% relative humidity. The outdoor air flows into the technical aisle at this temperature and it is mixed with indoor return air at 34 °C, 22% relative humidity. Next, the mixed air circulates in the fan coils to be cooled at 22.3 °C, 45% relative humidity. After that, the air is supplied into a data hall to cool off the computers to exit at 34 °C, 22% relative humidity. Fig. 3 shows the thermodynamic states and processes on the psychrometric chart.

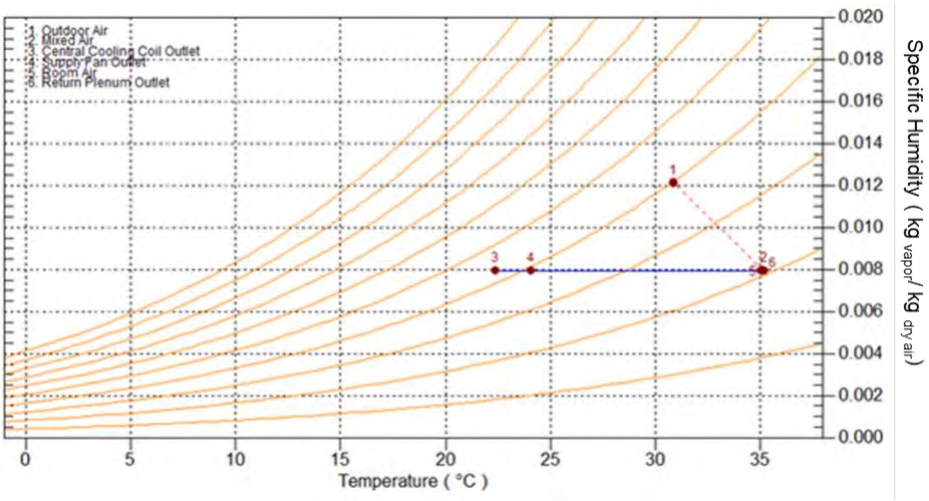

Figure 3: Thermal load of a simulation system seen in a psychrometric chart.

According to E20, a developed thermal simulation software by Carrier Corporation (Carrier Corporation, 2016), computers are accountable for 86% of the thermal load in such an environment.

Conventional air conditioning systems use electrically driven chillers operating day and night. Therefore, the maximum Thermal load is estimated and could selection the chiller for this building application in table 1.

Table 1: Chiller selection for this application. (TRANE, 2017)

Chiller Selections

Density (kW/m²)	Thermal Load (TR) - $C_{Tmáx}$	Chiller Selected (TR)	Chiller Comsuption Curve - y(C_T)
0,5	173,69	180,00	-2,00E-07 x³ + 4,00E-04 x² + -5,94E-02 x + 37,97
1,0	259,57	260,00	-7,00E-08 x³ + 3,00E-04 x² + -5,94E-02 x + 54,85
2,0	440,33	500,00	-2,00E-08 x³ + 1,00E-04 x² + -5,94E-02 x + 105,5
4,0	795,85	840,00	-7,00E-09 x³ + 9,00E-05 x² + -5,94E-02 x + 177,2
8,0	1506,88	1680,00	-2,00E-09 x³ + 4,00E-05 x² + -5,94E-02 x + 354,4

The power consumption by the chillers can be estimated by $y(\dot{C_T})$, according to Belizário (2018).

However, this paper proposes that during the day, when there is solar radiation, collected energy will be stored in a battery load bank at hours when the electricity prices are higher (In Brazil, the hours between 5:00 PM and 8:00 PM).

The first step is to obtain the PV panels efficiency (η_{sol_pow}). The calculation is presented in equation (1) (Huld *et al.*, 2010), where the *k*'s values are presented in Table 2.

$$\eta_{sol\_pow} = \{1 + k_1 \cdot \ln I_T + k_2 \cdot (\ln I_T)^2 + T_{panel} \cdot [k_3 + k_4 \cdot \ln I_T + k_5 \cdot (\ln I_T)^2] + k_6 \cdot T_{panel}^2\} \cdot \eta_{system} \quad \text{Eq. (1)}$$

Table 2: Constants for PV panels efficiency in equation (2) (Huld et al., 2010)

Constants for PV panels efficiency calculation in Eq. (2)					
k_1	k_2	k_3 (°C $^{-1}$)	k_4 (°C $^{-1}$)	k_5 (°C $^{-1}$)	k_6 (°C $^{-1}$)
-0,01716	-0,04029	-0,00468	0,000148	0,000169	0,000005

In addition, it should be estimated the superficial panel temperature T_{panel}, which can be done by equation (2), where both radiation and convection effects are considered (Belizário, 2018).

$$T_{panel} = TBS + \frac{I_T}{h_{conv_{air}}} \quad \text{Eq. (2)}$$

To calculate the efficiency of PV panels equations (1) and (2) are used to give equation (3).

$$\eta_{sol\_pow} = \left\{1 + k_1 \ln I_T + k_2(\ln I_T)^2 + (TBS + \frac{I_T}{h_{conv_{ar}}})[k_3 + k_4 \ln I_T + k_5(\ln I_T)^2] + k_6(TBS + \frac{I_T}{h_{conv_{ar}}})^2\right\}\eta_{System} \text{ Eq.(3)}$$

The PV power generation (W_{PV}), are estimated in equation (4) (Kalogirou, 2004). Other constants considered are $\dot{W_{STC}}$ e I_{pSTC}, respectively 150 Wm^{-2} e 1.000 Wm^{-2} obtained in laboratory tests.

$$\dot{W_{PV}} = \dot{W}_{STC} \cdot \frac{I_T}{I_{pSTC}} \cdot \eta_{sol\_pow} \quad \text{Eq. (4)}$$

After the generation, the energy will be stored in battery banks (W_{acum}) in equation (5). The variable t indicates the time of energy storing.

$$W_{acum} = \int_0^t \dot{W}_{PV}\, dt \quad \text{Eq. (5)}$$

In a previous schedule, those batteries will be discharged for powering the chillers. The available energy (W_{ava}) will be the accumulated energy (W_{acum}), less the power used for the batteries ($\dot{W_U}$) in a time of utilization t_u. The equation (6) show this function.

$$W_{ava} = W_{acum} - \int_0^{t_u} \dot{W_U}\, dt_u \quad \text{Eq. (6)}$$

5. PERFORMANCE ANALYSIS OF PHOTOVOLTAIC COOLING

The Thermal Load Accumulated (C_T) is provided by (ASHRAE, 2017) and the electrical consumption is calculated by the conventional equipment and by equations provided in Table 1. The results for a typical year are given in. Weather data presented in reference (ASHRAE, 2011) and the equipment data presented in (Otanicar, Taylorb and Phelanc, 2012) were used. Table 3 presents the accumulated monthly values in a typical year (ASHRAE, 2017).

It can be noticed that for different load densities, the consumption energy curve modifies.

Table 3: Electrical consumption by a conventional system

Conditions	Density electric charge from computers (kW/m^2)				
	0.5	1	2	4	8
Typical Month Summer (kWh)	75.96	145.59	190.51	415.08	641.31
Typical Month Winter (kWh)	74.32	143.07	187.83	412.83	639.73
All Year Non-Peak Hour (kWh)	807.81	1550.81	2031.83	4441.32	6869.62
All Year Peak Hour (kWh)	79.43	152.43	199.33	436.14	674.44
Total	887.24	1703.24	2232.49	4877.46	7544.06

It can be noticed that 2 kW/m² the Electrical chiller Coefficient of performance is better than other densities because, in this case, all the time the chiller works in the best operation ranges, between 60% and 95%.

In comparison, It must utilize the solar contribution (W_{ava}) calculated from Eq. (6). In cases that the available energy is lower than the energy required for cooling all thermal load, it is necessary to calculate the residual energy consumption (E_{PV}). This is obtained by solving the equation (7).

$$E_{PV} = \int_0^t y(\dot{C_T}) - W_{ava} \qquad \text{Eq. (7)}$$

Table 4 presents the residual consumption by a photovoltaic cooling system.

Table 4: Residual consumption by the photovoltaic cooling system

Residual consumption (E_{PV})					
Conditions	Electrical load density (kW/m^2)				
	0.5	1	2	4	8
Typical Month Summer (kWh)	49.71	119.34	164.25	388.80	615.04
Typical Month Winter (kWh)	66.20	134.96	179.92	404.71	631.61
All Year Non-Peak Hour (kWh)	688.06	1477.89	1969.16	4425.51	6866.51
All Year Peak Hour (kWh)	2.09	28.27	66.04	254.86	480.44
Total	690.15	1506.15	2035.19	4680.37	7346.95

Fig. 4 shows the economy provides by photovoltaic cells. This study shows that the solar contribution decreases when the thermal load density grows. The densities are lower than 4 kW/m² the contribution depends on the chosen chillers, because of the work compressor curve adapted better to the Thermal load.

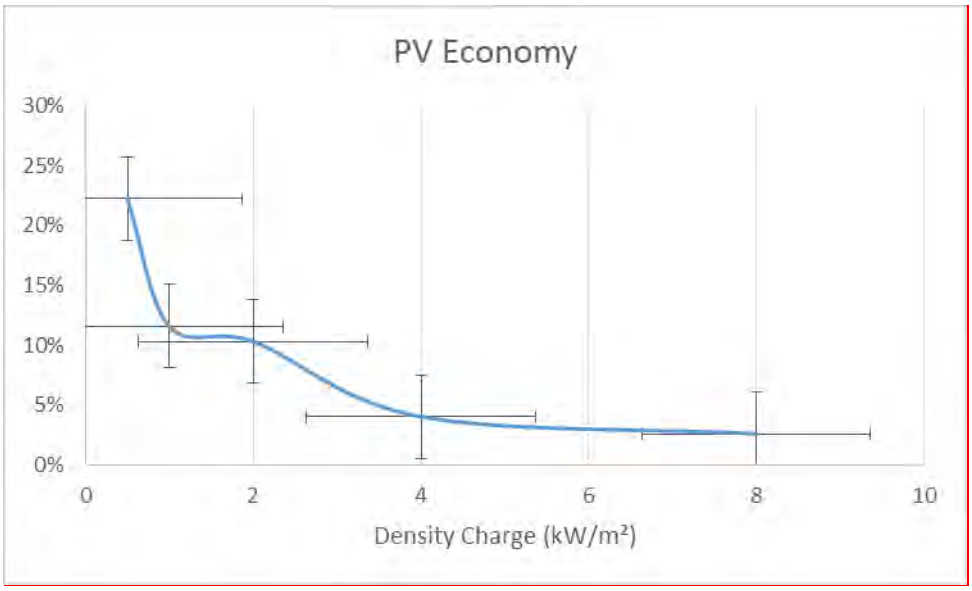

Figure 4: Evolution of energy savings according to the load density

6. CONCLUSION

An air conditioning system powered by electrical energy produced by photovoltaic means has been presented as a solution for energy saving in order to decrease the consumption from the electrical grid energy and, consequently, fossil fuel burn dependency. One advantage of this system is that the solar contribution is provided directly to the electrical energy consumption, without interfering with the thermal load and the working regime of the chiller.

In this paper, the thermal load was calculated at 5 densities charges in a generic IT room and their respective annual consumption for a typical year. For a density charge 0.5 kW/m² this system represents a 22% energy saving, for 1.0, 2.0. 4.0 and 8.0 kW/m² the savings represents 12%, 10%, 5% and 3%, respectively. The savings decreases when the density charges increases, except at 2.0

kW/m², where a system works in the optimum point of chiller efficiency. The results are better than results obtained by (Otanicar, et. al. 2012 and Porumb et. al, 2016) because the solar irradiance available in Brazil is better than Europe. Other studies have been developed since the begin of this decade in Brazil, although your results have not been published.

Nevertheless, these studies must be updated frequently, because the new and more efficient solar collector has been developed. Recent developments indicate that trend, as well as the reduction of the acquisition and maintenance costs of this equipment.

ACKNOWLEDGMENTS

The work was developed at SISEA - Alternative Energy Systems Laboratory from Escola Politécnica at Universidade de São Paulo. The second author thanks CNPq for the research scholarship.

NOMENCLATURE

$\dot{W}_c$	Electrical power of chiller (kW)	COP_E	Electrical chiller Coefficient of performance (-)
$\dot{C_T}$	Thermal load (kW)	η_{sol_pow}	PV panels efficiency (-)
k_1,k_2	Constants for photovoltaic panel	k_3, k_4, k_5, k_6	Constants for photovoltaic panel (°C^{-1})
T_{panel}	Temperature of surface panel (°C)	*TBS*	Dry bulb temperature of ambient air
I_T	Solar Irradiation (kW·m^{-2})	$h_{conv_{air}}$	Air convection coefficient (kW·°C^{-1}·m^{-2})
η_{System}	Electrical system efficiency (-)	$\dot{W_{PV}}$	Power generation by photovoltaic panels (kW)
$\dot{W}_{STC}$	Constant of photovoltaic panel (W·m^{-2})	I_{pSTC}	Constant of photovoltaic panel (W·m^{-2})
W_{acum}	Energy stored in battery banks (kWh)	t	Time os storage (h)
W_{ava}	Available energy (kWh)	$\dot{W}_U$	Power used for the batteries (kW)
t_u	Time of utilization (h)	$y(\dot{C_T})$	Chiller consumption (kW)
E_{PV}	Residual consumption		

REFERENCES

ANEEL (2015) *Understand the Electrical Taxes (In Portuguese: Entendendo a Tarifa) - ANEEL*, *Agência Nacional de Energia Elétrica*. Available at: http://www.aneel.gov.br/entendendo-a-tarifa (Accessed: November 21, 2017).

ASHRAE (2006) "ANSI/ASHRAE Standard 169-2006 - Weather Data for Building Design Standards." Atlanta: American Society of Heating, Refrigeration and Air Conditioning Engineering, p. 20.

ASHRAE (2011) "Ashrae Thermal Guidelines for Data Processing Environments." Atlanta: American Society of Heating, Refrigeration and Air Conditioning Engineering.

ASHRAE (2016a) *Data Center Power Equipment Thermal Guidelines and Best Practices*, *Technical Comitee 9.9 of American Society of Heating, Refrigeration and Air Conditioning Engineering*.

ASHRAE (2016b) *Thermal Guidelines for a Data Processing Environments*. Atlanta.

ASHRAE (2017) *Ashrae Fundamentals Handbook*. Atlanta: American Society of Heating, Refrigeration and Air Conditioning Engineering.

Baltus, C. W. A., Eikelboom, J. A. and Van Zolinge, R. J. C. (1997) "Analytical Monitoring of Losses in PV Systems," in *European Photovoltaic Solar Energy Conference*. Barcelona: ECN, pp. 1–5.

Belizário, A. C. (2018) *Financial and Energetic Evaluation to use air conditioning systems powered by solar energy in Critical Buildings for different regions (Avaliação energética e financeira para utilização de sistemas de ar condicionado acionados por energia solar em ambient*. Universidade de São Paulo.

Carrier Corporation (2016) “Hour Analyse Program E-20.” Farmington, USA, p. 100.

Ferreira, C. I. and Kim, D.-S. (2014) “Techno-economic review of solar cooling technologies based on location-specific data,” *International Journal of Refrigeration*, 39, pp. 23–37.

Fraunhofer Institute for Solar Energy Systems (2018) *Photovoltaic Reports*. Freiburg.

Hassan, H. Z. and Mohamad, A. A. (2012) “A review on solar cold production through absorption technology,” *Renewable and Sustainable Energy Review*, 16(5331–5348).

Huld, T. *et al.* (2010) “Mapping the performance of PV modules, effects of module type and data averaging,” *Solar Energy*, 84, pp. 324–338.

Kalogirou, S. A. (2004) “Solar Thermal collectors and applications,” *Prog. Energy Combust.* Sci, pp. 231–295.

Otanicar, T., Taylorb, R. A. and Phelanc, P. (2012) “Prospec of a solar cooling - An economic and environmental assessment,” *Solar Energy*, 86, pp. 1287–1299.

Papadopoulos, A. M., Oxidis, S. and Kyriakis, N. (2003) “Perspective of Solar Cooling in view of the development in the air conditionig sector,” *Renewable and Sustanable Energy Reviews*, 7, pp. 419–438.

Porumb, R., Porumb, B. and Balan, M. (2016) “Baseline evalution of potential to use solar radiation in air conditioning applications,” *Energy Procedia*, pp. 442–451.

Strutt, S. *et al.* (2012) “Data Center Efficiency and IT Equipment Reliability at Wider Operating Temperature and Humidity Ranges,” *The Green Grid*. Available at: https://energy.gov/sites/prod/files/2013/12/f5/data_center_efficiency_and_reliabilit_at_wider_operating_ranges.pdf (Accessed: November 20, 2017).

TRANE (2017) “Resfriadores de Líquido Tipo Parafuso Série R.” Araucária, PR: Trane, p. 257. Available at: http://www.trane.com/content/dam/Trane/Commercial/lar/br/produtos-sistemas/equipamentos/Chillers/Chillers_Parafuso/Condensacao_Agua/RTWD_RTUD-Serie_R/Catalogo_Produto-RTWD(RLC-PRC029-PT).pdf (Accessed: December 6, 2017).

Manuscript ID: 161
DOI: 10.18462/iir.icr.2019.0161

Theoretical and experimental studies on the influence of subcooling of the liquid in air-conditioning system

Liviu Geo DRUGHEAN[(a)], Mădălina Teodora NICHITA[(a)], Cătălin NEGRUȚIU[(b)], Răzvan CALOTĂ[(a)], Valentin CUBLEȘAN[(a)]

[(a)]Technical University of Civil Engineering Bucharest, 122-124, Lacul Tei, Bucharest 2, Zip code: 020396, Romania, mtn_76@yahoo.com

[(b)]Daikin Central Europe - Romania, 169A Calea Floreasca, Bucharest 1, zip code: 014459, Romania, cnegrutiu77@ygmail.com

ABSTRACT

The paper analyzes the influence of liquid subcooling on the performances of an air conditioning system. The nominal refrigeration power is 11.2 kW. The theoretical study was conducted for the next refrigerants: R410A, R134a, R407C, R22 and R32.

The plant's operating conditions are vaporization temperature 6°C, condensation temperature 45°C, vapor temperature at evaporator exit 13°C. The subcooling of the liquid is done with air in a subcooler.

The authors made a comparative analysis between theoretical and experimental results. The experimental stand consists in an air conditioning refrigeration system, type VRV (Variable Refrigerant Volume), which is part of the Thermodynamics and Thermal Equipment Laboratory from the Technical University of Civil Engineering Bucharest. The refrigeration system works with R410A refrigerant.

Keywords: Air Conditioning, Performance, Refrigerating Plant, Subcooling.

1. INTRODUCTION

Under ideal conditions the condensation process takes place in the refrigeration plant condenser, so that the resulting liquid is saturated. Likewise, in ideal conditions, the evaporation ends in the evaporator so that the vapors resulting therefrom are dry saturated. In fact, the vapor leaves the vaporizer in an overheated state.

It is well-known the beneficial effect of liquid subcooling on the mechanical compression plant's performances by reducing the mass enthalpy of the liquid before the throttling valve, with the result of increasing the mass cooling capacity, $\dot{q}_0$. This becomes more important when working with refrigeration fluids with low $\dot{q}_0$ as freons.

In the literature it is mentioned that a large subcooling value involve a smaller mass of refrigerant for the same cooling power.

In the present paper a theoretical and experimental analysis of the performances of a mechanical compression cooling system is performed using a refrigerant/ air heat exchanger liquid as subcooler.

We studied 5 refrigerants, respectively: R410A, R134a, R407C, R22 and R32. They are recommended for low-power air conditioning systems.

2. THEORETICAL AND EXPERIMENTAL STUDY ON THE SUBCOOLING EFFECT

2.1. General Data

The experimental study was carried out on a VRV (Variable Refrigerant Volume) system, located in the Thermodynamics and Thermal Equipment Laboratory part of the Technical University of Civil Engineering from Bucharest. The components of the system are: an

outdoor unit and two indoor units, a scroll inverter compressor, with refrigerant R410A. A general view of the experimental stand is in Fig. 1.
The system is used for air conditioning of the laboratory where the indoor units are mounted.

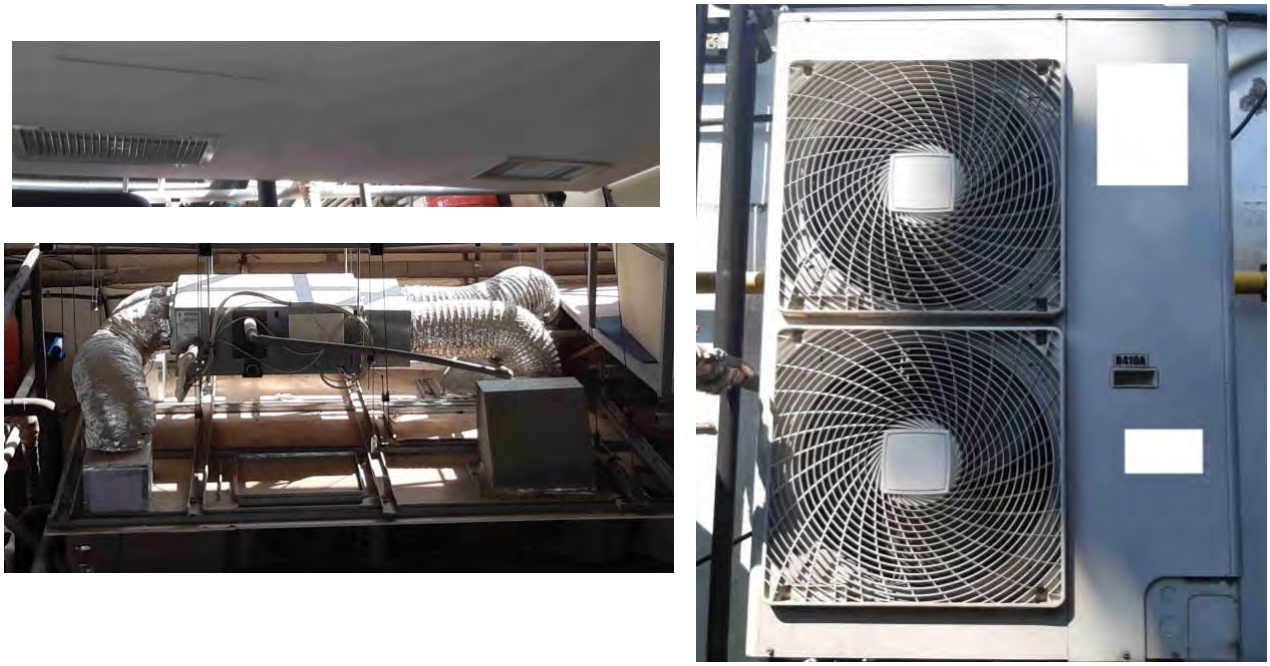

Figure 1: The experimental stand.l

2.2. Theoretical Study

The theoretical study was conducted for five refrigerants as follows: R410A, R134a, R407C, R22 and R32.
For the analysis, the following input data are considered:
- evaporating temperature $t_0 = 6℃$;
- condensing temperature $t_C = 45℃$;
- isentropic efficiency: 1;
- vapor temperature at the compressor inlet ($t_3 = 13℃$);
- the temperature of the refrigerant at the outlet of the subcooler ($t_7 = 40℃$).

The study aimed to calculate the value of the cooling system performance coefficient (EER) according to the refrigerant used. The thermodynamic cycles were represented with the Coolpack Program.
The theoretical EER values obtained from the calculations are shown graphically in Fig. 2.

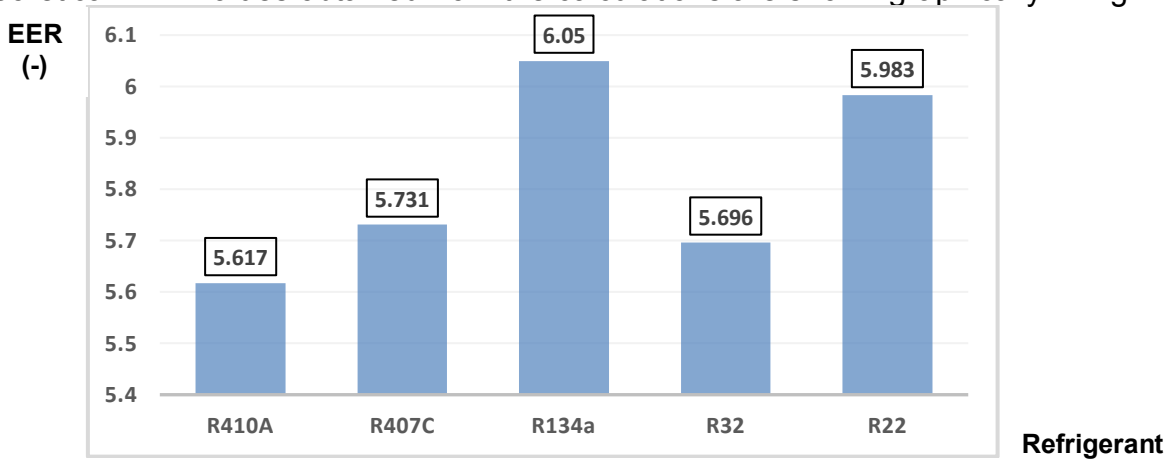

Figure 2: EER value to 5°C subcooling effect.

Fig. 3 shows the EER values of an air conditioning system with subcooling and an air conditioning system without subcooling.

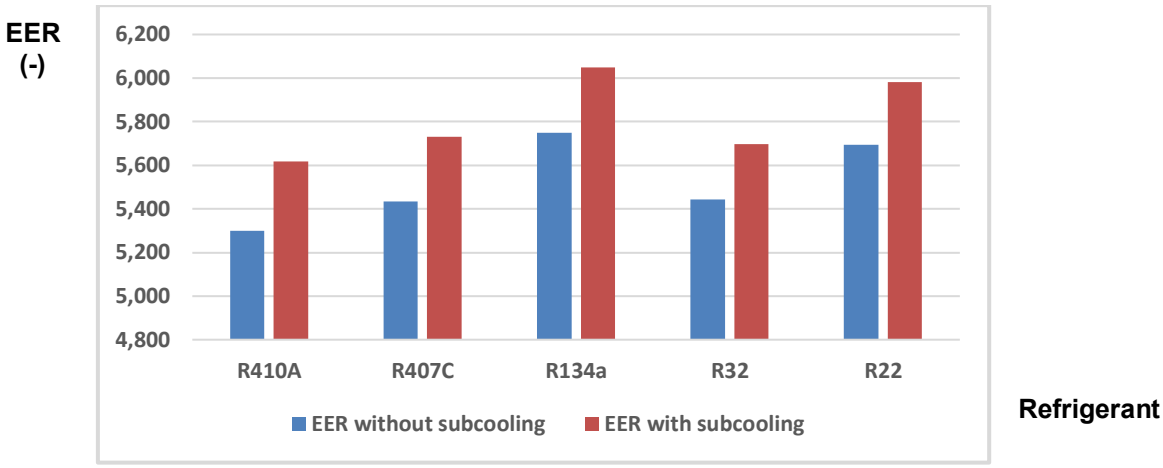

Figure 3: EER system with and without the subcooling.

Fig. 2 show that EER coefficient depend by type of refrigerant. It can be observed that for a subcooling of 5°C, the performance coefficient has the highest values, respectively 6.05 and 5.95 for R134a and R22.
Refrigerants R407C and R32 have appropriate performance coefficients, 5.73 and 5.70. The smallest values for the performance coefficient correspond to R410A refrigerant with a value 7.20% lower than the R134a.
Fig. 3 shows the subcooling effect for each analyzed refrigerant. EER values are higher for subcooling than those without subcooling. EER values are by 5% higher for a subcooling of 5°C.

2.3. Experimental Study

2.3.1. Experimental Stand and Data Acquisition System

The experimental stand contains a VRV (Variable Refrigerant Volume) refrigeration unit consisting of an outdoor unit to which two indoor units with a nominal refrigeration capacity of 2.8 kW and 4.5 kW. The refrigeration system is with refrigerant R410A.

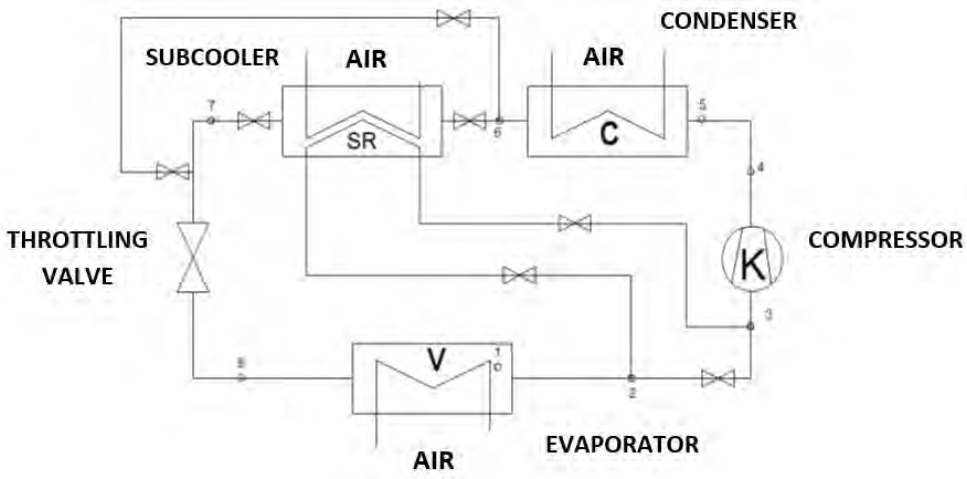

Figure 4: Experimental setup.

The experimental study was carried out for the system operating in different conditions:

- air inlet temperatures between 14 and 38°C;
- condensation temperatures between 29 and 48°C;

For data measures and registration, them was used a Data Acquisition System and a Service Checker. Service Checker made the control VRV, which enabled a real diagnosis of how the installed system follows the parameters. The system parameters were measured and monitored at the entrance and exit of each equipment.

2.3.2. Experimental Results

The recording of the experimental data took place in several measurement sessions so that the information is as varied as possible and provides a clear picture of the operation of the equipment. The experimental results are only for the R410A refrigerant.

There were performed measurements of air and refrigerant parameters.

On the air side there were measured:

- Inlet / outlet temperature of the condenser;
- Ambient temperature (t_{amb}).

On the refrigerant side there were measured:

- Inlet / outlet temperature of the compressor ($t_{inlet\ compressor}$/ $t_{outlet\ compressor}$);
- Saturation pressure and temperature in the condenser ($p_{saturation\ condenser}$/ $t_{saturation\ condenser}$);
- Different temperature at subcooling ($\Delta t_{subcooling}$).

A selection of different measured values is presented in Table 1.

Temperature sensors have a precision of $\pm$ 0.01°C. The air flow meter used for measuring air flow has an accuracy of $\pm$3%. The flow of refrigerant was measured with a Portaflow300 type ultrasonic flow meter with an accuracy of $\pm$ 4%.

The recording of the experimental data took place in several measurement sessions from the period (October 2017, March 2018, July 2018).

The results were plotted in the next Figs. 5 and 6, in order to highlight the importance of the subcooling.

Fig. 5 shows that the mass cooling capacity varies between 160 ÷ 230 kJ/kg for a maximum subcooling of 5°C. We observe the general the tendency of mass cooling capacity increasing with subcooling. This increase is up to 30% in compare to the variant without subcooling. An increase in subcooling by one degree, attracts an average increase in the mass cooling capacity with 5 ÷ 6 %.

Fig. 6 shows that the EER performance coefficient increases with the increase of subcooling. This coefficient varies between 4.90 and 7.50 for a subcooling of maximum 5°C. As with mass refrigeration, the subcooling effect leads to an increase in the system's performance coefficient. This increase is up to 34%.

Table 1. Measured values

No exp	t_{amb}	t_{inlet} compressor	t_{outlet} compressor	t_{outlet} condenser	$t_{saturation}$ condenser	Δt subcooling	$p_{saturation}$ condenser
	(°C)	(°C)	(°C)	(°C)	(°C)	(°C)	(bar)
1	13	5	49	25	28	3	16,6
2	14	5	48	30	31	1	18,2
3	14	5	48	30	31	1	18,2
4	14	5	48	30	31	1	18,2
5	15	5	55	36	36	0	21,1
6	14	5	51	35	37	2	21,6
7	14	5	51	35	37	2	21,6
8	14	5	51	35	37	2	21,6
9	15	5	56	37	39	2	22,8
10	15	5	56	37	39	2	22,8
11	15	5	56	37	39	2	22,8
12	15	5	56	37	39	2	22,8
13	15	5	56	37	39	2	22,8
14	15	5	56	37	39	2	22,8
15	14	6	55	36	39	3	22,8
16	14	6	55	36	39	3	22,8
17	14	6	55	36	39	3	22,8

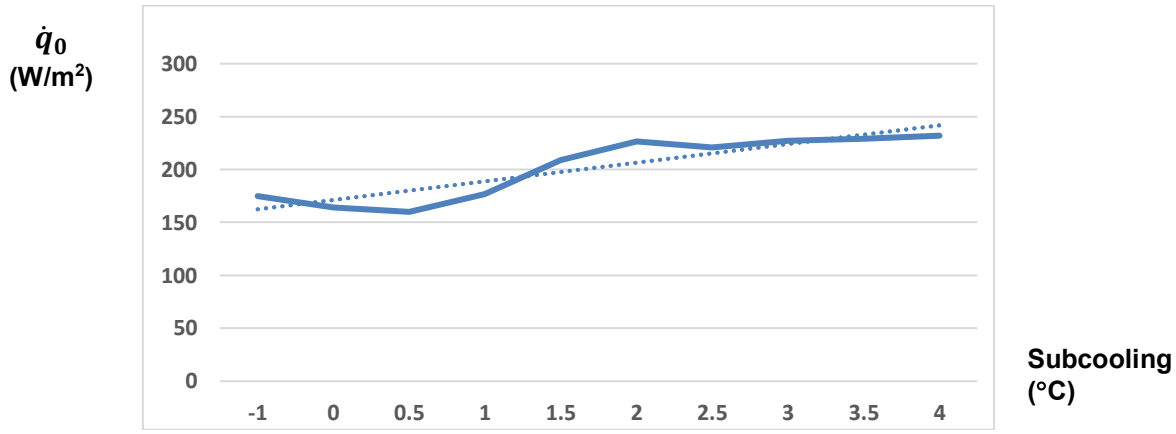

Figure 5: Mass cooling capacity versus subcooling.

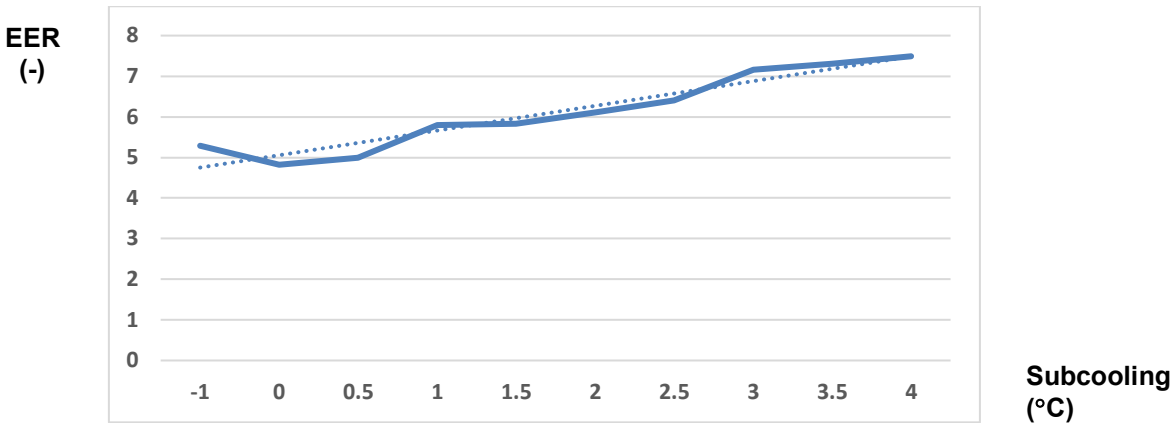

Figure 6: EER versus subcooling.

3. COMPARATIVE ANALYSIS

Comparative (theoretical / experimental) analysis was conducted for R410A refrigerant.
The comparative analysis was carried out between the theoretical study which is represented by the following parameters:
- Evaporating temperature: $t_0 = 6℃$;
- Condensing temperature: $t_C = 45℃$;
- Inlet compressor vapor temperature $t_3 = 13℃$;
- Refrigerant temperature at subcooler outlet: $t_7 = 40℃$;

And the experimental study which is represented by:
- Refrigerant temperature at subcooler outlet: between 25 and 37°C;
- Condensing temperatures between 29 and 48°C;
- Evaporating temperatures between 1 and 6°C.

Experimental and theoretical EER values are presented in table 2.

Table 2: EER experimental and theoretical

$\Delta t_{subcooling}$	$EER_{experimental}$	$EER_{theoretical}$	Deviation
(°C)	(-)	(-)	(%)
0	4.82	5.15	6.41
1	4.95	5.22	5.17
2	5.05	5.30	4.72
3	5.10	5.37	5.03

It can be seen from Table 2 that EER theoretical and experimental values increase with the increase in subcooling.
In the study, subcooling varied between 0 and 3°C. The EER experimental values varied between 4.82 and 5.10, and the EER theoretical values are ranged between 5.15 and 5.37.

4. CONCLUSIONS

By analyzing the processes presented in this paper, we can conclude that the effect of the subcooling, which takes place in a refrigerant/air heat exchanger, determine an increase of system's efficiency, EER.
However, from a constructive point of view, this solution is limited to a subcooling of maximum 5°C. The effect of subcooling depends on the refrigerant used. So, except of the refrigerant R32, a substantial increase in EER theoretical is observed, with values 5% higher for a subcooling of 5°C.
The mass cooling capacity increases with the refrigerant subcooling in the range 0÷3°C.
At 3°C subcooling the EER experimental coefficient increases with 5.50%.
The deviation EER theoretical/experimental is between 4.72÷6.41%.

ACKNOWLEDGEMENTS

The Technical University of Civil Engineering Bucharest provided the logistic support for the experimental tests for the doctoral thesis entitled "Contributions to the analysis of the evolution of the refrigeration systems with direct vaporization". We are grateful to the Department of Thermo-Technics and Thermic Equipment for its support.

REFERENCES

Negrutiu, G.C. 2018. Doctoral thesis entitled "Contributions to the Analysis of Evolution of Direct Vaporization Refrigeration Systems"

Ilie A., Girip A., Drughean L., Nichita T.M., 2015. Thermal calculation, cycles and schemes for the design of refrigeration plants with mechanical compression. ISBN 978-606-25-0116-7

Negrutiu, G.C., Hera D. 2016. Analysis of refrigerant subcooling in direct-evaporation refrigeration plants. Romanian Journal of Civil Engineering 86-99. ISSN 2068-3987

Revue Generale du Froid, collection year 2011

Coolpack Program.

Manuscript ID: 208
DOI: 10.18462/iir.icr.2019.0208

Dynamic Modeling and Control Strategy of a Transcritical CO2 Cycle for a Multi-Temperature Refrigerated Container System for Military Applications

Riley B. BARTA[(a,*)], Davide ZIVIANI[(a)], Jason J. HUGENROTH[(b)], Eckhard A. GROLL[(a)]

[(a)] Ray W. Herrick Labs, Purdue University Mechanical Engineering
West Lafayette, IN, 47906, USA, bartar@purdue.edu, dziviani@purdue.edu, groll@purdue.edu

[(b)] Inventherm, LLC
Baton Rouge, Louisiana, 37064, USA, Jason.hugenroth@inventherm.com

ABSTRACT

A transcritical carbon dioxide (CO_2) refrigeration cycle has been investigated for applications in U.S. Army Multi-Temperature Refrigerated Container Systems (MTRCS). The cycle configuration has been optimized to meet both environmental and energy efficiency targets. The proposed transcritical CO_2 cycle utilizes an axial multi-piston compressor-expander based on the Sanderson Rocker Arm Mechanism (S-RAM) that enables expansion energy recovery. The cycle features three compression stages, intercooling between the 2nd and 3rd compression stages, flash tank economization, and expansion work recovery. The numerical optimizations led to a maximum coefficient of performance (COP) of 1.0 at an ambient air temperature of 57.2 ºC. Due to the complexity of the cycle, a dynamic model of the system was developed to investigate different control strategies. Simulation results showed that the system was able to operate with adequate compressor suction superheats and flash tank liquid under excitations as well as varying operating conditions applied to both evaporators.

Keywords: Carbon Dioxide, Expansion Work Recovery, Multi-Temperature, Controls, Flash Tank Economizer

1. INTRODUCTION

The minimization of performance losses has been a focus of the heating, ventilation, air conditioning, and refrigeration (HVAC&R) industry in their pursuit of utilizing natural refrigerants such as Carbon Dioxide (CO_2). Despite the high pressures inherent of CO_2 during the rejection of heat to ambient in transcritical cycles, cycle enhancements and modifications enable performance competitive to cycles that utilize hydrofluorocarbon (HFC) refrigerants. With that being said, increasingly complicated cycles bring the need for understanding of cycle dynamics and associated control strategies for reliable operation. Analysis of the Multi-Temperature Refrigerated Container System (MTRCS) presented herein will provide insights into how the system reacts in transient conditions that will enable the development of control schemes for implementation. Lorentzen (1994) first suggested revisiting the use of CO_2 as a refrigerant, citing the fluid as inexpensive, non-flammable, and non-toxic as some of many advantages that would be beneficial in military application. Considering the MTRCS application will result in entry and exit into the cooled spaces numerous times, the ability to increase system capacity for a short time at the cost of power consumption will be beneficial.

Li and Groll (2004) performed a theoretical analysis of a U.S. Army Environmental Control Unit (ECU) utilizing a transcritical CO_2 cycle and concluded that the system out-performed the existing ECU with R-22 as a working fluid in all ambient conditions tested, which ranged from 31.7 ºC to 48.9 ºC. Robinson and Groll (1998) developed thermodynamic models to compare transcritical CO_2 cycles with and without expansion work recovery, concluding that the cycle with an expansion work recovery device at 60% isentropic efficiency had a 25% higher COP than the cycle with 100%-effective internal heat exchange. Agrawal et al. (2007) conducted the optimization of a two-stage transcritical CO_2 heat pump cycle and found that the cycles with either flash or compressor intercooling did not perform as well as cycles utilizing a flash-gas bypass. Xu et al. (2011) proposed and experimentally validated an R-410A vapor injection flash tank heat pump control strategy with

an electronic expansion valve (EXV) between high and intermediate pressures and a heater on the bypass gas line employed as the means of control of injection superheat. This combination with bypass line superheat as the only input proved to be an effective means of controlling flash tank liquid level, thus making the installed liquid level measurement redundant. Bertsch and Groll (2008) experimentally assessed the ability of a thermostatic expansion valve (TXV) to control the superheat of an injection line in a two-stage cycle utilizing closed economization and concluded that this solution was acceptable, but recommended an EXV in future experiments for better control.

The additional independent variable of high-side pressure in transcritical CO_2 cycles presented a significant gap in controls literature upon the revitalization of CO_2 as a refrigerant. Mcenaney and Hrnjak (2000) found potential COP improvements of up to 20% through experimental assessment of optimum cycling operation of a transcritical CO_2 cycle applied in automotive air conditioning. Rasmussen et al. (2002) compared both linear and non-linear transient models of a CO_2 air conditioning system in transcritical operation and concluded that the linearized model agreed with the 3rd order model as well as experimental data. Rasmussen (2012) conducted an in-depth literature review on dynamic vapor compression cycle modeling techniques, concluding that models that utilize a physics-based modeling approach provided a more useful tool than strictly empirical-based models. Additionally, heat exchangers have proven to be the primary challenge for dynamic modeling efforts, given that the two-phase thermal dynamics occur at a much slower rate than physical dynamics, such as pressure propagation and compressor pulsation, which are therefore considered instantaneous. Chen and Treado (2014) proposed a Simulink-based signal-oriented dynamic HVAC model that assessed the effects of controlling various numbers of physical parameters in building control, concluding that the tool could be used to effectively diagnose inappropriate control strategies, test and compare control strategies for higher efficiency, and detect faults if validated with experimental data.

This work presents a dynamic model of the MTRCS cycle is developed in Dymola using the TIL library from TLK-Thermo GmbH (2018). Sanderson-Rocker Arm Mechanism (S-RAM) is employed in the novel Energy Recovery Compressor (ERC) applied in the proposed MTRCS cycle. The S-RAM reduces sidewall losses common in wobble plate, swash plate, and crank shaft mechanisms during the conversion of reciprocating motion to rotary motion. Furthermore, variable capacity is possible through variation of the piston stroke without varying head clearance. Additional information on the ERC can be found in Kurtulus et al. (2012). Important control parameters for the MTRCS cycle are identified and discussed, as are results of the MTRCS dynamic reaction to varying operating conditions and excitations applied to the evaporators. The main purpose for this analysis is to ensure compressor suction superheats and the flash tank liquid level remain at safe values. Recommendations for control strategies are discussed, as is future work for continued improvement of the model.

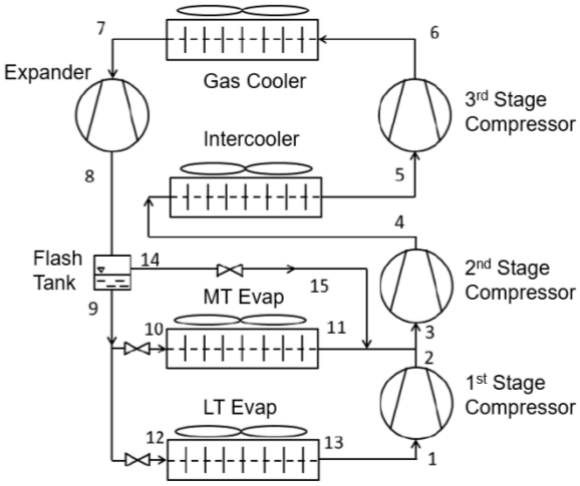

Figure 1: MTRCS cycle Schematic

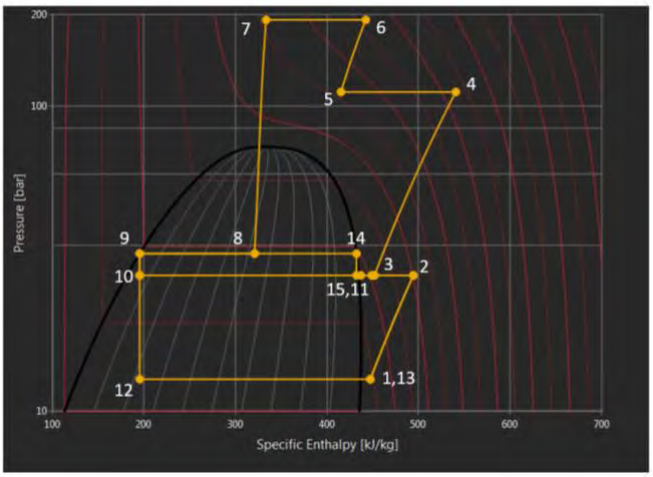

Figure 2: State points of MTRCS cycle in a P-h diagram

2. APPROACH

2.1 Design Overview

The transcritical CO_2 cycle for application in the MTRCS consists of three compression stages, two evaporators, a gas cooler, intercooling between the 2nd and 3rd stages of compression, flash tank economization, and expansion-work recovery. The 2nd and 3rd compression stages, along with the expander cylinders, are all connected to a common shaft inside the ERC. A schematic of the cycle is shown in Figure 1, and a pressure-specific enthalpy (P-h) diagram of the cycle state points operating at the design ambient temperature of 57.2 ºC is provided in Figure 2. The first stage of compression is completed with a single-stage compressor.

2.1 Modeling Overview

The transient modeling analysis for this work was conducted using Dymola in the Modelica language, and the cycle and model design in this environment is provided in Figure 3.

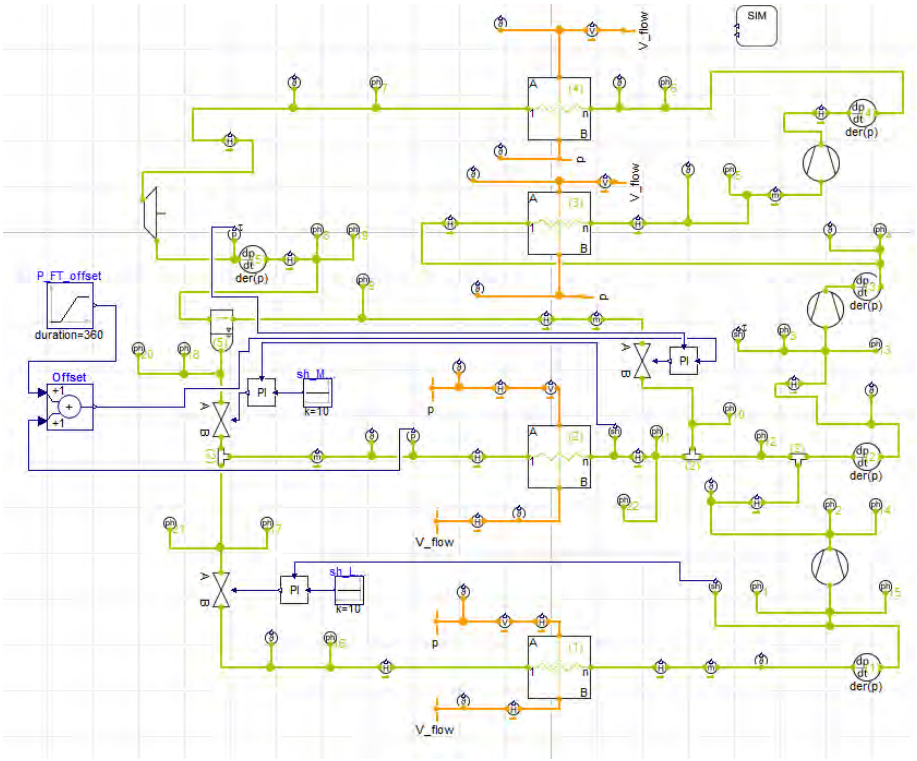

Figure 3: MTRCS model in Dymola by using the TLK library.

COP is calculated through the conventional ratio of cooling capacity to net power input, with recovered expansion work both increasing the potential cooling capacity of the system and decreasing the net-work input. All heat exchangers were treated as air-cooled with fixed volumetric air flow rates across them, and used fin-and-tube designs with constant heat diffusivity. The flash tank phase separation was modeled as ideal, and both the heat exchange and phase separation processes were modeled as isobaric. Experimental data was obtained for both expander and compressor operation of the ERC, but there was insufficient data to create an effective map for either operation. As a result, a conservative estimate was made for effective isentropic efficiency, $\eta_{is,eff}$, of 0.7 and 0.35 for compression and expansion, respectively, based off of the experimental values obtained. A constant volumetric efficiency, η_{vol}, of 0.8 and filling factor, φ_{FF}, of 2.5 was also assumed by this logic. These efficiencies are summarized in Eq. (1) through Eq. (4).

$$\eta_{is,eff,exp} = \frac{\dot{W}_{exp}}{\dot{m}(h_{in} - h_{out,s})} \qquad \text{Eq. (1)}$$

$$\eta_{is,eff,comp} = \frac{\dot{m}(h_{out,s} - h_{in})}{\dot{W}_{comp}} \quad \text{Eq. (2)}$$

$$\eta_{vol} = \frac{\dot{m}_{comp}}{\rho_{in} nVol_{comp}} \quad \text{Eq. (3)}$$

$$\varphi_{FF} = \frac{\dot{m}_{exp}}{\rho_{in} nVol_{exp}} \quad \text{Eq. (4)}$$

2.2 Operating Conditions Tested

Transient operation is vital to understand when designing a refrigeration system, particularly one as complex as the MTRCS, primarily because of the effects on component safety and system efficiency. The three primary areas of transients assessed herein are startup, evaporator condition variation, and system disturbances. Startup is when the system is initially turned on and brought from resting equilibrium to operating conditions. Evaporator condition variations are when the system operating condition changes and the evaporators are set to reach a different temperature. Given the operational purpose of the MTRCS, system disturbances were deemed worthwhile to assess and would primarily be due to the door opening and letting hot air into the refrigeration compartment, thus increasing the load on the evaporator cooling the compartment in question. The operating conditions for the MTRCS that were assessed in this analysis are summarized in Table 1.

The control scheme involves three EXVs controlled by proportional integral (PI) controllers. Referencing Figure 3, the EXV at the inlet to the low-temperature (LT) evaporator is used to maintain the suction superheat of the low-pressure compressor at $T_{sh} = 10$ ºC, while the EXV between the liquid outlet of the flash tank and the medium-temperature (MT) evaporator is to set the evaporator outlet superheat to that same target value in an effort to maintain at least 10 ºC of superheat at the medium-pressure compressor suction. The final EXV between the vapor outlet of the flash tank and the outlet of the MT evaporator is used to maintain a pressure differential of 5 bar between the MT evaporating pressure and the flash tank pressure. This value was attained to maximize both the range of operating temperatures where superheat can be attained at the MT evaporator outlet as well as the pressure differential across the expander to increase expansion work recovery.

Table 1: MTRCS Model Operating Conditions.

Ambient Temperature	℃	57.2
Medium-Temp. Compartment Target Temperature	℃	3.3
Medium-Temp. Evaporator Target Capacity	kW	3.8
Low-Temp. Compartment Target Temperature	℃	-20.6
Low-Temp. Evaporator Target Capacity	kW	1.9

Table 2: Evaporator Condition Variation Simulation Matrix.

Test #	Medium Temp. Evap. Set Point	Low Temp. Evap. Set Point
1	$3.3\ ℃ - 10\ ℃ = -6.7\ ℃$	$-20.6\ ℃$
2	$3.3\ ℃$	$-20.6\ ℃ - 10\ ℃ = -30.6\ ℃$
3	$3.3\ ℃$	$-20.6\ ℃ + 23.9\ ℃ = 3.3\ ℃$
4	$3.3\ ℃ - 23.9\ ℃ = -20.6\ ℃$	$-20.6\ ℃$

2.2.1 Startup

The aim of assessing the system startup behavior is to ensure that compressor suction ports avoid two-phase flow and pressures remain near maximum operating pressures. However, given the ambient condition for the MTRCS, the CO_2 will be at a superheated vapor state, therefore posing no risk of sending two-phase fluid into the compressor suction at first. However, this superheat could fail to be maintained if the controls on the EXVs fail to correct rapidly reducing superheat quickly enough. For this analysis, startup is defined as the time from turning on the system to when steady-state at the target operating condition has been achieved for 30 seconds.

2.2.2 Evaporator Conditions Variation

In this portion of the simulation, steady-state operating conditions are reached, then one or both of the evaporator air inlet temperatures are changed as inputs. The test matrix for this simulation is based off of the baseline parameters from Table 1 and includes the fours tests summarized in Table 2. Tests 1 and 2 are meant to show general reactions to smaller variations in temperature for both refrigeration (MT evaporator) and freezer (LT evaporator). Whereas, Tests 3 and 4 show how the system reacts to transitioning from the original refrigeration and freezer split design to both evaporators supplying air at refrigeration and freezer temperatures, respectively. All changes are applied in the form of a ramp down or up over a three-minute window. The analysis for evaporator condition variation effects brings compressor safety and flash tank starvation to take priority over efficiency, as rapid changes in evaporation pressure can have a significant effect on both of these parameters. As the evaporation pressure changes the flash tank pressures follow. Therefore, it is important to ensure that the liquid level does not get too low and risk send vapor into the evaporator inlet or too high and send liquid to the compressor suction.

2.2.3 System Disturbances

System disturbances are assumed to be a rapid change in evaporation pressure due to a sudden change in load on an evaporator in the low-side of the system. In practice, this could occur when the door into either the refrigeration or freezer section of the MTRCS is opened. The technique chosen to simulate this is to allow the system to arrive at steady state, then impart an increase in evaporation air inlet temperature of 15 ºC over 30 seconds before returning the evaporator air inlet temperature to its original temperature over the following 6 minutes.

3. RESULTS AND DISCUSSION

A steady-state P-h diagram of the MTRCS cycle at the operating conditions outlined in Table 1 is provided in Figure 2. With the given assumptions the cycle was able to reach a COP of 1.0 at these conditions, and the target superheat of 10 ºC at the medium-pressure and low-pressure compressor suction ports was retained in all tests except when both evaporators were transitioned to freezer operation.

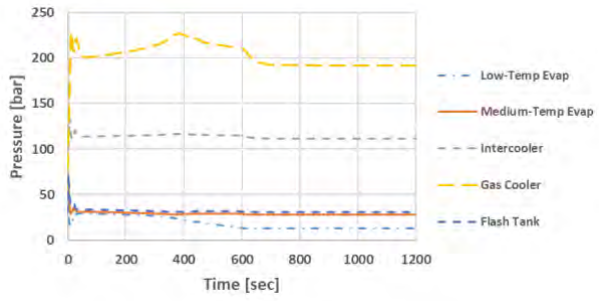

Figure 4: System Pressures – Startup.

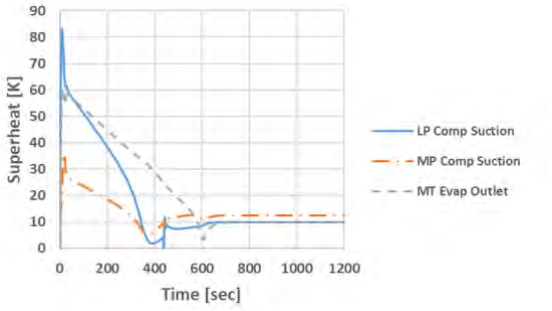

Figure 5: Key Superheats – Startup.

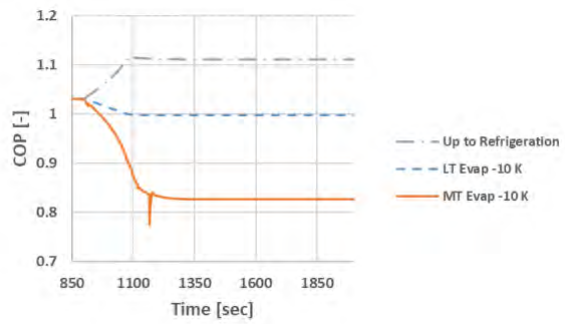

Figure 6: COP Variation with Evaporator Conditions.

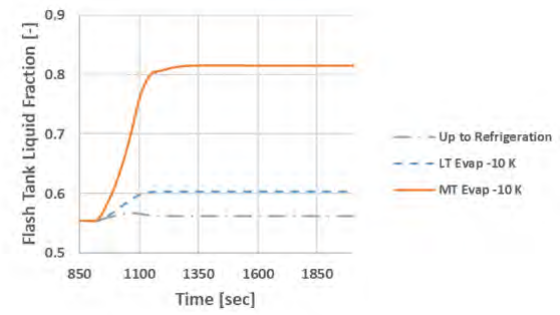

Figure 7: Flash Tank Liquid Volume Fraction Variation with Evaporator Conditions.

3.1 Startup

Given the high ambient temperature, the equilibrium values for the system were set to 57.2 ºC and 50 bar, which was an estimate of the equilibrium pressure from a low-fidelity charge inventory model independent from this dynamic study. This high temperature resulted in significant superheat at both compressor suction ports, which resulted in the EXVs operating at the edge of their set orifice opening ability. The EXV behavior is clear in Figure 4, which shows the system pressures over time and is supported by superheats of both compressor suction ports as well as the MT evaporator outlet plotted over the same time window in Figure 5. After initial startup the gas cooling pressure begins to decrease. However, it then begins to increase again until time $t = 400$ seconds, when it decreases once again. When compared to the superheat values of the low-pressure compressor suction at that time, it is clear that the low-pressure EXV is closing in an effort to reduce suction superheat of the low-pressure compressor as quickly as possible, with the unintended consequence of raising high-side pressure despite all of the thermal mass between the low-pressure EXV and gas cooler. Furthermore, the thermal inertia of the system causes the low-pressure compressor suction superheat to disappear temporarily at the conclusion of the rapid decrease in superheat. Other reactions in the system do not result in unsafe operating conditions for any components in this test. The system requires between 10 and 12 minutes to reach steady state from this startup condition.

3.2 Evaporator Condition Variation

The system was able to respond well to 3 of the 4 evaporator condition variation tests conducted, meaning that after disturbances were passed the system was able to return to steady-state with the target superheat at the low and medium-pressure compressor suction ports. Reducing the medium-temperature evaporating temperature to the freezer conditions, Test 4, resulted in a condition that the system could not recover from and resulted in two-phase at the outlet of the MT evaporator and thus the suction port of the medium-pressure compressor. To remedy this, two changes were implemented. The first was reducing the target superheat at both compressor suction ports from 10 ºC to 5 ºC. This alone was insufficient, prompting assessment of the expander. As the expander was modeled with a fixed-volume ratio designed to expand from the gas cooler outlet state at ambient conditions of 57.2 ºC to the MT evaporator pressure at 3.3 ºC, this volume needed to be reduced by 39% in order to retain superheat at the suction to both compressors when Test 4 was implemented. Given these modifications, the results from Test 4 are not meaningful in comparison and are therefore not presented in detail. The system pressures react proportionally to the temperature changes, and the superheat variations remain within 5 ºC in magnitude, lasting no more than two minutes. The more revealing aspects of this variation are found in COP and flash tank liquid level variations. Figure 6 shows the COP variation over time for the three successful tests, revealing that reduction in medium-temperature evaporation temperature by $10\ ℃$ can result in a 20% reduction in COP, among other results. From a design perspective, the independent reduction in evaporation temperatures in both evaporators results in a 5 to 25 % increase in liquid volume fraction, reaching a maximum of 80% liquid by volume. Plotted in Figure 7, these results show that an over-sized flash tank is a necessity in design, particularly when considering the cost of CO_2, and that the 1 Liter tank used in this simulation is under-sized. The temperature variation is applied at time $t = 900$ seconds.

3.3 System Disturbances

Both evaporators absorbed the disturbances with minimal impact to the system, suggesting that the EXV control strategy implemented was sufficient for these conditions. The liquid level in the flash tank was able to return to original operating conditions within 10 minutes of the beginning of the original disturbance, and the COP varied from its steady-state value by less than 10% over that same period of time. The increase in LT evaporation pressure during excitation had negligible effect on the high-side pressures of the system. However, given the flash tank pressure is controlled to vary directly with the MT evaporator pressure and that the expander is modeled to have a constant volume, the excitation on the MT evaporator increased the gas cooling pressure by more than 5%. Compressor suction superheats experienced more significant variation with the MT evaporator excitation than with the LT, with superheat variation up to 15 ºC observed. Plots of superheat over

time are provided in Figure 8 and Figure 9 for the MT and LT evaporators, respectively. The excitation is applied at $t = 1800$ seconds.

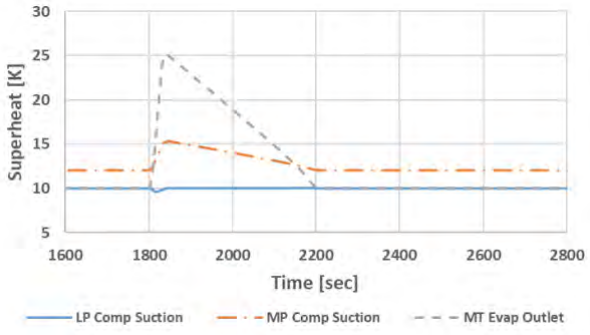

Figure 8: Superheat Variation with Medium-Temperature Evaporator Disturbance.

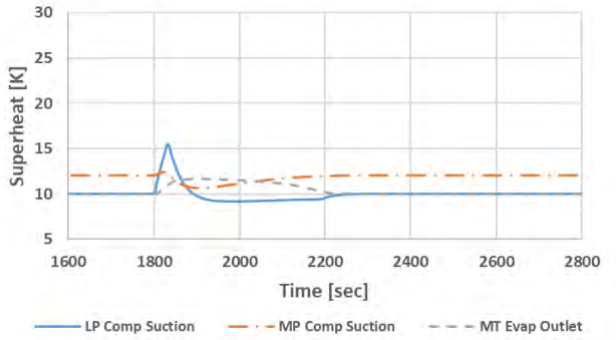

Figure 9: Superheat Variation with Low-Temperature Evaporator Disturbance.

4. CONCLUSIONS

This paper presented a theoretical analysis of the dynamic response of an MTRCS transcritical CO_2 cycle during startup, during evaporator condition variations, and when exposed to disturbances on the evaporator load. These simulations were conducted at an ambient temperature of 57.2 ºC and a COP of 1.0 was achieved at the initial ambient condition while meeting cooling targets in both the refrigeration and freezer sections. The system was able to retain suction superheat at both medium and low-pressure compressor suction ports, but resulted in a rise in gas cooler pressure above 200 bar as well as a 100% liquid level in the flash tank that would result in temporarily sending liquid to the compressor suction were it applied in a physical system. Both LT and MT evaporator excitations were absorbed effectively by the system, resulting in compressor superheat fluctuations of 5 ºC to 15 ºC in magnitude, and ultimately a 2% COP increase due to increased suction pressures. Temperature reductions of 10 ºC in the MT and LT evaporators caused a rise in flash tank liquid level and a decrease in COP, but did not result in irrecoverable system instability. The system was also able to transition from the design distribution of refrigeration and freezer temperatures between evaporators to conditions where both evaporators operated at refrigeration conditions, also causing an increase in COP as to be expected. However, transitioning to both evaporators operating at freezer operating conditions resulted in a loss of superheat at the medium-pressure compressor suction which could be remedied with a reduction in expander volume.

The control scheme utilized PI controllers through three EXVs to manage both evaporator outlet superheats and flash tank pressure. Dynamic responses were heavily impacted by EXV tuning methods, and results presented in this work represent results of a control scheme focused on sustainable operation and protecting compressors from receiving two-phase flow at the suction ports. Therefore, EXV control optimization for system efficiency will be a vital part of future work for this project. Additionally, moving-boundary heat exchanger heat transfer and pressure drop models, empirical expander and compressor maps, and experimental validation are in the future work.

ACKNOWLEDGEMENTS

The authors would like to thank the U.S. Department of Defense and S-RAM Dynamics for financial support through an SBIR grant.

NOMENCLATURE

Properties			**Subscript**	
h	Specific enthalpy	kJ kg^{-1}	1,2,3…	State points
$\dot{m}$	Mass flow rate	kg s^{-1}	$HTEvap$	High-temperature evaporator
p	Pressure	bar	$LTEvap$	Low-temperature evaporator
T	Temperature	℃	$Comp, 1st$	1st stage of compression
$\dot{W}$	Power	kW	$Comp, 2nd$	2nd stage of compression

$\dot{Q}$	Heat Transfer Rate	kW	$Comp, 3rd$	3rd stage of compression
N	Rotational Speed	Hz	Eff	Effective
Acronyms			is	Isentropic
COP	Coefficient of Performance		s	Isentropic State
GWP	Global Warming Potential		exp	Expansion
HFC	Hydrofluorocarbon		Vol	Volume
ERC	Energy Recovery Compressor		**Greek Symbols**	
TXV	Thermostatic Expansion Valve		Δ	Change
EXV	Electronic Expansion Valve		η	Efficiency
PI	Proportional-Integral		φ_{FF}	Filling Factor
MT	Medium-Temperature			
LT	Low-Temperature			

REFERENCES

Agrawal, N., Bhattacharyya, S., & Sarkar, J. (2007). Optimization of two-stage transcritical carbon dioxide heat pump cycles. *International Journal of Thermal Sciences*, *46*(2), 180–187. https://doi.org/10.1016/J.IJTHERMALSCI.2006.04.011

Bertsch, S. S., & Groll, E. A. (2008). Two-stage air-source heat pump for residential heating and cooling applications in northern U.S. climates. *International Journal of Refrigeration*, *31*(7), 1282–1292. https://doi.org/10.1016/J.IJREFRIG.2008.01.006

Chen, Y., & Treado, S. (2014). Development of a simulation platform based on dynamic models for HVAC control analysis. *Energy and Buildings*, *68*(PARTA), 376–386. https://doi.org/10.1016/j.enbuild.2013.09.016

Kurtulus, O., Yang, B., Lumpkin, D., Groll, E.A., and Jestings, L. (2012). Performance and Operating Characteristics of a Novel Rotating Spool Compressor. In *International Compressor Engineering Conference at Purdue*.

Li, D., and Groll, E. A. (2004). Theoretical Performance Evaluation of a Carbon Dioxide based Environmental Control Unit (ECU) with Microchannel Heat Exchangers. In *6th IIR Gustav Lorentzen Conf. on Natural Working Fluids*.

Lorentzen, G. (1994). Revival of carbon dioxide as a refrigerant. *International Journal of Refrigeration*, *17*(5), 292–301. https://doi.org/10.1016/0140-7007(94)90059-0

Mcenaney, R. P., & Hrnjak, P. S. (2000). SAE TECHNICAL Control Strategies for Transcritical R744 Systems, (724). https://doi.org/10.4271/2000-01-1272

Rasmussen, B., Alleyne, A., Bullard, C., Hrnjack, P., and Miller, N. (2002). Control-Oriented Modeling and Analysis of Automotive Transcritical AC System Dynamics. In *Proc. of American Control Conference*.

Rasmussen, B. P. (2012). Dynamic modeling for vapor compression systems-Part I: Literature review. *HVAC and R Research*, *18*(5), 934–955. https://doi.org/10.1080/10789669.2011.582916

Robinson, D. M., & Groll, E. A. (1998). Efficiencies of transcritical CO2 cycles with and without an expansion turbine: Rendement de cycles transcritiques au CO2 avec et sans turbine d'expansion. *International Journal of Refrigeration*, *21*(7), 577–589. https://doi.org/10.1016/S0140-7007(98)00024-3

TLK-thermo. (2018). TIL Suite simulates Thermal Systems. Retrieved from https://www.tlk-thermo.com

Xu, X., Hwang, Y., & Radermacher, R. (2011). Transient and steady-state experimental investigation of flash tank vapor injection heat pump cycle control strategy. *International Journal of Refrigeration*, *34*(8), 1922–1933. https://doi.org/10.1016/J.IJREFRIG.2011.08.003

Manuscript ID: 292
DOI: 10.18462/iir.icr.2019.0292

Investigation of two-phase injected compression with economization for high temperature application

Ammar M. BAHMAN[(a,*)], Davide ZIVIANI[(b)], Eckhard A. GROLL[(b)]

[(a)] Mechanical Engineering Department, College of Engineering and Petroleum, Kuwait University
P.O. Box 5969, Safat 13060, Kuwait, a.bahman@ku.edu.kw
[(b)] Ray W. Herrick Laboratories, School of Mechanical Engineering, Purdue University
West Lafayette, IN 47907-2099, USA, dziviani@purdue.edu, groll@purdue.edu

ABSTRACT

An economized two-phase injection (ETI) system has been investigated under extreme high ambient temperatures. An Environmental Control Unit (ECU) for military applications with a cooling capacity of 17 kW was retrofitted with a plate heat exchanger (PHX) economizer and an electronic expansion valve to control the injection state during the compression process. Two-phase injection was compared with both saturated vapor injection and no-injection (baseline) under different testing conditions up to an ambient temperature of 51.7 ºC (125 ºF). The experimental results show a significant reduction in compressor discharge temperature up to 11.4 K and an improvement in cooling capacity up to 10% while maintaining approximately the same COP. The increase in compressor power consumption suggested further potential for ETI optimization for air conditioning (AC) application at high ambient temperature.
Keywords: Two-phase injection, Economization, Air Conditioning, High Ambient Temperature, Experimentation.

1. INTRODUCTION

Military Environmental Control Units (ECU) are crucial equipment that is often required to operate in harsh climates and environments (e.g., desert conditions). Traditionally, ECUs are packaged air-conditioning systems featuring standard four-component vapor compression cycles. However, these single-stage systems being operated at high ambient temperatures lead to several unwanted conditions such as high compressor discharge temperature, loss of cooling capacity and COP among others. To this end, the use of vapor injection at an intermediate state of the compression process has been demonstrated to improve the system capacity and operation of the compressor at different conditions, and to reduce the compressor discharge temperature especially under extreme conditions (Tello Oquendo et al., 2016; Bahman et al., 2018). Nevertheless, experimental evaluations of the impact of the refrigerant injection quality on the performance of the compressor and the system are still limited.

In the literature, a few studies have been conducted to assess the impact of vapor- and two-phase injections for heating and cooling applications. For instance, Lee et al. (2013) numerically compared the vapor injection with two-phase injection for heating application. The results showed that the two-phase injection system not only reduced the discharged temperature, but also consumed less compressor power by up to 22.6% compared to vapor injection system. Kim et al. (2018) investigated numerically liquid, vapor, and two-phase injection for heat pump system at low ambient temperature up to -20 °C. The results showed that at optimum injection state, the two-phase injection system attained higher COP up to 3% compared to vapor injection system, while Kim et al. (2017) experimentally showed that the COP improved up to 5.8% for two-phase injection system.

This paper aims to assess the application of an economized two-phase injection (ETI) system in a packaged air conditioning (AC) unit to improve the performance at extreme ambient conditions. To evaluate the effectiveness of ETI in a packaged air conditioner, an R-407C Environmental Control Unit (ECU) with 17.6 kW cooling capacity was retrofitted with a plate heat exchanger (PHX) economizer and an additional expansion device to examine two-phase and saturated injections at different steady-state operating conditions in side-by-side psychrometric chambers. The cooling

capacity, COP, and compressor power and discharge temperature of the ETI system were evaluated and compared to the case without injection (baseline case).

2. EXPERIMENTAL METHODOLOGY

2.1. Experimental setup and procedures

An Environmental Control Unit (ECU) for military applications was retrofitted with an economized two-phase injection (ETI) system, as shown in Fig. 1, and tested under the same operating conditions in side-by-side psychrometric chambers to assess the implementation of two-phase injection and unit's performance improvement. The ECU has a rated cooling capacity of 17.6 kW (60,000 Btu hr^{-1}) and uses R-407C as a working fluid. Fig. 2 illustrates the original ECU system schematic as black solid lines and the retrofitted parts as colored lines. The compressor type is a hermetic scroll compressor with a single-port injection and a volumetric displacement rate of 14.1 m^3 h^{-1}. More details about the setup can be found in Bahman et al. (2018).

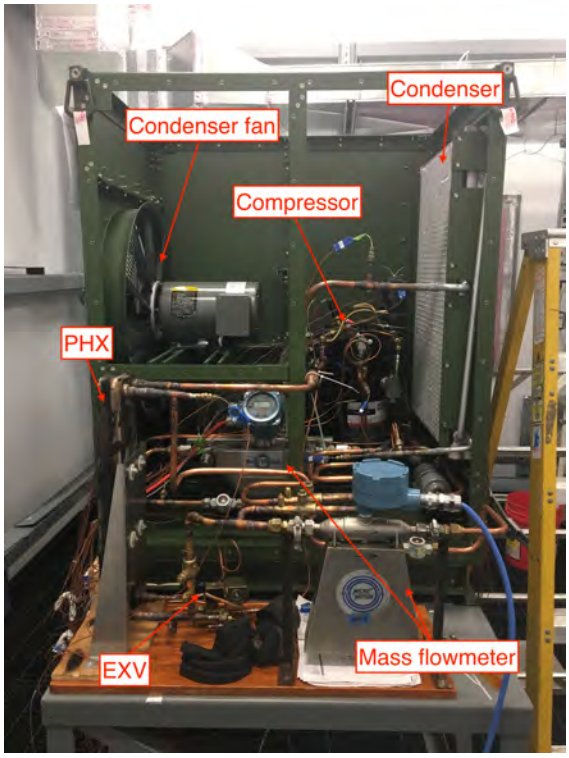

Figure 1: Environmental Control Unit (ECU) retrofitted with injected compressor, plate heat exchanger, electronic expansion device

To integrate the ETI system, the ECU was retrofitted with an economizer and an electronic expansion valve (EXV), as illustrated with colors in Fig. 2. Moreover, Fig. 2 shows that EVI system was configured with downstream injection (i.e., split line after the economizers outlet) according to the manufacturer's bulletin for optimal EVI injection control. The economizer is a brazed plate heat exchanger (PHX), which was over-sized for the purpose of this study (Mösch et al., 2016). After the PHX, a stepper motor-driven electronic expansion valve (EXV) is installed to facilitate and control the down-stream injection to the compressor. The EXV has been selected based on the nominal capacity of the PHX to control the injection flow. The EXV control is based on the injection quality that resulted from the energy balance on the PHX (i.e., enthalpy at the injection state, h_{inj}) using a PID control algorithm.

To accurately estimate the injection state, the enthalpy of the injected state is calculated based on the energy balance across the economizer (PHX) as shown in Eq. (1) and Eq. (2),

$$h_{inj} = \frac{\dot{m}_{r,tot}\left(h_{cond,out} - h_{PHX,out}\right) - \dot{Q}_{loss}}{\dot{m}_{r,inj}} + h_{PHX,out} \qquad \text{Eq. (1)}$$

$$\dot{Q}_{loss} = \mathrm{UA}(T_s - T_{amb}) \qquad \text{Eq. (2)}$$

where the heat leakage for the PHX was considered and estimated to have a constant overall heat conductance of UA = 13.56 W K^{-1}.

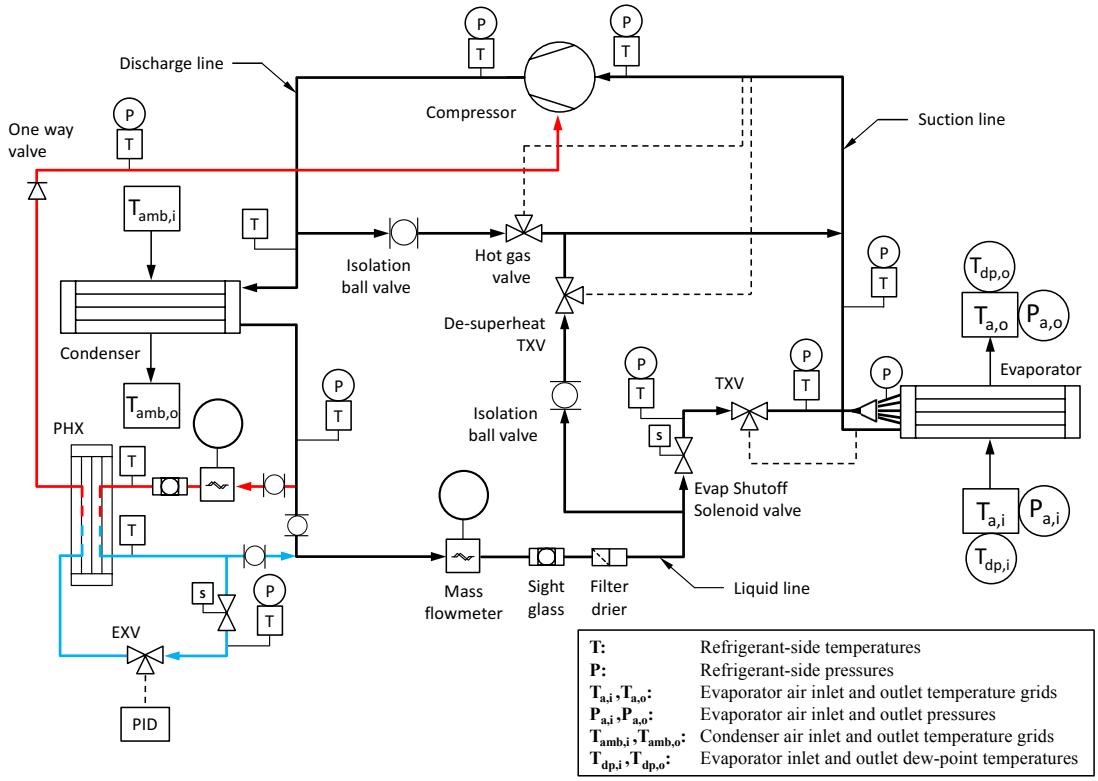

Figure 2: Schematic of ETI system with measured points

To be noted is that all the retrofitted parts are fully insulated to avoid any heat loss during testing. In addition, Fig. 2 shows the mounting position of each measuring instrumentation, while the respective accuracies of these instruments are listed in Table 1. Finally, the unit was charged with 5.01 kg (11.05 lb) of refrigerant.

Table 1. Measurement instrumentation and accuracy

Physical parameter	Instrument	Range	Accuracy
In-line temperature	SS T-type	-250-350 °C	± 1.1 °C
Surface temperature	T-type	-250-350 °C	± 1.1 °C
Refrigerant pressure (low/high)	Pressure transducer	0-1750, 0-3500, 0-7000 kPa	± 0.08% FS
Refrigerant pressure (econ)	Pressure transducer	0-3447 kPa	± 0.13% FS
Air humidity	Chilled mirror	-20-85 °C, 0-95%	± 0.2 °C
Air flow rate	ASHRAE nozzle box	2188-5107 m^3 hr^{-1}	± 6.66 m^3 hr^{-1}
Refrigerant flow rate (total)	Coriolis	0-2720 kg hr^{-1}	± 0.87 kg hr^{-1}
Refrigerant flow rate (suc)	Coriolis	0-680 kg hr^{-1}	± 0.18 kg hr^{-1}
Unit total power	Power transducer	0-40 kW	± 0.5% FS
	Current transducer	100:5 CR	± 1.5% FS
Compressor power	Power transducer	0-45 kW	± 0.25% FS
	Current transducer	1000:1 CR	± 0.3% FS
Fans power	Power transducer	0-2 kW	± 0.04% FS

2.2. Experimental methods

The experimental tests were performed in a pair of psychrometric chambers that simulate indoor and outdoor conditions, with the unit located in the outdoor chamber. The test conditions are listed in Table 2. The ECU was charged under the same operating condition of Test 4/A for testing the economized two-phase injection (ETI) system with no-injection (baseline), saturated-injection and two-phase-injection. To be noted is that Test Conditions 4/A, B and C are compliant with AHRI (2008), while Test Conditions 1 and 2 represent extreme ambient temperatures. After ensuring that the ECU reached steady-state conditions (typically after a run time of at least an hour), measurements were recorded every two seconds for 20 min. The average values of the data measurements were used in Section 3 to assess the ETI on improving the cooling capacity and COP as well as the reduction of compressor discharge temperature.

Table 2. Experimental test matrix

Test No.	Outdoor condition		Indoor condition	
	Dry-bulb ºC (ºF)	Wet-bulb ºC (ºF)	Dry-bulb ºC (ºF)	Wet-bulb ºC (ºF)
1	51.7 (125)	29.4 (85)	32.2 (90)	23.9 (75)
2	46.1 (115)	22.2 (72)	29.4 (85)	17.2 (63)
3	40.6 (105)	22.8 (72)	29.4 (85)	17.2 (63)
4/A	35 (95)	23.9 (75)	26.7 (80)	19.4 (67)
5	29.4 (85)	17.2 (63)	23.9 (75)	13.9 (57)
6	23.9 (75)	17.2 (63)	25 (77)	13.9 (57)
B	27.8 (82)	18.3 (65)	26.7 (80)	19.4 (67)
C	27.8 (82)	18.3 (65)	26.7 (80)	13.9 (57)

2.3. Data reduction

The cooling capacity and coefficient of performance (COP) were determined based on the air and the refrigerant enthalpy methods. Both methods were determined using thermodynamic property feature in the Engineering Equation Solver (EES) software (Klein and Alvarado, 2017) and compared to agree with each other within 6% per ANSI/AHRI Standard 210/240 (AHRI, 2008). The measured dry-bulb and dew-point temperatures, and the atmospheric pressure at a corresponding location were used to determine the air enthalpies, whereas the local temperature and pressure measurements were used to calculate the refrigerant enthalpies. Due to the fact that the available measurements cannot be used to calculate the refrigerant property at a two-phase mixture state, it was assumed a constant refrigerant enthalpy across the expansion valve. Note that for the air mass flow rate, the nozzle box setup calculation included the water vapor during test sampling. However, the air mass flow was corrected afterward during data reduction according to ASHRAE Standard 41.2 (ASHRAE, 1987) for laboratory airflow measurements. Since the tube between the compressor discharge port and the condenser inlet is relatively short, the pressure drop is neglected. Hence, the total cooling capacity measured on the refrigerant-side and the air-side is determined by Eq. (3) and Eq. (4), respectively. The cooling coefficient of performance (COP) is calculated by Eq. (5) where $\dot{E}_{tot}$ is the total power input, which includes the compressor, the fans, and the power used by the controllers.

$$\dot{Q}_{evap,r} = \dot{m}_{r,suc}\left(h_{r,out} - h_{r,in}\right) \quad \text{Eq. (3)}$$

$$\dot{Q}_{evap,a} = \dot{m}_a\left(h_{a,in} - h_{a,out}\right) - \dot{W}_{evap,fan} \quad \text{Eq. (4)}$$

$$\text{COP}_{sys} = \frac{\dot{Q}_{evap,a}}{\dot{E}_{tot}} \quad \text{Eq. (5)}$$

3. RESULTS AND DISCUSSION

The following sections discuss the experimental results for the economized two-phase injection (ETI) system based on the performance testing from Section 2. In addition, an uncertainty analysis of the performance results was carried out according to the Taylor and Kuyatt (1994) method by using the EES software (Klein and Alvarado, 2017). The analysis considered both the accuracy of the sensors and the propagation of sensors accuracies through the calculated properties.

3.1. Discharge Temperature

The economized two-phase injection (ETI) reduces the discharge temperature of the compressor due to the injection of cooler refrigerant during the compression process. Fig. 3 shows the absolute improvement to the compressor discharge temperature of the ETI system for different testing conditions. Note that the discharge temperature reduces significantly as more liquid injected to the compressor shell. For instance, the discharge temperature reduced up to 11.4 K at Test Condition 1. On the other hand, Fig. 3 shows that the discharge temperature had limited improvement for Test Condition 5 up to Test Condition C because the system was working at off-design points. Nevertheless, the minimum reduction in discharge temperature was around 4.1 K at Test Condition C.

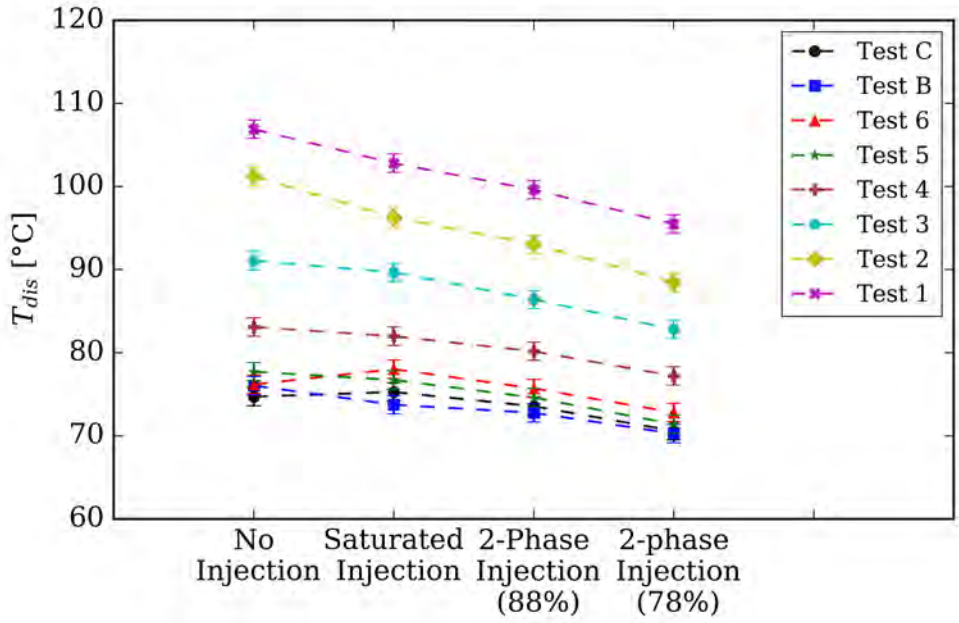

Figure 3: Comparison of compressor discharge temperature improvement using saturated and two-phase injections at different testing conditions

3.2. Cooling Capacity

The cooling capacity of the economized two-phase injection (ETI) system improved as a result of the increased subcooling in the economizer compared to the baseline cycle without injection. Fig. 4 shows that, for different testing conditions, the improvements in cooling capacity ranged from approximately 3% to 10% when saturated injection was applied. As more liquid is injected to the compressor, less refrigerant is flowing into the evaporator, and therefore a slightly decrease in the cooling capacity can be observed, as shown in Fig. 4. The maximum reduction in cooling capacity was approximately 2.4% at Test Condition 1. Otherwise, the reduction in cooling capacity remained less than approximately 1% for the other test conditions for two-phase injection (i.e., 78%).

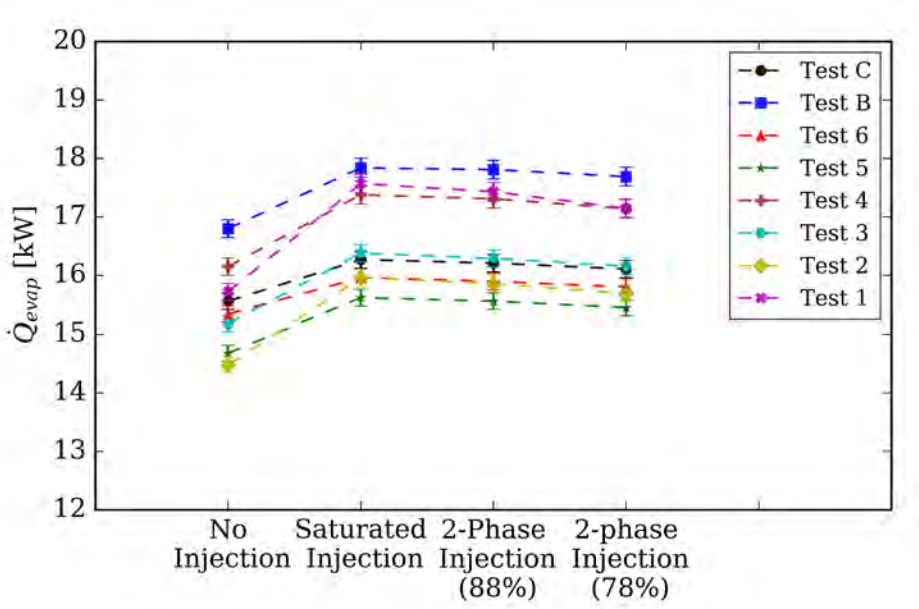

Figure 4: Comparison of cooling capacity variations using saturated and two-phase injections at different testing conditions

3.3. Compressor Power

Economized two-phase injection (ETI) affects the compressor performance and consequently the overall performance of the system. Fig. 5 compares the compressor power consumption for ETI system with respect to the baseline case (no injection) for all tested conditions. It can be noticed that the compressor power increased when more refrigerant was injected to the compressor. This can be clearly seen for Test Condition 4 up to Test Condition 1 because at those conditions the compressor was overloaded as more liquid was injected to the compressor. For instance, the power consumption increased up to approximately 18% at Test Condition 1. However, no significant increase in the compressor power can been seen for Test Conditions 5 to C. The increase in power consumption was below 10% compared to the baseline case (no injection). Note that for the cases of two-phase injection above 40.6 ºC (105 ºF) (i.e., Test 3 through Test 1), the maximum operating electrical current of 18 Amp was exceed because the compressor was not designed for air conditioning (AC) application, but for refrigeration application.

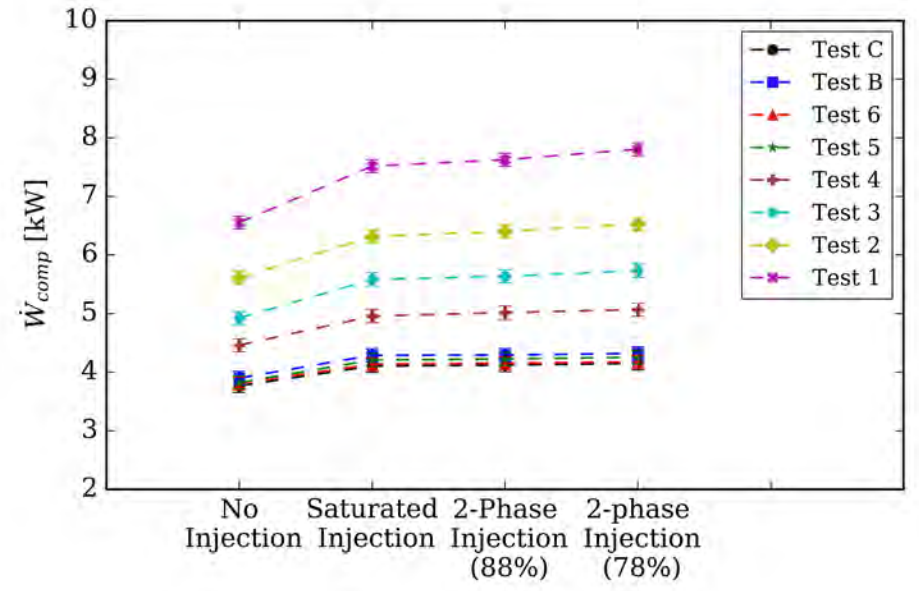

Figure 5: Comparison of compressor power consumption variations using saturated and two-phase injections at different testing conditions.

3.4. System COP

Due to the variation in compressor power and high cooling capacity of the ETI system, the system COP maintained almost constant, as shown in Fig. 6. Furthermore, Fig. 6 compares the system COP for the two-phase cases with the baseline (no-injection) case at different testing conditions. The system COP only varied from 2% to 5% when comparing the two-phase injection (78%) to the baseline case (no injection). Again, the ETI compressor was not optimized for AC applications. Rather, it was designed for refrigeration applications. This stipulates a potential for system optimization at high ambient temperature conditions.

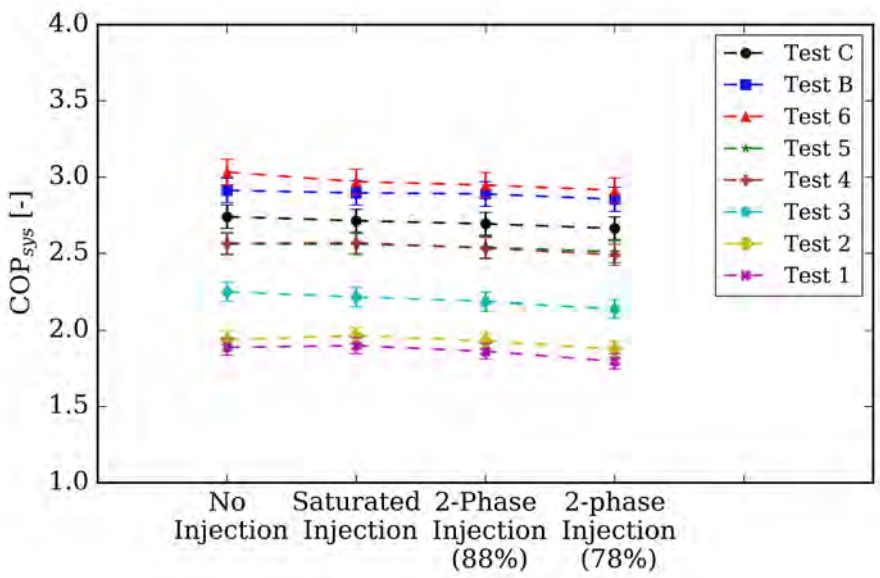

Figure 6: Comparison of system COP variations using saturated and two-phase injections at different testing conditions.

4. CONCLUSIONS

This paper presents an assessment of two-phase injection with economization in a packaged air conditioning (AC) unit to improve the performance under high temperature ambient conditions. The effectiveness of economized two-phase injection (ETI) system was investigated in a 17.6 kW Environmental Control Unit (ECU) with R-407C as working fluid. The ECU was retrofitted with a plate heat exchanger (PHX) as an economizer, and an additional expansion device to experimentally evaluate saturated and two-phase injections at extreme testing conditions. Comparisons of cooling capacity, COP, and compressor power and discharge temperature were analyzed with respect to the case of no injection. The results yielded the following conclusions:

- The ETI system was able to reduce the discharge temperature up to approximately 11.4 K.
- Despite the relative reduction in cooling capacity with two-phase injection, the ETI system improved the cooling capacity by up to 10% for saturated injection.
- Due to the design limitation of the ETI compressor for AC application, the system COP was maintained almost the same compared to no injection case.

The future work will consider optimizing the ETI system for optimal injection state to maximize its performance at high ambient temperature. Furthermore, a fully mechanistic cycle model could also be developed to resemble the real AC system operation.

ACKNOWLEDGEMENTS

The authors would like to acknowledge the support from the Center for High Performance Buildings (CHPB) at the Ray W. Herrick Laboratories.

NOMENCLATURE

h	specific enthalpy (kJ kg^{-1})	**Subscript**	
$\dot{m}$	mass flow rate (kg s^{-1})	*a*	*air*
P	pressure (kPa)	*comp*	*compressor*
$\dot{W}$	work rate (kW)	*cond*	*condenser*
T	temperature (°C/°F)	*dis*	*discharge*
Q	cooling capacity (kW)	*evap*	*evaporator*
AC	air conditioning (–)	*in*	*inlet*
COP	coefficient of performance (–)	*inj*	*injection*
ECU	environmental control unit (–)	*out*	*outlet*
ETI	economized two-phase injection (–)	*r*	*refrigerant*
EXV	electronic expansion valve (–)	*s*	*surface*
PHX	plate heat exchanger (–)	*suc*	*suction*
AC	air conditioning (–)	*sys*	*system*

REFERENCES

AHRI, 2008. ANSI/AHRI Standard 210/240. Performance rating of unitary A/C and air-source heat pump equipment.

ASHRAE, 1987. Standard 41.2–1987, standard methods for laboratory airflow measurement. American Society of Heating, Refrigerating and Air-Conditioning Engineers, Inc., Atlanta, GA.

Bahman, A.M., Ziviani, D. and Groll, E.A., 2018. Vapor injected compression with economizing in packaged air conditioning systems for high temperature climate. International Journal of Refrigeration, 94, pp.136-150.

Klein, S., Alvarado, F., 2017. Engineering Equation Solver, Academic Professional Version 10.273. F-Chart Software, Madison, WI.

Kim, B.G., Kim, D., Lee, D. and Kim, Y., 2017. Performance of a two-phase injection heat pump with the variation of injection quality and pressure. International Journal of Air-Conditioning and Refrigeration, 25(02), p.1750018.

Kim, D., Jeon, Y., Jang, D.S. and Kim, Y., 2018. Performance comparison among two-phase, liquid, and vapor injection heat pumps with a scroll compressor using R410A. Applied Thermal Engineering, 137, pp.193-202.

Lee, H., Hwang, Y., Radermacher, R. and Chun, H.H., 2013. Potential benefits of saturation cycle with two-phase refrigerant injection. Applied Thermal Engineering, 56(1-2), pp.27-37.

Mösch, T., Bahman, A. M., Groll, E. A., 2016. Performance testing of a vapor injection scroll compressor with R407C. In: Proceedings of the International Compressor Engineering.

Taylor, B., Kuyatt, C., 1994. NIST Technical Note 1279: Guidelines for Evaluating and Expressing the Uncertainty of NIST Measurements Results. National Institute of Standards and Technology, Washington DC.

Tello Oquendo, F. M., Peris, E. N., Macia, J. G., Corberán, J. M., 2016. Performance of a scroll compressor with vapor-injection and two-stage reciprocating compressor operating under extreme conditions. International Journal of Refrigeration, 63, 144-156.

Manuscript ID: 435
DOI: 10.18462/iir.icr.2019.0435

Development of a propane double duct room air conditioner

G. RIGHETTI[(a)], M. L. CAMPIDELLI[(b)], O. BOTTARO[(b)], C. ZILIO[(a)]

(a) Department of Management and Engineering, University of Padova,
Vicenza, I-36100, Italy, claudio.zilio@unipd.it

(b) Innova S.r.l.,Via 1° Maggio, 8 I-38089 Storo (Tn), Italy,
oreste.bottaro@innovaenergie.com

ABSTRACT

"Double duct" room air conditioners (DD-AC) are compact systems with no external heat exchanger unit. Outdoor air flow is conveyed through two ducts crossing external walls. Design and optimization of a DD-AC operating with R290 are reported. A suitable 3D simulation code was developed for the analysis of finned coils heat exchangers in order to optimize system efficiency, still minimizing refrigerant charge. In particular, the effect of refrigerant condensate subcooling on refrigerant charge and the optimal number of circuits on system performance were investigated. The R290 system performance was compared in summer conditions, according to EN 14511, with a similar off-the-shelf system operating with R410A. The results showed that, with a R290 charge lower than 150 g, it is possible to achieve at least the same energy efficiency with the same cooling capacity of the R410A system.

1. INTRODUCTION

Propane (R290) has been investigated as a viable substitute for R410A in several refrigeration applications, including air conditioners (Harby, 2017, Ribeiro and Barbosa, 2016, Wu et al, 2012) because of its low global warming potential (GWP~3 or less). The major limitation in use for R290 is surely its high flammability that requires a special design of the system components and, above all, refrigerant charge minimization. Compact air conditioning systems without external remote heat exchangers (as for example double duct air conditioners) offer promising opportunities for refrigerant charge minimization, given the relatively shortness of refrigerant lines.

It is worth to underline that in compact air conditioning systems, given the relatively small charge achievable also with HFC refrigerants, the indirect environmental impact, due to CO_2 emissions generated by energy consumption in use, is much larger than the direct effect consequent to the refrigerant release in ambient. Therefore, it is mandatory to maximize the energy efficiency of the air conditioner, keeping in mind that the key driver for a successful, in terms of safety, development of hydrocarbon air conditioners is linked to the refrigerant charge minimization. It is worth noticing that in compact air conditioners the condenser usually retains most of the refrigerant charge, depending on condenser design and on system lay-out (Wu et al, 2012). Accordingly, it is mandatory to reduce the volume of the two main heat exchangers (that operate can as condenser or as evaporator, depending on the type of operation: cooling or heating mode).

It is also well known that the heat exchangers design has a strong impact on the heat exchangers efficiency and consequently a marked effect on the energetic efficiency of the air conditioning machines. Hence, it is necessary to optimize the condenser and evaporator design not only from the point of view of charge reduction but also for an optimization of the thermal-hydraulic performance of the refrigerant during the phase change processes, considering the peculiar thermophysical properties of the refrigerant.

This paper presents the design optimization of a double duct compact room air conditioner operating with propane. A detailed simulation tool, validated on the basis of the experimental characterization of an off-the-shelf R410A system, is used to investigate the optimal number of circuits of the finned coil condenser and evaporator and to evaluate the effect of the condensate subcooling on the performance of a propane double duct room air conditioner.

2. IDEAL VAPOR COMPRESSION REFRIGERATION CYCLE

In order to gauge the performance potential of R290 vs R410A, the two refrigerants are compared in an idealized vapor compression refrigeration cycle. The cycle chosen is meant to be representative of typical comfort cooling operating conditions, and is specified by a constant condensation temperature of 55 °C, an evaporation temperature of 10°C, with 5 K vapor superheat 5 K and no condensate subcooling, 0.7 isoentropic compression efficiency.
The thermodynamic properties of R290 and R410A were evaluated with REFPROP 10.0 (Lemmon et al. 2018). Table 1 is comparing the main performances with R410A and R290 together with the saturated liquid density. The volumetric cooling capacity (VCC) is the product of the suction vapor density and the evaporator specific enthalpy change. The Coefficient Of Performance (COP) is the ratio of specific cooling capacity (per unit mass of fluid) and the compression work.

Table 1. Cycle performance with R410A and propane

	VCC (kJ/m^3)	COP (-)	Sat. liquid density (kg/m^3)
R410A	5340	2.92	865.5
R290	3217	3.26	438.8
Variation	-40%	+11%	-50%

In an ideal cycle, it is possible to make the following observations:

- First, the volumetric cooling capacity with R290 is about 40% lower. The R410A suction vapor is about 3 times denser while the refrigeration capacity per mass of R290 is about 1.8 times the R410A one, leading to 42% lower volumetric cooling capacity.
- Second, not reported in Table 1, the compression work is about 40 % lower with R410A. Considering that R290 has about 1.8 times larger refrigeration capacity per mass for R290, the COP with the hydrocarbon is +11%.
- Finally, the lower liquid density of the hydrocarbon permits to markedly reduce the refrigerant mass inventory in the circuit. However, in order to minimize the charge, it is mandatory to reduce the finned coil tubes diameter.

3. "REAL" VAPOR COMPRESSION REFRIGERATION CYCLE PERFORMANCE

In the present work, an off-the-shelf "Double Duct" room Air Conditioner (DD-AC) operating with R410A was taken as benchmark. DD-AC are compact systems with no external heat exchanger unit. Outdoor air flow is conveyed through two ducts crossing external walls. In the following, the two main finned coils heat exchangers (condenser/evaporator depending on the type of operation, i.e. heating or cooling mode) will be indicated as "indoor air coil" (IAC) and "outdoor air coil" (OAC). The main characteristics of the two finned coils are reported in Table 2.
As design criteria for the development of the R290 unit, it was decided to keep it as close as possible to the off-the-shelf R410A appliance. Therefore, the external overall dimensions, the fans and the air ducts were kept unchanged, as well as the overall heat exchangers dimensions. In order to reduce the refrigerant hold-up, commercially available copper microfin tubes with 5 mm nominal OD were adopted for R290 instead of the 7 mm OD ones, used for R410A.

3.1. Thermodynamic analysis

Cavallini et al. (2010) and Brown et al. (2014) clearly demonstrated that changing the refrigerant and/or the tube diameter, while keeping fixed all the other relevant geometrical features of the finned coil and the all the air side parameters, requires the optimization of the single circuit length. The authors used the criterion of minimizing the entropy generation for the definition of suitable performance evaluation criteria for in-tube condensation and boiling, like, for example, the Total Temperature Penalization (TTP). The reader may refer to the above mentioned papers for a proper definition of the TTP. The optimal circuit length is the one leading to minimum TTP.

Table 2. Finned coil heat exchangers geometry (R410A)

		Outdoor air coil (OAC)	Indoor air coil (IAC)
Tube arrangement		Staggered	Staggered
Tube material		Cu	Cu
Finned coil length	(m)	0.3	0.7
Outside tube diameter	(mm)	7	7
Inside tube diameter	(mm)	6.3	6.3
Longitudinal tube spacing	(mm)	12.7	12.7
Transverse tube spacing	(mm)	21	21
Fin geometry (material)		louvered (Al)	Louvered (Al)
Fin spacing	(mm)	1.4	1.3
Fin thickness	(mm)	0.1	0.1
Number of rows		4	2

The same approach was used here to compare R410A and R290 in reference conditions applicable for a DD-AC. The models used for the estimation of refrigerant-side parameters such as heat transfer coefficient, pressure drop, and void fraction are listed in Table 3. In Fig. 1a the TTP approach is used according to Cavallini et al (2010) for condensation while in Fig 1b. according to Brown et al. (2014) for boiling. All the assumptions are reported inside the figures. It is evident that, both with reference to condensation and boiling process, in order to achieve the minimum TTP values, it is mandatory to choose a proper circuit length. The optimal length is similar for R410A and R290, but propane performance is more sensible to the length. The circuit for evaporator should theoretically be shorter than that for the condenser. However, the TTP curves for the condenser are rather flat in the region close to the minimum so, once that the evaporator has been properly designed, it is possible to operate it as a condenser without remarkable thermodynamic penalization.

Table 3: Correlations used for the evaporator and the condenser

Evaporator refrigerant-side heat transfer coefficient	Cavallini et al (2006)
Condenser refrigerant-side heat transfer coefficient	Cavallini et al. (2009)
Refrigerant-side pressure drop	Cavallini et al. (2000)
Refrigerant void fraction	Rouhani and Axelsson (1970)
U-bend pressure drop	Equivalent length = 30D
Air-side heat transfer coefficient	Manufacturer proprietary data

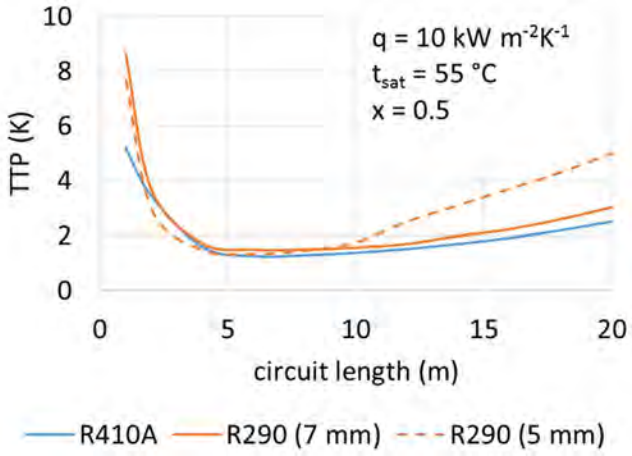

Figure 1a. Total Temperature Penalization (TTP) as a function of the circuit length for 55 °C of saturation temperature.

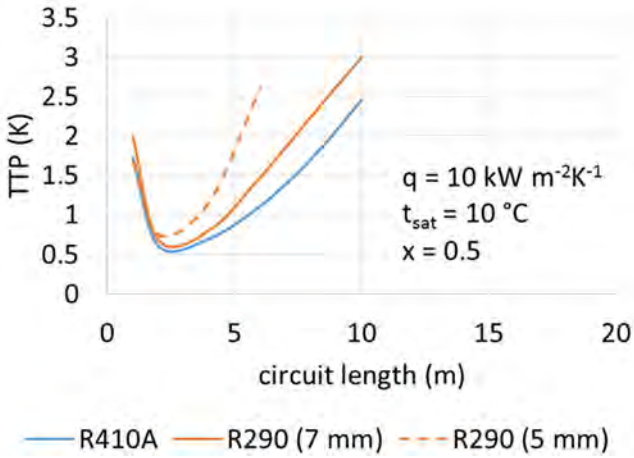

Figure 1b. Total Temperature Penalization (TTP) as a function of the circuit length for 10 °C of saturation temperature.

3.2. Detailed analysis

Starting from the above reported preliminary thermodynamic considerations, for the detailed analysis of the benchmark R410A unit and for the design of the new R290 unit, the numerical approach described in Casson et al. (2002) has been used with emphasis on the design the finned coil heat exchangers. The heat exchanger is discretized in a series of finite volumes, each element is calculated as small cross flow heat exchanger, and the conditions of both the primary refrigerant and secondary coolant are passed to the adjacent volume.
The correlations used for the refrigerant-side parameters such as heat transfer coefficient, pressure drop, and void fraction are listed in Table 3. The air-side heat transfer coefficients are calculated according to semi-empirical correlations developed from an experimental data base collected at Padova University. The air-side heat transfer coefficients are assumed to be constant and uniform in the whole heat exchanger. The main geometric characteristics are reported in Table 2 and are chosen according to a typical air-conditioning European production.
A simulation code of the whole chiller has been implemented based on the previously outlined simulation tools for the condenser and the evaporator. The compressor is characterized through its experimental compression efficiency (based on actual electric power consumption) and volumetric flow rate polynomials. A flow diagram of the code is shown in Fig. 2.
The inlet dry and wet bulb temperatures and mass flow rates of indoor and outdoor air are the input parameters to the simulation program, as well as the vapor superheat at the evaporator outlet. Starting from suction and discharge pressure initial guess, each component subroutine provides a refrigerant mass flow rate of the condenser, the evaporator and the compressor. When these mass flow differences are higher than the set tolerance (fixed by the user), the suction and discharge pressures are varied until the components' mass flow rates converge within the set tolerance.

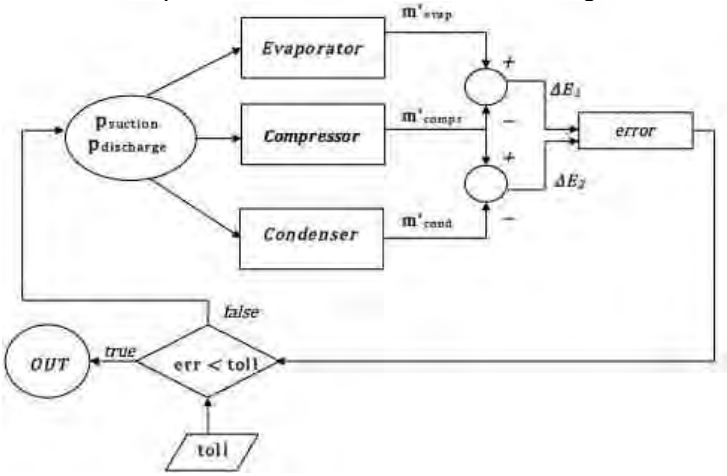

Figure 2: Simulation code flow chart

The present simulation tool was validated on the experimental performance data recorded for the benchmark R410A unit. Tests were run in a calibrated ambient double room type calorimeter according to EN 14511-2 and EN14511-3 specifications. The uncertainties of measurement fulfilled EN 14511-3 and the most relevant for the present paper are reported in Table 4. The experimental values are reported in Table 5. The measured condensate liquid subcooling was around 4 K.

Table 4 — Specification of the different measuring devices

Description	Uncertainty
Refrigerant temperature	±0.15 °C
Dry bulb air temperature	±0.3 °C
Wet bulb air temperature	±0.4 °C
Volumetric flow rate (air)	±5 %
Electric power	±1 %

The simulation tool was able to capture the rated heating and cooling capacities, the EER and the COP within 4%, hence it was considered calibrated and it was used for the design and analysis of the R290 unit.

Table 5 — Test results according to EN 14511-3

Description	Measurement	Unit
Standard rating conditions, indoor air dry bulb (wet bulb) temperature in cooling mode	27(19)	°C
Standard rating conditions, outdoor air dry bulb (wet bulb) temperature, in cooling mode	35(24)	°C
Rated capacity for cooling $P_{rated,c}$	2.35	kW
Rated power input for cooling P_{EER}	0.730	kW
Rated Energy Efficiency Ratio EER= $P_{rated,c}$/ P_{EER}	3.22	-
Indoor air flow rate	420	m^3/h
Outdoor air flow rate	500	m^3/h

4. ANALYSIS OF PROPANE DD-AC UNIT

Cavallini et al. (2014) demonstrated that, from a thermodynamic point of view, the overall compression efficiency of a compressor developed for R290 should be quite close to (if not better than) the efficiency of a R410A compressor. Accordingly, for the present analysis the polynomials used for R410A compressor characterization were adopted also for simulating the R290 compressor. Evidently, the compressor volumetric flow rate was increased to achieve with R290 the same cooling/heating capacity of the R410A unit.

The rating conditions and flow rates reported in Table 5 were investigated with a fixed vapor superheat at evaporator outlet of 5 K. Auxiliaries electric consumption was considered the same of the R410A unit. For simplicity, the connection vapor and liquid lines were considered adiabatic and with negligible pressure drops.

In order to assess the preliminary results of the thermodynamic analysis based on the TTP performance evaluation criteria, a detailed 3D simulation tool was used to analyze the IAC and OAC as stand-alone components. In particular, fixed condensation and evaporation temperatures (55 °C and 10 °C, respectively), 0 K condensate subcooling, and 5 K vapor superheat were considered. The length of each refrigerant circuit was increased from about 2 m to the maximum possible (14 m for IAC and 22 m for OAC). As mentioned before, 7 mm external diameter (OD) microfin tubes were used for R410A while 5 mm microfin OD pipes were considered for R290. Fig. 3a and Fig. 3b report the exchanged heat flow rate and the corresponding saturation temperature drop for OAC and IAC, respectively. The star bullets indicate the configuration adopted for the R410A unit, demonstrating that the benchmark system properly adopted an optimized circuitation of both the condenser and evaporator coils. The simulation of the evaporator at 10 °C saturation temperature, reported in Fig. 3b, indicates that R290 would require a shorter circuit length (i.e., higher number of circuits in parallel) in comparison to R410A. However, one should also consider that the two-phase fluid distribution in finned coil evaporators can be a heavy constraint for the designer. For this reason, since analyzing Fig. 3b it emerges that there is limited difference in the heat capacity between 2 m and 4 m for the IAC, a configuration with 4 circuits (i.e., length of the single circuit about 4 m) was adopted for both R410A and R290.

Furthermore, basing on the simulation results, the length of the circuits in the OAC (Fig. 3a) was slightly decreased from about 7 m (used for R410A, see star bullet) to about 5 m for R290.

Once fixed the circuitry configurations, the effect of condensate subcooling on system performance was analyzed. It is well known that subcooling occurs by flooding the terminal region of a condenser, with the consequence of an increase in the condensation pressure. In operation, this effect is controlled by the refrigerant charge in systems with a thermostatic expansion valve and no liquid receivers, like the one under investigation. It is common opinion that this practice brings about an improvement of COP (i.e., the benefit of larger specific (per mass unity) refrigerating effect outweighs the penalization arising from higher condensation pressure). From a theoretical point of view, this advantage can mostly be attributed to the reduction of exergy loss in throttling process, together with

a reduction of the heat transfer irreversibilities, due to the more favorable profiles of temperature of the two fluids along the heat exchanger. Hence, a larger benefit can be expected for propane having larger throttling losses than R410A and for operating conditions with a high temperature lift from evaporation to condensation.
In Fig. 5 the effect of subcooling is analyzed for the R410A and R290 in terms of EER and mass of refrigerant contained in the condenser during cooling operations, under the hypothesis of same cooling capacity for the two fluids. As expected, an optimal condensate subcooling that maximizes the EER (around 4-5 K for R410A and around 15 K for R290) exists for both the fluids. Propane benefits more for the larger subcooling, obtaining higher EER with the same cooling capacity of the R410A appliance, as presented in Fig. 6. However, the mass of hydrocarbon contained in the condenser increases from about 26 g at 0 K subcooling up to 45 g at 15 K subcooling. Given the much higher liquid density, the R410A charge is about 162 g at 0 K subcooling and it increases to 181 g at 4 K subcooling. According to Table 3, Rouhani and Axelsson (1970) void fraction model was used for the condenser charge estimation. Similar calculations were run for the evaporator. The liquid and vapor lines for the connection of different devices can be considered identical to the ones in use for the off-the-shelf R410A unit and the corresponding refrigerant charge can be easily evaluated once known the density of the single-phase fluid. The amount of refrigerant contained in the compressor during cooling operation can be estimated experimentally with a gravimetric method after quickly isolating the compressor during operation by means of rapid closing valves. Therefore, for the propane system under development, it was possible to estimate a total refrigerant charge of 138 g.

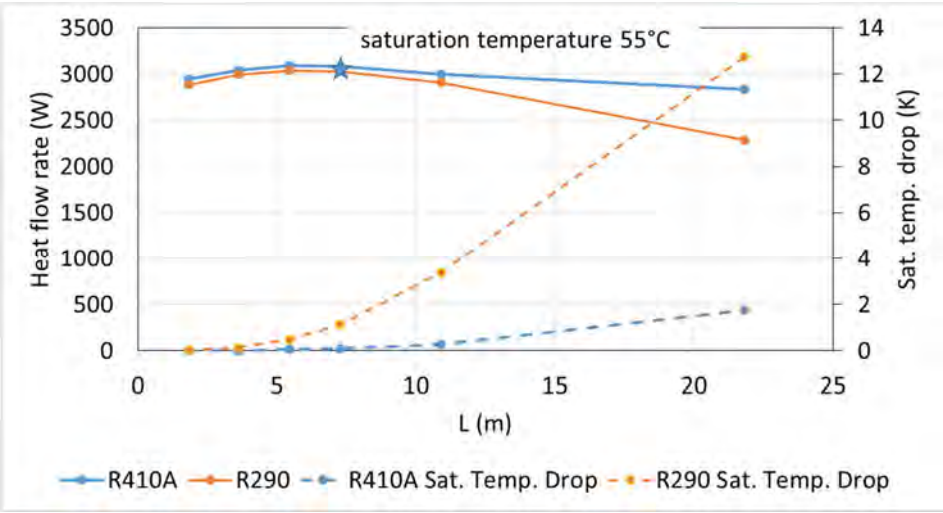

Figure 3a. Exchanged heat flow rate and saturation temperature drop of OAC (cooling mode)

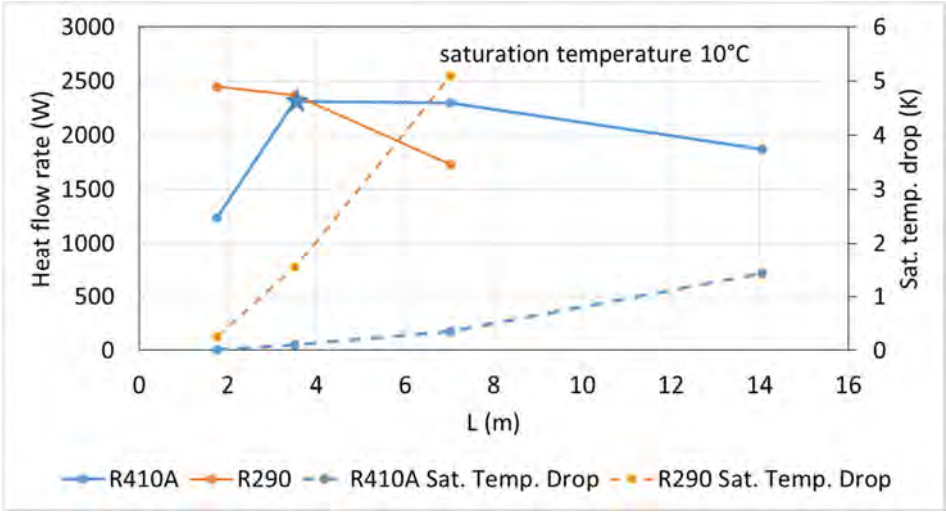

Figure 3b. Exchanged heat flow rate and saturation temperature drop of IAC (cooling mode)

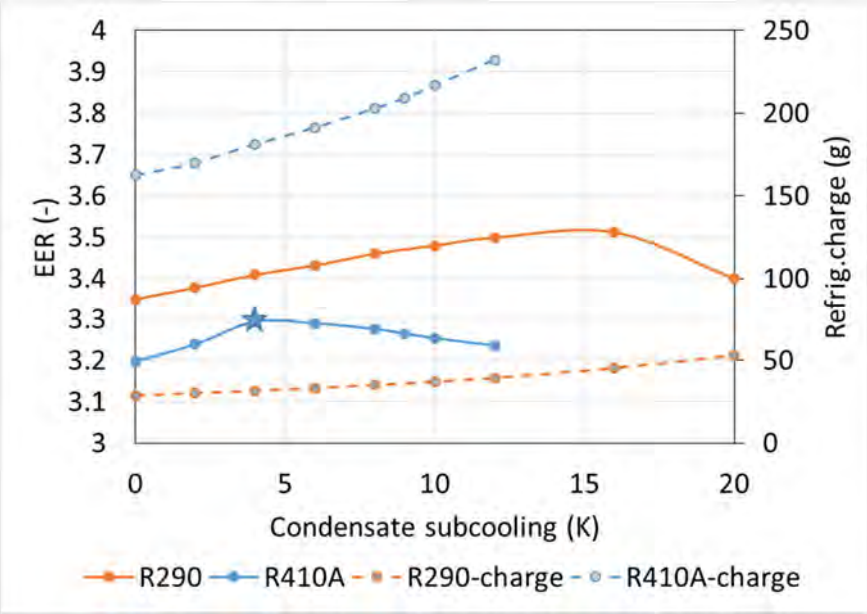

Figure 4. Effect of condensate subcooling on the EER, and on the mass of refrigerant inventory in the condenser (cooling mode) (star indicates the measured value for R410A unit).

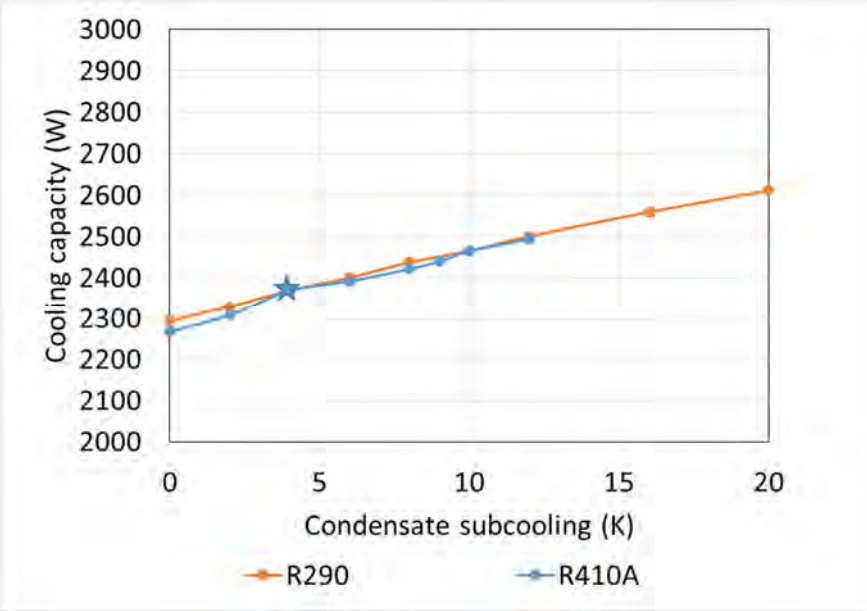

Figure 5. Effect of condensate subcooling on the air conditioner cooling capacity (star indicates the measured value for R410A unit).

5. CONCLUSIONS

In this paper a detailed simulation model was implemented and validated on the experimental analysis of a R410A double duct room air conditioner. The validated model was used for the design of an identical appliance (i.e. same overall dimensions, same fans, same cooling capacity) operating with propane as refrigerant. The analysis showed that is possible to design the unit operating with less than 150 g propane charge, able to achieve the same capacity of the R410A and equal or slightly higher performance (EER). The R290 system performance would benefit from a liquid condensate subcooling larger than the R410A system, but this have an impact on the propane charge in the system.

6. ACKNOWLEDGEMENTS

The financial support of European Commission within the project LIFE ZEROGWP (LIFE17 CCM/IT/000026) is acknowledged.

7. NOMENCLATURE

COP Coefficient of Performance (-)
EER Energy Efficiency Ratio (-)
VCC Volumetric cooling capacity (kJ m^{-3})

8. REFERENCES

Brown J.S., Zilio C., Brignoli R., Cavallini A., 2013. Heat transfer and pressure drop penalization terms (exergy losses) during flow boiling of refrigerants. Int. J. Energy Res. 37, 1669–1679.

Casson V., Dal Belin Peruffo G., Fornasieri E., Zilio C., 2003. Energy efficiency of a household air conditioner using new HFC refrigerants, 21st Int. Cong. Refrigeration IIF-IIR, Washington.

Cavallini, A., Del Col, D., Doretti, L., Longo, G.A., Rossetto, L., 2000. Heat Transfer and Pressure Drop during Condensation of Refrigerants Inside Horizontal Enhanced Tubes. Int. J. Refrigeration, 23, 4-25.

Cavallini, A., Del Col, D., Rossetto, L., 2006. Flow boiling inside microfin tubes: prediction of the heat transfer coefficient, Proc. of ECI Int. Conf. on Boiling Heat Transfer, Spoleto, Italy.

Cavallini, A., Del Col, D., Mancin, S., Rossetto, L., 2009. Condensation of pure and near-azeotropic refrigerants in microfin tubes: A new computational procedure. International Journal of Refrigeration, 32 (1), 162-174.

Cavallini, A., Brown J.S., Del Col D, Zilio C., 2010. In-tube condensation performance of refrigerants considering penalization terms (exergy losses) for heat transfer and pressure drop, Int. J Heat Mass Transfer, vol. 53: p. 2885-2896.

Cavallini, A., Zilio, C., Brown, J. S., 2014. Sustainability with prospective refrigerants, International Journal of Energy Research, 38, 285- 298

EN 14511-2, 2018. European Committee for Standardization, Air conditioners, liquid chilling packages and heat pumps for space heating and cooling and process chillers, with electrically driven compressors. Part 2: Test conditions

EN 14511-3, 2018. European Committee for Standardization, Air conditioners, liquid chilling packages and heat pumps for space heating and cooling and process chillers, with electrically driven compressors. Part 3: Test methods

Harby, K., 2017. Hydrocarbons and their mixtures as alternatives to environmental unfriendly halogenated refrigerants: An updated overview, Renew. Sustain. En. Rev., 73, 1247- 1264

Lemmon, E. W., Bell, I.H., Huber, M. L., McLinden, M. O., 2018. NIST Standard Reference Database 23, Reference Fluid Thermodynamic and Transport Properties (REFPROP), version 10.0, National Institute of Standards and Technology: Gaithersburg, MD

Ribeiro, G.B., Barbosa, J.R., 2016. Analysis of a variable speed air conditioner considering the R-290/POE ISO 22 mixture effect, Appl. Th. Eng., 108, 650–659.

Rouhani, S. Z., Axelsson, E., 1970. Calculation of volume void fraction in the subcooled and quality region, Int. J. Heat Mass Transfer, 13, 383–393.

Wu, J. H., Yang, L.D., Hou, J., 2012. Experimental performance study of a small wall room air conditioner retrofitted with R290 and R1270, Int. J. Refrigeration, 35, 1860–1868.

Manuscript ID: 509

DOI: 10.18462/iir.icr.2019.0509

First Measurement Results of Cooling and Heat-pump Operation of an Environmental Test Chamber using CO2 as Refrigerant

Andreas WAGNER[(a)], Thomas TANNERT[(a)], Ullrich HESSE[(a)]

[(a)] Bitzer-Professur für Kälte-, Kryo- und Kompressorentechnik, Technische Universität Dresden

Dresden, 01069, Germany, andreas_wagner@tu-dresden.de

ABSTRACT

The EU F-Gas Regulation brings a strict schedule for phase-down and a ban of synthetic high-GWP refrigerants. Small industry sectors like manufacturers of environmental simulation chambers are affected as well. Recent announcements of supply constraints and a massive price increase led to the question if new drop-in alternatives are available. CO_2 is a well-known and sustainable, alternative refrigerant. It becomes also an option for the environmental test chamber industry.

A former work shows a concept of an environmental test chamber using CO_2 as refrigerant. Its cooling cycle allows also to operate in a heat-pump mode. It was theoretically evaluated by a transient simulation model.

This study shall answer the question if the concept is working in reality. First measurements of a test rig containing the new concept cycle are made and presented.

The measurement results show a significant energy saving potential. Furthermore a lower chamber temperature can be achieved in comparison to a baseline chamber using R452A.

Keywords: Environment Simulation, Environmental Test Chamber, Carbon Dioxide, Cooling System, Heat-Pump, Energy Saving Potential, Measurement

1. INTRODUCTION

Environmental test chambers are used for individual stress tests of technical parts, assemblies or substances. These tests require predefined environmental conditions, which may include desired settings for temperature, humidity, sun load or further conditions. Test procedures such as temperature-time profiles are usually defined by published and proprietary standards. Hence, environmental test chambers need to be designed for desired temperature ranges and necessary temperature changing speed values to cover the specified test procedures. State-of-the-art environmental test chambers use vapor compression cycles for cooling and an electrical heater for heating.

Typical environmental test chambers for temperatures down to -40 °C use refrigerants like R404A or R507 with a significant global warming potential (GWP) of 3922 and 3985, respectively.

With respect to the EU F-Gas Regulation both refrigerants are not allowed to be used in new devices as of the year 2020 due to their very high GWP values. Various publications from the environmental simulation industry (Wagner (2017), Haack (2017), Weiss Umwelttechnik GmbH (2016) indicate that new low-GWP mixtures (e.g. R452A or R449A) will be used as alternative refrigerants for R404A and R507, respectively. However, the natural refrigerant CO_2 may also be an interesting alternative refrigerant, especially with regards to additional functionalities (as e.g. heat-pump operation).

This paper presents a new environmental test chamber with CO_2 as refrigerant for cooling and heat-pump mode. Measurement data from cooling and heating operation show in which temperature range the new CO_2 chamber can be operated properly. The energy consumption in cooling and heating mode are compared between a baseline chamber and the CO_2 chamber.

2. WORKING PRINCIPLE OF THE BASELINE AND CO_2-CHAMBER

2.1 Test chamber and baseline cooling cycle

The baseline chamber[1] was investigated in previous experimental and theoretical studies (Wagner *et al.,* 2017, Wagner *et al.,* 2018). Figure 1 shows a simplified diagram of the cooling cycle and the test chamber. The test chamber has a constant volume of 280 l and is working with a continuous, closed air loop that is driven by a radial fan at the top. The air circulates through the test chamber and the adjacent conditioning channel. The conditioning channel consists of a finned tube evaporator and an electrical heater. The utilized cooling unit (placed in the machine compartment below the test chamber) is a standard vapor compression cycle. The compressor has a nominal volume flow rate of 7.35 m^3/h. The finned tube condenser uses a constant speed fan that provides an ambient air flow of approximately 0.36 m^3/s. The liquid receiver has an inner volume of 3.1 l. The cycle uses two expansion devices. The first thermostatic expansion valve (TEV cooling) feeds the evaporator. A second thermostatic expansion valve (TEV after injection) cools down the suction gas for test chamber temperatures above 60 °C to protect the compressor. The total mass of R452A in the baseline environmental test chamber for lab tests is 2.5 kg.

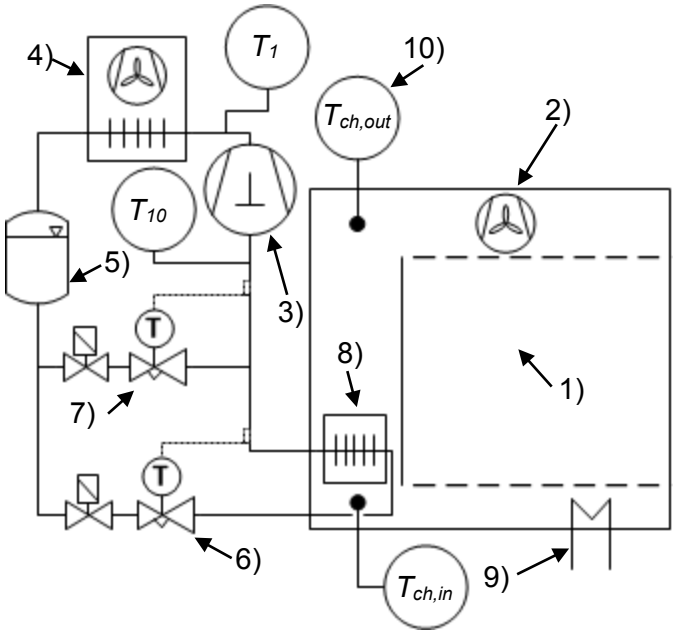

1) Test chamber
2) Chamber fan
3) Compressor
4) Condenser
5) Receiver
6) TEV cooling
7) TEV after injection
8) Evaporator
9) Electrical heater
10) Test chamber temperature

Figure 1: Schematic diagram of the state-of-the-art baseline test chamber and cooling cycle

[1] Type 3433/17, Feutron Klimasimulation GmbH

2.2 Cooling and Heating Cycle of the CO_2 Concept Chamber

The new CO_2 chamber represents a modification of the baseline chamber. Only the refrigeration cycle is changed. Figure 2 shows the simplified schematic diagram of the CO_2 refrigeration and heat-pump cycle.

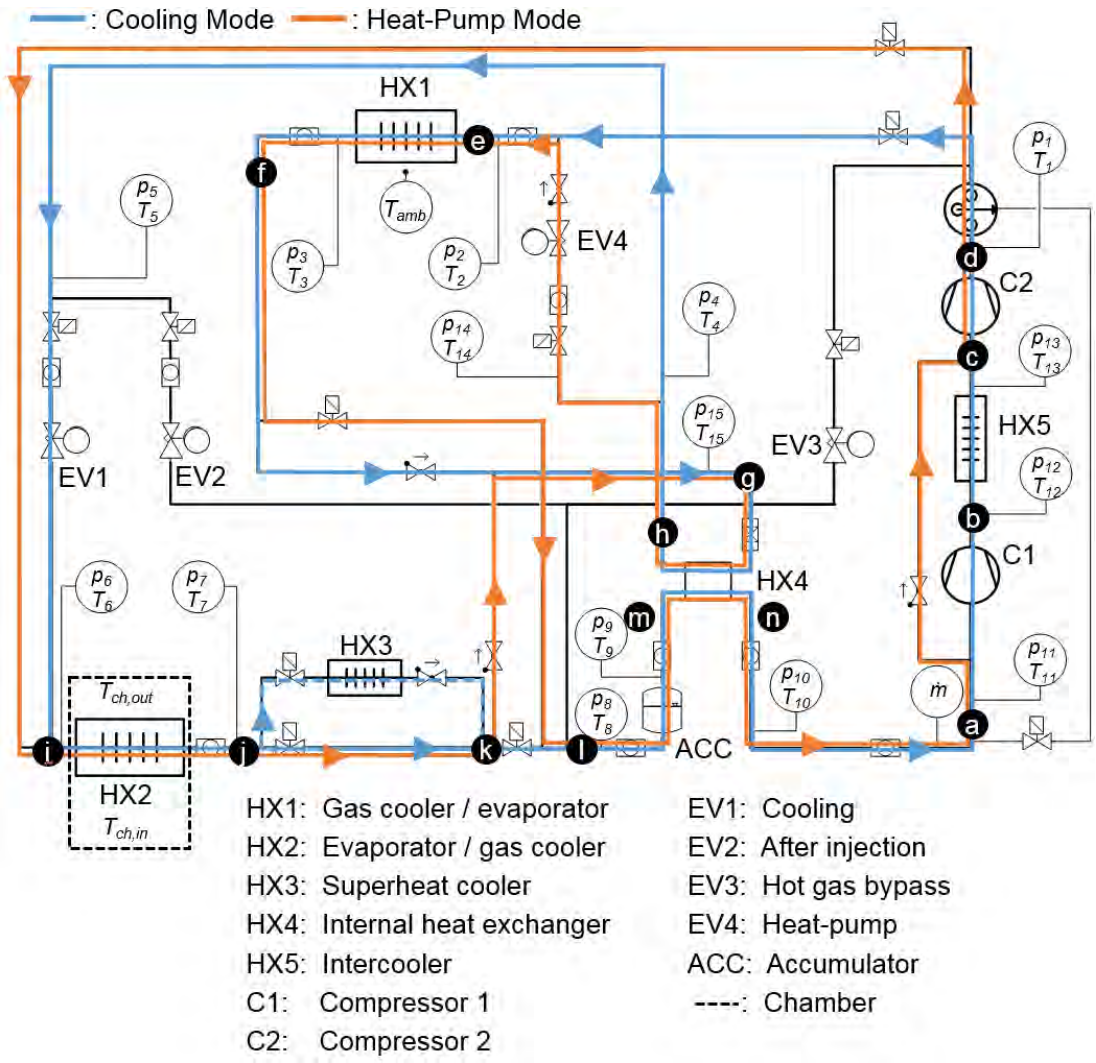

Figure 2: Schematic diagram of CO_2 cooling and heating cycle

The blue line represents the cooling mode. A two-stage compression (compressor 1 and 2) with an intercooler is used. This usually leads to higher cycle efficiencies but is mainly applied to reduce the discharge temperature at high pressure ratios. An internal heat exchanger (HX4) is applied to further cool down the high-pressure CO_2 behind the gas cooler (HX1) by using the cold suction gas. The CO_2 is then expanded in a throttle valve (EV1) and fed to the evaporator (HX2). The mass flow rate through the expansion valve is controlled to achieve an optimal cycle COP, which depends on the gas cooler outlet temperature and the high pressure (Reichelt (1996)). The refrigerant may leave the evaporator with temperatures above ambient temperature depending on the respective test chamber temperature. In this case the refrigerant can be cooled by an additionally implemented superheat cooler (HX3). The cooling power is provided by the environment. The evaporator can be bypassed in case the refrigerant leaves the evaporator with a temperature lower than ambient temperature. The high pressure control strategy and the one-stage expansion may lead to liquid CO_2 after the evaporator depending on the operational conditions. This is why an accumulator is incorporated and separates liquid from gas to avoid liquid refrigerant entering the compressor. The accumulator also

works as a liquid receiver, which balances the amount of refrigerant in the cycle. Behind the accumulator (ACC) the refrigerant enters the internal heat exchanger (HX4) and is superheated prior to the compression. For part-load operation EV2 controls the after injection behind the evaporator and EV3 controls the hot gas bypass.

The heat-pump mode is highlighted in orange. For this operation mode a single stage compression (C2) is applied. The first compressor of the cooling mode (C1) is therefore bypassed. The discharge temperatures are expected to be in a moderate range, because the pressure ratio in the heat-pump mode is lower compared to the cooling mode. After compression the refrigerant enters the evaporator of the cooling mode, which works now as gas cooler to heat the test chamber (HX2). The gas cooler of the cooling mode now works as evaporator (HX1) and uses the environment as a heat source. The evaporated refrigerant then enters the accumulator (ACC). Like in the cooling mode the internal heat exchanger (HX4) superheats the saturated vapor after the accumulator. An increase of the suction gas temperature also increases the heating capacity.

Figure 3 shows the different operation modes in a p-h diagram. The cycles are designed to run transcritical as well.

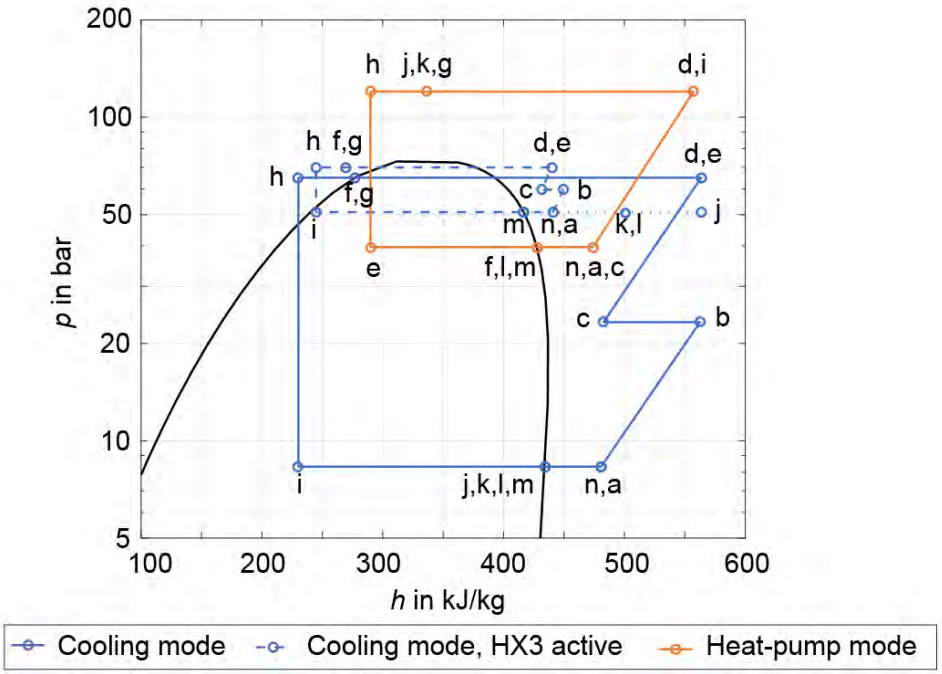

Figure 3: Operation modes of the CO_2 chamber

3. EXPERIMENTAL INVESTIGATION OF THE CO_2 CONCEPT CHAMBER

3.1 Test Setup

The CO_2 concept chamber is build up as a test rig. For a better accessibility and visibility the cooling cycle is placed in a separate rig (Figure 4). The cooling aggregate of an ordinary baseline environmental test chamber is installed in the machine compartment below the test chamber.

Both compressors in the CO_2 concept chamber test rig are hermetic with a displacement of 5 cm^3 and BLDC motors, which are controlled by inverters. An oil separator is placed behind compressor 2 and injects, depending on its oil level, oil into the suction line of compressor 1. The accumulator with a volume of 2 l can be used up to a pressure value of 100 bar. All heat exchangers, except HX4, are custom build fin-tube heat exchangers. HX4 is designed as a plate heat exchanger. Table 1

shows the design points of the heat exchangers. The expansion valves are driven by step motors and can be controlled externally via the data acquisition system. All components, except the accumulator, can operate on a pressure up to 120 bar. The refrigerant charge is 2 kg.

With a data acquisition system temperature values (thermocouples, type T), pressure values (transmitters accuracy ±0.07 bar calibrated in a range of 3 bar…72 bar) and the mass flow rate (Coriolis flowmeter accuracy ±0.13 %) of the refrigerant can be measured as shown in Figure 4. To evaluate the total electric energy consumption a Yokogawa WT330 power meter (accuracy ±0.5 %) is used. The test chamber in- and outlet temperature $T_{ch,in}$ and $T_{ch,out}$ are measured with PT100 sensors. The measuring data PT100 sensors is read out of the control unit of the chamber.



Figure 4: Picture of the CO_2 chamber test rig

Table 1: Design points of the heat exchangers

	$T'_{CO_2,in}$ in °C	$x_{CO_2,in}$ in -	$x_{CO_2,out}$ in -	$\dot{V}_{air}$ in m^3/s	$T_{air,in}$ in °C	$T_{air,out}$ in °C	$\dot{Q}$ in kW
Evaporator	-47	0.53	1	0.36	-40	-42.5	1.12
	p_{CO_2} in bar	$T_{CO_2,in}$ in °C	$T_{CO_2,out}$ in °C	$\dot{V}_{air}$ in m^3/s	$T_{air,in}$ in °C	$T_{air,out}$ in °C	$\dot{Q}$ in kW
Gas cooler	130	140	25	0.243	20	47	7.8
Intercooler	58.7	140	25	0.1215	20	50	4.29
Superheat cooler	26.5	150	25	0.09	20	52	3.44
	$p_{CO_2,2}$ in bar	$T_{CO_2,in,1}$ in °C	$T_{CO_2,out,}$ in °C	$p_{CO_2,2}$ in bar	$T_{CO_2,in,2}$ in °C	$T_{CO_2,out,2}$ in °C	$\dot{Q}$ in kW
Internal HX	130	25	6.4	26.48	-10.5	24.4	1.14

3.2 Measurement Procedure of Cooling and Heating Cycle

During the measurement the test chamber temperature T_{ch} is defined as the temperature of the air, which leaves the test chamber and enters the conditioning channel ($T_{ch,out}$ of Figure 1 and Figure 2). The procedure for the CO_2 chamber starts with cooling down from a test chamber temperature of 50 °C to the lowest possible temperature. Compressor 1 runs with 7200 rpm and compressor 2 runs with 2700 rpm. Afterwards the cycle is switched to heat-pump mode and only compressor 2 with 2700 rpm is activated. The procedure ends by reaching a chamber temperature of 55 °C.

3.3 Measurement Results of Cooling and Heating Cycle

The averaged ambient temperature during the measurement is 20.3 °C. Figure 5 a) shows the cooling and heat-pump cycle of the CO_2 chamber. The cooling cycle ends with a minimal test chamber temperature $T_{ch,out}$ of -50.5 °C. During that time the lowest measured pressure on the evaporator (HX2) outlet p_7 is 5.2 bar and the suction gas pressure p_{11} is 4.6 bar. Hence the suction gas pressure is below the triple point pressure of 5.18 bar (Lemmon *et al.*, 2013). In the sight glass close to p_7 liquid and gaseous refrigerant can be observed. The sight glass close to p_{11} shows only gaseous refrigerant. It is situated after the internal heat exchanger HX4 so the refrigerant is superheated in a range from 34.6 °C to 23.8 °C. Even if the refrigerant pressure is below the triple point no solid particles enter the compressor because of the superheating. It's unknown if there are solid particles in the cycle. They should be in the internal heat exchanger where the pressure loss leads to a pressures below the triple point. If there were blockings in the internal heat exchanger pressure fluctuations would occur in the evaporator. There are no pressure fluctuations observed.

Figure 5 a) also shows the discharge temperatures T_{12} and T_1 of both compressors. T_1 already exceeds a value of 140 °C on a test chamber temperature of -36.6 °C and reaches a maximum value of 191.3 °C. The discharge temperature T_1 shouldn't exceed around 140 °C because of the limited thermal stability of the oil. T_{12} reaches a maximum value of 128.7 °C, which is in an acceptable range. During heat-pump mode, starting after 52 minutes, T_1 reaches a maximum value of 126.5°C, which is also acceptable. A comparison to the measurement data (T_{amb} = 21.6 °C) of the baseline chamber in Figure 5 b) shows that the CO_2 chamber cools down much faster than the baseline chamber. During cooling the baseline chamber shows a moderate discharge temperature T_1 in a range from 104.9 °C to 68.2 °C.

To compare the total electrical energy consumption $E_{el,tot}$ it makes sense to look on different sequences. Reason for this is, that the baseline chamber only cools down to -40 °C instead of -50.5 °C and an electrical heater is used instead of a heat-pump. During the cool down procedure from 50 °C to -40 °C the CO_2 chamber saves 50 % of the total electric energy consumption compared to the baseline chamber. During the heat-pump operation starting from -40 °C to 55 °C a reduction of 49 % of the total electrical energy, compared to the baseline chamber, can be achieved. Reasons for that significant reduction of energy consumption during cool down mode can be found in the use of the two stage compression with intercooler and the internal heat exchanger. Beside this, the higher cooling capacity leads to a faster cooling procedure, which reduces the energy consumption of additional aggregates like fans and the control unit. The cooling procedure turns after 5.5 min from a transcritical to subcritical process. Higher ambient temperatures would result in a longer operating, transcritical cycle, which decreases the efficiency. Another reason for the faster cool down at the beginning of the procedure could be the heat-pump mode, which ran before the test procedure.

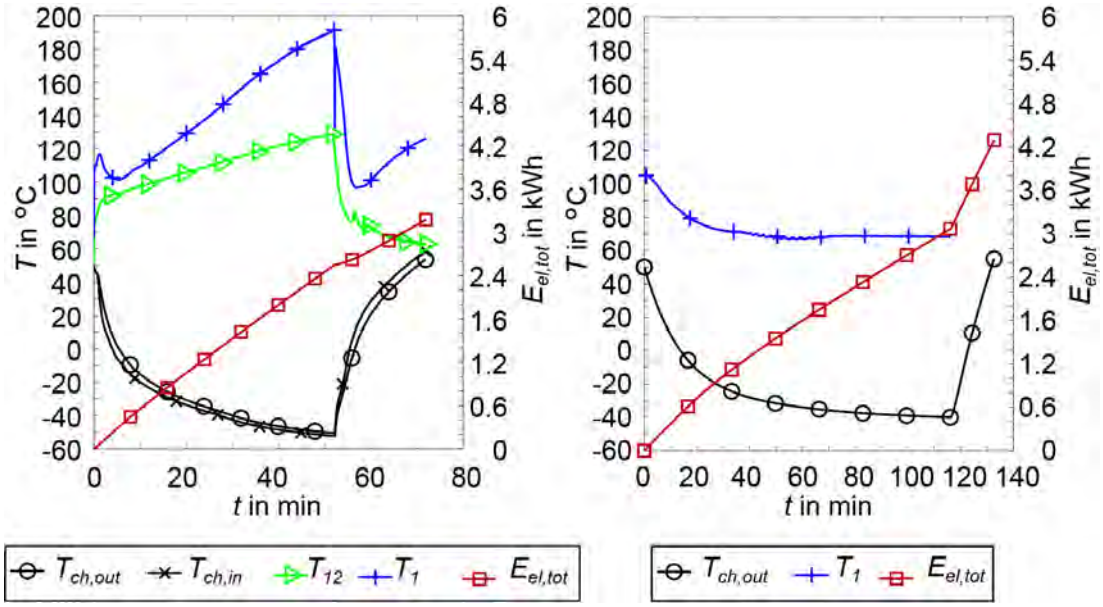

a) Cooling and heat-pump cycle of the CO_2 chamber

b) Cooling and el. heating cycle of the baseline chamber

Figure 5: Measurement results of the CO_2 and baseline chamber

3.4 Suggestions for improvement and future work

The measurement data of the CO_2 chamber show a large potential to use CO_2 in environmental test chambers. Furthermore different challenges can be identified.

The discharge temperature of compressor 2 T_1 is too high. To reduce the discharge temperature the middle pressure level has to increase. This can be realized by increasing the volume flow ratio between compressor 1 and 2. In the present configuration the compressor 1 runs at maximum speed and compressor 2 runs at minimal rotational speed, so the middle pressure level can't be increased in this configuration. Another possibility is the reduction of the size of the internal heat exchanger HX4. In the present measurement the internal heat exchanger leads to suction gas temperatures from 23.8 °C to 34.6 °C. A smaller internal heat exchanger reduces the suction gas temperature. A lower suction gas temperature brings a higher suction gas density, which increases the middle pressure level. Further the discharge temperature of compressor 1 decreases.

Another field of investigation is the oil management. In the present configuration the oil is separated from the refrigerant after compressor 2 and injected into the suction line of compressor 1. Both compressors are hermetic and they don't have an oil level control. The different rotational speeds and pressure ratios occur different values of the oil carry over rate of both compressors, which can result in an overfill or an underfill.

To realize defined cooling speed down to constant temperatures it's necessary to implement a part load control strategy.

CONCLUSIONS

In this work a new environmental test chamber with CO_2 as refrigerant is presented. First measurements of a cooling procedure show, that test chamber temperatures down to -50.5 °C can be reached. However test chamber temperatures below -36.6 °C cause very high discharge temperatures above 140 °C. The heating cycle with heat-pump mode shows moderate discharge temperatures. In comparison with a baseline chamber the new CO_2 chamber cools and heats much faster. During cooling and heating mode about 50 % of electrical energy can be saved in certain temperature ranges.

ACKNOWLEDGEMENTS

The author appreciates the collaboration with the company Feutron Klimasimulation GmbH which built up the CO_2 chamber. This project is a ZIM cooperation project and is funded by AiF Projekt GmbH (ZF4005606 – ecoKPK).

NOMENCLATURE

COP	coefficient of performance (-)	*amb*	Ambient
E	energy (kWh)	*ch*	test chamber
h	enthalpy (kJ/kg)	*in*	Inlet
p	pressure (kPa)	*out*	outlet
$\dot{Q}$	heat flow (kW)	*tot*	total
t	time (min)	ACC	accumulator
$\dot{V}$	volume flow (m^3/s)	C	compressor
x	vapor quality (-)	EV	electronic expansion valve
T	temperature (°C)	GWP	global warming potential
T'	evaporation temperature (°C)	HFO	hydrofluoroolefin
		HX	heat exchanger
		PI	proportional, integral
		SHC	superheat cooler
		TEV	thermostatic expansion valve

REFERENCES

Haack, C., 2017, Vorschriften für die Betreiber von Umweltsimulationsanlagen, GUS-Tagung, Karlsruhe, DE.

Lemmon, E.W., Huber, M.L., McLinden, M.O. 2013, REFPROP, NIST Standard Reference Database 23, Version 9.1, Boulder, USA.

Reichelt, J., 1996, Fahrzeugklimatisierung mit natürlichen Kältemitteln, C.F. Müller Verlag, Heidelberg, DE.

Wagner, A., Langebach, R., Hesse, U., 2017, Systematische Suche und Erprobung von Ersatzkältemitteln für Anwendungen in der Klimasimulation bis -40 °C, DKV-Tagung, Bremen, DE.

Wagner, A., Langebach, R., Hesse, U., 2018, Theoretical Evaluation of Cooling and Heat-pump Operation of an Environmental Test Chamber using CO_2 as Refrigerant, 13th IIR Gustav Lorentzen Conference, Valencia, ES.

Weiss Umwelttechnik GmbH, 2016, FAQs: F-gases, https://www.schunk-group.com/fileadmin/Redakteur/Mediathek/Zertifikate-Richtlinien/WeissTechnik/Weiss_Umwelttechnik/ClimeEvent-FAQ-EN.pdf.

Manuscript ID: 511
DOI: 10.18462/iir.icr.2019.0511

Optimal Operation of HVAC System Incorporated with Online Performance Evaluation Based on Operation Data

Wantao SHI[(a)], Xinqiao JIN[(a)], Xuejun ZHANG[(b)], Jiangqing WANG[(a)]

[(a)] School of Mechanical Engineering, Shanghai Jiao Tong University, Shanghai, 200240, P. R. China, xqjin@sjtu.edu.cn

[(b)] Institute of Refrigeration and Cryogenics, Zhejiang University, Hangzhou, 310027, P. R. China

ABSTRACT

With the higher requirement of intelligent operation of HVAC system and the more operation data being gathered, it is possible to use the operation data to intelligentize and optimize operation of HVAC system. This paper presents an optimal method for operation of chilled water system of HVAC. An online performance evaluation is set up and incorporated to guide the operation optimization. The evaluation benchmark is an optimal performance curve based on historical operation data and the time for optimization is determined by evaluation index. The optimization includes energy prediction and setpoints optimization, which are based on BP neural network and PSO, respectively. The proposed optimization method is validated by an actual chilled water system located in China, and it is compared with a conventional optimization method. The results show that the proposed method can save the energy consumption of the system without increasing the computation burden.

Keywords: Chilled Water, Energy Saving, Operation, Optimization

1. INTRODUCTION

Chilled water system has great influence on the energy efficiency of HVAC system (He et al., 2014). Recently, many optimization methods have been applied in the operation of chilled water system, which can save considerable energy consumption (Vakiloroaya et al., 2014). Those optimization methods can be categorized into two types according to used model: physical model based methods and data-driven based methods (Asad et al., 2017). The physical model based methods require detailed mathematical models to describe the thermal and physical relationships between each device. This method is complex, and solving the models usually consumes a lot of computation costs and memory resources (Nishiguchi et al., 2010). On the other hand, with the popularity of building energy management systems (BEMS), operational data which includes features of chilled water system becomes easy to collect (Xiao and Fan, 2014). The data-driven based methods are promising in modelling complicated systems and many applications have been studied (Fong et al., 2006).

Most of the proposed optimization methods have fixed optimization periods, that is, the optimization will be done at a predefined period. However, the operation conditions do not change periodically, and a fixed optimization period may not be energy-efficient for chilled water system. Although it can increase the optimization frequency to achieve better energy saving, the system may increase the computation burden (Wang et al., 2016). It is critical when the computation resources of the system are limited.

In order to achieve better energy saving in chilled water system without increasing the computation burden, this paper presents an optimization method incorporated with online performance evaluation. An optimal performance curve is used as the evaluation benchmark and the evaluation index is defined. The optimization is performed only if the evaluation index is less than the predefined value.

2. THE OPTIMIZATION METHOD

The principle of proposed optimization method is shown in Fig. 1, which includes two parts: online evaluation and online optimization. The online evaluation can determine whether chilled water system needs to be optimized, and the online optimization can output optimal setpoints under the current operation condition. What's more, the minimum time interval for optimization is used to keep the operation of chillers stably.

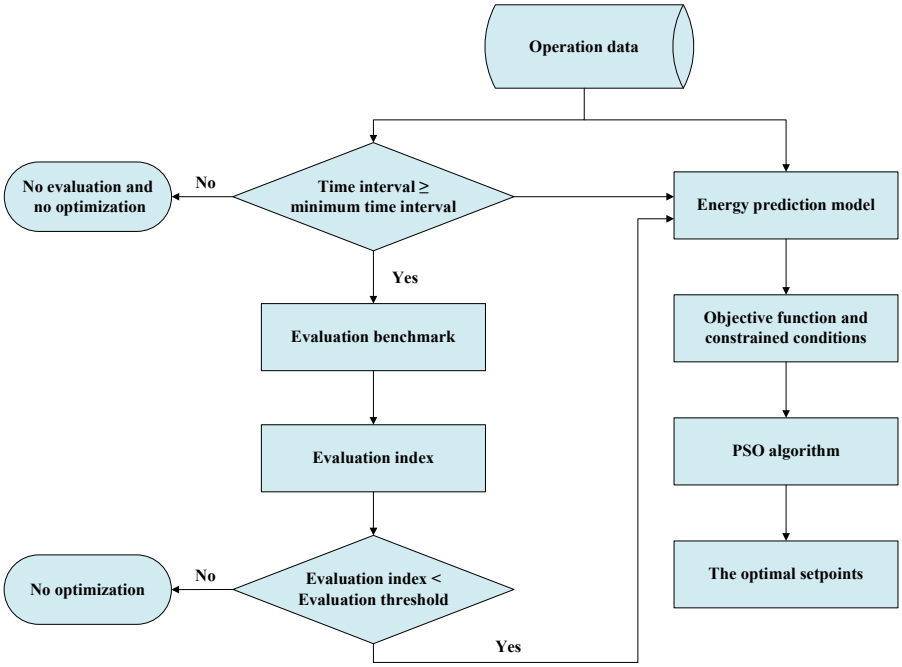

Figure 1: Schematic diagram of the proposed optimization method

2.1. Online evaluation

Chilled water system contains many devices, which are interrelated and interact on each other. The system coefficient of performance (SCOP) is defined and expressed in Eq. (1) to characterize the energy performance of the chilled water system.

$$SCOP = \frac{load}{P_{tot}} \quad \text{Eq. (1)}$$

Where P_{tot} is expressed by

$$P_{tot} = P_{ch} + P_{cdp} + P_{pchp} + P_{schp} + P_{ct} \quad \text{Eq. (2)}$$

Where *load* is the cooling load, *P* is the power, the subscripts tot, ch, cdp, pchp, schp and ct denote the entire system, chillers, cooling water pumps, primary chilled water pumps, secondary chilled water pumps and cooling towers, respectively.

2.1.1. Evaluation benchmark

The evaluation benchmark is the optimal performance curve. The optimal performance curve consists of the maximum SCOP under the different operation conditions. The steps for establishing the optimal performance curve are:

Step 1: According to the range of cooling load, the historical operation data is divided into *n* load intervals.

Step 2: If the amount of data in one load interval is enough (more than 5), the maximum SCOP of the load interval is obtained by moving-maximum method (Wang et al., 2017).

Step 3: If the amount of data in one load interval is scare (less than 5), an approximation value of the maximum SCOP is obtained by Lagrange interpolation.
Step 4: The maximum SCOP of each load interval constitutes the optimal performance curve.
Lagrange interpolation is one of polynomial interpolation methods. In the *k* th-dimensional search space (*k*=1,2,…,D), the Lagrange interpolation polynomial $L(x_k)$ passes through *n* different given points $(x_k^1, y_k^1), (x_k^2, y_k^2), \ldots, (x_k^n, y_k^n)$, *k*=1,2,…,D. Then the Lagrange interpolation polynomial is expressed in Eq. (3) (Huang et al., 2019).

$$\begin{aligned} L(x_k) = {} & y_k^1 \frac{(x_k - x_k^2)(x_k - x_k^3)\cdots(x_k - x_k^n)}{(x_k^1 - x_k^2)(x_k^1 - x_k^3)\cdots(x_k^1 - x_k^n)} \\ & + y_k^2 \frac{(x_k - x_k^1)(x_k - x_k^3)\cdots(x_k - x_k^n)}{(x_k^2 - x_k^1)(x_k^2 - x_k^3)\cdots(x_k^2 - x_k^n)} \\ & + \cdots \\ & + y_k^n \frac{(x_k - x_k^1)(x_k - x_k^2)\cdots(x_k - x_k^{n-1})}{(x_k^n - x_k^1)(x_k^1 - x_k^2)\cdots(x_k^n - x_k^{n-1})} \\ = {} & \sum_{i=1}^{n} y_k^i \prod_{j=1, j\neq i}^{n} \frac{x_k - x_k^j}{x_k^i - x_k^j} \end{aligned} \quad \text{Eq. (3)}$$

According to Eq. (3), the interpolation of the maximum SCOP on a load interval is obtained.

2.1.2. Evaluation index

The evaluation index is defined as the ratio of the actual SCOP to the maximum of SCOP values. The definition is shown in Eq. (4).

$$I_{\text{index}} = \frac{SCOP_{\text{act}}}{SCOP_{\text{max}}} \quad \text{Eq. (4)}$$

Where I_{index} is the evaluation index, and the $SCOP_{act}$ and $SCOP_{max}$ are the actual SCOP and maximum of SCOP, respectively.
The optimization condition is shown in Eq. (5). When the evaluation index is less than the evaluation threshold, the optimization needs to be done. On the contrary, when the evaluation index is larger than or equal to the evaluation threshold, there is no need for optimization.

$$I_{\text{index}} = \begin{cases} < I_{\text{thres}}, & \text{Optimization} \\ \geq I_{\text{thres}}, & \text{No optimization} \end{cases} \quad \text{Eq. (5)}$$

2.2. Online optimization

Online optimization includes energy prediction and setpoints optimization. Accurate energy prediction is the premise of optimization, and the energy consumption of the chilled water system can be saved by optimizing the control setpoints.

2.2.1. Energy prediction

BP neural network is used to predict energy consumption of chilled water system as its reliability and can be pre-programmed in many programs (Kumar et al., 2013). The architecture of BP neural network is shown in Fig. 2, which includes input layer, hidden layers and output layer. The input layer and output layer represent the input and output of the prediction model, while the hidden layers need to be trained by operation data.
Assuming that the main characteristic parameters that affect the SCOP are outlet chilled water temperature, inlet cooling water temperature, primary chilled water flow and cooling water flow, then the energy consumption of the system can be expressed as

$$P_{tot} = f(T_{\text{chw,out}}, T_{\text{cdw,in}}, m_{\text{chw,prim}}, m_{\text{cdw}}) \quad \text{Eq. (6)}$$

Where $T_{chw,out}$ is the outlet chilled water temperature, $T_{cdw,in}$ is the inlet cooling water temperature, $m_{chw,prim}$ is the primary chilled water flow and m_{cdw} is the cooling water flow.

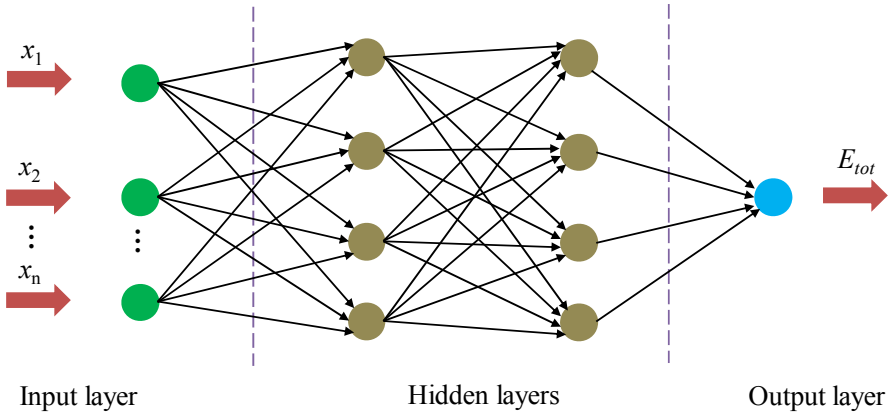

Figure 2: Architecture of BP neural network

2.2.2. Setpoints optimization

Particle swarm optimization (PSO) algorithm is used to optimize setpoints. PSO is a heuristic global optimization algorithm, which seeks the optimal solutions through cooperation and information sharing among individuals in the group (Wei et al., 2015). The optimization algorithm has advantages of fast convergence and less parameters setting. The objective function and the constraints are given by Eq. (7) and Eq. (8), respectively.

$$\max SCOP = \frac{load}{P_{tot}} = \frac{load}{f(T_{chw,out}, T_{cdw,in}, m_{chw,prim}, m_{cdw})} \quad \text{Eq. (7)}$$

$$\begin{aligned} T_{chw,out,min} &\le T_{chw,out} \le T_{chw,out,max} \\ T_{cdw,in,min} &\le T_{cdw,in} \le T_{cdw,in,max} \\ m_{chw,prim,min} &\le m_{chw,prim} \le m_{chw,prim,max} \\ m_{cdw,min} &\le m_{cdw} \le m_{cdw,max} \end{aligned} \quad \text{Eq. (8)}$$

where $T_{chw,out,min}$ and $T_{chw,out,max}$ are the minimum and maximum setpoints of $T_{chw,out}$, respectively; $T_{cdw,in,min}$ and $T_{cdw,in,max}$ are the minimum and maximum setpoints of $T_{cdw,in}$, respectively; $m_{chw,prim,min}$ and $m_{chw,prim,max}$ are the minimum and maximum setpoints of $m_{chw,prim}$, respectively; $m_{cdw,min}$ and $m_{cdw,max}$ are the minimum and maximum setpoints of m_{cdw}, respectively.

3. METHOD VALIDATION

3.1. The object of the optimization

An airport terminal's chilled water system is used for validation, which is located in the south of China. The chilled water system mainly consists of 4 chillers, 4 chilled water pumps, 4 secondary pumps, 4 cooling water pumps and 5 cooling towers. The operation time is 7:00-22:00 per day. The schematic diagram of the chilled water system is shown in Fig. 3. TRNSYS 17 is used to develop the simulation model (Fan et al., 2014). 7 days in August are selected for simulation. The outdoor temperature is shown in Fig. 4.

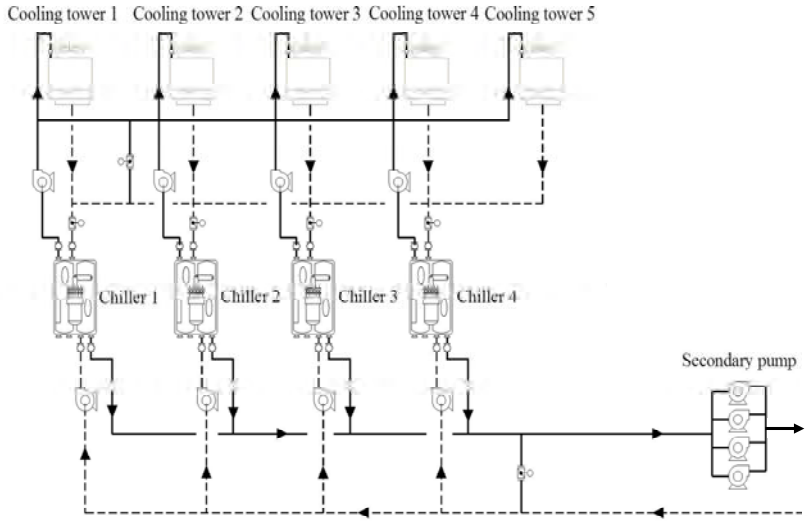

Figure 3: Schematic diagram of the chilled water system

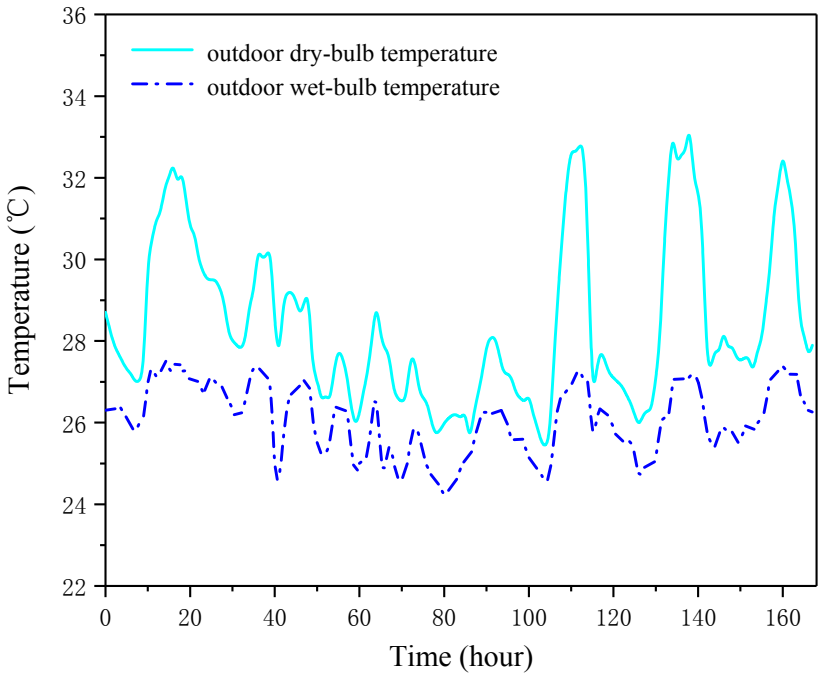

Figure 4: Outdoor temperature

3.2. Original control strategy

The original control strategy applies chillers sequence control (Fan et al., 2014):

a. When the load is less than the rated capacity of CH1, CH1 is turned on;
b. When the load is less than the sum of rated capacity of CH1 and CH2, CH2 is turned on;
c. When the load is less than the sum of rated capacity of CH1, CH2 and CH3, CH3 is turned on;
d. When the load is more than the sum of rated capacity of CH1, CH2 and CH3, CH4 is turned on.

The setpoints of the outlet chilled water temperature, the inlet cooling water temperature are 7℃ and 30, respectively.

3.3. Optimization methods

The proposed optimization method is compared with a conventional optimization method, which includes energy prediction and setpoints optimization based on BP neural network and PSO. The optimization period is 15 minutes.

In this study, $T_{chw,out,min}$ and $T_{chw,out,max}$ are set as 7℃ and 12℃, respectively; $T_{cdw,in,min}$ and $T_{cdw,in,max}$ are set as 26℃ and 30℃, respectively; $m_{chw,prim,min}$ and $m_{chw,prim,max}$ are set as 0 and 425 m^3/h, respectively; $m_{cdw,min}$ and $m_{cdw,max}$ are set as 0 and 540 m^3/h, respectively.
The initial parameter settings of PSO algorithm are listed in Table 1.

Table 1. Initial parameter settings of PSO algorithm

Particle number	Learning factors	Inertia weight	Maximum iterations
50	c_1=0.8; c_2=0.8	0.7	100

3.4. Results and analysis

The original control strategy is used as a reference. Fig. 5 shows the average energy saving of two methods and Fig. 6 shows the average optimization times of two methods. It can be seen that the average energy saving of the proposed optimization method is more than that of the conventional optimization method, while the average optimization times of the proposed optimization method is less than that of the conventional optimization method. This is because the proposed optimization method optimizes chilled water system at the right time, but the conventional optimization method optimizes the system at a predefined period, regardless of the change of operation conditions. As known, the lower the optimization times, the smaller the computation burden. Therefore, the proposed method can achieve better energy saving in chilled water system without increasing the computation burden.

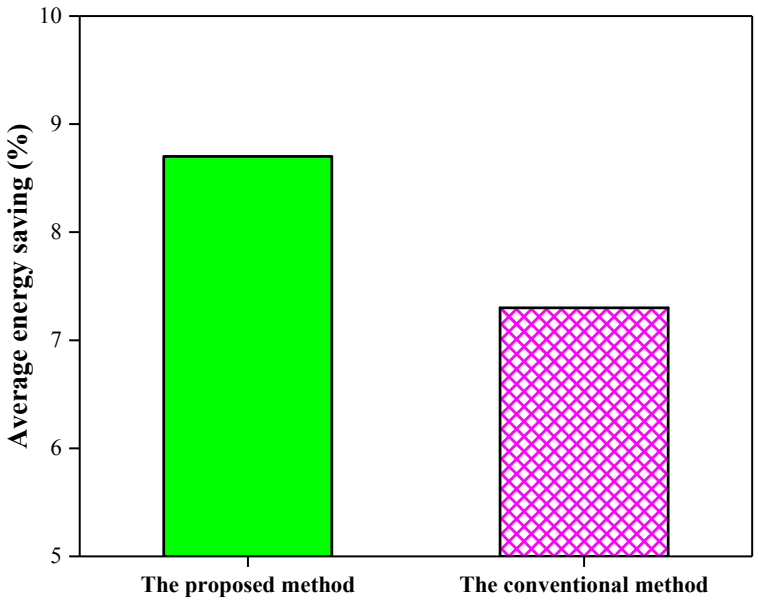

Figure 5: The average energy saving of two methods

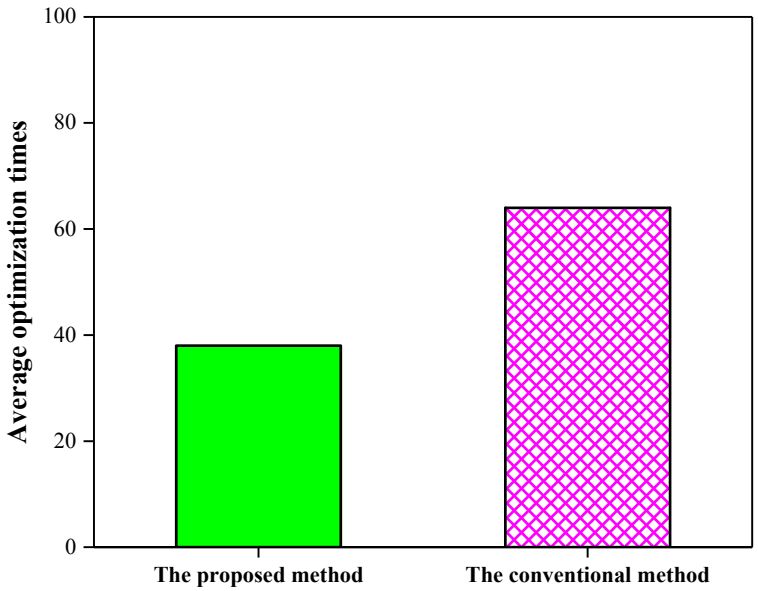

Figure 6: The average optimization times of two methods

4. CONCLUSIONS

This paper presents an optimization method incorporated with online performance evaluation in chilled water system. The evaluation benchmark is an optimal performance curve, and the evaluation index is defined. The proposed optimization method is compared with a conventional optimization method which has a fixed optimization period. Results show that the proposed optimization method can achieve better energy saving without increasing the computation burden.

ACKNOWLEDGEMENTS

The research work is financially supported by National Natural Science Foundation of China (No. 51776118).

NOMENCLATURE

load	cooling load (kW)	ct	cooling towers
P	power (kW)	I_{index}	evaluation index
tot	entire system	I_{thres}	evaluation threshold
ch	chillers	$T_{chw,out}$	outlet chilled water temperature
cdp	cooling water pumps	$T_{cdw,in}$	inlet cooling water temperature
pchp	primary chilled water pumps	$m_{chw,prim}$	primary chilled water flow
schp	secondary chilled water pumps	m_{cdw}	cooling water flow

REFERENCES

Asad, H.S., Yuen, R.K.K., Huang, G., 2017. Multiplexed real-time optimization of HVAC systems with enhanced control stability. Applied Energy 187, 640-651.

Fan, B., Jin, X., Fang, X., Du Z., 2014. The method of evaluating operation performance of HVAC system based on exergy analysis. Energy and Buildings 77, 332-342.

Fong, K.F., Hanby, V.I., Chow, T.T., 2006. HVAC system optimization for energy management by evolutionary programming. Energy and Buildings 38(3), 220-231.

He, X., Zhang, Z., Kusiak, A., 2014. Performance optimization of HVAC systems with computational intelligence algorithms. Energy and Buildings 81, 371-380.

Huang, Q., Zhang, K., Song, J., Zhang Y, Shi J., 2019. Adaptive differential evolution with a Lagrange interpolation argument algorithm. Information Science 472, 180-202.

Kumar, R., Aggarwal, R.K., Sharma J.D., 2013. Energy analysis of a building using artificial neural network: A review. Energy and Buildings 65(4), 352-358.

Wang, Y., Jin, X., Fang, X., 2017. Rapid evaluation of operation performance of multi-chiller system based on history data analysis. Energy and Buildings 134, 162-170.

Nishiguchi, J., Konda, T., Dazai, R., 2010. Data-driven optimal control for building energy conservation. Proceedings of SICE annual conference, Taipei, Taiwan, 116-120.

Vakiloroaya, V., Samali, B., Fakhar, A., Pishghadm, K., 2014. A review of different strategies for HVAC energy saving. Energy Conversion and Management 77(1), 738-754.

Wang, J., Huang, G., Sun, Y., Liu, X., 2016. Event-driven optimization of complex HVAC systems. Energy and Buildings 133, 79-87.

Wei, X., Kusiak, A., Li, M., Tang F., Zeng Y., 2015. Multi-objective optimization of the HVAC (heating, ventilation, and air conditioning) system performance. Energy 83, 294-306.

Xiao, F., Fan, C., 2014. Data mining in building automation system for improving building operational performance. Energy and Buildings 75, 109-118.

Manuscript ID: 565
DOI: 10.18462/iir.icr.2019.0565

A Novel Unitary Air Condition System Design for Flammable Refrigerants and Building Ventilation

Hanlong WAN[(a)], Tao CAO[(a)], Yunho HWANG*[(a)]

[(a)] 4164 Glenn Martin Hall Bldg., Center for Environmental Energy Engineering
Department of Mechanical Engineering, University of Maryland,
College Park, MD., 20742, United States, *yhhwang@umd.edu

ABSTRACT

Flammable refrigerants like R32 and R290 can be used as alternative refrigerants for energy efficient and environmentally friendly air conditioning systems. Nevertheless, the safety issue of such flammable refrigerants limits their market expansion. Moreover, enhancements in building envelop insulation have resulted in significant reduction in buildings' thermal loads and increased demands for ventilation. The objective of this study is to propose and develop a novel unitary air conditioning system design enabling flammable refrigerants usage and building ventilation. In this novel design, we minimized the refrigerant charge by using microchannel heat exchanger designs and reducing the liquid line length. In addition, advanced hybrid options were applied such as two-stage cycles and economizers. Moreover, the return air and condensate water from the evaporator were used to cool down the condenser. We investigated the performance of the new unitary system design and found that the annual performance factor can be increased up to 45%. This device can be used for building air conditioning and ventilation with high efficiency in a safe manner with environmentally friendly refrigerants.

Keywords: Flammable Refrigerants, Ventilation, Two-stage cycle, Energy Efficiency.

1. INTRODUCTION

Severe damage to the environment has been caused by many reasons including long-term usage of halogenated gases as the refrigerant in refrigeration, air conditioning and heat pumping systems. With the phasing out or phasing down of these refrigerants, the focus has been shifted to use low global warming potential (GWP) fluids. Replacement of currently used refrigerants requires safe, energy efficient and environmentally friendly characteristics (Calm, 2008). Nevertheless, no perfect alternative refrigerant was identified (Venkatarathnam and Murthy, 2012). Mota-Babiloni et al. (2015) wrote an overview and classification of current considerations about candidates to replace high-GWP refrigerants used in markets. R290 and R32 are two efficient and non-toxic alternatives, yet they are flammable. According to the literature (Cleland et al., 2009; Palm, 2008), it's the safety issue of such flammable refrigerants that limits their applications. These working fluids can be considered in non-occupied systems or low-refrigerant-charge applications. Moreover, enhancements in building envelop insulation have significantly reduced the buildings' thermal loads but increased needs for ventilation at the same time. Thus, guaranteeing the ventilation of the building is significant in HVAC system design, especially for those systems using flammable refrigerants. Researchers have also been studying ventilation parts of HVAC systems in the past three years. Lee et al. (2017) studied an outdoor processing (OAP) unit and optimized the supply air temperature. Im et a. (2016) tested the same building as Lee's. Park et al. (2017) compared a general energy recovery ventilation (ERV) system's performance with a dedicated outside air system (DOAS) Zhu et al. (2014) tested a roof top unit (RTU) and studied the setting supply air temperature and the part load ratio (PLR) of the OAP. Some details of these studies are summarized in Table 1.

Table 1. Recent literature about ventilation

Researcher (Year)	Solutions	Gross Floor Area	Design Flow Rate	Model	Validation	Control Logic	Max System COP
Lee et al. (2017)	OAP	300 m^2	0.189 m^3/s	Cooling /Heating	Simulation /Field Test	OA supply setpoint, Feedback control (RH indoor based)	Not mentioned
Park et al. (2017)	ERV/DOAS	5000 m^2	0.56 m^3/s	Cooling /Heating	Simulation /Field Test	Not mentioned	3.5
Im et al. (2016)	OAP/DOAS	300 m^2	0.189 m^3/s	Cooling	Field Test	Not mentioned	4.2
Zhu et al. (2014)	RTU(OAP)	4000 m^2	0.40 m^3/s	Cooling	Simulation /Field Test	OA supply setpoint, PLR of OAP	4-5

Current RTU systems and unitary HVAC systems use traditional refrigerants and are usually installed on the roof, attic or surrounding of the houses. Bourne et al. (2008) proposed a rooftop cooling unit, which is directed to packaged rooftop units that provide heating, ventilation, and air conditioning to buildings. This patent presents new RTU designs that include evaporative cooling of both ventilation air and a condensing refrigerant, as well as other features, to significantly improve RTU efficiency). Hwang et al. (2006) developed a unitary air conditioning system for individually cooling or heating the zone. Accordingly, cooling or heating operation is performed on each zone of the building. Simultaneously, additional individual heating or cooling operation can be performed on a specific space. By doing so, the operation cost can be reduced, and cooling or heating in the building can be efficiently performed. Wohlert (2013) studied a rooftop air conditioning unit having a centralized refrigeration system. The author proposed a system comprising a plurality of rooftop HVAC units having a centralized refrigeration unit, along with a method for retrofitting existing independent HVAC units into the proposed system. The resulting multi-unit system offers increased efficiency and reliability over independently operating HVAC units. However, these systems are unable to use flammable refrigerants due to safety concerns. These systems were designed to use non-flammable refrigerants. Moreover, they have no mitigation method in case the refrigerant leak. On the other hand, the energy efficiency can be increased. Our proposed device optimizes the refrigerant charge and contains safety dampers to prevent the refrigerant from entrancing the indoor environment in the case of refrigerant leaks. The device is also installed with an economizer to get free cooling during the shoulder reason, which the previous devices do not have. The device can be used for both residential buildings and commercial buildings. More specifically, the device is a safe unitary air conditioning system allowing the use of flammable refrigerants and building ventilation.

2. OBJECTIVES

The first objective of the invention is to be able to use flammable refrigerants. Various methods were adapted to guarantee safety. First, the refrigerant charge was minimized by using microchannel heat exchanger designs and reducing the liquid line length. Furthermore, two safety dampers were installed on the return air duct and supply air duct. When refrigerant leaks, the safety dampers are set to be closed to prevent refrigerant from entering the indoor environment. In addition, the device was designed as a unitary system installed outside of the building, which would make the system safer for customers. The system also aims at providing ventilation function due to high latent load as building envelope improves its thermal insulation. An economizer was added in the device to increase the energy efficiency and get free cooling during the shoulder season. Furthermore, the return air and condensate water from the evaporator was used to cool down the condenser. The third objective is to increase system efficiency. Besides the conventional vapor compression cycle, the option of using a two-stage cycle also investigated. Then we estimated and compared the performance of the new and existing system.

3. METHODOLOGIES

3.1 System Design

The device is comprised of two sections. The first section is the condensing unit, which includes the compressor, the condenser, and the condenser fan motor. The other section is the evaporating unit, which contains the evaporator, supply air fan motor, and dampers. Two refrigerants, R290 and R32, are considered in this paper.

3.1.1 Cycle

The two-stage vapor compression cycle has been reported to have 45% higher energy efficiency than the single-stage cycle (Bertsch and Groll, 2008; Wang, 2008; Xu, 2012; Xu et al., 2012). In this study, the device has two options which include a single-stage cycle and a two-stage cycle.

3.1.2 Description of the System

Fig. 1 illustrates the front view of the system including an outdoor unit (no. 15) and the duct which can be separated as the returned air duct (no. 16) and the supply air duct (no. 17). The outdoor unit (no. 15) is installed with an outdoor fan (no. 12). Fig. 1(a) shows the conventional system with a single-stage cycle. Fig. 1 (b) shows the refrigerant system including an optional two-stage refrigeration loop having a compressor (no. 5), a condenser (no. 1), a split unit, which also known as phase separator (no. 2), an internal heat exchanger (no. 3), the expansion valve (no. 4), a high-temperature evaporator (no. 6) and a low-temperature evaporator (no. 8). A drain pan (no. 7) to collect condensate water is installed under the evaporators. The condensate water is used to cool down the condenser by spraying to increase the efficiency of the system. A damper (no. 13) is installed on the duct (no. 17) to control the ambient air flow. Another damper (no. 14) is installed on the return air duct (no. 16) to control the exhaust air flow. A blower (no. 9) is installed in the supply air duct. To ensure safe system design and operations, two dampers (no. 10 and no. 11) are installed on the return air duct (no. 16) and the supply air duct (no. 17), respectively. When the flammable refrigerant sensor (shown as 19) detects a refrigerant leakage, the entire system would shut down, a warning alarm would be made, and the safety dampers would be closed. However, the outdoor fan (no. 12) could be kept on running to ventilate the refrigerant from the system. Fig. 2 illustrates the top view of the system. A small duct (no. 18) connects the return air duct (no. 16) and the outdoor unit (no. 15). The benefit of this design is to use partial return air to cool the condenser. Fig. 3 illustrates the left view of the system with ventilation dampers (no. 13 and no. 14) at different opening modes. Fig. 3a shows the case that both dampers are closed. There's no ambient air in and all the returned air is used as the supply air in this case. In Fig. 3 b, the supply air is composed by part of the return air and the ambient air. In Fig. 3 c, the return duct and supply duct are separated by the dampers so that all the supply air is from the ambient environment. This situation can happen during the shoulder season and free cooling can be achieved.

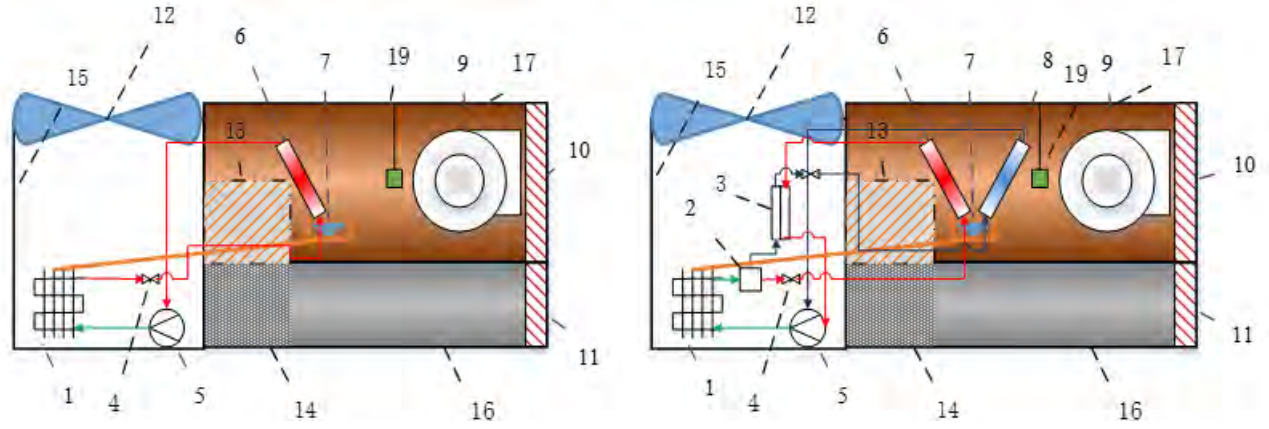

Figure 1: Front view of proposed system:
(a) Option 1: single stage system; (b) Option 2: two-stage system

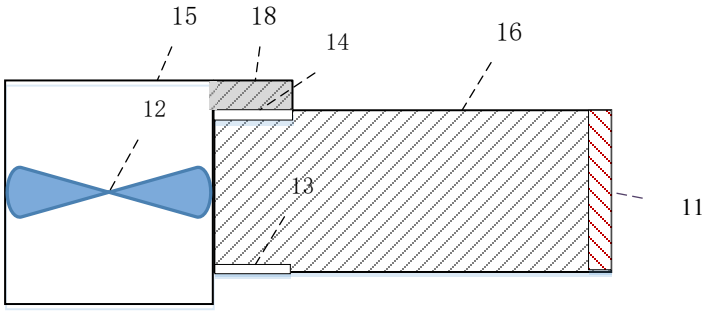

Figure 2: Top view of the proposed system

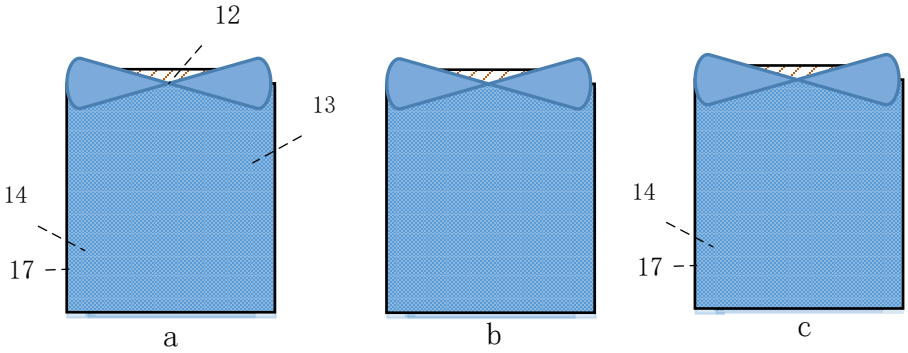

Figure 3: Left view of the proposed system

3.2 Basic assumption and modeling

Approach temperature method according to Thulukkanam (2013) was adopted to calculate the heat exchangers performance due to its simplicity and effectiveness. Xu (2012) did both experiment work and modeling work of a two-stage cycle of R32 using a single-stage cycle as a baseline. Based on his experimental data for the single-stage cycle, the approach temperatures of the evaporator and condenser were set at 5.7°C and 6°C, respectively. For the two-stage cycle, the approach temperature of the first evaporator, the second evaporator, and the condenser was set at 5.7°C, 5.7°C, and 6°C, respectively. The pressure drop of the condenser was set at 50 kPa, while for evaporator at 40 kPa. The mass flow rate of the fan of the evaporator and the condenser were 0.56 kg/s and 1.20 kg/s, respectively. In Xu et al.'s research (2012), the compressor isentropic efficiency didn't change a lot when the ambient temperature varied from 15°C to 35°C. It would decrease when the ambient temperature increased to 45°C. However, in this study, nearly all the ambient temperature (99% of the database) were below 35°C. Thus, we assumed the compressor isentropic efficiency to be a constant as 0.7. The process through the expansion valve was considered as isenthalpic. The pressure drop of the pipeline was ignored. The outdoor weather data is from TMY3 (Wilcox and Marion, 2008). The data of four different US cities (Baltimore, MD; Miami, FL; Houston, TX; and Chicago, IL) in 1980 was used in this research to represent four different climate zones in US. The indoor thermal load and the indoor temperature was set to be 10 kW and 26.7°C, respectively (ASHRAE, 2013). To evaluate the annual cooling performance of this system, temperature bin method was adapted (Erbs et al., 1983). The period considered for cooling was from May to October. The modeling work was performed in Engineering Equation Solver (EES, 2011).

4. RESULTS

Fig. 4 shows the cooling bin hour distribution for Baltimore, MD from the weather database. The x-axis is the ambient dry bulb temperature. Y-axis is the number of hours in a certain temperature bin. Fig. 5 shows the simulation results of the system's performance. The x-axis shows the ambient dry

bulb temperature, while the Y-axis is the system's COP from the simulation program. Different color of lines means different cycle option. These lines stand for the single stage cycle of R290, the single stage cycle of R32, the two-stage cycle of R290 and the two-stage cycle of R32, respectively. At 35°C ambient temperature, the COP of the R32 single-stage cycle is 3.3, which is the same as Pande et al.'s results (1996). It is observed that the system COP decreases with ambient temperature. In addition, the two-stage cycle has better performance (COP increased by 1% at 35°C ambient temperature) than the single stage cycle.

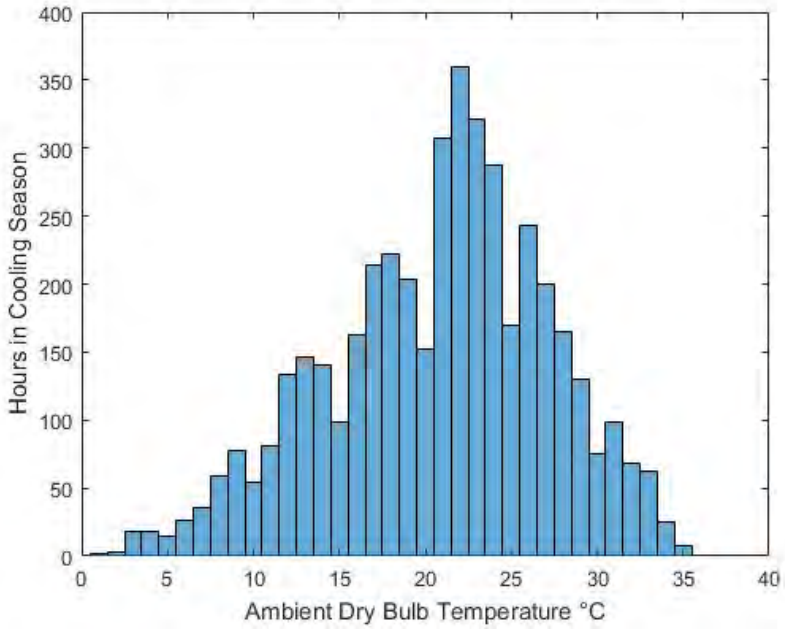

Figure 4: Temperature Bin Distribution for Baltimore, MD from TMY3

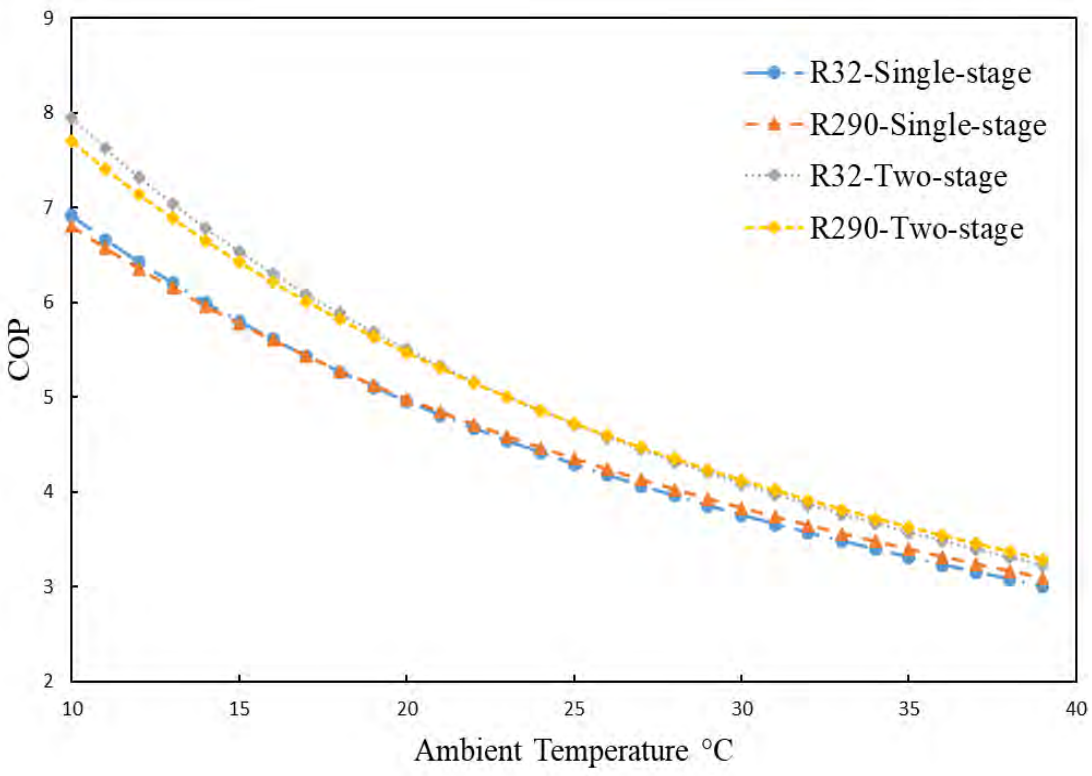

Figure 5: System COP simulation results

Table 2 shows the annual performance factor (APF) results for four US cities. With the adoption of the economizer, free cooling can be achieved under 18°C. This helps increase the efficiency of the system. Annual performance factors of each cycle with two refrigerants are shown in Table 2. The APF can be increased by 31% with economizer and by 45% with two-stager cycle and economizer in Chicago. The result of Miami shows that the economizer couldn't increase the performance because of high temperature all year round. The result of Houston shows that the economizer only has a limited effect on the APF as this city has a rather low temperature in the winter and the temperature is higher than 18°C during the shoulder season. According to this table, the new system with economizer can have the best performance to be used in a place has mild-and-warm weather condition like Baltimore and Chicago.

Table 2. APF results for four US cities

City	Refrigerant	One-stage cycle without economizer	One-stage cycle with economizer	Two-stage cycle with economizer
Baltimore	R290	4.84	5.79	6.31
	R32	4.80	5.72	6.31
Miami	R290	4.09	4.11	4.45
	R32	4.02	4.04	4.42
Houston	R290	4.25	4.66	5.05
	R32	4.19	4.59	5.03
Chicago	R290	5.14	6.78	7.41
	R32	5.12	6.71	7.42

5. CONCLUSIONS

In this study, a novel unitary air conditioning system's design concept allowing the use of flammable refrigerants and the building ventilation was proposed. We minimized the refrigerant charge by using microchannel heat exchanger designs and reducing the liquid line length. In addition, advanced hybrid options were also applied such as two-stage cycles, and economizer integrations. Moreover, the return air and condensate water from the evaporator was used to cool down the condenser. We simulated the performance of the new unitary system design and found that the APF can be increased by up to 45% as compared to existing design. This device could be used in residential and small commercial buildings as a high-efficiency design in a safe manner with environmentally friendly flammable refrigerants.

ACKNOWLEDGEMENTS

We gratefully acknowledge the support from Center for Environmental Energy Engineering (CEEE) at the University of Maryland.

NOMENCLATURE

COP	Coefficient of Performance	HVAC	Heating, Ventilation and Air Conditioning
DOAS	Dedicated Outside Air System	OAP	Outdoor Processing
ERV	Energy Recovery Ventilation	RTU	Roof Top Unit
GWP	Global Warming Potential		

REFERENCES

ASHRAE, 2013. Standard 55-2013. Thermal environmental conditions for human occupancy.

Bertsch, S.S., Groll, E.A., 2008. Two-stage air-source heat pump for residential heating and cooling applications in northern U.S. climates. International Journal of Refrigeration 31, 1282–1292.
Bourne, R.C., Lee, B.E., Berman, M.J., 2004. Hydronic rooftop cooling systems. US Patent Application No. 20050056042, March 2015.
Calm, J.M., 2008. The next generation of refrigerants–Historical review, considerations, and outlook. international Journal of Refrigeration 31, 1123–1133.
Cleland, D.J., Keedwell, R.W., Adams, S.R., 2009. Use of hydrocarbons as drop-in replacements for HCFC-22 in on-farm milk cooling equipment. international journal of refrigeration 32, 1403–1411.
EES, 2012. F-Chart Software
Erbs, D.G., Beckman, W.A., Klein, S.A., 1983. Estimation of degree-days and ambient temperature bin data from monthly-average temperatures. ASHRAE Journal 25(6).
Hwang, Y.J., Hyun, S.Y., Lee, W.H., Sim, J.H., 2006. Unitary air conditioning system. United States Patent No. US20060032929A1.
Im, P., Mini, M., Munk, J.D., Lee, J., 2016. Cooling season full and part load performance evaluation of Variable Refrigerant Flow (VRF) system using an occupancy simulated research building. Proceedings of the Int. Refrigeration Conference at Purdue, Purdue, IN.
Lee, J., Yoon, H., Im, P., Song, Y., 2017. Verification of Energy Reduction Effect through Control Optimization of Supply Air Temperature in VRF-OAP System. Energies 11(49).
Mota-Babiloni, A., Navarro-Esbrí, J., Barragán-Cervera, Á., Molés, F., Peris, B., Verdú, G., 2015. Commercial refrigeration-An overview of current status. International Journal of Refrigeration 57, 186–196.
Palm, B., 2008. Hydrocarbons as refrigerants in small heat pump and refrigeration systems–a review. International journal of refrigeration 31, 552–563.
Pande, M., Hwang, Y.H., Judge, J., Radermacher, R., 1996. An experimental evaluation of flammable and non-flammable high pressure HFC replacements for R-22, Proceedings of the Int. Refrigeration Conference at Purdue, pp. 21-27, Purdue, IN.
Park, D.Y., Yun, G., Kim, K.S., 2017. Experimental evaluation and simulation of a variable refrigerant- flow (VRF) air-conditioning system with outdoor air processing unit. Energy and Buildings 146, 122–140.
Thulukkanam, K., 2013. Heat exchanger design handbook. CRC press.
Venkatarathnam, G., Murthy, S.S., 2012. Refrigerants for vapour compression refrigeration systems. Resonance 17, 139–162.
Wang, X., 2008. Performance investigation of two-stage heat pump system with vapor-injected scroll compressor, PhD Thesis, University of Maryland, College Park, MD, USA.
Wilcox, S., Marion, W., 2008. Users manual for TMY3 data sets. National Renewable Energy Laboratory Golden, CO.
Wohlert, C.W., 2013. Roof top air conditioning units having a centralized refrigeration system. United States Patent No. US8353175B2.
Xu, X., 2012. Investigation of vapor injection heat pump system with a flash tank utilizing R410A and low-GWP refrigerant R32, PhD Thesis, University of Maryland, College Park, MD, USA.
Xu, X., Hwang, Y., RADERMACHER, R., Pham, H.M., 2012. Performance measurement of R32 vapor injection heat pump system, 14th International Refrigeration and Air Conditioning Conference at Purdue, Paper No. 2328.
Zhu, Y., Jin, X., Du, Z., Fan, B., Fang, X., 2014. Simulation of variable refrigerant flow air conditioning system in heating mode combined with outdoor air processing unit. Energy and Buildings 68, 571–579.

Manuscript ID: 573
DOI: 10.18462/iir.icr.2019.0573

Hydrocarbon refrigerant for building air conditioning application in Indonesia: performance and safety analysis

Ardiyansyah YATIM[(a)], M. Idrus ALHAMID[(a)], Agus PAMITRAN[(a)], Nandy S. PUTRA[(a)], Budihardjo BUDIHARDJO[(a)]

[(a)] Department of Mechanical Engineering, Universitas Indonesia
Depok, 16424, Indonesia, ardiyansyah@eng.ui.ac.id

ABSTRACT

Indonesia has taken an active role in the phase-out of ozone depleting substances and reduction of high global warming potential substances in HVACR systems. For air conditioning applications, the choice has been geared toward the use of natural refrigerant with hydrocarbons shows a great potential to be an alternative refrigerant. This paper presents review on the development of hydrocarbon refrigerant applications in Indonesia. As a case study, the installation, performance measurement and safety analysis of a hydrocarbon (R290) chiller for air conditioning application in an auditorium building at Universitas Indonesia is presented. Field measurement was performed on refrigerant, cooling water and air sides to obtain its performance at several cooling load conditions. The paper also presents analysis on the safety for the flammability aspects, charge limit as well as applicable national standards for its safe use and handling as well as benchmarking with international standard. The study showed that the hydrocarbon chiller is an energy efficient and safe option for air conditioning application in Indonesia.

1. INTRODUCTION

Indonesia is one of the fastest growing markets for air conditioning (AC) primarily for residential sector. The population of the AC system is depicted in Figure 1. As this sector is contributing to both ozon depletion and global warming both directly from the use of refrigerant and indirectly from its use of energy from fossil fuel sources. Indonesia has taken an active role in the phase-out of ozone depleting substances through ratification of Montreal Protocol since 1992 and its all amendments in 2006. As of 2008, the import of chlorofluorocarbons (CFC) has been prohibited and subsequent phase out of hydrochlorofluorocarbons (HCFC) is on the way. the use of different types of HCFC-based refrigerants has been decided to phase out by 2030 in all developed countries and by 2040 in developing countries, including Indonesia For refrigeration and air conditioning applications, the choice of environmentally friendly refrigerants has been geared toward the use of hydrofluorocarbons (HFC) due to its non-ozone depleting effects. However, the concern on its global warming potential has caused the search of refrigerants with both non-ozone

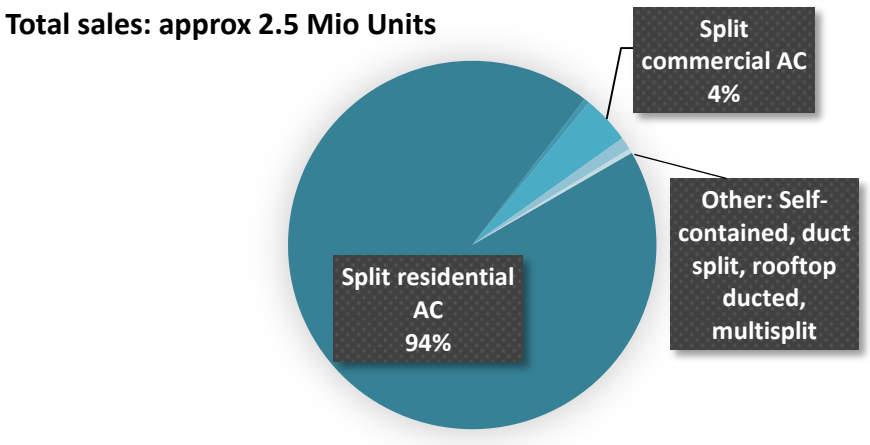

Figure 1: Population of AC system in Indonesia (GIZ, 2015)

depleting and low global warming impact properties. Recent Kigali amendment in 2016 set plan for HFC phase down in coming years. As a drop-in option, hydrocarbons refrigerants have a great potential to be an alternative refrigerant that is not only satisfy the above requirements but also improve energy efficiency and lower refrigerant charge for the equipment, leading to lower direct and indirect carbon dioxide-equivalent emission.

2. HYDROCARBON REFRIGERANT APPLICATIONS: PERFORMANCE ANALYSIS

The use of hydrocarbon (HC) refrigerants R600a (isobutane), R600 (normal-butane), R290 (propane), R1270 (propylene) and refrigerants mixed from three of them or replacements for HCFC's and HFC's continues around the globe and also in Indonesia. The R600a, R600, and R290, R1270 are commonly used as single, non-mixed refrigerant. They have ozone depletion potential (ODP) factors of zero and a very low global warming potential in comparison to incumbent HCFC or HCF refrigerants.

Neither of these refrigerants are "drop-in" replacements for HCFC's or HFC's. There are significant differences between R600a and R290, and the non-HC refrigerants that must be considered in handling, processing and application. These descriptions are offered to help understand these differences. Hydrocarbon refrigerant has found in Indonesian market derived from some of the manufacturer or brand (*Musicool, Petrozon, Hycool, Artek* and some brand import) to be distinguishable in the following types:

1. Hydrocarbon refrigerant for substituting R22, using a pure propane (R290)
2. Hydrocarbon refrigerant for substituting R134a, using a mixture of propane, iso butane, and normal butane with a particular composition.
3. Hydrocarbon refrigerant for substituting R12, using a mixture of propane, iso butane, and normal butane with a particular composition.
4. Hydrocarbon R600a (iso butane) & R600 (normal-butane), usually they are used in domestic refrigeration system.

Hydrocarbon refrigerant are miscible with and soluble in conventional mineral and synthetic oils used with a HCFC's. From the three types of product, the most common to find is R290 (Pure propane), certain amount of hydrocarbon are used as a substitute for R134a, but starting in 2014 there have been no found again hydrocarbon to substitute R12. As an illustration, a given displacement compressor with R600a will produce 50 to 60% of then capacity that it would with R134a. R290 will produce 85 to 90% compared to R404A. R600a and R290 are compatible with all materials used in All Products' hermetic compressors and condensing units that are designated for use with these refrigerants. The types of system which are using hydrocarbon refrigerants in Indonesia are: split air conditioning (office and housing), vehicle air conditioning (train, bus, and private transport), and chiller at building commercial, showcase refrigeration system and storage refrigeration system.

Refrigerant HCFC22 (R22), the most estimated currently, despite its low ODP, has a 1,810 GWP which is considered high. The limit on the use of R22 is 2030 for developed countries, and 2040 for developing countries. Therefore, R22 needs to be replaced with other environmentally friendly refrigerants (Tian et al., 2014, Aurora and Kaushik, 2008, Chen and Yu, 2008, Fuadi et al. 2018). Many studies have been dedicated to alternative refrigerant HC290 (R290) and several other refrigerant mixtures (Qian et al., 2016; Shaik and Babu, 2017; Sah et al., 2014; Wu et al., 2012). R290 has zero ODP with very low GWP, which is 3.3. The properties of R290 and R22 are shown in Table 1. The performance comparison between hydrocarbon refrigerant and R22 refrigerant is presented in Figure 2.

Table 1. Properties of R290 and R22

No.	Refrigerant	Boiling Point (ºC)	Critical Pressure (Mpa)	Critical Temperature (K)	ODP	GWP (in 100 years)
1	R22	-40.81	4.99	369.3	0.055	1760
2	R290	-42.11	4.2512	369.89	0	3

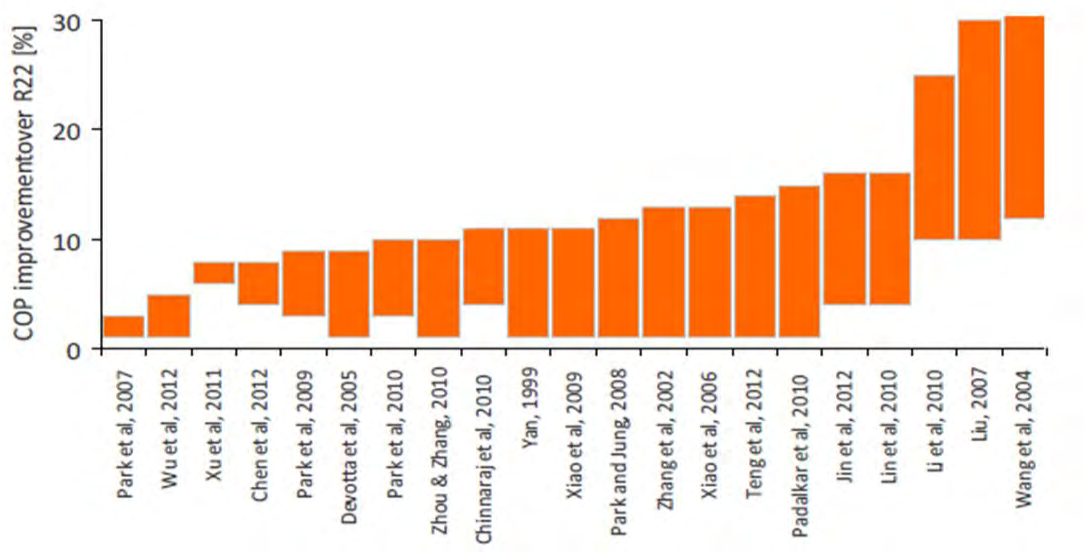

Figure 2: Comparison of Hydrocarbon and R22 performance (Opplet, 2015)

The hydrocarbon refrigerant application policy in Indonesia is associated of its energy performance characteristic, hence is included in energy conservation and environmental policy. In line with the issue of climate change, Indonesia is committed to reducing greenhouse gas (GHG) emissions amounting to 26% by 2020 from the level of business as usual (BAU) with its own business and reaching 41% if it receives international support. To realize this commitment, the President of Indonesia established Presidential Regulation Number 61/2011 concerning the National Action Plan for Reducing Greenhouse Gas Emissions. Energy conservation is a systematic, planned and integrated effort to preserve domestic energy resources and improve the efficiency of their use. In relation to energy conservation in order to achieve national energy security, the government has issued various regulations ranging from the highest, namely Law Number 30 of 2007 concerning Energy, Government Regulation Number 70/2009 concerning Energy Conservation, Presidential Instruction and various ministerial regulations as operational guidelines. In Government Regulation number 70/2009 concerning Energy Conservation, it is mandated that energy conservation is the responsibility of the government, regional government, employers and the community. In addition, national energy conservation covers all stages of energy management, namely the activities of supplying, exploiting and utilizing energy and conserving energy resources. Government Regulation Number 70/2009 concerning Energy Conservation requires that energy users who use energy equal to 6000 (six thousand) tons of oil per year to apply energy management which includes, appoint a certified energy manager, compile energy conservation programs, carry out periodic energy audits by certified auditors, carry out the results of the energy audit, and report on the implementation of energy management to the government. This regulation is supported by the Minister of Energy and Mineral Resources Regulation Number 14/2012 concerning Energy Management, which technically clarifies the steps and obligations that must be done in implementing energy management.

The national standard SNI 6390:2011 on energy conservation in building air conditioning systems addresses the energy efficiency recommendations for chillers in Indonesia. The standard applies to new and modified refrigeration systems and covers unitary and chiller systems, fans, pumps, ducting and insulation. In the Indonesian standard, the chiller system is defined as refrigeration systems with cooling capacities above 176 kW (50 TR). The standard also recommends several energy conservation measures to achieve energy efficiency. The implementation of standards mainly takes place in the building sector and has been defined by the Energy and Mineral Resources Ministry (ESDM 31/2005 and 14/2012), the Public Works Ministry (PU 29/2006 and 02/2015) and several municipal government regulations. Recent development for rating and testing is set in SNI 8476:2018. These standards are not yet mandatory, and, consequently also not enforced. Furthermore, the current standards only set full load requirements.

Table 2 Energy performance standard for air conditioning system in Indonesia

Refrigeration system	Compressor type	Capacity	Minimum Efficiency	
			COP (kW/kW)	EER (kW/TR)
Split		< 65.000 Btuh	2.70	1.303
Variable refrigerant volume			3.70	0.951
Split duct			2.60	1.353
Air cooled chiller	Reciprocating	< 150 TR	2.80	1.256
Air cooled chiller	Screw	< 150 TR	2.90	1.213
Air cooled chiller	Reciprocating	> 150 TR	2.80	1.256
Air cooled chiller	Screw	> 150 TR	3.00	1.172
Water cooled chiller	Reciprocating	< 150 TR	4.00	0.879
Water cooled chiller	Screw	< 150 TR	4.10	0.858
Water cooled chiller	Reciprocating	> 150 TR	4.26	0.826
Water cooled chiller	Screw	> 150 TR	4.40	0.799
Water cooled chiller	Centrifugal	> 150 TR	6.05	0.581

It can be deduced that the level of compliance to the standard is varied and there are chillers operating with energy efficiency below the requirement or chillers that have not been addressed in the national standard. In the global context, the US and Japan and latterly Europe have been the trendsetters in developing and implementing a comprehensive set of Minimum Energy Performance Standards and labels to drive the energy efficiency of refrigeration and air conditioning appliances, including chillers.

Table 3 Typical energy performance of RAC equipment in Indonesia

Industry Types	Description	Unit number	Typical EER/COP in 2012 Prior to HPMP	COP SNI 6390:2011
Commercial (<12hp)	Retail food service, Walk-in coolers/freezers and other commercial cold rooms	11,055	8.2 – 10.9 (EER)	
			2.4 – 3.2 (COP)	N/A
Industrial (> 12 hp)	Industrial cold rooms, chilling plants and refrigerated warehouse		8.2 – 12.6 (EER)	
			2.4 – 3.7 (COP)	N/A
Transport Refrigeration	Refrigerated truck and container van	15	8.2 – 10.9 (EER)	
			2.4 – 3.2 (COP)	N/A
Residential, Light Commercial and Commercial AC	Window-, split- and package-type AC	1.4 mil	8.2 – 12.6 (EER)	
			2.4 – 3.7 (COP)	2.6-3.7
Chiller	Water cooled and air cooled chillers	511	8.2 – 10.9 (EER)	
			2.4 – 3.2 (COP)	2.8-6.05

As a case study, an air conditioning system using R290 is discussed in the following section. The cooling system in Universitas Indonesia utilizing hydrocarbon refrigerant within academic institution is the first in Indonesia. The air-cooled reciprocating chiller is installed at the Auditorium Art Center in the university for the purpose of air conditioning the indoor of the Auditorium which is built for art performance and educational activities as shown in Figure 3. The building, particularly the auditorium, is functionally designed to cope with the incoming and outgoing of audience whenever there is on event being held. Outside the hours, the auditorium is closed to the public. The auditorium is able to house 400 people. The system is designed with a typical one-stage refrigeration cycle.

From the performance investigation, the following conclusions can be drawn, the maximum cooling effect at freeload condition is reached at 135.33 kW with energy consumption of 34.62 kW when the water temperature at inlet side is within 15.1ºC. At partial load during testing condition the obtained cooling capacity is 148.39 kW with power consumption for compressor work is 30.12 kW when the water temperature at inlet side is within 7.8ºC. The highest COP value during freeload is obtained when the water temperature at inlet side is within 8.9ºC. The maximum value of COP is 4.27 with cooling effect generated around 125.93 kW and compressor work of 30.06 kW. The optimum system at 64% cooling load from the chiller specification design. The maximum value of COP during partial load is reached at the value of 5.25 with cooling capacity obtained is 148.39 kW and the compressor work of 30.12 kW when the water temperature at inlet side is within 7.8ºC and the optimum chiller in the range of 75% loading.

Table 4 Specification of R290 chiller at Universitas Indonesia

Cooling Capacity:	56 TR 197.6 kW	Refrigerant Charge:	2 x 14 kg
Total Power Consumption:	55.9 kW (dual compressors)	Nominal Fluid Flow:	33.8 m^3/h
Refrigerant:	Propane HC290 (R-290)	Pressure Drop @ Nominal Flow:	30.0 kPa
Charging:	2 x 16.6 kg	Refrigerant Flow Control:	Thermostatic Expansion Valve with External Equalizer
Total Rated Ampere	101 A	Quantity (Circuit)	1 (2)
Complementary Measurement Tools : Refrigerant Side & Water Side Measurement, Pressure Transducer, Temperaturee Transducer, Refrigerant Flow Meter, Water Flow Meter, Water Temperaturee Inlet & Outlet Chiller, kWh Energy Monitoring.			

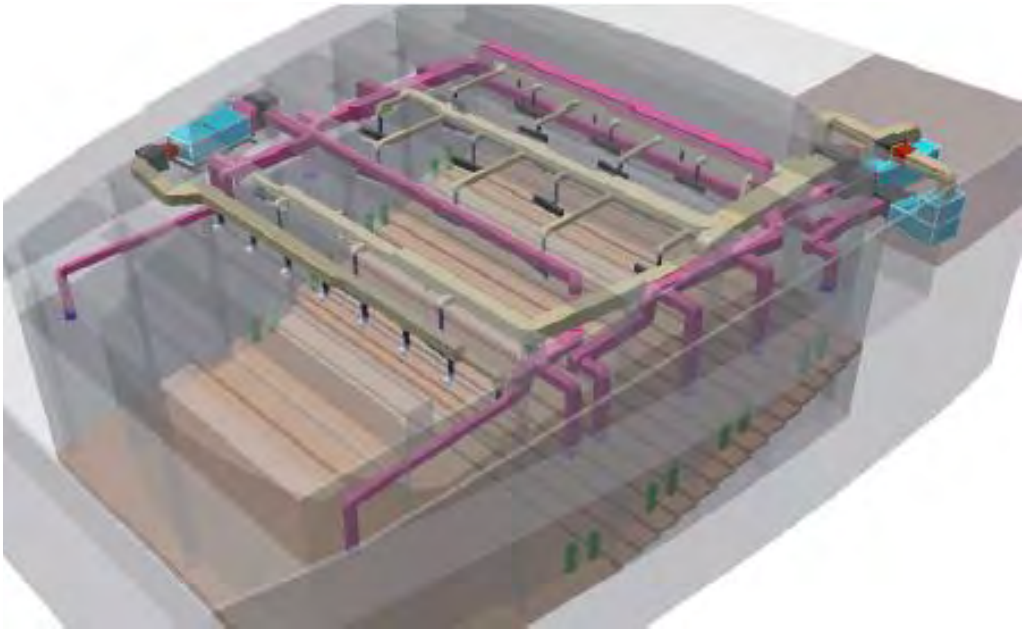

Figure 3: Art Center auditorium at Universitas Indonesia utilizing chiller with R290

3. HYDROCARBON REFRIGERANT APPLICATIONS: SAFETY CONSIDERATION

On the safety aspect, there are three main national standards related to safety aspects of hydrocarbon refrigerant applications in Indonesia. The national standard SNI 6500-2018[5] regulates the use of refrigerants for fixed refrigeration systems (including chiller applications). The second national standard SNI 6501.1-2000 lays out the safety guideline for refrigerants of the A3 safety group in regard to filling, storage and transportation processes. The safety guideline that specifically addresses the hydrocarbon refrigerant is SNI 7647:2010. These standards are discussed in the following section.

Indonesian standard on chiller safety measures is set in place by SNI 6500-2018: Refrigerants for fixed applications. The standard covers wide ranges of stationary chillers, including new and modified refrigeration systems, relocated systems, as well as system converted from the use of one refrigerant to an alternative refrigerant (retrofit). Referring to SNI ISO 817:2018, the national standard classifies the refrigerant into groups based on the flammability and the toxicity level. The flammability levels of the refrigerants are classified into Class 1 to 3 with increasing flammability. The values are based on the flame propagation behaviour when tested in air at 101 kPa pressure and temperatures between 18 to 21°C. Both the lower flammability limit (LFL) and calorific value of the refrigerants are considered to determine the flammability classification. The toxicity level is divided into A and B groups with increasing toxicity. The group A refrigerants have a toxicity level, in regards to lethal concentration, of LC50 value higher than 10,000 ppm, while the group B refrigerants have a LC 50 value lower than 10,000 ppm. Based on this standard, the refrigeration systems are also classified into high risk and low risk system based on the probability of the refrigerant being released into the occupied area. The room type classification is based on the accessibility to the occupants, the familiarity of occupants inside the room regarding the safety procedures of the room, and the ease of the occupant to be aware of the condition changes inside the room during emergency situations. Room type is divided into three groups based on the criteria mentioned above.

The maximum refrigerant charge is regulated for general A3 class refrigerant, including R290. The maximum mass charge is calculated as follow (Pasek, 2013):

$$m_{max} = 2{,}5 \times LFL^{5/4} \times h_o \times A^{1/2} \qquad \text{Eq. (1)}$$

or, minimum area

$$A_{min} = \left(\frac{m}{2{,}5 \times LFL^{5/4} \times h_o}\right)^2 \qquad \text{Eq. (2)}$$

Where m is the mass of refrigerant charge in kg, and A is area, in m^2.

To accommodate the use of every type of refrigerant on a type of system group installed in each of room type, SNI 6501.1-2000 has established 20 rules to follow. Hydrocarbon refrigerant may be used as a an alternative refrigerant in various sectors and it is available on the Indonesian market at competitive prices. However, the safety issues may limit the application of this substance. As a consequence of the missing safety measures, the following hazards can be found in Indonesia which could be avoided by adhering to advanced standards in line with international rules, such as the EN378, enhanced training and certification of technicians and enforcement of these requirements. In the global context, due to the advantage of natural refrigerants, in particular hydrocarbons, it is recommendable that these refrigerants become permissible as long as they can be safely handled. The standards serve to set the boundaries under which natural refrigerants can safely be used. The European Union has established EN 378 and EN 60335-2-40 harmonized standards. Internationally, the most elaborate and comprehensive international standard and standard framework in place allowing the use of natural refrigerants is the European Standard EN 378. The current Indonesian standard covers large parts of the EN 378. There are certain aspects included in the EN 378, not yet as comprehensively addressed under the SNI 7647:2010. These aspects include the handling potential sources of ignition, leak detection requirements and requirements on information instructions. The Indonesian Ministry of Environment Regulation No. 2/2007 also requires the retrofitting and recycling of refrigerants on chillers to be carried out by technicians holding a certification. However, to date, such certification has not been implemented or enforced in the market. It is recommended that a certification scheme for technician is established for retrofitting, recycling and the installation of chillers with flammable refrigerants.

4. CONCLUSIONS

This paper presents a review on hydrocarbon refrigerant application in Indonesia. Hydrocarbon refrigerant is a natural refrigerant with higher energy efficiency than conventional refrigerants. Applications in refrigeration and air conditioning of hydrocarbon refrigerants in Indonesia have been found in several sectors including initial (dedicated) machine and retrofitting. The policy and regulation of the refrigerant is associated to energy conservation and environmental consideration. Both national and international energy efficiency requirements were discussed. The national Indonesian standard SNI 6390:2011 on energy conservation in building air conditioning system contains the energy efficiency levels for air conditioning and chillers. A case study of building air conditioning using R290 is presented. The second part of the study discusses the safety aspects of its applications. The flammability aspects, material and equipment compatibility, and applicable standards for its safe use and handling in Indonesia are also addressed. With the SNI 7647:2010 Indonesia has a safety standard in place which allows the operation of chillers with natural refrigerants, including hydrocarbons. The study showed that the hydrocarbon chiller is an energy efficient and safe option for air conditioning application in Indonesia.

ACKNOWLEDGEMENTS

This research/article's publication is supported by the United States Agency for International Development (USAID) through the Sustainable Higher Education Research Alliance (SHERA) Program for Universitas Indonesia's Scientific Modeling, Application, Research and Training for City-centered Innovation and Technology (SMART CITY) Project, Grant #AID-497-A-1600004, Sub Grant #IIE-00000078-UI-1.
Part of the text has been presented at Quality in Research Conference in 2015 (Yatim and Adiwinata, 2015), however significant development has been updated here.

NOMENCLATURE

CFC	chlorofluorocarbons	*Max*	Maximum
HCFC	hydrochlorofluorocarbons	*Min*	Minimum
HFC	hydrofluorocarbons	*SNI*	National Standard of Indonesia
p	pressure (kPa)	*LFL*	Lower Flammability Limit
T	temperature (K)		

REFERENCES

Arora, A., & Kaushik, S. 2008. Theoritical Analysis of a Vapour Compression Refrigeration System with R502, R404A dan R507. International Journal of Refrigeration 31:998-1005.

Chen, J., & Yu, J. 2008. Performance of a New Refrigeration Cycle Using Refrierant Mixture R32/R134a for Residential Air Conditioner Aplications. Energi Building 40:2022-2027.

Fuadi, Z., A Yatim, R Rizky, N Aisyah, I Alhamid, B Budihardjo, N Putra 2018. Chiller performance study with refrigerant R290. AIP Conference Proceedings 2062 1, 020061

GIZ, 2015. Study on Green Chiller in Indonesia. Published Report.

Opplet, D. 2015. Green Chiller in Indonesia. in Green Chiller NAMA Workshop Indonesia

Pasek, A., 2013. Performance and Safety Consideration in Adopting Zero-ODP and Low-GWP Refrigerants, in 4th Ozone2Climate Technology Roadshow and Industry Roundtable, Manila.

Qian, S., et al 2016. Not-in-kind Cooling Technologies: A Quantitative Comparison of Refrigerans and System Performance. International Journal of Refrigeration. 62: 177-192.

Shaik, S.V., Babu, T.P.A., 2017 Theoretical Performance Investigation of Vapour Compression Refrigeration System Using HFC and HC Refrigeran Mixtures as Alternatives to Replace R22. International Conference on Recent Advancement in Air Conditioning and Refrigeration. 109: 235 – 242.

Sah, Ramesh P., Das, Ranadip K., Tiwari, Vidhika 2014 Analysis of Vapour Compression Refrigeration System with Refrigerans R134a, R143a, R152a, R290, and R32. International Journal of Innovative Research & Development Vol. 3 Issue 6 ISSN 2278 – 0211.

Tian, Q., Cai, D., Ren, L., Tang, W., Xie, Y., He, G., & Liu, F. 2014. An Experimental Investigation of Refrigeran Mixture R32/R290 as Drop-In Replacement for HFC410A in Household Air Conditioners. International Journal of Refrigeration 57:216-228.

Wu, J., Yang, L., & Hou, J. 2012. Experimental Performance Study of a Small Wall Room Air Conditioner Retrofitted with R290 and R1270. International Journal of Refrigeration 35:1860-1868.

Yatim, Ardiyansyah and A. Adiwinata. 2015. Hydrcarbon Refrigerant Applications in Indonesia. Proceeding of Quality in Research (QiR) 2015. Bali, Indonesia.

Manuscript ID: 598
DOI: 10.18462/iir.icr.2019.0598

Evaporative coolers of gases and liquids with a lowered level of cooling

Guangming CHEN[(a)], Aleksander DOROSHENKO[(b)], Kostyantyn SHESTOPALOV[(a,b)]

[(a)] Ningbo Institute of Technology, Zhejiang University, No 1 QuianHu South Road, Ningbo City, 315100, Zhejiang Province, China, gmchen@zju.edu.cn

[(b)] Institute of refrigeration, cryotechnology and eco-energy, Odessa National Academy of Food Technologies, 112 Kanatnaya str., Odessa, 65039, Ukraine, dor_av43@i.ua

ABSTRACT

This study is dedicated to the creation of the schematic solutions of the evaporative cooling and air conditioning systems, development of the heat and mass transfer equipment for such systems, experimental investigation and analysis of principle possibilities of such systems on the basis of carried out theoretical and experimental research. The theoretical modeling of the coupled heat and mass transfer process in indirect evaporative coolers of water and air is carried out. It is shown that the dew point temperature of the air flow entering the evaporative cooler can be served as a limitation of cooling. The difficulties connected with obtaining the cooling limitation for low-temperature cooling connected with the possible condensation of water vapor in the air flows, when the air flow contacting with water becomes fully saturated before going out from the heat and mass transfer device, are studied.

Keywords: Evaporative Coolers, Natural Cooling, Air-Conditioning, Energy Saving

I. INTRODUCTION

The interest to the possibilities of the evaporative cooling has been increased recently. It is caused by their small energy consumption and by their environmental loyalty (Chen et al., 2015; Doroshenko and Glauberman, 2012). Both direct evaporative coolers (DEC - air coolers and water coolers, cooling towers (CTW)) and indirect evaporative coolers (IEC) find a wide practical application. The capabilities of such coolers according to the achievable level of cooling are limited by wet bulb temperature of the outside air t_{wb}. This temperature is a natural limitation of cooling. The efficiency of such systems depends essentially on local climatic conditions. The evaporative coolers with decreased level of cooling have been intensively studied recently (Maisotsenko and Gillan, 2003; Pandelidis et al., 2015; USA Patent 2009/0007583; USA Patent 6,494,107). The purposes of the present study are the extension of the practical area of application of evaporative water and air coolers; design of the corresponding new solutions, and particularization of the conditions for realization of the low-temperature cooling, primarily, the determination of optimal ratios of contacting flows.

In IEC of air (Fig. 1), which have become the most widely used recently, the air flow (F) entering for cooling, is divided into two parts. The auxiliary air flow (A) enters the "wet" part of the cooler, where it contacts with water film, flowing down on the surface of the channel (water recirculates through the packing of the device). The evaporative cooling of water is realized here. The chilled water provides a contactless cooling of the main air flow (M) through the wall, which separates the channels. The main air flow is cooled at constant humidity content: this provides the advantages during construction of the air conditioning systems based on the IECa. Auxiliary air flow rejects the heat from the device, its temperature also decreases, and humidity content is increased. Temperature of water in the cycle is constant and it is a little higher than the wet bulb temperature of the outside air entering the IECa. This temperature depends on the ratio of the air flows in IECa, and it is considered as a limitation of cooling for both air flows.

Indirect evaporative coolers of gases can be of ordinary or regenerative types (Chen et al., 2015; Pandelidis et al., 2015; USA Patent 2009/0007583). In a regenerative cooler (Fig. 1A) the separation of the air flows takes place at the exit of the "dry" zone of the device (in the inner heat

exchanger). This system is marked as IEC-Rg (air chiller Chg). Here the auxiliary air flow enters the evaporative part of the cooler; it is already chilled at constant humidity content. Its cooling potential is substantially increased and the limitation of cooling is decreased theoretically to the dew point temperature of the ambient air t_{dp}^1. The concern to the capabilities of the solutions of Chg diagram in literature is large (Chen et al., 2015; Pandelidis et al., 2015; USA Patent 2009/0007583), but the results of the studies do not take into account the concomitant circumstances, which are to be discussed in the present study. In a polytropic process of the evaporative cooling of water in a water chiller (CTW) the limitation of evaporative cooling is determined by the wet bulb temperature of air entering the device. Fig. 1B represents the system where cooled and humid air is delivered to the room (Chg*); Fig. 1C represents the system where cooled air is delivered to the room (Chg), but its humidity content is not changed.
Fig. 2 presents the schematic diagrams of the indirect type water chillers (Chw) which are realized in combined (Fig. 2A) and separated modes (Fig. 2B). The water cooler IECw is similar to the air cooler IECg, but the main difference is that the main product flow in IECw is the chilled water. This design can be considered as a two-component cooling tower, in which the product water is chilled contactless. The process in "wet" channels is fully similar to IECg. In a chiller-water cooler Chw the limitation of cooling theoretically is also decreased to the dew point temperature of ambient air t_{dp}^1.

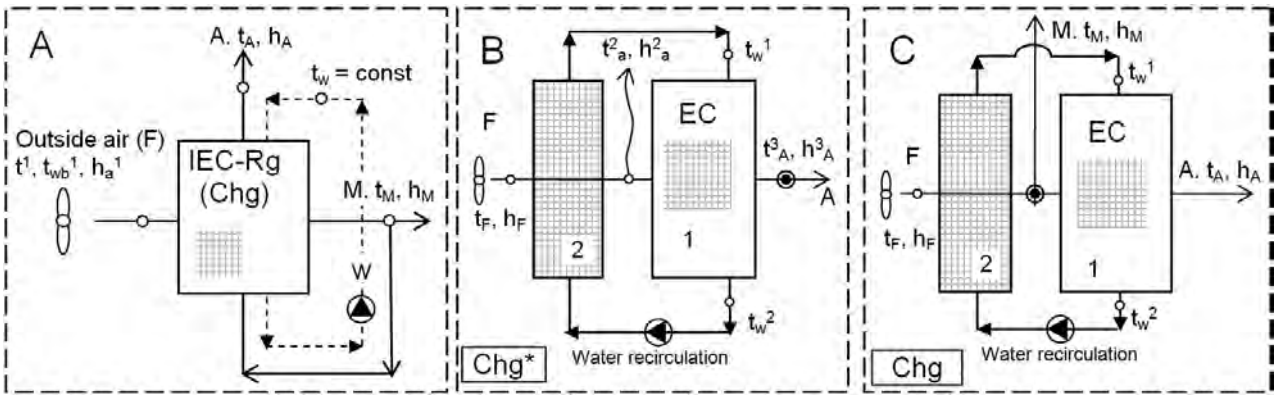

Figure 1: Transition from combined scheme of IEC-Rg (A) to separated schemes of air cooler Chg (B and C): 1 – evaporative air cooler; 2 – water-air heat exchanger

Based on the previously carried out studies (Chen et al., 2015; Chen et al., 2018; Doroshenko and Glauberman, 2012), it was determined, that the regularized symmetrical packing with vertical or inclined channels is the optimal choice for the design of the film evaporative heat and mass transfer devices (channels can be closed-loop or partially closed loop). The main problems for such design are: the packing layer should be unified, i.e. can be used for both counter flow and cross-current flow of air and water contact - this is particularly important for the indirect evaporative coolers; the packing should have a large specific surface with small resistance to air flow; the density of the layer is selected considering a stability of the system, as well as possible sedimentation on the working surfaces; the packing should have corrosion resistance to working fluids, it should be of a simple construction and manufacturable; the packing layer should assist the uniform input of liquid and its favorable distribution between neighboring channels (the problem of wettability of the multichannel packing surface) - the appropriate material for packing manufacturing should be selected. In recent decade, mainly the polymeric materials have been used for manufacturing the film type heat and mass transfer equipment: high density polyethylene, high-impact polystyrene, polyvinylchloride, polypropylene (Gómez et al., 2005; Martínez et al., 2011; Koltun et al., 2003).
Weak wettability of the polymeric materials can be compensated by manufacturing of the complex form of the surface by creation of microtoughness on the surface of the packing elements, and by application of various distributors of gases and liquids. One of the prospective materials for application for these purposes is a polycarbonate (PC). The honeycomb panels made from PC are characterized by high mechanical characteristics, such as solidity, persistence to impact influence at continuous exposition on open air.

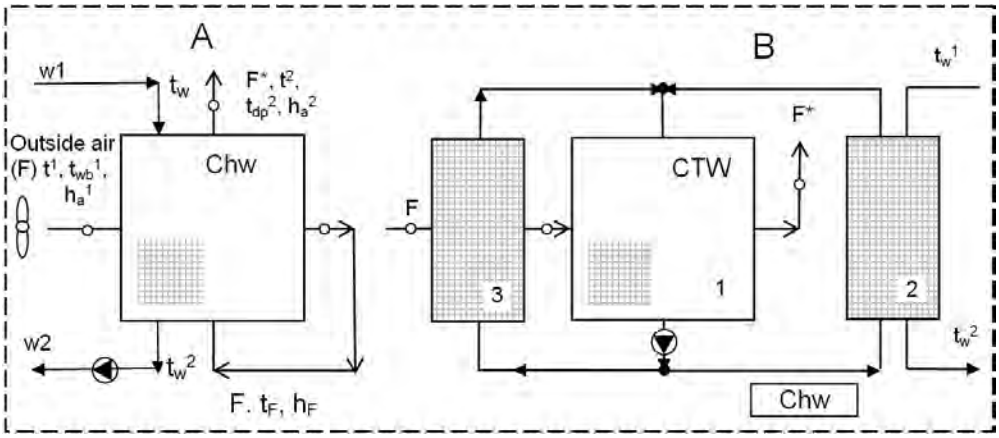

Figure 2: Schematic diagrams of indirect evaporative coolers of water: combined (A) and separated (B) schemes: 1 - cooling tower, 2 - loading heat exchanger (the object which is cooled by a chiller), 3 - water-air heat exchanger

II. MODELING OF THE PROCESS OF THE COUPLED HEAT AND MASS TRANSFER IN EVAPORATIVE AIR COOLER OF INDIRECT TYPE

The element of the packing with dimensions of $0 \le x \le H$, $-a \le y \le b$, $0 \le z \le L$ (Fig. 3A) is considered for description of the heat and mass transfer in IECg for the condition of material homogeneity of flows. The main flow of air is cooled through the separating wall on account of evaporative cooling of water flowing down if a form of film. The auxiliary air flow contacts directly with liquid (schemes of gases and liquids contacts in "wet" channels are considered as parallel flow as well as counter flow).

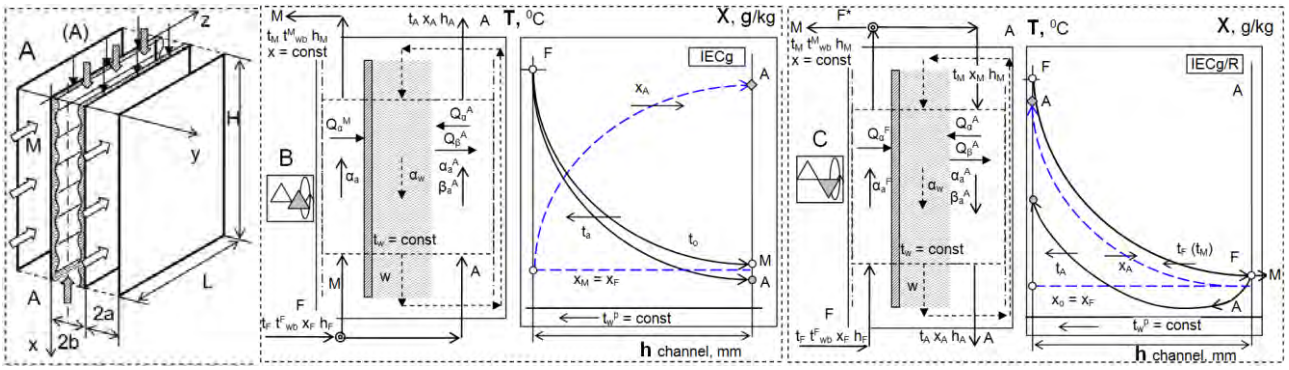

Figure 3: Modeling of the coupled heat and mass transfer in IEC of air: A - design scheme; B - IECg; C - IECg/R

The equation of coupled heat and mass transfer in IECg and corresponding matching conditions in a form of equations of boundary layer:

- for liquids ($0 \le x \le H$, $0 \le y \le h$ (h – the thickness of the liquid layer), $0 \le z \le l$), temperature $t_w = t_w\,(x, y, z)$ is determined from equation:

$$W_w(y)\frac{\partial t_w}{\partial x} = a_w \frac{\partial^2 t_w}{\partial y^2}, \qquad \text{Eq. (1),}$$

condition at entrance at $x = 0$, is: $t_w\,(0, y, z) = t_w^0$;

– for auxiliary air flow «A» ($0 \le x \le H$, $h \le y \le b$, $0 \le z \le l$), temperature $t_A = t_A\,(x, y, z)$ and partial pressure of vapor $p_v = p_v(x, y, z)$ is determined by the equations:

$$W_A(y)\frac{\partial t_A}{\partial x} = \frac{\partial}{\partial y}\left[(a_a + a_a^T)\frac{\partial t_A}{\partial y}\right], \qquad \text{Eq. (2)}$$

$$W_A(y)\frac{\partial p_n}{\partial x} = R_n T_A \frac{\partial}{\partial y}\left[(D_a + D_a^T)\frac{\partial p_n}{\partial y}\right], \qquad \text{Eq. (3)}$$

at $x = 0$: $t_A = t_B^0$, $p_V = p_n^0$; at $y = b$: $\frac{\partial t_A}{\partial y} = 0$, $\frac{\partial p_n}{\partial y} = 0$.

– for main air flow "M" ($0 \le x \le H$, $-a \le y \le 0$, $0 \le z \le L$) temperature $t_M = t_M(x, y, z)$ is determined from equation:

$$W_M(y)\frac{\partial t_M}{\partial x} = \frac{\partial}{\partial y}\left[(a_a + a_a^T)\frac{\partial t_M}{\partial y}\right], \qquad \text{Eq. (4)}$$

at $z = 0$: $t_M = t_M^0$; at $y = -a$: $\frac{\partial t_M}{\partial y} = 0$

– the matching conditions: on the wall at $y = 0$, $q_0 = k_\alpha(t_A - t_w)$, where q_0 – heat flow, k – heat transfer coefficient through the wall with thickness of δ_w and thermal conductivity λ_w:

$$k = \frac{1}{\frac{1}{\alpha_M} + \frac{\delta_w}{\lambda_w} + \frac{1}{\alpha_A}}; \qquad \text{Eq. (5)}$$

At $y = h$ $p_M = p''$, $q = q_\alpha + q_\beta$ (on the interface). The following set of equations can be obtained by averaging the above equations:

$$\begin{cases} \frac{\partial t_w}{\partial x} = a_1(t_A - t_w) + b_1(p - p'') + c_1(t_M - t_w) \\ \frac{\partial t_A}{\partial x} = a_2(t_w - t_A), \quad \frac{\partial p}{\partial x} = b_2(p'' - p) \\ \frac{\partial t_M}{\partial z} = c_2(t_w - t_M) \end{cases} \qquad \text{Eq. (6)}$$

The boundary conditions: at $x = 0$ $t_w = t_w^0$, $t_A = t_A^0$, $p = p_0$; at $z = 0$ $t_M = t_M^0$. Coefficients a_1, b_1, c_1, a_2, b_2, c_2 can be determined from the relations:

$$a_1 = \frac{\alpha}{c_w g_w}, \quad b_1 = \frac{r_D \beta_p}{c_w g_w}, \quad c_1 = \frac{k}{c_w g_w}, \quad a_2 = \frac{\alpha}{c_a g_A}, \quad b_2 = 1.61\frac{p_b \beta_p}{g_A}, \quad c_2 = \frac{k}{c_a g_M}.$$

Linear theory of the evaporative coolers is considered; coefficients a_1, b_1, c_1, a_2, b_2, c_2 are constants; for the partial pressure of the saturated vapor p'' the nonlinear relation was used:

$$p''(t) = 690.5 \exp(0.0608\, t). \qquad \text{Eq. (7)}$$

Equation (6) can be presented as following:

$$\begin{cases} \frac{\partial t_w}{\partial x} + c_0 t_w = a_1 \theta_A + b_1(p - p'') + c_1 t_M, \quad c_0 = a_1 + c_1 \\ \frac{\partial t_A}{\partial x} + a_2 t_A = a_2 t_w, \quad \frac{\partial p}{\partial x} + b_2 p = b_2 p'', \quad \frac{\partial t_M}{\partial z} + c_2 t_M = c_2 t_w \end{cases} \qquad \text{Eq. (8)}$$

Here we consider the numerical solution of the problem; the explicit difference scheme (method of Euler) was used as an algorithm:

$$\begin{aligned} t_{wj}^{i+1} &= (1 - c_0 \Delta x) t_{wj}^{i} + \left[a_1 t_{Aj}^{i} + b_1(p_j^i - p_j''^i) + c_1 t_{Mj}^{i}\right]\Delta x \\ t_{Aj}^{i+1} &= (1 - a_2 \Delta x) t_{Aj}^{i} + a_2 t_{wj}^{i} \Delta x, \\ p_j^{i+1} &= (1 - b_2 \Delta x) p_j^i + b_2 \Delta x\ p_j''^i \\ t_{Mj+1}^{i} &= (1 - c_2 \Delta z) t_{Mj}^{i} + c_2 \Delta z\, t_{wj}^{i} \end{aligned} \qquad \text{Eq. (9),}$$

where *i*, *j* determine the corresponding anchor point on axes *x* and *z*, and *Δx* and *Δz* – are the steps of difference grid. According to the boundary conditions for the boundary anchor points the following relations can be obtained:

$$t_{wj}^{0} = t_{w}^{0}\ ,\ t_{Aj}^{0} = t_{A}^{0}\ ,\ p_{j}^{0} = p_{0}\ ,\ j = 1, 2, n,\ t_{M0}^{i} = t_{M}^{0}\ ,\ i = 1, 2, m \qquad \text{Eq. (10)}$$

The representative profile changes of the main parameters of main "M" (temperature of the chilled flow at constant humidity content) and auxiliary "A" (temperature and humidity content) air flows in IECg and IEC-Rg by length and by height of the considered module are presented in Fig. 3.

III. EXPERIMENTAL STUDY OF THE PROCESSES OF EVAPORATIVE COOLING IN LOW-TEMPERATURE EVAPORATIVE COOLERS

The test rig provides the possibility of study the working processes: in direct evaporative water chiller (CTW) and low temperature cooler-chiller Chw, as well as air cooler IECg. The air is taken from the environment by fan, then it undergoes thermal and humidity handling, and is transferred to the working chamber, where the evaporative cooler is located. Dimensions of the chamber were: 460×400×180mm, full air flow capacity was 3500 $m^3\,hour^{-1}$. The flowmeter was placed on the air line; flow rate regulators were located on the bypass line. The pump with adjustable capacity provides the circulation of water. The water flow rate was determined by set of flowmeters. The packing of the heat and mass transfer device was made as a film type counter flow apparatus; the main element of the packing was two-layer multichannel PC plate with channels of complex configuration. A thin film of liquid is flowing down through the channels of the packing elements interacting with air flow. The shape of the channels is formed by multiple decussation of thin-walled polymeric plates placed under various angles; this provides accumulation of liquid and its retention in packing (fluid retention). A high reliability and stiffness of the whole construction of the packing is realized as well. Such configuration of the channel improves uniform distribution of liquid along the whole surface of the packing, and it provides approximation of the wetted surface to the construction surface of the device packing. Water collector consists of five pockets. This provides the differential measurement of the liquid flow rate along the whole cross section of packing module. The test rig provides the possibility to study the designed evaporative coolers with packing made from polymeric materials with multichannel regular structure. Preliminary calculations (Doroshenko and Glauberman, 2012; Foster and Dijkastra, 1996; McNab and McGregor, 2003; Stoitchkov and Dimirov, 1998; Zhao et al., 2008; Gómez et al., 2005) showed that the polymeric materials can be used in the construction of evaporative coolers without substantial decrease in efficiency of the device, because the thermal resistance of the walls of the channel is comparable to the thermal resistance of the liquid film located on the outer surfaces. This is confirmed by the data of the Australian study (McNab and McGregor, 2003). During the experiments, the value of the equivalent diameter of working channels was 22mm; the working velocities of the air motion in the channels of the packing were changed in the range of w_a = 1.0 – 4.0 $m{\cdot}s^{-1}$; water concentration (water spray rate) of packing was 5 - 18 $m^3{\cdot}(m^2{\cdot}h)^{-1}$; humidity content was changed in the range from 8 to 18 $g{\cdot}kg^{-1}$. Measurement error of the main values, caused by the accuracy of measurements, was calculated during data processing for each experiment; for the heat balance the error was 12%; experimental material was characterized by the reliable reproducibility. The program of the research covered to study hydro-aerodynamics and heat and mass transfer for various regimen of the evaporative cooling of air and water. A water-air heat exchanger was included to the test rig to study the chiller-water coolers Chw; part of the chilled water from the evaporative water cooler was delivered to a water-air heat exchanger for preliminary cooling of air flow.

IV. ANALYSIS OF OBTAINED RESULTS

In this section the analysis of operation of evaporative air cooler IECg is performed for various ratios of main and auxiliary air flows of $l^* = G_M/G_A$: 1 – 1.5; 2 – 1.0; 3 – 0.5; the influence of the temperature and humidity content of air at the entrance of IECg was studied as well. For IECg, the

wet bulb temperature t_{wb}^1 of total air flow can be considered as the natural limitation for evaporative cooling of main and auxiliary air flow, increased by a certain value depending on the ratio of the air flows $l^* = G_M / G_A$; $t^0 = t_{wb}^1 + \Delta t^*$. This is connected with the process of heat transfer from the main flow to the auxiliary flow through the dividing wall and flowing down liquid film on surface of the "wet" channel, as well as with corresponding increase in temperature of the liquid recirculating through the "wet" part of the device (t_w^{rec}); this temperature remains constant.
Thermal efficiency of IECg according to main and auxiliary air flows can be determined from:

$$E_M = (t_M^1 - t_M^2)/(t_M^1 - t^0);\ E_A = (t_A^1 - t_A^2)/(t_A^1 - t^0) \qquad \text{Eq. (11)}$$

$$E_M = f\,(l^* = G_M/ G_A,\ t_P,\ t^0);\ E_A = f\,(l^* = G_M/ G_A,\ t_P,\ t^0) \qquad \text{Eq. (12)}$$

The following values of the thermal efficiency of the process for the real values of the cooling limitation t^0 were obtained: $l^* = G_M / G_A = 1.5$, $E_M = 0.45$; $l^* = G_M / G_A = 1.0$, $E_M = 0.65$; $l^* = G_M / G_A = 0.5$, $E_M = 0.89$. The increasing in the portion of the auxiliary flow consistently increases the cooling level of the main flow; at the same time the specific energy consumption for the unit of "product" is increased. A comparison between operation of IEC of air and IEC-Rg was made. The analysis was carried out for the following condition: $l^* = G_M / G_A = 1.0$ or both schemes of IEC. The decreasing in temperature of the main air flow from $t_M = 26.5^0$C for IEC ($t_A = 25.5^0$C; $\varphi_A = 95\%$) to $t_M = 21.0^0$C for IEC-R (parameters of auxiliary air flow $t_A = 27.0^0$C, $\varphi_A = 100\%$). Attention should be paid to the parameters of the auxiliary air flow at the exit of the IEC-Rg. Unlike the processes in IECg, the changing in the condition of auxiliary air flow in IEC-Rg takes place along the line of $\varphi_A = 100\%$; this can result in decreasing of the efficiency of cooling. This circumstance is very important for the development of the evaporative cooling technique, but usually it is not considered in publications of recent years (Maisotsenko and Gillan, 2003; Pandelidis et al., 2015; USA Patent 2009/0007583; USA Patent 6,494,107); this can result in distortion of the obtained results. The correct selection of the correlation of $l^* = G_M / G_A$ influences the nature of the process in IEC-Ra. The ratio of auxiliary air flow and flow of recirculating water also plays an important role.
The comparative analysis of the operation of IEC and Chg (scheme is according to Fig. 1B) is presented in Fig. 4A. The analysis was carried out for the condition of $l^* = G_M / G_A = 1.0$ for both solutions. The conditional step analysis for Chg is presented: 1-2-3..., dash-and-dot line (1-3*, 1-3**, 1-3ch A, processes in evaporative cooler for auxiliary air flow); corresponding processes in heat exchanger (processes of cooling of main air flow "M" at constant humidity content) are presented by lines 1-2*, 1-2**, 1-2ch M. The changing in water temperature in the recirculating loop (t_w^2) are shown on the equilibrium curve; for each step they match the corresponding value of wet bulb temperature of auxiliary air flow entering the evaporative cooler which was previously cooled in a heat exchanger. The resulting process of main air flow cooling is shown by solid line 1-2ch M.
The following data was obtained (for initial conditions: $t_a^1 = 35^0$C, $x_a^1 = 11$g/kg, $t_{dp}^1 = 14^0$C):

IEC: $\underline{t_M = 26.5^0\text{C}}$, $t_A = 25.5^0$C; $\varphi_A = 95\%$;

Chg: $\underline{t_M = 19.5^0\text{C}}$, $t_A = 27.5^0$C, $\varphi_A = 100\%$.

Comparative capabilities of evaporative water chillers, CTWs, and Chw were studied (Fig. 4B). The background for comparative analysis was the experimental data. Packing multichannel polymeric structures were used as heat and mass transfer apparatus: CTWs and chillers. The flow ratios in the main cooling loops in water-water and water-air heat exchangers was $l^{**} = G^1_w / G^2_w$ at $l = G_a / G_{w\Sigma} = 1.0$ for all analyzed variants of operation of Chw (where $G_{w\Sigma} = G^1_w + G^2_w$). Processes in a cooling tower: 1-3 - for air, 5-6 - for cooling water. Processes in a Chw: 1-2-4 - for air, 7-8 - for cooling water. It can be seen that the degree of approximation to the cooling limitation (dew point temperature t_{dp}^1) is 9.5 *и* 6.0^{0}C for compared cases, respectively. The analysis was carried out for Chw for different ratios of water in main cooling loops at $l^{**} = G^1_w / G^2_w$. For initial conditions of $t_a^1 = 35^0$C, $x_a^1 = 11$g·kg^{-1}, $t_{dp}^1 = 14^0$C, the following data was obtained:

1. $l^{**} = G^1_w / G^2_w = 1.5$: $t_w^2 = 22.3^0$C; $\Delta t^{**} = 8.3\ ^0$C;
2. $l^{**} = G^1_w / G^2_w = 1.0$: $t_w^2 = 20.0^0$C, $\Delta t^{**} = 6.0\ ^0$C;
3. $l^{**} = G^1_w / G^2_w = 0.5$: $t_w^2 = 18.5^0$C, $\Delta t^{**} = 4.5\ ^0$C.

It can be seen clearly that the increase in cold water portion entering the heat exchanger of preliminary cooling of air (G^1_w) leads to decreasing in chilled water temperature t_w^2: the value of $\Delta t^{**} = (t^2_w - t_{dp}^1)$ is 4.5^{0}C for $l^{**} = 0.5$.

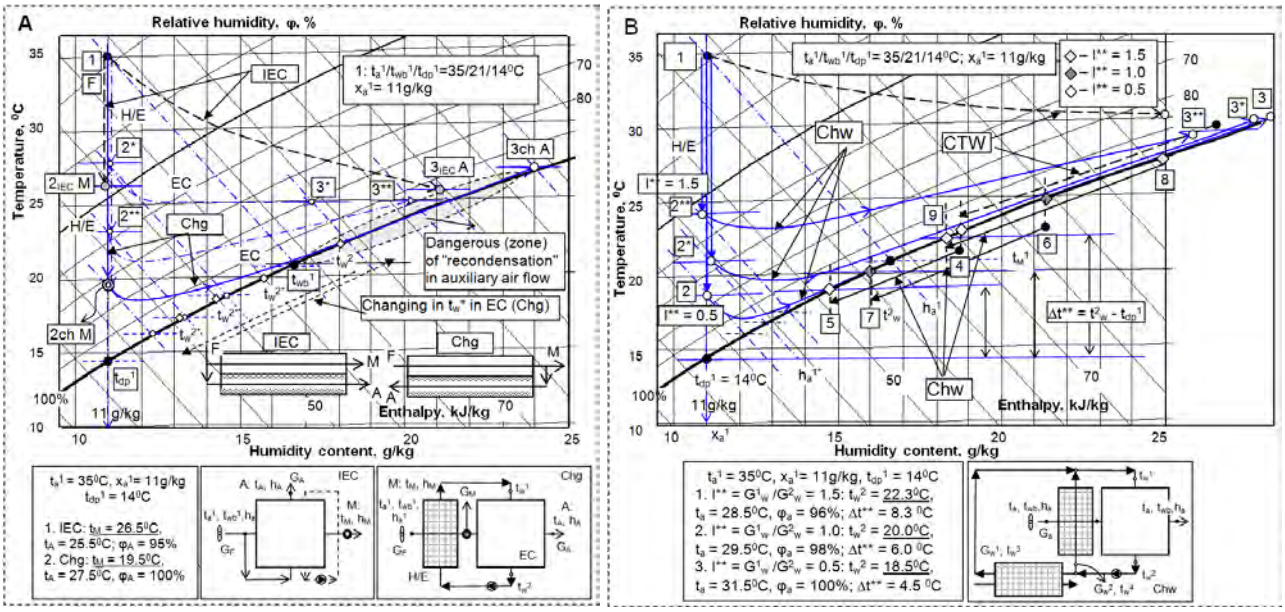

Figure 4: A - operation of indirect evaporative air cooler (IECg (dotted line) and low temperature air cooler Chg (dash-dotted line)); B - operation of water chiller Chw depending on water flow rate ratios in main cooling loops

The limit of cooling is related to the ratio of flow rates in evaporative cooler (CTW), and for the highest values of $I = G_a/G_w$ it almost equals the natural limit (in this case this is the value of t_{wb}^1); for Chw with maximal value of $I^{**} = G^1_w/G^2_w = 0.5$ the line representing the changing conditions of the air flow in evaporative cooler almost coincides with the line of $\varphi = 100\%$.

CONCLUSIONS

1. Compared to indirect evaporative cooling in IECg, the cooling of air flow in a chiller air cooler Chg decreases the cooling limit of the main air flow lower than the wet bulb temperature of the ambient air; this increases the capabilities of the evaporative methods of cooling.

2. Compared to CTW, the cooling in water chiller Chw can provide a considerable decrease in temperature of cooling; the limitation of cooling in this case will be the dew point temperature of the ambient air; this expands substantially the boundaries of the practical application of such coolers; the further approximation to the limitation of cooling in Chw provides the variation of the ratio of the liquid flows in main cooling loops $I^{**} = G^1_w/G^2_w$, and it can be decreased at the increase in $I = G_a/G^{\Sigma}_w$.

3. A transition to the "deep cooling" of water in Chw compared to CTW, will result in the increase in specific energy consumption; from this point of view, the study of optimal operation conditions of such water cooler is the most interesting, particularly, the study of the influence of contacting flow rate ratios of air and water $I = G_a/G_w$ on the efficiency of the process, as well as the influence of the value of $I^{**} = G^1_w/G^2_w$, flow rates of water in the main cooling loops of the chiller Chw.

ACKNOWLEDGEMENTS

The paper was financially supported in part by the Natural Science Foundation of China (Projects No. 51776187), Zhejiang Province Natural Science Foundation of China (Project No. LY16E060004), and by Ningbo Science and Technology Bureau from the International Cooperation Project No. 2017D10006.

NOMENCLATURE

δ	thickness (m)	*Chw*	chiller of liquids
Chg	chiller of gases	*CTW*	cooling tower

DEC	direct evaporative cooler	λ	thermal conductivity (W m^{-1})
E	thermal efficiency	*p*	pressure (Pa)
G	flow rate (kg m^{-3})	*PC*	polycarbonate
H	thickness of the liquid layer (m)	*Q*	heat flux (W)
IEC	indirect evaporative cooler	*q*	specific heat flow (W m^{-2})
h	specific enthalpy (kJ kg^{-1})	*x*	humidity content (g kg^{-1})
k	heat transfer coefficient (W×(m×°C)$^{-1}$)	*t*	temperature (°C)
L	length (m)	*φ*	relative humidity (%)
l	flow rate ratio	*w*	velocity (m s^{-1})

REFERENCES

Chen, G.M., Shestopalov, K., Doroshenko, A., Koltun, P., 2015 Polymeric materials for solar energy utilization: a comparative experimental study and environmental aspects, Polymer-Plastics Technology and Engineering 54, 796-805.

Chen, G.M., Doroshenko, A., Shestopalov, K., 2018. Solar absorption systems with heat and mass transfer apparatus with fluidized bed packing, Analysis and perspectives. Proceedings of the 6th International Conference on Cryogenics and Refrigeration, Shanghai, China, 413.

Doroshenko, A.V., Glauberman, M.A., 2012. Alternative energy. Refrigerating and Heating Systems, Odessa I.I. Mechnicow National University Press, 430p.

Foster, R.E., Dijkastra, E., 1996. Evaporative air-conditioning fundamentals: environmental and economic benefits worldwide. Proceedings of the IIR Conference on Applications for Natural Refrigerants, Aarhus, Denmark, IIF/IIR, 101-109.

Gomes, E.V., Martinez, F.J., Diez, F.V., Leyva, M.J., Martin, R.H., 2005. Description and experimental results of a semi-indirect ceramic evaporative cooler. Int. J. Refrigeration 28, 654-662.

Koltun, P., Ramakrishnan, S., Doroshenko, A., Kontsov, M., 2003. Life Cycle Assessment of a Conventional and Alternantive Air-Conditioning Systems. Proceedings of the 21^{h} International Congress of Refrigeration IIR/IIF, Washington, D.C, 45-57.

John, L., McNab, Paul, McGregor, 2003. Dual indirect cycle air-conditioner uses heat concentrated desiccant and energy recovery in a polymer plate heat exchanger. Proceedings of the 21 International Congress of Refrigeration, IIR/IIF, Washington.

Maisotsenko, V., Lelland, Gillan, M., 2003, The Maisotsenko Cycle for Air Desiccant Cooling. Proceedings of the 21st Int. Congress of Refrigeration, Washington, D.C.

Martínez, F.J., Gómez, E.V., García, C.M., Requena, J.F., Gracia, L.M., Navarro, S.H, Guimaraes, A.C., Gil, J.M., 2011. Life cycle assessment of a semi-indirect ceramic evaporative cooler vs a heat pump in two climate areas of Spain. Applied Energy 88, 914-921.

Pandelidis, D., Anisimov, S., William M. Worec, 2015. Performance study of the Maisotsenko Cycle heat exchangers in different air-conditioning applications. Int. J. of Heat and Mass Transfer 81, 207-221

Patent USA (Pub. No.: US 2009/0007583 A1, Pub. Date: Jan. 8, 2009). Indirect Evaporative Cooling Device.

Patent USA (Pub. No.: US 6,494,107 B2, Date: Dec. 24, 2002). Maisotsenko et al. Method and Apparatus of Indirect Evaporative Cooling.

Stoitchkov, N.J., Dimirov, G.J., 1998. Effectiveness of crossflow plate heat exchanger for indirect evaporative cooling. Int. J. Refrigeration 21(6), 463-471.

Zhao, X., Liu, S., Riffat, S.B., 2008. Comparative study of heat and mass exchanging materials for indirect evaporative cooling systems. Proceedings of the 43th Int. Conf. Building and Environment, 1902–1911.

Manuscript ID: 621
DOI: 10.18462/iir.icr.2019.0621

Energy and exergy analysis of flat plate solar air heater with micro-heat pipes arrays (MHPA)

Tingting ZHU[(a)] *, Yaohua ZHAO[(b)], Yanhua DIAO[(b)]

[(a)]Tianjin Key Lab of Refrigeration Technology, Tianjin University of Commerce, Tianjin, 300134, China, zhutingting@tjcu.edu.cn

[(b)]Beijing Key Laboratory of Green Built Environment and Efficient Technology, Beijing University of Technology, Beijing, 100124, China, diaoyanhua@bjcu.edu.cn

ABSTRACT

Solar energy is a clean and renewable energy resource, which can be used freely and safety. For the purpose of rural heating energy in the northeast of China, a novel solar air collector heating system based on micro-heat pipe arrays (MHPA) has been proposed.

In this paper, different working modes and the corresponding thermal performance of the novel solar air collector is investigated by experimental and energy analysis methods. The flat plate solar air heater is mainly composed of a set of 15 heat transfer components. The MHPA is a flat aluminum plate with several independent micro-heat pipes. Each heat transfer component contains an MHPAs unit whose condenser is attached to aluminum fins placed in the air duct, and the evaporator of MHPA is coated with absorber black film. The air flows inside the air duct and there occurred heat exchange between air and fins inside of the air duct. A detailed parametric study is conducted to examine the effects of various operation parameters on energy and exergy efficiencies. Results indicated that the energy efficiency of the collector is approximately 62% and corresponding exergy efficiency is about 1.014% with the air flow rate of 0.08 kg/s. As an energy saving and emission reduction product, MHPA-FPSAH provide a new approach.

Keywords: Micro-heat pipe arrays, Solar air heater, Performance, Efficiency, Exergy

1. INTRODUCTION

Solar energy is a clean and renewable energy resource, which can be used freely and safety. For the purpose of maximum utilization of solar energy, numerous devices have been developed. But, from the structure of rural heating energy in a certain area in the northeast of China (Fig. 1), solar energy utilization is so small. Solar air heaters as one type of solar energy thermal utilization devices have been widely concerned for the merits of simple structure, low cost, durability and reliability. Conventional solar air heaters are mainly the type of flat-plate solar air heaters (SAHs). The main drawback of an air heater is that the heat transfer coefficient between the absorber plate and the airstream is low and heat losses to environment is high, which results in a lower thermal efficiency (Mohamad, 1997). Therefore, several researchers have been conducted to improve the performance of solar air heaters, experimentally and theoretically. Some ways such as application of internal fins

attached to the absorber plate, roughness elements in the air duct and the changing recycling form of air (Fakoor Pakdaman et al., 2011, Ebrahim Momin et al.2002, Tanda, 2011, Hans et al., 2010, Zhu et al., 2017, Li rt al., 2018, Priyam and Chand, 2018, Abuşka and Şevik, 2017. Nemś, M. et al. 2018).

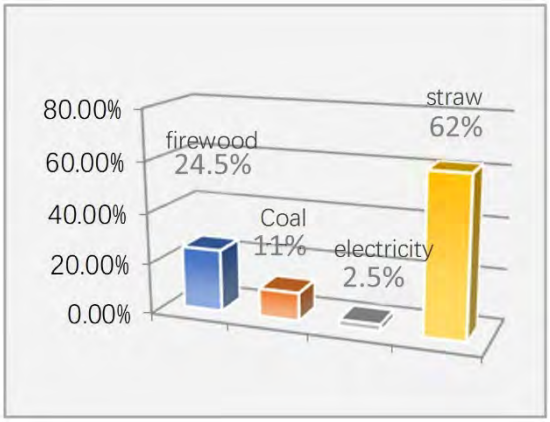

Figure 1: Diagram of rural heating energy structure in the northeast of China

Longitudinal fins can be attached to an absorber plate of a natural-convection solar air heater to enhance heat transfer effectively (Fakoor Pakdaman et al., 2011). In this manner, almost 66% increase in heat transfer area and 20% enhancement in heat transfer may be achieved in the investigation. Momin et al. (2002) explored the effects of the geometrical parameters of V-shaped ribs on heat transfer and fluid flow characteristics of rectangular duct of solar air heater with absorber plate having V-shaped ribs on its underside. The results revealed that effect of Reynolds number on Nusselt number and friction factor is stronger than that of the angle of attack. Tanda (2011) proposed different performance evaluation criteria to assess the heat transfer and friction characteristics of collectors with various rib configurations. Results show that repeated ribs is a good technique to improve the performance of a solar air heater. Hans et al. (2010) investigated the effects of the roughness of multiple V-shaped ribs on heat transfer coefficient and friction factor in an artificially roughened solar air heater duct. Momin et al. (2002) also explored the effects of the geometrical parameters of V-shaped ribs on heat transfer and fluid flow characteristics of rectangular duct of solar air heater with absorber plate having V-shaped ribs on its underside. The results revealed that effect of Reynolds number on Nusselt number and friction factor is stronger than that of the angle of attack.

In this paper, the detailed thermal behavior of the MHPA-based flat plate SAH, which was firstly proposed in Ref. (Zhu et al. 2017), and some basic conclusions were drawn. This paper constitutes an important contribution to the study and evaluation of the type of solar air heaters. Another important contribution is the expressions of the exergy efficiency which can be used as the useful tools for the optimization design of the type of heaters as well as for the performances improvement with different operating parameters. The objective of the current investigation is to make performance comparisons between the measured and calculated values under different working conditions. The experimental setup is installed at Beijing, China (39.9° (latitude) North and 116. 3° (longitude) East).

2. SOLAR AIR HEATER BASED ON MICRO-HEAT PIPE ARRAYS

The structure of FPSAH with MHPA studied in this paper is shown in Fig. 2. It is made up of by 15 collecting core units, an air duct and a fan. Each core unit consists of aluminum fin, MHPA and an absorber plate. The heater has an area of 1.8 m^2 and a flat plate absorber fabricated from a high efficient absorption black film galvanized iron sheet of thickness 1.5 mm. A glass cover (3.5 mm thick) with distance separation of 35mm from the absorber is used as the cover of the new air heater. The bottom of the heater is insulated by 25 mm layer of glass wool fixed with rubber sheet. In addition, the sides of the heater are insulated by rubber and plastic material.

For normal flat-plate SAHs, when strengthen the heat transfer between the heat-collecting surface and airflow, the heat loss of SAHs increased simultaneously. Thus, heat insulation and heat transfer cannot be simultaneously enhanced. However, the new MHPA-based flat-plate SAH separates the heat exchange of airflow from heat collection part, which can achieve effective heat transfer just in the air duct with fins shown as Fig.2. The air to be heated flows by the fins fixed on the condenser section of MHPA, where it gains thermal energy from the evaporator section connected with the absorber plate. The condenser section with fin makes heat exchange with air flow in the air duct. And working principle of the collecting core unit is showed in Fig. 2. MHPA working process is shown in Fig.3.

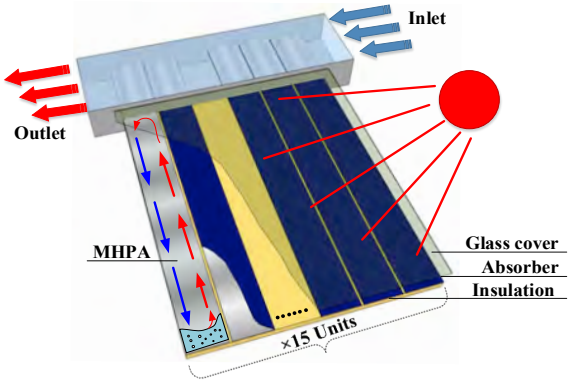

Figure 2: Flat plate solar air heater based on micro-heat pipe arrays (MHPA)

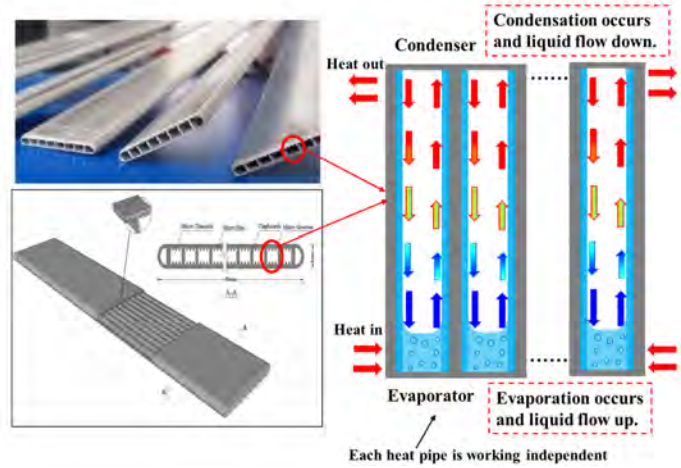

Figure 3: Micro-heat pipe arrays

2.1. Testing system

The experimental platform was constructed in Beijing University of Technology; the area surrounding the experimental platform is open and unsheltered. The experimental test system includes a new solar air heater, an axial flow fan, and other test instruments, including a weather station (total radiation meter, temperature and humidity sensor, and wind vane), thermal resistors, thermocouples, an Agilent data acquisition instrument, and a computer. Inlet and outlet air temperatures were measured with four well-insulated thermal resistors installed evenly on the cross section of the dust inlet and outlet at corresponding positions along the direction of air flow.

2.2 Data reduction

The instantaneous thermal efficiency of the solar air heater was calculated from the experimental data for each flow rate from daytime measurements using the equations below,

$$S = I\tau\alpha \cdot A \quad \text{Eq. (1)}$$

$$Q_u = c_p m\left(t_o - t_i\right) \quad \text{Eq. (2)}$$

$$\eta_{th} = \frac{Q_u}{S} \quad \text{Eq. (3)}$$

The exergy can be calculated as,

$$\Delta \mathrm{E} = \mathrm{m}\left[\left(h_o - h_i\right) - T_{\mathrm{a}}\left(s_o - s_i\right)\right] \quad \text{Eq. (4)}$$

$$\Delta \mathrm{E} = \mathrm{m}\mathrm{C}_{\mathrm{p}}\left[\left(T_o - T_i\right) - T_{\mathrm{a}}\mathrm{In}\frac{T_o}{T_i}\right] \quad \text{Eq. (5)}$$

Exergy efficiency of the heater can be express as:

$$\eta_{\mathrm{ex}} = \frac{\Delta E}{A_c I} = \frac{\Delta E}{C_{\mathrm{p}}\mathrm{m}\left(T_o - T_i\right)} \cdot \frac{C_{\mathrm{p}}\mathrm{m}\left(T_o - T_i\right)}{A_c I} \quad \text{Eq. (6)}$$

Where, m-mass flow rate of air, kg/s; A_c-total net heater area, m^2 ; T_o-outlet temperature, °C; T_i -inlet temperature, °C; c_p-specific heat of air, kJ/(kg· K); I-solar radiation, W/m^2; Q- volume flow rate, m^3/h; T_a- ambient temperature, °C; ΔT-temperature difference, °C; ΔP- pressure drop, Pa; ΔI- solar radiation difference, W/m^2; Qu - useful energy gain, W/m^2; ΔE- Exergy difference; h- enthalpy, kJ/kg; S- entropy, kJ/kg·K; η_{th}- thermal efficiency; η_{ex}- exergy efficiency.

2.3 Uncertainty analysis

The data recording type and accuracy based on the precision of the equipment used during experimentation are summarized in Table 1. The relative uncertainty of η can be determined by using the equation (7), Therefore, the uncertainty value in this study is about 7.2%.

$$\Delta\eta = \left[\left(\frac{\partial\eta}{\partial\dot{Q}}\Delta\dot{Q}\right)^2 + \left(\frac{\partial\eta}{\partial T_o}\Delta T_o\right)^2 + \left(\frac{\partial\eta}{\partial T_i}\Delta T_i\right)^2 + \left(\frac{\partial\eta}{\partial I}\Delta I\right)^2\right]^{1/2} \quad \text{Eq. (7)}$$

Table 1. Information and uncertainties about the test instruments

Device name	Global pyranometer	Thermocouple	Thermoresistance	Air volume cover
Model	TRT-2	WRNK-191	Pt100WZPK-293	TSI8371
Accuracy	<2%	I	A, 0.15 °C	±5%

3. RESULTS AND DISCUSSIONS

3.1. Energy efficiency

Fig.4 shows thermal efficiency variation with solar radiation with the mass flow rate of 0.08kg/s. The experimental tests were carried out on 15th, Dec. 2015. During the period of time (time: 9:15-15:15), solar radiation is ranged from 468 W/m^2 to 822 W/m^2, and the energy efficiency ranged from 40~80%, the average value is 62% with the air flow rate of 0.08kg/s. It can be found that thermal efficiency gradually increased as the solar radiation intensity increased. The solar radiation peak was observed at 12:35, and the thermal efficiency reached its peak at 13:05 during stable stage. The solar radiation fluctuated and decreased after 12:35, which caused the fluctuation of the efficiency. These findings can be attributed to the thermal inertia of the solar collector.

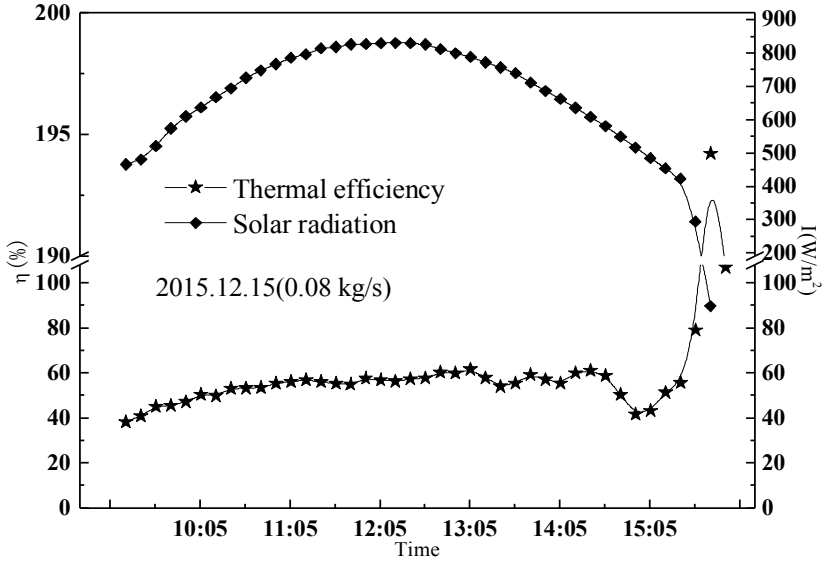

Figure 4: Thermal efficiency variations of MHPA SAH (0.08kg/s)

Fig.5 shows thermal efficiency variation with solar radiation with the mass flow rate of 0.053kg/s. The experimental tests were carried out on 3th, Dec. 2015. Fig.5 shows the average value is 59.2% with the air flow rate of 0.053kg/s. The solar radiation during the test (9:15–15:55) was between 49 and 729 W/m^2, the solar radiation peak was observed at 11:55, and there occur sudden increase in thermal efficiency after 15:25 which is caused by the sudden decrease of solar radiation as well as the heat transfer delay in the solar air collector. The thermal efficiency curve shows a gradual and slow climbing trend, totally. By comparing Fig. 4 and Fig. 5, it can be found that under these two flow

conditions, the heat transfer with a large flow rate is more enhanced, so the efficiency is higher than the lower flow rate working condition.

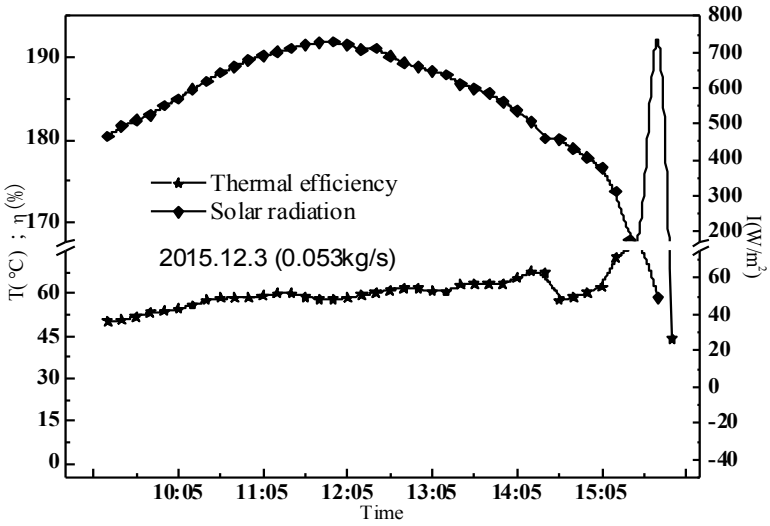

Figure 5: Thermal efficiency variations of MHPA SAH(0.053kg/s)

3.2. Exergy efficiency

For use of solar thermal energy, actually available energy is not the total heat energy collected by the collector, but is part of the total heat energy. Exergy is a physical quantity, which can evaluate power capability of the fluid medium (air) on the basis of the ambient temperature. Exergy efficiency of the collector can not only reflect the external exergy loss but also can reflect the various kinds of exergy loss caused by irreversible factors.

Fig.6 and Fig.7 shows exergy efficiency variation with solar radiation. Exergy efficiency ranged from 0.138%~1.542%, the average value is 1.014% with the air flow rate of 0.08kg/s. And the average value is 0.910% with the air flow rate of 0.053kg/s. The exergy efficiency of SAC was 0.341% at 9:15 and reached its first peak of 1.541% at 12:45. The average exergy efficiency during the testing period is 1.014% approximately. There are fluctuations of the exergy efficiency curve after 12:45, which is affect by the decrease of solar radiation and the fluctuations of the ambient temperature.

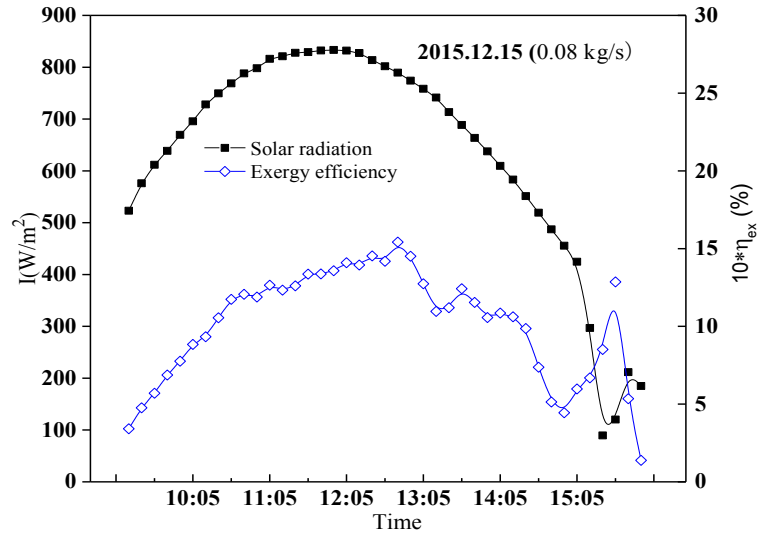

Figure 6: Exergy efficiency variations of MHPA SAH (0.08 kg/s).

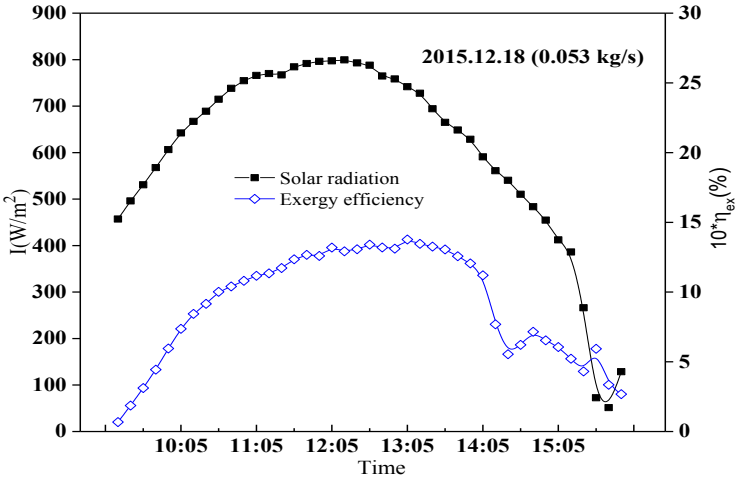

Figure 7: Exergy efficiency variations of MHPA SAH (0.053 kg/s).

The curve of the efficiency results shows that thermal efficiency and exergy efficiency of the heater increases with the increase of solar radiation and air flow rate. And with the quality concern the value of exergy efficiency is very small. It can be found that exergy efficiency was always lower than the energy efficiency throughout the operation process. It was caused by the exergy losses dissipated to the surrounding and exergy destruction within the process. And exergy accounts for the quality of energy which cannot be conserved during the heat exchange process. Potential for improvement of the performance of FPSAH with MHPA is exist. Generally, increasing the flow rate is an effective way to improve the thermal performance of a solar air collector, but it can result a high input of fan power. The variation of exergy efficiency η_{ex}, remind us it isn't an effective method always, it is based on the quality of the energy gained and the power input.

4. CONCLUSION

In this paper, the energy and exergy performance of FPSAH with MHPA is presented. The heat collecting component is the micro-heat pipe arrays (MHPA). The test data were analyzed from the aspects of energy thermal performance and exergy performance. The average thermal efficiency is 62% and exergy efficiency is 1.014% for the FPSAH with MHPA. Test results can also serve as an important basis for understanding the performance of the FPSAH with MHPA. Exergy efficiency can be used as one of the main criterion to evaluate the performance of MHPA-FPSAH.

ACKNOWLEDGEMENT

The authors gratefully acknowledge the financial support provided by the Scientific Research Project of Beijing Educational Committee (Grant No. 004000546315527), Scientific Research Project of Beijing Advanced Innovation Center for Future Internet Technology and Research Project of Tianjin University of Commerce (Grant No. 2017ZT010327-60104).

NOMENCLATURE

A_c	area of the absorber (m^2)	η	efficiency
c_p	specific heat at constant pressure, kJ/(kg·K)	α	absorptivity of the absorber plate
I	total radiation on tilted surface, W/m^2	τ	transmittance of glass cover
l	length of the air duct, m	ρ	density of air, kg/m^3
MHPA	micro-heat pipe arrays	η	efficiency
$\dot{m}$	air mass flow rate, kg/s	Subscript	
p	pressure, Pa	*a*	ambient
SAH	solar air heater	i	inlet
T:	temperature, °C	O	outlet
v	air velocity, m/s	th	thermal
V	volume, m^3	ex	exergy

REFERENCES

Mohamad, A. A., 1997. High efficiency solar air heater. Solar Energy 60(2), 71-76.

Fakoor Pakdaman, M., Lashkari A., Basirat Tabrizi H., Hosseini R., 2011. Performance evaluation of a natural-convection solar air-heater with a rectangular-finned absorber plate. Energy Conversion and Management 52,1215-1225.

Ebrahim Momin, A.-M., Saini, J.S., Solanki, S.C., 2002. Heat transfer and friction in solar air heater duct with V-shaped rib roughness on absorber plate. Heat and Mass Transfer 45(16) ,3383-3396.

anda, G.,2011. Performance of solar air heater ducts with different types of ribs on the absorber plate. Energy 36, 6651-6660.

Hans, V.S., Saini, R.P., Saini, J.S., 2010. Heat transfer and friction factor correlations for a solar air heater duct roughened artificially with multiple v-ribs. Solar Energy 84, 898–911.

Zhu, T.T., Diao, Y.H., Zhao, Y.H., Ma, C., 2017. Performance evaluation of a novel flat-plate solar air collector with micro-heat pipe arrays (MHPA). Applied Thermal Engineering118,1-16.

Li,X.L., Qin,H., Zhang, Y., Yao, W.X., Li,Y., Liu,H.M., 2018. Dust effect on the optical-thermal properties of absorber plate in a transpired solar air collector. Energy Conversion and Management 169,13–21.

Priyam, A., Chand, P., 2018. Effect of wavelength and amplitude on the performance of wavy finned absorber solar air heater. Renewable Energy 119, 690-702.

Abuşka,M., Şevik, S., 2017. Energy, exergy, economic and environmental (4E) analyses of flat-plate and V-groove solar air collectors based on aluminum and copper. Solar Energy 158, 259–277

Nemś, M., Kasperski, J., Nemś, A., Bać,A., 2018. Validation of a new concept of a solar air heating system with a long-term granite storage bed for a single-family house. Applied Energy 215,384–395.

Manuscript ID: 622
DOI: 10.18462/iir.icr.2019.0622

Heat transfer analysis of double U-tube ground heat exchanger of closed loop ground source heat pump system during space cooling application for Indian climatic conditions

Satish KUMAR[(a)], Jivlal PANDIT[(b)] and Krishnan MURUGESAN[(a*)]

[(a)] Department of Mechanical & Industrial Engineering, Indian Institute of Technology Roorkee, Roorkee – 247 667, INDIA

[(b)] Mangalore Refienery and Petrochemicals Limited, Mangalore, INDIA

ABSTRACT

Use of ground source heat pump system (GSHP) for spce cooling application results in significant reduction in electricity consumption as the temperature of heat rejection (ground) is lower than the ambient.The main focus of the present research is to investigate the heat transfer and temperature variation of heat transfer fluid in a double U-tube ground heat exchanger (GHE) of a 5-ton GSHP system installed in IIT Roorkee, Roorkee in the northern region of India. Thermal properties of the ground formation were obtained using thermal response test (TRT). An analytical model has been developed using thermal resistance concept for the computation of temperature and heat transer variation along the four legs of the GHE during space cooling operation. Results indicate 77% of heat is exchanged in the first U-tube and 23% in the second U-tube. Results are reported by assuming constant borehole temperature of 26°C. Comparison between theoretical prediction and experimental results obtained for heat transfer through GHX indicates that the theoretical model could predict the heat transfer rate through the GHX with 2 to 27% error depending on the inlet temperature of heat transfer fluid in the borehole.
Keywords: ground heat exchanger, heat transfer, temperature variation, ground source heat pump system, thermal response test, U-tube heat exchanger.

1. INTRODUCTION

Ground source heat pump system (GSHP) has played a vital role in the reduction of energy consumption in the Indian climatic conditions Sivasakthivel et al. (2015). GSHP is a renewable type of system that makes use of ground as a source/sink for exchanging heat. Due to a constant ground temperature throughout the year, the coefficient of performance of the system is high in cooling as well as in heating mode of operation. Therefore, use of the low temperature sink of the ground using GSHP results in less fossil fuel consumption and greenhouse gas emission to the environment as compared to the conventional air conditioning system Mustafa Omer (2008). For the analysis of GSHP, it is necessary to select the best possible configuration of pipe connection according to geographical location. Zeng et al.(2003) proposed an analytical model (quasi-3D model) for all possible configurations of vertical GHX. Based on borehole thermal resistance, they observed that the parallel configuration provides better performance as compared to series configuration because, in all possible configurations, parallel arrangement (1-3, 2-4) or (1-2, 4-3) yielded the lowest thermal resistance. In series category, arrangement (1-2-4-3) shows the lowest borehole thermal resistance and single U-tube the highest. Chang et al.(2016) evaluated the

thermal performance of vertical U-loop ground heat exchangers. It was suggested that increasing tube surface area or number of tubes, increases the efficiency and operating time of GSHP because increasing surface area of tube results in decrease in the mean temperature of the coolant. Zhai et al. (2017) carried out experimental analysis for different depths of GHX and found that the coefficient of performance for heating mode was lower than that of cooling mode. Zeng et al. (2018) evaluated the performance of GSHP in continuous and intermittent mode of operation and observed that heat accumulation in heating mode was more than heat accumulated in cooling mode of operation in ground near the GHX.This resulted in better coefficient of performance in cooling mode as compared to heating mode of operation.

The present research work is focused on the temperature response of the ground (TRT), temperature and heat transfer analysis by performing experiments on the GHX of a closed loop GSHP system. The main contribution of this paper is to analyze the Indian soil terrain condition, heat transfer capacity using double U-tube series connected, GSHP system. To analyze, the same, few experiments were carried out on a 5-ton capacity GSHP system connected with six boreholes. Reports are reported on heat transfer analysis using mathematical model as well as experimental work for cooling mode operation.

2. SYSTEM DESCRIPTION

In Indian climatic condition, due to extreme weather condition, the cooling mode duration is more than the heating mode. In the present work, the analysis of heat transfer into the ground (cooling mode) of a GSHP system of 5 TR capacity that is established at IIT Roorkee, Roorkee in northern part of India is discussed. The proposed model consists of 5 double U-tube series connected ground heat exchanger (GHX) that interact with the ground during cooling mode operation. The double U-tube is buried into ground at a depth of 120 m and a single U-tube GHX has been established to analyze the ground properties through thermal response test (TRT). Based on the heat exchanging capacity of soil terrain, the depth of each borehole has been taken as 120 m for each ton of refrigeration capacity. The geometrical properties of tube and borehole are given in Table 1.The proposed GSHP model includes heat pump, water pump, borehole heat exchanger as shown in Fig.1.Data are recorded during peak summer condition for two hours of continuous operation.

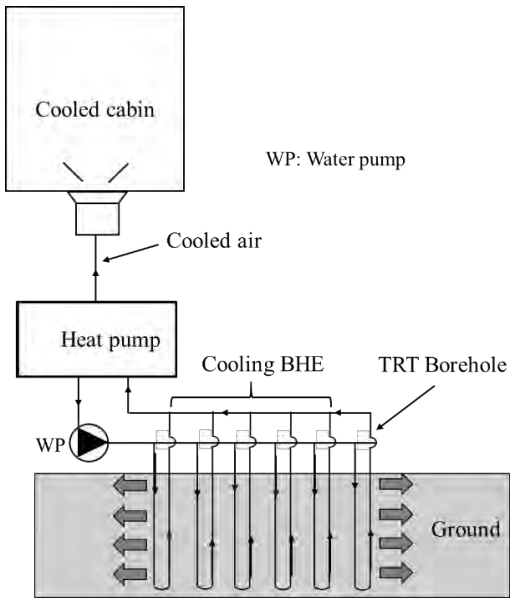

Figure 1: Proposed GSHP model

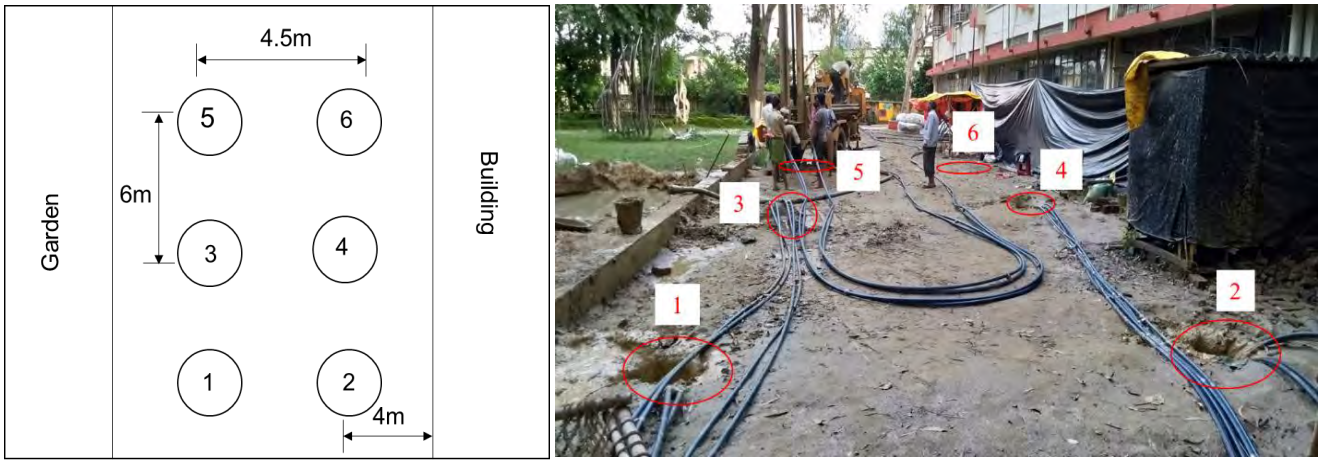

(a) (b)

Figure 2: (a) Proposed boreholes location (b) Installed boreholes

3. MATHEMATICAL MODELING

Figures 2(a) and (b) show the orientation of 5 double U-tube GHX and one single U-tube GHX for the TRT and the corresponding photograph during drilling of these boreholes at IIT Roorkee. The heat flow per unit length of all the legs of the tube can be obtained by applying energy balance principle across the tube and borehole wall. Therefore based on the methodology proposed by Hellström (1991) the heat transfer in each leg can be written as

$$T_{f1} - T_b = R_{11} q_1 + R_{12} q_2 + R_{13} q_3 + R_{14} q_4$$

$$T_{f2} - T_b = R_{21} q_1 + R_{22} q_2 + R_{23} q_3 + R_{24} q_4$$

$$T_{f3} - T_b = R_{31} q_1 + R_{32} q_2 + R_{33} q_3 + R_{34} q_4$$

$$T_{f4} - T_b = R_{41} q_1 + R_{42} q_2 + R_{43} q_3 + R_{44} q_4 \qquad \text{Eq. (1)}$$

Rearranging Eq.(1) leads to a quasi-3D model by assuming heat flow in axial direction also which is more practical approach of analyzing GHXs.

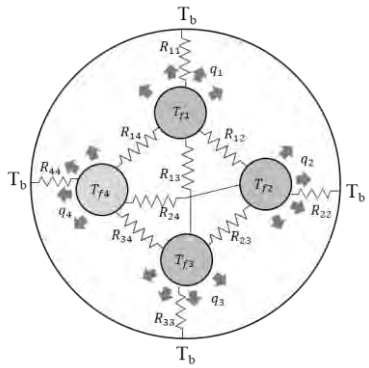

Figure 2: (c) Borehole placing

$$q_1 = \frac{T_{f1}-T_b}{R_1^{\Delta}} + \frac{T_{f1}-T_{f2}}{R_{12}^{\Delta}} + \frac{T_{f1}-T_{f3}}{R_{13}^{\Delta}} + \frac{T_{f1}-T_{f4}}{R_{12}^{\Delta}}$$

$$q_2 = \frac{T_{f2}-T_{f1}}{R_{12}^{\Delta}} + \frac{T_{f2}-T_b}{R_1^{\Delta}} + \frac{T_{f2}-T_{f3}}{R_{12}^{\Delta}} + \frac{T_{f2}-T_{f4}}{R_{14}^{\Delta}}$$

$$q_3 = \frac{T_{f3}-T_{f1}}{R_{13}^{\Delta}} + \frac{T_{f3}-T_{f2}}{R_{12}^{\Delta}} + \frac{T_{f3}-T_b}{R_1^{\Delta}} + \frac{T_{f3}-T_{f4}}{R_{12}^{\Delta}}$$

$$q_4 = \frac{T_{f4}-T_{f1}}{R_{12}^{\Delta}} + \frac{T_{f4}-T_{f2}}{R_{13}^{\Delta}} + \frac{T_{f4}-T_{f3}}{R_{12}^{\Delta}} + \frac{T_{f4}-T_b}{R_1^{\Delta}} \qquad \text{Eq. (2)}$$

where,

$$R_1^{\Delta} = R_{11} + R_{13} + 2R_{12}$$

$$R_{12}^{\Delta} = R_{11}^2 + R_{13}^2 + 2R_{11}R_{13} - 4R_{13}^2$$

$$R_{13}^{\Delta} = \frac{(R_{11}-R_{13})\left(R_{11}^2 + R_{13}^2 + 2R_{11}R_{13} - 4R_{13}^2\right)}{R_{13}^2 + R_{11}R_{13} - 2R_{12}^2} \qquad \text{Eq. (3)}$$

where T_{fi} *(i=1,2,3,4)* is the temperature of the flowing fluid in respective pipes, R_{ii} *(i=1,2,3,4)* is the thermal resistance between borehole wall and a particular pipe and R_{ij} *(i,j=1,2,3,4)* is the thermal resistance among different pipes. In practical application, all the tubes are placed symmetrically in the borehole as shown in Fig.2c. Therefore $R_{ij}=R_{ji}$, $R_{ii}=R_{jj}$ (e.g. $R_{12}=R_{14}, R_{32}=R_{34}$ and so on) is taken in general.

$$R_{11} = \frac{1}{2\pi k_b}\left[ln\left(\frac{r_b}{r_p}\right) - \delta\, ln\left(\frac{r_b^2 - D^2}{r_b^2}\right)\right] + R_{pipe}$$

$$R_{12} = \frac{1}{2\pi k_b}\left[ln\left(\frac{r_b}{\sqrt{2}D}\right) - \frac{\delta}{2} ln\left(\frac{r_b^4 + D^4}{r_b^4}\right)\right]$$

$$R_{13} = \frac{1}{2\pi k_b}\left[ln\left(\frac{r_b}{2D}\right) - \delta\, ln\left(\frac{r_b^2 + D^2}{r_b^2}\right)\right] \qquad \text{Eq. (4)}$$

where $\delta = \dfrac{k_b - k}{k_b + k}$

and k is thermal conductivity of ground formation around the borehole, while k_b is the thermal conductivity of grouting material, r_p is the inner radius of the tube and R_{pipe} is the heat transfer resistance from inside to outer surface of the pipe which includes convection resistance of fluid and conduction resistance of the pipe material.

Table 1 Geometrical properties of borehole and tube

r_b(m)	r_p(m)	H (m)	D (m)	k_b ($Wm^{-1}K^{-1}$)	k ($Wm^{-1}K^{-1}$)	$\dot{m}$ (kgs^{-1})	C ($Jkg^{-1}K^{-1}$)	Rp (mKW^{-1})
0.06	0.016	120	0.032	1.82	0.97	0.207	4187	0.1

4. RESULTS AND DISCUSSION

4.1. Thermal response test (TRT)

Thermal response test has been conducted for the northern part of India for 48 hours of continuous operation and calculation of thermal conductivity of ground formation is carried out.The graph shown in Fig.3 is plotted between mean temperature T_f ($=\frac{(T_i+T_o}{2}$) on y-axis and natural algorithm of time on x-axis. It is evident from this graph that initial data is unsuitable for deciding the slope of curve. So, initial 5 hours of data has been shaved off and the magnified view of the rest of the graph has been represented.

The slope has been determined by regression analysis by fitting a straight line for the experimental data. The slope 'a' of the line is obtained as 1.676. Hence from Eq. (5) Ingersoll et al. (1951), the thermal conductivity of ground formation is found as

$$k = \frac{\dot{Q}}{4\pi aH} \qquad \text{Eq. (5)}$$

$$k = \frac{4615.78}{4 \times \pi \times 1.67854 \times 120}$$

$$k = 1.823\ W \times m^{-1} \times K^{-1}$$

Now the above calculated thermal conductivity *($k = 1.823\ W \times m^{-1} \times K^{-1}$)* is used to calculate the heat transfer throughout the depth for different legs of ground heat exchanger.

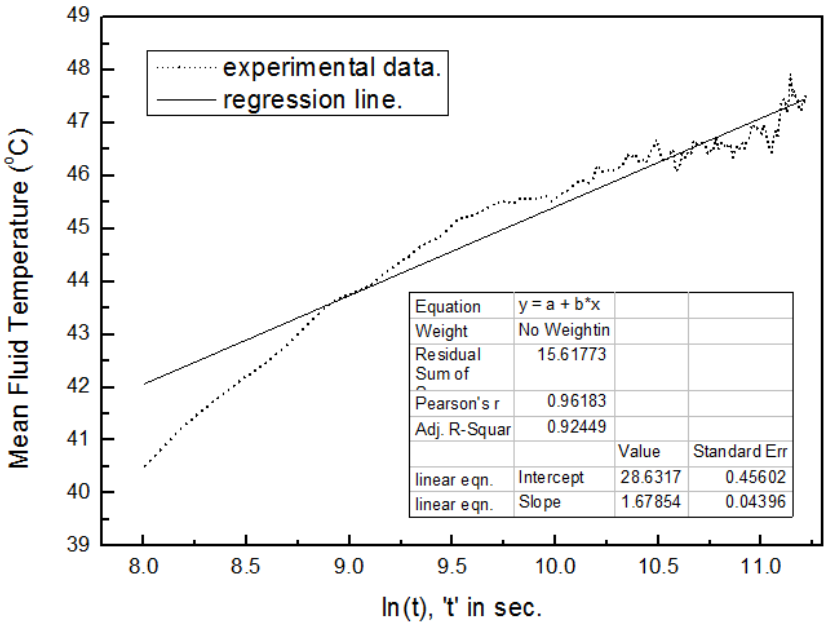

Figure 3: Mean water temperature on logarithmic time scale and regression analysis

4.2. Temperature analysis

4.2.1. Temperature distribution

In order to analyze the heat transfer rate through the boreholes, it is essential to evaluate the temperature distribution of working fluid in BHEs. Temperature distribution along the four legs of BHE has been calculated for 120 m depth of borehole using quasi-3D model, proposed by Zeng

et al. (2003) and the variation of temperature is depicted in Fig.4a.The theoretical temperature variation is plotted corresponding to different actual working conditions e.g. 34°, 35°, 36°C inlet and a fixed borehole temperature of 26 °C. It is observed from Fig.4a that maximum temperature drop is taking place in the first two legs and lowest in the last leg of the double U-tube GHX. The experimental observation of inlet and outlet temperatures is shown in Fig.4b for real-time working condition and it is observed that inlet (to borehole) and outlet (from borehole) temperature of the water increases as duration of the experiment increases, but the difference of these two temperatures remain almost constant ,e.g. 4.2°C, for two hours of experimental process.

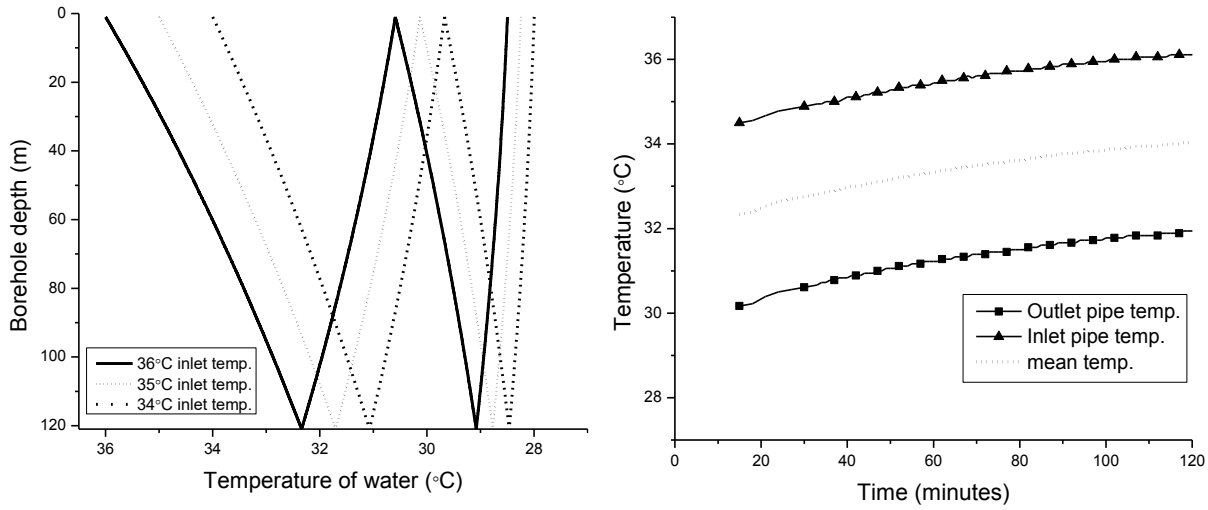

(a) (b)

Figure 4: (a) Temperature distribution of water in all legs BHE at different inlet temperature and (b) Variation of inlet (to borehole) and final outlet (from borehole) temperature (experimental)

4.2.2. Heat transfer analysis

The estimated ground property by thermal response test has been used to calculate local heat transfer rate in all the four legs of the tube as shown in Fig.5a. Eq. (1) is used to analyze the heat transfer rate at different inlet temperatures for a constant ground temperature of 26°C.It is observed from Fig.5a that the pattern of heat transfer is similar to the temperature drop, discussed in the previous section and about 77% of the total heat is transferred in the first U-tube whereas only about 23% is exchanged in the second U-tube. The experimental heat transfer rate for the present setup is shown in Fig.5b and can be observed that the heat transfer rate is nearly constant at 4 kW except some fluctuations in the initial stage. Heat transfer obtained from experiment is found to be 4 kW whereas the total heat transfer from theoretical calculation varies from 4.16 to 5.2 kW at different actual inlet temperature. Therefore, the heat transfer calculated from the proposed model shows a variation of 2 to 27% difference from the experimental results. This variation is due to the assumption of constant borehole temperature in theoretical calculation but in actual practice, it varies as the duration of the experiment in increased.

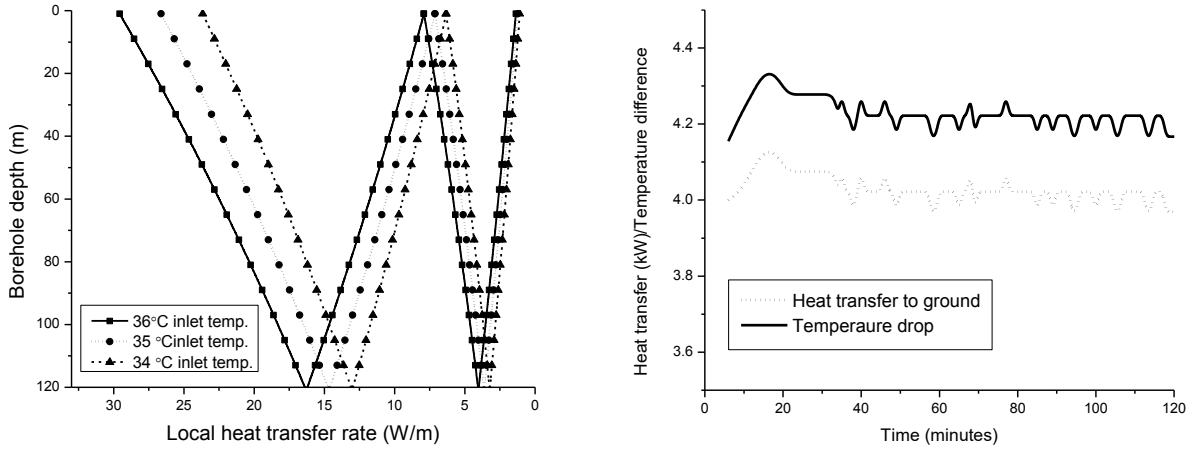

(a) (b)

Figure 5: (a) Local heat transfer from all legs of BHE and (b) Experimental total heat transfer rate to ground and temperature drop

5. CONCLUSIONS

In this study mathematical model of a series connected double U-tube GHX has been developed for a 5 TR refrigeration capacity with 5 boreholes of 120 m depth. Experiments were performed on one of the GHXs for effective heat transfer to the ground during space cooling mode operation of the GSHP system. Based on theoretical analysis as well as experimental results, the following observations are made:

(i) The temperature drop of water flowing inside the tube is plotted at different inlet temperature and it observed maximum temperature drop is taking place in first two legs least in last leg of the tube. Experimental results show an increase in inlet and outlet temperature of the borehole but their difference remains almost constant e.g.4.2°C.

(ii) Heat transfer analysis shows that is 77% of the total heat transferred in first tube whereas 23% is exchanged in second tube. From experimental procedure, the total heat exchange is found to be 4kW except some fluctuation at the initial stage.

(iii) The proposed theoretical model shows 2 to 27% variation from experimental observations of heat transfer of double U-tube series-connected configuration. This variation is because of constant borehole temperature assumption in theoretical calculation but in actual practice, it varies as the duration of experiment in increased.

ACKNOWLEDGMENTS

The first author is thankful to the Ministry of Human Resources and Development, Government of India, for providing the fellowship for pursuing PhD at Indian Institute of Technology Roorkee, Roorkee, India.

NOMENCLATURE

C	specific heat capacity of coolant($J \times kg^{-1} \times K^{-1}$)
D	half center distance(m)
H	depth of borehole(m)
k	thermal conductivity of ground formation($W \times m^{-1} \times K^{-1}$)

k_b	thermal conductivity of grouting material ($W \times m^{-1} \times K^{-1}$)
$\dot{m}$	Mass flow rate of water($kg \times s^{-1}$)
q	local heat transfer from tube($W \times m^{-1}$)
$\dot{Q}$	heater capacity of TRT setup(W)
R_b	thermal resistance of borehole ($m \times K \times W^{-1}$)
r_b	borehole radius(m)
R_{ii}, R_{jj}, R_{ij}	thermal resistance defined in Eq.(4)
r_p	tube radius(m)
R^{Δ}	thermal resistance defined in Eq.(1)
Tf	water temperature at different depth(°C)
Tb	borehole temperature(°C)
TR	ton of refrigeration

REFERENCES

Chang, K.S., Kim, M.J., 2016. Thermal performance evaluation of vertical U-loop ground heat exchanger using in-situ thermal response test. Renew. Energy 87, 585–591.

Hellström, G., 1991. Ground heat storage: Thermal analyses of duct storage systems. Lund Univ. 310.

Ingersoll,L.R.,Adler,F.T.,Plass,H.J.,Ingersoll,A.C.,1951.Theory of earth heat exchangers for the heat pump.ASHRE Trans,167-168.

Mustafa Omer, A., 2008. Ground-source heat pumps systems and applications. Renew. Sustain. Energy Rev. 12, 344–371.

Sivasakthivel, T., Murugesan, K., Sahoo, P.K., 2015. Study of technical, economical and environmental viability of ground source heat pump system for Himalayan cities of India. Renew. Sustain. Energy Rev. 48, 452–462.

Zeng, H., Diao, N., Fang, Z., 2003. Heat transfer analysis of boreholes in vertical ground heat exchangers. Int. J. Heat Mass Transf. 46, 4467–4481.

Zeng, Z., Zhao, Y., Lu, H., Wei, C., 2018. Experimental performance study of ground-coupled heat pump system for cooling and heating provision in karst region. Energy Build. 158, 971–986.

Zhai, X.Q., Cheng, X.W., Wang, R.Z., 2017. Heating and cooling performance of a minitype ground source heat pump system. Appl. Therm. Eng. 111, 1366–1370.

Manuscript ID: 642
DOI: 10.18462/iir.icr.2019.0642

Numerical modelling of thermal comfort for auditory halls

Aneta BOHOJŁO-WIŚNIEWSKA, Mirosława KOŁODZIEJCZYK, Dariusz BUTRYMOWICZ, Adam DUDAR, Michał ŁUKASZUK, Kamil ŚMIERCIEW

Bialystok University of Technology
Bialystok, 15351, Poland, d.butrymowicz@pb.edu.pl

ABSTRACT

At a time when energy saving is critical, one of the ways to reduce unnecessary energy losses is to provide a feeling of thermal comfort for people staying in closed utility rooms. It is important to properly determine and maintain indoor conditions to achieve the desired effect of the operation of ventilation, air conditioning or heating. In this type of issues, the numerical fluid mechanics comes to the aid. The paper presents the results of modelling of heat transfer process in the utility rooms and prediction of the thermal comfort by means of CFD code. Calculations were made for the auditorium in which measurements of inside air parameters were previously performed. Calculations were made for two turbulence models k-ε Standard, k-ε RNG. The differences between numerical and experimental values vary between 5 to 40 % depending on the locations of the measurement points.
Keywords: CFD, turbulence models, validation, thermal comfort

1. INTRODUCTION

At present, when energy saving is critical in all engineering activities, one of the ways to reduce unnecessary energy losses is to provide a thermal comfort for people staying in homes, offices and other building at the lowest possible cost. Poor indoor air quality can often lead to excessive natural ventilation, e.g. by opening windows. Often, the windows are opened when heating system is running. An increased supply of cold, fresh, outside air can overwhelm the heating system and reduce the air temperature inside the room. However, this leads to uncontrolled energy losses. It is important to properly determine and maintain indoor conditions. The effective operation of the ventilation, air conditioning or heating systems without unnecessary excessive energy consumption are desired. In such case, the numerical fluid mechanics by means of the CFD techniques comes to the aid, allows for numerical analysis ventilation issues at the design stage of buildings. This leads to lowering costs associated with possible design errors. Early detection of possible errors gives the opportunity to avoiding them in the next step. CFD also enables the analysis of existing rooms, e.g. to detect ventilation and air-conditioning problems related to the room architecture, without the need for long-term and expensive experimental research.
In numerical simulation of thermal comfort in the room two main challenges exists: modelling of the turbulent air flow and modelling of human impact on the indoor environment. According to the literature (Horikiri et al., 2015; Hajdukiewicz et al., 2013; Nada et al., 2016) there is no one specific turbulence model that would be recommended for modelling air flow in utility rooms. The literature shows that the most appropriate approach is to perform numerical calculations for several turbulence models to choose the one that best suits the specific case. Such approach is presented in this paper. Results obtained for two turbulence models k-ε Standard, k-ε RNG are presented. These models give the results the best fits to experimental ones, therefore, only these two are presented.
Taking into consideration the human impact on the indoor environment it can be found that in most of the cases the constant heat flux on the human skin surface is used as a boundary condition (Bohojlo and Kolodziejczyk, 2009; Capano et al., 2011; Hajdukiewicz et al., 2013; Heidarinejad et al. 2015; Koper, 2013; Nada et al., 2016; Schellen et al., 2013). Bohojlo-Wisniewska (2013), Cheng et al. (2012), Horikiri et al. (2015), Koper (2013) used constant temperature instead heat flux. Koper (2013) also considered the influence of the water vapor exhaled by the human. In

papers published by Bohojlo and Kolodziejczyk (2009), Bohojlo-Wisniewska (2013) the humidity was modelled as water vapor mass flow inlet boundary condition set on human skin surface.
The aim of this paper was to develop a computational model, for modelling the distribution of humid air parameters in an auditorium with group of people inside the room. On this basis the model was used to study the impact of external factors (e.g. settings of air conditioners) and internal factors (e.g., the number of people present in the room or their physical characteristics) on the thermal comfort. Consequently - obtaining a model that allows for proper determining of air parameters inside different kinds of rooms. For this purpose, numerical calculations for the auditorium were performed. The obtained results were compared with experimental results.

2. THERMAL COMFORT FACTORS

Recognizing that the various factors affecting thermal comfort of the occupants in a space will vary through the year, for example, due to changes in surface temperatures, changes in clothing, solar conditions, or high summertime temperatures in non-air-conditioned buildings, computer thermal modelling may be used to establish the percentage of time that different levels of operative temperatures are achieved. International standard ISO 7730, Ergonomics of the Thermal Environment, provides the basis for the determination of thermal comfort from a calculation of the Predicted Mean Vote (PMV), which is the average sensation of comfort experienced by a large group of people, and the Predicted Percentage (of occupants) Dissatisfied (PPD) at different temperatures. The Standard offers design criteria, related to the activity level indicated and for clothing of 0.5 clo during summer and 1.0 for winter conditions. When using PPD percentages it should be recognized that 5 to 10 per cent of people will be dissatisfied with any given internal environment. In addition, where people are able to adjust their clothing, they will remain comfortable over a wider range of temperatures.
Determination of an acceptable internal climate must take in many variables through the year and is a complex area to establish optimal design objectives. Where thermal modelling is based upon weather tapes to represent external conditions through the year it should be recognized that the data is derived from historical records and therefore makes no allowance for the effects of global warming and are therefore not necessarily representative of future conditions.
Fanger developed equation to calculate the predicted mean vote (PMV) in the seven-point in range -3, …, +3 thermal sensation scale

$$PMV = [0.303\exp(-0.036M) + 0.028] \times \{(M-W) - 3.05\cdot 10^{-3}\cdot[5733 - 6.99\cdot(M-W) - p_a] - 0.42\cdot[(M-W) - 58.15]$$

$$-1.7\cdot 10^{-5} M(5867 - p_a) - 0.0014M(34 - t_a) - 3.96\cdot 10^{-8}\cdot f_{cl}[(t_{cl}+273)^4 - (\overline{t_r}+273)^4] - f_{cl}h_c(t_{cl} - t_a)\} \quad \text{Eq. (1)}$$

$$t_{cl} = 35.7 - 0.028(M-W) - I_{cl}\{3.96\cdot 10^{-8}\cdot f_{cl}[(t_{cl}+273)^4 - (\overline{t_r}+273)^4] + f_{cl}h_c(t_{cl} - t_a)\} \quad \text{Eq. (2)}$$

$$\overline{t_r} = [(t_g + 273.15)^4 + 2.5\cdot 10^8 v_a{}^{0.6}(t_g - t_a)]^{0.25} - 273.15 \quad \text{Eq. (3)}$$

where: M – metabolic rate, W/m2 ; W – external work (assumed = 0), W/m2; I_{cl} – clothing insulation, (m2K)/W; f_{cl} – ratio of the surface area of clothed body to the surface area of exposed body; t_a – air temperature, °C; t_r – mean radiant temperature, °C; v_a – air velocity, m/s; p_a – partial pressure of water vapour in the surrounding air, Pa; h_c – heat transfer through convection, W/(m2K); t_{cl} – mean temperature of the clothed surface of human body, °C; t_g – black-globe temperature, °C.

The PPD can be calculated as follows:

$$PPD = 100 - 95\exp(0.03353PMV^4 + 0.2179PMV^2) \quad \text{Eq. (4)}$$

Numerical simulation using ANSYS FLUENT were performed to predict the thermal comfort in the auditorium. The PPD and PVM parameters were defined as User Defined Functions and used as global indicators of thermal comfort.

3. DESCRIPTION OF MODELLING QUARTERS

Numerical simulations were performed for existing auditorium located in Faculty of Mechanical Engineering, Bialystok University of Technology. Fig. 1 shows the geometry of this room. The volume of the analysed room was 147 m^3, the floor area 51 m^2, the window panes during the measurements were covered with vertical blinds that protected the room from direct solar radiation. The details concerning air outlet at the air conditioning unit that was operated during test in ventilation mode only were shown in Fig. 2.
All crucial elements affecting the airflow or thermal conditions were included in geometrical model. Few simplifications were made to limit the cells number, e.g. irrelevant elements such as paintings, baseboards were omitted. Such simplifications are widely used in numerical calculations of ventilation issues (Capano et al., 2011; Cheng et al., 2012; Cheong et al., 2003; Fathollahzadeh et al., 2015; Heidarinejad et al., 2015; Nada et al., 2016; Yao and Lin, 2014). The model was built in 1:1 scale

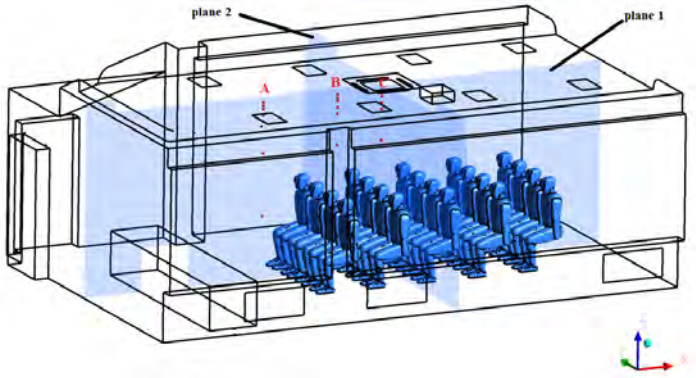

Figure 1: Room geometry with marked planes and measurement verticals

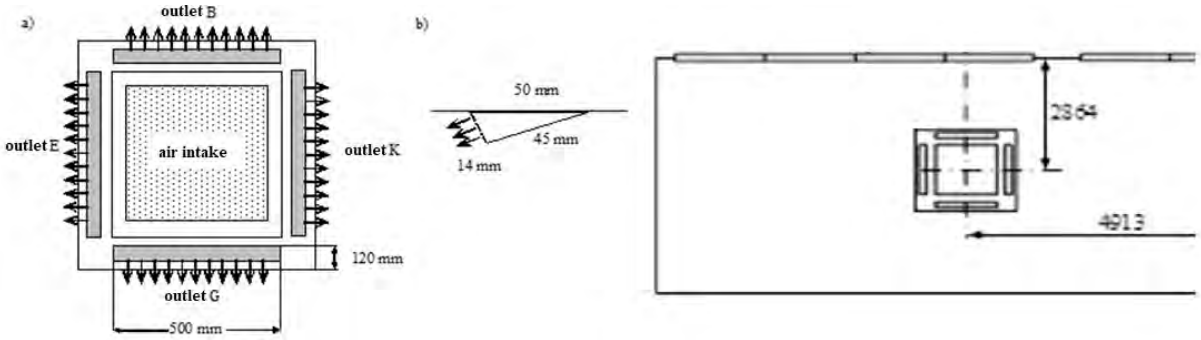

Figure 2. Air outlet location in the analysed room: a) geometry of the air conditioning unit; b) air outflow geometry and air conditioning unit location.

Presence of a human or group of people is an important factor in the numerical modelling of the indoor environment. In this paper, a group of 20 people was modelled in a direct way, i.e. keeping the approximate shape of people, then the boundary conditions were set on the surface of each silhouette. The room also includes heat gains from lighting, windows, ceiling, floor, multimedia projector, etc. Heat gains from solar radiation are not included. In the modelled case, the cassette ceiling air conditioner providing downward–upward air circulation. The AC indoor unit was equipped with four diffusers for cold air supply and one exhaust grill for return air.

4. NUMERICAL MODELLING

Simulations were performed using ANSYS Fluent 17.2 solver with six paralleled processes. Pressure-velocity coupling was modelled with SIMPLE (Semi-Implicit Method for Pressure Linked Equations) scheme. Calculations were performed as steady-state.
Initially the geometrical model was discretized with tetrahedral mesh built in ANSYS Workbench, later the mesh was converted into polyhedral cells in Fluent. Mesh conversion reduces the number of mesh cells and time of simulation. Final mesh density was 4.7 million of cells. During

discretization special attention was paid into crucial areas, e.g. supply air inlet and return air outlet, skin surface or in vicinity of a human mouth. The mesh was denser in these areas to better capture of occurring phenomena. Fig. 3 shows the numerical mesh create at two cross-sections.

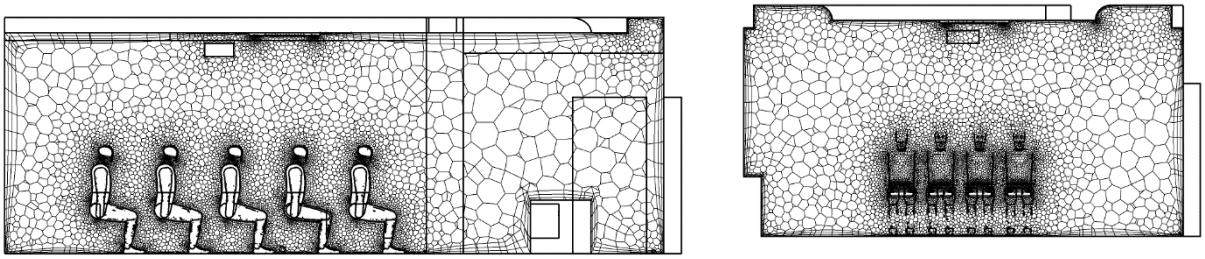

Figure 3: View on numerical mesh at two cross-sections: a) numerical mesh at location y = 3.098 m; b) numerical mesh at location x = 4.913 m

Humid air with perfect gas assumption was set as a working fluid. Air was modelled as a mixture of oxygen O_2, nitrogen N_2 and water steam. Thermodynamic properties were temperature dependent and were approximated with fourth degree polynomial. Coefficients for polynomial were taken from Fluent fluid database (species transport model without chemical reactions).
It was assumed that occupants have light summer clothes and they maintain light physical activity level at sitting position. On this basis factors affecting thermal comfort were as follows: thermal resistance of clothes I_{cl} = 0.1 (m2×K)/W; metabolic rate M = 70 W/m2; no external heat sources W = 0. Mean radiant temperature (MRT) was t_{MRT} = 26.75 °C. The MRT was estimated using a black-globe thermometer. The details concerning the measurement apparatus and procedure were not provided due to space limitation and may be found in Bohojło-Wiśniewska (2018)

Table 1. Boundary inlet conditions

Inlet condition	name	T [K]	Mass fraction [kg/kg]		turbulent intensity [%]	velocity v [m/s]
			water steam	oxygen		
velocity inlet	inlet B	300.15	0.011	0.2094	5	4.75
	inlet E					5.28
	inlet G					5.6
	inlet K					5.7
	mouth 1÷20	304.15	0.028	0.2094	5	$3 \cdot 10^{-9}$
pressure outlet	outlet	300.15	0.011	0.2094	5	negative gage pressure [Pa]
						-0.02
wall	human skin	303.15	0.0134			
	ceiling	299.25				
	lighting	346.15				
	windows	299.65				
	floor	297.25				
	multimedia projector	304.15				
	walls	298.25				

As a boundary conditions the air inlet and outlet parameters were set. Additionally, the temperature of surfaces imitating the heat sources were set. These parameters were established on the basis of experimental measurement conducted in the room. Boundary conditions details are given in Table 1. Heat and moisture load generated by the occupants were included. On the human faces the small circle surfaces imitating human mouth were applied. Velocity inlet was a boundary condition in this case. Velocity at level 3·10-9 m/s, temperature t_m = 31°C and relative humidity of 96% were set. Mass flow rate of air generated by individual human was close to zero and it was

irrelevant on the mass balance in the room, however, a non-zero value was necessary due to the type of the boundary condition. The temperature and relative humidity of air exhaled by the human were taken from Bogdan and Chludzinska (2008). On the human skin surface constant temperature and the mass fraction of water steam were set. The thermal comfort conditions outside the occupied zone were also analysed (e.g. air conditioning unit vicinity) since in this region possible application of the turbulence models may be validated

5. RESULTS

Results of simulation of the quantities describing all parameters of the thermal comfort, i.e. PMV and PPD were presented in this section. In Fig. 4 the PMV distributions for two tested turbulence models are shown. The PMV is plotted on the plane crossing the AC unit (plane 1 in Fig.1). It is seen from the figure that for *k-ε RNG* turbulence model the mean value of PMV in the room excluding the ceiling and walls vicinity areas is close to PMV_{mean} = 0.9. PMV at level of 1 according to the Fanger scale means that environmental thermal conditions are felt as slightly warm. The *k-ε Standard* turbulence model predicts slightly higher value of PMV in the occupied zone where PMV = 1.1. In close vicinity of human skin PMV = 1.2 is observed.

.

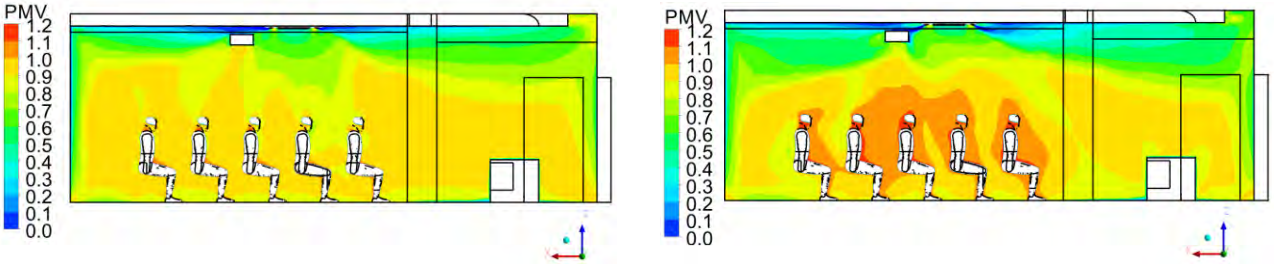

Figure 4: PMV distribution at plane 1 (*y* = 3.098 m): a) *k-ε RNG*, b) *k-ε Standard*

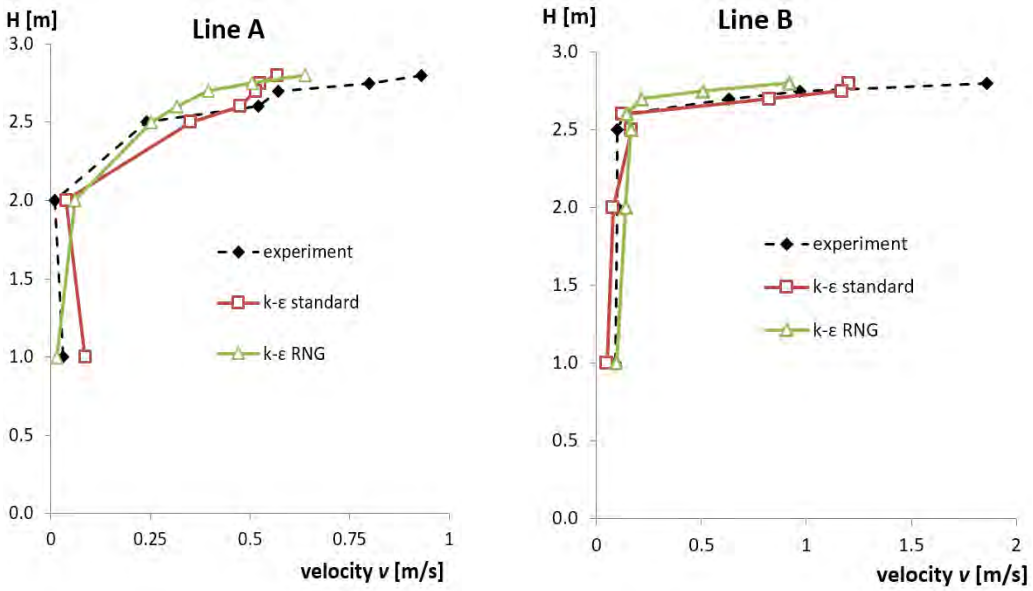

Figure 5: Vertical velocity distributions at lines A, B

Fig. 5 presents vertical velocity distributions for three measurement lines (marked as A, B, C in Fig. 1). The location of the measuring device is represented by dots in each row. Line C runs through the middle of the room, Line B runs between the first and the second row of sitting people, line A runs in front of the first row of people. For all tested lines both turbulence models predicting velocity with good accuracy. The largest differences between measurement and simulations velocities above H = 2.5 m are observed. Maximum velocity on line A is $v_{max,exp}$ = 0.93 m/s, while for turbulence models are $v_{max,standard}$ = 0.57 m/s and $v_{max,RNG}$ = 0.64 m/s. For line B maximum velocities are: $v_{max,exp}$ = 1.86 m/s, $v_{max,standard}$ = 1.20 m/s and $v_{max,RNG}$ = 0.92 m/s. For line C maximum

velocities are: $v_{max,exp}$ = 1.12 m/s, $v_{max,standard}$ = 0.54 m/s and $v_{max,RNG}$ = 0.55 m/s. In Fig. 6 the PPD distribution at plane in the middle of the room is presented. Location of this plane is presented in the Fig. 1 (marked as plane 2). It is clear in the figure, that *k-ε Standard* turbulence model is predicting less comfortable conditions. Predicted Percentage Dissatisfied exceeds 32% in the middle part of group of people. This is consistance with Fig 4b where higer value of PMV are observed. For *k-ε RNG* turbulence model the thermal conditions are more comfortable. The maximum value of PPD_{max} = 26% is achieved

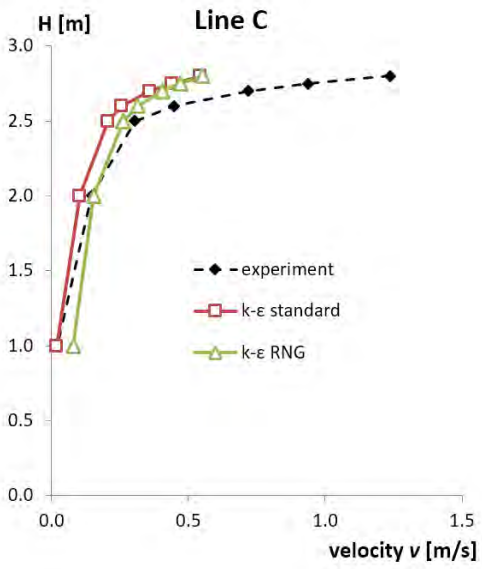

Figure 5 cont.: Vertical velocity distributions at line C

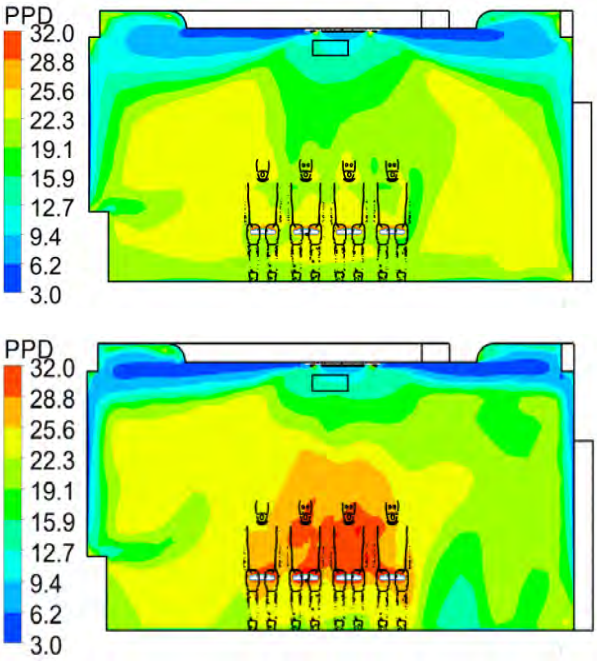

Figure 6: PPD distribution at plane 2 (x = 4.993 m): a) *k-ε RNG*, b) *k-ε Standard*

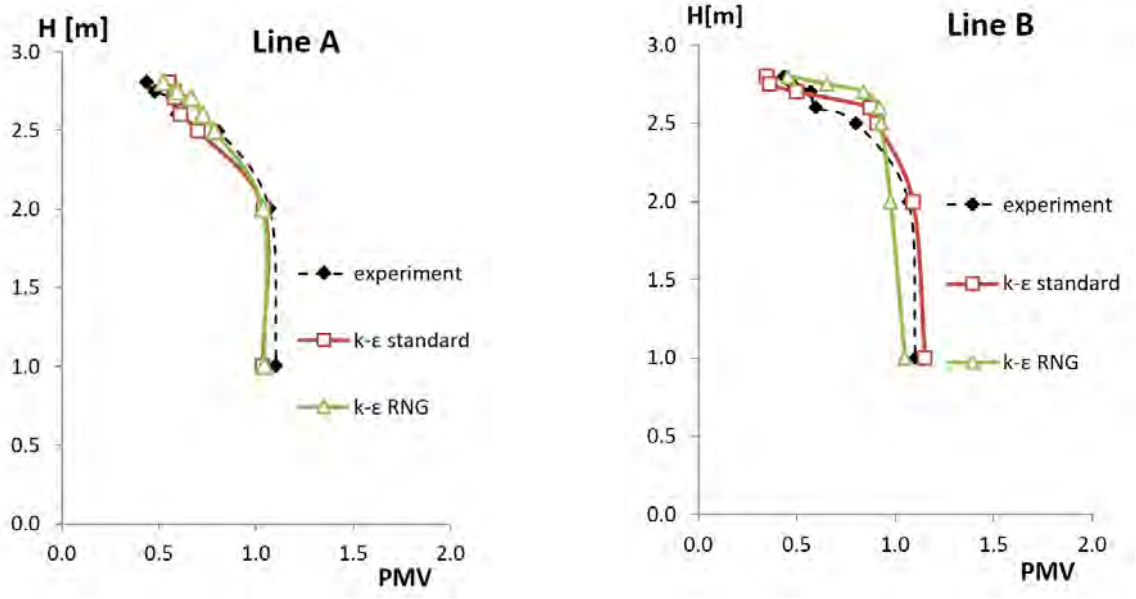

Figure 7: PMV distributions at lines A and B

In Fig. 7 vertical distributions of PMV indicator along measurement lines A, B and C are shown. Since only positive values were obtain in experiment and in simulation the abscissa axis has values above zero, regardless of Fanger scale. Both turbulence models give very good accuracy

with experiments for line A. Again, the highest differences between numerical and experimental results are observed above H = 2.5 m. For line B the *k-ε Standard* turbulence model in most of measurement points overpredicts values of the PMV, however, results for this model are closer to experimental one compared to *k-ε RNG.* The latter, overpredicts the PMV for H>2.5 an underpredicts the PMV for H<2.5. Similar trends are observed for line C. Analysis of the PMV distribution does not give a clear advantage to any of the turbulence models analyzed. In general, both tested models give similar results in velocity distribution, therefore, both can be equally recommended for modelling of the indoor thermal comfort. However, taking into consideration the PMV indicator, it can be concluded that the *k-ε standard* turbulence model better predicts the thermal comfort inside the group of people.

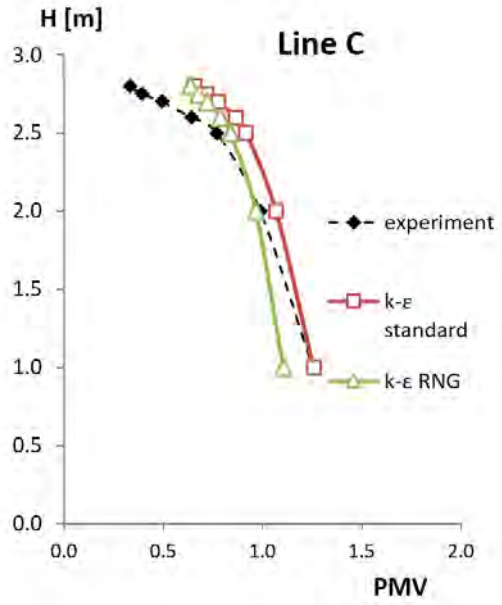

Figure 7 cont.: PMV distributions at line C

6. CONCLUSIONS

Based on presented results it can be summarized that proposed CFD approach can be applied for simulation of the thermal comfort in auditorium. The obtained numerical results agreed with experimental ones. Presented approach can have practical application in the design or evaluation of existing AC systems.

This paper presents an approach based on modelling individual people in the analyzed room. Such approach requires time needed to prepare the geometrical model and very accurate discretization. In the case of rooms or halls dedicated to large numbers of people this approach may not be considered as effective. More practical approach of modelling of thermal comfort in such room based on porous media model is presented in Bohojlo-Wisniewska (2017). Porous media core is applied instead the group of people. Proposed approach was experimentally validated. The results obtained confirmed practical utility of this approach. It is planned to apply porous media model for evaluation of the AC systems installed in cabins in the small yachts.

ACKNOWLEDGEMENTS

The research was carried out as part of research work no. S/WM/1/2018 at the Bialystok University of Technology and financed from a subsidy provided by the Minister of Science and Higher Education

NOMENCLATURE

f	ratio of the surface area of clothed to the surface area of exposed body	Subscript	
h	heat transfer coefficient	a	air
I	insulation	c	convection
M	metabolic rate ($W \times m^{-2}$)	cl	clothing
p_a	pressure (Pa)	g	black-globe
t	temperature (K)	r	radiant
v	velocity (m/s)		
W	external work ($W \times m^{-2}$)		

REFERENCES

Bogdan, A., Chludzińska, M. (2008). Human impact on the indoor environment. Heat engineering, heating, ventilation*,5,* 40-44 (in Polish).

Bohojło, A. & Kołodziejczyk, M. (2009). Numerical modeling of local thermal comfort parameters in a living room (in Polish). *Acta Mechanica et Automatica, 3(1),* 14-23.

Bohojło-Wiśniewska, A. (2013). Determination of thermal comfort parameters of a residential room in conditions of complex heat exchange (in Polish). *Ciepłownictwo, Ogrzewnictwo, Wentylacja, 4,* 168-172.

Bohojło-Wiśniewska, A. (2018). Modeling of distribution of internal air parameters in cooled rooms. (in Polish) Ph.D. Thesis. Bialystok University of Technology.

Campano, M. A., Sendra, J. J., Domínguez, S. (2011). Analysis of thermal emissions from radiators in classrooms in Mediterranean climates. *Procedia Engineering, 21*, 106 – 113.

Cheng, Y., Niu, J., Gao, N. (2012). Stratified air distribution systems in a large lecture theatre: A numerical method to optimize thermal comfort and maximize energy saving. *Energy and Buildings, 55,* 515–525.

Fanger, P. O. (1974). Thermal comfort. Arkady.

Hajdukiewicz, M., Geron, M., Keane, M. M. (2013). Calibrated CFD simulation to evaluate thermal comfort in a highly-glazed naturally ventilated room. *Building and Environment, 70*, 73-89.

Heidarinejad, G., Fathollahzadeh, M. H., Pasdarshahri, H. (2015). Effects of return air vent height on energy consumption, thermal comfort conditions and indoor air quality in an under floor air distribution system. *Energy and Buildings, 97*, 155–161.

Horikiri, K., Yao, Y.,Yao, J. (2015). Numerical optimisation of thermal comfort improvement for indoor environment with occupants and furniture. *Energy and Buildings, 88,* 303–315.

Koper, P. (2013). Modeling of the distribution of ventilation air in auditorium halls (in Polish). Silesian University of Technology, Gliwice.

Nada, S. A., El-Batsh, H. M., Elattar, H. F., Ali, N. M. (2016). CFD investigation of airflow pattern, temperature distribution and thermal comfort of UFAD system for theatre buildings applications. *Journal of Building Engineering, 6*, 274-300.

PN-EN ISO 7730:2006, Ergonomics of the thermal environment. Analytical determination and interpretation of thermal comfort using the calculation of PMV and PPD indicators and criteria of local thermal comfort

Schellen, L., Loomans, M. G. L. C., Kingma, B. R. M., Wit, M. H. de, Marken, Lichtenbelt, W. D. van, Frijns, A. J. H. (2013). The use of a thermophysiological model in the built environment to predict thermal sensation. Coupling with the indoor environment and thermal sensation. *Building and Environment, 59*, 10-22.

Yao, T. & Lin, Z. (2014). An experimental and numerical study on the effect of air terminal layout on the performance of stratum ventilation. *Building and Environment, 82, 75*-86.

Manuscript ID: 658
DOI: 10.18462/iir.icr.2019.0658

A Study on Cost-Efficiency Relationship Analysis of Air Conditioner in Korea

Daehoon Kim[(a)], Jinho You[(a)], Younsung Choi[(a)], Heejeong Kang[(a)], Jeongsik Seo[(a)], Wonyoung Park[(b)]

[(a)] Korea Refrigeration and Air-conditioning Assessment Center
Ansan, Gyeonggi-do, Korea, dhkim@kraac.or.kr
(b) Lawrence Berkeley National Laboratory
Sanfrancisco, United States, wypark@lbl.gov

ABSTRACT

This study is an analysis of energy efficiency improvement and manufacturing cost relationship of inverter type 3 ~ 6 kW wall-mounted air conditioner in Korea.

The analysis of manufacturing cost was based on the reverse engineering method. The efficiency of the system was measured by the combination of the indoor unit and the outdoor unit under the cooling standard conditions.

The results of the analysis were obtained the correlation equation by using the regression equation of cost and efficiency.

System efficiency increased by 19% and cost increased by 46% when the compressor efficiency increased by 20% in the reference model. In the reference model, the efficiency increased by 12% and the cost increased by 14% when the condenser cross-sectional area increased by 60%. As the evaporator cross section increases, system efficiency and cost increase. In the reference model, efficiency and cost increased by 1% as the evaporator cross-sectional area increased by 10%.

The manufacturing cost of air conditioner was increased as the efficiency increases. As the factors affecting the efficiency of the system, the manufacturing cost increased greatly.

Keywords:, Energy Efficiency, Efficiency-Cost Analysis, Engineering Analysis

1. INTRODUCTION

In modern society, as the level of living improves with the occurrence of environmental problems, a demand for a pleasant environment in the building is increasing. Accordingly, it is necessary to install air-conditioning equipment capable of controlling the air, and the amount of power used at home is also increasing. The Korean government is implementing various policies to regulate energy supply and demand, such as the Low Carbon Green Growth Basic Law, the Energy Law, the Rational Energy Use Law, the Collective Energy Business Act, and the Development, Use and Promotion of New Energy and Renewable Energy Act. As the industry develops and the standard of living grows, policies and consumers are demanding natural, energy-efficient devices. In the competitive system through rapid change of technology and efficiency improvement, it is necessary to formulate energy efficiency management system through more effective policy establishment. In order to establish such an efficiency management system, Research is needed to maximize efficiency. In addition, as the industry continuously develops technology and high-efficiency products are developed continuously according to various demands of consumers, a systematic efficiency standard operation method is required. In establishing the efficiency class, it is necessary to enhance the credibility of efficiency class formulation by collecting opinions of various stakeholders through standardized and open process.

These factors minimize risks to development schedules and costs, predict market entry and competitiveness, and improve the systematic and reliable operation of efficiency standard adjustment and operation methods.

Kang et al. (2) developed a high-speed technology for inverter rotary compressors to reduce costs and maximize efficiency with compact design of compressor. Based on the element design

technology, the partial load efficiency of the compressor was improved by 4% in the condition of using the air conditioner, and the compressor with high reliability was developed at the maximum 150 Hz operation. Kim (4) studied the heat transfer and pressure loss of a 7.0 mm microfin tube and found that the heat transfer rate increases with decreasing mass flow rate. Song et al. (5) developed a type of indoor unit of air conditioner as a circular form in a 4-way cassette, which resulted in a 13% higher thermal comfort index due to flow control and air distribution. The DOE document (6) US Department of Energy's Energy Efficiency Standards Program has played an important role in the operation of US energy efficiency policies to generate economic benefits and reduce greenhouse gas emissions through energy conservation. , Which has been evaluated as an energy policy with high investment cost.

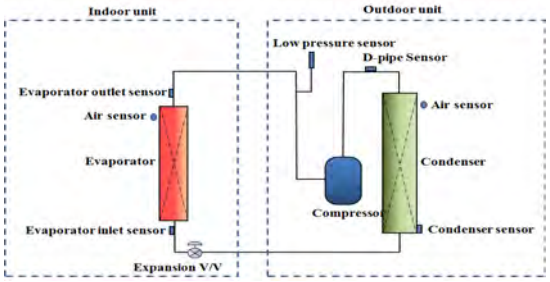

Figure 1 : Air conditioner of cycle diagram

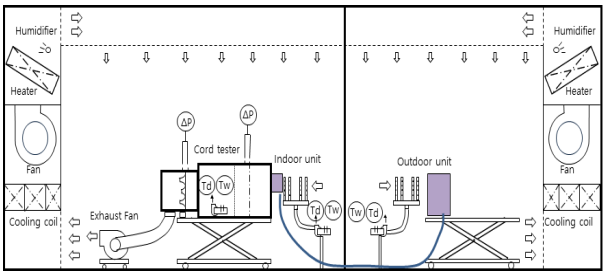

Figure 2 : Schematic diagram of psychrometric calorimeter

The purpose of this study is to analyze the correlation between system efficiency and cost by the most influential compressor capacity, condenser size, and evaporator size among various efficiency factors of air conditioner system. The efficiency of the system is determined experimentally by the system efficiency (EER, Energy Efficiency Ratio) according to each variable and the material cost of each system is checked by reverse engineering to analyze the relationship of cost according to the efficiency.

2. EXPERIMENTAL APPARATUS AND METHOD

Table 1. Air conditioner of Specification

General	No. of Indoor unit	1
	Refrigerant	R410A
Compressor	Type	Rotary
	No. of Compressor	1
	Capacity(Factor)	0.95 / 0.98 / 1* / 1.11
Indoor unit	Type	Wall mounted
	Row	2
	FPI	19
	Tube diameter[mm]	7
	Area(Factor)	0.62 / 1** / 1.05 / 1.12
Outdoor unit	Row	2
	FPI	14
	Tube diameter[mm]	7
	Area(Factor)	0.88 / 1*** / 1.02 / 1.24 / 1.56

* Compressor Reference Model Capacity : 4 800 W
** Indoor unit Reference Model Heat Transfer Area : 0.334 ㎡
*** Outdoor unit Reference Model Heat Transfer Area : 0.416 ㎡

2.1. Experimental Apparatus

This study analyzed the efficiency and cost of a split wall mounted air conditioner (less than 6 kW). The cycle of the air conditioner is a basic single-stage compression system. It is shown in Fig.1. Air enthalpy calorimeter was used for the performance test of the air conditioner. The schematic is shown in Fig.2.

The calorimeter used in this study is composed of a code tester, an air sampling unit and an air sampler, an AC power source, an air handling unit, Data acquisition system). Specification of calorimeter is cooling capacity 75 kW, dry bulb temperature is -20 ℃ ~ 60 ℃, relative humidity is 20% R.H. ~ 95% R.H. Is automatically controlled by the PID method of the controller. The calorimeter was manufactured in accordance with the KS C 9306 Air Conditioner (7) and ISO 5151 (8) standards.

The installation of the air conditioner was installed according to the specification of KS C 9306 air conditioner (9) and the installation manual of the manufacturer, and the amount of refrigerant charge was tested by applying the rated refrigerant amount required by the manufacturer.

2.2. Method of processing experimental results.

In this experiment, air conditioner with rated cooling capacity of 6 kW or less is used in Korea. The cooling capacity of the reference model is 4.8 kW. The parameters are as follows: compressor capacity, condenser size, and evaporator size. The ratio of each base to each base is shown in Table 1. The factor value is represented by the reference value divided by the changed value. Table 1 shows the details of the air conditioner used in the experiment and the ratio of the variables. Compressors were classified into four types according to their capacity, four types of evaporators according to their sizes, and five types of condensers according to their sizes. For the heat exchanger specifications, an evaporator, and for a condenser, a fin tube heat exchanger was used. The factors influencing cooling capacity, power consumption, and cost in the configuration of the air conditioner are shown in Fig.3. In this experiment, experiments were carried out by changing the capacity of the compressor, the sectional area of the condenser, and the sectional area of the evaporator, which have the greatest influence on the cooling capacity and power consumption in the air conditioner system. The experiment was carried out.

The experimental conditions were tested under the standard cooling condition of KS C 9306 air conditioner. The cycle of each combination was experimented with superheat of 3 ℃ ~ 5 ℃, and the RPM of the indoor fan and the outdoor fan were the same.

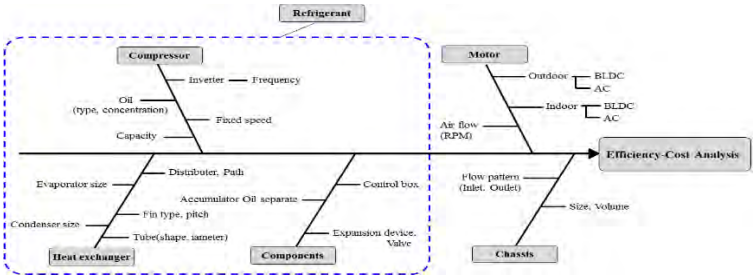

Figure 3 : Factor analysis (Fish-bone chart)

In this study, we derive the efficiency predictive correlations according to the experimental results. The system correlation equation was derived according to the method presented in the DOE document (9), assuming that the mixing system relation of each component has no influence on each other. The relationship between the cooling capacity of the system and the capacity of each component is shown in Eq. (1). The changes in cooling capacity are derived from the regression analysis of the system cooling capacity, the cooling capacity of the system with respect to the condenser cross section, and the cooling capacity of the system with respect to the evaporator cross sectional area. Here, superscripts a, b, and c represent constants for which the correlation equation is to be applied.

$$Q_{x,sys} = Q_{m,sys} \times F^{a}{}_{comp} \times F^{b}{}_{cond} \times F^{c}{}_{eva} \qquad \text{Eq. (1)}$$

The relationship between the power consumption of the system and the power consumption of each component is shown in Eq. (2). The change of the power consumption of the system is derived by the regression analysis of the power consumption result of the system with respect to the variation of the capacity of each component as a function of the exponential function type. Here, superscripts d, e, f, and g denote constants for which a correlation equation is to be applied.

$$P_{x,sys} = P_{m,sys} \times F^{d}{}_{comp,P} \times F^{e}{}_{comp,Q} \times F^{f}{}_{cond} \times F^{g}{}_{eva} \quad \text{Eq. (2)}$$

The EER (Energy Efficiency Ratio) correlation between the cooling capacity and the power consumption of the system is expressed by Eqs. (3) and (4). The efficiency correlation equation is shown by applying the correlation equation derived from equations (1) and (2).

$$EER_{x,sys} = EER_{m,sys} \times \frac{Q_{x,sys}}{Q_{m,sys}} \times \left(\frac{P_{x,sys}}{P_{m,sys}}\right)^{-1} \quad \text{Eq. (3)}$$

$$= \mathrm{EER}_{m,sys} \times (\mathrm{F}_{comp,Q})^{a-g} \times (\mathrm{F}_{comp,P})^{-f} \times (\mathrm{F}_{cond})^{b-h} \times (\mathrm{F}_{eva})^{c-i} \quad \text{Eq. (4)}$$

The cost analysis is expressed as a percentage by analyzing the material cost of products produced in Korea from 2010 to 2014. The cost analysis method was analyzed by reverse engineering 4) method presented in the DOE document. Reverse engineering is the process of discovering the technical principles of a device or system through its structural analysis, which involves fragmenting and analyzing objects (mechanical devices, electronic components, software programs, etc.). In this experiment, all parts of the air conditioner were disassembled and the cost of the disassembled parts was calculated considering the detailed processes such as the cost of raw materials, weight, size, and number of processes.

The correlation between the cost of the system and the cost of each component is shown in Eqs. (5) and (6). The cost and the processing cost of each component are analyzed by reverse engineering method and the results are divided into indoor and outdoor units. The factors influenced by the product size were derived in a one - dimensional linear form. The cost of the air-conditioning system is the sum of the indoor unit (5) and the outdoor unit (6). Eq. (5) is calculated by dividing the cost of indoor unit into molding, sheet metal, pipe, heat exchanger, drive, motor, and others. Equation (6) is calculated by dividing the cost of outdoor unit into molding, sheet metal, pipe heat exchanger, compressor, drive, motor and others.

$$\mathrm{Cost\,T}_{id} = \mathrm{Cost_{i,mol}} + \mathrm{Cost_{i,she}} + \mathrm{Cost_{i,pip}} + \mathrm{Cost_{i,hex}} + \mathrm{Cost_{j,dri}} + \mathrm{Cost_{j,mot}} + \mathrm{Cost_{i,oth}} \quad \text{Eq. (5)}$$

$$\mathrm{Cost\,T}_{od} = \mathrm{Cost_{o,mol}} + \mathrm{Cost_{o,she}} + \mathrm{Cost_{o,pip}} + \mathrm{Cost_{o,hex}} + \mathrm{Cost_{k,com}} + \mathrm{Cost_{k,dri}} + \mathrm{Cost_{k,mot}} + \mathrm{Cost_{o,oth}} \quad \text{Eq. (6)}$$

(7) and (9) for the indoor unit, and (8) and (10) for the outdoor unit, respectively, in the Eqs. (5) and (6) . And the constants for which the correlation equation is to be applied such as α, β, γ, δ, ω, κ, ρ, σ.

$$\mathrm{Cost}_{id} = \alpha \times Cost_{id,sys} + \beta \quad \text{Eq. (7)}, \qquad \mathrm{Cost}_{od} = \gamma \times Cost_{od,sys} + \delta \quad \text{Eq. (8)}$$

$$\mathrm{Cost}_{j} = \omega \times Exp(\pi \times Cost_{id,sys}) \quad \text{Eq. (9)}, \qquad \mathrm{Cost}_{k} = \rho \times Exp(\sigma \times Cost_{od,sys}) \quad \text{Eq. (10)}$$

In order to predict the cost - efficiency of air conditioners with various capacities, simulation was performed by applying the specifications of the air conditioner applied to the experiment. The simulation program was a DOE / ORNL Heatpump Design mode MARK VI program developed by Oak Ridge National Laboratory. The ORNL program was used to input the specifications of the compressor, expansion device, indoor heat exchanger, and outdoor heat exchanger, and the simulation was performed by inputting the refrigerant charge amount and the superheat degree data. Fig. 4 shows the comparison between the test results and the simulated values for the air

conditioning capacity of the air conditioner. The cooling capacity was expressed by fact value. The experimental result and the simulation value agreed well within ± 10%.

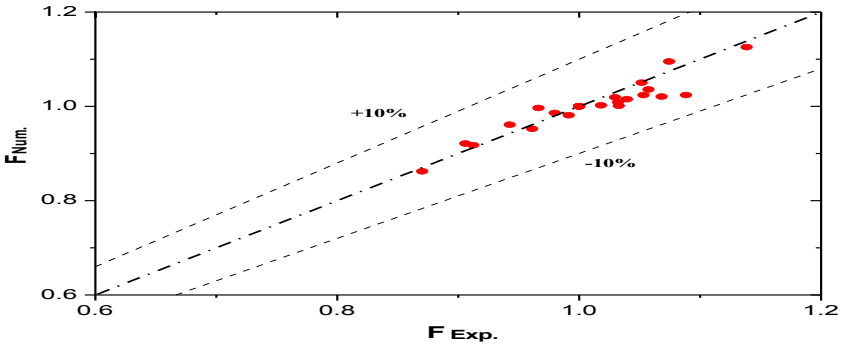

Figure 4 : Comparison of numerical results with experimental results

3. RESULTS AND DISCUSSION

3.1. Analysis of Cooling Capacity and Power Consumption Change for Capacity change of each Component.

For the analysis of the cooling capacity and power consumption change for each component, the reference model was selected and the experiment was performed by changing the compressor capacity, the condenser and the evaporator cross sectional area. In addition, the simulation was performed by applying the specifications of the air conditioner used in the experiment.

Fig. 5 shows the change in the system cooling capacity, the power consumption change, and the p-h diagram of the cycle for the compressor capacity change. The system capacity factor is the ratio to the capacity of the reference model. Experiments were carried out by changing the compressors of different capacities with the same number of revolutions of the condenser, evaporator, and fan. Fig. 5 (a) shows the change of the cooling capacity of the system with respect to the change of the compressor capacity by the experimental results and simulation results. The solid line is represented by the data obtained by the ORNL program. Fig. 5 (a) is a graphical representation of the cooling capacity change of the system with respect to compressor capacity change. As the capacity of the compressor increases, the capacity of the compressor and the amount of discharge increase, so that the cooling capacity is increased due to the increase of the refrigerant flow rate. In the reference model, the cooling capacity of the system increased by 4% when the compressor capacity increased by 5%, and that the cooling capacity of the system was lower than the performance of the single unit, which had an influence on the pressure loss of the condenser, evaporator and piping do. Fig. 5 (b) is a graphical representation of the power consumption change of the system with respect to compressor capacity change. As the compressor capacity increased, the refrigerant flow rate increased and the power consumption increased proportionally. In the reference model, when the compressor capacity was reduced by 5%, the power consumption decreased with the efficiency of the compressor. When the compressor capacity increased by 10%, the power consumption of the system increased by 14%. This is a result of an increase in the compression ratio and an increase in power consumption as the high-pressure-side pressure increases. Fig. 5 (c) is a P-h diagram of the change in the system for compressor capacity change. When the capacity of the compressor decreases, the refrigerant flow rate and the supercooling degree of the compressor are decreased and the cooling capacity is decreased.

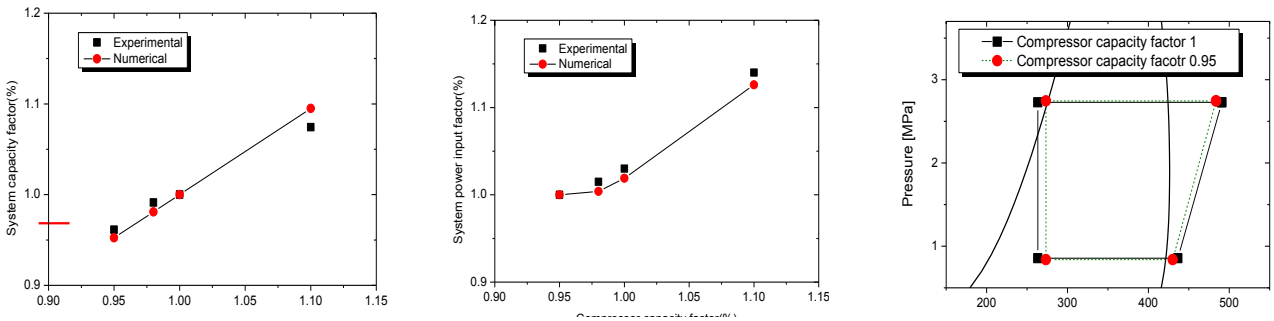

Figure 5 : System factor and p-h diagram of compressor capacity factor

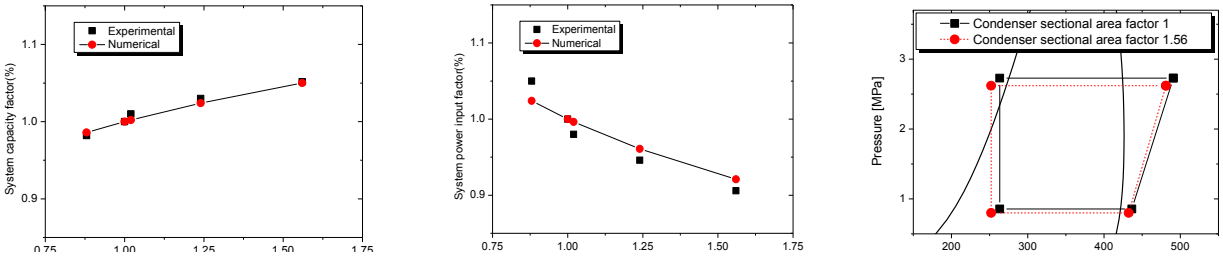

Figure 6 : System factor and p-h diagram of condenser sectional area factor

Fig. 6 shows the change in the cooling capacity of the system, the power consumption change and the P-h line of the cycle with respect to the change in the cross-sectional area of the condenser. Fig. 6 (a) graphs the change in cooling capacity of the system to the change in condenser cross-sectional area. As the cross - sectional area of the condenser increases, the heat exchange capacity increases. As the condenser outlet temperature decreases, the supercooling increases. The cooling capacity increased by 5% as the condenser cross-sectional area increased by 56% in the reference model. (b) is a graph of the power consumption variation of the system with respect to the change in the cross-sectional area of the condenser. As the cross-sectional area of the condenser increases, the heat exchange capacity of the condenser increases and the condensation pressure decreases. As a result, the compression ratio decreases and the power consumption decreases. When the condenser cross-sectional area increased by 56%, the power consumption decreased by 9.2%. On the other hand, when the condenser cross-sectional area decreased by 12%, the power consumption increased by 9%. (c) shows the change of the system with respect to the change in the cross-sectional area of the condenser in the P-h diagram. If the cross-sectional area of the condenser increases as in the P-h diagram, the condensation pressure decreases and the supercooling degree increases. As a result, the cooling capacity is increased and the power consumption is decreased due to the lowering of the high pressure side.

Fig. 7 is a graphical representation of the change in system for changing the evaporator cross-sectional area. Fig. 7 (a) is a graphical representation of the cooling capacity change of the system for varying the evaporator cross-sectional area. As the evaporator cross - sectional area increases, the heat exchange capacity increases and the cooling capacity increases. The system capacity increased by 5% as the evaporator cross-sectional area increased by 12% in the reference model.

In addition, when the evaporator cross-sectional area was reduced by 38%, the system capability was reduced by 13%. Fig. 7 (b) is a graphical representation of the power consumption variation of the system for varying the evaporator cross-sectional area. This is because the evaporator cross sectional area increases and the heat exchange capacity increases so that the low pressure side rises and the high pressure side rises accordingly. As the evaporator cross-sectional area increased by 12%, the power consumption of the system increased by 3.5%. On the other hand, when the evaporator cross sectional area decreased by 38%, the power consumption of the system decreased by 14%. The change of power consumption was smaller than that of evaporator cross section. Fig. 7 (c) is a P-h diagram showing the change of the system for changing the evaporator cross-sectional area. The P-h diagram shows that the supercooling is reduced due to the smaller cross-sectional area of the evaporator, resulting in reduced cooling capacity and reduced power consumption.

Table 2 shows the constants of the correlation equation for the cooling capacity and power consumption of the system. Where a, b, and c are constant values for calculating the cooling capacity

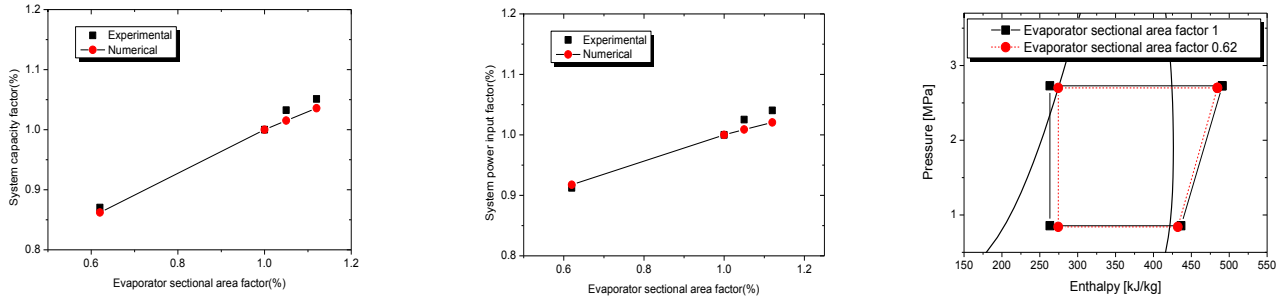

Figure 7 : System factor and p-h diagram of evaporator sectional area factor

of the system for Eq. (1), and d, e, f, and g are constants for power consumption calculation in Eq. (2). The final correlation was derived by applying this constant value.

Table 2. Constants of calculate to energy efficiency ratio

General	a	b	c	d	e	f	g
Constant	1.05	0.03	0.23	0.62	0.09	0.205	0.18

3.2. Analysis of efficiency and cost changes for capacity change of each component

The efficiency relation of the system to the capacity change of each component is derived as Eq. (11). Equation (11) is obtained by applying Equation (4) to the constant of Table 2.

$$\mathrm{EER}_{x,sys} = \mathrm{EER}_{m,sys} \times (\mathrm{F}_{comp,Q})^{0.96} \times (\mathrm{F}_{comp,P})^{-0.62} \times (\mathrm{F}_{cond})^{0.235} \times (\mathrm{F}_{eva})^{0.05} \quad \text{Eq. (11)}$$

Table 3. Constants of calculate to cost

General	α	β	γ	δ	General	ω	κ	ρ	σ
Molding	3 173	18 695	1 472	6 191	Drive	244	1.75	92	5.48
Sheet metal	733	3 409	4 694	17 999	Motor	84	4.14	74	5.55
Pipe	1 903	7 156	4 700	21 681	Compressor	-	-	87	5.21
HEX	3 969	17 724	7 186	34 886	Printing	73	1 017	-	-
The others	462	2 714	4 421	6 229	-	-	-	-	-

The cost analysis for the capacity change of each component was calculated by the reverse engineering method and the cost correlation formula was derived by analyzing the calculated data. The air conditioner disassembled both the indoor unit and the outdoor unit to create a BOM for each part, and the amount for each individual part was confirmed. The selection of the amount was based on the inflation information site and the website. The factors that influence the size and the factors that affect the efficiency are listed in Table 3. The classification of each category is α, β, γ, δrelated to the size. The constant values are derived, and ω, κ, $\rho$and σrelated to the efficiencies of Eqs. (9) and (10). Based on the results of the survey, we analysed the cost correlation through the relative increase ratio to the increase of the cost according to the variables.

Fig. 8 is a graphical representation of system efficiency and cost changes for each component change. Fig. 8 (a) graphs the efficiency and cost changes of the system due to increased compressor efficiency. As compressor efficiency increases, system efficiency increases proportionally. System efficiency increased by 19% and cost increased by 46% when the compressor efficiency increased by 20% in the reference model. The cost of the system increased as the compressor efficiency increased. In terms of efficiency and cost, the cost of system change was larger than that of system efficiency as the compressor efficiency increased. Fig. 8 (b) is a graphical representation of the efficiency and cost changes of the system for changing the condenser cross-sectional area. As the condenser cross section increased, the system efficiency increased and the

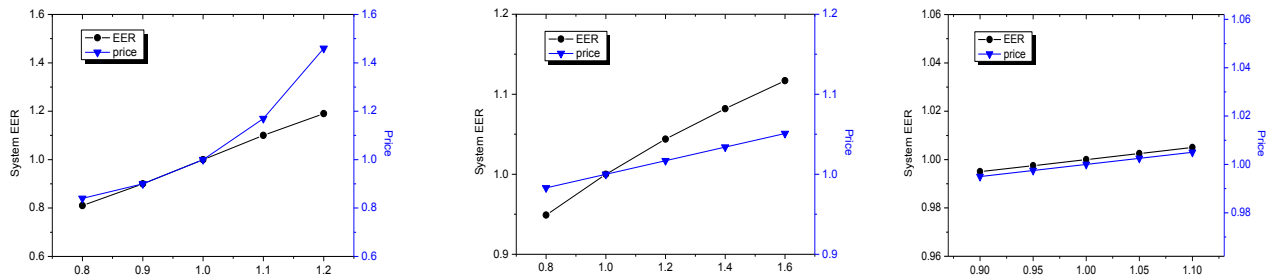

Figure 8 : System energy efficiency ratio factor, System price factor of AC component factor

cost increased as well. In the reference model, the efficiency increased by 12% and the cost increased by 14% when the condenser cross-sectional area increased by 60%. As the cross - sectional area of the condenser increases, the cooling capacity increases and the power consumption decreases. At this time, the cost also increased proportionally. Fig. 8 (c) is a graphical representation of the efficiency and cost changes of the system for changing the evaporator cross-sectional area. As the evaporator cross section increases, system efficiency and cost increase. In the reference model, efficiency and cost increased by 1% as the evaporator cross-sectional area increased by 10%. The efficiency and cost due to the increase of the evaporator cross sectional area increased proportionally and the effect on the system efficiency was negligible.

By developing a correlation formula for efficiency and cost, we can predict changes in cooling capacity, power consumption, efficiency, and cost due to capacity changes of each component.

4. CONCLUSION

In this study, the efficiency change of the system when the capacity of the component is changed for the air conditioner of 6 kW or less is experimented and the cost for each component is analyzed. Based on the results, we developed the efficiency and cost correlation equation for the capacity change of each component.

Experiments on the changes of each component and the correlations derived from this study will be able to predict the performance design and cost relationship of the air conditioner and the government predicts the efficiency and cost relationship when establishing the efficiency standard, It can be considered.

(1) The capacity of the compressor and the cooling capacity of the system have changed proportionally, and the costs have increased significantly to increase the efficiency of the system.

(2) The increase in the cross sectional area of the condenser was influential on the cooling capacity increase and the power consumption decreased. As a result, the effect on the system efficiency increase was largest and the cost rose proportionally.

(3) The changes in the evaporator cross - sectional area were proportional to the cooling capacity and power consumption, and the efficiency and cost also changed proportionally. However, the effect on system efficiency is reduced compared to other components.

(4) In the future, it is necessary to establish more effective and realistic results by establishing current technology level and scope of analysis.

REFERENCES

Korea Energy Agency, 2015 Korea Energy Handbook, pp. 11

Kang, S. M., Park, J. H., Shin, J. W., Lee, S. D., Yang., E. S., Ha., J. H., Son., Y. B. and Lee, B. C., Development of High Speed Inverter Rotary compressor for the Air-conditioning system, Proceeding of SAREK 2015 Winter Annual Conference, pp. 153-158.

Kim, Y.S., Yoo, S. Y. and Na, S. G., Study of compressor-performance improvement in automotive air-conditioning system, Proceeding of KSME 2015, Vol. 39, No. 9, pp. 713-718

Kim, N. H., Evaporation Heat Transfer and Pressure Drop of R-410A in a 7.0 mm O.D. Micro fin Tube at Low Flow Rates, Vol. 39, No. 9, pp. 761-772.

Song, W. S., Seo, H. J., Kim, J. M., Kim, Y. J, Seo, Y. H., Ju, Y. J. and Hwang, J., Development of High-efficiency Flow Control using Pressure Control Method, Proceeding of SAREK 2016 Summer Annual Conference., pp. 516-519.

Korean Standards Association, Airconditioners : KS C 9306, 2011

Non-ducted air conditioners and heat pumps – Testing and rating for performance : ISO 5151, 2010

Manuscript ID: 662
DOI: 10.18462/iir.icr.2019.0662

Marine application of waste heat to drive ejection refrigeration system

Dariusz BUTRYMOWICZ[(b)], Mateusz KĘDZIERSKI[(a)], Kamil ŚMIERCIEW[(b)], Jerzy GAGAN[(b)]

[(a)] Marine Projects Ltd.
Gdańsk, 80-605, Poland, m.kedzierski@marpro.pl
[(b)] Bialystok University of Technology
Bialystok, 15-351, Poland, d.butrymowicz@pb.edu.pl

ABSTRACT

Heat recovery is a common approach for effective energy management. Combustion engine is a main source for electric energy consumed be all electrical devices in ships and yachts. Currently, the classic compressor systems driven by electricity generated in generators are used for production of cold water used in AC units. With utilization of the waste heat the investment and operation costs can be reduced. In the paper a different solutions of waste heat recovery node from flue gases in the maritime industry are discussed. The proposed ejection system is an excellent example of an industrial application with a strong potential for implementation. The paper summarizes the first phase of the project dealing with developing of the ejection air-conditioning system driven by waste heat will be presented. Preliminary calculation of the proposed system operating with low-GWP working fluid will be presented and discussed. The geometry of the ejector designed for the specific case and performance operation line will also be shown.
Keywords: Waste heat, Ejector, Refrigeration, COP, Marine.

1. INTRODUCTION

Medium-speed piston engines are usually used on maritime vessels and yachts to propel the ship, and to drive generators to produce electricity. Piston engines works as a heat engine, converting the thermal energy of the fuel to mechanical work and further to electrical energy. Usually, the machinery systems fitted on ships and yachts are designed to work with maximum efficiency and run for long hours. Analysing data of various piston engine manufacturers, it can be concluded that engines have efficiency in the range of 30-50 %. Typical distribution of the waste heat for piston engine is shown in Table 1. This means that all the energy in the fuel cannot be converted into mechanical work and is converting for useful energy only partly. The most common and maximum energy loss from machinery is in the form of heat energy. This loss of heat energy has to be reduced or carried away by a cooling media, such as central cooling water system, to avoid malfunctioning or breakdown of the machinery. Utilization of the waste heat is a promising way for improvement the overall efficiency. Different types of waste heat recovery technologies and the potential for ship-owners to lower fuel costs, cut emissions are presented in Diesel (2011) and Shu et al (2013). The energy reclaimed from the engine depends to a great extent on the size of the main engine of the ship, its load and ambient temperatures. The engine size, operation route, loading condition and environment should be taken into consideration before choosing an appropriate way to waste heat utilization. Waste heat quantity, quality i.e., typical exhaust temperature, current recovery technologies and practices, and barriers to heat recovery should be taken into consideration. In any heat recovery situation, it is essential to know the amount of the recoverable heat and how it can be used. One of the commonly known application is use the waste heats to drive the absorption cooling unit. The main problem with absorption systems is that they are larger and heavier than conventional vapour-compression systems which adversely affects the vessel's parameters. This is because absorption systems have more components and as the heat and mass transfer of absorption equipment is poor, large heat transfer surface areas are required. Despite that absorption system can be used in naval ships, they are not suitable for small yachts due to its dimensions. Typical diagram of marine engine heat cooling system is shown in Figure 1.

It should be noted that not all of the heat sources listed can be recovered separately, rather as combinations, depending on the engine used. As showed in Table 1 part of heat from HT, jacket cooling circuits and exhaust gases can be recovered without major technical shortcomings intended for heating on maritime vessels. Also, due to promising temperature level of the waste heat source it is possible to use this heat as a motive source for ejection refrigeration system operating for air-conditioning purposes (Ezgi and Girgin, 2015). As shown by Butrymowicz et al. (2014) and Śmierciew et al. (2017) the ejection refrigeration systems can operate with low-temperature heat source. Moreover, the temperature requirements for air-condition system on the ship are favourable for ejection systems, since design temperature for summer is 24 ~ 28 C (Yan et al., 2011).

Table 1. The typical distribution of waste heat for piston engine

Energy source	Temperature	Portion of fuel energy
Exhaust gas	~ 400-500 °C	~ 30%
Jacket water	~ 85 °C	~ 6.5%
High-temperature air charger	~ 90 °C	~ 9%
Lubricating oil	~ 70 °C	~ 5.5 %
Low-temperature air charger	~ 40 °C	~ 4 %
Generator cooling (on gen-set)	~ 35 °C	~ 1.3%
Engine radiation	~ 35 °C	~ 1.5%

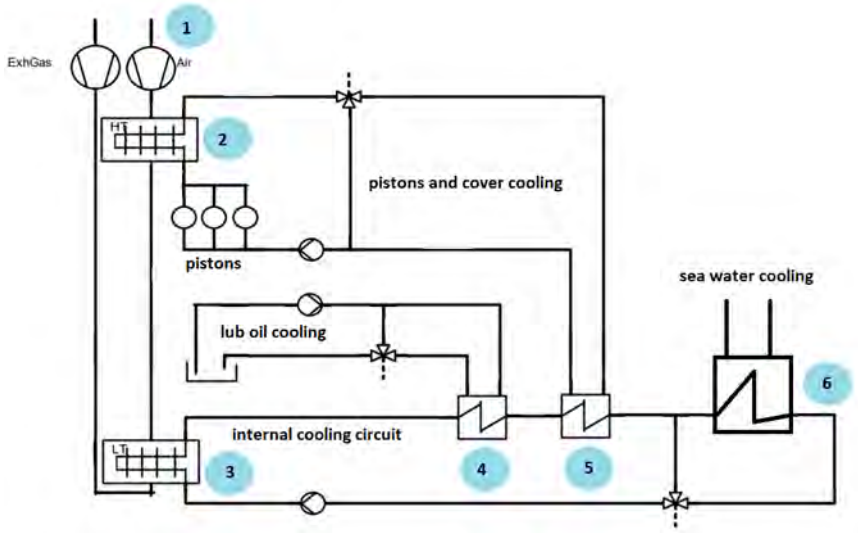

Figure 1: Marine engine heat cooling system 1-turbine; 2-hight temperature heat exchanger of charge air; 3-low temperature heat exchanger of charge air 4- exchanger of lubricating oil cooling; 5-heat exchanger of piston/jacket water cooling; 6-internal heat exchanger of cooling engine

2. MARINE APPLICATION OF WASTE HEAT TO DRIVE EJECTION REFRIGERATION SYSTEM

This paper presents the phase 1 of the project dealing with developing of the ejection air-conditioning system driven by waste heat. The potential application of the ejection refrigeration system operating for air-conditioning purposes and driven by waste heat from piston engine has been analysed. Also shown problems of used waste heat technology to the powered refrigeration system at ship. Preliminary calculation of the proposed system operating with environmentally friendly new HFO (*hydro-fluoro-olefins*) group refrigerant R-1234zeE are presented and discussed. Proposed fluid fulfils the requirements of Regulation of the European Parliament and the EU Council No. 517/2014 enacted on April 16th, 2014.

2.1. Exhaust Gas Heat Recovery

All devices present on ships must meet the relevant safety requirements. Therefore, it was necessary to design a heat recovery system that would transfer heat to the refrigerant without direct contact with the exhaust gas. Of course, intermediate systems using thermal oils are known. However, to completely protect the system from the danger of indirect fluid inflammation was used complete neutrality fluid in terms of any hazards related to flammability or the possibility of harmful chemical reactions occurring in the event of a possible failure of the system causing the leak. The working fluid in the presented system is water and water vapour. Another aspect that speaks for the possibility of using such a system is the operating pressure of the system is designed for values in the range of 1.3 - 2.0 bar. Moreover, taking into account the high enthalpy of water evaporation and the relatively small amounts of heat contained in the exhaust gases, the mass of water circulating in the system is negligible. With a power of 100 kW, it is about 0.035 kg what accounts for the possibility of its use in the exhaust systems of vessels.
System shown in figure 2 is used to recovery heat from exhaust gases for various heat consumers, including refrigeration systems. The system is designed for installation in the exhaust gas duct. The water vapour is generated as a result of the heat recovery from the exhaust gas heat exchanger 1. Then it passes through the liquid phase separator 2 to pressure reduction station 3, where the desired pressure is set due to the required temperature in the heat exchanger 4 where the heat is transferred to further work systems. From the heat exchanger 4, the condensate returns to tank 5 from where it is pumped to the heat exchanger 1 using the pump 6. The control valve 9 regulates the flow of condensate to the heat exchanger in exhaust gas duct, depending on the power demand. This results in protection of the system against uncontrolled pressure increase is doubled. First, if the pressure rises above the set limit, in the heat exchanger 1 the bleed valve 7 will work by which excess of refrigerant escapes into the condensate collector. An additional safety device is the safety valve 8.

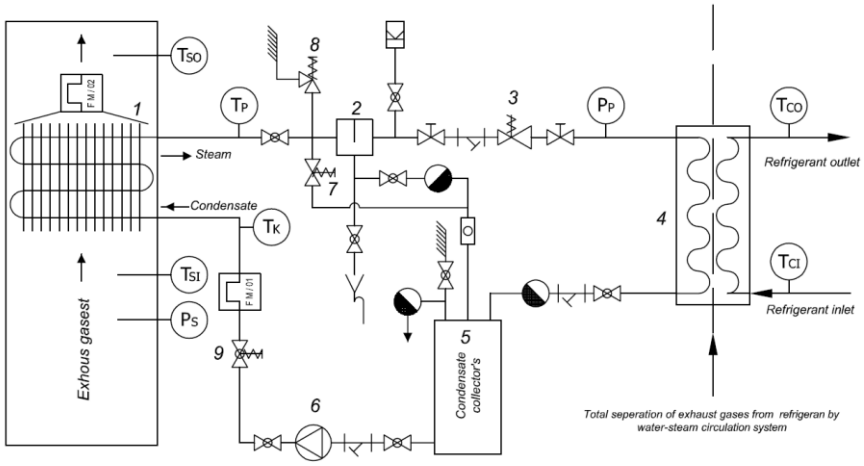

Figure 2: System of heat recovery heat from exhaust gases 1-Steam-exhaust heat exchanger, 2-phase separator, 3-pressure reduction, 4-steam compensator; 5-condensate tank, 6-pump, 7-bleed valve, 8-safety valve, 9-regulating valve

2.2. Formal Requirements for the Application of Maritime Refrigerant System

One of the key problems of refrigeration technology is the fulfilment of strict legal requirements regarding working factors: currently, classical working factors are being applied, which under European Union Directive 517/2014 on fluorinated greenhouse gases will have to be withdrawn from use soon. In air-conditioning systems as well as the entire refrigeration technology and heat pumps, the Directive enforces the use of agents with low potential for greenhouse effect. Ultimately, factors with GWP <150 will be allowed. However, the Directive does not apply to the maritime industry. Equivalent of the F-gas Directive for marine applications is the MARPOL Convention, Annex VI, Regulation 12 (MARPOL VI / 12). This document includes the requirements of refrigerant used and deliberate emission of substances that deplete the ozone layer and removal of these substances from the vessels. This Requirement applies only for refrigeration equipment supplied in separate parts, assembled and connected on board, regardless of size. It should be

noted that the requirements included in the MARPOL do not apply to equipment which is defined as permanently sealed. It means, there are no connections to fill up the refrigerant or potentially exchangeable parts. An example of such a device is home refrigeration equipment like fridge or air-conditioning devices.

2.3. Ejection refrigeration system

Ejector refrigeration system used for heat recovery is shown in Fig. 3. Instead of pressurizing the refrigerant by a mechanical compressor, an ejector compresses refrigerant vapour flowing from the evaporator and discharges it to the condenser. The motive vapour is generated in the vapour generator 3 which is heated by heat recovery system form piston engine. Recovery system consists of high-temperature heat-exchanger powered by exhaust gas and low-temperature heat-exchanger 2 powered by rest of thermal energy source from piston engine.
The performance of the ejector depends on several quantities such as: operating pressures and temperatures at the ejector inlets and outlet, working fluid properties and ejector geometry.

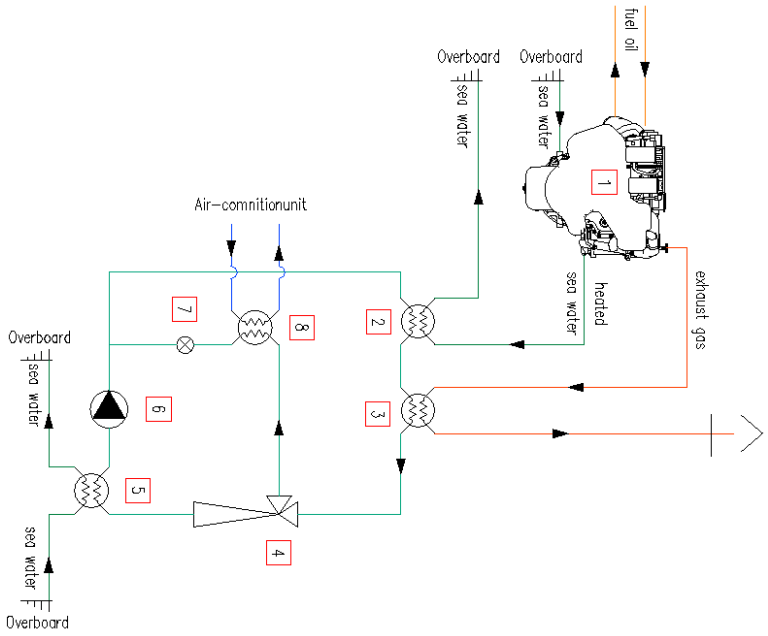

Figure 3: Schematic diagram of waste heat recovery system using ejector refrigeration system, 1-Piston engine; 2-heat exchanger; 3-steam generator; 4-ejector; 5-condenser; 6-pump; 7-expansion valve; 8-evaporator

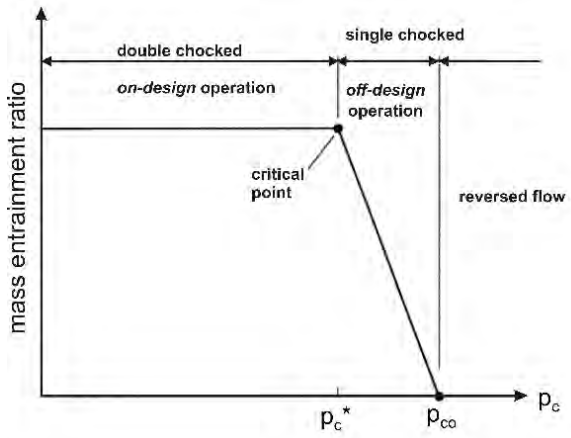

Figure 4: Performance curve and operational modes of the vapour ejector

A typical performance curve of vapour ejector for primary and secondary pressures (motive vapour pressure and evaporator pressure, respectively) is shown in Fig. 4. There are three operation modes distinguished. The most desirable operation mode is a critical mode, also called "on-design" operation mode. Under the critical mode ejector operates with maximum mass entrainment ratio. Independently of the type of operation mode the primary fluid reaches the supersonic speed during expansion in the motive converging-diverging nozzle. The flow is also chocked. In the critical operation mode secondary flow reaches the speed of sound because of favourable conditions related with momentum exchange and pressure difference between streams. When the secondary fluid achieves the speed of sound the flow is chocked. Now both fluids are chocked and remain in this state as long as the back-pressure is lower than critical pressure. In the critical mode, the shock wave, which creates the compression effect, is expected downstream the flow, either at the constant area mixing chamber or at the diffuser. However, if the back pressure increases the shock wave moves upstream the flow. For back-pressure lower than critical pressure the shock wave influences neither primary nor secondary mass flow rate. Therefore, the entrainment ratio is constant for back-pressures lower than critical pressure. When the back-pressure is equal to critical pressure the shock wave is located exactly where the secondary flow achieves the speed of sound and where it was chocked. With a further increase in the back-pressure the shock wave moves upstream into the suction chamber. As a result, the pressure of the primary and the secondary fluid increases and velocity of both fluids subsequently decreases. Secondary flow cannot reach the speed of sound and the mass flow of the fluid is lower than in the critical operation mode. This mode is also called "off-design". In this mode the mass flow rate of the secondary flow is described by the equation continuity equation. The increase in the back-pressure leads to decrease in the velocity of the secondary fluid. Consequently, the mass flow rate decreases. Primary flow in the off-design operation mode is still chocked. This is the reason why the mass entrainment ratio decreases with the increase in back-pressure in the subcritical or off-design operation mode. Under specific conditions, i.e. with the back pressure higher than breakdown pressure, the pressure in the suction chamber exceeds evaporation pressure and thus the reverse flow appears, whereas the ejector stop operating.

2.4. Analysis of the Performance of the Ejection Refrigeration System

Analysis of the performance of the ejection system in terms of mass entrainment ratio and compression ratio was performed for refrigerant R1234ze(E). Performance of the system operating with ejectors of two different geometries were tested. The first ejector geometry was developed based on model proposed by Huang et al. (1999), Chen et al. (2013) for assumed operating conditions: motive source heat flux Qg = 100 kW, motive temperature and pressure: tg = 130 ºC, pg = 4 MPa (supercritical conditions), expected cooling capacity Qe = 25 kW, evaporation temperature te = 5 ºC, superheating in evaporator ΔTe = 5 K. Thermodynamic cycle on pressure-enthalpy plot is shown in Fig 3.It was assumed that condenser will be cooled by sea water with temperature 35 ºC according to ISO 7547:2002(E). However, for calculation of the performance of the ejector condensation temperature was varied. It was also assumed that temperature increase in circulating pump is negligible. Second geometry was obtained by slight modification of the mixing chamber and diffuser dimensions. Results of obtained basic geometrical diameters two tested ejectors are shown in Table 2.

Table 2. Geometrical parameters of ejector

-	Geometry No.1	Geometry No.2
Nozzle throat diameter	5.7 mm	5.7 mm
Diameter of the nozzle outlet	11.8 mm	11.8 mm
Diameter of mixing chamber	20 mm	18 mm
Diameter of diffuser	60 mm	60 mm

Since motive parameters are constant diameters of the nozzle throat and nozzle outlet are the same for both geometries. The effect of the condensation temperature on mass entrainment ratio are shown in and Fig. 5.
The results show that for both tested geometries the performance line is typical for gas ejector. It is seen from this figure that for all investigated cases the ejector operates both under on-design and off-design conditions. However, for the cases with geometry No.1 ejector operate with higher mass

entrainment ratio. The maximum predicted by the model mass entrainment ratio is U_1 = 0.37. Simultaneously, the critical condensation temperature is tc_1* = 26 °C. With this critical condensation temperature, the ejector driven by tg = 130 °C starts to operate under off-design conditions. With a further increase of the condensation temperature the mass entrainment ratio consequently decreases. The slope of the performance line indicates that the ejector with geometry No. 1 will not operate for temperatures of condensation above 45 °C.

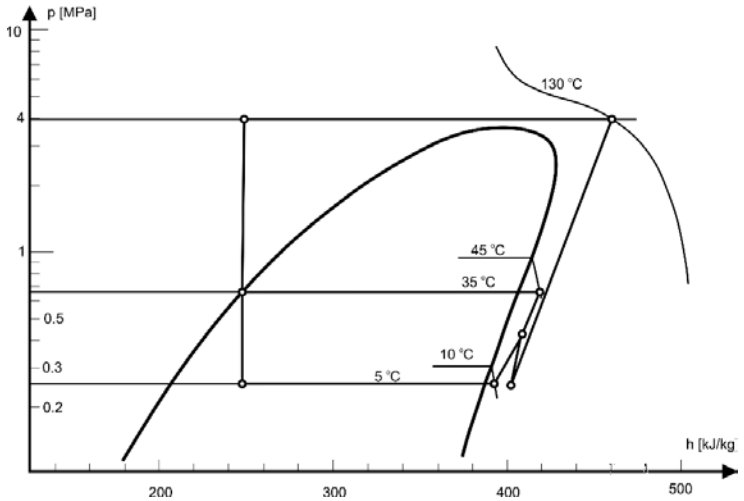

Figure 5: Effect of the condensation temperature on the mass entrainment ratio for various geometry

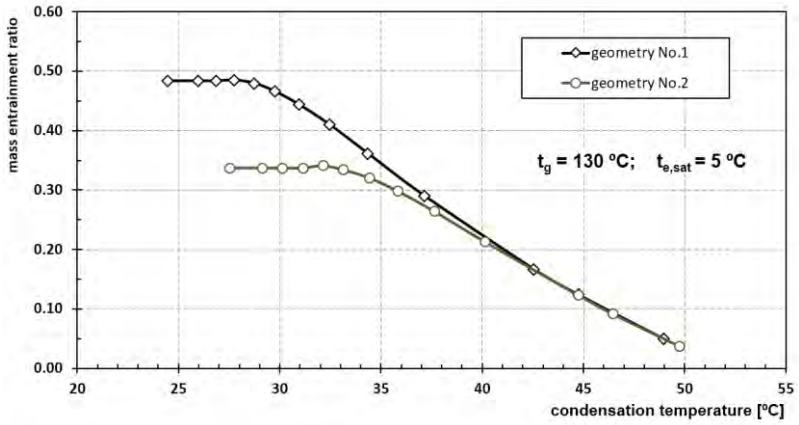

Figure 6: Effect of the condensation temperature on the mass entrainment ratio for various geometry

It must be noted that ejector is dedicated for A/C system for yachts therefore, high condensation temperature can be expected, especially in hot climate. Because of this the critical condensation temperature at level tc_1* = 26 °C can be though as moderate in proposed system. On the other hand, the mass entrainment ratio at level U_1 = 0.37 is relatively high compared to initially assumed value of U≈ 0.25. Therefore, the geometry was slightly modified in order to reduce mass entrainment ratio and extend the on-design operation of the ejector. The diameter of the mixing chamber was modified using trial-and-error method. The performance line for second geometry is also shown in Fig. 4. It is seen that decreasing of mixing chamber diameter reduces the mass entrainment ratio and extends the on-design operating regime, as expected. The maximum reported mass entrainment ratio was U2 = 0.25. For geometry No.2 the critical condensation temperature is tc_2* = 31 °C. Analogically as for geometry No. 1 the slope of the performance line predicted by the model indicates that the ejector with geometry No. 2 will not operate for temperatures of condensation above 45 °C.

Taking into consideration the requirements for air temperature in ship cabins during summer it can be postulate that evaporation of refrigerant at temperature 0 ºC is not necessary, because the temperature of fresh supply air should be approximately 19 ºC. Cooling the air up to temperatures slightly above 0ºC is not an effective solution, because in the next step the air should be heated up, to provide proper supply air temperature. The second reason why one should avoid excessive

cooling of the air is to reduce the potential risk of condensation of water vapour on cold air-cooler surface. Operation performance of ejector of both geometries was tested for evaporation temperature te_2 = 5 ºC. Again, the motive temperature was tg = 130 °C. Results are presented in Fig. 6. Results show that increasing of evaporation temperature increase the mass entrainment ratio. For ejector with geometry No.1 the mass entrainment ratio is U1 = 0.49 and the critical condensation temperature is approximately tc1* = 29 °C. The slope of the performance line in off-design regime indicates that ejector should operate for condensation temperature up to 50 °C. For the case of ejector with geometry No. 2 the maximum entrainment ratio is U2 = 0.33 and the critical condensation temperature is approximately tc2* = 34 °C. The temperature above which the ejector will not operate is predicted as 50 °C. It must be pointed out that performance of the both ejectors are very promising. The model predicts that on the off-design operating regime for temperature tc2 = 40 °C both ejector will have mass entrainment ratio at level of 0.20. Performance lines in terms on compression ratio vs mass entrainment ratio for te2 = 5 ºC are shown in Fig. 7.

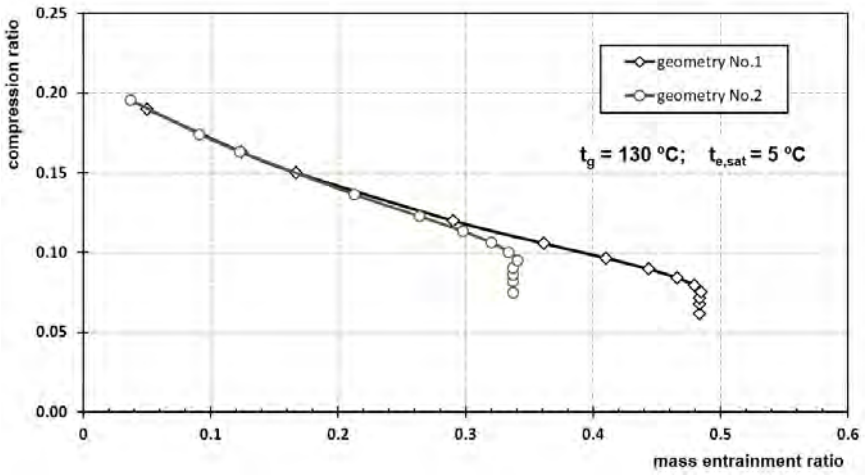

Figure 7: Compression ratio versus mass entrainment ratio for both geometries

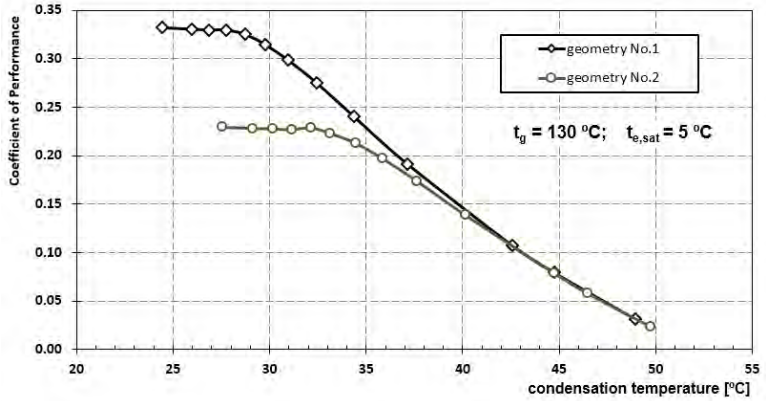

Figure 8: Coefficient of performance versus condensation temperature

The influence of the condensation temperature on the coefficient of performance *COP* of the ejector system is presented in Fig. 8. The coefficient of performance is directly related with mass entrainment ratio, therefore like in the case of mass entrainment ratio, the maximum level of *COP* = 0.33 was obtained for geometry No. 1 and condensation temperatures below t_{c1^*} = 29 °C (i.e. on-design operation regime). The lowest reported *COP* = 0.23 at the on-design operation was obtained for geometry No. 2. With mass entrainment ratio above the critical condensation temperature t_{c^*} the *COP* of the tested ejector consequently decreases, with subsequent increase in the condensation temperature.

3. CONCLUSIONS

The paper presents the results of application of the ejector refrigeration system for waste heat recovery in small yachts. Refrigerant R1234zeE was selected as a working fluid. A different formal approach in the field of application of refrigerant in cooling and air conditioning systems in marine vessels was indicated. The results show that proposed system can utilise the waste heat from piston engine as the motive source. Wide range of the disposable temperature of the source allows to use the supercritical state of refrigerant to drive the system. Reduction of mixing chamber diameter leads to extension of the on-design operating regime of the ejector. Require/ assumed coefficient of performance can be achieved for analysis operating conditions. Temperature tc1* = 29 °C and tc2* = 34 °C were predicted as the critical condensation temperatures for operating temperatures te = 5 ºC and tg = 130 ºC.

ACKNOWLEDGEMENTS

The research results presented in the paper were supported by the National Centre of Research and Development, Contract No. POIR 04.01.02-00-0135/16

REFERENCES

Diesel, MAN & Turbo, SE. (2011). Waste heat recovery system (WHRS) for reduction of fuel consumption, emissions and EEDI.

Shu, G., Liang, Y., Wei, H., Tian, H., Zhao, J., Liu, L. (2013). A review of waste heat recovery on two-stroke IC engine aboard ships. Renewable and Sustainable Energy Reviews 19, 385–401

Ezgi, C., (2014). Design and thermodynamic analysis of an H2OeLiBr AHP system for naval surface ship application, International Journal of Refrigeration 48, 153-165.

Ezgi, C., Girgin, I. (2015). Design and Thermodynamic Analysis of a Steam Ejector Refrigeration/Heat Pump System for Naval Surface Ship Applications, Entropy 17, 8152–8173

Butrymowicz D., Śmierciew K., Karwacki J., Gagan J. (2014). Experimental investigations of low-temperature driven ejection refrigeration cycle operating with isobutane, International Journal of Refrigeration 39, 196-209.

Śmierciew K., Gagan J., Butrymowicz D., Łukaszuk M., Kubiczek H. (2017). Experimental investigation of the first prototype ejector refrigeration system with HFO-1234ze(E), Applied Thermal Engineering 110, 115–125.

Yan, L., Li, J., Zhang, D., Liu, C. 2011. The Modeling and Simulation of Marine Air-condition, Procedia Engineering 12, 141–148.

Regulation (EU) No 517/2014 of the European Parliament and of the Council on fluorinated greenhouse gases and repealing Regulation (EC) No 842/2006.

Huang B.J., Chang J.M., Wang C.P., Petrenko V.A. (1999). A 1-D analysis of ejector performance, International Journal of Refrigeration 22, 354– 364.

ISO 7547:2002(E) Ships and marine technology - Air-conditioning and ventilation of accommodation spaces - Design conditions and basis of calculations.

Chen, W., Liu, M., Chong, D., Yan, J., Little, AB., Bartosiewicz, Y. (2013). A 1D model to predict ejector performance at critical and sub-critical operational regimes, International Journal of Refrigeration 36, 1750-1761

International Convention on the Arrangement of the State of the Sea by Ships, 1973/1978. MARPOL.

Manuscript ID: 672
DOI: 10.18462/iir.icr.2019.0672

Dynamic testing to better reflect real use for the seasonal performance of Air Conditioners

Carsten PALKOWSKI[(a)], Stefan VON SCHWARZENBERG[(b)], Anne SIMO*[(a)]

[a)] BAM Bundesanstalt für Materialforschung und -prüfung
Berlin, 12205, Germany, carsten.palkowski@bam.de
[(b)] TÜV SÜD Industrie Service GmbH Referat Kältetechnik
Olching, 82140, Germany, stefan.schwarzenbergvon@tuev-sued.de

ABSTRACT

In this contribution, a dynamic test method to determine the seasonal performance of inverter-type air conditioners has been developed and verified. In comparison to current test standards, where test modes for fixing the compressor speed are required, a dynamic approach is applied with unfixed compressor speed and thus better reflects the performance of air conditioners under real operating conditions.
The dynamic tests are conducted in two calorimeter chambers. The indoor chamber is kept at a constant temperature whereas the outdoor chamber is subjected to a temperature profile based on the climate BIN-distribution, representing the reference cooling demand. The proposed dynamic test considers the dynamic control of an air conditioner and delivers results which could indicate the units' performance in the field.
Keywords: Seasonal Performance Factor, Inverter-type Air Conditioner, Dynamic Test Method, Real Use Behavior.

1. INTRODUCTION

The worldwide domestic cooling demand is likely to increase due to climate change and the rise of the average global temperature. For instance, Casini (2009) showed that the electricity demand for cooling in the EU will be up to 72% higher by 2030. Similar observations were made by Miller et al. (2007), who analyzed the US market. Extensive research is being carried out in recent years, to improve the energy efficiency of air conditioners (ACs) as their energy consumption is found to account for more than 70% of the total carbon dioxide equivalent emissions based on the life cycle climate performance (Li, 2015). The quality of the control system of an AC has a large influence on the efficiency of the unit. Inverter-driven ACs are the prevalent type of split ACs. Under real operation conditions the inverter regulates the compressor speed to adjust the cooling capacity using pulse width modulation (PWM) or pulse amplitude modulation (PAM). The proper modulation of the capacity to the heat load reduces the power consumption of the AC, which was shown by Shao (2004). The major factor for the capacity modulation and thus the performance of the AC is the compressor operating frequency as found by Tu et al. (2018). Several experimental studies gave evidence for the influence of the compressor speed on the cooling capacity; control strategies via frequency adjustment of the compressor were developed within these studies (Choi and Kim, 2003; Jeong and Choi, 2014; Park et al., 2000; Wu et al., 2005). Furthermore, Hirota et al. (2014) showed that innovative control strategies like PFC (predictive function control) could significantly increase the average annual COP by 70% compared to PID control.
Methods for laboratory testing of ACs are described in several standards, such as the (DIN) EN 14825 (FNKä, 2016), AS/NZS 3823 (AS/NZS, 2014) and ANSI/AHRI Standard 201/240 (AHRI, 2008), ASHRAE 116-2010 (ASHRAE 2010), and JIS C9612 (JIS 2013). In those standards, the seasonal performance of ACs is evaluated under full load and various part load conditions, because the most frequent heat loads are lower than the rated capacity of the AC throughout a season. However, these standards require steady-state conditions, which are achieved by running the inverter at a certain frequency and thereby fixing the compressor speed, inactivating

the control of the AC. Fixing the compressor in an artificial operating mode, however, does not consider the effectiveness of the unit´s control and thus, the partial load characteristics cannot be obtained properly. Testing according to the current test standards is not possible without manufacturer support since a specific software or test modes are required to fix the compressor frequencies. As a consequence, the seasonal performance of ACs cannot be tested independently by testing institutes, for instance for certification purposes.

Therefore, the dynamic behavior and control of the unit play a crucial role for the evaluation of the energetic performance of ACs during daytime temperature changes and should be included in test methods. Only few examples from the literature can be found that describe methods or approaches for the dynamic testing of heat pump systems. Various simulation studies have been conducted to reproduce the seasonal performance of air conditioners and heat pumps (Gomes, 2013; Cuevas 2009), also considering operating parameters of the units' control, including the compressor frequency (Lee, 2018). Menegon et al. (2017) as well as Haller et al. (2013) developed dynamic tests for the laboratory characterization of heating systems. Riederer et al. (2009) developed a dynamic test for ground source heat pumps (GSHPs) which considers dynamic weather conditions, occupancy profiles and a reference building. Huchtemann et al. (2016) followed another approach and developed a dynamic test and a Hardware-in-the-Loop (HiL) test bench for GSHPs and air source heat pumps (ASHPs). The obtained results showed deviations between measured performance and the manufacturer declared performance according to test standards. Watanabe et al. (2009) introduced a load-based steady-state measurement and tested ACs with unfixed compressor speed. Several studies followed this pioneering approach for the seasonal performance of inverter-type ACs (Mavuri, 2015; Nakos et al., 2014). The seasonal performance was determined from the measurement results and the application of the BIN method, in which the operation duration corresponds to temperature intervals called bins. This method is well known for the consideration of climate conditions (ASHRAE, 2010), however, the seasonal performance is obtained from the interpolation of performance results under only four part load conditions and temperature changes are not considered. To adequately predict the seasonal performance of ACs, for instance for the temperate European climate, by means of laboratory tests, the whole temperature range 17°C – 39°C, which are 23 1K-temperature-steps, needs to be considered.
In this study, we propose a dynamic test method to determine the seasonal cooling performance of split ACs. This method consists of 23 load-based measurements and thus considers the whole temperature range during a cooling season for the average European climate. Additionally, the testing includes changes of the outdoor temperature to reflect the dynamic adjustment of cooling capacity for variable capacity units and thus could give a closer approximation to field behavior. This method could help to distinguish between efficient and less efficient ACs and could give impetus for manufacturers to optimize the control systems of their products.

2. DYNAMIC METHOD

This section defines the specific test procedure of the dynamic method and describes how to determine the seasonal energy efficiency ratio (SEER) of ACs. The laboratory tests consist of a temperature profiling at the condenser inlet. The design of the temperature profiling is explained in detail in section 2.1. It follows the requirements and conditions for the part-load ratios (PLRs) and related dry-bulb and wet-bulb temperatures for the indoor room and the outdoor room of the calorimeter according to test standard EN 14825. The requirements and the permissible deviations of the determined values from the set values, used in our tests, are shown in Table 1. The PLR is defined as the ratio of the cooling capacity in a defined part-load operating point and the rated cooling capacity (full load 100%) according to Eq. (1):

$$PLR = \frac{\dot{Q}_{C,PLR}}{\dot{Q}_{C,100\%}} \cdot 100\% \qquad \text{Eq. (1)}$$

The tests were carried out in two doubled calorimeter rooms, one room for the indoor unit and one

for the outdoor unit, respectively. The calorimeter rooms are equipped with cooling coils, heaters, humidifiers, fans and air mixers to ensure the described stable conditions in each room according to Table 1.

The evaporator inlet temperature θ_{ei} is kept constant at 27°C during the whole measurement. Therefore, the set temperature of the AC is set to 27°C via the unit's remote control and was only adjusted if the evaporator inlet temperature exceeded the permissible deviations given in Table 1. The condenser inlet temperature θ_{ci} was subjected to a temperature profile based on the BIN-distribution, which is shown in Figure 1. The room temperatures, θ_{1or} and θ_{1ir}, were allowed to deviate by more than ±10%, as they are identified to have a minor influence on the measurement results. The PLR of the cooling capacities of the tested ACs are given in Table 1. They follow a specific linear cooling curve which depends on the condenser inlet temperature θ_{ci} and the nominal cooling capacity $\dot{Q}_{c,100\%}$ at 35°C. For each θ_{ci} value we hereby define a correlating cooling capacity $\dot{Q}_{c,PLR}$. For each temperature sequence of the profile, a particular heating capacity (compensation load) is given by the test stand; the tested AC responds with the corresponding cooling capacity $\dot{Q}_{c,PLR}$. Due to the heat transmission losses of the test stand, the compensation load and the cooling capacity are not equal.

Table 1. Test conditions and permissible deviations from set values used for the dynamic method

Step #	PLR of cooling capacity (%)	Condenser inlet dry bulb temperature θ_{ci} (°C)	Evaporator inlet dry bulb temperature θ_{ei} (°C)	Evaporator inlet wet bulb temperature θ_{ei} (°C)	Permissible temperature deviation of the arithmetic mean values from set values (for dry bulb and wet bulb)	Permissible temperature deviations of each of the individual measured values from set values (for dry bulb and wet bulb)
1	5	17	27	19	± 1 K	± 1.5 K
2	16	19	27	19		
3	21	20	27	19		
4	32	22	27	19		
5	47	25	27	19		
7	58	27	27	19		
8	74	30	27	19		
9	121	39	27	19	± 2 K	± 3 K
10	116	37	27	19	± 1 K	± 1.5K
11	100	35	27	19		
12	89	33	27	19		
13	79	31	27	19		
14	68	29	27	19		
15	58	27	27	19		
16	47	25	27	19		
17	37	23	27	19		
18	26	21	27	19		
19	21	20	27	19		
20	11	18	27	19		
21	5	17	27	19		

The cooling capacity $\dot{Q}_c$ and the electric power consumption P_{el} are detected during the whole measurement process. From these measurement results we derive for the provided cooling energy Q_c and the electric energy consumption E_{el} of the test AC. The $SEER_{dyn}$ is calculated using an energy balance of the overall measurement time:

$$SEER_{dyn} = \frac{\int \dot{Q}_c}{\int P_{el}} \quad \text{Eq. (2)}$$

where $\int \dot{Q}_c$ is the cumulated cooling energy and $\int P_{el}$ the cumulated electric energy consumption. Standby is included during the ON/OFF behavior of the unit. It is observed that, the duration of standby differs for the different units which could better reflect the real control behavior, instead of considering a general assumption of standby duration for the different types of ACs. Other non-active modes can be included using the same conditions as described in the current test standards (e.g. EN 14825).

2.1 Design of the Temperature Profile

The temperature BIN-distribution weights the outdoor air temperatures (corresponding to our condenser inlet temperatures) by their occurrences per year to consider different climates. In this study, the tested ACs are subjected to a temperature profile based on the BIN-distribution for "average" climate conditions according to the climate in Strasbourg/France during the test. The active mode seasonal performance for "warmer" and "colder" climate can be easily calculated from the "average" temperature profile measurement by weighting the applicable climate BIN hours, as given in EN 14825.

For the condenser inlet temperature θ_{ci}-profile we further considered the following criteria:

- Variation of θ_{ci} sequences in the range of 17°C – 39°C to represent the average European climate based on the BIN distribution of the EN 14825, with each temperature being weighted as in the BIN distribution;
- Measurement time for each sequence should be at least 40 min in order to achieve representative average measurement values and to minimize the influence of local effects and thus increase the accuracy;
- The profile should consider both, the increase and decrease of θ_{ci};
- The overall measurement time is max. 6 days.

Based on these criteria the temperature-profile and the corresponding cooling capacity were designed as depicted in Figure 1. Starting from 17°C the temperature increases to 39°C and afterwards decreases back to 17°C again. At temperatures higher than 30°C the duration for each sequence is significantly shorter than at lower temperatures, most of the time the measurements are conducted at temperatures lower than 30°C.
To meet all the aforementioned criteria and to achieve a correct weighting of each temperature, six temperatures (24°C, 26°C, 28°C, 32°C, 34°C, 36°C and 38°C) were not considered. However, non-consideration of these temperatures has only little impact on the compliance with the average climate. The excluded temperatures do either I) have a small percentage share in the BIN distribution, II) do only show little differences in unit behavior compared to nearby temperature sequences which are considered in the profile or III) do meet both of the aforementioned criteria.

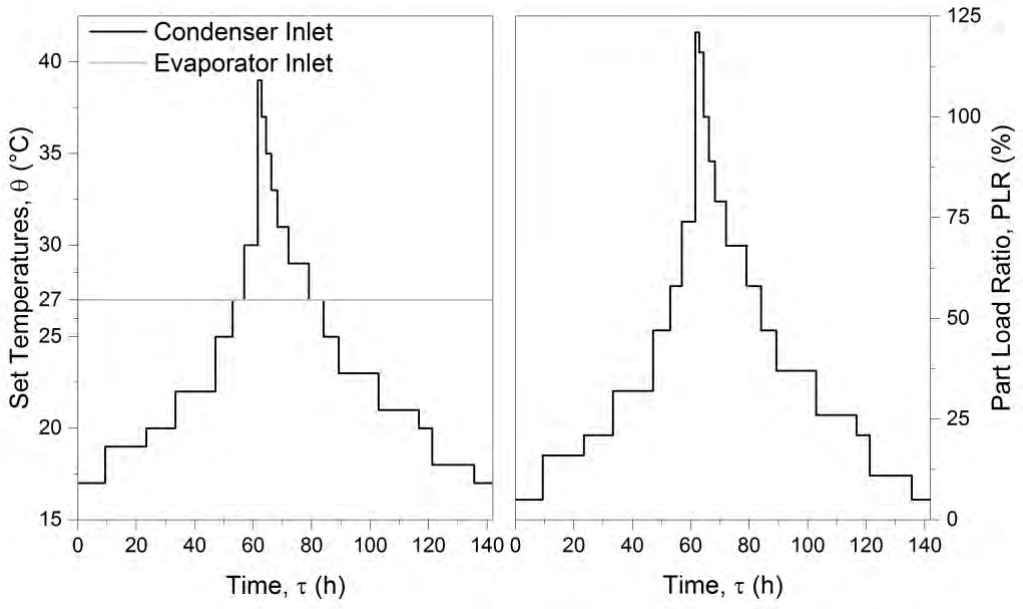

Figure 1: Temperature and cooling capacity profiling

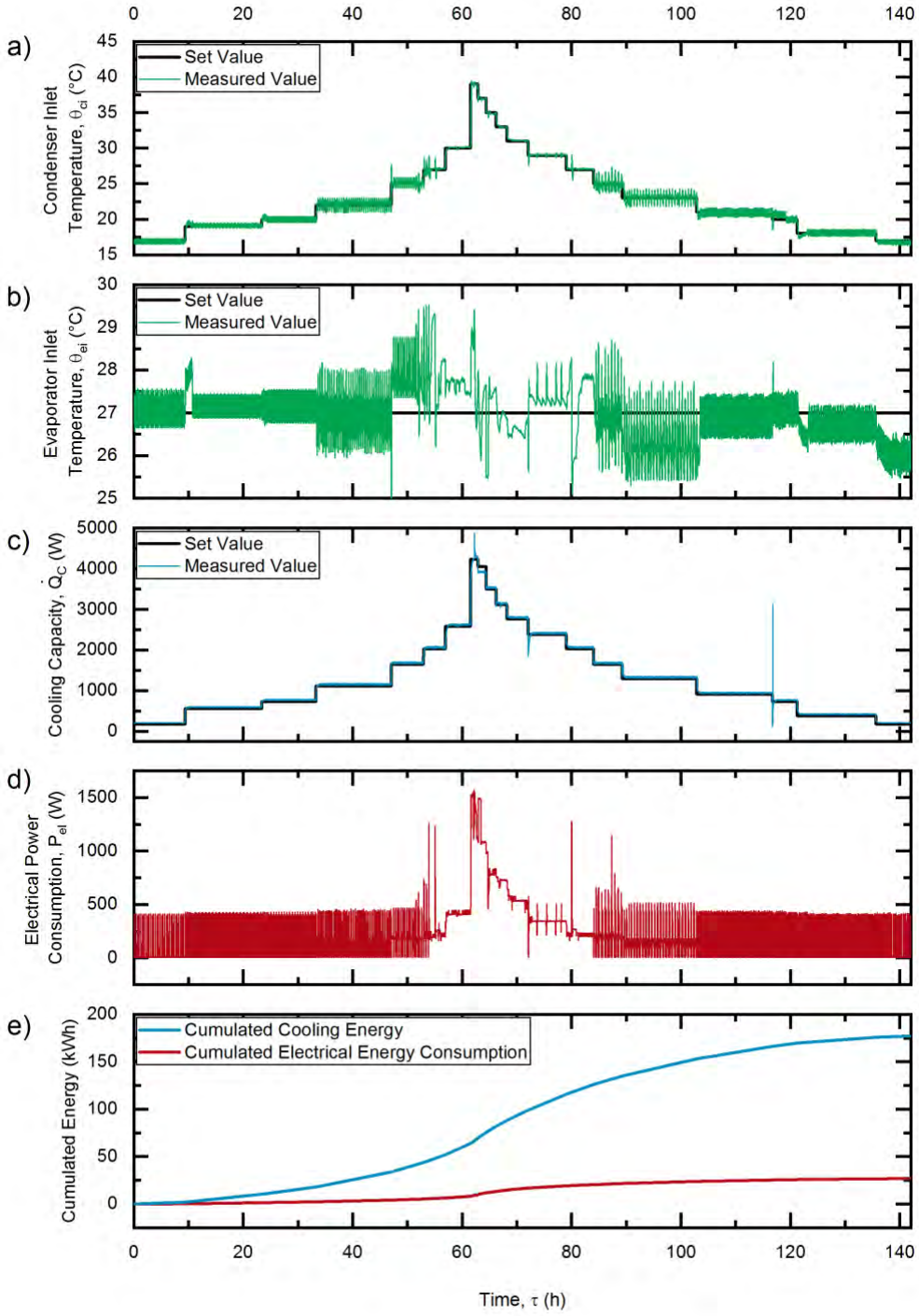

Figure 2: Results of the dynamic testing of AC#1

2.2 Implementation of the Temperature Profile

We tested two ACs, AC#1 and AC#2, according to the dynamic test method. The main properties of the tested ACs are given in Table 2.

Table 2. Tested air/air type AC models

AC device No.	Rated cooling capacity (kW)	Declared SEER (-)	Energy efficiency class	Refrigerant
1	3,5	8,5	A++	R410A

2	2,6	6,66	A++	R410A

During the test, the condenser inlet temperature, evaporator inlet temperature, the cooling capacity and the electric power consumption were recorded with a measurement intervals of 10 seconds. At the end of the test, the recorded cooling capacity and electric power consumption were integrated to determine the cumulated cooling energy Q_c and cumulated electric energy consumption E_{el}, respectively. Fig. 2 exemplarily shows the results of the dynamic test for AC#1. For the comparison of measured values and the set values, the latter are included in Fig. 2.
The measured temperatures and cooling capacity follow the set values according to the profiles shown in Fig. 1. The condenser inlet temperature (Fig. 2a) and the evaporator inlet temperature (Figure 2b) range within the permissible deviations according to Table 1. Only for cooling capacities with PLRs greater than 58% unpredicted fluctuations occurred and temperatures exceeded the permissible deviations at 80h (PLR = 58%). Hence, an adjustment of the permissible deviations for the temperatures for PLRs greater than 58% could be put up for discussion. The cooling capacity peaks (Fig. 2c) at 63h, 72h and 117h are artefacts from the test stand and are not attributed to the tested unit. Therefore, these particular single measured values were not considered for the evaluation of the measurement. The electric power consumption P_{el} (Fig. 2d) increases with increasing cooling capacity and vice versa, thus representing the different dependencies on the cooling demand. For PLRs lower than 58%, we observed ON/OFF-operation, with amplitude and frequency of the ON/OFF-cycles varying depending on the outdoor room temperature. However, despite the constant fluctuations in the electric power consumption, we achieve stable conditions at all times with measured values that are within the permitted deviations.
Fig. 2e shows the cumulated cooling energy (blue curve) and the cumulated electric energy consumption (red curve). During the whole measurement, the cumulated cooling energy is higher than the cumulated electric energy consumption. At the end of testing, AC#1 in total provided an amount of cooling energy of 101.16 kWh by consuming an electricity energy of 13.97 kWh. The energy balance according to Eq. 2 results in a $SEER_{dyn}$ of 6.6. CONCLUSIONS

Currently, energy efficiency testing for ACs is only possible in particular test modes, which fix the compressor speed. In consequence, tests cannot be conducted independently and additionally do not reflect the real use behavior of ACs. This study proposes a dynamic test method which could be used to test independently from manufacturers and closer to real use behavior to determine values for the declaration on the energy label.
The dynamic test method can be used for the same experimental setup as applied in current standards. The test conditions are based on the climate data already implemented in current standards. Following this climate data, a profile has been designed for condenser inlet temperature which is varied during the test. The evaporator inlet temperature is kept constant at 27°C. The AC is not fixed into a test mode but achieves the required test conditions by using its variable speed controller. The dynamic test method delivers results for the seasonal cooling performance by simply balancing the cumulated energies for use and effort and moreover has the following advantages:

- It can be conducted independently from manufacturer data and makes special test modes obsolete;
- It considers the whole temperature range from 17°C to 39°C, specifically those sequences which are commonly linearly interpolated in current standards.
- It makes linear interpolation and the prescription of invariables obsolete and hence gives a closer approximation for the field performance of ACs and could reduce the need for field tests;
- It considers the real control behavior of ACs hence enables a sound performance evaluation;
- Its testing duration was designed according to current standards (six days) and has the potential to be further shortened;
- It has the potential to achieve a high degree of automation and could be easily modified to new technologies.

The growing market penetration of ACs indicates the need for a performance test method for ACs which better reflects their units' capacity modulation.
The results obtained with the dynamic method provide useful information to improve the system´s control. In this way, the implementation of a dynamic testing offers an opportunity to give manufacturers an impetus to introduce more efficient products into the market.
In addition, the dynamic method has potential to be shortened by reducing the duration of the temperature sequences at low condenser inlet temperatures from 17°C to 25°C. The frequency of each temperature could be mathematically recovered after testing. The impact on the precision of the test method should be a particular objective of further investigations.

ACKNOWLEDGEMENTS

This project is financed as a part of the National Action Plan on Energy Efficiency (NAPE) of the German Federal Ministry for Economic Affairs and Energy.

NOMENCLATURE

EER_{PLR}	energy efficiency ratio at specific part load ratio (W x W^{-1})	E_{el}	electric energy consumption (Wh)
$\dot{m}_{w1}$	water mass flow (kg x s^{-1})	P_{el}	electric power consumption (W)
$P_{el,PLR}$	electric power consumption at specific part load ratio (W)	PLR	Part load ratio (%)
$\dot{Q}_c$	cooling capacity (W)	$\dot{Q}_{c,PLR}$	cooling capacity at specific part load ratio (W)
$\dot{Q}_{eh}$	heating capacity of electric heater (W)	Q_c	cooling energy (Wh)
$SEER$	seasonal energy efficiency ratio (W x W^{-1})	$SEER_{dyn}$	seasonal energy efficiency ratio of dynamic test (W x W^{-1})
θ_{ci}	condenser inlet temperature (°C)	θ_{ei}	evaporator inlet temperature (°C)
$\theta_{W1,in}$	water inlet temperature of fan coil (°C)	$\theta_{W1,out}$	water outlet temperature of fan coil (°C)
θ_{ir}	average indoor room temperature (°C)	θ_{or}	average outdoor room temperature (°C)
τ	time (h)		

REFERENCES

Air Conditioning, Heating and Refrigeration Institute, 2008. ANSI/AHRI 210/240:2008. Standard for Performance Rating of Unitary Air-Conditioning & Air-Source Heat Pump Equipment. Arlington, USA.

American Society of Heating, Refrigerating and Air-Conditioning Engineers Inc., 2010. ASHRAE, ANSI/ASHRAE Standard 116-2010 Methods of Testing for Rating Seasonal Efficiency of Unitary Air Conditioners and Heat Pumps. Atlanta, USA.

Casini, M, 2009. Advanced Materials and Nanotechnology to Improve Energy-Efficiency and Environmental Performance. , Woodhead Publishing Series in Civil and Structural Engineering (Elsevier).

Choi, J.M., Kim, Y.C., 2003. Capacity modulation of an inverter-driven multi-air conditioner using electronic expansion valves. Energy 28, 141-155.

DIN Normenausschuss Kältetechnik (FNKä), 2013.DIN EN 14511:2013-3 Air conditioners, liquid chilling packages and heat pumps with electrically driven compressors, for space heating and cooling Part 3: Test methods. Berlin, Germany.

DIN Normenausschuss Kältetechnik (FNKä), 2016. DIN EN 14825:2016 Air conditioners, liquid chilling packages and heat pumps, with electrically driven compressors, for space heating and cooling - Testing and rating at part load conditions and calculation of seasonal performance. Berlin, Germany.

Haller, M.Y., 2013. Dynamic whole system testing of combined renewable heating systems The current state of the art. Energy Buildings 66, 667-677.

Hirota, M., Iwata, Y., Sakuraba, I., Nagamatsu, K., Shinagawa, K., Katsuragi, H., Hoshino, H., Kasahara, S., Oka, M., Yabu, T., 2014. Research and development of innovative energy-saving controls of next-generation multiple air-conditioning systems for buildings. 11th IEA Heat Pump Conference, Montréal, Canada.

Huchtemann, K, Engel, H., Mehrfeld, P, Nürenberg, M., Müller, D., 2016. Testing method for evaluation of a realistic seasonal performance of heat pump heating systems: Determination of typical days. 12th REHVA World Congress: volume 3, Aalborg, Denmark.

Japanese Industrial Standards Committee, 2013. JIS C9612, 2013. Room Air Conditioners. Tokyo, Japan.

Jeong, K., Choi, J.M., 2014. Capacity modulation of a cascade heat pump with the variation of compressor speed and electronic expansion valve opening. Renew Sustain. Energy 6, 1-9.

Lee, S.H., Jeon, Y., Chung, H.J., Cho, W., Kim, Y., 2018. Simulation-based optimization of heating and cooling seasonal performances of an air-to-air heat pump considering operating and design parameters using genetic algorithm. Appl. Therm. Eng. 144, 362-370.

Li, G., 2015. Investigations of life cycle climate performance and material life cycle assessment of packaged air conditioners for residential application. Sustain Energy Technol. Assess. 11, 114- 125.

Mavuri, S., 2015. Field behaviour of inverter air conditioners effect on seasonal performance. Application or Innovation in Engineering and Management 4, 18-25.

Menegon, D., Soppelsa, A., Fedrizzi, R., 2017. Development of a new dynamic test procedure for the laboratory characterization of a whole heating and cooling system. Appl. Energy. 205, 976 -990.

Miller, N., Hayhoe, K., Jin, J, Auffhammer, M., 2007. Climate, extreme heat, and electricity demand in California. Appl Meteorol Climatol 47, 1834-1844.

Nakos, H., Haglund Stignor, C., Andersson, K., Lidbom, P., Thyberg, S., 2014. Air-to-air heat pumps evaluated for Nordic climates-trends and standards. 11th IEA Heat Pump Conference, Montréal, Canada.

Park, Y.C., Kin, Y.C., Min, M.K., 2000. Performance analysis on a multi-type inverter air conditioner. Energy Convers. Manage. 42, 1607-1621.

Riederer, P., Partenay, V., Raguideau, O., 2009. Dynamic test method for the determination of the global seasonal performance factor of heat pumps used for heating cooling and domestic hot water preparation. Proceedings of the 11th International IBPSA Conference, Glasgow, Scotland, 752-759.

Standards Australia and New Zealand Standards, 2014. AS/NZS 3823:2014 Performance of electrical appliances - Air conditioners and heat pumps. Sydney, Australia / Wellington, New Zealand.

Tu, Q., Zhang, L., Cai, W., Guo, X., Yuan, X., Deng, C., Zhang, J., 2018. Control strategy of compressor and sub-cooler in variable refrigerant flow air conditioning system for high EER and comfortable indoor environment. Appl. Therm. Eng. 141, 215-225.

Watanabe, C., Ohashi, E., Hirota, M., Nagamatsu, K., Nakayama, H., 2009. Evaluation of annual performance of multi-type air-conditioners for buildings. J. Therm. Sci. Tech.-JPN. 4, 483-493.

Wu, C., Zhou, X., Deng, S.M., 2005. Development of control method and dynamic model for multi evaporator air conditioners (MEAC). Energy Convers. Manage. 46, 451-465.

Manuscript ID: 679
DOI: 10.18462/iir.icr.2019.0679

Improvement of efficiency of a geothermal heat pump installation

Chantal MAATOUK[(a)], Pierre AZAR[(a),(b)]

[(a)] Saint Joseph University of Beirut, Faculty of Engineering, MarRoukoz, Lebanon, chantal.maatoukriachi@usj.edu.lb
[(b)] Lebanese University, Hadath, Lebanon

ABSTRACT

A vertical geothermal heat exchanger is made of a pair or two pairs of a U-shaped tubes in which circulates the coolant. The heat flux flowing from the soil to the coolant is limited by the grout physical properties.
The geotechnical works hold the highest cost in geothermal installations, reducing this cost is critical to the economic viability of the system. Market grouting products thermal conductivity limit is 2.08 $W.m^{-1}.K^{-1}$ leading to high heat exchanger length. Increasing the thermal conductivity of the grout material will result in reducing the heat exchanger length.
Laboratory tests were undertaken to determine the thermal conductivity of an aluminum, silica sand and cement mixture. A thermal modeling of the heat exchanger, grout and soil was conducted. The experimental results show that thermal conductivity of 5 $W.m^{-1}.K^{-1}$ can be achieved.
A heat pump, coupled to the vertical geothermal heat exchanger was modeled. The simulations showed that a reduction of 25% of the heat exchanger length can be achieved theoretically for the same heat load absorbed from the soil.
Keywords : geothermal, grout, thermal conductivity, heat pump, borehole, aluminum, vertical heat exchanger, thermal enhancing.

1. INTRODUCTION

The geothermal energy is a promising source of energy for the both near and far future, looking to the need of replacement of nuclear, coal-fired and fossil energies with more environmental choices. The geothermal energy appears to be a good alternative with unlimited energy production and use.
Geothermal heat pumps, also referred to as ground source heat pumps or geo-exchange, refer to systems that use the ground, groundwater, or surface water as a heat source or sink. Such system is made up of several key components including: Ground loop; Heat pump; Air or Water delivery system. The ground loop is a system of pipes that is buried in the shallow ground near the building. A fluid circulates through the ground loop to absorb or relinquish heat within the ground. In winter, the heat pump removes the heat from the fluid in the pipe, and transfers it to the building. This process is reversed in summer. The air delivery system uses conventional ductwork or pipe systems to distribute the heated or cooled air throughout the building.
There are two types of geothermal probes, the vertical heat exchangers and the horizontal heat exchangers. Most vertical probes drilled are installed at a depth between 50 and 200 meters to operate a heat between 10 to 20 °C. Generally, it would be better to drill down to reach higher

temperatures, but the chosen depth is usually a compromise between the cost of drilling and the amount of electricity needed to run the circulating pump.
For a well-insulated family home, a single drill between 120 and 150 m is usually sufficient, where a vertical geothermal probe is sealed in a double pipe that descends and goes up. The working fluid, usually water, is the heat transfer medium between the soil and the building. If the heat recovered is not sufficient, in this case two probes are installed. The material used for the realization of a geothermal probe is simple; it is composed of polyethylene pipes coated in a sealing grout called bentonite.
The bentonite provides a heat transfer medium between the geothermal probe and surrounding. The conventional commercial grout fillers has low thermal conductivity ranging from 1.73 to 2.08 $W.m^{-1}.K^{-1}$, which leads to high heat exchanger length. Increasing this thermal conductivity, permit the improvement of the heat transfer between the soil and the probe, thus reducing the heat exchanger length. Many studies where done in the last twenty years concerning the thermal conductivity of the grout and the performance of the heat exchanger. A series of simulations for different thermal conductivities and borehole depth shows that the conductivity of the grout is a determining factor for the depth and for the performance (Cassaso and Sethi,2014). Case studies with Carm-tool were compared to Ashrae recommendation for geothermal U-pipe heat exchanger was done without taking into consideration the effect of the thermal conductivity of the grout versus the drilling depth. Capozza et al., 2015 and Pouloupatis et al. 2016 have analyzed the performance of geothermal heat exchangers in Cyprus which theatrically has a close geological structure to Lebanon. Depth reduction while increasing the thermal conductivity that reached 4 $W.m^{-1}.K^{-1}$ of the grout was simulated and concluded that 6 $W.m^{-1}.K^{-1}$ is the optimum thermal conductivity (Maatouk (2016)).
As seen, most of the researches targeted the performance of the system while proposing theoretical thermal conductivities of the grout materials, from this point comes the strength of our research to improve and develop grouting materials that have good thermal quality and a low market price while being abundant and harmless for the soil and the underground water.
In this paper, an experimental study was performed studying the thermal conductivity of various grout mixture using recycled aluminum waste particules. Experimental results shows that thermal conductivity of the grout can be increased up to 5 $W.m^{-1}.K^{-1}$. A thermal modeling of the soil, the grout and the heat exchanger was conducted. The simulation results showed that the reduction in required borehole length was predicted theoretically for an example heat pump system and found to reach 40 %, depending on the soil thermal conductivity and borehole diameter.

2. EXPERIMENTAL APPARATUS

Several standards exist for measuring the thermal conductivity of materials, such as IEEE Standard 442-1981, ASTM Standard D5334-08 and others. Based on these standards, an experimental apparatus was built in order to measure the thermal conductivity of various composition of grout mixture. The objective of this experimental study is to improve the thermal conductivity of the sealing cement in order to enhance the heat flux exchanged between soil and geothermal probes.

2.1. Description of the Apparatus

The constructed apparatus is cylindrical having a diameter of 400mm and a height of 270mm including the sample insertion space, which have a diameter of 100mm and a height of 120mm. The insulation is made of three layers of Rockwool blankets to eliminate the radial heat flux, thus increasing the vertical heat flux and controlling the heat losses from the sample. The used Rockwool has a density equal to 24 $kg.m^{-3}$, a 50 mm thickness and thermal conductivity equal to 0.044 $W.m^{-1}K^{-1}$.

Two temperature sensors were installed on the outer insulation layer to monitor any heat losses threw the incubator. The measuring sensors were placed in the molds at a spacing of 30mm. The temperature sensors used are Type K Thermocouple. In this experiment an electrical heating source of 450 W and 220 V was used. The heating power was varied using a sliding coil voltage regulator with digital display for the output voltage from the regulator.

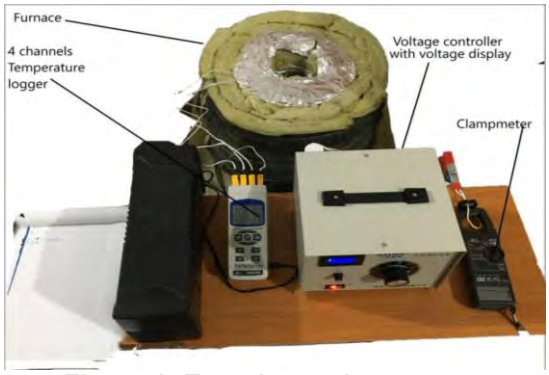

Figure 1: Experimental apparatus

2.2. Experimental Results

The experiments took place under room conditions; 26°C room temperature and a humidity varying between 65% and 78%. Prior to the measurement of the thermal conductivity of the samples, the apparatus and the different probes were calibrated. When the steady state is reached, thermal conductivity is calculated as following:

$$k = \frac{Q.\Delta x}{S.\Delta T} \qquad \text{Eq. (1)}$$

The tested mixtures are mainly composed of cement, sand, water and aluminum powder, varying the mass composition of the different components. Table 1 shows the average values of the measured thermal conductivity of the samples.

Table 1. Experimental results

Sample	1	2	3	4	5	6
Cement	48%	47.75%	47.75%	47.75%	47.75%	47.25%
Sand	52%	51.75%	51.75%	51.75%	51.75%	51.25%
Aluminum	0%	0.50%	0.50%	0.50%	0.50%	1.50%
Water*	0%*	0%*	5%*	10%*	15%*	15%*
Thermal conductivity ($W.m^{-1}K^{-1}$)	0.65	0.95	1.93	2.29	3.31	5.04

*of weight of solid materials

The maximum reached thermal conductivity in these experiments is for mix number 6 and is 5.01 $W.m^{-1}K^{-1}$. Results shows a bold increase of the thermal conductivity when adding aluminum particles to the mix, also it shows an increase of the thermal conductivity with the increase of water proportion. This result will be used to compare the difference between the existing market grout material and the mix 6 effects on the length of the borehole as well as on the COP.

3. THERMAL MODELING OF THE GEOTHERMAL HEAT EXCHANGER

The thermal behavior of the ground was modeled using Ansys Fluent. The objective is to calculate the linear power extracted from the soil for different thermal conductivity of the grout in order to determine the best aluminum proportion to be added to the mix. The case of the geothermal heat exchanger operating in both heating and cooling modes are investigated.

3.1. Modelling of the Ground Temperature Variation

3.1.1. Modeling of the Ambient Air Temperature

Daily ambient temperatures during a typical year were considered. To facilitate the use of these data, the temperature changes was represented as a cosine function of time (days). This function is considered as a boundary condition in the CFD model.

$$T(t) = T_{av} + A.\cos(\omega(t - t_0)) \quad \text{Eq. (2)}$$

Where ω is the angular frequency equal to 0.0172 rad.day^{-1}, which corresponds to a period of 365 days; T_{av} is the average annual temperature. A is the amplitude of the temperature variation; t_0 is the day of the year when the maximum temperature is reached.

3.1.2. Layout of the Modeled Geometry and Meshing

In this study we propose a geothermal probe composed of a polyethylene tube of 40 mm diameter and 4 mm thick, installed in a borehole of 30 cm in diameter. The tube is fixed by the grout. The vertical probe depth is 156 m. “Design builder”, a built in drawing software was used to create the geometry. The mesh is formed of 13519785 hexahedral shaped cells selected in order to decrease the time of the simulation without affecting the accuracy of the results. A mesh distribution strategy was used. Fluid domain and inner pipes and edges had the highest mesh concentration, followed by the grout mesh with slightly lowest mesh dimensions, soil mesh concentration is high on the edge linking to the grout and decreases as it goes out from the center. Fig. 2 shows the meshed geometry.

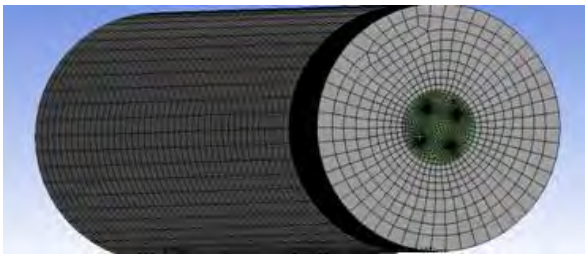

Figure 2: The geothermal heat exchanger, the grout and the soil mesh

3.1.3. Models and boundary conditions

The energy model and the k-epsilon model for turbulent flow were activated. Cell zone conditions were defined according to the material of each zone as fluid domains and solids, respectively assigning each material to the concerned zone. The boundary conditions were defined according to each zone limits, type, temperature, velocity inlet and wall. For cooling mode the entering water temperature is 315 K and for heating mode the entering water temperature is 278 K. The water flow per circuit is 0.045 l.s^{-1}.

3.2. Results and Discussions

The main concern of this study is to evaluate the heat transfer and the temperature gradient in the bore. Figure 3a and b shows the temperature contour for all domains of the heat exchanger with the geothermal heat pump in heating mode for K=5W.m^{-1}.K^{-1} and 1 W.m^{-1}.K^{-1} for depths

varying between 5 and 100 m, entering fluid temperature 4.85°C. Results shows that the temperature gradient is greater for higher thermal conductivity, leading to higher temperature at the outlet of the water flow.

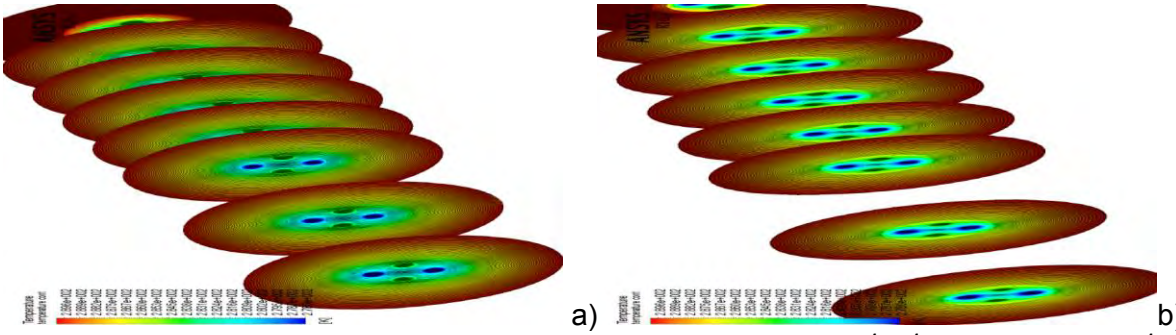

a) b)

Figure 3 : Temperature contour in heating mode for ; a) k=5W.m^{-1}.K^{-1} and b) k = 1 W.m^{-1}.K^{-1}

Same results were obtained in the cooling mode, where the heat flux extracted from the soil is much more interesting for higher thermal conductivity of grout. The thermal conductivity of the grout was increased to evaluate its effect on the heat transfer between the soil and the water flux. These results are presented in figure 4. For a conventional conductivity value, the thermal gradient observed in the grout is around 7 °C, and then decreases sharply to 2.5 °C at 5 W.m^{-1}.K^{-1}, and then stabilized to 1 °C for λ = 10 W.m^{-1}.K^{-1}. For this value of conductivity, the limiting factor is not the grout but the soil itself.

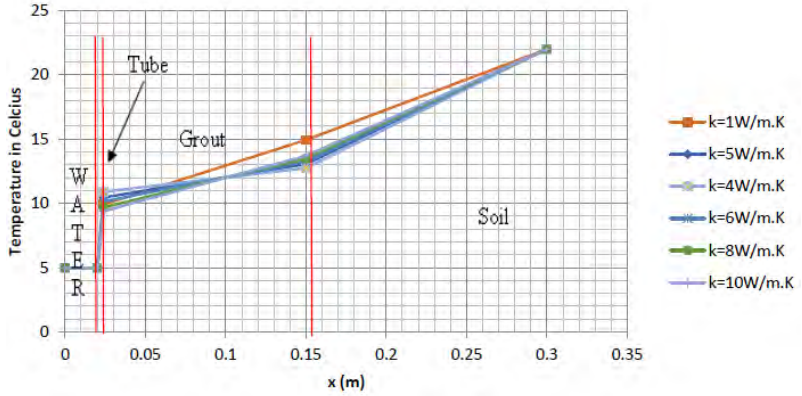

Figure 4 : Evolution of the temperature in the borehole for different k values for the grout

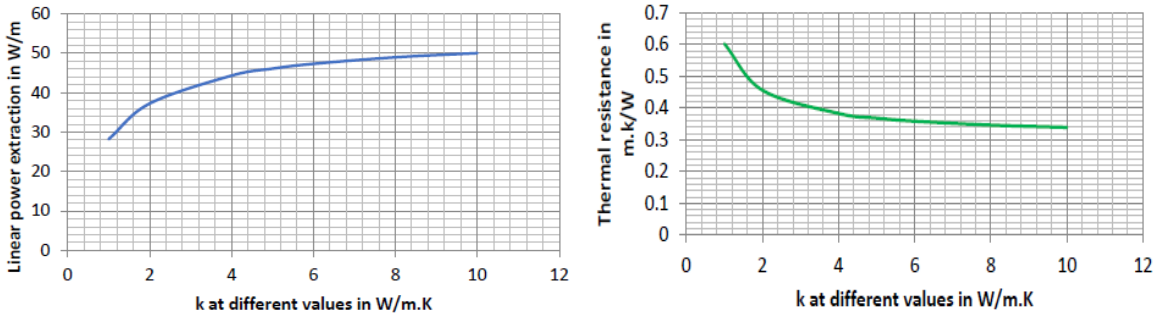

Figure 5: Thermal behavior of the borehole

We find this trend in figure 5, the overall thermal resistance of a conventional geothermal borehole decrease when the conductivity of grout increases to stabilize for a value of k around 5 W.m^{-1}.K^{-1}. The power extraction at k = 5 W.m^{-1}.K^{-1} is 61 % higher than the extraction at k = 1 W.m^{-1}.K^{-1}, while the raise at k = 10 W.m^{-1}.K^{-1} is limited at 77 %. As well, we can see from that the

thermal resistance of the borehole decreases sharply till k = 6 $W.m^{-1}.K^{-1}$ and then stabilizes relatively till k = 10 $W.m^{-1}.K^{-1}$. At this value, it is very clear that the grout is no longer the main thermal resistance of borehole and will allow as shown in figure 5, a significant gain of linear power extracted.

4. THERMAL MODELING OF THE GEOTHERMAL HEAT PUMP

A typical residential space was chosen and the cooling and heating demands were calculated using the hourly analysis program HAP. The proposed model is located in Beirut and has a typical construction. The peak cooling and heating loads are the determining loads to choose the equipment thus we will choose a unit that satisfies the cooling and heating peak loads being respectively 16.18 kW and 15.87 kW, a geothermal heat pump of 17 kW is chosen. A model for the geothermal heat pump was developed using Refprop library and Excel software. The model involved theoretical refrigeration cycle calculations.

4.1. COP at Constant Bore Depth

The cooling COP was calculated using Refprop software for different thermal conductivities of the grout, the acquired data was tabulated and generated the below graph (Fig. 6). As it can be seen the COP ascending curve becomes quasi-static starting k = 5 $W.m^{-1}.K^{-1}$, for our case study the initial COP for k= 1 $W.m^{-1}.K^{-1}$ was 3.878 and increased to 3.986 for k = 5 $W.m^{-1}.K^{-1}$being a raise of 2.78 %.

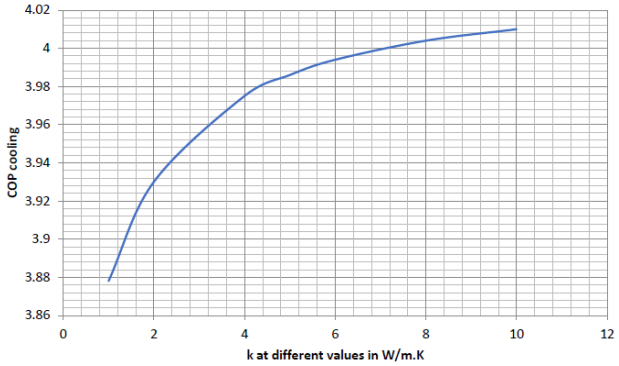

Figure 6 : COP vs. thermal conductivity

The same work was done for calculating the heating COP, the initial heating COP for k = 1 $W.m^{-1}.K^{-1}$was 4.26 and increased to 4.38 for k = 5 $W.m^{-1}.K^{-1}$being a raise of 2.81 %.

4.2. Bore depth reduction at constant COP

Studying the variation of the COP with the borehole depth unchanged revealed a slight increase both in cooling and heating modes, for that we will investigate the potential of depth reduction while leaving the initial COP of the geothermal heat pump unit. As stated in (Fig. 5), the linear power extraction has increased from 28.23 W/m at k = 1 $W.m^{-1}.K^{-1}$ to 46.15 $W.m^{-1}$ at k = 5 $W.m^{-1}.K^{-1}$ being a raise 61%. This step up in the linear power extraction and at constant COP, will decrease the borehole depth of 38.89% from 156 m to 95.5m leading to a huge cost reduction. Fig. 7 shows the reduction of the borehole depth versus the increase of the grouts' thermal conductivity, we remark that the sharp decrease it between k = 1 $W.m^{-1}.K^{-1}$ and k = 6 $W.m^{-1}.K^{-1}$ thus in our case for k = 5 $W.m^{-1}.K^{-1}$ we are in the optimal zone.

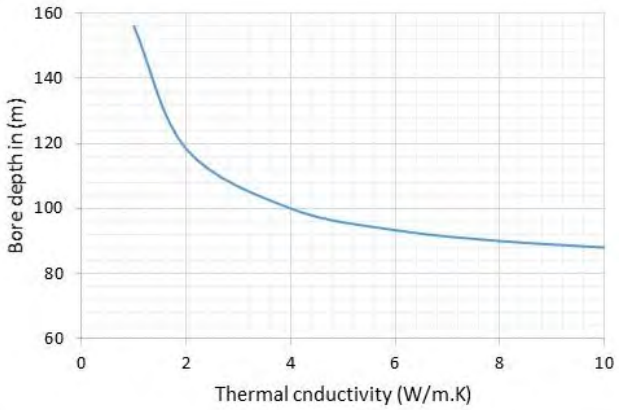

Figure 7: Bore depth versus thermal conductivity

5. ECONOMICAL STUDY

An economical study was performed in order to evaluate the feasibility of the project. In this section, the both cases are treated i.e. the fixed borehole depth with improved COP and reduced depth fixing the COP of the refrigeration system. Thus, we will calculate the costs and the payback time based on a 20 years project lifetime.

Table 2 shows the economic results obtained for a fixed and reduced depth of the borehole. It can be seen clearly that improving the COP of the machine is not interesting economically, whereas reducing the depth of the drill has much more economical impact.

Table 2. Economical results

	Fix depth/ Improved COP	Fix COP / Reduced depth
Drilling depth (m)	156	95.5
Cost of drilling ($.m^{-1})	65	65
Total cost of drilling ($)	10140	6207.5
Filling volume (m^3)	11	6.73
Filler price ($.m^{-3})	90	95.85
Total filler price ($)	990	645.07
Total cost ($)	11130	6852.57

If we compare the two cases, we will clearly conclude that the reduction of the bore depth is much more economic for this model. The electric bill reduction and the decrease in the initial installation cost for the second make the payback time for this project very quick.

6. CONCLUSIONS

In this paper, we investigated the importance of increasing the thermal conductivity of a geothermal heat exchanger borehole with abundant and cheap materials. A thermal conductivity of 5 $W.m^{-1}.K^{-1}$ was reached by doping the cement silica send mix with 1.5% in weight of sawdust aluminum. The benefits of using sawdust aluminum, is reducing the recycling scheme of the sawdust aluminum to a re-use scheme of that material. Re-using the aluminum will reduce the energy consumption to recycle it by 398 $kJ.kg^{-1}$ being 0.11 $kJ.kg^{-1}$ which is the latent heat of fusion of aluminum.

The thermal simulation showed an increase in power extraction, but showed as well a loss of performance inside the bore itself by recycling the energy between the pipes. From the simulation

we also learned that there is a boundary for increasing the thermal conductivity which is the thermal conductivity of the soil itself.
A model of the heat pump was created the assess the COP variation in both cooling and heating modes, the results came unsatisfactory with a maximum raise of 2.78% for the cooling COP and 2.81 % for the heating COP. The reduction of the borehole at constant COP was investigated and a reduction of 38.89 % can be achieved while keeping the system performance intact.
The earth temperature wasn't affected due to the balance of the heating and cooling load profiles of this model, another model with different load profiles might result in a variation of the earth temperature.
The economic evaluation turned to be satisfying with a payback time of 6.24 years in case the depth is kept and the aluminum is added to the grout, and a direct gain if the borehole depth is reduced with variation of the performance of the unit.

NOMENCLATURE

A	Amplitude	t_0	Day 1 of the year
k	Thermal conductivity ($W.m^{-1}.K^{-1}$)	T	Temperature (°C)
Q	Heat (W)	ΔT	Temperature variation (K) or (°C)
S	Surface (m^2)	ω	Angular frequency ($rd.day^{-1}$)
t	Time (day)	av	average

REFERENCES

Advanced Thermal Conductivity Testing for Geothermal Heating and Cooling Systems, U.S. Department of Energy, Small Business Vouchers Pilot http://www.sbv.org/a/pages/level3-geothermal-round1-2.

Alessandro Casasso (2014) Sensitivity analysis on the performance of a ground source heat pump equipped with a double U-pipe borehole heat exchanger

Antonio Capozza, (2015) Analysis of vertical ground heat exchangers: the new CaRM tool

ASTM Standard D5334-08 – Standard Test Method for Determination of Thermal Conductivity of Soil and Soft Rock by Thermal Needle Probe Procedure.

C.MAATOUK (2016),Improvement of thermal conductivity of grut mixture for geothermal heat pump systems

Claesson, (2011). An analytical method to calculate borehole fluid temperatures for time-scales from minutes to decades. ASHRAE Transactions.,

IEEE Standard 442-1981- IEEE guide for soil thermal resistivity measurements, 10.1109/IEEESTD.1981.81018

Marcotte,. (2010). The importance of axial effects for borehole design of geothermal heat-pump systems. Renewable Energy,

M. Benhammoul (2011), Modélisation de la température en profondeur du sol pour la région d'Adrar

M.L Brendt 2008, Improving the Performance of Geothermal Heat Pumps through Borehole Grout Materials, Australian Geothermal Energy Conference 2008, 157-162

Panayiotis D. Pouloupatis (2016)Parametric analysis of the factors affecting the efficiency of ground heat exchangers and design application aspects in Cyprus.

Manuscript ID: 722
DOI: 10.18462/iir.icr.2019.0722

Fast predicting method for maximum APF of heat pump type air conditioner

Tao REN[(a)], Jiamin SHEN[(a)], Guoming WU[(a)] , Yongxin ZHENG[(b)], Yifeng GAO[(b)], Ji SONG[(b)]

[(a)] Institute of Refrigeration and Cryogenics of Shanghai Jiao Tong University, Shanghai,200240, People's Republic of China, purple2511@sjtu.edu.cn

[(b)] International Copper Association Shanghai Office, Shanghai, 200240, People's Republic of China, kerry.song@copperalliance.asia

ABSTRACT

As APF (annual performance factor) becomes the energy efficiency index of heat pump type air conditioners, the amount of working conditions to be tested for each air conditioner has greatly increased from one to five, meaning experiment based maximization of the energy efficiency index may result in too heavy experimental tasks.
The purpose of this paper is to present a method to maximize the APF of a heat pump type air conditioner quickly. In this method, one set of experimental data of air conditioner performance is obtained at first, then the APF optimization equations is deduced from the theoretical cycle of refrigeration, and finally the experimental data are substituted into the APF optimization equations to calculate the best combinations of capacity and energy efficiency.
The new method is applied to a real HPAC, which shows a large amount of time and experimental work can be reduced to get the maximum APF.
Keywords: Room air conditioner, Numerical Model, APF, Maximum value.

1. INTRODUCTION

The heat pump type air conditioners have become the main products of air conditioners due to the dual functions of cooling in summer and heating in winter, accounting for nearly 70% of the global air conditioner market (Hui H et al., 2018). Many countries, such as China (GB/T 7725, 2004), Japan (JIS C 9612, 2005) and America (ISO 5151, 2004), have adopt the annual performance factor (APF) to evaluate the efficiency of air conditioners in their national standards. Their standards divide air conditioners into different efficiency classifications according to APF values.
To make HPAC reach an APF as high as possible, engineers have to improve the system match for each component repeatedly which cost large amount of time and resource (Kang E C et al., 2013). However, the wasting time and resource usually occur, since engineers don't know the maximum APF of the HPAC before they start to improve the system match. The air conditioner may already have a desirable system match and has little space for the further improvement, but engineers are still testing the air conditioner for a higher APF. These repeated APF tests will lead to a huge waste of time and resource, since every APF test of HPAC requires multiple experiments under 5 different working conditioners. To reduce the time and the resource waste, engineers need to know the maximum APF of the air conditioner before they improve the system match. While, no literature provides a method of predicting the maximum APF of HPAC.
The challenge of using the numerical simulation method to predict the maximum APF for heat pump air conditioners comes from the low predicting speed and the low predicting precision. The prediction of the maximum APF needs thousands of times of air conditioner simulation due to the large amount of APF iteration and multiple working conditions in every APF iteration, requiring a very fast calculation speed of air conditioner model to satisfy the engineering need. The traditional air conditioner models not only calculate the capacities and efficiencies that APF needs, but also calculate large amount of intermediate parameters which is irrelevant and useless for the APF calculation, such as temperature, pressure and performance of each component (Tomiyama K et al., 1998), leading to a time-consuming and slow-speed calculation (Mahlia T M I et al., 2001). Besides, to get a precise prediction, the air conditioner models still need to be modified by many specific parameters of air conditioner, such as heat transfer coefficient, compressor performance

and coupling characteristics of components, since the air conditioner models are initially set up based on the general theories of air conditioners. As for a new developed air conditioner, the air conditioner model lack the specific parameters of air conditioner to modify the simulation, generating as much as ±20% prediction error (Wu J H et al., 2017). So the traditional air conditioner models are hard to be used in the prediction of the maximum APF for HPAC.
The purpose of the paper is to propose a method of predicting the maximum APF of HPAC fast and precisely. To improve the calculation speed, the paper set up a simplified predicting model of capacities and efficiencies; to improve the prediction precision, one group of APF test data under 5 working conditions, including compressor efficient, condensing temperature, evaporating temperature, heat transfer capacity of outdoor unit and heat transfer capacity of indoor unit, are applied to modify the simplified predicting model.

2. PREDICTION PRINCIPLE OF MAXIMUM APF OF HPAC

The fast and precise prediction of the maximum APF of HPAC is realized by setting up a simplified predicting model to calculate the capacities and efficiencies fast and precisely, and deducing a simplified APF calculating formula to further accelerate the calculate speed of APF. Large amount of iterations are carried out between calculating the better air conditioner performance by the simplified predicting model of capacities and efficiencies and generating the higher APF by the simplified APF calculating formula, until the maximum APF of the HPAC is obtained, as shown in Fig. 1.

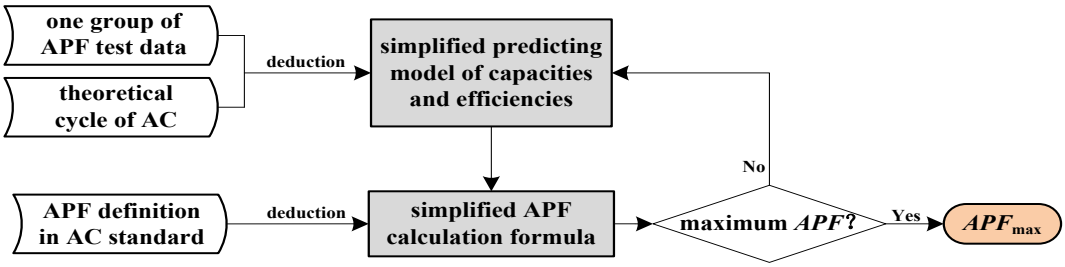

Figure 1: Principle of predicting maximum APF for heat pump air conditioner

3. SIMPLIFIED PREDICTING MODEL OF CAPACITIES AND EFFICIENCIES BASED ON ONE GROUP OF APF TEST DATA

The method of setting up the simplified predicting model is to 1) deduce the relationship between the efficiencies and the capacities according to one group of APF test data and the theoretical cycle of air conditioner, 2) determine the variation range of the capacities according to the regulations of the air conditioner standard, 3) set up the simplified predicting model by combining the variation range of the capacities and the relationship between the efficiencies and the capacities.

3.1. Deduction of relationship between efficiencies and capacities

The relationship between EER and heat transfer capacity is deduced from the theoretical cycle of air conditioner, as shown in Fig. 2.

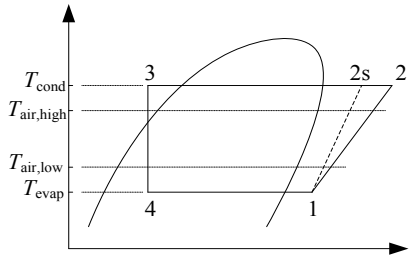

Figure 2: Theoretical cycle of air conditioner

EER is the ratio between the capacity and the energy consumption, as shown in Eq. (1). The EER is linearly related to evaporating temperature T_{evap} and condensing temperature T_{cond}, as shown in Fig. 3. The ratio can be fitted to a linear function of T_{evap} and T_{cond}, as shown in Eq. (2). EER can be transferred into the linear function of T_{evap} and T_{cond}, as shown in Eq. (3).

$$EER = \eta_{\mathrm{i}} \frac{h_1 - h_4}{h_{2s} - h_1} \quad \text{Eq. (1)}$$

$$\frac{h_1 - h_4}{h_{2s} - h_1} = (\mathrm{a} + \mathrm{b}\, T_{\mathrm{evap}})(\mathrm{c} + \mathrm{d}\, T_{\mathrm{cond}}) \quad \text{Eq. (2)}$$

$$EER = \eta_{\mathrm{i}} (\mathrm{a} + \mathrm{b}\, T_{\mathrm{evap}})(\mathrm{c} + \mathrm{d}\, T_{\mathrm{cond}}) \quad \text{Eq. (3)}$$

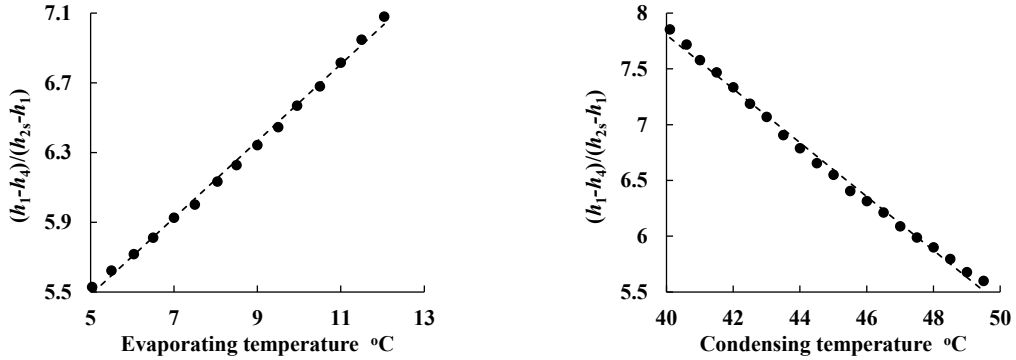

（a）Evaporating condition （b）Condensing condition

Figure 3: Relationship between $(h_1-h_4)/(h_{2s}-h_1)$ and evaporating or condensing temperature

The heat transfer capacities under the cooling condition includes the heat transfer capacity of evaporator, the heat transfer capacity of condenser and the relationship between EER and heat transfer capacities, which are deduced based on one group of APF tested data. The heat transfer capacities of evaporator and condenser are linear functions of temperature difference, as shown in Eq. (4a) and Eq. (4b). EER is a function of the heat transfer capacity of both evaporator and condenser, as shown in Eq. (4c).

$$\begin{aligned} \phi_{\mathrm{evap}} &= \frac{\phi_{\mathrm{evap,test}}}{T_{\mathrm{air,low}} - T_{\mathrm{evap,test}}} (T_{\mathrm{air,low}} - T_{\mathrm{evap}}) \qquad (a) \\ \phi_{\mathrm{cond}} &= \frac{\phi_{\mathrm{cond,test}}}{T_{\mathrm{cond,test}} - T_{\mathrm{air,high}}} (T_{\mathrm{cond}} - T_{\mathrm{air,high}}) \qquad (b) \\ EER &= \frac{\phi_{\mathrm{evap}}}{\phi_{\mathrm{cond}} - \phi_{\mathrm{evap}}} \qquad (c) \end{aligned} \quad \text{Eq. (4)}$$

The relationship between the EER and the cooling capacity is obtained by substituting Eq. (4) into Eq. (3) to eliminate intermediate parameters, such as T_{evap}, T_{cond} and Φ_{cond}, as shown in Eq. (5).

$$\begin{aligned} EER_{\mathrm{i}} = {} & \frac{\eta}{2}\left[\mathrm{a} + \mathrm{b}\, T_{\mathrm{air,low}} - \frac{\mathrm{b}\phi_{\mathrm{evap}}(T_{\mathrm{air,low}} - T_{\mathrm{evap.test}})}{\phi_{\mathrm{evap.test}}}\right]\left[\mathrm{c} + \mathrm{d}\, T_{\mathrm{air,high}} + \frac{\mathrm{d}\phi_{\mathrm{evap}}(T_{\mathrm{cond.test}} - T_{\mathrm{air,high}})}{\phi_{\mathrm{cond.test}}}\right] \\ & + \left\{\frac{\eta^2}{4}\left(\mathrm{a} + \mathrm{b}\, T_{\mathrm{air,low}} - \frac{\mathrm{b}\phi_{\mathrm{evap}}(T_{\mathrm{air,low}} - T_{\mathrm{evap.test}})}{\phi_{\mathrm{evap.test}}}\right)^2\left(\mathrm{c} + \mathrm{d}\, T_{\mathrm{air,high}} + \frac{\mathrm{d}\phi_{\mathrm{evap}}(T_{\mathrm{cond.test}} - T_{\mathrm{air,high}})}{\phi_{\mathrm{cond.test}}}\right)^2\right. \\ & \left. + \frac{\eta \mathrm{d}\phi_{\mathrm{evap}}(T_{\mathrm{cond.test}} - T_{\mathrm{air,high}})}{\phi_{\mathrm{cond.test}}}\left[\mathrm{a} + \mathrm{b}\, T_{\mathrm{air,low}} - \frac{b\phi_{\mathrm{evap}}(T_{\mathrm{air,low}} - T_{\mathrm{evap.test}})}{\phi_{\mathrm{evap.test}}}\right]\right\}^{\frac{1}{2}} \end{aligned} \quad \text{Eq. (5)}$$

The capacity of standard cooling condition is not less than 95% of nominal cooling capacity on the nameplate of air conditioner according to air conditioner standard GB/T 7725-2004. The capacity of standard heating condition is not less than 110% of nominal cooling capacity. The capacity of standard low temperature heating condition is not less than nominal cooling capacity. The capacities of intermediate conditions equal half of the capacities of standard condition.

3.2. Solution of simplified predicting model of capacities and efficiencies

By combing Eq. (5) and the variation range of capacities, the simplified predicting model of capacities and efficiencies is obtained, as shown in Eq. (6).

$$
\begin{aligned}
&\phi_{cr} \geq 95\%\,\phi_{cra},\quad \phi_{\mathrm{hr}} \geq 110\%\,\phi_{cra}\\
&\phi_{\mathrm{def}} \geq \phi_{cra},\quad \phi_{cm} = 0.5\,\phi_{cr},\quad \phi_{hm} = 0.5\,\phi_{hr}\\
&EER_{\mathrm{cr}} = E(\phi_{cr}, \eta, T_{\mathrm{evap,test}}, T_{\mathrm{cond,test}}, \phi_{\mathrm{evap,test}}, \phi_{\mathrm{cond,test}})\\
&EER_{\mathrm{cm}} = E(\phi_{cm}, \eta, T_{\mathrm{evap,test}}, T_{\mathrm{cond,test}}, \phi_{\mathrm{evap,test}}, \phi_{\mathrm{cond,test}})\\
&COP_{\mathrm{hr}} = C(\phi_{hr}, \eta, T_{\mathrm{evap,test}}, T_{\mathrm{cond,test}}, \phi_{\mathrm{evap,test}}, \phi_{\mathrm{cond,test}})\\
&COP_{\mathrm{hm}} = C(\phi_{hm}, \eta, T_{\mathrm{evap,test}}, T_{\mathrm{cond,test}}, \phi_{\mathrm{evap,test}}, \phi_{\mathrm{cond,test}})\\
&COP_{\mathrm{def}} = C(\phi_{\mathrm{def}}, \eta, T_{\mathrm{evap,test}}, T_{\mathrm{cond,test}}, \phi_{\mathrm{evap,test}}, \phi_{\mathrm{cond,test}})
\end{aligned}
\qquad \text{Eq. (6)}
$$

4. DEDUCTION OF SIMPLIFIED APF CALCULATING FORMULA

The deduction of simplified APF calculating formula includes two steps: 1) transfer the composite functions into an elementary function by eliminating intermediate parameters; 2) simplify the elementary function by numerical fitting to get the simplified APF calculating formula.

4.1. APF defined by composite functions in AC standard

APF is defined in GB/T 7725-2004 by many composite functions, as shown from Eq. (7) to Eq. (19). APF is the ratio between total capacity and the total power consumption in a whole year, as shown in Eq. (7). *CSTL* is the total cooling capacity; *HSTL* is the total heating capacity; *CSTE* is the power consumption under cooling season; *HSTE* is the power consumption under heating season.

$$APF = \frac{CSTL + HSTL}{CSTE + HSTE} \qquad \text{Eq. (7)}$$

$$CSTL = \sum_{j=1}^{12} BL_c(t_j) \times n_j + \sum_{j=13}^{15} \dot{\Phi}_{cr2}(t_j) \times n_j \qquad \text{Eq. (8)}$$

$$HSTL = \sum_{j=1}^{23} BL_h(t_j) \times n_j \qquad \text{Eq. (9)}$$

$$CSTE = \sum_{j=1}^{k} P_{clm}(t_j) + \sum_{j=k+1}^{12} P_{cm2}(t_j) + \sum_{j=13}^{15} P_{c2}(t_j) \qquad \text{Eq. (10)}$$

$$HSTE = \sum_{j=1}^{26} \dot{P}_h(t_j) \times n_j + \sum_{j=1}^{26} P_{RH}(t_j) \qquad \text{Eq. (11)}$$

$$BL_c(t_j) = \Phi_{\mathrm{cr}2a} \times \frac{t_j - 23}{35 - 23} \qquad \text{Eq. (12)}$$

$$\dot{\Phi}_{cr2}(t_j) = \Phi_{cr} + \frac{\Phi_{cr}(29) - \Phi_{cr}}{35 - 29}(35 - t_j) \qquad \text{Eq. (13)}$$

$$BL_h(t_j) = 1.39 \times 0.82 \times \Phi_{cra} \times \frac{17 - t_j}{17} \qquad \text{Eq. (14)}$$

$$\dot{P}_h(t_j) = \begin{cases} \dot{P}_{def3}(t_j) = \dfrac{BL_h(t_j)}{\dot{C}_{def3}(t_j)} & \text{above standard low Temp. heating capacity in frozen zone} \\ \dot{P}_{def2}(t_j) = \dfrac{BL_h(t_j)}{\dot{C}_{def2}(t_j)} & \text{above standard heating capacity in frozen zone} \\ \dot{P}_{defm}(t_j) = \dfrac{BL_h(t_j)}{\dot{C}_{defm}(t_j)} & \text{below intermediate heating capacity in frozne zone} \\ \dot{P}_{hm2}(t_j) = \dfrac{BL_h(t_j)}{\dot{C}_{hm2}(t_j)} & \text{between intermediate and standard heating capacity in frozne zone} \\ \dot{P}_{hlm}(t_j) = \dfrac{BL_h(t_j)}{\dot{C}_{hlm}(t_j)} & \text{below intermediate heating capacity in nonfrozne zone} \end{cases} \qquad \text{Eq. (18)}$$

$$P_{clm}(t_j) = \frac{BL_c(t_j) \times n_j}{\dot{E}_{clm}(t_j)} \quad \text{Eq. (15)}$$

$$P_{cm2}(t_j) = \frac{BL_c(t_j) \times n_j}{\dot{E}_{cm2}(t_j)} \quad \text{Eq. (16)}$$

$$P_{c2}(t_j) = \left[P_{c2} + \frac{P_{c2}(29) - P_{c2}}{35 - 29}(35 - t_j) \right] \times n_j \quad \text{Eq. (17)}$$

$$P_{RH}(t_j) = [BL_h(t_j) - \dot{\Phi}_{def3}(t_j)] \times n_j \quad \text{Eq. (19)}$$

4.2. APF transformation from composite functions to one elementary function

The method of transforming the composite functions into an elementary function is to 1) deduce *CSTL*, *HSTL*, *CSTE* and *HSTL* as elementary functions, 2) and bring *CSTL*, *HSTL*, *CSTE* and *HSTL* into Eq. 7 to obtain the elementary function of APF.

By substituting Eq. (8)-Eq. (19) into Eq. (7), the function of APF is deduced, as shown in Eq. (20).

$$\begin{aligned}
&\mathrm{APF} = 991.29 \times \Phi_{cr2} / (CSTE + HSTE) \\
&CSTE = \sum_{j=1}^{6} \frac{(t_j - 23) \times n_j \times \frac{13.848\Phi_{cr2a}}{\Phi_{cr2a} + 0.154\Phi_{crm}} \times \frac{EER_{cr2}}{EER_{crm}} \times P_{c2}}{16.725 \times (\frac{23\Phi_{cr2a} + 17.39\Phi_{crm}}{\Phi_{cr2a} + 0.154\Phi_{crm}} - t_j) + \frac{83.088\Phi_{cr2a}(t_j - 23)}{4.968\Phi_{cr2a} + 1.956\Phi_{crm}}} \\
&\quad + \sum_{j=1}^{12} \frac{(t_j - 23) \times n_j \times \frac{\Phi_{cr2a} - \Phi_{crm}}{\Phi_{cr2a} + 0.154\Phi_{crm}} \times \frac{EER_{cr2}}{EER_{crm}} \times P_{c2}}{(t_j - \frac{23\Phi_{cr2a} + 17.39\Phi_{crm}}{\Phi_{cr2a} + 0.154\Phi_{crm}}) \times \frac{EER_{cr2}}{EER_{crm}} + \frac{6.924\Phi_{cr2a}(35 - t_j)}{4.968\Phi_{cr2a} + 1.956\Phi_{crm}}} + 29.54 \times P_{c2} \\
&HSTE = \sum_{j=1}^{k} [0.067 \times (17 - t_j) \times \Phi_{cr2a} - (0.95668 + 0.021662 \times t_j) \times \Phi_{def}] \times n_j \\
&\quad + \sum_{j=1}^{p} \frac{0.067 \times (17 - t_j) \times n_j \times \Phi_{cr2a} (\frac{114\Phi_{cr2a} - 74.423\Phi_{hr2}}{6.7\Phi_{cr2a} + 1.685\Phi_{hr2}} - \frac{114\Phi_{cr2a} - 95.67\Phi_{def}}{6.7\Phi_{cr2a} + 2.166\Phi_{def}})}{\frac{88.79\Phi_{cr2a}}{75.9\Phi_{cr2a} + 12.84\Phi_{def}} \frac{\Phi_{def}}{P_{def}} (\frac{114\Phi_{cr2a} - 74.4\Phi_{hr2}}{6.7\Phi_{cr2a} + 1.69\Phi_{hr2}} - t_j) + \frac{69.07\Phi_{cr2a}}{67\Phi_{cr2a} + 8.81\Phi_{hr2}} \frac{\Phi_{hr2}}{P_{hr2}} (t_j - \frac{114\Phi_{cr2a} - 95.67\Phi_{def}}{6.7\Phi_{cr2a} + 2.17\Phi_{def}})} \\
&\quad + \sum_{j=p+1}^{l} \frac{0.067 \times (17 - t_j) \times n_j \times \Phi_{cr2a} (\frac{114\Phi_{cr2a} - 74.423\Phi_{hrm}}{6.7\Phi_{cr2a} + 1.685\Phi_{hrm}} - \frac{114\Phi_{cr2a} - 74.423\Phi_{hr2}}{6.7\Phi_{cr2a} + 1.685\Phi_{hr2}})}{\frac{69.1\Phi_{cr2a}}{67\Phi_{cr2a} + 8.81\Phi_{hr2}} \frac{\Phi_{hr2}}{P_{hr2}} (\frac{114\Phi_{cr2a} - 74.4\Phi_{hrm}}{6.7\Phi_{cr2a} + 1.7\Phi_{hrm}} - t_j) + \frac{69.1\Phi_{cr2a}}{67\Phi_{cr2a} + 8.81\Phi_{hrm}} \frac{\Phi_{hrm}}{P_{hrm}} (t_j - \frac{114\Phi_{cr2a} - 74.4\Phi_{hr2}}{6.7\Phi_{cr2a} + 1.7\Phi_{hr2}})} \\
&\quad + \sum_{j=l+1}^{m} \frac{0.067 \times (17 - t_j) \times n_j \times \Phi_{cr2a} (\frac{114\Phi_{cr2a} - 81.94\Phi_{hrm}}{6.7\Phi_{cr2a} + 2.57\Phi_{hrm}} - \frac{114\Phi_{cr2a} - 81.94\Phi_{hr2}}{6.7\Phi_{cr2a} + 2.57\Phi_{hr2}})}{\frac{84.3\Phi_{cr2a}}{75.6\Phi_{cr2a} + 12.9\Phi_{hr2}} \frac{\Phi_{hr2}}{P_{hr2}} (\frac{114\Phi_{cr2a} - 81.9\Phi_{hrm}}{6.7\Phi_{cr2a} + 2.57\Phi_{hrm}} - t_j) + \frac{84.3\Phi_{cr2a}}{75.6\Phi_{cr2a} + 12.9\Phi_{hrm}} \frac{\Phi_{hrm}}{P_{hrm}} (t_j - \frac{114\Phi_{cr2a} - 81.9\Phi_{hr2}}{6.7\Phi_{cr2a} + 2.57\Phi_{hr2}})} \\
&\quad + \sum_{j=m+1}^{n} \frac{0.067 \times (17 - t_j) \times n_j \times \Phi_{cr2a} (17 - \frac{114\Phi_{cr2a} - 81.94\Phi_{hrm}}{6.7\Phi_{cr2a} + 2.57\Phi_{hrm}})}{\frac{84.27\Phi_{cr2a}}{75.61\Phi_{cr2a} + 12.87\Phi_{hrm}} \times \frac{\Phi_{hrm}}{P_{hrm}} (17 - t_j) + \frac{1.114 \times \Phi_{hrm}}{P_{hrm}} (t_j - \frac{114\Phi_{cr2a} - 81.94\Phi_{hrm}}{6.7\Phi_{cr2a} + 2.57\Phi_{hrm}})}
\end{aligned} \quad \text{Eq. (20)}$$

4.3. APF simplification from elementary function to simplified calculating formula

The elementary function of APF shown in Eq. (20) still has complicated expression which need further simplification to accelerate the calculation speed. The idea of obtaining the simplified APF calculating formula is to make a proper fitting for complicated parameters *CSTE* and *HSTE* to get simplified $CSTE_{fit}$ and $HSTE_{fit}$, and bring $CSTE_{fit}$ and $HSTE_{fit}$ into Eq. (20) to get a simplified APF formula.

The fitting of *CSTE* includes the following 3 steps:

1）Determining the fitting forms of $CSTE_{fit}$. The variable $CSTE/P_{c2}$ is a non-dimensional number which is related to EER_{cr2}/EER_{crm}, as shown in Fig.4. The variable $CSTE_{fit}/P_{c2}$ can be fitted as a linear function of EER_{cr2}/EER_{crm}.

2）Determining variation range of independent variables. The value of EER_{cr2}/EER_{crm} changes between 0.6 and 1 according to the market survey of current air conditioners.

3）Determining fitting coefficients. The fitting results are shown in Eq. (21).

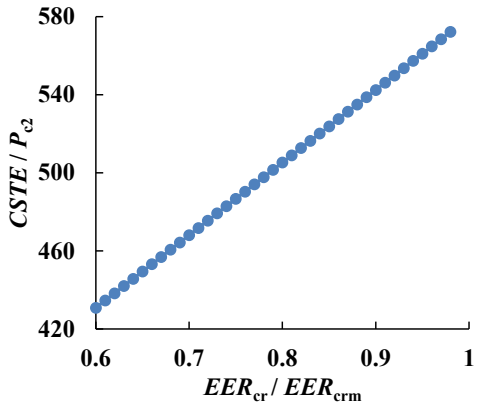

Figure 4: Relationship between CSTE/P_{c2} and EER_{cr2}/EER_{crm}

$$CSTE_{fit} = [209.37+369.95\times\frac{EER_{cr2}}{EER_{crm}}]\times P_{c2} \quad \text{Eq. (21)}$$

The fitting of *HSTE* includes the following 3 steps:

1）Determining the fitting forms of $HSTE_{fit}$. *HSTE* is linearly related to P_{hr}, P_{hm} and P_{def}. The variables of Φ_{hr}/Φ_{cr2} and Φ_{def}/Φ_{cr2} in *HSTE* are quadratic polynomial.

2）Determining variation range of independent variables. The value of Φ_{def}/Φ_{cr2} changes between 0.8 and 1.4; the value of Φ_{hr}/Φ_{cr2} changes between 1.1 and 1.6; the value of P_{hr} changes between 1000W~1500W; the value of P_{hm} changes between 400W~600W; the value of P_{def} changes between 1300W~1600W.

3）Determining the fitting coefficients. The fitting results are shown in Eq. (22).

$$HSTE_{fit} = [1570\text{-}1400\frac{\phi_{hr}}{\phi_{cr}}+390(\frac{\phi_{hr}}{\phi_{cr}})^2+736\frac{\phi_{def}}{\phi_{cr}}+162(\frac{\phi_{def}}{\phi_{cr}})^2+215\frac{\phi_{def}}{\phi_{cr}}\frac{\phi_{hr}}{\phi_{cr}}]\times p_{def} \quad \text{Eq. (22)}$$

$$+[-3692+6743\frac{\phi_{hr}}{\phi_{cr}}\text{-}2963(\frac{\phi_{hr}}{\phi_{cr}})^2]\times p_{hr}+[10980\text{-}18730\frac{\phi_{hr}}{\phi_{cr}}+8108(\frac{\phi_{hr}}{\phi_{cr}})^2]\times p_{hm}$$

By substituting Eq. (21) and Eq. (22) into Eq. (20), the simplified APF calculating formula is deduced, as shown in Eq. (23).

$$APF = \frac{991.29\times\Phi_{cr2}}{A+B+C}$$

$$A = [209.37+369.95\times\frac{EER_{cr2}}{EER_{crm}}]\times P_{c2} \quad \text{Eq. (23)}$$

$$B = [1570\text{-}1400\frac{\phi_{hr}}{\phi_{cr}}+390(\frac{\phi_{hr}}{\phi_{cr}})^2+736\frac{\phi_{def}}{\phi_{cr}}+162(\frac{\phi_{def}}{\phi_{cr}})^2+215\frac{\phi_{def}}{\phi_{cr}}\frac{\phi_{hr}}{\phi_{cr}}]\times p_{def}$$

$$C = [-3692+6743\frac{\phi_{hr}}{\phi_{cr}}\text{-}2963(\frac{\phi_{hr}}{\phi_{cr}})^2]\times p_{hr}+[10980\text{-}18730\frac{\phi_{hr}}{\phi_{cr}}+8108(\frac{\phi_{hr}}{\phi_{cr}})^2]\times p_{hm}$$

4.4. Error analysis on simplified APF calculating formula

The error of the simplified APF calculating formula derives from the fitting error of $CSTE_{fit}$ and $HSTE_{fit}$.The maximum fitting error of $CSTE_{fit}$ is 0.45% when EER_{cr2}/EER_{crm} equals 0.6.The maximum fitting error of $HSTE_{fit}$ is 0.2% when Φ_{def}/Φ_{cr2}, Φ_{hr}/Φ_{cr2}, P_{hr}, P_{hm} and P_{def} are respectively 1.18, 1.31, 1323W, 461W and 1538W. The maximum error of simplified APF calculating formula is less than the sum of the maximum error of $CSTE_{fit}$ and the maximum error of $HSTE_{fit}$. So the maximum error of simplified APF calculating formula is within 0.65%.

5. A PRACTICAL CASE OF PREDICTING MAXIMUM APF FOR HPAC

A practical case is provided on a normal domestic split HPAC in order to clearly illustrate how to predict the maximum APF. The cooling capacity of the HPAC is 3.5 kW. The HPAC use an inverter reciprocating compressor, a capillary tube with 1.3 mm inside diameter and 500 mm length.

Step 1: Determining the simplified predicting model of capacities and efficiencies by one group of APF test data shown in Table 1. The tested data are brought into Eq. (6) to obtain the exact

expressions of the simplified predicting model of capacities and efficiencies.

Table 1. One group of original APF test data

Conditions	Standard cooling	Intermediate cooling	Standard heating	Intermediate heating	Standard low Temp. heating
Compressor efficiency	0.68	0.75	0.66	0.78	0.65
Evaporating Temp. /°C	9.7	19.7	1.9	3.2	-2.5
Condensing Temp. / °C	44.3	40.6	48.6	30.0	36.9
Capacities /W	3507.4	1767.1	5155.7	2571.2	4006.3
Efficiencies /W	3.373	4.875	3.039	5.161	2.691
APF	3.798				

Step 2: Determine the simplified APF calculating formula. Eq. (23) is used to calculate the APF.
Step 3: Searching the maximum APF. The maximum APF is searched on the computer by solving the optimization function set shown in Eq. (24).

$$
\begin{aligned}
&APF = \frac{991.29 \times \Phi_{cr2}}{A + B + C} \\
&A = [209.37+369.95 \times \frac{EER_{cr2}}{EER_{crm}}] \times P_{c2} \\
\max: \quad &B = [1570-1400\frac{\phi_{hr}}{\phi_{cr}} + 390(\frac{\phi_{hr}}{\phi_{cr}})^2 + 736\frac{\phi_{def}}{\phi_{cr}} + 162(\frac{\phi_{def}}{\phi_{cr}})^2 + 215\frac{\phi_{def}}{\phi_{cr}}\frac{\phi_{hr}}{\phi_{cr}}] \times p_{def} \\
&C = [-3692 + 6743\frac{\phi_{hr}}{\phi_{cr}} - 2963(\frac{\phi_{hr}}{\phi_{cr}})^2] \times p_{hr} + [10980-18730\frac{\phi_{hr}}{\phi_{cr}} + 8108(\frac{\phi_{hr}}{\phi_{cr}})^2] \times p_{hm} \\
&\phi_{cr} \geq 95\%\,\phi_{cra};\ \phi_{\mathrm{hr}} \geq 110\%\,\phi_{cra};\ \phi_{\mathrm{def}} \geq \phi_{cra};\ \phi_{cm} = 0.5\,\phi_{cr};\ \phi_{hm} = 0.5\,\phi_{hr} \\
&EER_{\mathrm{cr}} = 24.14 + 4.57\phi_{cr} - 0.105\phi_{cr}^2 + \sqrt{0.472\phi_{cr}^4 + 2.754\phi_{cr}^3 - 2.47\phi_{cr}^2 + 42.55\phi_{cr} + 12.477} \\
&EER_{\mathrm{cm}} = 32.2 + 3.024\phi_{cm} - 0.254\phi_{cm}^2 + \sqrt{0.025\phi_{cm}^4 + 3.024\phi_{cm}^3 - 1.287\phi_{cm}^2 + 62.54\phi_{cm} + 35.5} \\
\text{s.t.} \quad &COP_{\mathrm{hr}} = 4.57 + 8.57\phi_{hr} - 0.524\phi_{hr}^2 + \sqrt{1.47\phi_{hr}^4 + 0.474\phi_{hr}^3 - 0.487\phi_{hr}^2 + 4.457\phi_{hr} + 1.452} \\
&COP_{\mathrm{hm}} = 24.5 + 8.11\phi_{hm} - 0.247\phi_{hm}^2 + \sqrt{3.414\phi_{hm}^4 + 0.875\phi_{hm}^3 - 1.54\phi_{hm}^2 + 2.68\phi_{hm} + 6.57} \\
&COP_{\mathrm{def}} = 28.6 + 4.66\phi_{def} - 0.678\phi_{def}^2 + \sqrt{5.69\phi_{def}^4 + 0.773\phi_{def}^3 - 3.67\phi_{def}^2 + 6.578\phi_{def} + 32.55}
\end{aligned}
\qquad \text{Eq. (24)}
$$

The maximum APF and the corresponding best capacities and efficiencies of 5 working conditions are obtained, as shown in Table 2. The calculation results show that the maximum APF predicted by the proposed method for a normal domestic HPAC is 7.08% higher than the initial test data of APF.

The prediction of the maximum APF is resolved on a normal computer configured with a CPU of 3.6GHz×4 cores and a memory stick of 1600MHz×4G, and consumes 12 seconds which is fast enough to satisfy the engineering requirement.

Table 2. Prediction of the maximum APF for HPAC

Type	Conditions	Standard cooling	Intermediate cooling	Standard heating	Intermediate heating	low Temp. heating
Predicted maximum APF data	Capacities /W	3325	1663	4224	2112	4305
	Efficiencies	3.501	4.991	3.365	5.29	2.565
	APF	4.067				

6. CONCLUSIONS

This paper proposes a method to predict the maximum APF for HPAC. The method is applied to a normal domestic HPAC. The main conclusions are as follows:

(1) The fast and precise prediction of maximum APF for HPAC is realized by setting up a simplified predicting model based on a group of APF test data to accelerate the speed and precision of

calculating capacities and efficiencies, and deducing the simplified APF calculating formula to accelerate the search speed of the maximum APF.
(2) The maximum APF predicted by the proposed method for a normal domestic HPAC is 7.08% higher than the initial test data of APF. The prediction of the maximum APF is resolved on a normal computer configured with a CPU of 3.6GHz×4 cores and a memory stick of 1600MHz×4G, and consumes 12 seconds which is fast enough to satisfy the engineering requirement.

ACKNOWLEDGEMENTS

This work is supported by the State Key Laboratory of Air-Conditioning Equipment and System Energy Conservation (Project No. SKLACKF201605), the National Natural Science Foundation of China (No.51504149), the Program of Shanghai Academic Research Leader (No. 16XD1401500), and the Foundation for Innovative Research Groups of the National Natural Science Foundation of China (No. 51521004). All the supports are greatly appreciated.

NOMENCLATURE

EER	efficiency of theoretical cycle	η_i	efficiency of compressor
h	Enthalpy(kJ×kg^{-1}×K^{-1})	T_{evap}	evaporating temperature(°C)
T_{cond}	condensing temperature(°C)	$T_{air,high}$	higher ambient temperature(°C)
$T_{air,low}$	lower ambient temperature(°C)	Φ_{evap}	heat transfer capacity of evaporator(W)
Φ_{cond}	heat transfer of condenser (W)	$\Phi_{evap,test}$	tested capacity of evaporator(W)
$T_{evap,test}$	tested evaporating temperature(°C)	$T_{cond,test}$	tested condensing temperature(°C)
t_j	outdoor ambient temperature(°C)	n_j	working hours(×3600s)
$\Phi_{cr2}(t_j)$	standard cooling capacity (W)	Φ_{cr2}	standard cooling capacity (m^3×mol^{-1})
Φ_{cr2a}	nominal cooling capacity (W)	$P(t_j)$	cooling power consumption(W)
$E(t_j)$	cooling efficiency	P_{c2}	standard cooling power consumption
$BL_c(t_j)$	cooling load of building(W)	$BL_h(t_j)$	heating load of building(W)
$P_h(t_j)$	heating power consumption(W)	$C_h(t_j)$	heating efficiency
$P_{RH}(t_j)$	power of electric heater(W)		

REFERENCES

Hui H, Ding Y, Zheng M, 2018. Equivalent Modeling of Inverter Air Conditioners for Providing Frequency Regulation Service. IEEE Transactions on Industrial Electronics (99):1-1.

ISO 5151, 2004. Non-ducted air conditioners and heat pumps- testing and rating for performance. International Organization for Standardization.

GB/T 7725, 2004. Room air conditioners. Standardization Administration of the People's Republic of China.

JIS C 9612, 2005. Room air conditioners. Japanese Standards Association.

Kang E C, Riederer P, Yoo S Y, Lee E J, 2013. New approach to evaluate the seasonal performance of building integrated geothermal heat pump system. Renewable Energy 54(6):51-54.

Tomiyama K, Daniel J P, Ihara S. , 1998 Modeling air conditioner load for power system studies [J]. IEEE Transactions on Power Systems, 13(2):414-421.

Mahlia T M I, Masjuki H H, Choudhury I A, et al, 2001. Potential CO 2, reduction by implementing energy efficiency standard for room air conditioner in Malaysia. Energy Conversion & Management 42(14):1673-1685.

Wu J H, Liu C P, Li H Q, Ouyang D, Cheng J H, Wang Y X, You S F., 2017. Residential air-conditioner usage in China and efficiency standardization. Energy 119:1036-1046.

Manuscript ID: 730
DOI: 10.18462/iir.icr.2019.0730

The application and risk assessment of R290 in split type household air conditioners

Guogeng HE[(a)], Wei SUN[(a)], Weier TANG[(a)], Dehua CAI[(a)] , Sai ZHOU[(a)]

[(a)] Huazhong University of Science and Technology
Wuhan, 430074, China, gghe@mail.hust.edu.cn

ABSTRACT

Nowadays, the natural substance R290 has been considered as a promising next generation refrigerant for split type household air conditioners (STHACs) owing to its excellent environmental and thermodynamic properties. However, the obvious shortcoming of R290 is flammable and explosive, which make the application of R290 needs more security precautions to ensure the safety. This study introduced the application and risk assessment of R290 in the STHACs. The refrigerant mass distribution in the components of R290 STHAC were carried out. In addition, the R290 concentration distribution after a leakage from the STAHC at different charge quantity and the diameter of leak hole was presented and the risk of R290 was analysed. Based on the results, a practical method by installing a solenoid valve to reduce the risk of R290 was proposed and verified.
Keywords: Air conditioner, Distribution, Leakage, R290, Safety.

1. INTRODUCTION

HCFCs are being phased out under the Montreal Protocol (1987), and the HFCs alternatives with high GWP values will also be phased down under the Kigali amendment (Höglund et al., 2017), which was signed in 2016 and will enter into force in 2019. Therefore, the application of environment-friendly hydrocarbons (HCs) in air conditioners has attracted worldwide attention. R290 (propane), as one of the HCs, has begun to be successfully applied in air conditioners in China and Europe for replacing R22. When used in air conditioners, R290 can provide higher energy efficiency (Wu et al., 2012), better heat transfer in heat exchangers (Sánchez et al., 2017), lower discharge temperature and reduce the power consumption (Padalkar et al., 2014), relative to R22. Besides, the charge quantity of R290 is approximately 50% of R22 in the same air conditioner system due to its much lower density (Teng et al., 2012) and although the cooling capacity of R290 is 4.7–6.7% lower the energy efficiency ratio (EER) could be 8.5% higher than that of R22 (Zhou and Zhang, 2010). Most importantly, the favorable environmental characteristics of R290 make it a viable long-term refrigerant option (Colbourne et al., 2015). As a part of the liquefied natural gas, R290 (propane) has the characteristics of flammable and explosive, it needs a series of safety precautions to avoid leakage and ensure the safety (Colbourne et al., 2013). In this paper, the R290 concentration distribution in the room are measured by series gas detectors. The influence of charge quantity and the diameter of leak hole on the R290 concentration distribution was discussed and compared. A new method of using a solenoid valve near the capillary to reduce the leaking rate was investigated. The results could provide valuable guidance for improving the indoor safety and accident prevention when using R290 as working fluid in the STHACs.

2. EXPERIMENTAL APPARATUS AND PROCEDURES

2.1. Experimental apparatus

Fig. 1 illustrates the schematic of the experimental apparatuses. Two identical indoor units with a width of 1.05 m were employed, the indoor unit (4) was connected to the corresponding outdoor unit while the experimental indoor unit (8) was separately mounted to imitate the R290 indoor leakage. The solenoid valve (2) was installed on the liquid delivery tube and near the capillary to investigate its effects on reducing the fire hazard of R290. The three-way tube (5) and hand valve (6) were

installed on the outlet pipe of the STHAC indoor unit (4) to exclude the impact of the liquid refrigerant. The flexible hose (7) with a length of 1.5 m and the inner diameter of 9.6 mm was connected to the hand valve (6) and acted as the delivery tube. In the R290 mass distribution experiments, the R290 in the indoor and outdoor unit was separated by the shut off valves (3), the flexible hose (7) delivers the refrigerant into the gas collection (13) and the mass of R290 was measured by the quasi-liquid nitrogen method (QLNM), which is a convenient method using the gas bag to measure the refrigerant mass. In the R290 leakage experiments, the port of flexible hose (7) was put inside the experimental indoor unit (8) to mimic the leakage point. It was located at the position of the u-tube junctions of the evaporator, which is the most likely leakage position inside the indoor unit according to the record by STHAC service engineers (Li, 2014, Colbourne et al., 2013). By these experimental methods, the pressure in the STHAC gradually decreases during the leakage process, which is close to the actual leakage conditions. According to Tang's research (Tang et al., 2018), when R290 leaks on the indoor unit side, the area where the R290 concentration exceeds the lower flammable limit is mainly concentrated in the area directly under the air conditioner. Therefore, the sensors are mainly placed in the area directly under the air conditioner to detect the leaked refrigerant concentration distribution.

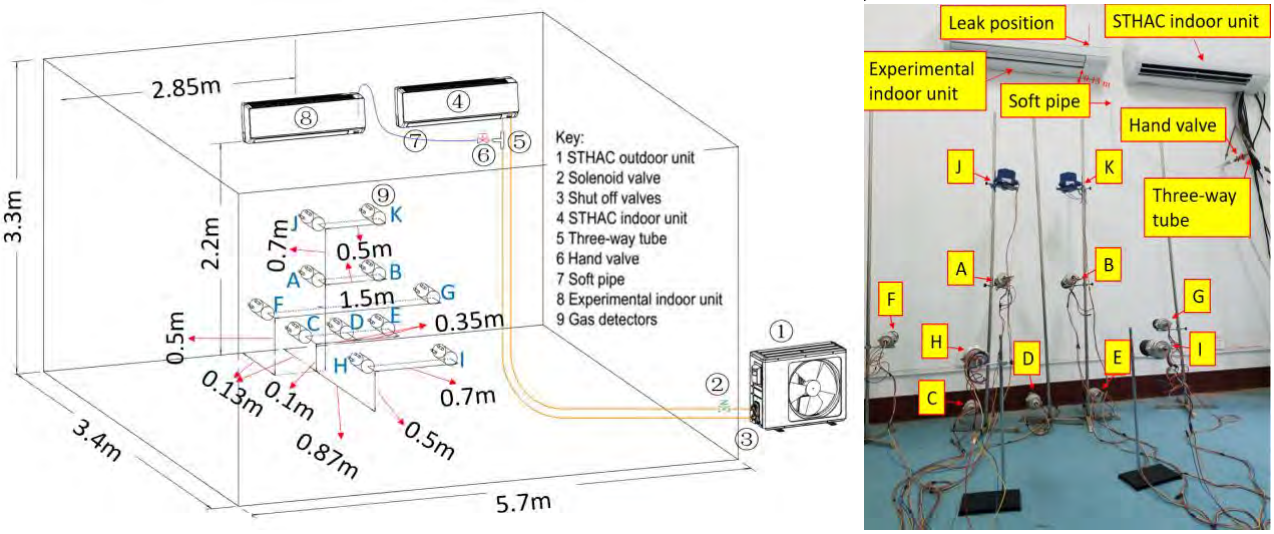

Figure 1: Schematic and photograph of the experimental apparatus

2.2. Quasi liquid nitrogen method (QLNM) for measuring refrigerant mass distribution

The famous methods for measuring refrigerant mass in components of a refrigeration system are liquid nitrogen method (LNM) and online measurement method (OMM). But the test system of LNM is very complicated. OMM, in which the components are placed on the balance and weighed directly, is convenient but less accurate. The measurement error while using LNM is 0.07–0.11% and that of OMM is 3–8% (Ding and Zhang, 2009). Combining these two methods, a method called quasi liquid nitrogen method (QLNM) was proposed, which is expected to be more convenient than LNM and more accurate than OMM. In QLNM, the refrigerant flows into a large plastic bag because of the higher pressure in the components. However, the actual mass of the refrigerant is different from the measurement result because of air buoyancy. The actual refrigerant mass in the plastic bag based on the Archimedes buoyancy formula is given by Eqs. (1) and (2)

$$G=\rho_r \cdot V_1 \cdot g = Fn + F = Fn + \rho_a \cdot V_1 \cdot g \quad \text{Eq. (1)}$$

$$\frac{G}{Fn} = \frac{G}{G-F} = \frac{\rho_r \cdot V_1 \cdot g}{\rho_r \cdot V_1 \cdot g - \rho_a \cdot V_1 \cdot g} = \frac{\rho_r}{\rho_r - \rho_a} \quad \text{Eq. (2)}$$

Where G is the actual weight of the refrigerant, Fn is the weight of the refrigerant measured by using the balance, F is the buoyancy force by the air, and V_1 is the volume of the plastic bag. Moreover, ρ_r is the density of R290 and ρ_α is the density of air. Fn can be read from the balance. The ambient temperature of the experimental situation is 32°C, and the atmospheric pressure is 1atm. Thus, ρ_r=1.7879kg/m^3 and ρ_α=1.1568 kg/m^3, $G = \frac{1.7879}{1.7879-1.1568}\text{Fn}=2.83\text{Fn}.$

3. RESULTS AND DISCUSSION

3.1. R290 mass distribution of the STHACs

As shown in Fig. 1, the flexible hose (7) was put into the gas collection (13) in the R290 mass distribution experiments, then the mass of R290 in the STHAC was measured by QLNM. The results were illustrated in Fig. 2. The R290 mass of the indoor unit included the evaporator and the delivery tubes, while the outdoor unit included the condenser and accumulator. It can be found in Fig. 2(a) that the R290 mass distribution in the outdoor unit accounted 57-80% of total charge when the STHAC is working for a long time; the reason is that most refrigerant will gather in the condenser with the liquid form or dissolved in the lubricating oil. From Fig. 2(b), the R290 mass distribution in the indoor unit accounted 66-73% of total charge when the STHAC does not work for a long time; the reason is that the part of the refrigerant is stored in the liquid form in the evaporator, and the refrigerant in the condenser is in the form of a gas. The results indicate that the refrigerant migrates from the condenser to the evaporator after the STHAC is shut down. This outcome is expected since the pressure in the condenser is higher than that in the evaporator when the STHAC is shut down. Hence, the refrigerant migrates from condenser to evaporator until the equilibrium pressure is reached. The phenomenon of refrigerant migration after STHAC shutdown raises safety concerns since the STHAC closed stage occupied most of time in the room. R290 will gather in the indoor unit after the STHAC cooling mode powered off. On the other hand, we can infer that in the heating mode, the potential indoor fire risk of STHAC will be reduced because R290 will gather in the outdoor unit. The results also indicated that if the connection of indoor unit and outdoor unit could be cut off after the STHAC shutdown, only 20-43% of total R290 charge quantity could leak off when the leakage accident occurs. The specific control method is that in the cooling mode, the STHAC is cut off immediately after the shutdown of the indoor unit and the outdoor unit; in the heating mode, the STHAC is turned off for a period of time to cut off the connection between the indoor unit and the outdoor unit.

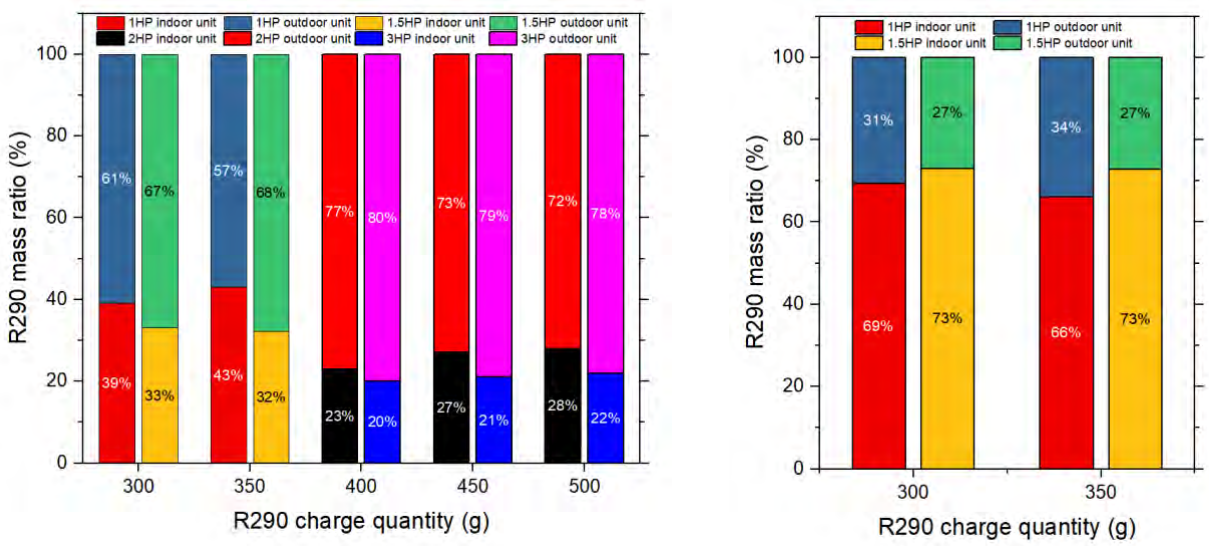

(a) (b)

Figure 2: R290 mass ratio of the indoor and outdoor unit; (a) the STHAC is working for a long time (more than 4 hours); (b) the STHAC does not work for a long time (more than 24 hours)

3.2. Indoor leakage of the R290 STHACs

3.2.1. Impact of the refrigerant charge quantity

To explore the relationship between different R290 charge quantity and concentration distribution in the room, two R290 charge quantity with 260 g and 350 g were selected in this study for 1HP STHAC. The results of R290 concentration distribution with different charge quantity and 0.5 mm leakage hole were shown in Fig. 3. Since the range of the gas detectors is 0-100% lower flammable limit (LFL). It could be convenient to find that the concentration of which detectors could exceed LFL in those figures.

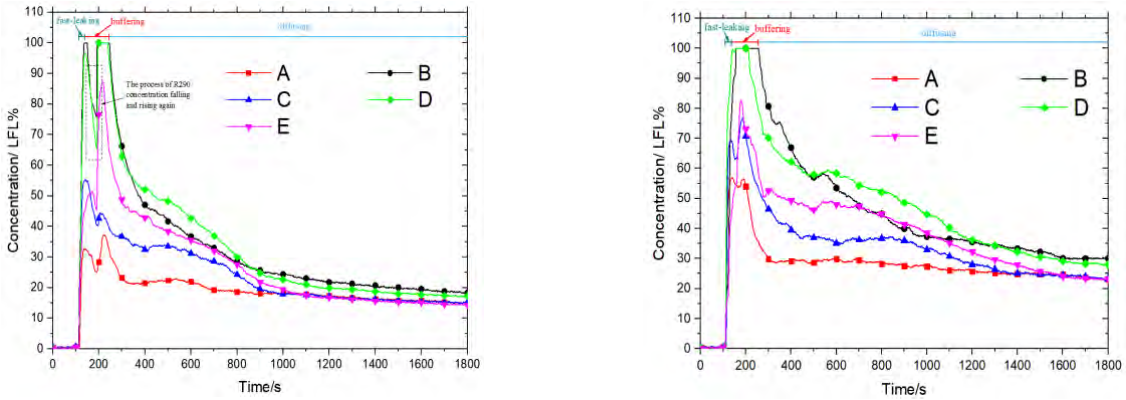

Figure 3. Concentration distribution results of 0.5 mm leakage hole for 1HP; (a) 260 g charge quantity; (b) 350 g charge quantity

The whole leakage process in Fig. 3 was summarized in three periods, which is the fast-leaking period, buffering period and diffusing period. It could be observed in Fig .3(a) that after the fast-leaking period, the R290 concentration of all detectors has a process of falling and rising again. The reason is that the leaked R290 in fast-leaking period reduced the pressure in the evaporator and leaking rate is also decreased, so the R290 concentration falling at the beginning of buffering period. After that the high pressure in the condenser will drive the R290 to migrate from condenser to evaporator through the capillary and liquid connect pipe then leaks off, the migrated R290 from condenser will raise the pressure in the evaporator and the leaking rate, and the R290 concentration in the room rising again. After the most of R290 in the STAHC leaks off and disperses in the room, the R290 concentration in the room will gradually decline and reach a stabilized level in the last. The stabilized R290 concentration level can be verified by the charge quantity. For Fig. 3(b), the trend of the R290 concentration curve is similar to Fig. 3(a). However, the duration time of fast-leaking period is extended since the evaporator gathers more liquid R290 in it, the concentration of detector D also reached LFL level in the fast-leaking period. The biggest difference between the two Figures is the duration time of concentration exceeds the LFL, which means the time of combustible zone appears in the room. The combustible zone's residence time in Fig. 3(a) and Fig. 3(b) are 53s and 99s, respectively. The major difference is that the combustible zone's residence time will be extended by increasing the refrigerant charge quantity. Taken together, it is increasing with the charge quantity, which implies the higher R290 charge quantity will bring the longer dangerous time in the room when R290 leakage occurs. Hence, it needs to strictly restrict the R290 charge quantity to ensure the safety. Another, the concentration distribution of Fig. 3 implies that the combustible zone is more likely appear in the region underneath and near to the leak position. Hence, the electrical components, such as the socket, should not install underneath the R290 STHAC to prevent the generation of accidental short circuit electric sparks in the combustible zone.

3.2.2. Influence of diameter of leakage hole

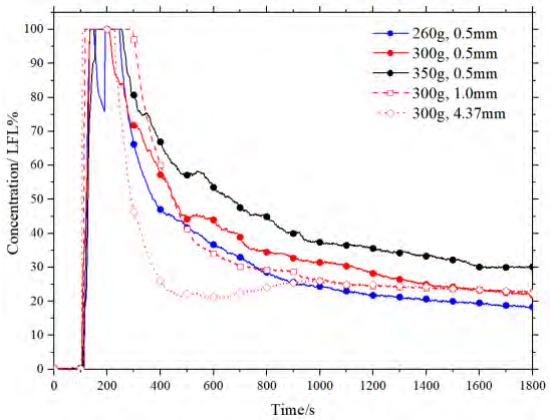

Figure 4: R290 concentration of detector B under different charge quantity and diameter of leakage hole

Three kinds of circular leakage hole with a diameter of 0.5 mm, 1.0 mm and 4.37 mm were chosen in this study to investigate the influence of different leakage hole on R290 concentration distribution in the room. The leakage hole with 0.5 mm diameter was to imitate the situation that tiny rupture on the tube, because it is difficult to drill a smaller diameter hole in the copper tube due to limitations imposed by process. At the same time, the 1.0 mm was to imitate the partial rupture on the tube while 4.37 mm was corresponding to a breakage of the pipe in this study. The 4.37 mm leakage hole was exactly a tube with 5.0 mm external diameter since the researchers in China have applied it to reduce the heat exchanger's inner volume for reducing the R290 charge quantity. Fig. 3 illustrated that the trend of the R290 concentration curve is similar in the whole leakage process and detector B always have the highest R290 concentration. Hence, R290 concentration in detector B under different situations were discussed and the results were shown in Fig. 4.

The results described in Fig. 4 show that the combustible zone's residence time will increase with the charge quantity, but not with the diameter of leakage hole. For example, in the condition of 300 g R290 charge quantity, the combustible zone's residence time under 0.5 mm, 1.0 mm and 4.37 mm diameter of leakage hole is 82 s, 178 s, and 115 s, respectively. The longest combustible zone's residence time appeared in the condition of 1.0 mm diameter of leakage hole, which is not 4.37 mm. The larger diameter of leakage hole brings the faster leaking rate and leads to more expansive combustible zone in the room, but it also leads to shorter leaking time in the same charge quantity at the same time. The combustible zone of 4.37 mm is more expansive than 1.0 mm (all detectors exceeded the LFL in 4.37 mm while detectors A and C cannot reach LFL level in 1.0 mm), but a shorter leaking time leads to the combustible zone's residence time of 4.37 mm (115s) is shorter than 1.0 mm (178s). The result of 0.5mm leakage hole remains the shortest combustible zone's residence time (82s) because its leaking rate is too low to maintain the R290 concentration exceed LFL for a long time. The longer leaking time and fast enough leaking rate results in the longest combustible zone's residence time under 1.0 mm diameter of leakage hole. Therefore, it is noteworthy that the size of the leakage hole is not positively related to the degree of risk, the certain leakage hole with long leaking time and fast enough leaking rate will bring the most dangerous situation in the room.

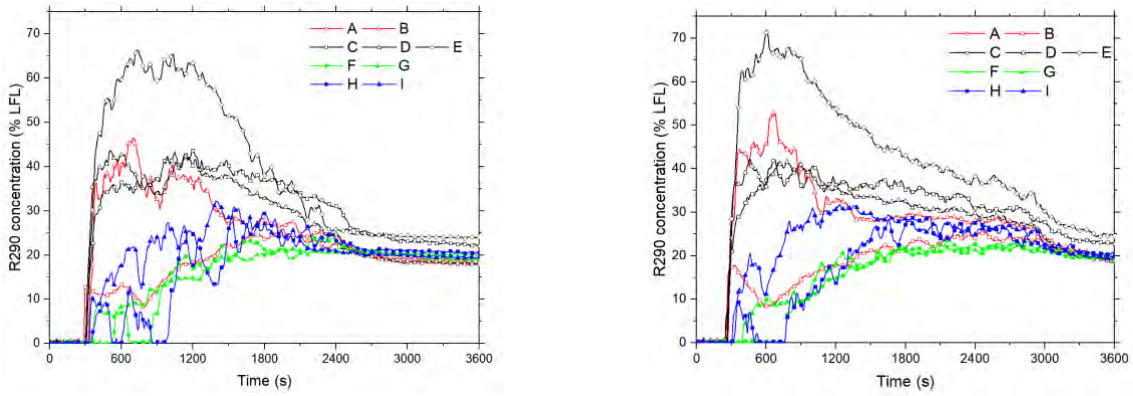

(a) (b)

Figure 5: Concentration distribution results of 500 g charge quantity and 0.5 mm leakage hole; (a) 2 HP STHAC; (b) 3 HP STHAC;

In addition, an unusual phenomenon was found when studying the diameter of leakage hole. It is that for 2HP and 3HP STHAC, all of the 0.5 mm leakage hole results showed that the R290 concentration will not approach the LFL, regardless of the quantity of refrigerant charge, as shown in Fig. 5. But in the results of 1 HP STHAC, the R290 concentration did reach the LFL with a 0.5 mm leakage hole, even though the R290 charge quantity was only 260g (as shown in Fig. 3). This outcome might be explained by the larger internal size of the indoor unit. The leaking refrigerant flow rate depends mainly on the pressure difference between inside and outside of leakage hole and the area of leakage hole, then if the pressure difference between inside and outside of leakage hole and the area of leakage hole are all same, the leaking refrigerant flow rate will be same and has nothing to do with the capacity of the unit. But the different capacities of the air-conditioner units need different size of indoor unit and outside unit. The larger capacity of the unit needs larger size indoor unit. In our experiments, the height and the width of the indoor unit of 1HP unit are same with that of

the indoor unit of 2HP and 3HP units, but the length of the indoor unit of 1HP unit is only about 800mm with the length of evaporator tube is 600 mm (Tang et al. 2018) and the length of the indoor unit of 2HP and 3HP units is 1000 mm with the length of evaporator tube is 805mm. When the saturation pressure in indoor unit and the leakage hole are same for air conditioner units with different capacities, the leaking refrigerant flow rate through the leakage hole would be the same. Because the leaked refrigerant will first diffuse inside the indoor unit and then flow into the room through the air outlet (length is same with the length of evaporator tube) of the indoor unit, the larger length of the air outlet could result in the lower refrigerant flow rate through the air outlet of the indoor unit, and the lower refrigerant flow rate into the indoor environment would cause the lower R290 concentration distribution. Hence, the R290 concentration of 2 HP and 3 HP STHAC with a 0.5 mm leakage hole will not exceed the LFL. Besides, the difference of the internal positioning, the direction of the leak jet and the location of the concentration sensors could also have the effect on the indoor R290 concentration distribution.

3.3. Reduce the risk of R290 leakage

The results of R290 mass distribution of the STHACs indicated that installing a solenoid valve near to the capillary could reduce the leaking rate by delay the R290 migrate from condenser to evaporator. Hence, the experiments with solenoid valve closed were carried out to investigate its effects on reducing the leaking rate. Fig. 6 illustrates that all detectors have reached the LFL level and the longest combustible zone's residence time (186s) since it has the largest charge quantity (350 g) and the longest leaking time (1.0 mm). However, the result of the situation that solenoid valve closed (Fig. 6(b)) shows that the region and residence time of the combustible zone were reduced, only detectors B and D have reached the LFL and the residence time was shortened to 85s. Fig. 6(a) and 6(b) show the comparison of solenoid valve opening or closed under the most dangerous situation in this study. Therefore, it could be concluded that closing the solenoid valve could greatly improve the safety of R290 STHAC.

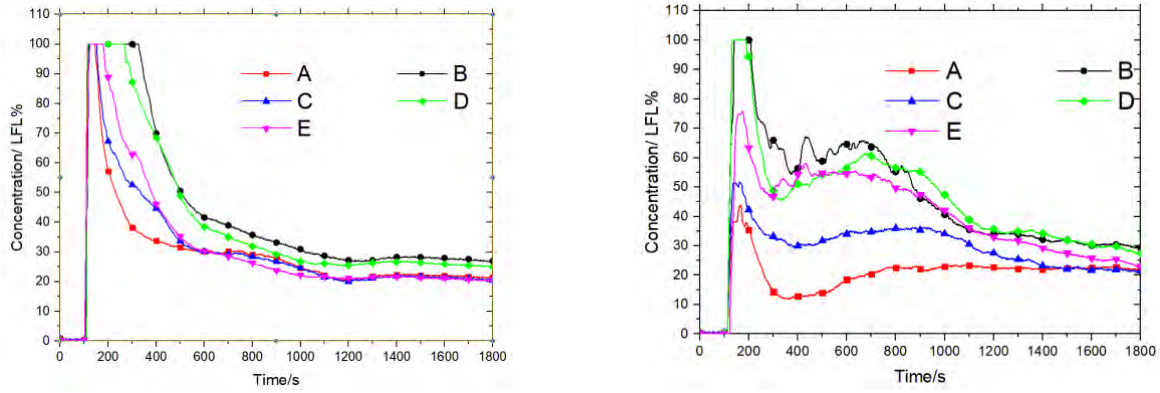

Figure 6: Concentration distribution results of 350g charge quantity with 1.0mm leakage hole; (a) solenoid valve opened; (b) solenoid valve closed;

Another, Fig. 7(a) illustrated the R290 concentration of 2 HP STHAC with a 400 g refrigerant charge quantity, 2.0 mm diameter leakage hole and solenoid valve (2) closed. The closed solenoid valve hinders the refrigerant migration process from the condenser to the evaporator and reduce the leaking rate, resulting that both the region and residence time of the combustible zone being decreased. It could be clearly observed from Fig. 7(a) that there is a distinct rise of R290 concentration (especially the gas detector E) in the buffering period. This means that there might exist other migration ways from condenser to evaporator when the solenoid valve closed. The experiment with shut off valve (3) of the 2 HP STHAC closed was therefore carried out to investigate it. Only the shut off valve (3) of the gas delivery tube was closed at beginning since the solenoid valve (2) was installed on the liquid delivery tube (Fig. 1), but it was reopened once the R290 concentration in the room was stable for a period. The solenoid valve (2) was kept closed during the whole leakage process and the results are shown in Fig. 7(b). The R290 concentration illustrated in Fig. 7(b) was clearly divided into two phases. Firstly, the refrigerant in the evaporator leaked out and raised the R290 concentration in the room. Then the average stabilized concentration at the moment

of 1200-1800 s in Fig. 7(b) was about 5% LFL. The shut off valve of the gas delivery tube was reopened at the 1800 s, then the R290 concentration in the room raised immediately and the final stabilized concentration value is the same as all the 450 g R290 had leaked into the room. From this phenomenon it could be inferred that the R290 migration process through the liquid delivery tube will be cut off by the closed solenoid valve, but the high pressure of the condenser will still drive the refrigerant to the evaporator through the clearances of the compressor and the gas delivery tube.

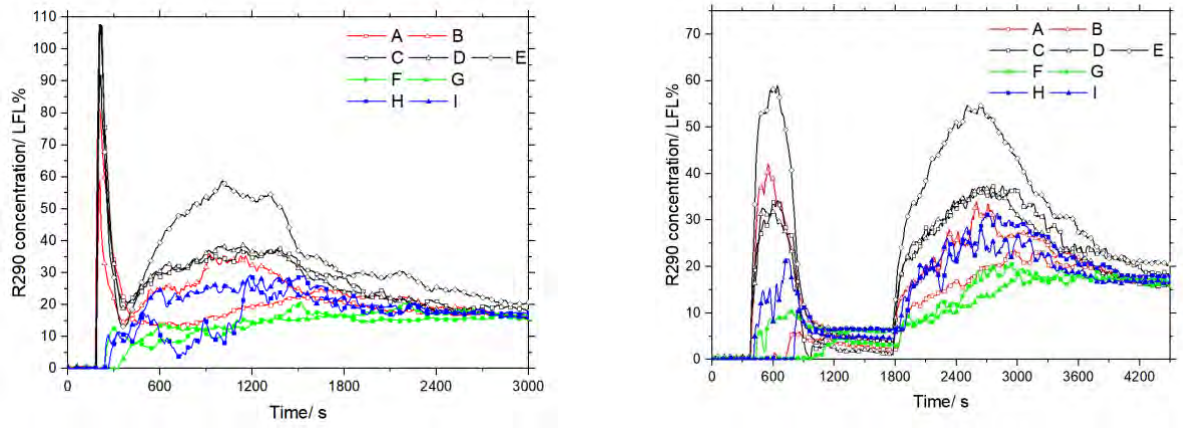

Figure 7: Concentration distribution results of 400 g charge quantity, 2.0 mm leakage hole and solenoid valve closed of 2 HP STHAC; (a) the shut off valve (3) was always open; (b) the shut off valve (3) was closed at the beginning but reopened at the 1800s

3.4. Summary of the results

Except for the above representative experimental results, many different experiments carried out to analyse the influence of the various factors. Table 1 lists the distribution of R290 concentrations in a room with several special cases. For 2HP and 3HP STHAC, whether the solenoid valve is closed, it is found that the room is relatively safe under the 0.5 mm diameter leak hole because all of the sensors do not detect the refrigerant concentration reaching the LFL. But for the 1HP STHAC, the refrigerant concentration in the area where the sensors are located does not reach the LFL only when the solenoid valve is closed. The range and residence time of the combustible zone was reduced after closing the solenoid valve for the 2 HP STHAC with a 2.0 mm leakage hole, but was extended for the 3 HP STHAC. This might be caused by the wider clearances of the 3 HP R290 rotary compressor on account of it being a prototype. After the solenoid valve closed, the refrigerant in the condenser will migrate through the clearances of the rotary compressor into the evaporator and then leak out; the leaking rate was reduced but the leaking time extended. As a comparison, the combustible zone's residence time of 2 HP STHAC was shortened because its leaking rate could only make the R290 concentration in the room to reach the LFL for a short time. As a mitigation, the manufacturing process of the 3 HP R290 rotary compressor needs to be improved so that clearances distances are reduced.

Table 1. Summary of the indoor leakage tests conditions and results

Type	1HP				2HP				3HP			
Leakage hole	0.5mm		1mm		0.5mm		2mm		0.5mm		2mm	
charge quantity	350g		350g		500g		500g		500g		500g	
Solenoid valve	open	close	open	close	open	close	open	close	open	close	open	close
Sensors NO. of exceeding LFL	BD	-	ABC DE	BD	-	-	ABCD EJK	ACJ	-	-	ABCD EJK	BCD EK
Residence time of measurement points exceeding LFL /s	99	0	186	85	0	0	123	33	0	0	157	153

Particular, there is an important observation cannot be ignored that within the fast-leaking period, R290 leakage is accompanied by a huge sound. This huge sound is similar to the sound at the start of the STHAC switching to the defrost mode from the heating mode. The difference is the huge sound is transitory in the defrost mode but continues in the whole leakage process, it will be quieter

in the buffering period but still could be clearly heard in the room. In addition, this huge sound can also be heard by the experimenter even in the tests that no detectors reach the LFL level such as under the condition that 0.5 mm leakage hole and solenoid valve closed. Hence, this observation could help the consumers to identify the flammable risk in the room where using R290 STHAC: if they heard the huge leakage sound, there probably exists fire risk in the room.

4. CONCLUSIONS

Based on the above experimental results, the following conclusions can be reached:

(1) Refrigerant charge quantity has a major influence on the R290 concentration distribution in the room. A higher R290 charge quantity will lead to a more extensive combustible zone and longer residence time in the room.

(2) A practical and achievable approach to significantly reduce the leaking rate and enhance the room safety is installing a solenoid valve behind the capillary, and simultaneously closing it as the STHAC shutdown. The results demonstrate that both range and residence time of the combustible zone were significantly reduced under the condition of solenoid valve closed.

(3) Potential ignition sources, such as switches and other electrical components should be avoided installed underneath the indoor unit of STHAC because it is the most probable region where combustible zone appears. The huge sound accompanied with the leakage might be the judgment whether the flammable risk appeared in the room.

REFERENCES

Montreal Protocol 1987. Montreal Protocol on Substances that Deplete the Ozone Layer, New York, USA, United Nations (UN) (1987 with subsequent amendments)

Höglund-Isaksson, L., Purohit, P., 2017. Cost estimates of the Kigali Amendment to phase-down hydrofluorocarbons. Environmental Science & Policy 75, 138-147.

Wu, J.H., Yang, L.D., 2012. Experimental performance study of a small wall room air conditioner retrofitted with R290 and R1270. Int. J. Refrigeration 35, 1860-1868.

Sánchez, D., Cabello, R., 2017. Energy performance evaluation of R1234yf, R1234ze(E), R600a, R290 and R152a as low-GWP R134a alternatives. Int. J. Refrigeration 74, 269-282.

Padalkar, A.S., Mali, K.V., 2014. Simulated and experimental performance of split packaged air conditioner using refrigerant HC-290 as a substitute for HCFC-22. Applied Thermal Engineering 62, 277-284.

Tang W, He G., 2018. Assessment of leakage and risk reduction of R290 in a split type household air conditioner. Int. J. Refrigeration 89: 70-82.

Teng, T.-P., Mo, H.-E., 2012. Retrofit assessment of window air conditioner. Applied Thermal Engineering 32, 100-107.

Zhou, G., Zhang, Y., 2010. Performance of a split-type air conditioner matched with coiled adiabatic capillary tubes using HCFC22 and HC290. Applied Energy 87, 1522-1528.

Colbourne D, Suen K O, 2015. Comparative evaluation of risk of a split air conditioner and refrigerator using hydrocarbon refrigerants. Int. J. Refrigeration 59, 295-303.

Colbourne D, Espersen L, 2013. Quantitative risk assessment of R290 in ice cream cabinets. Int. J. Refrigeration 36, 1208-1219.

G. Ding, X. Ma, P. Zhang, 2009. Practical methods for measuring refrigerant mass distribution inside refrigeration system. Int. J. Refrigeration 32, 327-334.

Li, T., 2014. Indoor leakage test for safety of R-290 split type room air conditioner. Int. J. Refrigeration 40, 380-389.

Colbourne D, Hühren R, 2013. Refrigerant leakage control for R-290 in split type refrigeration and air conditioning systems. Castá, Papiernicka, Proc. IIF-IIR.

Manuscript ID: 797
DOI: 10.18462/iir.icr.2019.0797

Experimental investigation of CO_2 systems for Indian supermarkets with parallel configuration of multiejectors (INDEE)

Krzysztof BANASIAK[(a)], Simarpreet SINGH[(b)], Armin HAFNER[(c)], Prakash M. MAIYA[(b)], Petter NEKSÅ[(a)], Ángel Á. PARDIÑAS[(c)]

[(a)] SINTEF Energi AS, Kolbjørn Hejes vei 1B, Trondheim, 7034, Norway, krzysztof.banasiak@sintef.no

[(b)] Indian Institute of Technology Madras, 600036, India

[(c)] Department of Energy and Process Engineering, NTNU, Trondheim, 7491, Norway

ABSTRACT

Experimental investigation of transcritical R744 pack for Indian supermarkets was performed. Parallel combination of expansion work recovery multiejector blocks was applied for optimization of energy performance of the whole pack. The discharge pressure control proved to be fully functional with parallel multiejector operation providing system stability over a broad range of ambient conditions. Energy performance of the pack measured in Indian conditions was at the level recorded in the NTNU/SINTEF laboratory for a reference R744 pack. High ambient temperatures might result in operation on the verge of the operational envelope for compressor discharge temperature, especially for the MT machines.
Keywords: Supermarket, R744, Ejectors.

1. INTRODUCTION

Refrigeration systems for supermarkets solely based on carbon dioxide are currently able to outperform HFC-based units for across Europe, thanks to the implementation of different technologies improving energy performance, such as overfed evaporators, vapour ejectors for unloading the medium-temperature (MT) compressors or AC production, Pardiñas et al. (2018a), as well as mechanical subcooling, Karampour and Salwaha (2018), among others. Still, that continuous adoption of more and more sophisticated technical solutions for boosting of energy performance made the system layouts and control strategies more complex, elevating the investment costs for 'all-in-one' R744 solutions above the level of typical HFC units, Gullo et al. (2018). This effect, together with the lack of knowledge and experience with transcritical systems and their performance in tropical conditions results in the total absence of R744 in the Indian supermarkets, hotels and cold chain industry, for the sake of HCFCs and HFCs.

Initial studies show however that potential for application is great, even in the regions of India characterized by very hot climate. Namely, Purohit et al. (2018) found in their theoretical study that properly designed 'all-in-one' R744 systems (integrated all CO_2 booster with multiejectors and flooded evaporators) always outperform conventional HFC systems with direct expansion and superheated evaporators.

Typical design profile of refrigeration loads for supermarkets of different size around Europe is defined by the refrigeration capacity ratio (called also load factor and defined as ratio of MT refrigeration load to LT refrigeration load), typically between 2 and 8, Gullo et al. (2017), for evaporating temperatures ranging from -10 °C to -2 °C for the MT section and from -35 °C to -25 °C for the LT section, correspondingly, Gullo et al. (2018). Integration of AC is desired, however not always accepted by the shop owners. Integration of heating is in practice a standard design.

In Indian conditions load factor is somewhat lower (between 3 and 4) and the effect of AC cannot be neglected since AC constitutes ca. 50% of the overall load, Purohit et al. (2018). Also, in order to effectively compete with HFC systems, integration of the AC load in the 'all-in-one' R744 system is

a must. Integration of heating will naturally only further boost up the energy performance, due to very advantageous properties of CO_2 for heat reclaim. Therefore, appropriate design of the integrated compressor pack for Indian supermarkets becomes an issue of particular importance. The purpose of this paper is to present the first results registered at a demo transcritical R744 facility, emulating compressor pack for a small-size Indian supermarket. A specific feature of the rig elevating the energy performance, apart from complete integration (freezing + cooling + air conditioning + heating), is maintaining the discharge pressure solely with the use of multiejectors, i.e., total elimination of the high-pressure expansion valves.

2. SYSTEM DESCRIPTION

A demo R744 test facility for supermarket applications of 3 kW LT, 10 kW MT and 20 kW AC cooling capacity was developed in cooperation with ENEX, Danfoss, Dorin, LUVE and Klimal, and installed at IIT Madras, India (Figure 1), within the scope of project INDEE. The cooling system is designed to maintain three different levels of temperatures at the three shell-and-tube evaporators: freezing temperature (LT) at -29°C, refrigeration temperature (MT) at -6°C and air conditioning (AC) at 7-9°C. The test facility is also equipped with the glycol-based heat recovery system to maintain a constant heat load to the system (heat reclaimed in gas coolers is effectively used to supply evaporators). The excess heat is rejected in an air-cooled fin-and-tube gas cooler. Outlet conditions of MT and LT evaporators are controlled by Electronic Expansion Devices (EEV). Propylene glycol and water solution is used as a heat transfer medium in the test facility. Two separate glycol loop circuits are arranged with different glycol concentrations; 42% for MT & AC load and 56% for LT load.

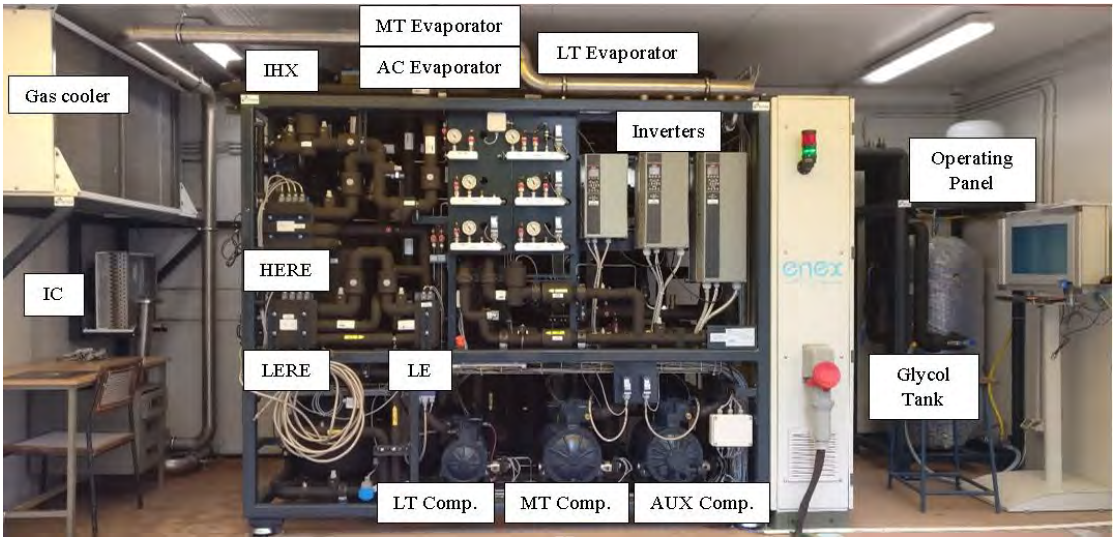

Figure 1: Layout of the transcritical R744 demo facility for Indian supermarkets at IIT Madras

Three piston compressors are arranged at various suction temperature levels (LT & MT and AUX compressors) to handle load as well as high amounts of flash gas. Two 4-cartridge vapour multiejector blocks by Danfoss (Multi Ejector Solution™) are installed in parallel, low entrainment ratio ejector (LERE) and high entrainment ratio ejector (HERE). One 2-cartridge liquid ejector block is also installed and connected to a suction accumulator to provide an excess feed to overflood the MT evaporators throughout the year (not indicated in Figure 2 for the sake of picture's clarity). Temperature sensors (PT1000), pressure sensors (piezoelectric cells), and flow meters (ultrasound flow meters for glycol circuits) are installed for system control and data acquisition.
The rig facilitates a few different operational modes to evaluate various possible configurations for supermarket application at high ambient temperature (up to 48 °C). Figure 2 shows the detailed schematic of the R744 test facility and various components installed in the system. The corresponding *p-h* plot for the present study is projected in Figure 3.

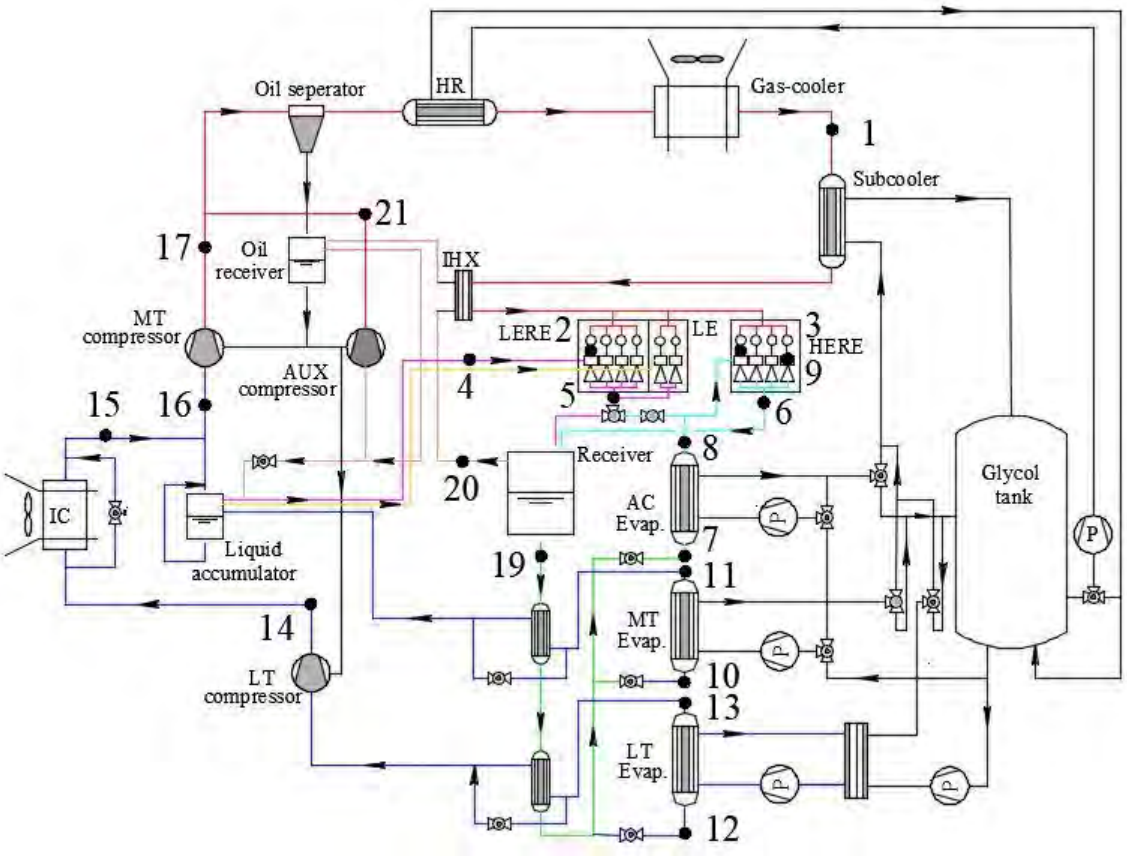

Figure 2: P&ID of the demo R744 system at IIT Madras. IC – intercooler (desuperheater), HR – heat reclaim, LERE – low-entrainment-ratio ejectors, HERE – high-entrainment-ratio ejectors, IHX – internal heat exchanger. For state points representation in *p-h* diagram see Figure 3

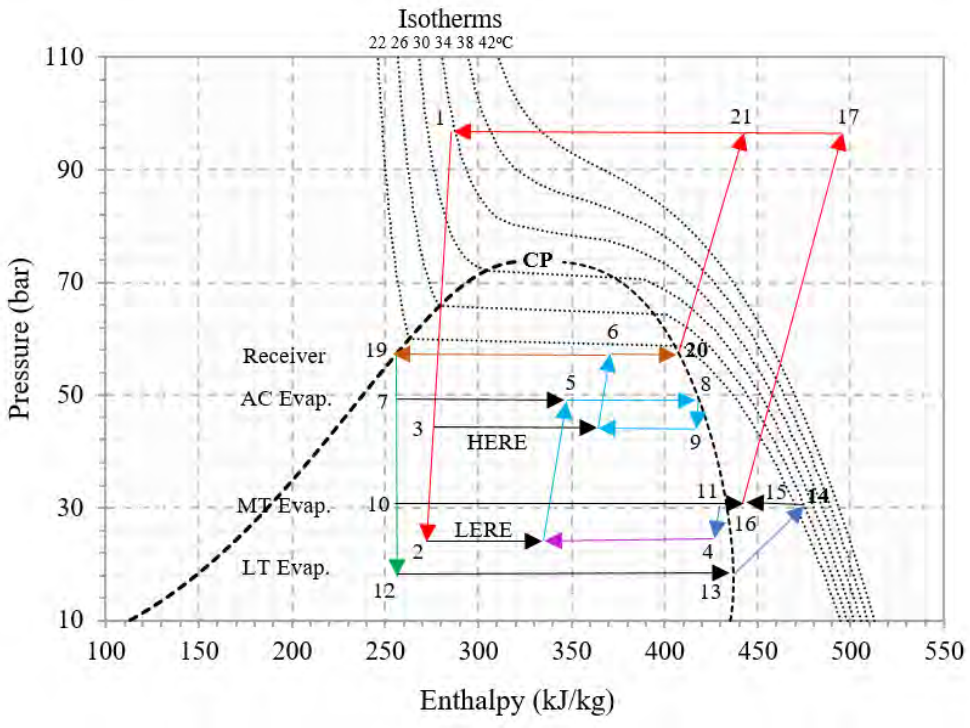

Figure 3. Cycle representation for the integrated LT, MT, and AC system for Indian supermarkets

3. TEST CONDITIONS

System layout investigated during the test campaign enabled maximum recovery of the expansion work potential available in the high-pressure gas cooler outlet stream, i.e., the potential available in the high-pressure stream leaving the gas cooler was effectively converted into suction effect in two independent multiejector blocks, HERE for AC production, and LERE for compressing part of the MT vapour to the receiver pressure.
The main device used to control discharge pressure were LERE ejectors (in auto mode) while HERE ejectors were switched on manually to invoke circulation in the AC evaporator. The range of operating conditions tested is given in
Table 1.

Table 1. Test conditions maintained during experimental campaign

Operating parameter	Units	Value/Range
Gascooler outlet temperature	°C	36 to 46
Gascooler outlet pressure	bar	86 to 108
AC evaporation temperature	°C	4 to 8
MT evaporation temperature	°C	-9 to -6
LT evaporator temperature	°C	-31 to -28
superheat	K	4 to 15
Receiver pressure	bar	43 to 46
IHX/heat reclaim	-	Bypassed/not included

4. ENERGY PERFORMANCE PARAMETER

The variety of technical solutions offered by manufacturers as an alternative to F-gases banned from 2020 (like R-404A) and the availability of very new integrated solutions for refrigeration and air conditioning based on CO_2 require a comparison of systems in terms of energy efficiency, rather than energy consumption. It claims for experimental methodologies, as consolidated and validated models for those systems are not yet available or affordable. Thus, a simplified approach based on measurement of power input and the comparison of the minimum ideal required power in the Carnot cycle is proposed. Namely, Power Input Ratio (PIR, see Figure 4) may be calculated for any ambient conditions and reference temperature levels of utilities (LT, MT, AC, heating, domestic hot water).

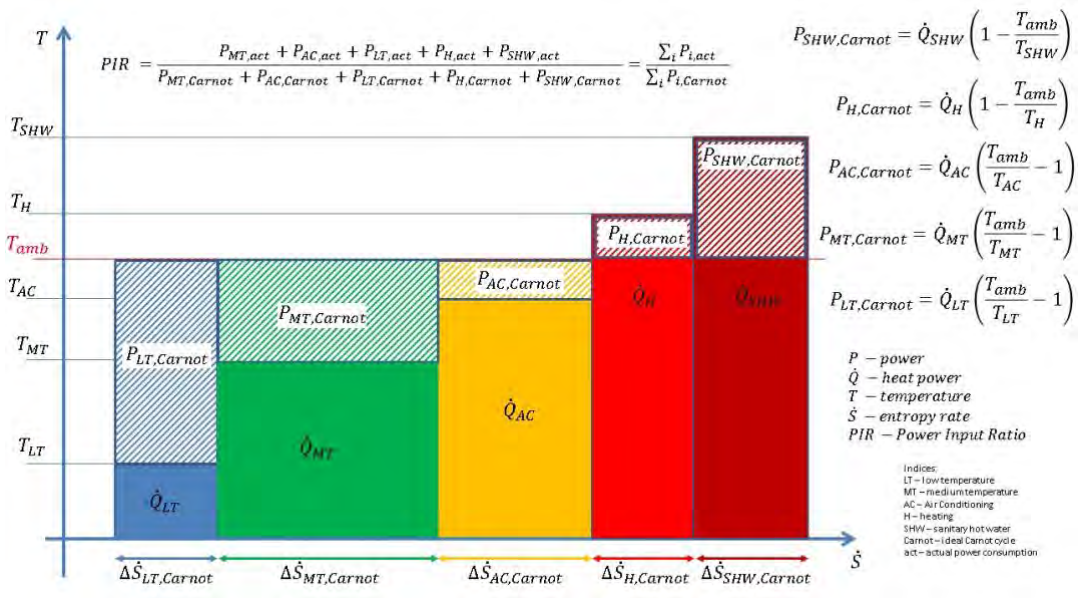

Figure 4. Definition of energy performance measure for integrated systems in supermarkets.

5. RESULTS

A dedicated test campaign was carried out for experimental investigation of (i) stability of discharge pressure control with two parallel multiejector blocks and (ii) energy performance of the system. 16 points were recorded, differentiated according to the emulated ambient conditions (it was assumed constant temperature approach in gas cooler equal to 3 K).

Table 2 presents an overview of the expansion duty distributed among various cartridges. It can be observed that fixing certain opening in the HERE block for AC generation does not reduce the ability of the LERE controller to maintain the requested discharge pressure, taken from the optimum energy performance curve. Average relative opening time less than 100% means that the ejector cartridge was actively adjusting the overall opening of the expansion nozzles in the block, being shut and open according to the steering signal sent by the discharge pressure controller. Thus, steady state test periods were in practice emulated with quasi-steady-state operation with discharge pressure fluctuating within certain narrow dead band (2 bar).

Table 3 shows basic parameters of the system in response to growing gas cooler outlet temperature. The most significant change one can observe is in the discharge temperature of the MT compressor, rising along with the ambient conditions, and reaching values close to not recommended by the compressor manufacturers due to the danger of thermal degradation of lubricant. At the same time, the energy performance, represented by PIR, reveals weak correlation to ambient conditions, showing even certain optimum around 37-39 °C.

Since the use of PIR has not been widespread so far, it is hard to find data for cross-checking whether the recorded values represent an up-to-date energy performance. Thus, own experimental data gathered in the course of the *Super-Smart Rack* project were utilized for comparison (Figure 5). For details on test rig and other experimental results on integrated R744 packs recorded during *Super-Smart Rack* see: Pardiñas et al. (2018b).

Table 2. Relative opening time of individual ejector cartridges for parallel operation of the HERE and LERE multiejector blocks

No.	Emulated ambient temp., °C	Gas cooler outlet temp., °C	Discharge pressure, bar	Average relative opening time (auto mode for LERE)				Average relative opening time (manual mode for HERE)			
				EJ1	EJ2	EJ3	EJ4	EJ1	EJ2	EJ3	EJ4
1	32.8	35.8	86.4	41%	12%	0%	0%	100%	0%	0%	100%
2	34.7	37.7	91.7	47%	44%	0%	0%	100%	100%	100%	0%
3	35.0	38.0	88.4	24%	25%	2%	0%	0%	100%	100%	0%
4	34.5	37.5	92.1	92%	6%	0%	0%	100%	0%	0%	100%
5	36.9	39.9	96.9	44%	56%	0%	0%	100%	100%	100%	0%
6	36.9	39.9	93.4	35%	17%	0%	0%	100%	100%	100%	0%
7	36.8	39.8	97.1	46%	54%	0%	0%	100%	0%	0%	100%
8	38.9	41.9	101.2	18%	82%	0%	0%	100%	0%	0%	100%
9	38.8	41.8	100.7	59%	0%	0%	0%	100%	0%	0%	100%
10	39.1	42.1	101.7	26%	74%	0%	0%	100%	0%	0%	100%
11	41.2	44.2	106.3	1%	99%	0%	0%	100%	0%	0%	100%
12	40.8	43.8	104.9	95%	1%	0%	0%	100%	0%	0%	100%
13	41.1	44.1	105.8	12%	88%	0%	0%	100%	0%	0%	100%
14	43.2	46.2	109.9	42%	58%	0%	0%	100%	0%	0%	100%
15	43.1	46.1	109.3	84%	1%	0%	0%	100%	0%	0%	100%
16	43.1	46.1	109.7	68%	32%	0%	0%	100%	0%	0%	100%

Table 3. Power Input Ratio of the system as a function of rising ambient conditions. Assumed utility temperatures: -18 °C for LT, +4 °C for MT, and +22 °C for AC

No.	Gas cooler outlet temp., °C	Receiver pressure, bar	MT discharge temp., °C	Evaporation temperature, °C			Load factor		PIR
				LT	MT	AC	$\frac{\dot{Q}_{MT}}{\dot{Q}_{LT}}$	$\frac{\dot{Q}_{AC}}{\dot{Q}_{MT}}$	
1	35.8	45.8	111.2	-29.9	-6.7	7.7	2.8	2.4	6.23
2	37.7	43.0	123.2	-29.8	-7.7	4.1	12.7	1.6	6.38
3	38.0	46.7	107.8	-28.4	-5.9	7.9	3.1	1.3	5.88
4	37.5	44.2	124.8	-29.2	-7.9	5.8	4.6	1.9	5.43
5	39.9	43.3	128.5	-29.4	-8.0	3.8	5.0	1.5	5.34
6	39.9	45.5	120.8	-29.3	-6.6	6.2	3.7	1.5	5.94
7	39.8	44.3	127.9	-26.8	-7.8	5.5	4.4	1.9	5.42
8	41.9	43.2	134.7	-29.3	-7.9	4.2	5.2	2.0	5.78
9	41.8	44.1	134.1	-29.0	-7.8	4.2	5.1	1.4	5.30
10	42.1	44.4	134.6	-29.1	-7.9	5.3	4.8	2.0	5.53
11	44.2	43.4	140.0	-29.2	-8.0	4.0	5.4	2.1	6.01
12	43.8	44.2	138.9	-29.3	-8.0	4.1	5.2	1.7	5.42
13	44.1	44.4	139.5	-30.8	-7.8	5.0	5.2	2.0	5.74
14	46.2	43.7	143.2	-28.2	-7.9	4.0	5.8	2.2	6.38
15	46.1	44.2	141.3	-29.2	-7.9	3.9	4.7	2.0	5.84
16	46.1	44.4	144.6	-27.7	-7.8	4.6	4.8	2.2	5.84

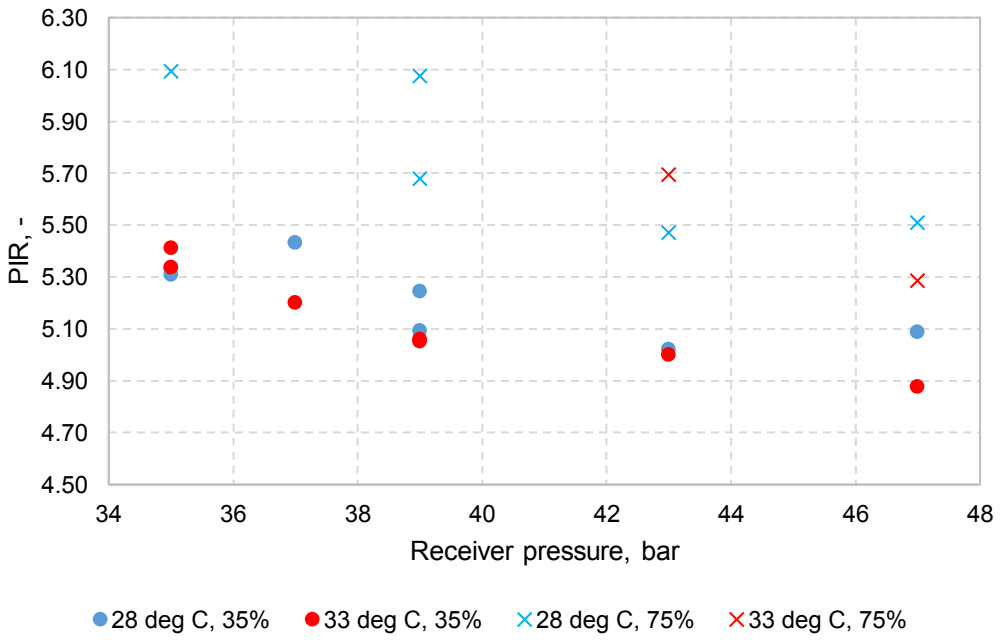

Figure 5. PIR for a reference transcritical R744 system investigated at SINTEF/NTNU laboratory during the KPN project *Super-Smart Rack*. Different colours denote gas cooler outlet conditions, while marker shape denotes load factor between AC and MT, according to the definition in Table 3. Load factor between MT and LT equal to 5; superheat conditions in all the evaporators

Points plotted in Figure 5 allow for comprehensive interpreting the results gathered in Table 3. Firstly, they confirm that the range of PIR values recorded during the INDEE-project test campaign does not differ significantly from what was recorded at a reference test facility. Secondly, it has been confirmed that PIR is practically not influenced by the ambient conditions. Finally, two important parameters that might have impact on PIR were revealed, namely (i) load factor between AC and MT, and (ii)

receiver pressure. Elevating the receiver pressure led to improvement in energy performance, at least in the investigated range, i.e., up to 47 bar. On the other hand, rising values of the AC/MT load factor deteriorate PIR. A possible explanation might be found in the fact that the AC load is burdened with greater specific entropy generation related to heat transfer between the evaporating refrigerant and the final utility. For example, the average temperature difference for data in Table 3 was equal to 11 K, 11.6 K, and 17 K for the LT, MT, and AC loads, correspondingly.

Nevertheless, an interesting point of the analysis could be making the integrated R744 cycle even more efficient, i.e., removing the main cycle inefficiencies. Apart from obvious features like using high-efficiency compressors or applying flooded evaporators (especially for ejector-supported AC evaporators where there is no danger of compressor flooding), an interesting aspect seems to be proper balancing of the receiver pressure. Firstly, due to the double-stage expansion layout, the intermediate pressure is one of the cycle degrees of freedom that should be optimized based on the overall energy performance, independently of the system complexity. Receiver pressure should be thus controlled according to the optimum-performance curve, like the discharge pressure. Secondly, the location of that optimum will be highly influenced not only by ambient conditions but also by actual performance of individual components like compressors and ejectors. For both compressors and ejectors the energy (and flow) performance is highly dependent mainly on requested pressure lift (or pressure ratio). For example, taking into consideration three quite similar test conditions according to the values of gas cooler outlet temperature, namely points, 2, 3, and 4, one can see that even small adjustments in the values of requested receiver pressure invoke non-negligible changes in PIR. The same observation applies to another pair, points 14 and 15.

Table 4. Compressor pressure ration for LT, MT and AUX machines together with pressure lift for HERE and LERE blocks

No.	Gas cooler outlet temperature, °C	Discharge pressure, bar	Receiver pressure, bar	Compressor pressure ratio			Pressure lift for HERE, bar	Pressure lift for LERE, bar	PIR
				LT	MT	AUX			
1	35.8	86.4	45.8	1.94	3.01	1.87	3.3	13.1	6.23
2	37.7	91.7	43.0	1.88	3.31	2.11	4.2	15.3	6.38
3	38.0	88.4	46.7	1.97	3.01	1.87	4.0	14.4	5.88
4	37.5	92.1	44.2	1.76	3.33	2.07	3.7	14.7	5.43
5	39.9	96.9	43.3	1.84	3.52	2.22	4.8	16.3	5.34
6	39.9	93.4	45.5	1.95	3.25	2.03	4.6	14.6	5.94
7	39.8	97.1	44.3	1.79	3.51	2.17	4.0	16.7	5.42
8	41.9	101.2	43.2	1.90	3.67	2.32	4.3	16.2	5.78
9	41.8	100.7	44.1	1.82	3.64	2.26	5.3	16.5	5.30
10	42.1	101.7	44.4	1.88	3.68	2.27	4.4	17.5	5.53
11	44.2	106.3	43.4	1.88	3.86	2.43	4.7	17.0	6.01
12	43.8	104.9	44.2	1.81	3.81	2.35	5.4	17.4	5.42
13	44.1	105.8	44.4	1.86	3.82	2.36	4.7	17.3	5.74
14	46.2	109.9	43.7	1.87	3.98	2.49	5.0	17.3	6.38
15	46.1	109.3	44.2	1.82	3.96	2.45	5.7	17.5	5.84
16	46.1	109.7	44.4	1.70	3.95	2.45	5.1	17.8	5.84

6. CONCLUSIONS

An initial test campaign of integrated transcritical CO_2 test facility designed to emulate typical working conditions in Indian supermarkets was carried out where parallel configuration of multiejector blocks was validated. The conducted experiments proved that parallel operation of HERE and LERE multiejectors is feasible and discharge pressure can be effectively maintained, regardless of ambient

conditions. Very high ambient temperature (above 43 °C) may though impose hazardous working conditions for the MT compressor section, due to excessive discharge temperature (above 140 °C). Recorded energy performance, expressed with the use of newly introduced parameter PIR, proved to be within range typical for integrated R744 packs for supermarkets tested in European conditions. Still, substantial energy performance improvements can be harvested thanks to certain simple measures like controlling the intermediate pressure according to the optimum performance curve or flooded evaporators.

ACKNOWLEDGEMENTS

The research was supported by a grant from the Norwegian Ministry of Foreign Affairs (MFA) under contract no. IND-15/0023.

REFERENCES

Gullo, P., Hafner, A., Cortella, G., 2017. Multi-ejector R744 booster refrigerating plant and air conditioning system integration – A theoretical evaluation of energy benefits for supermarket application. Int. J. Refrigeration 75, 164-176.

Gullo, P., Hafner, A., Banasiak, K. 2018. Transcritical R744 refrigeration systems for supermarkets applications: Current status and future perspectives. Int. J. Refrigeration 93, 269-310.

Karampour, M., Sawalha, S., 2018. State-of-the-art integrated CO_2 refrigeration system for supermarkets: A comparative analysis. Int. J. Refrigeration 86, 239-257.

Pardiñas, Á.Á., Hafner, A., Banasiak, K., 2018a. Novel integrated CO_2 vapour compression racks for supermarkets. Thermodynamic analysis of possible system configurations and influence of operational conditions. Appl. Therm. Eng. 131, 1008-1025.

Pardiñas, Á.Á., Hafner, A., Banasiak, K., 2018b. Integrated R744 ejector supported parallel compression racks for supermarkets. Experimental results. Refrigeration Science and Technology 2018-June, pp. 1173-1180.

Purohit, N., Sharma, V., Salwaha, S., Fricke, B., Llopis, R., Dasgupta MS., 2018. Integrated supermarket refrigeration for very high ambient temperature. Energy 165, Part A, 572-590.

Manuscript ID: 800
DOI: 10.18462/iir.icr.2019.0800

Energy and economic approach for the use of thermal energy storage on district cooling – impact of scenario and materials

Hong Minh HOANG [(a*)], Thomas DUFOUR [(a)], Veronique OSSWALD[(a)], Pascal CLAIN[(a,b)], Laurence FOURNAISON [(a)], Anthony DELAHAYE [(a)]

[(a)] Irstea, UR GPAN, Refrigeration Processes Engineering Research Unit, 1 rue Pierre-Gilles de Gennes, F-92761 Antony, France

[(b)] Leonard de Vinci Pôle Universitaire, Research Center, 12 avenue Léonard de Vinci, 92916 Paris La Défense, France

hong-minh.hoang@irstea.fr

ABSTRACT

Thermal energy storage allows shifting of energy production from high-peak to off-peak hours. This peak shaving could improve the system efficiency and reduce the energy consumption, components sizing and costs. However, the improvement depends on the choice in storage material and scenarios (full storage, load levelling, demand limiting). To assess the impact of these parameters on the system, a model of the cooling district using secondary refrigeration was developed by assembling component models: chiller, storage tank, circulation loop and users (heat exchanger). This model is able to predict the system dynamic behavior (fluid temperature evolution in loop, storage tank and heat exchangers), pumping power, energy consumption, investment and operation costs. The comparison of different storage materials (MPG, ice slurry, CO_2 hydrate slurry) and storage scenarios was performed to identify configurations with the best performance.
Keywords: Secondary refrigeration, CO_2 hydrate slurry, Ice slurry, COP, Energy efficiency.

1. INTRODUCTION

Exponential growth is expected in the refrigeration and air conditioning (RAC) sector in the following decades (Isaac and van Vuuren, 2009) because of both the global warming and the increasing cold demand in numerous sectors (HVAC in building, merchandise storage and distribution, data centers…). However, a strong development of RAC industry (already responsible for 15% of the consumed electricity (IIR, 2005) and 8% of the greenhouse gas (GHG) emissions (Cowan et al., 2010)) needs emerging solutions to overcome environmental sustainability issues. These issues can take two principal forms: direct impact due to refrigerant leakage and indirect impact related to energy consumption.

Two solutions have been proposed: 1-replacement of HFC by natural fluids (carbon dioxide, ammonia, hydrocarbon...) or alternative refrigerants (HFO blends…) and 2-processes that can limit refrigerant charge. While new refrigerants may undergo the uncertainty of cost and availability, secondary refrigeration is considered to be a promising alternative technology (Wang et al., 2010). Based on the use of environment-friendly secondary fluids which role is to transport the cold from the place of production (machine room) to places of use, secondary refrigeration allows the amount of primary refrigerant to be limited and confined. Moreover, the cold can be transported by two-phase secondary refrigerants (or slurries, composed of phase change material (PCM) particles in suspension in a liquid phase (Youssef et al., 2013) to increase the fluid energy density. The choice of secondary refrigerant can greatly impact the system design and performance. Indeed, each refrigerant has its own properties (energy density, viscosity, working temperature…) which can modify the tank volume, the pumping power and the chiller energy consumption. However, only few studies were proposed to analyze the performance of different slurries (Guilpart et al., 2006, Pons et al., 2018). A quantitative comparison between monophasic and diphasic refrigerants has not yet been carried out.

Secondary refrigerants (chilled water or slurries) can also be stored and used as reserves for refrigeration process. These storage tanks as thermal energy storage (TES) devices can enhance system design downsizing and energy demand management and thus improve the system's energy efficiency and flexibility (Hasnain, 1998). Secondary refrigeration coupling with TES device can thus become a solution that could limit both direct and indirect impacts of cold systems. TES utilization scenarios can be classified into 2 categories: "full storage" and "partial storage" (Hasnain, 1998). The first scenario, "full storage", consists in turning on the chiller during off-peak period (for example nighttime) to charge the TES tank; during on-peak period (daytime), the chiller is turned off and the cooling demand is totally assured by the TES device. This operation mode is also called "load shifting" strategy: the chiller load is totally shifted to the TES device during on-peak period. In "partial storage" scenario, the cooling power can simultaneously come from both the chiller and the TES device during on-peak period while the TES tank is charged by the chiller during off-peak period. Two strategies can be used: "load levelling"- the chiller runs at the same capacity (full capacity with the best performance) through 24h of the day; and "demand limiting" - the chiller also runs all day long but with reduced capacity during on-peak hours.

Refrigeration system with secondary loop, in particular, is a complex system composed of various interacting heat process equipment (compressor, evaporator, condenser, storage tank, heat exchanger…) which needs a systemic modelling approach. Modelling is a key tool for system design and control. For the design of new systems, models can be helpful for choosing the appropriate materials (type of secondary refrigerant/TES material), calculating the tank size, testing innovative architectural configurations, etc. For existing systems, models can simulate various supervisory and loop control strategies to improve the energy efficiency and support real time energy management decisions. A simulation tool modelling a secondary refrigeration system with TES device has been developed in previous work (Dufour et al., 2016) by integrating many modules: chiller, storage tank, circulation loop and users. This tool can be used for 2 main applications: sizing a new system or modelling the dynamic behavior of a given secondary loop.

The present study focuses on the impact of choice of materials and storage scenarios on a secondary refrigeration system sizing and energy consumption. Three materials are considered: MPG (monopropylene glycol), ice slurry and CO_2 hydrate slurry. The comparison between MPG and ice slurry will highlight the difference of performances between a monophasic and a diphasic refrigerant, both work at negative temperature. Moreover, the comparison between CO_2 hydrate slurry and ice slurry of two different solid fractions shows the influence of working temperature and solid fraction on the performance. Finally, the system sizing and energy consumption related to 3 storage scenarios: full storage, demand limiting and load leveling are also reported.

2. MATERIALS AND METHODS

The considered system (Fig. 1a) is composed of a chiller (cold production), a TES tank (storage device), a circulation loop to transport the secondary refrigerant and 3 users connected in series. Each user is simulated as a heat exchanger (fan convector unit) with a power demand of 100 kW. The pricking fluid coming from the secondary loop into the heat exchanger is taken downstream of the same heat exchanger and reinserted upstream (Figure 1b); this "treatment" allows stabilizing the secondary fluid temperature in the loop. The distance between the storage tank and the users is 100 m while a distance of 20 m is considered between two users. The chiller generates cold energy which can be stored by materials in the storage tank or be transferred directly to the users. The same material is used for secondary refrigerant and thermal energy storage. The coupling between the chiller and the tank determines the energy needed for cold production.

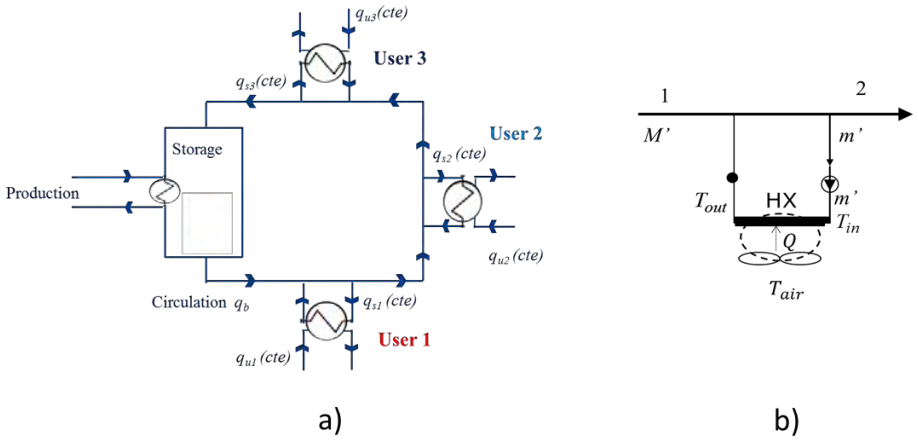

Figure 1: 2nd refrigeration system with TES device (a) and scheme of pricking (b)

2.1. Secondary Refrigerant and Storage Materials

Three secondary refrigerants are investigated in this study. While monophasic secondary refrigerants are used largely in industrial and commercial applications, diphasic secondary refrigerants can offer many advantages such as high energy density and temperature stabilization (due to the phase change process). Ice slurry (initially 30% mass fraction using ethyl alcohol EA as solute) and MPG are considered for negative temperature applications (for example cold room). CO_2 hydrate slurry (initially 15% mass fraction, positive phase change temperature) can be applied for higher temperature. The choice of initial fractions of ice and hydrate slurry is made according to expert recommendations. Moreover, other characteristics related to safety and practical problems need to be considered: flammability, corrosiveness, material compatibility, stability… The characteristics of many aqueous solutions were reported in Kauffeld et al. (2005). While MPG is only slightly flammable, solution using EA is highly flammable. CO_2 hydrate slurry is not flammable. However, as CO_2 hydrate slurry is formed and stored under pressure (up to 2.9 MPa for 15 % mass fraction), the storage material needs to be selected with caution. MPG, ice slurry (with EA as solute) and CO_2 hydrate slurry are reported to be not corrosive. The stability of the slurry depends mainly on two phenomena: the agglomeration of the crystals and the melting of crystals due to thermal losses. The presence of additives, agitation and insulation can reinforce the slurry stability. More details of these fluids can be found in literature and previous works (Weast et al., 1987, Guilpart et al., 2006, Youssef et al., 2013, Delahaye et al., 2018). Their properties are reported in the Table 1.

Table 1. Storage materials

-	MPG	Ice slurry (with EA as solute)	CO_2 hydrate slurry
Density (kg/m^3)	1000-1055	*f*(solute,xi,T) (Guilpart et al., 2006)	1000-1061
Cp (kJ/kgK)	3.6-4.2	*f*(solute,xi,T) (Guilpart et al., 2006)	2.1-4.2
Solid phase change enthalpy (kJ/kg)		333.6 (Weast et al., 1987)	374 (Kang et al., 2001)
Storage temperature range (°C)	From -12°C to -7°C	From -10°C to -7°C	From 0.1°C to 3.1°C
Flammability	slightly flammable (Kauffeld et al., 2005)	highly flammable (Kauffeld et al., 2005)	not flammable (National_Center_for_Biotechnology_Information)
Corrosiveness	Not corrosive (Kauffeld et al., 2005)	Not corrosive (Kauffeld et al., 2005)	Not corrosive (Tanupabrungsun et al., 2012)

2.2. Storage and User demand Scenarios

Three storage scenarios (Fig. 2a) are considered in the present study:

- full storage: the chiller runs during 6h at night (from 20h to 2h) to charge the TES tank, it is stopped during daytime
- partial storage - demand limiting: the chiller runs during 6h at night with higher power than during daytime.
- partial storage - load leveling: the chiller runs throughout the day with the same power.

These simplified scenarios allow testing three strategies of storage and chiller utilization. The first and the second scenarios propose a more important chiller work during nighttime (lower ambient temperature, higher chiller performance and lower electricity price) and using storage during daytime (higher electricity price). The third scenario suggests maintaining the same power (chiller nominal power) throughout the day as each chiller has a nominal regime at which it has the best performance. Three different user demand scenarios are also taken into account (Fig. 2b): the value 1 corresponds to the time when the refrigeration is requested. The demands are supposed to be off (level=0) between 2 and 9h for the 3 users.

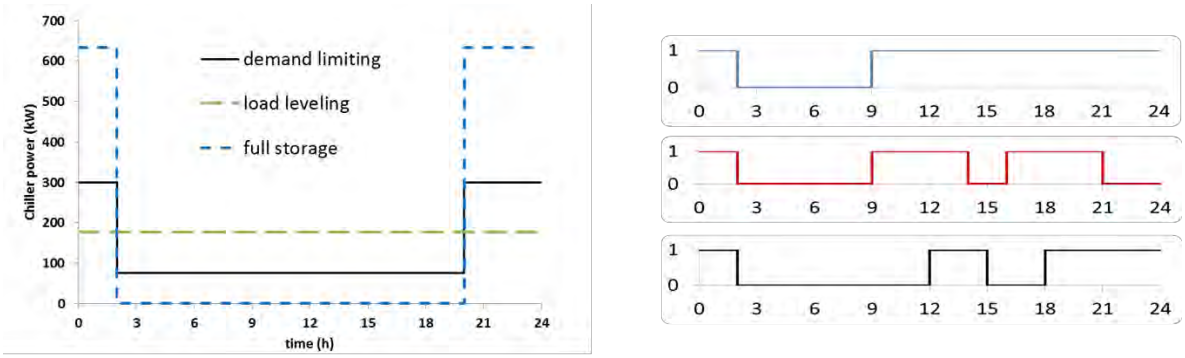

a) b)

Figure 2: Scenarios of storage (a) and user demand (b)

2.3. System Sizing

2.3.1. User sizing

The aim of the sizing is to ensure that all users received the required power (q_{ch} =100 kW). Thus the heat exchanger's surface (S) and the mass flow rate of the pricking ($\dot{m}_f$) are evaluated using this value (Eq.1 and 2). The choice has been made to fix the temperature variation of the secondary refrigerant through the heat exchanger ($\Delta T = T_{f,out} - T_{f,in}$) at 5 K for MPG (regular value for monophasic fluid). In the case of diphasic fluid the variation is set at 2 K because of the thermal stability brought by latent heat.

$$q_{ch} = \dot{m}_f c_{p,f} (T_{f,out} - T_{f,in}) \quad \text{Eq. (1)}$$

$$q_{ch} = \alpha \, S \, \Delta T_{LM} \quad \text{Eq. (2)}$$

With $\Delta T_{LM} = \frac{(T_{air,out} - T_{f,out}) - (T_{air,in} - T_{f,in})}{ln \frac{T_{air,out} - T_{f,out}}{T_{air,in} - T_{f,in}}}$

For the sizing, a constant heat transfer coefficient α = 100 W/m^{2}K is considered for all fluids.

2.3.2. Circulation loop sizing

In order to prevent too important pressure drops and stratified flow, the velocity is fixed at 1.2 m/s. In the same manner as for the heat exchanger sizing, the temperature variation along the loop (ΔT_{loop}) was fixed. This variation is set at 5 K for MPG and 2 K for diphasic fluid. Using the enthalpy balances of fluids at the inlet and outlet of the heat exchangers, the flowrate of the circulation loop

and the loop diameter are calculated using iteration process according to this criterion of temperature variation.

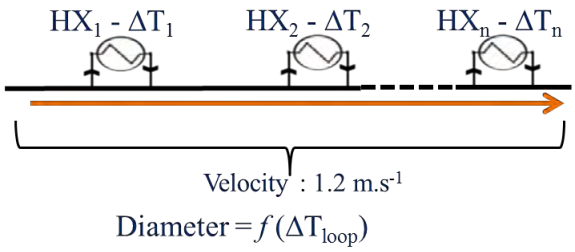

Figure 2: Scheme of the circulation loop sizing

2.3.3. Tank sizing

The tank sizing is performed so that the energy demanded by all users is ensured during a representative day (E_{store}). Other parameters are the fluid maximum temperature $T_{f,max}$ (defined by the sizing of the loop, cf. 2.3.2) and the fluid minimum temperature $T_{f,min}$ associated with the type of secondary refrigerant.

$$V_{tank} = \frac{E_{store}}{h(T_{f,max}) - h(T_{f,min})} \quad \text{Eq. (3)}$$

2.4. Energy Consumption (Chiller and Pumping)

The electricity consumption of the chiller is calculated using the required cooling energy (obtained from the user demand power q_{ch} and the user demand scenarios) and COP (coefficient of performance). The latter can be estimated from the outdoor and the setpoint temperatures; these temperatures decide the condenser and evaporator temperatures of the chiller.

$$\dot{W}_c = COP * q_{ch} \quad \text{Eq. (4)}$$

The pumping power can be evaluated as the product of the pressure drop and the volume flow rate:

$$\dot{W}_p = \Delta P * Q_v \quad \text{Eq. (5)}$$

The calculation of the pressure drop is reported in Dufour et al. (2016).

2.5. Economic Assessment

A preliminary analysis of the investment and operating costs was performed using the data listed in the following table. A total costs analysis taking into account all investment (tank, piping, pump, refrigerant…) and running costs (operation, maintenance, energy) will be the object of further studies.

Table 2. Investment and electricity cost (Vetterli and Benz, 2012, Yan et al., 2016)

-	Cost
Chiller	215 €/kW
Electricity - Regular hours	0.13
Electricity - Off peak hours	0.08
Electricity - Peak hours	0.25

3. RESULTS AND DISCUSSION

3.1. Impact of the Choice of Secondary Refrigerant on System Sizing

The results of the system sizing and the energy consumptions (chiller and pump, full storage scenario) for systems using MPG, ice slurry and CO_2 hydrate slurry are presented in Table 3. It is to be noted that these results were obtained with simplifying assumptions such as fixed temperature variations (ΔT) of the secondary refrigerant through the heat exchanger and through the circulation loop. A variation of (ΔT) will generate a variation of the secondary refrigerant flow rate and a variation of the circulation loop diameter (fluid velocity is fixed at 1.2 m/s).

3.1.1. Comparison between MPG and ice slurry

The use of diphasic secondary refrigerant (ice slurry) allows reducing significantly the tank volume (-49%), the diameter of the circulation loop (-21%), the loop flow rate (-38%) and the heat exchanger surface (-51%) compared to a monophasic fluid (MPG). Because of a higher viscosity, a small increase in energy consumption for pumping is observed for ice slurry (+2%). For systems using ice slurry (storage temperature between -10 and -7°C), the chiller can work at higher evaporator temperature than system with MPG (storage temperature between -12 and -7°C). Thus, the chiller energy consumption is reduced of 13% for ice slurry. A smaller diameter and energy consumption also lead to lower costs of circulation loop and daily electricity.

3.1.2. Comparison between ice slurry and CO_2 hydrate slurry

The comparison between ice slurry (initially 30% mass fraction) and CO_2 hydrate slurry (initially 15% mass fraction) was also performed in Table 3. A greater tank volume is needed for the CO_2 hydrate slurry due to the gas returning after hydrate dissociation and a lower fraction. Because of a lower energy density, CO_2 hydrate slurry needs a larger circulation loop, a greater flow rate and heat exchanger surface. However, the use of CO_2 hydrate slurry which is formed at positive temperature offers great advantage (-32%) related to the chiller energy consumption compared to ice slurry.

Table 3. System sizing and energy consumption

-	MPG	Ice slurry	CO_2 hydrate slurry
Tank volume (m3)	640.9	328.6	633.1
Diameter of circulation loop (m)	0.122	0.096	0.110
Loop flowrate (kg/s)	14.14	8.78	11.40
Surface of user heat exchanger (m2)	7.79	3.84	5.94
Daily pump energy consumption (GJ)	0.279	0.285	0.278
Daily chiller energy consumption (GJ)	8.30	7.26	4.87
Daily electricity cost (€)	184	161	108

3.2. Impact of the choice of storage scenario on system sizing

The choice of storage scenario can lead to different chiller and TES tank sizing. Table 4 presents the result of the sizing obtained for full storage scenario and 2 partial storage scenarios: demand limiting and load leveling. The secondary refrigerant is CO_2 hydrate slurry. The 2 partial storage

scenarios (the power demand during the daytime is shared by both the chiller and the TES device) allow the reduction of the tank volume compared to the full storage (the power demand during the daytime is assured only by the TES tank). Moreover, in order to charge completely the TES tank during only 6h at night, higher chiller capacity is needed in the full storage case. Between the 2 partial storage scenarios, the load leveling presents a more important reduction of tank volume and chiller capacity. However, the full storage scenario which takes more advantage of the nighttime condition (lower outdoor temperature and higher COP) consumes less energy than the partial storage scenarios.

Table 4. Tank and chiller sizing and energy consumption for different storage scenarios (system using CO_2 hydrate slurry)

-	Partial storage - demand limiting	Partial storage- load leveling	full storage
Tank volume (m3)	397.3	175.4	633.1
Daytime chiller power sizing (kW)	75	176.3	0
Nighttime chiller power sizing (kW)	300	176.3	634.1
Daily chiller energy consumption (GJ)	4.78	5.66	4.87

4. CONCLUSIONS

Secondary refrigeration system using TES device is a promising alternative technology to direct refrigeration. The present study has investigated the impact of the choice of secondary refrigerant and storage scenarios on the system sizing, cost and energy consumption. Diphasic refrigerants (ice slurry and CO_2 hydrate slurry) present important advantages compared to monophasic refrigerant (MPG) in terms of system downsizing and reduction of energy consumption. 3 storage scenarios (full storage, load leveling and demand limiting) are also considered. While lower energy consumption can be obtained with full storage, partial storage (load leveling and demand limiting) can reduce the required tank volume and chiller power.

ACKNOWLEDGEMENTS

This work was funded by the Agence Nationale de la Recherche (ANR) [Project CRISALHYD #ANR-14-CE05-0045].

NOMENCLATURE

α	heat transfer coefficient (W/m^{2}K)	ΔP	pressure drop (Pa)
c_p	heat capacity (J/kgK)	q_{ch}	users required power (kW)
COP	coefficient of performance	Q_v	volume flow rate (m^3/s)
E_{store}	energy demanded by all users during a representative day (J)	T	temperature (K)
h	specific enthalpy (J/kg)	S	heat exchanger surface (m^2)
		x_i	initial fraction
$\dot{m}$	mass flow rate (kg/s)	$\dot{W}_c$	chiller power (W)
MPG	monopropylene glycol	$\dot{W}_p$	pumping power (W)

REFERENCES

Cowan, D., Gartshore, J., Chaer, I., Francis, C.,Maidment, G. 2010. REAL Zero – Reducing refrigerant emissions & leakage - feedback from the IOR Project. Proc Institute Of Refrigeration.

Delahaye, A., Fournaison, L.,Dalmazzone, D. (2018). Use of hydrates for cold storage and distribution in refrigeration and air-conditioning applications. Gas Hydrates 2: Geoscience Issues and Potential Industrial Applications. Wiley-ISTE**:** 315-358.

Dufour, T., Oignet, J., Ben Abdallah, T., Hoang, H. M., Leducq, D., Delahaye, A., Fournaison, L.,Pons, M. 2016. Dynamic modelling of secondary refrigeration loop with co2 hydrate slurry. 11th IIR Conference on Phase Change Materials and Slurries for Refrigeration and Air Conditioning. Karlsruhe

Guilpart, J., Stamatiou, E., Delahaye, A.,Fournaison, L. 2006. Comparison of the performance of different ice slurry types depending on the application temperature. International Journal of Refrigeration. 29.5, 781-788.

Hasnain, S. M. 1998. Review on sustainable thermal energy storage technologies, Part II: cool thermal storage. Energy Conversion and Management. 39.11, 1139-1153.

IIR. 2005. Global warming: refrigeration-sector challenges. International Institute of Refrigeration.

Isaac, M.,van Vuuren, D. P. 2009. Modeling global residential sector energy demand for heating and air conditioning in the context of climate change. Energy Policy. 37.2, 507-521.

Kang, S.-P., Lee, H.,Ryu, B.-J. 2001. Enthalpies of dissociation of clathrate hydrates of carbon dioxide, nitrogen, (carbon dioxide + nitrogen), and (carbon dioxide + nitrogen + tetrahydrofuran). The Journal of Chemical Thermodynamics. 33.5, 513-521.

Kauffeld, M., Kawaji, M.,Egolf, P. W. (2005). Handbook on ice slurries : fundamentals and engineering. Paris, International Institute of Refrigeration.

National Center for Biotechnology Information, https://pubchem.ncbi.nlm.nih.gov/compound/carbon_dioxide#section=Flammable-Limits; last accessed on 30th april 2019

Pons, M., Hoang, H.-M., Dufour, T., Fournaison, L.,Delahaye, A. 2018. Energy analysis of two-phase secondary refrigeration in steady-state operation, part 1: Global optimization and leading parameter. Energy. 161. 1282-1290.

Tanupabrungsun, T., Young, D., Brown, B.,Nešic, S. 2012. Construction And Verification of Pourbaix Diagrams For CO2 Corrosion of Mild Steel Valid Up to 250°C. CORROSION 2012. Salt Lake City, Utah. NACE International

Vetterli, J.,Benz, M. 2012. Cost-optimal design of an ice-storage cooling system using mixed-integer linear programming techniques under various electricity tariff schemes. Energy and Buildings. 49. 226-234.

Wang, K., Eisele, M., Hwang, Y.,Radermacher, R. 2010. Review of secondary loop refrigeration systems. International Journal of Refrigeration. 33.2, 212-234.

Weast, R. C., Astle, M. J.,Beyer, W. H. (1987). Handbook of Chemistry and Physics. Boca Raton, Florida, CRC Press.

Yan, C., Shi, W., Li, X.,Zhao, Y. 2016. Optimal design and application of a compound cold storage system combining seasonal ice storage and chilled water storage. Applied Energy. 171. 1-11.

Youssef, Z., Delahaye, A., Huang, L., Trinquet, F., Fournaison, L., Pollerberg, C.,Doetsch, C. 2013. State of the art on phase change material slurries. Energy Conversion and Management. 65. 120-132.

Youssef, Z., Delahaye, A., Huang, L., Trinquet, F., Fournaison, L., Pollerberg, C.,Doetsch, C. 2013. State of the art on phase change material slurries. Energy Conversion and Management. 65.0, 120-132.

Manuscript ID: 845
DOI: 10.18462/iir.icr.2019.0845

Novel integration of latent heat storage in multi-split air conditioning systems

Timo KORTH*, Felix LOISTL and Christian SCHWEIGLER

CENERGIE Research Center Energy-efficient Buildings and Districts
Munich University of Applied Sciences, Department of Building Services Engineering,
Lothstr. 34, 80335 Munich, Germany
timo.korth@hm.edu

ABSTRACT

The increased use of renewable energy sources leads to a growing demand for storage systems. In heating and cooling huge potential is seen in latent heat storages (LHS).
The innovation presented in this paper combines the advantages of a Variable-Refrigerant-Flow system (VRF-System) with those of the LHS, operating at constant temperature level.
Loading and unloading of the LHS is realized by direct heat exchange with the refrigerant, which eliminates temperature losses by an intermediate heat carrier loop. Here an innovative coupling of the heat storage with two indoor units is described, with the aim of avoiding negative influence on the operating temperatures of the cycle. During loading the LHS is cooled by evaporation of refrigerant in parallel with the two indoor units, allowing for system operation at standard suction pressure. During unloading the storage serves as a condenser, connected in series between the two indoor units.
Experimental investigations confirm the feasibility of the novel coupling concept.
Keywords: Thermal storage, Latent heat storage, Phase change material, PCM, Air conditioning, VRF-System

1. INTRODUCTION

In the field of heating and cooling reversible heat pumps are widely used for an efficient and flexible provision of thermal energy. Especially in combination with the use of renewable energies, which is a worldwide concern, the mentioned attributes – efficiency and flexibility – ensure a steady growing usage of this technology in the sector of residential and non-residential buildings. For further improvement of these systems and to tap the full potential of the renewable energy sources storage technologies are inevitable.
Besides battery and chemical storage systems, thermal storages are used for this purpose. But storing thermal energy induces in any case a loss of temperature. This occurs because of the need of a temperature difference to develop thermal energy fluxes during loading and unloading. As a consequence a minimization of the temperature differences is worth striving for. Following this aspect, huge potential is seen in latent heat storages (LHS) as they meet the characteristic of heat pumps. LHS can serve as heat source or heat sink at an almost constant temperature level which meets the nature of the evaporator and condenser in heat pump systems. This is seen as the stand out characteristic of the LHS that results from the utilization of the phase change of the material selected. Additionally, in air conditioning systems using direct heat exchange between air and the refrigerant an additional heat carrier loop can be avoided.
Dincer and Rosen (2011) describe in detail the advantages and disadvantages of latent heat storage starting from the requirements giving the thermodynamic, kinetic, chemical, technical and economic criteria and ending up with several case studies.
The present paper gives a short overview of strategies to combine a LHS with air conditioning systems with direct integration in the internal refrigeration cycle, focusing on associated thermodynamic characteristics. This leads to a novel storage configuration allowing for a use of the LHS in the refrigerant cycle with minimal influence on the operating temperatures. Thus a reduction of energy losses is accomplished, as compared to conventional application of thermal storages.

The concept shall be applied for a Variable-Refrigerant-Flow heating and cooling system (VRF-System) which is driven by the electricity output of a PV generator. The core objective of the novel concept is to keep the setting of the operating parameters of the air conditioning system unchanged. This allows an operation of the system at design pressure lift of the compressor which sets the efficiency of the system.
To verify the feasibility of the concept experimental investigations for the direct heat exchange between refrigerant and LHS have been carried out. The used storage contains a paraffin wax as phase change material (PCM). For the usage in latent heat storages PCM are available with melting temperatures in a wide temperature range. Thus a good match with regard to the targeted application can be found. In addition, PCM have a high energy density and are widely compatible to common construction materials. As a consequence a very compact and cost-effective design is possible. To meet the technological challenges utilizing a LHS, above all the low heat conductivity, Mehling and Cabeza (2008) and Hauer et al. (2013) give an overview of different design concepts.

2. STATE OF THE ART

To take advantage of the phase change enthalpy for thermal storage systems several concepts have been investigated. Especially ice storage systems which use water as phase change material are widely known and developed up to commercial availability for the use in chilled water systems. However, improvements of this technology and appropriate concepts are still researched. Tam et al. (2018) present an economic comparison of a conventional split system with a packaged air conditioning system combined with an ice storage for residential buildings. It is pointed out that the optimal air conditioning and storage capacities are dependent on the combination of climate and variable utility rates for a given geographic location. Besides that it is clarified that an increase of the efficiency of the air conditioning system can significantly reduce the economic payback for both systems. Thiem et al. (2016) present the results of a model-based predictive control strategy for cold thermal energy storages using ice. This study also stresses one key characteristic of using an ice storage: The heat pump system has to operate at lower temperature during the charging process which requires more primary energy input. In addition to that several studies deal with the investigation and modelling of the charging and discharging process (Erek et al., 2007; Zhu et al., 2001).
In the field of LHS several investigations focus on the research of phase change materials with different phase change temperatures aiming at a characterization and realistic modeling of the process to optimize the design of the storages (Frazzica et al., 2017), (Fan et al., 2016), (Palomba et al., 2017). In these studies a heat carrier fluid is used to charge and discharge the storage. Figure 1 puts emphasis on the additional temperature differences required for loading and unloading of an ice storage in comparison to the operation without a storage. For an air conditioning system which shall provide an outlet temperature $\mathrm{T_{use}}$ of the conditioned air flow a two-step heat exchange from the air flow to the heat carrier fluid (T_{HCF}) and further to the evaporation temperature T_{e2} of the refrigeration cycle occurs. In total a driving temperature difference $\Delta\mathrm{T}_E + \Delta T_F$ has to be provided. Whereas when a heat storage is used, in both loading and unloading of the storage two additional temperature differences $\Delta\mathrm{T_G}$ and $\Delta\mathrm{T}_H$ have to be overcome. Consequently, to meet the desired air output temperature $\mathrm{T_{use}}$ the application of the storage system implicates a significant decrease $\Delta\mathrm{T}_e$ of the evaporation temperature (T_{e3}) compared to the design temperature T_{e2} without LHS. To avoid these additional temperature differences the loading and unloading by direct heat exchange with the refrigerant without an intermediate heat carrier loop is an appropriate concept.

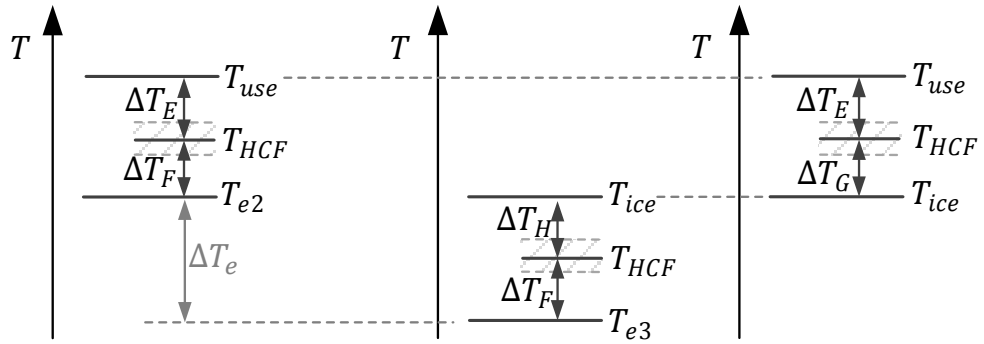

Figure 1: Temperature differences using an ice storage system with an additional heat carrier loop: Normal operation without storage (left), loading of the storage via decrease of the evaporating temperature by ΔT_e (middle), unloading of the storage (right)

Hai et al. (2006) developed an ice storage system to subcool the refrigerant in an air conditioning system. Thus, the storage is loaded during night-time through direct evaporation of the refrigerant with a decrease of the evaporation temperature. In unloading mode throughout the day the liquid refrigerant leaving the condenser is subcooled by heat transfer to the storage, resulting in an increase of refrigeration capacity while the refrigerant mass flow stays constant. Furthermore, a heat pump system has been developed and has been introduce into the market in which the LHS is directly loaded and unloaded by direct heat exchange with the refrigerant in order to improve the defrost mode of the air-source heat pump (Daikin). By this means, inversion of the refrigeration cycle in defrost mode is avoided, allowing for continuous operation of the heat pump and increased heating comfort. Yet, the thermal energy is not stored for direct heating or cooling purposes with the target of increased flexibility for the electric supply. In view of this objective, further investigations of the direct integration of a LHS in the refrigerant cycle of an air conditioning system have been carried out by Loistl et al. (2015) focusing on the evaluation of different concepts and potential energy savings by modeling and characterization of the heat transfer processes and the potential of energy shifting.

3. NOVEL CONCEPT FOR THE INTEGRATION OF A LATENT HEAT STORAGE IN A VAPOR COMPRESSION CYCLE

As discussed in the previous chapter the integration of a thermal storage in a heat pump system generally leads to a negative influence on the system's evaporation and condensing pressure and temperature. The presented concept avoids this as the novel interconnection of the components allows a system operation at the nominal temperature levels.

The novel concept comprises a LHS which is integrated in the refrigerant cycle of an air conditioning system. The concept is presented with regard to a cooling application, while the concept is analogously also suitable for a LHS on higher temperature level to store thermal energy for heating purposes. The regarded storage consists of a serpentine tube heat exchanger which is inserted in a cubic tank that is filled with a suitable PCM (e.g. paraffin wax). The air conditioning system with its main components compressor, condenser, expansion valve and evaporator is supplemented by integration of a LHS in the low pressure part of the cycle. The loading and unloading processes take place through direct evaporation and direct condensation of refrigerant in the heat exchanger embedded in the storage, respectively. The novel aspect of the proposed configuration is given by separation of the evaporator component in two parts and by switching of the hydraulic interconnection of the components: The loading process is realized in parallel connection of the two evaporator units (EU) and the LHS which allows a loading of the storage at the nominal evaporation temperature. To use the stored thermal energy with the provided temperature level of the storage, the unloading is effected with serial flow of the refrigerant through the evaporator units and the LHS, providing almost full capacity of the refrigeration system with substantially reduced operation of the compressor.

3.1. Loading of the Storage – Crystallisation of the PCM

During the loading mode, i.e. crystallization of the storage content, liquid refrigerant is supplied to the two evaporator sections and the LHS in parallel. The three expansion valves are controlled in order to ensure the desired superheating of the merged vapor flow entering the compressor. Figure 2 shows a simplified scheme of the process. Figure 3 depicts the process in the log(p)-h diagram, illustrating the common pressure level p_e of the three low-pressure components EU1, LHS, and EU2, allowing for operation of the air conditioning system under design pressure setting. With respect to the given state points the following steps take place:

1-2 Compression of the refrigerant vapor by the compressor
2-3 Condensation of the refrigerant with heat rejection to the environment in the condenser unit
3-4 Expansion of the refrigerant through the three expansion valves (EXV) to evaporation pressure
4-1 Evaporation of the refrigerant in parallel in both evaporator sections and in the LHS by absorption of heat from the room and by heat extraction from the LHS, resulting in a crystallization of the PCM.

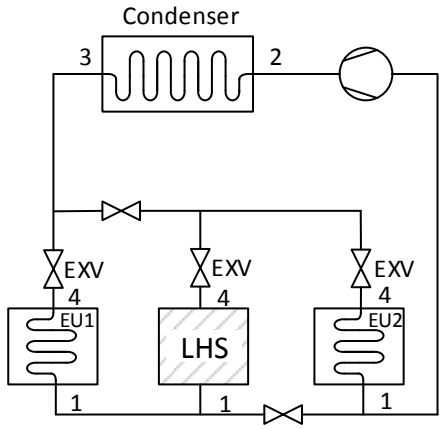

Figure 2: Loading the LHS in parallel interconnection with two evaporation units

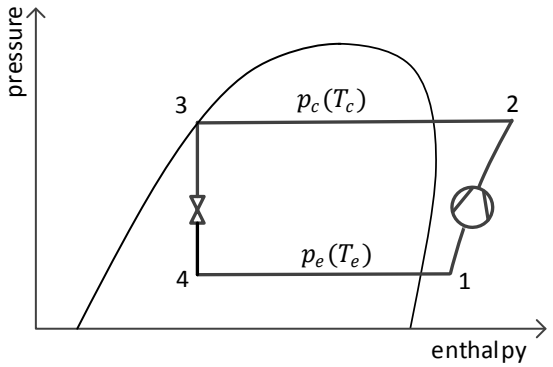

Figure 3: The loading process of the storage in the log(p)-h diagram

Based on the common pressure level, all three low-pressure components operate at identical evaporation temperature. In order to accomplish the desired storage effect, a suitable PCM with phase change temperature T_{PCM} above the evaporation level T_e together with an appropriate design of the heat exchanger has to be selected. The temperature levels during the loading process are shown in Figure 6 (left). T_{e2} denotes the evaporation temperature in normal operation and T_{PCM} the phase change temperature. The temperature difference $\Delta T_B$is the driving temperature difference for loading the storage. ΔT_A represents the temperature difference between the evaporating refrigerant and the air in the evaporation unit operated in parallel to the storage.

3.2. Unloading of the Storage – Melting of the PCM

Through the serial interconnection of the components in unloading mode an additional condensation of the refrigerant occurs. This gives the opportunity to double the cooling output from a given refrigerant flow by evaporating the refrigerant twice in one cycle: First the refrigerant evaporates on a higher temperature level and after condensing in the storage it evaporates on the lower nominal temperature level. Consequently, a reduced compressor speed is sufficient for providing the full cooling capacity. Figure 4 shows the serial configuration of the low-pressure components EU1 – LHS – EU2 in a simplified scheme. With regard to Figure 5 the process can be followed in the log(p)-h diagram. The following steps take place:

1-2 Compression of the refrigerant vapor through the compressor.
2-3 Condensation of the refrigerant with heat rejection to the environment in the condenser unit.
3-4 Expansion of the refrigerant through the expansion valve (EXV) to evaporation pressure

p_{e1} of EU1.

4-5 Evaporation of the refrigerant with heat absorption from the room in EU1.

6-7 Condensation of the refrigerant with heat rejection into the LHS on the same pressure level ($T_{e1} = T_{c;St}$), assuming that no pressure drops occur within the internal cycle.

7-8 Control of the refrigerant flow rate, avoiding retention of liquid refrigerant in the LHS.

8-1 Evaporation of the refrigerant with heat absorption from the room in EU2 at evaporation temperature T_{e2} that is equal to the evaporation temperature T_e during the loading process.

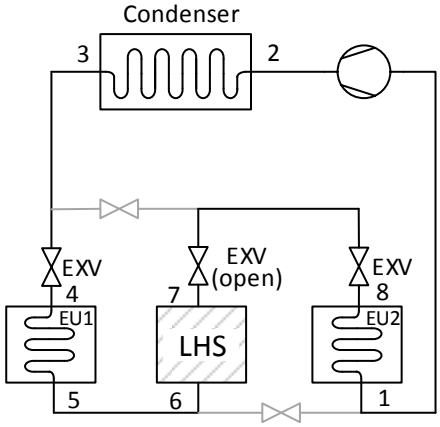

Figure 4: Unloading of the storage in a serial interconnection in the order EU1 - LHS – EU2

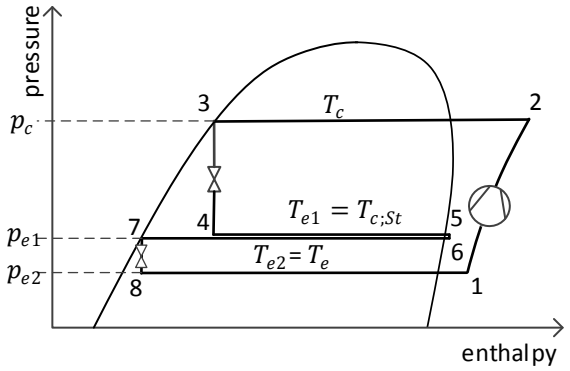

Figure 5: The Unloading process of the storage in the log(p)-h diagram

Using this interconnection the unloading of the storage takes place within the original pressure and temperature levels of the system ($T_{e2} = T_e$, cf. Figure 3). With regard to Figure 5 the phase change temperature of the PCM (T_{PCM}) lies between the upper and lower evaporation level: $T_{e1} > T_{PCM} > T_{e2}$. This defines the material selection of the PCM.

Figure 6 (right) shows the temperature levels during the unloading process. In this case ΔT_A and ΔT_D are determinative for the heat exchange between the air and the corresponding evaporation temperatures T_{e1} and T_{e2}. ΔT_C describes the temperature difference allowing the condensation of the refrigerant at the temperature $T_{c;St} = T_{e1}$ against the PCM with the temperature T_{PCM}. The process leads to different air outlet temperatures at the evaporator units resulting in an average outlet air temperature $T_{air;out;mean}$, assuming an equal air volume flow through both evaporating units.

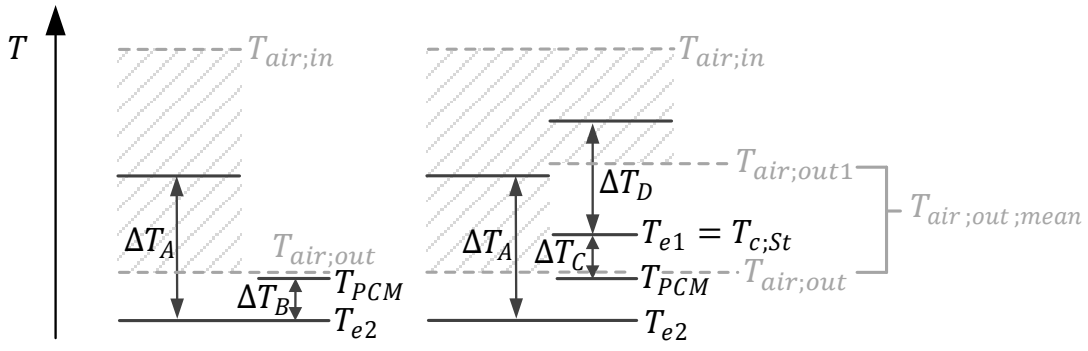

Figure 6: Temperature differences during the loading process (evaporation of the refrigerant in the LHS, left) and during the unloading process (condensing of the refrigerant in the LHS, right)

For the given conceptual description it has been assumed that the driving temperature differences are represented by the logarithmic mean values obtained from the inlet and outlet temperature of the air flow and the respective equilibrium temperature of the refrigerant, e.g. for the evaporator units EU1 and EU2 during the loading process of the LHS:

$$\Delta T_A = \frac{(T_{air;in} - T_{e2}) - (T_{air;out} - T_{e2})}{\ln\left(\frac{T_{air;in} - T_{e2}}{T_{air;out} - T_{e2}}\right)} \quad \text{Eq. (1)}$$

Furthermore the thermal capacity is given in equation 2.

$$\dot{Q} = UA * \Delta T \quad \text{Eq. (2)}$$

For the realization of the concept a minimization of the temperature differences is necessary. As a consequence the components have to be designed carefully to the application. Following Eq. (2), for instance, a thermal capacity of 3 kW which is equal to a common performance of an indoor unit an average UA value of 1 kW/K has to be accomplished in order to limit the driving temperature difference to 3 K. The design of the heat exchanger with appropriate measures to overcome the low conductivity of the PCM material has to be precisely defined.

The described concept allows an operation of the heat pump system at design pressure lift of the compressor as no decrease of the evaporation temperature T_{e2}, even during the loading of the LHS, occurs. Yet, as a consequence of the temperature differences ΔT_C and ΔT_D the outlet temperature ($T_{air;out1}$) of the air flow passing through EU1 is increased in comparison to the nominal operation of the system. Hereby ΔT_D describes the log mean temperature difference between the evaporation at T_{e1} and the air inlet and air outlet temperature. In this heat exchanger section no superheat of the refrigerant is required, because after evaporation the refrigerant is lead through the storage at the same pressure level, which leads to a condensation of the refrigerant at $T_{c;St} = T_{e1}$. As there is only a small driving temperature difference ΔT_C there will be only marginal subcooling of the refrigerant in the storage. The following pressure decrease can be realized by an expansion valve working with low pressure difference or a liquid receiver withholding the liquid refrigerant to provide a separation of pressure. The subsequent evaporation unit EU2 operates at the design suction pressure level provided by the compressor. To guarantee stable cycle operation by sufficient superheating of the refrigerant, the refrigerant flow through the entire EU1-LHS-EU2 configuration has to be controlled accordingly.

3.3. Laboratory Investigations

In the experiments the two principals of the novel concept for loading and unloading the storage are investigated. The main focus lies on the capacity of the storage working with small temperature differences and the dynamic behavior of the LHS. The used test rig for this purpose has been designed to investigate different modes of operation of latent heat storages in a refrigerant cycle operating with the refrigerant R410a. A detailed description of the setup is given by Loistl et al. (2016). The LHS consists of a serpentine tube heat exchanger which is inserted in a paraffin-filled cubic tank with transparent walls and a stable framework. The copper tube has a length of 20 m with a tube diameter of 0.015 m and a tube spacing of 0.05 m. The chosen paraffin is RT28HC with a melting temperature range of 27-29 °C and a latent heat of 200 kJ/kg. The heat conductivity of the pure material is 0.2 W/(m K). To overcome the low thermal conductivity of the PCM aluminum lamellas are integrated in the heat exchanger. The storage is equipped with 6 temperature sensors in the paraffin and 12 sensors in direct contact to the tubes along the heat exchanger.

Two experiments have been carried out to assess the available thermal capacity at small temperature differences: Firstly, direct evaporation of the refrigerant in the heat exchanger of the storage has been realized. Figure 7 and Figure 8 represent the results of the crystallization experiment. The test has been conducted in a heat pipe configuration, with integration of the storage and a water cooled condenser in a closed loop. The condenser is situated above the LHS. When the condenser is cooled by cooling water, a natural refrigerant circulation is established, in which the storage works as an evaporator with a small temperature difference to the phase change temperature. Secondly, condensation of the refrigerant in the storage is investigated (Figure 9 and Figure 10). To meet the characteristic of the novel concept, saturated vapor has been supplied to the inlet of the LHS. For this purpose the storage has been connected in series to a water cooled condenser in which the refrigerant vapor provided by the compressor has been de-superheated before entering the LHS.

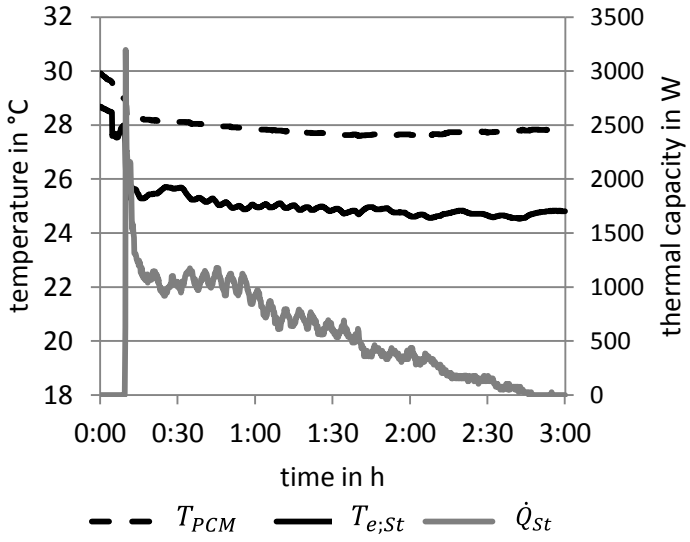

evaporation and PCM temperature (primary ordinate) and thermal capacity (secondary ordinate) vs. time

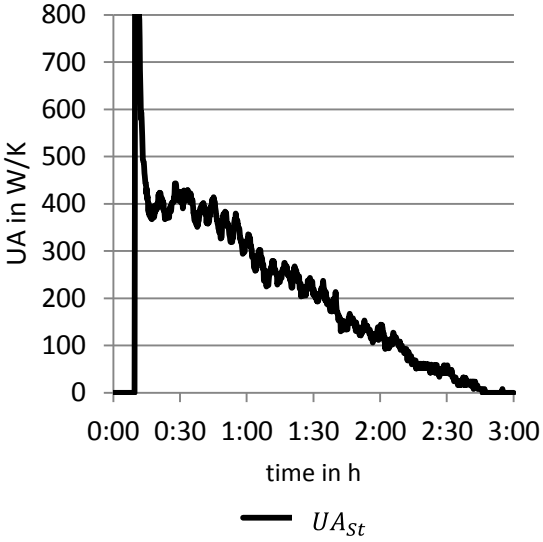

LHS: UA-value vs. time

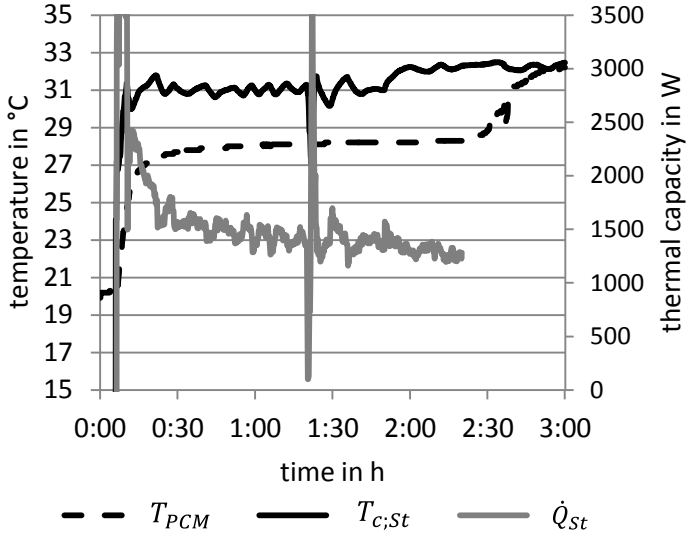

Condensation and PCM temperature (primary ordinate) and thermal capacity (secondary ordinate) vs. time

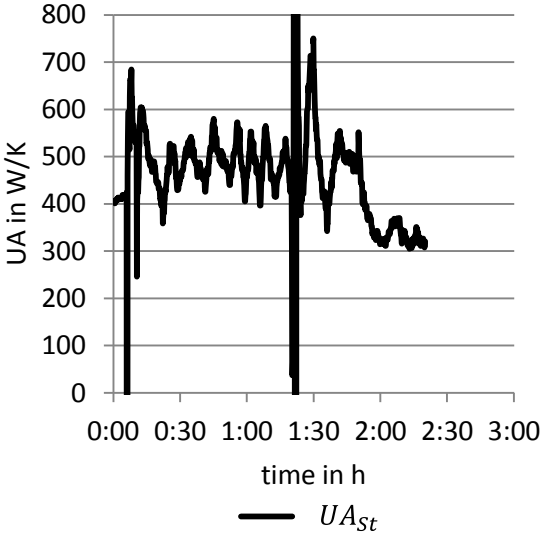

the LHS: UA-value vs. time

Figure 7 clarifies that a temperature difference of 3 K between evaporation and PCM is sufficient for a mean thermal capacity of the storage of about 700 W. With respect to Figure 6 this indicates that the loading of the storage with a small ΔT_B is feasible. Figure 8 states that the course of the UA value follows the capacity trend starting from around 400 W/K at constant operation at the beginning and declining down to 50 W/K after 2:30 h. The decrease of the thermal capacity is a result of the increase of the thermal resistance of the PCM when crystallized PCM builds up on the surface of the heat transfer fins. Consequently, the mass flow of the natural refrigerant circulation is decreased, reaching a standstill when the phase change is completed. In contrast to that Figure 9 shows only a slight decrease of the thermal capacity of the LHS with an average capacity of about 1500 W until the phase change is completed after 2:20 h. This rather stable behavior is attributed to the effect of convection, which supports heat transfer when the liquid layer between heat exchanger surface and PCM grows during the unloading of the storage. Again, the temperature difference between condensation and PCM – which is represented by ΔT_C in Figure 6 – amounts to 3-4 K. Accordingly, the UA value has a slightly decreasing trend starting with a value of about 690 W/K ending up with 330 W/K after 2:20 h.

4. CONCLUSIONS

A novel concept for the integration of a latent heat storage in the refrigerant cylce of a heat pump system is presented. The key feature is a novel flexible interconnection of the components: The loading process is realized in a parallel configuratoin of two evaporator units and the LHS, while during unloading the system is switched to a serial interconnection of the LHS with the two evaporator units. This concept allows for utilization of a heat storage in heat pump systems without negative influence on the pressure lift and COP. For the implementation of the concept small temperature differences for the heat transfer between the refrigerant and the LHS are required, as analyzed in the present work. Experimental investigations prove the feasibility of the concept by showing that a sufficient thermal capacity can be achieved at temperature differences of 3-4 K between the phase change temperature and the evaporation and condensation level, respectively. Further investigations in a pilot plant shall be conducted with regard to the control of the air conditioning system with integrated latent heat storage.

ACKNOWLEDGEMENTS

This work has been conducted within the research project "SolarSplit", funded by the German Federal Ministry for Economic Affairs and Energy (FKZ 0325900B).

NOMENCLATURE

p	pressure (bar)
T	temperature (°C)
$\dot{Q}$	thermal capacity (W)
ΔT	temperature difference (K)

Indices

c	condensation
e	evaporation
St	storage

REFERENCES

Dincer, I., Rosen, M.A., 2011. Thermal Energy Storage – System and applications, Second Edition, John Wiley & Sons, West Sussex, United Kingdom

Erek, A., Ezan M.A., 2007. Experimental and numerical study on charging processes of an ice-on-coil thermal energy storage system, International Journal of Energy Research, Wiley Inter Science

Fan, L., Zhu, Z., Xiao, S., Liu, M., Lu, L., Zeng, Y., Yu, Z., Cen,K., An experimental and numerical investigation of constrained melting heat transfer of a phase change material in a circumferentially finned spherical capsule for thermal energy storage, Applied Thermal Engineering, 2016

Frazzica, A., Palomba, V., La Rosa, D., Brancato, V., Experimental comparison of two heat exchanger concepts for latent heat storage applications, IRES, Düsseldorf 2017

Hai, X., et al., 2006. “Design and Research of the Commercial Digital VRV Multi-Connected Units With Sub-Cooled Ice Storage System”, International Refrigeration and Air Conditioning Conference, Nr. 759

Hauer, A., Hiebler, S., Reuß, M., 2013. Wärmespeicher, 5., vollständig überarbeitete Auflage, Fraunhofer IRB Verlag, Karlsruhe

Loistl, F., Schweigler, C., 2015. Integration of a latent heat storage in VRF systems for heating and cooling with enhances flexibility and efficiency, International Congress of Refrigeration, Yokohama, Japan

Loistl, F., Korth, T., Schweigler, C., 2016. Einsatz von Latentwärmespeichern in Klimageräten, DKV-Tagung, Kassel

Mehling, H., Cabeza, L. F., 2008. Heat and cold storage with PCM – An up to date introduction into basics and applications, Springer Verlag, Heidelberg

Palomba, V., Frazzica, A., Brancato, V., Experimental investigation of a latent heat storage for solar cooling applications, Applied Energy 2017

Thiem, S., Born, A., Danov, V., Schäfer, J., Hamacher, T., Optimized cold storage energy management – Miami and Los Angeles Case Study, Proceedings of the 5th International Conference on Smart Cities and Green ICT Systems (SMARTGREENS 2016), pages 271-278

Manuscript ID: 849
DOI: 10.18462/iir.icr.2019.0849

Cooling demand: a challenging issue for new buildings in moderate climates

Dorota A. CHWIEDUK

Institute of Heat Engineering, Faculty of Power and Aeronautical Engineering
Warsaw University of Technology, 00665 Warsaw, Poland, dchwied@itc.pw.edu.pl

ABSTRACT

This paper aims to illustrate the problem of summer overheating of rooms in specific locations with large windows in new well insulated buildings in moderate climates. Such problems did not exist in older buildings characterized by relatively high heat transfer through the building envelope. Solar energy gains can influence the thermal comfort of rooms with large windows significantly, causing high cooling energy demand even in moderate climates. A mathematical model of the energy balance of a building has been elaborated with the focus being on heat transfer through windows and solar energy passing through them. The results show that if the glazed surface of the west and south façade of a building is large, then the summer cooling demand can be twice the winter space heating demand. This is a new challenge for the energy supply and thermal comfort systems of new buildings.
Keywords: Energy Balance, Space Heating/Cooling Demand, Solar Energy, Building Overheating.

1. INTRODUCTION

Nowadays, buildings in Europe are constructed in accordance with existing standards. Specific regulations based on these standards formulate technical requirements for buildings and their location. At present, EU laws foster implementation of energy efficiency in buildings according to recommendations given by the Directive of the European Parliament and of the Council on the energy performance of buildings (Directive 2010/31/EU). The Directive entered into force in 2010. It obliges Member States to carry out analyses related to determining the energy characteristics of buildings. According to Article 9 of the Directive, from the year 2021 all new buildings will have to be nearly zero-energy buildings, and in the case of public utility buildings the rule has already come into force at the beginning of this year - 2019. It is good to notice that in Europe, adopting rules of nearly zero-energy construction technology is no longer just a concept for implementing general energy conservation principles and minimizing environmental footprint, but also a legal necessity. The EU boundary indices for final and primary energy consumption define limits for energy consumption for buildings depending on their typology. These indices are different in different EU countries depending on climate and energy mix in those countries. Thanks to well-designed envelopes and structures, nowadays buildings can considerably decrease their energy needs. Moreover, thanks to implementing highly efficient and reliable equipment and energy installations, the final energy demand also drops considerably. When renewable energy sources are utilized substituting coal, oil and gas then the primary energy consumption based on fossil fuels is reduced a lot.

At this point it is necessary to mention the specific situation of countries in a moderate climate. For many years high energy consumption in buildings in countries of such a climate was caused by high heat losses through buildings' envelopes. The space heating demand used to be the highest demand component of energy consumption in buildings and was responsible for about 70% of the total energy needs of buildings (https://ec.europa.eu/energy/, 2018). Therefore it is not surprising that recently the measures

focused on reduction of energy consumption in buildings have been put mainly on decreasing the space heating loads. For example in Poland from the year 2021, according to existing regulations (Rozporządzenie, 2013), the indices of primary energy consumption for space heating and domestic hot water of all newly constructed residential buildings, called nearly zero energy buildings, cannot exceed 70 $kWh \cdot m^{-2}a^{-1}$ or 65 $kWh \cdot m^{-2}a^{-1}$ for single family houses or multi-family apartment buildings, respectively. In addition the heat transfer coefficients for external walls must not be higher than 0.2 $W \cdot m^{-2} K^{-1}$. As a result external walls have thick insulation of high thermal quality (in the 70s the recommended thickness of thermal insulation was 6-8 cm, at present it is 20 - 25 cm) (Rozporządzenie, 2013). What is more, the heat transfer coefficients for windows should soon not be larger than 0.9 $W \cdot m^{-2} K^{-1}$and now they cannot be higher than 1.3 $W/(m^2K)$ (in the 70s it was 3.2 $W \cdot m^{-2} K^{-1}$). It must be noticed that there are no limits for cooling energy consumption in residential buildings. It is arbitrary assumed, that residential buildings in Poland as in other countries of moderate climate do not require cooling. However, supplying cooling energy to residential buildings is sometimes necessary to keep the thermal comfort at the required level. Summer cooling demand can be seen especially for south and west facing rooms with large windows. It turns out that cooling demand becomes a challenging issue for new buildings in moderate climates.

In old buildings the influence of solar radiation on the energy balance of a building was neglected in moderate climates. Heat gained due to solar radiation passing through glazing and absorbed inside rooms was quickly lost, because of poor thermal quality of buildings' envelopes. Nowadays, when buildings are very well insulated, very air-tight and solar energy absorbed by the internal elements of the interior of the building and converted into heat stays in the building; dictated by the basic rule limiting heat losses of a building as much as possible. It turns out that in Poland as in other countries in a moderate climate southern and western facing rooms are exposed to especially high solar irradiation. Solar energy gains can influence the thermal comfort of rooms with large windows significantly, causing high cooling energy demand even in moderate climates. To present how this problem can be significant for some room locations simulation studies of the energy balance of a building for Polish climatic conditions have been developed. First a mathematical model of the energy balance of air in a building has been formulated.

2. MODELLING ENERGY BALANCE OF A BUILDING

External walls constitute the majority of a building envelope. In residential buildings they are constructed with bricks, concrete or other solid construction materials and insulation layers. Nowadays, thermal and physical parameters of external walls are selected to assure very small heat flow through them. This heat flow in a well-designed building can be less than 10% of total heat exchanged through the envelope of the building and ventilation with outside environment during the whole year, even in a moderate climate. Glazing and ventilation become the most important elements for the energy balance of a building and they determine the energy exchanged with the surrounds. The energy flow through glazing includes energy transferred by solar radiation, which enters the interior of the building directly (as short wave electromagnetic radiation) and heat transfer caused by the temperature gradient between inside and outside.

The energy balance of air in a building can be written in a general form with lumped parameters, i.e.:

$$Vc_p\rho\frac{dT_{in}}{dt} = \sum \dot{Q}_{in}(t) - \sum \dot{Q}_{out}(t) \pm \sum \dot{Q}_{ven}(t) + \sum \dot{Q}_{qv}(t) \qquad \text{Eq. (1)}$$

The energy balance takes into account energy fluxes coming out or into the room/building, or heat sources existing in a building. During daytime solar energy always as an energy gain flowing into the building. Heat transferred through external walls, windows, roof, ground and ventilation may be directed outwards - heat losses, or inwards - heat gains. The heat transfer direction depends on ambient air temperature, interior air temperature and heat capacity of

the building. Usually there are also internal heat sources, e.g. people, electric equipment, lighting, etc. Thus, taking into account heat losses through the envelope and ventilation, and heat gains because of internal heat sources and solar energy gains, the energy balance Eq.(1) now can be written as follows:

$$Vc\rho\frac{dT_{in}}{dt} = \sum\dot{Q}_{walls}(t) + \sum\dot{Q}_{win}(t) + \sum\dot{Q}_{roof}(t) + \sum\dot{Q}_{gt}(t) - \sum\dot{Q}_{sol}(t) - \sum\dot{Q}_{qv}(t) \qquad \text{Eq. (2)}$$

Applying the general form of Eq. (2) with lumped parameters the individual energy flows may be mathematically formulated separately in more or less complex ways, depending on the aim of calculations. These energy flows can be also calculated separately with different accuracies. Assuming the temperature T_{in} of air inside a building to be the same in all the space (all rooms) and constant in time, the left side of Eq. (2) is equal to zero. This means that a heating/cooling system's operation follows variable ambient conditions to maintain constant indoor air temperature. The heating demand can be now determined using the general form of the energy balance given by Eq. (2), as:

$$\sum\ \dot{Q}_h(t) = \sum_j\dot{Q}_{j,wall}(t) + \sum_i\dot{Q}_{i,win}(t) + \dot{Q}_{ven}(t) - \sum_i\ \dot{Q}_{i,sol}(t) - \sum_n\dot{Q}_{n,qv}(t) \qquad \text{Eq. (3)}$$

When there are only heat gains (heat flows into a building), the energy balance equation takes the form for determination of the cooling demand:

$$\sum\ \dot{Q}_c(t) = \sum_j\dot{Q}_{j,wall}(t) + \sum_i\dot{Q}_{i,win}(t) + \dot{Q}_{ven}(t) + \sum_i\ \dot{Q}_{sol}(t) + \sum_n\dot{Q}_{n,qv}(t) \qquad \text{Eq. (4)}$$

Of course, other forms of equations of heating and cooling demand are also possible. For example due to the high thermal capacity of external walls heat can flow into a building, but because of the temperature gradient and low thermal capacity of windows the direction of the heat flow through windows can be opposite and there are heat losses through windows.
In the study presented in the paper the heat transfer through external walls, roof, floor (on the ground) has been considered as unsteady heat conduction through solid bodies. For every opaque partition assumed to consist of a few isotropic, homogeneous layers, the temperature field has been described by the partial differential equation (Fourier - Kirchhoff's equation). The model developed includes boundary conditions with fully detailed equations describing the radiation exchange between the ground, the sky and window, and wall, solar radiation absorption, transmission or reflection on all surfaces, and the effects of orientation and inclination on them.
Heating/cooling energy needed for ventilation has been calculated in a simplified way taking into account the averaged standardized volumetric flow of the ventilated air (exchanged in a given room in a quantity depending on the function of the room).
The mathematical model developed for this research study has been elaborated with the focus being on heat transfer through windows and solar energy passing through them. The heat flow through a window depends on air temperature gradient between inside and outside of the building and the thermal resistance of the window structure. Solar energy flow depends on irradiance, variable over time and position of the exposed surface of the glazing or other building's element. The optical behaviour of glazing has been taken into account to determine the solar flux coming directly into the room at a rate depending on the transmissivity of the glass pane system and effective absorptivity of the room cavity. Solar radiation incident on glazing and other elements of the building envelope have been determined using the anisotropic solar radiation HDKR model (Reindl, Beckman and Duffie, 1990). The ambient thermal state changes in time and it is described by variations of ambient air temperature and direct and diffuse solar radiation. A 'representative averaged' ambient temperature and solar radiation regime (taken as that of Warsaw) has been elaborated

(Chwieduk and Bogdańska, 2004).
Details of mathematical model of energy balance of a building and methods of describing all energy fluxes coming out or into a building have been described in the literature (Chwieduk, 2014).
Based on the mathematical model developed a numerical model of the energy balance of a building has been developed for numerical simulations using MATLAB. Numerical simulations of the dynamics of a building in changing climatic conditions throughout the year (for averaged ambient conditions for Warsaw with a time step of an hour) have been used to calculate the components of the energy balance of the building described by the general Eq.(2), or specific forms e.g. as Eqs. (3) or (4). Calculations have been performed for different examples of room locations and construction of envelope elements of the hypothetical building.

3. SOME RESULTS OF SIMULATION STUDIES OF ENERGY BALANCE OF A BUILDING

As has been mentioned, simulations studies have been performed to calculate all components of the energy balance of the hypothetical building. Some results of simulation studies are presented in this paper to show the evident impact of solar radiation on the energy balance of some rooms' locations. The rooms under consideration have 16 m^2 of floor area, 3m height, 1 window of 2 x 2 m^2 of total surface. The external wall is constituted of 3 layers with total heat transfer coefficient U equal to 0.2 $W \cdot m^{-2} K^{-1}$. The window is a compact type, double glazed with low emissivity coating and wooden frame, U is equal to 1.3 $W \cdot m^{-2} K^{-1}$. Because of the assumed and elaborated solar radiation representative model, 12 averaged days (one for each month) have been simulated (with different time steps for different elements of building envelope), each day being repeated enough times to ensure a steady solution.
As has been mentioned only some results of the simulation studies of the dynamics of the building are presented in the paper. Fig. 1 presents daily distribution of solar radiation transmitted directly through the window into the south room for every hour of averaged days of four summer months (June – September) of the averaged year for Warsaw climatic conditions.

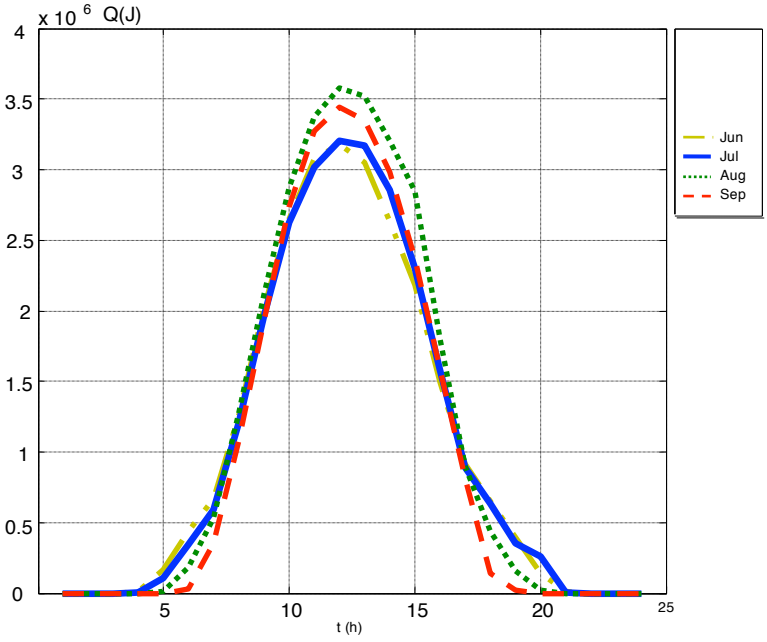

Figure 1: Distribution of solar radiation transmitted directly through the south window into the room for every hour of averaged day of four summer months of the averaged year for the Warsaw climate

Fig. 2 presents daily distribution (hour by hour) of total energy demand of the room for the considered averaged days of the four summer months. The positive values of energy demand indicate the necessity for supplying cooling energy to rooms, and negative values imply heating demands. It is evident that the curve of daily distribution of cooling demand during the day time correspond directly to the distribution of daily solar irradiation, which passes through the glazing of the room. When solar irradiance is small then the influence of solar energy on the energy balance is also small, and then the influence of temperature difference between outside and inside can be seen more easily. During nights the small need for heating energy can be seen, but the values are so small that of course the heating load can be neglected.

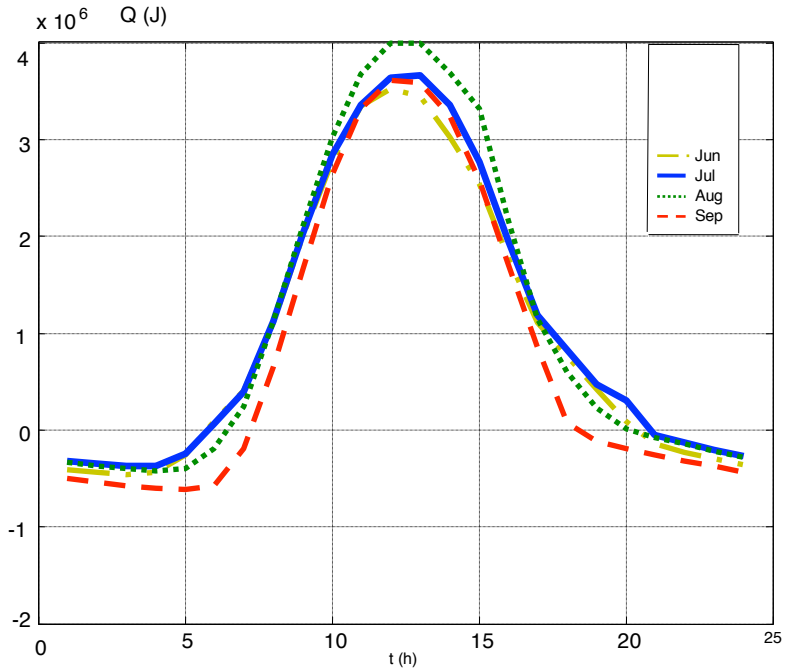

Figure 2: Daily distribution (hour by hour) of total energy demand of the south facing room under consideration for four summer months of the averaged year for Warsaw climate

Table 1 is presented to describe more cases of rooms with large glazing areas, showing the necessity of supplying cooling energy in summer. Table 1 shows results of calculations of annual heating/cooling loads and heating/cooling load indices for rooms of different aspect: south, east, west, east and north-facing, located at regular floors of a building and in an attic, and for the whole apartments consisting of all the considered rooms. The attic rooms have been taken into consideration, because nowadays attic apartments are fashionable in big cities. Building developers want to sell every square meter of a high-rise building, because the land in the city is expensive. So attics are sold as living area spaces, even if in the past nobody used to live in such space, because of extreme weather conditions, which can occur in both summer and winter. Table 1 presents also the energy losses/gains through the windows. These energy flows are crucial to understand why the cooling demand of some room cases is so large. It is necessary to recall that the calculations have been made with a one hour time step for averaged days of every month of the averaged year. It is also good to mention that because the average data of climatic conditions have been used they do not fully present the extreme summer conditions of ambient air temperature and solar irradiance, which can happen in moderate climate and can give more extreme picture of possible summer overheating of rooms.

Table 1. Annual heating/cooling loads and load indices for rooms of different aspect and for whole apartments with component of energy losses/gains through windows

Attic rooms	South	East	West	North	Apartment
Heating demand ($MJ \cdot year^{-1}$)	2008.8	3019.4	2681.3	3643.0	11352.5
Cooling demand ($MJ \cdot year^{-1}$)	6481.8	4503.9	5327.0	2790.9	19103.6
Energy losses through window ($MJ \cdot year^{-1}$)	1202.1	1898.8	1662.15	2504.0	7267.1
Energy gains through window ($MJ \cdot year^{-1}$)	6961.8	4730.7	5629.7	3051.2	20373.4
Heating load indices ($kWh \cdot m^{-2}a^{-1}$)	34.78	52.42	46.55	46,55	49.27
Cooling load indices ($kWh \cdot m^{-2}a^{-1}$)	112.5	77.5	92.5	47.5	82.91
Regular rooms	South	East	West	North	Apartment
Heating demand ($MJ \cdot year^{-1}$)	1884.2	3122.5	2802.8	3573.5	11383
Cooling demand ($MJ \cdot year^{-1}$)	4078.1	2944.7	3729.3	1568.0	8590,8
Energy losses through window ($MJ \cdot year^{-1}$)	1085.6	2011.8	1696.3	2365.7	7159.4
Energy gains through window ($MJ \cdot year^{-1}$)	4593.1	3186.5	3954.7	1749.5	13483.8
Heating load indices ($kWh \cdot m^{-2}a^{-1}$)	32.71	54.21	48.66	62,. 4	49.41
Cooling load indices ($kWh \cdot m^{-2}a^{-1}$)	70.80	51.12	64.74	27.22	37.29

The graphical interpretation of heating and cooling load indices given in Table 1 is also presented in graphical form in Fig. 3.

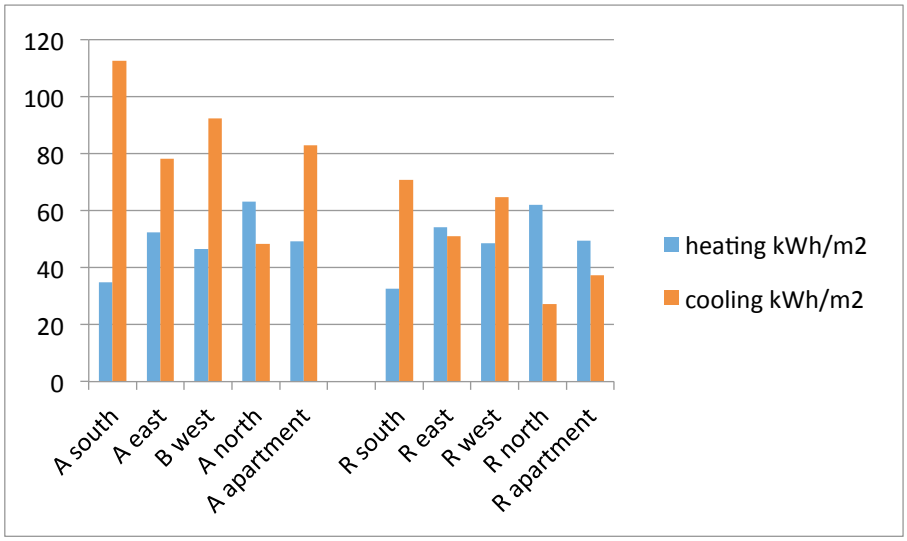

Figure 3. Annual heating/cooling load indices for rooms of different location and for whole apartments

Analysing Table 1 and Fig. 3 it is evident that heating demands for attic apartments and regular apartments are very similar. For regular rooms the heating demand is even slightly higher. However, cooling demands for attic apartments are much higher, i.e. 2.2 times more than for regular apartments. Such a situation is caused by very high energy gains resulting from too much solar radiation passing through the large roof windows, comparing vertical windows of the same size and the same optical and thermal parameters in summer.

At the beginning of the paper it was mentioned that according to Polish regulations the indices of primary energy consumption for heating (space and DHW) since the year 2021 for single family houses should not be higher than 70 kWh·m^{-2}a^{-}1 and for multifamily buildings than 65 kWh·m^{-2}a^{-1}. According to the simulation studies performed it turns out that for the hypothetical building the indices for heating demand for attic rooms are at level of - 34.78 kWh·m^{-2}a^{-1} - south, 52.42 kWh·m^{-2}a^{-1} – east, 46.55 kWh·m^{-2}a^{-1} – west, 46.55 kWh·m^{-2}a^{-1} – north and for the whole apartment – 49.27 kWh·m^{-2}a^{-1}. For regular rooms the indices are slightly higher as can be seen in Fig. 3. Of course the final energy consumption depends on the type of space heating system and its effectiveness. The indices of final energy consumption are usually higher, apart from the application of a heat pump (because the COP – coefficient of performance is taken into account as effectiveness of the device). Primary energy consumption depends on the type of energy source (fuel) used. It seems that for some type of heating systems and energy sources the required limits for primary energy indices can be fulfilled. However, a problem occurs in a case of the cooling energy needed to be supplied to keep the required thermal comfort. It turns out that cooling needs for attic rooms are quite large, i.e. for the south - 112.5 kWh·m^{-2}a^{-1}, west – 92.5 kWh·m^{-2}a^{-1}, east – 77.5 kWh·m^{-2}a^{-1}. Only for the north room they are evidently smaller - 47,5 kWh/(m^{2}year). For the whole apartment the cooling load indices are at level of 82.91 kWh·m^{-2}a^{-1}. Final and primary energy consumption is usually higher. If HVAC is supplied by electrically driven devices based on fossil fuels then the primary energy consumption is especially high. Taking into account an obligatory value of the conversion coefficient for electricity based on coal (equal to 3) the primary energy consumption index for the considered hypothetical attic apartment will be at very high level of about 250 kWh·m^{-2}a^{-1}. Unfortunately, some can say that such a situation is not a problem, because there are no official regulations and limits for energy consumption for cooling energy consumption in residential buildings in moderate climates.

4. CONCLUSSIONS

The simulation results show that overheating in summer due to the high solar irradiation can be a real problem for the design of some buildings even in moderate climates. To solve the problem it is necessary to use external shading devices. However, in a case of roof windows shading means usually utilization of external blinds, which block the whole spectrum of solar radiation including the visible light. Usually inhabitants do not like limitation of the daylighting availability. Perhaps windows changing their optical parameters with respect to the level of the solar irradiance (like electro-chromatic windows) would be a much better solution.
If summer cooling is necessary then perhaps the best solution is to use solar cooling systems, like traditional compressor cooling devises driven by PV panels, as has become quite fashionable nowadays (Chwieduk and Szelągowski, 2018). Another option could be the application of solar thermal cooling systems. Solar cooling (PV or thermal) technologies also have the advantage of using surplus renewable energy when there would otherwise be no use for it, improving the overall system economics.

NOMENCLATURE

c	specific heat (kJ kg^{-1} K^{-1})
Q_c	cooling energy flux supplied by the space cooling system (kW)
Q_h	heating energy flux supplied by the space heating system (kW)
Q_{in}	energy flux coming into a building (kW)
Q_{out}	energy flux coming out of a building (kW)
Q_{qv}	internal heat gains (kW)
Q_{roof}	heat flux transferred through a roof (kW)
Q_{gr}	heat flux transferred through a floor on the ground or basement (kW)
Q_{sol}	solar energy flux transmitted through windows into a building (kW)
Q_{ven}	heating/cooling energy flux needed for ventilation (kW)
Q_{wall}	heat flux transferred through walls (kW)
Q_{win}	heat flux transferred through windows (kW)
T	temperature (K)
t	time (s)
V	volume (m^3)
ρ	density (kg m^{-3})

REFERENCES

Directive 2010/31/EU of the European Parliament and of the Council of 19 May 2010 on the energy performance of buildings.

https://ec.europa.eu/energy/en/topics/energy-efficiency/heating-and-cooling (access on 4. 01. 2018)

Rozporządzenie Ministra Infrastruktury w sprawie warunków technicznych, jakim powinny odpowiadać budynki i ich usytuowanie Warszawa, Dziennik Ustaw dnia 13 sierpnia 2013 r. Poz. 926. National Regulation on technical conditions for buildings and their location with amendments (in Polish).

Reindl DT, Beckman WA, Duffie JA., 1990. Evaluation of Hourly Tilted Surface Radiation Models. Solar Energy. 45 (1), 9-17.

Chwieduk D., Bogdańska B., 2004. Some recommendations for inclinations and orientations of building elements under solar radiation in Polish conditions. Renewable Energy 29, 1569 –1581.

Chwieduk, D., 2014. Solar Energy in Buildings. Thermal Energy Balance for Efficient Heating and Cooling, Elsevier Academic Press, 362.

Chwieduk B., Szelągowski A., 2018. Savings resulting from coupling the PV with the space cooling system. SOLINA 2018 - VII Conference SOLINA Sustainable Development: Architecture - Building Construction - Environmental Engineering and Protection Innovative Energy-Efficient Technologies - Utilization of Renewable Energy Sources / Lichołai L. (Ed.), E3S Web of Conferences, vol. 49, EDP Sciences, 14.1-10.

Manuscript ID: 865
DOI: 10.18462/iir.icr.2019.0865

Control analysis of VRF air-conditioners for the evaluation of demand response

Kuniyasu MATSUMOTO[(a)], Kiyoshi SAITO[(b)], Seiichi YAMAGUCHI[(b)], Keisuke OHNO[(b)]

[(a)] The Kansai Electric Power Co., Inc.
AMAGASAKI, 661-0974, JAPAN, matsumoto.kuniyasu@d3.kepco.co.jp
[(b)]WASEDA University,
Tokyo, 169-8555, JAPAN, saito@waseda.jp, sei_yamaguchi@aoni.waseda.jp
k.ohno@aoni.waseda.jp

ABSTRACT

The number of renewable power plants has recently been increasing; hence, it is essential to maintain a balance between the supply and demand of electric power. We employ the technique of demand response (DR) through the manipulation of air conditioners. In summer, the electric demand for air conditioning consumes the majority of the available total electric power; therefore, regulating this demand compliments the requirements of peak-cut and load leveling. However, the manipulation of air conditioning impacts the user comfort and the stability of the machine. Moreover, the energy consumption of air-conditioners is uncertain owing to the operation conditions. Consequently, it is difficult to estimate the performance of the DR method. In this study, we focus on the variable refrigerant flow system, which is a popular air-conditioning system in Japan. We evaluate the performance of the demand response method using a simulation analysis and ensure that the amount of DR to regulate the air-conditioner is controlled quantitatively.
Keywords: Demand Response, Control, Cycle, Expansion Valve, Variable Volume.

1. INTRODUCTION

When the capacity of the electric supply in Japan declined immediately following the Great East Japan Earthquake, certain parts of the Kanto region were subjected to rolling blackouts. Because some electric power plants had stopped functioning, the electric power supply had to be regulated properly owing to the electric power demand. Several Japanese citizens were required to conserve electricity; improving efficiency came at the cost of their comfort in many cases. Recently, some nuclear power plants have begun to function again and the number of renewable power plants has also been increasing. Therefore, the necessity to conserve surplus electricity has decreased. However, it is important to maintain the balance between the electric demand and supply which is dependent on the prediction of the amount of electric power supply from the renewable power plants. This is required if the large power plants are subject to any disruptions or problems. As the number of renewable power plants is increasing, this effect is becoming an increasingly important factor. With this background, it is evident that the demand response (DR) can be controlled by the electric suppliers of the power plants and the users, as they can manipulate the quantity of the electric demand subjectively. In particular, the manipulation of the air conditioner's operation is a promising application of the DR technique, because it delivers a quick response and does not require the addition of an expensive investment. In Japan, almost all the air-conditioners can regulate their outlet capacity by controlling the inverter frequency. Therefore, manipulation of air-conditioners can be considered an efficient application of the DR method. In this study, we evaluate the feasibility of employing this DR method for air-conditioners using a simulation analysis.

2. SYSTEM OVERVIEW

In this study, we focus on the variable refrigerant flow (VRF) system, which is installed in the inverter devices allowing the compressor, fan, and all the indoor units to be controlled independently. Fig. 1 shows the system overview. This system can regulate the quantity of the refrigerant flow by

manipulating the compressor rotational speed. Moreover, there are expansion valves in every indoor unit. Therefore, all the indoor units can be controlled independently based on the user's manipulation.

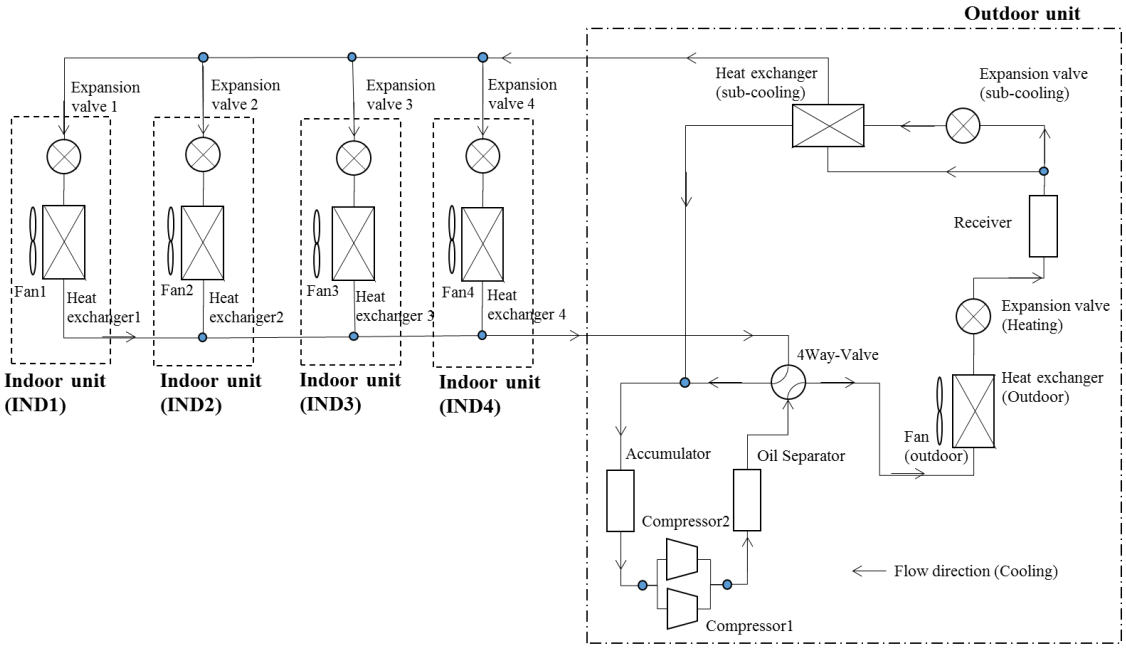

Figure 1: Overview of a VRF system

3. THE DEMAND RESPONSE METHOD

There are multiple types of technologies used to implement DR. Therefore, according to the Federal Energy Regulatory Commission, DR is defined as follows: "Changes in electric usage by end-use customers from their normal consumption patterns in response to changes in the price of electricity over time, or to incentive payments designed to induce lower electricity use at times of high wholesale market prices or when system reliability is jeopardized" (Balijepalli et al., 2011). Consequently, there are several ways to control the capacity or the shifting electric load using the energy storage systems to adjust the electric demand and supply. Fig. 2 shows the overview of DR.

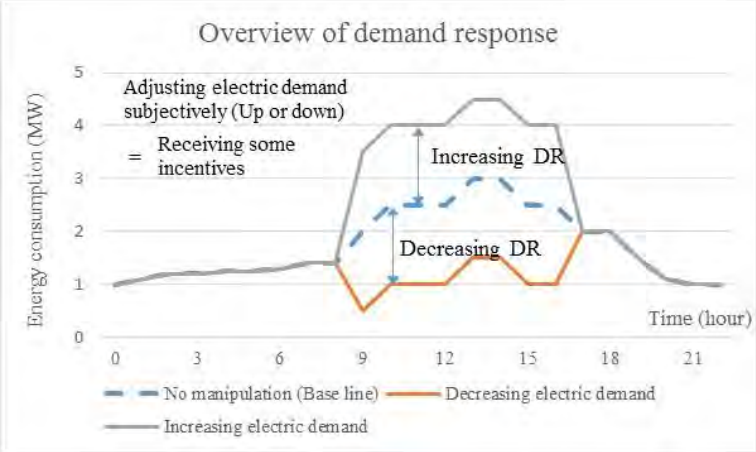

Figure 2: Overview of DR

Balijepalli et al. (2011) cited several technologies to control the functioning of air-conditioners. For example, Lu et al. (2011) adopted the smart grid system that turned both the water heater and air conditioner on and off using three types of strategies; these include stabilizing the electric voltage, stabilizing the electric frequency, and minimizing the electric cost. Some of the existing studies have evaluated the control of air-conditioners using energy resources. However, none of the studies have evaluated the physical aspects of air-conditioners in detail for the implementation of DR. Therefore, we have created a detailed simulation model and evaluated the VRF system quantitatively.

4. EVALUATING PERFORMANCE OF DR

The VRF system is flexible and has a wider load changing system. Because the compressor is connected to an inverter device, it is capable of regulating the quantity of refrigerant flow depending on the load change. In addition, each indoor unit contains an expansion valve. When the opening pulse is adjusted, the system is capable of appropriately regulating the amount of refrigerant circulating into the indoor unit. This enables a wide operation range of low to high loads, ultimately contributing to saving energy, and improving the user comfort with an independently controlled indoor unit.

In this study, we aim to evaluate the results obtained quantitatively after applying the VRF system in the implementation of DR. The power consumption of the air conditioner varies significantly depending on the load conditions, temperature, and the operation conditions of the indoor unit. Controlling the temperature is not feasible, and the driving situations vary frequently, rendering this method considerably uncertain. Therefore, we estimate the power consumption of the air-conditioner using a simulation model constructed by applying a physical formula. Moreover, we evaluate the performance of DR using the Monte Carlo simulation considering the uncertainty of the temperature and the load conditions

Details of the simulation analysis model of the air-conditioner are not covered in this study. Please refer to our previous studies (Matsumoto et al., 2015, 2016, 2019), where they have been described in detail. Fig. 3 presents a flowchart of the calculations performed.

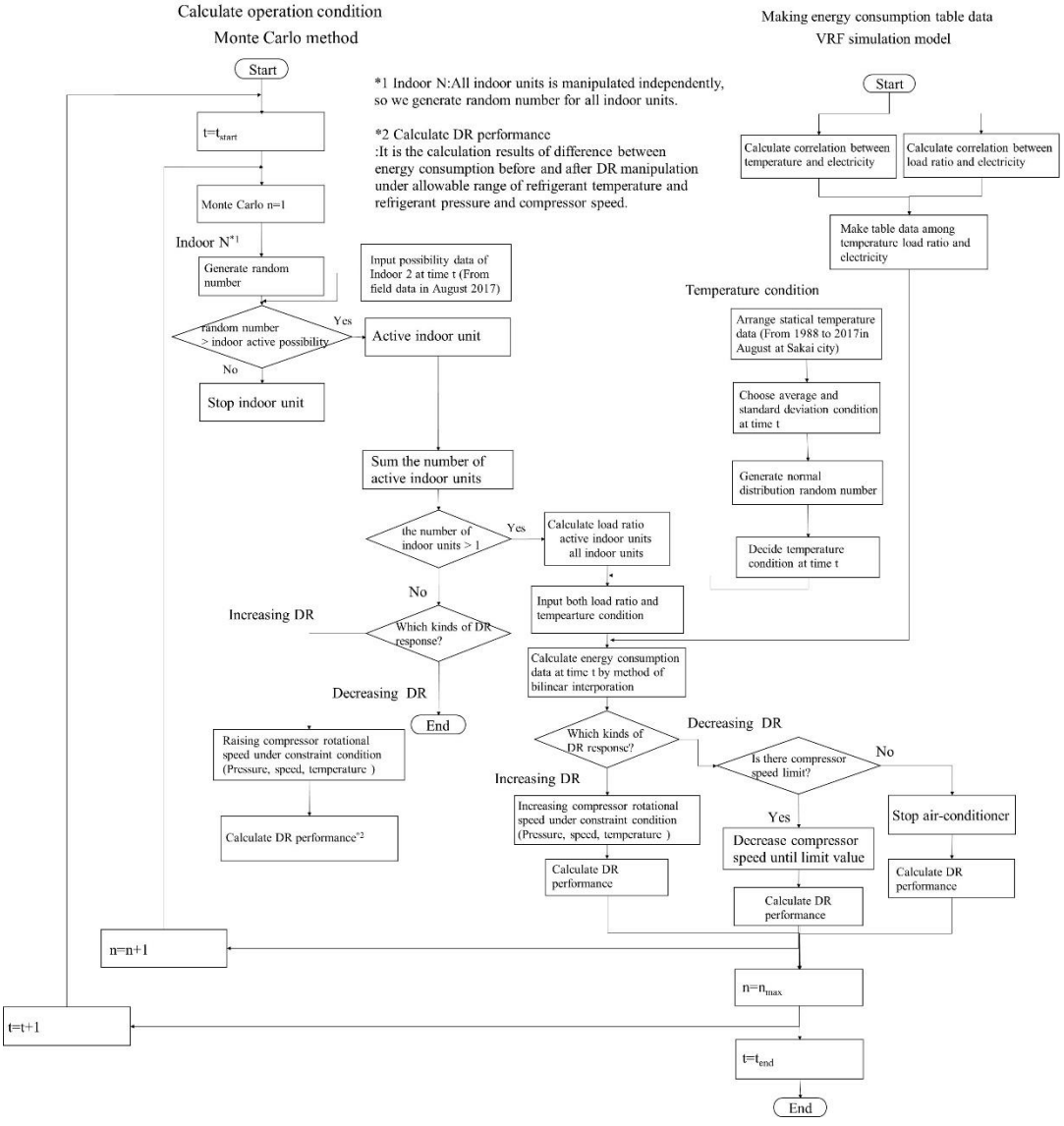

Figure 3: Flowchart of the calculations

4.1. Operating Characteristics of the VRF System

The air-conditioning system controls the rotational speed of the compressor and the open pulse of the expansion valve to maintain the stable operation of the equipment at high efficiency operation. The rotational speed of the compressor is manipulated depending on each indoor load using the feedback control method. Moreover, the open pulse of the expansion valve is manipulated by the degree of superheating at the evaporator outlet to avoid the liquid refrigerant flowing into the compressor. In this controlled background, we calculate the correlation among the energy consumption, capacity ratio, and the air temperature at the condenser. The calculations are defined as follows:

- Rated temperature operation conditions are defined as per the Japanese Industrial Standards. The outdoor temperature condition is 35 °C for dry bulbs and 24 °C for wet bulbs. The indoor temperature condition is 27 °C for dry bulbs and 19 °C for wet bulbs
- To protect the compressor, the degree of superheating at the evaporator outlet is constantly adjusted to be equal to the rated condition by manipulating the open pulse of the expansion valve.
- The allowable operating conditions are defined as follows. The degree of discharge temperature at the compressor outlet is maintained under 130 °C. The discharge pressure at the compressor outlet is maintained under 4.0 MPa. The range of the compressor rotational speed is maintained at 50% to 150% of the rated speed.

The results of the simulation analysis and the P－H diagram of three different conditions are presented in Figs. 4 and 5, respectively.

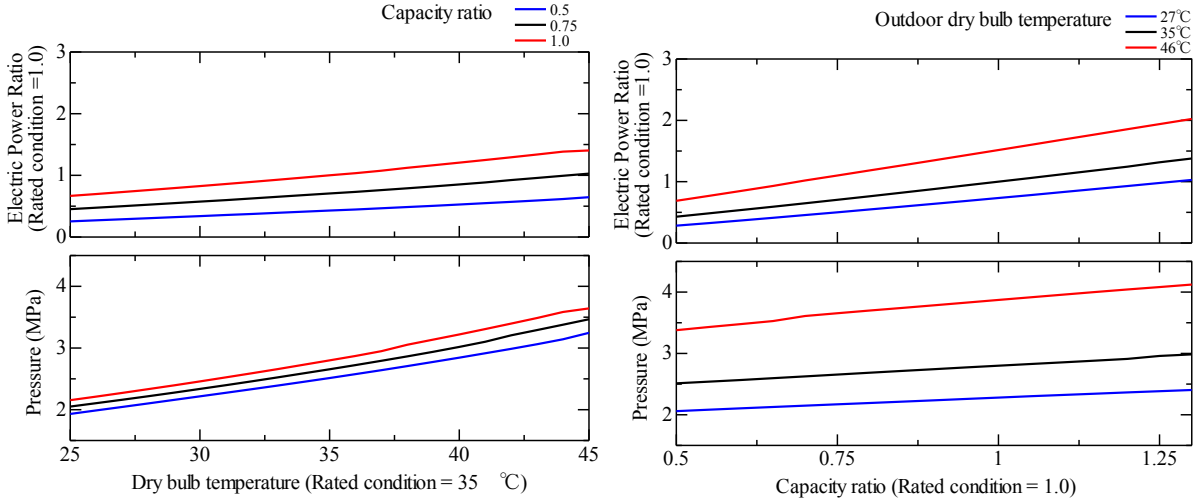

Figure 4: Simulation results (left: temperature characteristics; right: capacity characteristics)

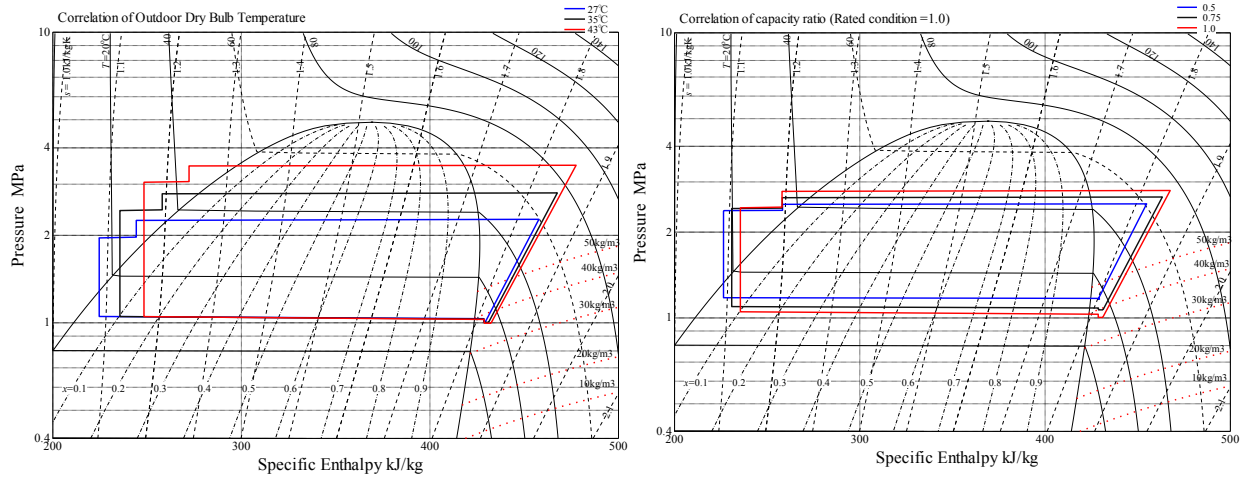

Figure 5: P－H diagram (left: temperature characteristics; right: capacity characteristics)

As shown in Fig. 4, the energy consumption and the refrigerant pressure decrease when the temperature and capacity ratio increase. Fig. 6 shows the integration of Fig.4 for the energy consumption, temperature, and the capacity ratio.

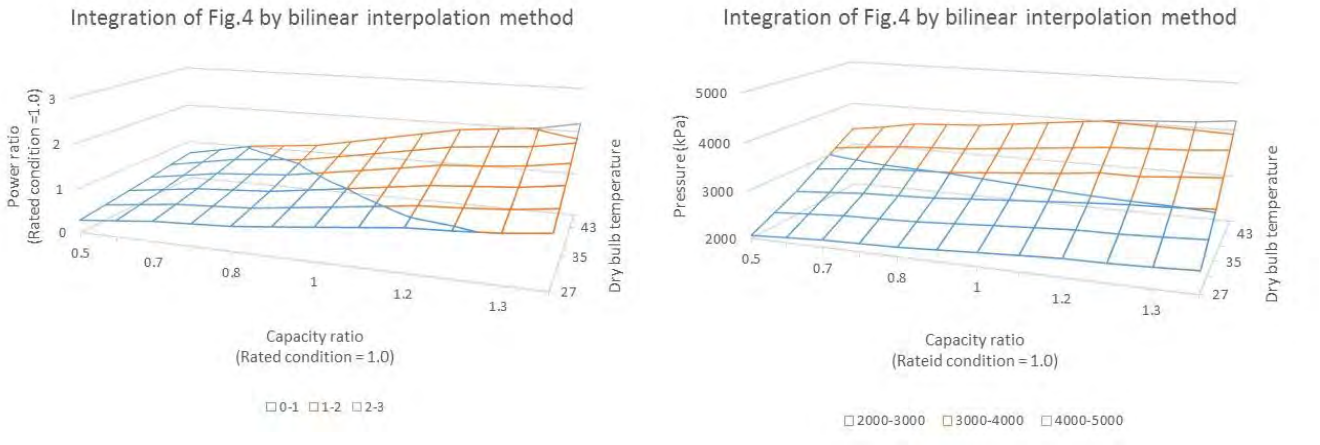

Figure 6: Integration of Fig.4 by bilinear interpolation method

As shown in Fig. 6, the correlation among the energy consumption, temperature, and the capacity ratio exhibits nonlinearity. When the temperature is higher than 45 °C and the capacity ratio is greater than 115%, the discharge pressure exceeds the allowable pressure. Due to limited calculation time, we evaluate the energy consumption using the bilinear interpolation method.

4.2. Data Collection from a Building

In the previous section, the power consumption characteristics of the load ratio and the temperature are calculated using a simulation analysis. In this section, we perform the evaluations using a building with an installed VRF system. The feasibility of DR is evaluated by extracting the driving situations and the temperature conditions of the indoor unit. Table 1 outlines the specifications of the air-conditioning equipment. Fig. 7 shows a portion of the room layout.

Table 1. Installation specifications of the VRF system

No.	Floor	Capacity (kW)	Number of indoor units	Number of indoor rooms	Remarks
AC 1	1st	28.0	10	4	1: Wide Office room 3: Narrow Meeting rooms
AC 2	2nd	45.0	7	3	1: Wide Office room 2: Narrow Meeting rooms
AC 3		56.0	6	1	1: Wide Office room (AC 2 is shared)
AC 4	3rd	56.0	6	2	1: Wide Office room 1: Narrow Meeting room
AC 5	4th	56.0	9	3	1: Wide Office room 2: Narrow Meeting rooms
AC 6		33.5	4	1	1: Wide Office room
AC 7	5th	45.0	5	3	1: Wide Office room 2:Narrow Meeting rooms
AC 8	7th	56.0	5	3	1: Wide Office room 2: Narrow Meeting rooms

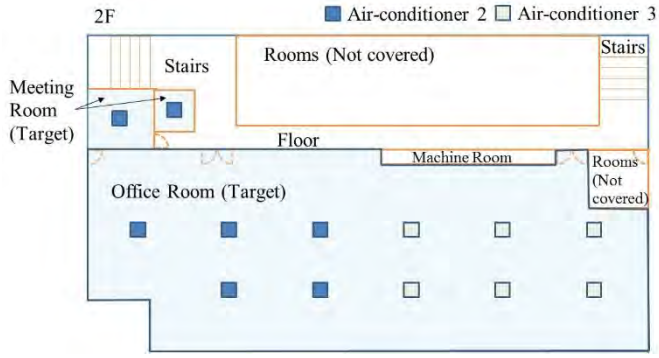

Figure 7: Room layout (2nd floor with AC2 and AC3)

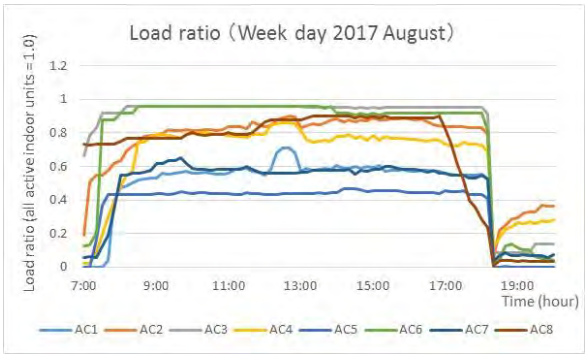

Figure 8: Load ratio data (average values for the weekdays in August 2017)

The building is primarily occupied by office workers; therefore, the air-conditioners are operated during relatively regular timeframes. However, the operation time differs depending on the purposes for which a particular room is used. Therefore, we have collected the indoor unit's operation data for one month during August 2017. Because the weekday and holiday schedules are different, we have only selected data for weekdays. Fig. 8 shows the evaluation results.
In addition, the data of the outside air temperature around the building during the month of August for over 30 years from 1988 to 2017 is already available. We assume that the data displays a tendency close to the normal distribution.

4.3. Monte Carlo Method

The Monte Carlo method performs a simulation analysis using random numbers and is extensively used. The operation probability and the temperature conditions of the indoor unit are defined in the previous section. In this section, random numbers are generated to simulate the operation state of the air-conditioner and the effect of DR is then evaluated. Fig. 9 shows an image of obtaining the operation state of the indoor unit. The temperature condition is determined by generating a random number based on the normal distribution. This number determines whether the indoor unit is active. Fig. 9 shows the condition generating a random number; the load ratio is defined using Eq. (1). Fig. 10 shows the generation of a random number for determining temperature conditions.

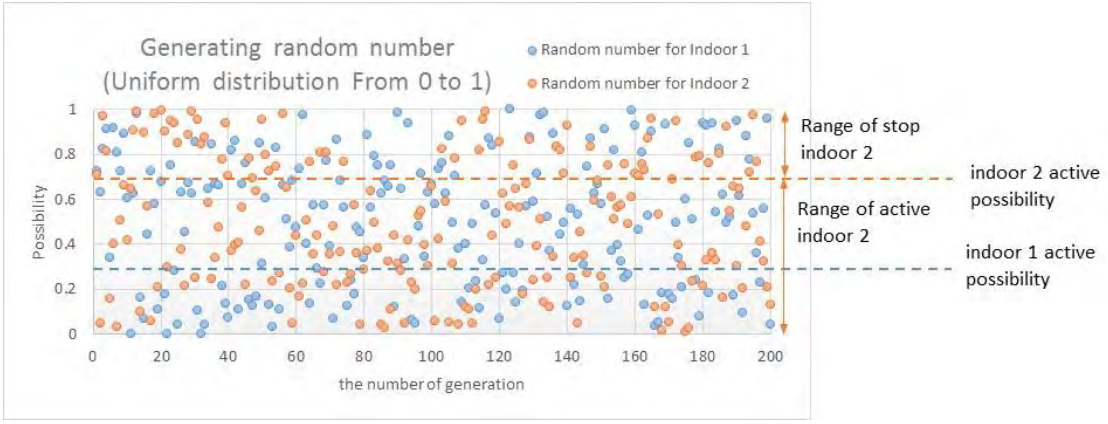

Figure 9: Generation of a random number

$$Load\ Ratio \equiv \sum Active\ Indoor\ Units / Number\ of\ indoor\ units \qquad \text{Eq. (1)}$$

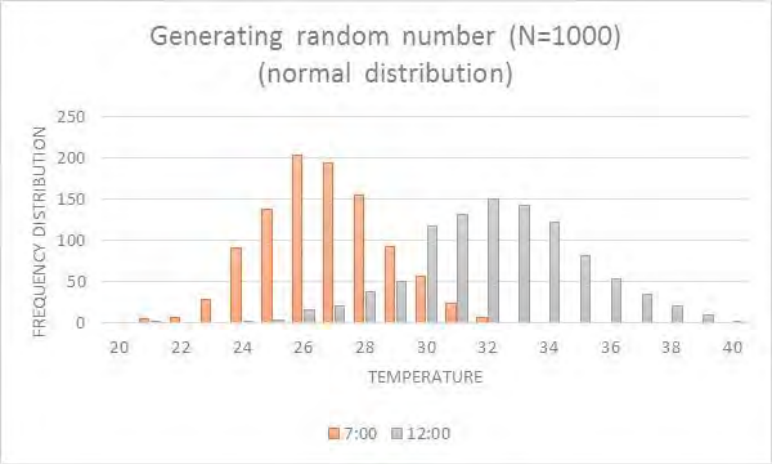

Figure 10: Generation of a random number for determining temperature conditions

5. CONCLUSION AND CONSIDERATION

A random number, defined as N = 200, is generated in each time zone from 7 to 20. The calculation results are obtained by evaluating the performance of the increased and decreased DRs, as shown in Fig. 11 at 14:00.

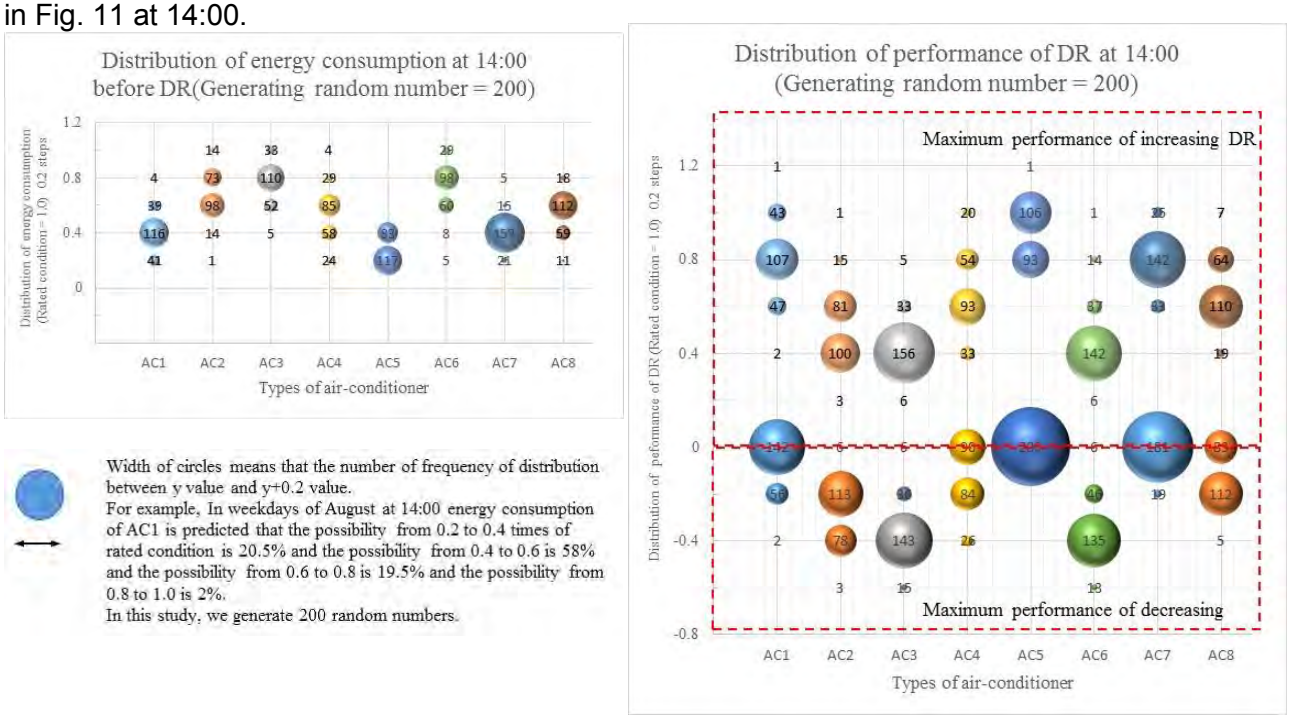

Figure 11: Evaluation of the performance of DR at 14:00

The left diagram is the distribution of energy consumption at 14:00 before DR manipulation. The right diagram is the distribution of the maximum performance of DR. A positive value indicates the performance of an increasing DR and a negative value indicates a decreasing DR. The performance of DR is calculated using the difference between energy consumption before and after DR manipulation under an allowable range of refrigerant temperatures, refrigerant pressures, and compressor speed.

Because the air-conditioners are turned off early in the morning and at night, the possibility of an increase in DR is expected and a decrease DR is not. Although the temperature conditions and the operating conditions of the indoor unit are different, depending on the effect of aggregation it is expected that the variances will become smaller. Fig. 12 shows the weighted distribution values, which are considered as the capacity differences in all the VRF systems. In this case, the performance of an increasing DR is expected to be approximately 60% of the rated operation and the performance of a decreasing DR is expected to be approximately 20%.

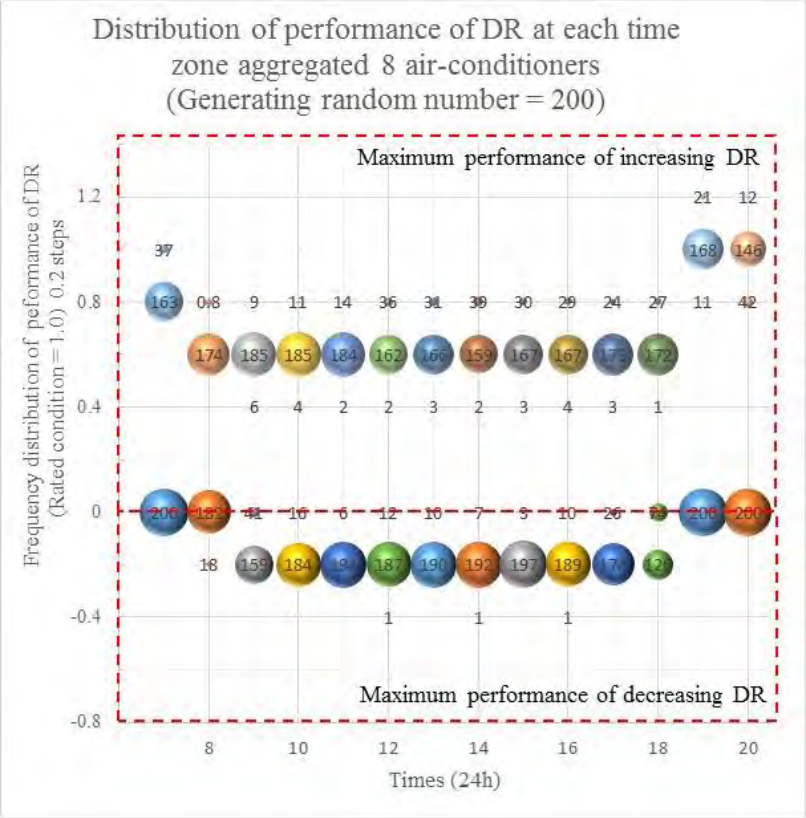

Figure 12: Distribution of performance of DR for each time zone aggregated for 8 air-conditioners

6. SUMMARY AND FUTURE STUDY

A detailed analysis model of an air-conditioner was constructed and the effect of DR was evaluated in detail, considering the manipulation of rotational speed of the compressor and the open pulse of the expansion valve. Moreover, the Monte Carlo method was employed to quantitatively evaluate the effect of DR considering the changes in the temperature and operating conditions of the indoor unit. A new evaluation method with a detailed analysis can be expected in the future. However, this study does not consider the indoor condition. In fact, the air-conditioner is turned on and off primarily according to the indoor temperature. It is assumed that the duration of DR is influenced, as the control to operate the activation is built-in. In future investigations, it will be necessary to perform the evaluations considering these influences.

REFERENCES

V. S. K. Murthy Balijepalli, Vedanta Pradhan, S. A. Khaparde., 2011. Review of Demand Response under Smart Grid Paradigm. IEEE PES Innovative Smart Grid Technologies – India, 236-243

S. Lu, N. Samaan, R. Diao, M. Elizondo, C. Jin, E. Mayhorn, Y. Zhang, H. Kirkham, 2011 Centralized and decentralized control for demand response, in Proc. of IEEE Innovative Smart Grid Technologies (ISGT), 1-8

K. Matsumoto, K. Ohno, K. Saito, T. Kishimoto, 2015 Evaluate VRF Compression Heat-pump System under Steady-State Analysis －1st Report: Analysis of Numerical Simulation and Experimental Study Focusing on Changing the Number of Active Indoor Units－, Trans. of the JSRAE, Vol.32, No.2, 95-107

K. Matsumoto, K. Ohno, K. Saito, 2016 Numerical Analysis of VRF Compression Heat-pump System under Unsteady-State Condition －Analysis of Special Unsteady State Characteristics of VRF Compression Heat-pump System, Trans. of the JSRAE, Vol.33, No.2, 155-164

K. Matsumoto, K. Ohno, S. Yamaguchi, K. Saito, 2019 Numerical analysis of control characteristics of variable refrigerant flow heat-pump systems focusing on the effect of expansion valve and indoor fan, Int. J. Refrigeration, Vol.99, 440-452

Manuscript ID: 927
DOI: 10.18462/iir.icr.2019.0927

Experimental investigation on a novel semi-coupled desiccant heat pump system

Fanli LU, Tianshu GE*, Yong LI, Yanjun DAI, Ruzhu WANG

Institute of Refrigeration and Cryogenics, Shanghai Jiao Tong University
Key Laboratory of Power Mechanical Engineering, MOE China
800 Dongchuan Road, Shanghai, 200240, China
*Email: baby_wo@sjtu.edu.cn, Tel: +86-(0)21-34206335, Fax: +86-(0)21-34206335

ABSTRACT

A novel semi-coupled desiccant heat pump (SCDHP) system in which a desiccant coated evaporator (DCE) and a conventional evaporator (CE) operate in series is proposed to overcome the disadvantages of integrated solid desiccant heat pump (IHP) system. An experimental setup is established and tested to obtain the performance of SCDHP system. Results show that under Shanghai conditions, on the one hand, SCDHP system can inherit the high COP of IHP system, which can reach to higher than 4; on the other hand, when an auxiliary CE is installed in series with DCE, the average temperature drop of process air is about doubled, then corresponding cooling capacity increases by more than 50%, and the variation range of outlet air temperature reduces by about 70%, moreover, the coordination between outlet air temperature and humidity can be improved significantly.

Key words: Desiccant coated heat exchanger; Conventional evaporator; Operate in series.

1. INTRODUCTION

At present, dominant air conditioning system is still based on vapor compression (VC) cycle. In such a system, in order to handle sensible and latent load together, evaporation temperature needs to be set lower than dew point temperature, which results in lower coefficient of performance (COP).
Recently, integrated solid desiccant heat pump (IHP) system is proposed to increase evaporation temperature and then to improve COP. In the IHP system, two fin-tube heat exchangers (evaporator and condenser) in traditional VC system are replaced by two desiccant coated heat exchangers (DCHE). Tolga et al. (2010) experimentally investigated the IHP system under American conditions. Results show that the latent load removal of IHP system can meet needs and COP can reach 5.0. However, the sensible load removal is relatively weak. Then, Napoleon et al. (2011) tested the performance of IHP system under Asia-Pacific summer conditions. Results show that COP can reach 2.8~5.7 which is higher than that of traditional VC system operating under same conditions. The humidity ratio of process air can be reduced by about 50% while the temperature of process air only can be reduced by 10%~20%, in other words, the sensible load removal of IHP system is much weaker than the latent load removal. Lingji et al. (2018) experimentally investigated the feasibility of improving the sensible load removal of IHP system by prolonging switching time. It is found that when this strategy is adopted, the improvement of sensible load removal is not obvious but COP decreases significantly. Yaodong et al. (2017) proposed a weakly coupled control strategy for IHP system. In such a strategy, firstly, evaporation temperature is set according to the sensible load, then switching time is set according to the latent load. However, experimental results reveal that the IHP system with this control strategy still shows the characteristics of inadequate sensible load removal. In addition, all of above-mentioned researches indicate the large fluctuation and the incongruity of supply air in the IHP system. Based on these works, it can be concluded that the COP of IHP system is obviously higher than traditional VC system and the latent load removal is adequate. But the disadvantages of such system are also obvious: (1) the removal of sensible load cannot meet needs; (2) the large fluctuation and the incongruity of supply air.

In this paper, a novel semi-coupled desiccant heat pump (SCDHP) system in which a desiccant coated evaporator (DCE) and a conventional evaporator (CE) operate in series is proposed to overcome the drawbacks of IHP system. And an experimental setup is built up to investigate performance of this novel system under typical conditions.

2. EXPERIMENTAL SETUP OF SEMI-COUPLED SOLID DESICCANT HEAT PUMP

2.1 Working Principle

Fig. 1(a) shows the schematic diagram of SCDHP system. The refrigerant cycle is shown in Fig. 1(b): refrigerant is compressed in compressor from state a to b, then flows into desiccant coated condenser (DCC) in which it can be cooled from state b to c, afterwards expands in throttle valve from state c to d, at last vaporizes from state d to e (in CE) and from state e to a (in DCE) successively. The air handling process is shown in Fig. 1(c): air first flows through DCE in which it is dehumidified and cooled from state 1 to 2, then is further cooled by CE from state 2 to 3. Simultaneously, condensation heat provides a reliable heat resource for the regeneration of the desiccant coated on the surface of DCC. In the SCDHP system, DCE and DCC are switched periodically to realize continuous dehumidification, and CE keeps operating mode to remove sensible load.

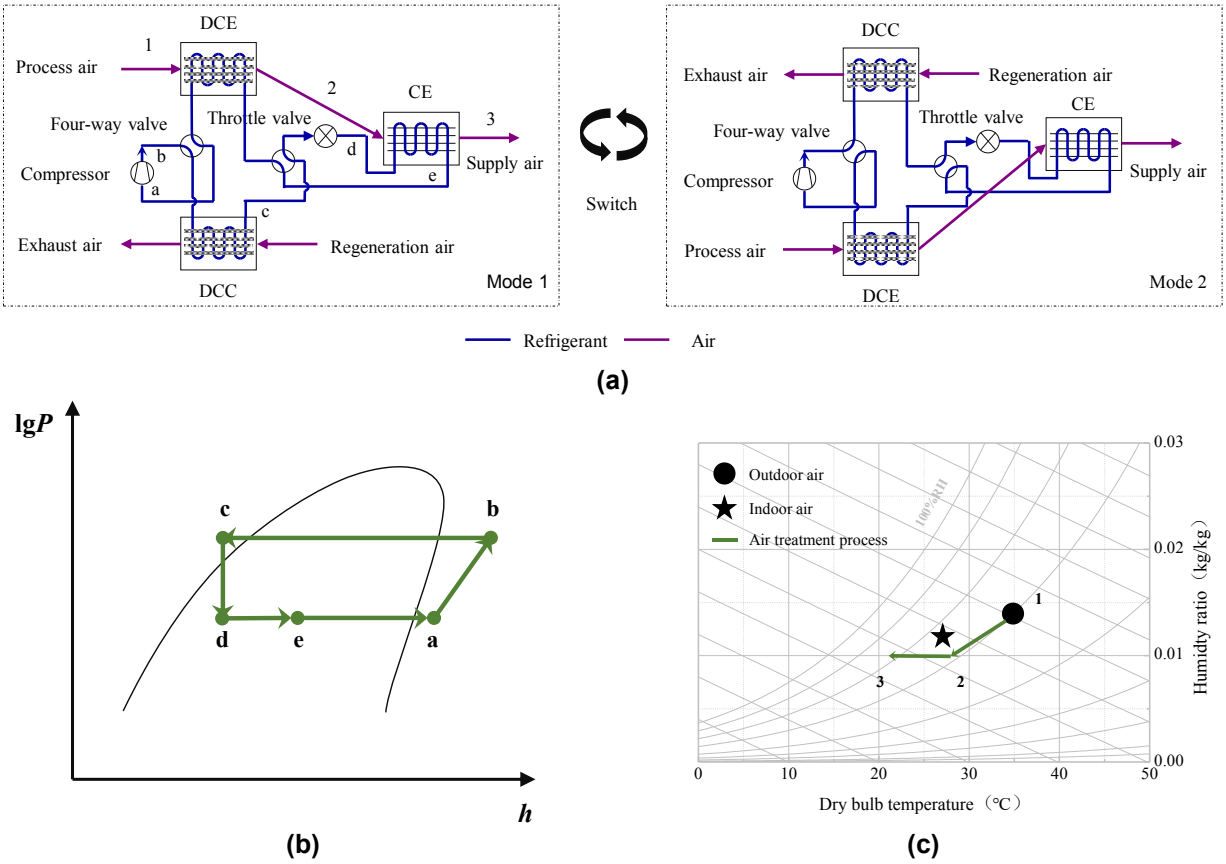

Figure 1: The (a) schematic diagram of SCDHP system (b) refrigerant cycle of IHP system (c) air handling process

2.2 Experimental Setup and Measurement

An experimental system as shown in Fig. 2 is established to test the performance of SCDHP system. Fig. 2(a) is the schematic figure of experimental system and Fig. 2(b) is the picture of experimental setup. The system includes refrigerant cycle and air flow path. For the refrigerant cycle, a frequency conversion compressor, an electronic expansion valve, a four-way valve and four one-way valves are installed to adjust and switch the refrigerant cycle. For the air flow path, four frequency conversion fans and eight electric air valves are installed to adjust air flow rate and to switch the air flow path. There are two operation modes: Mode 1 and Mode 2. In Mode 1, four-way valve is de-energized and air valves 1/2/3/4 are open while air valves 5/6/7/8 are closed: process air (state 1)

is first dehumidified and cooled by DCHE1 to state 2, then further cooled by CE to state 3, meanwhile the regeneration air (state 4) is humidified and heated by DCHE2 to state 5. When system switches from Mode 1 to Mode 2, the four-way valve is energized to reverse the function of two DCHEs, and CE keeps operating as an evaporator. In the meantime, the air flow path is changed by closing air valves 1/2/3/4 and opening air valves 5/6/7/8. Process air (state 1) is first dehumidified and cooled by DCHE2 to state 2, then further cooled by CE to state 3, meanwhile the regeneration air (state 4) is humidified and heated by DCHE1 to state 5. The parameters of heat exchangers are summarized in Table 1 and the specifications of other main components are shown in Table 2. The locations of test sensors are also shown in Fig1. (a) and the detailed specifications of test sensors are listed in Table 3. All data are collected and saved by PLC with the sample time of 2s. In order to simulate different air conditions, experimental setup is placed in a room which can provide air temperature from -10℃ to 40℃ with a precision of ±2℃ , and air relative humidity from 30% to 90% with a precision of ±5%.

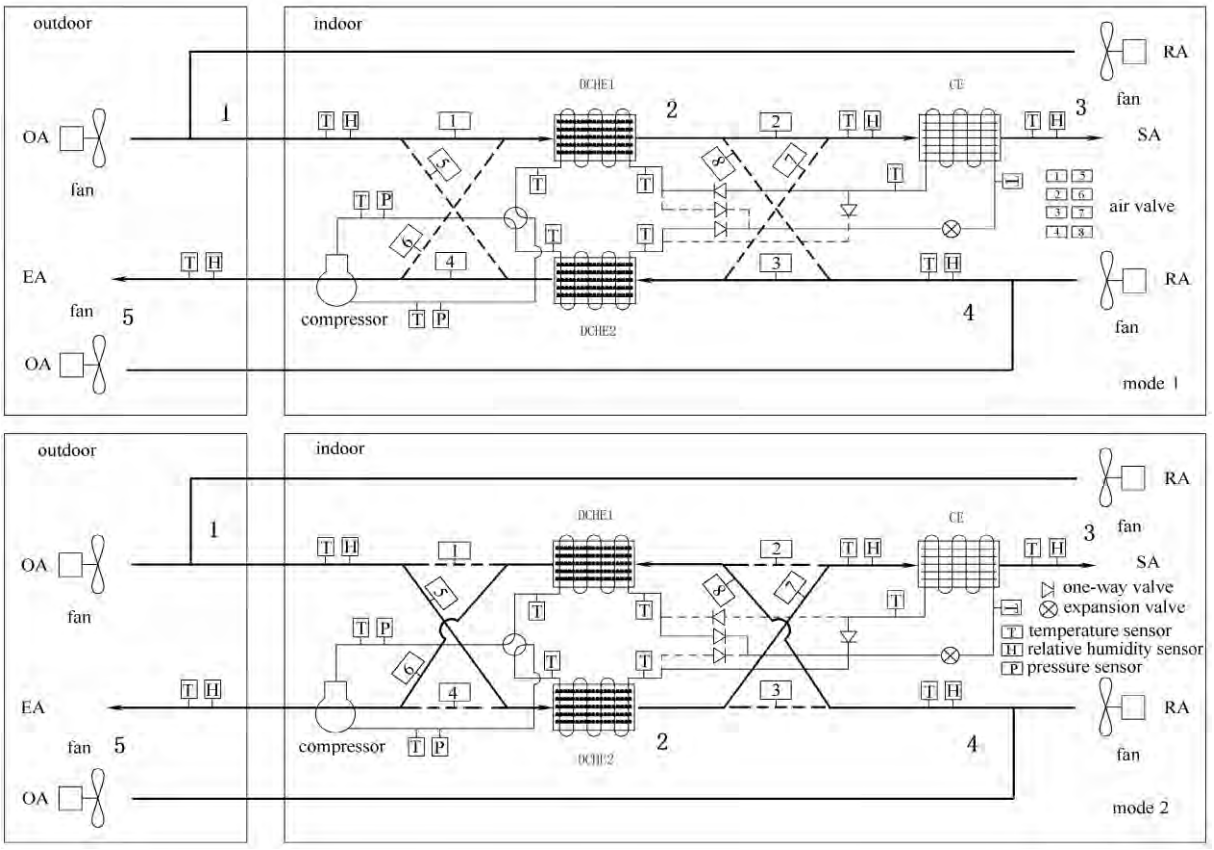

(a)

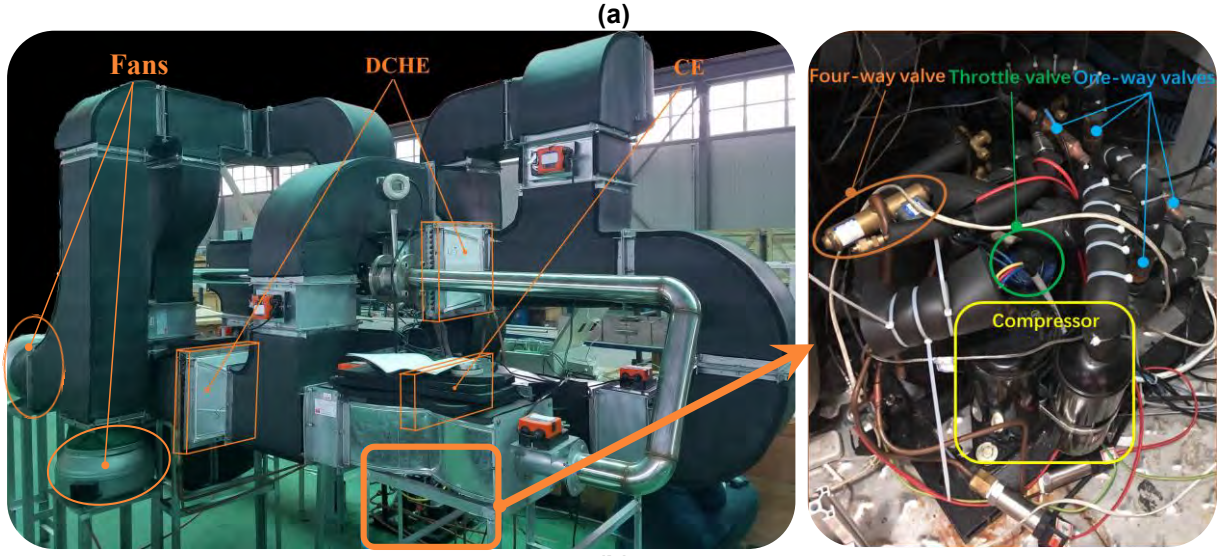

(b)

Figure 2: The (a) schematic diagram (b) picture of experimental system

Table 1. Structure parameters of heat exchangers

Specifications of heat exchangers	DCHE	CE
Inner diameter of copper tube (mm)	6.3	
Outer diameter of copper tube (mm)	7	
Transverse tube pitch (mm)	21	
Longitudinal tube pitch (mm)	12.7	
Fins thickness (mm)	0.115	
Fins spacing (mm)	2	1.5
Size (mm^3)	379*336*25.4	379*168*38.1
Mass of desiccant (g)	735	—

Table 2. The specifications of main components

Main components	Specifications	Number
Compressor	Refrigerant: R410A Capacity: 3.4KW	1
Throttle valve	Capacity (10%~100%): 2~19.3KW	1
Four-way valve	Capacity: 2.8~11.4KW	1
One-way valve	Capacity: 4.2KW; 32.9KW	4
Fans	Maximum flow rate: 600m^3/h	3
	Maximum flow rate: 1500m^3/h	1

Table 3. The specifications of sensors

Parameters	Sensors	Range	Accuracy
Temperature of air	Temperature and relative humidity sensor	-50~100℃	±0.1℃
Relative humidity of air		0~100%	±0.8%RH
Air flow rate	Hot-film anemometer	0~30m/s	±0.015m/s
Power of compressor	Power meter	0~9999W	±0.5%
Pressure of refrigerant	Pressure transmitter	0~6Mpa	±0.5%
Temperature of refrigerant	PT100	0~200℃	±0.1℃

3. PERFORMANCE INDICIES AND ERROR ANALYSIS

The performance of SCDHP system is evaluated by two groups of indices. The first group describes the temperature and humidity ratio of supply air, indicating load removal and supply air state. In this group, the temperature of the outlet air from DCE $t_{a,\,DCE,\,out}$, the temperature of the outlet air form CE $t_{a,\,CE,\,out}$, the humidity ratio of the outlet air from DCE $d_{a,\,DCE,\,out}$, the humidity ratio of the outlet air form CE $d_{a,\,CE,\,out}$ and power consumption $P_{com+fans}$ can be obtained directly. Besides, the average temperature drop of process air ($TD_{a,\,DCE}$, $TD_{a,\,DCE+CE}$) and the average humidity ratio drop of process air ($HD_{a,\,DCE}$, $HD_{a,\,DCE+CE}$) are adopted to describe sensible load removal and latent load removal more clearly (Eq. (1)-(4)). The variation range of outlet air temperature ($\Delta t_{a,\,DCE,\,out}$, $\Delta t_{a,\,CE,\,out}$) and the variation range of outlet air humidity ratio ($\Delta d_{a,\,DCE,\,out}$, $\Delta d_{a,\,CE,\,out}$) are adopted to describe outlet air stability (Eq. (5)-(8)).

$$TD_{a,DCE} = t_{a,DCE,in} - t_{a,DCE,out} \quad \text{Eq. (1)}$$

$$TD_{a,DCE+CE} = t_{a,DCE,in} - t_{a,CE,out} \quad \text{Eq. (2)}$$

$$HD_{a,DCE} = d_{a,DCE,in} - d_{a,DCE,out} \quad \text{Eq. (3)}$$

$$HD_{a,DCE+CE} = d_{a,DCE,in} - d_{a,CE,out} \quad \text{Eq. (4)}$$

$$\Delta t_{a,DCE,out} = t_{a,DCE,out,max} - t_{a,DCE,out,min} \quad \text{Eq. (5)}$$

$$\Delta t_{a,CE,out} = t_{a,CE,out,max} - t_{a,CE,out,min} \quad \text{Eq. (6)}$$

$$\Delta d_{a,DCE,out} = d_{a,DCE,out,max} - d_{a,DCE,out,min} \quad \text{Eq. (7)}$$

$$\Delta d_{a,CE,out} = d_{a,CE,out,max} - d_{a,CE,out,min} \quad \text{Eq. (8)}$$

The second group considers the overall performance of system. The air-side cooling capacity ($Q_{a,\ DCE}$, $Q_{a,\ DCE+CE}$) and COP of system can be calculated by Eq. (9)-(11).

$$Q_{a,DCE} = \dot{m}_a (i_{a,DCE,in} - i_{a,DCE,out}) \quad \text{Eq. (9)}$$

$$Q_{a,DCE+CE} = \dot{m}_a (i_{a,DCE,in} - i_{a,CE,out}) \quad \text{Eq. (10)}$$

$$COP = Q_{a,\ DCE+CE} / P_{com+fans} \quad \text{Eq. (11)}$$

The error analysis of indices is conducted by Eq. (12)-(13).

$$\Delta y = \left[(\frac{\partial f}{\partial x_1})^2 (\Delta x_1)^2 + (\frac{\partial f}{\partial x_2})^2 (\Delta x_2)^2 + \cdots + (\frac{\partial f}{\partial x_n})^2 (\Delta x_n)^2 \right]^{1/2} \quad \text{Eq. (12)}$$

$$\frac{\Delta y}{y} = \left[(\frac{\partial f}{\partial x_1})^2 (\frac{\Delta x_1}{y})^2 + (\frac{\partial f}{\partial x_2})^2 (\frac{\Delta x_2}{y})^2 + \cdots + (\frac{\partial f}{\partial x_n})^2 (\frac{\Delta x_2}{y})^2 \right]^{1/2} \quad \text{Eq. (13)}$$

where f is the function of independent variables; x_1, x_2, etc. stand for independent variables; Δx_1, Δx_2, etc. are the absolute error of corresponding variables; $\Delta y/y$ is the relative error. The relative errors of $TD_{a,\ DCE}$, $TD_{a,\ DCE+CE}$, $HD_{a,\ DCE}$, $HD_{a,\ DCE+CE}$, $\Delta t_{a,\ DCE,\ out}$, $\Delta t_{a,\ CE,\ out}$, $\Delta d_{a,\ DCE,\ out}$, $\Delta d_{a,\ CE,\ out}$, $Q_{a,\ DCE}$, $Q_{a,\ DCE+CE}$ and COP are ±2.6%, ±1.2%, ±7.1%, ±5.9%, ±2.6%, ±1.2%, ±7.1%, ±5.9%, ±3.9%, ±2.8% and ±2.9% respectively.

4. RESULTS AND DISCUSSIONS

In order to demonstrate the feasibility of SCDHP system, dynamic performance in terms of outlet air state, cooling capacity and power consumption are tested and analyzed. The detailed operating conditions are listed in Table 4. The state of indoor air is chosen according to GB 50736 (2012) and the state of outdoor air is chosen according Zhengyan et al. (2014). Condition1 refers to the mild condition in Shanghai and condition2 refers to the humid condition in Shanghai. Process air flow rate is 200 $m^3\ h^{-1}$, and regeneration air flow rate is 440 $m^3\ h^{-1}$ (220 $m^3\ h^{-1}$ comes from outdoor and 200 $m^3\ h^{-1}$ comes from indoor). Firstly, compressor and throttle valve are adjusted to ensure that evaporation temperature is close to 15ºC and condensation temperature is close to 45ºC, then superheated degree and subcooled degree are fine-tuned to obtain optimal performance. Switching time is the duration of each mode.

Table 4 Operating conditions

Parameters \ Air conditions		Condition 1	Condition 2
Outdoor	Temperature (ºC)	35	30
	Relative humidity (%)	40	60
Indoor	Temperature (ºC)	25	
	Relative humidity (%)	60	
Evaporation temperature (ºC)		14.6	12.9
Condensation temperature (ºC)		47.2	42.2
Superheated degree (ºC)		11.6	9.4
Subcooled degree (ºC)		4.6	3.4
Switching time (s)		185	

4.1 Condition 1: the mild condition in Shanghai

System performance under condition 1 is shown in Fig. 3, and it can be seen that the qualitative trends which are related to DCE and CE are similar. For outlet air humidity ratio, Fig. 3(a) shows that it firstly increases, then declines to minimum value, at last ascends back tardily. The reasons for the first increase can be attribute to two reasons: (1) the high temperature of DCE which has negative influence on adsorption) (2) the mixture with remained regeneration air in air duct. The second increase of outlet air humidity ratio can be explained by the fact that as dehumidification process goes on, the humidity difference between air and desiccant gets smaller, therefore, the latent load removal attenuates. For outlet air temperature, Fig. 3(b) shows that it firstly increases to maximum value then gradually decreases. This phenomenon can be explained by three factors: two factors are same to those result in the first increase of outlet air humidity ratio and another is adsorption heat. The variable trends of cooling capacity and electricity consumption are plotted in Fig. 3(c). Generally, cooling capacity firstly decreases to minimum valve, next gradually increases, at last declines slightly. In the preliminary period, both the outlet air humidity ratio and temperature increase continually, therefore, the cooling capacity decreases. When it comes to the second period, both the outlet air humidity ratio and temperature begin to decrease, as a result, cooling capacity increases. As process goes on, the decrease of latent load removal is more significant than the increase of sensible load removal, therefore, there is a small drop of cooling capacity in the third period. The power consumption of system rapidly descends to minimum value then ascends gradually due to the reconstruction of operating condition.

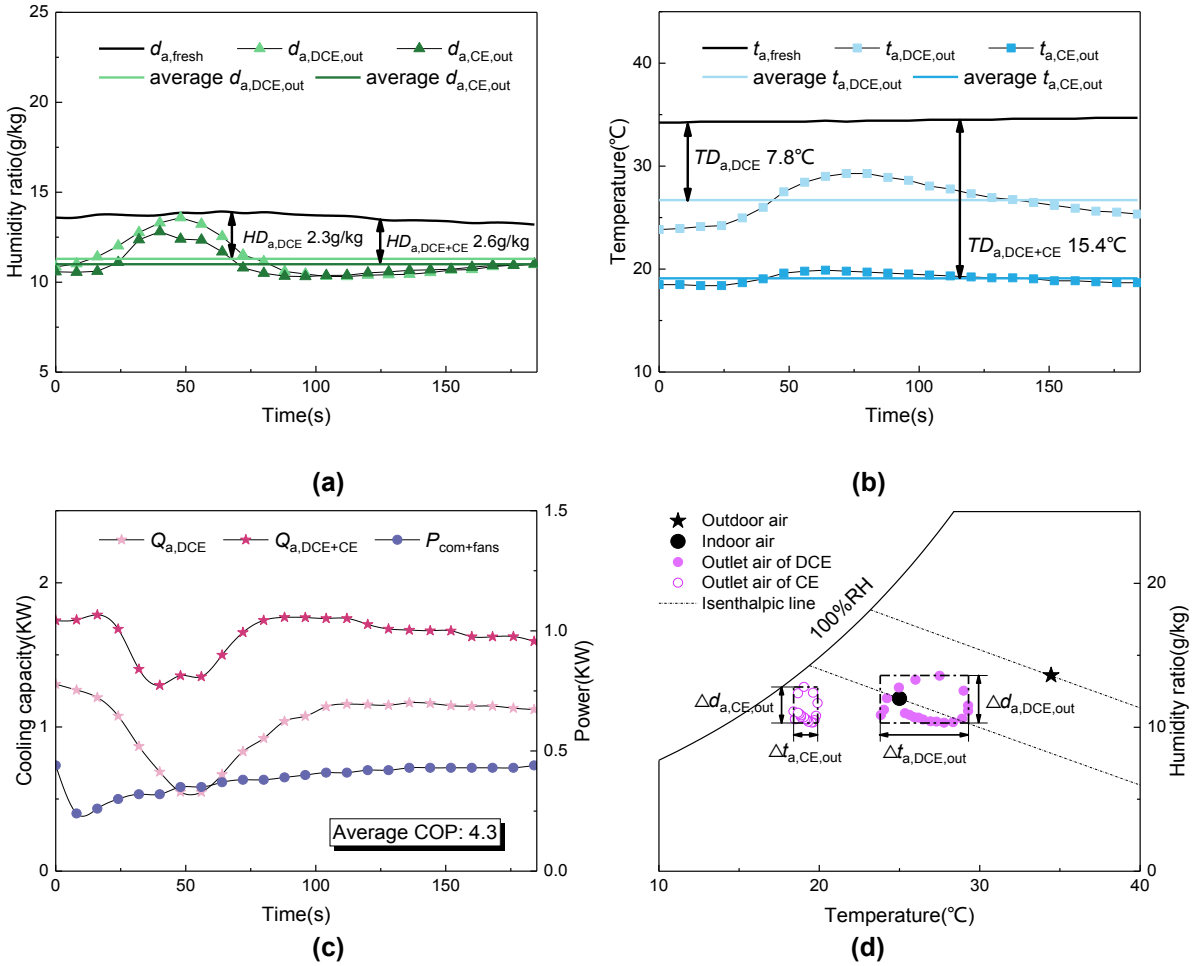

Fig. 3 (a) Outlet air humidity ratio (b) outlet air temperature (c) cooling capacity and COP (d) psychrometric chart of transient outlet air state under condition 1

Besides, it can be found that the CE contributes a lot to system performance in terms of the sensible load removal and outlet air state as Fig. 3(a), Fig. 3(b) and Fig. 3(d) illustrate. Due to the excellent sensible load removal of CE, average $t_{a,\,CE,\,out}$ is about 19.1°C while average $t_{a,\,DCE,\,out}$ is as high as 26.7°C, in other words, when process air further flows through CE, the average temperature drop of process air is about doubled. Fig. 3(d) shows that $\Delta t_{a,\,CE,\,out}$ is 1.5°C which is only 27% of $\Delta t_{a,\,DCE,\,out}$. This can be explained by the fact that when the outlet air temperature of DCE is high, the temperature difference between process air and CE is large, and the heat transfer between process

air and CE can be enhanced, which will reduce maximum outlet air temperature. Since CE is not set for dehumidification, average $d_{a,\,DCE,\,out}$ and average $d_{a,\,CE,\,out}$ are almost same ($d_{a,\,DCE,\,out}$: 11.3g/kg; $d_{a,\,CE,\,out}$: 11g/kg). It is worth noting that $\Delta d_{a,\,CE,\,out}$ is 2.5g/kg which is about 75% of $\Delta d_{a,\,DCE,\,out}$. This phenomenon mainly results from that the outlet air of DCE is humid in the first period and dew point temperature is even higher than the temperature of CE, therefore, condensation dehumidification will reduce maximum outlet air humidity ratio. In addition, when the outlet air humidity reaches minimum value (about 80s), $t_{a,\,DCE,\,out}$ is as high as 29.3ºC which means the temperature is not in keeping with the low humidity, but $t_{a,\,CE,\,out}$ is only 19.7ºC which means the coordination between temperature and humidity is improved significantly by CE. In sum, the cooling capacity produced by two heat exchangers (DCE and CE) is 59% larger than that of only one DCE and the system COP is 4.3.

4.2 Condition 2: the humid condition in Shanghai

System performance under condition 2 is tested and illustrated in Fig. 4. It shows that the trend of each index is similar to that in Fig. 3. Average outlet air temperature is 24.3ºC for $t_{a,\,DCE,\,out}$ and 17ºC for $t_{a,\,CE,\,out}$ while average outlet air humidity ratio is 12g/kg for $d_{a,\,DCE,\,out}$ and 11.6g/kg for $d_{a,\,CE,\,out}$. In other words, $TD_{a,DCE+CE}$ is 2.3 times as big as $TD_{a,DCE}$ and $HD_{a,DCE+CE}$ is almost same to $HD_{a,DCE}$. Also, it can be seen in Fig. 4(d) that $\Delta t_{a,\,CE,\,out}$ is obviously smaller than $\Delta t_{a,\,DCE,\,out}$, and the stability of outlet air humidity ratio is also improved. Fig. 4(c) illustrates that the integration of DCE and CE can provide a 54% higher cooling capacity than only one DCE and the system COP is 4.1.

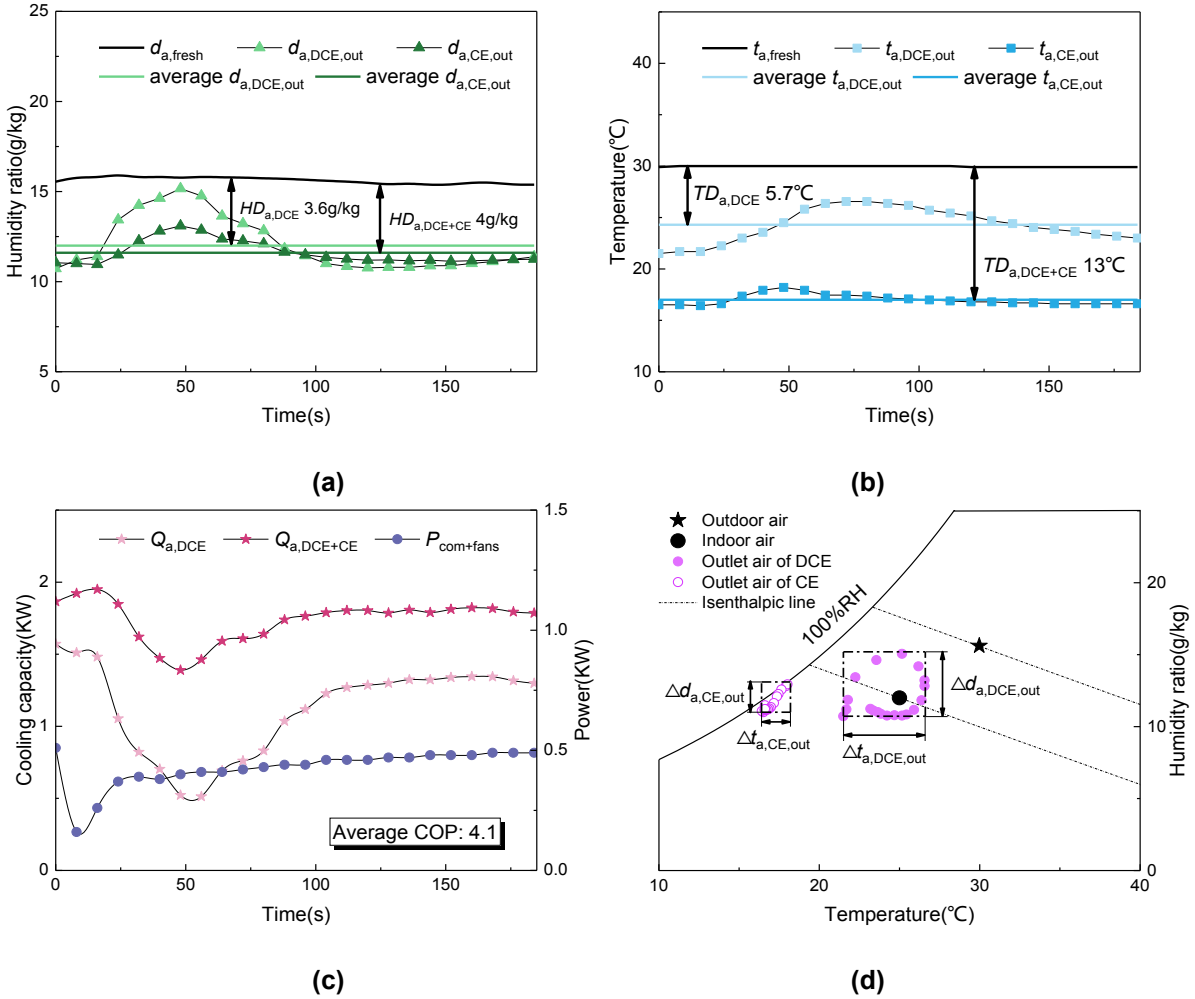

Fig. 4 (a) Outlet air humidity ratio (b) outlet air temperature (c) cooling capacity and COP (d) psychrometric chart of transient outlet air state under condition 2

5. CONCLUSION

Based on the presented experimental results, it can be found that on the one hand, SCDHP system inherits the merit of high COP of IHP system (higher than 4); on the other hand, when an auxiliary

CE is installed in series with DCE, the average temperature drop of process air is about doubled, then corresponding cooling capacity increases by more than 50%, and the variation range of outlet air temperature reduces by about 70%, moreover, the coordination between outlet air temperature and humidity can be improved significantly.

ACKNOWLEDGMENT

The authors acknowledge the financial support from the National Natural Science Foundation of China (Grant No. 51576121) also the Foundation for Innovative Research Groups of the National Natural Science Foundation of China (Grant No. 51521004).

NOMENCLATURE

COP	Coefficient of performance
d	Humidity ratio of the air (g kg^{-1}r)
HD	Humidity ratio drop (g/kg)
i	Enthalpy (J kg^{-1})
m	Mass flow rate of the air (kg s^{-1})
P	Power consumption (W)
Q	Cooling capacity (W)
t	Temperature (℃)
TD	Temperature drop (℃)

Subscripts

a	Air side
ads	Adsorption
CE	Conventional evaporator
com	Compressor
DCE	Desiccant coated evaporator
fans	Fans
in	Inlet
out	Outlet
reg	Regeneration

Abbreviation

ARI	Air-conditioning and Refrigeration
CE	Conventional evaporator
DCC	Desiccant coated condenser
DCE	Desiccant coated evaporator
DCHE	Desiccant coated heat exchanger
IHP	Integrated solid desiccant heat pump
SCDHP	Semi-coupled desiccant heat pump
VC	Vapor compression
VRV	Variable refrigerant volume

REFERENCE

GB 50736-2012, Design code for heating ventilation and air conditioning of civil buildings.

Lingji, H., Yu, J., Tianshu, G., Ruzhu, W., 2018. Experimental investigation on a novel heat pump system based on desiccant coated heat exchangers. Energy 142: 96-107.

Napoleon, E., Kunio, M., Yohei, M., Takayuki, A., Noriomi, O., 2011. Experimental evaluation of the new solid desiccant heat pump system in Asia-Pacific climatic conditions. Appl. Therm. Eng 31(2-3), 243-257.

Tolga N, A., Yunho, H., Radermacher, R., 2010. Integration of variable refrigerant flow and heat pump desiccant systems for the cooling season. Appl. Therm. Eng 30(8-9), 917-927.

Yaodong, T., Ruzhu, W., Tianshu, G., Xu, Z., 2017. Comfortable, high-efficiency heat pump with desiccant-coated, water-sorbing heat exchangers. Scientific Reports 7, 40437.

Yu, J., Tianshu, G., Ruzhu, W., Yan, H., 2014. Experimental investigation on a novel temperature and humidity independent control air conditioning system, Part I: Cooling condition. Appl. Therm. Eng 73(1), 782-791.

Zhengyan, T., Yong, L., Dong L., Yanjun, D., Ruzhu, W., 2014. Experimental investigation on novel rotary desiccant cooling system. Acta Energiae Solaris Sinica 35(4), 656-663

Manuscript ID: 936

DOI: 10.18462/iir.icr.2019.0936

Effects of cooling surface micro-machining shapes on frosting curves

Haruka AGUI [(a)], Hidetoshi OHKUBO [(b)], Sho MATSUSHITA[(c)]

[(a)] Mechanical Engineering Major, Graduate School of Engineering, Tamagawa Univ.
Machida City, 194-8610, Japan, aguih4is@engs.tamagawa.ac.jp
[(b)] Mechanical Engineering Major, Graduate School of Engineering, Tamagawa Univ.
Machida City, 194-8610, Japan, ohkubo@eng.tamagawa.ac.jp
[(c)] R&D Center, Mayekawa Mfg.Co., Ltd.
Moriya City, 302-0118, Japan, sho-matsushita@mayekawa.co.jp

ABSTRACT

Naturally formed frost on heat exchangers of low temperature devices is a cause for both increased resistance to air-passage and heat transfer. Therefore, defrosting operations will be needed when frost has collected excessively to avoid the deterioration of the heat exchanger efficiency. Focusing on the size of the droplets, the authors' group artificially changed the characteristics of the cooling surface by machining grid shapes of 100 microns order on the cooling surface. By doing so, they have succeeded in producing zones with no frost-crystal growth on the surface. In this study, the effects of the groove patterns on the frosting phenomenon under natural convection condition were investigated by varying the cooling surface temperature from -75 °C to -10 °C.
Keywords: Mass Transfer, Frost Crystal, Ice

1. INTRODUCTION

When a frost layer, which is a mixture of ice and moist air, forms on the heat exchanger of a low-temperature device, it acts as a thermal as well as a flow resistance causing the heat exchanger performance to deteriorate. To address this issue, Ohkubo et al (Ikemoto, S., 2011). have proposed a mechanical frost removal method. The force required to scrape the frost layer in this method could be reduced by using a cooling surface with micro-machined lattice structure when frosting occurs in the region I (of temperatures t_w between -40.1 °C and 0 °C) of the frosting curve. Further, the micro-machined surface showed a 75% reduction in the cooling surface area where frost crystals are formed and grow compared a flat cooling surface.
This study focuses on the reduction of frost layer thickness and frost deposition in regions I and II (-75 °C< t_w < -40.1 °C) when the cooling surface is micro-machined, and the results obtained are presented below.

2. EXPERIMENTAL APPARATUS AND METHODS

Figure 1 shows a schematic diagram of the experimental apparatus. Experiments of this study were conducted within an experimental chamber. The humidity and temperature of the chamber were controlled and maintained constant by using combination of a cooler, heater and dehumidifier. The temperature and humidity of the chamber were measured by using an Asman Ventilated psychrometer. A rectangular oxygen-free copper plate of 50 mm × 50 mm in size and 1 mm in thickness was used as the cooling surface, and it was oriented vertically. A grid pattern was micro-machined by making grooves on the cooling surface and the pattern has the following dimensions: the sides of a square pattern on the surface and width of grooves are each 0.25mm, and the grooves and squares each have a pitch of 0.5 mm. The cooling surface was bonded to an oxygen-free cooling block with an epoxy adhesive. To measure the cooling surface temperature, CA thermocouples (of 100 μm wire dia.) were fixed to the rear side of the copper plate using a conductive adhesive and secured to the plate using epoxy adhesive. The thermocouples are located at distances y = 12.5, 25.0 and 37.5 mm from the leading edge of the cooling surface, and

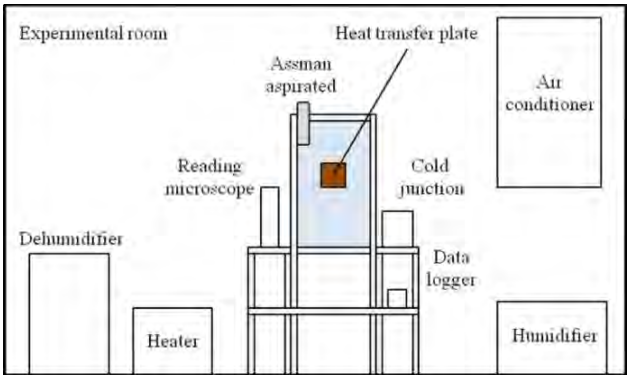

Figure 1: Experimental apparatus I

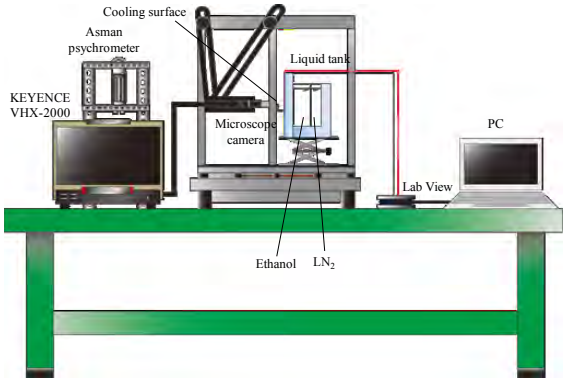

Figure 2: Experimental apparatus II

these measurements were used to control the cooling surface temperature. In this work, the thickness and quantity of frost formed and continued to grow on the cooling surface were measured. The frost layer thickness was measured every 10 min from the start of the experiment at a distance y = 25 mm using a measurement microscope. The experiments were repeated more than three times for each condition and the average of the measurements was considered as the experimental value of frost layer thickness. The frost deposition was measured by scraping and collection of frost. In this collection method, frost formed on the cooling surface was scraped after a desired time interval using a plastic scoop, and then collected on a filter paper and enclosed quickly in a Tupperware container before the frost would sublimate. Further, paper Kim wipes (of Nippon Paper Crecia Co. Ltd.) and threads were used to scrape off frost crystals in grooves and those strongly stuck onto the cooling surface. These wipes were enclosed in other Tupperware containers and the total weight of the containers was obtained using an electronic balance. Next, by deducting the pre-measured weights of Tupperware, paper filter, paper wipes and threads from the previous total weight, the amount of frost deposition was established. The measurements were conducted 3 times under the same conditions, and the average of these measurements was taken as the experimental value of the frost deposition.

In order to grasp the processes of frost crystal formation and growth on the cooling surface in the regions I and II of the frosting curve, a digital microscope (KEYENCE Co., VHX 2000) was used for carrying out the observations. The schematic diagram of the experimental set-up used for the observations is shown in Figure 2. Experiments were conducted under the following conditions: air temperature t_a = 25 °C, absolute humidity of air x_a = 0.0099 kg/kg', cooling surface temperature t_w = -75 ~ -15 °C, time interval $\tau \leqq$ 2hr.

3. RESULTS

3.1 Observation Results

Figure 3 shows the observation results on frost crystal formation and growth in regions I and II of the frosting curve.

In region I, super-cooled droplets are first formed, which would then coalesce and grow. After the super-cooling state is passed, multiple number of frost crystals would grow from the protruding crystals on the surface. It could be observed that as the frost crystal grew on the vertical cooling surface, parts of growing crystals would break away under the influence of gravity. As a result, the frost crystal thickness decreases.

On the other hand, in the case of region II, it was observed that clusters of droplets condensed within the boundary layer become solidified, getting attached to the cooling surface as snow. However, the frost layer that grows from these seeds will be weakly attached to the surface, and therefore will be fragile. Thus, breakages of the frost layer could be observed.

In the case of the micro-machined surface, it was observed that grooves did not have frost formations in them for the region I of the frosting curve. This can be attributed to the small vortexes that are formed near the grooves, preventing the movement of water vapour towards the grooves.

In the region II of the frosting curve, it was observed that snow crystals are formed even inside the grooves. However, their growth is slower compared to the growth from frost crystals on the protruding parts of the cooling surface. Thus, it was revealed that the porosity of frost layer near the

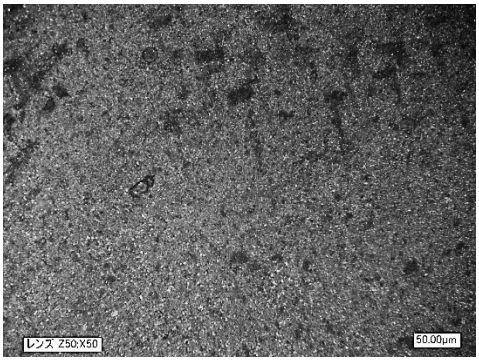

t_w = -15 °C 1mm

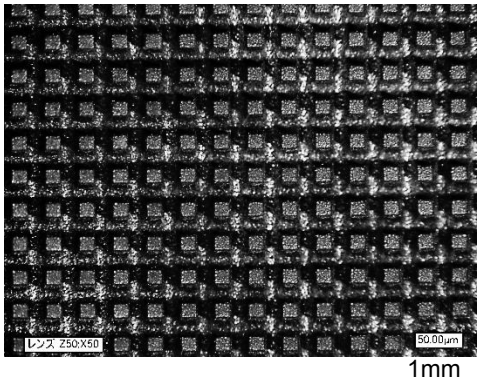

t_w = -15 °C 1mm

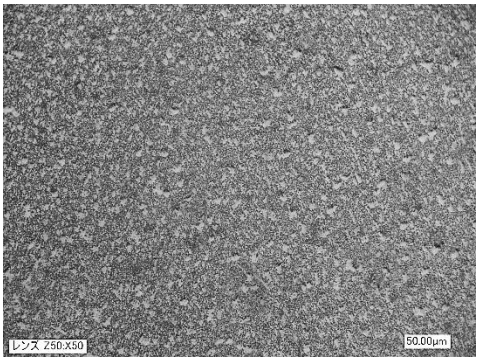

t_w = -60 °C 1mm
Flat (τ = 1 min)

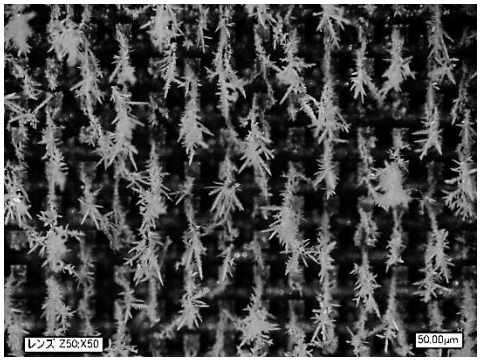

t_w = -60 °C 1mm
Lattice (τ = 1min)

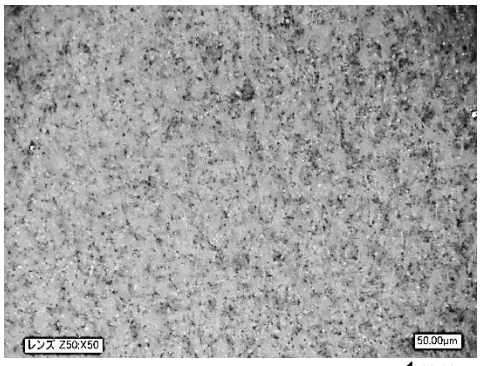

t_w = -15 °C 1mm

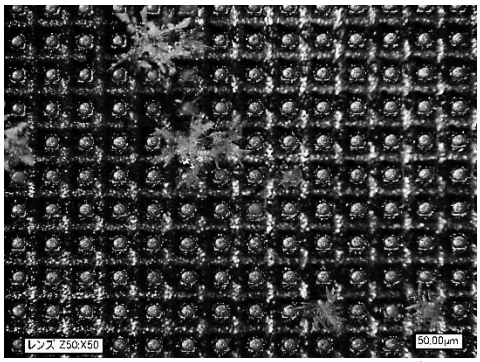

t_w = -15 °C 1mm

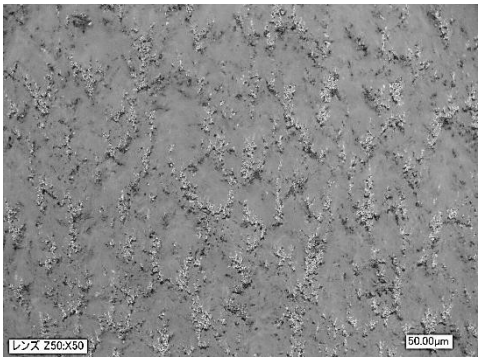

t_w = -60 °C 1mm
Flat (τ = 5 min)

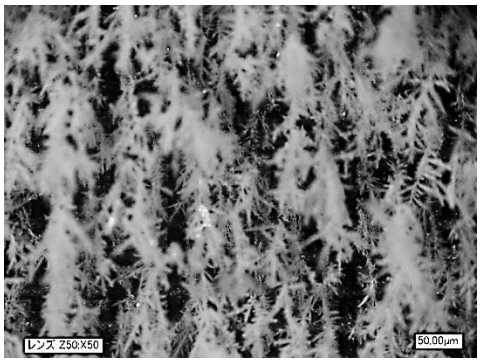

t_w = -60 °C 1mm
Lattice (τ = 5 min)

Figure 3: Observation results of frost crystal (t_a = 25 °C, x_a = 0.0099 kg/kg')

cooling surface is higher compared to the case of a flat cooling surface; a similar trend in porosity could be also observed for the region I.

3.2 Frost layer thickness

This section describes the findings of the effect of the cooling surface characteristics on the frost layer thickness. Two types of cooling surfaces were considered, one being a flat surface and the other being a surface with a micro-machined lattice pattern on it. Figure 4 shows the effect of the cooling surface type on the frost layer thickness by the use of frosting curve. The figure also includes the values of frost layer thickness obtained from predictive equations developed by considering several influencing factors. These predictive equations are shown below (Agui, H., 2018). These equations are for a flat surface, and a multiplication factor of 0.85 is used to evaluate the values for the micro-machined surface.

$\tau \leqq$ 1hr, $t_a \geqq 25\,^{\circ}\mathrm{C}$, $5\mathrm{K} \leqq \Delta T_w \leqq 75\mathrm{K}$

$$l_f = (-0.00028\Delta T_w^{\,2} + 0.087\,\Delta T_w + 1.2)\,\tau^{0.75} \times (2.12\times 10^{5} x_a^{\,3} - 1.06\times 10^{4} x_a^{\,2} + 1.81\times 10^{2} x_a - 3.45\times 10^{-3}) \times 2.07 t_a^{-0.226} \times (y/100)^{-0.25+0.25\tau} \quad \text{Eq. (1)}$$

$\tau >$ 1hr, $t_a \geqq 25\,^{\circ}\mathrm{C}$, $5\mathrm{K} \leqq \Delta T_w \leqq 75\mathrm{K}$

$$l_f = (-0.00028\Delta T_w^{\,2} + 0.087\,\Delta T_w + 1.2)\,\tau^{0.45} \times (2.12\times 10^{5} x_a^{\,3} - 1.06\times 10^{4} x_a^{\,2} + 1.81\times 10^{2} x_a - 3.45\times 10^{-3}) \times 2.07 t_a^{-0.226} \quad \text{Eq. (2)}$$

where, l_f is frost layer thickness [mm], x_a is absolute humidity of air [kg/kg'], y is the distance from the leading edge [mm], ΔT_w is the degree of super-cooling, τ is time [hr] and t_a is air temperature [°C].

Figure 4 shows that the frost layer thickness increases both in regions I and II when the cooling surface temperature T_w decreases (or in other words, when degree of super-cooling ΔT_w increases). Further, the predicted results are in good agreement with the experimental results. The results show that the micro-machined surface is effective in reducing the frost layer thickness by about 15 %

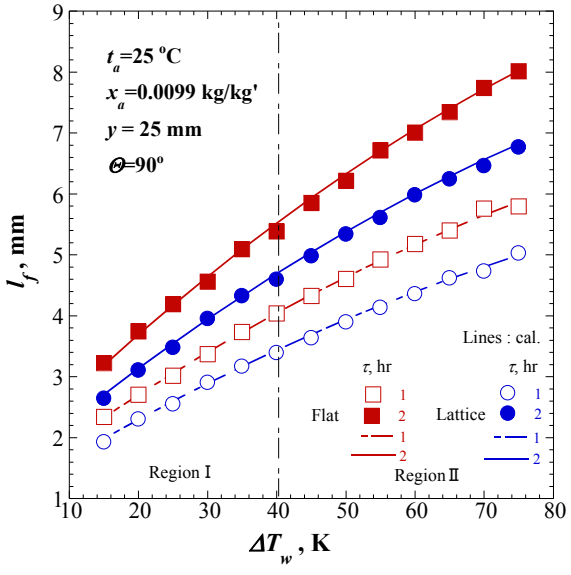

Figure 4: Frosting curve of frost layer thickness

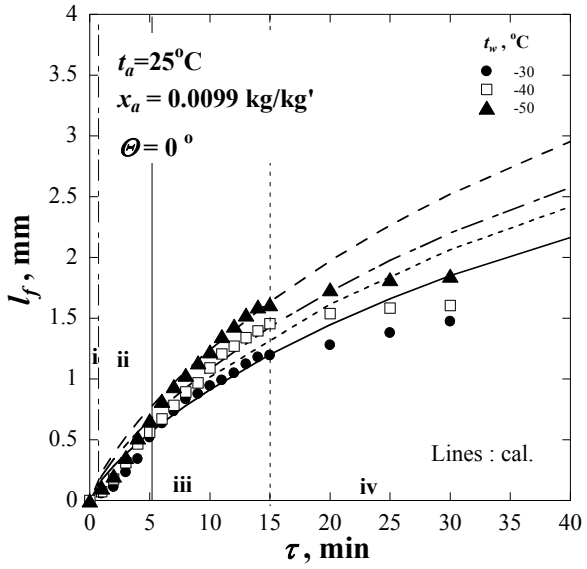

Figure 5: Relationship between frost layer thickness l_f and time τ

compared to that of a flat surface. The reason for the micro-machined cooling surface to reduce the frost layer thickness can be attributed to the fact that the surface area available for frost crystal growth is reduced to about 75 % of the projected cooling surface area.
Figure 5 shows the frost layer thickness as a function of time for the micro-machined cooling surface at different cooling surface temperatures T_w. The frost thickness variation can be categorized into four regions. For example, consider the case of t_w = -30 °C: in region i, super-cooled liquid droplets are formed and grown; in region ii, after the super-cooling of the droplets disappear, frost crystals will grow; in region iii, as the frost layer grows, its surface temperature increases and as a result, the rate of growth of frost film decreases; and, on further growth of the frost layer, in region iv, breakage of the frost layer becomes pronounced, leading to a partly collapsed state of the frost layer. Now, in the case of t_w = -40 °C, the region i is very small, while in the case of t_w = -50 °C, the region i did not exist. Further, it was observed that when the cooling surface temperature is reduced, effects of the collapse of frost crystals and their detachments become pronounced.

3.3 Amount of frost deposition

This section investigates the effect of cooling surface characteristics on the amount of frost deposition. Figure 6 shows the frosting curve of the amount of frost deposition for two types of cooling surfaces, namely, the flat surface and micro-machined surface. The figure also shows the frost depositions obtained from the predictive equations, which were developed considering appropriate influencing factors (Agui, H.,2018). The predictive equations for the average frost depositions in the regions I and II are as follows:

＜Average＞Region I (5K ≦ ΔT_w ≦ 40.1K)

$$m_f = (0.000257\Delta T_w^2+0.238\Delta T_w+170) \times 0.065L^{-0.25} \times x_a \times \tau \qquad \text{Eq. (3)}$$

＜Average＞Region II (40.1 K < ΔT_w ≦75K)

$$m_f = (-0.0139\Delta T_w^2+1.12\Delta T_w+158) \times 0.065L^{-0.25} \times x_a \times \tau \qquad \text{Eq. (4)}$$

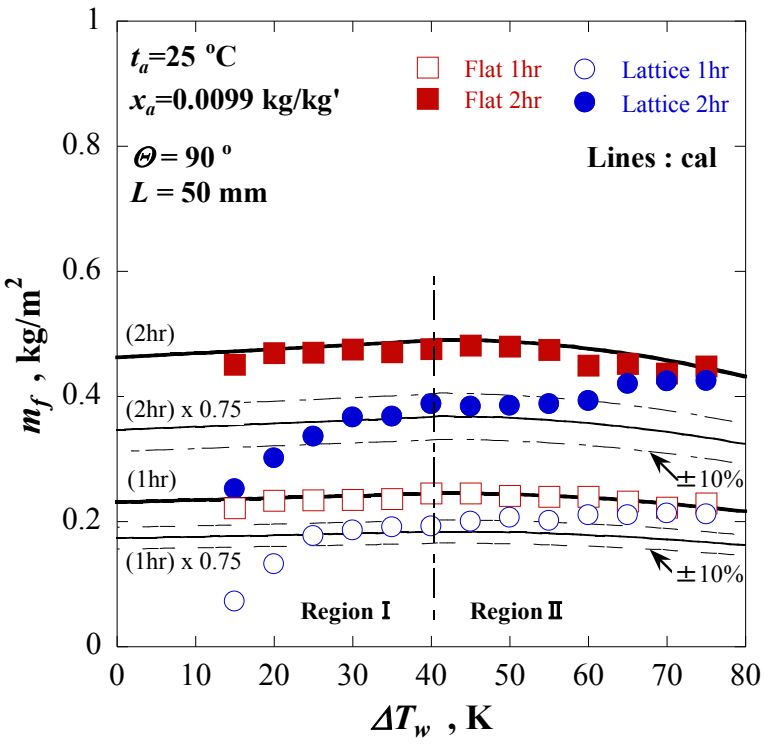

Figure 6: Relationship between mass of frost m_f and ΔTw

where, m_f is frost deposition per unit surface area [kg/m^2], ΔT_w is the degree of super-cooling [K], L is the dimension of cooling surface [m], x_a is absolute humidity of air [kg/kg'], and τ is time [hr].

Figure 6 shows that in the region I, the frost deposition decreases drastically when the degree of super-cooling ΔT_w decreases (or in other words, when the cooling surface temperature t_w increases). On the other hand, in the region II, it is clear that a micro-machined surface would reduce the amount of frost deposition to some extent, but its effect is not as drastic as in region I. The reason for this difference could be attributed to the differences in the frost crystal formation mechanisms in the two regions.

4. CONCLUSIONS

In this study, effect of cooling surface characteristics on the frosting phenomenon in the regions I and II of frosting curve was investigated by micro-machining a grid structure on the cooling surface. The followings are the findings of this study.

(1) When a grid structure is formed on the cooling surface by micro-machining the surface, the frost layer thickness showed a reduction of about 15% compared that of a flat surface.
(2) In the region I, the frost deposition decreases drastically when the degree of super-cooling ΔT_w decreases (or in other words, when the cooling surface temperature t_w increases). On the other hand, in the region II, it is clear that a micro-machined surface would reduce the amount of frost deposition to some extent, but its effect is not as drastic as in region I.
(3) It was observed that when the cooling surface temperature is reduced, effects of the collapse of frost crystals and their detachments become pronounced.

ACKNOWLEDGEMENTS

This work was supported by JSPS Grant-in-Aid for Scientific research (A) 15H02220 and (C) 16K06130.

REFERENCES

Ikemoto, S., Ohkubo, H. and Matsushita, S., (2011) : "Reduction of Frost Formation under Natural Convection", *Proceedings of the 2011 JSRAE Annual Conference*, pp.445-446.

Agui, H., Ohkubo, H. and Matsushita, S., (2018) : "Effect of cooling surface micro-machining shape on frosting phenomenon on vertical plate", *The 29th International Symposium on Transport Phenomena* (ISTP29), No.82 (USB).

Manuscript ID: 944
DOI: 10.18462/iir.icr.2019.0944

Formation and growth of frost crystals on micro-sized objects placed in boundary layer

H. Ohkubo[(a)], S. Yokoyama[(b)], H. Agui[(c)], S. Matsushita[(d)]

[(a)] Mechanical Engineering Major, Graduate School of Engineering, Tamagawa University
6-1-1 Tamagawagakuen, Machida, Tokyo 194-8610, Japan, ohkubo@eng.tamagawa.ac.jp
[(b)] Dept of Engineering , Tamagawa University
6-1-1 Tamagawagakuen, Machida, Tokyo 194-8610, Japan, ykyms5is@engs.tamagawa.ac.jp
[(c)] Mechanical Engineering Major, Graduate School of Engineering, Tamagawa University
6-1-1 Tamagawagakuen, Machida, Tokyo 194-8610, Japan, aguih4is@engs.tamagawa.ac.jp
[(d)] R&D Center, Mayekawa Mfg. Co., Ltd.
2000, Tatsuzawa, Moriya, Ibaraki 302-0118, Japan, sho-matsushita@mayekawa.co.jp

ABSTRACT

When a solid surface is cooled below the solidification temperature of water, vapor condenses on the solid surface forming frost. The frost formation is a transient phenomenon where heat and mass transfer take place simultaneously. In this study, we attempted not to allow frost crystals to grow on the cooling surface. This was attempted by forming super-cooled liquid in the boundary layer so that frost crystal growth would occur away from the cooling surface. To do so, we placed micro objects within the boundary layer and frost crystals were allowed to grow in the boundary layer. Results show that we can control the growth of frost crystals by this method.
Keywords: Frost, Mass transfer, Heat transfer, Ice.

1. INTRODUCTION

Frosting is a phenomenon in which both heat and mass transfers take place simultaneously, and it is also a transient one in that frost crystals are formed and then grow from the cooling surface to form a frost layer on the surface. Thus, it is a complex phenomenon, and a systematic clarification of the effects of influencing factors will be of great significance both industrially and academically. With a systematic understanding of the phenomenon, a reduction in energy consumption in low temperature devices can be achieved through the prevention and control of the problematic frost formation and growth in heat exchangers of such devices. Further, such efforts will also lead to the development of novel technology. Although there are many proposed models on frost layer growth, a model to elucidate the phenomenon systematically has not yet been put forward, which is partly due to the lack of experimental results on the mechanism of frost crystals formation and growth, in addition to the lack of those on the effects of influencing factors. Further, although many studies on the prevention or control of artificial frost formation and growth have been reported, they have not led to practical implementation of the technology. By contrast, in order to understand the frosting phenomenon systematically, the authors have proposed a frosting curve (S. Ikemoto, 2011) and used it to investigate the effects of the factors influencing the frosting phenomenon under natural convective conditions.
The authors have proposed and tested several methods to reduce the mass transfer towards the cooling surface without hindering the surface heat transfer. The methods and their effects are as follows: (1), the cooling surface was micro-machined to control the deposition of frost in the grooved parts of the cooling surface, limiting the frost crystal formation and growth to the protruded parts of the surface (H. Ohkubo, 2014), micro-objects were fixed either on the cooling surface or in the temperature boundary layer to control the formation of frost crystals on the cooling surface by making frost crystals to form and grow on the micro-objects (H. Ohkubo, 2018); and (3), frost crystal near the cooling surface were sublimated to lift the frost layer, which showed the possibility of frost

layer removal by sublimation (M. Kato, 2018).
With the above background in mind, the present study carries out fundamental research on the method (2) focusing on reducing the frost deposition in the region I (-40.1°C ≤ t_w<0°C: where t_w is cooling surface temperature). The results obtained are presented below.

2. EXPERIMEMTAL APPARATUS AND METHOD

It is not possible to completely eliminate the region where frost crystals would grow in the case of the micro-machined cooling surfaces. The region where frost crystals form is in fact in the protruded part of the micro-machined surface. This means that if the protruded part of the surface is fixed within the boundary layer, it will be possible to control the frost crystal formation on the cooling surface. In the present study, a wire-mesh made of SUS304 was placed inside the boundary layer, and the following quantities were experimentally investigated: namely, frost layer thickness, amount of frost deposition, and frost layer surface temperature and the temperature distribution within the boundary layer.
The experimental apparatus can be broadly classified into the followings: a cooler, heater, de-humidifier and humidifier, which will control to maintain constant temperature and humidity within the experimental room and a small experiment chamber; and a series of instruments for measurements. To measure the humidity and temperature within the experimental room and the small chamber within the experimental room, an Asman ventilated psychrometer was used. The heating block used here was one end of a copper block made of oxygen-free copper having surface dimensions of 50mm in length, and 50mm in width, and a copper plate of 1mm thickness was attached to the copper block with epoxy adhesive to use it as the cooling surface. The cooling surface was given a mirror finish and its temperature was measured at distances y=12.5, 25 and 37.5mm from the leading edge of the surface, using CA thermocouples (of 100μm wire dia.), which were attached to the rear side of the plate using a conductive adhesive and fixed in place by using epoxy adhesive. The sides of the cooling surface were insulated using Polyurethane foam and a silicon adhesive. The cooling block was then placed inside a small chamber, which was made using corrugated plastic sheets. The cooling surface was oriented in vertical orientation.
In the case of the experiments where a SUS304 wire-mesh was used, a wire mesh (with 150μm opening, 100-mesh size, and 100mm wire dia.) was fixed inside the thermal boundary layer of the surface. To measure the surface temperature distribution of the wire mesh, CA thermocouples of 100μm dia. were spot-welded onto the mesh at distances y=12.5, 25 and 37.5mm from the leading edge of the surface. The temperature of the cooling surface was controlled by filling the liquid storage behind the cooling surface with ethanol and cooling ethanol by liquid nitrogen. The wire-mesh used here was photographed using a commercial microscope (KEYENCE, VHX 2000), and a 3D image was composed using depth-based information, which is shown in Figure 1.
Frost thickness was measured every 10min using the reading microscope in the middle of the cooling surface at distances y=12.5, 25 and 37.5mm from the leading edge of the surface.
The frost deposition were used for measuring the amount of frost formation, depending on the difference in cooling surface.Frost deposited during a fixed time interval was first scraped by using a plastic spatula, then collected using a filter paper and finally sealed quickly in a Tupperware container before it could sublimate. Further, paper Kim wipes (of Nippon Paper Crecia Co. Ltd), frost in the grooves and flakes stuck on the surface were removed and collected. Then, these wipes/towels were sealed in a different Tupperware container, and the total mass of the containers was measured using an electronic balance. In the case of a wire mesh surface, the wire mesh was removed from the surface of the cooling surface 2 hours after the start of the experiment, and the frost layer and the wire mesh were sealed in Tupperware. The amount of frost deposition was then obtained by deducting from the measurements the total weights of Tupperware, filter paper, and other wipes, which have been pre-measured. Experiments were conducted more than three times under each condition to obtain an average value for the frost deposition.
The surface temperature of frost layer was measured using a commercially available infrared thermometer (Minolta, HT-11) and thermocouples. The emissivity was set to that of frost layer ε_f= 0.98.
The schematic diagram of the experimental apparatus is shown in Figure 2. A K-type thermocouple of 0.1mm wire diameter, which is Teflon coated is used in the (frost layer surface temperature) measurements. The temperature measurement parts of the wires were welded together after removing the Teflon insulation of the wires, and the Teflon insulated parts of wires were stretched on

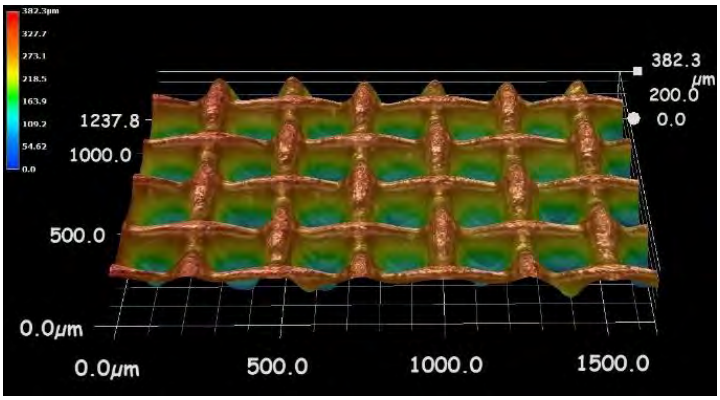

Figure 1: Dimensions of wire mesh

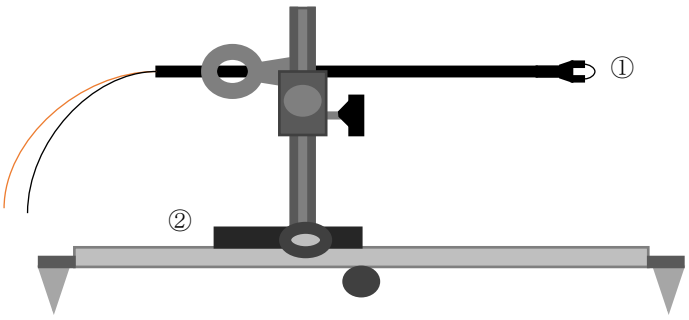

① Thermocouple ② Traverse device

Figure 2: Experimental apparatus

a Bakelite support section to form a bow shape. The Bakelite part was then fixed onto a supporting copper rod, which was attached onto a traverse device (see Figure 2), which made it possible to move the thermocouple horizontally and vertically. This traverse device positioned the thermocouple so that it could measure the temperature within the boundary layer as well as the frost layer surface temperature, which was defined here as the temperature of the humid air at the location where the frost layer thickness was measured.
Experiments were conducted at air temperature t_a of 25°C, air humidity x_a of 0.0099kg / kg' and for cooling surface temperatures t_w between -15°C and -40°C.

3. EXPERIMENTAL RESULTS AND DISCUSSION

3.1 Observations of Crystals

To investigate the process of formation and growth of frost crystals on the cooling surface, first we carried out observations by a microscope. The experiments were carried out at cooling surface temperatures t_w between -15°C and -40°C, which are within the range of temperatures of the region I (from -40.1°C to 0°C) of the frosting curve. The frost crystal formation and growth on the cooling surface were observed by a microscope (KEYENCE, VHX-2000). Figure 3 (a) and (b) show the observations results of frost crystal formation and growth on the flat cooling surface and SUS304 wire-mesh fixed onto the cooling surface, respectively. The results shown here are for t_w=-25°C. It is know that, in the region I of the frosting curve, super-cooled droplets are first formed and grown, and next, once their super-cooled state disappears, the crystals at the crest will cause the formation of many frost crystals (Ohkubo, 2014). From the observation results, it could be confirmed that droplets coalesce and grow from both the flat surface and wire-mesh, after the formation of super-cooled droplets on them. However, the process of crystal growth becomes drastically different when the super-cooled state of droplets is over.

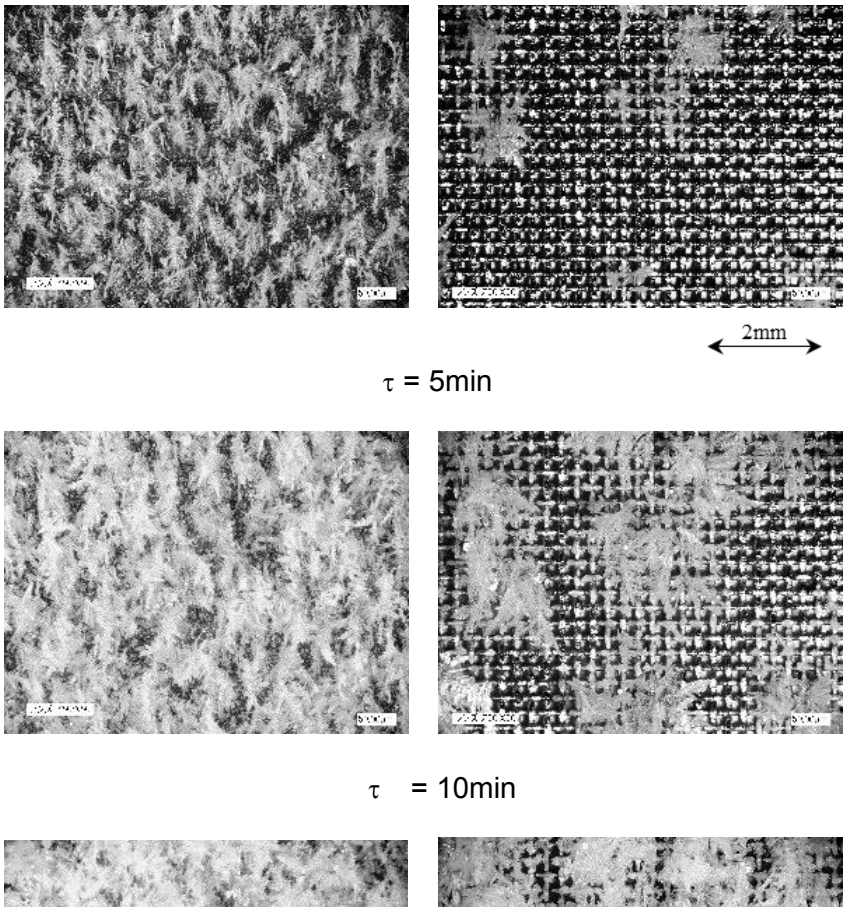

Figure 3: Observation of frost crystal

As a result, the porosity of frost layer close to the surface of wire-mesh became larger compared to that of the frost layer growing on the flat surface. Under the condition of t_w=-25°C, frost crystals show a dendroid structure. Further, in the case of the vertically oriented surface, it could be observed that growing frost crystals would collapse under the influence of gravity. Further, the rate of growth of frost crystals differed considerably from the flat surface to the wire-mesh surface.

3.2 Frost Layer Thickness

Figure 4 shows the thickness of frost layer that grew on the flat surface as a function of time at different distances from the leading edge of the vertical cooling surface. Previously, the authors (H. Agui, 2018) have developed a predictive equation for the frost layer thickness in the case of a vertical flat surface under natural convective condition by investigating the effects of factors that affect the frosting curve of frost layer thickness, and these equations are shown below by Eq. (1) and (2). Figures 4 and 5 show the values obtained from these equations. In the case of the flat

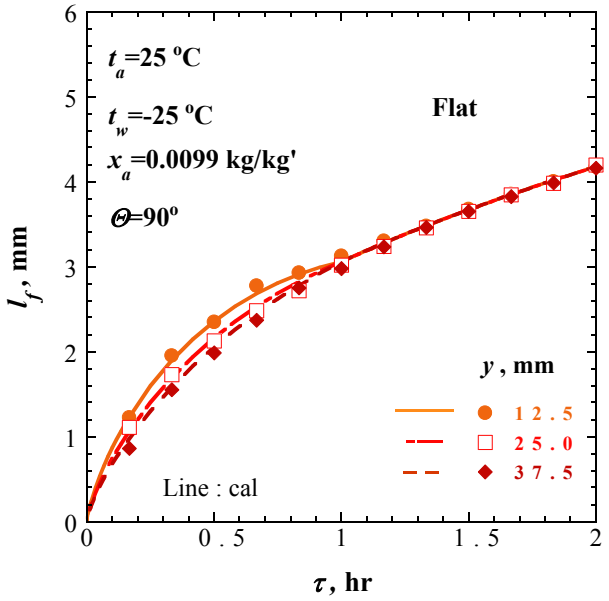

Figure 4: Relationship between l_f and τ I

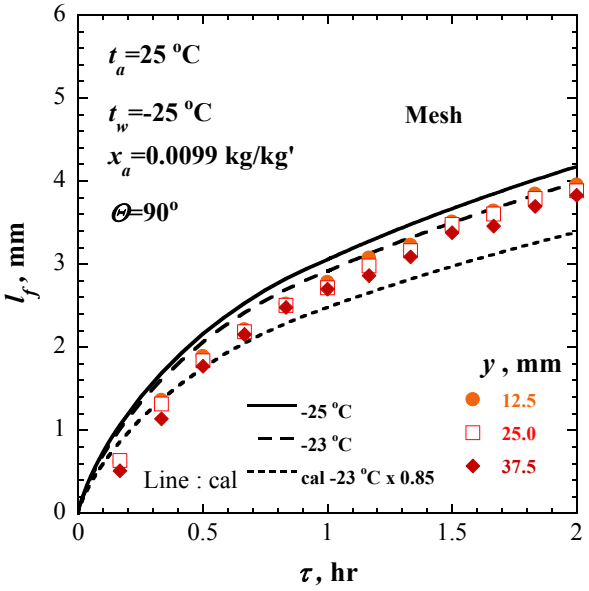

Figure 5: Relationship between l_f and τ II

surface, the agreement between the calculated and experimental results is fairly good, and within the frost deposition time interval less than 1 hr, the frost layer thickness shows a tendency to decrease with the distance from the leading edge. After the frost deposition time has passed 1hr, the frost deposition becomes asymptotic and independent of the distance from the leading edge. Next, Figure 5 shows the time dependence of the thickness of frost layer formed and developed on the metal wire-mesh. In this case, an effect due to the distance from the leading edge of the cooling surface on the frost layer thickness cannot be observed. Further, the compared to the thickness of the frost layer formed on the micro-machined surface, which are shown by the solid lines obtained from Eq. (1,2), the reduction effect is small.

$$\tau \leqq 1\text{hr}, \quad t_a \geqq 25\ ^{\circ}\text{C}, \quad 5\text{K} \leqq \Delta T_w \leqq 75\text{K}$$

$$l_f = (-0.00028\Delta T_w^2 + 0.087\,\Delta T_w + 1.2)\tau^{0.75} \times (2.12 \times 10^5 x_a^3 - 1.06 \times 10^4 x_a^2 + 1.81 \times 10^2 x_a - 3.45 \times 10^{-3}) \times 2.07 t_a^{-0.226} \times (y/100)^{-0.25+0.25\tau} \qquad \text{Eq. (1)}$$

$$\tau > 1\text{hr}, \quad t_a \geqq 25\ ^{\circ}\text{C}, \quad 5\text{K} \leqq \Delta T_w \leqq 75\text{K}$$

$$l_f = (-0.00028\Delta T_w^2 + 0.087\,\Delta T_w + 1.2)\tau^{0.45} \times (2.12 \times 10^5 x_a^3 - 1.06 \times 10^4 x_a^2 + 1.81 \times 10^2 x_a - 3.45 \times 10^{-3}) \times 2.07 t_a^{-0.226} \qquad \text{Eq. (2)}$$

where, l_f is frost layer thickness [mm], x_a is absolute humidity of air [kg/kg'], y is the distance from the leading edge [mm], ΔT_w is the degree of super-cooling [K], τ is time [hr] and t_a is air temperature [°C].

3.3 Frosting Curve

Figure 6 is the frosting curve based on frost layer thickness. The degree of supercooling ΔT_w was first obtained for each of the surfaces, the flat surface and meshed surface, by using the surface temperature of flat surface and that of metal wire mesh. Then, ΔT_w values were used in Eq. (1) and (2) to obtain the frost deposition on a flat surface, which is shown in Figure 6 together with the value of the frost deposition scaled down by a multiplication factor R to account for the frost deposition reduction. As seen from the figure, the calculated results match very well with the experimental

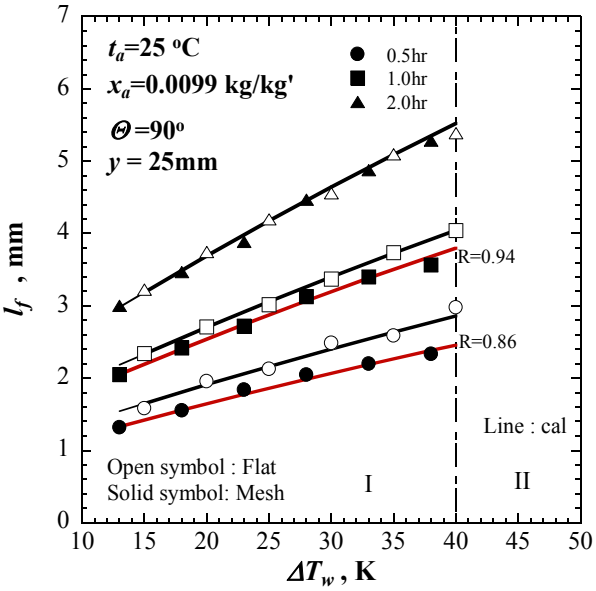

Figure 6: Relationship between l_f and ΔT_w

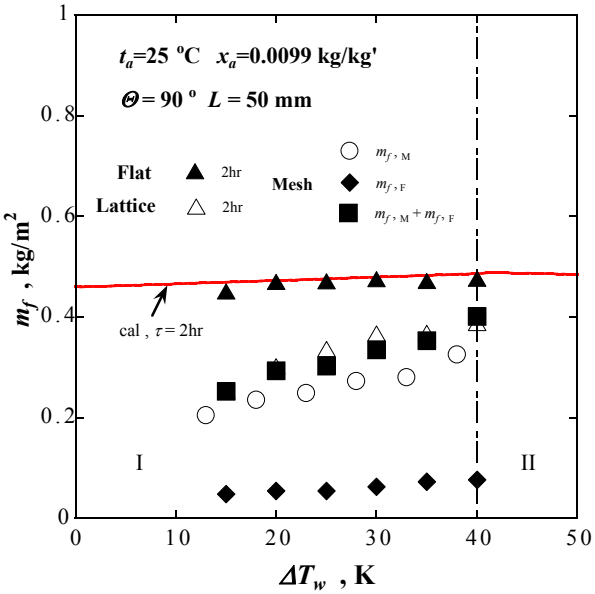

Figure 7: Relationship between mass of frost *mf* and ΔT_w

results. Thus, it can be stated that the frosting curve will be an effective tool to predict frost deposition on a metal wire mesh.

In the cases of different cooling surfaces, Figure 7 shows the measurements of frost depositions on: a flat surface, a surface with micro-machined lattice structure reported in a previous work (H. Agui, 2018), a metal wire mesh fixed onto a cooling surface, and the cooling surface when a metal wire-mesh is fixed onto the cooling surface. The figure also shows the predicted frost depositions obtained from using Eq.(3), which was developed by the authors (H.Ohkubo, 1995) by considering the effects of influencing factors on frost deposition in the case of a vertical surface under natural convective conditions. The figure shows that the agreement between the frost deposition obtained from Eq. (3) and the measurements for a flat surface is excellent. Further, the frost deposition on a micro-machined surface is known to be less than that on a polished surface, in the range of the present experiments. Here, it is clear that the frost deposition on a surface with a metal wire-mesh is even less than that on a micro-machined surface. However, when the frost deposition on the wire-mesh and amount of frost crystal formation on the cooling surface that carries the metal wire-mesh is added together, the frost deposition for the case of wire-meshed surface was found to be more or less the same as that formed on a micro-machined surface.

Region I (5K ≦ΔT_w≦ 40.1K)

$$m_f = (0.000257\Delta T_w^2 + 0.238\Delta T_w + 170) \times 0.065 L^{-0.25} \times x_a \times \tau \qquad \text{Eq. (3)}$$

here, m_f is amount of frost deposition per unit area [kg/m^2], ΔT_w is the degree of surface super-cooling [K], L is dimension of cooling surface[m], x_a is absolute humidity of air [kg/kg'], and τ is time [hr].

3.4 Surface Temperature of Frost Layer

The surface temperature of the frost layer was measured using both a radiation thermometer and thermocouples, and the first measurement type is called here Exp. 1 and the second type is called Exp. 2. In Exp. 2, temperature distribution in the humid air within the boundary layer was measured, and using this temperature distribution, the surface temperature of frost layer was obtained. Figure 8 shows the time variation of temperature distribution within the temperature boundary layer, with x_{ft} being the perpendicular distance measured from the frost-layer surface formed on a mirror-finished flat surface; x_{ft} =0 indicates the frost layer surface. The figure also includes the analytical temperature distribution of Fujii et al. (T. Fuji, 1958) shown by Eq. (4) and thermal boundary layer

thickness given by Eq. (5). The figure shows that the agreement between the calculated and experimental results is fairly good. Finally, Figure 9 shows the temperature distribution within the thermal boundary layer in the case of the metal wire-mesh, with the reference for the distance taken as the surface of the frost layer formed on the wire mesh. Even in this case, the agreement between the calculated and experimental results is fairly good. The results show that even when a metal wire-mesh is fixed, the air flow and temperature distribution under natural convective conditions are similar to those under natural convective conditions for a smooth flat surface.

$$T_\theta = (1 - x_{ft} / \delta_t)^2 \times (T_w - T_a) + T_a \qquad \text{Eq. (4)}$$

$$\delta_t = 3.93 \times \{ (0.952 + Pr)/Pr \}^{0.25} \times (1/Ra_y)^{0.25} \times y \qquad \text{Eq. (5)}$$

where, T_θ is temperature within boundary layer [K]; x_{ft} is the perpendicular distance measured from the frost-layer surface [mm]; δ_t is temperature boundary layer thickness; t_w is cooling surface temperature [K]; y is distance from leading edge of cooling surface [mm]; t_a temperature of air [K]; T_f is temperature of frost surface [K]; v is kinematic viscosity [mm^2/s]; α is thermal diffusivity [mm^2/s]; Pr is Prandlt number; and Ra_y is Raynold's number.

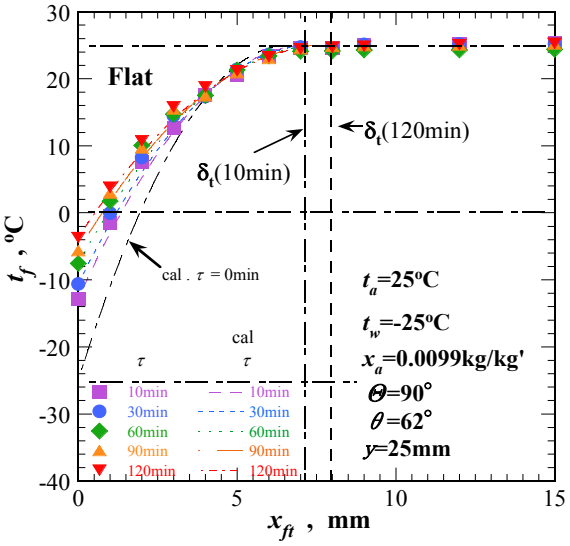

Figure 8: The temperature boundary layer I

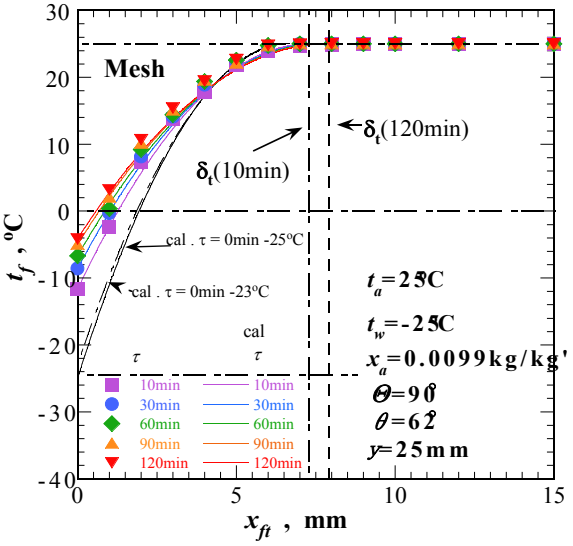

Figure 9: The temperature boundary layer II

4. CONCLUSION

In this study, frost formation and growth on a smooth flat surface and a metal mesh surface were investigated, and the following conclusions are made:

1. Visual observations showed that void fraction of frost film formed and grown on a metal mesh surface is greater than that on a smooth flat surface. At t_w=-25°C, the frost crystals are of dendroid shape. Further, in the case of a vertical cooling surface, the frost crystals grown on the surface would collapse under the influence of gravity.
2. In the case of metal wire-mesh, the frost layer thickness is not greatly affected by the distance from the leading edge of the cooling surface. Further, in comparison with the frost layer formed and grown on a micro-machined cooling surface, the wire-mesh has only a minor effect on reducing the frost layer thickness.
3. The amount of frost formation on the metal mesh surface is smaller than that on a micro-machined surface. On the other hand, when the two components of frost depositions, namely the frost deposition on the wire-mesh and the amount of frost crystals formed on the

cooling surface where the metal wire-mesh is fixed, are added together, the frost deposition in the case of the metal wire mesh was found to be more or less equal to that formed on a micro-machined surface.

4. The air flow under natural convective conditions and temperature distribution in the temperature boundary layer in the case of a metal-mesh covered surface are similar to those under natural convective conditions for a smooth flat surface.

ACKNOWLEDGMENT

The authors would like to acknowledge the funding from the Grants-in-Aid for fundamental research (C)(16K06130) provided by Japan Society for the promotion of science, for this research.

REFERENCES

S. Ikemoto, H. Ohkubo and S. Inoue, “Reduction of frost formation under natural convection”, *Proceedings of the 2011 JSRAE Annual Conference*, 2011, No.445, CD-ROM.

H. Ohkubo and S. Matsushita, “Reduction of frost crystal formation using micro-machined surfaces”, *Transactions of the Japan Society of Refrigerating and Air Conditioning Engineers*, 2014, Vol.31, No.1, pp.19-26.

H. Ohkubo, T. Suzuki and S. Nakajima, “Reduction of frost formation using phase change at boundary layer”, *Proceedings of the 2018 JSRAE Annual Conference*, 2018, No.835, CD-ROM.

M. Kato, S. Matsushita, K. Nishida, H. Ohkubo: “Separation Phenomenon between a Frost Layer and a Cooling Surface Using Sublimation under Low Temperature Forced Convection”, *Transactions of the Japan Society of Refrigeration*, 2017, Vol.34, No.4, p69.

H. Ohkubo, S. Matsushita, S. Saitou: “Effect of Cooling Surface’s Orientation on Thickness of Frost Layer”, *Transactions of the Japan Society of Refrigeration*, 2014, Vol.31, No.2, pp.199-206.

H. Agui, A. Koyama, N. Sugiura and H. Ohkubo, “Influence of cooling surface on frosting phenomena under natural convection”, *Proceedings of the 52nd JSRAE Annual Conference* , 2018, No.39 , CD-ROM.

H. Agui, H. Ohkubo and S. Matsushita, “Effect of cooling surface micro-machining shape on frosting phenomenon on vertical plate” *International Symposium on Transport Phenomena* , 2018, No.82 , USB.

H. Ohkubo, T. Tajima: “Effect of Surface Temperature on Frosting Phenomena” *Transactions of the Japanese Association of Refrigeration* , 1995, 12-3, 285.

T. Fuji , Transactions of the JSME, 1958, 24, 973.

Manuscript ID: 1056
DOI: 10.18462/iir.icr.2019.1056

Experimental study on oil charge impact on a scroll compressor energy performance

Ghady ABOU RACHED[1,2], Joelle RIZK[2], Assaad ZOUGHAIB[1], Bruno DEBOUX[2]

[1]MINES ParisTech, PSL Research University,
Paris, France, ghady.abou_rached@mines-paristech.fr
[2] DYNAES, Paris, France

ABSTRACT

Refrigeration and air conditioning systems consume about 17% of the global electricity generation. In addition, global efforts are put toward phasing out high GWP refrigerants with sometime contradictory results on the energy consumption leading to a systemic analysis of the environmental impact. Efforts to put in place to reduce this consumption must be first directed towards improving the compressor's performance.
Scroll and rotary compressors are widely used in small refrigeration systems and in air/air air conditioners. They have reached a high isentropic and volumetric performance with a continuous improvement. The oil charge in the crankshaft is specified by the manufacturer in a conservative way considering large circuits and the risk of bad oil return.
In this paper an experimental analysis on the oil charge impact on a small capacity water chiller coefficient of performance is performed.
The analysis of the experimental results shows an important increase in electricity consumption when the oil charge increases.

Keywords: Energy Efficiency, Experimentation, Lubrication, Scroll Compressor

1. INTRODUCTION

As time goes on, the world is becoming more conscious of its electric consumption. Air conditioning and refrigeration systems account for 17% of global electricity generation. In order to reduce the consumption, it is essential to improve the compressor's (which is the main consuming component of an air conditioning system and where the highest losses are observed) performance by studying its different components.
Oil is an important component of a compressor and plays a crucial role in its functioning. Its primary function is to lubricate the different rotating parts in order to reduce wear. It also plays a part in limiting noise, evacuating chemical impurities and cooling of rotating components (Youbi-Idrissi & Bonjour, 2008). Therefore, different parameters must be accounted for to choose the best oil possible, such as oil chemical stability, viscosity, as well as oil level and type.
By failing to play its primary role (due to lack of oil quantity or having a low viscosity oil), the compressor could break.
(Shin, Park, & Chang, 1998) studied the oil supply system in scroll compressors. They concluded that the higher oil level is, the higher the ratio between oil flow rate and refrigerant flow rate. Similarly,(Drost & Quesada, 1992) found that in varying the oil level from 0.5 to 4 inches, the oil flow rate to refrigerant flow rate ratio varies from 0.2 to 1.2. Their findings are important, because the more oil passes through the piping, the higher probability is it will stick to the evaporator, reducing the overall efficiency of the system (Youbi-Idrissi & Bonjour, 2008). In fact, the global exchange coefficient is reduced, meaning less heat is evacuated from the evaporator.

(Afshari, Comakli, Lesani, & Karagoz, 2017)tested oil with different viscosities, to correlate its viscosity to the compressor power consumption. They concluded that the oil with the lowest viscosity provides the highest coefficient of performance, consequently, lowest electrical consumption.
(Sarntichartsak, Monyakul, Thepa, & Nathakaranakule, 2006) studied the effects of oil circulation in air conditioning systems. They tested 2 different oil levels (0.8 and 1l) and found that the circulating oil flow rates decreases with lower oil charge. The 0.8l oil level showed better performance than the 1l oil level.
(Nam, Lee, Lee, Kwon, & Lee, 2015) studied the optimization of oil charge in scroll compressors inside eco-friendly cars. They varied the amount of oil inside the compressor and tested its performance. They found that for low oil level, leaks occur inside the compressor and the volumetric efficiency decreases. Oppositely, for a high oil level, the refrigerant mass flow rate decreases (circulated oil increases) thus reducing the efficiency of the compressor. (Nam et al., 2015) varied their oil charge from 40 to 120g by 20g steps. They found for low oil levels a decrease in the backpressure, but for 80g and above it remained constant. They deduced an optimal level of 80g of oil inside the compressor.

The main difference between our study and (Nam et al., 2015) is the architecture of the compressor. In this study, we are using a vertical semi hermetic compressor.

Our study aims to examine the effect of oil charge impact on a small air cooled water chiller scroll compressor. The motor driving the scroll is submerged with the lubricating oil and the low pressure vapour. Oil is sucked to the scroll rotating part via a lubricating tube. The oil used is the Polyolester (POE) oil. The aim is to find whether a compromise between a safety margin on the oil reserve and compressor performance exists.

2. EXPERIMENTAL SETUP, DESCRIPTION AND ANALYSIS

In this section, we will discuss the experimental setup and protocol, as well as the instrumentation. Results will be then presented and discussed.

2.1. Experimental study

A small capacity R4010A Copeland scroll compressor used in an air cooled water chiller with a classic thermodynamic cycle (view figure 1). The cycle is made of two loops: The water loop and the chiller loop. In this study, the chiller was retrofitted to R-32.
Water in the water loop is driven by a pump; it exchanges heat in the evaporator with the refrigerant, then it discharges in a water storage tank where the return temperature is controlled. The heat extracted from the water permits us to determine the cooling capacity of the chiller. The outlet water is maintained at 7°C. The heat added in the water tank is controlled in a way that the chiller operates at full load avoiding the start and stop cycles. Temperatures and flow are measured by PT100 sensors and flow meter. Data is collected and saved.
The chiller loop is composed of the compressor, evaporator, condenser and the expansion valve. The components are put in a climatic room that controls the ambient temperature. It is maintained at 35°C.
A set of PT100 temperature sensors and thermocouples are placed in different points of the circuit to monitor the different parameters' evolution: compressor, evaporator and condenser's inlet and outlet. Pressure sensors were put at the low and high pressure (inlet and outlet of the compressor). Temperature and pressure data is acquired through Agilent software at a time step of 1sec. Power consumption is directly measured at the compressor's terminals using PEL wattmeter and saved using the corresponding software.
The compressor is filled with a certain oil mass corresponding to a certain level inside the crankshaft. The compressor runs till the chiller reaches a steady regime. This first step aims to set a reference point for each oil level. Once the steady state is attained, data is collected for a minimum of 10 working minutes. Then the chiller's performance is evaluated. For each temperature/pressure/flow data, a mean value is taken over the whole running time. Once the point is set, and all data collected and evaluated, a new operating regime is to be determined. The oil level in the compressor is changed by drainage. The mass drained helps to determine the remaining mass/level existing inside the compressor. Once the oil mass balance is done, the compressor is restarted and the procedure is iterated.

Different oil mass charge is tested from 265g to 2077g in order to determine the relation between oil level inside the compressor and its performance. The oil used is the lubrication oil present inside the compressor; the POE Emkarate oil.

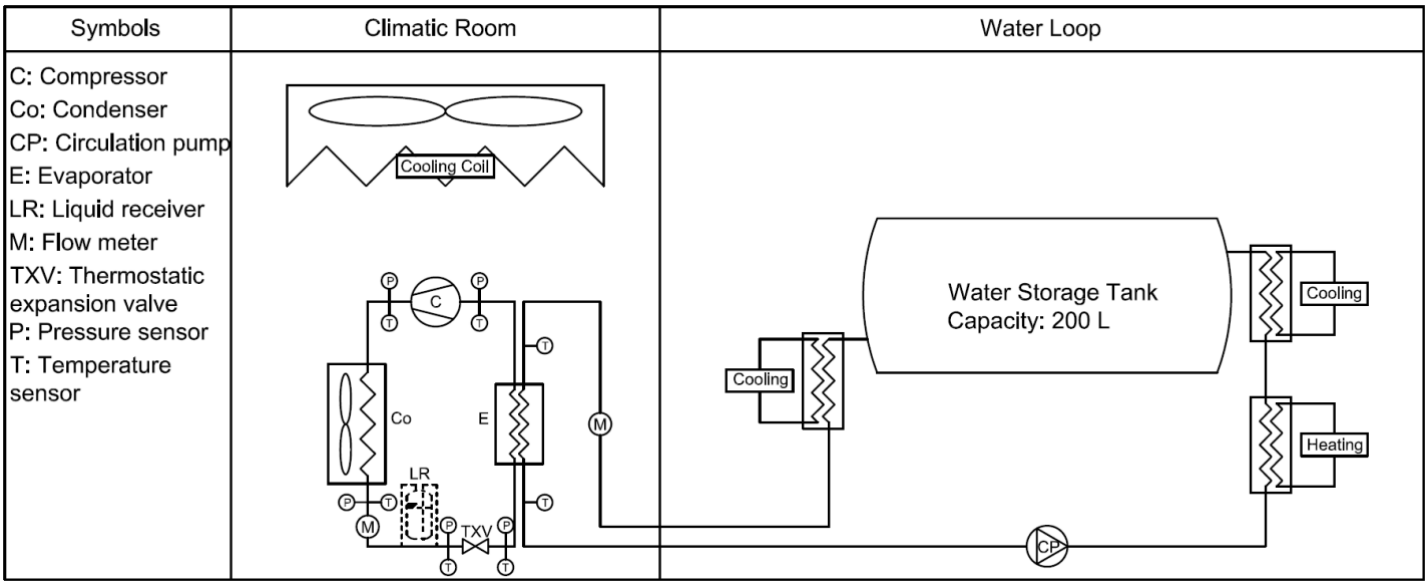

Figure 1: Experimental setup

2.2. Mathematical equations

In order to evaluate the performance of the chiller, the following equations are used. Equations 1 & 2 determine the cooling capacity of the compressor, while equation 3 computes the COP.

$$Q_{evap} = \dot{m}_{water} C_p (T_{water,in} - T_{water,out}) \quad \text{Eq. (1)}$$

$$Q_{evap} = \dot{m}_f (h_{f,in} - h_{f,out}) \quad \text{Eq. (2)}$$

$$COP = {}^{Q_{evap}}/_{W} \quad \text{Eq. (3)}$$

The refrigerant mass flow rate is estimated by equating eq. (1) and (2). The enthalpies are estimated using thermodynamic tables for R32 for the corresponding pressure and temperature.

2.3. Results

A series of twelve experiments were conducted. The compressor runs till equilibrium is reached: stabilization of temperatures and pressures. The data collected are summarized in table 1. Figures 2 to 6 show the variation of compressor input power, cooling capacity, HP and LP, compressor discharge temperature and COP as a function of oil mass respectively.

Table 1. Summary data of all tests

Test	m (g)	Q_{evap} (W)	P (W)	COP	$T_{comp,outlet}$(°C)	LP (bars)	HP (bars)
1	2077	9260.5	3811	2.430	117.04	8.92	33.3
2	1882	9311.1	3780	2.463	118.32	9.02	33.4
3	1681	9325.4	3720	2.507	118.38	9.02	33.5
4	1480	9312.5	3718	2.505	118.32	9.03	33.5
5	1273	9324.2	3722	2.505	118.03	9.03	33.5
6	1071	9318	3715	2.508	117.93	9.02	33.4
7	869	9327	3712	2.513	117.85	9.02	33.4
8	667	9271.4	3700	2.506	116.96	9.06	33.7
9	265	9227.7	3696	2.497	118.25	8.93	33.2

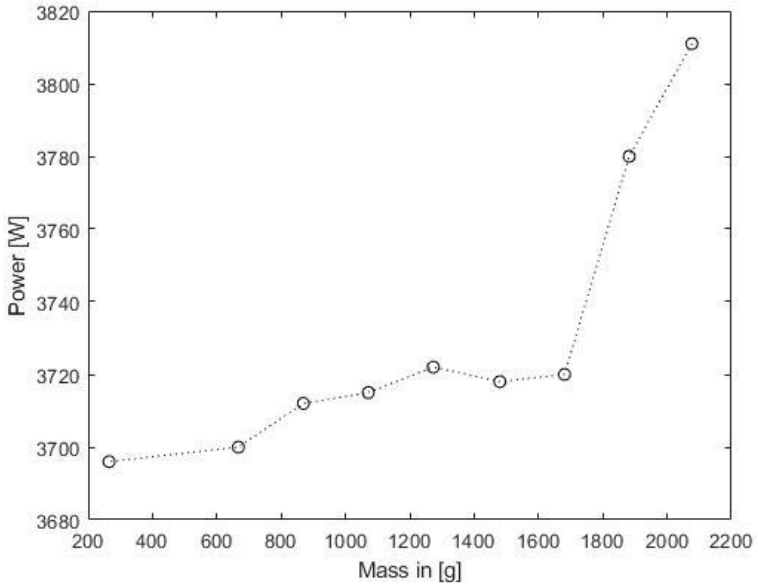

Figure 2: Power consumption variation of as a function of oil mass in the crankshaft

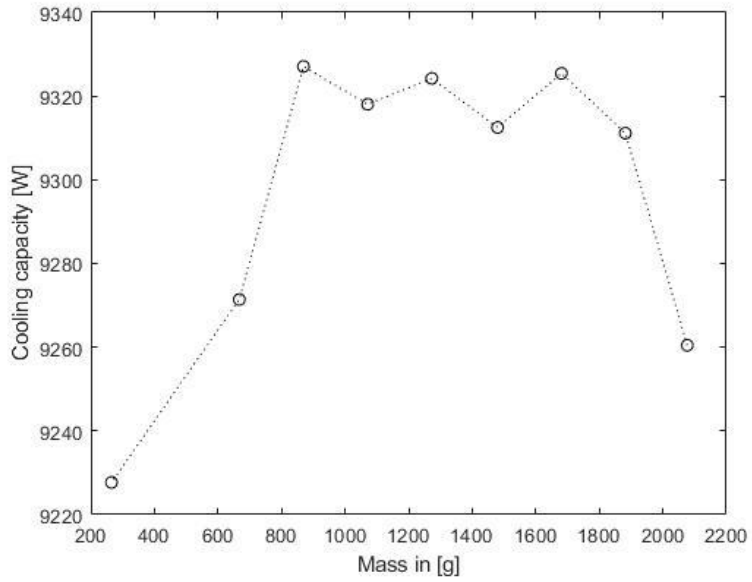

Figure 3: Cooling capacity variation as a function of oil mass in the crankshaft

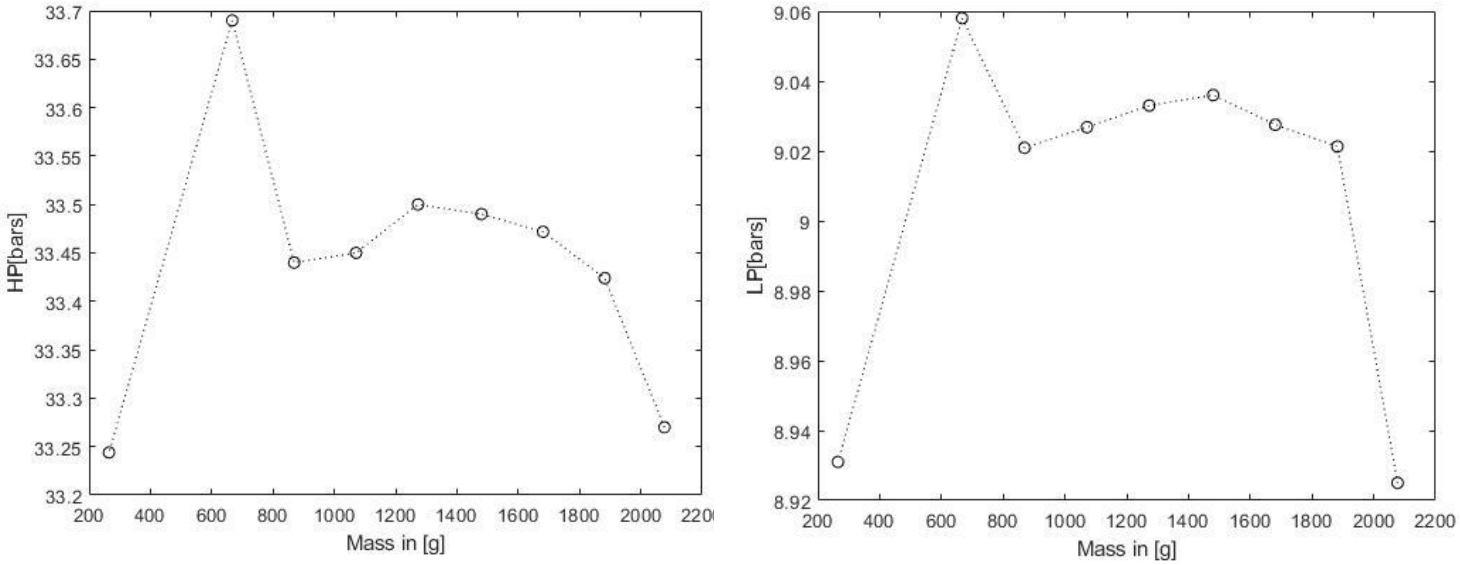

Figure 4: HP and LP variation as a function of oil mass in the crankshaft

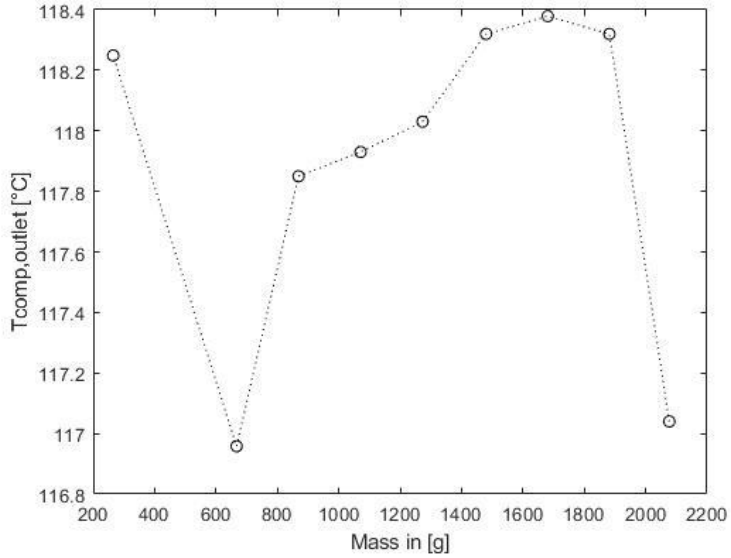

Figure 5: Compressor discharge temperature as a function of oil mass in the crankshaft

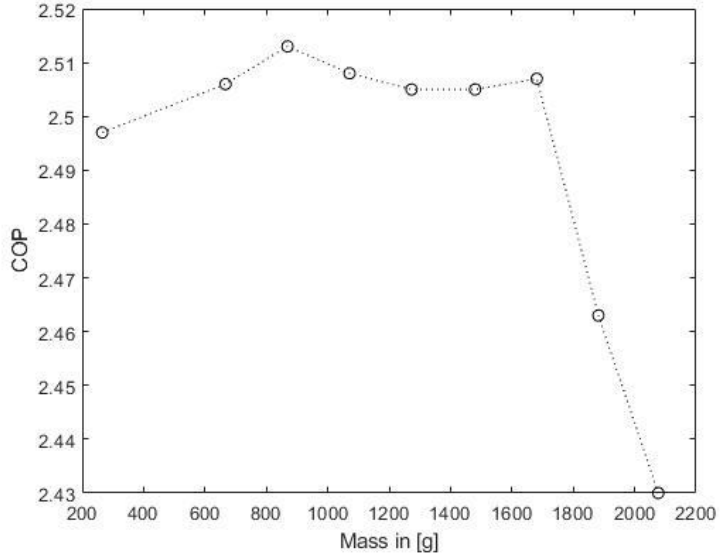

Figure 6: COP variation as a function of oil mass in the crankshaft

2.4. Results discussion

Let us first consider the compressor's power consumption. As shown in figure 2 and table 1, power remains almost constant for low oil mass. A sudden increase in consumption is to be found for larger quantities. More accurately, for quantities exceeding 1500g, power consumption jumps from 3700 W to 3800 W (figure 2). The more oil existing inside the compressor, the more power consumption increases: this may be explained by the power lost to compensate the friction viscous forces caused by the lubricating oil reserve inside the crankshaft; for a certain oil level, the rotation of the motor is opposed by the oil, whilst for lower levels it rotates in the vapour zone. In addition to having a positive effect, such as improved lubrication, reducing vapor leakage through the scroll, the oil generates a negative effect due to the viscous resistance to the motor rotation. Thus, a balance between positive and the negative effects is observed.

Cooling capacity has a distinctive behavior (figure 3). It increases with the increase of oil mass inside the crankshaft (passes from 9220 to 9300 W), till it reaches a flat behavior then it decreases (9260 W). However, it is hard to say whether this variation is significant because the range of variation is rather small, around 2%, which is close to the accuracy of our measurements. Nevertheless, the trend is interesting: For low oil masses, the basic function of the oil, which is leakage prevention, is not completely fulfilled due to the low oil quantity. With increasing oil mass, we get better lubrication and a better leak tightness which explains the increase in cooling capacity. For large oil masses, the behavior is different: The scroll compressor in this study is driven by an electric motor bathing inside the crankshaft filled with oil. With increasing oil quantities, the asynchronous machine (the motor) is subjected to an increasing shear stress which may cause the machine to slow down. The swept volume is then decreased and the refrigerant flow rate decreases, causing a reduction of cooling capacity. This phenomenon is not clear for lower oil quantities, because the shear stress created does not affect the motor's speed for lesser oil level. This behavior is not fully studied; it should be the subject of further investigations.

Both negative effects on power consumption and cooling capacity found for large oil masses explain the sudden decrease of the COP (figure 6). It goes from 2.5 to 2.37 (4.8% decrease).

The high and low pressures (Table 1 & figure 4) have no significant change which means there is no modification of the heat transfer due to the presence of oil. This behavior may be studied for longer tests which are not the aim of this work where the focus is on the compressor behavior. Similarly, for the outlet compressor temperature, no significant variation exists (figure 5).

The optimal oil mass is found to be 870 g. For this quantity, cooling capacity is maximal and power is constant (negative effects are compensated by the positive ones). The electrical power consumption is found to be 3700W, cooling capacity around 9300W and COP about 2.51.

For oil mass exceeding 1500g the increase in input power is notable.

3. CONCLUSION

The main aim of this work is to study the effect of oil level and mass inside a scroll compressor to determine its performance. It is found, that power consumption remains constant along different mass quantities, till it reaches a threshold. For an oil level exceeding this threshold, the compressor power increases drastically and significantly. The cooling capacity has an optimum for mid-range oil level. For extremely low oil level, the cooling capacity is minimal; this is probably due to bad gap sealing. For high oil levels, cooling capacity decreases; this is most probably due the oil viscous resistance to motor rotation, thus reducing its speed and its swept volume. For oil mass exceeding 1500g the COP degradation is noticeable. The performance of the compressor is deteriorated due to the increase of friction forces.
For future studies, it is important to find an optimum oil level inside the compressor that is able to ensure the best lubrication and gap sealing without actually harming the compressor's performance. They should also focus on the cooling capacity behaviour for great oil masses.

NOMENCLATURE

Comp,outlet	Compressor outlet	*COP*	Coefficient of performance
C_P	Specific heat capacity (J/kg×K)	*f*	Refrigerant fluid
h	Enthalpy (kJ/kg)	*HP*	High pressure (bars)
In,out	Inlet , outlet	*LP*	Low pressure (bars)
$\dot{m}$	Mass flow rate (kg/s)	*P*	Power consumption (Watts)
T	temperature (°C,°K)	Q_{evap}	Cooling capacity (Watts)

REFERENCES

Afshari, F., Comakli, O., Lesani, A., & Karagoz, S. (2017). Characterization of lubricating oil effects on the performance of reciprocating compressors in air–water heat pumps. *International Journal of Refrigeration*, *74*, 505-516. https://doi.org/10.1016/j.ijrefrig.2016.11.017

Drost, R. T., & Quesada, J. F. (1992). Analytical and experimental investigation of a scroll compressor lubrication system.

Nam, D., Lee, P., Lee, G., Kwon, Y., & Lee, J. (2015). Optimization of an oil charge amount on electric driven scroll compressor for eco-friendly vehicle. *International Journal of Refrigeration*, *57*, 54-61. https://doi.org/10.1016/j.ijrefrig.2015.05.009

Sarntichartsak, P., Monyakul, V., Thepa, S., & Nathakaranakule, A. (2006). Simulation and experimental evaluation of the effects of oil circulation in an inverter air conditioning system using R-22 and R-407C. *Applied Thermal Engineering*, *26*(14), 1481-1491. https://doi.org/10.1016/j.applthermaleng.2006.01.002

Shin, C. J., Park, J. S., & Chang, Y. I. (1998). An analytical study of the oil supply system in scroll compressors.

Youbi-Idrissi, M., & Bonjour, J. (2008). The effect of oil in refrigeration: Current research issues and critical review of thermodynamic aspects. *International Journal of Refrigeration*, *31*(2), 165-179. https://doi.org/10.1016/j.ijrefrig.2007.09.006

Manuscript ID: 1102
DOI: 10.18462/iir.icr.2019.1102

Modelling and dynamic simulation of a liquid desiccant system coupled to a heat pump for air conditioning

Juan PRIETO, Antonio ATIENZA-MÁRQUEZ, Alberto CORONAS

Universitat Rovira i Virgili, Mechanical Engineering Department, CREVER. Avda. Països Catalans 26, Tarragona, 43007, Spain, juan.prieto@urv.cat

ABSTRACT

In applications where latent loads or ambient humidity are high, liquid desiccant systems combined with vapor compression systems are a suitable alternative to conventional HVAC systems because they can efficiently control air temperature and humidity. In this sense, an optimal integration in terms of working conditions and energy management of both systems is required in order to maximize the overall performance when they are coupled.
This study analyses, by means of the modelling and dynamic simulation with TRNSYS, the seasonal performance of a liquid desiccant system coupled to a vapor compression heat pump for an HVAC application.
The developed model is then used to optimize to overall performance in terms of energy consumption and seasonal COP. Different operational conditions and control strategies are evaluated.
Results show that evaporator/absorber and condenser/regenerator temperatures are the variables that mainly affect the seasonal COP of the system.

Keywords: Liquid desiccant system, vapor compression heat pump, dynamic simulation, control optimization

1. INTRODUCTION

Liquid desiccant systems (LDS) are interesting thermally driven air conditioning (HVAC) systems when dehumidification has an important role in the thermal loads. These systems can both achieve a low level of humidity and be driven by low-grade heat sources (Mohammad et al., 2013; Misha et al., 2012). The combination of LDS with vapor compression refrigeration systems is called hybrid liquid desiccant system (HLDS). In these systems, the LDS typically handles the latent load and the vapor compression systems the sensible load. As a result, the HLDS handles the temperature and humidity control more efficiently than conventional HVAC systems (see Figure 1). The cooling demand to achieve the supply air conditions of temperature and humidity for HLDS is lower than for conventional systems and post-heating is not required (Prieto, 2016). Additionally, the evaporator of the vapor compression chiller may operate at higher temperatures, what enhances the COP of the system. Moreover, the heating from the condenser can be used to regenerate the solution.

To optimize the performance of the overall system, a good matching between the LDS and the vapor compression heat pump is required in terms of thermal capacities and operational conditions. In this way, the electrical consumption of the system will be affected by these conditions and the thermal capacities by increasing the overall COP (combined of the LDS and the vapor compression heat pump) and reducing, at the same time, the waste heat to the ambient. Regarding this optimization, Niu et al. (Niu et al., 2012) tried to find out the best way to match the two systems with the control, by actuating through the rotation speed of the compressor, the solution flow rate and the air flow rate in the condenser.

The main objective of this paper is to optimize the operational conditions of a HLDS (working temperatures and liquid desiccant mass fraction) in terms of seasonal performance (minimizing the annual electrical consumption of the compressor and the number of hours at discomfort conditions). To obtain this, the HLDS that operates in a locker room of a sports center in Taipei (Taiwan) has been modelled and simulated on TRNSYS.

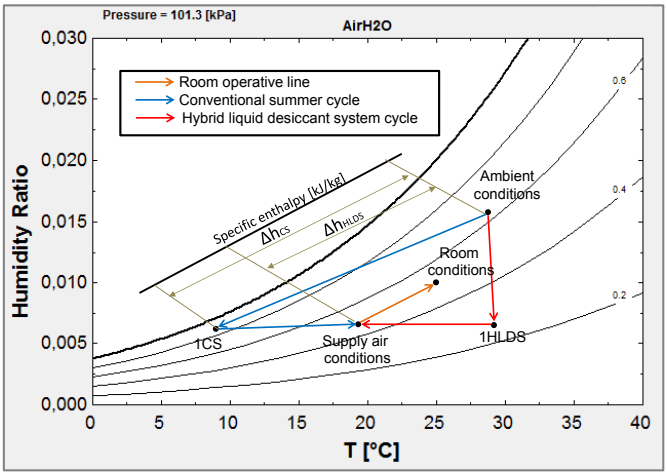

Figure 1: Conventional air handling unit cycle and HLDS cycle to control humidity and temperature separately

2. MAIN SECTION

2.1. Description of the HLDS

Fig. 2 illustrates a simple scheme of the demonstration unit of the HLDS studied which is coupled to a vapor compression heat pump that provides, at the same time, heating to the regenerator and cooling to the absorber. In addition, an air handling unit, of the variable air volume type, controls the supply air temperature, with a cooling/heating coil, and the air flow rate, with the air fans. Return air is used to regenerate the solution through the regenerator.

The system can operate either in summer or winter conditions because the hydraulic circuit can provide either chilled water from the evaporator or hot water from the condenser of the vapor compression heat pump to the coil inside the air handling unit.

Figure 2:

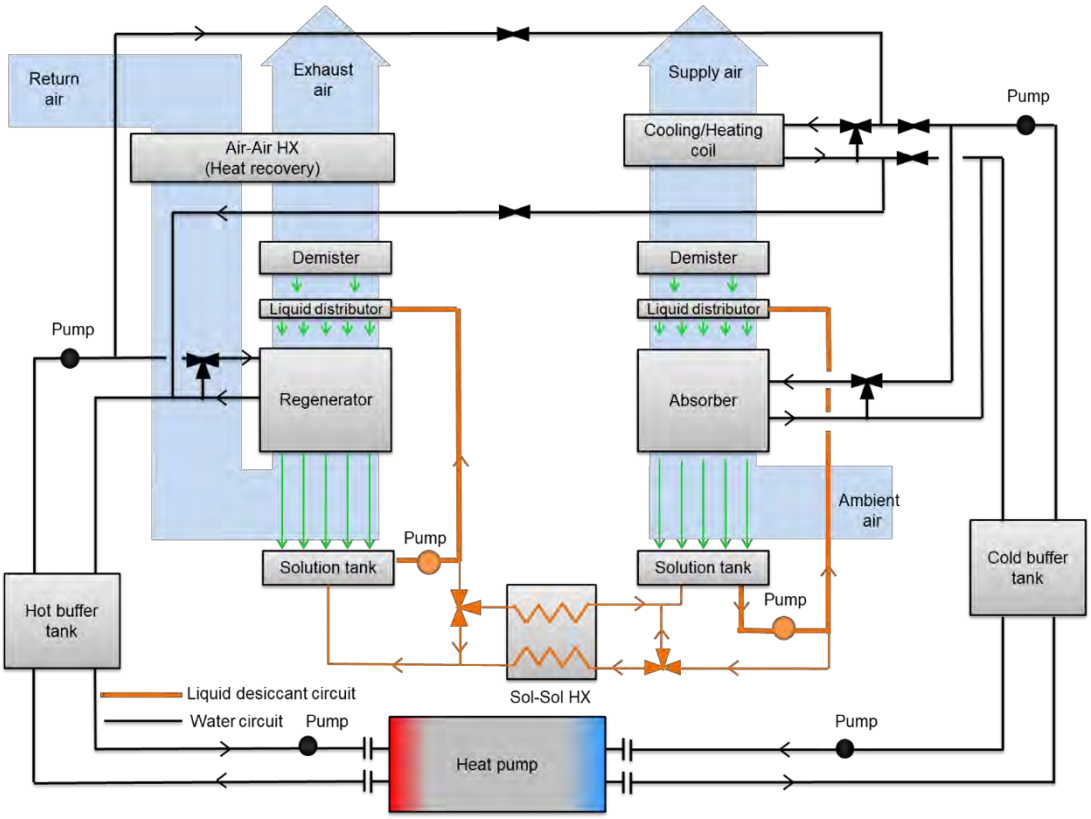

Schematic layout of the studied HLDS

2.1.1. Liquid desiccant system

The main components of a LDS are the absorber and the regenerator, where the moist air is dehumidified and the liquid desiccant is regenerated, respectively. Both processes take place by direct contact between the moist air and the liquid desiccant. The liquid desiccant system (LDS) contains non-adiabatic air-solution contactors of the falling-film with horizontal tubes type made of titanium, which can endure the corrosion with the liquid desiccant material used, the $LiCl/H_2O$ solution. Both air-solution contactors, absorber and regenerator, have the same dimensions. Table 1 shows their main specifications.

Table 1. Specifications of the air-solution contactors

Tube Material	Titanium
Contact surface (m^2)	41.18
Tube thermal conductivity (W/m·°C)	22.0
Tube length (m)	0.68
Tower width (m)	0.47
Inside tube diameter (mm)	5.10
Outside tube diameter (mm)	6.50

Other components of the LDS are: a solution heat exchanger that preheats the solution going from the absorber to the regenerator; two solution tanks; two solution pumps and two three-way valves.

2.1.2. Vapor Compression Heat Pump

Since chilled water is required for the absorber and the cooling coil (if the system is working in summer conditions) and hot water is required for the regenerator (or the coil if the system is operating in winter conditions), a water-to-water heat pump was decided to be used. The main problem while using a standard water-to-water heat pump is to manage the different energy loads that will appear when the system is operating. To solve this problem, a flexible vapor compression heat pump was chosen. This heat pump contains two evaporators and two condensers. One evaporator and one condenser are water cooled/heated and the others are air cooled/heated. In this way, the compressor of the heat pump operates to follow the maximum load. This means that if the cooling load is the highest, the compressor will operate to handle it, the water-cooled condenser will transfer part of the heating and the air-cooled condenser will transfer the rest to the ambient, and the opposite. The heat pump has not inverter, what means that the compressor operates in on/off. Figure 3 shows the vapor compression heat pump COP as a function of the condenser outlet water temperature (T_{cond}) and the evaporator outlet water temperature (T_{chi}). At nominal conditions (T_{chi}=7ºC and T_{cond}=30ºC), the cooling capacity of the heat pump is 56 kW, the heating capacity is 60 kW and the COP is 3.0. The maximum hot supply temperature of the condenser is 55ºC due to the system high pressure limitations.

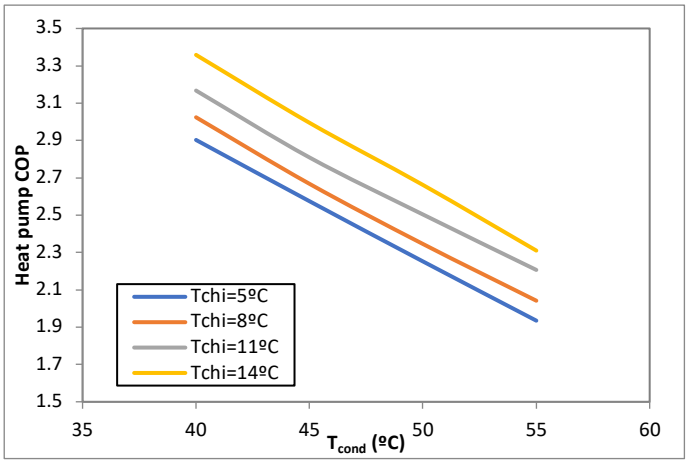

Figure 3: COP of the vapor compression heat pump as a function of the condenser outlet water temperature and the evaporator outlet water temperature.

2.1.3. Air Handling Unit

The air handling unit oversees both, supplying the moist air at the required conditions and regenerating the liquid desiccant with the return air circuit. The main components of the system are two fans coupled to frequency drivers, a heating coil and a cooling coil. The maximum volumetric air flow rate is 2500 m^3/h.

2.1.4. Hydraulic circuit

The hydraulic circuit provides the cooling and the heating from the evaporator and the condenser of the vapor compression heat pump to the absorber, regenerator, heating coil and cooling coil. This circuit is comprised of pumps, three-way valves, two-way valves and two buffer tanks.

2.1.5. Control system

The control of the system can be divided into four subsystems:

- Absorber, for the humidity control through a PID control that actuates on a three-way valve for the chilled water.
- Regenerator, for the liquid desiccant regeneration control with a differential on/off controller as a function of the LiCl mass fraction at the entrance of the absorber.
- Fans of the air handling unit, for the return air temperature control through a frequency driver.
- Heating and cooling coil, for the supply air temperature control through a PID control that actuates on a three-way valve.

2.2. Case Study

The case study is a locker room of a sports center in Taipei (Taiwan), which is an application with very high internal latent loads in a city with a warm and humid climate.

2.2.1. Internal loads

Left graph of Figure 4 shows the monthly internal loads (sensible cooling, sensible heating, and latent cooling) of the room, which are gotten from two locker rooms of a sports center in Taipei, Taiwan. The locker rooms are closed in February for one week, for two weeks in August and for three weeks in December. As it is observed from this graph, latent loads are always present and represent a significant amount of the total loads. However, sensible heating is more important from January to March and sensible cooling from April to November.

2.2.2. Weather conditions

The weather conditions are taken from Energy + Weather data available on their website. As a summary of this data, the right graph of Figure 4 shows the monthly average ambient temperature and humidity ratio. As can be observed from this graph, from May to October the weather is humid and warm, these conditions are the most suitable for a liquid desiccant system. During the other months, the weather is colder and dryer.

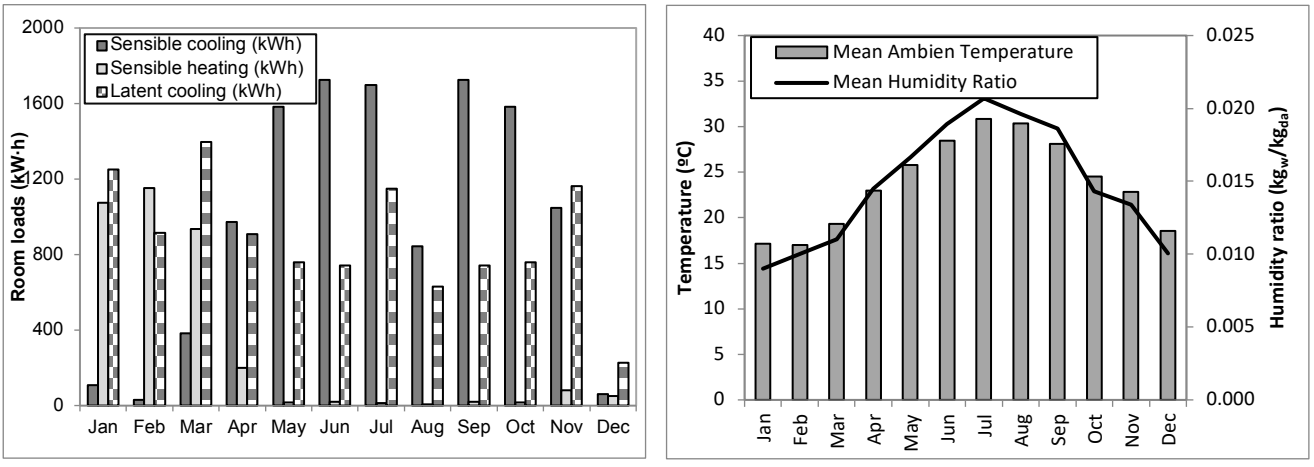

Figure 4. Monthly internal loads (left) and monthly mean ambient temperature and humidity ratio (right)

2.3. Modelling

2.3.1. Modelling of the air-solution contactors

A new component of a non-adiabatic air-solution contactor has been developed. The physical processes in the absorber and the regenerator are very similar, but the inverse. For instance, heating

is required to regenerate the solution while cooling to dehumidify the air. For this reason, the same equations have been used for both components.

The mathematical model is based on that described by Hellmann and Grossman (1995). This means that the same equations inputs and outputs have been considered in the model. The main reason why this model has been used is its relative simplicity because it can be modelled with algebraic equations. Moreover, the model is experimentally validated by Gommed et al. (2004); and Gommed et al. (2015). Furthermore, the thermo-physical properties of LiCl/H_2O brine (the density, the enthalpy, the specific heat capacity and the viscosity) have been adopted from Conde (2004) formulations.

The input values required in the mathematical model are: the inlet moist air dry bulb temperature, the inlet moist air humidity ratio, the inlet moist air mass flow rate, the inlet water temperature, the inlet water mass flow rate, the inlet solution temperature, the inlet solution mass fraction and the inlet solution mass flow rate. On the other hand, 12 variables are calculated: the outlet water temperature, the outlet moist air humidity ratio, the outlet moist air temperature, the outlet solution mass flow rate, the outlet solution temperature, the outlet solution mass fraction, the air-solution interface temperature at the top, the air-solution interface mass fraction at the top, the air-solution interface humidity ratio at the top, the air-solution interface temperature at the bottom, the air-solution interface mass fraction at the bottom and the air-solution interface humidity ratio at the bottom. The multivariable Newton-Raphson method has been used to solve the system of equations.

The model requires the heat and mass transfer coefficients to obtain the outlet parameters. For the tube-solution heat transfer, a value of 675 W/m^2·ºC has been used. For the tube-solution mass transfer coefficient, a value of 0.05 kg/m^2·s has been chosen. These are the values experimentally achieved by Gommed et al. (2015).

2.3.2. Modelling of the solution tanks

A model of the solution tanks has been also developed. The storage capacity of the solution tanks is related not only to the temperature of the liquid desiccant but also by the liquid desiccant mass fraction. Consequently, the model of the liquid desiccant tanks must consider a changeable mass inside them, as well as a variable liquid desiccant mass fraction.

The solution tanks model is based on energy and LiCl and total mass balance equations. Moreover, complete mixing has been assumed. For the calculation of the water mass in each time step, it is considered the amount of water content in the previous time step and the mass balance of water in the tank in that time. For the calculation of the tank temperature in each time step, the energy balance in the tank is formulated considering the temperature of the tank in the previous time step.

2.3.3. Modelling of the other components

The rest of the components have been gotten from standard libraries and TESS libraries (TESS 2014) available on TRNSYS. The solution heat exchanger and the air-air heat exchanger have been modeled with the standard component of TRNSYS Type91. The cooling/heating coil has been modeled with the standard component of TRNSYS Type5d. Pumps are modeled with the Type3b from the standard libraries of TRNSYS. This is a pump with a constant flow rate. The liquid desiccant flow rate has been set at 2.5 kg/s, which agrees with the measured values of the presented HLDS. Diverting valves are modeled with the Type647 from the TESS libraries. Finally, the vapor compression heat pump has been modelled with the Type668, which allows to include the performance curves of a single stage water-to-water vapor compression heat pump.

2.4. Results

2.4.1. Sensitivity analysis

The model has been used to perform a sensitivity analysis of three operational variables of the system: the minimum LiCl mass fraction at the entrance of the absorber (a variable that is used to activate the regeneration process), the inlet water temperature in the absorber and the inlet water temperature in the regenerator. In this sense, the system has been simulated at 45 operational conditions. The inlet water temperature in the absorber ranges from 11 °C to 15 °C and inlet water temperature in the regenerator ranges from 50 °C to 54 °C. These temperature values agree with the working temperatures that can provide the vapor compression heat pump. The maximum LiCl mass fraction ranges from 25 % to 35 %. Maximum LiCl mass fraction at the entrance of the absorber

(a variable that is used to stop the regeneration process) has been set as 2.5 % higher than the minimum LiCl mass fraction.

The following annual variables of the system are analyzed:

- The number of hours at discomfort conditions, which is counted whenever the room temperature is higher than 26 ºC or lower than 22 ºC or whenever the room humidity ratio is higher than 0.012 kg_w/kg_{da}. These criteria are in agreement with the suggested by ASHRAE (ANSI/ASHRAE 2010).
- The annual wasted thermal energy to the ambient, which is calculated as the sum of the wasted energy in the evaporator and the wasted energy in the condenser.
- The seasonal COP (SCOP) of the global system, which is calculated as the annual thermal energy provided by the HLDS divided by the annual electric consumption of the heat pump compressor:

$$\mathrm{SCOP} = \frac{\int \dot{Q}_a \cdot dt}{\int \dot{W}_c \cdot dt} \qquad \text{Eq. (1)}$$

- The annual electrical consumption of the heat pump compressor.

Figure 5 shows the results gotten from the sensitivity analysis performed. The number of hours at discomfort conditions mainly depends on the maximum LiCl mass fraction: the lower the mass fraction the lower the number of hours of discomfort. This effect is mainly due to a higher cooling capacity in the HLDS. The annual wasted thermal energy to the ambient is also mainly affected by the LiCl mass fraction but in a reverse way. This is, the higher the LiCl mass fraction the lower the waste heat to the ambient. In this case, this effect is due to more heating is required from the heat pump to keep high LiCl mass fraction in the LDS, what reduces the condenser wasted heat to the ambient.

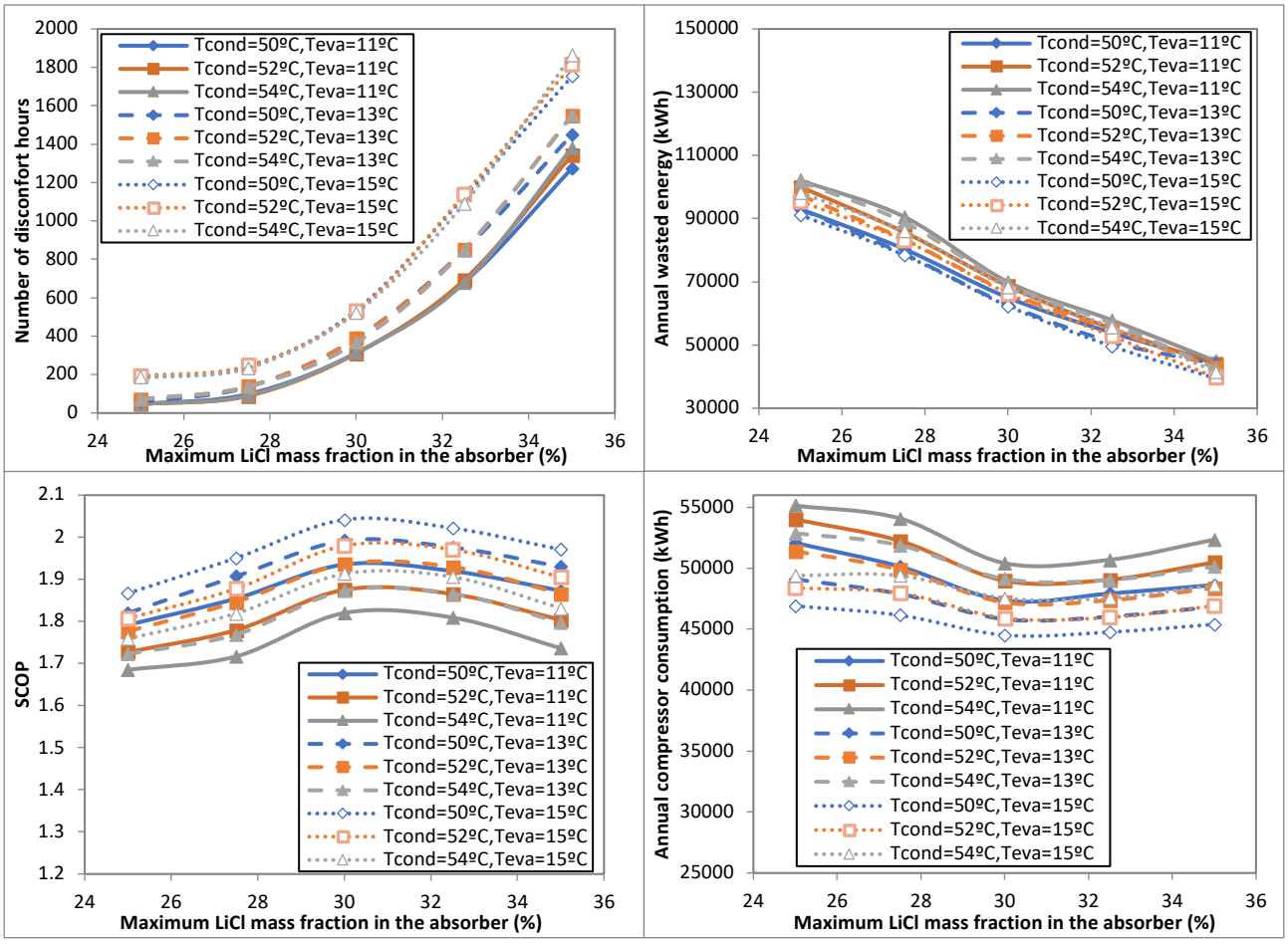

Figure 5. Sensitivity analysis of the HLDS.

On the other hand, the SCOP of the system is mainly affected by the inlet regenerator water temperature and the inlet absorber water temperature. The lower the regenerator water temperature and the higher the absorber water temperature, the higher the SCOP. In this case, the higher cooling capacity of the system with low LiCl mass fractions is compensated by the higher waste heat to the ambient, what means that there is a maximum SCOP for LiCl mass fractions in the range of 30%. In the same way, the electrical consumption of the heat pump compressor is also mainly affected by the operational temperatures. The reasons are the same as for the SCOP.

2.4.2. Optimization and monthly results

To select the operational conditions that optimize the seasonal performance of the system, the results of the previous sensitivity analysis have been used in a multi-objective optimization analysis. Figure 6 illustrates the electrical consumption of the compressor and the number of hours at discomfort conditions of the simulated cases. Since the two variables should be minimized, the Pareto front multi-objective optimization method can be used in this case. Darker points represent the operational conditions that coincide with the Pareto front in both graphs.

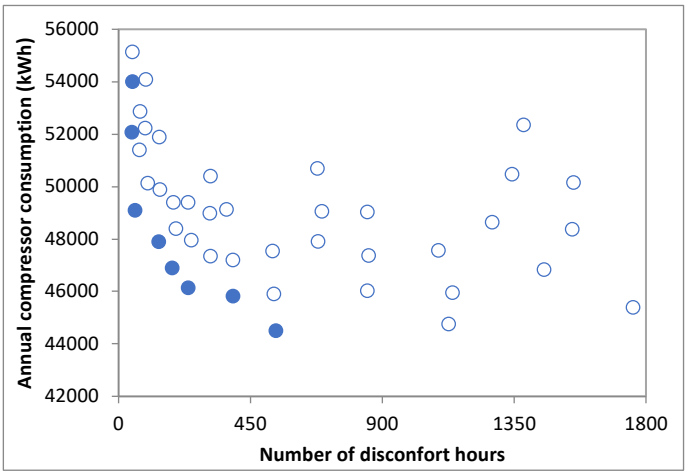

Figure 6. Electrical consumption of the compressor vs. the number of discomfort hours. The selected point corresponds to a chilled water temperature equal to 13ºC, a hot water temperature equal to 50 °C and a minimum LiCl mass fraction equal to 22.5 %.

Figure 7 shows the monthly results of the selected working conditions. It can be observed that the system performance is very affected by the weather conditions. Moreover, the energy wasted in the condenser mostly occurs in summer and the wasted energy in the evaporator during winter. The annual wasted energy in the condenser doubles the annual wasted energy in the evaporator.

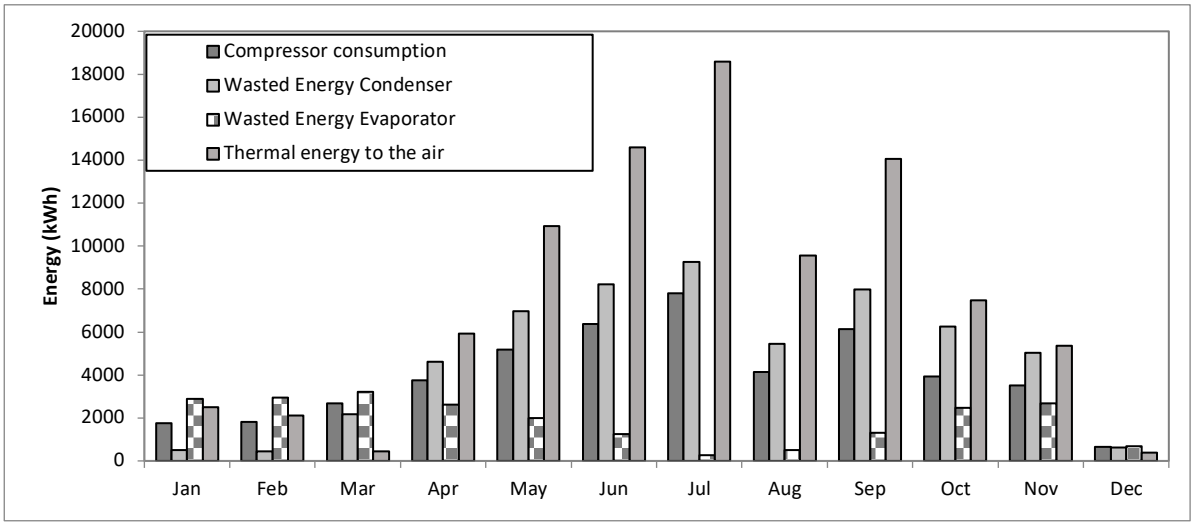

Figure 7. Monthly results for the selected case

3. CONCLUSIONS

A model of a HLDS developed on TRNSYS has been used to perform a sensitivity analysis in terms of number of hours of discomfort conditions, the annual wasted heat, the SCOP and the annual power consumption of the heat pump compressor as a function of three operational variables: the chilled water temperature, the hot water temperature and the maximum LiCl mass fraction at the entrance of the absorber. The LiCl mass fraction mainly affects the number of hours of discomfort and the annual waste heat. In this sense, the lower the mass fraction the lower the number of hours of discomfort and the higher the waste heat. The chilled water temperature and the hot water temperature mainly affect the SCOP and the power consumption of the compressor. In this case, the lower the hot water temperature and the higher the chilled water temperature, the higher the SCOP and the lower the power consumption of the heat pump compressor.

The operational conditions that minimize the number of hours out of comfort conditions and the power consumption of the heat pump compressor have been determined by a multi-objective optimization analysis. The selected point corresponds to a chilled water temperature equal to 13 °C, a hot water temperature 50 °C and a minimum LiCl mass fraction equal to 22.5 %.

NOMENCLATURE

LDS	Liquid desiccant system	*SCOP*	Seasonal COP of the HLDS
HLDS	Hybrid liquid desiccant system	*T*	Temperature (ºC)
$\dot{Q}_a$	Thermal energy ratio provided to the air (kW)	$\dot{W}_c$	Power of the heat pump compressor (kW)

REFERENCES

ANSI/ASHRAE. 2010. “Standard 55.” In , 3–6.

Conde, M R. 2004. Properties of Aqueous Solutions of Lithium and Calcium Chlorides: Formulations for Use in Air Conditioning Equipment Design. *Int. J. of Thermal Sciences* 43, 367–82.

Gommed, K, G Grossman, and F Ziegler. 2004. Experimental Investigation of a LiCl-Water Open Absorption System for Cooling and Dehumidification. *J. of Solar Energy Engineering* 126, 710–15.

Gommed, Khaled, Gershon Grossman, Juan Prieto, Jordi Ortiga, and Alberto Coronas. 2015. Experimental Comparison between Internally and Externally Cooled Air-Solution Contactors. *Science and Technology for the Built Environment* 21 (3), 267–74.

Hellmann, H, and G Grossman. 1995. Simulation and Analysis of an Open-Cycle Absorption Chiller for Low-Grade Heat Utilization. *Int. J. of Refrigeration* 18 (3), 177–89.

Misha, S, S Mat, M H Ruslan, and K Sopian. 2012. Review of Solid/Liquid Desiccant in the Drying Applications and Its Regeneration Methods. *Renewable and Sustainable Energy Reviews* 16 (7), 4686–4707.

Mohammad, Abdulrahman Th., Sohif Bin Mat, M.Y. Sulaiman, K. Sopian, and Abduljalil A. Al-abidi. 2013. Survey of Liquid Desiccant Dehumidification System Based on Integrated Vapor Compression Technology for Building Applications. *Energy and Buildings* 62, 1–14.

Niu, Xiaofeng, Fu Xiao, and Zhenjun Ma. 2012. Investigation on Capacity Matching in Liquid Desiccant and Heat Pump Hybrid Air-Conditioning Systems. *Int. J. of Refrigeration* 35 (1), 160–70.

Prieto, Juan. 2016. Theoretical and Experimental Study of a Dehumidification System Based on Liquid Desiccants for Air Conditioning Applications. Universitat Rovira i Virgili.

TESS libraries. 2014. Component Libraries General Descriptions.

Manuscript ID: 1112
DOI: 10.18462/iir.icr.2019.1112

Simulation and optimization of water-based hybrid VRF systems with bifurcating bare-tube heat exchangers

Ransisi HUANG [(a)], Zhiwei HUANG [(b)], Jiazhen LING [(a)], Vikrant AUTE [(a)]

[(a)] Center for Environmental Energy Engineering, University of Maryland
College Park, 20740, United States
[(b)] Johnson Control Inc.
Norman, Oklahoma, United States

ABSTRACT

Hybrid VRF (hVRF) systems enjoy reduced refrigerant charge and wider selection of refrigerants compared to traditional VRF systems. However, due to relatively low heat transfer rate in the indoor coil, hVRF system COP is 10% lower than a traditional VRF system COP. To solve the COP degradation problem of hVRF system, a bi-objective optimization method was proposed for a water-based hVRF system that uses bifurcating bare-tube heat exchangers (bBTHX) as the indoor coils. The two objectives are minimizing bBTHX envelop volume and maximizing system COP. The optimization problem is separated into two steps. First, refrigerant loop parametric analysis was performed to determine the optimal water loop operating conditions. Next, bBTHX optimization was conducted subjected to the constraints of capacity requirements from step one and dimension limitations. Then we simulated the entire hVRF system with the optimal bBTHX designs and obtained the Pareto front between system COP and bBTHX volume.
Keywords: Hybrid System, Compact Heat Exchanger, Optimization, COP.

1. INTRODUCTION

Hybrid variable refrigerant flow (hVRF) system is a new type of VRF system that hasn't been widely investigated and applied. Unlike traditional VRF systems (Fig. 1) that circulate refrigerants in indoor units, hVRF systems (Fig. 2) circulate water (or other type of coolants) in indoor units. The refrigerant exchanges heat with water in a heat exchanger (usually a plate heat exchanger inside the heat recovery unit). This configuration eliminates the refrigerants inside the building. Thus, hVRF system enjoys reduced refrigerant charge, wider selection of refrigerants and lower refrigerant-related maintenance cost.

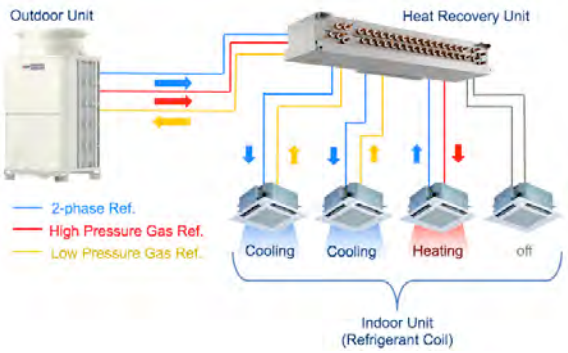

Figure 1: Traditional VRF system

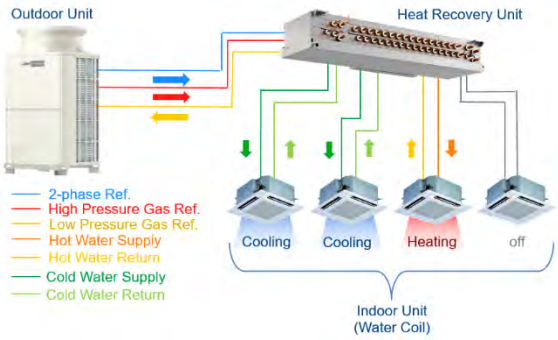

Figure 2: Hybrid VRF system

Takenake *et al.* (2017) conducted a field test and found that despite all the benefits as stated above, the hVRF system suffers from about 10% COP degradation comparing with the traditional VRF system due to low water-side heat transfer in the indoor coils. They concluded that the indoor coil design is crucial to improve the system efficiency. Huang *et al*. (2016) proposed a nature inspired

novel heat exchanger based on finless bifurcating bare-tubes. The two key novelties of the coil design are: (1) finless design with small diameter tube (0.5 - 5 mm) and (2) bifurcated tubes. Huang *et al*. concluded that the bifurcation enhanced air-side heat transfer by creating 3D flow and improved water-side heat transfer by boundary layer interruption and redevelopment. This novel heat exchanger consists of two sections of tubes: the main tubes and the branch tubes as shown in Fig. 3. Main tubes are all vertical tubes whose outer diameter is noted as D_1. The outer diameter of the branch tubes is noted as D_2. Longitudinal tube pitch (P_L) is defined as the center-to-center distance of two adjacent main tubes. The transverse tube pitch (P_t) is then defined as the center-to-center distance of two adjacent rows, as shown in Fig. 4. Bifurcation angle (θ) is the angle between branch tube and the center line.

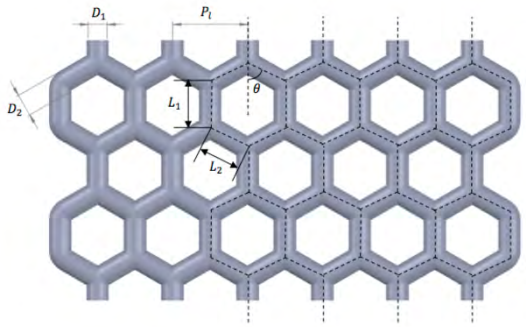

Figure 3: Bifurcated tube structure

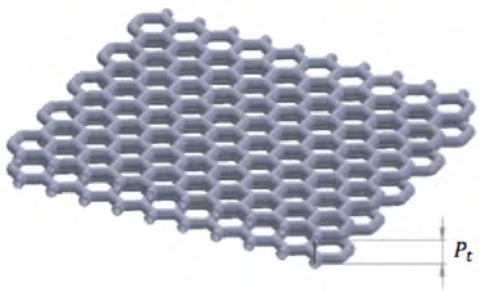

Figure 4: BTHX staggered pattern

Huang et al. (2018) applied the bifurcated bare-tube heat exchanger (bBTHX) as the hVRF indoor coil to enhance the water-side heat transfer to solve the hVRF COP degradation problem. They used multi-scale approximation-assisted optimization (Abdelaziz, 2009) for bBTHX design optimization. The optimal bBTHX design has 65% lower envelop volume and 70% lower material volume than those of traditional tube-fin heat exchanger (TFHX) while delivering the same capacity. The system simulation results showed that by replacing TFHX with the optimal bBTHX design, hVRF system COP can be increased by 10%, but is still 3% lower than the traditional VRF system COP.
The design optimization by Huang et al. (2018) was not conducted on the system level. Therefore, the simulation work mentioned above does not guarantee that the hVRF system design was optimal. To further improve the COP of the hVRF system, the current study proposes a two-step strategy for hVRF system optimization. The objective is to find the optimal bBTHX designs that will result in the maximum system COP. In the main section, the hVRF system design and the modelling approaches for each component were described. Then the two-step hVRF system optimization method was presented. Lastly, the optimization results were discussed.

2. MAIN SECTION

2.1. Hybrid VRF System Design and Component Models

Fig. 5a shows the schematic of the water-based hybrid VRF system. It consists of a refrigerant (R410A) loop on the top and a water loop in the bottom. The two parts are coupled by a plate heat exchanger (PHX) through which the refrigerant and the water exchange heat. According to AHRI VRF testing standard (AHRI, 2010), VRF systems should have at least two indoor units. Therefore, in current study, two bBTHX indoor units are designed. The piping designs follow the hVRF system data book (Mitsubishi, 2012). Pipe 1 (suction pipe) and pipe 2 (liquid pipe) are refrigerant pipes and their lengths are 110 m. The diameters of pipe 1 and 2 are 16 mm and 9.5 mm, respectively. Pipe 3 and pipe 4 are water pipes. Their lengths are 60m, and diameters are 22 mm. The two water pipes are both being elevated from the ground by 15 m.

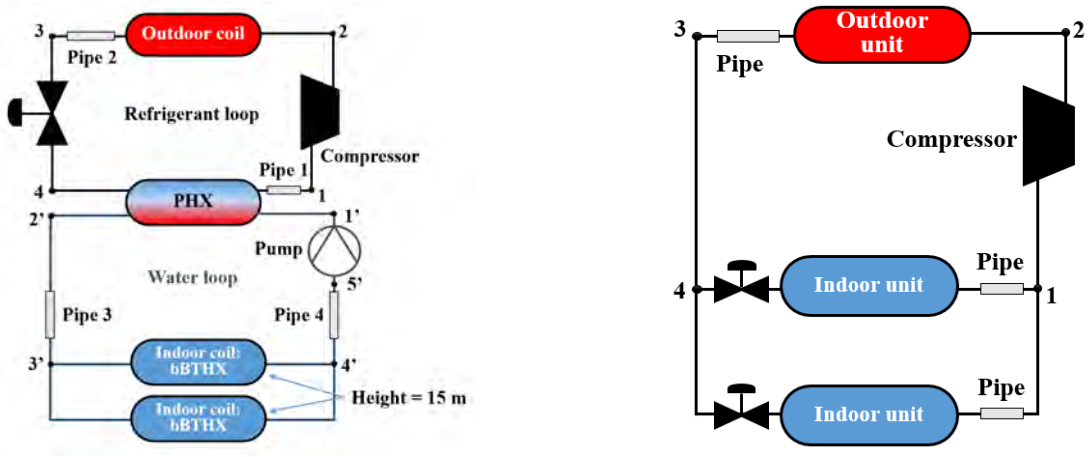

(a) (b)

Figure 5: Schematic: (a) hVRF System, (b) VRF System

The modelling approach for each component in the hVRF system is as follows. The compressor model is an isentropic efficiency-based model. The outdoor coil is modelled with the three-zone approach. The plate heat exchanger is modelled with the finite-volume approach (Qiao *et al*, 2013). The bBTHX indoor coil is modelled with ε-NTU method. The air- and water-side pressure drop and heat transfer metamodels were generated from CFD simulations. Details about bBTHX simulation can be found in Huang *et al.* (2017). The pump power consumption is evaluated by

$$W_{pump} = \dot{V}_w \Delta P_w / \eta_{pump} \quad \text{Eq. (1)}$$

where $\dot{V}_w$ is the water volume flow rate, η_{pump} is the pump efficiency, assumed to be 0.5. ΔP_w is the water loop pressure drop, which is the pressure difference between point 1' and 5'. The system COP is defined as

$$COP = \frac{Q}{W_{comp} + W_{pump}} \quad \text{Eq. (2)}$$

2.2. Optimization Approach

The design variables and their ranges for the hVRF system optimization are listed in Table 1. Tubes per segment is the number of honey-comb structure along the longitudinal tube pitch (P_L) direction (see Fig. 3). The problem formulation is as follows:

Objectives:
max COP
min V_{bBTHX}
S.T.
H ≤ 250 mm
L ≤ 900 mm
D ≤ 100 mm

Table 1. Design variables and the ranges

Variable type	Discrete			Continuous				
Design variable	Tubes per segment	Number of rows	Number of segments	D_1 (mm)	P_L/D_1	P_t/D_1	θ (deg)	L_1/L_2
Range	2-1000	2-15	2-20	0.5-5	1.5-3	1.5-3	5-85	1.5-7.5

The optimization problem is to find the bBTHX designs with the minimum envelop volume that will result in the maximum system COP, while satisfying the hVRF indoor unit dimension limitation (H ≤

250 mm, L ≤ 900 mm, D ≤ 100 mm) that follows the hVRF system data book (Mitsubishi, 2012). The bBTHX design affects the system COP by influencing the water loop steady-state operating conditions, particularly the PHX water inlet temperature and water loop mass flow rate. Therefore, the optimization can be split into the following two steps.

1. Refrigerant loop parametric analysis

The first step is the parametric analysis of the refrigerant loop on the water loop operating conditions. We simulated the performances of the refrigerant loop in Fig. 5 at various water temperatures ($T_{1'}$) and water mass flow rates ($\dot{m}_{1'}$). In this step, system capacity is the capacity of the PHX. The water loop pressure drop (ΔP_w) in Eq.(2) is estimated by

$$\Delta P_w = \Delta P_{PHX} + 2\Delta P_{pipe3} + \Delta \tilde{P}_{bBTHX} \quad \text{Eq. (3)}$$

where ΔP_{PHX} is the pressure drop of the PHX, $2\Delta P_{pipe3}$ is the estimation of the total water pipe pressure drop (assuming the pressure drops of pipe 3 and pipe 4 are similar), and $\Delta \tilde{P}_{bBTHX}$ is the assumed bBTHX pressure drop, which is 25 kPa. Then a series of optimum values of $T_{1'}$ and $\dot{m}_{1'}$ were selected according to the simulation results of step one.

2. bBTHX optimization and baseline design

The second step is the bBTHX design optimization using the genetic algorithm. The baseline design of the indoor unit is a tube-fin heat exchanger (TFHX), whose specification is shown in Table 2.

Table 2. Baseline design of indoor unit: tube-fin heat exchanger

Tube per bank	Tube bank #	Circuit #	Tube length (m)	Tube OD (mm)	Tube ID (mm)	Tube spacing (mm)	FPI	H × L × D (mm^3)	Volume (cm^3)
422	1	7	0.25	5	4.6	21	22	250 × 899 × 11.4	2562.1

The optimization formulation is as follows:

$$\text{Objectives :}$$
$$\text{Min } V_{bBTHX}$$
$$\text{S.T.}$$
$$0.98\ Q_{target} \le Q_{bBTHX} \le 1.02\ Q_{target}$$
$$H \le 250 \text{ mm}$$
$$L \le 900 \text{ mm}$$
$$D \le 100 \text{ mm}$$
$$\Delta P_{bBTHX} \le \Delta \tilde{P}_{bBTHX}$$

where Q_{target} is the system capacity calculated from step one. bBTHX water-side inlet conditions are the outlet conditions of pipe 3 calculated from step one. The design optimization was conducted multiple times because, for each pair of $T_{1'}$ and $\dot{m}_{1'}$, there is a corresponding optimal bBTHX design. Then, the entire hVRF system (refrigerant and water loop) with the optimized bBTHX designs was simulated to obtain the Pareto front between bBTHX volume and system COP.

2.3. Results and Discussion

2.3.1. Parametric analysis of water loop operating conditions

Fig. 6 shows the effect of water mass flow rate ($\dot{m}_{1'}$) and PHX water inlet temperature ($T_{1'}$) on the system capacity. As the value of $\dot{m}_{1'}$ increases, system capacity first increases and then plateaus. This trend is consistent for all water temperatures. At small values of $\dot{m}_{1'}$, the increase of water mass flow rate results in larger water flow velocity in the PHX and thus better heat transfer. Therefore, the larger water mass flow rate, the larger the system capacity. When $\dot{m}_{1'}$ is increased to a certain value, the refrigerant side outlet temperature in the PHX reaches the water inlet temperature ($T_{1'}$), and thus the system capacity can no longer increase with the increase of $\dot{m}_{1'}$. On the other hand, the increase

of $T_{1'}$ always leads to a larger capacity because of the larger refrigerant-water temperature difference and higher refrigerant exit temperature in the PHX.

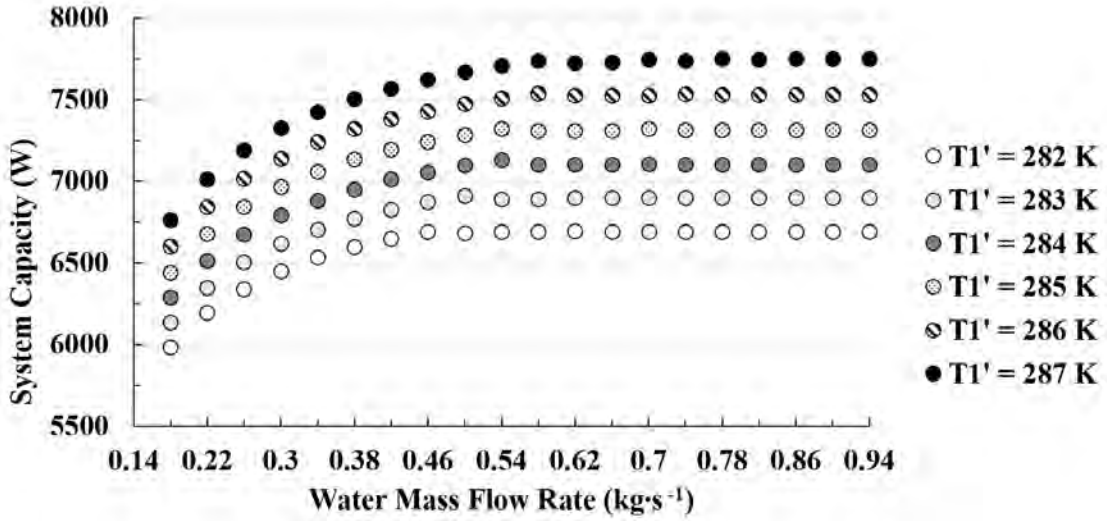

Figure 6: Effect of water mass flow rates and water temperatures on system capacity

Fig. 7 shows the effect of water mass flow rate ($\dot{m}_{1'}$) and PHX water inlet temperature ($T_{1'}$) on the system COP. As previously discussed, the increase of water mass flow rate ($\dot{m}_{1'}$) would result in larger capacity at small $\dot{m}_{1'}$. On the other hand, larger water mass flow rate would result in higher water loop pressure drop, and thus larger pump power consumption. Therefore, the system COP first increases with $\dot{m}_{1'}$ and then decreases. For each value of water temperature, the system COP peaks at the water mass flow rate of 0.3 kg·s $^{-1}$.

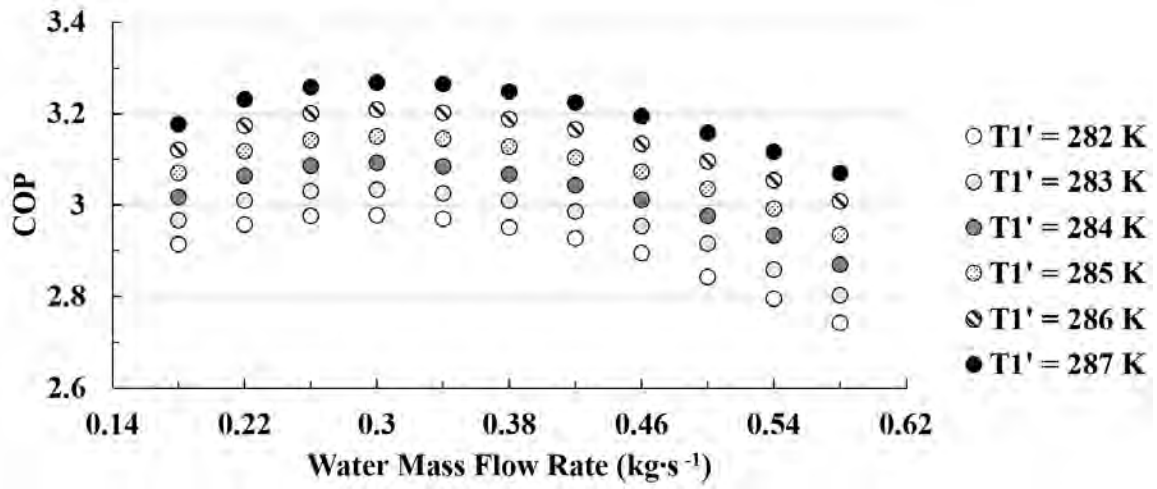

Figure 7: Effect of water mass flow rates and water temperatures on system COP

The results of the parametric analysis indicate that to increase the system COP, the water loop should be operated with water mass flow rate of 0.3 kg·s $^{-1}$ and $T_{1'}$ as high as possible. However, higher COP is associated with larger system capacity, and should result in larger volume of the bBTHX design. To obtain the Pareto front between system COP and the bBTHX volume, we selected 6 operating conditions to perform bBTHX optimization, as shown in Table 3. The target capacity for each bBTHX is half the system capacity, since there are two identical indoor units in the hVRF system. $T_{3'}$ and $P_{3'}$ is the inlet water temperature and inlet water pressure of the bBTHX.

Table 3. Selected operating conditions for bBTHX optimization

No.	$T_{1'}$ (K)	$\dot{m}_{1'}$ (kg·s $^{-1}$)	Q_{system}	bBTHX Q_{target} (W)	$T_{3'}$ (K)	$P_{3'}$ (Pa)
1	282	0.3	6443.47	3221.73	276.89	273835.87
2	283	0.3	6613.49	3306.75	277.76	274015.63
3	284	0.3	6786.16	3393.08	278.62	274190.55
4	285	0.3	6961.46	3480.73	279.47	274360.81
5	286	0.3	7139.40	3569.70	280.33	274526.60
6	287	0.3	7320.22	3660.11	281.19	274688.11

2.3.2. Optimization results of the hVRF system

Table 4 shows the optimization results of bBTHX and the hVRF system using the optimized bBTHX design. The results demonstrate that as the system operates at higher COP, the volume of the optimized bBTHX design also increases. Therefore, the higher the system efficiency, the higher the HX size and cost. Fig. 8 shows the Pareto front between the system COP and bBTHX volume, together with the simulation result of the baseline indoor unit design (tube-fin heat exchanger). The results show that largest bBTHX design brings 5.5% COP improvement and 50% HX volume reduction comparing to the baseline result.

Table 4. bBTHX optimization results and hVRF system results

No.	Optimized bBTHX design			System results	
	Height (mm)	Length (mm)	Volume (cm^3)	COP (-)	Q (W)
1	226	767	257.20	2.957	6383.34
2	234	731	376.28	3.025	6579.28
3	243	754	407.48	3.089	6772.75
4	249	806	513.99	3.146	6940.55
5	220	879	891.68	3.223	7163.25
6	227	858	1287.16	3.251	7259.07

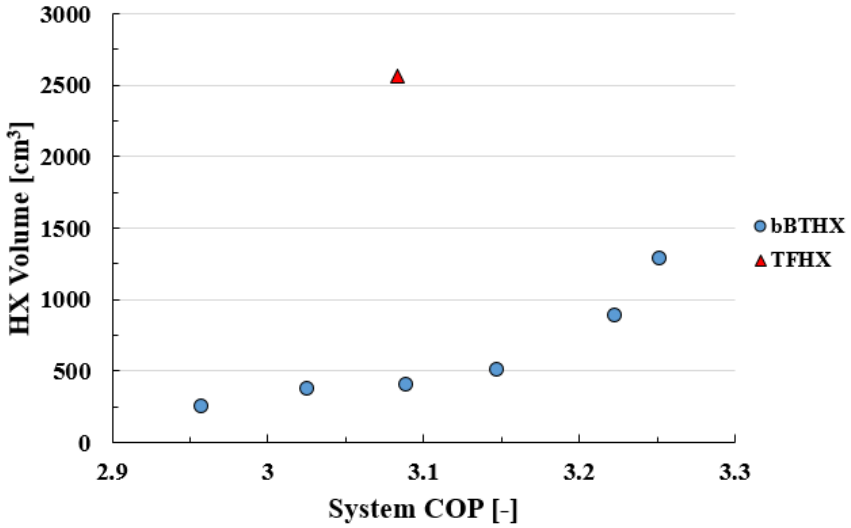

Figure 8: Pareto front between system COP and bBTHX volume

Table 5 shows the comparison among 3 cases: VRF direct expansion system, hVRF system with TFHX as indoor unit design, and hVRF system with bBTHX. Comparing with VRF direct expansion system, hVRF system suffers 10% COP degradation with tube-fin indoor unit, and 4% COP degradation along with 50% HX volume reduction with bBTHX design.

Table 5. Comparison between VRF and hVRF system results

No.	System Configuration	Indoor HX design	COP	HX Volume (cm^3)
1	VRF (Fig. 5b)	TFHX	3.39	2562.1
2	hVRF (Fig. 5a)	TFHX	3.08 (-10%)	2562.1
3	hVRF (Fig. 5a)	bBTHX	3.25 (-4%)	1287.2 (-50%)

To verify the consistency between the two steps of the hVRF system optimization, Table 6 compares the refrigerant loop parametric analysis results and the hVRF system results with optimized bBTHX designs. The values of $T_{1'}$ and $\dot{m}_{1'}$ from the two steps are highly consistent with each other. There is slight deviation (<1%) in the system capacity and therefore system COP. This is due to the 2% relaxation in the inequality constraint of the target bBTHX capacity.

Table 6 Comparison between the parametric analysis and the final results

Parametric analysis results				Final system results			
$T_{1'}$ (K)	$\dot{m}_{1'}$ (kg·s $^{-1}$)	COP	Q (W)	$T_{1'}$ (K)	$\dot{m}_{1'}$ (kg·s $^{-1}$)	COP	Q (W)
282	0.3	2.978	6443.47	281.7	0.3	2.957	6383.34
283	0.3	3.034	6613.49	282.9	0.3	3.025	6579.28
284	0.3	3.091	6786.16	284.0	0.3	3.089	6772.75
285	0.3	3.149	6961.46	285.0	0.3	3.146	6940.55
286	0.3	3.208	7139.40	286.2	0.3	3.223	7163.25
287	0.3	3.267	7320.22	286.7	0.3	3.251	7259.07

3. CONCLUSIONS

Hybrid VRF systems use water in the indoor units and thus enjoys reduced refrigerant charge, wider selection of refrigerants and lower maintenance cost comparing with traditional VRF systems. However, the field test results by Takenaka *et al.* (2017) and the simulation results by Huang *et al*. (2018) both show that the hVRF system COP is at least 10% less than the COP of traditional VRF system.

To solve the COP degradation problem, a bi-objective optimization method was proposed for the hVRF system that uses bifurcated bare-tube heat exchangers (bBTHX) as the indoor coil. The two objectives are minimizing bBTHX envelop volume and maximizing system COP. The optimization method consists of two steps. The first step is the parametric analysis of the refrigerant loop to determine the optimal water loop operating conditions. The second step is bBTHX optimization subject to the constraints of envelop limitation and capacity requirements. The required capacity, and the inlet conditions for bBTHX in step two are calculated from the first step.

The results of the parametric analysis show that to increase the system COP, the water loop should be operated with water mass flow rate of 0.3 kg·s $^{-1}$ and the controller water-side inlet temperature as high as possible. However, higher COP is associated with larger system capacity, and thus would result in larger volume of the bBTHX design. We selected 6 operating conditions from the parametric analysis to perform bBTHX optimization. Then the entire hVRF system was simulated with the optimal bBTHX designs to obtain the Pareto front between system COP and the bBTHX volume. Compared with TFHX indoor unit design, the optimal bBTHX designs show at least 50% of envelop volume savings. Compared with VRF direct expansion system, hVRF system suffers 10% COP degradation with tube-fin indoor unit, and at least 4% COP degradation with bBTHX designs. Lastly, the final results of the hVRF system were found to agree with the results from the refrigerant loop parametric analysis.

The future work of this research may include the investigation of optimal indoor unit designs for multiple operating modes, and for both full and part load conditions.

ACKNOWLEDGEMENTS

This work is supported by the Modelling and Optimization Consortium (MOC) at the University of Maryland.

NOMENCLATURE

bBTHX	bifurcated bare tube heat exchanger	D	depth (mm)
D_1	main tube diameter (mm)	D_2	branch tube diameter (mm)
H	height (mm)	hVRF	hybrid variable refrigerant flow
L	length (mm)	L_1	main tube length (mm)
L_2	branch tube length (mm)	$\dot{m}$	mass flow rate ($kg \cdot s^{-1}$)
P	pressure (Pa)	PHX	plate heat exchanger
P_l	longitudinal tube pitch (mm)	P_t	transverse tube pitch (mm)
ΔP	pressure drop (Pa)	Q	capacity (W)
V	volume (mm^3)	$\dot{V}$	volumetric flow rate ($m^3 \cdot s^{-1}$)
W	power consumption (W)	T	temperature (K)
TFHX	tube-fin heat exchanger	θ	bifurcation angle (deg)
η	efficiency (-)		

REFERENCES

Abdelaziz, O., Aute, V., Azarm, S., Radermacher, R., 2010. Approximation-assisted optimization for novel compact heat exchanger designs. HVAC&R Research 16(5), 707-728.

AHRI, 2010. Standard for Performance Rating of Variable Refrigerant Flow (VRF) Multi-Split Air-Conditioning and Heat Pump Equipment, AHRI Standard 1230.

Beshr, M., Aute, V., & Radermacher, R., 2016. Steady State Modeling of Advanced Vapor Compression Systems. International Refrigeration and Air Conditioning Conference. Paper no. 1588.

Huang, Z., Ling, J., Hwang, Y., Aute, V., Radermacher, R., 2016. Design and Numerical Parametric Study of Fractal Heat Exchanger, International Refrigeration and Air Conditioning Conference. Paper no. 1723.

Huang, Z., Ling, J., Hwang, Y., Aute, V., Radermacher, R., 2017. Design and numerical parametric study of a compact air-cooled heat exchanger. Science and Technology for the Built Environment 23:6, 970-982.

Huang, Z., Huang, R., Ling, J., Aute, V., Hwang, Y., 2018. Applicability of A Bifurcated Bare-tube Heat Exchanger in Water-based Hybrid VRF System, International Refrigeration and Air Conditioning Conference. Paper no. 2518.

Qiao, H., Aute, V., Lee, H., Saleh, K., & Radermacher, R., 2013. A new model for plate heat exchangers with generalized flow configurations and phase change. international journal of refrigeration 36(2), 622-632.

Takenake, N., Ikeda, S., Wakamoto, S., Motomura, Y., Yamashita, K., 2017. Development of water-based hybrid VRF system for building. In ASHRAE winter conference.

Manuscript ID: 1126
DOI: 10.18462/iir.icr.2019.1126

Improving the performance of a rechargeable personal cooling system with low GWP refrigerants

Rohit DHUMANE [(a)], Yiyuan QIAO [(a)], Jiazhen LING [(a)], Vikrant AUTE [(a*)], Yunho HWANG [(a)], Reinhard RADERMACHER [(a)]

[(a)] Center for Environmental Energy Engineering, 4164 Glenn L. Martin Hall
Mechanical Engineering Department, University of Maryland, College Park, United States 20742
dhumane, yyqiao, jiazhen, vikrant, yhhwang, raderm}@umd.edu

ABSTRACT

Personal cooling systems (PCS) enable 10-30% saving in building energy consumption, which takes up 41% of US primary energy. An innovative PCS called Roving Comforter (RoCo) uses R134a based vapour compression cycle (VCC) to provide cooling. To reduce environmental impact, it is necessary to evaluate RoCo performance with low GWP refrigerants.
The condenser heat of VCC is stored in a phase change material (PCM) storage, which limits the cooling operation duration. A recharge operation is conducted after the cooling operation.
A validated dynamic model (using Modelica) of VCC integrated with PCM is used to simulate the cooling operation with R32, R1234yf, R1234ze(E) and R290.
The change in COP is +8%, -12% and -5% and -5% with R32, R1234yf, R1234ze (E) and R290 respectively. Dynamic pressure, mass flow rates, temperature and power are presented.
Keywords: Refrigeration, Low GWP Refrigerants, PCM, Personal Cooling.

1. INTRODUCTION

Portable personal conditioning systems (Dhumane et al. 2017) have the potential for providing energy saving in space heating and cooling loads with improved thermal comfort. Roving Comforter (RoCo) is one such system which uses a vapour compression cycle (VCC) to provide personal cooling (Dhumane et al. 2019). The condenser heat from VCC is stored in a phase change material (PCM) storage. Schematic of the operation of the latest RoCo prototype with heat pump operation and graphite enhanced PCM is shown in Figure 1.
R134a is used as the refrigerant for the VCC. It is a hydrofluorocarbon (HFC) with zero ozone depletion potential. However, it has a global warming potential (GWP) of 1430. The Kigali Agreement under the Montreal Protocol will bring restriction on the use of R134a and it is necessary to evaluate the performance of RoCo with other refrigerants. R32, R1234yf, R290 and R1234ze(E) have been selected for this study. The current study models the latest prototype for both cooling and recharge modes and four refrigerants.
Modelica (Modelica Association 2019) will be used for the analysis of the cooling mode of RoCo. Model development for cooling mode is presented in Dhumane et al. (2019) will not be repeated for brevity. Experimental validation for the cooling mode of this new prototype is presented here for the first time. Details of the experiment conducted on this prototype are presented in Qiao et al. (2019). Finally, results from both cooling mode and recharge mode for all the refrigerants are obtained from simulation and analysed.
The new prototype of RoCo uses a heat pump operation for recharge (see Fig.1) instead of thermosiphon operation in the previous prototype (Dhumane et al. 2018a). This eliminates the need for a receiver and reduces the total refrigerant charge which is beneficial towards meeting safety requirements for low GWP refrigerants for flammability. Additionally, a serpentine microchannel heat exchanger is used for evaporator instead of a round tube plate fin type. This reduces the internal volume of the system even more. A new model is developed for modelling this microchannel heat exchanger, which is used as the evaporator of RoCo.

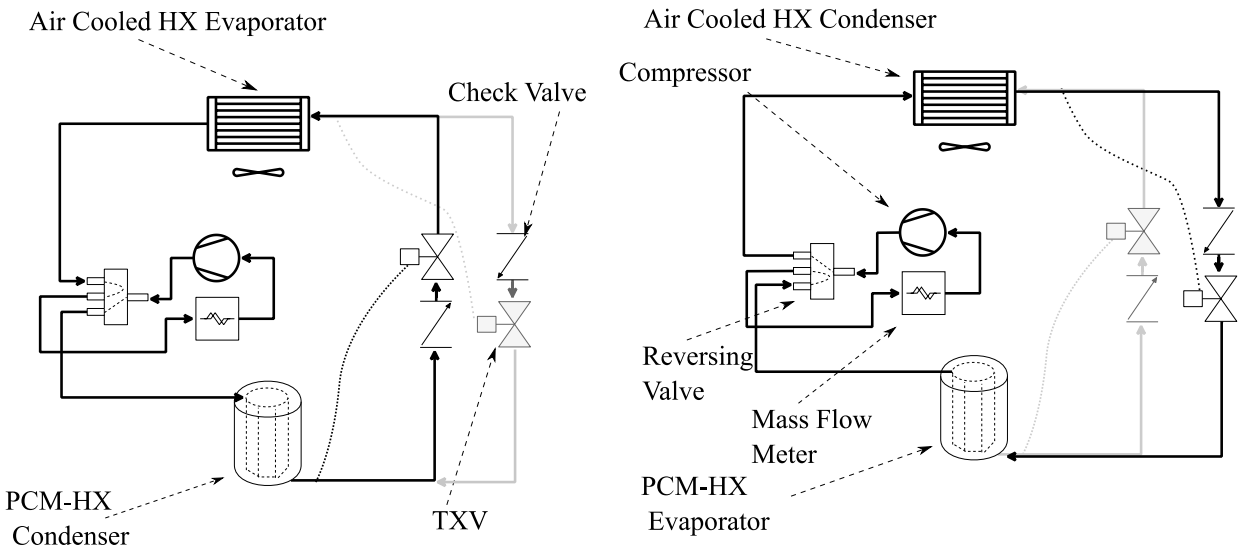

Figure 1: Operating modes of RoCo; (left) cooling mode, (right) recharge mode

2. MODELING AND VALIDATION

The system simulation is carried out using Modelica. Model diagram for the simulation is shown in **Error! Reference source not found.**. Details for modelling cooling system of RoCo can be found in Dhumane et al. (2019).

A graphite enhanced PCM is used for the present investigation. Due to the lack of natural convection based flows, the heat transfer can be modelled as a pure conduction problem. Details of this approach and modelling have been shown in Dhumane et al. (2018b), while the test results can be found in Qiao et al. (2018). For the current application, discretization is also carried out along the refrigerant flow direction. Implementation details for these can be found in Alexiades and Solomon (1993) and Patankar (1980). The PCM used is a commercial product containing 20% wt. graphite and 80% wt. PCM. Its thermo-properties were evaluated using Eq. (1) to Eq. (6). The results are summarized in Table 1. The correlation in Eq. (6) and Eq. (7) is obtained from the experimental work of Py et al., (2001).

$$\rho_{bulk} = \gamma \rho_{gr} \quad \text{Eq. (1)}$$

$$\gamma = \frac{V_{gr}}{V_{tot}} \quad \text{Eq. (2)}$$

$$\rho_{eff} = (1-\gamma)\rho_{PCM} + \gamma \rho_{gr} \quad \text{Eq. (3)}$$

$$c_{eff} = (1-\gamma)\frac{\rho_{PCM}}{\rho_{eff}} c_{PCM} + \gamma \frac{\rho_{gr}}{\rho_{eff}} c_{gr} \quad \text{Eq. (4)}$$

$$L_{eff} = (1-\gamma)\frac{\rho_{PCM}}{\rho_{eff}} L_{PCM} \quad \text{Eq. (5)}$$

$$k_{rad} = 3\left(\frac{\rho_{bulk}}{46}\right)^{4/3+0.17} \quad \text{Eq. (6)}$$

$$k_{len} = 3\left(\frac{\rho_{bulk}}{46}\right)^{2/3}\left[2 - \left(\frac{\rho_{bulk}}{46}\right)^{0.17}\right] \quad \text{Eq. (7)}$$

Table 1. Thermo-physical properties of PCM

Graphite bulk density	Graphite volume fraction	Density	Specific heat capacity	Latent heat	Conductivity
($kg \times m^{-3}$)	(%)	($kg \times m^{-3}$)	($J \times kg^{-1} \times K^{-1}$)	($J \times kg^{-1}$)	($W \times m^{-1} \times K^{-1}$)
182.6	8.1	1028.2 (solid) 954.7 (liquid)	1945.4 (solid) 2264.8 (liquid)	173000	23.8(rad), 5.5(len)

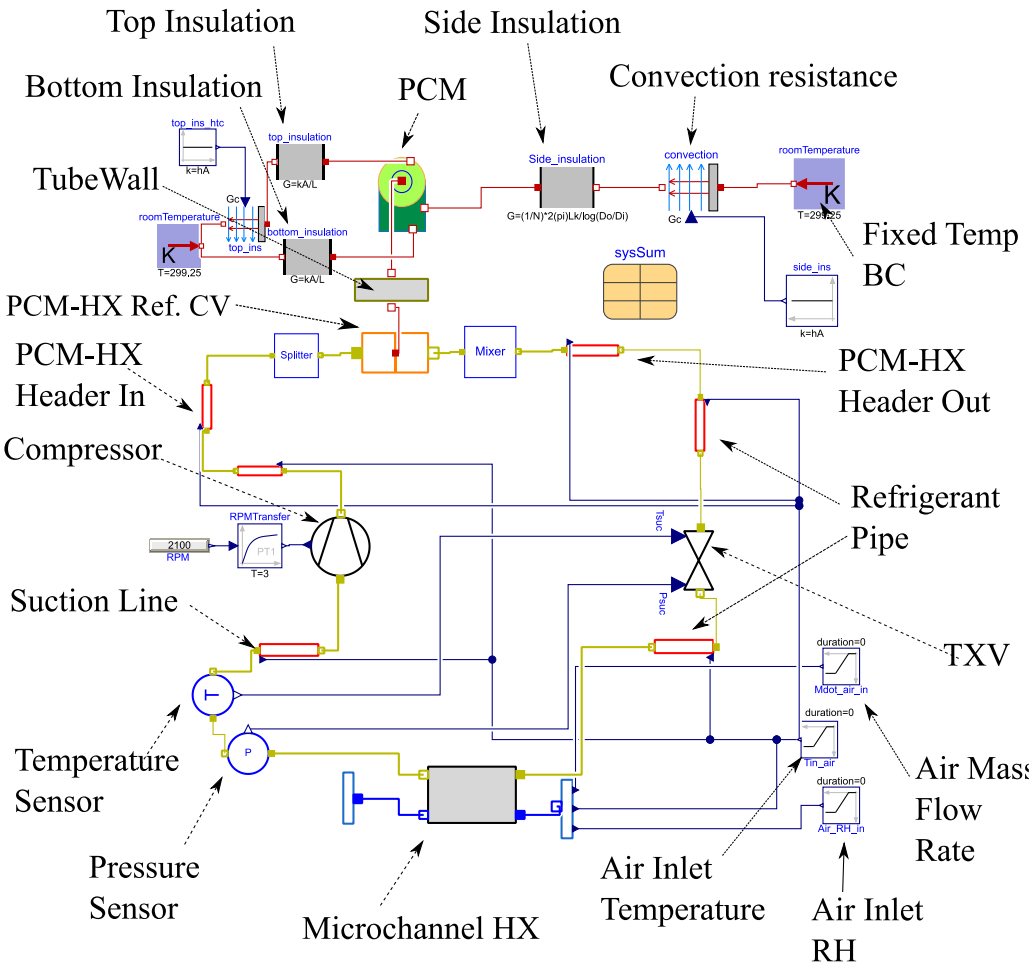

Figure 2: Model diagram

The experiment setup includes a thermal expansion valve (TXV). Detailed physics-based model of TXV requires information about its internal geometry. Due to its unavailability, the spring force balance is calibrated using the experimental data to provide the required amount of superheat temperature.

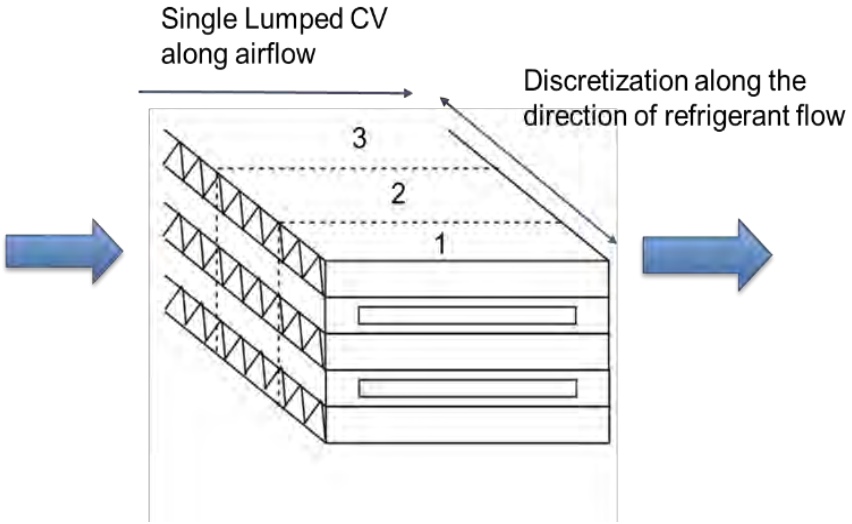

Figure 3: Assumptions in Microchannel Model

The evaporator is a serpentine microchannel with louvered fins. All the refrigerant tubes have fins on either side. End plates are present to clamp the outermost fins. The heat transfer areas and other parameters necessary for its performance calculations are calculated based on the equations presented in Shah and Sekulic (2003). The microchannel model is discretized along the refrigerant flow direction and the airflow direction is modelled as lumped (See Figure 3). As per this assumption, all the refrigerant ports are combined into a single equivalent passage with an equivalent hydraulic diameter. The two-phase boiling heat transfer coefficient is evaluated using Kim and Mudawar (2013a), two-phase pressure drop using Kim and Mudawar (2013b) correlation. Chang and Wang (1997) is used to calculate airside heat transfer from the louvered fins. Fin efficiency is evaluated as per the methodology presented by Hong and Webb (1996). All the fins (except those surrounding end plates) are assumed adiabatic at the centre and provide heat transfer to adjacent refrigerant tubes. The first and last refrigerant tube are modelled separately since they have more fin area for heat transfer. The heat transfer area of end plates is also added to these refrigerant tubes. The efficiency of heat transfer of end plates is assumed to be equal to that of the fins.
The results of the simulation are shown in Figure 4. The results are validated with experimental data, where the cooling mode was run for 5.5 hrs before switching to the heat pump mode.

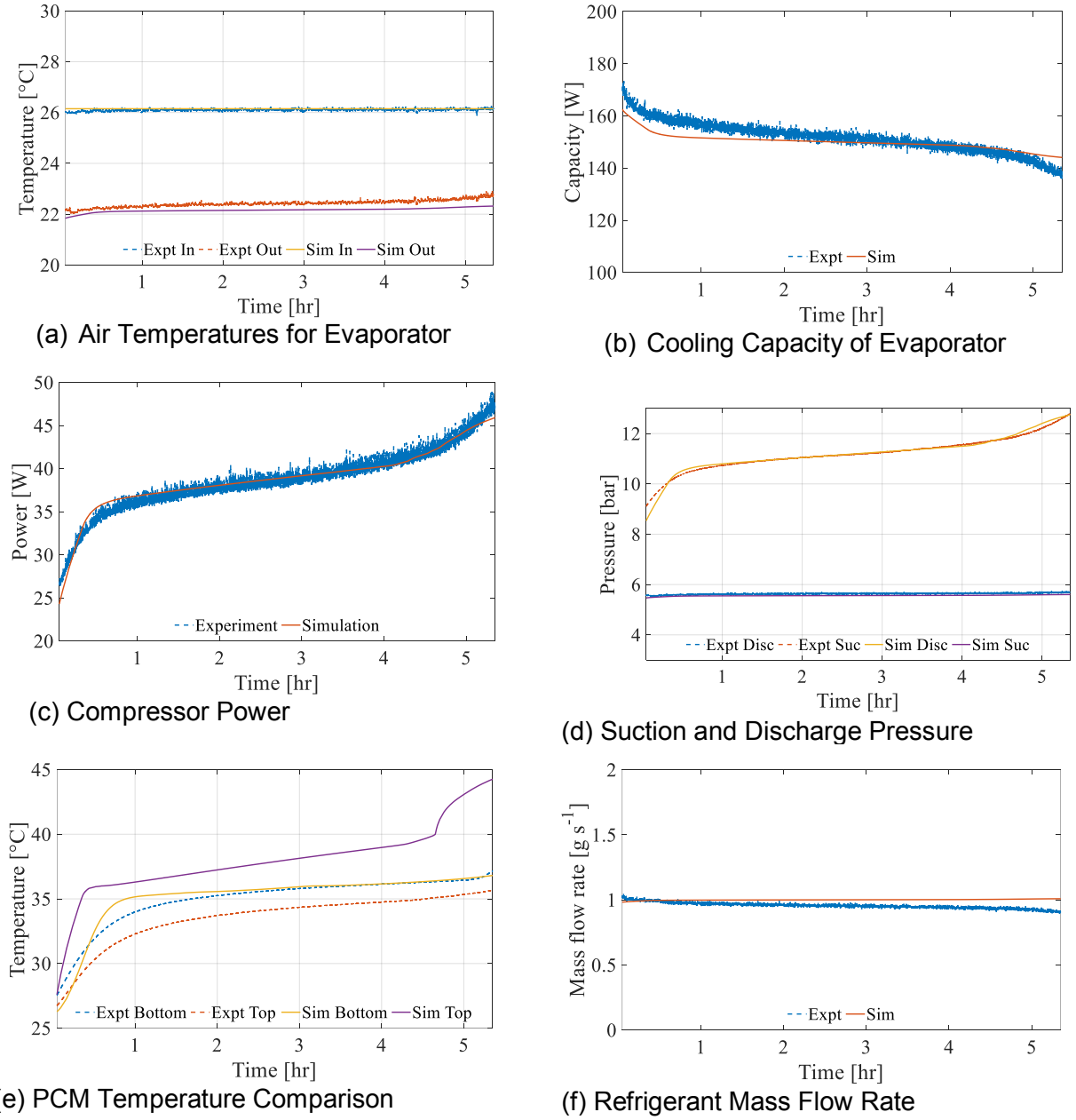

(a) Air Temperatures for Evaporator

(b) Cooling Capacity of Evaporator

(c) Compressor Power

(d) Suction and Discharge Pressure

(e) PCM Temperature Comparison

(f) Refrigerant Mass Flow Rate

Figure 4: Validation for cooling mode of RoCo

The air inlet and outlet temperatures for the microchannel are plotted in Fig. 4(a). It can be seen that the values match the experimental data within measurement uncertainty. The airside and refrigerant side capacity matches exactly in the simulation, but in the experiment, the airside capacity is slightly smaller due to losses, which may also explain the deviations. The refrigerant side measurements are used to calculate the total capacity in the experiment and are compared with the simulation in Fig. 4(b). The compressor model uses fixed efficiency values, which are calibrated to match the power in Fig. 4(c). The suction and discharge pressures also show a good match (Fig. 4(d)). The PCM control volume is discretized into 4 segments along the radial direction and 10 segments along the tube direction. The temperatures from [4,1] and [4,10] control volumes are compared with experimental data with thermocouples which were placed at 1 inch from top and bottom towards the side of the PCM. Details of PCM geometry and thermocouple placement are available in Qiao et al. (2019). The temperatures show a significant difference. The temperature transforming model (Cao and Faghri 1991), which is used for modelling the PCM, distributes the latent heat equally over the temperature glide range. However, in reality, this profile needs to be obtained from DSC measurements. The properties of PCM composite also vary from sample to sample and also based on the rate of phase change. Finally, the refrigerant mass flow rate is compared in Fig. 4(f).
The coefficient of performance (COP) for the experiment for the cooling operation is evaluated to be 3.82, while that for simulation is 3.75 for the period of 5.5 hours. Fan power is not included in the evaluation of the coefficient of performance.

3. SIMULATION WITH LOW-GWP REFRIGERANT

To compare the performance of RoCo with different refrigerants, it needs to be initialized with the same state as the R134a system. The ambient of the environmental chamber is 79°F (26.1°C). So, the initial refrigerant pressure of the system is the saturation pressure of the refrigerant at this temperature (shown in Table 2). Refrigerants having a higher enthalpy of vaporization will require lesser mass flow to provide the same cooling. Also, higher thermal conductivity leads to better heat transfer and lower viscosity leads to lesser pressure drops. Thus, the interplay of several parameters makes it hard to predict the behaviour of the system. The resultant system behaviour is analysed using system simulation, where the same amount of cooling capacity and the same superheat is provided by each refrigerant. The system is initialized with the same refrigerant quality distribution.

Table 2: Properties of refrigerants (At 26.1°C)

Name	Saturation pressure	Vaporization enthalpy	Liquid specific heat capacity	Vapour Density	Liquid viscosity	Liquid thermal conductivity	GWP
	(kPa)	($kJ \times kg^{-1}$)	($kJ \times kg^{-1} \times K^{-1}$)	($kg.\ m^{-3}$)	($Pa \times s^{-1}$)	($W \times m^{-1} \times K^{-1}$)	(-)
R134a	688	176.8	1.429	33.4	1.917e-4	0.083	1430
R32	1741	268.6	1.949	48.9	1.161e-4	0.122	650
R290	979	333.8	2.749	21.2	0.973e-4	0.094	3
R1234yf	704	144.4	1.3974	39.1	1.52e-4	0.063	4
R1234ze (E)	515	166.1	1.397	27.2	1.874e-4	0.075	6

The operating conditions of RoCo with different refrigerants are shown in Figure 5. The interactions of the various parameters from Table 2 on the system can now be easily evaluated. From Fig. 5(a), we can observe that R32 and R290 operate at higher refrigerant pressures to provide similar performance as R134a. But R1234yf and R1234ze(E) have almost similar operating pressures as R134a. The suction and discharge temperatures are plotted in Fig. 5(b). All the refrigerants have a similar suction temperature. This is because the refrigerant side heat transfer coefficient is much higher than the airside. So the differences in the heat transfer coefficients do not cause a pronounced difference. However, on the discharge side, these differences can be observed. Fig. 5(c) shows the

refrigerant mass flow rates required to provide the same cooling capacity. The trend is inversely proportional to the latent heat of vaporization (Table 2, third row). The cooling capacities were matched as the requirement for comparison of the system and it can be seen that they match closely on visual inspection (Fig. 5(d)). Also plotted in Fig. 5(d) is the compressor power.

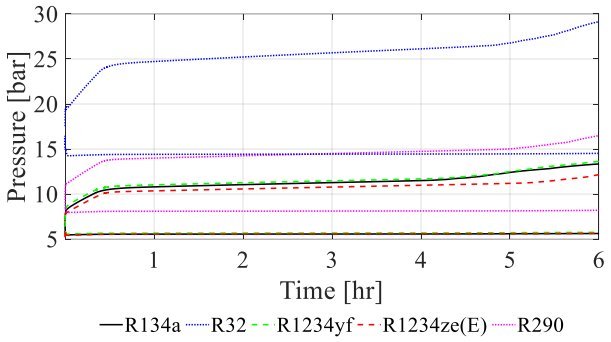

(a) Suction and Discharge Pressures

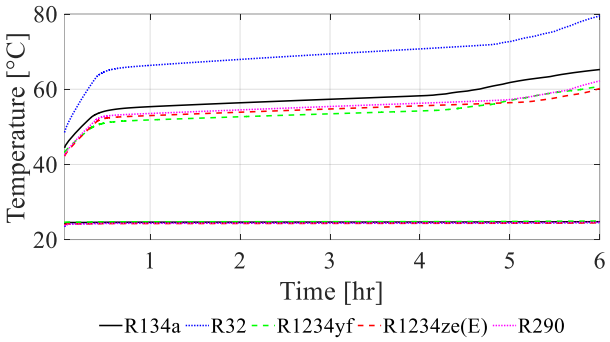

(b) Suction and Discharge Temperatures

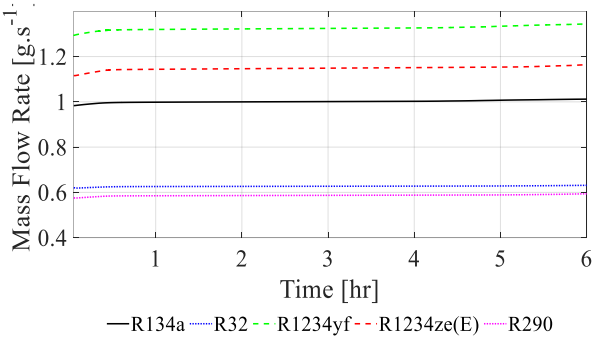

(c) Refrigerant Flow Rate

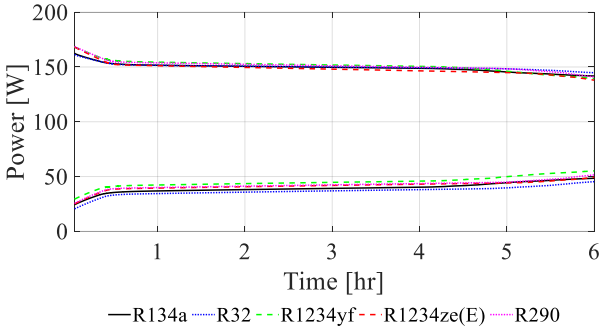

(d) Cooling Capacity and Compressor Power

Figure 5: Comparison of transient variables for RoCo with different refrigerants

The homogenous void fraction model is used for modelling the refrigerant flow. This model relatively poor prediction of the total refrigerant charge. So, it is used only for qualitative comparisons here. Since the base system is R134a, the charge amount is calculated with the R134a system charge for normalization. COP of the system is also evaluated using the transient cooling capacity and compressor power. The comparison of charge and COP is shown in Figure 6. It can be observed that R290 requires the least system charge for operation. This is because of its highest latent heat of vaporization among the refrigerants. Additionally, it can be seen that among the low GWP refrigerants, R32 has the highest COP. From the operation point of view, R1234yf has the closest operating pressures as R134a. This would mean that this could be used as a drop-in substitute.

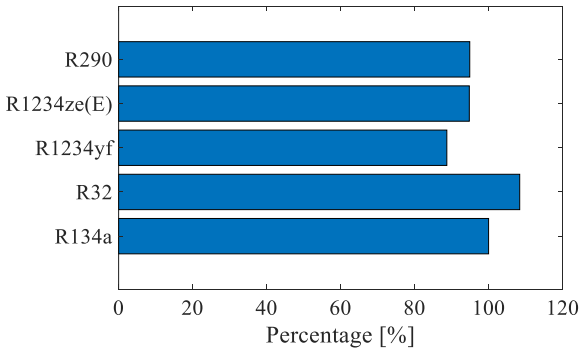

(a) Coefficient of Performance

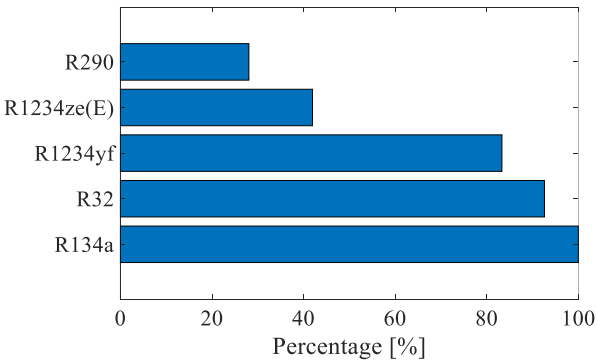

(b) Refrigerant Charge

Figure 6: Comparison of system variables

4. CONCLUSIONS

The system model of cooling operation of RoCo is developed using Modelica and validated with experimental data. A new model for microchannel is developed and used for modelling the cooling mode of RoCo. The results are validated with experimental data conducted with R134a. Finally, simulation is conducted to study the drop-in performance of RoCo with different refrigerants. R1234yf operates at very close pressure values as R134a, while R32 has the highest COP. Propane R290 system requires the least charge for providing the same cooling capacity.

ACKNOWLEDGEMENTS

This research was supported by the Advanced Research Projects Agency - Energy (ARPA-E) under Award DE-AR0000530 and Center for Environmental Energy Engineering (CEEE). The authors acknowledge the support of the team members of the Roving Comforter Project.

NOMENCLATURE

c	specific heat capacity ($J \times kg^{-1} \times K^{-1}$)	L	latent heat capacity ($J \times kg^{-1}$)
k	thermal conductivity ($W \times m^{-1} \times K^{-1}$)	V	volume (m^3)

Greek

γ	volume fraction of graphite (-)	ρ	density (8.314472 $J \times mol^{-1} \times K^{-1}$)
T	temperature (K)	V	molar volume ($m^3 \times mol^{-1}$)

Subscript

len	along length of tube	*gr*	graphite
bulk	PCM-graphite composite	*PCM*	phase change material
eff	effective	*rad*	radial

REFERENCES

Alexiades, Vasilios, and Alan Solomon. 1993. *Mathematical Modeling of Melting and Freezing Processes*. Taylor & Francis. https://doi.org/10.1201/9780203749449.

Cao, Y, and A Faghri. 1991. “Performance Characteristics of a Thermal Energy Storage Module: A Transient PCM / Forced Convection Conjugate Analysis.” *International Journal of Heat and Mass Transfer* 34:93–101.

Chang, Yu-Juei, and Chi-Chuan Wang. 1997. “A Generalized Heat Transfer Correlation for louver Fin Geometry.” *International Journal of Heat and Mass Transfer* 40 (3). Elsevier:533–44.

Dhumane, Rohit, Jiazhen Ling, Vikrant Aute, and Reinhard Radermacher. 2017. “Portable Personal Conditioning Systems: Transient Modeling and System Analysis.” *Applied Energy* 208. Elsevier:390–401.

Dhumane, Rohit, Anne Mallow, Yiyuan Qiao, Kyle R Gluesenkamp, Samuel Graham, Jiazhen Ling, and Reinhard Radermacher. 2018a. “Enhancing the Thermosiphon-Driven Discharge of a Latent Heat Thermal Storage System Used in a Personal Cooling Device.” *International Journal of Refrigeration* In Press. Elsevier.

Dhumane, Rohit, Yiyuan Qiao, Jiazhen Ling, Jan Muehlbauer, Vikrant Aute, Yunho Hwang, and Reinhard Radermacher. 2019. “Improving System Performance of a Personal Conditioning System Integrated with Thermal Storage.” *Applied Thermal Engineering* 147 (25 January 2019). Elsevier:40–51.

Dhumane, Rohit, Yiyuan Qiao, Jan Muehlbauer, Jiazhen Ling, Vikrant Aute, and Yunho Hwang. 2018b. “Evaluating Recharge Options for Phase Change Material Storage of a Personal Conditioning System.” In *5th International High Performance Buildings Conference*, Paper 302.

West Lafayette, IN: Purdue University.

Hong, Kwang Taek, and Ralph L Webb. 1996. “Calculation of Fin Efficiency for Wet and Dry Fins.” *HVAC&R Research* 2 (1). Taylor & Francis:27–41.

Kim, Sung-Min, and Issam Mudawar. 2013a. “Universal Approach to Predicting Saturated Flow Boiling Heat Transfer in Mini/Micro-Channels–Part II. Two-Phase Heat Transfer Coefficient.” *International Journal of Heat and Mass Transfer* 64. Elsevier:1239–56.

Kim, Sung-Min, and Issam Mudawar. 2013b. “Universal Approach to Predicting Two-Phase Frictional Pressure Drop for Mini/Micro-Channel Saturated Flow Boiling.” *International Journal of Heat and Mass Transfer* 58 (1–2). Elsevier:718–34.

Modelica Association. 2019. “Modelica.” https://www.modelica.org/.

Patankar, Suhas. 1980. *Numerical Heat Transfer and Fluid Flow*. CRC press.

Py, Xavier, Régis Olives, and Sylvain Mauran. 2001. “Paraffin/Porous-Graphite-Matrix Composite as a High and Constant Power Thermal Storage Material.” *International Journal of Heat and Mass Transfer* 44 (14):2727–37. https://doi.org/10.1016/S0017-9310(00)00309-4.

Qiao, Yiyuan, Yilin Du, Jan Muehlbauer, Yunho Hwang, and Reinhard Radermacher. 2019. “Experimental Study of Enhanced PCM Exchangers Applied in a Thermal Energy Storage System for Personal Cooling.” *International Journal of Refrigeration*. Elsevier.

Qiao, Yiyuan, Anne Mallow, Jan Muehlbauer, Yunho Hwang, Jiazhen Ling, Vikrant Aute, Reinhard Radermacher, and Kyle R Gluesenkamp. 2018. “Experimental Study on Portable Air-Conditioning System with Enhanced PCM Condenser.” In *17th International Refrigeration and Air Conditioning Conferenc*. West Lafayette, IN.

Shah, Ramesh K, and Dusan P Sekulic. 2003. *Fundamentals of Heat Exchanger Design*. John Wiley & Sons.

Manuscript ID: 1135
DOI: 10.18462/iir.icr.2019.1135

Performance Characteristics of a Residential Air Conditioning System with Subcooling Control

Bruno Yuji KIMURA DE CARVALHO[(a)], Pega HRNJAK[(a)(b)]

[(a)] ACRC, University of Illinois at Urbana-Champaign,
Urbana, Illinois, USA, brunoykc@illinois.edu
[(b)] Creative Thermal Solutions Inc.
2209 Willow Rd. Urbana, Illinois, USA, pega@illinois.edu, pega@creativethermalsolutions.com

ABSTRACT

Superheat control of refrigerant flow using thermostatic expansion valves (TEV) has been widely employed in residential air conditioning and heat pump (RAC&HP). Subcooling control is an alternative for refrigerant flow metering focusing on maximizing COP/HPF or capacity. An electronic expansion valve (EEV) adjusts subcooling while an accumulator prevents liquid return. The paper provides an experimental analysis on the performance of a RAC system with subcooling control. Performance of the system was evaluated at different conditions, at nominal charge. Superheat and subcooling control are compared. Refrigerant charge was also optimized at a single condition for both superheat and subcooling control. Results show a 10.1% increase in COP using subcooling control for indoor/outdoor temperatures of 20°C/40°C. Subcooling control provides a balance between the increase in specific compression work and the increase in specific refrigerating effect.
Keywords: Air Conditioning, Electronic Expansion Valve, Optimization, Subcooling.

1. INTRODUCTION

Current RAC systems rely on superheat control to regulate refrigerant flow and prevent liquid intake at the compressor suction. This method provides acceptable performance at relatively low cost, but it is not optimal since superheat generates a dryout region in the evaporator reducing heat exchanger effectiveness. Pottker and Hrnjak (2015a) have previously shown that controlling subcooling can potentially increase system performance by 2.7%-8.4% in simulations comparing different refrigerants. This increase in system efficiency by controlling subcooling is backed by theoretical analyses (Sebas, 2006; Pottker and Hrnjak, 2012) showing that there exists an optimal subcooling value capable of maximizing COP, as shown in Fig. 1 and equations 1, 2 and 3. An increase in subcooling leads to higher condensing pressures and lower enthalpies at the expansion device inlet. These two effects cause an increase in specific compression work and refrigerating effect, respectively. A trade-off between the increase in compressor power and cooling capacity thus leads to a maximum COP at a defined subcooling value. Automotive air conditioning systems have been using integrated receivers and subcoolers (Yamanaka et al., 1997) to improve system performance for a long time. Nevertheless, this component has not been adopted by residential system manufacturers due to limitations with reversible cycles.

$$COP' \approx COP\left(1 + \frac{\Delta q}{q} - \frac{\Delta w}{w}\right) \quad \text{Eq. (1)}$$

$$COP = \frac{q}{w} \quad \text{Eq. (2)}$$

$$COP' = \frac{q + \Delta q}{w + \Delta w} \quad \text{Eq. (3)}$$

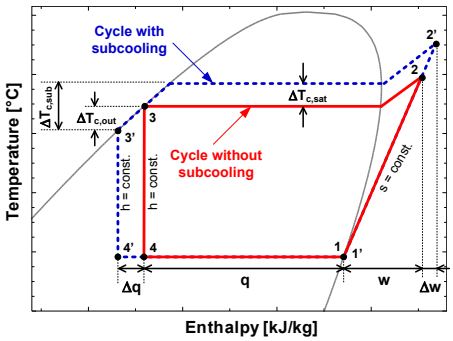

Figure 1: Schematic of cycles with/without subcooling in a T-h diagram (Pottker and Hrnjak, 2012)

Pottker and Hrnjak (2015b) also showed that the use of an internal heat exchanger reduces the overall performance improvement from controlling subcooling since it competes towards mitigating throttling losses. Xu and Hrnjak (2014) also investigated the use of subcooling control through a RAC R410-A system experimentally and using validated. The authors showed that the COP improvement is inversely proportional to the condenser size. They showed that control based on a linear function of ΔT_{in} can provide an acceptable control strategy. Pitarch et al. (2017a, b, c) have also studied subcooling control in heat pump water heaters using natural refrigerants and concluded that optimal subcooling may be obtained as a function of the temperature lift of the secondary fluid or a fixed pinch point temperature difference may be used as a simpler control strategy to keep performance close to optimal levels.
This paper aims to experimentally evaluate the impact of subcooling control on the performance of a R410-A system. Refrigerant charge influence on the air conditioning system was investigated and a fair comparison between the use of a thermostatic valve passively controlling superheat and an electronic expansion valve actively controlling subcooling was performed.

2. FACILITY

The facility, shown in Fig. 2, is comprised of two environmental chambers that can maintain outdoor and indoor temperatures within ± 0.5°C and absolute humidity ±2%. Each chamber uses a variable speed wind tunnel with electric heaters and cooled glycol heat exchangers to simulate a range of operating conditions. Humidity in the chambers can be controlled through steam injection.

4WV: 4-way valve
ABL: Air blender
ACC: Accumulator
AIR: Air
BL: Blower
CC: Charge compensator
CD: Condenser
CP: Compressor
DP: Differential pressure transducer
DPS: Dew-point sensor
EGC: Ethylene glycol chiller
EGHX: Ethylene glycol heat exchanger
ERH: Electric resistance heater
EV: Evaporator
EXV: Electronic expansion valve
FN: Flow nozzle
MF: Muffler
MFM: Mass flow meter
P: Absolute pressure transducer
SI: Steam injection
T: Type-T thermocouple
TCG: Thermocouple grid
TXV: Thermostatic expansion valve
VFD: Variable frequency drive

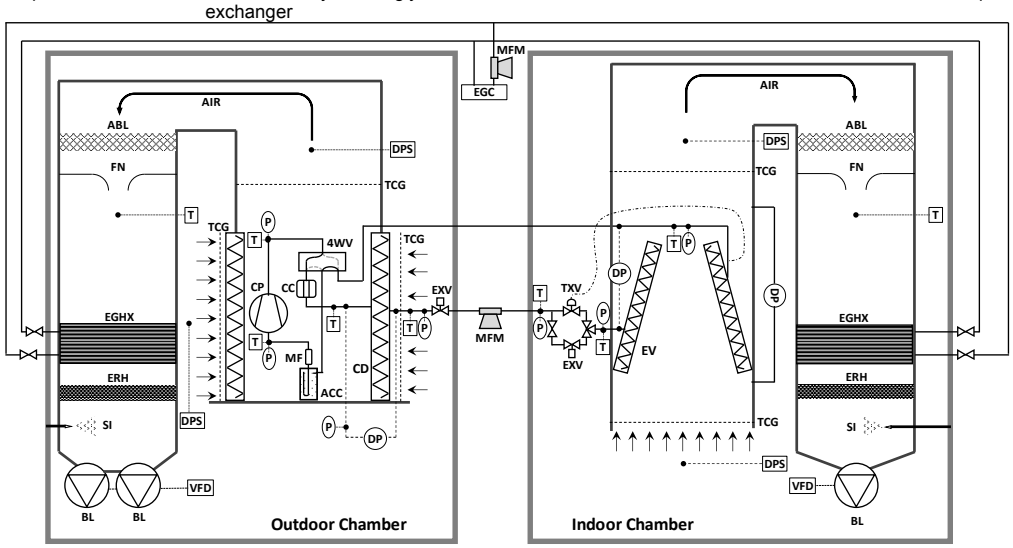

Figure 2: Layout of facility for performance evaluation

The capacity is currently determined by both air side energy balance, and refrigerant side energy balance. The average uncertainty for compressor, heaters and blowers power measurement is within ±0.2%. Air-side and refrigerant side capacity calculations have an expanded uncertainty of around ±4% and COP uncertainty is calculated to be ±5%.
The 2 Ton (7kW) R410-A residential reversible system used has a round-tube A-coil indoor heat exchanger with a thermostatic valve (TXV) and a round-tube horizontal condenser with an electronic expansion valve (EXV) for heat pump operation. Two EXVs were installed in the system in parallel with its present expansion devices to allow subcooling control in both A/C and H/P operation modes. Fig. 3 shows a diagram of the system cycle only. Table 1 shows the specifications for the heat exchangers on the outdoor and indoor chamber.

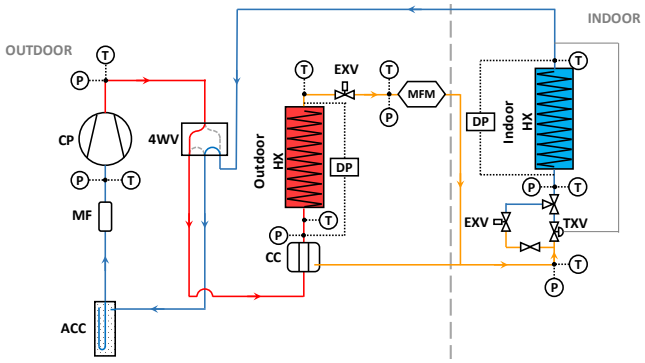

Figure 3: Schematic drawing of the air-conditioning system evaluated

Table 1. Residential system heat exchanger specifications

	Outdoor heat exchanger	Indoor heat exchanger
Description	Two rows, eight circuits, fin pitch 1.27 mm (20 fpi)	Two slabs, three staggered rows, eight circuits, fin pitch 1.75 mm (14.5 fpi)
Face area	2.81 m^2 (30.25 sqft)	0.689 m^2 (7.42 sqft)
Core depth	0.038 m	0.056 m
Core volume	0.1068 m^3	0.03858 m^3
Air side area	153.53 m^3	40.1 m^3
Refrigerant side area	4.61 m^3	2.39 m^3
Material	Aluminum louvered fins, copper tubes, vapor line O.D. = 22 mm, liquid line O.D. = 9.5 mm	

3. RESULTS AND DISCUSSION

3.1 Test conditions

Three outdoor air temperatures were selected to evaluate the improvement obtained by subcooling control at different outdoor conditions. Table 2 summarizes the test matrix for the baseline data. Indoor temperature was fixed at 20°C.The experiments followed the load requirements assuming a linear load with its maximum at 40°C. Compressor speed was controlled through the system interface although the control logic hard-limits maximum compressor speed to prevent excessive wear on the compressor. These baseline test at 40°C were done at different refrigerant charges to determine the optimal charge for the system using a thermostatic valve and compare it to a subcooling-controlled system at its optimal charge.

Table 2. Test conditions

Condition	T_{cai} (°C)	T_{eai} (°C)	Indoor air flow rate (SCFM / m^3/s)	Outdoor air flow rate (SCFM / m^3/s)	Compressor setting (%)	Compressor speed (RPM)
A	35	35	900 / 0.425	2100 / 0.9912	65	1950
B	38	38	900 / 0.425	2100 / 0.9912	85	2720
C	40	40	900 / 0.425	2100 / 0.9912	100	3240

3.2 Refrigerant charge effect on subcooling control

To provide a fair comparison between superheat and subcooling control the optimal refrigerant charge with a thermostatic valve at the baseline condition C was determined. Evaporator superheat was regulated by the thermostatic valve which kept superheat at 3°C ± 0.5°C, and the optimal charge found was of 8050 g. Using this charge as a baseline subcooling was then controlled by an EXV. Refrigerant charge was added to the system to verify its effect on subcooling control performance, Fig. 4 shows COP behavior with subcooling control at three different refrigerant charges. COP-maximizing subcooling increases as more charge is added to the system. At higher refrigerant charges the system can operate at its COP-maximizing subcooling with a flooded evaporator. The use of a thermostatic valve, on the other hand, suffers a significant penalty as charge is increased beyond its optimal condition because overall evaporator performance does not change significantly since dryout is always present, but compressor power is further increased. The optimal charge for the system with TXV yields a COP-maximizing subcooling close to the one obtained at 9300g with subcooling control, meaning that even with a small amount of dryout the optimal value of subcooling is close when outdoor and indoor conditions are kept the same. Subcooling control with the higher refrigerant charge can still achieve a 10.1% increase in COP when compared to a charge-optimized TXV system.

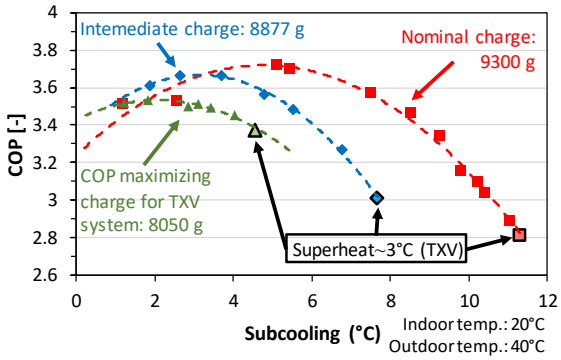

Figure 4: COP as a function of subcooling for three different refrigerant chargers

Fig. 5a and 5b, show the cooling capacity and compressor power vs. subcooling at condition C with three different refrigerant charges. Since subcooling is being regulated by the expansion valve both high-side and low-side pressures are affected by it, thus a maximum cooling capacity is observed when the evaporator is flooded at the lowest evaporation pressure. Compressor power increases monotonically with subcooling as expected due to rise in pressure difference as the expansion valve is closed. The refrigerant charge seems to have a diminishing effect on cooling capacity as the evaporator becomes fully flooded at the optimal subcooling, thus not yielding much change at the higher charges. Compressor power also stabilizes at higher charges because keeping subcooling at its optimal level results in the excess charge being stored in the accumulator.

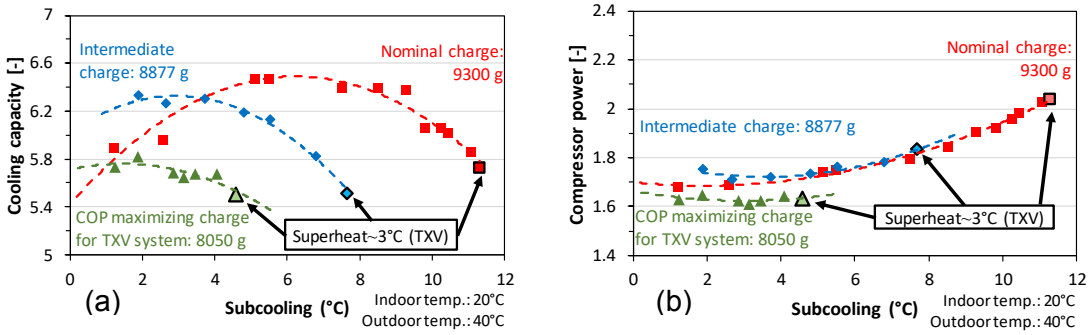

Fig. 5: Cooling capacity reaches a plateau as charge is increased at lower subcooling level (a), while compressor power increases monotonically with subcooling (b)

The evaporator inlet pressure at COP-maximizing subcooling rises by 60 kPa from the lowest charge to the nominal charge of 9300g, shown in Fig. 6a. This translates to an increase in 2°C of saturation temperature, from 6.6°C to 8.6°C. Change in condenser inlet pressure at optimal subcooling is less pronounced with an increase of only 40 kPa from the lower charge to the higher charge, meaning a

saturation temperature difference of approximately 0.6°C, as seen on Fig. 6b. These results further indicate that once the appropriate charge to optimize subcooling control is reached the excess will be stored in the accumulator and any further increase will not affect system performance significantly.

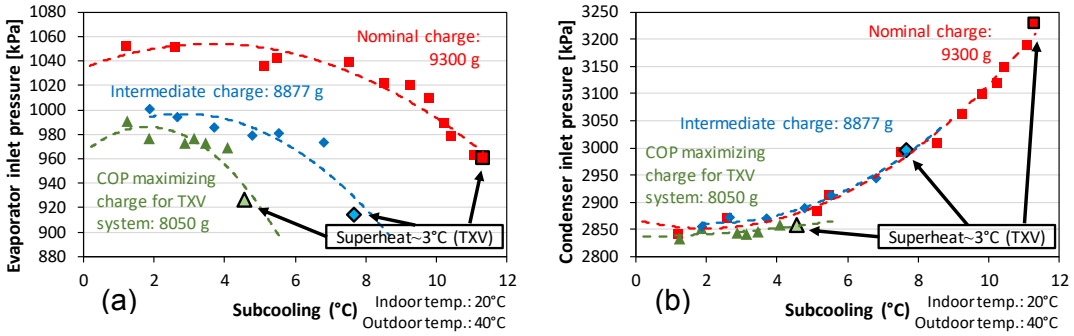

Fig. 6: Cooling capacity reaches a plateau as charge is increased at lower subcooling level (a), while compressor power increases monotonically with subcooling (b)

The P-h diagrams of the system running at its COP-maximizing subcooling with three different charges, and with a TXV at its optimal charge are shown in Fig. 7. The temperature difference between condenser outlet and outdoor air inlet almost coincide at the optimized system with TXV and the COP-maximizing subcooling controlled system at the nominal charge of 9300g. This behavior may be similar to what was observed by Pitarch et al. (2017a) where the optimal subcooling is obtained at a specific temperature difference between condenser refrigerant outlet and secondary fluid inlet which matches the temperature difference at the pinch point in the condenser. This effect must be further investigated as it may allow system optimization through subcooling control based on an indirect measurement of this temperature difference. Xu (2014) concluded that subcooling could be modeled as a linear function of the difference between condensing temperature and outdoor air inlet temperature, but implementation would still require computing subcooling, which can be difficult due to its dependence on the measurement of the saturation pressure at condenser outlet.

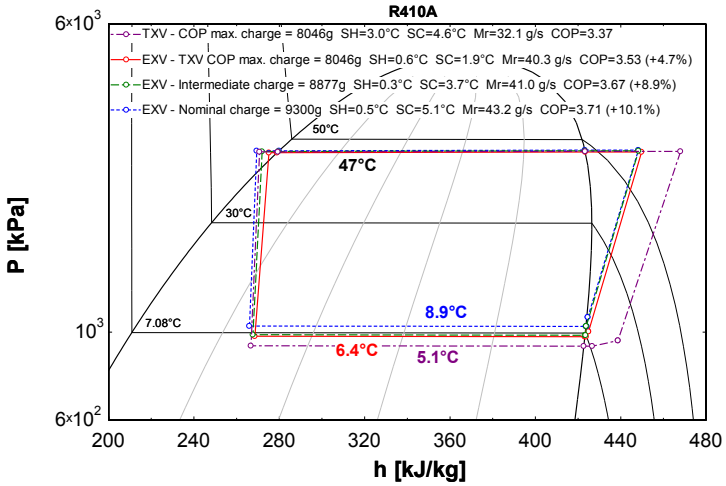

Fig. 7: Operation of the system in two control modes: COP-maximizing subcooling controlled system (at three different charges) and TXV system at its optimal charge

Specific compressor work is affected by the suction pressure change as the refrigerant charge is increased, while high-side pressure rises only slightly. The accumulator also influences the performance using a TXV. The superheat at compressor suction is around 13°C, therefore air-side heat transfer between evaporator outlet and compressor inlet is significant.

3.3 Effect of subcooling control on performance

By controlling subcooling at the condenser outlet it's possible to achieve maximum COP due to a balance between the increase in specific cooling capacity and specific compression work. But when comparing improvements obtained from subcooling control with modeling and experimental results

the benefits in real application are generally more significant due to several effects that are neglected to simplify models. This was observed by Feng and Hrnjak (2016) when analyzing a mobile heat pump with subcooling control.

Figs. 8a and 8b show the evaporator outlet superheat and quality, and evaporator effectiveness as a function of the subcooling. As previously mentioned, the evaporator will have a slightly wet outlet when operating at the COP-maximizing subcooling. Evaporator outlet superheat measurement becomes inaccurate at subcooling below 9°C because the temperature measurement of two-phase flow outlet is too close to the saturation temperature defined by the evaporator outlet pressure measurement. Slightly wet conditions seem to occur between 4°C and 9°C of subcooling. The flooded evaporator will have a significant improvement in effectiveness which allows for higher evaporation pressure, thus a lower specific compression work. At the COP-maximizing subcooling the effectivess is around 75%, or about 25% higher than when the system operates with a TXV. Because the outlet quality is still very close to 1 liquid intake should not pose threat to the scroll compressor if the accumulator is large enough to store the excess charge. The 4 l accumulator used in this system is oversized to protect the compressor during heat pump startup at low outdoor temperature, when most of the charge will migrate to the outdoor unit.

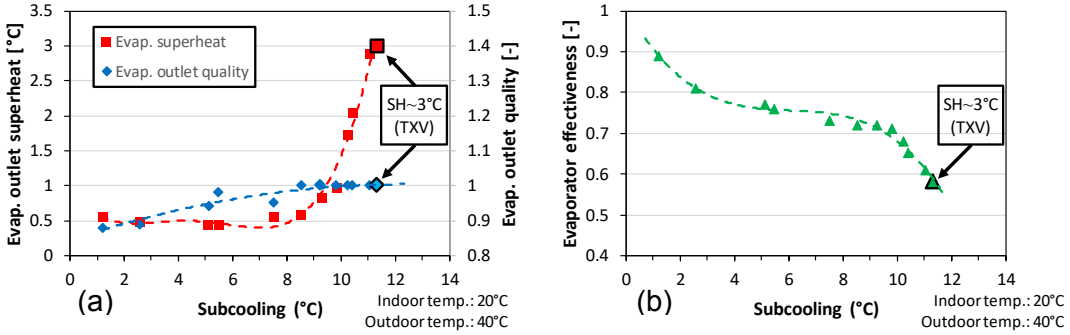

Fig. 8: Evaporator outlet is slightly wet at COP-maximizing subcooling (a), evaporator effectivess is at 75% when COP is maximized, once dryout starts it drops (b)

Pressures remain almost constant when the evaporator is fully flooded, as it's more dependent on the indoor air temperature, and the excess charge in the accumulator mitigates any changes in pressure as the expansion valve is closed. As subcooling is further increased and the accumulator is emptied both high and low side pressures become dependent on the subcooling, once this point is reached the system is already above its COP-maximizing subcooling.

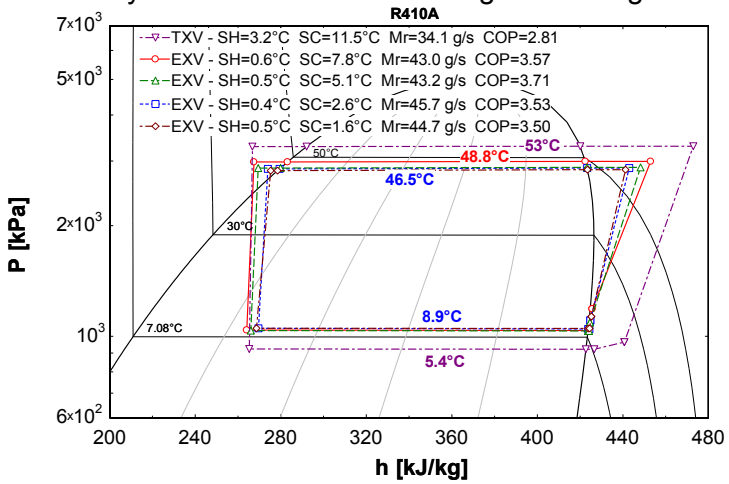

Fig. 9: The accumulator dampens pressure changes at lower subcooling, but as the EXV is closed the operating pressure becomes more dependent on subcooling

Subcooling has a stronger effect on the decrease of specific compression work than on the reduction in specific cooling effect. This was also shown in Fig. 5, as the relative increase in cooling capacity is about 13.2% while the decrease in compressor power was around 14.5%, and the mass flow rate increased by 26.7%. As the pressure ratio is decreased with lower subcooling the compressor's global efficiency should increase. The combined effects of increased evaporator effectiveness and

compressor efficiency lead to greater gains in performance from controlling subcooling when compared to the use of a thermostatic expansion valve.

3.4 Effect of outdoor conditions on subcooling control

Based on the charge optimization procedure done at condition C a comparison between TXV and COP-maximizing subcooling was done. Fig. 10 shows the performance at three different outdoor air temperatures. Compressor speed was matched to provide the capacity following cooling load with a TXV and a refrigerant charge of 9300 g. Subcooling control can provide maximum COP, but it also significantly increases cooling capacity. By actively controlling the compressor speed an even greater increase in performance could be obtained. When comparing COP with the charge-optimized TXV system average COP increase is 8.5%.

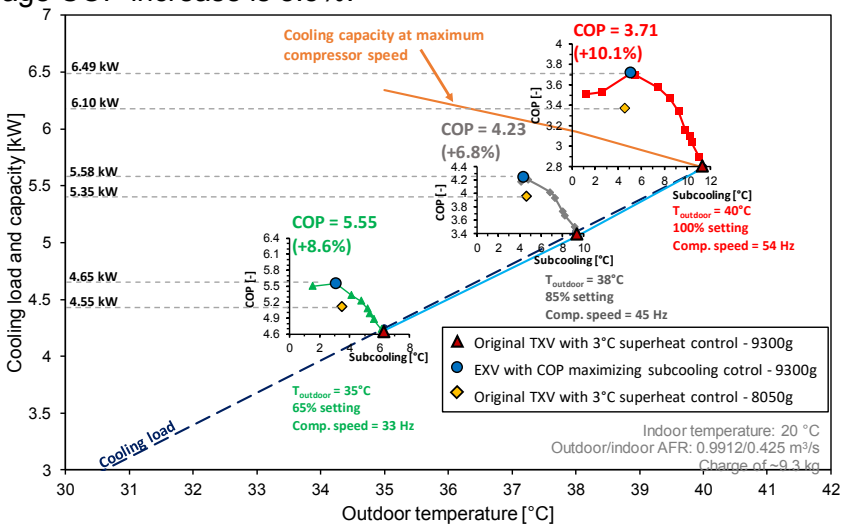

Fig. 10: COP for 3 different outdoor ambient temperatures following the cooling load.

Refrigerant charge was only optimized for the outdoor temperature of 40°C, thus results at lower outdoor temperature may not reflect the best possible condition for a superheat-controlled system. Nevertheless, the COP increase achieved through subcooling control is significant even at lower ambient temperatures and shows a very promising development which requires only the use of an electronic expansion valve and proper control strategy. COP-maximizing subcooling decreases from 5.1°C down to 3.1°C as the outdoor temperature is lowered from 40°C to 35°C.

Table 3 shows a brief comparison of relevant variables for COP-maximizing subcooling control and superheat control at the optimal charge for condition C. These results are very promising as they show that improvement from subcooling control is significant even at lower ambient temperatures. Cooling capacity at these conditions are also above the original cooling load defined for the system. A further reduction in compressor speed would provide even greater COP while still fulfilling the required cooling load.

Table 3. Comparison between subcooling control with EXV at 9300g and with TXV at 8050g

T_{cai} (°C)	40		38		35	
	EXV	TXV	EXV	TXV	EXV	TXV
Q_e (kW)	6.48	6.1	5.58	5.35	4.65	4.55
W_{cp} (kW)	1.74	1.81	1.32	1.35	0.84	0.89
M_r (g/s)	43.2	34.4	35.3	30.0	25.7	23.7
T_{evap} (°C)	8.4	4	8.6	5.4	10.8	8.1
T_{cond} (°C)	47.2	48.1	44.8	44.7	40.3	40.8
ΔT_{sup} (°C)	0.5	3.0	0.9	2.7	0.8	2.8
ΔT_{sub} (°C)	5.1	4.6	4.4	4.6	3.1	3.5
COP (-)	3.71	3.37	4.23	3.96	5.55	5.11

4. CONCLUSIONS

This paper presented an experimental analysis of subcooling control on a residential air conditioning system. Refrigerant charge improves the performance of subcooling control until an excess amount

refrigerant can be kept in the accumulator at the optimal subcooling level for the condition tested. Subcooling control with an electronic expansion valve required 15.5% more charge than the use of a thermostatic valve to reach optimal performance. By keeping subcooling at its optimal level the evaporator operates at a higher effectiveness since its outlet is slightly wet and compressor power is reduced due to lower pressure difference/ratio. When comparing subcooling control with an EXV at different outdoor ambient temperatures with a charge optimized system using a TXV an average increase in COP of 8.6% was observed. The temperature difference between condenser refrigerant outlet and outdoor air temperature was kept almost constant with only a slight reduction. This parameter may be used to indirectly control subcooling and maximize either COP or cooling capacity without the requirement of pressure measurements.

Since pressure transducers can increase the cost of RAC system a thorough investigation on a control strategy requiring only temperature measurements and further study of other effects on subcooling control, such as air face velocity on both heat exchanger and different indoor ambient temperature must be done to validate this approach COP-maximizing approach.

ACKNOWLEDGEMENT

This work was supported by the Air Conditioning and Refrigeration Center at the University of Illinois at Urbana-Champaign. Support from ACRC members and sponsors are gratefully acknowledged.

NOMENCLATURE

A/C	Air conditioning	evap	evaporation (subscript)	SH	superheat
AFR	Air flow rate ($m^3\ s^{-1}$)	EXV	Electronic expansion valve	sub	subcooling (subscript)
cai	condenser air inlet (subscript)	h	Enthalpy ($kJ\ kg^{-1}$)	sup	superheat (subscript)
cond	condensation (subscript)	H/P	Heat pump	T	Temperature (°C)
cp	compressor (subscript)	M	Mass flow rate ($kg\ s^{-1}$)	TXV	Thermostatic expansion valve
COP	Coefficient of performance	Q	Capacity (kW)	w	Specific work ($kW\ kg^{-1}$)
ΔT	Temperature difference (°C)	r	refrigerant (subscript)	W	Work/Power (kW)
e	evaporator (subscript)	RAC	Residential air conditioning		
eai	evaporator air inlet (subscript)	SC	Subcooling		

REFERENCES

Feng, L., Hrnjak, P. (2016). Experimental and Numerical Study of a Mobile Reversible Air Conditioning-Heat Pump System. *Proceedings of the 16th International Refrigeration and Air Conditioning Conference at Purdue, West Lafayette*, *USA* (2569). West Lafayette, USA. Purdue University.

Pitarch, M., Navarro-Peris, E., Gonzalvez-Macia, J., Corberan, J.M. (2017a). Experimental study of a subcritical heat pump booster for sanitary hot water production using a subcooler in order to enhance the efficiency of the system with a natural refrigerant (R290). *International Journal of Refrigeration, 73, 226-234.*

Pitarch, M., Navarro-Peris, E., Gonzalvez-Macia, J., Corberan, J.M. (2017b). Evaluation of different heat pump systems for sanitary hot water production using natural refrigerants. *Applied Enerty, 190, 911-919.*

Pitarch, M., Navarro-Peris, E., Gonzalvez-Macia, J., Corberan, J.M. (2017c). Evaluation of optimal subcooling in subcritical heat pump systems. *International Journal of Refrigeration, 83, 18-31.*

Pottker, G. and P. S. Hrnjak, (2012). Potentials for COP increase in Vapor Compression Systems, ACRC TR 294. University of Illinois at Urbana-Champaign.

Pottker, G., Hrnjak, P. (2015a). Effect of the condenser subcooling on the performance of vapor compression system. *International Journal of Refrigeration, 50, 156-164.*

Pottker, G., Hrnjak, P. (2015b). Thermoeconomic optimization of subcooler and superheated vapor compression refrigeration cycle. *Energy, 31, 2108-2128.*

Selbas, R., Kizilkan, O., Sencan, A. (2006). Experimental investigation of the effect of condenser subcooling in R134a and R1234yf air conditioning systems with and without internal heat exchanger. *International Journal of Refrigeration, 50, 104-113.*

Xu, L., Hrnjak, P. (2014). Potential of Controlling Subcooling In Residential A/C System. *Proceedings of the International Refrigeration and Air Conditioning Conference at Purdue, West Lafayette*, *USA.* West Lafayette, USA (2387). Purdue University.

Xu, L. and P.S. Hrnjak, (2014). Potential of Controlling Subcooling in Residential Air Conditioning System ACRC TR311. University of Illinois at Urbana-Champaign.

Yamanaka, Y., Matsuo, H., Tuzuki, K., Tsuboko, T., 1997, Development of Sub-cool system, SAE Technical Paper Series, paper 970110.

Manuscript ID: 1149
DOI: 10.18462/iir.icr.2019.1149

Experimental research on the heating performance of a flat-heat-pipe heating system integrated with phase change material and thermoelectric unit

Hongli Sun[(a)], Borong Lin[(a)], Haitian Zhao[(a)], Xiaoming Ma[(a)]

[(a)] Department of Building Science, Tsinghua University, Beijing 100084, China, 541421129@qq.com

ABSTRACT

In this research, flat-heat-pipe heating system using phase change material (PCM) and thermoelectric unit was firstly proposed. The flat heat pipe was utilized as a heating terminal in this system, which made it have potential to achieve intermittent radiant heating for specialized applications. Furthermore, the proposed system would be able to use solar energy to achieve a higher energy efficiency owing to the integrated PCM. In addition, the thermoelectric unit, which acted as an auxiliary heat source, was innovatively integrated with PCM and flat heat pipe. This structure increases the heating coefficient of performance of thermoelectric unit and makes it possible to apply the thermoelectric unit in the field of heating. The different components of the heating system complemented each other and meant that intermittent heating could be achieved at any time. The experimental results show that the heating terminal could be heated in only 500 s. Moreover, the PCM was able to guarantee a heating temperature above 40 °C for 2520 s. When the heat supplied by the PCM was insufficient, the thermoelectric unit provided the needed heat with a coefficient of performance greater than 1.70. In addition, the thermoelectric unit had a heating coefficient of performance of 1.35 to 1.54 when there was no heat stored in the PCM. Overall, this novel heating system is capable of highly efficient intermittent heating.
Keywords: Heating System, Flat Heat Pipe, Phase Change Material, Thermoelectric Unit

1. INTRODUCTION

The building sector accounts for almost 20% of the total energy consumption in China (Huo et al., 2018), most of which is related to heating-ventilation-air-conditioning (HVAC) systems. Thus, it is very important to apply appropriate HVAC systems with high energy efficiencies in the building sector. Among the various HVAC systems in the market, radiant heating systems have been widely used in the building sector in recent years owing to their potential for higher energy savings and the greater thermal comfort they provide (Imanari et al., 1999). Therefore, an increasing number of people in China prefer radiant heating systems, especially in areas with hot summers and cold winters. There are primarily two types of radiant heating systems that are widely used in China: one is the electric radiator, which has a small thermal inertia but a low heating coefficient of performance (COP), and the other uses heated water as the radiant source and thus has a higher COP but larger thermal inertia (Ren et al., 2008). However, some regions in China, such as hot summer and cold winter area, require intermittent heating rather than continuous heating (Chen et al., 2011). Generally, the air temperature differences between days and nights are large and the heating demand often occurs at night and the heating measures are often taken at night, especially around 7 pm to 10 pm. Moreover, the intermittent heating demands show more potential in some Tibetan areas. It is very warm during the day owing to abundant solar energy, but it is extremely cold at night (Sun et al., 2015). Therefore, intermittent heating is encouraged by the government in these areas to balance the needs for energy saving and thermal comfort. Hence, radiant systems with both acceptable COPs and small thermal inertia show great potential to be deployed in these areas.

In this research, we proposed an intermittent radiant heating system that includes both a terminal and heat source. One of the novelties of this heating system is that the flat heat pipe, which is mainly

applied in the heat transfer optimization field, was utilized as a heating terminal in the intermittent heating system. The high heat transfer efficiency of the flat heat pipe makes the system having the potential achieving the intermittent radiant heating. The other is that this system has a novel structure of integrating the PCM and flat heat pipe with the thermoelectric unit. Although the thermoelectric unit has higher heating COP than electric heating, the heat source at the cold side and the dissipation at the hot side of the thermoelectric unit are the key points when applying thermoelectric unit in the heating system. The application of PCM at the cold side and the flat heat pipe at the hot side enhances the coefficient of performance of the thermoelectric unit significantly.
The radiant terminal is formed by a flat heat pipe with a microchannel structure, which allows it to be heated rapidly. Meanwhile, the heat sources comprise a passive-heating phase change material (PCM) and an active-heating thermoelectric unit. In areas requiring intermittent heating, heating systems are not operated continuously. Thus, excess energy (e.g. solar energy) available during the day time could be stored when there is no demand for heating. Accordingly, using a PCM shows potential to yield energy savings in situations where there is a time difference between energy acquisition and consumption (Moreno et al., 2014); in this research we thus used a PCM as a heat source. However, considering the energy storage quantity of the PCM could be insufficient, an active-heating measure was also included in our system. The thermoelectric component functions via the Peltier effect without any moving parts or refrigerant and can be heated rapidly within a few seconds. It absorbs heat from the cold side and heats the hot side when it is in operation. Hence, it has a higher COP than electric heating. In this system, these two heat sources work harmoniously with a flat heat pipe terminal, allowing us to achieve intermittent heating with a high response speed and high energy efficiency.

2. MAIN SECTION

The aim of this research was to study a flat heat pipe radiant heating system integrated with a thermoelectric unit and PCM for intermittent radiant heating for use in specialized locations. In this research, an experimental system was built and its working characteristics were analyzed for a comprehensive set of conditions. For the flat heat pipe, the heat response speed and heating uniformity were studied and analyzed. Meanwhile, the thermoelectric unit was turned on when there was not enough energy storage in the PCM. During operation, a heating COP analysis was performed and the heat transfer process was also analyzed. For the PCM, both the energy storage and release process were studied. This research provides a radiant heating system for areas where intermittent heating is required.

2.1. Experimental Method

The flat heat pipe heating system was built in a laboratory room where the indoor temperature was controlled between 23 and 24 °C. A schematic and a photograph of the experimental heating system are shown in Figs. 1 and 2. This heating system was driven by two water pumps, connected by circulation water pipes and two three-way valves. The heating system consisted of three parts: the heating terminal, the PCM heat storage unit, and the heater. The heating terminal (top panel of Fig. 1) had three main parts, namely the heat exchange tank, the thermoelectric unit, and the flat heat pipe. The thermoelectric unit (TEC12706) had two sides, the hot side and cold side, with dimensions of 0.04 m × 0.04 m × 0.005 m (L × W × H). The hot side was connected to the bottom of the flat heat pipe (dimensions of 0.5 m × 0.04 m × 0.2 m), while the cold side was in contact with the heat exchange tank (Fig. 3). Both interfaces were covered uniformly with a thermal grease compound for better heat conductivity. When heated water flowed through the heat exchange tank, the heat was transferred to the flat heat pipe through the thermoelectric unit. When the water was insufficiently heated, and the set heating temperature could not be reached, a steady DC power was applied to the thermoelectric unit and it could supply the heat deficit.
The PCM heat storage unit was a passive heat source in the system; the PCM heat storage unit was made of stainless steel (0.3 m tall and 0.06 m in diameter). The circulation water flowed into the PCM heat storage through a tube and was then divided into eight streams (bypasses) in separate tubes (Fig. 4) for better heat transfer. The PCM heat storage unit was filled with the PCM, namely inorganic salt and various additives. The main physical properties of the PCM are shown in Table 1. The PCM used here is solid at room temperature and begins to absorb heat and liquefy when the ambient temperature reaches 54 °C. There are two reasons we chose this PCM: one is that 54 °C is a common temperature for solar-heated hot water, which makes it possible to simulate the

application of solar energy. The other is that 54 °C is close to common heating temperatures. Therefore, this PCM was chosen as an energy storage unit. The PCM heat storage unit provided the storage and supply of energy in this system, the heat transfer process of which was accomplished by heat transfer with the water circulation system.
The heater was a water tank with an electric heater, the power of which was adjustable. It simulated the heat exchange with the external environment, in particular energy acquisition processes, such as via solar energy conversion. When the heating system was not working, the system collected the solar energy and stored it in the PCM heat storage unit. Overall, it worked as the energy exchange (with the external environment) component of this system. Characteristics of the key components of the heating system are listed in Table 1.

Table 1. Physical characteristics of the PCM

Component	Crystallization temperature(°C)	enthalpy (KJ/kg)	density (g/cm^3)
inorganic salt, additives	54-58	225	1.28(liquid) 1.40(solid)

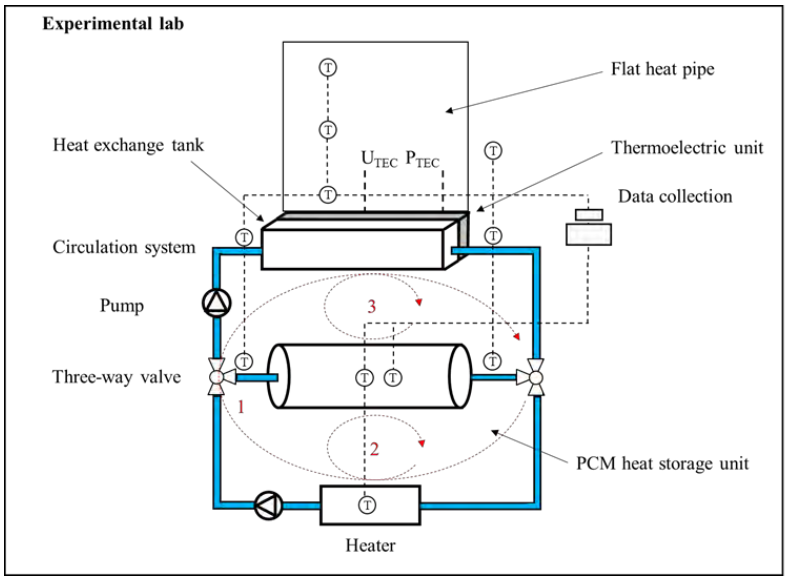

Figure 1: Schematic of the experimental system

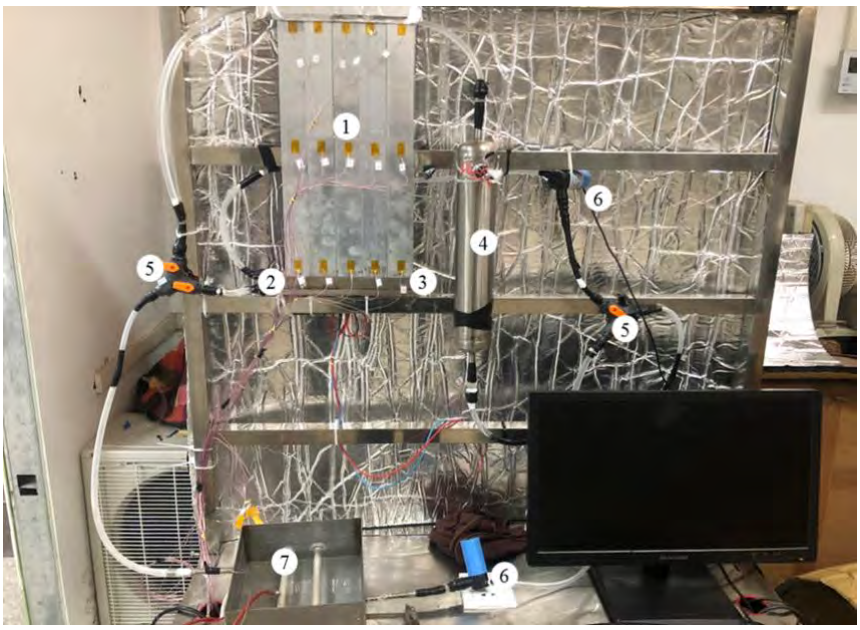

Figure 2: Photograph of the experimental system

1 flat heat pipe 2 thermoelectric unit 3 heat exchange tank

4 PCM heat storage unit 5 three-way valve 6 pump 7 heater

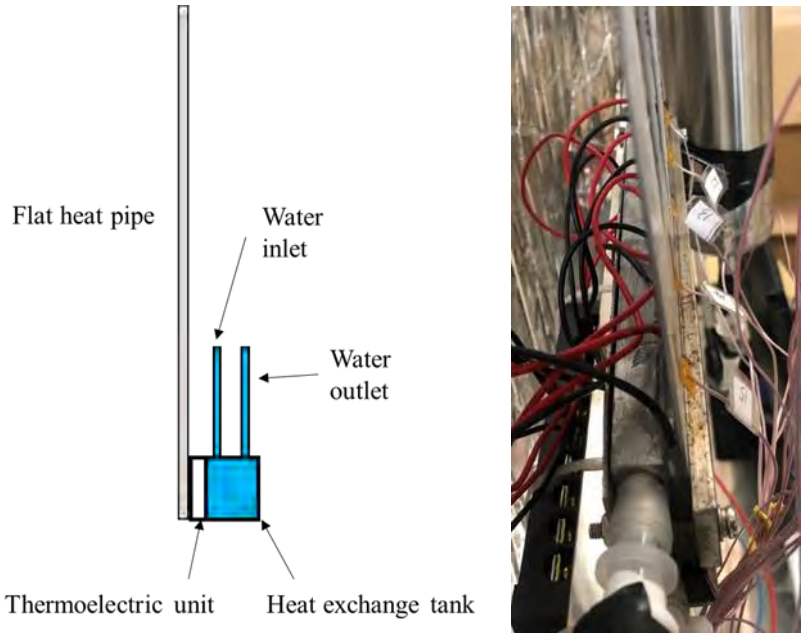

Figure 3: The heating terminal of the system

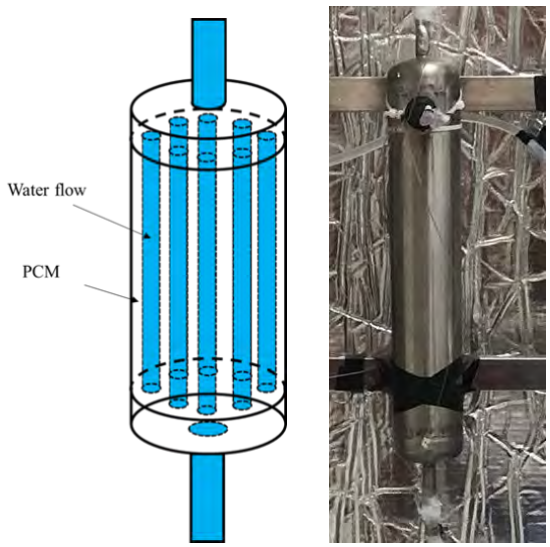

Figure 4: The PCM heat storage unit

2.2. Experimental Conditions

The heating system was designed for locations where there is a demand for intermittent heating, such as in the Tibetan area in China. The air temperature difference between day and night is large and the heating demand often occurs at night. Additionally, solar energy sources are adequate during the daytime. Thus, several working conditions of this heating system were proposed for efficient intermittent heating during the whole heating season.

During the daytime, solar energy was adequate and the water in the circulation system was heated. When there was an indoor heating demand, the heated circulation water flowed into the heating terminal and heated the indoor environment through the flat heat pipe. With the assumption that there is no heat loss from the TEC unit to the environment (less than 2%), the heat (Q_{hc}) was conducted from the heat exchange tank to the flat heat pipe through the thermoelectric unit; this process can be describe by

$$Q_{hc} = K_0 F(T_w - T_f) \quad \text{Eq. (1)}$$

where K_0 is the total thermal conductance between the heat exchange tank and the flat heat pipe [Wm^{-2} K^{-1}]; F represents the heat exchange area between the flat heat pipe and the tank [m^2]; and T_f and T_w represent the average temperature of the flat heat pipe and the circulation water [K]. The heat was ultimately dissipated from the flat heat pipe to the indoor environment by radiation and the convection described by

$$Q_{hc} = hA(T_f - T_0) \quad \text{Eq. (2)}$$

where h is the averaged coefficient of the heat transfer of the flat heat pipe, which was measured in [34] to be 5.73 [W m^{-2} K^{-1}]; A represents the dissipation area of the flat heat pipe; and T_0 is the indoor air temperature [K]. This heating circulation is indicated by loop 1 in Fig. 1. When there was no heating demand or excess solar energy was available, the heated circulation water was distributed into the PCM heat storage unit, which is indicated by circle 2 in Fig. 1. The PCM was heated and the excess energy was stored in the PCM heat storage unit.

At night, there might be a demand for heating in the room. If there was energy stored in the PCM heat storage unit, circle 3 in Fig. 1 started running. The water flowed into the PCM heat storage unit and was heated via a heat exchange. The heated water then flowed into the heating terminal, and the temperature of the flat heat pipe rose rapidly to achieve intermittent heating. When the heat stored in the PCM heat storage unit was not sufficient to satisfy the required heating demand, the active heating system, namely the thermoelectric unit, was turned on to compensate. When the thermoelectric unit was working, it absorbed heat (Q_c) from the heat exchange tank and released heat to the flat heat pipe (Q_h). According to the simplified energy equilibrium model [24], Q_c and Q_h can be expressed as

$$Q_c = \alpha I T_c - 0.5 I^2 R - K(T_h - T_c) \quad \text{Eq. (3)}$$

$$Q_h = \alpha I T_h + 0.5 I^2 R - K(T_h - T_c). \quad \text{Eq. (4)}$$

where α is the Seebeck coefficient of the thermoelectric material [V/K]; I represents the current through the thermoelectric unit [A]; T_c and T_h are the cold and hot side temperature of the thermoelectric unit, respectively [K]; R is the electrical resistance of the thermoelectric unit [Ω]; and K is the thermal conductance of the thermoelectric unit [W m^{-2} K^{-1}]. Therefore, the input electric power (P_{TEC}) of the thermoelectric unit can be described as

$$P_{TEC} = Q_h - Q_c = I^2 R + \alpha I (T_h - T_c). \quad \text{Eq. (5)}$$

Furthermore, the heating coefficient of performance (COP_h) is given by:

$$\mathrm{COP}_h = Q_h / P_{TEC}. \quad \text{Eq. (6)}$$

When the thermoelectric unit was in operation, the heat acquired by the flat heat pipe mainly consisted of two parts: the thermoelectric unit heat (Q_h) and the heat conduction from the heat exchange tank (Q_{hc}). The heat equilibrium of the flat heat pipe is thus given by:

$$Q_{hc} + Q_h = hA(T_f - T_0) \quad \text{Eq. (7)}$$

If there was no heat stored in the PCM heat storage unit, circle 1 in Fig. 1 would be taken into operation. The cold side of the thermoelectric unit absorbed heat from the circulation water system and transferred the heat to the hot side to heat the flat heat pipe. The circulation water exchanged heat with the external environment through the heater, which in an actual application could be a solar hot water pipe.

In this experiment, the surface temperature of the flat heat pipe was measured by the thermocouples with an accuracy of 0.1°C and the temperature of the PCM was measured by the thermal resistance with an accuracy of 0.2°C.

Several operation conditions are summarized in Table 2.

Table 2. Experimental operation conditions of the heating system

Condition	PCM heat storage unit	Thermoelectric unit	Heater	Circle in Fig.1
Direct heating from heater: there is heating demand in daytime	Affluent energy for charging	Off	On	1
PCM charging: affluent energy is stored in the PCM during the daytime	Charging	Off	Off	2
PCM discharging for heating: the energy stored in PCM is utilized for intermittent heating at night	Discharging	Off	Off	3
PCM discharging with thermoelectric concurrent heating: the energy in the PCM is insufficient	Discharging	On	Off	3
Thermoelectric heating: there is no thermal storage in the PCM.	-	On	Heat exchange	1

2.3. Experimental Results

2.3.1. "Direct heating from heater" condition

This condition simulated a heat demand in the daytime, and the heating terminal was heated by the heater directly. When the flat heat pipe was heated, the surface temperatures at the bottom, middle, and upper section of the pipe (T_1, T_2, and T_3) were tested. The experimental heating procedure was roughly divided into 5 stages, which are illustrated in Fig. 5. In the first 600 s of stage 1, the water in the heater was heated to around 65 °C (± 0.2), which simulated water in a solar heater. Once there was indoor heat demand, the circulation water system started up and the heated water was pumped into the heat transfer tank, which then heated the flat heat pipe. Stage 2 showed the initial heating

stage of the flat heat pipe. The flat heat pipe was heated rapidly. However, there was a decrease in the rate at which the temperature rose owing to the water in the heater and circulation system mixing. Thereafter, the mixed water was heated to a set temperature, and the temperature of the flat heat pipe rose further to a stable state. The temperature rise in both stage 1 and 2 took less than 500 s to reach a steady state, thus executing intermittent heating excellently. During stage 4 with its stable heating, the average heating temperature was around 44 °C. In addition, there was a vertical temperature difference of 1.7 °C on the surface of the flat heat pipe. When ending indoor heating, the water circulation system was stopped, and the flat heat pipe allowed to cool naturally. Stage 5 in Fig. 5 shows that the flat heat pipe could cool down naturally in less than half an hour. Overall, the flat heat pipe achieved intermittent heating when heated by the heater directly.

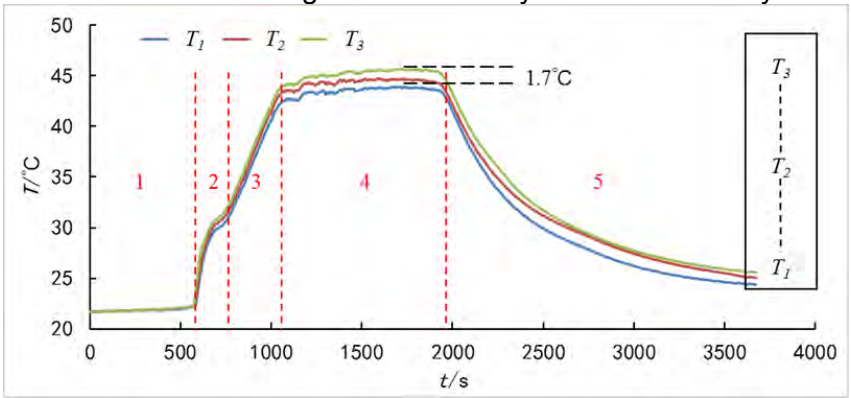

Fig. 5. Heating characteristics of the flat heat pipe when heated from the heater directly

2.3.2. PCM discharging for heating

At nightfall, the heat stored in the PCM heat storage unit can be released to the indoor environment through the flat heat pipe. In this experimental condition, the charging process of the PCM is completed in advance. Then the circulation water system is turned on to carry heat from the PCM to the flat heat pipe. Fig. 6 illustrates the discharging process of the PCM when it releases heat to the flat heat pipe. In this experiment, the hysteresis of melting and solidification for the PCM is neglected for its time scale is relatively smaller. The trends in the temperature changes were similar, but also considerably faster compared with the natural discharging process. The T_4 refers to temperature of the inner position of the PCM unit while the T_5 refers to the outside position. The temperature of the PCM dropped to 49.2 °C in the first 920 s, namely the sub-cooling stage. Then the PCM was further heated to 55.8 °C by the heat generated by the phase transition, before it was cooled down to the natural indoor environment.

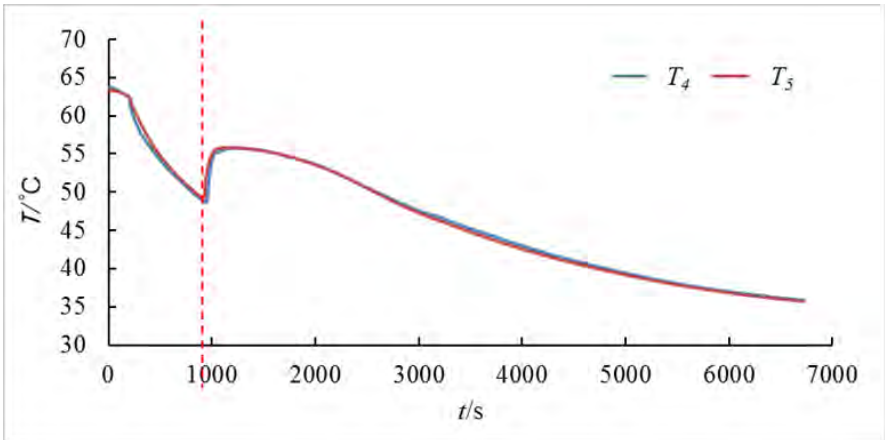

Fig. 6. Discharge characteristics of the PCM heat storage unit

The reason the PCM discharged faster was that it heated the flat heat pipe at the same time. Fig. 7 shows the heating characteristics of the flat heat pipe heated by the PCM storage unit. When the heated water flowed into the heat exchange tank, the flat heat pipe was heated in 400 s. The surface temperature of the flat heat pipe changed with the change in temperature of the PCM, and both curves showed the same trend. Further, there were almost no differences in the temporal

temperature change characteristics between the PCM and the flat heat pipe. In other words, the flat heat pipe had good heat response characteristics and could deliver intermittent heating. In addition, the flat heat pipe had an average heating temperature of 40 °C in the first 2040 s with a vertical surface temperature difference of 1.1 °C.

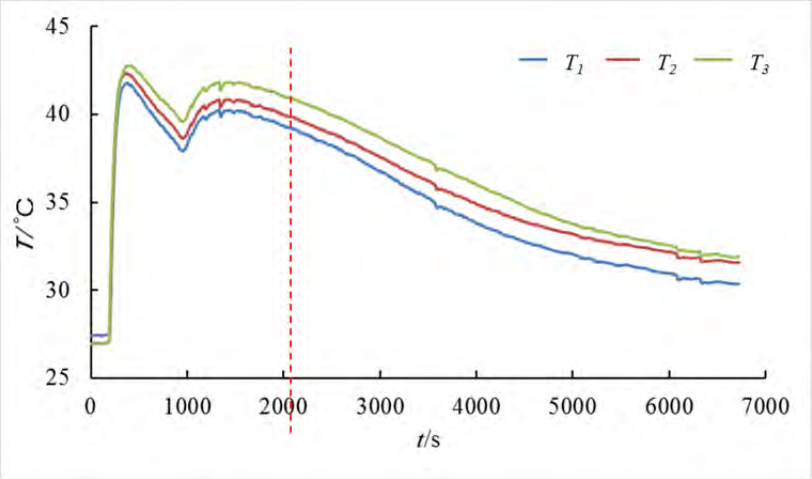

Fig. 7. Heating characteristics of the flat heat pipe heated by the PCM heat storage unit

2.3.3. PCM discharge concurrent with thermoelectric heating

As the discharging process of the PCM continued, the average temperature of the PCM decreased, which made the heating temperature of the flat heat pipe decrease as well. Thus, over time the heating temperature could not satisfy the indoor heating demand and an auxiliary heat source was necessary. The thermoelectric unit worked as an auxiliary heat source in this system that absorbed heat from the PCM and increased the temperature of the flat heat pipe further. Fig. 8 shows the heating and working characteristics of the system. The temperature is displayed on the left ordinate, while the voltage (V), power (W), and COP are shown on the right ordinate. The COP was calculated by the Eq. (6) based on the Q_h and the power measured in the experiment. It can be seen from the temperature curve that the thermoelectric unit was switched on when the average surface temperature of the flat heat pipe was below 40 °C at 2520 s. Then, the average surface temperature was controlled to around 40 °C by adjusting the voltage of the thermoelectric unit.

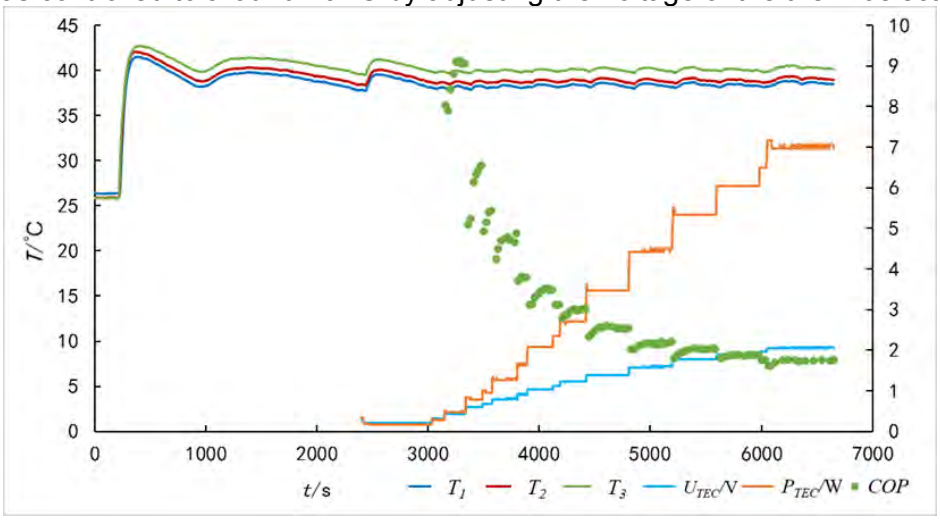

Fig. 8. Heating and working characteristics of the system concurrent with thermoelectric heating

The voltage of the thermoelectric unit (U_{TEC}) increased from 0 to 2.05 V during the experimental process as the power (P_{TEC}) changed from 0 to 6.97 W. The heat the flat heat pipe gained was owing to heat conductance from the heat exchange tank (Q_{hc}) and from the thermoelectric unit (Q_h). As the temperature of the PCM decreased, Q_{hc} decreased while Q_h increased. The calculated heat COP of the thermoelectric unit is also shown in Fig. 10. At the position of the thermoelectric unit, the heating

COP was very high, which was caused by the high hot side temperature (T_h) and the small temperature difference between the hot side and the cold side. As the U_{TEC} increased, more heat was supplied by the thermoelectric unit and the heat COP decreased fast initially and then slowly. After 6090 s, the thermoelectric unit had a heating COP of 1.70. Without the thermoelectric unit, the average surface temperature would decrease to 30 °C. Overall, the thermoelectric unit was a good auxiliary heat source owing to its practical feasibility and high heating COP.

2.3.4. Thermoelectric heating

In an actual intermittent heating application, the situation might occur that no energy is stored in the PCM. We tested for this, and when there was a heating demand, the thermoelectric unit was turned on. It absorbed heat from the water circulation system and heated the flat heat pipe. Further, the water circulation system exchanged heat with the external environment through the heater, which worked as a heat exchanger with the environment in this system.

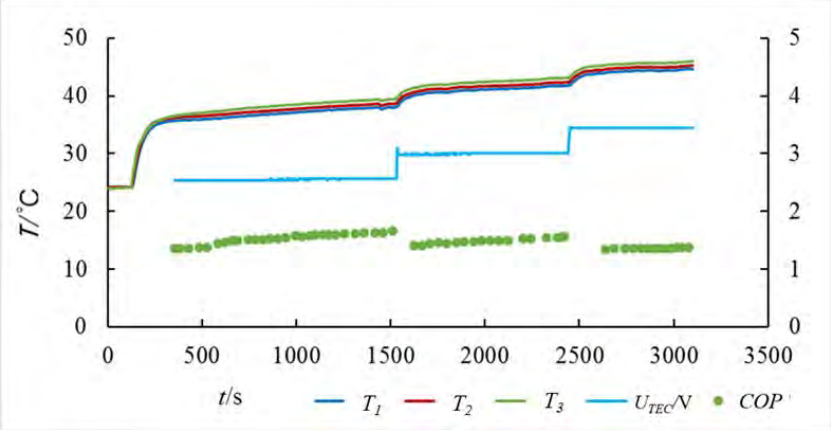

Fig. 9. Heating and working characteristics when the thermoelectric unit worked alone

For this experimental condition, three different voltages were set for the thermoelectric unit in the experiment, namely 2.5, 3.0, and 3.5 V. When the thermoelectric unit turned on, the flat heat pipe reached a stable heating state in 320 s. For 2.5 V, the heating COP of the thermoelectric unit was around 1.54 and the flat heat pipe reached a heating temperature of 38.5 °C. For 3.0 V, the heating COP decreased to 1.49 while the heating temperature increased to 42.5 °C. As the temperature difference between the cold side and hot side of the thermoelectric unit increased, the COP decreased. When the voltage was increased to 3.5 V, the heating temperature increased to 45.6 °C. Meanwhile, the heating COP of the thermoelectric unit decreased to 1.35. During the whole experimental process, the flat heat pipe had a vertical surface temperature of 1.3 °C. Overall, this heating system was able to heat intermittently (with an activation time of below 320 s) and had a comparatively acceptable heating COP above 1.35.

3. CONCLUSIONS

A flat heat pipe intermittent heating system integrated with a PCM and thermoelectric unit was proposed and experimentally studied in this research. This heating system had a rapid heating response during radiant heating and has the advantage of being able to use solar energy during the day based on the local climate. In addition, the application of the thermoelectric unit as an auxiliary heat source allows the heating system to function at any time with an acceptable heating COP. In addition, the thermoelectric unit has advantages of compact in size and high installability. In this research, an experimental rig was set up and the working characteristics of the heating system were analyzed; it was found to have the following benefits:

- Rapid radiant heating response time of less than 500 s
- The PCM guaranteed a heating temperature greater than 40 °C for 2520 s.
- The thermoelectric unit had a heating COP greater than 1.70 when working as an auxiliary heat source, while the COP was 1.35 to 1.54 when working alone.

The heating COP of the thermoelectric unit increased as the temperature of the cold side increased. Thus, the combination of the thermoelectric unit and the PCM increased the heating COP and made it possible to apply the thermoelectric unit in real applications. Moreover, the combination of heat pump and this system might show greater performance for the reason that the heat pump could produce hot water with higher efficiency. This heating system can store solar energy during the day and releases that heat to the indoor environment at night through the flat heat pipe. Several working conditions of the heating system were studied in this research. Overall, this heating system is applicable to hot summer and cold winter and Tibetan areas, which has abundant solar energy and which has a large difference in the air temperature between day and night.

ACKNOWLEDGEMENTS

The study has been supported by the China National Key R&D Program "Solutions to heating and cooling of buildings in the Yangtze river region" (Grant No. 2016YFC0700303)

NOMENCLATURE

T	The measured temperature [K]	*Tf*	The average temperature of the flat heat pipe [K]
Tw	The average temperature of the circulation water [K]	*T0*	The indoor air temperature [K]
Tc	The cold-side temperature of TEC unit [K]	*Th*	The hot-side temperature of TEC unit [K]
Qc	The heat absorbed from environment by TEC unit [W]	*Qh*	The heat released to flat heat pipe from TEC unit [W]
Qhc	The heat conducted from the heat exchange tank to the flat heat pipe [W]	*PTEC*	The power of TEC unit [W]
I	Electric current [A]	*UTEC*	The voltage power [V]
R	Electrical resistance of TEC unit [Ω]	*K0*	The total thermal conductance between the heat exchange tank and the flat heat pipe [Wm−2 K−1]
h	The averaged coefficient of the heat transfer of the flat heat pipe [W m−2 K−1]	*F*	The heat exchange area between the flat heat pipe and the tank [m2]
A	The dissipation area of the flat heat pipe [m2]	*t*	Experimental time [s]
α	Seebeck coefficient of the thermoelectric unit [V/K]		

REFERENCES

Catalina, T., Virgone, J., Kuznik, F., 2009. Evaluation of thermal comfort using combined CFD and experimentation study in a test room equipped with a cooling ceiling. Building and Environment 44: 1740-1750.

Chen S, Li N., Yoshino, H., et al. Statistical analyses on winter energy consumption characteristics of residential buildings in some cities of China[J]. Energy & Buildings, 2011, 43(5):1063-1070.

Grynning, S., Goia, F., Rognvik, E., et al. Possibilities for characterization of a PCM window system using large scale measurements., 2013. International Journal of Sustainable Built Environment 2(1):56-64.

Guarino, F., Athienitis, A., Cellura, M., et al., 2017. PCM thermal storage design in buildings: Experimental studies and applications to solaria in cold climate. Applied Energy 185:95-106.

Huo, T., Ren, H., Zhang, X., et al., 2018. China's energy consumption in the building sector: A Statistical Yearbook-Energy Balance Sheet based splitting method[J]. Journal of Cleaner Production.

Imanari, T., Omori, T., Bogaki, K., 1999. Thermal comfort and energy consumption of the radiant ceiling panel system.: Comparison with the conventional all-air system[J]. Energy & Buildings 30(2):167-175.

Lei, J., Yang, J., Yang, E, H., 2016. Energy performance of building envelopes integrated with phase change materials for cooling load reduction in tropical Singapore. Applied Energy 162:207-217.

Lin, B., Wang, Z., Sun, H., et al., 2016. Evaluation and comparison of thermal comfort of convective and radiant heating terminals in office building. Building and Environment 106(9):91-102.

Moreno, P., Castell, A., Solé, C., et al., 2014. PCM thermal energy storage tanks in heat pump system for space cooling[J]. Energy & Buildings 82(82):399-405.

Niu, J, L., Zhang, L, Z., Zuo, H, G., 2002. Energy savings potential of chilled-ceiling combined with desiccant cooling in hot and humid climates. Energy & Buildings, 2002, 34(5):487-495.

Rao, Z., Wang, Q., Huang, C., 2016. Investigation of the thermal performance of phase change material/mini-channel coupled battery thermal management system. Applied Energy 164:659-669.

Ren, X, F., Meng, Y., Liu, Y., et al., 2008. Study on the Control Methods of Radiant Air Conditioning System[J]. Refrigeration Air Conditioning & Electric Power Machinery.

Stetiu, C., 1999. Energy and peak power savings potential of radiant cooling systems in US commercial buildings[J]. Energy & Buildings 30(2):127-138.

Sun, H., Leng, M., 2015. Analysis on building energy performance of Tibetan traditional dwelling in cold rural area of Gannan[J]. Energy & Buildings 96:251-260.

Tsinghua University Building Energy Saving Research Center: Annual Report on China Building Energy Efficiency., 2017. China Architecture and Building Press, Beijing.

Manuscript ID: 1159
DOI: 10.18462/iir.icr.2019.1159

Performance Evaluation and Strategies of Subcooling Control in Residential Heat Pump Systems

Bruno Yuji KIMURA DE CARVALHO[(a)], Pega HRNJAK[(a)(b)]

[(a)] ACRC, University of Illinois at Urbana-Champaign,
Urbana, Illinois, USA, brunoykc@illinois.edu
[(b)] Creative Thermal Solutions Inc.
2209 Willow Rd. Urbana, Illinois, USA, pega@illinois.edu, pega@creativethermalsolutions.com

ABSTRACT

In most residential heat pump systems, the refrigerant flow has been controlled with focus on preventing liquid intake at the compressor suction. The use of electronic expansion valves allows new control methods to be employed. One of the methods proposed is to control subcooling at the condenser outlet keeping the system at maximum efficiency or capacity. The paper presents an investigation based on ideal cycle analysis and experimental data of a residential heat pump system on the performance and possible subcooling control strategies. Subcooling control was able to improve performance by 8.6%, 7.4% and 5.9% for outdoor ambient temperature of, 0C, -5C and -10C, respectively. A simple linear regression of the subcooling and discharge superheat based on the condensation and evaporation temperature difference can be used to achieve maximum efficiency. The use of discharge superheat to indirectly control subcooling provides an accurate and stable method of maximizing heating performance factor, but requires correction based on the refrigerant charge of the system.
Keywords: Air Conditioning, Control (Generic), Domestic Heat Pump, Electronic Expansion Valve, Optimization, Subcooling.

1. INTRODUCTION

Cost reduction of electronic expansion valves (EXV) have enabled the widespread use of these components in residential air conditioning and heat pump systems. Despite the ability to fully control the expansion device to possibly maximize efficiency or capacity, most implementations still rely solely on superheat control. While controlling superheat can deliver acceptable performance and prevent any liquid intake at the compressor suction, it also presents some issues with minimum stable superheat which may lead to hunting (Chen et al., 2002). Performance improvement ranging from 2.7%-8.4% for mobile air conditioning systems have been obtained by Pottker and Hrnjak (2012 and 2015). The authors also showed that the potential for increase in coefficient of performance is inversely proportional to the size of the condenser. Xu and Hrnjak (2014) also obtained COP improvement in a residential air conditioning system with subcooling control when compared to the use of a conventional thermostatic expansion valve (TXV).

Heating performance factor (HPF) improvement by means of subcooling stems from the overall greater relative increase in specific heating capacity as opposed to the specific compression work as the condensation pressure rises with higher subcooling. Fig. 1 and Eq. (1) and 2 illustrate the change as subcooling is increased in a T-h diagram, as the high-side pressure increases the enthalpy change on the condenser will be improved by the lower expansion device inlet enthalpy and higher discharge enthalpy, while only the increase in discharge enthalpy will boost specific compression work.

$$\Delta q_{cond} = \Delta q + \Delta w \qquad \text{Eq. (1)}$$

$$HPF' = \frac{q_{cond} + \Delta q_{evap} + \Delta w}{w + \Delta w} \qquad \text{Eq. (2)}$$

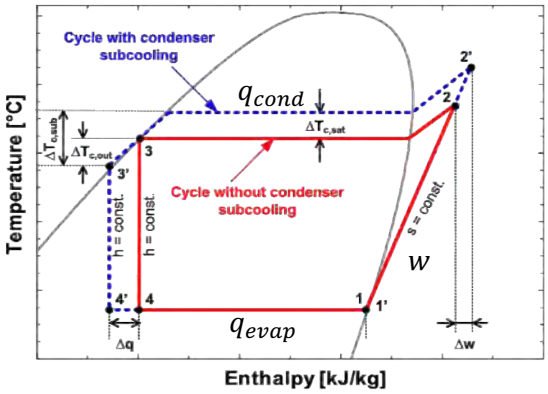

Figure 1: Schematic of cycles with/without subcooling in a T-h diagram (Pottker and Hrnjak, 2012)

Subcooling control in a heat pump water heater was able to significantly improve HPF when compared to a zero subcooling system (Pitarch et al., 2017). The authors also determined the higher performance was a consequence of higher exergy efficiency on the condenser and expansion device due to overall lower temperature difference between refrigerant and water in the condenser and decreased enthalpy at the expansion valve inlet.

Subcooling control may also be done indirectly through different variables, such as keeping a constant condenser approach (Hervas-Blasco et al., 2018) or even controlling discharge superheat (Tanawittayakorn et al., 2012; Menken et al., 2014).

In this paper the performance characteristics of a residential heat pump with subcooling control were assessed, and possible alternative subcooling control strategies were investigated. Results at the system's optimal points were compared to the data with evaporator outlet superheat control.

2. FACILITY

Figure 2 shows the full schematic for the facility used in this study. Two environmental chambers simulate indoor and outdoor conditions and can keep temperatures within ± 0.5°C and absolute humidity ±2%.

4WV: 4-way valve
ABL: Air blender
ACC: Accumulator
AIR: Air
BL: Blower
CC: Charge compensator
CD: Condenser
CP: Compressor
DP: Differential pressure transducer
DPS: Dew-point sensor
EGC: Ethylene glycol chiller
EGHX: Ethylene glycol heat exchanger
ERH: Electric resistance heater
EV: Evaporator
EXV: Electronic expansion valve
FN: Flow nozzle
MF: Muffler
MFM: Mass flow meter
P: Absolute pressure transducer
SI: Steam injection
T: Type-T thermocouple
TCG: Thermocouple grid
TXV: Thermostatic expansion valve
VFD: Variable frequency drive

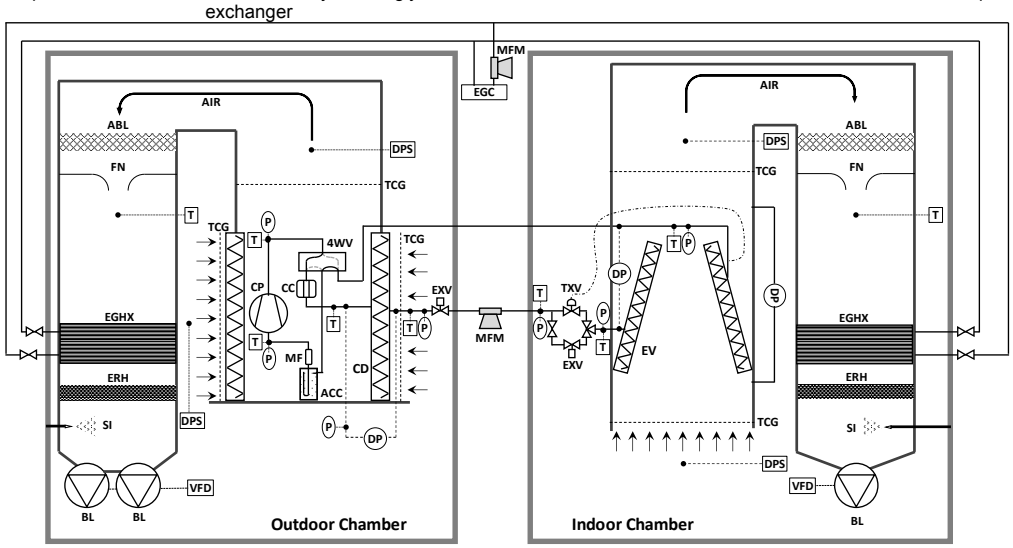

Figure 2: Layout of facility for performance evaluation

Compressor, heaters and blowers power measurement is within ±0.2% and the expanded uncertainty for air-side and refrigerant side capacity calculations of approximately ±4%. Heating performance expanded uncertainty is estimated to be around ±5%.

An off-the-shelf reversible residential 2 Ton (7kW) R410-A system with a round-tube A-coil indoor heat exchanger and a round-tube horizontal condenser with an electronic expansion valve (EXV) was installed in the facility. A separate EXV was installed on the outdoor unit to allow full control over the expansion process and the charge compensator was closed off from the system to prevent it from destabilizing subcooling control. The cycle diagram is shown in figure 3, the TXV on the indoor unit acts as a check valve during heat pump operation. Specifications for the indoor and outdoor heat exchangers are shown in Table 1.

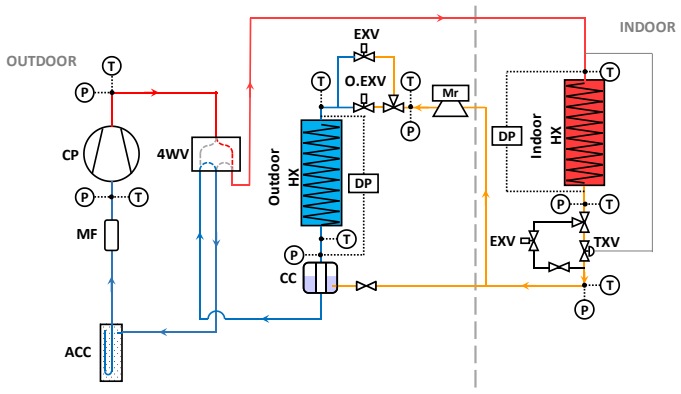

Figure 3: Schematic drawing of the air-conditioning system evaluated

Table 1. Residential system heat exchanger specifications

	Outdoor heat exchanger	Indoor heat exchanger
Description	Two rows, eight circuits, fin pitch 1.27 mm (20 fpi)	Two slabs, three staggered rows, eight circuits, fin pitch 1.75 mm (14.5 fpi)
Face area	2.81 m^2 (30.25 sqft)	0.689 m^2 (7.42 sqft)
Core depth	0.038 m	0.056 m
Core volume	0.1068 m^3	0.03858 m^3
Air side area	153.53 m^3	40.1 m^3
Refrigerant side area	4.61 m^3	2.39 m^3
Material	Aluminum louvered fins, copper tubes, vapor line O.D. = 22 mm, liquid line O.D. = 9.5 mm	

3. RESULTS AND DISCUSSION

3.1 Ideal cycle analysis of potential benefits from subcooling control in heat pump systems

To evaluate the potential for HPF improvement in a heat pump cycle a similar analysis as the one performed by Pottker and Hrnjak (2012) was implemented based on the cycle represented in Fig. 1. Eq. (3) shows an approximation for the increase in specific heating capacity for an ideal cycle assuming constant evaporation pressure and an increase in subcooling, as well as condensation pressure. Eq. (4) shows the original specific heating capacity and finally eq. (5) is the relative increase in specific heating capacity based on the higher subcooling.

$$\Delta q_{cond} \cong \overbrace{h_{2'} - h_2}^{\Delta w} + \overbrace{\overline{cp}_{l.c}\left(\Delta T_{c,o}\right)}^{\cong \Delta q_{evap}} \quad \text{Eq. (3)}$$

$$q_{cond} = h_2 - h_{c,sat,v} + h_{fg.c} \quad \text{Eq. (4)}$$

$$\frac{\Delta q_{cond}}{q_{cond}} = \frac{h_{2'} - h_2 + \overline{cp}_{l.c}\left(\Delta T_{c,o}\right)}{h_2 - h_{c,sat,v} + h_{fg.c}} \quad \text{Eq. (5)}$$

Considering an increase in subcooling of 5 K, and an increase in condensation temperature of 1 K table 2 shows the resulting relative increase in specific compression work, heating and cooling capacities. An initial condensation temperature of 45°C and evaporation temperature of 5°C were used in this analysis. The relative improvement in specific heating capacity is about 10% lower than the increase obtained for the cooling capacity. This decreased benefit in performance is mostly due to the overall larger initial heating capacity. Generally, a lower liquid specific heat and enthalpy of condensation leads to greater improvement from subcooling. The fluid used in this study's

experimental analysis is R410a, which shows the highest relative increase in specific heating capacity among the refrigerants included in this analysis.

Table 2. Ideal cycle analysis of performance improvement from subcooling for a heat pump

Refrigerant	$Cp_{l.c}$ (kJ kg^{-1}K^{-1})	hfg_e (kJ kg^{-1})	hfg_c (kJ kg^{-1})	$\frac{\Delta w}{w}$ (%)	$\frac{\Delta q_{cond}}{q_{cond}}$ (%)	$\frac{\Delta q_{evap}}{q_{evap}}$ (%)
R410a	2.002	215.1	148.4	2.256	6.055	6.696
R134a	1.516	194.7	157.6	2.155	4.996	5.499
R1234yf	1.431	160.7	128.6	2.079	6.043	6.681
R290	2.97	367.5	295.8	2.168	5.202	5.749
R717	4.967	1244	1075	2.463	2.376	2.357
R600a	2.575	350.1	305.1	2.149	4.668	5.104

The analysis was also done for lower evaporation temperatures to evaluate how much improvement could be obtained as the heat pump load in increased due to lower outdoor ambient temperatures. Fig. 4a and 4b show the change in relative change of the heating capacity and specific compression work as the saturation temperatures are varied, respectively. For a fixed condensation temperature, the decrease in $\Delta q_{cond}/q_{cond}$ as the evaporation temperature drops is not as significant as the decrease in $\Delta w/w$ which should lead to potentially higher performance improvement as the outdoor air ambient temperature is decreased. Since this analysis is based on an ideal cycle the isentropic efficiency of the compressor is not considered, but the effect obtained at lower evaporation temperatures should mitigate the decrease in compressor efficiency due to higher compression ratios and possibly lead to good performance improvement even at low outdoor ambient temperatures.

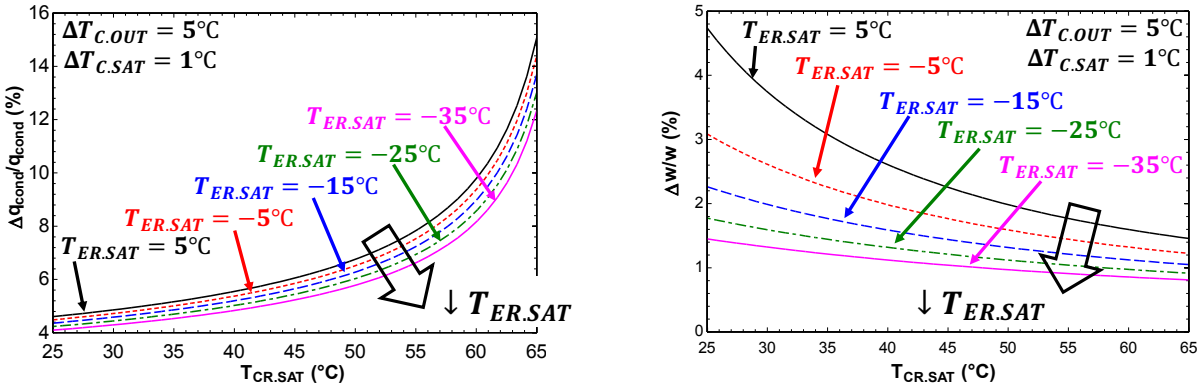

(a) (b)

Figure 4: Relative change in specific heating capacity and compression work as a function of condensation and evaporation temperatures

3.2 Test conditions

The heat pump system was tested at three different outdoor ambient temperature 0°C, -5°C and -10°C. The outdoor chamber was initially run with the glycol chiller to dehumidify it and mitigate frosting on the evaporator allowing for near-dry test conditions. The refrigerant charge of 6685g was selected to maximize HPF at -5°C, and to guarantee enough subcooling at -10°C to achieve its optimal point. Indoor temperature was fixed at 21.1°C by using the glycol loop chiller and a PID controlled electric heater. Compressor speed was set based on the maximum speed as a function of the outdoor ambient temperature per the manufacturer's data. This system maxes out its compressor speed at -5°C to protect the compressor when running at low outdoor ambient temperatures. The baseline selected was a charge optimized system using an EXV with 3K evaporator superheat control.

Table 2. Test conditions

Condition	T_{cai} (°C)	T_{eai} (°C)	Indoor air flow rate (SCFM / m^3/s)	Outdoor air flow rate (SCFM / m^3/s)	Compressor speed (RPM)
A	21.1	0	900 / 0.425	2000 / 0.944	4500
B	21.1	-5	900 / 0.425	2000 / 0.944	5700
C	21.1	-10	900 / 0.425	2000 / 0.944	5700

3.3 Effect of subcooling control on heat pump performance

Condition B was used to analyze the effect of subcooling control on heat pump performance, figure 5 shows the heating capacity, HPF and compressor work as a function of subcooling. This condition presented the highest capacity between all three conditions and thus resulted in a HPF-maximizing subcooling of 6.5 K. The heating capacity and HPF were improved by 17.6% and 7.4%, while the compressor power increased by 9.5% when compared to the charge optimized 3K superheat-controlled system.

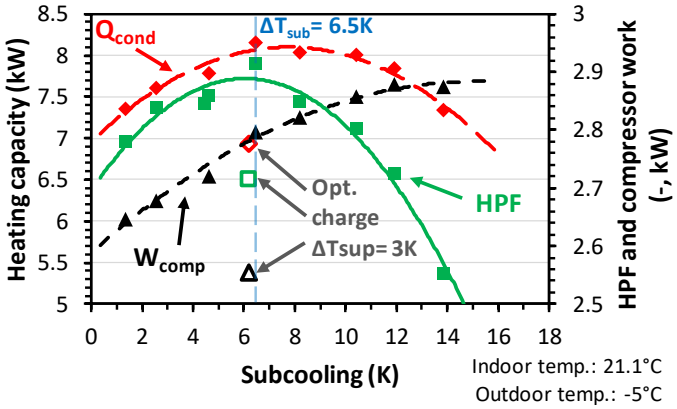

Figure 5: Heating capacity, HPF and compressor work vs. SC for condition B

The charge optimized superheat control results in approximately the same HPF-maximizing subcooling as the one achieved with active subcooling control indicating that a evaporator/compressor suction superheat based control should only be able to provide maximum HPF at the condition it was charge optimized. Compression ratio at the optimal points is close, but the mass flow rate is significantly reduced for a superheat-controlled due to the higher specific volume at the compressor suction.

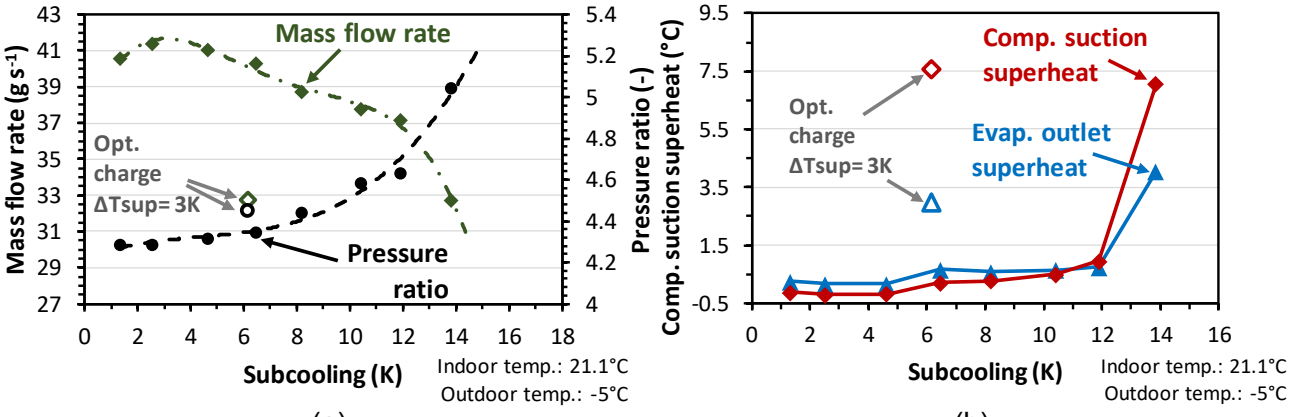

Figure 6: a) Mass flow rate and compression ratio, b) Compressor suction and evaporator outlet superheat, vs. subcooling for condition B

Figure 7 shows the P-h diagram comparing the HPF-maximizing subcooling point (6.5 K) with the evaporator outlet superheat controlled point (3°C). Evaporation pressure was increased by about 50 kPa while the condensation pressure was reduced by approximately 75 kPa. These changes in pressure results in a significant reduction of the compression ratio which leads to higher compressor efficiencies and increased mass flow rate. These results indicate that by controlling subcooling the overall evaporator and condenser heat transfer coefficients can be improved thus reducing the

temperature difference between refrigerant and air. The improvement in capacity also means that the further reduction in compressor speed can further improve performance while matching the required load for the system.

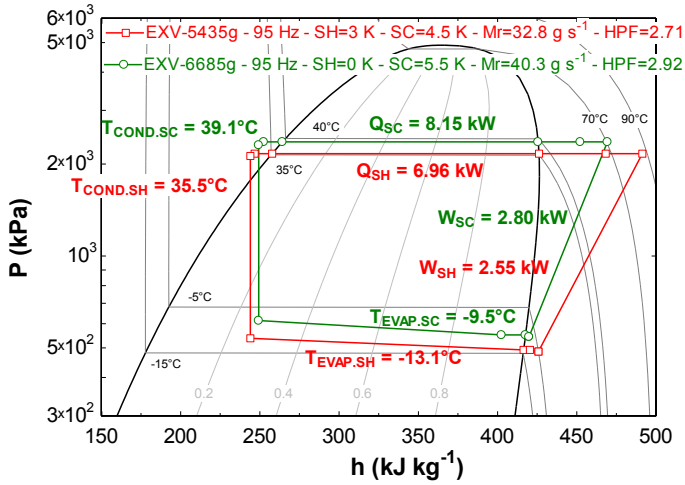

Figure 7: P-h diagram for the HPF-maximizing SC and the charge-optimized SH-controlled point at condition B

Discharge superheat control may also be used as a variable to indirectly control subcooling and maximize performance and/or capacity. Figure 8a shows the relationship between discharge superheat and subcooling for the system under three different refrigerant charges. Because both variables follow a monotonic function it should be possible to use them interchangeably to optimize the system. Control based on discharge superheat should have lower sensitivity to temperature sensor uncertainty and no issues with stability since its minimum value is always greater than zero, but its dependency on charge must to be considered to generalize the control strategy. Subcooling control, on the other hand, is not significantly affected by refrigerant charge allowing for optimal control without requiring self-correction based on the system charge, as shown in figure 8b.

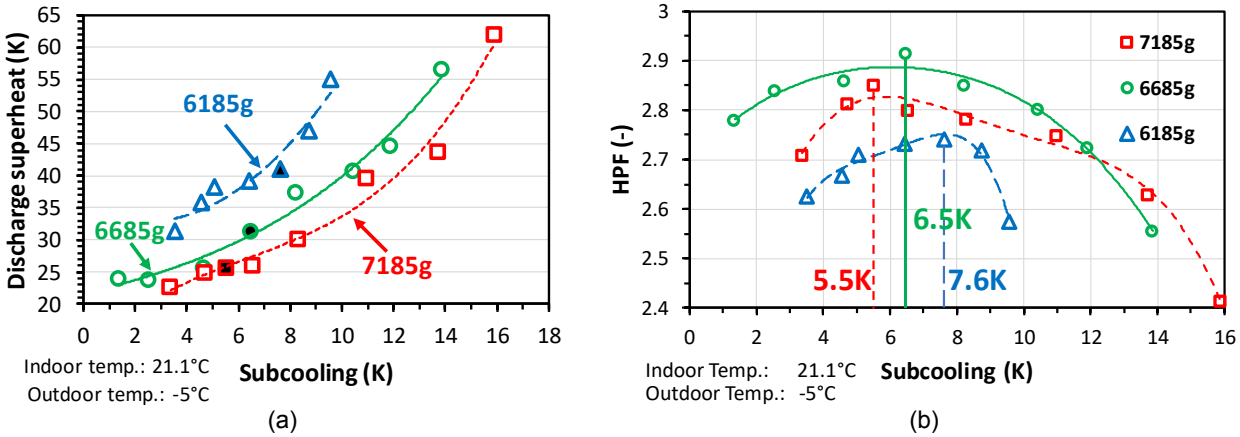

Figure 8: Compressor discharge superheat vs. subcooling for condition B

3.4 Subcooling control of a heat pump system under different outdoor conditions

The HPF-maximizing subcooling is directly correlated to the load or heating capacity on the system, as shown in the comparison between subcooling control in conditions A, B and C (Fig. 9a and 9b). Figure 9b shows that the maximum heating capacity decreases at condition C due reduced mass flow rate caused by the limitation of compressor speed to 5700 RPM (95 Hz), which is the same speed as condition B. Overall HPF improvement when compared to a 3°C superheat-controlled system is of 8.6%, 7.4% and 5.9% for conditions A, B and C, respectively. Heating capacity is improved by 12.0%, 17.6% and 12.5% for conditions A, B and C, respectively, due to the increased mass flow rate since the evaporator is flooded and the compressor suction is admitting refrigerant with qualities in the range of 0.95-0.99.

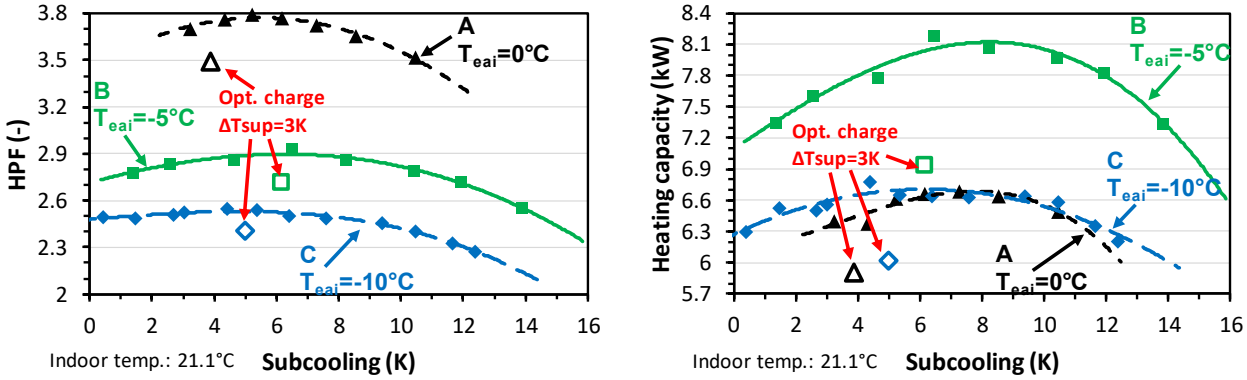

Fig. 9: HPF (a) and heating capacity (b) vs. subcooling for conditions A, B and C.

HPF results differ from the ideal cycle analysis partly because the compressor speed is fixed for conditions B and C and also because compressor efficiency drops significantly as a function of the increased pressure ratio when outdoor ambient temperature is decreased while indoor air temperature is kept constant, shown in figure 10a. Figure 10b shows that the discharge superheat for all three conditions follows a monotonic trend as a function of subcooling and its HPF-maximizing value increases as the outdoor temperature is decreased.

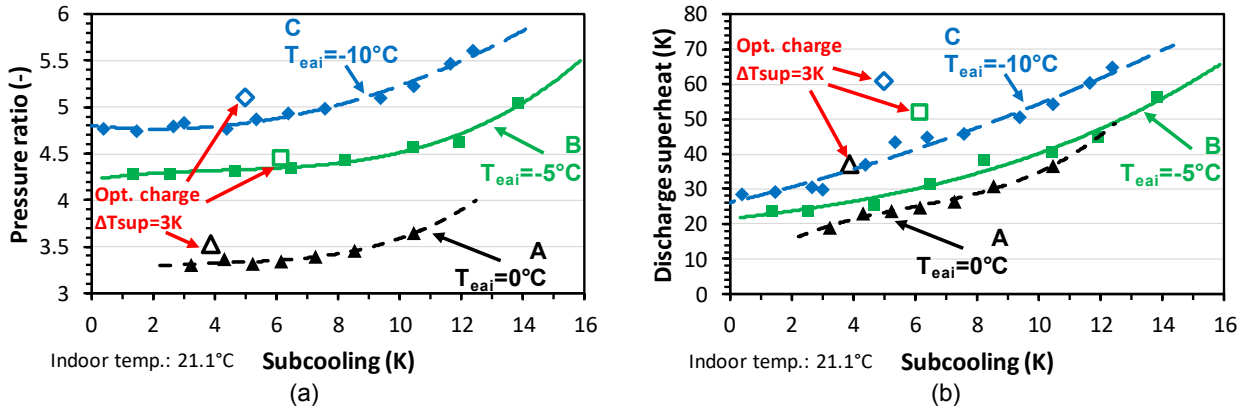

Fig. 10: Pressure ratio (a) and discharge superheat (b) vs. subcooling for A, B and C.

Based on these results two different control strategies can be derived to provide a simple HPF-maximizing method: subcooling or discharge superheat based on the saturation temperature difference. These approaches should provide a control method based on the current capacity of the system considering the limitation of compressor speed at lower outdoor ambient temperatures. Eq. (6), (7) and (8) define the variables used in these two control methods and figure 11 shows a linear regression for subcooling and discharge superheat.

$$\Delta T_{sub.cro} = T_{cro.sat} - T_{cro} \quad \text{Eq. (6)}$$

$$\Delta T_{sup.cpro} = T_{cpro} - T_{cpro.sat} \quad \text{Eq. (7)}$$

$$\Delta T_{sat} = T_{cr.sat} - T_{er.sat} \quad \text{Eq. (8)}$$

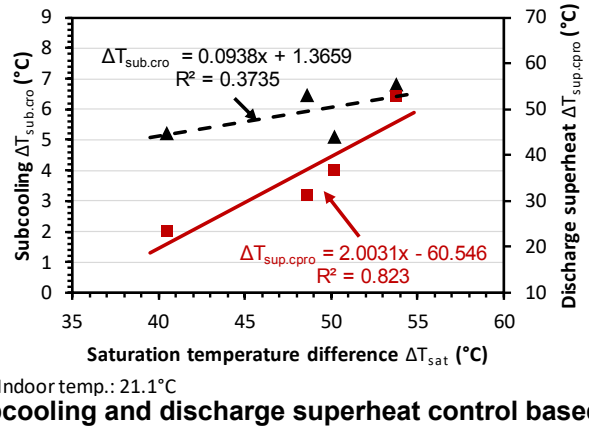

Fig. 10: Subcooling and discharge superheat control based on ΔT_{SAT}

Discharge SH control can provide a more precise control based on ΔT_{SAT} while also being more stable since it cannot be zero and has a higher value, minimizing its sensitivity to the sensors' uncertainties. But it's dependent on the refrigerant charge, thus requiring a correction based on the charge of the system. SC control is less sensitive to the charge, but the control is less accurate and less stable due to its proximity to the saturation point. Because both strategies are based on refrigerant side variables, which could lead to instability during startup, the initial control may be based on suction SH and later switched to the strategies presented.

4. CONCLUSIONS

This paper investigated the performance and possible strategies of a SC-controlled residential heat pump system. The ideal cycle analysis showed that as the outdoor temperature decreases the performance improvement from SC also increases. Experimental results presented an HPF increase of 8.6%, 7.4% and 5.9% for outdoor ambient temperature of, 0C, -5C and -10C, respectively. The HPF improvement decreases as the load increases, or outdoor ambient temperature, drops because higher pressure ratios lead to a decline in compressor efficiency. Finally, a control strategy based on discharge SH as a function of ΔT_{SAT} was shown to provide more precise control while also being more stable due to its non-zero condition, and less sensitive to temperature sensor uncertainties due to its higher values, but due to its charge-sensitivity it must be corrected based on the refrigerant charge of the system.

ACKNOWLEDGEMENT

This work was supported by the Air Conditioning and Refrigeration Center at the University of Illinois at Urbana-Champaign. Support from ACRC members and sponsors are gratefully acknowledged.

NOMENCLATURE

a	Air (subscript)	fg	vaporization (subscript)	sat	saturation (subscript)
cond	condensation (subscript)	h	Enthalpy (kJ kg^{-1})	SC	subcooling (K)
c	condenser (subscript)	HPF	Heating performance factor (-)	SH	superheat (K)
$\overline{cp}$	Specific heat (kJ kg^{-1}°C^{-1})	i	inlet (subscript)	sub	subcooling (subscript) (K)
cp	compressor (subscript)	l	liquid (subscript)	sup	superheat (subscript) (K)
COP	Coefficient of performance	M	Mass flow rate (kg s^{-1})	T	Temperature (°C)
ΔT	Temperature difference (°C)	o	outlet (subscript)	TXV	Thermostatic expansion valve
e	evaporator (subscript)	q	Specific capacity (kJ kg^{-1})	v	vapor (subscript)
evap	evaporation (subscript)	Q	Capacity (kW)	w	Specific work (kW kg^{-1})
EXV	Electronic expansion valve	r	refrigerant (subscript)	W	Work/Power (kW)

REFERENCES

Chen, W., Zhijiu, C., Ruiqi, Z., Yezheng, W., 2002. Experimental investigation of a minimum stable superheat control system of an evaporator. *Int. J. Refrigeration,* 25, 1137-1142.

Menken, J.K., Weustenfeld, T., Köhler, J., 2014. Experimental Comparison of the Refrigerant Reservoir Position in a Primary Loop Refrigerant Cycle with Optimal Operation. *Proceedings of the International Refrigeration and Air Conditioning Conference at Purdue, West Lafayette*, *USA.* West Lafayette, USA (1397). Purdue University.

Pitarch, M., Navarro-Peris, E., Gonzalvez-Macia, J., Corberan, J.M., 2017. Evaluation of optimal subcooling in subcritical heat pump systems. *Int. J. Refrigeration, 83, 18-31.*

Pottker, G., Hrnjak, P. S., 2012. Potentials for COP increase in Vapor Compression Systems, ACRC TR 294. University of Illinois at Urbana-Champaign.

Pottker, G., Hrnjak, P., 2015. Effect of the condenser subcooling on the performance of vapor compression system. *Int. J. Refrigeration, 50, 156-164.*

Tanawittayakorn, W., Phrajunpanich, P., Siwapornphaisam, S., 2012. Heat Pump Efficiency Improvement by Discharge Superheated Control. *Proceedings of the International Refrigeration and Air Conditioning Conference at Purdue, West Lafayette*, *USA.* West Lafayette, USA (1197). Purdue University.

Xu, L., Hrnjak, P.S., 2014. Potential of Controlling Subcooling in Residential Air Conditioning System ACRC TR311. University of Illinois at Urbana-Champaign.

Hervas-Blasco, E., Pitarch, M., Navarro-Peris, E., Corberán, J.M., 2018. Study of different subcooling control strategies in order to enhance the performance of a heat pump. *Int. J. Refrigeration, 88, 156-164.*

Manuscript ID: 1195
DOI:0.18462/iir.icr.2019.1195

Experimental investigation and mathematical modelling of the desiccant wheel of a hybrid air conditioning system

Manoj KUMAR[(a)], Manish MISHRA[(a)], Pradeep K. SAHOO[(b,*)]
[(a)]Mechanical and Industrial Engineering Department
IIT Roorkee, 247667, India, Email: mkumar5@me.iitr.ac.in
[(b)]Mechanical, Energy and Industrial Engineering Department
BUIST, Private Bag 16, Palapye, Botswana, Email: sahoop@biust.ac.bw

ABSTRACT

The performance of a hybrid solid desiccant (combination of desiccant wheel and vapor compression) system depends on heat recovery from the condenser of vapor compression system, the performance of the desiccant wheel and heat wheel. The performance of the desiccant wheel depends on regeneration temperature, wheel speed, flow rate and flow area for hot and cold fluids. Some research works have been carried out to increase the performance of hybrid desiccant cooling system with various affecting parameters. However, the heat recovery from the condenser exhaust has very limited experimental work. Keeping these things in mind, an attempt has been made to study the effect of the heat recovery from the condenser. It is observed that heat recovery from the condenser is not sufficient to meet the heating requirement for regeneration air. However it can reduce the heating requirement. As a result, the COP of the system increases from 2.8 to 3.45 for 100% fresh air. This result corresponds to regeneration temperature of 60ºC for hot and humid climate in Roorkee, India.

Keywords: desiccant, regeneration, air condition, hybrid

1. INTRODUCTION

Air-conditioning (AC) demands efficient control of both temperature and humidity. Hybrid cooling systems combines more than two cooling systems so that overall system performance can be improved with the use of low grade thermal energy sources. In the present study, a hybrid system which combines vapor compression air conditioning system with solid desiccant wheel and heat (enthalpy) wheel system is investigated. The removal of latent heat and sensible heat loads are taken care separately by the system. Solid desiccant wheel removes latent load whereas vapor compression and heat wheel are used to remove sensible load. To reduce the consumption of electrical energy and to achieve a higher energy efficiency, hybrid solid desiccant cooling system is proposed as an alternative to conventional vapor compression system. These systems will be cost effective where 100% fresh air is required.

Our system consists of solid desiccant wheel, a sensible heat wheel heat exchanger, electrical heater and vapor compression air conditioning system. Process air after desiccant wheel gets dehumidified with the increment of its temperature as heat of adsorption is released to it. The heated process air exchanges sensible heat with heat wheel and consequent sensible cooling by vapor compression system and then it is supplied to the room. Exhausted heat from the condenser of vapor compression air conditioning system is used to preheat the regeneration air going to the desiccant wheel after electrical heater.

Desiccant dehumidifier is a device by which moisture from wet air gets removed without air being cooled below its dew point. Instead, it relies on the ability of hygroscopic adsorption of water on to its surface. In the process of adsorption, a thin layer of molecules of water vapor formed and adheres to the substrate surface of desiccant material. On one operation (dehumidification), the desiccant material becomes saturated with water and has to be regenerated through a drying process on another operation (desorption).

The literature review reveals that various authors differ in their evaluation of the effectiveness of these systems. This seems to be due to different methods of modelling of dehumidifier and differences in the operating conditions of the cycles employed.

Several researchers have worked on different types of hybrid systems (Burns et al. 1985; Sheridan Mitchell 1985; Maclaine-Cross and Banks 1972). The performance of a first generation prototype

desiccant integrated hybrid system was investigated by Worek and Moon (1972) through establishing a numerical model of the system. They used their system to utilize waste heat rejected from a vapor compression cycle, to directly activate a solid desiccant dehumidification cycle. They found that at the same level of dehumidification, 60% performance improvement over vapour compression system was obtained at Air-conditioning and Refrigeration Institute (ARI) design conditions. As the outdoor humidity ratio was increased the performance of hybrid system decreased. Analysis of the performance of four hybrid cycles for a typical hot-dry and hot humid weather, based on the analogy method of Maclaine-Cross and Banks (1972) were done by Dhar and Singh (2001). Subramanyam et al. (2004a, 2004b) studied the effect of design variables and also the application of desiccant wheel to control humidity. System coefficient of performance was found sensitive to regeneration temperature and humidity ratio (Jani et al. 2015). Jani et al. (2016a, 2016b, 2016c, 2016d, 2016e, 2016f) studied the suitability of the solid desiccant cooling to supplement the traditional VCR system for hot and humid climate. Effect of room sensible heat factor, ventilation mixing ratio, and regeneration temperature were analysed. Yadav et al. (2013, 2014, 2015) intensively studied operating parameters of solid desiccant wheel. The effect of change in ambient conditions as well as effectiveness of desiccant wheel and sensible regenerator were studied by Panaras et al. (2010), on overall performance of desiccant cooling system. Results show that solid desiccant-based hybrid air conditioning systems can give substantial energy savings, compared to the conventional vapour compression refrigeration based air-conditioning systems.

Considering literature reviews, we found a scarcity of research in the area where the heat of condenser exhaust being used for the regeneration of desiccant wheel. So, an effort has been made to examine experimentally the performance of hybrid solid desiccant air conditioning system. Along with the performance of the hybrid air conditioning system in terms of COP, variations of other parameters such as moisture removal rate (MRR) of desiccant wheel, effectiveness of desiccant wheel and heat wheel were also studied.

2. EXPERIMENTAL SETUP

In this paper, a hybrid desiccant dehumidification system that recovers the condensing heat from the vapor compression air conditioning unit to remove moisture from the air (typically hot and humid weather condition) is experimentally investigated. Figure 1 shows the schematic diagram of the hybrid air-conditioning system which operates on ventilation mode. It consists of rotary solid desiccant dehumidification wheel, a heat wheel as counter flow heat exchanger and a conventional vapor compression air conditioning unit. In present study, hybrid solid desiccant cooling system has three air streams. First one is process air (1-2-3-4-5) through desiccant wheel, heat wheel and evaporator of vapor compression system. Second one is the regeneration air (6-7-8-9) for desorption of the desiccant wheel. Third one (6-10) is passed through heat wheel to precool the process air from desiccant wheel. Five fans are used in for air circulation. One is at outlet of desiccant wheel on process side (at state 2), another one is at outlet on regeneration side (at state 9). One is at the outlet of heat wheel at state 10. There are 2 others fans in cooling coil assembly (one is after cooling coil and another is for condenser) whose power consumption is small have been neglected.

3. TEST PROCEDURE

Initially, humid air (state 1) gets dehumidified (state 2). The effect of heat of adsorption and heat transferred from the regeneration air stream due to rotation of desiccant wheel increase the temperature of the dehumidified process air after desiccant wheel (state 2). This results in higher temperature at the exit than at the inlet (state 1).

Heated processed air after dehumidifier gets cooled by the heat wheel, acting as heat exchanger with the ambient air to state 3 and then is allowed to pass through the cooling coil of conventional vapor compression air conditioning system for further sensible cooling to attain the required comfort temperature for the space (state 4). On the regeneration side, ambient air after recovering the heat from the condenser of conventional vapor compression air conditioning system, passes through electrical heater where it is heated to a specific temperature (state 8). After this, heated air is passed through the desiccant wheel to regenerate the wheel by desorption process and exhausted to ambient (state 9). In desiccant wheel, flow area for the process side is three times more than that of

regeneration side whereas in heat wheel, sectorial flow area is equally divided for process and regeneration air. The regeneration air temperature is controlled with an adjustable 3.6 kW electrical heater. The third air stream drawn from the ambient is forced by a fan to pass through a cross-flow heat wheel, to pre-cool the process air from the desiccant wheel and then is allowed to escape to ambient as exhaust (state 10). When temperature and humidity of the system attains steady state conditions, various measurements are taken. It takes about thirty minutes for the system to reach steady state.

As per ASHRAE (1997), for human comfort, the desired condition is 26°C and 50%. In the present

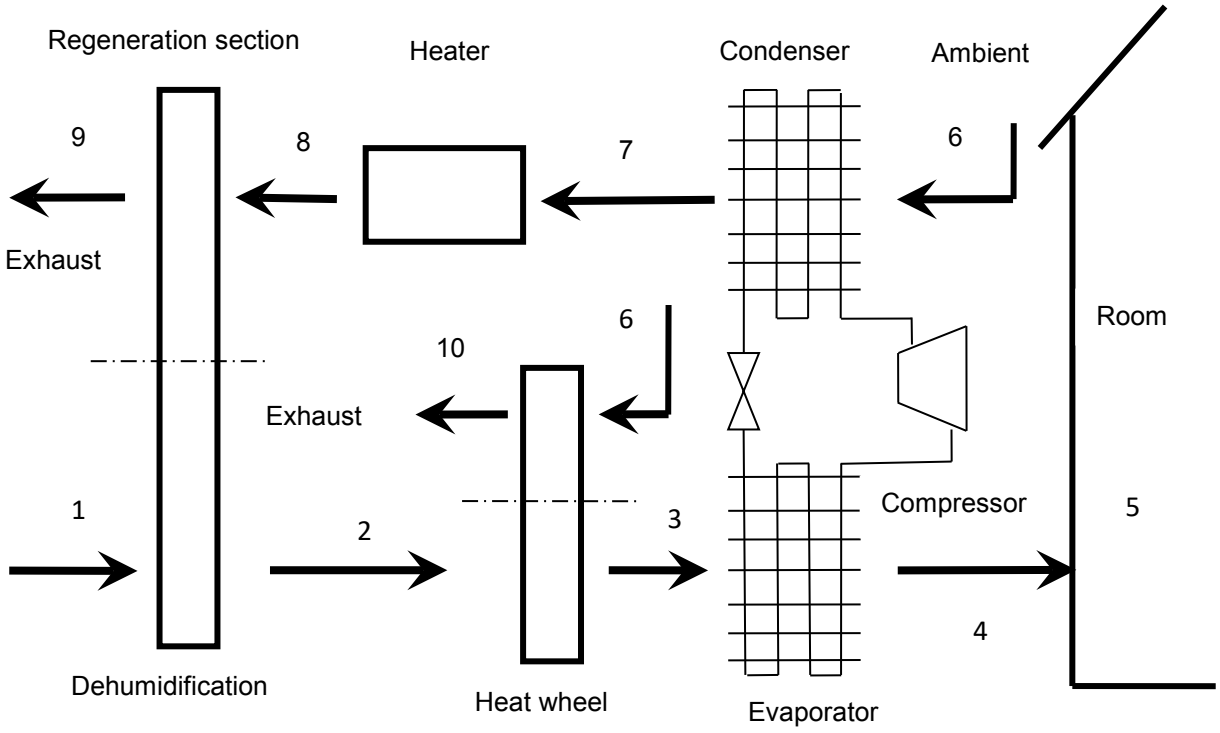

Figure 1 Hybrid solid desiccant cooling system with use of condenser exhaust for regeneration

case, a test room having volume 37.6 m^3 has been selected for the experimental study. Total cooling load of the test room was calculated to be 2.1 kW out of which 1.7 kW is sensible load and latent load is 0.4 kW (Kulkarni et al. 2011). The capacity of the cooling coil assembly is 2.8 kW.
Experiments were carried out by simultaneous measurements of temperature, relative humidity and flow rate with the help of multifunctional digital transmitters connected via Masibus-85XX microcontroller based scanner along with control panel to control and operate the system. The inaccuracies in measurement of temperature, relative humidity and flow rate were found to be ±0.3 K, ±2.0% and ±1.5% respectively. The desiccant used in the desiccant wheel is synthesized metal silicate. The size of the desiccant wheel is 360 mm diameter and 100 mm width. The rotational speed of the dehumidifier is kept constant as 20 rph.

4. THEORETICAL CONSIDERATION

The coefficient of performance is defined to evaluate the energy efficiency of the system as

$$\text{COP} = \frac{\dot{Q}_{cool}}{\dot{Q}_{reg}+\text{W}_\text{c}+\text{W}_\text{fans}} = \frac{\dot{m}_\text{p}(h_1-\text{h}_4)}{\dot{m}_\text{r}(\text{h}_8-h_7)+\text{W}_\text{c}+\text{W}_\text{fans}} \qquad \text{Eq.(1)}$$

Where $\dot{Q}_{cool}$ is the rate of heat removed from the cooled room, $\dot{Q}_{reg}$ is the rate of regeneration heat supplied to the unit, $\dot{m}_\text{p}$ is the mass flow rate of process air, $\dot{m}_\text{r}$ is the mass flow rate of regeneration air and *h* is the enthalpy of moist air. The state numbers refer to Fig.1 throughout this paper.

Moisture removal rate (MRR) by desiccant wheel is defined by the following relation given by as

$$\mathrm{MRR} = \dot{m}_p(\omega_1 - \omega_2) \quad \text{Eq.(2)}$$

The performance relation for the desiccant wheel is expressed in terms of specific humidity given by Van den Bulck et al. (1988) as

$$\varepsilon_{DW} = \frac{(\omega_1 - \omega_2)}{(\omega_1 - \omega_{2,ideal})} \quad \text{Eq.(3)}$$

Where $\omega_{2,ideal}$ is the humidity ratio at the wheel exit in the ideal case. Its value may be taken to be zero since an ideal wheel will completely dehumidify the air.
The effectiveness of the heat wheel may be expressed as given by Jani et al (2016f),

$$\varepsilon_{HW} = \frac{(T_2 - T_3)}{(T_2 - T_6)} \quad \text{Eq.(4)}$$

where T is the dry bulb temperature of moist air where subscripts refers to state points in the system. For practical purposes, forms of low grade energy like solar thermal energy or waste thermal energy from process industries can be used, though in the present study an electrical heater is used for the regeneration air heating.

5. RESULTS AND DISCUSSION

Table 1 shows the relevant data which were measured and used in calculation of the other parameters i.e. COP of the system and effectiveness of the system.

Table 1. Measured velocity and calculated mass flowrates of Hybrid System

	Duct Diameter (m)	Velocity (m/s)	Mass Flow Rate (kg/s)
Process Air	0.110	13.1	0.136
Regeneration Air	0.095	8.5	0.063

Table 2 lists the measured dry bulb temperature, relative humidity and calculated properties for the process and regeneration air during a typical steady state operation for the regeneration temperature of 90°C. The corresponding state points in the psychrometric chart are shown in Fig. 2.

Table 2. Steady state properties at various state points for regeneration temperature of 90°C.

	Dry Bulb Temperature(°C)	Relative Humidity(%)	Humidity Ratio (g/kg da)	Specific Enthalpy (kJ/kg da)
1	29.1	80.0	21.0	83.1
2	50.5	19.1	15.8	91.7
3	42.3	31.2	16.9	86.2
4	10.4	90.8	7.3	29.1
5	27.4	47.8	11.3	56.2
6	29.1	79.9	21.0	83.1
7	43.5	34.9	20.3	96.0
8	90.0	5.7	20.4	138.1
9	40.7	52.4	26.4	108.6
10	38.0	45.9	19.9	89.3

Use of hybrid solid desiccant cooling system helps to manage latent heat and sensible heat separately. The desiccant wheel manages latent heat and vapour compression refrigeration system

manages sensible cooling. But the variation of ambient temperature and relative humidity put restrictions on prescribed and desired performance of the whole system. From Table 2 and Fig. 2, one can observe deviations from ideal behaviour of a desiccant system. State points 1 and 6 represent ambient condition. State point 2 is the usual point after dehumidification in the desiccant wheel. In this process, temperature of the process air rises due to heat of adsorption released to air, whereas the humidity ratio and relative humidity decreases. State point 3, is the outlet of heat wheel, its temperature was found decreased as usual but the humidity ratio got increased slightly. Ideally this process is a sensible heat exchange process between the hot stream, leaving the desiccant wheel, and the cold ambient air. From the experimental result, it is observed that the humidity ratio at state point 3 is slightly higher than that of state point 2. This happens as some of the cold air having higher humidity trapped in the rotating wheel near the partition of the wheel enters the supply air side. Similarly, some of the supply air also enters the cold air side, which reduces its humidity ration. For this reason, the humidity ration of the state point 10 is lower than that of state point 6. Comparing state point 1 and 3, one can observe that the enthalpy oat state point 3 is higher than the enthalpy at state point 1. This increases the load on the AC but it is sensible load which can be taken care by the AC without maintaining it at very load temperature for carrying out condensation. Thus, in a well-designed system, air can be cooled without condensation of moisture. At the same time, it removes the post heating requirement, which also saves the energy.

State point 4 is the supply condition to the test room after passing through the cooling coil of vapour compression system. Cooling coil was supposed to handle only sensible load but for hot and high humidity ambient condition, it is very difficult to get the desired humidity ratio only by dehumidifier wheel. When a conditioned space experiences a net addition of both sensible and latent heat from interior and exterior loads, the supply air must enter the conditioned space at a state where both the temperature and humidity ratio is lower than the values to be maintained in the space. It is strongly desired and recommended that only sensible heat transfer should take place between the air and cooling coil. This is possible if the dew point temperature of air at state 3 is lower than the evaporator

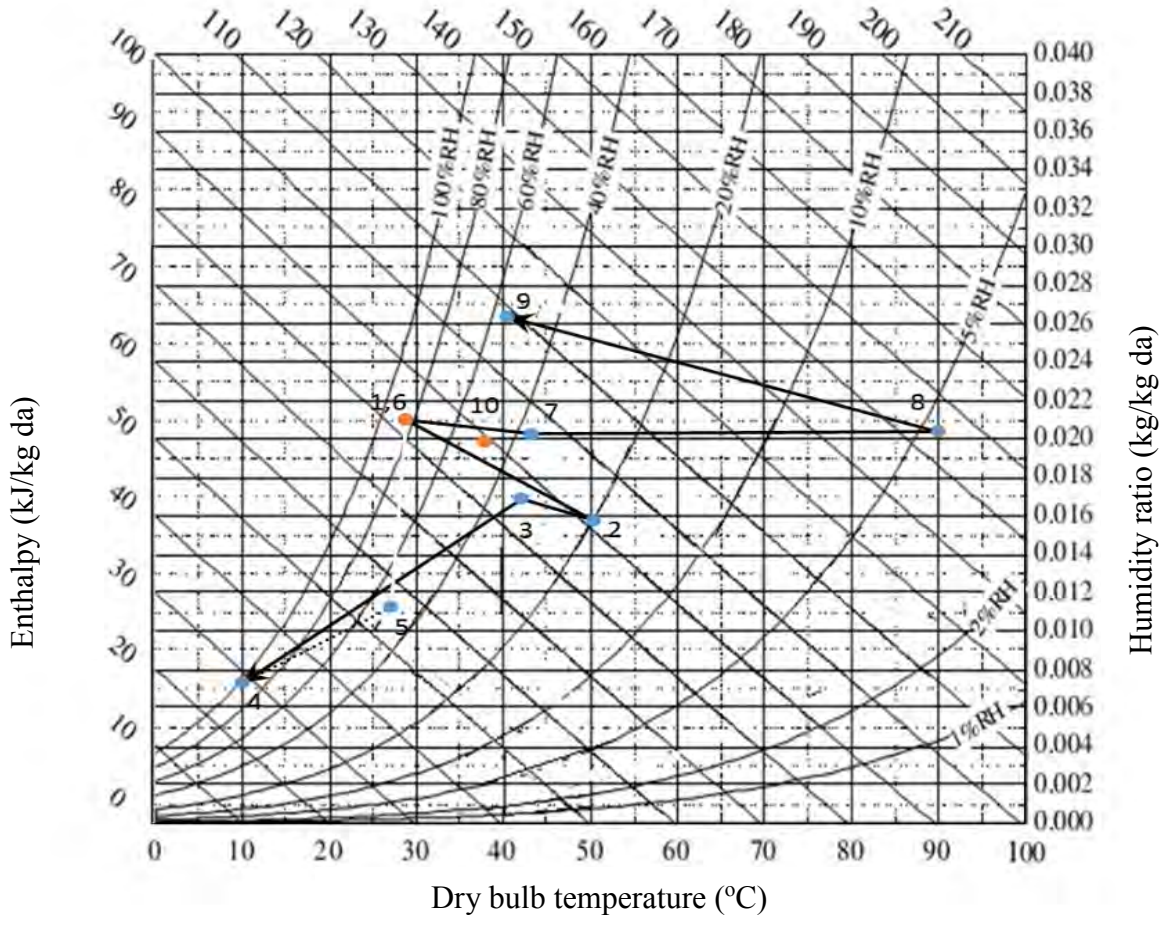

Figure 2 State points corresponding to Table 2 on psychrometric chart

temperature. Point 5 is steady state condition prevalent inside the conditioned room. Point 7 show the state of air after condenser exhaust which passes through the electrical heater where it is sensibly heated and then passes through the dehumidifier to regenerate it. Air exiting from dehumidifier on the regeneration side (state 9) has high humidity ratio due to desorption of desiccant wheel.

The power consumption by fans are 0.28 kW. Figure 3 shows the variation of COP with T_{reg} for a system with and without condenser exhaust heat use. From Fig. 3, it is clear that as regeneration temperature increases, COP of the system goes on decreasing. Also it is clear that when condenser exhaust heat is used to regenerate the desiccant wheel, there is always gain in COP of hybrid system. The gain is higher at lower regeneration temperature. At low regeneration temperature, the contribution of condenser exhaust have significant proportion compared with that of electrical heater. Hence, the two curves diverge as regeneration temperature decreases. For high regeneration temperature, proportion is insignificant and hence the two curves tend to meet each other. The percent increase with decreasing temperature is show in Fig. 4. It is about 10% at 90°C and 23% at 60°C.

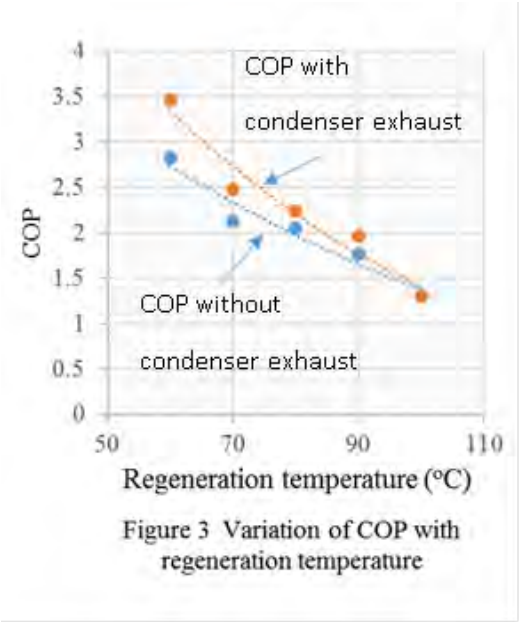

Figure 3 Variation of COP with regeneration temperature

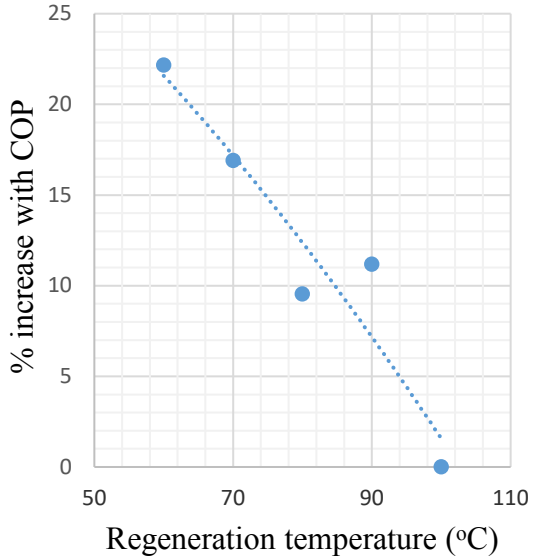

Figure 4 Variation of % increase of COP with regeneration temperature with condenser exhaust heat use

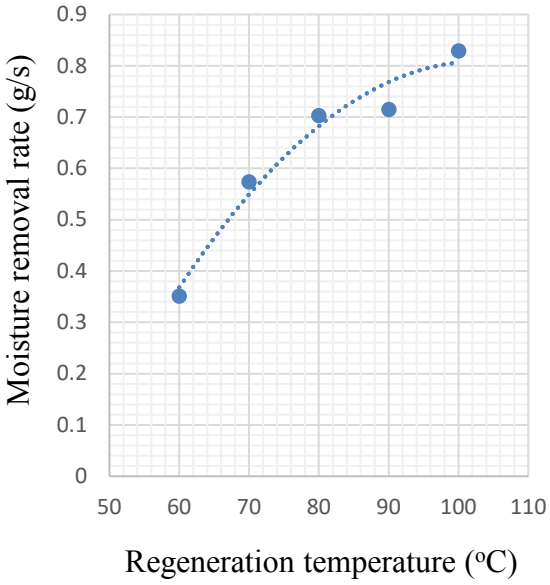

Figure 5 Variation of MRR with regeneration temperature

Figures 5 and 6 show the variation of MRR and effectiveness of desiccant wheel with respect to $T_{reg.}$ As regeneration temperature increases, rate of increment of MRR decreases. This can be explained by the fact that at higher regeneration temperature, heat which is carried with the matrix of desiccant wheel from regeneration side to process side becomes potential enough so that it renders the dehumidification capacity of the desiccant wheel nearly around a maximum and optimum value. Figure 6 shows the variation of effectiveness of the desiccant wheel with regeneration temperature. It is clear that as regeneration temperature increases, effectiveness of desiccant wheel increases. At higher regeneration temperature, desiccant wheel is regenerated better on regeneration side so that its dehumidifying capability increases for the process side. Figure 7 shows the variation of effectiveness of heat wheel with regeneration temperature. It is found that effectiveness is not affected by regeneration temperature and remains constant at about 0.4.

Some of the minor results were also observed along with above results. Among them, the temperature of delivery air to the conditioned space was found to increase with outdoor temperature. Temperature at all the points on the process side increases with outdoor temperature and so the delivery temperature. Also, regeneration temperature has the potential to affect process side outlet conditions of the desiccant wheel. Lowering the regeneration temperature lowers the outlet wheel temperature with higher humidity as evident from Fig. 5.

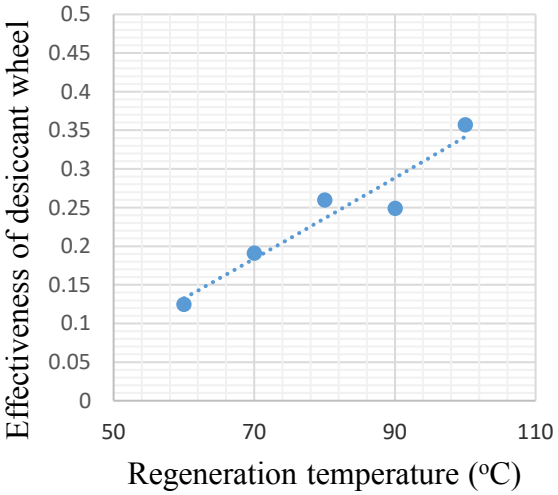

Figure 6 Variation of effectiveness of desiccant wheel with regeneration temperature

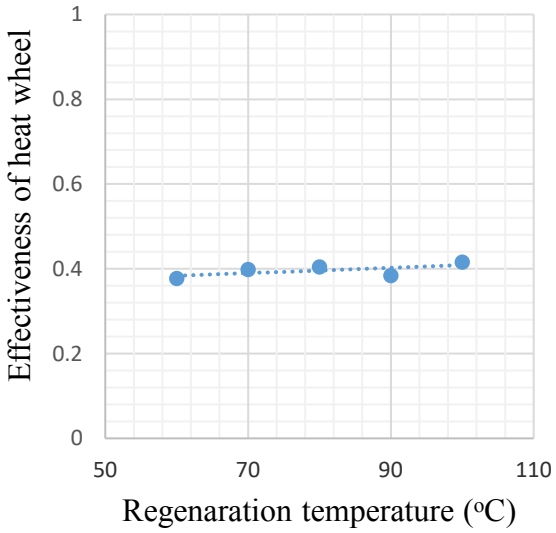

Figure 7 Variation of effectiveness of heat wheel with regeneration temperature

6. CONCLUSIONS

Hybrid solid desiccant cooling system with condenser exhaust heat recovery to regenerate the desiccant wheel was experimentally studied to investigate the behaviour and performance at different regeneration temperature varying from 60°C to 100°C. Some salient results are summarised below:

- As regeneration temperature increases, COP of the system with or without condenser exhaust decreases.
- COP of the system is always higher when condenser exhaust is used for regeneration of the desiccant wheel as that of the case when condenser exhaust is not used.
- At low regeneration temperature, curves of COPs with and without condenser exhaust diverge from each other, whereas for high values of regeneration temperature, they seem to assume closer values.
- Rate of increment of moisture removal rate (MRR) slows down as regeneration temperature is increased.
- Effectiveness of desiccant wheel increases with regeneration temperature.
- Effectiveness of the heat wheel is not affected by regeneration temperature.
- Moisture removal by single desiccant wheel is insufficient for high humid climate. Hence, a double desiccant dehumidification will be more appropriate.

ACKNOLEDGEMENT

The authors are thankful to the department of Mechanical and Industrial Engineering, Indian Institute of technology Roorkee for providing the financial support and facilities to conduct the experiment at refrigeration and air conditioning laboratory.

NOMENCLATURE

COP	Coefficient of performance
h	Enthalpy of moist air (kJ/kg of da)
$\dot{m}_p$	Mass flow rate of process air (kg/s)
$\dot{m}_r$	Mass flow rate of regeneration air (kg/s)
$\dot{Q}_{cool}$	Cooling load (kJ)
$\dot{Q}_{regen}$	Rate of regeneration heat supplied to the unit (kJ)
T	Dry bulb temperature of moist air (^oC)
W_c	Work done by compressor (kJ)
W_{fans}	Work done by fans (kJ)
ε_{DW}	Effectiveness of desiccant wheel

REFERENCES

ASHRAE.1997. *ASHRAE Handbook of Fundamentals*. American Society of Heating, Refrigerating and Air Conditioning Engineers, Atlanta.

Burns, P. R., Mitchell ,J. W., Beckman, W. A. 1985. Hybrid desiccant cooling systems in super market applications. *ASHRAE Trans* 91(1B), 457–468.

Dhar, P. L., Singh, S. K.. 2001. Studies on solid desiccant based hybrid air-conditioning systems. *Applied Thermal Engineering* 21, 119–134

Jani, D. B., Mishra, M., Sahoo, P. K., 2015. Performance studies of hybrid solid desiccant-vapor compression air-conditioning system for hot and humid climates. *Energy and Buildings*. 102, 284-292

Jani, D. B., Mishra, M., Sahoo, P. K., 2016a. Performance prediction of rotary solid desiccant dehumidifier in hybrid air-conditioning system using artificial neural network. *Appl. Therm. Eng*. 98 , 1091–1103.

Jani, D. B., Mishra, M., Sahoo, P. K., 2016b. Performance analysis of hybrid solid desiccant–vapor compression air conditioning system in hot and humid weather of India. *Build. Serv. Eng. Res*. Tech. 1–16.

Jani, D. B., Mishra, M., Sahoo, P. K., 2016c. Solid desiccant air conditioning – a state of the art review, *Renew. Sustain. Energy Rev*. 60, 1451–1469.

Jani, D. B., Mishra, M., Sahoo, P. K., 2016d. Performance prediction of solid desiccant–vapor compression hybrid air-conditioning system using artificial neural network. *Energy* 103, 618–629.

Jani, D. B., Mishra, M., Sahoo, P. K., 2016e. Experimental investigation on solid desiccant–vapor compression hybrid air-conditioning system in hot and humid weather. *Applied Thermal Engineering* 104, 556–564.

Jani, D. B., Mishra, M., Sahoo, P. K., 2016f. Exergy analysis of solid desiccant–vapour compression hybrid air conditioning system. *Int. J. Exergy.* Vol. 20, No. 4.

Kulkarni, K., Sahoo, P. K., and Mishra, M., 2011. Optimization of cooling load for a lecture theatre in a composite climate in India. *Energy and Buildings* 43, 1-30.

Maclaine-Cross, I. L., Banks, P. J., 1972. Coupled heat and mass transfer in regenerators predictions using an analogy with heat transfer. *Int. J. of Heat and Mass Transfer* 15, 1225–1241.

Panaras, G., Mathioulakis, E., Belessiotis, V., Kyriakis, N., 2010. Experimental validation of a simplified approach for a desiccant wheel model. *Energy Build*. 42, 1719–1725.

Sheridan, J. C., Mitchell ,J.W., 1985. Hybrid solar desiccant cooling system. *Solar Energy* 34(2), 187–193.

Subramanyam N, Maiya, M. P., Murthy, S. S., 2004a*, Parametric studies on a desiccant assisted air-conditioner*, Applied Thermal Engineering 24, 2679–2688.

Subramanyam N, Maiya, M. P., Murthy, S. S., 2004b, *Application of desiccant wheel to control humidity in air-conditioning systems*, Applied Thermal Engineering 24, 2777–2788

Van Den Bulck, E., S. A. Klein, J. W. Mitchell. 1988. Second law analysis of solid desiccant rotary dehumidifiers. *ASME Journal of Heat Transfer* 110, 2–9.

Worek, W. M., Moon, C. J., 1988. Desiccant integrated hybrid vapour compression cooling performance sensitivity to outdoor conditions. *Heat Recovery Systems and CHP* 8(6), 489–501.

Yadav, A., Bajpai, V.K., 2013. Numerical and experimental investigation of operating parameters of solar–powered desiccant wheel in India. *Heat Transfer*, Asian Research. Vol. 42 (1), 1-30.

Yadav, A., Yadav, L., 2014. Comparative performance of desiccant wheel with effective and ordinary regeneration sector using mathematical model. *Heat and Mass Transfer*, Springer Berlin Heidelberg. Vol. 50 (10), 1465-1478.

Yadav, A., Yadav, L.,2015. Comparative Performance of Different Sector Arrangement in a Desiccant Wheel Using a Mathematical Model*. Heat Transfer,* Asian Research. Vol. 44 (2), 133-153.

Manuscript ID: 1228
DOI: 10.18462/iir.icr.2019.1228

Covering peak loads with phase change materials in a geothermal and desiccant assisted air conditioning system

Finn RICHTER[(a)], Peter NIEMANN[(a)], Gerhard SCHMITZ[(a)]

[(a)] Hamburg University of Technology, Institute of Engineering Thermodynamics
Hamburg, 21073, Denickestraße 17, Germany, finn.richter@tuhh.de

ABSTRACT

In a geothermal and desiccant assisted air conditioning system at Hamburg University of Technology covering thermal peak loads by means of phase change materials (PCM) is investigated. In the consequence of high ambient temperatures the cooling power of the soil can be exceeded and a backup system is necessary. In this study experimental data of a backup system consisting of PCM encapsulated in plates and placed in a rack is presented. A computer case fan is used to induce a volume flow through the PCM rack. Results show that the PCM rack is able to locally focus cooling operation and as a result improve thermal comfort perception. An air temperature reduction of approximately 0.7 – 0.9 °C at an average cooling power of 26.58 W can be achieved. The COP accounts for 6.65 with a corresponding electricity consumption of 4 W.
Keywords: Air Conditioning, Desiccant Wheel, Geothermal, Thermal Peak Loads, PCM, Local Cooling, Thermal Comfort.

1. INTRODUCTION

Increasing ambient temperature due to global warming matched with higher incomes results in a growing demand for thermal comfort and air conditioning systems (Davis and Gertler, 2015). The estimated increase from approximately 4 billion in 2016 to 9.3 billion in 2050 air conditioning systems in the residential and commercial sector (International Energy Agency, 2018) shows the necessity of energy efficient space cooling.

To achieve thermal comfort, latent and sensible loads need to be removed from the outside air. In conventional systems air is cooled below dew point temperature by a vapour compression cycle to remove moisture. Thus, removing latent and sensible loads is coupled within the process. In desiccant assisted systems the energy intensive dehumidification process is replaced by a solid or liquid desiccant and therefore separated from sensible cooling. As a result higher tempered heat sinks, e. g. shallow geothermal energy, can be used to remove sensible loads. Due to high ambient temperatures the cooling power of the soil can be exceeded and comfortable room temperatures may not be maintained (Casas and Schmitz, 2005). This implicates an oversizing of the geothermal system (Speerforck and Schmitz, 2016) or another backup system is necessary. In this study phase change materials (PCM) are investigated experimentally as backup system.

The usage of PCM for space cooling is well-known. The application ranges from free-cooling with PCM encapsulated in plates and placed in air ducts of the ventilation system (Zalba et al., 2004) to heat pipes incorporated in PCM to enhance the cooling power (Turnpenny et al., 2000). Many different encapsulations (Raj and Velraj, 2010) and system designs, e. g. PCM implemented in the building facade and ceiling (Álvarez et al, 2013), have been investigated. Additionally, different designs of cooling ceilings have been studied and monitored extensively (Weinläder et al., 2016, Weinläder et al., 2017).

In addition to PCM the idea of personal ventilation or local cooling is increasing. Local cooling describes the attempt to achieve a comfortable microenvironment around a person despite the uncomfortable uniform room environment (Melikov, 2004). There is a huge variety of approaches to implement local cooling. Varying the direction of fresh air flow can obtain cooling sensation (Kalmár and Kalmár, 2013). Different devices, e. g. cooled wristpad, deskfan, cooled chair (Luo et al., 2018), ventilated mattress or local bed ventilation (Melikov, 2016), can improve thermal comfort perception. Additionally to achieving higher comfort, local cooling is able to reduce energy use for air conditioning applications. (Zhang et al., 2010) simulated a reduction of energy use by only cooling hands and

face of up to approximately 29 % compared to a conventional air conditioning system. (Veselý and Zeiler, 2014) give an overview of different local cooling systems with energy savings of up to 45 %. Combining both, PCM and local cooling, is part of recent studies. (Lu et al., 2015) and (Kang et al., 2018) investigated uniforms incorporated with PCM and ventilation fans. (Dhumane et al., 2018) and (Dhumane et al., 2019) used PCM to store heat of the condenser of a vapour compression cycle used in a personal conditioning system. In this study, the combination of a geothermal and desiccant assisted air conditioning system and a backup system consisting of PCM is investigated experimentally. Therefor PCM is encapsulated in plastic plates and placed in a rack to locally cool and enhance thermal comfort in case of thermal peak loads.

2. EXPERIMENTAL STUDY

The investigated test facility as well the concept of local cooling is described. The performance and limitations of the PCM rack design are analysed. To evaluate thermal comfort a comfort measurement device according to DIN EN ISO 7726 is utilized.

2.1. Test Facility

The test facility is built of eight 20 ft. containers and is located on the campus of Hamburg University of Technology. The four upper containers (56 m²) are used as office and conference room and the lower containers contain the air handling unit and technical installations.

2.1.1. System Concept

In Fig. 1 a simplified system layout of the open cycle desiccant assisted air conditioning system with borehole heat exchanger is depicted. In summer operation the outside air is dehumidified by a desiccant wheel (1-2). After precooling the air in a rotary thermal wheel (2-3) supply air temperature (22 °C) is adjusted by a dry cooling coil (3-4). In order to regenerate the desiccant wheel the heat recovery wheel preheats extract air from the reference room (5-6). To reach the required regeneration temperature, a water to air heat exchanger is utilized (6-7). In a final step moisture is removed from the desiccant (7-8) before the air is emitted to the environment. In the reference room a cooling ceiling is implemented to remove sensible loads. One double U-tube borehole heat exchanger is used to cover the cooling demand of the cooler and the cooling ceilings.

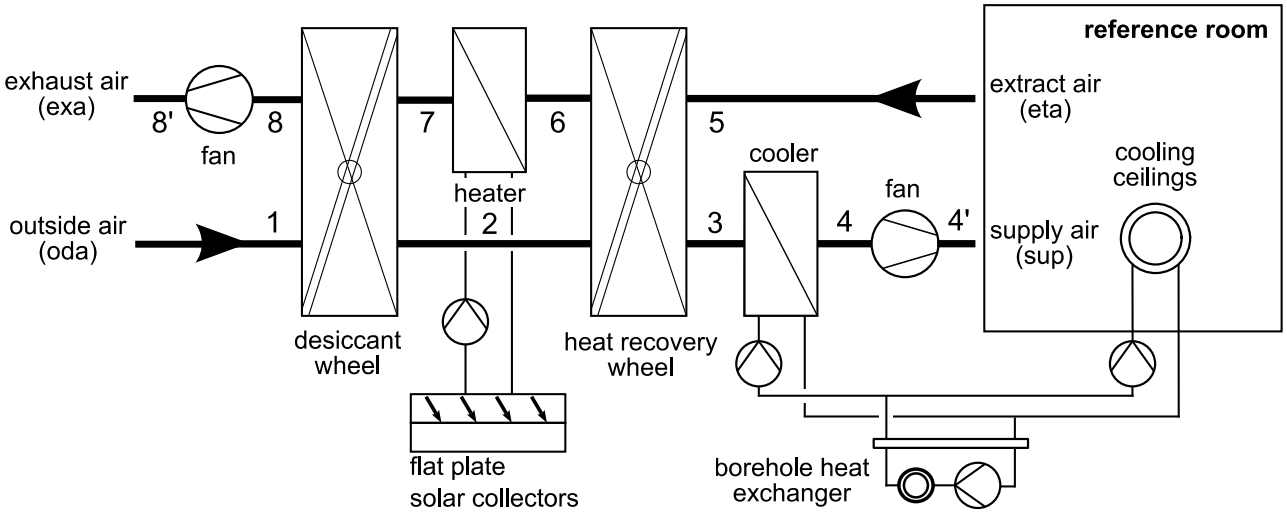

Figure 1: Simplified system layout of the test facility

2.1.2. Thermal Comfort Measurement

The objective of the system concept is to achieve comfortable indoor air conditions according to DIN EN 15251. This implicates to keep indoor temperature between 21 °C and 25.5 °C and relative humidity between 30 % and 50 %. Therefor the system is operated during common office hours from 7 am to 10 pm. In addition to general data acquisition to monitor the performance of test facility, a thermal comfort measurement device according to DIN EN ISO 7726 is set up. The measurement device is shown in Fig. 2.

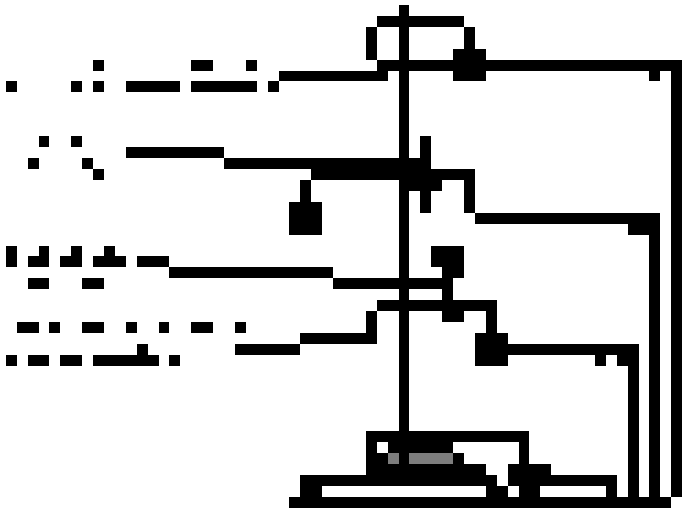

Figure 2: Schematic layout of the thermal comfort measurement device

At the height of head, abdomen and ankle, corresponding to sitting or standing position of human beings, the air temperature and the mean radiant temperature is measured. The air velocity is quantified by an omnidirectional hot-wire anemometer. Using a capacitive sensor the relative humidity is assessed. Measurement devices in use and the related uncertainties are listed in Table 1.

Table 1. Measurement sensors used by the thermal comfort measurement device

Measured property	Sensor type / measuring principle	Measurement uncertainty
Resistance thermometer	Pt100 (accuracy class W 0.1)	$\pm 1/3 \cdot (0.3 + 0.005 \cdot T)$ °C
Black-globe thermometer	Pt100 (accuracy class W 0.1)	$\pm 1/3 \cdot (0.3 + 0.005 \cdot T)$ °C
Anemometer	Hot-wire sensor	± 1.5 % m.s^{-1} of reading
Hygrometer	Capacitive sensor	± 2 % r.h. for 10 … 90 % r.h.

Utilizing the measurement device it is possible to objectively and comparably assess thermal comfort referred to DIN EN ISO 7730. Within this study the air temperature and the draught rate (DR) will be evaluated. According to DIN EN ISO 7730 the DR is calculated as follows.

$$DR = (34 - T_{\mathrm{l}}) \cdot (v_{\mathrm{a}} - 0.05)^{0.62} \cdot (0.37 \cdot v_{\mathrm{a}} \cdot Tu + 3.14) \qquad \text{Eq. (1)}$$

2.2. PCM Backup System

In the described system shallow geothermal energy is used to cool the supply air and to remove sensible loads by means of a cooling ceiling. A previous study has shown that a maximum temperature level of approximately 18 °C is required to accomplish thermal comfort inside the reference room at any time (Speerforck and Schmitz, 2016). Due to the slow regeneration of the soil around the borehole heat exchanger through conduction, shallow geothermal energy is not inexhaustible regarding a limited period of time. Thus, in the consequence of high cooling loads during hot periods in summertime the outlet temperature of the borehole heat exchanger can raise above the desired value. As a result, indoor room air temperatures above 25.5 °C can occur. Therefore, a PCM rack is used to cover the occurring thermal peak loads by locally reducing the temperature.

2.2.1. PCM Material and Encapsulation

The PCM used is AXIOTHERM® ATS 25. It is an inorganic PCM with melting temperature in the range of 22 – 25 °C and a heat storage capacity (temperature range of 15 – 30 °C) of 195 kJ.kg^{-1}. Solidification temperature range lays in between 21 – 24 °C. Due to its corrosive nature on metal, the capsule material is plastic with dimensions of (0.175 x 0.235 x 0.006) m^3 (l x w x h). The surface

area of one plate is 0.091 m^2 with a maximum PCM layer thickness of 0.008 m. The filled volume of PCM inside one plate is 0.00014 m^3, resulting in approximately 0.217 kg of PCM per plate.

2.2.2. PCM Rack Design

To achieve local cooling a PCM rack containing the PCM plates was designed. The rack consists of 5 compartments, each containing 50 PCM plates in 2 rows with 25 plates each. According to its cooling purpose in an office building, the height of the PCM rack correlates to the head location in sitting position (1.10 m). The PCM rack is depicted in Fig. 3.

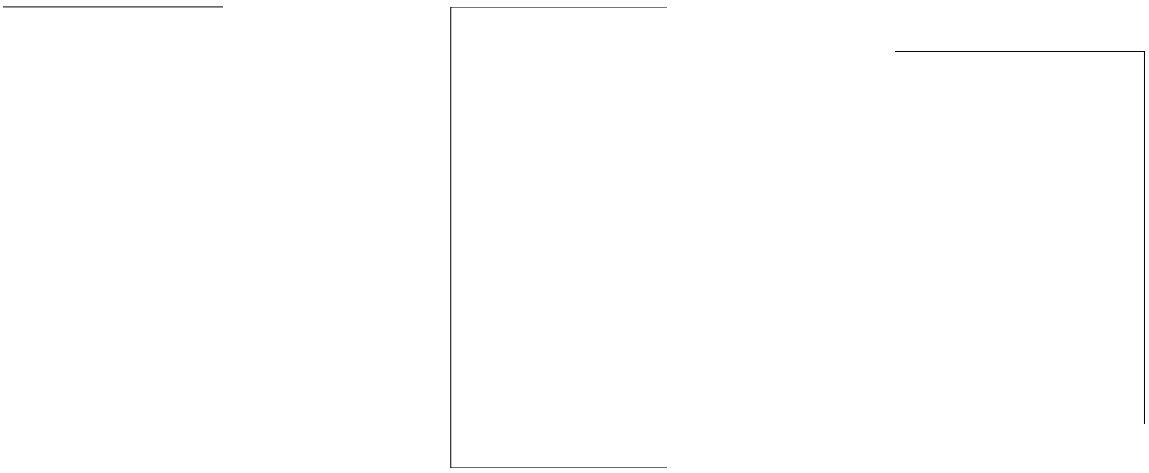

Figure 3: PCM rack: back view (left), front view (middle), top view (right)

Each compartment is equipped with a computer case fan inducing a volume flow of 38.68 $m^3.h^{-1}$ in cooling and regeneration mode. By means of an Arduino Uno and two temperature sensors (marked with circles in Fig. 3) the PCM rack is able to independently control the fans. In general, three operating modes can be differentiated: standby mode, cooling mode and regeneration mode. During cooling mode, the PCM will change phase from solid to liquid and therefor account for sensible cooling of the induced air flow. The cooling mode will be entered if the room temperature exceeds 24.5 °C for a certain amount of time. Cooling mode is continued until either the room temperature falls below the threshold value or the cooling power of the PCM rack is below 50 W. In case of room temperatures below 23 °C the regeneration mode will start. In this mode the phase changes from liquid to solid and prepares the PCM for the next cooling cycle. Regeneration mode is running until either the room temperature rises above the threshold temperature, a set amount of time is passed or the temperature difference between the inlet and the outlet is small. The PCM rack is only powered by electricity. The supply voltage is 12 V and the power consumption is 1 W in standby mode and 20 W in active mode, respectively. To evaluate the performance of the PCM rack 6 temperature sensors are placed at the top compartment (marked with arrows in Fig. 3). The specifications of the measurement devices and the related uncertainties can be found in Table 3. Prior to installation all temperature sensors have been calibrated using an oil bath.

Table 3. Measurement sensors used by the thermal comfort measurement device

Measured property	Sensor type / measuring principle	Measurement uncertainty
Resistance thermometer	Pt100 (accuracy class F 0.15)	$\pm(0.15 + 0.002 \cdot T)$ °C
Volume flow	Vane anemometer (0.06 m)	$\pm(0.2 + 1.5\ \%$ of reading) $m.s^{-1}$

2.3. Measurement Results

In order to evaluate the capability of the PCM rack to locally increase thermal comfort, temperatures above 25.5 °C are artificially induced by the ceiling surface heat exchanger in the reference room of the test facility. The PCM rack is faced towards the comfort measurement device in a distance of 1 m. A schematic view of the placements in the reference room is shown in Fig. 4.

2.3.1. PCM Rack Evaluation

The cooling power of the PCM rack is calculated simplified for the top most compartment. Therefor the properties of air are approximated and set as constant within the calculations:

- Specific heat capacity: $c_{\mathrm{p}} = 1007$ J.kg^{-1}.K^{-1}
- Density: $\rho = 1.19$ kg.m^3

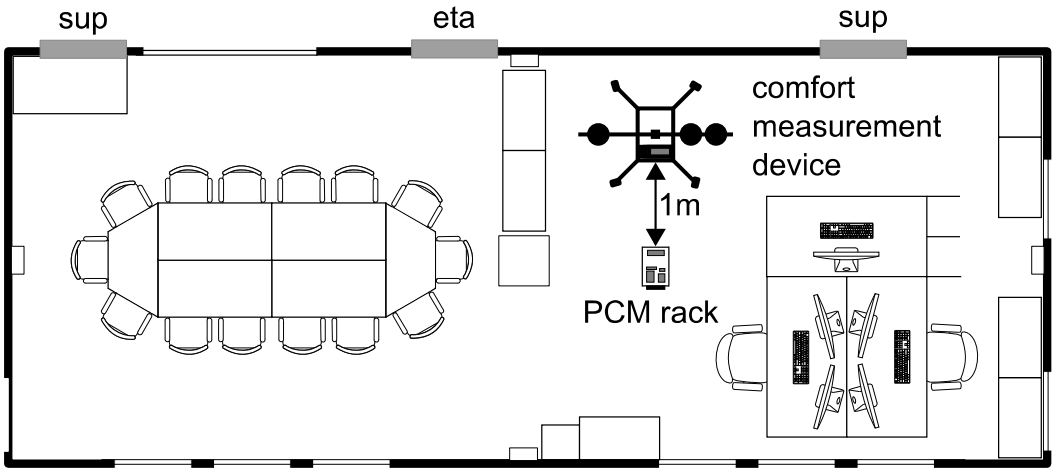

Figure 4: Schematic view of the reference room

By means of three resistance thermometers the outlet temperature of the PCM rack is measured (as illustrated with arrows by Fig. 3). Thus, the mean outlet temperature is used for calculation and shown in all figures. The cooling power and the COP are calculated as follows:

$$\dot{Q}_{\mathrm{cool}} = \dot{V} \cdot \rho \cdot c_{\mathrm{p}} \cdot (T_{\mathrm{in}} - T_{\mathrm{out}}) \qquad \text{Eq. (2)}$$

$$COP = \frac{\dot{Q}_{\mathrm{cool}}}{P_{\mathrm{el}}} \qquad \text{Eq. (3)}$$

In Fig. 5 the measured temperature profile and the according cooling power in the course of a day are depicted. It can be assumed that at the start of the measurement the PCM is fully solidified.

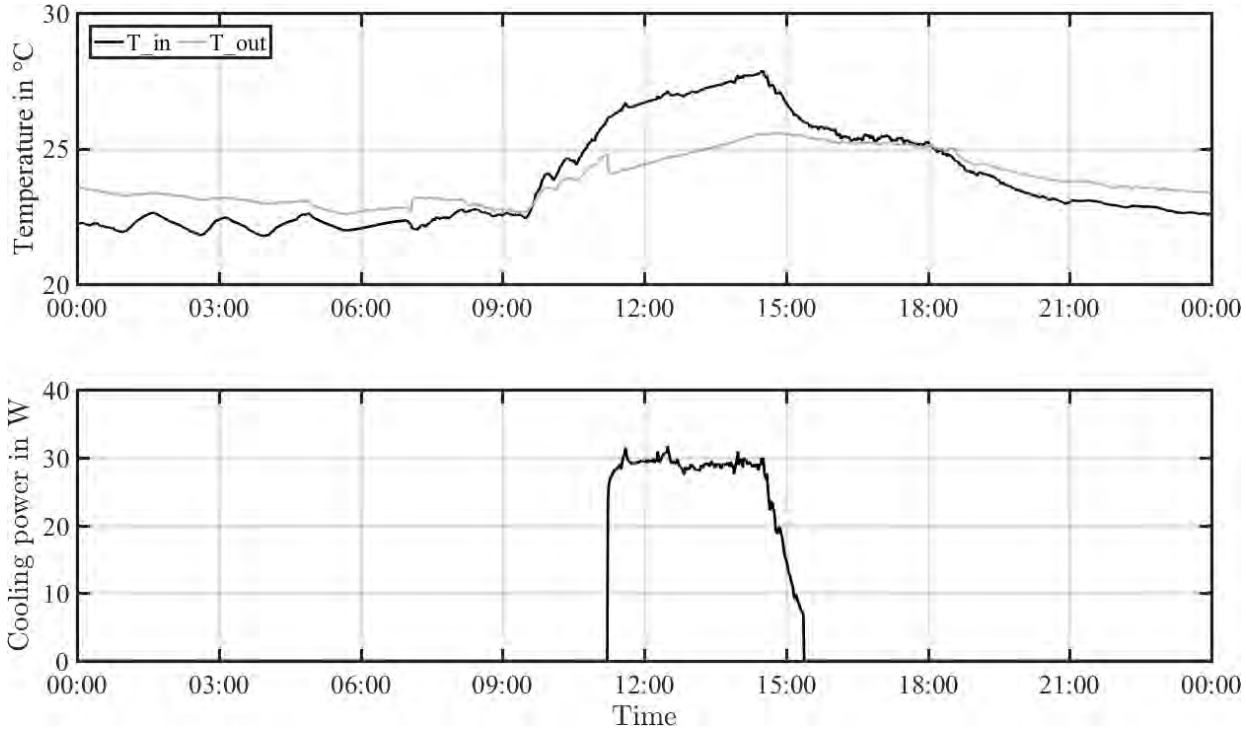

Figure 5: Temperature profile (top) and cooling power (bottom) of the top compartment

During the runtime of 4 hours an average cooling power of 26.58 W and an average COP of 6.65 could be achieved. It must be pointed out that the decrease in cooling power towards the end of the runtime is not a result of near PCM exhaustion, but of the decline in room temperature and therefor a reduced temperature difference between room temperature and PCM melting temperature. At maximum the cooling power reached a value of (31.69 ± 4.91) W with a COP of 7.92 ± 1.23 was reached.

2.3.2. Thermal Comfort Evaluation

As described in Section 2.3.1., the outlet temperature of the PCM rack is lower than the ambient room temperature. Therefore, an increase in thermal comfort can be assumed. In Fig. 6 the measured temperatures of the thermal comfort measurement device for the same day as in Fig. 5 are shown.

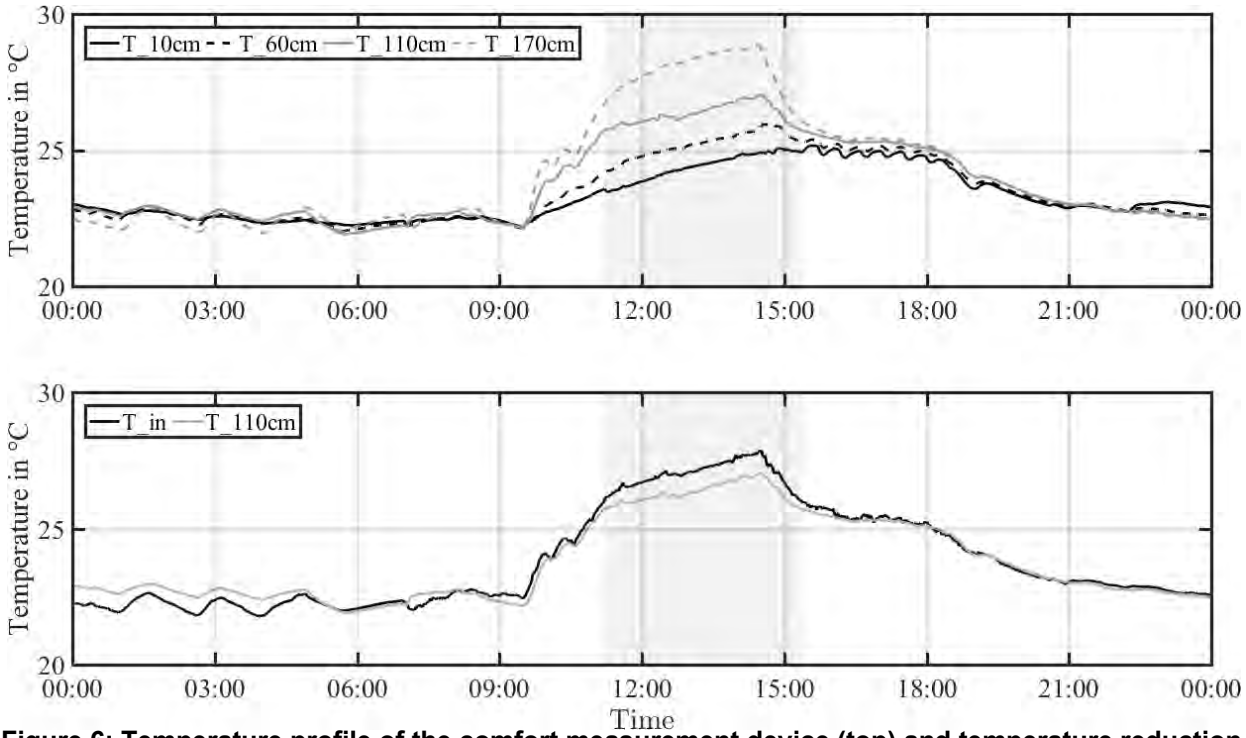

Figure 6: Temperature profile of the comfort measurement device (top) and temperature reduction achieved by the PCM rack (bottom). The grey background indicates the runtime of the PCM rack in cooling mode.

At start-up of the PCM rack the gradient change of the temperature graph in the height of 110 cm is clearly visible. A temperature reduction of approximately 0.7 – 0.9 °C could be achieved. The upper temperature measurement position at 170 cm is not affected by the PCM rack due to its maximum height of 110 cm. The different effects on the measurement position show the ability of the PCM rack to locally focus cooling operation. Due to the artificially created high air temperatures, stratification inside the room can be observed. Therefore, the lower compartments cannot offer significant cooling power because the inlet temperature at that height is at the same level as the PCM melting temperature. Besides the positive effects on local temperature, the influence of the induced air flow needs to be evaluated. In Fig. 7 the measured air velocity of the comfort measurement device and the calculated DR are depicted. It can be seen that there is no negative impact due to the induced air flow.

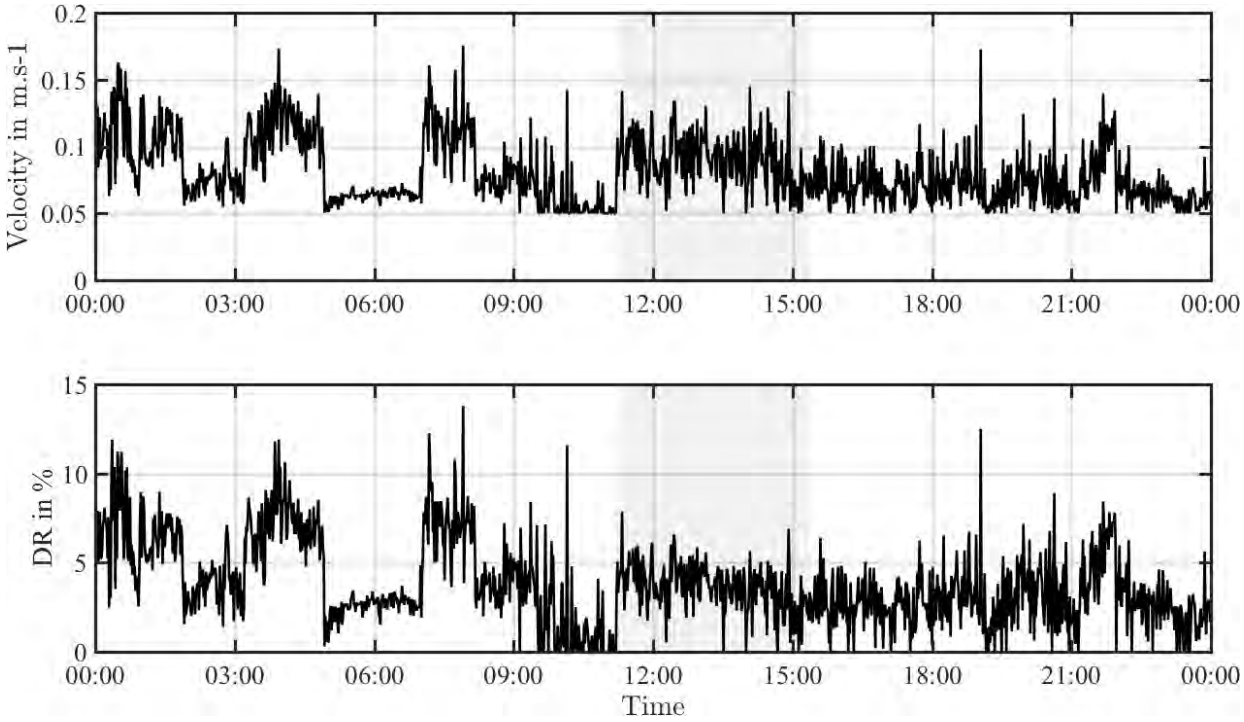

Figure 7: Air velocity profile (top) and corresponding DR (bottom) during the measurements. The grey background indicates the runtime of the PCM rack in cooling mode.

3. CONCLUSIONS

Local cooling by means of the PCM rack can improve thermal comfort perception by reducing the air temperature about approximately 0.7 – 0.9 °C. The low electricity demand of 4 W per compartment offers the possibility to save energy compared to a uniform air conditioning approach. During 4 hours of operation mode an average cooling power of 26.58 W with a COP of 6.65 is provided by only one compartment. Due to its construction out of compartments, the PCM rack is scalable and offers the possibility to adapt the rack to different cooling tasks. However, analysis of the rack regarding regeneration time and the resulting energy efficiency ratio is required.

ACKNOWLEDGEMENTS

This work is being conducted in the frame of a project funded by the Federal Ministry for Economic Affairs and Energy (www.bmwi.de), cf. project funding reference number 03ET1421A.

NOMENCLATURE

c_p	specific heat capacity (J.kg^{-1}.K^{-1})	COP	coefficient of performance (-)
DR	draught rate (%)	P	electrical power (W)
$\dot{Q}$	thermal power (W)	T	temperature (°C)
Tu	intensity of turbulence (%)	$\dot{V}$	volume flow (m^3.s^{-1})
v_a	local mean air velocity (m.s^{-1})	ρ	density (kg.m^{-3})
cool	cooling	el	electrical
eta	extract air	exa	exhaust air
in	inlet	l	local
oda	outside air	out	outlet
sup	supply air		

REFERENCES

Álvarez, S., Cabeza, L.F., Ruiz-Pardo, A., Castell, A., Tenorio, J.A., 2013. Building integration of PCM for natural cooling of buildings. Applied Energy 109, 514-522.

Casas, W., Schmitz, G., 2005. Experiences with a gas driven, desiccant assisted air conditioning system with geothermal energy for an office building. Energy and Buildings 37(5), 493-501.

Davis, L.W., Gertler, P.J., 2015. Contribution of air conditioning adoption to future energy use under global warming. Proceedings of the National Academy of Sciences 112 (19), 5962-5967.

Dhumane, R., Mallow, A., Qiao, Y., Gluesenkamp, K.R., Graham, S., Ling, J., Radermacher, R., 2018. Enhancing the thermosiphon-driven discharge of a latent thermal storage system used in a personal cooling device. International Journal of Refrigeration 88, 599-613.

Dhumane, R., Qiao, Y., Ling, J., Muehlbauer, J., Aute, V., Hwang, Y., Radermacher, R., 2019. Improving system performance of a personal conditioning system integrated with thermal storage. Applied Thermal Engineering 147, 40-51.

International Energy Agency, 2018. The Future of Cooling. OECD/IEA, Paris.

Kalmár, F., Kalmár, T, 2013. Alternative personalized ventilation. Energy and Buildings 65, 37-44.

Kang, Z., Udayraj, Wan, X., Wang, F., 2018. A new hybrid personal cooling system (HPCS) incorporating insulation pads for thermal comfort management: Experimental validation and parametric study. Building and Environment 145, 276-289.

Lu, Y., Wei, F., Lai, D., Shi, W., Wang, F., Gao, C., Song, G., 2015. A novel personal cooling system (PCS) incorporated with phase change materials (PCMs) and ventilation fans: An investigation on ist cooling efficiency. Journal of Thermal Biology 52, 137-146.

Luo, M., Arens, E., Zhang, H., Ghahramani, A., Wang, Z., 2018. Thermal comfort evaluated for combinations of energy-efficient personal heating and cooling devices. Building and Environment 143, 206-216.

Melikov, A.K., 2004. Personalized ventilation. International Journal of Indoor Environment and Health 14(7), 157-167.

Melikov, A.K., 2016. Advanced air distribution: improving health and comfort while reducing energy use. International Journal of Indoor Environment and Health 26(1), 112-124.

Raj, V.A.A., Velraj, R., 2010. Review on free cooling of buildings using phase change materials. Renewable and Sustainable Energy Reviews 14(9), 2819-2829.

Turnpenny, J.R., Etheridge, D.W., Reay, D.A., 2000. Novel ventilation cooling system for reducing air conditioning in buildings. Part I: testing and theoretical modelling. Applied Thermal Engineering 20(11), 1019-1037.

Veselý, M., Zeiler, W., 2014. Personalized conditioning and its impact on thermal comfort and energy performance – A review. Renewable and Sustainable Energy Reviews 34, 401-408.

Weinläder, H., Klinker, F., Yasin, M., 2016. PCM cooling ceilings in the Energy Efficiency Center – passive cooling potential of two different system designs. Energy and Buildings 119, 93-100.

Weinläder, H., Klinker, F., Yasin, M., 2017. PCM cooling ceilings in the Energy Efficiency Center – Regeneration behavior of two different system designs. Energy and Buildings 156, 70-77.

Zalba, B., Marín, J.M., Cabeza, L.F., Mehling, H., 2004. Free-cooling of buildings with phase change materials. Int. J. of Refrigeration 27(8), 839-849.

Zhang, H., Arens, E., Kim, D., Buchberger, E., Bauman, F., Huizenga, C., 2010. Comfort, perceived air quality, and work performance in a low-power task-ambient conditioning system. Building and Environment 45(1), 29-39.

Manuscript ID: 1244
DOI: 10.18462/iir.icr.2019.1244

Identification of vapour compression air conditioning system behaviour using Bayesian regularization neural network

SHOLAHUDIN[(a)], Keisuke OHNO[(b)], Seiichi YAMAGUCHI[(a),(b)], Kiyoshi SAITO[(a),(b)]

[(a)]Department of Applied Mechanics and Aerospace Engineering, Waseda University Tokyo, 169-8555, Japan, sholahudin@fuji.waseda.jp
[(b)]Interdisciplinary Institute for Thermal Energy Conversion Engineering and Mathematics, Waseda University, 3-4-1 Okubo, Shinjuku-ku, Tokyo, 169-8555, Japan, sei_yamaguchi@aoni.waseda.jp

ABSTRACT

Identification for system dynamic behaviour is necessary to develop control strategy. In this paper, the dynamic performance of air conditioning (AC) system is predicted using artificial neural network (ANN) approach. The ANN is developed to predict exergy efficiency, coefficient of performance (COP), and cooling capacity. The controllable parameters including compressor speed and evaporator and condenser fan speed are considered as the input. The datasets for prediction are generated by AC system simulator. The system was simulated by randomly varying compressor speed and evaporator and condenser fan speed with N-sample signal input. The dynamic ANN configuration with Bayesian regularization is proposed to predict one-step ahead of system performance behaviour. The results show that the developed ANN in present study yields good prediction accuracy for all outputs. Accordingly, ANN can be further applied for predictive control application in AC system to control cooling capacity while maintaining system efficiency.
Keyword: System Identification, Air Conditioning, Neural Network, Exergy.

1. INTRODUCTION

Today, air conditioning and refrigeration system becomes the important part in life as the result of increasing in population growth, economic, and living standard. The huge demand of AC and refrigeration system brought the people to concern about the raise of energy consumption and its negative impact to the environment. Increasing AC system efficiency has a large contribution in reducing building energy consumption. Vapour compression cycle (VCC) is one of the system that has been used in many buildings and industrial application. The development of VCC system has almost reached the maximum performance and hard to improve due to its limitation such as compressor and heat exchanger technology (Nishijima, 2016). The solution that can be proposed to improve the system operation efficiency is on control development. A system with high efficiency will be useless if it is not equipped with proper control strategy. Hence, developing control strategy which considers the system efficiency is necessity for system operation.

The control strategy using on/off and PI has been widely applied in VCC system for either AC or refrigeration (Ng, 2014). In on/off control, the system is operated by setting the compressor speed in one level. Consequently, it generates overshoots and undershoots and consumes a lot of energy. For PI control, the compressor speed can be regulated in various levels to maintain the desired room temperature with less energy input. However that control strategy can be applied in limited range operation condition and has poor performance if the cooling load is very small and set point changes from the designed point (Nam, 2017).

A model predictive control (MPC) strategy can be chosen as alternative solution to improve efficiency of system operation. The first important thing in MPC development is system identification. The output performance of system should be precisely predicted according to various actuator signal. It can be performed by physical-based approach which includes a lot of equation and assumption in the model to achieve accurate estimation. However it is very complex and takes a long computation time due to many equations that should be solved. Modelling with artificial neural network (ANN) offers lower complexity and less computational task as compared to physical model since it involves

input and output data only. The applicability of ANN for dynamic system modelling and MPC application has been proven in several studies (Li, 2013; Yang, 2016; Muñoz, 2017). In those works, ANN is developed to predict room temperature and humidity without considering efficiency parameter. In this paper, ANN model is developed to predict system dynamic behaviour of split AC system under modulation of evaporator fan, condenser fan, and compressor speed. The proposed ANN model is developed to capture the dynamic performance behaviour of system namely COP, exergy efficiency, and cooling capacity.

2. METHODOLOGY

2.1 System Description

Single stage VCC system is used for air conditioning purpose in present study. The schematic diagram of system is depicted in Fig. 1. The system has variable speed compressor, electronic expansion valve (EEV), one indoor and one outdoor unit. The refrigerant of R410A is used as the medium to transfer the heat from conditioned space Q_E at room temperature T_R to the environment at temperature T_A through the condenser as Q_C. The system performance behavior is simulated by Energy flow+M software which is developed using physical model and has been validated with actual system in steady and unsteady condition (Matsumoto, 2016). The detail of mathematical models for each component are presented in (Saito, 2018). The system characterization is performed by varying manipulated parameters including compressor speed, fan speed at evaporator and condenser. N-sample signal type is introduced to demonstrate system performance behavior in unsteady condition. Input and output data applied for system identification is shown in Fig. 2. During the simulation, PI controller is applied to maintain superheat temperature T_{SH} at 5 °C. Totally, there are 2000 pairs of input and output data generated by simulator with sampling time of 30 s. The first 1500 data is used for training and the rest is employed for validation. So the data set used for validation is totally different with the data used in training phase.

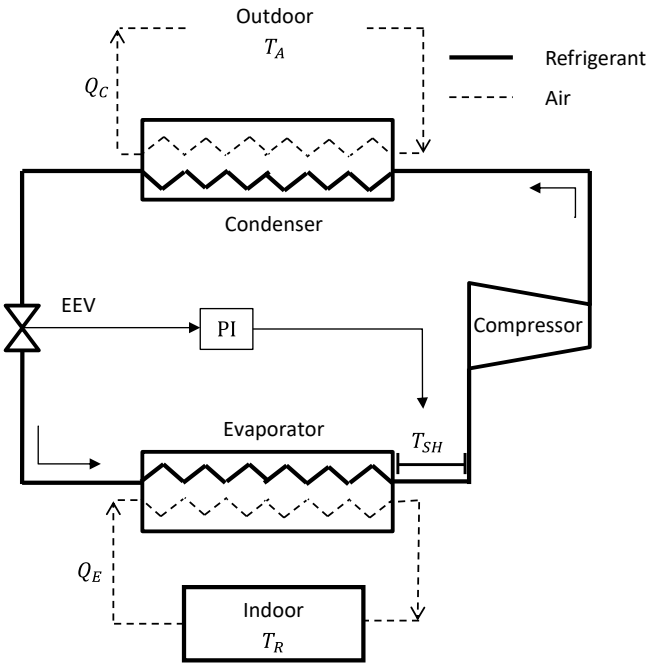

Figure 1: Schematic diagram of vapor compression AC system

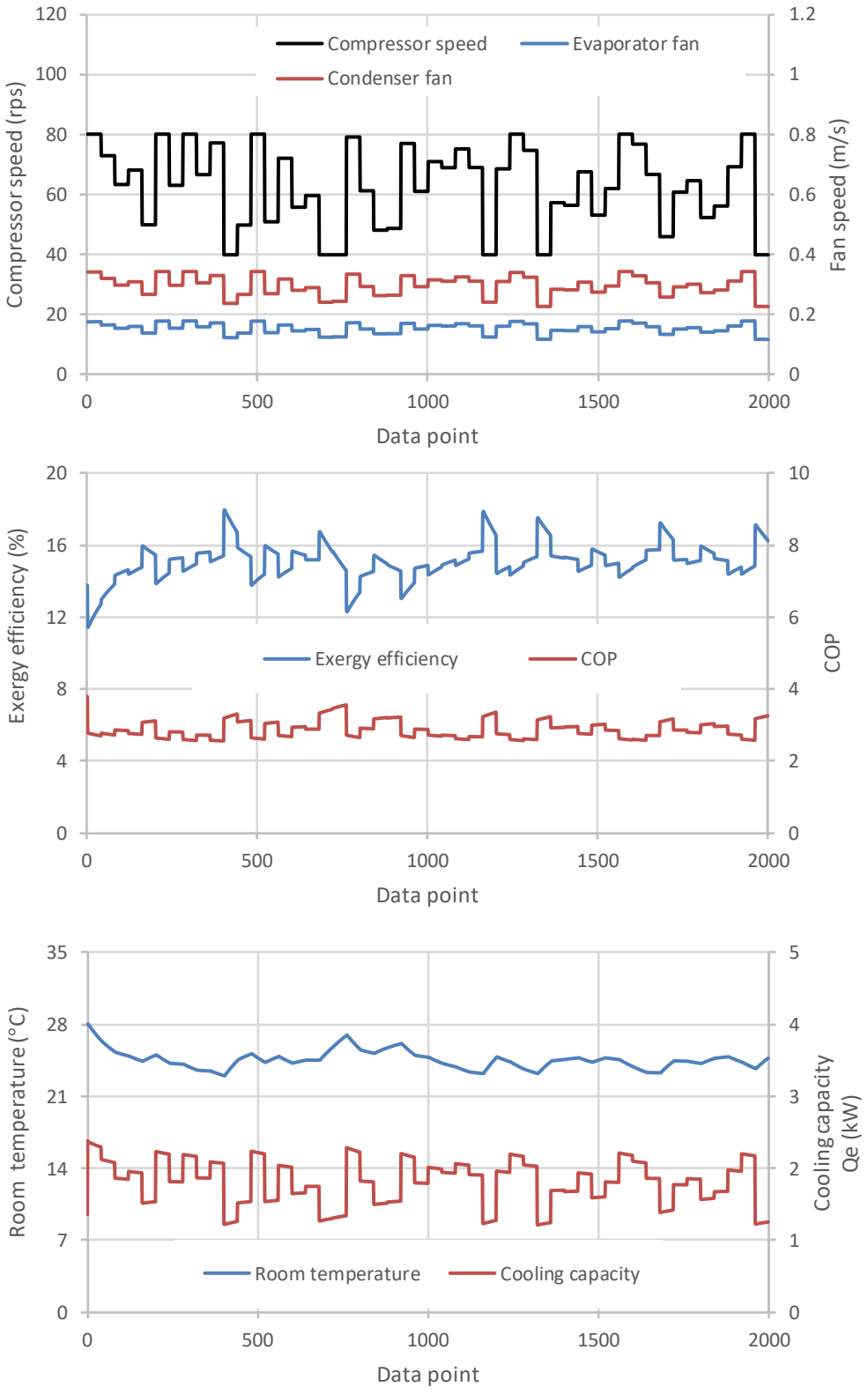

Figure 2: Input output pattern used for identification

2.2 Artificial Neural Network

Artificial neural network (ANNs) is kind of machine learning tool which can formulate the relationship between inputs and outputs via mathematical function. This technique has been successfully used to predict the static and dynamic output response in building application (Sholahudin, 2015;

Sholahudin, 2016). The structure of ANN is generally consisted of input, hidden, and output layer. In hidden layer, there is one or more neurons which build up the relationship between input and output through some mathematical function. Mathematically, the learning process of ANN can be seen in Fig. 3. The network is trained by adjusting the weight (w_1, w_2) and bias (b_1, b_2) coefficient to produce the ANN output as the actual output. Combination of Levenberg-marquardt and Bayesian regularization is proposed to determine the weight and bias coefficient by minimizing objective function which consists of prediction error and weight and bias coefficients. These coefficients are minimized to avoid over fitting during training phase.

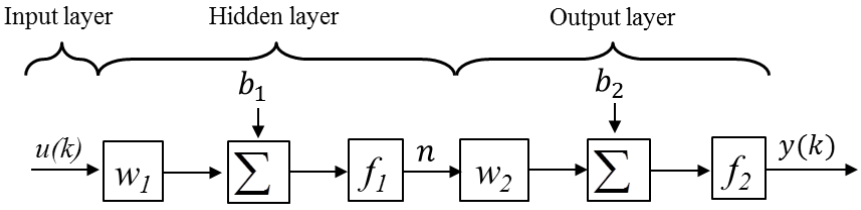

Figure 3: Diagram block of ANN calculation

Fig. 4 shows the structure of dynamic ANN. Performance parameter including cooling capacity (Q_e), coefficient performance (COP), and exergy efficiency (η_{ex}) at time t is predicted using previous manipulated parameters (compressor speed N_{comp}, evaporator fan speed F_{evap}, condenser fan speed F_{cond}) and state variable of room temperature T_R with number of time delay represented by *nu*.

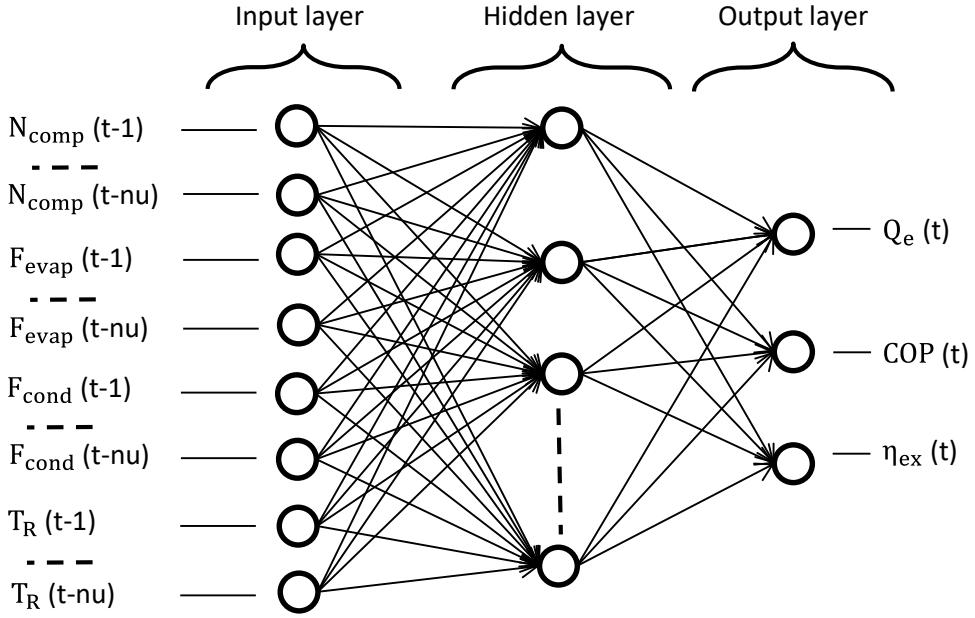

Figure 4: Structure of dynamic ANN

The prediction accuracy of ANN model is measured by root means square error (RMSE) and coefficient of variation (CV) written in Eq. (1) and Eq. (2) respectively.

$$\mathrm{RMSE} = \sqrt{\frac{\sum_{i=1}^{n}(x_i - y_i)^2}{n}} \quad \text{Eq. (1)}$$

$$\mathrm{CV} = \frac{RMSE}{\sum_{i=1}^{n} x_i} \times 100 \quad \text{Eq. (2)}$$

Where xi and yi shows original and predicted data by ANN respectively. Notation n indicates number of data.

2.3 Sensitivity Analysis

The sensitivity of each input is investigated to show how significant its influence on prediction. Four ANN models represented by network1 to network4 have been trained with the same configuration and different input parameters. Table 1 shows the prediction error for each model. The higher CV value represents the lower prediction accuracy. The highest CV value is shown by Network1 where compressor speed is not included in training. It indicates that compressor speed is the most sensitive parameter in prediction followed by room temperature and both fan speed. The error difference between network1 and others is quite large. Meanwhile there is no significant change in accuracy when either evaporator or condenser fan speed is not included in training. Based on this analysis, it can be concluded that compressor speed and room temperature is more sensitive than both fan speeds for prediction.

Table 1. Performance of ANN model with various input combinations

ANN model	Input variables				Prediction accuracy (CV)		
	N_{comp}	F_{evap}	F_{cond}	T_R	Q_e	η_{ex}	COP
Network 1	NI	I	I	I	3.31	1.50	1.09
Network 2	I	NI	I	I	3.27	1.41	0.96
Network 3	I	I	NI	I	3.27	1.44	0.98
Network 4	I	I	I	NI	3.25	1.42	0.95

I: Included ; NI: not included

2.4 Optimal Number of Time Delay Lines

Input time delay plays important role in developing dynamic ANN model due to the future output is highly affected by the present and previous inputs and state outputs. In this section, the effect of number of delayed inputs for compressor speed and room temperature denoted by *du* and fan speed at evaporator and condenser shown by *dy* is investigated. Fig. 5 shows the accuracy of several ANN models developed by using different number of time delay combination. Time delayed inputs are varied from 2 to 7 which generates 36 different ANN models. The change of number of time delayed input affects the prediction accuracy greatly. The optimal number of time delay is determined by investigating the 3D graph presented in Fig. 5. Based on the graph, the lowest RMSE value for three prediction outputs is shown by five *du* (time delay for compressor speed and room temperature) and two *dy* (time delay for evaporator and condenser fan speed). Accordingly, this structure is considered as the optimal model.

2.5 Optimal Number of Neurons

Furthermore, the final parameter that should be determined for ANN configuration is number of neurons. The optimized time delayed inputs with 5 *du* and 2 *dy* is trained using various number of neurons. The training is carried out by varying number of neurons from 1 to 20 neurons incrementally and the results are summarized in Fig. 6. In the beginning, when one neuron is used for training, the model has highest error. Then the error goes down drastically and has no significant change in accuracy after 2 neurons. The ANN model with one neuron has very few weight and bias coefficients. Consequently, the network is not flexible to fit the data and has poor accuracy. In the other hand, the network with many neurons will potentially cause overfitting. Based on the results depicted in Fig. 6, the ANN model with 3 neurons is selected as the optimal model where it has good accuracy and the other reason is to avoid overfitting.

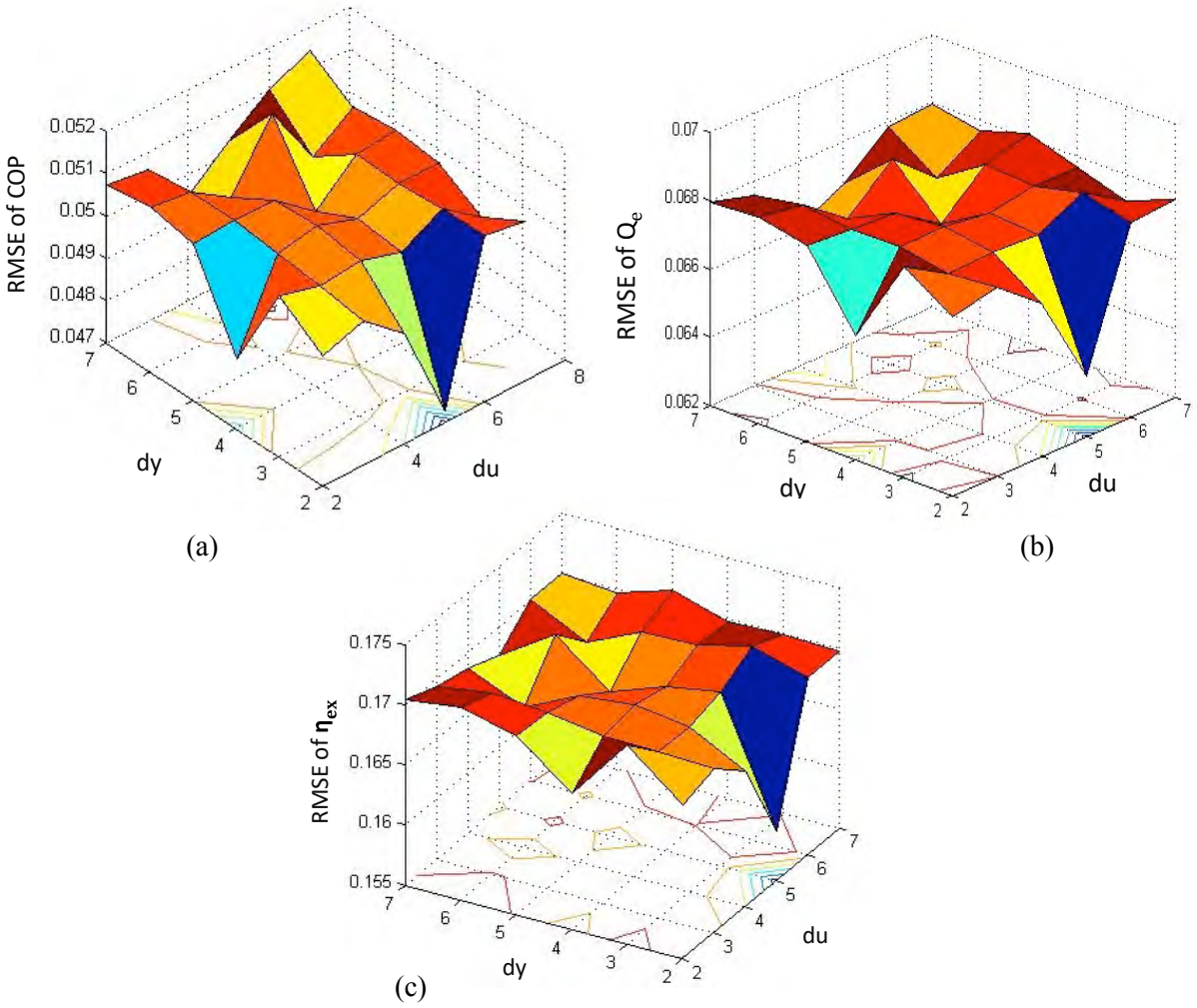

Figure 5: Effect of number of time delay lines on prediction accuracy

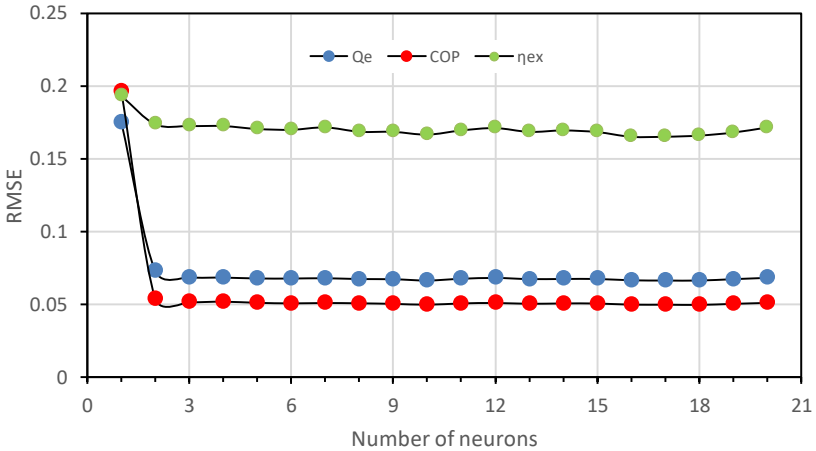

Figure 6: Effect of number of neurons on prediction accuracy

2.6 Prediction Results

In previous section, the optimal ANN configuration is obtained with 5 *du*, 2 *dy* and 3 neurons. The prediction results by this network can be seen in Fig. 7. The results show good prediction accuracy for all outputs with RMSE value 0.07, 0.05, 0.17 and CV 3.3%, 1.44%, 0.94% for exergy efficiency,

cooling capacity, and COP respectively. This result proves that the developed ANN model can capture the dynamic behaviour of A/C system under modulation of compressor speed and evaporator and condenser fan speed. Accordingly, it can be applied for predictive control application to control cooling capacity with considering system efficiency.

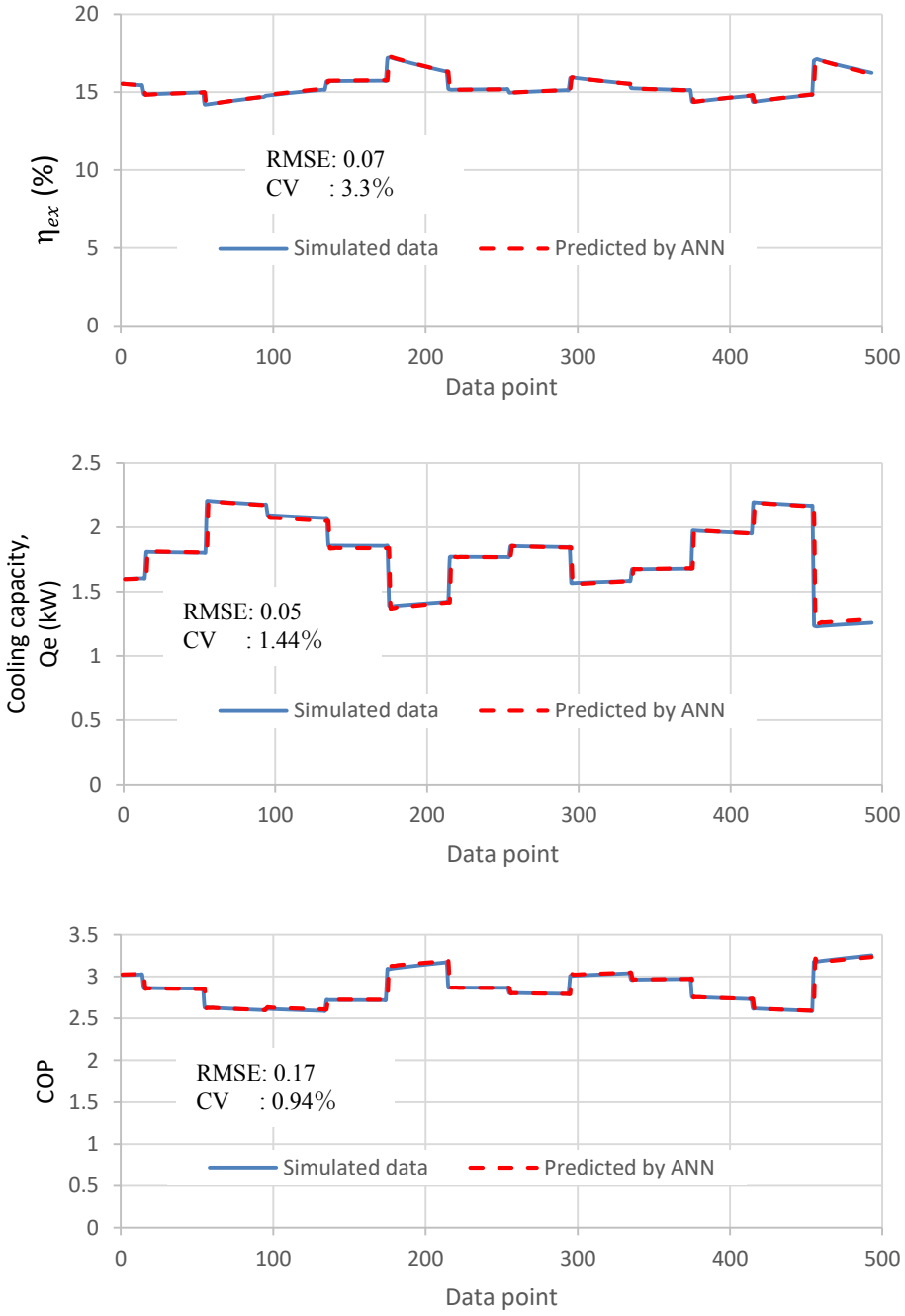

Figure 7: Prediction results; (a) exergy efficiency; (b) cooling capacity; (c) COP

3. CLONCUSIONS

A dynamic ANN model has been developed for system identification in vapor compression A/C system. Among four input variables, compressor speed and feedback input of room temperature are more sensitive than evaporator and condenser fan speed on prediction accuracy. This work shows that, ANN model can predict system dynamic behaviour through the proper number of time

delayed inputs and neurons. In the future study, the developed ANN model can be implemented to control cooling capacity while considering first and second law thermodynamic efficiency

ACKNOWLEDGEMENT

The author would like to acknowledge the financial support provided by LPDP (Indonesia Endowment Fund for Education).

REFERENCES

Li, N., et al., 2013. On-line adaptive control of a direct expansion air conditioning system using artificial neural network. Applied Thermal Engineering 53(1), 96-107.

Matsumoto, K., et al., 2016. Numerical analysis of VRF Compression Heat-pump System under Unsteady-State Condition, Trans. of the JSRAE 33(2), 155-164.

Muñoz, F., et al., 2017. Real-time neural inverse optimal control for indoor air temperature and humidity in a direct expansion (DX) air conditioning (A/C) system. International Journal of Refrigeration 79, 196-206.

Nam, S., et al., 2017. Real-time Air Conditioner Zone Temperature Control by Cascaded Intelligent PI. 2017 17th International Conference on Control, Automation and Systems (ICCAS 2017) Oct. 18–21, Ramada Plaza, Jeju, Korea.

Ng, B.C., et al., 2014. Dynamic modelling of an automotive variable speed air conditioning system using nonlinear autoregressive exogenous neural networks. Applied Thermal Engineering 73(1), 1255-1269.

Nishijima, D., 2016. Product lifetime, energy efficiency and climate change: A case study of air conditioners in Japan. Journal of Environmental Management 181, 582-589.

Saito, K. and K. Ohno, 2018. Performance analysis of lower GWP refrigerants for air-conditioning systems using Energy flow+M. JRAIA International Symposium.

Sholahudin, S. and H. Han, 2015. Heating Load Predictions using The Static Neural Networks Method. International Journal of Technology, 6(6), 946-953.

Sholahudin, S. and H. Han, 2016. Simplified dynamic neural network model to predict heating load of a building using Taguchi method. Energy 115, 1672-1678.

Yang, Q., et al., 2016. Simultaneous control of indoor air temperature and humidity for a chilled water based air conditioning system using neural networks. Energy and Buildings 110, 159-169.

Manuscript ID: 1247
DOI: 10.18462/iir.icr.2019.1247

Development of an ice storage integrated into a mono-split air conditioning system for increase of photovoltaic self-consumption

Carsten HEINRICH[(a)], Myrea RICHTER [(a)], Felix STELZER[(b)], Tobias FRANZKY[(a)], Mathias SAFARIK[(a)], Ralf HERZOG[(a)]

[(a)] Institute of Air Handling and Refrigeration (ILK Dresden), Dresden, 01309, Germany, carsten.heinrich@ilkdresden.de

[(b)] Technische Hochschule Nürnberg Georg Simon Ohm, Nuremberg, Germany, felix.stelzer@gmx.de

ABSTRACT

Photovoltaic-driven air conditioning systems offer a lot of advantages over solar-thermal driven cooling systems. An open issue is the missing linkage between PV and AC system regarding the different temporal peaks of electricity generation and cooling demand. The paper present results and experiences from experimental investigations of an ice storage coupled with a mono-split air-conditioning unit.
Keywords: PV-cooling, ice storage

1. INTRODUCTION

The number of installed air-conditioning (AC) systems is rapidly increasing worldwide. About 130 million units a year are sold (Holley, 2014). The majority (about 120 million) are lower capacity units. A number of unfavorable effects are associated with the desired gain in comfort: (1) increasing electricity demand and thereby an increasing emission on greenhouse gases (indirect emissions), (2) direct greenhouse gas emissions due to usage of refrigerants with high global warming potential (GWP), (3) distinct peak loads in the grid.

To reduce these impacts solar-driven cooling technologies have been developed and applied in the last ten to fifteen years. In the past the focus was set to solar-thermal systems, due to the use of natural refrigerants (mainly water/lithium bromide) and the cost benefits of thermal collectors. The number of solar-thermal driven cooling systems increased but on low level. Only about 1000 systems are installed worldwide (Mugnier, 2015). A higher dissemination is impeded by high investment costs and complexity of those systems.

On the opposite distinct cost reductions have been achieved in the photovoltaic (PV) sector. Present electricity generation costs of PV-systems turn PV-driven cooling systems into an economic scenario. Investigations within the EvaSolK project revealed lower carbon dioxide abatement costs for PV-driven compression refrigeration systems compared to solar-thermal driven single stage refrigeration systems (Wiemken et al., 2012).

An issue of the majority of existing PV-driven cooling systems is the missing linkage of PV and AC system. Generally the PV-system is operated grid-connected, feeding in electricity during the period of high solar radiation around midday. In residential area AC-systems start operation in the late afternoon when people come home (see Figure 1, left figure). Hence, in countries with a high dissemination of rooftop PV-systems (e.g. Australia (Council, 2016)) the demand peak of AC systems is not noticeable reduced, but during midday an oversupply of electricity is fed in into the grid.

To balance the temporal divergence between electricity generation and cooling demand an integrated energy storage is required. Thermal cold storages offer a number of advantages compared to batteries: Materials are inexpensive and free of risk to the environment. Thermal losses can be regarded as far less relevant if storage is located in the air conditioned room. Using ice storages the required volume can be decreased to suitable sizes. Depending on the concept, maximum cooling capacity provided to the room can be significantly increased in case of parallel operation of storage discharge and outdoor unit.

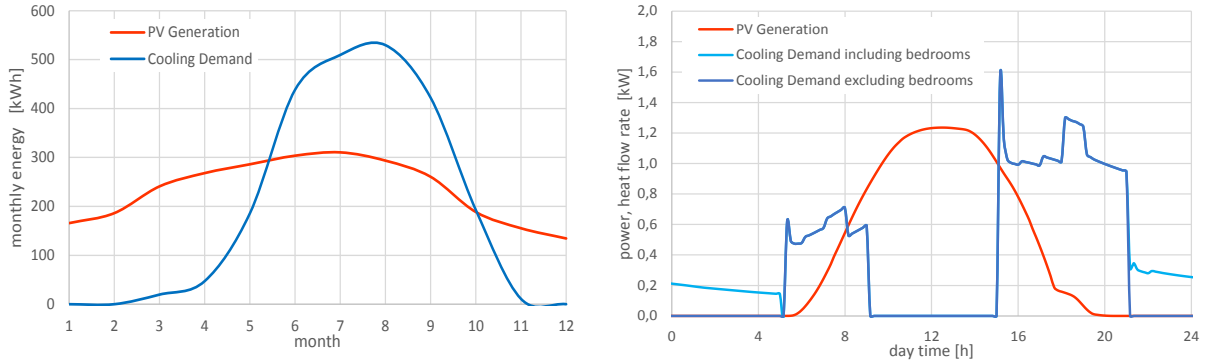

Figure 1: Seasonal (left figure) and daily (right figure) PV electricity generation and cooling demand in a residential building. Source: ILK Simulation results for a residential building in Lisbon / Portugal using Modelica - BuildingsLibrary

2. SYSTEM CONCEPTS AND STORAGE DIMENSIONING

2.1. System Concepts

A standard mono-split AC system consists respectively of an outdoor and an indoor installed unit, linked by a low pressure liquid and low pressure suction gas tube. From refrigeration side the outdoor unit contains compressor, condenser and electric expansion valve and the indoor unit the air-cooling evaporator.

Integration options of an ice storage into mono-split-AC-system can be characterized by

- storage position (outdoor, indoor or inside indoor unit)
- charging by direct evaporation process or via secondary cycle (brine, refrigerant)
- discharging using direct air contact (integration into indoor unit), external melting process (water cycle using the water of the ice storage) or an integrated heat exchanger (using the refrigeration or brine cycle)
- realization of direct cooling mode by usage or by bypassing the storage

Varying the mentioned characteristics lead to a number of cycle options which even increases if valves, bypasses or pumps are taken into account to achieve a more flexible operation.

A number of boundary conditions resulting from market situation and trends, legal regulations and technical standards influences the selection process. Some main aspects are discussed below:

- Required technical solutions are not yet available on the market or in a reasonable cost ranges: Discharge process using the ice storage water by external melting process can be combined with standard air cooler units. But using water in the air cooler is not common in Mono-Split systems so far. Discharge process using the refrigeration cycle requires very low capacity refrigerant pumps with a high pressure rating. There are no standard refrigeration products including such pumps on the market.
- Efficiency requirements arising from legislation and quality labels: The European product regulation requires seasonal cooling efficiency ratios (SEER) calculated according to DIN EN 14825 of > 7 and > 8.5 from 01.01.2019 for air conditioning units with a cooling capacity of less than 12 kW. The German quality label Blauer Engel requires an EER Cooling > 4.6. The direct cooling operation will be the minor operation mode of a mono-split-unit with integrated ice storage.
- Requirements to refrigerant usage: European F-Gas Regulation requires the usage of refrigerants with a global warming potential < 750 from 01.01.2025 in small scale air-conditioning units. Blauer Engel requires the usage of non-halogen refrigerants. Within a progressive intensification of regulations the usage of natural refrigerants gain in importance. Almost all refrigerant with a GWP < 750 that can be applied in split systems are flammable. Therefore the refrigerant charge needs to be limited.

Based on an assessment matrix using the upper characteristics further theoretical and experimental analysis were focused on a small number of preferred options. Table 1 contains three promising options, including their advantages and drawbacks.

Table 1: Preferred integration options . system description and remarks

system description	remarks
option 1: 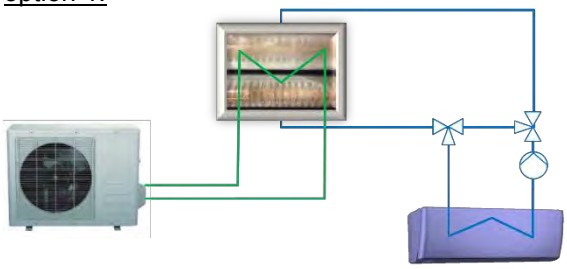 - direct charging using an evaporator in the ice storage - discharge using the water of the storage in a hydraulic cycle with a standard fan coil as indoor unit	advantages: - standard products can be applied - cost efficient solution - simple control - ice melting direction inverse to freezing direction - air cooler surface temperature can be controlled by return flow addition in the water cycle for controlled dehumidification drawbacks: - poor cooling efficiency in direct cooling mode - thermally inertial system, especially not recommendable for heating mode
option 2: 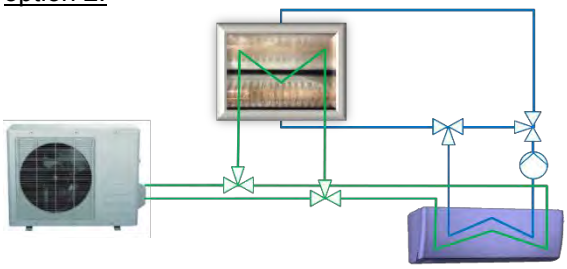 - option 1 is extended by an parallel refrigerant cycle to the indoor unit.	advantages: - direct cooling and heating mode as efficient as in common mono-split systems - extended operation flexibility (e.g. parallel operation of direct cooling and storage discharge is possible) drawbacks: - non-standard indoor unit required - more complex control algorithms required
option 3: 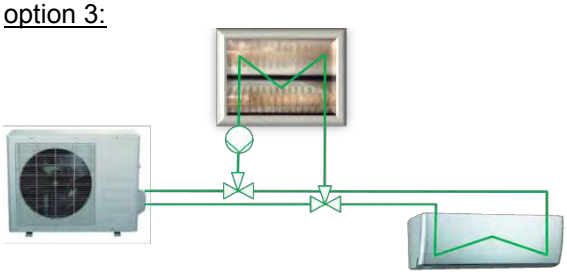 - option 2 is extended by an additional refrigerant pump for discharge process, indoor unit is changed to standard split indoor unit, water cycle is removed	advantages: - standard indoor unit - no water cycle - direct cooling and heating mode as efficient as in common mono-split systems drawbacks: - refrigerant pump availability - discharge process probably less efficient - difficult dehumidification control - complex control

2.2. Storage Dimensioning

The mono-split unit including an ice storage is connected to a photovoltaic system as well as to the grid, increasing photovoltaic self-consumption and decreasing grid peak loads. The storage should allow equalizing the daily shift between solar irradiation and cooling demand. For economic and energy efficiency reasons it is not appropriated to avoid grid demand at all. A simple algorithm for reasonable storage size estimation is presented in (Richter 2016). For an example building, a single family house according to the German building standard EnEV2016 situated at German site Mannheim, the algorithm leads to a cold storage size of about 5 kWh. Hereby grid demand for cooling production can be reduced from 138 to 38 days a year. For the remaining 38 days the cooling demand with electricity consumption from the grid is largely reduced.

3. EXPERIMENTAL INVESTIGATIONS

3.1. Motivation and experimental set up

Characteristic data for mono-split-AC-units are limited to air conditioning conditions and are only available as function of room and ambient conditions. Ice growth on evaporator during charging mode and melting during discharging mode represent non-uniform, three dimensional and dynamic processes. Furthermore, mono-split-AC-units include a number of implemented operation and safety

algorithms, designed for building cooling (and heating) and dehumidification only. Hence, an evaluation of the operation of a mono-split-AC-unit with integrated ice storage requires experimental analysis.

Experimental investigations focused on

- evaluation of operation control and safety algorithm issues connected with the operation with lower evaporation pressure and non-corresponding response signals from indoor unit
- operational limits of the outdoor unit in case of lower evaporation pressures
- cooling capacity and cooling efficiency under different operation modes
- application of PV-power-supply and forecast-based control algorithms

For the experimental investigations, a test rig was built. It is designed to investigate a number of different integration options. A simplified piping and installation is shown in Figure 2. It includes the outdoor unit, ice storage vessel, with ice storage evaporator and an air measurement section including to indoor units. Discharge process can be realized by a hydraulic cycle (blue lines) or and refrigeration cycle including a small refrigerant pump (green cycle). A number of valves are included to allow different operation modes.

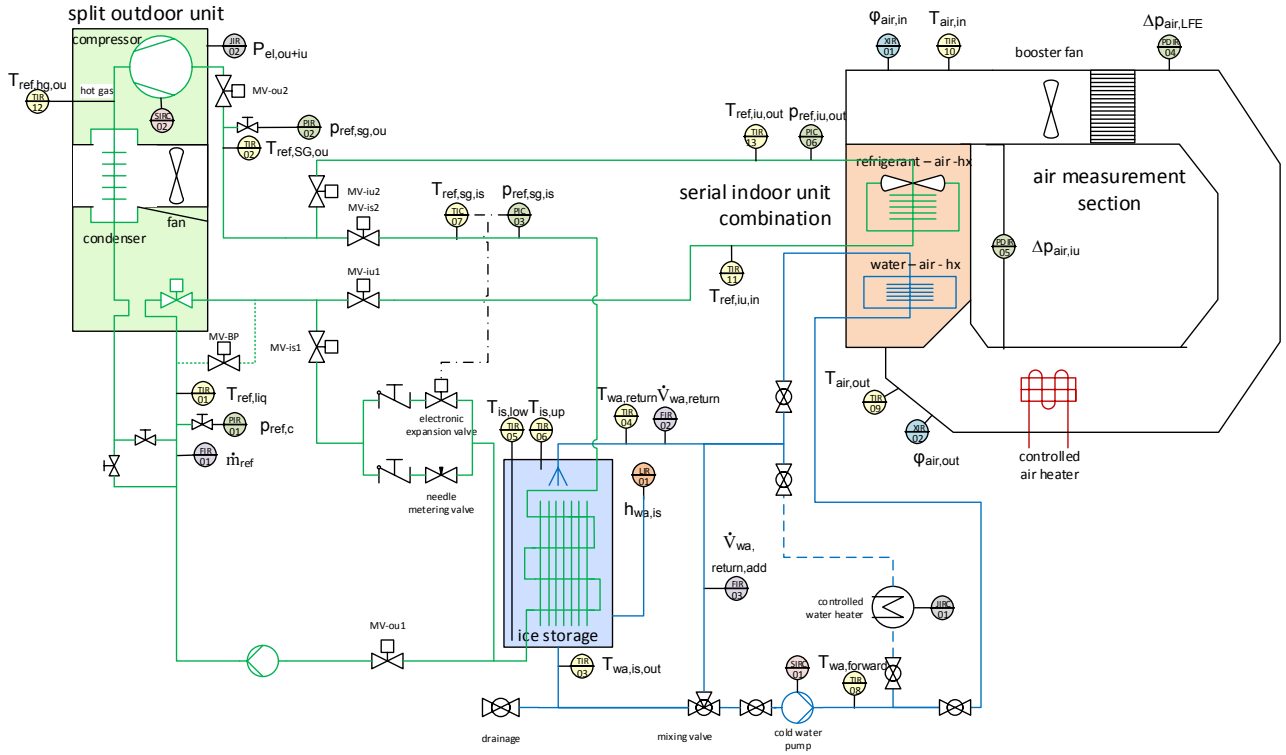

Figure 2: Piping and installation scheme of test rig to investigate the integration option 1 - direct charge process and discharge process applying external melting

Component dimensioning was carried out according to the results of a residential building simulation. A maximum cooling capacity of 2.5 kW is required. An oversized mono-split-outdoor-unit with a rated cooling capacity of 4.0 kW (Fujitsu AOYG 14LMCA) was selected to compensate the required lower evaporation temperature. The installed test rig is shown in Figure 3. Three different evaporator types are investigated (see Table 2). The selection criteria focused on market availability and price.

Table 2: Relevant geometry parameters of evaporators investigated

	tube and fin	finned tube	wire and tube
tube length	2 x 6.2 m, in series	4 x 4.95 m, in parallel	4 x 7.63 m, in parallel
tube outside surface	0.39 m²	0.51 m²	0,43 m²
fin water side area	2.32 m²	0.91 m²	1.54 m²
total water side area	2.71 m²	1.42 m²	1.97 m²
mean fin length	9.8 mm	11.1 mm	25 mm
refrigerant volume	0.58 l	0.50 l	0,22 l

Refrigerant cycle operation is measured by high pressure liquid medium temperature in front of expansion valve inlet $T_{ref,liq}$, suction gas temperature at evaporator outlet $T_{ref,sg,is}$, hot gas temperature as tube surface temperature at compressor outlet $T_{ref,hg}$, condensing pressure p_{refc} in front of expansion valve inlet, evaporation pressure $p_{\mathrm{ref,sg,ou}}$ in suction tube in front of outdoor unit inlet and refrigerant mass flow rate $\dot{m}_{ref}$ in front of expansion valve inlet. Furthermore, split-unit power input $P_{el,ou+iu}$, which includes power demand for compressor / inverter, electronic control unit and fan of indoor and outdoor unit. Compressor speed n_{Comp} and expansion valve opening is taken from split unit service tool, connected to electronic control unit.
Storage and water cycle is measured by upper and lower storage water temperature $t_{is,up}$ and $T_{is,low}$, return water temperature at storage inlet $T_{wa,return}$, supply water temperature at storage outlet $T_{wa,is,out}$, water volume flow rate $\dot{V}_{wa}$ in front of storage inlet and storage liquid level height by an optical system $y_{wa,is}$. Additionally the power input of electrical heater $P_{el,heater}$ is measured.
If not mentioned differently, temperatures are measured using PT100 sensors, directly in the fluid.

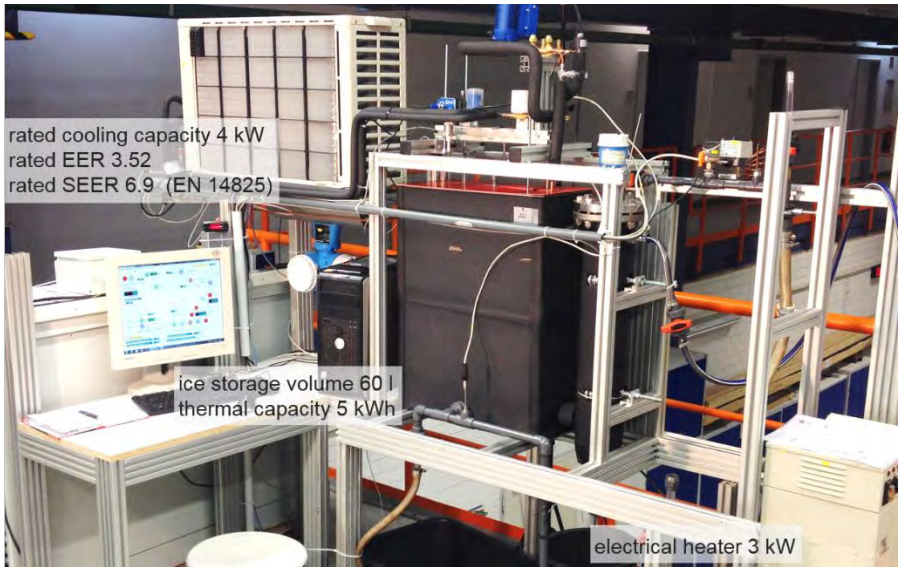

Figure 3: Photo of the test rig

3.2. Data post processing

Cooling capacity $\dot{Q}_{\mathrm{ref,charge}}$ during charge process is calculated under the assumption of subcooled condenser outlet and superheated evaporator refrigerant state.

$$\dot{Q}_{\mathrm{ref,charge}} = \dot{m}_{\mathrm{ref}} \cdot \left(h_{\mathrm{gas}}\left(p_{\mathrm{ref,sg,ou}},\ T_{\mathrm{ref,sg,is}}\right) - h_{liq}\left(p_{\mathrm{ref,c}}, T_{\mathrm{ref,liq,ou}}\right)\right) \quad \text{Eq. (1)}$$

Energy efficiency ratio of charging process EER_{charge} is calculated using cooling capacity and total power consumption of split unit and an optional pump to enforce heat transfer in the storage.

$$EER_{\mathrm{charge}} = \dot{Q}_{\mathrm{ref,charge}} \,/\, \left(P_{\mathrm{el,iu+ou}} + P_{\mathrm{el,pump}}\right) \quad \text{Eq. (2)}$$

Ice fraction x_{ice} of the storage is calculated based on the density difference between liquid and solid phase of water. A reference temperature T_{R} is defined for reference conditions of storage level height $y_{\mathrm{wa,is,TR}}$ and liquid water density $\varrho_{\mathrm{W,TR}}$.

$$x_{ice} = \left(y_{wa,is}/y_{wa,is,TR} - 1\right)/\left(1 - \varrho_{wa,TR}/\varrho_{ice}\right) \quad \text{Eq. (3)}$$

Discharge capacity $\dot{Q}_{\mathrm{discharge}}$ is calculated by the enthalpy difference resulting from the temperature difference between storage inlet and outlet.

$$\dot{Q}_{\mathrm{discharge}} = \dot{\mathrm{V}}_{\mathrm{wa,return}} \cdot \varrho_{\mathrm{wa}}\left(T_{wa,return}\right) \cdot \left(h_{\mathrm{wa}}\left(T_{\mathrm{wa,return}}\right) - h_{W}\left(T_{\mathrm{wa,is,out}}\right)\right) \quad \text{Eq. (4)}$$

All media properties for water and the refrigerant R410A are calculated using CoolProp (Bell et al., 2014).

3.3. Results – Charging Process

The charging process is investigated for tube and fin and for finned tube evaporator types varying the outdoor unit part load factor. Initial storage temperature is kept constant at 18 °C. Test rig is located in the main test hall of the institute. Ambient temperature depend on test hall temperature and varied in the measuring period between 20 and 25 °C. The charging process is terminated in case of ice fraction of 75 % or in case a further ice growth could lead to storage damages.

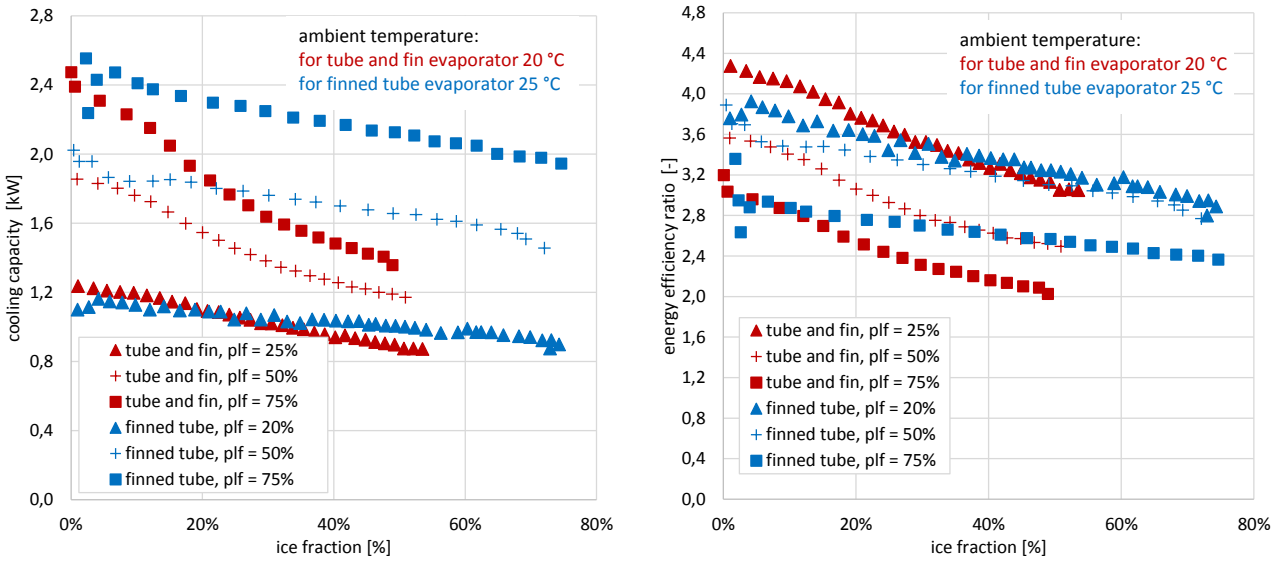

Figure 4: Ice storage charging process - cooling capacity and energy efficiency ratio versus ice fraction with variation of outdoor unit part load factor

Figure 4 (left) shows the cooling capacity versus ice fraction for both evaporator types and for varying outdoor unit part load factor (plf). Maximum achieved ice fractions are 75 % for the finned tube evaporator and 55 % for the tube and fin evaporator. The cooling capacity decreases with increasing ice fraction and with decreasing outdoor unit part load factor. The decreasing cooling capacity as function of ice fraction is more distinct for the tube and fin evaporator. The cooling capacity decreases from 0 to 50 % ice fraction to about 60 to 65 %. For the finned tube evaporator the cooling capacity decrease for the same ice fraction range to about 80 to 85 %.
Figure 4 (right) shows the energy efficiency ratio (EER) of the charging process versus ice fraction for both evaporator types and for varying outdoor unit part load factor. The EER varies between 2 and 4.4. It decreases with increasing part load factor and increasing ice fraction. The EER for the split-unit at a part load factor of 75 %, an ambient temperature of 25 °C and an indoor temperature 25 °C can be estimated using the catalog data (Swegon, 2016) and the info sheet for SEER calculation according to eco design regulation (Fujitsu, 2015) to 6.0.
In Figure 5 charging time and average energy efficiency ratio between a storage temperature of 15 °C and an ice fraction of 50 % are shown as function of outdoor unit part load factor.

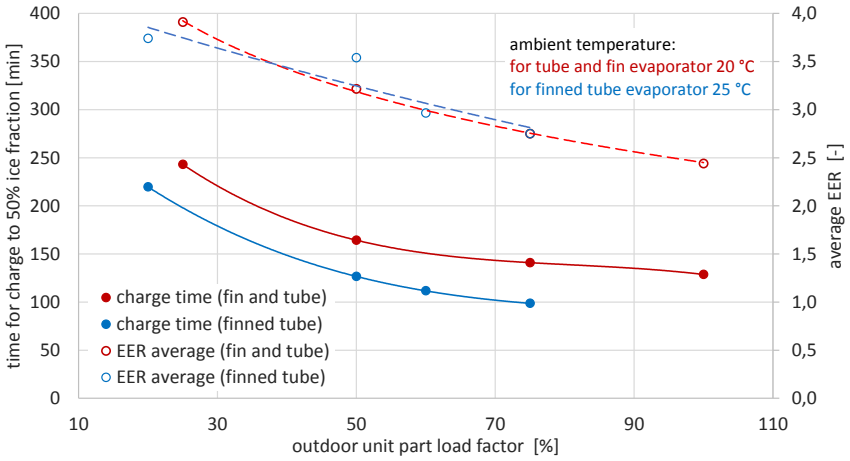

Figure 5: Charge time and average energy efficiency ratio versus outdoor unit part load factor

Charging times for the finned tube evaporator are 40 to 45 minutes lower compared to the fin and tube evaporator for the same part load factors. For part load factors lower than 60 % a strong dependency between charging time and part load factor can be observed. A further increase of the part load factor result in only minor reductions of the charging time.
Average energy efficiency ratios for the defined charging range and ambient temperature of 20 and 25 °C vary between 2.4 and 3.9. Outdoor unit part load factor and average energy efficiency ratio show approximately a linear dependency.

3.4. Results – Direct Cooling Mode

In direct cooling mode the cooling capacity supplied by the outdoor-unit is directly transferred to the water cycle. Ideally no change of storage state of charge occurs. Cooling capacity is limited by the heat transfer conditions in the storage. Heat transfer is characterized by forced convection due to the storage water flow rate. Evaporation temperature has to be limited to avoid ice growth on the surface. In this case the cooling capacity supplied by the outdoor-unit exceeds the cooling capacity transferred to the water cycle.
Figure 6 shows the maximum cooling capacity and the corresponding energy efficiency ratio depending on the storage volume flow rate for the finned tube evaporator. Maximum cooling capacity increases with increasing water flow rate, due to the improving heat transfer conditions. Energy efficiency ratio decreases with increasing cooling capacity due to the higher part load factor in the outdoor unit.

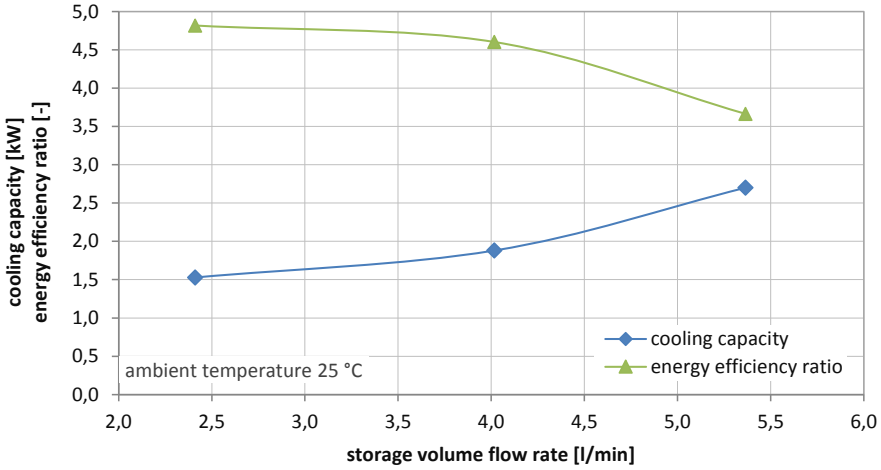

Figure 6: Maximum cooling capacity and energy efficiency ratio versus water volume flow rate for finned tube evaporator

4. CONCLUSIONS

Based on daily characteristic of cooling demand and photovoltaic electricity generation in residential buildings the integration of a cold storage into the AC-system can significantly increase photovoltaic self-consumption. Integrating the ice storage into a mono-split-AC-system is a potential option. The system benefits from the high energy efficiency and low investment cost of mono-split-systems. Using an assessment matrix approach the large number of conceivable integration options is reduced to a few technically promising and economically feasible options. Three basic options were presented and discussed. Experimental investigations have been carried out for all three options. Here the results of the charging process including operation experiences are discussed.
No additional modifications of the outdoor-unit were required. Only a mass flow sensor was implemented between condenser and expansion valve. A successful interaction, an efficient and stable operation of the outdoor unit with the connected storage was achieved after installation of additional refrigeration and electronic components. The required refrigerant charge had increased by about 100 g of R410A. As mono-split-units are designed to operate at evaporation temperatures above 0 °C, some protection functions had to be outwitted.
Charging process at part load factors between 20 and 75 %, ambient temperatures between 20 and 25 °C result in energy efficiency ratios between 2.0 and 4.4. In direct cooling mode in case of maximum achievable cooling capacity at given water flow rate and an ambient temperature of 25 °C energy efficiency ratios between 3.5 and 4.8 were achieved.

The efficiency during charging process is acceptable as in many cases there are not a lot of other applications for self-consumption during the day. For direct cooling mode the required efficiency ratio of 4.6 according to the German quality label Blauer Engel (EER = 4.6 at 27 °C room temperature and 35 °C ambient temperature) will be achieved only in low part load ranges.
Option 2 and 3 are more sensitive to the amount of refrigerant charge. Especially toggling from ice storage to indoor unit evaporator is challenging as refrigerant is adhered in the evaporator due to low temperature level around. Further investigations on discharge process using an adapted pump in the refrigerant cycle are carried out, now.

ACKNOWLEDGMENT

The investigations were carried out in the SolarSplit project (funding code 0325900A). It is managed by the project management organization Jülich (PTJ) and financially supported by German Federal Minister of Economics and Technology (BMWI) within the 6th Energy Research Program of the German Federal Government.

NOMENCLATURE

p	pressure (kPa)	x_{ice}	ice fraction
T	temperature (°C)	$\dot{m}$	mass flow rate [kg/s]
h	specific enthalpy [J/(kg.K)]	$\dot{V}$	volume flow rate [m³/s]
ϱ	density [kg/m³]	$\dot{Q}$	heat flow rate, cooling capacity [kW]

indices

ref	refrigerant	wa	water
iu	indoor unit	ou	outdoor unit
is	ice storage	ice	ice
sg	suction gas	hg	hot gas
liq	liquid	c	condensing state

REFERENCES

Bell, I.H., Wronski, J., Quoilin, S., Lemort, V., 2014. Pure and Pseudo-pure Fluid Thermophysical Property Evaluation and the Open-Source Thermophysical Property Library CoolProp. Industrial & Engineering Chemistry Research 53, 2498–2508.

Fujitsu, 2015. Information Sheet (Lot. 10) - ASYG14LMCA / AOYG14LMCA. Swegon - Fujitsu.

Holley, A.M., 2014. Global Trends in Air Conditioning. Chillventa.

Mugnier, D., 2015. Worldwide overview on Solar cooling and SHC tasks 48, 53, in: Chinese Solar Cooling Conference.

Nytsch-Geusen, C., Inderfurth, A., Moeckel, J., Mucha, K., Tugores, C.R., Raedler, J., Thorade, M., 2017. Modelica BuildingSystems Library (Version 2.0.0-beta).

Richter, M., 2016. SolarSplit: Gebäudeenergiebedarf und Rückschlüsse auf notwenige Speichergrößen (No. ILK-B-5-16-0369). ILK Dresden.

Swegon, 2016. Montage- und Betriebsanleitung Wärmetauschersteuerung INV-DX Fujitsu Single-Split.

Wiemken, E., Safarik, M., Zachmeier, P., Schweigler, C., Nienborg, B., Elias, A.R.P., 2012. Evaluierung der Chancen und Grenzen von solarer Kühlung im Vergleich zu Referenztechnologien, in: EuroSun 2012, ISES-Europe Solar Conference. Rijeka, Croatia.

Manuscript ID: 1354
DOI: 10.18462/iir.icr.2019.1354

A novel dehumidification system using zeotropic refrigerants

Xingru LIU[(a)], Xiangfei LIANG[(a),(b)*], Mingyue HUANG[(a)]

[(a)] Refrigeration Institute, Gree Electric Appliances, Inc. of Zhuhai,

Zhuhai, 519070, China

[(b)] National Engineering Research Center of Green Refrigeration Equipment,

Zhuhai, 519070, China

*Email: liangxf@cn.gree.com

ABSTRACT

Dehumidifier of vapor compression type is widely used to remove moisture of air in small capacity situations of dehumidification because of such advantages as lower price and very convenience. However, lower evaporating temperature than dew-point of air supply resulting in low energy efficiency is the main drawback. To overcome the barrier, a novel dehumidification system with zeotropic refrigerants has been proposed in the paper. The proposed system can achieve dual evaporating temperature and dual condensing temperature by using one regular single-stage compressor. Based on verified models, the performance for the proposed dehumidification system under different conditions has been investigated. The results implied that (1) compared to regular dehumidification system, the proposed system can enhance COP by 10.6%~14.5% and dehumidification efficiency by 7%~13.6% under different conditions; (2) the proposed system has good potential for small capacity dehumidification applications.
Keywords: Dehumidification System, Component Separation, Zeotropic Refrigerants, Simulation.

1. INTRODUCTION

Conventional dehumidification systems are used to cool and remove moisture from hot and humid indoor air. Low energy efficiency is the main drawback because of lower evaporating temperature than dew point (Liu et al., 2016). To overcome the barrier, many solutions were proposed. The most efficient way is separate sensible and latent cooling system (SSLC).

Much work in this area was focus on using a vapor compression cycle to conduct the sensible load and the solid or liquid desiccant system to remove the latent load (Jia et al., 2006). As a result, the hybrid system can achieve more than 40% improvement on energy saving over that of conventional dehumidification system. However, a relatively high temperature heat source is necessary to regenerate the desiccant, which severely constrains its further application (Neti and Wolfe, 2000). Actually, using electricity to regenerate is common and convenient, which substantially eliminates the merits of the hybrid system.

To break through the limitation, SSLC system using two independent separate cycles with two separate compressors is developed (Ling et al., 2010). Investigated results presented 30% improvement on COP is realized compared to that of conventional system. However, expensive initial investment compels that it is hard to use for small capacity dehumidification situations. To improve the economy, twin rotary compressor in one shell with two suction structures was applied to replace two separate compressors (Cao et al., 2017). Though this technology indeed reduced the initial investment and enhanced the energy efficiency, it was still too expensive and complicated to use for small capacity dehumidifier.

In general, many SSLC technologies can solve the issue of low energy efficiency for regular dehumidification system, but all of them are not suitable to use in small capacity dehumidifier. Consequently, a novel dehumidification system using zeotropic refrigerants for dehumidifier is proposed. The proposed system, using one regular single stage rotary compressor, can achieve dual condensing temperatures and dual evaporating temperature by utilizing the component

separation in two phase balance status and temperature glide of zeotropic refrigerants. Furthermore, the system simulation platform including distributed parameter models of rotary compressor and fin-and-tube heat exchangers is built and verified. Based on verified models, the performance research on the proposed system is conducted.

2. NOVEL DEHUMIDIFICATION SYSTEM

Fig.1 shows the schematic diagram of the novel dehumidification system. As shown as Fig. 1, the novel system includes one regular single stage rotary compressor, two condensers, two evaporators, flash tank and two expansion devices. The high temperature refrigerant from the discharge port of compressor (2) enters the high temperature condenser into two phase refrigerant (gas quality: roughly 0.5) and further flows into the flash tank (3). The gas refrigerant in the flash tank flowing in low temperature condenser (3') turns into subcooled liquid refrigerant (4) that is throttled by the expansion device. The low temperature refrigerant (5) from the expansion device flows into the low temperature evaporator becoming the superheat gas refrigerant (6). The middle temperature refrigerant (7) from the bottom of flash tank throttled by the expansion device and the outlet refrigerant of the low temperature evaporator (6) gather together into the high temperature evaporator. The superheat gas refrigerant (1) evaporating in the high temperature evaporator is sucked by the suction port of compressor.

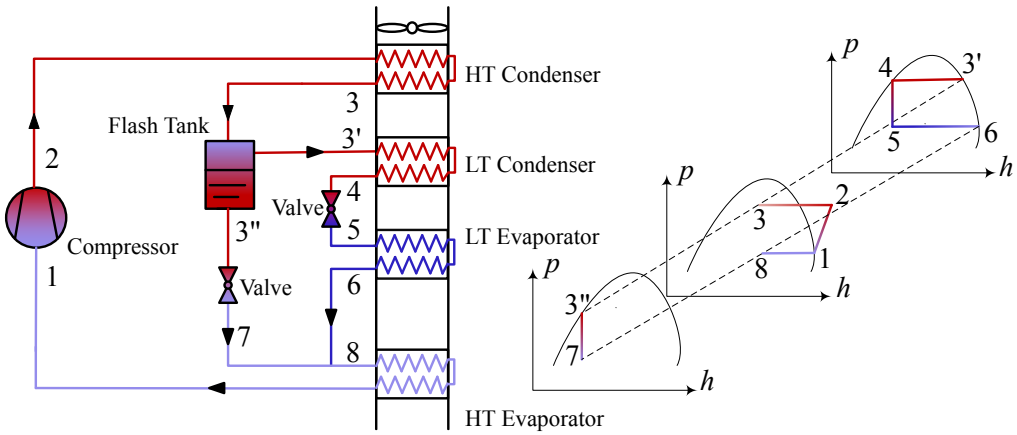

Figure 1: Schematic diagram of novel dehumidification system

The proposed system can realize two evaporating temperatures and two condensing temperatures by using the characteristic of component separation of zeotropic refrigerants in two phase status. Actually, the refrigerant of high boiling point will condense easily and the one of low boiling point is hard to condense in the high temperature condenser. Consequently, the liquid refrigerant in the flash tank will enrich the component of high boiling point and inversely the low boiling point refrigerant is enriched in the gas refrigerant. By using the principle of component separation, separating refrigerants of different boiling point in the flash tank flow into different evaporators. Because refrigerants with different mass fraction of high or low boiling point composition under the equal pressure have different saturated temperature, the dual evaporating temperatures for the proposed dehumidification system can be achieved.

Generally, by using the component separation and temperature glide of zeotropic refrigerants, the novel dehumidification system can realize stepped cooling and dehumidifying and is close to Lorenz cycle. Compared to conventional SSLC technologies, the system structure is considerably simplified and the initial investment is reduced substantially. Because of the merits of simple structure and low cost, the proposed system has a remarkable application prospect and is expected to use for small capacity dehumidifier.

3. METHODOLOGY AND RESEARCH CONDITION

To evaluate the effects of the proposed system, a system simulation platform was established. For improving the computational accuracy and analyzing internal heat transfer characteristics of zeotropic refrigerants, the distributed parameter models for rotary compressor and fin-and-tube heat exchangers were considered (Liu et al., 2016). Furthermore, the experimental data including compressor, fin-and-tube heat exchangers and systems were connected to verify the deviation of models (Liu et al., 2018).

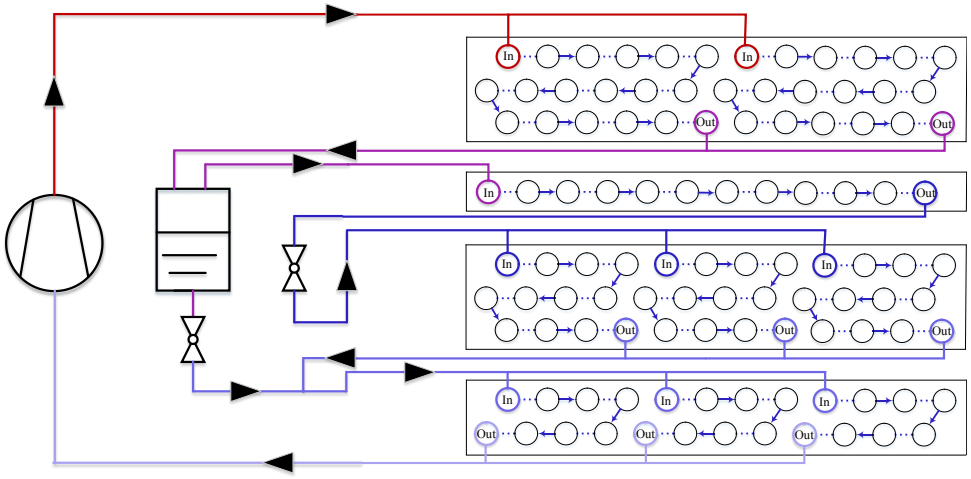

Figure 2: Designation diagram of novel dehumidification system

Table 1. Structure parameters of rotary compressor

Cylinder radius (mm)	Rotor radius (mm)	Eccentric rate (-)	Thickness of cylinder (mm)	Angle of suction port (rad)	Angle of discharge port (rad)
23.2	18.56	0.2	23.2	0.69	5.96

Table 2. Structure parameters of heat exchangers

High temperature evaporator							
Flow paths (-)	Pipe rows (-)	Number of row (-)	Length (mm)	Distance of pipe (mm)	Distance of row (mm)	Pipe diameter (mm)	High of louver (mm)
3	2	12	260	12.7	19.05	7.4	0.7
Low temperature evaporator							
Flow paths (-)	Pipe rows (-)	Number of row (-)	Length (mm)	Distance of pipe (mm)	Distance of row (mm)	Pipe diameter (mm)	High of louver (mm)
3	3	12	260	12.7	19.05	7.4	0.7
Low temperature condenser							
Flow paths (-)	Pipe rows (-)	Number of row (-)	Length (mm)	Distance of pipe (mm)	Distance of row (mm)	Pipe diameter (mm)	High of louver (mm)
1	1	12	260	12.7	19.05	7.4	0.7
High temperature condenser							
Flow paths (-)	Pipe rows (-)	Number of row (-)	Length (mm)	Distance of pipe (mm)	Distance of row (mm)	Pipe diameter (mm)	High of louver (mm)
2	3	12	260	12.7	19.05	7.4	0.7

Based on verified models, the proposed system including the rotary compressor, the heat exchangers and other devices was designed. The numbers of rows and path-flowing for the heat exchangers were optimized. Fig. 2 shows the designation diagram. As shown as Fig. 2, all of the heat exchangers were designed as counter flow. The numbers of row and path-flowing for the high temperature condenser were confirmed as 3 and 2, respectively. The low temperature condenser was designed as 1row and 1path-flowing. The two evaporators were fixed as 3 path-flowing. Actually, the capacities of heat exchange for the low temperature condenser and two evaporators are roughly equal, but the areas of heat exchangers have an obvious difference. The reason is that the low temperature evaporator has a very small temperature difference of heat exchange compared to that of the low temperature condenser. According to the optimized results, the parameters for the compressor and heat exchangers can be described as Table 1 and Table 2.
In this paper, the air temperature is fixed as 27°C because the proposed dehumidification system is expected to use for small capacity dehumidifier which is commonly placed in the indoor. The mass flowrate of air and subcooling degree of the low temperature condenser are fixed too. However, the superheat degrees for the two evaporators are not fixed simultaneously under different conditions. Finally, the working conditions are confirmed as Table 3. As a comparison of the novel system, a regular dehumidification system which numbers of row for the condenser and evaporator are respectively equal to 5 and 4 was also designed. R407C and R134a were used for the novel system and regular system, respectively. The refrigerants properties are calculated by call the functions of REFPROP (Lemmon et al., 2007) in the simulation software.

Table 3. Working conditions

Air temperature (℃)	Humidity ratio of air (g/kg)	Mass flowrate of air (m^3/h)	Subcooling degree (℃)
27	10.39	300	10
27	11.39	300	10
27	12.39	300	10
27	13.39	300	10
27	14.39	300	10
27	15.39	300	10
27	16.39	300	10
27	17.39	300	10
27	18.39	300	10

4. RESULTS AND DISCUSSION

4.1. Internal Heat and Mass Transfer

As mentioned above, when the refrigerant into the flash tank is two phase status, the phenomenon of component separation will happen. Fig. 3 presents the component separation in the flash tank (gas quality: 0.5). As shown as Fig. 3, the liquid refrigerant in the flash tank has a higher mass fraction of high boiling point component (R134a) and a lower mass fraction of low boiling point component (R32) than those of the inlet refrigerant. Inversely, mass fraction of R32 is higher and R134a is lower in the gas refrigerant.
Because of the component separation of zeotropic refrigerants at two phase status, separating refrigerants in the flash tank under the same pressure present two different temperatures. The refrigerants enriching low boiling point into the low temperature condenser result in lower temperature compared to the high temperature condenser as Fig. 4a. Similarly, the refrigerants from the low temperature condenser into the low temperature evaporator have a lower evaporating temperature over those of high temperature evaporator under the same pressure as Fig. 4b. In general, compared to conventional dehumidification system, the proposed system has a matching heat exchange process and can remarkably reduce the heat transfer loss.

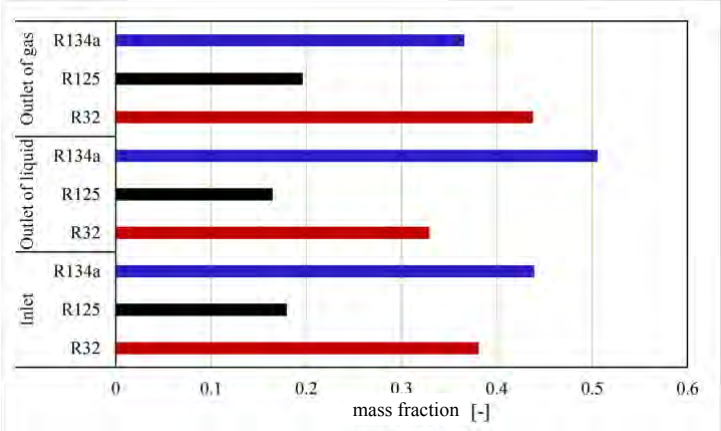

Figure 3: Phenomenon of component separation in flash tank

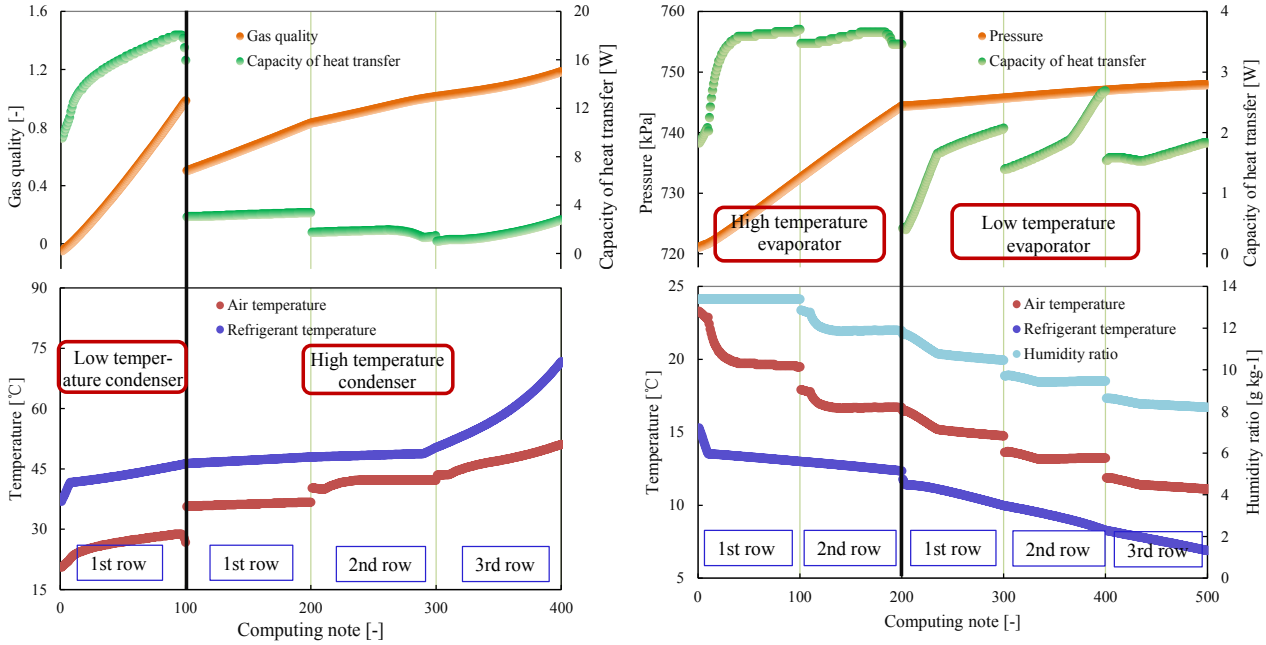

(a) Condenser **(b) Evaporator**

Figure 4: Heat transfer process in condensers and evaporators

4.2. System Performance under Varying Conditions

Fig. 5 shows the temperature parameter changes for refrigerant and air under different conditions. Actually, under the condition of comparative cooling capacity, the temperature difference of air between the outlet and the inlet will decrease with the increase of humidity ratio of the inlet air because of the increase of latent heat proportion. In this research, the compressor speed is fixed as 50Hz. With the increase of humidity ratio, the temperature differences of heat transfer in the evaporators are increasing. Then the evaporating temperature is increasing with the increase of humidity ratio as Fig. 5a. The outlet temperatures of air at all of heat exchangers are also increasing as Fig. 5b. The reason can be attributed to the increase of latent heat sector with the increase of humidity ratio. Actually, the heating capacity at condenser will increase with the increase of evaporating temperature under the fixed compressor speed. The increases of heating capacity and latent heat ratio both result in the increasing condensing temperature as Fig. 5a. Besides, the gas quality in the flash tank presents a slowly increasing tendency but keeps almost constant around 0.5.

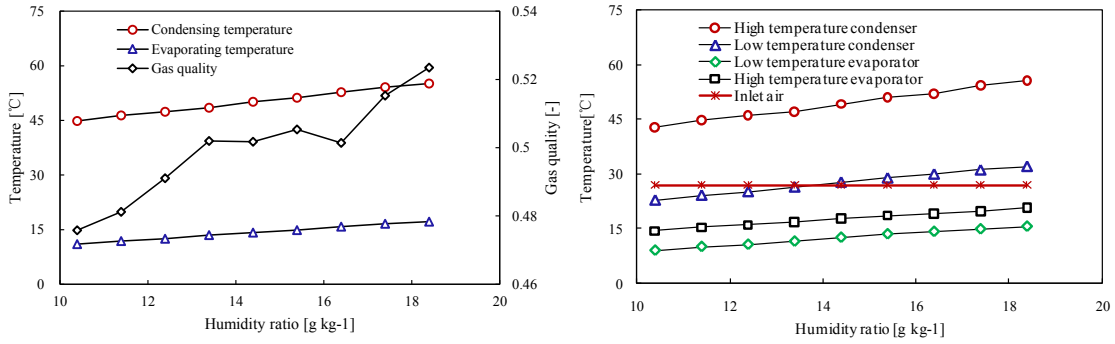

(a) Refrigerant **(b) air**

Figure 5: Temperature parameter changes under different conditions

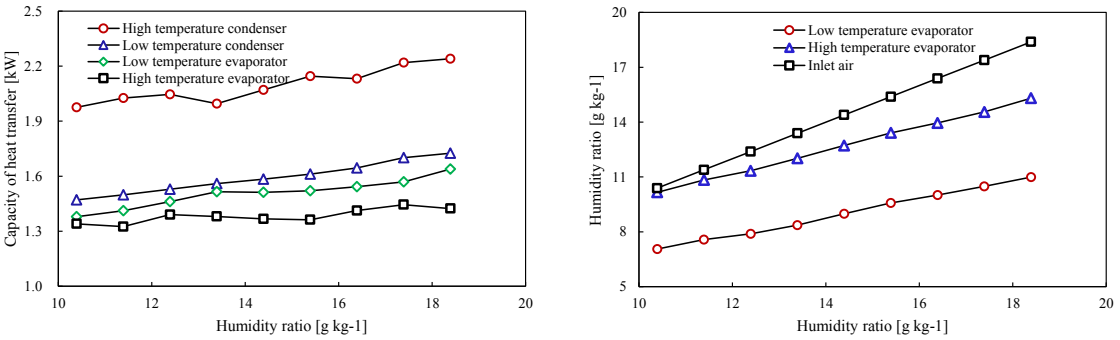

(a) Heat transfer **(b) Dehumidification**

Figure 6: Capacities of heat transfer and dehumidification under different conditions

Because gas quality in the flash tank is around 0.5 as Fig. 5a, the capacities of heat transfer for the low temperature condenser and evaporators should be similar as Fig. 6a. As shown as Fig. 6a, high temperature condenser has a highest capacity of heat transfer. The reason is the discharge refrigerant has a larger superheat degree. With the increase of humidity ratio, the capacities of heat transfer for the heat exchangers are increasing as the increase of the evaporating temperature as Fig. 5a. Fig. 6b shows the dehumidification capacities of two evaporators. With the increase of humidity ratio, the latent heat proportion for the high temperature evaporator is increasing but keeps almost same for the low temperature evaporator as Fig. 6b.

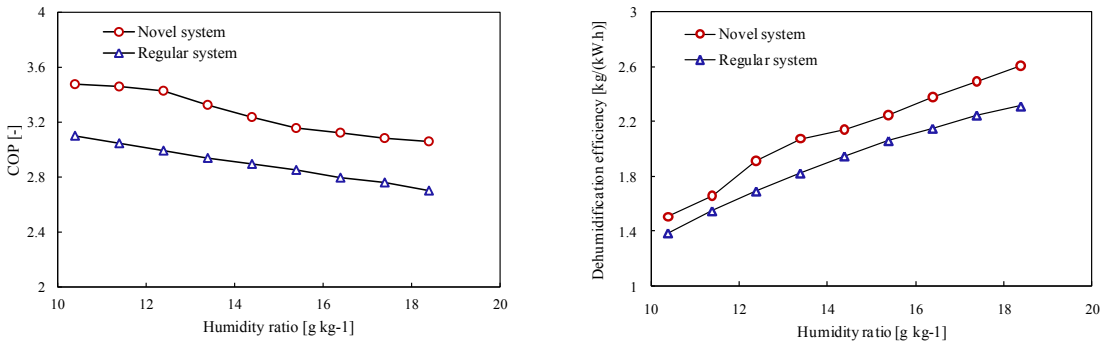

(a) COP **(b) Dehumidification efficiency**

Figure 7: System performance under different conditions

To evaluate the performance of the proposed dehumidification system, a comparative research has been done. A regular dehumidification system using the same as parameters of compressor and areas of heat exchangers with the novel system is considered as comparison. The path-flowing and

number of rows for the condenser and evaporator of the regular system are optimized. The compressor speed of the regular system is varying under different conditions to insure the comparative dehumidification capacity with the novel system. Fig. 7 shows the simulation results. The results indicate that the proposed dehumidification system presents improvements on COP by 10.6%~14.5% as Fig. 7a and dehumidification efficiency by 7%~13.6% as Fig. 7b under different conditions over the regular dehumidification system.

5. CONCLUSIONS

Separate sensible and latent cooling system is confirmed as a promising solution to replace regular dehumidification systems. Currently, many technologies for separate sensible and latent cooling system were developed, but all of them are too expensive or complicated to suit for small capacity dehumidification situations. In this paper, a novel dehumidification system using zeotropic refrigerants has been proposed. The proposed dehumidification system can realize dual evaporating temperatures by using one single cylinder rotary compressor. Compared to current SSLC system, the proposed system has the merits of simpler structure and lower price. Based on verified models, the heat transfer process and system performance of the novel dehumidification system were analyzed and evaluated. The results show:

(1) Compared to conventional dehumidification system, the proposed dehumidification system has a more matching heat exchange process;

(2) Compared to regular dehumidification system, the proposed dehumidification system can enhance COP by 10.6%~14.5% and dehumidification efficiency by 7%~13.6%;

(3) The proposed system has good potential for small capacity dehumidification situations.

REFERENCES

Cao, X., Zhang, C.L., Zhang, Z.Y., 2017. Stepped pressure cycle – A new approach to Lorenz cycle, International Journal of Refrigeration, 74, 283-294.

Jia, C., Dai, J., Wang, R., 2006. Analysis on a hybrid desiccant air conditioning system. Applied Thermal Engineering 26, 2392-2400.

Lemmon, E.W., Huber, M.L., McLinden, M.O, NIST Reference Fluid Thermodynamic and Transport Properties Database, NIST 23, (REFPROP), Version 8.0, National Institute of Standards and Technology: Gaithersburg, MD, 2007.

Ling, J.Z., Hwang, Y.H., Radermacher, R., 2010. Theoretical study on separate sensible and latent cooling air-conditioning system. International Journal of Refrigeration, 33, 510-520.

Liu, C., Zhang, H.F., Zhang, L., 2016. Development of a Novel Structure Rotary Compressor for Separate Sensible and Latent Cooling Air-Conditioning System, 23rd International Compressor Engineering Conference at Purdue, July 11-14.

Liu, X.R., Liang, X.F., Wu, Y.W., 2018. Performance investigation on ASHP of two-stage compression with flash tank using R32/R41 refrigerant mixtures, 9th Asian Conference on Refrigeration and Air-conditioning, June 10-13,Sapporo, Japan.

Liu, X.R., Wang, B.L., Shi, W.X., 2016. Comparative research on air conditioner with gas-injected rotary compressor through injection port on blade, Applied Thermal Engineering 106(2016) 67-75.

Neti, S., Wolfe, E., 2000. Measurements of effectiveness in a silica gel rotary exchanger. Applied Thermal Engineering 20, 309-322.

Manuscript ID:1459
DOI: 10.18462/iir.icr.2019.1459

Comparative analysis of vacuum membrane distillation regenerator and traditional regenerator in liquid desiccant air conditioning system

Junming ZHOU, Xiaosong ZHANG,

School of Energy and Environment, Southeast University, Nanjing 210096, China,
230179378@seu.edu.cn

ABSTRACT

In order to solve the problem of poor regeneration performance of the solar solution dehumidification air conditioning regeneration system under high temperature and high humidity weather conditions. In this paper, a novel vacuum membrane distillation (VMD) solution regeneration method was proposed for a solution desiccant air conditioning system, and a theoretical study of this novel regenerator is performed. Through the analysis of heat and mass transfer, the mathematical model of VMD regeneration is established, and the mathematical model is verified by experiments. The results indicated that VMD regenerator not only could increase the regenerate rate, but also could exhibit higher energy utilization efficiency. At the same concentration, the VMD regenerator has a higher regeneration performance, and the regeneration rate is 1.6-2.4 times that of the internal heat type regenerator,and the 4.5-6 times that of the adiabatic regenerator.
Keywords: Liquid Regeneration, Modeling, Heat and Mass Transfer, VMD.

1. INTRODUCTION

Solar Liquid Desiccant Air Conditioning System (SLDAS) is a novel air conditioning system with good energy saving potential, which has the characteristics of environmental protection and low-grade thermal energy drive. The traditional solution regeneration method relies heavily on the conditions of the surrounding environment. Yin and Qian (2014) concluded that under the conditions of high temperature and high humidity, the regeneration effect cannot meet the demand for dehumidification. In order to ensure the stability of the solar solution regeneration system under high temperature and high humidity weather, it is necessary to find a new regeneration process. It is worth noting that (Chen and Xu,2017) analysis shows that the energy consumption of the solution regeneration process accounts for more than 75% of the total energy consumption of liquid dehumidification air conditioners(LDAC). Therefore, seeking a method with low energy consumption and higher regeneration efficiency is critical to the system performance of LDAC.

Membrane distillation (MD) is a novel membrane separation technique combining membrane separation with evaporation. MD is a thermally driven process that utilizes the vapor pressure differential across the hydrophobic porous membrane as a driving force to achieve membrane separation of solute and solvent. Compared with the traditional heat regeneration process, MD regeneration can be operated with a lower heat source (40-80°C) (Drioli and Macedonio, 2015). The water flux of VMD is usually larger than that of other MD because only the diffusion flux of water vapor exists in the membrane pores (Luo and Lior, 2017). In addition, another advantage of VMD is that the heat loss is small because the insulation layer cannot be conducted through the membrane by vacuum. Therefore, heat transfer through the membrane is negligible (Chiam and Sarbatly, 2013). Different from the seawater desalination process of VMD regeneration and drinking water production, the regeneration of the dehumidification solution involves the removal of only a small amount of water in the higher concentration solution.

Membrane distillation technology is mostly applied in seawater desalination and wastewater treatment processes. Recently, membrane distillation technology in solution dehumidification air conditioners has also been investigated (Duong et al., 2017). Duong et al.(2018) evaluated the ability of three commonly used liquid desiccant solutions for membrane distillation (MD) regeneration in LDAC. The results indicate that the polarization effect has a considerable effect on the process water flux during the MD regeneration of these desiccant solutions. (Lefers et al., 2018) describe the testing

of a vacuum membrane distillation system for liquid dehumidification. It was found that a 30 wt% magnesium chloride solutions obtained an average flux of 8 $\mathrm{kg/m^2 \cdot h}$ at a temperature of 50℃. (Chen et al., 2018) studied a vacuum multi-effect membrane distillation system (V-MEMD) for liquid desiccant regeneration. Compared to existing liquid desiccant regeneration systems, specific energy consumption is reduced by 10-50%. (Abdel-Salam et al., 2014) reviewed the application, energy saving, economic and environmental impact of liquid-air membrane energy exchangers (LAMEE) in dehumidification applications. The conclusion is that the LAMEE system has the potential to reduce the capital and operating costs of HVAC systems by reducing energy consumption and component size. The solution-side effectiveness of LAMEE as a regenerator was evaluated (Moghaddam et al., 2014). The current research finds that it is feasible to use membrane distillation technology for solution regeneration, but there are few studies on the influence of various parameters on the performance of the distillation process of vacuum membrane distillation solution. Therefore, research in this area must be able to promote understanding of the parameter control and performance of membrane distillation-based solution regeneration systems.
In this paper, the mathematical model of VMD regeneration was established and the mathematical model was verified. Using the established numerical model of the hollow fiber VMD to evaluate the performance of VMD regeneration. This has provided support for the application of VMD regeneration in solution desiccant air conditioning systems, especially in hot and humid areas.

2. SYSTEM DESCRIPTION AND MATHEMATICAL MODEL

2.1. System Description of Solar VMD Regeneration System

This paper presents a solar VMD regeneration system shown in Fig.1a. The system consists of solar collectors, VMD regenerator (Fig.1b), concentrated solution tanks, vacuum pumps, condensers etc. The dilute solution first flows into the solar collector and is heated. In the VMD regenerator tube, a hollow fiber membrane is established. A vacuum pump is utilized to draw a vacuum on the cold side of the membrane to increase the pressure difference between the vapor on both sides of the membrane, thereby obtaining a higher distillation flux. The system effectively uses solar energy and can still regenerate the dehumidification solution stably and efficiently under high temperature and high humidity conditions.

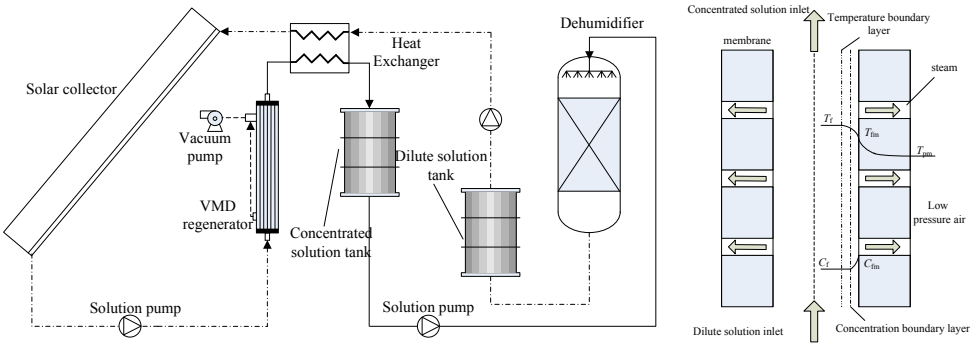

(a)Schematic diagram of system (b) Schematic of VMD heat and mass transfer

Figure1: The solar VMD regeneration system

2.2. Mathematical Model

2.2.1. Heat and mass transfer mathematical model of VMD regeneration

The dilute solution flows in the tube side of the hollow fiber membrane in the VMD regenerator. The shell side is in a negative pressure environment. In this paper, based on the heat and mass transfer equation of the solution in the hollow fiber membrane tube, the mathematical model of the VMD regeneration process is established.
Convective heat flux in the tube side
The heat of the solution is transferred to the inside of the membrane by convective heat transfer.

$$q_f = h_f(T_f - T_{fm}) \qquad \text{Eq. (1)}$$

Transmembrane heat transfer flux

The heat reaching the surface of the membrane is mainly transmitted to the outside through the latent heat of vaporization, and at the same time, part of the heat is transferred to the outside through the heat conduction of the membrane.

$$q_m = NH + \lambda_e (T_{fm} - T_{pm}) \quad \text{Eq. (2)}$$

The thermal conductivity of the membrane is composed of the gas thermal conductivity in the pores of the membrane and the thermal conductivity of the solid membrane.

$$\lambda_e = \varepsilon\lambda_a + (1-\varepsilon)\lambda_m \quad \text{Eq. (3)}$$

For steady-state solution regeneration, the fluxes of equation (1) and equation (2) are equal.
Heat transfer on the shell side
The shell side is in a negative pressure environment. Since the gas is drawn faster from the cold side of the membrane, the shell-side gas temperature gradient is small, so the temperature change is ignored.

2.2.2. VMD water flux and diffusion coefficient

The diffusion mechanism of the gas in the membrane during VMD regeneration is determined by the mean free path λ of the molecular motion and the size of the membrane pores. The Knudsen number is described as the ratio of the mean free path (λ) of the molecule to the pore diameter of the membrane (d): kn=λ/d.
If kn is between 0.01 and 10, diffusion mechanism for the transition zone, both the collision of gas molecules with the pore wall and the collision between gas molecules should be considered. The molar flow rate can be represented by the following equation:

$$N = \left[\frac{2}{3} \left(\frac{8M}{\pi RT} \right)^{\frac{1}{2}} \frac{\varepsilon r}{\delta \tau} + \frac{1}{8\mu} \frac{\varepsilon r^2}{\delta \tau} \frac{MP_{avg}}{RT} \right] \Delta p \quad \text{Eq. (4)}$$

2.2.3. Performance indexes

In general, the regeneration rate (mw) is used to determine the amount of vapor removed from the solution in the regenerator, which is calculated as Eq. (5):

$$m_w = N \bullet A / 3600 \quad \text{Eq. (5)}$$

The regeneration rate reflects the direct benefit of the regenerator regeneration process. The VMD regeneration process requires energy compensation. The total input of heat of the VMD regenerator can be expressed as Ep. (6) (Sarbatly and Chiam, 2013):

$$Q_s = m_s Cp (T_{s,in} - T_{s,out}) \quad \text{Eq. (6)}$$

In order to describe the energy utilization efficiency of the regeneration process, the energy efficiency of the regeneration process is generally defined to measure energy use efficiency:

$$\eta = \frac{m_w H}{Q_s} \quad \text{Eq. (7)}$$

The concentration polarization phenomenon will reduce the mass transfer during membrane distillation and concentration polarization coefficient can be expressed as: $\mathrm{CPC} = \frac{C_{fm}}{C_f}$ .Temperature polarization coefficient can be expressed as: $\mathrm{TPC} = \frac{T_{fm}}{T_f}$.

2.3. Simulation Calculation Process

The heat and mass transfer process of vacuum membrane distillation solution regeneration ware simulated by MATLAB software. The solution procedure is as follows: (1) Input membrane structural parameters and the dilute solution inlet state parameters. (2) Assume the initial temperature and

solution concentration of the solution. (3) Calculate the heat transfer coefficient, diffusion coefficient and membrane flux in the solution. (4) Solving linear equations to obtain the temperature and concentration of the solution.

3. VALIDATION OF MODELS

Lefers et al. (2004) show that the membrane distillation flux varied primarily as a function of the solution vapor pressure, while the type of inorganic salt used was not influential. The relevant parameters of the experiment in Lefers et al.(2004) and Alsalhy et al.(2017) are given in Table 1. This paper uses the LiCl solution as a desiccant. Under the same equilibrium relative humidity conditions, the simulation results of the established mathematical model are compared with the experimental data in (Lefers et al.(2004) and Alsalhy et al.(2017 as shown in Fig.2. It can be observed in Fig. 2a that the simulated flux of LiCl solution is basically the same as the experimental flux of CaCl2 and MgCl2 solutions, and the maximum error is less than 15%. Fig 2b shows the experimental value of the VMD Regenerator at different flow rates, where the membrane flux is between±15%, respectively, compared to the calculated values.The results show that the mathematical model of VMD regeneration can be used to obtain accurate results under experimental conditions.

Table1. The simulation parameters used for the model validation of VMD

Source	temperature	Flow rate	liquid	Vacuum pressure	No. of fiber	Inside/outside diameter	length	pore size
Lefers et al.(2004)	30℃	0.83m.s^{-1}	$MgCl_2/CaCl_2$	3 mbar	1	1.8/2.6 mm	0.47 m	0.2um
Alsalhy et al.(2017)	40-65℃	0.2-1 m.s^{-1}	H_2O	4 kPa	40	0.6/0.87 mm	0.4 m	0.29um

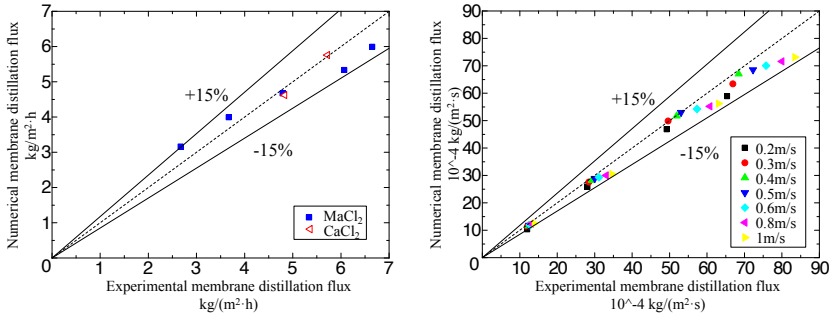

Figure 2: Comparison of the VMD simulation data and the experimental data

4. RESULTS AND DISCUSSION

The most widely used solution regeneration is the packed tower regeneration model. The physical model of the heat source side solution regeneration is generally used, and the research on such physical models is extensive. Yin et al. (2010) compared the adiabatic regenerator to an internal thermal regenerator that emphasized regeneration rate and regenerative thermal efficiency to evaluate the performance of both regenerators. The dimensions of the regenerator were as follows: the width of the regenerator (W) was 0.3 m and the height (H) was 1 m. The width of the channel II (d) was 0.024 m。 In the case of the same volume, the membrane shell has a length of 1 m, a shell diameter of 0.135 m, and an inner diameter of 0.095. The parameters of the membrane fibre under the same regeneration area are: the size of the hollow fiber membrane tube of the membrane tube regenerator: the inner diameter is 0.0048 m, the thickness is 0.4 mm, and the length is 0.5 m. The component filling rate in engineering applications is usually between 0.063 and 0.689, and the value of this paper is 0.139.The number of fibres was calculated to be 40 using the filling rate formula.
In order to investigate the characteristics of VMD solution regeneration, this paper will analyze the influence of the size of the hollow fibre membrane, solution inlet parameters, and vacuum degree on the VMD regeneration effect, cost and energy utilization efficiency. The cost mainly includes the cost of materials and equipment, as well as the electricity bill generated during the operation. The cost of materials and equipment is mainly composed of solar collectors and membranes; the operating costs are mainly composed of the electricity costs of the solution pump and the vacuum pump. Calculated

according to 8 hours of work per day, the total cost of the year includes the cost of equipment and materials as well as the electricity cost of the solution pump and vacuum pump. The relevant parameters are shown in Table 2 (Sarbatly and Chiam, 2013;Guo et al., 2004)

Table 2. Parameters of cost analysis for vacuum membrane distillation

Parameter	value	Parameter	value	Parameter	value
solar collector	185\$.m^{-2}	Electricity price	0.12\$.kwh^{-1}	η_{TH}	70%
Membrane material	90\$.m^{-2}	η_p	80%	G	700W.m^{-2}

By comparing the parameters of the membrane distillation solution regenerator with the parameters of the adiabatic and internal heat regenerator solutions, it is possible to gain an in-depth understanding of the internal operating rules and characteristics, to facilitate the discovery of their respective advantages and disadvantages, and to provide conceptual guidance for the dimensional design of the equipment. .The values of the operating conditions of Yin et al. are shown in Table 3.(Yin and Zhang , 2010)

Table 3 Operating condition parameter values

Ta(℃)	Wa(g.kg^{-1})	Ma(kg.s^{-1})	Ms(kg.s^{-1})	Ts(℃)	Xs(%)	Tw(℃)	Mw(kg.s^{-1})
30	11.5	0.015	0.004	65	37	65	0.02

(1) Influence of solution flow state on regeneration performance

Fig.3a shows that when flow rate increases gradually from 1g.s-1 to 31g.s-1, the solution outlet temperature rises from 23.2°C to 59.3°C and the concentration decreases from 42% to 37.7%. When flow rate is greater than 10g.s-1, the change of temperature and concentration gradually becomes gentle with the increase of flow rate and tends to the inlet solution state parameter. TPC and CPC are also gradually gradual. This is because flow rate increases, the lower the residence time for a solution of a unit mass. Fig 3b shows the regeneration efficiency and regeneration rate of the adiabatic, internal heat regenerator and VMD solution regenerator as a function of flow rate. When the solution flow rate is low (1g.s-1), the regeneration efficiency and regeneration rate of the adiabatic regenerator are both negative, which means that the dehumidification process is carried out in the adiabatic regenerator because the solution is supplied when the flow rate is low. The heat of the regeneration process is less, and then the temperature of the solution rapidly drops after entering the regenerator, and the partial pressure of water vapor on the surface of the solution begins to be lower than the partial pressure of the air water vapor. The internal heat type regenerator can provide heat to maintain the regeneration process at a lower flow rate, and the low flow rate of the solution can effectively avoid the carrying of solution droplets in practical applications. Moreover, the regeneration efficiency and the regeneration rate were also maintained at 68% and 0.11 g.s-1, respectively, with the change in flow rate. The regeneration rate of the VMD solution regenerator increased from 0.1g.s-1 to 0.5g.s-1 as the solution flow rate increased, and the VMD solution regeneration efficiency increased from 94% to 97.6%. The increase of the flow rate increases the disturbance of the solution in the membrane, reduces the heat and mass transfer resistance, and increases the membrane regeneration rate and the regeneration efficiency. The maximum regeneration rate of membrane is 4 times that of the internal heat type regenerator. The heat lost by the solution through the membrane tube is less, and the membrane regeneration heat efficiency is higher than that of the internal heat type regenerator. The cost of regeneration increased from 38\$ to 84\$, because as the flow rate increased, the power consumption of the solution pump increased, and the area of the solar panel used to heat the solution also increased, resulting in an increase in cost.

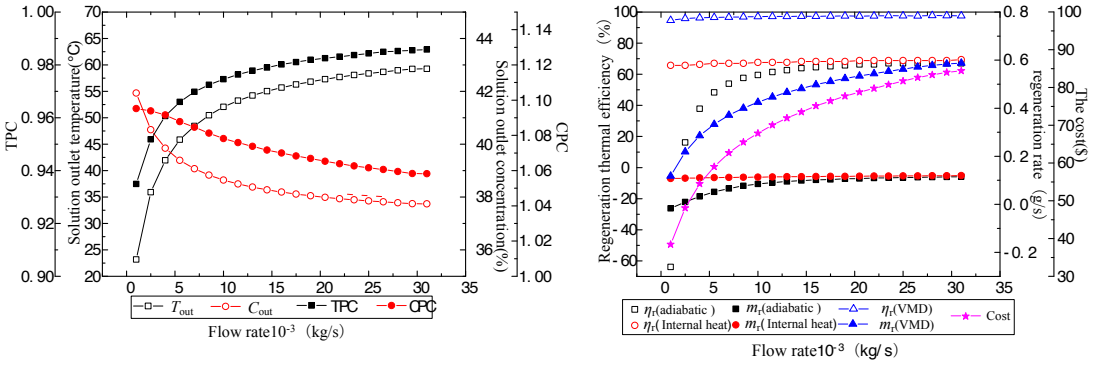

(a)Solution outlet parameters (b)The cost and energy utilization efficiency

Fig.3 Effect of solution inlet concentration on regeneration performance

(2) Influence of solution inlet temperature on regeneration performance

It is easy to seen from Fig.4a that when the solution inlet temperature is increased from 50°C to 100°C, the temperature of VMD regeneration outlet solution rises linearly with it, but the outlet temperature variation is smaller than the inlet temperature variation. The outlet concentration of the solution also increases with increasing temperature. And the increase in the temperature of the solution inlet causes the TPC to decrease linearly and the CPC to increase linearly. When the temperature is greater than 70°C, the rate of increase of the outlet concentration of the solution increases significantly. This is due to the fact that as the temperature of the solution increases, the vapor pressure of the solution increases exponentially with the temperature. The effect of solution inlet temperature on the regeneration rate and regeneration efficiency is seen in Fig 4(b). It is not difficult to see that when the solution inlet temperature is increased from 50℃ to 100℃, the regeneration rate of the adiabatic, internal heat regenerator and VMD regenerator increases as the solution temperature increases. The regeneration rate of the internal heat regenerator is 1.6-20 times that of adiabatic, and the regeneration rate of the VMD regenerator is 2.5 times that of the internal heat regenerator. The regeneration efficiency of the three regenerators increased with the increase of the solution temperature. The VMD regeneration efficiency was always higher than the internal heat type and the adiabatic type, and the regeneration efficiency was as high as 97%. When the regeneration rate was 0.27g.s-1, the regeneration temperature and efficiency of the internal heat type regenerator were 100℃ and 91%, respectively, and the temperature and efficiency of the VMD regenerator solution were 64℃ and 96%, respectively. It can be seen that the VMD regenerator reduces the unfavorable heat to the dehumidification process during regeneration. The cost has increased from 40$ to 98$. This is because in order to heat the solution to a higher temperature, a larger solar heat collection area is required, resulting in an increase in the total cost.

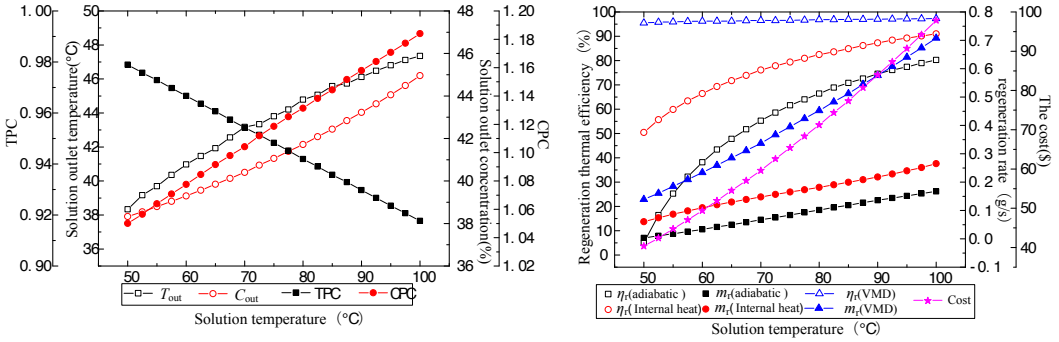

(a)Solution outlet parameters (b)The cost and energy utilization efficiency

Fig.4. Effect of solution inlet temperature on regeneration performance

(3) Influence of solution inlet concentration on regeneration performance

Fig.5a shows the effect of solution inlet concentration on the temperature and concentration of the VMD regeneration outlet solution. When the solution inlet concentration increased from 30% to 40%, the corresponding solution outlet temperature increased from 33 to 47°C, and the solution outlet concentration increased from 33.3% to 42.3%. It can be seen that the concentration difference of the inlet and outlet solutions decreases with the increase of the inlet concentration of the solution, but the difference between the inlet and outlet concentrations only decreases by 0.01%. This is because as the concentration of the inlet solution increases, the mass transfer driving force on both sides of the membrane gradually decreases. Fig. 5b shows the changes of regeneration rate and regeneration efficiency during the change of solution concentration. The calculation results show that the regeneration rate and regeneration efficiency of the three regenerators decrease with the increase of concentration. Mainly because the surface water vapor partial pressure decreases with the increase of the inlet concentration of the lithium chloride solution, the mass transfer power between the two sides of the membrane decreases, and the evaporation amount decreases, resulting in a decrease in the regeneration rate. The heat at the inlet of the solution does not change much, and the amount of water evaporated as the concentration of the solution increases, and the less the portion of the heat converted into latent heat of steam, the lower the energy utilization efficiency. At the same concentration, the VMD regenerator has a higher regeneration performance, and the regeneration rate is 1.6-2.4 times that of the internal heat type regenerator. The VMD regeneration cost is reduced from 65$ to 48$ as the concentration of the inlet solution increases.

This is because as the concentration of the solution increases, the specific heat capacity of the solution decreases. When the dilute solution is heated to the same temperature, the solar heat collecting area is required to be reduced, and the total cost is reduced.

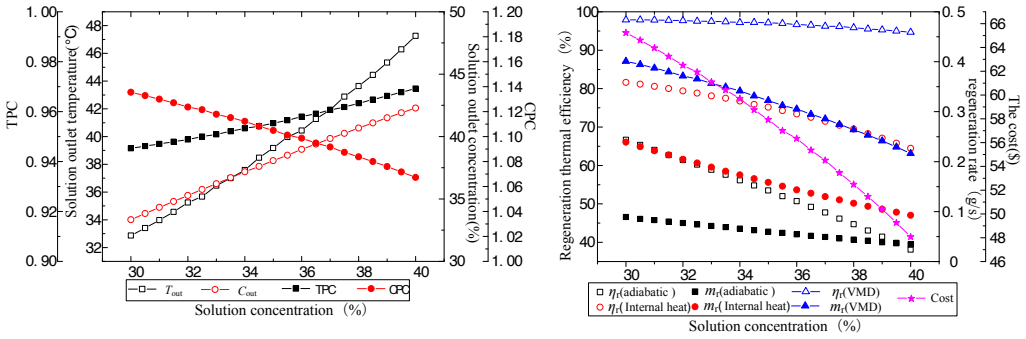

(a)Solution outlet parameters (b)The cost and energy utilization efficiency

Figure 5: Effect of solution inlet concentration on regeneration performance

5. CONCLUSION

(1) The VMD regenerator maintains high regenerative performance at higher flow rates with a regeneration efficiency of up to 97% and avoids drift.
(2) At the same concentration, the VMD regenerator has a higher regeneration performance, and the regeneration rate is 1.6-2.4 times that of the internal heat type regenerator,and the 4.5-6 times that of the adiabatic regenerator.

ACKNOWLEDGEMENTS

This work was supported by National Natural Science Foundation of China (No. 51520105009).

NOMENCLATURE

A	area (m^2)
C	Concentration(%)
C_p	Specific heat capacity($kJ\cdot(kg\cdot k)^{-1}$)
H	Evaporation heat of vapor($kJ\cdot kg^{-1}$)
k	Thermal conductivity of solution($J\cdot m^{-1}\cdot K^{-1}\cdot s^{-1}$)
m	mass flow rate ($kg\cdot s^{-1}$)
M	Molecular weight
N	membrane water flux ($kg\cdot m^{-2}\cdot h^{-1}$)
P	pressure(kPa)
Q	Heating capacity (kW)
R	Hollow fiber membrane radius(m)

Greek letter

δ	thickness
η	Thermal efficiency
λ	Molecular free path(m)
τ	tortuosity
ε	Porosity

Subscripts

fm	Solution side of the membrane
in	inlet
out	outlet

REFERENCES

Abdel-Salam M R H, Fauchoux M, Ge G, et al. Expected energy and economic benefits, and environmental impacts for liquid-to-air membrane energy exchangers (LAMEEs) in HVAC systems: A review[J]. Applied Energy, 2014, 127(127):202-218.

Aoyi L., Noam Lior.Study of advancement to higher temperature membrane

distillation.Desalination,2017. 419(1)88-100

Chel-Ken Chiam, Rosalam Sarbatly.Vacuum membrane distillation processes for aqueous solution treatment—A review. Chemical Engineering and Processing:Process Intensification,74(2013)27-54

Chen Q.,M.Kum Ja, Y.Li, K.J.Chu.Thermodynamic optimization of a vacuum multi-effect membrane distillation system for liquid desiccant regeneration.Applied Energy. 2018, 230 (11) :960-973

Cheng Q., Xu W..Performance analysis of a novel multi-function liquid desiccant regeneration system for liquid desiccant air-conditioning system.Energy, 140(2017)240-252

Duong H C, Álvarez I R C, Nguyen T V, et al. Membrane distillation to regenerate different liquid desiccant solutions for air conditioning[J]. Desalination, 2018, 443:137-142.

Drioli E., Ali A., Macedonio F., Membrane distillation: recent developments andperspectives, Desalination. 35 (2015)56–84.

Guo Y, Ma Z, Al-Jubainawi A, et al. Using electrodialysis for regeneration of aqueous lithium chloride solution in liquid desiccant air conditioning systems[J]. Energy & Buildings, 2016, 116:285-295.

Hung C. Duong, Faisal I. Hai, Ali Al-Jubainawi, Zhenjun Ma, Long D. Nghiem.Liquid desiccant lithium chloride regeneration by membrane distillation for air conditioning.Separation and Purification Technology, 2017.177(28)121-128

Lefers R , Srivatsa Bettahalli N M , Fedoroff N , et al. Vacuum membrane distillation of liquid desiccants Utilizing Hollow Fiber Membranes[J]. Separation and Purification Technology, 199(2018):57-63..

Li Y., Lu J.. Electrolyte solution theory[M]. Tsinghua University Press. Beijing.2005:401-420

Moghaddam D G, Besant R W, Simonson C J. Solution-side effectiveness for a liquid-to-air membrane energy exchanger used as a dehumidifier/regenerator[J]. Applied Energy, 2014, 113(6):872-882.

Qusay F. Alsalhy.Salah S.Ibrahim.Samraa R.Khaleel.Performance of vacuum poly(propylene) membrane distillation (VMD) for saline water desalination.Chemical Engineering and Processing - Process Intensification.120(2017):68-80

Sarbatly R, Chiam C K. Evaluation of geothermal energy in desalination by vacuum membrane distillation[J]. Applied Energy, 2013,112(112):737-746.

Yin Y , Zhang X . Comparative study on internally heated and adiabatic regenerators in liquid desiccant air conditioning system[J]. Building & Environment, 2010, 45(8):1799-1807.

Yin Y., Qian J., Zhang X..Recent advancements in liquid desiccant dehumidification technology.Renewable and Sustainable Energy Reviews,2014,31(3)38-52

Zhou J., Lu X., Wang Y., Shi J..Molecular dynamics study on ionic hydration.Fluid Phase Equilibria, 194–197(2002)257-270

Manuscript ID: 1496
DOI: 10.18462/iir.icr.2019.1496

The performance of a proposed hyper-gravity dehumidifier

Yangyang Gu[(a)], Xiaosong Zhang[(a)]

[(a)] School of Energy and Environment, Southeast University, Nanjing 210096, China
guy_seu@163.com

ABSTRACT

Liquid desiccant air conditioning systems have received more attention in recent years for their lower energy consumption. A counter current-flow hyper-gravity dehumidifier using a rotating packed bed was proposed in this paper. Rotating packed bed (RPB) uses a rotating part to create an artificial centrifugal force which is stronger than gravity. The gas-liquid heat and mass transfer process will be intensified in the hyper-gravity field. A mathematical model was established in this work. An experimental apparatus is established to verify the mathematical model. The results show that good agreement between the theoretical model and the experimental results was achieved in the present study. The moisture removal rate can be enhanced by increasing the air flow rate, solution flow rate, and rotating speed. And the dehumidification effectiveness can be improved by raising the solution flow rate and rotating speed.
Keywords: Liquid Desiccant, Rotating Packed Bed (RPB), Hyper Gravity, Dehumidifier.

1. INTRODUCTION

The world requirement of equipment for heating, ventilation, and air-conditioning (HVAC) has increased in the last few decades. Rising comfort requirements and increasing population have led to a significant increase in energy consumption for air-conditioning systems. Temperature and humidity control are essential and vital parameters for the indoor environment and human comfort. It is feasible to regulate temperature and humidity by conventional vapor compression cycles. During regulating the humidity they dehumidify the supplied air through cool-reheat processes. In these cycles, the latent load of moisture content is reduced by reducing the temperature of the air. The air temperature drops below the dew-point temperature which typically is lower than the set point, thus a reheat coil is used to increase the sensible temperature of the air back to its set point.

Liquid desiccant air-conditioning systems have shown promising potential and application in the controlling of temperature and humidity by its lower energy consumption and higher indoor comfort (Misha et al., 2012). Therefore liquid desiccant dehumidification systems have drawn more and more attention in recent years. Koronaki et al. (2013) established a counter-flow dehumidifier and compared the performance of LiCl desiccant solution with it of LiBr rich desiccants solution. Bai et al. (2017) investigated experimentally the performance of a cross-flow membrane liquid desiccant dehumidification system using $CaCl_2$ solution. Yang et al. (2014) proposed an ultrasonic atomization dehumidification system which expanded the specific surface area of the desiccant solution in dehumidifier dramatically by the ultrasonic atomization technology. Membrane liquid desiccant air conditioning systems were promoted which used liquid-to-air membrane energy exchangers (LAMEEs) instead of conventional direct-contact dehumidifiers (Zhang, 2012). Air and solution streams are separated from each other in LAMEEs using hydrophobic semipermeable membranes. There is an additional resistant for mass transfer in the LAMEE caused by the membrane which results in the worse performance of mass transfer compared with the direct-contact dehumidifiers. The membrane accounts for 6-12% and 26-43% of the overall heat and mass transfer resistance, respectively, depending on the width of the air channel (Ge et al. 2017).

Hyper-gravity technology was originally proposed by Ramshaw and Mallinson (1981) as a process intensification, which was regarded by using a rotating packed bed (RPB) and referred as “HIGEE”. In the last three decades, the application of the hyper-gravity technology and its device the rotating packed bed (RPB) have been used for process intensification in the field of chemical, energy, environment and process engineering, especially in gas-liquid absorption, gas-liquid separation,

liquid-liquid extraction, heat transfer, reactive crystallization and nanomaterial synthesis. HIGEE devices use a rotating packed bed to create artificial centrifugal force which is 200-1000 times stronger than gravity in order to enhance mass-transfer and up to 1-2 orders of magnitude, allowing for a reduction in size of up to 10 times with respect to conventional packed bed for the same separation (Rao et al. 2004; Zhao et al. 2010). In the hyper-gravity field, liquid splits into a thin film and tiny droplets. Consequently, the heat and mass transfer can be enhanced compared with traditional packed towers because of an enormous contact area and intensive mixing between gas and liquid phases (Wang et al. 2008) and better self-cleaning of the rotor, which avoids plugging in the system, and being unaffected by a moderate disturbance in its orientation (Tan et al. 2006). Meanwhile, hyper-gravity relaxes flooding limits of the column that allows operation at higher gas velocities. The entrainment liquid droplets generated from liquid film and tiny droplets will be separated from air stream on account of the strong artificial centrifugal force. With these advantages, extensive studies have been conducted to research the performance of absorption such as CO_2 (Wu et al. 2017), H_2S (Guo et al., 2014), NO_x (Li et al., 2010) and VOC (Hsu et al., 2012).

This study applied the RPB in the field of liquid desiccant. The rotating packed bed was employed as a dehumidifier. A mathematical model was established. To verify the feasibility of the proposed RPB liquid desiccant dehumidification system, a testbed for counter-flow RPB dehumidifier using LiCl solution as the liquid desiccant was established, and the effects of the air flow rate, solution flow rate and rotating speed on the moisture removal rate and dehumidification effectiveness were experimentally studied.

2. MATHEMATICAL MODEL

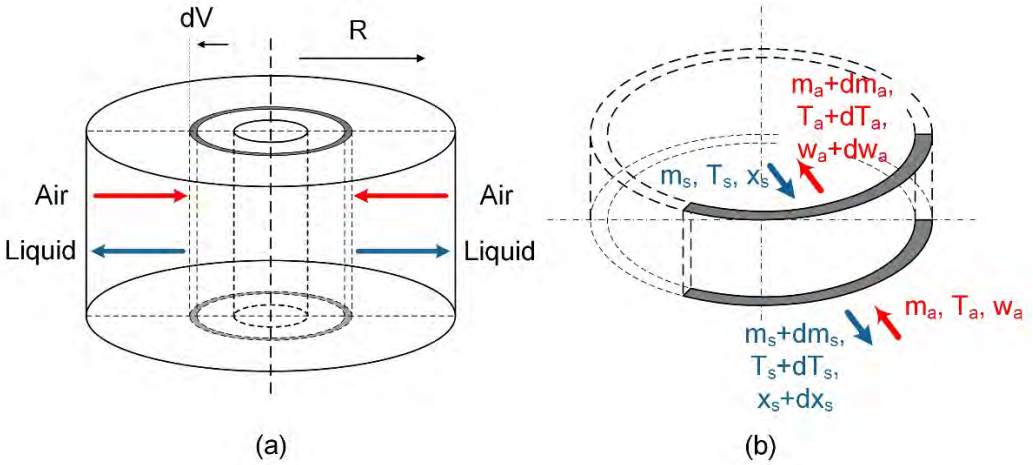

Figure 1: (a) Schematic of the RPB dehumidifier model; (b) Control volume for the model.

In this section, a mathematical model was established to describe gas-liquid heat and mass transfer for the liquid desiccant system in an RPB dehumidifier. The desiccant solution is distributed into the rotating packed bed (RPB) and absorbs water vapor through direct contact with the air, as shown in Fig 1. A theoretical model based on the finite volume method (FVM) to predict liquid desiccant in RPB performance is developed. As illustrated in Fig. 1, the RPB is divided into n control volumes along the radius. Considering the space between two adjacent packing layers as volume element for the liquid desiccant system, energy and mass balance between air and solution in the control volume can be expressed as following differential equations:

$$m_s \mathrm{d}h_s + h_s \mathrm{d}m_s = m_a \mathrm{d}h_a \qquad \text{Eq. (1)}$$

$$\mathrm{d}m_s = m_a \mathrm{d}\omega_a \qquad \text{Eq. (2)}$$

The heat and mass transfer equations between liquid desiccant and air in the control volume are defined respectively in Eqs. (3) and (4):

$$m_a \, \mathrm{d}h_a = h_c A_v \, \mathrm{d}V \left(T_s - T_a\right) + r_{T_s} m_a \, \mathrm{d}\omega_a \qquad \text{Eq. (3)}$$

$$m_a \, \mathrm{d}\omega_a = h_d A_v \, \mathrm{d}V \left(\omega_e - \omega_a\right) \qquad \text{Eq. (4)}$$

The mass transfer coefficient can be expressed as (Chen et al., 2006):

$$\frac{h_d A_v}{D_G a_t^2}\left(1 - 0.9\frac{V_o}{V_t}\right) = 0.023 \mathrm{Re}_G^{1.13} \mathrm{Re}_L^{0.14} \mathrm{Gr}_G^{0.31} \mathrm{We}_L^{0.07} \left(\frac{a_t}{a_p'}\right)^{1.4} \qquad \text{Eq. (5)}$$

The Le number which is usually assumed to be one (Gandhidasan et al., 1986) is defined as:

$$\mathrm{Le} = \frac{h_c}{h_d c_{pa}} \qquad \text{Eq. (6)}$$

On the basis of Eqs. (1)-(6), the outlet parameters of the air and solution can be calculated using the model and the moisture removal rate and dehumidification effectiveness are obtained.

3. EXPERIMENTAL SETUP

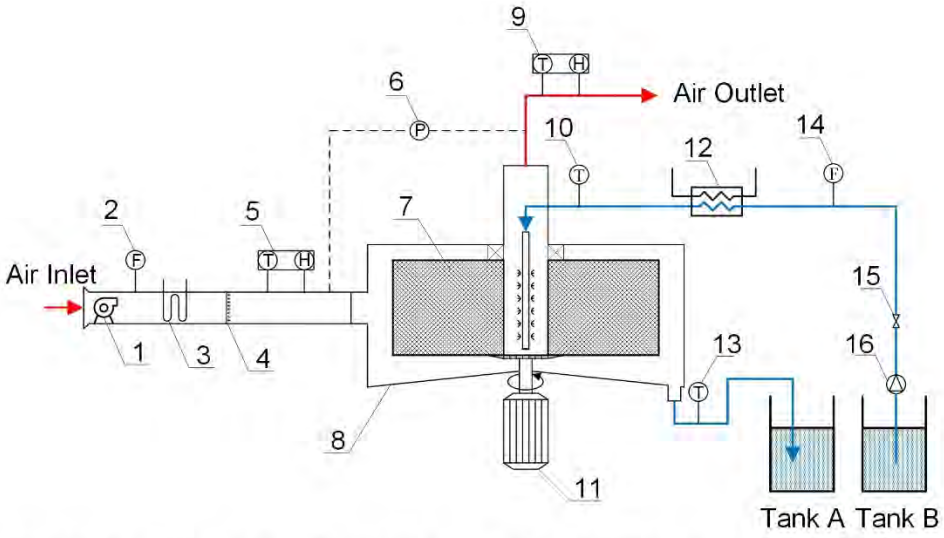

Components: (1) Fan; (2) Air flow meter; (3) Heat Exchanger; (4) Humidifier; (5) Integrated temperature and humidity sensor; (6) Differential pressure gauge; (7) RPB; (8) RPB shell; (9) Integrated temperature and humidity sensor; (10) PT100; (11) Motor; (12) Heat Exchanger; (13) PT100; (14) Liquid flow meter; (15) Valve; (16) Pump.

Figure 2: Testbed for the novel high-gravity liquid desiccant dehumidifier.

3.1. Testbed for the Countercurrent-Flow Rotating Packed Bed Dehumidifier

A testbed for a counter current-flow rotating packed bed dehumidifier using LiCl solution as the liquid desiccant was established, shown in Fig. 2. The RPB dehumidifier comprised a stationary housing and a doughnut rotor that was driven by a motor. The inner and outer radiuses of the rotor were 6 and 18 cm, respectively, and the axial height was 4 cm which was packed up with foamed nickel with the specific surface area of 500 $m^2.m^{-3}$ and the porosity of 93%.

3.2. Measuring instruments

Table 1: Specification of the different measuring devices

Devices	Parameters	Accuracy	Range
Air flow meter	Flow rate ($m^3.h^{-1}$)	±2.5%@20 °C & 1 atm	0-180 $m^3.h^{-1}$
Thermometer	Temperature (°C)	±0.15 °C@23 °C±5 °C	-50-100 °C
Integrated temperature and humidity sensor	Temperature (°C) & RH (%)	±0.2 °C & ±1.0% (0-90 RH%) ±1.7% (90-100 RH%)	-40-80 °C & 0-100 RH%
Solution flow meter	Flow rate ($L.h^{-1}$)	±2.5%@20 °C & 1 atm	0-240 $L.h^{-1}$
Densitometer	Density ($kg.m^{-3}$)	±1 $kg.m^{-3}$@0-40 °C	0-2000 $kg.m^{-3}$

Parameters of the RPB dehumidifier were measured before and after the dehumidifier with the devices listed in Table 1. The positions of measurement devices are shown in Fig. 2. Mass fraction of LiCl solution can be calculated based on the measurement results of density and temperature of LiCl solution (Conde et al. 2004).

4. RESULTS AND DISCUSSION

4.1. Evaluation Indexes of Dehumidification Performance

For the hyper-gravity liquid desiccant dehumidification system, the moisture removal rate (M) of moist air presents the water amount separated from the humid air and is selected to indicate the quantity of the mass transfer between the humid air and LiCl solution in the dehumidifier, shown in Eq. (7).

$$M = m_a \left(\omega_{a,in} - \omega_{a,out} \right) \quad \text{Eq. (7)}$$

Dehumidification effectiveness (η) has been widely used to evaluate the mass transfer performance of the dehumidifier in previous studies (Liu et al. 2006 & Bassuoni et al. 2011). The dehumidification effectiveness (η) is defined as the ratio of actual different of the humidity ratio between the inlet and outlet air to the maximum possible change, shown in Eq. (8).

$$\eta = \frac{\omega_{a,in} - \omega_{a,out}}{\omega_{a,in} - \omega_e} \quad \text{Eq. (8)}$$

4.2. Effects of Inlet Parameters and Operation Condition on the Performance

The effects of the air flow rate, solution flow rate, and rotating speed on the moisture removal rate and dehumidification effectiveness of the RPB dehumidifier were studied. Table 2 shows the inlet parameters and operation condition of experimental conditions in Figs. 3–5.

Table 2: Experimental conditions of hyper gravity liquid desiccant dehumidification

	$X_{s,in}$ (%)	$\omega_{a,in}$ ($g.kg^{-1}$)	m_a ($kg.s^{-1}$)	m_s ($kg.s^{-1}$)	$T_{a,in}$ (°C)	$T_{s,in}$ (°C)	N ($r.min^{-1}$)
Fig. 3	35.0±0.2	16±0.3	0.0286 ±0.0005	0.0267 ±0.0005	32.0±0.3	28.0±0.3	-
Fig. 4	35.0±0.2	16±0.3	0.0286 ±0.0005	-	32.0±0.3	28.0±0.3	1000
Fig. 5	35.0±0.2	16±0.3	-	0.0267 ±0.0005	32.0±0.3	28.0±0.3	1000

4.2.1. Rotating speed of RPB

The hyper-gravity dehumidifier was tested at five different rotating speed. Fig. 3 shows the effect of rotating speed on the moisture removal rate and dehumidification effectiveness of air in the dehumidifier. It is apparent that the experimental results are in good agreement with the predicted

values of the model. Both the moisture removal rate and dehumidification effectiveness of the air goes up as rotating speed increases from 500 to 1500 r.min^{-1}. As a result, the lower humidity level to which the air can be dehumidified and dehumidification effectiveness can be higher at higher rotating speed. This may because the growth of rotating speed increases the dispersion degree of the desiccant solution and therefore increases the effective contact area between the solution and air. Besides, increasing rotating speed increases the solution flow rate in the rotor which leads to the improvement of the heat and mass transfer coefficients between the air and desiccant solution.

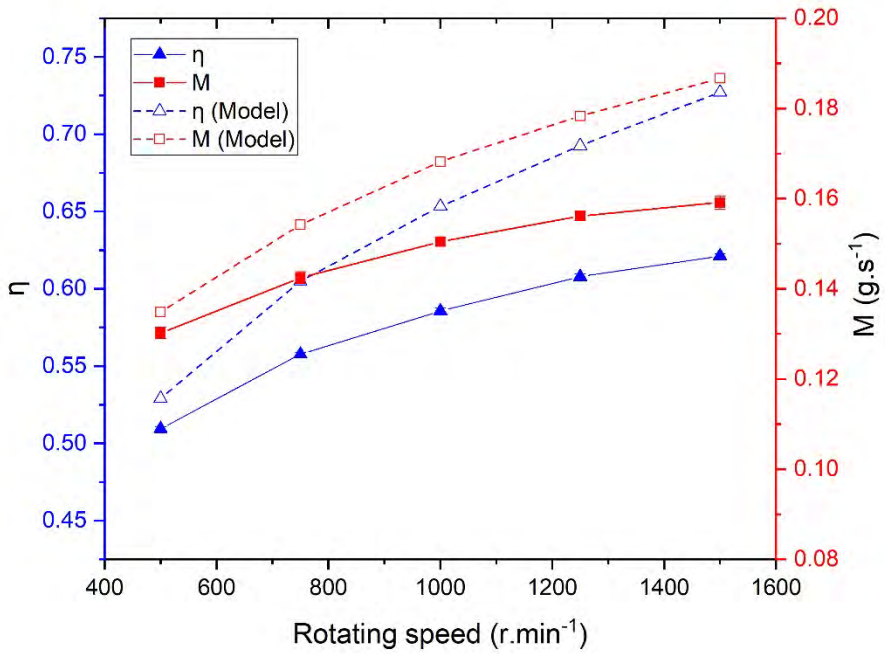

Figure 3. Moisture removal rate and dehumidification effectiveness under different rotating speed

4.2.2. Solution flow rate

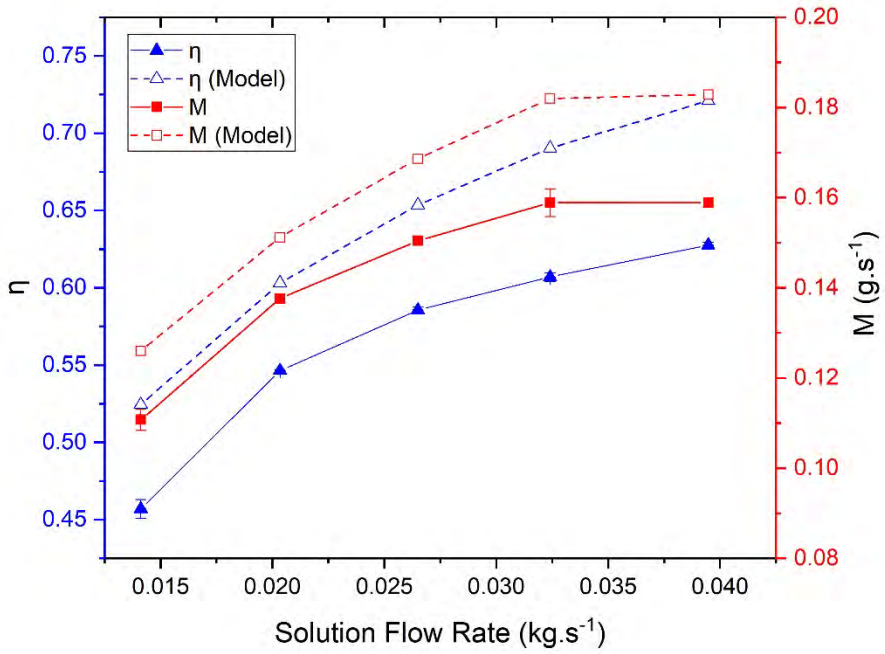

Figure 4. Moisture removal rate and dehumidification effectiveness under different solution flow rate

As shown in Fig. 4, in both the experimental condition and the model, the moisture removal rate and the dehumidification effectiveness increases with the flow rate of solution changing from 0.014 to 0.039 kg.s^{-1}. In general, the experimental data was in line with the results of the model. It can be explained as follows. The increase of solution flow rate decreases the mean surface vapor pressure of the solution through the RPB dehumidifier and increases the mean vapor pressure difference between the solution and air. In addition, increasing the solution flow rate increases the mass transfer coefficients and also increases the effective contact area between the solution and air. Due to these three reasons, the dehumidification effectiveness and moisture removal rate increases remarkably with the growth of the solution flow rate.

4.2.3. Air flow rate

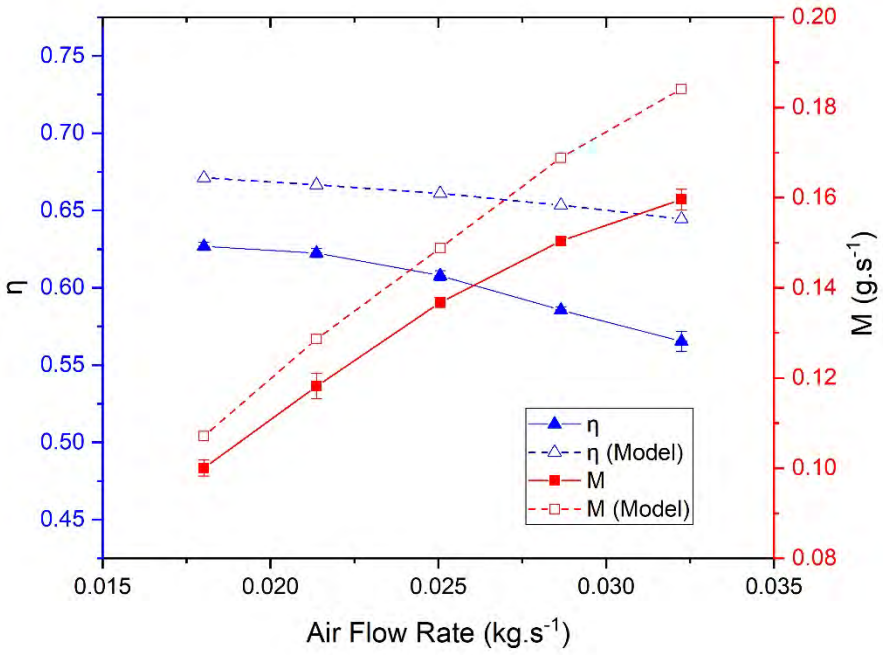

Figure 5. Moisture removal rate and dehumidification effectiveness under different solution inlet concentrations.

Fig. 5 displays the effect of air flow rate on dehumidification effectiveness and moisture removal rate in RPB dehumidifier. As shown in Fig. 5, it is apparent that the experimental values were in good agreement with the results of the model. The moisture removal rate increases while the dehumidification effectiveness decreases with the air flow rate changing from 0.018 to 0.032 kg.s^{-1} under a certain rotating speed. This may because increasing the air flow rate leads to the increase of the heat and mass transfer between the air and solution, meanwhile, the mean vapor pressure difference is enlarged. Finally, the growth of the air flow rate increases the moisture removal rate. The decrease of air residence time in the RPB dehumidifier increases the outlet air humidity ratio which leads to the decrease of dehumidification effectiveness.

5. CONCLUSIONS

This paper proposes a rotating packed bed dehumidifier. The mathematic model of the RPB dehumidifier was established. An investigation on the RPB dehumidifier is carried out experimentally to verify the mathematic model. The moisture removal rate and dehumidification effectiveness are employed as the performance indexes. Experiments are conducted to discover the effects of the air flow rate, solution flow rate and rotating speed on the moisture removal rate and dehumidification effectiveness. The RPB dehumidifier can improve its preference by increasing the rotating speed of RPB. Experimental results show that dehumidification effectiveness can reach 0.621 at the rotating

speed of 1500 r.min^{-1}. Good agreement between the theoretical model and the experimental results was achieved in the present study. Besides rotating speed, the moisture removal rate can be enhanced by increasing the air flow rate, solution flow rate. The dehumidification effectiveness can be improved by raising the solution flow rate.

ACKNOWLEDGMENTS

This work is supported by the National Natural Science Foundation of China (No.51876034).

NOMENCLATURE

A_v	specific area of the packing, [$m^2.m^{-3}$]	c_{pa}	specific heat capacity of air, [$kJ.kg^{-1}.°C^{-1}$]
h_a	enthalpy of air, [$kJ.kg^{-1}$]	h_c	heat transfer coefficient, [$kW.m^{-2}.°C^{-1}$]
h_d	mass transfer coefficient, [$kg.m^{-2}.s^{-1}$]	h_s	enthalpy of solution, [$kJ.kg^{-1}$]
m_a	mass flow rate of air [$kg.s^{-1}$]	m_s	mass flow rate of solution [$kg.s^{-1}$]
M	moisture removal rate [$g.s^{-1}$]	N	rotating speed of RPB [$r.min^{-1}$]
r_{Ts}	enthalpy of dilution at solution temperature T_s, [$kJ.kg^{-1}$]	T_a	temperature of air [°C]
T_s	temperature of solution [°C]	V	volume of the packing, [m^3]
$X_{s,in}$	concentration of inlet solution [%]	$\omega_{a,in}$	humidity ratio of inlet air [$kg.kg^{-1}$]
$\omega_{a,out}$	humidity ratio of outlet air [$kg.kg^{-1}$]	ω_e	equilibrium humidity ratio of air
η	dehumidification effectiveness		

REFERENCES

Bai, H. Y., Zhu, J., Chen, Z. W., Ma, L. N., Wang, R. Z., Li, T. X., 2017. Performance testing of a cross-flow membrane-based liquid desiccant dehumidification system. Appl. Therm. Eng. 119, 119-131.

Chen, Y. S., Lin, F. Y., Lin, C. C., Tai, C. Y., Liu, H. S., 2006. Packing Characteristics for Mass Transfer in a Rotating Packed Bed. Ind. Eng. Chem. Res., 45, 6846-6853.

Gandhidasan, P., Kettleborough, C. F., & Ullah, M. R., 1986. Calculation of heat and mass transfer coefficients in a packed tower operating with a desiccant-air contact system. .J. Sol. Energy Eng. Trans-ASME, 108, 123–128.

Ge, G. M., Abdel-Salam, A. H., Abdel-Salam, M. R. H., Besant, R. W. Simonson, C. J., 2017. Heat and mass transfer performance comparison between a direct-contact liquid desiccant packed bed and a liquid-to-air membrane energy exchanger for air dehumidification. Sci. Technol. Built Environ. 23(1), 2-15.

Ge, G. M., Abdel-Salam, M. R. H., Besant, R. W., Simonson, C. J., 2013. Research and applications of liquid-to-air membrane energy exchangers in building HVAC systems at University of Saskatchewan, A review. Renew Sustain. Energy Rev. 26, 464-479.

Guo, K., Wen, J. W., Zhao,Y., Wang, Y., Zhang, Z. Z., Li, Z. X. Qian, Z., 2014. Optimal Packing of a Rotating Packed Bed for H2S Removal. Environ. Sci. Technol. 48(12), 6844-6849.

Hsu, L. J., Lin, C. C., 2012. Binary VOCs absorption in a rotating packed bed with blade packings. J. Environ. Manage. 98, 175-182.

Koronaki, I. P., Christodoulaki,R. I., Papaefthimiou V. D., Rogdakis, E. D., 2013. Thermodynamic analysis of a counter flow adiabatic dehumidifier with different liquid desiccant materials. Appl. Therm. Eng. 50(1), 361-373.

Li, Y., Y. Liu, Z., Zhang, L. Y., Su, Q., Jin, G. L., 2010. Absorption of NOx into Nitric Acid Solution in Rotating Packed Bed. Chin. J. Chem. Eng. 18(2), 244-248.

Liu, X. H., Zhang, Y., Qu K. Y., Jiang, Y., 2006. Experimental study on mass transfer performances of cross flow dehumidifier using liquid desiccant. Energy Convers. Manag. 47(15-16), 2682-2692.

Luo, Y., Chu, G. W., Zou, H. K., Zhao, Z. Q., Dudukovic, M. P., Chen, J. F., 2012. Gas-Liquid Effective Interfacial Area in a Rotating Packed Bed. Ind. Eng. Chem. Res. 51(50), 16320-16325.

Luo, Y. M., Yang, H. X., Lu, L., Qi, R. H., 2014. A review of the mathematical models for predicting the heat and mass transfer process in the liquid desiccant dehumidifier. Renew Sustain. Energy Rev. 31, 587-599.

Misha, S., Mat, S., Ruslan, M. N., Sopian, K., 2012. Review of solid/liquid desiccant in the drying applications and its regeneration methods. Renew Sustain. Energy Rev. 16(7), 4686-4707.

Mondal, A., Bhowal, A., Datta, S., 2013. Gas-Liquid Sensible Heat Transfer in Spray and Packed Bed under a Centrifugal Field. Ind. Eng. Chem. Res. 52(1), 499-506.

Ramshaw, C., Mallinson, R. H., 1981. Mass Transfer Process. US Patent. 4 283 255. 4 283 255, 4 283 255.

Rao, D. P., Bhowal, A., Goswami, P. S., 2004. Process intensification in rotating packed beds (HIGEE), An appraisal. Ind. Eng. Chem. Res. 43(4), 1150-1162.

Su, M. J., Luo, Y., Chu, G. W., Liu, W., Zheng, X. H., Chen, J. F., 2018. Gas-Side Mass Transfer in a Rotating Packed Bed with Structured Nickel Foam Packing. Ind. Eng. Chem. Res. 57(13), 4743-4747.

Tan, C. S. Chen, J. E., 2006. Absorption of carbon dioxide with piperazine and its mixtures in a rotating packed bed. Sep. Purif. Technol. 49(2), 174-180.

Vestrelli, F., 2006. Study on membrane contactors, performances analysis, system simulations and fields of application. Doctor, University of Genoa.

Wang, G. Q., Xu, Z. C., Yu, Y. L., Ji, J. B., 2008. Performance of a rotating, zigzag bed-A new HIGEE. Chem. Eng. Process. 47(12), 2131-2139.

Wu, S. Y., Zhang, L. L., Sun, B. C., Zou, H. K., Zeng, X. F., Luo, Y., Lo, Q., Chen, J. F., 2017. Mass-Transfer Performance for CO2 Absorption by 2-(2-Aminoethylamino)ethanol Solution in a Rotating Packed Bed. Energy Fuels 31(12), 14053-14059.

Yang, Z., Zhang, K., Yang, M. Lian, Z., 2014. Improvement of the ultrasonic atomization liquid desiccant dehumidification system. Energy Build. 85, 145-154.

Zhang, L.Z., 2012. Coupled heat and mass transfer in an application-scale cross-flow hollow fiber membrane module for air humidification. International Heat Mass Transf. 55, 5861–5869.

Zhang, L. Z., 2012. Progress on heat and moisture recovery with membranes, From fundamentals to engineering applications. Energy Conv. Manag. 63, 173-195.

Zhao, H., Shao, L., Chen, J. F., 2010. High-gravity process intensification technology and application. Chem. Eng. J. 156(3), 588-593.

Manuscript ID: 1514
DOI: 10.18462/irr.icr.2019.1514

Analysis on potential to enhance the energy efficiency of inverter air conditioners

Mengdi CUI[(a)], Baolong WANG[(a)], Lianrui DING[(a)], Wenxing SHI[(a)], Xianting LI[(a)]

[(a)] Department of Building Science, Tsinghua University, Beijing, 100084, P.R. China, wangbl@tsinghua.edu.cn

ABSTRACT

The inverter air conditioner has been widely implemented due to higher energy efficiency and better thermal sensation. Because the frequency of the compressor is modulated in a large range according to the variation of the working conditions, the working states of the air conditioner varies a lot. The thermodynamic potential should be analyzed to enhance the annual performance.
In this research, exergy analysis of experimental data is conducted for evaluating the irreversible loss distribution of inverter air conditioners in different operating states, which shows that most exergy loss in low frequency occurs in the evaporator and the compressor. Furthermore, thermal resistance analysis on the evaporator illustrates that the inner thermal resistance is almost equal to the external when it operates in low frequency.
This work clarifies that heat transfer enhancement on the refrigerant side of evaporators is the key to improve the refrigeration efficiency of inverter air conditioners.
Keywords: inverter air conditioner, exergy analysis, evaporator, heat resistance, low-frequency, partial load

1. INTRODUCTION

As one of widely used energy consumers in buildings, the air conditioners have consumed more and more energy. According to statistic data published by International Energy Agency (IEA, 2018), space cooling used about 10% of total electricity globally in 2016. Among types of air-conditioning systems, mini-split air conditioner and multi-split air conditioner shared 77% of total stock capacity end that year. As a typical air conditioner, inverter air conditioners can adjust the operating frequency according to the indoor and the outdoor environments, which leads to a higher energy efficiency and a better thermal comfort than constant speed air conditioner. As a result, the inverter air conditioners are sharing more and more air conditioner market. Further improving the energy efficiency of inverter air conditioners has become an important research topic.
Exergy analysis is an effective methods to identify weak points in energy utilization system. Yumrutaş et al. (2002) obtained the expressions for the exergy losses and pressure losses for the individual processes that make up the vapor compression refrigeration cycle (VCRC). Ahamed et al. (2011) reviewed on the possibilities of researches in the field of exergy analysis in various usable sectors where vapor compression refrigeration systems (VCRS) are used. Recently, exergy analyses on VCRS mostly focus on the rated condition or simulated variable condition (Baakeem et al., 2018) (Rostamzadeh et al., 2018). Less attention has been paid to exergy losses of individual components with varying frequency in the actual operation. In fact, inverter air conditioners operate at low frequency most of time because of the larger selection capacity meeting the need for rapid cooling. For instance, Murakami et al. (2016) illustrated that an invert air conditioner of an ordinary office operated at 50% or less load rate for about 90% of the annual operation time. As we know, the coefficient of performance (COP) of inverter air conditioner does not continuously increase with the decreasing frequency, which illustrates that exergy loss of inverter air conditioners will change with operating frequency. Therefore, in order to investigate the potential to enhance the energy efficiency, the exergy analysis on inverter air conditioners at full operating frequency is urgently needed.

Fin-and-tube heat exchangers are applied to air conditioners generally. Because the heat transfer coefficient (HTC) of two-phase refrigerant is much larger than that of air flow in the rated condition, heat transfer enhancement of air side has been drawing more attention than that of refrigerant side. Especially, the fourth-generation technology utilizing longitudinal vortex generators (LVGs) greatly improves the heat transfer performance of air side (Awais and Bhuiyan, 2018;Li et al., 2015). However, the mass flow of refrigerant decreases with reduced operating frequency, which influences the uniformity of refrigerant distribution among multiple paths. These phenomena both have strong effect on the HTC of refrigerant side. Comparatively, HTC of air flow mainly relies on the airflow rate rather than operating frequency. Consequently, as for inverter air conditioners at the low operating frequency most of time, it is necessary to identify the thermal resistance distribution between the air side and the refrigerant side.

In this paper, the procedures of exergy destruction and thermal resistance is expounded firstly. Then the experiment of the inverter air conditioner is conducted at full operating frequency. Based on the experiment data, exergy loss and thermal resistance are analyzed successively. The results illustrate key points of the potential to enhance the energy efficiency of inverter air conditioners.

2. EXERGY ANALYSIS FOR AIR CONDITIONERS

2.1. Drivers of Exergy Loss in Air Conditioners

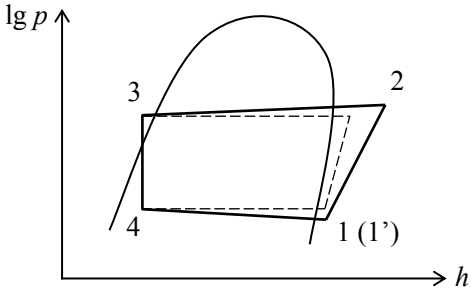

Figure 1: Schematic of VCRC in air conditioner

Based on the VCRC, a common inverter air conditioner consists of a compressor, a condenser, a throttling device, an evaporator and some connecting pipes. Fig. 1 provides the refrigeration cycle on the logarithmic pressure-enthalpy diagram, which comprises the following processes: a) compression (1 → 2) in the compressor: the vapor enters the compressor at state1 and exits with higher temperature and pressure at stage 2; b) heat rejection (2 → 3) in the condenser: when rejecting heat to the ambient air, the vapor at state 2 cools down and condenses to liquid-vapor two-phase flow and leaves the condenser as subcooled liquid at state 3; c) throttling process (3 → 4) in the expansion value: the liquid at state 3 turns into the liquid-vapor mixture at isoenthalpic state 4 with decreasing pressure and temperature; d) heat absorption (4 → 1') in the evaporator: when absorbing heat from indoor air, the liquid-vapor mixture at state 4 evaporates and exits as superheated vapor at state 1'.

Due to the irreversibility of actual process, exergy losses occurs in each process. Compressor loss is from impacts of clearance volume, internal friction, thermal loss, flow drag, etc., which results in the non-isentropic compression process. Evaporator loss and condenser loss mainly derive from the heat transfer with limited temperature difference combined with pressure drop of refrigerant. Throttling process is a typical irreversible process because of mechanical mechanism, which causes entropy generation with isoenthalpic line. Otherwise, exergy loss also occurs in connecting pipes attributing to pressure drop and thermal leakage.

2.2. Exergy Balance Analysis

In order to obtain the quantitative expression of exergy loss, exergy balance analysis is applied to each component based on the principle of exergy-anergy conversion and energy destruction. For the inverter air conditioner, these hypothesizes are taken account of as follows.

a) Refrigerant flow is considered stable and its kinetic energy and potential energy are ignored.
b) The influence of other power consumption components except the compressor on the exergy efficiency of the system is not considered.
c) The ambient state is used as a reference state for the exergy analysis.

Regarding the individual component as the opening system, the exergy balance can be written as

Eq. (1). The exergy carried by refrigerant flow enters the control volume at the inlet. In addition, some external exergy is also input the system. The motor provides electricity for the compressor. As the process is conducted, the system outputs some exergy as the harvest term accompanied by the irreversible exergy loss. Subsequently, the refrigerant leaves the system carrying some exergy:

$$ex_{in} + ex_{ip} = ex_{out} + ex_{op} + \pi_x \quad \text{Eq. (1)}$$

Exergy loss of each component can be derived from Eq. (1). Then, because exergy loss of the whole system consists of separate losses of individual components, exergy efficiency of the whole system and the relative exergy loss of each component can be gotten from Eq. (2) and Eq. (3) respectively.

$$\eta_{ex} = \frac{ex_{op}}{ex_{ip}} = 1 - \frac{\sum \pi_x}{ex_{ip}} \quad \text{Eq. (2)}$$

$$\Omega_x = \frac{\pi_x}{ex_{ip}} \quad \text{Eq. (3)}$$

For instance, as for the compressor, the electricity provided by motor is the input exergy, one part of that is utilized to compress refrigerant vapor and the other is dissipated. Substituting the input exergy into Eq. (1), exergy balance of the compressor can be rewritten as Eq. (4).

$$ex_1 + \frac{P}{M_r} = ex_2 + \pi_{12} \quad \text{Eq. (4)}$$

According to Eq. (4), exergy loss of compressor can be derived as in Table 1. Analogously, exergy balance of other components can be described without input exergy. Especially, the expression of evaporator contains the output exergy term, which is the cooling exergy for the air conditioner. Table 1 presents the exergy loss of individual components derived from exergy balance.

Table 1. Exergy loss expressions of air conditioner

Terms	Quantitative Value	Relative Value
Cooling Exergy	$ex_{q_0}=\left(\frac{T_o}{T_i}-1\right)(h_{1'}-h_4)$	$\eta_{ex}=\frac{ex_{q_0}}{P/M_r}\times 100\%$
Exergy Loss in Compressor	$\pi_{12}=\frac{P}{M_r}-(h_2-h_1)+T_o(s_2-s_1)$	$\Omega_{12}=\frac{\pi_{12}}{P/M_r}\times 100\%$
Exergy Loss in Condenser	$\pi_{23}=h_2-h_3-T_o(s_2-s_3)$	$\Omega_{23}=\frac{\pi_{23}}{P/M_r}\times 100\%$
Exergy Loss in Throttling device	$\pi_{34}=T_o(s_4-s_3)$	$\Omega_{34}=\frac{\pi_{34}}{P/M_r}\times 100\%$
Exergy Loss in Evaporator	$\pi_{41'}=T_o\left(1-\frac{T_e}{T_i}\right)(s_{1'}-s_4)$	$\Omega_{41'}=\frac{\pi_{41'}}{P/M_r}\times 100\%$
Exergy Loss in Other Components	$\pi_{oth}=\frac{P}{M_r}-ex_{q_0}-\Sigma\pi$	$\Omega_{oth}=\frac{\pi_{oth}}{P/M_r}\times 100\%$

3. THERMAL RESISTANCE ANALYSIS FOR HEAT EXCHANGER

The total thermal resistance of the fin-and-tube heat exchanger is composed of refrigerant-side resistance, tube wall resistance, dirtiness resistance, thermal contact resistance and air-side resistance. Eq. (5) indicates the correlation between the total resistance and the separate resistance concisely. In order to analyze the distribution of the thermal resistance, the separation from different sides is a necessary approach.

$$R_{tot} = R_{ref} + R_{wal} + R_{dir} + R_{con} + R_{air} \quad \text{Eq. (5)}$$

3.1. Method of Thermal Resistance Separation

Because of the complexity of the convective heat transfer and the phase change heat transfer, the HTC are mainly obtained from experimental correlation equations. Especially for the two-phase flow, the HTC depends on numerous variable factors that are difficult to measure directly such as flow pattern, quality, etc. Furthermore, the mass flow of refrigerant will change with the variable operating frequency, which impacts on the refrigerant distribution among paths.

In this research, thermal resistance separation is conducted based on the experimental data. Firstly, some key data can be acquired from experiment, such as state parameters of refrigerant, air temperature, airflow rate, heat exchange capacity, etc. Then, logarithmic mean temperature difference (LMTD) method is adopted to calculate total thermal resistance and air-side thermal resistance. Finally, the data reduction of refrigerant-side thermal resistance can be realized based on the composition of thermal resistance as presented Eq. (5).

3.2. Data Reduction for Thermal Resistance

In order to discover characteristics at variable operating frequency, the main thermal resistance is emphasized neglecting the slight parts. Several hypotheses are considered as following.

a) Thermal contact resistance is ignored because the tube expanding process was applied to the fin-and-tube heat exchanger.
b) Dirtiness resistance is slight enough to be neglected because the inverter air conditioner is new utilized in the test and the dust removal function was attached to that.
c) Compared with the tube wall resistance, the refrigerant-side resistance and the air-side resistance account for a quite larger proportion of the total thermal resistance.

For the fin-and-tube heat exchanger, the total LMTD can be separated into the internal part and the external part. If the refrigerant is saturated in the tube, the separation for dry condition is conducted following Eq. (6) ~ Eq. (8):

$$R_{tot} = \frac{\left[\left(t_{air,in} - t_{ref,out}\right) - \left(t_{air,out} - t_{ref,in}\right)\right] \Big/ \ln\left[\left(t_{air,in} - t_{ref,out}\right) \Big/ \left(t_{air,out} - t_{ref,in}\right)\right]}{\Phi} \quad \text{Eq. (6)}$$

$$R_{air} = \frac{\left[\left(t_{air,in} - t_{wo,out}\right) - \left(t_{air,out} - t_{wo,in}\right)\right] \Big/ \ln\left[\left(t_{air,in} - t_{wo,out}\right) \Big/ \left(t_{air,out} - t_{wo,in}\right)\right]}{\Phi} \quad \text{Eq. (7)}$$

$$R_{ref} = R_{tot} - R_{air} \quad \text{Eq. (8)}$$

For the dewing condition, Threlkeld method (Wang et al., 2007) is adopted to analyze the thermal resistance of fin-and-tube heat exchangers, which proposed the logarithmic mean enthalpy difference method. The temperature in LMTD is replaced to the equivalent enthalpy. The equivalent enthalpy of tube wall equals to the saturated air enthalpy at the wall temperature. Analogously, the equivalent enthalpy of refrigerant is ascertained based on the refrigerant temperature.

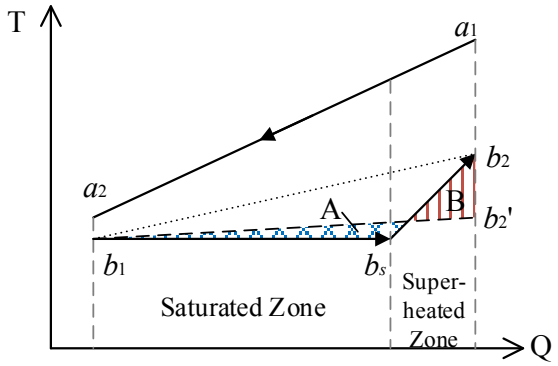

Figure 2: Correction schematic for refrigerant temperature in superheated condition

If the superheated state occurs in the evaporator, the refrigerant temperature at outlet of the tube in the LMTD should be corrected, otherwise the total thermal resistance would be smaller than the actual value as shown in Fig. 2. In detail, the calculated refrigerant temperature at the outlet is ascertained according to the principle of equal area in the T-Q diagram. When the area of shaded zone A equals to that of shaded zone B, the calculated outlet temperature is located on b_2'.

4. ACTUAL MEASUREMENT FOR INVERTER AIR CONDITIONER

4.1. Test System for Actual Measurement

The actual operating performance of the inverter air conditioner typed KFR-26 was tested in the air enthalpy difference laboratory. In order to acquire the characteristic parameters of refrigeration cycle, key measuring points were selected at the inlets and outlets of several main components. The specific layout of measuring points is shown in Fig. 3.

The WTP program was used for testing, which meant testing the power of the compressor, the temperature and pressure of each measuring point, the mass flow of circulating refrigerant, air flow through the evaporator. In order to acquire the actual state parameters of refrigerant, drop-in pressure sensors were installed at the inlets and outlets of compressor and condenser respectively. To avoid leakage of refrigerant, temperature sensors were stuck on the tube wall. Therefore, temperatures of refrigerant can be corrected based on the difference between the tube wall temperature and the saturation temperature corresponding to the pressure in the two-phase region.

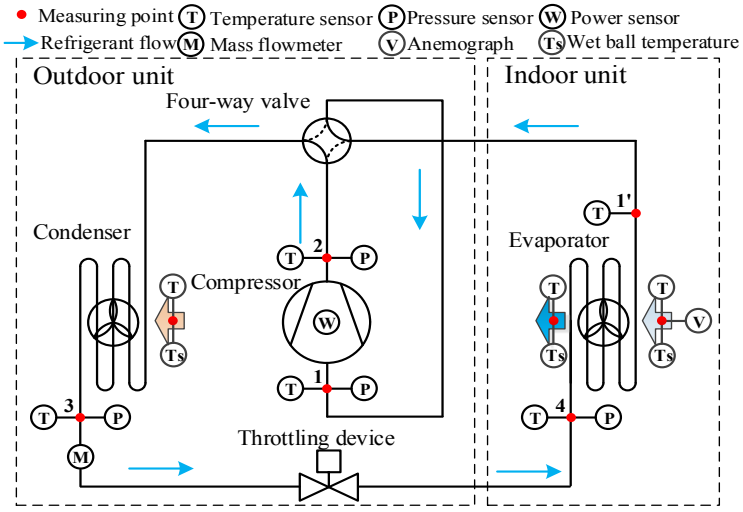

Figure 3: Test system diagram

4.2. Test Condition

In actual operation, the operating frequency depends not only on the operating condition, but also on the cooling load. It is hard to acquire the accurate relation between the operating frequency and the operating condition. In addition, exergy value changes with the variable ambient temperature. Therefore, in order to illustrate characteristics with variable operating frequency, a constant operating condition was selected. The indoor dry / wet bull temperature is 27 / 19 ℃ and the outdoor dry / wet bull temperature is 35 / 24 ℃. At the constant operating condition, the operating frequency was locked every 10Hz from 80Hz to 10Hz. When the inverter air conditioner operated at steady states, the test data would be recorded.

5. RESULTS AND DISCUSSION

5.1. Exergy Loss Distribution

Fig. 4 presents the distribution of exergy loss among the main components. As operating frequency reduces, the total exergy loss and individual exergy loss decreases except the state at 10 Hz, which reflects the decreasing energy consumption with the reduced cooling demand. The increasing evaporating temperature and the decreasing condensing temperature lead to the reduced pressure ratio, compressor loss and throttling loss. Furthermore, heat transfer losses of heat exchangers also decrease because of the decrescent heat transfer temperature difference. Pressure losses of heat exchangers diminish with the decreasing mass flow of refrigerant. For the state at 10 Hz, very low operating frequency leads to the wet compression, which deteriorates the compression efficiency.

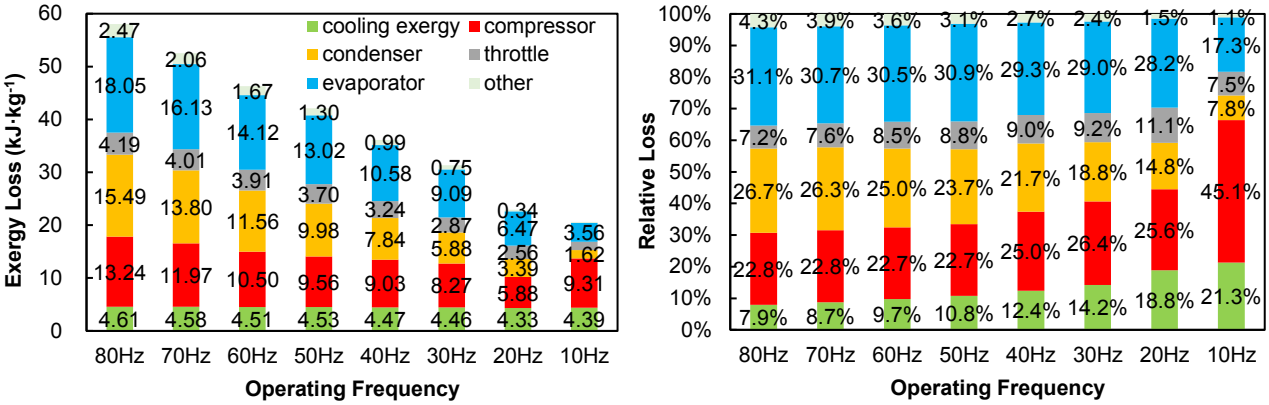

Figure 4: Distribution of exergy loss among different components

As for the relative loss, most of the exergy loss occurs in the compressor, the evaporator and the condenser. Moreover, the compressor loss proportion gradually increases with the reduced operating frequency when the operating frequency is lower than 50 Hz. Compared with the useful work, effects of exhaust loss, internal dissipation, and motor loss largen, which leads to the compressor loss ratio increases. For the evaporator, it is worth noting that the loss ratio just decreases a little except the state at 10 Hz. This is because mass flow of refrigerant decreases, which leads to the HTC decreases. The bad factor weakens the benefit of the decreasing temperature difference between the inside and the outside in the evaporator. The similar effect also happens in the condenser. However, when the operating frequency reduces, the condenser loss ratio decreases significantly. When the frequency is as low as 20 Hz, the condenser loss ratio is lower than 15%, which is the result of the slighter impact on the condensation process of refrigerant vapor compared with the evaporation process. Therefore, the compressor and the evaporator are the main components of exergy loss at low frequency.

5.2. Thermal Resistance Distribution

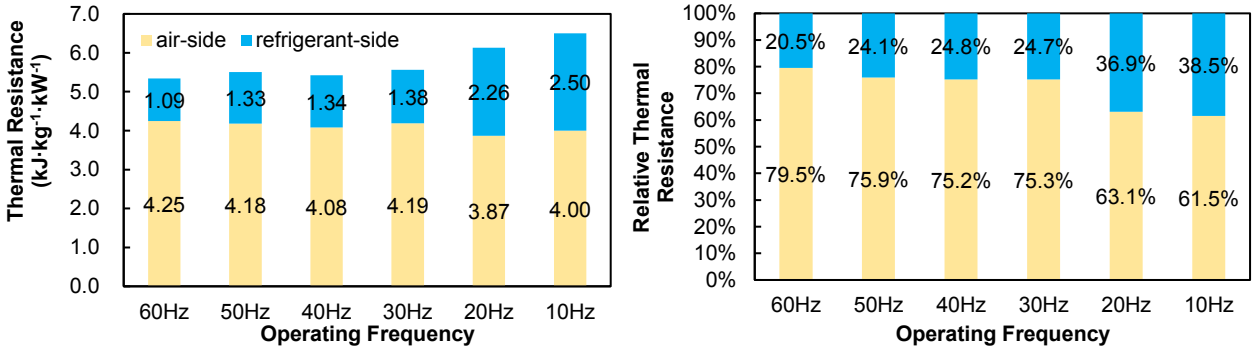

Figure 5: Distribution of thermal resistance of the evaporator

Fig. 5 presents the distribution of thermal resistance of the evaporator between the air-side and the refrigerant-side. When the operating frequency is as high as 60 Hz, the thermal resistance ratio between the air-side and the refrigerant-side is close to 8:2, which is accordant with the commence sense for the fin-and-tube heat exchanger. However, the thermal resistance proportion of the refrigerant-side obviously increases with the reduced operating frequency. At the very low frequency, for instance, the refrigerant-side proportion is close to 40% at 10 Hz. First, the decreasing mass flow of refrigerant deteriorate the HTC of the convective evaporation. Second, the maldistribution of refrigerant between two paths gets obvious as presented in Fig. 6. The temperature difference between two refrigerant paths of the evaporator and the condenser were respectively recorded. Compared with the condenser, the temperature different of the evaporator obviously increase at 30 Hz, which is because the very small mass flow impacts on the distribution of two-phase refrigerant between these two paths. Instead, the steep dropping temperature difference of the condenser illustrates that the one path is at two-phase state and the other path is at subcooled state when the operating frequency is high enough. When the operating frequency is lower than 50 Hz, the mass flow of refrigerant is small enough to make the subcooled states both in these two paths.

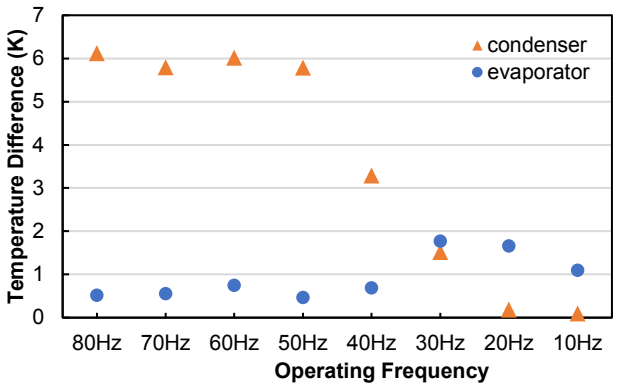

Figure 6: Temperature difference between two refrigerant paths

6. CONCLUSION

In this work, the actual measurement was conducted in a wide range of variable operating frequency. Exergy loss distribution among several main components and thermal resistance of the evaporator both change with the operating frequency. The following conclusions are revealed:

a) At low or very low operating frequency, most of exergy loss occurs in the compressor and the evaporator. Compared with the condenser, the evaporator should be taken more attention to enhance the energy efficiency of the inverter air conditioner.

b) When the operating frequency decreases, the refrigerant-side thermal resistance increases rapidly. At low or very low frequency, the refrigerant-side thermal resistance is even equal to the air-side thermal resistance. Therefore, internal heat transfer enhancement for the evaporator at low operating frequency is the potential to improve the performance of the inverter air conditioner.

ACKNOWLEDGEMENTS

This research was funded by the China National Key R&D Program “Solutions to Heating and Cooling of Buildings in the Yangtze River Region” (Grant No. 2016YFC0700304).

NOMENCLATURE

ex	exergy, ($kJ \cdot kg^{-1}$)
h	specific enthalpy of refrigerant, ($kJ \cdot kg^{-1}$)
M_r	mass flow of refrigerant, ($kg \cdot s^{-1}$)
P	input power of compressor, (kW)
R	thermal resistance, ($k \cdot W^{-1}$ or $℃ \cdot W^{-1}$)
s	specific entropy of refrigerant, ($kJ \cdot kg^{-1} \cdot K^{-1}$)
T	temperature, (K)
t	temperature, (℃)
Greek symbols	
η_{ex}	exergy efficiency
π	exergy loss, ($kJ \cdot kg^{-1}$)
Φ	heat exchange capacity, (W)
Ω	relative value of exergy loss
Subscripts	
12	compression process
23	condensation process
34	throttling process
41’	evaporation process
air	air-side
i	indoor
in	inlet
ip	input
o	outdoor
op	output
oth	connection lines
out	outlet
q_0	cooling capacity
ref	ref-side
wo	outside wall of the tube
tot	entirety
dir	Dirtiness-side
con	Thermal-contact-side
wal	Wall-side

REFERENCES

Ahamed, J.U., Saidur, R., et al., 2011. A review on exergy analysis of vapor compression refrigeration system. Renew. Sust. Energy Rev. 15, 1953-1600.

Awais, M., Bhuiyan, A.A., 2018. Heat transfer enhancement using different types of vortex generators (VGs): A review on experimental and numerical activities. Therm. Sci. Eng. Prog. 5, 524-545.

Baakeem, S.S., Orfi, Jamel., et al., 2018. Optimization of a multistage vapor-compression refrigeration system for various refrigerants. Appl. Therm. Eng. 136, 84-96.

IEA, 2018. The future of cooling: opportunities for energy-efficient air conditioning. International Energy Agency (IEA), Paris, 21-23 p.

Li, L., Du, X.Z., et al., 2015. Numerical simulation on flow and heat transfer of fin-and-tube heat exchanger with longitudinal vortex generators. Int. J. Therm. Sci. 92, 85-96.

Murakami, Y., Kitaura, H., et al., 2016. High efficiency inverter scroll compressors. 23rd International Compressor Engineering Conference, Purdue University, USA, 1081(1)-1081(6).

Rostamzadeh, H., Rostamzadeh, J., et al., 2018. Novel dual-loop bi-evaporator vapor compression refrigeration cycles for freezing and air-conditioning applications. Appl. Therm. Eng. 138, 563-582.

Wang, C.C., 2007. Heat Transfer Design. Wunan Book Publishing co. LTD, Taipei, 204-221 p.

Yumrutas, R., Kunduz, M., et al., 2002. Exergy analysis of vapor compression refrigeration systems. Int. J. Exergy 2, 266-272.

Manuscript ID: 1538
DOI: 10.18462/iir.icr.2019.1538

Two stage high speed centrifugal blower flow characteristics via CFD simulation

Wun-Huei Chih[(a)], Kuo-Shu Hung[(b)], Yean-Der Kuan[(a)], Huang-En Lin[(a)], Jeng-Min Huang[(b)], Chung-Che Liu[(b)]

[(a)]National Chin-Yi University of Technology, Taichung City, 41170, Taiwan

ydkuan@ncut.edu.tw , jmh@ncut.edu.tw ,

s4a716002@student.ncut.edu.tw , s4a616002@student.ncut.edu.tw

[(b)]Industrial Technology Research Institute, Hsinchu, 31057, Taiwan

kshung@itri.org.tw, CCLiu@itri.org.tw

ABSTRACT

As the demand significantly increases in diversified applications, the development of high performance higher speed centrifugal blowers has reached urgency. Therefore, to understand the flow behaviour inside the blower becomes very important in the design stage. In order to reach a higher pressure ratio, the two stage centrifugal blower is desired. This paper adopts transient computational fluid dynamics (CFD) software with the sub-grid geometry resolution (SGGR) technique to predict the pressure-air flowrate (P-Q) curve of a two stage high speed centrifugal blower. The axial work as well as the corresponding efficiency based on the CFD results are also calculated and obtained. As the flow inside a high speed blower would be highly unstable, the design should avoid the circulation occurring inside the blower. In addition, the matching between the first and second stage also plays an important role. The CFD simulation could provide clear observation of the flow behavior which could help to improve the design and increase the blower performance.
Keywords: Centrifugal Blower, Energy Efficiency, Mass Flow Rate, Pressure Ratio

1. INTRODUCTION

This study uses CFD software to probe into the internal flow behaviour of a high-speed blower. As the fluid motion behaviour is closely bound up with the efficiency of blower, the flow behaviour of fluid in the blower can be observed clearly by using CFD simulation software (Benini and E and Toffolo,2003).

Two-stage pressure is used in this study to increase the blower pressure ratio. However, matching Stage 1 and Stage 2 in a multistage pressure blower is very important (Clements et al,1987). The data from Stage 1 are closely related to the Stage 2 boundary conditions. If the internal flow field of the first stage blower is unstable, the two-stage operation will be unstable accordingly. If the behaviours of Stage 1 and Stage 2 can be known using the CFD simulation, the blower operating range can be identified. In addition, this study follows the development planning of previous blower model generations. The blower operating range and efficiency are increased by geometric changes. The flow effect on the whole blower can be known using CFD simulation. The whole flow field is steadiest at the design point and the efficiency is the best. When the flow decreases from the design point, the flow field remains stable within certain limits. Recirculating flow is generated after the range is exceeded. The recirculating flow consumes internal energy; the efficiency is reduced, leading to a surge. Once the surge occurs the blower is severely damaged. Therefore, the blower operating flow range is obtained by simulation, preventing the surge phenomenon (Rainer Kurz, 2016), which is helpful to future experiments to some extent.

2. MAIN SECTION

2.1. Research Method

In the fluid machinery development process, the efficiency, flow work and shaft work are the foremost design reference frame. To know whether the blower design is superior or not the outlet/inlet temperature, outlet/inlet pressure and inlet air volume are monitored in CFD software to work out the flow work (Siva Reddy et al,2005), shaft work and efficiency.

Pressure ratio (P_r):

$$P_r = P_{out}/P_{in} \quad \text{Eq. (1)}$$

Flow power (W_{flow}):

$$W_{flow} = \frac{k}{k-1} * P_{in} * \dot{Q}_{in} * \frac{1}{60} * \left(P_r^{k-1/k} - 1\right) \quad \text{Eq. (2)}$$

The W_{flow} herein is flow power, the unit is watt, P_{in} is the inlet pressure, the unit is pascal, $\dot{Q}_{in}$ is the inlet air volume, the unit is CMM, k: gas constant, the gas constant of air is 1.4

Shaft power P_t:

$$P_t = 2 * \pi * N * \frac{1}{60} * Torque \quad \text{Eq. (3)}$$

P_t is the shaft power (w) of fluid machinery, N is the speed, the speed is 185000rpm in this study, the Torque unit is N-m.

Efficiency (η_b):

$$\eta_b = W_{flow}/P_t \quad \text{Eq. (4)}$$

However, the design in this study is a two-stage pressure blower. The boundary conditions of the second stage pressure must depend on the simulated outlet temperature and outlet pressure of the first stage. Therefore, the first stage pressure data must be relatively precise. The error must be reduced as much as possible. In the CFD simulation the grid analysis is performed under Stage 1 full load, the data errors are compared for grid selection.

2.2. General description of model

In this study, the blower uses two-stage pressure technique, the pressure ratio of blower is increased. However, this blower is designed as back to back design in this study, two rotors can be strung by one bearing, the duplex bearing mechanical equipment is not required. Therefore, one-forward one-backward design is used, Stage 1 rotates anticlockwise, and Stage 2 rotates clockwise. The results are shown in figure3-5.

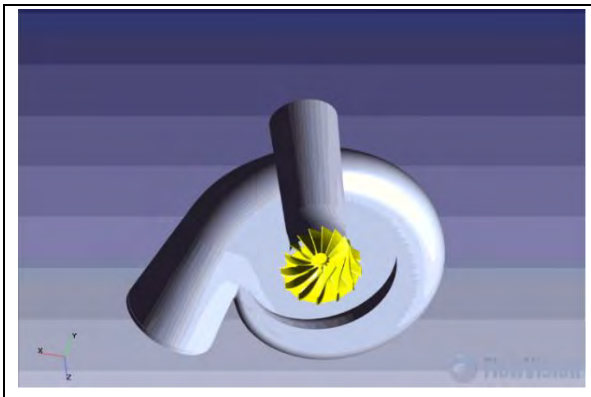

Figure 1a: First stage compressor model

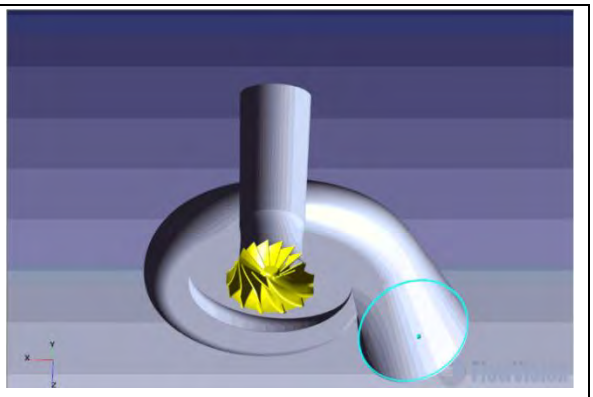

Figure1b: Second stage compressor model

2.3. Establishment of boundary conditions

This study reduces the flow in turn according to the percentage of mass flow rate, till the flow field of blower has surge flow. The CFD simulation is stopped in this interval. The boundary conditions of the second stage blower are the monitored values of the first stage blower.
Boundary conditions of the first stage blower in this study:

Speed:18500rpm
Initial ambient temperature: 293k
Initial ambient pressure: one atm
Inlet pressure: -825Pa
Turbulence model : k-εmodel
Wall: wall function
Step number :4000
Software: Flowvision

Mass flow rate: 2.16kg/s (100%), 1.944kg/s (90%), 1.728kg/s (80%), 1.512kg/s (70%), 1.296kg/s (60%), 1.08kg/s (50%), 0.864kg/s (40%) Grid building and analysis.

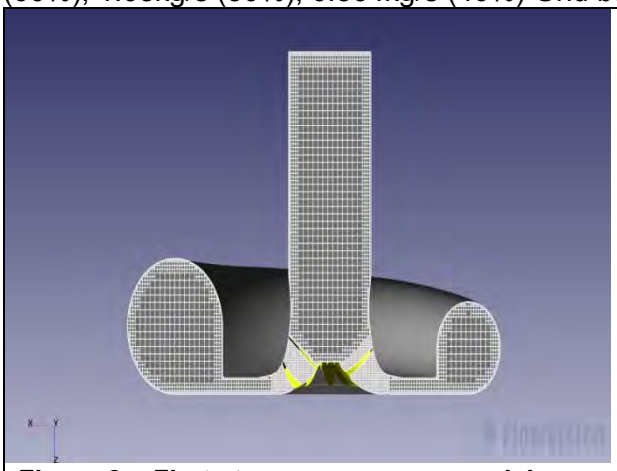

Figure 2a: First stage compressor model

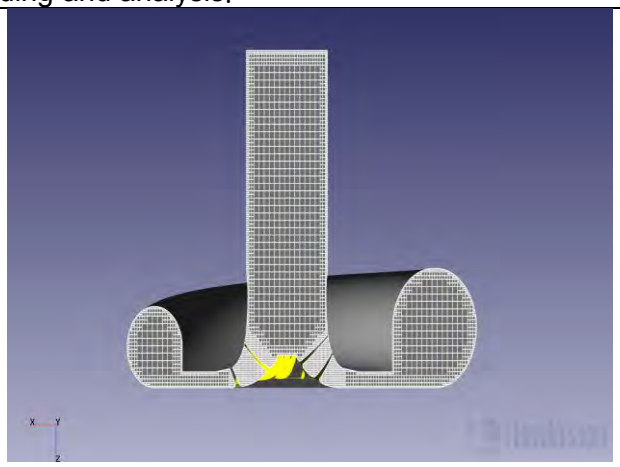

Figure 2a: Second stage compressor model

2.4. Simulation results and analysis

2.4.1. First stage blower

The influence of flow on the whole blower can be known by simulation. When the flow decreases from the mass flow rate 1.512kg/s (70%), a little small recirculating flow occurs at the upper end of the vaneless diffuser. however, the impeller rotation is not influenced. The backwash is not detected in the impeller part, so the impeller flow and shaft work are not influenced. There is little influence on the blower efficiency. However, when the mass flow rate is 1.296kg/s (60%), a part of fluid on one side of impeller has surged back to the rotating rotor region. The blower pressure ratio is increased slightly, but some fluid is found unable to flow out of the blower. This may be close to the surge flow point. As expected, at mass flow rate 1.08kg/s (50%), the blower pressure ratio drops immediately and the impeller region backwash phenomenon becomes very apparent. Therefore, this blower is in the range of 1.296-2.16kg/s (60%-100%) in the first stage blower simulation. As the flow field remains stable the surge flow occurs out of the range, adverse to the blower operation.
The CFD simulation data of the first stage blower are monitored in the simulation process, including outlet/inlet pressure, outlet/inlet air volume, outlet temperature and torque. The boundary conditions of Stage 2, pressure ratio, mechanical power of fluid, shaft power and efficiency are obtained from the aforesaid monitoring data. The results are shown in figure3-5.

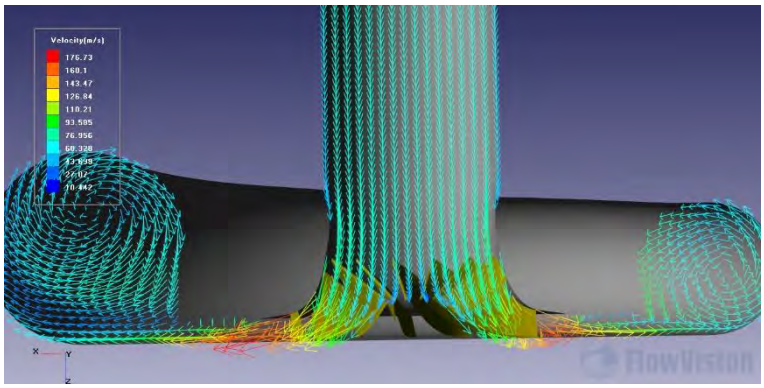

Figure 3: mass flow rate 1.512kg/s (70%) flow phenomenon

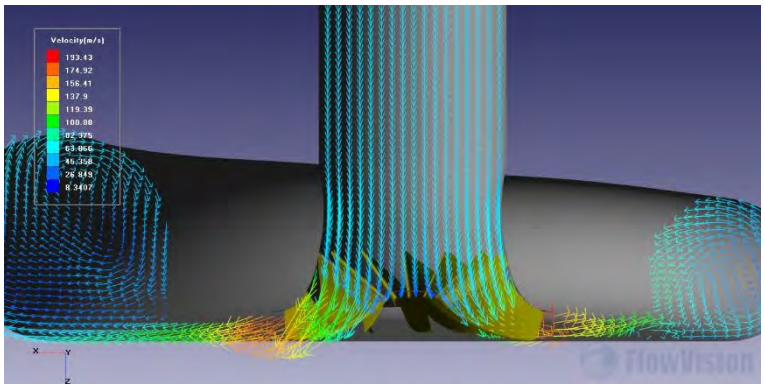

Figure 4: mass flow rate 1.296kg/s (60%) flow phenomenon

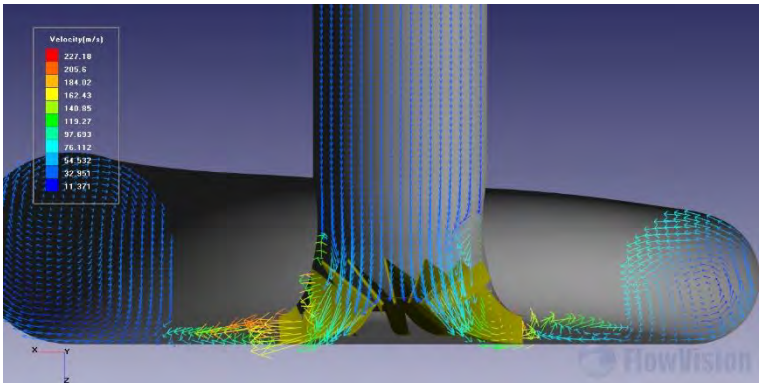

Figure 5: mass flow rate 1.08kg/s (50%) flow phenomenon

2.4.2. Second stage blower

Following the simulated data of Stage 1, the monitored outlet temperature and outlet pressure of Stage 1 are set as the boundary conditions of the second stage blower, so as to implement two-stage pressure. The ambient temperature is also set as 293k, the atmospheric pressure is set as the CFD software set value which is one atm. The results are shown in Table 1

Table 1. Second stage blower inlet boundary condition

Simulation result	100%	90%	80%	70%	60%
Inlet Pressure (Pa)	125785.4	128250.4	130674.4	134374.3	135099.5
Inlet Temperature(k)	299.3	300.89	301.37	304.19	305.28

As the second stage compressor operation is limited to the flow at the first stage surge flow point, the mass flow rates are 2.16kg/s (100%), 1.944kg/s (90%), 1.728kg/s (80%), 1.512kg/s (70%), 1.296kg/s (60%).

According to the Stage 2 simulation flow phenomenon, when the mass flow is 1.296-2.16kg/s (60%-100%), the pressure ratio increases as the fluid mass flow rate decreases. Since the mass flowrate of 1.08 kg/s (50%) was already evaluated in the first stage, it is unnecessary to test the lower flow rate. However, when the partial mass flow rate of the second stage was 1.296 kg/s (60%) the turbulent flow phenomenon does not occur. From the first and second stage simulation results, it's safe to conclude that the two stage compressor mass flowrate is 1,295 kg/s (60%) and the most efficient, in which the blower operation is safer. The results are shown in figures 6-8.

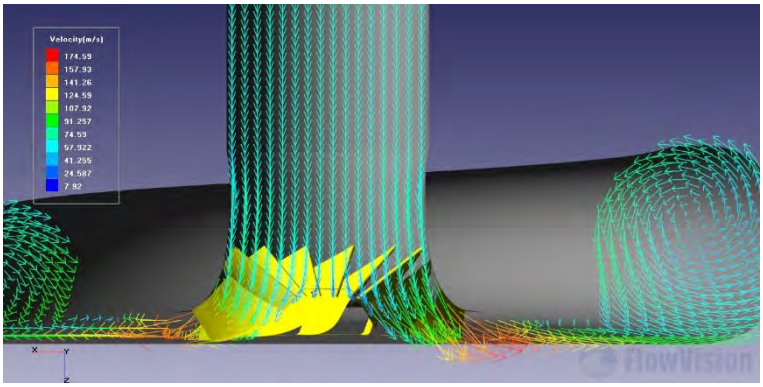

Figure 6: mass flow rate 1.728 kg/s (70%) flow phenomenon

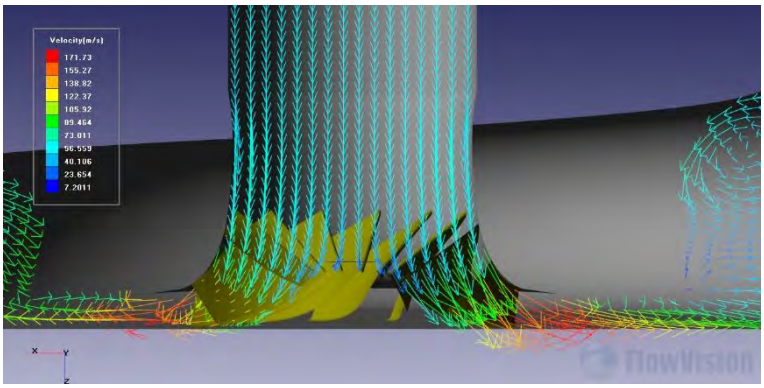

Figure 7: mass flow rate 1.512kg/s (70%) flow phenomenon

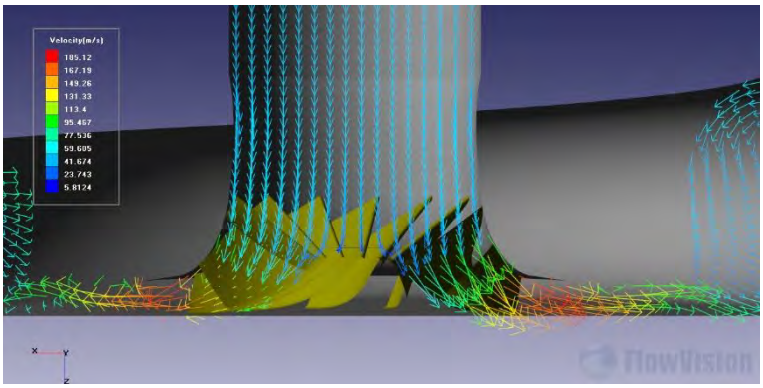

Figure 8: mass flow rate 1.296kg/s (60%) flow phenomenon

2.5. Results Analysis

The pressure ratio, flow work, shaft work and efficiency of each blower stage are calculated according to the aforesaid equation. However, this blower is a two-stage blower. The pressure ratio of this blower must be calculated using Eq. (4). The results are shown in Table 2 and figures 4-6. Overall Pressure ratio ($P_{r,total}$)

$$P_{r,total} = P_{r1} * P_{r2} \quad \text{Eq. (5)}$$

Table 2. Look-up table for pressure ratios corresponding to various blower stages and mass flow rates

Pressure ratio / Mass flow rate	First stage Pressure ratio	Second stage Pressure ratio	Overall Pressure ratio
2.16kg/s (100%)	1.257	1.255	1.578
1.944kg/s (90%)	1.281	1.284	1.646
1.728kg/s (80%)	1.306	1.303	1.702
1.512kg/s (70%)	1.342	1.321	1.772
1.296kg/s (60%)	1.349	1.336	1.802
1.08 kg/s (50%)	1.326		

In this equation, η_{b1} and η_{b2} are the efficiency of Stage 1 and Stage 2 respectively, the two efficiencies are multiplied to obtain the total efficiency of this blower. The overall Pressure ratio is expressed as Eq. (5). The mass flow rates are compiled in Table 3.

$$\eta_{total} = (W_{flow,total}/(P_{t1} + P_{t2}) \quad \text{Eq. (6)}$$

Table 3. Look-up table for efficiencies corresponding to various blower stages and mass flow rates

Efficiency / Mass flow rate	Efficiency of Stage 1	Efficiency of Stage 2	Total efficiency
2.16kg/s (100%)	81.93%	85.85%	82.02%
1.944kg/s (90%)	82.34%	86.38%	83.64%
1.728kg/s (80%)	84.47%	85.56%	85.93%
1.512kg/s (70%)	85.40%	85.65%	83.42%
1.296kg/s (60%)	81.01%	85.80%	78.38%
1.08 kg/s (50%)	60.40%		

According to the total efficiency and overall pressure ratio in the data of Stage 1 and Stage 2, the best efficiency point of this first stage blower occurs at mass flow rate 1.512-1.728kg/s (70-80%), that of Stage 2 occurs at 1.944-2.16kg/s (90-100%). The best efficiency point of this second stage blower is in the mass flow rate interval 1.512-1.728kg/s (70-80%). The total efficiency in the interval is 72.27-73.15%, and the pressure ratio exceeds the design value 1.7. Therefore, the operation in this interval is the steadiest and the efficiency is the highest. Figures 9-11 show the overall characteristic curves of Stage 1 and Stage 2 respectively.

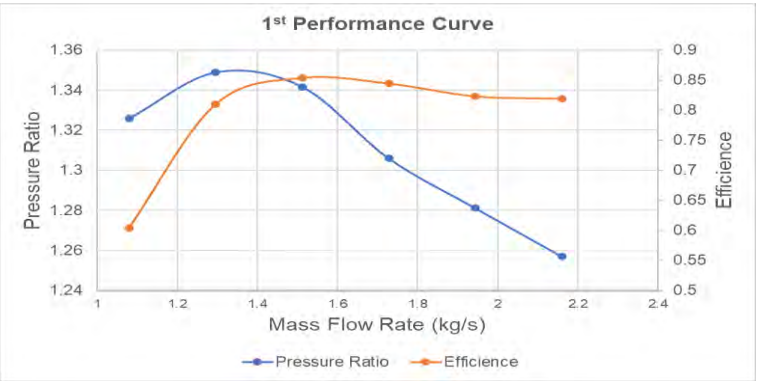

Figures 9: 1st performance curve

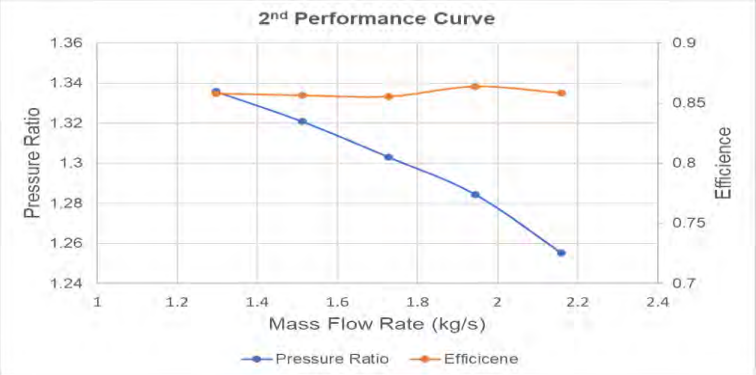

Figures 10: 2nd performance curve

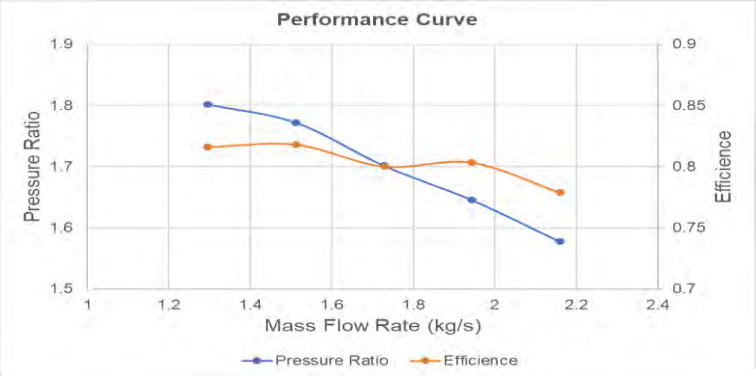

Figures 11: Total performance curve

3. CONCLUSIONS

The blower performance was simulated successfully using CFD software. This study proposed some improvement guidelines for the research subject. If a runner can be built to connect the outlet of Stage 1 to the inlet of Stage 2, the boundary conditions between Stage 1 and Stage 2 are set. The simulated data are closer to real data, and the man-induced record carry is unlikely to influence the simulation result. In addition, the CFD simulation shows that the outlet temperature of the second stage blower is relatively high. In some cases with requirements for temperature, the outlet temperature of this blower may be inapplicable. However, this problem can be solved by placing an intercooling system between Stage 1 and Stage 2.

In addition, the fluid surge flow points of Stage 1 and Stage 2 were determined using CFD simulation successfully in this study. The blower operating flow range and matching degree were obtained and the surge phenomenon prevented. For the blower, the machine body can be protected using system protectors to prevent human negligence or accidents from influencing the blower operation. The

operating efficiency point of this blower is known by the blower characteristic curve. The results of this study can provide a good reference frame for future blower improvement or design.

ACKNOWLEDGEMENTS

The authors sincerely appreciate for the financial support from the Industrial Technology Research Institute's under the project number: A06903022.

REFERENCES

Benini, E. and Toffolo, A.2003, Centrifugal compressor of a 100 kW micro turbine: Part 2 - Numerical study of impeller-diffuser interaction, American Society of Mechanical Engineers International Gas Turbine Institute, Turbo Expo (Publication) IGTI, p 699-705

Clements, W. and Artt, D. W.,1987, Performance prediction and impeller diffuser matching for vaneless diffuser centrifugal compressor, I.Mech E Conference Publications, Institution of Mechanical Engineers), 1987, p 183-198

Sato, T, Oh, J.M.; 2005, experimental and numerical investigation of the flow in a vaneless diffuser of a centrifugal compressor stage. Part 1: Experimental investigation, Proceedings of the Institution of Mechanical Engineers, Part C: Journal of Mechanical Engineering Science, p 1053-1059

Siva Reddy, T.C.,2005, Some studies on low solidity vaneless diffusers of a centrifugal compressor stage, Proceedings of the ASME Turbo Expo, v 6 PART B, Proceedings of the ASME Turbo Expo 2005, p917-925

Manuscript ID: 1566
DOI: 10.18462/iir.icr.2019.1566

Performance investigation of a fresh air pre-handling system integrated with pipe-embedded envelopes by utilizing shallow geothermal energy

Weihua Lyu, Xianting Li*, Shuai Yan

Department of Building Science, School of Architecture, Tsinghua University
Beijing, 100084, China, e-mail: xtingli@tsinghua.edu.cn

ABSTRACT

Traditionally, shallow geothermal energy is utilized by ground source heat pump. Actually, the temperature of shallow geothermal energy is much suitable for the cooling/heating of the building envelope and fresh air in most of time. To utilize shallow geothermal energy more efficiently, an integrated system combined pipe-embedded walls, pipe-embedded windows, and fresh air pre-handling system is proposed based on the temperature comparison among the indoor air, envelopes, fresh air and the undisturbed soil. The simulation model of the integrated system is developed on the platform of TRNSYS. The free-running temperature of the integrated system applied in an office building in Shanghai is investigated. The results show that the free-running temperature of the integrated system is always higher than 15 °C throughout the year, the free-running temperature that higher than 30 °C accounts for a fewer ratio and the non-air conditioning period extends approximately 20% compared with the conventional GSHP system.
Keywords: Shallow Geothermal Energy, Free-Running Temperature, Pipe-Embedded Envelope, Fresh Air Pre-Handling, Building Energy Efficiency.

1. INTRODUCTION

Shallow geothermal energy, as a renewable energy, is popular in the HVAC field. At present, the ground source heat pump (GSHP) system has been regarded as an energy efficient way of utilizing shallow geothermal energy. In the conventional application, the ground heat exchanger (GHX) is always integrated with a heat pump unit to generate high-grade hot water or chilled water for space heating and cooling (Bakirci, 2010; Soni et al., 2016; Sivasakthivel, et al., 2017). Though the GSHP system has been widely used to build the energy efficient HVAC system (Aikins and Choi, 2012), the energy consumption of GSHP system is still at a relatively high level. The good characteristic of shallow geothermal energy, i.e., warm in winter and cold in summer, has not yet fully been utilized by the GSHP system.

In fact, the temperature of shallow geothermal energy is much suitable for the cooling and heating of envelopes and fresh air in most time of a year. Taking the temperature ranges in Beijing as an example, the temperature relationship of the soil with indoor and outdoor temperature is clearly described in Figure1. The differences between the soil temperature and outdoor fresh air temperature as well as the envelope temperature are much larger than that between soil and indoor temperature. According to Manz (2004), the temperature of the blinds in a traditional double glass window can be heated to 60 °C by absorbing solar radiation. The larger temperature difference should benefit a more efficient utilization of shallow geothermal energy. Unfortunately, the larger temperature differences have not yet been fully exploited. Moreover, the large temperature differences between the soil and outdoor fresh air as well as the envelope also can be utilized for heating. As shown in Figure1, the temperature difference between the soil and the fresh air temperature would be larger than 20 °C in most time of the heating season. That means shallow geothermal energy can also have great potential of direct utilization in winter. Therefore, the shallow

geothermal energy should be preferred to eliminate the building load caused by building envelopes and the fresh air.

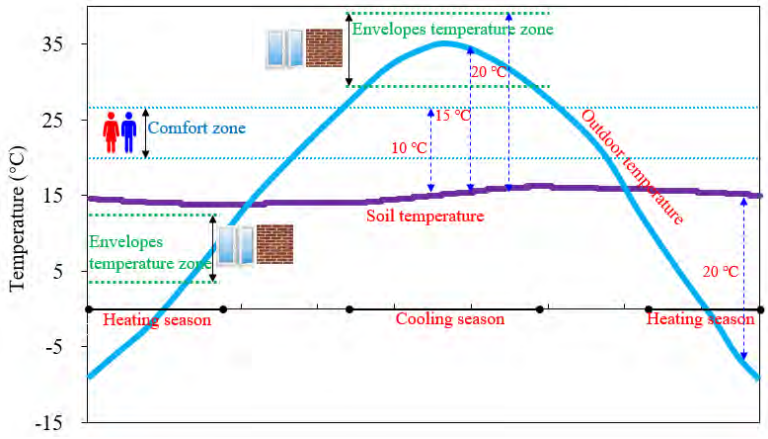

Figure 1: Temperature relationship between soil and ambient conditions

Based on analyzing the temperature relationship between indoor air, building envelope, fresh air and the stable soil, an integrated system that can utilize shallow geothermal energy more efficiently is proposed in this study. The integrated system combines pipe-embedded walls, pipe-embedded windows, and the fresh air pre-handling system. To demonstrate the capability of the integrated system, the simulation model of the integrated system is built on the platform of TRNSYS. The free-running temperature is calculated, based on which the non-air conditioning extension ratio is obtained by comparing with the conventional building.

2. PRINCIPLE OF THE INTEGRATED SYSTEM

The schematic of the integrated system is shown in Figure 2. The integrated system includes a sub-system of pipe-embedded walls, a sub-system of pipe-embedded windows, and a sub-system of fresh air pre-handling. The air-water heat exchanger (AWHX) is fixed in the air handling unit (AHU) for the pre-handling of fresh air. The water inlets of pipe-embedded walls, pipe-embedded windows, and the AWHX are connected with the distributor. The water outlets of them are connected with the collector. Therefore, the outlet water of the GHX can be delivered to these three parts based on the control strategies.

With the effects of pipe-embedded walls, pipe-embedded windows and the fresh air pre-handling system, the free-running temperature of the room may be maintained at the comfortable zone without turning on the conventional air conditioning system. The non-air conditioning period is calculated according to the simulation of free-running temperature. The non-air conditioning period refers to the comfortable period that the conventional air conditioning system does not need to operate. When the free-running temperature cannot meet the thermal comfort, the conventional air conditioning system will be turned on to remove the rest building load.

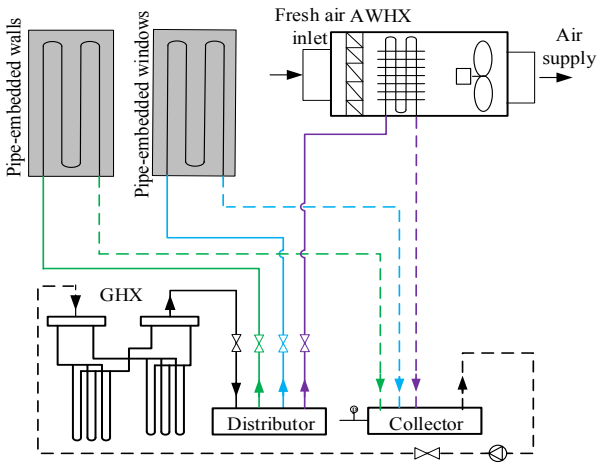

Figure 2: Schematic of the integrated system

3. METHODS

To investigate the performance of the integrated system, the system model is built based on a case study of an office building in Shanghai, China. These models of the key components and the evaluation indexes are interpreted briefly in this section.

3.1. Building Outlines

A three-story office building in Shanghai is chosen as the serviced object of the integrated system. The building is 40 meters long from north to south, 10 meters wide from west to east, and 10.5 meters high. The occupant density is 8 m^2·$person^{-1}$. Each person has a printer and a computer with the total power of 140 W. The lighting power is 13 W·m^{-2}. All the heat gains inside the selected room spaces are on/off controlled according to the regular occupancy schedule, which is set from 8:00 am to 18:00 pm.

Pipes are embedded in the concrete layer of external walls and the roof in serpentine pattern. Windows are fixed in the south and north walls and the window-wall ratio is 0.3. The windows are designed with double glasses and pipes are embedded in the cavity of the double glasses. A traditional office building with the same settings, same building envelopes except for the pipes, is utilized as the baseline. The configurations of the traditional double glass window and the pipe-embedded window are set according to Shen and Li (2016) and the main difference is the pipes.

3.2. Model of the Pipe-Embedded Wall

By referencing to Li et al., (2016), the parameters of the pipe-embedded wall are listed in Table 1. The water pump of the pipe-embedded wall system is on-off controlled. In the cooling condition, when the indoor temperature is larger than 25 °C and the inlet water temperature of the pipe is smaller than the inside surface temperature of the wall, the water pump is turned on. Similarly, in the heating condition, the water pump is activated when the room temperature is smaller than 21 °C and the inlet water temperature is larger than the inside surface temperature of the wall.

According to the simulation, the internal surface temperature of each wall can be obtained. The hourly heat flux, Q_{wall}, through the wall to indoor space can be calculated by Eq. (1).

$$Q_{wall}=h_{sur}\cdot A_{wall}\cdot(t_{sur}-t_{room}) \quad (1)$$

Compared with the traditional wall, the hourly building load reductions caused by the pipe-embedded wall are calculated as:

$$\Delta Q_{wall}=Q_{wall,trad}-Q_{wall,pipe} \quad (2)$$

The hourly heat capacity of the pipe-embedded wall, Q_{pwall}, can be calculated as:

$$Q_{pwall} = C_w \cdot m_w \cdot (t_{wall,o} - t_{wall,i}) \quad (3)$$

Table 1. Parameters of the pipe-embedded walls

Items	Pipe spacing (mm)	Pipe inner diameter (mm)	Pipe shell thickness (mm)	Water flow rate ($m \cdot s^{-1}$)
Values	150	16	2	0.5

3.3. Model of the Pipe-Embedded Window

The structure of the pipe-embedded window that used in this study refers to Shen and Li (2016). The analytic models of the traditional double glass window and the pipe-embedded window are obtained based on the heat transfer network which was interpreted in reference (Yan et al., 2018) in detail. In this study, both the analytic models of the traditional double glass window and the pipe-embedded window are obtained based on the analytic method. All the short-wave solar heat, conductive, convective and long-wave radiative heat transfers were considered in the analytic models.

The pipe-embedded windows system can be activated when the solar radiation is larger than 200 $W \cdot m^{-2}$ in the cooling condition. In the heating condition, pipe-embedded windows system does not work, i.e., no water is pumped to the pipe-embedded windows and the heat transfer performance of the pipe-embedded window is regarded as the same with the traditional double glass window with conventional blinds. With the specific structure of the pipe-embedded window, the analytic model that used to describe the heat gains through the window to indoor space can be expressed as follows.

For the traditional double glass window, the hourly heat gains in per square meter window area that caused by convection can be expressed by Eq. (4).

$$q_{conv\_trad} = 1.6 \cdot (t_{out} - t_{room}) + 0.25 \cdot I \quad (4)$$

For the pipe-embedded window, the hourly heat gains in per square meter window area that caused by convection can be expressed by Eq. (5) and Eq. (6). The hourly heat capacity of the pipe-embedded window is calculated by Eq. (7) and Eq. (8).

$$q_{conv\_pipe} = 2.77 \cdot (t_{out,e} - t_{room}) + 0.05 \cdot I \quad (5)$$

$$t_{out,e} = 0.15 \cdot t_{out} + 0.85 \cdot t_w \quad (6)$$

$$Q_{pwin} = (8 \cdot (t_{out,e} - t_w) + 0.5 \cdot I) \cdot A_{win} = C_w \cdot m_w \cdot (t_{win,o} - t_{win,i}) \quad (7)$$

$$t_w = (t_{win,i} + t_{win,o}) / 2 \quad (8)$$

The short wave radiation heat gains of the traditional double glass window are the same with that of the pipe-embedded window because of the same arrangement of blinds. For the specific windows, the short wave radiation heat gains in the cooling condition are calculated as:

$$q_{rad} = 0.1 \cdot I \quad (9)$$

The heat gains caused by the window are added to the building model in the form of convective and radiative heat exchange with indoor space. Compared with the traditional double glass windows, the hourly building load reductions caused by the pipe-embedded window are calculated as equation (10).

$$\Delta Q_{win} = (q_{conv,trad} - q_{conv,pipe}) \cdot A_{win} \quad (10)$$

3.4. Model of the AWHX

The fresh air volume is set as 30 $m^3 \cdot (h \cdot person)^{-1}$ for the air conditioning system. As described in section 2, the fresh air is pre-handled by the AWHX in the AHU. The design air pre-handling temperature difference is 8 °C and design water temperature difference is 3 °C.

The hourly heat exchange capacity of the AWHX is expressed as Eq. (11).

$$\Delta Q_{AWHX} = abs(C_a \cdot \frac{F \cdot \rho}{3600} \cdot (t_{ao} - t_{ai})) \quad (11)$$

Compared with the baseline system, the hourly building load reductions caused by the fresh air pre-handling system equal to the heat exchange capacity of the AWHX.

3.5. System Design

The analytical model of the pipe-embedded window is implanted in the building model (i.e. Type 56) on TRNSYS (Solar Energy Laboratory, 2004). Thus, the new building envelopes can be built with the model of the pipe-embedded window and the existing model of thermal active layer inside of Type 56. The complete simulation model of the integrated system can be built on the platform of TRNSYS according to section 2.

The ground heat exchanger is used as the heating and cooling source and the type 557a, a model of Duct Ground Heat Storage, in TRNSYS is used to simulate its heat transfer process. The accuracy of this dynamic model has been validated in a detailed study (Bo and Hellström, 2000). The single U-tube vertical GHX is utilized and the primary design parameters are listed in Table 2.

Table 2. Design parameters of the GHX

Items	values
Borehole depth (m)	100
Initial soil temperature (°C)	14.56
Soil thermal conductivity (W/(m·°C))	1.4
Soil heat capacity (kJ/(m3·°C))	2016
Soil density (kg/m3)	1857
Ground thermal conductivity (W/(m·°C))	1.4
Radius of U–tube pipe (mm)	16

3.6. Evaluation index

To evaluate the energy performance of the integrated system, the available heat transfer temperature difference is estimated first, and the non-air conditioning ratio is defined based on the free-running temperature.

The available heat transfer temperature difference is defined as:

$$\Delta t\_i = t_i - t_{soil} \tag{12}$$

where i refers to “wall”, “win”, “a”, and “room”.

The non-air conditioning ratio is defined as:

$$\gamma = \frac{T_{non-AC}}{T_{occupied}} \times 100\% \tag{13}$$

where $T_{non\text{-}AC}$ is the non-air conditioning period, which means that the free-running temperature is between 20-26 °C without the operation of the heat pump system; $T_{occupied}$ is the period during which the office room is occupied.

4. RESULTS AND DISCUSSION

The feasibility of the integrated system is investigated from the following two parts: analyzing the available temperature difference in different heat transfer process; calculating the free-running temperature and the non-air conditioning ratio.

4.1. Available Heat Transfer Temperature Difference

To have a better understanding of the design purpose of the integrated system, the available temperature difference in different heat transfer process is analyzed to demonstrate the advantage of the integrated system. The temperature distribution of the baseline system in the occupied time is shown in Figure 3. For the baseline building, the soil temperature changes a little throughout the year. The cavity temperature of the traditional double glass window can be over 60 °C in the cooling season, which is caused by much solar radiation absorbed by the conventional blinds. In the heating season, the fresh air temperature is much lower than the soil temperature. That means the shallow geothermal energy can be used to heat the fresh air efficiently.

The temperature difference between the soil and the wall mainly distributes in 10-15 °C in the cooling season and 0-10 °C in the heating season. The temperature difference between the soil and the window that is larger than 20 °C accounts for approximately 80% in the cooling season. The available temperature difference between the soil and the fresh air is between 10-20 °C at most of time both in the cooling season and heating season. The available temperature difference distribution frequency indicates that shallow geothermal energy would perform well to cool the window, the wall, and the fresh air directly in the cooling season. Moreover, the integrated system also has some effects on preheating the fresh air and intercepting the heat transfer through the wall.

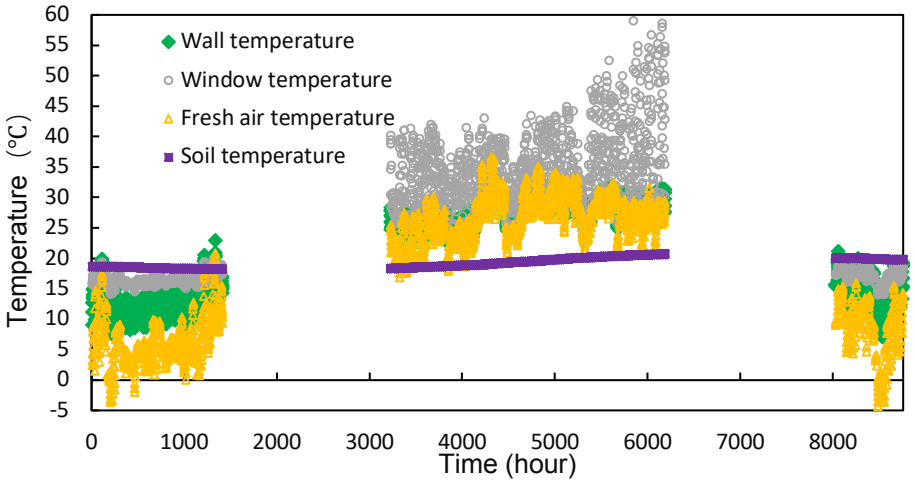

Figure 3: The temperature distribution of the baseline system in the occupied time

4.2. Increase of Non-Air Conditioning Ratio

To investigate the increase of non-air conditioning ratio, the free-running temperature of both the integrated system and the baseline system are simulated. The free-running temperature of the corner room in the top floor is taken as an example. As shown in Figure 4, for the baseline office room, the period that free-running temperature is lower than 15 °C or larger than 30 °C accounts for more than 60% of a year. It means that the room temperature is terribly uncomfortable in most time of the year without the operation of conventional heat pump system. When the outlet water of the GHX is directly delivered to the pipe-embedded windows, pipe-embedded walls, and the AWHX, the period that free-running temperature is smaller than 15 °C disappears and that is larger than 30 °C is reduced apparently. The ratio of the free-running temperature in the comfortable zone (i.e. temperature is 20-26 °C) is more than 30% in the integrated system but less than 15% in the traditional baseline system.

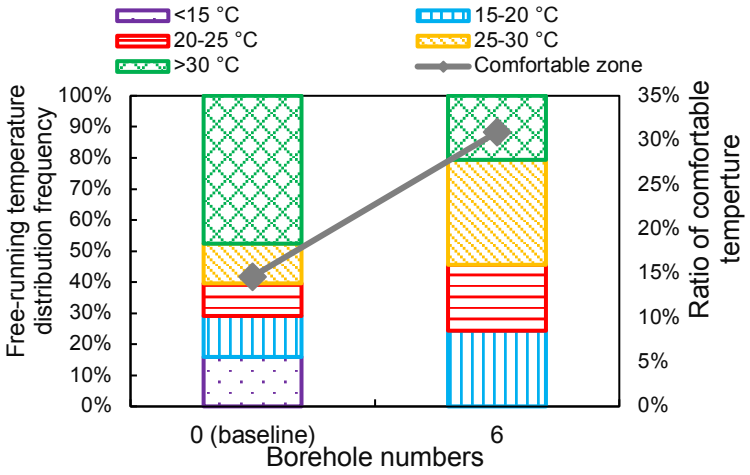

Figure 4: Free-running temperature distribution frequency

The free-running temperature distribution of the baseline and the integrated system are illustrated in Figure 5. In the baseline system, the free-running temperature would be over 40 °C in the cooling

season. With the effect of the pipe-embedded walls, pipe-embedded windows, and the fresh air pre-handling system, the free-running temperature of the integrated system is reduced. The conventional air conditioning system also should be operated to maintain the thermal comfortable. However, the peak cooling load can be reduced by the pipe-embedded walls pipe-embedded windows and the fresh air pre-handling system. Consequently, the system capacity of the conventional air conditioning system can be reduced significantly. It is obvious that if the integrated system is applied for a residential building with small indoor heat gains, the period with acceptable thermal comfort will be much longer.

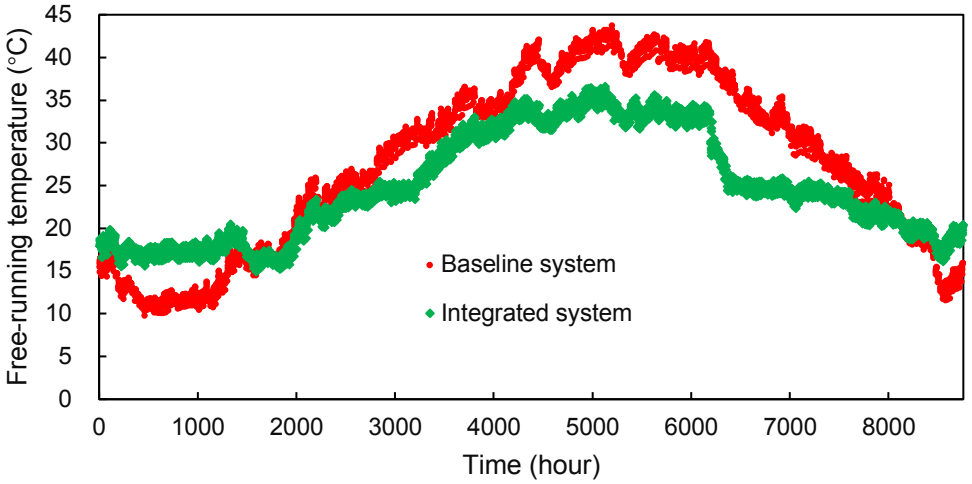

Figure 5: The free-running temperature distribution of the baseline and the integrated system

5. CONCLUSIONS

The shallow geothermal energy is not fully utilized by the conventional GSHP system. To improve the usage efficiency of shallow geothermal energy, an integrated system combined pipe-embedded walls, pipe-embedded windows, and fresh air pre-handling system is proposed based on the analysis of the temperature relationship between the envelopes, fresh air, indoor air and the undisturbed soil. The performance of the integrated system is investigated in terms of the increase of non-air conditioning ratio. The conclusions based on the case study are as follows:

(1) The available temperature differences between the undisturbed soil and the building envelopes as well as the fresh air can exceed 20 °C in most of time, which provide a way to utilize the shallow geothermal energy efficiently.

(2) The free-running temperature of the integrated system is always above 15 °C throughout the year, and the non-air conditioning ratio increases approximately 20% compared with the conventional system.

(3) The integrated system can contribute to the capacity decrease of conventional air conditioning system.

ACKNOWLEDGEMENTS

This study was supported by the China National Key R&D Program “Solutions to heating and cooling of buildings in the Yangtze river region” (Grant No. 2016YFC0700302) and the National Natural Science Foundation of China (Grant No. 51578306 and Grant No. 51638010).

NOMENCLATURE

C	Specific heat capacity, $kJ\cdot(kg\cdot°C)^{-1}$	q	Heat gains in per square meter area, $W\cdot m^{-2}$
h	Convection heat transfer coefficient, $W\cdot(m^2\cdot°C)^{-1}$	m	Water flow rate, $kg\cdot s^{-1}$
K	Heat transfer coefficient, $W\cdot(m^2\cdot°C)^{-1}$	t	Temperature, °C

Subscripts

a	Fresh air	pwall	Pipe-embedded wall
base	Baseline system	pwin	Pipe-embedded window
conv	Convection heat transfer	rad	Radiation
e	Equivalent	sur	Inner surface
i	Inlet	trad	Traditional
inte	Integrated system	w	Water
o	Outlet	win	Window

REFERENCES

Aikins, K. A. and Choi, J. M., 2012. Current status of the performance of GSHP (ground source heat pump) units in the Republic of Korea. Energy 47(1): 77-82.

Bakirci, K, 2010. Evaluation of the performance of a ground-source heat-pump system with series GHE (ground heat exchanger) in the cold climate region. Energy 35(7): 3088-3096.

Bo, N. and Hellström, G., 2000. High temperature solar heated seasonal storage system for low temperature heating of buildings. Solar Energy 69(6): 511-523.

Li, A., Xu, X. and Sun, Y., 2016. A study on pipe-embedded wall integrated with ground source-coupled heat exchanger for enhanced building energy efficiency in diverse climate regions. Energy and Buildings 121: 139-151.

Manz, H, 2004. Total solar energy transmittance of glass double façades with free convection. Energy and Buildings 36(2): 127-136.

Shen, C. and Li X., 2016. Solar heat gain reduction of double glazing window with cooling pipes embedded in venetian blinds by utilizing natural cooling. Energy and Buildings 112: 173-183.

Yan, S, Shen, C., Li, X., Lv, W., 2018. Predicting method for annual dynamic performance of pipe-embedded windows. HV&AC (in Chinese) 48(2): 18-23.

Sivasakthivel, T., Philippe, M., Murugesan, K., Verma, V. and Hu, P., 2017. Experimental thermal performance analysis of ground heat exchangers for space heating and cooling applications. Renewable Energy 113: 1168-1181.

Solar Energy Laboratory, U. o. W.-M, 2004. TRNSYS 17 User Mannual. Madison.

Soni, S., Pandey, M. and Bartaria, V., 2016. Hybrid ground coupled heat exchanger systems for space heating/cooling applications: A review. Renewable and Sustainable Energy Reviews 60: 724-738.

Manuscript ID: 1587
DOI: 10.18462/iir.icr.2019.1587

Investigation on the feasibility of using wood pulp fiber paper as substrate of rotary desiccant wheel for dehumidification

Xuannan WU, Tianshu GE*, Yanjun DAI, Xiaoqiang ZHAI

Institute of Refrigeration and Cryogenics, Shanghai Jiao Tong University, Key Laboratory of Power Mechanical Engineering of M.O.E
Shanghai, 200240, P.R. China, baby_wo@sjtu.edu.cn

ABSTRACT

The objective of this work is to investigate the feasibility of using wood pulp fiber paper (WPFP) as substrate of rotary desiccant wheel for dehumidification. The sample WPFP coated with silica gel was fabricated using impregnation method. The water vapor adsorption isotherm of the sample was tested. Additionally, an experimental system was set up to test dehumidification performance of the rotary desiccant wheel with WPFP as substrate. The results show that the water adsorption capacity of the sample WPFP coated with silica gel is close to that of pure silica gel under the condition of 20°C, RH < 70%. In winter condition, the maximal dehumidification capacity of the rotary desiccant wheel with WPFP as substrate can be 0.91 $g \cdot kg^{-1}$ under revolving speed of 47 $r \cdot h^{-1}$ and process air flow rate of 245 $m^3 \cdot h^{-1}$. The investigation results indicate that the WPFP can be an alternative for the substrate of desiccant wheel.

Keywords: WPFP, Substrate, Desiccant Wheel, Dehumidification, Silica Gel, Adsorption Isotherm.

1. INTRODUCTION

With the development of social economy and the improvement of people's living standard, people pay more attention to comfort and health of their residential environment. To keep the indoor air healthy, much fresh air is introduced into living and working place. And the introduced fresh air needs to be cooled and dehumidified in hot and humid climate to meet people's demands. Generally, conventional air conditioning system is used to achieve space cooling and dehumidification. The dehumidification principle of conventional air conditioning system is lowering the temperature of process air to below its dew point and then the moisture in the process air will be condense into liquid water, which makes the indoor air be cooled and dehumidified. However, this method wastes large amounts of electricity and even causes urban heat island effect.

To solve those problems, many researchers started to investigate adsorption method for dehumidification. Zhao et al. (2014) adopted experimental method to investigate the dehumidification performance of silica gel coated fin-tube heat exchanger. Zheng et al. (2015) coated silica gel-LiCl composite desiccant on heat exchanger for dehumidification. Besides, Zheng et al. (2015) tested the adsorption kinetics curves of SAPO-34 and FAPO-34. Chen et al. (2015) developed a composite material by combining silica gel with both polyacrylic acid and sodium polyacrylate and applied it in air conditioning systems. Al-Alili et al. (2015) experimentally investigated the performance of a desiccant wheel cycle utilizing novel Zeolite desiccant material. And there are also researches about investigating the dehumidification performance of desiccant wheel dehumidification systems (Mandegari et al., 2017; Tu et al., 2018; Yadav et al., 2018). However, the above researches mainly focused on the investigation about different adsorbent itself or the dehumidification performance of desiccant wheel dehumidification systems. In fact, the desiccant and substrate are integrated into a whole in a desiccant wheel. Therefore, the investigation on the water adsorption performance of the whole integrated desiccant material with substrate has an important significance.

In this paper, silica gel was selected as desiccant material for a rotary desiccant wheel, and WPFP was selected as possible substrate. Firstly, raw WPFP and silica sol were prepared, and then the sample WPFP coated with silica gel was made by impregnation method. Secondly, the water vapor adsorption isotherms of WPFP coated with silica gel and pure silica gel were tested and analyzed. Thirdly, a desiccant wheel made of WPFP and coated with silica gel was fabricated, and its

dehumidification performance was tested and analyzed. It is hoped that this study will provide guidance for substrate selection of rotary desiccant wheel.

2. EXPERIMENTAL DESCRIPTION

2.1. Preparation of WPFP Coated with Silica Gel

Materials used in this experiment mainly included silica sol and raw WPFP. The adopted silica sol was purchased from Qingdao Maike silica gel desiccant Co., Ltd (in China), and its parameters were listed in Table 1. The raw WPFP was manufactured by Shanghai Mingguan Purification Materials Co., Ltd (in China), and its thickness is 0.595mm.

Table 1. Parameters of silica sol used in this work

Type	Grain diameter (nm)	Na_2O (%)	SiO_2 (%)	Density ($g \cdot cm^{-3}$)	pH	Viscosity (mPa·s)	Technology
JN-30	14	≤0.3	30-31	1.19-1.20	8.9-9.0	8.0-9.0	Ion exchange method

Next, impregnation method was adopted to coat silica gel on raw WPFP. In this paper, the specific process of this method was conducted as follow: (1) a piece of raw WPFP mentioned in the above text with the size of 100mm*100mm was prepared and weighed in an electronic balance; (2) the raw WPFP was put into a glass dish which was filled with enough silica sol, and the raw WPFP was submerged absolutely. Meanwhile, the glass dish should be covered with preservative film to prevent the silica sol from absorbing water vapor from ambient air; (3) after 6 hours, the raw WPFP was taken out from the glass dish carefully and dried in an oven at the temperature of 100°C until its weight remained unvaried, and its final weight was recorded; (4) the sample WPFP coated with silica gel was obtained, and the weight of the sample was recorded. The above steps of coating silica gel on raw WPFP is illustrated in Fig. 1. To coat more silica gel on raw WPFP, the step (2) to (4) can be repeated for more times. Coating ratio is defined as the mass of silica gel coated on the sample per unit volume of raw WPFP, which is used to evaluate coating capacity of different substrates. The coating ratio of the sample is given by the following Eq. (1):

$$\lambda = (m - m_0) / V \qquad \text{Eq. (1)}$$

where λ is the coating ratio based on the volume of the raw WPFP in $g \cdot cm^{-3}$, m_0 is the original weight of the raw WPFP in g, m is the total weight of the sample coated with silica gel in g, and V is the volume of the raw WPFP in cm^3.

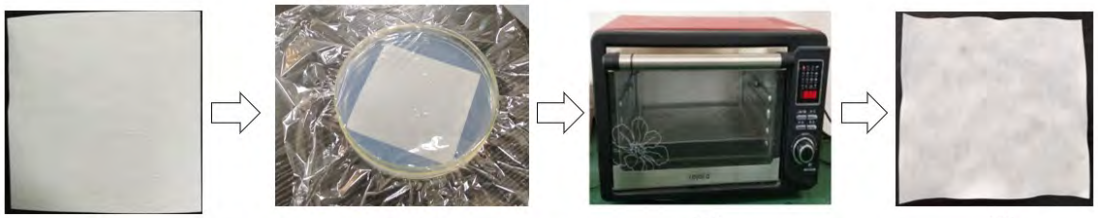

Figure 1: The silica gel coating process for WPFP: (1) raw WPFP; (2) coating; (3) drying; (4) WPFP coated with silica gel

2.2. Adsorption Test

In general, the instrument ASAP2020 is used to test microcosmic pore structure parameters (like specific surface area, pore volume, pore size distribution and so on) with nitrogen as adsorbate. In this paper, the ASAP2020 system was improved by attaching a water vapor generator, a jacketed beaker and a thermostatic water bath (Zheng et al., 2015). The thermostatic water bath and jacketed beaker work together to control the temperature of water vapor delicately. Besides, the two attached apparatuses can also eliminate the effect of temperature change caused by adsorption heat. Therefore, the isothermal adsorption process can be realized. By using the improved ASAP2020 system, water vapor adsorption isotherms of WPFP coated with silica gel was tested at 20°C.

2.3. Description of Rotary Desiccant Wheel Dehumidification System

An experimental system was set up to test the dehumidification performance of the rotary desiccant wheel, which is showed in Fig. 2. The system mainly consists of three parts, namely rotary desiccant wheel, process air passage and regeneration air passage. The rotary desiccant wheel is the core of the system, which is used to realize air dehumidification. The substrate of this rotary desiccant wheel is WPFP, and silica gel is used as adsorbent. The thickness and diameter of the rotary desiccant wheel are 100mm and 250mm, respectively. In addition, an electric motor is adopted in the system to drive the rotary desiccant wheel, and the revolving speed of the electric motor is controlled by a frequency converter. The cross section of the rotary desiccant wheel is divided into two parts by adiabatic clapboard, namely dehumidification area and regeneration area, and the area ratio of dehumidification area and regeneration area is 3:1. In the process air passage, an induced draft fan (namely process fan) is installed at the exit to drive the process air flow. In regeneration air passage, besides an induced draft fan (namely regeneration fan) installed at the exit, a heater with the maximum power of 10.8 kW is installed at the entrance of the regeneration air passage.

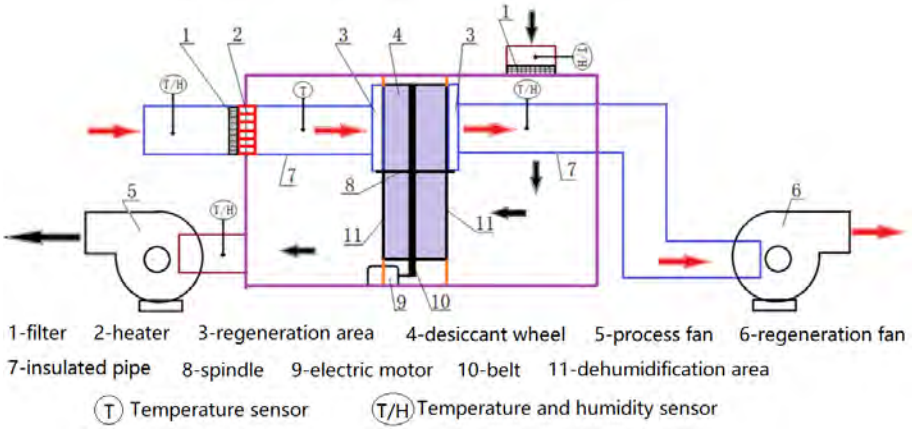

Figure 2: Experimental setup

2.4. Measurement

To evaluate the dehumidification performance of the rotary desiccant wheel using WPFP as substrate, the inlet and outlet temperature and relative humidity of process air should be measured and recorded. In this experiment, two types of sensors were applied as shown in Table 2. It is noted that one type of sensor (PT100) is used to measure temperature and the other type of sensor (temperature and humidity sensor) is used to measure relative humidity of process air.

The dehumidification performance of the rotary desiccant wheel was evaluated by dehumidification capacity, which is calculated by the following Eq. (2):

$$\Delta d = d_{in} - d_{out} \qquad \text{Eq. (2)}$$

where Δd is the dehumidification capacity in g·kg^{-1}, d_{in} and d_{out} are humidity ratio in the inlet and outlet of process air passage in g·kg^{-1}, respectively.

Table 2. List of the instruments

Instruments	Type	Range	Accuracy
PT100	WZPK-191	–200-450°C	±0.5°C
Temperature and humidity sensor	HF33-D (ROTRONIC)	–40-60°C; 0-100%RH	±0.5°C; ±2%RH

3. RESULTS AND DISCUSSION

3.1. Silica Gel Coating Analysis

In rotary desiccant wheel, it is the desiccant material that adsorbs moisture from process air, and the substrate mainly provides support for desiccant material. Therefore, the coating ratio of WPFP has an important effect on dehumidification capacity. The relation of coating ratio about silica gel and coating times for WFPF is shown in Fig. 3. It can be observed that the coating ratio increases all the time with the increasing of coating time, and the coating ratio can be 1.4 g·cm^{-3} when the coating time reaches to six. However, the increment of coating ratio decreases gradually with the increasing of coating time. Compared with the fifth coating, the coating ratio of WPFP in the sixth coating increases only by 4.8%. Because silica sol can enter the big pores of WPFP in the first or second coating, the fiber bundles are wrapped with silica gel and most of the big pores are filled with silica gel, which makes the coating ratio increase sharply. With the coating time increasing, silica gel heaps on preceding silica gel layer, which not only leads to coating ratio decreasing but also results in unstable coating. After the sixth coating, it was found from the actual experiment that some silica gel powder can easily fall off from the samples. Therefore, six times is recommended as the maximum number for coating.

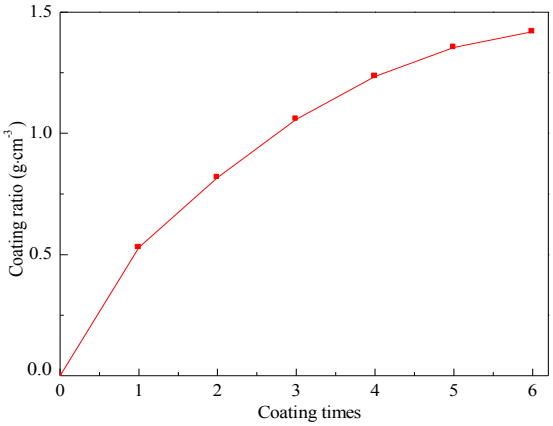

Figure 3: The coating ratio of WPFP

3.2. Adsorption Isotherm

To investigate the feasibility of using WPFP as substrate of desiccant wheel, water vapor adsorption isotherm of WPFP coated with silica gel after the first coating was tested in the improved ASAP2020 system at the temperature of 20°C, and the water vapor adsorption isotherm of pure silica gel was tested as comparison. The adsorption isotherms were plotted in Fig. 4.

It can be witnessed from Fig. 4 that the water adsorption capacities of the two samples increase slowly with the increasing of relative humidity in low relative humidity area (RH < 40%), and the two curves rise rapidly in medium relative humidity area (40% < RH < 75%). In high relative humidity area (75% < RH < 97%), the water vapor adsorption isotherm of pure silica gel becomes relatively flatter, but the water adsorption isotherm of WPFP coated with silica gel still increases obviously. Under the relative humidity of 97%, the saturated adsorption capacity of pure silica gel is 0.235 g·g^{-1}, and that of WPFP coated with silica gel is 0.240 g·g^{-1}. When the relative humidity is close to 100%, the adsorption isotherm of WPFP coated with silica gel increases precipitously and is difficult to reach saturated state. The reason is that some of the water vapor begins to condense into liquid when the relative humidity is close to 100%. At the same time, a certain number of big pores exist in WPFP coated with silica gel, which can be filled with liquid water. However, silica gel belongs to mesoporous material and there are rare big pores in it. Hence, the adsorbed water vapor molecules can only be condensed in the mesoporous, which can't make the adsorption isotherm rise dramatically.

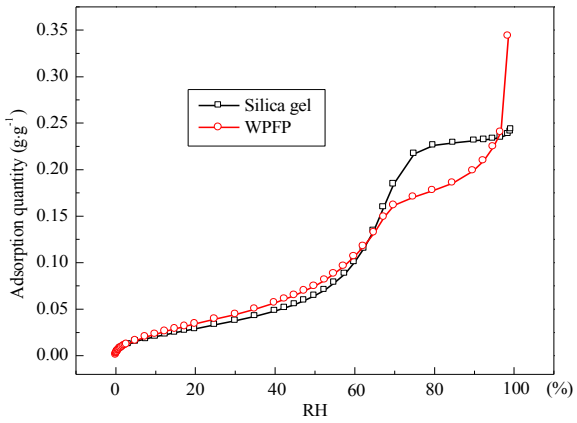

Figure 4: Water vapor adsorption isotherms of pure silica gel and WPFP coated with silica gel after the first coating

3.3. Dehumidification Performance of the Rotary Desiccant Wheel

To test the dehumidification performance of the rotary desiccant wheel using WPFP as substrate, the rotary desiccant wheel dehumidification system described in Chapter 2.3 was operated in a laboratory. In addition, the test was conducted in winter condition, and the inlet air condition of process air was 12ºC and 35%RH. The volume flow rate of regeneration air was set as 73 $m^3 \cdot h^{-1}$.

3.3.1. Effect of Regeneration Temperature

Fig. 5 shows the effect of regeneration temperature on the dehumidification capacity under different revolving speed of the rotary desiccant wheel. The flow rate of process air was set as 304 $m^3 \cdot h^{-1}$. It can be witnessed that the dehumidification capacity increases greatly with the increasing of regeneration temperature under the revolving speed of 47 $r \cdot h^{-1}$ and 180 $r \cdot h^{-1}$. But the increasing trend is not obvious under very low revolving speed (10 $r \cdot h^{-1}$). The reason is that the regenerated part of the rotary desiccant wheel stays in dehumidification area for a long time when the revolving speed of the rotary desiccant wheel is too low. The part of the rotary desiccant wheel which reaches adsorption equilibrium can't enter regeneration area timely. Therefore, increasing regeneration temperature has little effect on the improvement of the dehumidification capacity when the revolving speed of the rotary desiccant wheel is too low. Additionally, it can be also found that the dehumidification capacity will decrease under the same regeneration temperature if the revolving speed of the rotary desiccant wheel is too high, which means that there is an optimal revolving speed for the rotary desiccant wheel. In this experiment, the obtained maximal dehumidification capacity is 0.82 $g \cdot kg^{-1}$ air. This is because of too low inlet humidity ratio (3.03 $g \cdot kg^{-1}$ air) and high flow rate (304 $m^3 \cdot h^{-1}$) of process air.

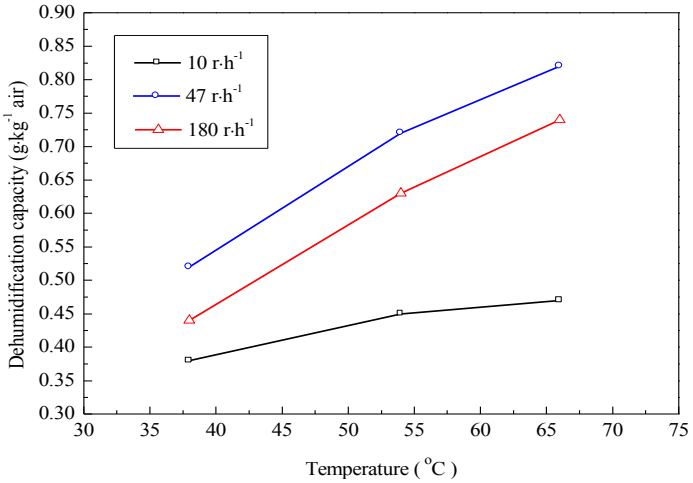

Figure 5: Effect of regeneration temperature on dehumidification capacity

3.3.2. Effect of Flow Rate of Process Air

Fig. 6 shows the effect of flow rate of process air on the dehumidification capacity under different revolving speed of the rotary desiccant wheel. The regeneration temperature was set as 66°C. It can be seen that the dehumidification capacity decreases greatly with the increasing of flow rate of process air under different revolving speed of the rotary desiccant wheel. Besides, the variation trend is approximately linear. When the flow rate of process air increases, the flow velocity in the air channel of desiccant wheel will increase accordingly. So, the time of contact between process air and desiccant material decreases, which leads to the decline of dehumidification capacity. Under meeting the requirement of ventilation rate, the flow rate of process air needs be decreased to obtain large dehumidification capacity. Under the revolving speed of 47 $r \cdot h^{-1}$ and process air flow rate of 245 $m^3 \cdot h^{-1}$, the maximal dehumidification capacity can be 0.91 $g \cdot kg^{-1}$ air. The dehumidification capacity is relatively low, because inlet humidity ratio (3.03 $g \cdot kg^{-1}$ air) of process air is very low. The experimental results indicate that WPFP can be an alternative for the substrate of desiccant wheel. In addition, it is also observed from Fig. 6 that the dehumidification capacity increases with the increasing of the revolving speed when the revolving speed varies from 10 $r \cdot h^{-1}$ to 47 $r \cdot h^{-1}$, but the dehumidification capacity decreases when the revolving speed reaches to 180 $r \cdot h^{-1}$.

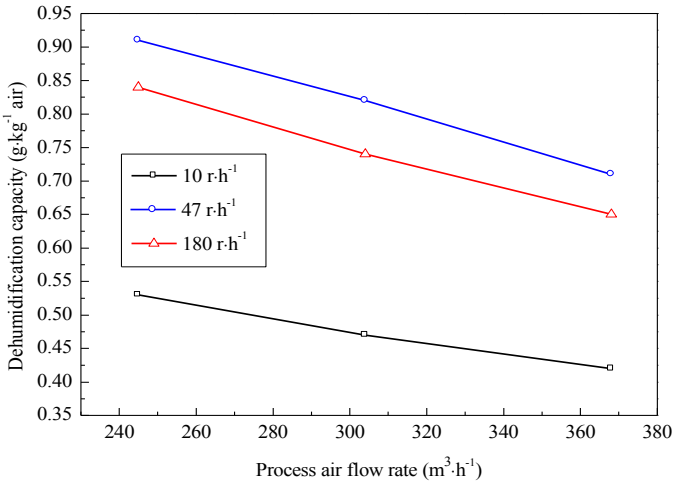

Figure 6: Effect of flow rate of process air on dehumidification capacity

4. CONCLUSIONS

In this paper, silica gel was selected as desiccant material for a rotary desiccant wheel, and WPFP was selected as potential substrate. Firstly, the sample WPFP coated with silica gel was fabricated using impregnation method. Secondly, the adsorption isotherms of WPFP coated with silica gel was tested and analyzed. In the end, a rotary desiccant wheel dehumidification system was set up and the dehumidification performance of the rotary desiccant wheel made of WPFP and silica gel was tested and analyzed. Some conclusions were summarized as follow:

(1) For WPFP, the coating ratio increases gradually with the increasing of coating time, but the increment of coating ratio decreases gradually with the increasing of coating time. Six times is recommended as the maximum number for coating.

(2) The water vapor adsorption isotherm of the sample WPFP coated with silica gel increases obviously with the increasing of relative humidity. Under the relative humidity of 97%, the saturated adsorption capacity of the sample WPFP coated with silica gel is 0.240 $g \cdot g^{-1}$.

(3) The dehumidification capacity of the rotary desiccant wheel with WPFP as substrate increases greatly with the increasing of regeneration temperature, but the increasing trend is not obvious under too low revolving speed (10 $r \cdot h^{-1}$).

(4) The dehumidification capacity of the rotary desiccant wheel with WPFP as substrate decreases greatly with the increasing of flow rate of process air.

(5) The experimental results obtained in winter condition indicate that WPFP can be an alternative for the substrate of desiccant wheel.

ACKNOWLEDGEMENTS

The authors acknowledge the financial support of the National Natural Science Foundation of China (Grant NO.51576121) and support from Shanghai Pujiang Program (NO.18PJD021).

NOMENCLATURE

Δd	dehumidification capacity ($g \cdot kg^{-1}$)	V	volume (cm^3)
d_{in}	humidity ratio in the inlet of process air passage ($g \cdot kg^{-1}$)	WPFP	wood pulp fiber paper
d_{out}	humidity ratio in the outlet of process air passage ($g \cdot kg^{-1}$)		
m	the total weight of the sample coated with silica gel (g)	Greek symbols	
m_0	the original weight of the raw WPFP (g)	λ	the coating ratio based on the volume of the raw WPFP ($g \cdot cm^{-3}$)
RH	relative humidity		

REFERENCES

Al-Alili, A., Hwang, Y., Radermacher, R., 2015. Performance of a desiccant wheel cycle utilizing new zeolite material: experimental investigation. Energy 81, 137-145.

Chen, C.H., Hsu, C.Y., Chen, C.C., Chen, S.L., 2015. Silica gel polymer composite desiccants for air conditioning systems. Energy build. 101, 122-132.

Mandegari, M. A., Farzad, S., Angrisani, G., Pahlavanzadeh, H., 2017. Study of purge angle effects on the desiccant wheel performance. Energy Convers. Manage. 137, 12-20.

Tu, R., Hwang, Y., Cao, T., Hou, M., Xiao, H., 2018. Investigation of adsorption isotherms and rotational speeds for low temperature regeneration of desiccant wheel systems. Int. J. Refrig. 86, 495-509.

Yadav, L., Yadav, A., 2018. Effect of different arrangements of sector on the performance of desiccant wheel. Heat Mass Transfer 54(1), 7-23.

Zhao, Y., Ge, T.S., Dai, Y.J., Wang, R.Z., 2014. Experimental investigation on a desiccant dehumidification unit using fin-tube heat exchanger with silica gel coating. Appl. Therm. Eng. 63(1), 52-58.

Zheng, X., Ge, T.S., Hu, L.M., Wang, R.Z., 2015. Development and characterization of mesoporous silicate–LICL composite desiccants for solid desiccant cooling systems. Ind. Eng. Chem. Res. 54(11): 2966-2973.

Zheng, X., Ge, T.S., Jiang, Y., Wang, R.Z., 2015. Experimental study on silica gel-LiCl composite desiccants for desiccant coated heat exchanger. Int. J. Refrig. 51, 24-32.

Zheng, X., Wang, R.Z., Ge, T.S., Hu, L.M., 2015. Performance study of SAPO-34 and FAPO-34 desiccants for desiccant coated heat exchanger systems. Energy 93, 88-94.

Manuscript ID: 1619
DOI: 10.18462/iir.icr.2019.1619

Numerical stduy on performance comparison for sub-cooling methods using a sub-cooler in a multi-split variable refrigerant flow(VRF) system

Taemin LEE[(a)], Byungchae MIN[(a)], Gyungmin CHOI[(a)], Heunghee BAE[(b)]

[(a)] School of Mechanical Engineering, Pusan National University
Busan, 46283, Republic of Korea, choigm@pusan.ac.kr
[(b)] SAC Research/Engineering Division, H&A Solution company, LG Electronics
84, Wanam-ro, Seongsan-gu, Changwon-si, Gyengsangnam-do51554, Republic of Korea,
heunghee.bae@lge.com

ABSTRACT

In this study,the performance of the VRF systems applying a bypass cycle and injection cycle using a sub-cooler is compared by numerical method. In the simulation for a multi-split variable refrigerant flow(VRF) system, it is important to predict the input power and mass flow rate of a scroll compressor with considering the refrigerant injection process in a compression chamber, and pressure drop and heat transfer in pipe lines between an outdoor unit and indoor units. Therefore, the simulation for a multi-split VRF system was developed with considering those, and validated with experimental data. The bypass and refrigerant injection have improvement potential to increase the cooling capacity due to increasing enthalpy difference in an evaporator. The refrigerant injection cycle has more improvement potential of performance than bypass cycle. Sub-cooling degree at inlet of EEV is above 10°C degree in two cycles, which can avoid flash gas generation.
Keywords: Multi-Split VRF System, Flash Gas, Bypass Cycle, Injection, Subcooling.

1. INTRODUCTION

A multi-split VRF consists of indoor and outdoor devices and is connected by pipe between them. The length of the pipe is usually 150m (Afify, 2008), and the pressure drop in pipe is caused by the loss of fluid flow and heat transfer to the ambient air. A pipe that passes by liquid refrigerant is called a liquid pipe, and the liquid refrigerant may change to flash gas under any conditions due to pressure drop. The flash gas generation in the liquid pipeline leads to noise in EEVs, decrease of the mass flow rate through the EEV, and yields lower system efficiency and reliability (Kang and Yoo, 2012).
In multi-split VRF system, the sub-cooler heat exchanger (or intermediate heat exchanger, IHX) is a device that prevents the generation of flash gas, reduces the discharge temperature of the compressor, and increases the cooling capacity. There are two methods of multi-split VRF using sub-cooler. As shown in Figure 1, one is bypass cycle and the other is injection cycle. In bypass cycle, the IHX refrigerant cools the main stream refrigerant by heat exchange with the main stream refrigerant, which is at a higher temperature, and the heated IHX refrigerant is mixed with the refrigerant flowing from the evaporator. Unlike bypass cycle, the IHX refrigerant in the injection cycle enters the compression chamber of the compressor directly.
The objective of this study is to develop a numerical simulation to compare and analyze the improvement potential of the multi-split VRF system using bypass and injection methods under cooling mode.

2. MATHEMATICAL MODELS

To develop numerical analysis simulations, each component of the multi-split VRF system is modelled. Modeling targets include scroll compressor, heat exchangers (condenser, evaporator, sub-cooler), pipeline, electronic expansion valve(EEV) and multi-split VRF system.

2.1. Scroll compressor

To simulate the performance of a compressor, three models were considered, namely, the semi-empirical model (Sun et al., 2017; Zhu et al. 2013; Shao et al. 2012), map-based model(10-efficient Air Conditioning, Heating, and Refrigeration Institute (AHRI) compressor map), and the geometry-based model(Kwon et al., 2017). The semi-empirical and map-based models have been used in most previous studies because these models are better to reducing the numerical simulation time. However, these models are not suitable for the simulation of refrigerant injection compressor. This is because the refrigerant injection into a compressor occurs continuously, as shown in Fig. 1. In this study, the geometry-based model was applied to the simulation of the multi-split VRF system with a sub-cooler in order to take into account the refrigerant injection process and degree of suction superheating.

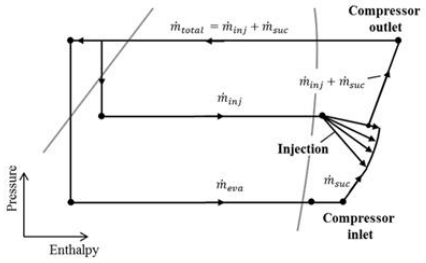

Figure 1: P-h diagram of injection cycle with a scroll compressor

The governing equations for the numerical model of a scroll compressor include changes in mass, enthalpy, pressure, and temperature in a compressor chamber, as respectively indicated by Eq. (1) - (2) (JSRAE, 2018):

$$\frac{dm}{d\theta} = \frac{dm_{in}}{d\theta} - \frac{dm_{out}}{d\theta} + \frac{dm_{inj}}{d\theta} \quad \text{Eq. (1)}$$

$$M\frac{dh}{dt} = \dot{m}_{in}(h_{in} - h) - \dot{m}_{out}(h_{out} - h) + \dot{m}_{inj}\left(h_{inj} - h\right) + Q + V\frac{dP}{dt} \quad \text{Eq. (2)}$$

where Q is heat transfer rate between the wrap wall and the refrigerant in a compressor chamber.

Mass flow rates in a scroll compressor, such as suction, injection, and discharge flows, are predicted by Eqs. (3) - (5).

$$\dot{m} = C_d A\sqrt{\left(\frac{2k}{(k-1)}P_u\rho_u\right)\left\{(P_r)^{2/k} - (P_r)^{\frac{k+1}{k}}\right\}} \quad \text{Eq. (3)}$$

$$P_{cr} = \left(\frac{2}{k+1}\right)^{\frac{k}{k-1}} \quad \text{Eq. (4)}$$

when $\mathrm{P_r} < \mathrm{P_{cr}}$, then

$$\dot{m} = CP_u A\sqrt{\frac{2k}{(k-1)}P_u\rho_u}\left\{\left(\frac{2}{k+1}\right)^{\frac{k+1}{k-1}}\right\} \quad \text{Eq. (5)}$$

$$\rho_{tp} = \rho_l + x\left(\rho_g - \rho_l\right) \quad \text{Eq. (6)}$$

Eq. (6) is a homogeneous model for two-phase flow.

The indicated work of a compressor can be predicted by the variation in pressure and volume of the compressure chambers from the suction to the discharge processes, as indicated by Eq. (7).

$$W_{ind} = \oint P\, dV \quad \text{Eq. (7)}$$

Finally, the compressor input power is calculated using Eq. (8), including the motor and mechanical efficiencies. The motor, mechanical, and volumetric efficiencies are obtained from compressor calorimeter tests.

$$W_{comp} = W_{ind}/\eta_{motor}\eta_{mech} \quad \text{Eq. (8)}$$

2.2. Heat Exchagner

2.2.1. Condenser and Evaporator

The fin of the heat exchanger were adopted as louver fin. The tube-by-tube method was applied to the heat exchanger simulation to calculate the heat transfer and pressure drop. The heat transfer was calculated using the effectiveness-NTU method. The heat transfer rate and pressure drop were obtained through the correlation equations (Table 1).

2.2.2. Sub-cooler

The sub-cooler used in this simulation of the multi-split VRF system is a tube-in-tube heat exchanger type, which consists of one outer tube and seven inner tubes. The heat transfer and pressure drop was calculated in the same ways as the condenser and evaporator.

2.3. Pipelines

The liquid pipeline and gas pipeline are connected between the outdoor and indoor units. To accurately perdict system performace, heat transfer and pressure drop of pipelines were calculated. The correlation equations used for the model of the pipelines are summarized in Table 1.

Table 1. Correlations of heat transfer and pressure drop coefficients for the refrigerant and air sides

	Refrigerant side	Air side
Heat transfer coefficient	- Single phase : Gnielinski (1976) - Two phase : Condensation : Shah (1979) Evaporation : Kandlikar (1990)	Wang (1999)
Pressure drop coefficient	- Single phase : Churchill (1977) - Two phase : Condensation : Lockhart-Martinelli (1949) Evaporation : Gronnerud (1979)	

2.4. Electronic expansion valve (EEV)

The mass flow rate flowing through an EEV can be predicted by the orifice equation,

$$\dot{m}_{EEV} = C_v A\sqrt{\rho_{EEV,in}\Delta P_{EEV}} \quad \text{Eq. (9)}$$

where A is the flow area, ΔP_{EEV} is the pressure difference between the inlet and outlet of the EEV, $\rho_{EEV,i}$ is the refrigerant density at the inlet, and C_v is the flow coefficient which is obtained from the literature (Zhu et al., 2013).

2.5. Multi-split VRF system equipped with a sub-cooler

The laws of mass, energy and momentum conservation of the VRF system should be satisfied, as indicated by Eqs. (10) - (12).

$$\dot{m}_{comp} - \sum \dot{m}_{EEV} - \dot{m}_{inj} = 0 \quad \text{Eq. (10)}$$

$$W_{in,comp} + \sum_{i=1}^{n} Q_{eva,n} - Q_{cond} = 0 \quad \text{Eq. (11)}$$

$$P_{suc} + \Delta P_{EEV} = P_{dis} \quad \text{Eq. (12)}$$

Fig. 2 shows the flow chart of the simulation logic for the multi-split sVRF system which can satisfy the governing equations of the VRF system.

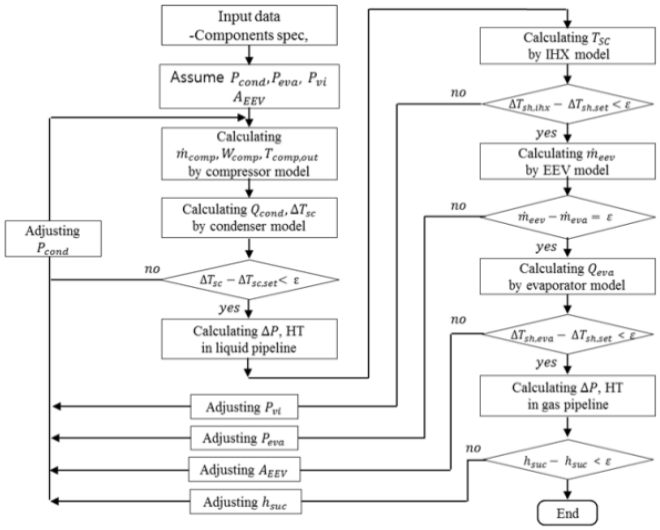

Figure 2: Flow chart of the simulation logic

3. RESULTS AND DISCUSSION

3.1. Validation of the simulation

3.1.1. Compressor simulation validation

Figs 3a and 3b show the validation results for the scroll compressor without the refrigerant injection. As shown in Fig. 3, the simulation results for the input power and the mass flow rate of the scroll compressor without the refrigerant injection show a similar tendency with the results of the calorimeter test, and are within 15% and 5%, respectively.

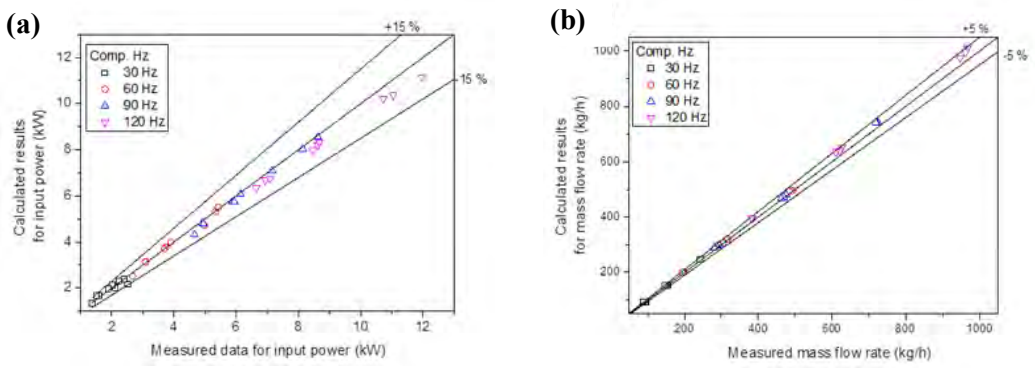

Figure 3: Validation results for the scroll compressor without the refrigerant injection (a) Input power (b) Mass flow rate

3.1.2. Compressor simulation validation

Fig 4a shows the validation results for the simulation of the multi-split VRF system without injection in the cooling mode with variation in the part load. As shown in Fig 4a, the simulation results for the cooling capacity and input power of the multi-split VRF system in cooling mode are consistent with experimental data within 15%. The validation results for the simulation of the system with an injection cycle in heating mode are indicated in Fig 4b and show a similar tendency with expermental data (maximum error of 10.3%).

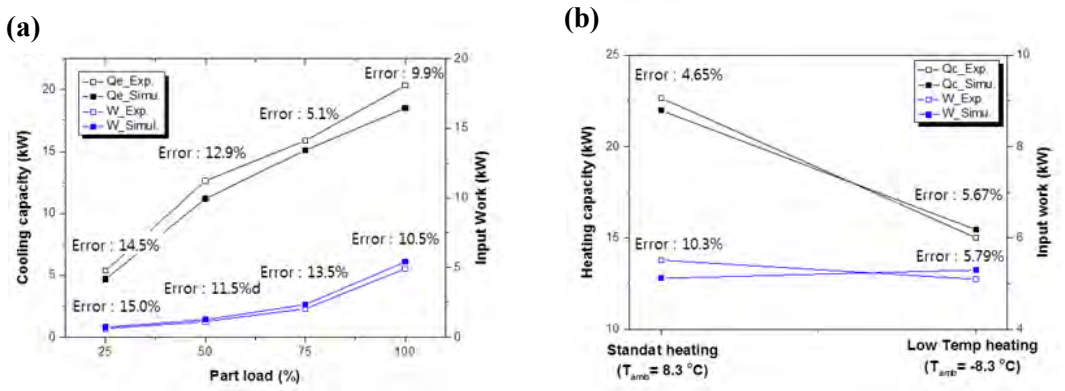

Figure 4 : Validation results for the simulation for the multi-split VRF system (a) Cooling mode (b) Heating mode

3.2. Performance Comparison for a Multi-split VRF System using Bypass and Injection Cycles as Sub-Cooling Methods

The performance of a multi-split VRF system was compared according to the variations of the bypass and injection ratios when the sub-cooling methods were employed in the same configuration. This simulation was calculated by fixing the sub-cooling degree at the outlet of the condenser and superheating degree at the outlet of the evaporators as input data.

3.2.1. Sub-cooling degree at the inlet of EEV and superheating degree

For the bypass and injection cycles, the sub-cooling degree at the inlet of the EEV and the superheating degree of IHX stream refrigerant(at exit to bleeding line) are considerably influenced by the bypass and injection ratios, as shown in Figs 5a and 5b.

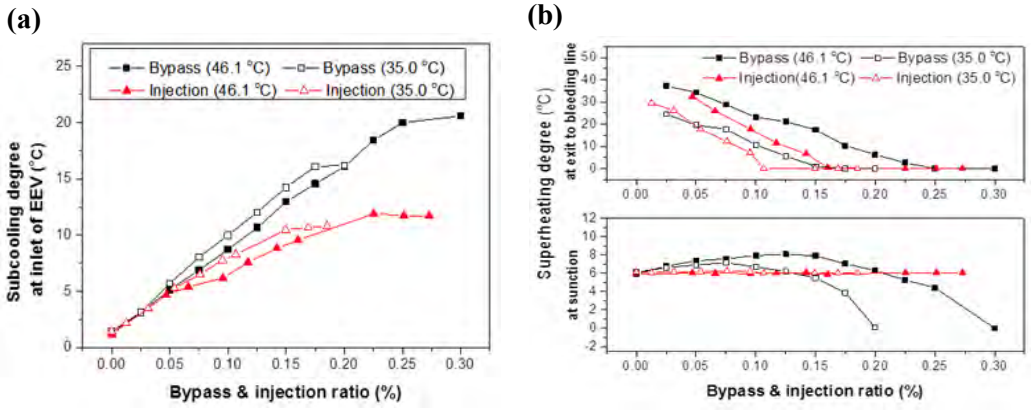

Figure 5 : (a) Sub-cooling degree at the inlet of EEVs (b) Superheating degree at exit of bleeding line and suction

The sub-cooling degree at the inlet of the EEV increases as the bypass and injection ratios increases. This is because the two-phase heat transfer area in the sub-cooler increases as the degree of superheating at the exit of the bleeding line decreases. The increase of the two-phase heat transfer area in the sub-cooler means that the overall heat transfer coefficient is enhanced. However, after the superheating degree at the exit of the bleeding line reaches 0 ℃, the subcooling degree at the

inlet of the EEV is maintained at a constant value because the overall heat transfer coefficient is unchanged.
The sub-cooling degree of the bypass cycle is higher than that of the injection cycle because the bled refrigerant in the bypass line is reached near the evaporating pressure. In injection cyle, the injection line pressure is higher than the suction pressure to inject the refrigerant into the compression chamber. The high bled refrigerant pressure means that the temperature of the bled refrigerant is high, thus the subcooling effect of main stream refrigerant reduces.

3.2.2. Mass flow rate and Discharge temperature

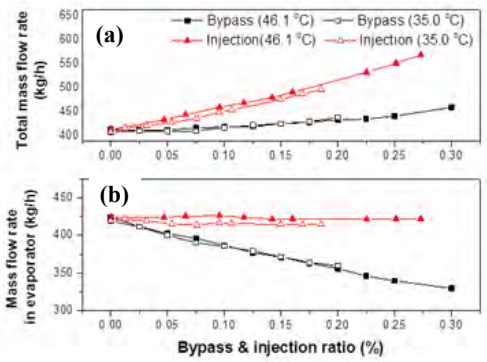

Figure 6 : Mass flow rate (a) total (b) in the evaporator

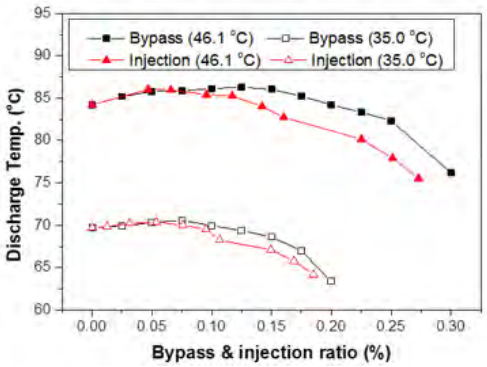

Figure 7 : Discharge temperature

Fig 6 shows the total mass flow rate and the mass flow rate in the evaporators. In the case of the bypass cycle, the total mass flow rate is not changed significantly at the beginning of the bypass, but is increased slightly because of the decrease of the degree of the suction superheating. The mass flow rate in the evaporators decreases of the increase of the bypassed mass flow rate. In the case of the injection, the total mass flow rate increases because the injected refrigerant is added to the suction mass flow rate. The evaporating pressure is not affected by the injection ratio.
Fig 7 shows the discharge temperature for the two cycle and the two ambient temperature conditions as a function of the bypass and injection ratios. The temperature starts to decrease as the bypass and injection ratios increase further. The reason for the decrease of the discharge temperatures is different for each cycle. In the bypass cycle, the discharge temperature was influenced by the suction temperature. However, in the injection cycle, it is influenced by the temperature of the injection refrigerant owing to the intercooling effect.

3.2.3. Mass flow rate and Discharge temperature

Fig 8a shows the cooling capacities for both cycles at two ambient temperature conditions. In the bypass cycle, the cooling capacity increases with the increase of the bypass ratio at the onset of the bypass. However, it decreases from the specific bypass ratio. This is because the mass flow rate in the evaporators decreases continuously. In the injection cycle, the cooling capacity increases since the mass flow rate in the evaporators are almost constant despite the increase of the injection ratio, while the sub-cooling degree increases as the injection ratio increases.
The input power is also influenced by the bypass and injection ratios in Fig 8b. In the case of the

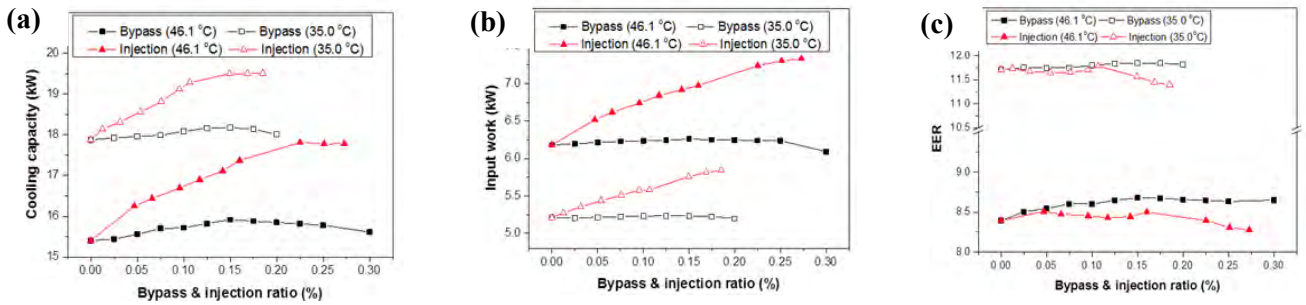

Figure 8: The operating characteristics of the system with variation of bypass and injection ratio (a) Cooling capacity (b) Input power (c) EER

bypass cycle, the input power increases slightly with increases of the bypass ratio because of the increase of the suction temperature and the total mass flow rate. but it decreases as the bypass ratio increases further owing to the decrease of the suction temperature. but, the input power in the injection cycle increases continuously because of the increase of the total mass flow rate.
Fig 8c shows energy efficiency ratio (EER). The EER for the bypass cycle increases gradually with the bypass ratio, but the EER decreases from the specific bypass ratio because the cooling capacity in the two cases of different temperatures decreases. In the injection cycle, The EER of the injection cycle decreases at the beginning of the refrigerant injection because the degree of superheating for the injected refrigerant is high. However, The EER of the injection cycle slightly increases when the degree of superheating at the injection line is reached to 0 ℃ because of the decrease of specific volume of the injection refrigerant.

3.3. Performance Comparison for the Bypass and Injection Cycles with the same Cooling Capacities

As shown in Fig 8a, the cooling capacity of the injection cycle is relatively higher than that of the bypass cycle. To compare the performance of the system using the injection to that using bypass under same cooling capacity. The compressor frequency was adjusted for two outdoor temperatures. Fig 9a shows that input power of injection cycle is less than of bypass cycle by 4.45 % and 2.32 % respectively in two different outdoor temperature. Therefore, the COP of injection cycle is better than that of the bypass cycle by 5.08 % and 2.38 % respectively as shown in Fig 9b.

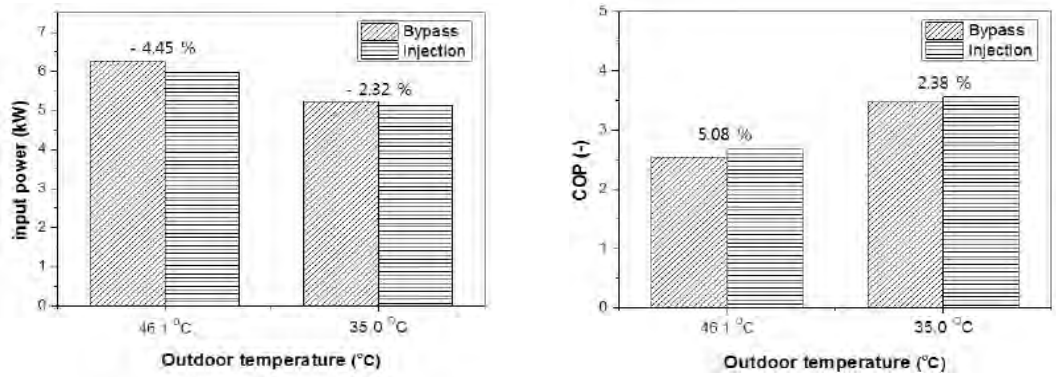

Figure 9: The operating characteristics of the system with variation of the bypass and injection ratio (a) Input power (b) COP

4. CONCLUSIONS

Subcooling methods of a sub-cooler can be divided into by bypass method and injection method. The operating characteristics of the VRF system using bypass and injection was compared. The sub-cooling degree is influenced by the bypass and injection. The discharge temperature of the compressor decreases when the bypass and injection ratios increase. Both the bypass and injection cycles yield improvements in the potential of the cooling capacities. In the bypass cycle, the cooling capacity decreases beyond the optimum bypass ratio owing to decreases of the mass flow rate in the evaporators. In the injection cycle, the cooling capacity is enhanced as the injection ratio increases because of the constant mass flow rate in the evaporators and the increase of the sub-cooling degree at inlet of the EEV. The application of the injection cycle reduces the input power. In addition, the injection cycle is more effective in reducing the discharge temperature at high-ambient temperature conditions.

ACKNOWLEDGEMENTS

This work was supported by "Human Resources Program in Energy Technology" of the Korea Institute of Energy Technology Evaluation and Planning (KETEP), granted financial resource from

the ministry of Trade, Industry & Energy, Republic of Korea. (No. 20184010201660)

NOMENCLATURE

h	Enthalpy (kJ/kg^{-1})	k	Ratio of specific heat (-)
P_{cr}	Critical pressure (kPa)	$\dot{m}$	Mass flow rate (kgs^{-1}
P_r	Pressure ratio (-)	Q	Capacity (kW) and heat transfer rate
R	Gas constant ($kJkg^{-1}K^{-1}$)	R_{ini}	Injection ratio (-)
υ	Specific vloume (m^3kg^{-1})	W	Work (kW)

Greek symbols

η	Efficiency (%)	θ	Angle (°)
ρ	Density (kgm^{-3})		

Subscript

avr	average	byp	bypass	comp	compressor
cond	condenser	dis	discharge	eev	electronic expansion valve
eva	evaporator	g	gas phase	ihx	internal heat exchanger
sc	sub-cooling	ind	indicated	inj	injection
l	liquid phase	sh	super-heating	m	mass
mech	mechanical	u	upstream	vi	vapor-injection
p	pressure	suc	suction		

REFERENCES

Afify, 2008, Designing VRF systems, ASHRAE Journal, 50, 52-55.

Churchill, S. W., Bernstein, M., 1977, A correlating equation for forced convection from gases and liquids to a circular cylinder in crossflow, Journal of heat transfer, 99(2), 300-306.

Gnielinski, V., 1976. New equations for heat and mass transfer in turbulent pipe and channel flow, Int. Chem.Eng., 16(2), 359-368.

Gronnerud, R., 1972, Investigation of liquid hold-up, flow-resistance and heat transfer in circulation type evaporators, part Ⅳ: two-phase flow resistance in boiling refrigerants, Bull. De l'Inst. Du Froid, Annexe, 1.

JSRAE, 2018. Compressors for Air Conditioning and Refrigeration, Technical Book Series, Japan Society of Refrigeration and Air Conditioning Engineers.

Kandlikar, S. G., 1990, A general correlation for saturated two-phase flow boiling heat transfer inside horizontal and vertical tubes, Journal of heat transfer, 112(1), 219-228.

Kang, H., Joo, Y., 2012. Effects of flash gas generation at the expansion device inlet on the dynamic characteristics of a refrigeration system, International Journal of Refrigeration, 31(3), 396-403.

Kwon, C., Kim, M.S., Choi, Y.G., 2017. Performance evaluation of a vapor injection heat pump system for electric vehicles, International Journal of Refrigeration, 74, 138-150.

Lockhart, R. W., Martinelli, R. C., 1949, Proposed correlation of data for isothermal two-phase, two-component flow in pipes, Chem. Eng. Prog, 45(1), 39-48.

Shah, M. Ml., 1979, A general correlation for heat transfer during film condensation inside pipes, International Journal of heat and mass transfer, 22(4), 547-556.

Shao, S., Xu, H., Tian, C., 2012. Dynamic simulation of multi-unit air conditioners based on two phase fluid network model, Applied Thermal Engineering, 40, 378-388.

Sun, H.S., Hu, H., Ren, T., Xia, G., Wu, G., 2017. A general simulation model for variable refrigerant flow multi-split air conditioning system based on graph theory, International Journal of Refrigeration, 82, 22-35.

Wang, C. C., Lee, C. J., Chang, C. T., Lin, S. P., 1999, Heat transfer and friction correlation for compact louvered fin and tube heat exchangers, International journal of heat and mass transfer, 42(11), 1945-1956.

Zhu, Y., Du, Z., Fan, B., Fu, S., 2013. Generic simulation model of multi-evaporator variable refrigeration flow air conditioning system for control analysis, International Journal of Refrigeration, 36, 1602-1615.

Manuscript ID: 1626
DOI: 10.18462/iir.icr.2019.1626

Assessing fresh air rate for theatre buildings using particle mass balance principle

Yuchen SHI [(a)], Xiaofeng LI [(a)]

[(a)]Tsinghua University
Beijing, 100084, China, syc17@mails.tsinghua.edu.cn

ABSTRACT

In order to maintain a good indoor environment, fresh air is essential for audience in theatre buildings due to the high occupant density. Apart from mechanical fresh air, uncontrolled air leakage across building exterior (i.e., air infiltration) is also a source of outdoor fresh air. Therefore, assessing air infiltration rate is very necessary for determining total fresh air rate and avoiding excessive ventilation. However, the commonly used method to assess infiltration rate is very complex to implement. In this paper, we propose a convenient method to assess infiltration rate based on the mass balance of particulate matters. Given the ubiquity of particulate matters in the outdoor environment and being cost-free, this method is able to avoid the disadvantages of traditional methods. PM2.5 is chosen to establish the mass balance. Infiltration and total fresh air rates of a concert hall were measured and analyzed using the proposed method.
Keywords: Fresh Air Rate, Infiltration, Particle Mass Balance, Ventilation.

1. INTRODUCTION

To maintain a satisfying indoor air quality, sufficient fresh outdoor air for building occupants is vital, especially for audience in theatre buildings due to the high occupant density (Wargocki et al., 2000; ASHRAE, 2016). China's standard of fresh air rate for theatre buildings is 15 – 25 $m^3 \cdot h^{-1}$ per person (MOHURD, 2016). To reach the standard, mechanical ventilation systems are generally used in theatre buildings. Actually, apart from mechanical ventilation, air infiltration, which means the uncontrolled air leakage across a building envelop, is also a source of outdoor fresh air. Unlike mechanical fresh air rate that can be measured in air ducts, infiltration rate cannot be measured directly. Besides, infiltration brings outdoor particulate matters indoors and directly influences indoor air quality, especially when the outdoor air is highly polluted. Therefore, assessing infiltration rate is very necessary for determining total fresh air rate, avoiding excessive ventilation and improving indoor air quality.

The most commonly used method to measure infiltration rate is the tracer gas method (ASTM 2010). The tracer gas method uses tracer gas dilution for calculating a single zone's air change rate with the outdoors. There are three kinds of techniques used in the tracer gas method: concentration decay, constant injection, and constant concentration. Among them concentration decay is the most widely used one, which has been used in office buildings (Reardon et al., 2002), residential buildings (Almeida et al., 2017), classrooms (Almeida et al., 2017) and retail stores (Chan et al., 2015). The test procedure of tracer gas method consists of the release, mixture, and monitor of suitable tracer gas. The method is very complex to implement and takes several hours to get one result (ASTM, 2010). Besides, the cost of tracer gas is relatively high, especially if the space volume is large. Hence, a simpler method is urgently needed for assessing infiltration rate.

During the past decade, haze pollution in China is very serious (Huang et al., 2014). The main component of haze is fine particulate matters, which are particles with a maximum diameter of 2.5 μm (abbreviated as PM2.5) and can be inhaled into the lungs (Gao et al., 2015). As mentioned before, particles will infiltrate indoors. In order to keep a low indoor PM2.5 concentration, air filters for particulates are extensively used in the mechanical ventilation systems in China (Jiang et al., 2017). Besides, due to people's sustained attention to PM2.5, the measuring instruments and on-line monitoring of PM2.5 are prevalent and of mature technology.

In this paper, we propose a convenient method to assess infiltration rate based on the mass balance of particulate matters. Given the ubiquity of particulate matters in the outdoor environment and being cost-free, this method is able to avoid the disadvantages of the tracer gas method. PM2.5 is chosen

to establish the mass balance. Considering that PM2.5 deposits indoors, sensitivity analysis is conducted for PM2.5 deposition rate. Infiltration rates of a concert hall were measured using our proposed method when the mechanical fresh air was supplied or not. Then the total fresh air rates were analyzed for different ventilation conditions.

2. METHOD

2.1. PM2.5 Mass Balance

Taking the internal room space as a control body, the PM2.5 mass balance is shown in Fig. 1.

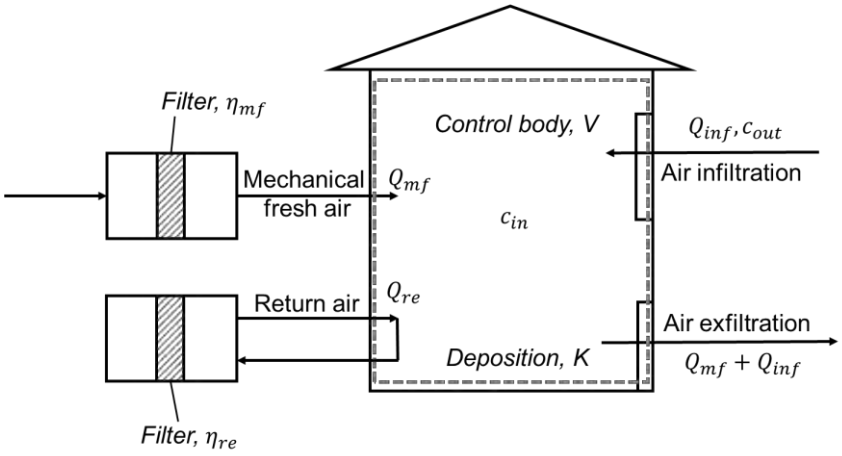

Figure 1: Indoor PM2.5 mass balance

There are two ways for PM2.5 to enter indoors: PM2.5 transported through mechanical fresh air gets indoors after filtration; and PM2.5 transported through air infiltration gets indoors directly. After getting indoors, part of the particles deposits on indoor surfaces, part of them is filtered by the return air unit, and the remaining PM2.5 exits the control body through air exfiltration. If outdoor PM2.5 concentration is constant for a given time period, the indoor PM2.5 concentration will eventually come to a steady state. The steady-state PM2.5 mass balance equation is expressed as

$$PQ_{inf}c_{out} + Q_{mf}(1-\eta_{mf}) = Q_{re}\eta_{re}c_{in} + (Q_{inf}+Q_{mf})c_{in} + KVc_{in} \quad \text{Eq. (1)}$$

where P is penetration factor, dimensionless; Q_{inf} is infiltration rate, $m^3 \cdot h^{-1}$; c_{out} is outdoor PM2.5 concentration, $\mu g \cdot m^{-3}$; Q_{mf} is mechanical fresh air rate, $m^3 \cdot h^{-1}$; η_{mf} is filtration efficiency of mechanical fresh air unit, dimensionless; Q_{re} is mechanical return air rate, $m^3 \cdot h^{-1}$; η_{re} is filtration efficiency of mechanical return air unit, dimensionless; c_{in} is indoor steady-state PM2.5 concentration, $\mu g \cdot m^{-3}$; K is PM2.5 deposition rate, h^{-1}; and V is volume of the control body, m^3.
The I/O ratio of PM2.5 for the steady state is given by Eq. (2) (Monn et al., 1997):

$$I/O_{ratio} = \frac{c_{in}}{c_{out}} \quad \text{Eq. (2)}$$

Substituting Eq. (2) into Eq. (1), infiltration rate is calculated by the following equation:

$$Q_{inf} = \frac{Q_{re}\eta_{re} \times I/O_{ratio} + Q_{mf}(I/O_{ratio} + \eta_{mf} - 1) + KV \times I/O_{ratio}}{P - I/O_{ratio}} \quad \text{Eq. (3)}$$

According to Eq. (3), when I/O ratio, mechanical ventilation rates, filtration efficiencies, room volume, deposition rate, and penetration factor are determined, infiltration rate can be calculated. Among them, I/O ratio, mechanical ventilation rates, filtration efficiencies, and room volume are obtained by measurements. Researchers have found that indoor deposition rate is 0 – 0.5 h−1 for PM2.5 and the penetration factor is very close to 1 and usually set to 1 (Thatcher and Layton, 1995; Ozkaynak et al., 1996; Wallace, 1996).
Then, total fresh air rate is

$$Q_t = Q_{inf} + Q_{mf} \quad \text{Eq. (4)}$$

where Q_t is total fresh air rate, $m^3 \cdot h^{-1}$.

2.2. Sensitivity Analysis

As mentioned before, the variation range of PM2.5 deposition rate in previous researches is 0 – 0.5 h^{-1}. In this study, PM2.5 deposition rate is set to 0.25 h^{-1}. Then, sensitivity analysis is conducted for deposition rate within the range of 0 – 0.5 h^{-1}.
According to Eq. (3), infiltration rate can be divided to the ventilation and deposition parts:

$$F = \frac{Q_{re}\eta_{re} \times I/O_{ratio} + Q_{mf}(I/O_{ratio} + \eta_{mf} - 1)}{P - I/O_{ratio}} \quad \text{Eq. (5)}$$

$$D = \frac{KV \times I/O_{ratio}}{P - I/O_{ratio}} \quad \text{Eq. (6)}$$

where F is the ventilation part which means infiltration rate calculated by mechanical ventilation and filtration, $m^3 \cdot h^{-1}$; and D is the deposition part which means infiltration rate calculated by particle deposition ($m^3 \cdot h^{-1}$).
Substituting Eqs. (5) and (6) into Eq. (3), infiltration rate is calculated by

$$Q_{inf} = F + D \quad \text{Eq. (7)}$$

Also according to Eq. (3), infiltration rate and deposition rate are linearly positive correlated. Thus, the impact of deposition rate on infiltration rate is

$$\delta = \frac{D_{0.25} - D_0}{F + D_{0.25}} = \frac{D_{0.5} - D_{0.25}}{F + D_{0.25}} = \frac{D_{0.5}/D_{0.25} - 1}{F/D_{0.25} + 1} \quad \text{Eq. (8)}$$

where δ is the impact of deposition rate on infiltration rate, dimensionless; D_0, $D_{0.25}$ and $D_{0.5}$ are deposition parts when PM2.5 deposition rates are 0, 0.25 and 0.5 h^{-1}, respectively.
According to Eq. (8), the relationship between $F/D_{0.25}$ and δ is illustrated in Fig. 2, which indicates that the impact of deposition rate on infiltration rate will be lower than 10% when the ventilation part is more than 10 times the deposition part. In other words, in order to reduce the impact of deposition rate (which cannot be directly measured) on the calculated result of infiltration rate and to enhance the calculating accuracy, mechanical ventilation rate and filtration efficiency should be as high as possible.

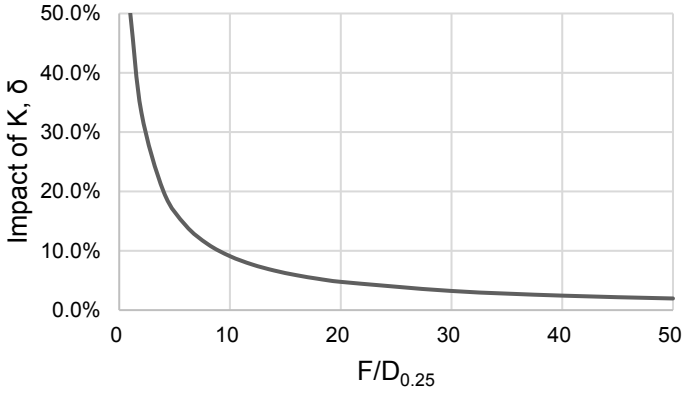

Figure 2: Relationship between $F/D_{0.25}$ and δ

3. RESULTS

The proposed method was used to assess fresh air rate for a concert hall which has a measured volume of 6950 m^3 and 510 seats (as shown in Fig. 3). Infiltration and total fresh air rates of two ventilation conditions were measured. Instruments used in the measurements are listed in Table 1.



Figure 3: The measured concert hall

Table 1. Instrument list

Instrument	Model	Accuracy	Usage
Tape measure	Tajima Hilock-25	± 0.5 mm	Measuring room volume and mechanical ventilation rates
Hot wire anemometer	TSI 962	± 0.015 m/s or ± 3% of reading	Measuring mechanical ventilation rates
PM2.5 concentration monitor	TSI AM510	/	Measuring indoor and outdoor PM2.5 concentrations

Measurements were conducted on May 4, 2017. The concert hall has two air handling units (AHUs), one for stage area (AHU1) and another for audience area (AHU2). Mechanical ventilation rates of AHUs were measured in air ducts using hot wire anemometer. The measured air supply rates of the two AHUs under difference ventilation conditions are listed in Table 2. There were twelve measuring points indoors for PM2.5 concentrations and two outdoors. Indoor PM2.5 measuring points were evenly distributed.

Table 2. Mechanical ventilation rate

Ventilation condition	All return air	Fresh and return air
AHU1 (stage area)	13213 $m^3 \cdot h^{-1}$ (return air)	13213 $m^3 \cdot h^{-1}$ (return air)
AHU2 (audience area)	14461 $m^3 \cdot h^{-1}$ (return air)	11354 $m^3 \cdot h^{-1}$ (fresh air) 3746 $m^3 \cdot h^{-1}$ (return air)
Filtration efficiency	75.5%	

First, the two AHUs were adjusted to 'All return air' model, under which circumstances there was no mechanical fresh air and the mechanical return air rate was 27674 $m^3 \cdot h^{-1}$ in total. The indoor and outdoor PM2.5 concentrations are shown in Fig. 4. As illustrated in this figure, the outdoor PM2.5 concentration is stable during the test period. That is because horizontal static wind is one of the main reasons for the formation of hazy weather and can cause a steady outdoor concentration of PM2.5 for a period of time (Zhou, 2015), which also validates our assumption for Eq. (1). Indoor PM2.5 concentration declines and reaches a stable value after turning on the AHUs for half an hour. The steady-state PM2.5 I/O ratio is 0.09 and the infiltration rate calculated by Eq. (3) is 2241 $m^3 \cdot h^{-1}$, which is also the total fresh air rate. By Eqs. (5) and (6), the ratio between the ventilation and deposition parts ($F/D_{0.25}$) is 15, thus the impact of deposition rate on infiltration rate is lower than 7% and is ignored.

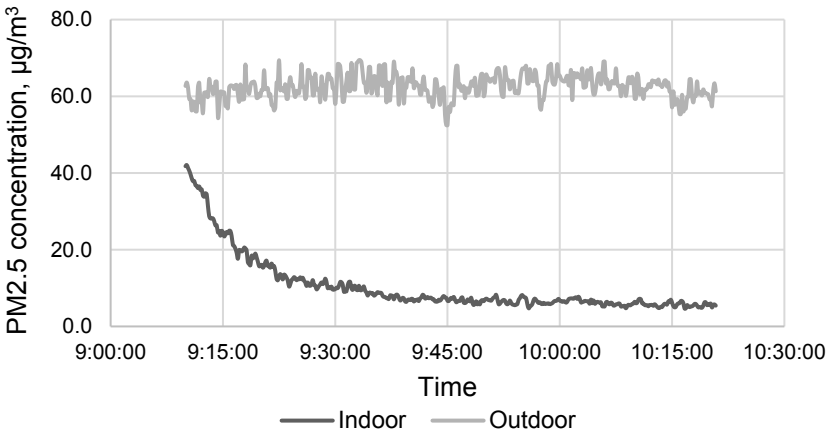

Figure 4: PM2.5 concentration (All return air)

Then, AHU2 was adjusted to 'Fresh and return air' model, with AHU1 unchanged. In this case, the mechanical fresh and return air rates were 11354 and 16959 $m^3 \cdot h^{-1}$. The indoor and outdoor PM2.5 concentrations are shown in Fig. 5. The steady-state PM2.5 I/O ratio is 0.11 and the infiltration rate calculated by Eq. (3) is 124 $m^3 \cdot h^{-1}$. Hence, the total fresh air rate is 11478 $m^3 \cdot h^{-1}$.

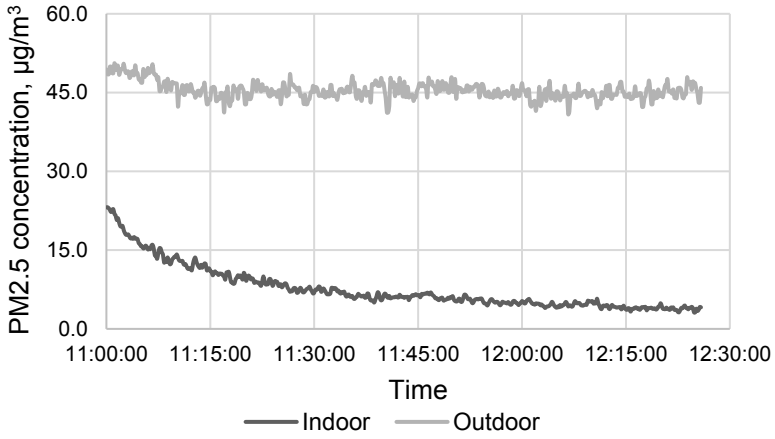

Figure 5: PM2.5 concentration (Fresh & return air)

Results of the above measurements are listed in Table 3. As mentioned in the Introduction, China's standard of fresh air rate for theatre buildings is 15 – 25 $m^3 \cdot h^{-1}$ per person. Therefore, the measured concert hall needs 7650 – 12750 $m^3 \cdot h^{-1}$ of fresh air. Under the first ventilation condition ('All return air'), infiltration is the only source of fresh air, but the infiltration rate is much lower than standard. This ventilation model can be used during rehearsals. While, when the audience is present, mechanical fresh air should be supplied. Under the second ventilation condition (Fresh & return air), the infiltration rate reduces sharply. This is because mechanical fresh air contributes to maintaining the positive pressure indoors and restraining air infiltration (Sapkota et al. 2005, ASHRAE 2009). Many researches assume that when a room is supplied with mechanical fresh air, infiltration rate will be zero (Cetin and Novoselac 2015). However, our results indicate that the relationship between infiltration and mechanical fresh air rates needs to be further studied. In order to determine the total fresh air rate, infiltration rate under certain mechanical fresh air rate needs to be assessed. According to our results, the second ventilation model provides adequate fresh air for audience.

Table 3. Test results

Ventilation condition	All return air	Fresh and return air
Mechanical fresh air rate ($m^3 \cdot h^{-1}$)	0	11354
Mechanical return air rate ($m^3 \cdot h^{-1}$)	27674	16959
Outdoor PM2.5 concentration ($\mu g \cdot m^{-3}$)	63.0	45.1
Indoor steady-state PM2.5 concentration ($\mu g \cdot m^{-3}$)	5.7	5.0
I/O ratio	0.090	0.112
Infiltration rate ($m^3 \cdot h^{-1}$)	2241	124
Total fresh air rate ($m^3 \cdot h^{-1}$)	2241	11478

4. CONCLUSIONS

Due to high occupant density, sufficient fresh outdoor air for audience in theatre buildings is vital. Mechanical ventilation and air infiltration are two sources of outdoor fresh air. In order to determine total fresh air rate, avoid excessive ventilation and improve indoor air quality, it is necessary to assess mechanical ventilation and air infiltration rates. Mechanical ventilation rate can be measured in air ducts, but infiltration rate cannot be directly measured. The commonly used method to assess infiltration rate is very complex to implement. This paper proposes a convenient method to assess infiltration rate based on the particle mass balance principle. Considering that particles deposit indoors, sensitivity analysis is conducted for particle deposition rate. It is concluded that in order to reduce the impact of deposition rate on infiltration rate, mechanical ventilation rate and filtration efficiency should be as high as possible.

The proposed method was used to assess infiltration and total fresh air rates for a concert hall. When mechanical fresh air is not supplied, infiltration is the only source of fresh air, which is not enough for audience but can be applied during rehearsals. When mechanical fresh air is supplied, infiltration rate reduces sharply (from 2241 to 124 $m^3 \cdot h^{-1}$), which proves that mechanical fresh air contributes to maintaining the positive pressure indoors. The relationship between infiltration and mechanical fresh air rates needs to be further studied.

In conclusion, in order to determine the total fresh air rate, infiltration rate under certain mechanical fresh air rate needs to be assessed. Our proposed method provides a convenient way to assess infiltration rate, which avoids the disadvantages of traditional methods.

REFERENCES

Almeida, R. M. S. F., Barreira, E., & Moreira, P., 2017. Assessing the variability of the air change rate through tracer gas measurements. Energy Procedia, 132, 831-836.

Almeida, R. M. S. F., Pinto, M., Pinho, P. G., & Luís T. de Lemos, 2017. Natural ventilation and indoor air quality in educational buildings: experimental assessment and improvement strategies. Energy Efficiency, 10(4), 839-854.

ASHRAE, 2009. ASHRAE handbook—Fundamentals: Ventilation and Infiltration, American Society of Heating, Refrigerating and Air Conditioning Engineers, Inc.

ASHRAE, 2016. Standard 62.1-2016 Ventilation for Acceptable Indoor Air Quality, American Society for Heating, Refrigeration, and Air-Conditioning Engineers, Inc.

ASTM, 2010. Standard Test Method for Determining Air Change in a Single Zone by Means of a Tracer Gas Dilution, ASTM Standard E741, American Society of Testing and Materials, Philadelphia.

Cetin, K. S., & Novoselac, A., 2015. Single and multi-family residential central all-air HVAC system operational characteristics in cooling-dominated climate. Energy and Buildings, 96, 210-220.

Chan, W. R., Cohn, S., Sidheswaran, M., Sullivan, D. P., & Fisk, W. J., 2015. Contaminant levels, source strengths, and ventilation rates in California retail stores. Indoor Air, 25(4), 381-392.

Gao, J., Tian, H., Cheng, K., Lu, L., Zheng, M., Wang, S., ... & Wang, Y., 2015. The variation of chemical characteristics of PM2.5 and PM10 and formation causes during two haze pollution events in urban Beijing, China. Atmospheric Environment, 107, 1-8.

Huang, R. J., Zhang, Y., Bozzetti, C., Ho, K. F., Cao, J. J., Han, Y., ... & Zotter, P., 2014. High secondary aerosol contribution to particulate pollution during haze events in China. Nature, 514(7521), 218.

Jiang, Y., Yang, X., Li, X., Yan, D., Wei, Q. & Shi, W., 2017. Annual Report on China Building Energy Efficiency. Tsinghua University, Building Energy Research Center.

Zhou, J., 2015. Analysis of causes and hazards of China's frequent hazy weather. The Open Cybernetics & Systemics Journal, 9(1).

MOHURD, 2016. Code for Design of Theater Building (JGJ57-2016) Ministry of Housing and Urban-Rural Development of the People's Republic of China, Beijing, China Architecture & Building Press.

Monn, C. H., Fuchs, A., Högger, D., Junker, M., Kogelschatz, D., Roth, N., & Wanner, H. U., 1997. Particulate matter less than 10 μm (PM10) and fine particles less than 2.5 μm (PM2. 5): relationships between indoor, outdoor and personal concentrations. Science of the Total Environment, 208(1-2), 15-21.

Ozkaynak, H., Xue, J., Spengler, J., Wallace, L., Pellizzari, E., & Jenkins, P., 1996. Personal exposure to airborne particles and metals: results from the particle team study in riverside, California. Journal of Exposure Analysis and Environmental Epidemiology, 6(1), 57-78.

Reardon, J. T., Atif, M. R., & Chia-yu, S., 2002. Tracer gas measurements for ventilation, air movement and air infiltration in a four-sided atrium office building. International Journal of Ventilation, 1(1), 13-22.

Sapkota, A., Williams, D., & Buckley, T. J., 2005. Tollbooth workers and mobile source-related hazardous air pollutants: how protective is the indoor environment? Environmental Science & Technology, 39(9), 2936-2943.

Thatcher, T. L., & Layton, D. W., 1995. Deposition, resuspension, and penetration of particles within a residence. Atmospheric Environment, 29(13), 1487-1497.

Wallace, L., 1996. Indoor particles: a review. Journal of the Air & Waste Management Association, 46(2), 98-126.

Wargocki, P., Wyon, D. P., Sundell, J., Clausen, G. & Fanger, P. O., 2000. The Effects of Outdoor Air Supply Rate in an Office on Perceived Air Quality, Sick Building Syndrome (SBS) Symptoms and Productivity. Indoor Air, 10(4), 222-236.

Manuscript ID: 1627
DOI: 10.18462/iir.icr.2019.1627

Simulation study for transcritical R744 refrigeration system with ejector installed

Gu Hwang KANG [(a)], Sun Ik NA [(b)], Min Soo KIM [(c)]

[(a)] Department of Mechanical & Aerospace Engineering, Seoul national university
Seoul, 08826, Korea, hardly11@nate.com
[(b)] Department of Mechanical & Aerospace Engineering, Seoul national university
Seoul, 08826, Korea, happy8earth@gmail.com
[(c)] Department of Mechanical & Aerospace Engineering, Seoul national university
Seoul, 08826, Korea, minskim@snu.ac.kr

ABSTRACT

The regulations on high global warming potential (GWP) refrigerants are being intensified in recent years. Thus, the researches with respect to alternative refrigerants are actively carried out. The R744 is representative natural refrigerant with low GWP, however, the pressure of R744 cycle is very high, and the coefficient of performance (COP) tends to be lower than conventional cycles. Therefore, in this study, experimental study for transcritical R744 refrigeration system with ejector installed is progressed. Ejector geometry and optimal operating conditions are provided to find an optimal COP. In addition to this, experiments are conducted at various conditions to investigate the optimal operating situation.

The cycle shows the best performance when the ejector geometry and operating conditions are well matched. Performance of ejector is enhanced as the gas cooler pressure elevates. While the compressor work is also increases. Therefore, optimal operation conditions should be thoroughly determined.

Keywords: Refrigeration, Carbon Dioxide, COP, Ejector.

1. INTRODUCTION

As global warming gets worse, temperatures of earth have risen dramatically. For this reason, air conditioner becoming an indispensable product in the current generation. However, the refrigerant using in air conditioner has high GWP. Therefore, the use of air conditioner accelerates the global warming, and we need more air conditioner. To break a vicious circle, there must be a new alternative. Though natural refrigerants, such as carbon dioxide, ammonia, and hydrocarbon etc., are classical refrigerants, natural refrigerants are substituted because those has some problems to use. However, the global warming problems of CFC, HFC, and HCFC refrigerants lead a new emergence of natural refrigerants. Natural refrigerants have very low GWP.

In this paper, representative natural refrigerant, carbon dioxide is analysed. GWP of carbon dioxide is just 1, and ODP is zero. However, as I mentioned before, carbon dioxide has problem to use as refrigerant. That is low COP. Therefore, research on performance improvement is important in carbon dioxide refrigeration system.

Yoon et al. carried out fundamental study about heat transfer and pressure drop characteristics of carbon dioxide at the supercritical region. And many researchers devise new carbon dioxide cycle to get performance improvement. Dai et al. studied energetic performance of transcritical CO_2 refrigeration cycles with mechanical subcooling using zeotropic mixture as refrigerant, and Zhang et al. studied double-compression transcritical CO_2 cycle, and get performance improvement at various conditions. Song et al. investigated the transcritical CO_2 refrigeration system using capillary tube with experimental study.

There is also a paper on the ejector. Basic ejector cycle is appeared in Fig. 1. Li et al. conducted visualization of two phase ejector through experimental study, and Palacz et al. carried out CFD calculation of CO_2 gas ejector and get entrainment ratio of ejector at various conditions. Taslimi Taleghani et al. conducted two-phase ejector modelling for on-design and off-design condition.

In this study, the simulation study for transcritical R744 refrigeration system with ejector is conducted.

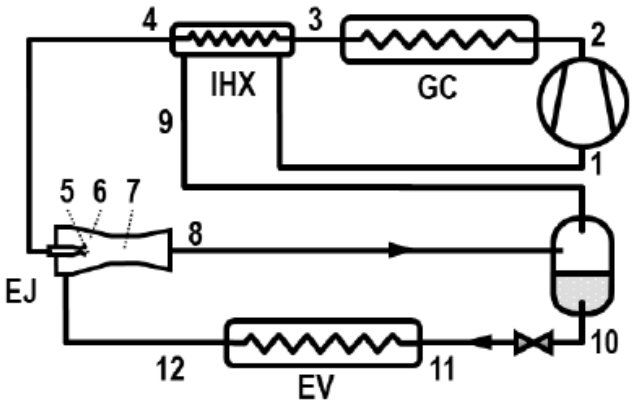

Figure 1: General transcritical R744 refrigeration cycle with ejector

2. SIMULATION STUDY

2.1. Ejector

Ejector has converging nozzle and diverging nozzle. Refrigerant get in ejector compressed and mixed with suction flow and discharged. In the process, pressure is decreased and restored. This is key point of ejector. By using the ejector, the mass flow rate of evaporator is reduced. Because of that, cooling capacity of system is reduced compared by non-ejector system. However, refrigeration pressure is restored and the refrigerant is heated at inlet of compressor. Therefore, compressor work is lowered. COP is calculated by Eq. (1)

$$\mathrm{COP} = \frac{Q_e}{W_c} \qquad \text{Eq. (1)}$$

Consequently, performance is improved as using ejector.

2.2. Heat Transfer Characteristics of Carbon Dioxide

T_{pc} is the temperature that has maximum specific heat. Characteristics of carbon dioxide shows drastic change before and after the pseudo critical temperature. Therefore, the heat transfer calculation method has to be divided.

$$\mathrm{Nu} = 0.013 * \mathrm{Re} * \mathrm{Pr}^{-0.05} * \left(\frac{\rho_{pc}}{\rho}\right)^{1.6} \quad \text{for } T \le T_{pc} \qquad \text{Eq. (2)}$$

$$\mathrm{Nu} = 0.14 * \mathrm{Re}^{0.69} * \mathrm{Pr}^{0.66} \quad \text{for } T \le T_{pc} \qquad \text{Eq. (3)}$$

Using Nusselt number according to Eq. (2) and Eq. (3), heat transfer rate of carbon dioxide is calculated.

2.3. Simulation Condition

The main parameter of simulation is compressor speed, and the iteration values in simulation are entrainment ratio of ejector, pressure of internal heat exchanger and separation ratio of phase separator. The flow chart of simulation represented in Fig. 2.
Outdoor temperature is 35℃, and indoor temperature is 27℃. In order to maintain a certain condition, the air temperature at exit of evaporator is fixed as 12℃. Other conditions, such as length, are given in the following Table 1.

Table 1. Condition of simulation

Parameter	Value
Outdoor temperature	35℃
Indoor temperature	27℃
Air temperature at evaporator	12℃
Gas cooler length (fin-tube)	37 m
Internal heat exchanger length (doubled-tube)	10 m
Evaporator length (fin-tube)	21 m
DSH	15 to 19

From the Table 1, DSH is relatively high than general refrigeration system. This is feature of this system. Refrigerant in this system is cooled down in evaporator and pass ejector and IHX. Therefore, temperature of refrigerant is comparatively lower. This effect lead to rise of DSH.

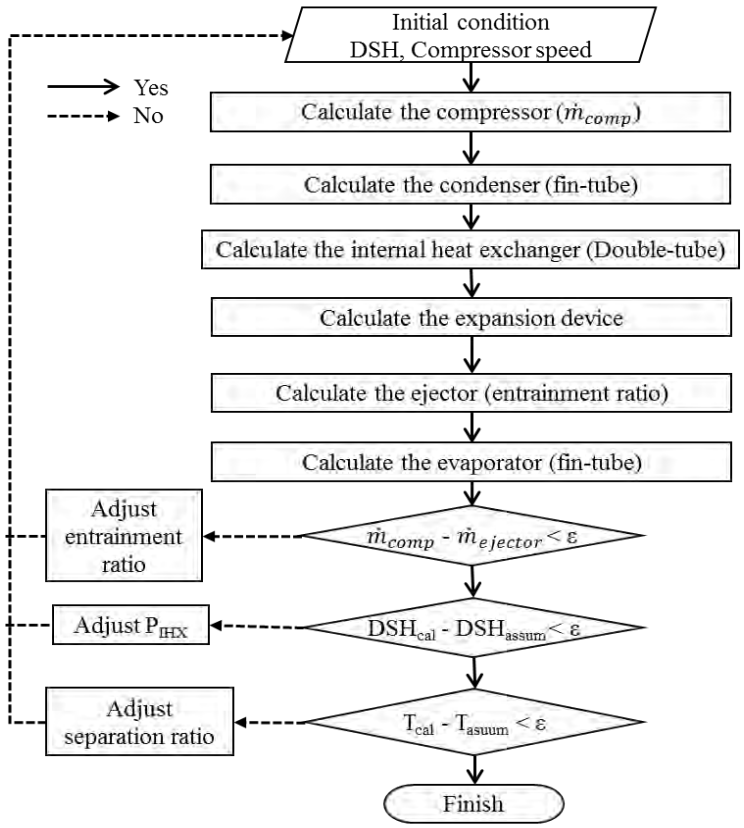

Figure 2: Flow chart of simulation

3. RESULT AND DISCUSSION

3.1. Temperature contour and density contour

This section shows temperature contour and density contour in gas cooler and evaporator. Contours are calculated through MATLAB. All the figures are selected at the same case. DSH is 18, and compressor speed is 70 Hz. The translucent black region appear flow path in heat exchanger, and

translucent white arrow shows the flow direction. Fig. 3 is temperature contour in gas cooler, and Fig. 4 is density contour in gas cooler.

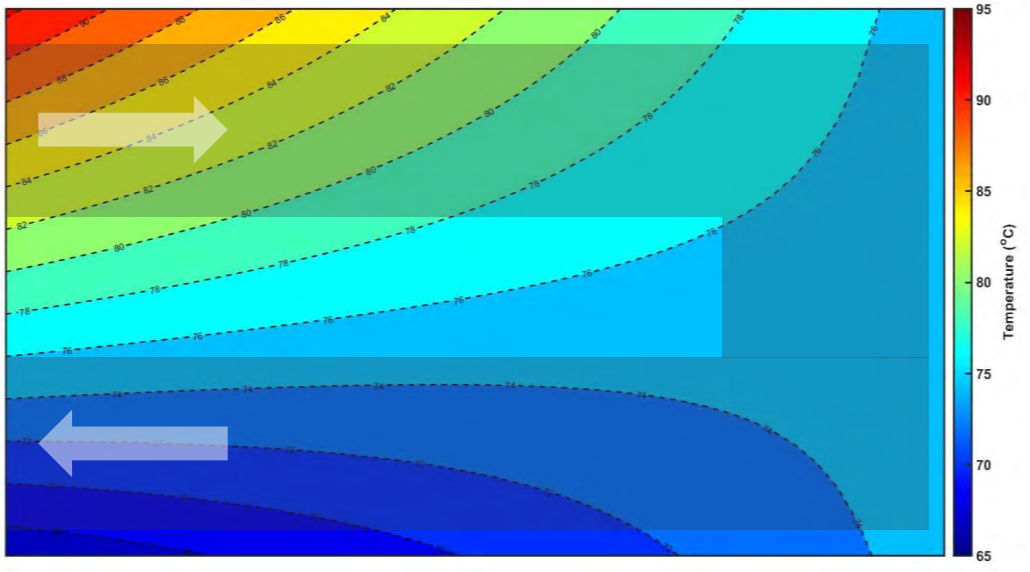

Figure 3: Temperature contour in gas cooler

As the flow progresses, temperature becomes decreases and density becomes increases. And at the curved section, temperature and density are stagnated.

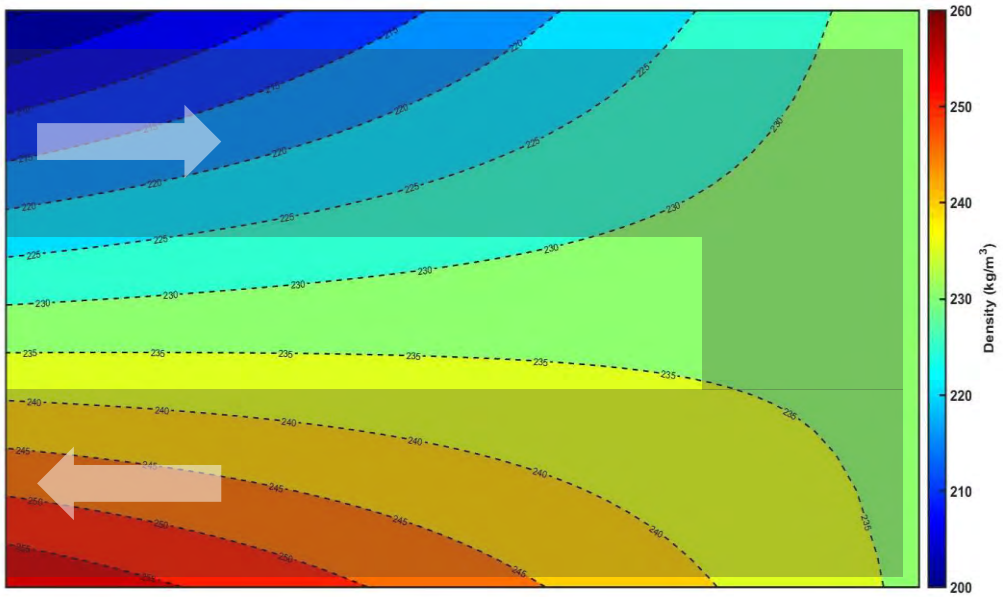

Figure 4: Density contour in gas cooler

Fig. 5 is density contour in evaporator. Temperature in evaporator shows similar values with each other, the temperature contour in evaporator does not appear in this paper.

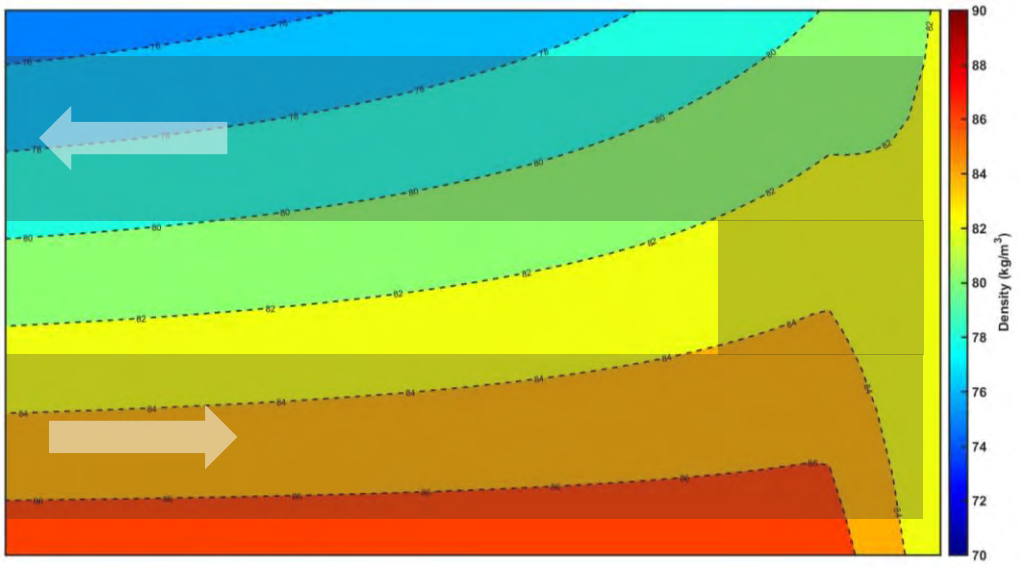

Figure 5: Density contour in evaporator

As the flow progresses, density becomes decreases. And at the curved section, temperature and density are stagnated.

3.2. Coefficient of Performance

3.2.1. Compressor speed

The COP of transcritical R744 refrigeration cycle with ejector with respect to compressor speed is represented in Fig. 6.

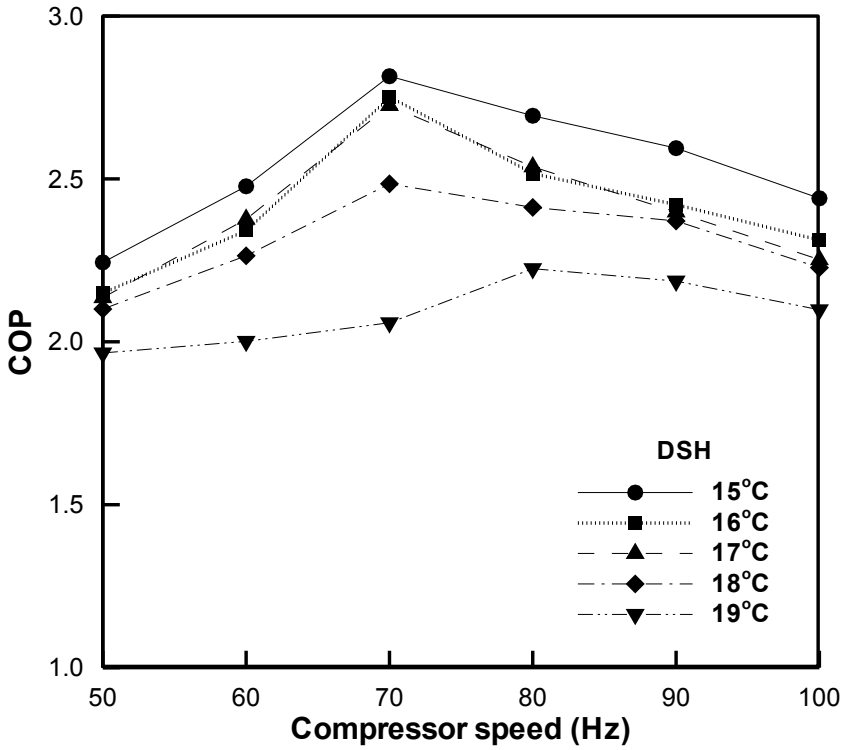

Figure 6: COP with compressor speed

COP is grows bigger as compressor speed increases until about 70 Hz or 80 Hz, and COP decreases as compressor speed increases. In this simulation, five DSH conditions selected, and except DSH is 19 case, all cases have maximum COP at compressor speed is 70 Hz.

3.2.2. DSH

The COP of the

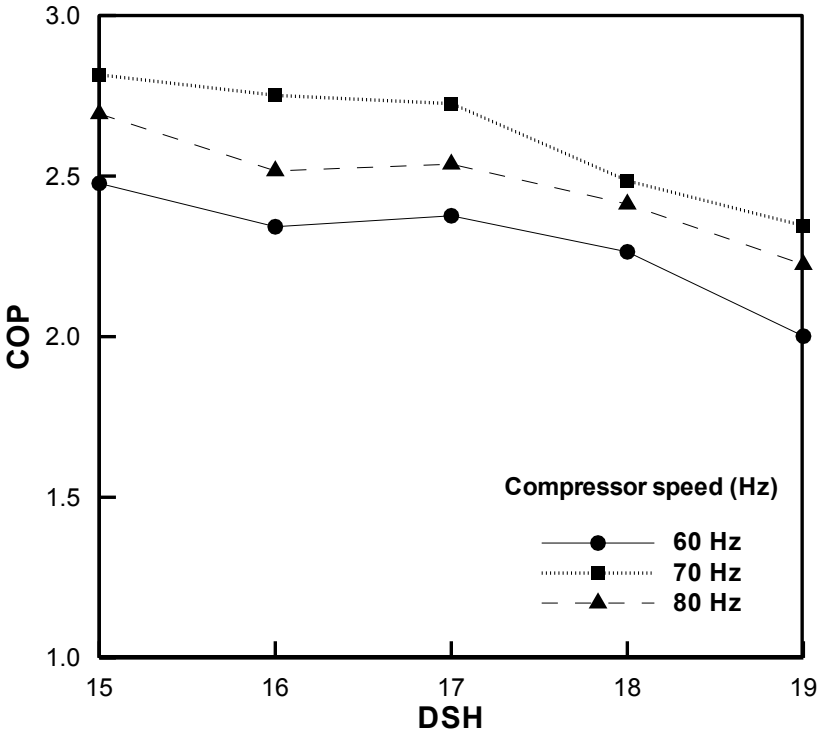

Figure 7: COP with DSH

As I mentioned before, DSH of transcritical R744 refrigeration cycle with ejector is relatively high. Academically, the lower DSH, the better. However, lower DSH can cause wet compression. Wet compression is the phenomenon that compressor inhale liquid refrigerant and compressed it. This can be lead break-up of compressor. From the Fig. 7, COP decreases as DSH grow bigger. Furthermore, compressor speed is 70 Hz case is optimal case.

4. CONCLUSIONS

In this paper, transcritical R744 refrigeration cycle with ejector is analysed. Using simulation study, temperature distribution and density distribution are obtained as contour figure. Further on, the COP with compressor speed and COP with DSH are calculated. And using this results, operating condition that maximize the COP is gained. In this simulation condition, compressor speed is 70 Hz, and DSH is 15 case show optimal value.

ACKNOWLEDGEMENTS

The authors are very thankful for the support from the Brain Korea 21 Plus Project (F14SN02D1310) of the Ministry of Education And the support from the Basic Science Research Program through the National Research Foundation of Korea (NRF) funded by the Ministry of Science, ICT & Future Planning (2016R1A2A1A05005510), and this project is supported by the ‘‘R&D Center for reduction of Non-CO2 Greenhouse gases (2017002430001)” funded by Korea Ministry of Environment (MOE) as ‘‘Global Top Environment R&D Program”.

NOMENCLATURE

DSH	Degree of superheat	GWP	Global Warming Potential
IHX	Internal heat exchanger	Nu	Nusselt number
ODP	Ozone Depletion Potential	Pr	Prandtl number
Q	Heat (kW)	Re	Reynolds number
T	temperature (℃)	W	Work (kW)

GREEK SYMBOLS

ρ	Density ($\mathrm{kg \cdot m^{-3}}$)

SUBSCRIPTS

c	Compressor	e	Evaporator
pc	Pseudo critical		

REFERENCES

Dai, B., Liu, S., Li, H., Sun, Z., Song, M., Yang, Q., & Ma, Y., 2018. Energetic performance of transcritical CO 2 refrigeration cycles with mechanical subcooling using zeotropic mixture as refrigerant. Energy, 150, 205-221.

Li, Y., Deng, J., Ma, L., & Zhang, Y., 2018. Visualization of two-phase flow in primary nozzle of a transcritical CO2 ejector. Energy Conversion and Management, 171, 729-741.

Llopis, R., Nebot-Andrés, L., Sánchez, D., Catalán-Gil, J., & Cabello, R., 2018. Subcooling methods for CO2 refrigeration cycles: A review. International Journal of Refrigeration, 93, 85-107.

Palacz, M., Haida, M., Smolka, J., Plis, M., Nowak, A. J., & Banasiak, K., 2018. A gas ejector for CO2 supercritical cycles. Energy, 163, 1207-1216.

Song, Y., Wang, J., Cao, F., Shu, P., & Wang, X., 2017. Investigation on the adaptivity of the transcritical CO 2 refrigeration system with a capillary. International Journal of Refrigeration, 79, 183-195.

Taslimi Taleghani, S., Sorin, M., & Poncet, S., 2018. Modeling of two-phase transcritical CO 2 ejectors for on-design and off-design conditions. International Journal of Refrigeration, 87, 91-105.

Yoon, S. H., Kim, J. H., Hwang, Y. W., Kim, M. S., Min, K., & Kim, Y., 2003. Heat transfer and pressure drop characteristics during the in-tube cooling process of carbon dioxide in the supercritical region. International Journal of Refrigeration, 26(8), 857-864.

Zhang, Z., Wang, H., Tian, L., & Huang, C., 2016. Thermodynamic analysis of double-compression flash intercooling transcritical CO2 refrigeration cycle. The Journal of Supercritical Fluids, 109, 100-108.

Manuscript ID: 1706
DOI: 10.18462/iir.icr.2019.1706

Comparison of two indirect cooling processes to produce cold water

Yi JIANG[(a)], Xiaoyun XIE[(a)]

[(a)] Building Energy Research Center, Tsinghua University
Beijing, 100084, China, jiangyi@tsinghua.edu.cn

ABSTRACT

Indirect evaporative cooling technology to produce cooling water (called IEC chiller) is proved to be most predicable with lower outlet temperature of cooling energy and lower transportation power consumption. There are different process structures of IEC chillers. However there are not good methods and principles to compare and choose different processes. In this paper, two typical IEC chillers with different process structures are compared, by field testing results, theoretical analysis and simulation analysis. Based on the field-testing analysis and theoretical analysis, the comparisons by simulation are carried out with the same NTU and the same cooling capacity. The comparison results are obtained, which changes with the size of NTU. The main reasons are discussed and the principle of choosing different processes are primarily obtained.
Keywords: Cold Water, Efficiency, Evaporative System, Optimization, Testing.

1. INTRODUCTION

Evaporative cooling technologies have been used more and more widely in building cooling systems, data centre cooling systems, different factory cooling processes and so on as its benefits on low energy consumption and zero CFCs emissions.

Considering the basic cooling processes, the evaporative cooling technology can be divided into two kinds, direct evaporative cooling technologies (DEC) and indirect evaporative cooling technologies (IEC) (Duan, 2012). For DEC processes, the limit outlet temperature is inlet wet bulb temperature. While for IEC processes, the limit outlet temperature is inlet dew point temperature (Wicker,2003, Jiang and Xie, 2010, Mahmood, 2016). For dry climates, the dew point is about 8~10K lower than wet bulb temperature. Thus, IEC technology can be used in wider climates and applications (Bom, 1999).

Considering the working medium for supplying cooling energy, the evaporative cooling technology can be divided into two kinds, DEC/IEC processes to produce cooling water (Jiang and Xie, 2010) or DEC/IEC processes to produce cooling air (Watt, 1987, Singh,1999, Al-Juwayhel,2004). First, the transportation energy consumption for cooling water system can only be 1/4 to 1/10 of cooling air system. Second, the cooling water system is more sensible to realize local cooling where heat emits. Thus, cooling water systems can be used in wider applications.

Accordingly, IEC technology to produce cooling water process is the most competitive technology. IEC technology to produce cooling water, also called IEC chiller is prompted (Jiang and Xie, 2010) more than ten years ago in about 2002 and has been used in a lot of real projects in northwest of China for buildings cooling systems. After that, several kinds of IEC chiller processes are prompted. The different IEC chiller processes are composed of different sensible heat transfer processes, different heat and mass transfer processes and different connections of these processes. Thus, how to choose the better processes of IEC chiller is a key and basic problem, for finding the most suitable processes for real applications. Accordingly, two basic IEC chiller processes is compared in this paper, including comparisons of both theoretical analysis results and real testing results. Based on the comparisons, the principle of comparing different processes is discussed and obtained primarily.

2. PRINCIPLES OF TWO IEC CHILLER PROCESSES

2.1. IEC Chiller Process I

Fig. 1 shows the structure of IEC chiller process I, which is put forward in 2002 (Jiang and Xie, 2010). As shown in Fig. 1a, the main components are a counter current air cooler and a counter current padding tower. The inlet air is cooled by one part of the outlet cold water, from O to A, as Fig. 1(b) shows. Then the air at conditions A is extracted into the padding tower and is carried heat and mass transfer process with the spraying water, and finally is heated and humidified to conditions E. The outlet cooling water at the condition $t_{w,O}$ of the padding tower is divided into two parts, one part is pumped into the air cooler to cool the inlet air and the other is pumped into the users. The two parts of return water are mixed to the condition $t_{w,sp}$ and sprayed on the top of the tower and then contacts with air for direct evaporative cooling processes and finally to be cooled to the outlet condition $t_{w,O}$.

For this IEC chiller process I, when the ratio of the two parts water flow rate is designed to be a suitable value, the air-water sensible heat transfer process and the air-water evaporative cooling process can be both matching heat transfer processes. Further, when the heat transfer area of the two main components is designed to be infinite, the limit outlet temperature of the cooling water is the inlet dewpoint temperature (Jiang and Xie, 2010).

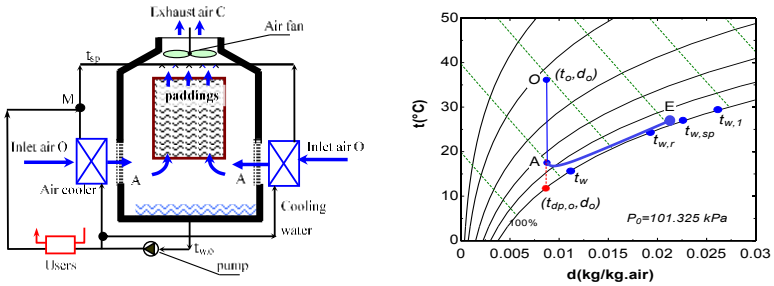

(a) structure of the process (b) process to produce cooling water

Figure 1: IEC chiller process I

2.2. IEC Chiller Process II

Fig. 2 shows the structure of IEC chiller process II. The main components of this process are crosscurrent air-air heat exchangers and counter current air-water evaporative cooling modules, as shown in Fig. 2(a). The inlet air is first cooled by the exhaust air, from O to A as Fig. 2(b) shows. Then the cooled air A is extracted into the air-water heat and mass transfer modules to be humidified to the condition E to produce cooling water at the condition $t_{w,O}$. The inlet water at the condition $t_{w,in}$ is sprayed on the top of the evaporative cooling modules and then contacts with the air to carry out heat and mass transfer processes and finally is cooled to be $t_{w,O}$. The outlet air of the evaporative cooling modules at the condition E is heated by the air-air heat exchangers to be the condition F and finally exhausted out.

For this IEC chiller process, the outlet water temperature cannot reach the inlet dew point temperature even if the air-air heat transfer processes and the air-water heat and mass transfer processes are both matching designed and the heat transfer area is large enough to be infinite. While for this process, all of the cooling water produced by the padding tower is transported to users.

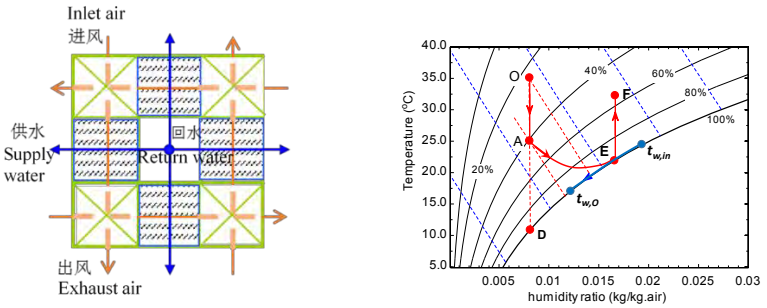

(a) Structure of the process (b) process to produce cooling water

Figure 2: IEC chiller process II

2.3. Performance Description Method of IEC Chillers

Each table First, to express the basic performance-the outlet temperature of the cooling water of the IEC chillers introduced above, the efficiencies of the basic two kinds of components are used to obtain the outlet temperature, as shown by Eq. (1)~(3):

$$t_{w,o}=t_{wr}-\eta_{ev}[t_{wr}-(t_{sO}-\eta_c(t_{sO}-t_{dpO})]] \quad \text{Eq. (1)}$$

$$\eta_c=(t_{sO}-t_{sA})/(t_{sO}-t_{dpO}) \quad \text{Eq. (2)}$$

$$\eta_{ev}=(t_{wr}-t_w)/(t_{wr}-t_{sA}) \quad \text{Eq. (3)}$$

Where η_c represents the air cooling efficiency of the sensible heat transfer process, η_{ev} represents the water cooling efficiency of the heat and mass transfer process.
Where $t_{w,O}$ represents the outlet water temperature of the IEC chiller; t_{wr} represents the return water temperature of cooling water; t_{sO} represents the wet bulb temperature of the inlet air; t_{sA} represents the wet bulb temperature of the outlet air of the air cooling processes; t_{dpO} represents the dew point temperature of the inlet air.
If η_c and η_{ev} were both reaching 1, the outlet temperature of the cooling water would reach the inlet dew point temperature.
Second, the output quantity of cooling energy for unit inlet air flow rate can be expressed by Eq. (4).

$$q_w=G_w*c_{pw}*(t_{w,r}-t_{w,o})/G_a \quad \text{Eq. (4)}$$

Where G_w represents the output water flow rate to users; c_{pw} represents the specific heat capacity of water, G_a represents the inlet air flow rate.

3. FIELD TESTING RESULTS OF TWO IEC CHILLERS

3.1. Field Testing Results of IEC Chiller I



(a) Developed IEC chiller I

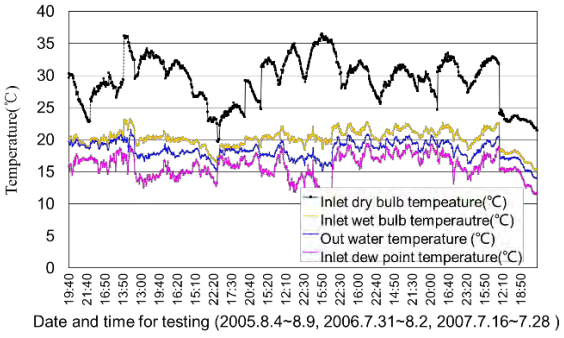

(b) Testing outlet water temperature of the chiller

Figure 3: Testing results of IEC chiller I

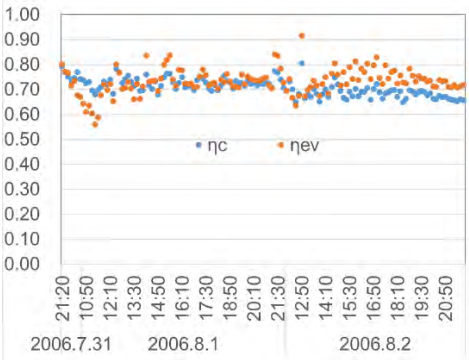

Figure 4: Testing efficiencies of IEC chiller I

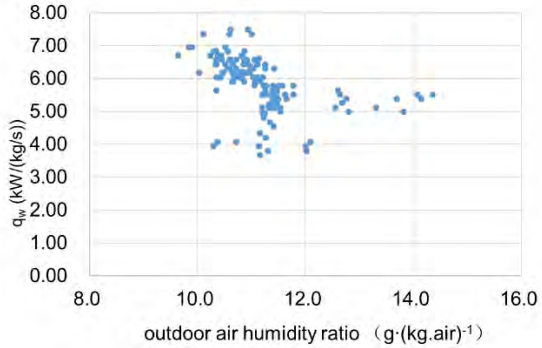

Figure 5: Testing cooling energy of IEC chiller I

The IEC chiller I is developed and applied in real buildings, as shown in Fig. 3a. As Fig. 3b shows, the tested outlet water temperature of the chiller is lower than inlet wet bulb temperature and higher than inlet

dew point temperature, and more or less at the average value of inlet wet bulb and dew point temperature (Jiang and Xie, 2010).
The tested efficiencies η_c and η_{ev} is shown in Fig. 4, η_c and η_{ev} are both at about 0.7~0.8. The output cooling energy of unit inlet air flow rate is at about 4~7 kW·kg^{-1}·s^{-1}).

3.2. Field testing results of IEC chiller II

The testing results of IEC chiller II is shown in Table 1. Fig. 6 and Fig. 7 shows the processes of working condition 1 and working condition 2. The tested efficiencies η_c and η_{ev} is shown in Table. 1. η_c is at about 0.3, which is much lower than that of IEC chiller I. η_{ev} is higher than 0.9, which is a little higher than that of IEC chiller II.

Table 1. Testing results of IEC chiller II

Working condition	t_O (℃)	t_{sO} (℃)	t_{dpO} (℃)	t_A (℃)	t_{sA} (℃)	t_E (℃)	d_E (g·(kg. air)$^{-1}$)	t_F (℃)	$t_{w,in}$ (℃)	$t_{w,o}$ (℃)	η_c	η_{ev}	q_w kW·kg^{-1}·s^{-1}
Working condition 1	32.2	17.9	8.4	24.9	15.3	19.2	11.61	26.6	21.7	15.8	0.27	0.92	6.3
Working condition 2	40.4	22.4	13.4	30.1	19.3	22.1	13.75	32.4	21.7	19.4	0.34	0.98	2.4

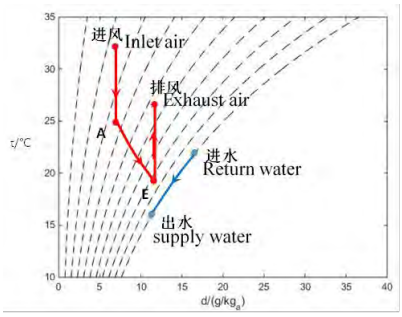

Figure 6: Working conditon 1 of IEC chiller II

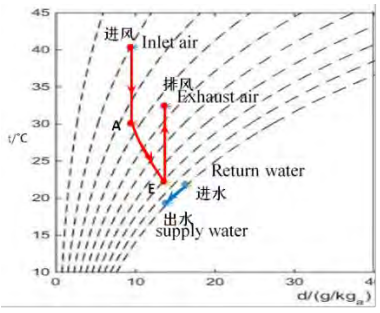

Figure 7: Working condition 2 of IEC chiller II

4. IDEAL PERFORMANCE OF TWO IEC CHILLERS BY THEORETICAL ANALYSIS

For one process, when the internal heat transfer processes, and heat and mass transfer processes are both designed to be flow rate matching processes, and the heat transfer area is tended to be infinite, the processes reaches its ideal performance. For different process structures, the ideal performances are different. The ideal processes of IEC chiller I and IEC chiller II are shown in Fig. 8. and Fig. 9.

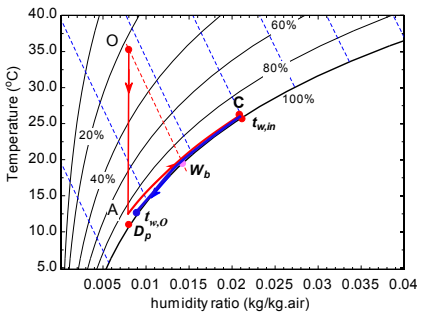

Figure 8: The ideal performance of IEC chiller I

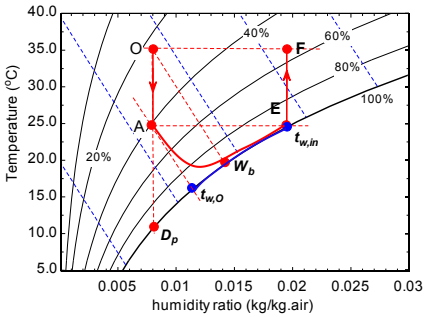

Figure 9: The ideal performance of IEC chiller II

The comparison is shown in Table 2.

Table 2 Comparison of ideal performances of the two IEC chillers

	IEC chiller I	IEC chiller II
Ideal $t_{w,o}$	$t_{dp,o}$	t_{sA}, where t_A=$t_{w,in}$ and d_A=d_O, which is higher than $t_{dp,o}$

q_w $kW \cdot kg^{-1} \cdot s^{-1}$	$q_{wI}=G_{wI}c_{pw}(t_{w,in}-t_{dpO})/G_a$	$q_{wII}=G_{wII}c_{pw}(t_{w,in}-t_{wo})/G_a=r_0(d_{w,in}-d_O)$

For IEC chiller I, the ideal outlet temperature is inlet dew point temperature $t_{dp,o}$, the ideal output cooling energy q_{wI} depends on the return water temperature $t_{w,in}$ and $t_{dp,o}$. The higher the $t_{w,in}$, the higher the q_{wI}. For this process, the ideal $t_{w,o}$ is independent of q_{wI}.
For IEC chiller II, the ideal outlet temperature is the wet bulb temperature of air with the dry bulb temperature equals to $t_{w,in}$ and the humidity ratio equals to inlet air humidity d_O, which is higher than $t_{dp,o}$. The ideal output cooling energy q_{wII} depends on $t_{w,in}$ and d_O. For this process, $t_{w,o}$ not only depends on d_o, but also depends on $t_{w,in}$. The lower the $t_{w,in}$, the lower the $t_{w,o}$, while the lower the $t_{w,in}$, the lower the q_{wII}. The ideal $t_{w,o}$ is related to q_{wII}.

Furthermore, if the saturation line is assumed to be a linear line, which can be described by Eq. (5).

$$d_s=at_s+b \quad \text{Eq. (5)}$$

where t_s represents the dry bulb temperature of the saturated air, and d_s represents the humidity ratio of the saturated air, a is the linear factor.
In addition, for matching design of each heat transfer processes, the relation of the flow rates of air and water for IEC chiller I can be expressed by Eq. (6)~(8).

$$G_{wb}c_{pw}=G_ac_{pa} \quad \text{Eq. (6)}$$

$$(G_{wI}+G_{wb})c_{pw}=G_ac_{pea} \quad \text{Eq. (7)}$$

$$c_{pea}=c_{pa}+r_0a \quad \text{Eq. (8)}$$

Where G_a represents the air flow rate of inlet air, G_{wb} represents the water flow rate of the air cooler, G_{wI} represents the water flow rate of the user, c_{pa} represents the specific heat capacity of air, c_{pw} represents the specific heat capacity of water, c_{pea} represents the equivalent specific heat capacity of air for evaporative cooling process.
By using Eq. (5)~(8), the output cooling capacity q_{wI} can by expressed by Eq. (9).

$$q_{wI}=G_{wI}c_{pw}(t_{w,in}-t_{dpO})/G_a=r_0a(t_{w,in}-t_{dpO}) \quad \text{Eq. (9)}$$

For matching design of IEC chiller II, the flow rates of air and water can be expressed by Eq. (10)

$$G_{wII}c_{pw}=G_ac_{pea} \quad \text{Eq. (10)}$$

Where G_{wII} represents the cooling water flow rate for users.
The output cooling energy of IEC chiller II q_{wII} can be expressed by Eq. (11).

$$q_{wII}=G_{wII}c_{pw}(t_{w,in}-t_{wo})/G_a=r_0(d_{w,in}-d_O)=r_0a(t_{w,in}-t_{dpO}) \quad \text{Eq. (11)}$$

Thus, we can see that, for the ideal performances, the cooling capacity of the two IEC chillers are equal to each other, while the output cooling water temperature of IEC chiller I is lower than IEC chiller II. Accordingly, IEC chiller I is better than IEC chiller II for ideal performances.

5. RESULTS AND DISCUSSION

5.1. Comparison by Field Testing Results

The simulation procedures of IEC chiller I and IEC chiller II were both set up by EES, which can be used to compare the two IEC chillers under the same inlet air conditions. Thus, the performance of IEC chiller I is simulated under the testing inlet air conditions of IEC chiller II for comparison. Table 3 shows the comparison results.

Table 3. Comparison results under field tested inlet air conditions

	Working condition 1	Working condition 2

performance	t_O (℃)	$t_{dp,o}$ (℃)	$t_{w,in}$ (℃)	$t_{w,o}$ (℃)	η_c	η_{ev}	q_w kW·kg^{-1}·s^{-1}	t_O (℃)	$t_{dp,o}$ (℃)	$t_{w,in}$ (℃)	$t_{w,o}$ (℃)	η_c	η_{ev}	q_w kW·kg^{-1}·s^{-1}
IEC chiller I	32.2	8.4	21.7	13.0	0.75	0.8	>7.0	40.4	13.4	21.7	16.9	0.75	0.8	7.0
IEC chiller II	32.2	8.4	21.7	15.8	0.27	0.92	6.3	40.4	13.4	21.7	19.4	0.34	0.98	2.4

From Table 3, under the same tested working conditions, the performance of IEC chiller I is better than IEC chiller II as well, with lower $t_{w,o}$ and higher q_w. The comparison results of field testing results not only depend on the different structure of IEC chillers, but also depends on NTU of internal heat transfer processes and the running air-water flow rate ratio, which are shown in Table 4.

Table 4. NTU and air-water flow rate ratio of real tested IEC chillers

-	NTU of sensible heat exchanger	NTU of padding tower	air-water flow rate ratio
IEC chiller I	4.5	2.5	3.3
IEC chiller II	1.66	1.66	3.9

From Table 4, the NTU of the sensible heat exchanger and the padding tower of IEC chiller I are both higher than that of IEC chiller II. The air-water flow rate ratio of IEC chiller I is lower. Thus, it is difficult to say that IEC chiller I is better than IEC chiller II for real performances. To fairly compare the two different structures under finite heat transfer area, it is better to carry out the comparison under the same NTU and the same air-water flow rate ratio, which is discussed in the flowing part.

5.2. Comparison under the Same NTU and the Same Flow Rate Ratio

The simulation models of IEC chiller I and IEC chiller II are set up and verified by the field testing results. Using the simulation models of IEC chiller I and IEC chiller II, the comparisons are carried out under the conditions as Table 5 shows. Given the same NTU of both air coolers and padding towers of the two kinds of IEC chillers and to produce the same cooling energy, to compare the temperature level of the output cooling water, the lower the better.

The two kinds of IEC chillers are compared under three working conditions, with different NTU levels and different cooling capacity demands. The comparison results are shown in Fig. 10~Fig. 11. From Fig. 11. It is can be seen that, when the NTU of the two main components is low, as for working condition 1, the $t_{w,o}$ of IEC chiller I is higher than that of IEC chiller II, and at this moment, IEC chiller II is better than IEC chiller I. While when the NTU is high enough, as for working condition 2 and working condition 3, the $t_{w,o}$ of IEC chiller I is lower than that of IEC chiller II, which indicates that IEC chiller I is better than IEC chiller II.

Table 5. The comparison conditions

Given parameters	Working condition 1		Working condition 2		Working condition 3	
NTU of padding towers	2.5		3.75		5.0	
NTU of air coolers	2.5		3.75		5.0	
	IEC chiller I	IEC chiller II	IEC chiller I	IEC chiller II	IEC chiller I	IEC chiller II
Cooling capacity (kW·kg^{-1}·s^{-1})	7.8	7.8	9.0	9.0	9.6	9.6
air flow rate (kg·s^{-1})	1.0					
Water flow rate (kg·s^{-1})	0.4					
Inlet air t_O (℃)	35.0					
Inlet air d_O (g·(kg.air)$^{-1}$)	8.0					

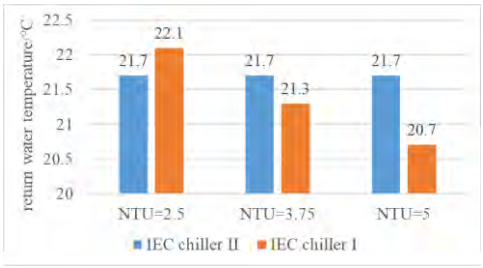

Figure 10: The inlet water temperature $t_{w,in}$

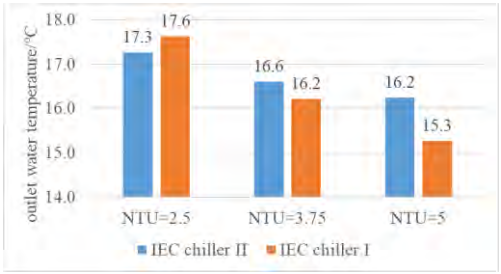

Figure 11: The outlet water temperature $t_{w,o}$

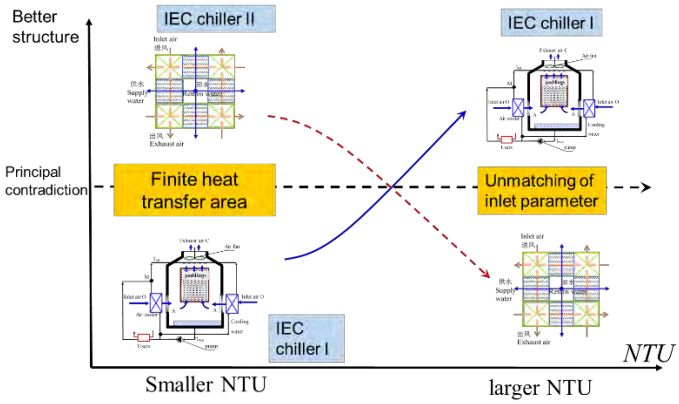

Figure 12: The comparison results

5.3. Analysis of the Comparison Results

From Fig. 10 to Fig. 11, we can see that, the comparison result of the two different structures depends on the level of NTU. Fig. 12 shows the main reason. For IEC chiller I, as Fig. 8 shows, the inlet air can be cooled near the saturation line by the air cooler, thus the following evaporative cooling process can be both flow rate matching and parameter matching process. However, the quantity of the transferred heat of the air cooler and the padding tower are both larger than that of IEC chiller II, which needs more heat transfer area. While, for IEC chiller II, as the air after the air-air heat exchanger is far from the saturation line, the evaporative cooling process cannot be realized to inlet parameters matching, and when the heat transfer area is large enough, the influence of unmatching is more prominent.

Thus, when the NTU is low enough, the principal contradiction is the finite heat transfer area, the process with lower quantity of total transferred heat is better, and when the NTU is high enough, the principal contradiction is the matching performance, the process with better matching performance is better. This is why the IEC chiller II is better than IEC chiller I when the NTU is low and when the NTU is high enough, the IEC chiller I is better. The comparison results of processes with different structures depends on the principal contradictions which will change with the size of NTU.

6. CONCLUSIONS

In this paper, two typical kinds of IEC chillers are compared, both by field testing results, theoretical analysis and simulation analysis. The main results are:

1. From field testing results of real equipment, IEC chiller I is better than IEC chiller II, with lower outlet temperature of cooling water $t_{w,o}$ and higher cooling capacity q_w.
2. From theoretical analysis for ideal performance, IEC chiller I is better than IEC chiller II, with lower $t_{w,o.}$ The cooling capacity q_w is equal to each other for the two processes.
3. By using the verified simulation models, IEC chiller I and IEC chiller II are compared under the same NTU and the same demand of q_w. When the NTU is low enough, IEC chiller II is better than IEC chiller I, and when the NTU is high enough, IEC chiller I is better than IEC chiller II. This is due to the different features of the two IEC chillers. IEC chiller I is a matching process with both flow rate matching and inlet parameter matching, while with higher quantity of total transferred heat. IEC chiller II is an unmatching process for inlet parameter as the cooled air after the air-air heat exchanger is far from the saturation line, while with lower

quantity of total transferred heat. As the NTU is changing from low to large, the principal contradiction is changing from the finite heat transfer area to unmatching performance, which makes the comparison results change. The comparison results gives us the choosing principle of different structure of IEC chillers.

ACKNOWLEDGEMENTS

The authors gratefully acknowledge the support from the National Natural Science Foundation of China (grant numbers 51306098, 51138005), the innovative Research Groups of National Natural Science Foundation of China (grant number 51521005), and Tsinghua University Initiative Scientific Research Program (No. 20151080470).

NOMENCLATURE

t	temperature (℃)	subscripts	
q	cooling capacity ($kW \cdot kg^{-1} \cdot s^{-1}$)	w	water
η	cooling efficiency	dp	dew point temperature
G	Mass flow rate ($kg \cdot s^{-1}$)	c	air cooler
c_p	Specific heat capacity ($kJ \cdot kg^{-1} \cdot K^{-1}$)	ev	evaporative cooling process
d	humidity ratio($g \cdot (kg.air)^{-1}$)	O	outdoor air
NTU	number of heat transfer unit		

REFERENCES

Al-Juwayhel, F., El-Dessouky, H., Ettouney, H., et al., 2004. Experimental evaluation of one, two, and three stage evaporative cooling systems. Heat Transfer Engineering 25(6): 72-86.

Bom, G.J., Foster, R., Dijkstra, E., Tummers, M., et al.,1999. Evaporative Air-Conditioning, Applications for Environmentally Friendly Cooling. World Bank Technical Paper, No 421, March.

Duan, Z.Y., Zhan, C.H., Zhang, X.X., et al., 2012. Indirect evaporative cooling: Past, present and future potentials. Renewable and Sustainable Energy Reviews 16(9), 6823-6850.

Jiang, Y., Xie, X.Y., 2010. Theoretical and testing performance of an innovative indirect evaporative chiller. Solar Energy 84(12), 2041-2055.

Mahmood, M.H., Sultan, M., Miyazaki, T., et al, 2016. Overview of the Maisotsenko cycle - A way towards dew point evaporative cooling. Renewable and Sustainable Energy Reviews, 66, 537-555.

Singh, S. P., Tulsidasani T. R., Sawhney R. L., et al., 1999. Recent research on an indirect evaporative cooler. Part VI: evolution of design pattern for indirect evaporative cooler. International Journal of Energy Research 23(7): 557-561.

Watt, J. R., 1987. Nationwide Evaporative Cooling Is Here. ASHRAE Transactions. 93(1):1237-1251.

Wicker, K., 2003. Life below the wet bulb: The Maisotsenko cycle. Power 147(9):29.

Manuscript ID: 1709
DOI: 10.18462/iir.icr.2019.1709

A novel indirect evaporative chiller system to realize anti-freezing of cooling tower used in data centre systems

Xiaoyun XIE[(a)*], Hua CAI[(a)], Yi JIANG[(a)]

[(a)] Building Energy Research Centre, Tsinghua University
Beijing, 100084, China, xiexiaoyun@tsinghua.edu.cn

ABSTRACT

Data Centres have been developed quickly in recent years. For water cooled data centre cooling system, the freezing of cooling tower in winter is a big problem and very hard to solve. In this paper, a novel system using indirect evaporative chillers to solve the freezing problem is put forward. The running mode and the switch point from refrigeration to free cooling is discussed for the new system. The performance of the recommended system in both winter and summer conditions is analysed both by simulation and by field testing. Upon the results, the ice problem can be solved thoroughly in winter, and the out water temperature of the indirect evaporative chiller can be 6~9K lower than common cooling towers in summer. From a real case study, compared with common water-cooled systems, the free cooling time can be 1000 hours increase and the electricity consumption can be 30~60% reduced.
Keywords: Cooling Tower, Data Centre, Evaporation, Free Cooling, Freezing.

1. INTRODUCTION

Recently, along with the development of IT industry, more and more data centres are built all over the world. As the heat production density is very high in data centres, the heat load is increasing to be 5kW/m^2 or more. For a large scale data centre, the supplied power can be reached to 600,000kW, equivalently as the output of a medium scale power station, or as the power consumption of a million population city. From the statistical data, the power consumption of the data centres in China takes more than 1% of the total power consumption of the country (Gu et al.,2011). To decrease the electricity consumption of data centres is the active demand.
The power consumption of air conditioning systems can be 30~40% of that of the IT equipment. To reduce the power consumption of air conditioning systems, most of the data centres are set up in cold climates, and further for large-scale data centres, water cooled systems are mostly applied to fully use the temperature difference between the air dry bulb and wet bulb temperature and to realize free cooling in transition seasons and winters using cooling towers.
However, for the water cooled systems in cold climates, a big problem is that the freezing of cooling towers in winters, as Fig. 1 shows.



Figure 1: Freezing of the cooling towers running in winters

Freezing of water always appears at the air inlet of the cooling tower, and make the air inlet blocked and the air flow rate reduced to zero, which strongly influence the safe running of the cooling system as well as the data centres. To solve the freezing problems, there exists some measures. For some data centres, independent dry air coolers are set up to be used to cool water in winters instead of cooling towers. However, using this measure, the system cost would be increased a lot, and furthermore, the switching between the dry air cooler and the refrigeration system according to the air temperature difference between the daylight and night would be very complicated. For some data centres, internal cooling towers are used (Gong and Lin, 2013), which working as a cooling tower in

summers and working as a dry air cooler in winters. However, using this method, the performance is worse than ordinary cooling tower in winter and it would encounter all the problems of dry air coolers stated above. In additions, for most of the data centres, electric heat tracing systems are used for anti-freezing, which cannot avoid the freezing of air inlet and also consume a lot of electricity. Besides, some assistant measures are used such as the air dampers and so on (Jiang et al., 2010). As there are not good methods to solve the freezing problem, it can only depend on manual removing the ice. Thus, it is a strong demand to find a good method to solve the freezing problem.

Accordingly, in this paper, a new method using indirect evaporative cooling technology to realize anti-freezing of cooling tower in winter is introduced. An indirect evaporative cooling device to produce cooling water (Jiang and Xie, 2010), also called IEC chiller is used instead of cooling tower, which can both realize anti-freezing in winter and decrease the cooling water temperature in summer. The IEC chillers have been used in air conditioning systems of large public buildings very well (Jiang et al., 2009; Xie, 2009) in dry climates to replace ordinary mechanical chillers, such as northwest of China. The energy consumption can be 40~70% reduced compared with common air conditioning systems. While for these existed applications, the IEC chillers are just used in summer season, for air conditioning systems of buildings. Thus, it is a new attempt to use IEC chillers for data centres for all over the year, also the cooling water temperature for data centres is different from that for building air conditioning systems. The joint system of IEC chiller and mechanical chiller is introduced as well as the principle of running mode for different seasons. The anti-freezing principle is detailed analysed and the real testing results in winter conditions are shown. Final a design case is shown, to give the comparison results of the recommended system and other common systems in electricity consumption, free cooling hours and switching conditions for mechanical cooling to free cooling.

2. COMBINED IEC CHILLER AND MECHINICAL CHILLER SYSTEM

To realize the whole year cooling for data centres, a combined system of an IEC chiller and a mechanical chiller is prompted. The principle of the combined system is introduced first. Then the anti-freezing process of using the IEC chiller is analysed in detail, the anti-freezing performance is tested in winter air conditions and the results are shown. The performance of the IEC chiller using in summer conditions is discussed as well, to show its advantage compared with common cooling towers.

2.1. Principle of the Combined System

The combined system of an IEC chiller and a common mechanical chiller is shown in Fig. 2. The system is composed of an IEC chiller, a mechanical chiller and a plate heat exchanger. The cooling water is produced by the IEC chiller and then is pumped to the plate heat exchanger (PHE) to transfer heat with the cold water, after the PHE, the cooling water is pumped into the condenser of the mechanical chiller to absorb heat, and finally is pumped back to the IEC chiller. In the IEC chiller, the return cooling water of the system is first pumped into an air-water heat exchanger to transfer heat with air, and then is pumped to the top of the padding tower for spraying. In the padding tower of the IEC chiller, the heat and mass transfer process is carried out to produce output cooling water. In the IEC chiller, the inlet air is first extracted into the air-water heat exchanger to transfer heat with the return cooling water, and then is extracted into the padding tower to carry heat and mass transfer with the spraying water and finally is exhausted out of the device. For the cold water system, the return cold water from terminal air condition systems is first pumped into the PHE, and then is pumped to the evaporator of the mechanical chiller to get the outlet cold water. There are two switching valves in the cold water system, valve 1 and valve 2, as Fig. 2 shows. The two valves are responsible for the two modes switching, cold water pumped into the PHE or not, which represents using free cooling or not.

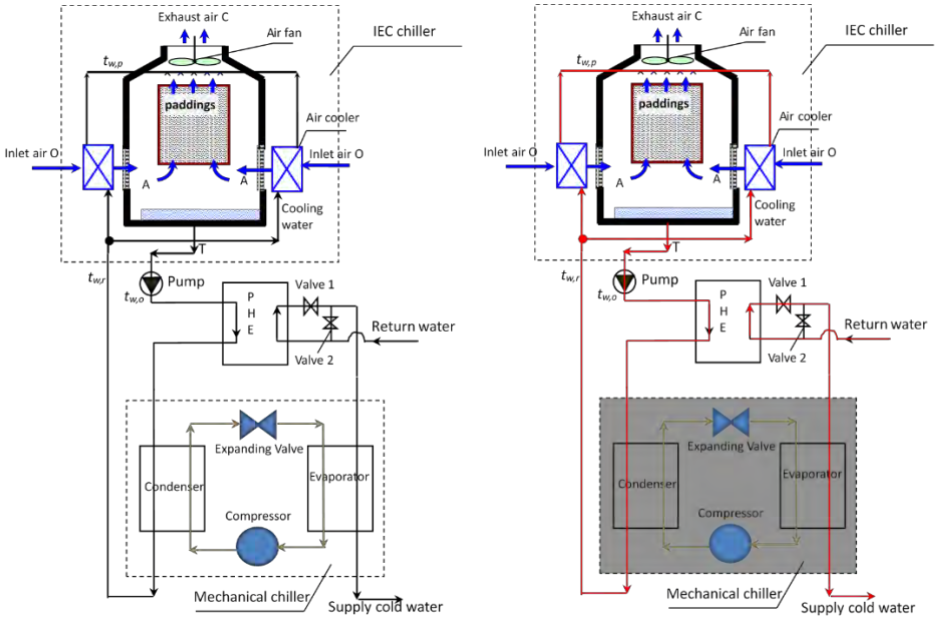

(a) Principle of the system (b) running mode in winter

Figure 2: The combined system of the IEC chiller and the mechanical chiller

In summer conditions, the IEC chiller is used to exhaust heat of condenser, valve is off and valve 2 is open. The function of the IEC chiller is just as the common cooling tower, only the cooling water temperature is lower, as part 2.3 shows.
In winter conditions, the mechanical chiller is turned off, and valve 1 is open and valve 2 is off. Free cooling mode is turned on. The IEC chiller is used as the cooling source of the system. The produced cooling water is used to cool the cold water to the demanded temperature. The water cycle is as Fig. 2 (b) shows. As the inlet air can be heated by the return cooling water through the air-water heat exchanger, the anti-freezing of the cooling tower can be realized, as part 2.2 shows.
In transition seasons, if the output cooling water is lower than the return cold water temperature but higher than the demanded supply cold water temperature, at this moment valve 1 is open and valve 2 is closed, the IEC chiller and the mechanical chiller is combined to produce the demanded outlet cold water.

2.2. Anti-Freezing Performance of the IEC Chiller

In winter conditions, as Fig. 2(b) shows, as the temperature of the inlet air is low, always lower than zero in very cold climates, and lower than the return cooling water, thus the inlet air is heated by the return cooling water to the temperature higher than zero or even higher than 10℃ if the return cooling water higher than 10℃. Then the heated air is directly contacted with the spaying water for evaporative cooling processes in the padding tower, the freezing problem can be thoroughly solved. On the other hand, the cooling water is cooled by the air-water heat exchanger and the padding tower together, which can save the water consumption compared with common cooling towers. To maintain the stable outlet cooling water temperature, the air fan frequency is adjusted along with outdoor air conditions, which can ensure to avoid the freezing problem all over the winter.
A case under extreme cold outdoor conditions in winter is shown by Table 1 and Fig. 3.

Table 1. The air and water conditions in an extreme cold case

t_O	t_A	$t_{s,A}$	t_C	t_{wr}	t_{wp}	t_{wo}	$m_{a\text{-}w}$
℃	℃	℃	℃	℃	℃	℃	
-40	13.8	2.5	11.0	14	11.1	10	0.23

Where t_o represents the inlet air temperature, t_A represents the outlet air dry bulb temperature of air-water heat exchanger, $t_{S,A}$ represents the outlet air wet bulb temperature of air-water heat exchanger, t_C represents the exhaust air temperature of the padding tower, t_{wr} represents the return cooling

water temperature, t_{wp} represents the outlet cooling water temperature of the air-water heat exchanger, t_{wo} represents the outlet cooling water temperature of the IEC chiller, $m_{a\text{-}w}$ represents the air water mass flow rate ratio.

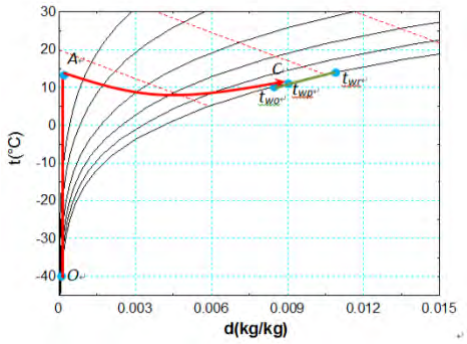

Figure 3: The process of an extreme cold condition in winter

From Table 1 and Fig. 3 we can see, even the inlet air temperature is low to -40℃, the inlet air can be heated to 13.8℃, the wet bulb of inlet air of the padding tower can be higher than 0℃, which can avoid the freezing of cooling tower thoroughly. Meanwhile, the water temperature in the air-water heat exchanger varies between 14~11.1℃, which can avoid the freezing of water in the air-water heat exchangers as well if the air-water heat exchanger is designed to be countercurrent or quasi countercurrent heat transfer processes.

The anti-freezing performance was also tested in winter conditions for a real developed IEC chiller. For the testing conditions, the cooling energy output was stable at 120kW, the inlet air dry bulb temperature varied between -12~-15℃, the inlet wet bulb temperature varied between -13.4~-16.3℃, the inlet dew point temperature varied between -23.1~-26.9℃. The testing results of a typical working condition are shown in Fig. 4. The inlet air dry bulb temperature is at -14.4℃ and wet bulb at -16.0℃. After the air-water heat exchanger, the air is heated to 12.8℃, the exhaust air is at about 10.0℃ and the relative humidity is at about 93.9%. The return cooling water is at about 14.6℃ and the outlet water temperature of air-water heat exchanger is at about 11.7℃. The outlet cooling water temperature maintained at about 9.7℃ with the fan frequency adjusted with the changing of inlet air temperature. There were no freezing of water for the padding tower and the air-water heat exchanger. The surface temperature of the air-water heat exchanger at the inlet air surface was tested, as Fig. 4 shows, the surface temperature was at 5~9.6℃ and no freezing of air-water heat exchanger.

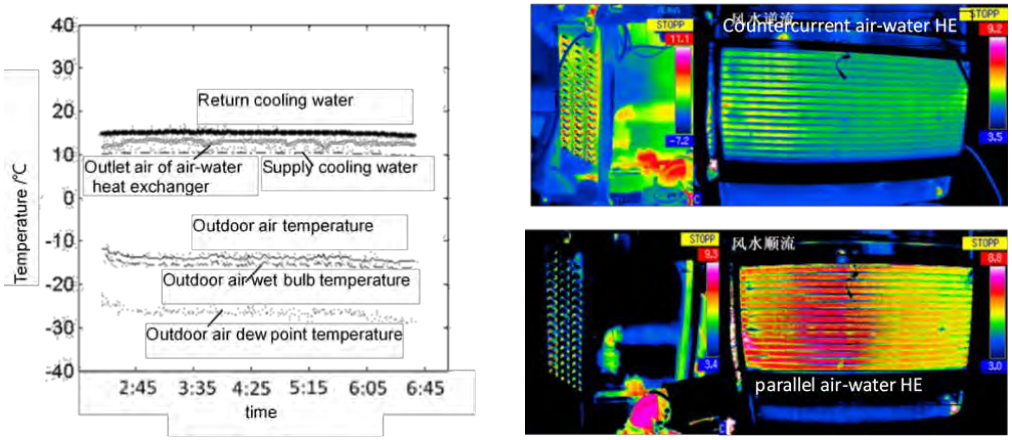

(a) Air and water temperature (b) surface temperature of air-water temperature

Figure 4: Testing performance of IEC chiller in winter conditions

2.3. Performance of the IEC Chiller in Summer Season

For the IEC chiller used in summer seasons, as the outdoor air is high to 30~40℃, which is higher than the outlet cooling water and even higher than the return cooling water of the system. Thus the inlet air is cooled by the cooling water through the air-water heat exchanger, accordingly, the air wet bulb temperature is decreased and then for the following air-water evaporative cooling processes,

the outlet cooling water temperature can be reduced as well. When the IEC chiller process is designed to the structure as Fig. 5(a) shows (Jiang and Xie, 2010), also called parallel structure as the water pumped into the air-water heat exchanger and the user are of parallel relation, the ideal outlet temperature of the IEC chiller can be near the inlet dew point temperature, as Fig. 5(b) shows. The testing outlet temperature of a developed parallel IEC chiller is shown in Fig. 6 (Jiang and Xie, 2010), for a real developed IEC chiller, the outlet water temperature is lower than the inlet wet bulb temperature and higher than the inlet dew point temperature, and more or less at the middle value of dew point and wet bulb temperature. As the outlet temperature of the common cooling tower is always 3~4℃ higher than the wet bulb temperature, the outlet cooling water temperature of the IEC chiller is 6~9℃ lower than that of the common cooling towers. Thus the COP of the mechanical chiller of the recommended system in this paper in summer would have a prominent increase compared with common systems using common cooling towers.

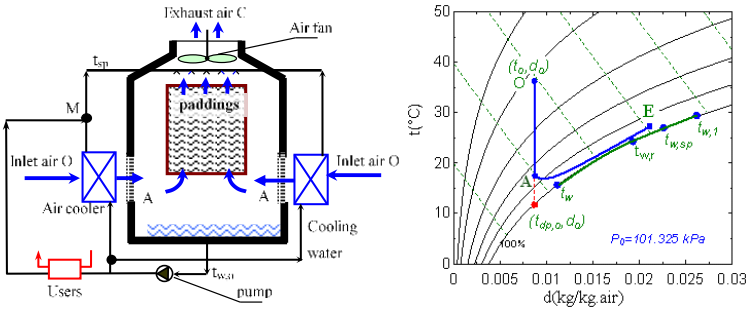

Figure 5: The working principle of IEC chiller under summer conditions

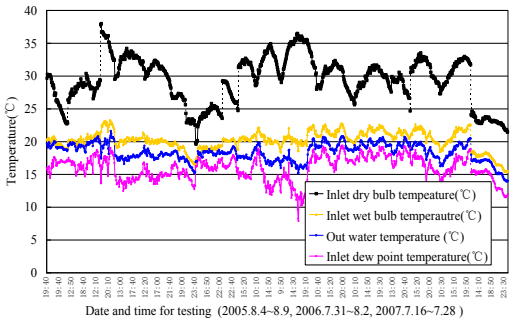

Figure 6: Testing performance of IEC chiller in summer conditions

3. CASE STUDY OF USING IEC CHILLER

To clearly show the whole year performance of the recommended system, a real case is given here to compare the novel system with common systems, to show the advantage of the supposed system.

3.1. Case Conditions and Comparison Systems

The case is for a data centre in Lanzhou of China. The quantity of heat production of the data centre is 14.4 MW. The climate data of Lanzhou for a whole year is shown in Fig. 7. Two kinds of IEC chiller combined mechanical chiller systems are discussed, as Fig. 8 shows, one is the serial structure of IEC chiller, the other is the parallel structure of IEC chiller. The comparison systems are the two recommended systems using IEC chillers, common water cooled system (that is mechanical chiller with common cooling tower) and common air cooled system (that is air cooled mechanical chiller) .

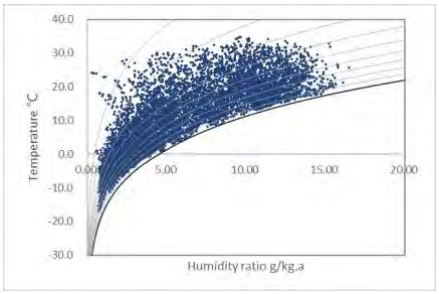

Figure 7: The climate data of Lazhou city

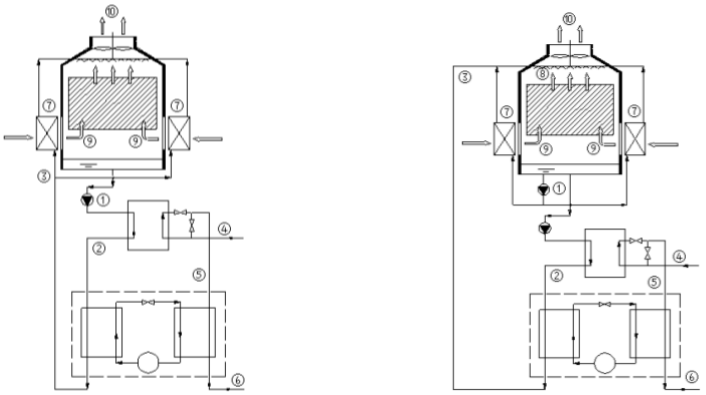

(a)serial structure (b) parallel structure

Figure 8: Two systems of with different IEC chiller structures

3.2. Comparison Results

As the demand cold water temperature of the data centre cooling system is one of the most important factor to influence the electricity consumption of the whole system, the comparison results are given for different cold water levels, as Fig. 9 and Fig. 10 show.

Fig. 9 gives the free-cooling hours of the discussed systems, and Table 2 gives the switching conditions of free-cooling for different systems.

From Fig. 9, the free-cooling hours of all the systems are increased along with the increase of the demanded cold water temperature, while for the recommended IEC chillers, the increase is the largest. If the demanded supply/return cold water temperature is increased to 22/28℃, the mechanical chiller can be cancelled for IEC chiller systems, and free cooling can be realized all over the year. Second, using the recommended IEC chiller system with parallel structure, the free cooling hours is always 1000 hours longer than the common water-cooled chiller systems, and is 1000~2700 hours longer than the common air-cooled chiller systems. The higher the demanded cold water temperature, the larger difference with the air cooled chiller systems.

Fig. 10 shows the electricity consumption of the compared systems. Using the recommended IEC chiller systems, about 30~60% of electricity consumption is saved compared with common water cooled chiller system, and about 50~80% of electricity consumption is saved compared with common air cooled chiller system.

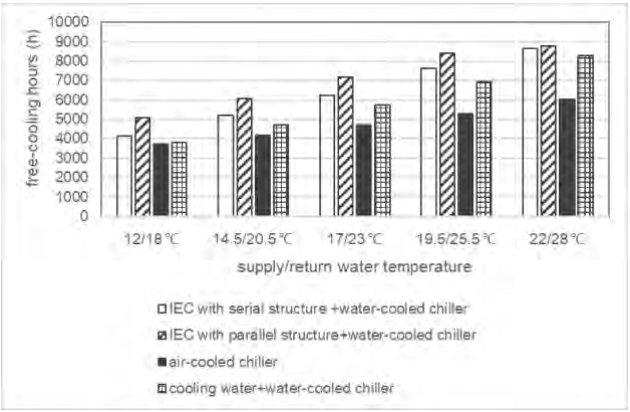

Figure 9: Free cooling hours of the systems

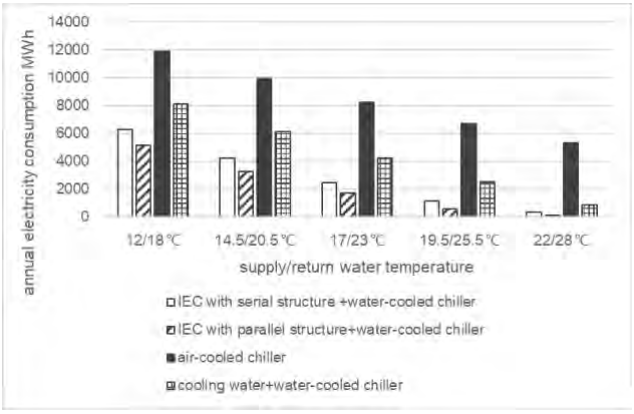

Figure 10: Electricity consumption of the systems

Table 2. The switching condition of free cooling for different systems

Systems	12/18 ℃	14.5/20.5 ℃	17/23 ℃	19.5/25.5 ℃	22/28 ℃
1	$t_m \leqslant 3.0^\circ$ C	$t_m \leqslant 7.0^\circ$ C	$t_m \leqslant 10.7^\circ$ C	$t_m \leqslant 14.0^\circ$ C	$t_m \leqslant 17.3^\circ$ C
2.	$t_m \leqslant 6.8^\circ$ C	$t_m \leqslant 10.1^\circ$ C	$t_m \leqslant 13.4^\circ$ C	$t_m \leqslant 16.3^\circ$ C	$t_m \leqslant 19.3^\circ$ C
3	$t_{s,O} \leqslant 4.1^\circ$ C	$t_{s,O} \leqslant 7.6^\circ$ C	$t_{s,O} \leqslant 10.8^\circ$ C	$t_{s,O} \leqslant 14.1^\circ$ C	$t_{s,O} \leqslant 17.2^\circ$ C
4	$t_O \leqslant 7.9^\circ$ C	$t_O \leqslant 10.2^\circ$ C	$t_O \leqslant 12.5^\circ$ C	$t_O \leqslant 14.7^\circ$ C	$t_O \leqslant 17.1^\circ$ C

Where sytem1 represents IEC chiller with parallel structure combined with water cooled chiller system, sytem2 represents IEC chiller with serial structure combined with water cooled chiller system, system 3 represents common water cooled chiller system, system 4 represents common air cooled chiller system. Where tm represents the average temperature of outdoor wet bulb temperature and outdoor dew point temperature, $t_{s,O}$ represents the outdoor wet bulb temperature, t_O represents the outdoor dry bulb temperature.

4. CONCLUSIONS

In this paper, a novel IEC chiller combined with mechanical chiller system is introduced to realize anti-freezing of cooling tower in winter, and to decrease the output cooling water temperature in summer conditions as well. The process structure of the recommended system is introduced. The anti-freezing principle is discussed in detail. The main results are:

(1) For the anti-freezing performance of the IEC chiller, an extreme case is designed with outdoor air temperature low to -40°C, the inlet air can be heated to 13.4°C by the air-water heat exchanger for evaporative cooling processes, to avoid the freezing of cooling tower reliably.
(2) The anti-freezing performance is tested for a real device under outdoor air temperature at about -16°C, the inlet air can be heated to12.8℃, and the surface of the air-water heat exchanger with lowest temperature reached 5~9.6℃, the padding tower and the air-water heat exchanger can both realize anti-freezing safely.
(3) For the performance of the IEC chiller in summer climates, the outlet water temperature can be lower than outdoor wet bulb temperature, thus can be 6~9°C lower than that of common cooling towers.
(4) From the case study, compared with common water cooled chiller systems, the free cooling hours of the novel system is always 1000 hours longer and 30~60% of electricity consumption can be saved; compared with common air cooled chiller systems, the free cooling hours of the novel system is 1000~2700 hours longer and 50~80% of electricity consumption can be saved.

The higher the demanded cold water temperature, the more above advantages of the recommended IEC chiller system.

ACKNOWLEDGEMENTS

The authors gratefully acknowledge the support from the National Natural Science Foundation of China (grant numbers 51306098, 51138005), the innovative Research Groups of National Natural Science Foundation of China (grant number 51521005), and Tsinghua University Initiative Scientific Research Program (No. 20151080470).

NOMENCLATURE

t	temperature (℃)	*s*	wet bulb temperature
m	air-water mass flow rate ratio	*m*	Average of wet bulb and dewpoint temperature
Subscripts		*w*	water
O	outdoor air		

REFERENCES

Gu, L.J., Zhou, F.Q., Meng, H., 2011. The study of China data centre energy consumption and energy efficiency. Energy of China 32(11), 42-45.

Gong, Y.X, Lin C.F.,2013. Closed cooling towers used in data centre air conditioning systems. Refrigeration and Air conditioning 13(8), 23-24.

Jiang, Y., Xie, X.Y., 2010. Theoretical and testing performance of an innovative indirect evaporative chiller. Solar Energy 84(12), 2041-2055.

Jiang, Y., Xie, X.Y.,2009. The applications of indirect evaporative cooling technology in China northwest regions. HVAC 39(9),1-4.

Jiang, X.R., Wang, W.M., Li, J.S., et al, 2010. Anti-freezing device for cooling tower, has macromolecule shutter. China, CN101881573A.

Xie, X.Y.,2009. Research on Indirect evaporative cooling systems. Doctoral Thesis, Bejing: Tsinghua Univeristy.

Manuscript ID: 1721
DOI: 10.18462/iir.icr.2019.1721

Discrete modeling of fin-tube heat exchangers accounting for cross-fin conduction

Omer SARFRAZ[(a)] *, Christian K. BACH[(b)], Craig R. BRADSHAW[(c)]

[(a) (b) (c)] Oklahoma State University, Mechanical & Aerospace Engineering, Stillwater, OK 74075, USA

[(a)] sarfraz@okstate.edu, [(b)] cbach@okstate.edu, [(c)] craig.bradshaw@okstate.edu

ABSTRACT

Heat exchanger coil models are a critical component for developing a predictive simulation platform which allows for model-based design of new equipment. Most residential and commercial heating, ventilation, and air-conditioning (HVAC) systems utilize fin-tube heat exchanger coils. Many of the current state-of-the-art heat exchanger models do not include cross-fin conduction and struggle with predictive accuracy of these coils under non-uniform flow and especially with large temperature difference between adjacent tubes.

This paper presents a segment-by-segment model of a fin-tube heat exchanger that includes cross-fin conduction between all adjacent tube segments through the fins (e.g. cross-fin conduction). The physics of the model also accounts for both refrigerant and air phase transitions as well as the ability to account for air and refrigerant maldistribution.

The model's predictions are compared against experimental results collected on an industrial heat exchanger test facility for an air-to-water heat exchanger. A preliminary set of results confirm that cross-fin conduction accounts for large discrepancies in predicted coil performance, particularly with large temperature differences in walls of adjacent tubes.

Keywords: Conduction, Finned Tube, Heat Exchanger, Modelling

1. INTRODUCTION

The vapor compression system is the most commonly used cooling system type in heating, ventilation, and air-conditioning (HVAC) applications. The four basic components in a vapor compression system are: two heat exchangers i.e. an evaporator and a condenser, a compressor, and an expansion device. Air-to-refrigerant heat exchangers are most commonly used in vapor compression systems. Fin-and-tube heat exchangers are most widely used in HVAC applications because they are easily manufacturable and have reliable performance. The fin-and-tube heat exchangers consist of tubes with extended outside area (fins) to enhance the heat transfer.

The computer simulation models to design heat exchangers have been developed and updated continuously since the 1980s. Each new model adds more complexity to the calculation procedures or covers increased range of refrigerants. The heat exchanger model has a substantial influence on the overall accuracy and fidelity of vapor compression systems. The four main control volume based modeling approaches for heat exchangers are: Lumped approach, moving boundary approach, tube-by-tube approach, and segment-by-segment approach. The overall fidelity and computational time increases from lumped approach to segment-by-segment approach. Figure 1 shows the control volume for different modeling approaches.

Cross-fin conduction is a heat exchange between adjacent tubes conducted through the connecting fin sheets in a fin-and-tube heat exchanger and is an important phenomenon that substantially affects the heat exchanger thermal performance. It will be shown that for maximum accuracy for the highest fidelity models, this phenomenon needs be incorporated in the heat exchanger models, particularly for part-load simulation. Figure 2 shows the cross-fin conduction between two tubes of a fin-and-tube heat exchanger.

Romero-Méndez et al. (1997) developed an analytical model for fin-and-tube heat exchanger to investigate the cross-fin conduction. They found a capacity degradation of up to 20% due to decrease in heat transfer as a result of cross-fin conduction.
Domanski et al. (2007) experimentally analysed the effect of cross-fin conduction on the heat exchanger performance using 5 kW fin-and-tube heat exchanger. They found a capacity degradation of 20% in slit fin-and-tube heat exchanger (heat exchanger with slit fins) compared to the slit split (tube depth rows separated by fin cuts) heat exchanger for 16.7°C evaporator superheat.

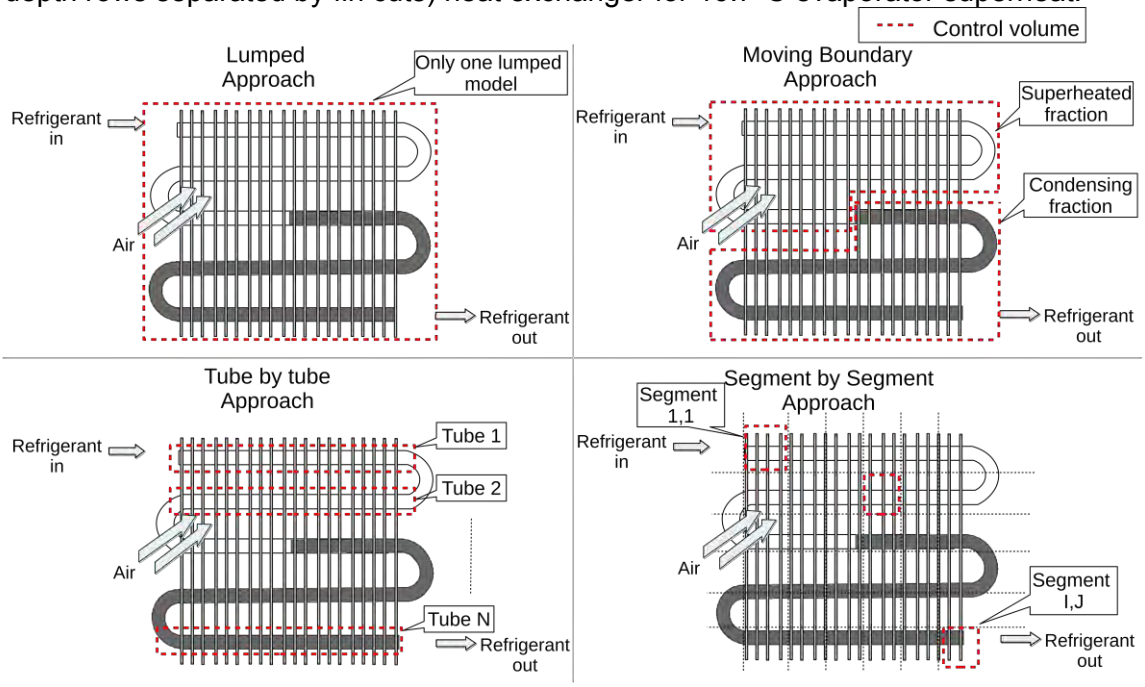

Figure 1: Control volume for different modeling approaches (Sarfraz, 2018)

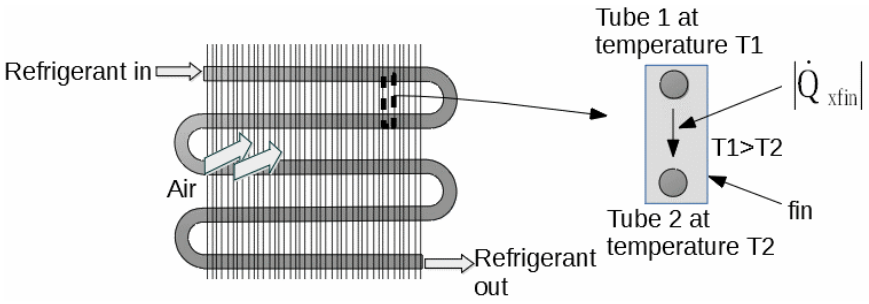

Figure 2: Cross-fin heat conduction phenomenon in a heat exchanger

Although cross-fin conduction is an important phenomenon affecting the heat exchanger performance, only few models include it. One reason for this may be that including cross-fin conduction substantially increases both the complexity and computational cost of the model. Cross-fin conduction is more prominent in commercial multi-circuit heat exchangers due to no refrigerant flow in the circuit(s) when the system operates at part load condition.

2. DETAILED SEGMENT-BY-SEGMENT HEAT EXCHANGER MODEL

The segment-by-segment solver is comprised of two sub-solvers. A segment solver (i.e. a low-level solver) solves the heat exchanger segment and a coil solver (i.e. an upper-level solver) solves the heat exchanger by connecting and solving the segments in the refrigerant flow direction.

2.1. Segment Solver

A segment is a heat exchanger element obtained by dividing heat exchanger into small elements. A segment includes a tube segment with associated fins as shown in Figure 3.

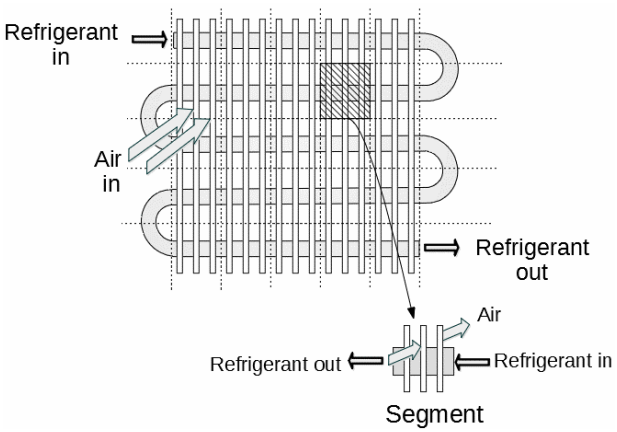

Figure 3: A schematic representation of a fin-and-tube heat exchanger with a segment highlighted

Each segment is assumed to be of uniform properties and operating at steady-state with negligible conduction along the axis of refrigerant flow. Therefore, the segment energy and mass balances can be integrated into a one-dimensional, lumped element, thermal resistance network. The resistance network can be used to characterize the interaction between each segment and the adjacent segments in the heat exchanger. The resistance network for a segment with the cross-fin conduction included is shown in Figure 4. It can be seen that the wall temperatures of all the tube segments in the heat exchanger are needed for cross-fin conduction calculation. The calculation of wall temperatures for all the tube segments adds another variable to iterate for, thereby, increasing the overall computational time to solve a heat exchanger.

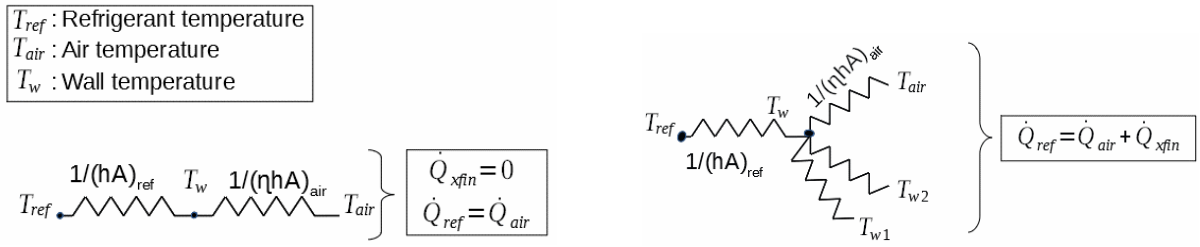

(a) No cross-fin conduction **(b) Including cross-fin conduction**

Figure 4: Resistance network for a heat exchanger segment

The heat exchanger segment can be in evaporator or condenser mode based on the air and refrigerant inlet temperatures. The different refrigerant inlet phases and phase change transitions in a segment included in the model are shown in Figure 5. The refrigerant phase change transition in a segment is found using a moving boundary approach (Sarfraz et al., 2018).

The heat transfer, in W, on the refrigerant, $\dot{Q}_{ref}$ and airside, $\dot{Q}_{air}$ is calculated assuming each segment is a uniform lump and applying a lumped analysis using $\varepsilon - NTU$ method and are given by Eq. (1) and Eq. (2),

$$\dot{Q}_{ref} = \varepsilon_{ref}\, \dot{m}_{ref} c_{p,ref} \left(T_{ref,i} - T_w\right) \quad \text{Eq. (1)}$$

$$\dot{Q}_{air} = \varepsilon_{air}\, \dot{m}_{air} c_{p,air} \left(T_{air,i} - T_w\right), \quad \text{Eq. (2)}$$

where ε is the effectiveness, $\dot{m}$ is the mass flow rate in Kg.s^{-1}, c_p is the heat capacity in J.Kg^{-1}.K^{-1}, and T_w is the segment wall temperature in K. It is important to note that the effectiveness is a function of the condition (single-phase or two-phase refrigerant) of the segment (per Figure 5) and uses an appropriate analysis corresponding with this condition.

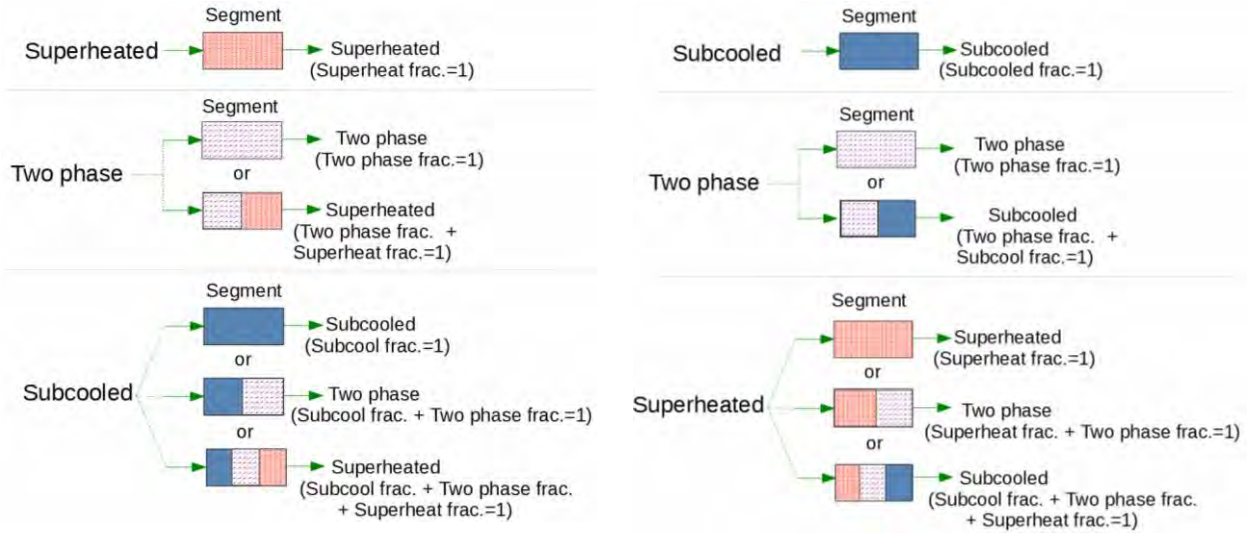

(c) Evaporator **(d) Condenser**

Figure 5: Different inlet phases and phase change transitions modelled in a heat exchanger segment. Sub-cooled/Superheated/Two phase – "frac." is the fraction of segment length that is sub-cooled/superheated/two phase.

The airside analysis includes the influence of latent effects through a humid air analysis. Each segment is considered either fully dry or fully wet on the airside. If the air dew point temperature at the inlet of the segment is below the wall temperature of the segment, segment is considered fully dry else segment is considered fully wet. The dry segment analysis follows that presented in Harms et al. (2003). The wet segment heat transfer analysis is performed using the dehumidification model from Harms et al. (2003) and Braun (1989).

The calculation of cross-fin conduction, $\dot{Q}_{xfin}$ requires the following information:

- Conduction shape factor.
- Wall temperatures of neighboring segments of each tube segment in a heat exchanger.
- Distance of each tube from its neighboring tube.

A simplified conduction shape factor, S for plain and wavy fins is given by Lee and Domanski (1997) as $S = \frac{tD}{d}$, where t is fin thickness in m, D is the tube diameter in m, and d is the distance of the tube from its neighboring tube in m. The cross-fin conduction in W, $\dot{Q}_{xfin}$ for N-neighboring tubes is calculated by Eq. (3),

$$\dot{Q}_{xfin} = tKDN_{fins}\sum_{n=1}^{N}\frac{T_{wn} - T_{w0}}{d_n} \qquad \text{Eq. (3)}$$

where K is the thermal conductivity in W.m^{-2}.K^{-1} , N_{fins} is the number of fins, T_{w0} is the wall temperature of the tube under consideration in K, T_{wn} is the wall temperature of neighboring tubes in K, and d_n is the distance of the tube from its neighboring tubes in m.

2.2. Coil Solver

The coil solver is a generic algorithm that solves the entire coil by simultaneously solving all the segments using refrigerant circuitry and neighboring tubes information.

The following information is needed in the coil solver:

- The refrigerant circuitry information, and
- Information on the neighboring tubes i.e. wall temperatures and distances.

The refrigerant circuitry information is provided by adopting the algorithm developed by Jiang et al. (2006). This algorithm requires a user input of junction-tube connectivity matrix where junction is

formed when two or more tubes are joined together. The connectivity matrix describes the location relationship between tubes and junctions

It is assumed that only tubes immediately adjacent to the tube of interest (first-order neighbour) contributes to the cross fin conduction phenomenon. This is because conduction between the tubes through fins is inversely proportional to the distance between the tubes and it decreases with the increase in the distance between the tubes (Bergman et al., 2011). Also, the second order neighbors are partially obstructed by the direct (first order) neighbors. Therefore, adding second or third order neighboring tube segments in the analysis will result in an increased complexity in overall solving process that will result an increase in the overall computational time with little potential benefit in overall model accuracy. The number of neighboring tubes varies from three to eight tubes for tubes in in-line configuration. While for staggered-convergent or staggered-divergent tube configuration, number of neighboring tubes can vary from two to six depending on the tube location.

Figure 6 shows the neighboring tubes for two different tube locations for different heat exchanger configurations.

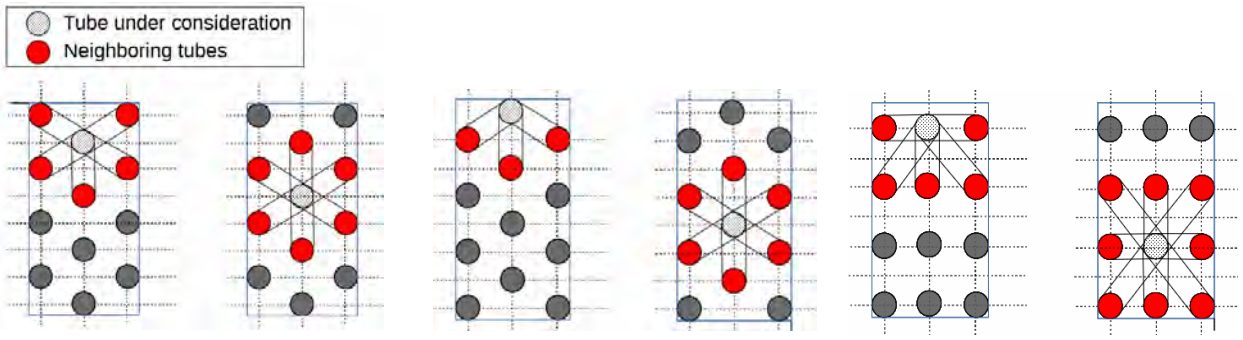

Figure 6: Neighboring tubes for two tube locations for different heat exchanger configurations

The coil solver is illustrated in the flow chart in Figure 7. The geometrical and operational parameters are given as an input. The coil solver is comprised of two sub-solvers. The first sub-solver is a pre-conditioner and provides the guess values for wall temperatures of all the tube segments as well as air temperature and humidity after each segment. The second sub-solver is the main solver that uses the guess values provided by the pre-conditioner to calculate the heat exchangers performance.

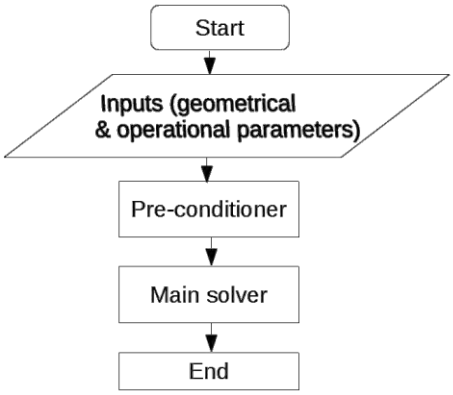

Figure 7: Flow chart for coil solver

2.3. Results and Discussions

The air-to-water coil shown in Figure 8 was tested in an industrial experimental facility. The coil is comprised of two systems (water flow rate can be independently controlled for each system): system 1 and system 2. System 1 consists of 13 circuits while system 2 has 12 circuits. The geometrical parameters of the coil are listed in Table 1.

The coil was operated in simulated heating mode using a coil calorimeter. The experimental design allowed the two systems to operate independently so that one system could be “active”, meaning water is flowing through the system circuit while the second is “inactive” with no water flow. The coil was operated with either 1 or 2 systems “active”. The experimental data was provided by Kolekar (personal communication, September 11, 2017). The data contained the air and refrigerant side capacities with the associated experimental uncertainties. The experimental uncertainty is the combination of standard (related to instrument) and random (related to variation in experimental data) uncertainty.

Table 1: Geometrical parameters of air-to-water coil

No. of rows	4
No. of tubes per row	25
No. of water systems	2
No. of tubes per circuit	4
No. of circuits in system 1	13
No. of circuits in system 2	12
Tube outer diameter	0.00953 m
Tube spacing	0.0254× 0.0219 m
Tube length	0.762 m
Fin type	Wavy fins
Fin thickness	1.14×10^{-4} m
Fins spacing	1.57×10^{-3} m
Fin projected length	5.41×10^{-3} m
Fin pattern depth	2.17×10^{-3} m

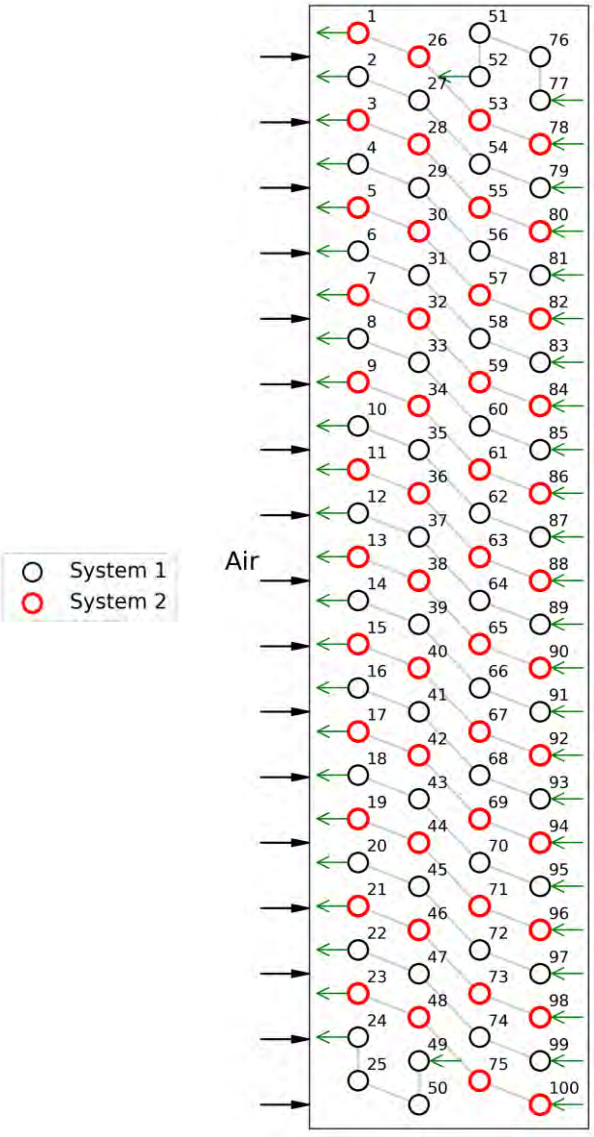

Figure 8: Air-to-water coil

The operational parameters for the case where air is heated is by the water are listed in Table 2.

Table 2: Operational parameters

Tube fluid	Water
Water inlet temperature	321.85 K
Air inlet temperature	294.25 K
Water mass flow rate	0.625 kg/s
Air velocity at coil face	0.49 to 2.93 m/s

2.3.1. Both systems active

The model is first compared against the experimental data with both the systems active for different air velocities. Figure 9 shows the comparison of the detailed segment-by-segment model with the experimental data with and without the consideration of cross-fin conduction for different air velocities. The maximum absolute difference in heat transfer of model from the experiment when cross-fin conduction is considered is within 7.5% while it is greater than 10% when cross-fin conduction is not considered.

The absolute difference in heat transfer between the model with and without cross-fin conduction is within 7% when both systems are active for different air velocities. Overall, the model with no cross fin-conduction has a bias to underpredict the capacity, and the addition of cross fin conduction to the model reduces that bias.

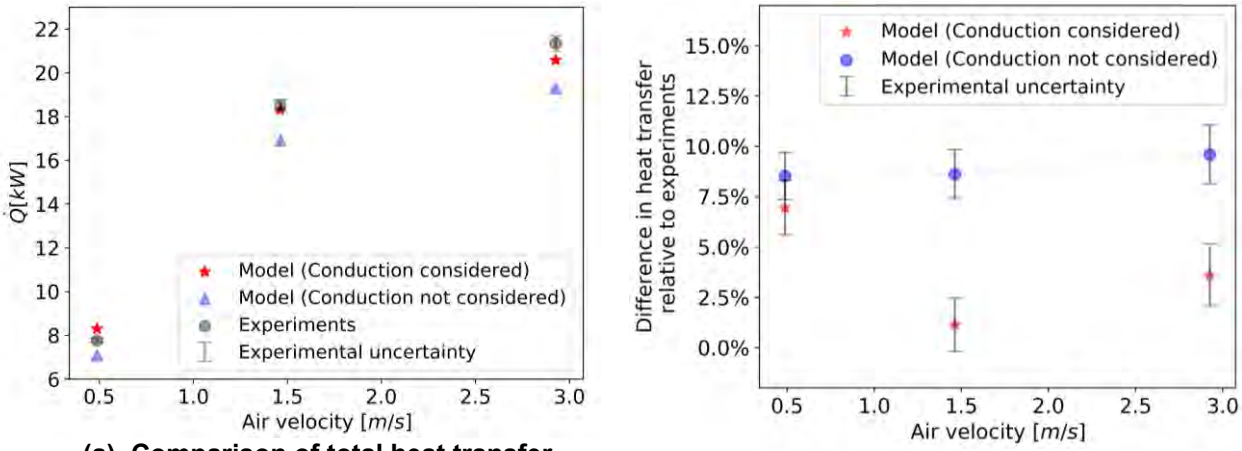

(a) Comparison of total heat transfer

(b) Difference in heat transfer relative to experimental data

Figure 9: Comparison of model with and without cross-fin conduction with experimental data for different air velocities, both systems active

2.3.2. System 2 active and system 1 inactive

Figure 10 shows the comparison of the model with the experimental data with and without accounting for the cross-fin conduction with only one system active for different air velocities.

The maximum absolute difference in overall heat transfer of the model from experimental data is within 9% when cross-fin conduction is considered in comparison to greater than 25% when cross-fin conduction is not considered.

The increased percentage difference in heat transfer from experimental data for the model with no cross-fin consideration is due to the increased difference in wall temperatures between the neighboring tubes e.g. an absolute difference of greater than 15 K (in comparison to 9 K when both systems were active) for an air velocity of 2.93 m/s. The increased difference in wall temperatures is due to the flow of water in active system tubes while there is no water flow in the inactive system tubes. Overall, the model with no cross fin-conduction has an increased bias to underpredict the capacity when one system is inactive. However, the addition of cross fin conduction to the model reduces that amount of underprediction.

The results show that neglecting the cross-fin conduction particularly when system(s) of a heat exchanger is/are inactive can result in less accurate prediction of overall heat exchanger capacity.

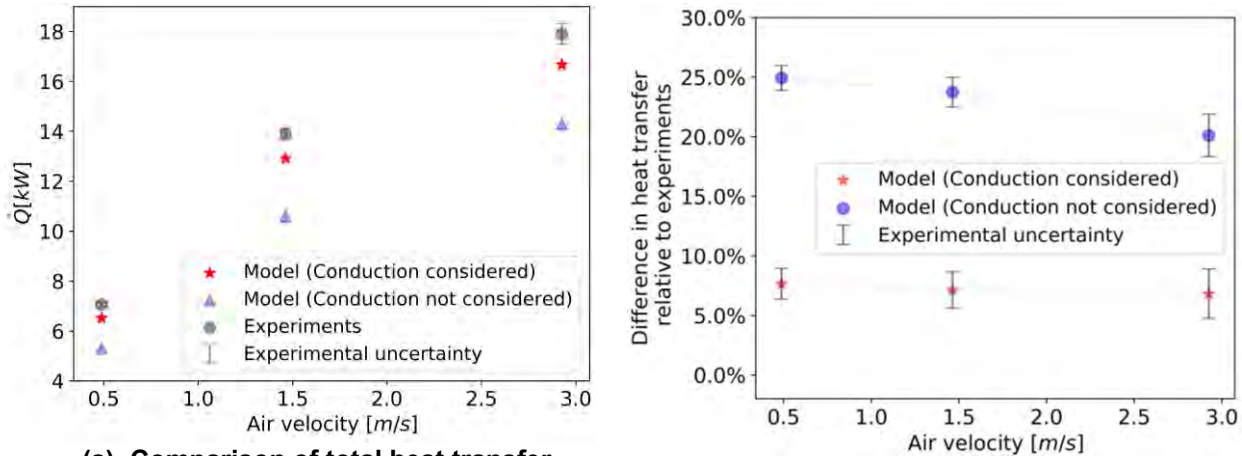

(a) Comparison of total heat transfer

(b) Difference in heat transfer relative to experimental data

Figure 10: Comparison of model with and without cross-fin conduction with experimental data for different air velocities, system 2 active

3. CONCLUSIONS

This paper presents the development of a detailed segment-by-segment model with cross-fin conduction functionality. The model is compared against experimental data of air-to-water coil with and without consideration of cross-fin conduction for different air velocities. The effect of cross-fin conduction on the overall heat transfer was found to be less than 10% of overall heat transfer, when both the water systems were active. Cross-fin conduction becomes even more relevant i.e. maximum difference of >20% of the overall heat transfer when one system was inactive. Overall, the model with no cross fin-conduction has an increased bias to underpredict the capacity when one system is inactive and addition of cross fin conduction to the model reduces that amount of bias.
Therefore, neglecting cross-fin conduction when heat exchanger system(s) is inactive will results in less accurate prediction of overall coil capacity.
The maximum difference of 10% in capacity predicted by the model with cross-fin conduction included relative to the experimental capacity might be due to simplifications, including

- Considering uniform air flow rate and air temperature and humidity at the coil face,
- Assuming same water flow rate at the inlet of each active circuit,
- Neglecting the effect of airside pressure drop, and
- Using simplified conduction shape factor in the model.

Future work includes validation with high fidelity refrigerant-to-air experimental data. This will allow to isolate the effects of the above simplifications.

ACKNOWLEDGEMENTS

This research was supported by Oklahoma Center for the Advancement of Science and Technology (OCAST) under project number and title: AR17-040-1/2. The authors would also like to gratefully acknowledge the technical and in-kind support of Johnson Controls, Norman, Oklahoma.

REFERENCES

Braun, J. E. (1988). Methodologies for the design and control of central cooling plants. Ph.D. dissertation, University of Wisconsin, Madison.

Domanski, P. A., Choi, J. M., & Payne, W. V. (2007). Longitudinal heat conduction in finned-tube evaporators. 22nd IIR International Congress of Refrigeration, Beijing, China.

Bergman, T. L., Incropera, F. P., DeWitt, D. P., & Lavine, A. S. (2011). Fundamentals of heat and mass transfer. John Wiley & Sons.

Harms, T. M., Groll, E. A., & Braun, J. E. (2003). Accurate charge inventory modeling for unitary air conditioners. HVAC&R Research, 9(1), 55-78.

Jiang, H., Aute, V., & Radermacher, R. (2006). CoilDesigner: a general-purpose simulation and design tool for air-to-refrigerant heat exchangers. International Journal of Refrigeration, 29(4), 601-610.

Kolekar, R. (2017, September 11). Personal communication (email).

Lee J, Domanski P. A. Impact of air and refrigerant mal-distributions on the performance of finned-tube evaporators with R-22 and R-407C, 1997, ARTI MCLR Project, DOE/CE/23810-81.

Romero-Méndez, R., Sen, M., Yang, K. T., & McClain, R. L. (1997). Effect of tube-to-tube conduction on plate-fin and tube heat exchanger performance. International journal of heat and mass transfer, 40(16), 3909-3916.

Sarfraz, O., Bach, C. & Bradshaw, C. (2018). A Literature Review of Numerical Modeling Techniques for Vapor Compression Systems with Focus on Heat Exchanger Modeling. International Refrigeration and Air Conditioning Conference. Purdue, USA.

Manuscript ID: 1761
DOI: 10.18462/iir.icr.2019.1761

Study on risk assessment of air conditioner using R290

Atsushi BABA[(a)], Kenji TAKAICHI[(a)], Shigeharu TAIRA[(a)], Tsutomu IMOTO[(a)], Shyunji ITAKURA[(a)], Hironori MORI[(a)], Hiroaki MAKINO[(a)], Koji YAMASHITA[(a)], Hiroichi YAMAGUCHI[(a)]

[(a)] The Japan Refrigeration and Air Conditioning Industry Association
Minato-ku, Tokyo, 105-0011, Japan, atsushi.baba@glb.toshiba.co.jp

ABSTRACT

Nowadays, further phase-down of HFC is expected to encourage the use of lower GWP refrigerants, but the majority of the refrigerants with low GWP values tend to have high flammability and there is a danger of explosion that may cause fire. In general, the occurrence of an ignition event of a flammable refrigerant has much to do with the development of flammable cloud and the existence of ignition sources such as static electricity and electric sparks. For risk assessment, therefore, it is necessary to determine the volume and duration of flammable cloud following refrigerant leakage. In this paper, CFD simulations was undertaken to evaluate the volume and duration of flammable cloud generated by leaked refrigerant from an outdoor unit under several sets of given conditions. The CFD results indicated flammable regions stagnated so long that ignition risks may be intolerable under certain circumstances.
Keywords: Air Conditioner, Flammability, R290, R32, Refrigerant.

1. INTRODUCTION

In order to mitigate global warming, refrigerant replacement of R410A with R32 is in progress in residential air conditioners and light commercial air conditioners in Japan. However, we will be facing further reduction of GWP levels in response to the Kigali Amendment to the Montreal protocol. One of the most extensively studied refrigerants is a highly flammable refrigerant R290. Several researchers have assessed flammability risk of R290 residential air conditioners and evaluated ignition frequency of leaked refrigerant for different charge sizes, different room dimensions, and unit fan ON/OFF operation (Colbourne and Suen, 2018). In these studies, however, outdoor units positioned at floor level are merely considered and there is no detail description as to how leaked refrigerant will disperse under several installation conditions. Considering these previous studies, the Japan Refrigeration and Air Conditioning Industry Association (JRAIA) has been working on risk assessment of R290 residential air conditioners. This paper addresses how flammable regions change in the event of leaks through CFD analysis and sources of ignition around outdoor units.

2. CALCULATION METHOD OF IGNITION FREQUNECY

Ignition frequency was calculated based on the assumption that an ignition event occurs when a flammable mixture and a source of ignition coexist at the same location at the same time. Assuming that they are randomly positioned within a reference space and the size of the source of ignition is negligibly small compared to that of the flammable cloud, the number of occurrence of the ignition event per unit time under a set of conditions j can be expressed as Eq. (1).

$$P_{\mathrm{j}} = P_{\mathrm{r}} \times k_{\mathrm{j}} \times \left\{ \frac{V_{\mathrm{f}}}{V_{\mathrm{ref}}} \times \left[1 - \left(1 - \frac{T_{\mathrm{f}} + T_{\mathrm{s}}}{T_{\mathrm{ref}}} \right)^{n} \right] \right\}_{\mathrm{j}} \qquad \text{Eq. (1)}$$

Where P_j is the ignition frequency per unit time, P_r is the refrigerant leakage frequency per unit time, V_{ref} is the reference volume, T_{ref} is the reference time, V_f is the volume of flammable cloud, T_f is the duration of flammable cloud, T_s is the duration of an ignition source, n is the typical number of occurrences of the ignition source per unit time. In general, V_f changes with time, but time averaged volume is used to simplify the calculation. V_{ref} is the volume of the extent where leaked refrigerant can travel. k_j is the weighting factor of the condition j. k_j varies depending on the number of persons or objects with the same kind of ignition source, unit fan operation, installation conditions, and weather conditions etc. Eq. (1) indicates that it is necessary to quantitatively evaluate the volume and duration of flammable cloud when calculating ignition frequency.

3. CFD ANALYSIS OF REFRIGERANT LEAKAGE

3.1. Installation Conditions of Outdoor Unit

Installing outdoor units on balconies in addition to installation in open space is common practice, especially in high rise apartments, in Japan. In a balcony, an outdoor unit is placed on a floor, a wall, or eaves with mounting brackets. Moreover a steel stand is sometimes used for installing two outdoor units. In Japan, a balcony usually has a fence and partitions which can block the line of sight adequately. The fence has sometimes openings. Also, there are also sometimes gaps under the fence and the partitions. However, there are some cases where three sides of a balcony can be seen as wall with no gap under itself or no openings. In such a situation, the balcony is not in a well-ventilated state and leaked refrigerant concentration is expected to be relatively high. Fig. 1 shows three installation conditions that were considered in this study. The first is floor mounted. The second is steel stand mounted. The third is eaves mounted. The typical outdoor unit with cooling capacity of 4.0 kW was chosen as an outdoor unit. In addition to these installation conditions, the effect of the unit fan operation or when there is a partition gap or natural wind were evaluated.

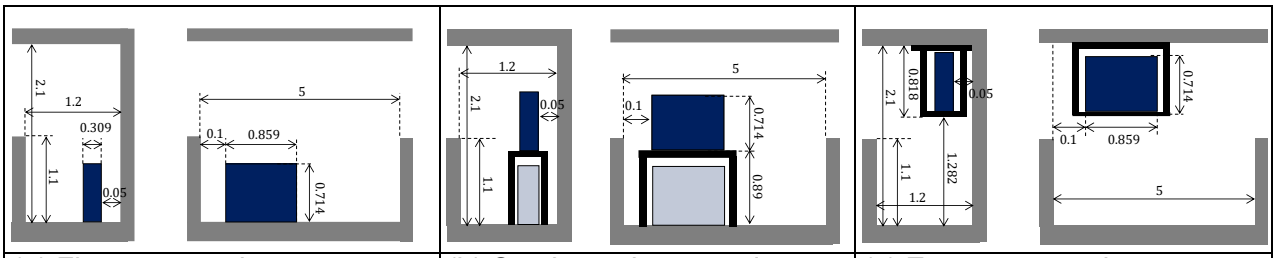

(a) Floor mounted | (b) Steel stand mounted | (c) Eaves mounted

Figure 1: Three installation conditions of outdoor unit in a balcony

3.2. Analysis Models and Conditions

The leak rates for various refrigerant charge sizes of R290 are shown in Table 1. The refrigerant charge sizes considered are 0.2 kg, 0.5 kg, and 1.0 kg. The charge size of 0.2 kg means the maximum allowable charge stipulated by the IEC standards for the floor area of 7 m^2. The charge size of 0.5 kg is required charge amount to achieve drop-in replacement for a R32 residential air conditioner. The 1.0 kg is charge amount corresponding to refrigerant charge boundary “m2” stipulated by the IEC Standards. The refrigerant amount leaked was assumed to be equal to the refrigerant amount charged. The leak rate for each charge size was taken as constant during leakage. Only a vapour leak was considered and the leak was completed in 4 minutes. To simulate the leak dispersion, commercial 3D CFD software “STREAM” was used. On the basis of Reynolds number calculation, turbulent flow field analysis was carried out with the standard k-ε turbulence model. In these calculations, R290 was assumed to leak uniformly from the air intake side of the heat exchanger of the outdoor unit. In other words, uniform concentration and velocity profile were given as inlet boundary conditions. Considering outdoor installation, outdoor wind environment was also factored into leak dispersion simulations. Fig. 2 shows the CFD model. In this study, the floor area of a balcony was set to 6 m^2 and the height of the fence (front wall) was set to 1.1 m. It was assumed that there was no drainage outlet. Also, no gaps under the walls and no openings in the walls exist for default settings.

仕様 時間 （可燃域継続時間 4分）
ベランダ_床置き 5秒 4分後（冷媒漏えい終了） ４分1秒後

Table 1. R290 leakage conditions

冷媒	Leakage amount
	Leak rate R290
冷媒漏えい速度	R290 density (25°C
	125g/min
	Leakage area
エアコン風量	Leakage concentratio
	1700m3/h（最小風量）

仕様 時間 （可燃域継続時間 4分）
ベランダ_床置き 5秒 4分後（冷媒漏えい終了） ４分1秒後

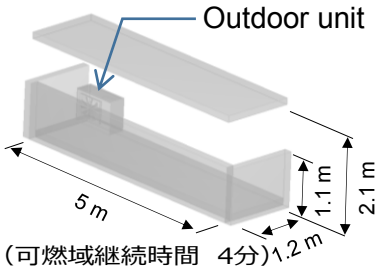

Figure 2: CFD model of balcony

3.3. Results of CFD Analyses

3.3.1. Flammable region for each installation

Fig. 3 shows CFD results for three different charge sizes in three installation conditions. The concentration distribution, the duration of flammable regions (the area where refrigerant concentration is between the lower flammability limit (LFL) and the upper flammability limit (UFL)), and the time averaged flammable volume are shown. In each of the installation conditions, the duration of the flammable region became longer as the charge amount increased. For each of the three charge sizes, the duration of the flammable region became longer as the installation height became lower. The duration of the flammable region reached as long as 3546 sec for the condition that the outdoor unit with 1.0 kg charge was installed on the floor. Leaked refrigerant from an outdoor unit installed in a high place entrains air, accelarates due to gravity force against buoyancy effect, and spreads while falling toward the floor. As a result, the concentration of refrigerant at the floor level becomes thinner. For this reason, when the outdoor unit with 0.2 kg charge was installed on the eaves (at the height of 1.282 m from the floor), the duration of the flammable region was approximately one third of that of the case where it was installed on the floor. However, increased charge amount tends to lessen that effect. On the other hand, the time averaged flammable volume for the installation on the floor with the 1.0 kg charge was smaller than that with the 0.5 kg charge. This was because the UFL volume, which means the volume of space where refrigerant concentration is UFL or higher, increased. This UFL volume increase was also seen in the condition where the outdoor unit was installed on the steel stand.

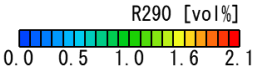

*Note: White colour indicates the area with UFL or more

Installation Condition	Leakage Amount	0.2 kg		0.5 kg		1.0 kg	
	Time	240 sec	600 sec	240 sec	600 sec	240 sec	600 sec
Floor mounted	Concentration distribution	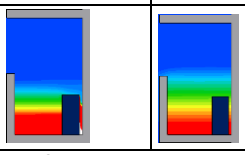		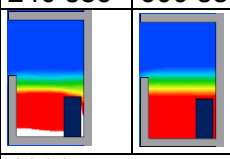		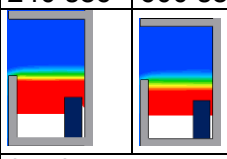	
	Duration	776 sec		1900 sec		3546 sec	
	Averaged volume	1.22 m^3		2.96 m^3		2.73 m^3	
Steel stand mounted	Concentration distribution	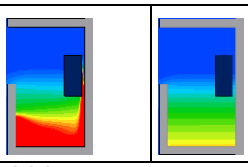		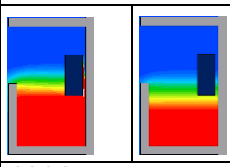		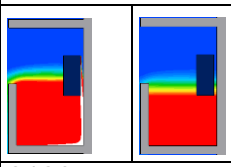	
	Duration	292 sec		1206 sec		2126 sec	
	Averaged volume	0.20 m^3		2.83 m^3		3.87 m^3	
Eaves mounted	Concentration distribution	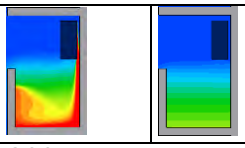		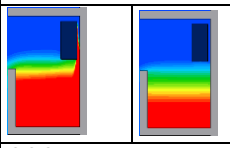		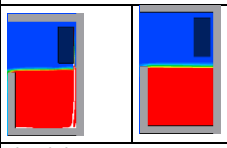	
	Duration	260 sec		939 sec		1711 sec	
	Averaged volume	0.05 m^3		2.47 m^3		3.73 m^3	

Figure 3: Concentration distribution, the duration and time averaged volume of flammable region within the balcony for different installation conditions

3.3.2. Generation of the flammable region during unit fan operation

Leak dispersion is considerably affected by airflow generated by the outdoor unit fan. CFD analysis was made for the air flow volume rate of 0.472 $m^3 \cdot s^{-1}$, which is the minimum value of the outdoor unit fan. As a result, the flammable region was not generated for the charge size of 0.5 kg. For the charge size of 1.0 kg, a tiny size of flammable region was generated only during the leakage, and the flammable region disappeared immediately after the leak ended. These results indicate airflow by an outdoor unit fan is effective at preventing the generation of flammable cloud. Therefore, we took the operation time of a residential air conditioner into consideration in carrying out risk assessment.

3.3.3. Effect of gap under the partition plate

Fig. 4 shows the construction of a typical balcony of high rise apartments in Japan. The balcony has usually a partition on each of its two sides. It can be kicked down in an emergency to secure an evacuation route. It has also a gap under itself and leaked refrigerant from an outdoor unit flows into the adjacent balcony (balcony 2). Also, as the adjacent balcony has also partitions, the leaked refrigerant flows into its adjacent balcony (balcony 3). In this study, all the gaps were set to 0.1 m, which is a typical value from the our survey results in Japan. Fig. 5 shows CFD results for three different charge sizes. The concentration distribution, the duration of the flammable regions, and the time averaged flammable volume are shown. The duration of the flammable regions and the time averaged flammable volume within the balcony 1, where the outdoor unit was installed, decreased for all of the charge sizes considered. The duration of the flammable region for 1.0 kg charge size is 1211 sec, which is about 1/3 of the case where there is no gap. Although a small size of flammable region was generated in the next balcony and no flammable region was generated in the next to the next balcony for the 0.2 kg charge, flammable regions were generated in the next balcony for the charge sizes of 0.5 kg and 1.0 kg.

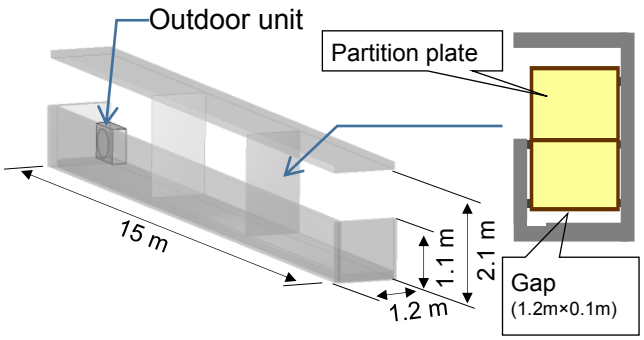

Figure 4: The construction of a typical balcony

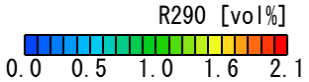

*Note: White colour indicates the area with UFL or more

Leakage amount			Balcony 1	Balcony 2	Balcony 3
0.2 kg	Concen-tration distribution	240 sec	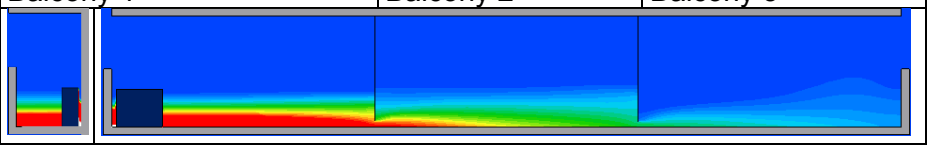		
	Duration		418 sec	175 sec	0 sec
	Averaged volume		0.51 m^3	0.01 m^3	0 m^3
0.5 kg	Concen-tration distribution	240 sec	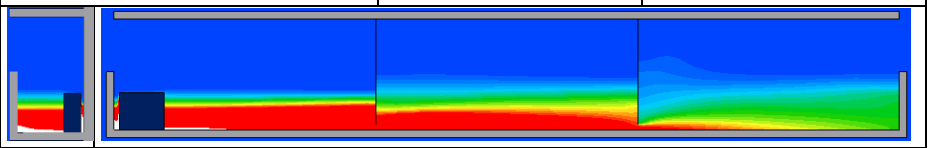		
	Duration		701 sec	582 sec	269 sec
	Averaged volume		1.32 m^3	0.71 m^3	0.07 m^3
1.0 kg	Concen-tration distribution	240 sec	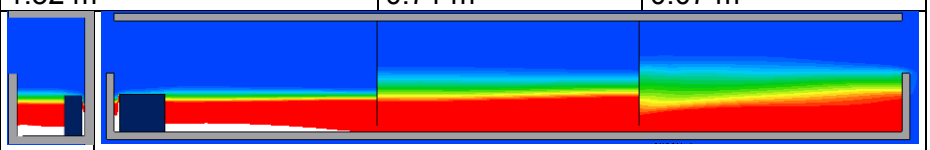		
	Duration		1211 sec	1132 sec	1059 sec
	Averaged volume		2.16 m^3	2.32 m^3	2.20 m^3

Figure 5: Concentration distribution, the duration and time averaged volume of flammable regions within each balcony with partition plates

3.3.4. Effect of natural wind

CFD simulations have been ususally carried out in a quiescent room in the case of a refrigerant leak from an indoor unit despite the occurrence of infiltration due to outdoor wind enviroment. This implies wind velocity is set to 0 m·sec^{-1}. In our CFD simulations for the balcony, therefore, zero wind velocity was adopted as the default value. But leaked refrigerant would be stirred by natural wind entering the balcony. Fig. 6 shows the appearance time lengths of wind speeds in 16 major cities in Japan. There are some differences between cities, but wind velocity of 1.0 m·sec^{-1} to 2.0 m·sec^{-1} appears frequently. These data produces a 0.5 % probability that windless weather will occur. Therefore, CFD analyses were carried out for the cases when natural wind blows around the outdoor unit. Fig. 7 shows the CFD model of a balcony in side win
0.3 m·s^{-1}, and 0.5 m
three different winc
duration of the flam
flammable volume
In the case of 0.5
region became abc
wind, and its flam
Factoring these results into risk assessment, decreased total ignition frequency by a factor of approximately 100

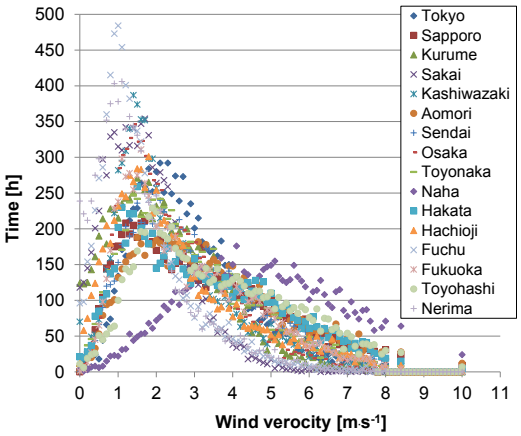

Figure 6: The appearance time length of each wind velocity in 16 cities in Japan

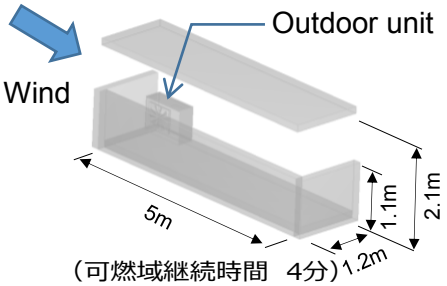

Figure 7: The CFD model of a balcony with side wind

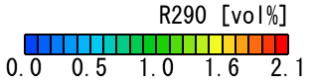

*Note: White colour indicates the area with UFL or more

Wind velocity		0.0 m·sec^{-1}	0.1 m·sec^{-1}	0.3 m·sec^{-1}	0.5 m·sec^{-1}
Concentration distribution	240 sec	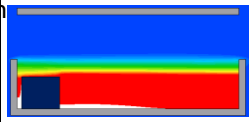	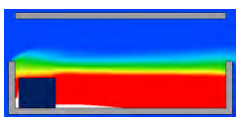	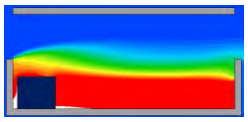	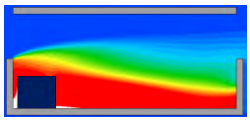
	600 sec	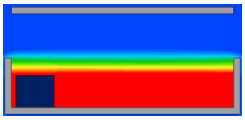	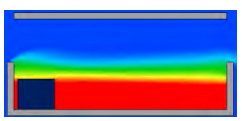	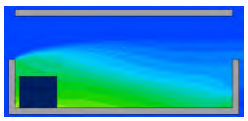	
Duration		1900 sec	926 sec	496 sec	391 sec
Volume		2.96 m^3	2.75 m^3	2.06 m^3	1.39 m^3

Figure 8: The influence of wind velocity on duration and time averaged volume of flammable regions within the balcony (Leakage amount: 0.5 kg)

3.3.5. Effect of the analysis model

The standard k-ε turbulence model is based on fully developed isotropic turbulent flow. In the turbulent flow, refrigerant diffusion due to concentration gradients arises in a different manner from laminar diffusion. In general, turbulent diffusion coefficients are much larger than laminar ones. If the flow within a balcony is not this type of turbulent one, leaked refrigerant may really diffuse slower than the CFD results. There is a possibility that the transition from turbulent flow to laminar flow might occur sometime after the completion of leakage. For comparison, therefore, we carried out CFD simulations using the laminar model for leakage from the outdoor unit with 0.5 kg charge which was installed on the floor in the windless weather. In this simulation, the balcony has no gap. The result indicated that the flammable region remained for as long as 60740 sec (16 hr. 52 min. 20 sec.), which means the duration of the flammable region increased by a factor of 30 in comparison with the case of the turbulence model (1900 sec). The real duration will fall somewhere in between the two values and leak dispersion tests are needed.

4. IGNITION SOURCES

Table 2 shows the typical duration of the state where each ignition source is active per occurrence, and the typical height of the location of each ignition source. Smoking by users, open flames of gas/oil water heaters, and electric sparks associated with the other air conditioners were considered an ignition source. Electrostatic discharge is listed as an ignition source in the EN1127-1 and the IEC60079-32-1. They point out that users must always consider electrostatic ignition risks. People experience electrostatic discharge shocks when wearing/taking off clothes, or touching a metal door knob. Electrostatic discharge may occur even in outdoor environment, when a person on whom electrostatic charge has built up touches a conductive object. The frequency of these behaviours, however, is considered significantly small. For cigarettes, some past risk assessments were carried out based on the fact that the smouldering can't ignite a flammable mixture, but the lighting pieces can be considered a source of ignition (Colbourne and Suen, 2016). The previous study in Japan, (Nakayama et al., 2016), however, shows that cigarettes per se do not ignite a flammable mixture. Therefore, there remain a possibility that the lighting might ignite a flammable mixture. For gas/oil water heaters, open flames within such equipment may not be considered an ignition source, because their blowing fans are operating before ignition. Also, there is a literature reporting that an outdoor unit located in a flammable mixture caused no ignition. We need to give further consideration to sources of ignition. We have a plan to investigate them in corporation with academic institutions.

Table 2. The typical duration and the typical location height of each ignition source

Name	Ignition sources	Duration T_S (sec)	Height h_S (m)
Smoking by users	Open flame	4.5×10^{1}	≤ 0.172
Gas/oil water heater (stationary type)	Open flame	3.0×10^{2}	≤ 0.06
Outdoor unit of AC	Electric spark	5.0×10^{-3}	≤ 0.714
Static electricity	Electrostatic spark	5.0×10^{-6}	-

5. CONCLUSIONS

The sizes and duration of flammable cloud are necessary for risk assessment of a R290 outdoor unit and they were determined through CFD analysis for various conditions including weather conditions etc. The results are as follows.

(1) Flammable regions stagnated so long that ignition risks may be intolerable when three conditions come into alignment. The three conditions are that three sides of a balcony can be seen as a wall with no gaps under itself or openings, that windless weather occurs, and that the outdoor unit is installed on the floor.
(2) Larger charge sizes didn't always lead to larger sizes of flammable regions. This was due to the fact that refrigerant concentration exceeds UFL.
(3) Gaps under partitions reduced the sizes and the duration of the flammable regions within the balcony where the outdoor unit was installed. In contrast to this, flammable regions were generated in the next balconies.
(4) The outdoor unit fan operation helped to reduce the sizes of flammable regions greatly. Natural wind with wind speeds of more than 0.5 $m \cdot s^{-1}$ also reduced them, which may reduce the ignition frequency by a factor of approximately 100.
(5) Ignition source candidates were listed for outdoor units installed on a balcony. There is mixed information with regard to ignition sources, and It is necessary to further investigate whether these ignition source candidates can really ignite leaked refrigerant.

ACKNOWLEDGEMENTS

This study was carried out by member companies of JRAIA, Panasonic, Daikin, Toshiba Carrier, Hitachi Johnson Controls, Fujitsu General, Mitsubishi Heavy Industries Thermal Systems, and Mitsubishi Electric Corporation. Observers from each company are Akira Hiwata, Tomoatsu Minamida, Takeshi Watanabe, Shunji Sasaki, Toshiyuki Fuji, and Akira Maeda, who cooperated with this study. The authors would like to deeply appreciate these members support.

NOMENCLATURE

P_j	ignition frequency per unit time	P_r	refrigerant leakage frequency per unit time
V_{ref}	reference volume (m^3)	T_{ref}	reference time (sec)
V_f	volume of flammable cloud (m^3)	T_f	duration of flammable cloud (sec)
T_s	duration of ignition source (sec)	n	occurrence frequency of ignition source
k_j	weighting factor	h_s	height of the location of ignition source (m)

REFERENCES

Colbourne, D., Suen, K.O., 2004. Appraising the flammability hazards of hydrocarbon refrigerants using quantitative risk assessment model Part 1: modelling approach, Proc. International Journal of Refrigeration 27(7), 784-793

Colbourne, D., Suen, K.O., 2016. RISK ASSESSMENT OF R22 AIR CONDITIONERS USING R290. Proc. 12th IIR Gustav Lorentzen Natural Working Fluids Conference, Edinburgh, 1004

Colbourne, D., Suen, K.O., 2018. R290 CONCENTRATIONS ARISING FROM LEAKS IN ROOM AIR CONDITIONERS. Proc. 13th IIR Gustav Lorentzen Conference, Valencia, 1103

Nakayama, T., Nakada, H., Mochizuki, M., Toriya, S., 2016. Study on the Ignition Properties of Various Types of Flammable Gas, Report of Fire Technology and Safety Laboratory of Tokyo Fire Department 53, 86-94. (in Japanese)

EN 1127-1: 2011. Explosive atmospheres. Explosion prevention and protection. Basic concepts and methodology.

IEC 60079-32-1 Ed. 1.1: 2017. Explosive atmospheres - Part 32-1: Electrostatic hazards, guidance

Manuscript ID: 1788
DOI: 10.18462/iir.icr.2019.1788

The effects of antifreeze in the circulating water on the operation performance of ground heat exchangers

Xiuqin YANG[(a)], Xiang ZHOU[(a)], Xu ZHANG[(a)]*
[(a)]School of Mechanical Engineering,
Tongji University, 4800 Caoan Road,
Shanghai, 201804, China

ABSTRACT

Ground-coupled heat pump (GCHP) systems often require antifreeze in the circulating water in locations with significant heating seasons, such as Northern China. In this study, the effects of antifreeze in the circulating water on operation performance of ground heat exchangers (GHEs) was investigated. A theoretical model was derived to analyze the antifreeze effect. Then the model was validated by an experimental system. Based on the effects of antifreeze solution on heat transfer performance and friction loss, the correction factor of flowrate and friction loss are given. In addition, the design method for GHEs in cold regions are also discussed.
Keywords: Ground Heat Exchanger, Antifreeze, Correction Factor, RC Model.

1. INTRODUCTION

Ground heat exchangers (GHEs) are applied to transfer heat to/from the ground in ground-coupled heat pump (GCHP) systems. Heat can be extracted from the ground of relatively higher temperature, and then be sent into the conditioned space by supplying heat pumps in winter. Therefore, GCHP technology can offer higher energy efficiency for air-conditioning than conventional air-conditioning systems (Self et al., 2013). A number of investigations have been conducted on the operation performance of GCHP systems. Healy and Ugursal (1997) investigated the effect of various system parameters on GCHP performance using a computer model. Hepbasli et al. (2003) reported the performance evaluation of a vertical GCHP system in the heating mode. Pulat et al. (2009) investigated the performance of the horizontal GCHP system including the effect of leaving temperature of GHE unit and outdoor temperature for winter climatic condition.

In winter, GCHP systems operate under the heating mode. In order to prevent the circulating water below freezing, aqueous solution of ethylene glycol is usually required as the antifreeze solution. Its chief attributes are its ability to efficiently lower the freezing point of water, its low volatility, and its relatively low corrosively when properly inhibited. The physical properties of the antifreeze solution are different from those of water, which could affect the conventional design of piping systems.

Some researchers have carried out theoretical or experimental studies on the addition of antifreeze to heat exchange equipment. İnallı and Esen (2004) observed that the increasing of the mass flow rate of the antifreeze solution increased the electric power required to run the heat pump and consequently decreased the coefficient of performance (COP) of the system. Casasso and Sethi (2014) observed that the antifreeze and its concentration heavily influenced the energy performance of GCHPs, in particular the borehole resistance and the power consumed by auxiliary plants. Moreover, Tang and Nowamooz (2019) showed that working fluids influenced differently the COP of heat pump due to their different physical properties.

So far, researches on antifreeze lacked relevant experimental data, and most of them focused on heat exchangers in the refrigerator rather than GHE (Bakirci, 2010). And in general, the selection of the circulation pump is based on the friction loss, but equipment manufacturers rarely provide correction factors when piping systems adopt the antifreeze solution.

This paper presents an analysis of operation performance of a vertical GHE, which used antifreeze solution as working fluid for heating modes. An experimental system was constructed and tested, theoretical analysis was also performed. The heat exchange rate and friction loss of the GHE were

determined from experimental and theoretical results. Results derived from theoretical methods agreed well with the experimental results. The influence of antifreeze solution on operation performance of the GHE were examined and correction factors were given accordingly.

2. THEORY

In the existing models of GHEs, numerical models lead to extensive computation time and a substantial effort in terms of pre-processing work (Congedo et al., 2012). On the contrary, analytical models offer simple, parameter input-based modeling and cost short computation time. But they usually disregard transient effects of heat and mass transport in the borehole and hence are not suitable for the prediction of short-time behavior (Lamarche and Beauchamp, 2007). Two-dimensional thermal resistance and capacity (RC) model has advantages of rapid and accurate calculation compared with analytical and numerical models (Bauer et al., 2011). The soil outside the borehole can be divided into several layers by several regions, and the thermal capacity of the soil outside the borehole and grouting material are both considered (Tu et al., 2017). Heat balance method is applied on each temperature node to simulate heat transfer process of GHEs. A module for freezing soil is added, in order to study the heat transfer characteristics of GHEs in cold climate regions. The effective heat capacity method takes latent heat as a large heat capacity in a small temperature range (Kim et al., 2008). It is assumed that the thermal conductivity and specific heat follow Eq. (1) and (2) within a temperature range of T_m-$\Delta T \leq T_m \leq T_m$+$\Delta T$:

$$\lambda = \begin{cases} \lambda_{\mathrm{fr}} & (T < T_{\mathrm{m}} - \Delta T) \\ \lambda_{\mathrm{fr}} + \left(T - T_{\mathrm{m}} + \Delta T\right)\dfrac{\lambda_{\mathrm{ufr}} - \lambda_{\mathrm{fr}}}{2\Delta T} & (T_{\mathrm{m}} - \Delta T \leqslant T \leqslant T_{\mathrm{m}} + \Delta T) \\ \lambda_{\mathrm{ufr}} & (T > T_{\mathrm{m}} + \Delta T) \end{cases} \quad \text{Eq. (1)}$$

$$C = \begin{cases} \dfrac{C_{\mathrm{fr}}}{\rho} & (T < T_{\mathrm{m}} - \Delta T) \\ \dfrac{H \cdot W}{2\Delta T} + \dfrac{C_{\mathrm{ufr}} + C_{\mathrm{fr}}}{2\rho} & (T_{\mathrm{m}} - \Delta T \leqslant T \leqslant T_{\mathrm{m}} + \Delta T) \\ \dfrac{C_{\mathrm{ufr}}}{\rho} & (T > T_{\mathrm{m}} + \Delta T) \end{cases} \quad \text{Eq. (2)}$$

where λ_{fr} and λ_{ufr} are the thermal conductivities of frozen and unfrozen material in W.m^{-1}.K^{-1}, C_{fr} and C_{ufr} are the volume heat capacity of frozen and unfrozen material in J.m^{-3}.K^{-1}. ΔT is a small temperature range, which can be assumed as 0.5 K, H is the latent heat of the liquid in J.kg^{-1}, W is the moisture content of soil in %. ρ is the density in kg.m^{-3} and c is the specific heat of the material in J.kg^{-1}.K^{-1}.

The viscosity and density of the antifreeze solution increase with its concentration, so that the friction loss will increase at the same pipe diameter and flow rate. The power consumption for transporting working fluid increase as a result. The friction loss per unit length can be calculated by Eq. (3).

$$\Delta p_{\mathrm{m}} = 0.158 \times \rho^{0.75} \times \mu^{0.25} \times d_{\mathrm{i}}^{-1.25} \times v^{1.75} \quad \text{Eq. (3)}$$

Where Δp_{m} is the friction loss per unit length in Pa.m^{-1}, μ is the viscosity in N.s.m^{-2}, d_{i} is pipe inner diameter in m, v is the velocity of working fluid in m.s^{-1}.

3. MATERIALS AND METHODS

An experimental system was constructed and tested in Shanghai, China. As shown in Fig. 1, the system consisted of an air-cooled refrigerator (outlet temperatures range from -15 to 10°C), a vertical

single U-tube heat exchanger, a water tank with the volume of 3 m^3, a chemical pump and a computer to record data. The refrigerator could produce low-temperature fluid to simulate the inlet temperatures of the GHE under extreme conditions in winter heating modes. Temperatures of inlet and outlet fluids were measured by platinum resistance temperature sensors. Pressures of inlet and outlet pipes were measured by pressure gages. Flow rate of the GHE was measured by a turbine flow meter.

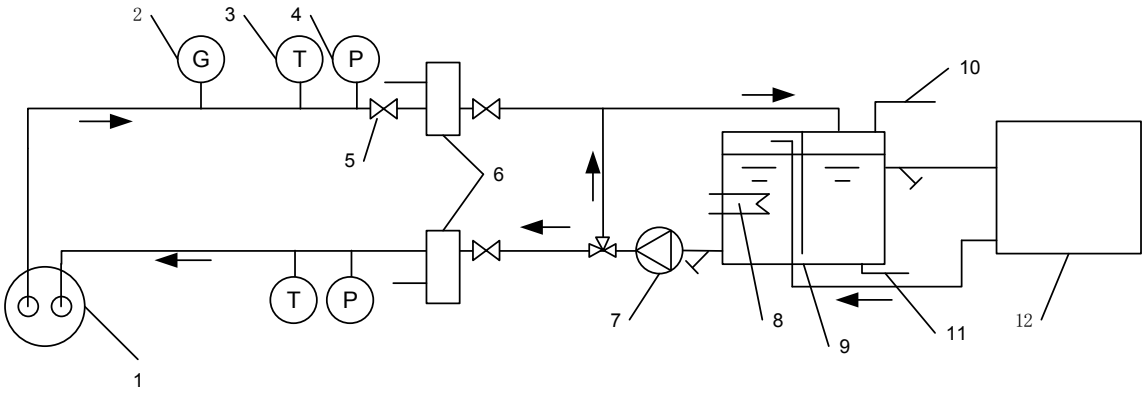

1-Borehole; 2-Turbine flowmeter; 3-Platinum resistance temperature sensor; 4-Pressure gage; 5-Valve; 6-Manifold; 7-Chemical pump; 8-Electric heating; 9-Water tank; 10-Water replenishing pipe; 11-Water drain pipe; 12-Refrigerator

Figure 1: Diagram of experimental system

Characteristics of the GHE were as below:
Pipe thermal conductivity, λ_p=0.6 W. m^{-1}. K^{-1}.
Pipe outer diameter, d_o=0.032 m.
Pipe inner diameter, d_i=0.025 m.
Borehole diameter, d_b=0.16 m.
Bore depth, L=100 m.
According to ASHRAE handbook(ASHRAE, 2017), physical properties for antifreeze solution are listed in Table 1 to 4.

Table 1. Density of aqueous solutions of ethylene glycol

	Concentrations in volume percent					
Temperature, °C	5%	10%	15%	20%	25%	30%
-10	--	--	--	--	--	1054.31
-5	--	--	--	1036.85	1044.98	1053.11
0	1009.32	1018.73	1027.20	1035.67	1043.73	1051.78
5	1008.69	1017.57	1025.97	1034.36	1042.35	1050.33
10	1007.99	1016.28	1024.61	1032.94	1040.85	1048.76

Table 2. Specific heat of aqueous solutions of ethylene glycol

	Concentrations in volume percent					
Temperature, °C	5%	10%	15%	20%	25%	30%
-10	--	--	--	--	--	3560
-5	--	--	--	3757	3666	3574
0	4075	3937	3853	3769	3679	3589
5	4074	3946	3863	3780	3692	3603
10	4073	3954	3873	3792	3705	3617

Table 3. Thermal conductivity of aqueous solutions of ethylene glycol

	Concentrations in volume percent					
Temperature, °C	5%	10%	15%	20%	25%	30%
-10	--	--	--	--	--	0.411
-5	--	--	--	0.458	0.438	0.417
0	0.532	0.512	0.489	0.466	0.445	0.423
5	0.541	0.520	0.496	0.472	0.451	0.429
10	0.551	0.528	0.504	0.479	0.457	0.435

Table 4. Viscosity of aqueous solutions of ethylene glycol

	Concentrations in volume percent					
Temperature, °C	5%	10%	15%	20%	25%	30%
-10	--	--	--	--	--	0.00619
-5	--	--	--	0.00365	0.00434	0.00503
0	0.00193	0.00208	0.00255	0.00302	0.00359	0.00415
5	0.00167	0.00179	0.00217	0.00254	0.00301	0.00348
10	0.00143	0.00156	0.00187	0.00218	0.00257	0.00295

The temperature of the tank was adjusted by the refrigeration. When the temperature of the tank became stable, the pump was started to circulate the working fluid in the GHE. The data logger was used to monitor the inlet and outlet fluids temperature and pressure. The refrigerator's outlet temperature was continuously adjusted to achieve the stability of GHE's inlet temperature. After the ground temperature was measured to be stabilized, results were identified by the average of recorded data in 2 hours.

4. RESULTS AND DISCUSSION

After adding the antifreeze, the physical properties of the working fluid are different from pure water, which affect the heat transfer between the circulating fluid and the ground. At the same time, the viscosity and density of the antifreeze solution increase with its concentration. The power consumption for transporting working fluid increase consequently.

4.1. Heat Transfer Performance

The heat exchange rate was calculated according to recorded temperatures of inlet and outlet fluids and flow rate of the GHE in the experiment. On the other hand, the aforementioned RC model was used to simulate the heat exchange rate under the same conditions as the experiment. Relative errors between experimental and simulation results were within acceptable range of ±10%, as shown in Table 5. Therefore, the subsequent research was performed by the simulation model.

Table 5. Heat exchange rate of experiment and simulation

-	Inlet temperature t=10°C			Inlet temperature t=5°C		
Concentration of antifreeze solution	Heat exchange rate per unit length, W.m^{-1}		Relative error	Heat exchange rate per unit length, W.m^{-1}		Relative error
	experimental	simulation		experimental	simulation	
5%	26.0	27.3	4.9%	43.8	42.1	-4.0%
10%	25.8	27.1	4.9%	42.6	42.4	-0.5%
15%	25.7	27.2	5.7%	39.8	42.1	5.6%

In this paper, the degradation coefficient for heat transfer D_q was defined as the ratio of the heat exchange rate after adding the antifreeze to the heat exchange rate without antifreeze. D_q could indicate the influence of antifreeze on the heat exchange performance of the GHE. The degradation coefficient changed with the physical properties of antifreeze solution, and the physical properties of antifreeze solution were affected by its concentration and temperature. Therefore, the degradation coefficient can be related to the concentration of antifreeze solution at the same temperature. The heat exchange rate of different inlet temperatures were simulated by the simulation model. GHE parameters of the simulation model were the same as the experiment, and the physical properties parameters of antifreeze were set according to Table 1 to 4. The degradation coefficients for heat transfer D_q are shown in Fig. 2.

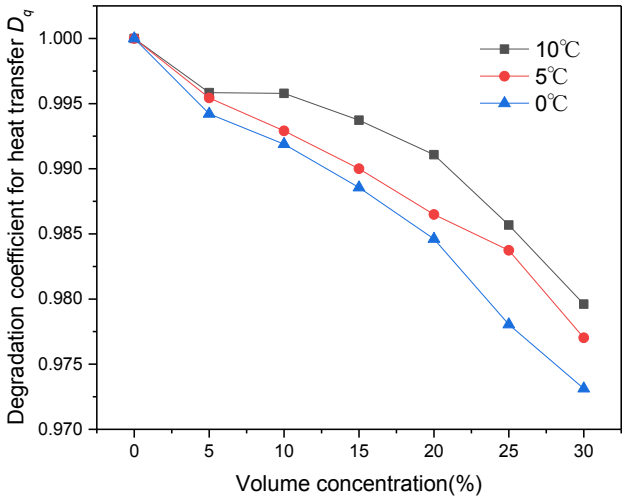

Figure 2: Degradation coefficients for heat transfer D_q

At the same concentration, the degradation coefficient for heat transfer increased with the inlet temperature. At the same inlet temperature, the degradation coefficient for heat transfer changed linearly with the concentration. For every 5% increase in concentration, the heat exchange rate decreased by about 0.4%. Among the simulation results, the degradation of heat exchange rate was the largest at inlet temperature of 0°C with the concentration of 30%, and the degradation coefficient was 0.973.

Four physical properties of the heat transfer fluid were considered to affect the heat exchange rate of GHEs, including density ρ, specific heat c, thermal conductivity λ and viscosity μ. They were analyzed by the simulation model constructed above. The physical properties parameters were determined by the temperature and concentration of antifreeze solution. The control variable method was applied, in order to study the effect of single physical parameter. To be specific, one parameter was determined separately according to the temperature and concentration of antifreeze solution, and the rest parameters were set according to pure water at the same temperature. The simulation results are shown in Fig. 3 to 5.

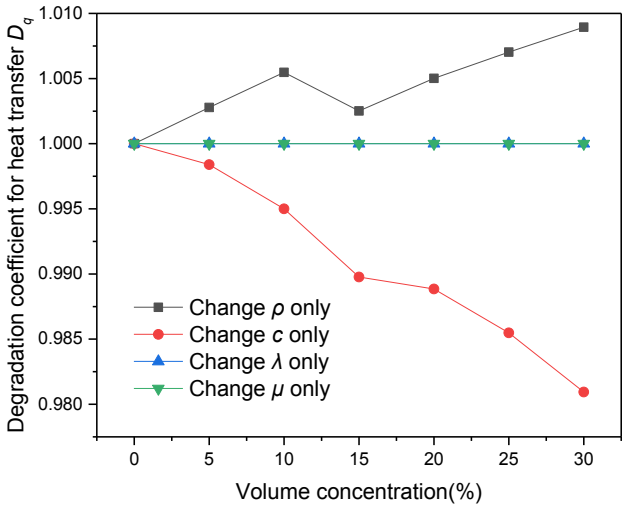

Figure 3: Influence of physical properties when inlet temperature *t*=10°C

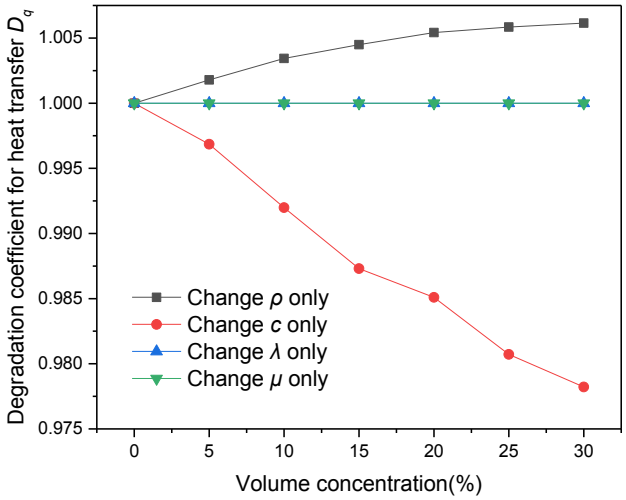

Figure 4: Influence of physical properties when inlet temperature *t*=5°C

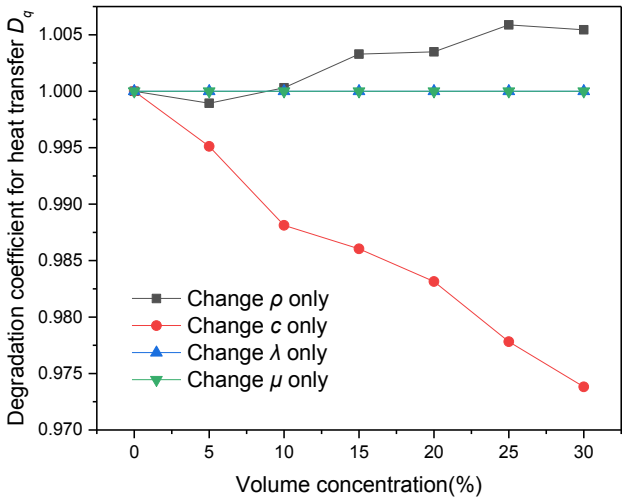

Figure 5: Influence of physical properties when inlet temperature *t*=0°C

Results indicated that only change of the thermal conductivity λ or the viscosity μ would not affect the heat exchange rate. It is because thermal conductivity λ and viscosity μ only affect the convective heat transfer coefficient inside GHEs, which occupies a relatively small proportion of the total thermal resistance (Bauer et al., 2011). The density ρ increased with the concentration of antifreeze solution. However, the temperature difference between the inlet and outlet of the GHE decreased in the simulation. Therefore, the degradation coefficients for heat transfer fluctuated at some points, but most of them were greater than 1 and showed an upward trend. The specific heat c was the main factor causing the decrease of heat exchange rate. As the concentration of antifreeze solution increased, the specific heat c decreased as well as the ability to transfer heat.

From the above analysis, heat transfer capacity of working fluid with the same volume was decreased after the addition of antifreeze. In general, the working fluid in GHEs should be guaranteed in turbulent state (ASHRAE, 1995). However, the increase in viscosity caused the decrease of Reynolds number. In comprehensive consideration, it is recommended to increase the flow rate for preventing the degradation of heat exchange rate of GHEs. For the same heat exchange rate at the same temperature difference, the correction factor of flow rate is shown in Table 6. The flow rate is suggested to be corrected according to Table 6 to ensure that the heat exchange rate meet the acquirement after the addition of antifreeze.

Table 6. Correction factors of flow rate

	Concentration in volume percent				
Inlet temperature, °C	10%	15%	20%	25%	30%
-10	--	--	--	--	1.122
-5	--	--	1.081	1.100	1.119
0	1.050	1.064	1.079	1.097	1.116
5	1.049	1.063	1.077	1.095	1.113

4.2. Friction loss

Since there was a few valves and section changes in the pipelines of this experiment, the flow fitting loss could be neglected. Pressure on the inlet and outlet pipes and flow rate were recorded by a data logger, and friction loss per unit length was calculated at every measuring time. In addition, Eq. (3) was used for theoretical calculation, and the friction loss per unit length was obtained under the same conditions as the experiment (Table 7). The relative errors between the experimental and theoretical results were within the acceptable range of ±10%, so the following study was carried out using Eq. (3).

Table 7. Friction loss for experiment and theory

-	Inlet temperature t=10°C			Inlet temperature t=5°C		
Concentration of antifreeze solution	Friction loss per unit length, Pa.m^{-1}		Relative error	Friction loss per unit length, Pa.m^{-1}		Relative error
	experimental	theoretical		experimental	theoretical	
5%	144	150	4.1%	145	153	5.4%
10%	162	161	-0.6%	167	165	-1.2%
15%	164	168	2.4%	168	174	3.5%

Eq. (3) indicated that friction loss per unit length was only related to the density and viscosity of the working fluid when the pipe diameter and velocity remaining the same. The correction factors of friction loss were calculated according to the physical property parameters of different concentrations and temperatures of antifreeze solution, as shown in Table 8.

Table 8. Correction factors of friction loss

	Concentration in volume percent				
Inlet temperature, °C	10%	15%	20%	25%	30%
-10	--	--	--	--	1.419
-5	--	--	1.228	1.290	1.346
0	1.053	1.115	1.170	1.229	1.282
5	1.014	1.069	1.120	1.175	1.226

Accordingly, after adding antifreeze to GHEs, in order to prevent the degradation of heat exchange rate, the flow rate should be corrected. Then the corrected flow rate should be used to calculate the friction loss. Finally, the friction loss after adding antifreeze could be obtained by multiplying the correction factor given in Table 8. The corrected friction loss per unit length is the basis for pump selection.

5. CONCLUSIONS

In this paper, the effects of adding antifreeze on the heat transfer and flow friction loss of GHEs were studied. The results and discussion could provide a reference for GHEs design under low-temperature conditions. The following conclusions could be drawn:

1) The heat exchange rate degradation of different concentrations and temperatures of antifreeze solution was discussed. Higher concentration and lower inlet temperature caused greater degradation of heat exchange rate.

2) Heat transfer capacity of working fluid with the same volume was decreased after the addition of antifreeze. It is recommended to increase the flow rate by multiplying the given correction factor of flow rate, in order to prevent the degradation of the heat exchange rate.

3) The corrected flow rate is suggested to be used to calculate the friction loss. Since the density and viscosity of antifreeze solution are higher than those of pure water, the friction loss is suggested to be corrected by multiplying the given correction factor of friction loss as well.

ACKNOWLEDGEMENTS

This research and the associated scientific investigations are supported by the National Natural Science Foundation of China (Grant No. 51678418).

NOMENCLATURE

C_{fr}	volume heat capacity of frozen material ($J\times m^{-3}\times K^{-1}$)	C_{ufr}	volume heat capacity of unfrozen material ($J\times m^{-3}\times K^{-1}$)
c	specific heat ($J\times kg^{-1}\times K^{-1}$)	d_b	borehole diameter (m)
d_i	pipe inner diameter (m)	d_o	pipe outer diameter (m)
H	latent heat ($J\times kg^{-1}$)	L	bore depth (m)
p_m	friction loss per unit length ($Pa\times m^{-1}$)	T	temperature (K)
t	inlet temperature (°C)	v	velocity ($m\times s^{-1}$)
W	moisture content (%)	λ_{fr}	thermal conductivity of frozen material ($W\times m^{-1}\times K^{-1}$)
λ_p	pipe thermal conductivity ($W\times m^{-1}\times K^{-1}$)	λ_{ufr}	thermal conductivity of unfrozen material ($W\times m^{-1}\times K^{-1}$)
ρ	density ($kg\times m^{-3}$)	μ	viscosity ($N\times s\times m^{-2}$)

REFERENCES

ASHRAE, 1995. Commercial/Institutional Ground-source Heat Pump Engineering Manual. ASHARE, Inc., Atlanta.
ASHRAE, 2017. ASHRAE handbook: Fundamentals. ASHRAE, Inc., Atlanta.
Bakirci, K., 2010. Evaluation of the performance of a ground-source heat-pump system with series GHE (ground heat exchanger) in the cold climate region. Energy 35, 3088-3096.
Bauer, D., Heidemann, W., Müller-Steinhagen, H., Diersch, H.J.G., 2011. Thermal resistance and capacity models for borehole heat exchangers. International Journal of Energy Research 35, 312-320.
Casasso, A., Sethi, R., 2014. Efficiency of closed loop geothermal heat pumps: A sensitivity analysis. Renewable Energy 62, 737-746.
Congedo, P.M., Colangelo, G., Starace, G., 2012. CFD simulations of horizontal ground heat exchangers: A comparison among different configurations. Applied Thermal Engineering 33-34, 24-32.
Healy, P.F., Ugursal, V.I., 1997. Performance and economic feasibility of ground source heat pumps in cold inmate.
Hepbasli, A., Akdemir, O., Hancioglu, E., 2003. Experimental study of a closed loop vertical ground source heat pump system. Energy Conversion and Management 44, 527-548.
İnallı, M., Esen, H., 2004. Experimental thermal performance evaluation of a horizontal ground-source heat pump system. Applied Thermal Engineering 24, 2219-2232.
Kim, K., Zhou, W., Huang, S.L., 2008. Frost heave predictions of buried chilled gas pipelines with the effect of permafrost. Cold Regions Science and Technology 53, 382-396.
Lamarche, L., Beauchamp, B., 2007. A new contribution to the finite line-source model for geothermal boreholes. Energy and Buildings 39, 188-198.
Pulat, E., Coskun, S., Unlu, K., Yamankaradeniz, N., 2009. Experimental study of horizontal ground source heat pump performance for mild climate in Turkey. Energy 34, 1284-1295.
Self, S.J., Reddy, B.V., Rosen, M.A., 2013. Geothermal heat pump systems: Status review and comparison with other heating options. Applied Energy 101, 341-348.
Tang, F., Nowamooz, H., 2019. Factors influencing the performance of shallow Borehole Heat Exchanger. Energy Conversion and Management 181, 571-583.
Tu, S., Zhang, X., Zhou, X., 2017. A revised thermal resistance and capacity model for the ground heat exchanger under freezing soil conditions and thermal performance analysis. Procedia Engineering 205, 19-26.

Manuscript ID: 1795
DOI: 10.18462/iir.icr.2019.1795

A new approach for dehumidifying air under refrigerator temperature situations: Dehumidification with proton exchange membrane (PEM)

Ronghui QI[(a,*)] Tao LI[(a)], Li-zhi ZHANG[(a,b)]

[(a)] Key Laboratory of Enhanced Heat Transfer and Energy Conservation of Education Ministry, School of Chemistry and Chemical Engineering, South China University of Technology, Guangzhou 510640, China, qirh@scut.edu.cn

[(b)] State Key Laboratory of Subtropical Building Science, South China University of Technology, Guangzhou 510640, China

ABSTRACT

A dehumidifier with Polymer electrolyte membrane (PEM), consisting of five layers of electrolyte, is suitable for the high-accuracy, limited-space humidity control for food storage, pharmaceutical and other chemical industries. It can be powered by low-voltage electric field (~3V), and has advantages such as ultra-compact (a few cm^3), fast response, no drainage and no moving parts. In this study, the system performance of dehumidifying moist air below 0 °C with this innovation PEM is investigated experimentally, with our self-built test rig. At a sub-zero temperature of -5.5°C, the moisture removal rate increases almost proportionally with the increase in applied voltages at the range of 2~4V, which provides practical potentials for accurate controlling the novel dehumidifier by varying the voltages. When the voltage increases, the dehumidification efficiency also increased. Therefore, the new approach of dehumidifying moist air with PEM element can be a promising alternative for small-scale, high-requirement dehumidification under low temperature for refrigerators.

Keywords: Air Dehumidification, Proton Exchange Membrane, Sub-zero, Experiments, Energy Efficiency.

1. INTRODUCTION

In beverage and food storage, pharmaceutical and several other chemical industries, dehumidifying moist air at low temperature is usually required, which the common refrigerator temperature range is about -10~10 °C. And the operation space is very limited, requiring an ultra-compact handling method. More specifically, there exist cases that demand a sub-zero dew point, even up to -40 °C. Condensing-based dehumidifiers have been widely used in industrial and commercial applications. However, it is limited by freezing phenomenon occurring when the dew point at 0 °C. In addition, the presence of liquid water generated during condensation can damage food and pharmaceutical systems. Desiccant absorption is capable of handling the low-temperature air, but it usually has a big volume and large thermal inertia. Furthermore, thermal energy (around 60 to 260°C) is required to regenerate the desiccant, which limits its applications.

Electrolytic dehumidification with proton exchange membrane (PEM) is an innovative independent humidity control technology. It was firstly proposed by Iwahara et al. (2000), by using the solid electrolyte material SrCeO ceramics for dehumidification and verifying its feasibility under DC voltage. Sakuma et al. (2009, 2010) proved its possibility at room temperature (20~40°C), and developed an empirical formula. Previous research of our research group found that under 3V electric field, the outlet humidity of air flow could reduce from 90% to 30% (Qi, et al., 2017, 2018). And the energy efficiency of moisture removal was $2.0\sim3.0\times10^{-2}$ g/(J·m^2), which was competitive with other dehumidification methods, i.e. 2.0×10^{-2} g/(J·m^2) for electro-osmotic dehumidification (Yan et al. 2012) and 2.4×10^{-2} g/(J·m^2) for thermoelectric dehumidification (Shen et al. 2016). Furthermore, it is ultra-compact without any cooling/regeneration devices, which the volume could be as small as a few cm^3, as shown in Fig.1.

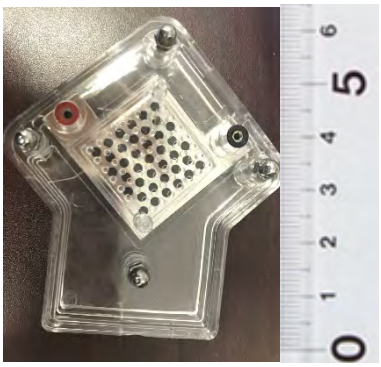

Fig. 1. Façade of an air dehumidifier based on PEM

Literature review indicated that the novel air dehumidifier with PEM could drive the moisture transport directly by the electric field rather than the difference of temperature or water vapor partial pressure, which means that it has potential to be operated efficiently under low temperature situations. In this paper, with our self-developed test rig, the performance of PEM-based electrolytic dehumidification was investigated experimentally under various operating conditions, under a low-temperature environment.

2. METHODS

2.1. Experimental rig

A PEM-based electrolytic experimental rig was established. The PEM assembly is composed of a PEM in the middle, a porous Pt cathode and an IrO_2 anode catalytic layers composed of metal particles, and carbon fiber paper as a diffusion layer on both sides. The air channel, with the thickness of 2mm, is assembled on the outermost side. When a DC voltage is applied, the following reactions occur.

Anode: $H_2O \rightarrow 2H^+ + 2e^{-1} + 0.5O_2$ (1)

Cathode: $2H^+ + 2e^{-1} + 0.5O_2 \rightarrow H_2O$ (2)

At the anode side, water vapor in the air is decomposed, producing H+ protons. The H+ protons are driven toward the cathode side through the PEM and react with oxygen to form water at the cathode side. The vapor generated at cathode side is taken away by the gas. This completes the transport of moisture from the anode-side air to the cathode-side air, as shown in Fig. 2.

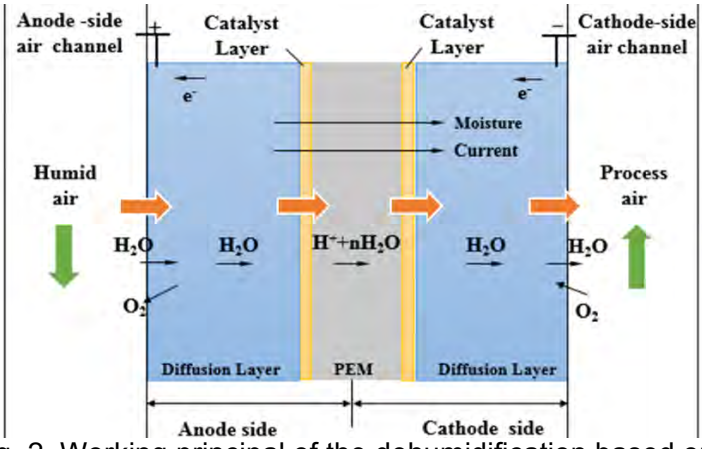

Fig. 2. Working principal of the dehumidification based on PEM

The schematic diagram of the test rig is shown in Fig. 3, which is similar to the test rig developed in our previous study (Qi. et al. 2017). The differences are that 1) the air was pre-cooled to reach the required sub-zero temperature; 2) the whole system was placed in a constant temperature& humidity chamber, to maintain the required low temperature situation.

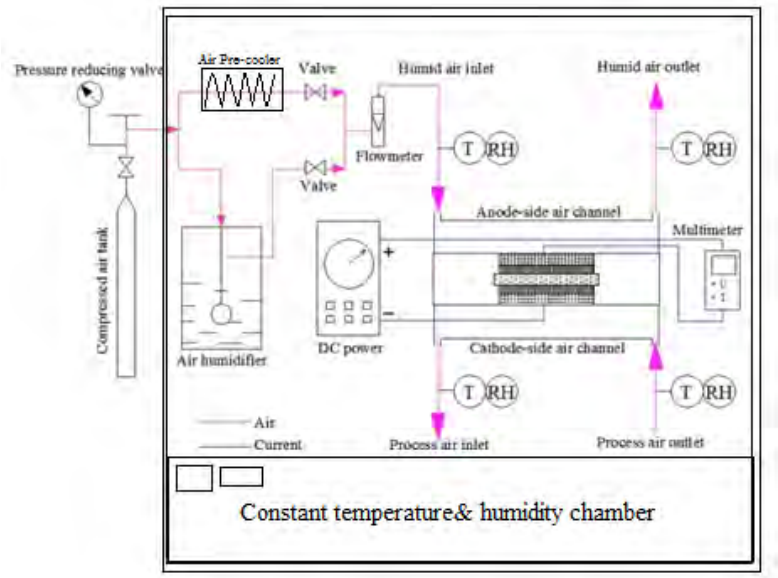

Fig.3. Schematic of the test rig

The inlet and outlet temperature and humidity was recorded by electronic sensors, with the errors of ±1°C and ±3%RH, respectively. The operating voltage and current were recorded by the multi-meter, with the measurement error of ±2mV. The experimental procedures were as follows. 1) The air pump, pre-cooler and humidifier were adjusted according to the set value, and was opened 1 hour before the experiment to let the air reach the steady condition; 2) The chamber was set at a sub-zero temperature, 1 hour before the experiment; 3) The DC power was opened and adjusted to the set value; 4) After the device reached a steady state, the operational data were recorded by the Agilent data logger every 5 seconds.

2.2. Performance index

During the experiments, the moisture removal rate of the electrolyte membrane could be calculated by Eq. (3). The dehumidification efficiency could be calculated by Eq. (4).
Several performance indexes for evaluating the system performance were defined as follows.

Moisture removal rate (g/s): $m_{removal} = m_{aA}(\omega_{aA,out}+\omega_{aA,in})$ Eq. (1)

Current density (mA/cm^2) : $i = I / A_{area}$ Eq. (2)

Dehumidification efficiency (g/(h·V·m^2)): $_{V} = m_{removal} / (V \cdot A_{area})$ Eq. (3)

Energy efficiency(-): $\eta_{energy} = \Upsilon \times m_{removal}/(P \times A_{area})$ Eq. (4)

where m is mass flow rate, ω is moisture content, A_{area} is membrane area, P is power, A is anode, η is energy efficiency and a is air. ϒ is the latent heat of vaporization of water vapor. The subscripts "in" and "out" stands for the inlet and outlet parameters.

3. RESULTS

During the experiments under refrigerator temperatures, the operation conditions of experiments are summarized in Table 1.

Table 1. Operation conditions of PEM dehumidification

Electric Field (V)	Air inlet of Anode side			Air inlet of Cathode side		
	m_a (g/s)	t (°C)	RH (%)	m_a (g/s)	t (°C)	RH (%)
2,3,4	0.0218	-5.5	60±2	0.0219	-5.5	58±5

The time-series parameters, including the current, moisture removal rate (Eq. (1)), dehumidification efficiency (Eq. (3)) and energy efficiency (Eq. (4)), under various voltages during dehumidification processes are summarized in Fig. 4 and 5. As shown in Fig. 4(a), with the increase in applied electric field, the moisture removal rate increases almost proportionally. It provides practical potentials for accurate controlling the novel air dehumidifier by varying applied voltages. Besides, in Fig. 4(a), the startup time of the dehumidification based on the PEM, which is the time to reach the steady state, is about 4 to 12 minutes. This startup time is obviously shorter at higher applied voltages, which the time under 4V is 3 times that under 2V, possibly due to the more intense chemical reactions under high applied voltages.

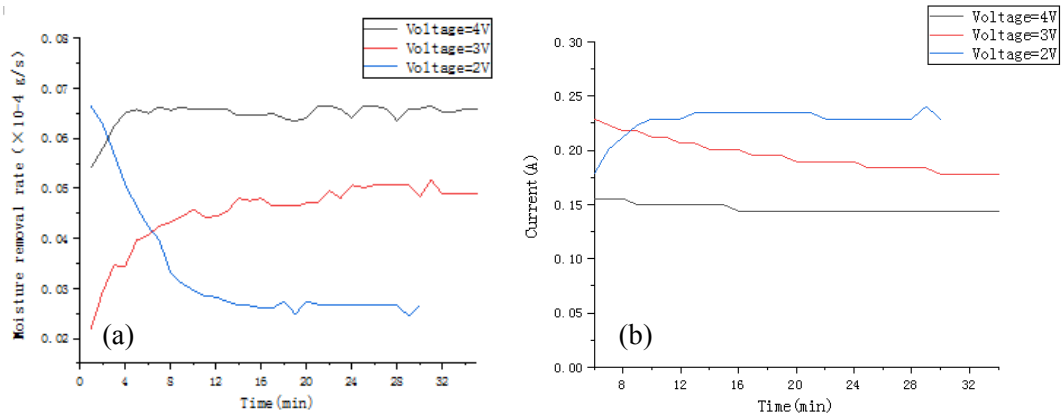

Fig. 4 Time-series parameters under various voltages (a) Current and (b) Moisture removal rate

However, in Fig. 4 (b), the operating current during dehumidification decreases, rather than increases, with the increase in the electrical field. These results are confusing, and also different from the current data in our previous study at room temperature (Qi. et al. 2017). Possibly reason is that a startup voltage, around 1.5V, is required for the electrolysis of water vapor at the anode side. Thus, under a low electric field such as 2V, the vapor decomposition occurs ineffectively, which means that the main overpotential of PEM element is the Ohmic effect. However, at higher voltages such as 3V and 4V, the activation overpotential plays the most significant role, which is several times higher than the Ohmic effect. Thus, at the low-voltage conditions, though the operating current is high, the dehumidification rate is actually lower compared to those at high-voltage conditions. This phenomenon is more obvious at low air temperature conditions, which will be further investigated in our future work.

Then, the energy efficiency and dehumidification efficiency during dehumidification are shown in Fig. 5. It could be found that generally, the increase of voltage results in an increase of both efficiencies. The dehumidification efficiency is around 4~5g/(h·V·m^2) during our experiments. Thus, if this novel dehumidification element is practically applied, it could remove 0.7g moisture one day under a 3V voltage, for a 4×4cm^2 PEM element. It is competitive with the commercial PEM-based element, which is 1g/per day at the room temperature. Furthermore, in Fig. 5(b), it could be found that the energy efficiency is relatively low, which may be caused by the small PEM area (3.5×3.5cm^2) used in our experiments.

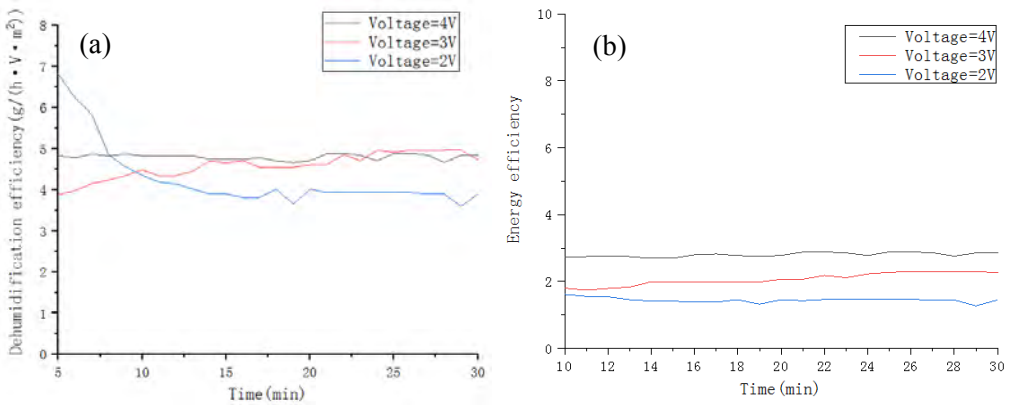

Fig. 5 Time-series parameters under various voltages (a) Dehumidification efficiency and (b) Energy efficiency

4. CONCLUSIONS

A dehumidifier with Polymer electrolyte membrane (PEM), consisting of five layers of electrolyte, is suitable for the high-accuracy, limited-space humidity control for food storage, pharmaceutical and other chemical industries. It can be powered by low-voltage electric field (~3V), and has advantages such as ultra-compact (a few cm^3), fast response, no drainage and no moving parts.As the moisture transport is driven by the electric field rather than the difference of temperature or water vapor partial pressure, it has potential to be operated efficiently under low temperature even sub-zero situations. In this paper, with our self-developed test rig, the performance of PEM-based electrolytic dehumidification was investigated experimentally under various operating conditions, under a low-temperature environment. Results showed that at an operation temperature of -5.5°C, the moisture removal rate increases almost proportionally with the increase in applied voltages at the range of 2~4V, which provides practical potentials for accurate controlling the novel dehumidifier by varying the voltages. Furthermore, the dehumidification efficiency also increased with the voltage, which is competitive compared with the commercial element under room temperature. Therefore, the new approach of dehumidifying moist air with PEM element can be a promising alternative for small-scale, high-requirement dehumidification under low temperature for refrigerators.

ACKNOWLEDGEMENTS

The project is supported by National Key Research and Development Program (No. 2016YFB0901404), National Natural Science Foundation of China (51876067). It is also supported by the Science and Technology Planning Project of Guangdong Province: Guangdong-Hong Kong Technology Cooperation Funding Scheme (TCFS), No.2017B050506005.

NOMENCLATURE

m	Mass flow rate (kg/s)	RH	Relative humidity (%)
t	Temperature (°C)	ω	Moisture content (kg/kg)
A_{area}	Effective area (m^2)	P	Power (kJ)
I	Current (A)	η	Efficiency
Subscripts			
a	Air	w	Water
A	Anode	C	Cathode
In	Inlet	Out	Outlet

REFERENCES

B. Li, Y.Y. Yan, 2011, Solid Desiccant Dehumidification Techniques Inspired from Natural Electroosmosis Phenomena, Journal of Bionic Engineering, 8, 90-97

L. Cheng, et al., 2017. Household frost-free appliances humidity control principle and practical application (in Chinese), Journal of appliance science & technology 2017; (04): 56-59.

X. Liu, et al., 2015. Performance improvement in air dehumidifiers: From ideal to actual (in Chinese), Chin Sci Bull 2015, 60: 2631–2639

H. Iwahara, et al., 2000. Electrochemical dehumidification using proton conducting ceramics, Solid State Ionics 2000, Vol: 136-137 pp. 133-138.

K. Onda, et al., 2005. Polymer Electrolyte Dehumidifying Cell and Its Application to Air Conditioners, Journal of applied electrochemistry 2005; 152(12): A2369-A2375.

S. Sakuma, et al., 2009. Water transfer simulation of an electrolytic de-humidifier, J Appl Electrochem 2009; 39(6):815-825

S. Sakuma, et al., 2010. Estimation of dehumidifying performance of solid polymer electrolytic dehumidifier for practical application, J Appl Electrochem 2010; 40(12): 2153-60.

R. Qi, et al., 2017. Experimental study on electrolytic dehumidifier with polymer electrolyte membrane for air-conditioning systems, Energy Procedia; 142: 1908–1913.

R. Qi, D.J. Li, H.Y. Li, et al., 2018, Heat and mass transfer in a polymeric electrolyte membrane-based electrochemical air dehumidification system: Model development and performance analysis, International Journal of Heat and Mass Transfer, 126 (Part B), 888-898.

Q. Chen, et al., 2019. A dehumidification process with cascading desiccant wheels to produce air with dew point below 0 °C, Applied Thermal Engineering, 148: 78-86.

Manuscript ID: 1808
DOI: 10.18462/iir.icr.2019.1808

Numerical simulation for heat transfer performance of a prefabricated ceiling radiant cooling panel with air layer

Dong XIE[(a)], Jinzhi LIU[(a)]*, Hanqing WANG[(a)]

[(a)]University of South China
Hengyang, 421001, China, nhxiedong@126.com

ABSTRACT

A novel prefabricated radiant cooling panel with air layer which has uniform surface temperature distribution is proposed in order to improve the performance of radiant cooling ceiling. The purpose of this study is to research the influence of the thickness of air layer and chilled inlet water temperature on the surface temperature and cooling capacity of this panel using numerical simulation. A simplified mathematical heat transfer model using CFD technology is developed for the numerical simulation of fluid-flow and heat transfer inside the 3-D radiant panel. The simulation results of prefabricated radiant panel are in good agreement with the value of experimental results. The simulated results demonstrated that the novel prefabricated radiant ceiling cooling panel has the potential of condensation control due to natural convection in the air layer. Cooling capacity of ceiling panel decreases with increase of air layer thickness and supply water temperature.
Keywords: Prefabricated Radiant Cooling Panel, Numerical Simulation, Surface Temperature Distribution, Cooling Capacity.

1. INTRODUCTION

Prefabricated construction, as novel mode of building construction, is being vigorously promoted recently. The radiant ceiling cooling system is applied in the prefabricated construction for its thermal comfort, improved energy efficiency and reduced building energy consumption. A radiant cooling system can be defined as a high temperature cooling system, which has higher efficiency for total chilling system compared with low temperature system.The vertical temperature gradient in the room of radiant cooling system has achieved more uniform than that of conventional air-conditioning (Yasin et al., 2015). Besides, the results of energy consumption calculation show that the radiant system is more efficient than all-air systems (Lin et al., 2015).

However, it is inevitable that the condensation problem on the radiant panel surfaces is found to hinder the extensive application of radiant cooling in hot and humid areas (Baisong et al., 2016; Haida et al., 2017; Rabanillo-Herrero et al., 2018). The general radiant ceiling panels are faced with serious condensation problems because the minimum surface temperature of panel surfaces is easily lower than indoor dew point temperature (Moon Keun and Hansjürg, 2014). In order to avoid condensation risk, the panel is required to increase chilled water temperature to raise minimum temperature of panel surfaces. Thus, cooling capacity of panels is not sufficient to meet requirements of indoor thermal comfort. On the other hand, to prevent condensation risk and solve the problem of limited cooling capacity, we would use a dehumidification system to remove indoor partial sensible load and all latent heat load. Melanie Fauchoux et al. (2010) built the simulation model of a new panel. The results illustrated that this panel can transfer heat and remove indoor moisture moderating indoor humidity. Radia Eldeeb et al. (2013) developed a novel heat and moisture transfer panel which could control the relative humidity and reduce the total energy consumption. Moon Keun Kim et al. (2018) studied a radiant cooling system in series with a decentralized air convector. The results showed that this radiant system has potential of dehumidification of indoor air and increasing temperature of panel surfaces. Jungmin et al. (2014) investigated the possibility of a coupling outdoor air cooling with radiant floor cooling by a simulation method. It's indicated that the proposed system can save more than 20% of cooling energy in during the hot and humid climate. Haida et al. (2016) proposed a mathematical model for obtaining the departure duration of the droplet, which was verified by measured results.

Typically, the pipes inside the metal radiant cooling panel are closely connected to the metal ceiling.

Therefore, the lowest temperature of the metal ceiling is about the same as the temperature of chilled inlet water in the tubes (Kang and Xiaohua, 2014). Moreover, the radiant ceiling cooling system types like the pipes in the concrete or capillary have the disadvantage of post-maintenance difficulties if the tubes of panels occur leakage. In addition, these radiant systems need some form of air treatment system to keep the indoor air dry enough and decrease indoor air temperature. Research on avoiding condensation problem and improving the uniformity of panel surfaces mainly focused on the increasing chilled water temperature and ventilation systems (Esmail M et al., 2014; Angelo et al., 2014). Little research has been found on internal structure of the radiant cooling panel for preventing condensation.

This paper presents the performance of a prefabricated radiant cooling panel with straight tube and air layer as it potentially has three key advantages: higher quality, simple operation and better flexibility. In addition,the existence of air layer is found to improve the uniformity of surface temperature on the radiant ceiling panel (Baisong et al., 2016). The radiant cooling panels with uniform surface temperature have higher cooling capacity, when minimum surface temperature is higher than indoor dew point temperature (Baisong et al., 2016). The main purpose of this study is to investigate influence of supply water temperature and thickness of air layer on surface temperature and cooling capacity. The heat-transfer process of liquid-solid coupling and gas-solid coupling are realized by numerical simulation method. The uniformity of prefabricated radiant cooling panel with air layer and the potential for resistance to condensation have been evaluated.

2. METHODOLOGY

2.1. Physical Model

The structure of prefabricated radiant cooling panel with air layer is shown in Fig.1. Half of copper tube is exposed in the air layer and half of that is embedded in the insulation layer. The copper tubes are not in close contact with metal ceilings (called aluminium plate). The heat transfer inside this panel is through radiation, convection and conduction. The material properties used in the prefabricated radiant cooling ceiling are summarized in Table 1.

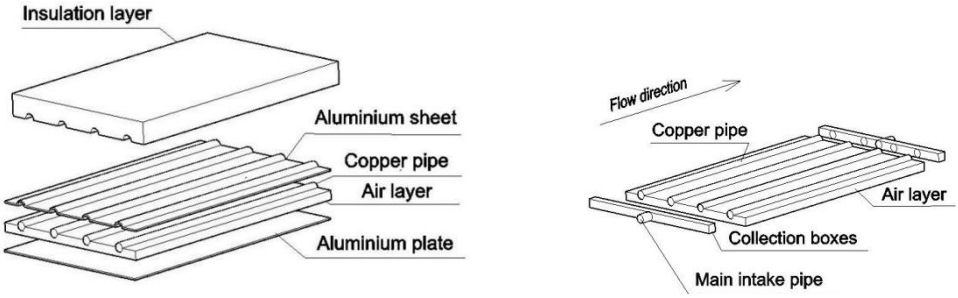

Figure 1: Three-dimensional decomposition drawing

Fig. 2. shows heat transfer between aluminum plate surface and indoor thermal environment. Heat transfer process of this panel from chilled water to room environment includes the four parts:

(1) Convective heat exchange between chilled water and inside surface of tubes.

(2) Heat conduction between external surface of pipes and aluminum sheet.

(3) Convective and radiation heat transfer occur within air layer affected by factors of aluminum sheet, pipe outside surface and internal surface of aluminum plate.

(4) Heat transfer between panel surface and indoor thermal environment.

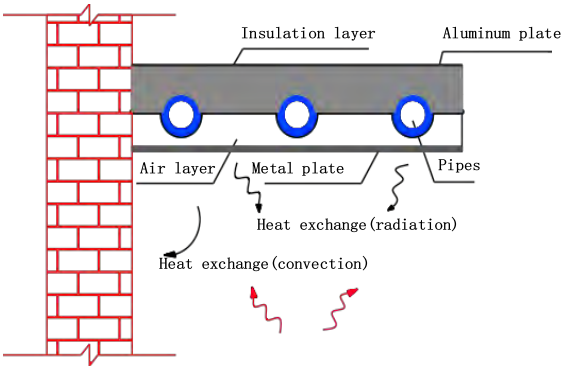

Figure 2: Diagram on heat transfer mechanism of the panel

Table 1. Material properties of mathematical heat transfer model

Structural layers	Thermal conductivity (W·m $^{-1}$ K $^{-1}$)	Thickness (mm)
Copper pipes	401	1.5
Insulating layer	0.035	40
Aluminum sheet	237	1.5
Air layer	0.023	8-16
Aluminium plate	237	1.5

2.2. Theoretical Analysis

Due to complexity of heat transfer process, we simplify the model of heat transfer. The model assumes that 1) the external aluminum sheet surface is treated as adiabatic because of well-insulated insulation, 2) the external air has no effect on the air flow in the cavity due to well-sealed enclosure, 3) the cooper tubes are considered as stabilized. Their physical property parameters are not changed with temperature, 4) heat transfer in the panel is steady state. According to the calculation results of Reynolds number, the state of flow in tubes is turbulent. The $k-\varepsilon$ model is set to solve the turbulent flow in the core region.

2.3. Heat Transfer in Radiant Cooling System

The heat transfer between cooling panel surface and indoor thermal environment mainly includes convection heat transfer of indoor air, radiative heat exchange between radiation surface and enclosure structure. The total sensible heat flux (q_{total}) of the panel can be expressed by the sum of radiative heat fluxes (q_r) and convective heat fluxes (q_c). The equation is (Xing et al., 2010):

$$q_{total} = q_r + q_c \quad \text{Eq. (1)}$$

$$q_r = 5\times10^{-8}\left[(AUST+273.15)^4-(T_p+273.15)^4\right] \quad \text{Eq. (2)}$$

$$q_c = 2.13(T_a-T_p)\left|T_a-T_p\right|^{0.31} \quad \text{Eq. (3)}$$

where (Radia et al., 2013; Karadag, 2009):

$$h_c = 2.13(T_a-T_p)^{0.31} \quad \text{Eq. (4)}$$

where T_a is indoor temperature, T_p is mean panel surface temperature. According to the method of mean radiative heat transfer in the radiation air-conditioning room based on ASHRAE Handbook, the other interior surfaces in the room are assumed to be a surface except for ceiling cooling panel. The temperature of the imaginary surface is area-weighted average uncooled temperature (AUST). Through simultaneous calculation of equations (1-4), the convective heat transfer coefficient (h_c) is 4.2 W·m^{-2}·K^{-1} ,and then, the value 4.2W·m^{-2}·K^{-1} of h_c is used in numerical simulation.

3. VALIDATION OF THE MODELING SIMULATION

Experiments of the ceiling cooling system were carried out in a test chamber with stable environment in June 2018. The dimensions of the internal chamber are 4.0 m (length)×3.8 m (width)×3.0 m (height). The walls of experimental chamber were made of thick insulation layer embedded in steel with good insulation performance. The radiant cooling system consists of cooled and heated source, pipeline transportation and radiant ceiling panels. The top of panels was installed with 20-mm-thick thermal insulation materials of cystosepiment with small thermal conductivity. The metal radiant panel had an air layer thickness of 10 mm. Inner diameter of embedded pipes of PPR material was 4 mm. To test metal panel surfaces temperature, there were 12 measuring points in the ceiling panel under different supply chilled water parameter. The panel surface temperature was measured by infrared radiation thermometer. The inlet and outlet temperature and the flow rate of the chilled water were measured by temperature sensors and turbine flow meter, respectively.

The results of numerical simulation and experiment are listed in Table 2. We can see that the relative error of temperature distribution in the panel is within 10%, and the numerical results agreed well with measured results. The parameters of supply water in the experiment are used as input boundary conditions of numerical simulation. As shown in the Table, the maximum temperature difference between the numerical and measured values is 1.4 ℃.

Equation(5) shows the errors between simulation and experiment. Relative error ξ is expressed as:

$$\xi = \frac{|t_m - t_e|}{t_e} \times 100\% \qquad \text{Eq. (5)}$$

Where t_m is mean surface temperature of numerical simulation, t_e is mean measured surface temperature.

Table 2. Comparison of numerical and measured values under different supply water parameters

Experimental condition	Inlet water temperature (℃)	Outlet water temperature (℃)	Water flow rate($m^3 \cdot h^{-1}$)	Ceiling surface temperature		Relative error (%)
				Measured	Numerical	
Case 1	15.0	15.7	0.376	23.5	23.6	0.4
Case 2	14.5	15.8	0.301	22.8	23.7	3.9
Case 3	16.3	17.3	0.320	23.1	24.5	6.1
Case 4	15.1	15.9	0.290	24.6	23.6	4.1

4. RESULTS AND DISCUSSIONS OF SIMULATION

4.1 Effect of the Air Layer Thickness on the Temperature and Cooling Capacity of Radiant Cooling Panel

Fig.4 shows the temperature field of ceiling panels under two thickness of air layers. Distance of tube spacing was 100 mm and length of the panel was 1200 mm. As shown in Fig.4, temperature fluctuations mainly come from increasing thickness of air layer. This was because the increase of air layer thickness would cause the enhancement of convective heat transfer. When thickness of air layer reached 16 mm, the difference between average surface temperature of cooling ceiling panel and chilled inlet water temperature was 4.2 ℃.

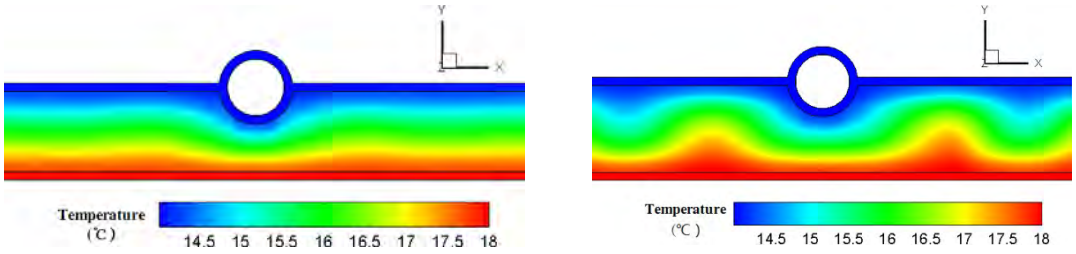

$\delta = 14$ mm $\qquad$ $\delta = 16$ mm

Figure 4: Temperature gradient of three-dimensional model

A linear negative correlation on the cooling capacity of ceiling panel with the increase of air layer thickness is shown in Fig. 5. *Q* and *T* were the cooling capacity and mean surface temperature of radiant cooling panel, respectively. When air layer thickness increased from 8 mm to 16 mm, the decrement value of cooling capacity was about 16.7 $W \cdot m^{-2}$ at inlet water temperature of 14℃. The air thickness layer has little influence on the average ceiling temperature when air layer thickness was less than 12 mm.

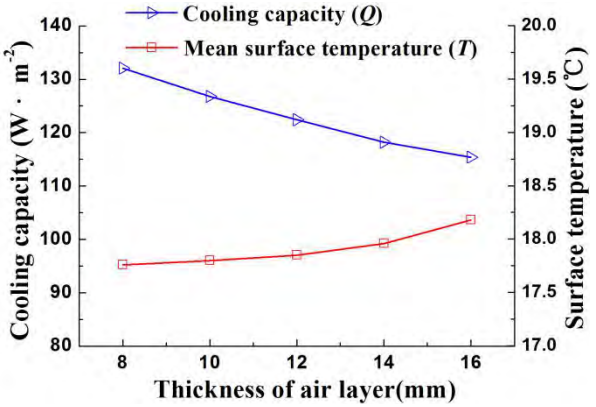

Figure 5: Influence of different air layer thickness on performance of radiant cooling panel

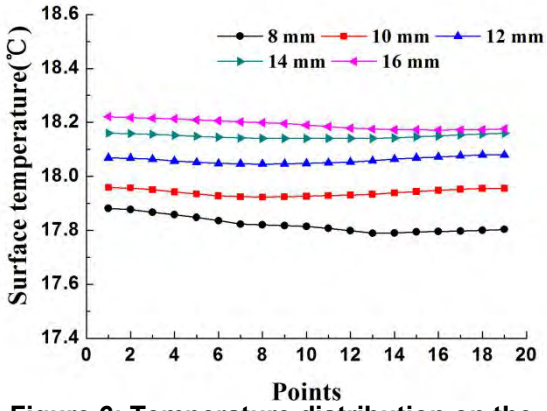

Figure 6: Temperature distribution on the surface of the novel radiant cooling panel

The temperature distribution of prefabricated ceiling radiant cooling panel with different air layer thicknesses was presented in Fig. 6. A novel prefabricated radiant cooling panel with air layer inside was of great significance on the uniformity of surface temperature distribution. It has been known that large non-uniformity of surface temperature distribution would rise up the risk of condensation. It has been found that the prefabricated ceiling radiant cooling panel with straight tubes has uniform temperature distribution, which means enhancement of convective heat transfer is beneficial to improve the uniformity of surface temperature. The maximum difference between the lowest surface temperature and the average surface temperature was 0.08℃and the mean surface temperature was 17.7℃, when thickness of air layer was 8 mm. We also found that mean surface temperature of the panel in 12 mm-thick air layer was 18.06 ℃， and the biggest surface temperature difference was 0.03 ℃. The room air dew-point temperature was 17.8℃ on the condition of indoor air temperature of 26℃ and relative humidity of 60%. Therefore, the radiant panel with air layer thickness of 8 mm had the possibility risk of condensation due to the lowest surface temperature was lower than room air dew-point temperature.

4.2 Effect of the Supply Water Temperature on the Temperature and Cooling Capacity of Radiant Cooling Panel

The supply water temperature played an important effect on the surface temperature and cooling capacity of the radiant cooling panel. As shown in Fig. 7, T_1 was the lowest temperature and T_2 was the average surface temperature of the bottom surface of radiant panel. The lowest temperature values were very close to the average temperature values of radiant panel with 12 mm-thick air layer. When the supply water temperature increased from 14 ℃ to 18 ℃, the surface temperature would increase, while the cooling capacity would decrease at water velocity of 0.6 ℃. Compared to the water velocity of 1.2 m·s^{-1}, the value of cooling capacity was reduced by 8.3 W·m^{-2}. The lowest surface temperature of radiant panel was 18.0 ℃ at the supply water temperature of 14 ℃, which is higher than room air dew-point temperature(17.8℃).

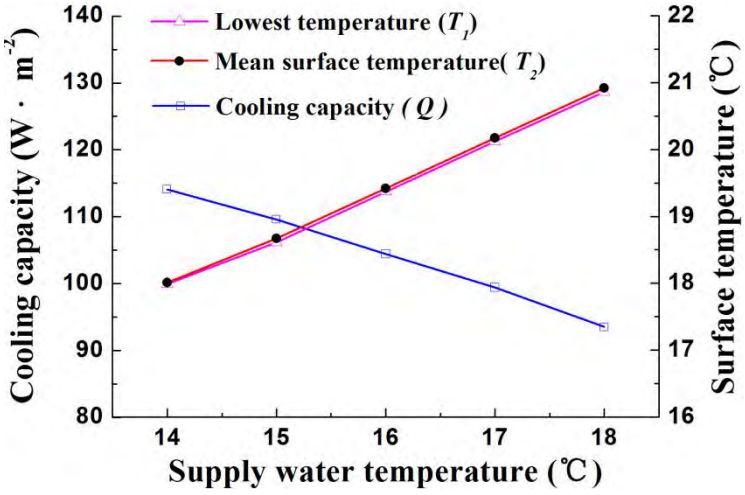

Figure 7: Influence of different supply water temperature on performance of radiant cooling panel

4.3 Effect of the Air Layer Thickness on the Air Movement Inside Radiant Cooling Panel

The thickness of air layer also had the significance influence on velocity streamline diagram. Fig. 8. showed that the cooling pipes were used as cold source to transfer cooling load to the air of the

sealed air layer. Due to the effect of temperature difference inside air layer, colder air sinks and hotter air rises. Then, air circumfluence in confined layer was emerged. The increase of air layer thickness was expected to enhance convective heat transfer in ceiling air layer.

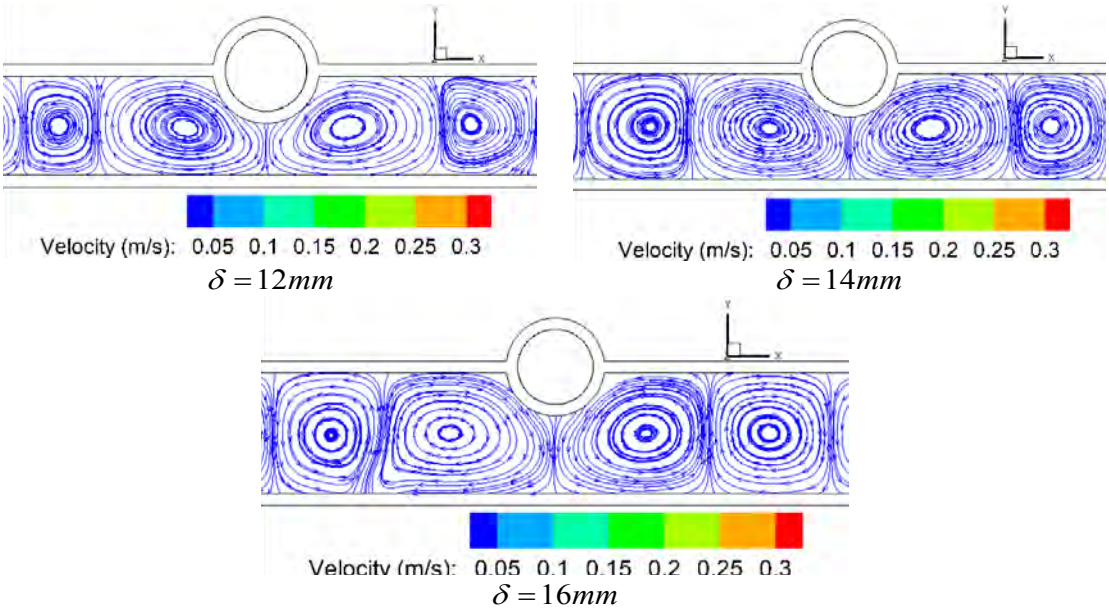

Figure 8: Air velocity streamlined diagram in ceiling cooling panel on the conditions of air layer thickness: 12 mm,14 mm and 16 mm

5. CONCLUSIONS

The numerical model of prefabricated ceiling radiant cooling panels with air layer was implemented by CFD software and was validated by the experiment. A small radiant panel was chosen for the simulation and experimental verification. The experimental error may come from the precision of controlled instruments for the chilled water temperature and the water flow rate. Based on the comprehensive analysis of simulation results, we can conclude that thickness of air layer and supply water temperatures have an important influence on the heat transfer of radiant panel.

The natural convection in the air layer is beneficial to improve the uniformity of the surface temperature distribution on the radiant cooling panel. The reason is that: the increasing air layer thickness is expected to enhance convective heat exchange. Surface temperature of radiant cooling panel decreases with the increase of air layer thickness and supply water temperature. Cooling capacity has a negative correlation with air layer thickness and supply water temperature. Chilled inlet water temperature has great influence on cooling capacity. When the thickness of air layer increases from 8 mm to 16 mm, cooling capacity of radiant panel is decreased by 12.4%.

It has been found that the lowest surface temperature of cooling panels can be better controlled. And the cooling capacity can be increased and uniform surface temperature distribution can be obtained through improving the structure of radiant panels.

ACKNOWLEDGEMENTS

This research was supported by Key Lab of Hunan for the technologies of Energy Conservation in Prefabricated Buildings (Project No. 2017SK2394).

NOMENCLATURE

q_{total}	total heat flux (W×m^{-2})	T_a	indoor air temperature (℃)
q_r	radiative heat flux (W×m^{-2})	T_p	mean panel surface temperature(℃)
q_c	convective heat flux (W×m^{-2})	h_c	convective heat transfer coefficient (W×m^{-2}×K)
AUST	area-weighted average uncooled temperature (℃)		

REFERENCES

Angelo Zarrella, Michele De Carli, Clara Peretti., 2014. Radiant floor cooling coupled with dehumidification systems in residential buildings: A simulation-based analysis, Energ Convers Manage. 85, 254-263.

Baisong N, Youming C, Hui L, Shunbo Z.,2016. Cooling capacity improvement for a radiant ceiling panel with uniform surface temperature distribution. Build Environ. 102, 64-72.

E.M. Saber, R. Iyengar, M. Mast, F. Meggers, K.W. Tham, H. Leibundgut., 2014. Thermal comfort and IAQ analysis of a decentralized DOAS system coupled with radiant cooling for the tropics, Build Environ. 82, 361-370.

Haida T, Tao Z, Xiaohua L, Yi J.,2017. Theoretical and experimental study of departure duration of condensate droplets from radiant cooling ceiling surfaces. Build Environ,114, 445-454.

Haida T, Xiaohua L, Haoyue L, Yan Z., 2016. Study on the reduction of condensation risks on the radiant cooling ceiling with superhydrophobic treatment. Build Environ, 100, 135-144.

Jungmin Seo , Doosam Song b , Kwang Ho Lee.,2014. Possibility of coupling outdoor air cooling and radiant floor cooling under hot and humid climate conditions. Energy Build, 81, 219-226.

Kang Z, Xiaohua L., 2014. Analysis of surface temperature uniformity of radiant panels, Acta Energiae Solaris Sinica. 35, 2475-2483.

Karadag Refet., 2009. The investigation of relation between radiative and convective heat transfer coefficients at the ceiling in a cooled ceiling room. Energ Convers Manage. 50, 1-5.

Lin S, Nianping L, Xuhan Z, Yeyao S., 2015. Heat transfer and cooling characteristics of concrete ceiling radiant cooling panel. Appl Therm Eng, 84, 170-179.

Moon Keun Kim, Hansjürg Leibundgut., 2014. Advanced Airbox cooling and dehumidification system connected with a chilled ceiling panel in series adapted to hot and humid climates,Energy Build, 85, 72-78.

Melanie Fauchoux, Mohit Bansal , Prabal Talukdar, Carey J. Simonson, David Torvi., 2010. Testing and modelling of a novel ceiling panel for maintaining space relative humidity by moisture transfer. Int J Heat Mass Transf, 53, 3961- 3968.

Moon Keun Kim, Jiying L, ShiJie C., 2018. Energy analysis of a hybrid radiant cooling system under hot and humid climates: A case study at Shanghai in China, Build Environ, 137, 208-214.

Radia Eldeeb , Melanie Fauchoux, Carey J. Simonson., 2013. Applicability of a heat and moisture transfer panel (HAMP) for maintaining space relative humidity in an office building using TRNSYS. Energy Build, 66, 338-345.

Rabanillo-Herrero Mario, Padilla-Marcos Miguel á, Feijó-Muñoz Jesús., 2018. Effects of the radiant heating system location on both the airflow and ventilation efficiency in a room, Indoor Built Environ. 1-12.

Xing J , Xiaosong Z, Yajun L., 2010. Numerical simulation of radiant floor cooling system: The effects of thermal resistance of pipe and water velocity on the performance. Build Environ. 45, 2545-2552.

Yasin Khan, Vaibhav Rai Khare, Jyotirmay Mathur, Mahabir Bhandari., 2015. Performance evaluation of radiant coolingsystem integrated with air system under different operational strategies, Energy Build. 97,118-128.

Manuscript ID: 128
DOI: 10.18462/iir.icr.2019.0128

Numerical performance investigation of a CO_2 heat pump and refrigeration system for a Nordic hotel

Silje Marie SMITT, Armin HAFNER

Norwegian University of Science and Technology,
Kolbjørn Hejes vei 1D, 7491 Trondheim, Norway,
silje.smitt@ntnu.no, armin.hafner@ntnu.no

ABSTRACT

This article evaluates the first adaptation of a CO_2 supermarket unit as an integrated solution for hotel applications. The system consists of a single unit for heating, ventilation, air conditioning (HVAC) and domestic hot water (DHW). The heat pump and chiller unit is installed in Northern Europe and has a heating and cooling capacity of 280 and 75 kW, respectively. Included in the thermal system is a 6 m^3 DHW storage for peak load shaving. A dynamic model of the system is developed in the *Modelica* programming language and the validity of the model is discussed. The model behavior is similar to actual system performance. The operational benefits of applying fixed-speed compressors are evaluated through simulations. The results show that the overall efficiency of the complete thermal system is improved by 3.8% when compared to using the current variable speed drive (VSD) control strategy.

Keywords: CO_2 heat pump and AC, combined heating and cooling systems, hot thermal energy storage, hot tap water production

1. INTRODUCTION

The interest for environmentally friendly thermal energy systems is steadily growing within the Nordic hotels sector and is becoming an important element in hotel branding (Lee *et al.* (2010), Bohdanowicz (2005)). Energy for heating purposes is the greatest contributor to the overall energy demand within the Nordic hotel sector. On an average basis, hotels in Norway require approximately 240 kWh/m^2 per year, where the share of DHW demand is about 16 % of the total energy demand (NVE, 2016). A study of water consumption in hotel chains in Europe show that 70 % of the hotel facilities use 151–250 liter of water/guest-night (Bohdanowicz *et al,* 2007). The hot water consumption follows a specified schedule depending on the occupancy and the daily activities (showering) e.g. in the morning (from 6 to 8 a.m.) and the evening (from 7 to 9 p.m.), which generates large consumption peaks (Deng *et al.* (2002), *Standard Norway* SN/TS 3031 (2016)). Very few energy systems installed in Nordic hotels take actions to reduce the peak power demand that occur following these time periods of large DHW consumption.

In order to satisfy future legislation and environmental goals, efficient and profitable energy systems must be implemented to reduce the large energy demand and environmental footprint of the sector. Integrated CO_2 heat pump and chiller systems is a solution that meets these standards and can cover all thermal needs of the hotel. CO_2 is an environmentally friendly and natural refrigerant, which has no ozone depleting potential (ODP) and a negligible global warming potential (GWP) compared to synthetic refrigerants. It is widely available, inexpensive, and is neither toxic nor flammable. Due to its temperature glide when operating in a transcritical cycle, CO_2 as a refrigerant is excellent for heating tap water and the technology for residential water heaters is well established (Zhang et al., 2015). Currently, CO_2 transcritical cycles with heat recovery are mainly applied within the supermarket sector, where excess heat obtained from the gas cooling process is used for space heating, air handling units (AHU) and DHW production (D'Agaro *et al* (2019), Hafner and Banasiak (2016)).

The first combined CO_2 heat pump and chiller unit for hotels in cold climates was installed in Norway in 2018 (Smitt *et al*, 2019). The system is equipped with 6 m^3 integrated thermal energy storage to reduce DHW consumption peaks. The buffer storage offers two important benefits as it supplies extra hot water during peak hours and enables continuous production and accumulation of DHW, which stabilizes the operation of the heat pump unit. There are generally large variations in the heating demand of the hotel during the spring/fall season. The current accumulation strategy in these instances is to charge for short periods, typically 6-8 hours, at high loads (~100 kW). When charging the storage over a longer period, however, the heat load could be reduced by taking advantage of the continuous accumulation that the storage provides. An alternative charging strategy is to accumulate based on available compressor load when operating the compressor at optimum conditions at fixed speed. Moreover, an on/off control of the compressors would reduce the inefficiencies associated with VSD regulation. This paper investigates the operational influence of using a fixed speed compressor compared to a VSD controlled device. System efficiencies are evaluated according to the optimal compressor operation and continuous DHW accumulation.

2. SYSTEM DESCRIPTION

The hotel building was established close to Trondheim, Norway, in 1987. Until 2018, it has been equipped with a heating system consisting of an electric boiler (for base load coverage) and an oil boiler (to cover peak loads). Fig. 1 shows the CO_2 heat pump and chiller unit, which provides the hotel with space heating, DHW and AC cooling. The heating capacity of the system is 280 kW. The heat pump design is based on a typical single-stage supermarket refrigeration unit equipped with heat recovery. The CO_2 unit is composed of four single-stage compressors arranged in parallel, where one compressor is equipped with a VSD. The high pressure and load control of the heat pump is based on feedback signals from the different thermal demands, such as hot tap water, heat towards ventilation- and radiators circuits. The building side supplies these signals to the heat pump controller, which optimizes the high-pressure level within specific constraints, such as the different setpoint temperatures.

The CO_2 heat pump is equipped with four 50 kW air/CO_2-evaporators, at -15 ºC evaporation temperature. In case of simultaneous cooling and heating demands, it is possible to recover heat from a 75 kW chilled water heat exchanger (HX) for AC cooling. The combination of the chiller unit and the heat pump is beneficial, as it reduces the overall operational cost for the hotel operators while satisfying the heating and cooling demands. Heat is delivered to two secondary hydronic circuits through the two gas coolers (GC1 and GC2) in series, where the appropriate temperature adaptation to each secondary circuit is achieved by the CO_2 temperature glide in the supercritical region. The high temperature (HT) circuit is mainly used to reheat tap water through the reheat HX by the use of the recovered high temperature heat from GC1. A radiator backup interface is also installed in the HT circuit and acts as an interface between the two secondary circuits. The mid temperature (MT) circuit provides heat primarily to ventilation heat exchanger batteries and a radiator circuit. The remaining heat is used to elevate the tap water temperature from approximately 8 to 25℃ through the preheat HX. Next, the MT fluid is recirculated back to GC2. The CO_2 temperature is thereby further reduced and the efficiency of the cycle is considerably enhanced. For winter season operations, it is possible to employ the defrost HX in the MT circuit for defrost of the air evaporators.

Hot tap water can be produced continuously in both preheat and reheat HXs when there is a need for ventilation heating. An optimum sized water storage is a key factor for a high system efficiency, as the working range in which the heat pump can operate in optimal conditions is larger. A hot water buffer configuration is especially advantageous in hotel facilities since the DHW consumption curve is characterized by enormous peaks during a few hours in the mornings and evenings. Yet, if DHW is continuously generated, it can be stored for later usage in order to handle these peaks. The hot water storage system consists of tanks in series with a storage capacity of 6 m^3. During charging, DHW is directed to the storage, where it moves through the series of tanks as the buffer is gradually charged from right to left. Cold water is drawn from the last tank (no. 8) and is sent through the heating process. The thermal storage is fully charged when the normally stratified tanks have a high and uniform temperature throughout the buffer.

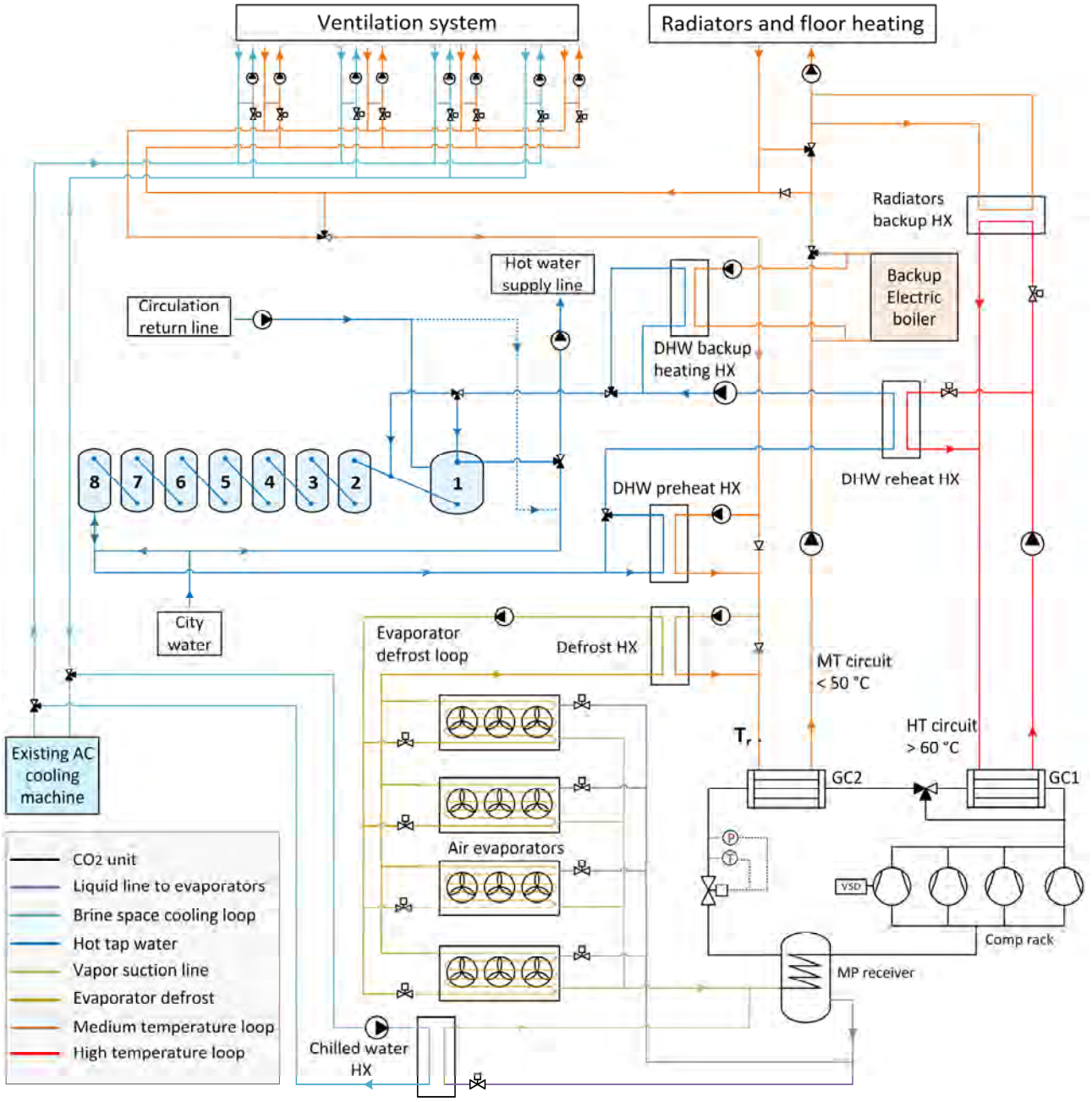

Figure 1: Circuit diagram of CO_2 unit with HVAC and DHW

3. SIMULATION MODEL

A model of the entire thermal system was created in the *Modelica* programming language. The programming environment *Dymola* was used to simulate the quasi-dynamic system with variations of 20 minutes intervals in the setpoint temperatures, heating and cooling loads and DHW usage. The model was built using components from the thermodynamic library, *TIL-Suite*, developed by TLK-Thermo GmbH**.** TIL-Suite is an advanced library for transient simulations of fluid systems and is especially applicable for heat transfer modelling purposes, i,e. heat pumps, refrigeration, cooling and heating systems. Among the components that are included in the library are compressors, pumps, valves and HXs. These can be connected in the oriented physical modeling interface, Dymola, to construct complex models. Each physical element in the diagram structure represent a real physical element in the system. When the component elements are connected in the model structure, the mathematical equations in all components constitute the behavior of the model. All components used in the simulation model of the heat pump and chiller system are specified according to manufacturer description. Plate HXs are used for all heat exchange between the different internal circuits. The VDI

heat transfer model in TIL-library (Martin, 2010) is used to describe the transfer properties of all single-phase liquids in the system. The pressure losses are assumed to be quadratic and mass flow dependent. Constant heat transfer coefficient of 3000 $W.m^{-2}.K^{-1}$ and 2500 $W.m^{-2}.K^{-1}$ are used for the CO_2-side of the gas coolers and evaporators, respectively. TIL-library correlations for quadratic pressure drop in pipes describe the pressure losses in the fin-and-tube evaporators (Wagner, 2001). TIL-Media library is applied for the simulation of the fluids used in the model, which includes refrigerant CO_2, water, glycol and dry air. External data for boundary conditions, heating and cooling loads are imported to the model with the program *TIL-FileReader*. All external data inputs to the model have the resolution of one hour. Dampening transitions are included to increase the stability of the model by reducing rapid changes. The set of model equations are solved with the *DASSL* algorithm.

3.1. Boundary conditions and controlling

The control of the components in the model is achieved according to the specification given by the manufactures of the CO_2 heat pump and chiller unit. PI-controllers operate all the active components in the model, such as compressors, pumps, fans and valves. Each component in the model is controlled according to setpoints in the system. All the important parameters in the hotel thermal system are measured and logged at irregular intervals. As the system is not operating in a controlled environment, irregular data points may occur. A 72-hour period of system operation (3rd – 6th November 2018) was chosen in order to validate the behavior of the Dymola model. This period was selected as it best reflects the specified and typical behavior of the system. Fig. 2 shows the ambient temperatures recorded at the hotel location during the correspondent period. The data was obtained from the Norwegian Meteorology Institute Database. Hourly mean ambient temperatures are applied as model input in evaporators and are used to define the setpoint temperatures of the hotel building (Fig. 3). Curve fittings are applied to the building setpoints that are used in the model.

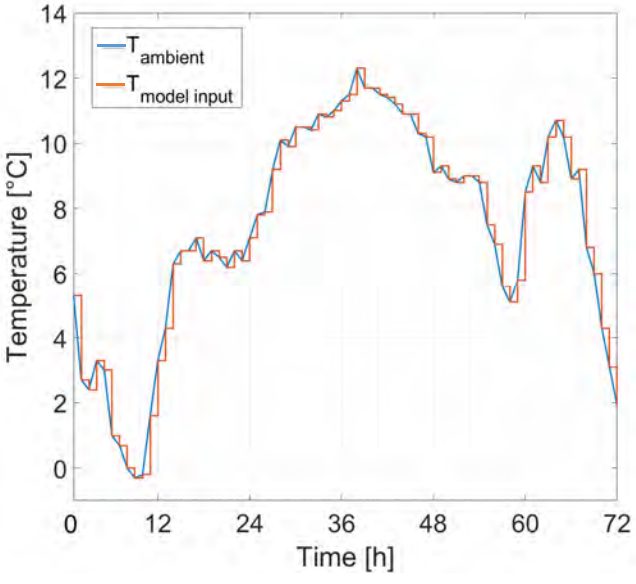

Figure 2: Ambient temperatures and model input

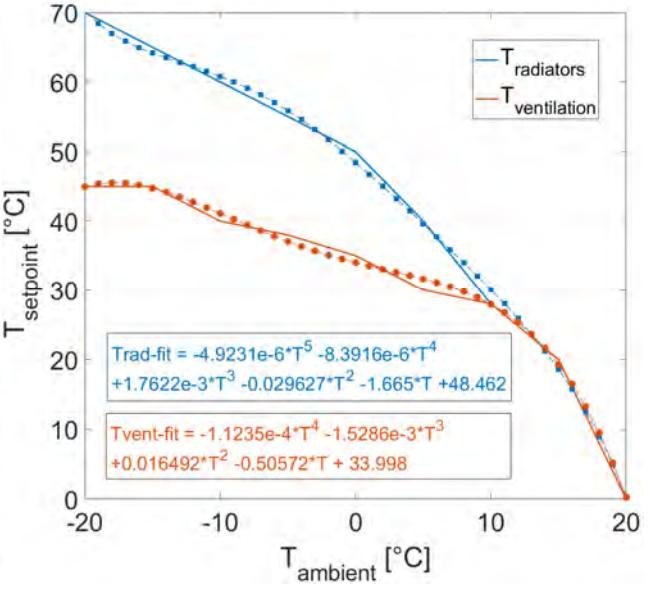

Figure 3: Hotel setpoint temperatures model fitting

The modeled requested compressor load is defined in Eq.(1), where the ratio is approximated based on logged data from the system. The VSD compressor is controlled from a frequency of 30 to 70 Hz, dependent on the required capacity. The three remaining compressors in the rack are controlled by on/off switching. The requested capacity of the model will be increased in steps of 0.05 (5% of total system capacity) if the required temperatures in the system are not reached. The displacement will continue until the temperature setpoints in Fig. 3 are satisfied. A similar strategy is used to reduce capacity should the ventilation supply temperature become considerably higher than the setpoint temperature. The compressors are turned off during low load operations if the setpoints in the model are satisfied.

$$\text{Requested compressor load ratio} = \frac{0.24708(\dot{Q}_{vent} + \dot{Q}_{rad} + 1.0335)}{100} + \text{state} * 0.16 \qquad \text{Eq. (1)}$$

State in Eq.(1) is a variable that is assigned values from 0 to 2 based on the energy remaining in the DHW storage. When the temperatures in the DHW storage becomes lower than a threshold, the requested heating capacity of the thermal system is increased as *state* is no longer zero. Fig. 5 shows the simplified control logic used in the Dymola model to recreate the charging behavior in the system. *State 1* is triggered by the requirements described in path *A*. If the demand for DHW is greater than what is supplied to the storage, more heat input is necessary. Path *C* is then activated resulting in *state 2*. Path *D* is included as a temperature restricting of the fluid returning to GC2 (T_r in fig. 1) to limit the CO_2 gas cooler outlet temperature. Only when the storage is fully charged is path *B* triggered and the system returns to normal operations. Fig. 5 shows the specific heat demands applied to the model over the 72 hour period. The data are calculated based on logged power output in the hotel thermal system, where the mean measured values per 20 minutes are used as input to the model. Momentary power peaks and rapid changes are therefore not included. However, the same sum amount of energy per 20 minutes is applied. No AC cooling demand occurred over this time period.

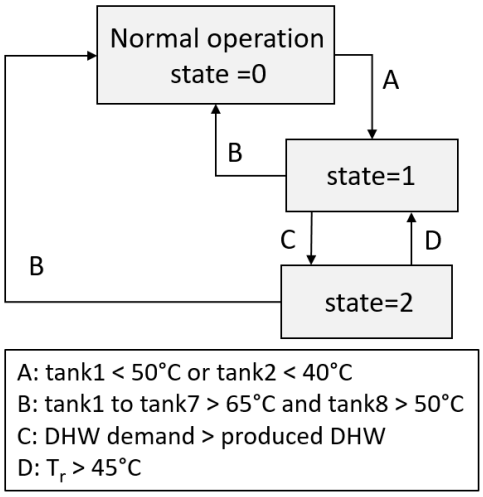

Figure 4: Simplified charging strategy for the DHW storage

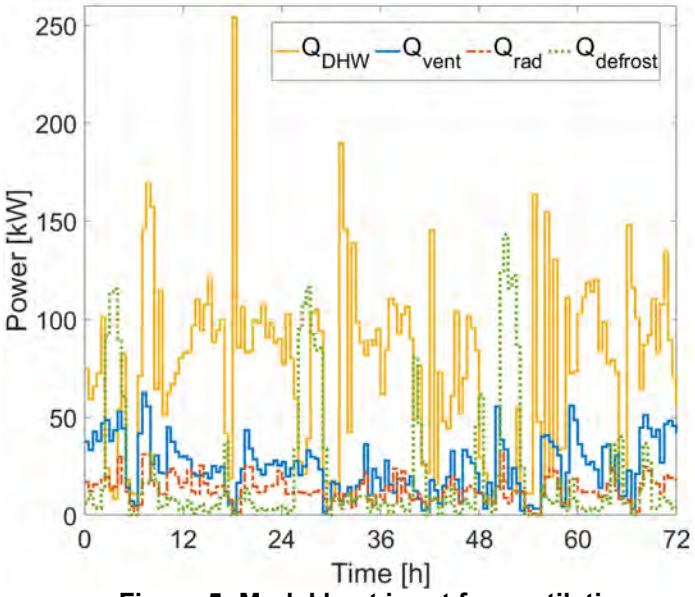

Figure 5: Model heat input for ventilation, radiators, DHW and defrost (hourly changes)

3.2. Model validation

A model of the entire thermal system is simulated for a 72-hour period with the input values described in the previous section. Fig. 6 shows the simulated and measured power input to the hot water subsystem, where the area represents the heat input. These values are equivalent to DHW heat input through the preheat and reheat HXs (see Fig. 1). The figure also displays the percentage energy charge in the storage. 50 and 400 kW are used to define the range between 0-100%. Fig. 7 shows the heat power input to the thermal system through the two gas coolers. The hourly root mean square deviation (RMSD) is 37.1 and 39.0 for the simulated values in Fig. 6 and Fig. 7, respectively. This would be considered high errors were the goal of the model to predict the exact system point values. However, the model behavior is similar to the actual system trends as the heat input (area) occurs at approximately the same time over the period. This is also reflected in the storage energy as chagrining and discharging are cooccurring during the period. A certain delay is observed in the simulated data, which has a large influence on the RMSD values. As the data is investigated over a long time interval, external factors might influence the system behavior. The largest deviation between the simulated and measured data is the magnitude of the power. As it can be seen in Fig. 6 and Fig. 7, the simulated data does not achieve the high power peaks that is observed in the measured data. The underprediction of power input could be explained by model simplification, i.e. neglecting heat losses. This behavior is of little consequence as it is undesirable, and can be explained by the interval length mean values used as model input (Fig. 5). A reduction of the interval would be a possible solution that would decrease the power error. However, the important aspect of the simulation results is that the model is able to fulfill all demand inputs during the period. In addition,

all minimum setpoint temperatures are satisfied during active model operation. The model responds similarly during the same occurrences, i.e. when there is demand for charging the DHW storage and during the low load operations.

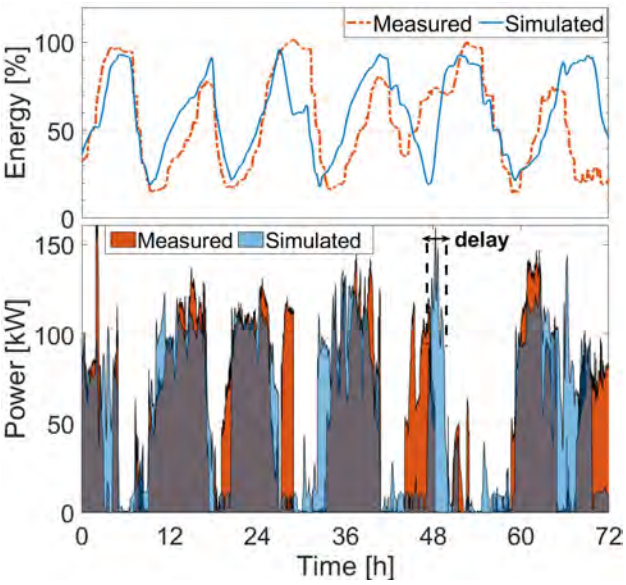

Figure 6: Storage charge, power and heat to the DHW system

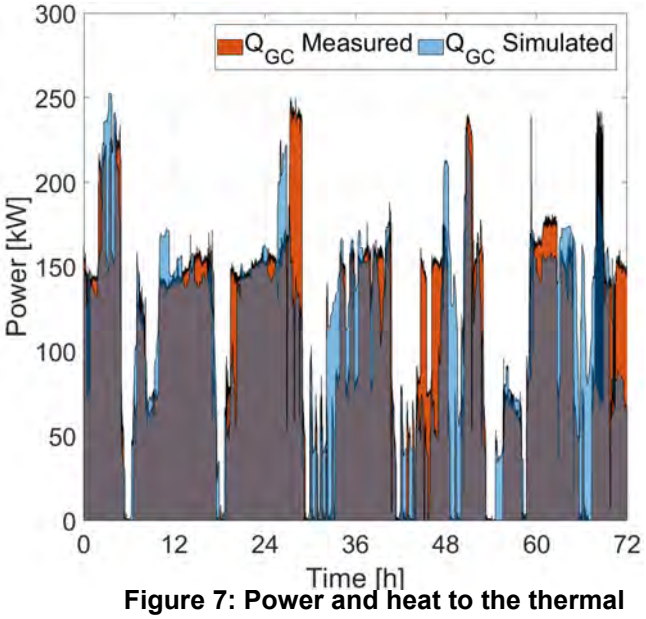

Figure 7: Power and heat to the thermal system through the gas coolers

Eq.(2) defines the energy efficiency of the system over the period as total amount of heat supplied to the thermal system divided by the sum of all power inputs. Table 1 lists the measured and simulated energy efficiency to be comparable. This is indicates that experimental and numerical results are in a good agreement. This is further confirmed when considering the total heat accumulations over the period. Table 1 depicts accumulated heat deviations between the numerical and experimental data of 5.1% (DHW subsystem, Fig.6) and 4.7% (entire thermal system, Fig.7).

Table 1: Measured and simulated produced heat and efficiencies

Parameter	Values	Period (72 h)
Total DHW heat input [kWh]	Measured	4079
	Simulated	4285
	% Error	5.1
Total thermal system heat input [kWh]	Measured	8041
	Simulated	8418
	% Error	4.7
Mean energy efficiency	Measured	2.94
	Simulated	2.92

$$\text{Energy efficiency (E. E.)} = \frac{Q_{GC1} + Q_{GC2}}{\sum W_{compressors} + \sum W_{fans} + \sum W_{pumps}} \qquad \text{Eq. (2)}$$

3.3. Alternative DHW accumulation and compressor control

Constant frequency of 50 Hz is applied to all compressors in the model and the control strategy of the system is modified in order to investigate possible operational benefits. The DHW storage is charged with available heat when the compressors are operating in optimum conditions. The requested capacity is defined by Eq.(1). However, *state* is zero at all times. The compressors will operate with the same off-conditions at low loads when setpoints are satisfied. If the setpoints temperatures in the system are not satisfied, a second compressor will be activated. This will also be the case if condition *A* (Fig. 4) is satisfied. If this is still not sufficient to charge the storage, a third compressor will be switched on as condition *C* is satisfied. Similar as the behavior presented in Fig. 4, the number of compressors activated by the storage is reduced to normal when the storage is fully charged, during which the number of active compressors again is defined by Eq.(1).

4. SIMULATION RESULTS AND DISCUSSION

A fixed-speed compressor control strategy is applied to the model and simulations are conducted for a 72-hour period. No additional model modifications are made. Setpoints, boundary conditions and input values are as stated in section 3.1. Fig. 8 shows the power and heat (area) to the DHW subsystem and the instantaneous energy charge (%) in the storage. Fig. 9 shows the power and heat to the entire thermal system. It is observed from both figures that the heat area and peak power values are reduced compared to the simulations with VSD regulation. The desired model behavior of heat recovery over a longer period at lower intensity is achieved. The buffer is charged over a longer period by using available load in the compressors. The storage capacity is higher for longer periods due to continuous DHW accumulation. The total heat energy accumulated over the period is 4275 kWh and 8420 kWh for the fixed-speed compressor case in Fig. 8 and Fig. 9, respectively. This is a slight increase compared to results from the simulation with VSD, which confirms that the fixed-compressor operational strategy is a functional alternative to VSD-regulation. All thermal demands are fulfilled and all minimum temperature setpoints are satisfied during the operating time of the system.

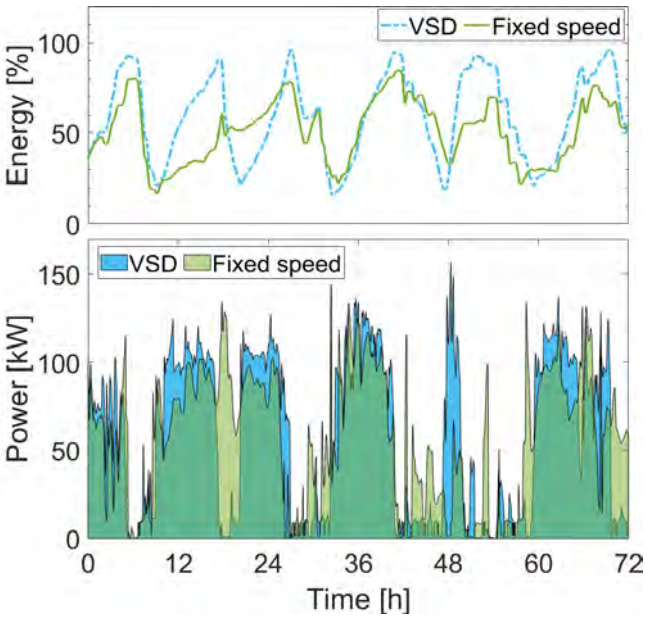

Figure 8: Storage charge, power and heat to the DHW system with fixed-speed compressors

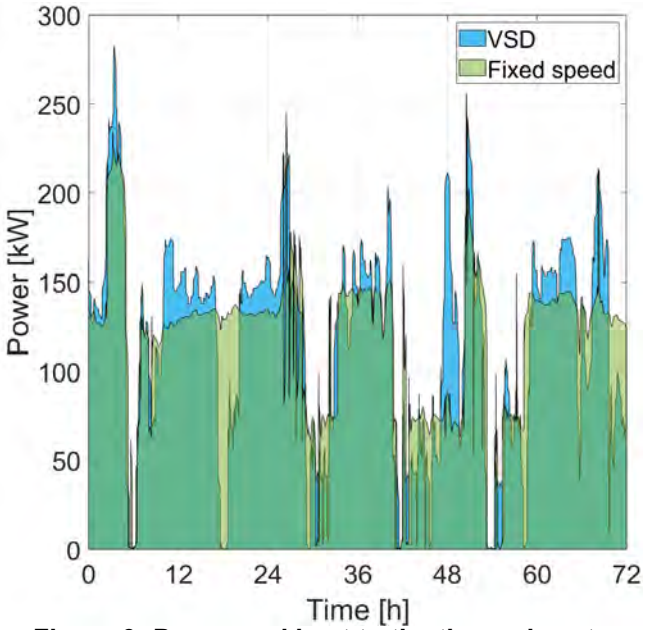

Figure 9: Power and heat to the thermal system through the gas coolers with fixed-speed compressors

The mean energy efficiency of the entire thermal system is 3.03 for the period, which is a 3.8% increase in relation to the reference validation case (E.E. = 2.92) with VSD controlled compressors. For both simulations, only three of the four compressors in the rack are activated during the 72-hours. However, the maximum compressor motor power input is reduced with 22.6 kW (from 99.2 kW to 76.6 kW) in the fixed-speed investigation. The overall energy input to the compressors are reduced from 2726 kWh to 2601 kWh, which is a difference of 125 kWh or about 4.6% for the entire period. A 108 kWh or 3.6% reduction in work energy input to the complete thermal system is achieved (from 3034 kWh to 2926 kWh) in relation to the VSD regulation results. The energy consumption of the entire thermal system is thus reduced whilst there is an increase in total heat output. The operating time of the compressors are increased from 91% to 94% or with about 3 hours over the interval. Heat recovery from the AC chiller unit is normally limited, as heating and cooling demands are generally not synchronized. However, fixed-speed compressor control allows for DHW accumulation over longer periods. A larger amount of heat could therefore potentially be recovered from the AC ice water as the operating period is increased. Combined heat pump and chiller mode is not investigated in this paper, as a cooling demand is not recorded in the selected time interval. This investigation only reveals the benefits of fixed-speed compressors for periods with similar system operation and behavior. A broader selection of operational scenarios should therefore be investigated to fully reveal the potential benefits of fixed-speed compressor control in systems with thermal storage.

5. CONCLUSIONS

This work investigates the operational strategy and design of the first CO_2 heat pump and chiller unit installed in a Nordic hotel. A dynamic simulation model of the entire thermal system is constructed with the Modelica programming language. A 72-hour period of system operation is selected to validate the model behavior. Variations with 20 minute intervals in the ambient temperatures, setpoint temperatures, heating and cooling loads and DHW usage are applied to the model. The simulation results show high RMSD values, which are mainly caused by mismatch due to delay in model behavior. The model responds similarly to the system during events, which is the consequential aspect of the model validation. All demands and all minimum setpoint temperatures are satisfied with 4.7% error in total heat energy accumulated over the period.

The thermal storage enables accumulation of DHW based on available load when operating the compressors, which is currently applying VSD to one compressor. An alternative fixed-speed compressor control strategy is therefore evaluated. The mean energy efficiency of the complete thermal system increases by 3.8% to 3.03. The maximum compressor motor power input is reduced with 22.6 kW in the fixed-speed investigation. The overall energy demand (wihtin the investigated period of 72 h), to the compressors is reduced with 125 kWh or about 4.6%. For the model of the entire thermal system, a 3.6% reduction in energy input is observed. The energy consumption of the entire thermal system is reduced with a similtanous increase in the total heat output. The results show that a fixed-speed compressor control is beneficial and should be considered in future systems.

NOMENCLATURE

Q	Work Input (kW)	W	Heat Input (kW)

REFERENCES

Bohdanowicz, P., 2005. European hoteliers' environmental attitudes: Greening the business. Cornell Hotel and Restaurant Quarterly 46, 188–204.

Bohdanowicz, P., Martinac, I., 2007. Determinants and benchmarking of resource consumption in hotels - Case study of Hilton Int.ernational and Scandic in Europe. Energy and buildings, 39(1), 82-95.

D'Agaro, P., Coppola, M.A. and Cortella, G., 2019. Field tests, model validation and performance of a CO2 commercial refrigeration plant integrated with HVAC sustem. International Journal of Refrigeration, accepted manuscript, january 2019.

Deng, S. M., Burnett, J., 2002. Water use in hotels in Hong Kong. International Journal of Hospitality Management, 21(1), 57-66.

Lee, J.-S., Hsu (Jane), L.-T., Han, H., Kim, Y., 2010. Understanding how consumers view green hotels: how a hotel's green image can influence behavioural intentions. Journal of Sustainable Tourism 18 (7), 901-914.

Hafner, A., Banasiak, K., 2016. R744 ejector technology future perspectives. Journal of Physics: Conference Series, 745(3), 032157.

Martin, H., 2010. N6 pressure drop and heat transfer in plate heat exchangers. In VDI Heat Atlas. Springer, Berlin, Heidelberg, 1515-1522.

Norwegian Water Resources and Energy Directorate (NVE). Analyse av energibruk i yrkesbygg. Report No. 24 (2016), Oslo, 36-40.

Standard Norway SN/TS 3031, 2016. Energy performance of buildings – Calculation of energy needs and energy supply. Report No. 1 (2016), Oslo, 41-43.

Smitt, S. M., Hafner, A., Hoksrød, E., 2019. Presentation of the first combined CO2 heat pump, air conditioning and hot tap water system for a hotel in Scandinavia. IIR Conference on Ammonia and CO_2 Refrigeration Technologies. Ohrid, Republic of Macedonia, April 11-13, 2019.

Zhang, J. F., Qin, Y., Wang, C. C., 2015. Review on CO2 heat pump water heater for residential use in Japan. Renewable and Sustainable Energy Reviews, 50, 1383-1391.

Wagner, W., Strömung und Druckverlust, 5. Auflage, Vogel Buchverlag, 2001. d

PAPER ID: 155
DOI: 10.18462/iir.icr.2019.0155

Photovoltaic/Thermal (PV/T) to drive a dual source heat pump (ground and PV cooling): performance analysis in a real application

RenatoLAZZARIN[(a)], MarcoNORO[(b)]

Department of Management and Engineering – University of Padova
Vicenza, 36100, Italy
[(a)] renato@gest.unipd.it [(b)] marco.noro@unipd.it

ABSTRACT

A large fraction (more than 80%) of the solar radiation impinging a PV panel is lost. A Photovoltaic/Thermal (PV/T or PVT) module allows not only to partially recover the otherwise lost heat, but also to cool the PV and increase its electrical efficiency. A retrofitted building located in Northern Italy will be equipped by a PVT dual source heat pump, operating with the ground as source/sink, whereas the PVT drives the heat pump compressor and acts as a dual source. When the heat pump does not need heat or operates for summer air conditioning the ground is the heat sink both for the heat pump and for the PVT cooling.
A dynamic simulation allowed to size the plant, revealing high values of heat pump coefficient of performance for the favorable thermal levels of the heat source, and better thermal levels of the ground source that receives heat from the PVT panels when it is not required by the heat pump.Very high efficiency and low primary energy consumption are demonstrated for the whole plant, thanks the high energy independency from the grid.
Keywords: dual source heat pump; ground regeneration; ground source heat pump; multisource heat pump; PVT

1. INTRODUCTION

The residential sector is responsible for about 40% of energy demand in Europe. When insulating technologies and the new heating and cooling equipment are considered, this datum is surprising. Nowadays, a building can be realized with a minimum requirement of traditional fuels and electricity. These buildings are referred to as nearly Zero Energy Buildings (nZEB). The retrofitting of a school building located near Feltre in Northern Italy allows utilizing several modern technologies with the purpose of realizing something more of a nZEB, that is a Plus Energy Building.This is a building which is not only energy self sufficient on a yearly basis, but it can provide energy to nearby buildings, or to the grid.
Some proposed technologies are well known: ground heat pump, PV modules, thermal solar collectors, thermal bridges reduction, careful thermal insulation, heat recovery on ventilation air. The novelty in this study is in the coupling of the different components, with a control logic conceived to exploit all the energy contributions.
A particular novelty is the use of photovoltaic cogeneration (PV/T or PVT). A PV module turns, say, 18% of solar radiation into electricity. As a matter of fact, 82% is then lost (Figure 1).Moreover, its dissipation is detrimental for the efficiency as it produces an increase in the PV cell temperature. As a consequence, cell efficiency is reduced of the order of 0.2-0.5% for every 1 °C rise.
A PVT module exploits the thermal fraction, as the PV cells are connected to a device that exchanges heat with a fluid (usually air or water) (Chow, 2010). The thermal levels can provide domestic hot water (DHW) or ambient heating, but a better compromise between the useful energy and a moderate PV temperature indicates a better utilization as heat pump source. Bertram et al. (2012) reported a possible improvement from 4.2 to 5.4 for the seasonal performance factor for a dual source heat pump system ground-PVT with respect to only ground source. The penalization for the PV electricity production was estimated at 5%. They used unglazed PVT. Instead, in this

study glazed PVTs are used, as the Authors believe that a glazed PVT can give the best results once the PV cells temperature is controlled by a proper coupling with the ground heat exchanger.

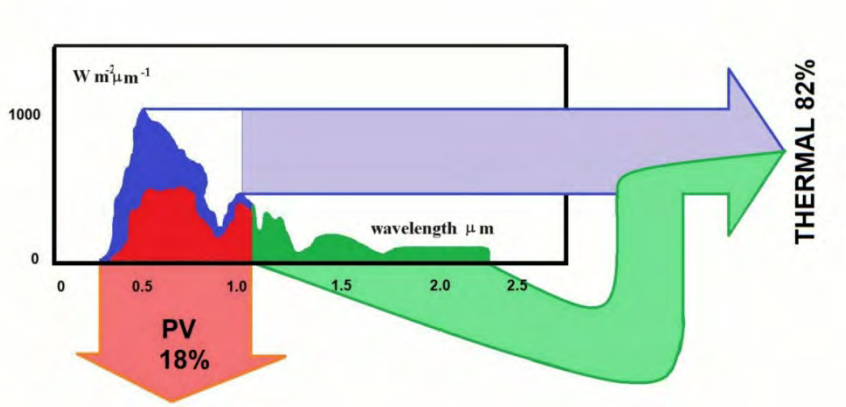

Figure 1: A possible share of solar irradiation between electricity and thermal effect for a PV module

2. METHODS

2.1. Building thermal loads

The building to be retrofitted has a total floor area of 2435 m^2 (two storey), with an outward surface area of 2505 m^2, and an enclosed gross heated volume of 11060 m^3. The insulation is designed to allow obtaining an average thermal transmittance of 0.15 W m^{-2} K^{-1} for outer walls and roof, 0.7 W m^{-2} K^{-1} for the windows.

A careful evaluation of thermal loads was obtained by dynamic simulation (TRNSYS 17). The monthly energy needs are represented in Figure 2, subdivided into ambient heating, air conditioning, and ventilation (heating and air conditioning). A considerable load is due to DHW,as a part of the retrofitted building is a large gym with showers. The hot water demand is estimated in 2000 $Lday^{-1}$.Whereas in winter the demand is governed by ambient and DHW heating, in summer, apart the constant DHW demand, air conditioning is the main load with a contemporary ventilation heating and cooling demand, as a post heating is provided.

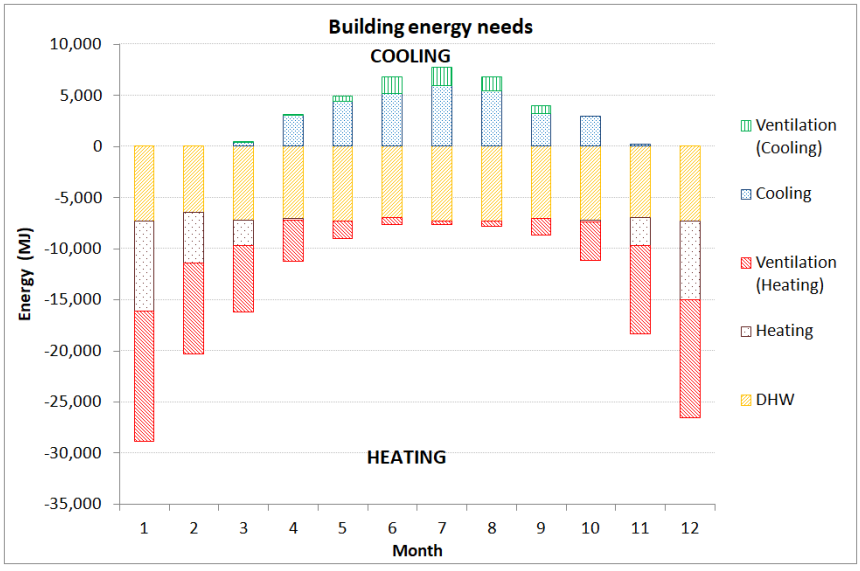

Figure 2: Monthly energy needs in terms of heating, cooling, ventilation (hot and cold coils of AHUs), and DHW

The peak heating load (-44.6 kW) occurs towards the end of January, whereas the peak cooling load (21.6 kW) is observed at the beginning of June. As the gym is used mainly in the late afternoon and in the evening, the DHW demand is concentrated in few hours every day, and this feature must be considered in the plant design providinga suitable storage.

2.2. The HVAC plant

The original feature of the HVAC plant is the solar section composed of PVT and plain PV that drive a heat pump which satisfies all the loads, safe that when possible the PVT thermal component provides DHW heating or at least preheating. The heat pump is a dual source with PVT or vertical tube ground boreholes. The PVT excess heat (mainly in summer) recharges the ground. A simplified scheme of the plant is represented in Figure 3, where the various components are connected via suitable storage tanks. A radiant floor provides space heating in the large gym, which is cooled by an all air cooling that gives the ventilation service (6600 m^3 h^{-1}) by an air handling unit (AHU). The other rooms (small gym, bar, laboratories and offices) are heated and cooled by fan coils, whereas toilets are heated only (by radiators), and laboratories are served also by an independent AHU (7000 m^3 h^{-1}) for ventilation.

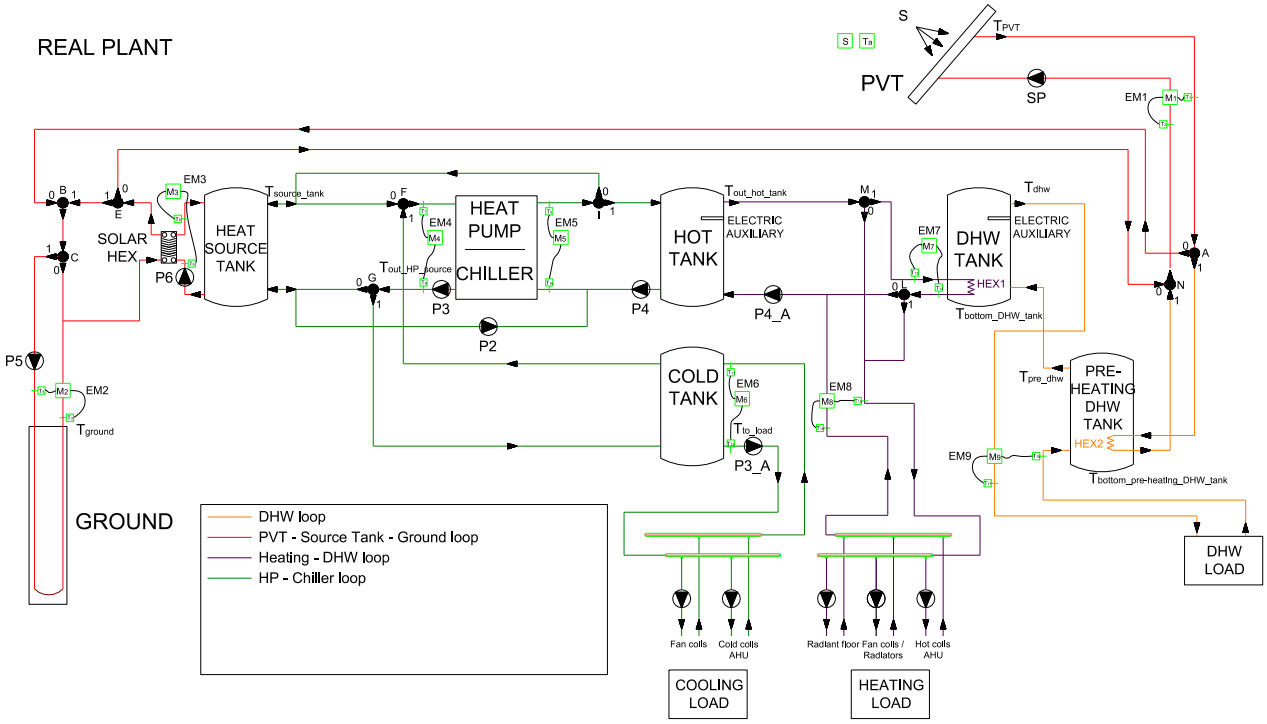

Figure 3: Simplified functional diagram of the HVAC plant

On the right of Figure 3two storage tanks are committed to the DHW service. Water from the mains arrives at the Pre-Heating DHW Tank, where a possible contribution is offered by the PVT. The heating till the consumption set point is completed in the DHW Tank, supplemented via a heat exchanger by the Hot Tank. The latter satisfies the heating load, receiving heat by the heat pump condenser. The heat pump evaporator takes heat from the Heat Source Tank, which is alimented either by the ground or by the PVT.

The Cold Tank is dedicated to cooling loads. It is cooled by the heat pump evaporator. During the heat pump operation as a chiller, useful heat for post-heating or DHW heating can be provided by the heat pump condenser. In summer, the eventual excess heat from the PVT or heat pump condenser cooling is used to recharge the ground, maintaining at an acceptable temperature the glazed PVT.

The control logic is based on a survey of solar radiation intensity, determining an operation threshold between 50 and 100 W m^{-2}, and on a comparison between the various suitable tanks set-points and the available temperatures in the different circuits (here not reported for sake of brevity).

3. RESULTS AND DISCUSSION

A full system energy performance evaluation is fundamental for a rational sizing of the various plant components, first of all PVT area, length of the geothermal probes, and tanks capacities.

The main results of a monthly analysis is here proposed for the sizing alternative that appeared preferable on an energy and economical basis. The alternative considers three ground probes, 100 m each, and 60 m^2 PVT plus other 60 m^2 of plain PV. A water-water heat pump was selected with 35 kW heating capacity, 27 kW cooling capacity. The claimed coefficient of performance (COP) at 12/7 °C cold source and 40/45 °C heating is 4.5. As regards the storage tanks capacities, the following values were chosen:

- Pre-Heating DHW Tank 2 m^3;
- DHW Tank 1 m^3;
- Hot Tank 2 m^3;
- Cold Tank 1 m^3;
- Heat source Tank 2.5 m^3.

3.1. Energy analysis of the preferred alternative

The presentation of results is based on energy balance of the different plant components.
A solar energy balance is given in Figure 4 for the PVT. The balance brakes down the positive input, that is the solar radiation, into five fractions:

- Thermal losses, that is the largest fraction;
- Electric energy;
- Contribution as heat pump heat source;
- Thermal energy to the DHW pre-heating;
- Ground recharging.

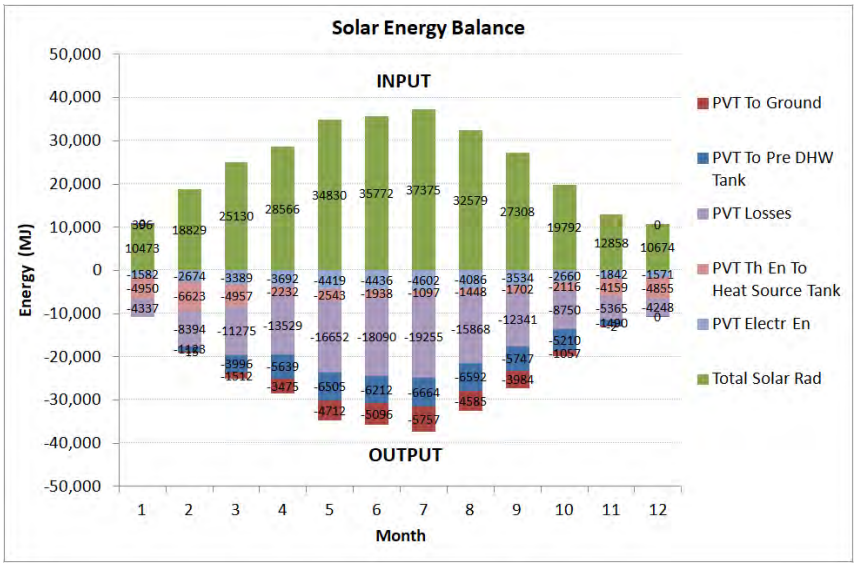

Figure 4: Monthly PVT solar energy balance

Even if thermal losses generally exceed the other items, a good contribution is offered in winter as heat pump heat source. In the most unfavorable month, January, 1,374 kWh are available for the heat pump at a temperature higher than the ground source, against 1,204 kWh of thermal losses and 439 kWh electricity.
In July, the produced electricity is of 1,278 kWh, with 1,851 kWh to DHW pre-heating and 1599 to ground recharging. In July, the overall useful energy supplied by PVT is almost comparable to the heat losses, with a 48% overall monthly efficiency (electrical efficiency 12% and thermal efficiency 36%).
The significant contribution of PVT to DHW heating is well represented in Figure 5. Here, the negative component of the balance is the load plus a small heat amount due to the tank thermal losses. PVT satisfies from 70% to more than 90% of DHW demand for the whole period from April to October.

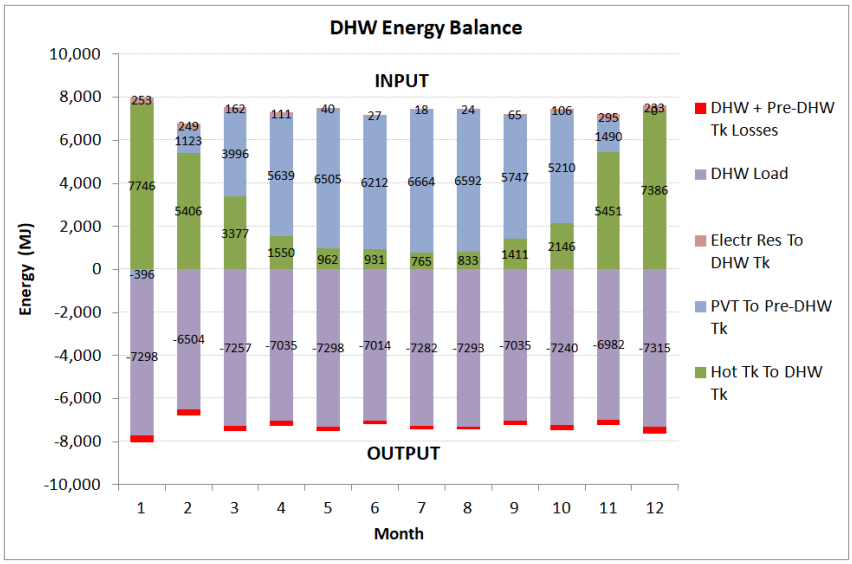

Figure 5: Monthly DHW energy balance

As far as the heat pump behavior is concerned, during the cold months the best observation point is the balance of the Hot Tank (Figure 6). Here the positive component is the contribution of the heat pump condenser to the tank. This is split into the satisfaction of the heating load and the integration of DHW from the pre-heating temperature to the set point (45 °C). An almost negligible fraction must be attributed to Hot Tank losses. A further insight is allowed by Figure 7 that reports the balance of the Heat Source Tank. During the cold months, this tank receives the two positive contributions from the ground and from the PVT: this energy is found in practice entirely as output of the heat pump evaporator.

However, during the other months the balance is complicated as the heat pump condenser releases to the tank the energy not requested by the DHW heating (mainly satisfied by PVT), or for the AHU post-heating. The output of the tank is then mainly towards the ground, even if a small fraction happens to be supplied for short periods of the month to the heat pump evaporator.

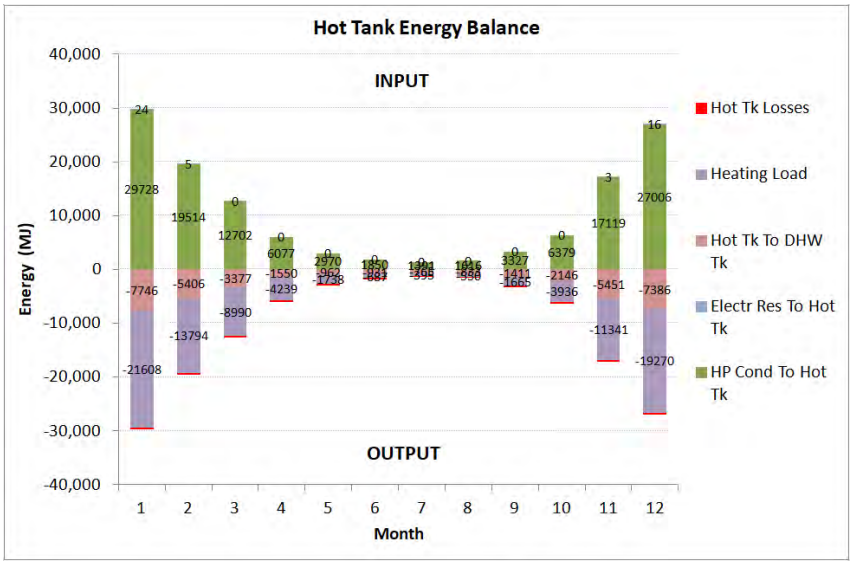

Figure 6: Monthly Hot Tank energy balance

For sake of brevity, other meaningful balances are omitted. One of them is the ground energy balance. On a yearly basis, the withdrawal is of 14,695 kWh, whereas the injection is of 19,722 (8,383 supplied by PVT and 11,339 by the heat pump condenser). Then the average ground temperature should slightly increase in the long run.

Figure 8 illustrates the efficiency parameters of the heat pump and of the whole system. They were evaluated as COP for the heat pump operation, and as energy efficiency ratio (EER) for the chiller operation. The correspondent values for the system, that is taking into account the parasitic power of pumps, were considered as well. This produces a noticeable reduction for the EER when the

longer circuits between PVT and boreholes are more active. Both COP and EER maintain high values during the whole year. The primary energy ratio (PER) is particularly high (around 5) for the combined operation of the heat pump producing simultaneously useful heating and cooling for a long period during the year. Note in Figure 8 the considerable increasing of the efficiency of the whole plant ($PER_{\_plant}$),that is taking into account the PVT thermal contribution for DHW heating.

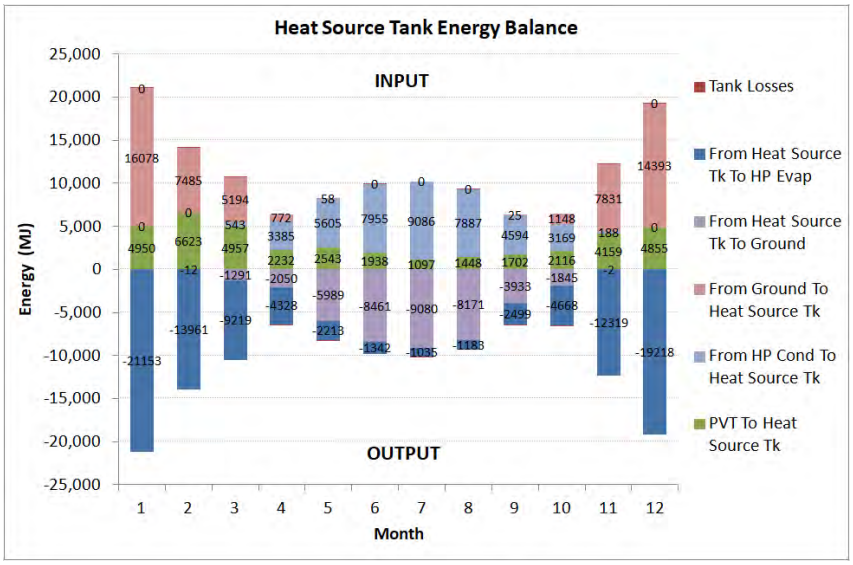

Figure 7: Monthly Heat Source Tank energy balance

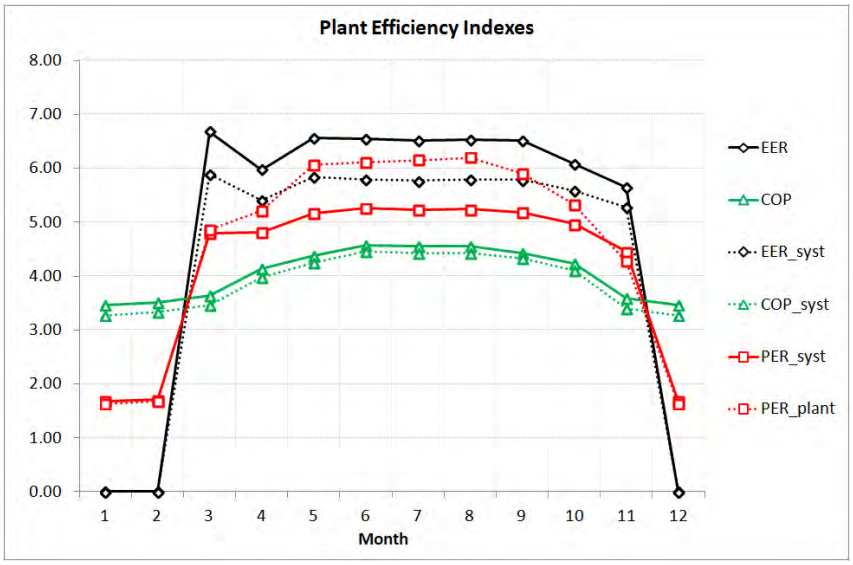

Figure 8: Heat pump efficiency indexes with pump parasitic energy (subscript _syst) or without. PER of the whole plant is represented as well (subscript _plant)

The obtained results regarding the energy balance of the building show that it is completely self sufficient for the energy on a yearly basis, rather making available electricity for the nearby buildings of the same complex, or for the grid. The electricity external dependency from the grid can be observed only in January and December, whereas in February and November the self produced electricity is clearly prevailing. In the other months, no external electricity is required, and electricity can be exported (Figure 9).

3.2. Energy comparison with a conventional system

A comparison has been carried out in energy terms between the proposed plant and a conventional one equipped with a natural gas fired condensing boiler (100% efficiency on lower heating value) and an air cooled chiller. The comparison is illustrated in Figure 10 in terms of primary energy, with a 1.95 factor for the electricity from the grid (average electricity production efficiency 51.3%). The monthly bars reveal a relevant negative item due to natural gas demand of the conventional plant, with a comparatively small consumption of the air cooled chiller. The

proposed plant takes some electricity from the grid only in the cold months, offering from March to October an energy surplus to be exported.

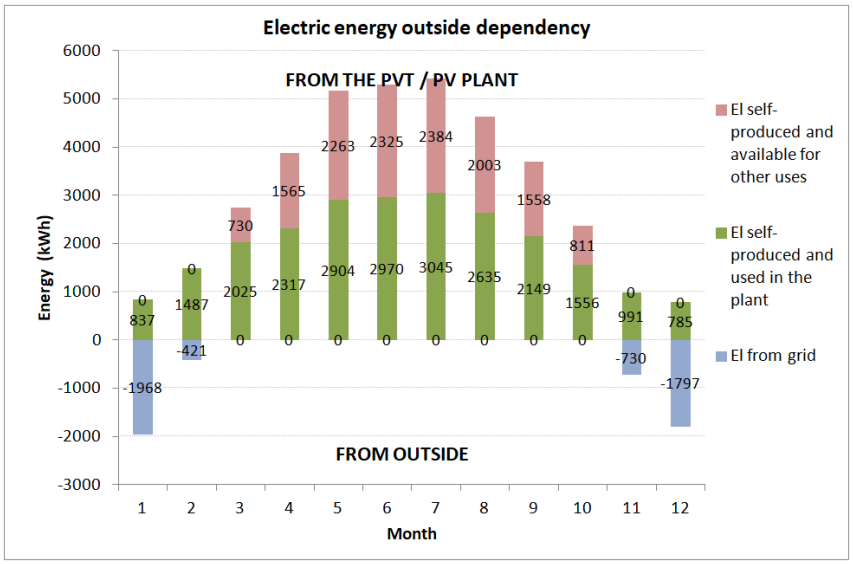

Figure 9: Monthly electricity balance for the building

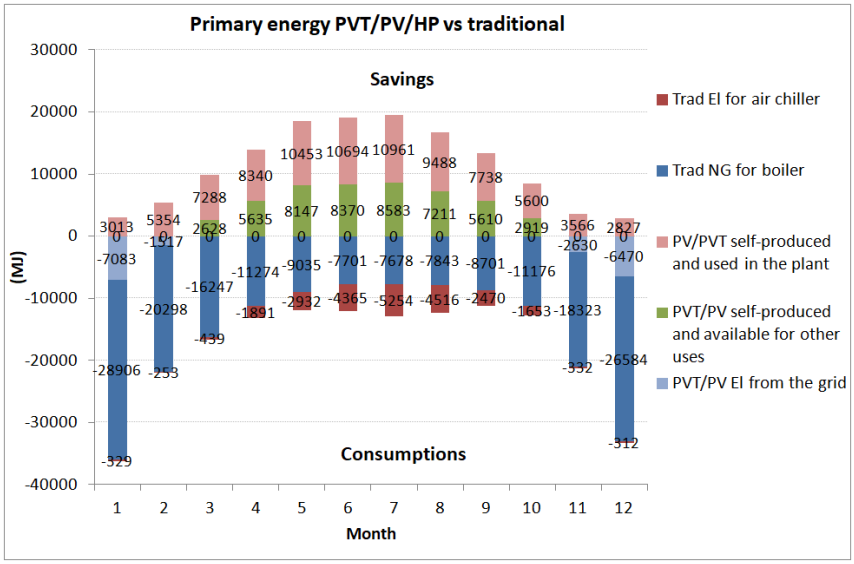

Figure 10: Monthly comparison between the proposed plant and a conventional plant in terms of primary energy

3.3. Energy comparison of different alternatives

As mentioned at the beginning of the paper, the results are referred to a “preferred” alternative. In fact,five different alternatives were studied with different combinations of PVT area and ground probes length:

- 20 m^2 PVT - 500 m boreholes;
- 40 m^2 PVT - 300 m boreholes;
- 40 m^2 PVT - 400 m boreholes;
- 60 m^2 PVT - 300 m boreholes;
- 60 m^2 PVT - 500 m boreholes.

Each alternative provides also 60 m^2 of plain PV. The five alternatives are compared in Figure 11between them on yearly basis in terms of primary energy savings, each with the counterpart of a traditional solution. The increment of savings is less than proportional to the PVT area as already at 40 m^2 the thermal contribution is in excess of the demand in various summer days, and obviously more often for 60 m^2.Instead, it is worth to realize that no advantage is offered by an increase in borehole length from 300 to 500 m. The fact is that for a shorter length the ground recharging is more effective, and this balances the slightly higher or lower temperature that longer probes may offer to the evaporator or condenser heat pump respectively.

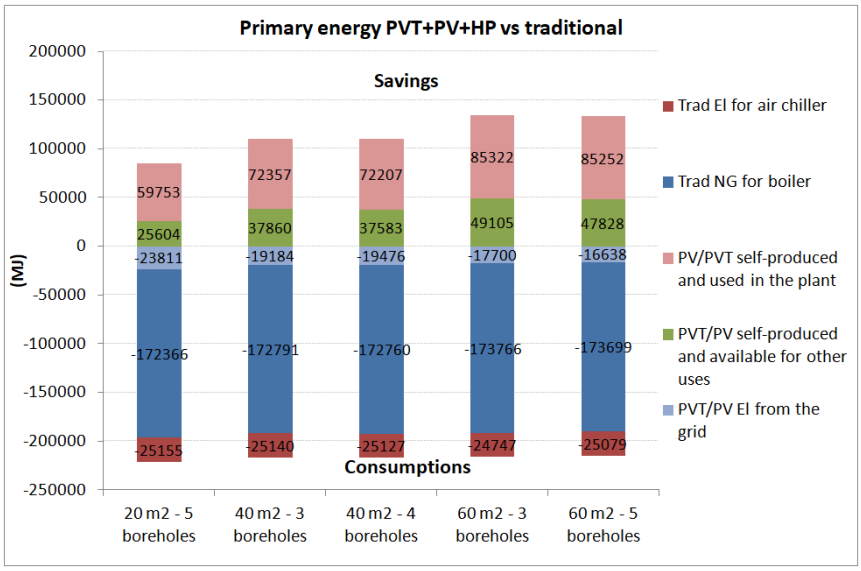

Figure 11: Primary energy comparison between the five considered different alternatives, each compared with the conventional solution

4. CONCLUSIONS

PVTs represent really a small niche in the actually huge PV market. The possibility of producing at the same time heat and electricity was conceived in the late 1976 (Wolf, 1976). However, in the beginning the main purpose was a PV cooling to increase the electric efficiency. A first proposal of using a PVT panel to supply a heat pump (Ito et al., 1997) appeared not economically viable. The attractive feature of PVT was essentially the best use of a limited area for collecting solar energy (Zondag et al., 2003). The high cost of PV and the absence of commercial PVT limited the researches mainly to computer simulations, with few experimentsrelated above all to DHW heating (Kalogirou, 2006). Most of the considered solutions were unglazed for fear of a possible overheating of the PV cells. A recent market survey supplied a short list of manufacturers, most of them with unglazed products (de Keizer et al., 2017). The very interesting energy performance of the plant designed in this study for a retrofitted building, coupled to the impressive PV (and then PVT) cost reduction and the possibility of prevent the overheating in a dual source heat pump combination, indicate that the use of glazed PVT offers a technical solution really suitable in view of nZEB design.

ACKNOWLEDGEMENTS

Authors would like to kindly thank Luigino Tonus and GirolamoBilotta (General Service Dept of the Belluno Province Administration), and GianlucaVigne (Areatecnica) for the data provided.

REFERENCES

Bertram, E., Glembin, J., Rockendorf, G., 2012. Unglazed PVT collectors as additional heat source in heat pump systems with borehole heat exchanger, Energy Procedia; 30: 414 – 423

Chow, TT., 2010. A review on photovoltaic/thermal hybrid solar technology. Appl Energy; 87:365–79.

de Keizer, C., Bottse, J., de Jong M., 2017. PVT inSHaPe benchmark 2017, SEAC, Partners in solar energy solutions.

Ito, S, Miura, N, Wang, JQ., 1997. Heat pump using a solar collector with photovoltaic modules on the surface. J Sol Energy Eng; 119: 147–51.

Kalogirou, SA, Tripanagnostopoulos, Y., 2006. Hybrid PV/T solar systems for domestic hot water and electricity production. Energy Convers Manage; 47(18– 19): 3368–82.

Wolf, M., 1976. Performance analysis of combined heating and photovoltaic power systems for residences. Energy Convers; 16:79–90.

Zondag, HA, de Vries, DW, van Helden, WGJ, van Zolingen, RJC., 2003. The yield of different combined PV-thermal collector designs. Sol Energy; 74: 253–69.

PAPER ID: 156
DOI: 10.18462/iir.icr.2019.0156

Solar thermal and ground source absorption heat pump: energy analysis for a nearly Zero Energy Building

RenatoLAZZARIN[(a)], MarcoNORO[(b)],Oscar ZANNI[(c)]

Department of Management and Engineering – University of Padova
Vicenza, 36100, Italy
[(a)]renato@gest.unipd.it,[(b)]marco.noro@unipd.it, [(c)]oscar.zanni@studenti.unipd.it

ABSTRACT

The retrofitting of an existing gymnasium building located in Northern Italy is simulated by TRNSYS-17 environment. The retrofitting allows to reduce heating and cooling needs of the building, as to convert it to a nearly zero energy building (nZEB). It is equipped with a solar thermal and ground source absorption heat pump system, operating with the ground as source/sink. Besides the direct use for domestic hot water and for heating, solar thermal energy is used as heat source for the heat pump, or as regeneration of ground when the system operates for summer air conditioning. In this case, condensation heat from the absorption chiller can be usefully directed to post-heating coils of the air handling units, or to regenerate the ground as well. The system simulation allows to size the plant and to evaluate its performance in terms of solar ratio and primary energy ratio.
Keywords: solar thermal collector; dual source heat pump; ground regeneration; ground source heat pump; multisource heat pump; absorption heat pump

1. INTRODUCTION

The concept of nZEBis based on the reductionof the primary energy demand through a high insulation level, theuse of high efficiency heating/cooling systems and the integrationof renewable energy sources into the building plant. In this regards, heat pump isone of the most advantageous systems to be considered in theheating, ventilating and air conditioning (HVAC)plant. As it is well known, designing a heat pump system needsa particular care concerning the selection of both the heating system(in order to lower heat supply temperature) and the heat source(outside air is the most widespread but the worst from thermodynamic point of view as the buildings heating loads generallyincrease as air temperature decreases). In particular, this secondaspect should be carefully evaluated when designing a heat pumpsystem as the potential benefits of alternative heat sources couldbe significant. That is why the interest in dualsource systems has been increasing during the last decades both theoretically and experimentally.
The present paper deals with an example of good integration of thejust mentioned three elements (building's high insulation, use of heat pump and integration of renewable energy sources). The building is part of an old school in North Italy that will be deeply retrofitted to become a nZEB. A dualsource (solar + ground) absorption heat pump system is here considered for the HVAC plant. Several scenarios are assessed with respect to primary energy consumption by means ofdynamic simulations in TRNSYS environment. The key issue of thispaper is to determine whether it is better to use ground source heat pump, or to integrate it by solar energy into amulti-source heat pump based system, to face the heating, cooling and domestic hot water (DHW) loads of the building. The analysis is carried out both on energy and economic basis.

2. METHODS

2.1. Building retrofitting and thermal loads

The building that is going to be retrofitted in 2019 is part of an old (completed in 1960) high school building of Feltre, situated in the province of Belluno, northern Italy. The climate is rather severe in wintertime (3100 degree-days). The gym and the laboratories will be retrofitted in order to become

a nZEB.The retrofitting will be operated by the Belluno Province Administration, a public Authoritycharged with the public education service.The main part of the retrofitted building is a largegym (33 m x 25 m x 8.40 m,expandingon two levels).Changing rooms, bathrooms with toilet and showers, and technical rooms are located at ground floor;an office, a small gym and a bar are at first floor. At second floor, six laboratories will be retrofitted and made newly available.
The total floor area is 2435 m^2, with an outwardsurface area of 2505 m^2, and an enclosed gross heated volume of11060 m^3.During the retrofit intervention, the envelope will be well insulated, with outer walls androof allowing for an average thermal transmittance of approximately0.15 W m^{-2} K^{-1}, floor tothe ground of 0.5 Wm^{-2} K^{-1}, and glazing system of 0.7 W m^{-2} K^{-1}.
Based on Trnsys17 (Klein et al., 2010) dynamic simulation, each thermal zone of the building is defined by means of scheduling of presence of people, type of activity, lighting and other internal gains, and humidity and air temperature set points. The HVAC system provides ventilation by two air handling units (AHU), space heating and cooling, and DHW production. Figure 1 reports monthly energy needs, obtained by summarizing the heating and cooling loads calculated with a 0.25 h simulation time step.

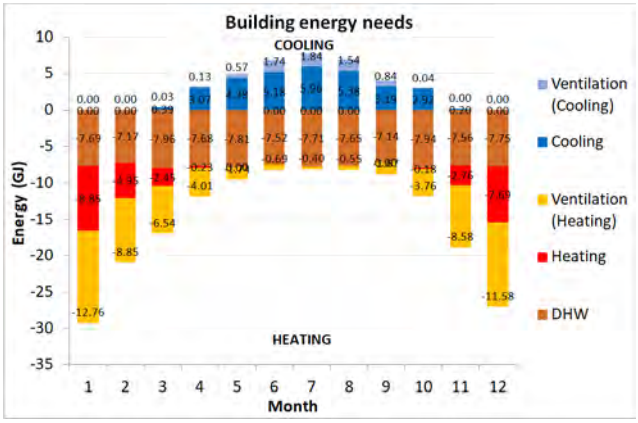

Figure 1: Monthly energy needs in terms of heating, cooling, ventilation (hot and cold coils of AHUs), and DHW

The maximum cooling load (21.6 kW) occurs at the beginning of June, when the school is still fully operating (open to students and professors, gyms open to extra-school activities as well). The maximum heating load (-44.6 kW) occurs in the second half of January.However,even during summer months post heating ventilation requires some heat. Ventilation needs in heating season are prevailing with respect to heating needs, as a consequence of the very high thermal insulation of the retrofitted building, and minimization of thermal bridges. Moreover,DHW needs(2000 L per day at 45 °C) are a large quota of the total heat request. They are concentrated in short periods mainly during the evening.

2.2. The HVAC plant

Through dynamic simulation using Trnsys environment, different solutions are evaluated with respect to the HVAC system. In another paper of this conference (Lazzarin and Noro, 2019), a multisource electric vapour compression heat pump coupled to photovoltaic/thermal collectors is studied. In this paper, a multisource gas-fired absorption heat pump systemis designed to fulfil the needs of the building, utilising ground and solar energy. Absorption heat pumps needa smaller and less expensive borehole fields, as the ratio between the thermal input from the source and the thermal output is much lower than for electric compression heat pumps. The model selected is a Robur GAHP-WS type, with modulating natural gas burner and stainless steel condensation heat recovery, able to produce alternatively or simultaneously hot water (till 65 °C) and cold water (till 3 °C) (Table 1).
The HVAC system in the large gym provides space heating by means of a radiant floor, and space cooling by air conditioner units, while ventilation is realized by means of anair handling unit (AHU)(6600 m^3 h^{-1}) serving a single-duct system. The other spaces (small gym, bar, laboratories and offices) are heated and cooled by fan coils, whereas toilets are heated only (by radiators), and laboratories are served also by an independent AHU (7000 m^3 h^{-1}) for ventilation. For sake of simplicity, a reduced functional diagram of the plant is shown in Figure 2. The system is equipped with one gas-fired absorption heat pump. An integration air/water electric chiller (rated capacity

10.5 kW, rated EER 2.75 at A30W7 condition) covers the cooling peak load, and operates as backup.
The ventilation is satisfied by two AHUs equipped with heating and cooling coils,served by hot and cold main collectors in the central plant (Figure 2). A heat recovery is provided in AHUs through sensible cross-flow heat exchangers, whose efficiency is limited to 50% in order to avoid frosting drawbacks.
The thermal source for the heat pump can be either the ground (nx100 m in a row of vertical tube U heat exchangers with an outer diameter of 32 mm and a thickness of 2.9 mm, with n=2-3-4 as a function of the solar field area as described in section 3), or solar collectors. Evacuated tube and flat plate collectors are considered in the simulation. Solar collectorsfirstly servethe DHW Tank, then the Hot Tank (for direct heating), and finally can regenerate the ground.Main characteristics of solar collectors are reported in Table 2. Table 3reports the rated electric consumption of main circulation pumps, computed after an evaluation ofpressure drops along the different circuits.

OPERATING AS HEAT PUMP	
Gas Utilization Efficiency (GUE)	174 %
Heating power (condenser) [kW]	43.9
Heat source power (evaporator) [kW]	18.7
OPERATING PRODUCING USEFUL HEAT AND COOL	
Total efficiency index	248 %
OPERATING AS CHILLER	
Cooling power (evaporator) [kW]	18.7
Heating power (condenser) [kW]	43.9
Thermal power burner [kW]	25.2
Electric power [kW]	0.41

Table 1. Main technical characteristics of the absorption HP/chiller (Robur, 2017)

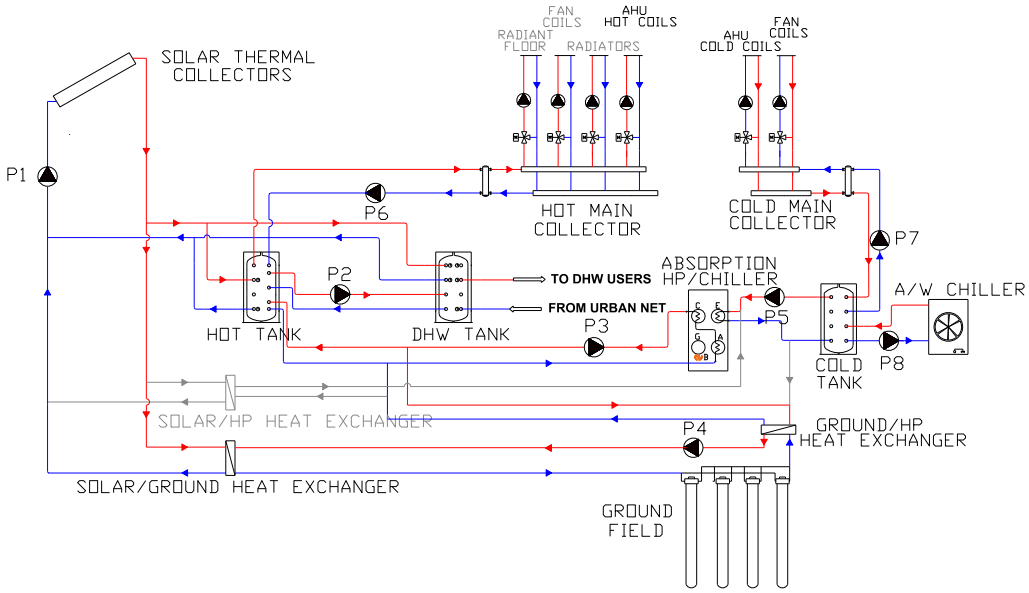

Figure 2: Simplified functional diagram of the HVAC plant. The mass flows of the main circuits (ground, solar, tanks, hot and cold collectors) are shown (in grey the part of the plant operating during heating season only)

Table 2. Main technical characteristics of solar collectors (Kloben Industries, 2017)

	Evacuated tube	Flat plate
Absorption area [m^2]	2.55	1.84
η_0 [@ 1000 W m^{-2}]	72.10 %	78.50 %
a_1 [W m^{-2} K^{-1}]	1.051	3.594
a_2 [W m^{-2} K^{-2}]	0.004	0.014
IAM [50°]	1.09	0.94

Pump	Electric power in heating operation [kW]	Electric power in cooling operation [kW]
P1	0.1	0.15
P2	0.03	0.03

Table 3. Electrical rated power of the main circulation pumps

P3	0.1	0.15
P4	0.5	0.5
P5	0.15	0.05

2.3. Control logic of the HVAC plant

The need for sensible heating of the AHUs depends directly on the outdoor air temperature and on the ventilation flow, which is constant for every AHU. The large gym AHU is scheduled to work from 8 am to 10 pm every day, that of the laboratories from 8 am to 6 pm from Monday to Friday. The solar system is activated whenever the measured global solar radiation on the plane of collectors (tilt 18°, orientation South-East) exceeds a threshold radiation (100 W m^{-2}). This is the radiation that provides the minimum acceptable efficiency once fixed the solar field characteristics, the minimum average temperature desired and the outdoor temperature (Busato et al., 2013a) (Busato et al., 2013b) (Busato et al., 2015). Solar energy is always firstly directed to DHW Tank, and successively to Hot Tank. When the two tanks exceed a temperatureat the top of 45 °C and 50 °C respectively and the solar circuit outlet fluid temperature is above 15 °C, the flow is directed to the ground field to regenerate it. In this case, when the absorption machine is operating as heat pump (heating season), the heat pump evaporator is supplemented by the solar section when its outlet temperature is lower than 30 °C. DHW Tank is firstly served by solar energy. If solar energy is not enough, thermal energy is provided by Hot Tank. Hot Tank is fed by the solar circuit, and by the HP condenser. In both tanks, an electric auxiliary is present. Absorption HP/chiller is activated once the Hot/Cold Tank temperature falls below/above the given set points (50 °C and 7 °C respectively).

3. RESULTS AND DISCUSSION

A full system energy performance evaluation isundertaken at the design stage. Firstly, the energy analysis results are reported on a monthly basis for one of the alternatives considered (Table 4). Subsequently, the annual results are reported in order to select the mostviable mixed solution, and to optimize the size of the solar and ground fields. As the ground field extension can be reduced when increasing the solar field area, a first attempt of economic analysis is reported in order to evaluate the viability of the proposed solutions.

Table 4. Different alternatives simulated by Trnsys with solar field, ground boreholes and storage tanks dimension

Alternative	Type of collector	Solar field area [m^2] – Ground boreholesdeep [m]	DHW Tank [L]	Hot Tank [L]	Cold Tank [L]
A1	-	0	1500	1500	1000
A2	Evacuated tube	20 - 400	1500	2000	1000
A3	Evacuated tube	40 - 300	3000	3000	1000
A4	Evacuated tube	60 - 200	5000	5000	1000
A5	Flat plate	50 - 300	3000	5000	1000

3.1. Energy analysis

Some first results are here reported on a monthly basis (Figure 3-Figure 5), referring to A3 case only(40 m^2 evacuated tube – 300 m ground probes)to stay within the paper length limits. Solar energy is used to provide hot water for heating (yellow in Figure 3a) and sanitary uses (grey) during the year, and to regenerate the ground mainly in summer months (orange). While the latter quota increases proportionally to the increasing of solar field area, the former increases less than proportionally, due to the very small heating demand in summer. The quota of solar energy directed to the HP evaporator is negligible in Figure 3a. This is true for all the evacuated tube alternatives, whereas for A5 a meaningful quota used as heat source is present. This is due to the lower thermal efficiency of flat plate collectors in winter conditions with respect to evacuated tube. Then outlet solar circuit temperatures lower than Hot Tank or DHW Tank temperatures more frequently occur.

Figure 3b reports the absorption HP/chiller energy balance:the limited use of solar energy as heat source of the HP is confirmed. The highest efficiency (1.83) is reported during mid seasons (April and October), whereas during cooling season the GUE is between 0.74 and 0.79.

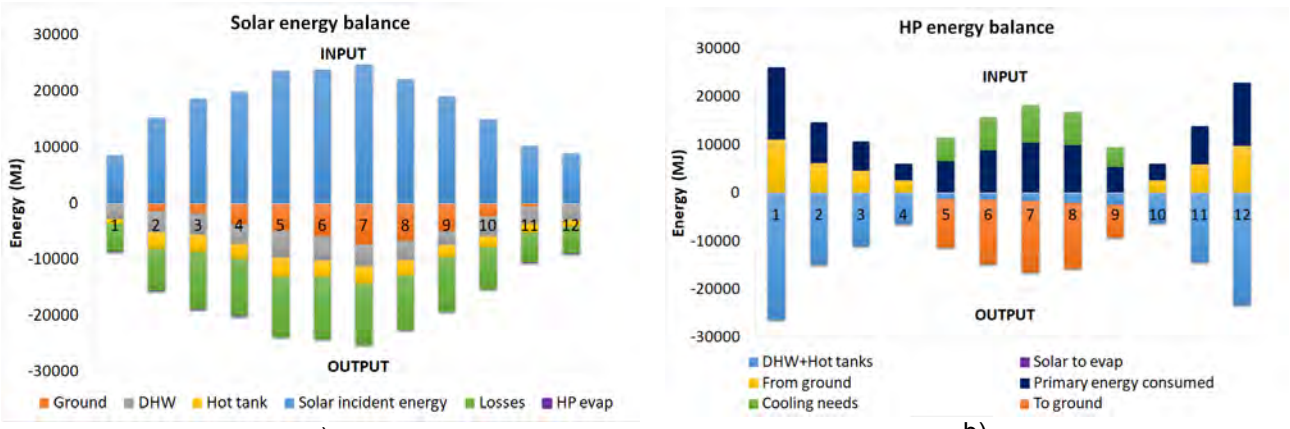

a) b)

Figure 3: Solar energy balance (a) and absorption HP/chiller energy balance (b) for A3 alternative

Figure 4 reports the energy balance of DHW Tank and Hot Tank. Solar energy assures an appreciable contribution to DHW demand, even if the Hot Tank contribution prevails above all in the colder months.

Electric auxiliaries contribution is quite limited, and mainly during summer or mid season. This is because in winter the absorption machine operates as HP, and it is controlled by the Hot Tank set point temperature. In this way, also DHW tank is satisfied mainly by solar energy and Hot Tank. Instead, during summer or mid season the absorption machine operates as chiller, controlled by the Cold Tank set point temperature. Then heat recovered by the condenser is available from the absorption machine only when it is on.

The Hot Tank is quite fully satisfied by solar energy (red in Figure 4b) during summer months.

Figure 5 reports the percentage covering of different heat generators (solar collectors, absorption HP, and electric auxiliaries), and the primary energy ratio (PER) for A3 alternative. PER is defined as the ratio between useful energy produced by the plant (energy from the three tanks to the main collectors of Figure 2) and the total no-renewable requested primary energy. The latter includes natural gas (NG) supplied to the absorption machine, and electricity to the auxiliaries of Hot Tank and DHW Tank, and to the A/W chiller. According to Italian standard DM 26/06/2015, such electricity consumptions are converted to primary energy by no-renewable primary factor $f_{p,nren}$=1.95.

During winter months, PER is always greater than 1.94, that is the nominal value of HP GUE. Heat pump covers the largest fraction of heating+DHW demand. Instead, during summer months the lowest values of PER are reported. This is due to low GUE of the absorption machine in chiller mode, and to low contribution of the heat recovered by the chiller to the heating+DHW demand.

As a matter of fact, the demand is nearly fully satisfied by solar energy. The highest values of PER are recorded during mid season, as heating demand is lower than in winter and solar collectors can largely satisfy it. Moreover, absorption machine is still operating as HP, with higher GUE than in chiller mode.

Figure 6 reports the annual energy balance for all the alternatives considered. Ground energy balance is always positive when solar collectors are installed (all alternatives except for A1), that is energy injected into the groundexceeds the energy extracted. The larger the solar field area, the greater the energy from solar collectors directed to regenerate the ground (grey in Figure 6a), and the lower the energy extracted from the ground for heating purpose (red). In all the cases, the cooling energy from the A/W electric chiller and its electricity consumption are quite limited. As a matter of fact, this equipment is for backup use only.

The annual PER is reported in Figure 6b, also considering the electricity consumption by the circulation pumps (PER^*). The latter is not negligible at all, mainly due to the pressure drops of the ground circuit. For example, for A3 case the annual pumps electricity consumption is around 1650 kWh: this is 3 % of the total thermal and cooling useful energy, and around 11 % of the total primary energy supplied to the plant.

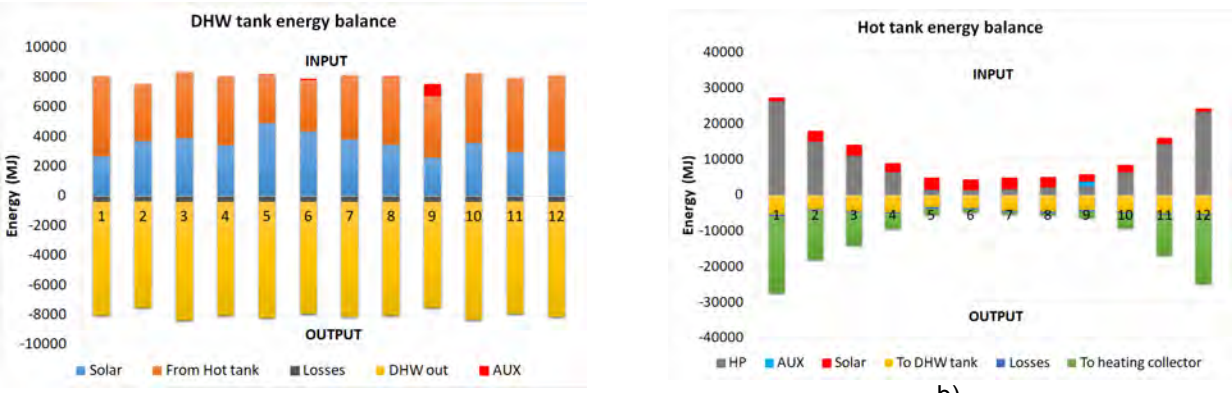

a) b)

Figure 4: Energy balance for DHW (a) and Hot (b) tank for A3 alternative

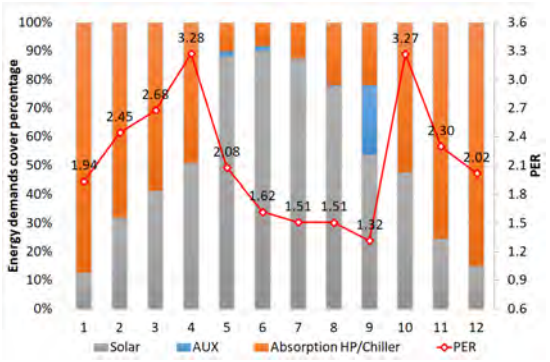

Figure 5: Energy demand percentage covering of different energy sources, and PER for alternative A3

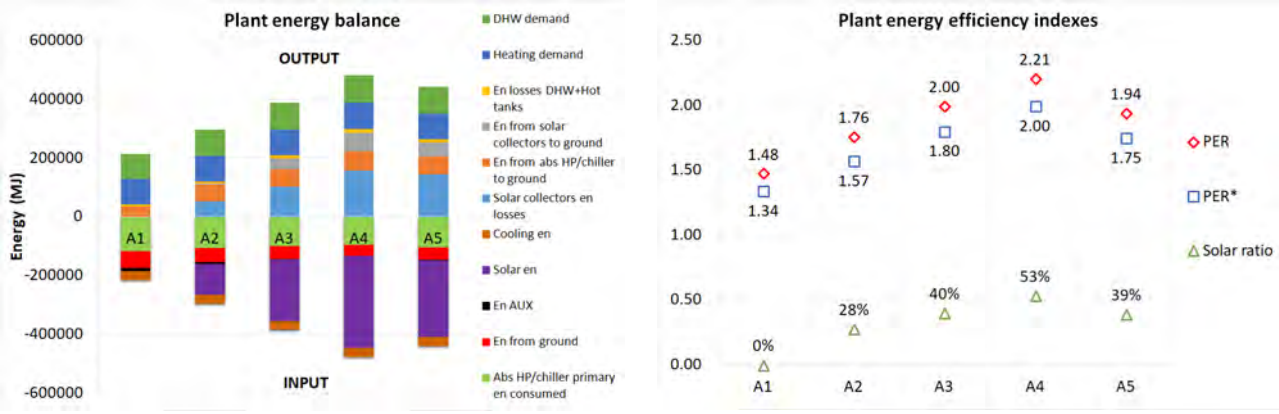

a) b)

Figure 6: (a) Plant energy balance for the different alternatives; (b) PER, PER*(considering also the circulation pumps electricity consumption)and solar ratio (the latter with reference to heating+DHW needs only) for the different alternatives

Such a percentage is consistent with data find in previous Authors' work in similar multi-source heat pump plants (Busato et al., 2013a) (Busato et al., 2013b). Then auxiliary distribution systems weight on the global energy consumption is not negligible. PER rises above PER* values above all in mild months, as the direct solar heating contribution becomes higher, and the solar section operates for many hours, also in ground recharging mode. With A5 alternative, HP operates for longer time during winter months with respect to A3 solution (light green in Figure 6a), as flat plate collectors feature lower efficiency than evacuated tube. For example, the plant with 50 m^2flat plate collectors cannot reach the same energy performance in terms of PER of that with 40 m^2 evacuated tubes.

As one of the more important advantages of multi-source HP plant with solar is the possibility to regenerate the ground, a simulation over ten years long was performed in order to evaluate such an effect on ground temperature. Average ground temperature for A3 case during the first years of simulation appreciably increases, starting from 7 °C and stabilizing around 10 °C at the end of the

period. Differently, in case of no-ground regeneration (alternative A1) the ground temperature varies around the initial value but with a slight decreasing trend during the ten years period. It is apparent the beneficial effect of ground regeneration using solar energy that exceeds direct use.

3.2. Economic analysis

High initial costs are common to many renewable energy installations.This is particularly the case of multi-source heat pump plants. With regards to investment costs, referring to literature and manufacturers average values (Lazzarin, 2014; Infante Ferreira and Kim, 2014; Weiss et al., 2017, Robur, 2017; Kloben Industries, 2017) a reasonable estimate of absorption single effect machine cost, evacuated tube and flat plate solar collectors specific cost is 26500 €, 545 € m^{-2} and 310 € m^{-2} respectively. A reasonable hypothesis concerns the cost of other equipment (pumps, tubes, boiler, valves, etc.), and considering a 30 % discount on price catalogue values, allows to calculate the total investment cost for solar thermal plant reported in Table 5.Cost of the ground field is calculated considering 10000 € of fixed cost plus 25 € per meter of ground heat exchanger. The same table reports also the value of the economic incentive ("Conto Energia Termico 2.0"), that is defined as 65 % of the plant total investment cost for retrofitting of nZEB (MISE,2016). For public buildings like schools, such an incentive can be allocated onceat the beginning of the intervention. Other parameters useful for the economic analysis are: NG cost fixed at 0.70 € Nm^{-3}, electricity cost at 0.22 € kWh^{-1}, real interest rate 0.565 %, period of the economic analysis 20 years.

Table 5. Investment cost of the plant, and "Contotermico 2.0" incentive

Alternative	Plant cost (solar field+pumps, tubes, etc.) [€]	Ground field cost [€]	Abs HP/chiller cost [€]	Installation cost [€]	Total invest. cost [€]	Total incent. (65%) [€]
A1	11600	20000	26500	8715	66815	43430
A2	24013	20000	26500	10577	81090	52708
A3	37310	17500	26500	12197	93507	60779
A4	54243	15000	26500	14361	110104	71568
A5	36687	17500	26500	12103	92790	60314

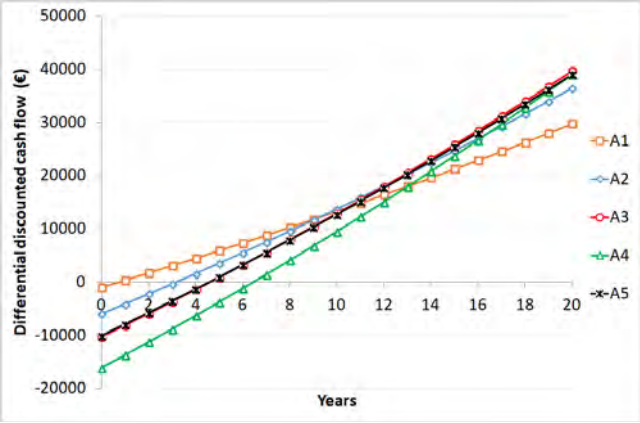

Figure 7: Annual discounted differential cash flows between the A1-A5 alternatives and the traditional one (A0)

An economic analysis in terms of net presentworth (NPW) and discounted payback period (DPB) of the different solutions is carried out with respect to a "reference solution" A0, whose cost is evaluated in 26910 €(three 25 kW NG condensing boilers with efficiency 100 %, and anaircooled electric vapor compression chiller). In terms of DPB, multi-source is not so profitable: the only-ground HP plant (A1) allows to get the shortest payback, around one year, whereas the most efficient solutions(A3, A4) feature longer payback periods (5 and 7 years respectively) (Figure 7). However, consider that the shortest DPB criterion is short sighted for a HVAC plant. Instead, in terms of differential (with respect to A0) discounted NPW, the most advantageous solution is a multi-source HP plant with 40 m^2 of evacuated tube and 300 m boreholes (A3), that allows to get around 40 k€ in 20 years. Increasing the solar field is a favorable solution in NPW terms, as A3, A4 and A5 alternatives feature higher NPW than A1 and A2.This is due to the possibility to reduce the ground field extension when increasing the solar field area, as confirmed also by previous Authors' study (Busato et al., 2015).

4. CONCLUSIONS

The paper describes the design of the functional scheme and the control logic of a multi-source absorption heat pump system coupled to a nZEB. The integration of different heat sources greatly increases the efficiency of the system in terms of primary energy consumption.
The solar heat contributes with a meaningful fraction of the space heating and DHW needs, and the use of the solar source to regenerate the ground plays an important role in maintaining the heat pump performance at high level during the years. Instead, the contribution of solar energy to the evaporator of the heat pump is negligible. This is mainly due to the control logic here proposed, as solar energy isdirectly used as HP heat source when its temperature is between 15 °C and 30 °C and if, at the same time, HP is in operation. One possible improvement of this configuration could be the use of a tank at the HP evaporator side, collecting warm water from solar collectors when the HP is off.
All the alternatives here considered varying the sizes of solar and ground fields perform better than the only-ground solution. For example, the best alternative from the economic point of view (40 m^2 evacuated tube – 300 m boreholes) features an annual PER of 2.0 and a solar ratio of 40 %. The circulation pumps consumption is an important part of the primary energy consumption, as taking it into account PER decreases to 1.8.
From the energy point of view all the multi-source alternatives here considered are viable and efficient solutions. However,the incentive of 65 % of the investment cost is essential for their economic viability.

ACKNOWLEDGEMENTS

Authors would like to kindly thank Luigino Tonus and Girolamo Bilotta (General Service Dept of the Belluno Province Administration), and GianlucaVigne (Areatecnica) for the data provided.

REFERENCES

Busato, F., Lazzarin, R., Noro, M., 2013a. Two years of recorded data for a multisource heat pump system: A performance analysis. Applied Thermal Engineering, 57, 39-47.

Busato, F., Lazzarin, R., Noro, M., 2013b. Multisource heat pump system from design to operation: the case study of a new school building. International Journal of Low-Carbon Technologies, 8, 88–94.

Busato, F., Lazzarin, R., Noro, M., 2015. Ground or solar source heat pump systems for space heating: Which is better? Energetic assessment based on a case history. Energy and Buildings, 102, 347–356.

Klein, S.A., et al., 2010. TRNSYS 17: a transient system simulation program, Solar Energy Laboratory, University of Wisconsin, Madison, USA, <http://sel.me.wisc.edu/trnsys>, (accessed 12.08.18).

Kloben Industries S.r.l., 2017. Priced catalogue 2017, Italy, http://www.kloben.it, (accessed 12.08.18).

Infante Ferreira, C.A., Kim, D.S., 2014. Techno-economic review of solar cooling technologies based on location-specific data. Int. J. Refrig. 39, 23–37.

Lazzarin, R., 2014. Solar cooling: PV or thermal? A thermodynamic and economical analysis. Int. J. Refrig. 39, 38–47.

Lazzarin, R., Noro, M., 2019. Photovoltaic/Thermal (PV/T) to drive a dual source heat pump (ground and PV cooling): performance analysis in a real application. Proceedings of ICR 2019 - The 25th IIR International Congress of Refrigeration, Montréal, Québec, Canada.

MISE (Italian Ministry of Economic Development), 2016. DM 16/02/2016 – Contotermico 2.0 (Thermal incentive 2.0), Italy, http://www.gse.it/servizi-per-te/efficienza-energetica/conto-termico, (accessed 18.10.18).

Robur S.p.A., 2017. Design manual 2017, Italy, http://www.robur.it, (accessed 12.08.18).

Weiss, W., Spörk-Dür, M., Mauthner, F., 2017. Solar Heat Worldwide. Detailed Market Figures 2015. Global Market Development and Trends in 2016. AEE – Institute for Sustainable Technologies; IEA – International Energy Agency.

Manuscript ID: 214
DOI: 10.18462/iir.icr.2019.0214

Experimental analysis of a gas-fired absorption heat pump with a refrigerant cooled flue gas heat exchanger

Philipp WAGNER, René RIEBERER

Institute of Thermal Engineering, Graz University of Technology
Inffeldgasse 25/B, 8010 Graz, Austria, philipp.wagner@tugraz.at

ABSTRACT

Residential heating has a significant potential in the reduction of energy consumption and CO_2 emissions. A relevant contribution can be expected from gas-fired ammonia/water absorption heat pumps (GAHPs).
Commonly the return flow of the heat distribution system is used to cool the combustion gas below the dew point to condensate water vapour and to minimize latent heat losses. Especially in retrofit applications the temperature of the heat distribution system is too high to condensate water vapour. To use the latent heat under all operating conditions, a GAHP can be equipped with a refrigerant cooled flue gas heat exchanger between the evaporator and the absorber. Therefore, an increase in efficiency can be achieved.
Measurements were carried out to determine the increase in efficiency using a refrigerant cooled flue gas heat exchanger. The GAHP was operated at different operating conditions and different cycle configurations.
Keywords: Ammonia/Water, Cycle Design, Efficiency, Flue Gas Heat Exchanger, Space Heating

1. INTRODUCTION

The energy consumption for residential heating has a crucial share on the total energy consumption. For instance, in the European Union around 26 % of the total energy consumption was used for residential heating in the year 2012 (Fleiter et al., 2016). In order to reach the ambitious climate targets, a significant reduction of the European and global energy consumption and CO_2 emissions are necessary. Especially, the heating demand of buildings has to be reduced and the efficiency of heating technologies has to be increased. Currently the heating demand is mainly covered by condensing gas boilers. In Germany gas and oil boilers had a market share of 68 % in the year 2012 which is still growing (Umweltbundesamt, 2016).
Condensing boilers provide the heating demand by burning fossil fuels (e.g. gas, oil) and cooling the combustion gas by the return flow of the heat distribution system. If the return flow temperature is below the dew point of the combustion gas, latent heat can be utilized by water vapour condensation. In this way, with state-of-the-art condensing gas boilers an efficiency of up to 109 % (based on the lower calorific value), which is already the limit, can be achieved (Wolff et al., 2004).
For a further increase in efficiency a new technology is necessary. A worthwhile contribution can be expected from directly gas-fired absorption heat pumps (GAHPs). Recently, a lot a research has been carried out in this field. A GAHP is driven by a high-temperature heat source (combustion of natural gas) and utilizes low-temperature heat from the ambient (e.g. air, ground, water) and releases the sum of both heat flows to the heat distribution system at a medium temperature. Due to the utilization of ambient heat - which is “free of charge” - with this technology an efficiency of up to 180 % (based on the lower calorific value) is possible (Wechsler et al., 2016). A reduction of the energy consumption and CO_2 emissions of more than 40 % compared to state-of-the-art condensing boilers is possible. It has to be noted, that such high efficiencies are only possible in combination with a low-temperature heating system (e.g. floor heating system) and if the low-temperature heat from the ambient is supplied at a moderate level.
But right here an issue with the realistic achievable efficiencies exists. For example, in Germany around three quarters of the residential buildings were built more than 30 years ago. In this particular case the return temperature of the hydronic heat distribution system is around 55 °C under usual operating conditions (Recknagel et al., 2011). But the dew point of a natural gas combustion with an air-fuel equivalence ratio of $\lambda = 1.3$ is around 55 °C, which means in most applications the

condensing boiler technology cannot be used because water vapour condensation in the combustion gas does not take place and thus latent heat dissipates into the environment.
To use the condensing boiler technology under all operating conditions the combustion gas has to be cooled with a low-temperature medium. In a GAHP the lowest temperature occur at the evaporator, which results in the possibility of cooling the combustion gas with the refrigerant by modifying the standard GAHP cycle. As it is not useful to (partially) replace the evaporator with a refrigerant cooled flue gas heat exchanger, it makes sense to install it after the evaporator or depending on the cycle design after a refrigerant heat exchanger (internal heat exchanger). Generally, after the evaporator or the refrigerant heat exchanger the temperature is around -15 °C to +20 °C, which is lower and independent from the temperature of the heat distribution system, which ensures water vapour condensation under all operating conditions. Wagner and Rieberer (2017) have shown a simulation study of a GAHP with a conventional water cooled flue gas heat exchanger (cooled by the heat distribution system) compared to a GAHP with a refrigerant cooled flue gas heat exchanger (cooled by the refrigerant). This study has shown the possibility to increase the efficiency of a GAHP by up to 12 % depending on the operating conditions and the cycle configuration by installing a refrigerant cooled flue gas heat exchanger. Due to the new cycle design the influence of strongly superheated ammonia vapour entering the absorber on the absorption and the overall heat pump process was investigated by Wagner and Rieberer (2018).
Within this work a GAHP prototype with ammonia/water as working pair and a nominal heating capacity of 18 kW was equipped with a refrigerant cooled flue gas heat exchanger between the evaporator and the absorber and experimentally investigated. Different cycle configurations were investigated and a comparison between a GAHP with a refrigerant cooled flue gas heat exchanger and a GAHP with a water cooled flue gas heat exchanger was performed.

2. SYSTEM DESCRIPTION

Fig. 1 shows a schematic flow chart of the analysed GAHP cycle. Rich solution (rso) with a relatively high ammonia mass fraction (x_{rso}) enters the generator (GEN) at state point 15, where it is partially evaporated by the heat supplied by a natural gas burner. Depending on the operating condition, the combustion gas leaves the generator at around 130 °C to 150 °C ($t_{combustiongas}$). To reduce energy losses, the combustion gas can be additionally cooled by either the water cooled (FlueHX1) or the refrigerant cooled (FlueHX2) flue gas heat exchanger. By analysing the GAHP cycle with the water cooled flue gas heat exchanger the return flow of the heat distribution system is preheated (from $t_{sink,in}$ to $t_{sink,FlueHX1,out}$) before entering the condenser (CON) and the water cooled absorbers (ABS-1 & ABS-2). If the GAHP cycle is analysed with a refrigerant cooled flue gas heat exchanger the refrigerant can be further heated by the combustion gas, before it enters the solution cooled absorber (ABS-3).

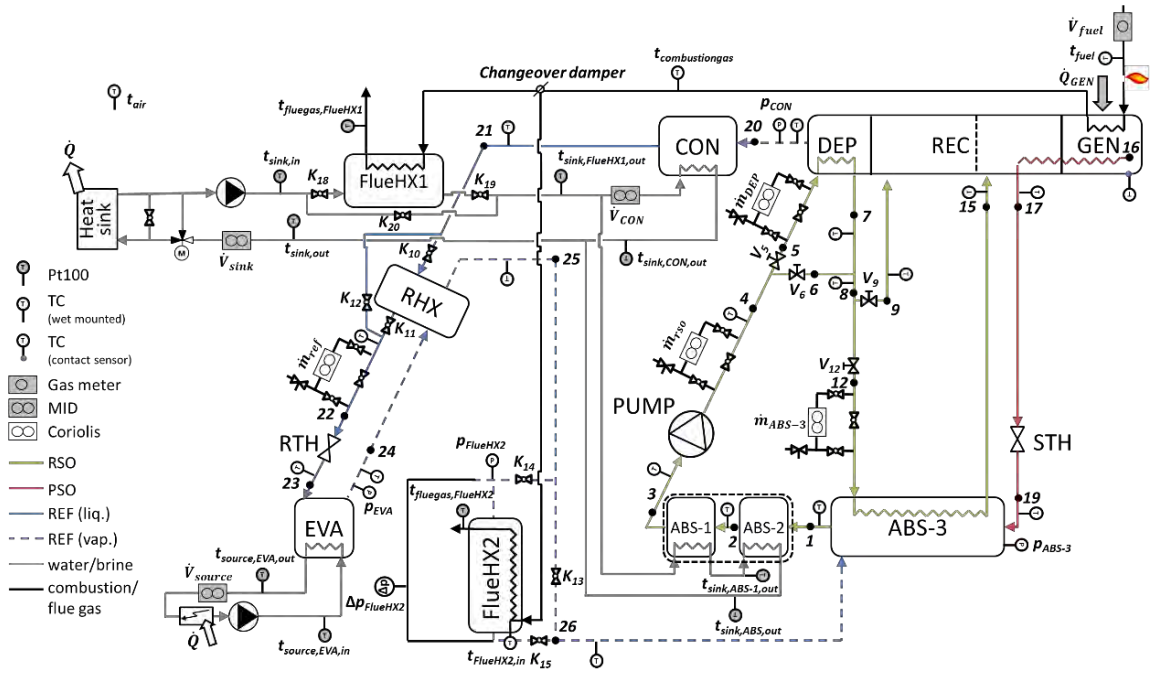

Figure 1: Schematic flow chart of the analysed absorption heat pump cycle

In principle the refrigerant cooled flue gas heat exchanger prototype is designed like a counterflow fin and tube heat exchanger with a heat transfer area of approx. 16 m². The cold refrigerant enters the flue gas heat exchanger at the top and the hot combustion gas (leaving the generator) enters at the bottom. On each level the refrigerant flows through two to three parallel pipes in series before it flows down to the next level. After 24 levels the refrigerant exits the flue gas heat exchanger at the bottom at a high temperature. The hot combustion gas flows upwards while getting cooled and exits at the top of the flue gas heat exchanger as flue gas. There is a huge difference in the heat transfer area compared to the water cooled flue gas heat exchanger with approx. 0.5 m². This difference is caused by the limited convective heat transfer of superheated refrigerant, which is substantially lower than the one of liquid water.
The ammonia vapour evaporated in the generator rises upwards to the rectification column (REC) where it is in contact with the liquid solution flowing downwards. Thus, the ammonia mass fraction (x) increases due to heat and mass transfer. Subsequently, the vapour enters the dephlegmator (DEP) where it is cooled by the rich solution and the less volatile vapour component (water) condenses. This condensate is used as the required reflux for the rectification column. The dephlegmator can be bypassed to investigate the influence of the dephlegmator on the refrigerant ammonia mass fraction (x_{ref}) and on the efficiency. After the dephlegmator, the vapour enters the condenser, where it is liquefied by releasing heat to the heat sink. In the following refrigerant heat exchanger (RHX) the refrigerant can be subcooled before it expands in the refrigerant throttle (RTH) to the low pressure (evaporation pressure p_{EVA}). For the investigation of the influence of the refrigerant heat exchanger on the efficiency it can be bypassed. Subsequently, the refrigerant enters the evaporator (EVA) and evaporates by extracting heat from the heat source. If the refrigerant heat exchanger is not bypassed, the refrigerant is further heated.
After partly evaporation of ammonia vapour in the generator, the poor solution (pso) with a relatively low ammonia mass fraction (x_{pso}) is taken from the bottom (state point 16) and cooled by a solution recirculation. After being expanded in the solution throttle (STH), the poor solution enters the solution cooled absorber, where it absorbs the refrigerant. A complete absorption of the refrigerant by the poor solution takes place in the water cooled absorbers. The resulting rich solution is brought to the high pressure (condensation pressure p_{CON}) by means of an electrical solution pump (PUMP).

3. MEASUREMENTS

Measurements with a GAHP have been conducted. Different cycle configurations and operating conditions have been investigated. The mass flow rate of the refrigerant ($\dot{m}_{ref}$), the rich solution ($\dot{m}_{rso}$), through the dephlegmator ($\dot{m}_{DEP}$) and through the solution cooled absorber ($\dot{m}_{ABS-3}$) were measured using Coriolis flow meters. By applying a mass balance at the solution cooled absorber the missing mass flow rate of the poor solution ($\dot{m}_{pso}$) can be calculated. The condensation pressure (p_{CON}) was measured at the condenser inlet (state point 20) and the evaporation pressure (p_{EVA}) was measured at the evaporator outlet (state point 24). The pressure loss of the refrigerant cooled flue gas heat exchanger ($\Delta p_{FlueHX2}$) was determined using a differential pressure transmitter. The “internal temperatures” (refrigerant & solution, except state point 16) and the combustion gas temperature ($t_{combustiongas}$) were measured by means of wet-mounted thermocouples. The temperature at the generator bottom was calculated as an average of the temperatures measured using three contact sensors (thermocouples) mounted at the outer wall approx. where the poor solution enters the solution recirculation pipe. The “external” temperatures at the heat sink and heat source and the flue gas temperature ($t_{fluegas}$) were measured using wet-mounted Pt100 sensors. The volume flow rates at the heat sink ($\dot{V}_{sink}$, $\dot{V}_{CON}$) and source ($\dot{V}_{source}$) were measured using MID flow meters. The fuels’ volume flow ($\dot{V}_{fuel}$) rate was measured using a gas meter.

3.1. Methodology

In order to compare the different cycle configurations and the different flue gas heat exchangers, measurements were taken at a constant natural gas flow rate. For the experimental investigation different heat source temperatures were combined with a constant heat sink temperature. To investigate the influence of different ammonia mass fractions in the refrigerant investigations were performed with (DEP) and without (nDEP) the dephlegmator. The effects of the refrigerant heat exchanger on the overall efficiency were analysed by investigations with (RHX) and without (nRHX) the refrigerant heat exchanger. Table 1 shows an overview of the varied parameters of the experimental investigation.

Table 1. Overview of the varied parameters

Parameter	Values
Natural gas flow rate ($\dot{V}_{fuel,norm}$) in m³/h	0.75
Heat source in/outlet temperature ($t_{source,EVA,in/out}$) in °C	+10/+7, -5/-8
Heat sink in/outlet temperature ($t_{sink,in/out}$) in °C	45/55
Dephlegmator	with (DEP), without (nDEP)
Refrigerant heat exchanger	with (RHX), without (nRHX)
Flue gas heat exchanger	FlueHX1 (water cooled), FlueHX2 (refrigerant cooled)

The evaluation of the measurement data was performed with the software Engineering Equation Solver (EES, 2018). The substance data of ammonia/water was taken from the equation of state formulated by Ibrahim and Klein (1993), which is implemented in EES as a predefined function. All measurement uncertainties indicated by error bars in the following figures were calculated by means of Gaussian error propagation rule implemented in EES (2018).
The following assumptions were made within the evaluation:

- The ammonia concentration of the poor solution (x_{pso}) at the generator bottom (state point 16) and of the refrigerant (x_{ref}) at the dephlegmator outlet (state point 20) were calculated as a function of the measured temperatures at those state points and the condensation pressure by assuming saturated conditions.
- The heat flow rates at the water cooled flue gas heat exchanger, condenser, evaporator and water cooled absorbers were determined using the measured values at the external (water) circuits due to the smaller measurement uncertainty.
- Pressure losses were neglected, except the refrigerant side pressure loss in the refrigerant cooled flue gas heat exchanger as well as when determining the theoretically achievable efficiency ($GUE_{FlueHX2,th}$, see below).
- Heat losses were neglected with the exception of the combustion gas heat losses between the generator outlet and the inlet of the refrigerant cooled flue gas heat exchanger when determining the theoretically achievable efficiency ($GUE_{FlueHX2,th}$, see below). The heat losses to the ambient ($\dot{Q}_{loss,pipe,FlueHX2}$) were estimated according to Eq. (1). U_{pipe} was calculated using the thermal conductivity of the insulating material ($\lambda_{Insulation}$) and the convective heat transfer coefficients of the combustion gas ($\alpha_{combustiongas}$) and the air (α_{air}) as shown in Eq. (2). Due to the high thermal conductivity of aluminium and the small thickness of the pipe the thermal conductivity was neglected which means that it was assumed that the temperature outside the aluminium pipe corresponds to the one inside the pipe. Separate temperature measurements at the beginning ($t_{combustiongas}$) and at the end of the pipe ($t_{FlueHX2,in}$) were taken to verify the calculation of the heat losses according to Eq. (1).

$$\dot{Q}_{\mathrm{loss,pipe,FlueHX2}} = U_{pipe} \cdot L_{pipe} \cdot (t_{combustiongas} - t_{air}) \qquad \text{Eq. (1)}$$

$$U_{\mathrm{pipe}} = \frac{1}{\frac{1}{d_{inner} \cdot \pi \cdot \alpha_{combustiongas}} + \frac{1}{2 \cdot \pi} \cdot \frac{1}{\lambda_{Insulation}} \cdot \ln\left(\frac{d_{outer}}{d_{inner}}\right) + \frac{1}{d_{outter} \cdot \pi \cdot \alpha_{air}}} \qquad \text{Eq. (2)}$$

For the assessment of the heat pump process the ratio of the total heating capacity and the fuel input is relevant. DIN EN 12309-1 (2015) defines the Gas Utilization Efficiency as an appropriate value for the evaluation of GAHPs as shown in Eq. (3). In this consideration, the energy consumption of the solution pump is neglected.

$$\mathrm{GUE} = \mathrm{GUE_{Hs}} = \frac{\dot{Q}_{\mathrm{sink}}}{\dot{Q}_{\mathrm{fuel,norm,H_s}}} = \frac{\dot{Q}_{\mathrm{sink}}}{\dot{V}_{\mathrm{fuel,norm}} \cdot H_{\mathrm{s,norm}}} \qquad \text{Eq. (3)}$$

$$\mathrm{GUE_{Hi}} = \frac{\dot{Q}_{\mathrm{sink}}}{\dot{Q}_{\mathrm{fuel,norm,H_i}}} = \frac{\dot{Q}_{\mathrm{sink}}}{\dot{V}_{\mathrm{fuel,norm}} \cdot H_{\mathrm{i,norm}}} \qquad \text{Eq. (4)}$$

$$\mathrm{GUE_{FlueHX2,th}} = \frac{\dot{Q}_{\mathrm{sink}} + \dot{Q}_{\mathrm{loss,pipe,FlueHX2}}}{\dot{Q}_{\mathrm{fuel,norm,H_s/H_i}}} + \underbrace{(\mathrm{GUE_{FlueHX1}} - \mathrm{GUE_{FlueHX1,\Delta pFlueHX2}})}_{\text{consideration of pressure loss in FlueHX2}} \qquad \text{Eq. (5)}$$

A fair comparison of GAHPs with traditional condensing boilers is not possible due to different reference values. The lower calorific value (H_i) is taken as the reference value for the calculation of the efficiency of traditional condensing boilers, whereas for GAHPs the calorific value (H_s) is taken.

For that reason in the figures that show the efficiency of the GAHP an additional ordinate is plotted which shows the efficiency based on the lower calorific value (H_i) according to Eq. (4). The theoretically achievable efficiency $GUE_{FlueHX2,th}$ was calculated according to Eq. (5) and should show which efficiency could be achieved if the combustion gas heat losses occurring between the generator and the refrigerant cooled flue gas heat exchanger as well as the pressure losses can be omitted.

3.2. Results

In Figs. 2 - 9 the measurement results regarding the flue gas temperature at the outlet of the flue gas heat exchanger ($t_{fluegas}$), the recovered latent heat flow rate in the flue gas heat exchangers ($\dot{Q}_{fluegas,lat}$), the Gas Utilization Efficiency (GUE) and the pressure loss ($\Delta p_{FlueHX2}$) in the refrigerant cooled flue gas heat exchanger with its effect on the GUE at different cycle configurations (with/without RHX, with/without DEP) and different operating conditions (t_{sink}, t_{source}) are shown.
Fig. 2 shows the flue gas temperature with RHX, Fig. 3 without RHX for different heat source temperatures with (DEP) and without (nDEP) the dephlegmator. The flue gas temperature at the water cooled flue gas heat exchanger ($t_{fluegas,FlueHX1}$) shows only minor changes due to the independence of the flue gas temperature on the heat source temperature and the cycle configuration. It can be seen, that the flue gas temperature at the refrigerant cooled flue gas heat exchanger ($t_{fluegas,FlueHX2}$) is dependent on the cycle configuration and the heat source temperature. If a dephlegmator was used, an ammonia mass fraction in the refrigerant of around 0.99 could be achieved. Without using a dephlegmator an ammonia mass fraction of 0.96 to 0.98 was achieved. A lower ammonia mass fraction in the refrigerant results in a higher temperature glide during evaporation and a lower vapour quality after the evaporator as well as after the refrigerant heat exchanger. Due to the lower vapour quality basically a higher heat flow rate can be transferred in the refrigerant cooled flue gas heat exchanger and a lower flue gas temperature ($t_{fluegas,FlueHX2}$) can be achieved, e.g. 17 °C instead of 45 °C (compare SRC 10/7 DEP & SRC 10/7 nDEP in Fig. 2). It also turned out, that the flue gas temperature $t_{fluegas,FlueHX2}$ for $t_{source,EVA,in/out}$ = 10/7 °C is lower compared to $t_{source,EVA,in/out}$ = -5/-8 °C, even though the refrigerant inlet temperature into the flue gas heat exchanger - which cools the combustion gas - is higher. This issue is caused by the lower refrigerant mass flow rate for $t_{source,EVA,in/out}$ = -5/-8 °C which can recover less heat. At the operating condition SRC -5/-8 DEP the heat flow rate transferred to the refrigerant was limited due to the low refrigerant mass flow rate which caused a slight increase of the flue gas temperature. Without dephlegmator (SRC -5/-8 nDEP) a slight decrease of the flue gas temperature was achieved which was caused by the lower ammonia mass fraction in the refrigerant. Without RHX the refrigerant enters the refrigerant cooled flue gas heat exchanger at a lower temperature and a lower vapour quality. This leads to a higher recovered heat flow rate in the flue gas heat exchanger, which results in a lower flue gas temperature, e.g. 29 °C instead of 45 °C (compare Fig. 2 & Fig. 3: SRC 10/7 DEP). Due to the low refrigerant mass flow rate for $t_{source,EVA,in/out}$ = -5/-8 °C only a small decrease of the flue gas temperature occurred without RHX (compare SRC -5/-8 DEP & SRC -5/-8 nDEP with RHX (Fig. 2) and without RHX (Fig. 3)).

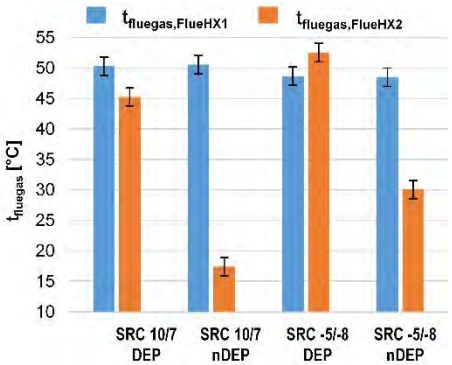

Figure 2: Flue gas temperature for $t_{sink,in}/t_{sink,out}$ = 45/55 °C with RHX

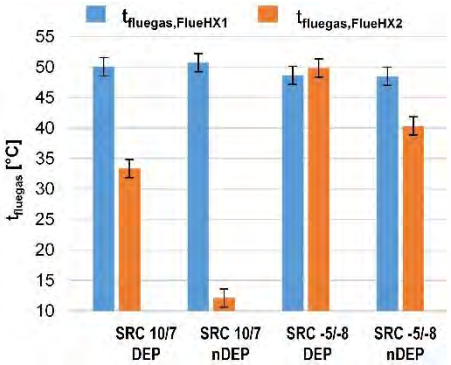

Figure 3: Flue gas temperature for $t_{sink,in}/t_{sink,out}$ = 45/55 °C without RHX

The great benefit of the refrigerant cooled flue gas heat exchanger is the lower flue gas temperature and therefore the higher water condensate mass flow rate. As the sensible heat has only a minor effect on the heat flow rate transferred in the flue gas heat exchanger the focus will be on the recovered latent heat flow rate ($\dot{Q}_{fluegas,lat}$). The latent heat flow rate with RHX is shown in Fig. 4 and without RHX in Fig. 5. It was calculated with the measured amount of condensate during the

measurement period (generally 15 minutes) and the condensation enthalpy of water. Due to the similar flue gas temperatures, the latent heat flow rates recovered by the water cooled flue gas heat exchanger is independent of both, the cycle configuration and the heat source temperature. Comparing the flue gas temperatures (Fig. 2 & Fig. 3) and the recovered latent heat flow rates (Fig. 4 & Fig. 5), an inverse trend can be seen. A lower flue gas temperature causes a higher condensation mass flow rate and therefore a higher recovered latent heat flow rate. E.g., the recovered latent heat flow rate increased from around 260 W to around 420 W while the flue gas temperature decreased from 50 °C to 45 °C (see Fig. 2 & Fig. 4: SRC 10/7 DEP). Since the majority of the recovered heat flow rate transferred to the refrigerant in the refrigerant cooled flue gas heat exchanger is released to the heat sink in the water cooled absorbers a higher heating capacity is achieved, which influences the GUE positively.

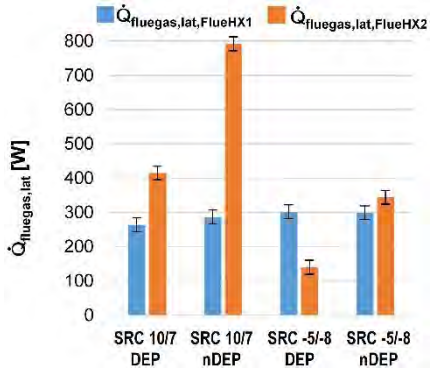

Figure 4: Recovered latent heat flow rate for $t_{sink,in}/t_{sink,out}$ = 45/55 °C with RHX

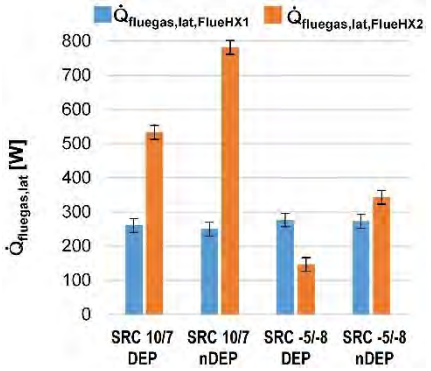

Figure 5: Recovered latent heat flow rate for $t_{sink,in}/t_{sink,out}$ = 45/55 °C without RHX

The achieved GUEs at different heat source temperatures and different cycle configurations are shown in Fig. 6 (with RHX) and Fig. 7 (without RHX). With the water cooled flue gas heat exchanger the highest GUEs can be achieved with dephlegmator and with RHX. With RHX the refrigerant cooled flue gas heat exchanger does not show a benefit at a higher ammonia mass fraction in the refrigerant (see Fig. 6: SRC 10/7 DEP & SRC -5/-8 DEP), compared to the water cooled flue gas heat exchanger. This issue has two main reasons. On the one hand, the heat losses between the generator outlet and the refrigerant cooled flue gas heat exchanger reduced the heat flow rate transferred to the refrigerant and therefore the heat flow rate transferred to the heat sink. On the other hand, the refrigerant side pressure loss in the refrigerant cooled flue gas heat exchanger had a negative effect on the GUE, which will be explained in Fig. 8 and Fig. 9. Without RHX the GUE with the water cooled flue gas heat exchanger decreased slightly due to the lower evaporator capacity caused by the higher vapour quality after the expansion and the non-existing heat transfer between the state points 24 and 25 which resulted in a reduced heat flow rate transferred to the heat sink in the water cooled absorbers. With the refrigerant cooled flue gas heat exchanger the non-existing heat transfer in the RHX was partly compensated. For example, at the operating condition SRC 10/7 DEP the recovered latent heat flow rate ($\dot{Q}_{fluegas,lat}$) increased from 420 W (see Fig. 4: SRC 10/7 DEP) with RHX to 530 W (see: Fig. 5: SRC 10/7 DEP) without RHX, whereby the $GUE_{FlueHX2}$ was similar with 1.28 (see Fig. 6 and Fig. 7: SRC 10/7 DEP). The highest increase of the GUE from 1.23 ($GUE_{FlueHX1}$) to 1.27 ($GUE_{FlueHX2}$), i.e. by around 3 % can be seen at SRC 10/7 nDEP without RHX (see Fig. 7).

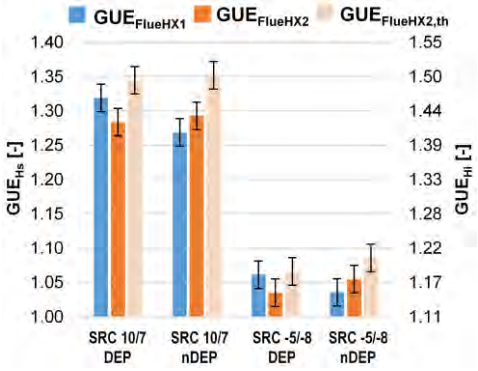

Figure 6: GUE for $t_{sink,in}/t_{sink,out}$ = 45/55 °C with RHX

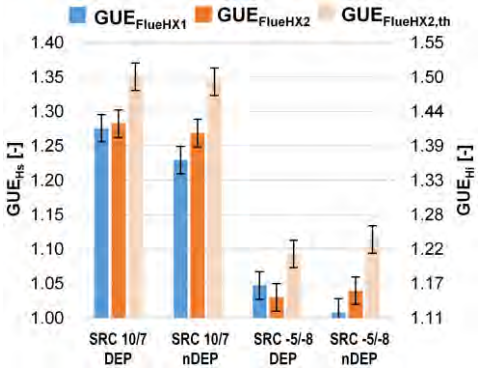

Figure 7: GUE for $t_{sink,in}/t_{sink,out}$ = 45/55 °C without RHX

Fig. 8 shows the refrigerant side pressure loss in the refrigerant cooled flue gas heat exchanger at different cycle configurations and $t_{source,EVA,in/out}$ = 10/7 °C. Due to the higher pressure loss at a higher refrigerant mass flow rate, these operating conditions are used to show the influence of the pressure loss on the GUE, which is shown in Fig. 9. Due to the pressure loss between the evaporator and the absorber the ammonia mass fraction in the rich solution decreases (assuming same heat sink temperature). This issue results in a lower refrigerant mass flow rate evaporated in the generator, which has a negative effect on the efficiency. The pressure loss of around 0.025 MPa (see Fig. 8: SRC 10/7 DEP, RHX), which is nearly independent of the cycle configuration, caused a decrease of the GUE from 1.32 ($GUE_{FlueHX1}$) to 1.27 ($GUE_{FlueHX1,\Delta pFlueHX2}$), i.e. by 4 % (see Fig. 9: SRC 10/7 DEP, RHX). A detailed explanation of the impact of pressure losses within an absorption heat pump can be found in Niebergall (1981). If the heat losses are added to the heating capacity and if the pressure losses can be reduced to a minimum without reducing the transferred heat flow rate in the flue gas heat exchanger a theoretical GUE ($GUE_{FlueHX2,th}$) can be calculated according to Eq. (5) which is shown in Fig. 6 and Fig. 7. E.g., for the operating condition SRC 10/7 DEP with RHX a GUE of 1.33 could be achieved by adding the GUE reduction due to the pressure loss ($GUE_{FlueHX1}$ – $GUE_{FlueHX1,\Delta pFlueHX2}$) of 0.05 to the measured $GUE_{FlueHX2}$. By additionally reducing the heat loss ($\dot{Q}_{loss,pipe,FlueHX2}$) between the generator outlet and the inlet of the flue gas heat exchanger, which was 0.17 kW by a heating capacity of 11.2 kW, a $GUE_{FlueHX2,th}$ of 1.35 would be possible, which means an increase by 6 % at this operating condition compared to a GAHP with a water cooled flue gas heat exchanger. The highest theoretical increase of the GUE, from 1.23 ($GUE_{FlueHX1}$) to 1.34 ($GUE_{FlueHX2,th}$), i.e. by around 9 % can be seen at SRC 10/7 nDEP without RHX (see Fig. 7).

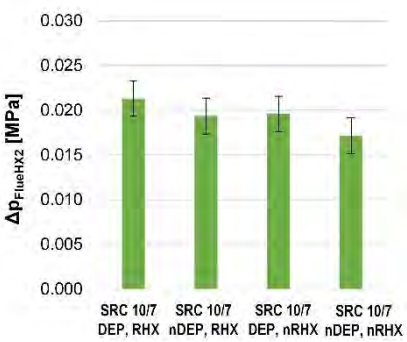

Figure 8: Pressure loss in FlueHX2 for $t_{sink,in}/t_{sink,out}$ = 45/55 °C with RHX

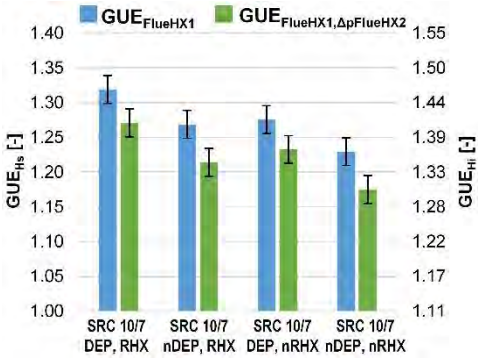

Figure 9: Effect of the pressure loss in FlueHX2 on the GUE for $t_{sink,in}/t_{sink,out}$ = 45/55 °C with RHX

4. CONCLUSION AND OUTLOOK

A gas-fired absorption heat pump (GAHP) with a conventional, i.e. water cooled, flue gas heat exchanger was compared to a GAHP with a novel refrigerant cooled flue gas heat exchanger. The influence of the dephlegmator and the refrigerant heat exchanger on the recoverable heat from the combustion gas as well as the Gas Utilization Efficiency (GUE) were analysed.

First measurements showed that a lower flue gas temperature could be achieved and a higher latent heat flow rate could be recovered in the refrigerant cooled flue gas heat exchanger. The highest benefits could be achieved at a lower ammonia mass fraction in the refrigerant. The measurements also pointed out, that the pressure loss in the refrigerant cooled flue gas heat exchanger had a significant impact on the efficiency. Due to that and the heat losses between the generator and the refrigerant cooled flue gas heat exchanger an increase in efficiency of only approx. 3 % could be achieved, which could be increased to 9 %, if the pressure and heat losses could be reduced.

Hence further efforts are required to reduce the combustion gas heat losses as well as the pressure losses. The know-how gained from this experimental analysis will be considered in a simulation model of the GAHP.

ACKNOWLEDGEMENTS

This work has been conducted in the course of the cooperative project “FluePump” (FFG-Project No.: 853579). The project is funded by the Austrian Climate and Energy Fund and carried out within the Austrian Energy Research Program 2015. The authors would like to thank the project partner E-Sorp GmbH to make this work possible.

NOMENCLATURE

1…i	state point	liq	liquid
α	heat transfer coefficient ($W \cdot m^{-2} \cdot K^{-1}$)	$\dot{m}$	mass flow rate ($kg \cdot s^{-1}$)
ABS-1, ABS-2	water cooled absorber	norm	referred to standard conditions
ABS-3	solution cooled absorber	out	outlet
CON	condenser	p	pressure (Pa)
Δ	difference	pso	poor solution
d	diameter (m)	PUMP	solution pump
DEP	dephlegmator	$\dot{Q}$	heat flow rate (W)
EVA	evaporator	RHX	refrigerant heat exchanger
FlueHX1	water cooled flue gas heat exchanger	REC	rectification column
		ref	refrigerant
FlueHX2	refrigerant cooled flue gas heat exchanger	rso	rich solution
		RTH	refrigerant throttle
fuel	fuel (natural gas)	sink	heat sink
GAHP	gas-fired absorption heat pump	source	heat source
GEN	generator	SRC	source temperature level
GUE	Gas Utilization Efficiency (-)	STH	solution throttle
H_i	lower calorific value ($kJ \cdot m^{-3}$)	t	temperature (°C)
H_s	calorific value ($kJ \cdot m^{-3}$)	th	theoretical
in	inlet	U	heat transmission coefficient ($W \cdot m^{-1} \cdot K^{-1}$)
K_i	ball valve	$\dot{V}$	volume flow rate ($m^3 \cdot s^{-1}$)
λ	air-fuel equivalence ratio	V_i	valve
$\lambda_{Insulation}$	thermal conductivity ($W \cdot K^{-1}$)	vap	vapour
L	length (m)	x	ammonia mass fraction ($kg \cdot kg^{-1}$)
lat	latent		

REFERENCES

DIN EN 12309-1, 2015. Gas fired sorption appliances for heating and/or cooling with a net heat input not exceeding 70 kW - Part 1: Terms and definitions.

EES, 2018. Engineering Equation Solver. V10.439. F-Chart Software, Madison, USA.

Fleiter, T., Steinbach, J., Ragwitz, M., Arens, M., Aydemir, A., Elsland, R., Frassine, C., 2016. Mapping and Analyses of the Current and Future (2020 – 2030) Heating/Cooling Fuel Deployment (Fossil/Renewables). Work Package 1: Final Energy Consumption for the Year 2012. European Commission, DG Energy, Brussels.

Ibrahim, O.M., Klein, S.A., 1993. Thermodynamic Properties of Ammonia-Water Mixtures, ASHRAE Transactions 99(1), 1495-1502.

Umweltbundesamt, 2016. Marktdaten: Bereich Wohnen. http://www.umweltbundesamt.de/daten/private-haushalte-konsum/gruene-produkte-marktzahlen/marktdaten-bereich-wohnen (2016/06/29)

Niebergall W., 1981. Sorptions-Kältemaschinen. Springer-Verlag, Heidelberg.

Recknagel, H., Sprenger, E., Schramek, E.-R., 2011. Heizung + Klima Technik, 75. Auflage. Oldenburg Industrieverlag GMBH, Oldenburg.

Wagner, P., Rieberer, R., 2017. Untersuchung einer neuartigen Abgaswärmeübertragereinbindung für gasbefeuerte Absorptionswärmepumpen, Proc. Deutsche Kälte-Klima-Tagung 2017, Bremen, Germany.

Wagner, P., Rieberer, R., 2018. Untersuchung der Auswirkungen einer hohen Kältemitteltemperatur auf das Absorptionsverhalten, Proc. Deutsche Kälte-Klima-Tagung 2018, Aachen, Germany.

Wechsler, R., Rieberer, R., Emhofer, J., Zottl, A., Köfinger, C., 2016. Experimentelle Untersuchung einer Gasabsorptionswärmepumpe unter Labor- und Feldtestbedingungen sowie Vergleich mit Simulationsergebnissen, Proc. Deutsche Kälte-Klima-Tagung 2016, Kassel, Germany.

Wolff, D., Teuber, P., Budde, J., Jagnow, K., 2004. Felduntersuchungen: Betriebsverhalten von Heizungsanlagen mit Gasbrennwertkesseln. Fachhochschule Braunschweig Wolfenbüttel, Wolfenbüttel, 14 p.

Manuscript ID: 242
DOI: 10.18462/iir.icr.2019.0242

High temperature heat pump using HFO and HCFO refrigerants – system design and experimental results

Cordin ARPAGAUS[(a)], Ralph KUSTER[(a)], Manuel PRINZING[(a)], Frédéric BLESS[(a)], Michael UHLMANN[(a)], Elias BÜCHEL[(a)], Stefan FREI[(a)], Jürg SCHIFFMANN[(b)], Stefan S. BERTSCH[(a)]

[(a)] NTB University of Applied Sciences of Technology Buchs, Institute for Energy Systems, Werdenbergstrasse 4, 9471 Buchs, Switzerland, cordin.arpagaus@ntb.ch
[(b)] Ecole Polytechnique Fédérale de Lausanne, Laboratory for Applied Mechanical Design, Rue de la Maladière 71b, 2002 Neuchâtel, Switzerland

ABSTRACT

High temperature heat pumps (HTHP) with heat sink temperatures of 100 to 160 °C will increasingly become commercialized in the coming years, especially for industrial drying, sterilization and evaporation processes. In particular, the HFO R1336mzz(Z) and the HCFOs R1233zd(E) & R1224yd(Z) are low GWP (< 10) replacement refrigerants for R245fa and R365mfc. This study examines the experimental performance of R1336mzz(Z) and R1233zd(E) in a laboratory HTHP with 5 to 10 kW heating capacity. The developed heat pump is single-stage, operates with a variable speed piston compressor, and contains a continuously adjustable internal heat exchanger (IHX) for superheating control. The performance data were measured at 30, 50, and 70 K temperature lift (40 to 80°C heat source, 80 to 150°C heat sink). At W60/W110 the experimental results with R1233zd(E) showed a COP of 2.8 (basic cycle) and 3.1 with IHX integration (+15%). For R1336mzz(Z) a COP of 2.4 and 3.0 was reached (+24%). At higher temperatures tested, the deviations between the measured COP with R1336mzz(Z) and R1233zd(E) were within the measurement uncertainty. Moreover, R1336mzz(Z) achieves potentially higher condensing temperatures due to its higher critical temperature. By increasing the heat sink temperature glide from 5 to 30 K, a further 15% COP increase was achieved.
Keywords: High temperature heat pump, HFO, HCFO, R1336mzz(Z), R1233zd(E), R1224yd(Z), efficiency, COP

1. INTRODUCTION

High temperature heat pumps (HTHP) with heat sink temperatures in the range of 100 to 160 °C will become increasingly available on the market in the coming years (Arpagaus et al., 2017, 2018b, 2018c). Potential applications for HTHP are found in various industrial processes such as drying, sterilization, steam generation, papermaking, food preparation, and heat recovery. Waste heat at a low temperature can be efficiently converted into usable process heat. The replacement of fuel driven steam boilers by heat pumps would be a significant contribution (Nilsson et al., 2017). In addition, multi-temperature heat pumps using multiple heat sources and heat sinks with different temperature levels are potential systems to further increase system efficiency (Arpagaus et al., 2016).

There is a high level of research activity in the field of HTHP technology development at the international level. The main research objectives are the extension of heat source and sink temperatures to higher values, the improvement of heat pump efficiency, the testing of new environmentally friendly refrigerants, and in particular the scale-up from laboratory to industrial scale. With the stricter F-Gas regulation, only refrigerants with a global waring potential (GWP) of less than 150 may be used in new commercial heat pumps starting from 2022. The greenhouse effective hydrofluorocarbon (HFC) refrigerants R245fa and R365mfc (GWP of 858 and 804) are therefore subject to a "phase-down" (i.e. reduction of production and consumption) in most industrialised countries. Replacement refrigerants are currently being developed and researched. Natural refrigerants such as water (R718) or hydrocarbons (e.g. R600 and R601) are promising environmentally friendly substitutes. However, special heat pump cycles with multi-stage

compression (e.g. vapour recompression) or sophisticated safety measures due to flammability are required, which can increase system costs.

In recent years, various hydrofluoroolefins (HFO) and hydrochlorofluoroolefins (HCFO) have been developed which exhibit very low GWP, are non-combustible and have great potential for use as refrigerants in HTHPs. Table 1 lists some suitable HFO and HCFO refrigerants including their thermodynamic, environmental and safety parameters. R1233zd(E) with a critical temperature of 166.5 °C and a critical pressure of 36.2 bar is available as Solstice®zd from Honeywell or Forane®HTS 1233zd from ARKEMA. Although R1233zd(E) contains chlorine, its ODP is extremely small (0.00034) and the atmospheric lifetime is only 40.4 days (Patten & Wuebbles, 2010). The advantages of R1336mmz(Z) are the higher critical temperature of 171.3°C at a feasible pressure of 29.0 bar. Its safety class is A1, and it has a GWP of 2, an ODP of 0, and an atmospheric life of only 22 days (Myhre et al., 2013). Chemours commercialized R1336mzz(Z) under the brand Opteon™MZ. Polyolester oil (POE) with high viscosity is recommended as lubricant, as it is fully miscible over wide ranges of temperatures and compositions (Kontomaris, 2014a, 2014b). R1224yd(Z) is another non-combustible (A1) HCFO refrigerant designed for use in heat pumps for waste heat recovery. AGC Chemicals (Asahi Glass) markets the refrigerant as Amolea®1224yd (AGC Chemicals, 2017). With an ODP of almost zero (0.00012, atmospheric lifetime of 21 days) and a GWP < 1, it has a low environmental impact. The physical properties are close to R245fa and R1233zd(E). Relatively little information is available on R1234ze(Z), which has a critical temperature of 150.1°C and a critical pressure of 35.3 bar (Kondou and Koyama, 2015). Its GWP is < 1 (Myhre et al., 2013) and its flammability is rated with A2L (Fukuda et al., 2014). R1234ze(Z) is assessed as a promising “drop-in” substitute for R114 in HTHP applications (Brown et al., 2009).

Table 1. Properties of HFO and HCFO refrigerants suitable for HTHP (bold: refrigerants tested in this study, HFC refrigerants R365mfc and R245fa for comparison)

Refrigerant	Brand (manufacturer)	T_{crit} (°C)	p_{crit} (bar)	ODP (-)	GWP_{100} (-)	Lifetime (days)	SG	NBP (°C)
R1336mzz(Z)	**Opteon™MZ (Chemours)**	**171.3**	**29.0**	**0**	**2**	**22**	**A1**	**33.4**
R1234ze(Z)	not yet available	150.1	35.3	0	<1	18	A2L	9.8
R1233zd(E)	**Solstice®zd (Honeywell)** Forane®HTS 1233zd (ARKEMA)	**166.5**	**36.2**	**0.00034**	**1**	**40.4**	**A1**	**18.0**
R1224yd(Z)	AMOLEA®1224yd (AGC Chemicals)	155.5	33.3	0.00012	<1	21	A1	14.0
R365mfc	Solkane®365mfc (Solvay)	186.9	32.7	0	804	8.7 years	A2	40.2
R245fa	Genetron®245fa (Honeywell)	154.0	36.5	0	858	7.7 years	B1	14.9

Table 2 shows an overview of experimental studies published in the literature on HTHPs with R1336mzz(Z) and R1233zd(E). The heating capacities range from about 1.8 to 12 kW for the laboratory prototypes (Arpagaus et al., 2018a; Fleckl et al., 2015; Fukuda et al., 2014; Helminger et al., 2016). The commercial HeatBooster S4 from Viking Heat Engines (2018) represents the industrial benchmark with heat sink outlet temperatures of up to 160 °C using R1336mzz(Z) and up to 200 kW heating capacity (Nilsson et al., 2017; Viking Heat Engines, 2018). Four piston compressors are connected in parallel to increase the capacity. Helminger et al. (2016) reported a highest heat sink outlet temperature of 156.3 °C (condensation at 160°C) in a single-stage laboratory HTHP with IHX with a coefficient of performance (COP) of 2.67 and a temperature lift of 47.4 K. In a previous study, Fleckl et al. (2015) reached 150°C with a basic cycle at a COP of 2.4 and a temperature lift of 70 K.

Table 2. Published experimental research studies testing HFO refrigerants in HTHP systems

Organisation partners	Refrigerant	Heat sink/ source T (°C)	Heating capacity (kW)	Com-pressor	Cycle	References
AIT, Chemours, Bitzer	R1336mzz(Z)	75-160/30-110	12	Piston	1-stage with IHX	(Helminger et al., 2016)
Viking Heating Engines AS	R1336mzz(Z)	80-160/35-110	75-200	Piston (4 parallel)	1-stage with IHX	(Nilsson et al., 2017)
NTB Buchs,	R1233zd(E)	70-150/40-80	3-10	Piston	1-stage with	(Arpagaus et

SCCER EIP					adjustable IHX	al., 2018a)

In our previous study, first experimental results of a single-stage laboratory HTHP system using R1233zd(E) (Solstice®zd from Honeywell) have been presented. At the reference point conditions (W60/W110) a COP of 2.43 was achieved (Arpagaus et al., 2018a). The system was capable of testing heat source temperatures of 40 to 80 °C and sink temperatures of 80 to 150 °C.
This paper continues these studies and examines the performance of R1336mzz(Z) (Opteon™MZ from Chemours) and R1233zd(E) (Solstice®zd from Honeywell) in the same laboratory HTHP plant after improved insulation of some components (e.g. oil separator, liquid receiver, and suction line accumulator) with Armaflex®HT insulation. The system design with the integration of an IHX into the cycle and the experimental test results of a parameter study are presented and compared with literature data. In particular, the COP is investigated as a function of the temperature lift between the heat source and the heat sink, the temperature glide on the heat sink side and the refrigerant charge.

2. EXPERIMENTAL DESIGN AND TEST PROCEDURE

Figure 1 illustrates the developed HTWP laboratory plant (A) with the schematic diagram (B) and the two pressurized water loops for the heat source and heat sink (C). The HTHP is single-stage and operates with a variable-speed semi-hermetic piston compressor (Bitzer, 2DES-3Y New Ecoline). An integrated temperature sensor prevents overheating of the motor with a switch-off temperature of approx. 110°C. The heat pump contains an IHX for increasing the suction gas temperature (T_1), which ensures dry compression and simultaneously subcools the refrigerant after condensation.
The superheat for controlling the expansion valve (EXV) is measured after the evaporator at state point 6 (before the IHX) and was set to 5 K for all experiments ($\Delta T_{SH} = T(p_5) - T_6$). The liquid subcooling after the condenser was calculated by $\Delta T_{SC} = T(p_3) - T_4$.
The refrigerant mass flow through the IHX is continuously adjustable from 0% to 100% via a 3-way valve (Siemens). A receiver serves as a refrigerant collector after condensation and ensures liquid refrigerant prior to the expansion valve. An oil separator is installed on the high pressure side, which returns the collected oil back to the compressor via a cooling pipe. The heat exchangers are compact plate heat exchangers with low pressure drops. The heat source inlet temperature ($T_{Source,in}$) can be varied between 40 and 80 °C and the heat sink outlet temperature ($T_{Sink,out}$) between 70 and 150 °C. The heat source circuit simulates potentially available waste heat from an industrial process and includes a controllable electrical heater (Backer ELC, 10 kW), a water pump with adjustable flow rate, and an expansion vessel with safety valve. The heat sink represents a potential HTHP application (e.g. steam generation or drying process) and includes a water cooler to dissipate the generated heat to the environment. The electrical heater controls the heat source inlet temperature ($T_{Source,in}$) and a control valve (BELIMO, 2-way zone valve with rotary actuator) at the inlet of the water cooler the heat sink inlet temperature ($T_{Sink,in}$) into the condenser.
The temperatures are measured with calibrated thermocouples (type K, class 1) with an accuracy of ± 0,1 K. Differential temperature measurement is used at the input and output of the heat pump (ΔT_{Sink}, ΔT_{Source}). A Coriolis flow meter (E+H, Promass F300) measures the water mass flow in the heat sink circuit with an accuracy of ± 0.05 %. A power transmitter (Infratek, ITL-101) measures the electrical power consumption of the compressor with an accuracy of ± 3 %. A CompactRIO® cRIO-9022 from National Instruments in combination with LabVIEW™2017myRio is used for data acquisition and control. All components are commercially available without modifications.

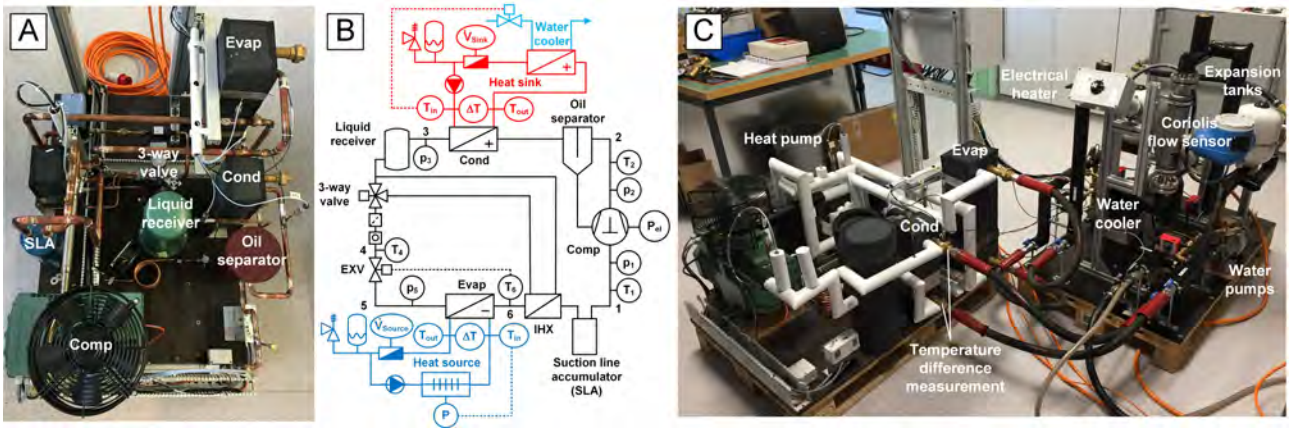

Figure 1: (A) Experimental setup, (B) schematic diagram, and (C) hydraulic loops (heat source and heat sink) of the developed laboratory scale HTHP plant

More details on the components and sensors are described in the paper of Arpagaus et al. (2018a). The filling quantities for the refrigerants R1233zd(E) and R1336mzz(Z) were 4.2 kg and 4.1 kg, respectively. To achieve sufficient lubrication at high operating temperatures, POE oil (Reniso Triton SE170) was selected with a kinematic viscosity of 173 mm^2/s at 40°C (17,6 mm^2/s at 100 °C).

After heating up the HTHP to the desired heat source and heat sink temperatures, the water flow rates in the two hydraulic circuits were adjusted by the pumps to receive constant temperature differences of 3.0 ± 0.1 K at a heat source (ΔT_{Source}) and 5.0 ± 0.1 K at the heat sink (ΔT_{Sink}). Mean values of at least 5 minutes under stationary conditions were used for the data analysis. The heating COP was determined from the measured heating capacity ($\dot{Q}_{Sink}$) and the electrical power consumption of the compressor (P_{el}) according to Eq. (1). The 2nd Law efficiency was determined by Eq. (2). The temperature dependence of the specific heat capacity of water was taken into account.

$$COP_H = \dot{Q}_{Sink}/P_{el} = \left(\dot{m}_{H_2O} \cdot c_{p,H_2O}(T) \cdot \Delta T_{Sink}\right)/P_{el} \quad \text{Eq. (1)}$$

$$_{2nd} = COP_H/COP_{Carnot} \text{ with } COP_{Carnot} = T_{Sink,out}/\left(T_{Sink,out} - T_{Source,in}\right) \quad \text{Eq. (2)}$$

3. EXPERIMENTAL RESULTS AND DISCUSSION

3.1. Results with R1233zd(E)

The most important measurement results of the parameter study with R1233zd(E) are illustrated in Figure 2 (A) to (F). Figure 2 (A) shows the experimentally measured COP_H of the laboratory plant as a function of the investigated heat sink outlet temperature ($T_{Sink,out}$) at different temperature lifts ($\Delta T_{Lift} = T_{Sink,out} - T_{Source,in}$) from 30 to 70 K. As expected, the COP increased with smaller temperature lift and higher heat sink outlet temperature according to the Carnot relationship (Eq. 2). At the reference point (Ref) W60/W110 (50 K temperature lift) a COP of 2.8 ± 0.2 was measured with the basic cycle. The better insulation of the heat pump compared to the earlier studies by Arpagaus et al. (2018a) led to an increase in efficiency of about 15%. In comparison to the basic cycle, the integration of the IHX into the circuit led to a further COP increase of approx. 15% to 3.1. Since the suction gas superheat is achieved in the IHX and not in the evaporator, the evaporation temperature in the IHX circuit is higher than in the basic cycle. This results in a higher refrigerant density at the compressor inlet and an increased efficiency. The maximum heat sink temperature tested was 150°C, whereby a COP of 2.1 was achieved with a heat source of 80°C (70 K lift). The slightly decreasing COP curve at 70 K lift is the result of the narrower two-phase region for condensation near the critical point and the increasing heat losses ($\dot{Q}_{Loss}$) of the system due to natural convection and radiation of the uninsulated parts (i.e. compressor).

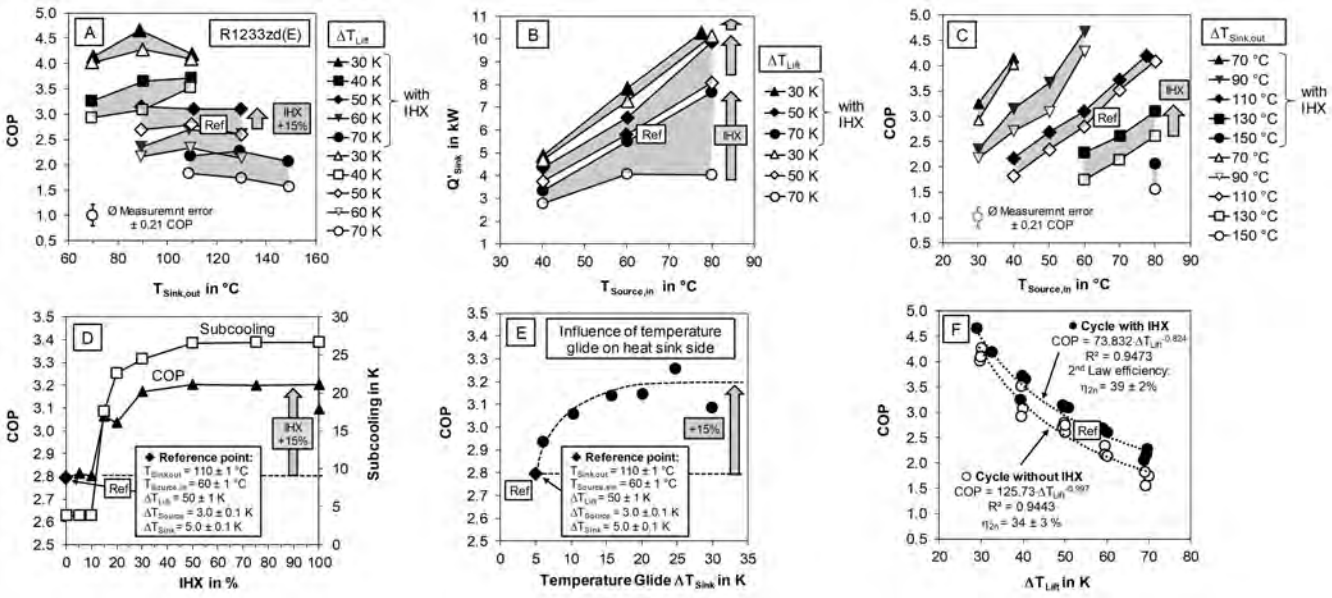

Figure 2: Experimental results with the refrigerant R1233zd(E). (A) Operating map, (B) heating capacity, (C) COP vs. heat source temperature with and without IHX, (D) influence of the IHX on the COP at the reference point (W60/W110), (E) efficiency increase with higher temperature glide on the heat sink side, (F) curve fit of the COP measurement data vs. temperature lift

Heat losses of about 21 ± 7 % could be estimated from the energy balance of the heat pump ($\dot{Q}_{Loss} \approx \dot{Q}_{Source} + P_{el} - \dot{Q}_{Sink}$) leading to a 2nd Law efficiency of about 39 ± 2 % (with IHX in the cycle) (see Figure 2, F). In other words, there is still potential for optimisation in insulation (especially at the compressor) and possibilities for increasing efficiency. For large-scale application, the relative heat losses will be significantly lower due to higher energy density of the heat pump.

Figure 2 (B) illustrates the heating capacity ($\dot{Q}_{Sink}$) as a function of the heat source inlet temperature ($T_{Source,in}$) at constant temperature lifts (ΔT_{Lift}). The heating capacity increased steadily with temperature according to Carnot's relationship (Eq. 2). At Ref conditions, the heating capacity was about 5.8 kW and increased to about 10 kW at W80/W110. At this operating point, the heat pump reached its experimental capacity limits.

Figure 2 (C) provides an overview of the entire operating map of the HTHP with and without IHX at the same experimental temperature conditions. The increase in efficiency with the use of the IHX is evident. For example, the COP at W80/W150 increased from 1.6 to 2.1 or at W60/W110 (Ref) from 2.8 to 3.1. For W80/W130, the suction (T_1) and discharge (T_2) temperatures were 112 °C and 161 °C, respectively, and thus close to the temperature limit of the compressor motor. Excessively high discharge gas temperatures are limited by the compressor switch-off temperature.

Figure 2 (D) shows the influence of the IHX on the COP from 0 to 100 % opening degree of the 3-way valve at the reference point (W60/W110). Compared to the basic heat pump cycle, the suction gas is additionally superheated in the IHX and the liquid refrigerant subcooled. When the IHX is integrated, both the suction gas (T_1) and discharge gas (T_2) temperatures as well as the COP increased due to the higher heating capacity. The COP levelled off with increasing flow through the IHX, indicating a sufficiently large IHX heat exchanger. The integration of the IHX provides additional flexibility in superheat control for future applications with alternative low GWP refrigerants that require high superheat (strongly overhanging two-phase region to the right in the log(p)-h diagram).

The graph in Figure 2 (E) shows the effect of a higher heat sink temperature glide (ΔT_{Sink}) on the COP varied from the Ref conditions as an example of a potential process heating application. With increasing temperature glide from 5 to 30 K (at constant $T_{Source,out}$) the heat transfer in the condenser improves, which led to a 12 % higher heating capacity and approx. 15 % higher COP.

Figure 2 (F) shows the determined COPs of the entire measurement data as a function of the respective temperature lift between heat source and sink. The COP values decrease with higher temperature lift and correspond to a curve with 39 ± 2 % and 34 ± 3 % 2nd Law efficiency (η_{2nd}) for the IHX cycle and the basic cycle, respectively.

3.2. Results with R1366mzz(Z)

The experimental results with R1336mzz(Z) are shown in Figure 3 (A) to (E). Figure 3 (A) presents the system performance as a function of the investigated heat sink outlet temperature ($T_{Sink,out}$) at different temperature lifts (ΔT_{Lift}) from 30 to 70 K. At the reference point (Ref) W60/W110, a COP of 2.4 was achieved with the basic cycle. The integration of the IHX into the circuit significantly increased efficiency across the entire operating map, e.g. up to +47% at W80/130 (50 K temperature lift). This is in line with Helminger et al. (2016) where an efficiency increase of 4 to 10 % and 19 to 47 % at about 20 K and 45 K temperature lift was observed with the integration of an IHX.

Figure 3 (B) shows the heating capacity ($\dot{Q}_{Sink}$) as a function of the heat source inlet temperature ($T_{Source,in}$) at constant temperature lifts (ΔT_{Lift}). The IHX significantly increases the heating capacity compared to the basic cycle, especially for high temperature lifts between heat source and heat sink. The heating capacity under Ref conditions was approx. 3.4 kW and increased to approx. 7.8 kW at W80/W110 with IHX cycle. Overall, the heating capacity of R1336mzz(Z) was about 46 to 76% lower than that of R1233zd(E). This is due to the lower volumetric heating capacity (VHC) of R1336mzz(Z). A larger compressor would be required to achieve similar heating capacities as R1233zd(E). This is in agreement with simulation studies by Arpagaus et al. (2018b), where at 60 °C/130 °C (evaporation/condensation temperatures) VHC values of 1'779 kJ/m^3 and 2'594 kJ/m^3 (+46%) were calculated for R1336mzz(Z) and R1233zd(E), respectively.

Figure 3 (C) shows the operating map without and with IHX in the cycle at the same experimental temperature conditions as in Figure 3 (A). The increase in efficiency with the use of the IHX is evident as in the operating map of R1233zd(E) (see Figure 2, C). For example, at operating point W80/W150 (70 K lift) a COP of 1.8 could be measured.
Figure 3 (D) shows the suction (T_1) and discharge (T_2) temperatures as a function of the heat sink outlet temperature. Overall, the suction temperature in the basic cycle (Δ) was well below the motor shut-off temperature of approx. 110°C (indicated by a grey line). With the IHX cycle, the suction temperature (○) exceeded the motor limit temperature at a heat sink outlet temperature of about 130°C and higher. However, short-term experiments over several minutes were still possible to run, especially at 150°C.
Figure 3 (E) illustrates the influence of refrigerant charge for R1336mzz(Z) on COP under reference conditions with the IHX cycle. With increasing refrigerant charge, the COP reached a plateau and the performance became almost independent of the charge. This result is of practical interest, as the experimental tests were carried out with a charge of 4.1 kg. The liquid receiver (5.6 L volume) ensured liquid refrigerants prior of the expansion valve. In addition, the sight glass in the liquid line between condenser and expansion valve was inspected to be clear (no presence of gas bubbles), as a rough check for sufficient refrigerant charge.
Figure 3 (F) shows the measured COP data of the basic and IHX cycle as a function of the temperature lift. Positive effects on the COP are a small temperature difference between heat source and heat sink. 2nd Law efficiencies of 34 ± 3 % and 29 ± 3 % were obtained, respectively. For comparison, Fleckl et al. (2015) reported values of about 35 to 50 % in a laboratory single-stage heat pump with R1336mzz(Z).

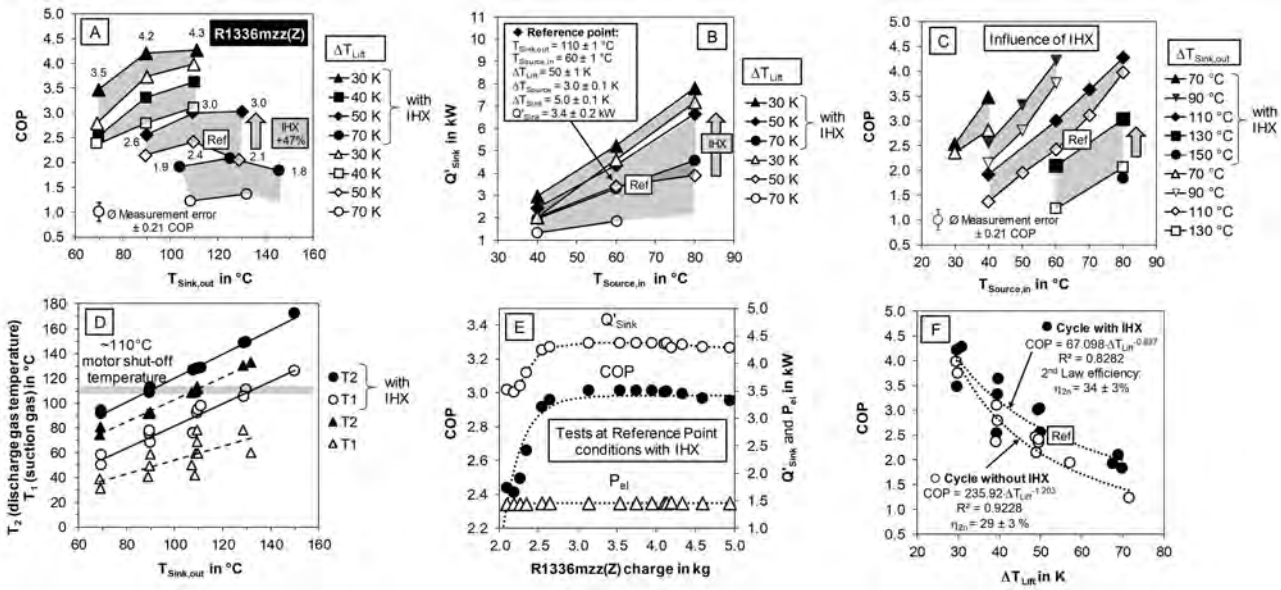

Figure 3: Performance figures with the refrigerant R1336mzz(Z). (A) Operating map, (B) heating capacity, (C) COP vs. heat source temperature with and without IHX, (D) discharge and suction gas temperatures, (E) influence of the refrigerant charge on the COP at the reference point (W60/W110), (F) curve fit of the COP measurement data vs. temperature lift

Figure 4 (A) compares the measured operating maps of the refrigerants R1233zd(E) and R1336mzz(Z) in the HTHP with the IHX cycle at the same temperature conditions (Figure 2 A and Figure 3 A). The comparison indicates that the heat pump was capable of achieving a slightly higher COP with R1233zd(E) than with R1336mzz(Z) at heat sink outlet temperatures of up to about 110°C.
This is attributed to the smaller heating capacity of R1336mzz(Z), which means that the relative heat losses are more significant. Thereafter the deviations are in the measurement uncertainty of the experiments. At higher temperatures, both refrigerants have comparable efficiency. R1336mzz(Z) achieves potentially higher condensing temperatures due to the higher critical temperature of 171.3°C (compared to 166.5 °C of R1233zd(E)). In this study, the maximal tested heat sink temperature was 150 °C.

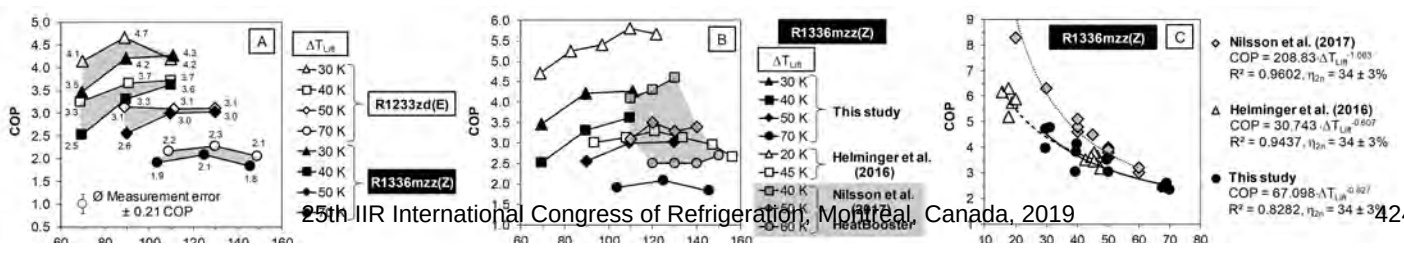

Figure 4: (A) Comparison of the operating maps of (A) R1233zd(E) vs. R1336mzz(Z). (B) and (C) Comparison of the R1336mzz(Z) operating map with literature data from Helminger et al. (2016) (laboratory scale setup) and Nilsson et al. (2017) (HeatBooster from Viking Heating Engines)

Figure 4 (B) and (C) compare the performance map of R1336mzz(Z) at different temperature lifts with literature data from Helminger et al. (2016) and Nilsson et al. (2017). Helminger et al. (2016) reported heat sink temperatures of up to 156.3°C and a COP of almost 2.7 with a temperature lift of about 45 K. The 2nd Law efficiency of the laboratory setup corresponded to 34 ± 3%, thus similar to our study. The commercial HeatBooster technology achieves a higher efficiency with a 2nd Law efficiency of 41 ± 3 %. Even at 60 K temperature lift, a COP of 2.5 is achieved. This increase in performance is partially attributable to a larger temperature glides tested on the heat sink side of 10 and 20 K, compared to 5 K in this study, which leads to an increase in efficiency. In addition, with larger heating power the relative heat losses are smaller.

4. CONCLUSIONS

The operating maps of a laboratory HTHP system with the refrigerants R1233zd(E) and R1336mzz(Z) could be experimentally examined at 40 to 80 °C heat source and 70 to 150 °C heat sink temperatures. The integration of an IHX in the heat pump cycle significantly increased the efficiency and the heating capacity over the entire operating map. At W60/W110 (reference point) a heating COP of 2.8 was achieved for R1233zd(E) with the basic cycle and 3.1 with IHX integration (+15%). For R1336mzz(Z) a COP of 2.4 was reached with the basic and 3.0 with the IHX cycle (+24%). Up to a heat sink outlet temperature of about 110°C, R1233zd(E) delivered a slightly higher COP than R1336mzz(Z) due to higher heating capacity and smaller relative heat losses at the same temperature conditions. At the higher temperatures tested, the deviations between the measured COP with R1336mzz(Z) and R1233zd(E) were within the measurement uncertainty (± 0.21 COP). R1233zd(E) provided a heating capacity on 5.8 kW at the reference point and approx. 10 kW at W80/W110, which corresponded to the capacity limit of the laboratory plant. With R1336mzz(Z) a maximum heating capacity of 7.8 kW could be achieved. For R1336mzz(Z) a larger compressor would be required to achieve similar heating capacities as R1233zd(E). Moreover, R1336mzz(Z) achieves potentially higher condensing temperatures due to its higher critical temperature of 171.3 °C. An increase in the temperature glide on the heat sink side from 5 to 30 K raised the COP by another +15%, which is promising in process with low return temperatures. A larger temperature glide improved the heat transfer in the condenser. As expected, the COP curves decreased with increasing temperature lift and corresponded to an average Carnot efficiency (2nd Law efficiency) of 39% for R1233zd(E) and 34% for R1336mzz(Z) with the IHX cycle. These values are comparable with the results of Helminger et al. (2016) in another HTHP laboratory setup, but lower than with the commercial HeatBooster technology, which achieves an average efficiency of approx. 41% at 20 kW (Nilsson et al., 2017). The experimental results are promising as the developed HTHP system allows testing alternative HFO and HCFO refrigerants like R1224yd(Z), R1336mzz(E) and R1233zd(E) with stabilizing additives in the future. Temperature-resistant compressors and lubricating oils are decisive components for the further development and commercialization of HTHPs.

ACKNOWLEDGEMENTS

This research project is part of the Swiss Competence Center for Energy Research SCCER EIP of the Swiss Innovation Agency Innosuisse.

NOMENCLATURE

COP	coefficient of performance (–)	Lift	temperature lift from heat source to sink
c_p	specific heat capacity (kJ/kg-K)	ODP	ozone depletion potenial
ΔT	temperature difference (K)	p, T	pressure (bar), temperature (°C)
η_{2nd}	2nd Law efficiency ($\eta_{2nd} = COP_H/COP_{Carnot}$)	P_{el}	electrical power (kW)
GWP_{100}	global warming potential, 100 years	POE	polyolester oil
HCFO	hydrochlorofluoroolefin	$\dot{Q}$	heating capacity (kW)
HFC	hydrofluorocarbon	Ref	reference point conditions
HFO	hydrofluoroolefin	SC, SH	subcooling, superheating

HTHP	high temperature heat pump	SG	safety group classification
IHX	internal heat exchanger	Sink, Source	heat sink, heat source
in, out	inlet, outlet	VHC	Volumetric heating capacity (kJ/m^3)

REFERENCES

AGC Chemicals, 2017. AMOLEA® 1224yd, Technical Information, ASAHI Glass Co., Ltd.

Arpagaus, C., Bless, F., Schiffmann, J., Bertsch, S.S., 2016. Multi-temperature heat pumps: A literature review. Int. J. Refrig. 69, 437–465.

Arpagaus, C., Bless, F., Schiffmann, J., Bertsch, S.S., 2017. Review on High Temperature Heat Pumps – Market Overview and Research Status. In: International Workshop on High Temperature Heat Pumps, September 9, 2017, Copenhagen, Denmark. pp. 1–25.

Arpagaus, C., Bless, F., Uhlmann, M., Büchel, E., Frei, S., Schiffmann, J., Bertsch, S.S., 2018a. High temperature heat pump using HFO and HCFO refrigerants - System design , simulation, and first experimental results. In: 17th International Refrigeration and Air Conditioning Conference at Purdue, July 9-12, 2018. pp. 1–10.

Arpagaus, C., Bless, F., Uhlmann, M., Schiffmann, J., Bertsch, S.S., 2018b. High temperature heat pumps: Market overview, state of the art, research status, refrigerants, and application potentials (Lizenz-/Genehmigungsnummer: 4432121433391). Energy 152, 985–1010.

Arpagaus, C., Bless, F., Uhlmann, M., Schiffmann, J., Bertsch, S.S., 2018c. High temperature heat pumps: Market overview, state of the art, research status, refrigerants, and application potentials. In: 17th International Refrigeration and Air Conditioning Conference at Purdue, July 9-12, 2018. pp. 1–10.

Brown, J.S., Zilio, C., Cavallini, A., 2009. The fluorinated olefin R-1234ze(Z) as a high-temperature heat pumping refrigerant. Int. J. Refrig. 32, 1412–1422.

Fleckl, T., Hartl, M., Helminger, F., Kontomaris, K., Pfaffl, 2015. Performance testing of a lab-scale high temperature heat pump with HFO-1336mzz-Z as the working fluid. In: European Heat Pump Summit 2015, October 20-21, Nuremberg, Germany. pp. 1–25.

Fukuda, S., Kondou, C., Takata, N., Koyama, S., 2014. Low GWP refrigerants R1234ze(E) and R1234ze(Z) for high temperature heat pumps. Int. J. Refrig. 40, 161–173.

Helminger, F., Kontomaris, K., Pfaffl, J., Hartl, M., Fleckl, T., 2016. Measured Performance of a High Temperature Heat Pump with HFO-1336mzz-Z as the Working Fluid. In: ASHRAE 2016 Annual Conference, St. Louis, Missourii, 25-29 June 2016. pp. 1–8.

Kondou, C., Koyama, S., 2015. Thermodynamic assessment of high-temperature heat pumps using low-GWP HFO refrigerants for heat recovery. Int. J. Refrig. 53, 126–141.

Kontomaris, K., 2014a. Zero-ODP, Low-GWP, Nonflammable Working Fluids for High Temperature Heat Pumps. In: ASHRAE Annual Conference, Seattle, Washington, July 1, 2014. pp. 1–40.

Kontomaris, K., 2014b. HFO-1336mzz-Z: High Temperature Chemical Stability and Use as A Working Fluid in Organic Rankine Cycles, Paper 1525. Int. Refrig. Air Cond. Conf. Purdue, July 14-17, 2014.

Myhre, G., Shindell, D., Bréon, F.-M., Collins, W., Fuglestvedt, J., Huang, J., Koch, D., Lamarque, J.-F., Lee, D., Mendoza, B., Nakajima, T., Robock, A., Stephens, G., Takemura, T., Zhang, H., 2013. Anthropogenic and natural radiative forcing. In: Climate Change 2013: The Physical Science Basis. Contribution of Working Group I to the Fifth Assessment Report of the Intergovernmental Panel on Climate Change. Cambridge University Press, Cambridge, United Kingdom and New York, NY, USA, pp. 659–740.

Nilsson, M., Risla, H.N., Kontomaris, K., 2017. Measured performance of a novel high temperature heat pump with HFO-1336mzz-Z as the working fluid. In: 12th IEA Heat Pump Conference 2017, Rotterdam. pp. 1–10.

Patten, K.O., Wuebbles, D.J., 2010. Atmospheric lifetimes and Ozone Depletion Potentials of

trans-1-chloro-3,3,3-trifluoropropylene and trans-1,2-dichloroethylene in a three-dimensional model. Atmos. Chem. Phys. 10, 10867–10874.

Viking Heat Engines, 2018. HeatBooster HBS4: Industrial heat pump for clean energy production up to 160 °C.

Manuscript ID: 252
DOI: 10.18462/iir.icr.2019.0252

Novel high-efficient open sorption system using multilevel cascade reactors for space heating

Y.N. Zhang, R.Z. Wang*

Institute of Refrigeration and Cryogenics and Key Laboratory of Power Mechanical Engineering, Shanghai Jiao Tong University
Shanghai, 200240, China, zyn1126@sjtu.edu.cn

ABSTRACT

An innovative high-efficient 1.3 kW open sorption thermal storage (STS) prototype using multilevel cascade reactors is experimental investigated for space heating. It can solve the performance degradation problem of traditional STS systems, by cascading two reactors which was packed with activated alumina/LiCl composite and $SrBr_2 \cdot H_2O$, respectively. Its performance under different relative humidity (60%, 80% RH) and flow rate (30, 39 m^3/h) of inlet air at 20 ^oC were tested, whose results were compared with that of the same size reactor packed with only activated alumina/LiCl composite. The results prove that the cascaded reactor with different sorbents can increase the storage density from 191 kWh/m^3 to 252 kWh/m^3 under the condition of 20 ^oC and 80% RH. It also indicates that the output temperature (from 35 to 40 ^oC) and power (from 120 to 200 W) can be adjusted by changing the relative humidity and flow rate of the inlet air.
Keywords: Thermal energy storage, Modular cascade reactor, Water vapour, Mass and heat transfer.

1. INTRODUCTION

The energy demand for space heating is continuously growing with the increase of population and technology (Henning, 2007), which leads to the serious problems of adding the burden of power system. And it also brings environmental pollution since the heat for space heating is still mainly comes from the burning of fossil fuels. However, the existing space heating devices like air-driven heat pump and electric heater cannot solve the above two problems at the same time. Recently, sorption thermal energy storage (STES) is receiving burgeoning interests as a novel technology applied for space heating by utilizing off-peak electricity (Aydin et al., 2016 & Zhang et al., 2017). It can relieve the burden of the power system by store the off-peak electricity for the usage in peak load duration. Furthermore, it can reduce the depletion of fuel fuels. It has prominent advantages of alleviating the mismatch between energy supply and demand and not damaging the environment (Donkers et al., 2017).

Recently, the open sorption thermal storage (STES) devices are still in the lab-scale investigation stage. And its large-scale application requires higher energy storage density stable working performance. The ordinary reactor which bulked with one type sorbent encounters the performance degradation problem (Aydin et al., 2016 & Zhang et al., 2017 & Nonnen et al., 2016 & Xu et al., 2018), which is caused by the varied parameters of the flowing air along the reactor. In former study (Zhang et al., 2017), an open sorption reactor with two modules packed with activated alumina/LiCl composites was experimentally investigated. The results indicated that compared with the former reactor module, the second reactor module showed extremely worse performance with lower sorption capacity and smaller storage density. Besides, the two reactor modules need the same charging temperature, but smaller heat is provided to the second reactor module since the first reactor module receive the desorption heat in priority. In consequently, it takes longer to finish the charging process and reduce the system efficiency.

In this study, a 1.3 kWh compact open sorption prototype using multilevel cascade reactors is experimentally studied and analysed. Activated alumina/LiCl composites with regeneration temperature of 110 ^oC and strontium bromide monohydrate ($SrBr_2 \cdot H_2O$) with regeneration temperature of 80 ^oC are packed inside the first reactor module and the second reactor module,

respectively. Experimental results show that the combination of multilevel sorbents can contribute to better performance compared with open sorption reactor packed only with Activated alumina/LiCl composites.

2. SORBENTS SELECTION

Sorbents are the most significant issues to enhance the energy storage density, heat and mass transfer and system efficiency of the open sorption system. Considering the practical requirement, the selected sorbent should possesses the following properties: high volumetric energy storage density, large water uptake amount, strong mechanical strength, high thermal conductivity, good heat transfer and good mass transfer. Besides these basic requirements, two different types of sorbents with multilevel charging temperature are needed. The sorbents packed inside the first reactor module should have higher regeneration temperature than that of the sorbents packed inside the second reactor module. The sorbents packed inside the second reactor is preferred to have stronger moisture adsorption ability to ensure quick water uptake under the condition of high temperature and low relative humidity.

Composite sorbents have promising advantages of high storage density and good heat and mass transfer. Generally, the commercial porous materials used for developing composite sorbents are silica gel, zeolite and natural minerals. All of them cannot satisfy the requirement of high thermal conductivity, high volumetric storage density and strong mechanical strength, as shown in Table 1. Novel activated alumina/LiCl composite which surpasses the above composite sorbent have been developed and measured in our previous study (Zhang et al., 2018). In this study, activated alumina/LiCl composite with salt content of 14.7% is used for the first reactor module. Its regeneration is about 110 ^{o}C. So the sorbents for the second reactor module should have regeneration lower than 110 ^{o}C and stronger water adsorption ability than activated alumina/LiCl composite. Hydrophilic salts $SrBr_2 \cdot H_2O$ is chosen for its regeneration temperature of 80 ^{o}C and stronger moisture capture ability.

Table 1. Comparison of characteristic properties of common commercial porous matrix with low charging temperature (80~120 ^{o}C) (cited from (Zhang et al., 2018))

Porous matrix	Bulk density (kg/m^3)	Thermal conductivity (kg/m^3)	Pore volume (cm^3/g)	Mechanical strength
Silica gel	415	0.174	0.4~0.9	Easy to crash into powder
Activated alumina	908	0.279	0.39	Excellent
Expanded vermiculite	128	0.064	4.8 (macropore)	Easy to distortion at pressure

3. WORKING PRICIPLE AND DEVICE

3.1. Working principle

The open sorption system works based on the interaction forces between the sorbents and moisture. The system consists of four main components: a humidifier, a fan, an electrical heater and a modular reactor. The sorbents are packed inside the reactor. Its whole working cycle comprises a charging process and a discharging process, as presented in Fig. 1:

(1) In charging mode (off-peak electricity duration in night), cold room air is blown into the prototype by the fan and then heated to the charging temperature at the function of the electrical heater. The obtained hot air enters the reactor, where the packed sorbents are regenerated. Meanwhile, the adsorbed water vapour is released and flows into the flowing air, thus wet hot air is received, which is further mixed with cold room air to obtain warm wet air for comfortable space heating at the reactor exit. In this process, the off-peak electricity is stored in the form of chemical potential of the dry sorbents inside the reactor.

(2) In discharging mode (peak electricity duration in day-time), the indoor air is humidified by the humidifier and then flows into the reactor, where its moisture content is adsorbed by the sorbents. Related with the water adsorption process, a large amount of sorption heat is released to heat the flowing air. As a result, warm air with temperature of 40~45 ^{o}C is release to the room for

comfortable space heating. In this process, the stored off-peak electricity is released for space heating without additional electricity consumption used to heat the room air.
In all, during both the charging process and discharging process, warm air is able to be supplied for comfortable space heating. That is to say, the open sorption system can sustainably meet the space heating demands of the users during a whole day.

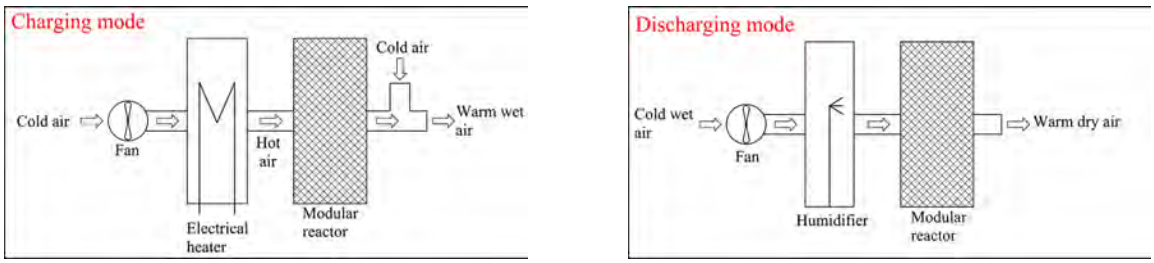

Figure 1: Charging-discharging cyclic working modes of open sorption system.

3.2. Device Design

The photo and schematic of the 1.3 kWh prototype is shown in Figure 2. It has compact vertical structure, and a humidifier, a fan, an electrical heater and a modular reactor is arranged from bottom to the top. The modular reactor is the core component, which comprises three cuboid-shaped reactor modules with size of 300 mm*300 mm*35 mm. The fan is used to drive the room air flow into the reactor, which can change the flowing velocity of the inlet air by its connected frequency transformer. The humidifier is used to increase the moisture content of the inlet air during discharging mode, and the supplied moisture content can be changed according to the required relative humidity of the inlet air. The electrical heater is utilized to heat the room air to regeneration temperature powered by heat sources. And its heating power can be adjusted by the connected potential transformers and intelligent temperature control meter.
The temperature and relative humidity of the inlet air and outlet air of each reactor module are measured by three high-temperature thermos-hygrometers (Rotronic HC2-IC102) with accuracy of ±0.1 ^{o}C and ±0.8% RH, respectively. The sorbent temperature at the middle layer of each reactor module is measured three Pt100 temperature sensors with accuracy of 0.15 ^{o}C settled in its medial section. The air speed is measured at the system outlet tube with a diameter of 100 mm, using a hot-wire anemometer (Kanomax 6533) with a resolution of ±0.015 m/s.
The experimental procedure is as follows: the prototype works in charging mode firstly. Room air is introduced to the electrical heater by the fan, where the room air will be heated to regeneration temperature. Then the hot air with regeneration temperature flows into the reactor, and the adsorbed water of the sorbents is released. Thus the electricity is stored in the obtained dry sorbent. It is assumed that the charging process is finished when the temperature difference between the inlet air and outlet air doesn't change. After the sorbents inside the reactor cool down to the room temperature, the discharging process is started. Room air is humidified by the humidifier, and then flows into the reactor at the driving force imposed by the fan. In the reactor, the contented moisture of the flowing air is adsorbed by the sorbents, and the flowing air is thus heated by the related released heat. The discharging process is ended when the outlet air decreases to room temperature.

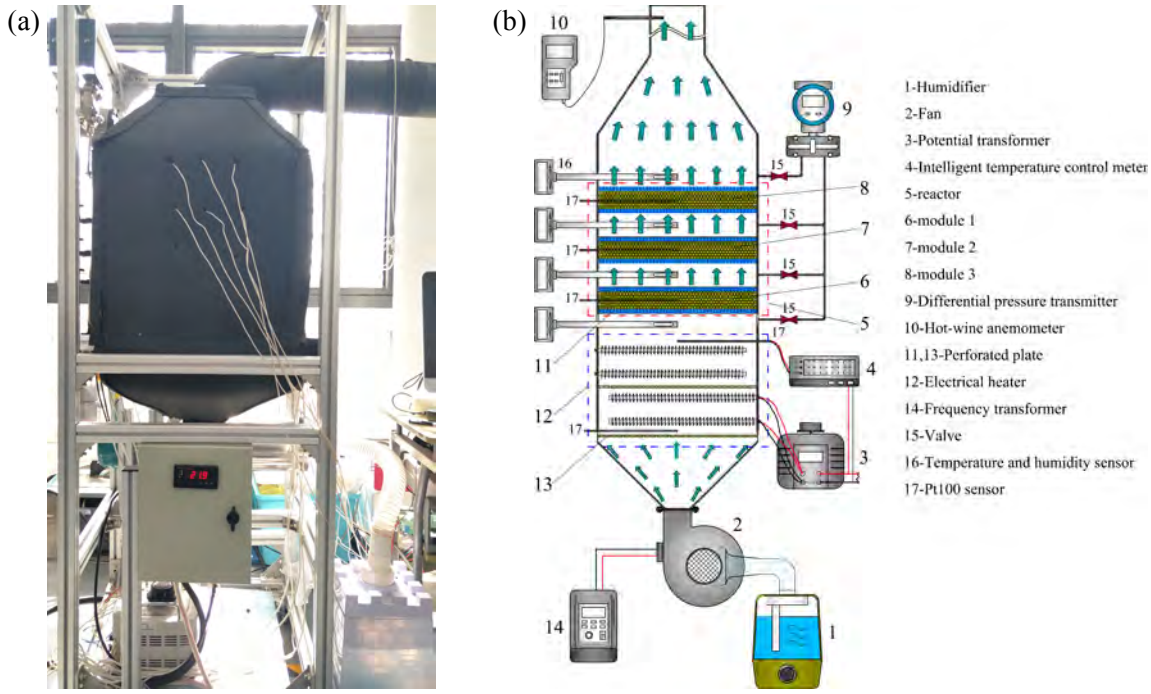

Figure 2: (a) Photo of the prototype; (b) Schematic of the open sorption thermal storage prototype.

3.3. Analysis method

Parameters reflecting the prototype performance including temperature lift of the inlet air (ΔT), water uptake capacity (x_{total}), sorption heat (Q_{sor}), desorption heat (Q_{des}) and volumetric energy storage density (Q_v) are calculated based on the measured air temperature, sorbent temperature, flow rate and relative humidity of the inlet and outlet air. The calculation equations are as follows:

$$\Delta T = T_o - T_i \quad \text{Eq. (1)}$$

$$x_{total} = \int_0^{t_{sor}} q_m (d_i - d_o) dt \quad \text{Eq. (2)}$$

$$Q_{sor} = \int_0^{t_{sor}} q_m C_p (T_o - T_i) dt \quad \text{Eq. (3)}$$

$$Q_{des} = \int_0^{t_{des}} q_m C_p (T_i - T_o) dt \quad \text{Eq. (4)}$$

$$Q_v = Q_{sor} / V_{reactor} \quad \text{Eq. (5)}$$

Where T_i and T_o is the temperature of inlet air and outlet air, respectively. d_i and d_o is the moisture content of the inlet air and outlet air, respectively. q_m is the flow rate of the flowing air. C_p is the specific heat capacity of the flowing air. $V_{reactor}$ is the volume of the reactor.

4. RESULTS AND DISCUSSIONS

4.1. Comparisons with traditional open sorption reactor

Experimental results demonstrate that the open sorption reactor packed with two types of sorbents show obvious better performance compared with that of the reactor with the same size packed with only one type of sorbent, as shown in Figure 3. Under the working condition of 20 ^{o}C, 70% RH and 30 m^3/h, the device packed with activated alumina/LiCl composites can reach volumetric storage density of 146.1 kWh/m^3. Although the volumetric energy storage density of its first module is 201 kWh/m^3, the volumetric storage density obtained by its second module is only 90.5 kWh/m^3. When the activated alumina/LiCl composites inside the second reactor module, the volumetric storage density of the second reactor module can be as high as 276.2 kWh/m^3, thus the total energy storage density of the whole device can reach to as high as 221.3 kWh/m^3.

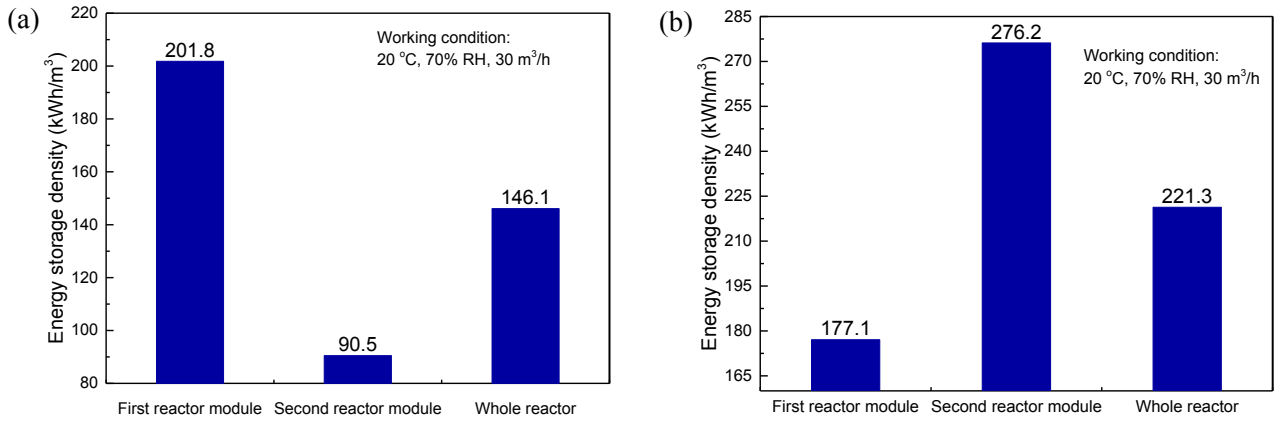

Figure 3: Comparison of the volumetric energy storage density of open sorption reactor using: (a) one type of sorbents (activated alumina/LiCl composites); (b) two types of sorbents (activated alumina/LiCl composites and SrBr2·H2O).

4.2. Performance under different working conditions

The practical application of the open sorption system needs to adjust the performance according to varied demands of the users. Experiment results indicate that the output temperature and space heating time can be easily adjusted by changing the relative humidity and flow rate of the inlet air. The experimental performances of the 1.3 kWh open sorption prototype under conditions of different relative humidity and flow rates are shown in Figure 4a &b, respectively. As presented in Figure 4a, the output temperature increases from 35.1 to 38.1 °C when the relative humidity increases form 60% RH to 80% RH. It is noted that the lasting time of the space heating process does not change with the increased relative humidity. As shown in Figure 4b, the output temperature does not change with the varied flow rate. And the lasting time of the space heating process decreases with the increased flow rate. Correspondingly, the output power increases with the increased flow rates of the inlet air.

In conclusion, the open sorption system can easily satisfy the varied demands for space heating. The output temperature, output power and operation time for space heating in buildings can be adjusted by changing the relative humidity and flow rate of the inlet air.

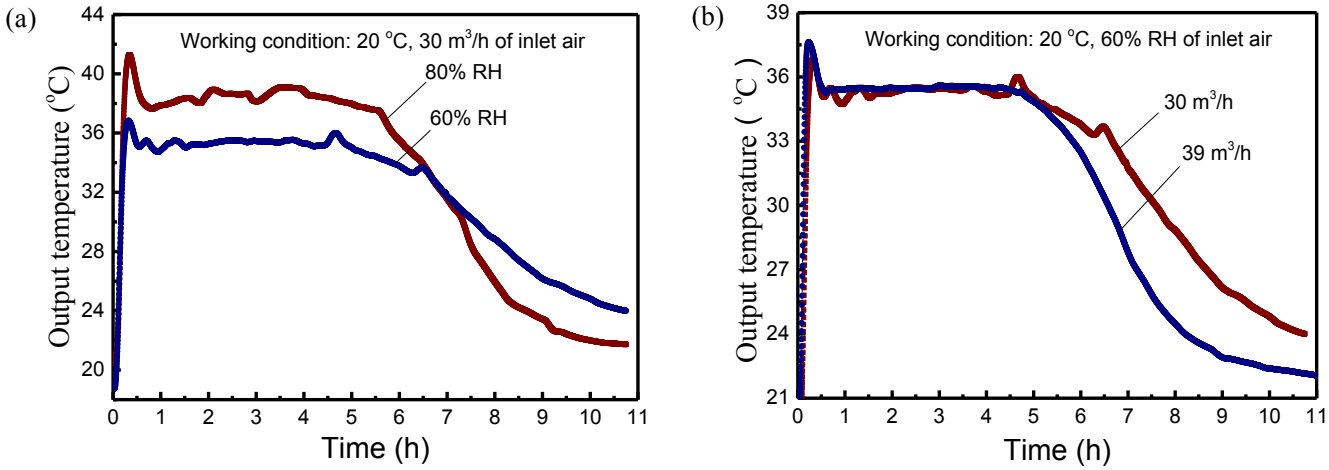

Figure 4: Performance under working conditions of: (a) different relative humidity; (b) different flow rate.

5. RESULTS AND DISCUSSIONS

This study proposes a novel open sorption system using multilevel cascade reactors for space heating. Through using different types of sorbents inside different reactor modules, the degradation problem of the traditional using only one type of sorbent caused by the varied parameters of the following air is solved. The volumetric storage density the novel system is 1.5 times that of the traditional system. The volumetric energy storage density of the 1.3 kWh prototype can be as high

as 252 kWh/m^3 under the working condition of 20 ^{o}C and 80% RH. Besides, the novel can adjust to varied demands of the users by changing the relative humidity and flow rate of the inlet air. It indicates that the value of output temperature (from 35.1 to 38.1 ^{o}C) and power (from 120 to 200 W) can be adjusted by changing the relative humidity and flow rate of the inlet air.

ACKNOWLEDGEMENTS

This work was supported by the Foundation for Innovative Research Groups of the National Natural Science Foundation of China under the contract No.51521004.

NOMENCLATURE

ΔT	temperature lift of the inlet air pressure (^{o}C)	x_{total}	total water uptake capacity during discharging process (g)
Q_{sor}	released sorption heat during discharging process (kJ)	Q_{des}	input desorption heat during charging process (kJ)
Q_v	volumetric energy storage density (kWh/m3)	T_i	temperature of the inlet air (^{o}C)
T_o	temperature of the outlet air (^{o}C)	d_i	moisture content of the inlet air (g/kg dry air)
d_o	moisture content of the outlet air (g/kg dry air)	q_m	massive flow rate of the flowing air (kg/s)
C_p	specific heat capacity of the flowing air (kJ/(kg·K))	$V_{reactor}$	volume of the reactor (m^3)

REFERENCES

Henning, H.M., 2007. Solar assisted air conditioning of buildings - an overview. Appl. Therm. Eng. 27(10):1734-49.

Aydin, D., Casey, S.P., Chen, X., Riffat, S., 2016. Novel “open-sorption pipe” reactor for solar thermal energy storage. Energy Convers. Manage. 121:321-34.

Zhang, Y.N., Wang, R.Z., Li, T.X., 2017. Experimental investigation on an open sorption thermal storage system for space heating. Energy 141:2421-33.

Donkers, P.A.J., Pel, L., Adan, O.C.G., 2017. Dehydration/hydration of granular beds for thermal storage applications: A combined NMR and temperature study. Int. J. Heat Mass Transfer 105:826-30.

Nonnen, T., Beckert, S., Gleichmann, K., Brandt, A., Unger, B., Kerskes, H., et al. 2016. A Thermochemical Long‐Term Heat Storage System Based on a Salt/Zeolite Composite. Chem. Eng. Technol. 39(12):2427-34.

Xu, C., Yu, Z., Xie, Y., Ren, Y., Ye, F., Ju, X., 2018. Zeolite/MgSO4-Study of the hydration behavior of zeolite-MgSO4 composites for long-term heat storage. Appl. Therm. Eng. 129:250-9.

Zhang, Y.N., Wang, R.Z., Li, T.X., 2018. Thermochemical characterizations of high-stable activated alumina/LiCl composites with multistage sorption process for thermal storage. Energy 156:240-9.

Manuscript ID: 259
DOI: 10.18462/iir.icr.2019.0259

High temperature heat pumps – Theoretical study on low GWP HFO and HCFO refrigerants

Cordin ARPAGAUS[(a)], Manuel PRINZING[(a)], Ralph KUSTER[(a)], Frédéric BLESS[(a)], Michael UHLMANN[(a)], Jürg SCHIFFMANN[(b)], Stefan S. BERTSCH[(a)]

[(a)] NTB University of Applied Sciences of Technology Buchs, Institute for Energy Systems, Werdenbergstrasse 4, 9471 Buchs, Switzerland, cordin.arpagaus@ntb.ch
[(b)] Ecole Polytechnique Fédérale de Lausanne, Laboratory for Applied Mechanical Design, Rue de la Maladière 71b, 2002 Neuchâtel, Switzerland

ABSTRACT

High temperature heat pumps with heat sink temperatures of 100 to 160 °C have great application potential in the food, paper, and chemical industries for heat recovery and process heat generation in drying, sterilization, and evaporation processes. The present study compares the theoretical performance of the low GWP refrigerants R1336mzz(Z), R1224yd(Z), R1234ze(Z), and R1233zd(E) in common one- and two-stage heat pump cycles (internal heat exchanger, economizer, flash tank, cascade) at different temperature levels. The thermodynamic simulations reveal that, depending on the refrigerant and cycle, a trade-off between system complexity (e.g. control, number of components), efficiency, and volumetric heating capacity (VHC) has to be found. Optimal COPs are reached depending on the refrigerant and its heat outlet temperature. R1336mzz(Z) is suggested as the closest drop-in replacement for R365mfc, while R1224yd(Z), R1234ze(Z), and R1233zd(E) are closer to R245fa in terms of COP and VHC. A two-stage cascade with IHX and R1336mzz(Z) in both stages achieved the highest efficiency for high temperature lifts.
Keywords: COP, Cycle, Efficiency, HFO, HCFO, High temperature heat pump, Low GWP refrigerant

1. INTRODUCTION

Industrial high temperature heat pumps (HTHP) with heat sink temperatures in the range of 100 to 160 °C are expected to increasingly replace fuel-driven steam boilers for the generation of vapor, hot water and hot air (Arpagaus et al., 2018). The selection of the refrigerant is a key element in the design of HTHPs. The refrigerant must be safe to the environment, future-proof according to F-gas regulations, thermodynamically suitable, efficient, and commercially available. In addition, no or only low flammability (safety groups A1 or A2) are beneficial to reduce the complexity of the safety devices and thus the equipment costs of the heat pump. The critical temperature needs to be high enough to enable subcritical cycle operation, which is often required in industries.
Besides natural refrigerants, synthetic hydrofluoroolefins (HFOs) and hydrochlorofluoroolefins (HCFOs) are considered as part of the fourth generation of low GWP refrigerants to replace hydrofluorocarbons (HFCs) (Calm, 2008). Commercialized members of the HFO family are for instance R1234yf and R1234ze(E) and are possible substitutes for R134a in automotive air conditioners, refrigerators and freezers. The capacities and efficiencies are comparable. Recently, fluorinated butenes such as R1336mzz(Z) and chlorinated compounds like R1233zd(E) or R1224yd(Z) were introduced as attractive replacements for R245fa and R365mfc in HTHPs and Organic Rankine Cycle (ORC) applications. Although HCFOs are chlorinated, their ozone depleting potential (ODP) is negligibly small (~ 0.00034) due to their short lifetime in the atmosphere (AGC Chemicals, 2017; Patten and Wuebbles, 2010).
Table 1 compares the fundamental thermodynamic, environmental and technical characteristics of the mentioned refrigerants. Figure 1 illustrates their T-s and p-T diagrams, as well as the heating COP as a function of the condensation temperature for a basic heat pump cycle calculation at 50 K temperature lift between condensation and evaporation (5 K subcooling, 15 K superheat, 70% isentropic compressor efficiency). The simulated COPs rise to an optimum and decrease with the narrowing of the two-phase region (smaller condensation enthalpy) up to the critical temperature.

Table 1. Properties of selected HFO and HCFO refrigerants for HTHP applications (⁺for comparison, *40 to 90 °C temperature lift, **fluid properties not yet available in the software EES)

Refrigerant	T_{crit} (°C)	p_{crit} (bar)	$p_{Sat,40°C}$ (bar)	$p_{Sat,90°C}$ (bar)	p_{Ratio}* (-)	ODP (-)	GWP_{100} (-)	Lifetime (days)	SG	NBP (°C)	M (g/mol)
R1336mzz(Z)	171.3	29.0	1.3	5.6	4.3	0	2	22	A1	33.4	164.1
R1233zd(E)	165.6	35.7	2.2	8.3	3.9	0.00034	1	40.4	A1	18.0	130.5
R1224yd(Z)	155.5	33.4	2.5	9.3	3.8	0.00012	<1	21	A1	14.0	148.5
R1234ze(Z)	150.1	35.3	2.9	10.8	3.7	0	<1	10	A2L	9.8	114.0
R1336mzz(E)**	137.7	31.5	3.2	12.2	3.8	0	18	90	n.a.	7.5	164.1
R1234ze(E)	109.4	36.3	7.7	24.8	3.2	0	<1	16.4	A2L	-19.0	114.0
R1234yf	94.7	33.8	10.2	30.8	3.0	0	<1	11	A2L	-29.5	114.0
R134a⁺	**101.0**	**40.6**	**10.2**	**32.5**	**3.2**	**0**	**1300**	**13.4 years**	**A1**	**-26.3**	**102.0**
R365mfc⁺	**186.9**	**32.7**	**1.0**	**4.6**	**4.6**	**0**	**804**	**8.7 years**	**A2**	**40.2**	**148.1**
R245fa⁺	**154.0**	**36.5**	**2.5**	**10.1**	**4.0**	**0**	**858**	**7.7 years**	**B1**	**14.9**	**134.0**

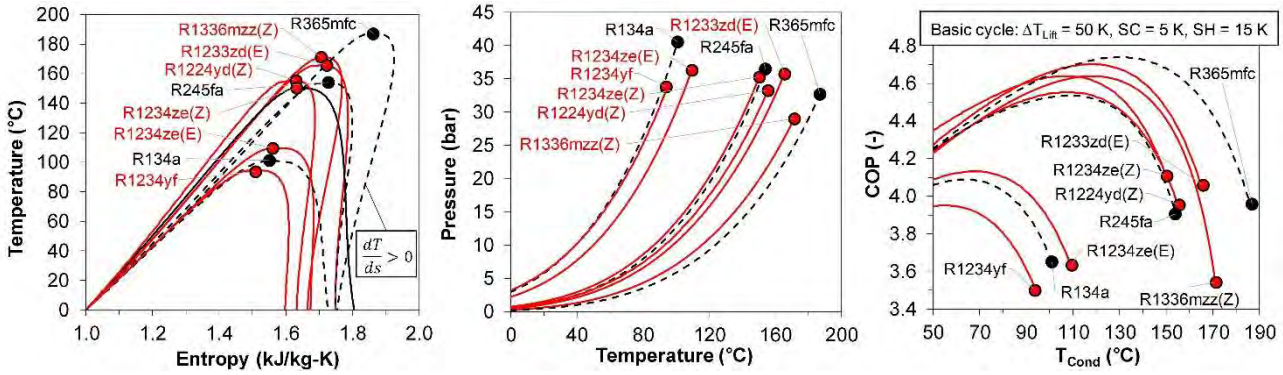

Figure 1: T-s, p-T diagrams, and simulated COP of selected HFO and HCFO refrigerants

R365mfc offers the highest COP over the entire temperature range, followed by R1233zd(E) and R1336mzz(Z). R1234ze(Z) and R1224yd(Z) are comparable to R245fa, while R1234yf and R1234ze(E) are similar to R134a. Among the HFO refrigerants, R1336mmz(Z) offers the highest critical temperature of 171.3 °C at a relatively low pressure of 29 bar. It is non-flammable (A1), has zero ODP, a GWP of about 2, and an atmospheric life of 22 days. According to Kontomaris (2014) it is stable up to 250 °C and therefore suitable for applications in waste heat recovery, ORC, and steam generation. Its isomer R1336mzz(E) has a GWP of about 18, a critical temperature of 137.7 °C and offers a higher volumetric heating capacity (VHC) (Juhasz, 2017). The VHC is an important performance parameter for the compressor design as it determines its size and cost. Little information is available on R1234ze(Z) (Fukuda et al., 2017, 2014; Kondou and Koyama, 2014), which is considered mildly flammable (A2L, burning velocity of ≤ 10 cm/s) but difficult to ignite.

A characteristic feature of some of the mentioned refrigerants is a positive slope (dT/ds > 0) of the saturated vapor curves (see Fig. 1, left). Sufficient superheating is thus required to ensure dry compression.

A cycle design with an internal heat exchanger (IHX) appears to be the most promising. Various studies demonstrated that a one-stage cycle with an IHX is an efficient configuration at temperature lifts up to about 40 K (Arpagaus et al., 2018; Bamigbetan et al., 2018; Frate et al., 2019; Helminger et al., 2016; Juhasz, 2017; Kontomaris, 2014; Mateu-Royo et al., 2018; Nilsson et al., 2017). As the temperature lift rises, a two-stage cycle becomes a more efficient system configuration. As shown in Table 2, several studies investigated the theoretical efficiency of HFO and HCFO refrigerants in different heat pump configurations. Efficiency optimizations are achieved in particular by the introduction of IHXs, two-stage cycles, and multi-stage extraction cycles.

The simulations of Mateu-Royo et al. (2018) in two-stage cycles and heat sink temperatures of up to 150 °C showed the highest COP using R601 (n-pentane), followed by R1336mzz(Z) and R1233zd(E). Mota-Babiloni et al., (2018) presented a theoretical study of a two-stage cascade using R1233zd(E), R1336mzz(Z), R1224yd(Z) and pentane in the high-stage (HS) and R1234yf, R1234ze(E), R600 (butane), R600a (isobutene) and R290 (propane) in the low-stage (LS). The highest efficiency was reached with the refrigerant pair pentane/butane (HS/LS). For HFO

refrigerants the combination R1336mzz(Z)/R1234ze(E) (HS/LS) achieved the highest COP, whereas R1224yd(Z)/R1234yf showed the lowest efficiency among the investigated refrigerants.
Cao et al. (2014) conducted thermodynamic and economic analyses of various two-stage cycles with refrigerant R152a and showed that a two-stage heat pump with flash tank provided highest COPs and lowest payback times. Hu et al. (2017) analysed two-stage and three-stage compression systems with R1234ze(Z) for waste heat recovery in industrial processes up to 120 °C. Compared to a one-stage cycle, the COP improvements were between about 9% and 15%. Kondou and Koyama (2014) explored different multi-stage and cascade cycles for upgrading waste heat from 80 to 160 °C and compared the efficiencies of R365mfc, R1234ze(E), and R1234ze(Z). A three-stage extraction cycle with R1234ze(Z) achieved the highest efficiency thanks to reduced exergy losses in the expansion valve and the condenser. A two-stage cascade cycle with R365mfc/R1234ze(Z) also provided high COPs and practical benefits (i.e. compressor control, lubricant selection).

Table 2. Theoretical studies with HFO and HCFO refrigerants in different HTHP cycles

HFO and HCFO refrigerants										Basic cycle	1-stage with IHX	2-stage with IHX	2-stage with economizer and	2-stage with flash tank and	2-stage extraction	2-stage cascade extraction	2-stage cascade with IHX	Triple tandem with IHX	3-stage with flash tanks	3-stage extraction	Reference
R1336mzz(Z)	R1233zd(E)	R1224yd(Z)	R1234ze(Z)	R1234ze(E)	R1336mzz(E)	R1234yf	R365mfc	R245fa													
	X		X	X			X	X		X					X					X	(Fukuda et al., 2017, 2014)
	X		X	X			X	X							X	X		X		X	(Kondou and Koyama, 2015)
X				X	X	X		X		X											(Juhasz, 2017; Kontomaris, 2014)
X											X										(Helminger et al., 2016)
X	X	X		X		X											X				(Mota-Babiloni et al., 2018)
			X							X			X						X		(Hu et al., 2017)
X	X	X	X				X			X											(Frate et al., 2019)
X	X							X			X	X									(Mateu-Royo et al., 2018)
X	X		X	X			X	X		X											(Bamigbetan et al., 2018)
X	X	X	X	X			X	X			X										(Arpagaus et al., 2018)
X	**X**	**X**	**X**	**X**		**X**	**X**	**X**			**X**		**X**	**X**			**X**				**This study**

As Table 2 shows, a comprehensive comparison of HFO and HCFO refrigerants with low GWP in different heat pump cycles is still a research gap. As a follow-up study to the review paper by Arpagaus et al. (2018), this study examines the suitability of the working fluids R1336mzz(Z), R1233zd(E), R1224yd(Z), R1234ze(Z), R1234ze(E) and R1234yf for HTHP application and presents simulations in the following heat pump cycles:

- One-stage cycle with IHX
- Two-stage cycle with economizer and IHX
- Two-stage cycle with flash tank and IHX
- Two-stage cascade with two IHX

The goal of this study is the evaluation of the thermodynamic efficiency (COP), volumetric heating capacity (VHC), pressure ratio, and discharge temperature of the selected HFO and HCFO refrigerants in the different heat pump cycles (see Table 2). In the two-stage cascade cycle, 24 refrigerant pairs are compared with each other. Finally, the results are compared with today's HFC refrigerants R365mfc, R245fa, and R245fa/R134a for potential drop-in replacements.

2. SIMULATION MODEL

Simplified thermodynamic cycle models have been developed in Engineering Equation Solver Software (EES, Version 10.268) (Klein, 2017). Figure 2 shows the schematics of the investigated cycles with the corresponding log(p)-h diagrams and the temperature profiles in the heat exchangers. The approach temperatures were considered constant for all operating conditions and are summarized in Table 3. The cycles were simulated in steady state conditions for several temperatures and refrigerant combinations using the following basic assumptions:

- No parasitic heat losses and pressure drops
- Isenthalpic expansion
- Constant compressor isentropic efficiency of $\eta_{is} = 0.7$
- Intermediate pressure in the two-stage economizer and flash tank cycle calculated as the geometric mean (square root) of the evaporation and condensation pressures

The operating point W60/W110 (50 K temperature lift) was considered as reference point (Ref) with constant temperature glides in the heat source and sink of 10 K. A parameter study was performed by varying the heat sink outlet temperature from 70 to 160 °C and the heat source inlet temperature from 40 to 90 °C (i.e. potential waste heat from an industrial process).
Finally, the COP was calculated as the ratio from the heating capacity and the total compressor work (i.e. in the IHX cycle: $COP = (h_2-h_3) / (h_2-h_1)$). The VHC was calculated in the IHX cycle as the product of the enthalpy difference supplied to the heat sink and the suction vapor density ($VHC = (h_2-h_3)\cdot\rho_1$)). It allows an estimation of the compressor size.

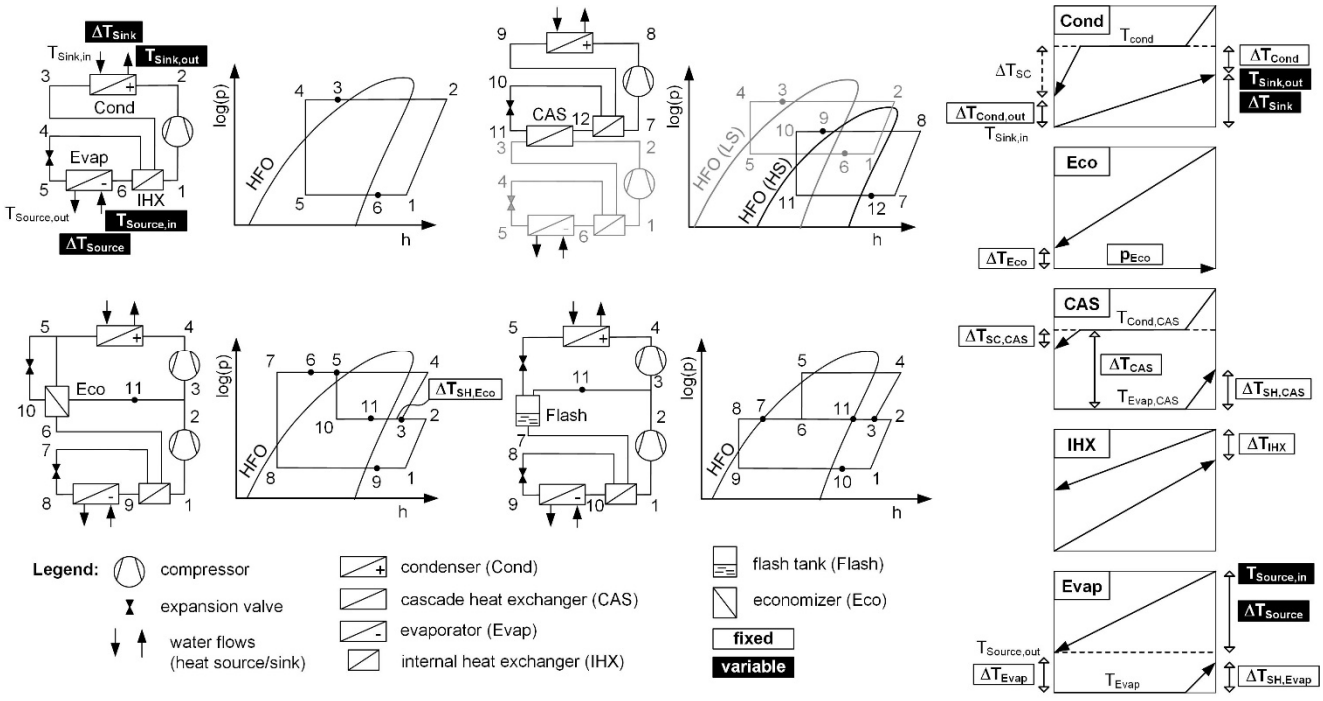

Figure 2: Investigated heat pump cycles with log(p)-h diagrams and approach temperatures in the heat exchangers (Cond, Eco, CAS, IHX, Evap)

Table 3. Fixed parameters, reference conditions and variation range of the variable parameters (*12 K superheat for R1336mzz(Z) and R365mfc to assure dry compression)

Fixed parameters				Variable parameters	Reference	Range
ΔT_{Cond}	2 K	ΔT_{Eco}	2 K	$T_{Sink,out}$	110 °C	70 to 160 °C
$\Delta T_{Cond,out}$	5 K	$\Delta T_{SH,Eco}$	5 (12*) K	$T_{Source,in}$	60 °C	40 to 90 °C
$\Delta T_{SC,CAS}$	1 K	ΔT_{IHX}	3 K	ΔT_{Lift} ($T_{Sink,out}$ - $T_{Source,in}$)	50 K	30 to 70 K
ΔT_{CAS}	3 K	ΔT_{Evap}	3 K	ΔT_{Sink}	10 K	5 to 30 K
$\Delta T_{SH,CAS}$	3 K	$\Delta T_{SH,Evap}$	5 K	ΔT_{Source}	10 K	5 to 30 K

3. SIMULATION RESULTS AND DISCUSSION

Table 4 compares the cycle performances of the investigated HFO and HCFO refrigerants at reference conditions in the IHX, economizer, and flash tank cycles. The values in brackets indicate the relative comparison to R245fa. The data show that the COP and the pressure ratio of R1336mzz(Z) are the highest among the investigated HFO and HCFO refrigerants, and the lowest for R1234ze(Z). However, the variation of the COPs from 3.72 to 3.96 stays within a few percent. Compared to R245fa, the COPs are also very similar. The calculated pressure ratios of 4.8 to 5.7 are considered manageable for common compressors. The VHC of R1336mzz(Z) and R365mfc are significantly lower than for the other substances due to the lower suction vapor densities (ρ_1), which in practice, will result in larger compressors to achieve comparable heating capacity. Compared to a basic cycle, the IHX provides additional superheating of the suction gas, which in turn increases the discharge gas temperature of the compressor and the potential heating capacity of the heat pump application. On the other side, too high temperatures can lead to overheating of the compressor motor and thermal decomposition of the lubricant oil. As a conservative hypothesis the compressor oil temperature should not exceed 180 °C (Frate et al., 2019).

Table 4. Comparison of the main performance parameters for the selected refrigerants in the IHX cycle, two-stage economizer cycle and two-stage flash tank cycle at reference conditions.

Parameter	R1336mzz(Z)	R1233zd(E)	R1224yd(Z)	R1234ze(Z)	R365mfc	R245fa
One-stage cycle with IHX (% relative to R245fa)						
COP_H (-)	3.96 (+4%)	3.86 (+1%)	3.82 (0%)	3.72 (-2%)	3.98 (+5%)	3.81
VHC (kJ/m^3)	1'600 (-43%)	2'412 (-15%)	2'639 (-7%)	3'093 (+9%)	1'329 (-53%)	2'830
ρ_1 (kg/m^3)	8.8 (-37%)	11.8 (-17%)	15.3 (+8%)	13.9 (-1%)	6.3 (-55%)	14.1
p_{Ratio} (-)	5.7 (+9%)	5.0 (-5%)	4.9 (-6%)	4.8 (-8%)	6.0 (+15%)	5.2
$T_{Discharge}$ (°C)	154 (-6%)	170 (+4%)	164 (0%)	189 (+15%)	154 (-6%)	164
Two-stage cycle with economizer and IHX (*temperature difference compared to IHX cycle)						
COP_H (-)	3.95	3.90	3.84	3.85	3.99	3.82
$p_{Ratio,HS}$, $p_{Ratio,LS}$ (-)	2.4	2.2	2.2	2.2	2.5	2.3
$T_{Discharge,HS}$ (°C)	116 (-38 K)*	118 (-52 K)	116 (-49 K)	125 (-63 K)	116 (-38 K)	116 (-48 K)
$T_{Discharge,LS}$ (°C)	100	107	105	115	100	105
Two-stage cycle with flash tank and IHX (*temperature difference compared to IHX cycle)						
COP_H (-)	4.00	3.98	3.93	3.90	4.03	3.91
$p_{Ratio,HS}$, $p_{Ratio,LS}$ (-)	2.4	2.2	2.2	2.2	2.5	2.3
$T_{Discharge,HS}$ (°C)	120 (-34 K)*	134 (-36 K)	129 (-36 K)	148 (-41 K)	120 (-34 K)	103 (-35 K)
$T_{Discharge,LS}$ (°C)	98	105	103	113	98	103

Figure 3 illustrates the results of the parameter study in the one-stage IHX cycle for the HFO and HCFO refrigerants over the entire operating range. The graphs provide a more qualitative comparison of the examined refrigerants. In general, the COP increases with heat sink temperature, heat source temperature, and smaller temperature lift. The VHC increases with increasing heat sink temperature and smaller temperature lift. A higher VHC is advantageous for positive displacement compressors, as it requires a smaller swept volume at a given capacity, and thus smaller size and investment costs. Common values are between 3'000 and 6'000 kJ/m^3 (Arpagaus et al., 2018). Overall, the analyses indicate that R1336mzz(Z) is the most suitable replacement fluid for R365mfc, whose COP and VHC are comparable (similar COP and 20% higher VHC). R1233zd(E), R1223yd(Z), and R1234ze(Z) are closest to R245fa in terms of COP and VHC. When selecting a refrigerant for a HTHP application, it is necessary to make a compromise between efficiency and capacity. As soon as the VHC becomes a decision parameter, R1233zd(E) becomes favorable. An efficiency loss of about 3% compared to R1336mzz(Z) is compensated with approximately 50% higher VHC. This is consistent with the calculations of Frate et al. (2019) in a basic cycle.

High compressor discharge temperatures ($T_{Discharge}$) can be observed especially for R1234ze(Z). To mitigate the relatively high discharge temperatures in the one-stage cycle with IHX, a two-stage cycle design with economizer functions is a valuable option. As shown in the Table 4, the two-stage cycles significantly reduce the discharge temperatures in the upper compressor stage (i.e. 34 to 41 K and 38 to 63 K reduction for the flash tank and closed economizer cycle). In the economizer, a certain amount of two-phase refrigerant is fed into the suction line of the high-stage compressor, where it is mixed with the discharge gas of the low-pressure compressor. This enables precise control of a

specified superheat value at the inlet of the high-stage compressor (e.g. 5 K superheat, or 12 K for R1336mzz(Z) and R365mfc, which exhibit a saturation curve dT/ds > 0). The flash tank system achieves slightly higher efficiency (1 to 3%) and about 2 K additional reduction in discharge temperature (see Table 4). Here, saturated vapor is pulled from the top of the flash tank and is fed to the suction line of the high-stage compressor. The superheat is controlled by mixing the saturated vapor with the discharge gas of the first-stage compressor.

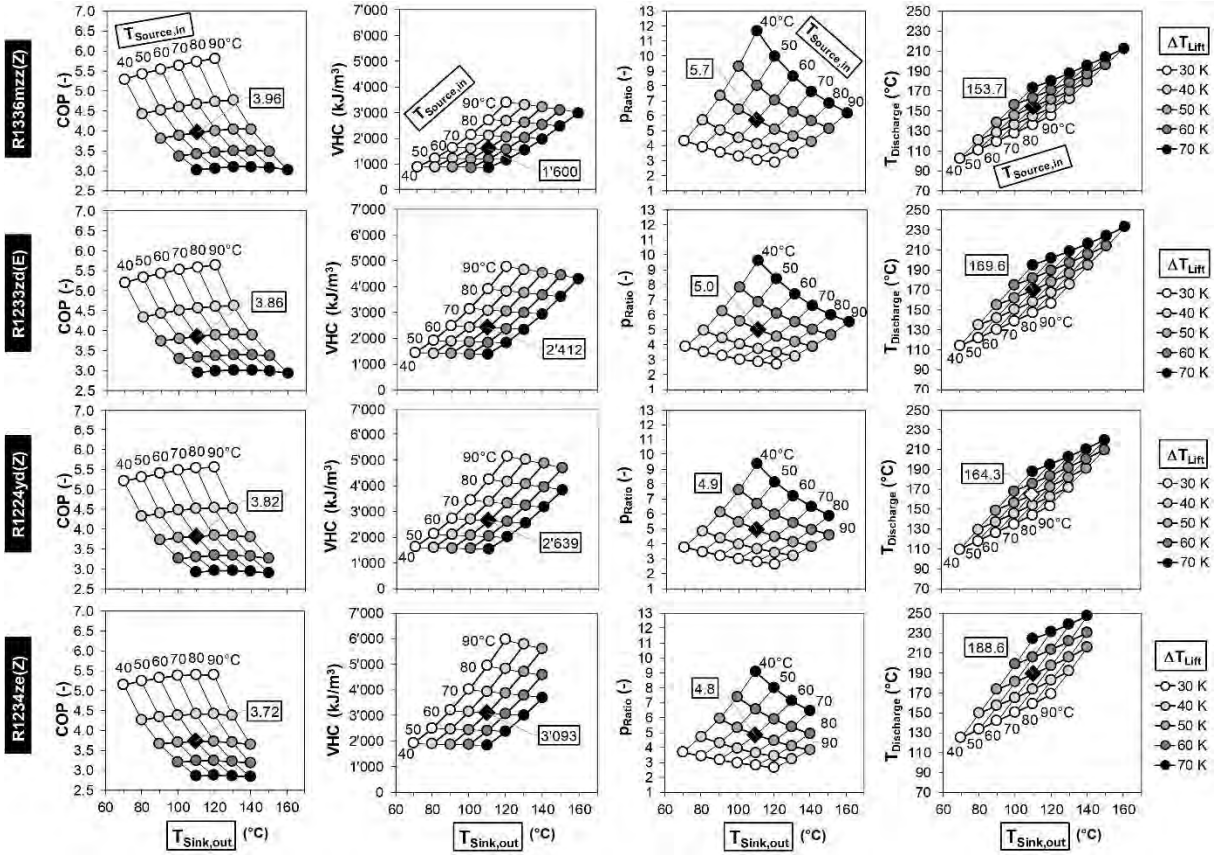

Figure 3: Operating maps of the one-stage cycle with IHX for different HFO and HCFO refrigerants. (A) COP, (B) VHC, (C) pressure ratio, (D) discharge temperature.

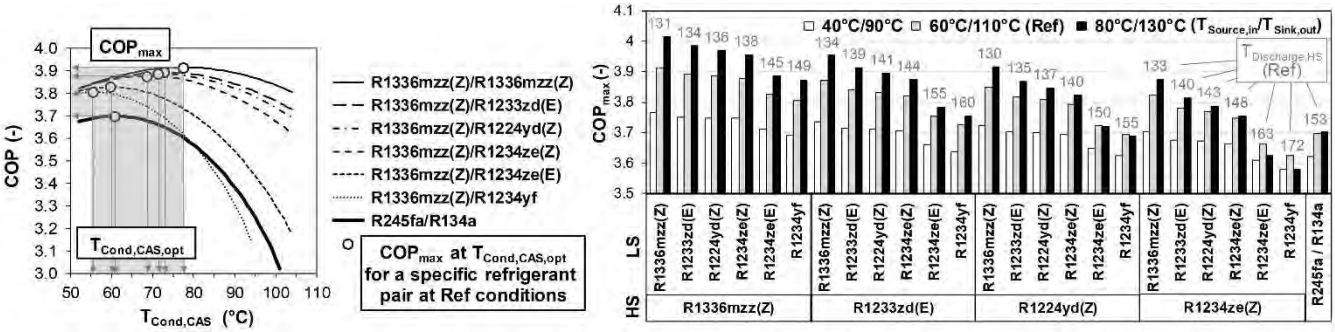

Figure 4: Maximum COP in the two-stage cascade cycle with IHX for different refrigerant pairs

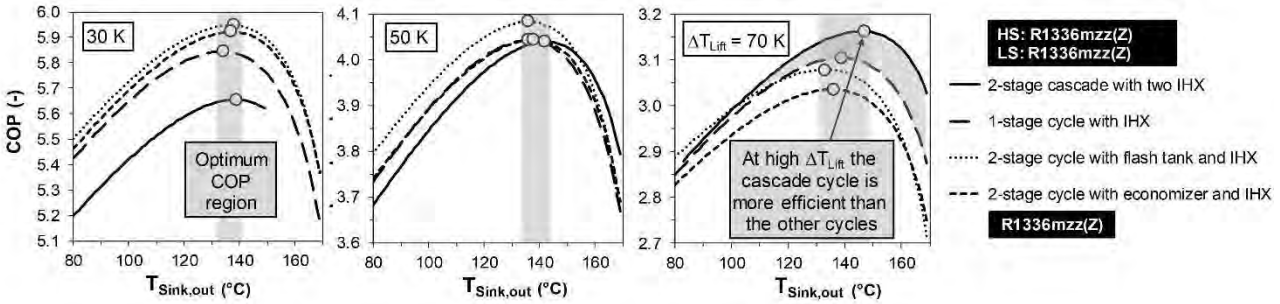

Figure 5: COP of the investigated cycles using R1336mzz(Z) at different temperature lifts

The two-stage cascade cycle enables testing different refrigerant combinations in the LS and HS cycles. Compared to a one-stage system, the pressure ratio per stage is lower and the efficiency higher, so that a higher COP can be achieved (Figure 5). In addition, there are no oil management issues between the two stages, which may compensate for higher installation and maintenance costs. A disadvantage is the temperature gap in the intermediate CAS heat exchanger (ΔT_{CAS} = 3 K) reducing efficiency. Depending on the operating conditions and refrigerant combination, an optimum intermediate temperature needs to be found to achieve maximum COP. The approach used in this study utilizes the Min/Max optimization method (Golden Section) of EES to find a COP maximum depending on the condensation temperature of the LS cycle ($T_{Cond,CAS}$).

Figure 4 (left) shows some COP curves for different refrigerant pairs as a function of $T_{Cond,CAS}$ at reference point condition. The optimal values are in the range of about 55 to 78 °C. Figure 4 (right) compares the optimal COPs of 24 pairs of HFO and HCFO refrigerants. R1336mzz(Z), R1233zd(E), R1224yd(Z), and R1234ze(Z) were selected for the HS, R1336mzz(Z), R1233zd(E), R1224yd(Z), R1234ze(Z), R1234yf, and R1234ze(E) for the LS. The presented results are calculated at a constant temperature lift of 50 K. The highest COP was achieved using R1336mzz(Z) in both stages (COP of 3.91 at Ref conditions 60 °C/110 °C, grey bars), followed by R1336mzz(Z)/R1233zd(E), R1336mzz(Z)/R1224yd(Z), and R1336mzz(Z)/R1234ze(Z) with a similar COP of 3.9. R1336mzz(Z)/R1234ze(E) presented a slightly higher performance than R1336mzz(Z)/R1234yf which is in agreement with simulations by Mota-Babiloni et al. (2018). Compared to a HTHP cascade with HFC refrigerants R245fa/R134a, the combination of R1336mzz(Z)/R1336mzz(Z) resulted in a 6% higher COP. The discharge temperatures were between 130 and 172 °C and thus lower than in the one-stage cycle with IHX, but higher than in the two-stage economizer and flash tank cycle.

Figure 5 shows the COP for the different cycles with refrigerant R1336mzz(Z) as a function of the heat sink outlet temperature for 30, 50, and 70 K temperature lift. As can be seen, the two-stage flash tank and economizer cycles are more efficient for small and medium lifts. With a higher lift, the two-stage cascade compensates for the losses of the cascade heat exchanger and clearly achieves the highest efficiency at 70 K lift.

4. CONCLUSIONS

The simulation results show that R1336mzz(Z) achieves the highest COP of all HFO and HCFO refrigerants in the temperature range from 120 to 160 °C, no matter which heat pump cycle is used. Each refrigerant achieves an optimal COP at a heat sink temperature of about 30 K below the critical temperature. A compromise must be found between COP and VHC when selecting refrigerants. R1336mzz is proposed as the next replacement for R365mfc, while R1233zd(E), R1224yd(Z), R1234ze(Z), R1234yf, and R1234ze(E) are closer to R245fa. The use of an IHX in the cycle is recommended to ensure dry compression, a two-stage cascade cycle for high temperature lifts of 70 K and higher. In further studies, the calculations can be extended to multi-stage extraction cycles and cycles with subcooler, ejectors, or multi temperature cycles to further increase efficiency.

ACKNOWLEDGEMENTS

This research project is part of the Swiss Competence Center for Energy Research SCCER EIP of the Swiss Innovation Agency Innosuisse.

NOMENCLATURE

CAS	cascade heat exchanger	*in, out*	inlet, outlet
Cond	condenser	*Lift*	temperature lift from heat source to sink
COP	coefficient of performance (-)	*ODP*	ozone depletion potential
ΔT	temperature difference (K)	*opt, max*	optimal, maximum
Eco	economizer	*p*	pressure (bar)
Evap	evaporator	*SC, SH*	subcooling, superheating
HFO	hydrofluorolefin	*SG*	safety group classification
HCFO	hydrochlorofluoroolefin	*Sink, Source*	heat sink, heat source
HS, LS	high-stage, low-stage	*T*	temperature (°C)
IHX	internal heat exchanger	*VHC*	volumetric heating capacity (kJ/m^3)

REFERENCES

AGC Chemicals, 2017. AMOLEA® 1224yd, Technical Information, ASAHI Glass Co., Ltd.

Arpagaus, C., Bless, F., Uhlmann, M., Schiffmann, J., Bertsch, S.S., 2018. High temperature heat pumps: Market overview, state of the art, research status, refrigerants, and application potentials. Energy 152, 985–1010.

Bamigbetan, O., Eikevik, T.M., Nekså, P., Bantle, M., Schlemminger, C., 2018. Theoretical analysis of suitable fluids for high temperature heat pumps up to 125 °C heat delivery. Int. J. Refrig. 92, 185–195.

Calm, J.M., 2008. The next generation of refrigerants - Historical review, considerations, and outlook. Int. J. Refrig. 31, 1123–1133.

Cao, X.-Q., Yang, W.-W., Zhou, F., He, Y.-L., 2014. Performance analysis of different high-temperature heat pump systems for low-grade waste heat recovery. Appl. Therm. Eng. 71, 291–300.

Frate, G.F., Ferrari, L., Desideri, U., 2019. Analysis of suitability ranges of high temperature heat pump working fluids. Appl. Therm. Eng. 150, 628–640.

Fukuda, S., Kondou, C., Takata, N., Koyama, S., 2014. Low GWP refrigerants R1234ze(E) and R1234ze(Z) for high temperature heat pumps. Int. J. Refrig. 40, 161–173.

Fukuda, S., Kondou, C., Takata, N., Koyama, S., 2017. Thermodynamic Analysis on High Temperature Heat Pump cycles using Low-GWP refrigerants for Heat recovery. In: 12th IEA Heat Pump Conference 2017, Rotterdam. pp. 1–7.

Helminger, F., Kontomaris, K., Pfaffl, J., Hartl, M., Fleckl, T., 2016. Measured Performance of a High Temperature Heat Pump with HFO-1336mzz-Z as the W orking F luid. In: ASHRAE 2016 Annual Conference, St. Louis, Missourii, 25-29 June 2016. pp. 1–8.

Hu, B., Wu, D., Wang, L.W., Wang, R.Z., 2017. Exergy analysis of R1234ze(Z) as high temperature heat pump working fluid with multi-stage compression. Front. Energy 1–10.

Juhasz, J.R., 2017. Novel Working Fluid HFO-1336mzz(E) for Use in Waste Heat Recovery Application. In: 12th IEA Heat Pump Conference, Rotterdam, May 14-17, 2017. pp. 1–10.

Klein, S.A., 2017. Engineering Equation Solver (Version V10.268): F-Chart Software.

Kondou, C., Koyama, S., 2014. Thermodynamic Assessment of High-Temperature Heat Pumps for Heat Recovery. In: 15th International Refrigeration and Air Conditioning Conference at Purdue, July 14-17, 2014. pp. 1–10.

Kondou, C., Koyama, S., 2015. Thermodynamic assessment of high-temperature heat pumps using low-GWP HFO refrigerants for heat recovery. Int. J. Refrig. 53, 126–141.

Kontomaris, K., 2014. Zero-ODP, Low-GWP, Nonflammable Working Fluids for High Temperature Heat Pumps. In: ASHRAE Annual Conference, Seattle, Washington, July 1, 2014. pp. 1–40.

Mateu-Royo, C., Navarro-Esbrí, J., Mota-Babiloni, A., Amat-Albuixech, M., Molés, F., 2018. Theoretical evaluation of different high-temperature heat pump configurations for low-grade waste heat recovery. Int. J. Refrig. 90, 229–237.

Mota-Babiloni, A., Mateu-Royo, C., Navarro-Esbrí, J., Molés, F., Amat-Albuixech, M., Barragán-Cervera, Á., 2018. Optimisation of high-temperature heat pump cascades with internal heat exchangers using refrigerants with low global warming potential. Energy 165, 1248–1258.

Nilsson, M., Risla, H.N., Kontomaris, K., 2017. Measured performance of a novel high temperature heat pump with HFO-1336mzz-Z as the working fluid. In: 12th IEA Heat Pump Conference 2017, Rotterdam. pp. 1–10.

Patten, K.O., Wuebbles, D.J., 2010. Atmospheric lifetimes and Ozone Depletion Potentials of trans-1-chloro-3,3,3-trifluoropropylene and trans-1,2-dichloroethylene in a three-dimensional model. Atmos. Chem. Phys. 10, 10867–10874.

Manuscript ID: 286
DOI: 10.18462/iir.icr.2019.0286

Overview on HCFO-R1233ZD(E) use for high temperature heat pump application

Nikhilkumar N. SHAH[(a)], Donal COTTER[(a)], Neil J. HEWITT[(a)]

[(a)] Centre for Sustainable Technologies, Ulster University
Newtownabbey, BT37 0QB, N. Ireland, U.K., n.shah@ulster.ac.uk

ABSTRACT

A high temperature heat pump has substantial potential for industrial waste heat recovery and upgrading of which there is a potential of 370 TWh in Europe. R1233zd(E) is a potential alternative to R245fa due to low GWP and ODP to achieve high temperatures in a range of 140°C and above. This paper presents review on R1233zd(E) and comparative thermodynamic simulation of high temperature heat pump based on selected compressor and between temperature range of 85°C to 135°C. In addition, details about high temperature heat pump test facilities and discussions on operational experiences and difficulties of high temperature heat pump test-rig development in terms of components and their limitations has been discussed. The initial experimental results from test rig are presented to demonstrate such operational challenges in terms oil cooling and expansion valve. Outcomes of this paper will provide indicators for future applications of high temperature heat pumps using alternative refrigerants.

Keywords: High temperature, heat pump, R1233zd, Industrial heat pump, HCFO

1. INTRODUCTION

Energy efficiency and waste heat recovery in industrial sector has a huge potential of 370 TWh (waste heat) per year in Europe alone (Panayiotou et al., 2017) which could help in a drive towards greenhouse gases emission (GHGs) reduction and to protect ozone layer. To support this drive, widely used refrigerant such as R134a, R410A, R407C and R245fa should be phased out due to high global warming potential (GWP) and ozone depletion potential (ODP) as a part of F-gas regulation in the EU and Montreal Protocol.

Table 1 Important parameter comparison between R1233zd(E) and R245fa (Yang et al., 2018)

Parameters	*R12233zd(E)*	*R245fa*
Chemical formula	$CF_3CH=CHCF_3$	$CF_3CH_3CF_2$
Pc (kPa)	3570	3650
Tc (°C)	165.6	154.01
Boiling point (°C)	17.97	14.81
Slope	Dry	Dry
ODP	0.00034	0
GWP100yr	7	1030
Atmosphere life time	7.7	0.07
Flammability	Non-flammable	Non-flammable
ASHRAE std 34 safety class	A1	B1

R1233zd(E) is one of the promising alternatives to replace R245fa which is widely used for waste heat recovery in Organic Rankine Cycle (ORC) or High Temperature Heat Pump (HTHP). R1233zd(E) belongs to HCFO family and has comparatively low GWP and ODP. Although R1233zd(E) contains one chlorine atom in the molecule, the contribution to stratospheric ozone depletion is expected to be negligible because of its very short-atmospheric lifetime. Table 1 shows

main parameter comparison between R1233zd(E) and R245fa. It is evident that R12233zd (E) can be used for HTHP up to 150°C and as a direct replacement of R245fa.
There are limited investigations related to R1233zd(E) use for HTHP in scientific literature and most investigations/literature are very recent. Fig. 1 illustrates the number of publications in the SCOPUs (75) and Web of Science (63) online database with search keyword “R1233zd” (keywords, title and abstracts). In addition, similar search was carried out in SCOPUS using same search key word in all field to find any literature that mentioned this word and found around 200 publications. Hence, scientific investigation/publication are at very early stage related to R1233zd(E).

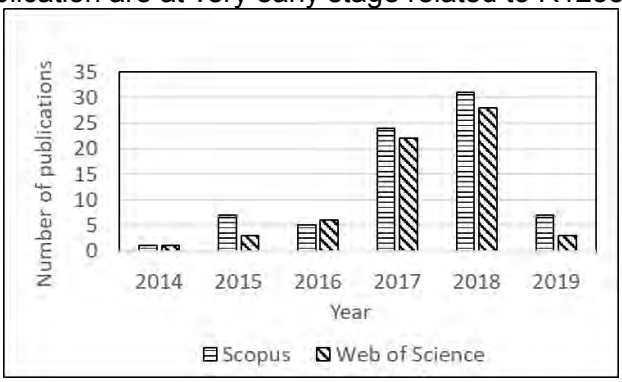

Figure 1: Publications related to R12333zd(E)

This paper aims to gather information related to R1233zd(E) use and application for HTHP through scientific literature. Thermodynamic simulation and comparative analysis for R245fa and R1233zd(E) is presented based on selected compressor and temperature range. In addition, initial experience of HTHP operation and preliminary results from HTHP test rig is presented for analysis purpose.

2. LITERATURES ON R1233ZD(E)

Detailed literature search on R1233zd(E) showed that most articles focused on properties of refrigerant, heat/flow transfer and ORC application. Most of ORC and/or HP investigations were based on mathematical model/simulation/theoretical analysis. Table 2 shows numbers of articles based on subject area and type of investigation. Overview and investigation of properties R1233zd(E) and other low GWP refrigerant has been widely covered by Bobbo et al. (2018). There were four investigations related to heat pump applications. For example, Ju et al. (2017) assessed heat pump water heater with mixture of R1233zd(E) with R290 and R1270 showed that R1233zd(E) can help to overcome the shortcoming of flexibility of HCs and modelling result showed 2 to 10 % higher COP compared to R22 or R134a and irreversibility of system components varies (except compressor) with mass fraction of R1233ZD(E) in a blend. Zuhlsdorf et al. (2018) showed that in a case of booster heat pump, mixture of R1233zd(E) and R1234yf would give higher COP compared to R1233zd (E) alone at design conditions. Although it was still lower compared to other refrigerant mixtures such as Iso-Butane and Pentane. Arpagaus et al. (2018) have presented extensive overview on HTHP showing waste heat recovery potential, state of the art, research status and refrigerant. A list of industrial HTHP was presented (28 kW to 20 MW) but none of industrial HP uses R1233zd(E) yet. Potential benefits of R1233zd(E) in terms reduced compressor size and trade-off between VHC and COP for HTHP application have been discussed by Frate et al. (2019) and Bamigbetan et al. (2018).
However, long term stability, thermal performance and interaction with other material (e.g. oil, copper, etc) is also important for R1233zd(E). In terms of suitable oil for R1233zd(E), some oil manufactures and researchers have shown suitability (e.g. miscibility) with POE (e.g. Fuchs, Climalife) whereas others suggest the use of mineral oil (e.g.Honeywell) (Suemitsu, et al., 2017) (Majurin, et al., 2017) or both (e.g. Arkema). In addition, Eyerer et al. (2018) showed an interesting analysis on the subtility of polymers (used on O-ring etc.) and their experimental and theoretical results showed that PTFE is the most compatible polymer which can be used with R1233zd(E) whereas special attention should be given if other polymers are used. Hence selection of suitable oil and other materials is crucial for R1233zd(E).

Table 2 Type of investigation and numbers of literatures

Are of investigation		Type of investigation	
Main subject	Sub-subject	Experimental	Theoretical/ modelling/simulation
Flow regime	pressure drop	4	2
Heat transfer	flow boiling, film condensation, nucleate boiling, condensation, supercritical pressure, high temperature	12	
Ejector	vapour-liquid, critical/sub-critical model, refrigeration system working fluid		3
ORC	scroll expander, various application, cycles configuration, with solar, with ejector, evaluation system, fluid comparison	5	26
Material	compatibility between refrigerant and polymer	1	
Properties	liquid viscosity, surface tension, solubility, diffusion, thermal conductivity, PvT, film thickness, heat capacity, speed of sound, liquid density	13	
Heat pump	booster, water heater (ref mixture), centrifugal chiller		3
Combined system	ORC+HP, absorption compression, trigeneration,		3

3. EXPERIMENTAL SETUP AND THERMODYNAMIC ANALYSIS

3.1 Test setup description

A HTHP test rig was developed in order to understand performance and behaviour of R1233zd(E) for high temperature application. The heat pump was designed at T_{con}=125°C and T_{evp}= 50°C with SH=20K (evaporator + liquid-suction heat exchanger) and SC=9K. At design condition, HP can provide 13.8 kW of condensing capacity. Commercially available components were used for the development of the test-rig. Figure 2 shows HTHP test-rig which was developed at Centre for Sustainable Technologies (Ulster University). Left side of test rig is accommodated with refrigeration side components such as compressor, condenser, evaporator, EEV etc whereas right side of test rig is for heat transfer fluid (water/oil) temperature management which helps to maintain constant temperature at outlet of condenser and inlet of evaporator as required. Table 3 shows main components used in development test-rig. Due to high temperature, thermal oil was used as a heat transfer fluid on secondary side of condenser whereas water was used on the evaporator secondary side. The compressor was driven by variable speed drive which can manage speeds between 750 to 1750 rpm for the compressor.

In order to monitor performance of the heat pump system variables such as temperature (refrigerant, oil and water)(inline and surface PT100), flow (refrigerant, oil and water), pressure (refrigerant), power (motor) were measured with sensor accuracy of ±0.2°C, ±1% (electromagnetic flow meter) / ±1.5% (pulse meter for oil), ±1% and ±1% respectively. All data were measured at interval of 30s using two data acquisition system and stored in a dedicated PC for data analysis purpose.

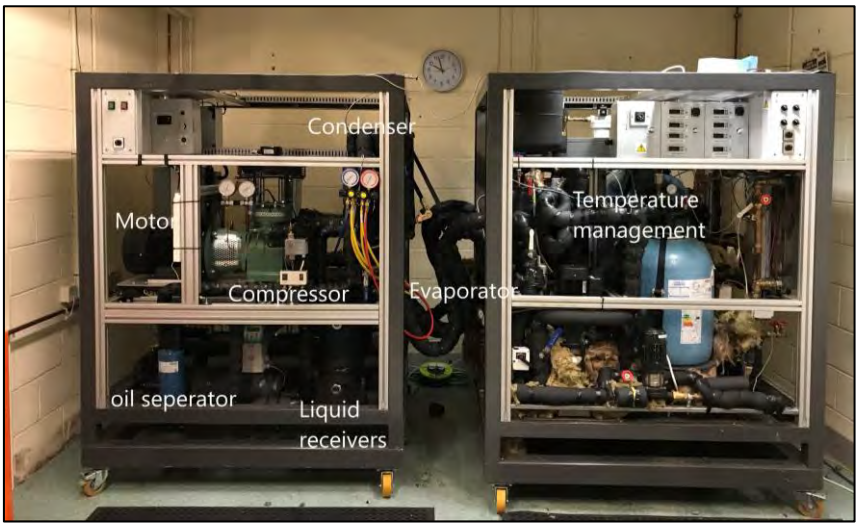

Figure 2 Test-rig development for HTHP

Table 3 List of components used for test-setup

Components	Details
Compressor	Bitzer: Open type Dis: 28 m3/h @50 Hz (1450 rpm)
Drive	EMI motor with Danfoss FC103 drive
Condenser	SWEP BPHE BT25Thx50
Evaporator	SWEP BPHE N80Hx26
Expansion valve	Danfoss EEV ETS12.5 with EKC316A
Oil separator	ESK OS22
Receiver	Bitzer FS102
Heat transfer fluid	Water and Therminol66

3.2 Test methodology and thermodynamic analysis

3.2.1 Test methodology

The system performance will be evaluated for condensing temperature between 85 to 135°C at an interval of 10K with fixed evaporation temperature of 50°C. First test will be carried out at design condition were flow rate on oil and water side will be set and it will be kept constant for other test condition in order to obtain change in heating/cooling capacity with respect to temperature difference. Similar test will be carried for evaporation temperature between 45 to 85°C at an interval of 10K while keeping the condensing temperature at 105,115,125 & 135°C. Compressor speed will be maintained at 50 Hz (1450 rpm). All variables such as temperature, pressure, flow rate and electric power will be measured on refrigeration/water/oil side.

3.2.2 Thermodynamic analysis

In order to estimate system performance and for comparative analysis, thermodynamic simulation is carried out for R1233zd(E) and R245fa at same temperature lift condition as mentioned above. The following assumptions were made for thermodynamic analysis:

- Heat dissipation with the ambient is ignored.
- Pressure drops in the evaporation and condensation processes are negligible.
- The compression process is adiabatic while the throttling process in expansion valve is isenthalpic.
- The heat transfer in the condenser or evaporator is of counter-flow
- The refrigerant at the outlet of the condenser is saturate liquid, and at the outlet of the evaporator is saturated vapor.
- LSH provides constant 15K superheat after evaporator

Properties of refrigerant were obtained using NIST-Refprop software and whereas compressor map of existing fluid (from manufacture) was used as reference to evaluate isentropic and volumetric

efficiency rather than fixed values. In order to evaluate system performance, a list of the assumptions/parameter and equations used are shown in Table 4 and Table 5. In equations, enthalpy difference at the inlet and outlet was used to calculate capacity for major components (such as evaporator, compressor, condenser, etc).

Table 4 Parameters used/assumed in thermodynamic simulation

Parameters	Values / Details
Refrigerant	R1233zd (E) and R245fa
Condensing temperature (C)	85,95,105,115,125,135
Evaporation temperature (C)	45,55,65,75
Superheat @evp and subcooling @cond (K)	5 and 5
Superheat using LSH (K)	15
Isentropic efficiency (%)	Based on compressor map: temperature lift
Volumetric efficiency (%)	Based on compressor map: temperature lift

Table 5 Equations used for thermodynamic simulation

Calculated parameters	Equation
For heat exchanger output (kW): Condenser, evaporator, LSH	$Q = m_{ref} * \Delta h$
Isentropic efficiency (compressor) (%):	$\eta_{is} = \frac{\Delta h_{is}}{\Delta h}$
Compressor power (kW):	$P = m_{ref}\,\Delta h = m_{ref} * \frac{\Delta h_{is}}{\eta_{is}}$
Refrigeration side COP:	$COP = \frac{Q_c}{P}$

4. RESULTS AND DISCUSSION

4.1 Result of thermodynamic analysis

The system performance was evaluated thermodynamically at various evaporation temperatures and condensing temperatures as describe earlier for R12333zd(E) and R245fa. Figure 3 shows comparative analysis of system performance for R245fa and R1233zd(E). Performance analysis is presented in terms of condensing capacity, compressor power and COP with varying condensing and evaporating temperature conditions.

It is evident that for similar temperature lift conditions, the heat output for R245fa is higher compared to R1233zd(E) but the compressor power consumption is also higher which ultimately results in a negligible reduction in COP compared to R1233zd(E) This is mainly due to density/pressure difference at those temperature condition which, results in a higher enthalpy difference for R245fa. The evidence suggests that R1233zd(E) gives a higher COP in the range of 1 to 9% but lower heat output in the range of 8 to 15%. This may result in an increase to the heat exchanger size and volumetric area for R1233zd(E) if used as a direct replacement for R245fa.

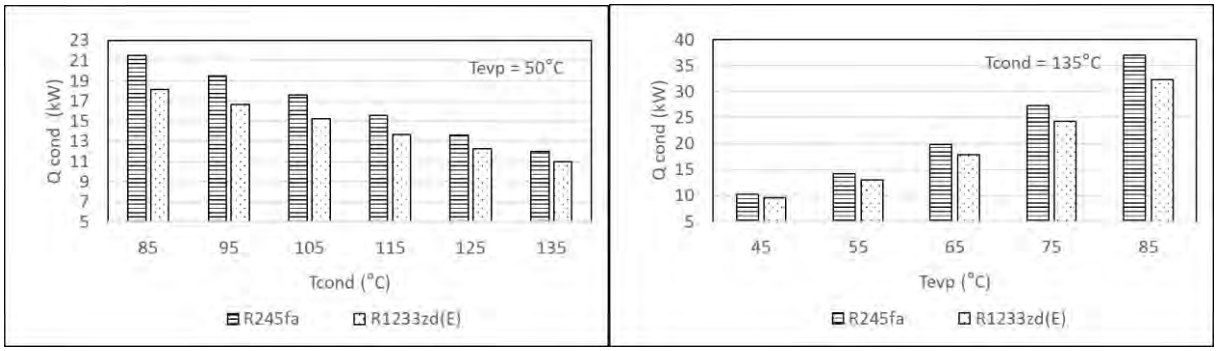

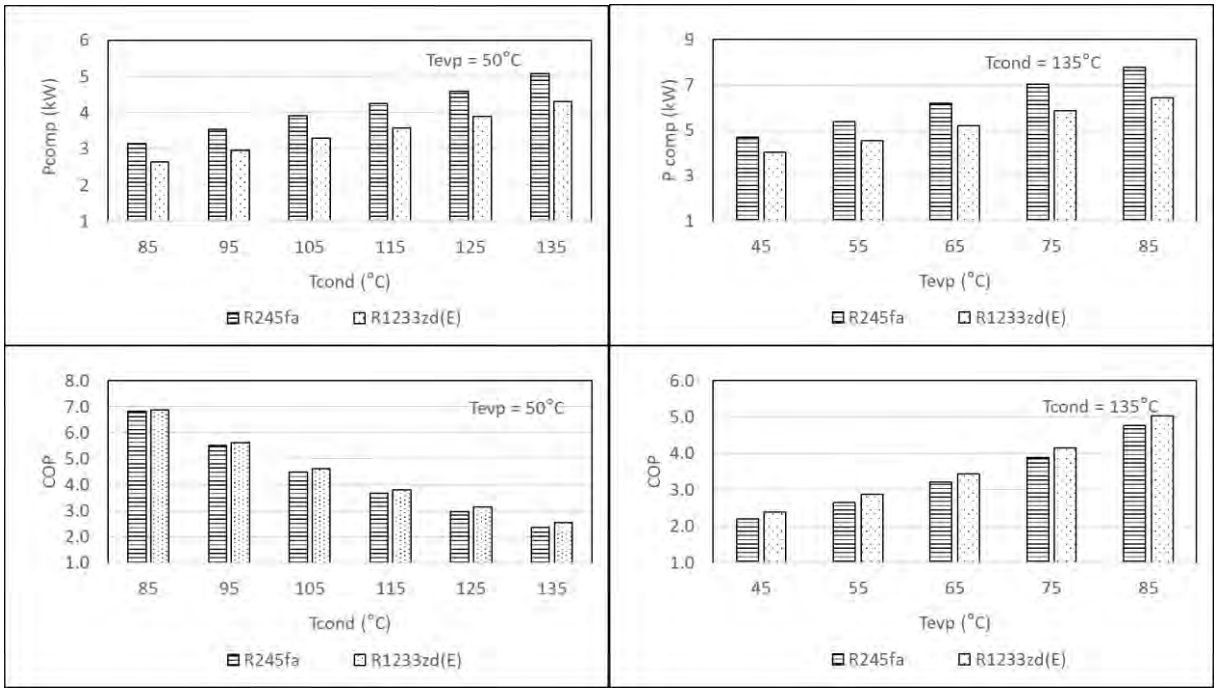

Figure 3 Comparative analysis for R245fa & R1233zd(E): Left: variation in T_{cond}, Right: variation in T_{evp}

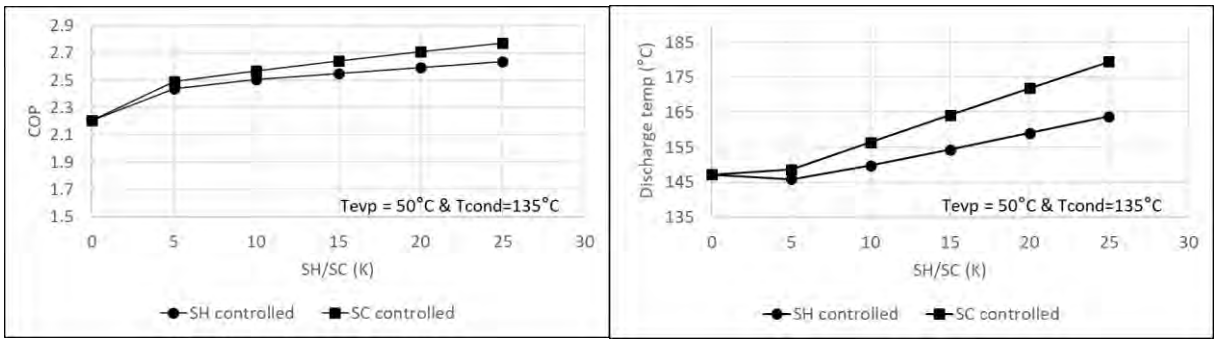

Figure 4 COP and discharge temperature variation with SC & SH controlled method using intermediate heat exchanger for R1233zd(E)

Above comparison was made while keeping LSH at 15K. However, further analysis carried out to understand benefits of controlling SH and SC for LSH assuming constant isentropic and volumetric efficiency at T_c=135°C & T_{evp}=50°C (with SH=SC=5K at condenser and evaporator). Figure 4 shows that if SC is controlled rather than SH then it could provide higher COP. However, discharge temperature puts limit on how much SC can be achieved in order to get improvement in COP.

4.2 Initial experience of test rig operation

For HTHP test rig, extensive time was spent on pre-commissioning before actual testing could take place as per test regime. There were several difficulties encountered mainly on: expansion valve and oil temperature side due to high temperature operation. Commercially available EEV needs additional cooling or EEV with stainless steel body is required for HTHP. In addition, oil viscosity at high temperature was a challenge as the oil temperature increased to 90°C while operating at 105°C condensing temperature. Hence, the test rig was modified to accommodate oil cooling to maintain temperatures with the range of 60-80°Cwhen operating at condensing temperature above 100°C. Figure 5 shows oil temperature rise with respect to $T_{con\ oil\ outlet}$ and $T_{evp\ water\ inlet}$ and addition of the I heat exchanger added to the compressor for oil cooling. However, oil temperature must be 5-10K higher than the suction temperature. Additional cooling was also provided to the expansion valve for safe working of the stepper motor as during initially commissioning the A stepper motor failed due to overheating issues.

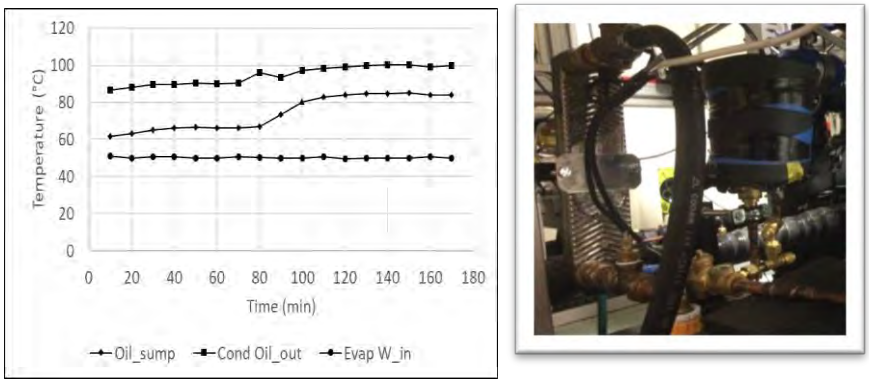

Figure 5 Oil sump temperature rise (left) and addition of oil cooler (right)

A few initial tests were carried out using R245fa as a reference in order to find component performance and controls required for safe working conditions. Figure 6 shows performance of the HTHP using R245fa at a fixed evaporation temperature and at varying condensing temperatures. Overall, the system COP remained between 2.3 to 4.3 and the condensing capacity between 10 to 14 kW. Although system performance is satisfactory, it is however lower compared to simulation results mainly due to several heat losses on primary side and refrigeration side. In addition, experimental results present system COP whereas simulation results provide the enthalpic COP.

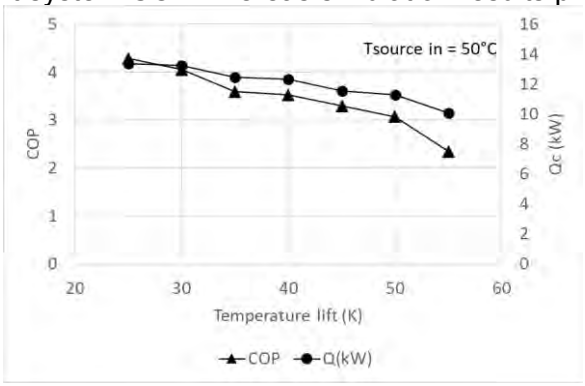

Figure 6 Initial test results of HTHP using R245fa

Before system performance can be evaluated further with R245fa and R1233zd(E), several other modifications will be carried out in terms of system temperature control, lubrication and insulation in order to optimise system performance. One of the biggest challenges for HTHP is commercially available parts, cost and suitable lubrication and cooling.

5. CONCLUSION

HTHPs have huge potential to use waste heat from industrial and commercial application. A literature search for R1233zd(E) has shown that there is limited investigation on the use of R1233zd(E) for HTHP, with most investigation focusing on simulation study and use in ORC applications. Simulation results and comparison between R245fa and R1233zd(E) showed a higher COP up to 8% when compared to R245fa. However, if R1233zd(E) is used as a direct replacement then careful consideration should be given to sizing of components (e.g. condenser, compressor) as it gives less heating/cooling capacity. Initial experience from this experiment showed the necessity for oil cooling due to high condensing temperatures which might be a limiting factor for safe compressor operation based on manufacture recommendations. In addition, if a commercially available standard EEV is used then it might need cooling to operate at high temperatures for prolonged periods. Suitable lubricant for R1233zd(E) is an area of debate as some refrigerant manufactures suggest POE whereas others suggest mineral oil. Oil miscibility data with POE is available for certain oil and temperature ranges but there is no readily available information for mineral oil. Long term performance and thermal stability with various materials requires further investigation for R1233zd(E). As a part of this ongoing CHESTER project, further investigation will be carried out to find suitable oil, properties (viscosity, miscibility, solubility) and temperature control for HTHP

application. However, increasing development in HTHP area calls for more open and readily available information, development of components and knowledge sharing platform.

ACKNOWLEDGEMENTS

The authors gratefully acknowledge the support of Engineering and Physical Sciences Research Council (EPSRC) through the Interdisciplinary Centre for Storage, Transformation and Upgrading of Thermal Energy (i-STUTE) (Grant No. EP/K011847/1) and the European Unions' Horizon 2020 research and innovation programme through the Compressed Heat Energy Storage for Energy from Renewable Sources (CHESTER) project (Grant No. 764042).

NOMENCLATURE

c/con	Condenser	*Δh*	Enthalpy difference (inlet & outlet) (kJ/kg)
comp	compressor	*T*	temperature (°C)
EEV	Electronic expansion valve	*η*	efficiency
evp	Evaporator	*HTHP*	High temperature heat pump
is	Isentropic	*Q*	heat energy (kW)
LSH	Liquid-suction heat exchanger	*COP*	Coefficient of performance
m_{ref}	Refrigerant mass flow rate (kg/h)	*P*	Compressor power (kW)
ORC	Organic Rankine Cycle	*HCFO*	Hydro-chloro-fluoro-olefins
SH/SC	Superheat/Subcooling	*PTFE*	Polytetrafluoroethylene
VHC	Volumetric heating capacity	*POE*	Polyol-ester
W	Water	*in/out*	inlet / outlet

REFERENCES

Arpagaus, C. et al., 2018. High temperature heat pumps: Market overview, state of the art, research status, refrigerants, and application potentials. Energy 152, 985-1010.

Bamigbetan, O. et al., 2018. Theoretical analysis of suitable fluids for high temperature heat pumps up to 125 °C heat delivery. International Journal of Refrigeration 92, 185-195.

Bobbo, S. et al., 2018. Low GWP halocarbon refrigerants: A review of thermophysical properties. International Journal of Refrigeration 90, 181-201.

Eyerer, S. et al., 2018. Theoretical analysis and experimental investigation of material compatibility between refrigerants and polymers. Energy 163, 782-799.

Frate, G., Ferrari, L. & Desideri, U., 2019. Analysis of suitability ranges of high temperature heat pump working fluids. Applied Thermal Engineering 150, 628-640.

Ju, F. et al., 2017. Performance assessment of heat pump water heaters with R1233zd(E)/HCs binary mixtures. Applied Thermal Engineering 123, 1345-1355.

Majurin, J., Sorenson, E. & Steinke, D., 2017. Chemical Stability Assessments of R-514A and R-1233zd(E). ASHRAE Winter Conference, Las Vegas

Panayiotou, G. et al., 2017. Preliminary assessment of waste heat potential in major European industries. Energy Procedia 123, 335-345.

Suemitsu, R. et al., 2017. Development of centrifugal chiller and heat pump using low GWP. Rotterdam, 12th IEA Heat Pump Conference, Rotterdam.

Yang, J., Sun, Z., Yu, B. & Chen, J., 2018. Experimental comparison and optimization guidance of R1233zd(E) as a drop-in replacement to R245fa for organic Rankine cycle application. Applied Thermal Engineering 141, 10-19.

Zuhlsdorf, B. et al., 2018. Improving the performance of booster heat pumps using zeotropic mixtures. Energy 154, 390-402

Manuscript ID: 293
DOI: 10.18462/iir.icr.2019.0293

A novel air-source heat pump system with integrated desiccant for electric vehicles

Li ZHANG[(a)], Katsumi HASHIMOTO[(a)], Hiromi HASEGAWA[(a)], Michiyuki SAIKAWA[(a)]

[(a)] Central Research Institute of Electric Power Industry
2-6-1 Nagasaka, Yokosuka City, Kanagawa Prefecture, 240-0196, Japan,
zhangli@criepi.denken.or.jp

ABSTRACT

In this study, we proposed a novel air-source heat pump system with integrated desiccant for electric vehicles (EVs), in which the heat pump absorbs atmospheric thermal energy to heat the cabin and the desiccant dehumidifies the cabin interior to prevent windshields from fogging up. The proposed system can reduce the amount of incoming fresh air needed and the cabin heat demand, consequently saving on the electricity consumption of batteries. The calculation results show that compared to conventional EV heat pumps, the cabin heat load and compressor electric power of the proposed system decline by 42 and 38% at an ambient air temperature of -20°C. Furthermore, the defrosting process of the proposed system saves electricity, since it utilizes the adsorption heat of the desiccant.
Keywords: Electric vehicle, Heat pump, Desiccant, Anti-fogging, Heating, Defrosting.

1. INTRODUCTION

The automobile air conditioning (AC) system, an essential vehicle subsystem, ensures thermal comfort for passengers, but also contributes to the anti-fogging of windows, which increases the active safety factor. AC systems for vehicles generally operate in one of three modes: cooling, heating and dehumidification-reheating. Compared to conventional vehicles, EVs have no waste heat from combustion engines available for heating and dehumidification-reheating modes, hence additional heat sources, such as fuel-fired heaters, viscous heaters, positive temperature coefficient (PTC) heaters and heat pumps, are proposed to cover the heat demand at low ambient temperatures. Among these, the PTC heater and heat pump are commonly adopted for EVs. Although the former could provide sufficient heat energy to warm the cabin, it comprises a considerable proportion of the total electricity consumed by the vehicle and thus significantly reduces the EV cruising range.

Much research has focused on heat pump air-conditioning systems in EVs (Suzuki 1996, Kondo 2011, Kwon et al., 2017). Suzuki (1996), for example, proposed a heat pump system for EVs, which could provide cooling, heating and dehumidification and have cooling and heating capacities of 2.9 and 2.3kW under ambient temperatures of 40 and -10°C, respectively. Experimental results revealed coefficients of performance (COP) during cooling and heating operations of 2.9 and 2.3, respectively.

Although the heat pump is a promising way to meet both heating and cooling demands of passengers and anti-fogging of windows, its electricity consumption increases sharply at low ambient temperatures due to the increased heat demand. In conventional EV air-conditioning systems, to prevent windshields from fogging up, an all-fresh-air heating mode is used in winter, the introduction of which generates a large heating load due to the fresh air introduction, with a ratio of 60% to the total heating load (Hagiwara, 2011). Accordingly, operating on the premise of anti-fogging decreasing the fresh-air ratio can effectively reduce EV energy consumption.

In this study, we proposed a heat pump system for EVs, in which a desiccant-coated heat exchanger is adopted to dehumidify the inside cabin air. Accordingly, anti-fogging of the windshield becomes possible under interior-air recirculation, allowing less fresh air into the vehicle cabin and thus reducing heat loss.

Another crucial technical barrier to applying the air-source heat pump for EVs is the development of an efficient defrosting method (Steiner, 2015). There are two defrosting methods: reverse cycle

defrost and hot gas defrost. The former switches the refrigerant cycle from heating to cooling mode, in which hot refrigerant under high pressure from the compressor enters the external heat exchanger to melt the frost. The latter utilizes a bypass valve, channelling the hot gas from the compressor directly to the external HE to melt the frost. Comparing the two defrosting methods, the former seems to show higher defrosting performance because the cabin air can be used as a heat source, whereas the hot-gas defrosting uses only the electrical energy from the compressor. The drawback of the former is the cold wind supply to the cabin during the defrosting process and the higher heat demand in the subsequent heating mode. Furthermore, a means of preventing the windshield from fogging up during the defrosting process is also a challenge for EV AC systems.
In the proposed system, the adsorption heat is utilized to remove the frost, whereupon the electrical energy consumption is reduced. Another advantage is the dehumidified cabin air allowing anti-fogging, even during the defrosting operation. Moreover, the temperature of the cabin air does not decrease sharply, as happens during the reverse cycle defrost.
In this paper, we give the system description and simulation results of the proposed system.

2. SYSTEM DESCRIPTION

Note that the proposed system can also operate in cooling and dehumidification-reheating modes. In this paper, we mainly introduce the working principle and analyze the system performance during heating and defrosting modes at low atmospheric temperatures.

2.1. Heating mode

A schematic diagram of the heat pump with integrated desiccant for EVs is shown in Fig. 1, with the process illustrated in a pressure-enthalpy diagram of the refrigerant and a psychometric chart in Figs. 2 and 3. The system comprises a compressor, a four-way valve (F-W valve), an internal heat exchanger (internal HE), four dampers (D1-D4), a desiccant-coated heat exchanger (DCHE), two expansion valves (V1 and V2), a gas-liquid separator (Separator) and an external heat exchanger (external HE). The DCHE is capable of dehumidifying the cabin air, which makes it possible to prevent the windshield from fogging under interior-air recirculation. Once the DCHE dehumidification capacity goes below a pointed value or when passengers want some fresh air, fresh air will be introduced into the cabin to regenerate the DCHE or meet passenger demand. With respect to the switch between interior and fresh air, the system operation can be classified into two modes: interior-air recirculation mode (Interior-Air-Mode) and fresh air introducing mode (Fresh-Air-Mode).
In Interior-Air-Mode, as shown in Fig. 1 (a), the system places the damper (D1) in position “b” and the dampers (D2-D4) are closed, meaning the return air (RA) traverses the DCHE and Internal HE sequentially before flowing back into the cabin. The RA is dehumidified and heated at the DCHE and Internal HE, respectively. For the refrigerant cycle, the two expansion valves (V1 and V2) are throttled, meaning the internal HE functions as a condenser, while the DCHE and external HE function as evaporators at two different evaporation temperatures. The refrigerant leaving the compressor in state “1” releases its condensation heat into the dry air (DA) at the internal HE, so the hot air (HA) is obtained and supplied to the vehicle cabin. After the refrigerant leaves the internal HE, it is expanded to intermediate pressure (P_{mid}) by flowing through the V1. The RA is dehumidified at the DCHE due to the desiccant adsorption process, whereupon the adsorption heat is used to vaporize part of the refrigerant. The refrigerant from the DCHE in state “4” flows into the separator, where the refrigerant liquid and vapor are separated. The saturated refrigerant liquid at point “6” flows into the external HE after it has been throttled to the required evaporator pressure (P_{low}) by traversing V2. The saturated refrigerant vapor at point “5” is fed into the compressor and compressed via condensation pressure (P_{high}). At the external HE, the refrigerant is vaporized by absorbing heat from the ambient air. The refrigerant from the external HE at point “8” is then fed back to the compressor where two-stage compression is conducted: P_{low} to P_{mid} for the refrigerant, m_{r2}; and P_{mid} to P_{high} for the total refrigerant, $m_{r1}+m_{r2}$.
The moisture-adsorbing capacity of the desiccant will decrease and eventually expire throughout the adsorption process, which means the humidity ratio and dew point of the cabin air will gradually increase. When the dew point of the cabin air exceeds the inside surface temperature of the windshield, the windshield fogs up and the desiccant should be regenerated (desorbed). Correspondingly, Fresh-Air Mode is started. As mentioned above, the Fresh-Air Mode can also be started by passengers at any time.

During Fresh-Air Mode, as shown in Fig. 1 (b), with the damper (D1) in position “a” and dampers (D2-D4) opened, outdoor air (OA1 and OA2) are introduced into the cabin and heated at DCHE and Internal HE respectively, before finally being discharged in an EA state. For the refrigerant cycle, the expansion valve (V1) is opened and V2 throttled, so the internal HE and DCHE work as condensers and the external HE as an evaporator. The refrigerant leaving the compressor in the “1” state releases part of the condensation heat to OA2 at the internal HE. The hot air (HA2) at the internal HE outlet has a low humidity ratio and dew point and is blown toward to the windshield to prevent fogging. After leaving the internal HE, the refrigerant in the “2” state traverses the opened V1 with constant temperature and pressure and flows into the DCHE. At the DCHE, the desiccant is heated by the condensation heat of the refrigerant and discharges moisture into the outdoor air (OA1). Consequently, the desiccant is regenerated (desorbed) and the OA1 is heated and humidified to the HA1 state. Because the hot air (HA1) has a relatively high dew point and may fog up the windshield, it is blown toward passengers and heats the cabin, before being finally exhausted. The refrigerant exiting the DCHE in the state of “4” traverses the separator, is expanded at the V2 and flows into the external HE. At the external HE, the refrigerant is then evaporated by extracting thermal energy from the ambient air and fed back to the compressor.
Once the desiccant is completely regenerated, the Fresh-Air Mode may end and the Interior-Air Mode may be restarted.

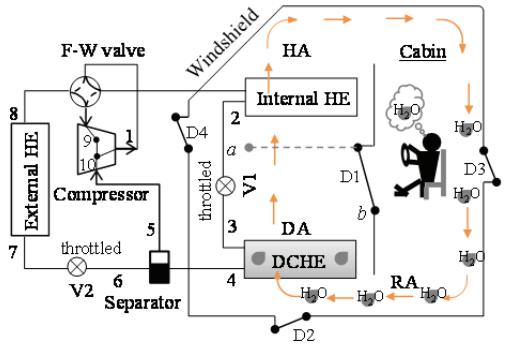

(a) Interior-Air Mode

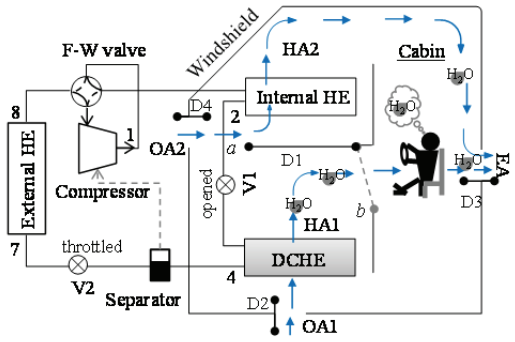

(b) Fresh-Air Mode

Figure 1: Schematic diagram during heating mode

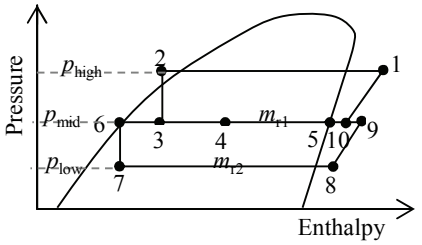

(a) Interior-Air Mode

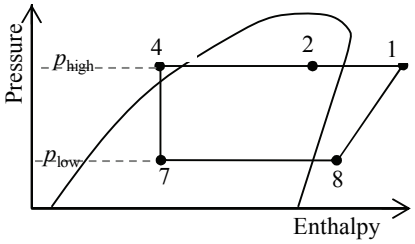

(b) Fresh-Air Mode

Figure 2: Pressure – enthalpy of refrigerant

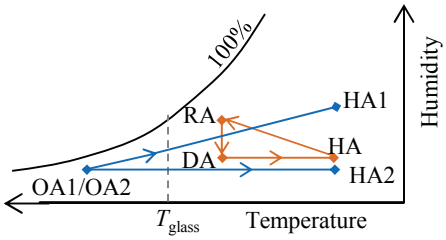

Figure 3: Air state change during Interior-Air and Fresh-Air modes

2.2. Defrosting mode

During defrosting mode, as shown in Fig. 4, with the damper (D1) in position “b” and D2-D4 closed, the RA traverses the DCHE and feeds back into the cabin. The F-W valve changes the refrigerant flow direction, in which the hot refrigerant leaving the compressor in state “1” flows into the external HE. The expansion valve (V1) is opened and V2 throttled, so the external HE and DCHE function as condenser and evaporator, respectively. The refrigerant releases its condensation heat to melt the frost on the surface of the external HE. The refrigerant exiting the external HE in the state of “7” is expanded at the V2 and flows into the DCHE. At the DCHE, the RA is dehumidified due to the desiccant adsorption process and the adsorption heat is used to vaporize the refrigerant. Here the evaporation temperature of the refrigerant (Fig. 5(a)) is controlled and made equivalent to the RA

temperature, so the temperature of the supplying air (DA) remains constant (Fig. 5(b)). In other words, the latent (adsorption) heat of the cabin air is utilized to remove the frost, with no sensible heat (temperature) loss of the cabin air. Furthermore, the cabin air is dehumidified, which means the anti-fogging of the windshield can be maintained, even in defrosting mode. The refrigerant exiting the DCHE passes through the V1 and internal HE is then fed back to the compressor.

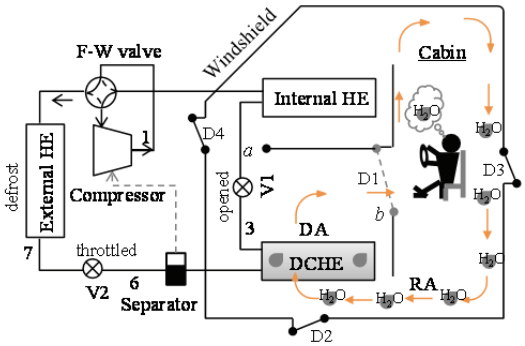

Figure 4: Schematic diagram during defrosting mode

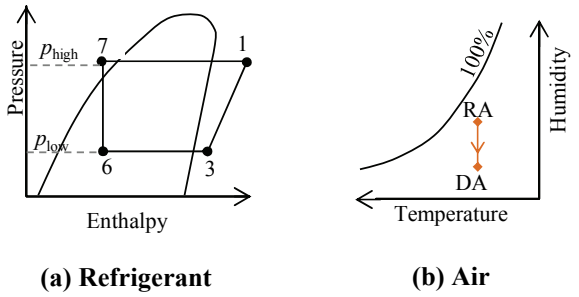

(a) Refrigerant **(b) Air**

Figure 5: State changes of refrigerant and air

3. MATHEMATICAL MODEL

A simulation was performed to analyze and evaluate the performance of the proposed system during heating and defrosting modes, respectively.

3.1. Heating mode

As mentioned above, while in heating mode, the system is operated in interior-air and fresh-air modes alternately. Correspondingly, the mathematical model is given separately.

(1) For Interior-Air Mode

As shown in Figs. 1(a) and 2(a), there are two evaporators: DCHE and the external HE, in which the refrigerant evaporation temperatures ($T_{eva,1}$ and $T_{eva,2}$) are obtained by Eqs. (1-2).

$$T_{eva,1} = T_{ra}\ [°C] \quad \text{Eq. (1)}$$

$$T_{eva,2} = T_{oa} - \Delta T_1\ [°C] \quad \text{Eq. (2)}$$

The internal HE functions as a condenser and the refrigerant condensation temperature (T_{con}) is calculated by Eq. (3).

$$T_{con} = T_{ra} + \Delta T_2\ [°C] \quad \text{Eq. (3)}$$

The evaporation loads (q_{eva1} and q_{eva2}) and condensation load (q_{con}) are obtained by Eqs. (4-6).

$$q_{eva,1} = (m_{r1} + m_{r2})(i_4 - i_3)\ [kW] \quad \text{Eq. (4)}$$

$$q_{eva,2} = m_{r2}(i_8 - i_7)\ [kW] \quad \text{Eq. (5)}$$

$$q_{con} = (m_{r1} + m_{r2})(i_1 - i_2)\ [kW] \quad \text{Eq. (6)}$$

The electric power consumption during the low and high pressure stages is calculated by Eqs. (7) and (8), while the total electric power of the compressor is obtained by: $w_{com,int}=w_{low}+w_{high}$, [kW].

$$w_{low} = m_{r2}(i_9 - i_8)\ [kW] \quad \text{Eq. (7)}$$

$$w_{high} = (m_{r1} + m_{r2})(i_1 - i_{10})\ [kW] \quad \text{Eq. (8)}$$

The evaluation criteria for anti-fogging of windshields is given as:

$$DP_{air,glass} < T_{glass} \quad \text{Eq. (9)}$$

Here, T_{glass} is the inside surface temperature of windshields and calculated by Eq. (10),

$$T_{glass} = T_{cab} - \frac{K_g(T_{cab}-T_{oa})}{h_{ci}} \text{ [°C]} \quad \text{Eq. (10)}$$

where K_g is the overall heat transfer coefficient of glass and h_{ci} is the heat transfer coefficient inside the cabin, [kW $(m^2 \cdot k)^{-1}$]. T_{cab} and T_{oa} are the cabin and ambient air temperatures.
$DP_{air,glass}$ is the dew point of the air blown toward to the windshield, equal to the dew point of the DCHE outlet air that is a function of the humidity ratio of the DCHE outlet air (X_{da}). X_{da} is calculated by Eq. (11).

$$X_{da} = X_{ra} - \eta_{x,ad}(X_{ra} - X_{d,eq}) \text{ [kg·vapor (kg·dry air)}^{-1}\text{]} \quad \text{Eq. (11)}$$

where $\eta_{x,ad}$, the adsorption effectiveness of the desiccant, is assumed as 0.7 in this study; $X_{d,eq}$, the air humidity ratio in equilibrium with the desiccant, is calculated by $X_{d,eq}=0.622(R_p \cdot P_s)/(101325-R_p \cdot P_s)$. Here, R_p, the relative pressure of the desiccant, is a function of the desiccant moisture content (C_w) and obtained from the adsorption isotherm of the desiccant. In this study, we selected Z02 (a kind of desiccant belonging to the zeolite family, developed by Mitsubishi Chemical Corporation) as the desiccant. As the adsorption process proceeds, C_w, R_p, $X_{d,eq}$ and $DP_{air,glass}$ increase. When the anti-fogging criteria expressed at Eq. (9) can no longer be satisfied, Interior-Air Mode ends and Fresh-Air Mode is started.

(2) For Fresh-Air Mode

As shown in Figs. 1(b) and 2(b), two condensers: DCHE and Internal HE, have the same condensation temperature determined by Eq. (3), while the evaporation temperature of the external HE is determined by Eq. (2). The evaporation load of the external HE and the condensation loads of the DCHE and Internal HE are obtained by Eqs. (12-15).

$$q_{eva} = m_r(i_8 - i_7) \text{ [kW]} \quad \text{Eq. (12)}$$

$$q_{con,1} = m_r(i_1 - i_2) \text{ [kW]} \quad \text{Eq. (13)}$$

$$q_{con,2} = m_r(i_2 - i_4) \text{ [kW]} \quad \text{Eq. (14)}$$

The electric power of the compressor is calculated by Eq. (21).

$$w_{com,fre} = m_r(i_1 - i_8) \text{ [kW]} \quad \text{Eq. (15)}$$

While in Fresh-Air Mode, the desiccant is regenerated and the C_w decreases. When the C_w is equal to the moisture content at the starting point of Interior-Air Mode, Fresh-Air Mode is finished and one cycle of the heating mode is completed.

3.2. Defrosting mode

While in defrosting mode, the condensation temperature of the external HE is equal to that of the interior HE in the heating mode and calculated by Eq. (3). The evaporation temperature of the DCHE is equal to the cabin air temperature and the evaporation load of the DCHE ($q_{eva,def}$) is obtained by Eq. (16),

$$q_{eva,def} = m_{vap} \cdot \gamma \text{ [kW]} \quad \text{Eq. (16)}$$

where m_{vap} is the moisture adsorption rate of DCHE, decided by the states of the desiccant and cabin air, [kg s^{-1}].γ is the adsorption heat, [kJ kg^{-1}].
The electric power of the compressor ($w_{com,def}$) is calculated by Eq. (17).

$$w_{com,def} = m_r(i_1 - i_3) \text{ [kW]} \quad \text{Eq. (17)}$$

The condensation load used to remove the defrost ($q_{con,def}$) is the sum of $q_{eva,def}$ and $w_{com,def}$.

4. SIMULATION RESULTS AND ANALYSIS

The specifications of the EV (Nissan Leaf 24s, 2017) are shown in Table 1. R134a is used as a working fluid in this system, the thermophysical properties of which were calculated using REFPROP7.0 (NIST, 2007).

Table 1. EV specifications

Parameters		Values
EV specifications	Body length, width and height [mm]	4445, 1770, 1550
	Battery capacity [kWh]	24
	Electricity consumption (AC off) [kW km^{-1}]	0.114
	Cruising range (AC off) [km]	228

4.1. Simulation results during heating mode

Calculations were performed using the above mentioned methods and a time step of one second and the results at an ambient air temperature of -10°C are shown in Figs. 6-9. Figure 6 shows the variations of the dew point of air with elapsed time for a single cycle. It emerges that the dew point of air blown toward to the windshield ($DP_{air,glass}$) increases over time during Interior-Air Mode and is ultimately equivalent to the interior windshield temperature (T_{glass} of -2.3°C). For Fresh-Air Mode, $DP_{air,glass}$ is constant at -16°C and equivalent to the dew point of outdoor air. The dew point of air blown toward passengers ($DP_{air,passenger}$) increases over time due to obtaining moisture from the DCHE desorption process. Furthermore, the operation times for Interior-Air and Fresh-Air modes are 13.5 and 10.25 minutes, separately.

The calculated cabin heat loads (q_{cab}) during Interior-Air and Fresh-Air modes are shown in Fig. 7. q_{cab} during Interior-Air mode is approximately 3.5 times smaller than that during Fresh-Air Mode. Figure 8 shows the heat loads of the internal HE, DCHE and external HE during Interior-Air and Fresh-Air modes. The internal HE functions as a condenser independent of operation modes and has a virtually constant 1.15kw heat load, while DCHE transfers from an evaporator to a condenser when the operation mode changes from Interior-Air to Fresh-Air modes. The evaporation and condensation heat loads of the DCHE are approximately 0.3 and 3.3kW, separately and decrease over time. The electric power of the compressor (w_{com}) for a single cycle is shown in Fig. 9. w_{com} in Interior-Air Mode is about five times smaller than that in Fresh-Air Mode due to the low cabin heat load during Interior-Air Mode, which is why the proposed system saves more energy compared to conventional EV heat pumps. In the following section, we provide detailed comparison results.

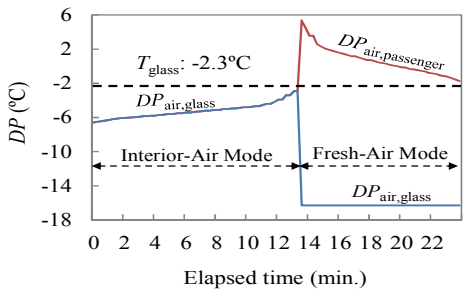

Figure 6: Variations in the dew point of air with elapsed time for a single cycle

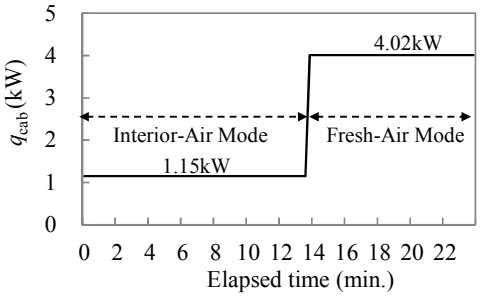

Figure 7: Variations in the cabin heat loads (q_{cab}) with elapsed time for a single cycle

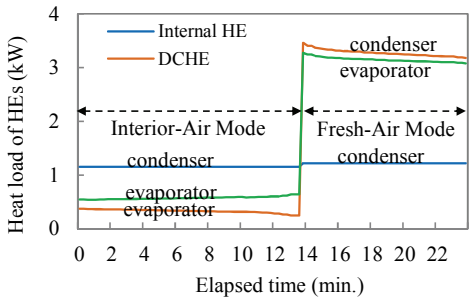

Figure 8: Variations in the heat load of heat exchangers with elapsed time for a single cycle

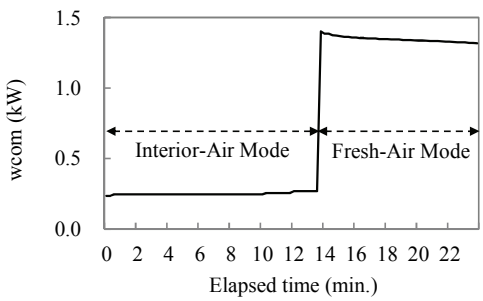

Figure 9: Variations of the electric power (w_{com}) with elapsed time for a single cycle

4.2. Energy saving compared to conventional EV heat pumps during heating mode

Fig. 10 show the average compressor electric power ($w_{com,ave}$, obtained by Eq. (18)) of the proposed system (HP-Prop) and conventional heat pumps (HP-Conv). Results show that $w_{com,ave}$ of HP-Prop are lower 0-38% compared to those of HP-Conv under an ambient air temperature of -20 - 10°C.

$$w_{com,ave} = \frac{\int w_{com,int} d\tau_{int} + \int w_{com,fre} d\tau_{fre}}{\tau_{int} + \tau_{fre}} \text{ [kW]} \qquad \text{Eq. (18)}$$

We attempt to compare the cruising range of an EV under different heating methods, including electric heater (heater), conventional heat pump (HP-Conv) and the proposed heat pump (HP-Prop). The EV has the specifications shown in Table 1 and the ambient air temperature is assumed to be -20°C. The calculation results are shown in Fig. 11. Compared to the cruising range of 228kW when leaving air-conditioning (AC) off, the cruising range decreases by 54, 32 and 25% respectively, when the AC is turned on with three kinds of heating methods: heater, HP-Conv and HP-Prop. The decreasing range of the proposed heat pump is obviously the smallest of the three heating methods.

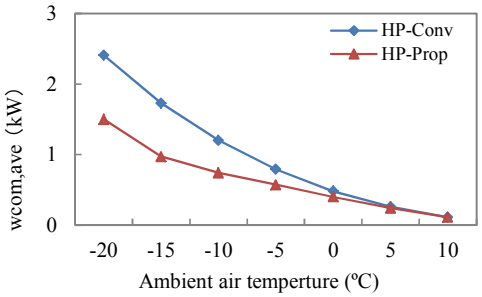

Figure 10: Comparison of the electric power of compressor between conventional and proposed systems

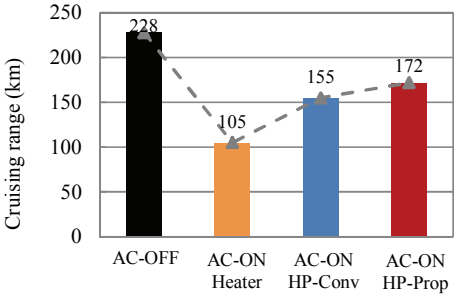

Figure 11: Cruising range comparison of different AC methods at an ambient air temperature of -20°C

4.3. Simulation results during defrosting mode

While in defrosting mode, the evaporation and condensation temperatures of the heat pump are 25 and 45°C, separately. The coated desiccant amount of the DCHE is assumed to be 0.75kg and the operation time of the defrosting mode is 5 minutes. Calculation results at an ambient air temperature of -10°C are shown in Figs. 12-13. Figure 12 shows the condensation heat load (q_{con}), evaporation heat load (q_{eva}) and electric power of the compressor (w_{com}) are approximately 0.4, 0.36 and 0.04kW, separately. We found that the 90% of the defrosting heat can be obtained from the adsorption heat of the desiccant (q_{eva}). Furthermore, the dew point of the cabin air (DP_{air}) is lower than the surface temperature of windshields (T_{glass}), meaning anti-fogging can also be maintained, even during defrosting mode.

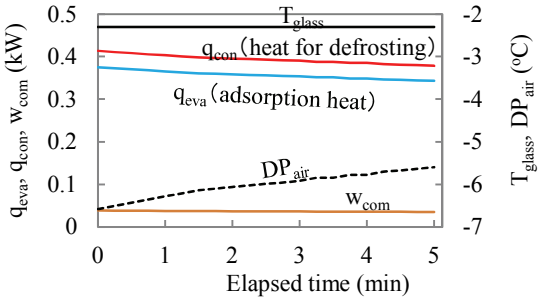

Figure 12: Calculation results of the proposed system during defrosting mode

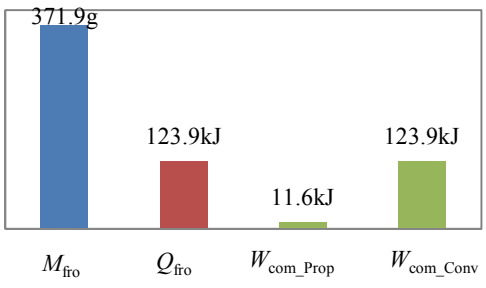

Figure 13: Comparison of the electric power consumption required for defrosting between conventional and proposed heat pump systems

Fig. 13 shows the total removed frost amount (M_{fro}), required defrosting heat amount (Q_{fro}) and electrical energy consumption (W_{com_Prop}) of the proposed system are 371.9g, 123.9kJ and 11.6kJ. Note that the heat required to remove 1kg frost is assumed to be 333.4kJ. The electrical energy consumption of the conventional hot gas bypass defrosting method (W_{com_Conv}) is also shown in Fig. 13. We found that the proposed system can reduce the consumption of electrical energy by around 90% compared to the conventional defrosting method.

5. CONCLUSIONS

In this study, we proposed a heat pump system for EVs, in which a DCHE is adopted to dehumidify the cabin air and remove the frost effectively. Calculation results show that compared to conventional EV heat pumps, the cabin heat load and compressor electric power of the proposed system are decreased by 42 and 38% at an ambient air temperature of −20°C. Moreover, the electrical energy consumption required for defrosting is reduced by around 90% compared to that of the conventional hot gas bypass defrosting method.

NOMENCLATURE

C_w	moisture content of desiccant [(kg·moisture) (kg·dry desiccant)$^{-1}$]	DP	dew point of air (ºC)
m	Mass flow rate (kg s^{-1})	m_{vap}	moisture removal rate of desiccant (kg s^{-1})
P	pressure (Pa)	q	heat load (kW)
T	temperature (ºC)	w	electric power (kW)
X	humidity ratio of air ((kg·vapor) (kg·dry air)$^{-1}$)	τ	time (s)

REFERENCES

Kondo T., 2011. Development of automotive air-conditioning systems by heat pump technology. Mitsubishi Heavy Ind. Tech. Rev. 48 (2), pp. 27–32.

Kwon C., Kim M.S. Choi Y., Kim M.S., 2017. Performance evaluation of a vapor injection heat pump system for electric vehicles. Int. J. Refrigeration 74, 136-148.

Hagiwara, Y., 2011. Features and trends of an air-conditioning system for electric vehicles. Denso Tech. Rev. 16, pp. 83–89 (In Japanese).

Nissan Leaf 24s: http://ev.nissan.co.jp/LEAF/PDF/leaf specifications.pdf (Accessed June 2017).

NIST: NIST reference fluid thermodynamic and transport properties - REFPROP: Version 8.0 (2007).

Steiner A., 2015. Simulation based identification of the idea defrost start time for a heat pump system for electric vehicles. Int. J. Refrigeration 57, pp. 87-93.

Suzuki T., 1996. Air-conditioning system for electric vehicles. SAE technical paper No. 960688.

Manuscript ID: 308
DOI: 10.18462/iir.icr.2019.0308

Experimental investigation of a heat pump assisted drum drying system using propane (R290) as working fluid

Espen STORSLETT[(a)], Trygve M. EIKEVIK[(b)]
[(a)] Norwegian University of Science and Technology, Dept. of Energy and Process Engineering Trondheim, NO-7491, Norway, espen.storslett@gmail.com
[(b)] Norwegian University of Science and Technology, Dept. of Energy and Process Engineering Trondheim, NO-7491, Norway, trygve.m.eikevik@ntnu.no

ABSTRACT

This study experimentally investigates the suitability of R290 in replacement of R134a as refrigerant in a mass-produced heat pump assisted drum dryer. A heat pump assisted drum dryer designed for R134a is instrumented and rebuilt by replacement of the compressor and in turn the capillary tube. The effect of R290 charge optimization and capillary tube accommodation is investigated. Input power, refrigerant pressure and temperature as well as temperature and humidity of the airstream is logged. By replacing only the compressor, the R290 system obtained the same level of efficiency as the original R134a system. Subsequent to replacement of the capillary tube 6% increase in COP was observed, maintaining the same level of SMER as with R134a.

Keywords: Drying, heat pump, propane, R290

1. INTRODUCTION

Drum dryers has been used for drying of fabric for a long time. Conventional drum dryers rely on heating air by an electric heater and rejecting moisture along with heated air to the ambient. This means of drying is highly energy demanding, thus having negative effect on the environment. By closing the air loop and utilizing a heat pump to heat air as well as condensing moisture, significantly higher energy efficiency may be obtained. Unfortunately, modern heat pump assisted drum dryers utilizes HFC gases with high GWP (Global Warming Potential). By replacing the HFC gases used in HPDD's (Heat Pump assisted Drum Dryers) with HC's (hydrocarbons) reduced environmental impact may be obtained.

Through this study, experimental investigation a mass produced HPDD originally utilizing R134a has been performed. The HPDD has been rebuilt to utilizing R290 by replacing the compressor, and in turn the capillary tube. Instrumentation and manual controls has been added to the HPDD prior to the rebuild, allowing for investigation of performance while utilizing R134a to establish the baseline of performance for comparison.

1.1. The Heat Pump Assisted Drum Drying Process

The HP (Heat Pump) assisted drying process utilizes the heat pumps ability to extract heat at low temperatures and reject heat at high temperatures. Moist air coming from the drum it utilized as the heat source for the evaporator, while air cooled by the evaporator is reused as the heat sink for the condenser. By extracting heat from relatively low temperature moist air condensation of water are obtained. By reheating the chilled air low RH (Relative Humidity) of the air is obtained at high temperature. The low RH air is blown across wet fabrics, absorbing moisture due to the difference in vapor pressure relative to the near saturated air close to the wet fabric. Subsequent to absorbing moisture, the moist air is refed into the HP evaporator by use of a closed air loop.

Utilizing a heat pump to condense water and reheat the air are found to theoretically offer energy savings up to 69% compared to traditional air vented dryers (Gopalnarayanan and Radermacher 1997).

The IX-diagram in Fig. 1 provide the basic understanding of the physics behind a closed loop drum drying process. The air initially at state 1 absorbs moisture from point 1 to point 2. Assuming adiabatic drying, moisture extracts energy from the air in order to evaporate, thus maintaining constant enthalpy. This causes RH to increase and temperature to decrease. As the air is cooled by the evaporator from point 2 to point 3, moisture condenses at the evaporator surface at point 4. Due to energy being extracted by the evaporator, temperature and enthalpy decreases. The air is then reheated at constant mixing ratio by the condenser from point 3 to point 1, causing the temperature and enthalpy to increase.

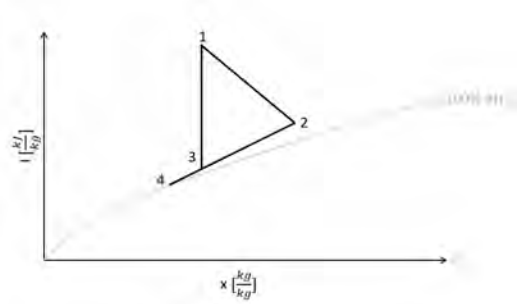

Figure 1. IX diagram explaining the drying process

Due to the nature for air – water vapor mixtures, the most efficient drying is obtained at high temperatures in the right side of the IX diagram. As the airs ability to hold water increases exponentially at increased temperatures, more water may be removed by the same amount of air. This reduces the amount of air that needs to be moved by the drum fan, thus reducing overall energy consumption. Consequently, higher Coefficient of Performance (COP) of the heat pump does not directly translate to increased overall energy efficiency.

1.2. Environmental Effects

The positive environmental effect caused by increased efficiency and energy savings of heat pump assisted drum dryers are diminished by the use of environmental unfriendly refrigerants. Ozone depletion caused by high ODP (Ozone Depletion Potential) CFC's, global warming contribution from high HFC's and the unknown environmental consequences of HFO's are concerns related to the use of traditional refrigerants. Natural refrigerants such as propane are not inflicted by these concerns. The ODP and GWP of R290 is respectively 0 and 3. In comparison the ODP and GWP of R134 are respectively 0 and 1340 (UN 1989, EU 2014, Ciconkov 2018).

2. MATERIALS AND METHOD

2.1. Collection of Data

Data has been collected using a standard Bosch Serie 4 WTW86298SN drum dryer. It is a HPDD (Heat Pump assisted Drum Dryer) using R134a as working fluid. Initial to the study, the original instrumentation and control module of the drum dryer were removed. To obtain satisfactory control of the process, manual switches were used to turn the compressor, drum motor and drum fan on/off. Suitable instrumentation was added to the drum dryer. Temperature is measured at six points of the HP cycle, as well as at three points of the air cycle. RH of the air is measured along with the temperature. Pressure is measured before and after the HP compressor. Additionally, the input power to the compressor and auxiliary components are measure separately. Fig. 2 shows a schematic of the instrumentation, as well as the drum dryer.

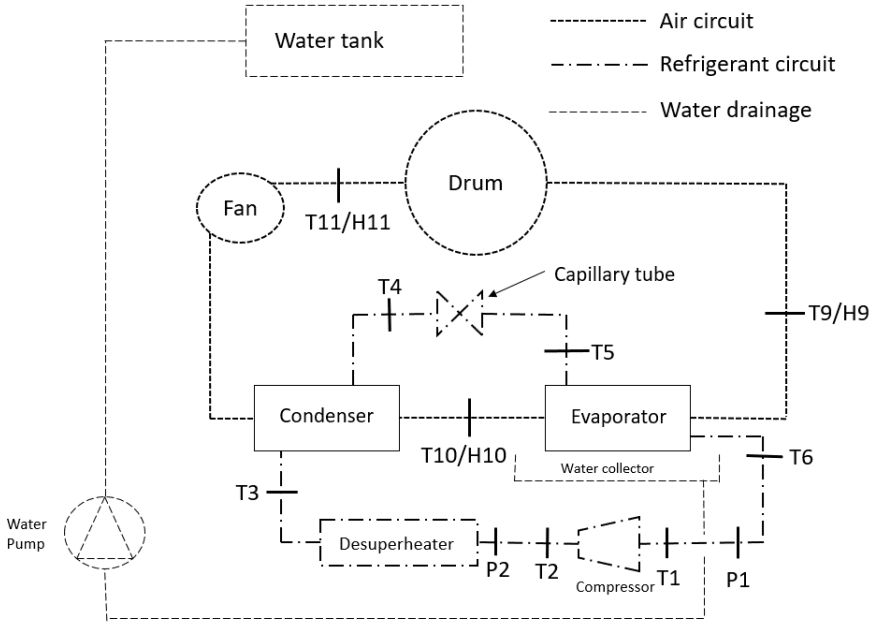

Figure 2. Schematic of the HPDD including instrumentation. P1 and P2 are pressure transmitters. T1-T6 are thermistors. T9/H9, T10/H10 and T11/H11 are combined humidity and temperature sensors.

T1 – T6 represents the six thermistors used to measure the temperatures of the HP circuit. The thermistors are attached to the outside of the tubes by aluminium tape and insulated from the ambient by cellular rubber. T9/H9, T10/H10 and T11/H11 represents the remote probes of the VAISALA humidity and temperature transmitters used to measure temperature and humidity of the airstream. Conversion formulas provided by VAISALA are used to convert the relative humidity measured by the probes to mixing ratio and absolute humidity. P1 and P2 are pressure transmitters, respectively DRUCK PTX 110/W at the low-pressure side and Endress+Hauser Cerabar PMC731 at the high-pressure side.

The weight of the dried fabric was measured before and after experiments using a Mettler Toledo XS32001LX scale. The measured weight was collected manually, while parameters measured by the sensors adapted to the drum dryer were automatically saved to a log file approximately every third second throughout the experiments.

2.2. Experimental Parameters

The following test parameters were chosen for the comparison to R290; A test load of 2.642 kg fabric consisting of various cotton, soaked and centrifugally treated at 1400 rpm in an AEG LN58460 washing machine. The initial state of the system was set to be in equilibrium with the ambient air in the laboratory. Equilibrium were defined by the temperature measurements to being equal to ambient temperature, and the pressure measured by the pressure sensors equal to saturation pressure at ambient temperature. The length of the experiments were set to 80 minutes, as initial experiments revealed residual moisture of 3-5% at that time.

The baseline for evaluation of the performance of R290 were established by performing experiments on the original R134a system. Due to the need of draining the system to install pressure transmitters, the system was recharged with 220g R134a. The charge after installation were equal to the factory charge stated by markings on the dryer. Experiments were performed before and after recharge to ensure that the recharge did not affect performance.

2.3. R290 Rebuild

To ensure adequate and unharmful operation the original R134a compressor was substituted for a Tecumseh AE4430U-FZ1A compressor. The AE4430U-FZ1A is a hermetic reciprocating compressor developed for use with R290. Efforts were made to fit the larger outer dimensions of the R290 compressor within the original casing of the dryer, ensuring relatively unaltered insulation and heat loss as well as suction and exhaust tube lengths. A service valve was fitted to the process port of the compressor, allowing for alternating refrigerant charge. Instrumentation were refitted and reinsulated as similar to prior as possible. Comparison of rated parameters of the original and substitute compressor is found in Table 1.

Table 1. Rated parameters of the original R134a compressor and the replacement R290 compressor

Producer	Modell no.	Type	Refrigerant	Displacement	Input power	Frequency
Rechi Precision	39E073B	Hermetic Reciprocating	R134a	7.5 ccm	300 W	50 Hz
Tecumseh	AE4430U-FZ1A	Hermetic Reciprocating	R290	6.12 ccm	315 W	50 Hz

A series of experiments were performed on the R290 system with unaltered capillary tube at different charge levels. Subsequent to obtaining a satisfactory amount of data, the capillary tube was replaced. The internal diameter of the capillary tube was kept constant at 1.00mm. The length of the capillary tube was increased by 53%, from 78.5cm to 120.0cm. The replacement capillary tube was soldered into place, maintaining the same length of insertion into the connecting tubes as before. No modifications were made to the tube and fin types condenser or evaporator. Due to the safety regulations in IEC 60335-289:2010 the maximum refrigerant charge is 150g. At the maximum charge of 150g R290 the global warming potential equivalents 0.450kg CO_2. The original charge of 220g R134a equivalents 295kg CO_2.

2.4. Experiments matrix

A total of 23 experiments form the data basis for the results and discussion. Parameters and number of experiments are presented in Table 2. The parameters of the experiments are selected based on calculations and investigative experiments. Excess of three repetitions at each set of parameters are initiated by excessive variance and deviations in the results after three repetitions.

Table 2. Matrix of experiments providing the data basis for results and discussion

Reference no.	Refrigerant	Capillary tube diameter	Capillary tube length	Refrigerant charge	Number of experiments
		[mm]	[cm]	[g]	
#1	R134a	1.00	78.5	220	3
#2	R290	1.00	78.5	100	3
#3	R290	1.00	78.5	115	5
#4	R290	1.00	78.5	125	4
#5	R290	1.00	78.5	135	3
#6	R290	1.00	120.0	150	5

3. RESULTS AND DISCUSSION

The system is evaluated in terms of COP, SMER (Specific Moisture Extraction Rate) and MER (Moisture extraction Rate). COP are calculated from sensor readings, while SMER and MER are calculated from the weight of the fabric before and after drying. Intermediate values of SMER and MER are calculated from hygrometer readings, calibrated against fabric weight for each individual experiment.

3.1. Optimization

A series of experiments (Ref. no #2, #3, #4, #5) were performed to investigate the ideal R290 charge while maintaining the original capillary tube. It is seen in Table 3 that the highest COP was obtained at 125g charge, while the highest SMER was obtained at 115g. By regression analysis the ideal charge in respect to COP was found to be 123g of R290.

Table 3. System performance at different R290 charge levels. The compressor is replaced while maintaining the original capillary tube.

Reference no.	Refrigerant charge	COP	SMER	MER
#2	100g	3.88	1.68	0.887
#3	115g	3.93	1.71	0.896
#4	125g	3.96	1.67	0.892
#5	135g	3.92	1.69	0.911

The length of the capillary tube was increased from 78.5 cm to 120cm by replacement. Due to excessive overheating at the evaporator outlet subsequent to the replacement, the charge was increased until reaching the maximum limit of 150g. At 150g adequate overheating were obtained. Table 4 shows that increased COP was obtained at this state, while SMER and MER did not deviate significantly compared to previous experiments. While the performance parameters of the R134a system is also seen in Table 4, characteristics of the original R134a system is compared to the R290 system at 120 cm capillary tube and 150g charge in the following subchapters.

Table 4. System performance of the original R134a system and the rebuild R290 system. For the R290 system the compressor and the capillary tube has been replaced while the charge is 150g

Reference no.	Refrigerant	COP	SMER	MER
#1	R290	3.80	1.69	0.914
#6	R134a	4.03	1.70	0.912

3.2. Heat Exchange and Temperature Development

The development of the Log Mean Temperature Difference (LMTD) throughout the experiment is plotted in Fig 3. The plotted value the average for the experiments performed on the R134a (#1) system, and the average for the experiments performed on the R290 (#6) system. The LMTD is calculated based on condensation and evaporation pressure derived from condensation and evaporation pressure through saturation tables. The LMTD equation does not allow for applying subcooling or overheating to the equation. The plot shows that the LMTD of the evaporator decreased when charged with R290 compared to R134a, indicating slightly superior heat transfer characteristics of R290.

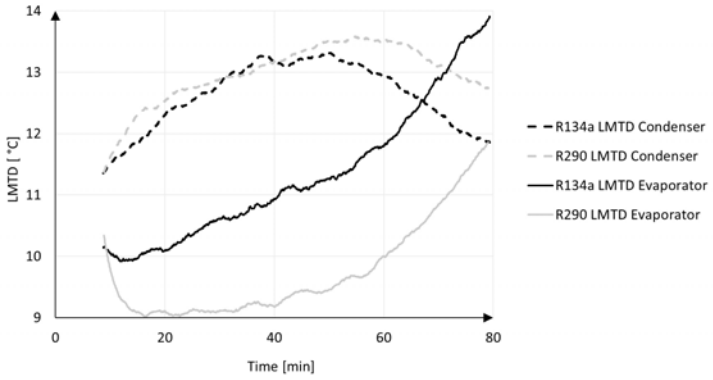

Figure 3. LMTD of the Condenser and Evaporator of the R134a (#1) system and the R290 (#6) system

Towards the end of the experiments the Evaporator LMTD of both refrigerants increases significantly, while the Condenser LMTD decreases. The decrease in evaporator LMTD is a result of decreased moisture ratio of the air coming from the drum, seen in Fig. 4. Moist air inhibits

improved heat transfer characteristics compared to dry air, providing lower LMTD while the air is moist. The decrease in Evaporator LMTD while charged with R290 suggests that the refrigerant side (tubing) of the evaporator may be reduced when designing a HPDD utilizing R290.

The Condenser LMTD is influenced by the amount of subcooling at the condenser outlet. Increased subcooling implies that a larger part of the condenser contains refrigerant at temperatures below condensation temperature. This requires the smaller part of the condenser filled with refrigerant at condensation temperature to transfer more heat through a smaller surface area, demanding increased temperature difference. Due to decrease in subcooling at the condenser outlet towards the end of experiments, a corresponding decrease in the LMTD is observed.

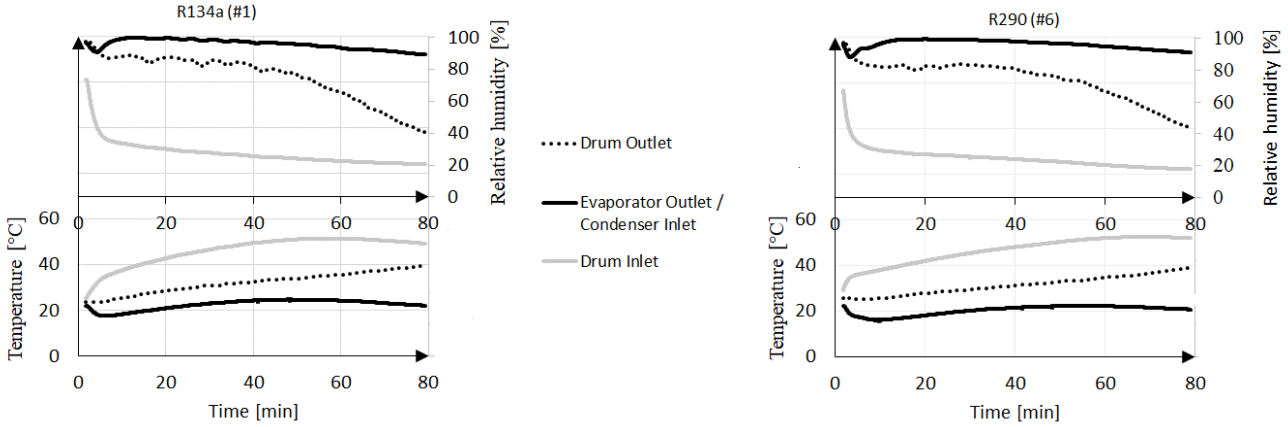

Figure 4 - Air cycle temperature and RH. R290 (#6) to the right and R134a (#1) to the left.

As the humidity of the drum exhaust air declines, increase in the temperature difference between the drum exhaust air going into the evaporator and the air leaving the evaporator is observed. As less moisture is available in the drum, less energy is taken from the air to evaporate water providing elevated temperatures at the drum outlet. In the evaporator less energy is available in the air as the humidity declines, due to the latent heat of evaporation of water. To maintain heat flow to the evaporator, the sensible cooling of air must increase.

3.3. System performance

As observed by Table 3 and Table 4 the highest SMER is observed while the R290 system was charged with 115g R290 and the original capillary tube maintained. Statistically, no difference between the measured SMER values were found ($P>0.05$). The highest COP was observed after capillary tube replacement, while charged with 150g R290. The increase in COP was found to be statistically significant ($P<0.05$). Compared to the original R134a system, the COP increase was 6%. The development of the COP throughout the experiments are shown in Fig. 5, while the efficiency of the compressor is shown in Fig. 6. Due to the increase in LMTD of the condenser and evaporator discussed earlier, the COP is reduced even though the compressor efficiency increases. Increased temperature difference requires more work to be done by the compressor.

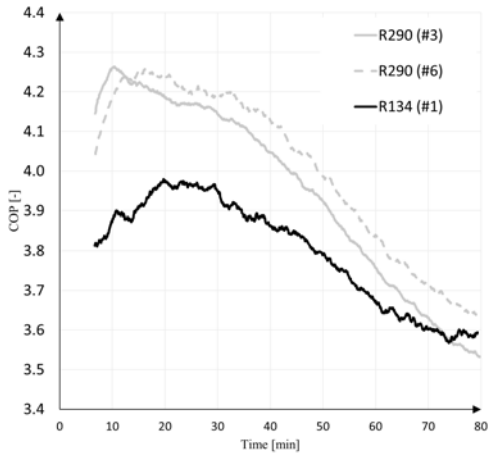

Figure 5. COP of the HP pump vs. time

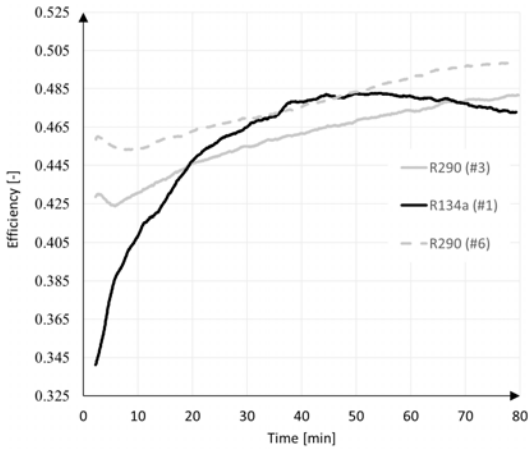

Figure 6. Efficiency of the compressor vs. time

The SMER relies on the energy consumption of the drum fan and drum motor, as well as the COP of the HP. Maximum SMER and maximum COP is not observed at the same time. This is caused by the increased efficiency of the drying process at elevated temperatures. As the temperature increases, the drying process is moved to the right in the IX-diagram, where more moisture can be held by a given amount of air. This reduces the need for work to be done by the fan to remove the same amount of moisture. As the fan and drum is run by the same motor at constant speed, the measured energy consumption relatively constant. The energy consumption for the compressor increases along with the drying rate. By summation of the components, the total energy consumption per unit of moisture removed is at its lowest at relatively high temperatures and high drying rates.

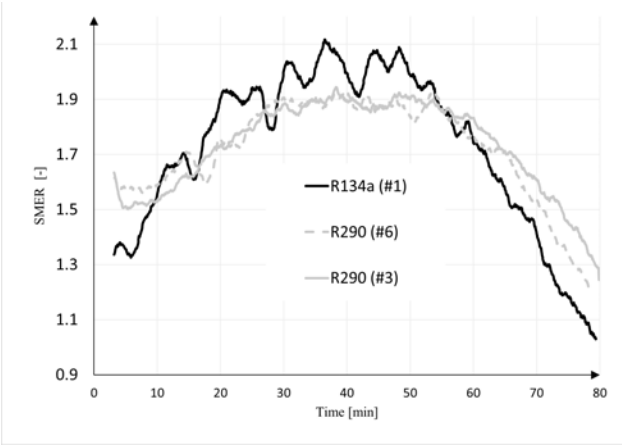

Figure 7. SMER vs. time

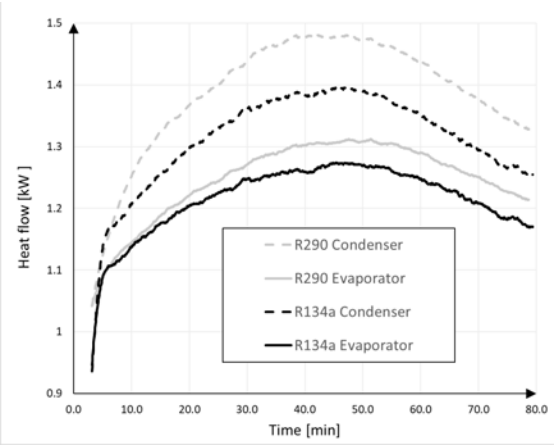

Figure 8. Condenser and Evaporator heat flow vs. time for the R134a (#1) system and the R290 (#6) system

As seen by Fig. 7 and Fig. 8**Figure *8*** the maximum SMER is obtained simultaneously with the highest heat flow through the evaporator and condenser. It elucidates that the HPDD overall efficiency relies on minimum energy to be used for moving air and rotating the drum per unit of moisture extracted by the heat pump. The SMER as well as the heat flow increases as long as close to constant relative humidity of the air leaving the drum is maintained. Reduction in humidity of the air leaving the drum causes rapid decrease in both SMER, drying rates and heat flow.

4. CONCLUSIONS

By substituting no other components than the compressor, R134a was replaced with R290 without diminishing energy efficiency, reliability or drying rates. Subsequent to replacing the capillary tube, 6% increase in the heat pumps COP was observed. Due to lowered drying temperatures, no significant increase in SMER were observed. The maximum charge of 150g R290 set by the IEC 60335-2-89:2010 was not exceeded.

It is possible to conclude that successful substitution of R134a for R290 in heat pump assisted drum dryers may be accomplished without making excessive changes to system design or challenging charge regulations. Providing compressor replacement, the same level of energy efficiency and reliability is obtained. By proper replacement of the capillary tube, increased energy efficiency may be obtained.

The climate affect caused by leakage or improper handling of used refrigerant is reduced tremendously by utilizing R290.

REFERENCES

Ciconkov, R. (2018). "Refrigerants: There is still no vision for sustainable solutions." International Journal of Refrigeration **86**: 441-448.

EU (2014). REGULATION (EU) No 517/2014 OF THE EUROPEAN PARLIAMENT AND OF THE COUNCIL of 16 April 2014 on fluorinated greenhouse gases and repealing Regulation (EC) No 842/2006. 842/2006. Official Journal of the European Union.

Gopalnarayanan, S. and R. Radermacher (1997). Heat-pump assisted dryer using refrigerant mixtures -- Batch mode drying, American Society of Heating, Refrigerating and Air Conditioning Engineers, Inc., Atlanta, GA (United States).

UN (1989). Montreal Protocol on Substances that Deplete the Ozone Layer (with annex). Concluded at Montreal on 16 September 1987. U. N.-T. Series. Montreal, United Nations.

Manuscript ID: 325
DOI: 10.18462/iir.icr.2019.0325

Investigation of an air source heat pump water heating system working at wide temperature scale

Jianyong CHEN[(a,b)], Ying CHEN[(a,b)], Xianglong LUO[(a,b)], Zhi YANG[(a,b)]

[(a)] School of Material and Energy, Guangdong University of Technology
Guangzhou, 510006, China, e-mail: jianyong@gdut.edu.cn
[(b)] Guangdong Provincial Key Laboratory of Functional Soft Condensed Matter
Guangzhou, 510006, China

ABSTRACT

Water heating represents significant energy use and accounts for a high proportion of total energy consumption in residential section. Air source heat pump water heater (ASHPWH) has been recognized as a very promising technology with advantages of energy-saving, safe in use, low cost, etc. The current heat pump systems are subjected to inefficient operation all year around. A novel ASHPWH is proposed for wide temperature scale. It consists of four different operating modes. The mathematical model is established and integrated with refrigerant properties from REFPROP. Results show that the switch strategies of ambient temperature for optimum COP are distinguished. At outlet water temperature of 41 ^{o}C, the switch ambient temperature is -18 ^{o}C and 16.5 ^{o}C for Mode A, Mode B and Mode D. Its application in typical cities has superior performance to each individual cycle. In Guangzhou, the proposed system shows the highest improvement. The experimental study of Mode C and Mode D indicates that the later one has better COP at ambient temperature of -25 ^{o}C and -12°C.
Keywords: COP, Efficiency, Heat Pump, Operating Mode, Ambient Temperature.

1. INTRODUCTION

Water heating consumes a significant percentage of total end-use energy in residential sections, which accounts for 15% in China, 18% in USA, 25% in UK, 30% in Australia and 20% in Canada (Guo et al. 2019). Heat pump is able to generate much more heat with the same amount of electricity used for conventional heaters, and it only use 40%-100% energy of electric heating units and 30%-50% of gas units. It is very helpful to reduce the consumption of electricity and fossil energy. Air source heat pump water heater (ASHPWH) makes a better use of the energy from air that is an excellent source in terms of availability. With benefits of comparably low initial cost, energy saving, effectiveness and environmental benign, it has gained the increasing popularity for water heating application.

Numerous investigations on heat pump water heater have been carried out with focus on various heat pump cycles, such as single-stage cycle, vapor-injection cycle, two-stage cycle and cascade cycle. Ji et al. (2005) proposed a single-stage heat pump cycle having multi-functions of three operating modes, namely water-heating, space-heating and space-cooling, under the ambient temperature (T_{air}) of 2.8 ^{o}C. The energy-saving was confirmed. Cho and Choi (2013) carried experiments on a similar heat pump cycle under various operating modes in which the heating mode was operated at the T_{air} of 5 ^{o}C. They found that the cooling-hot water mode had the highest COP. To improve the heating performance at low T_{air}, the vapor-injection compressor is rapidly developed and implemented since only one compressor is used to achieve high pressure differences. Heo et al. (2011) studied four different vapor-injection cycles at T_{air} of -15 ^{o}C and discovered that they had equivalent COP, but the vapor-injection cycle with a flash tank had superior heating capacity. Two-stage heat pump cycle employs two compressors with the cooled temperature at the second stage compressor suction. Cao et al. (2014) comparatively studied the thermodynamic and economic heat pump performance of a single-stage cycle and five two-stage cycles for high condensation temperatures. It is concluded that the two-stage cycle with flash tank was favorited due to high COP and less initial investment. Regarding the cascade cycle, it consists of two single-stages working with different refrigerants, aiming to get even larger

temperature difference. Jung et al. (2013) verified that the cascade heat pump had more stable air and water heating operations and higher water outlet temperatures than the single-stage one under the evaporation temperature of 0 °C. Shen et al. (2018) presented a heat pump by changing operation mode between single stage cycle and cascade cycle to satisfy the heating demand under different T_{air} in the range from -12 °C to 10 °C, and claimed that the COP curves of different modes crossed each other, leading to the optimal control method. Moreover, Bertsch and Groll (2008) compared three heat pump cycles (two-stage with intercooler/economizer and cascade) and pointed out that the cascade cycle had the better performance at T_{air} between -30 °C to 10 °C. Roh and Kim (2014) revealed that the applications of vapor-injection to up and/or low stages of cascade heat pump cycle could enhance heating capacity by 12% but decrease COP by 6.6%. In general, different cycles have their preferable operating conditions.

ASHPWH has optimal performance only under certain operating conditions, especially for a fixed structure. At low T_{air}, the single-stage cycle has high compressor discharge temperature, leading to compressor shut down because of its protection. Moreover, it has significantly degraded COP when lowering T_{air}. Hence the two-stage cycle are mostly applied. At high T_{air}, the two-stage cycle has to operate intermittently to reduce the heating capacity, while for cascade cycle neither the up-stage nor the low-stage can work solely because of the connection of intermediate heat exchanger. Thus the single-stage cycle is recommended. In a word, no individual heat pump cycle can generally serve for wide temperatures with high efficiency. Given the fact that the considerable variations of year-round T_{air}, how to keep heat pump operation efficiently at different seasons is of necessity to solve and to enhance the system feasibility.

In this paper, a novel ASHPWH system is proposed, which has four different cycles coded by four operating modes. The objective is to improve the heat pump efficiency throughout the entire year that has large variations of T_{air}. The system operating modes are identified and its performance is evaluated at four cities in China. Preliminary experiments are also conducted and analyzed. The study is useful to provide guidance for selecting suitable cycles and control designing of the proposed novel ASHPWH.

2. SYSTEM DESCRIPTIONS AND FORMULATIONS

Fig. 1a schematically shows the proposed ASHPWH system. Basically, it is the combination of a vapor-injection cycle and a cascade cycle. The vapor-injection cycle and a single-stage cycle are located at the up-stage and low-stage, respectively, in the cascade cycle, and they are connected by an intermediate heat exchanger acting as evaporator for up-stage and condenser for low-stage. More interestingly, they have a mutual evaporator. By opening/closing the valves (V1-V3), it can operate at four modes corresponding to four cycles, namely single-stage cycle (Mode A), vapor-injection cycle (Mode B), cascade cycle (Mode C) and vapor-injection cascade cycle (Mode D), as listed in Fig. 1b. To be specific, it is a single-stage heat pump as Mode A when vapor-injection line (V1), intermediate heat exchanger line (V2) and the low-stage are closed. The vapor-injection cycle is realized by closing V2 and low-stage. Regarding cascade cycle, V1 and V3 are closed. For injection-cascade cycle, only V3 is closed. It aims to achieve the relatively superior annual efficiency by switching among different modes to work at own optimal T_{air}.

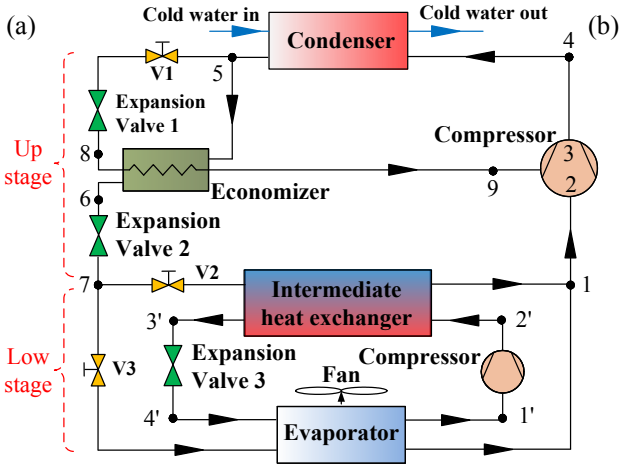

Operating modes		Up stage	Low stage	On/Off Valve		
				V1	V2	V3
Mode A	Single-stage	ON	OFF	OFF	OFF	ON
Mode B	Vapor-injection	ON	OFF	ON	OFF	ON
Mode C	Cascade	ON	ON	OFF	ON	OFF
Mode D	Injection cascade	ON	ON	ON	ON	OFF

Figure 1: Proposed heat pump system (a) schematic diagram (b) its operation modes

For simplicity, the assumptions in the theoretical calculations are made as: the system operates steady; the pressure drop and heat loss are neglected. The temperature differences are set as constants. The system performance is evaluated based on the conservations of mass and energy. Therefore, the following equations are used:

$$Q_{con}=\dot{m}_4\cdot(h_4-h_5) \quad \text{Eq. (1)}$$

$$W_{up,I}=\dot{m}_4\cdot(h_4-h_1) \quad \text{Eq. (2)}$$

$$W_{up,I}=\dot{m}_1\cdot(h_2-h_1)+\dot{m}_4\cdot(h_4-h_3) \quad \text{Eq. (3)}$$

$$W_{low}=\dot{m}_{1'}\cdot(h_{2'}-h_{1'}) \quad \text{Eq. (4)}$$

$$\dot{m}_1\cdot(h_7-h_1)=\dot{m}_{1'}\cdot(h_{2'}-h_{3'}) \quad \text{Eq. (5)}$$

$$\dot{m}_1\cdot(h_5-h_6)=\dot{m}_9\cdot(h_9-h_8) \quad \text{Eq. (6)}$$

For mode A $$COP=Q_{con}/W_{up,I} \quad \text{Eq. (7)}$$

For mode B $$COP=Q_{con}/W_{up,II} \quad \text{Eq. (8)}$$

For mode C $$COP=Q_{con}/(W_{up,I}+W_{low}) \quad \text{Eq. (9)}$$

For mode D $$COP=Q_{con}/(W_{up,II}+W_{low}) \quad \text{Eq. (10)}$$

$$APF=\Sigma Q_{con,i}/\Sigma W_i=\Sigma f_i\cdot COP_i \quad \text{Eq. (11)}$$

where Q_{con} is heating capacity in kW, $W_{up,I}$, $W_{up,II}$ and W_{low} are compressor electricity consumptions in kW at single-stage, vapor-injection and low-stage, respectively. $\dot{m}$ is mass flowrate in kg/s, h is specific enthalpy in kJ/kg. COP is coefficient of performance, which is calculated accordingly for these four modes. The subscripts are in consistent with Fig. 1. APF, i.e. annual performance factor, is applied to evaluate the performance throughout a year. The subscript i represents T_{air}=i °C and f_i is the frequency of T_{air}=i °C in total hours of a year.

3. EXPERIMENTAL SETUP

To confirm the effectiveness of proposed ASHPWH system, an experimental prototype was constructed as shown in Fig. 2a. A vapor-injection scroll compressor having a displacement of 12.8 m^3/h and a rotary compressor with a displacement of 7.3 m^3/h were equipped, in which R134a and R410A were used, at the up stage and low-stage, respectively. Moreover, three plate heat exchangers were employed as the condenser, intermediate heat exchanger the economizer. The cooperative evaporator was modified from a double-row fin-and-tube heat exchanger. All expansion devices were electronic expansion valves (EEV) due to its convenience for adjustments. Other auxiliaries, such as receiver, liquid-vapor separator, sight glasses, were also installed to facilitate system operation.

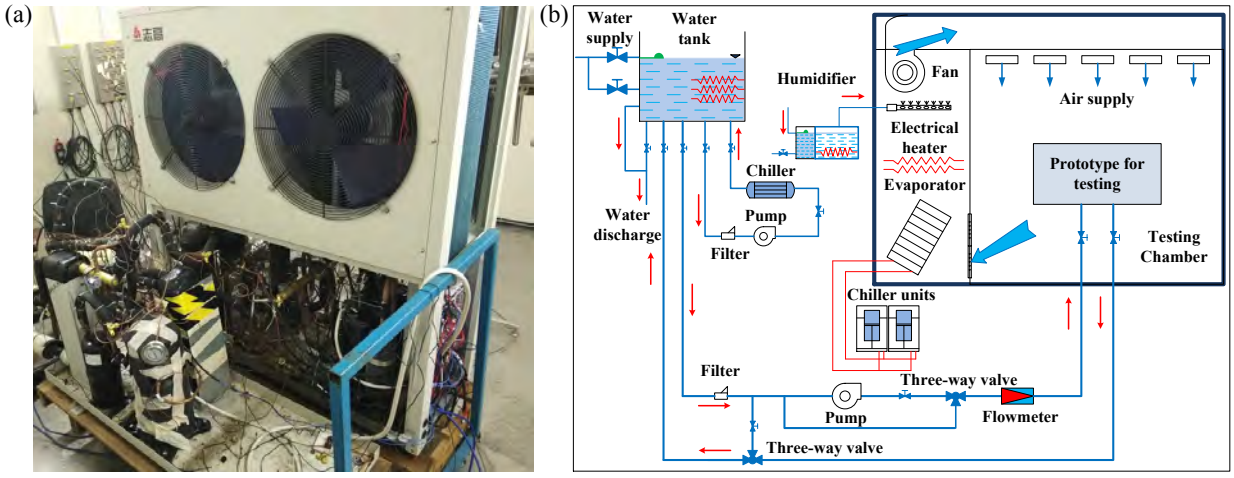

Figure 2: (a) Heat pump prototype (b) schematic of testing lab

The testing lab is schematically illustrated in Fig. 2b. The temperature of testing room can be controlled in the range from -25 °C to 60 °C by the evaporator of a chiller units and the electrical heater, while its relative humidity is regulated by the humidifier in the range of 30%-90%. The testing prototype is connected to a water tank. The water temperature (4-80 °C) and flowmeter

are automatically maintained. The testing lab is able to measure the heating capacity of 1.5-25 kW. In the present testing, the heating capacity, the compressor power consumption and COP are directly recorded with uncertainties of ±1.5%, ±0.2% and ±1.5%, respectively.

4. RESULTS AND DISCUSSIONS

To discover the characteristics of the proposed ASHPWH system, the effects of ambient temperature (T_{air}) are firstly evaluated at different water outlet temperatures ($T_{water,out}$) in order to identify its optimum operation of the four modes and determine the T_{air} switching strategy. Then it is applied to four different cities from North to South in China to reveal its superiority in terms of APF. R134a and R410A are employed in the up-stage and low-stage, respectively, as same as in the experiments. The empirical correlations of the compressor isentropic efficiencies were provided by the manufactures in the experiments. The other operating conditions in theoretical calculations are constantly set as listed in Table 1. A MATLAB program is compiled to calculate the system performance. The fluids (R134a, R410A, water and air) are taken from refrigerant property database (REFPROP 10.0).

Table 1. Conditions in the calculation

Parameters	Value
Temperature difference between ambient and evaporator	10 °C
Temperature difference between water outlet and condenser	7 °C
Temperature difference in the intermediate heat exchanger	8 °C
Temperature difference in the economizer	5 °C
Subcooling at the intermediate heat exchanger and condenser	0 °C
Superheating at the intermediate heat exchanger outlet	10 °C
Superheating at evaporator outlet	5 °C
Up-stage compressor displacement	12.8 $m^3 \cdot h^{-1}$
Low-stage compressor displacement	7.3 $m^3 \cdot h^{-1}$

Preliminary experiments are mainly carried out according to Chinese standard (GB/T 25127.2-2010), in which the nominal operating condition is specified as: T_{air} of dry bulb and wet bulb are kept at -12 °C and -14 °C, respectively, meanwhile $T_{water,out}$ is 41 °C and water flowrate is 0.172 m^3/h. It is noted that in the paper only Mode C and Mode D are attempted to be examined, while Mode A and Mode B are not discussed since they are still under calibrations.

4.1 Performance Evaluation for Different Operating Modes

Fig. 3 depicts COPs of the four modes at various T_{air} (from -25 °C to 35 °C) and $T_{water,out}$ (41 °C, 50 °C, 60 °C and 70 °C) with the eliminations of some data that have the compressor discharge temperature higher than 140 °C. As expected, COPs of all modes increases with the increasing of T_{air} and the decreasing of $T_{water,out}$. Due to various sensitivity of the four modes subjected to T_{air}, COPs curves of the operating modes are crossed. Clearly, Mode A has the most significant variation rate of COP, followed by Mode B and then Mode C, while Mode D is the least. As a result, each mode has its optimal operating conditions, which fulfills the intension of the proposed ASHPWH system that is to widen the operation conditions without serious penalty of COP relative to any individual cycle. For instance, at $T_{water,out}$=41 °C, when T_{air} is higher than 16.5 °C, the single-stage cycle has the best COP; when T_{air} is between -18 °C to 16.5 °C, the vapor-injection cycle has the best COP; when T_{air} is lower beyond -18 °C, the injection-cascade has the best COP. In other words, the operation of proposed system at $T_{water,out}$=41 °C should be as following: Mode D is in action as $T_{air} \leq$ -18 °C; Mode B is in action as -18 °C $\leq T_{air} \leq$ -16.5 °C; Mode A is in action as $T_{air} \geq$ 16.5 °C. With this switching strategy, the proposed ASHPWH system could have the superior performance. Similarly, at $T_{water,out}$=50 °C, the switching temperature points are T_{air} at -8 °C and 28 °C among Mode D, Mode B and Mode A. As for $T_{water,out}$=60 °C and 70 °C, only Mode D and Mode B are in operation with the switching temperature of T_{air} at -5 °C and 0 °C, respectively. Interestingly, the switching T_{air} also increases with the increasing of $T_{water,out}$, which means that the precise control is of great importance for specific operating conditions. Moreover,

it seems that Mode C is not covered in the operation because of its moderate performance.

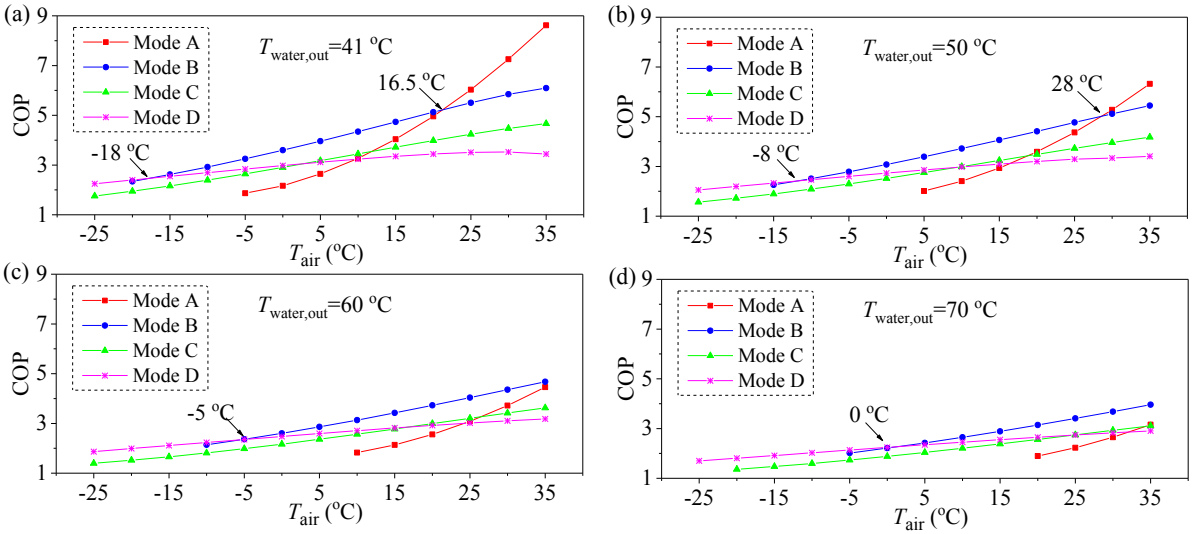

Figure 3: Variations of COP of different modes with ambient temperature

4.2 System Performance at Different Cities

Different cities have their specific climate characteristics and its T_{air} changes dramatically. As shown in Fig. 4 of climate temperature data for four cities in China, namely Shenyang, Beijing, Wuhan and Guangzhou (Meteomanz 2019), the biggest temperature difference between the minimum and maximum ones can be up to 55 °C. As indicted, an individual heat pump cycle cannot operate with its optimal performance throughout the whole year. Moreover, the duration of each temperature ranges are significantly differentiated from these cities. The north city Shenyang has major T_{air} lower than 0 °C that accounts for 35.2% of all 8760 hours a year, and it also has extra low T_{air} of -24 °C. Beijing has the most T_{air} in the range -5 °C to 30 °C, and T_{air} of Wuhan are mostly from 5 °C to 30 °C. As for the south city Guangzhou, it is typical subtropical climate and has an average T_{air} of 22 °C with no exception of lower than 0 °C.

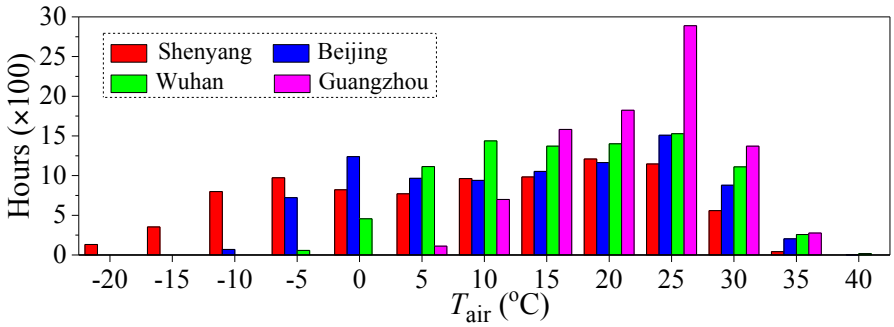

Figure 4: Hours of ambient temperatures at four cities in China

The proposed ASHPWH system is attempted in these four cities by means of comparing APF to that of each individual cycle. At the scenario of $T_{water,out}$=41 °C, the switching T_{air} of the proposed system are -18 °C and 16.5 °C, as indicated in Fig. 3(a). Moreover, the single-stage cycle at T_{air} < -5 °C is exclusively feasible due to the extremely high compressor discharge temperature, which means it does not work. Under such circumstances, the electrical heater has to be used. Meanwhile, its efficiency is considered to be equal to one at these conditions. The values of APF are presented in Table 2. Since the four cities are from north to south with an increase annual average T_{air}, APFs of the four individual cycles (single-stage, vapor-injection, cascade and injection-cascade) and the proposed system are also increased. Furthermore, the vapor-injection cycle has superior APFs among the four cycles, which is explained by its widest range of T_{air} for optimal COP, i.e. Mode B in the proposed system. By integrating Mode A and Mode D at their corresponding optimum conditions, the proposed system has even more preferable APF that is 4%, 6.3%, 7.4% and 9.0% higher than that of vapor-injection cycle at Shenyang, Beijing, Wuhan and Guangzhou, respectively.

Table 2. APF when $T_{water,out}$=41 °C for different modes

City	Single-stage (Mode A)	Vapor-injection (Mode B)	Cascade (Mode C)	Injection-cascade (Mode D)	Proposed system (Switch mode)
Shenyang	3.58	4.30	3.39	3.16	4.47
Beijing	4.23	4.64	3.64	3.27	4.93
Wuhan	4.67	4.88	3.82	3.35	5.24
Guangzhou	5.46	5.25	4.07	3.44	5.72

4.3 Experimental Results

By carefully adjusting the refrigerant charges and the openings of electronic expansion valves of the prototype at Mode D, the optimum COPs are obtained based on cascade cycle under nominal operating condition (T_{air}=-12 °C and $T_{water,out}$=41 °C) according to Chinese standard (GB/T 25127.2-2010). Moreover, the extra low T_{air} of -25 °C is also tested for both Mode C and Mode D. The experimental results are listed in Table 3. It is found that Mode D has improved Q_{con} of 3.0% and 5.8% than those in Mode C at T_{air} of -12 °C and -25 °C, respective, and it also has higher COPs of 3.3% and 6.8%. This indicates that Mode D is more effective at the lower T_{air}. Moreover, Q_{con} at T_{air} = -25 °C is much lower than that at T_{air} = -12 °C at both modes.

Table 3. Experimental results at ambient temperature -12 °C and -25 °C

T_{air}	Operating mode	Q_{con} (kW)	W (kW)	COP
-12 °C	Mode C	8.761	4.766	1.838
	Mode D	9.290	4.894	1.898
-25 °C	Mode C	6.189	4.354	1.422
	Mode D	6.994	4.604	1.519

More experiments are targeted to the various operating conditions of Mode C that is relatively well calibrated. The results of COPs are shown in Fig. 5. Obviously, COP decrease with enlarged temperature, i.e. the reducing of T_{air} and the increasing of $T_{water,out}$. It is more sensitively influenced by T_{air} than $T_{water,out}$. For example, a 1 °C change in T_{air} leads to an average 0.027 change of COP, while a 1 °C change in $T_{water,out}$ results in an average COP variation of 0.011. Moreover, effects of $T_{water,out}$ on COP at low T_{air} are less significant than at high T_{air}. The similar characteristic is also found for the effects of T_{air} at different $T_{water,out}$. Therefore, it is more preferred at larger temperature differences.

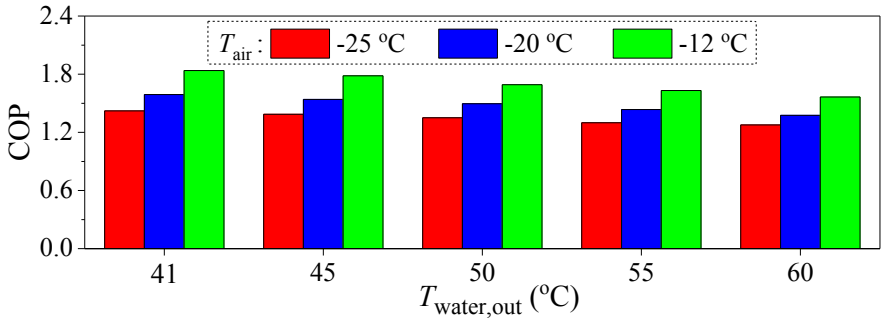

Figure 5: Experimental COP of Mode C at different operating conditions

Fig. 6 depicts the variations of heat capacity (Q_{con}) from the experiments. Similarly, Q_{con} increases with the increasing of T_{air}. When T_{air} rises from -25 °C to -12 °C, Q_{con} improves ranges from 29.2% from 41.5% in the considered conditions. This can be explained by the variations of refrigerant mass flowrate at different T_{air}. A higher T_{air} causes a higher evaporating temperature in the evaporator, hence the compressor suction pressure increases as well, which means the specific volume is reduced. Consequently, more refrigerant can be entered to the compressor, i.e. higher mass flowrate. Moreover, for a certain T_{air}, Q_{con} is insignificantly impacted by $T_{water,out}$. This is

contributed by the regulated water side during the experiments.

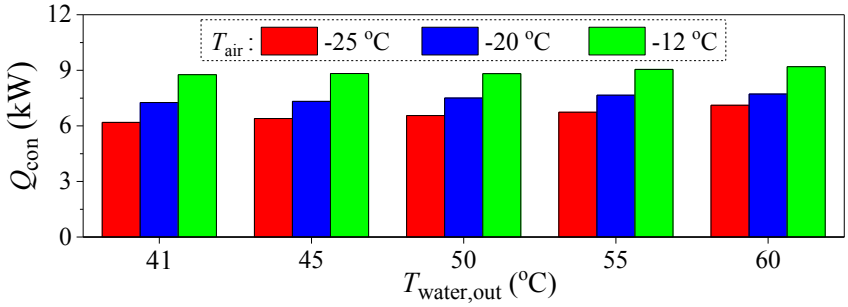

Figure 6: Experimental heating capacity of Mode C at different operating conditions

5. CONCLUSIONS

A novel ASHPWH system with different operating modes is proposed to have wide operating conditions. The theoretical evaluations and experimental studies are conducted. The main findings are addressed as:

(1) Each individual cycle has different sensitivities, and they fail to cover the wide ambient temperature ranges with optimal COPs.
(2) The proposed system has various operating modes and switching strategy of ambient temperatures when the water outlet temperature is different.
(3) The proposed system has the superior APF compared to any individual cycle. Its application to Guangzhou is most promising with the enhanced APF of 9.0%.
(4) The experiments reveal the COP of injection-cascade is 3.3% higher than cascade cycle when ambient temperature is -12 °C. The improvement is more obvious at 6.8% at the ambient temperature of -25 °C.

ACKNOWLEDGEMENTS

This study is supported by National Natural Science Foundation of China (51706047) and Science and Technology Program of Guangzhou (201704030108).

NOMENCLATURE

APF	annual performance factor	Subscripts	
COP	coefficient of performance	air	ambient
f	typical temperature frequency	con	condenser
h	specific enthalpy (kJ·kg^{-1})	i	normalized temperature
$\dot{m}$	mass flow rate (kg·s^{-1})	low	low-stage in cascade
Q	heat load (kW)	up	up-stage in cascade
T	temperature (K)	1-9 and 1'-	locations in Fig. 1
W	compressor power consumption (kW)		

REFERENCES

Bertsch, S.S., Groll, E.A., 2008. Two-stage air-source heat pump for residential heating and cooling applications in northern U.S. climates. Int. J. Refrigeration 31(7), 1282-1292.

Cao, X.Q., Yang, W.W., Zhou, F., He, Y.L., 2014. Performance analysis of different high-temperature heat pump systems for low-grade waste heat recovery. Appl. Therm. Eng. 71(1), 291-300.

Cho, C., Choi, J.M., 2013.Experimental investigation of a multi-function heat pump under various operating modes. Renew. Energ. 54, 253-258.

GB/T 25127.2, 2010. Low ambient temperature air source heat pump (water chilling) packages –

part 2: heat pump (water chilling) packages for household and similar application (in Chinese).

Guo, X., Ma, Z., Ma, L., Zhang, J., 2019. Experimental study on the performance of a novel in–house heat pump water heater with freezing latent heat evaporator and assisted by domestic drain water. Appl. Energ. 235, 442-450.

Heo, J., Jeong, M.W., Baek, C., Kim, Y., 2011. Comparison of the heating performance of air-source heat pumps using various types of refrigerant injection. Int. J. Refrigeration 34(2), 444-453.

Ji, J., Pei, G., Chow, T., He, Wei., Zhang, A., Dong, J., Yi, H., 2005. Performance of multi-functional domestic heat-pump system. Appl. Energ. 80(3), 307-326.

Jung, H.W., Kang, H., Yoon, W.J., Kim, Y., 2013. Performance comparison between a single-stage and a cascade multi-functional heat pump for both air heating and hot water supply. Int. J. Refrigeration 36(5), 1431-1441.

Lemmon, E.W., McLinden, M.O. and Huber M.L., 2018. NIST standard reference database 23: reference fluid thermodynamic and transport properties-REFPROP, Version 10.0. Gaithersburg (USA): National Institute of Standards and Technology, Standard Reference Data Program.

Meteomanz 2019. http://www.meteomanz.com/index?l=1 (Accessed January 5, 2019).

Roh, C.W., Kim, M.S., 2014. Effect of vapor-injection technique on the performance of a cascade heat pump water heater. Int. J. Refrigeration 38, 168-177.

Shen, J., Guo, T., Tian, Y., Xing, Z., 2018. Design and experimental study of an air source heat pump for drying with dual modes of single stage and cascade cycle Appl. Therm. Eng.129, 280-289.

Manuscript ID: 400
DOI: 10.18462/iir.icr.2019.0400

Implementation of a 25kW NH_3-H_2O absorption resorption refrigeration unit in the heating, cooling and refrigeration network of a supermarket

Oliver ZIEGLER[(a)], Ullrich HESSE[(a)], Christiane THOMAS[(a)]

[(a)] Bitzer-Professur für Kälte-, Kryo- und Kompressorentechnik, Technische Universität Dresden
Dresden, 01069, Germany, oliver.ziegler@tu-dresden.de

ABSTRACT

In the scope of a demonstration project, an absorption resorption refrigeration system (RRS) has been further developed from the functional to the prototype status. The RRS was integrated into the heating, cooling and refrigeration structure of a supermarket. The main purpose of the integration was the increase in the annual efficiency of the Cogeneration plant (CHP) and the reduction of electrical energy consumption of the cooling system in the A/C level (3°C to 9°C) and medium temperature refrigeration (-6°C to 6°C).
To distribute the cooling capacity a secondary refrigerant cycle is used, which allows additional R290 refrigeration units. A PCM cold storage unit was installed to further increase the flexibility of the generation of power, heating and cooling capacity.
The implementation of the RRS is presented and the achieved cooling capacities are discussed depending on selected boundary conditions.
Keywords: Resorption, Absorption, Ammonia-water, Supermarket, Cogeneration.

1. INTRODUCTION

In all scenarios of the transition to a regenerative-based energy supply, the use of the advantages of highly efficient cogeneration plants (CHP) is one of the recognized methods (BMWi, 2014). To this end, the potential of a combined heating, power and cooling system (CHCP) must be exploited to provide a guaranteed and efficient cooling for storage in the food industry as well as for industrial and technological processes. In order to further increase the operating hours of combined heat and power plants (CHP plants), the low temperature waste heat can be used in the summer and transitional months to provide refrigeration capacity even in the range below 0 °C. The resorption technology offers a promising technical alternative to conventional CHCP plants. Within the scope of the ResoField project a new absorption resorption refrigeration system for combined heating, power and cooling supply (CHCP) with a maximum cooling capacity of 25 kW was thermodynamically optimized. In order to demonstrate the plant technology and to compare the economic efficiency with other thermally driven refrigeration plants, a resorption plant was designed, manufactured, implemented in a reals supermarket and operated for a period of 6 months up to now. After a brief outline of the functional principle of resorption technology, the integration of a resorption plant into the system network of heat and cold generators of a supermarket and their mode of operation is illustrated by means of suitable tables and figures.

2. RESORPTION REFRIGERATION PROCESS

2.1. Distinction from the Absorption Process

The technology of refrigeration by resorption is as old as that of absorption and its implementation was already described by Altenkirch in 1954 (Altenkirch, 1954). The significant difference to absorption is that the refrigerant always occurs in solution with the absorbent and therefore another solution circuit with an absorber and a desorber replaces the condenser and the evaporator. As a result, the system pressure can be reduced and cost-intensive components such as the rectification column can be omitted, especially in systems with ammonia-water as the working fluid pair. This

results in safety-related and economic advantages, which have made the implementation of absorption chillers of low capacity (<100 kW) unprofitable so far.

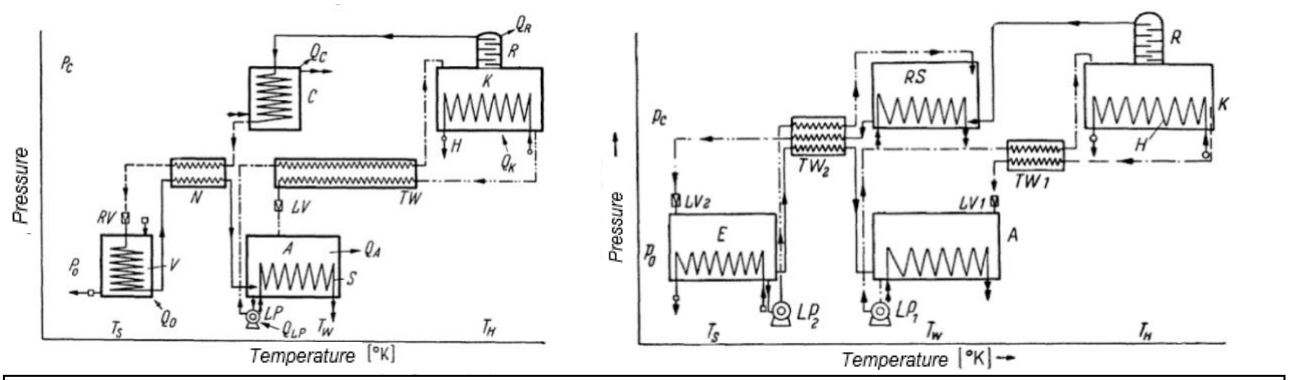

K…desorber, C…condenser, V…evaporator; A…absorber; E…degasser (cold desorber), RS…resorber; LV/RV…throttle valve; R…rectification; LP…solution pump; TW/N…internal heat

Figure 1: Comparison of the interconnection of absorption (left) and resorption refrigeration (right) systems according to Niebergall (1981).

However, if no rectification column is implemented for working fluid pairs with too small differences between their normal boiling points (e.g. NH_3-H_2O) a carryover of absorbents into the cold part of the plant. Ziegler et al. (2017) and Ziegler and Hesse (2018) investigated the influence of these concentration shifts, presented their effects on operational safety and presented solutions to prevent a shift respectively an adjustment.

2.2. Thermodynamic of the Resorption Process

As mentioned in section 2.1, the resorption chiller is characterized by its second solution circuit and the resulting duplication of the components absorber, desorber, internal heat exchanger, throttle valve and solution pump, which eliminates the need of the evaporator and the condenser. The process is illustrated in the lg p - - 1/T diagram in Fig. 2. Thus, the decrease of the pressure levels (condensation pressure: $p_c \rightarrow p_{d,h}$ and evaporation pressure: $p_0 \rightarrow p_{d,c}$) as a result of the exclusive presence of the refrigerant in solution becomes obvious which has decisive impacts on safety and system design.

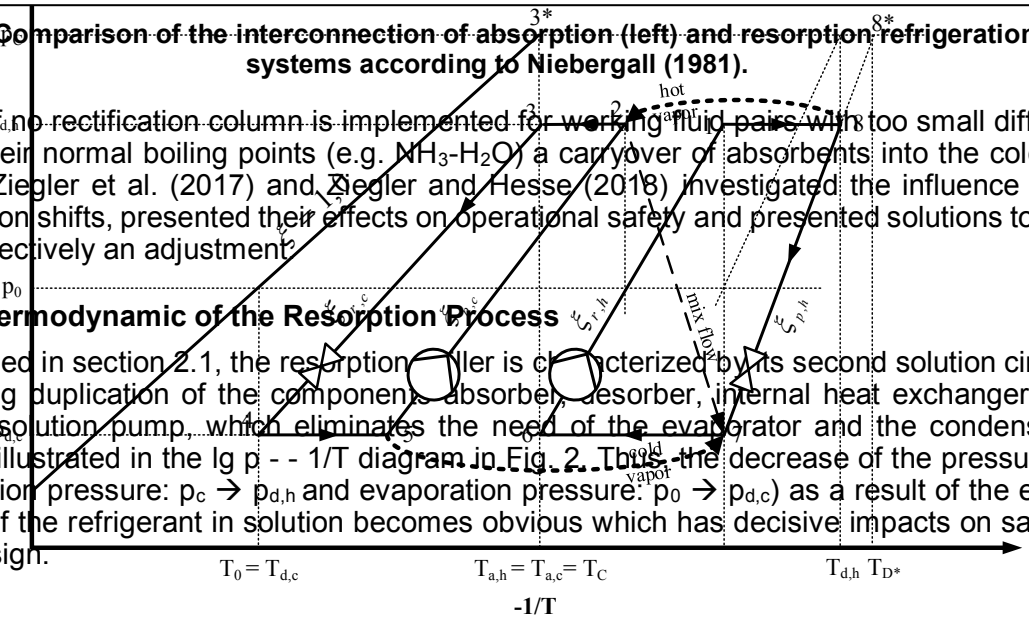

Figure 2: Illustration of the resorption refrigeration process in the lg p - -1/T diagram.

2.3. Boundary Conditions during the Operation of Absorption/Resorption Refrigeration Systems

As in absorption plants, a heat source is required for the operation of resorption plants. This is typically required in a temperature range between 70 and 95 °C, which corresponds to the waste heat temperature level of numerous industrial processes, electrical energy generators (CHPs) or other energy consumers. The technology can thus be used as an interface technology where even small amounts of waste heat are generated and also refrigeration is required. Due to the possibility of shifting the concentration of the refrigerant between the two solution circuits, a direct adjustment to the external boundary conditions is also quickly possible, which emphasizes the flexibility of the system technology.

The dependency of the achievable cooling capacity is strongly bound to the recooling conditions in both resorption and absorption refrigeration systems and is accordingly influenced by the type of recooling unit. For this reason, adiabatic recooling units (wet recoolers) are favourable. For smaller systems, the environmental and maintenance requirements are comparatively too high, therefore dry recoolers are usually used.

Due to the dependency of absorption and resorption chillers on the external boundary conditions, daily and seasonal fluctuations have an impact on the achievable cooling capacity, which run contrary to the cooling load in most cases. In the supermarket sector, for example, a higher capacity

must be provided for air conditioning, especially in summer, in addition to the almost constant cooling load for food cooling. This is contrary to the operating conditions of absorption chillers. Thus, to ensure the supply security of the cooling capacity and cold chain of the goods, redundancy of the cooling systems is required. A stand-alone absorption or resorption refrigeration system, without being oversized by magnitudes, would not be able to provide the necessary cooling capacity on hot summer days, which in certain circumstances would lead to significant product losses. An absorption or resorption system can preferably be installed in the area of supermarkets as an additional unit in order to relieve the existing conventional compression refrigeration systems

3. INTEGRATION OF A RESORPTION SYSTEM INTO THE COOLING AND HEATING NETWORK OF A SUPERMARKET

3.1. Heating and Cooling Supply at the Supermarket

The studied supermarket located near Stuttgart (Germany) is a supermarket with a sales area of approx. 1300 m^2 and a total area of approx. 1700 m^2. Before retrofitting of the store (refrigeration and air-conditioning systems, cooling cabinets and installation of a CHP-unit), the total annual electricity consumption (2011 - 2014) was approx. 500 MWh and the heat consumption approx. 130 MWh, which led to annual energy costs of approx. 90.000 € (see Fig. 3).
Due to the relatively high electricity consumption, it was considered to use a CHP unit with a maximum power capacity of 48 kW_{el} in addition to redesigning and retrofitting the market. However, in order to increase the nominal load hours of the CHP unit to cover the electrical power requirement, an additional heat sink is required to avoid emitting the generated heat to the environment. This scenario favours the use of a thermally driven refrigeration system. After the retrofitting, the market has several temperature levels at which cold or heat is required. Several heat generators and refrigeration units are available for the supply of the different temperature levels (see Table 1).

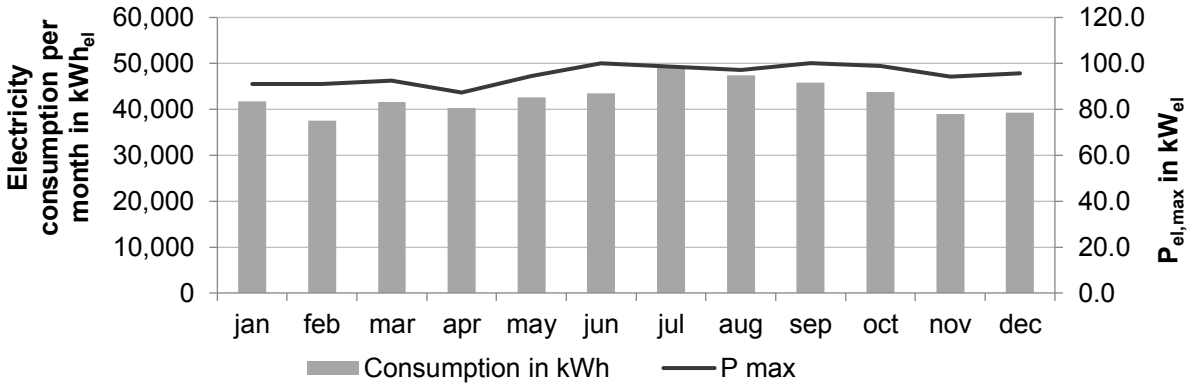

Figure 3: Monthly power consumption and peak load of *EDEKA Neukauf* Moeglingen in 2014 (Korn, 2016)

Table 1: Temperature levels and cooling capacities of the refrigeration units

	Temperature level	Aggregate/ refrigerant	Cooling capacity in kW_{th}
Freezing refrigeration (FR)	- 22 °C (direct expansion)	Cascade with 3 compressors (R744)	18
Normal refrigeration (NR)	-4 / 0 °C	Parallel operation of 2 chillers (R290)	2 x 25
Air-conditioning (A/C)	4 / 10 °C	1 Chiller (R290)	1 x 44
Air-conditioning/ normal refrigeration	-6 °C to 10 °C	Resorption refrigeration system (R717/R718)	1 x 25

Due to EDEKA's efforts to primarily use natural refrigerants for cooling and air-conditioning and the decision to use propane (R290), an outdoor installation of the units in a container was chosen. The decoupling of the cold in the NR and A/C sectors in the market is therefore not carried out via direct expansion, as in the case of most CO_2 refrigeration systems, but by a distribution via a brine circuit.

One advantage of this solution is that it is possible to integrate other refrigeration units, such as a resorption refrigeration system. For the additional decoupling of demand and generation as well as for peak load coverage, several storage tanks were integrated (see Table 2).

Table 2: Storage units at the supermarket

	Storage Type	Temperature Level	Volume
AC-Storage Tank	Sensitive	6 – 10 °C	1 m³
NR-Storage Tank	Sensitive	-4 – 0 °C	3 m³
Ice-Storage Tank	Latent	-2 – 0 °C	4 x 0,6 m³
Hot Water Storage Tank	Sensitive	70-90 °C	2 m³

3.2. Design and Construction of the Resorption Refrigeration System

The ResoField project was preceded by a BMWi-funded project called ResoFreeze (FKZ: 03ET1121B), in which the resorption plant was tested in the laboratories of the Technische Universität Dresden. After successful completion of the investigations and significant performance increases through various modifications (e.g. fluid distribution systems for the absorbers designed as plate heat exchangers), it was possible to design a resorption plant that could withstand the requirements of use in field applications. Particular attention was paid to the development of a control concept for the daily and seasonally dependent fluctuations of the recooling temperatures, as well as in the technically challenging process of the starting phase. The construction of the resorption plant at Moeglingen does not differ fundamentally from the one at the TU Dresden, but was extended by significant elements and optimized under operational safety aspects. A CAD model of the TU system is shown in Fig. 4, where the red coloured system parts represent the hot solution circuit and the blue coloured system parts represent the cold solution circuit, each with an absorber, desorber, internal heat exchanger and a solution pump.
Due to the use of ammonia-water as the working fluid pair, particular attention had to be paid to safety aspects with regard to the installation site of the plant. For this purpose, a concept was developed which included the installation as a container solution. At the same time, this allowed the possibility of installing the new CHP unit, including the hot water and air-conditioning buffer storage, in the close proximity of the resorption plant to omit long pipes and heat losses. A CAD model of the 40-foot container with the corresponding plant components is shown in Fig. 4.

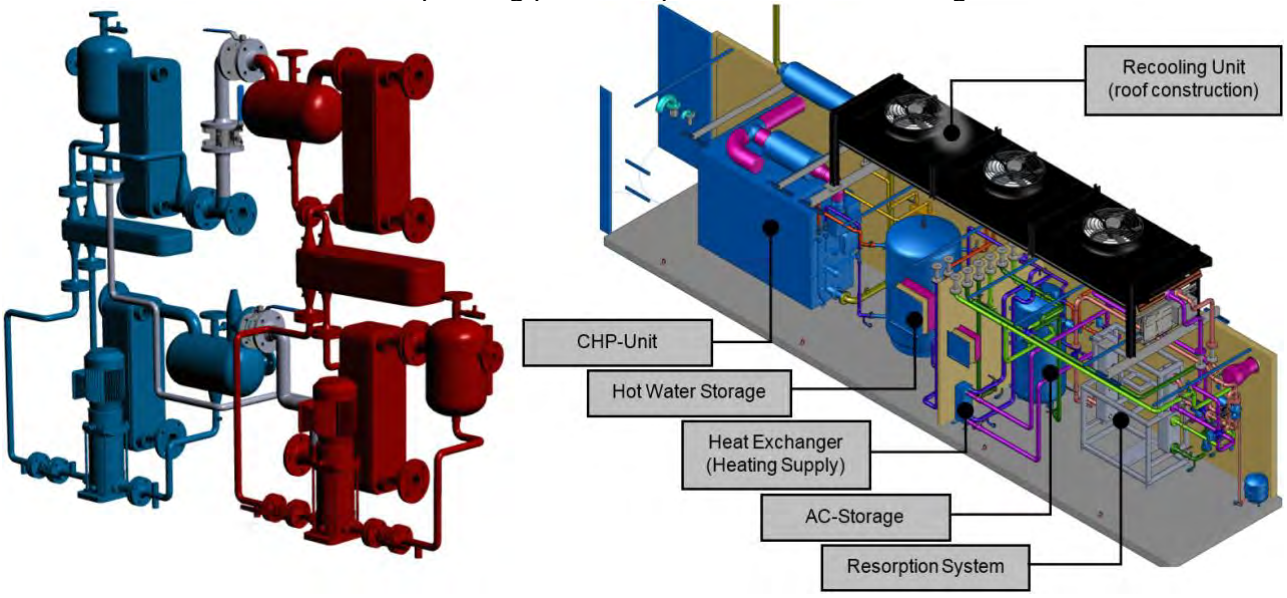

Figure 4: CAD model of the resorption system at the TU Dresden (left) and 40-ft standard-container with components, systems and piping at the supermarket in Moeglingen (right).

4. OPERATING CHARACTERISTICS OF THE RESORPTION REFRIGERATION PLANT IN THE SYSTEM NETWORK

4.1. Operating Conditions and Load Cases of the Resorption System

The resorption plant of the supermarket in Moeglingen is part of a network of heat and cold generators. It has to cover different load cases in order to guarantee the supply of cold for the market on the one hand and to be operated under economic aspects on the other hand. During the commissioning, corresponding load cases were implemented in the control program, which are shown in Table 3.

Table 3: Load cases for the operation of the resorption system and dependence on the heating demand of the supermarket

Load Case	Condition 1	Condition 2	Condition 3
Supply of NR-Cold	Ambient Temperature < 22 °C	Heating demand < 35 kW	
Supply of A/C-Cold	Temperature A/C-Storage > 8 °C	Heat consumption RRS > 20 kW	
Charging Ice Storage	Between 21:00 pm – 06:00 am	Ambient Temperature > 5 °C	Ice storage is unloaded
Supply of heating heat	heating delivery temperature < 70 °C		

4.2. Operating Characteristics

Resorption plants ensure base load supply and are designed to produce cold in continuous operation. For peak load coverage, systems that can quickly achieve a stationary operation point or/and thermal storages are required. Due to the relatively large masses and heat capacities, however, slow temperature changes occur in sorption plants, which increases the duration of the starting procedure.

Starting Procedure

Fig. 5 shows the procedure for starting the resorption plant. In order to couple the cold and hot parts of the plant, the pressure levels must be adjusted. It can be seen that the amount of consumed heat increases at the beginning of the procedure. This is necessary in order to heat up the hot part of the plant and thus achieve the corresponding high pressure level. The cold part of the system is cooled down after a short delay in order to adjust the low-pressure level which becomes evident by a

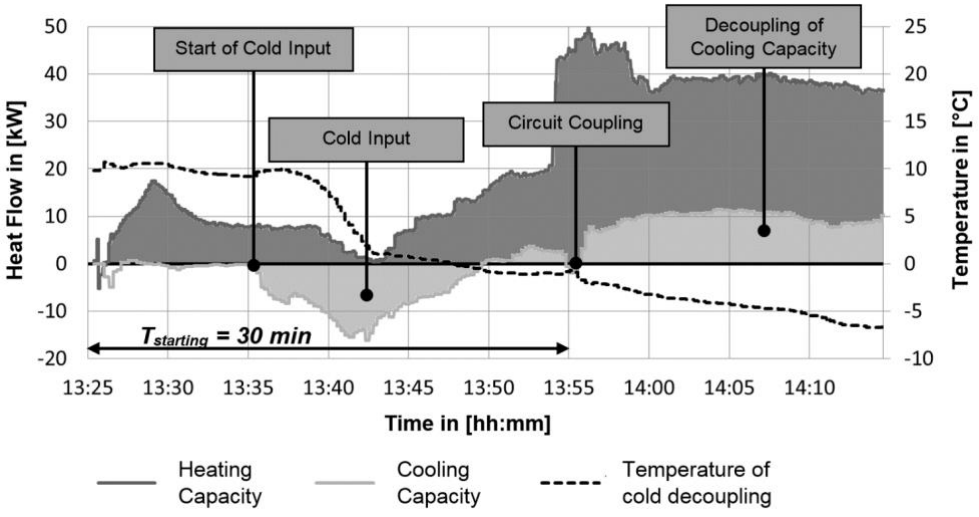

Figure 5: Sequence of the starting procedure

negative cooling capacity (*cold input*). For this purpose, it is possible to access the NR storage. After adjusting the pressure levels, the two solution circuits can be coupled (*circuit coupling*) and the external boundary conditions can be adjusted. Thus, cooling capacity is generate, which can be seen in the reduction of the temperature of the *decoupling of cooling capacity*.

4.3. Typical Daily Load Profiles

In Fig. 6, Fig. 7 and Fig. 8, typical load profiles are plotted as daily curves. For better clarity, the cooling capacity is not shown as a continuous curve, but as the amount of heat per hour. In addition, the connection to the achievable COP (Coefficient of Performance) of the system can be deduced from the cooling water temperature depending on the outside temperature and the temperature of the cold decoupling.

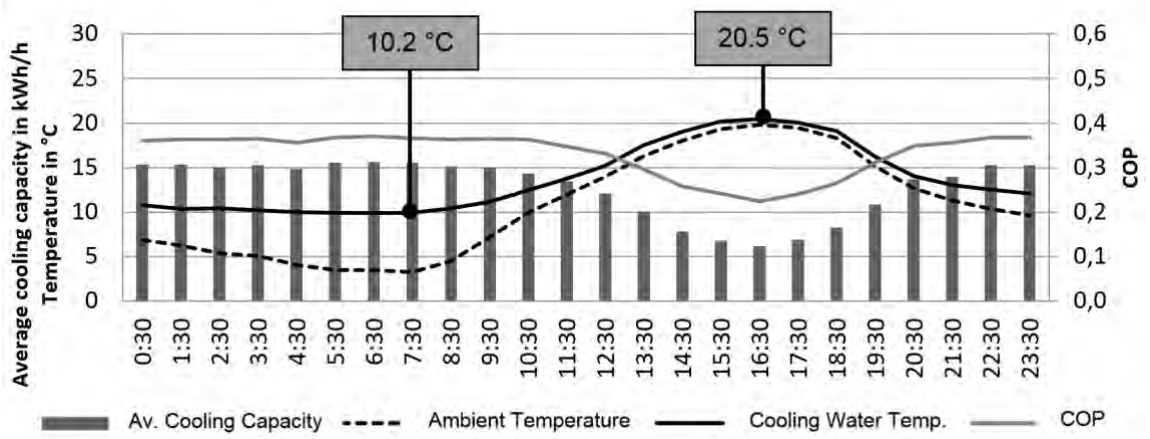

Average ambient temperature: 10.7 °C; Average hot water temperature: 82.5 °C; Average cold decoupling temperature: -3.9 °C; Average cooling capacity: 12.8 kW

Figure 6: Load profile autumn day in NR-mode (26th Sept. 2018).

Fig. 7 shows a significant increase of the COP between 8:30 a.m. and 9:30 a.m. while the cooling water temperature increases. This is related to a switch from load case NR cooling to A/C cooling,

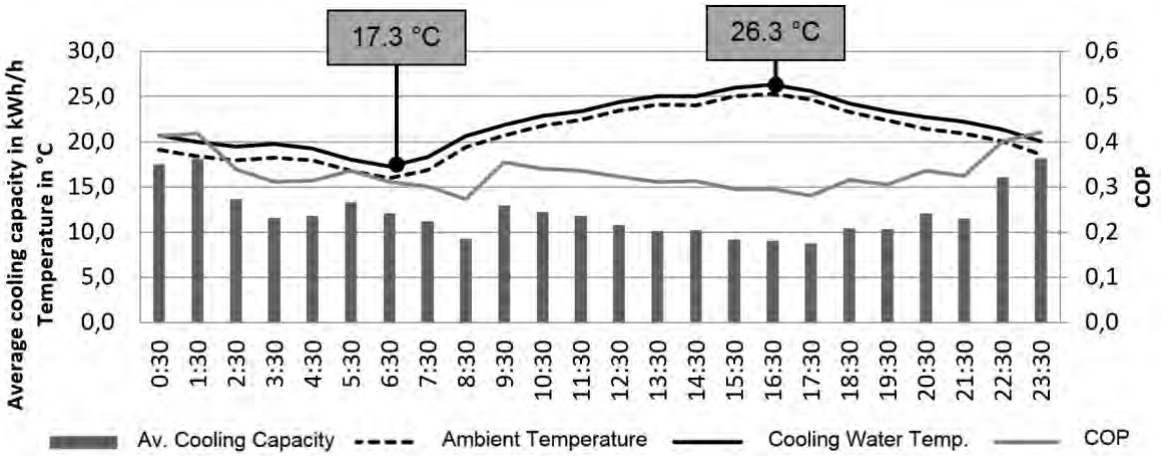

which is automatically performed by the implemented control system based on the evaluation of measured variables such as ambient temperature and achievable cooling capacity. If this switching is not performed, which was intentionally disabled for the measurement in Fig 8, the system is shut down between 14:30 and 19:30 due to an insufficient cooling capacity within that period.

Average ambient temperature: 20.8 °C; Average hot water temperature: 85.5 °C; Average cold decoupling temperature (NR/AC): -2.1/4.8 °C; Average cooling capacity: 12.2 kW

Figure 7: Load profile summer day WITH switching between NR- and A/C-mode (14th Aug. 2018).

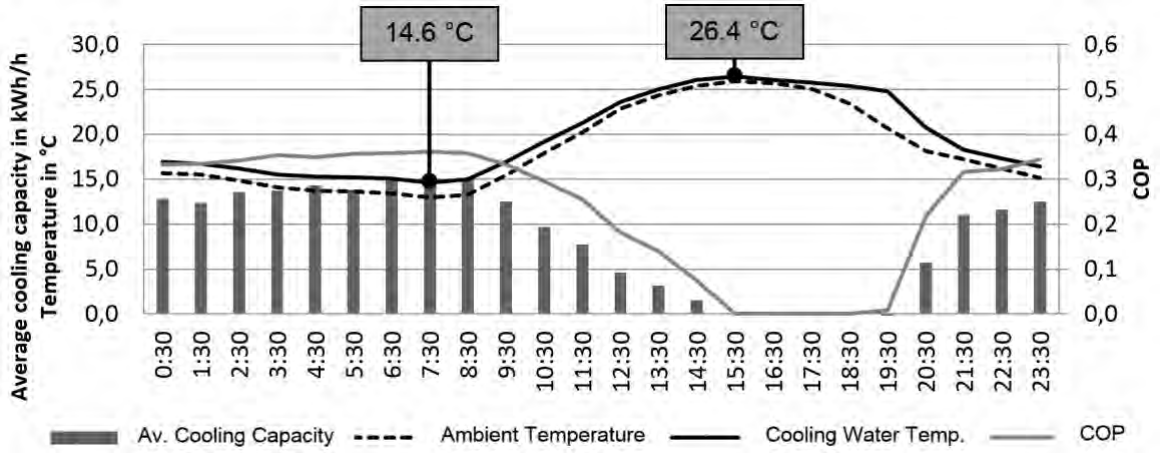

Average ambient temperature: 18.4 °C; Average hot water temperature: 83.2 °C; Average cold decoupling temperature: -2.8 °C; Average cooling capacity: 8.6 kW

Figure 8: Load profile summer day WITHOUT switching between NR- and A/C-mode (12th Oct. 2018).

4.4. Carnot Efficiency Ratio

In order to compare the RRS in Moeglingen with other systems, the Carnot efficiency ratio for the external boundary conditions should be used. Table 4 shows the temperatures and heat flows used in this case. The calculation of the external Carnot efficiency ratio has to be applied because the external volume flows (cooling water, hot water, cold brine) have different values depending on the used system and therefore a simple comparison of the heat flows is not sufficient.
According to Niebergall (1981), the external Carnot heat ratio for resorption plants is calculated according to equation 1. (The description and nomenclature of the indices is listed in table 4.)

$$\xi_{Ca} = \left(\frac{1}{T_{CW,A}} - \frac{1}{T_{m,HW}}\right) \Big/ \left(\frac{1}{T_{Brine}} - \frac{1}{T_{CW,RS}}\right) \quad \text{Eq. (1)}$$

With the heat ratio for resorption plants according to equation 2

$$\xi = \frac{\dot{Q}_0}{\dot{Q}_H} \quad \text{Eq. (2)}$$

the external Carnot efficiency ratio of resorption refrigeration systems can be derived to equation 3

$$\eta_{Ce} = \frac{\xi}{\xi_{Ce}} \quad \text{Eq. (3)}$$

Table 4: Descriptions, Nomenclature and quantities for the calculation of the external Carnot efficiency ratio and exemplary values of one measuring point of the RRS in Moeglingen

Description	Nomenclature	RRS Moeglingen
Average heat input temperature	$T_{m,HW}$	$353\ K$ (80 °C)
Cooling water temperature at the absorber outlet	$T_{CW,A}$	$299\ K$ (26 °C)
Cooling water temperature at the resorber outlet	$T_{CW,RS}$	$297\ K$ (24 °C)
Temperature of the brine at the degasser outlet	T_{Brine}	$270\ K$ (−3 °C)
Supplied hot heat flow	$\dot{Q}_H$	$28{,}2\ kW$
Cooling capacity	$\dot{Q}_0$	$6{,}5\ kW$
External Carnot heat ratio	ξ_{Ce}	1,57
Heat ratio	ξ	0,230
External Carnot efficiency ratio	$\boldsymbol{\eta_{Ce}}$	$\mathbf{14{,}7}$ %

5. CONCLUSIONS

Within the scope of the ResoField project, a resorption refrigeration system with the working fluid pair ammonia-water was installed as an additional thermally driven refrigeration machine for the refrigeration supply of a supermarket. In close cooperation with the Resotec GmbH, the resorption system was further developed and designed in the laboratories of the TU Dresden, manufactured and finally installed as a container solution in Moeglingen. During the commissioning, a PLC control program was developed that was specifically adapted to the local conditions. The plant was integrated into the supermarket's network of refrigeration and heat generators in March 2018. Since then, it has been supplying the market reliably with normal and climatic cooling, using the waste heat from a CHP unit that was installed specifically for the supermarket's electricity and heat supply.

ACKNOWLEDGEMENTS

The presented results were achieved within the scope of the project RESOFIELD supported by the German Federal Ministry for Economic Affairs and Energy (BMWi) (Contract FKZ: 03ET1338A). The authors express their gratitude to the BMWi and the companies EDEKA Handelsgesellschaft Südwest mbH and Resotec GmbH for their financial and energetic support.

NOMENCALTURE

p	pressure	$P_{el,max}$	Maximum Electrical Power Consumption (kW)
$T_{starting}$	Start-up time	FKZ	project code number
T	temperature (°C)	BMWi	German Federal Ministry for Economic Affairs and Energy
$T_{m,HW}$	Average heat input temperature	A/C	Air Conditioning
$T_{CW,A}$	Cooling water temperature at the absorber outlet (°C)	NR	Normal Refrigeration
$T_{CW,RS}$	Cooling water temperature at the resorber outlet (°C)	$\dot{Q}_H$	Supplied hot heat flow (kW)
T_{Brine}	Temperature of the brine at the cold desorber outlet (°C)	$\dot{Q}_0$	Cooling capacity (kW)
η_{Ce}	External Carnot efficiency ratio	ξ_{Ce}	External Carnot heat ratio
ξ	Heat ratio	COP	Coefficient of Performance

REFERENCES

BMWi Bundesministerium für Wirtschaft und Energie), 2014, Abschlussbericht zum Projekt I C 4 - 42/13, Potenzial- und Kosten-Nutzen-Analyse zu den Einsatzmöglichkeiten von Kraft-Wärme-Kopplung (Umsetzung der EU-Energieeffizienzrichtlinie) sowie Evaluierung des KWKG im Jahr 2014, Berlin

Altenkirch E., 1954. Absorptionskältemaschinen, VEB Verlag Technik, Berlin

Niebergall W., 1981. Handbuch der Kältetechnik Band 7 - Sorptionskältemaschinen, Springer, Berlin Heidelberg New York

Ziegler O., Hesse U., Thomas C., Grund M., Weimer T., 2017. Influence of the recirculation of the solution on the performance of a resorption refrigeration system, Ohrid

Ziegler O., Hesse U., 2018. Theoretical and Experimental Investigations on the Recirculation of the Solution (Mix-Flow) in a NH_3-H_2O-Absorption Resorption Refrigeration System, West Lafayette

Korn, O., 2016. Energiecontrolling für Möglingen. EDEKA Handelsgesellschaft Südwest mbH, Offenburg

Manuscript ID: 415
DOI: 10.18462/iir.icr.2019.0415

Operating characteristics of heat pump type ventilation heat recovery system in winter

Lei WANG[(a)], Guoyuan MA[(a)] , Anna MA[(a)], Feng ZHOU[(a)], Fuping LI[(b)]

(a) College of Environmental and Energy Engineering, Beijing University of Technology, Beijing 100124, China

(b)College of Mechanical Engineering and Applied Electronics Technology, Beijing University of Technology, Beijing 100124, China

ABSTRACT

The study on the operating characteristics of heat pump in ventilation heat recovery system can point out the way of improvement for heat pump in this application. An experimental platform was set to conduct a comprehensive study on the heat pump ventilation heat recovery system in winter conditions. The results show that under the experimental conditions, the system pressure ratio, power input and refrigerant mass flow rate decrease with the decrease of outdoor temperature; the recovered heat, temperature effectiveness and COP (coefficient of performance) increase with the decrease of outdoor temperature. Increasing the mass flow rate of the system can be an effective way to improve the performance of heat pump type ventilation heat recovery system.

Keywords: heat pump, ventilation, heat recovery, operating characteristic, improvement, mass flow rate

1. INTRODUCTION

With the development of economy, people begin to put forward higher requirements for the comfort of the living environment, so the HVAC industry has been developed and improved. However, while people are enjoying the comfortable indoor environment, they bring heavy pressure to the natural environment. In 2017, the world's primary energy consumption is 135.112 million tons of oil equivalent, while China's is 313.22 million tons of oil equivalent, accounting for 23% of the world's primary energy consumption, ranking first in the world (British Petroleum, 2018). Statistics show that in some European and American countries, the energy consumption of heating, ventilation and air conditioning accounts for about 30% of the national energy consumption (Long,1999). In China, the total energy consumption of civil buildings has been maintained at 20%-25% in the last ten years (Tsinghua University, 2015), the energy consumption of air conditioning can reach 60% of the total building energy consumption (Sun,2000), and the fresh air load generally accounts for the 30% of the total air conditioning load (Chen,2004). The tense situation of the world's environment and energy makes energy conservation and environmental protection becomes the theme of the world. Low-energy buildings and green buildings have become a hot topic of research. In winter, the indoor exhaust air temperature can be 10 °C ~ 40 °C higher than the outdoor environment. Adding heat recovery device in the ventilation system can be an effective way to save energy for air conditioning system, and then reduce building energy consumption.

At present, the heat recovery devices in the ventilation system mainly include: rotary wheel, plate exchanger, heat pipe, run-around system and heat pump. Different types of heat recovery devices have their own advantages and disadvantages. Many scholars have also made researches on different types of heat recovery devices from different aspects. Among all the ventilation heat recovery devices, the heat pump system has the unique characteristic that the temperature effectiveness can be greater than 100% under certain conditions. A lot of research had been made on the operating characteristics of the heat pump system, which indicated the direction for the heating performance of the heat pump (Yan, 2016; Heo, 2011; Kim, 2015; Li, 2014). However, there is no research on the characteristics of heat pump system in heat recovery application under different operating conditions. In the application of heat recovery, the analysis of the operating characteristics of system can find the problems of heat pump heat recovery system, and provide a way to improve the system.

Therefore, this paper conducts experimental tests of the heat pump type ventilation heat recovery system, and studies the changes of various operating parameters and performance of the system with the outdoor temperature decrease in winter, and points out the primary direction for the system improvement in the future.

2. HEAT PUMP HEAT RECOVERY SYSTEM PRINCIPLE AND EXPERIMENTAL METHOD

2.1 System Principle

Fig. 1 shows the cycle of heat pump ventilation heat recovery system. The refrigerant is compressed in the compressor, in which the temperature and pressure of the refrigerant are improved. The refrigerant releases heat to the low-temperature outdoor fresh air and condensing in condenser, the heat obtained by the fresh air comes from the heat absorbed by the refrigerant from the high-temperature indoor exhaust, and part of it comes from the compressor's work on the refrigerant. After throttling process, the refrigerant passes through the evaporator and is finally inhaled by the compressor.

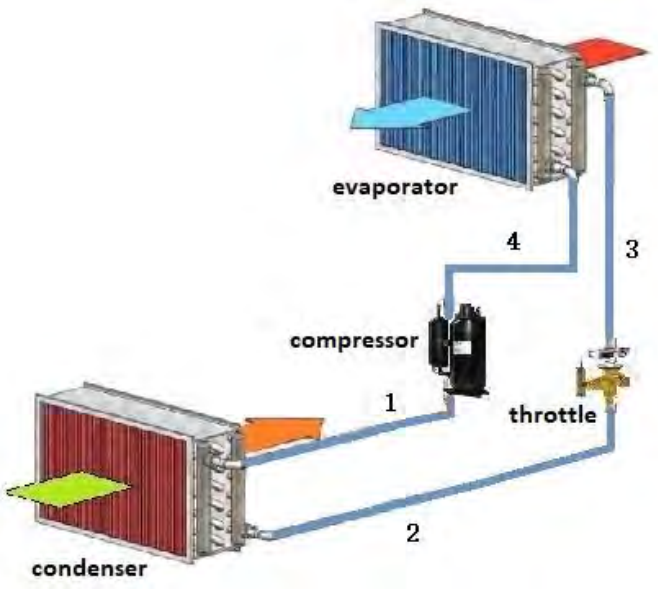

Fig.1 Heat pump type ventilation heat recovery system

2.2 Experimental Method

Fig. 2 is a schematic diagram of the experimental setup of the heat pump heat recovery system. The condenser and evaporator of the heat recovery system were placed in the outdoor simulation room and the indoor simulation room of the enthalpy laboratory, respectively. The air in the outdoor simulation room is regarded as the outdoor low-temperature fresh air introduced by the fresh air duct in the ventilation heat recovery scene. The air discharged from the condenser can be regarded as the fresh air discharged into the room after being heated by the ventilation heat recovery system. The air in the indoor simulation room is regarded as the indoor air taken in by the exhaust air duct in the ventilation heat recovery scene, and the air discharged from the evaporator can be regarded as the air discharged to the outdoor environment after the heat recovery by the ventilation heat recovery system. In this experiment, the compressor is 220V, 50Hz, standard discharge volume is 24.6cm^3/rev. The refrigerant used in the heat recovery system is R410A. The performance of the heat recovery system was tested and the system operating state parameters were collected in the outdoor simulation room from 15℃ to -20℃ with an interval of 5℃, and the temperature of the indoor simulation room was constant at 20℃.

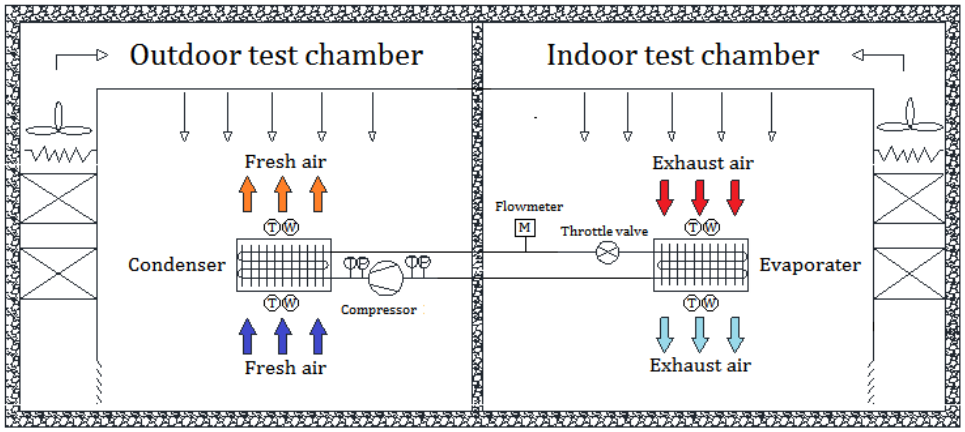

Fig.2 Schematic of heat pump heat recovery setup

The thermal properties of the air can be obtained indirectly from the parameters collected by the sensors arranged in the air duct. The fresh air volume can be indirectly calculated through the cross-sectional area of the air duct and the wind speed measured by the air meter. The system's heating capacity for fresh air can be calculated by the following formula:

$$Q = \frac{q_{vi} C_{pa} (t_{f2} - t_{f1})}{v'_n (1 + W_n)} \quad \text{Eq. (1)}$$

The temperature effectiveness of the heat recovery system was calculated by the following formula:

$$\eta = \frac{t_{f2} - t_{f1}}{t_{e1} - t_{f1}} \quad \text{Eq. (2)}$$

The performance coefficient (COP) of the whole heat recovery system was calculated with the following formula:

$$\mathrm{COP} = \frac{Q}{W_C + W_F} \quad \text{Eq. (3)}$$

3. RESULTS AND DISCUSSION

3.1 Operating state of the system

Fig.3 shows the temperature changes of fresh air and exhaust air outlets during the experiment. As the outdoor temperature decreases, the fresh air temperature at the condenser outlet and the exhaust air temperature at the evaporator outlet are continuously decreasing, but the temperature lift of the outdoor fresh air from the condenser inlet to the outlet is constantly increasing.

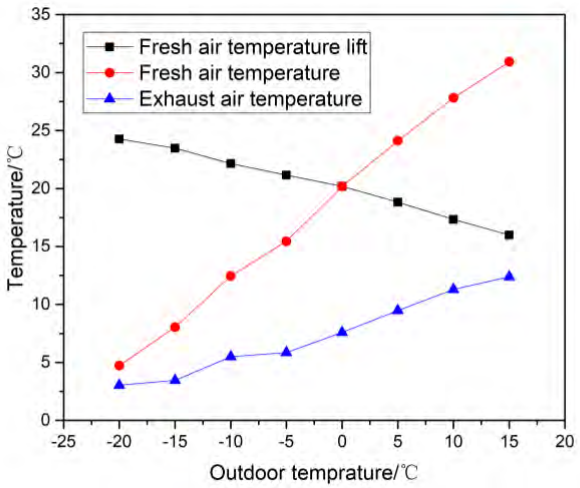

Fig.3 Temperature changes of fresh air and exhaust air

Fig.4 shows the changes of evaporation pressure and condensation pressure during the experiment. With the decrease of outdoor environment temperature, both evaporation pressure and condensation pressure are gradually decreased, and the difference between condensation pressure and evaporation pressure is constantly decreased. The decrease of condensing pressure is mainly due to the continuous decrease in the temperature of the fresh air entering the condenser. The temperature of the air entering the evaporator is constant, so the decrease in the evaporation pressure is due to the continuous decrease in the temperature of the air at the outlet of the evaporator. The decrease in the difference between the condensing pressure and the evaporation pressure will result in a decrease in the pressure ratio of the system. The change of pressure ratio is completely different from that of the conventional heat pump heating system. In the conventional heat pump heating system, when the indoor temperature is kept constant and the outdoor temperature is decreasing, the pressure ratio of the system will continuously increase.

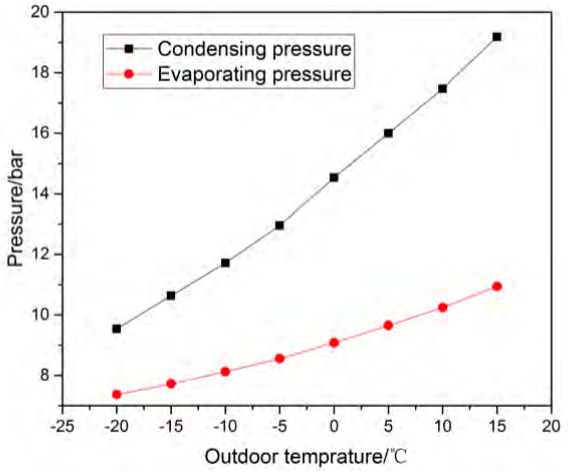

Fig.4 Pressure changes of system

Fig.5 shows the mass flow rate changes of the heat recovery system. As the outdoor temperature drops, the mass flow rate in the heat pump heat recovery system also decreases. In the heat pump system, the evaporation pressure is directly related to the circulation mass flow rate. Since the evaporation pressure is continuously decreasing, the system circulation flow also shows a decreasing trend. The heat pump recovery system and the conventional heat pump heating system are the same in the mass flow rate change law. Therefore, like the conventional heat pump heating system, the decrease of the circulating mass flow rate and its adverse effects when the outdoor environment temperature is too low are also the real problems faced by the heat pump heat recovery system.

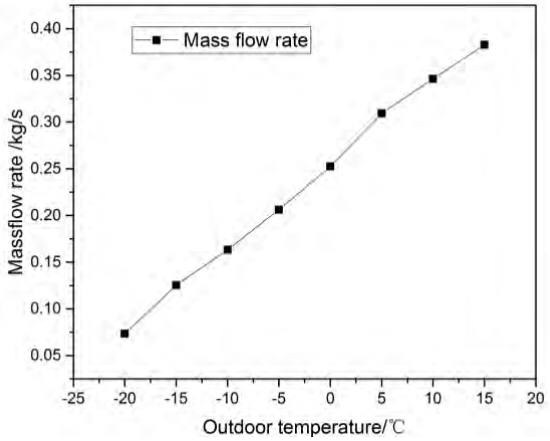

Fig.5 Mass flow rate changes of system

Fig.6 shows the variation of power input at different outdoor temperatures. It can be found that the power input decreases with the decrease of outdoor temperature. It can be found that the power input of heat pump heat recovery system decreases with the decrease of outdoor temperature. The power input of fans in the system can be considered constant, so the total power input is only related to the compressor. From the analysis of Fig.4, the pressure ratio of the system decreases with the decrease of the outdoor temperature. For the compressor, the pressure ratio of the compressor is positively correlated with the power consumed, so the power input of the system tends to gradually decrease as the outdoor temperature decreases. The power input of the system in conventional heating system increases as the outdoor temperature decreases, because the pressure ratio of the conventional heat pump heating system increases as the outdoor temperature decreases. The characteristic of power input varies with outdoor temperature in heat pump heat recovery system is opposite to that of conventional heat pump heating system.

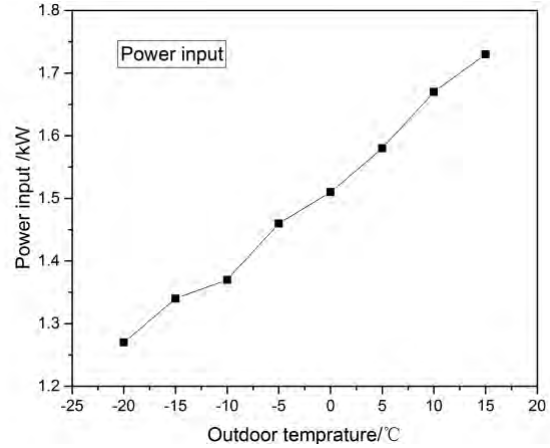

Fig.6 Power input changes of system

3.2 Operating performance of the system

The temperature effectiveness of the system as the outdoor temperature decreases is shown in Fig.7. The temperature effectiveness decreases with the decrease of outdoor temperature. The heat pump heat recovery system relies on the circulating refrigerant in the system. From the analysis of Fig.5, it is found that the circulating mass flow rate of the system gradually decreases as the outdoor temperature decreases, so that the degree of heat recovery from heat source is inevitably weakened. When the temperature effectiveness is more than 100%, it can be considered that the exhaust heat is completely recovered and released into the fresh air. This is the characteristic of the heat pump heat recovery system different from other kinds of heat recovery devices. In this condition, the fresh air of the heat recovery system can be directly discharged into the room without secondary heat treatment. It can makes the fresh air load zero or even negative.

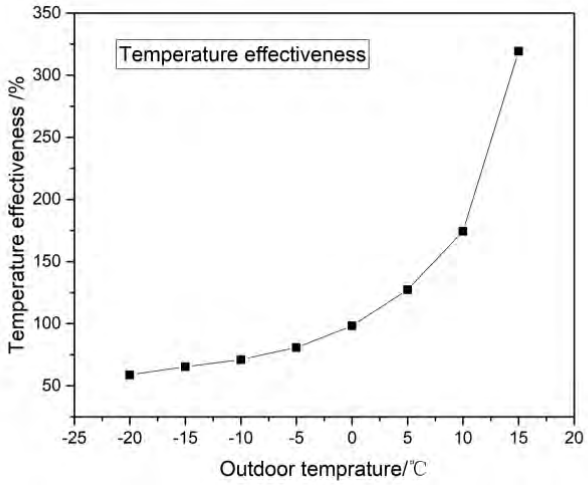

Fig.7 Temperature effectiveness change of system

Fig.8 shows variation of recovered heat with different outdoor temperatures. With the outdoor temperature decreases, the recovered heat of the system increases gradually. The evaporation pressure of traditional heat pump heating system decreases with the decrease of outdoor temperature, and the mass flow rate of the system decreases. Therefore, the heating ability of heat pump system decreases with the decrease of outdoor temperature. However in the application of heat recovery system, as the outdoor temperature gradually decreases, the heat transfer temperature difference of the condenser becomes larger and the cooling effect of the refrigerant in the condenser becomes stronger. The dryness fraction of the refrigerant after throttling is greatly reduced. So the refrigerant will absorb more heat from the exhaust air in the evaporator. This will increase the heat recovery ability of the system and increase the recovered heat. Considering two factors, the recovered heat will increase with the decrease of outdoor temperature under the experimental conditions. If the mass flow rate of the system can be increased by other means, it can further improve the heating capacity of the fresh air, which can be used as the main research direction for improving the performance of the heat pump heat recovery system in the future.

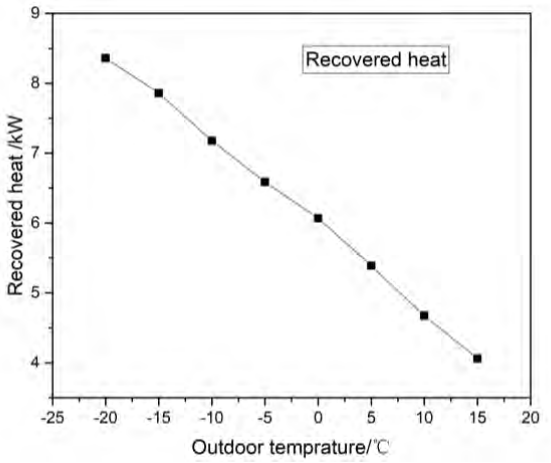

Fig.8 Recovered heat change of system

Fig.9 shows the COP of heat pump heat recovery system changing with outdoor temperature. With outdoor temperature drop, the COP of the system is increased gradually, when the outdoor temperature decreased from 15℃ to -20℃, the COP of the system increases from 3.35 to 7.58 with a increase rate of 126.27%. However, the COP of the traditional heat pump system decreases with the decrease of the outdoor temperature. The characteristics of the COP in the heat pump heat recovery system are contrary to the conventional heat pump system. However, the COP of the traditional heat pump system decreases with the decrease of the outdoor temperature. The characteristic of the COP in the heat pump heat recovery system is contrary to the conventional heat pump heating system. This is mainly determined by the change of the recovered heat and the change of the power input.

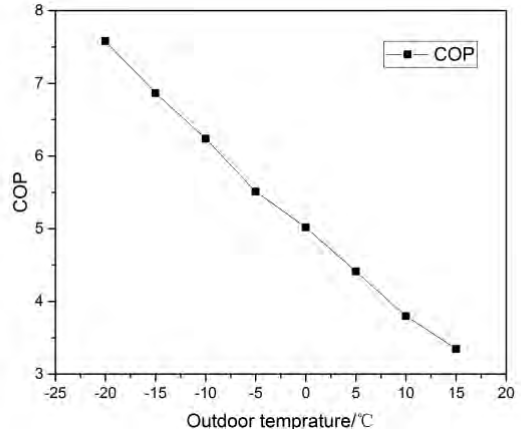

Fig.9 COP change of system

4. CONCLUSION

In this paper, the experimental platform of heat pump heat recovery system was set up. Through the experiment of the system in winter, the operation characteristics of heat pump heat recovery system were found and summarized. The main conclusions are as follows:

(1)The air temperature of fresh air and exhaust at the outlet of heat exchangers, the system pressure ratio, the circulation mass flow rate, the power input and the temperature effectiveness of the heat pump heat recovery system all decrease with the decrease of the outdoor temperature; the heating capacity of the fresh air and the system COP are all increased with the decrease of the outdoor temperature.

(2)As an air source heat pump system, only the change rule of the mass flow rate in heat recovery application is consistent with the conventional heat pump system in the process of outdoor temperature decline. Improving the circulating mass flow rate of refrigerant can be a direction to improve the performance of heat pump heat recovery system.
(3)With the decrease of outdoor temperature, except mass flow change law, the heat pump heat recovery system shows that the lower the outdoor temperature, the more conducive to the performance of the system. It shows that heat pump heat recovery system is a kind of heat recovery system which is very suitable for low temperature environment. Under the experimental conditions, the COP of the system reaches 7.58 when the outdoor temperature is -20℃ and the indoor temperature is 20℃.

NOMENCLATURE

Q	total heating capacity (W)	W_n	absolute humidity of air (kg/kg)
q_{vi}	air-volume flow rate of fresh air duct (m3/s)	t_{e1}	temperature of air entering the exhaust air duct(℃)
C_{pa}	specific heat capacity of air (J/kg℃)	η	temperature effectiveness (%)
t_{f2}	temperature of air leaving the fresh air duct (℃)	t_{f1}	temperature of air entering the fresh air duct (℃)
COP	coefficient of performance	W_C	input power of compressor (W)
v_n'	specific volume of air (m3/kg)	W_F	input power of fans (W)

REFERENCES

British Petroleum, 2018. BP Energy Outlook, https://www.bp.com/zh_cn/china/reports-and-publications/_bp_2018-_.html.

Long, W., 1999. New concepts of building energy conservation. Hv & Ac, 29(1):10-13.

Tsinghua University, 2015. 2015 annual report on China building energy efficiency. China Architecture & Building Press.

Sun Z., Li S., 2000.Energy saving analysis about recovery of waste heat in the air conditioner system. Beijing Energy Conservation, (2):20-22.

Chen P., 2004. Building air-conditioning technology and practical basis. China Electric Power Press

Yan G., Jia Q., Bai T., 2016. Experimental investigation on vapor injection heat pump with a newly designed twin rotary variable speed compressor for cold regions. International Journal of Refrigeration, 62:232-241.

Heo J., Min W., Baek C., et al, 2011. Comparison of the heating performance of air-source heat pumps using various types of refrigerant injection. International Journal of Refrigeration, 34(2):444-453.

Kim J., Lee J., Choi H., et al, 2015. Experimental study of R134a/R410A cascade cycle for variable refrigerant flow heat pump systems. Journal of Mechanical Science & Technology, 29(12):5447-5458.

Li Z., Nan Z., Shuai D., 2014. A thermodynamic analysis of an auto-cascade heat pump cycle for heating application in cold regions. Energy & Buildings, 82:621-631.

Manuscript ID:444
DOI: 10.18462/iir.icr.2019.0444

A hardware-based heat pump water heater design model for quasi-steady-state simulation

Bo SHEN[(a)], Kashif NAWAZ[(a)], Ahmed ELATAR[(a)], Van BAXTER[(a)]

[(a)]Oak Ridge National Laboratory[1]
Oak Ridge, TN 37831-6070, USA, shenb@ornl.gov

ABSTRACT

A storage heat pump water heater (HPWH) comprises a vapor compression system and a hot water tank. It can lead to more than 70% energy saving, compared to electric resistance heating. HPWH usually uses a wrapped-tank coil as the water heater. The wrapped coil has a strong interaction with the water tank and impose a new challenge for the engineering design and simulation study. Based on the US DOE/ORNL Heat Pump Design Model (HPDM), a component-based thermal system modelling platform, a segment-to-segment wrapped-tank coil model and a one-dimensional stratified water tank model were developed, which facilitates modeling and design HPWHs having various configurations and components. In the paper, the new HPWH system design model was used to investigate effects of compressor size, refrigerant charge, water draw pattern, and refrigerant type, etc., for predicting 24-hour energy factors and first-hour rating. The HPWH system model was proved to be an effective equipment design tool.
Key Words: Heat Pump Water Heater, Low GWP Refrigerant, Modelling, Wrapped-Tank Condenser

1. INTRODUCTION

The DOE Buildings Energy Databook (Department of Energy, 2010) reported that water heating consumed 12.9% source energy in the residential sector of U.S. in 2010, making it the third largest energy end use for residences, after the space heating and cooling. Electric heat pump water heaters (HPWH) are the most promising technology to replace water heaters using all electric resistance, because the vapor compression cycle absorbs heat from ambient or indoor air with an air-to-refrigerant evaporator, a compressor elevates the refrigerant pressure, temperature, and discharges the high-grade heat to the domestic hot water through a condenser. HPWHs can achieve energy savings up to 70%. Nowadays, high efficiency HPWHs have energy factors above 3.5, able to compete with gas heating in terms of source energy. Therefore, HPWHs will not only lead to great energy reduction, also decrease greenhouse gas emission.

Condensers of HPWHs fall into two categories: 1) forced flow heat exchangers like tube-in-tube and brazed plate heat exchangers coupled with a water circulation pump; and 2) a water heating coil either wrapped-around the water tank or submerged inside the water tank (no water pump required). Unlike a submerged coil, a wrapped-tank coil has no water scaling problem since it has no direct contact with the hot water. Therefore, wrapped-tank water heating coils are the most common in the current HPWH products. The wrapped-tank coils use either D-shape tubes or microchannel flat tubes.

An accurate computer modelling tool is much needed for HPWH engineering design and energy simulation, to simulate the interaction between a stratified hot water tank and a HPWH system having a wrapped-around coil. The modelling tool for such purposes should be hardware-based, with

[1] Notice: This manuscript has been authored by UT-Battelle, LLC, under contract DE-AC05-00OR22725 with the US Department of Energy (DOE). The US government retains and the publisher, by accepting the article for publication, acknowledges that the US government retains a nonexclusive, paid-up, irrevocable, worldwide license to publish or reproduce the published form of this manuscript, or allow others to do so, for US government purposes. DOE will provide public access to these results of federally sponsored research in accordance with the DOE Public Access Plan (http://energy.gov/downloads/doe-public-access-plan).

detailed inputs of heat exchanger geometry and compressor performance representations, etc. It should reasonably predict the effects of component sizes and heat exchanger configurations, etc. In addition, it should be fast enough to accommodate 24-hour energy factor simulations, etc. It should complete a 24-hour simulation in minutes than days like some CFD models do. This paper describes modelling methodologies and simulation cases of a baseline HPWH.

2. MODEL DISCRIPTION

Development of a quasi-steady-state HPWH system model was based on a public-domain thermal system modelling platform, i.e. the Heat Pump Design Model (HPDM) developed and maintained by the Oak Ridge National Laboratory (ORNL). The HPDM has been a reliable, public-domain platform for design, optimization and analyses of heat pump systems with varying complexities for both residential and commercial applications. Some existing component models that can be used directly for the HPWH system model are introduced below.

For air-to-refrigerant heat exchangers, HPDM uses a segment-to-segment modelling approach, which divides a single tube into numerous mini segments. Each tube segment has individual air-side and refrigerant-side entering states and considers possible phase transition; the ε-NTU approach has been used for heat transfer calculations within each segment. In addition to the functionalities of the segment-to-segment fin-tube condenser, the evaporator model can simulate the dehumidification process. The method proposed by Braun et al., (1989) was used to simulate cases of water vapor condensing on an evaporating coil, where the driving potential for heat and mass transfer is the difference between enthalpies of the inlet air and saturated air at the refrigerant temperature.

AHRI 10-coefficient compressor maps have been used to calculate mass flow rate and power consumption. Compressor shell heat loss, relative to the power input, is considered to simulate the refrigerant side and air side energy balance. For modelling various refrigerants, while using one map developed from a baseline refrigerant, it is assumed that the compressor would maintain the same volumetric and isentropic efficiencies at the same suction and discharge pressures, i.e. converting the original compressor map to a pressure-based efficiency map.

Improved Stratified Water Tank Model

EnergyPlus is an open-source, building energy simulation software developed by the U.S. Department of Energy. The EnergyPlus stratified water tank model is a one-dimensional model, simulating water temperature stratification up to 10 nodes. Each node is a control volume, having uniform temperature and water property values. It models water piston flow, i.e. bulk water flow from a make-up port to a supply port, heat conduction between water nodes and natural convection up-flow and mixing. It was widely verified being adequately accurate in simulating tank shell losses, placements of electric heater elements, thermostats, etc.

To validate the EnergyPlus stratified water tank model, the tank node temperature profile measured by Murphy et al. (2011) was used. It was observed that the EnergyPlus tank model tends to over-estimate the water temperature stratification, i.e. the predicted temperature difference between the top and bottom was larger than the measured value, especially when there is a big water draw. It was speculated that the tank model failed to account for bulk mixing during big water draws. Large bulk water flows cause whirls leading to bulk mixing effects between tank nodes. A CFD tank model can more accurately represent the physics of the tank mixing phenomena, etc.; however, it is too slow for HPWH energy simulations. A 1-D stratified tank model is fast enough, but it can't describe mixing mechanisms due to two-dimensional or three-dimensional flow. It is necessary to bridge the simplified tank model with a detailed CFD model or experimental measurements. Thus, an empirical bulk mixing term, a calibration factor, is introduced to adjust the simplified tank model. The calibration accounts for the energy transfer between the tank average and nodal temperatures caused by the whirls, as shown in Eq. 1.

$$q_{bulkmix,n} = Ratio_{bulkmix} \times (T_{avg,tank} - T_n) \times m_n \times Cp \qquad \text{Eq. (1)}$$

where $Ratio_{bulkmix}$ (ratio of nodal water mass exchanging energy with the bulk flow) is an empirical factor to correlate the mixing effect, it can be derived by calibration against measured data or CFD simulation. $Ratio_{bulkmix}$ should be different values with/without water draw. $T_{avg,tank}$ (K) is the tank average water temperature at each time step. T_n (K) and m_n (kg·s^{-1}) are temperature and water mass in each individual node, Cp (J/kg·K^{-1}) is the water specific heat. $q_{bulkmix,n}$ (W) is the energy transfer rate to each node, caused by the bulk mixing effect of the backflow whirls. If more detailed

experimental or CFD simulation data are available, $Ratio_{bulkmix}$ can be derived specific to different regions of a water tank, for example, a bulk mixing ratio may be larger, if adjacent to a flow disturbance, i.e. the supply and return water ports; but smaller, if away from a flow disturbance. For this case, $T_{avg,tank}$ [K] should be an average of the node temperatures in the region having the same bulk mixing ratio.

Using the measured data from Murphy et al. (2011), the figures below compare the measured water temperature stratification from the top node to the bottom mode, with the model predictions. Fig. 1 shows the comparison to the un-calibrated model and Fig. 2 shows the comparison to the calibrated model. The calibrated model was adjusted using 0.15% tank water bulk mixing ratio during a 3 GPM (0.001136 $m^3 \cdot minute^{-1}$) water draw, and zero bulk mixing when no draw. It can be seen that the calibrated model matches the measured water profile closely, with a reasonable calibration factor. In the two figures, the biggest temperature differences between the top and bottom are at the start of the 3 GPM (0.001136 $m^3 \cdot minute^{-1}$) water draws.

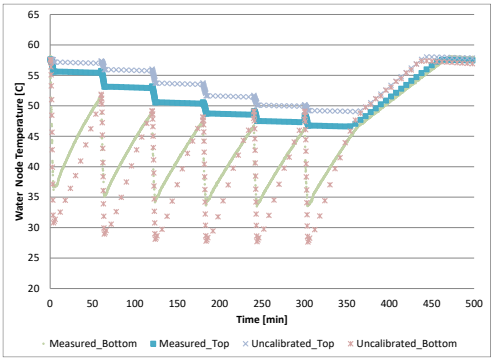

Figure 1: Compare water stratifications of measured and predicted by the uncalibrated 1-D tank model.

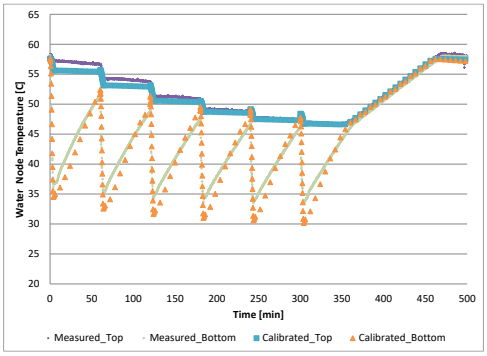

Figure 2: Compare water stratifications of measured and predicted by the calibrated 1-D tank model.

Segment-to-Segment Wrapped Tank Condenser Model

To reveal the interaction between a stratified water tank and the wrapped-tank coil, a new wrapped-tank condenser model was developed, using a segment-to-segment modelling approach. Each single condenser coil tube is divided to numerous segments, and each segment is allocated to its geometrical location on the tank. The heat transfer and pressure drop in each segment is calculated along the refrigerant flow direction. In the segment where phase change occurs, the phase transition point is determined. Figure 3 illustrates the overall heat transfer of one segment. It comprises the refrigerant side condensing heat transfer, the conductive resistance due to the tube and tank wall thickness, and the natural convective heat transfer between the water node and tank wall. The heat transfer is driven by the difference between the average refrigerant temperature in the segment and the temperature of the water node where the tube segment is located. The arrows in Fig. 3 indicate the refrigerant flow direction.

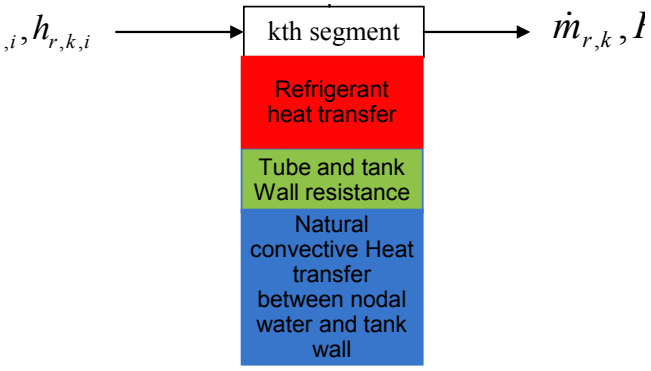

Figure 3: Overall heat transfer between a tube segment in a wrapped-tank coil and a water node.

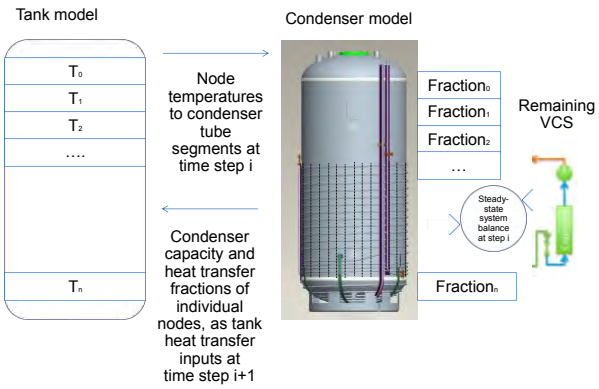

Figure 4: Information flow between tank, wrapped-tank coil and heat pump system in one time step.

At the refrigerant side, the flow-pattern-dependent heat transfer correlation published by Thome (2003) was used to calculate the condenser two-phase heat transfer coefficient. The single-phase heat transfer was calculated using the Dittus-Boelter correlation (Dittus and Boelter, 1930). The two-phase pressure drop was modelled using the correlation published by Kedzierski (1999), and the single-phase pressure drop was modelled as fully-developed turbulent internal flow in a smooth tube, as described in the Moody diagram (Moody, 1944). A non-circular tube is approximated as a round tube by inputting the hydraulic diameter. The contact surface area between the refrigerant tube and the tank wall is a user input, as this is subject to using thermal adhesive or not. The natural convective heat transfer between the water and the tank wall is simulated by Churchill and Chu (1975), assuming natural convective heat transfer from a vertical plate.

Fig. 4 describes the information flow between the water tank and the wrapped-condenser coil models in one quasi-steady-state simulation step. The dashed lines indicate separations of the tube segments. At the beginning of each time step, the water node temperatures are treated as boundary conditions to drive the heat transfer in individual tube segments associated with the tank nodes via geometrical locations. The condenser model balances with the other components in the VC cycle model to calculate steady-state system balance points at one moment. As a result, the condenser capacity is determined and the heat transfer fractions are distributed to individual nodes by accumulating the heat transfer rates of tube segments in each node. At the end of the time step, the new water node temperatures are calculated based on the condenser heat fractions. Then, the updated node temperatures become new boundary conditions to the condenser coil for the next time step. It should be noted, for a tank node having no condenser tubes at the location, the condenser heat fraction is zero. If multiple tubes are wrapped on the same tank node, the nodal temperature to the tubes is assumed the same.

As mentioned, both the evaporator and condenser models use the segment-to-segment modelling approach, which calculate and accumulate the refrigerant charge at the segment level specific to vapor phase, liquid phase and two-phase. To calculate the two-phase refrigerant density, the Hughmark (1962) void fraction model is adopted.

3. ENERGY STANDARD FOR RATING WATER HEATERS

The US test procedure of water heaters was recently modified, i.e. from the previous Energy Factor (EF) to the new Unified Energy Factor (UEF). The two test procedures require the same air side conditions, i.e. setting the surrounding air at 67.5°F (19.7°C) temperature and 50% relative humidity. The make-up water temperature is controlled at 58°F (14.4°C). The difference between the two test procedures is due to the water draw pattern and supply water temperature setting. The previous EF test procedure starts when an average internal tank temperature reaches 135°F ± 5°F (57.2 ± 2.7°C), and applies 6 equal water draws of ~10.7 gallons (40.5 L), each spaced equally during the first five hours, and no more water draws until the end of the 24-hour test period. The new UEF test procedure starts when an average internal tank temperature reaches 125°F ± 5°F (51.7± 2.7°C), and its water draw profiles vary with the usage pattern. Typically, a 50-gallon (189 L) water heater is related to the medium water use pattern, which comprises 12 water draws: 1. at 0:00, draw 56.8 L at a flow rate of 6.5 L·minute^{-1}; 2. at 0:30, draw 7.6 L at a flow rate of 3.8 L·minute^{-1}; 3. at 1:40, draw 34.1 L at a flow rate of 6.5 L·minute^{-1}; 4. at 10:30, draw 34.1 L at a flow rate of 6.5 L·minute^{-1}; 5. at 11:30, draw 18.9 L at a flow rate of 6.5 L/minute; 6. at 12:00, draw 3.8 L at a flow rate of 3.8 L·minute^{-1}; 7. at 12:45, draw 3.8 L at a flow rate of 3.8 L·minute^{-1}; 8. at 12:50, draw 3.8 L at a flow rate of 3.8 L·minute^{-1}; 9. at 16:00, draw 3.8 L at a flow rate of 3.8 L·minute^{-1}; 10. at 16:15, draw 7.6 L at a flow rate of 3.8 L·minute^{-1}; 11. at 16:45, draw 7.6 L at a flow rate of 6.5 L·minute^{-1}; 12. at 17:00, draw 26.5 L at a flow rate of 6.5 L·minute^{-1}. The total volume drawn per day is 208 L.

The EF and UEF are defined as the ratio of the total heat supplied to the tank water during the test to the total power required to operate the system.

$$UEF = \sum_{k=1}^{n} \frac{M_k c_p (T_s - T_i)}{W_i} \quad \text{Eq. (2)}$$

In Eq. 2, k represents individual hot water draw while n represents the total number of draws during the test. Note that n can vary according to the draw pattern used for the test (small, medium and large usage pattern), M is the total mass drawn for respective draw. T_s, T_i and W_i represent the supply water temperature, inlet water temperature and the total energy consumed by the heat pump (power times the heat pump run time) respectively.

The 24-hour energy factor tests rate energy efficiency of water heaters. First Hour Rating (FHR) is a measure of the available hot water capacity of the WH (in gallons). It is determined by the water tank's storage volume, the heat pump and supplemental resistance heating capacity. The previous test procedure starts when an average internal tank temperature reaches 135°F ± 5°F (57.2 ± 2.7°C). The hot water is drawn at a 3.0 GPM flow rate (11.4 $L \cdot min^{-1}$), and the water draw continues until the supply water temperature drops to 25R (13.9K) below the maximum water supply temperature as observed. The water draw is recovered when the thermostat senses the water temperature rises back to 135°F ± 5°F, and terminated again when the water temperature drops by 25R. This process is repeated for one hour. At the end of the hour, if a draw is ongoing, the draw is allowed to complete normally. If a draw doesn't start, a final draw is started and then terminated when the outlet water temperature reaches the same outlet temperature that the previous draw was terminated at. The new FHR test procedure keeps everything the same, except having the average internal tank temperature at 125°F ± 5°F (51.7± 2.7°C), and the water draw terminated when the temperature drops by 15R (8.3K).

4. SIMULATION-DRIVEN DESIGN

A baseline 50-gallon heat pump water heater was selected for the simulation study. It originally uses R-134a, a wrapped-tank condenser coil having 32 tubes (wraps) split to two circuits. The condenser uses D-shape aluminium tubes with a 0.31 inch (7.9 mm) outside diameter, and the tube wall thickness is 0.04 inch (1.0 mm). The tank's steel wall thickness is 0.064 inch (1.6 mm). The evaporator coil has 28 aluminium tubes split into two parallel circuits in two rows. The evaporator tubes have a 0.375 inch (9.5 mm) outside diameter, and the tube length is 17.0 inches (0.43 m) with the fin density of 240 fins/foot (787 fins/meter). The evaporator frontal flow area is 1.65 square feet (0.15 square meter). The evaporator blower is installed downstream of the evaporator coil, while the compressor is installed upstream. The air flow picks up the compressor shell heat before entering the evaporator coil. The blower consumes 13 Watts and drive 150 CFM (4.25 cubic meter per minute) flow. A thermo-expansion valve serves as the expansion device controlling a 10R (5.6K) superheat degree at the evaporator exit. The compressor map of a rotary compressor was provided by the manufacturer. The compressor displacement volume is 8.6 ml per revolution. The tank insulation results in a 90% energy factor if using all electric resistance heaters. It is assumed that the compressor shell loss is 40% relative to its power input under the standard WH rating condition. The water tank has two resistance probe heaters. The upper one, of 5 kW capacity, is inserted at the 65% height, and the lower one is placed at the bottom. The lower heater is used for emergency, when the heat pump fails to start. A temperature sensor for controlling both the top resistance heater and the heat pump is located at the same level as the top heater.

4.1 Compare Test Procedures of Energy Factor and Unified Energy Factor

Since it is a recent modification from the EF test procedure to the UEF test procedure, most WH manufacturers only have the previous EF and FHR test results and didn't report the UEF and FHR numbers following the new test procedure, yet. A use case of the quasi-steady-state HPWH model is to have the model calibrated against a previous EF test, based on which the manufacturer can predict the UEF and FHR following the new standard.

With respect to the baseline 50-gallon heat pump water heater, when tested under the previous EF procedure, the heat pump is ON when the temperature sensor measures the node temperature < 130°F (54.4°C), and is OFF when the temperature reaches 135°F (57.2°C); the top resistance heater is ON when the node temperature is below 110°F (43.3°C), and is OFF when reaching 135°F. Under the new UEF standard, the heat pump is ON when the temperature sensor measures the node temperature < 120°F (48.9°C), and is OFF when the temperature reaches 125°F (51.7°C); the top resistance heater is ON when the node temperature is <110°F, and is OFF at 125°F.

The figures below present the 24-hour EF and UEF HPWH simulations, respectively. They depict ten water nodal temperature profiles (water nodes in the tank evenly distributed from top to bottom, numbered from 0 to 9), the draw moments and heat pump power consumption. It demonstrates that the UEF draw pattern is less regular in comparison to the six equal draws of the EF procedure. The heat pump operations respond to the water draws, but last longer to recover the tank water temperature. At a water draw moment, the tank temperature stratification is most significant. The heat pump operation promotes water mixing. When there are no draw and heat pump operation, the water nodal temperatures deviate due to the natural convection and heat loss to the surrounding. At 19:00 during the 24-hour EF test in Fig. 5, the heat pump was called to recover the tank temperature

when there was no draw. The top resistance heater was never called for both the 24-hr simulations. As a result, the predicted EF is 3.69, and the predicted UEF is 3.76. The UEF is higher, due to its lower temperature setting.
The first-hour ratings were also predicted for the two test procedures. Following the previous EF test procedure, the FHR water draw amount is 53.3 gallons (202 L); following the new UEF test procedure, the FHR is 58.4 gallons (221 L). The new UEF test gives higher FHR, because it requires a smaller temperature increment from 58°F (14.4°C) to 125°F (51.7°C) than from 58°F to 135°F (57.2°C) in the previous procedure. Additionally, the FHR is dominated by the top resistance heater because of its much larger capacity (5 kW) than the heat pump.

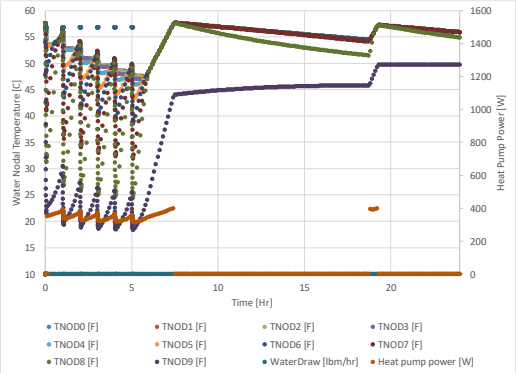

Figure 5: Temperature profiles, water draw patterns and heat pump power consumption of previous 24-hr EF test.

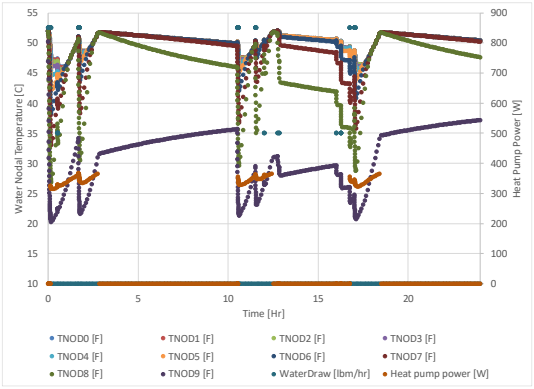

Figure 6: Temperature profiles, water draw patterns and heat pump power consumption of new 24-hr UEF test.

4.2 Vary Refrigerant Charge

Refrigerant charge optimization is required for developing all vapor compression systems. Normal practice is to gradually increase the system charge and locate the best performance point. The charge optimization process can be tedious, while it is more time consuming for HPWHs as having to do 24-hour tests repeatedly. The model-based design makes it more efficient. In a HPWH using a TXV, addition of refrigerant charge mainly goes to the wrapped-tank coil, which lowers the condenser exit liquid temperature and increases the evaporator cooling capacity, also promotes the water temperature stratification. However, adding charge causes higher compressor discharge pressure and temperature, which degrades the compressor efficiency. Fig. 7 illustrates the predicated heat pump run time and the UEF when changing the system charge from 0.5 kg to 0.9 kg. Adding charge enlarges the heat pump capacity, and thus decreases the heat pump run time. When increasing the charge from 0.5 kg to 0.7 kg, the enhancement in UEF is noticeable. Beyond the 0.7 kg, the efficiency trend becomes flat.

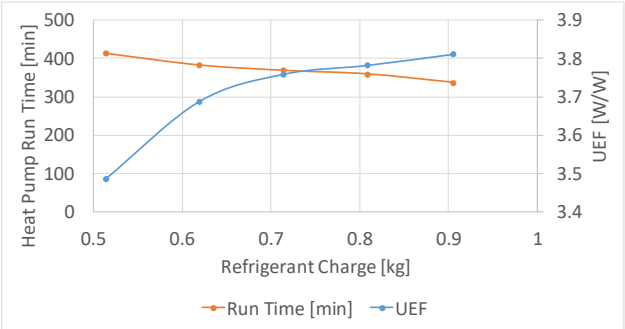

Figure 7: Heat pump run time and UEF varying with charge.

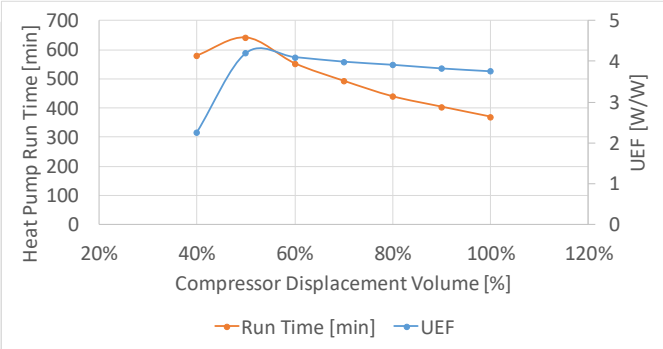

Figure 8: Heat pump run time and UEF varying with compressor displacement volume.

4.3 Vary Compressor Displacement Volume

It is easy to switch the compressor map for compressor selection. On the other hand, compressors of varied displacement volumes (capacity) from one manufacturer tend to have similar efficiencies. Thus, using one baseline map, engineers can scale the compressor displacement volume to

optimize the HPWH performance. Reduced compressor displacement volume results in smaller refrigerant mass flow rate and unloads the heat exchanger to achieve better effectiveness. On the other hand, it decreases the heat pump capacity and leads to longer run time. If the heat pump capacity is too small, and can't meet the temperature setting, the resistance heater will kick in, which degrades the performance quickly.
Figure 8 illustrates the heat pump run time and UEF with decreasing the compressor volume from 100% to 40%. The volume reduction enhances the UEF and extends the run period. With further reduction to 40%, dramatic drops occur in both the UEF and the heat pump run time, because the top resistance heater was called, which accelerated the water heating but impaired the energy factor. The analysis suggests that use of a two-stage compressor may result in superior HPWH efficiency. When there is a water draw, the high stage will run to satisfy the quick hot water demand. When the water draw is off, the lower stage can be used for slow heating with a better efficiency.

4.4 Vary Refrigerant Type

R-134a is the most used refrigerant for HPWH. However, its global warming potential (GWP) is very high, i.e. 1430. R-134a should be phased out soon to protect our environment. The candidates of direct drop-in replacement, i.e. using the same compressor and heat exchangers, include R-1234yf (GWP of 4), R-1234ze (GWP of 2) and propane (R290, GWP of 3).
Assuming the same volumetric and isentropic efficiencies at the same suction and discharge pressures when varying the refrigerant, 24-hour UEF simulations were conducted for these four refrigerants. In order to compare the system charges, it is assumed that the required charge leads to 20% liquid phase ratio in the condenser for each individual refrigerant. Figure 9 compare the UEF, heat pump run time and required system charges, relative to the baseline R-134a. R-1234ze has the longest running time, indicating that the refrigerant has the smallest volumetric capacity. With reducing the capacity, the heat exchangers are unloaded, consequently, R-1234ze achieves the highest UEF. R-290 results in the shortest runtime with the highest volumetric capacity, which degrades its efficiency. R-1234yf's performance is slightly worse than R-134a. R-1234yf, R-1234ze and R-134a have similar refrigerant system charges. R-290 requires 50% less charge, due to its smaller molecular weight. Figure 10 compares the highest compressor discharge temperatures in the 24-hour run, the alternative refrigerants lead to similar temperatures, with R-1234yf and R-1234ze even lower, and R-290 slightly higher. It implies that the compressor lubricant can accommodate the refrigerant change.

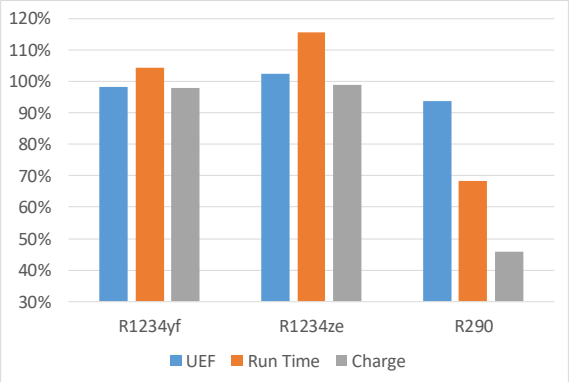

Figure 9: Performance indices of alternative refrigerants relative to R-134a.

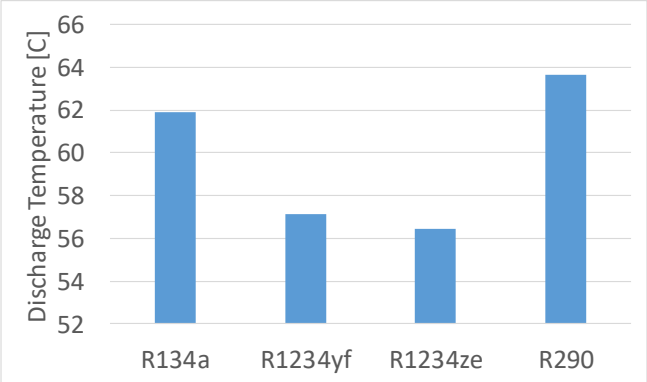

Figure 10: Compressor discharge temperatures of four refrigerants.

Vary Tube Connection and Locations

The HPWH modelling and design tool uses a segment-to-segment modelling approach to simulate the wrapped-tank coil, which allows users to edit locations and flow path of the tube wraps. Engineers can use it to optimize the heat exchanger design. Here is to show a simple example, i.e. combining the two circuits (refrigerant flow paths) (32 tubes) into one circuit with the tube locations unchanged. There is a trade-off in combining the refrigerant flow paths, where the refrigerant mass flux is doubled, and thus, the heat transfer coefficient is augmented, with the refrigerant pressure drop increased as a penalty. The model predicted the related saturation temperature drop in the two-circuit condenser is 1.3K, however, the saturation temperature drop in the one-circuit condenser is 6.7K. Overall, the one-circuit condenser results in slightly higher average condensing temperature,

i.e. 53.3°C versus 51.7°C led by the two-circuit condenser, and a slightly lower UEF, i.e. 3.75 versus 3.76.

4 CONCLUSIONS

The well-regarded, public-domain ORNL Heat Pump Design Model was upgraded to model and design heat pump water heaters for quasi-steady-state simulations. The EnergyPlus stratified tank model was improved to predict water temperature profiles with introducing a bulk mixing mechanism, and a new segment-to-segment wrapped-tank condenser coil model was added to the HPDM component model library. The system model is able to run one 24-hour simulation within 5 minutes, and predict the HPWH performance fairly accurate. It can serve as an effective design tool to predict energy factors and first-hour rating with respect to extensive design parameters, e.g. compressor size, heat exchanger configuration, tube locations, refrigerant charge, water draw pattern, etc. Furthermore, it can simulate HPWHs using low GWP refrigerants.

5 ACKNOWLEDGEMENTS

The authors are grateful to Mr. Antonio Bouza, Technology Development Manager of the U.S Department of Energy, Building Technologies Office for supporting this work.

6 REFERENCES

Braun. J.E., Klein. S.A, Mitchell, J.W., 1989. Effectiveness models for cooling towers and cooling coils, ASHRAE Transactions, 95(2), 164-174.

Churchill, S.W., Chu, H.H.S., 1975. Correlating Equations for Laminar and Turbulent Free Convection from a Vertical Plate, International Journal of Heat and Mass Transfer 18, 1323..

Dittus. F. W., Boellter, L. M. L,1930. University of California, Berkeley, Publications on Engineering2, 443

Department of Energy (DOE), 2013. Water Heater Test Procedure Rulemaking: Development Testing Preliminary Report, November
(https://www1.eere.energy.gov/buildings/appliance_standards/pdfs/water_heater_test_report_111413.pdf).

EnergyPlus Engineering Reference, Version 8.1, DOE, 2016
(http://apps1.eere.energy.gov/buildings/energyplus/energyplus_documentation.cfm).

Hughmark, G. A., 1962. Holdup in gas-liquid flow, Chem. Eng. Progress.58, 62-65

Kedzierski, M. A. Choi J. Y., 1999 A generalized pressure drop correlation for evaporation and condensation of alternative refrigerants in smooth and micro-fin tubes", NISTIR 6333.

Moody, L. F., 194. Trans ASME, 66, 671.

Murphy, R. W., Baxter V. D., Vineyard, E. A.,Linkous, R. L. 2011. Drop-in evaluation of refrigerant r1234yf in a residential integral heat pump water heater," Proceedings of the 10th International Energy Agency Heat Pump Conference.

Shen, B., Rice, K., 2018. DOE/ORNL Heat Pump Design Model (http://hpdmflex.ornl.gov/).

Thome J. R., El Hajal, J., Cavallini, A. 2003.Condensation in Horizontal Tubes, Part 2: New Heat Transfer Model Based on Flow Regimes, International Journal of Heat and Mass Transfer 46(18), 3365-3387.

Manuscript ID: 453
DOI: 10.18462/iir.icr.2019.0453

Modeling and Optimization for the External Heat Exchanger of CO2 Heat Pump applied for Electric Vehicles

Yiyu CHEN[(a),(b),(c)], Huiming ZOU[(a),(b)*], Junqi DONG[(d)], Changqing TIAN[(a),(b),(c)]

[(a)] Cas Key Laboratory of Cryogenics, Technical Institute of Physics and Chemistry, CAS, Beijing, 100190, China
[(b)]Beijing Key Laboratory of Thermal Science and Technology, Technical Institute of Physics and Chemistry, Beijing, 100190, China
[(c)]University of Chinese Academy of Sciences, Beijing, 100049, China
[(d)]SANHUA Holding Group Centre Research Center, Hangzhou, 310018, China

ABSTRACT

CO2 heat pump is a promising system for electric vehicles to improve its heating performance in cold region. The external heat exchanger is a key component acting as evaporator on heating mode and gas cooler on cooling mode, respectively. In this paper, the simulation model of a kind of micro-channel heat exchanger for CO2 heat pump is setup and validated. The maximum errors of heat capacity and refrigerant-side pressure drop between the simulated results and experimental results are within 8.5% and 11.6%, respectively. Based on the simulation model, the performance of this heat exchanger with different structure layout is analyzed under different working conditions. Accordingly, an optimized structure of the micro-channel heat exchanger for CO2 heat pump is presented to get the optimal performance in electric vehicles.
Keywords: Modeling, Optimization, Heat Exchanger, CO2 Heat Pump, Electric Vehicles

1. INTRODUCTION

Air source heat pump system is a promising development direction for electric vehicle air conditioning due to the benefits of high efficiency and low energy consumption. However, the heating capacity and performance of a traditional air source heat pump employed HFC-134a or HFO-1234yf as refrigerant diminish significantly while the ambient temperature decreases. As a result, the heat pump system cannot provide enough heat for the passenger compartment in extreme cold region. CO2 heat pump is a promising system for electric vehicles to improve its heating performance in cold region (Lorentzen and Pettersen, 1993).The external heat exchanger (EHX) of a CO2 air source heat pump is a crucial component acting as evaporator on heating mode and gas cooler on cooling mode, respectively. The EHX needs to adapt to wide temperature range and multiple working conditions as the operating conditions are switched. Its performance which is easily affected by ambient condition has a strong effect on the heat pump system performance. Thus, it is important to improve the performance of cooling and heating modes comprehensively.

Din et al. 2015 developed a mathematical model to predict the performance of the EHX which using HFC-134a as refrigerant, and analyzed the structure parameters' effect on the performance on the EHX, especially the frosting characteristics. Zhang et al. 2016 experimentally studied the influence of flat pipes layout of the microchannel HX (horizontal/ vertical) on the performance of heat pump air-condition system, environmental refrigerant HFO-1234yf was chosen as the media. There were several researches focusing on the compatibility of the EHX between cooling mode and heating mode. However, those researches were all based on HFC-134a or HFO-1234yf which worked as sub-critical cycles. When it comes to the performance of the EHX using in trans-critical cycle, there were no related reports.

The purpose of this paper was to develop a simulation model for EHX which is validated by experimental data. Based on the developed simulation model, the performance of this heat exchanger with different structure layout was analyzed under different working conditions, aiming to find an optimized structure of the micro-channel heat exchanger for CO2 heat pump.

2. MODEL DEVELOPMENT

The research object was aluminum parallel flow microchannel heat exchanger, which was widely used in the field of automotive air conditioning. Fig. 1 was a schematic diagram of the structure of the heat exchanger. It was consisted of 56 horizontal flat tubes and the louvered fins attached to the tubes.

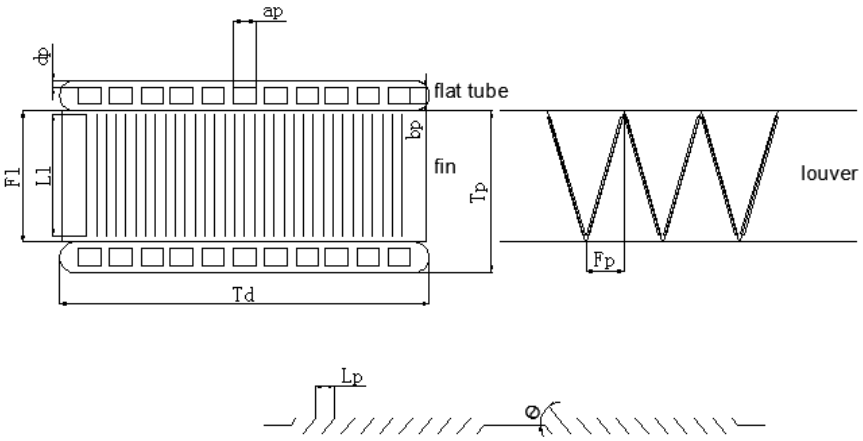

Figure 1: The schematic diagram of the external heat exchanger

By using finite element approach, a distributed parameter model is developed. The refrigerant port was divided into 20 equal length elements along the CO2 flow direction while the air side channel was composed of two semi-fins symmetrically distributed on both sides of the flat tube. Then thermodynamic analysis on each segment was performed.
Some reasonable assumptions were made to simplify the calculation process. (1) The heat exchanger was working in steady state. (2) Air passed through the surface of the flat tube evenly. (3) There was little heat conduction along the axial direction of the flat pipe. (4) The flow rate of the refrigerant in each flow channel of the flat pipe was evenly distributed.

2.1. Governing Equations

For the i-th segment, the conservation equations of energy mass between air and refrigerant were given in Table 1.

Table 1: The governing equations used in the model

Heat transfer process	Equations
Energy conservation in refrigerant side	$Q_{r,i} = m_r(h_{rout,i} - h_{rin,i})$
Convective heat transfer between refrigerant and wall	$Q_{r,i} = \alpha_r A_{r,i}(T_{win,i} - T_{r,avr,i})$
Heat conduction between the inner wall surface and the outer wall surface	$Q_{w,i} = \lambda A_{w,i}(T_{wout,i} - T_{win,i})$
Convective heat transfer between refrigerant and wall	$Q_{a,i} = \alpha_a A_{a,i}(T_{a,avr,i} - T_{wout,i})$
Energy conservation in air side	$Q_{a,i} = \alpha_a A_{a,i}(T_{a,avr,i} - T_{wout,i})$
Energy balance between the refrigerant flow and the air flow	$Q_{r,i} = Q_{w,i} = Q_{a,i}$

2.2. Heat Transfer Coefficient and Pressure Drop

Table 2 gave the correlations of heat transfer coefficient and pressure drop that employed to develop the distribution parameters model.

2.2.1. Refrigerant side

According to different working conditions and different exit state of the EHX, the refrigerant flow can be divided into two working modes and three regions: evaporating and gas cooling modes, two-phase, superheat and super-critical regions.

In two-phase region, the flow boiling heat transfer coefficient and pressure drop has always been a research hotspot. Fang (2013a) established a new high-precision CO2 tube flow boiling heat transfer model, based on 2956 experimental data points. The friction factor is calculated from Kim and Bullard (2001) correlation. In superheat region, the heat transfer coefficient is calculated using the Gnielinski (1976) correlation and the friction factor is calculated by Churchill (1977) correlation. In super-critical region, the thermodynamics properties of carbon dioxide vary greatly with temperature, especially when the temperature is near to the critical temperature. Therefore, the effect of wall temperature cannot be ignored. Pital (2002) introduced the influence of wall temperature on physical properties by means of average Nusselt number and proposed a modified heat transfer correlation, where Nu is calculated from Gnielinski (1976) correlation. Fang (2013b) introduced the characteristics of the supercritical zone and proposed a new correlation to predict the friction factor based on the adiabatic flow resistance correction equation.

2.2.2. Air side

According to different working conditions, the air side could be three different working condition: dry, wet or frost condition. In dry condition, the heat transfer factor and friction factor are calculated from the basic equations of the louver fins directly. If the temperature of the outer wall is lower than the dew point temperature of air but higher than the freezing point of water, then it comes to wet condition. And the impact of condensation should be considered (Kim and Bullard, 2001). Otherwise, if the temperature of the outer wall is lower than both of the dew point temperature of air and the freezing point of water, then the frost and defrost problem should be considered. Xia (2010) provided a simplified model to characterize the effects of frosting on the heat transfer of louvered-fin, flat-tube heat exchangers. The effect of frost on heat transfer was characterized as a correction factor. In this correlation, Γ was the non-dimensional frost thickness, defined as frost thickness normalized with respect to the fin pitch.

Table 2: Correlations of heat transfer coefficient and pressure drop

Refrige-rant side	Two-phase region	Nu	$Nu = 0.00061(S+F)Re_l Fa^{0.11}\,\mathrm{Pr}^{0.4}/\ln(1.024\mu_{l,f}/\mu_{l,w})$ $S = 41000Bo^{1.13} - 0.275 \quad F = [x/(1-x)]^a(\rho_l/\rho_g)^{0.4}$
		f	$\phi_{\mathrm{Lo}}^2 = 1 + (4.3\Gamma^2 - 1)[Nx^{0.875}(1-x)^{0.875} + x^{1.75}]$
	Superheat region	Nu	$Nu = \frac{(f/8)(\mathrm{Re}-1000)\,\mathrm{Pr}}{1+12.7\sqrt{f/8}(\mathrm{Pr}^{2/3}-1)}$
		f	$f = [1.82\ln(\mathrm{Re}) - 1.64]^{-2}$
	Supercritical region	Nu	$\overline{Nu} = (\frac{Nu_w + Nu_f}{2}) \times \frac{k_w}{k_f}$
		f	$f = f_{iso}(\frac{\mu_w}{\mu_b})^{0.49(\frac{\rho_f}{\rho_{pc}})^{1.31}}$ $f_{iso} = 1.613\{\ln[0.234(\frac{\varepsilon}{D})^{1.1007} - \frac{60.525}{\mathrm{Re}^{1.1105}} + \frac{56.291}{\mathrm{Re}^{1.0712}}]\}^{-2}$
Air side	Dry condition	j	$j = \mathrm{Re_a}^{-0.49}(\frac{\theta}{90})^{0.27}(\frac{F_p}{L_p})^{-0.14}(\frac{F_l}{L_p})^{-0.29}(\frac{T_d}{L_p})^{-0.23}(\frac{L_l}{L_p})^{0.68}(\frac{T_p}{L_p})^{-0.28}(\frac{\delta_f}{L_p})^{-0.05}$
		f	$f = 3.208\,\mathrm{Re}_a^{-0.384}(\frac{L_p}{F_p})^{-0.196}$
	Wet condition	j	$j = \mathrm{Re_a}^{-0.512}(\frac{\theta}{90})^{0.25}(\frac{F_p}{L_p})^{-0.17}(\frac{F_l}{L_p})^{-0.29}(\frac{T_d}{L_p})^{-0.25}(\frac{L_l}{L_p})^{0.68}(\frac{T_p}{L_p})^{-0.28}(\frac{\delta_f}{L_p})^{-0.05}$
		f	$f = \mathrm{Re}_a^{-0.798}(\frac{\theta}{90})^{0.395}(\frac{F_p}{L_p})^{-2.635}(\frac{F_l}{L_p})^{-1.22}(\frac{T_d}{L_p})^{0.832}(\frac{L_l}{L_p})^{1.97}$
	Frost condition	j	$j/j_0 = 1.0 - 3.020\Gamma + 2.719\Gamma^2$

2.3. Procedure for Modeling

The EHX was divided into *n* segments (20 segments here) along the flow direction of refrigerant each pass. Figure 2 showed the procedure for analyzing the energy and mass balance for the i-th segment. According to the correlations listed in Table 1 and Table 2, the inside wall temperature (Tw_in) and heat flux (q) are inevitable in the heat transfer correlation. On the other hand, the outer wall temperature (Tw_out) was also critical to accurately determine the operating conditions on the air side. If we made hypothetical iterations on each of the above three key parameters, the calculation process would be very inefficient. In order to improve the efficiency of calculation, the refrigerant outlet enthalpy of refrigerant (hrout) was selected as the only initial iteration value. The iterative process was shown in Fig. 2. Assuming that the outlet enthalpy has been known, the heat flux (q) could be determined easily. Then the outlet parameters of air side could be known, which provided a basis for judging the air side working conditions. And we could get the wall outer and inner wall temperature (Tw_out, Tw_in) from the air side convection heat transfer and flat tube wall heat conduction equations. Since the heat flux (q) and inner wall temperature (Tw_in) were no longer uncertain, the working condition and convective heat transfer equations could be solved out.

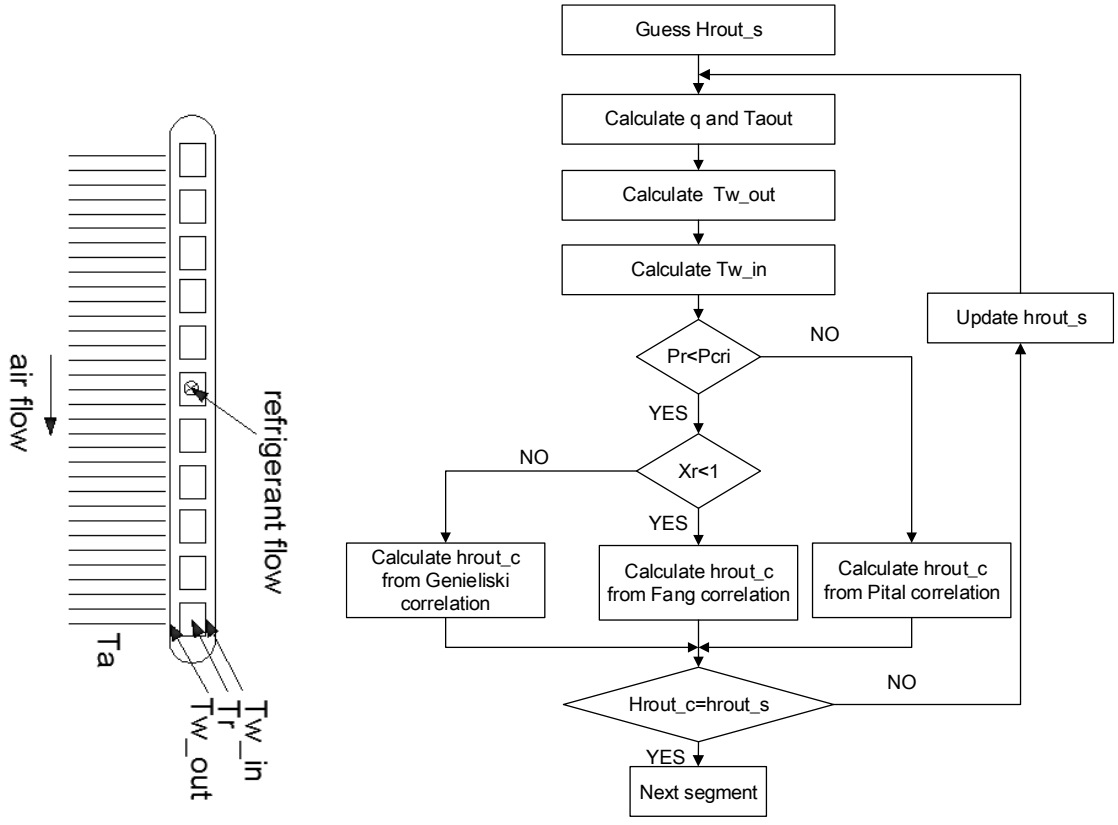

Figure 2: The calculation process of the i-th segment. (a) The schematic diagram of the i-th segment. (b) The algorithm of modeling

Considering that hundreds of iterations might be required in the calculation process, the thermal properties of carbon dioxide would be called repeatedly. Employing the Nist Database directly would result in a lot of time to be consumed, even dozens of minutes. In order to ensure the computational efficiency, the explicit physical property calculation equations (Hu, 2008) were selected to develop a subroutine. And the calculation efficiency has been increased nearly 50 times while the calculation accuracy almost has not been affected.

2.4. Model Validation

The model validation was conducted by the experimental data for a parallel flow microchannel heat exchanger. Figure 3 showed the comparison between the experimental data and calculated result. Fig. 3(a) illustrated that the calculation error was within ±15% in the heating mode while Fig. 3(b)

showed that the maximum error was not exceed 10% in the cooling mode, and the developed model could predict the performance of the EHX well.

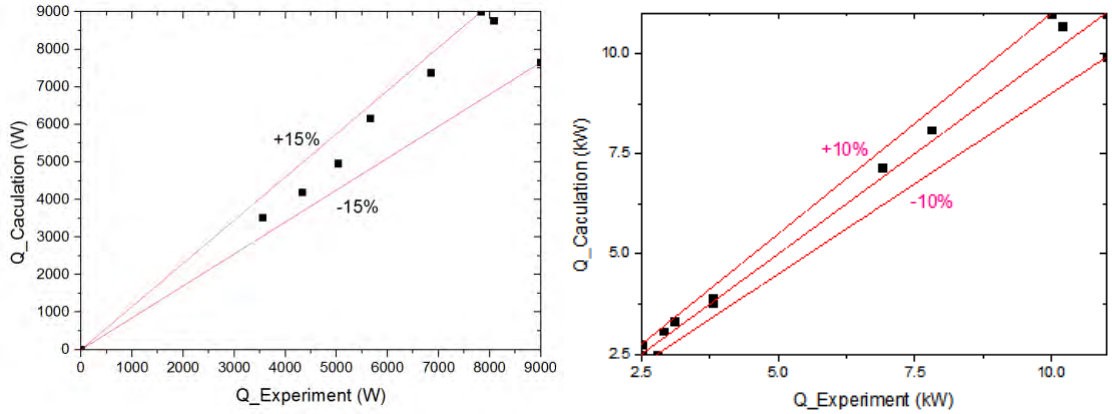

(a) (b)

Figure 3: Comparison of calculated and measured heat capacities. (a) Heating mode, (b) Cooling mode.

2.5. Optimization of the EHX

The next step was to employ the developed model to analyze the performance of the EHX with difference structure layout in wide temperature range. Considering the practical application of the EHX, a heat exchanger which has two passes is selected as the basic research object. Three distribution schemes of 1:1 (marked as No.1 scheme), 1:2 (marked as No.2 scheme) and 1:3 (marked as No.3 scheme) have been analyzed respectively. Fig. 4 was the simplified schematic diagram of the three layout structures, and the 56 flat tubes were simplified to 16. The main difference between the three schemes was the different positions of the baffles, which were important for refrigerant flow distribution.

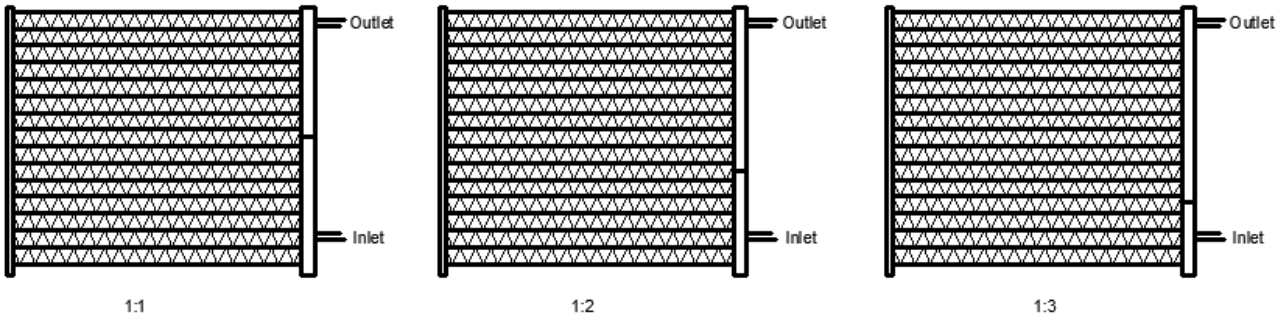

Figure 4: The simplified schematic diagram of the layout structures

The distributed parameter method completed the simulation analysis of the entire heat exchanger by means of segment-by-segment calculation. And if could give the distribution of the parameters of each segment. Fig. 5 showed the distribution of quality and temperature along the refrigerant flow direction. The refrigerant reached superheat region at 80% of the total length of the heat exchanger. From the perspective of heat transfer, the performance of No.3 structure was a good choice as the refrigerant entered the superheat region firstly. However, as shown in Fig. 5(b), the saturation temperature of refrigerant in No.3 structure was greatly affected by pressure drop.

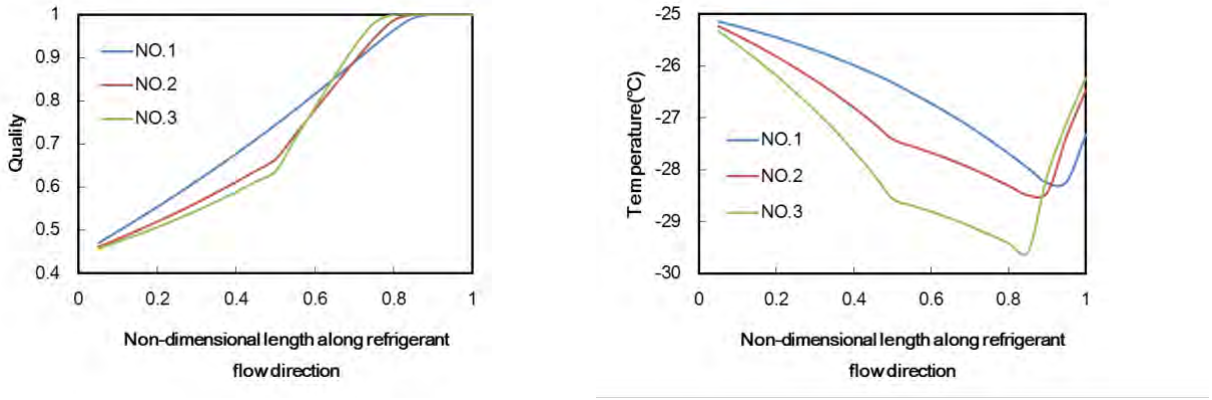

(a) (b)

Figure 5: The distribution of quality and temperature along the refrigerant flow direction. Ta=-25 °C, Mr =62.21 kg/h, Va=5 m/s.

In the optimization process of the heat exchanger, the increase of the heat exchange rate was always accompanied with the increase of pressure drop. Evaluating the merits of a solution required a comprehensive consideration of both heat transfer and pressure drop, it was best to use a dimensionless number to characterize the optimization effect. Eq. (1) gave us such an opportunity to evaluate the merits of each scheme.

$$\eta = \frac{Q / Q_0}{\Delta P / \Delta P_0} \qquad \text{Eq. (1)}$$

Where η was non-dimensional enhancement factor, defined as the ratio of the heat transfer per unit flow resistance of a scheme to that of NO.1 structure. The dimensionless optimization factors for the three optimization schemes at different operating temperatures were shown in Fig. 6. Fig. 6(a) showed that NO.2 structure was the best one whose η was 10% higher than the 1st in heating mode while the 3rd structure had a little advantage in the extremely cold region than the NO.1. However, when it was employed as a gas cooler in the cooling mode, both NO.2 and NO.3 were not good choices, which could be seen in Fig. 6(b). The main reason resulting in the great difference is that the quality and density of the refrigerant were gradually increasing as it evaporated along the refrigerant flow direction in heating mode, while the temperature and density of the refrigerant were gradually decreasing as it was cooled in cooling mode. The great difference in thermodynamics properties changing trend between different working conditions leaded to the unbalanced performance between summer and winter season.

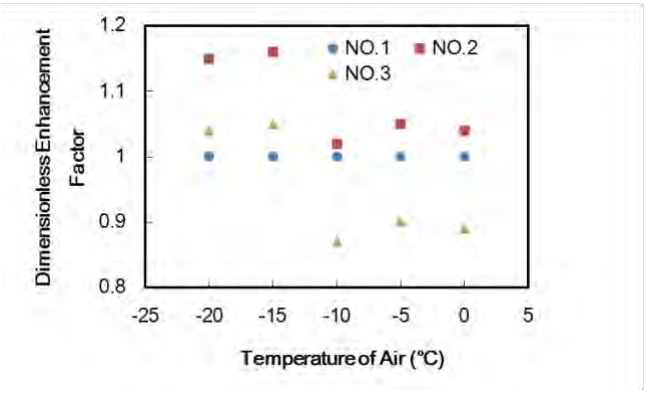

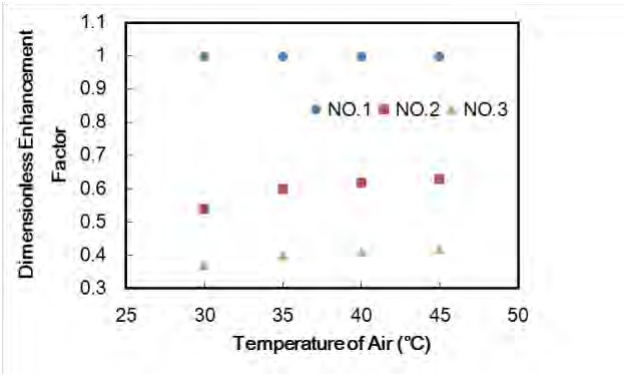

(a) (b)

Figure 6: Dimensionless optimization factors for the three optimization schemes at different operating temperatures. (a) Heating mode, (b) Cooling mode

Considering the significant difference between the two modes, exchange the inlet and outlet collectors of refrigerant as an optimal solution. Fig. 7(a) showed the dimensionless optimization factors for the three optimization schemes at different operating temperatures with exchanging the inlet and outlet collectors. The η of No.2 and No.3 layout structure were both optimized significantly comparing to those without exchanging collectors (shown as Fig. 6(b)). Fig. 7(b) gives an implementation to exchange the inlet and outlet collectors of the EHX. Only one additional four passes valve was employed to achieve the aim to exchanging the inlet and outlet collectors.

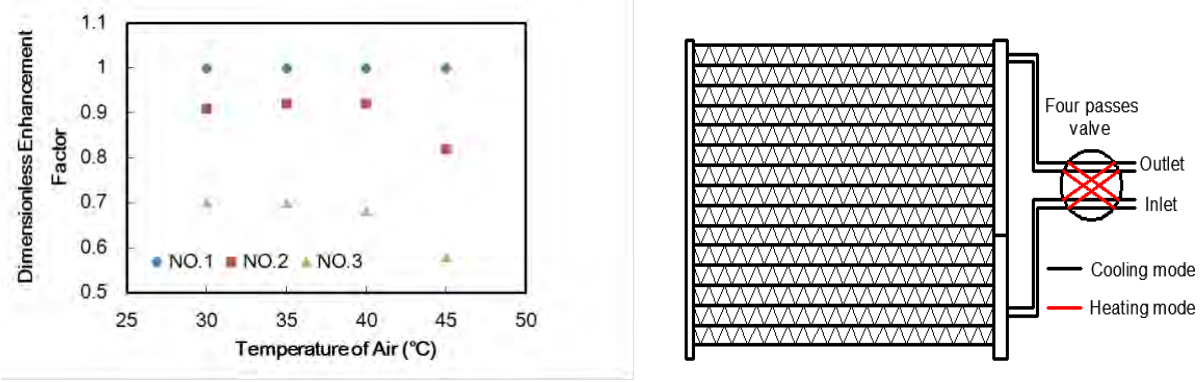

(a) (b)

Figure 7: (a) Dimensionless optimization factors for the three optimization schemes at different operating temperatures with exchanging the inlet and outlet collectors, (b) An implementation to exchange the inlet and outlet collectors

3. CONCLUSIONS

A distribution parameter model was developed to simulate the performance of the external heat exchanger of CO2 heat pump applied for electric vehicles and validated by experimental results. The main conclusions are listed as follows:

(1) A simulation model of a kind of parallel-flow heat exchanger for CO2 heat pump is setup and validated. The maximum errors of heat capacity and refrigerant-side pressure drop between the simulated results and experimental results are within 8.5% and 11.6%, respectively.

(2) Three distribution schemes of 1:1 (marked as NO.1 scheme), 1:2 (marked as NO.2 scheme) and 1:3 (marked as No.3 scheme) have been analyzed respectively. In heating season, the NO.2 structure has the highest dimensionless enhancement factor. However, in cooling season, both NO.2 and NO.3 have obviously negative effects.

(3) An optimal design by exchanging the inlet and outlet collectors was given out. Besides, a structure to achieve the aim was proposed by employing a four passes valve.

ACKNOWLEDGEMENTS

We would like to thank the support by the National Key Research and Development Program of China (No. 2018YFB0105400) and the Natural Science Foundation of China (No. 51676201)

NOMENCLATURE

A	area (m^2)	*Nu*	Nusselt number
Bo	Bond number	*h*	enthalpy (kJ/kg)
f	friction factor	*P*	pressure (Pa)
F	Fang number	*Q*	heat capacity (W)
Fd	fin depth (m)	*Re*	Reynolds number
Fl	fin length (m)	*T*	Temperature (K)
Ll	louver length (m)	*x*	quality
Lp	louver pitch (m)	*m*	mass flow rate (kg/s)

Greek letters

α	heat transfer coefficient ($W/m^{2*}K$)	θ	louver angel
λ	thermal conductivity (W/m*K)	Γ	non-dimensional frost thickness
η	non-dimensional enhancement factor	δ f	fin thickness (m)

Subscript

a	air	*crit*	critical
in	inlet	*out*	outlet
r	refrigerant	*w*	wall

REFERENCES

Fang X., Xu Y., Su X., 2012. Pressure drop and friction factor correlations of supercritical flow. Nuclear Engineering & Design 242:323-330.

Fang X., Zhou Z., Li D., 2013. Review of correlations of flow boiling heat transfer coefficients for carbon dioxide. Int. J. Refrigeration 36(8): 2017-2039.

Gnielinski V., 1976. New equations for heat and mass transfer in turbulent pipe and channel flow. Int. chem. Eng. 16(2): 8-16.

Din J., Zhao L., Yang Z., 2015. Analysis of refrigerant side structure in the automobile heat pump's exterior heat exchanger. Refrigerant Technology 34(3): 25-31.

Kim M H., Bullard C W., 2001. Development of a microchannel evaporator model for a CO2 air-conditioning system. Energy 26(10):931-948.

Kim M H., Bullard C W., 2002. Air-side performance of brazed aluminum heat exchangers under dehumidifying conditions. Int. J. Refrigeration 25(7):924-934.

Pital S., Groll E A., Ramadhyani S., 2002. New correlation to predict the heat transfer coefficient during in-tube cooling of turbulent supercritical CO2. Int. J. Refrigeration 25(7):887-895.

Pettersen J., Lorentzen G., 1993. A new efficient and environmentally benign system for automobile air conditioning. SAE Trans 102(5): 135-145.

Zhang X., Xue Q., Zou H., Liu J., Tian C., 2017. Influence of heat exchanger tube layout on performance of heat pump system for electric cars. Energy Procedia 105, 5085-5090.

Manuscript ID:467
DOI: 10.18462/iir.icr.2019.0467

Research Progress of Air source Heat Pump Heating System Suitable for Cold Area Applications

Anna MA[(a)] , Guoyuan MA[(a)] , Lei WANG[(a)] , Mingjian JIANG[(a)] , Xianghui YAN[(a)]

(a)College of Environmental and Engineering, Beijing University of Technology, Beijing 10024, China

ABSTRACT

Air source heat pump is a kind of circulatory system that utilizes the low energy in the environment, high efficiency, environmental protection, energy saving and convenient operation, however, the system is greatly affected by the climate and environment. The article mainly analyzes the technology and development status of various air source heat pump systems in building heating in cold regions, and provides reference for further optimization of the system.
Key words: air source heat pump; cold area; energy saving

1.INTRODUCTION

Air source heat pump has the advantages of abundant resources, environmental protection, simple installation, convenient operation and maintenance, etc. However, the application of the air source heat pump is susceptible to the climatic environment. In view of the limitations of traditional air source heat pumps used in cold regions, experts and scholars at home and abroad have conducted a lot of research and analysis, and proposed different solutions, including: two-stage compression heat pump system, quasi-secondary compression heat pump system with economizer, cascade heat pump system, two-stage coupled heat pump system and liquid-cooled heat pump system.

In this paper, the author will conduct a detailed discussion on various the air source heat pump heating systems in cold areas above, and provide a reference for further improvement of the air source heat pump using in low temperature.

2.TWO-STAGE COMPRESSED AIR SOURCE HEAT PUMP

In the two-stage compression heat pump cycle, the refrigerant is compressed twice by the low pressure stage and the high pressure stage cylinders of the compressor, respectively, to complete the compression process. This type of compression not only adjusts the pressure ratio of each stage, reduces power consumption, but also reduces the exhaust temperature and increases the service time of the compressor.

Cuifeng C (2013) studied the low temperature application of single-machine and two-stage screw compressor. Sichao Z et al. (2013) proposed a single-machine and two-stage rolling piston compressor heat pump system with intermediate gas supplement, which proved that reasonable parameter control could significantly improve system performance. The system flow chart was

shown in Fig. 1. Shuxue X et al. (2014) used jet and enhanced enthalpy technology to prove that the two-cylinder rolling piston type two-stage compression heat pump system could greatly improve the overall performance of the system and meet the indoor comfort in winter.

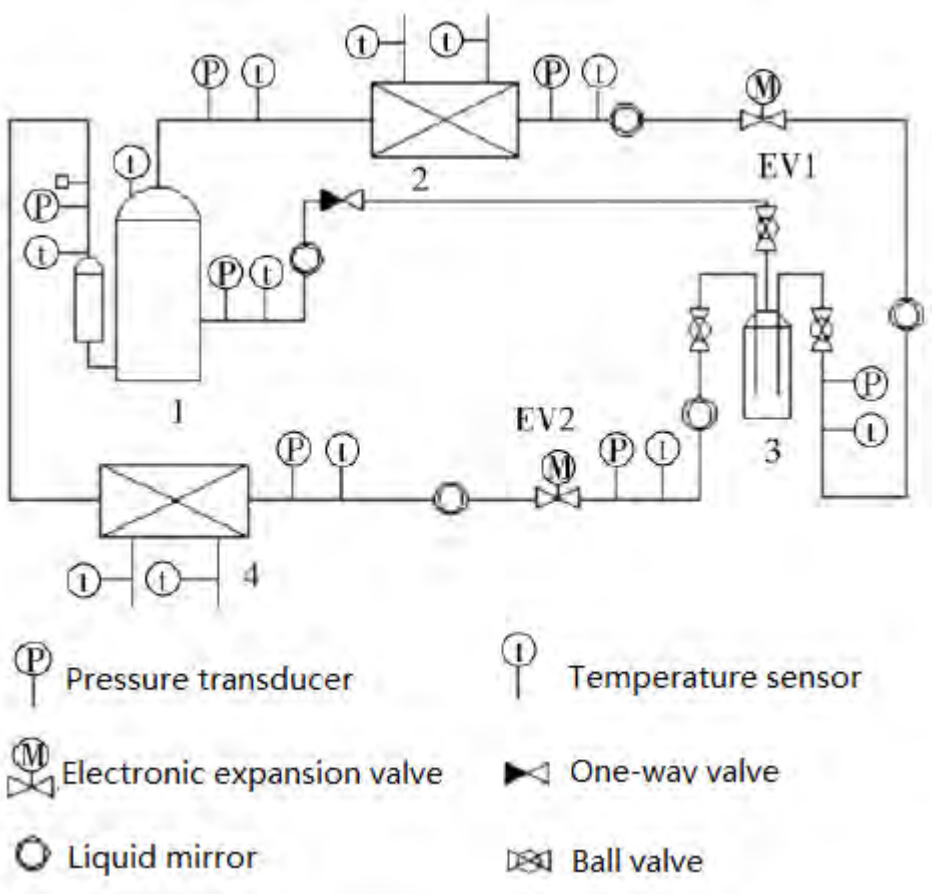

Figure 1: Single-machine and two-stage rolling heat pump system

According to the above analysis, it can be found that the heating performance of the two-stage air source heat pump system in low temperature environment has certain application advantages, but the system will still have the problem of heating attenuation with further reduction of the environment temperature, which also affects its development in ultra-low temperature fields.

3.QUASI-SECONDARY COMPRESSED AIR SOURCE HEAT PUMP TECHNOLOGY

The main feature of quasi-secondary compression heat pump system is the use of a compressor with an auxiliary inlet to form a parallel circuit between the condenser and the compressor. By strengthening gas supplement into the working chamber of the compressor, the compression process inside the heat pump is improved, thereby improving the low temperature adaptability of the system.

Guoyuan M et al. (2014) proposed a quasi-secondary heat pump system for a vortex compressor with an auxiliary air inlet, and used a sub cooler to assist system circulation. In the low temperature environment of -10 ° C ~ -15 ° C, the system still had a high heating capacity, and the heating performance was remarkable.

Yupeng C et al. (2017) compared the single-stage conventional heat pump system with gas supplement system for a vortex compressor with a flasher with R134a as the working fluid, and

pointed out that the quasi-secondary heat pump system had improved performance in all aspects under low temperature. In the further study, in order to recover the energy of the gas supplement circuit of the ordinary quasi-secondary compression heat pump system, Shuxue X et. al. (2010) proposed a quasi-secondary compression-jet heat pump system. The improvement of the system was that the injector was used to replace the common throttling element, and the system air inlet was designed to the place that compressor suction chamber just closed. The test proved that the heating capacity and heating coefficient of the system were improved compared with the common gas supplement system. Fig. 2 was a system diagram.

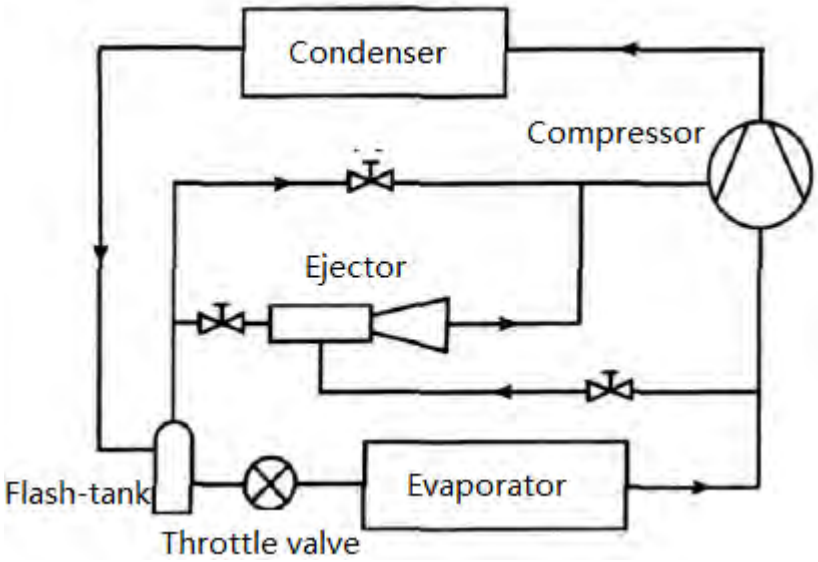

Figure 2: Diagram of the quasi-secondary compression-injection heat pump system

Roh C W et al. (2011,2012) proposed to install a gas-liquid separator on the pipeline between the evaporator and the compressor, and connected it to the gas supply circuit. The test results shown that the system could effectively reduce the exhaust temperature of the compressor.

4.TWO-STAGE COUPLE HEAT PUMP TECHNOLOGY

The new coupled two-stage heat pump heating system consisting of an air source heat pump and a water source heat pump is energy-saving and clean, and can replace the traditional heating method in cold regions.

Zuiliang M and Wei W et al. (2005,2008) had simulated the two-stage coupled heat pump system through computer to study the influence of heat exchanger area on system performance. The simulation results shown the reasonable heat exchange area played a key role in improving the system performance. In recent years, Zuiliang M and Long M.et. al. (2016) had established a jet and enhanced enthalpy two-stage coupled heat pump unit, and added a domestic hot water module. Through the simulation, the operating performance of the unit under different working conditions was analyzed to determine the reliability of the system operating in a low temperature environment.

5.THE MULTI-LAYER CIRCULATING AIR SOURCE HEAT PUMP TECHNOLOGY

The multi-layer circulating air source heat pump can be divided into two types of systems, one is a common multi-layer heat pump system that couples two single-stage heat pump cycles through a

condensing evaporator, and the other one is self-multiplying system formed by azeotropic mixing of working mediums. Both systems have their own cycle characteristics in improving the low temperature adaptability of air source heat pump systems.

5.1 The common multi-layer heat pump system

The system consists mainly of two single-stage circulation systems, each cycle being carried out independently according to the Reverse Carnot cycle, connected by a condensing evaporator, which is both an evaporator for high temperature circulation and a condenser for low temperature circulation. The system mainly achieves the purpose of increasing the working temperature difference of the system by reducing the pressure ratio of each stage of the compressor.

Dong et al. (2016,2013,2014) had established a mathematical model for the multi-layer heat pump system with R134a / R410a as the working mediums to find the best theoretical intermediate pressure to adapt to the system. Xi C et al. (2016) mainly studied the cascade heat pump air source heat pump system with NH3 / CO2 as the working mediums, and established the mathematical model to understand the operating state of the system, and hope to find the optimal operating parameters of the system cycle.

Although the cascaded heat pump system has a larger working range and a wider application field, there is still not a better solution to determine its intermediate temperature in different environments in the domestic. Therefore, it is a key factor that need to be broken for future development.

5.2The self-multiplying air source heat pump technology

The self-multiplying heat pump mainly utilizes the different boiling point characteristics of non-azeotropic mixed working mediums at the phase equilibrium point, and realizes automatic separation of high and low boiling point working mediums through condenser and gas-liquid separator to carry out separate refrigeration cycle and then multiplying.

Weirong X et al. (2009) established a mathematical model of the self-stacking heat pump system with R123/R134a as the working mediums, and found the optimal operating parameters of the system operation through simulation calculation, which provided a powerful theoretical tool for coming test demonstration.

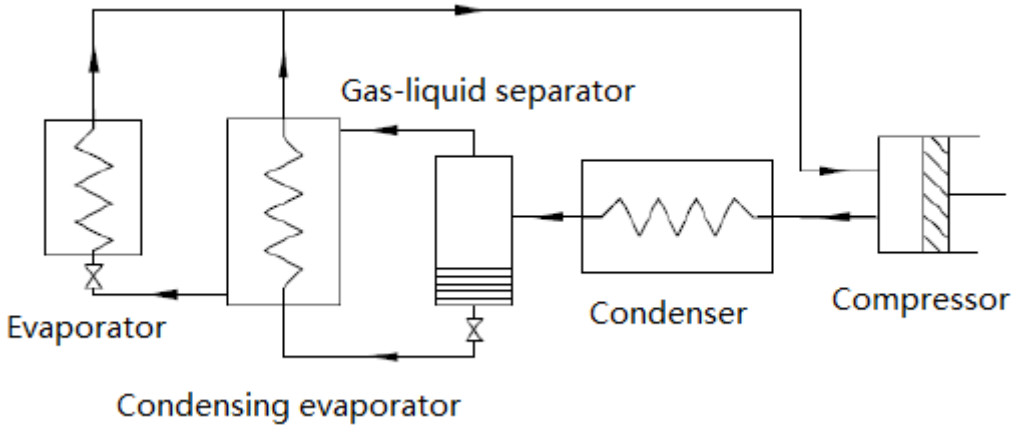

Figure 3: Single-stage compression single-stage condensation cycle diagram

Maoqiong G et al. (2000) carried out an experimental analysis on a single-stage compression multi-stage solidification self- multiplying heat pump system, which proved that the system could effectively improve the separation effect of mixed working mediums and lubricating oil, which

prevented the system from blocking the event of throttle elements in the low temperature side.
The self- multiplying air source heat pump system brings great benefits to production and life. However, due to the great variability of the combination and concentration ratio of the mixed working mediums in the system and the leakage problem of the mixed working mediums, the study on the system still needs further research.

6. SPRAY-COOLED AIR SOURCE HEAT PUMP TECHNOLOGY

The principle of the spray-cooled heat pump system is similar to that of the strengthening gas supplement heat pump system, which is to supplement a certain amount of refrigerant through the compressor auxiliary circuit, thereby changing the compressed state inside the compressor and increasing the working temperature difference of the system. The different of both is the state of supplemental working medium.
Japan's Hagimoto K et al. (1992,1997,2001) proposed a scroll compressor system with a spray bypass. Until 2017, Hagimoto K and others had been focusing on how to solve the problem of excessive exhaust gas temperature during heating at low temperature conditions and taken long-term research.
Through the above analysis, it can be found that no matter which types of liquid discharge cycles, the suction liquid in the low temperature can effectively decrease the exhaust temperature of the compressor, but also It can also be found that most of the spray-cooled heat pump systems are not ideal for improving the heat and energy consumption, so further research and analysis are needed.

7. CONCLUSION

In view of the current national conditions of serious energy consumption and urgent need to solve environmental pollution problems. It has certain practical significance to research and applicate air source heat pump system which is suitable for winter heating in cold regions of northern China. This paper reviews the development of low temperature heat pump systems and provides a reference for further optimization of the system.

REFERENCES

Cuifeng C, 2013. Application of single machine two-stage screw compressor refrigeration system. Int. J. Public Communication of Science & Technology, (2), 139+135.

Sichao Z, Guoyuan M, Shuxue X ,2013. Experimental investigation on working performance of two - stage compression heat pump system with vapor injection. Int. J. Cryogenics & Superconductivity,41 (5),409-43.

Shuxue X, Guoyuan M, 2014. Experimental study on two stage compression refrigeration /heat pump system with dual-cylinder rolling piston compressor. Int. J. Applied Thermal Engineering, 62(02),803-808.

Guoyuan M, Shuangquan S, 2002. Research on heat pump cycle for air conditioning in cold regions. Int. J. Acta Energiae Solaris Sinica, (1),17-21.

Yupeng C, Guoyuan M, Shuxue X et al., 2017. Experimental Research on Quasi Two-stage Compression Heat Pump with Flash Tank Vapor-injection Using R134a. Int. J. Journal of Refrigeration,38 (2),11-16.

Shuxue X, Guoyuan M, Long P, 2010. Experimental research and design of quasi two-stage heat pump system coupled with ejector. Int. J. Chemical Engineering (China),38 (1),99-102.

Roh C W, Kim M S,2011. Effects of intermediate pressure on the heating performance of a heat pump system using R410A vapor-injection technique. Int. J. International Journal of Refrigeration, 34(08),1911-1921.

Roh C W, Kim M S,2012. Comparison of the heating performance of an inverter-driven heat pump system using R410A vapor injection into accumulator and compressor. Int. J. International Journal of Refrigeration, 35(02),434-444.

Wei W, Zuiliang M, Yuemei Z, 2005. Optimize zation of heat exchanger area for double-stage coupling heat pump heating systems. Int. J. Heating Ventilating & Air Conditioning,35 (10),71-75.

Wei W, Zuiliang M, Yang Y, 2008. Development of the Optimal Middle Water Loop Temperature for the Double-stage Coupled Heat Pumps Heating System. Int. J. Fluid Machinery,36(1),66-69.

Long M, Zehua L, Xiaohong Z, et al.,2016. Design and Thermodynamic Optimization of Enhanced Vapor Injection Technology in Double Stage Coupling Heat Pump. Int. J. Building Energy & Environment,35(2),17-21.

Dong H.K, Han S. P, Min S. K,2013. Optimal temperature between high and low stage cycles for R134a-R410a cascade heat pump based water heater system. Int. J. Experimental Thermal and Fluid science, 47,172-179.

Dong H. K, Han S. P, Min S. K,2014. The Effect of the refrigerant charge Amount on Single and Cascade cycle heat pump system. Int. J. International Journal of refrigerant ion, 40,254-268.

Han S. P, Dong H. K, Min S. K,2013. Thermodynamic analysis of optimal intermediate temperature R134a-R410a cascade refrigerant systems and its experimental verification. Int. J. Applied Thermal Engineering, 54(1),319-327.

Xi C, Jun W, Haixia W, et al.,2016. Thermodynamic analysis of NH3 /CO2 cascade refrigeration system. Int. J. Cryogenics & Superconductivity, (3),55-59.

Weirong X, Kai D, 2009.Thermodynamic calculation and analysis on auto-cascade heat pump system. Int. J. Cryogenics,117(5),31-36.

Maoqiong G, Luo E R, Zhou Y,2000. Research on a mixed- refrigerant J- T at refrigerator used for cryosurgery , proceeds dings of ICEC 18, Bombay, India , 8,413.

Afjei T, Suter P, Favrat D,1992. Experimental Analysis of an Inverter-Driven Scroll Compressor with Liquid Injection. Int. A.2,541-550.

Yanagisawa T, Fleming John S, Dutta A K, et al.,1997. A study of a refrigerant cycle driven by a liquid refrigerant injected compression. Int. A. Proceedings of the ASME Advance Energy System Division, 337,295-302 .

Asity K, Tadashi Y, Mitsuhiro F, 2001. An investigation of the performance of a scroll compressor under liquid refrigerant injection. Int. Inter Journal of refrigeration, 24, 577-587 .

Manuscript ID:473
DOI: 10.18462/iir.icr.2019.0473

Thermodynamic Performance of Triple-loop Heat Pump Ventilation Recovery System

Anna MA[(a)], Guoyuan MA[(a)], Lei WANG[(a)], Feng ZHOU[(a)], Mingjian JIANG[(a)], Xianghui YAN[(a)]

(a)College of Environmental and Engineering, Beijing University of Technology, Beijing 10024, China

ABSTRACT

In order to improve the performance of the heat pump system under large temperature difference, this paper proposed a triple-loop heat pump ventilation recovery scheme, and an energy recovery performance test platform was set up based on the exhaust energy recovery of the building air-conditioning system. The performance of the single-loop and triple-loop heat pump systems were tested under different outdoor temperature conditions in winter and summer through experiments. The results showed that the overall performance of the triple-loop system was significantly higher than the single-loop under all operating conditions. Under winter conditions, the COP of the triple-loop system had reached to 11.19, when the indoor and outdoor temperature difference was 40 °C, and the COP of the triple-loop was 54.8% higher than the single-loop. Under summer conditions, the growth rate of the COP of the triple-loop system had reached to 89.8%, when the temperature difference was 13 °C, and the COP of the triple-loop was 74.6% higher than the single-loop.

Key words**:** Air Source Heat Pump, Exhaust Heat Recovery, Triple-loop System, Coefficient of Performance.

1.INTRODUCTION

The improvement of people's living standards makes the air-conditioning penetration rate increase year by year, and the energy consumption brought by air-conditioning operation has also been rising. Since the indoor exhaust has a certain amount of heat or cooling energy relative to the outdoor air, recycling air conditioning exhaust heat has become a hot spot for people to pursue energy saving in air conditioning systems.

The air source heat pump is a kind of air conditioning systems with energy saving benefits and environmental protection benefits, and is one of the feasible technologies for the sustainable development of air conditioners, which has been widely used in China. But the performance of air source heat pumps is easily affected by the outdoor environment.

In recent years, on the basis of improving the performance of traditional air source heat pumps, many scholars have gradually used air source heat pump systems for exhaust energy recovery in public building air conditioning systems.

Yiping W *et al*. (2004) proposed an air source heat pump system using air conditioning exhaust as a low temperature heat source, and analyzed the performance and energy saving of the system.

Yuhua Z (2014) proposed to use the energy of exhaust air for the heat exchange of the outdoor heat exchanger of the air source heat pump to strengthen the heat exchange intensity, and analyzed the performance and power consumption of the system. Xiaolei L *et al*. (2016) proposed a new type of solar low-temperature heat recovery air source heat pump combined heating system. Chen *et al.* (2015) compared the heat pump heat recovery system with the runner heat recovery and the plate heat recovery system, and concluded that the heat pump heat recovery system had greater energy saving potential. Fracastoro *et al.* (2010) had found that the efficiency of the heat pump system using building exhaust as a heat source was much higher than that of the ground source, and the installation cost of the system was lower.

In order to further improve the performance of the air source heat pump system in the large temperature difference environment, the author proposed a triple-loop heat pump ventilation system based on the exhaust air energy recovery of the building air conditioning, and built a system performance test platform to test the performance of the system through experimental methods, and discusses the heat transfer characteristics and performance improvement of the triple-loop system.

2.SYSTEM CYCLE MECHANISM

The system flow chart of the heat pump ventilation recovery system is shown in Figure 1. The system mainly includes fresh air heat exchangers (2a~2c), exhaust heat exchangers (3a~3c), and liquid storage tank (1#), throttle valves (4a~4c), four-way reversing valves (5a~5c), shut-off valves (1~18) and compressors (1a~1c).

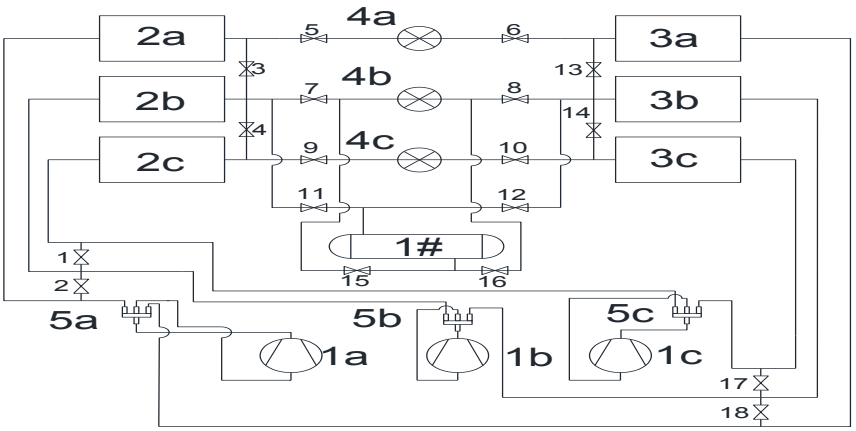

Fig. 1: System flow chart of the air source heat pump ventilation recovery system

By adjusting shut-off valves 1~18, different loop systems can be formed. By adjusting 5a~5c, the flow direction of the system refrigerant can be changed to meet the different requirements of the system in winter and summer. System flow chart shown in Fig.2 and Fig.3. The working process is as follows: The compressor sucks the low-temperature and low-pressure refrigerant vapor, compresses it into high-temperature and high-pressure steam, and sends it to the exhaust heat exchanger (or fresh air heat exchangers). After the heat is released from the cooling medium in the exhaust heat exchanger, it is condensed into a high-temperature and high-pressure liquid. After that, the refrigerant is throttled into a low-temperature and low-pressure liquid through a throttle valve, and enters the fresh air heat exchanger (or exhaust heat exchangers) to absorb heat and vaporize, and then is sucked by the compressor to form a complete circulation system.

During the whole cycle, the refrigerant absorbs heat from the outdoor fresh air in the fresh air heat exchanger, cools the fresh air, and then discharges the fresh air to the indoor. After that, the refrigeration in the indoor exhaust air is recovered to make the refrigerant exchange heat in the exhaust heat exchanger. The refrigerant condenses into a high-pressure liquid, which realizes energy recovery as a whole and improves energy utilization.

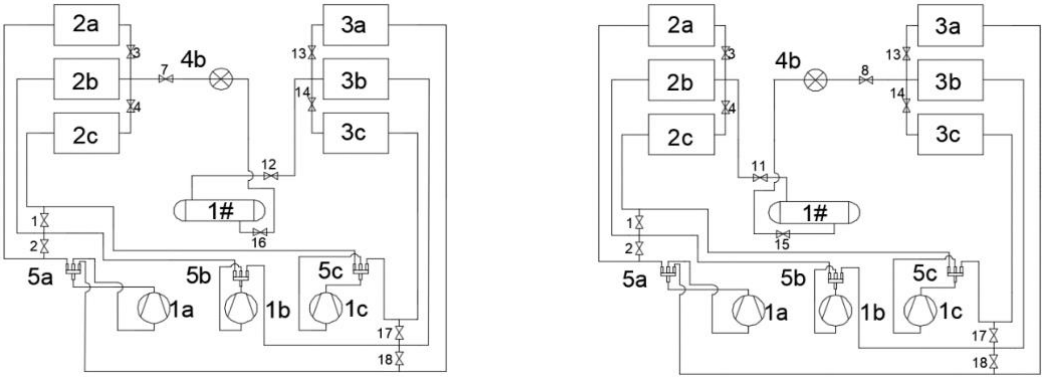

(a) Summer condition **(b) Winter condition**

Fig. 2 Flow chart of the single-loop air source heat pump system in summer and winter conditions

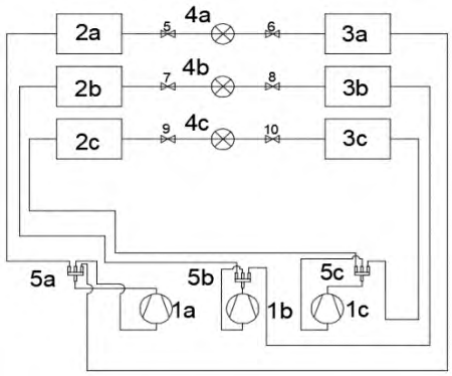

Fig. 3 Flow chart of the three-loop air source heat pump system in summer and winter conditions

3.EXPERIMENTAL METHODS AND SYSTEM PERFORMANCE ANALYSIS

Single-loop and triple-loop air source heat pump systems used the same heat exchangers which was placed at the same height. In the direction of air circulation, there were three rows of pipes, and the supporting fan of the heat exchanger was an axial flow fan with a rated power of 72W.

The experiment was carried out in a laboratory with test rooms of different enthalpy conditions, and constant temperature and humidity conditions were provided in each test room. Exhaust air conditions and fresh air conditions are provided in the indoor test room and the outdoor test room, respectively. Before the experiment, the experimental conditions were determined by consulting the relevant specifications.

During the experiment, we controlled the oncoming wind speed，air volume of fresh air heat exchanger and exhaust heat exchanger under various working conditions (air mass flow rate), refrigerant mass flow rate and refrigerant type remain unchanged. R410A was selected for all the circulating refrigerants, and the total refrigerant flow of the system remained unchanged. The compressors were all 1HP GMCC rotor compressors of the same type with a frequency of 50HZ.

Wherein, the compressor power and the fan power of the heat exchanger could be measured by a digital power meter. The heat exchange amount of the system was equivalent to the heat exchange amount of the exhaust heat exchanger, so h_1 and h_2 were the enthalpy values of the inlet and outlet air of the exhaust heat exchanger. Three samplers were installed at the inlet and outlet of the fresh air heat exchanger and at the inlet and outlet of the exhaust heat exchanger, and the dry and wet bulb temperatures of the inlet and outlet of the fresh air heat exchanger and the exhaust heat exchanger were collected by the data collector, and then the enthalpy and density of air inlet and outlet could be calculated; the wind speed test device could measure the wind speed of the inlet and outlet of the fresh air heat exchanger and the exhaust air heat exchanger, and the inlet and outlet areas of the heat exchangers could be inquired through the product specifications by calculating the mass flow rates of the inlet and outlet air of the heat exchangers. The specific calculation formulas were as follows:

$$Q = \dot{m}(h_2 - h_1) \quad \text{Eq. (1)}$$

$$\dot{m} = \rho \upsilon A \quad \text{Eq. (2)}$$

$$COP = Q/(W_1 + W_2 + \sum W_n) \quad \text{Eq. (3)}$$

4.EXPERIMENTAL RESULTS AND ANALYSIS

4.1 Winter Operation Mode

With changes in outdoor temperature，the comparison results between the single-loop and triple-loop systems about the compressor power and the coefficient of performance COP were shown in Figure 4.

From the trend of Fig. 4(a), we could see when the indoor temperature was kept at 20 ° C, as the outdoor temperature gradually decreases，the compressor power of two systems both showed a downward trend. When the temperature difference was 5°C, the compressor powers of the single-loop and triple-loop system were 1.77kW and 1.61kW, respectively. When the temperature difference was 40°C, they were 1.38kW and 1.12 kW, respectively. Two systems were reduced by 22% and 30.4%, respectively. Because the total power consumption of the system was the sum of the power consumption of the fresh air and exhaust heat exchanger fan and the compressor, during the experiment, the oncoming wind speed and air volume were constant, so the power of the fans was constant, too. As a result, the power of the solid system was consistent with the change trend of the input power of the compressor. And because the exhaust heat recovery system was characterized by the fact that when the outdoor air temperature changed, the compressor power was mainly affected by the change of the condenser (or evaporator) load, which was consistent with the operating characteristics of the compressor under this system operating condition.

From Fig. 4(b) as the outdoor temperature decreased, the COP of the two systems gradually increased, which was the opposite of the conventional heat pump system, and was also related to the operating characteristics of this system which the fresh air heat exchanger was treated by outdoor fresh air, the decrease in outdoor temperature caused a decrease in the condensing temperature, so the COP of the system would increase as the outdoor temperature decreased. When the temperature difference was 5 °C, the COPs of the triple-loop system and the single-loop system were 3.34 and 3.88, respectively. When the temperature difference was 40 °C, the COPs of two systems were 7.23 and 11.19, respectively. The increments of two systems were

3.89 and 7.31, respectively. This suggested that the greater the indoor and outdoor temperature difference is, the more obvious the advantages of the triple-loop system are. On the one hand, the overall heat transfer effect of the triple-loop system was more obvious than that of the single-loop system; on the other hand, the compressor power consumption of the triple-loop system was lower, and the overall downward trend was also higher. Therefore, the performance coefficient of the triple-loop system was better than the single-loop, and when the indoor and outdoor temperature difference reached to 40 °C, the COP of the triple-loop was 54.8% higher than that of the single-loop.

4.2 Summer Operation Mode

We could see from the trend of Fig. 5(a), remaining the indoor temperature unchanged, as the indoor and outdoor temperature difference gradually increasing, the compressor power of two systems both showed a growth trend. The values (1.16kW, 2.38kW, 1.45 kW) can not be read from Fig.5 (a). The compressor powers of two systems were increased by 28% and 25%, respectively, but the power of the triple-loop system was lower, which was consistent with the operating characteristics of the compressor under this system operating condition.

The COP of both systems gradually increased with the increase of indoor and outdoor temperature difference from Fig. 5(b), because in summer, the increase of outdoor temperature would cause the evaporation temperature to rise. When the temperature difference was 3 °C, the COPs of the triple-loop system and the single-loop system were 1.5 and 2.06, respectively. When the temperature difference was 40 °C, the COPs of two systems were 2.24 and 3.91, respectively, and the growth rates were 89.8% and 49.3%, respectively. Through analysis, it could be seen that due to the temperature difference between indoor and outdoor was relatively small in summer, although the triple-loop system changed the heat transfer temperature difference distribution of the heat exchanger, the overall heat transfer of the two loop systems were not much different. Therefore, the main reason for affecting COP was the total power consumption of the triple-loop system. The reason of winter condition was as similar as in summer. Since the overall power consumption of the triple loop system is higher, the growth rate of COP is higher. When the temperature difference of indoor and outdoor was 13 °C, the triple-loop COP was 74.6% higher than single-loop.

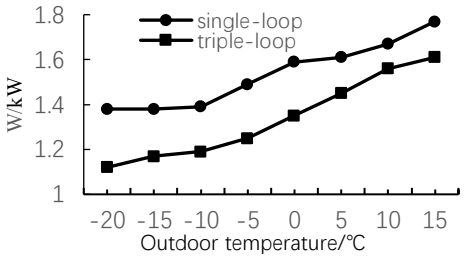

(a) Compressor power W/kW

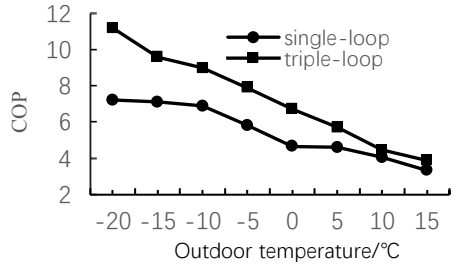

(b) System performance coefficient

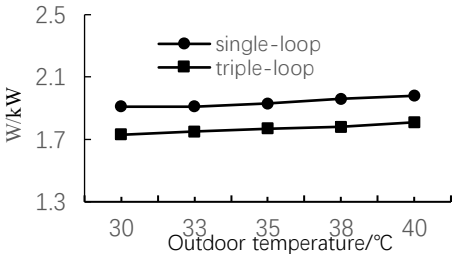

(a) Compressor power W/kW

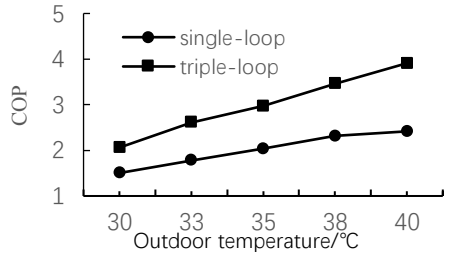

(b) System performance coefficient

Fig. 4 Performance comparison of single-loop system and triple-loop system under winter condition

Fig. 5 Performance comparison of single-loop system and triple-loop system under summer condition

5.CONCLUSION

(1) No matter in winter or summer conditions, the triple-loop system was significantly higher than the single-loop in the overall performance.

(2) With the increase of indoor and outdoor temperature difference, the COP growth rate of triple-loop and single-loop systems reached 1.88 and 1.16 respectively under winter condition, the compressor power consumption decreased by 30.4% and 22%, respectively, and when the indoor and outdoor temperature difference was 40°C, the COP of triple-loop was 54.8% higher than the single-loop; Under summer conditions, the COP growth rates of two systems were 89.8% and 49.3%, respectively, and the compressor power consumption increased by 25.0% and 28.0%, respectively. When the indoor and outdoor temperature difference was 13 °C, the COP of the triple-loop increased 74.6% comparing with the single-loop, which also indicated that the heat recovery rate of the triple-loop system was higher.

NOMENCLATURE

h_1	exhaust air heat exchanger inlet air enthalpy(kJ/kg)	h_2	exhaust air heat exchanger outlet air enthalpy(kJ/kg)
W_1	fresh air heat exchanger fan power(kW)	W_2	exhaust air heat exchanger fan power(kW)
$\sum Wn$	compressor total power(kW)	Q	exhaust air heat exchanger heat exchange capacity(kW)
ρ	exhaust side air density(kg/m3)	υ	exhaust side air speed(m/s)
$\dot{m}$	exhaust side air mass flow(kg/s)	A	exhaust side exhaust air heat exchanger area(m^2)

REFERENCES

Yiping W, Youngun Y, Guangxiao Y,2004. Analysis of energy-saving characteristics of air source heat pump based on air conditioning exhaust. Int. J. Construction Machinery for Hydraulic Engineering & Power Station, 26(5), 26-28.

Qihua Z, 2014.The depth of energy-saving air source heat pump air conditioning based on exhaust air. Int. J. Refrigeration and Air-Conditioning, 14(3),7-10.

Xiaoyong L, Yong W,2016. Design and calculation method of heat collection side for combined heating system of solar and low temperature heat recovery air-source heat pump. Int. J. Heating Ventilating & Air Conditioning, 46(10),99-103.

Chen A, Liu H, Ran C, et al.,2015 Economic analysis on application of exhaust air heat recovery in existing public buildings in the severe cold regions. Int. C. International Forum on Energy, Environment Science and Materials.

Fracastoro G V, Serraino M, 2010. Energy analyses of buildings equipped with exhaust air heat pumps (EAHP) . Int. J. Energy and Buildings,42(8),1283-1289.

Air-air energy recovery device: GBT 21087-2007. Int. S.

Code for design of ventilation and air conditioning for mining: GB 50019-2003. Int. S.
Gian V. F, Matteo S, 2010. Energy analyses of buildings equipped with exhaust air heat pumps (EAHP) . Int. J.Energy and Buildings, 42(8),1283-1289.

Manuscript ID: 495
DOI: 10.18462/iir.icr.2019.0495

Waste heat recovery from urban electrical cable tunnels

Akos REVESZ[(a)], Gareth DAVIES[(a)], Graeme MAIDMENT[(a)], Joanna KULESZO[(b)], Rob LIDDIARD[(b)], Hector ALTAMIRANO[(b)], Alex DAVENPORT[(c)], Boris YAZADZHIYAN[(c)]

[(a)] London South Bank University, [(b)] University College London, [(c)] UK Power Networks
London, SE1 0AA, United Kingdom, revesza2@lsbu.ac.uk

ABSTRACT

Electrical power distribution within cities is most often distributed through underground cables located just below the road surface. Due to steadily increasing electricity demands, many power suppliers are making large investments in housing these cables in underground tunnels. These urban cable tunnels often extend to many kilometres in length. Through the electrical loading of the cables a significant amount of heat is generated. Often this heat has to be removed through ventilation in order to avoid overheating the cables and to provide safe conditions for access. As opposed to rejecting the heat to the atmosphere, this low grade energy could potentially be recovered, upgraded if necessary, and distributed to nearby heat users above ground. This paper discusses possible heat recovery methods applicable for urban electricity distribution networks, i.e. transformers and cable tunnels. It also presents results from a modelling-based preliminary feasibility study which used cable tunnels in London as a case study.
Keywords: Heat recovery, Transformers, Cable tunnels, Heat networks, Urban energy systems

1. INTRODUCTION

The Climate Change Act (2008) sets UK wide targets for reducing carbon emissions by 80% of its 1990 baseline level by 2050, and was established to meet the requirements of the Kyoto Protocol (1998). The carbon reduction measures adopted to date include the phasing out of coal fired power stations, the increased use of renewable energy resources, together with improvements in the efficiency of vehicles, electrical and electronic equipment and new building performance requirements. Current data suggest that these measures have ensured that the UK is on track to achieve the interim 2020 carbon reduction target (Committee on Climate Change, 2018). However, achieving the UK's 2050 carbon emissions target is likely to be more difficult and will require significantly more radical solutions than the measures and technologies considered to date. In order to meet its emission targets, the UK Government has put forward a strategy for mitigating future carbon emissions from heating and cooling, as described in, for example, the 2050 Pathways Analysis (DECC, 2010) and The Future of Heating: Meeting the Challenge (DECC, 2013).
One of the key areas for reducing carbon emissions is the implementation of low carbon heating and cooling networks, especially in cities. For example, The Mayor of London has set a target for London to generate 25% of its heat and power requirements through the use of local, decentralised energy systems by 2025 (Mayor of London, 2013). Renewable decentralised energy opportunities include the use of energy from secondary sources such as sewers, electricity cable tunnels or underground railways (URs). These urban infrastructure systems, are potent and untapped energy sources, are often in close proximity to areas of high heat demand and could potentially provide a year-round heat supply. It has been shown that the total heat that could be delivered from secondary sources in London is of the order of 71 TWh/ year, which is more than the city's total estimated heat demand of

66 TWh/yr in 2010 (GLA, 2013). Some of these secondary heat sources have the limitation that their location is too far from where the heat is needed or that they are only available at a particular period of the year. However, parts of electrical distribution networks such as substation transformers and underground cable tunnels are often in close proximity to areas of high heat demand and could potentially provide a year-round heat supply.

London South Bank University's (LSBU's) Centre for Air conditioning and Refrigeration Research team and University College London (UCL) are currently undertaking a research project called LUSTER (London Sub-Terrain Energy Recovery). This involves evaluating a range of secondary waste heat sources to determine their potential for recovery and reuse. As part of the LUSTER project, LSBU and UK Power Networks have undertaken a feasibility study to investigate the effects of cooling and heat recovery for electrical cable tunnels, and substation transformers in London. The paper first summarizes heat recovery potential from transformers and preliminary results from the feasibility study concerning the combined cooling and heat recovery from cable tunnels.

2. COOLING AND HEAT RECOVERY FOR ELECTRICITY DISTRIBUTION NETWORKS

If it is feasible to capture and use the heat generated by electricity distribution network losses, the overall energy efficiency of electricity distribution can be improved and this may also be economically viable in some cases. There are opportunities, particularly in urban areas, to consider the benefits from using any heat that has a commercial value. This may be implemented as a retrofit solution, or may be engineered into the overall network design when new equipment is required. This section of the paper reviews the potential for extracting heat from urban electrical distribution networks, i.e. substation transformers and cable tunnels.

2.1. Heat Recovery Potential from Electrical Substation Transformers

Transformer energy losses can be classified as: (i) no-load losses; or (ii) load losses. The former are constant for all transformer operating points and are related to core losses whilst the latter are proportional to transformer loadings and are associated with winding losses. Transformer winding losses produce heat which without effective cooling will increase transformer temperatures. In the case of very high temperatures, the insulation can be carbonised and produce gasses, and can significantly reduce the lifetime of the transformer. Therefore, effective cooling of transformers and rejection of heat is essential. The heat losses are normally dependent upon the transformer's rating, peak load, load factor and efficiency. Often these losses can be calculated for the full operation range using nominal operating loss values provided by the transformer manufacturer. Figure 1 illustrates typical heat outputs at different loading conditions for a 240 MVA transformer in London (Modern Power Systems, 2016). It can be seen in Figure 1 that the transformer heat losses increase at an accelerating rate as the loading percentage increases. The loading percentage will, of course, vary according to the fluctuation of electricity demand. It is therefore necessary to determine or estimate the transformer loading throughout the year in order to calculate the potential quantity of heat that could be recovered annually, and to size the heat recovery equipment appropriately. Waste heat from transformers could typically be captured through their cooling system. Table 1 compares commonly used transformer types based on their cooling methods and their potential for implementing a heat recovery application. It can be seen in Table 1 that there are a number of different transformer cooling systems currently in use. These systems vary in complexity and in their effectiveness of meeting the preliminary objective of cooling the transformer. The two main categories are the dry and oil-immersed types cooling methods. Dry type solutions are normally used for cooling smaller transformers rated up to 1.5 MVA. The oil immersed type cooling systems are generally used for larger units, e.g. those rated up to several hundreds of MVA. The top section of transformer tanks is normally cooled by either a water or air cooling system. In many cases, the heat captured by these coolants is dissipated into the atmosphere and wasted. However, in densely populated urban areas, this waste heat could serve a different purpose. For example, it could be supplied to a local district heating scheme. At times when there is no heat demand, freestanding cooling banks mounted on the substation roof could be used to dissipate the heat and maintain cooling of the transformer or the heat could be stored for later use.

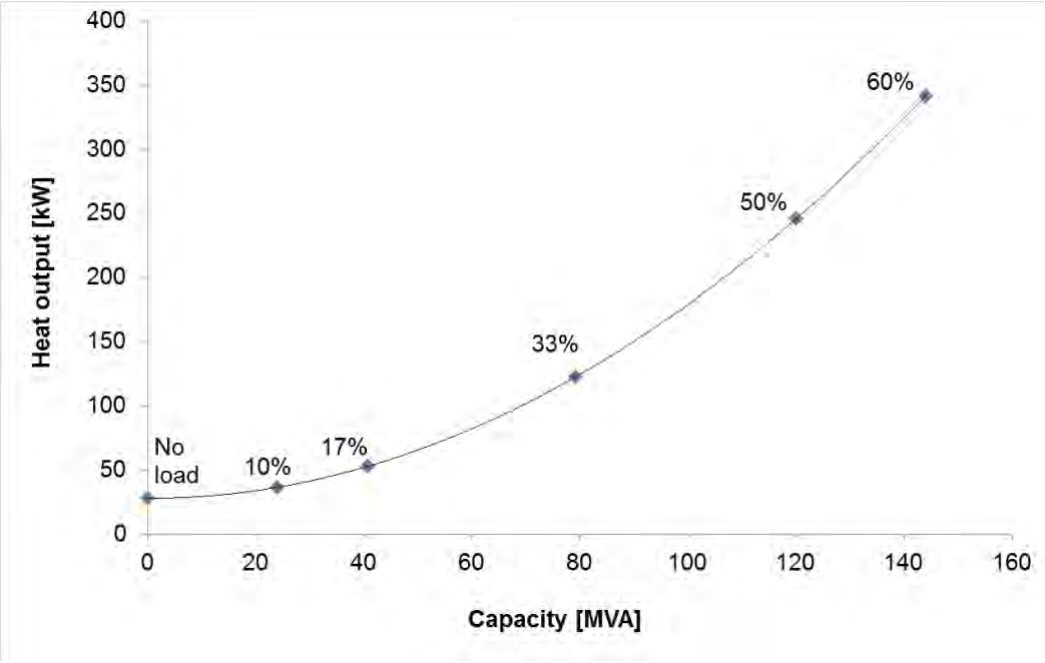

Figure 1: A typical 240 MVA transformers' heat output at different loading levels

Table 1. Summary of transformer types and their potential for heat recovery

Transformer type / cooling method		Potential for heat recovery	Comment
Dry type	Air Natural (AN): This method is used for cooling the smallest output transformers rated up to 1.5 MVA	Low (~ < 15 kW)	• Heat recovery (HR) system could be non-intrusive making it easier to retrofit • Could be cost effective for existing transformers with an adjacent heat user requirement • For natural air cooling, only low control of HR is possible • If forced air is used then medium control of HR could be achieved
	Air Forced (AF): This method is used for transformer rating up to 15MVA.	Medium (~20-60 kW)	
Oil immerse type	Oil Natural Air Natural (ONAN) This type of cooling is used for the transformer rating up to 30 MVA.	Low to Medium (~ 50-100 kW)	• It would require major intrusion into the cooling system for connecting additional heat exchangers (HEXs) • Low control of HR
	Oil Natural Air Forced (ONAF) Used for the cooling of the transformer of rating up to 60 MVA.	Medium (~80-120 kW)	• It would require major intrusion for connection of additional HEXs • Medium control of HR
	Oil Forced Air Forced (OFAF) Rating more than 60 MVA.	Medium to High (~>120 kW)	• This type of cooling system would still require major intrusion for connection of HEXs • Greater control of HR due to the forced nature of oil circulation
	Oil Forced Water Forced (OFWF) This type of method is suitable for large capacity of the transformer having rating as several hundred MVA or where banks of transformers are installed.	High (Could be more than 300 kW)	• This type of transformer currently offers the greatest opportunity for large scale HR • Generated heat is captured by the cooling water of the oil-water cooler • Permits less intrusive solutions for connecting additional HEXs • Offers a high degree of control HR

There are hundreds of primary substation transformers across the UK providing a significant quantity of excess energy and an overall heat recovery potential that is larger than 30MW in capacity (Davies *et.al.* 2018) The LUSTER project team is conducting further works to investigate the potential for heat recovery from electrical substation in London.

2.2. Heat Recovery Potential from Urban Electrical Cable Tunnels

Electrical network operators transmit electrical power through cables, many of which are housed in networks of tunnels, particularly in cities such as London. Many cable tunnels are large enough e.g. of the order of 2.5 m diameter, to permit human access for maintenance and repairs. The cables produce significant quantities of heat, particularly at high electrical power loadings, and cooling needs to be provided, for example by forced ventilation of the tunnels using outside air. Once air is supplied into the tunnels its temperature increases as it travels to the air extraction point. The air flow rate and electrical power loadings used are selected on the basis of limiting the exhaust tunnel air temperature to a maximum of around 44°C (designated as the limit for human access to the tunnel). If network operators could reduce the air temperatures in their cable tunnels (and cables) e.g. by introducing additional cooling, the electrical loadings on the cables could be increased. Additionally, the heat generated in cable tunnels represents a significant heat resource, which the operator could recover and potentially sell for reuse.

3. FEASIBILITY STUDY FOR COMBINED COOLING AND HEAT RECOVERY FROM CABLE TUNNELS

A typical tunnel section of length 1.8 km and 2.5 m in diameter, in central London, was selected for this study. The financial calculations included, a UK government environmental programme, the Renewable Heat Incentive (RHI), which provides financial incentives to increase the uptake of renewable heat by businesses, the public sector and non-profit organisations. Eligible installations receive quarterly payments over 20 years based on the amount of heat generated, therefore it could support the uptake of innovative energy solutions in cities and elsewhere. Two heat recovery methods were considered for the cable tunnel location selected, namely: (i) a combined cooling and heat recovery system, which has been termed a “cold led heat recovery system” (CLHR); and (ii) a heat recovery only system, which has been termed a “heat led heat recovery system” (HLHR). For the CLHR method it is assumed that an air to water heat exchanger is installed at the supply end of the ventilation system. The water exiting the heat exchanger transfers the recovered heat to a heat pump, which may be located either close to the point of recovery or at the end-user site. This configuration is illustrated in Figure 2 (a). It can be seen that the ambient air supplied is cooled by the water circuit of the heat recovery heat exchanger. This heat exchanger could provide benefits for both the electrical network operator, due to its cooling impact on the tunnel environment, and to any nearby end users, who are able to utilise the heat recovered. Figure 2 (b) shows the HLHR scheme, where the heat recovery heat exchanger is located at the head of the exhaust ventilation shaft.

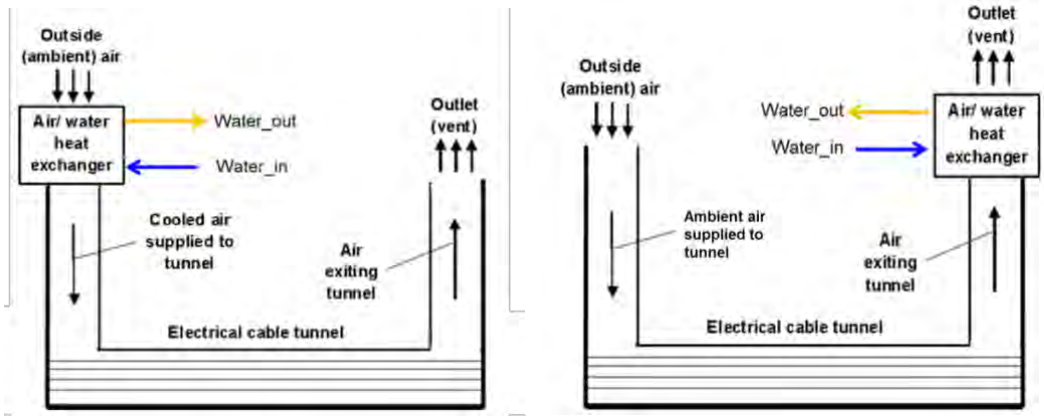

(a) CLHR method **(b)HLHR method**

Figure 2: Heat recovery options

3.1. Calculation of Heat recovery potential from electrical substation transformers

A spreadsheet based calculation has been conducted in order to estimate the heat exchanger performance with different air temperature reductions across the heat exchanger. The assumptions used during the calculations are summarised in Table 2.

Table 2: Summary of key assumptions

<table>
<tr><td rowspan="8">Configuration, supply temperature, cost and carbon</td><td>CLHR</td><td>HLHR</td></tr>
<tr><td>Heat was recovered using a fan coil heat exchanger located at the head of the air supply shaft.</td><td>Heat was recovered with a fan coil heat exchanger at the head of the exhaust shaft</td></tr>
<tr><td colspan="2">The heated water was transported through pipes to the heat pump, which was located 10 m from the point of recovery.</td></tr>
<tr><td colspan="2">The water temperature was then upgraded using the heat pump for delivery at 65°C.</td></tr>
<tr><td>The degree of cooling of the outside air prior to supply to the tunnels (ΔT) depends on the outside air temperature.</td><td>The tunnel exhaust air temperatures, which were based on measured data, were found to be steady (i.e. 27.6 to 32.7°C) for the period considered (June to November)</td></tr>
<tr><td>The ΔT was selected to ensure that the heat pump operated with a COP > 3.</td><td>A constant ΔT of 10 K was used.</td></tr>
<tr><td colspan="2">The cost for delivery of 1 MWh of heat, for recovered heat (with and without RHI), was compared to that for a gas boiler.</td></tr>
<tr><td colspan="2">RHI was applied to recovered heat at a tariff of 2.69 p per kWh.</td></tr>
<tr><td colspan="2">% carbon saving for recovered heat compared to that for a gas boiler was also calculated. Carbon factors used were 0.41 kg CO_2e per kWh for electricity and 0.18 kg CO_2e per kWh for gas (DEFRA, 2016).</td></tr>
<tr><td rowspan="5">For the air to water fan coil heat exchanger</td><td>CLHR</td><td>HLHR</td></tr>
<tr><td colspan="2">An approach temperature (air side to water side) of 2K.</td></tr>
<tr><td colspan="2">Water side temperatures of less than 0˚C can be achieved using a water/glycol mixture.</td></tr>
<tr><td colspan="2">A temperature gain on the water side of 5K in each case.</td></tr>
<tr><td colspan="2">A pressure drop on the air side of the heat exchanger of 0.3 bar.</td></tr>
<tr><td rowspan="2">For the cable tunnel</td><td>CLHR</td><td>HLHR</td></tr>
<tr><td colspan="2">The outside air temperatures based on UK meteorological data for London, averaged for each month during the year.</td></tr>
</table>

3.1.1. Results of CLHR method

The results obtained using the spreadsheet model applied to the CLHR method are shown in Table 3, which shows that the quantity of heat recovered from outside air varied from 64.1 to 310.8 kW during the year, and that heat recovery was lowest in winter and highest in summer. A heat pump COP of > 3 was achieved for delivery of the upgraded heat at 65°C, in each case. The cost of delivery includes the total energy costs including heat pump, pumping power and heat losses. It can also be seen in Table 3 that the cost for delivery of 1 MWh of recovered heat was much less than that for a gas boiler when RHI was included. The calculated results also showed carbon savings of > 50% for the heat recovery system compared with gas boiler heating. It should be noted that the total economic benefits of the cooling of the cable tunnel air and cables combined with simultaneous heat recovery from the outside air, have not been included in the results shown in Table 3 i.e. only the heat recovery benefits have been considered. Due to the large variation in heat output, it is likely that this scheme would need to form part of a hybrid scheme with supplementary heating from other sources being used when required, to make up any shortfall.

Table 3: CLHR from cable tunnels

Month	T_{air} (°C)	T_{sup} (°C)	ΔT (K)	Q_{dot} (kW)	T_{evap} (°C)	COP_h (65°C)	E_{in} (kW)	Q_{del} (kW)	Cost of 1 MWh (-RHI)	Cost of 1 MWh (+RHI)	Cost of 1 MWh (gas)	% CO_2e saving
1	6.3	4.3	2	64.1	-2.7	3.0	31.6	95.7	£32.98	£14.95	£24.4	53.3
2	5.7	3.7	2	64.3	-3.3	3.0	32	96.3	£33.28	£15.33	£24.4	52.9
3	7.5	4.5	3	95.8	-2.5	3.0	46.9	142.7	£32.88	£14.83	£24.4	53.5
4	11.2	6.2	5	157.5	-0.8	3.1	74.2	231.8	£32.03	£13.75	£24.4	54.7
5	13.3	8.3	5	156.4	1.3	3.2	70.2	226.6	£30.99	£12.42	£24.4	56.1
6	16.3	6.3	10	309.5	-1.7	3.0	148.9	458.4	£32.48	£14.31	£24.4	54
7	19.5	9.5	10	306.2	1.5	3.2	136.8	443	£30.88	£12.29	£24.4	56.3
8	17.6	7.6	10	308.2	-0.4	3.1	143.9	452.1	£31.84	£13.50	£24.4	54.9
9	15.1	5.1	10	310.8	-2.9	3.0	153.6	464.5	£33.08	£15.08	£24.4	53.2
10	12.5	7.5	5	156.8	0.5	3.1	71.7	228.6	£31.39	£12.93	£24.4	55.6
11	9	4	5	158.8	-3	3.0	78.7	237.4	£33.13	£15.15	£24.4	53.1
12	9.8	4.8	5	158.3	-2.2	3.0	77	235.4	£32.73	£14.64	£24.4	53.7

T_{air} (°C) = Outside ambient air temperature (°C)
T_{sup} (°C) = Air supply temperature to cable tunnel (°C)
ΔT (K) = Cooling temperature difference (for air)
Q_{dot} (kW) = Heat recovery by fan coil heat exchanger
T_{evap} (°C) = HP evaporator temperature
COP_h (65°C) = COP heating for delivery at 65°C
E_{in} (kW) = Electrical energy input required for HP
Q_{del} (kW) = Heat delivered at 65°C

3.1.2. Results of HLHR method

The results from the model showing the calculated quantities of heat recovered from the 1.8 km cable tunnel section and the costs for delivering this heat at 65°C are shown in Table 4.
The results presented in Table 4 show that heat recovery was fairly constant (at approximately 300 kW) for the period considered i.e. June to November. It is seen that for delivery at 65°C, a heat pump COP close to 4 was achieved, in each case. The cost for delivery of 1 MWh of recovered heat is seen to be about the same as that for a gas boiler without RHI. However, very significant cost savings for the recovered heat are possible, if RHI is available. Carbon savings of 62-65.6% were calculated for the recovered heat system compared to the carbon emissions for gas boiler heating to deliver the same quantity of heat.

Table 4: HLHR from cable tunnels

Month	T_{ext} (°C)	T_{out} (°C)	ΔT (K)	Q_{dot} (kW)	T_{evap} (°C)	COP_h (65°C)	E_{in} (kW)	Q_{del} (kW)	Cost of 1 MWh (-RHI)	Cost of 1 MWh (+RHI)	Cost of 1 MWh (gas)	% CO_2e saving
6	27.6	17.6	10	298	9.6	3.7	109.5	407.4	£26.87	£7.19	£24.4	62
7	28.6	18.6	10	297	10.6	3.7	106.4	403.4	£26.38	£6.57	£24.4	62.7
8	32.7	22.7	10	293	14.7	4.1	94.2	387.2	£24.33	£3.98	£24.4	65.6
9	30.7	20.7	10	294.9	12.7	3.9	99.9	394.8	£25.30	£5.20	£24.4	64.2
10	29	19	10	296.5	11	3.8	105	401.5	£26.14	£6.28	£24.4	63
11	27.6	17.6	10	298	9.6	3.7	109.6	407.6	£26.88	£7.21	£24.4	62

T_{ext} (°C) = Cable tunnel exhaust air temperature (°C)
T_{out} (°C) = Temperature of air ejected to outside
ΔT (K) = Cooling temperature difference (for air)
Q_{dot} (kW) = Heat recovery by fan coil heat exchanger
T_{evap} (°C) = HP evaporator temperature
COP_h (65°C) = COP heating for delivery at 65°C
E_{in} (kW) = Electrical energy input required for HP
Q_{del} (kW) = Heat delivered at 65°C

3.1.3. Identified benefits of a combined cooling and heat recovery solution

The results of the study showed that a combined cooling and heat recovery solution can result in a range of benefits for electrical cable operators. These include:

(i) Provision of significant quantities of waste heat from a single cable tunnel ventilation shaft for delivery to low temperature energy networks: The results of the investigation showed that substantial amounts of heat can be recovered and delivered to end users in the vicinity of the ventilation shafts. The quantity of deliverable heat would depend on the method of heat recovery. For cold led heat recovery, it was estimated that between 96 and 460 kW of heat can be delivered, depending on the season. For heat lead heat recovery, the deliverable heat values remained relatively constant through the investigation period, at approximately 400 kW.

(ii) Revenues from the sale of the recovered waste heat: If the heat recovery system is located in an urban area, it may be possible to sell heat to neighbouring buildings such as offices, hospitals, hotels or leisure centres. Recovered heat can also be sold for use in district heating, urban farms, greenhouse heating and swimming pools.

(iii) Reduced operational costs i.e. through reduced ventilation loads: for example, if the tunnel air is being cooled by implementing the CLHR method.

(iv) Increased loading of the cables: For example, if the cables are being cooled by implementing the CLHR method. A reduction in cable temperature could also result in lower electricity distribution losses, producing additional carbon and cost savings.

(v) Contributions towards low carbon sustainable development: The London Plan (Mayor of London, 2016) focuses on securing a low carbon energy supply for London and sets a target of achieving 25% of London's heat energy supply from decentralized or district energy schemes, by 2025. Heat recovery from cable tunnels can contribute towards these targets. Also, a shift towards using electrical energy for space heating and hot water, it is likely to add to the need for increased distribution network capacity, thus making more waste heat available for repurposing.

4. CONCLUSIONS

A preliminary investigation was carried out to investigate heat recovery potential from electricity conversion and distribution networks. The paper first summarised energy recovery potential from the losses of substation transformers. It was described that the oil immersed type transformer cooling systems which are generally used for larger units, have the highest heat recovery potential. It was shown that more than 300 kW of waste heat can be captured from these types of transformers. The paper then described a more detailed study of the combined cooling and heat recovery potential for the air supplied to cable tunnels. Two heat recovery methods were considered for the cable tunnel location selected, namely: (i) a combined cooling and heat recovery system, which has been termed a CLHR system; and (ii) a heat recovery only system, which has been termed a HLHR system. In each case, an air to water heat exchanger was utilised. Results from a spreadsheet based calculation showed that between 60 and 300 kW of heat can be recovered this way, depending on the ambient air temperature supplied to the shaft (which varies seasonally) and the applied temperature difference (ΔT) used within the heat exchanger. Using a heat pump, the recovered heat could be upgraded, transported and distributed to nearby heat users. Therefore, both substation transformers and cable tunnels offer the opportunity of a useful heat source, which is comparable to (and in some cases superior to) many other waste heat sources being considered for LSBU's EPSRC sponsored LUSTER project e.g. sewers, canals, data centres and underground railway tunnels. Further work, within the LUSTER project, will investigate the matching of the local heat demand to the heat available from cable tunnels, using demand modelling and geospatial techniques. This will be covered in future publications.

ACKNOWLEDGEMENTS

The authors would like to express their gratitude for the support by Engineering and Physical Science Research Council (EPSRC) and LUSTER - London Urban Sub-Terrain Energy Recovery project

[EP/R001294/1]. Thanks also go to the Innovation team at UK Power Networks, for general support and the provision of data.

REFERENCES

Climate Change Act 2008: Elizabeth II. (2008) London, Stationery Office.

Committee on Climate Change (2018) Reducing carbon emissions: How the UK is progressing. Online at: https://www.theccc.org.uk/tackling-climate-change/reducing-carbon-emissions/how-the-uk-is-progressing/ Accessed 15-11-18

Davies, G., Boot-Handford, N., Grice, J., Dennis, W., Ajileye, A., Revesz, A. and Maidment, G. G. (2018) Heat Recovery Potential from Urban Underground Infrastructures, in: Chicago: London South Bank University.

DECC (2010) 2050 Pathways Analysis, Department of Energy and Climate Change, UK
DECC (2013) The Future of Heating: Meeting the Challenge, Department of Energy and Climate Change, UK.

DEFRA (2016) UK Government GHG Conversion Factors for Company Reporting Department for Environment, Food and Rural Affairs. Online at: https://www.gov.uk/government/publications/greenhouse-gas-reporting-conversion-factors-2016 Accessed 1-02-19

Kyoto Protocol (1998) Kyoto Protocol to the United Nations Framework Convention on Climate Change 2303 UNTS 148/[2008] ATS 2/37 ILM 22 (1998)

Mayor of London (2013) London's Zero Carbon Energy Resource: Secondary Heat. Mayor of London Report. Online at: https://www.london.gov.uk/sites/default/files/gla_migrate_files_destination/031250%20GLA%20Secondary%20Heat%20-%20Summary%20Report_0.pdf Accessed 4-12-18

Mayor of London (2016), The London Plan, Spatial Development Strategy for London, Greater London Authority, London, UK.

Modern Power Systems (2016) Transformers as district heating boilers. Online at: https://www.modernpowersystems.com/features/featuretransformers-as-district-heating-boilers-4816181/ Accessed 29-01-19

The Greater London Authority (GLA), Buro Happold (2013) London's zero carbon energy resource, Online at: http://www.london.gov.uk/sites/default/files/031250%20GLA%20Secondary%20Heat%20-%20Summary%20Report.pdf Accessed 12-11-18

Manuscript ID: 497
DOI: 10.18462/iir.icr.2019.0497

Experimental study of residential air-to-air heat pump performances in the field

Cong Toan TRAN [(a)], Philippe RIVIERE [(a)], Dominique MARCHIO [(a)], Assaad ZOUGHAIB [(a)], Christine ARZANO-DAURELLE[(b)]

[(a)] MINES ParisTech, PSL Research University, CES (Center for Energy efficiency of Systems)
5, rue Léon Blum, 91120 Palaiseau, France
cong-toan.tran@mines-paristech.fr

[(b)] EDF R&D, Moret/Loing, France

ABSTRACT

Air-to-air heat pump (AAHP) is regarded as one of the energy saving technologies in the building sector. However, experimental studies on AAHP performances in the field are still insufficient. In order to investigate practical performances, in situ experiments are carried out on a split residential AAHP. The measurements are mainly realized on the indoor unit side, including air velocity (via hot wire sensors), dry and wet bulb temperatures and atmospheric pressure. The performances are analyzed in different operational modes, especially the unsteady-state operation and the defrosting phase. The paper proposes a measurement procedure for the AAHP seasonal coefficient of performance and discusses the optimum recorded data rate. Finally, the results of this study could provide useful guidelines to check in situ performances, since performance checking will be more and more required to ensure the energy gains and the economic benefits that the end-user expects when purchasing an AAHP.
Keywords: Air-to-air heat pump, operational performance, in situ test, moist air, hot-wire sensor, seasonal coefficient of performance

1. INTRODUCTION

With a view to reducing energy consumption and greenhouse gas emissions, the use of heat pumps (HPs) is considered a promising solution. HP performances are measured in laboratory conditions. They are tested in particular under steady state conditions and their capacity controls are by-passed. Therefore, their performances in the field and in the laboratory may differ. Moreover, the performances in the field also depend on the installation quality, the system design, user behavior as well as performance deterioration due to lack of appropriate maintenance.
Therefore, it is necessary to develop a measurement method for HP performances in the field. The method should be applicable at the customer's house over a long period (one season) without disturbing overall comfort. The method could be used for future building regulations based upon performance guarantee, or by third parties to check performance and verify the energy gains and economical benefits that the user expects when purchasing a HP.
The main difficulty in HP performance measurement is the evaluation of heating energy delivered. The latter is relatively easy in the field in presence of water-to-water or air-to-water HPs (by measuring the energy supplied to the water circuit through water temperature and water flow rate measures), but it is not the case for air-to-air HPs due to the difficulty of measuring the air flow rate and air enthalpy in the field over a long period.
A review of airflow measurement techniques is given in (McWilliams, 2002). The most common technique in the field is as follow: the air flow is led into a duct and then measured directly by an anemometer. The latter may be either of helix type, or of Pilot-tube type or calibrated capillary type as shown in (Howell and Sauer, 1990), (Francisco and Palmiter, 2003) and (Rivière et. al, 2012). However, this technique is cumbersome so that it cannot be used at a customer's dwelling for a long period of time. In addition, the measurement installation interferes with the HP operation

because it causes pressure losses which significantly change the air flow rate. A fan can be used to compensate pressure losses but in the field there is no way to check if this compensation does occur correctly.
As demonstrated (Ichikawa et al., 2007), a multi point measurement of air temperature, humidity and velocity was performed to determine air enthalpies. In particular, the air velocity field was identified, and then corrected to fit the value of air flow rate provided by the manufacturer. The main issue with this method is the likely evolution of HP performances over time, which cannot be evaluated.
Paper (Tran et al., 2013) proposed an alternative method based on a measurement of the air velocity field via hot wires sensors. By comparing an in-laboratory ducted measurement with the hot wire sensor results, it was concluded that the method is accurate in steady state conditions.
In this context, the present work is intended to test the method (Tran et al., 2013) in the field. The objectives are to check unsteady-state conditions, to analyze the impacts of operation conditions and frost-defrost cycles on performances, and to make recommendations based on measurement procedures in the field.

2. METHODOLOGY

2.1. In situ instrumentation

The HP tested is a residential air-to-air split type with a wall mounted indoor unit. All measurements used are shown in Fig. 1. The method requires the measurement of air enthalpies and mass flow rate in the indoor heat exchanger (condenser). Four PT100 thermometers (sensors T1, 2 , 3, 4) are installed at the inlet side and two other ones (T5,6) are located at the outlet side in order to determine the average dry air temperatures. Since the humidity ratio is constant during the heating process, it is only measured on one side. In our test, a capacitive hygrometer measuring relative humidity (sensor RH, Fig. 1) is installed on the inlet side where the humidity field is more homogeneous than on the outlet side. A measurement of the atmospheric pressure (sensor P1) is added to allow a better determination of the enthalpies.

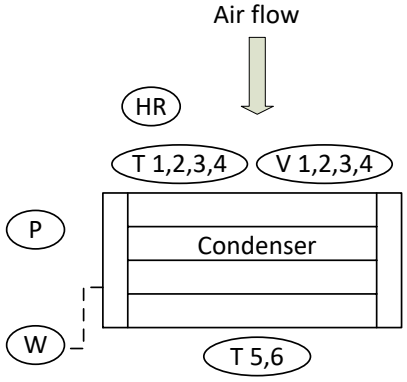

T: dry temperature sensor; V: hot-wire sensor
P: atmospheric pressure sensor;
HR: humidity ratio sensor; E: electricity meter;

Figure 1: Schematic view of the instrumentation

Air flow velocity field at the inlet side is determined via a multi point measurement via 4 hot-wire sensors (V1, 2, 3, 4). The mass flow rate is then calculated from the air flow area and the air temperatures. It is worth remarking that the number of sensors used and their position in the air flow are determined according to the air velocity distribution which may not be homogeneous (Weng et al., 2007). Moreover, the air flow rate should be measured at the inlet side rather than the outlet side because of the following two reasons: the temperature field is generally more homogeneous on the inlet side; so integration over the flow area is easier; besides, the velocity field is less stable at the outlet side because the HP usually allows the user to control the exhaust air flow direction.
Fig. 3 shows the positioning of temperature and hot-wire sensors used in the test. At the outlet side, the sensors are equi-distributed. At the inlet side their position results from a velocity field measurement carried out previously in the laboratory. The blue lines represent the air velocities at different measurement points when the internal fan is set at a low velocity level mode. Velocities vary insignificantly along the horizontal axis. However, the velocity distribution can be divided into two zones along the vertical axis: first, the velocities decrease almost linearly until

Table 1. Instrument accuracies of measured variables

Variable	***Relative accuracy***	***Absolute accuracy***
Pressure	0.25 %	-
Air velocity	3 %	-
Air dry temperature	-	0.2 K
Relative humidity	-	5 %
Electric power	3 %	-
Data acquisition system	1 %	

the middle of the axis (100 mm), and then they remain fairly constant. The same shape velocity distribution is observed for the high velocity level. This explains why four velocity sensors are used and located at cells C3, C5, F3 and F5:

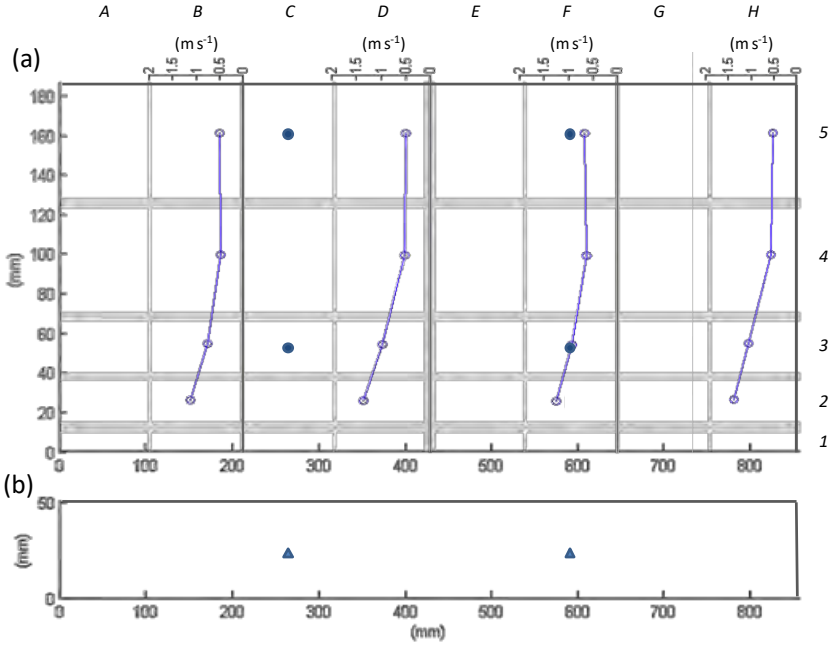

Figure 2: (a) Positioning of temperature and velocity sensors and air velocity distribution at the inlet side; (b) Positioning of temperature sensors at the outlet side

- the measurements at rows 3 and 5 measure the average velocity at each zone.
- the measurements are duplicated along the horizontal axis for a better determination of the total average velocity.

The inlet temperature is measured in the same positions, as the hot-wire sensor used is a "double" type (measuring both air velocity and temperature). Finally, an electricity meter (W, Fig. 1) is used to measure the HP electric power. The accuracies of measured variables and data acquisition system are shown in Table 1. The variables are recorded with a sampling rate of 2 seconds.

2.2. Calculation Method

The average of the four measured velocities represents the mean velocity v over the condenser air section (part 2.1). The air volume flow rate is then calculated as $\dot{V} = Av$, where *A* is the air section area, after deduction of the grille (Fig. 2).

The dry air temperatures T_{in} at the inlet side and T_{out} at the outlet side are computed as an average of the measured values. At the inlet side, the specific enthalpy h_{in} (kJ (kg dry air)$^{-1}$), specific volume υ_{in} (m^3 (kg dry air)$^{-1}$) and humidity ratio w_{in} (kg water (kg dry air) $^{-1}$) are then computed from the dry air temperature T_{in}, relative humidity RH_{in} and atmospheric pressure p_{atm}. It is noted that *h* refers to the specific enthalpy of the moist air, which encompasses dry air and water vapor. The dry air mass flow rate is expressed as $\dot{m}_{da} = \dot{V} / \upsilon_{in}$ where subscript *da* refers to dry air. The humidity ratio at the outlet side can be determined as $w_{out} = w_{in}$ (humidity conservation). The

$$v = \frac{v_1 + v_2 + v_3 + v_4}{4}$$

$$\dot{V} = Av$$

$$T_{in} = \frac{T_1 + T_2 + T_3 + T_4}{4}$$

$$T_{out} = \frac{T_5 + T_6}{2}$$

$$T_{in}, RH_{in}, p_{atm} \rightarrow h_{in}, \upsilon_{in}, w_{in}$$

$$\dot{m}_{da} = \frac{\dot{V}}{\upsilon_{in}}$$

$$w_{out} = w_{in}$$

$$T_{out}, W_{out}, p_{atm} \rightarrow h_{out}$$

$$\dot{Q} = \dot{m}_{da}\left(h_{out} - h_{in}\right)$$

$$COP = \frac{\dot{Q}}{\dot{W}_{HP}}$$

in: inlet side; out: outlet side

Figure 3: Calculation flow chart of the method

air properties h_{out} and υ_{out} are then computed from $T_{out}, W_{out}, p_{atm}$, and the heating power is expressed as $\dot{Q} = \dot{m}_{da}\left(h_{out} - h_{in}\right)$. Finally, COP is defined as a ratio of heating power and HP electric power: Air thermodynamic properties are calculated using ASHRAE equations (ASHRAE, 2001). The calculation method is summarized in Fig. 3.

2.3. Reference for COP Comparison

Reference values are required to validate the results obtained in the field. The references used here are the COP values of the same HP model measured in the laboratory. The reference method, based on refrigerant intrusive measures (temperature, pressure and flow rate), is of good accuracy (Tran et al., 2012). The tests were performed in stationary conditions where different outdoor temperatures were tested but the same indoor temperature (around 21 °C) was fixed. In addition, the tests were carried out with two levels of internal fan speed. Fig. 4 shows COP values obtained which is thus correlated with the outdoor temperature (in °C) $COP^{ref} = 2.58 + 0.074 T_{ext}$, with a coefficient R^2=0.96.

This correlation is used to compare the COP determined in situ because the same operating mode (maximum compressor speed allowed by the HP control) was used in both tests - laboratory and in situ. It must be noted that the indoor temperature differs during two tests, and that may introduce small differences between the 2 measurements.

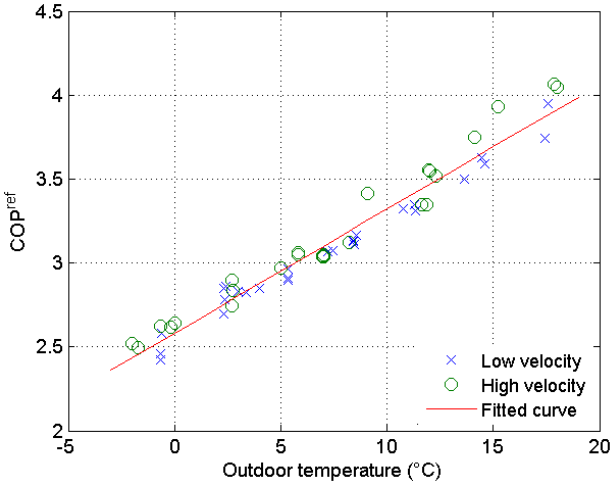

Figure 4. Coefficient of performance measured in laboratory

3. EXPERIMENTAL RESULTS IN THE FIELD

The tests were carried out in an experimental house over 15 days where the outdoor temperature varied between -2 and 16 °C. The internal fan speed was in the automatic mode (i.e. the HP selected an appropriate speed level depending on dynamic operating conditions).

Hereafter, we study separately the phenomenon affecting HP performances, including the defrosting phase and the unsteady-state operation. Then, we present the HP performance map according to the outdoor temperature. Finally, we discuss the required time period for the acquisition sampling rate for long duration test in the field. The compressor electric consumption is only measured to get a better understanding of HP behavior; this variable is not necessary to compute the COP.

3.1. Defrosting Phase

Fig. 5 shows the results derived over a defrosting phase, which can be split into 3 periods:

- Preparatory period (between points 1 and 2): the compressor electric power begins to decrease (in other words the compressor rotation speed slows down), but the indoor fan remains at its operating speed. When the compressor stops, the fan still operates. Thus, the energy in the condenser is drawn before the beginning of the inversion cycle. Consequently, the instantaneous COP is artificially high, especially at the end of the period.
- Inversion cycle (between points 2 et 3): the indoor fan stops to avoid any production of cold air. Thus, the COP is obviously equal to zero.
- Transitory period (between points 3 and 4): the compressor stops for a while, then increases its speed step by step. At the beginning, the COP remains at zero because the indoor fan doesn't start immediately, then the COP increases gradually up to the level before the defrosting phase.

The defrosting phase lasts about 12 minutes and the instantaneous COP ranges from 0 to a very high value.

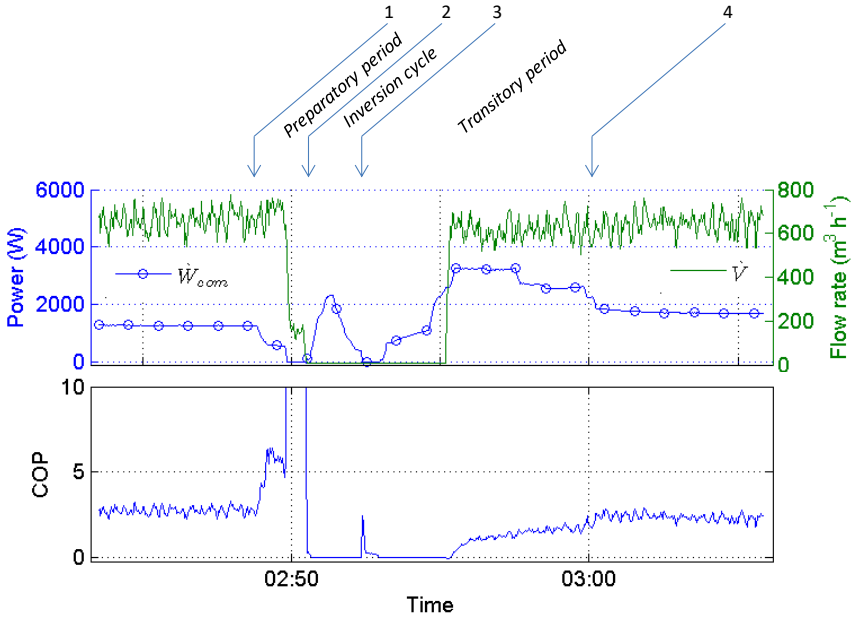

Figure 5. Time evolution of the compressor electric power, the air flow rate and the instantaneous COP during a defrosting phase

3.2. Unsteady-state operation due to the HP control

We sometimes observe unsteady-state operations only due to the HP control performance. Fig. 6 shows the results over fifteen minutes when the indoor and outdoor temperatures are almost constant but the compressor speed is changed. First, the COP is stabilized at around 4. At point 5 the compressor speed increases. The COP simultaneously falls to 2 then increases progressively, because of a delay in the heating power. Inversely, while the compressor speed decreases (point 6), the COP increases rapidly up to 5, then decreases to 4.

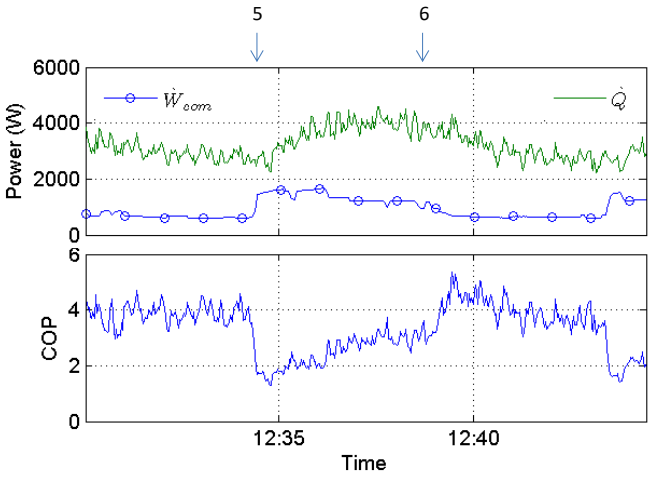

Figure 6. Time evolution of the compressor electric power, the heating power and the COP during an unsteady phase

Therefore, the HP is not always in steady-state operation even if the indoor and outdoor temperatures are stable. The reason why couldn't be clarified, but the phenomenon makes the COP vary around an average value and causes, as shown in the next part: performance deteriorations.

3.3. Performance Map

Fig. 7a shows all measurement points (a sampling rate of two seconds). To obtain an appropriate scale, the points with a COP of more than 8 are not presented (as shown in part 3.1, the COP can reach an artificial high value during the defrosting phase). Therefore, the results derived in the field are coherent, compared to the reference values.

The points which are located far from the reference correspond to the unsteady-state operations, including the defrosting phase, the compressor stop phase (stand-by) or simply the unsteady phase due to HP control. In these conditions, the condenser's internal energy has an important impact on the instantaneous COP. Indeed, the color represents the variation in refrigerant

temperature at the condenser outlet T_r (in K s^{-1}), it refers roughly to the variation in condenser's internal energy. Thus, the COP is lower when T_r increases. This can be explained by the fact that part of the heating energy produced is used to increase the condenser's internal energy. Similarly, the COP is higher when the temperature decreases. To avoid this ambiguity, it is better to average the COP over a longer period of time. Fig. 7b shows the results with a COP defined as:

$$COP = \frac{\sum_{t_0} \dot{Q} \Delta t}{\sum_{t_0} \dot{W} \Delta t} \qquad \text{Eq. (1)}$$

where the sums are calculated over a period t_0=10 minutes and Δt is sampling rate (2 seconds). Therefore, the sums are still gathered around the reference point but are more concentrated. It also indicates that when the HP is in unsteady-state conditions, there really are performance deteriorations (up to 50 % compared to the value obtained in the same temperature condition). In our test, about 4 % of the points are related to these conditions.

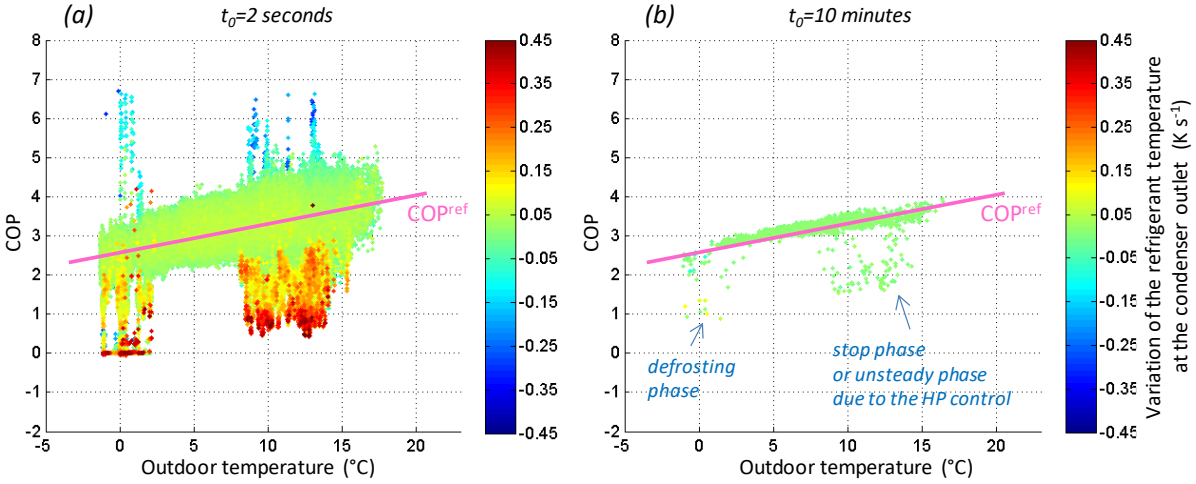

Figure 7. Coefficient of performance according to the outdoor temperature

3.4. COP Uncertainty

Uncertainty around the COP measured mainly depends on the precision of the air flow rate determination. If the air velocity field is accurately established, allowing the velocity sensors to be placed in the optimum positions, precision of the flow rate can reach ±10 % according to the laboratory tests of (Tran et al., 2013). Then, COP uncertainty is approximately equal to 12.5%, including all sensor accuracies and the heterogeneity of air temperature fields.

In view of tests undertaken in the field, it may be difficult to measure the entire velocity field, resulting in a higher COP uncertainty. In an extreme situation when the velocity field is not determined at all and the sensors are randomly placed around the middle of the air grille (row 4 Fig. 2), precision of the air flow rate determination ranges from -25% to +12%.

3.5. Optimum Recorded Data Rate

In view of the long testing period in the field, it is necessary to optimize the recorded data rate to reduce the data storage volume required, without affecting the precision of measurement variables. In our test, the variables are recorded at a high rate (two seconds). We aim to evaluate the measurement precision when the rate is slowed. The calculation is carried out for slower rates, named hereafter: sampling rate Δt, by counting only data which correspond to the rates considered (in other words, data between time steps are not taken into account). Fig. 8 shows the errors as a function of Δt, compared to Δt =2 seconds. In particular, we consider heating capacity and electric consumption of the HP over a period of time t_p, which are defined as:

$$Q = \sum_{t_p} \dot{Q} \Delta t$$

$$W = \sum_{t_p} \dot{W}_{HP} \Delta t \qquad \text{Eq.(2)}$$

Two different periods are analyzed in order to distinguish the impacts of the following 2 issues:

- Change in climatic condition: the calculation is performed over a period t_p=12 hours when the HP works only in the standard heating operation (without defrosting cycle and compressor stop) and the outdoor temperature increases slowly from 4 °C to 16 °C. There are no significant errors up to Δt=5 minutes (Fig. 8).
- Defrosting cycle or on/off cycle: we examine a period t_p= 6 hours when the defrosting operation occurs (once an hour on average) and the outdoor temperature is fairly constant. As shown on Fig. 8, the electric consumption error becomes significant when Δt reaches 3 minutes, which is roughly equal to the duration of the inversion cycle (Fig. 5). The heating capacity error becomes significant when Δt reaches 5 minutes, the value corresponding to the null heating power period (Fig. 5).

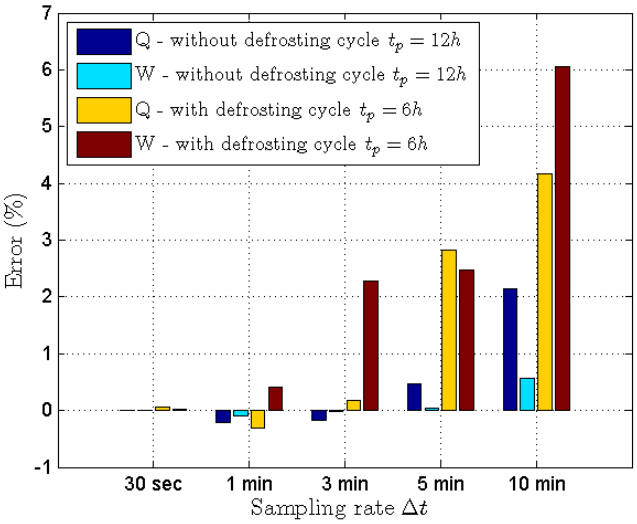

Figure 8: Error evolutions of the heating capacity Q and electric consumption W in function of the sampling rate

So, in our tests a recorded data rate of 1 minute or better should not have any meaningful impact on measurement precisions.

3.6. Measurement procedure for a seasonal test in situ

In order to measure the seasonal coefficient of performance, value of the best advantage for the end-user, an on-site test is required for at least one season. The measurement method presented above can be used for such needs. Indeed, since the method provides an acceptable uncertainty and the measurement installation satisfies visual criteria without causing any major discomfort for house occupants. The following measurement procedure is proposed:

- Equipment conditioning: Fig. 1 shows all sensors required, with an accuracy specified in Table 1 (all sensors commercially available). The number of thermometers and hot-wire sensors results from the temperature and velocity range determined in a preparatory test (next step).
- Preparatory test: this step is intended to determine the sensor arrangement. The air temperature and velocity fields are measured at different points of the flow. The results obtained will allow a choice of the best sensor arrangement, providing correct flow rate measurements with an optimum number of sensors. The air velocity should be measured on the inlet side rather than on the outlet side.
- Performance test: the optimum sensor arrangement is used, and the measurement installation is left in the user's house for a long duration test. The optimum recorded rate is around 1 minute.

4. CONCLUSION

A test campaign was undertaken to measure the performances of an air-to-air HP in the field. The method was based on the measurement on the air side, in particular the air flow rate was determined from hot wire sensors.

Based on the results obtained, the following conclusions can be reached:

- The performances measured in the field concord with the performances expected.
- The HP operation is not always stable even in steady-state conditions. This is due to the bad performance of the HP control, and can lead to a lower than expected energy performance.
- When the HP is in unsteady-state operations, the instantaneous COP could vary from null to a very high value, resulting from condenser thermal energy inertia.

- There are actually performance losses in the defrosting phase or in the compressor stop phase.
- The optimum recorded data rate depends on climatic conditions and HP behavior in frosting conditions. In our tests, it is around 1 minute.
- The method is suitable for long duration tests in the field. It provides an acceptable precision.

The main drawback is related to the determination of the sensor arrangement (step 2 of the measurement procedure, part 3.6). Indeed, it is not considered easy to measure correctly the air velocity field and then to deduce the best sensor arrangement from it. That requires the expertise of an installation technician as there is no common method for every HP due to a wide variety of indoor unit types (geometric shapes, types of fan …).

NOMENCLATURE

			Subscrips	
A	area	m^2	atm	atmospheric
h	enthalpy	J kg^{-1}	com	compressor
$\dot{m}$	mass flow rate	kg s^{-1}	da	dry air
p	pressure	Pa	ext	exterior/outdoor
Q	heating capacity	J	in	inlet side
$\dot{Q}$	heating power	W	out	outlet side
RH	relative humidity	-	r	refrigerant
T	temperature	°C	ref	reference
v	velocity	m s^{-1}		
$\dot{V}$	volume flow rate	m^3 $hour^{-1}$		
w	humidity ratio	-	Abbreviations	
W	electric consumption	J	COP	coefficient of performance
$\dot{W}$	electric power	W	HP	heat pump
υ	specific volume	m^3 kg^{-1}		

REFERENCES

ASHRAE. (2001). Fundamentals Handbook.

Francisco, P. W., & Palmiter, L. (2003). Field evaluation of a new device to measure air handler flow. Ashrae annual meeting. Kansas City, USA.

Howell, R. H., & Sauer, H. J. (1990). Field measurement of air velocity : pitot traverse or vane anemometer? ASHRAE journal .

Ichikawa, T., Won, A., & Yashida, S. (2007). Study on Running Performance of a Split-type Air conditioning System Installed on a University Campus in Subruban Tokyo. Climat 2007 WellBeing Indoors.

McWilliams, J. (2002). Review of Airflow Measurement Techniques, Contract for U.S. Department of Energy, Contract No. DE-AC03-76SF00098.

Rivière, P., Arzano-Daurelle, C., Tran, C. T., & Nordman, R. (2012). Survey of completed and ongoing field measurements of air-to-air heat pumps, Projet SEPEMO, Contract for the European Communities, Contract No. IEE/08/776/SI2.529222.

Tran, C. T., Rivière, P., Marchio, D., & Arzano-Daurelle, C. (2013). In Situ Measurement Methods Of Air To Air Heat Pump Performance. International Journal of Refrigeration, vol 36 n°5 , 1142-1455.

Tran, C. T., Rivière, P., Marchio, D., & Arzano-Daurelle, C. (2012). Refrigerant-based measurement method of heat pump seasonal performances. International Journal of Refrigeration 35 , 1583-1594.

Weng, W.-B., Ding, H.-Y., & Li, D. (2007). Research on temperature and velocity field of room for wall-mounted air-conditioner. Journal of University of Shanghai for Science and Technology , 378-382.

Manuscript ID: 533
DOI: 10.18462/iir.icr.2019.0533

A new self-driven loop heat pipe used in HVAC systems: feasibility analysis

Xiaorui YANG, Penglei ZHANG*, Xingwang LI, Dalin ZHANG

Institute of Air Conditioning and Refrigeration, Nanjing University of Aeronautics and Astronautics, Nanjing 210016, P.R. China, plzhang@nuaa.edu.cn

ABSTRACT

Two-phase thermosyphon loop (TPTL) has been widely used in industrial applications for energy conservation. However, the circulation of two-phase thermosyphon depends on the gravity, and the condenser must be higher than the evaporator by a certain height, which brings about significant difficulties in design and application. In this paper, a self-driven loop heat pipe (SDLHP) without the assistance of gravity is proposed. The working principle of SDLHP is described, and a performance simulation model has been developed. Based on the model, heat transfer rate, mass flux, the mass distribution of the working fluid, thermal resistance distribution and the flow parameters along the loop of SDLHP are simulated and compared to a traditional TPTL without height difference. The simulation results show, compared to the traditional TPTL without height difference, by utilizing the thermal potential difference between the heat source and the heat sink to generate driving force, SDLHP can enhance the circulation flow to optimize the refrigerant distribution in the evaporator and the condenser, and the heat performance improves significantly. Meanwhile, based on a theoretical analysis, the proposed SDLHP is thermodynamically feasible. Because of no need for the height difference, the SDLHP greatly expands the application of heat pipes in various industrial applications.

Key words: heat pipe, self-driven, two-phase thermosyphon loop, numerical simulation

1. INTRODUCTION

Two-phase thermosyphon loop (TPTL), also called wickless loop heat pipe, is a high-efficiency facility which can transfer heat over a relatively long distance. And it is a natural circulation without extra driving, such as a pump or a compressor. Owing to its characters of flexibility, simplicity, no energy consumption and high heat transfer efficiency, it has been widely used in HVAC systems for energy conservation. Liu et al. (Liu et al., 2006), Zhang et al. (Zhang et al., 2015c) utilized TPTL heat exchangers to recover heat from exhaust air; Byrne et al. (Byrne et al., 2011a, b) recovered waste heat to carry out defrosting for an air-source heat pump by a TPTL; Tu et al. (Tu et al., 2011) and Samba et al. (Samba et al., 2013) used TPTL for free cooling of Internet data centres. In short, it has been proved that TPTL is a high-efficiency and reliable option for the optimum use of natural and recovered energy.

A TPTL is a closed loop which is comprised of a gas line, a liquid line, a condenser and an evaporator, shown in Fig. 1. The working fluid absorbs heat and evaporates in evaporator, then the vapor from evaporator flows to condenser through the gas line, after releasing heat and condensing in condenser, the liquid in condenser flows back to the evaporator through the liquid line by the force of gravity. Because the circulation of TPTL must depend on gravity, it's essential that the condenser should be higher than the evaporator by a certain height (as Fig. 1 shown). And the height difference between the condenser and the evaporator is the essential driving source and a key factor in heat transfer performance of TPTL (Zhang et al., 2018; Zhang et al., 2015b). Zhang et al. found through experiments, when the height difference between the condenser and the evaporator is small, the working fluid in the condenser can't return to the evaporator, both the evaporator superheating and the condenser flooding phenomena are significant, the heat transfer performance of TPTL is poor (Zhang et al., 2018) ,as Fig. 2 as shown. Naturally when the condenser and the evaporator are at the same height, because of the lack of driving force for

circulation, the loop can't operate normally, which brings about significant difficulties in TPTL design, and restricts the promotion and application of TPTL.

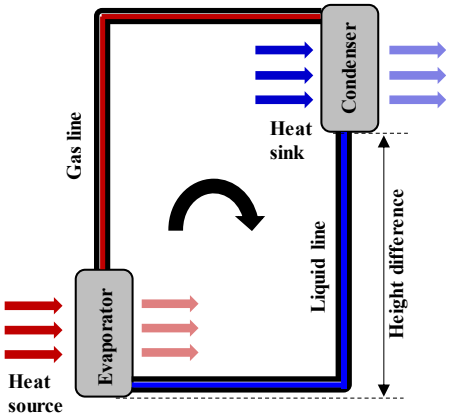

Figure 1:TPTL

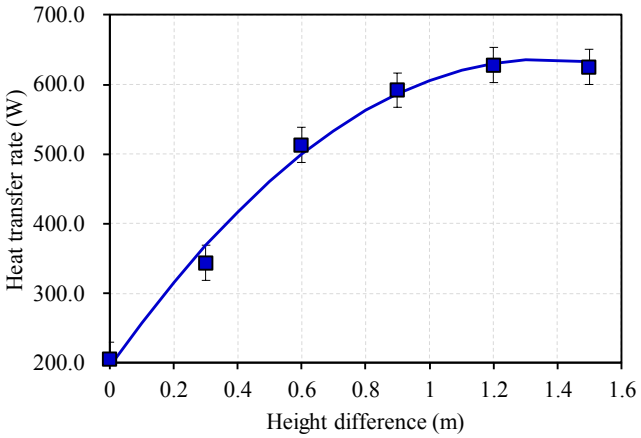

Figure 2: Performance vs. height difference

In this paper, a self-driven loop heat pipe (SDLHP) without the assistance of gravity is proposed. The details of SDLHP is described, the theoretical analysis and performance modelling are developed. The heat transfer rate, mass flux, mass distribution of the working fluid, thermal resistance distribution and the flow parameters along the loop are simulated and compared with a traditional TPTL. Finally, the feasibility and performance of the proposed SDLHP is discussed thoroughly.

2. DESCRIPTION OF SDLHP

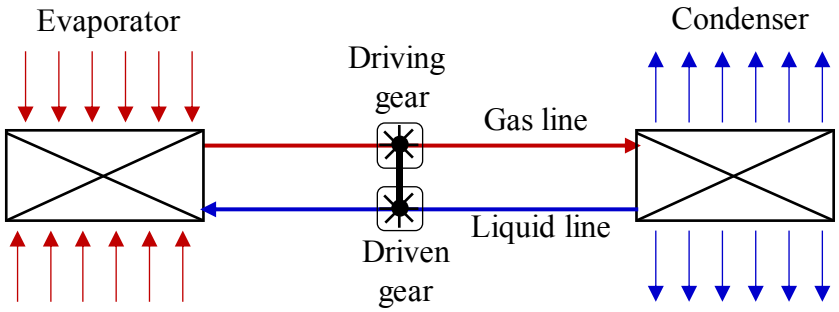

Figure 3: The self-driven loop heat pipe heat exchanger

A SDLHP is comprised of an evaporator, a condenser, a gas line, a liquid line, a driving gear, a shaft and a driven gear, as shown in Fig. 3. By connecting evaporator with condenser through gas line and liquid line, the whole system becomes a closed loop, the working fluid is charged into the closed loop. Specially, a driving gear is installed in the gas line, a driven gear is installed in the liquid line, and the driving gear and the driven gear are mounted on the same shaft. During the operation, the evaporating temperature is relatively higher than the condensing temperature. The working fluid in evaporator is changed into the gas phase, because of the thermal potential difference between the evaporator and the condenser (the saturated temperature difference corresponding to the saturated pressure difference), the vapor in the evaporator flows to the condenser through the gas line. The vapor in the gas line drives the driving gear to rotate, the driving gear drives the driven gear to rotate through the rotation shaft, and the driven gear drives the liquid to return to the evaporator.

Because of the coaxial rotation of the driving gear and the driven gear, the power of the driving gear N_g (Eq. 1) is approximately equal to the power of the driven gear N_l (Eq. 2). And because of the continuity of the flow (Eq. 3), finally the pressure head obtained by the liquid ΔP_l is calculated as shown in Eq. 4. Notably, the density of the vapor ρ_g is far less than the density of the liquid ρ_l, hence the pressure head obtained by the liquid ΔP_l is much larger than the pressure loss of the

vapor ΔP_g, and the pressure head obtained by the liquid is sufficient to overcome the flow resistance to drive the loop. For example, taking R134a as the working fluid, when temperature difference is 30ºC, approximately 12000 Pa pressure head is required in the liquid line to make a traditional TPTL with 1 m height difference operate normally ($\Delta P=\rho_l gh\approx$12000 Pa). So for the SDLHP under the same operation condition, the driven gear in liquid line should generate 12000 Pa pressure head (ΔP_l=12000 Pa). For R134a, the density ratio of liquid and vapor is approximately 60; and the transmission efficiency η_m from the driving gear to the driven gear is set to be 0.2, which is feasible in practical engineering. Calculated by Eq. 5, only 1000 Pa pressure head is consumed at the driving gear to generate 12000 Pa pressure head at the driven gear to drive the loop. It's noteworthy that the SDLHP has a self-regulation ability: when heat-transfer requirements improves (the temperature difference increases), the saturated pressure difference between the evaporator and the condenser increases as well, which leads an increase of volume flow to satisfy the heat-transfer requirements.

$$N_g = Q_{V,g}\Delta P_g \quad \text{Eq. (1)}$$

$$N_l = Q_{V,l}\Delta P_l \quad \text{Eq. (2)}$$

$$Q_{V,g}\rho_g = Q_{V,l}\rho_l \quad \text{Eq. (3)}$$

$$\Delta P_l = \frac{\rho_l}{\rho_g}\Delta P_g \quad \text{Eq. (4)}$$

$$\Delta P_l = \frac{\rho_l}{\rho_g}\Delta P_g \eta_m \quad \text{Eq. (5)}$$

In the whole, by installing the driving gear, the driven gear and the shaft, the thermal potential difference between the heat source and the heat sink can be effectively utilized to drive the working fluid. When the vapor flows spontaneously to the condenser, the driving gear in the gas line is driven. Meanwhile, the driven gear in the liquid line is driven by the driving gear to drive the liquid flow to the evaporator, the whole loop is completed. The SDLHP gets rid of the dependence of the gravity, the evaporator is no longer restricted by the condenser, the applied range of which is wider.

3. MODELLING

A steady-state distributed-parameter model of a SDLHP is developed in this paper. The loop is divided into 400 elements and heat transfer and pressure drop are calculated for each element, correspondingly the thermodynamic parameters of each node along the loop are achieved. For single-phase flow, momentum and heat transfer correlations are consistent and exact (not explained here). And for two-phase flow, there are some different momentum and heat transfer correlations for different conditions respectively, in this paper, the correlations which are selected for SDLHP are shown in Table 1. And the details of chosen mathematical models and correlations can be found in reference (Zhang et al., 2015a).

Table 1. Empirical correlations used in two-phase flow modelling

Item	Correlations
Frictional pressure gradient (two-phase)	Lockhart and Martinelli (Lockhart and Martinelli, 1949)
Vapor void fraction	Thom (Thom, 1964)
Boiling heat transfer	Khodabandeh(Khodabandeh, 2005)
Condensation heat transfer	Nusselt (Nusselt, 1916)

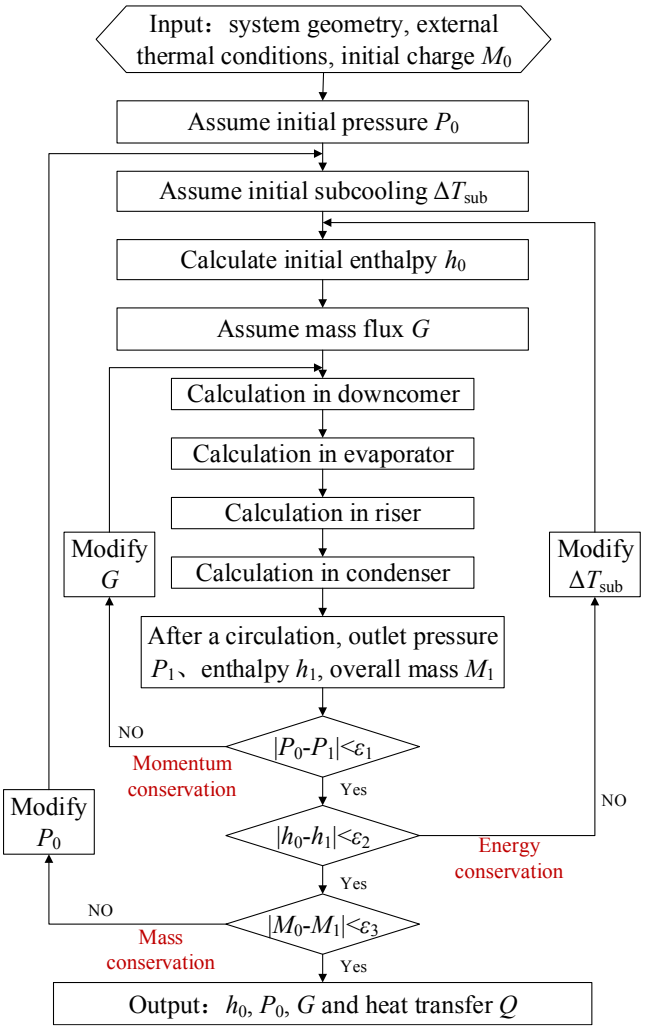

Figure 4: System-solving flowchart for the modelling

The detailed system-solving flowchart is shown in Fig. 4, the sequential module method is used. Three iterations based on the conservation of momentum, energy and mass are used to figure out three unknown initial flow parameters. And to simulate the effect of the driving gear and the driven gear, the pressure ratio *P*r between the front and rear of the driving gear and the transmission efficiency η_m from the driving gear to the driven gear are settled before the calculation. When the simulation proceeds to the node before the driving gear, the pressure before the driving gear is known, the pressure loss of the vapor at the driving gear ΔP_g can be figured out by *P*r, and the flow parameters at the node after the driving gear can also be figured out corresponding to the pressure at this node. Similarly, the pressure head obtained by the liquid ΔP_l can be figured out by Eq. 5, and the flow parameters at the node after the driven gear is also clear. At this point, the simulation along the whole loop is continuous and obeys three conservation laws. Furthermore, when Pr is equal to 0, the developed model actually is the model for the TPTL without height difference between the condenser and the evaporator. The refrigerant thermodynamic properties are collected from Refprop 8. The model is developed based on MATLAB.

The simulated heat exchangers are air-to-air heat exchangers and the specifications of which are shown in Table 2. The operation conditions of the simulated SDLHP are shown in Table 3. R134a is used as the working fluid. The filling ratio is defined as the ratio between the filling refrigerant volume and the whole system volume.

Table 2. Heat exchanger specifications

Items	Evaporator/condenser
Tube bundle specification	3 rows, 28 tubes/row Tube length: 700 mm

Tube size	Tube pitch: 25.4 mm; Row pitch: 22.2 mm Outer diameter: 9.52 mm; Inner diameter: 8.88 mm
Fin specification	Wavy fin; Pitch: 1.814 mm; Thickness: 0.105 mm

Table 3. Simulation conditions

Parameter	Value	Parameter	Value
Pipe length	10 m	Heat sink temperature	10°C
Pipe diameter (inner)	12mm	Filling ratio	0.3
Pipe diameter (outer)	15.8 mm	Pr	1.001
Heat source temperature	30°C	η_m	0.8

4. RESULTS

To analyze feasibility of the proposed SDLHP, the performance of a traditional TPTL without height difference and the SDLHP are simulated and compared under the same operation conditions by the developed model. Fig. 5(a) and (b) shows the heat transfer rate and mass flux of which, compared to the TPTL, the circulation flow of SDLHP increases significantly, which leads an improvement of heat transfer rate. And refer to reference (Zhang et al., 2018), the heat transfer rate of the SDLHP is near to the heat transfer rate of “ideal cycle” under the same operation conditions. The specific effects of the SDLHP can be revealed by the parameters shown in Fig. 5(c) (d) and Fig. 6.

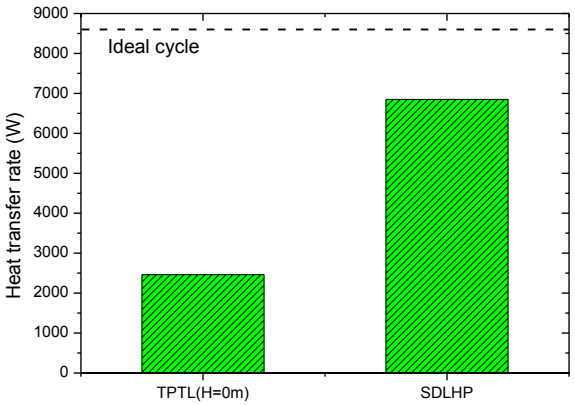

(a) Heat transfer rate mass flux

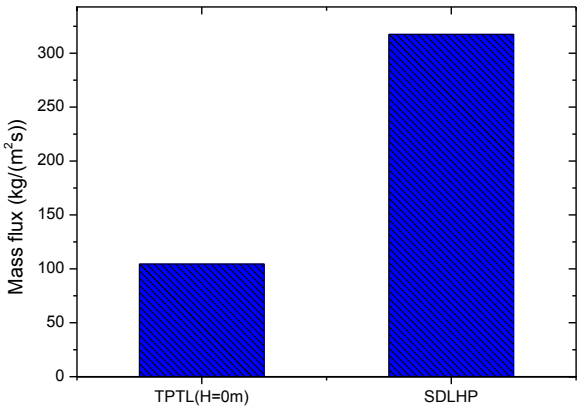

(b) Mass flux

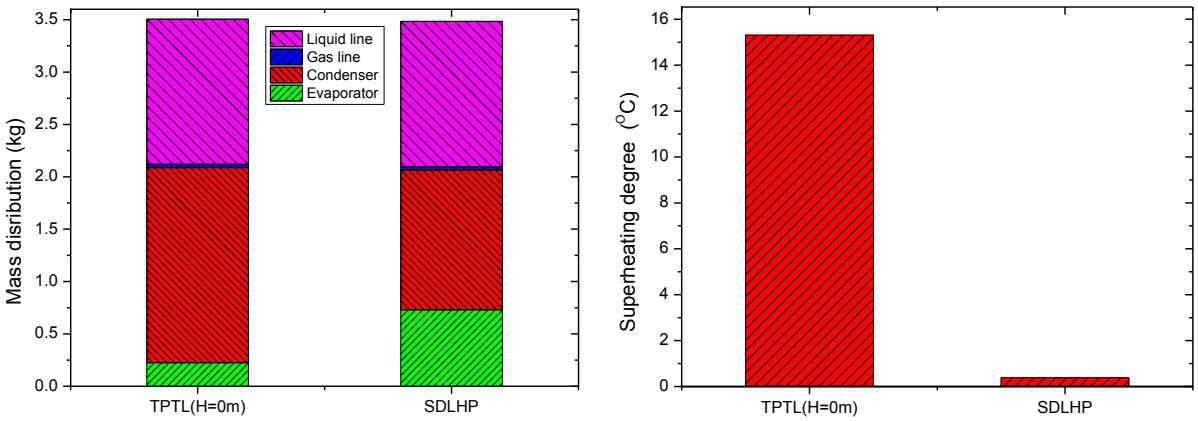

(c) Mass distribution (d) Superheating degree

Figure 5: Thermal performance of TPTL and SDLHP

Fig. 5(c) presents the mass distribution of refrigerant along the loop, Fig. 5(d) shows the evaporator outlet superheating degree. Fig. 6 shows the distribution of pressure (*P*), temperature (*T*), vapour quality (*x*) and the void fraction (*α*) in two-phase flow along the loop.

For the TPTL without height difference, the refrigerant mass in evaporator is relatively small (Fig. 5(c)), the evaporator outlet superheating degree is large (Fig. 5(d)), which indicates the refrigerant in evaporator is insufficient and superheating phenomenon is significant in the evaporator. Just as shown in Fig. 6(a), after a little part behind the evaporator inlet, the refrigerant has been transferred into gas (corresponding *x* exceeds 1), the refrigerant temperature begins to increase in evaporator because of single-phase heat transfer. Meanwhile, the flooding phenomenon is significant in the condenser: after the middle of the condenser, the refrigerant has been transferred into liquid (corresponding *x* is less than 0), and the refrigerant temperature reduces to the heat sink temperature. Therefore, for TPTL without height difference, because of the lack of the driving force, the refrigerant in the condenser can't return to the evaporator, circulation flow is insufficient, and the heat transfer performance is poor.

By works of the driving gear and the driven gear to increase the circulation flow, the heat transfer rate of SDLHP increases significantly. Fig. 5(c) shows, compared to the TPTL, the mass of refrigerant reduces in condenser and increases in evaporator, which indicates that more refrigerant in condenser is driven back to the evaporator by the driven gear. Consequently, as Fig. 6(b) shown, compared to the TPTL, the area of two-phase region (corresponding *x* ranges 0 to 1) increases, the refrigerant temperature mostly stabilizes in constant (corresponding to the saturation temperature), which indicates and superheating phenomenon and flooding phenomenon are alleviated. Just as Fig. 5(d) shown, the superheating degree of SDLHP is reduced to near 0°C.

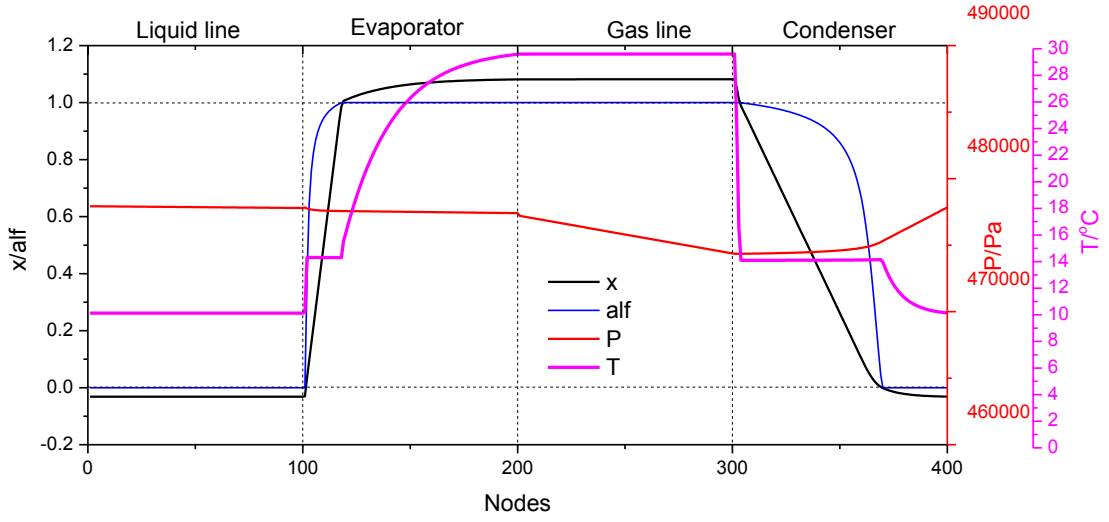

(a) TPTL (H=0m)

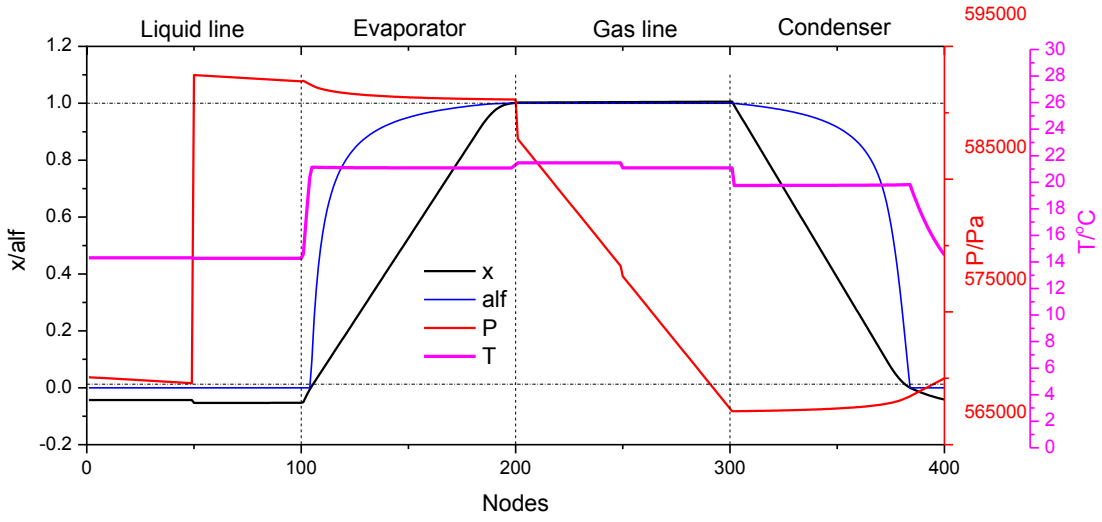

(b) SDLHP

Figure 6: Parameters distribution along the loop

To explain the effect of SDLHP more clearly, refer to reference (Zhang et al., 2018), the thermal resistance from the heat source to heat sink can be defined and divided into three parts: thermal resistance in the evaporator Re, which represents the heat transfer performance in evaporator; thermal resistance in heat transfer process Rt, which is caused by the pressure loss along the gas line，the larger pressure loss，the larger Rt is; thermal resistance in the condenser Rc, which represents the heat transfer performance in condenser. And Fig. 7 shows the thermal resistance distribution of TPTL and SDLHP. For TPTL, the evaporator superheating and the condenser flooding phenomena are significant, Re and Rc are large; and because the flow velocity is low, the pressure loss along the gas line is slight, i.e. Rt is slight. For SDLHP, the driving gear increases the pressure loss along the gas line to drive the driven gear, which leads to an increase of Rt; however, the increasing circulation flow optimizes the refrigerant distribution in heat exchangers, both superheating phenomenon and flooding phenomenon are alleviated, Re and Rc decreases and the total thermal resistance decreases, which leads to an improvement of heat transfer performance. However, the increase of Rt caused by the increase of the pressure loss is inevitable. Hence, even the operation of the evaporator and the condenser reaches the requirement of the “ideal cycle” (no overheating, subcooling, and pressure loss, i.e. Re and Rc remains minimum, and Rt=0), the performance of the whole loop can’t reach the “ideal cycle”.

The effect on pressure of the SDLHP can be found in Fig. 6. For the TPTL, because of the lack of the driving force and low flow rate, the variation of the pressure is slight (Fig. 6(a)). For the SDLHP, as Fig. 6(b) shown, there is a little rapid decrease of pressure in the middle of the gas line because of the work of driving gear, consequently the liquid gets a high pressure head in the middle of the liquid line, which is sufficient to overcome the flow resistance of the whole loop.

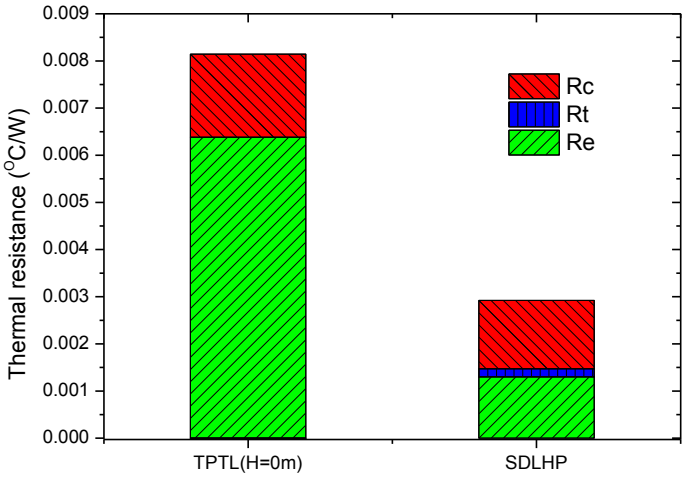

Figure 7: Distribution of thermal resistance

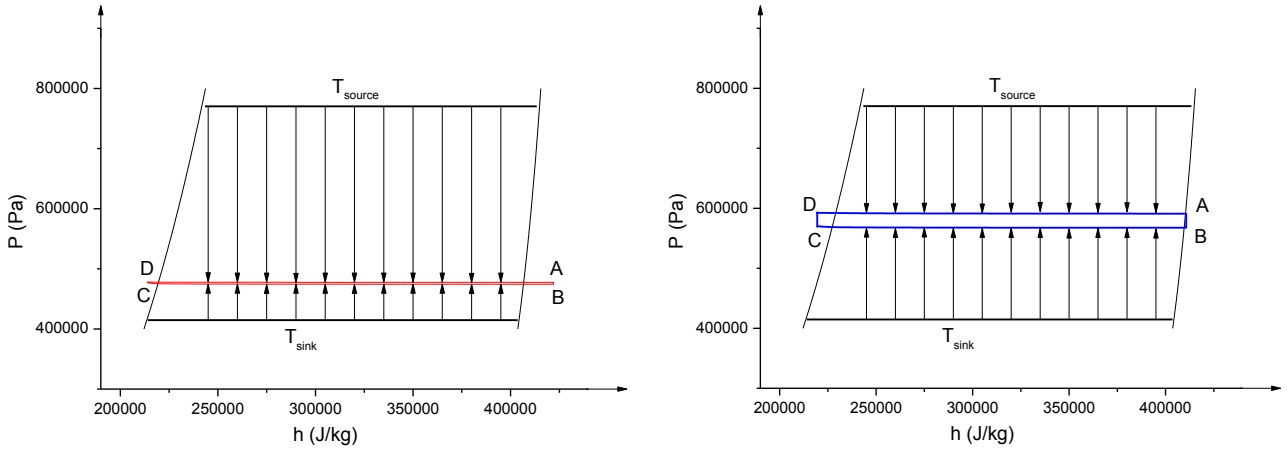

(a) TPTL (H=0 m) (b) SDLHP

Figure 8: The pressure-enthalpy diagram of two loops

Essentially, the mechanism of SDLHP is that, by sacrificing a small part of the temperature difference between the heat source and the heat sink, the driving gear works to improve the circulation flow to solve the difficulty of returning the working fluid. Actually, for the TPTL, the pressure-enthalpy diagram of which is shown in Fig. 8(a), the temperature difference (which can be used in heat transfer) between the heat source and the heat sink is 20°C, only a little part of which is consumed by the saturated temperature difference between the evaporator and the condenser, which is caused by the pressure loss along the gas line. And for SDLHP, as Fig. 8(b) shown, because of the pressure loss at the driving gear, more part of the temperature difference between the heat source and the heat sink which can be used in heat transfer is consumed by the saturated temperature difference to generate mechanical energy. Consequently, although the temperature difference which is used in heat transfer reduces, the flow rate is remarkably enhanced, and the heat transfer performance improves significantly.

To verify the thermodynamics feasibility of the SDLHP, the Carnot efficiency of the driving gear should be compared with the actual efficiency of which. The refrigerant temperature before the driving gear T_1=294.5 K, the refrigerant temperature behind the driving gear T_2=294.1 K, hence the Carnot efficiency η_c is 0.0014 (η_C=1- T_2/T_1). The power of the driving gear N_g is 0.7431 W, the heat transfer rate of the loop Q is 6849 W, hence the actual efficiency of the driving gear η_a is 0.000108 (η_a= N_g/ Q). Therefore, the actual efficiency of the driving gear is far less than the Carnot efficiency, which indicates the proposed SDLHP is thermodynamically feasible. The refrigerant temperature and pressure used to calculate above two efficiency values are taken from the node at the middle of gas line in Fig. 6(b).

5. CONCLUSIONS

In this paper, a self-driven loop heat pipe (SDLHP) without the assistance of gravity is proposed. The performance modelling of which is developed. And to analyse the feasibility of the proposed SDLHP, the performance of which is compared with a traditional TPTL without height difference.

The simulation results show, compared to the traditional TPTL without height difference, by utilizing the thermal potential difference between the heat source and the heat sink to generate driving force, SDLHP can enhance the circulation flow to optimize the refrigerant distribution in the evaporator and the condenser, consequently the heat transfer rate improves from 2460W to 6850 W. Meanwhile, the Carnot efficiency of the driving gear of SDLHP is 0.0014, and the actual efficiency of which is 0.000108, which indicates the SDLHP is thermodynamically feasible.

In the whole, the proposed SDLHP has an excellent performance in heat transfer, and no need of gravity to drive the loop, which greatly expands the application of heat pipes in various industry applications, especially in zero-gravity and anti-gravity field.

ACKNOWLEDGEMENT

This work was supported by the National Natural Science Foundation of China (No. 51806101) and Natural Science Foundation of Jiangsu Province, China (No. BK20180425).

NOMENCLATURE

N	power (W)	P	pressure (Pa)
P_r	pressure ratio at the driving gear (-)	Q_v	volume flow rate ($m^3\ s^{-1}$)
Re	thermal resistance in the evaporator (°C W^{-1})	Rc	thermal resistance in the condenser (°C W^{-1})
Rt	equivalent thermal resistance in the transport (°C W^{-1})	SDLHP	self-driven loop heat pipe
T	temperature (ºC)	T_{source}	temperature of heat source (ºC)
T_{sink}	temperature of heat sink (ºC)	*TPTL*	two-phase thermosyphon loop
x	vapor quality in two-phase flow (-)	ρ	density (kg m^{-3})
η	efficiency (-)	m	mechanical
g	gas	l	liquid

REFERENCES

Byrne, P., Miriel, J., Lenat, Y., 2011a. Experimental study of an air-source heat pump for simultaneous heating and cooling – Part 1: Basic concepts and performance verification. Applied Energy 88, 1841-1847.

Byrne, P., Miriel, J., Lenat, Y., 2011b. Experimental study of an air-source heat pump for simultaneous heating and cooling – Part 2: Dynamic behaviour and two-phase thermosiphon defrosting technique. Applied Energy 88, 3072-3078.

Khodabandeh, R., 2005. Heat transfer in the evaporator of an advanced two-phase thermosyphon loop. International Journal of Refrigeration 28, 190-202.

Liu, D., Tang, G.-F., Zhao, F.-Y., Wang, H.-Q., 2006. Modeling and experimental investigation of looped separate heat pipe as waste heat recovery facility. Applied Thermal Engineering 26, 2433-2441.

Lockhart, R., Martinelli, R., 1949. Proposed correlation of data for isothermal two-phase, two component flow in pipes. Chem. Eng. Prog 45, 39-48.

Nusselt, W., 1916. Die Oberflachenkondesation des Wasserdamffes the surface condensation of water. Zetrschr. Ver. Deutch. Ing. 60, 541-546.

Samba, A., Louahlia-Gualous, H., Le Masson, S., Nörterhäuser, D., 2013. Two-phase thermosyphon loop for cooling outdoor telecommunication equipments. Applied Thermal Engineering 50, 1351-1360.

Thom, J.R.S., 1964. Prediction of pressure drop during forced circulation boiling of water. International Journal of Heat and Mass Transfer 7, 709-724.

Tu, R., Liu, X.-H., Li, Z., Jiang, Y., 2011. Energy performance analysis on telecommunication base station. Energy and Buildings 43, 315-325.

Zhang, P., Shi, W., Li, X., Wang, B., Zhang, G., 2018. A performance evaluation index for two phase thermosyphon loop used in HVAC systems. Applied Thermal Engineering 131, 825 - 836.

Zhang, P., Wang, B., Shi, W., Han, L., Li, X., 2015a. Modeling and performance analysis of a two-phase thermosyphon loop with partially/fully liquid-filled downcomer. International Journal of Refrigeration 58, 172-185.

Zhang, P., Wang, B., Shi, W., Li, X., 2015b. Experimental investigation on two-phase thermosyphon loop with partially liquid-filled downcomer. Applied Energy 160, 10-17.

Zhang, P., Wang, B., Wu, W., Shi, W., Li, X., 2015c. Heat recovery from Internet data centers for space heating based on an integrated air conditioner with thermosyphon. Renewable Energy 80, 396-406.

Manuscript ID: 540
DOI: 10.18462/iir.icr.2019.0540

Development of a photovoltaic driven thermodynamic chiller. Application to solar air conditioning and cooling storage

Philippe ESPARCIEUX[(a)], Olivier BAUP[(a)], Christophe MARVILLET[(b,c)] Christophe WEBER[(c)], Daniel MUGNIER[(d)]

[(a)] ATISYS CONCEPT, Toulon, 83210, France, p.esparcieux@atisys.fr

[(b)] CNAM/IFFI, Paris, 75141, France, christophe.marvillet@lecnam.net

[(c)] NEOTHERM, Le Bourget du Lac, 73375, France, christophe.weber@greth.fr

[(d)]TECSOL, Perpignan, 66004, France, daniel.mugnier@tecsol.fr

ABSTRACT

This paper presents a smart design named PV COOLING to produce solar cooling using low GWP heat pump system coupled with a standard photovoltaic power plant. Optimum autonomy is achieved with proper chiller power management real-time adapted with PV production, a light battery pack and iced water tank for cold storage. For this, a test rig has been developed and installed on the building roof in the south of France with the originality to be entirely real-time controlled in terms of building thermal load. Thereafter, this new system goal is to be used as air-conditioning device (mainly in office buildings) or alternatively as a positive cold storage device in food preservation with a view to reducing post-harvest losses in developing countries.
Current presentation deals with thermal/electrical performances of our test facility with the purpose to air-conditioning a building by means of several sensors and meters.
Keywords: solar cooling, air-conditioning, cold storage, food preservation photovoltaic, heat pump, self-consumption, batteries, thermal tank, glycol water, low GWP, R290.

1. INTRODUCTION

Traditional PV economic model in France was for a long time based upon feed-in tariff. However this trend is currently moving toward on-site self-consumption. PV self-consumption can be used in a straightforward manner for domestic purposes: lighting, heating, domestic hot water heating (DHW), cooking, domestic appliances, etc.
An example of application consists in using solar power to directly drive a thermodynamic device with a target to producing cooling or refrigeration. It can be noted that PV production perfectly matches cooling needs during daytime. Besides, in many countries all over the world, summer comfort in buildings becomes necessary in order to allow employees to work in good condition (Tom C., 2008).
The use of renewable energy for powering heat pumps can solve environmental problems due to the ways of producing energy (e.g. CO2 emissions by coal thermal plants in China). Even if the energy problem is settled, it remains the issue of refrigerant fluid leakage which represents a non-negligible share of the greenhouse effect. Therefore, conjunction use of low refrigerant load and low Global Warming Potential (GWP) fluid in thermodynamic system allows to reducing carbon footprint of the process.

2. THE ADOPTED STRATEGY

At first glance, compressor power may be adapted with PV output power. This may work within a certain range until a minimum threshold is reached where chiller compressor has to be stopped. When PV output power is back, the main issue is to be sure that power remains sufficiently stable and reliable to start compressor again, avoid short-cycle or more drastically abort chiller starting process. Indeed, the problem of driving a chiller compressor with PV lies in the fact that it may happen that irradiation may be temporary obstructed by some peculiar clouds, and this is not predictable.

Use of variable-frequency drive can solve the problem of high inrush current during compressor run-up. For the intermittent energy problem, storage using batteries or other electricity supply can easily sort this problem out. It also is highly recommended to mix with thermal storage system which is a shorter-term storage mode. Both electricity and thermal storage allow storing a sufficient energy when PV production exceeds actual need and use stored cold when cooling demand becomes higher than PV production may provide.
To enhance environmentally friendly character of PV COOLING, propane (R290) has been chosen as refrigerant for this project. This very low GWP refrigerant (GWP < 10) combined with an original configuration allows a significant reduction of refrigerant amount. To maximize the self-consumption, the inverter has to allow both electric powers issued from PV and batteries.
Project goal consisted of developing a test facility using PV COOLING principle. Rig is installed on the building roof in the south of France. For a better understanding of the system behavior, instead of cooling the building, cooling is distributed into a chilled water tank in which is fitted a power controlled heating resistor which simulates all sorts of building thermal load configurations.

3. PROMOTING SOLAR PHOTOVOLTAIC ON NEW MARKET SEGMENTS

3.1. Air-conditioning for the tertiary sector

To avoid an unfair competition with cheap traditional heat pump produced at ten millions samples yearly, PV COOLING will be suitable for medium/high power in the tertiary sector and according to certain criteria. The criteria to lead the market study are classified into three main contextual families (climatic, economic and regulatory) and are summarized through a “bubble chart” (Figure 1). These criteria are expressed inside the chart as:

- cooling demand expressed in *cooling-degree-days* (CDD) on the x-axis;
- annual *global horizontal irradiation* (GHI) per square meter on the y-axis;
- market size of mid-sized / large heat pump in the tertiary sector is expressed by the percentage of the worldwide unit demand through the surface size of the bubble;
- electricity price in the tertiary sector as a driver of renewable investment is expressed by the “coloring” of the country, with cheap costs in light and high costs in black;
- Self-consumption policy and fiscal incentives which are positive for renewables (e.g. feed-in-tariffs, subsidies, solar obligations) are marked with (+); others with (-) and unclear situation with (?).

Figure 1 shows only the final result of an ambitious market study. Indeed, several countries have been removed from previous “bubble charts” because of following weaknesses. First of all, many countries in Europe have an insufficient radiation like Germany and even if the radiation is enough like in South Europe, the cooling needs are only present during summer. Among countries which gather good natural conditions (both radiation and cooling needs), the low electricity price doesn’t allow for photovoltaic to be profitable (e.g. Saudi Arabia).
Countries that appear qualitatively as the most mature to accommodate a short-term photovoltaic air-conditioning system according to Figure 1 are mainly countries with a tropical climate. Indeed, under this kind of climate, the cooling needs are constant during the whole year. Electricity price appears as an important criterion which participates to have a quick return on investment.
The market size is not an essential criterion because PV COOLING can find its place in a market niche where the tertiary sector is not as developed as in high-income countries. However, more and more African cities tend to offer services moving towards European standard for a category of population which are increasingly financially secure.
Self-consumption policy and fiscal incentives are the last criterion which may help PV solutions to be more attractive especially the right to self-consume. But it is difficult to be entirely exhaustive in each country because the PV policy changes quickly. PV outlooks show that many governments trend towards the smart way to consume photovoltaic which is self-consumption model. Besides, a lot of PV self-consumption projects take place in countries where no PV policy exists particularly in Western Africa. That means PV policy is not a necessary criterion to have the right to self-consume.

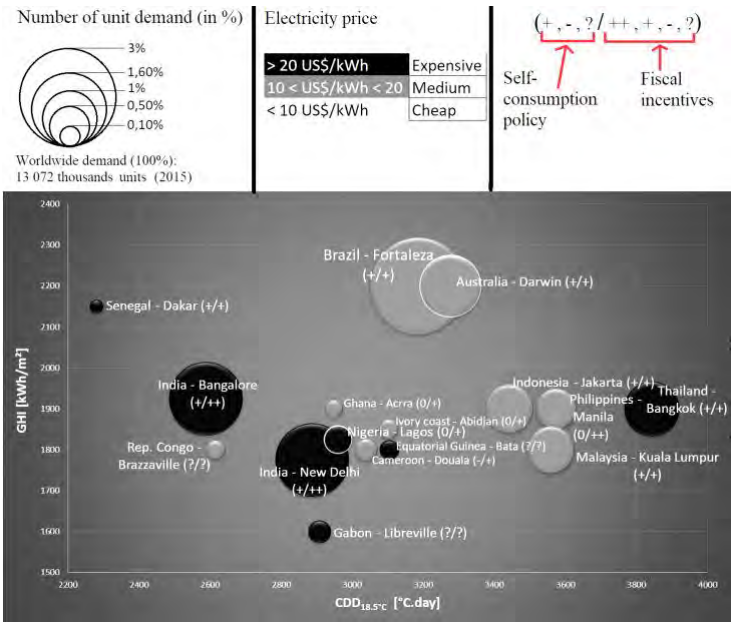

Figure 1 : Graph illustrating the attractiveness of cooling markets for PV COOLING

3.2. Cold room for perishables foods in industrial sector

An industrial sector which matches quite well the natural conditions is agricultural & food industry, and more specifically storage for perishable food items with positive cold storage or refrigerated warehouse. A perishable foodstuffs which require positive cold storage to maintain a longer lifetime are mostly fruits & vegetables and roots & tubers. Countries with tropical climate and low/middle income appear to be regions where due to lack of proper cold storage and cold management (a problem enhanced in many African remote regions by lack of reliable grid) food post-harvest losses is a major problem (*Gustavsson* et al., 2011).
As the air-conditioning study market, the “bubble chart” underlines the fact that tropical countries appear to be the most attractive for PV COOLING usage for positive cold storage food.

4. R&D CARRIED OUT FOR A PROPERLY SIZED SYSTEM

Actual PV COOLING innovation mainly consists of setting together in a clever way, components which actually are highly improved, but never have been set together in a single goal system: PV plant dedicated to driving a thermodynamic fluid chiller as shown in Figure 2.
This is the fruit of two years co-operation with 3 French companies, with several decades of expertise: in solar energy (TECSOL), heat exchangers technology and thermodynamic equipment design (NeoTherm Consulting) and designing & implementing innovative systems (ATISYS).
Furthermore, this R&D project also has an academic issue in France with an expert in cold industry from the Conservatoire National des Arts & Métiers (CNAM-Paris).

4.1. Overall PV COOLING architecture

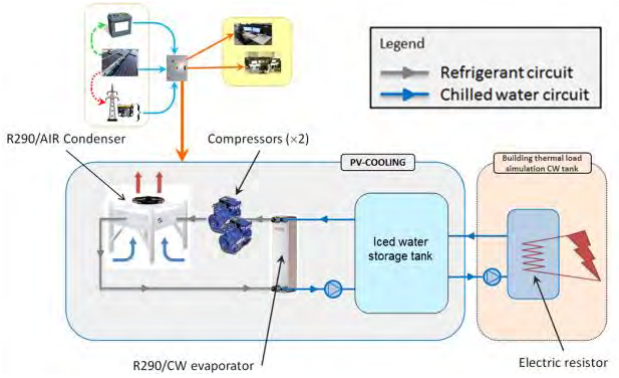

Figure 2 : Schematic architecture of PV-COOLING system

4.2. Layout description

The first test bench, installed on the ATISYS head-office roof-top, is located in Toulon area (South East of France, lovely site in French Riviera).



Figure 3 : Global view of 18 mono-crystalline PV plant and chiller unit on ATISYS headquarters roof

In the pilot testing system, electrical production is delivered by 18 mono-crystalline photovoltaic modules (280 Watts peak (Wp) for each module) as illustrated on Figure 3, which represents a total power of 5.0 kW_p. This power is quite enough for driving chiller compressors and all ancillary equipment dimensioned for 10 kW_{th} chilling power (condenser fan and chilled water circulation pump).
These photovoltaic panels are connected to a three-phase wired inverter along with batteries bank. The four selected 12-Volt batteries are connected in series to obtain a voltage of 48V. Their 150Ah capacity each with a 50% depth of discharge (DOD) allows obtaining useful electrical storage energy about 3.6kWh. This is enough to drive the full load power installation at least for one hour.
For a real operational system, battery capacity may be chosen according to actual need.
In order to limit the inrush current during compressor run-up, a variable-frequency drive has been installed downstream from the inverter which makes possible to divide the inrush current by 6.
Two parallel-mounted semi-hermetic compressors were selected and adapted for propane. Each compressor can provide from 2.4 to 5.4 kW of cooling by varying its rotation frequency from 30 to 70 Hz. This allows a cooling capacity between 2.4 and 10.8 kW. For the future, commercial PV COOLING systems will be able to reach high cooling power till 300 kW using bigger compressors. It is enough to size the other equipment accordingly.
The major innovation regarding the heat pump system lies in the use of low Global Warming Potential (GWP) refrigerant. The choice fell on propane (R290) with (<10) GWP, which is considerably low compared to a common refrigerant (e.g. 1300 GWP for R134a).
The fluid that transports the refrigerating capacity from the cold unit to the chilled water tank is water/methyl propylene glycol (MPG) mixture, so as to avoid any freezing risk.



Figure 4 : Picture of the global chiller installation installed on ATISYS top roof

For this test bench, the chilled water tank is representative of a typical building whose thermal load is simulated with an electrical resistor heating the 180L chilled water tank. That gives the advantage to fully control the building loads and consequently simulate several conditions which correspond to different building utilization/insulation and climate conditions.
A monitoring system has been set up with a view to monitoring performances of the system according to the needs throughout the year. Monitoring is powered by PV-COOLING itself.

4.3. PV COOLING management

For the automatic control of heat pump management, several approaches are tested between two main paradigms. The first one is the **economy mode** (also designated as **"eco" mode**) in which compressor driving power is adapted to PV output power. The second one is the **comfort mode** in which set point value consists in keeping constant chilled water feedback temperature (12°C) and if necessary take complementary power from the grid when both PV and batteries power are insufficient.
Building thermal load is estimated and real-time adapted as follows:

$$P_{Build-Load}(t) = G \times V \times \left[T_{ext}(t) - T_{set}(t)\right] + K \times S_{Build} P_{Sol.Ir}(t) * \delta(t-\tau) \qquad \text{(Eq. 1)}$$

where T_{ext} is outdoor measured temperature, T_{set} is indoor set point temperature, G is volume heat loss coefficient [W/m^3.°C] chosen as G=2.5 (poorly insulated building, here), V is the cooled volume (here, V=325 m^3), $P_{Sol.Ir}$ is measured power of solar irradiation [W/m^2], S_{Build} is time average wall surface of building exposed to solar irradiation (chosen to 40 m^2), K is solar power absorption sensitivity of building walls [non-dimensional, $0 \leq K \leq 1$, here K= 0.20], $\delta(t-\tau)$ is delay function (Dirac), corresponding to building's thermal inertia to solar irradiation (τ = 1 hour)

5. EXPERIMENTAL RESULTS

PV COOLING test bench has been tested during several months with monitoring sequences of several days from June to September 2017. The electrical resistance of the heater has been controlled to model a 350 m^3 building (i.e. 135m² with a high ceiling of 2.60m). To match with reality and upgrade in real-time building thermal load (according to Eq. 1), outside temperature and irradiation sensors and monitoring were fitted. Major monitoring data and performance results are presented hereby, for both **"eco"** and **"comfort"** modes, and under both **sunny** and **intermittently disrupted sunny/cloudy** conditions.

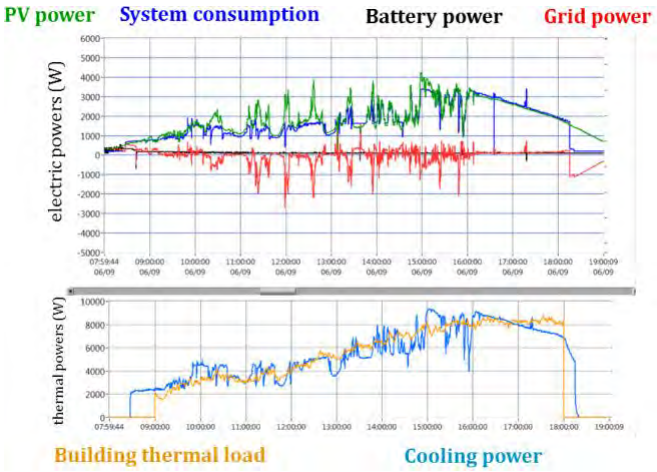

Figure 5 : Electric and thermal powers time history (Sept 6th 2017 – TOULON) – "eco" mode

On following graphical displays (Figure 5 and Figure 6), negative values of grid electric powers means that power in injected by PV system into the grid (red curve). For battery (black curve), it is the opposite (this was done for legibility). Data and performances results were obtained on a daily basis, from 8 a.m. up to 7 p.m. Those data may permit one to appreciating PV COOLING efficiency especially EER: ratio of thermal energy produced to grid energy consumption (Figure 7).

5.1. “eco” mode

Figure 5 displays a quite significant case of ”eco” mode efficiency : Sept 6th was quite a disrupted sunny/cloudy day until 4:00 p.m. and in can be seen that system consumption (and thus cooling power) is adapted PV power. One can notice that despite disrupted conditions, Sept 6th cooling power this day matches quite well thermal load history. This case gives **EER = 44** (see Figure 7).

5.2.”comfort" mode

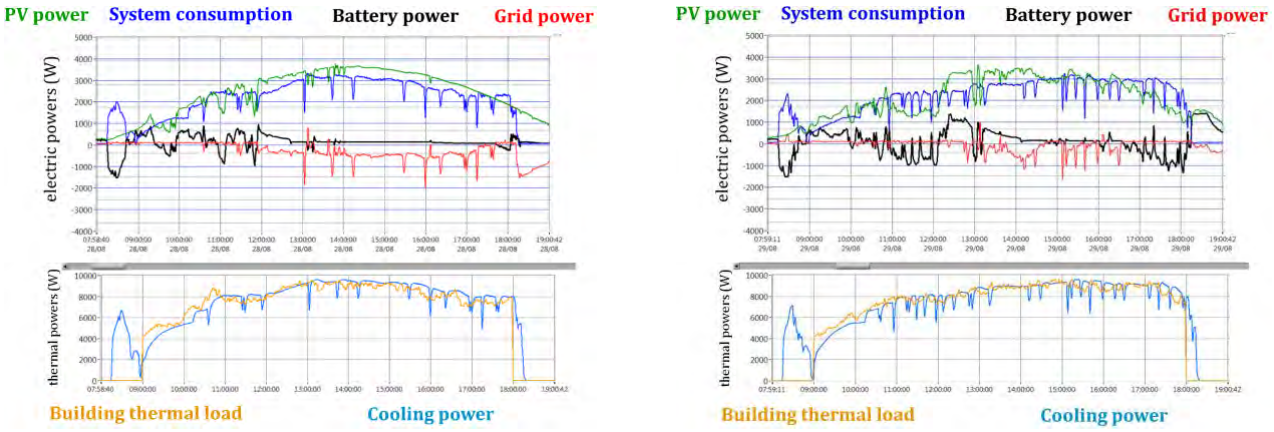

Figure 6 : : Electric and thermal powers time history (Aug. 28th and. 29th 2017 – TOULON) – “comfort” mode

Figure 6 (above) displays PV-COOLING results obtained on Aug. 28th 2017. It was quite a sunny day with high thermal load (71.15 kWh). High cooling production (75.46 kWh) was achieved and with low grid contribution (0.47 kWh) which yields to **EER = 161.93** (see Figure 7). The next day (Aug 29th), solar irradiation was much more disrupted than previous example and still exhibits high thermal load (72.04 kWh) a high cooling production (75.14 kWh) and a low grid consumption (0.78 kWh). Here **EER = 95.82** (see Figure 7).

On all those examples, one can see that priority is given to battery as external supply (at the condition that battery charge level is sufficient).

Figure 7 below is a synthetic table of significant values which permit one to appreciating PV-COOLING performances. Surprisingly high values of EER are the result of very low grid consumption and have to be interpreted with humility: in fact, comparing EERs on Aug. 28th and 29th (respt. 162 and 96) is only du to 0.31 kWh difference in 11 hours !

	"ECO" mode		"COMFORT" mode		
DATA	sept 5th	sept 6th	Aug. 28th	Aug. 29th	Aug. 30th
overall electric consumption(kWh)	14,52	17,87	22,62	22,22	25,24
PV electric consumption (kWh)	14,11	16,64	21,29	19,26	15,95
PV energy production (kWh)	26,56	19,94	25,88	22,94	18,72
consumption from battery (kWh)	0,00	0,01	0,87	2,18	6,13
Q_{grid}: consumption from GRID (kWh)	**0,40**	**1,22**	**0,47**	**0,78**	**3,15**
building thermal load (kWh)	38,64	51,74	71,15	72,04	75,99
Q_{th}: cooling production (kWh)	**43,03**	**53,87**	**75,46**	**75,14**	**77,89**
compressor COP	3,40	3,36	2,91	2,96	2,82
"PV COOLING" COP	2,96	3,02	2,72	2,76	2,64
PV COOLING "EER" (Q_{th}/Q_{grid})	**106,34**	**44,11**	**161,93**	**95,82**	**24,71**
SELF CONSUMPTION RATE (%)	**53**	**83**	**82**	**84**	**85**
SELF PRODUCTION RATE (%)	**97**	**93**	**94**	**87**	**63**

Figure 7 : Summary off significant values for different weather and management conditions

As a result of those examples, it may be concluded that PV-COOLING concept can be considered as efficient and quite acceptable values of EER were obtained which demonstrate possibility to run PV-COOLING independently from grid.

6. DISCUSSION ON ENVIRONMENTAL AND ECONOMIC BENEFIT

From 2017 summer measurements, an attempt has been done with a view to estimating environmental and economic benefit due to PV COOLING. This was done considering thermal cooling need for days when cooling is required, and the monthly rate of days of for which cooling is needed. This yields to monthly cooling energy (kWh).

Figure 8(a) below shows the result in terms of cooling energy (kWh) and electricity induced CO_2 (kg) during the period from April to September for our 135 m^2 office building in south of France (French Riviera): 232 kg; although Figure 8(b) produces same results considering southern Italy : 1270 kg.
In France (Figure 8(a)), the required 7.7 MWh induces 232 kg CO_2 and in southern Italy (Figure 8(b)), 12 MWh correspond nearly to 1.3 ton of CO_2.

	kWh(th) per day	Nb days	rate of use (%)	kWh (thermal)	kg CO2/kWh (elec)	CO2 benefit (kg)
april	20	30	20%	120	0,09	4
may	40	31	50%	620	0,09	19
june	60	30	85%	1 530	0,09	46
july	75	31	100%	2 325	0,09	70
aug.	65	31	90%	1 814	0,09	54
sept.	50	30	70%	1 050	0,09	32
oct.	30	31	30%	279	0,09	8
TOTAL				7 738		232

(a)

	kWh(th) per day	Nb days	rate of use (%)	kWh (thermal)	kg CO2/kWh (elec)	CO2 benefit (kg)
april	30	30	30%	270	0,32	29
may	50	31	70%	1 085	0,32	116
june	80	30	100%	2 400	0,32	256
july	95	31	100%	2 945	0,32	314
aug.	80	31	100%	2 480	0,32	265
sept.	75	30	80%	1 800	0,32	192
oct.	50	31	60%	930	0,32	99
TOTAL				11 910		1 270

(b)

Figure 8 : : **Elements of estimate of the environmental and economic benefit (a): in southern France (French Riviera) ; (b): in southern Europe (southern Italy)**

A transposition is done considering a 1000 m^2 office building over a 15 years duration, and by considering 2 hypothesis:

i. PV COOLING COP = 3
ii. Expected average cost increase of electric energy evaluated as 3 % per annum.

Transposition to a 1000 m^2 office building shows the following:

- CO_2 saving of 25,8 tons in France and 141 tons in southern Italy
- Energy saving cost of 30 k€ in France and 121 k€ in southern Italy.

The disparity is due to the fact that in Italy, as in many Europeans countries (and unlike “nuke” France), grid power rests upon embodied energy and consequently carbon footprint is much higher than in France.
Similar remarks may be done and for the same reasons regarding cost considerations where PV COOLING may induce 121 k€ in Italy although the same PV COOLING may only induce 30 k€ in southern France.

7. CONCLUSIONS

To conclude, the developed and tested PV-COOLING concept allows bringing following conclusions:

- PV-COOLING demonstrates that it is possible to combine improved technologies which are photovoltaic (PV) power plant to drive vapour compression thermodynamic system for the sake of producing cooling energy ;
- Securing PV plant with external power supply to drive thermodynamic system was successfully demonstrated ;
- Part of efficiency results in possibility to real-time adapting cooling power to solar irradiation ;
- EER obtained values shows that only a limited amount of grid supply is necessary and consequently, external generator may efficiently be substituted to grid ;
- Proper management permits one to consider fully autonomous systems disconnected from grid.

Technically, existing system is planned to further investigate clever ways of using PV excessive power. This concerns mainly investigating cold storage (as shown on Figure 2), but also electric storage and compare which is better to improve autonomy of PV-COOLING.

Comparison of Italy vs France benefits of PV COOLING shows that energy cost and current grid power carbon footprint is a drastic parameter for environmental and economic efficiency. In this respect, France is far from holding the best position for developing a renewable energies policy.
The marketing plans carried out target PV COOLING as a development tool in sunny and/or tropical regions for both air-conditioning system and positive food storage. Eventually, PV-COOLING concept open wide perspective for insulated areas and may constitute a tool for land-use planning, and especially in the developing world.

AKNOWLEDGEMENTS

Authors greatly aknowledge French Ministère de l'Ecologie, du Développement durable et de l'Energie (now Ministère de la transition écologique et solidaire) and the Agence de l'Environnement et de la Maîtrise de l'Energie (ADEME) for financial support of the project.

REFERENCES

Tom, S., 2008, Managing Energy and Comfort, ASHRAE Journal, June.

Gustavsson, J., Cederberg, C., Sonesson, U., van Otterdijk, R., Meybeck, A., 2011. *Global food losses and food waste – Extent, causes and prevention*. Report of Food and Agriculture Organization of the United Nations (FAO).

Manuscript ID: 543
DOI: 10.18462/iir.icr.2019.0543

Ammonia - carbon adsorption heat pump development

Robert CRITOPH, Steven METCALF, Angeles RIVERO-PACHO

University of Warwick
Coventry, CV4 7AL, UK, R.E.Critoph@warwick.ac.uk

ABSTRACT

The overall objective of the research is to develop a domestic air source gas-fired heat pump to replace standard condensing boilers cost-effectively. The working pair is ammonia and active carbon. A succession of sorption generators have been prototyped, culminating in the 'kebab' design in which monolithic carbon is compressed between aluminum fins on a steel tube containing pressurized water that either heats or cools the adsorbent in a two-bed cycle with heat and mass recovery.
A 10 kW system was built and tested. Initial results were poor with Coefficient of Performance (COP) a little above 1. This was due to mass transfer resistance in adsorption being too high, due to an excessive binder fraction.
A new formulation has been tested in a single 'kebab' and the results are consistent with an internal COP of 1.40 when delivering 10 kW at 50°C and evaporating at 0°C or 1.34 when delivering 20 kW.
Keywords: Adsorption, Ammonia, Domestic Heat Pump, Performance

1. INTRODUCTION

The University of Warwick is currently developing a very compact carbon-ammonia adsorption cycle gas fired heat pump to be a box-for-box exchange with a conventional domestic gas boiler, with much reduced size and capital cost compared to alternative machines on the market (<4 times). Also for ease of retrofit, it is an air source machine. It must provide at least 10 kW of heat output, which is the requirement for an average semi-detached UK household. The working conditions of the machine are heating water to >50°C for low temperature radiators, and the evaporating temperatures vary with the ambient temperature but can range from 0 to 10°C. The target of internal COP achieved by the machine should be higher than 1.4 so that the gas utilization efficiency (GUE) is higher than 1.25. With this predicted delivered COP, the machine will reduce the household gas consumption by 30% compared to a conventional condensing boiler.
The refrigerant used is ammonia since it has the ability to operate below 0°C evaporating temperature which makes it suitable for air source operation. Also, the high working pressures of the ammonia in the system enables a compact machine and the achievable power density is almost entirely heat transfer, rather than mass transfer limited. Ammonia is paired with active carbon, as adsorbent, which has been chosen since it is stable at high driving temperatures. It does have lower and more gradual concentration change than adsorbents with S-shaped curves or salts, but does not suffer from a sudden 'switch off'.
Fig. 1 shows the schematics of the heat pump. On the left hand side there is the burner that provides heat to the heat transfer fluid (pressurized water). The heat transfer fluid, at a high and at a low temperature, is pumped through two sorption generators, one being cooled, adsorbing ammonia, and the other being heated, desorbing ammonia. The ammonia that has been desorbed from Bed 1 first passes through the condenser, releasing heat to the house heating system, then through the expansion valve, then through the evaporator, where it evaporates and absorbs heat from the ambient air, and finally it is adsorbed in Bed 2. After (typically) two or three minutes the beds are switched, Bed 2 being heated and Bed 1 being cooled. Additionally there is heat and mass recovery between the beds to improve the COP.
The sorption generator is effectively a thermally driven compressor and is the most critical part of the design. The challenge is to design and build a sorption generator that has excellent heat transfer, not just to reduce the size and cost of the machine but also to allow effective transfer of heat between the beds in a high COP regenerative cycle. However, it must also have low thermal mass since it is repeatedly cycled in temperature and the sensible heat used, whilst partly recoverable is not multiplied by the heat pump COP. In addition, the generator must be capable of reliable mass production at a

cost of at most a few tens of Euros. Without this challenge being met it is unlikely that a domestic adsorption heat pump to replace a gas boiler will ever be viable.

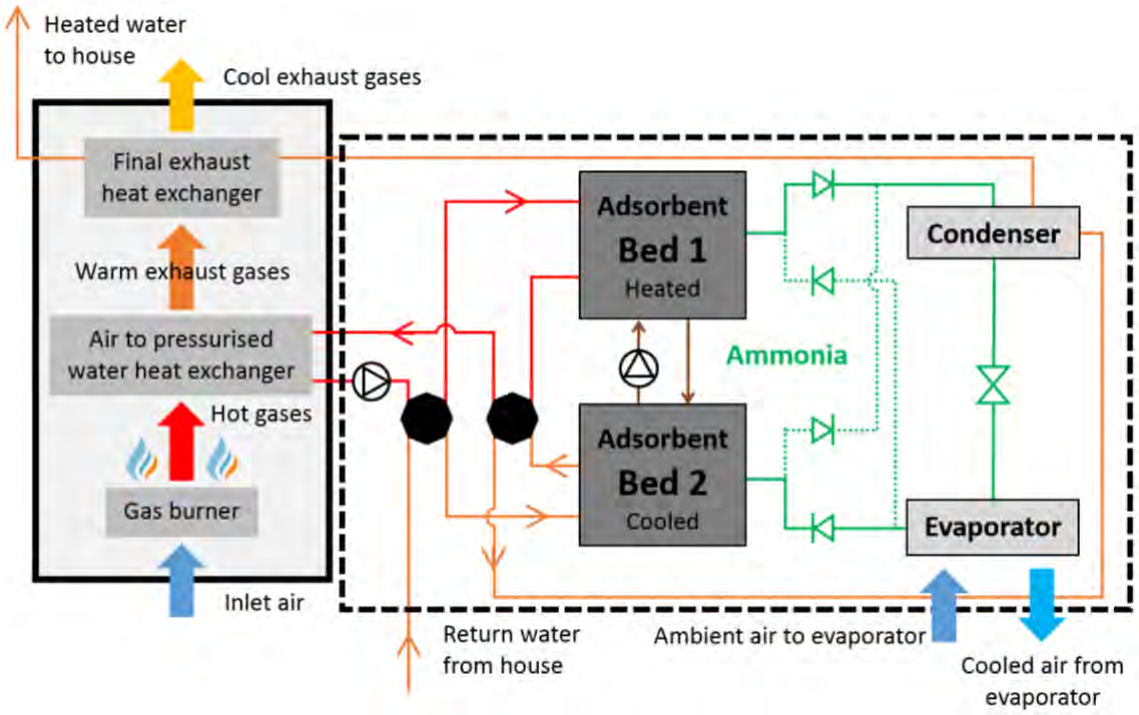

Figure 1: Warwick adsorption heat pump schematic

The geometry of the adsorption generators that contain the sorbent and that have previously been used at Warwick have over 1000 water tubes of 1.2 mm diameter on a 3 mm pitch, shown in Fig. 2. (Critoph and Metcalf, 2011).This geometry had been not optimised and a dynamic simulation program was written to determine how far from optimal the design is and also whether alternative designs or materials offer advantages (Rivero-Pacho et al., 2017). They investigated active carbon bound with silanes, activated carbon in an Expanded Natural Graphite matrix and activated carbon with an organic binder. The carbon - organic binder combination was found to be superior in all cases studied, having reasonable thermal conductivity together with low thermal mass. The preferred adsorbent was then modelled in both shell and tube and shell and finned tube arrangements.

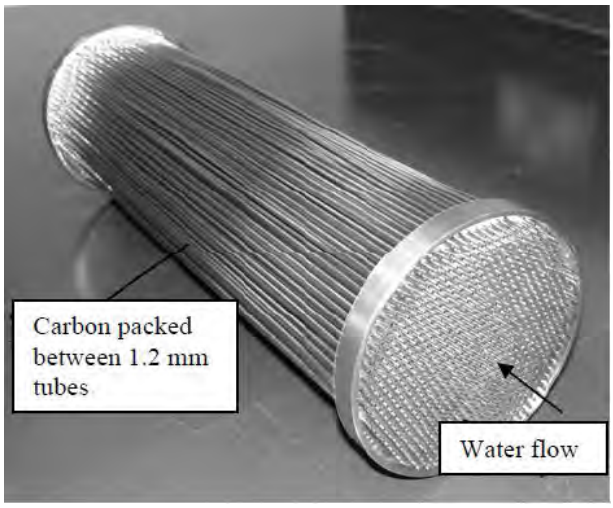

Figure 2: Shell and (micro) tube sorption generator

2. SIMULATION AND OPTIMISATION

2.1. Model with idealised condenser and evaporator

The shell and tube configuration of Fig. 2 was not far from optimal. Fig. 3 shows the cycle COP (heat output / heat input from gas flame) and SHP for a number of simulations. In this and all other simulations the cooling phase assumes an inlet water temperature of 50°C, heating water inlet at 170°C, evaporating at 5°C and condensing at 50°C in order to compare designs. Each of the points of similar colour show a combination of heating/cooling time and heat recovery time for a particular (triangular) tube pitch. The envelope of all points of the same colour represents the best combination of times, i.e. control strategy to use in operating the system and represents the best trade-off between COP and power.

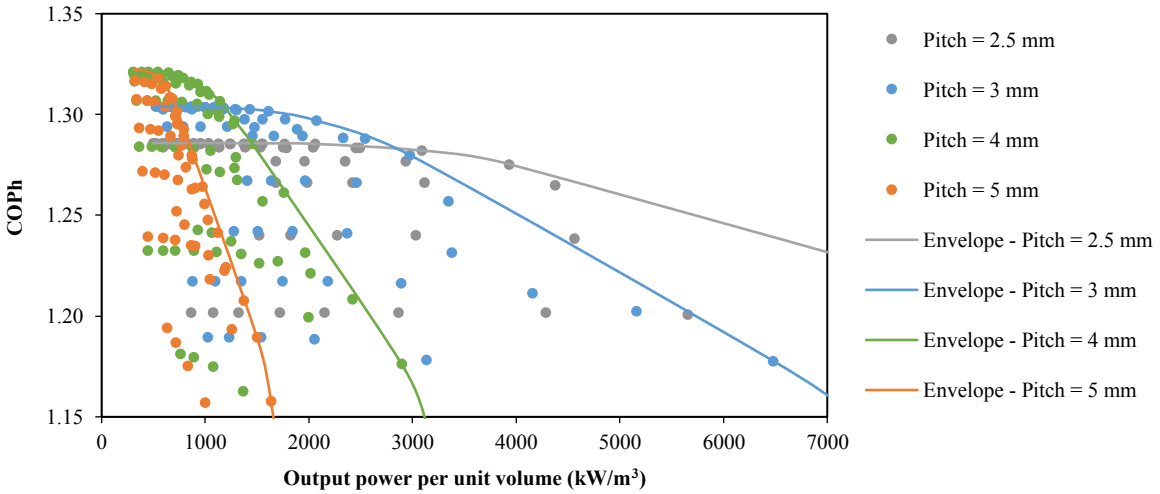

Figure 3: COP v. SCP for 208C carbon + organic binder with 1.2 mm OD tube and a range of pitches

The shell and tube configuration was tested but not further developed for a combination of reasons. Firstly the nickel brazed generator was too expensive to produce and secondly the effective material conductivity achieved was less than in the bulk material. A finned tubes in shell design is much lower cost and the adsorbent conductivity is equal to the bulk value.

The 'kebab' design uses aluminum fins on a stainless steel tube with carbon-binder mixture compressed between the fins, as shown in Figs. 4 and 5.



Figure 4: 'Kebab' schematic

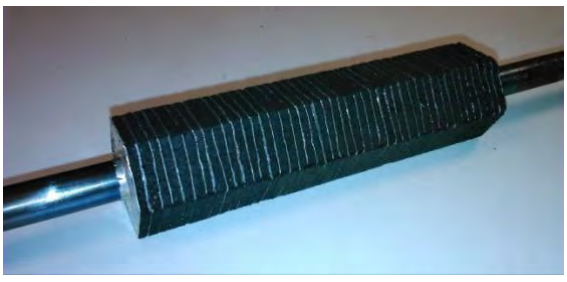

Figure 5: Sample 'kebab'

A two dimensional finite difference simulation model in MATLAB was written to explore how varying the geometry of the generator, dimensions and control parameters affect the Coefficient of Performance (COP) and power output under specified conditions and sorption materials. The adsorbent thermal properties used in the simulation were the ones previously tested and presented.

The unit cell is a cylindrical section as shown in Fig. 6. The lengthwise cell is split into nl axial sections and the carbon is split into nr equal radial sections. The pressurised water used to heat or cool the steel has only one radial element, but the water can be subdivided into multiple numbers of axial elements if the mass flow rate specified is so high that an element of water could flow past more than one axial element of steel in one time step.

In order to keep the simulation stable whilst the heat transfer in the metallic segments was modelled and whilst keeping the total computation time reasonable, a time step of roughly 0.05 times that of the carbon was used for all the metallic elements. The geometric variables that can be changed in this model are the inner and outer tube diameter and the tube pitch in addition to the fin thickness and the carbon thickness between fins.

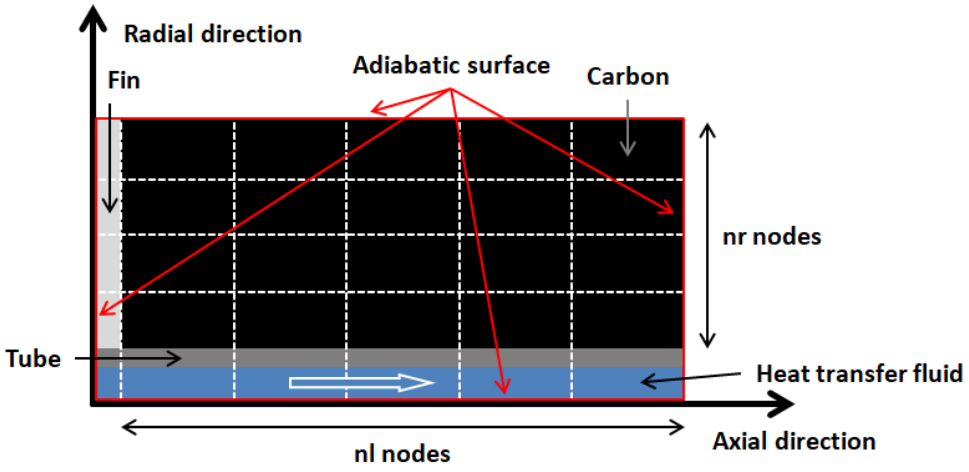

Figure 6: Finned tube unit cell

A typical compilation of simulated COP v SCP is shown in Fig. 7 which explores the effect of using different tube pitches for a particular tube diameter and fin pitch. Using the optimal pitch it is noticeable that the COP does not drop off rapidly with increasing power output, e.g. COP of 1.39 at 10 kW reducing to 1.35 at 20 kW.

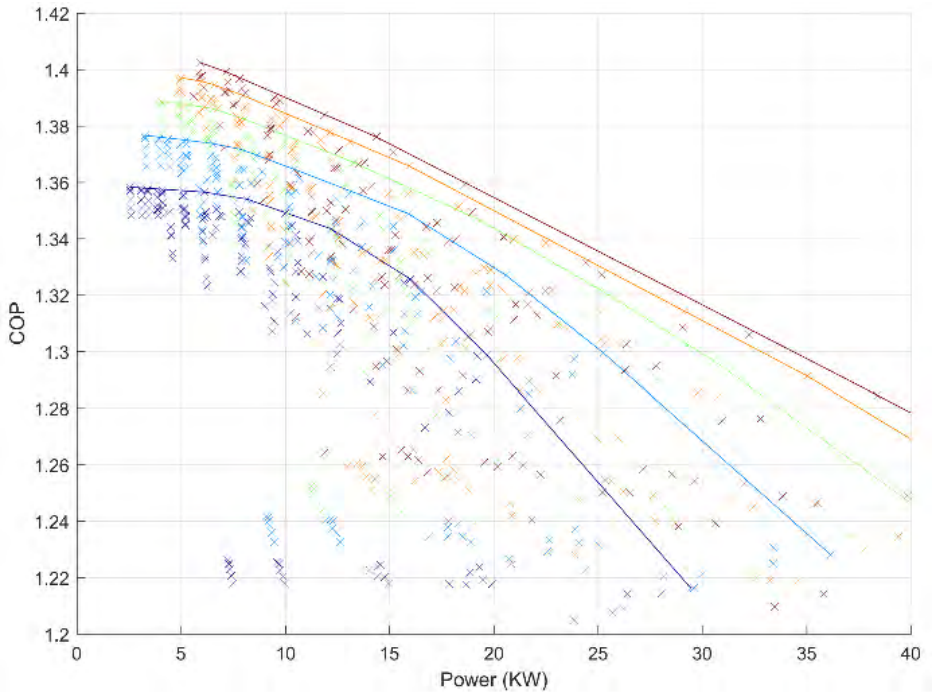

Figure 7: COP v. power for 208C carbon + organic binder 'kebab' with a range of pitches

2.1. Model with 'real' condenser and evaporator

This behavior is probably exaggerated. Work has recently begun to realise a fully functional prototype with a gas burner and this has required a more realistic model that takes into account the gas burner and heat exchanger and the heat transfer coefficients of the condenser and evaporator to load and environment rather than assuming fixed temperature boundary conditions. Fig. 8 plots GUE (Gas utilization efficiency) v. power for a condenser of 2.5 kW/K and evaporator 1.45 kW/K with ambient

temperature 10°C and water return temperature 50°C. The GUE is based on the higher calorific value. The gas to pressurized water heat exchanger is modelled as a series of sections with varying heat transfer coefficients. The overall efficiency of gas higher heating value to the pressurized water varies but is normally close to 80%. There is an additional assumption that the exhaust leaving that heat exchanger will provide a further 10% of higher heating value to the load via the final exhaust heat exchanger as shown in Fig. 1.

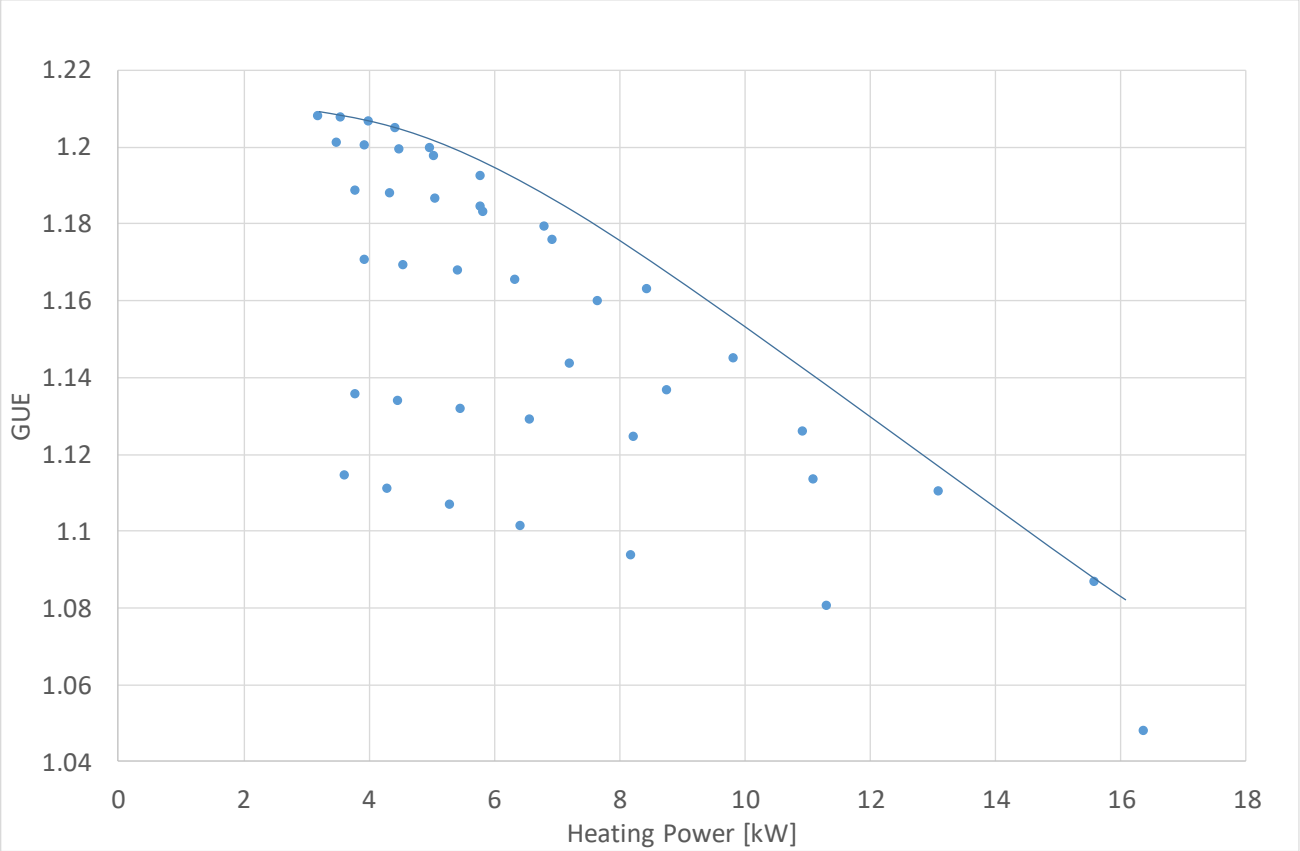

Figure 8: GUE v. SCP for final design of 208C carbon + organic binder 'kebab'

It is clear that the sensitivity of GUE to power output has increased but there is still the prospect of achieving an average GUE of > 1.2 in UK climatic conditions. Whether this is commercially acceptable will depend crucially on the production cost. Previous 4-bed configurations with enhanced internal heat recovery [Critoph and Metcalf, 2011] show a GUE of 1.4 to be possible but at the expense of greater complexity and cost. Our aim is to explore simpler, low cost options if at all possible.

An initial set of 'kebab' generators were built and tested in 2018. The results were very poor, desorption being rapid and in line with predictions but adsorption being very slow. This was found to be due to an excess of binder leading to high mass transfer resistance. A new method of production was found enabling a much lower mass fraction of binder and acceptable mass transfer resistance.

At the time of writing a full set of generators is being manufactured and will be tested in the laboratory in the test facility shown in Fig. 9 in which the pressurised water is electrically heated rather than by combustion of gas. This was previously used successfully for evaluating shell and tube generators.

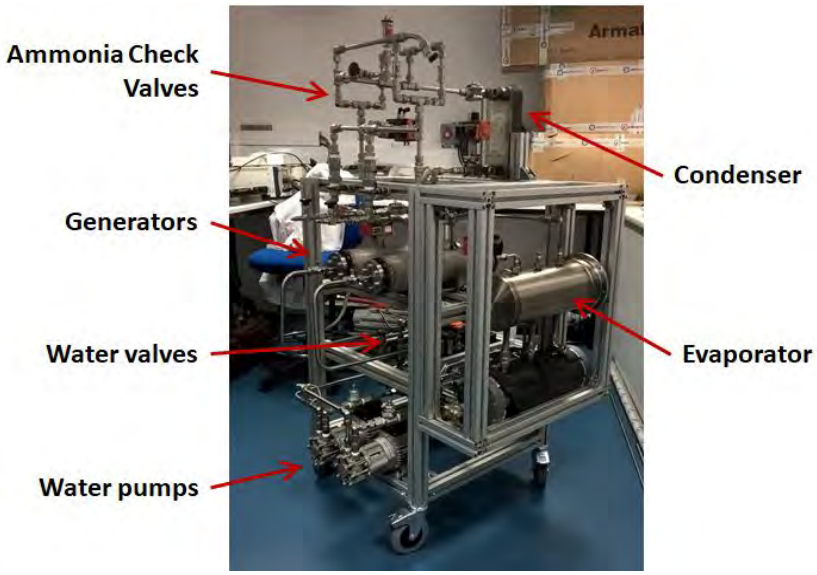

Figure 9: Laboratory heat pump test rig

A single 'kebab' with the new formulation has been made and tested in a Large Temperature Jump (LTJ) test apparatus. A sample 'kebab' is located in the main vessel of the LTJ. This main vessel is connected to a reservoir vessel containing ammonia gas and pressure and temperatures in different parts of the system are recorded throughout the experiment. Once the heat transfer fluid that flows through the tubes of the heat exchanger suddenly increases its temperature, the ammonia adsorbed in the carbon composite desorbs increasing the pressure of the system. This increase in pressure is recorded and matched to a simulation program in MATLAB that predicts the thermal properties of the sample.

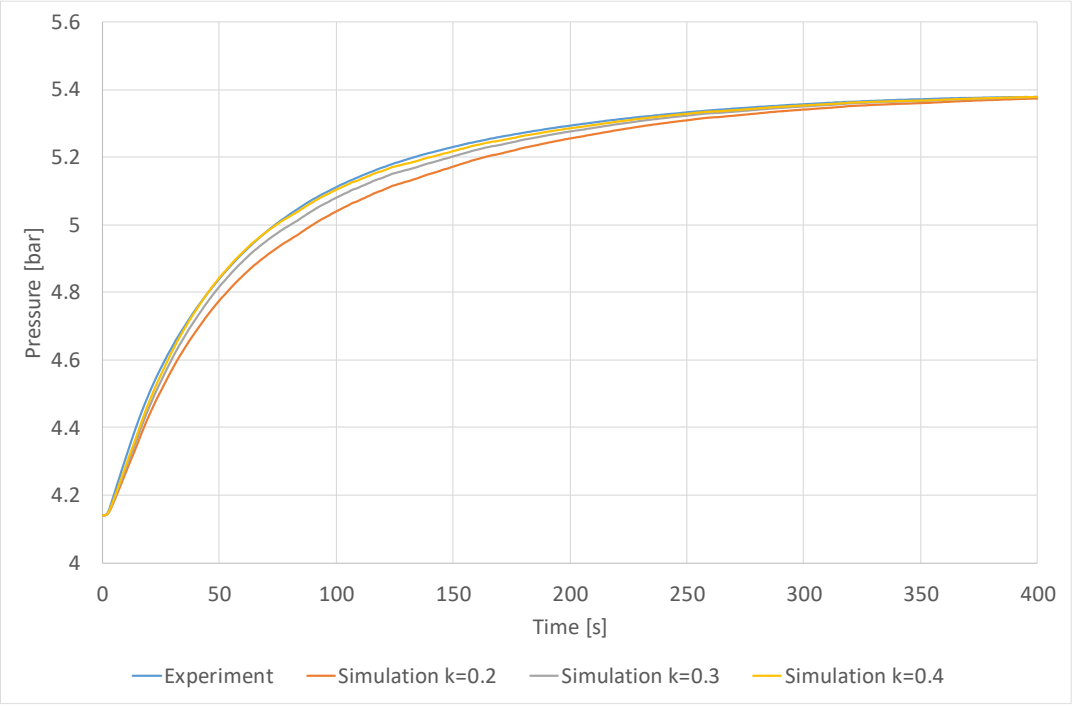

Figure 10: Comparison between large temperature jump experiment and computational model.

Fig. 10 shows the comparison and the match between the large temperature jump experiment and the model in desorption. Adsorption results are very similar. 'k' in the plot is the assumed effective thermal conductivity of the bound carbon in $Wm^{-1}K^{-1}$. There is clearly a good match between the two. The simulations reported above used a conductivity of 0.3 $Wm^{-1}K^{-1}$ (based on previous fabrication methods

and the sample results suggest a conductivity of at least 0.4 $Wm^{-1}K^{-1}$, giving some confidence that the desired performance can be achieved.

3. CONCLUSIONS

The challenge in developing a cost effective adsorption heat pump is to design a sorption generator that has low thermal mass combined with good heat transfer and mass transfer. Three different types of binder have been evaluated for use with active carbon adsorbent and an organic binder selected. Micro tube and shell designs have been fabricated and tested but are too costly to manufacture and the effective conductivity was below that of the bulk composite. A finned-tubes in shell configuration offers low cost manufacture combined with adequate heat transfer and thermal mass. Simulation has been used to identify a good combination of tube diameter and pitch plus fin thickness and pitch. A single finned tube has been fabricated and tested in a Large Temperature Jump apparatus. Analysis of the results shows an effective adsorbent thermal conductivity of at least 0.4 $Wm^{-1}K^{-1}$ which is sufficient to achieve the required performance in the full system currently being built.

ACKNOWLEDGEMENTS

The work presented here has been supported by RCUK grant EP/K011847/1, Interdisciplinary Centre for Storage, Transformation and Upgrading of Thermal Energy (i-STUTE) and Department for Business, Energy and Industrial Strategy, BEIS Low Carbon Heating Technology Innovation Fund grant 'Adsorption gas heat pump'.

NOMENCLATURE

COP Coefficient of Performance = Heat output / heat input (-)
GUE Gas utilization efficiency = Heat output / higher heating value of gas input (-)
k Thermal conductivity ($Wm^{-1}K^{-1}$)
SCP Specific Cooling Power (kWm^{-3})

REFERENCES

Critoph, R. E., Metcalf S., 2011, Development of a Domestic Adsorption Gas-fired Heat Pump, Proc. Inst. R. (2011-12) 1.1 – 1.7.

Rivero-Pacho, A.M., Critoph, R.E., Metcalf, S., 2017, Alternative monolithic/composite carbons for adsorption generators and simulation for optimal performance, Applied Thermal Engineering, 126, 350-357.

Manuscript ID: 547
DOI: 10.18462/iir.icr.2019.0547

Efficiency evaluation of borehole heat exchangers in Nunavik, Québec, Canada

Nicolò GIORDANO[(a)], Luca RIGGI[(b)], Simone DELLA VALENTINA[(b)], Alessandro CASASSO[(b)], Giuseppe MANDRONE[(c)], Jasmin RAYMOND[(a)]

[(a)] Institut national de la recherche scientifique – Centre Eau Terre Environnement, Québec, G1K 9A9, Canada, nicolo.giordano@ete.inrs.ca
[(b)] Politecnico di Torino – Dipartimento di Ingegneria dell'Ambiente, del Territorio e delle Infrastrutture, Torino, 10129, Italy
[(c)] Università degli Studi di Torino, Dipartimento di Scienze della Terra, Torino, 10125, Italy

ABSTRACT

Remote northern communities of Nunavik rely on fossil fuels for space heating and domestic hot water production. The capital Kuujjuaq is characterized by 8500 heating degree days and discontinuous permafrost. Numerical simulations taking into account latent heat effects due to water-ice phase changes demonstrated that the 10-year performance of small-diameter borehole heat exchangers is as valuable as conventional diameters. Moreover, owing to the cold underground, deeper boreholes perform significantly better than shallow ones. A heat extraction rate of 35 W m^{-1} can be sustainably maintained by a 300-m borehole. The financial analysis showed that ground-source heat pumps are a viable alternative to fossil fuels. Absorption heat pump is the most interesting technology, but only district-scale applications could justify high drilling and installation costs of vertical ground heat exchangers. Payback time of 15 years was found at the current costs, but less than 10 years can be achieved at 150 CAD m^{-1} drilling cost.
Keywords: Ground-source Heat Pumps, Permafrost, Freeze-thaw Cycles, Feflow, Nunavik.

1. INTRODUCTION

Nunavik is the Québec territory north of the 55th parallel that hosts 14 Inuit and 1 Cree villages, with a total population of around 12 300 people (SHQ, 2014). All of these off-grid communities currently rely on fossil fuels to provide both electricity and heat. Hydro-Québec, the provincial electricity provider, produces electricity with community diesel power plants at costs ranging from 0.6 to 1.5 CAD kWh^{-1} (Canadian dollars; Hydro-Québec, 2011). Space heating (SH) and domestic hot water (DHW) are autonomously provided by each building with oil furnaces, with the cost of heating oil amounting to 2.03 CAD l^{-1} in 2018 (Makivik, 2018). Subsidies from the Government of Québec allow the beneficiaries to pay 0.058 CAD kWh^{-1} up to an electricity consumption of 900 kWh $month^{-1}$ and then 0.38 CAD kWh^{-1}, as well as 1.63 CAD L^{-1} for the heating oil (Karanasios and Parker, 2016). To this regard, the study of possible alternatives is of utmost importance to reduce the costs and environmental impacts of energy production in these communities (e.g. Yan et al., 2019). Among the suitable renewable technologies, ground source heat pumps (GSHP) are under study to evaluate the potential contribution of shallow geothermal energy to provide SH and DHW.
GSHP have already been studied and tested in cold climates (e.g. Wu et al., 2013; You et al. 2016; Garber Slaght et al., 2017) and few works on shallow geothermal technologies have also been conducted in Nunavik (e.g. Fontaine et al., 2011; Belzile et al., 2017; Giordano et al., 2018). Strongly heating dominated buildings and permafrost conditions are the main issues to face in arctic to subarctic environments. The unbalanced heat extraction from the ground surrounding the vertical (or horizontal) heat exchangers can reduce the GSHP performance in the long term. On the other hand, a temperature decreasing trend is desirable in permafrost maintenance applications, with the heat being regarded to as a by-product only (e.g. McFadden 2007; Instanes and Instanes 2008). However, in both cases, frequent freezing-thaw cycles must be avoided to safeguard building foundations and grout integrity of borehole heat exchangers (BHE; e.g. Kirschbaum et al., 2018).
Besides the technical issues, drilling activity is the most expensive element of GSHP systems and in Nunavik this is a critical factor that can negatively affect the development of the technology. In the last 10-15 years, drilling firms have developed in Nunavik to provide services to mining exploration

companies. A local company can drill 3-inch (NQ diamond drilling standard) and 4-inch (HQ diamond drilling standard) boreholes up to 300-400 m with a cost of around 300 CAD m^{-1}, but usually the rigs are outside Kuujjuaq to work in prospection areas and the helicopter transportation in town can double the price. Alternatively, a firm in Iqaluit (Nunavut) can drill conventional 6-inch boreholes (CO), but with transportation and manpower travel expenses they cannot work it out for less than 400 CAD m^{-1}.
In the light of this situation, the objective of the present contribution is twofold. First, numerical simulation of BHEs with different diameters and lengths were carried out to evaluate the long-term technical performance of NQ vs. CO borehole diameter. Second, a financial analysis was conducted in order to assess the economic feasibility of three different GSHP systems, by taking into account that Hydro-Québec currently forbids the use of electricity to provide SH and DHW; the payback times (PBT) of these scenarios have been compared as a function of the drilling cost in order to define a threshold of financial sustainability.

2. METHODOLOGY

2.1. Geological, Climate and Energy Setting

Kuujjuaq (58.10°N, -68.42°E) is the administrative capital of Nunavik and it is home to around 2375 people (SHQ, 2014). Mainly marine and glacial deposits constitute the quaternary cover of a Precambrian bedrock whose main lithologies are diorites and paragneisses (Giordano et al., 2018 and references therein). Kuujjuaq presents a subarctic climate with average annual air temperature of -5.8 °C and 8500 heating degree days (1981-2010 Climate Normals, Government of Canada, 2018). Winter shallow ground temperature clearly shows the insulating effect of snow cover (Fig. 1). The presence of discontinuous but widespread permafrost is reported in the region and it strongly depends on the local geological conditions (Lemieux et al., 2016). A reference building simulated by Kanzari et al. (2018) displayed a total heating load of 33.6 MWh, SH and DHW included.

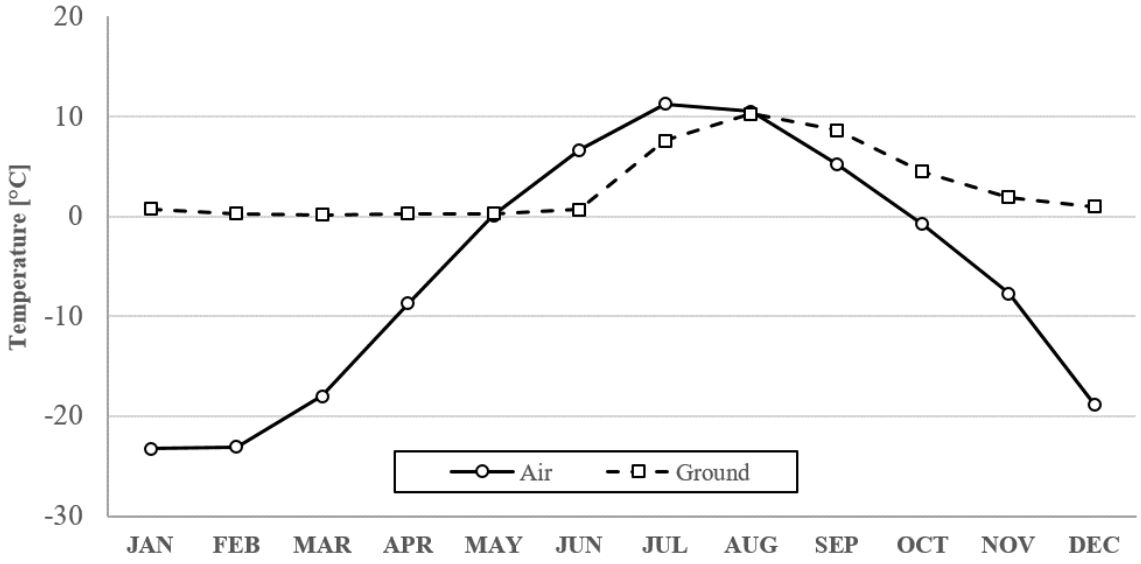

Figure 1: Monthly air and ground (0.25 m below ground level (b.g.l.)) temperature

2.2. Numerical Simulations

The commercial code FEFLOW (Diersch, 2014) was used to simulate the long-term behaviour of borehole heat exchangers. An open-source plug-in developed by Anbergen et al. (2015) was included in the calculations in order to take into account the phase change of water at 0 °C, with transition zone between 0 °C and 1 °C, and monitoring the freeze-thaw cycles occurring in the underground. A 3D model 190 × 190 × 350 m was built and spatially discretized with a mesh of 65 750 triangular prismatic elements, refined nearby the BHE and progressively coarser towards the model boundaries. The refinement around the BHE consisted in 6 nodes according to the methodology described by Diersch et al. (2011) in order to have an optimal nodal distance of 0.45 m

and thus ensure numerical stability and accuracy. Two different nominal borehole diameters were considered here: NQ (2.97 inches, 75.4 mm) with a pipe outer diameter of 26.67 mm and CO (6 inches, 152.4 mm) with a pipe outer diameter of 33.40 mm. CO borehole is equipped with a double-U heat exchanger, while NQ can only host a single-U pipe owing to the limited space. For both of them, 100-m and 300-m lengths were tested by applying 9-month constant heating loads of 1 kW, 3.5 kW (100 m), and 7 kW, 10 kW (300 m). A total of 8 simulations were run for 10 years; the automatic time-step control scheme was adopted to allow the solver to choose the appropriated length depending on the change of the primary variables. Geological stratigraphy consists of 25 m of saturated marine deposits (λ 1.5 W m^{-1} K^{-1}, Cv 3.0 MJ m^{-3} K^{-1}, Φ 0.35; Giordano et al., 2017) overlying highly conductive diorites (λ 3.0 W m^{-1} K^{-1}, Cv 2.4 MJ m^{-3} K^{-1}, Φ 0.05; Miranda et al., 2018). A temperature profile measured in a well in Kuujjuaq was set as temperature initial condition (IC) to the whole model; the IC is free of frozen ground (Della Valentina et al., 2018). One-year temperature recordings at 0.25 m below the ground level (b.g.l.; Fig. 1) were assigned as time-series Dirichlet boundary condition (BC) at the top of the model and geothermal heat flux of 0.045 W m^{-2}, estimated by Miranda et al. (2018), was given as Neumann BC at the bottom. Since no specific information is available, no groundwater flow was considered in these simulations, but the whole column is saturated by water since groundwater table in town is commonly less than one meter b.g.l.

2.3. Financial Analysis

Three different heating scenarios were considered to offer a GSHP alternative to the business-as-usual (BAU) diesel furnaces above described:

1. An absorption heat pump (absHP) with energy to run the thermal compressor provided by a diesel furnace (efficiency η 0.78) similar to the ones already existing in each building in Kuujjuaq. The GAHP-WS from Robur S.p.A. (cost 15 000 CAD) was chosen for this study and a COP of 1.25 was adopted based on the minimum expected entering water temperature;
2. A compression heat pump (compHP_DgHR) with energy provided by a diesel generator (η 0.35; cost 20 000 CAD) with 50 % heat recovery. The ACTEA SI from Rossato Group srl (cost 15 000 CAD) with a COP of 3.5 was chosen;
3. A compression heat pump (compHP_Dpp) with energy provided by the community diesel power plant (η 0.35). Even if currently forbidden, this scenario was studied to evaluate the possible gain of using high-efficiency heat pump in place of diesel furnaces.

The underground part of the system was calculated with BHEs of 100 m with NQ diameter to cover the 70 % of the total SH and DHW demand. According to the GPOT method (Casasso and Sethi, 2016), such a BHE can provide on average 110 kWh m^{-1}y^{-1} of thermal energy in Kuujjuaq, considering a minimum BHE temperature of -10 °C. According to the ASHRAE sizing method (Philippe et al., 2010; ASHRAE, 2015), total drilling lengths of approximately 50 m, 100 m and 150 m would be necessary for scenarios absHP, compHP_DgHR and compHP_Dpp, respectively; peak hourly ground loads amount to 1 kW, 2.3 kW and 3.5 kW, respectively.

A 10-dwelling case (demand calculated as single-dwelling's heating load x 10) was also considered in order to share the investment costs on heat pumps and diesel generators, and to decrease the PBT. According to the G.POT method, a BHE with the same configuration as before but 300-m long can provide on average 130 kWh m^{-1}y^{-1}. For absHP, compHP_DgHR and compHP_Dpp the ASHRAE sizing method outputs drilling lengths of 400 m, 1000 m and 1400 m, and peak hourly loads of 9.9 kW, 24 kW and 35.4 kW, respectively.

3. RESULTS AND DISCUSSION

3.1. Numerical Simulations

The results show that the minimum BHE average fluid temperature reaches an equilibrium before the 10-year term for both the heating loads applied to the 300-m-BHE and for the 1kW case for the 100-m-BHE (Fig. 2). Conversely, the 100m_3.5 kW case still presents a decreasing trend at the end of the simulation time. The two end members belong to the 100-m BHE, being clearly under-designed when only 10 W m^{-1} of heat extraction rate is applied, but over-designed for 35 W m^{-1}, with the average BHE temperature lower than -10 °C for the most part of the season already at year 3. The BHE fluid temperature decreases more with NQ diameter rather than CO over the long term as expected (Fig. 3), due to its higher borehole thermal resistance (0.1 m K W^{-1} vs 0.06 m K W^{-1}

according to Claesson and Hellström, 2011). However, the difference is small in both cases (0.2 °C at 3.5 kW and 0.7 °C at 10 kW). Owing to the cold shallow underground, geothermal gradient and heat flow become more influent with respect to warmer climates. Longer boreholes are therefore more suitable in the Kuujjuaq conditions, and 35 W m^{-1} seems to be the maximum threshold for sustainable heat extraction. It can also be said that single-U NQ boreholes can provide the same amount of energy of conventional diameters with a not-significant impact on both the long-term sustainability of the underground resource and performance of the GSHP system.

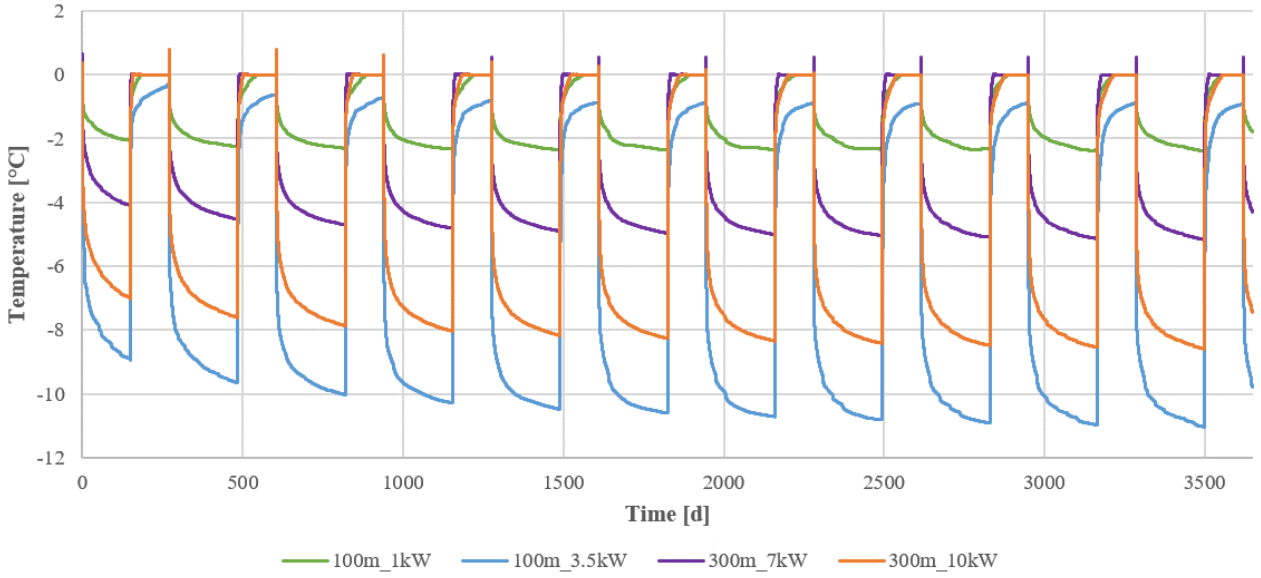

Figure 2: NQ BHE average fluid temperature over the 10-year simulation

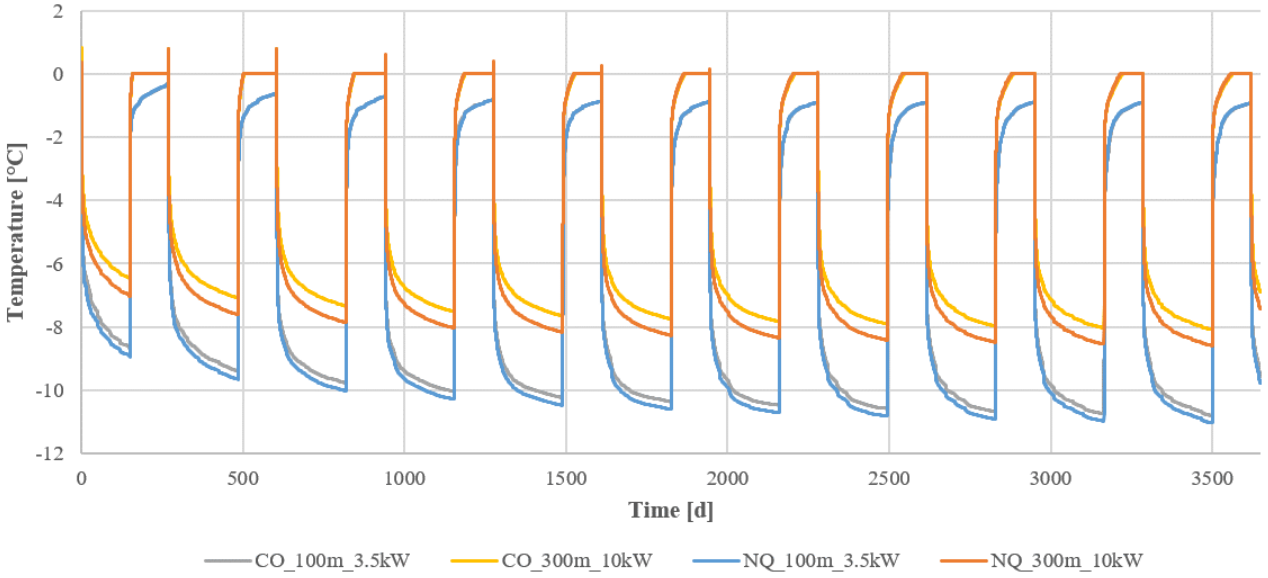

Figure 3: Comparison of NQ and CO BHE average fluid temperature over the 10-year simulation

The underground temperature evolution at 5-m depth clearly shows the influence of the phase change water-ice occurring in the surrounding of the BHE (Fig. 4). During the heat extraction, the ground freezes and latent heat is released generating a temperature increase in the nearby volume. This phenomenon is visible in all the heating load scenarios with spikes along the decreasing temperature curves. Cases with 1 kW (100 m) and 7 kW (300 m) heat extraction show a general increasing trend of the maximum temperature meaning that the BHE heat extraction is under-designed. Spikes also occur with 7 kW heat extraction along the ascending temperature curve as a result of the absorption of the latent heat of fusion. The ground volume in a radius of 2 m from the BHE reaches a permanent frozen condition after year 4 for the 3.5 kW scenario (100 m). However, at radius > 2 m freeze-thaw cycles are likely to happen. Conversely, the 300-m BHE with 10 kW heat

extraction shows that water phase changes are only concentrated close to the BHE and it reaches an equilibrium between heat extraction and recharge from the top of the model. The results prove that freeze-thaw cycles occur in both the low (10-20 W m^{-1}) and high heat extraction rates (30-35 W m^{-1}) simulated here. However, with a deeper borehole the phenomenon is localized within a 2-m radius from the BHE and 35 W m^{-1} can be sustainably extracted without negatively affecting the buildings' pressure bulb (ground volume influenced by the weight of the building).

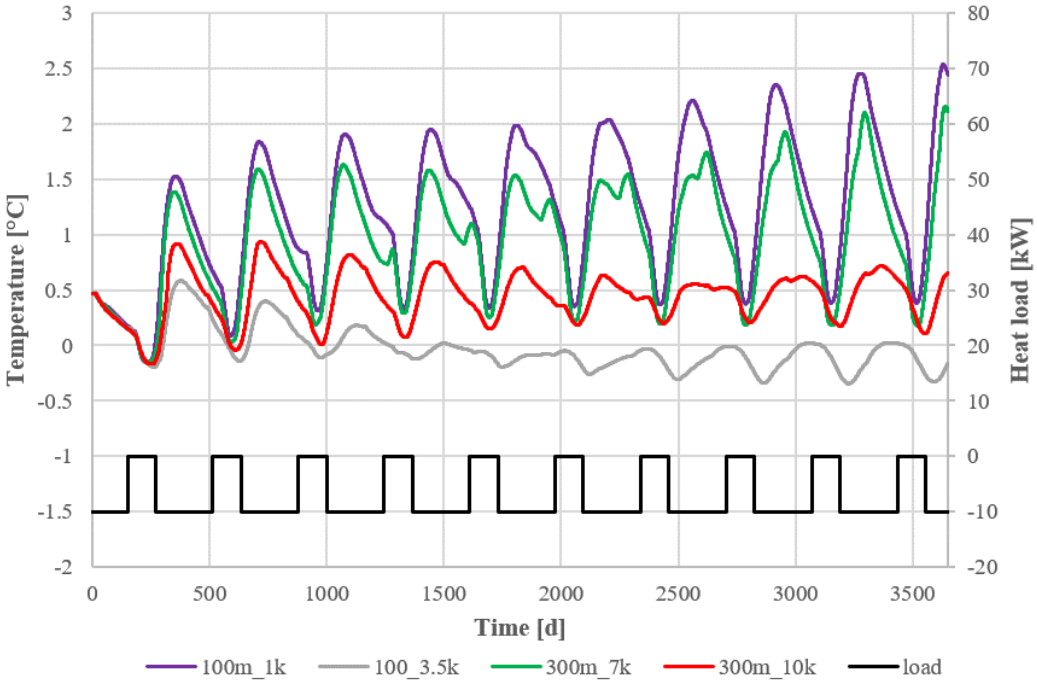

Figure 4: Comparison of temperature at 2-m distance from the BHE and 5-m depth for the four different NQ diameter scenarios. An example of heat load is also shown

3.2. Financial Analysis

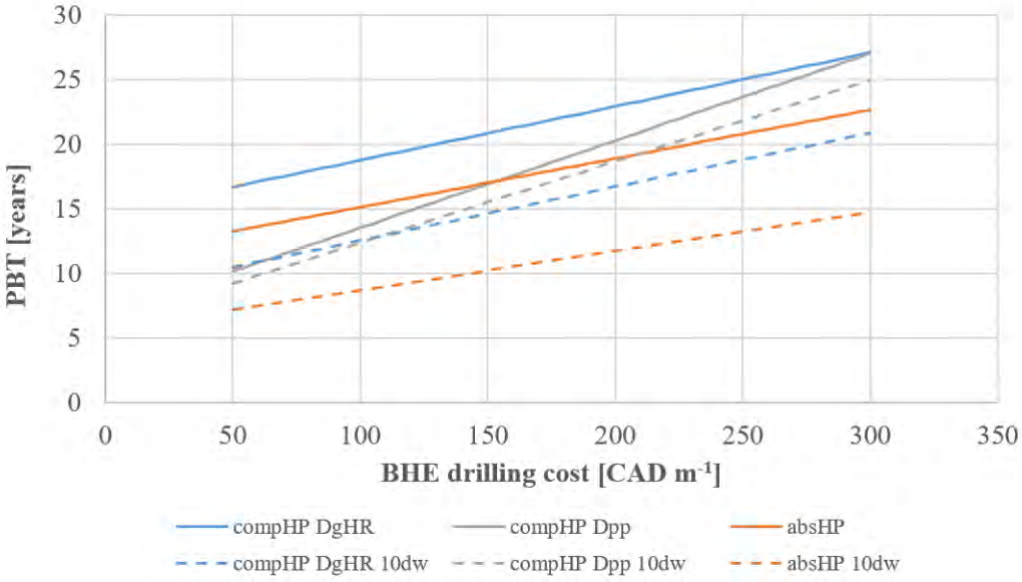

Figure 5: Payback time vs. drilling costs

The PBT for the single-dwelling case range from 10 to 17 years with optimistic drilling costs (50 CAD m^{-1}), but achieve 23-27 years at 300 CAD m^{-1} (Fig. 5). The 10-dwelling case would allow to reduce PBT to 7-10 years and 15-25 years, respectively, thanks to the significant advantage of sharing the cost of heat pumps and diesel generators among several home-owners. In both cases, compression heat pump shows to be the most expensive technology due to higher COP, which

requires more drilling length compared to an absorption heat pump. The choice of installing a diesel generator to locally produce electricity would be profitable only if the GSHP installation was done at the scale of a district or small residential area. Indeed, this scenario is more desirable than using the electricity from the power plant already at drilling costs of 100 CAD m^{-1}. Generally, the absorption technology can guarantee the best investment opportunity in both the single and 10-dwelling cases, with the latter showing interesting PBT even at the maximum drilling cost considered in this study.
The government's perspective was calculated through the annual subsidies that have to be corresponded and the greenhouse gas (GHG) emission savings provided by each scenario compared to BAU (Tab. 1). No subsidies were considered for the purchase of heat pumps or diesel generators: for simplicity, only the current subsidies on diesel and electricity consumption were used. The compression GSHP system fed by the power plant would require the highest subsidies, as expected, but it would guarantee the highest amount of CO_2 savings. The absoprtion system would generate benefits for both the home-owners and the government, with 26 % less annual operating costs and subsidies, but the smallest CO_2 reduction. 48 % financial savings and 3.9 tons of CO_2 reduction would be generated by installing a diesel generator to feed the compression GSHP system.

Table 1. Financial analysis of GSHP operation

Scenario	GSHP		Furnace	Home-owner		Annual government's subsidies (kCAD)	GHG saving (t CO_2)
	Electricity (kWh)	Diesel (L)	Diesel (L)	Investment (kCAD)	Annual operating costs (kCAD)		
BAU	-	-	3081	-	5.02	1.23	-
compHP_DgHR	-	687	924	35.00	2.63	0.64	3.9
compHP_Dpp	22 400	-	924	15.00	2.81	17.96	5.7
absHP	-	1346	924	15.00	3.70	0.91	2.1
BAU_10dw	-	-	30 813	-	5.02	1.23	-
compHP_DgHR_10dw	-	687	9244	20.09	2.63	0.64	38.8
compHP_Dpp_10dw	22 400	-	9244	13.42	2.81	17.96	56.9
absHP_10dw	-	1346	9244	7.50	3.70	0.91	21.4

4. CONCLUSIONS

This contribution presented the 10-year performance evaluation of borehole heat exchangers in the subarctic climate of Kuujjuaq, Nunavik. In parallel, a financial analysis was carried out to evaluate GSHP as alternative solution to the diesel furnaces currently used in all the autochthonous communities for providing SH and DHW.
The numerical simulations showed that 3-inch diameter borehole equipped with a single U-pipe heat exchanger can extract a similar amount of energy than 6-inch conventional boreholes, without significant impact on both the underground temperature and the GSHP performance. Moreover, owing to the cold underground in Kuujjuaq, deeper BHE are preferable in order to restrict the occurrence of freeze-thaw cycles within 2 m surrounding the BHE. Therefore, no negative influence on the buildings' pressure bulb is foreseen if safety distance is kept (e.g. 5 m). BHE grout's integrity to prevent infiltration of surface water along the borehole can however be expected and needs to be further investigated. A heat extraction rate of 35 W m^{-1} for a 300-m borehole was finally shown as the maximum threshold for a sustainable heat extraction in these subarctic conditions.
The financial analysis revealed that ground-source absorption heat pumps installed for a single dwelling can be a valid alternative for both home-owners and government's perspective at optimistic drilling costs only (50 CAD m^{-1}). Subsidies could help purchase the system or support the drilling activity in order to reduce PBT. If district-scale systems were built, both compression and absorption GSHP would guarantee PBT lower than 15 years at drilling costs of 150 CAD m^{-1}. The absorption technology, provided that it can operate on diesel, provides the most interesting opportunity from the

economical point of view. As expected, the compression heat pump generates the best GHG savings and the lowest subsidies with on-site diesel generators, but it is financially unprofitable for home-owners at the current drilling costs.
In conclusion, GSHP systems can be a viable alternative to fossil fuels in Kuujjuaq, but a decrease of the drilling cost is crucial to aim at a widespread utilization of the technology. Future activities will encompass the study of BHEs' interaction, the influence of the groundwater flow and the performance evaluation with colder underground temperature in the northernmost communities of Nunavik.

ACKNOWLEDGEMENTS

The authors would like to thank the Institut Nordique du Québec (INQ) that supported the research described in the manuscript through the "Chaire de recherche sur le potentiel géothermique du Nord". The Ministère des Relations internationales et de la Francophonie of Québec and the Italian Ministero degli Affari Esteri e della Cooperazione Internazionale are also thanked for supporting the mobility of Luca Riggi in the framework of the cooperation project n. QU17MO07 involving INRS, UNITO and POLITO. The "Fonds de recherche québécois - nature et technologies", through the sustainable mining development program, has additionally contributed to this research. The Centre d'études nordiques, the Nunavik Mineral Exploration Funds, the Makivik Corporation and the Kativik Regional Governments are acknowledged for helping with field logistics.

NOMENCLATURE

Cv	heat capacity (MJ m^{-3} K^{-1})	Φ	Porosity (-)
λ	thermal conductivity (W m^{-1} K^{-1})	T	temperature (°C)
η	efficiency (-)		

REFERENCES

Anbergen, H., Rühaak, R., Frank, J., Sass, I., 2015. Numerical simulation of a freeze-thaw-testing procedure for borehole heat exchanger grouts. Canadian Geotechnical Journal, 52(8), 1087-1100.

ASHRAE, 2015. Geothermal Energy, in: ASHRAE (Ed.), ASHRAE Handbook - HVAC Applications. American Society of Heating, Refrigerating and Air-Conditioning Engineers, Atlanta, 34.

Casasso, A., Sethi, R., 2016. G. POT: A quantitative method for the assessment and mapping of the shallow geothermal potential. Energy, 106: 765-773.

Claesson, J., Hellström, G., 2011. Multipole method to calculate borehole thermal resistances in a borehole heat exchanger. HVAC & R Research 17: 895 – 911

Della Valentina, S., Chicco, J., Giordano, N., Casasso A., Sethi, R., Mandrone, G., Raymond, J., 2018. Mapping the geothermal potential of a borehole heat exchanger in Kuujjuaq, Québec, Canada. Proceedings Resources for Future Generations, June 16-21, Vancouver, Canada.

Diersch, H.J.G., Bauer, D., Heidemann, W., Rühaak, W., Schätzl, P., 2011. Finite element modeling of borehole heat exchanger systems Part 2. Numerical simulation. Computers & Geosciences, 37(8): 1136-1147.

Diersch, H.J.G., 2014. FEFLOW: Finite element modeling of flow, mass and heat transport in porous and fractured media. Berlin, Germany, Springer.

Fontaine, P-O., Marcotte, D., Pasquier, P., Thibodeau, D., 2011. Modeling of horizontal geoexchange systems for building heating and permafrost stabilization. Geothermics, 40(3): 211-220.

Garber-Slaght, R., Craven, C., Peterson, R., Daanen, R.P., 2016. Ground source heat pump demonstration in Fairbanks, Alaska. Cold Climate Housing Research Center, Fairbanks, United States, 39 p.

Giordano, N., Kanzari, I., Miranda, M.M., Dezayes, C., Raymond, J., 2017. Shallow geothermal resource assessments for the northern community of Kuujjuaq, Québec, Canada. IGCP636 Annual Meeting, Santiago de Chile, Chile, 3 pp.

Giordano, N., Kanzari, I., Miranda, M.M., Raymond, J., Dezayes, C., 2018. Thermal energy storage in subarctic climates: a feasibility study conducted in Kuujjuaq (QC, Canada). Research Conference Proceedings, IGSHPA Research Conference, September 18-19, Stockholm, Sweden, pp. 150-159, doi: 10.22488/okstate.18.000024.

Hydro-Québec, 2011. Réseaux autonomes, portrait d'ensemble et perspectives d'avenir. Demande R-3776, HQD-13, 35 pp.

Instanes, B., Instanes, A., 2008. Foundation design using a heat pump cooling system. Ninth International Conference on Permafrost. U.S. Permafrost Association. Fairbanks, AK.

Kanzari, I., Giordano, N., Miranda, M.M, Raymond, J., Dezayes, C., 2018. Conception préliminaire et évaluation du potentiel d'installations géothermiques superficielles au Nunavik. Proceedings 2e Journée de la recherche nordique, January 24, Montréal, Canada.

Karanasios, K., Parker, P., 2016. Recent developments in renewable energy in remote aboriginal communities, Québec, Canada. In: Papers in Canadian Economic Development. University of Waterloo, Canada, 16: 98-108, doi: 10.15353/pced.v16i0.

Kirschbaum, A., Kuckelkorn, J.M., Hagel, K., 2018. Vertical hydraulic conductivity of borehole heat exchanger systems before and after freeze-thaw cycle stress. Research Conference Proceedings, IGSHPA Research Conference, September 18-19, Stockholm, Sweden, pp. 422-430, doi: 10.22488/okstate.18.000032.

Lemieux, J-M., Fortier, R., Talbot-Poulin, M-C., Molson, J., Therrien, R., Ouellet, M., Banville, D., Cochand, M., Murray, R., 2016. Groundwater occurrence in cold environments: examples from Nunavik, Canada. Hydrogeology Journal, 24: 1497-1513.

Makivik Corporation, 2018. Rise in the cost of gasoline. Press release, Kuujjuaq, Canada. https://www.makivik.org/rise-in-the-cost-of-gasoline/

McFadden, T., 2007. Supplemental research report on the foundation stabilization using a heat pump cooling system at 728 Constitution Drive Fairbanks, Alaska. Permafrost Technology Foundation. Fairbanks, AK.

Miranda, M.M., Giordano, N., Raymond, J., Kanzari, I., Dezayes, C., 2018. Geothermal gradient and heat flow estimation in New Québec Orogen (Labrador Trough), Northern Québec, Canada. Proceedings of 20th International Sedimentological Congress, August 13-17, Québec City, Canada.

Philippe, M., Bernier, M., Marchio, D., 2010. Sizing calculation spreadsheet: Vertical geothermal borefields. Ashrae Journal, 52(7): 20-28.

Société d'habitation du Quebec. 2014. Le logement au Nunavik - Document d'information. Gouvernement du Québec, Québec, Canada, 40 pp. http://www.habitation.gouv.qc.ca/fileadmin/internet/publications/0000023767.pdf

Wu, W., Wang, B., You, T., Shi, W., Li, Z., 2013. A potential solution for thermal imbalance of ground source heat pump systems in cold regions: ground source absorption heat pump. Renewable Energy, 59: 39-48.

Yan, C., Rousse, D., Glaus, M., 2019. Multi-criteria decision analysis ranking alternative heating systems for remote communities in Nunavik. Journal of Cleaner Production, 208: 1488-1497.

You, T., Wu, W., Shi, W., Wang, B., Li., X., 2016. An overview of the problems and solutions of soil thermal imbalance of ground-coupled heat pumps in cold regions. Applied Energy, 177: 515-536.

Manuscript ID: 584
DOI: 10.18462/iir.icr.2019.0584

Performance evaluation and validation of a novel heat pump water heater with rotary compressor and D-shaped condenser coils

Ce SHI[(a) (b)], Pega HRNJAK[(a)(b)]

[(a)] Department of Mechanical Science and Engineering,
University of Illinois at Urbana-Champaign
1206 West Green Street, Urbana, IL 61801, United States
Phone: (217) 721-1755, Email: ces3@illinois.edu
[(b)] Creative Thermal Solutions, Inc., 2209 N Willow Rd, Urbana, IL, 61802, United States
Phone: (217) 721-1755, Email: pega@illinois.edu

ABSTRACT

This paper presents the model of the heat pump water heater that has two interdependent parts: water in the storage tank of a heat pump water heater and the steady-state vapor compression system.

System performance is modelled by Engineering Equation Solver (EES) while computational fluid dynamics (CFD) is used for the water tank. These models are linked to simulate the performance in the transient, warm-up period.

The iterations between the EES-CFD linked model exchange the data though the interface of the water and tank wall until obtaining the matched solutions for both models. This EES-CFD linked model is found to be in good agreement with the experimental results conducted in the same activity and can predict the temperature distribution of the vapor compression system and transient behavior of the thermal storage tank.

Keywords: CFD, Modelling, Heat Pump, Water Heater.

1. INTRODUCTION

Modelling a HPWH system is a challenge due to the complexity of various sub-systems and the integration between the vapor-compression cycle and the water tank. Therefore, a EES-Fluent linked model has been developed and used to simulate the transient heating-up process of the HPWH system. The CFD model exports the thermal and momentum profiles in the water tank while the EES model simulates the vapor compression cycle. The EES system model outputs the heat flux profile as a boundary condition of coil segments in the CFD model. Therefore, the EES system model and CFD tank model exchange the information via the tank wall. By iterating the data between EES system model and CFD model, the solutions from the two models can be matched. This method is proposed by Shah and Hrnjak (2014) and refined by Li and Hrnjak (2018). Since the OCR is within 0.3% which is fairly small during the heating up process, the oil effect on the HPWH system performance is assumed to be neglected, the thermodynamic properties in the model is set to be those of the pure refrigerant.

2. MODELLING

2.1 Vapor compression cycle system model

A quasi-steady-state EES system model contains three sub-systems to simulate and predict the thermal behaviour of the condenser, evaporator and compressor. The Electronic Expansion Valve is set to be isenthalpic.

2.1.1 Compressor model

AHRI 10-coefficient compressor maps are used to obtain refrigerant mass flow rate through the compressor and compressor power consumption. The performance map of a single-speed rotary compressor obtained from manufacturer is used in the compressor model. Eq. (1) and (2) shown below are flow rate and power as functions of evaporating and condensing temperatures.

$$\dot{m} = \alpha_1 + \alpha_2 T_{evap} + \alpha_3 T_{cond} + \alpha_4 T_{evap}^2 + \alpha_5 T_{evap} T_{cond} + \alpha_6 T_{cond}^2 + \alpha_7 T_{evap}^3 + \alpha_8 T_{evap}^2 T_{cond} + \alpha_9 T_{cond}^2 T_{evap} + \alpha_{10} T_{cond}^3 \quad \text{Eq. (1)}$$

$$\dot{W} = \beta_1 + \beta_2 T_{evap} + \beta_3 T_{cond} + \beta_4 T_{evap}^2 + \beta_5 T_{evap} T_{cond} + \beta_6 T_{cond}^2 + \beta_7 T_{evap}^3 + \beta_8 T_{evap}^2 T_{cond} + \beta_9 T_{cond}^2 T_{evap} + \beta_{10} T_{cond}^3 \quad \text{Eq. (2)}$$

Where, T_{cond} and T_{evap} are the discharge and suction saturation temperature of the compressor. Discharge temperature is estimated based on the difference between actual and isentropic work. Actual suction state is considered here to correct the compressor map mass flow prediction by using Dabri and Rice (1981) method.

$$\dot{m}_{actual} = \left[1 + F_{mass}\left(\frac{v_{ARI-map}}{v_{actual}} - 1\right)\right] m_{ref,ARI-map} \quad \text{Eq. (3)}$$

Where empirical correction factor $F_{mass} = 0.75$. $\frac{V_{ARI-map}}{V_{actual}}$ is the ratio of specific volume at compressor map to the specific volume at actual superheat. Discharge temperature is estimated based on the difference between actual and isentropic work.

2.1.2 Heat Exchanger models

The HPWH system model uses the finite element by using a segment-to-segment method similar to Li and Hrnjak (2016), the single tube is divided into finite elements. Each tube element has refrigerant side and other side entering flow states, and phase changes are considered, therefore, the Effectiveness-Number of Transfer Unit (ε-NTU) method is used for heat transfer calculations between the refrigerant and air (water) side within each element.

Heat exchanger effectiveness ε is shown in Eq. (4) as a dimensionless ranging between 0 and 1.

$$\varepsilon = \frac{Actual\ heat\ transfer}{Theoretical\ maximum\ heat\ transfer} = \frac{q_{act}}{q_{max}} \quad \text{Eq. (4)}$$

Where q_{max} is the maximum possible heat transfer for the heat exchanger, as shown in Eq. (5) and Eq. (6).

$$q_{max} = C_{min}\,(T_{h,i} - T_{c,i}) \quad \text{Eq. (5)}$$

$$q_{act} = \varepsilon\, C_{min}\,(T_{h,i} - T_{c,i}) \quad \text{Eq. (6)}$$

The number of transfer unit (NTU) is used to represent the sensible heat transfer in heat exchanger.

$$NTU = \frac{UA}{C_{min}} \quad \text{Eq. (7)}$$

Where C_{min} is the minimum thermal capacity (the maximum temperature difference), UA is the overall heat transfer coefficient which can be obtained by

$$\frac{1}{UA} = \frac{1}{h_{hot}A_{hot}} + \frac{\delta}{kA_{hot/cold}} + \frac{1}{h_{cold}A_{cold}} \quad \text{Eq. (8)}$$

The effectiveness of the cross-flow heat exchanger of the HPWH system can be obtained and

validated by using Navarro and Cabezas-Gomez (2007) method shown in Eq. (9):

$$\varepsilon = 1 - \exp\{\left(\frac{C_{max}}{C_{min}}\right) \cdot NTU^{0.22} \cdot [\exp\left(-(\frac{C_{min}}{C_{max}}) \cdot NTU^{0.78}\right) - 1]\} \quad \text{Eq. (9)}$$

2.1.3 Evaporator

The fin-and-tube evaporator is used in the Heat Pump Water Heater System. The effect of fin needs to be taken into consideration, therefore equation can be modified to Eq. (10):

$$\frac{1}{UA} = \frac{1}{\eta_{fin} h_{hot} A_{hot}} + \frac{\delta}{k A_{hot/cold}} + \frac{1}{h_{cold} A_{cold}} \quad \text{Eq. (10)}$$

Where η_{fin} is the surface efficiency of the evaporator fins.

Air-side heat transfer coefficient h_{air} is obtained by using correlations from Wang et al. (2001) Equation presents the Coburn j-factor for a slit evaporator fin design as shown in Eq. (11):

$$\mathrm{j} = 0.086 \cdot Re_{D_C}^{j_1} \left(\frac{F_p}{D_C}\right)^{j2} \left(\frac{F_p}{D_h}\right)^{j_3} \left(\frac{F_p}{P_t}\right)^{-0.93} N^{j_4} \quad \text{Eq. (11)}$$

Therefore, Eq. (12) presents the air side heat transfer coefficient

$$h_{air} = j \cdot G_{air} \cdot c_{p,air} \cdot {P_r}_{air}^{-0.667} \quad \text{Eq. (12)}$$

On the refrigerant side, to calculate the single-phase heat transfer coefficient, the correlation proposed by Gnielinski is used for turbulent flow heat transfer through circular tubes, which the effects of tube wall roughness can be taken into consideration, as shown in Eq. (13) and (14):

$$h_{ref} = \frac{Nu_D \cdot D}{k_{ref}} \quad \text{Eq. (13)}$$

$$Nu_D = \frac{(f/8)(Re_D - 1000)Pr}{1 + 12.7(f/8)^{1/2}(Pr^{2/3} - 1)} \quad \text{Eq. (14)}$$

Where *f* denotes the Darcy friction factor, which can be obtained from Moody chart or for smooth tubes from Cooper correlation shown in Eq(15):

$$f = (0.790\ lnRe_D - 1.64)^{-2} \quad \text{Eq. (15)}$$

For the two-phase heat transfer coefficient, Wattelet et al. (1994) proposed the asymptotic model shown in Eq. (16) considering two components that make up the two-phase heat transfer coefficient h_{tp}: nucleate boiling $h_{nb}$and convective boiling h_{cb}.

$$h_{tp} = [h_{nb}^n + h_{cb}^n]^{1/n} \quad \text{Eq. (16)}$$

Where exponent n is considered to be 2.5. Nucleate boiling $h_{nb}$and convective boiling h_{cb} are calculated by

$$h_{nb} = 55 q''^{0.67} {W_m}^{-0.5} Pr_{ref}^{0.12} [-\log_{10} Pr_{ref}]^{-0.55} \quad \text{Eq. (17)}$$

$$h_{cb} = (1 + 1.925 X_{tt}^{-0.83})(0.023 \frac{k_{ref,liq}}{D} Re_{liq}^{0.8} Pr_{liq}^{0.4}) R \quad \text{Eq. (18)}$$

Where q'' is the heat flux, W_m is refrigerant mole weight, Pr_{ref} is reduced pressure.

The single-phase pressure drop is obtained by using the correlation of Churchill et. al (1977) friction factor:

$$f_c = \left([2.475(\frac{1}{(\frac{7}{Re})^{0.9} + \frac{0.27\varepsilon}{D}})]^{16} + (\frac{37530}{Re})^{16} \right)^{-1/8} + \frac{8}{Re} \quad \text{Eq. (19)}$$

The two-phase pressure drop in a horizontal tube can be divided into two parts: Frictional pressure drop ΔP_f and acceleration pressure drop ΔP_a.To calculate the acceleration pressure drop ΔP_a, the following momentum balance shown in Eq. (20) can be applied:

$$\Delta P_a = G_{ref}^2 \left\{ \left[\frac{x_o^2}{\rho_v \alpha_o} + \frac{(1-x_o)^2}{\rho_l (1-\alpha_o)^2} \right] - \left[\frac{x_i^2}{\rho_v \alpha_i} + \frac{(1-x_i)^2}{\rho_l (1-\alpha_i)^2} \right] \right\} \quad \text{Eq. (20)}$$

Where α_i and α_o are the void fraction for the inlet and outlet. This void fraction shown in Eq. (21) is calculated by using the correlation from Rouhani and Axelsson (1970):

$$\alpha = \frac{x}{\rho_v} \left\{ [1 + 0.2(1 - x)] \left[\frac{x}{\rho_v} + \frac{1-x}{\rho_l} \right] + \frac{1.18}{G_{ref}} \left[\frac{\sigma_{ref} g (\rho_l - \rho_v)}{\rho_l^2} \right]^{0.25} \right\}^{-1} \quad \text{Eq. (21)}$$

To calculate the frictional pressure drop for the two-phase refrigerant flow, a correlation proposed by Muller et al. (1986) can be used based on the flow quality, which is shown in Eq. (22)

$$\left(\frac{\partial P}{\partial z}\right)_g = f_g \frac{G_{ref}^2}{2 \rho_g D_h} \quad \text{Eq. (22)}$$

The frictional gradient of total refrigerant liquid flow can be obtained by Eq. (23):

$$\left(\frac{\partial P}{\partial z}\right)_{lo} = G_{ref} (1 - x)^{1/3} + \left(\frac{\partial P}{\partial z}\right)_g x^3 \quad \text{Eq. (23)}$$

2.1.4 Condenser model

This HPWH unit contains a wrapped around coil condenser. Two parallel circuits of tube coils are wrapped around the water tank wall. Each circuit contains 16 coils and the refrigerant flow inside the coils is going upward. In order to simplify the modelling process, it is assumed that the two condenser circuits split the refrigerant entering the condenser and there is no maldistribution, so the two circuits have identical states of refrigerant. Therefore, in the model, these two circuits are simplified as one circuit which contains doubled contact area with tank wall as well as doubled cross-sectional area.

Fig. 1 shows that the condenser contains N coils in the Finite Volume Method, and to simplify the model, each coil is wrapped around the tank horizontally without any slopes. Furthermore, in order to realize interaction between the tank and coil, the model uses a segment-to-segment method that each coil has been divided into M elements, as it shown in Fig. 1. Since each coil has been discretized into M elements, Fig. 2 shows the simulation of each element. Heat transfer and pressure drop can be calculated along refrigerant upward flow. Each single coil segment has its own corresponding segment of tank wall and water segment, these three segments compose area for refrigerant side heat transfer, thermal resistance from tube to tank wall thickness, and natural convection heat transfer between water element and tank wall.

Fig. 3 shows model reduction of refrigerant coils and tank wall. They are simplified to fins and the arrow indicates the heat

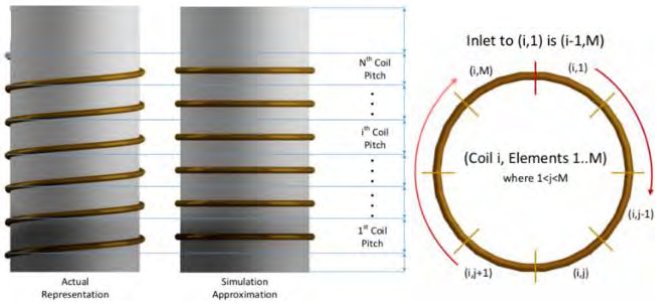

Fig. 1: Adaptation of coils windings in modelling and discretization of each coil into elements

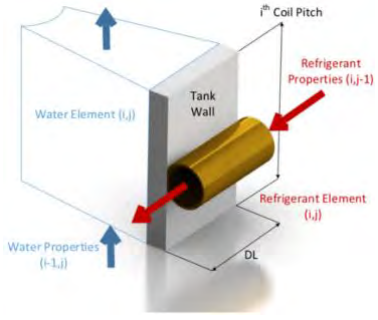

Fig. 2: Single element of condenser

transfer direction. This heat transfer is driven by the temperature difference between the refrigerant segment and water element corresponding to that refrigerant segment. On refrigerant side, same correlations used in evaporator are chosen to calculate the single-phase heat transfer and pressure drop in the condenser.

For the two-phase heat transfer correlation, Xiao and Hrnjak (2017)'s model is applied.

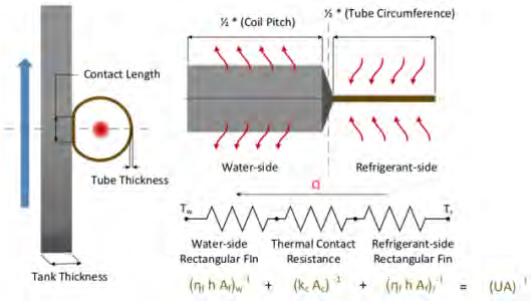

Fig. 3: Simplification of element level modelling and description of heat path

In their model, superficial quality for void fraction is introduced to account for non-equilibrium effects of tube condensation.

On the water side, the heat transfer coefficient is calculated by using the heat transfer correlation based on the external laminar flow through a flat plate.

$$\mathrm{Nu} = 0.664 Re^{1/2} Pr^{1/3} \qquad \text{Eq. (24)}$$

where the characteristic length is the thickness of the upward flow layer which will be discussed later.

2.2 Water Side CFD Model

The temperature and velocity profiles in the water tank are simulated by using the CFD model in ANSYS Fluent. This CFD model is designed as a Two-Dimensional axisymmetric domain that simulates heating process of the water tank, as it shown in Fig. 8.6. One axisymmetric boundary represents centerline of water tank, and the other three boundaries corresponds to the tank walls including the top, bottom and side wall.

Due to the buoyancy effect, the water nearby the tank wall flows in an upward direction and is heated by the tank wall conduction.

An "upward flow layer" is then defined to account for the upward flow velocity component in the nearby wall area and is set to be 1 cm, as it shown in Fig. 4. 54280 cells are used in the CFD quadrangular mesh to better obtain the thermal and momentum profiles between the water side and tank wall.

As it shown in Fig. 5, each line segment represents one of 16 condenser coils, the length of each segment equivalents to the coil pitch. Heat flux is assumed to be uniform on each segment's surface and it is specified by the User Defined Function file that obtained from the quasi steady state vapor compression system model.

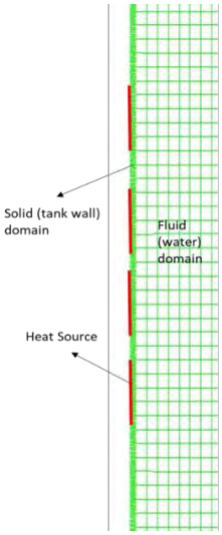

Fig. 4: Zoom in the near-wall area

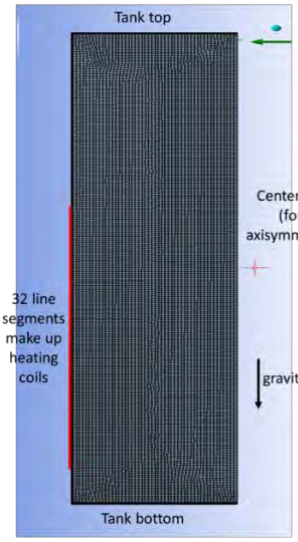

Fig. 5: Geometry and mesh of the water tank CFD model

It is assumed that the density of the tank water has a linear relation with the temperature, and the buoyancy driven flow is set to be laminar flow. Based on the assumptions that made before, governing equations are solved by using Finite Volume Method and pressure based solver. SIMPLE (semi-implicit method for pressure-linked equations) scheme has been applied to pressure-velocity coupling, Green-Gauss Node Based has been chosen as the gradient, and Second Order scheme

is used for the pressure accuracy. To improve the accuracy, Second Order Upwind has been applied for momentum and energy. The convergence standard has been taken as 1e-06 for the pressure residual, and for the continuity residual, 1e-3 has been selected.

2.3 EES-CFD Linked model

The CFD model outputs the near-wall water temperature and velocity of each segment coil to the EES system model for heat transfer calculation. The EES system model outputs the heat flux profile as a boundary condition of coil segments in the CFD model. Therefore, the EES system model and CFD tank model exchange the information via the tank wall. By iterating the data between EES system model and CFD model, the system performance solutions from two models can be matched. First, the iteration begins with a guessed value of coil segment heat flux. With the heat flux profile in UDF, the CFD model simulates the first heating-up process. After that, CFD model outputs the near-wall water temperature and velocity profiles to the EES system model, then, the system model generates a new heat flux profile for CFD model for next simulation. This linked model runs iteratively and exchanges the profile internally until the heat flux becomes stable (change within 1% variation).

3. RESULTS

The temperature contours and velocity trajectories at 60, 120 and 180 min are given in Figs. 6 and 7. Combining the two Fig.s, it can be observed that the upward flow is restricted in a thin layer that near the tank wall. The water flows upward while the outside water flows downward, the water temperature in that layer is also higher than the outside water temperature. From the three charts in Fig 7, it is shown that the flow patterns at different time point remain relatively similar, only velocity magnitude changes slightly with time. However, for the three charts in Fig. 8, there is a significant difference among temperature contours at different time. The thermal stratification is getting intensive and obvious with time that a thicker thermocline is achieved with longer heating time. The temperature difference between tank top and bottom is over 20 ℃ at 180 mins that Boussinesq approximation may not be applicable to that high temperature difference.

For a better insight of the interaction between the vapor compression system and the water tank, Figs 8 and 9 plot the average temperature and velocity profile at each corresponding coil segment in the upward flow layer, at several heating-up times. It is proved that stratification becomes more intensive as the heating time

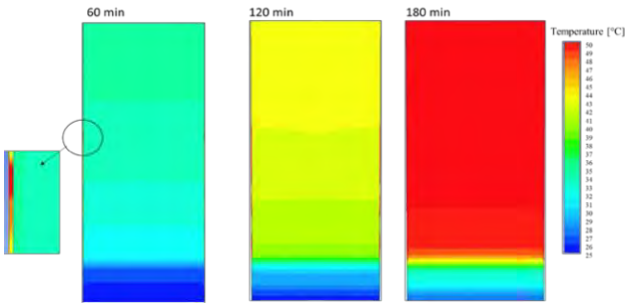

Fig. 6: Temperatures at t = 60, 120, and t= 180 min

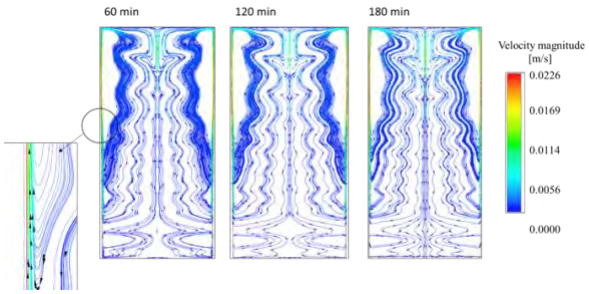

Fig. 7: Velocities at t = 60, 120 and t= 180 min

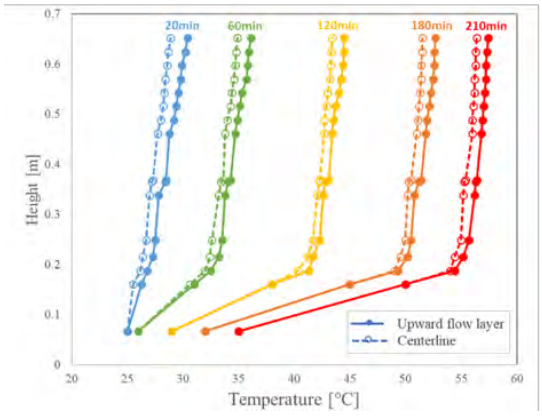

goes longer. Furthermore, the temperature in the upward flow layer is 0.5℃ - 2.5℃ higher than the tank centerline temperature. From Fig. 9, the velocity profiles at different time have quite similar trend, this coincides well with the velocity trajectories that the water flow in the tank is stable during the heating up process.

Near-wall velocities at different heating time show similar trends and increase with the coil height. The velocity decreases with time at first three coils from bottom, and increases with time at upper coil level.

The linked model is able to capture the thermal behavior of the water in the tank. As it has been described, three series of thermocouples are placed at three different location inside the tank to record temperature change during heating-up. Therefore, temperatures at each corresponding thermocouple location are obtained from CFD model to validate experimental temperature profiles.

Fig. 8: Temperatures in the upward flow layer is 0.5℃ - 2.5℃ higher than the tank centerline temp.

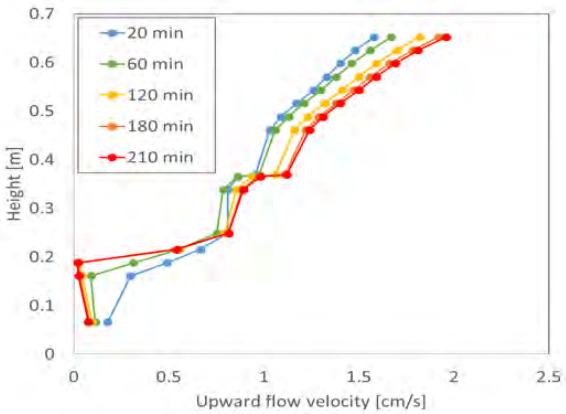

Fig. 9: Velocity decreases with time at lower coil level and increases with time at upper coil level

The average temperature of the tank is compared with the vertical thermocouple series, and two horizontal series with the average temperature at the corresponding heights in the tank model. The comparison between the CFD model and experimental data is shown in Fig. 10. It indicates that predicted water temperatures match the experimental within a deviation of 2℃.

The model validation of the capacities of condenser and evaporator, the compressor work and COP is given in Fig. 11. The system model predictions coincide well with the experimental data. The prediction of COP matches the experimental COP well that the deviation is within 4.5% while the average deviation is 1.0%. The average deviation of condenser capacity and compressor work is 0.79%. However, deviation of the evaporator capacity is 12.5%, and this might due to some imperfections in manufacturing which are not considered in the system model.

Fig. 12 presents the comparison between the measured and predicted results of the refrigerant flow pressure drop in the condenser and evaporator. It shows that the model can properly predict the condenser pressure drop within ±10% deviation. However, the model underestimates the refrigerant pressure drop on evaporator, the predicted results are much smaller than experimental data. This additional pressure drop may due to the brazed joints at the end of each horizontal tubes.

Fig. 13 gives comparison between experimental data and measurements of the refrigerant at the inlet and outlet of the evaporator and condenser. It shows that the prediction deviations of refrigerant temperatures at the inlet and outlet of the evaporator are within 0.5℃. For the condenser, the prediction deviation is within 2℃ and it could be found that most of the predictions are within 0.5℃.

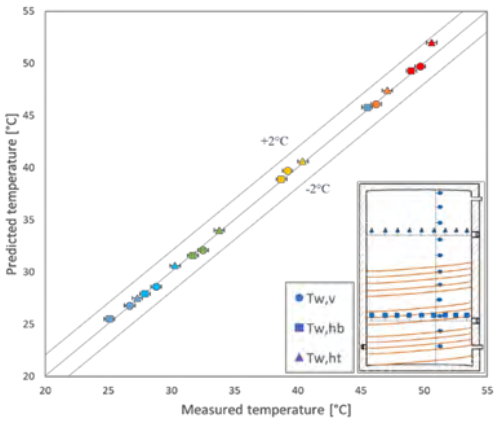

Fig. 10: Predicted water temperatures match the experimental data, deviations are within 2℃.

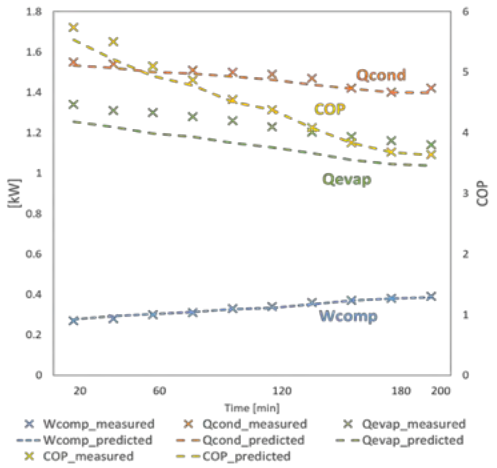

Fig 11: The model match well with experimental data.

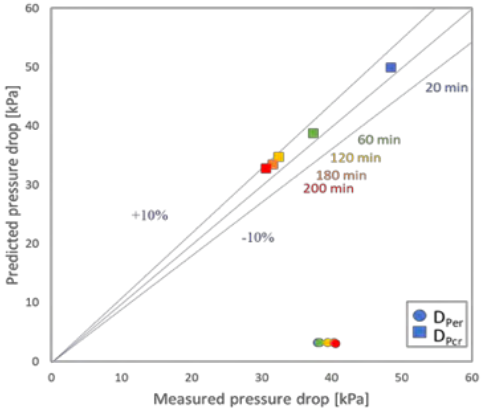

Fig. 12: Model predicts refrigerant pressure drop in condenser within 10%, but underestimates evap.

It could also be explained by the U-bend effect on the flow regime. In the model the friction factor is determined with the pressure drop in the U-bend region being neglected. Besides, the imperfectness in manufacturing would also cause the pressure drop, which is not considered in modelling.

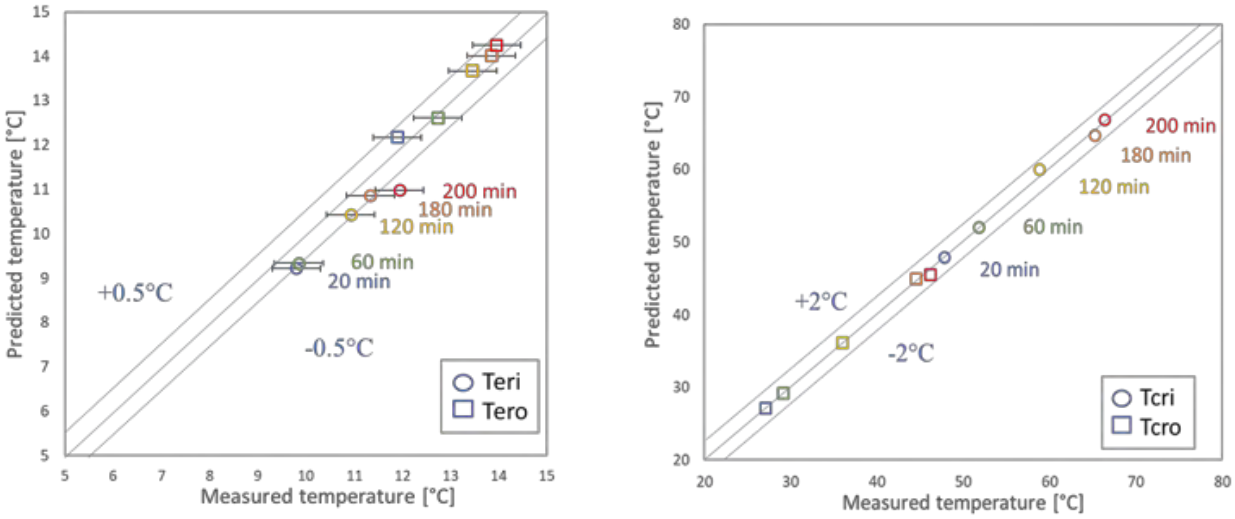

Fig. 13: Model predicts refrigerant temp. at the inlet and outlet of the evap. and cond. within 0.5℃ and 2℃.

CONCLUSION

A linked EES-CFD model has been developed to simulate the transient warm-up period of a Heat Pump Water Heater. The CFD model describes the heat transfer and fluid dynamics on the water side, while EES system model describes the vapor compression cycle. The model is found to be in good agreement with experimental results conducted in the same heat-up, and it is capable of predicting the temperature distribution of the vapor compression system and transient behavior of the thermal storage tank. The deviations of the refrigerant temperatures in two heat exchangers and water temperature in the storage tank are within 2℃, and the model predicts the system power and capacities within the average deviation of 4.1%. The predicted pressure drop in condenser is within 10% deviation, however, the model underestimates the pressure drop in evaporator due to the local pressure loss due to defects from manufacturing which is not counted in the system model.

REFERENCES

Churchill, S.W., 1977. Friction-factor equation spans all fluid flow regimes, Chem. Eng., No. 7, pp.91-92.

Dabiri, A.E., Rice, C.K., 1981. A compressor simulation model with corrections for the level of suction gas superheat. ASHRAE Trans, 87(2), 771-782.

Li, J., Hrnjak, P., 2016. Separation of Liquid and Vapor in Header of MCHE. Int. Ref. Air Cond Conf. Purdue, # 2248.

Li, W., Hrnjak, P., 2018. Experimentally validated model of heat pump water heater in heating-up transients. International Journal of Refrigeration, 88, 420-431.

Navarro, H.A., Cabezas-Gómez, L.C., 2007. Effectiveness-ntu Computation with a Mathematical Model For Cross-Flow Heat Exchangers. Brazilian Journal of Chemical Engineering, 24(4), 1678-4383.

Rouhani, S.Z., Axelsson, E., 1970. Calculation of void volume fraction in the sub cooled and quality boiling regions. International Journal of Heat and Mass Transfer, 13, 383–393, 1970.

Shah, T., Hrnjak, P., 2014. Linked modelling of heat pump water heater vapor compression system and water tank. International Refrigeration and Air Conditioning Conference at Purdue, Paper 1481.

Wang, C.C., 2001. A comparative study of compact enhanced fin-and-tube heat exchangers. International Journal of Heat and Mass Transfer, 44, 3565-3573.

Xiao, J., Hrnjak, P., 2017a. A new flow regime map and void fraction model based on the flow characterization of condensation. Int. J. Heat and Mass Transfer, 108, 443-452.

Xiao, J., Hrnjak, P., 2017b. A heat transfer model for condensation accounting for non-equilibrium effects. Int. J. Heat and Mass Transfer, 111, 201-210.

Manuscript ID: 603
DOI:10.18462.iir.icr.2019.0603

Heat and mass transfer characteristics of a molded activated carbon/methanol pair for adsorption cooling

Chieko SHIBATA[1], Akio KODAMA[2], Hidenori HIGASHI[2], Takafumi SETO[2], Yoshio OTANI[2], Mikio KUMITA[2]

[1] Graduate School of Science and Technology, Kanazawa University
Kanazawa, 920-1192 Japan, chieko080@stu.kanazawa-u.ac.jp

[2] Institute of Science and Engineering, Kanazawa University
Kanazawa, 920-1192, Japan, kumita@se.kanazawa-u.ac.jp

ABSTRACT

Using alkali activated carbon fiber and powder with a large specific area of around 3000 $m^2\ g^{-1}$ as starting material, we prepared a molded adsorbent with a small amount of polytetrafluoroethylene (PTFE) binder for adsorption cooling by a mechanical compression at ordinary temperature. PTFE nanofibers played an important role in the retention of the shape of the molded adsorbent. Adsorption equilibria of methanol vapor on the prepared high-density activated carbons (HDACs) were found to be expressed by the Dubinin-Astakhov equation. Experimental results showed that the denser HDAC rapidly adsorbed methanol vapor, and heat of adsorption was earlier removed. The temporal changes in the methanol uptake and the temperature of HDACs could be estimated through numerical analysis based on a one-dimensional heat and mass transfer model. Therefore, the prepared compression-molded activated carbon would be a promising material for adsorption cooling, and the established calculation model would aid the design of molded adsorbents.
Keywords: Adsorption cooling, Activated carbon, Compression-molded adsorbent, Methanol vapor, Heat and mass transfer

1. INTRODUCTION

Adsorption heat pumps and chillers are high energy-saving heat transformers driven by low-temperature waste heat and/or solar energy. Adsorption chillers using silica gel/water or zeolite/water pairs have been in practical use, and a downsizing and performance improvement of adsorption chiller is needed to extend a further spread of them. The cooling performance of adsorption chiller is affected by some factors such as nature of adsorbent/refrigerant pair, heat and mass transfer in an adsorbent heat exchanger, the temperatures of heat sources, and the adsorption-desorption cycle operation. The selection of adsorbent material is of particular importance for a high-performance adsorption chiller. Recently, new materials such as aluminophosphates, metal-organic frameworks

and porous material-metal salt composites have been examined for their applicability to adsorption cooling (Henninger et al., 2017; Ma L. et al., 2016; Simooka et al., 2007; Suwa et al., 2016).
Activated carbon is one of the potential adsorbent candidates for adsorption chillers because they have a large adsorption capacity of refrigerant vapors such as ammonia and lower alcohols. The authors prepared a molded adsorbent with high apparent density using activated carbon fiber (ACF) having a quite large surface area exceeding 3000 $m^2\ g^{-1}$ as a starting material, aimed to increase the cold output per unit volume of adsorption chillers in the previous study (Kumita et al., 2018). This high-density activated carbon fiber (HDACF) could be obtained through a simple dry preparation process consisting of kneading a mixture of ACF and a low dose of polytetrafluoroethylene (PTFE), and mechanically compressing the kneaded mixture at ordinary temperature. In the present study, we attempted to prepare compression-molded adsorbent using activated carbon fiber and activated carbon powder (ACP) in order to further increase its apparent density. The molded activated carbons with different densities were examined for their adsorption capacities and adsorption rates of methanol vapor, both experimentally and theoretically.

2. EXPERIMENTAL

2.1. Preparation of molded activated carbon adsorbent

We used alkali activated carbon fiber and powder (Kansai Coke and Chemicals Co., Ltd.) as a starting material for production of molded adsorbent (Fig. 1). The mean fiber diameter of ACF was 18 μm and the mean particle diameter of ACP was 84 μm. The BET specific surface areas and pore volumes were 3346 $m^2\ g^{-1}$ and 1.81 $cm^3\ g^{-1}$ for ACF, and 2973 $m^2\ g^{-1}$ and 1.57 $cm^3\ g^{-1}$ for ACP, respectively.

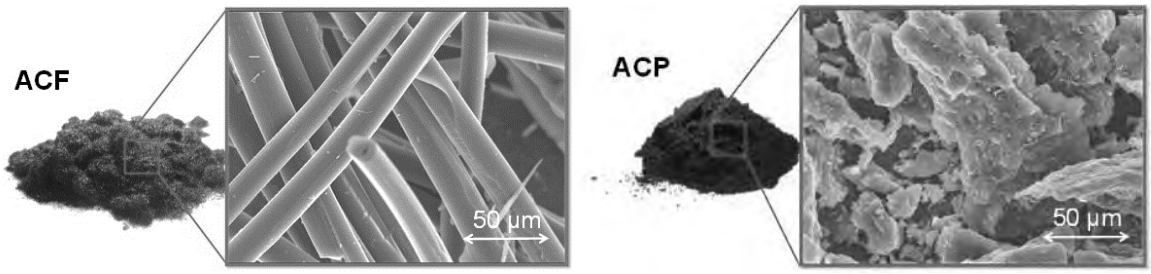

Figure 1: SEM images of activated carbon fiber and powder

First, the ACF and ACP were placed in a mortar at a given mass ratio, and then PTFE powder (Du Pont-Mitsui Fluorochemicals Co., Ltd.) was added to this mixture at the ratio of 5 wt%. The PTFE powder with a mean particle diameter of 470 μm will easy fibrillated by being subjected to an external shear force. The mixture of ACF, ACP and PTFE was kneaded at 100 rpm for 20 min. Subsequently the kneaded mixture was charged in a cylindrical steel mold 10 mm i.d. in diameter and then compressed at a given load using an oil hydraulic press. A coin-shaped activated carbon compact (HDAC: high-density activated carbon) was obtained through this procedure. The apparent density

of the HDAC was determined from its weight and dimensions after drying at 100°C for 12 h.

2.2. Methanol vapor adsorption

A schematic diagram of an experimental apparatus for methanol vapor adsorption on the HDACs is shown in Fig. 2. The apparatus was composed of an evaporator, a vapor reservoir and an adsorption chamber, which were connected through valves. The HDAC was placed on a stainless-steel flat wall maintained constantly at 30°C in the adsorption chamber. K-thermocouples were attached on both the upper and lower surfaces of the HDAC. After the vapor pressure of methanol was set at a given value in the reservoir, the adsorption experiment started by introducing the methanol vapor into the adsorption chamber. During the experiment, the vapor pressure in the chamber and temperatures of the HDAC were continuously monitored until the system reached a condition of adsorption equilibrium. The methanol uptake by the HDAC was determined from the change in vapor pressure.

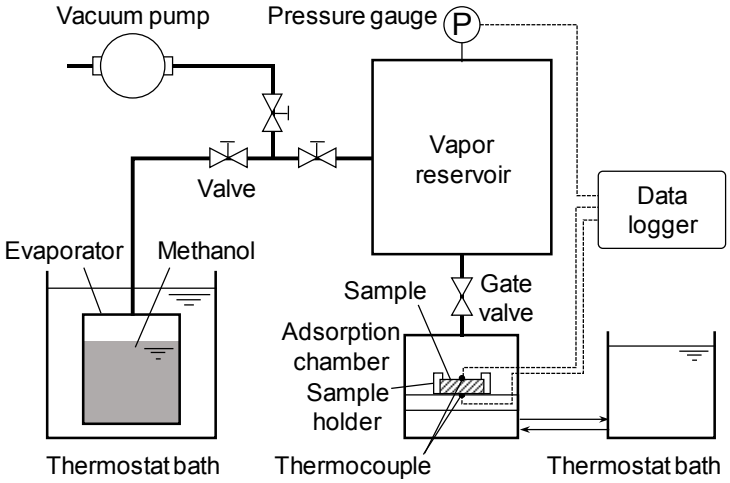

Figure 2: Schematic diagram of experimental apparatus

3. THEORETICAL ANALYSIS

In order to evaluate the HDAC/methanol pair for its transient adsorption behaviors, a numerical analysis was carried out based on a one-dimensional heat and mass transfer model for the adsorption pair. The governing equations (Kariya et al., 2006; Kumita et al., 2018) were shown as follows:

Heat and mass transfer equations

$$\left\{\varepsilon\rho_{\mathrm{g}}c_{pg}+\left(1-\varepsilon\right)\rho_{\mathrm{a}}c_{ps}\right\}\frac{\partial T}{\partial t}=\lambda_{\mathrm{e}}\frac{\partial^2 T}{\partial x^2}+\rho_{\mathrm{a}}\Delta H_{\mathrm{ad}}\frac{\partial q}{\partial t} \qquad \text{Eq. (1)}$$

$$\frac{\partial\left(\rho_{\mathrm{g}}u_{\mathrm{g}}\right)}{\partial x}=\varepsilon\frac{\partial\rho_{\mathrm{g}}}{\partial t}+\rho_{\mathrm{a}}\frac{\partial q}{\partial t} \qquad \text{Eq. (2)}$$

The velocity of methanol vapor, u_{g} was determined from the Darcy's equation and Blake-Kozeny equation,

$$u_g = -\frac{K}{\mu_g}\frac{\partial P}{\partial x} \quad \text{where} \quad K = \frac{\varepsilon^3}{150\left(1-\varepsilon^2\right)} D_f^2 \qquad \text{Eq. (3)}$$

Adsorption rate equation (Linear driving force model)

$$\frac{\partial q}{\partial t} = D\left(q^* - q\right) \qquad \text{Eq. (4)}$$

q^* is the equilibrium amount of methanol adsorption, which is given by the Dubinin-Astakhov (D-A) equation,

$$q^* = q_{max} \exp\left[-\left\{\frac{RT}{E}\ln\left(\frac{P^s}{P}\right)\right\}^n\right] \qquad \text{Eq. (5)}$$

In this study, the temporal changes in the amount of methanol adsorption and temperature of the HDAC for adsorption process in the relative pressure range from 0.12 to 0.25 were calculated numerically using a finite difference method.

4. RESULTS AND DISCUSSION

4.1. High-density activated carbon

Fig. 3 shows an SEM image of the cross-section of HDAC with a mixing ratio, $m_{ACP}/(m_{ACP}+m_{ACF})$ of 0.5. The ACF and ACP are obviously entangled in PTFE nanofibers as shown in this image, so that the PTFE fibers play an important role in the retention of the shape of HDAC.

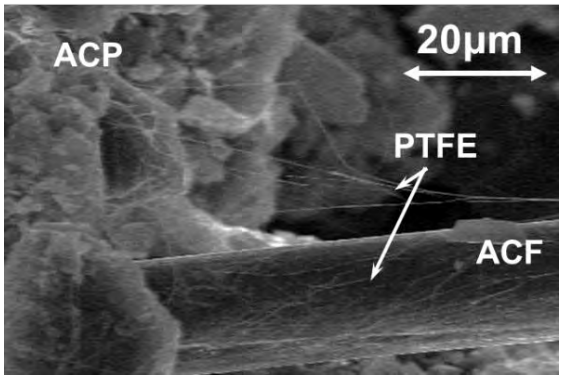

Figure 3: SEM image of HDAC

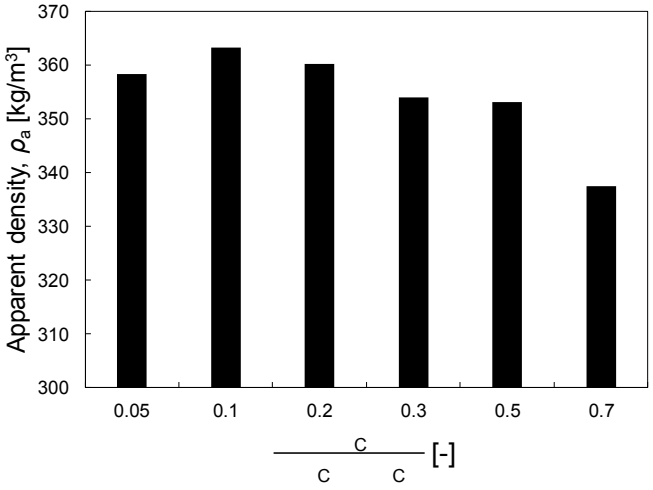

Figure 4: Relationship between apparent densities of HDACs and mixing ratio

Fig. 4 represents the relationship between the apparent density of HDAC, ρ_a and the mixing ratio. The apparent density of HDAC varies with the mixing ratio. The value of ρ_a reaches a maximum of 363 kg m^{-3} at the ratio of 0.1 and decreases with increase in the mixing ratio. We confirmed that

unfortunately it is hard to produce the coin-shaped HDACs at mixing ratios below 0.7 because of poor fibrillation of the PTFE powder. These results indicate that a certain amount of ACF is required for adequate fibrillation of the PTFE powder in the kneading process.

4.2. Adsorption capacity of methanol vapor on HDAC

Two HDACs having apparent densities of 311 and 345 kg m^{-3} and approximately the same thickness were evaluated volumetrically for their adsorption capacities of methanol vapor at 30°C. Fig. 5 shows the methanol vapor adsorption isotherms on the HDACs. The vertical axis is the equilibrium amount of methanol adsorption per unit apparent volume of the HDAC, q^*, and the horizontal axis is the relative pressure, φ, which is defined as the ratio of the equilibrium vapor pressure to the saturated vapor pressure at 30°C. The amount of methanol vapor adsorbed on the HDAC increases with increasing the relative pressure, and its value becomes larger for the denser HDAC. The adsorption equilibrium obtained experimentally can be expressed by the D-A equation as shown in this figure. The maximum amount adsorbed, q_{max}, activation energy, E, and Dubinin-Astakhov constant, n is 487 kg m^{-3}, 1.57 kJ mol^{-1}, and 1.59 for 311-kg m^{-3} HDAC, and 484 kg m^{-3}, 1.47 kJ mol^{-1}, and 1.66 for 345-kg m^{-3} HDAC respectively, which were determined on the basis of the experimental data.

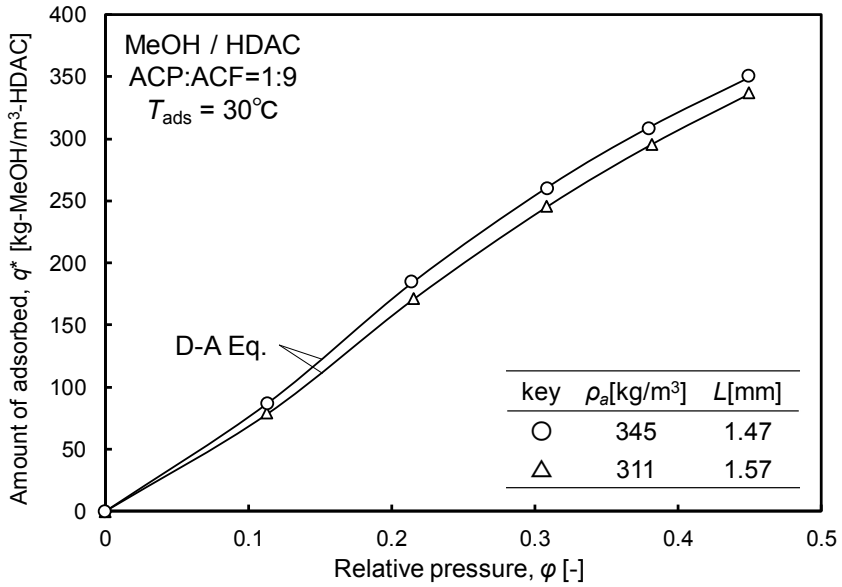

Figure 5: Adsorption isotherms of methanol vapor on HDACs with different apparent densities at 30°C

4.3. Transient behaviors of methanol adsorption

In the relative pressure range from 0.12 to 0.25, methanol vapor adsorption on 311- and 345-kg m^{-3} HDACs were conducted both experimentally and theoretically. Fig. 6 shows the comparison between the experimental and calculated results of the temporal changes in the amount of methanol adsorption and the upper-surface temperature of the HDAC during the adsorption process. The amount adsorbed is represented as the normalized value, $(q-q_1)/(q_2-q_1)$, where q_1 and q_2 are

the equilibrium amounts of methanol adsorption at φ_1 = 0.12 and φ_2 = 0.25. In the numerical calculation, the adsorption rate constant, D and the contact heat transfer coefficient, h_c at the interface between the bottom surface of the HDAC and the heat-exchange wall were determined by comparing the experimental and calculated results. The effective thermal conductivities: λ_e = 0.179 W m^{-1} K^{-1} for 311-kg m^{-3} HDAC and 0.229 W m^{-1} K^{-1} for 345-kg m^{-3} HDAC were estimated based on the measured values by a steady-state method (Kumita et al., 2018; Kuwata et al., 2015).

As shown in Fig. 5, the amount of methanol adsorption on HDAC increases rapidly after the onset of the adsorption process and then gradually reaches the equilibrium value. According to the experimental results, the two HDACs shows of similar adsorption rate. The calculated results are in general agreement with the experimental ones, but the adsorption rate calculated for 345-kg m^{-3} HDAC is slightly faster than that for 311-kg m^{-3} HDAC. On the other hand, the upper-surface temperature of the HDAC immediately increases and reached a maximum due to the evolution of heat of adsorption after the introduction of methanol vapor. Then, it gradually decreases to the heat-exchange wall temperature of 30°C. The effective thermal conductivity of adsorbent layer makes a direct impact on the heat transfer in the layer. Therefore, the removal of heat of adsorption for 345-kg m^{-3} HDAC would proceed smoothly due to a large thermal conductivity, compared with 311-kg m^{-3} HDAC. The experimental data of the temperature variations are also reproduced generally by the numerical calculation. These results indicate that the calculation model could approximately predict the transient behaviors of the adsorption of methanol vapor and the heat transfer in the activated carbon layer.

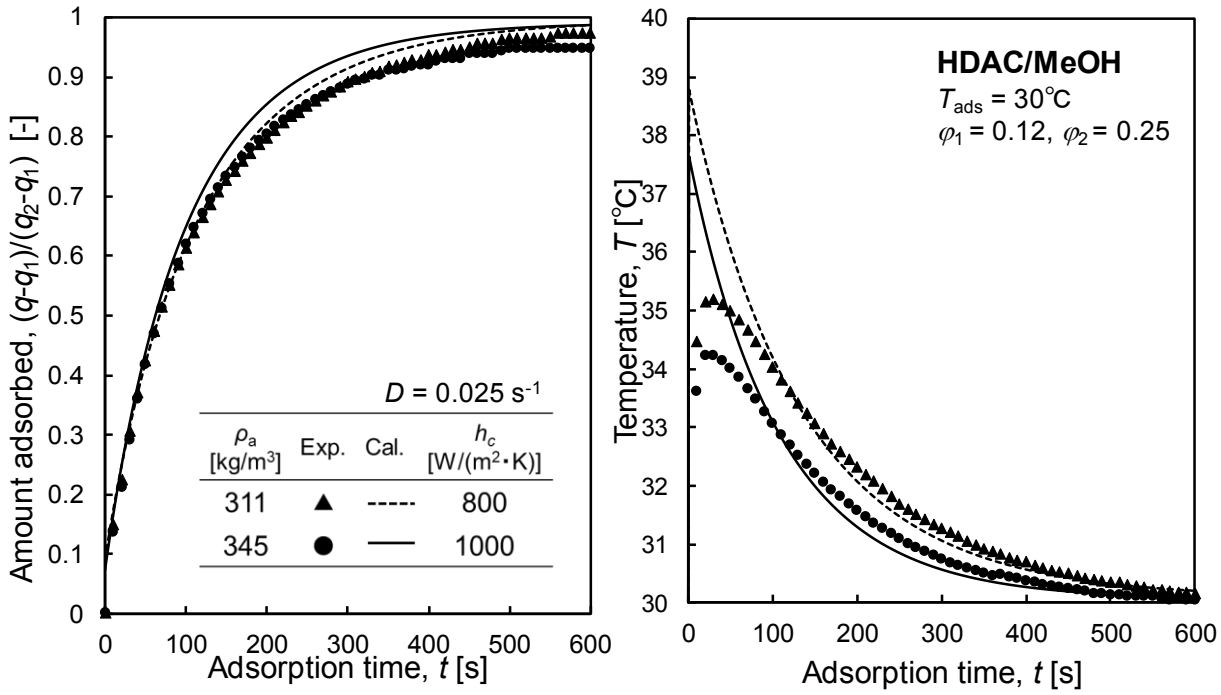

Figure 6: Temporal changes in amount of methanol adsorption and upper-surface temperature for 311- kg/m^3 and 345-kg/m^3 HDACs

5. CONCLUSIONS

Compression-molded adsorbents consisting of activated carbon fiber and powder could be prepared by the addition of a small amount of PTFE. The PTFE powder fully fibrillated in the kneading process, thereby causing it to serve as a binder of the molded activated carbon, and the presence of a certain amount of ACF in the starting material brought about the promotion of fibrillation of the PTFE powder. The adsorption equilibrium of methanol vapor onto the molded adsorbent consisting of ACF and ACP could be expressed by the Dubinin-Astakhov equation. Experimental results showed that the removal rate of heat of adsorption for the denser molded activated carbon became faster. The temporal changes in the amount adsorbed and the temperature of HDACs could be estimated generally by the numerical calculation on the basis of a one-dimensional heat and mass transfer model.

ACKNOWLEDGEMENTS

The authors are grateful to Kansai Coke and Chemicals Co., Ltd. for providing the activated carbon fiber and powder. We also thank Prof. N. Kobayashi at Nagoya University for the measurement of the thermal conductivities of HDACs.

NOMENCLATURE

c_p	isobaric specific heat (J kg^{-1} K^{-1}))·	t	time (s)
D	rate constant of adsorption (s^{-1})	T	temperature (K)
D_f	mean diameter of ACF (m)	u	velocity (m s^{-1})
D_p	mean particle diameter of ACP (m)	x	distance from upper surface of HDAC in thickness direction (m)
E	activation energy (J mol^{-1})	Greek symbols	
h_c	contact heat transfer coefficient (W m^{-2} K^{-1})	ε	void fraction (-)
ΔH_{ad}	heat of adsorption (J kg^{-1})	φ	relative vapor pressure (-)
K	permeability (-)	λ_e	effective thermal conductivity of HDAC (W m^{-1} K^{-1})
L	thickness of HDAC (m)	μ	viscosity (Pa s)
n	constant in Dubinin–Astakhov equation (-)	ρ	density (kg m^{-3})
P	vapor pressure (Pa)	ρ_a	apparent density of HDAC (kg m^{-3})
P^s	saturated vapor pressure (Pa)	Subscripts	
q	amount adsorbed (kg kg^{-1})	g	gas phase (methanol vapor)
q_{max}	maximum amount adsorbed (kg kg^{-1})	s	solid phase (ACF)
R	gas constant (J mol^{-1} K^{-1})	*	equilibrium

REFERENCES

Henninger, S.K., Ernst, S.-J., Gordeeva, L., Bendix, P., Fröhlich, D., Grekova, A.D., Bonaccorsi, L., Aristov, Y., Jaenchen, J., 2017. New materials for adsorption heat transformation and storage. Renew. Energy 110, 59-68.

Kariya, K., El-Sharkawy, I.I., Suda, K., Saha, B.B., Kuwahara, K., Koyama, S., 2006. Study on adsorption process of ethanol vapor to activated carbon fibers. Trans. Jpn. Soc. Refrig. Air Cond. Eng. 23, 355-363.

Kumita, M., Yamawaki, N., Shinohara, K., Higashi, H., Kodama, A., Kobayashi, N., Seto, T., Otani, Y., 2018. Methanol adsorption behaviors of compression-molded activated carbon fiber. Int. J. Refrig. 94, 127-135.

Kuwata, K., Kobayashi N., Fuse, T., 2015. Heat and mas transfer rate of $SrCl_2$ ammine complex formation. Trans. Jpn. Soc. Refrig. Air Cond. Eng. 32, 393-402.

Ma, L., Rui, Z., Wu Q., Yang H., Yin Y., Liu Z., Cui Q., 2016. Performance evaluation of shaped MIL-101-ethanol working pair for adsorption refrigeration. Appl. Therm. Eng. 95, 223-228.

Shimooka S., Oshima K., Hidaka H., Takewaki T., Kakiuchi H., Kodama A., Kubota M., Matsuda H., 2007. The evaluation of direct cooling and heating desiccant device coated with FAM. J. Chem. Eng. Japan 40, 1330-1334.

Suwa Y., Kumita M., Noki R., Kodama A., Otani Y., 2016. Water vapor sorption characteristics of calcium chloride-anodized alumina composites. J. Chem. Eng. Japan 49, 274-279.

Manuscript ID: 613
DOI: 10.18462/iir.icr.2019.0613

Performance optimization of ground water heat pump system for space heating and cooling applications

Mahalingesh SATALAGAON[(a)], Krishnan MURUGESAN[(b*)], Hywel R. THOMAS[(c)]

[(a)] Subros Limited, Noida, India.
[(b)] Department of Mechanical and Industrial Engineering, Indian Institute of Technology Roorkee, Roorkee -247667, Uttarakhand, India.

[c] Geoenvironmental Research Centre, Cardiff University, Cardiff, UK, krimufme@iitr.ac.in

ABSTRACT

Ground water heat pump systems (GWHP) provide better coefficient of performance (COP) because it makes use of ground water whose temperature is lower and higher than the atmosphere during summer and winter respectively. The present research focusses on determining optimum levels of operating and design parameters of an 8-ton GWHP for space heating and cooling mode operations assuming different combination of cooling and heating periods. Six variables at three levels are considered for optimization using Taguchi method and utility concept. An L_{27} orthogonal array has been used to obtain the levels of variables for 27 trial runs for space cooling and heating modes of operations. The effectiveness of plate heat exchanger is found to be the most influencing variable on COP followed by the ground water temperature. The COP increases with increase in the priority of mode of operation with 4.6 and 3.8 COP for cooling and heating modes respectively.
Keywords: Ground Water Heat Pump, Heating and Cooling Mode, Plate Heat Exchanger, COP, Taguchi, Utility Concept, Optimization, Weighing Factor.

1. INTRODUCTION

Ground water heat pump systems (GWHP), ground source heat pump (GSHP) systems and solar assisted ground source heat pump systems (Soni et al., 2015; ASHRA, 2011; Ozyurt et al., 2011; Wang et al., 2013; Cakir et al., 2013) to the conventional systems because they interact with the constant heat source/sink, that is ground instead of atmosphere which is subjected to diurnal variation. The GWHP also known as open loop GSHP systems make use of ground water as heat sink/source and hence the heat interaction with the heat transfer fluid in the heat pump is achieved effectively though a plate heat exchanger (PHE). Choi et al. (2006) proposed an optimum operation method for open loop ground heat exchangers (GHX) considering the subsurface temperature gradient. A series of thermal response tests and artificial heating/cooling operations were carried out along with monitoring temperatures in the standing column well (SCW). It was found out that the temperature distribution with depth is opposite to the natural underground condition. Kim et al. (2015) presented a research work in which the head and power of submersible pumps, heat pump units, piping, and heat exchangers are expressed as polynomial equations, and these equations are solved numerically to determine the system performance. Their results showed that system performance dropped as the water level in the bore well dropped, and the lowest flow rates generally achieve the highest system performance. The system COPs were almost unchanged or gradually changed in the low flow rate region with

increase in flow rate. However, in the higher flow rate region, the system heating and cooling COPs decreased rapidly as the flow rate increased. The heating COPs increased with warmer ground water temperatures, similarly, the system cooling COPs increased with cold groundwater temperatures. Increasing the UA value of the heat exchanger universally improved the system heating and cooling COPs. Rode et al. (2015) conducted a numerical parameter study of combined extraction- injection one-well systems. Numerical models of ground water flow and heat transport were carried out to check the influence of various hydro-geological and technical parameters. They concluded that the efficiency or feasibility of combined extraction injection one-well systems are strongly dependent on pumping rates and possible distance of the well screens. Wang et al. (2012) proposed two new design options that can improve open loop surface water heat pump system (SWHP) efficiency. A numerical model pertaining to a SWHP system was presented and parameters such as fluid intake temperature and energy saving rate of heat pump system were analyzed and compared with experimental measurements. When the cooling water temperature difference were 5°C and 10°C, they estimated 8.72% and 7.34% of theoretical energy saving rate respectively. There are very limited number of literature available on the optimization and thermal design of ground water heat pump systems and hence the present research focuses on the methodology of thermal design of GWHP (Ground Water Heat Pump) system and optimization of the design and operating parameters using Taguchi method. The utility concept is employed in order to predict the optimum conditions for varying periods of cooling heating mode operations.

2. THERMAL DESIGN OF GWHP SYSTEM

Fig. 1 shows the schematic diagram of the GWHP system for space cooling mode and heating is provided in the room using the reversing valve during the space heating mode operation. In the case of space cooling application the heat is removed from the room and it is rejected to the ground through the continuous supply of water from the extraction well. The heat to be removed from the room is given by:

$$Q_C = Q_H - W_{comp} \quad \text{Eq. (1)}$$

where Q_C is the heat to be removed from the room, Q_H is the heat to be rejected into the ground using the ground water and plate heat exchanger and W_{comp} is work input to the heat pump in kW. Similarly, the heat to be supplied to the room for space heating also can be computed. The main objective of an efficient thermal design is to achieve maximum overall COP of the GWHP system defined as:

$$COP_{overall\ system} = \frac{Q}{W_{comp}+W_{pump}+W_{fcu}} \quad \text{Eq. (2)}$$

where W_{comp} is the work supplied to the heat pump, W_{pump} is the pump work and W_{fcu} is fan coil unit work. In the case of GWHP system the main heat interaction between the heat pump and the ground water is achieved through a plate heat exchanger (PHE). For 28 kW cooling load capacity, the PHE, the mass flow rate of refrigerant and other parameters are designed following the standard procedure. In the PHE, the fluid flow pattern is much closer to counter flow stream unlike in shell and tube heat exchangers. In the present research the governing equations and the formulae used for designing of plate heat exchanger as discussed in Kakac and Liu (2002) have been used. The details of the thermal design of GWHP is explained in Fig.2 through a computational flow chart.

3. TAGUCHI TECHNIQUE

Six parameters, extraction well water temperature, flow rate of ground water, flow rate of heat transfer fluid (water) in chiller, heat transfer area in PHE, effectiveness of PHE and depth of well have been considered as influencing parameters at three levels. Taguchi optimization forms the matrix of experimental trial combinations by using standard orthogonal arrays. The parameter

combinations from the matrix is used to calculate the values of the objective function (i.e., system COP) and signal to noise (S/N) ratios are used to calculate the contribution pattern of the control parameters on the objective function. This technique provides maximum information from minimum number of experiments and the best level of each parameter to achieve better objective function value. The following relation is used to decide the minimum number of experiments to be conducted:

$$N_{Taguchi} = 1 + NV(L-1) \quad \text{Eq. (3)}$$

where $N_{Taguchi}$ is the number of experimental trials required to be conducted, NV is the number of variables or influencing parameters and L is the number of levels selected. In the present research work, NV = 6 and L = 3. According to Eq. (3), 12 number of experiments have to be conducted. However, e the standard orthogonal arrays (OA), L_{27} is selected for the experimental trials to satisfy the condition of three-level arrays suggested by Ross [1988] and each experimental trial is carried out according to the parameter combination given by the L_{27} array. Signal/Noise ratios are calculated based on larger the better concept to achieve maximum value for the COP of system.
For larger the better concept the signal to noise ratio [Ross, 1988]:

$$S/N(dB) = -10log_{10}\left(\frac{1}{n}\sum_{i=1}^{n}\frac{1}{y_i^2}\right) \quad \text{Eq. (4)}$$

where, y_i is response value, *'n'* is trial number and *'i'* is number of repetitions in a trial.

4. UTILITY CONCEPT

From Taguchi method, two different sets of control parameters have been obtained to achieve optimum COP of the system for space heating and cooling modes, now it is necessary to obtain a single set of control parameters which works better for both space cooling and space heating applications in GSHP system. This can be achieved by using utility concept. In optimization of GSHP system utility concept computes the utility value of individual performance parameters to a single performance index. The overall utility function (U) is given by:

$$U(R_1, R_2, .. R_n) = f(U(R_1), U(R_2), .. U(R_n)) \quad \text{Eq. (5)}$$

where $U(R_1, R_2, .. R_n)$ is overall utility of n performance parameters. According to required applications, performance parameters can be given weights. Different weighting factors are assigned to each performance parameter. The general equation of weighting utility is:

$$U(R_1, R_2, .. R_n) = \sum_{i=1}^{n} W_i U_i(R_i) \quad \text{Eq. (6)}$$

where W_i is the weight assigned to the performance parameters and the sum of all weights of all parameters should be equal to 1. The following conditions have to be satisfied to assign weighting factors for calculating COP of system:

$$\sum_{i=0}^{n} W_i = W_{cooling} + W_{heating} = 1 \quad \text{Eq. (7)}$$

where $W_{cooling}$, $W_{heating}$ are the weights assigned to the utility values calculated. In Asian countries there is requirement of heating for only 3-4 months compared to cooling requirement of 7-9 months, so cooling is given more priority than heating. For cooling, 0.7 and for heating, 0.3 weighting factors are assigned and the overall utility is computed as:

$$U = \sum_{i=0}^{n} W_i P_i \quad \text{Eq. (8)}$$

Where:

$P_i = Preference\ number = A \times log\left(\frac{y_i}{y_i'}\right)$ and $A = 9/log\frac{y_i^*}{y_i'}$

And *'A'* is a chosen arbitrary constant, y_i^* is the optimum value of y_i (i.e., COP in this work), y_i' is minimum possible value of system COP.

5. RESULTS AND DISCUSSION

5.1. Thermal Performance of GWHP

Thermal performance calculations of the GWHP were computed assuming an 8 TR space cooling capacity system. The details of the thermal performance calculations are demonstrated using the flow chart shown in Fig. 2. The PHE acts as the intermediate heat exchanger between the heat pump and the ground water source.

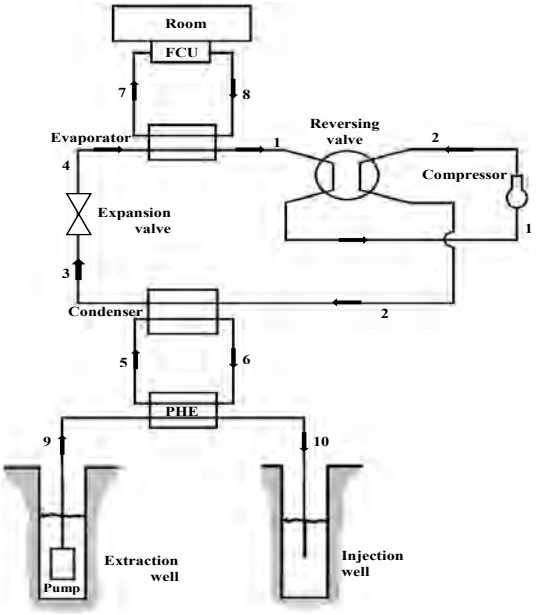

Figure 1: Schematic diagram of GWHP system for cooling application.

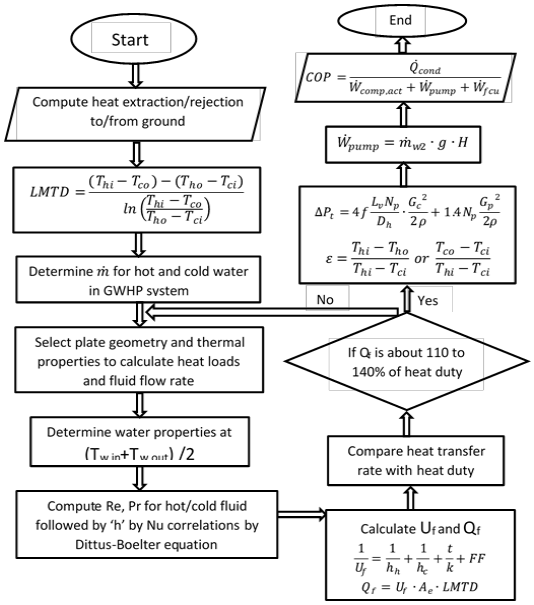

Figure 2: Flow chart for thermal design.

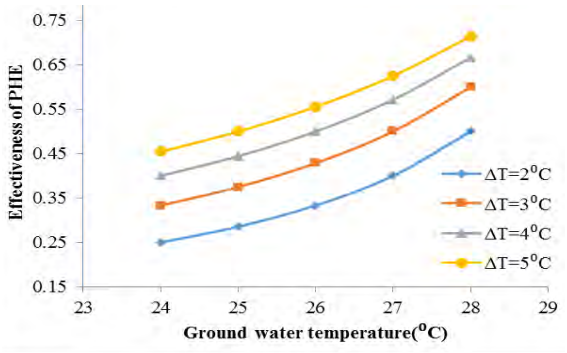

(a)

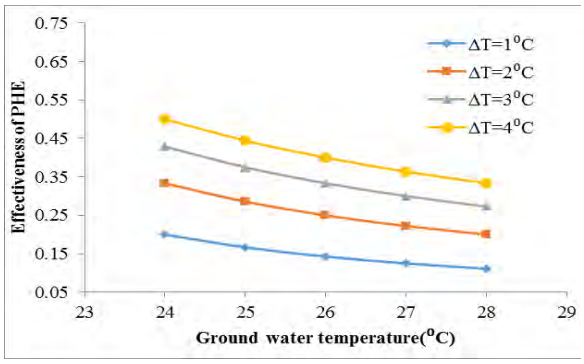

(b)

Figure 3: Variation of effectiveness of PHE with ground water temperature and ground water temperature difference for space (a) cooling and (b) heating.

Hence the effectiveness of PHE directly affects the performance of the system. Fig.3a shows the variation of effectiveness as a function of ground. water temperature for different ΔTs during cooling mode operation. For a given ΔT, with increase in ground water temperature the

effectiveness increases because for a fixed ΔT of cold water (ground water), the denominator of temperature ratio that defines effectiveness ($\varepsilon = \frac{T_{co}-T_{ci}}{T_{hi}-T_{ci}}$), keeps decreasing. This trend is repeated for all the ΔTs considered in this work. There is a difference of about 0.2 at the lower and upper ends of these curves. While performing these calculations a limit of 30°C is assumed for T_{ho}, that is the outlet temperature of chiller fluid coming from the PHE. Fig.3b depicts the variation of effectiveness for space heating mode at different ΔTs. In this case there is a continuous decrease in the effectiveness with increase in the ground water temperature because in this case ($\varepsilon = \frac{T_{hi}-T_{ho}}{T_{hi}-T_{ci}}$), in which the chiller fluid is the cold fluid and ground water becomes the hot fluid in the PHE. For a fixed ΔT of hot fluid, that is ground water temperature, increase in the inlet of hot fluid increases the denominator of temperature ratio in the definition of effectiveness, thus resulting in lower values of effectiveness. Hence in order to achieve an optimum overall COP of the GWHP system, the PHE has to be designed so that it operates at an optimum effectiveness. Fig. 4 shows the variation of COP with actual ground water temperature for both cooling and heating modes of operations with solid line for cooling and dotted line for heating mode. It can be noted that with increase in ground water temperature, the thermal potential of ground water to act as a source of heat supply increases resulting in increased heating effect and hence the COP increases. The opposite trend is observed for the case of cooling mode operation, because when the ground water temperature increases its potential to act as a sink to absorb heat from the chiller fluid through the PHE, decreases, resulting in decrease in the COP of the system and these trends are correctly depicted in the above figure. It is interesting to note that at 25°C, both the lines cross each other at a COP value of about 3.8, which is common for both cooling and heating modes of operations. These characteristic curves help one to estimate the expected COP of the system when the ground water temperature is known. The effect of mass flow rate of ground water on COP is depicted in Fig.5 for both cooling and heating modes of operations with solid line for cooling and dotted line for heating mode. As can be seen from this figure, the variation of COP for both cooling and heating modes is not very significant, however, cooling mode is more sensitive to change in mass flow rate of ground water compared to the heating mode. Here again both the curves cross each other at a COP of about 3.9 for 1.5 kg×s^{-1} of flow rate.

5.2. Optimization of Thermal Performance of GWHP System

For the purpose of application of Taguchi and Utility concept a table with values of levels of

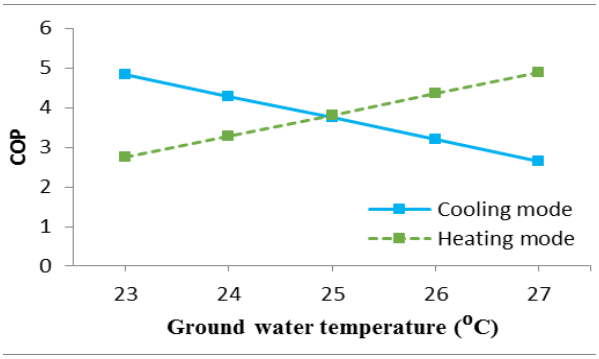

Figure 4: Variation of system COP with ground water temperature for cooling and heating mode.

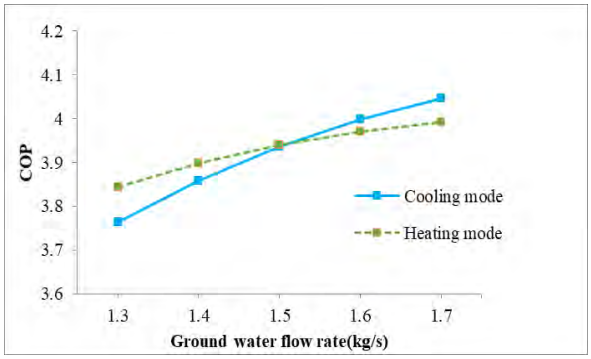

Figure 5: Variation of system COP with ground water flow rate for cooling and heating modes.

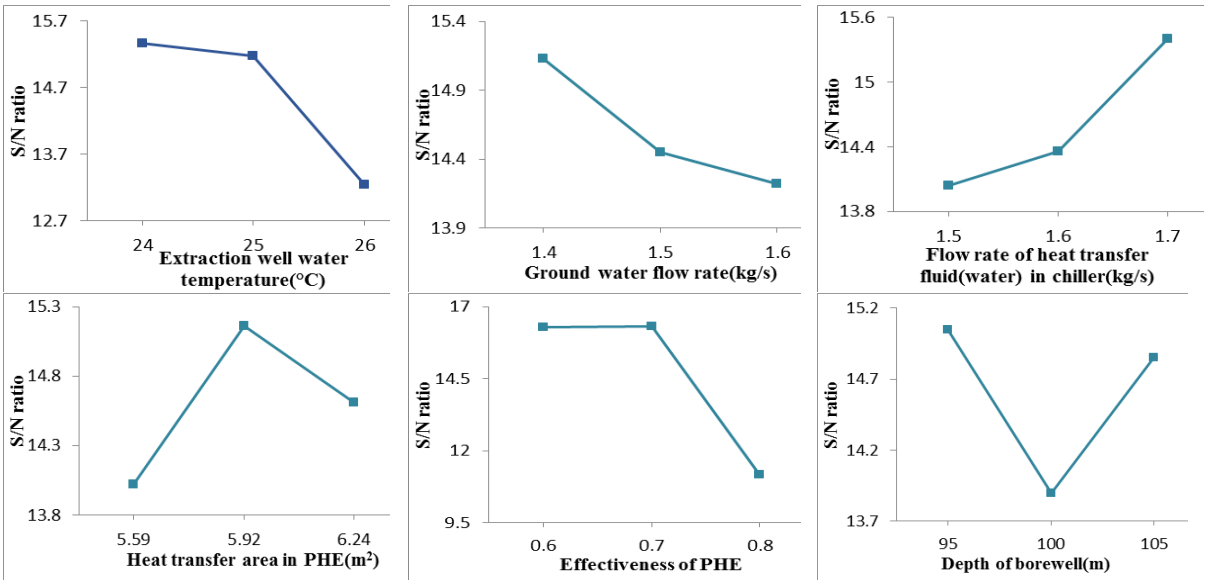

Figure 6: Utility Signal to noise ratio (S/N) for COP of system.

different parameters of the L_{27} orthogonal array (OA) has been prepared. Each set of values of parameters represent the data that to be fixed for the respective experimental trial run. A program in FORTRAN has been developed to compute the signal to noise ratio, S/N and other parameters of the ANOVA (Analysis of variance) for each trial run while computing the COP of the overall system for both cooling and heating mode of operations. From the plots of S/N for all the six parameters for cooling/heating modes, the levels of each parameter corresponding to the larger the better concept are selected for both cooling and heating mode operations. Now two set of these six variables are available for cooling and heating mode separately. However, as the same system will be used for both space cooling and heating mode operations, it is essential to determine single set of parameters that will provide maximum COP during both cooling as well as heating mode operations. For this purpose, utility concept has been implemented which requires the weighting function. Fig.6 shows the S/N plots for all the six parameters considered

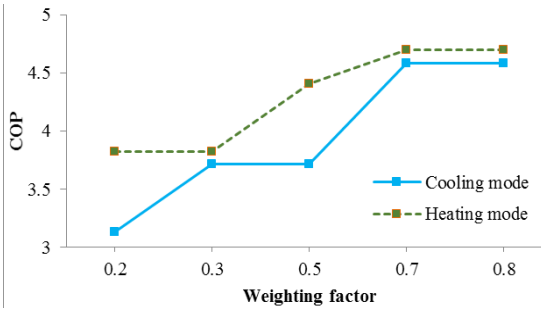

Figure 7: Variation of system COP with weighting factors for cooling and heating modes.

for the utility concept. A horizontal line in these plots indicates that particular parameter does not have any influence on the performance of the system. It is evident from this figure that all the six parameters have some influence on the COP of the GWHP system. The period of operation of GWHP system during cooling and heating mode operations is considered as the weighting function and is given as a ratio. Fig.7 shows the variation of COP of the GWHP system during cooling and heating mode operations for different weighting functions 0.2, 0.3, 0.5, 0.7 and 0.8. For example, for weighting function 0.3 corresponding to cooling curve, it indicates 30% of the

total time of operation of the GWHP system in a year, is the cooling period and the remaining 70% is the heating period. Heating mode always achieves higher COP compared to the cooling mode and is more predominant for weighting factors 0.2 and 0.5.

6. CONCLUSIONS

The basic thermal energy equations and design of plate heat exchanger and procedure to compute the overall system COP are discussed in detail. Some of the important design and operating parameters are optimized using Taguchi method and utility concept to achieve maximum system COP for both cooling and heating modes of operations. Based on the detailed study on the thermal performance and optimization of the ground water heat pump system for cooling and heating applications, the following observations are made:

(i) Increase in ground water temperature results in increase in the effectiveness of plate heat exchanger for space cooling because during space cooling increase in ground water temperature which is the cold fluid results in decrease in the value of maximum possible heat transfer, thus resulting in increase in the effectiveness.

(ii) In the case of space heating mode, the ground water temperature becomes the hot fluid in the plate heat exchanger and hence increase in the hot fluid inlet temperature will result in increase in the value of maximum possible heat transfer from the heat exchanger, thus resulting in decrease in effectiveness with increase in ground water temperature.

(iii) With increase in ground water temperature difference, the COP of the GWHP system increases linearly and the COP for heating mode is always higher than that of cooling mode of operation, however, the difference is only 5%.

(iv) With increase in exit temperature of chiller heat transfer fluid during cooling mode, the COP increases linearly, however, the COP decreases linearly with increase in exit water temperature for space heating mode.

NOMENCLATURE

A_{ch}	channel flow area (m^2)	Re	Reynolds number
b	mean flow channel gap (m)	t	thickness of plate (m)
D_h	hydraulic diameter (m)	T	Temperature (°C)
FF	fouling factor	U_f	Overall heat transfer coefficient ($W \times m^{-2} \times K^{-1}$)
G	mass velocity ($kg \times m^{-2} \times s^{-1}$)		**Greek letters**
G	mass velocity ($kg \times m^{-2} \times s^{-1}$)	ε	effectiveness of PHE
h	heat transfer coefficient ($W \times m^{-2} \times K^{-1}$)	ρ	density of water ($kg \times m^{-3}$)
h	specific enthalpy ($kJ \times kg^{-1}$)		**Subscripts**
H	height of water column (m)	a	air
k	thermal conductivity of plate ($W \times m^{-1} \times K^{-1}$)	act	actual
L_p	length of plate (m)	c	cold
$\dot{m}$	mass flow rate of water ($kg \times s^{-1}$)	comp	compressor

$\dot{m}_{ch}$	mass flow rate per channel(kg $\times s^{-1}$)	dest	destruction
N_{cp}	channels per pass	fcu	fan coil unit
N_e	effective no. of plates	h	hot
N_p	number of passes	i	inlet
N_t	number of plates	o	outlet
Nu	Nusselt number	pump	pump
p	plate pitch (m)	r	refrigerant
P	Pump power (kW)		
Pr	Prandtl number		
ΔP_t	Pressure drop (kPa)		
Q_f	Actual heat transfer rate (kW)		
Q_r	Heat duty (kW)		

REFERENCES

ASHRAE. 2011. ASHRAE handbook: HVAC application. Atlanta, GA, USA.

Cakir, U., Comakli, K., Comakli, O., Karsli, S. 2013. An experimental exergetic comparison of four different heat pump systems working at same conditions: as air to air, air to water, water to water and water to air. Energy 58, 210–219.

Choi, H.J.,Park,S., Lee, H., Pham, Khanh L. N.,Ryu,H., Choi,H.,2016. Optimum operation of open-loop ground heat exchanger considering subsurface temperature gradient. International Journal of Energy Research 40, 651–661.

Kakac, S., Liu, H.,2002. The gasketed plate heat exchangers , Text book for Heat exchangers selection, rating and thermal design, Second edition, 373-412.

Kim, J., Nam,Y.2015.A numerical study on system performance of groundwater heat pumps. Energies 9(1), 1-14.

Ozyurt, O., Ekinci,D.A.,2011. Experimental study of vertical ground source heat pump performance evaluation for cold climate in Turkey. Applied Energy 83, 1257–1265.

Rode,A.,Liesch,T.,Goldscheider,N.,2015. Open-loop geothermal heating by combined extraction–injection one-well systems: A feasibility study. Geothermics, 56,110-118.

Ross, P. J., 1988. Taguchi techniques for quality engineering, Loss function, orthogonal experiments, parameter and tolerance design, 73-75 and 172-173.

Soni, S.K., Pandey, M., Bartaria, V.N., 2015. Ground coupled heat exchangers: A review and applications. Renewable and Sustainable Energy Review 47, 83-92.

Wang, H.J. Zhao, Q., Wu, J., Yang, B., Chen, Z., 2013. Experimental investigation on the operation performance of a direct expansion ground source heat pump system for space heating. Energy and Buildings 61,349–355.

Wang,Y., Wong, K.K.L., Liu, Q., Jin, Y., Tu, J.,2012. Improvement of energy efficiency for an open-loop surface water source heat pump system via optimal design of water-intake. Energy and Buildings 51, 93-100.

Manuscript ID: 645
DOI: 10.18462/iir.icr.2019.0645

Integration of a compact two fluid PCM heat exchanger into the hot superheated section of an air source heat pump cycle for optimized DHW generation

Johann EMHOFER[(a)], Tilman BARZ[(a)], Klemens MARX[(a)], Felix HOCHWALLNER[(a)], Luisa F. CABEZA[(b)], Gabriel ZSEMBINSZKI[(b)], Andreas STREHLOW[(c)], Birgo NITSCH[(c)], Michael WEISS[(d)]

[(a)] AIT Austrian Institute of Technology, Center for Energy, 1210 Wien, Austria, johann.emhofer@ait.ac.at
[(b)] GREiA Research Group, INSPIRES Research Centre, Universitat de Lleida, 25001 Lleida, Spain, lcabeza@diei.udl.cat
[(c)] AKG Verwaltungsgesellschaft mbH, 34369 Hofgeismar, Germany, andreas.strehlow@akg-gruppe.de
[(d)] OCHSNER Wärmepumpen GmbH, 4020 Linz, Austria, michael.weiss@ochsner.com

ABSTRACT

This contribution presents a concept for the direct integration of a refrigerant/water Heat Exchanger (HEX) with a Phase Change Material (PCM) in the hot superheated section of an R32 - air source compression Heat Pump (HP) cycle, for optimized Domestic Hot Water (DHW) generation in multi-family houses. The concept takes advantage of the PCMs high thermal storage capacity integrated into a high performance compact enhanced plate-and-fin aluminium HEX. On the refrigerant side, it works as a de-superheater for DHW generation during heating and cooling operation whereas the process water is connected to decentralized DHW storages located in single apartments of a low energy building. We present results from simulations at a system level for typical operating conditions and corresponding seasonal and annual performances. Compared to conventional systems, the results indicate savings up to 11% of electric energy over the year for DHW generation in average climate.

Keywords: domestic hot water, energy efficiency, heat pump, heating, hot gas, phase change material.

1. INTRODUCTION

Today's commercially available air source HPs work highly efficient and make a valuable contribution to reach climatic goals as the reduction of CO_2 in our atmosphere. To further increase the efficiency of HPs many different concepts using latent heat thermal energy storage technologies were proposed recently. The aim is to decrease the size of buffer tanks and to avoid the oversizing of HPs reducing thermal peak loads by shifting heating and cooling demands in time (Pardiñas *et al.*, 2017), to optimize integration of solar thermal collectors (Kapsalis *et al.*, 2016), to enhance the storage density of DHW storages (Zou *et al.*, 2017) or to enhanced the defrosting performance of air source HPs (Song *et al.*, 2018). Recent studies showed further that a wide spectrum of PCMs are available to be used in such storages at different temperature levels (Cabeza *et al.*, 2011).

This contribution employs latent heat thermal energy storage technology to increase the efficiency of air source HP systems in multi-family houses for DHW generation. The key idea is to optimally use the available exergy of the refrigerant during operation all over the year. This means that thermal energy at a high temperature level in the superheated section of the HP cycle is stored in a PCM to be used later for high temperature DHW generation rather than being used at intermediate temperatures for heating or even being wasted in the case of cooling operation. The optimal assignment of high temperature heat during conventional operation is realized by the direct

integration of a refrigerant (R)/water (W) heat exchanger (HEX) with phase (P) change material – in short: RPW-HEX . The compact RPW-HEX is integrated in the hot refrigerant flow exiting the compressor of a compression HP on the primary side and in the process water flow on the secondary side. From the secondary side of the RPW-HEX, the process water delivers the thermal energy to decentralized DHW storages located in the individual apartments of a multi-family house. The RPW-HEX also manages flexible DHW demands and by this minimizes the operation of the air source HP in the highly non-efficient direct DHW operating mode. Furthermore, it adds the necessary flexibility by decoupling the high temperature high power energy streams (for DHW generation) and the low temperature and low power energy stream (for heating). To guarantee high heat transfer coefficients between the hot gaseous refrigerant and the PCM, between the PCM and the process water and between the refrigerant and the process water, with a minimum of refrigerant mass, a plate and fin aluminium heat exchanger design is used. The present study answers the question, how much of the heat can be stored in the RPW-HEX and therefore delivered to the decentralized DHW storages in a typical application. Furthermore, possible savings in electric energy are quantified and compared to a reference system without the RPW-HEX. For doing so, simulation studies at selected operating points were carried out. Annual efficiencies for the proposed system and the reference system without RPW-HEX were calculated by summing up steady states over one year on an hourly basis.

2. CASE STUDY AND OPERATION MODES

The case study considers an application with three apartments located in average climate conditions in Europe and an air source HP. The main purpose is heating in winter and DHW generation all over the year. Through switching into reverse mode, cooling during summer is also possible.

The proposed system distinguishes between six operating modes (a-f) whilst a conventional system distinguishes between mainly three operating modes, namely heating, cooling and DHW generation which have similar efficiencies as (d,e,f) in the proposed system,

(a) heating operation and charging the RPW-HEX ($0 < SoC \uparrow \leq 1$)

(b) cooling operation and charging the RPW-HEX ($0 < SoC \uparrow \leq 1$)

(c) energy efficient DHW generation by discharging the RPW-HEX ($0 \leq SoC \downarrow \leq 1$)

(d) conventional (inefficient) direct DHW generation ($SoC = 0$)

(e) heating operation when the RPW-HEX is fully charged ($SoC = 1$)

(f) cooling operation when the RPW-HEX is fully charged ($SoC = 1$)

where SoC refers to the state of charge of the RPW-HEX (Barz *et al.*,2018). Figure 1 (a)-(d) show the operation modes (a)-(d) in a system sketch, where the conventional operation modes (e), (f) are omitted for the sake of brevity. The HP is connected to the apartments with two hydraulic lines and the switching between charging the decentralized DHW storages and heating/cooling takes place in the apartments. During heating mode (a), most of the sensible energy in the superheated hot gas charges the RPW-HEX (R). The amount of transferred heat depends on the hot gas temperature, the refrigerant mass flow, the phase transition temperature of the (solid/liquid) PCM, and the overall heat transfer coefficients of the RPW-HEX. Hot gas temperature and refrigerant mass flow result from the operating point whereas the switching temperature range of the PCM and the heat transfer capabilities of the RPW-HEX are design inherent (design parameters). For the proposed concept, R32 as a refrigerant was used and Rubitherm PCM RT64HC as PCM with a phase change temperature of 64℃ and a narrow phase transition temperature range was selected (Rubitherm, 2019). R32 has a rather high hot gas temperature when compared to other refrigerants. To limit the compressor discharge temperature at low temperatues, liquid refrigerant from the condenser exit is injected into the compressor (which is able to handle a small amount of liquid refrigerant) entrance by means of a liquid injection valve (B). In doing so, the hot gas temperature can be limited to ≈115℃. Furthermore, an additional HEX (F) is introduced to ensure that the refrigerant is in the liquid phase at the expansion valve (X) entry. Via the condenser (C), the heat is delivered to the apartments by the heating distribution system (H). In cooling mode (b), the four-way valve (W) switches to reverse mode and the evaporator (E) acts as a heat sink, whereas the condenser (C) cools the building via the heating and cooling network (H). Because the four-way valve (W) is located after the RPW-HEX, the PCM is also charged by the hot gas during cooling operation. Note that contrary to heating mode,

where it would also be possible to use the energy stored in the PCM for heating (of course with a low exergy efficiency), the energy stored in the RPW-HEX during cooling is usually not used in a conventional system. Once, the RPW-HEX is fully charged (SoC =1) by mode (a) or (b), the HP system switches to DHW generation mode (c). Contrary to direct DHW-generation mode (d), the condensing temperature, and therefore the COP, remains at the values for heating mode in (c). Therefore, the process water from the return line of the decentralized DHW storages (S) is pre-heated by the condenser at a beneficial COP. Subsequently the process water is boosted to the DHW set-point temperature ($\vartheta_w \approx 62$ °C) by discharging the RPW-HEX (R). During this operation mode, additionally the hot gas will transfer its sensible energy via the RPW-HEX (R) to the process water. Once the RPW-HEX is discharged, the HP switches back to heating or cooling mode, respectively.

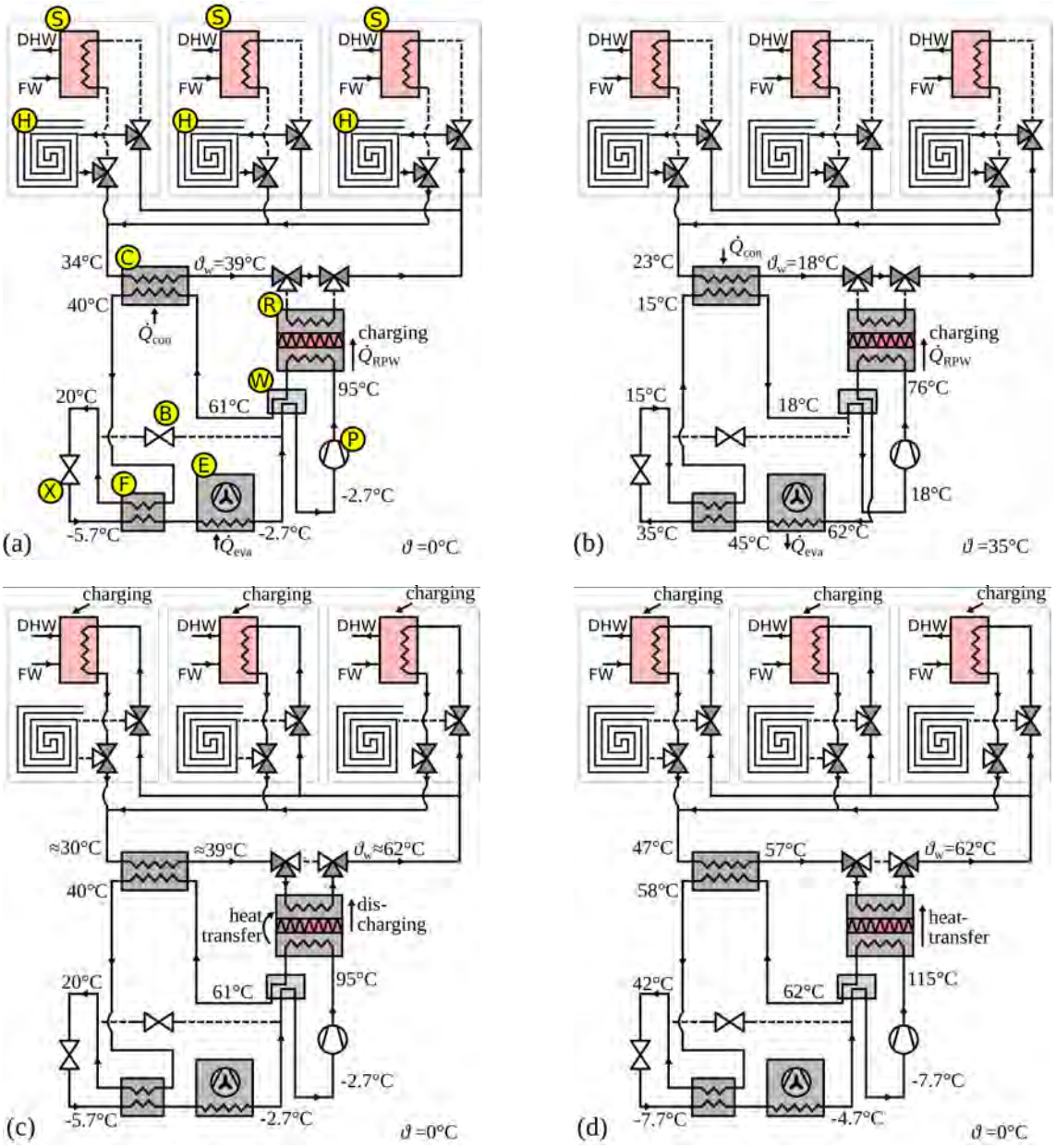

Figure 1: Concept of the proposed system for a scenario with three apartments during: (a) heating operation, (b) cooling operation, (c) energy efficient DHW generation by discharging the RPW-HEX and (d) direct DHW. (S) Decentralized sensible DHW storage, (H) low- or intermediate temperature heating system, (C) condenser, (R) RPW-HEX, (W) four way valve, (B) bypass expansion valve, (X) regular expansion valve, (F) fluid phase heat exchanger, (E) evaporator and fan, (P) compressor. The temperatures indicated in (a),(b) and (d) were taken from steady-states at an SoC of 20% and 50% for heating and cooling, respectively, whereas they were taken shortly after switching from mode (a) to (c) in (c). The ambient temperature (ϑ) was 0°C in (a,c and d) and 35°C in (b).

In the case that the thermal energy for DHW generation cannot be provided entirely by operating mode (c), e.g. during spring, the HP has to switch to the direct DHW generation mode (d). In this mode, similar to a conventional system, DHW has to be generated by increasing the condensing temperature to values suitable for DHW. The RPW-HEX acts in this case solely as HEX and transfers the sensible energy of the hot gas directly to process water. In operating mode (e) and (f) the RPW-HEX is fully charged and the modes are comparable to conventional heating and cooling modes.

3. METHODOLOGY

3.2 Simulation models

Simulation studies were carried out for both, the novel system and the reference system without RPW-HEX. The following performance indicators were computed to calculate the annual efficiencies: Coefficient of Performance related to the hot side of the HP for heating and cooling: COP_h, Coefficient of Performance related to the hot side of the HP for DHW: COP_{DHW} and RPW-HEX utilization factor: ε_{RPW}. The simulations were carried out in the Dymola/Modelica modelling environment using ThermoCycle library components (Quoilin *et al*., 2014). Additionally, models for the RPW-HEX, the outdoor unit and the four way valve were developed in.house (Emhofer *et al.*, 2018, Frazzica *et al.*, 2018). Thermodynamic properties were taken from the CoolProp library (Bell *et al*., 2014). The performance indicators were derived from the dynamic simulation when the system is in steady-state or when the SoC reached 20% or 50% for heating and cooling, respectively. Defrosting operation was neglected, and electric power consumption for COP calculations solely reflects the consumption of the compressor and the fan of the outdoor unit. All HP geometry/component design parameters, efficiencies and heat transfer coefficients were taken from design sheets or calculated from well-established equations and were later experimentally validated with measurements of the prototype air source HP used in the H2020 project HYBUILD (HYBUILD, 2017) without RPW-HEX.

3.2 Annual Energy Efficiency Calculations

A quasi-static approach to estimate the annual energy demand of the systems was adopted. Performance parameters at different ambient temperature levels were considered for heating, cooling and DHW generation mode (a), (b) and (d) on an hourly basis over one year or 8760 hours. Please note, that pre-heating of the process water with the condenser in operation mode (c) is not considered in the following because this process is highly dynamic and can't be handled with this quasi-static approach. Hence, the entire energy for energy efficient DHW generation is always taken from the RPW-HEX. The assumed scenario is defined by ambient temperatures (ϑ) from Strasbourg in an hourly resolution (Meteonorm, 2016). A function for the feed water temperature to the heating distribution system (ϑ_w) see Eq. (1), was fitted to the ambient temperatures as defined in the EN14825 (2016), using variable outlet temperatures for heating and for cooling ceiling applications:

$$\vartheta_{\mathrm{w}}(\vartheta) = \begin{cases} -0.577 \times \vartheta + 39.1\,^{\circ}\mathrm{C}, & \vartheta \leq 2^{\circ}\mathrm{C} \\ -1 \times \vartheta + 40\,^{\circ}\mathrm{C}, & 2^{\circ}\mathrm{C} \leq \vartheta \leq \vartheta_{\mathrm{on,h}} = 16^{\circ}\mathrm{C} \\ 18\,^{\circ}\mathrm{C}, & \vartheta \geq \vartheta_{\mathrm{on,c}} = 20^{\circ}\mathrm{C} \end{cases} \quad \text{Eq. (1)}$$

Note that heating starts below $\vartheta_{on,h}$ = 16 °C and cooling starts above $\vartheta_{on,c}$ = 20 °C, respectively. Because the condenser is connected to the heating and cooling distribution system (c.f. Fig. 1 (a,b)), $\dot{Q}_{con}$ is used to describe the heating and cooling demand of the building which needs to be covered by the HP at all times. The design point of the HP is defined by a heating demand of $\dot{Q}_{con} = 2$ kW per apartment at ϑ=$\vartheta_{design,h}$=-10°C, typical for a low energy building. As the main purpose of the system is heating, the design cooling load ($\dot{Q}_{con}(\vartheta_{design,c})$) is calculated from the definitions from heating by considering solely heat conduction between the apartment and the ambient air while neglecting solar radiation. This approach will underestimate the cooling demand but was used to be able to work without a detailed building model. The design cooling load is given in Eq. (2):

$$\dot{Q}_{\mathrm{con}}(\vartheta_{\mathrm{design,c}}) = \mathrm{UA}\,(20^{\circ}\mathrm{C} - \vartheta_{\mathrm{design,c}}) = \frac{\dot{Q}_{\mathrm{con}}(\vartheta_{\mathrm{design,h}})}{\vartheta_{\mathrm{on,h}} - \vartheta_{\mathrm{design,h}}}\,(\vartheta_{\mathrm{on,c}} - \vartheta_{\mathrm{design,c}}) \quad \text{Eq. (2)}$$

where $\vartheta_{design,c}$=35 °C. With Eq. (2) one finds a cooling load of 1.15 kW per apartment at 35 °C. The part load behaviour $\dot{Q}_{con}(\vartheta)$ is obtained assuming a linear dependence between $\vartheta_{on,h}$ and $\vartheta_{design,h}$, and between $\vartheta_{on,c}$ and $\vartheta_{design,c}$, respectively (EN14825, 2016), as shown in Eq. (3):

$$\dot{Q}_{con}(\vartheta) = \begin{cases} \frac{\vartheta - \vartheta_{\mathrm{on,h}}}{\vartheta_{\mathrm{design,h}} - \vartheta_{\mathrm{on,h}}} \times \dot{Q}_{\mathrm{con}}(\vartheta_{\mathrm{design,h}}), & \text{heating}, \vartheta \leq 16℃ \\ \frac{\vartheta - \vartheta_{on,c}}{\vartheta_{\mathrm{design,c}} - \vartheta_{\mathrm{on,c}}} \times \dot{Q}_{\mathrm{con}}(\vartheta_{\mathrm{design,c}}), & \text{cooling}, \vartheta \geq 20℃ \end{cases} \quad \text{Eq. (3)}$$

The amount of heat transferred to the RPW-HEX $\dot{Q}_{RPW}$, is calculated using a utilization factor ε_{RPW} which relates to the total thermal energy transferred at the hot side $\dot{Q}_{hot}(\vartheta)$ as shown in Eq. (4):

$$\dot{Q}_{\mathrm{RPW}}(\vartheta) = \varepsilon_{\mathrm{RPW}}(\vartheta)\, \dot{Q}_{\mathrm{hot}}(\vartheta) \quad \text{Eq. (4)}$$

where the heat transferred on the hot and cold side of the heat pump are given by Eq.(5) and Eq.(6):

$$\dot{Q}_{\mathrm{hot}}(\vartheta) = \begin{cases} \dot{Q}_{\mathrm{con}} + \dot{Q}_{\mathrm{RPW}}, & \text{heating, DHW generation} \\ \dot{Q}_{\mathrm{eva}} + \dot{Q}_{\mathrm{RPW}}, & \text{cooling} \end{cases} \quad \text{Eq. (5)}$$

$$\dot{Q}_{\mathrm{cold}}(\vartheta) = \begin{cases} \dot{Q}_{\mathrm{eva}}, & \text{heating , DHW generation} \\ \dot{Q}_{\mathrm{con}}, & \text{cooling} \end{cases} \quad \text{Eq. (6)}$$

Note that ε_{RPW} in Eq. (4) strongly depends on the temperature conditions. In the reference system ε_{RPW} is zero and therefore, the entire thermal energy on the hot side (Eq. (5)) is transferred to the condenser during heating or to the evaporator during cooling, respectively.

Furthermore a daily DHW consumption of Q_{DHW}^{d} =5.845 kWh per apartment is assumed, which is comparable to a medium water consumption as defined in the EN16147 (2017). The load profile is also taken from the standard, and it is assumed that the energy stored in the RPW-HEX can always be delivered to the decentralized water storages without thermal losses in space and time.

The annual energy efficiency ratios (EER) for heating and cooling are calculated by means of Eq. (7) and Eq. (8), similarly to the basic definitions for the $SCOP_h$ and $SCOP_c$ in the EN14825 (2016):

$$EER_{\mathrm{heating}} = \frac{Q_{\mathrm{heating}}^{y}}{W_{\mathrm{heating}}^{y}} = \frac{\sum_{j=1}^{8760} Q_{con}(\vartheta_j)}{\sum_{j=1}^{8760} \left(\frac{Q_{con}(\vartheta_j)}{COP_h(\vartheta_j)} \right)} \quad \text{Eq. (7)}$$

$$EER_{\mathrm{cooling}} = \frac{Q_{\mathrm{cooling}}^{y}}{W_{\mathrm{cooling}}^{y}} = \frac{\sum_{j=1}^{8760} Q_{\mathrm{con}}(\vartheta_j)}{\sum_{j=1}^{8760} \left(\frac{Q_{\mathrm{con}}(\vartheta_j)}{COP_h(\vartheta_j) - 1} \right)} \quad \text{Eq. (8)}$$

where the superscript y indicates the annual demand and W ist the electric energy demand of the compressor and the fan. In the reference as well as in the proposed HP system in direct heating mode (d), the COP for DHW generation COP_{DHW} will be significantly lower than the COP for heating due to the higher temperature difference between evaporator and condenser. The electric energy consumption at a certain ambient temperature ϑ_j at a certain hour of the year h_j is given in Eq. (9):

$$W_{\mathrm{DHW}}(\vartheta_j, h_j) = \frac{Q_{\mathrm{DHW}}(h_j)}{COP_{\mathrm{DHW}}(\vartheta_j)} \quad \text{Eq. (9)}$$

With the aid of the RPW-HEX, a certain amount of thermal energy can be generated with a better with COP_h instead of COP_{DHW} leading to a reduction of the electric energy demand. The situation is

different in cooling mode. In the reference system, the total energy transferred on the hot side dissipates in the evaporator and is lost. Therefore, DHW is not only generated with a better COP with the RPW-HEX, but for free, as waste heat is utilized. The reduction of electric energy demand compared to direct DHW generation is therefore given in Eq. (10):

$$\Delta \mathrm{W}_{\mathrm{DHW,RPW}}(\vartheta_j, h_j) = \begin{cases} Q_{\mathrm{RPW}}(\vartheta_j)\left(\frac{1}{COP_{\mathrm{DHW}}(\vartheta_j)} - \frac{1}{COP_{\mathrm{h}}(\vartheta_j)}\right), & \text{heating} \\ \frac{Q_{\mathrm{RPW}}(\vartheta_j)}{COP_{\mathrm{DHW}}(\vartheta_j)} & \text{cooling} \end{cases} \quad \text{Eq. (10)}$$

where $\dot{Q}_{RPW}$ follows from Eq. (4) for heating and cooling. With Eq. (9) and Eq. (10), the anual efficiency for DHW generation reads:

$$\Delta EER_{DHW} = \frac{Q^{y}_{\mathrm{DHW}}}{W^{y}_{\mathrm{DHW}}} = \frac{\sum_{j=1}^{8760} Q_{\mathrm{DHW}}(\mathrm{h_j})}{\sum_{\mathrm{j=0}}^{8760}\left(W_{\mathrm{DHW}}(\vartheta_j, h_j) - \Delta W_{\mathrm{DHW,RPW}}(\vartheta_j, h_j)\right)} \quad \text{Eq. (11)}$$

4. RESULTS AND DISCUSSION

4.1 Performance indicators obtained from simulation studies

Figure 2 shows results of the performance indicators obtained from the simulations for different constant ambient temperatures. For annual calculations missing values between the depicted points were calculated by linear interpolation. As expected the COPs significantly decrease for low (heating) and high (cooling) ambient temperatures due to the high temperature lift between evaporator and condenser. The COPs of both system are almost equal although the sensible heat of the hot gas can be used for heating in the reference heating case and doesn't need to be cooled by the outdoor air in the cooling case for the novel system. Heating, cooling and direct DHW behaviour in Fig. 2(a) corresponds to operating modes (a),(b) and (d) for the novel system. Note that if the RPW-HEX can be charged, DHW can be generated with operating mode (c) with the better COPs "heating and RPW-DHW" and "cooling and RPW-DHW", respectively, instead of "direct DHW" generation. The RPW-HEX is able to store energy for ambient temperatures below 10 °C and above 30 °C (Fig. 2(b)). Between 10 °C and 30 °C, the hot gas temperature is too low ($\lesssim 64$ °C). Below ≈ -5 °C, the liquid injection valve starts to work and therefore, the hot gas temperature is limited to ≈ 115 °C. The storable energy from superheated refrigerant then only depends on the mass flow of the refrigerant.

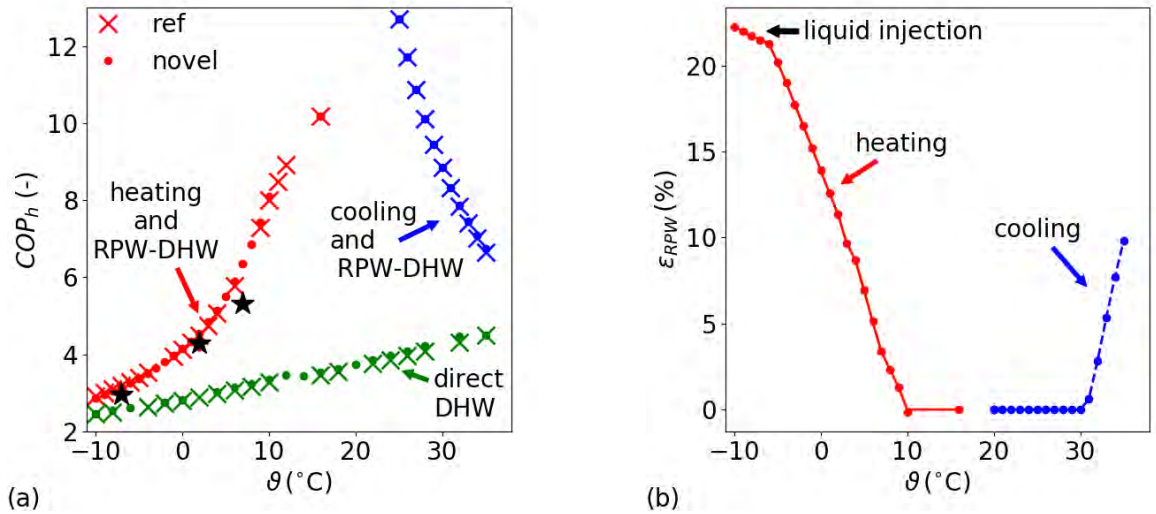

Figure 2: Performance indicators of the HP system in relation to the ambient temperature. The black stars in (a) denote the values from the measurements of the prototype HP without RPW-HEX.

4.2 Annual energy efficiency

The resulting annual heating and cooling demands are $Q^{\mathrm{y}}_{\mathrm{heating}}$=12 847 kWh and $Q^{\mathrm{y}}_{\mathrm{cooling}}$=1 093 kWh, respectively. Furthermore, the annual heating demand for DHW is $Q^{\mathrm{y}}_{\mathrm{DHW}}$ = 6 400 kWh. Figure 3 shows how much thermal energy can be provided by the RPW-HEX for DHW generation on a daily basis. During winter times in 17 days the RPW-HEX can deliver more than necessary to cover the DHW consumption. Hence, the surplus thermal energy might be shifted to the decentralized DHW storages. Due to the relatively low hot gas temperature in summer times, and the low amount of hot days (only 30 hours with temperatures above 30 °C) the RPW-HEX will not contribute significantly to the DHW generation given the climatic scenario selected here.

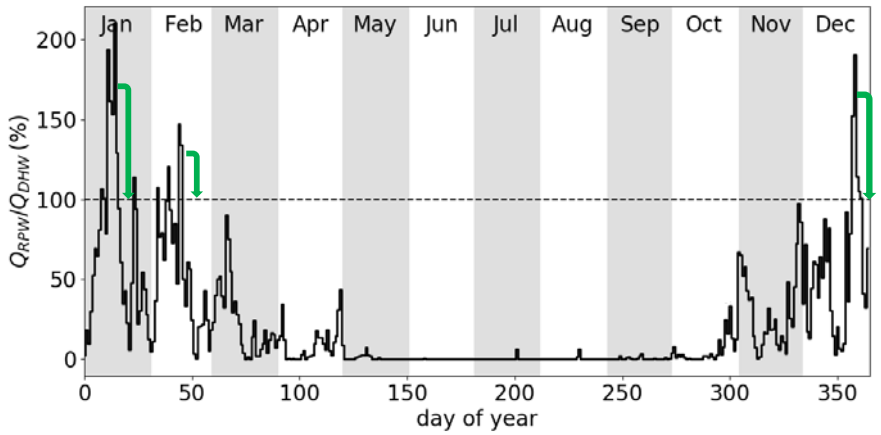

Figure 3: Coverage ratio of energy for DHW provided by the RPW-HEX. Note that, for the calculated annual performance indicators, it is assumed that surplus energy gained from the RPW-HEX can be stored for usage during the days to come (green arrows).

Table 1 summarizes the annual performance indicators and the electric energy consumption of the reference and the novel system. The annual performance for heating EER_h and cooling EER_c are almost equal whereas, the annual performance for DHW is about 11 % higher for the novel system compared to the reference system. To sum up, the novel concept saves 200 kWh electricity per year which results in 4.3 % lower annual total electric energy consumption.

Table 1: Calculated annual energy efficiencies

	$Q^{\mathrm{y}}_{\mathrm{RPW}}$(kWh)	W_{sum}(kWh)	W_{h}(kWh)	W_{c}(kWh)	W_{DHW}(kWh)	EER_{h}	EER_{c}	EER_{DHW}
Reference	0	4654	2586	105	1963	4.97	10.4	3.26
Novel	1389	4456	2583	105	1768	4.97	10.4	3.62

5. CONCLUSIONS AND OUTLOOK

Technical details and economic benefits are presented for a novel heat pump system, with a Refrigerant/PCM/Water Heat EXchanger (RPW-HEX) directly integrated in the hot gas section of an air source HP, for energy efficient DHW generation. Annual calculations indicate for average climatic conditions, intermediate heating temperatures and medium DHW consumptions, estimated savings of about 4.3 % of electric energy when compared to conventional air source HP systems. These energy savings result from a 11 % better performance for DHW generation with the novel system. The case study considers three apartments located in a low energy building, each with a heat demand of 2 kW per apartment at -10 °C and a DHW demand of 5.825 kWh per day. The absolute savings amount in this case is 200 kWh of electric energy with the proposed system per year.

The average energy price per kWh was 0.22 €/kWh for households in the Euro area in 2018 (EUROSTAT, 2018) which means a cost saving of 44 € per year. If we assume a latent storage density of 70 Wh/kg and would like to discharge the RPW-HEX after 2 hours of heating/cooling operation, we would need around 1.5 kWh storage capacity for three apartments or around 21 kg

PCM to deliver the daily DHW demand to the decentralized storages. For a typical price of 5 € per kg PCM, the PCM costs therefore about 105 €. Based on the design used for the prototype, the aluminium and manufacturing costs are around 200 € and 500 €, respectively. Summing everything up one can estimate investment costs of about 805 € for the RPW-HEX what gives a payback time of around 18 years for the given example. Next steps will include the assessment of the annual performances for other climatic conditions, building conditions and PCM materials, as the yearly performance and therefore the payback time strongly depend on these constraints. Furthermore, solar radiation needs to be included in the calculations for heating and cooling demand and experiments with the experimental air source HP and the RPW-HEX will be carried out in the months to come.

ACKNOWLEDGEMENTS

The authors thank C. Köfinger, M. Lauermann, W. Pink and A. Zottl for critical discussion.This project has received funding from the European Union's Horizon 2020 research and innovation programme under grant agreement No 768824 (HYBUILD). GREiA is certified agent TECNIO in the category of technology developers from the Government of Catalonia. The authors would like to thank the Catalan Government for the quality accreditation given to their research group (2017 SGR 1537).

NOMENCLATURE

COP	Coefficient of Performance (-)	W	Electric energy (kWh)
EER	Energy Efficiency Ratio (-)	ε_{RPW}	Utilization factor of the RPW-HEX (-)
Q	Thermal energy (kWh)	ϑ	Temperature (°C)
UA	Thermal conductance (kW/K)		

REFERENCES

Barz, T., Seliger, D., Marx, K., Sommer, A., Walter, S. F., Bock, H. G., Körkel, S., 2018, State and state of charge estimation for a latent heat storage, Control Engineering Practice, 72, 151-166.

Bell, I. H., Wronski, J., Quoilin, S., Lemort, V., 2014, Pure and Pseudo-pure Fluid Thermophysical Property Evaluation and the Open-Source Thermophysical Property Library CoolProp, Industrial & Engineering Chemistry Research, 53 (6), 2498--2508.

Cabeza, L.F., Castell, A., Barreneche, C., de Gracia, A., Fernández, A.I., 2011, Materials used as PCM in thermal energy storage in buildings: A review, Renew Sust Energ Rev, 15, 1675–1695.

Emhofer, J., Barz, T., Palomba, V., Frazzica, A., Sergi, F., Varvagiannis, S., Karellas, S., Oró, E., Zsembinszki, G., Cabeza, L.F., Deliverable D3.1 of the HYBUILD-Project: Modular flow sheet simulation of the hybrid (sub-)system, 2018. [Online]. Available: http://www.hybuild.eu/publications/deliverables/

EN 16 147: Heat pumps with electrically driven compressors - Testing, performance rating and requirements for marking of domestic hot water units, EN 16 147, 2017-01

EN 14 a825: Air conditioners, liquid chilling packages and heat pumps, with electrically driven compressors, for space heating and cooling — Testing and rating at part load conditions and calculation of seasonal performance, EN 14 825, 2016-03

EUROSTAT, Electricity price statistics - Statistics Explained, 2018, https://ec.europa.eu/eurostat/statistics-explained/index.php/Electricity_price_statistics#Electricity_prices_for_household_consumers, accessed Apr. 30, 2019

Frazzica, A., Palomba, V., Sergi, F., Ferraro, M., Cabeza. L.F., Zsembinszki, G., Oró E., Karellas, S., Varvagiannis, S., Emhofer, J., Barz, T, 2018, Dynamic Modelling of a Hybrid Solar Thermal/electric Energy Storage System for Application in Residential Buildings. Proceedings of the 12th International Conference on Solar Energy for Buildings and Industry, Raperswil, Switzerland.

HYBUILD, Innovative compact hybrid storage systems for low energy buildings, 2017, http://www.hybuild.eu/, acessed Jan. 22, 2019.

Kapsalis, V., Karamanis, D., 2016, Solar thermal energy storage and heat pumps with phase change materials,Applied Thermal Engineering, 99, 1212-1224.

Meteonorm, Irradiation data for every place on Earth, 2016. [Online] Available: http://www.meteonorm.com/en/

Pardiñas, A.A., Alonso, M.J., Diz, R., Kvalsvik, K.H., Fernández-Seara, J., 2017, State-of-the-art for the use of phase-change materials in tanks coupled with heat pumps, Energy and Buildings, 140,28-41.

Quoilin, S., Desideri, A., Wronski, J., Bell, I., Lemort, V., 2014. ThermoCycle: A Modelica library for the simulation of thermodynamic systems, in: Proc. of the 10th Int. Modelica Conference. Lund, Sweden.

Song, M., Deng, S., Dang, C., Mao, N., Wang, Z., 2018, Review on improvement for air source heat pump units during frosting and defrosting, Applied Energy 211, 1150-1170.

Pardiñas, A.A., Alonso, M.J., Diz, R., Kvalsvik, K.H., Fernández-Seara, J., 2017, State-of-the-art for the use of phase-change materials in tanks coupled with heat pumps, Energy and Buildings, 140,28-41.

Rubitherm, Rubitherm GmbH, 2019, https://www.rubitherm.eu/en/ acessed Jan. 30, 2019

Zou, D., Ma, X., Liu, X., Zheng, P., Cai, B., Huang, J., Guo, J., Liu, M., 2017, Experimental research of an air-source heat pump water heater using water-PCM for heat storage, Applied Energy, 206, 784-792,

Manuscript ID: 647
DOI: 10.18462/iir.icr.2019.0647

Performance of ground source heat pump that uses direct expansion method for supplying hot water

Ryoichi NISHIZAWA[(a)], Tetsuaki TAKEDA[(b)], Shuhei ISHIGURO[(a)], Yuki MARUMO[(a)]

(a) University of Yamanashi, Integrated Graduate School of Medicine, Engineering, and Agricultural Sciences, 4-3-11 Takeda, Kofu, Yamanashi, 400-8511, Japan
g18tm021@yamanashi.ac.jp

(b) University of Yamanashi, Graduate School of Engineering
4-3-11 Takeda, Kofu, Yamanashi, 400-8511, Japan
ttakeda@yamanashi.ac.jp

ABSTRACT

This study investigates the performance of a ground source heat pump that uses the direct expansion method for hot water supply. The performance of cooling and heating/hot water supply systems of a ground source heat pump that uses the direct expansion method is better than that of the conventional ground source heat pump. Considering actual usage conditions, an experiment was conducted using R32 refrigerant. The length of the underground heat exchanger was 30 m. We investigated the maximum value of the amount of extracted heat from the ground by a single underground heat exchanger. The experiment was continued until the temperature of hot water in the tank reached approximately 65 °C. When the discharge amount of hot water was 200 L, the average Coefficient of Performance COP during the experiment was 2.4. When the discharge amount was 300 L, the average COP was 2.3.
Keywords: Borehole, COP, Direct Expansion, Ground-Source System, Hot Water, R32.

1. INTRODUCTION

Ground source heat is low-temperature thermal energy that is deeper than 10 m from the ground surface and shallower than 100–150 m underground. The temperature in the ground is not affected by temperature fluctuations and is almost constant throughout the year. The underground temperature is higher than the outside air temperature in the winter and lower in the summer. Therefore, a ground source heat pump is highly efficient compared with an air-conditioner. It is an energy-saving system that can provide both air conditioning and hot water supply (Hokkaido University, 2007). Tsuchiya, et al. (2017) and Marumo, et al. (2018) reported the performance of hot-water supply heat pumps using a ground source heat pump that uses the direct expansion method. The heat pump thereof is a system that directly exchanges heat with the underground by extending the circulation piping of a refrigerant such as R32 to the underground. Therefore, the heat exchanger performance is superior to the ground source heat pump using brine, which has already been implemented.

In the ground source heat pump using the direct expansion method, it is difficult to obtain the amount of heat because the refrigerant is accompanied by condensation/evaporation. However, in the hot-water supply system, because the heat quantity can be measured from the waterside inlet/outlet temperature and the flow rate of the water/refrigerant heat exchanger, improvement in accuracy can be expected compared with the heat quantity measured on the refrigerant side.

Therefore, in this study, we aim to clarify the performance at the time of hot-water generation using the ground source heat pump that uses the direct expansion method.

2. EXPERIMENTAL APPARATUS, CONDITION, AND EVALUATION METHOD

2.1 Experimental Apparatus

Fig. 1 shows the experimental apparatus. The experimental apparatus is composed of a compressor, a water/refrigerant heat exchanger, an expansion valve, and an underground heat exchanger. In this research, a hot-water supply experiment of a ground source heat pump using the direct expansion method was performed using a ground heat exchanger that is inserted in one closed-type vertical buried-type borehole. The depth of the borehole was 30 m. A casing pipe of outer diameter 165.2 mm and inner diameter 155.2 mm was inserted into the borehole. The bottom end of the casing pipe was closed and the pipe was filled with water. The refrigerant was filled with 1.0 kg of R32 and lubricating oil. A capillary tube-coupled heat transfer tube was adopted for the water/refrigerant heat exchanger. The output of the outdoor unit was 5.0 kW. A water storage tank with a capacity of 460 L was installed.

Fig. 2 shows a schematic of the underground heat exchanger. The underground heat exchanger was buried in the ground to exchange heat with the ground. The ground source heat exchanger is of different shapes for efficiently exchanging heat. It consists of three copper pipes connected at the bottom to one copper pipe resembling a U-shape. The outer diameter of the copper tube is 6.35 mm.

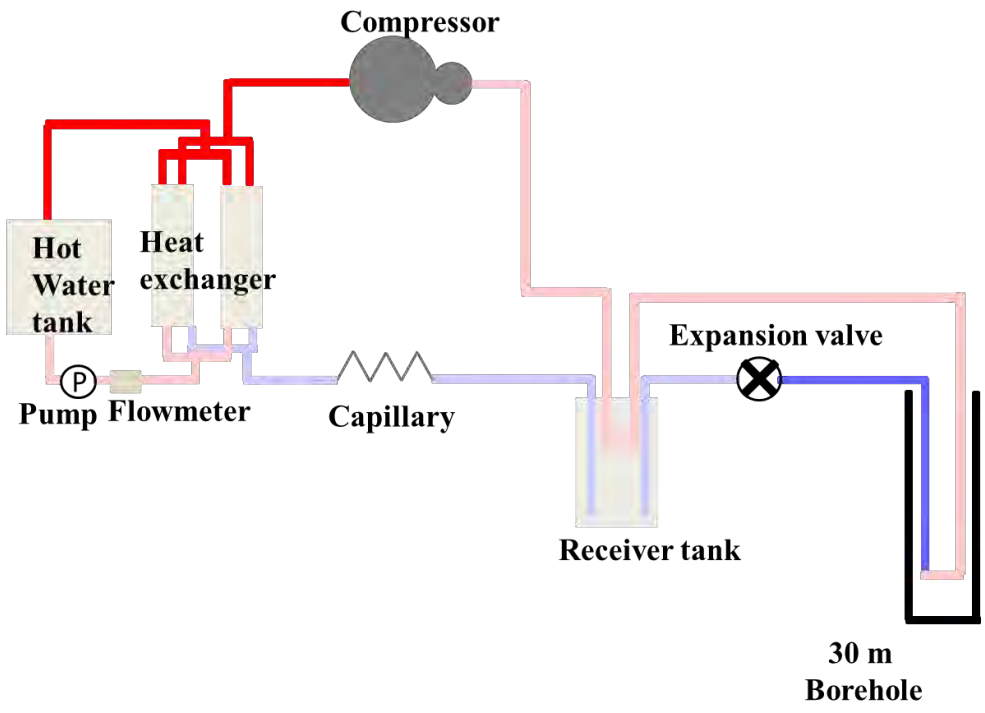

Figure 1: Flow sheet of the ground source heat pump system using direct expansion method

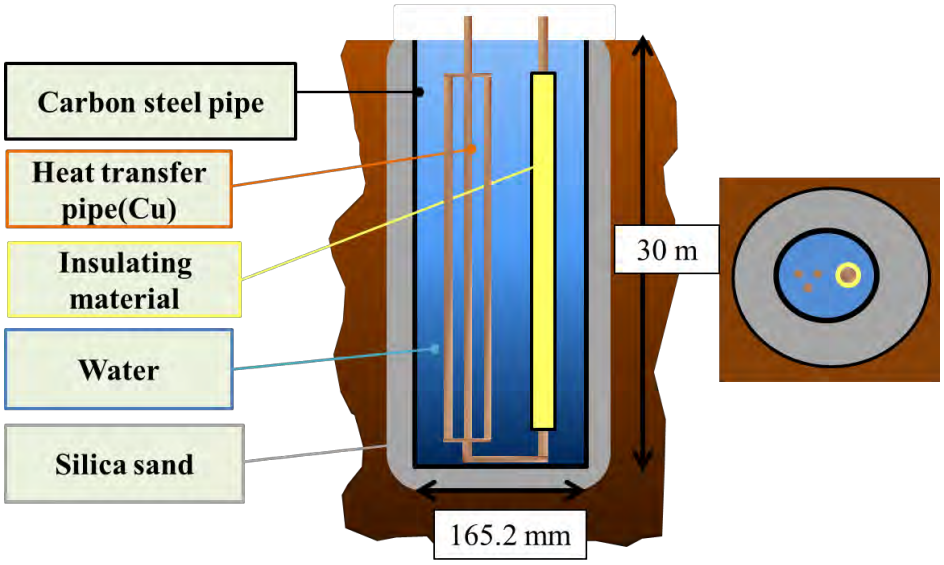

Figure 2: Schematics of the underground heat exchanger

2.2 Experimental Condition

Considering actual use conditions, in this experiment, 200 L of hot water with a set temperature of 40 °C was discharged and the water temperature in the hot water storage tank unit was increased by midnight electric power; this was conducted for seven consecutive days. The experiment was continued until the hot-water temperature in the tank reached approximately 65 °C.

Table 1: Experimental conditions

Experimental date	From November 7th to November 14th, 2018	From December 6th to December 13th, 2018
Discharge amount of hot water	200 L	300 L
Borehole depth	30 m	
Borehole diameter	155.2 mm	
Filled material	Silica sand	
Refrigerant	R32 (1.0 kg)	
Water storage capacity	460 L	
Pre-set temperature	65 °C	

2.3 Evaluation Method

In this study, we calculated the coefficient of performance (COP) as the performance of the ground source heat pump that uses the direct expansion method for hot water supply. COP is a value expressing the cooling/heating capacity for every 1 kW of power consumption. The larger this value, the better is the energy-saving performance. As described above, in the direct expansion method, the refrigerant is a two-phase flow of gas–liquid; therefore, it is difficult to measure the flow rate of the refrigerant on the underground side. Therefore, the COP was measured using the waterside inlet/outlet temperature and flow rate of the water/refrigerant heat exchanger.

$$COP = cpq(t_{out} - t_{in}) \cdot W^{-1}, \quad \text{Eq. (1)}$$

where c is the specific heat of water in $kJ\times(kg\times K)^{-1}$, ρ is the density of water in $kg\times m^{-3}$, q is the water/refrigerant heat exchanger inlet water flow rate in $m^3\times s^{-1}$, t_{out} is the water/refrigerant heat exchanger outlet water temperature in K, t_{in} is the water/refrigerant heat exchanger inlet water temperature in K, and W is the power consumption in kW.

3. EXPERIMENTAL RESULTS AND DISCUSSIONS

3.1 Underground Temperature

Figs. 3 and 4 show the underground temperature when the discharge amounts of hot water are 200 and 300 L, respectively. When the discharge amount was 200 L, the underground temperature on the first day of the experiment was 14.8 °C at the 10 m point, 15.3 °C at the 20 m point, and 16.0 °C at the 30 m point. On the 7th day, it was 15.0, 15.5, and 16.1 °C at the 10, 20, and 30 m points, respectively. When the discharge amount was 300 L, the underground temperature on the first day of the experiment was 14.9, 15.6, and 15.9 °C at the 10, 20, and 30 m points, respectively. On the 7th day, it was 14.2, 14.9, and 15.5 °C at the 10, 20, and 30 m points, respectively. When the discharge amount was 200 L, the underground temperature became almost the same at the start and end of the experiment. This indicated that the underground temperature was recovering. However, when the discharge amount was 300 L, the underground temperature at the end of the experiment was approximately 0.5 °C lower than at the start of the experiment. Therefore, the recovery of the underground temperature is insufficient with the discharge amount of 300 L. This result indicates that a long-term operation without a water injection system is difficult if the discharge amount of hot water increases.

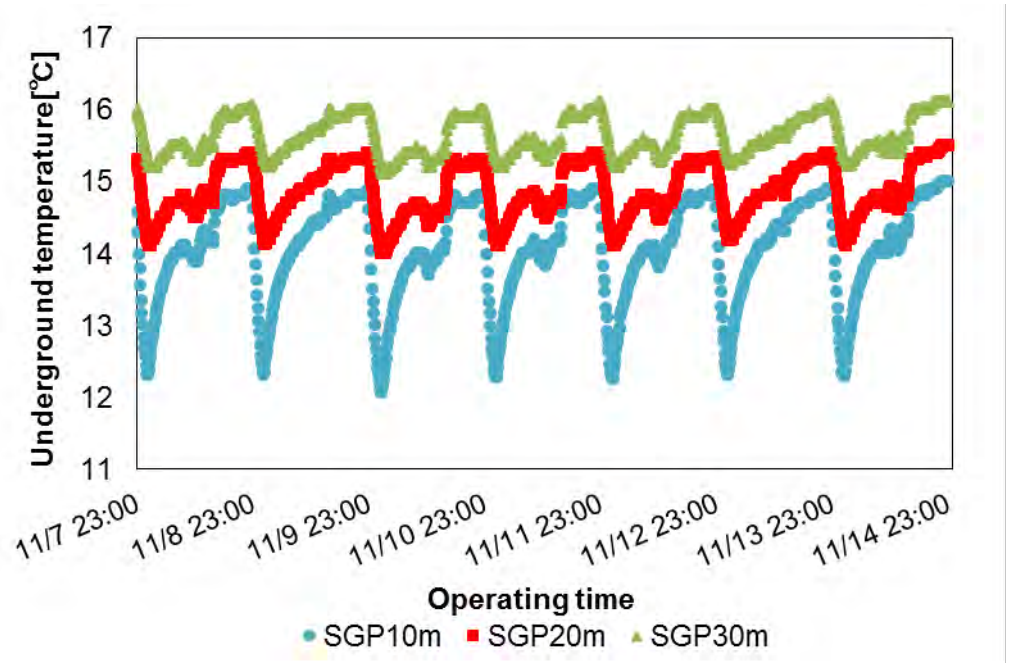

Figure 3: Underground temperature (200 L)

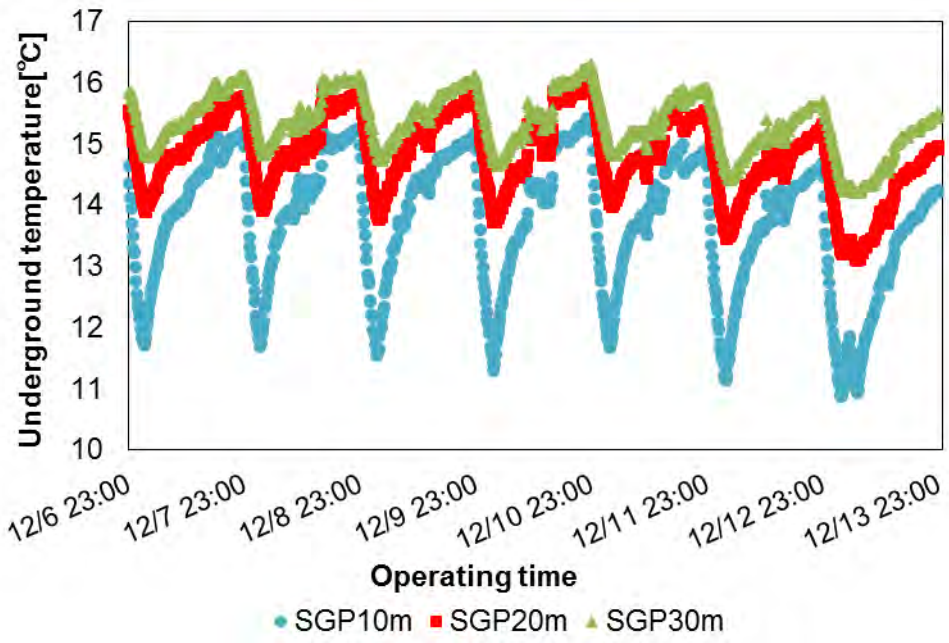

Figure 4: Underground temperature (300 L)

3.2 Performance Evaluation

Figs. 5 and 6 show the COP, output power, and power consumption with respect to the operation time when the discharge amounts of hot water are 200 and 300 L, respectively. In this experimental apparatus, the power consumption was almost constant throughout the operation period because it was controlled to operate at a constant speed of the compressor. When the discharge amount was 200 L, the average power consumption during the operation period was 1.3 kW, the average COP was 2.4, and the average output power was 3.2 kW. With the discharge amount of 300 L, the average power consumption during the operation period was 1.3 kW, the average COP was 2.3, and the average output power was 3.2 kW. In both cases, the output power decreased with decreased underground temperature. Consequently, the COP decreased. Furthermore, the sudden decrease in output power at the discharge amount of 200 L was attributed to the activated control for protecting the compressor. In previous experiments (Marumo, et al., 2018), the output power was approximately 0.15 kW/m, whereas in this experiment, it was approximately 0.1 kW/m. Although the output power per meter was decreasing, the load in the underground per unit depth was reduced. When the discharge amount was 300 L, a reduction in the underground temperature by 0.5 K did not affect the COP. It is necessary to perform a long-term operation to investigate how reducing the underground temperature affects the performance.

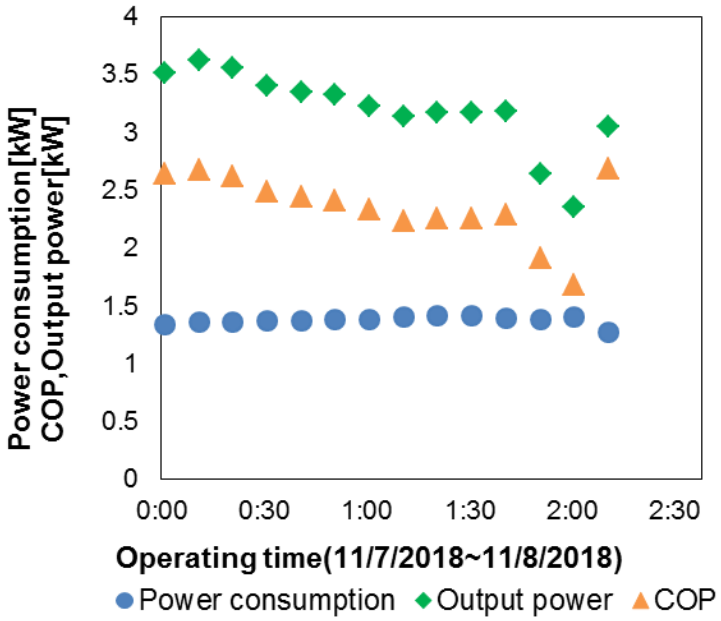

Figure 5: Performance evaluation (200 L)

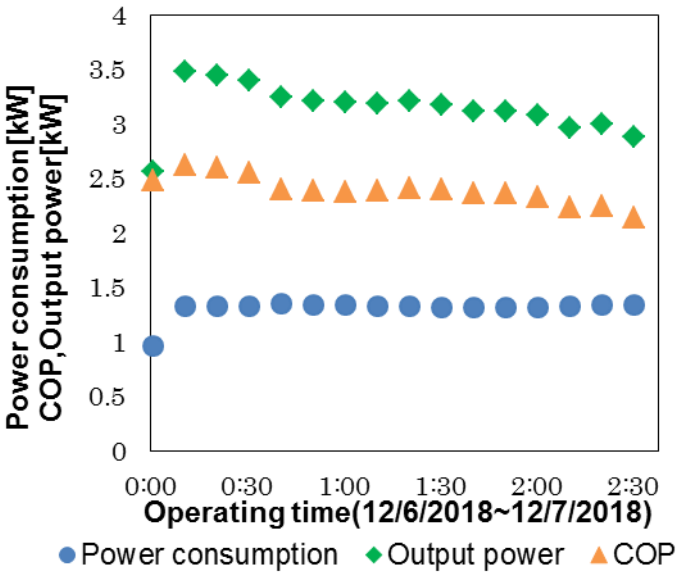

Figure 6: Performance evaluation (300 L)

4. CONCLUSION

An experiment on a hot-water supply system by a ground source heat pump that used the direct expansion method was performed using a single borehole of depth 30 m. The obtained experimental results were as follows.

1. With the discharge amount of 200 L, the average power consumption during the operation period was 1.3 kW, the average COP was 2.4, and the average output power was 3.2 kW.
2. With the discharge amount of 300 L, the average power consumption during the operation period was 1.3 kW, the average COP was 2.3, and the average output power was 3.2 kW.
3. In previous experiments, the output power was approximately 0.15 kW/m, whereas in this experiment, it was approximately 0.1 kW/m. Although the output power per meter was decreasing, the load in the underground per unit depth was reduced.

NOMENCLATURE

c	specific heat of water ($kJ\times(kg\times K)^{-1}$)	t_{out}	water/refrigerant heat exchanger outlet water temperature (K)
ρ	density of water ($kg\times m^{-3}$)	t_{in}	water/refrigerant heat exchanger outlet water temperature (K)
W	power consumption (kW)	q	water/refrigerant heat exchanger inlet water flow rate ($m^3\times s^{-1}$)

REFERENCES

Hokkaido University, 2007. Ground Source Heat Pump System. Ohm Company, Tokyo, Japan, pp.19-20.

Tsuchiya, M., et al., 2017. Performance Evaluation of Ground Source Heat Pump Using Direct Expansion Method –In case of Hot Water Supply System-. Thermal and Fluids Engineering Conference, Okinawa, Japan, No. G0800202 (2017).

Marumo, Y., et al., 2018. Study on round source heat pumps that use direct expansion method for hot water supply system. Proceedings of the 9th Asian Conference on Refrigeration and Air Conditioning, Sapporo, Japan, ACRA2018-D115.

Manuscript ID: 649
DOI: 10.18462/iir.icr.2019.0649

Thermal performance of underground heat exchanger for ground source heat pump that uses direct expansion method

Ryosuke OKAZAWA[(a)], Tetsuaki TAKEDA[(b)], Shuhei ISHIGURO[(a)]

[(a)] University of Yamanashi, Integrated Graduate School of Medicine, Engineering, and Agricultural Sciences,
4-3-11 Takeda, Kofu, Yamanashi, 400-8511, Japan,
g18tm006@yamanashi.ac.jp

[(b)] University of Yamanashi, Graduate School of Engineering,
4-3-11 Takeda, Kofu, Yamanashi, 400-8511, Japan,
ttakeda@yamanashi.ac.jp

ABSTRACT

The specifications of an underground heat exchanger used for a ground source heat pump that uses the direct expansion method could not be established thus far because the refrigerant flowing in the underground heat exchanger is a gas–liquid two-phase flow accompanying evaporation and condensation that exhibits a complicated behavior. Therefore, an experiment was conducted using a U-shaped heat exchanger in which one 3/8-inch copper tube and multiple 1/4-inch copper tubes were connected at the bottom as a heat-collecting tube. In this experiment, parallel underground heat exchangers were used. We introduce this underground heat exchanger into the air-conditioner used for an actual agricultural vinyl house and describe the results of the demonstration test. The coefficient of performance in the cooling and heating operations were approximately 4.0 and 3.5, respectively, and the primary energy consumption reduction rates compared with the conventional system were 20% and 43%, respectively.
Keywords: Borehole, COP, Direct expansion, Ground source system, Heat exchanger, R410A

1. INTRODUCTION

Currently, global warming and the exhaustion of energy resources have become serious; thus, energy saving and effective use of energy are required in all fields worldwide. In this research, we focused on a ground source heat pump that can yield better energy saving effects than the conventional air heat pump. Ground source heat pumps can be categorized into two types: indirect method and direct expansion method. Researcher at Yamanashi University have been studying the development of a ground source heat pump that uses the direct expansion method, which is considered to be superior in heat exchange performance to the conventional indirect method (Watanabe et al., 2018) (Muramatsu et al., 2018). Especially in the cooling operation, we have obtained experimental results in which the coefficient of performance (COP) exceeded 10. As a result of the achievement, an air-conditioning facility using a ground source heat pump that uses the direct expansion method has been introduced in Yamanashi Prefecture in which the university has been conducting research as an air-conditioned house for summer/autumn strawberry business. In this report, to contribute to the promotion of ground source utilization in the next-generation agriculture field, we evaluated the cooling and heating air-conditioning performances and the effect of reducing the primary energy consumption and demonstrated its effectiveness.

2. OUTLINE OF EXPERIMENT and EXPERIMENTAL APPARATUS

2.1. Ground Source Heat Pump System

Fig. 1 shows a simplified diagram of the indirect method and direct expansion method. Ground source heat pumps can be categorized into two types: indirect method and direct expansion method. The indirect method installs a resin or metal heat exchanger between a heat pump and an underground heat exchanger and collects it indirectly from the ground through circulating water or antifreeze. Meanwhile, in the direct expansion method, as shown in Fig. 1, a refrigerant tube of a heat pump is buried in the ground and heat exchange is performed directly with the underground. Compared with the indirect method, the operation efficiency of the heat pump is high and the power of the circulation pump for the antifreeze is unnecessary; therefore, the energy-saving effect tends to be high (Hokkaido University, 2007).

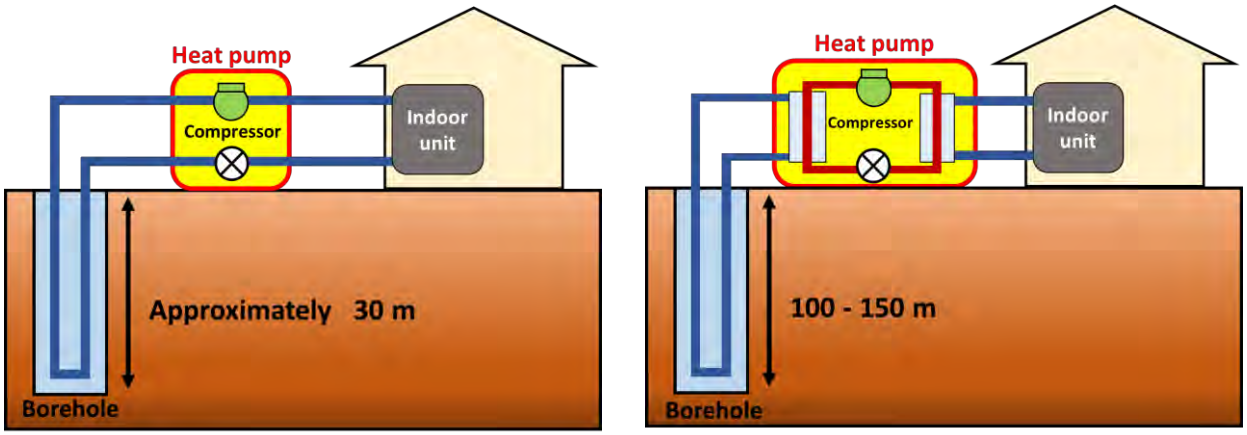

Figure 1: Simplified diagram of indirect method (left) and direct expansion method (right)

2.2. Outline of Experiment

In this experiment, a refrigerant (R410A) is circulated in the underground heat exchanger, and a demonstration experiment of a system that performs the evaporation and condensation of the refrigerant between the indoor unit and underground heat exchanger, and performs cooling and heating was conducted. Furthermore, to maintain the temperature inside the heat exchanger, a system for injecting well water according to operating conditions was provided.

In this system, the required temperature of the crop to be cultivated was set based on the operation record in the house where the air heat pump was installed. This project aims to cultivate summer and autumn strawberries, but the planned area was highland; thus far, no air-conditioning in the summer was necessary. However, owing to the effect of global warming in recent years, the temperature, especially the nighttime temperature, did not decrease. Thus, the fruiting of strawberry was affected and cooling was necessitated. In addition, because the ground source heat pump could be used for cooling and heating, we studied the possibility of further energy cost reduction by using it as an aid for hot air generation utilizing fossil fuel in the winter.

2.3. Experimental Apparatus

Fig. 2 shows the outline of the verification test system and the picture of the vinyl house. The altitude of the planned site was approximately 800 m highland, and we introduced two ground source heat pumps that use the direct expansion method for cooling primarily in the summer. It operated as a set of three underground heat exchangers of φ100 mm × 30 m each. The equipment capability was assumed as the ability to provide the temperature required by summer and autumn strawberries cultivated in the planning building: the cooling output was 12.5 kW, and the heating output was 14 kW. The direct expansion method exhibited excellent underground heat exchange efficiency; therefore, there was a concern that the heat release to the ground by heat exchange and heat extraction from the ground would significantly affect the underground temperature fluctuation. We adopted a method of supplementing the amount of heat collection of the ground by placing a well for water injection and injecting it into the borehole. We had confirmed that the

amount of groundwater available was abundant owing to the operating condition of the existing wells in the premises and the well data of neighboring areas. The water pumping volume used for water injection was at the most 3 L/min per heat exchanger, and 18 L/min as a whole; therefore, it was less than those of household wells. We adopted a method to infiltrate the overflow after injection and reduced it to the underground.

Fig. 3 shows the structure of the underground heat exchanger used in this experiment. The underground heat exchanger consists of a borehole, steel gas pipe, water, no. 2 silica sand, and collected heat pipe. A casing tube closed at the bottom was placed in a borehole of 30 m in depth, filled with water, and a copper heat-sink tube was inserted in it. To disperse the load on the ground when releasing heat, a parallel method was adopted. A steel gas pipe was used for the casing pipe, and the periphery was filled with no. 2 silica sand. The collected heat pipe was a U-shaped copper pipe divided into one side and three sides. In addition, one side was wrapped with insulation to prevent heat extraction from the ground and heat radiation.

Regarding the circulation direction of the refrigerant, it was circulated from the three sides to the one side during the cooling operation, and vice versa during the heating operation, referring to past experimental results (Muramatsu et al., 2018).

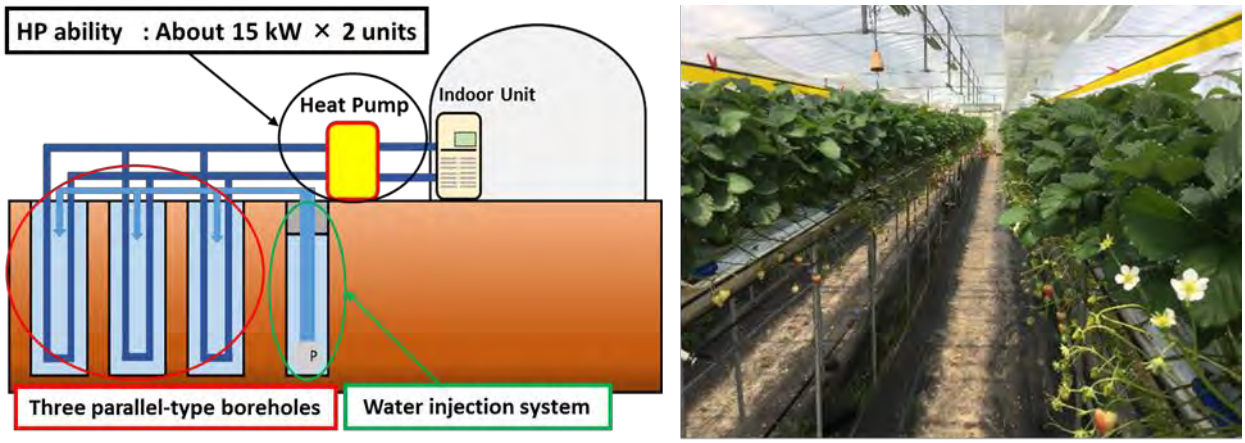

Figure 2: Outline of the verification test system and a photograph of the house

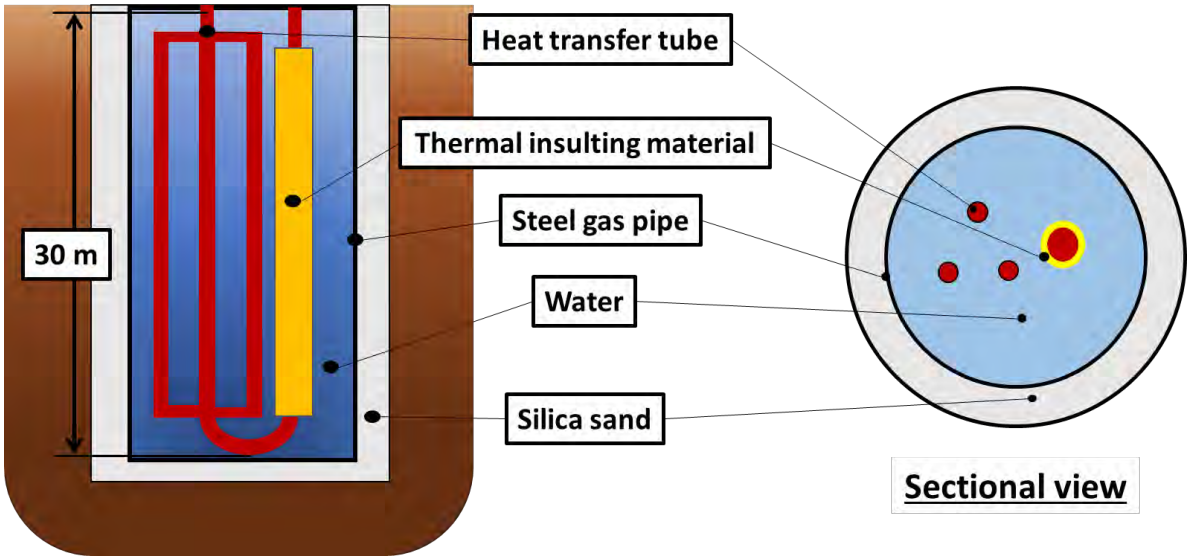

Figure 3: Underground heat exchanger

2.4. Evaluation Method

For the performance evaluation of the heat pump, the COP representing the cooling/heating capacity per power consumption was used. The larger the value, the better was the consumption efficiency. As it was difficult to measure the flow rate of the refrigerant on the underground heat exchanger side, in this study, calorimetry was performed on the indoor unit side, and the COP was calculated using Eq. (1).

$$COP = \frac{Outout\ power}{Power\ consumption} = \frac{\Delta h \times \rho \times A \times v}{P \times 6}, \quad \text{Eq. (1)}$$

where Δh is the enthalpy difference between the indoor unit intake port and exhaust port in $kJ \cdot kg^{-1}$, ρ is the air density in $kg \cdot m^{-3}$, A is the indoor unit discharge duct area in m^2, v is the wind speed $m \cdot s^{-1}$, and P is the power consumption (cumulative value for 10 min) in kWh. The enthalpy difference necessary for obtaining the output power was obtained by measuring the temperature and humidity at both the indoor unit suction port and discharge port using the psychometric diagram of the Japan Refrigeration and Air-Conditioning Association. For the performance evaluation of the heating operation, instead of Δh, a value obtained by multiplying the temperature difference ΔT in °C between the indoor unit discharge port and intake port by the air specific heat c in $J \cdot kg^{-1} \cdot ºC^{-1}$ was used.

3. EXPERIMENTAL RESULTS and DISCUSSION

3.1. Performance Evaluation in Cooling Operation

In this experiment, the cooling operation period during the summer was approximately 38 days from July 20th to August 26th, 2018. Fig. 4 shows the temperature inside the house and the outside air temperature on July 24th, which was a relatively hot day even during the cooling operation period performed at that time. The temperature inside the house increased with the increasing outside air temperature, and the cooling operation began at approximately 9 AM from the inverter control. It can be confirmed that the outside air temperature increases as time progresses to approximately 35 °C at 15 o'clock. At this time, the inside temperature of the house was approximately 32 °C, and it could be maintained at approximately 3 °C lower than the outside air temperature. However, because we were cooling the heating house that was originally a heating facility, the load was extremely large. Furthermore, if we considered the growing environment of strawberries, capacity shortage must be considered. In this experiment, two indoor units were used to cool the inside of the house; however, in the initial plan, four indoor units were required for the existing vinyl house. Hence, it was necessary to add an indoor unit to ensure the necessary amount of heat dissipation.

Fig. 5 shows the performance values of the cooling operation on July 24th. Soon after the operation began, the released heat increased to approximately 16 kW, the power consumption was approximately 4 kW, and the COP was approximately 4. The inside temperature of the house during the day was 30 °C or higher and the load was extremely large; therefore, the released heat and power consumption always exhibited high values and operated at the maximum output during the cooling operation. Although the rated energy consumption efficiency of the air heat pump to be compared was approximately 3.2, even in an extremely heavy load environment such as that in the experiment, the COP in the direct expansion method was approximately 4, which was superior to the conventional air heat pump system.

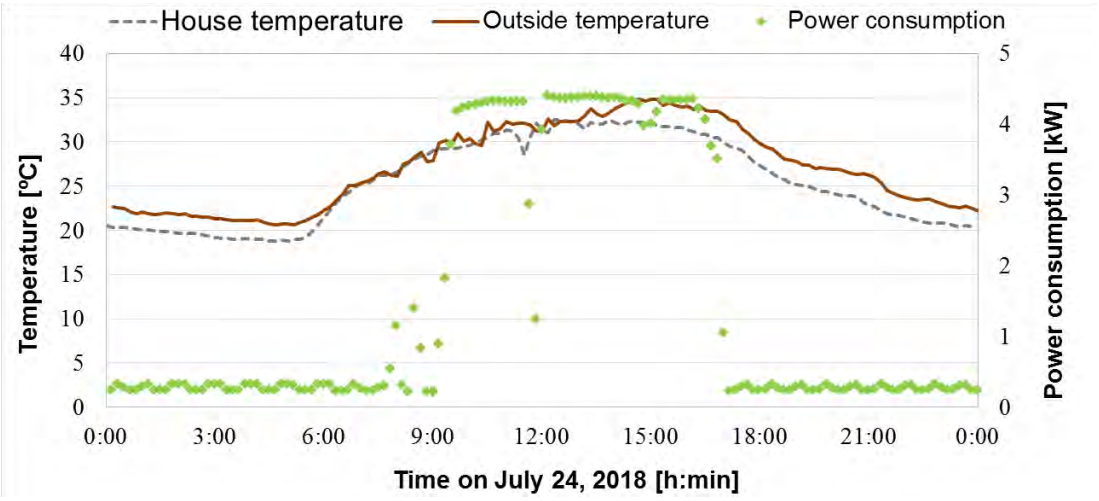

Figure 4: House temperature and outside temperature

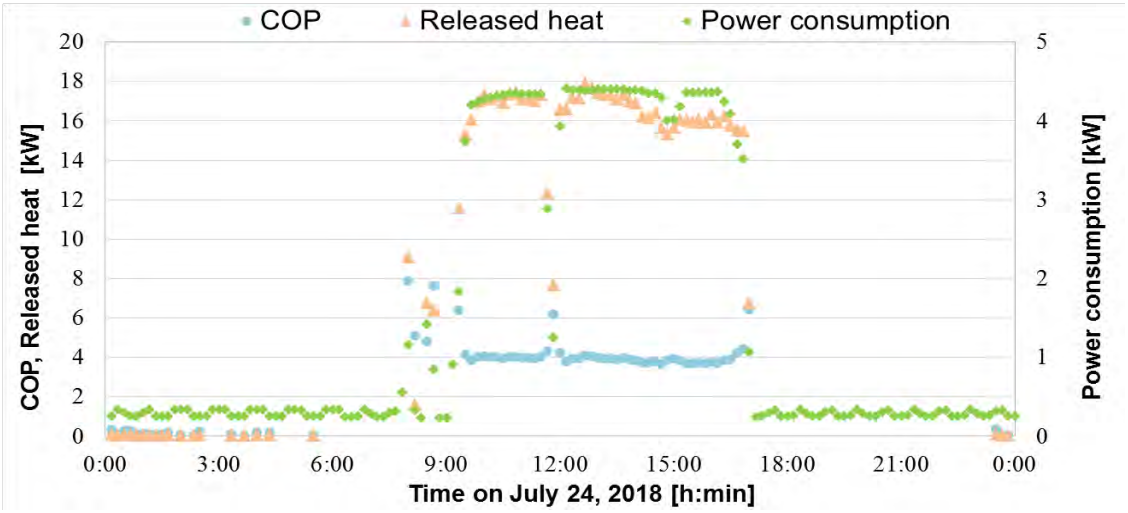

Figure 5: COP, released heat, and power consumption

3.2. Performance Evaluation in Heating Operation

In this study, an evaluation was conducted from November 17, 2018 to December 31, 2018, in which winter heating was performed.

Fig. 6 shows the temperature inside the house and the outside air temperature on December 28, when the average temperature per day was the lowest among the heating operation periods performed at that time. The temperature inside the house was approximately 10 °C at 15 o'clock before the start of the heating operation, and when the heating operation was started from 15 o'clock, the temperature recovered to 20 °C. Subsequently, the temperature inside the house decreased with the decrease in the outside air temperature, and it was stable at approximately 15 °C at night. Compared with the cooling operation, no significant capacity shortage was indicated.

Fig. 7 shows the performance values of the heating operation on December 28th. Shortly after the operation began, the output power increased to approximately 16 kW, the power consumption increased to approximately 5 kW, and the COP was approximately 3.4. It could be confirmed that the output power and power consumption were increased slightly from 3 am to 6 pm when the outside air temperature reached –5 °C. However, the parameters were almost constant from the start to the end of operation outside the time range above. The planned area was high ground and the outside temperature had reached below freezing; therefore, it did not the planned initial performance value was not attained. In the experiment conducted this time, the number of indoor units was two; as such, the load per unit was extremely large. Therefore, the load per unit can be

reduced, e.g., by adding an indoor unit; it is thought that further improvements in performance will be achieved.

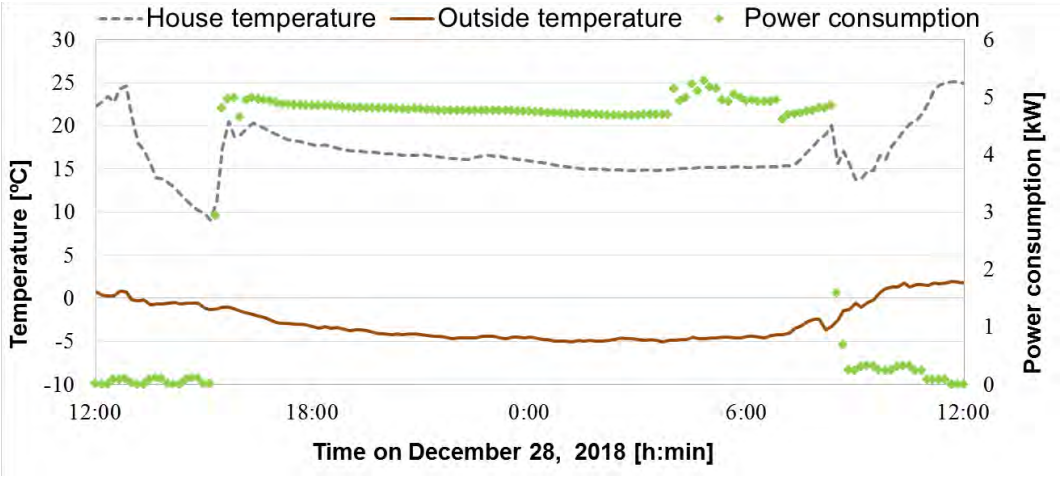

Figure 6: House temperature and outside temperature

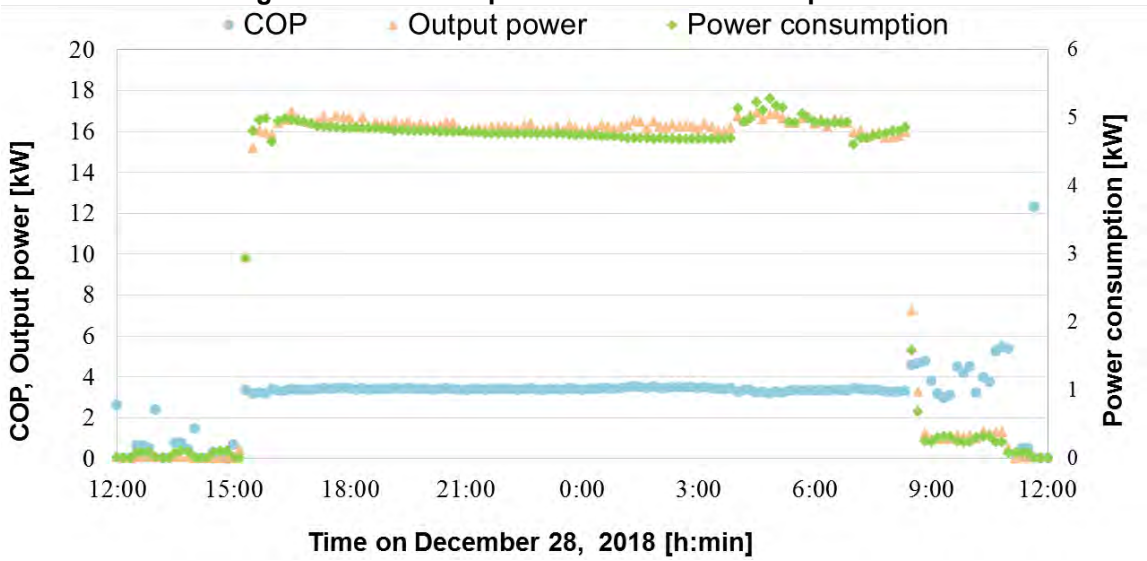

Figure 7: COP, output power, and power consumption

3.3. Primary energy consumption reduction effect and carbon dioxide emissions

Fig. 8 shows the primary energy consumption and carbon dioxide emissions when using the air heat pump and ground source heat pump that use the direct expansion method. The values shown in Fig. 8 are cumulative values for 43 days including the test runs. The power consumption of the air heat pump was calculated using the rated capacity and power consumption. Crude oil consumption and carbon dioxide emissions were calculated using the conversion factor described in the guidelines issued by the Tokyo Metropolitan Government Bureau of Environment (Tokyo Metropolitan Government Bureau of Environment, 2018).

The amount of power consumption in the cooling operation was 3276 kWh for the air heat pump and 2614 kWh for the ground source heat pump, and the reduction amount was 661 kWh. Converting this into crude oil, the amount of crude oil used was 842 L in the air heat pump and 672 L in the ground source heat pump, and the reduction amount was 170 L. As for the carbon dioxide emissions, 1251 kg-CO_2 was obtained for the air heat pump and 998 kg-CO_2 for the ground source heat pump, and the reduction amount was approximately 252 kg-CO_2. Consequently, the overall reduction rate of the cooling operation was 20.2%. Originally, because the vinyl house was a facility for warming, the amount of power consumption in the ground source heat pump is calculated only when the load was extremely large, and it caused a significant decrease in energy

consumption efficiency. Therefore, if the ground source heat pump could be operated under the same load condition as the rated value, the reduction rate could be further improved.

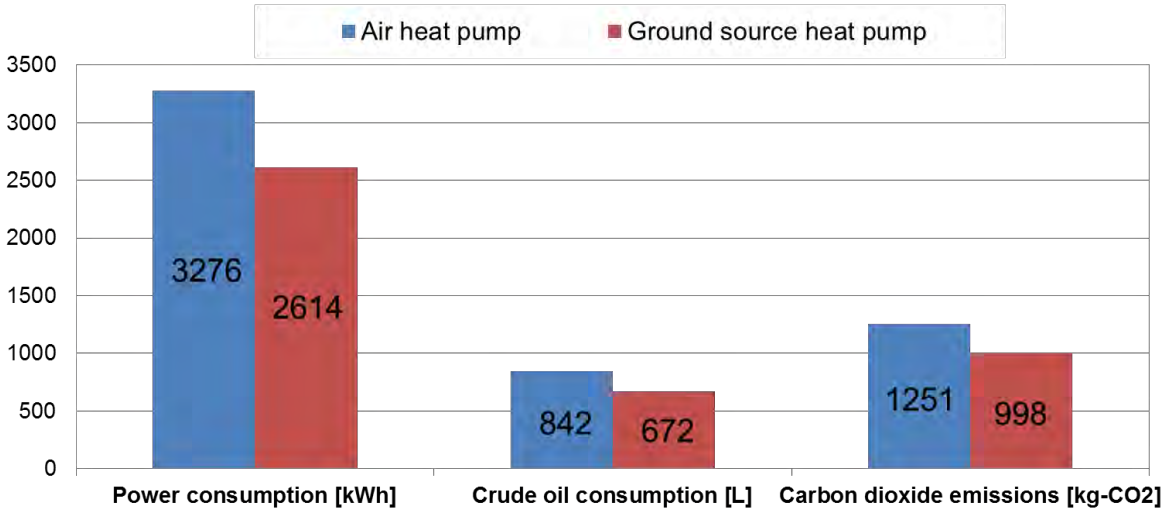

Figure 8: Primary energy consumption and carbon dioxide emissions in cooling mode

Fig. 9 shows the primary energy consumption and carbon dioxide emissions of the A heavy oil boiler that is the existing heating systems and ground source heat pump using the direct expansion method. A total of 70 days including the trial run was calculated. The crude oil equivalent amount and carbon dioxide emissions were obtained using the conversion factor described in the guidelines of the Tokyo Metropolitan Government Bureau of Environment (Tokyo Metropolitan Government Bureau of Environment, 2018).

Regarding the primary energy consumption in the heating operation, the crude oil equivalent amount was 3635 L for the A heavy oil boiler and 2049 L for the ground source heat pump, and the reduction amount was 1585 L. The crude oil reduction rate was approximately 43%. With regard to carbon dioxide emissions, it was 9635 kg-CO_2 for the A heavy oil boiler and 3275 kg-CO_2 for the ground source heat pump; the reduction amount was 6359 kg-CO_2. The reduction rate of carbon dioxide emissions was approximately 66%. Both crude oil and carbon dioxide emissions achieved high reduction rates. However, in the cooling operation, the load in the use environment was extremely large; therefore, the original performance might not have been achieved. As the outside air temperature sometimes decreased to near –10 °C during the winter nighttime, considerable effort was required to maintain a warm house. Therefore, to increase the energy consumption efficiency and improve the reduction rate, the load per indoor unit must be reduced.

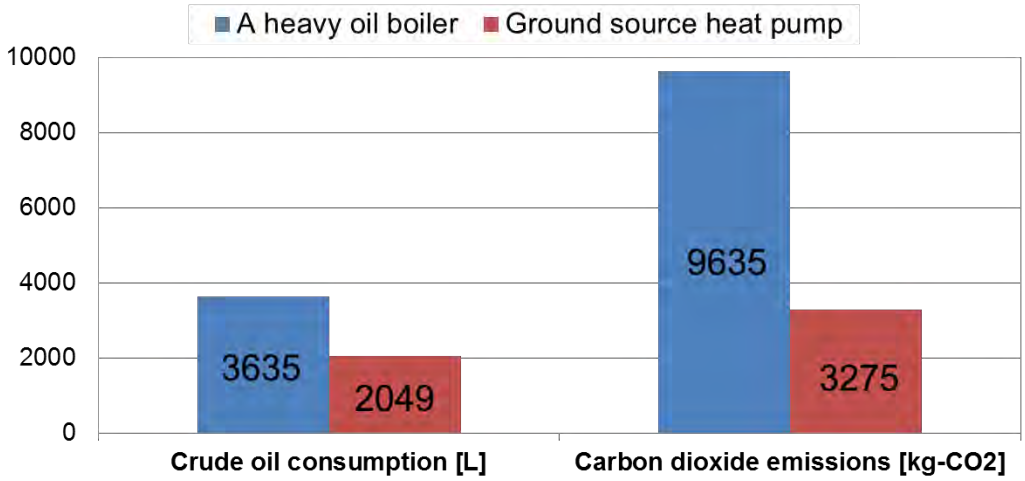

Figure 9: Primary energy consumption and carbon dioxide emissions in heating mode

4. CONCLUSION

In this study, by introducing a ground source heat pump that used the direct expansion method as an air-conditioning equipment in the agricultural field, the following conclusions were drawn after examining cooling and heating air-conditioning performance and evaluating the primary energy consumption reduction effect:

[1] The COP was approximately four in the cooling operation and approximately 3.4 in the heating operation; it demonstrated excellent performance considering the load size owing to the operating environment.

[2] The primary energy consumption reduction rate compared to the conventional air-conditioning equipment was 20% in the cooling operation and 43% in the heating operation.

[3] The reduction rate of carbon dioxide emissions was 20% in the cooling operation and 66% in the heating operation; in particular, an excellent reduction rate was obtained in the heating operation.

Future research plans include demonstrating the effectiveness of the energy-saving system in an agricultural house by calculating the operating cost from the cooling and heating performances requested this year and clarifying the cost amortization period from the initial investment cost.

NOMENCLATURE

Δh	enthalpy difference (kJ×kg^{-1})	ρ	air density (kg×m^{-3})
T	temperature (°C)	A	sectional area (m^2)
v	wind speed (m×s^{-1})	P	power consumption (kWh)

REFERENCES

Hokkaido University, 2007, Ground Source Heat Pump System, Ohm Company, Tokyo, Japan, pp.31-32.

Muramatsu, N., et al., 2018, “Thermal performance of ground source heat pump using direct expansion method”, Proc. of the 9th JSME-KSME Thermal and Fluids Engineering Conference, Oct. 28-30, Okinawa, Japan, TFEC9-1243.

Tokyo Metropolitan Government Bureau of Environment, 2018, “Guidelines for calculating of an amount of specific greenhouse gas emissions regarding emissions reduction obligations and emissions trading scheme”, Tokyo Metropolitan Government Bureau of Environment, Tokyo, Japan, p.69, p.71 and p.75, in Japanese.

Watanabe, S., et al., 2018, “Thermal performance of underground heat exchanger for ground source heat pump”, Asian Conference on Refrigeration and Air Conditioning, Sapporo, Japan, ACRA2018-D116.

Manuscript ID: 689
DOI: 10.18462/iir.icr.2019.0689

Gas dynamic analysis of a rotary compressor with vapor injection

Wei SUN[(a)], Guogeng HE[(a)], Dehua CAI[(a)], Sai ZHOU[(a)], Yu GAO[(a)]

[(a)] Huazhong University of Science and Technology
Wuhan, 430074, China, gghe@mail.hust.edu.cn

ABSTRACT

Air source heat pump heating has been widely used for energy conservation especially in cooler climes. Compressor displacement directly affects the heating capacity of an air source heat pump system. The application of enhanced vapor injection in an air source heat pump can greatly increase the compressor displacement in low temperature environments. In this paper, in order to analyse the internal flow and suction and exhaust conditions of the rotary compressor with vapor injection, a three-dimensional dynamic numerical model was built up by using the commercial CFD (computational fluid dynamics) solvers FLUENT and dynamic grid technique. And the theoretical model is used to verify the correctness of the simulation model. The simulation results of rotary compressor with and without the injection port are compared and analysed. The effect of the injection port on suction and discharge of the rotary compressor has been investigated in this study.
Keywords: CFD, Energy efficiency, Heat pump, Intermediate injection, Rotary compressor.

1. INTRODUCTION

China has been suffering from smog and haze pollution for a long time, especially in the winter, a large amount of coal combustion that is used for heating causes serious atmospheric pollution (Li et al., 2014). Where the low temperature air source heat pump (LTHP) technology, which is an energy-saving and efficient heating technology, can effectively reduce the atmospheric pollution caused by coal combustion for heating (Zhang et al., 2018). However, as the outdoor temperature decreases, the outdoor unit heat exchange capacity decreases, resulting in a decrease in the suction amount of the compressor relative to the normal suction amount, and the compressor compression efficiency is lowered (Jeon et al., 2016). Enhanced vapor injection technique can supplement the refrigerant in the compression process of the compressor, thereby increasing the discharge amount of the compressor, increasing the circulating refrigerant amount of the indoor heat exchanger, and increasing the heating capacity (wang et al., 2009). So this technology is very suitable for use in cold areas. Where enhanced vapor injection technique has been successfully applied to screw compressors and scroll compressors. In recent years, a few researchers have proposed applying this technique to rolling piston type rotary compressors with lower cost and comparable efficiency (Heo et al., 2013, Yan et al., 2016, Wang et al., 2018). Meanwhile, screw compressors and scroll compressors are generally used in middle or large heat pump systems, and rolling piston type rotary compressors are more suitable for small heat pump systems. Therefore, it is significant to study the rolling piston type rotary compressor with vapor injection for improving the heating performance of small heat pump systems.

Where CFD simulation technology, which can realistically simulate the compression process of the compressor, is a cost-effective product development tool. By using CFD simulation technology, it is visual for the changes in the distribution of pressure, streamtraces and temperature of the compressor during compression. If this technology is applied to a compressor with vapor injection, it will be very helpful to optimize the design of the compressor. Geng et al. (2004), and Ding et al. (2014) have conducted a detailed study of the internal flow process of a compressor without vapor injection, and the simulation results are in good agreement with the experimental results. Additionally, Farkas et al. (2015) respectively used the unstructured grid and the structured grid to simulate the compression process of the compressor, and compared the two models. The results show that the structured grid has a great advantage in computational efficiency. And by using dynamic grid technique, Ba et al. (2016) has been successfully used to simulate the transient flow mechanism of the rotary compressor and could predict the performance of the compressor with a reasonable

precision by comparing with experiment. Most of the previous scholars have carried out simulation studies on rotary compressors without injection port, and there have been few simulation studies on rotary compressors with injection port. It is significant to study the internal flow process of compressor with vapor injection.

2. GRID GENERATION AND NUMERICAL SETUP

The purpose of this work is to propose a CFD procedure for predicting and optimizing the internal refrigerant flow process of a rotary compressor with refrigerant vapor injection. The reasonable choice of flow area and the physical model has an important impact on the accuracy of the simulation. In particular, there is a quite challenging for the handling of the mesh motion and the mesh generation of the flow area.

2.1. Schematic and geometry of a rolling piston compressor

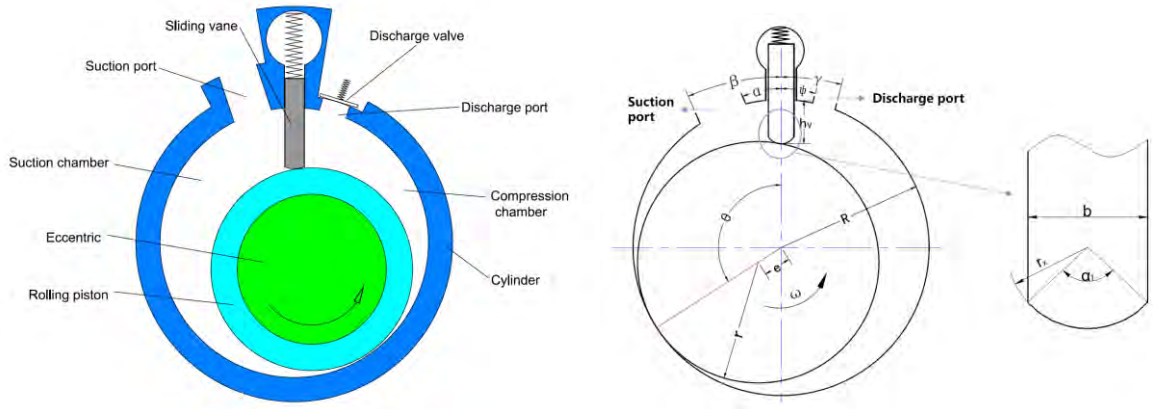

Figure 1: Schematic and geometry of a rolling piston compressor

As shown in Fig. 1, the mechanical components of the rolling rotor compressor to achieve the gas compression process are mainly composed of the cylinder block, eccentric, rolling piston, sliding vane, and discharge valve. The movement of the rolling piston is driven by the rotation of the crankshaft, the outer surface of the rolling piston is in contact with the inner surface of the cylinder block, and the sliding vane is closely attached to the surface of the rolling piston by the elastic force of the spring. Then, the chamber of the compressor is divided into a compression chamber and a suction chamber by the sliding vane and the rolling piston. When the pressure in the compression chamber reaches the discharge pressure, the discharge valve is opened due to the pressure difference between the compression chamber and the condenser, thereby releasing the compressed gas.

2.2. Grid Generation and Dynamic Grid Method

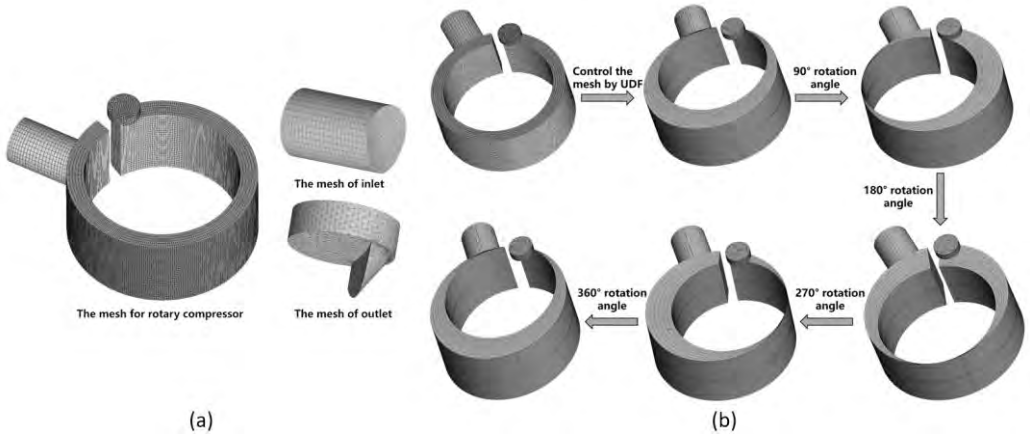

Figure 2: (a) Mesh of the whole compressor and details of the inlet and outlet; (b) The dynamic mesh changes process

According to the characteristics of the CFD solvers and the working mechanism of the rotary compressor, the fluid calculation domain as shown in Fig. 2(a) is established. By using meshing software of ANSYS ICEM, a structured meshing method (O-grid generation technique) is used for the cylinder block and the suction port, and an unstructured meshing method is used for the discharge port. Then the three parts are assembled by using the interface technique. Final mesh of the whole compressor and details of the inlet and outlet is shown in Fig. 2(a).
In order to simulate the movement process of the compressor piston, the dynamic mesh technology is required. The dynamic mesh changes process that controlled by UDF (user-defined function), which is used to control the motion of the mesh nodes, is shown in Fig. 2(b). Since dynamic mesh problems require that at least one layer remains in order to maintain the topology, a small clearance will be created between the compression chamber and the suction chamber. Where the presence of the clearance causes the refrigerant in the compression chamber to leak into the suction chamber through the clearance, which will affect the accuracy of the simulation. Fortunately, there is also a radial clearance leakage from the high pressure side to the low pressure side through the clearance during the actual operation of the compressor. Therefore, as long as the radial clearance is reasonably controlled, the accuracy of the calculation can be guaranteed to be consistent with the actual situation. In addition, the leakage losses through piston faces clearances between the upper and lower end faces of the rolling piston and head walls of the cylinder, the leakage losses through clearances between the upper and lower end faces of the sliding vane and head walls of the cylinder, and the leakage losses through clearances between the sides of the sliding vane and side walls of the chutes inside the cylinder is ignored for simplifying the model.

2.3. Governing Equations and Numerical Setup

In this study, the choice of physical models are mass, momentum and energy conservation equations, respectively. According to the ANSYS Fluent Theory Guide, these three equations are expressed as follows.

$$\frac{\partial \rho}{\partial t} + \nabla \bullet \left(\rho \vec{v} \right) = 0 \qquad \text{Eq. (1)}$$

$$\frac{\partial}{\partial t}\left(\rho \vec{v} \right) + \nabla \bullet \left(\rho \vec{v} \vec{v} \right) = -\nabla p + \nabla \bullet \left(\bar{\bar{\tau}} \right) + \rho \vec{g} + \vec{F} \qquad \text{Eq. (2)}$$

$$\frac{\partial}{\partial t}\left(\rho E \right) + \nabla \bullet \left(\vec{v} \left(\rho E + p \right) \right) = -\nabla \bullet \left(\sum_j h_j J_j \right) + S_h \qquad \text{Eq. (3)}$$

Since the RNG k-εtwo-equation model is more suitable and accurate for simulating the compression process of the compressor than other turbulence models, the RNG k-εtwo-equation model is chosen to account for turbulence. And the equations are shown in follows.

$$\frac{\partial}{\partial t}\left(\rho k \right) + \frac{\partial}{\partial x_i}\left(\rho k u_i \right) = \frac{\partial}{\partial x_j}\left(\alpha_k \mu_{eff} \frac{\partial k}{\partial x_j} \right) + G_k + G_b - \rho \varepsilon - Y_M + S_k \qquad \text{Eq. (4)}$$

$$\frac{\partial}{\partial t}\left(\rho \varepsilon \right) + \frac{\partial}{\partial x_i}\left(\rho \varepsilon u_i \right) = \frac{\partial}{\partial x_j}\left(\alpha_\varepsilon \mu_{eff} \frac{\partial \varepsilon}{\partial x_j} \right) + C_{1\varepsilon} \frac{\varepsilon}{k}\left(G_k + C_{3\varepsilon} G_b \right) - C_{2\varepsilon} \rho \frac{\varepsilon^2}{k} - R_\varepsilon + S_\varepsilon \qquad \text{Eq. (5)}$$

In order to make the process of simulating refrigerant gas compression more realistic, the NIST real gas model is chosen. And the fluid material from the REFPROP database can be loaded into Fluent. Then R32 and R125, which are the constituents of R410A, are selected for simulation calculation. Therefore, all physical properties (density, specific heat, thermal conductivity, viscosity and so on) of R410A used in the simulation are close to real physical properties of R410A, which makes the simulation results more authentic.

Table 1. Summary of boundary conditions

Suction port	Injection port	Discharge port	Remaining
Pressure inlet	Pressure inlet	Non-slip and adiabatic wall ($P_{compression}$<=$P_{discharge}$) Pressure outlet ($P_{compression}$>=$P_{discharge}$)	Non-slip and adiabatic wall

As shown in Table 1, the boundary conditions of the suction port and the injection port are set as pressure inlet. Since the movement process of the reed valve of discharge port is difficult to simulate, the motion of the reed valve is not considered in this study. Instead, the discharge port is set to the pressure outlet, and only when the pressure in the compression chamber is greater than the exhaust

pressure, the pressure outlet is open, otherwise the pressure outlet is closed. The remaining boundary conditions are set as non-slip and adiabatic wall.
For this case, the mesh counted about 120000 cells. Since the 3D dynamic grid unsteady computations proved to be extremely time consuming, the simulation time for a complete revolution for a 3D case at 50Hz rotational speed took approximately 3.5 days on a PC with twelve-core Intel Xeon CPU at 3.4GHz.

3. RESULTS AND DISCUSSION

3.1. Theoretical Analysis of Rotary Compressor Without Vapor Injection

Geometry of the rolling piston compressor is shown in Fig. 1. According to the kinetic characteristics and geometric structure of the rotary compressor, the variation of the volume of the compression chamber and the suction chamber with the rotation angle can be obtained, as follows:

$$\varepsilon = \frac{e}{R} \quad \text{Eq. (6)}$$

$$v_s = bL\left(h_v - 2r_x \sin^2\frac{\alpha_1}{4}\right) + \frac{1}{2}Lr_x^2\left(\alpha_1 - \sin\alpha_1\right) \quad \text{Eq. (7)}$$

$$h_v = R\varepsilon\left(1 - \cos\theta + \frac{1}{2}\frac{\varepsilon}{1-\varepsilon}\sin^2\theta\right) \quad \text{Eq. (8)}$$

$$v_x = \frac{1}{2}R^2L\varepsilon(2-\varepsilon)\theta - R^2L\varepsilon\left[\left(1-\varepsilon\right)\sin\theta + \frac{1}{4}\varepsilon\sin\left(2\theta\right)\right] - \frac{1}{2}v_s \quad \text{Eq. (9)}$$

$$v_y = R^2L\varepsilon(2-\varepsilon)(\pi - \frac{1}{2}\theta) + R^2L\varepsilon\left[\left(1-\varepsilon\right)\sin\theta + \frac{1}{4}\varepsilon\sin\left(2\theta\right)\right] - \frac{1}{2}v_s \quad \text{Eq. (10)}$$

Where v_s is the volume of the sliding vane, and v_x and v_y respectively are the volume of the suction chamber and the compression chamber.
The compression process can be regarded as an ideal adiabatic compression process since the compression process of the compressor lasts for a short time. Hence, the compression process must conform to the following equations.

$$pv^k = \text{constant value} \quad \text{Eq. (11)}$$

$$\frac{p_2}{p_1} = \left(\frac{v_1}{v_2}\right)^k \quad \text{Eq. (12)}$$

$$\frac{T_2}{T_1} = \left(\frac{v_1}{v_2}\right)^{k-1} \quad \text{Eq. (13)}$$

$$\frac{T_2}{T_1} = \left(\frac{p_2}{p_1}\right)^{\frac{k-1}{k}} \quad \text{Eq. (14)}$$

Where k denotes the adiabatic exponent of the vapor refrigerant. When the volume variation law of the compression chamber is known, the relationship between the pressure, temperature and density of the compression chamber as a function of the rotation angle can be obtained by the above equations.

3.2. Comparison of Theoretical and Simulation Results of Rotary Compressor Without Vapor Injection

In order to verify the correctness of the simulation model, the compression process of the rotary compressor without vapor injection is simulated. By comparing the simulation results with the theoretical results, it is easy to know whether the setting of the simulation model is reasonable and reliable.
In the simulation, the suction and discharge pressures are set to 0.573MPa and 3.206MPa respectively. And R410A was chosen as the refrigerant for the compressor. Analysis of the

simulation results found that the solution becomes periodical after about 2 revolutions. The comparison of theoretical and simulation results of rotary compressor without vapor injection is shown in Table 2. From Table 2, it is easy to see that the difference in mass flow rate between suction and discharge port is within 1%, which indicates that the calculation results have been relatively stable. In addition, both of the suction and discharge mass flow rates of the simulation results are relatively small relative to the theoretical values. And the simulation results are about 11% smaller than the theoretical calculation results. The reason for the difference between the simulation results and the theoretical results is that there is a radial clearance in the simulation, which causes the relatively high-pressure refrigerant gas of the compression chamber to leak into the relatively low-pressure suction chamber through the radial clearance. But in the theoretical calculation, the radial clearance is not considered. In fact, the volumetric efficiency of the compressor is generally about 90%. Therefore, it is reasonable for the simulation results to be smaller than the theoretical calculation results.

Table 2. Comparison of Theoretical and Simulation Results of Rotary Compressor without Vapor Injection

Calculation method	Theoretical results	Simulation results
Mass flow rate of suction port per revolution (g/r)	0.411	0.363
Mass flow rate of discharge port per revolution (g/r)	0.411	0.366

During the simulation, by monitoring the mass flow rate of the suction and discharge ports, the suction and discharge pressure, temperature and density, the variation of these parameters with the rotation angle can be obtained. Fig. 3 plots the variation of the mass flow rate and pressure including theoretical results and simulation results with the angle of rotation. Nevertheless, the mass flow rate curve of simulation results fluctuating and less than the theoretical calculation results. This is because of that the pressure of the suction chamber is smaller than the suction pressure in the actual process, and it is not equal to the suction pressure. In the theoretical calculation, the pressure of the compression chamber is equal and equal to the suction pressure. Therefore, the simulated value of the refrigerant gas mass flow rate of the suction port is smaller than that of theoretical calculation value. In addition, there is leakage of refrigerant gas in the clearance between the compression chamber and the suction chamber, resulting in the mass flow rate of the suction port being lower than the theoretical calculation results. When the compressor begins to compress, there is a backflow of refrigerant gas at the suction port, which causes mass flow rate fluctuations near the suction port. And the reasons for that the pressure curve of simulation results fluctuating and less than the theoretical calculation results are similar. In general, according to the curves in Fig. 3, it is pretty straightforward to know that the simulation results are in good agreement with the theoretical calculation results, which means that the model used to simulate the internal compression process of the compressor is very suitable.

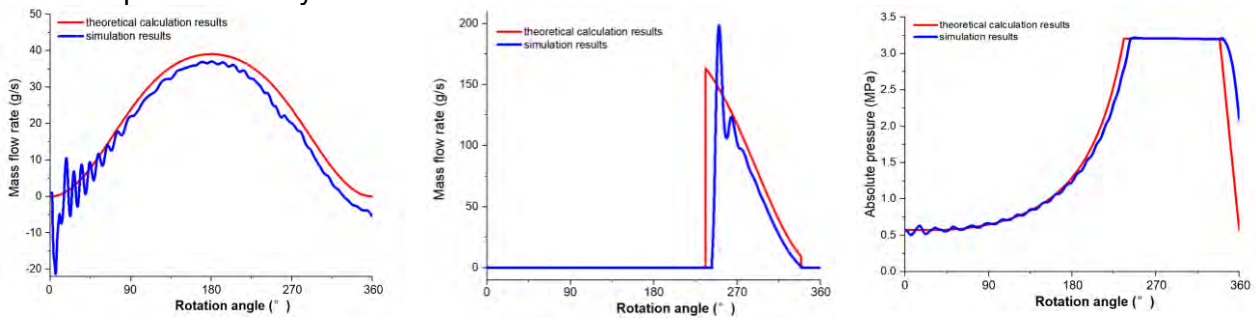

(a) (b) (c)

Figure 3: Comparisons of theoretical calculation results and simulation results; (a) Variation of refrigerant gas mass flow rate of suction port with rotation angle; (b) Variation of refrigerant gas mass flow rate of discharge port with rotation angle; (c) Variation of refrigerant gas pressure with rotation angle in compression chamber;

3.3. Simulation Results of Rotary Compressor with Vapor Injection

For the simulation model of the rolling piston compressor with vapor injection, the only difference for the simulation model without vapor injection is the addition of the injection port. Since the model has a good effect on the simulation of the compression process of the compressor without vapor injection,

the simulation model should also be able to accurately predict the processes of the suction, compression and discharge of the compressor with vapor injection.
For the simulation of compressor with vapor injection, the suction, injection and discharge pressure are set to 0.573MPa, 1.355MPa and 3.206MPa respectively. The simulation results with vapor injection are shown in Table 3. According to Table 3, it is found that the simulation result of the suction mass flow rate with the injection port is 11.3% smaller than that without the injection port, but the discharge mass flow rate is 3.2% larger.

Table 3. Comparison of simulation results with or without injection ports

With or without injection port	Without injection port	With injection port
Mass flow rate of suction port per revolution (g/r)	0.363	0.322
Mass flow rate of injection port per revolution (g/r)	0	0.052
Mass flow rate of discharge port per revolution (g/r)	0.366	0.378

Additionally, the comparisons of simulation results with or without the injection port are shown in Fig. 4. From Fig. 4(a), whether or not the injection port has a great influence on the suction mass flow rate since the simulation results of the suction mass flow rate are so different. It is difficult to distinguish the difference between the two from Fig. 4(b) because of the difference in the discharge is only 3%. Furthermore, Fig. 4(c) shows the variation of injection mass flow rate with rotation angle.

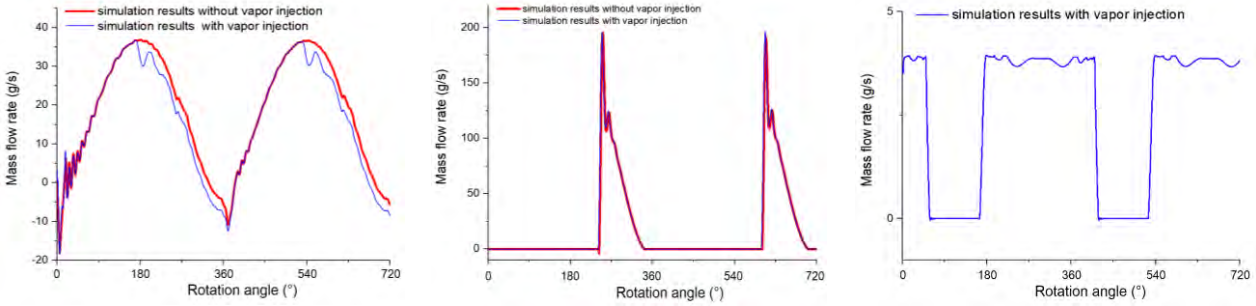

Figure 4: Comparisons of simulation results with or without injection ports; (a) Variation of refrigerant gas mass flow rate of suction port with rotation angle; (b) Variation of refrigerant gas mass flow rate of discharge port with rotation angle; (c) Variation of refrigerant mass flow rate of injection port with rotation angle;

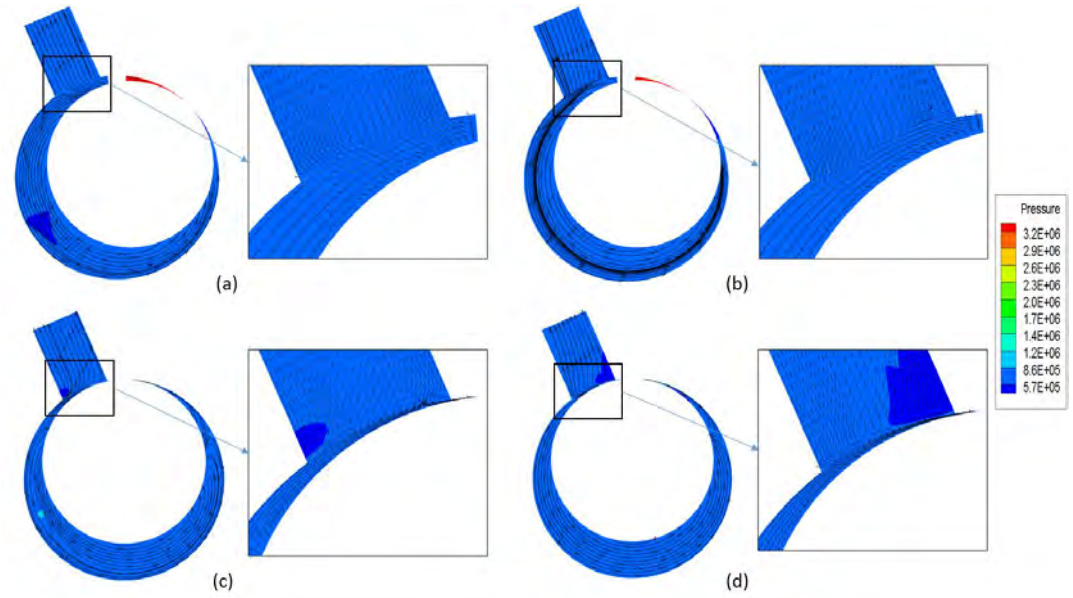

Figure 5: Distribution of streamtraces and velocity vector; (a) 360°+315°, with injection port; (b) 360°+315°, without injection port; (c) 360°+360°, with injection port; (d) 360°+360°, without injection port

Fig. 5 shows the distribution of pressure, streamtraces and velocity vector. By comparing Fig. 5(a) and Fig. 5(b), it can be clearly found that when the compressor is operated to the same angle (360°+315°), there is a backflow at the suction port of the compressor with injection port, but there is no backflow at the suction port of the compressor without injection port. In addition, by comparing Fig. 5(c) and Fig. 5(d), it is easy to know that whether there is injection port or not, there will be backflow at the suction port of the compressor when the compressor is operated to about 360 degrees. Therefore, the injection port has a large influence on the flow state of the compressor suction port. In the process of designing the compressor with vapor injection, it is very meaningful to properly set the position of the injection port to reduce the backflow of the suction port for reducing the power consumption of the compressor.
Fig. 6 shows the streamtraces distribution of different rotation angles of the compressor with vapor injection in 3D. It is easy to see the internal refrigerant gas flow path of the compressor, which is very helpful in analyzing the effect of the injection port on the internal flow of the compressor. At the same time, this also provides some reference for designing the compressor with vapor injection.

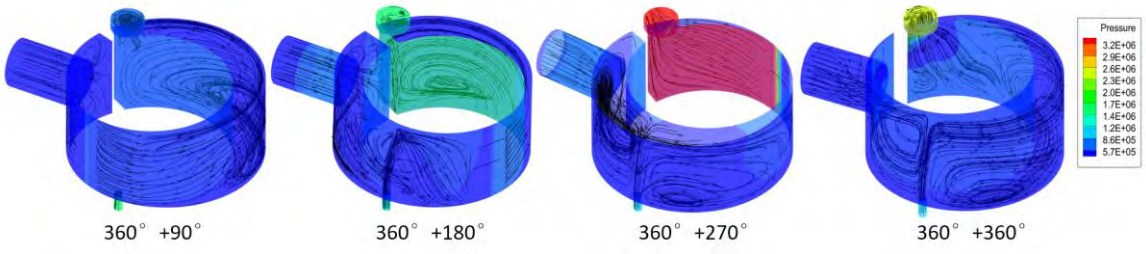

Figure 6: Streamtraces distribution of different rotation angles of the compressor with vapor injection in 3D

Pressure and temperature distribution of different rotation angles of the compressor with vapor injection are shown in Fig. 7. From Fig. 7, it can be clearly seen that the pressure in the compression chamber of the compressor is gradually increased until the pressure reach to discharge pressure, and the pressure distribution in both the compression chamber and the suction chamber is uniform. Similarly, the temperature of the compression chamber is gradually increased, but the difference is that the temperature distribution is not as uniform as the pressure distribution, and it is obvious that the high-temperature refrigerant gas leaks into the relatively low-temperature suction chamber from compression chamber and clearance volume. The reason for the difference in temperature distribution and pressure distribution is that the pressure balance propagates at the speed of sound, while the temperature balance propagates with convection and diffusion, and the propagation speed of the two are not on the same order of magnitude.

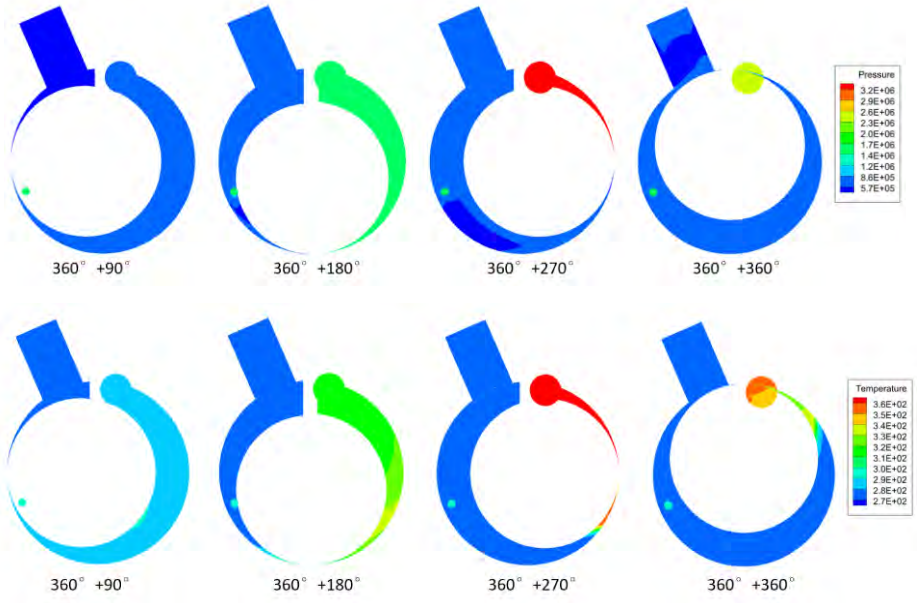

Figure 7: Pressure and temperature distribution of different rotation angles of the compressor with vapor injection

4. CONCLUSIONS

A three-dimensional dynamic numerical model was established to simulate the transient process of internal flow, suction and discharge of the rolling piston compressor by using the commercial CFD solvers FLUENT and dynamic grid technique in this paper. And the distribution of temperature, pressure and streamtraces of the compressor with and without injection port were carried out at different rotation angles, as well as the variations of refrigerant mass flow rate of suction, injection and discharge port with rotation angle. By comparing the simulation results with the theoretical results of the compressor without vapor injection, it is found that the simulation results can be better agreement with the theoretical results, which verifies the reliability and practicality of the model. Meanwhile, the simulation results with and without the injection port are compared and analysed, including the distribution of streamtraces and refrigerant mass flow rate of suction and discharge ports. The simulation results show that the injection port has a great influence on the internal flow field and the mass flow rate of suction port and discharge port of the rolling piston compressor.

NOMENCLATURE

p	pressure (kPa)	v	volume (m^3)
b	thickness of sliding vane (m)	e	eccentricity (m)
h	length of the sliding vane into the cylinder (m)	k	adiabatic exponent
L	height of the cylinder (m)	r	outer radius of rolling piston (m)
R	inner radius of the cylinder (m)	T	temperature (K)
θ	Rotation angle of compressor (°)		

REFERENCES

Li, L., Liu, D. J., 2014. Study on an air quality evaluation model for Beijing City under haze-fog pollution based on new ambient air quality standards. Int. J. Environmental Research and Public Health 11(9), 8909-8923.

Jingchao, Z., Kotani, K., & Saijo, T., 2018. Public acceptance of environmentally friendly heating in Beijing: A case of a low temperature air source heat pump. Energy Policy, 117, 75-85.

Jeon, Y., Lee, S. H., Kim, W., Jung, J., & Kim, Y., 2017. Numerical study on the optimal design of injection-hole geometries of a twin rotary compressor in a liquid injection heat pump. Applied Thermal Engineering, 113, 1178-1188.

Wang, X., Hwang, Y., & Radermacher, R., 2009. Two-stage heat pump system with vapor-injected scroll compressor using R410A as a refrigerant. Int. J. Refrigeration 32(6), 1442-1451.

Heo, J., Yun, R., & Kim, Y., 2013. Simulations on the performance of a vapor-injection heat pump for different cylinder volume ratios of a twin rotary compressor. Int. J. Refrigeration 36(3), 730-744.

Yan, G., Jia, Q., & Bai, T., 2016. Experimental investigation on vapor injection heat pump with a newly designed twin rotary variable speed compressor for cold regions. Int. J. Refrigeration 62, 232-241.

Wang, B., Liu, X., Ding, Y., & Shi, W., 2018. Optimal design of rotary compressor oriented to end-plate gas injection with check valve. Int. J. Refrigeration 88, 516-522.

Geng, W., Liu, C. H., & Wang, Y. Z., 2004. The performance optimization of rolling piston compressors based on CFD simulation. West Lafayette, America, ICECP, C013

Ding, H., & Gao, H., 2014. 3-D Transient CFD Model For A Rolling Piston Compressor With A Dynamic Reed Valve. West Lafayette, America, ICECP, 1548

Farkas, B., Szente, V., & Suda, J. M., 2015. Dynamic meshing strategies to model fluid flow in rolling piston compressors. Budapest, Hungary, CMFF

Ba, D. C., Deng, W. J., Che, S. G., Li, Y., Guo, H. X., Li, N., & Yue, X. J., 2016. Gas dynamics analysis of a rotary compressor based on CFD. Applied Thermal Engineering 99, 1263-1269.

Manuscript ID:712
DOI: 10.18462/iir.icr.2019.0712

Pore-scale 2D modeling of sensible thermal heat storage in a packed bed

Peiyu HU[(a)], Shugang WANG[(a)], Jihong WANG[(a)], Shuang JIANG[(b)], Tengfei ZHANG[(a)] Zhenjun MA[(c)]

[(a)] Faculty of Infrastructure Engineering, Dalian University of technology
Dalian, 116024, China, sgwang@dlut.edu.cn
[(b)] College of Civil Engineering, Dalian Minzu University
Dalian, 116600, China, shjiang@foxmail.com
[(c)] Sustainable Buildings Research Centre, University of Wollongong
Wollongong, 2522, Australia, zhenjun@uow.edu.au

ABSTRACT

The flow and heat transfer characteristics of packed beds, integral in heat recovery technologies, are particularly dependent on corresponding pore structures. However, the meso-structure is always neglected to simplify the issues in related studies. Therefore, this paper presents a novel 2D pore-scale CFD simulation method to investigate the influence of design and operating parameters on the performance of the thermal energy storage system. The proposed method is performed based on structurally typical sections picked up from 3D realistic packed bed models in virtue of two-point correlation. Validation of the computation results with the experimental data has shown a good agreement. Additionally, cases were run to systematically analyze the combined effect including, particle size and compaction degree. Accordingly, when the reciprocal of the vessel-to-particle-diameter ratio, 1/N, is decreased 0.035, the mean steady temperature of the system increases by approximately 1.2% and the pressure drop increases by approximately 35%.
Keywords: sensible heat storage; packed bed; heat transfer; pressure drop.

1. INTRODUCTION

The thermal energy storage (TES) has become one of the main topics of interest in the field of building energy efficiency because TES has a promising potential in effectively exploits renewable energy (Diaz-Gonzalez et al, 2012) and waste heat capture, which would enable the application of advanced energy utilization schemes to HVAC in buildings (Mehling and Cabeza, 2008). The currently available TES technologies can be summarized into the sensible heat storage and latent heat storage (Zhang et al, 2016). Sensible TES, especially sensible heat stored by the packed bed, has been widely developed for commercial implementation and extensively used because of its remarkable characteristics, such as a long service life, economic efficiency and good compatibility with other systems. To enhance the operation performance further, many experiments exploring sensible heat storage in packed beds have been conducted (Anderson et al, 2014, McTigue, 2016). However, the development of sensible TES requires investigating many factors, including the geometry, thermophysical properties and operational parameters, in order to complete an optional design in some sense (Marti et al, 2018). The numerical method is an effective and practical way to cope with this serious difficulty. The current published researches on the simulation of heat transfer in a packed bed can be classified into two categories: (1) modeling without considering the pore structure and (2) modeling with a realistic physical structure. The most popular mathematic model of the first category, which was first developed by Schuman (Schumann, 1929), still has a wide access in simulating the heat storage in a packed bed (Hänchen et al, 2011, He et al, 2017). However, the inhomogeneous bed structure leads to significant wall effects, local backflows and, hence, to large axial and radial gradients of velocity, pressure and temperature (Handley and Heggs, 1969). Neglecting the pore structure of the packed bed seriously limits the ability of the model in analyzing and optimizing the system. Moreover, the heat transfer coefficients in the models of the first category are always determined by an empirical equation, which makes a specific model not credible when the storage mediums change. In the second category, modeling with a realistic structure has recently become available with advancements in computed tomography technology (Johnson et al, 2017).

Packed beds with ordered structure (Li et al, 2017, Wang et al, 2018) and limited particle amount less than 500 (Dong et al, 2017) have been modeled and the pore-scale flow and heat transfer in the packed bed have also been studied. However, the modeling with a realistic physical structure remains challengeable for pilot-scale reconstruction model because of the difficulty in meshing with a complex geometry boundary and an enormous computing time.
In brief, although modeling without pore structure are still used in engineering applications, they are gradually losing competitiveness in the development and optimization of storage systems. Additionally, the enormous workload and computation make it less practical to simulate the storage process with a realistic 3D physical structure at the system scale. Hence, this paper proposes a novel modeling approach to bridge the two currently existing categories, which balances the computational cost and the physical reality. In the present study, physical models are built by simulating the falling and packing process of uniform spherical particles with Discrete Element Method (DEM). Then, the most representative section is selected through a structural analysis with a two-correlation function and validated by the numerical method. Moreover, a 2D two-phase model based on the chosen section is developed. Finally, the proposed model is applied to predict the dynamic thermal performance of the packed bed on a pore scale.

2. GEOMETRAICAL MODEL

2.1. 3D Physical Model of the Packed Bed

The 'pipe in pipe' system used in this paper is depicted schematically in Fig. 1 (a, b). The inner pipe is cylindrical vessel containing the storage particles (aluminium particles) and the outer pipe is equipped with insulations. For the purpose of obtaining the realistic physical packed bed structure, the process of pouring particles into the inner vessel, is simulated with DEM method. Additionally, the static friction coefficient is further studied to generate a preferable physical structure. The static friction coefficient among particles is set to 0.06 (Etsion et al, 2005) and the static friction coefficient between the particle and flat is set to 0.3 (Zhang et al, 1995). Fig. 1 (c) illustrates the pore structure of packed bed generated by the DEM simulation.

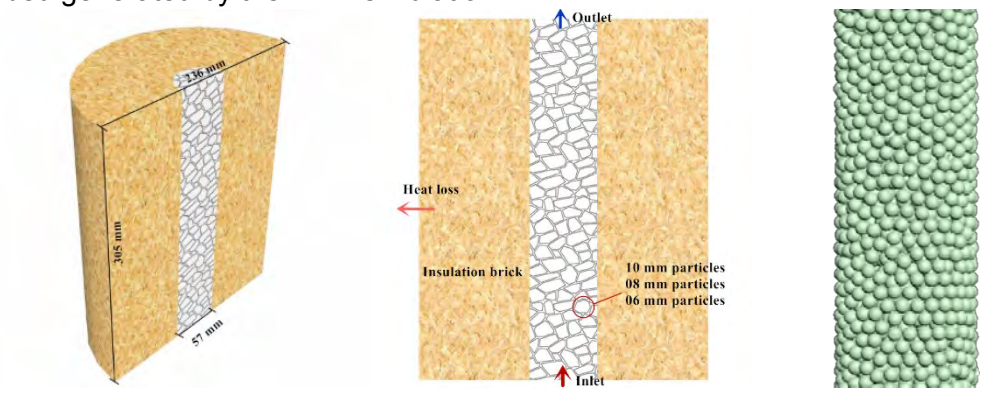

(a) **(b)** **(c)**

Figure 1: Schematic of the thermal energy storage (a, b) and structure of the packed bed (c)

2.2. 2D Structurally Typical Section

If the packed bed structure is an isotropic, a 2D structurally typical section could be picked up with two-point correlation function. The structural characteristics of the selected section determines that whether the flow and heat transfer process based on the section is representative of that in 3D model. Therefore, the analysis can be simplified into storage based on a 2D typical section and it will be verified in the 4.1. The structural analysis is applied to the packed bed along the ring direction, which is achieved by a two-point correlation function given by Berryman (Berryman and Blair, 1986):

$$S_2(r) = < f(x) \cdot f(x+r) > \quad \text{Eq. (1)}$$

where the brackets <·> indicate a volume average over spatial coordinate *x*, *r* is the distance of the two points and *f(x)* is a characteristic function with a value of either 0 or 1. For a two-phase porous media, we can define the void phase with a value of *f(x)* = 1, whereas the solid phase has a value of

f(x) = 0. The most important aspects for the present application of the two-point correlation function are as follows (Berryman 1985):

$$S_2(0) = \phi;\ \lim_{r\to\infty} S_2(r) = \phi^2 \qquad \text{Eq. (2)}$$

where ϕ is the porosity. As r increases, the correlation of the two points drops from approximately ϕ to ϕ^2. The two-point correlation are applied to the 6 cross-sections captured from 0° to 150° with a step of 30°, shown in Fig. 2, which is the top view of the Schematic of the vessel.

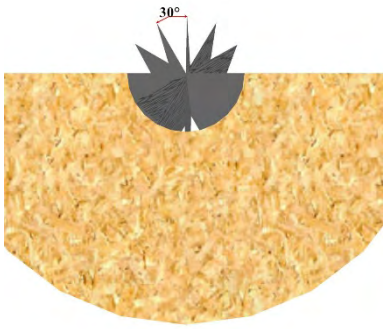

Figure 2: Schematic of the employed sections in the packed bed for structural analysis

3. MATHEMATICAL MODEL

The proposed model analyzes the flow and the heat transfer in the packed bed with reasonable assumptions, including that the heat fluid (compressed air) satisfies the ideal gas law and the flow is considered to be laminar. Standard conservation formulations of momentum, mass and energy are applied using the commercial CFD software FLUENT. Moreover, the natural convection on the outer wall is calculated in the form of the third boundary condition whose heat transfer coefficient is related to the vertical height growth. The heat transfer coefficient is preliminarily calculated by Eqs. (4, 5) proposed by Fevre (LeFevre, 1956) and further modified by Eq. (6) proposed by Tetsu (Tetsu and Haruo, 1970). Additionally, the heat transfer between heat fluid and storage particles is determined by the coupled condition, which calculates the heat transfer directly.

$$\mathrm{Nu}(x) = \left[\frac{7\mathrm{Gr}(x)\,\mathrm{Pr}_{\mathrm{air}}^2}{100+105\,\mathrm{Pr}_{\mathrm{air}}}\right]^{1/4} + \frac{4(272+315\,\mathrm{Pr}_{\mathrm{air}})}{35(64+63\,\mathrm{Pr}_{\mathrm{air}})}\frac{x}{D_{\mathrm{out}}} = \frac{h_{\mathrm{wall}}x}{k_{\mathrm{air}}} \qquad \text{Eq. (4)}$$

$$\mathrm{Gr}(x) = \frac{g(T_{\mathrm{surface}} - T_\infty)x^3}{\upsilon^2(T_{\mathrm{surface}} + T_\infty)} \qquad \text{Eq. (5)}$$

$$(\mathrm{Nu})_{\mathrm{c}} = (\mathrm{Nu})_{\mathrm{p}} + 0.435\frac{x}{r_{\mathrm{w}}},\ \frac{x}{r_{\mathrm{w}}} \le 0.7(\mathrm{Nu})_{\mathrm{p}} \qquad \text{Eq. (6)}$$

In order to assess the grid independency, the Grid Convergence Index (GCI) analysis (Celik et al, 2008) is applied to the case utilizing 3 different meshes, consisting of (1) 1283082; (2) 701005; and (3) 382285 cells. The element ratio for the 3 meshes, N_{i+1}/N_i, is approximately 1.35. The operating conditions used for the GCI analysis refer to the case utilizing the laminar model with the boundary conditions and physical properties set mentioned above. The four parameters, the mean temperature and mean velocity at the outlet and the medial plane, are present in Table 1.

Table 1. Grid Independency

	Temperature at outlet (K)	Temperature at medial plane (K)	Velocity at outlet (m/s)	Velocity at medial plane (m/s)
Φ_1	383.691	388.759	0.349	0.459
Φ_2	383.698	388.753	0.347	0.4534
Φ_3	383.801	388.772	0.338	0.4326
P	8.91	4.24	5.37	4.35
GCI (%)	1.55×10^{-4}	4.46×10^{-4}	0.13	0.41

The results show that asymptotic behaviors of both the temperature and velocity are reached with the GCI below 1%. According to Table 2, the mesh (2) (N_2 = 701005) is adopted for the analysis performed in this study. Moreover, simulations are performed until the normalized residuals fall below 1×10^{-5} (1×10^{-7} for energy equations) for all equations. The transient solutions are obtained by applying coupled algorithms to solve the momentum and community equations together in a relatively large time step of 200 s between each set of results.

4. RESULT AND DISCUSSION

4.1. Validation

The predictions of 2D CFD model with a realistic structure were first demonstrated to be reasonable by comparing the heat transfer in different sections of the same packed bed. Then, the simulation result were compared with the experimental data to further validate the proposed model.
Firstly, it is necessary to verify that the simulated storage process based on the selected section is representative. The two-point correlations of different sections of the same packed bed are shown in Fig. 3 (a). Regarding the correlation, the 60° section and the 120° section are the two closest sections to the average, indicating that these two items have the most similar structure with the 3D packed bed, statistically, while 0° section deviates from the average, symbolizing the most unrepresentative section. These 3 sections were utilized to prove that modeling based on a typical section is rational. As shown in Fig. 3 (b), the real-time heat flux on the particle surfaces of the 3 sections are close on the whole. Nevertheless, the heat transfer of the 0° section is considerably lower at the beginning of the storage process because of the slightly dense packed structure compared with the other two sections. However, it gradually draws closer to the others over time.

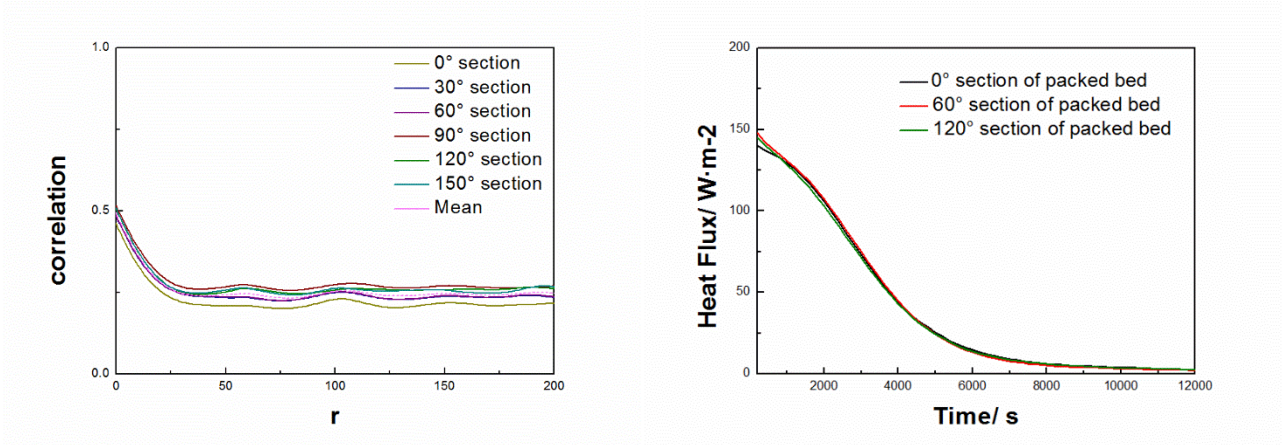

(a) (b)

Figure 3: (a) Two-point correlation of different sections (left). (b) Average heat flux of employed sections (right)

In the second part, to further prove the reliability of the presented method, the numerical data is compared with the experimental data from Anderson (2014). As seen in Fig. 4, the axial temperature distribution predicted by the model coincides well with the experimental data at different stages of the storage process. The model is capable of predicting the storage performance of the packed bed.

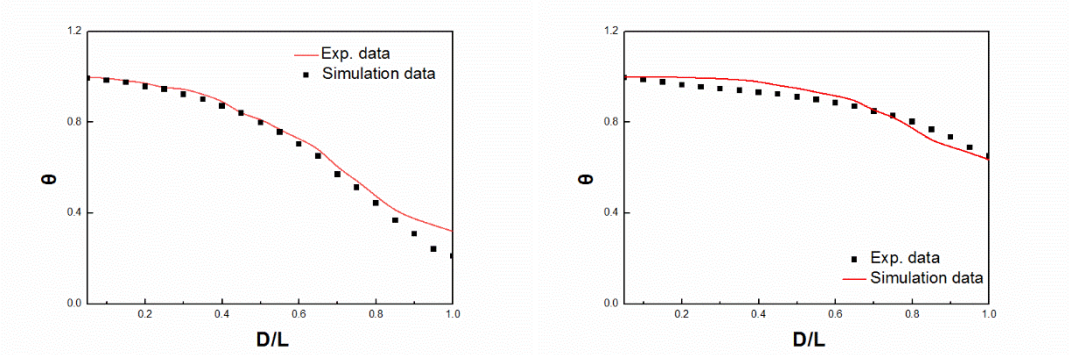

(a) (b)

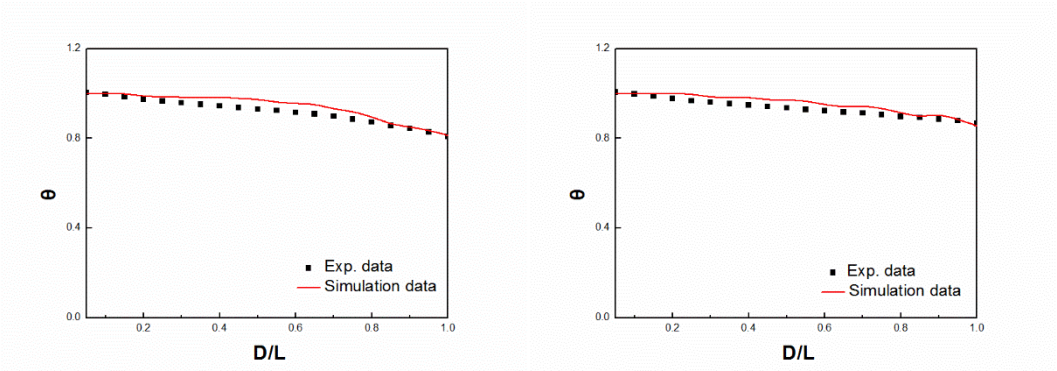

Figure 4: Comparison of the simulated axial averaged temperature profiles (lines) with experimental measurements (a) 2000 s, (b) 3000 s, (c) 4000 s and (d) steady state

4.2. Particle Size

The size of constituent uniform particles not only results in various porosity but also a series of clearly distinct parameters, including void configuration, specific surface area, and pore size distribution. These differences all influence the flow and heat transfer in the packed bed to some degree. Therefore, 6-, 8- and 10-mm particles are employed to pack under the same force, and the corresponding simulation results are illustrated in Fig. 5. Comparisons of the predicted pressure drop and the Ergun solutions (Ergun, 1952) are presented in Fig. 5 (a). As shown, all three models provide a reasonable pressure drop that match well with the Ergun equation, in which the models with smaller particles (6 and 8 mm) are virtually identical with the analytical solutions. Additionally, the pressure drop of a 10-mm packed bed shows that the packed bed with higher *N*, the ratio of the vessel diameter and particle diameter directly lead to higher boundary effect, higher porosity in near wall region, which results in the deviation pronounced at the section simulation. Additionally, when *1/N* decreases 0.035, the pressure drop increases approximately 35%, i.e., a larger flow resistance. The pressure drop is drastically influenced by the slight fluctuations of the porosity. Fig. 5 (b) shows the transient average heat flux at the particle-fluid surface and Fig. 5 (c-d) plots the axial temperature profile and the instantaneous exit temperature, respectively. The average heat flux drops as the particles diameter decreases due to the larger specific surface area, which also contributes to a relatively slower and longer storage process. Moreover, the 6-mm particle packed bed has a smaller void region, which determines a higher steady temperature than other two models, partly because of the larger specific surface area and partly because of the larger storage volume. When *1/N* decreases 0.035, the mean steady temperature of the system increases approximately 1.2%. However, it is questionable to pack with particles as small as possible, as it sacrifices the smooth stream for a slight improvement in storage ability.

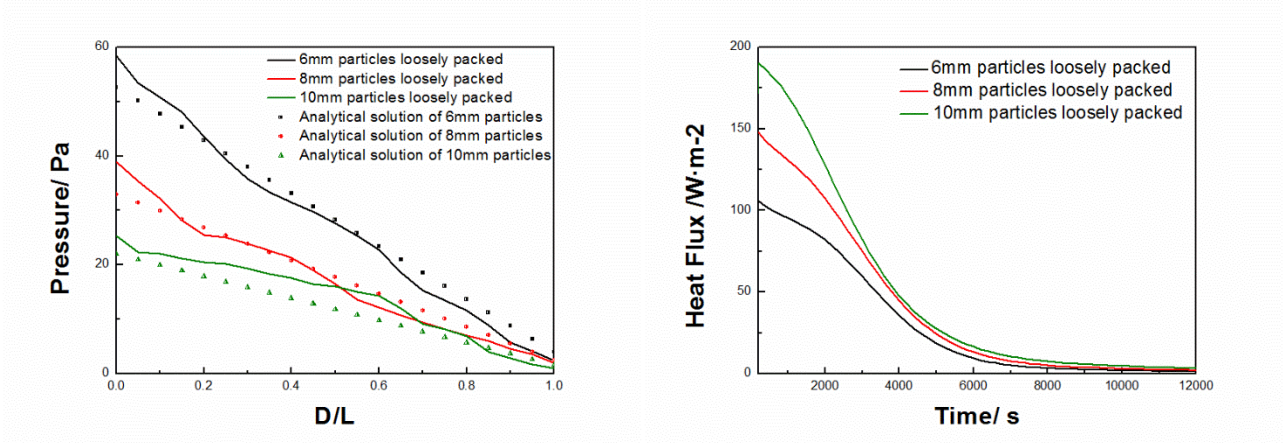

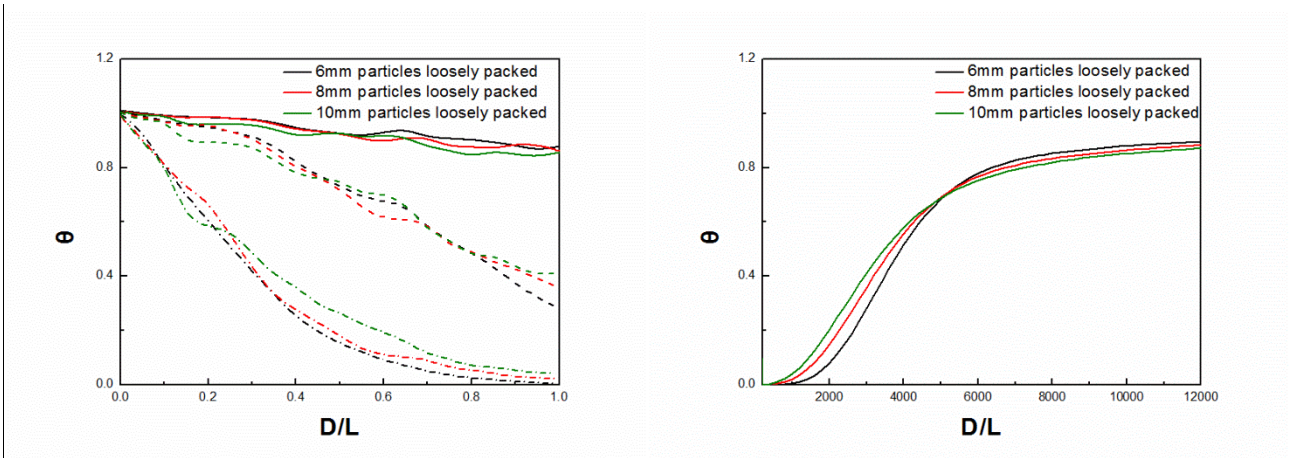

Figure 5: (a) Comparison of the axial averaged pressure profiles (lines) with the Ergun equation, (b) average heat flux at the particle surface, (c) axial averaged temperature profiles with lines representing 2000 s, 4000 s and steady state from left to right, respectively and (d) the exit temperature as a function of time.

4.3. Compaction Degree

Different stresses acting on the same size particles directly give rise to packed beds with different porosities, which is crucial for the sensible heat storage performance. Three models that are generated under various suppositional accelerations of gravity, 9.8, 98 or 980 m/s², are employed to represent free falling, loose and dense packed beds. As shown in Fig. 6 (a), the pressure drop increases with the enhanced compaction degree. However, they do not show a linear correlation. Fig. 6 (b) illustrates the axial temperature distribution of the 3 models at different times. As shown, there are not obvious differences among the steady temperature of the system. On one hand, the smaller porosity arising from less stress leads to a larger flow resistance in the packed bed, which is usually negative for the heat transfer between the particle and heating fluid (Anderson et al, 2014). On the other hand, the enhanced specific surface area is positive in respect to the heat storage. Therefore, under the combined influences of the porosity and the specific surface area, the steady axial temperature distributions of the 3 beds are similar. Additionally, a denser packed bed is always heated slower, particularly in the region nearby that exist during the storage period, which means it requires a relatively longer time to reach the steady state.

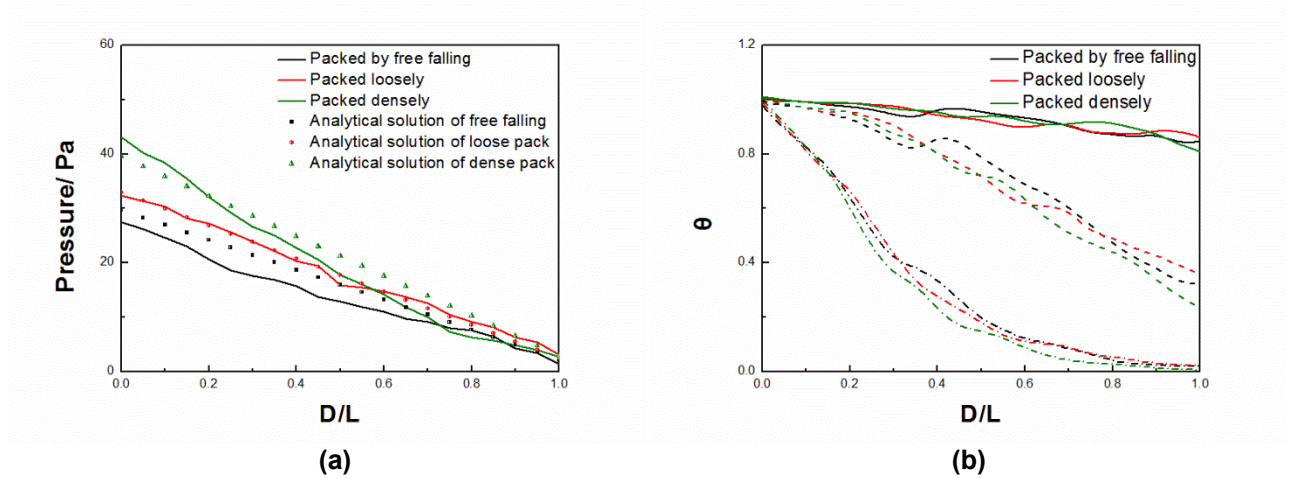

Figure 6: (a) Comparison of axial averaged pressure profiles (lines) with the Ergun equation, (b) axial averaged temperature profiles with lines representing 2000 s, 4000 s and steady state from left to right, respectively.

5. CONCLUSIONS

A novel 2D fluid-solid coupling model with a realistic pore structure is presented for reasonably predicting the flow and heat transfer in a packed bed thermal energy storage vessel using

compressed air as the heating fluid and aluminium particles as storage medium. The presented model is performed on a structurally typical section, extracted from a physically realistic 3D model in virtue of two-point correlation. Meanwhile, the physically realistic 3D model is obtained by simulating the packing process of the particles with DEM. Good agreement is found between the numerical and measured axial temperature profiles collected in a packed bed. Additionally, the simulated pressure drop is consistent with the analytical solutions calculated by the Ergun equation, which is a semiempirical correlation. The proposed method considers considerably more effective factors, including the particle size, specific surface area, mesoscopic structure, and temperature gradient inside the particles, instead of a single structural parameter, i.e., porosity, that makes the model advanced in the optimal design of the storage vessel. For packed beds whose vessel-to-particle-diameter ratio, N ranges from 5 to 10, the pressure drop and the mean steady temperature are proportional to the particle size. When 1/N is increased 0.035, the mean steady temperature of the system decreases by approximately 1.2% and the pressure drop decreases by approximately 35%.

ACKNOWLEDGEMENTS

The authors acknowledge financial support from The National Natural Science Foundation of China (Grant No. 51774181) and National Key R&D Program of China (Grant No. 2018YFC0807902).

REFERENCES

Anderson, R., S. Shiri, H. Bindra and J. F. Morris, 2014. Experimental results and modeling of energy storage and recovery in a packed bed of alumina particles. Applied Energy 119, 521-529.

Berryman, J. G., 1985. Measurement of Spatial Correlation-Functions Using Image-Processing Techniques. Journal of Applied Physics 57(7), 2374-2384.

Berryman, J. G. and S. C. Blair, 1986. Use of digital image analysis to estimate fluid permeability of porous materials: Application of two-point correlation functions. Journal of Applied Physics 60(6), 1930-1938.

Celik, I. B., U. Ghia, P. J. Roache and C. J. Freitas, 2008. Procedure for estimation and reporting of uncertainty due to discretization in CFD applications. Journal of Fluids Engineering-Transactions of the Asme 130(7).

Diaz-Gonzalez, F., A. Sumper, O. Gomis-Bellmunt and R. Villafafila-Robles, 2012. A review of energy storage technologies for wind power applications. Renewable & Sustainable Energy Reviews 16(4), 2154-2171.

Dong, Y., B. Sosna, O. Korup, F. Rosowski and R. Horn, 2017. Investigation of radial heat transfer in a fixed-bed reactor: CFD simulations and profile measurements. Chemical Engineering Journal 317, 204-214.

Ergun, S., 1952. Fluid Flow through Packed Columns. chemical engineering progress 48(2), 89-94.

Etsion, I., O. Levinson, G. Halperin and M. Varenberg, 2005. Experimental Investigation of the Elastic–Plastic Contact Area and Static Friction of a Sphere on Flat. Journal of Tribology 127(1), 47.

Hänchen, M., S. Brückner and A. Steinfeld, 2011. High-temperature thermal storage using a packed bed of rocks – Heat transfer analysis and experimental validation. Applied Thermal Engineering 31(10), 1798-1806.

Handley, D. and P. J. Heggs, 1969. The effect of thermal conductivity of the packing material on transient heat transfer in a fixed bed. International Journal of Heat and Mass Transfer 12(5), 549-570.

He, W., J. H. Wang, Y. Wang, Y. L. Ding, H. S. Chen, Y. T. Wu and S. Garvey, 2017. Study of cycle-to-cycle dynamic characteristics of adiabatic Compressed Air Energy Storage using packed bed Thermal Energy Storage. Energy 141, 2120-2134.

Johnson, T. F., P. R. Levison, P. R. Shearing and D. G. Bracewell, 2017. X-ray computed tomography of packed bed chromatography columns for three dimensional imaging and analysis. J Chromatogr A 1487, 108-115.

LeFevre, E., 1956. Laminar free convection from a vertical plane surface. Proc. 9th Int. Congress Applied Mechanics 4, 168-174.

Li, L., X. H. Yan, J. Yang and Q. W. Wang, 2017. Numerical investigation on band-broadening characteristics of an ordered packed bed with novel particles. Applied Energy 185, 2168-2180.

Marti, J., L. Geissbühler, V. Becattini, A. Haselbacher and A. Steinfeld, 2018. Constrained multi-objective optimization of thermocline packed-bed thermal-energy storage. Applied Energy 216, 694-708.

McTigue, J., 2016. Analysis and optimisation of thermal energy storage, Department of Engineering, University of Cambridge.

Mehling, H. and L. F. Cabeza, 2008. Heat and cold storage with PCM, Springer.

Schumann, T. E. W., 1929. Heat transfer: A liquid flowing through a porous prism. Journal of the Franklin Institute 208(3), 405-416.

Tetsu, F. and U. Haruo, 1970. Laminar natural-convective heat transfer from the outer surface of a vertical cylinder. International Journal of Heat and Mass Transfer 13(3), 607-615.

Wang, J., J. Yang, Z. Cheng, Y. Liu, Y. Chen and Q. Wang, 2018. Experimental and numerical study on pressure drop and heat transfer performance of grille-sphere composite structured packed bed. Applied Energy 227, 719-730.

Zhang, H. L., J. Baeyens, G. Caceres, J. Degreve and Y. Q. Lv, 2016. Thermal energy storage: Recent developments and practical aspects. Progress in Energy and Combustion Science 53, 1-40.

Zhang, Z. F., L. C. Zhang and Y. W. Mai, 1995. Particle effects on friction and wear of aluminium matrix composites. Journal of Materials Science 30(23), 5999-6004.

Manuscript ID: 732
DOI: 10.18462/iir.icr.2019.0732

Modelling and experimental evaluation of a condenser for a heat-pump tumble dryer

Nada PETELIN[(a)], Pero GATARIĆ[(b)], Andrej KITANOVSKI[(a)], Alojz POREDOŠ[(a)]

[(a)] Faculty of Mechanical Engineering, University of Ljubljana
Ljubljana, 1000, Slovenia, nada.petelin@fs.uni-lj.si
[(b)] Gorenje Group
Velenje, 3320, Slovenia, pero.gataric@gorenje.com

ABSTRACT

This article reports on the development of a mathematical model for a finned tube condenser, which is a part of the heat exchanger in a heat-pump tumble dryer. The purpose of this model was to determine the number of tube rows with respect to the minimal mass and volume of the condenser, while maintaining the energy efficiency. The analysis was based on the Ɛ-NTU method, which was further evaluated by the experimental data obtained from measurements performed on a commercial heat-pump tumble dryer. The model can be broadly used for different geometries, refrigerants and air velocities to evaluate the condenser's performance. The numerical results show good agreement with the experimental data; the difference between the predicted and measured outlet air temperatures being less than 4.5%. According to the numerical results, a new condenser, with a 28.5% reduction in the initial size, was designed and tested.
Keywords: Condenser, Finned Tube, Heat Exchanger, Heat Pump, Heat Transfer, Modelling.

1. INTRODUCTION

In the modern world, tumble dryers represent a quick solution for high-density living conditions in cities, air pollution and a rapid method of drying clothes that is independent of daily weather changes. Since a considerable amount of energy is used for clothes drying, the demand for more energy-efficient tumble dryers has increased. The integration of a heat-pump represents a very interesting option from the perspective of energy and cost savings. Heat-pump tumble dryers consume up to 50% less energy compared to conventional condenser dryers (Bush et. al, 2007). This significant improvement in energy efficiency has increased their domestic use considerably: in the US and EU, trends show a growing number of households with a tumble dryer. While in 2015, over 92.5 million US households owned a tumble dryer, an increase to 105.8 million is expected by 2025 (U.S. Energy Information Administration, 2017). The heat-pump tumble dryer's performance and energy efficiency as well as the drying time have been actively investigated either with experiments or with computer models. Braun et al. (2002) used simple models to compare the energy efficiency of heat-pump tumble dryers with conventional air-vented dryers. TeGrotenhuis et al. (2017) developed a computational model to design a hybrid heat-pump clothes dryer. This model predicted an energy-factor increase of more than 90% compared to a standard electric vented clothes dryer. The energy factor was determined as the ratio of dry load weight to the total power consumed during the drying cycle. Based on 27 experimental tests with heat-pump tumble dryer, Gatarić et al. (2018) developed linear-regression models for fan speed, drum speed and mass load, as well as their impact on the energy consumption and the drying time. They found that a large mass load, a high drum speed, and a low fan speed contributed to the highest energy efficiency. Jiang el al. (2006) presented a detailed simulation tool for design and optimization of air to refrigerant heat exchangers. A combination of modelling and experimental set-ups for heat-pump system development was investigated by Pal and Khan (2008), Saensabai and Prasertsan (2003), Bengtsson et al. (2014) and Peng et al. (2017). In this paper, a similar approach to condenser modeling as presented by Pal and Khan (2008) and Parise and Tiecher (2012) will be presented.

2. EXPERIMENTAL SETUP

The experimental setup consisted of a commercial heat-pump tumble dryer with a maximum dry load capacity of 8kg. All the tests were performed according to the standard procedure for tumble dryers, IEC 61121 (2013). For this reason, a walk-in thermostatic chamber was applied to maintain the ambient conditions of 23 ± 2°C and 55 ± 5%, respectively. All the sensors were connected to a DEWE-50-USB2-8 data-acquisition system and a computer for the data recording, monitoring and processing. The data was recorded at one-second intervals. In order to verify the mathematical model, nine thermocouples of type T (±1°C uncertainty) were used, located as shown in Fig. 1. The condensing and evaporating pressure were measured using Cerabar T PMC 131 (± 0.2 bar uncertainty) pressure transducers. The electrical current of the compressor was measured using Dewetron PNA-CLAMP-5 (± 0.5% uncertainty) current clamps. Before starting the measurements, the conditioned cotton test load (7934g) was wetted and spin dried with a washing machine to reach a textile moisture content of 60% ±1%. The textiles were inserted into the drum in a certain order, always following the same procedure, as described by Gatarić et al. (2018). All the tests were performed using the standard cotton drying program (IEC 61121). The moisture content of the textiles after drying had to be equal to 0%±3%, to be considered dry, otherwise the test was not considered to be valid.

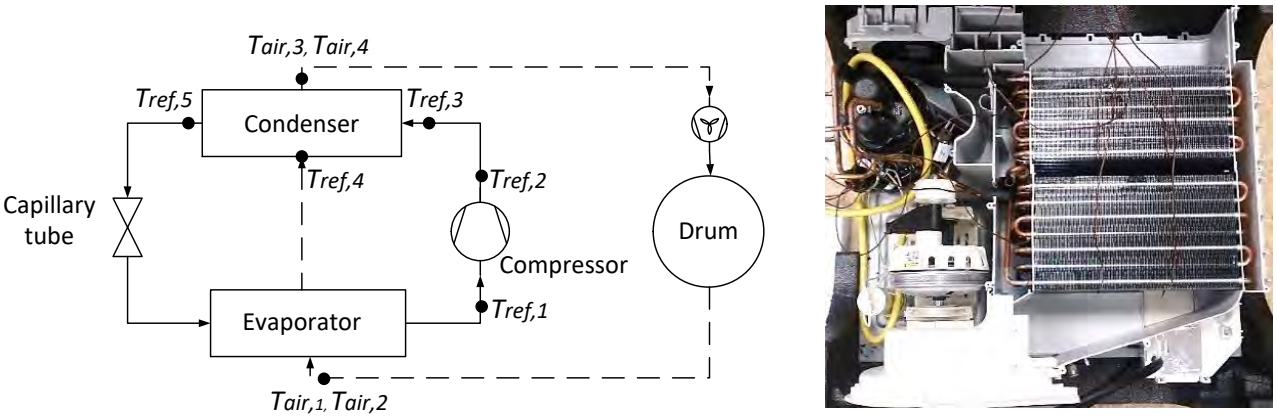

Figure 1: Scheme of the heat-pump system in a commercial tumble dryer

A heat-pump tumble dryer consists of the air and refrigerant circuits, as shown in Fig. 1. The refrigerant circuit, also known as the vapour-compression cycle (Fig.2), combines four main components: an evaporator, a compressor, a condenser and a capillary tube. The refrigerant enters the compressor (2a) as a slightly superheated vapour, where it is compressed to a higher pressure and consequently a higher temperature, as illustrated in Fig. 2. At the condenser inlet (3), the refrigerant is in the thermodynamic state known as a superheated vapour. The condensation starts as a result of the heat rejection to the cooled, dehumidified air (3a). A subcooled refrigerant at the condenser outlet (4a) enters the capillary tube, where it is throttled to the evaporator pressure (1). After expansion, a low-quality saturated mixture enters the evaporator, where the liquid part of refrigerant evaporates by absorbing latent and sensible heat from the air. A superheated vapour at the evaporator outlet enters the compressor (2a), thereby repeating the cycle.

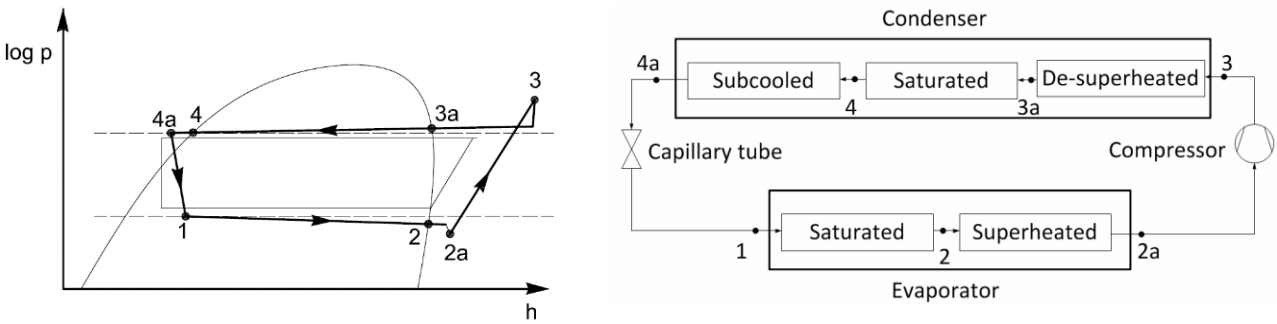

Figure 2: log p-h and block diagram for refrigerant phase changes inside the condenser

2.1. Condenser

The condenser consists of seven tube rows in the direction of the air flow and forms a cross-flow heat exchanger. The internal surface of the tubes is grooved, while the air-side heat transfer is increased with wavy aluminium fins arranged along the tube's length. The condenser's specification can be found in Table 1. A new condenser, with five tube rows and with the same geometry specifications as the existing condenser, was designed from the results of the mathematical modelling. The only difference between the condensers, besides the number of tube rows, was in the refrigerant charge. In order to compare the condenser's performance, the same superheating during the drying cycle must be ensured. Therefore, the refrigerant charge was adjusted from 340 g for the condenser with 7 tube rows to 310 g for the five-tube-rows condenser.

3. MODELLING THE CONDENSER

The condenser was modelled using Python (Python Software Foundation, version 2016.1.1.), while the thermodynamics properties of the refrigerant and the air were calculated using an open-source thermophysical library CoolProp (Bell et al., 2014). The developed model could predict the air outlet temperature and the heating power for different geometries. The number of tube rows for the existing condenser was gradually reduced to find the optimal size. The modelling procedure is presented as a flow chart in Fig. 3 and the input parameters are shown in Table 1.

3.1. Assumptions

To develop the mathematical model, the following assumptions were made:

- The refrigerant pressure drop through the heat exchanger is negligible
- The heat transfer in the fin's z- direction can be neglected
- The air temperature along the y-direction is constant
- The air can be treated as an ideal gas
- The downstream rows have a negligible effect on the heat transfer from the upstream rows
- The analysis is performed under steady-state conditions
- The heat losses to the surroundings and the air leakages of the internal system to the surroundings are neglected

Table 1. Input data for modelling

Input data		Heat exchangers parameters [mm]			
Air flow rate [m^3/h]	[190-230]	Height	150	Fin thickness	0.12
Refrigerant mass flow rate [g/s]	13.7	Width	273	Microfin height	0.24
Inlet air temperature [°C]	33.5	Depth	165	Tube thickness	0.25
Refrigerant outlet temperature [°C]	56.6	Finned length	273	Tube pitch	21.65
Condensing temperature [°C]	61.7	Tube outer diameter	7.37	No. of tubes rows	7
Refrigerant type	R134a	Fin spacing	1.8	No. of tubes in height	6

Each control volume of the condenser is treated as a single cross-flow heat exchanger, where the outlet air and the refrigerant temperatures were determined using the ε - NTU method. The numerical calculation is divided into three phases, namely, the de-superheated, the condensation and the subcooled phase, as shown in Fig. 2. In the first phase, the refrigerant enters the condenser as a superheated vapour, and during the second phase, the heat is removed from the refrigerant, causing the vapour to change into a liquid. When most of the vapour has been condensed, the final phase starts. During this stage, the refrigerant is subcooled and enters a capillary tube in liquid form, allowing the capillary tube to work properly.

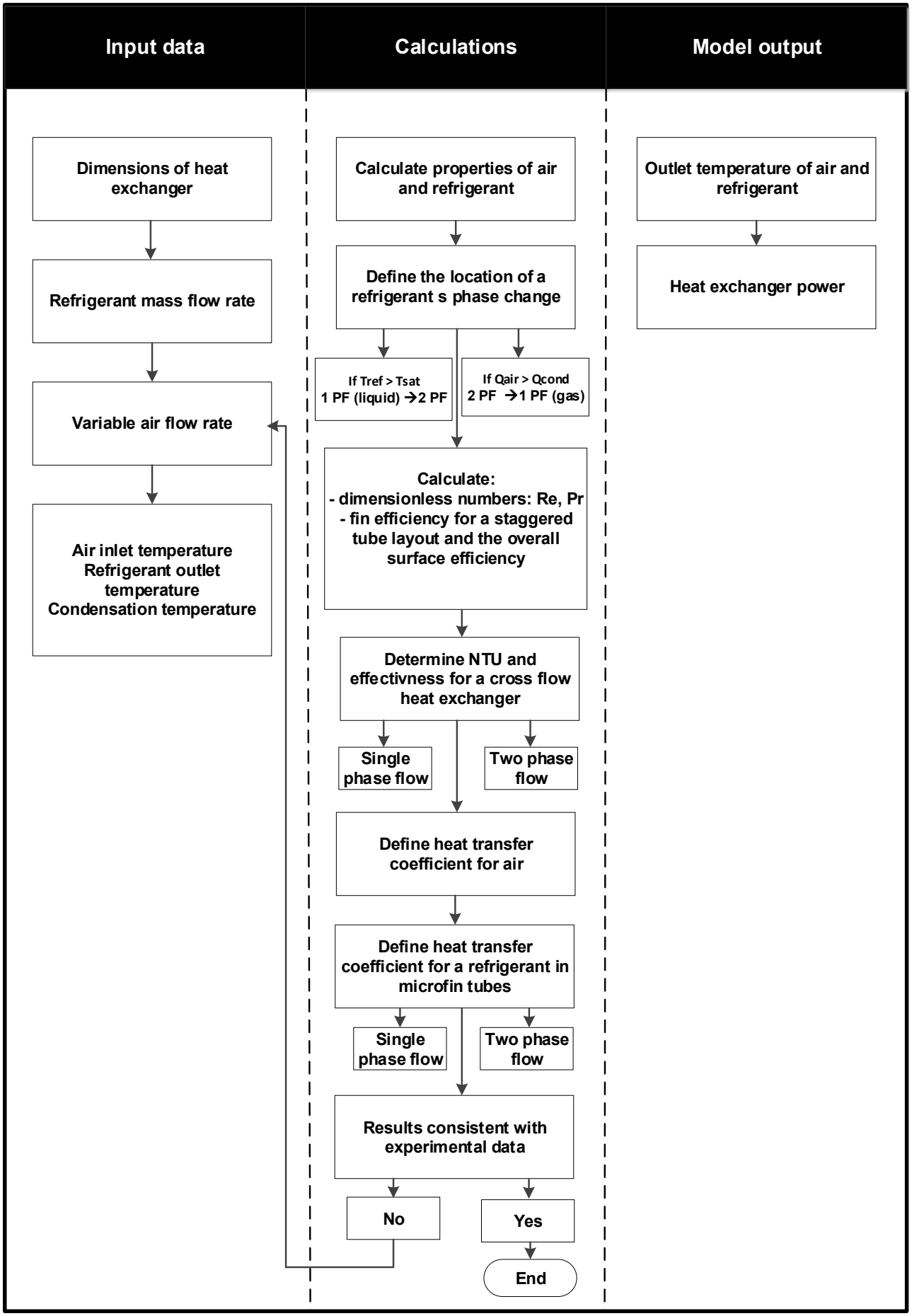

Figure 3: Flow chart for the modelling process of the condenser

A numerical calculation starts with a control volume at the refrigerant outlet in the direction of the air flow, as illustrated in Fig. 4. The condenser domain is divided into seven control volumes, each having six sub-dividable segments that represent the tube rows. If the refrigerant undergoes a phase change within the tube, tube is divided into two separated parts. For the plain fin and the tube heat exchanger with a staggered tube layout, the fins are approximated with hexagons, as suggested by Schmid (1945). The calculated outlet temperatures of the air and the refrigerant for control volume i represent the input values for the control volume i+1. In the first control volume, the Ɛ-NTU equations for the single phase flow are used to determine the heat transfer between the fluids. When the refrigerant's outlet temperature is higher than the condensation temperature, the location of a refrigerant's phase change is defined and so the tube is divided into two segments. The outlet temperatures are calculated following the work of Cavallini et al. (2009) for two-phase flow. When the total condensation heat flux ($\dot{Q}_{con} = \dot{m}_{ref}\, h_{lg}$) is used for heating the air, the condensation segment ends and the calculation for the de-superheated phase starts.

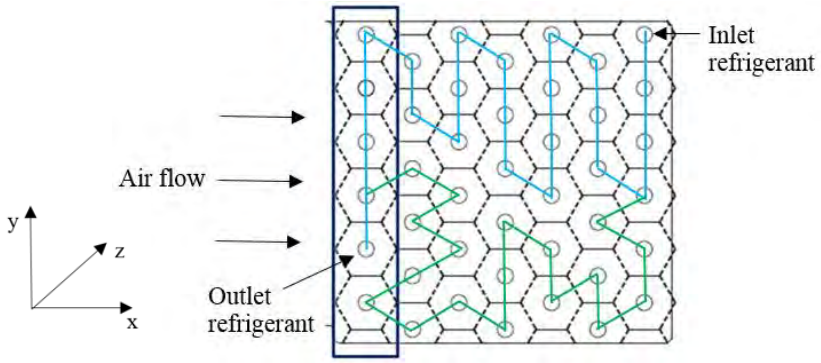

Figure 4: Control volume divided into 6 segments with a hexagon shape.

Table 2. Correlations used in this paper

Description	Author
The number of transfer units and the effectiveness for a cross-flow heat exchanger – single-phase flow, two-phase flow	Shah and Sekulić (2003)
The fin efficiency for a staggered tube layout	Schmid (1945)
Colburn factor correlation for air-side heat-transfer coefficient for herringbone wave fins	Youn and Kim (2007)
The heat-transfer coefficient for a single-phase flow in internally finned tubes	Ravigururajan and Bergles (1996)
The heat-transfer coefficient for a two-phase flow in internally finned tubes	Cavallini et al. (2009)

4. RESULTS

The mathematical model was employed to simulate the condenser's performance, as well as the phase state of the working fluid inside the condenser tubes. This helped us to determine and reduce the condenser's size for subcooling, condensation and de-superheating. As previously mentioned, the mathematical model of a condenser was divided into seven main control volumes, with six sub-divided segments. In Table 3, the average air and refrigerant temperatures for individual control volumes are shown for the 100th minute of the drying time. For the analysed cross-flow heat exchanger, the first control volume represents the air inlet, while the defined temperature of the refrigerant in the first control volume corresponds to a condenser outlet. As shown in Table 3, condensation takes place in more than 70% of the total condenser's area. Therefore, subcooled and de-superheated phases represent a smaller part of the condenser's area, i.e., 10% and 20%, respectively.

Table 3. Results obtained with the mathematical model

Condenser with 7 tube rows						Condenser with 5 tube rows					
CV	Refrigerant		Air			CV	Refrigerant		Air		
	T_{in} [°C]	T_{out} [°C]	T_{in} [°C]	T_{out} [°C]			T_{in} [°C]	T_{out} [°C]	T_{in} [°C]	T_{out} [°C]	
1	56.6	61.7	33.5	46.1	SC/C	1	59	64.1	33.4	46.9	SC/C
2	61.7	61.7	46.1	54.4	C	2	64.1	64.1	46.9	56.0	C
3	61.7	61.7	54.4	58.3	C	3	64.1	64.1	56.0	60.3	C
4	61.7	61.7	58.3	60.1	C	4	64.1	64.1	60.3	62.3	C
5	61.7	61.7	60.1	61.0	C	5	64.1	64.5	62.3	63.3	C/ SH
6	61.7	62.4	61.0	61.3	C/ SH						
7	62.4	64.0	61.3	61.7	SH						

*SC – subcooling, C – condensation, SH – de-superheating

The results obtained with the mathematical model for the seven-row condenser showed that the air outlet temperature in the fourth control volume is already close to the refrigerant's condensing temperature. It can be seen from Table 3 that the air outlet temperature increased by less than 1°C between CV 4 and CV 5, and only by 0.3 °C between CV5 and CV 6. Therefore, the remaining part of the heat exchanger (CV 5 and CV 6) intended for condensation is unnecessary and does not contribute greatly to the airflow heating. Based on this assumption, a new condenser with five tube rows was designed, experimentally tested and numerically analysed. To verify the performance of a tumble dryer with a reduced-size condenser, the new condenser was integrated and tested in a heat-pump tumble dryer. The Fig. 5 and Fig. 6 compared the superheating, the COP, the temperature profiles at the condenser outlet and the evaporating and condensing pressure from the experimental setup, for a condenser with 7 and 5 tube rows, respectively. As previously mentioned, superheating affects the specific heating capacity of the system and in order to compare the performances of both condensers, the same superheating during the drying cycle must be ensured first (Fig. 5). To obtain this, the refrigerant charge was reduced for the condenser with 5 tube rows, from 340 g to 310 g. The COP for a heat pump is determined as:

$$\mathrm{COP_{HP}} = \frac{\dot{Q}_{con}}{P_c} = \frac{\dot{m}_{ref}\ (h_{con,in} - h_{con,out})}{P_{com}} \qquad \text{Eq. (1)}$$

The condenser outlet air temperature has a great impact on the drying process and the drying time. With a higher air temperature, the drying time decreases. Figure 6 shows that the difference in the outlet air temperature between the 5- and 7-row condensers is negligible, which indicates that the additional rows do not have a significant effect on the air conditions. Therefore, the assumption of the mathematical model proves to be correct. However, the experimental results show a reduction in the COP by approximately 13%, compared to the existing heat-pump dryer. The basic reason lies in the fact that the condensing pressure increased, as did the compressor's electrical power (Fig. 6). A possible improvement should be found in the optimization of different components in the vapour-compression cycle, for example, refrigerant charge, different compressor, and capillary tube.

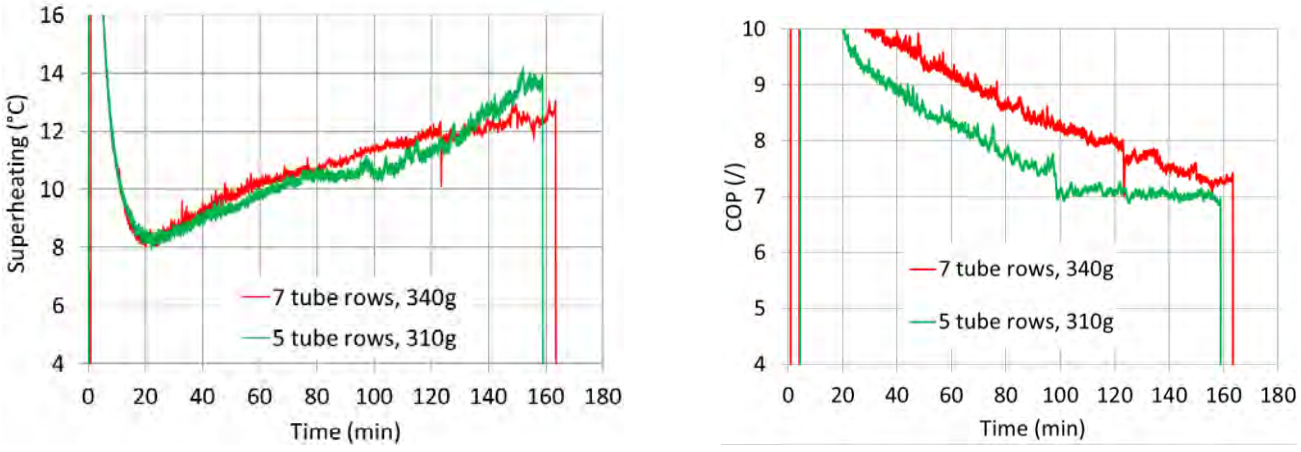

Figure 5: Superheating at the compressor inlet and COP_{HP} for 7- and 5-row condensers

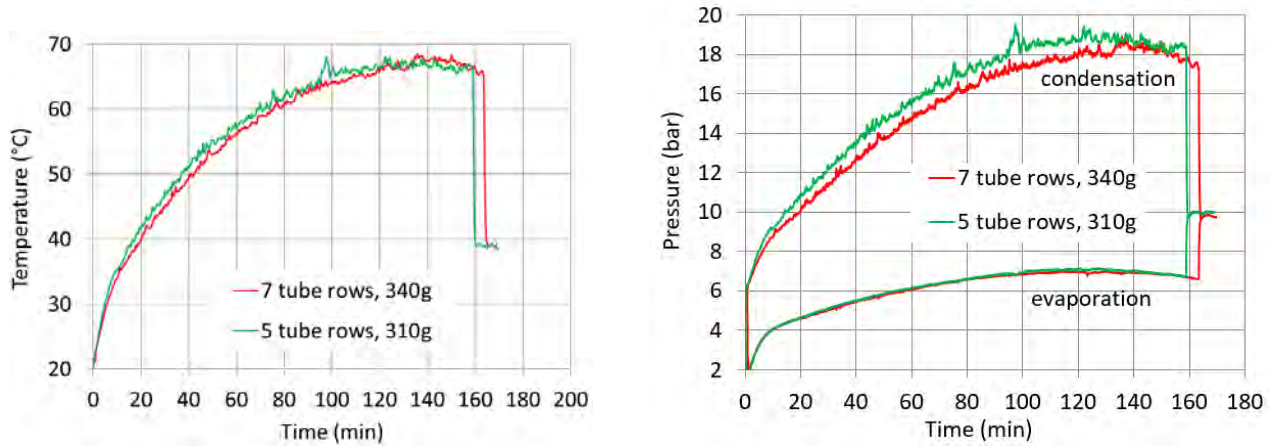

Figure 6: Temperature profiles at condenser outlet and pressure conditions for 7- and 5-row condensers

The results from the mathematical model and the experiment were compared for the 100th minute of the drying time (Table 4). The model's prediction of the outlet air temperature for the 7- and 5-row condensers is satisfactory, with an accuracy of 4.4% and 1.4%. However, comparing the refrigerant temperature, the model underestimated the outlet temperature ($T_{ref,out}$) by 16.5% in the case of a condenser with seven tube rows, and by 19.7% for a condenser with five tube rows. When comparing the results from the model, it is important to point out that the air flow rate was not measured during the drying cycle, but an approximate range of values was used as the input data. By measuring the air volume flow, the accuracy of the model could be improved, although the air flow rate is not constant during the cycle and it strongly depends on the air-pressure distribution. The volume of the textiles inside the drum is changing during the drying time, which affects the pressure distribution and therefore the air volume flow is difficult to measure.

Table 4. Comparison of experimental and numerical results

No. rows	$T_{air,\,out}$ model [°C]	$T_{air,out}$ experiment [°C]	Percentage Error [%]	$T_{ref,out}$ model [°C]	$T_{ref,out}$ experiment [°C]	Percentage Error [%]
7	61.7	64.4	4.4	64	74.6	16.5
5	63.3	64.2	1.4	64.5	77.2	19.7

5. CONCLUSIONS

This study was focused on the development of a mathematical model of a condenser in a commercial heat-pump tumble dryer. The results obtained from the modelling served to reduce the number of tube rows for the existing condenser. Namely, an oversized heat exchanger unnecessarily increases the volume, mass, refrigerant charge and price of the system. The output of the model showed that the condensation area for a seven-row condenser is too extensive and does not contribute considerably to the airflow heating. Therefore, a new condenser with five rows was designed and tested. The experimental results showed the difference in the outlet air temperature between the 7- and 5-row condensers is negligible. The model prediction of the outlet air temperature for the 7- and 5-row condensers is satisfactory, with an accuracy of 4.4% and 1.4%, respectively. The above model will be helpful for the design and performance evaluation of finned-tube condensers.

NOMENCLATURE

C	heat capacity (kJ×kg^{-1}×K^{-1})	$\dot{Q}$	heat-transfer rate (W)
COP	coefficient of performance (-)	$\mathcal{E}$	effectiveness (-)
Cr	heat-capacity ratio (-)	Subscript	
CV	control volume (-)	c	cold
h	specific enthalpy (J×kg^{-1})	com	compressor
h_{lg}	latent heat of condensation(J×kg^{-1})	con	condenser
$\dot{m}$	mass flow rate (kg×s^{-1})	h	hot

NTU	number of transfer units (-)	*in*	inlet
P	electrical power (W)	*max*	maximum
PF	phase flow (-)	*out*	outlet
T	temperature (K)	*ref*	refrigerant

REFERENCES

Bell, I. H., Wronski, J., Quoilin, S., Lemort, V., 2014. Pure and Pseudo-pure Fluid Thermophysical Property Evaluation and the Open-Source Thermophysical Property Library CoolProp. Industrial & Engineering Chemistry Research 53(6), 2498-2508.

Bengtsson, P., Berghel, J., Renström, R., 2014. Performance Study of a Closed-Type Heat Pump Tumble Dryer Using a Simulation Model and an Experimental Set-Up. Drying Technology 32(8), 891-901.

Braun, J. E., Bansal, P. K., Groll, E. A., 2002. Energy efficiency analysis of air cycle heat pump dryers. Int. J. Refrig. 25(7), 954-965.

Bush, E., Attali, S., Brunner, C.U., 2007. Topten - Best of Europe. How do best products perform and why aren't they sold across Europe? ECEEE Summer study proceedings, La Colle sur Loup, France, ECEE, 1331–1341.

Cavallini, D., Del Col, D., Mancin, S., Rossetto, L., 2009. Condensation of pure and near-azeotropic refrigerants in microfin tubes: A new computational procedure. Int. J. Refrig. 32(1), 162-174.

Gatarić, P., Širok, B., Hočevar, M., Novak, L., 2018. Modeling of heat pump tumble dryer energy consumption and drying time. Drying Technology, 1-9. In press. DOI: 10.1080/07373937.2018.1502778.

IEC 61121, 2013. Tumble Dryers for Household Use - Methods for Measuring the Performance.

Jiang, H., Aute, V., Radermacher, R., 2006. CoilDesigner: a general-purpose simulation and design tool for air-to-refrigerant heat exchangers. Int. J. Refrig. 29(4), 601-610.

Kim, N. H., Yun, J. H., Webb, R.L., 1997. Heat Transfer and Friction Correlations for Wavy Plate Fin-and-Tube Heat Exchangers. Journal of Heat Transfer 119(3), 560-567.

Pal, U.S., Khan, M. K., 2008. Calculation steps for the design of different components of heat pump dryers under constant drying rate condition. Drying Technology 26 (7), 864-872.

Parise, J. A. R., Tiecher, R. F. P., 2012. A Simulation Model for the Application of Nanofluids as Condenser Coolants in Vapor Compression Heat Pumps. Proceedings of the International Refrigeration and Air Conditioning Conference, Purdue, Indiana, Purdue University, 1-10.

Peng, J., Zhang, C., Cao, X., 2017. Modeling and Analysis of a Heat Pump Clothes Dryer. Proceedings of the 12th IEA Heat Pump Conference, Rotterdam, Netherlands, IEA, 1-10.

Ravigururajan, T. S., Bergles, A. E., 1996. Optimization of in-tube enhancement for large evaporators and condensers. Energy 21(5), 421-432.

Saensabai, P., Prasertsan, S., 2003. Effects of Component Arrangement and Ambient and Drying Conditions on the Performance of Heat Pump Dryers. Drying Technology 21(1), 103-127.

Schmid, T. E., 1945. The Heating Capacity of Finned Tubes. Bulletin of International Institute of Refrigeration Annex G-5.

Shah, R.K., Sekulić, D.P., 2003. Fundamentals of Heat Exchanger Design. John Wiley & Sons, Inc., New Jersey, 97-231.

TeGrotenhuis, W., Butterfield, A., Caldwell, D., Crook, A., Winkelman, A., 2017. Modeling and design of a high efficiency hybrid heat pump clothes dryer. Appl Therm Eng 124, 170-177.

U.S. Department of Energy, Energy Information Administration Annual Energy Outlook 2017. Available from: https://www.eia.gov/outlooks/aeo/data/browser/#/?id=30-AEO2017

Manuscript ID: 734
DOI: 10.18462/iir.icr.2019.0734

Industrial Heat Pumps in the UK
Current Constraints and Future Possibilities

Neil J. Hewitt, Donal Cotter, Ming Jun Huang, Nikhilkumar Shah
Ulster University
Centre for Sustainable Technologies
Shore Road, Newtownabbey, Co. Antrim, Northern Ireland, BT370QB, UK, nj.hewitt@ulster.ac.uk

ABSTRACT

Industrial heat pumps are not common in the UK. However, there is a large and untapped waste heat energy resource that could be upgraded to useful heat in buildings and industrial processes, but there is confusion as to the amount of this heat that is available. Industrial Heat is approximately 300 TWh/year in 2016 (DUKES – ECUK, 2017) and the available waste Heat = 1/6th available for waste heat recovery (Element Energy, 2014) i.e. 50 TWh/year. If this was used for future district heating networks, 28 TWh/year would be utilised in new networks (Element Energy, 2014). Assuming a current household gas price of 3.69p/kWh (British Gas), the utilisation of 28 TWh/year will displace over £1Bn of gas purchases annually. However, UK industrial electricity prices for large energy users are almost 60% higher than the EU-15 median, while for medium and small/ medium users, the price differential is over 40%. Higher performing heat pumps may provide an answer.
Keywords: Industrial Heat Pumps

1. INTRODUCTION

Heat pumps are undoubtably an element of decarbonisation of heating. Exceptions include high temperature processes (steel, cement etc.) where biogas and/or hydrogen may be more suited in a near zero carbon future. However, despite clear indications that near decarbonisation is a possibility in the UK, there are considerable challenges for lower temperature heat processes that would consider using heat pumps.

1.1 UK energy pricing – a challenge for Electrically Driven Heat Pumps?

Energy price data from Eurostat (2018) reveals electricity and gas price comparisons for industry across Europe (Figure 1). While the UK does not have the worst comparator of electricity versus gas price (UK = 3.39, Italy > 4.04), it is none the less second placed in this league table and as a consequence, gas price is low relative to electricity price. In fact, the UK has the second lowest unit price in Europe at 2.594p/kWh for gas with Denmark the highest at 6.478p/kWh (149% higher). For electricity, the UK has the 10th most expensive rates at 8.794p/kWh with Cyprus the highest at 16.661p/kWh (89.45% higher). For this analysis, the comparator is of interest. Furthermore, given the increased capital cost of an electrically driven vapour compression heat pump versus a gas boiler of similar heating capacity, a heat pump seasonal performance factor (SPF) of 2.71 is the break even in terms of running costs, taking no account of any capital cost differences. This SPF is that necessary to overcome the price differential between electricity and gas when operating an electrically driven vapour compression heat pump to provide a heating demand when compared to providing heat from a heat pump when compared to providing heat from a conventional gas boiler. The latter is the most common approach of industrial space and process heating in the UK.

However, the Renewable Heat Incentive in the UK can provide some assistance in capital cost challenges with a 500 $kW_{thermal}$ heat pump operating for 5000 hours per annum receiving over £2000/annum of additional support. However, an industrial air source heat pump will cost approximately £140/$kW_{thermal}$ versus a gas boiler of £50/$kW_{thermal}$ and would require a payback period

of approximately 20 years at the break-even SPF of 2.71. Therefore, an important factor is the Seasonal Performance Factor.

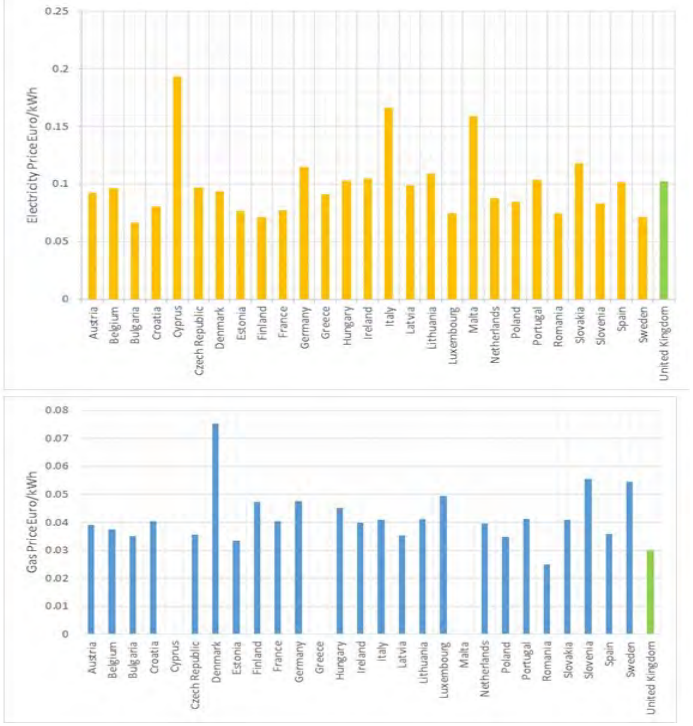

Figure 1: Electricity and Gas Price Comparison for UK Industry

1.2 Performance of UK Industrial Heat Pumps

Hughes (2018) analysed the performance of 19 monitored trials of commercial and industrial heat pumps in the UK. These were a mixture of ground source and air source units and seasonal performance factors were considered ranging from the heat pump itself, the heat pump and its internal fans and pumps, and the overall system performance including all auxiliary elements. Figure 2 illustrates the impacts of this review in terms of SPF. Regarding SPF, SPFH1 – Heat Pump only, SPFH2 – Heat Pump and Pumps/fans etc., and SPFH4 – System performance including all auxiliaries. Keeping in mind the approximate estimate of break-even SPF as being 2.71, the vast majority of heat pumps are above this point, recognising that this is very application dependant. These are noted in Figure 2 as SPFH1 (heat pump performance).



Figure 2: SPF Comparison of Monitored Commercial and Industrial Heat Pumps in the UK

However, the challenge is in the system and auxiliary components design and use. Therefore, in the following analysis, improvements to the heat pump, improvements to the fans and pumps and overall auxiliaries will be considered. The scatter in the examples of Figure 3 tends to indicate that there are

huge improvements in both heat pump and its installation, but a general improvement is in the lower the temperature lift (application dependant) and increasing the heat delivery heat transfer area i.e. underfloor heating and/or larger radiators (building dependant). These are well known but need constant reiteration coupled with end-user acceptability reinforcement to a different style of space heating delivery.

2. Improving an Industrial Heat Pump

In operating industrial heat pumps, a number of elements are considered. These include improving the overall performance of those operating under traditional space heating conditions to extending the range for process heating applications. The role of alternative heat sources must also be addressed.

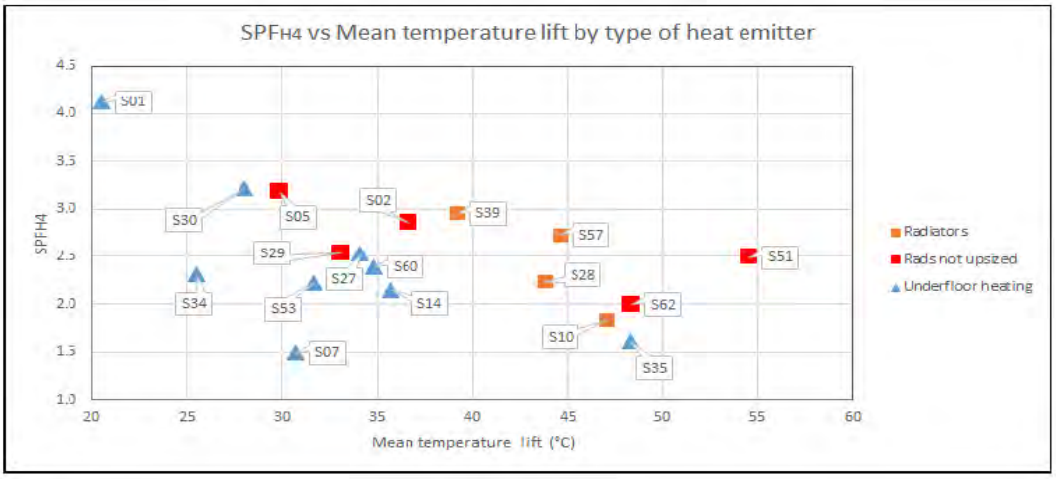

Figure 3: Space Heating Applications for UK Commercial and Industrial Applications

2.1 Replacing R410a in Industrial Applications

In considering how to improve heat pumps, low Global Warming Potential (GWP) working fluids must be utilised. A traditional heat pump i.e. that heating an underfloor hydronic system may replace R410a with R32. This will see a drop in GWP from 2088 to 675 and the use of R32 will deliver a COP that is similar to R410a e.g. Alabdulkarem et al (2015) or superior to R410a e.g. Mota-Babiloni et al (2017). Heat pumps that utilise existing high temperature hydronic radiators could utilise R410a at the lower temperatures encountered e.g. <60˚C but see superior performance with R32 with its superior critical temperature, heat transfer and lower pressure drop (Botticella et al, 2018). R32 compares favourably to other proposed replacements as the modelled results indicate (Figure 4).

2.2 Utilisation of Low Temperature Heat Networks for Industrial Applications

A low temperature heat network (or 4th Generation heat network) is one that can supply low-temperature district heating for space heating, domestic hot water and process heating to buildings and industry. A 4th Generation Heat Network will have low grid losses, be able to utilise waste heat from low-temperature sources and integrate renewable energy sources such as solar and wind as part of a smart energy system to be flexible in the future (Lund et al, 2014). Low temperature is defined by the Danish as >50˚C and ultra-low networks as <45˚C (Danish Energy Agency, 2014). The latter would require heat pumps for upgrading to traditional space heating temperatures, for domestic hot water use (booster heat pumps) and beyond to industrial process applications. UK low grade waste represents a significant energy resource. While there are discrepancies on the actual values, industrial heat represents 300 TWh/year in 2016 (DUKES, 2016) and 1/6th of the waste heat is available for waste heat recovery (Element Energy, 2014) i.e. 50 TWh/year. Furthermore, 28 TWh/year has been identified for “potential” district heating networks and assuming a current household gas price of 3.69p/kWh, utilisation of 28 TWh/year will displace over £1Bn of gas purchases annually. However, the UK has the equivalent of 13 TWh of existing heat networks (BEIS,

2016) and assuming network construction costs are £1500/MWh, new network costs for 15 TWh/year lead to £22Bn investment. As gas is assumed to produce 0.19 kg/kWh of CO_2 and If the UK can utilise 28 TWh of waste heat displacing gas for space heating, 5,320,000 tonnes of CO2 will be saved. As an example, if this was utilised for domestic space heating, UK residential buildings currently emit 63.4 Million tonnes of CO_2/year,10% of residential CO_2 emissions can be saved if waste heat is fully utilised.

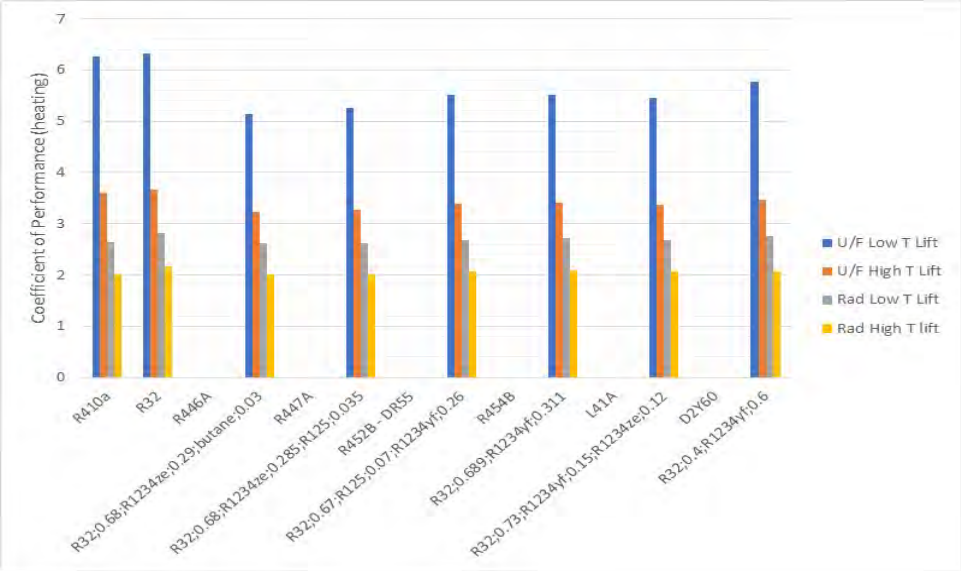

Figure 4: R410a Replacement Comparisons.

With respect to heat pump development for waste heat recovery, the EU is cutting the availability of hydrofluorocarbons (HFCs) by 79% between 2015 and 2030 (BEIS, 2015) due to high Global Warming Potential and alternative fluids must be evaluated. The vapour compression heat pump operating in conjunction with lower grade heat networks e.g. about 30°C, can uplift such heat to underfloor heating temperatures (<40°C) with a coefficient of performance >10 (very low running costs) and provide domestic hot water temperatures avoiding legionella concerns (~60°C) with a coefficient of performance >5.0 with current refrigerants e.g. R410a. However revised heat exchangers must be developed (Lee et al, 2013). For thermal networks, alternative fluids such as R245fa have realised coefficients of performance of >7.0 for ~60°C (Figure 5).

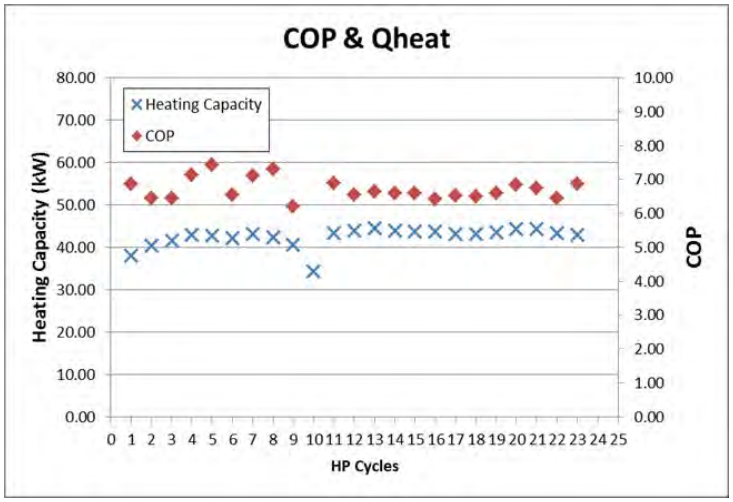

Figure 5: R245fa Performance in a Seasonal Thermal Storage Operation

Extending the temperature lift further sees low GWP fluids such as R1233zd (Ju et al, 2017) being able to upgrade low grade waste heat to process temperatures. Higher temperature heat pumps have been successful and new fluids such as R1233zd (>150°C, low GWP) are looking promising

(Figure 6). However, compressor lubrication strategies for higher temperatures with existing equipment have not been explored to give commercial confidence.

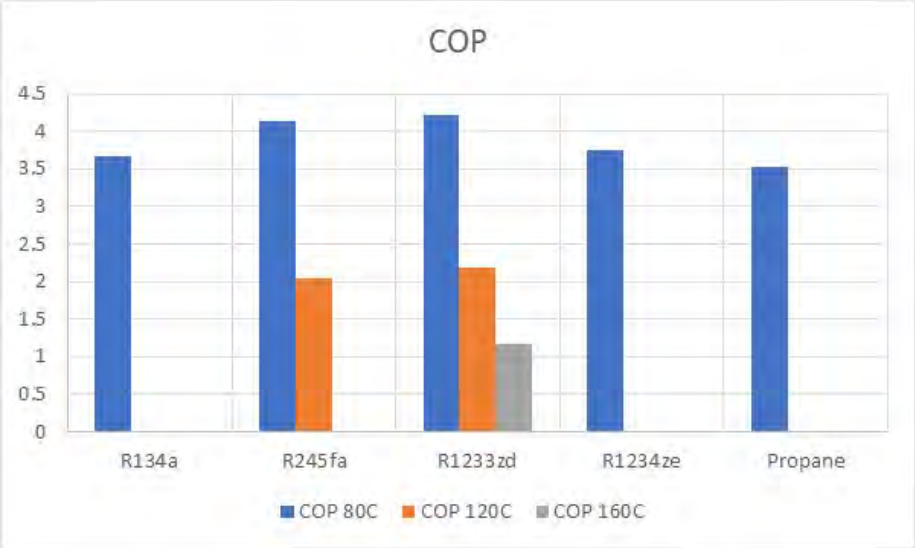

Figure 6: Alternative Refrigerant Performance at High Temperatures

3. High Temperature Heat Pumps Using R1233zd(E)

Hydrofluro-Olefins (HFO) R1233zd is an A1, non-toxic, non-flammable refrigerant with a GWP of 4.5 (under AR4). R1233zd is normally described as zero-ODP due to its very low ODP and is measured at 0.00034. Its physical properties are similar to R245fa and like R245fa, when used in a R134a compressor, both R245fa and R1233zd have higher specific volumes and therefore require larger components e.g. compressor and heat exchangers. They also require a suction line heat exchanger due to the re-entrant nature of the compression process at low superheats. The HFC gases that have been used so far for high temperature applications are R134a, R152a and R245fa and their GWP is 1300, 140 and 1030 respectively. Honeywell has developed a number of HFOs for high temperature applications with a very low GWP (<1). Working fluids such as HFO-1234ze(Z), HFO-1234ze and HFO-1233zd with critical temperatures higher than 94°C are the main candidates for high temperature applications (Longo, 2014). In addition, natural refrigerants have been always an interesting topic for heat pump developers due to their inexistent GWP and low cost. However, their flammability is very high and requires special safety equipment.

3.1 High Temperature Heat Pump Working Fluid Evaluation

Typically, a high temperature heat pump normally has a range of supply temperatures >80°C with typical heat source temperatures 20°C to 70°C. These heat pumps use low grade waste heat from primary processes as the source within a HP cycle to achieve higher secondary supply temperatures. Industries where this type of heat pump may be used range from paper, chemical, mechanical and textile industries. The Ulster University test facility (Figure 7) was built into a specially designed rig and uses mainly off the shelf components with some modification to mitigate against higher temperatures developed within the working system (Bitzer Heat Pump 1-stage cycle, Danfoss expansion valve and an optimization by IHX). A separate Thermal Balancing Rig (TBR) was also designed, which incorporates bespoke control systems to manage thermal loads within the secondary and tertiary hydraulic circuits. The combined systems of heat pump and TBR forms an integrated system and has fitted a range of controls and sensing devices necessary to operate and derive data for experimental analysis. Baseline performance was achieved with R245fa and is illustrated in Figure 8. Comparing R245fa and R1233zd(E) reveals the following analysis (Figure 9) and seems to suggest that R245fa performs slight better at higher temperature demands. However, these are preliminary results.



Figure 7: Ulster University High Temperature Heat Pump Test Facility

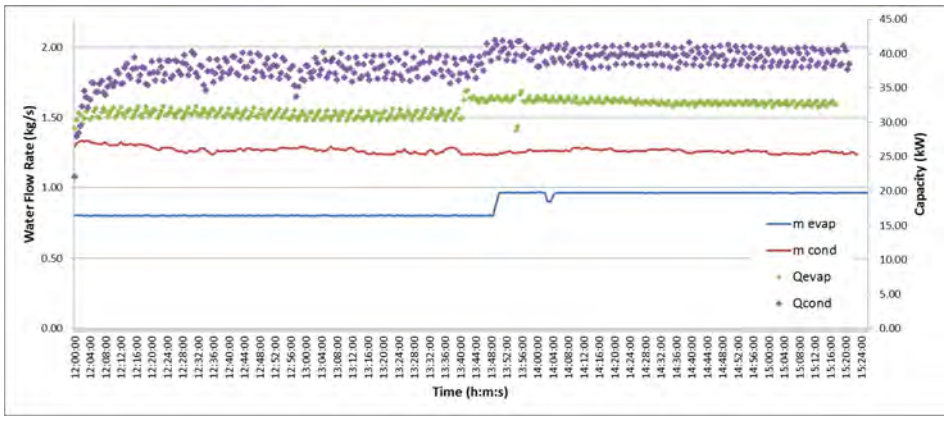

Figure 8: R245fa Baseline Performance

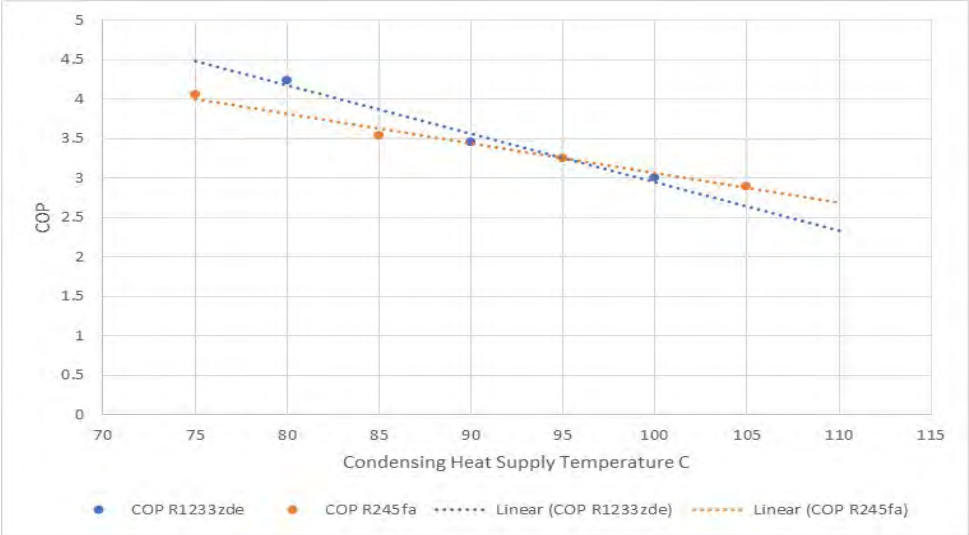

Figure 9: COP Comparison

3.2 Compressor Lubricant Oil Observations

During initial setup the compressor was ramped up gradually to condenser temperatures above 120°C, a small leak from the outer housing was observed. The OEM guidance does suggest that a small amount of oil may pass through the seals dependant on operating conditions. However, this leak gradually increased over several tests and a decision was made to check and replace seals. To repair the leak new seal kit was installed. This required the separation of the motor from the heat pump and careful removal of the damaged seals and installation of the new kit. There was no apparent visual damage to the outer seals, but the inner seal rubber was hardened compared to the new seal. The oil sump-plug magnetic core did pick up some swarf but was not excessive and maybe attributable to the running in process of the compressor. The refrigerant filter was removed and again a visual examination completed, this showed a small quantity of particles around the inlet but no major build-up of dirt. The pressure drop across the filter was about 0.2 bar during operation, which

was only a slight amount higher than when first installed. The filter was replaced as a precaution and checked for leaks prior to operation. The compressor was refilled with POE68 oil to the required levels considering the additional requirement of 0.6l as specified for the oil separator. Upon running the compressor over a period of 6 months the same grey film has not reappeared on the glass surface. Polyester oil HARP POE68 was recommended by the suppler for higher temperature applications exceeding DIN51503 part 1 (Bitzer). Based on technical guidance (Figure 10) for this oil, the viscosity ranges from 65.5 cSt at 40°C to 9.3 cSt at 100°C, providing a guide to viscosity assuming liner response between the temperature bandwidth. During the maintenance service, compressor oil was removed to assess the state of degradation. This was done visually without testing of any type. The visual examination compared a sample of new oil against the oil removed. There was a marked changed in the clarity from the clear yellowish-brown tone when new to a dark cloudy black to grey colour when removed from the compressor. It may be possible to speculate that the internal run-in period of the compressor had deposited carbon like deposit into the oil creating almost a graphite type appearance within the oil. The inspection port on the side of the compressor had also completely clouded over with this deposit, blocking the view of oil levels completely. This required the removal of the side viewing port to thoroughly clean these deposits off the glass. The compressor was refilled with POE68 oil to the required levels considering the additional requirement of 0.6l as specified for the oil separator. Upon running the compressor over a period of 6 months the same grey film has not reappeared on the glass surface.

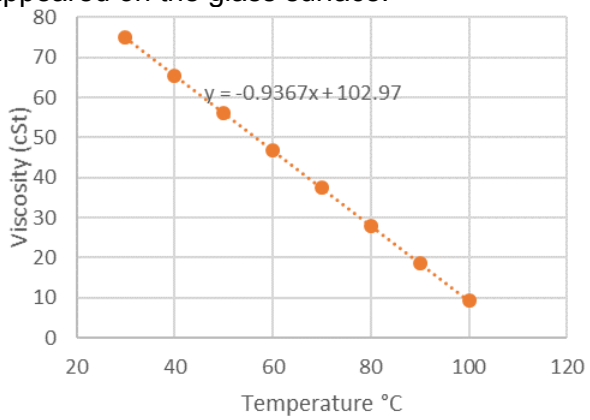

Figure 10. Viscosity Vs Temperature based on product technical data (HARP)

During the initial start-up the compressor goes through a phase whereby the oil and refrigerant mix readily (as seen in the oil levels and colour within the compressor sump - Figure 11). Once the evaporator and condenser temperatures start to stabilise and setpoints are reached, a rapid drop in both pressure and temperature in the sump occurs. In this compressor it takes approximately one hour to reach stability. Therefore refrigerant/oil interactions need further investigation.



Figure 11: System Start Oil Observations

4. Discussion and Conclusions

A number of observations can be made from this work from a UK context. Energy pricing and subsidy support are not yet sufficiently favourable for wide scale deployment of electrically driven vapour compression heat pumps. The current gas price is sufficiently low, and boilers are of low capital cost to ensure boilers are the heating system of choice. However, there are cases were that trend can be overcome. UK Government energy statements such as “near 100% decarbonisation” by 2050 will see a rise in renewable electricity dependency and a need to decarbonise the gas network

(biomethane or hydrogen for example) to reduce expensive electricity network upgrades and to utilise an existing and wide-reaching gas infrastructure. However, if hydrogen were utilised, there would be a significant requirement to improve the performance of electrolysers and safety concerns would limit hydrogen to the low-pressure gas distribution network. Of course, thermal storage has not been mentioned as a useful system addition to electrically driven heat pumps so that such heat pumps can utilise off-peak or excess renewably generated electricity. There is an emerging literature that suggests higher temperature heat pumps would benefit from thermochemical storage due to higher energy densities at higher temperatures. Thermal storage would facilitate demand side response and distributed energy management. UK industrial heat pumps (and indeed heat pumps in general) also suffer from performance challenges. These are invariably brought about by the overall system performance and not necessarily by the heat pump itself. Given the capital cost differential between boilers and heat pumps and the relative simplicity of boiler operation, the added expertise in fully understanding an installation challenge can be sometimes underestimated. There are great examples of excellently performing heat pumps but unfortunately there are others which are not doing so well. A challenge is of course the operating regime. District heating is not a common option in the UK but if there are serious efforts to address the available waste heat. Booster heat pumps upgrading the heat from low temperature, low loss networks are possible. R410a and R245fa were potential candidate fluids for space heating and process heating applications but their global warming potential is unacceptable. R32 appears to be an excellent candidate for R410a replacement (accepting a small safety risk) and R1233zd(E) has potential to replace R245fa. Initial results are promising but compressor lubrication and transportation (solubility and miscibility) requires further investigation.

Acknowledgements

The authors would like to acknowledge the support of EPSRC i-STUTE, EPSRC 4s-DHW, EPSRC Lot-NET, FP7 Einstein, H2020 CHESS-SETUP, H2020 CHESTER and INTERREG VA SPIRE 2 to facilitate the bringing together of these concepts.

References

Abdullah Alabdulkarem, Radia Eldeeb, Yunho Hwang, Vikrant Aute, Reinhard Radermacher (2015) Testing, simulation and soft-optimization of R410A low-GWP alternatives in heat pump system, International Journal of Refrigeration, Volume 60, December 2015, Pages 106-117

F. Botticella, F. de Rossi, A.W. Mauro, G.P. Vanoli, L. Viscito (2018) Multi-criteria (thermodynamic, economic and environmental) analysis of possible design options for residential heating split systems working with low GWP refrigerants, International Journal of Refrigeration 87 131–153

Guidelines for Low-Temperature District Heating, A deliverable in the project financially supported by the Danish Energy Agency in the R&D programme EUDP (Energiteknologisk Udviklings-og Demonstration Program): “EUDP 2010-II: Full-Scale Demonstration of Low-Temperature District Heating in Existing Buildings”, April 2014

F. Ju et al (2017) Performance assessment of heat pump water heaters with R1233zd(E)/HCs binary mixtures, Applied Thermal Engineering, Volume 123, August 2017, Pages 1345-1355,

Lee et al (2013) Experimental investigation of novel heat exchanger for low temperature lift heat pump, Energy, Volume 51, 1 March 2013, Pages 468-474,

Henrik Lund, Sven Werner, Robin Wiltshire, Svend Svendsen, Brian Vad Mathies (2014) 4th Generation District Heating (4GDH): Integrating smart thermal grids into future sustainable energy systems, Energy, Volume 68, 15 April, Pages 1-11

Adrián Mota-Babiloni, Joaquín Navarro-Esbrí, Pavel Makhnatch, Francisco Molés (2017) Refrigerant R32 as lower GWP working fluid in residential air conditioning systems in Europe and the USA, Renewable and Sustainable Energy Reviews 80 1031–1042

https://www.gov.uk/government/statistics/energy-chapter-1-digest-of-united-kingdom-energy-statistics-dukes

https://www.gov.uk/guidance/hfc-phase-down-in-the-eu-how-it-works-and-exemptions

https://www.gov.uk/government/publications/summary-evidence-on-district-heating-networks-in-the-uk

The potential for recovering and using surplus heat from industry, Final Report for DECC, 05/03/2014, Led by Element Energy Limited

Manuscript ID: 750
DOI: 10.18462/iir.icr.2019.0750

Sorption heat pump for flue gas condensation of biomass-fired boilers

Tina HERMANN[(a)], Julian GEIER-PIPPIG[(a)], Christian SCHWEIGLER[(a)]

[(a)] CENERGIE Research Center Energy-efficient Buildings and Districts
Munich University of Applied Sciences, Department of Building Services Engineering,
Lothstr. 34, 80335 Munich, Germany
tina.hermann@hm.edu

ABSTRACT

Extracting heat from hot flue gas by utilization of condensing technology leads to a significant increase in boiler efficiency. Conventional systems are often limited by unfavorably high return temperatures of the heating system which preclude the use of the extensive potential of the sensible and especially latent heat of the flue gas.
In this research the integration of an absorption heat pump (AHP) into the heating system of a wood chips fired boiler is investigated. This allows cooling of the flue gas down to temperatures around 25 °C and serves for upgrading the low grade heat for further utilization in conventional heating systems. Therefore, increases in fuel utilization rate up to 20 % can be achieved.
The concept of the heat pump cycle for integration with the biomass boiler is presented, followed by thermodynamic modelling and thermal design of a flue gas-coupled evaporator of the heat pump.
Keywords: Absorption, Biomass, Energy Efficiency, Heat Pump, Heat Transfer, Latent Heat, Water-Lithium Bromide

1. INTRODUCTION

Heat recovery of flue gas reduces the flue gas losses and increases the boiler efficiency. Cooling the flue gas down to temperatures below the dew point allows the transfer of energy released by sensible heat and by latent heat. Condensing the vapor fraction of a flue gas flow is an established technology for heat recovery of gas and oil fired boilers. To ensure the full utilization of the heat content of the flue gas, low cooling temperatures are required. Commonly, the return flow of the heating network is used to cool the flue gas down. Thus, the heat gain is limited by the temperature level of the heating system. For standard local heating networks with return flow temperatures of 50 °C and closest approach temperature (CAT) between flue gas and heating medium of 15 K, compared to manufactural data (Rennergy Systems AG, 2016; Fröling GesmbH, 2017), condensation process hardly starts. Wood chips fired boilers show high losses due to flue gas outlet temperatures of around 150 °C and water vapor contents of 0.65 kg per kg wood even for combustion of biomass fuel with low water content (w=20 %) (Hartmann et al., 2004). Heat recovery can increase conventional boiler efficiencies from 85–90 % to over 100 %, if use of latent heat content is accomplished. When heat recovery is supported by a heat pump, cooling temperatures independent of return flow temperatures of the heating system can be provided. Absorption heat pumps (AHP) require only a fraction of electrical energy needed by compression heat pumps for upgrading the low-temperature heat. In the given application the driving heat for the heat pump cycle can be supplied by the biomass boiler. Thus, heat pump operation is almost completely based on renewable energies.
Figure 1 shows the boiler efficiency based on lower heating value with respect to flue gas temperature. For the combustion of wood with a water content of 30 % and an air-fuel ratio of λ=1.5 the boiler efficiency for flue gas outlet temperatures of 140 °C is around 90 %. By cooling down to 65 °C, feasible through common heat exchanger and the temperature level of the return flow, boiler efficiency is increased to 96 %. Cooling down to 25 °C, by using an AHP, results in a further increase to roughly 110 %. The sharp increase at around 55 °C is caused by the onset of condensation when flue gas temperature falls below the dew point. (Kaltschmitt et al., 2009; Joos, 2006)

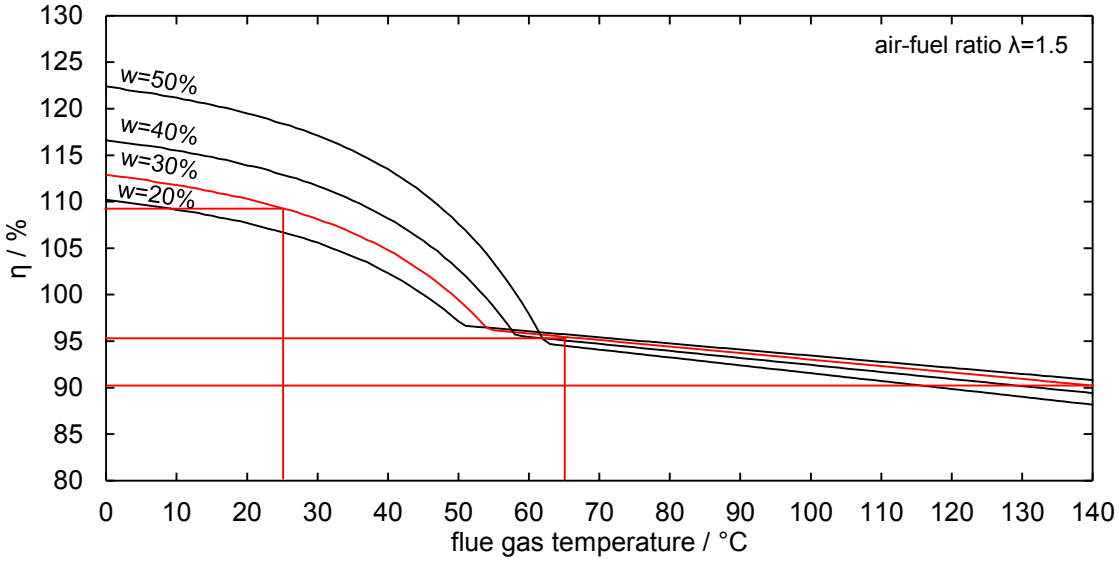

Figure 1: Boiler efficiency based on lower heating value with respect to flue gas temperature (parameter: water content w=20…50%), for atmospheric pressure (1013 mbar) and ambient temperature (0 °C) and average composition of wood ($CH_{1.44}O_{0.66}$)

2. INTEGRATION OF AN ABSORPTION HEAT PUMP INTO A HEATING SYSTEM

The integration of the AHP into the heating system aims at cooling the flue gas down to 25 °C. For further use in the heating network, the AHP upgrades the recovered heat flow and transfers it to the return flow of the heating system. The concept of integration is shown in Figure 2 (Hermann et al., 2018). Standard district heating networks are operated with supply temperature of about 70 °C and return water at 50 °C. A wood chips fired boiler producing hot water of 95 °C can serve as heat supply for the network and provide the driving heat for the generator (G) of the AHP. Extracted heat from cooling and condensation of the flue gas with an outlet temperature of 140 °C is transferred to the refrigerant of the AHP in the evaporator (E). Heat output from absorber (A) and condenser (C) is released to the return flow at a temperature level above 50 °C. As an alternative, the sensible heat content of the flue gas in the temperature range down to about 70 °C can be transferred to the heating system directly. Further heat recovery then has to be accomplished by the AHP, as described above. Final design of the system may be found with regard to heat exchanger cost and system complexity.

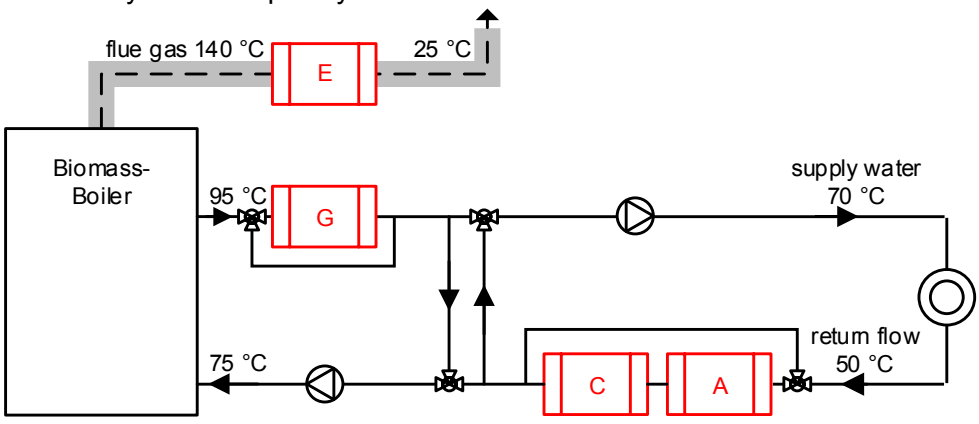

Figure 2: Heating network with integrated AHP

Figure 3 shows the sorption process in the solution field (van't Hoff) of the working pair water/lithium-bromide and provides pressure, internal temperature and concentration of the sorbent solution. Internal process data are set to match heat transfer from/to flue gas (t_E), heating system return flow (t_A) and driving heat (t_G) at external temperature levels t_E, t_A and t_G respectively. The refrigerant evaporates at around 21 °C and 2.4 kPa. For the given temperature levels, the AHP operates with moderate concentration of the solution and safe distance to the crystallization

limit, marked by a dotted line in lower right corner of the solution field. (Alefeld and Radermacher, 1994)

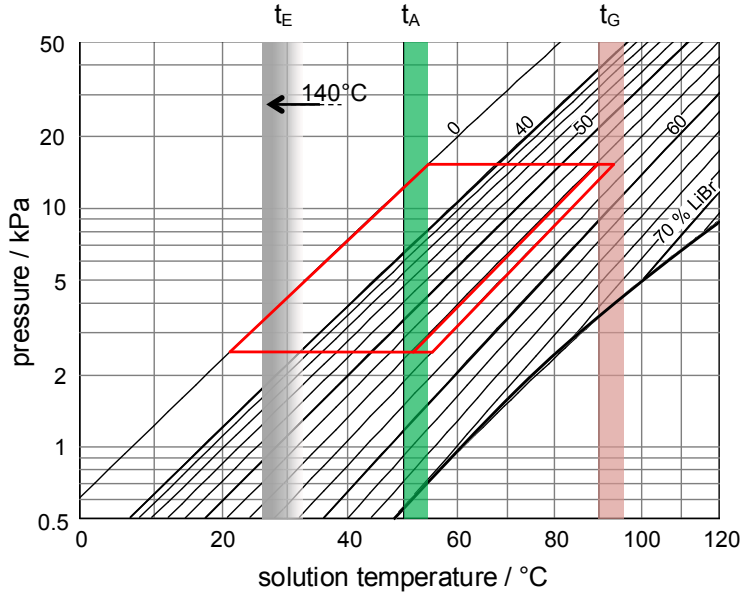

Figure 3: Solution field of water/lithium-bromide (van't Hoff)

3. CONCEPT OF THE ABSORPTION HEAT PUMP

The development of the main components of the AHP aims at a robust operation with simple control and lowest use of additional devices. Figure 4 shows the concept of the AHP with sorbent and refrigerant cycle. In the evaporator the refrigerant evaporates at low temperature and pressure level extracting heat from the flue gas. The generated vapor is absorbed by the concentrated sorbent solution with heat release from the absorber to the return flow of the heating network. The dilute solution is preheated in the solution heat exchanger (SHX) by heat transfer from the concentrated solution before entering the generator. In the generator the solution is heated up to its boiling temperature at higher pressure and temperature level to boil off the refrigerant (thermosiphon). The required driving heat is extracted from the hot water cycle of the boiler. The desorbed refrigerant vapor is separated from the concentrated solution and transferred to the condenser, where the refrigerant is condensed while rejecting heat to the return flow. The remaining concentrated solution in the generator leaves at high temperature and returns to the absorber passing the SHX.

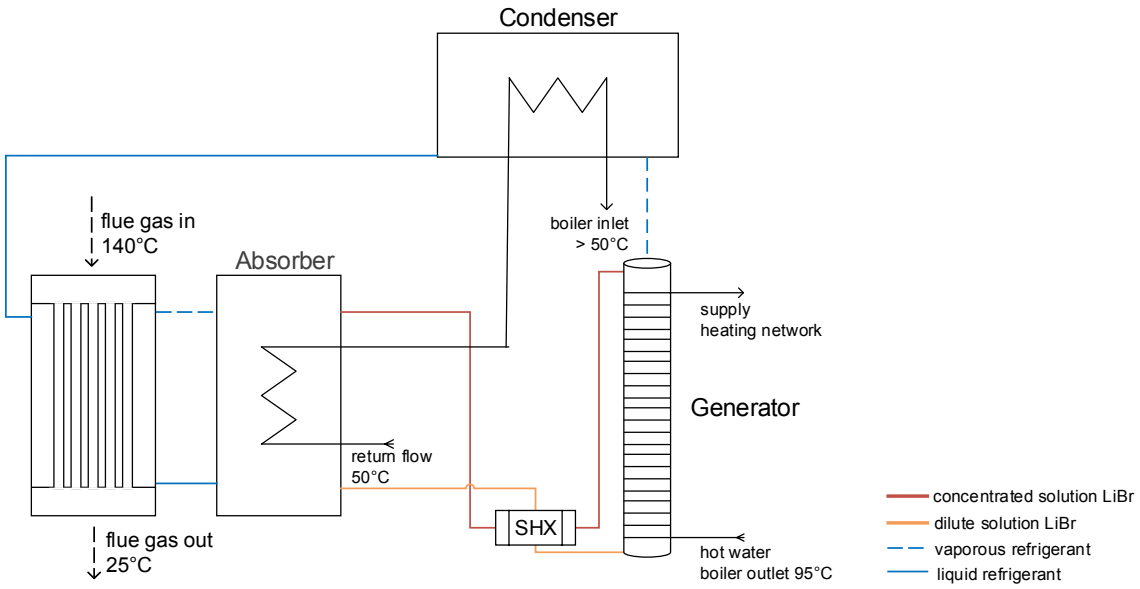

Figure 4: Cycle process of AHP

For the design of the heat exchangers a conventional falling film absorber and a plate heat exchanger for condensing shall be applied. To avoid the electrical consumption a solution pump, a natural circulation of sorbent between generator and absorber by means of a thermosiphon-desorber is intended, based on previous studies investigating related applications (Kren, 2008). In the evaporator the extracted heat from cooling and condensation of the flue gas is directly transferred to the refrigerant. Therefore, a new design has to be found that integrates a flue gas coupled heat exchanger into the process of the AHP.

4. DESIGN OF FLUE GAS-COUPLED EVAPORATOR

Falling film evaporators show low pressure drops on refrigerant side and are widely used for AHPs to enable high performances. For the design of the flue gas-coupled evaporator, the corrosive characteristics of the flue gas and the high content of particles have to be considered. In order to avoid deposition of particles, a high flow velocity and an even flow profile are favourable. The selected material must be acid-resistant. Using a tube bundle heat exchanger, flue gas can be directed through shell side or tube side. For shell side flue gas flow, baffles are needed to maintain a proper flue gas velocity. The access for cleaning is thereby limited although higher deposition rates are expected due to uneven velocity distribution. The evaporation of refrigerant inside the tubes affects unfavourable pressure drops. Figure 5 (left) shows the design for the evaporator with baffles and shell side flue gas flow. Figure 5 (right) shows the design with a tube side flue gas flow and shell side evaporation. Flue gas is directed downstream to facilitate discharge of condensate and particles. This configuration makes mechanical cleaning and periodical water injection possible.

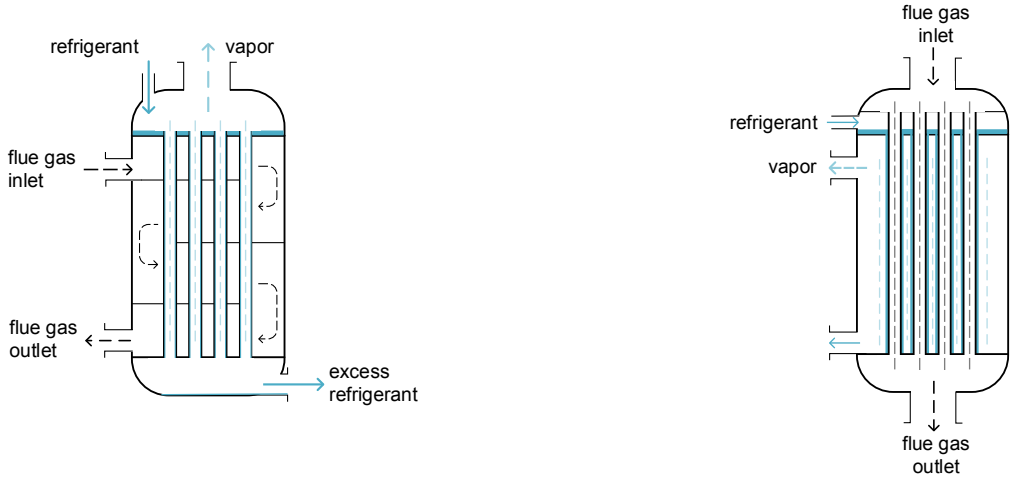

Figure 5: Evaporator design

5. MODELLING OF THE FLUE GAS-COUPLED EVAPORATOR

First, the shell side evaporation of the refrigerant is described. The heat transfer coefficient is calculated according to Schnabel (Schnabel, 2013) for heat transfer to falling films at vertical surfaces. The Reynolds number Re is calculated by

$$Re = \frac{\dot{m}_{ref}}{\mu} \qquad \text{Eq. (1)}$$

with the mass flow rate of refrigerant per unit circumference $\dot{m}_{ref}$ in kg $m^{-1}s^{-1}$ and dynamic viscosity μ. To avoid dry parts of the heat transfer area mass flow rates of 0.0138–0.0416 kg $m^{-1}s^{-1}$ are suggested, forming a continuous laminar film down the surface (Kraume, 2012). Regarding a biomass boiler with a thermal output of 50 kW, the capacity transferred in the evaporator is about 10 kW according to evaporation of 0.004 kg s^{-1} refrigerant. Thereby, a circumference of 0.29 m can be wetted to meet the requirements of the given mass flow rate. The Nusselt number for a laminar flow is calculated as a function of the Reynolds number.

$$Nu_{lam} = 0.9\, Re^{-\frac{1}{3}} \qquad \text{Eq. (2)}$$

The heat transfer coefficient h_{evap} results from the calculation of Nusselt number.

$$Nu_{lam} = \frac{h_{evap}}{\lambda}\left(\frac{\nu^2}{g}\right)^{\frac{1}{3}} \quad \text{Eq. (3)}$$

with thermal conductivity λ, kinematic viscosity ν and the gravitational constant g. The results show heat transfer coefficients of 4800 W $m^{-2}K^{-1}$ for mass flow rates of 0.0138 kg $m^{-1}s^{-1}$ decreasing to 3300 W $m^{-2}K^{-1}$ for 0.0416 kg $m^{-1}s^{-1}$. Increasing film thickness leads to higher thermal resistance and therefore to the reduction of the heat transfer coefficient. Data from literature (Schnabel, 2013) confirm the calculated range of values for heat transfer. Due to experimental data (Schweigler, 1999), a conservative design with lower values is considered. In an experimental setup will further be examined, if the technical requirements with particular regard to the surface wetting can be met. Aiming at a reduction of mass flow down to the mass flow related to the evaporation capacity, the wetting behavior of the surface has to be improved. The use of tubes with modified surfaces promises a complete wetting and minimal film thickness. Due to missing fundamental equations for heat transfer to different structured surfaces, experimental studies will be conducted in order to provide a basis for the dimensioning of the heat exchanger.

The heat transfer from the flue gas is described separately for the dry part and wet part of the heat exchanger. In the dry part the flue gas is cooled down from the hot outlet temperature of the biomass boiler down to the dew point. The heat transfer in this section is calculated according to forced convective heat transfer in pipe flows (Gnielinski, 2013). The Reynolds number is calculated as a function of flow velocity w and kinematic viscosity ν of the flue gas.

$$Re = \frac{w\, d_i}{\nu} \quad \text{Eq. (4)}$$

The correlation of the Nusselt number is a function of Reynold, Prandtl and geometric dimensions.

$$Nu = 0{,}0214(Re^{0.8} - 100)\, Pr^{0.4}\left[1 + \left(\frac{d_i}{l}\right)^{\frac{2}{3}}\right] \quad \text{Eq. (5)}$$

with internal diameter d_i and tube length l. Finally, the heat transfer coefficient h_g is obtained from

$$Nu = \frac{h_g\, d_i}{\lambda} \quad \text{Eq. (6)}$$

The maximal flow velocity of the flue gas is set to 15 m s^{-1} to avoid erosion problems inside the tubes. Consequently, with 2300<Re<10000 the flow is found to be in the transition region between laminar and turbulent flow.

For flue gas temperature falling below the dew point, the heat transfer is calculated referred to the condensation of vapor in the presence of an inert gas (Numrich, 2013). The coupled heat and mass transfer for condensation is described by the heat transfer coefficient h_{eff}.

$$h_{eff}(\mathrm{T}_G - \mathrm{T}_F) = h_g(\mathrm{T}_G - \mathrm{T}_F) + \dot{m}_C \Delta H_{(\mathrm{T}_F)} \quad \text{Eq. (7)}$$

with heat transfer coefficient of gas phase h_g, locally condensing mass flow $\dot{m}_C$ (kg $m^{-2}s^{-1}$), evaporation enthalpy ΔH, flue gas temperature T_G and condensate film temperature T_F. The locally condensing mass flow is a function of the mass transfer coefficient β_G, density ρ_G and mole fractions of vapor y_G and y_F in the core flow of flue gas and on the surface of the condensate film, respectively.

$$\dot{m}_C = \beta_G \rho_G (y_G - y_F) \quad \text{Eq. (8)}$$

The heat transfer coefficient of the gas phase is calculated equivalent to Eq. (6) for forced convective heat transfer in pipe flows. The occurrence of mass transfer besides heat transfer is considered by the Ackermann correction. The transfer area is determined by the energy balance for the heat transfer from cooling and condensation of the flue gas to the coolant.

$$\dot{Q} = \Delta\dot{M}_C \Delta H_{vap} + \dot{M}_G c_P \Delta T = UA\, \Delta T_{log} \quad \text{Eq. (9)}$$

with mass flow of condensate $\Delta\dot{M}_C$, evaporation enthalpy ΔH_{evap}, flue gas mass flow $\dot{M}_G$, specific heat capacity c_P, temperature difference ΔT, overall heat transfer coefficient U, transfer area A and logarithmic temperature difference ΔT_{log}.
The overall heat transfer coefficient U is described by heat transfer coefficients of flue gas h_{eff} and condensate h_C, conductivity of pipe wall λ_{tube} and heat transfer coefficient of evaporation h_{evap}.

$$U = \left(\frac{1}{h_{eff}} + \frac{1}{h_C} + \frac{d_o \ln \frac{d_o}{d_i}}{2\,\lambda_{tube}} + \frac{d_o}{d_i h_{evap}} \right)^{-1} \quad \text{Eq. (10)}$$

An estimation of pressure losses is given by

$$\Delta p = \xi \frac{l}{d_i} \frac{\rho w^2}{2} \quad \text{Eq. (11)}$$

with tube length l, flue gas density ρ, flue gas velocity w and resistance coefficient ξ.

$$\xi = \frac{0{,}3164}{\sqrt[4]{Re}} \quad \text{Eq. (12)}$$

for 3000<Re<100000. (Kast, 2013)

6. RESULTS

Based on the preceding equations, a parametric study has been conducted to design a flue gas coupled evaporator for a biomass fired boiler of 50 kW. The boundary conditions for the calculation are listed in Table 1.

Table 1: Boundary conditions of heat exchanger design

$\dot{Q}$ kW	λ -	w_{wood} %	$\vartheta_{dewpoint}$ °C	$\dot{M}_G$ kg·s^{-1}	$\vartheta_{G,in}$ °C	$\vartheta_{G,out}$ °C	h_{evap} W·m^{-2}K^{-1}	d_i mm
50	1.5	30	54	0.04	140	25	3300	16

As a result of the calculation the mole fraction of water vapor and heat transfer coefficient of the flue gas are shown in Figure 6. Starting from the tube inlet at the top, the mole fraction of water vapor is constant until temperature falls below dew point. With starting condensation the mole fraction of water vapor decreases along with the gas temperature until outlet is reached at 25 °C. Finally, the flue gas contains only 20 % of initial water content. The heat transfer coefficient shows low values with little decline alongside the dry part of the heat exchanger tube, followed by a sharp increase to comparatively high values, when condensation process starts. The sudden increase results from the different characteristics for dry and condensing part of the heat exchanger. In practical applications it is expected to have a transition area with partial condensation in the cold boundary layer of the gas flow, while the core still stays above dew point. The temperature profile of the flue gas flow and the accumulated heat flux are shown in Figure 8. The temperature of the coolant side is set constant, assuming homogeneous evaporation at 21 °C along the entire height of the heat exchanger. The slope of the heat flux curve indicates the recoverable heat per tube length. According to the profile of the heat transfer coefficient, the amount of recovered heat per tube length significantly increases with starting condensation but then flattens off along the condensing part, due to decreasing temperature difference between flue gas flow and coolant side. Consequently, considerably potential savings in tube length can be obtained by accepting slightly higher flue gas outlet temperatures.

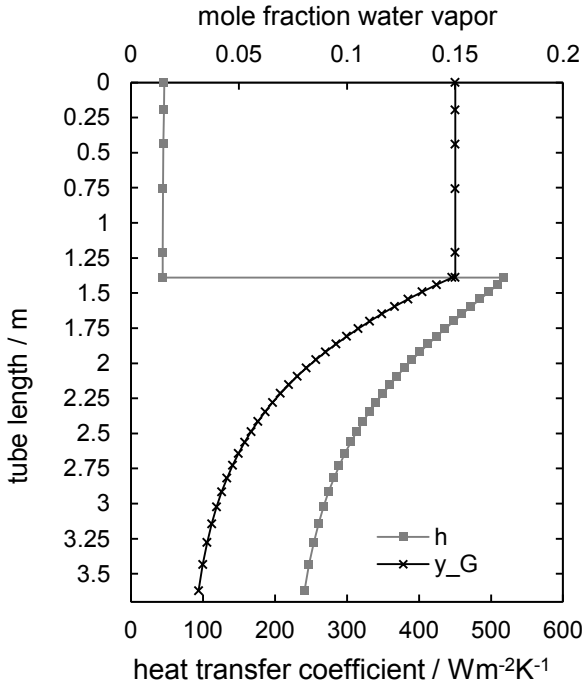

Figure 6: Characteristics of flue gas

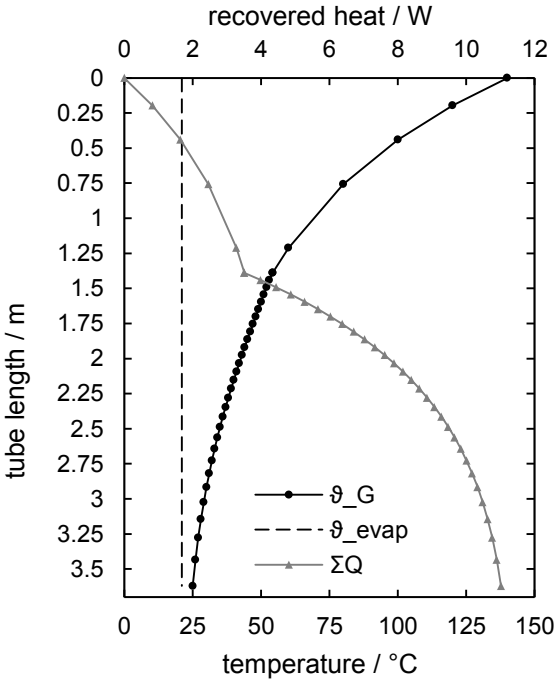

Figure 7: Recovered heat and temperature profile

Decisive criterion for dimensioning the heat exchanger is the selection of the tube diameter and the number of parallel tubes forming the flue gas flow section. Figure 8 shows the result of the design study again for a flue gas inlet/outlet temperature of 140/25 °C, inner tube diameter of 16 mm and a number of parallel tubes varying from 5 to 50. The overall heat transfer coefficient, representing the average value for the dry part and the condensing part (Fig. 8) together with the total length of the apparatus and the resulting pressure drop is given (Fig. 9). The result is strongly influenced by the flue gas velocity, which varies with the number of parallel tubes. For practical implementation the flue gas velocity should not exceed 15 ms^{-1}, hence, turbulent flow characteristics are not achievable. With increasing tube number the overall heat transfer coefficient decreases, as a result of reduced flue gas velocity. Generally, the values for the condensing part are significantly higher. Taking into account the substantially higher heat transfer coefficient on coolant side, the surface area is clearly determined by the heat transfer coefficient of flue gas side. As can be read from Figure 9 the increase of heat exchanger surface area by means of additional tubes yields an only marginal decrease of required tube length. This effect is due to the dependency of the heat transfer coefficient on the flow velocity. Respecting practical limitations for the pressure drop in the flue gas flow of about 5 mbar the apparatus should be designed with about 20 parallel tubes, resulting in a tube length of roughly 3 m. Thus, a two pass design or a cascaded configuration of dry and wet section may be taken into consideration, to match typical dimensions of the biomass boiler.

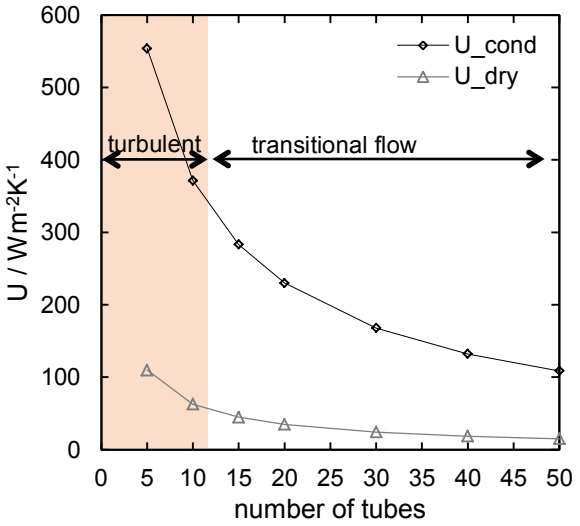

Figure 8: Overall heat transfer coefficient

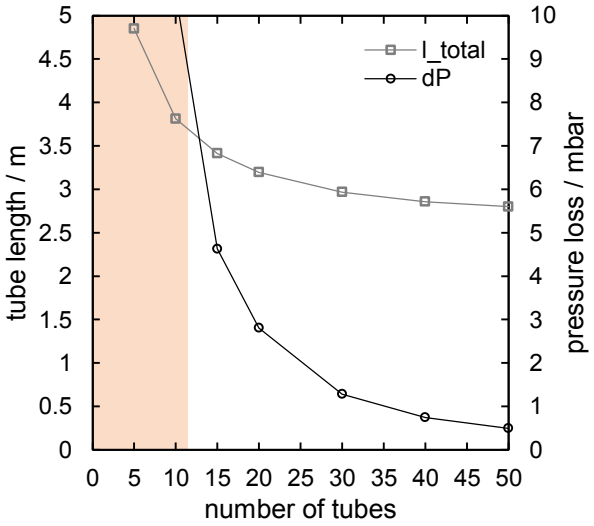

Figure 9: Tube bundle design

7. CONCLUSION

The integration of a lithium bromide/water absorption heat pump into a heating system with a wood chips fired boiler and outputs above 50 kW have been investigated. The use of an AHP for heat recovery allows cooling of the flue gas down to 25 °C. For wood chips with 30 % humidity, the recovery of condensing heat provides an improvement in efficiency up to 19 % related to no recovery. Heat recovery with direct heat exchange to the return flow of the heating system achieves only 5 % (CAT=15 K).

The developed concept for an optimized thermo-hydraulic integration of the AHP allows reduction of flue gas losses and further use of recovered heat in the heating system. In the cycle concept of the AHP innovative technical designs for a thermosiphon-desorber with natural circulation of sorbent between absorber and generator and a flue gas coupled evaporator are involved. The design of a falling film evaporator was developed, with cooling and condensation of the flue gas flow downwards in vertical tube bundles transferring energy to shell-side evaporation of refrigerant. Thermodynamic modelling results in heat transfer coefficients of evaporation around 3300 W $m^{-2}K^{-1}$. Heat transfer coefficients of flue gas flow provide average values around 45 W $m^{-2}K^{-1}$ for the dry part of the heat exchanger and improve up to 370 W $m^{-2}K^{-1}$ with beginning condensation. Increasing the surface of the heat exchanger by additional parallel tubes for the flue gas flow leads to a lower gas velocity and therefore lower heat transfer coefficients, yielding only a marginal reduction of the overall length of the apparatus.

REFERENCES

Alefeld, G., Radermacher, R., 1994. Heat conversion systems. CRC Press, Boca Raton, 295 p.

Fröling GesmbH, 27.03.2017. Montage- und Bedienungsanleitung für T4 24-50 | M1520317_de. Grieskirchen, retrieved from https://www.froeling.com.

Gnielinski, V., 2013. G1 Durchströmte Rohre. In: VDI-Wärmeatlas (11th ed.). Springer-Verlag, Berlin Heidelberg, 785-792.

Hartmann, H., Roßmann, P., Link, H., Marks, A., 2004. Erprobung der Brennwerttechnik bei häuslichen Holzhackschnitzelfeuerungen mit Sekundärwärmetauscher. Technologie- und Förderzentrum Straubing, Straubing, 49 p.

Hermann, T., Geier-Pippig, J., Schweigler, C., 2018. Brennwertnutzung an Biomassekesseln mittels angekoppelter Absorptionswärmepumpe. Proceedings of the DKV Conference, Aachen, Germany

Joos, F., 2006. Technische Verbrennung. Verbrennungstechnik, Verbrennungsmodellierung, Emissionen. Springer-Verlag, Berlin Heidelberg, 907 p.

Kaltschmitt, M., Hartmann, H., Hofbauer, H., 2009. Energie aus Biomasse. Grundlagen, Techniken und Verfahren (3rd ed.). Springer-Verlag, Berlin Heidelberg, 1867 p.

Kast, W., 2013. L1.2 Druckverluste in durchströmten Rohren. In: VDI-Wärmeatlas. (11th ed.). Springer-Verlag, Berlin Heidelberg, 1223-1226.

Kraume, M., 2012. Transportvorgänge in der Verfahrenstechnik. Grundlagen und apparative Umsetzungen (2nd ed.). Springer-Verlag, Berlin Heidelberg, 646 p.

Kren, C., 2008. Flue gas fired absorption chillers (doctoral dissertation). TUM, München. 253 p.

Numrich, R., 2013. J2 Kondensation von Mehrstoffgemischen. In: VDI-Wärmeatlas. (11th ed.). Springer-Verlag, Berlin Heidelberg, 1029-1039.

Rennergy Systems AG, 2016. Produktdatenblatt-Thermic Remover. Buchenberg, retrieved from https://www.rennergy.de.

Schnabel, G. 2013. M3 Wärmeübergang an senkrechten Rieselfilmen. In: VDI-Wärmeatlas (11th ed.). Springer-Verlag, Berlin Heidelberg, 1475-1482.

Schweigler, C., 1999. Kälte aus Fernwärme. Konzept, Auslegung und Betrieb der Single-Effect/Double-Lift-Absorptionskälteanlage (doctoral dissertation). TUM, München. 239 p.

Manuscript ID: 753
DOI: 10.18462/iir.icr.2019.0753

Multi-objective optimization of water tank of carbon dioxide heat pump water heater based on improved nondominated sorting genetic algorithm

Yingjie XU[(a)], Enteng LI[(a)]*, Yuangong HUANG[(b)], Xiaohong HAN[(c)], Qin WANG[(c)], Guangming CHEN[(c)]

[(a)] Institute of Process Equipment and Control Engineering, Zhejiang University of Technology, No. 288 Liuhe Road Hangzhou, 310014, China
xuyingjie@zjut.edu.cn, [(*)] entengli.199@gmail.com
[(b)] Zhejiang Zhenglishengneng Co. Ltd., Wenzhou, China
[(c)] Institute of Refrigeration and cryogenics, Zhejiang University, Hangzhou, China

ABSTRACT

CO_2 heat pump water heater (CHPWH) is a hot topic due to its merit in energy and environment. However, study on water tank considering energetic, economic, environmental and practical performances at one time, has been rarely reported. Therefore, a multi-objective optimization analysis, considering the above 4 aspects, is conducted under typical Chinese climate. The study is conducted with tank size range of 100-500 L. The elitist non-dominated sorting genetic algorithm (NSGA-II) is used with important factors considered, such as heat leak. Finally, a Pareto front of multi-objective solutions is obtained. The optimized system can save about 10% of electricity and 12% economic cost under nominated condition.
Keywords: Heat Pump, Carbon Dioxide, Water Tank, Algorithm, Neural Networks, Optimization.

1. INTRODUCTION

In China, domestic hot tap water energy demand accounted for about 32% of total building energy consumption during 2014, but more than 90% was directly generated by combustion of fossil fuel that caused serious environmental problems (CABEE, 2018). Therefore, with the concern of energy saving and emission reduction (Xu et al., 2018), the development of high performance CO_2 heat pump water heater (HPWH) has recently received a lot of attention (Zhang et al., 2015). Carbon dioxide (CO_2) is a non-flammable, non-toxic gas with zero ozone depletion potential and low global warming potential (GWP=1), which is harmless to environment. Moreover, using CO_2 in refrigerating systems has great advantages in heating high temperature hot water; thereby CO_2 HPWH has the potential to be used in residential applications.

For the CO_2 heat pump (HP) system, the pioneering study by Lorentzen et al. (1994) had confirmed that the transcritical system using CO_2 can reach the needs of high temperature hot water production. Michiyuki and Shigeru (2016) theoretically studied an ideal vapor compression cycle for tap water heating and calculated the upper limit of the COP for single-stage compression heat pump cycle with various refrigerants. The results showed the refrigerant which achieved the highest COP for supplying hot water was CO_2. A system associated with the interaction of the CO_2 HPWH and the water tank built by Nicholas et al. (2010) and a performance evaluation was conducted to study the effect of ambient temperature and hot water temperature on the COP in three different situations of residential hot water operation. Results show that the COP was maximized at higher ambient temperatures and at lower hot water temperatures. In order to reduce the degradation of the system performance due to the area of tepid water in the storage tank expands; Masashi et al. (2015) developed water heating systems, each of which is composed of a CO_2 heat pump and a hot water storage tank.

Additionally, optimization is an essential task to improve system performance and reduce cost. Thermodynamic study on ejector-expanded CO_2 refrigeration system with advanced exergy analysis (Bai et al., 2016 showed that compressor with the most avoidable endogenous exergy destruction possessed the highest improvement priority. Energy and cost effective transcritical CO_2

HP was defined by Farivar and Tatiana (2014), who recommended the use of economizers as an auxiliary component of the one-stage transcritical CO_2 heat pump to reduce the total cost by approximately 14%. Saber et al. (2018) applied thermoeconomic optimization to the improved transcritical CO_2 refrigeration cycle where multiple criteria for cooling capacity and annual cost are two objective functions. An artificial neural network (ANN) was used to establish an optimization model. The results showed that the cooling capacity has increased by 4.6% and the annual cost has decreased by 60.6%. However, this article replaced the entire optimization model with a neural network method, which may impair the thermodynamic connection of the model and expands the instability and non-universality of the model. Recently, the optimization of the CO_2 heat pump from the perspectives of energetic, exergetic, economic and exergoeconomic analyses has been extensively studied (Kashif et al., 2018). Nevertheless, there are few studies have considered the interaction between the water tank and the CO_2 heat pump, yet the water tank has a significant impact on the overall optimization.

The current study considers the interaction between a CO_2 heat pump and a water tank in system optimization. In order to obtain the optimized total cost and the tank volume of the proposed system, an economic and practical analysis is carried out. A thermodynamic prediction model of the CO_2 heat pump is developed using a back propagation artificial neural network (BP-ANN) with black box characteristics to reduce the complexity of the model. The Pareto optimal solution of the system is obtained using NSGA-Ⅱ algorithm based multi-objective optimization.

2. HPWH SYSTEM AND ANN MODEL

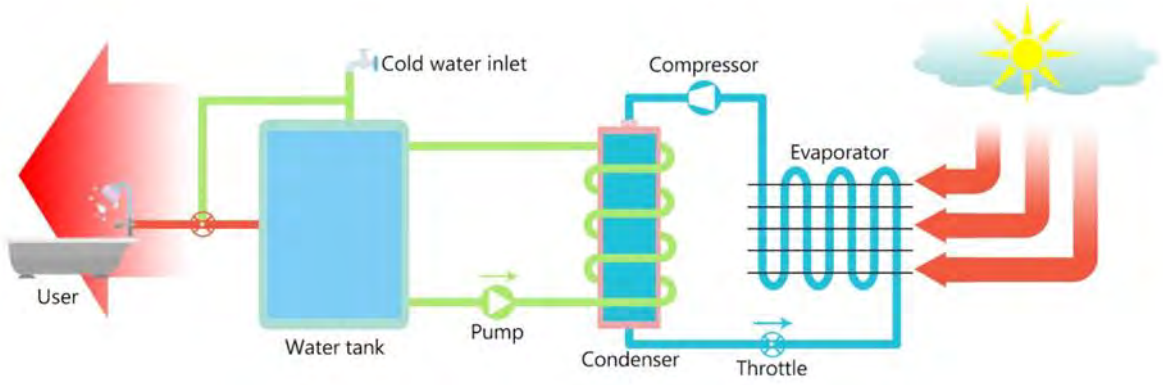

(a)

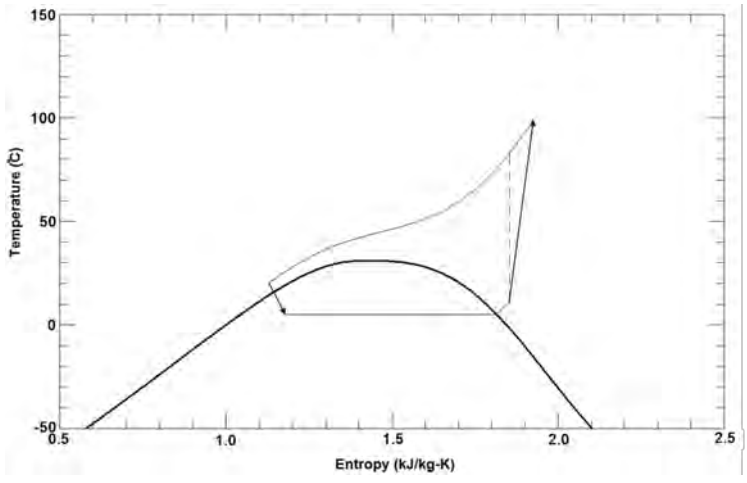

(b)

Figure 1: Schematics of CO_2 transcritical cycle (a); T-s diagram (b).

As shown in Fig. 1a, compressor, gas cooler, evaporator throttling valve, and etc constitute the transcritical heat pump cycle, which upgrades the heat energy from air and provides high-

temperature heat to cold feed water. On the left side of the heat pump cycle lies a hot water tank, which receives and stores hot water from gas cooler, and also supplies hot water to users. Fig. 1b shows the T-s diagram of the transcritical cycle. With a constant hot water demand, larger tank can store more hot water which is produced during off-peak period of power grid, reducing economic cost for electricity. However, the larger tank also leads to higher capital cost, larger area for installation and more heat leakage. There are also other parameters, such as temperature difference in gas cooler (ΔT_m), thickness of thermal insulation (δ), which can affect both energy consumption for operation and investment cost of the system. Therefore, an optimization work for HPWH, considering the water tank is important.

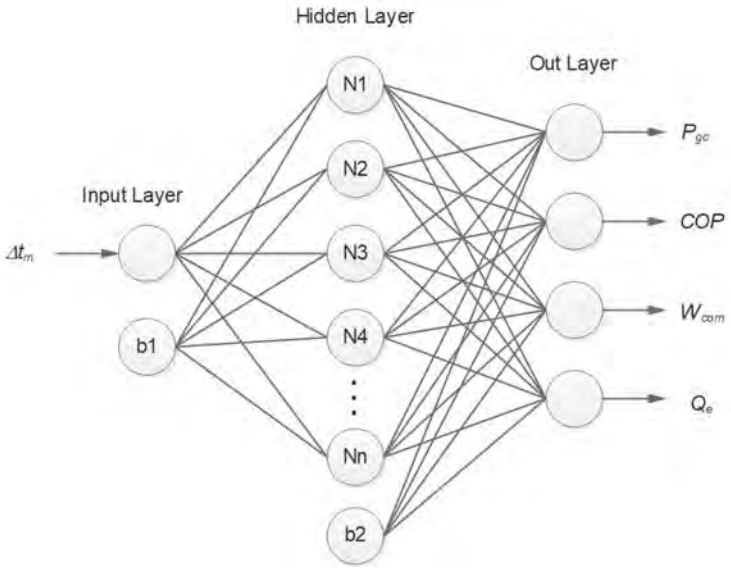

Figure 2: Structure of ANN of this paper.

To conduct the optimizing work, ANN technology is used, the topology of the ANN is shown in Fig. 2 which can precisely model the performance of HPWH with very fast calculation, as thermo physical properties of refrigerant no longer need to be calculated. It is very suitable for optimization study with a lot of iteration computation. In this paper, plenty of sets of data calculated by an HPWH model are used to train the ANN model, which has a one-dimensional input layer (ΔT_m) and an out layer with 4 elements (pressure in gas cooler P_{gc}, Coefficient of performance COP, compressor power W_{com}, and cooling capacity Q_e). The number of hidden layer neurons is set to be 6, which reveals good precision without overfitting, after some tests. As shown in Fig. 3, the predicted results match target value (actual value) well.

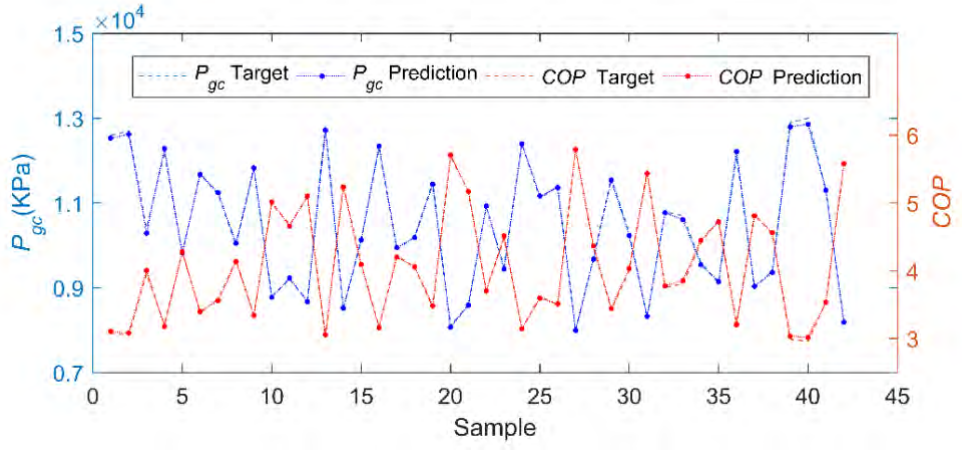

Figure 3: Predicted data comparing the target of pressure in gas cooler and COP.

3. ECONOMIC EVALUATION AND OPTIMIZATION METHOD

As discussed previously, temperature difference in gas cooler (ΔT_m), height of tank (H), diameter of tank (D), and thickness of insulation (δ) are chosen as optimized parameter, in this paper. The volume of tank is used as one of the objective variables, since the tank size has significant effects on system insulation and placing area, which is important especially in high-rise building in city. The other objective various is total annual cost (TAC). The two variables show economic performance and practicability, respectively. Specified values of the calculation are listed in Table 1.

Table 1. Specified values

Items	Value
Daily hot water demand	500 L
Supplying water temperature	65 ℃
Feed water temperature	15 ℃
Ambient temperature	20 ℃
Temperature difference in evaporator	10 ℃
Annual interest rate	12%
System lifetime	15 years
Night electricity cost	0.12 \$·kWh^{-1}
Day electricity cost	0.062 \$·kWh^{-1}

The total annual cost of overall system is given by Eq. (1), consisting of the investment and maintenance costs ($\dot{Z}_{inv+main}$, Eq. (2)), operational cost ($\dot{Z}_{op}$), and the penalty cost ($\dot{Z}_{env}$) due to CO_2 emission.

$$\dot{Z}_{TAC} = \dot{Z}_{inv+main} + \dot{Z}_{op} + \dot{Z}_{env} \quad \text{Eq. (1)}$$

$$\dot{Z}_{inv+main} = CRF \cdot \varphi \cdot \sum Z_k \quad \text{Eq. (2)}$$

$$CRF = \frac{i(1+i)^n}{(1+i)^n - 1} \quad \text{Eq. (3)}$$

where *CRF* is capital recovery factor, φ is maintenance factor, which is assumed 1.06, and the terms i and n represent interest rate and system lifetime, respectively. The investment and maintenance costs of the system is the sum of investment costs of each component, which are calculated with equations presented in literature (Farivar and Tatiana, 2014) and Eqs. (4) to (9).

$$Z_{wt} = 51.4\pi \times ((D+\delta)\cdot(2H+D+\delta) + \delta^2/2) \quad \text{Eq. (4)}$$

$$Z_{ins} = 105.4\pi\delta \times ((D+2\delta)\cdot H + (D+2\delta)^2/2) \quad \text{Eq. (5)}$$

$$Z_{evap} = 318.5 \times A_{evap}^{0.89} \quad \text{Eq. (6)}$$

$$Z_{gc} = 318.5 \times A_{gc}^{0.89} \quad \text{Eq. (7)}$$

$$Z_{exv} = 51.7 \times (P_{gc}/P_{evap})^{0.68} \quad \text{Eq. (8)}$$

$$Z_{com} = 1421.3 \times (W_{com})^{0.46} \quad \text{Eq. (9)}$$

The impact of CO_2 emissions due to electricity consumption will also be considered as penalty cost and as shown in Eq. (10):

$$\dot{Z}_{env} = C_{CO_2} m_{CO_2} \quad \text{Eq. (10)}$$

Where C_{CO_2} is the cost of unit carbon dioxide emission. As the value is generally between 0.022 \$·kg^{-1} to 0.130 \$·kg^{-1} (Bo et al., 2016). And the volume of water tank is given by:

$$V_{wt} = \pi D^2 H / 4 \quad \text{Eq. (11)}$$

In the optimization, the following assumptions are used.

- The system is running under steady state.
- Hot water demand is a constant value as given in Table 1.

- All the connection pipes of the system are well insulated.
- Time period for optimization is 1 day (24 hours), with ambient temperature keeping the same.
- Nighttime (Off-peak period) is prioritized for system operating to fill the water tank. When stored water is empty, the system then works in daytime.

In general, multi-objective optimization mathematical model can be described as:

$$f(x) = (f_1(x), f_2(x), \cdots, f_p(x))^T \quad \text{Eq. (12)}$$

$$s.t. \quad h_i(x) = 0 \quad (i = 1, 2, \cdots, m) \quad \text{Eq. (13)}$$

$$g_j(x) \geq 0 \quad (j = 1, 2, \cdots, l) \quad \text{Eq. (14)}$$

$$x \in \Omega \subset R^n \quad \text{Eq. (15)}$$

Where $x \in R^n$ is decision variables, Ω is feasible domain, $h_i(x)$ and $g_j(x)$ are constraint functions, $f(x)$ is the objective function vector consisting of p objectives.
For any two decision variables x_1, $x_2 \in \Omega$, The definition of dominant solution is $f(x_1)$ dominates $f(x_2)$, if solution $f(x_1)$ is no worse than $f(x_2)$ in all objectives and solution $f(x_1)$ is strictly better than $f(x_2)$ in at least one objective.
Given a set of solutions, the non-dominated solution (Pareto-optimal solution) set is a set of all the solutions that are not dominated by any member of the solution set. The boundary defined by the set of all point mapped from the Pareto optimal set is called the Pareto-optimal front.
The NSGA-II was proposed by Deb et al. (2002). It is a multi-objective optimization genetic algorithm based on the Pareto optimal concept of Goldberg's thinking. Compared with traditional genetic algorithms, this algorithm introduces a new selection mechanism based on the concept of pareto and non-dominated solutions. This selection mechanism performs non-dominated sorting of the population, which means that the smaller the number of individuals dominated by other individuals, the higher the non-dominated level and the higher the probability of being selected. For a series of individuals be classified as the same non-dominated rank, the greater the degree of crowding distance, the greater the probability of being selected. Finally, the pareto solution set of multi-objective optimization is obtained.

4. RESULTS AND DISCUSSION

In this paper, the total annual cost (Eq. (1)) of the whole CO_2 HPWH system and the tank volume (Eq. (11)) are minimized as the two objective functions considered. Optimization results of HPWH are shown in Figs. 4 to 7. Pareto front with optimized tank volume range of 0.02 to 0.52 m^3 and TAC range of 928 to 995 \$·$year^{-1}$, as given in Fig. 4. The corresponding operating parameters are given in Fig. 6. Most of the thickness of insulation is between 0.07 and 0.09 m, while the height of tank is uniformly distributed within the given range. And the optimized diameter of tank and temperature differences of gas cooler are mostly lies near 0.8 m and 14 ℃, respectively.

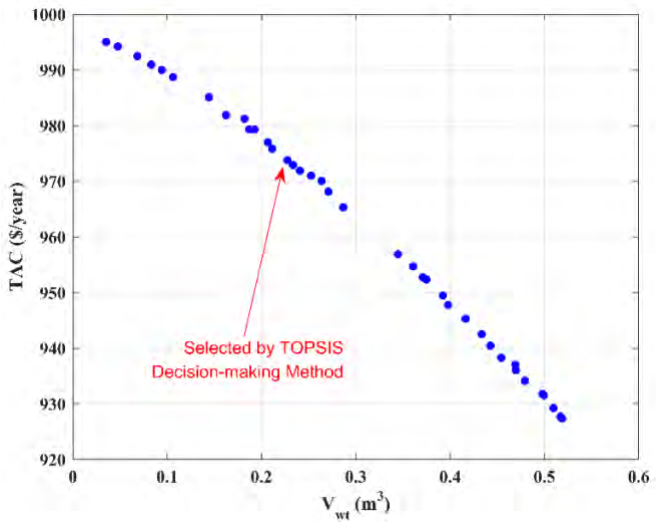

Figure 4: Pareto front of multi-objective optimization of HP water heater system.

The optimization result is normalized, and its non-dimensional pareto front is obtained. In Fig. 5, ideal point is on the bottom left, Non-ideal point is on the top right. The recommended optimized solution by TOPSIS (Technique for Order Preference by Similarity to an ideal solution) method is listed in Table 2. TOPSIS is a multi-objective decision making method that employs techniques that approximate the ideal solution. The idea of this method is to define the ideal solution and the non-ideal solution of the decision problem, and then find a solution in the feasible solution, which is closest to the ideal solution and farthest from the negative ideal solution.

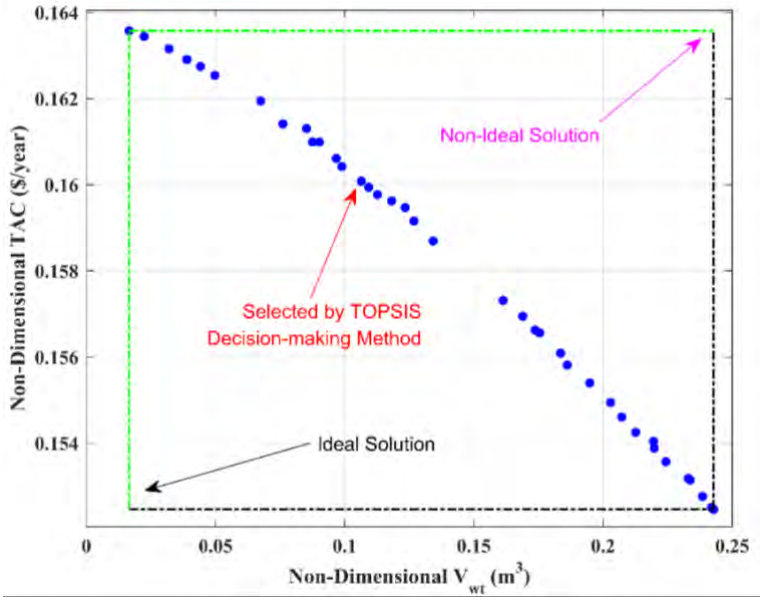

Figure 5: Non-dimensional pareto front of multi-objective optimization of HP water heater system.

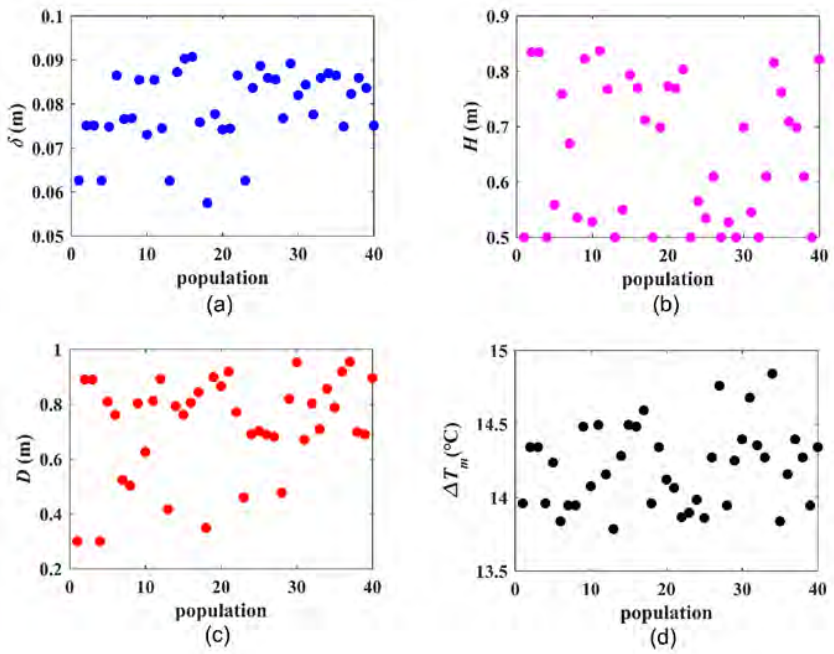

Figure 6: Optimized parameters.

Table 2. Results of the selected optimized solution

δ (m)	H (m)	D (m)	ΔT_m (°C)	V_{wt} (m^3)	TAC (\$·year^{-1})	Z_{inv} (\$·year^{-1})
0.086	0.61	0.69	14.27	0.23	973.8	551.6
T_{night} (hour)	T_{day} (hour)	P_{gc} (KPa)	COP	W_{com} (Watt)	Q_e (Watt)	Z_{op} (\$·year^{-1})
2.05	2.56	7974.6	5.50	1172.7	5045.5	278.9

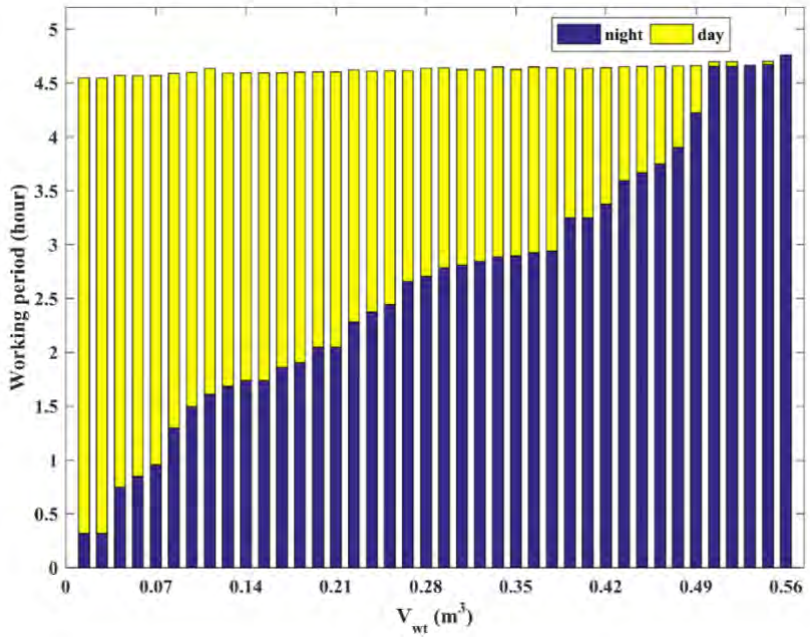

Figure 7: Comparison of working periods in day and night for optimized results.

In Fig. 7, it can be found that total running period almost keeps unchanged as water tank volume varies. However, the working hours in off-peak time (night) increases significantly as the tank volume increases, which causes a decrease in operating cost and further the decrease in TAC. Finally, according to optimized results, the system of this paper can reduce about 12% operating cost and 10% electricity consumption, comparing against modeling result of traditional HPWH with a compressor model of Xu et al's. (2018) work.

5. CONCLUSIONS

This paper presents a multi-objective optimization of the system, considering the interaction between a CO_2 heat pump and a water tank. temperature difference in gas cooler (ΔT_m), height of tank (H), diameter of tank (D), and thickness of insulation (δ) are chosen as optimized parameters. A Pareto front of optimized tank volume from 0.02 to 0.52 m^3 and TAC from 928 to 995 $/year is obtained. The optimized system can reduce about 12% operating cost and 10% electricity consumption.

ACKNOWLEDGEMENTS

This work is financially supported by the National Natural Science Foundation of China (Grant No. 51706202) and Zhejiang Provincial Natural Science Foundation of China (Grant No. LQ17E060001).

NOMENCLATURE

D	Diameter(m)	ΔT	Temperature difference (℃)
H	Height(m)	Z	Cost ($)
m	Mass (kg)	δ	Thickness (m)
Subscript			
com	Compressor	gc	Gas cooler
evap	Evaporator	ins	Insulation
exv	Expansion valve	wt	Water tank

REFERENCES

Bai, T., Yu, J. l., Yan, G., 2016. Advanced exergy analyses of an ejector expansion transcritical CO_2 refrigeration system. Energ. Convers. Manage 126, 850-861.

Bo, C., Michaela, M., John, R., Dieter, P., Thomas, R., 2016. Replacing traditional materials with polymeric materials in solar thermosiphon systems –Case study on pros and cons based on a total cost accounting approach. Sol. Energy 125, 294-306.

CABEE (China Association of Building Energy Efficiency). 2018. China Building Energy Research Report. Tsinghua University Press. Beijing. 246 p.

Farivar, F., Tatiana, M., 2014. Exergoeconomic analysis of carbon dioxide transcritical refrigeration machines. Int. J. Refrig 38, 128-139.

Kashif, N., Bo, S., Ahmed, E., Van, B., Omar, A., 2018. Performance optimization of CO_2 heat pump water heater. Int. J. Refrig 85, 213-228.

Lorentzen, G., 1994. Revival of carbon dioxide as a refrigerant. Int. J. Refrig 17(5), 292-300.

Michiyuki, S., Shigeru, K., 2016. Thermodynamic analysis of vapor compression heat pump cycle for tap water heating and development of CO_2 heat pump water heater for residential use. Appl. Therm. Eng 106, 1236-1243.

Masashi, O., Ryohei, Y., Takuya, N., Tetsuya, W., 2015. Numerical analysis on performance enhancement of a CO_2 heat pump water heating system by extracting tepid water. Energy 87, 435-447.

Nicholas, F., Yunho, H., Reinhard, R., 2010. Comparison of CO_2 heat pump water heater performance with baseline cycle and two high COP cycles. Int. J. Refrig 33(3), 635-644.

Saber, K., Mohsen, G., Shoaib, K., Hadi, G., 2018. Thermoeconomic modeling and multi-objective evolutionary-based optimization of a modified transcritical CO_2 refrigeration cycle. Therm. Sci. Eng. Prog 5, 86-96.

Xu, Y J., Guo, F Y., Song, M J., Jiang, N., Wang, Q., Chen, G G., 2018. Exergetic and economic analyses of a novel modified solar-heat-powered ejection-compression refrigeration cycle comparing with conventional cycle. Energ. Convers. Manage. 168, 107-118.

Xu, Y J., Jiang N., Wang Q., Mao N, Chen G M., Gao Z., 2018. Refrigerant evaluation and performance comparison for a novel hybrid solar-assisted ejection-compression refrigeration cycle. Sol. Energy 160: 344-352.

Yue, Z L., 2011. A method for group decision-making based on determining weights of decision makers using TOPSIS. Appl. Math. Model 35(4), 1926-1936.

Zhang, J F., Qin, Y., Wang, C C., Chi Chuan, W., 2015. Review on CO_2 heat pump water heater for residential use in Japan. Renew. Sust. Energ. Rev 50, 1383-1391.

Manuscript ID: 761

DOI: 10.18462/iir.icr.2019.0761

Simulation of the ammonia-water absorption heat pump system

Yuxue GUO, Weixing YUAN*, Yu LI, Bo YANG

Laboratory of Ergonomics and Environmental Control, School of Aeronautic Science and Engineering, Beihang University, Beijing 100191, China, *yuanwx@buaa.edu.cn

ABSTRACT

This paper writes a new simulation program for the ammonia-water absorption system using c# language in Visual Studio software. In this program, the properties of ammonia-water solution and the governing equations of each component and the whole system are solved simultaneously. As an example, an ammonia-water absorption heat pump system of 1000kW with a regenerator and an over-condenser is designed. The ammonia-water absorption program is used to simulate the steady-state operation performance of the system. It is found that the coefficient of performance (COP) of the system decreases with increasing condensation pressure and increases with increasing evaporation pressure. The calculation results of the program are consistent with the theoretical analysis which basically validates the program. This program is convenient for simulating absorption systems with varied configurations by adding new components and the corresponding equations, providing a simple and fast calculation method for the design of an ammonia-water absorption system.

Keywords: Ammonia-water, Heat Pump, Miniaturization, Simulation

1. INTRODUCTION

In current society, the challenges faced by human beings in environmental and social development have become increasingly severe. At present, the world's energy is mainly primary non-renewable energy such as coal, oil, and natural gas. This energy consumption mode cannot meet the requirements of sustainable development (Xiaohui and Junjun, 2014). Absorption heat pump technology is an energy-saving technology with high efficiency that can make use of low-temperature waste heat from industrial residual heat and other low temperature heat, and achieve the effect of energy conservation. It has advantages of less moving parts, low noise, low power consumption, and low wear and tear (Jianmin, 2004). It has become the focus of energy application research.

There are mainly two kinds of working fluids in absorption heat pump system, namely LiBr-H_2O solution and NH_3-H_2O solution. The former uses water as a refrigerant and lithium bromide as an absorbent, and the latter uses ammonia as a refrigerant and water as an absorbent. The LiBr-H_2O absorption system has many advantages, but the refrigeration temperature cannot be lower than 0°C because its refrigerant is water. An NH_3-H_2O absorption system is needed when the working environment is below 0°C. NH_3-H_2O absorption heat pump system can not only use the coldness above zero degree, but also can use the sub-zero cooling capacity, which has a wider application prospect than LiBr-H_2O absorption heat pump system. However, the traditional NH_3-H_2O absorption heat pump suite also has the disadvantages of large volume, large equipment, large metal consumption, high manufacturing cost, and the like. How to reduce the volume of the NH_3-H_2O absorption heat pump system, promote the miniaturization of the absorption heat pump system, and improve the performance of the system at the same time are the key points in promoting the application of NH_3-H_2O absorption system.

Ammonia-water absorption system has a wide range of operating temperature, thus is suitable to be used as an air source heat pump. However, it is difficult to extend the application due to its large volume. In order to facilitate the study of ammonia-water absorption system, promote miniaturization of the system and expand its application, a simulation model for simulating ammonia-water absorption system is established in this paper.

2. ABSORPTION HEAT PUMP TECHNOLOGY

Absorption heat pumps can be used to recover waste heat and produce high-temperature water, which is used for civil heating and various production occasions. It plays an important role in saving primary energy. According to the conversion form of the three heat sources in the heat pump, it can be divided into two types.

The first one is the absorption heat pump (AHP), which is characterized in that the temperature of hot water in the outlet is lower than that of the driving heat source. Its operating principle is shown in Fig. 1(a).The system absorbs the heat from the high-temperature heat source supplied to the generator and the heat from the low-temperature heat source of evaporator simultaneously, and transfers the heat to the condensate in the absorber and the condenser to obtain medium-temperature hot water. This heat pump technology utilizes a high-temperature heat source to increase the temperature of the low-temperature heat source to medium temperature, thereby improving the energy efficiency.

The second type is a temperature-increasing absorption heat pump or an absorption heat transformer (AHT), which is characterized in that the temperature of hot water in the outlet is higher than the temperature of the driving heat source. Its operating principle is shown in Fig. 1(b). In contrast to absorption refrigeration systems, the generator and condenser are in the low pressure zone, while the absorber and evaporator are in the high pressure zone. The heat source medium is connected in parallel to the generator and evaporator. In the absorber, the solution releases heat when water vapor is absorbed under high pressure and the temperature is higher than that of hot water, so that the hot water is heated when passing through the tube. A single-stage absorption heat pump can raise the temperature of hot water by about 30°C. This kind of heat pump is also known as a heat converter for the purpose of temperature increase (Yongqing, 2001).

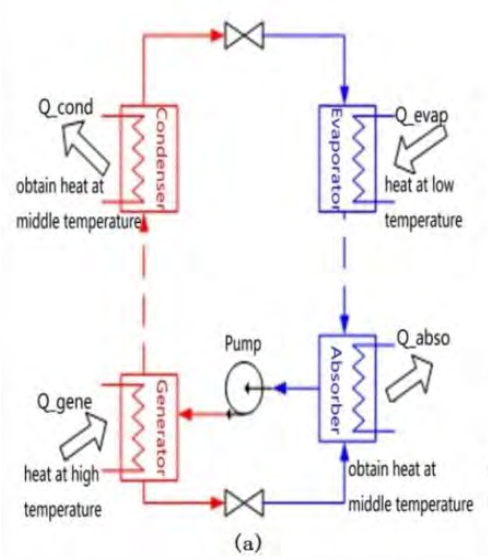

Figure 1: (a) The first type of absorption heat pump

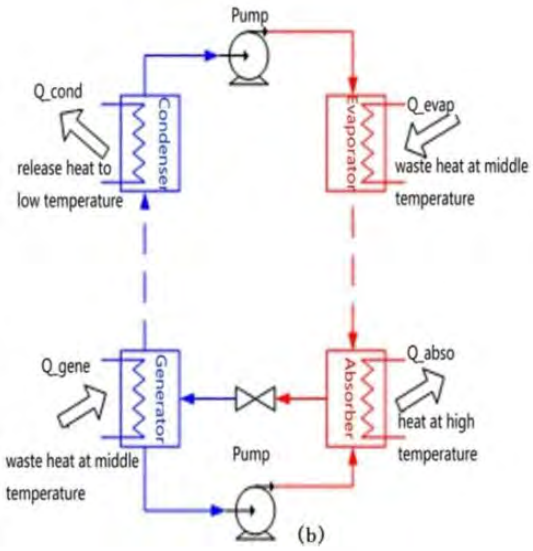

Figure 1: (b) The second type of absorption heat pump

3. SIMULATION MODELS OF ABSORPTION HEAT PUMP SYSTEM

According to the first law of thermodynamics, the second law of thermodynamics, heat transfer equations and property equations of the working solution, each component in the system should comply with the following control equations in the process of analysing absorption heat pump systems:

(1)The total mass conservation equation:

(2)The mass of the individual component (ammonia-water) is conserved:

(3)Energy conservation:

(4)Heat transfer relationship:

(5)Pressure-temperature-concentration relationship of gas-liquid equilibrium:

The above (5) is the relationship between the pressure, temperature, and concentration when ammonia-water solution is in equilibrium, which can be calculated from the physical properties of ammonia-water (Pátek and Klomfar, 1995).

In this paper, using c# language in Visual Studio software, a new program capable of solving absorption heat pump system is written. The program establishes the above governing equations for each component in the system, and then integrates all components to solve the equations. At the same time, the program compiles the physical property equation of ammonia-water into a subprogram, which is called in the process of solving equations. For such a large nonlinear system of equations, the program has written the code of Newton iterative solution. The basic solution process is as follows: (1) Input the structural parameters of all components (2) Set initial values for all variables (3) Simultaneous component governing equations and call physical property equations (4) Solve equations(5) Output the result (6) Analyze data.
This program is a general program that can freely simulate ammonia-water absorption heat pump system. This method can conveniently solve different ammonia-water absorption systems, has fast convergence speed and convenient addition of components. It can also provide a simple and quick calculation method for the design of the ammonia-water absorption system, and has wide application in aspects of reducing the volume of the absorption heat pump and improving the performance coefficient of the absorption heat pump system. Using this program, the performance of different absorption heat pump systems can be simulated, and the influence of operating parameters on system performance can be analyzed.
In the fourth and fifth parts of this paper, a system with regenerator and overcondenser is calculated, and the performance of the system under different working conditions is analyzed by this program.

4. SIMULATION PROGRAM OF AMMONIA-WATER ABSORPTION HEAT PUMP SYSTEM

4.1. Working process of the ammonia-water absorption heat pump system

The absorption heat pump system studied in this paper is a basic air source ammonia-water absorption heat pump system with ammonia-water as refrigerant and water as absorbent. The main system flow is shown in Figure 2. The main cycle of the system is divided into five parts:
(1) Generation and rectification process: The high-temperature heat source of the generator adopts the high-temperature flue gas of the natural gas boiler. This process heats the concentrated ammonia-water solution from the absorber. The ammonia-water evaporates due to the low boiling point, and the separated ammonia-water vapour is further purified by the rectifier. The remaining dilute solution is returned to the absorber.
(2) Condensation process: The ammonia-water vapour that flows into the condenser after purification by the rectification tower heats the external cooling water, and its temperature decreases, and liquid ammonia-water flows into the over-condenser for further cooling, and then enters the evaporator after throttling.
(3) Evaporation process: The liquid ammonia-water gets temperature and pressure reduced by the throttle valve and evaporates in the evaporator, and at the same time absorbs the heat from the low-temperature heat source, and the generated low-temperature and low-pressure steam enters the absorber.
(4) Absorption process: The dilute solution generated by the generator flows back to the absorber and the ammonia-water vapour from the evaporator are used for heat and mass transfer. The heat is released during the absorption process to heat the external cooling water.
(5) A solution heat exchanger is installed between the generator and the absorber for heat exchange between the dilute solution after the occurrence and the concentrated solution after absorption, and the performance of the generator and the absorber can be effectively improved.

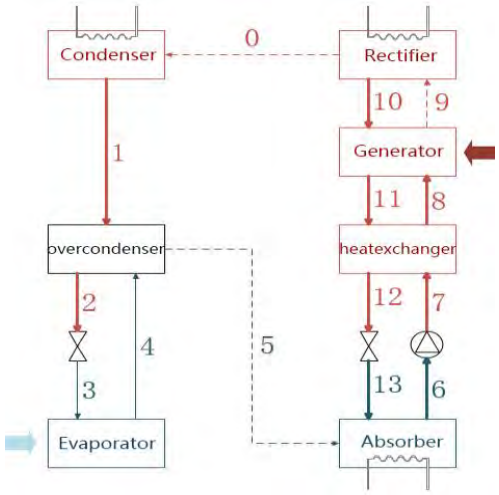

Figure 2: Ammonia-water absorption heat pump system

4.2. Condition assumptions of the system

In the calculation of the basic ammonia-water absorption heat pump, the following assumptions are made about the state of the process:
1) The system is in steady state operation;
2) Aqueous dilute solution at the generator outlet is saturated liquid;
3) The reflux solution at the rectifier outlet is a saturated liquid;
4) The concentrated ammonia-water solution at the outlet of the absorber is a saturated liquid;
5) Ignore heat loss.

4.3. Designed Parameters of the system

The heat source of evaporator is air, the heat source of generator is high-temperature flue gas, and the cold sources of condenser, absorber, and rectifier are all cooling water.UA values of each heat exchanger and mass flow rates of each fluid are shown in table 1.

Table 1 Typical operating conditions simulation data

Exchanger	UA (kW/K)	Fluid	Mass Flow Rate (kg/s)
Condenser	20.664	Water-condenser	18.656
Evaporator	46.479	Air	79.754
Absorber	74.702	Water-absorber	32.677
Generator	23.287	Flue gas	41.027
Rectifier	2.4248	Water-rectifier	4.088
Heat exchanger	18.688	Concentrated solution	1.11
Over-condenser	1.747	-	-

5. SIMULATION ANALYSIS OF PERFORMANCE UNDER DIFFERENT WORKING CONDITIONS

In this chapter, the ammonia absorption heat pump system program established in this paper is used to study the effects of low temperature heat source temperature, hot water inlet temperature and driving heat source temperature on the performance and internal parameters of the heat pump system in a large range of operating conditions.

5.1. Influence of Low Temperature Heat Source on System Performance

The low temperature heat source of evaporator is air. When the temperature of flue gas is 180 °C, the inlet temperature of hot water is 40 °C, and the temperature of the air increases from - 10 °C to 20 °C, the deflation range of the ammonia-water solution increases from 0.179 to 0.279, the refrigerant flow rate also increases from 0.235kg/s to 0.383kg/s, thus the heat rate of each heat exchanger increases, as shown in Fig. 3(a).

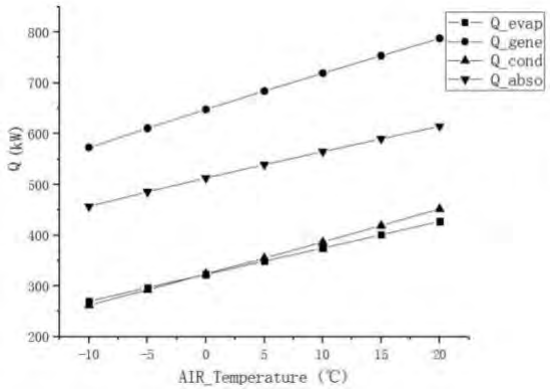

Figure 3: (a) heat rate varies with air source temperature

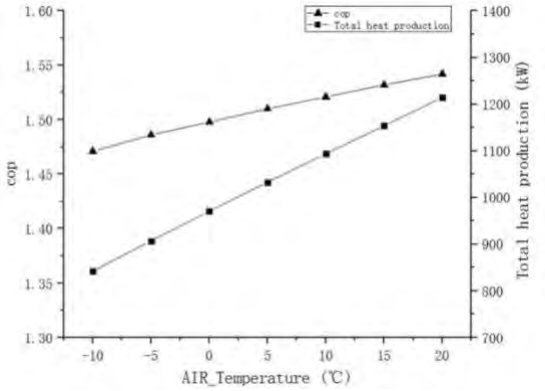

Figure 3: (b) COP and heat generation varies with temperature

The increase of air temperature is beneficial to the absorption heat pump system. And its COP increases from 1.471 to 1.542, and heat production increases from 842.406kW to 1214.566kW. The changes are shown in Fig. 3(b). The effect of evaporation pressure on COP is shown in figure 4. The increase of air temperature will make evaporation pressure larger, which is conducive to improving COP.

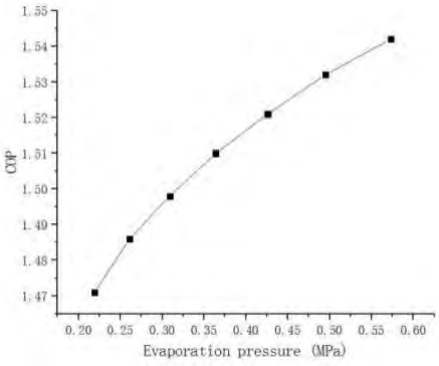

Figure 4: COP varies with evaporation pressure

5.2. Influence of Inlet Temperature of Cooling Water on System Performance

When the temperature of the air is 0 °C and the temperature of the flue gas is 180 °C. The COP of the system is reduced from 1.516 to 1.471, and the heat production is reduced from 1175.973 kW to 756.729kW in the process of raising the inlet temperature of cooling water from 30 °C to 50 °C, as shown in Fig. 5(a).

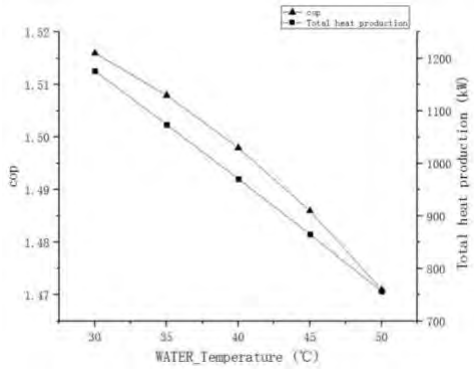

Figure 5: (a) COP and heat generation varies with water inlet temperature

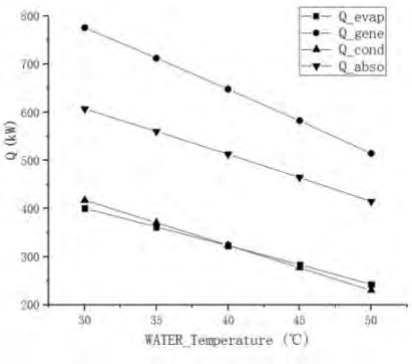

Figure 5: (b) heat rate varies with water inlet temperature

The condensation pressure increases, the deflation range of the system decreases, and the refrigerant flow rate decreases when the temperature of cooling water rises. Thus adversely affects system performance. The reduction of the refrigerant flow rate will inevitably reduce the heat rate of each heat exchanger, which is shown in Fig. 5(b).

5.3. Influence of High Temperature Heat Source on System Performance

When the temperature of air is fixed at 0 °C, the cooling water temperature is 40 °C, and the flue temperature increases from 130°C to 190°C, the deflation range of the system increases continuously, the refrigerant flow rate also increases from 0.146kg/s to 0.298kg/s, and the heat rate of each heat exchanger also increases all the time, as shown in Fig. 6 (a). The influence of heat source temperature on the COP and heat production of the system is shown in Fig. 6 (b). When the heat source temperature is 130 °C, the system COP is 1.495, then gradually increases, and after 160 °C, the system COP slightly decreases. The heat production increased from 508.407kW to 993.002kW with the increase of the heat source temperature. Because as the temperature of the flue increases, the flow rate of refrigerant gradually increases. The evaporator can absorb more heat from the low-temperature heat source, thus contributing to the increase of the COP of the system. When the temperature of the heat source increases to a certain range, more water vapor will evaporate from the generator, thus causing some of the heat to be absorbed by the water vapor and wasted, so COP will not continue to grow or even slightly decrease.

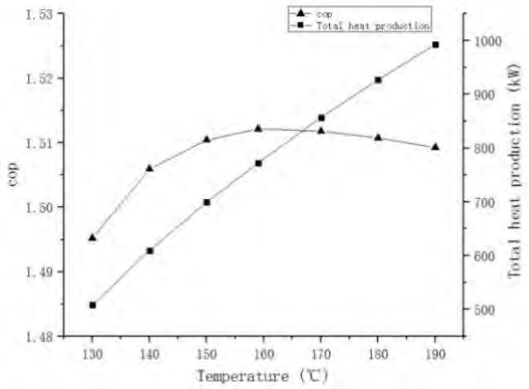

Figure 6: (a) COP and heat generation varies with driven temperature

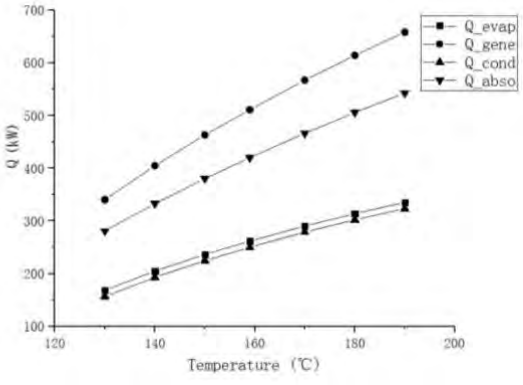

Figure 6: (b) heat rate varies with driven temperature

6. CONCLUSIONS

This paper introduces the working process of air source ammonia-water absorption heat pump system, and establishes a program to calculate the performance of the system. The calculated results of the program are consistent with the theoretical analysis. The program will be further improved in the later period, which will provide some references for the development and progress of ammonia-water absorption heat pump technology. The main results are as follows:

(1) A simulation program of ammonia-water absorption system is established. The program uses simultaneous solution of equations to simulate the steady state of the circulation system, which has the advantages of fast convergence speed and good expansibility. The parameters of each state point, heat rate and COP of each component of the system can be obtained by the program in this paper, which has strong practicability.

(2) The ammonia-water absorption heat pump system with a heat production capacity of 1000kW is simulated. The system performance and the variation rules of internal parameters of the system under different working conditions are analysed. The simulation results are analysed theoretically to verify the reliability and feasibility of the system. It is found that the COP of the system increases with the increase of the evaporator heat source temperature; increases first and then decreases slightly with the increase of the generator heat source temperature, and decreases with the increase of the inlet temperature of the heating water.

(3) Using this program, thermodynamic and heat transfer system simulation can be more conveniently carried out for ammonia-water absorption heat pump systems with different processes, such as basic ammonia-water cycle, basic GAX cycle and branch GAX cycle.

NOMENCLATURE

P	pressure (MPa)	*m*	mass flow rate (kg/s)
T	temperature (K)	*C*	mass fraction (%)
H	enthalpy(kJ/kg)	*Q*	heat transfer(kW)
Cp	specific heat capacity		

REFERENCES

Jianmin L. 2004. Performance analysis of GAX cycle for ammonia absorption refrigeration. Doctoral dissertation, Southeast University.

Pátek J, Klomfar J. 1995. Simple functions for fast calculations of selected thermodynamic properties of the ammonia-water system. International Journal of Refrigeration. 18(4), 228-234.

Xiaohui Z, Junjun G. 2014. Absorption heat pump technology and application. Metallurgical Industry Publishers, Beijing, 1-3

Yongqing D. 2001. Lithium bromide absorption refrigeration technology and application. Mechanical Industry Publishers, Beijing, 2-6

Manuscript ID: 775
DOI: 10.18462/iir.icr.2019.0775

Thermodynamic analysis of a novel high-temperature heat pump for low-grade waste heat recovery

Carlos MATEU-ROYO, Joaquín NAVARRO-ESBRÍ, Adrián MOTA-BABILONI, Francisco MOLÉS, Marta AMAT-ALBUIXECH

ISTENER Research Group, Department of Mechanical Engineering and Construction, Universitat Jaume I, Campus de Riu Sec s/n, E12071 Castelló de la Plana, Spain
mateuc@uji.es

ABSTRACT

This paper analyses the experimental preliminary results of a high-temperature heat pump (HTHP) prototype for low-grade waste heat recovery. HFC-245fa was selected as a working fluid to establish the baseline operation for future analyses of low global warming potential (GWP) alternative refrigerants. The HTHP experimental test reached a production temperature of 140 ºC. Moreover, the theoretical analysis shows the expected performance and the influence of the IHX for heat sources from 70 to 100ºC, the typical temperature range for the refrigeration jackets fluid of CHP systems. The theoretical IHX influence analysis shows that heating capacity and COP increase by about 22% and 16.5%, respectively, with the use of this component. Finally, the experimental setup gets a coefficient of performance (COP) of 2.23 for waste heat temperature (heat source) of 80 ºC and production temperature (heat sink) of 140 ºC.
Keywords: vapour compression, energy efficiency, low-GWP refrigerants, climate change, internal heat exchanger (IHX)

1. INTRODUCTION

Heat pumps can substitute boilers powered with fossil fuels and can contribute to improve the energy efficiency and decarbonise different types of the energy-intensive industries. However, their main drawbacks are the still the associated high initial costs and the lack of maturity in the technology (Wesseling et al., 2017). (Bataille et al., 2018) included industrial heat pumps as a possible technology to make consistent this type of industries with Paris Agreement.
(Arpagaus et al., 2018) performed a comprehensive review of the heat pumps with heat sink temperatures up to 150 °C, also named high-temperature heat pumps (HTHPs). The status of development of HTHPs configurations is still mostly limited to theoretical analysis, like those analysed by (Mateu-Royo et al., 2018) that considered external heat exchanger, in one and two-stages, or those by (Mota-Babiloni et al., 2018), who considered HTHP cascades. About experimental studies, the research is being performed using HTHP prototypes that use different component technologies and working fluids in basic cycle configurations. (Chamoun et al., 2014) used a twin-screw water HTHP equipped with plate condenser, an electrical expansion valve, a flash tank and a falling film evaporator. (Bobelin et al., 2012) constructed an HTHP with scroll compressors, to provide heat up to 125 °C with a developmental mixture fluid. For evaporating and condensing temperatures of 50 and 100 °C, respectively, the COP was 4.48.

Therefore, the HTHPs technology is in an earlier stage, in which the results of the prototypes are being published. Additionally, it is not ready to reach higher production temperatures that can be adapted to a wide range of industrial processes. This paper presents the first results of an HTHP experimental setup designed to test low synthetic GWP refrigerants and reach heat sink temperatures of 140 °C. The components of the vapour compression loop and secondary circuits, the test methodology exposed, and the measurements are described. Then, the first measurements with HFC-245fa are presented and discussed, to evaluate the performance that can reach this system and validate the first results. Finally, the theoretical IHX influenced analysis and compared with the HFC-245fa experimental results.

2. THEORETICAL EVALUATION

In order to analyse the influence of the operating parameters (evaporating temperature, condensing temperature, discharge temperature, and the use of IHX) on the heating capacity and the COP, a previous simple theoretical study is carried out, as shown Fig. 1.

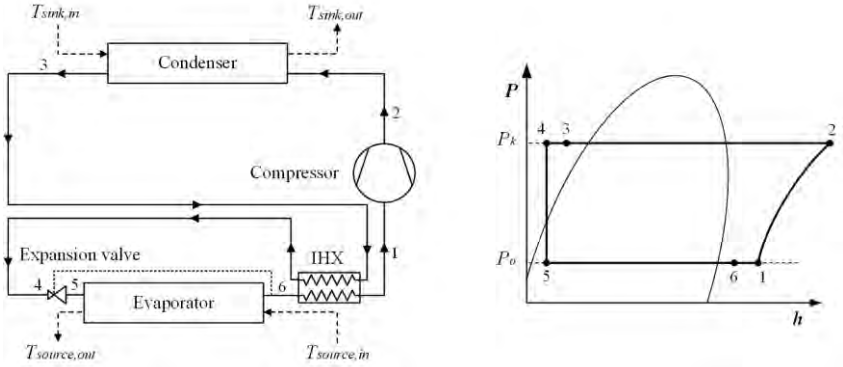

Figure 1: Schematic and P-h diagram of the single-stage cycle with IHX.

Around 30% of the input energy in a CHP is rejected as heat to the ambient. Typically, these CHP systems use a fluid refrigerant through the jackets to maintain the combustion chamber in an optimal operating temperature. These heat rejected to the ambient could be recovered using a high-temperature heat pump (EPA, 2012). Thus, heat source temperatures in the theoretical evaluation are considered between a range of 70-100 ºC to simulate the refrigerant fluid from CHP jackets whereas the heat sink temperature is considered 140 ºC in order to simulate the thermal level of an industrial process. In this theoretical study the following assumptions are made:

- A constant compressor isentropic efficiency of 0.75, the volumetric efficiency of 0.95 and electro-mechanic efficiency of 0.7 are considered.
- Sub-cooling degree of 2 K is considered at the condenser outlet.
- Superheating degree of 5 K is considered at the evaporator outlet
- Pitch point is considered 3 K at the evaporator and 10 K at the condenser.
- ΔT between inlet and outlet of the secondary circuits is considered 15 K at the evaporator and 10K at the condenser.
- The IHX effectiveness is considered 0.5.
- Isenthalpic process is considered at the expansion valve.
- No pressure losses and heat losses in any components are neglected.

The refrigerant mass flow rate ($\dot{m}_{ref}$) is calculated as follows:

$$\dot{m}_{ref} = \rho_{suc}\, V_c\, \eta_{vol} \left(\frac{N}{60}\right) \qquad \text{Eq. (1[MV1])}$$

where N is the compression rotation speed in rpm, and ρ_{suc} is the density of the refrigerant at the compressor suction.
The heating capacity ($\dot{Q}_k$) is defined as the product of the refrigerant mass flow rate and the refrigerating effect (enthalpy difference between evaporator outlet and inlet):

$$\dot{Q}_k = \dot{m}_{ref}\,(h_{k,in} - h_{k,out}) \qquad \text{Eq. (2)}$$

The vapour suction temperature is calculated using Eq. (3).

$$\varepsilon_{\mathrm{IHX}} = \frac{h_{suc} - h_{o,out}}{h_{k,out} - h_{o,out}} \qquad \text{Eq. (3)}$$

The electric power consumption of the compressor (W ̇_C), is expressed in Eq. (4) as the product of the mass flow rate and the isentropic enthalpy difference at the compressor divided by the isentropic and electromechanical efficiencies.

$$\dot{\mathrm{W}}_{\mathrm{C}} = \frac{\dot{m}\,\Delta h_{is,c}}{\eta_{is}\,\eta_{em}} \qquad \text{Eq. (4)}$$

To compare the influence of the volumetric flow rate at the compressor suction and the heating capacity, the volumetric heating capacity (VHC) is calculated using Eq. (5).

$$VHC = \frac{\dot{\mathrm{Q}}_{\mathrm{k}}}{\dot{m}_{ref}}\eta_{vol}\rho_{suc} \qquad \text{Eq. (5)}$$

The theoretical COP only depends on thermodynamic states at the inlet and outlet of the evaporator and the compressor and is defined as:

$$COP = \frac{\dot{Q}_k}{\dot{\mathrm{W}}_{\mathrm{C}}} \qquad \text{Eq. (6)}$$

3. EXPERIMENTAL SETUP AND PRELIMINARY RESULTS

The experimental tests are carried out considering a test bench that is represented in Fig. 2, which contains the main components, sensors and configurations. It is composed of the main vapour compression circuit and two closed secondary circuits, for the heat source and heat sink along with a closed water cooler circuit. While the heat source circuit simulates potentially waste heat available from industrial processes, the heat sink represents the high-temperature utilisation.
The vapour compression circuit consists of a scroll open-type compressor with a variable-speed electric motor of 7.5 kW nominal power and displacement of 121.1 cm^3 per revolution (2900 rpm at 230 V and 50 Hz), magnetically coupled to each other. The polyester oil with a viscosity of 40 mm^2/s (at 60 ºC) is used to ensure the required compressor lubrication at high operating temperatures. All the heat exchangers (condenser, sub-cooler, evaporator and internal heat exchanger, IHX) are brazed plate type. Liquid receiver between condenser and sub-cooler is used to ensure the absence of bubbles before the expansion process. Due to the lack of development of electronic expansion valves for high-temperature applications, the manual expansion valve is selected to control the correct superheating degree at the outlet of the evaporator.
The secondary circuits are used to set the targeted evaporation and condensation temperatures. The heat sink circuit uses thermal oil as the secondary fluid and is cooled by a closed-type cooling system that allows the control of the thermal oil temperature. Moreover, the volumetric flow rate can be adjusted using a variable-speed pump. This cooling water system is composed of a Proportional Integrative Derivative (PID) controlled dry cooler to ensure the temperature stability of the heat sink circuit. The

waste heat simulation system (heat source circuit) also regulates the secondary thermal oil temperature through a set of immersed PID controlled electrical resistances.

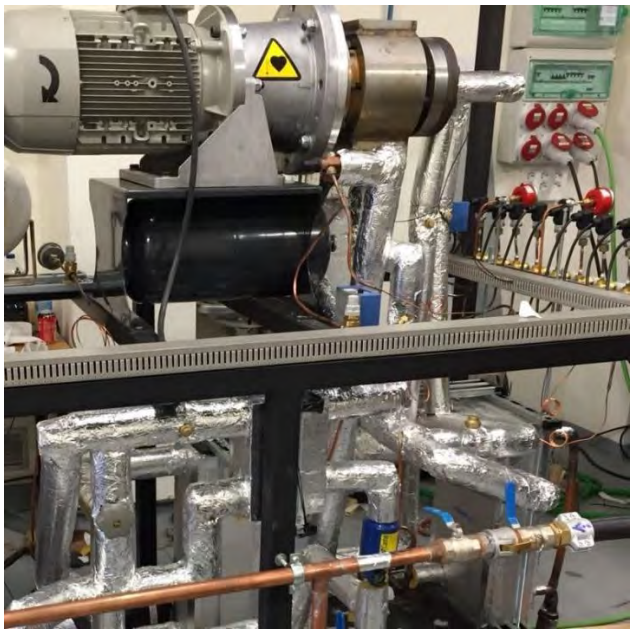

Figure 2: Photo of the experimental prototype (ISTENER, Universitat Jaume I, Spain)

The thermodynamic states of the refrigerant are calculated using pressure and temperature measurements in the required locations of the system. These values are obtained with calibrated thermocouples and pressure transducers. The refrigerant mass flow rate is measured by a Coriolis mass flow meter located at the liquid line while the power compressor consumption is measured using a digital wattmeter. In the secondary circuits, temperature and volumetric flow rate are measured. Table 1 shows the characteristics of the sensors and their uncertainty. Finally, the thermodynamic properties are calculated using the REFPROP software (Lemmon et al., 2018).

Table 1: Summary of measurement sensors and uncertainties

Measured parameters	Sensor	Uncertainty
Temperatures	J-type thermocouples	± 0.3 K
Pressures	Piezoelectric pressure transducers	± 0.04% of reading
Refrigerant mass flow rate	Coriolis mass flow meter	± 0.17% of reading
Heat source volumetric flow rate	Vortex flow meter	± 0.5% of reading
Heat sink volumetric flow rate	Vortex flow meter	± 0.028 $m^3 h^{-1}$
Compressor power consumption	Digital wattmeter	± 1.55%

The test operating conditions for the start-up of the HTHP system are described in Table 2.

Table 2: Operating conditions in the start-up experimental test

Controlled parameters	Values
Heat sink outlet temperature	140 ºC (413.15 K)
Heat source inlet temperature	80 ºC (353.15 K)
Superheating degree (SH) with IHX	35 K
Compressor drive frequency	50 Hz

The process for the selection of a steady state test consists of measuring for a time period of 40 min, with a sample period of 1 s, in which the condensing and evaporating pressure are within an interval of 3.5 kPa. During the test, all the temperatures are within a deviation of ± 0.25 K and the refrigerant mass flow rate is within ± 0.0007 kg·s^{-1}. Then, once the steady-state operation is achieved (with 2400 direct measurement), the data is processed with an algorithm in order to find the steady-state period of 10 min (600 direct measurements) with the highest precision and accuracy

In order to check the accuracy of the measurements, a comparison between the heat load removed by the refrigerant and the heat supplied by the brine at the evaporator is carried out. So, Fig. 3 shows a comparison between the cooling capacity measured at the refrigerant side and the propylene glycol brine side, including all the experimental tests used in this work with both refrigerants.

The heating capacity at the refrigerant side is obtained using the Eq. (2) moreover, the heating capacity at the heat sink side is obtained using the measured thermal oil flow rate ($\dot{m}_{heat\ sink}$) and the temperatures at the evaporator inlet ($T_{heat\ sink,in}$) and outlet ($T_{heat\ sink,out}$):

$$\dot{Q}_{sink} = \dot{m}_{sink}\, C_{p,sink}(T_{sink,out} - T_{sink,in}) \qquad \text{Eq. (7)}$$

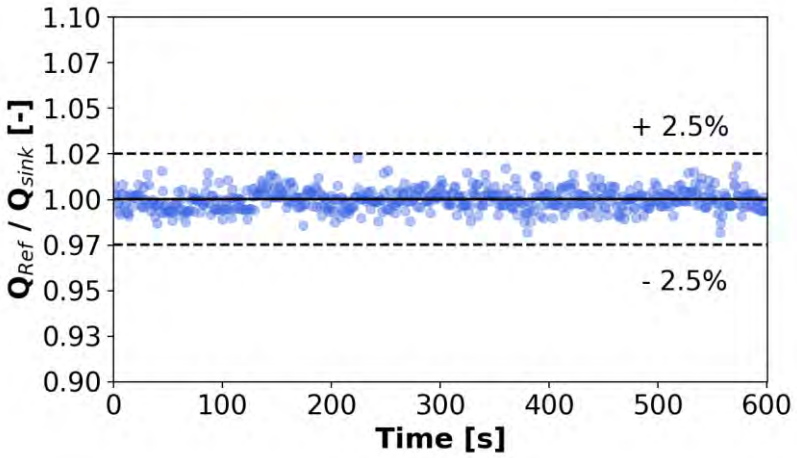

Figure 3: Heating capacity at the condenser (comparing refrigerant and brine sides)

The uncertainty propagation of the characteristic parameters is obtained by the root-sum-of-squares (RSS) method, taking into account both the uncertainty of the measurements (95% of confidence level) as the uncertainty of the measuring devices (Taylor and Kuyatt, 1994). Table 3 shows the uncertainties of the calculated parameters due to the uncertainties propagation of the test performed.

Table 3 Summary of measurement sensors and uncertainties

Uncertainty	$\dot{W}_C$ (kW)	$\dot{Q}_k$ (kW)	COP
Absolute	± 0.135	± 0.5623	± 0.0816
Relative	± 1.72%	± 3.21%	± 3.66%

4. THEORETICAL AND EXPERIMENTAL RESULTS

The experimental performance parameters are calculated with the equation shown above whereas the isentropic, volumetric and total compressor efficiencies were calculated using the Eq. (8), Eq. (9) moreover, Eq. (10), respectively. Finally, second law efficiency is calculated using Eq. (11) to illustrate the experimental performance results with the ideal Carnot COP. Table 4 shows the summary of results for the main experimental energy performance parameters

$$\eta_{is} = \frac{h_{dis,is} - h_{suc}}{h_{dis} - h_{suc}} \quad \text{Eq. (8)}$$

$$\eta_{vol} = \frac{\dot{m}_{ref}}{V_C \, \rho_{suc} \, (\frac{N}{60})} \quad \text{Eq. (9)}$$

$$\eta_{total} = \frac{\dot{m}_{ref} \ (h_{dis} - h_{suc})_{is}}{\dot{W}_c} \quad \text{Eq. (10)}$$

$$\eta_{2n\,law} = \frac{COP}{COP_{carnot}} = \frac{COP}{T_{sink,out}} (T_{sink,out} - T_{source,in}) \quad \text{Eq. (11)}$$

Table 4: Summary of the preliminary experimental results

Performance parameters	η_{is}	η_{vol}	$\dot{m}_{ref}$	T_{dis}	$\dot{W}_c$	$\dot{Q}_k$	VHC	COP	η_{total}	$\eta_{2n\,law}$
HFC-245fa (Experimental)	0.79	0.96	0.13	159.85	7.85	17.5	3125.8	2.23	0.55	0.32

Theoretical and experimental results are presented together as shown in Fig. 4 and Fig. 5. The experimental power consumption with IHX in the steady-state studied is 7.85 kW. The theoretical results illustrate similar values of this parameter using IHX, and therefore, the theoretical calculation without IHX shows that this component increases the compressor power consumption of about 4.75%, as shown in Fig. 4a. Similarly, Figure 4b shows that the IHX increase the heating capacity of around 22%.

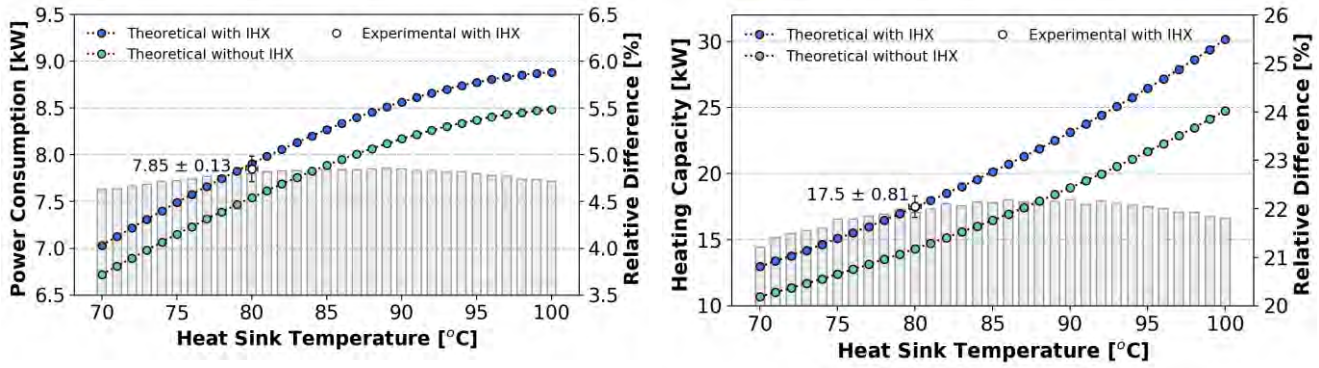

(a) (b)

Figure 4: Experimental and theoretical result and IHX influence of: (a) Compressor power consumption and (b) Heating Capacity

Strongly related with the previous energy parameters analysed, experimental and theoretical results of COP are presented in Fig. 5. The experimental COP is situated close to the theoretical results with the value of 2.23. The theoretical IHX in these parameters shows that about 16.5% energy performance increase is expected with the use of this component. Thus, this theoretical results promotes the use of IHX in HTHPs, and therefore, more experimental studies about IHX influence in HFC-245fa and alternative low-GWP refrigerants are required.

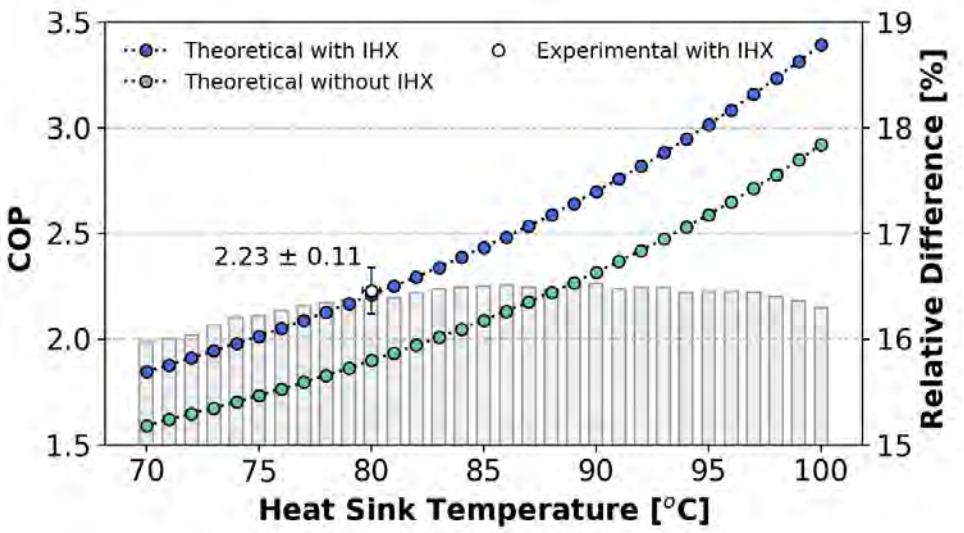

Figure 5: Experimental and theoretical result and IHX influence of COP

5. CONCLUSIONS

This paper describes and analyses the preliminary experimental results of a novel high-temperature heat pump (HTHP) based on a scroll compressor adapted to high-temperature applications with HFC-245fa. The baseline operation for future analyses of low global warming potential (GWP) alternative refrigerants is established. The HTHP experimental test with HFC-245fa reached a production temperature of 140 ºC.

The theoretical analysis shows the expected performance and the influence of the IHX for heat sources from 70 to 100ºC, the typical temperature range of the jackets refrigeration fluid in CHP systems. A heating capacity increases of 22% is expected with the use of IHX whereas the COP shows an increase of 16.5%. This theoretical result promotes the use of IHX in HTHPs, and therefore, more experimental studies about IHX influence in HFC-245fa and alternative low-GWP refrigerants are required.

Finally, the experimental setup gets a coefficient of performance (COP) of 2.23 for waste heat temperature (heat source) of 80 ºC and production temperature (heat sink) of 140 ºC. These promising experimental results illustrate that high-temperature heat pump will perform a crucial role in the decarbonisation and climate change mitigation.

ACKNOWLEDGEMENTS

The authors acknowledge the Spanish Government for the financial support under projects ENE2015-70610-R and grant FJCI-2016-28324. Furthermore, the authors acknowledge the Universitat Jaume I for the financial support under the project P1-1B2015-38 and Carlos Mateu-Royo acknowledges the funding received through the PhD grant PREDOC/2017/41.

NOMENCLATURE

ε	effectiveness	$\dot{Q}_k$	heating capacity (kW)
h	enthalpy (kJ·kg^{-1})	$\dot{W}_c$	compressor power consumption (kW)
$\dot{m}$	mass flow rate (kg·s-1)	T_{dis}	Discharge temperature (ºC)
η	efficiency	VHC	Volumetric heating capacity (kJ·m^{-3})
P	Pressure (kPa)		

Subscripts

dis	discharge	ref	refrigerant
in	inlet	sink	heat sink
is	isentropic	source	heat source
o	evaporating	suc	suction
out	outlet	vol	volumetric

Abbreviations

COP	Coefficient Of Performance	HFC	hydrofluorocarbon
GWP	Global Warming Potential	HCFO	hydrochlorofluoro-olefin
HFO	hydrofluoro-olefin	IHX	Internal Heat Exchanger
HTHP	High-Temperature Heat Pump		

REFERENCES

Arpagaus, C., Bless, F., Uhlmann, M., Schiffmann, J., Bertsch, S.S., 2018. High temperature heat pumps: Market overview, state of the art, research status, refrigerants, and application potentials. Energy 152, 985–1010. https://doi.org/10.1016/J.ENERGY.2018.03.166

Bataille, C., Åhman, M., Neuhoff, K., Nilsson, L.J., Fischedick, M., Lechtenböhmer, S., Solano-Rodriquez, B., Denis-Ryan, A., Stiebert, S., Waisman, H., Sartor, O., Rahbar, S., 2018. A review of technology and policy deep decarbonization pathway options for making energy-intensive industry production consistent with the Paris Agreement. J. Clean. Prod. 187, 960–973. https://doi.org/10.1016/J.JCLEPRO.2018.03.107

Bobelin, D., Bourig, A., Peureux, J., 2012. Experimental results of a newly developed very high temperature industrial heat pump (140°C) equipped with scroll compressors and working with a new blend refrigerant. Int. Refrig. Air Cond. Conf.

Chamoun, M., Rulliere, R., Haberschill, P., Peureux, J.-L., 2014. Experimental and numerical investigations of a new high temperature heat pump for industrial heat recovery using water as refrigerant. Int. J. Refrig. 44, 177–188. https://doi.org/10.1016/j.ijrefrig.2014.04.019

EPA, 2012. Evaluation of Combined Heat and Power Technologies for Wastewater Facilities. U.S. Environmental Protection Agency (EPA).

Lemmon, E.W., Bell, I.H., Huber, M.L., McLinden, M.O., 2018. NIST Standard Reference Database: Reference Fluid Thermodynamic and Transport Properties-REFPROP, Version 10. Natl. Inst. Stand. Technol. Stand. Ref. Data Program, Boulder, CO.

Mateu-Royo, C., Navarro-Esbrí, J., Mota-Babiloni, A., Amat-Albuixech, M., Molés, F., 2018. Theoretical evaluation of different high-temperature heat pump configurations for low-grade waste heat recovery. Int. J. Refrig. https://doi.org/10.1016/j.ijrefrig.2018.04.017

Mota-Babiloni, A., Mateu-Royo, C., Navarro-Esbrí, J., Molés, F., Amat-Albuixech, M., Barragán-Cervera, Á., 2018. Optimisation of high-temperature heat pump cascades with internal heat exchangers using refrigerants with low global warming potential. Energy 165, 1248–1258. https://doi.org/10.1016/j.energy.2018.09.188

Taylor, B.N., Kuyatt, C.E., 1994. Guidelines for Evaluating and Expressing the Uncertainty of NIST Measurement Results. Natl. Inst. Stand. Technol.

Wesseling, J.H., Lechtenböhmer, S., Åhman, M., Nilsson, L.J., Worrell, E., Coenen, L., 2017. The transition of energy intensive processing industries towards deep decarbonization: Characteristics and implications for future research. Renew. Sustain. Energy Rev. 79, 1303–1313. https://doi.org/10.1016/J.RSER.2017.05.156

Manuscript ID: 778
DOI: 10.18462/iir.icr.2019.0778

Theoretical and experimental investigation on a very high temperature heat pump with water refrigerant

Di WU, Bin HU, R.Z. WANG

Institute of Refrigeration and Cryogenics, Shanghai Jiao Tong University
Shanghai, 200240, China, hb1223@sjtu.edu.cn

ABSTRACT

Vapor compression very high temperature heat pumps (VHTHPs) with low-GWP refrigerants have attracted enormous attention for waste heat recovery. To yield high temperature output, a water vapor screw compressor with water-injection is developed and a VHTHP prototype is established to conduct the experimental investigation. The results show that when condensation temperature T_c increases from 110 to 150°C and evaporation temperature T_e is 75°C, 80°C and 85°C, COP of this VHTHP ranges between 1.85-4.03, 1.89-4.88 and 1.96-6.10, respectively. COP can reach the highest value 6.10 with heating capacity of 284.7 kW at T_e=85°C, T_c=117°C. What's more, the highest condensation temperature of this water vapor VHTHP can reach 150°C with the COP of 1.96 when T_e=85°C. So the water vapor VHTHP can supply pressured hot water or high temperature steam when the user is favourable. Considering the characteristic of high energy efficiency and environment friendly, this VHTHP is highly desirable and competitive.
Keywords: Water Refrigerant, High Temperature Heat Pump, System COP, Water Injection.

1. INTRODUCTION

Heat pumps are highly attractive energy conversion technologies in industrial production, since they offer efficient ways to reduce primary energy consumption by utilizing waste heat or any kind of low grade thermal heat (Bless *et al*., 2016). Vapor compression heat pumps are widely used and available in a large variety of sizes for different industrial applications. Because of the various of heat sources and supplying temperature, the vapor compression heat pump can be classified as conventional heat pump (HP), high temperature heat pump (HTHP) and very high temperature heat pump (VHTHP), as shown in Fig.1 (Bobelin and Bourig, 2012; Bless *et al*., 2018). VHTHP can supply heat temperature over 100°C with the heat source between 60 and 100°C. According to a study of the International Energy Agency (IEA) (Eisentraut and Brown, 2014), industry is the largest heat-consuming final sector with 79 EJ in 2011, accounting for nearly 46% of the world total energy use for heat in that year. And great application potential for VHTHPs has been identified in the paper, food, beverages, metal and chemical industries, in particular in drying processes. Many researchers are investigating VHTHPs using simulation and experimental methods and the refrigerants investigated are mainly R1336mzz(Z), R245fa, R1234ze(Z), R600, and R601 (Kondou *et al*., 2014; Ochsner, 2015; Nilsson, 2017; Haasteren *et al*., 2017).

However, as shown in Fig.2 (Calm and Hourahan, 1999; Calm, 2008), with the development of time, the requirement of refrigerant is different. Water is the representative of natural refrigerant in the

fourth stage with 0 ODP and GWP. Its thermodynamic properties such as high critical temperature (374.15°C) at pressure (22.13 MPa) make it more suitable for heat pump applications with high temperature. There are some researchers who are interested in using water refrigerant in the HTHP systems. Chamoun *et al*. (2011) presented a water vapor HTHP system. Although they performed both experimental and numerical investigations into the performance of this heat pump, they didn't give actual operation performance of this heat pump at certain working conditions (Chamoun *et al*., 2014). Shen *et al*. (2014) designed and analyzed a HTHP system with a water-jet screw vapor compressor. Using water spray makes the discharge water vapor reach a saturation point and meet the requirements of high temperature rise. Because of no actual experimental performance of HTHP with water refrigerant presented, the feasibility of it isn't verified.

In this paper, a water vapor compression VHTHP was designed and simulated. Then a prototype of this HTHP with water refrigerant was set up to validate the feasibility of this VHTHP.

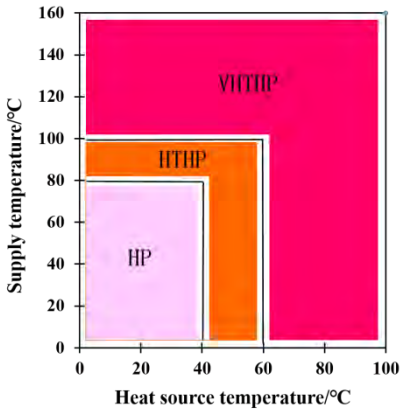

Figure.1 The classification of vapor compression heat pumps

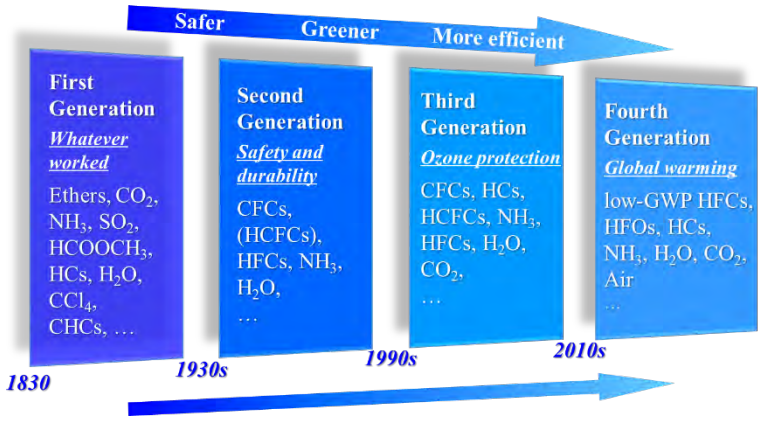

Figure.2 The development of refrigerants at different time

2. WATER VAPOR COMPRESSION VHTHP SYSTEM

Fig.3 shows the schematic diagram of the water vapor compression VHTHP system and its p-h diagram, which includes an evaporator, a flash tank, a compressor, a condenser, a liquid collector, an expansion valve, a circulating water pump and an injection water pump.

In the water vapor VHTHP cycle, the overheated water vapor from the evaporator at state1 flows into the flash tank and releases heat to saturation state. Part of the water in the flash tank absorbs the heat of overheating to evaporate into vapor. Then water vapor in the flash tank is sucked into the water vapor compressor at saturation condition, state 2. The low pressure and low temperature water vapor is compressed to a middle pressure and temperature state in the working chamber of water vapor compressor. During the compression process, the low temperature water at state 9 which comes from external environment is injected into the water vapor compressor by the injection water pump. The compressed water vapor in former stage mixes with the injected water and recompressed in the later stage. The injected water absorb the sensible heat of the compressed overheated water vapor and evaporate in the next working chamber of the water vapor compressor. The biphasic mixture is compressed and discharged at high pressure and temperature at state 3. Afterwards, the high pressure and temperature water vapor flows into the condenser and is cooled by the cooling water from the user side. The condensate water at state 4 is collected in the liquid collector and the water at state 5 expands to low pressure and temperature mixture through an expansion valve. The water and vapor mixture at state 6 flows into the flash tank. Part of the water

in the flash tank (state 7) is pumped into the evaporator by the circulating water pump. The water pumped into the evaporator (state 8) absorbs the waste heat from the heat source and evaporates into water vapor with certain temperature and pressure. Finally, the overheated water vapor at state1 flows back into the flash tank and will be sucked into the compressor in the next cycle.

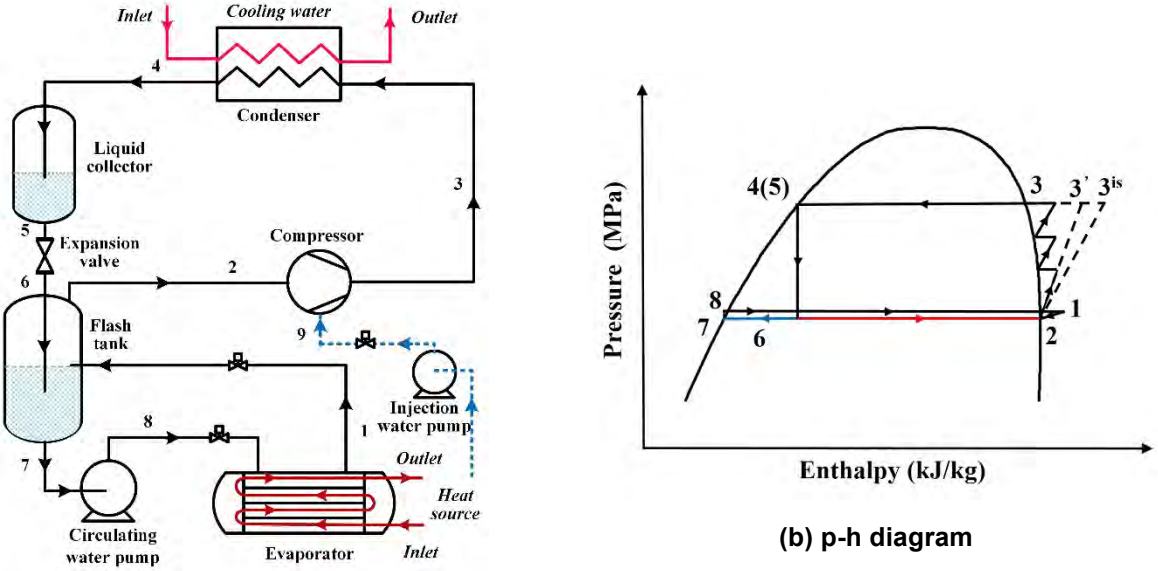

(a) schematic diagram **(b) p-h diagram**

Figure. 3 The water vapor compression VHTHP system

SIMULATION AND EXPERIMENT

2.1. Simulation model

The compressor volumetric efficiency, $_{vol}$, is defined in Eq. (1).

$$\eta_{vol} = V \cdot V_{th}^{-1} \quad \text{Eq. (1)}$$

where V is the compressor actual volume flow rate in $m^3 \cdot r^{-1}$, V_{th} is the compressor theoretical volume flow rate in $m^3 \cdot r^{-1}$.

The refrigerant mass flow rate of the compressor outlet is *m* in $kg \cdot m^{-1}$, shown in Eq. (2).

$$m = \rho \cdot n \cdot V_{th} \cdot \ _{vol} \quad \text{Eq. (2)}$$

where ρ is the refrigerant density in the suction side in $kg \cdot m^{-3}$, n is the rotation speed of the compressor in rps.

The compressor isentropic efficiency, $_{is}$, is defined in Eq. (3).

$$_{is} = (h_{act} - h_e) \cdot (h_{is} - h_e)^{-1} \quad \text{Eq. (3)}$$

where h_{act} is the actual compression enthalpy of refrigerant in $kJ \cdot kg^{-1}$, h_{is} is the isentropic compression enthalpy of refrigerant in $kJ \cdot kg^{-1}$, h_e is the enthalpy of refrigerant in the suction side in $kJ \cdot kg^{-1}$.

The power consumption of compressor is *W* in kW, shown in Eq. (4).

$$W = m \cdot (h_{is} - h_2) \cdot \quad _{is}^{-1} \qquad \text{Eq. (4)}$$

where h_2 is the enthalpy of refrigerant in the suction side in kJ·kg^{-1}.
The heating capacity of heat pump system is *Q* in kW, shown in Eq. (5).

$$Q = m \cdot (h_3 - h_4) \qquad \text{Eq. (5)}$$

where h_3 is the enthalpy of refrigerant in the suction side of condensor in kJ·kg^{-1}, h_4 is the enthalpy of refrigerant in the discharge side of condensor in kJ·kg^{-1}.
The COP of the system is shown in Eq. (6).

$$COP = Q \cdot (W + W_{pump})^{-1} \qquad \text{Eq. (6)}$$

where W_{pump} is power consumption of the circulating water pump and injection water pump in kW.

2.2. Experimental set up

In order to verify the precision of the simulation model and the feasibility of the VHTHP with water refrigerant, a prototype of the water vapor compression VHTHP was built based on the schematic diagram, as shown in Fig.4. In this prototype, a special designed twin-screw oil-free water vapor compressor was used. And there are three water-injection point in the compression chamber, as shown in Fig.5. Besides, the internal compression ratio and the rotation speed of this compressor are 7 and 5000 rpm respectively. The rated heating capacity of plate condenser and falling film evaporator are 300 kW and 240 kW respectively. To maintain water vapor supply and provide enough space to flash, the volume of the flash tank is 2.5 m^3. An electrically controlled expansion valve is adopted in which the condensation pressure is used as controlling signals.



Figure.4 The prototype of the water vapor VHTHP

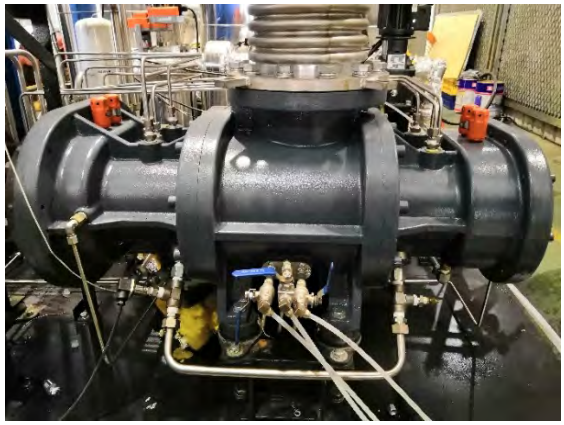

Figure.5 The photo of the water vapor compressor

The temperatures are measured using PT100 temperature senor with an accuracy of ±0.2°C. System pressures are measured using pressure transducers (accuracy, ±0.5% of full scale) with a measuring range of 0~0.16 MPa for the low pressure (below ambient) side and 0~1.6 MPa for the high pressure side. The volume flow rate of supply water is measured by a pipeline vortex flowmeter (accuracy, ±0.5% of reading) with a measurement range of 0~1100 m^3·h^{-1}. The mass flow rate of injected water is measured by a metal tube float flowmeter (accuracy, ±0.5% of reading) with a

measurement range of 0~63 $L \cdot h^{-1}$. All the experimental data, such as temperature, pressure, water mass flow rate and electrical power are collected and recorded by a PLC-200 control system.

3. RESULT AND DISCUSSION

The simulation was conducted to investigate the performance of this water vapor VHTHP system under different working conditions, such as different condensation and evaporation temperatures. And experimental investigation are also under the same conditions with the highest condensation temperature upto 150°C. The results comparison are shown in the following figures, in which $T_{e,exp}$ means experiment evaporation temperature, $T_{e,sim}$ means simulation evaporation temperature, $T_{lift,exp}$ means experiment temperature lift and $T_{lift,sim}$ means simulation temperature lift.

The performances of this twin-screw oil-free compressor in actual operation are shown in Fig.6 and Fig.7. Fig.6 shows that the volumetric efficiency of compressor has a negative correlation with the condensation temperature at the same evaporation temperature. With the increase of pressure difference, the increase of leakage between compression chamber and exit leads the decrease of volumetric efficiency. And as shown in Fig.7, the adiabatic efficiency of compressor also approximately decreases as the condensation temperature increases.

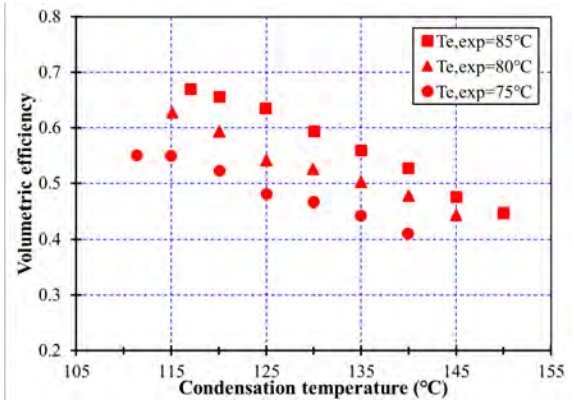

Figure.6 The change of volumetric efficiency with condensation temperature at different evaporation temperature

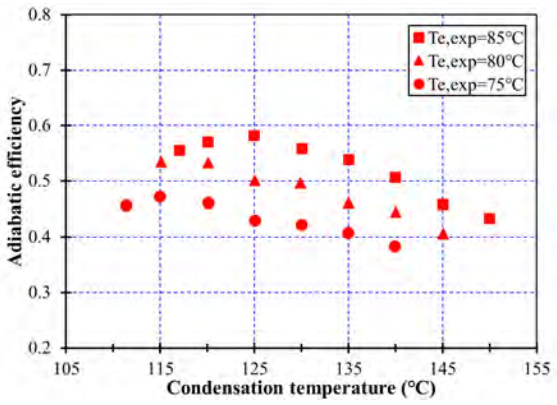

Figure.7 The change of adiabatic efficiency with condensation temperature at different evaporation temperature

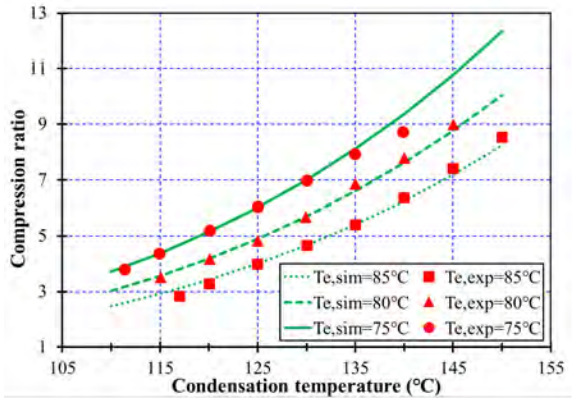

Figure.8 The change of compression ratio with condensation temperature at different evaporation temperatures

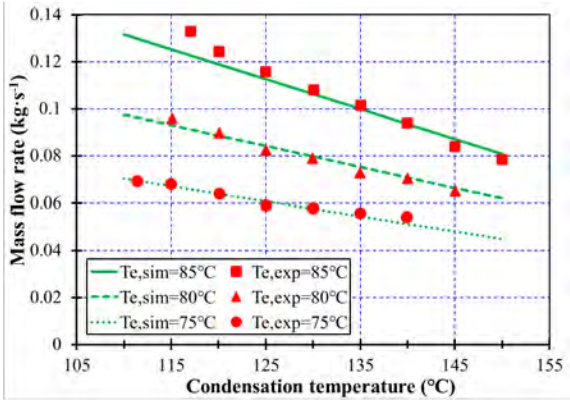

Figure.9 The change of mass flow rate with condensation temperature at different evaporation temperatures

Fig.8 shows that when the evaporation temperature is kept at 75°C, 80°C and 85°C, the compression ratio ranges between 2.8 to 9.0 as the condensation temperature increases from 110 to 150°C. The highest compression ratio 9 is reached at T_e=80°C and T_c=145°C.

Fig.9 illustrates that when the condensation temperature increases from 110 to 150°C and the evaporation temperature is kept at 75°C, 80°C and 85°C, the mass flow rate of water vapor in the system varies between 0.054-0.069 kg·s^{-1}, 0.065-0.096 kg·s^{-1} and 0.078-0.133 kg·s^{-1}, respectively. On account of the decrease of compressor volumetric efficiency and density of the water vapor, the mass flow rate of the system decreases with the increase of condensation temperature at constant evaporation temperature.

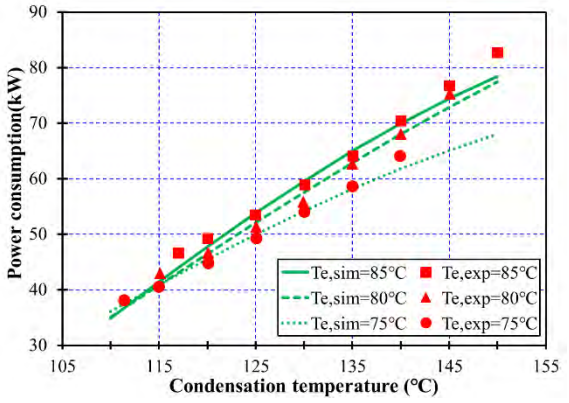

Figure. 10 The change of power consumption with condensation temperature at different evaporation temperature

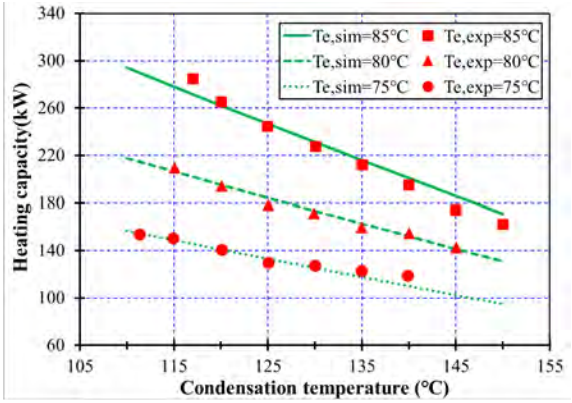

Figure.11 The change of heating capacity with condensation temperature at different evaporation temperature

Fig.10 presents that as the condensation temperature increases from 110 to 150°C and the evaporation temperature is kept at 75°C, 80°C and 85°C, compressor power of the water vapor VHTHP increases from 38.2 to 64.2 kW, 42.9 to 75.3 kW and 46.7 to 82.7 kW, respectively. At the same evaporation temperature, power consumption shows positive correlation with condensation temperature. In spite of the fact that the mass flow rate has a negative correlation with the condensation temperature, the increase of enthalpy difference and the decrease of compressor adiabatic efficiency lead the increase of power comsumption.

The heating capacity change with the condensation temperature is illustrated in Fig.11 at various evaporation temperature 75°C, 80°C and 85°C. With the condensation temperature increasing from 110 to 150°C, the heating capacity of the water vapor VHTHP increases from 118.8 to 155.0 kW, 142.6 to 209.3 kW and 162.3 to 284.8 kW at T_e=75°C, 80°C, 85°C, respectively. Due to Eq.(5), the heating capacity of this water vapor VHTHP is mainly determined by the latent heat and the mass flow rate of water vapor. However, the p-h characteristic of water decides that at operation conditons, the latent heat of water keeps almost constant. Based on the above, the heating capacity is determined by the mass flow rate of water vapor, and it has positive correlation with the mass flow rate of water vapor. In view of the negative correlation between the mass flow rate and the condensation temperature, the heating capacity shows negative correlation with the condensation temperature when evaporation temperature is constant.

The variety of COP with condensation temperature at T_e=75/80/85°C is shown in Fig.12. When the condensation temperature increases from 110 to 150°C, the COP of the water vapor VHTHP ranges between 1.85-4.03 (T_e=75°C), 1.89-4.88 (T_e=80°C) and 1.96-6.10 (T_e=85°C). The trend of COP curve illustrates that the COP of this heat pump has negative correlation with the condensation temperature, and it decreases more slowly as the condensation temperature

increases. This is mianly due to the decrease of the heating capacity and the increase of the power consumption. Fig.13 illustrates the variety of COP with constant temperature lift at different condensation temperature. At the same temperature lift, the COP increases with the increase of condensation temperature, because the heating capacity increases faster than the power consumption. When the evaporation temperature is 85°C with 32°C temperature lift, the COP reach 6.10. Even though the temperature lift reach 65°C and the condensation tempreature reach 150°C, the COP can still achieve 1.96.

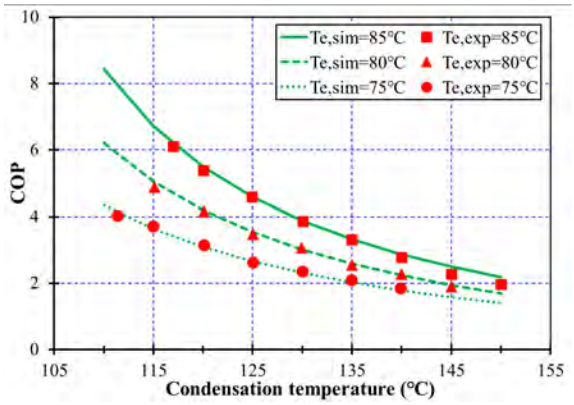

Figure.12 The change of COP with condensation temperature at different evaporation temperature

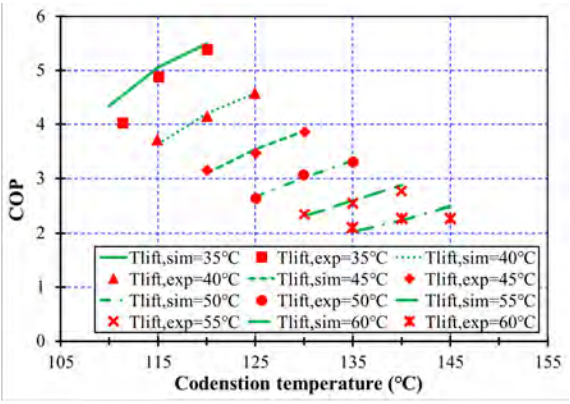

Figure.13 The change of COP with condensation temperature at different temperature lift

4. CONCLUSIONS

In this paper, a new VHTHP with water refrigerant is proposed and a VHTHP prototype is set up to validate the feasibility of this heat pump. The experimental results show that the natural refrigerant water is a promising working medium for heat pump system with very high temperature output. And twin-screw oil-free compressor with water-injection is suitable for compressing water vapor and decreasing the discharge temperature in this VHTHP. The performance of this water vapour VHTHP is excellent. When the condensation temperature increase from 110 to 150°C and the evaporation temperature is 75°C, 80°C and 85°C, the COP of this water vapor VHTHP ranges between 1.85-4.03, 1.89-4.88 and 1.96-6.10, respectively. When the evaporation temperature is 85°C and the condensation temperature is 117°C, COP can reach the highest value 6.10 with heating capacity of 284.7 kW and compression ratio of 2.84. What's more, the highest condensation temperature of this water vapor VHTHP can reach 150°C with the temperature lift of 66°C and COP of 1.96.

According to a study of the IEA, industry is the largest heat-consuming final sector and accounts for nearly 46% of the world total energy use for heat in 2011. Potential heat demand in industry are for space heating (>35°C), drying processes (>70°C) or process heat (120-150°C). Besides hot water, water vapor with high temperature and pressure also accounts a large proportion in the heat demand. And this water vapor VHTHP with the highest supply temperature of 150°C can not only supply hot water but also water vapor with high temperature and pressure. So great application potential for this water vapor VHTHPs is identified in the paper. In addition, natural refrigerant water is the representative working medium in the fourth stage low-GWP refrigerants with unexceptionable environmental protection property.

Combining the advantages of VHTHP and water refrigerant, water vapor VHTHP is highly desirable due to the characteristic of energy efficiency and environment friendly. It is a promising and competitive technology in future industrial applications.

ACKNOWLEDGEMENTS

This research was supported by the National Natural Science Foundation of China (51706131) and National key R&D program of China (2016YFB0601200).

REFERENCES

Arpagaus, C., F. Bless, J. Schiffmann, et al., (2016). Multi-temperature heat pumps – A literature review. International Journal of Refrigeration 69, 437-465.

Arpagaus, C., F. Bless, M. Uhlmann, et al., (2018). High temperature heat pumps: Market overview, state of the art, research status, refrigerants, and application potentials. Energy 152, 985-1010.

Bobelin, D., A. Bourig., (2012). Experimental Results of a Newly Developed Very High Temperature Industrial Heat Pump (140°C) Equipped With Scroll Compressors and Working With a New Blend Refrigerant. Proceedings of the International Refrigeration and Air Conditioning Conference, West Lafayette, 1-10.

Calm, J. M., (2008). The next generation of refrigerants – Historical review, considerations, and outlook. International Journal of Refrigeration 31(7), 1123-1133.

Calm, J. M., G. C. Hourahan., (1999). Physical, safety, and environmental data for refrigerants. HPAC Heating, Piping, Air Conditioning 71(8), 27-29.

Chamoun, M., R. Rulliere, P. Haberschill, et al., (2011). Water vapour as refrigerant for a new high temperature heat pump. Japanese Journal of Radiological Technology 49(6), 1879-1887.

Chamoun, M., R. Rulliere, P. Haberschill, et al., (2014). Experimental and numerical investigations of a new high temperature heat pump for industrial heat recovery using water as refrigerant. International Journal of Refrigeration 44(16), 177-188.

Eisentraut, A., A. Brown, (2014). Market Developments and Policy Considerations for Renewable Heat.

Fukuda, S., C. Kondou, N. Takata, et al., (2014). Low GWP refrigerants R1234ze(E) and R1234ze(Z) for high temperature heat pumps. International Journal of Refrigeration 40(3), 161-173.

Nilsson M, R. H., Kontomaris K., (2017). Measured performance of a novel high temperature heat pump with HFO-1336mzz-Z as the working fluid. Proceedings of 12th IEA Heat Pump Conference. Rotterdam, 1-10.

Ochsner, K., (2015). High temperature heat pumps for waste heat recovery. Proceedings of 8th EHPA European Heat Pump, Forum, 1-10.

Shen, J., Z. He, Z. Xing, (2014). Design and performance analysis of high temperature heat pump using water-jet screw type steam compressor. Refrigeration and Air-Conditioning. 14 (2), 95-98.

Wemmers, A. K., A. W. M. B. van Haasteren, P. Kremers et al., (2017). Test results R600 pilot heat pump. Proceedings of 12th IEA Heat Pump Conference, Rotterdam, 1-9.

Manuscript ID: 789
DOI: 10.18462/iir.icr.2019.0789

Absorption cooling system with optimized heat exchange network for efficient waste heat recovery

Zhenyuan XU[(a)], Ruzhu WANG[(a)], Chun YANG[(b)]

[(a)] Institute of Refrigeration and Cryogenics, Shanghai Jiao Tong University
Shanghai 200240, China, xuzhy@sjtu.edu.cn
[(b)] School of Mechanical and Aerospace Engineering, Nanyang Technological University
Singapore 639798

ABSTRACT

Industrial waste heat utilization by absorption cooling systems is an energy-saving option, especially in tropical areas. However, waste heat conditions vary under different scenarios, and optimization is always important. To make full use of the waste heat, there are two aspects. First, the waste heat exchange network should be optimized by minimizing the irreversible loss. Second, the absorption system should properly couple to the optimized heat exchange network. In this paper, the two-step method is presented together with a real case study. Extra heat of 5250-8020 kW with temperature of 108-83℃ is obtained through the optimization, and is used for absorption cooling. The first law and second law efficiencies are increased by 54.0% and 67.7% respectively. Considering the 8000 h/yr operation of the system per year, the system could generate 3.2×10^7 kWh cooling output. Estimated with the local tariff, the payback period is about 2.2 years.
Keywords: Absorption system, Heat pump, Waste heat recovery, Optimization.

1. INTRODUCTION

Industry processes consume enormous energies and release large amount of waste heat. With the modern energy conversion technologies, the waste heat can be recovered to produce electricity and chilled water(Brückner et al., 2015). In a waste heat recovery and conversion system, the energy input is waste heat instead of commonly used electricity or fossil fuel, the waste heat recovery system is energy-saving, economical and environmentally friendly, and thus has attracted researchers' great attention.

The available technologies for waste heat recovery mainly include heat to power conversion, heat to refrigeration conversion and heat upgrading. The heat to power conversion includes the Rankine cycle, Organic Rankine cycle (Carcasci et al., 2014; Kaşka, 2014; Sprouse and Depcik, 2013) and Kalina cycle (Bombarda et al., 2010; Mirolli, 2005; Ogriseck, 2009). The heat to refrigeration conversion includes the absorption refrigeration (Kalinowski et al., 2009; Khaliq et al., 2012; Mone et al., 2001), adsorption refrigeration (Saha et al., 2001; Wang and Oliveira, 2006; Wang et al., 2011) and desiccant cooling (Dai et al., 2001; Daou et al., 2006). The heat upgrading includes the absorption heat pump (Sözen et al., 2002; Wu et al., 2014), absorption heat transformer (Donnellan et al., 2015; Ma et al., 2003; Zhang et al., 2014) and vapor compression heat pump (Fatouh and Elgendy, 2011; Yilmaz, 2003). If there is time or space mismatch between waste heat supply and user demand, use of heat storage (Kuravi et al., 2013; Yu et al., 2013) is necessary. Despite so many technologies for waste heat recovery, no general guide is available in terms of how to select a proper technology for a given waste heat system.

In this paper, a case study is given to show how to optimize the waste heat recovery with absorption cooling system and heat exchange network optimization. The original system is located in the tropical area and provides demineralized water to industrial users. First, we conduct a heat exchange network optimization analysis using the second law of thermodynamics based pinch point method such that the temperature and amount of the available waste heat can be evaluated with the optimized heat exchange network. Second, we provide a detailed implementation plan to make better utilization of the waste heat. At last, economic benefit of the optimized system is analyzed to show the practicability.

2. OPTIMIZATION OF THE WASTE HEAT RECOVERY SYSTEM

This case study aims to accomplish an optimal design for the waste heat system using absorption cooling system. To achieve the project goal, the analysis of the original system, technology selection, optimized system design are carried out in sequence.

2.1. Analysis of the Original System

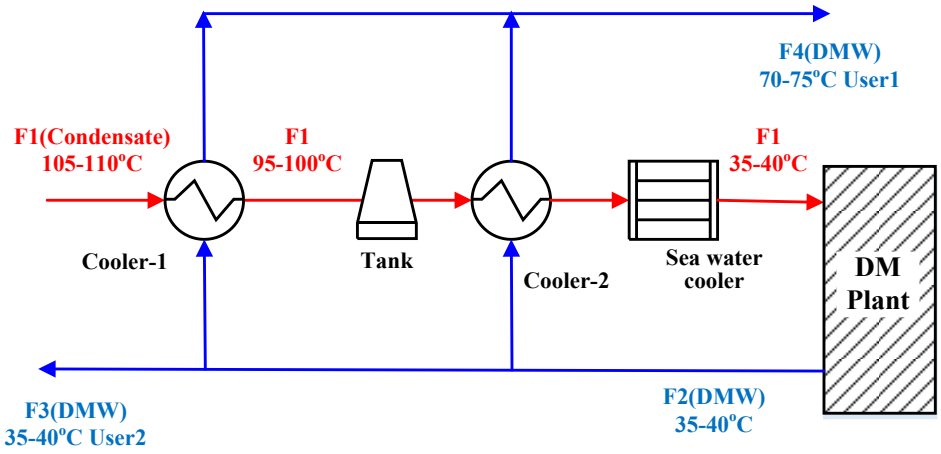

Figure 1: Schematic of the original system

Fig.1 depicts a schematic of the original system located in the tropical area which provides demineralized water (DMW) to industrial users through demineralized plant (DM plant). The hot steam condensate (F1) is sequentially cooled by cooler-1, cooler-2 and seawater cooler before it flows into the DM plant. The heat dissipation in two coolers is recovered for heating the DMW to user 1 (F4), but the heat dissipation in seawater cooling process is wasted. In the original system, there are three sets of operation conditions shown in Table 1. In order to obtain the optimal design of the waste heat recovery system, the waste heat recovery in the original system is analyzed first. The heat flows in each heat exchange process are calculated from the given temperatures and flow rates. A medium temperature in the given temperature range (for example 108 °C in 105~110 °C) is used in calculation.

Table 1. Flow rates in different operating conditions

Condition	Flow rate F1 (t/h)	Flow rate F2 (t/h)	Flow rate F3 (t/h)	Flow rate F4 (t/h)
1	275±5	450	205	245
2	275±5	450	130	320
3	180	275	205	70

Assuming that the pinch point of the heat exchange network is decreased to 10 °C (easy to be achieved), the optimal design for waste heat recovery can be obtained with the pinch point technology. At the same time, such design should meet other requirements by the users as shown below:

(1) Temperature of F1 into the DM plant is lower than 40 °C;

(2) Temperature of F4 to user 1 is maintained between 70 °C and 75 °C.

The heat exchange processes under condition 1 are calculated from Table 1 and shown in Table 2 and Fig. 2. The temperature changes and flow rates of hot/cold flows are presented for each heat exchange process. The discharged heat (i.e., the thermal energy dissipated by seawater cooler) has a temperature of 76.8 °C. The smallest temperature approaches in cooler-1 and cooler-2 are 35 °C and 25 °C respectively. The largest temperature approaches in cooler-1 and cooler-2 are 60 °C and 38.8 °C respectively. From a thermodynamic viewpoint, larger temperature approaches mean higher level of irreversible losses in the preheating process of DMW.

Table 2. Heat exchange processes in condition 1

	Hot flow	Temp. (°C)	Rate (t/h)	Cold flow	Temp. (°C)	Rate (t/h)
Cooler-1	Condensate	108→98	275	DMW	38→73	78.6
Cooler-2	Condensate	98→76.8	275	DMW	38→73	166.4
Seawater cooler	Condensate	76.8→35	275	Seawater	-	-

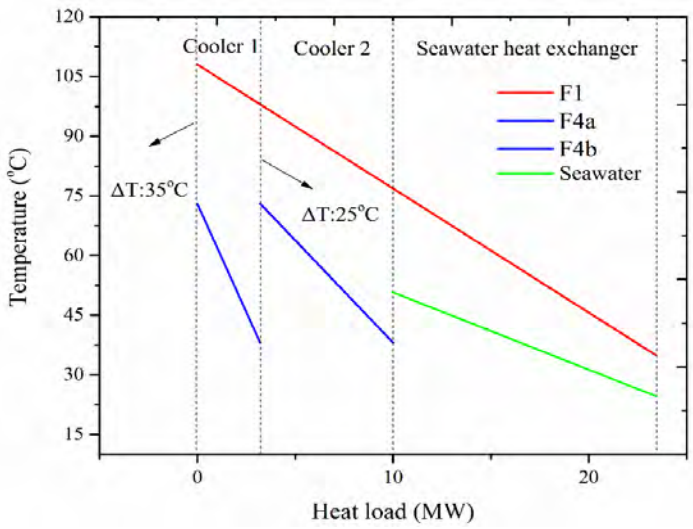

Figure 2: Temperature-heat load diagram in three heat exchangers：Condition 1

In order to enhance the waste heat recovery, the irreversible loss can be reduced and more waste heat can be utilized (with less discharged heat of lower temperature). Through the optimization using the pinch point technology, we obtain the optimal design. Table 3 shows the heat exchange processes after the optimization for condition 1. The temperature of discharged heat is reduced from 76.8 °C to 51.8 °C. As a result, hot water with a temperature range of 108 to 83°C is available and the available thermal power is 8020kW.

Table 3. Optimal design for condition 1

	Hot flow	Temp(°C)	Rate (t/h)	Cold flow	Temp(°C)	Rate (t/h)
Available	**Condensate**	**108→83**	**275**	-	-	-
Cooler	Condensate	83→51.8	275	DMW	38→73	245
Seawater cooling	Condensate	51.8→35	275	Seawater	-	-

2.2. Technology Selection

Based on the above analyses, the temperature ranges of the thermal power are 108→83°C, corresponding to the qualities of the available thermal power as 8020 kW. Considering the local demand, chilled water and electricity are preferred. The proper technology for the available waste heat recovery should have the following features: (1) activated by the heat source of its temperature range from 108 to 83 °C, (2) a large scale application, (3) be able to convert the waste thermal power into chilled water or electricity. Below is our selecting procedure:

(1) We first select the proper options for low grade heat recovery. According to the heat source temperature and demand, the available technologies mainly include: absorption cooling, adsorption cooling, organic Rankine cycle and thermoelectric conversion.

(2) Among those four technologies, the adsorption cooling and the thermoelectric conversion are not proper for large scale applications. Only the absorption cooling and the organic Rankine cycle are suitable.

(3) There is strong cooling demand in tropical area, so we compare the cooling efficiency of two technologies, the absorption cooling and the adsorption cooling. Typical absorption cooling with the current heat source temperature has the COP of 0.7, while the efficiency of the organic Rankine cycle driving vapor compression cooling is around 0.5. Therefore we choose the absorption cooling with higher efficiency.

2.3. Optimized System with Absorption Cooling

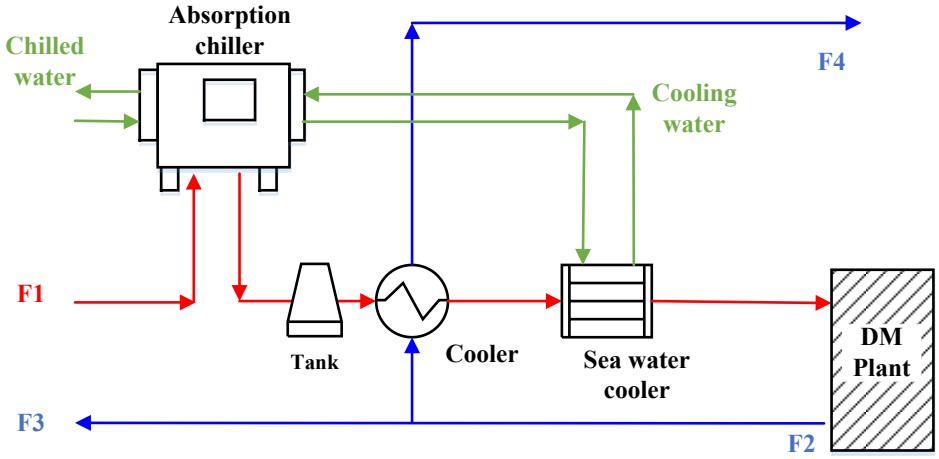

Figure 3: Schematic of our proposed heat recovery design after optimization

In our plan, steam condensate flow (F1) is used to activate a Lithium-Bromide (LiBr)-water absorption chiller first, and then to heat the DMW flow (F4). Fig.3 depicts a schematic of our proposed design after optimization. The steam condensate (F1) flows sequentially through the chiller, the cooler and the seawater cooler. The absorption chiller is cooled by the seawater cooler.

Fig.4 shows the heat exchange processes of our improved design under condition 1. The condensate provides 8.02 MW of heat input to the chiller, 10MW heat input to the cooler and has 5.4MW heat dissipation to the seawater cooler. This will lead to the cooling power of 5.6MW produced.

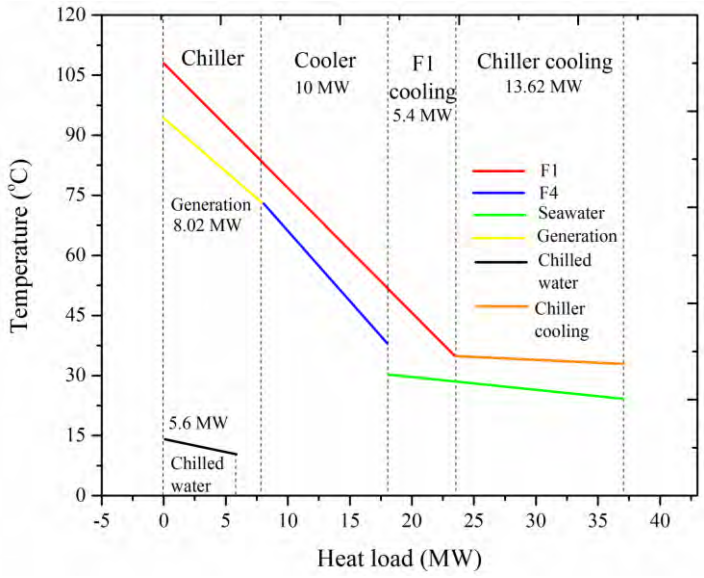

Figure 4: Temperature-heat load diagram of the improved construction: condition 1

2.4. Consideration of other Working Conditions

Except for condition 1, the other two conditions shown in Table 1also need to be investigated to see whether this plan works or not. With the same methodology shown above, condition 2 and condition 3 are analyzed and optimized. The heat exchange processes under condition 2 and condition 3 are provided in Fig. 5, and the heat exchange processes after the optimization are shown in Fig. 6.

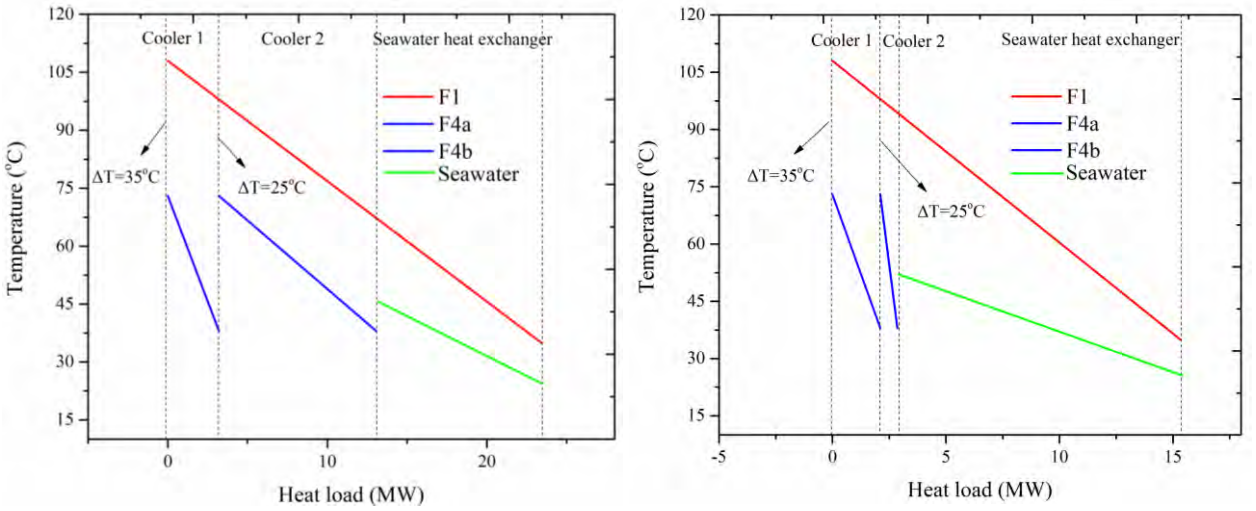

Figure 5: Temperature-heat load diagram of the original system: (a) condition 2 and (b)condition 3

As shown in Fig. 5(a) and Fig. 6(a) for condition 2, the inlet of the seawater cooler has a temperature of 67.3 °C. The smallest temperature approaches in cooler-1 and cooler-2 are 35 °C and 25 °C respectively. The largest temperature approaches in cooler-1 and cooler-2 are 60 °C and 29.3 °C respectively. After the optimization, the temperature at the inlet of the seawater cooler is reduced from 67.3 °C to 48 °C. Thus hot water with a temperature range from 108°C to 88.7°C is now available, and the available thermal power is 6192 kW. Similarly, as shown in Fig. 5(b) and Fig. 6(b) for condition 3, the temperature at the inlet of the seawater cooler is reduced from 94.4°C to 69.4°C. Thus, hot water with a temperature range from 108 to 83°C is now available, and the available thermal power is 5250 kW.

The energy flows after optimization could are also clearly shown in Fig. 6. For condition 2, the condensate provides 6.19 MW of heat input to the chiller, 13.07 MW heat input to the cooler and has 4.17 MW of heat dissipation to the seawater cooler after improvement. This will lead to a cooling power of 4.33 MW being produced. For condition 3, the condensate provides 5.25 MW of heat input to the chiller, 2.86 MW heat input to the cooler and has 7.22 MW of heat dissipation to the seawater cooler. This will lead to a cooling power of 3.67 MW being produced after improvement.

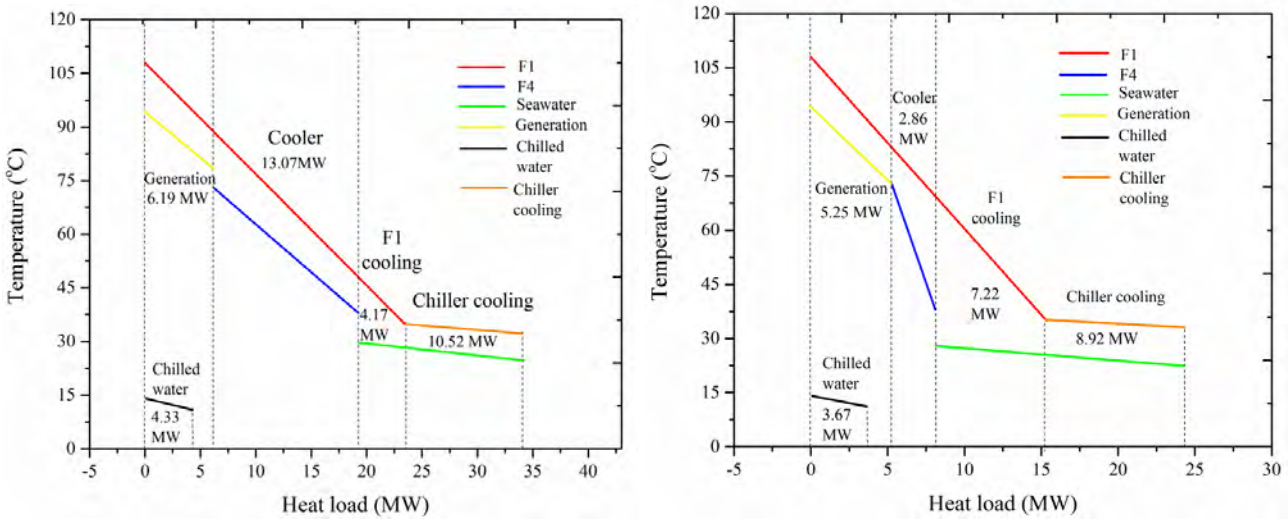

Figure 6: Temperature-heat load diagram of the improved system: (a) condition 2 and (b) condition 3

Table 4 summarizes the features of the optimal heat recovery: (1) The heat dissipation power (through seawater cooling) in the improved design has a range from 4170 kW to 7224 kW. Compared to the heat dissipation in the original design, the improved design reduces the heat

dissipation by 60%-42%. (2) Heat source with its temperature range from 108°C to 83°C is available with the thermal power of 5250-8220kW. It is utilized by the LiBr-water absorption chiller and can be utilized to produce a cooling power of 3675-5614 kW.

Table 4. Optimal design for condition 1

Condition	Input power of chiller (kW)	Power of cooler (kW)	Power of heat dissipation (kW)	Original heat dissipation (kW)
1	8020	10010	5390	13410
2	6192	13057	4170	10362
3	5250	2856	7224	12474

3. EVALUATION OF THE OPTIMIZED SYSTEM

In section 2, three major conditions are evaluated to check the feasibility of the optimized design. In the real operation, flow rate and temperature of F1 also change from time to time, which makes the average condition different from the major working condition. In this section, the evaluation of the optimized system is carried out based on the average working condition, which describes the long-term performance for this system.

3.1. Energy Flow for the Average Working Condition

Limited by the paper length, results for only condition 1 is shown in this section. According to the historical data, condition 1 under average F1 flow rate/temp. has the following parameters: F1 flow rate of 258 t/h and temperature of 106 °C, and F3/F4 flow rates of 205/245 t/h. Thermal energy with temperatures ranging from 106 °C to 80 °C and a capacity of 7826 kW can be recovered by the absorption chiller. Detailed thermal and mass balances are shown in Table 5. Cooling output of 5478 kW can be achieved by the absorption chiller. Cooling loads of 13304 kW and 3552 kW are required respectively for the absorption chiller and F1 into DM plant.

Table 5. Optimal design for Condition 1 under average F1 flow rate/temp.

	Hot flow	Temp.(°C)	Rate (t/h)	Cold flow	Temp(°C)	Rate (t/h)
Chiller	**Condensate F1**	**106→80**	**258**	-	-	-
Heat exchanger	Condensate F1	80→46.8	258	DMW	35→70	320
Cooling tower	Condensate F1	46.8→35	258	-	-	-

Fig. 7 shows the first law and second analyses for condition 1 under average F1 flow rate/temp. Available thermal power is calculated from reference temperature of 31.5 °C. First law efficiencies are 44.6% and 68.7% for the original and improved systems respectively. First law efficiency improvement of 54.0% is achieved. Exergy rate is also calculated from reference temperature of 31.5°C. The exergy efficiencies are 26.9% and 45.1% for the original and improved systems respectively. Second law efficiency (output exergy rate/input exergy rate) improvement of 67.7% is achieved.

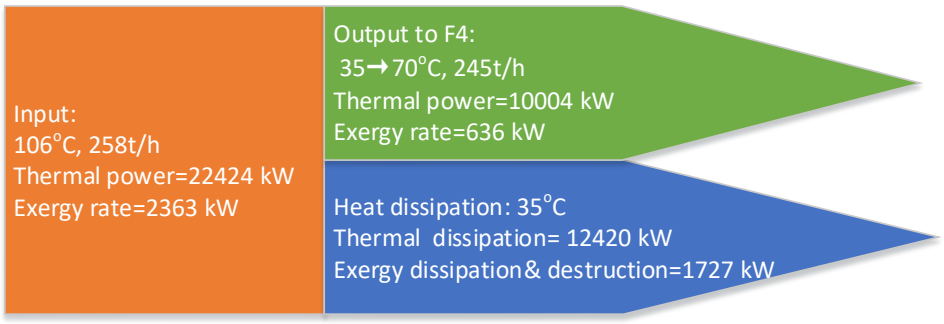

(a)

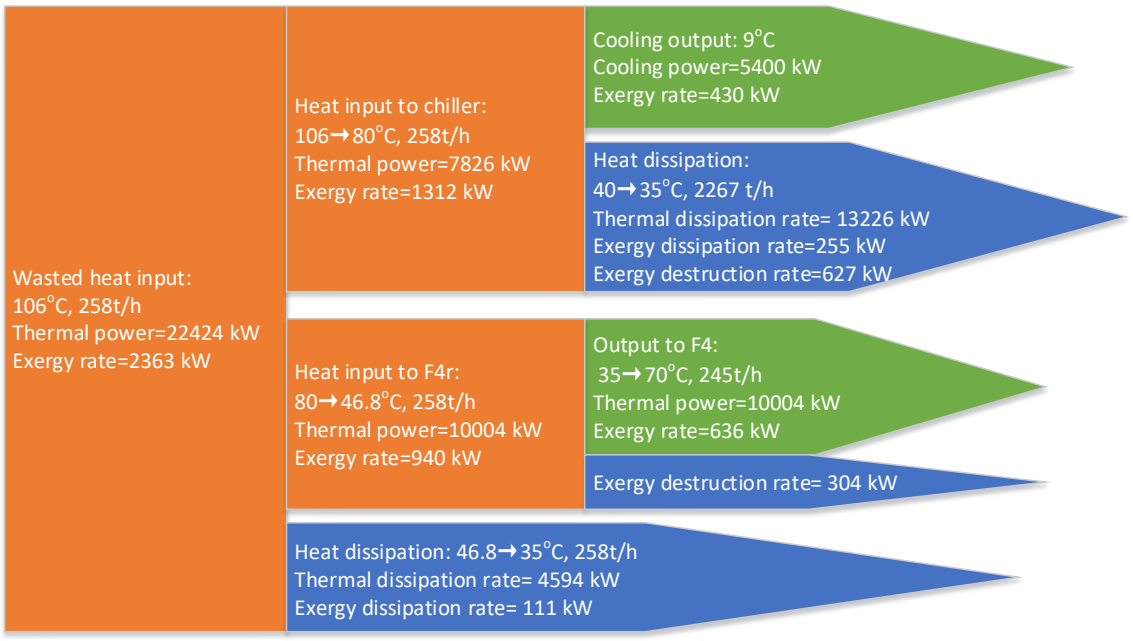

(b)

Figure 7: Energy and exergy flow of Condition 1 under average F1 flow rate/temp (Reference temperature =31.5°C), (a) Analysis before improvement; (b) Analysis after improvement

3.2. Economic Analysis for the Long-term Operation

According to historical data, the system is expected to operate for 8000h/year. Considering the operation period and average cooling output for conditions 1- 3, the maximum cooling power delivered by the system per year is about 3.3×10^7 kWh. Considering the fluctuation of working conditions, 3.2×10^7 kWh of cooling output should be delivered. Considering a COP of 4.0 for commercial compression cooling system, 8×10^6 kWh of electricity consumption will be saved every year. Based on the local tariff in the last five years, the electricity price of 0.15 USD/kWh could be used for economic analysis, and economic benefit per year is 1200k USD.

Investments for the project include the costs for absorption chiller, extra heat exchanger, pumps, installation, operation and manpower. The total cost could be covered by investment of 2600k USD, thus ensuring a payback period of 2.2 years.

4. CONCLUSION

In this paper, we discuss the procedure of waste heat recovery optimization with absorption cooling in two steps including the heat exchange network optimization via pinch point technology and the design of optimized waste heat recovery system. A case study is involved to illustrate the two steps and also the energy/economic benefit obtained from the optimization. Results show that both the first law efficiency and second law efficiency of the system could be increased significantly. Besides, short payback period also proves the economic feasibility of such optimization.

ACKNOWLEDGEMENTS

This research is supported by National Key Research and Development Program of China (Grant No. 2016YFB0601200).

REFERENCES

Bombarda, P., Invernizzi, C.M., Pietra, C., 2010. Heat recovery from Diesel engines: A thermodynamic comparison between Kalina and ORC cycles. Applied Thermal Engineering 30(2), 212-219.

Brückner, S., Liu, S., Miró, L., Radspieler, M., Cabeza, L.F., Lävemann, E., 2015. Industrial waste heat recovery technologies: An economic analysis of heat transformation technologies.

Applied Energy 151, 157-167.
Carcasci, C., Ferraro, R., Miliotti, E., 2014. Thermodynamic analysis of an organic Rankine cycle for waste heat recovery from gas turbines. Energy 65, 91-100.
Dai, Y.J., Wang, R.Z., Zhang, H.F., Yu, J.D., 2001. Use of liquid desiccant cooling to improve the performance of vapor compression air conditioning. Applied Thermal Engineering 21(12), 1185-1202.
Daou, K., Wang, R., Xia, Z., 2006. Desiccant cooling air conditioning: a review. Renewable and Sustainable Energy Reviews 10(2), 55-77.
Donnellan, P., Cronin, K., Byrne, E., 2015. Recycling waste heat energy using vapour absorption heat transformers: a review. Renewable and Sustainable Energy Reviews 42, 1290-1304.
Fatouh, M., Elgendy, E., 2011. Experimental investigation of a vapor compression heat pump used for cooling and heating applications. Energy 36(5), 2788-2795.
Kalinowski, P., Hwang, Y., Radermacher, R., Al Hashimi, S., Rodgers, P., 2009. Application of waste heat powered absorption refrigeration system to the LNG recovery process. International journal of refrigeration 32(4), 687-694.
Kaşka, Ö., 2014. Energy and exergy analysis of an organic Rankine for power generation from waste heat recovery in steel industry. Energy Conversion and Management 77, 108-117.
Khaliq, A., Agrawal, B.K., Kumar, R., 2012. First and second law investigation of waste heat based combined power and ejector-absorption refrigeration cycle. International journal of refrigeration 35(1), 88-97.
Kuravi, S., Trahan, J., Goswami, D.Y., Rahman, M.M., Stefanakos, E.K., 2013. Thermal energy storage technologies and systems for concentrating solar power plants. Progress in Energy and Combustion Science 39(4), 285-319.
Ma, X., Chen, J., Li, S., Sha, Q., Liang, A., Li, W., Zhang, J., Zheng, G., Feng, Z., 2003. Application of absorption heat transformer to recover waste heat from a synthetic rubber plant. Applied Thermal Engineering 23(7), 797-806.
Mirolli, M.D., 2005. The Kalina cycle for cement kiln waste heat recovery power plants, Cement Industry Technical Conference, 2005. Conference Record. IEEE, pp. 330-336.
Mone, C., Chau, D., Phelan, P., 2001. Economic feasibility of combined heat and power and absorption refrigeration with commercially available gas turbines. Energy Conversion and Management 42(13), 1559-1573.
Ogriseck, S., 2009. Integration of Kalina cycle in a combined heat and power plant, a case study. Applied Thermal Engineering 29(14), 2843-2848.
Saha, B., Akisawa, A., Kashiwagi, T., 2001. Solar/waste heat driven two-stage adsorption chiller: the prototype. Renewable Energy 23(1), 93-101.
Sözen, A., Altıparmak, D., Usta, H., 2002. Development and testing of a prototype of absorption heat pump system operated by solar energy. Applied Thermal Engineering 22(16), 1847-1859.
Sprouse, C., Depcik, C., 2013. Review of organic Rankine cycles for internal combustion engine exhaust waste heat recovery. Applied thermal engineering 51(1), 711-722.
Wang, R.Z., Oliveira, R.G., 2006. Adsorption refrigeration—an efficient way to make good use of waste heat and solar energy. Progress in Energy and Combustion Science 32(4), 424-458.
Wang, R.Z., Xia, Z.Z., Wang, L.W., Lu, Z.S., Li, S.L., Li, T.X., Wu, J.Y., He, S., 2011. Heat transfer design in adsorption refrigeration systems for efficient use of low-grade thermal energy. Energy 36(9), 5425-5439.
Wu, W., You, T., Wang, B., Shi, W., Li, X., 2014. Simulation of a combined heating, cooling and domestic hot water system based on ground source absorption heat pump. Applied Energy 126, 113-122.
Yilmaz, M., 2003. Performance analysis of a vapor compression heat pump using zeotropic refrigerant mixtures. Energy conversion and Management 44(2), 267-282.
Yu, N., Wang, R.Z., Wang, L.W., 2013. Sorption thermal storage for solar energy. Progress in Energy and Combustion Science 39(5), 489-514.
Zhang, X., Hu, D., Li, Z., 2014. Performance analysis on a new multi-effect distillation combined with an open absorption heat transformer driven by waste heat. Applied Thermal Engineering 62(1), 239-244.

Manuscript ID: 802
DOI: 10.18462/iir.icr.2019.0802

Simulation and optimization analysis of a dual-source R744 two-stage parallel compression hot water heat pump system

Yiming WANG[(a,#)], Hongxia ZHAO[(a,#,*)], Xinli WANG[(b)], Zeting YU[(a)], Jitian HAN[(a)]

[(a)] School of Energy and Power Engineering, Shandong University
Jinan 250061, P. R. China, hongxia.zhao@sdu.edu.cn
[(b)]School of Control Science and Engineering, Shandong University
Jinan 250061, P. R. China
[#]These authors contributed to the work equally and should be regarded as co-first authors.

ABSTRACT

An advanced dual-source R744 two-stage parallel compression hot water heat pump system (DEPC) was proposed by combining a dual-source system with a two-stage parallel compression system. Both air and ground heat were taken as the heat sources, which can effectively improve the stability and system performance of heat pump system. The model of the system was analysed and established, and then programs were written in MATLAB to simulate the system. Taking COP as the main criterion, the maximum COP and optimal state point of the system were found out. Furthermore, the system was compared with the conventional dual-evaporator system (DE), and the superiority of the optimized system was presented.
Keywords: Carbon Dioxide, Dual Source, Heat Pump, Optimization.

1. INTRODUCTION

In residential, industrial and commercial areas, heat pump water heater is the focus of application and research currently because of its advantages of good energy saving and mature technology. Heat pump system can transform low-grade energy in air or soil into water by consuming less high-grade energy. It is an effective way to reduce energy waste and improve energy efficiency. In addition, with the improvement of human awareness of environmental protection and the impact of environmental deterioration, R744 as a natural refrigerant has been widely concerned by scholars at home and abroad. R744 has many advantages that traditional refrigerants do not have, such as non-toxicity, easy access, etc. The ODP of R744 is zero and its GWP value is only 1. Many countries use R744 as an effective means to reduce global warming in heat pump water heater, such as Norway and Japan. However, the critical temperature of R744 is low. When the hot water temperature to be produced is high, the system will operate transcritically. Lorentzen (1994), Nekså (2002), Kim (2004), Ma et al. (2013), Gullo et al. (2018) and many other researchers have made outstanding contributions to the application characteristics and advantages of R744 in transcritical cycles. Nawaz et al. (2018) pointed out that in order to provide high-temperature hot water, the R744 system must run across critical conditions. Mancini et al. (2011) compared R744 transcritical cycle with R134a subcritical cycle, and they showed that R744 transcritical cycle has better matching and performance for high temperature water generation. R744 has the ability to produce high temperature hot water with high heat transfer coefficient, which makes it one of the best alternatives to HFCs refrigerants.

Changing the structure of transcritical system is a very effective way to improve heat pump system performance. Reasonable system design can sufficiently adapt to design conditions and improve COP (Coefficient of Performance). One of the approach is to adopt dual-source, which is one of the hotpots in current research. Using double heat sources to absorb heat in heat pump system can improve the efficiency of heat supply, avoid the shortcomings of single heat source and improve system stability. At present, there are two main forms of dual-source heat pump systems, which are series system and composite evaporator. For series systems, solar energy is often used as an auxiliary heat source. Lazzarin (2012) studied the combination of solar collector with air source heat pump and ground source heat pump respectively. When the ambient temperature is low in winter, solar energy or air source heat pump alone cannot meet the heating demand very

well. If the solar energy is used in series as an additional part of the heat pump system, the heating demand can be well met and the COP of the system can be effectively improved. Chargui and Sammouda (2015) put forward a method of residential heating coupled with solar heating and heat pump system, and describes the house mathematically on TRNSYS. The simulation results show that the system can meet the heating needs of local buildings or greenhouses. Buker and Riffat (2016) summarized some research results of solar assisted heat pump (SAHP) system for hot water production. They concluded that the combination of solar energy and heat pump system has strong environmental adaptability and stability. Chen et al. (2012) presented an air-water dual-source series heat pump system to produce hot water. Water is preheated in waste water first, and then it enters the heat pump system to continue absorbing heat. The dimensionless correspondence analysis method is used to analyse the system and the results proved that the COP of the series system is higher than that of the single heat source system, and it is more suitable for the cold environment in winter. Wang et al. (2015b) studied and tested the dual-source coupled heat pump system in an office building in Shenyang. The results show that the COP of heat pump is better and more stable when it is in the form of dual heat source.

Another approach to enhance system performance and stability is to adopt two-stage compression. It is well known that two-stage compression systems have higher system performance than series systems. Bertsch and Groll (2008) simulated and experimentally studied a two-stage compression heat pump system for air or water heating. The results show that the performance of the two-stage system is obviously better than that of commercial single-stage compression system. Kwon et al. (2013) studied a two-stage compression heat pump system for waste heat recovery. It was pointed out that when the pressure difference of the system was large, the two-stage compression would be more efficient than the single-stage compression system, and the system performance would be greatly improved. Shuxue and Guoyuan (2014) established a two-stage compression heat pump system model with vapour injection, and the heating performance of the system was studied experimentally. The results show that the COP of two-stage compression is 10% -12% higher than that of single-stage compression. Gullo et al. (2016) evaluated the R744 two-stage system from an energy and environmental perspective and added a parallel compressor to the system. The results show that both have a significant improvement in system performance.

Because there are many variable parameters in two-stage system, the analysis and optimization of these parameters is an important step to improve performance, and is also one of the focuses of many scholars. White et al. (2002) simulated the R744 heat pump water heater system, and obtained that the gas cooler pressure has a great influence on the system performance, and has an optimum pressure to make the best performance. Agrawal et al. (2007) studied and found that for R744 two-stage system, there exists an optimum gas cooler pressure and intermediate pressure, resulting in the maximum COP of the system. Cavallini et al. (2005) analysed the effect of two-stage compression intercooling system on cycle efficiency from both simulation and experiment, and analysed the optimum gas cooler pressure and influence of intercooler efficiency on cycle performance. From the above, the gas cooler pressure and intermediate pressure of the transcritical two-stage system are the key parameters affecting the performance.

From the above literature review, to the best of the authors' knowledge, no studies were reported on the combination of two-stage parallel compression with air-ground dual source hot water heat pump system. On the basis of the above researches, this paper proposes a system which combines air-ground dual-source with two-stage parallel compression heat pump system. The system can separately use two different temperature heat sources under different evaporation temperature to strengthen the performance improvement effect. Following that, this paper will carry out mathematical modelling and optimization of the system, and analyse the influence of gas cooler pressure and intermediate pressure on the system.

2. SYSTEM UNDER ANALYSIS

2.1. System Description

After the above analysis, a two-stage parallel compression heat pump system with dual-evaporator (DEPC) was proposed and the system scheme of DEPC system is shown in Fig. 1(a). The two evaporators in the system can absorb heat from air and soil separately for the purpose of dual-source utilization. In addition, the parallel compressor compresses the refrigerant more efficiently, which can reduce the system's power consumption and improve the performance of the system.

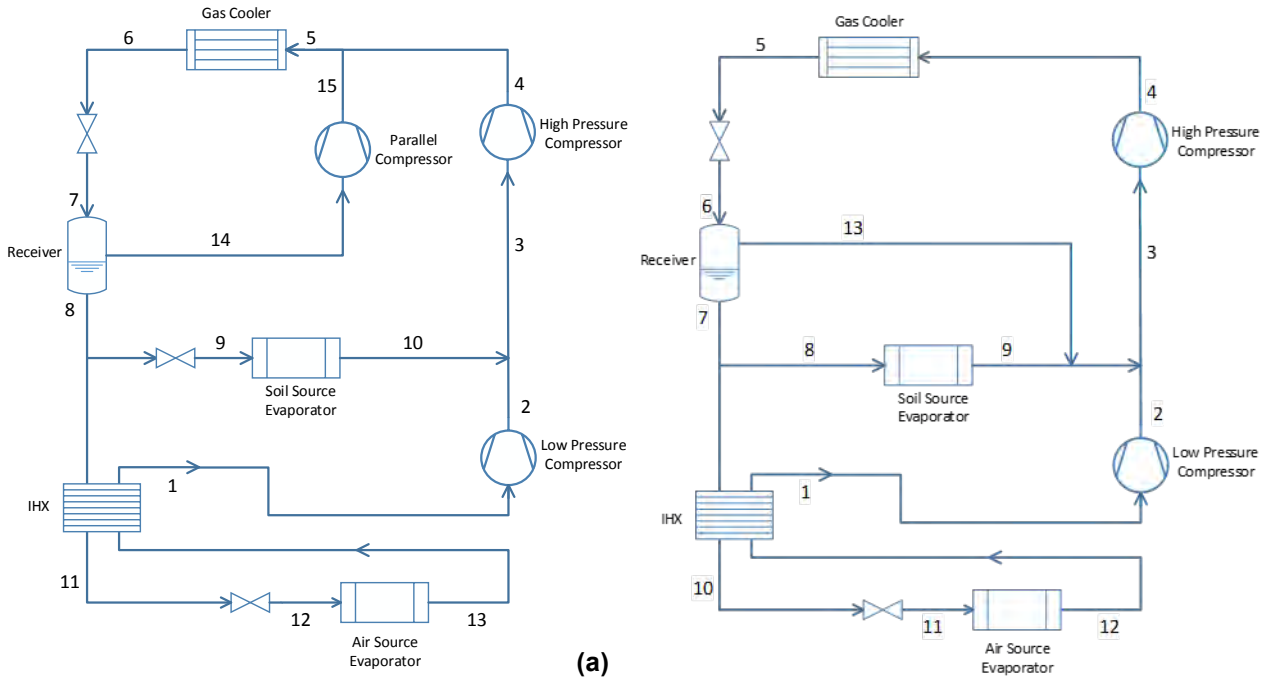

Figure 1: (a) Dual-evaporator and parallel compressor system (DEPC) (b) Conventional dual-evaporator system (DE)

In contrast, as mentioned in the previous literatures, in a conventional R744 two-stage dual-evaporator compression system (DE) shown in Fig. 1(b), there is usually only one intermediate pressure (refrigerant at the gas cooler outlet is throttled to intermediate pressure) and no parallel compressor. Based on this, the DEPC system is compared to a DE system at the same operating conditions.

2.2. Operating Conditions and Assumptions

Both systems are assumed to operate in northern China for water heating. On the hot water demand side, the system is applied in commercial water heaters, which can heat 300L of water per hour from 25 °C to 70 °C, and the gas cooler load is 1.57×10^4W. The systems and simulation methods are simplified for theoretical research under the following assumptions:

1) Saturated vapor at both evaporator outlet, and superheat at point 1 is maintained to 5K. (Pitarch et al., 2016)
2) Approach temperature of the gas cooler and IHX is fixed at 3 K. (Cecchinato et al., 2009)
3) According to the local climate conditions, the evaporation temperatures of two evaporators are respectively -10 °C and 5 °C
4) Because the soil source temperature is higher, the more refrigerants flow into the soil source evaporator, the better the system performance will be. However, due to the higher cost of installation and maintenance of soil source evaporator, this paper assumes that the mass flow rate of refrigerant entering air source evaporator and soil source evaporator is the same from the economic point of view.
5) The pressure drop of refrigerant in the heat exchangers and connecting pipes are negligible.

3. SIMULATION AND ANALYSIS METHOD

3.1. Simulation Models

The refrigerant in gas cooler is in transcritical state and releases heat to the external water. As mentioned above, the minimum heat transfer temperature difference of gas cooler is 3 K. Because the water is heated to 70 °C, the refrigerant temperature at the inlet of gas cooler (t_5) should be

greater than or equal to 73 °C. This is one of the criteria for judging whether the system is feasible or not. The pressure in the gas cooler (P_h) is a variable and this parameter has an important influence on the system performance. This paper will analyze the impact of P_h on system performance when its value changes between 80 bar and 110 bar. The heat release power of refrigerant in gas cooler can be calculated as:

$$\mathrm{Q}_c = \mathrm{M}_{gc} \times (h_{gc,in} - h_{gc,out}) \quad \text{Eq. (1)}$$

The refrigerant at the outlet of gas cooler enters the receiver in a two-phase state after isenthalpic throttling. The pressure at the receiver (P_{rec}) is another variable that has a great impact on system performance. The range of values of P_{rec} can be obtained from the system conditions: greater than P_{ev2} and satisfying the refrigerant condition at the receiver inlet to be two-phase. To this end, an intermediate pressure coefficient C_1 is introduced.

$$C_1 = \frac{P_{rec}}{P_{ev2}} \quad \text{Eq. (2)}$$

Because P_{ev2} has been determined, C_1 is proportional to P_{rec}. The value range of C_1 is greater than 1, and further optimization analysis is needed.

For compressors, the system involves high pressure compressor, low-pressure compressor and parallel compressor. Their isentropic efficiency can be expressed Eq. (3). (Liao et al., 2000)

$$\eta = 1.003 - 0.121 \times \frac{\mathrm{P}_{\mathrm{out}}}{\mathrm{P}_{\mathrm{in}}} \quad \text{Eq. (3)}$$

The equation was obtained by best fitting the experimental data of a R744 compressor made by Danfoss A/S. Therefore, the thermodynamic process of refrigerant in compressor can be expressed as Eq. (4)

$$\mathrm{h}_{\mathrm{out}} = h_{in} + \frac{h_{out,s} - h_{in}}{\eta} \quad \text{Eq. (4)}$$

3.2. Analysis Method

Through the above modeling, we can see that the gas cooler pressure (P_h) and intermediate pressure (P_{rec}) in DEPC system are two variables, and they have a significant impact on the system performance. Therefore, it is necessary to optimize these two variables. In this paper, the system performance is simulated when P_h and C_1 change in a reasonable range of values as mentioned above. A computation code is programmed in MATLAB to do system simulation and optimization. Firstly, an initial value of P_h and C_1 is given. Then, the values of P_h and C_1 are changed one by one and iterated in MATLAB.

After calculating in the above way, all possible situations of the system can be involved. Based on COP, this paper evaluates and analyses the performance of DEPC system, and finds the optimal state point of the system and its corresponding P_h and C_1 values.

4. RESULTS AND DISCUSSIONS

Through the above calculation results, this section presents and analyses the system performance when P_h and C_1 change in detail, and finds the optimal state point of the system. In addition, this part also makes a comparative analysis of DEPC system and DE system to reflect the superiority of the improved DEPC system. The COP is the most direct measurement of system performance calculated from the ratio of heating load to system work consumption, which is defined by Eq. (5).

$$COP = \frac{Q_c}{W} = \frac{Q_c}{W_{HP} + W_{LP} + W_{PC}} \quad \text{Eq. (5)}$$

4.1. Optimal Analysis of DEPC System

Fig. 3 shows the COP value of DEPC system intuitively when P_h and C_1 change. As can be seen from the three-dimensional graph shown in figure, COP value varies from about 2.9 to 3.9. In all the range of values, the COP value presents a form of high in the middle and low around, and

there is a maximum value. It can be concluded that both P_h and C_1 have a significant impact on COP, and there is a combination point that maximizes COP of DEPC system.

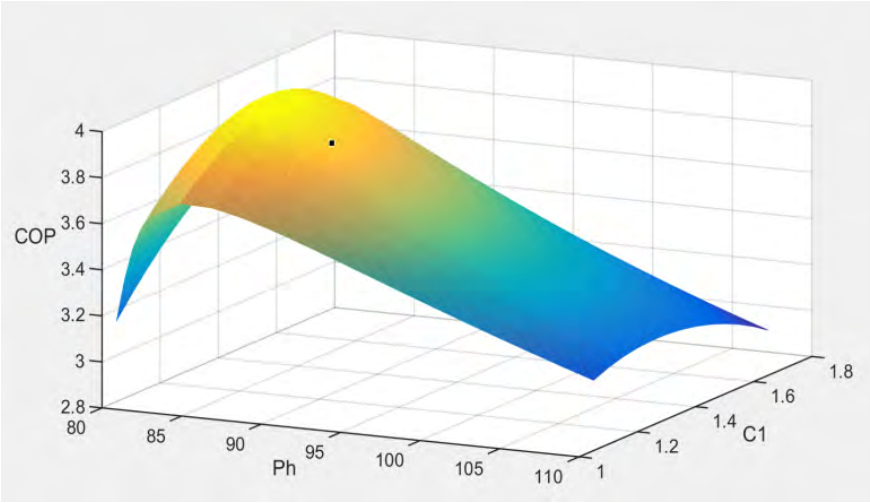

Figure 3: Relationship between COP and P_h and C_1

Through analysis, the optimal state point of the system is the point when P_h = 86bar, C_1 = 1.25, COP = 3.85, as shown in the black dot in Fig. 3. It should be noted in particular that the optimal state point of the system is not the maximum point of COP value shown in Figure 3. Because, as mentioned above, the refrigerant temperature at the gas cooler inlet should be greater than 73°C. This is the limitation of checking whether the system meets the requirements of design conditions, and other points with COP greater than 3.85 do not meet the above restrictions and therefore do not have the conditions to heat water to 70 °C. On the other hand, when the temperature of hot water demand is lower, other points with larger COP values can be considered.

For the optimal state point when P_h=86 bar, C_1=1.25, COP=3.85, the P-h diagram and detailed performance parameters at this time are shown in Fig. 4 and Table 1. It can be seen from the table that the total compressor power consumption is only 4.07 kW when the heating load is 15.7 kW, because the COP value of DEPC system is large at this point and the system has a high energy efficiency ratio. Moreover, the refrigerant temperature at the inlet of the gas cooler is 73.62 ℃, which meets the design condition of the system.

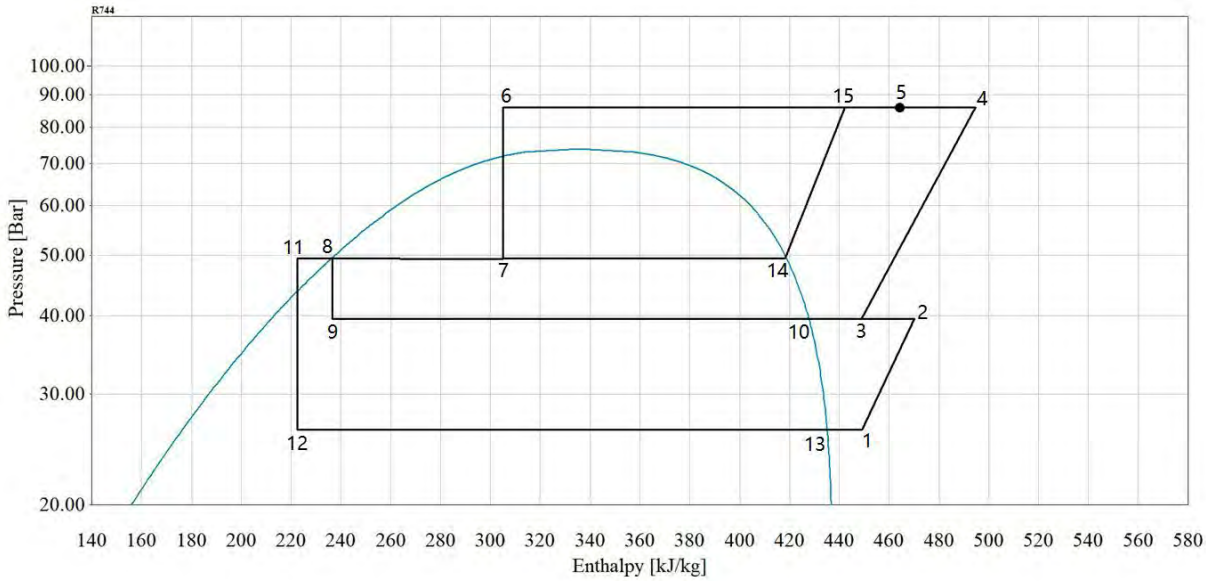

Figure 4: P-h diagram of the optimal state point

From the power consumption ratio of the three compressors, the power of the high pressure compressor is 2.64 kW, accounting for 64.7% of the total compressor power consumption. The power of the low pressure compressor and the parallel compressor is only 14.8% and 20.5% of the

total power of the compressors. It can be seen that the high pressure compressor is the main power-consuming component of the system, which provides guidance for maintenance in practical application and further optimization in the future.

Table 1. Detailed performance parameters of the optimal state point

P_h (bar)	C_1	COP	$t_{gc,in}$ (℃)	W(W)	W_{LP} (W)	W_{HP} (W)	W_{PC} (W)	M($kg \times s^{-1}$)
86	1.25	3.85	73.62	4071.6	602.58	2635.1	833.96	0.0923

4.2. Comparison of DEPC System and DE System

Compared with the conventional two-stage compression system (DE) with only one intermediate pressure, DEPC system proposed in this paper optimizes throttling pressure and adds a parallel compressor to the system, which can theoretically improve system performance. In this part, the COP values of the two systems will be compared and analyzed to reflect the superiority of DEPC system. Since P_h and C_1 are the two main variables affecting the system performance, this part analyses the COP values when P_h or C_1 changes separately. The fixed values of P_h and C_1 in this part are the values of the optimal state point, namely P_h=86 bar, C_1=1.25.

It should be pointed out that DE system does not optimize the throttling intermediate pressure. The throttling pressure is the same as the evaporation pressure of soil source. That is to say, the middle throttling coefficient C_1 = 1 of DE system all the time. Thus, when P_h is fixed, the COP of DE system is fixed. Fig. 5 (a) and 5 (b) below show the COP values of the two systems when P_h or C_1 are fixed.

As can be seen from Fig. 5 (a), the value of C_1 in DE system is constant to 1, so COP does not change with the change of C_1, and COP value is constant to 3.61. For DEPC systems, COP shows a trend of increasing first and then decreasing with the increase of C_1, and there is a maximum value. The COP value range of DEPC system is about 3.65~3.81. It can be seen that the minimum COP value of DEPC system is larger than that of DE system. As can be seen from Fig. 5 (b), the trend of COP change with P_h in the two systems is basically the same, showing a form of increasing first and then decreasing. Moreover, under different P_h values, COP of DEPC system is always larger than that of DE system, and the maximum increase is about 15%.

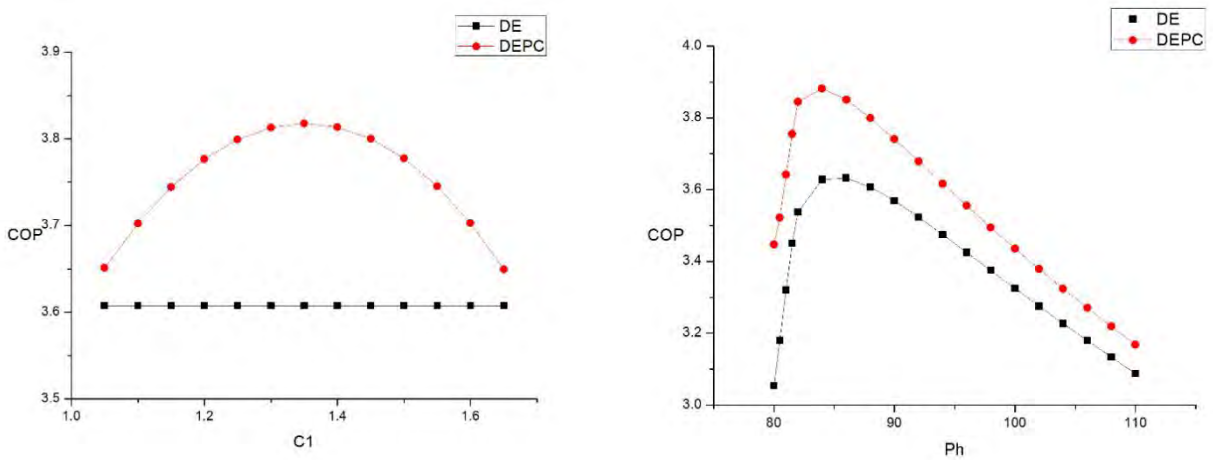

Figure 5: COP of the two systems when P_h are fixed (a) and C_1 are fixed (b)

It can be concluded that adding parallel compressor and optimizing intermediate throttling pressure in the system can effectively enhance the COP of the system. By adding a parallel compressor to the system, a part of the refrigerant can be directly compressed from the intermediate throttling pressure (P_m) to the gas cooling pressure (P_h). Although this will reduce the inlet temperature of the gas cooler to some extent, the advantage is that the compressor power consumption of DEPC

system can be significantly reduced. In addition, because the system optimizes the throttling intermediate pressure (P_m), throttle loss can be effectively reduced, and the inlet pressure of parallel compressor is also optimized. Integrating the influence of various factors, the system performance of DEPC can be significantly improved.

5. CONCLUSIONS

In this paper, a dual-source R744 two-stage parallel compression hot water heat pump system with dual-evaporator (DEPC) for commercial water heater is proposed, which improves the conventional simple two-evaporator system (DE). The system variables of P_h and C_1 are analysed, and the system is optimized by the method of iterative calculation. After that, DEPC system was compared with DE, and the superiority of the DEPC was analysed. The conclusions obtained are as follows:

(1) DEPC system can combine dual-source heat pump system with two-stage compression heat pump system, and can meet the heating demand of commercial water heaters.

(2) In MATLAB, the maximum COP can be accurately found when two variables change at the same time by using the method of iteration calculation and taking the maximum value.

(3) When P_h=86bar, C_1=1.25, the system has the maximum COP that meets the design conditions and is the optimal state point of the system. At this time, the COP value is 3.85.

(4) The performance of the optimized DEPC system is higher than that of the conventional two-stage compression system. COP can be increased by about 20%.

ACKNOWLEDGEMENTS

This work was supported by the National Natural Science Foundation of China (Grant No. 51776110) and the Fundamental Research Funds of Shandong University under the Grant No. 2017JC037.

NOMENCLATURE

C_1	intermediate pressure coefficient	*COP*	coefficient of performance
DE	dual-evaporator system	*DEPC*	dual-evaporator with parallel compression system
h	specific enthalpy ($kJ \times kg^{-1}$)	*IHX*	internal heat exchanger
M	mass flow rate ($kg \times s^{-1}$)	*P*	pressure (bar)
Q_C	gas cooler load (W)	*W*	compressor work (W)
x	vapor quality of two-phase fluid		
Greek symbols		η	compressor isentropic efficiency
Subscripts and superscripts			
1-15	state points of heat pump system	ev1	air source evaporation
ev2	soil source evaporation	gc	gas cooler
h	high pressure	HP	high pressure compressor
in	inlet	LP	low pressure compressor
m	intermediate	out	outlet
PC	parallel compressor	rec	receiver
s	isentropic process		

REFERENCES

Agrawal, N., Bhattacharyya, S., Sarkar, J., 2007. Optimization of two-stage transcritical carbon dioxide heat pump cycles. Int J Therm Sci 46, 180-187.

Bertsch, S.S., Groll, E.A., 2008. Two-stage air-source heat pump for residential heating and cooling applications in northern U.S. climates. Int. J. Refrigeration 31, 1282-1292.

Buker, Mahmut S., Riffat, S.B., 2016. Solar assisted heat pump systems for low temperature water heating applications: A systematic review. Renew Sust Energ Rev 55, 399-413.

Cavallini, A., Cecchinato, L., Corradi, M., Fornasieri, E., Zilio, C., 2005. Two-stage transcritical carbon dioxide cycle optimisation: A theoretical and experimental analysis. Int. J. Refrigeration 28, 1274-1283.

Cecchinato, L., Chiarello, M., Corradi, M., Fornasieri, E., Minetto, S., Stringari, P., Zilio, C., 2009. Thermodynamic analysis of different two-stage transcritical carbon dioxide cycles. Int. J. Refrigeration 32, 1058-1067.

Chargui, R., Sammouda, H., 2015. Numerical Simulation of a Residential House Coupled with a Dual Source Heat Pump System. International Letters of Chemistry, Physics and Astronomy 55, 150-159.

Chen, Z., Tao, W., Zhu, Y., Hu, P., 2012. Performance analysis of air-water dual source heat pump water heater with heat recovery. Science China Technological Sciences 55, 2148-2156.

Gullo, P., Elmegaard, B., Cortella, G., 2016. Energy and environmental performance assessment of R744 booster supermarket refrigeration systems operating in warm climates. Int. J. Refrigeration 64, 61-79.

Gullo, P., Hafner, A., Banasiak, K., 2018. Transcritical R744 refrigeration systems for supermarket applications: Current status and future perspectives. Int. J. Refrigeration 93, 269-310.

Kim, M., 2004. Fundamental process and system design issues in CO_2 vapor compression systems. Prog Energ Combust 30, 119-174.

Kwon, O., Cha, D., Park, C., 2013. Performance evaluation of a two-stage compression heat pump system for district heating using waste energy. Energy 57, 375-381.

Lazzarin, R.M., 2012. Dual source heat pump systems: Operation and performance. Energ Buildings 52, 77-85.

Liao, S.M., Zhao, T.S., Jakobsen, A., 2000. A correlation of optimal heat rejection pressures in transcritical carbon dioxide cycles. Appl Therm Eng 20, 831-841.

Lorentzen, G., 1994. Revival of carbon dioxide as a refrigerant. International Journal of Refrigeration 17, 292-301.

Ma, Y., Liu, Z., Tian, H., 2013. A review of transcritical carbon dioxide heat pump and refrigeration cycles. Energy 55, 156-172.

Mancini, F., Minetto, S., Fornasieri, E., 2011. Thermodynamic analysis and experimental investigation of a CO_2 household heat pump dryer. Int. J. Refrigeration 34, 851-858.

Nawaz, K., Shen, B., Elatar, A., Baxter, V., Abdelaziz, O., 2018. Performance optimization of CO_2 heat pump water heater. Int. J. Refrigeration 85, 213-228.

Nekså, P., 2002. CO_2 heat pump systems. Int. J. Refrigeration 25, 421-427.

Pitarch, M., Navarro-Peris, E., Gonzalvez, J., Corberan, J.M., 2016. Analysis and optimisation of different two-stage transcritical carbon dioxide cycles for heating applications. Int. J. Refrigeration 70, 235-242.

Shuxue, X., Guoyuan, M., 2014. Experimental study on two-stage compression refrigeration/heat pump system with dual-cylinder rolling piston compressor. Appl Therm Eng 62, 803-808.

Wang, H., Liu, X., Feng, G., Kang, Z., Luo, Y., Bai, B., Chi, L., 2015b. Simulation and Analysis of Air-Ground Dual source Heat Pump Operating Efficiency. Procedia Engineering 121, 1413-1419.

White, S.D., Yarrall, M.G., Cleland, D.J., Hedley, R.A., 2002. Modelling the performance of

a transcritical CO_2 heat pump for high temperature heating. Int. J. Refrigeration 25, 479-486.

Manuscript ID: 832
DOI: 10.18462/iir.icr.2019.0832

Decarbonization of industrial processes with heat pumps

Veronika WILK[(a)], Michael LAUERMANN[(a)], Franz HELMINGER[(a)]

[(a)] AIT Austrian Institute of Technology GmbH
Vienna, 1210, Austria,
veronika.wilk@ait.ac.at, michael.lauermann@ait.ac.at, franz.helminger@ait.ac.at

ABSTRACT

To counteract climate change the efficient use of energy in industry becomes increasingly important. Heat pumps enable decarbonized industrial processes by replacing fossil fuels with electricity. DryFiciency develops and demonstrates high temperature heat pumps using OpteonMZ as refrigerant to supply hot water up to 160°C. Heat pumps will be installed in drying processes for starch and bricks in two Austrian companies in spring 2019. We present design considerations for high temperature heat pumps, as well as the expected CO_2 reductions and primary energy savings. Calculations are based on numerical process simulation. At the two demo-sites CO_2 emission reductions up to 40-90% and primary energy reduction from 20-80% can be achieved compared to natural gas. If the heat pump technology is spread out to 50% of all drying processes in the EU, they would contribute 3-7% of the CO_2 emission reduction necessary to achieve the EU climate targets. Heat pumps improve the energy efficiency of industrial processes significantly. The demonstrators are an important step in the development of viable industrial solutions.
Keywords: CO_2 Emission, Design, Drying, Energy Efficiency, R1336mzz(Z), Simulation.

1. INTRODUCTION

Recently, the International Panel on Climate Change published a special report pointing out the importance to drastically reduce the CO_2 emissions to stabilize global warming at 1.5°C. This implies changes in behaviour and lifestyle worldwide. Concerning the impact of industry, pathways limiting global warming to 1.5°C project CO_2 emissions from industry to be about 65–90% lower in 2050 relative to 2010. Such large reductions require substantial efforts and combinations of new and existing technologies and practices, including increasing energy and process efficiency, electrification, hydrogen, sustainable bio-based feedstocks, product substitution, and carbon capture, utilization and storage (IPCC 2018). Almost nine out of ten of all national contributions submitted to the 2015 climate summit in Paris mention energy efficiency (IEA 2016). The European Union (EU) set itself the target of reducing greenhouse gas emission by 40% below 1990 level, increasing energy efficiency by 32.5% and raising the share of renewable energy to 32% of total energy consumption by 2030 (European Parliament 2018a, European Parliament 2018b).
Heat pumps for industrial applications can make an important contribution to increasing the efficiency of industrial processes and reducing CO_2 emissions and enable decarbonized industrial processes by replacing fossil fuels with electricity. In this paper, the CO_2 emission and primary reduction potential of high temperature heat pumps for industry is presented based on the development of two prototypes for drying processes.

2. HIGH TEMPERATURE HEAT PUMPS FOR DRYING

The focus of the H2020 project DryFiciency is the development and demonstration of high temperature heat pumps for industrial drying and dehydration processes. The heat pumps use industrial waste heat as the heat source and supply hot water up to 160°C. Two heat pumps prototypes will be installed in drying processes for starch and brick in the first quarter of 2019.
The heat pumps are designed as closed compression heat pumps with a heating capacity of around 400 kW. R-1336-mzz(Z) is used as refrigerant, that was already successfully been tested at AIT in a lab-scale heat pump prototype (Fleckl et al. 2015). It is marketed by Chemours under the trade name OpteonMZ and is a synthetic refrigerant based on HFO (hydrofluoro-olefin) developed for high-

temperature applications up to 160°C. It has a low GWP value of 2 (Global Warming Potential). Two different kinds of compressors are used for the heat pump prototypes, screw and piston compressors. Fuchs Schmierstoffe GmbH develops a suitable lubricant for both compressors, which fulfils all necessary requirements with regard to lubrication and viscosity. Furthermore the challenge is to find a lubricant which is chemically and thermally stable at high temperatures with the refrigerant. Bitzer Kühlmaschinen GmbH adapted their HS screw compressor for high temperature applications. The HS screws are suitable for multiple refrigerants, such as R134a, R404A, R507A, R407C and R22 and others. Most commonly, the compressors are used in refrigeration plants and heat pumps with evaporation temperatures from -50 to 12°C and condensation temperatures in the range of 45 to 70°C. The maximum suction gas temperature is 30°C and the maximum discharge gas temperature amounts to 100°C. The adapted version of the HS compressor can be applied for suction gas temperatures up to 100°C and discharge temperature of 160°C. It has a swept volume of 300 m³/h at 60 Hz. Two screw compressors are used to supply about 400 kW of process heat. The piston compressors integrated in the second demonstrator are developed and supplied by Viking Heat Engines AS. The compressor design is based on an ORC (Organic Rankine Cycle) expander used for heat recovery applications with an overall design temperature of 215°C. The expander has already been extensively tested at high temperatures and achieves high efficiencies. The compressor designed is 90% the same as the ORC and built on the same piston bottom-end, only the cylinder head is different. Over the past five years, the piston expander has undergone a comprehensive development program to achieve a long service life and high durability at very high temperatures. Today, this piston machine technology is equally capable of operating in organic Rankine cycles (ORCs) as well as vapour compression heat pump systems. The compressor is designed for use with OpteonMZ, but have also been used with commonly applied HFC e.g. R135a, R245fa and several HFO e.g. R1336mzz-E, R1234ze, R1233zd. One piston compressor has a swept volume of 55 m³/h at 60 Hz. A total of eight compressors arranged in two modules of four are used to supply 400 kW of process heat.

Drying processes are among the most important process steps in the food industry, pulp and paper and chemical industry and require intensive use of energy. Estimates show that 12-25% of the national industrial energy consumption in developed countries is attributable to industrial drying (Mujumdar (2006), Kemp (2012), Minea (2011)). Currently, most of this energy is supplied by fossil fuels with no or only limited recovery of waste heat streams. The energy saving opportunities by the use of more efficient low grade waste heat recovery technologies was estimated to 12% savings for the chemical industry and 4% for petroleum refineries in energy consumption by 2030 according to Chan and Kantamaneni (2015). Hence, there is a great potential for more efficient and environment-friendly technologies for industrial drying processes. In the following, the starch drying process and the drying of bricks in which the high temperature heat pumps will be integrated are described in more detail.

2.1. Starch Drying

Agrana Starch GmbH operates many dryers in its 54 sugar and starch factories for product and by-product drying. In Pischelsdorf in Austria, at their integrated bioethanol and wheat starch production site, the starch dryer will be equipped with a high temperature heat pump. The starch drying process is a continuous process with an entrained flow dryer. Drying air is preheated in a water-air heat exchanger using heat from a heat recovery cycle, which is fed from other drying processes. In the original set up without heat pump, the drying air is heated to around 160°C in a second heat exchanger with steam. Steam is provided in a natural gas-fired power plant. Figure 1 shows the integration of the heat pump. After preheating the drying air, the heat recovery circuit is also used as the source for the evaporator of the heat pump system. The inlet temperature is about 70°C. In the condenser heat is transferred to the drying air via an intermediate water circuit and a water-air heat exchanger. The heat supply temperature of the heat pump is up to 160°C. With the heat pump, the use of steam in the third heat exchanger can be reduced or completely eliminated depending on the selected heat supply temperature of the heat pump. Thereby, the heat recovery cycle can be used to a larger extent and the use of natural gas is reduced.

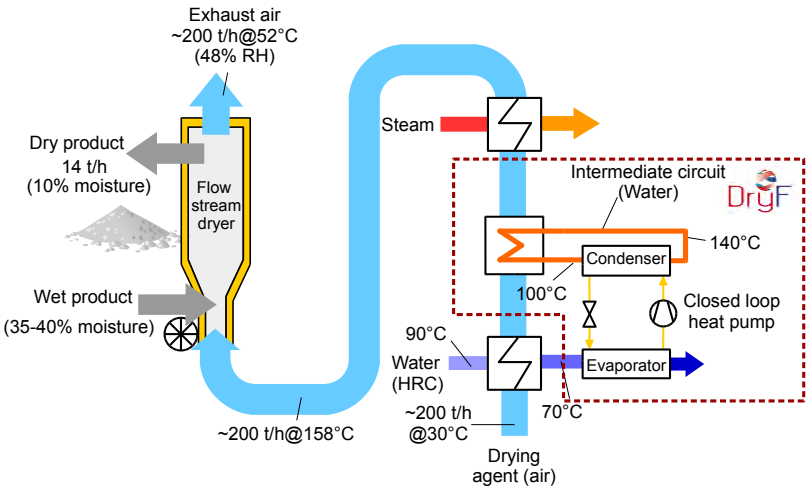

Figure 1: Starch drying process with high temperature heat pump

2.2. Brick Drying

Wienerberger AG, the world's largest brick producer, operates about 200 brick dryers. In the brick factory in Uttendorf in Austria, a high temperature heat pump will be integrated to supply heat for the drying process. In brick production, the bricks are first formed, dried and then fired. The drying process takes place in a continuous tunnel dryer shown in Figure 2. Air is used as the drying agent, which moves in a counter-current flow through the dryer. The bricks enter the dryer with 28% moisture and are dried to 2%. The drying air in the tunnel is heated by internal heat exchanger surfaces, which are supplied with 90°C hot water provided by a heat recovery circuit. The heat pump also uses this circuit as the heat source, the evaporator is placed in front of the heat exchangers. The heat pump supplies hot air via an intermediate water circuit, where heat supply temperatures of up to 160°C can be achieved. The hot air is fed into the outlet zone of the tunnel dryer, where the highest temperatures are required for drying.

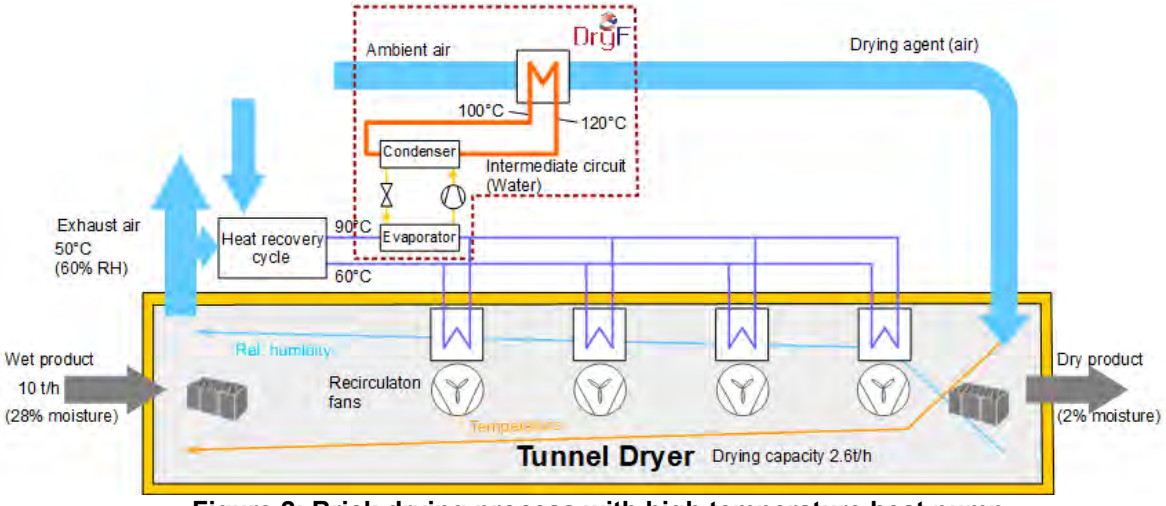

Figure 2: Brick drying process with high temperature heat pump

3. METHODOLOGY

3.1. Numerical Simulation of Heat Pump and Drying Process

A simulation model of two heat pump demo plants was created in the simulation package Dymola/Modelica. For the thermal modelling of the heat pump components the TIL library was used, which is widely used in refrigeration (Richter, 2008).

The modelling of the screw compressor and the piston compressor was based on measured data with an efficiency-based approach. The compressor is described by the isentropic and volumetric efficiency, which are a function of the pressure ratio and the condensation or evaporation temperature. The isentropic efficiency is based on the ideal isentropic compression and also considers the suction and pressure side pressure losses, internal leakage, re-expansion of the compressed fluid and mechanical friction. The volumetric efficiency describes the ratio between the geometrically possible mass flow and the actual mass flow through the compressor. For the screw compressor no measurement curves with R-1336mzz(Z) are available yet, therefore measurement data with R134a have been used, since both refrigerants have a similar isentropic exponent. For the description of the piston compressor, measurement data from Viking Heat Engines AG with R-1336mzz(Z) for volumetric and isentropic efficiency are available and were implemented in the model. The heat exchangers are modelled using the Number of Transfer Units method (NTU) and the pinch point as an input parameter enabling a reliable and robust calculation of the exchanged heat.

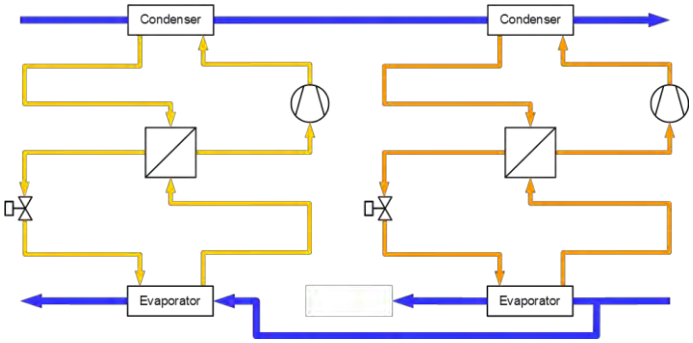

Figure 3: Schematic view of a twin cycle heat pump with parallel source

Figure 3 shows the configuration of the heat pump. It is a twin cycle set up, where each compressor module is located in a single refrigerant cycle. The condensers are arranged in series, the evaporators in parallel. Thus, the temperature lift is reduced somewhat for one of the two cycles and about one half of the heating capacity is provided at a higher COP. The twin cycle layout is also beneficial in terms of safety, start up procedure and official permits because of the smaller amount of refrigerant in the cycles. One cycle is equipped with a single Bitzer compressor or four Viking Heat Engines compressors. Due to the thermodynamic properties of the refrigerant, an internal suction gas heat exchanger is used to ensure dry compression.
The following boundary conditions were applied for the simulation based on the two heat pump demo plants: The source inlet temperature is 70°C for the Agrana heat pump, two screw compressors with the Bitzer characteristic and a constant speed of 60 Hz were used in this simulation. For the Wienerberger heat pump, the inlet temperature of the heat source is 90°C, eight piston compressors with the Viking Heat Engines characteristic and a constant speed of 60 Hz were used. For both demo plants, the condenser outlet temperatures were varied (110, 120, 140, 160°C). The spread at the condenser is set to 40 K. The pinch of the heat exchangers (evaporator and condenser) was assumed to be constant at 3 K. The suction gas superheat in the evaporator is 5 K, the hot gas superheat is 10 K.

3.2. CO_2 emission and primary energy calculation

Potential reduction in CO_2 emissions and primary energy consumption are calculated by comparing the original process to the process with the heat pump. In the original process at Agrana, heat is supplied by steam boilers fired by natural gas. At Wienerberger, a natural gas burner is used to heat the drying air. With the use of the heat pump, natural gas consumption is reduced but electricity is needed for the compressor. The CO_2 emission factor relates the amount of CO_2 emitted into the atmosphere to the end energy available as process heat. In case of the CO_2 equivalent, also other greenhouse gases such as methane are considered. According to GEMIS 2013, the CO_2 equivalent factor is 7-10% higher than the CO_2 factor for CO_2 emissions only. The primary energy factor shows how much energy is needed for extraction, processing, storage, transport, conversion, transmission, and distribution to provide end energy. The primary energy factor can be split in the renewable primary energy factor and the non-renewable factor. Here the total primary energy factor is used.

CO_2 emissions and primary energy consumption for electricity mainly depend on the energy carriers used for electricity generation. In Table 1, the CO_2 factors and in Table 2 the primary energy factors are compiled that are used for this calculation. They differ in their regional scope and reference year. If the reference year was not indicated in the publication, the publication year was given and marked with "p". The CO_2 factor for natural gas is in the range of 236 to 290 g/kWh, values calculated for Austria are slightly lower than those for EU. The CO_2 factor for electricity in Austria is 248 – 300 g/kWh. Austrian electricity production is mainly based on hydropower (60% in 2017), wind and photovoltaics amount to about 10%. Therefore the CO_2 emissions are lower than those for electricity generation in the EU. The primary energy factors show similar dependencies. Fritsche and Greß (2015) assessed that the EU-28 electricity primary energy factor was rather stable in the years 2010-2013 and was dominated by the non-renewable primary energy use. Recently the European Parliament amended the primary energy factor to be used for the calculation of the energy efficiency targets to 2.1 kWh/kWh for electricity (European Parliament, 2018c).

Table 1. CO_2 emission factors for natural gas and electricity

CO_2 emissions		Natural gas			Electricity		
data set	g/kWh	factor	source	year	factor	source	year
Austria 2011	CO_{2eq}	249	GEMIS 2013	2011	300	GEMIS 2013	2011
Austria 2015	CO_2	236	OIB 2015	2015 p	276	OIB 2015	2015 p
Austria 2018	CO_{2eq}	271	Umweltbundes-amt 2018	2018	248	Umweltbundes-amt 2018	2018
EU 2014	CO_2	277	EN15603	2008 p	363	EControl 2014	2014 p
EU 2018	CO_{2eq}	290	EN ISO 52000	2018 p	420	ENISO 52000	2018 p

Table 2. Primary energy factors for natural gas and electricity

Primary energy		Natural gas			Electricity		
data set		factor	source	year	factor	source	year
Austria 2011	kWh/kWh	1.18	GEMIS 2013	2011	1.79	GEMIS 2013	2011
Austria 2015	kWh/kWh	1.17	OIB 2015	2015 p	1.91	OIB 2015	2015 p
EU 2013	kWh/kWh	1.36	Fritsche and Greß 2015	2010	2.46	Fritsche and Greß 2015	2013
EU 2018	kWh/kWh	1.1	EN ISO 52000	2018 p	2.1	European Parliament 2018c	2018 p

Relative savings Δx in CO_2 emissions and primary energy are calculated according equation 1 using the respective factors for natural gas (g) and electricity (el). η_{ref} is the efficiency of the fossil energy supply system used for the calculation (Agrana = 0.93, Wienerberger 0.9), the COP is the coefficient of performance of the heat pump (ratio of supplied heat and electricity).

$$\Delta x = \frac{\eta_{ref}}{f_g}\left(\frac{f_g}{\eta_{ref}} - \frac{f_{el}}{COP}\right) \qquad \text{Eq. (1)}$$

4. RESULTS

4.1. Reductions on Prototype level

Figure 4 show the results on prototype level. Heat pump assisted drying allows for substantial CO_2 emission and primary energy reductions for all kinds of factors that were discussed in chapter 3. In the brick drying process, the reductions are higher, because the temperature of the heat source is 90°C compared to 70°C for starch drying. All reductions are strongly dependant on the heat supply temperature that was varied between 110 and 160°C because the prototypes will be operated in a broad range of operation conditions. For the highest heat supply temperatures the most electricity is required resulting in lower reductions. The results are calculated with the isentropic efficiency curves that are expected for the prototypes. The maximum isentropic efficiency for the Bitzer compressor is reached at the pressure ratio of 3 corresponding to a heat supply temperature of 110°C. The maximum for the Viking compressors is reached at a heat supply temperature of 140°C (pressure ratio of 6). In other operation conditions the efficiency is lower. For high temperature heat pumps that should be operated in a specific operation point e.g. a heat supply temperature of 160°C, both

types of compressors can be adjusted to have the highest efficiency at the required pressure ratio of the application (screw compressor: geometry and location of the discharge port, piston compressor: valves and dead volume adjustment). Therefore it can be assumed that even higher emission reductions can be achieved.

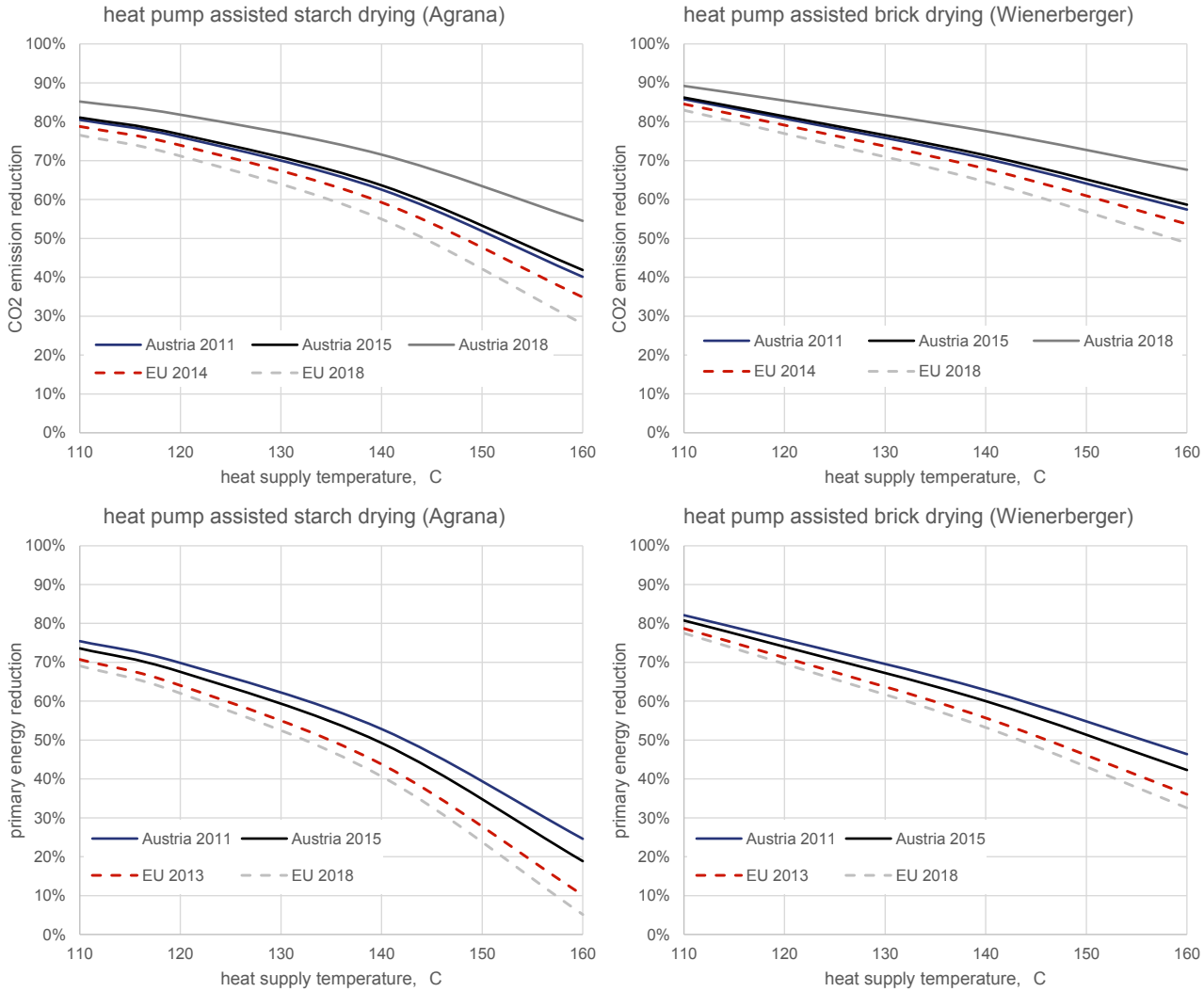

Figure 4: CO_2 and primary energy reduction on prototype level

4.2. Reductions on EU level

In the following, the savings of the prototypes are extrapolated to their potential contribution to the EU climate goals, if heat pumps for drying are wide spread in industry. As mentioned before, drying accounts for 10-25% of the total industrial energy use in most developed countries (Mujumdar (2006), Kemp (2012), Minea (2011)). In 2015, 12630 TWh/a of final energy were consumed in EU28 (Eurostat 2018a). The share of industry amounts to 25% or 3211 TWh in 2015. If drying consumes 10% of the total industrial energy use, it results in 321 TWh. If the share is 25%, drying consumes 803 TWh in the EU28. 10% and 25% are used to describe the range of potential.
It is assumed that 50% of all drying processes can be equipped with a heat pump similar to the heat pump prototypes developed in DryFiciency. The heat pumps for this consideration provide process heat and have an average COP of 3. This is the calculated value for the Agrana demonstrator at a heat source temperature of 70°C and a heat supply temperature of 140°C. This heat pump can be used for all kinds of applications requiring a similar lift, the heat supply temperature itself can be higher or lower resulting in the same COP. The heat pump replaces natural gas burners with an assumed efficiency of 95% and provide 161-401 TWh of process heat. Thus, heat pump assisted drying processes would consume 54-134 TWh of electricity, converting 107-268 TWh of waste heat into usable process heat.

Energy efficiency: The aim to increase energy efficiency is measured by the final energy and primary energy consumption in 2030, which should be as low as 956 Mtoe of final energy and 1273 Mtoe primary energy (European Parliament 2018b). Based on the final energy consumption 2015, 130 Mtoe (1512 TWh) of final energy have to be reduced by 2030 (Eurostat 2018a). The heat pump assisted drying processes allow for 107-268 TWh of energy consumption reduction, which corresponds to a contribution of 7-18% to the climate target. For the calculation the EU2018 dataset in Table 2 was used. In 2015, 17933 TWh primary energy were consumed, resulting in 269 Mtoe (3128 TWh) of primary energy reduction until 2030 (Eurostat 2018b). The heat pump assisted drying processes would reduce the primary energy consumption by 74-184 TWh, which is a contribution of 2-6% to this target.
CO_2 emissions: The EU target aims to reduce the CO_{2eq} emissions to 40% below the level of emissions in 1990 (European Parliament 2018a). In 2030, 3444 million t CO_{2eq} can be emitted. In 2015, 4461 million t CO_{2eq} were emitted resulting in 1017 million t CO_{2eq} that have to be reduced to reach the climate target. The manufacturing sector (NACE C) including manufacturing of food and other products where drying is a common process, emitted 843 million t CO_{2eq} in 2015, which is 19% of all CO_2 emissions (Eurostat 2018c). It is assumed the share of emissions among the sectors remains constant until 2030, therefore 19% of the emission reduction has to be contributed by the manufacturing sector, which are 192 million t CO_{2eq}. For the calculation the EU2018 dataset in Table 1 was used. With 50% of heat pump assisted dryers, the emissions would be reduced by 27-66 million t CO_{2eq}/a. The heat pump assisted drying processes contribute 14-35% to this target for the manufacturing sector or 3-7% of the total emission reduction that has to be achieved until 2030.

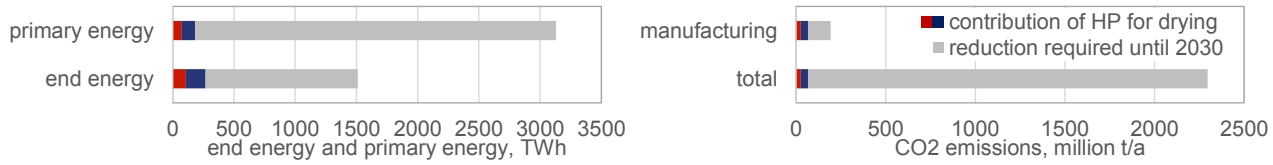

Figure 5: Contribution to EU climate targets

5. CONCLUSION

Heat pumps improve the energy efficiency of industrial processes significantly. At the two demo-sites of the DryFiciency project, CO_2 emission reductions up to 40-90% and primary energy reduction from 20-80% are expected for the drying processes compared to natural gas. If the heat pump technology is spread out to 50% of all drying processes in the EU, they would contribute 3-7% of the CO_2 emission reduction necessary to achieve the EU climate targets. The demonstrators are an important step in the development of viable industrial solutions. The heat pumps will be installed in drying processes for starch and bricks in two Austrian companies in spring 2019 and will be monitored and optimized for about one year. The high temperature heat pump solution can be multiplied not only for drying processes, but for all kinds of applications requiring hot media up to 160°C, such as the food industry (brewing, dairy, sugar, etc.), pulp and paper and the chemical industry (boiling processes, distillation, etc.).

ACKNOWLEDGEMENTS

The project has received funding from the European Union's Horizon 2020 programme for energy efficiency and innovation action under grant agreement No. 723576.

REFERENCES

Chan, Y. and Kantamaneni, R, 2015. Study on Energy Efficiency and Energy Saving Potential in Industry and on Possible Policy Mechanisms. https://ec.europa.eu/energy/en/studies/study-energy-efficiency-and-energy-saving-potential-industry-and-possible-policy-mechanisms

EN15603. Energy performance of buildings - Overall energy use and definition of energy ratings Edition: 2008-07-01.

EN ISO 52000. Energy performance of buildings - Overarching EPB assessment - Part 1: General framework and procedures (ISO 52000-1:2017), Edition: 2018-02-01

EControl, 2014. Energie-Control Austria (2014) Stromkennzeichnungsbericht. https://www.e-control.at/documents/20903/-/-/206f7f9f-f3a9-42f0-a874-4403a6d153a2 (access 2019-01-21)

European Parliament, 2018a, Directive (EU) 2018/2001 of the European Parliament and of the council of 11 December 2018 on the promotion of the use of energy from renewable sources (Text with EEA relevance.) PE/48/2018/REV/1, OJ L 328, 21.12.2018, p. 82–209

European Parliament, 2018b, Directive (EU) 2018/2002 of the European Parliament and of the Council of 11 December 2018 amending Directive 2012/27/EU on energy efficiency (Text with EEA relevance.) PE/54/2018/REV/1, OJ L 328, 21.12.2018, p. 210–230

European Parliament, 2018c, Position of the European Parliament, 13 November 2018, first reading 2016/0376(COD) adopted at first reading on 13 November 2018 with a view to the adoption of Directive (EU) 2018/… of the European Parliament and of the Council amending Directive 2012/27/EU on energy efficiency (EP-PE_TC1-COD(2016)0376).

Eurostat, 2018a. Simplified energy balances - annual data [nrg_100a] (access 2018-12-11)

Eurostat, 2018b. Primary Energy consumption [t2020_33], (access 2018-12-11)

Eurostat, 2018c. Greenhouse gas emission statistics – air emission accounts, Statistics explained, Date extracted in May 2018. https://ec.europa.eu/eurostat/statistics-explained/index.php/Greenhouse_gas_emission_statistics_-_air_emissions_accounts (access 2019-01-21)

Fleckl, T., Hartl, M., Helminger, F., Kontomaris, K. and Pfaffl, J., 2015. Performance testing of a lab-scale high temperature heat pump with HFO-1336mzz-Z as the working fluid. In European Heat Pump Summit 2015, Nuremberg, Germany, October 20-21

Fritsche, U. and Greß, HW., 2015. Development of the Primary Energy Factor of Electricity Generation in the EU-28 from 2010-2013 prepared for the European Heat Pump Association (EHPA), IINAS International Institute for Sustainability Analysis and Strategy.

GEMIS, 2013. Globales Emissions-Modell integrierter Systeme, Version Gemis-Österreich 4.81, Gas-Kessel-A-Konversionsfaktoren, El-KW-Park-A+Importe-2011, June 2013.

IEA, 2016. World Energy Outlook 2016 Special Report: Energy and Air Pollution, 266 pp.

IPCC, 2018: V. Masson-Delmotte et al. (eds.). Summary for Policymakers. In: Global warming of 1.5°C. An IPCC Special Report on the impacts of global warming of 1.5°C above pre-industrial levels and related global greenhouse gas emission pathways, in the context of strengthening the global response to the threat of climate change, sustainable development, and efforts to eradicate poverty. World Meteorological Organization, Geneva, Switzerland, 32 pp.

Kemp, I.C. 2012. Fundamentals of Energy Analysis of Dryers. In: Modern Drying Technology Volume 4: Energy Savings, First Edition. Tsotsas E. and Mujumdar A.S. (Edt.), Wiley-VCH.

Minea, V. 2011. Industrial Drying Heat Pumps. In: Larsen, M. E. (Edt.) Refrigeration. Theory, technology, and applications. Mechanical engineering theory and applications. New York: Nova Science Publishers 2011

Mujumdar, A.S. 2006. Principles, Classification, and Selection of Dryers. In: Mujumdar, A. S. (Edt.): Handbook of industrial drying. Boca Raton, FL: CRC 2007

OIB, 2015. Österreichisches Institut für Bautechnik, Richtlinie 6, Edition March 2015.

Richter, C. 2008. Proposal of New Object-Oriented Equation-Based Model Libraries for Thermodynamic Systems. PhD Thesis, Technische Universität Carolo-Wilhelmina, Braunschweig.

Umweltbundesamt, 2018. Online calculator for CO2 emissions in Austria, http://www5.umweltbundesamt.at/emas/co2mon/co2mon.html (access 2019-01-21).

Manuscript ID: 884
DOI: 10.18462/iir.icr.2019.0884

Application of R1224yd(Z) as R245fa alternative for high temperature heat pump

Takenobu KAIDA[(a)], Masato FUKUSHIMA[(b)], Koichiro IIZUKA[(c)]

[(a)] Central Research Institute of Electric Power Industry (CRIEPI)
Yokosuka, 240-0196, Japan, kaida@criepi.denken.or.jp
[(b)] AGC Inc., Ichihara, 290-8566, Japan
[(c)] Kobe Steel, Ltd., Kako, 675-0155, Japan

ABSTRACT

This paper discusses the suitability of R1224yd(Z) as R245fa alternative for high temperature heat pump. A drop-in test was performed when R245fa was replaced with R1224yd(Z) in a commercialized high temperature heat pump for industrial use. The test was performed by just replacing the refrigerant without changing any other components. In addition, the compatibility data with refrigeration oil, O-ring and motor insulation were obtained. The drop-in test result indicates better performance than the predicted thermodynamic simulation. As for the compatibility with refrigeration oil, O-ring and motor insulation, there were no significant differences between R1224yd(Z) and R245fa. Overall, R1224yd(Z) can be used as R245fa alternative for high temperature heat pump because of its good thermodynamic and environmental properties.

Keywords: Drop-in, HFO, High Temperature, Industrial Application, Performance.

1. INTRODUCTION

Heat pumps are among the key technologies for primary energy saving and greenhouse gas reduction. They are presently used mainly on air-conditioning and hot water heater in residential and commercial sectors, and then are expected to spread to industrial heating processes. For expanding the heat pump application range, some high temperature heat pumps with supply temperatures more than 100°C have been commercialized and are expected to become increasingly developed in the coming years.

Many of the commercialized high temperature heat pumps are used R245fa as the refrigerant (Arpagaus et al., 2018). However, R245fa has a high Global Warming Potential (GWP) of 858 and will be phased down in the foreseeable future. As the alternative refrigerant with lower GWP, R1224yd(Z) have been developed (Fukushima, 2015).

This paper discusses the suitability of R1224yd(Z) as R245fa alternative for high temperature heat pump. A drop-in test was performed when R245fa was replaced with R1224yd(Z) in a commercialized high temperature heat pump for industrial use. In addition, the compatibility data with refrigeration oil, O-ring and motor insulation were obtained.

2. CHARACTERISTICS OF R1224YD(Z)

2.1. Physical Properties

The physical properties of R1224yd(Z) is shown in Table 1 compared to R245fa. The normal boiling point and critical temperature of R1224yd(Z) are very close to the R245fa values, which implies that the thermodynamic performances would be similar. R1224yd(Z) is classified as A1 in ASHRAE Standard 34 safety group classification, which indicates low-toxicity and non-flammability. Ozone Depletion Potential (ODP) is 0.00023 and Global Warming Potential (GWP) is only 0.88 (Tokuhashi et al., 2018), which indicates that R1224yd(Z) is environmental-friendly refrigerant.

Table 1: Physical properties of R1224yd(Z) and R245fa

	R1224yd(Z)	R245fa
Molecular Formula	$CF_3CF=CHCl$	$CHF_2CH_2CF_3$
Molar mass [g/mol]	148.49	134.05
Normal Boiling Point [°C]	14.62	15.05
Critical Temperature [°C]	155.54	153.86
Critical Pressure [MPa]	3.34	3.65
OEL [ppm]	1,000	300
Flammability Range [%]	None	None
ASHRAE Safety Classification	A1	B1
ODP	0.00023	0
GWP (AR5)	0.88	858

Figure 1 (a) compares the saturated vapor pressure of R1224yd(Z) to R245fa. The saturated vapor pressure of R1224yd(Z) is very close to the R245fa value at low temperature region but becomes somewhat lower at higher temperature. This implies that the use of R1224yd(Z) in high temperature heat pump at a given operating temperatures would enable lower pressure ratio operation.

Figure 1 (b) and (c) show the comparisons of pressure-enthalpy diagram and temperature-entropy diagram, respectively. R1224yd(Z) latent heat are smaller than the R245fa value. Similarly to R245fa, R1224yd(Z) shows a saturated vapor line with a positive slope ($dT/ds > 0$, except near the critical point). In the case of ideal compression, namely isentropic process, discharge superheat would be smaller than suction superheat. As a result, for preventing wet fluid compression and compressor damage, high temperature heat pump cycle with R1224yd(Z) would require sufficient superheat at the compressor inlet to ensure dry compression.

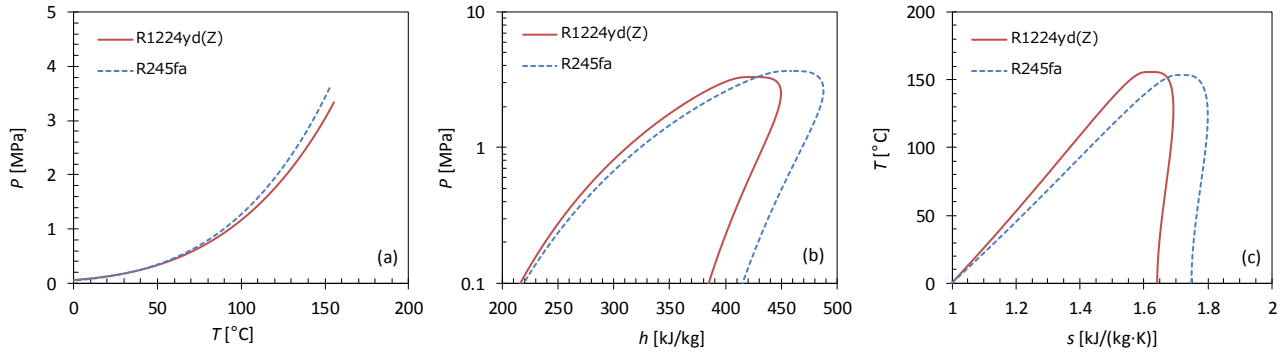

Figure 1: Comparison of (a) P-T, (b) P-h, (c) T-s diagrams

2.2. Predicted Thermodynamic Performance

The theoretical refrigerant cycle of R1224yd(Z) was calculated compared to R245fa refer to REFPROP program (Lemmon et al., 2018). The prediction was performed for simple heat pump cycle under the following conditions; condenser saturation temperature T_{cnd} = 120°C, evaporator saturation temperature T_{evp} = 60°C, discharge superheat $\Delta T_{sh,d}$ = 15 K, subcooling ΔT_{sc} = 10 K, compressor adiabatic efficiency η_{ad} = 0.8. This indicates that it is assumed that compressor, condenser and evaporator have the same performance between R1224yd(Z) and R245fa.

Table 2 and Figure 2 show the results. The coefficient of performance for heating, *COP*, with R1224yd(Z) would be similar to with R245fa. However, the volumetric heating capacity, *VHC*, with R1224yd(Z) would be 8% lower than with R245fa.

Table 2: Predicted thermodynamic performance of theoretical heat pump cycle
(T_{cnd} = 120°C, T_{evp} = 60°C, $\Delta T_{sh,d}$ = 15 K, ΔT_{sc} = 10 K, η_{ad} = 0.8)

	R1224yd(Z)	R245fa
Suction Pressure P_s [MPa]	0.44	0.46
Discharge Pressure P_d [MPa]	1.75	1.93
Pressure Ratio P_d/P_s[-]	3.97	4.17
Coefficient of Performance for Heating *COP* [-]	4.38	4.36
Volmetric Heating Capacity *VHC* [MJ/m^3]	3.21	3.49

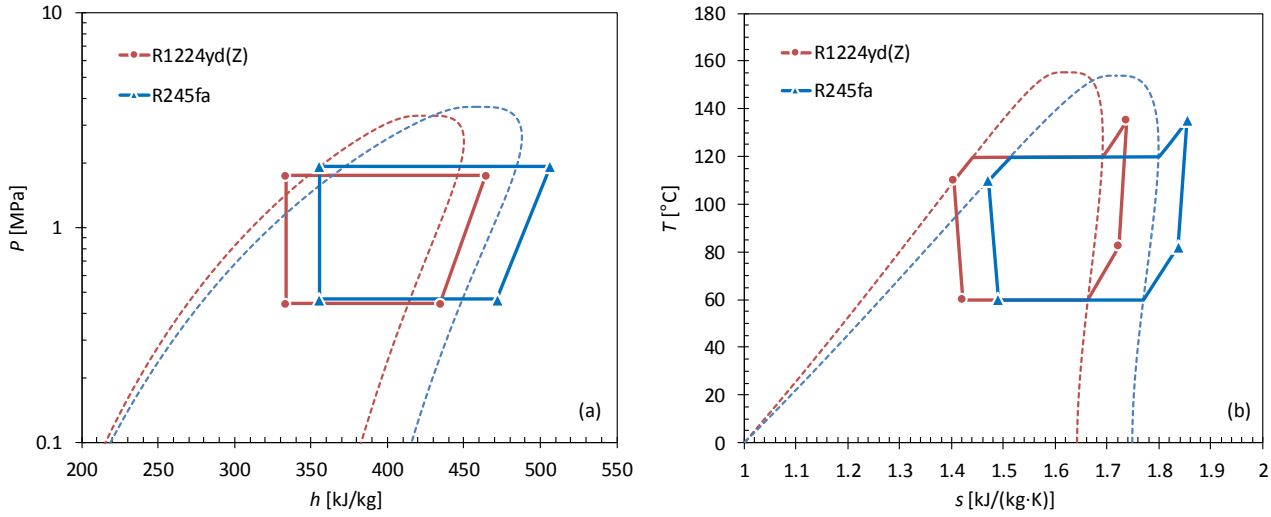

Figure 2: Comparison of (a) P-h, (b) T-s diagrams in predicted thermodynamic performance

3. PERFORMANCE EVALUATION

For surveying the actual performance including compressor, condenser and evaporator performances, a drop-in test was performed when R245fa was replaced with R1224yd(Z) in a commercialized high temperature heat pump for industrial use.

3.1. Test Method

A commercialized high temperature heat pump, HEM-HR115, which is the heat pump unit of SGH165, was used for the drop-in test. Originally, a mixture of R245fa and R134a was used as the refrigerant for HEM-HR115 (Iizuka and Maeda, 2011). In order to simply compare R1224yd(Z) to R245fa, the experimental tests were performed with pure R245fa and pure R1224yd(Z).

The test was performed with the HEM-HR115 installed at the large capacity heat pump evaluating apparatus in Central Research Institute of Electric Power Industry (Kaida et al., 2015). The apparatus can control the heat source water temperature from 10 to 90°C, simulating warm water effluents over a wide temperature range. The apparatus also can control the heat sink water or steam temperature up to 200°C.

Figure 3 shows the schematic cycle diagram of the test equipment, which is composed of a single-stage twin-screw compressor, a condenser, an evaporator, an internal heat exchanger, an economizer, a main expansion valve and an economizer expansion valve. All heat exchangers are plate type and two expansion valves are electronic automatic type. The same refrigerant weight of 140 kg was charged. Each of the inlet-outlet water temperatures, T_{c1}, T_{c2}, T_{h1}, T_{h2}, each of the water flow rates, V_c, V_h, and the power consumption, W were measured for evaluating the heating capacity, Q_h, and coefficient of performance, COP_h. The refrigerant pressures, P_s, P_d, P_{eco}, and the refrigerant temperatures, T_{r1}-T_{r9}, were also measured for reference.

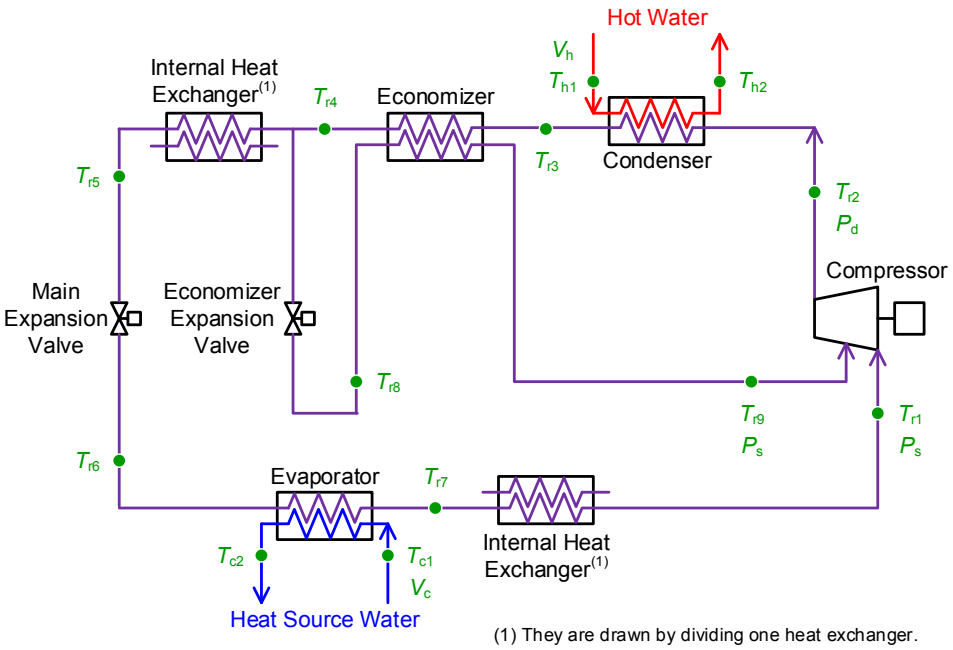

Figure 3: Schematic diagram of test equipment

Table 3 shows the test conditions. The test was performed in the compressor rotational speed fixed state to 100% with a difference of 5 K between outlet water temperature and inlet water temperature. The performances are evaluated under the same discharge superheat by controlling the main expansion valve. The economizer expansion valve was open and controlled at the economizer outlet superheat of about 20 K in Case 1, whereas was closed in Case 2 and Case 3.

Table 3: Test conditions

($\Delta T_c = T_{c1} - T_{c2}$ = 5 K, $\Delta T_c = T_{c1} - T_{c2}$ = 5 K, Compressor rotational speed = 100%)

	T_{c1} [°C]	T_{h2} [°C]	$\Delta T_{sh,d}$ [K]	Economizer
Case 1	70	115	15	Open
Case 2	70	95	25	Closed
Case 3	50	95	27	Closed

3.2. Test Results

Figure 4 shows the test results as the relative value of R1224yd(Z) to R245fa. The COP_h of R1224yd(Z) was nearly equal to or higher than the R245fa value. The Q_h of R1224yd(Z) was nearly equal to or smaller than the R245fa value. These indicate better performances than predicted. Figure 5-7 show the comparisons of cycle diagrams. In all the case, the temperature lift, $T_{cnd} - T_{evp}$, with R1224yd(Z) was decreased by 3-5%. This would be one reason for the higher COP_h.

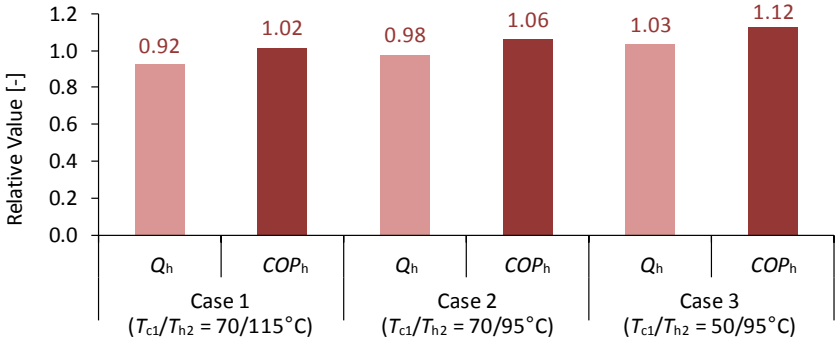

Figure 4: Actual performance of R1224yd(Z) relative to R245fa

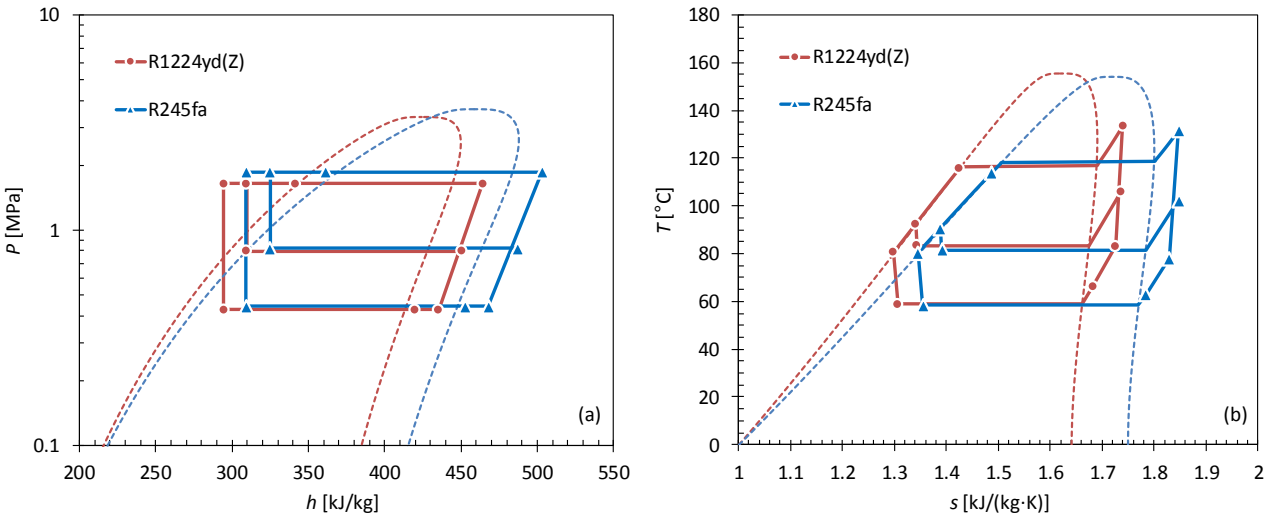

Figure 5: Comparison of (a) P-h, (b) T-s diagrams in actual performance (T_{c1}/T_{h2} = 70/115°C)

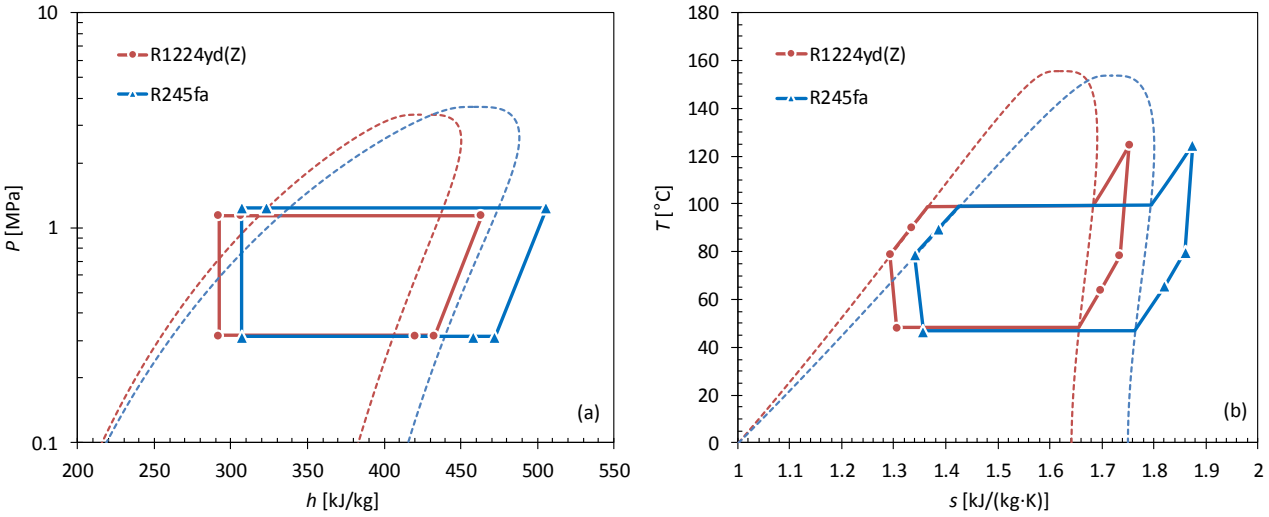

Figure 6: Comparison of (a) P-h, (b) T-s diagrams in actual performance (T_{c1}/T_{h2} = 70/95°C)

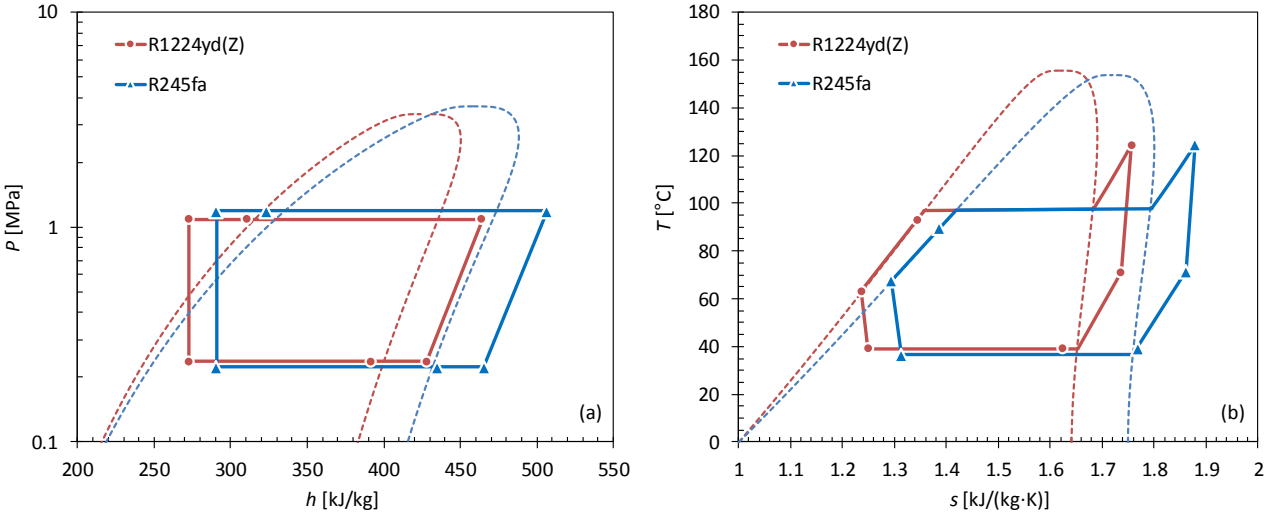

Figure 7: Comparison of (a) P-h, (b) T-s diagrams in actual performance (T_{c1}/T_{h2} = 50/95°C)

3.3. Discussion

It cannot be explained only decreasing the temperature lift about the reason for the higher COP_h. Other reason for the higher COP_h is discussed. The compressor adiabatic efficiency has the maximum value at the pressure ratio of around 3 (Iizuka, 2014). In all the cases, by decreasing the pressure ratio, the compressor adiabatic efficiency of R1224yd(Z) would be larger than the R245fa value. This also results in the higher COP_h.

Next, the reason for the more Q_h than predicted is discussed. Although the heating effect of R1224yd(Z) was smaller than the R245fa value due to the smaller latent heat by 13-16%, the refrigerant flow rate of R1224yd(Z) was larger than the R245fa value by 6-23%. It is considered that the increase of refrigerant flow rate would moderate the decrease of heating capacity. Moreover, when the effect of increasing refrigerant flow rate was greater, the Q_h of R1224yd(Z) could be larger than the R245fa value.

The increase of refrigerant flow rate also leads to the enhancement of condensation and evaporation heat transfer coefficient. This would one reason for decreasing the temperature lift. Regarding transport properties, both liquid thermal conductivity and liquid viscosity of R1224yd(Z) is smaller than the R245fa value. The decrease degree is more of liquid viscosity. As a result, the heat transfer might be also enhanced from the viewpoint of transport properties.

4. CHEMICAL STABILITY AND COMPATIBILITY

The chemical stability of R1224yd(Z) with refrigerant oils, naphtene, alkylbenzene (AB) and polyolester (POE), had been evaluated (Fukushima, 2015, Soga et al., 2017). In this study, the chemical stability of R1224yd(Z) with the polyalkylene glycol (PAG) used in HEM-HR115 was tested. The compatibility of R1224yd(Z) with O-ring and motor insulation material was also tested.

4.1. Chemical Stability with Refrigerant Oil

The chemical stability of R1224yd(Z) with a PAG oil in the presence of metals was tested by sealed tube testing compared to R245fa. Each tube was prepared at 60 g refrigerant and 60 g oil, and included the three metal catalysts representing the system materials of construction; steel (SS), copper (Cu) and aluminium (Al). Each tube was aged in a heated oven at 150°C for 14 days.

The refrigerant purity was measured by gas chromatography analysis. The acidity of refrigerant was measured by alkalimetric determination (minimum limit of detection: 0.2 ppm). The concentration of fluoride ion (F) and chloride ion (Cl) was measured by ion chromatography (minimum limit of detection: 0.2 ppm). These can be interpreted as indicators of the degree of degradation. Moreover, the acid number of oil was measured by titration (minimum limit of detection: 0.01 mgKOH/g). The color of oil was also measured. These can be interpreted as indicators of the degree of reactivity. Furthermore, the weight change of each metal was measured.

Table 4: Chemical stability of R1224yd(Z) and R245fa with PAG oil in the presence of metals
(Temperature: 150°C, Duration: 14days)

		R1224yd(Z)	R245fa
Refrigerant	Purity change [%]	99.8 → 99.5	99.9 → 99.9
	Acidity [ppm]	< 0.2	< 0.2
	F [ppm]	< 0.2	< 0.2
	Cl [ppm]	< 0.2	< 0.2
Oil	Acid number [mgKOH/g]	0.05	0.03
	Color of oil (ASTM)	L0.5	L0.5
Metal	SS weight change [mg]	< 0.01	< 0.01
	Cu weight change [mg]	< 0.01	< 0.01
	Al weight change [mg]	< 0.01	< 0.01

Table 4 shows the results. Although the acid number and the color of the PAG oil with R1224yd(Z) was slightly larger than the R245fa value, there were no significant differences between R1224yd(Z) and R245fa.

4.2. Compatibility with O-ring and motor insulation material

The compatibility of R1224yd(Z) with two types of O-rings, hydrogenated-nitrile-butadiene rubber (HNBR) and ethylene-propylene-diene rubber (EPDM), and motor insulation material was tested by sealed tube testing compared to R245fa. Each tube was prepared at 80 g refrigerant and included each material. Each tube was aged in a heated oven at 150°C for 7 days. The refrigerant purity, the acidity of refrigerant, and the concentration of fluoride ion and chloride ion were measured. In addition, the weight change of each material was measured. Regarding O-rings, the wire diameter change and volume change were also measured.

Table 5 and Table 6 show the results. As shown in Table 5, both R1224yd(Z) and R245fa made O-rings expand slightly. The degrees of expansion were the same level. The expansion change rate of HNBR was larger than the EPDM value regardless of refrigerants. As shown in Table 6, both R1224yd(Z) and R245fa made motor insulation material heavy slightly. The degrees of weight change were the same level. As a result, there were no significant differences between R1224yd(Z) and R245fa.

Table 5: Compatibility of R1224yd(Z) and R245fa with O-ring
(Temperature: 150°C, Duration: 7days)

		R1224yd(Z)		R245fa	
Refrigerant	Purity change [%]	99.8→99.5	99.8→99.5	99.9→99.9	99.9→99.9
	Acidity [ppm]	< 0.2	< 0.2	< 0.2	< 0.2
	F [ppm]	0.2	< 0.2	< 0.2	< 0.2
	Cl [ppm]	< 0.2	< 0.2	< 0.2	< 0.2
O-ring	Type	HNBR	EPDM	HNBR	EPDM
	Wire diameter change [%]	3.3	1.3	4.3	0.7
	Volume change [%]	9.6	3.6	14.4	2.5
	Weight change [%]	13.7	7.2	16.9	2.8

Table 6: Compatibility of R1224yd(Z) and R245fa with motor insulation material
(Temperature: 150°C, Duration: 7days)

		R1224yd(Z)	R245fa
Refrigerant	Purity change [%]	99.8 → 99.7	99.9 → 99.9
	Acidity [ppm]	< 0.2	< 0.2
	F [ppm]	< 0.2	< 0.2
	Cl [ppm]	< 0.2	< 0.2
Motor insulation material	Weight change [%]	0.54	0.63

5. CONCLUSIONS

In order to evaluate the suitability of R1224yd(Z) as R245fa alternative for high temperature heat pump, a drop-in test with a commercialized industrial heat pump was performed. The test result indicates better performance than the predicted thermodynamic simulation. As this reason, (1) the enhancement of compressor adiabatic efficiency by decreasing pressure ratio, (2) the increase of heating capacity by increasing refrigerant mass flow rate, (3) the decrease of temperature lift by the enhancement of condensation and evaporation heat transfer coefficient due to increasing refrigerant mass flow rate and decreasing liquid viscosity, are considered. The heat transfer characteristics of R1224yd(Z) compared to R245fa needs to be examined further.

In addition, the chemical stability of R1224d(Z) with PAG oil in the presence of metals and the compatibility of R1224yd(Z) with O-ring and motor insulation were tested compared to R245fa. There were no significant differences between R1224yd(Z) and R245fa.

Overall, R1224yd(Z) can be used as R245fa alternative for high temperature heat pump because of its good thermodynamic and environmental properties.

NOMENCLATURE

AB	alkylbenzene	ad	adiabatic
c	cooling, heat source water	cnd	condenser
COP	coefficient of performance [-]	*VHC*	volumetric heating capacity [MJ/m^3]
d	discharge	eco	evaporator
EPDM	ethylene-propylene-diene rubber	evp	evaporator
h	heating, hot water	GWP	global warming potential
h	specific enthalpy [kJ/kg]	HNBR	hydrogenated-nitrile-butadiene rubber
ODP	ozone depletion potential	*P*	pressure [MPa]
PAG	polyalkylene glycol	POE	polyoester
Q	capacity [kW]	r	refrigerant
s	suction	*s*	specific entropy [kJ/(kg·K)]
sc	subcooling [K]	sh	superheat [K]
T	temperature [°C]	*V*	flow rate [m^3/s]
W	electric power consumption [kW]	η	efficiency [-]

REFERENCES

Arpagaus, C., Bless, F., Uhlmann, M., Schiffmann, J., Bertsch, S., 2018. High temperature heat pumps: Market overview, state of the art, research status, refrigerants, and application potentials. Energy 152, 985-1010.

Kaida, T., Sakuraba, I., Hashimoto, K., Hasegawa, H., 2015. Experimental performance evaluation of heat pump-based steam supply system. Proceedings of 9th International Conference on Compressors and their Systems, London, 077.

Fukushima, M., 2015. Development of low-GWP alternative refrigerants. Proceedings of JSRAE Annual Conference, Tokyo, D332. [in Japanese]

Fukushima, M., 2018. Next generation low-GWP refrigerants “AMOLEA™.” Proceeding of JRAIA International Symposium, Kobe, 319-323.

Iizuka, K., Maeda, M., 2011. Development of high efficiency steam supply systems “Steam Grow Heat Pump.” Mechanical Engineering Congress, Tokyo, W091008. [in Japanese]

Iizuka, K., 2014. High efficiency steam supply systems using by heat pump cycle. JSRAE Journal 89 (1039), 13-18.

Lemmon, E., Bell, I., Huber, M., McLinden, M., 2018. Reference Fluid Thermodynamic and Transport Properties Database (REFPROP): Version 10, National Institute of Standards and Technology (NIST).

Soga, T., Hayamizu, H., Fukushima, M., 2017. Compatibility of low-GWP refrigerant HCFO-1224yd(Z). Proceedings of JSRAE Annual Conference, Tokyo, F312. [in Japanese]

Tokuhashi, K., Uchimaru, T., Takizawa, K., Kondo, S., 2018. Rate constants for the reactions of OH radical with the (E)/(Z) isomers of $CF_3CF=CHCl$ and $CHF_2CF=CHCl$. The Journal of Physical Chemistry A 122, 3120-3127.

Manuscript ID: 905
DOI: 10.18462/iir.icr.2019.0905

Thermal performance of ground source heat pump using steel pipe pile for house

Tomoya AOKI [(a)], Tetsuaki TAKEDA [(b)], Shuhei ISHIGURO [(a)], Osamu YODA [(c)], Hiroji OKUBO [(c)]

[(a)] University of Yamanashi, Integrated Graduate School of Medicine, Engineering, and Agricultural Sciences, 4-3-11 Takeda, Kofu, Yamanashi, 400-8511, Japan, g18tm001@yamanashi.ac.jp

[(b)] University of Yamanashi, Graduate School of Engineering 4-3-11 Takeda, Kofu, Yamanashi, 400-8511, Japan, ttakeda@yamanashi.ac.jp

[(c)] Fujishima Co, Ltd., 1-13-5 Misono, Midori-ku, Saitama, Saitama, 336-0972, Japan

ABSTRACT

Now-a-days, ground source heat pump (GSHP) are attracting attention as an energy saving technology in cooling and heating systems. The objective of this study is to evaluate the performance of a GSHP that uses the direct expansion method, in cooling and heating air conditioning applications. This pump utilizes the steel pipe foundation pile of the house to accommodate its heat exchanger. To achieve the same, 12 underground heat exchangers were inserted into the foundation piles. Experiments were conducted to study its performance in both cooling and heating operations, and the coefficient of performance (COP) was obtained by measuring the amount of heat transferred and the electricity consumption for running the GSHP. From the experimental result obtained, the COP was approximately 4.0 in the cooling operation and approximately 4.8 in the heating operation. Additionally, no performance deterioration was observed in the intermittent cooling or heating operation for 5 days.
Keywords: COP, Direct Expansion, Energy Consumption, Ground-Source System, Heat Exchanger.

1. INTRODUCTION

In recent years, the ground source heat pump (GSHP) that utilizes the ground source heat energy is attracting significant attention as an energy saving technology in heating and cooling systems. Ground source heat energy is low temperature thermal energy existing below the ground up to a depth of about 100 m, where the temperature is almost constant throughout the year. Hence, when compared to the outside ambient temperature, the ground source heat temperature is lower in summer and higher in winter. In addition, the ground source heat energy can be used across a wide area. A GSHP using the ground source heat energy as a heat source has superior efficiency and energy saving performance in air conditioning and hot water supply systems to a conventional air source heat pump.

Generally, a GSHP can operate on either an indirect or a direct expansion method. In the indirect expansion method, a heat exchanger is installed between the heat pump and the underground heat exchanger, and the heat of the refrigerant in the heat pump indirectly exchanges heat with the ground via water or an antifreeze. On the other hand, in the direct expansion method, the heat of the refrigerant in the heat pump directly exchanges heat with the underground. This is accomplished by introducing the refrigerant pipe of the heat pump directly into the ground. Therefore, the direct

expansion method can, more efficiently, utilize the ground source heat energy than the indirect method and offer better heat exchanger performance.
Takeda (2014, 2018) and Ishiguro (2018) have reported on the performance of a GSHP using the direct expansion method in air conditioning and hot water supply systems. While constructing a house or a building in areas where the ground is weak due to the nature of the soil, it is necessary to lay a foundation pile to support the construction. In this case, if an underground heat exchanger of a GSHP is inserted into the foundation pile, heat from the underground can be released and extracted through the foundation pile easily. Finally, the initial cost of digging the borehole can be reduced in comparison with the conventional type. The purpose of this study is to evaluate the performance of a cooling and heating air conditioning system with a GSHP employing the direct expansion method and utilizing the foundation steel pipe piles meant for a house.

2. EXPERIMENTAL SETUP AND EVALUATION METHOD

2.1. Experimental Setup

Fig. 1 shows the schematic view of the experimental setup. In this study, the GSHP uses a vertically buried steel pipe pile. We have used 12 steel pipe piles of 10 m depth as the underground heat exchanger. Each steel pipe pile was filled with water and a heat collection pipe was inserted into the same. Fig. 2 shows the underground heat exchanger. The heat collection pipe is U-shaped with one copper pipe and two copper pipes connected at the bottom as shown in the Fig. There are a total of 12 heat collection pipes and 3 header lines. The heat collection pipes are connected in groups of four to the headers lines.
The output of this system has a cooling capacity of 4.0 kW and a heating capacity of 4.5 kW. Furthermore, this system uses 1.8 kg of refrigerant R32 and is connected to one indoor unit. The air conditioning area is 15.3 m^2. We conducted the experiment with the unit temperature set at 27 ºC for cooling operation and at 20 ºC for the heating operation.

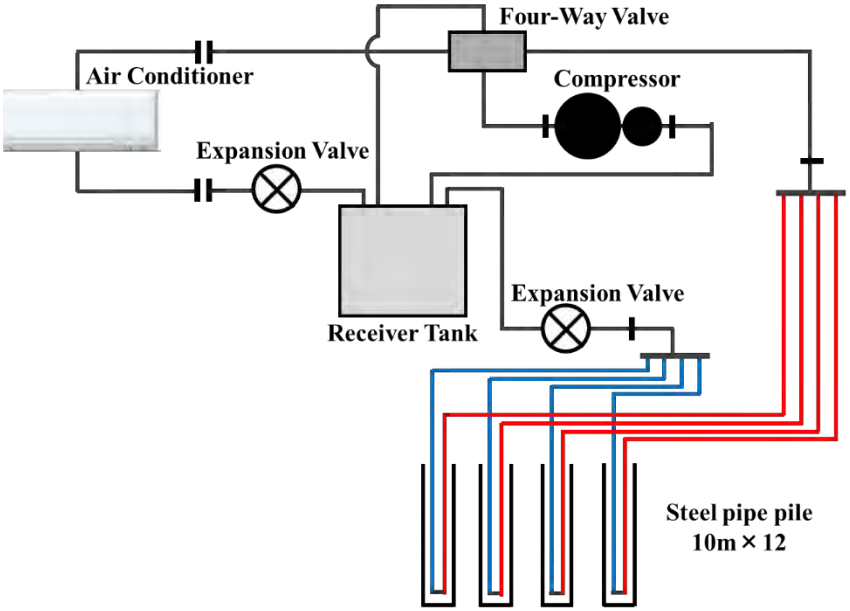

Figure 1: Schematic of the direct expansion method GSHP

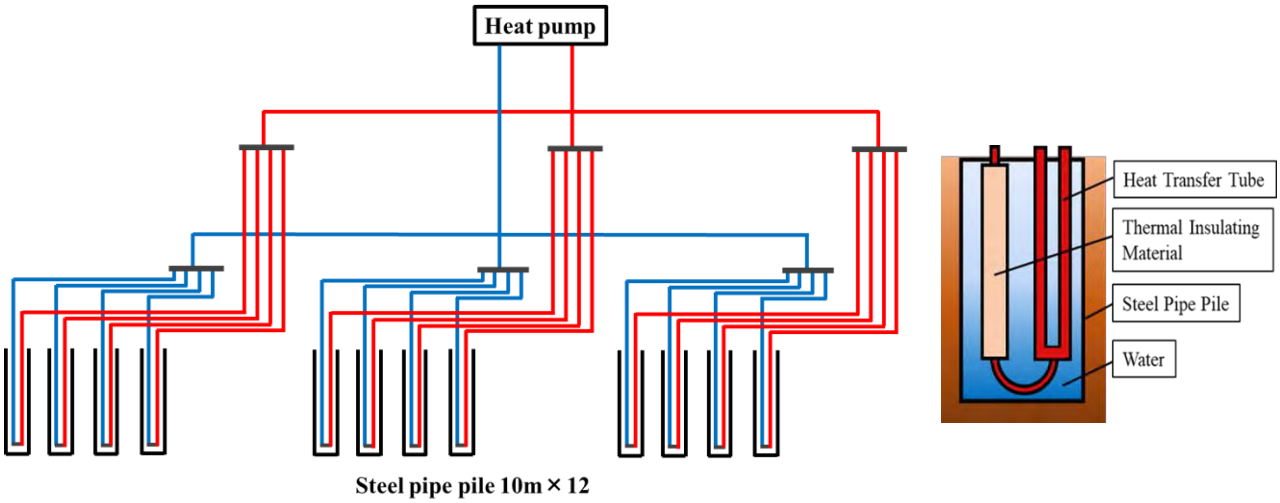

Figure 2: Schematic of the underground heat exchanger

2.2. Evaluation Method

Generally, Coefficient of Performance (COP) is used for the performance evaluation of a heat pump. COP is a numerical value of the cooling or heating capability obtained per kW of power consumption. Larger the value of COP, more efficient is the production of cooling or heating. In this study as well, COP of the direct expansion method GSHP was evaluated. In the direct expansion method heat pump, the underground heat exchanger is a condenser / evaporator. For this reason, the refrigerant becomes a two-phase flow with a phase change, and it is not easy to accurately measure the flow rate of the refrigerant on the underground heat exchanger side. Therefore, the amount of heat transferred is obtained at the suction and discharge ports on the indoor unit side. Equation (1) shows the formula for the calculation of COP.

$$COP = \frac{P}{W} = \frac{\Delta h \times \rho \times A \times v}{W} \qquad \text{Eq. (1)}$$

Where P is the amount of heat transferred in kW; Δh is the specific enthalpy difference of air flow in kJ.kg^{-1}; ρ is the density of air in kg.m^{-3}; A is the area of the duct outlet in m^2; v is the air speed in m.s^{-1}; and W is the power consumption in kW.

Fig. 3 shows the measurement system installed in the indoor unit. The enthalpy difference Δh was obtained by measuring the temperature and humidity at the suction and discharge ports of the indoor unit and referring to a psychrometric chart. In this experimental study, a simple duct was installed at the discharge port of the indoor unit, and four hot wire anemometers were installed at a spacing of 124 mm to measure the air speed. The air speed was calculated from the average of the four hot wire anemometer readings.

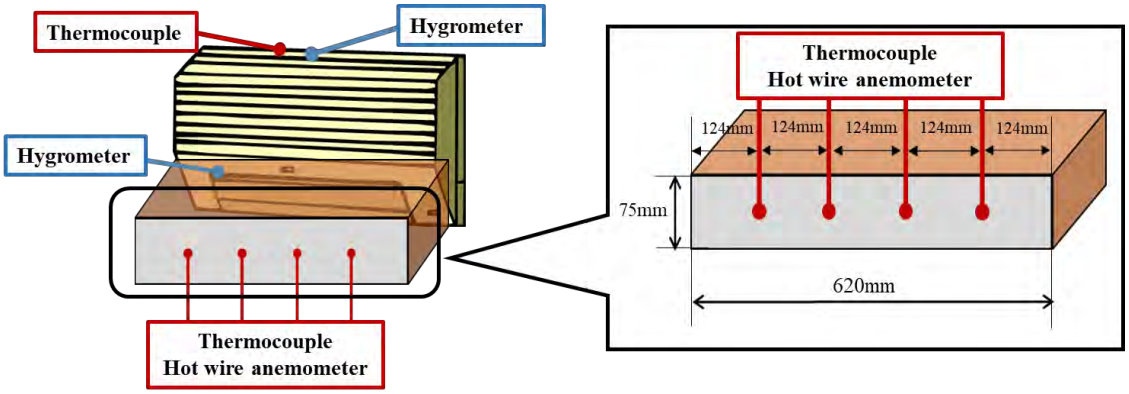

Figure 3: Measurement system in an indoor unit

3. EXPERIMENTAL RESULT

3.1. Cooling Operation

The first of the test cases involved a cooling operation for 8 h per day for 5 days from July 16 to July 20, 2018. Fig. 4 shows the variation of COP, amount of heat transferred, and power consumption from 8:40 to 16:30 h. on the first day of the operation, i.e., July 16, 2018. The operation was observed to be unstable for 1 h from the start of cooling operation after which it stabilized. From 9:40 to 10:30 h., an average COP of approximately 4.0, an average amount of heat transfer of approximately 2.46 kW, and an average power consumption of approximately 0.62 kW were observed. Towards the end of the cooling operation, from 15:40 to 16:30 h., the average COP was approximately 3.9; the average amount of heat transferred was approximately 2.56 kW; and the average power consumption was approximately 0.66 kW. During the operation period, it was found that the amount of heat transferred was steady at approximately 2.4 to 2.6 kW. In addition, the power consumption was approximately 0.6 kW, and did not increase significantly during the operation period.
Fig. 5 shows the variation of the same parameters for 8 h of intermittent cooling operation each day over the 5 days mentioned above. Table 1 shows averaged values of COP, heat transferred and power consumption for this case in numerical format. These values were averaged over each day of the operational period after the initial stabilization period. It may be inferred from the experimental results that the possibility of performance degradation is small even if the cooling operation is performed every day.

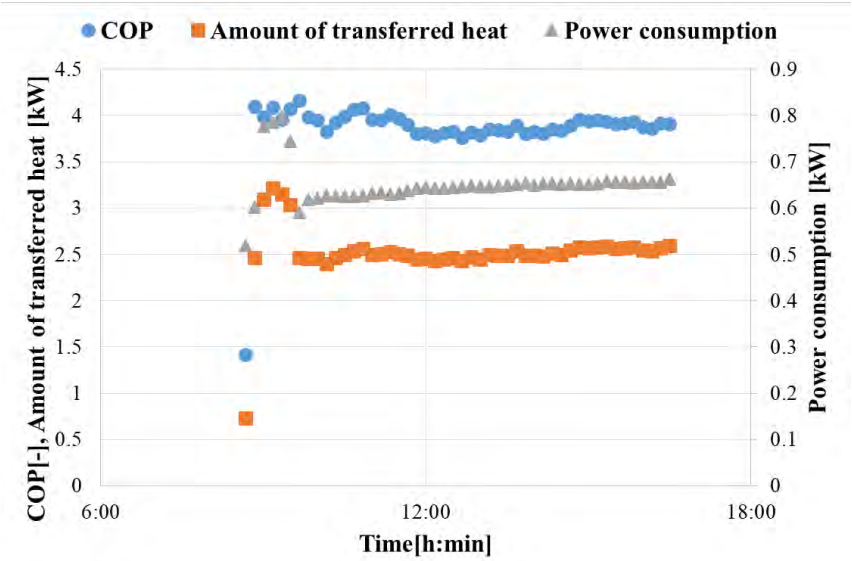

Figure 4: COP, amount of heat transferred, and power consumption in cooling mode (July 16, 2018)

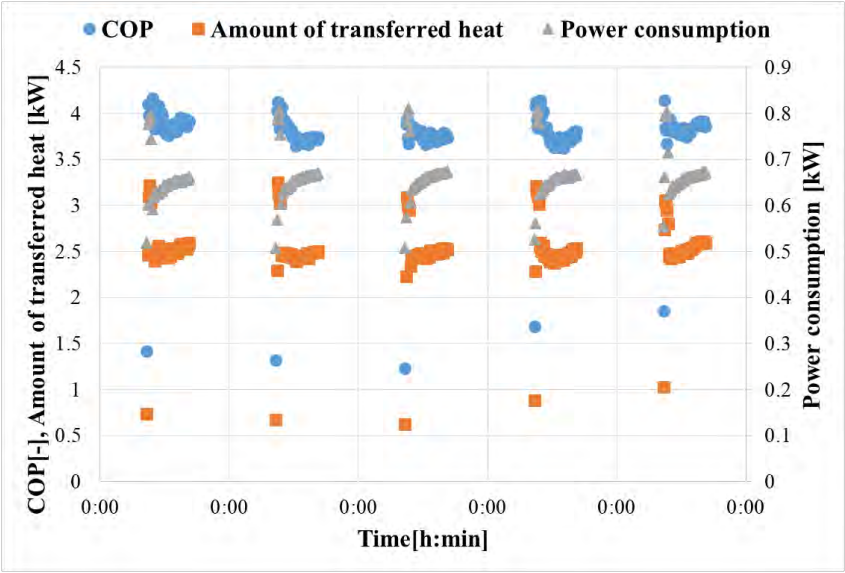

Figure 5: COP, amount of heat transferred, and power consumption in cooling mode (July 16 to July 20, 2018)

Table 1. Average COP, average amount of heat transferred, and average power consumption (July 16 to July 20, 2018)

-	Average COP (No unit)	Average amount of transferred heat (kW)	Average power consumption (kW)
July 16, 2018	3.9	2.50	0.64
July 17, 2018	3.8	2.46	0.65
July 18, 2018	3.8	2.47	0.66
July 19, 2018	3.8	2.46	0.65
July 20, 2018	3.8	2.52	0.66

3.2. Heating Operation

The second test case involved heating operation for 7 h per day over 5 days from December 10 to December 14, 2018. Fig. 6, similar to Fig. 4, shows the time change in COP, amount of heat transferred, and power consumption from 8:40 to 15:30 hrs. on the first day of operation. Shortly after the start of the operation, from 8:50 hrs. to 9:40 hrs., the average COP was approximately 4.8; the average amount of heat transferred was approximately 3.59 kW; and the average power consumption was approximately 0.74 kW. Towards the end of the operation, from 14:40 hrs. to 15:30 hrs., these parameters were calculated to be 4.7, 3.45 kW, and 0.74 kW respectively.

Fig. 7 shows the variation of the same three parameters for 7 h of intermittent heating operation every day over all the 5 days mentioned above. Table 2 shows averaged values of these parameters for each of these five days. It should be mentioned that on each day, the first 10 minutes of operation was excluded from the calculations. As in the earlier test case, here too, it may be inferred from the experimental results that the possibility of performance deterioration is small even if the heating operation is performed every day.

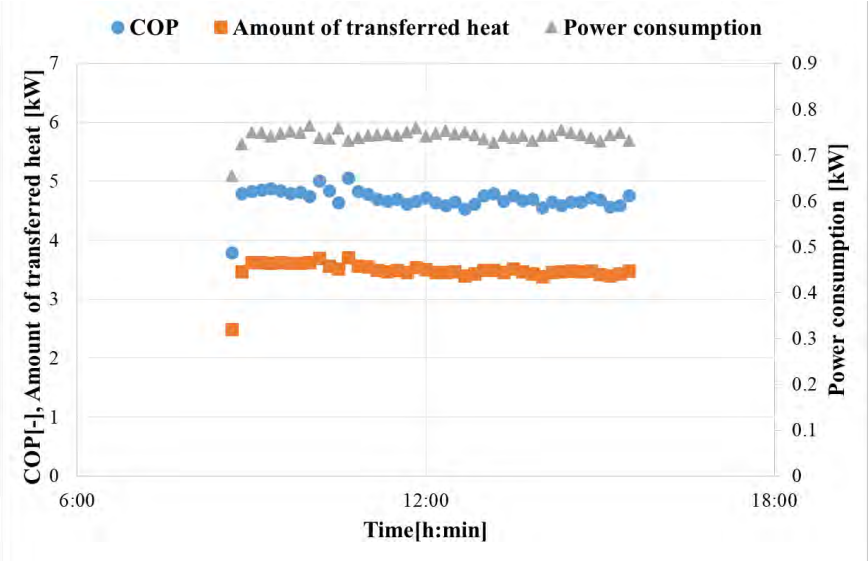

Figure 6: COP, amount of heat transferred, and power consumption in heating mode (December 10, 2018)

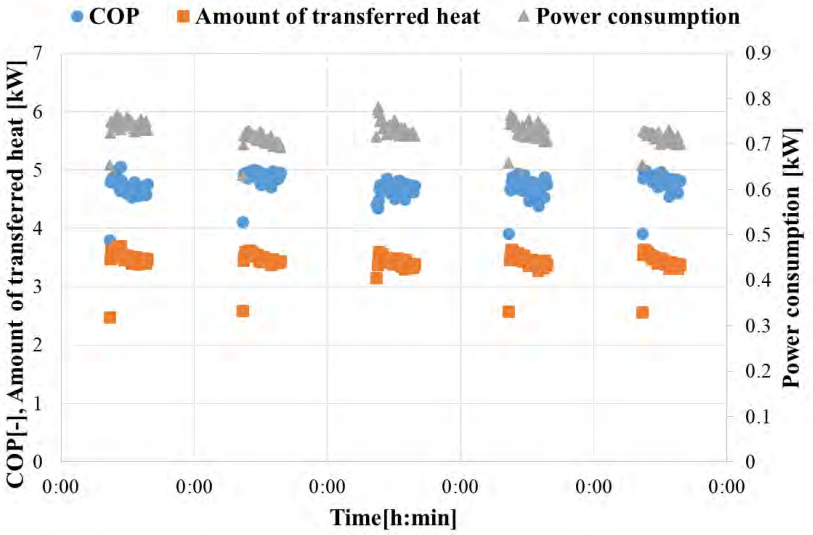

Figure 7: COP, amount of heat transferred, and power consumption in heating mode (December 10 to December 14, 2018)

Table 2. Average COP, average amount of heat transferred, and average power consumption (December 10 to December 14, 2018)

-	Average COP (No unit)	Average amount of transferred heat (kW)	Average power consumption (kW)
December 10, 2018	4.7	3.51	0.74
December 11, 2018	4.9	3.49	0.71
December 12, 2018	4.7	3.43	0.73
December 13, 2018	4.7	3.46	0.73
December 14, 2018	4.8	3.46	0.71

4. CONCLUSIONS

In this study, we have evaluated the performance of a GSHP employing the direct expansion method, and using 12 underground heat exchangers inserted in steel pipe foundation piles of the house. From the experiment, the following results were obtained.

1) In the cooling operation, the amount of heat transferred was stable, the power consumption hardly varied, and the COP was approximately 4.0.

2) In the heating operation, the amount of heat transferred was stable, the power consumption hardly varied, and the COP was approximately 4.8.

3) Performance did not decrease in intermittent cooling or heating operation over a 5-day period. Therefore, we infer that the possibility of performance deterioration would be small even if we performed cooling or heating operation every day.

NOMENCLATURE

P	amount of transferred heat (kW)	W	power consumption (kW)
Δh	specific enthalpy difference of air flow ($kJ \times kg^{-1}$)	ρ	density of air ($kg \times m^{-3}$)
A	area of the duct outlet (m^2)	v	wind speed ($m \times s^{-1}$)

REFERENCES

Ishiguro, S., et al, 2018. Study on Ground Source Heat Pump That Use Direct Expansion Method Using Foundation Pile, Proceedings of the 9th Asian Conference on Refrigeration and Air-conditioning, ACRA2018, Sapporo, Japan, ACRA2018-D114.

Ishiguro, S., Takeda, T., 2018. STUDY ON UNDERGROUND HEAT EXCHANGER FOR GROUND SOURCE HEAT PUMP THAT USE DIRECT EXPANSION METHOD, Proceedings of the 16th International Heat Transfer Conference, IHTC-16, Beijing, China, IHTC16-23415

Takeda, T., et al, 2014. EXPERIMENTAL STUDY OF GROUND SOURCE HEAT PUMPS THAT USE THE DIRECT EXPANSION METHOD, Proceedings of the 15th International Heat Transfer Conference, IHTC-15, Kyoto, Japan, IHTC15-8940

Takeda, T., et al, 2018. THERMAL PERFORMANCE OF GROUND SOURCE HEAT PUMPS THAT USE DIRECT EXPANSION METHOD USING FOUNDATION PILE, Proceedings of the 16th International Heat Transfer Conference, IHTC-16, Beijing, China, IHTC16-23590

Manuscript ID: 960
DOI: 10.18462/iir.icr.2019.0960

Development of water-lithium bromide absorption chillers based on asymmetric plate heat exchangers

Lutz RICHTER[(a)], Carsten HEINRICH[(a)], Christian KEMMERZEHL[(b)], Mathias SAFARIK[(a)], Mike OTTO[(b)], Gregor WEIDNER[(b)], Bodo BURANDT[(a)], Ralf HERZOG[(a)]

[(a)] Institute of Air Handling and Refrigeration (ILK Dresden), Dresden, 01309, Germany
lutz.richter@ilkdresden.de

[(b)] EAW Energieanlagenbau Westenfeld GmbH, Römhild, Germany
ckemmerzehl@wegra-anlagenbau.de

ABSTRACT

Water/lithium bromide (LiBr) absorptions chillers typically use horizontally arranged tube bundles for the heat exchangers. The use of plate heat exchangers is hampered by the low vapor density and low permissible pressure losses in the steam flow. Objective of the work was the development of an absorption chiller in which all heat exchangers are designed as plate heat exchangers.

A new asymmetric plate heat exchanger was developed with a channel height also appropriate for the conditions of the absorber and evaporator which represent the low pressure side of an absorption chiller.

Applying this new heat exchanger a complete absorption chiller was designed and built. At nominal conditions of heating water 86/71 °C, cooling water 27/32 °C, chilled water 15/9 °C the chiller reached a cooling capacity of 65 kW which is about 20 % more than expected. The volume of the chiller was reduced by 40 % compared to a chiller with the same capacity using tube bundle heat exchangers.

Keywords: absorber, heat exchanger, lithium-bromide, R718

1. INTRODUCTION

Higher costs and larger construction volumes of absorption refrigeration systems complicate their use compared to compression refrigeration systems. However absorption chillers have high potentials within polygeneration systems - the coupled generation of electrical, heating and cooling energy or the conversion of waste heat into cooling. In addition the natural refrigerant water is used in water/LiBr absorption refrigeration systems.

Steadily rising copper prices are hampering the use of absorption chillers. At present all producers of water/LiBr absorption chillers use straight or spiral copper or steel tube bundles as heat exchangers except for the solution heat exchanger. Plate heat exchangers are more compact than shell and tube heat exchangers and can be significantly cheaper.

Water/LiBr absorption chillers operate in a rough vacuum (10...100 mbar_a). Therefore the pressure losses of the refrigerant vapor need to be low because absolute pressure differences in the cycle are very small. Due to the high specific volume of water vapor large flow cross sections are necessary which preclude a compact system design. Depending on the saturation temperature the specific volume of water vapor is 1,000 to 2,500 times greater than R134a vapor. On the other hand small flow dimensions are required for the external fluid (heating, cooling and chilled water) in water cooled and hot water driven absorption chillers for a good heat transfer.

Conventional plate heat exchangers which have the same channel heights on both sides are therefore not usable in water/LiBr absorption chillers. Different channel heights are required. But asymmetric plate heat exchangers which meet the special requirements for use in water/LiBr absorption chillers did not exist so far.

Inside absorption chillers (symmetric) plate heat exchangers have been used so far as solution heat exchanger (Safarik et al. 2004) and high temperature generator in double effect chillers (Marcos et al. 2009, Safarik et al. 2013). Within an R&D-project asymmetric plate heat exchangers designed for air to water heat transfer have been used as generator and condenser in a single-effect absorption chiller (Kemmerzehl et al. 2017).

2. DEVELOPMENT TARGETS

Asymmetric plate heat exchangers have different channel heights for the two fluids - liquid on one side and vapor on the other. This allows optimum heat transfer conditions on both sides.

The objective was to develop new asymmetric plate heat exchangers with different optimal channel heights for the two sides and with a stamping pattern that improves the flow conditions and plate wetting. These plate heat exchangers are to be used as absorber, generator, evaporator and condenser in the water/LiBr absorption chillers. Targeted overall heat transfer coefficients of the plate heat exchangers at design conditions were for evaporation: 1,500 W/(m^2K), for condensation: 3,000 W/(m^2K), for absorption 600 W/(m^2K) and for desorption 800 W/(m^2K).

3. ASYMMETRICAL PLATE HEAT EXCHANGERS

The term asymmetry in asymmetric plate heat exchangers refers to the different heat capacity flows, enthalpy flows or volume flows on the primary and secondary side. This means that a mass flow and/ or the heat capacity of one fluid is significantly greater compared with the other fluid as it is the case in gas-liquid heat exchangers. The special requirement for asymmetric plate heat exchangers is to optimize flow control and pressure loss on each side. For this purpose differently sized free cross-sectional areas for the flow are required on the primary and secondary side. The previously available asymmetric heat exchangers have been primarily developed for gas-liquid heat transfer in the chemical process industry and for the extraction of exhaust gas heat. Another field of application is the evaporation and condensation of synthetic refrigerants. However there are no known asymmetric plate heat exchangers that have been designed both for a two-phase mixture and for a two-component mixture as it is the case in the absorption and desorption in absorption chillers. So far no asymmetric plate heat exchangers have been available on the market which meet the special requirements of absorption refrigeration systems with the refrigerant water.

With the accomplished development this gap was closed. The developed asymmetric plate heat exchanger is copper brazed. The external fluid flows through the heat exchanger in channels with a small channel height. The channel height of the product side (internal fluid, falling film side) is more than twice as high as that of the external fluid side. Figure 1 shows a partial view of a section in the asymmetric plate heat exchanger. The differently sized cross sections are recognizable. Also the graphical result of a numerical flow simulation of the external side is shown.

Numerical flow simulations were used to evaluate a homogeneous, well-formed channel flow of the external fluid (one computation with pure water and another one with a mixture of 65V% water and 35V% ethylene glycol, 20 °C). The calculations for the test models took into account different barriers and dimple arrangements on the plate. A preferred variant was selected for the construction of the test model. Criteria of the evaluation were the avoidance of too high local flow velocities, the reduction of flow shadows behind the dimples as well as the avoidance of bypass flows. A homogeneous fluid distribution was sought.

For producing the plates of the asymmetric plate heat exchanger of the test models a cutting and stamping tool has been developed. Due to the dimples a heat transfer area increase of approx. 20 % was achieved. The media connections and barriers in turn reduce the heat exchanger surface by approx. 10%. The external media sides were carried out one-pass and more-passes. One-pass means all channels are flowed through in parallel. In order to improve the flow velocities more passes are required in particular in the evaporator and generator. The channels for internal fluid are always in one-pass.

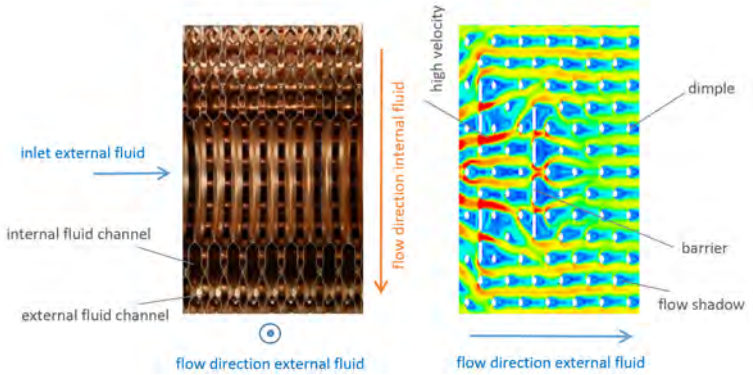

Figure 1: Partial view of a section in the asymmetric plate heat exchanger and example of the flow simulation for the external fluid of a variant for optimizing the plate design

4. MEASUREMENT OF ASYMMETRIC PLATE HEAT EXCHANGERS

The test models were measured under vacuum conditions in the functions evaporator, condenser, generator and absorber. For all measurements of this article the same test model was used (12 plates, 1 pass on both sides). The overall heat transfer coefficients were calculated for all apparatus'. Pressure losses on the media side were determined and the inert gas removal and liquid distribution on the product side were investigated.

Figure 2 shows the pressure losses for the external fluid (water 20°C) as a function of the flow velocity in the channel. For a quick calculation of the pressure loss of a plate heat exchanger with 1 pass a pressure loss coefficient of $\zeta = 100$ can be used. As result of the pressure loss measurement it was concluded that evaporator and generator must be made multi-passes on the external fluid side (ζ is for a heat exchanger with 2 passes 160 and for 3 passes 230). In general the plate heat exchanger causes low external pressure losses. This is important especially in the cooling water circuit to ensure a high EER_{el} value of the refrigeration system. The EER_{el} of an absorption chiller is the quotient of the cooling capacity to the electrical auxiliary energy (electrical energy for solution pumps, external pumps, re-cooling and so on).

In further measurements the dependencies of the overall heat transfer coefficients on the falling film flow rate and the flow velocity of the external fluid were determined. In addition the inlet temperatures of the external fluid and the solution and the solution concentrations were varied.

Table 1 contains the general conditions of the measurements. The fluid inlet temperature in the evaporator and in the condenser has been set in terms of practical values. The results are shown in Figure 3 to Figure 6.

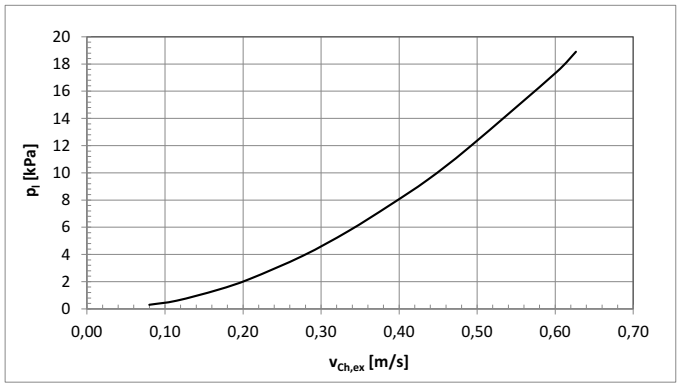

Figure 2: Pressure losses for the external fluid (water, 20°C) of the test model as a function of the flow velocity in the channel

Table 1: *General conditions of the measurements of figures 3 to 6 (distribution version 2)*

Component	$t_{ex,F,i}$ [°C]	$t_{s,H2O}$ [°C]	$\Delta t_{SC,S,i}$ [K]	$\Delta \xi_{S,i}$ [kg_{H2O}/kg_S]	$v_{Ch,ex}$ [m/s]
Evaporator	$t_{s,H2O}$ + 6 K	in figure 3: 9,0 in figure 4: 14,0	-	-	0,11
Condenser	$t_{s,H2O}$ - 4 K	34,0	-	-	-
Absorber	27,0	9,0	in figure 3: 2,0 in figure 4: 1,0	0,46	0,40
Generator	75,0	34,0	0,5	0,48	0,25

The overall heat transfer coefficient is determined with k = /(A_{ht}*Δt_m). Here is Δt_m the logarithmic temperature difference for counter flow, $\Delta t_m = (\Delta t_{max} - \Delta t_{min}) / LN(\Delta t_{max} / \Delta t_{min})$.

Figure 3 shows the overall heat transfer coefficients of evaporation, absorption and desorption and the absorption efficiency of the absorber as a function of falling film flow rate. The absorption efficiency is the quotient of the real concentration accumulation in the solution to the maximum possible at saturation state.

With increasing falling film flow rate the overall heat transfer coefficient increases but the absorption efficiency in the absorber decreases as more heat is withdrawn from a larger solution mass flow and the falling film surface on which the refrigerant vapor is absorbed remains the same. The overall heat transfer coefficients as a function of the flow rate of the external fluid in the A channel for evaporation, condensation, absorption and desorption are shown in Figure 4.

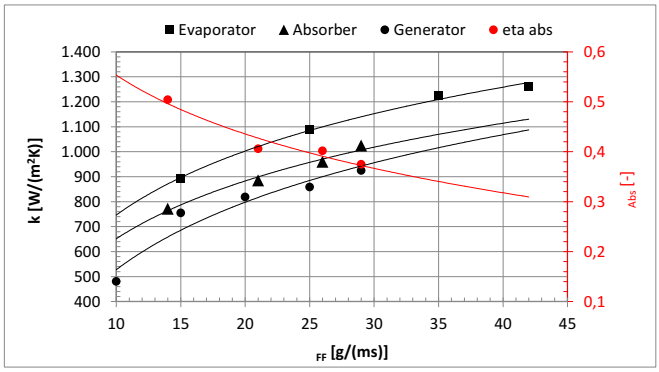

Figure 3: Heat transfer coefficients of evaporation, absorption and desorption and absorption efficiency as a function of falling film flow rate

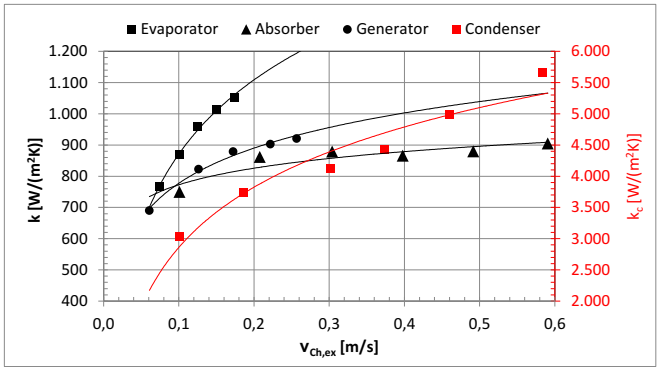

Figure 4: Heat transfer coefficient as a function of the flow velocity of the external fluid in the A channel for evaporation, condensation, absorption and desorption

The influence of the subcooling of the entering solution in the absorber and generator on the heat transfer coefficient can be seen in Figure 5. Higher subcoolings are favorable in the absorber, disadvantageous in the generator. Figure 5 confirms the need for a sufficiently dimensioned and well-functioning solution heat exchanger within an absorption refrigeration plant. If the solution heat

exchanger works poorly, the subcooling of the poor solution too small and the subcooling of the rich solution too large, the absorber and generator will not work well either.

Three distribution versions for the liquids were investigated. All versions used a pressurized distribution box with outlet holes. In version 1 the liquid was distributed directly into the flow channels (cells of internal channels) and in version 2 on the plate edges and in so-called distribution hollows formed by the plate stampings. In version 3 the liquid was passed directly onto the plate edges of the heat exchanger.

In the measurements for Figure 3 to Figure 6 the distribution version 2 was used. The distribution was optimized and the liquid in distribution version 3 was brought via a fine distribution directly to the heat exchanger surface. The improvements achieved can be seen in Figure 6. At the evaporation the heat transfer coefficients were increase by approx. 30%.

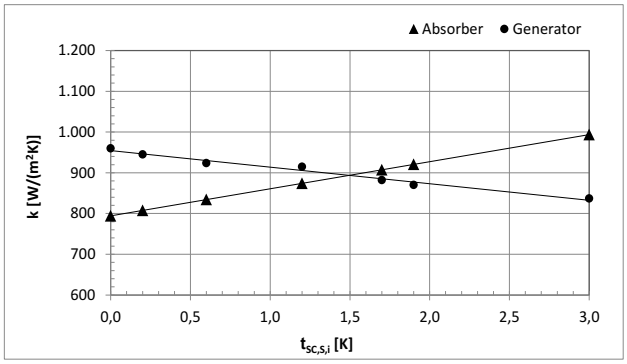

Figure 5: Heat transfer coefficient as a function of the subcooling of the entering solution for absorption and desorption

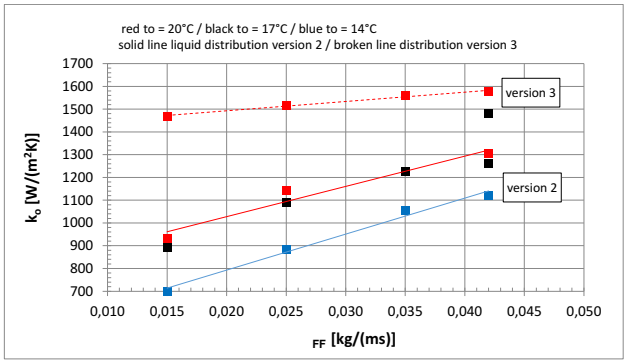

Figure 6: Heat transfer coefficients of evaporation as a function of falling film flow rate for 2 different liquid distribution devices

Figure 7 summarizes the results of the measurement of the test models of the achieved, average k-values in comparison with the intended target values. The results can be summarized as follows. The developed asymmetric plate heat exchangers work very satisfactorily in the functions evaporator, absorber, condenser and generator as well as in the corresponding functional units. At the mean k-values of the apparatus the target values were achieved.

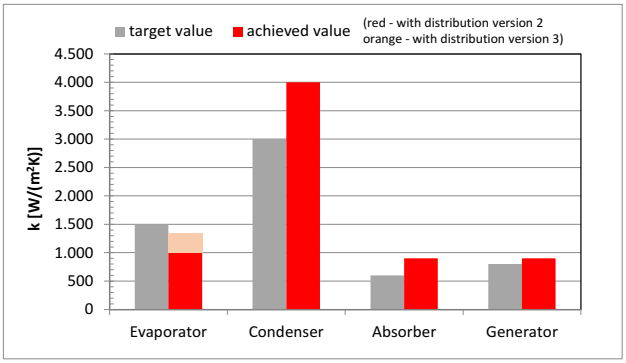

Figure 7: Comparison of the achieved average heat transfer coefficients with the target values

The de-aeration of the external channels is ensured by the fluid flow. The removal of inert gas from the condenser and absorber is ensured by a vacuum pump. This can also be done during the operation of the heat exchangers. The pressure losses of the external media are low. A good liquid supply is guaranteed but some improvement potential remains. The falling film flow rate in the internal channel of the plate heat exchanger should be > 40 g/ms for a good wetting. The flow velocity of the external fluid in the external channel should be > 0.4 m/s for a good heat transfer. By appropriate inhibition a sufficient protection against corrosion can be ensured. This is associated with a long service life of the heat exchanger.

5. APPLICATION OF ASYMMETRIC PLATE HEAT EXCHANGERS IN ABSORPTION REFRIGERATION SYSTEMS

Following the successful development of the asymmetric plate heat exchangers EAW's absorption chiller product range has been revised. The new plate heat exchangers were integrated into the systems. The result is a completely new generation of water/LiBr absorption chillers.

Three initial systems with 15, 30 and 65 kW cooling capacity were set up, successfully tested and measured. The new plate heat exchangers can be used to manufacture absorption chillers up to a cooling capacity of 400 kW. Figure 8 shows the simplified scheme of single-stage absorption chillers with the exclusive application of plate heat exchangers. Figure 9 shows views of the absorption chiller with 30 kW nominal cooling capacity without and with enclosure. The market entry of the new series was launched in October 2018.

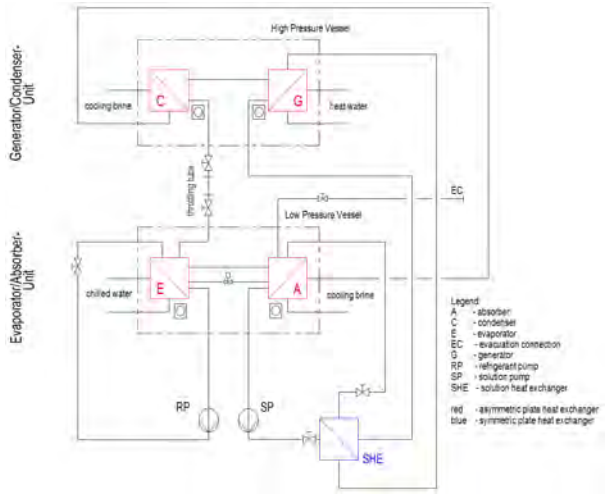

Figure 8: Simplified flow diagram of the novel series of water/LiBr absorption chillers with the exclusive use of plate heat exchangers

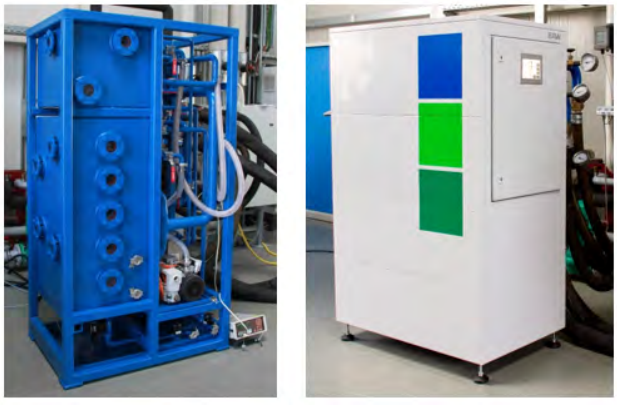

Figure 9: Views of the water-/LiBr absorption chillers with 30 kW rated cooling capacity without and with enclosure

For the absorption refrigeration systems nomograms have been created from which the achievable cooling capacity can be quickly determined as a function of the temperatures of cooling brine inlet, heating water inlet and chilled water outlet. Figure 10 contains the nomogram for the system with a nominal cooling capacity of 65 kW.

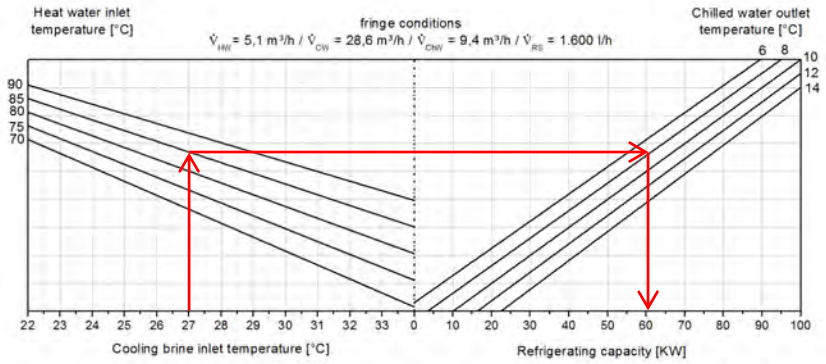

Figure 10: Power nomogram of the AKM with 65 kW nominal refrigerating capacity

Figure 11 shows the cooling capacity and the EER_{th} of the absorption chiller with 65 kW cooling capacity as a function solution flow rate. A high efficiency of 0.75 ... 0.8 could be achieved. EER_{th} is the quotient of cooling capacity and heating capacity.

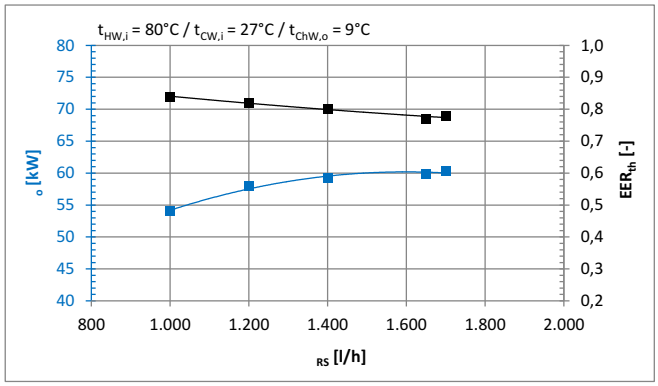

Figure 11: Cooling capacity and EER_{th} of the chiller with 65 kW nominal cooling capacity as a function of the volume flow of the refrigerant rich solution for measuring point 80/27/9

Figure 12 shows that these absorption chillers can also be used in district heating networks or in waste heat recovery systems where high temperature spreads (low return temperature) are required. With 80°C heating water inlet and 27°C cooling water inlet a chilled water of 11°C can be generated even with 25 K heating water temperature difference (heating water return temperature: 55°C). However the cooling capacity is reduced compared to the nominal condition - with a heating water return temperature of 70°C to 66 % of the nominal capacity.

The new plants can be used not only as absorption chillers but also as absorption heat pumps or heat transformers. The new series has the name Maral.

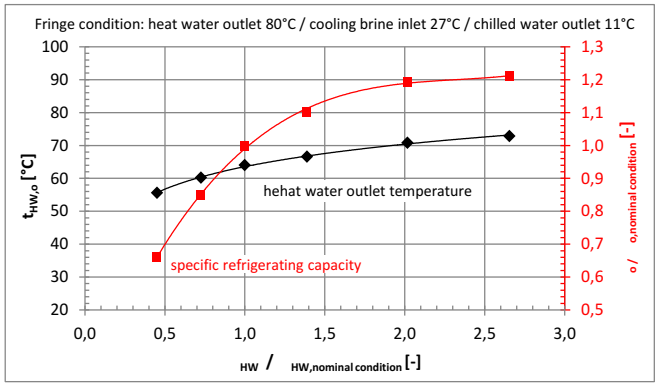

Figure 12: Heating water outlet temperature and change in cooling capacity as a function of the heating water volume flow (measured at chiller with 15 kW nominal capacity – transferable to chillers with same design and higher capacities)

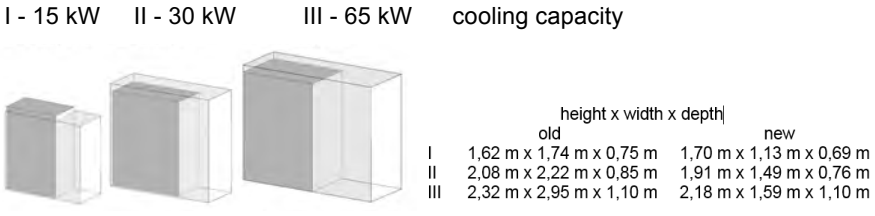

	height x width x depth old	new
I	1,62 m x 1,74 m x 0,75 m	1,70 m x 1,13 m x 0,69 m
II	2,08 m x 2,22 m x 0,85 m	1,91 m x 1,49 m x 0,76 m
III	2,32 m x 2,95 m x 1,10 m	2,18 m x 1,59 m x 1,10 m

(transparent - old design / shadowed - new design)

Figure 13: Size comparison of the old and new plant design

The results are very positive. In terms of design and channel height, the plate heat exchangers are unique on the world market and can be used for the refrigerant water in the generator, condenser, evaporator and absorber function. Compared with the use of tube bundle heat exchangers the cost of the new type of absorption chillers are considerable reduced while at the same time improving plant compactness (reducing the volume to around 60%). Figure 13 compares the size of the old and the new plant design. Based on the new plate heat exchanger a series of seven absorption chillers with capacities ranging from 15 … 400 kW have been designed, see Figure 14.

ILK and the company EAW 2018 received the German Refrigeration Award for the development of asymmetric plate heat exchangers and their application in a new generation of water/LiBr absorption refrigeration systems. The development project was funded by the Federal Ministry for Economic Affairs and Energy via the funding program INNO-KOM-OST.

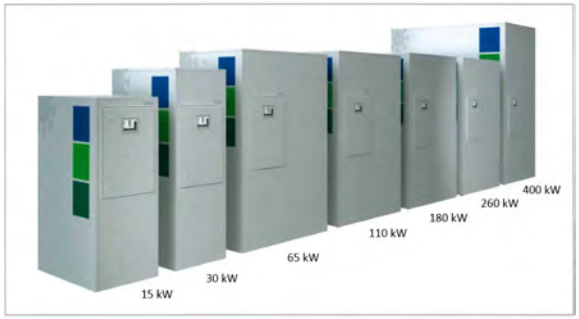

Figure 14: Series of EAW's new absorption chillers Maral 1 to 7

6. SUMMARY

Water/LiBr absorption chillers work under low pressure conditions. Therefore pressure losses of the refrigerant vapor needs to be low because absolute pressure differences in the cycle are very small. Due to the high specific volume of water vapor large flow cross sections are necessary which preclude a compact system design. On the other hand small flow dimensions are required for the

external media (heating, cooling and chilled water) in water cooled and hot water driven absorption chillers for a good heat transfer. Conventional plate heat exchangers which have the same channel heights on both fluid sides are therefore not usable in water/LiBr absorption chillers. Different channel heights are required. But asymmetric plate heat exchangers which meet the special requirements for use in water-/LiBr absorption chillers did not exist so far. Within a R&D cooperation of ILK Dresden, EAW and a heat exchanger manufacturer asymmetric plate heat exchangers have been developed which have different channel heights for the two media flows, liquid side and product side. The plate design is adapted on the conditions of water/LiBr absorption chillers with the functions absorber, generator, evaporator and condenser. Optimum flow and thus heat transfer conditions of the media and favorable plate wetting are achieved in the apparatus. Following the development and production of the adapted asymmetric plate heat exchangers three initial plants of water/LiBr absorption chillers were built with cooling capacities of 15, 30 and 65 kW at the nominal point. The systems were successfully tested and measured. They are extremely compact. The size reduction is on average 40 %. The manufacturing costs have been reduced. With the new plate heat exchangers plants can be built up to a refrigerating capacity of 400 kW. The new plants can also be used as absorption heat pumps, heat transformers or as resorption refrigerating plants for cold temperatures around 0 °C.

7. NOMENCLATURE

A	surface	m^2	pressure loss coefficient	-
EER	energy efficiency ratio	kW/kW	falling film intensity	kg/(ms)
k	heat transfer coefficient	$W/(m^2K)$	concentration	M%
p	pressure	Pa	difference	unit
	heating capacity	kW	efficiency	- or %
t	Celsius temperature	°C	heat ratio	-
v	velocity	m/s		
	volume flow	m^3/s		

Indices

A, Abs	absorber	G	generator (desorber)	o	cold, evaporation
c	condenser	HW	heating water	o	outlet
Ch	channel	ht	heat transfer	PS	poor solution
ChW	chilled water	i	inlet	RS	riche solution
CW	cooling water	l	loss	s	saturation
el	electrical	m	middle	S	solution
ex	external	max	maximal	SC	subcooling
F	fluid	min	minimal	th	thermal
FF	falling film				

8. REFERENCES

Kemmerzehl, C., Richter, M: 2017. Absorptionskälte mit Wasser als Kältemittel – kompaktere und leistungsfähigere Anlagen durch neue Wärmeübertragerkonzepte. (*Absorption cooling with water as refrigerant – more compact and more powerful chillers with new heat exchanger concepts.*) in: Dresdner Kolloquium der Kältetechnik, Dresden, Germany

Marcos, J.D., Izquierdo, M., Lizarte, R., Palacios, E., Infante Ferreira, C. 2009. Experimental boiling heat transfer coefficients in the high temperature generator of a double effect absorption machine for the lithium bromide/water mixture. Int. J. of Refrigeration, 32(4), 627-637

Safarik, M., Richter, L., Heinrich, C., Otto, M. 2004. Small capacity water/lithium bromide absorption chiller for solar cooling applications, in: EuroSun 2004, 14. Int. Sonnenforum. Freiburg, Germany.

Safarik, M., Richter, L. 2013. Development and demonstration of a 50 kW double-effect absorption chiller in combination with a parabolic trough collector. in: 5th Int. Conf. Solar Air-Conditioning, Bad Krozingen, Germany

Manuscript ID: 970
DOI: 10.18462/iir.icr.2019.0970

Comparison of configurations of high-temperature heat pumps for biogas-upgrading

Franz HELMINGER[(a)], Michael LAUERMANN[(a)], Alexander BAUM-HAKEL[(b)], Gerwin DREXLER-SCHMID[(a)]

[(a)] AIT Austrian Institute of Technology GmbH,
Center for Energy, Sustainable Thermal Energy Systems,
Giefinggasse 2, 1210 Wien, Austria, franz.helminger@ait.ac.at

[(b)] Frigopol Kälteanlagen GmbH
Gamser Straße 21, 8523 Frauental a.d. Laßnitz,
Austria, alexander.baumhakel@frigopol.com

ABSTRACT

High temperature heat pumps in industrial processes can enable an increase of their energy efficiency. The temperature swing adsorption process (TSA) enables an efficient separation of carbon dioxide. An essential part of the TSA process is a heat distribution concept, for which high temperature heat pumps are a good choice, since heat must be removed at low temperature (evaporation 35-50°C) and supplied at high temperature (condensation 110-125°C). With this aim different heat pump configurations have been numerically investigated using Dymola/Modelica™. A number of heat pump configurations, varying pre-selected refrigerants, circuit configurations, etc., have been simulated in order to compare the results by compressor size and an internal suction gas superheater (IHX).
The results show the relative displacement volume of each heat pump configuration and give recommendations of the use of the IHX as basis for investment costs and economical solutions.
Keywords: High-Temperature Heat Pump, Industrial Application, Heat Recovery.

1. INTRODUCTION

The use of high temperature heat pumps in industrial processes has been accelerated for several years. Use temperatures of 90°C is state of the art. As development progressed, both the usage temperatures and the thermal performance of the heat pumps were increased. Despite a growing interest in heat pump technology, knowledge about it and its possible applications is not widespread in industry. The present paper shows technical aspects of heat pump development when used in a so-called temperature swing adsorption process (TSA process for short). Of course, the results can also be applied to other industrial processes in order to implement energy efficiency measures in industrial processes.
At the TSA process, carbon dioxide is adsorbed on an adsorbent at a low temperature (about 45 to 60°C) and desorbed at a higher temperature (about 95 to 115°C), regenerating the adsorbent. The appropriate temperature levels and the corresponding separation efficiency between adsorption and desorption depend essentially on the affinity for adsorption of carbon dioxide. Similarly high affinities should be achieved in the TSA process as in amine washing, the energy requirement should be considerably lower. The TSA process has been successfully researched in climate protection research for several years. (Xu, Song, Andresen, Miller, & Scaroni, 2002) and (Sonnleitner, Schöny, & Hofbauer, 2017)
Preliminary investigations have shown that there is great potential for the TSA process, provided that suitable continuous process control with separate adsorption and desorption zones can be implemented. It must be continuously cooled (adsorption zone in the adsorber) and heated (desorption

zone in the desorber). High temperature heat pumps are very well suited for this purpose. (Vogtenhuber, et al., 2017)
When designing heat pumps for use in the TSA process, source temperatures between 35°C and 55°C and sink temperatures between 105°C and 115°C must be assumed. The selection and design of high temperature heat pumps raises a number of questions. The high operating temperatures at the desorber compared to products available on the market, the resulting temperatures in the heat pump condenser (condenser for short), the operating temperatures at the adsorber and the resulting temperature differences between heat pump evaporators (evaporators for short) are the basis for analyzing possible high temperature heat pumps and comparing them with each other.

2. GENERAL DESIGN ASPECTS

In order to design high temperature heat pumps, the know-how of cooling systems and heat pumps for room heating and hot water preparation is used. The main differences to heat pumps in the range up to 80°C utilization temperature lie in the refrigerants used and the requirements placed on the single components in the refrigeration cycle. For the application of high temperature heat pumps in industrial processes, there are different refrigerants that are better or less suitable for each area of application. Tailored to the aforementioned application of the separation of carbon dioxide (Drexler-Schmid, Lauermann, Baumhakel, & Helminger, 2018) and (Helminger, Lauermann, Baumhakel, & Drexler-Schmid, 2018) describe the selection of potential refrigerants, the selection of refrigeration cycle configurations and aspects of the heating and cooling capacities of different configurations. The selection of potential refrigerants was based on technical, economic and ecological aspects. Refrigeration cycle configurations were modelled, configured and simulated for the intended operating conditions. The mentioned documents focus on the presentation of different configurations of high temperature heat pumps and expected operating parameters, which provide the basis for economic evaluations of the operation. In the present paper, aspects of design and thus investment costs are also dealt with. Each refrigeration cycle consists of the main components evaporator, compressor, condenser and expansion valve. In some refrigeration cycle configurations, additional components such as economizers or ejectors can be found. In this article, the costs of the compressors and the use of an internal suction gas superheater (IHX) are examined in more detail.
The thermal performance in the evaporator and condenser and the electrical power consumption of the high temperature heat pump are determined by the mass flow of the refrigerant in the refrigeration cycle and depend on the displacement volume of the compressor. The displacement volume and thus the compressor size is of essential importance for the costs of a high temperature heat pump.
Depending on their thermodynamic properties, refrigerants suitable for high temperature heat pumps carry the risk that, in the event of insufficient suction gas superheating, compression into the wet steam area could occur, which would damage the compressor. The required suction gas superheating is low at low temperatures and increases as the temperature difference between evaporator and condenser increases. As a rule, a suction gas superheating of about 5 K prevails in the evaporator. In order to ensure additional suction gas superheating, internal suction gas superheaters (IHX) are used, which cause additional costs. It must therefore be decided at the design process of the high temperature heat pump, depending on the operating conditions, whether this additional component is to be installed or not.

3. OPERATING CONDITIONS, MODELLING, AND SIMULATIONS

The operating parameters for the present investigation are determined by the mode of operation of the TSA process. It is essential that both the required cooling capacity at the adsorber and the heating capacity at the desorber are provided by the high-temperature heat pump. For the high-temperature heat pump, the source and lower inlet and outlet temperatures are decisive in the first step of the investigation. The thermal performance is mainly determined by the delivery volume of the compressor(s) and can be determined by suitable selection of the compressor(s) or influenced by its operating frequency. For further investigation it is assumed that suitable compressors are available

and the focus is on operating temperatures. The operating temperatures are shown in Fig. 1 (Drexler-Schmid, Lauermann, Baumhakel, & Helminger, 2018). This results in a total of 180 operating points, which are defined as follows:

- Source in temperature (evaporator) of 35, 40, 45, 50 and 55°C,
- Source temperature difference (evaporator) of 3, 5, 7.5 and 10 K,
- Sink in temperatures (condenser) of 95, 97.5 and 100°C,
- Sink out temperatures (condenser) of 105, 110 and 110°C and
- Heating capacity at condenser of 140 kW at source in temperature of 50°C, source temperature difference of 7.5K, Sink in temperature of 100°C and Sink out temperature of 115°C

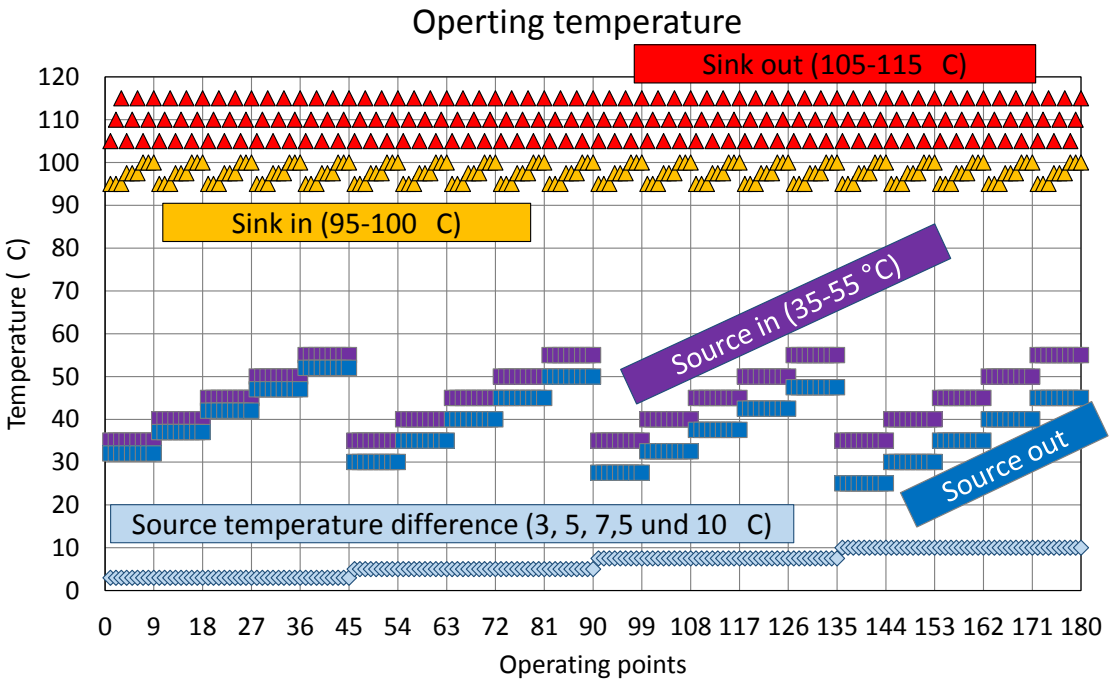

Figure 1: Expected operating range and operating conditions for heat source and heat sink (Drexler-Schmid, Lauermann, Baumhakel, & Helminger, 2018)

The following diagrams in Figure 2 show the investigated refrigeration cycle configurations. The main components of the refrigeration cycles are given at the refrigeration cycle “Single stage” and are the compressor (Co), the condenser (C), the expansion valve (ExV) and the evaporator (E). In the "EVI" refrigeration cycle (marked with b) in Figure 2), an economizer is installed which provides a vaporous refrigerant for injection into the compressor. The refrigeration cycle configuration “Two cycle” (marked with c) in Figure 2) consists in principle of two refrigeration cycles “Single stage”, in which each compressor circulates half the refrigerant. In this way, one of the two refrigerant circuits does not have to overcome the entire temperature difference between the heat source and the heat sink. The use of an ejector is a method of increasing the efficiency and reducing losses. In contrast to the refrigeration cycle configuration "Single stage", the compressor does not have to overcome the entire pressure ratio between condenser and evaporator. “Cascades” (marked with d) in Figure 2) are divided into a low temperature refrigeration cycle (low temperature cycle for short) and a high temperature refrigeration cycle (high temperature cycle for short). In the “Cascade”, each individual refrigeration cycle has to overcome a lower pressure ratio than in the "Single stage" configuration. This means that the compressor in each refrigeration cycle can be operated closer to its design point and thus a higher compression efficiency can be achieved. Both refrigeration cycles are connected by a heat exchanger (so-called evaporator condenser) in which the refrigerant of the low temperature cycle condenses and the refrigerant of the high temperature cycle evaporates simultaneously. In the refrigeration cycle "COS-ejector" (marked with e) in Figure 2), the refrigerant evaporates in two evaporators marked with E1 and E2. The cycles are described in more detail in (Drexler-Schmid,

Lauermann, Baumhakel, & Helminger, 2018) and (Helminger, Lauermann, Baumhakel, & Drexler-Schmid, 2018).

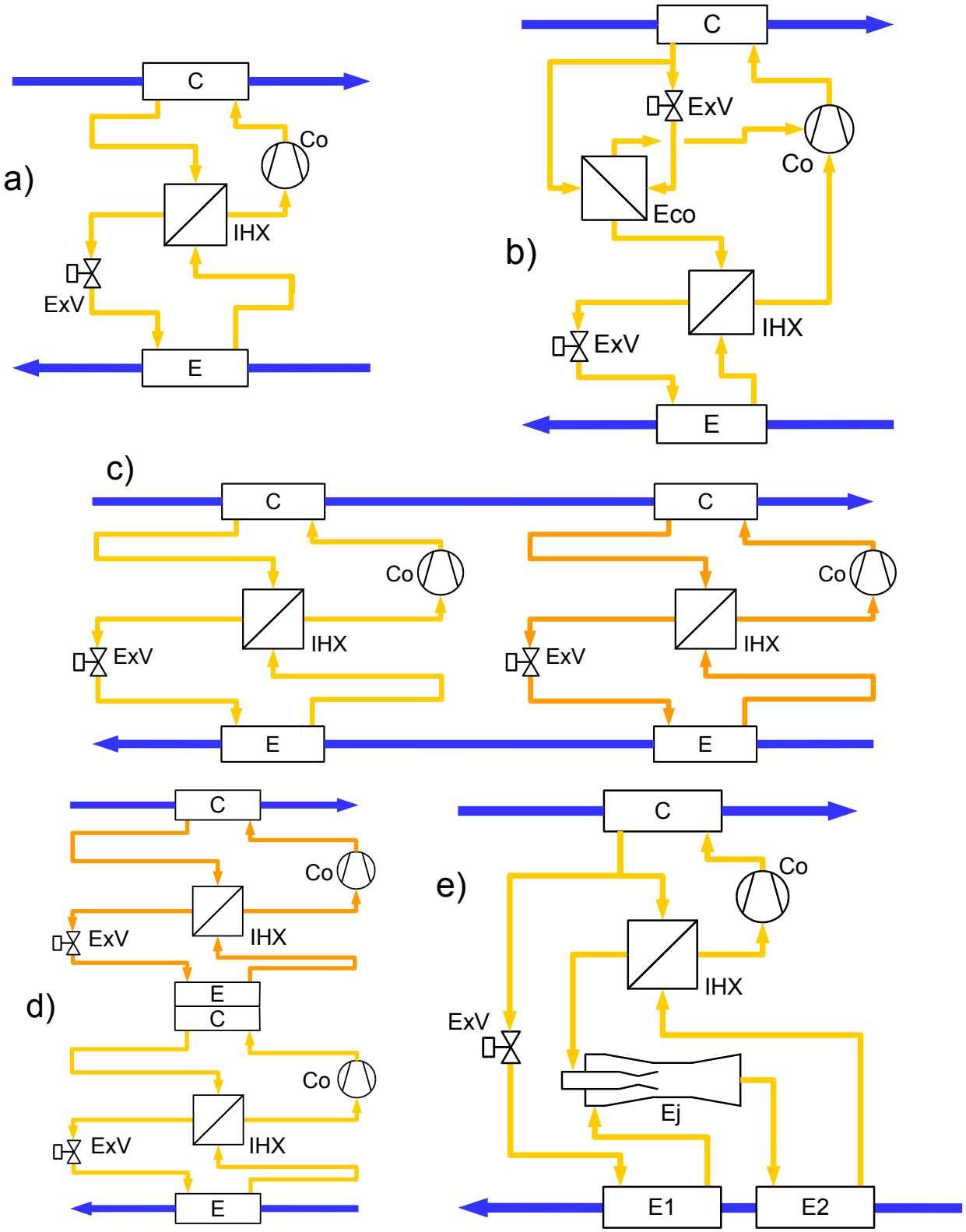

Figure 2: Schematic sketch of refrigeration cycles a)„Single stage“, b)„EVI“, c)„Two cycle“, d)„Cascade“ and e)“COS-Ejector“ (Drexler-Schmid, Lauermann, Baumhakel, & Helminger, 2018)

In all refrigeration cycle configurations optional internal suction gas superheaters (IHX) were provided. In the simulation, the function of the IHX is only activated if this is necessary for operation. Preselected refrigerants are assigned to the investigated refrigeration cycle configurations, resulting

in 14 configurations, which are summarized in Table 1. The modelling and simulation was done with models in Modelica™. The TIL-library was used for the thermal modelling, which is widely used in refrigeration engineering. (Helminger, Lauermann, Baumhakel, & Drexler-Schmid, 2018)

Table 1: Refrigerants and regrigeration cycles given by (Drexler-Schmid, Lauermann, Baumhakel, & Helminger, 2018) and (Helminger, Lauermann, Baumhakel, & Drexler-Schmid, 2018)

Refrigeration cycle	Refrigerants
Single stage	R600 R1234ze(Z)
EVI (enhanced vapour injection)	
Two cycle	
COS-Ejector	
Cascade Low temperature cycle/high temperature cycle	R717/R1234ze(Z) R1234ZE(E)/R1234ze(Z) R717/R600 R600a/R600 R600a/R1234ze(Z) R717/R1336mzz-Z

4. RESULTS REGARDING COMPRESSOR SIZE AND IHX

In this section the different compressor sizes are compared based on the displacement volume. The displacement volume of the refrigerant circuit "Single stage" with the refrigerant R600 is used as a reference and the other 13 variants are compared. The required heating capacity in the TSA process is 140 kW at 50°C evaporator inlet temperature (source in) and 115°C condenser outlet temperature (sink out, see chapter 3). Figure 3 shows the relative displacement volume of each configuration to the reference configuration (circle with white filling). For all configurations (except the reference configuration) the overall displacement volume is shown as a black diamond. In the "Two cycle" configurations with R600 and R1234ZE(Z) the displacement volume of each refrigerant cycle is shown as a diamond with a white filling. For the cascades, the displacement volume of the low temperature cycle is shown as a square and the displacement volume of the high temperature cycle as a triangle.

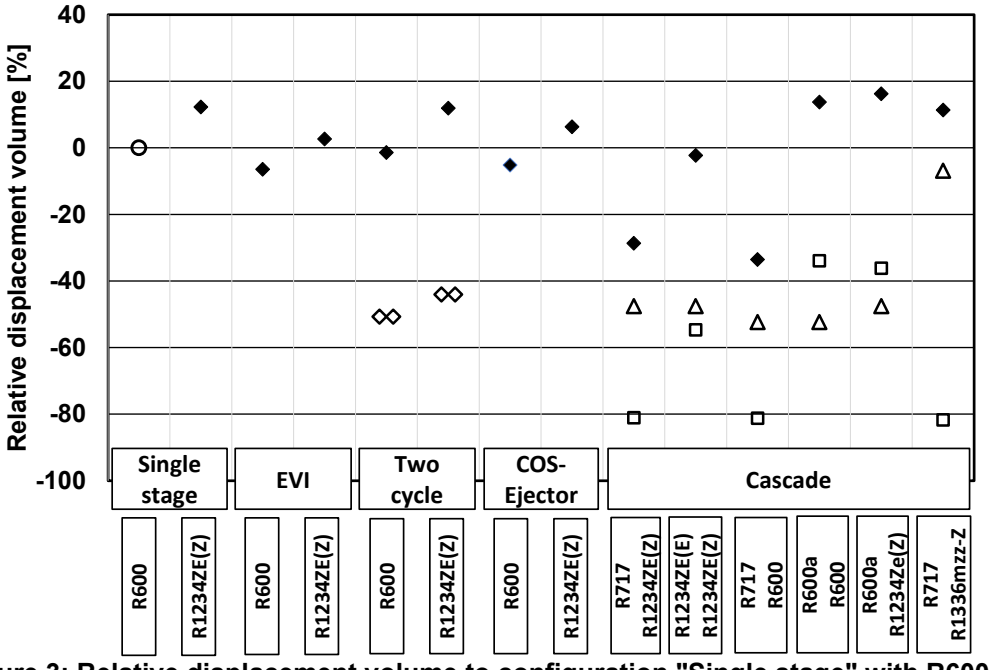

Figure 3: Relative displacement volume to configuration "Single stage" with R600

The use of the IHX in each configuration is analyzed on the basis of the calculated suction gas superheating. Figure 4 shows how the suction gas superheating behaves in the configuration “Single stage” with R600 at each operating point. It is shown how the calculation results are distributed depending on the operating temperatures.

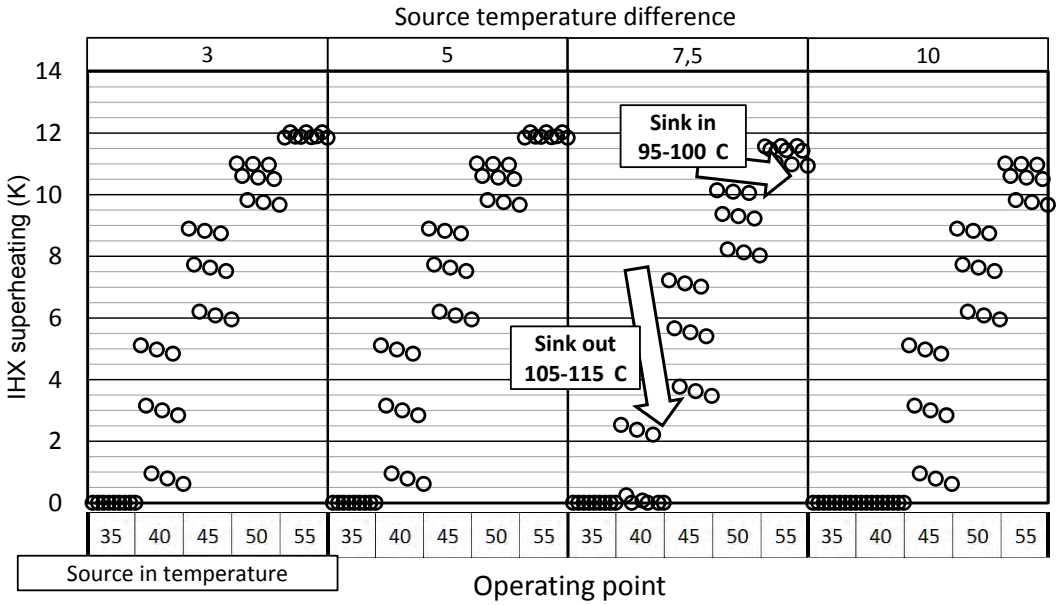

Figure 4: Suction gas superheating in the IHX of the configurations "Single stage" with R600

Figure 5 shows the suction gas superheating for each operating point of the configurations "Single stage", "EVI", "Two cycle" and "COS-Ejector" with R600 and R1234ZE(Z), respectively. Operating points where no suction gas superheating is required are not shown.

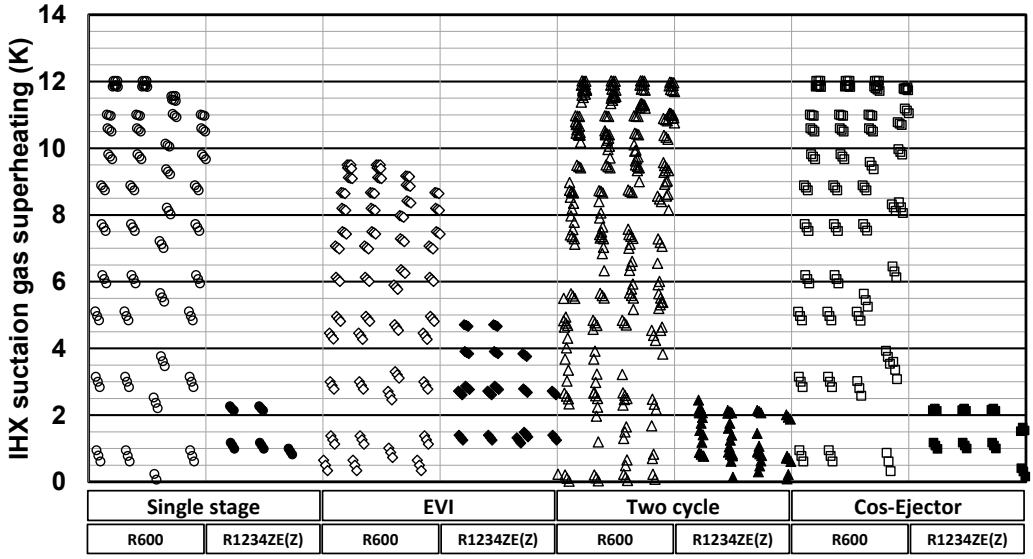

Figure 5: Suction gas superheating in the IHX of the configurations „Single stage“, „EVI“, „Two cycle“ and „COS-Ejector“ with R600 and R1234ZE(Z)

The calculation results of the required suction gas superheating in each low temperature and high temperature cycles of the cascades are summarized in Figure 6. The operating points that do not require suction gas superheating are also shown. For refrigerant circuits with R717, this is expected to be the case at all operating points.

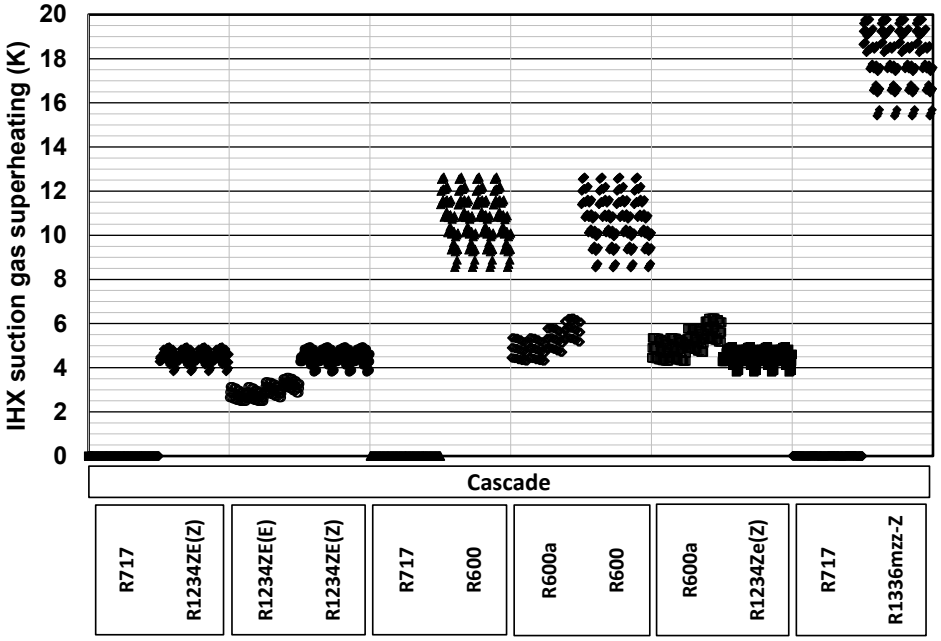

Figure 6: Suction gas superheating in the IHX in "Cascade" configurations

5. CONCLUSIONS

As expected, the evaluation of the displacement volume in Figure 3 of the compressors shows that the refrigeration cycle configurations "Single stage", "EVI", "Two cycle" and "COS-Ejector" with R1234ZE(Z) require a slightly larger displacement volume than refrigeration cycle configurations with R600. A lower displacement volume is required for the "EVI" and "COS-Ejector" refrigeration cycle configurations. In the case of cascades, the total displacement volume can be significantly lower in some cases compared to the reference by using R717 in the lower temperature cycle. Only the cascade R717/R1336mzz-Z requires a slightly higher overall displacement volume, which is due to the displacement volume of the high temperature cycle with R1336mzz-Z. The cascade with R1234ZE(E)/R1234ZE(Z) results in approximately the same total displacement volume. The cascades R600a/R600 and R600a/R1234ZE(Z) require a slightly higher total displacement volume.

When evaluating the suction gas superheating, IHX for refrigeration cycles with a required suction gas superheating below 3K can be omitted ("Single stage", "Two cycle" and "COS-Ejector" with R1234ZE(Z)). If the suction gas superheating is between 3 and 6K ("EVI" with R1234ZE(Z)), it should be checked if the operating range can be restricted and whether an IHX is still required. For suction gas superheating above 6K (R600), an IHX is recommended unless a significantly restricted operating range indicates a low required suction gas superheating. As expected, no IHX is required for cascades with R717 in the low temperature cycle. For cascades with suction gas superheating of about 5 K, either the low temperature cycle or the high temperature cycle could be equipped with an IHX and the IHX in the other cycle could be omitted. The high temperature cycles with R600 or R1336mzz-Z in the respective cascades should be equipped with an IHX.

The numerical assessment of the heat pump configurations in this work, the influence of the different heat pump cycles and different refrigerants is shown. The results provide information on the necessary compressor capacity and the question whether or not a suction gas superheater is needed for the specific application of biogas upgrading. Both of these components play a significant role in investment costs.

ACKNOWLEDGEMENTS

This publication was developed within the framework of the project "bioCH4.0" (FFG project number 853612). This project is funded by the Austrian Klima- und Energiefonds and will be carried out as part of the Energieforschungsprogramm 2. Ausschreibung 2016.

NOMENCLATURE

C	Condenser	Co	Compressor
COS	Condenser outlet split	E	Evaporator
Eco	Economizer	Ej	Ejector
EVI	Enhanced vapour injection	ExV	Expansion valve
IHX	Internal suction gas superheater	TSA	Temperature swing adsorption

REFERENCES

Drexler-Schmid, G., Lauermann, M., Baumhakel, A., Helminger, F., 2018. Konfigurations- und Leistungsvergleich von Hochtemperaturwärmepumpen zur Biogas-Aufbereitung. Proceedings of EnInnov. Graz, Austria.

Helminger, F., Lauermann, M., Baumhakel, A., Drexler-Schmid, G., 2018. Konfigurations- und Leistungsvergleich von Hochtemperaturwärmepumpen zur Biogas-Aufbereitung. Proceedings of DKV. Aachen, Germany.

Sonnleitner, E., Schöny, G., Hofbauer, H., 2017. Assessment of zeolite 13X and Lewatit® VP OC 1065 for application in a continuous temperature swing adsorption process for biogas upgrading. Biomass Conversion and Biorefinery (8), 379 - 395.

Vogtenhuber, H., Hofmann, R., Schöny, G., Pirklbauer, J., Fraubaum, M., Helminger, F., Werner, A., Hofbauer, H., 2017. Development of an Efficient Heat Balance Concept for a TSA-Process Considering Heat-Pump Integration. Proceedings of the 10th International Conference on Sustainable Energy and Environmental Protection. Renewable Energy Sources, Bled, Slovenia: University of Maribor Press.

Xu, X., Song, C., Andresen, J.M., Miller, B.G., Scaroni, A.W., 2002. Novel polyethylenimine-modified mesoporous molecular sieve of MCM-41 type as high-capacity adsorbent for CO2 capture. Energy and Fuels (16).

Manuscript ID: 973
DOI:10.18462/iir.icr.2019.0973

Turbo-compressors for R-718: Experimental evaluation of a two-stage steam compression cycle

Michael BANTLE[(a)], Christian SCHLEMMINGER[(a)], Cecilia GABRIELII[(a)] Marcel AHRENS[(b)]

[(a)]SINTEF Energy Research
Kolbjørn Hejes vei 1D, Trondheim, 7465, Norway, michael.bantle@sintef.no
[(b)] Norwegian University of Science and Technology
Trondheim, 7465, Norway

ABSTRACT

Water (R-718) is a safe and energy-efficient refrigerant. Mechanical vapour recompression (MVR), an open-loop heat pump using R718, can significantly reduce the energy consumption for steam-heated processes like drying, pasteurization, evaporation or distillation. However, the existing compression technology is not cost-efficient, especially in the capacity range from 500 kW to 4 MW. Therefore, a novel two-stage turbo-compressor system, developed for application in industrial superheated steam drying and based on mass-produced automotive turbocharger technology, was developed. Its performance was evaluated in a test facility, showing that it is possible to compress superheated steam from atmospheric pressure up to 3 bar, delivering 300 kW at 133°C, with a COP of 5.9, an isentropic efficiency of 74% and a Carnot efficiency of 48%. With an estimated investment cost of 150 €/kW installed heating capacity, the system clearly has the potential of being a cost-effective solution for heat recovery in steam-heated industrial processes.
Keywords: R718, turbo-compressor, mechanical vapour recompression, heat pump, steam drying

1. INTRODUCTION

Industrial heat pumps available on the market today normally operate with a heat delivery (heat sink) temperature of not more than 70 °C - 100 °C, depending on technology and refrigerant applied. In this temperature range, air or water is often used as a secondary heat carrier. There are, however, numerous industrial processes with heat demands at temperatures above 100 °C, such as drying, evaporation, pasteurization, sterilization or distillation, for which steam is used as a heat transport medium (Elmegaard et al., 2017).

Industrial drying processes require intensive use of energy. Estimates show that 12 % to 25 % of the national industrial energy consumption in developed countries is attributed to industrial drying, with limited utilization of waste heat streams. There is an accordingly large potential for more efficient and environmentally friendly technologies within industrial drying processes. By integrating a heat pump system, the specific energy demand can be reduced with up to 80% (Sannan et al., 2016., Kang and Ryu, 2016).

Heat pumps operating with heat sinks above 100 °C are normally classified as high-temperature heat pumps (HTHP). The choice of refrigerant for a HTHP is limited. Water (R718) is one of the few alternatives that is not only thermodynamically effective but also environmental-friendly, non-flammable, non-toxic and cost-effective (Larminat et al., 2014). Since water vapor (steam) is used as energy source in numerous plants its industrial acceptance is very high. Disadvantages include high specific volumes, as well as a large volume change and superheating during compression.

Mechanical vapour recompression (MVR) is an open-loop heat pump technology using R718. The MVR technology has the potential of significantly reducing the energy consumption for steam-heated processes. However, MVR is today normally applied only for thermal capacities higher than 10 MW because the specific investment costs (cost per kW installed capacity) for smaller systems can be as high as 1000€/kW (Bantle et al., 2018). To be an economically feasible alternative for the industry

an investment cost of 100 – 200 €/kW is required (Elmegaard et al., 2017). Steam compressor technology is today the main cost component in MVR systems and for capacities between 500 kW and 4 MW there is no cost-efficient technology available on the market (Elmegaard et al., 2017). Turbo-compressor technology is however considered as a potentially cost-effective and efficient alternative to conventional compressors in this capacity range. High impeller speeds allow a compact design with low material consumption. Turbo-compressors are normally used for compression of air and about 95% of all diesel cars are equipped with a "turbocharger" (Weel et al., 2013).
There are a several research projects focused on developing cost-effective R718 compressors for use in HTHPs. Larminat et al. (2014), Chamoun et al. (2014) and Madsboell et al. (2015) all present compressor technology development to supply 500 kW - 700 kW heat at a condensing temperature of 130 °C. Meroni et al. (2018) compared different HTHP cycles and compressor designs for steam generation at 150 °C and conclude that direct compression of steam (i.e. MVR) in a two-stage cycle out-performed the closed loop cascade cycles using other refrigerants. Zühlsdorf et al. (2018) suggests design recommendations for two-stage R718 turbo-compressors, to obtain lower investment costs and efficient de-superheating.
In the present work, a system with two-stage turbo-compression of steam was conceptualized, constructed and evaluated in a test facility. The objective is to investigate the potential of using an MVR heat pump with a turbo-compressor system based on mass produced components from the vehicle industry, in order to find a cost-efficient solution for waste heat recovery in industrial processes such as steam drying. By performing measurements with varying impeller speeds and mass flow rates the compressor performance map and system efficiency are determined, enabling an assessment of operating area and energy efficiency. In section 2, the test facility and experimental procedure are presented followed by a description of the method used for performance evaluation in section 3. The results are presented, discussed and concluded in section 4 and 5.

2. EXPERIMENTAL SETUP

2.1 Test facility system

In Fig. 1 the essential components and measuring points of the test facility are presented. The two-stage turbo-compressor system is designed for an industrial steam dryer providing up to a ton of excess steam per hour at atmospheric pressure and 10-20 K superheat. Drying conditions are simulated by means of a steam generator and steam cooler.

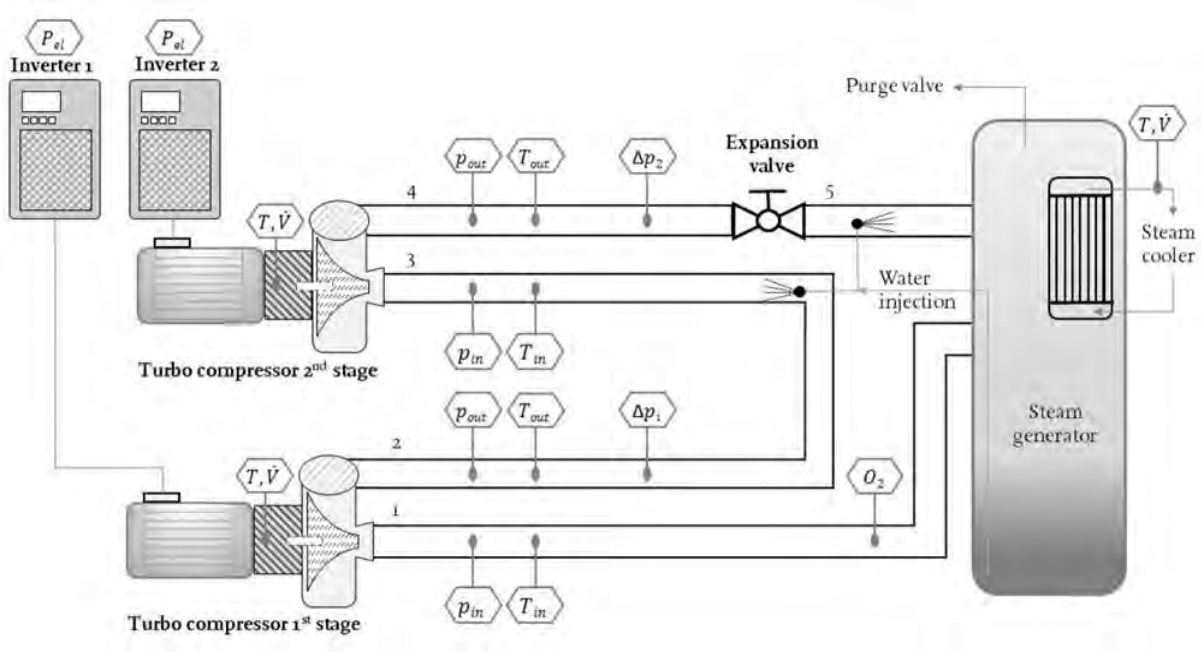

Figure 1: Schematic representation of the experimental setup of the MVR heat pump system.

The inlet of the first turbo compressor stage (1) is connected to the steam generator. After the first compression stage (1-2) a controlled amount of water is injected to reduce the steam superheat to around 20 K before the second stage inlet (2-3). After the 2nd compression stage (3-4) the pressure of the superheated steam is reduced to atmospheric conditions in the expansion valve (4-5). To minimise thermal stress on the steam generator, water injection is applied after the expansion valve. A steam cooler connected to the steam generator cools the system (i.e. simulates the dryer) by de-superheating the steam before it enters the 1st compression stage (5-1) at atmospheric pressure and 20 K superheat. To minimise mechanical stress of the compressor, all piping work was constructed to ensure compensation for thermal expansion during start-up and operation. The piping is insulated by 50 mm mineral wool (k=0.05 W/m·K). DN100 piping was used to minimize system pressure drop.

2.2 Turbo-compressor setup

Two identical turbo-compressors are installed in series to achieve a total pressure ratio of 3. A planetary gearbox, enabling a high transmission ratio of 7.5 with a mechanical efficiency of 98%, is mounted on the drive shaft of each turbo-compressor. The planetary gearbox is equipped with an internal oil pump and an external water-cooled oil cooler. A 650 V water cooled DC-motor is placed directly on the drive shaft of the gearbox, enabling a rotational speed of up to 90 000 rpm at the impeller. The motor is controlled by an inverter which can deliver 59 kW at an efficiency of 97%.
The turbo-compressor prototype is a further development of a conventional radial turbocharger from the automotive industry (i.e. designed for air), adapted by the manufacturer for use in steam compression systems. The modifications aimed at achieving a larger pressure ratio at a high isentropic efficiency and improving the durability for long-term continuous operation. The modified prototype includes an impeller designed in titanium with a diameter of 100 mm (the rest of the casting is in alumina) and a reinforced sealing between compression chamber and gear box.
It represents a compact and light-weighted design, with a total weight of the complete unit (turbo-compressor, gearbox, DC-motor) of about 40 kg and dimensions of 50 cm in length, 40 cm in width and 35 cm in height. More detailed design conditions are presented in Bantle et al. (2018). Based on costs for this turbo-compressor set-up the MVR heat pump investment cost is estimated to around 150 €/kW installed condenser capacity.

2.3 Data aquisation and measurement uncertainity

Steam temperature, pressure, mass/volume flow rate and oxygen content are measured at different points in the experimental facility, as shown in Fig. 1. Electric power of each inverter is recorded, as well as cooling capacity of the steam cooler and the respective water coolers, and the amount of injected cooling water. The accuracy of the sensors is between ±0.5 to ±0.75%, and the sampling rate of the data acquisition system is 1-5 seconds.
Measurement uncertainties are determined in accordance with ISO-5167-1:2003 and ISO-5167-2:2003, including primarily instrumental inaccuracy. For a pressure ratio of above 1.5 the uncertainty is less than 1.5 %. However, by error propagation, the calculated isentropic efficiency may vary by up to 5%, mainly due to the measuring inaccuracy of the pressure sensors. At higher pressures the uncertainity is significantly reduced.

2.4 Experimental procedure and operating conditions

Since the impeller is sensitive to droplets the system cannot be started with saturated steam. Instead it is started in an air atmosphere and heated up to a temperature of 110 °C, with excess heat from the compressor. Water is then injected through the de-superheaters and immediately evaporated, filling the system with superheated steam by replacing the air through the condenser purge valve. The system is considered completely filled with steam when the oxygen content is less than 0.1%.
Variation in operating points is achieved by changing the impeller speed of the two stages and changing the expansion valve opening posistion. An operating point is defined as stable when measurement variance over a period of 5 minutes is less than determined measurement uncertainty. The maximum investigated impeller speed was 81 000 rpm for the 1st stage and 72 000 rpm for the 2nd stage. Full speed of 90 000 rpm was not reachable due to a too high temperature of the gear box cooling oil. Impeller speeds below 54 000 rpm were not analysed since the corresponding operating conditions are industrially irrelevant due to the small pressure ratio achieved.

3. PERFORMANCE EVALUATION METHOD

3.1 Compressor performance map

A compressor performance map is a commonly used graph to represent, compare and analyze the performance at various operating conditions. Fig. 2 shows a typical performance map for turbo-compressors illustrating the relationship between mass/volume flow rate, pressure ratio, isentropic efficiency and impeller speed. Unstable operating points are represented by the "surge line" and "choke line". Surge behaviour occurs when the fluid flows back from the high-pressure to the low-pressure side, while choke behaviour is characterised by a rapid drop in pressure ratio.

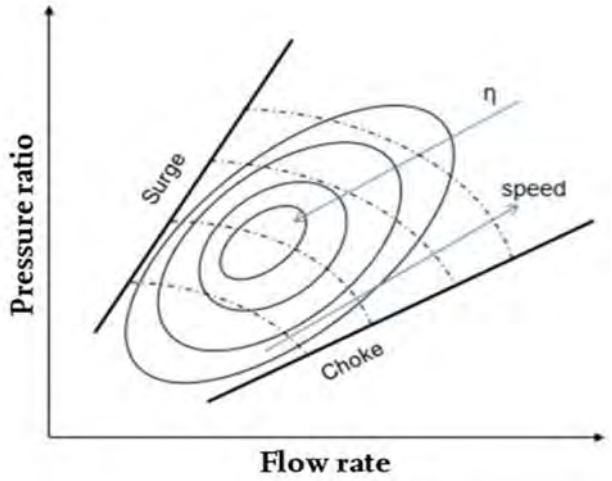

Figure 2: Schematic representation of a typical performance map for a turbo compressor

The determination of the performance map for the investigated turbo-compressor system was made as follows. All measured operating points are calculated back to a standardised reference point (i.e. a defined pressure and temperature). This is especially important for steam (R718) whose density is strongly reduced with reduced pressure. It is also recommended to adjust the impeller speed to correct for temperature influence (Hafaifa et al., 2014). These corrections enable a comparison of different operating points in the same performance map. Otherwise, the respective input parameters, e.g. temperature, pressure and flow rate, must be indicated for each point in the map.
Isentropic efficiency (η_{is}) is calculated from the ratio of enthalpy difference over the compressor for isentropic and real operating conditions (given from temperature and pressure measurement at inlet and outlet);

$$\eta_{is} = \frac{h_{out,is} - h_{in}}{h_{out} - h_{in}} \qquad \text{Eq. (1)}$$

Pressure ratio (Π_t) is given from the ratio of discharge and suction pressure of each compressor stage;

$$\Pi_t = \frac{p_{t\,out}}{p_{t\,in}} \qquad \text{Eq. (2)}$$

The corrected mass flow rate ($\dot{m}_{red}$) in Eq. 3 is achieved by calculating the mass flow rate back to the suction side reference point (van Essen, 1998), which was set to 1.013 bar and 120°C (corresponding to typical dryer conditions). In addition, the temperature measurements are corrected for heat losses (T_{hl}) between the measuring point and the actual compressor inlet/outlet.

$$\dot{m}_{red} = \dot{m}_t \cdot \frac{\sqrt{\left(T_{hl\,in}/T_{ref}\right)}}{\left(p_{t\,in}/p_{ref}\right)} \qquad \text{Eq. (3)}$$

The corrected volume flow rate is then given by using the density of R718 at the reference point (ρ_{ref} = 0,565 kg/m^3);

$$\dot{V}_{red} = \frac{\dot{m}_{red}}{\rho_{ref}} \quad \text{Eq. (4)}$$

The corrected impeller speed (N_{red}) is given from Eq. 5 where N_{set} is the set speed at the inverter.

$$N_{red} = \frac{N_{set}}{\sqrt{\left(T_{hl\ in}/T_{ref}\right)}} \quad \text{Eq. (5)}$$

The speed corrected pressure ratio (Π_{rel}), mass and volume flow rate ($\dot{m}_{rel}$, $\dot{V}_{rel}$) are then calculated as:

$$\Pi_{rel} = \Pi_t \cdot \frac{N_{set}}{N_{red}} \quad \text{Eq. (6)}$$

$$\dot{m}_{rel} = \dot{m}_{red} \cdot \frac{N_{set}}{N_{red}} \quad \text{Eq. (7)}$$

$$\dot{V}_{rel} = \dot{V}_{red} \cdot \frac{\mathrm{N_{set}}}{N_{red}} \quad \text{Eq. (8)}$$

3.2 Energy efficiency

The coefficient of performance (COP) of the turbo-compressor system is defined as the ratio between condenser cooling capacity and total electricity consumption of the system;

$$COP = \frac{\dot{Q}_{cond}}{\sum \dot{P}_{el}} \quad \text{Eq. (9)}$$

The COP determined from Eq. 9 considers all losses in the system; such as pressure drop (piping, measuring instruments, water nozzles, heat exchangers), losses of inverter, motor and gear unit, heat losses of the complete plant and compression losses of both turbo compressors.
The maximum theoretical COP, COP_{Carnot}, is determined according to Eq. 10. $T_{cond.,HP}$ and $T_{cond.,LP}$ is the condensing temperature [K] on the high pressure and low pressure side, respectively.

$$COP_{Carnot} = \frac{T_{cond.,HP}}{T_{cond.,HP} - T_{cond.,LP}} \quad \text{Eq. (10)}$$

Finally, the maximum system efficiency, the Carnot efficiency, is given as the ratio between the measured COP and the maximum COP;

$$\eta_{Carnot} = \frac{COP}{COP_{Carnot}} \quad \text{Eq. (11)}$$

4. RESULTS

4.1 Experimental compressor performance map

A performance map of the two-stage turbo compressor system was determined based on 87 measured stable operating points and is shown in Fig. 3. It can be observed that the second stage (blue dots) operates more closely to the surge line and is thus limiting the operating area of the system. An identical impeller design was used for both stages, which is not an optimal solution due to the change in steam volume flow between the two stages. A smaller design of the 2nd stage impeller is needed to obtain stable operation with a good safety margin to the surge line. Fig. 3 also shows the maximum achieved pressure ratio for the two stages; 1.95 at 81 000 rpm for the 1st stage

and 1.7 at 72 000 rpm for the 2nd stage. Due to the limitation of the gear box cooling oil temperature this is currently the highest possible pressure ratios that can be achieved in the test facility.

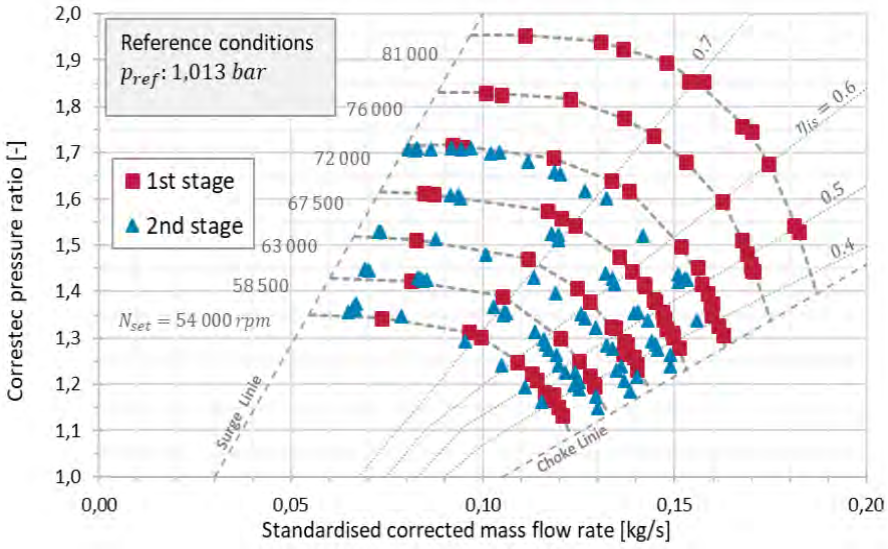

Figure 3: Experimentally determined performance map for the 1st and 2nd compressor stage

To analyze the system behavior when operating the two stages at either equal or unequal impeller speed, six operating points were selected for further evaluation. In Fig. 4, the three solid arrows (1-4) represent the connections between operating points for the 1st and 2nd stage at equal impeller speed, while the dashed arrows (5-6) represent the connections at unequal impeller speed.

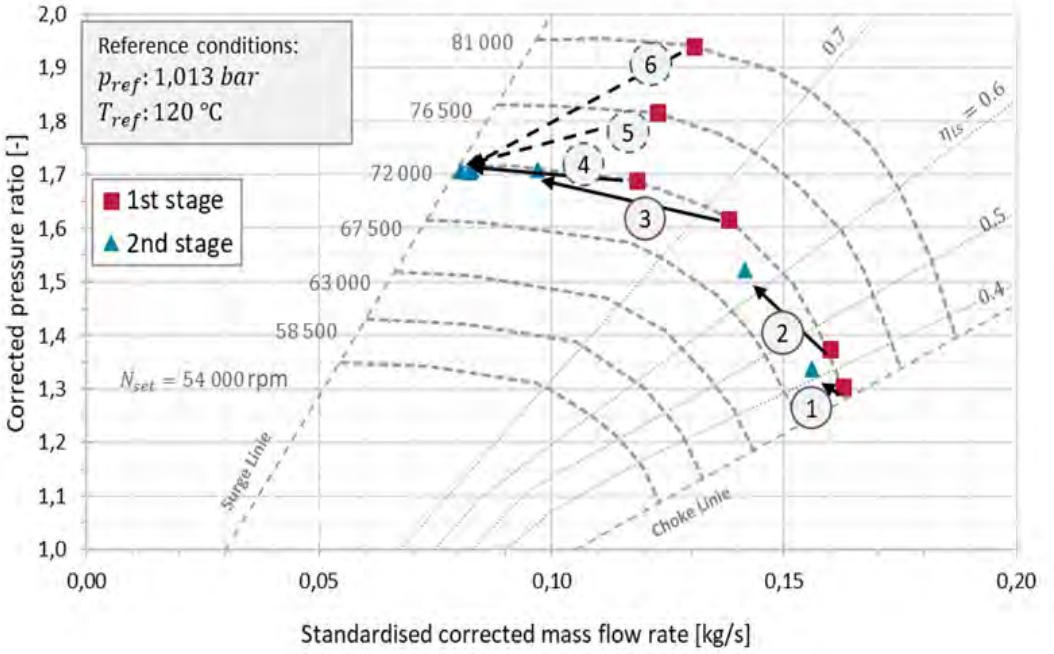

Figure 4: Dependencies (shown as arrows) between the 1st and 2nd stage for six operating points.

In point 1-4 both compressor stages are operated at 72 000 rpm. When then the expansion valve is successively more closed (moving left in the diagram), the pressure ratio and isentropic efficiency is improved for both stages, while the mass flow, and thus the condensing capacity, is reduced. In point 5 and 6 the impeller speed of the 1st stage is increased in relation to the 2nd stage. This leads to a larger pressure ratio for the 1st stage, while the mass flow remains almost unchanged. The operating point of the 2nd stage remains in a nearly constant position, close to the surge line, as when operating at equal impeller speeds (point 4). Both stages remain in the range of an isentropic

efficiency of 0.72 to 0.74. With different impeller speeds it is therefore possible to operate the system with higher pressure ratio and flow rate (condensing capacity) as well as a higher isentropic efficiency.

4.2 System efficiency

Table 1 shows the results from the performance analysis of the six operating points (#1 - #6) presented in Fig. 4. For point 1-4 (operation at equal impeller speed) an increased pressure ratio results in both a lower condensing capacity and a lower COP. When operating the 1st stage with a higher impeller speed (points 5-6) the total pressure ratio and condensing capacity are increased at the same time. For the desired pressure ratio of 3.0, a condensing capacity of 300 kW (steam flow of 500 kg/h) was achieved at a COP of 5.9, and a Carnot efficiency of 48 %. Even if the compressors account for the largest losses the isentropic efficiency is above 70%, which in principle is a satisfactory result. More notable is the observed heat losses, contributing to above 20% of the total losses, despite the use of thermal insulation. However, the compressor outlet temperature can be up to 230 °C, i.e. a temperature difference of up to 200 degrees to the environment, while the insulation thickness is only 5 cm.

Table 1: Summary of performance analysis for the six selected operating points (shown in Fig. 4).

#	N_{set} $(1/\mathrm{min})$	$\dot{m}_t$ $(\mathrm{kg/s})$	Π_t $(-)$	T_{sat} (°C)	T_{lift} (K)	$\dot{Q}_{Kond.}$ (kW)	P_{el} (kW)	COP $(-)$	COP_{carnot} $(-)$	η_{System}
1.	72.000 – 72.000	0,167	1,4	110,4	10,4	373,1	52,9	7,1	36,8	19,2%
2.	72.000 – 72.000	0,164	1,8	116,6	16,6	362,5	52,4	6,9	23,5	29,3%
3.	72.000 – 72.000	0,141	2,5	127,7	27,7	306,8	47,4	6,5	14,4	45,1%
4.	72.000 – 72.000	0,125	2,6	129,5	29,5	272,3	42,1	6,5	13,6	47,8%
5.	76.500 – 72.000	0,130	2,8	131,8	31,8	282,4	45,8	6,2	12,7	48,7%
6.	81.000 – 72.000	0,138	3,0	133,5	33,5	299,5	50,7	5,9	12,1	48,8%

5. CONCLUSIONS

This paper presents an experimental investigation of a two-stage turbo compressor MVR system, consisting of two identical impellers and developed for application in industrial superheated steam drying. A performance evaluation shows that the novel system has a clear potential of being a cost-effective alternative to conventional vapour compression systems. With the possibility of using series-produced components from vehicle industry, the estimated investment cost for the MVR system is 150 €/kW installed heating capacity. Stable operating conditions were documented for impeller speeds up to 81 000 rpm for the 1st compressor stage and 72 000 for 2nd stage. The desired total pressure ratio of 3.0 was reached, with an isentropic efficiency of 74 % for both stages. For the application of an atmospheric superheated steam dryer a steam flow of 500 kg/h at a condensing temperature of 133 °C was achieved, delivering 300 kW heating capacity with a system COP of 5.9 and a Carnot efficiency of 48%. The 2nd stage operates close to the surge line, implying that the design of the impellers should be adjusted to the targeted pressure and volume flow conditions at each stage, to ensure stable operation of both stages near the optimum operation point.

ACKNOWLEDGEMENTS

This work is a part of the DryFiciency project (www.dry-f.eu). DryFiciency receives funding from the European Commission under the Horizon 2020 programme - grant number 723576.

NOMENCLATURE

Abbreviations

COP	Coefficient of performance
HP	High pressure
HTHP	High temperature heat pump
LP	Low pressure
MVR	Mechanical vapour recompression

Roman

h	specific enthalpy	[J·kg^{-1}]
$\dot{m}$	mass flow	[kg·s^{-1}]
N	impeller speed	[min^{-1}]
$\dot{P}$	power	[W]
p	pressure	[Pascal]
$\dot{Q}$	heat flow	[W]
T	temperature	[K]
$\dot{V}$	volume flow	[m^3·s^{-1}]

Greek

η	efficiency	[-]
Π	pressure ratio	[-]
ρ	density	[kg/m^3]

Subscripts

cond	condenser
el	electrical
hl	heat losses
in	inlet
is	isentropic
out	outlet
red	reduced or standardised
ref	reference conditions
rel	relative
sat	saturated
t	total

REFERENCES

Bantle, M., Schlemminger, C., Tolstorebrov, I., Ahrens, M., Evenmo, K., 2018. Performance evaluation of two stage mechanical vapour recompression with turbo-compressors. 13th IIR Gustav Lorentzen Conference on Natural Refrigerants. Valencia, Spain.

Chamoun, M., Rulliere, R., Haberschill, P., Peureux, J.-L., 2014. Experimental and numerical investigations of a new high-temperature heat pump for industrial heat recovery using water as refrigerant. Int. J. Refrigeration 44, 177-188.

Elmegaard, B., Zühlsdorf, B., Reinholdt, L., & Bantle, M. (Eds.), 2017. Book of presentations of the International Workshop on High Temperature Heat Pumps. Kgs. Lyngby: Technical University of Denmark (DTU).

Hafaifa, A., Rachid, B., Mouloud, G., 2014. Modelling of surge phenomena in a centrifugal compressor: experimental analysis for control. Systems Science & Control Engineering, II, 632-641.

Larminat, P., Arnou, D., Sausse, P., Clunet, F., Peureux, J.-L., 2014. A high temperature heat pump using water vapor as working fluid. *11th IIR Gustav Lorentzen Conference on Natural Refrigerants.* Hangzhou, China.

Madsboell H., Weel M., Kolstrup A., 2015. Development of a water vapor compressor for high temperature heat pump applications *24th IIR International Congress of Refrigeration* Yokohama, Japan.

Meroni, A., Zühlsdorf, B., Elmegaard, B., Haglind, F., 2018. Design of centrifugal compressors for heat pump systems. Applied Energy (232), 139-156.

Sannan, S., Bantle, M., Lauermann, M., 2016. *D1.2* Specification of performance indicators and validation requirements. EU Project No. 723576 DryFiciency - Waste Heat Recovery in Industrial Drying Processes. H2020-EE-2016-2017-PPP

van Essen, H., 1998. Modelling and Model Based Control of Turbomachinery. PhD Thesis, Technical University of Eindhoven.

Weel, M. et al., 2013. Energy efficient drying with a novel turbo-compressorbased high-temperture heat pump. 6th Nordic Drying Conference 5-7 June 2013. Copenhagen, Denmark.

Zühlsdorf, B., Schlemminger, C., Bantle, M., Evenmo, K., Elmegaard, B., 2018. Design recommendations for R-718 heat pumps in high temperature applications. 13th IIR Gustav Lorentzen Conference. Valencia, Spain.

Manuscript ID: 978
DOI: 10.18462/iir.icr.2019.0978

Energy conservation effect based on the change of supercooling in water flow rate exchanging heat in condenser of refrigerated cabinet(s) using PCM

Toshiyasu WATANABE[(a)], Tatsutoshi NAKAMURA[(a)], Akira YASUKOCHI[(a)] , Sangchul BAE[(a)], Masafumi KATSUTA[(a)]

[(a)] Waseda University, Department of Modern Mechanical Engineering, Tokyo, 169-8555, Japan, watanabet@toki.waseda.jp, n.toshismile2564@ruri.waseda.jp, akira0610@akane.waseda.jp, scbae@aoni.waseda.jp, katsuta@waseda.jp

ABSTRACT

In this study, we focused on the way of waste heat utilization to supercooling in refrigerated cabinet(s) by cold heat of PCM (Phase change material) in the case of supermarket fields. In this experiment, we installed a heat exchanger after the condenser of the refrigerated cabinet to control the supercooling degree using the PCM cold storage tank. We changed supercooling water flow rate throughout the year to measure and compare the supercooling degree and power consumption of each season. We measured the energy conservation effect of supercooling by PCM in the refrigerated cabinet(s). As the result of this experiment, the exhaust heat utilization to supercooling by PCM was effective for energy conservation in the summer and the intermediate seasons. On the other hand, we confirmed that the effect of supercooling by PCM could be lost when the outside temperature was 16 Celsius and below.
Keywords: Heat Recovery, PCM, Supercooling, Supermarket.

1. INTRODUCTION

Activities to reduce energy consumption have become increasingly important in recent years from the viewpoint of taking countermeasures against environmental problems such as global warming. The United Nations has set itself an objective of "Climate Action" as the thirteenth objective of the Sustainable Development Goals (SDGs) in Paris Agreement.
Concept of an effective utilization of Energy Management Systems (xEMS) for commercial facilities with high energy consumption out of the concepts such as ‘Smart City technology’, ‘Realization of energy management technology based on Information Communication Technology (ICT)’ are highly required to achieve sustainable cities and communities.
The xEMS technology can be utilized in both cities and suburbs in consideration of not only "Climate Action" in SDGs, but also social problems such as hyper-aging society and depopulation in Japan. In suburbs, an idea of "Compact City" could be becoming popular to solve those problems (as illustrated by Figure 1).

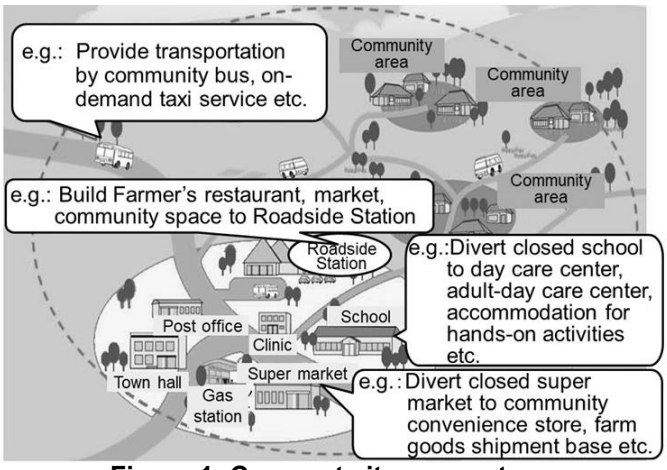

Figure 1: Compact city concept

In the previous research, we researched the possibility of mutual use of electricity and thermal energy, especially heat recovery, assuming a compact city in the suburbs with many business forms including Supermarket.
We constructed a 1/15 scale model to consider utilization Combined Heat and Power (CHP) assuming a complex of supermarket and restaurant in a compact city (Figure 2).

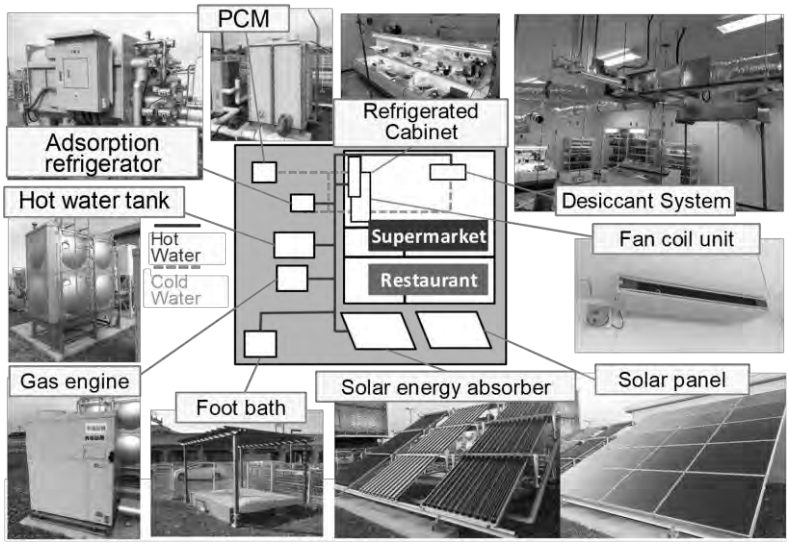

Figure 2: 1/15 scale model of supermarket and restaurant

In this study, we examined the possible countermeasures of energy conservation in supermarket facility, on the assumption that the waste heat from CHP is converted to cold water by adsorption refrigerator. We focused on reducing the electricity consumption by extending the supercooling degree of the condenser in refrigerated cabinet since it was confirmed that refrigerated cabinet accounts for about 60% of the total electricity consumption of supermarket facilities in general. We changed supercooling water rate throughout the year to measure and compare the supercooling degree and power consumption of each season.
The purpose of this study is to conduct experiments which focus on how much supercooling effect can be obtained by utilizing PCM as cold heat storage material.

2. APPROACH

We constructed an indoor environment simulating a supermarket facility to conduct experiments within the environment using an actual refrigerated cabinet. We constructed an experimental apparatus for supercooling the refrigerant between the condenser outlet of the refrigerated cabinet and the expansion valve by installing a heat exchanger between the expansion valve and the condenser of the refrigeration cycle of the refrigerated cabinet (Figure 3).

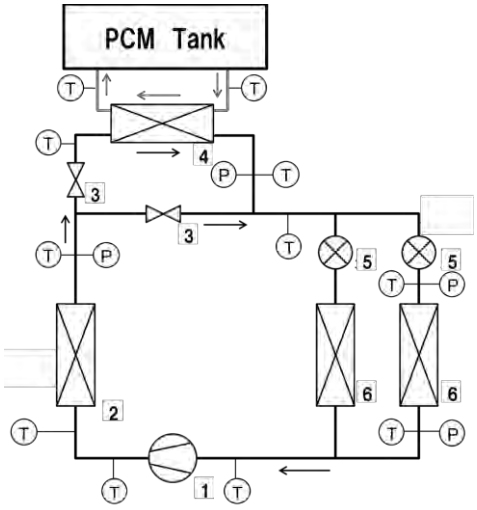

1 : Compressor
2 : Condenser
3 : Valve
4 : Plate heat exchanger
5 : Expansion valve
6 : Evaporator

Refrigerant : R404A
PCM: Paraffin Type
(JXTG Nippon Oil & Energy Corporation)
Melting Point 9, Freezing Point 10
Heat Storage Capacity 181 [kJ/kg]

Figure 3: Schematic diagram of experimental apparatus

The apparatus shows that the heat exchange is performed by cold water generated by the chiller, realizing supercooling of the refrigerant located after the condenser. In addition, the refrigerant used in this experiment is R404A which is widely used for refrigerated cabinet in general. Figure 4 shows the P-h diagram of the refrigeration cycle.

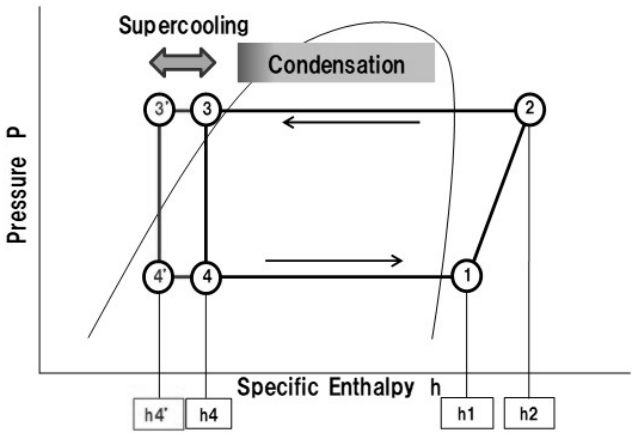

(i) Case of Normal Operation
- Refrigeration-cycle operation without supercooling experiment

$$COP = \frac{h1 - h4}{h2 - h1}$$

(ii) Case of with Supercooling (with PCM)
- Supercooling experiment conducted with PCM (PCM tank filled with maximum amount of PCM)

$$COP = \frac{h1 - h4'}{h2 - h1}$$

Figure 4: P-h diagram of experimental apparatus

In this experiment, the energy saving effect of supercooling is confirmed by comparison of the power consumption of normal operation and with PCM of the refrigerated cabinet.
This experiment was conducted to compare results measured during the summer, winter and intermediate season. Also, since the energy consumption of the refrigerated cabinet is greatly affected by the outside air temperature, we will grasp the relationship between the outside temperature and the effect of supercooling.
The experiment was scheduled to be conducted between 10:00 AM and 6:00 PM time period in which the actual supermarket facility is open for business and also the sun is out throughout the time period.
In the case of with PCM, we keep the tank temperature at 8℃ after placing the PCM into the tank. Circulating the cooling water from 10:00 AM to conduct heat exchange with the condenser of the refrigeration cabinet by using the PCM thermal energy storage amount.
We circulate cooling water at 3.6 L/min and 7.2 L/min between the PCM tank and the heat exchanger to confirm the effect of rate of water flow.
The purpose of this experiment is to conduct analysis with the results of comparison of energy consumption reduction rate to examine to what extent the supercooling effect PCM tank contributes to energy saving. Figure 5 shows pictures of the experimental apparatus.

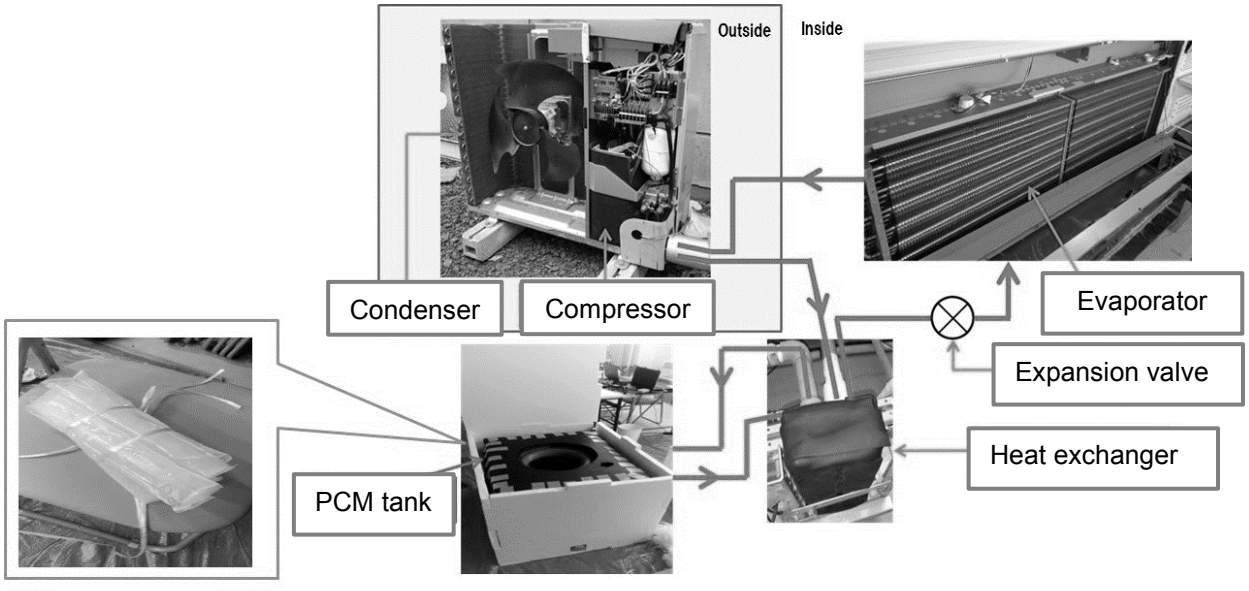

Figure 5: Pictures of experimental apparatus

2.1. Energy Conservation Effect of Supercooling by PCM

Figures 6-8 are graphs summarizing the comparison of energy consumption of refrigerated cabinet throughout the year. The line graphs have shown that there are no large difference in outside air temperature throughout the day. This is because days with stable weather conditions were selected for the measurements in order to ensure the supercooling effect was distinguishable with PCM.
The bar graphs have shown the energy-consumption result of each seasons in the case of normal operation, circulating cooling water between the PCM tank and the heat exchanger at 3.2 L/min and 7.2 L/min. The graphs were used to examine the effect on the refrigerated showcase brought by supercooling effect of the refrigeration cycle.
The experimental results have shown that the summer season had the highest power consumption throughout the year. Also, comparison result of the performance of the refrigerated showcase under different conditions have shown that the amount of effect of energy consumption reduction amount with PCM was the highest in summer throughout the year to compare with normal operation.
In the case of intermediate season, it was about half of the energy consumption compared to summer. Compared to its normal operation, the result has shown that even though the power consumption with PCM is smaller than that in summer, it has shown the effect.
Also, the energy consumption is the smallest in winter throughout the year. The result has shown that there is almost no difference in energy consumption reduction with PCM compared to its normal operation.

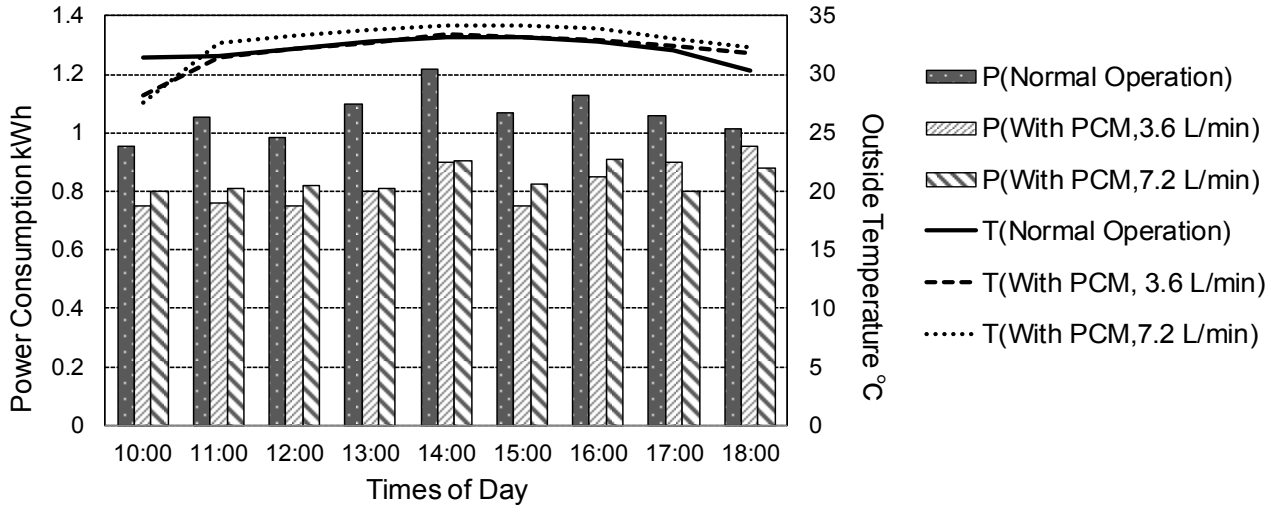

Figure 6: Power consumption in summer

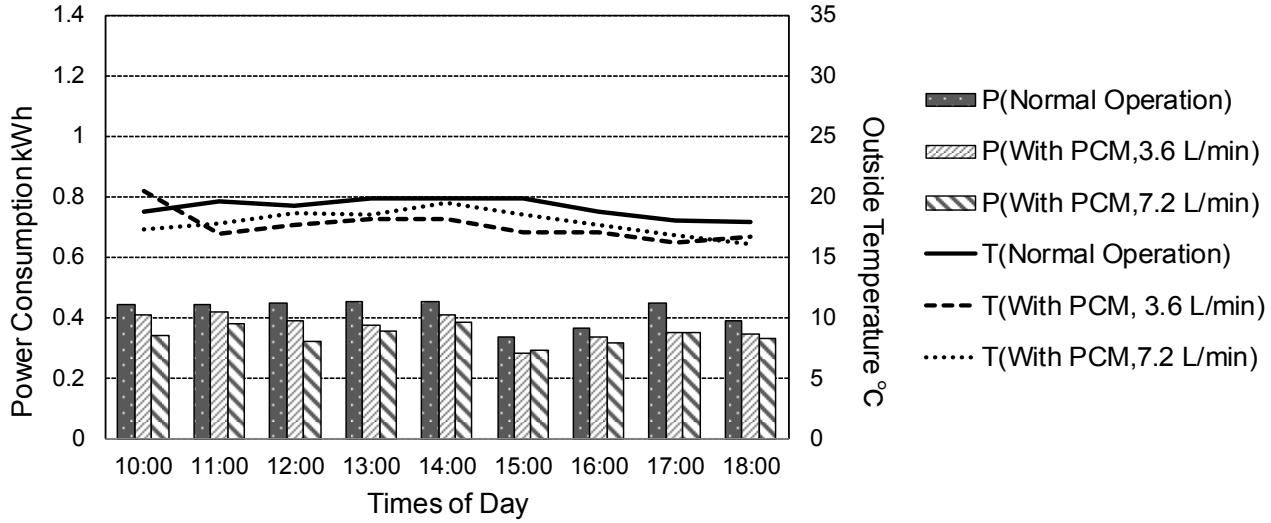

Figure 7: Power consumption during intermediate period

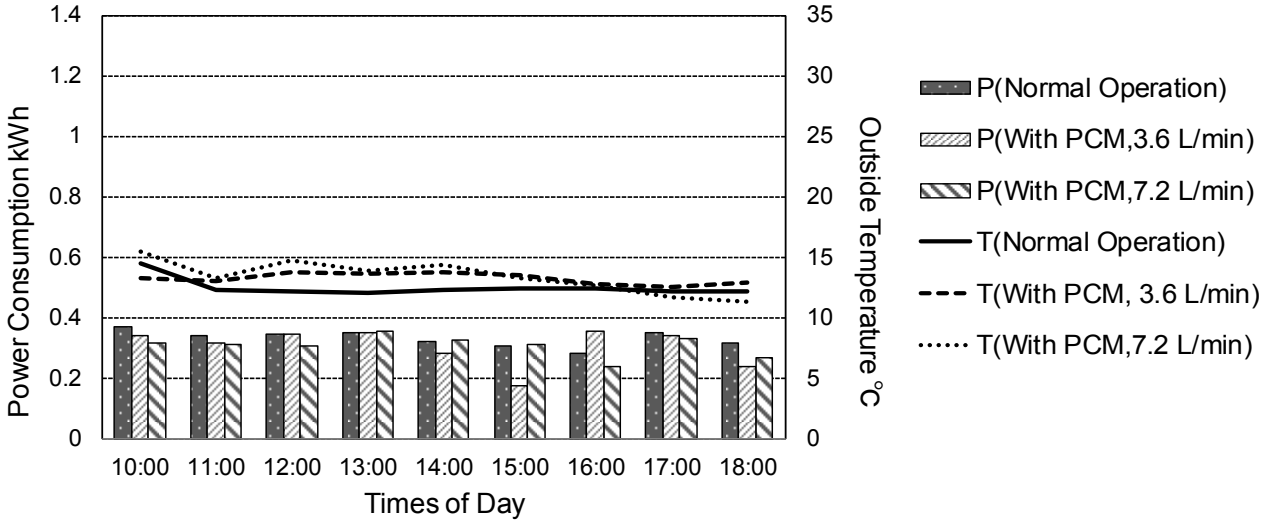

Figure 8: Power consumption in winter

2.2. Effectiveness on Cold Water Flow Rate Difference on Power Consumptions

Table 1 summarizes the energy consumption reduction and the reduction rate of each supercooling experiment result for each season. The result of this experiment has confirmed that supercooling effect is the most effective in summer, reaching to 22% of power reduction rate at 3.6 L/min and 7.2 L/min as well compared with normal operation.

We confirmed that the effectiveness of energy consumption reduction at the flow rate of 3.6 L/min was lower than at that of 7.2 L/min. In the total power consumption viewpoint between 10:00 AM and 6:00 PM time period, the amount of power consumption reduction difference between at 3.6 L/min and 7.2 L/min was 0.1kWh which meant few difference among them.

Table 1. Summary of supercooling test for each season

		Supercooling ℃		Power Consumption kWh	Reduction amount kWh	Reduction rate %
		at 11:00	at 14:00			
Summer	Normal Operation	—	—	9.6	—	—
	With PCM(3.6L/min)	9.8	2.2	7.4	2.2	22.0
	With PCM(7.2L/min)	9.2	1.2	7.5	2.1	22.0
Intermediate Period	Normal Operation	—	—	3.8	—	—
	With PCM(3.6L/min)	9.1	6.8	3.6	0.2	5.6
	With PCM(7.2L/min)	9.6	8.9	3.7	0.1	2.9
Winter	Normal Operation	—	—	3.0	—	—
	With PCM(3.6L/min)	8.0	7.8	2.7	0.2	8.1
	With PCM(7.2L/min)	7.2	4.5	2.8	0.2	7.7

Focusing on the summer where the most effective energy consumption reduction by PCM compared with normal operation, it was confirmed that time to maintain supercooling at the flow rate of 7.2L/min was earlier than that of 3.6L/min (Figure 9).

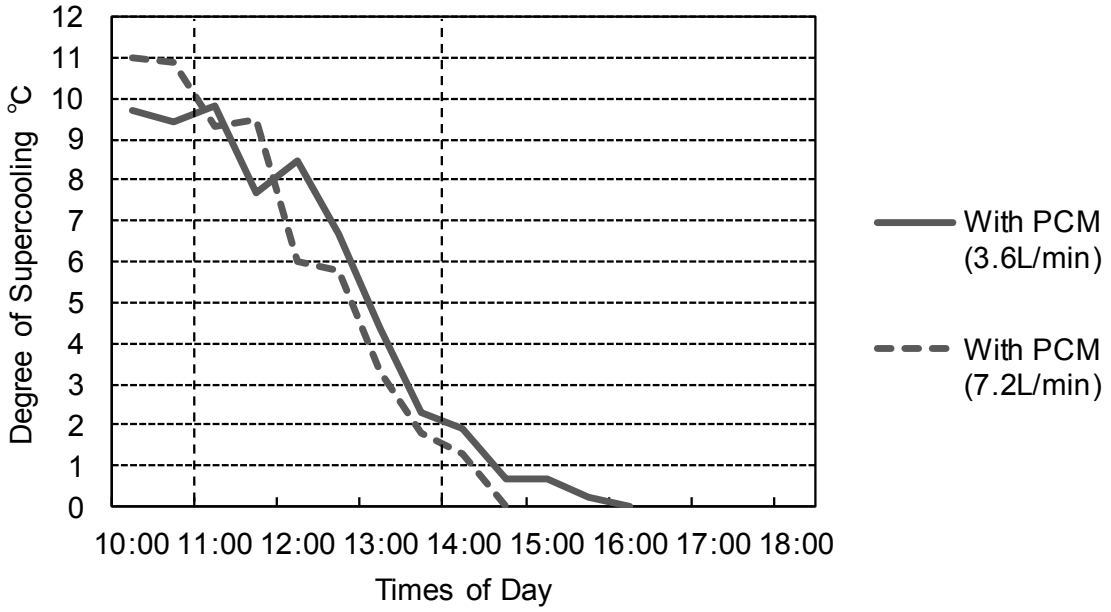

Figure 9: Supercooling trends in summer

This is because the amount of heat exchange on condenser with the cooling water at 7.2L/min was higher than the case of 3.6L/min. In other words, it means that the latent heat of the PCM tank in the case of 7.2L/min was used earlier than that of 3.6 L/min. Therefore, if the capacity of PCM tank would have a sufficient amount to be supercooling during business hours in the summer, it is suggested that the power reduction effect at 7.2L/min would be higher than 3.6L/min.
We confirmed that how much time will be covered as supercooling by PCM with cooling water could be the one of the parameter of sizing to PCM tank.

2.3. Relationship between Outside Air Temperature and Energy Consumption

Relationship between the outside air temperature and the energy consumption through the year was examined to clarify the effects of the supercooling or not. In the previous study[2)], we confirm that outside temperature was one of the key factor to confirm the tendency of power consumption of refrigerated cabinet.
Figure 10 illustrates a plot of energy consumption in the approximation formula as linear in the case of normal operation and with PCM at 3.2 L/min and 7.2 L/min as well. X = 16.3 was obtained as the result when examined the intersection of two approximate lines. Therefore, it can be considered that the energy conservation effect by supercooling utilizing PCM disappears when the temperature is lower than approximately 16°C.
It was confirmed that the supercooling effect of PCM disappeared compare to its normal operation even if the flow rate of cold water by PCM be changed from 3.6L/min to 7.2L/min.

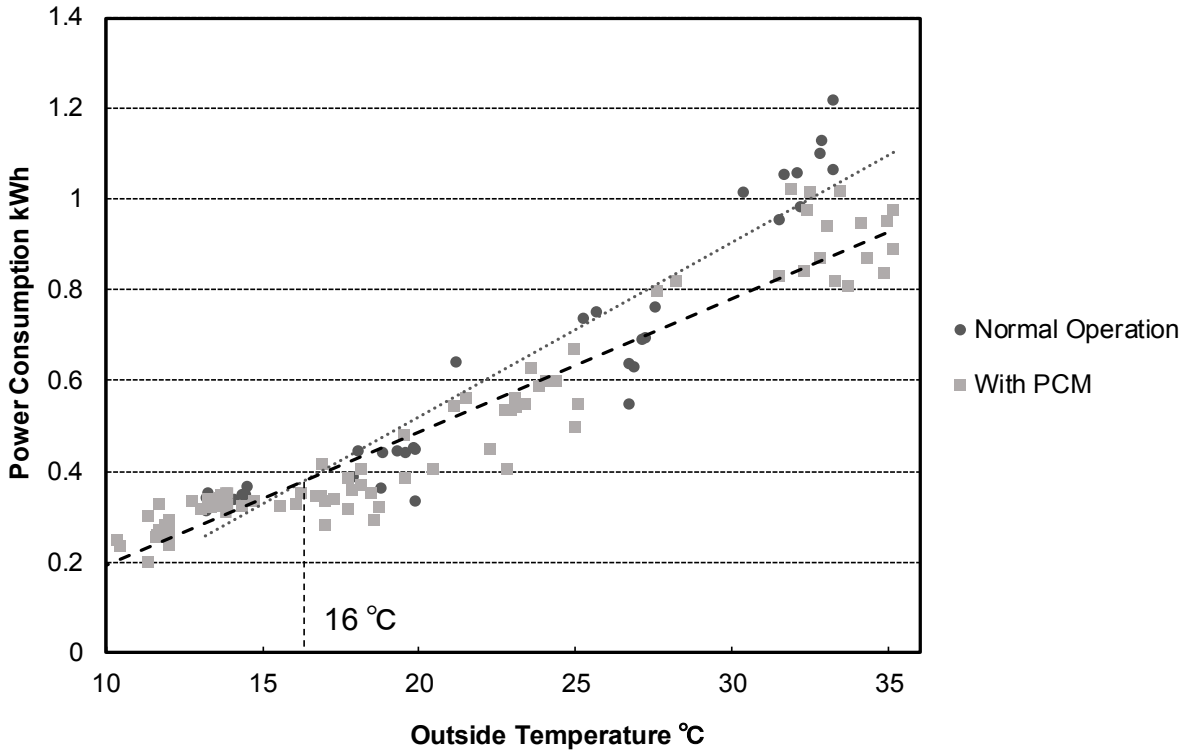

Figure 10: Relationship between power consumption and outside temperature

3. CONCLUSIONS

It was confirmed that the effect of supercooling by utilizing the PCM tank was highest in the summer throughout the year.
The experiment results have shown that the supercooling effect brought by PCM, at which meant that the energy consumption reduction effect can be obtained when the outside air temperature is at 16 ºC and over even if changing the flow rate from 3.6 L/min to 7.2 L/min.
Therefore the condition where the outside temperature is higher than 16 ºC could be utilized as one of the index when considering the installation of PCM to the actual supermarket facility.

REFERENCES

Cabinet Office, Government of Japan. 2015. Aging Society White Paper 2015. Chapter 1. (in Japanese).

Watanabe, T., Shikano, T., Bae, S., Katsuta, M., 2015.Energy Management System utilizing Exhaust Heat Recovery on Distributed Generation in Supermarket and Restaurant. 24th Int. Cong. of Refrig., Yokohama, Japan, 1772 - 1777.

Watanabe, T., Nakamura, T., Bae S., Katsuta, M., 2018. Integrated Energy Management System in Supermarket Assuming Utilization of Exhaust Heat for Subcooling by PCM to Achieve Sustainable Cities and Communities. Transactions of the Japan Society of Refrigeration and Air Conditioning Engineers, J-STAGE.

Shiraishi, K., 2010. Scenario and Policy Recommendations on Energy Reduction in Residential and Non-Residential Buildings for Low Carbon Society Part 12 Grasping the Actual Condition of Energy Consumption Structure in Food Supermarkets. Abstracts of Papers Presented at the Architectural Institute of Japan, 1003 -1004 (in Japanese).

Saito, R., Kuniyoshi, K., The Japan Society of Mechanical Engineers 2007. Annual Conference Papers (2) Temperature Characteristics in a Rack in a Refrigerated Showcase, 301-302.

Manuscript ID: 979
DOI 10.18462/iir.icr.2019.0979

Thermochemical heat transformer for waste heat recovery: consideration of dynamic aspects for design

Benoît MICHEL [(a)], Marc CLAUSSE [(a)]

(a) Univ. Lyon, CNRS, INSA Lyon, CETHIL, UMR5008, Villeurbanne, F-69621, France, Université Lyon 1, F-69622, France, benoit.michel@insa-lyon.fr
(b)

ABSTRACT

Waste Heat Recovery in the industrial sector often requires to upgrade the temperature of the heat fluxes in order to make them useful for the process. Thermochemical Heat Transformer can play a major role as they can provide high temperature lift when compared to alternative technologies.
The aim of the presented work is twofold:

- to identify suitable working pairs using water as working fluid taking into account three criteria: COP, temperature lift and equilibrium drop (difference of the operating temperature and pressure to their value at equilibrium)
- to run a parametric study, thanks to a dynamic 2-salt/2-reactor model, to identify optimal specific heat power as a function of cycle time, working pairs and reactor heat transfer coefficient.

For waste heat temperature at 90 °C and a cold source at 30 °C, the $CaCl_2/H_2O$ and $Ca(NO_3)_2/H_2O$ working pairs were identified as promising. The achieve temperature lift is as high as 90 K for a theoretical COP of 0.42. In dynamic operating, a specific heat power of 325 W/kg was found.
Keywords: Thermochemical Heat Transformer, Waste Heat, Salt Screening.

1. INTRODUCTION

As reported by Ademe, waste heat valorization is a promising solution to dramatically increase the energy efficiency of the industrial sector (ADEME, 2015). According to this report, heat to electricity conversion (e.g. ORC) becomes competitive for temperatures of recovered heat above 150 °C whereas a huge amount of waste heat is available at lower temperature. While sorption systems are industrially available for heat to cold conversion, there is today a great challenge for heat to heat conversion, i.e. to upgrade waste heat temperature from 90-100°C to 150°C and above.
Compared to Electrical Heat Pumps (EHP) and Absorption Heat Transformers (AHT), Thermochemical Heat Transformer (THT) is a far less mature technology (Li et al., 2013; Wu et al., 2017). However, THT could potentially tackle the issues of EHP and AHT by achieving high temperature lifts with 1-stage heat driven system without any crystallization or corrosion issues (Li et al., 2013). Furthermore, 2-salt technology (Figure 1a), also called resorption heat pump, allows a reduction of the high-pressure lift occurring in AHT when high temperature lifts are sought (Yu et al., 2008). In this case, the evaporator and the condenser are replaced by two reactors filled with a so-called low temperature salt (LT salt). Salt/ammonia pairs have been extensively studied for THT applications while there have been some evaluations of salt/methanol, salt/H_2O and salt/CO_2 pairs with encouraging results for the latter two (Yu et al., 2008). In such systems, a main issue is to select the appropriate salt pair for given operating temperatures (T_L, T_m & T_H), to achieve high performance.
Hence, the first objective of this paper is to perform a salt screening for industrial waste heat upgrade thanks to a static thermodynamic approach. The second objective is to study the dynamic behavior of the THT for pre-selected pairs. The model developed and validated for this purpose is presented as well. Furthermore, it was chosen to focus on water as working fluid.

2. STATIC THERMODYNAMIC APPROACH FOR SALT SCREENING

In this section, a static thermodynamic approach is used to perform a rapid screening of available salt-H_2O pairs (N'Tsoukpoe et al., 2014; Visscher et al., 2004). It is based on the following set of

equations. Eq. 1 states the hydration equation of a salt (S) by a vapour (G). The reaction equilibrium is given by Eq. (2), where p_{eq} is the equilibrium pressure at T_{eq} as shown in Eq. (3).

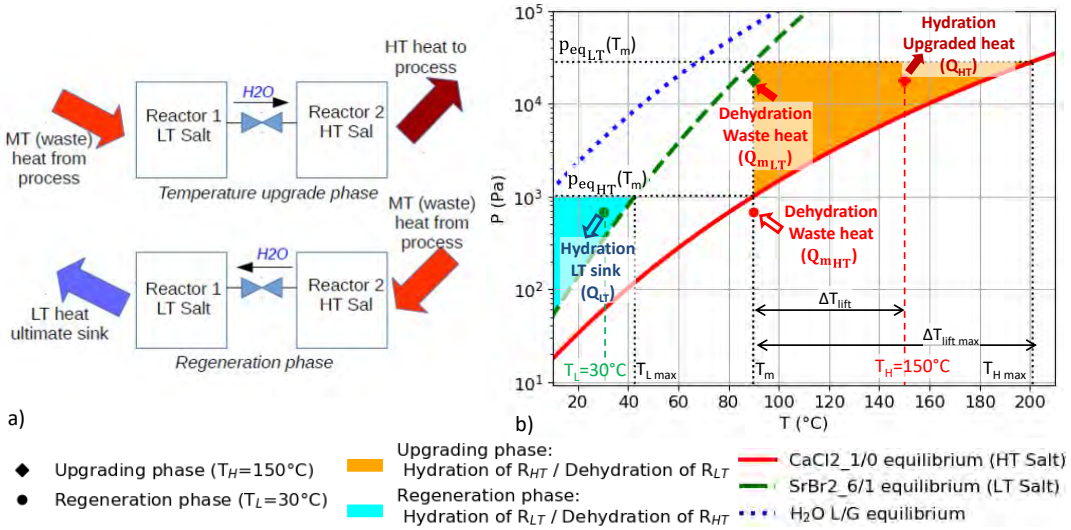

Figure 1: a) Working principle of a two-salt THT. b) Clapeyron diagram representation of the operating areas during hydration and dehydration for the $CaCl_2$/$SrBr_2$ pairs

$$\mathbf{S} + \boldsymbol{\nu}\mathbf{G} = \mathbf{S}' + \boldsymbol{\nu}\boldsymbol{\Delta h_r^0} \qquad \text{Eq. (1)}$$

$$\boldsymbol{\Delta g_r} = \boldsymbol{\Delta g_r^0} + \boldsymbol{RT_{eq} ln\left(\frac{p_{eq}}{p^0}\right)^{\nu}} = \boldsymbol{\nu \Delta h_r^0 - \nu T_{eq} \Delta s_r^0 + RT_{eq} ln\left(\frac{p_{eq}}{p^0}\right)^{\nu}} = \mathbf{0} \qquad \text{Eq. (2)}$$

$$\boldsymbol{p_{eq} = p^0 e^{-\frac{\Delta h_r^0}{RT_{eq}} + \frac{\Delta s_r^0}{R}}} \qquad \text{Eq. (3)}$$

For the sake of clarity, the work presented in this paper is focused on given heat source temperatures representative of operating conditions suitable for heat upgrading in the industry. The cold source temperature is chosen at T_L = 30 °C, the waste heat temperature at T_m = 90 °C and a high temperature source at T_H = 150 °C.

As shown on Fig. 1a, during the regeneration phase (phase 1), waste heat at T_m is supplied to the HT reactor and the LT salt is connected to a heat sink at T_L. In order to allow simultaneously the hydration of the LT salt and the dehydration of the HT salt, the operating conditions (vapor pressure and temperature) of the LT reactor must be in the blue zone presented on Fig. 1b. Therefore, this reactor has to be connected to a heat sink at $T_L < T_{Lmax}$ (i.e. the equilibrium pressure of the LT salt at T_L must be inferior to the equilibrium pressure of the HT salt at T_m). In the case of T_L is superior to $T_{L,max}$, the operating conditions do not allow the hydration of the LT salt and the dehydration of the HT salt. At the end of this phase, the reactive LT salt is fully hydrated and the HT salt is fully dehydrated.

During the temperature upgrade phase (phase 2), the LT reactor is connected to the waste heat at T_m. In order to achieve the dehydration of the LT reactor and the hydration of the HT reactor, the operating condition of the HT reactor must be in the orange zone of the Fig. 1b, thus the HT reactor temperature must be inferior to T_{Hmax} (i.e. the equilibrium pressure of the LT salt at T_m have to be superior the equilibrium pressure of the HT salt at T_H). Therefore, this phase allows to supply heat at high temperature (T_H). Finally, at the end of this phase, the reactive LT salt is fully dehydrated and the HT salt is fully hydrated, requiring the beginning of a new regeneration phase.

From these considerations, a simple numerical tool was developed to perform a first selection for LT and HT salts by checking whether the temperature conditions are satisfied ($T_L < T_{Lmax}$ and $T_H < T_{Hmax}$). 77 pairs were identified from 66 initial reactions.

A second step to discriminate between possible pairs is to consider the achievable performance in terms of COP and maximum temperature lift.

Using the thermodynamic considerations previously presented, neglecting heat accumulation by the salts (heat capacities are low compared to reaction enthalpies) and assuming that there are no heat losses, the theoretical maximal COP of the 2-salt THT is given by:

$$COP_{max} = \frac{Q_{HT}}{Q_{m_{LT}} + Q_{m_{HT}}} = \frac{\Delta h^0_{r_{S_{HT}}}}{\Delta h^0_{r_{S_{LT}}} + \Delta h^0_{r_{S_{HT}}}} \quad \text{Eq. (4)}$$

With $\Delta h^0_{r_{S_n}}$ the reaction enthalpy of the salt *n* (in J/mol$_v$).

The maximal temperature lift is achieved for adiabatic operation and therefore corresponds to the theoretical maximum lift attainable by the HT salt during the temperature upgrade phase: T_{Hmax}-T_m. For the targeted high and waste heat temperatures (150 & 90 °C), a minimum temperature lift of 60 K is then required. To take into account the temperature pinches required in the HT reactor for the heat transfer to occur in finite time, only pairs achieving a minimum temperature lift of 80 K are considered on Fig. 2.

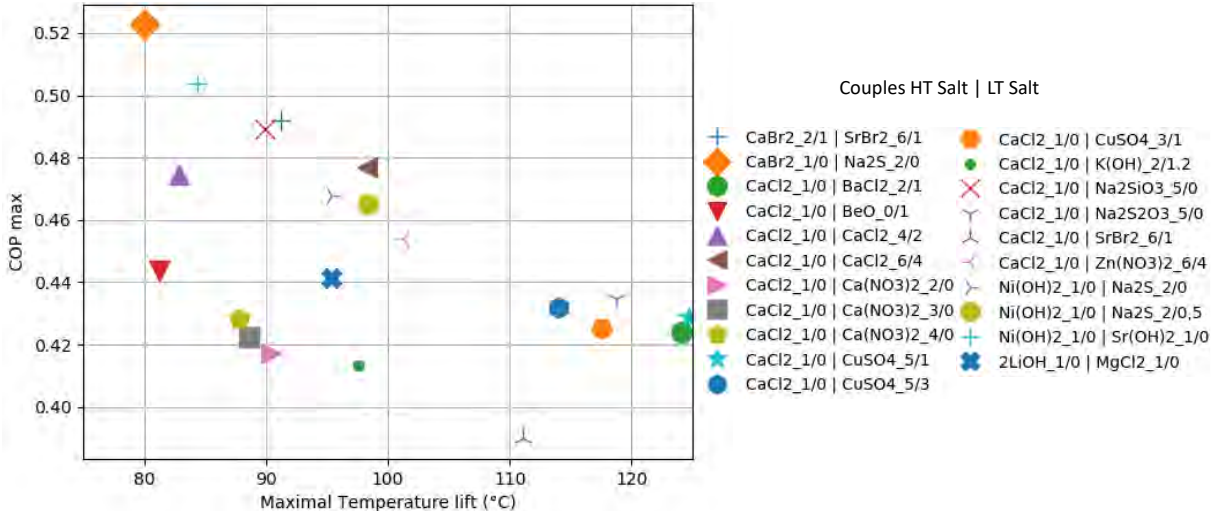

Figure 2: Maximal COP versus theoretical maximal temperature lift, for T_{LT}=30°C and T_m=90°C

From these results, 21 of the 77 promising reaction couples are kept. A large discrepancy between ΔT_{max} values is observed, from 80 K to 125 K (for the $CaCl_2/CuSO_4/H_2O$ pair) with a COP_{max} ranging from 0.39 to 0.52. Besides the static thermodynamic considerations, dynamic aspects have also to be taken into account in order to estimate specific heating power.

3. DYNAMIC MODEL

3.1 Governing Equation

Several modeling of solid/gas reactor, with different approaches (local, global) and complexity levels (1/2D, stationary/dynamic, …) have been presented in the literature (Castaing-Lasvignottes and Neveu, 1997; Nagel et al., 2016). Most of the reported works refer to cooling or heat storage applications and only few models deal with THT applications, especially for those based on 2-salt cycles.

Thus, from modeling approaches of a solid/gas reactor developed by Lebrun and Spinner (1990), a simple and original model of 2-salt THT reactor has been developed in the frame of this work. It should allow to study the dynamic behavior to estimate its performances, mainly heating capacity, and temperature lift. The following assumptions are made:

a) Uniform temperature (T_{SLT} and T_{SHT}) and local thermal equilibrium between the gas and solid phases is assumed in the reactors.
b) Heat accumulation in the gas phase and heat losses are neglected.
c) The heat capacities are considered constant during the reaction.
d) In closed thermochemical systems (working with pure gas), the mass transfer usually does not limit reaction kinetic. Thus, the vapor pressure is assumed uniform inside the reactor.
e) The assumptions (a) and (b) imply that the salt reaction advancement (X_S) is uniform in each reactor. X_S equals 0 when the salt is hydrated and 1 when is dehydrated
f) The kinetics of the solid/gas reactions depends only on the reaction advancement and on the equilibrium drop. This drop corresponds to the difference of the operating temperature and pressure to their value at equilibrium.

3.1.1 Energy balance

According to assumptions (a), (b) and (c), the energy balances of the HT and LT salt reactors are respectively written as:

$$\left[\boldsymbol{m_{S_n}}\left(\mathbf{1}-\left(\mathbf{1}-\boldsymbol{X_{S_n}}\right)\boldsymbol{\nu_{S_n}}\frac{\boldsymbol{M_v}}{\boldsymbol{M_{S_n}}}\right)\boldsymbol{c_{S_n}}+\boldsymbol{m_{exch_n}}\boldsymbol{c_{exch_n}}\right]\frac{\boldsymbol{dT_{S_n}}}{\boldsymbol{dt}}=\boldsymbol{\dot{q}_{S_n}}+\boldsymbol{\dot{m}_{htf_n}}\boldsymbol{c_{htf_n}}\left(\boldsymbol{T_{i_{htf_n}}}-\boldsymbol{T_{o_{htf_n}}}\right) \quad \text{Eq. (5)}$$

with:

$$\boldsymbol{\dot{q}_{S_n}}=-\boldsymbol{\dot{m}_{v_{S_n}}}\boldsymbol{\Delta h^0_{r_{S_n}}}=\boldsymbol{\nu_{S_n}}\frac{\boldsymbol{dX_{S_n}}}{\boldsymbol{dt}}\frac{\boldsymbol{m_{S_n}}}{\boldsymbol{M_{S_n}}}\boldsymbol{\Delta h^0_{r_{S_n}}} \quad \text{Eq. (6)}$$

With $\boldsymbol{\dot{m}_{v_{S_n}}}$ the source ($\boldsymbol{\dot{m}_{v_{S_n}}>0}$ in dehydration phase) or sink ($\boldsymbol{\dot{m}_{v_{S_n}}<0}$ in hydration phase) of vapor due the reaction of the salt *n*.

The outlet temperature of the heat transfer fluid is given by:

$$\boldsymbol{T_{o_{htf_n}}}=\frac{\left(\boldsymbol{T_{i_{htf_n}}}-\boldsymbol{T_{S_n}}\right)}{\boldsymbol{e^{\frac{UA_{S_n}}{\dot{m}_{htf_n}c_{htf_n}}}}}+\boldsymbol{T_{S_n}} \quad \text{Eq. (7)}$$

3.1.2 Kinetics of the solid/gas reaction

According to the assumption (f), the reaction kinetic depends on the reaction advancement and on the equilibrium drop. Mazet et al., (1991) have shown that it can write as a 1st order kinetic law:

$$\frac{\boldsymbol{dX_{S_n}}}{\boldsymbol{dt}}=\boldsymbol{k_{cin_{S_n}}}\boldsymbol{Y_{S_n}}\left(\mathbf{1}-\frac{\boldsymbol{p_{eq}(T_{S_n})}}{\boldsymbol{p_v}}\right) \quad \text{Eq. (8)}$$

where: $Y_{S_n}=\left(1-X_{S_n}\right)$ in hydration phase and $Y_{S_n}=X_{S_n}$ in dehydration phase.

3.1.3 Operating vapor pressure

The vapor operating pressure of the interconnected HT and LT salt reactors, p_v, is defined such as the vapor mass flow rate caught/released by the HT salt reactor is equal to the vapor mass flow rate respectively released/caught by the LT salt reactor. Thus, using Eq. (6) and Eq. (8), the vapor pressure writes:

$$\boldsymbol{p_v}=\frac{\boldsymbol{A\,p_{eq_{S_{HT}}}(T_{S_{HT}})-p_{eq_{S_{LT}}}(T_{S_{LT}})}}{\boldsymbol{A-1}},\ \textbf{with: }\boldsymbol{A}=-\frac{\boldsymbol{m_{S_{HT}}M_{S_{LT}}\nu_{S_{HT}}k_{cin_{HT}}(1-X_{S_{HT}})}}{\boldsymbol{m_{S_{LT}}\nu_{S_{LT}}k_{cin_{LT}}X_{S_{LT}}M_{S_{HT}}}} \quad \text{Eq. (9)}$$

Note that in case of the kinetic coefficients of both reactive salts are equals and if the salts masses are chosen in a balanced way (i.e. in a way that the overall of both reactive salts could react, cf. § 3.2), we have *A = -1*. Therefore, the operating vapor pressure is equal to the average of the equilibrium pressure of each salt:

$$p_v=\frac{p_{eq_{S_{HT}}}(T_{S_{HT}})+p_{eq_{S_{LT}}}(T_{S_{LT}})}{2} \quad \text{Eq. (10)}$$

3.2 Model Parameters

3.2.1 Reactor heat transfer coefficient (UA)

The global heat transfer coefficient of the reactor has been identified from experimental results of Esaki et al., (2017) obtained with a prototype of THT using $CaCl_2/H_2O$ as working pair. Although UA depends on the reactor geometry and on the reactive material used, we will suppose in this paper, that the change of the reactor scale and reactive material does not affect the heat transfer characteristics. The following specific heat transfer coefficient has been evaluated:

$$\frac{UA_{S_n}}{m_{S_n}}=131.36e^{-3.35X_{S_n}} \quad \text{Eq. (11)}$$

3.2.2 Kinetic parameter

The kinetic constant, k_{cin}, lumps the heat and mass transfers in the solid pores and the intrinsic kinetics of the reaction. A value of 68.10^{-4} s^{-1} has been identified from an experimental hydration of a THT using $CaCl_2$ as reactive salt (Esaki et al., 2017).

As shown by Michel et al. (2014), this value indicates that the kinetic is not the main limitation of the thermochemical reaction. In the following, this constant value of k_{cin} has been used for all the studied working pairs.

3.2.3 Mass of salts

In order to avoid that one of the two reactive salts limits the reaction of the other one, the mass of each salts should be chosen in a way that both reactive salts could totally react. Thus, each salt must allow to catch (respectively release) the water vapor released (respectively caught) by the other salt:

$$m_{v_{HT}} = m_{v_{LT}} \Leftrightarrow \nu_{S_{HT}} \frac{m_{S_{HT}}}{M_{S_{HT}}} = \nu_{S_{LT}} \frac{m_{S_{LT}}}{M_{S_{LT}}} \Rightarrow m_{S_{LT}} = m_{S_{LT}} \frac{\nu_{S_{HT}}}{\nu_{S_{LT}}} \frac{m_{S_{HT}}}{M_{S_{HT}}} \quad \text{Eq. (12)}$$

3.3 Model Validation

The model has been validated using experimental results of a $CaCl_2 \cdot 2H_2O$ THT prototype (Esaki et al., 2017). Fig. 3 presents simulations that fit adequately to experimental results. The difference between experimental and simulated reaction rates and outlet heat transfer fluid temperature is rather low: at X=0.5, it is respectively of 9% and 0.5%. These results demonstrate that this simple model predicts in a satisfactory way the thermal behavior of a reactor.

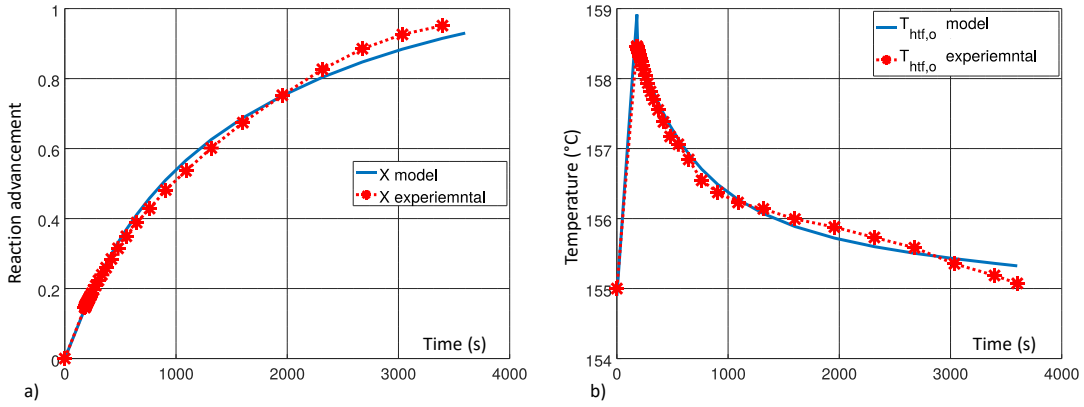

Figure 3: Experimental and simulated results of the hydration of the THT (A type reactor, (Esaki et al., 2017)) a) Reaction advancement vs. time during. b) Outlet heat transfer fluid temperature vs. time.

4. SALT SELECTION CONSIDERING DYNAMIC ASPECTS

In a real cycle an equilibrium drop must be considered in order to realize the thermochemical reaction. This parameter influences the heat and mass transfer rates and therefore the reaction kinetics (Mazet and Lu, 1998; Obermeier et al., 2015). Thus, any change in the operating temperature (T_L, T_m or T_H) results in a change in the equilibrium drop and then in the reaction kinetic. However, as indicated by Obermeier et al. (2015), the equilibrium drop is not an independent parameter and equal values do not produce the same heat and mass transfer rates for different reaction systems.

This parameter can be related to the chemical potential difference which represents the thermodynamic driving force of the reaction. Usually, the greater the driving force, the greater the reaction kinetic is. Under the assumptions of pure substances and ideal mixtures, the driving force can be described by the Gibbs free energy of the reaction (Obermeier et al., 2015). Thus according to the eq. (2) and (3) this parameter can be writes as:

$$F_m = \frac{\Delta G_r}{\nu RT} = \ln\left(\frac{p_v}{p_{eq}}\right) \quad \text{Eq. (13)}$$

In order to take into account the thermal resistances inside the reactors of a 2-salts THT, the reactor temperature must be evaluated for each reactor. Thus, assuming that the heat accumulation is negligible compared to the reaction enthalpy, the eq. (6), (7) and (8) lead:

$$T_{S_n}\left(1-e^{\frac{-UA_{S_n}\left(T_{ohtf_n}-T_{ihtf_n}\right)}{k_{cin_{S_n}}Y_{S_n}\left(1-\frac{peq\left(T_{S_n}\right)}{pv}\right)\Delta h^0_{rS_n}}}\right)-T_{ohtf_n}+T_{ihtf_n}e^{\frac{-UA_{S_n}\left(T_{ohtf_n}-T_{ihtf_n}\right)}{k_{cin_{S_n}}Y_{S_n}\left(1-\frac{peq\left(T_{S_n}\right)}{pv}\right)\Delta h^0_{rS_n}}}=0 \qquad \text{Eq. (14)}$$

Thus, assuming a reaction advancement of 0.5, determining the vapor pressure using eq. (10) and imposing a heat transfer fluid pinch (5°C for the HT reactor and 1°C for LT reactor), the temperature of each reactor has been determined and then the reaction driving forces have been evaluated.

Fig. 4 presents a comparison of the driving force of the hydration of the LT and HT reactors for different reactive couples (i.e. a comparison of the driving force during the regeneration and the upgrading temperature phases). A large discrepancy between F_m values is observed, from 0.001 to 0.35. However, promising reactive pairs are identified, as $CaCl_2/Ca(NO_3)_2$, $CaCl_2/SrBr_2$ and $CaCl_2/K(OH)$. They present high driving forces whose values are close between each cycle phase. This allows to avoid large reaction times gap between these phases.

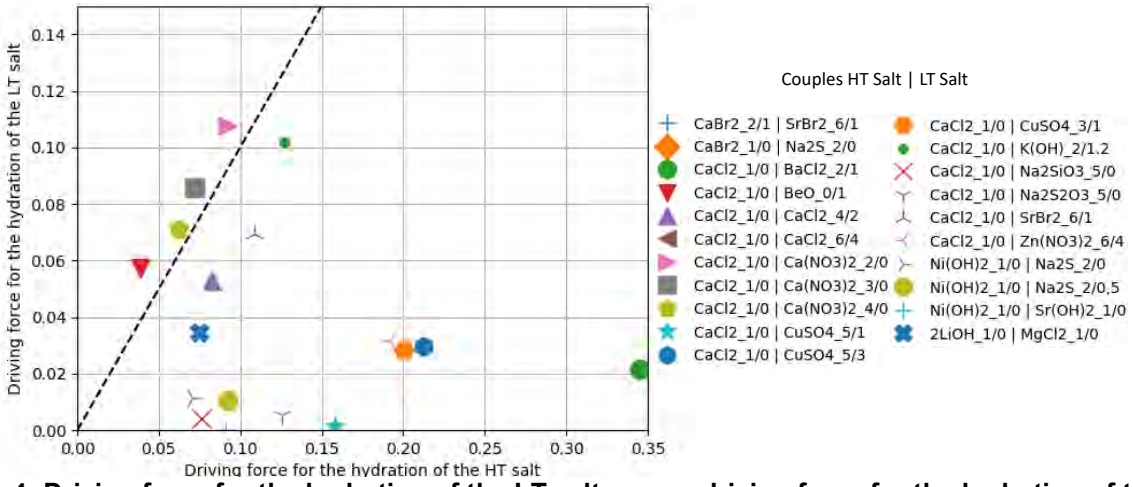

Figure 4: Driving force for the hydration of the LT salt versus driving force for the hydration of the HT salt (for X_{Sn}=0.5, T_L=30°C, T_m=90°C, T_H=150°C, $\Delta T_{htf,HT}$=5°C and $\Delta T_{htf,LT}$=1°C).

5. CYCLE PERFORMANCES

This part aims at analyzing the dynamic behavior and performances of a 2-salt THT. Three key parameters allowing to define the performance of the system are studied: the system heating power (during the upgrading phase), the COP and the temperature lift. The cyclic behavior of the two LT and HT reactors is simulated with successive heating and cooling. The results are given at cyclic steady state and optimal cycle time (maximum heating power).

5.1 Dynamic Behavior

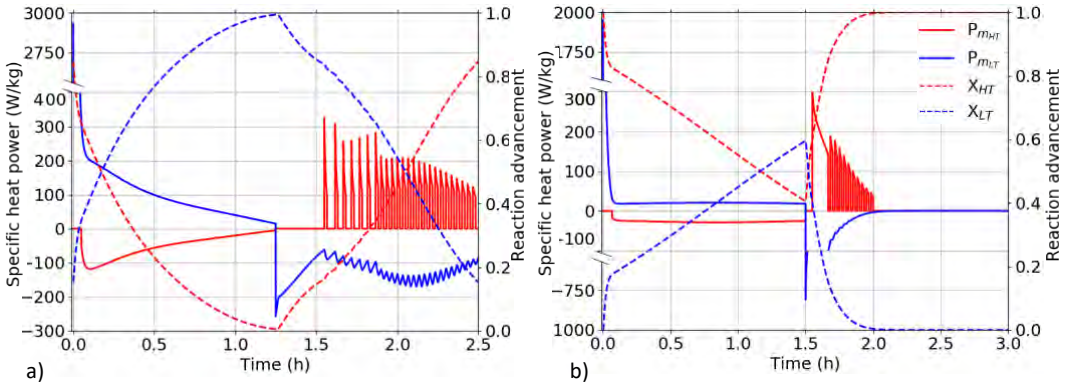

Figure 5: Specific heat power and reaction advancement versus time of 2-salt THT operating with: a) $CaCl_2$/ $Ca(NO_3)_2$ working pairs. b) $CaCl_2$/ $BaCl_2$ working pairs.

The dynamic behavior for $CaCl_2/Ca(NO_3)_2$ and $CaCl_2/BaCl_2$ reactive couples is presented Fig. 5a and b. Maximal specific heat power respectively of 325 W/kg and 300 W/kg have been reached during the temperature upgrade phase, corresponding to average specific heat power of 49 W/kg and 26.9 W/kg. Furthermore, due to the system regulation, the temperature and specific heat power are not stable, especially during the temperature upgrade phase.
In agreement with the driving forces presented in the Fig. 4, the reaction advancement evolution shows that the reaction kinetic of each phase is quite equilibrated for the $CaCl_2/Ca(NO_3)_2$ THT, while the temperature upgrade phase is much faster than the other phase for the system using the $CaCl_2/BaCl_2$ couple (30 min instead of 1.5h). In this last case, the system performances are therefore limited by the regeneration phase, especially due to the adverse operating conditions.

5.2 Sensitivity to Operating Temperatures

Simulations have been performed to study the sensitivity of the operating temperatures. Their influence to the average specific heat power and the reaction driving forces is presented on Fig. 7. The impact of the operating temperatures clearly depends to the driving force values. Thus, although the diminution of T_L increases the driving force associated to the generation phase, no significant change of the specific heat power is observed. As contrary, the increase of T_H (and then of the driving force associated to the temperature upgrade phase) allows in a first time to significantly increase the system performances. This is because in the reference case, the temperature upgrade phase corresponds to the lower driving force value. This phase is therefore the limiting phase, which is subject to the most unfavourable conditions on which it is necessary to play in priority.
Other limitations, as the heat transfer or the kinetic reaction can impact the system performances. However, this is out the scope of this paper. Note that in the studied cases, these parameters are weakly limiting.

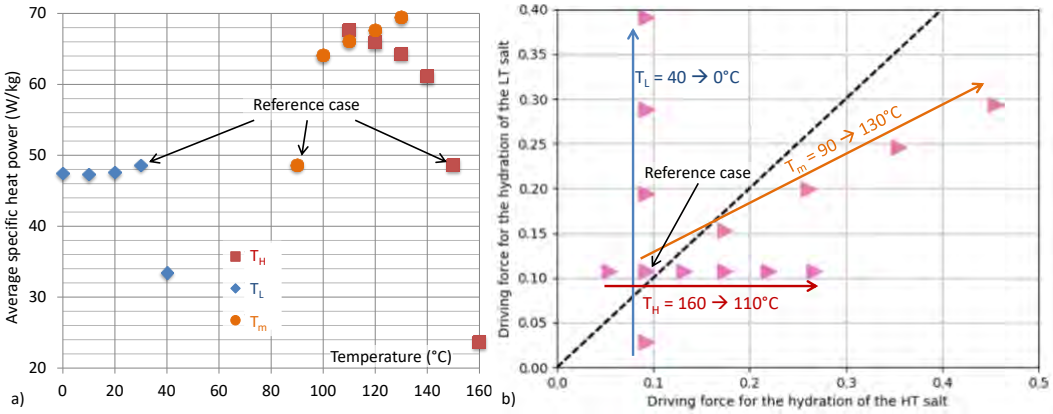

Figure 6: Impact of the operating temperatures. a) Evolution of the driving forces. b) Specific heat power release during the upgrading temperature phase. Case of the $CaCl_2/Ca(NO_3)_2$ reactive couples.

6. CONCLUSION

A screening of salt couples was performed to design a 2-salt Thermochemical Heat Transformer for waste heat recovery. For the sake of clarity a representative case was considered with a low temperature source at 30 °C, an intermediate at 90 °C and a high temperature source at 150 °C.
A first tool was developed to discriminate pairs using a static thermodynamic approach insuring cycle feasibility. From the selected 77 pairs, 21 were kept considering a minimum requirement in temperature lift. The last step was based on dynamic consideration (driving force) and allows to identify three candidates: $CaCl_2/Ca(NO_3)_2$, $CaCl_2/SrBr_2$ and $CaCl_2/K(OH)$.
Cycle operation was simulated for the most promising pair $CaCl_2/Ca(NO_3)_2$. An average specific heating power as high as 49 W/kg is achieved.

ACKNOWLEDGEMENT

The authors wish to thank the INSA LYON (BQR FATAL RECUP) for funding this study.

NOMENCLATURE

c	heat capacity ($J.kg^{-1}\cdot K^{-1}$)	Δs_r^0	standard entropy of reaction ($J\cdot mol^{-1}{}_v\cdot K^{-1}$)
COP	coefficient of performance *(-)*	ν	stoichiometric coefficient (mol_v/mol_s)
F_m	Driving force *(-)*	*Indices*	
k_{cin}	kinetic constant (s^{-1})	*eq*	solid/gas equilibrium
M	molar weight ($kg\cdot mol^{-1}$)	*exch*	exchanger
m	mass (kg)	*i*	inlet
$\dot{m}$	mass flow rate ($kg\cdot s^{-1}$)	*htf*	heat transfer fluid
$\dot{m}_v$	sink or source of gas ($kg\cdot s^{-1}$)	*H*	high temperature
p	pressure *(Pa)*	*HT*	high temperature salt
P_m	specific power ($W\cdot kg^{-1}$)	*L*	low temperature
$\dot{q}$	sink or source of heat ($J\cdot s^{-1}$)	*LT*	low temperature salt
Q	heat exchanged *(J)*	*m*	medium
R	ideal gas constant ($J\cdot mol^{-1}\cdot K^{-1}$)	*max*	maximum
T	temperature *(K or °C)*	*n*	HT or LT salt
UA	heat exchange coefficient ($W\cdot m^{-2}\cdot K^{-1}$)	*v*	vapor
X	reaction advancement *(-)*	*s*	salt
Greek symbols		o	outlet
Δg_r	free Gibbs energy ($J\cdot mol^{-1}{}_s$)	*Exponents*	
Δh_r^0	standard enthalpy of reaction ($J\cdot mol^{-1}{}_v$)	0	reference

REFERENCES

ADEME (2015). La chaleur fatale industrielle.

Castaing-Lasvignottes, J., Neveu, P., 1997. Development of a numerical sizing tool applied to a solid-gas thermochemical transformer-II. Influence of external couplings on the dynamic behaviour of a solid-gas thermochemical transformer. Appl. Therm. Eng. *17*, 519-536.

Esaki, T., Yasuda, M., Kobayashi, N., 2017. Experimental evaluation of the heat output/input and coefficient of performance characteristics of a chemical heat pump in the heat upgrading cycle of CaCl 2 hydration. Energy Convers. Manag. *150*, 365-374.

Lebrun, M., Spinner, B., 1990. Models of heat and mass transfers in solid—gas reactors used as chemical heat pumps. Chem. Eng. Sci. *45*, 1743-1753.

Li, T., Wang, R., Kiplagat, J.K., 2013. A target-oriented solid-gas thermochemical sorption heat transformer for integrated energy storage and energy upgrade. AIChE J. *59*, 1334-1347.

Mazet, N., Lu, H.-B., 1998. Improving the performance of the reactor under unfavourable operating conditions of low pressure. Appl. Therm. Eng. *18*, 819-835.

Mazet, N., Amouroux, M., Spinner, B., 1991. Analysis and experimental study of the transformation of a non-isothermal solid/gas reacting medium. Chem. Eng. Commun. *99*, 155-174.

Michel, B., Neveu, P., Mazet, N., 2014. Comparison of closed and open thermochemical processes, for long-term thermal energy storage applications. Energy *72*, 702-716.

Nagel, T., Beckert, S., Lehmann, C., et al., 2016. Multi-physical continuum models of thermochemical heat storage and transformation in porous media and powder beds - A review. Appl. Energy *178*, 323-345.

N'Tsoukpoe, K.E., Schmidt, T., Rammelberg, H.U., Watts, B.A., Ruck, W.K.L., 2014. A systematic multi-step screening of numerous salt hydrates for low temperature thermochemical energy storage. Appl. Energy *124*, 1-16.

Obermeier, J., Müller, K., Arlt, W., 2015. Thermodynamic analysis of chemical heat pumps. Energy *88*, 489-496.

Visscher, K., Veldhuis, J., Oonk, H.A.J., et al., 2004. Compacte chemische seizoensopslag van zonnewarmte.

Wu, S., Li, T.X., Yan, T., et al., 2017. Experimental investigation on a novel solid-gas thermochemical sorption heat transformer for energy upgrade with a large temperature lift. Energy Convers. Manag. *148*, 330-338.

Yu, Y.Q., Zhang, P., Wu, J.Y., et al., 2008. Energy upgrading by solid-gas reaction heat transformer: A critical review. Renew. Sustain. Energy Rev. *12*, 1302-1324.

Manuscript ID: 995
DOI: 10.18462/iir.icr.2019.0995

NEW TAP WATER HEAT PUMP USING PROPANE REFRIGERANT

Per Henrik Pedersen[(a)], Asbjørn Vonsild[(b)]

[(a)]Danish Technological Institute
Gregersensvej 2, DK-2630 Taastrup, Denmark, prp@teknologisk.dk
[(b)]Vonsild Consulting
Grejsdalsvej 239, DK-7100 Vejle, Denmark, vonsild@vonsild-consulting.com

ABSTRACT

A Danish manufacturer of tap water heat pumps has been producing appliances with HFC-134a for more than two decades.
After the implementation of the EU ecodesign criteria and the EU energy labelling scheme for water heaters in September 2015, the demand for heat pump water heaters has been increasing. The interest in high energy classes and products using natural refrigerants is increasing as well.
Two sizes of new products have been developed; a small unit with a 166-liter water tank using 140 grams of R290 and a bigger unit with a 270-liter tank using 350 grams of R290.
This paper describes the construction of the heat pumps. Test results according to EN16147 are also provided. Moreover, the paper describes a method to handle the R290 refrigerant with a charge above 150 g. The method uses a ventilated enclosure in which the refrigeration system is placed.

Keywords: Tap Water Heat Pump, Propane, Energy Efficiency, Ecodesign, Energy Label

1. INTRODUCTION

A Danish manufacturer of tap water heat pumps is producing around 10,000 units per year. Each heat pump is filled with 0.9 kg R134a. The product heats tap water for sanitary purposes for a family house and is equipped with a 270 l water tank.
This type of tap water heat pumps takes energy from exhaust air from e.g. a bathroom and makes the ventilation of the house.
The price for HFC refrigerant has been rising very fast in the past because of the limited availability caused by the EU F-gas regulation with phase down schedules and quotes. This is one of the reasons why a new generation of tap water heat pumps with natural refrigerants was wanted.

1.1. Aim of the project and the project organisation

The aim of the project was to:

- Develop and test a new generation with natural refrigerant
- To increase the efficiency
- To develop a product that is competitive and reliable.



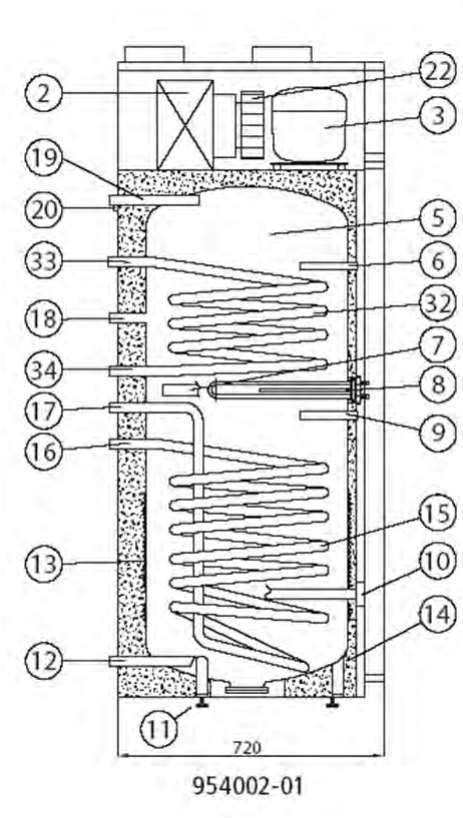

Figure 1a: Photo from the production site of tap water heat pumps. Figure 1b: Drawing of the tap water heat pump. Compressor and evaporator (and a fan) are placed in the upper part. The condenser (point 13) is wrapped around the lower part of the water tank. Cold tap water inlet is point 12. The warm tap water outlet is point 19. The appliance can be delivered with two, one or no spiral pipes inside the tank. The spiral pipes can be used for supplying solar heating and/or a heat exchanger for heating a (small) toilet floor.

Danish Technological Institute (DTI) was managing the project which also includes the manufacturer of hot water heat pumps, a global producer of fans and a consulting company with expertise in handling flammable refrigerants.
The project was started in January 2016 and finalized in October 2018.
The Danish Environmental Protection Agency (the “MUDP”-program) has been funding the project.

2. DEVELOPING AND TESTING PROTOTYPES

The first prototype was delivered for test at DTI in the summer of 2016, and the test was a little disappointing. Analysis showed that liquid refrigerant droplets were going to the compressor causing efficiency losses.
After the test of the first prototype, a lot of tests were done to minimize the charge of refrigerant in the system by using smaller pipes etc. It was shown that it is possible to reduce the charge of R290 to 150 grams by using “flat” condenser pipes and other improvements. But this also showed to have an influence on the energy efficiency. The idea to use max.150 gram R290 was dropped, and the aim for the refrigerant charge was to use a limited charge ensuring a high energy efficiency.
At the same time is was decided to develop a new small model for flats and to use max. 150 grams of R290 for this small model.
The second normal size prototype was installed with an internal heat exchanger and charged with 350 grams of R290. This model worked much better and had an efficiency of the same level as the HFC based unit. It turned out that there was a problem with the control of the unit.
Therefore, a third prototype was built by the manufacturer and tested in an accredited laboratory at DTI after EN16147:2017 and the “XL”-tap program.

The result of the test is COP = 3.52 which is 12 % better than the R134a-model. The sound level was measured to be within the EU Ecodesign criteria.
A small model was built by the manufacturer and was tested in the accredited laboratory at DTI after EN16147:2017 at the “L” tap program, and the result is COP = 3,20 which is fine for such a small machine. The sound level was measured to be within the EU Ecodesign criteria.
Both the normal size and the small model are in energy class A+ according to the EU energy labelling regulation for water heaters.
The compressor is a NLU8.8 (8.8 cm^3) for R290. The compressor for the small model is a DL6.5 (6.5 cm^3) for R290.

3. STANDARDS AND RISK ASSESSMENT

Vonsild (ref 11 and 12) describes the standards covering small domestic heat pumps. Figure 2 shows the relation between these standards and the EU legislation. The relevant safety directive is the Low Voltage Directive.

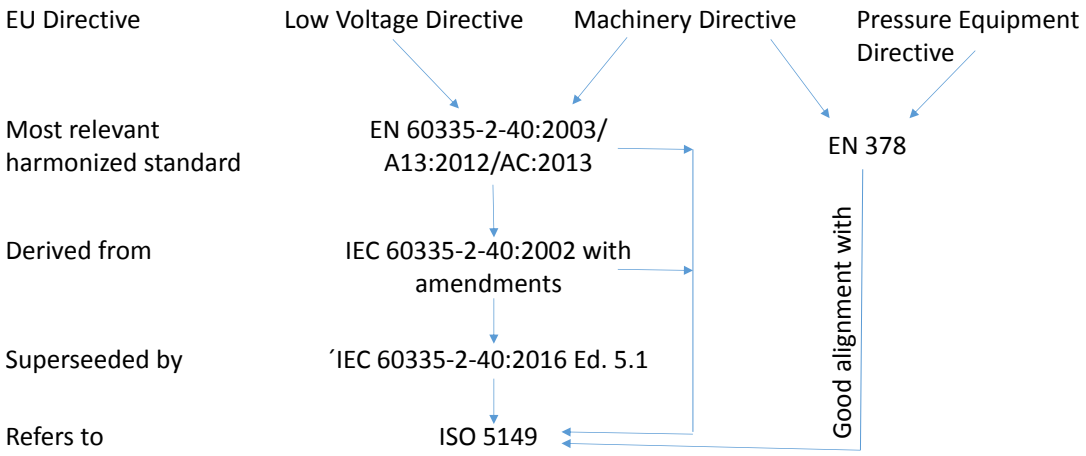

Figure 2: Relation between the standards and EU legislation.

Mechanical Ventilation Within the Appliance Enclosure
EN and IEC 60335-2-40 use the term “mechanical ventilation within the appliance enclosure” to cover a box surrounding the refrigerating system which is ventilated through a ventilation duct to the outside and prevents air from moving from the refrigerating system to the room outside the box.

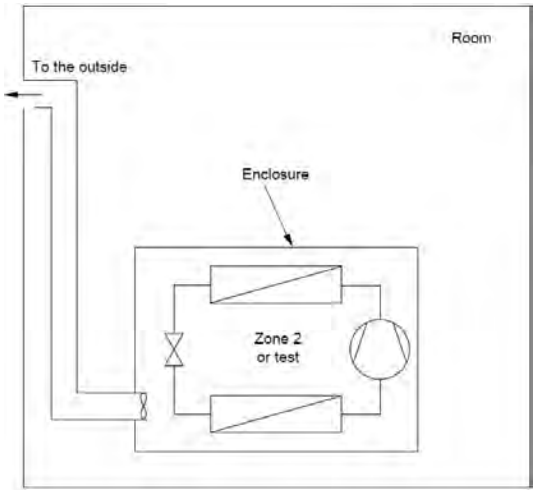

Figure 3: Illustration of ventilated enclosure from IEC 60335-2-40.
The reason for using this ventilated enclosure is that leaking refrigerant is much less dangerous if ventilated to the outside, and the system builder is rewarded by being allowed 5 times larger

flammable refrigerant charges than would normally be allowed indoors in very large rooms. This is enough to cover most heat pump applications.
To ensure that the refrigerant doesn't leak out of the enclosure, the standards require that the ventilation needs to create a negative pressure of at least 20 Pa, and the ventilation rate needs to be high enough to remove the total refrigerant charge within 1 minute, but not less than 2 m^3/h. The ventilation needs to be monitored, and if the ventilation fails, then the compressor needs to be switched of.
From a practical point of view, todays energy efficiency requirements make continuous ventilation difficult. Even for sanitary hot water heaters and heat pumps doing heat reclaim where ventilation air is feed through the heat pump, it can be difficult to maintain ventilation when heating is not needed.
This leads to look at alternatives with a risk assessment for evaluating that the amount of refrigerant charge is safe.
For ventilated enclosures the risk assessment approach can for instance be used if the required ventilation rate or the required negative pressure cannot be achieved without too large an impact to the energy efficiency or cost of the system.

3.1. Risk assessment

The system contains 350 g of R290 refrigerant. It has a machinery compartment which houses the compressor and evaporator, and a pipe coil which is wound around a vessel containing water to be heated.
When the compressor runs there is a fan which pushes air from the machinery compartment out of a ventilation outlet. The ventilation outlet is to be connected to a ventilation duct leading to the outdoors.
From the machinery compartment also runs a pipe to a drain to transport compensated water away. This pipe is fitted with a drain trap.
The electrical control box, which could potentially contain ignition sources, is placed outside the machinery compartment. The cables are lead through holes in the machinery compartment, and these holes are placed below the electrical control box.

Realistic worst case leak size
For simulating the consequences of leaked refrigerant, it is necessary to have values for the range of leak sizes which are relevant. Both the largest foreseeable leak and the smallest leak which is large enough to potentially create an intolerable risk.
The largest leak which is to be expected from the system has been estimated: Traditionally human comfort systems have been assumed to be able to leak the entire charge in 4 minutes under worst case conditions. Although this is much higher that what is usually possible to get out of a system. But it was agreed to since there was consensus that it is highly unlikely that a leak gets any larger. With a 350 g charge the leakage rate from a 4 minutes leak is 1,46 g/s.
Very small leaks do not present a risk. For instance, a very small closed volume of 5 m^3 needs 190 g of R290 to have a whole room flammable, and with one air change per hour and only 350 g R290, a flammable atmosphere can be maintained for less than 2 hours, after which the system the system would be empty.
In the proposal for the 7th edition of IEC 60335-2-40 the highest leak, which is still small enough to be safe, is calculated based on the historical acceptance of 150 g of flammable refrigerant, combined with a leak at 2,2 m and the hole charge leaking in 4 minutes: (2,2m/0,6m) × (150g/240s) = 0,17 g/s. For lower heights than 2,2 m it is proposed to scale the leak down with falling installation height, but not lower than 0,6 m.
A test evaluates whether this leak rate is safe for this specific application: A leak was created from the system through a 0,2 mm diameter whole, which at 20 bar (equivalent to 60 C) would create a leak of 0,17 g/s gas. The leak was at room temperature, but contained a mix of gas and liquid, so it was probably larger than 0,17 g/s. However, the leak leads to 130 % of LFL in a 5 m^2 airtight room (with 2,2m to the sealing), indicating that the real "largest safe leak" may be a factor smaller than 0,17 g/s due to the installation in a very small room, but it is not a factor 10 lower. This means that any leak taking more than 4 hours to empty the system is too small to worry about. Note that the installation room is required to be somewhat greater than 5 m^2, so the test does not directly show that the system is unsafe.
The leaks that the manufacturer actually sees in the field are smaller than the 4 hour leak, except for leaks occurring during transport. Leaks during transport occur in very large rooms or in the

outdoors and do not present a risk. Although large leaks are not seen in the field, it is still prudent to consider the effects if they should happen.
The tests supporting this report have all been done by simulating leaks into the machinery compartment from a bottle of R290.

Leak testing
Several leakage tests were carried out with a leak into the machinery compartment. The flow patterns of leaked refrigerant were investigated outside the machinery compartment by measuring the concentration. Sometimes manually by moving the gas detector around.
Refrigerant concentration was measured at the electrical box multiple times during testing, and the concentration never exceeded LFL and generally only started to increase after the leak started mixing in the room. The concentration was also measured below the electrical box, and the measurements clearly show that the refrigerant leaks from the machinery compartment through the wire conduit holes below the electrical box behind the front cover of the heat pump. The leak flows down from these holes and not up to the electrical box. The baffles behind the front panel force the leaked refrigerant to exit through the holes in the front panel. This is a process driven by gravity and it leads to an increasing refrigerant concentration at the floor.
The conclusion is that the worst case concentration will be at floor level. It is known that the concentration at floor level is likely to be very even and that the electrical box is not where leaked refrigerant flows or accumulates.

Leak in system with fan on and the outlet connected to the outdoors
This scenario is included in EN 378-2 as the concept of ventilated enclosure and in IEC 60335-2-40 as mechanical ventilation within the appliance enclosure. In both standards, 4,94 kg R290 is allowed in these types of applications. More than 10 times the amount in the system covered by this work.
If a leak happens, the air flow will force the leak refrigerant to the outdoors, where it will be diluted below any hazardous levels.
To verify that the system will be safe when the fan is on at the lowest speed and the outlet is connected to the outdoors, a test was carried out with the system in a 1 m^2 tent: The system was placed in a corner of the laboratory and a 1 m^2 tent was created around the system. See figure 4 below.
The tent was made tight with duct tape, just as for the other tests in this report. However, a 10 x 10 cm hole was cut above the unit to allow make-up air to replace what the fan blows out of the exhaust.
The air intake was deliberately placed above the unit since all tests and theoretical knowledge show that leaked refrigerant will flow down and accumulate near the floor. Having the make-up air come from above the unit is therefore seen as the worst case.



Figure 4: System placed in a 1 m^2 tent with the 10 x 10 cm air intake cut above the unit and the exhaust pipe on the upper right. The box on the right is not associated with the test.

The concentration was measured at floor level while leaking 350 g R290 gas into the unit from a bottle. In the first couple of minutes the gas is leaked at a rate equivalent to leaking all the charge in 4 minutes, but after the 3rd minute the bottle was not able to keep the flow rate as the rapid release requires liquid to boil in the bottle lowering the temperature and pressure in the bottle. This causes the total leak to take 5 minutes, which is still much faster than any expected leak. The concentration at floor level was measured every 15 seconds until the leak stopped, at which point the concentration stopped increasing: The maximum concentration measured was 20 % of LFL at floor level, showing that a small amount does leak out from the system, even with the fan on at lowest speed. However, the amount is very small and not enough to cause a hazardous atmosphere.
It should be noted that 20 % of LFL is equivalent to 7,6 g of R290 per m^3, and in a 1 m^2 room the unit takes up the majority of the volume, leading to the conclusion that the amount of refrigerant leaking out of the unit is just a few grams.
The conclusion is that the system will be safe in this scenario regardless of the room size.

Leak in system with fan off

If a leak occurs inside the machinery compartment when the fan is off, then the leak can get through the cracks of the enclosure and flow to the outside.
When the fan is off, the compressor is also off, since the compressor is switched off before the fan. This means that there are no moving parts or airflow inside the machinery compartment, therefore no vibrations in the system to create a leak. The machinery compartment is encapsulated in a PU foam shell which prevents mechanical impacts from the outside. This means that holes in the refrigerating system can only occur through corrosion or stress caused by temperature variations. The manufacturer has not seen this type of leak but has seen leaks through bad soldering connections. These leaks are estimated to take 3-5 years to cause the system to leak enough refrigerant to malfunction. Therefore, the leak rate is much too low to create a dangerous situation. The lack of airflow means that a leak can flow to the outside of the unit and potentially create flammable gas pooling at the floor.
To simulate a very small leak, a leak was created from the system through a 0,2 mm diameter hole (0,03 mm^3), and the refrigerant was leaked from the system through an on/off valve into the machinery compartment. The room size was 5 m^2 with a ceiling height of 2,2 m.
Two tests were conducted:

1) During the first test the leak created a haze in the machinery compartment, indicating that it was a mix of liquid and gas leaking out and that it is most likely pure refrigerant at the inlet. The haze could, however, also be oil mist from the lubricant of the system. During this test,

the concentration at the floor reached a flammable level after 3 ½ minute and kept increasing after that and topping at 130 % of LFL. The rapid increase of the concentration at floor level also indicates that the refrigerant is in liquid state at the inlet of the leak hole, because a liquid leak gives much higher mass flow than a gas leak.

2) The test was repeated with a small modification. The compressor was switched on for 5 minutes before the test to ensure that the leak would be refrigerant in gas phase. This also heats the oil which reduces the amount of refrigerant being retained in the system when it leaks. Also during this test, the concentration reached a flammable level at the floor. This time after 7 ¼ minute and it kept increasing until topping at 124 % of LFL after 20 minutes and falling below the lower flammability limit after 45 minutes.

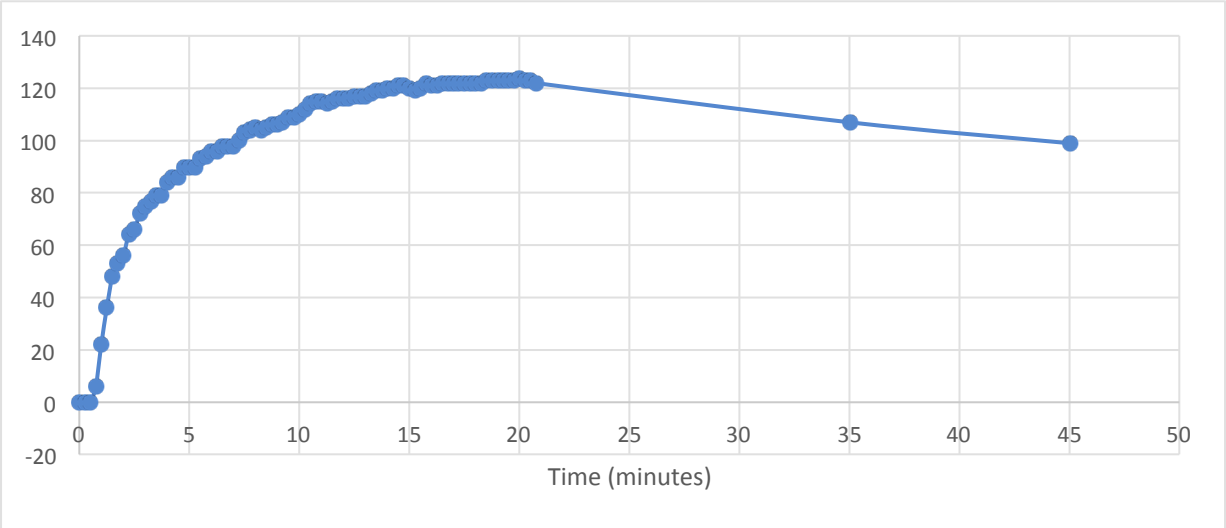

Figure 5: Plot of concentration at floor level in % of LFL from a refrigerant leak in a 5 m2 room.

Since the floor concentration will be equally distributed across the floor, and the room is only 5 m^2, increasing the room volume a little will scale the floor concentration down linearly. I.e. from the first test a room of 1,3 x 5 m^2 = 6,5 m^2 can be expected to reach a floor concentration of 130 % / 1,3 = 100 %.
Based on these tests it is concluded that the system will be safe in this scenario if installed in a room with at least 7 m^2 area. It is however noted that the type of leak considered is hard to imagine and never seen in practice, but the conservatism ensures safety.

Leak without drain trap
A test was conducted with a 4-minute leak, that is around 1,5 g/s, and the fan off. The tests show that the leak is lead through the drain pipe down to the floor and creates a high R290 concentration on the floor within seconds.
This allows the R290 to pool on the floor creating a flammable atmosphere. This is a situation that should be avoided since dilution of the pool can be slow and there is a risk of ignition sources at floor level. A drain trap is required to prevent leaks to lead to pooling at floor level.
A detailed report has been made with the risk assessment for the specific hot water heat pump (Vonsild, 2018).

CONCLUSIONS

A new generation of tap water heat pumps has been developed and tested. A “big” model with 270 liters water tank has the energy efficiency COP = 3,52 which is 12 % better than the similar HFC-model. This model uses 350 grams R290.
A “small” model for apartments with a water tank of 166 litters has been developed and tested, and the energy efficiency is COP = 3,20. This model is charged with 150 grams R290.
Risk assessments for the big model tell us that the heat pump is safe in all reasonably foreseeable scenarios, under the conditions that:

- The system installed in a 7 m^2 room or larger, and
    - common best practices are used during service as mandated by European legislation, and
    - a drain trap is installed, and
    - installing the outlet duct is not required for the system to be safe.

Or, alternatively:

- The system is installed in a room of any size, and
    - common best practices are used during service as mandated by European legislation, and
    - a drain trap is installed, and
    - the fan is running continuously at the lowest speed or higher, and
    - the outlet duct is installed.

The manufacturer is now working for commercialization of the two new products.

ACKNOWLEDGEMENTS

The work behind this paper was part of the project “Energy efficient tap water heat pump” under the Danish EPA programme MUPD (Miljøteknologisk Udviklings- og DemonstrationsProgram).
The authors wish to thank the Danish EPA for support.
The authors also wish to thank Mr. Torben Lauridsen, Vesttherm A/S for cooperation and support during the work.

REFERENCES

Pedersen, “Energy efficient tap water heat pumps using natural refrigerants”, October 2018. Publication in Danish from Danish Environmental Protection Agency: https://mst.dk/service/publikationer/publikationsarkiv/2018/nov/energieffektive-brugsvands-varmepumper-med-naturlige-koelemidler/

EN 60335-2-40:2003/A13:2012/AC:2013. Household and similar electrical appliances – Safety – Part 2-40: Particular requirements for electrical heat pumps, air-conditioners and dehumidifiers.

EN 378:2016 Refrigerating systems and heat pumps -- Safety and environmental requirements, all 4 parts.

EU Blue Guide, The ‘Blue Guide’ on the implementation of EU products rules 2016 (2016/C 272/01), European Commission.

IEC 60335-2-40:2002 Ed. 4. Household and similar electrical appliances – Safety – Part 2-40: Particular requirements for electrical heat pumps, air-conditioners and dehumidifiers.

IEC 60335-2-40:2016 Ed. 5.1. Household and similar electrical appliances – Safety – Part 2-40: Particular requirements for electrical heat pumps, air-conditioners and dehumidifiers.

ISO 5149:2014. Refrigerating systems and heat pumps -- Safety and environmental requirements, all 4 parts.

Low Voltage Directive, Directive 2014/35/EU of The European Parliament and of The Council of 26 February 2014 on the harmonisation of the laws of the Member States relating to the making available on the market of electrical equipment designed for use within certain voltage limits (recast).

Machinery Directive, Directive 2006/42/EC of the European Parliament and of the Council of 17 May 2006 on machinery, and amending Directive 95/16/EC (recast) (Text with EEA relevance).

Pressure Equipment Directive, Directive 2014/68/EU of the European Parliament and of the Council of 15 May 2014 on the harmonisation of the laws of the Member States relating to the making available on the market of pressure equipment (recast) (Text with EEA relevance).

Vonsild, “Flammable refrigerants, trends, legislation and standards for the Heat Pump Industry”, Heat Pump Centre Newsletter, IEA Heat Pump Centre, Vol. 34 No. 1/2016.

Vonsild, “Charge Limits for Heat Pumps with Flammable Refrigerants”, Heat Pumping Technologies Magazine, IEA Heat Pump Centre, Vol. 34 No. 2/2016.

Vonsild, “Risk Assessment for Hot Water Heat Pump”, September 2018.

Manuscript ID: 1013
DOI: 10.18462/iir.icr.2019.1013

Heat from Underground Energy London (Heat FUEL)

Henrique R. P. LAGOEIRO[(a)], Daniel CURRY[(b)], Gareth FAULKS[(b)], John BIELICKI[(b)], Akos REVESZ[(a)], Gareth DAVIES[(a)] and Graeme MAIDMENT[(a)]

[(a)]London South Bank University, London, United Kingdom, roscoeph@lsbu.ac.uk
[(b)]London Underground Limited, London, United Kingdom

ABSTRACT

This paper provides an analysis of a heat recovery scheme that collects waste heat from the London Underground, a large potential source that produces significant amounts of heat throughout the year. The heat is captured by an air-to-water heat exchanger located within a ventilation shaft of the London Underground, then upgraded using a heat pump and used as a low carbon energy source for a local district heating network. This work introduces some of the key aspects of the technical design of this novel urban heat recovery and delivery system, as well as compares it to similar solutions that recover heat from urban underground railways. The theoretical performance of the system is evaluated and compared to the previous heating method used for the buildings supplied by the network. This paper also provides recommendations for the implementation of future installations for secondary heat recovery and reuse in cities.

Keywords Heat networks, heat pumps, low carbon heat, London Underground, waste heat recovery

1. INTRODUCTION

The United Kingdom has achieved significant reduction of Greenhouse Gas (GHG) emissions in recent years, cutting them by 43% since 1990 (CCC, 2018), as a result of the Climate Change Act (2008), which established a target to reduce carbon emissions by 80% of its 1990 baseline level by 2050. In order to keep track of the UK's progress in tackling climate change, the Act also set carbon budgets to be measured every five years. Despite having met its 1st (2010), 2nd (2015) and 3rd (2020) carbon budgets, the UK will require much greater efforts if it is to meet the 4th (2025) and 5th (2030) targets, especially from the heating and cooling and transport sectors, since the results to date can be mainly attributed to the transformation of the power sector, which has achieved a considerable reduction in the use of coal as an energy source and an increase in the use of renewable sources. Approximately one third of carbon emissions and around half of the energy consumption in the UK can be traced back to heating and cooling (BEIS, 2018a). Despite having a considerable impact in energy consumption in Britain, very little of heating and cooling is provided with renewable energy. In 2017, only 4.5% of heating in buildings came from low-carbon sources (CCC, 2018). Lack of sustainable heating is also a problem at city level, with gas-fired boilers representing 90% of the heating used in London, making a significant contribution to both the carbon footprint and the air pollution in the city. Recent developments based on Combined Heat and Power (CHP) systems have been introduced across the country as a cost-effective way of producing low-carbon heat. However, as the national electricity grid decarbonises, the carbon savings relating to CHP are declining and there is increasing evidence of their adverse impacts on air quality. The Greater London Authority (GLA) (2018), has set the ambitious goal of London becoming zero carbon by 2050. Decarbonising the heating sector will be crucial to achieve this target, as London's 3.5 million homes produce one third of the capital's total GHG emissions and nearly three quarters of the energy consumed by homes is used for space and hot water heating. Meanwhile, the energy used to power and heat London's workplaces accounts for approximately 40% of the city's emissions, with 51% of that energy being used for space and hot water heating (GLA, 2018).

2. HEAT NETWORKS

Heat networks, or district heating networks (DHNs), represent an interesting alternative to deliver cost-effective low carbon heat. They are very flexible, being able to incorporate new buildings and heat sources as the network grows, and are particularly attractive in densely populated urban areas. DHNs also enable the use of different generating technologies to feed heat into the network, avoiding

a lock-in to technologies that may become obsolete in future decades. It also permits multiple heat sources to be used simultaneously in order to deliver heat to the network, providing a key mechanism to allow a smooth transition from current fossil fuel based heat to future low carbon heat sources. Nowadays only around 2% of the overall heating demand in the UK is met using heat networks (BEIS, 2018a), whilst London has 6% of its energy requirements supplied via local networks (GLA, 2018). However, it is already possible to identify some governmental initiatives to promote the use of low-carbon district energy within the UK. London, for instance, has already set a target of meeting 15% of its energy demand using district schemes and renewable sources by 2030 (GLA, 2018). It is likely that DHNs will play a key role in this process, as they can accommodate any heat source of sufficient temperature, enabling the use of waste heat sources to provide heating. The recovery of waste heat involves capturing heat that would otherwise be rejected during a given process, such as the heat that is generated during the operation of many urban infrastructures, e.g. sewage systems, electricity substations and cables, data centres, and railway tunnels. This paper analyses one such application for heat networks that will soon be operational in London, known as the Bunhill Waste Heat Recovery System or Bunhill 2, an extension of the Bunhill Heat Network which involves the recovery of waste heat from the Underground. The analysis entails comparing state-of-the-art technologies that could be applied to recover heat from railway tunnels, as well as describing the Bunhill system as a whole, its key components and expected performance.

3. HEAT GENERATION IN THE LONDON UNDERGROUND

As London is home to the world's first metro system, with a network length of 402 km (45% in tunnels) and 1.35 billion passengers per year (TfL, 2019), underground railways represent a particularly good option for secondary heat recovery in the city. The Metropolitan Integrated Cooling and Heating (MICAH) project investigated how the London Underground (LU) network remains relatively warm in most locations throughout the year and that the system could also deliver cooling to the tunnels when required (Davies et al., 2017). The Underground represents a great opportunity for waste heat recovery, as the operation of the trains requires considerable energy, which ends up being degraded and released as waste heat. Over 80% of the heat introduced into the network can be traced back to mechanical losses, related to the running of the trains; mainly, braking friction and resistive losses in the traction-control system, whilst the remainder can be attributed to commuters and station and tunnel systems (Botelle et al., 2010). The London clay surrounding the tunnel walls, which is the main heat sink, has gradually become heated, leading to higher temperatures for both the surrounding soil and the air in the tunnels. By exploiting the opportunity to recover waste heat from the Underground, it is also possible to deliver cooling to the tunnels, which is also beneficial.

4. WASTE HEAT RECOVERY FROM RAILWAY TUNNELS

A number of recent studies have addressed the potential to recover waste heat from railway tunnels, focusing on different technologies that could be applied to effectively retrieve the energy that is dissipated in the form of heat during the operation of underground trains. Botelle et al. (2010) showed how groundwater based air handling units (AHU), using either seepage water or aquifer groundwater, have already been applied to cool stations of the LU network. Seepage groundwater is particularly interesting as over 30 million litres of water already need to be constantly pumped out of the Underground network. Therefore, using it for cooling/heating represents an efficient solution energy wise, as shown by Ampofo et al. (2011), who investigated the performance of a groundwater cooling trial based on 3 fan coil units at Victoria station. Although the warmed water represents a large potential source for waste heat recovery, this technology might be limited to use at station platforms only, as the deep tunnels of the London Underground are too narrow to fit fan coil units.

Geothermal energy technologies, which are based on the capacity of the soil to store and provide heat, have also been investigated as a means of recovering waste heat from underground rail networks, resulting in innovative solutions that are both environmentally friendly and cost-effective. Brandl (2006) and Adam and Markiewicz (2009) investigated how foundations and underground structures, including tunnels, can be designed as thermo-active structures, enabling them to capture heat from their surrounding environment. Brandl (2006) researched how absorber pipes could be applied to bearing structures, such as bored piles, diaphragm walls and foundation slabs, in order to capture waste heat from railway tunnels and stations in Vienna. Both Adam and Markiewicz (2009) and Brandl (2006) also highlighted the potential of heat extraction based on absorber pipes attached

to an energy geocomposite placed between the outer and inner linings of a tunnel. The geotextile can also be connected to energy anchors, an important structural element that supports the tunnel excavation and could be applied as a new energy active element. In Stuttgart, Germany, a similar heat recovery trial was conducted on the city's metro system, where absorber pipes were attached to a geotextile and placed between the tunnel linings (Buhmann et al., 2016).

Nicholson et al. (2014) looked at the design of underground rail tunnels with absorber pipes embedded within segments of the tunnel lining, providing cooling to the Crossrail tunnels in London whilst harvesting waste thermal energy to heat nearby buildings. A similar system was proposed by Barla et al. (2016), which numerically analysed the feasibility of developing an energy tunnel in Turin. The proposed design also consisted of embedding pipes within the precast concrete lining and could operate in cooling and heating modes. Tunnels designed in this way can achieve high heat extraction rates, however, these technologies can only be applied to new underground railway developments and are not suitable to recover heat from the existing deep tunnels of the LU network. Revesz et al. (2019) proposed a different approach to recover the excess heat that is generated in railway tunnels in London, suggesting the use of ground source heat pumps (GHSPs) connected to geothermal heat exchangers (GHEs) to collect the heat that is conducted into the surrounding soil during the operation of trains due to the heat sink effect. As for the Bunhill Waste Heat Recovery System, an air-to-water heat exchanger will be applied so as to capture heat from a ventilation shaft within the LU network. The technology and its operation will be further described in the following sections of this paper. Davies et al. (2017) also investigated the potential to recover waste heat from ventilation shafts, identifying the benefits of applying this technology to a different shaft of the network.

Table 1 – Potential technologies for waste heat recovery from underground railway tunnels.

Technology	Location	Heat Source Medium	Heat Source Temperatures	Heat Extraction Rate	Service Disruption	Reference
Embedded absorber pipes in tunnel segments	London, UK	Air	17 to 36°C	7 to 30 W/m^2 of tunnel surface area	High	Nicholson et al. (2014)
	Turin, Italy	Air/ ground	14°C	53 W/m^2 of tunnel surface area	High	Barla et al. (2016)
Diaphragm and energy pile walls	Vienna, Austria	Air/ ground	>20°C	30 W/m^2 of earth-contact area	High	Brandl (2006)
Energy foundation slabs	Vienna, Austria	Ground	>20°C	10 to 30 W/m^2 of earth-contact area	High	Brandl (2006)
Pipes attached to geotextile between tunnel linings	Stuttgart, Germany	Air	6.5°C	20 W/m^2 of tunnel surface area	High	Buhmann et al. (2016)
Groundwater used in platform air handling units	London, UK	Air	22 to 32°C	50 kW/unit	Medium	Ampofo et al. (2011), Botelle et al. (2010)
Ground source heat pumps installed next to tunnels	London, UK	Ground	20 to 30°C	20 to 29 W/m of borehole length (depending on the GHE configuration)	Low	Revesz et al. (2016), Revesz et al. (2019)
Heat exchangers connected to ventilation shafts	London, UK	Air	20 to 28°C	900 kW/shaft	Low	Davies et al. (2017)

Table 1 summarises a range of previously investigated technologies that involve waste heat recovery from underground railway tunnels. The table also indicates the location where the technology was implemented/simulated; the temperatures and medium considered for the heat source; the calculated heat extraction rates; and the related risk of service disruption when installing each of the technologies. It also includes references to the authors reporting each study. Regarding the "risk of

service disruption" category in the table, a low risk means that the implementation does not hinder or slightly affects the operation of the trains, while a medium risk represents the need for a partial disruption of the transport service, and a high risk implies the need to suspend operation during the installation of the related technology. As it can be seen in Table 1, extracting heat from ventilation shafts represents a great opportunity, as significant heat can be extracted while keeping service disruptions to a minimum.

5. THE BUNHILL HEAT NETWORK

The Bunhill Heat Network was an initiative from Islington Council, aimed at providing locally produced cost-effective, low carbon heat for nearby housing estates and service buildings. The project consists of two different stages: Bunhill 1, the original DHN launched in 2012, and Bunhill 2, an extension to the existing heat network that will involve utilising recovered waste heat. The concept for Bunhill 1 was to use a gas-fired CHP system, producing both electricity and heat, which is linked to a heat distribution network in order to supply heating for the local community. The Energy Centre for Bunhill 1 comprises a 1.9 MW_e/2.3 MW_{th} gas fired CHP and a 115 m^3 thermal store. The network currently operates with flow and return temperatures of 95°C and 75°C, respectively.

In an effort to further expand the supply of low cost and low carbon heat to its residents, Islington Council started to research potential extensions to the Bunhill Scheme, which led to the opportunity of developing Bunhill 2, a waste heat recovery system based on heat capture from the London Underground, implemented in a partnership with Transport for London (TfL) and the GLA. This project is the first of its kind in Europe and is part of the EU CELSIUS Project, which aims to promote the use of sustainable heating and cooling in European cities. The decision to use waste heat sources is also related to the decreasing carbon efficiency of CHP systems due to the growing decarbonisation of electricity in the UK. Bunhill 2 will collect heat from one of the shafts that constitute the ventilation system of the Underground network. The heat will then be upgraded using a heat pump before being transferred into the DHN, which will be extended to connect new buildings to the new Energy Centre. The Energy Centre consists of the heat pump, a thermal store and two CHP engines, which will be added to the system so as to provide resilience and flexibility to the heat network. The development of Bunhill 2 will shed light on how London can become a truly smart city, showing how DHNs and heat pumps can be fundamental in future smart energy infrastructures, both at district and ultimately city levels, by allowing the capture of urban waste heat. As this paper aims to research the novelty related to the system, only the Bunhill 2 network will be presented, focusing on the first trial to recover waste heat from the London Underground.

6. THE OPERATION OF THE BUNHILL WASTE HEAT RECOVERY SYSTEM

The Energy Centre of Bunhill 2 is expected to meet an annual average heat output of 1,033 kW_{th}, with 780 kW of heat being recovered from the ventilation shaft and then upgraded by a two-stage heat pump, which will add the remaining 253 kW to the heat that is delivered to end users through the DHN. The two CHP units, each with an output of 237kW_e/372kW_{th}, will power the heat pump and also add resilience and flexibility to the Energy Centre, although its output heat could be dumped if not needed. A thermal store of 77.5 m^3 will also be installed in order to add flexibility, helping to manage peak demand. The air that exhausts through the ventilation shaft has temperatures varying from around 18°C to 28°C. Thus, the first water loop, which transports the heat from the vent shaft to the heat pump, will also work with flow and return temperatures that vary according to the season of the year. The expected operating flow and return temperatures vary from 11 to 18°C and 6 to 13°C, respectively. The heat will be then upgraded and distributed with a flow temperature of 75°C, being returned to the heat pump at 55°C. Figure 1 shows a schematic of the Bunhill 2 heat network.

6.1. Heat Exchanger

The first stage of the system involves capturing the heat using an air-to-water heat exchanger in the City Road ventilation shaft. The heat exchanger used for this waste heat recovery system is a fan coil unit. A head house, where the coils were installed, was built on top of the ventilation shaft, which was upgraded to accommodate the variable speed reversible fan that enables the system to work in both Extract and Supply modes. The benefits of operation in these two different modes have been previously investigated by Davies et al. (2017) and consists of reversing the flow direction of the fan, allowing the system to operate by either extracting hot air from the Underground, which can then be

used to warm the water in the coils, or using ambient air, which would be cooled by the coils and then supplied to the Underground, with the heat extracted being recovered by the heat exchanger. Extract mode would be used during the colder months of the year, when the heat demand is at its peak and the underground air is warmer. Supply mode would be used to supply cooling to the Underground during the summer, when ambient temperatures are higher. Throughout the year, heat can be collected at average temperatures between 17 and 25°C, which explain the varying flow and return operating temperatures of the DHN. The coils have an annual average operating cooling duty of 780 kW and consist of 6 modules with 6 rows of copper tubes, resulting in a total of 36 rows of tubes - comprising the coil heat exchanger. The coils were built up in modules to make maintenance simpler and minimise downtime for cleaning. Figure 2 shows a schematic of the ventilation shaft and the head house, showing the coil heat exchanger and the reversible fan.

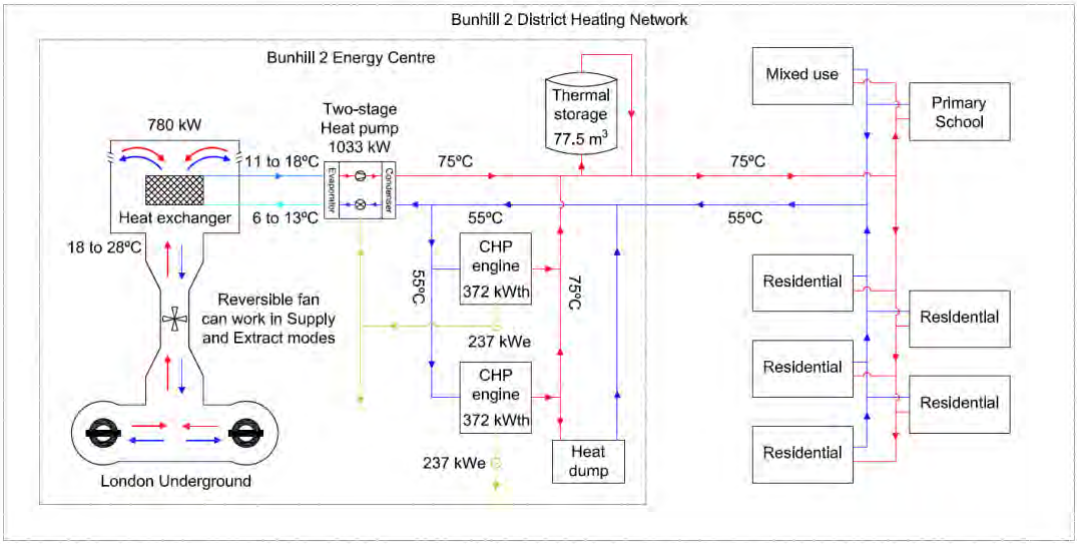

Figure 1 – Schematic of the Bunhill Waste Heat Recovery System.

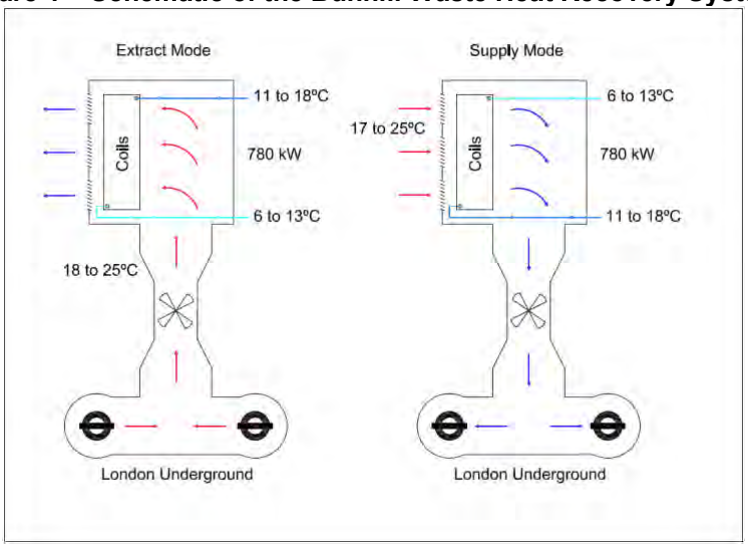

Figure 2 – Schematic of the heat exchanger and the ventilation shaft of the Bunhill Energy Centre 2.

6.2. Heat Pump

Before being delivered to the district heating network, the heat collected by the heat exchanger has to be upgraded by a two-stage water-to-water heat pump, which was designed based on the flow and return DHN temperatures of 75°C and 55°C, respectively. For district heating purposes, as the evaporator and the condenser operate with a large temperature difference, deploying single-stage heat pumps could lead to lower compression efficiency and decrease the overall system performance (Kwon et al., 2013). Two-stage compression represents a more flexible system, being able to operate at different capacities, and with greater efficiency. One advantage is that it allows intercooling, which decreases the necessary work input to the compressors, delivering high temperature lifts with a high Coefficient of Performance (COP) (Arpagaus et al., 2016). The flash

intercooler also improves the efficiency of the system by allowing flash gas to be removed before the refrigerant enters the evaporator, increasing its heat transfer rate. The two-stage heat pump installed at Bunhill 2 operates differently according to the season of the year, due to the varying temperatures of its heat source. Table 2 shows the design parameters of the two-stage heat pump.

The refrigerant used in the heat pump is R717 (ammonia). The low stage includes a compressor that can run at a wide range of capacities in order to accommodate the variation in ventilation temperatures exhausted from the LU shaft. The high stage includes two compressors, which can also accommodate varying capacity, while maintaining the desired outlet water temperature at 75°C. The heated water from the first water loop will deliver heat to the heat pump's evaporator, with an approach temperature (ΔT) of 5°C, however, the cooling duty increases slightly, as higher temperature water enters the evaporator, to between 778 kW and 784 kW, with an annual average of 780 kW. By varying the cooling duty, the power input to the compressors can be minimised without compromising the design outlet temperatures. This results in higher COPs as cooling duty is increased, with an annual average COP of 3.76. The heat pump includes a heating circuit with 5 shell and plate heat exchangers, which are the flooded evaporator, a condenser, a subcooler and two desuperheaters. Figure 3 shows a schematic of the two-stage water-to-water heat pump installed at the Energy Centre of the Bunhill 2 heat network.

Table 2 – Design parameters for the two-stage ammonia heat pump installed at Bunhill 2.

Design Parameters	Operating Mode 1	Operating Mode 2	Operating Mode 3
Cooling Duty - Qe (kW)	778	780	784
First Loop Water Flow Temp. (°C)	11	13	18
First Loop Water Return Temp. (°C)	6	8	13
Heating Duty - Qc (kW)	1042	1033	1012
Estimated Shaft Power (kW)	264	253	228
Estimated Electrical Consumption (kW)	286	275	248
Cooling COP	2.72	2.84	3.16
Heating COP	3.64	3.76	4.08

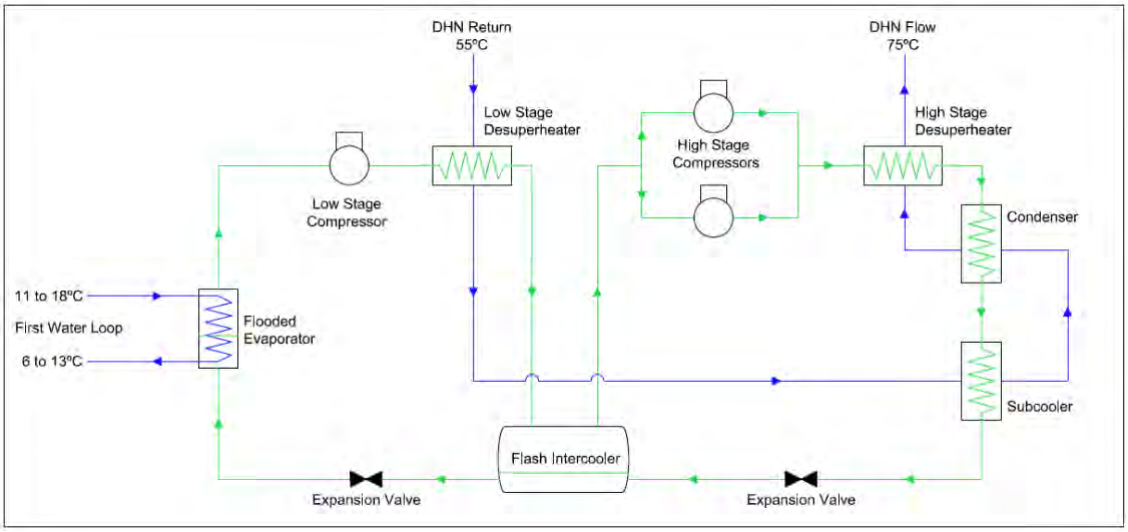

Figure 3 – Schematic of the two-stage heat pump of the Bunhill Energy Centre 2.

6.3. Thermal Storage

In order to provide flexibility, a thermal storage tank filled with 77.5 m^3 of water will be installed at the Energy Centre. Storing thermal energy is crucial to manage peak demand, securing the reliability of the system when it is most requested. The thermal store also avoids short cycling of the heat pump, enhancing its efficiency, since frequent start/stop operation can harm the system and increase its need for maintenance.

6.4. Heat Distribution Pipework

The heat distribution network will have an approximate length of 2.4 km and will utilise two parallel insulated pipes, for the flow, i.e. heat delivery, and return water streams. Water will leave the heat

pump outlet at a design flow rate of 37.2 kg/s. The network has different pipe diameters, varying from DN 80 for local building connections to DN 250 for the main flow/return pipes, which distribute the heated water from the heat sources to local circuits, which feed one or more buildings connected to the network. The scheme is expected to provide heating to 455 dwellings in 5 building blocks of a local housing estate and to a primary school. A new mixed use building complex that is currently being developed will also be connected to Bunhill 2, adding to the network 720 residential units, a 160-bed student accommodation and a 125-bed hotel, as well as areas for offices, retail and restaurants as new end users. The expected annual heat demand of the network is 11,358 MWh.

7. BENEFIT ANALYSIS

In order to assess the benefits of this new waste heat recovery system in terms of carbon and cost savings, a spreadsheet based model was developed and used. The method aims to provide a high-level appraisal of the system's benefits based solely on energy input costs and carbon emissions related to heat delivered from the heat pump, and does not include any other operational costs, such as for staff support and maintenance. The analysis compares a scenario where all the heat demand is met by the heat pump to the previous heating method based entirely on communal gas boilers. The calculations were based upon a 25-year design life (2019-2043) and the following assumptions: gas boiler efficiency of 80% for the previously used boilers (BRE Group, 2018), carbon factors of 0.184 $kgCO_{2e}$/kWh for gas and 0.145 $kgCO_{2e}$/kWh for electricity, based on the averages of annual projections for the design life of the system (BEIS, 2018b), fuel tariffs of 3.89 p/kWh for natural gas and 14.22 p/kWh for electricity, considering the average values of central annual projections for public sector tariffs during the design life of the project (BEIS, 2018b), and distribution losses of 10% related to the primary heat network fed by the heat pump. The results of the analysis can be seen in Table 3, which shows that a heat pump based system results in yearly carbon savings of 2,133 tCO_{2e}, a decrease of 82% in emissions, demonstrating how waste heat recovery could reduce the carbon footprint associated with heating. This is due to the high energy efficiency of heat pumps and similar carbon factors for natural gas and electricity, which has considerably decarbonised in the UK in recent years. The cost analysis demonstrated how heat pumps can lead to annual savings of £79,778 or 14%, indicating how waste heat recovery systems can be financially attractive.

Table 3 – Calculated annual carbon and cost savings for a heat pump based heat recovery system.

Energy Consumption				
Technology	Efficiency/COP	Heat Demand (MWh)	Annual Energy Spent (MWh)	
Gas Boilers	80%	11,358	14,198	
Heat Pump	3.76		3,323	
Carbon Savings				
Technology	Carbon Factor ($kgCO_{2e}$/kWh)	Emissions (tCO_{2e})	Annual Savings	
			(tCO_{2e})	%
Gas Boilers	0.184	2,615	2,133	82%
Heat Pump	0.145	482		
Cost Savings				
Technology	Energy Tariff (p/kWh)	Costs (£)	Annual Savings	
			£	%
Gas Boilers	3.89	552,283	79,778	14%
Heat Pump	14.22	472,505		

8. CONCLUSIONS

The results obtained show the importance of investing in waste heat recovery systems, as they can lead to significant carbon savings compared to conventional heating methods and could become a key technology in minimising climate change, especially as electricity is expected to keep on decarbonising in the coming years. Despite leading to operational cost savings, the conducted economic assessment did not consider the capital costs related to heat pumps or the utilisation of the other heat sources within the Energy Centre, which can impact the overall financial performance of the scheme considerably. Even though the costs of implementing district scale heat pumps are known to be high, it is anticipated that they may become more attractive in the near future. As their deployment becomes more popular, the capital costs related to waste heat recovery tend to become

lower. In addition, as natural gas reserves diminish over the next decades and possible new carbon taxes are introduced, gas prices are likely to rise, making heat pumps a viable alternative for heating. Further studies on the Bunhill Heating Scheme will be undertaken as part of a PhD project, which will study the overall system particularly with regard to its technical and financial performance. Bunhill 2 is expected to become operational in 2019. The study will involve investigating the network components and their performances in detail, comparing the design performance with the actual operation of the system. The benefits of the system will also be looked into in more detail, considering seasonal variations, capital costs and other operational costs and issues, as well as any other challenges that might be encountered after Bunhill 2 starts running.

ACKNOWLEDGEMENTS

The authors would like to acknowledge the support from London South Bank University, Transport for London and the Engineering and Physical Sciences Research Council (EPSRC) sponsored project Low Temperature Heat Recovery and Distribution Network Technologies (LoT-NET). The authors are also grateful to Rodrigo Matabuena, Stephen Mirkovic, Graeme Low and James Wilson of the London Borough of Islington for their support in providing valuable information for this project.

REFERENCES

Adam, D., and Markiewicz, R., 2009. Energy from Earth-Coupled Structures, Foundations, Tunnels and Sewers. Géotechnique 59(3), 229–236.

Ampofo, F., Maidment G.G. and Missenden J.F., 2011. Application of Groundwater Cooling Scheme for London Underground Network. Int. J. Refrigeration 34(8), 2042–2049.

Arpagaus, C., Bless, F., Schiffmann, J. and Bertsch, S.S., 2016. Multi-temperature heat pumps: A literature review. Int. J. Refrigeration 69, 437–465.

Barla, M., Di Donna, A., and Perino, A., 2016. Application of Energy Tunnels to an Urban Environment. Geothermics 61, 104–113.

Botelle, M., Payne, K. and Redhead, B., 2010. Squeezing the heat out of London's Tube. Proceedings of the Institution of Civil Engineers – Civil Engineering 163, 114-122.

Brandl, H., 2006. Energy Foundations and Other Thermo-Active Ground Structures. Géotechnique 56(2), 81–122.

BRE Group, 2018. Standard Assessment Procedure, version 10 (SAP 10). Available from: https://bregroup.com/sap/sap10 [Accessed 26.11.2018].

Buhmann, P., Moormann, C., Westrich, B., Pralle, N. and Friedemann, W., 2016. Tunnel Geothermics — A German Experience with Renewable Energy Concepts in Tunnel Projects. Geomechanics for Energy and the Environment 8, 1–7.

Committee on Climate Change (CCC), 2018. Reducing UK emissions – 2018 Progress Report to Parliament. United Kingdom.

Davies, G., Boot-Handford, N., Grice, J., Dennis, W., Rami, R., Nicholls, A. and Maidment, G.G., 2017. Metropolitan Integrated Cooling and Heating. ASHRAE Winter Conference. Las Vegas, USA.

Department for Business, Energy & Industrial Strategy (BEIS), 2018a. Heat Networks Investment Project, Introduction to the Scheme. United Kingdom.

Department for Business, Energy & Industrial Strategy (BEIS), 2018b. Green Book supplementary guidance: valuation of energy use and greenhouse gas emissions for appraisal. Available from: https://www.gov.uk/government/publications/valuation-of-energy-use-and-greenhouse-gas-emissions-for-appraisal [Accessed 26.01.2019].

Greater London Authority (GLA), 2018. London Environment Strategy. London, UK.

Kwon, O., Cha, D. and Park, C., 2013. Performance evaluation of a two-stage compression heat pump system for district heating using waste energy. Energy 57, 375–381.

Nicholson, D.P., Chen, Q., de Silva, M., Winter, A. and Winterling, R., 2014. The Design of Thermal Tunnel Energy Segments for Crossrail, UK. Proceedings of the Institution of Civil Engineers – Engineering Sustainability 167(3), 118-134.

Revesz, A., Chaer, I., Thompson, J., Mavroulidou, M., Gunn, M. and Maidment, G., 2016. Ground Source Heat Pumps and Their Interactions with Underground Railway Tunnels in an Urban Environment: A Review. Applied Thermal Engineering 93, 147–154.

Revesz, A., Chaer, I., Thompson, J., Mavroulidou, M., Gunn, M. and Maidment, G., 2019. Modelling of Heat Energy Recovery Potential from Underground Railways with Nearby Vertical Ground Heat Exchangers in an Urban Environment. Applied Thermal Engineering 147, 1059–1069.

Transport for London (TfL), 2019. Facts & Figures. Available from: https://tfl.gov.uk/corporate/about-tfl/what-we-do/london-underground/facts-and-figures [Accessed 14.01.2019].

Manuscript ID: 1055
DOI: 10.18462/iir.icr.2019.1055

Screening of heat pump performance improvements obtained through gradual heating using a tank system

René KOFLER[(a)], Brian ELMEGAARD[(a)], Claus MADSEN[(b)], Lars OLSEN[(b)], Wiebke B. MARKUSSEN[(a)]

[(a)] Technical University of Denmark, Kgs. Lyngby, 2800, Denmark, renekof@mek.dtu.dk
[(b)] Danish Technological Institute, Taastrup, 2630, Denmark, clma@teknologisk.dk

ABSTRACT

Many industrial processes require both cooling and heating of process streams. The use of a co-generation heat pump system enables the simultaneous production of both utilities within one single, electrically driven unit.
Within this work, the addition of a tank system at the hot end of different heat pump systems was investigated. The tank system consists of a stratified storage tank for the storage of hot water and a smaller charge tank, which allows for multiple circulations of the water through the condenser. This leads to a gradual heating of the water, leading to a higher COP compared to heating in one step.
Using numerical modelling and simulation, a screening was carried out investigating the influence of different working fluids and heat pump configurations, different temperature glides in the heat sink and different temperature lifts on the performance of the heat pump system. The largest improvement, compared to a conventional heat pump, was achieved with a one-stage heat pump with R600a, increasing the COP by 35 %.
Keywords: Heat pump, COP, Energy Efficiency, Working Fluid, Tank.

1. INTRODUCTION

Many countries aim to reduce the use of fossil fuels. The long-term Danish energy policy aims for a fossil fuel free society by 2050. This includes all sectors, including the heating and transport sector. Bühler et al. (2016) conducted an energy and exergy analysis of the Danish industry sector. The results show potentials for reduction of fossil fuel use and exergy losses through waste heat recovery and the use of alternative technologies.
Heat pumps (HPs) allow for an efficient, fossil fuel free production of heat, when using electricity from renewable energy carriers like wind and solar. Additionally, HPs allow for process integration by using waste heat streams, which have to be cooled down, while heating another stream at a higher temperature level. The cooled stream could be a warm stream, which is cooled down to ambient conditions before releasing it to the environment. It could also be a stream used for cooling purposes within the same process.
Units, providing heating and cooling capacity are referred to as co-generation HPs. The efficiency of such units is limited due to the high temperature lift between the cold and hot process water. In order to improve the efficiency of these systems, different cycle configurations, working fluids or new system designs can be used. One interesting approach is serial or gradual heating of water. Gradual heating leads to lower condensing temperatures on average and hence to higher coefficient of performance (COP) compared to heating in one step with conventional heat pumps.
Wang et al. (2010) conducted a comparison between a one-stage cycle, a two-stage cycle with intercooler and serial heating by two serial, one-stage HPs. The results show that below a specific temperature lift, the two-stage cycle achieves the highest COP, while the a configuration with two HPs in series is the most efficient above the threshold. Ommen et al. (2015) investigated the technical and economic feasibility of serially connected industrial HPs. It is shown that serial connection of two or three HPs leads to higher COPs and lower net present values (NPV) compared to one single HP.
Serial heating can also be realized by using storage tanks instead of several HPs in series. This approach is presented by Rothuizen et al. (2014) and Olsen et al. (2015) termed the ISEC concept and by Löffler and Griessbaum (2014) termed the trapezoid cycle. In both concepts, two storage tanks are used, where one tank is charged gradually, until it is fully charged with water of the wanted

supply temperature. In the meanwhile, the second tank is discharged, delivering hot water to the process from the top of the tank, while colder return water is filled into the bottom of the discharge tank.
The ISEC concept shows an improvement potential of up to 25 % in COP compared to a conventional HP, where a one-stage HP working with ammonia (R717) was used to heat water from 40 °C to 80 °C with an evaporation temperature of 22 °C (Rothuizen et al., 2014). The ISEC concept was furthermore tested experimentally, investigating the performance of the HP and the stratification in the storage tanks (Rothuizen et al., 2015 and Olsen et al., 2016).
Experimental investigations of the trapezoid cycle show COP improvements of 10 % - 50 % for water inlet temperatures at the condenser between 12 °C – 37 °C. The supply temperature of the hot water and the inlet temperature to the evaporator were kept constant at 42 °C and 10 °C, respectively. A one-stage HP using R134a was used for the experiments (Löffler and Griessbaum, 2014).
In this work, a system similar to the described systems using storage tanks was investigated. The main difference of the new system to the ones proposed by Rothuizen (2014) and Löffler (2014) was a different setup of the storage tanks.
In the previous works investigating gradual heating, only specific cases using specific HP configurations, working fluids, temperature sets etc. are considered. The aim of the screening is to reveal which of the investigated parameters mainly influence the possible performance improvements through gradual heating, and to identify the most promising system setups and system boundaries. The screening considered different heat pump configurations, different working fluids and different temperature sets.

2. METHODS

In the following sections, the new design is introduced, different HP configurations used for the screening are shown, the modelling strategy and the models of the different components of the systems are described and the assumptions for the different screening cases are explained.

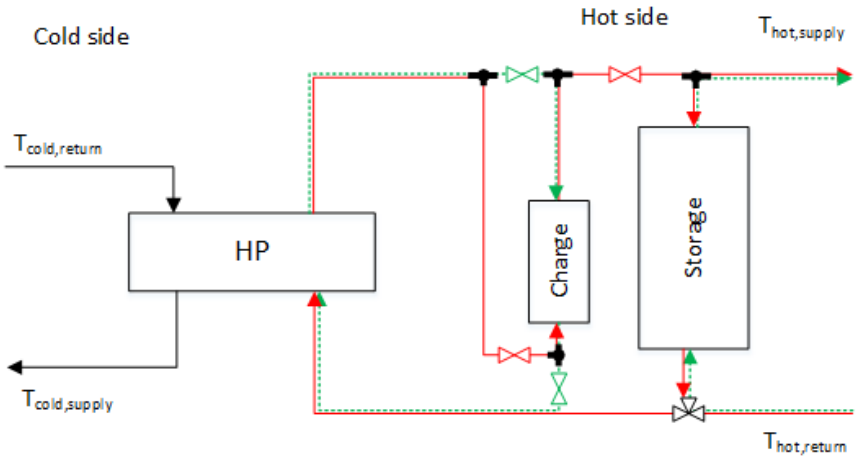

Figure 1: Principle sketch of the system. The green dashed line at the hot side denotes the flow during the charging process of the charge tank and the red solid line the one during discharging

2.1. The Concept

The main novelty of the proposed system is the tank setup, shown in Figure 1. Instead of using two tanks of the same size, one smaller charging tank and a bigger storage tank are used. This setup introduces two advantages compared to the previously described systems with two charging tanks of the same size. Firstly, the new system requires less three-way valves than the ISEC concept, which will reduce the investment costs. Secondly, many existing HP systems for industrial processes already use buffer tanks in order to compensate for varying heat loads over time. These tanks can be used as storage tanks for the new system. This allows for increasing the efficiency of existing HP systems by adding only one smaller charge tank, reducing the investment costs compared to the ISEC concept.
In Figure 1, the two different operation modes of the tank system at the hot side are depicted. The green dashed lines show the water flow during the charging process of the charge tank. In this

period, colder water is taken from the bottom of the charge tank, heated in the condenser of the HP and the hot water is returned to the top of the charge tank. In the meanwhile, hot process water at the required supply temperature is delivered to the process from the top of the stratified storage tank. The cold water returning from the process is fed to the storage tank at the bottom in order to insure stratification within the tank. When the charge tank is filled completely with water at the required supply temperature, the operation mode is switched to discharge the charge tank. This is shown in Figure 1 with red solid lines. In this mode, the return water from the process flows together with water from the bottom of the storage tank to the condenser of the HP. The heated water is then fed to the bottom of the charge tank. This leads through the stratification within the charge tank that the hot water at the top is supplied to the process. A part of the flow goes into the storage tank in order to refill it. When all the water at supply temperature has left the charge tank, the charging process of the charge tank starts again.

2.2. Heat Pump Configurations

This work aims at the investigation of the influence of different factors on the improvement potential though gradual heating. One of these factors is the HP configuration. In Figure 2, the investigated HP configurations are depicted.
In Figure 2, left, a simple one-stage cycle consisting of an evaporator, compressor, condenser and throttling valve is shown. The condenser is divided into two separated heat exchangers for desuperheating and condensation. This division is connected to the modelling approach, as explained in the following sections. The technical realization can be both, in two separate heat exchangers or one component for the whole process.
Figure 2, middle shows a one-stage cycle with regeneration heat exchanger (RHE), often called liquid-suction or internal heat exchanger. This component is often used for refrigeration or heat pump cycles with HFCs, hydrocarbons or similar working fluids.
A two-stage cycle with open intercooler is depicted in Figure 2, right. This setup is commonly used for refrigeration or heat pump cycles with large temperature lifts. It allows for an increase in efficiency and for higher pressure ratios between the evaporation and condensation pressure.

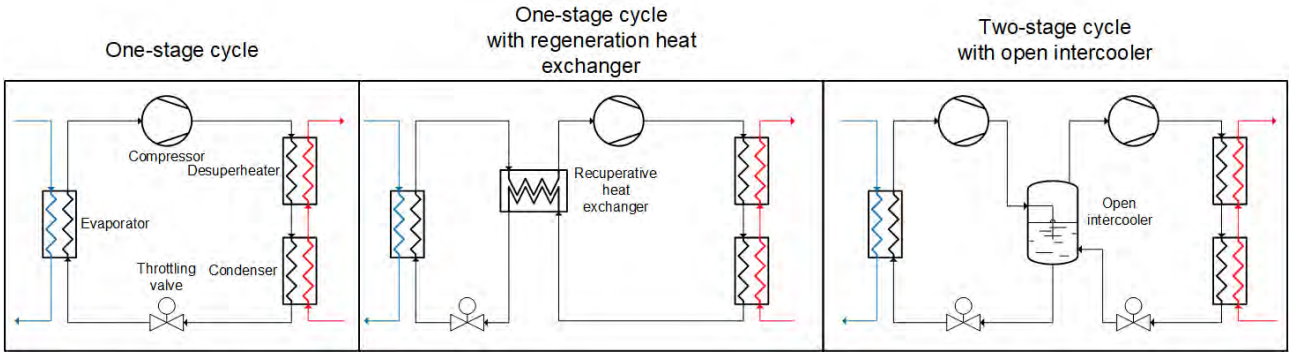

Figure 2: Different heat pump configurations examined in this work. Left: simple one-stage cycle. Middle: one-stage cycle with regeneration heat exchanger. Right: two-stage cycle with open intercooler

2.3. Modelling Strategy

For this work, a robust model for quick calculations of different cases was built. With the system, water was heated gradually in N circulations from a defined return temperature to a defined supply temperature. From a model-point-of-view, the first circulation was seen as a design circulation. For the first circulation, the minimum temperature differences in the evaporator and the condenser and quality of the working fluid between the condenser and desuperheater were defined. From these, the UA-values of the three heat exchangers were derived and kept constant for the following circulations. The UA-value of the RHE was determined by fixing the heat exchanger effectiveness during the first circulation.
The compressors were working at constant displacement during all circulations and the water mass flow through the condenser and desuperheater was also kept constant. The constant water mass flow rate allowed for an equal time period of each circulation. For the energy balance of the HP, one degree of freedom is required for the heat input from the heat source at the cold side. Here the return and supply temperatures were set constant, leading to the water mass flow to be variable between the different circulations. The ratio of displacement between the low- and high-stage compressor for

the two-stage cycle was determined by defining the intermediate pressure at the intercooler with the geometrical mean value, calculated as the square root of the product of evaporation and condensation pressure.

2.4. Component Models

As shown in section 2.2, all HP cycles consist of the following components: compressors, heat exchangers, throttling valves, intercooler (if applicable). All components were modelled based on steady state mass and energy balances. Heat losses in all components were neglected. The compressors were modelled by volumetric and isentropic efficiency. For both efficiencies, polynomials in dependency of the evaporation and condensation temperatures were used. The throttling valves were modelled as isenthalpic processes. The heat exchanger models were based on the logarithmic mean temperature difference (LMTD) and a constant UA-value. In order to calculate the UA-value of the evaporator and the condenser, the minimum temperature difference between water and working fluid within the heat exchanger was fixed. In the evaporator, the minimum temperature difference was found to be between the outlet temperature of the water and the evaporation temperature of the working fluid. The condenser was divided into two heat exchangers, one for desuperheating of the working fluid and one for condensation, as shown in Figure 2. A UA-value for each of the two heat exchangers was determined. The minimum temperature difference was found to be between the condenser and the desuperheater. Additionally, the inlet quality to the condenser was fixed. In this work, no subcooling of the working fluid within the condenser was included. The size of the RHE was determined by fixing the heat exchanger effectiveness, which describes the ratio between the transferred heat over the theoretical maximum heat transfer. The open intercooler was completely determined through the mass and energy balances. Complete interstage cooling within the intercooler was assumed, meaning that the outlet quality of the vapour going to the high-stage compressor was set to one.
The tank system was modelled by quasi-static mass and energy balances. Further, we assumed both - charging and storage tank, to be ideally stratified, i.e. without mixing of layers and heat transfer between layers and through the tank walls. In order to account for the increasing energy consumption of the water pump with increasing water mass flows, a simple pump model based on a constant pressure loss within the condenser, the water volume flow and a constant isentropic efficiency was used.

2.5. Test Cases for Screening

In this work, different screenings were conducted. The first screening investigated the performance of the system for different working fluids and cycle configurations for different numbers of circulations per charging cycle of the charging tank. For this screening, cold water was cooled from 20 °C to 10 °C while heating water from 20 °C to 60 °C at the hot side. The number of circulations was varied from 2-15 and then compared to the direct heating HP without a tank system. The examined working fluids were R134a, R290, R600a and R717. For all working fluids, calculations with a simple one-stage HP were conducted. For R717, a two-stage cycle with open intercooler and for the other working fluids, a one-stage cycle with RHE were investigated additionally.
In the next screening, the influence of the temperature glide in the heat sink was examined. The temperature glide in the heat sink is defined as the difference between the return and supply temperature on the hot side. For the variation, the supply temperature was held constant at 60 °C, while the return temperature was varied from 20 °C to 55 °C. The temperature of the heat source was kept constant.
Finally, the influence of the temperature lift was examined by varying the hot supply temperature between 40 °C and 80 °C while keeping the temperature glide in the heat sink at 20 K. The temperature lift of the process is defined as the difference between the supply temperature and the return temperature of the cold water. By keeping the cold side at the supply temperature of 10 °C and a return temperature of 20 °C, temperature lifts of 20 K to 60 K were investigated.
For the cases using ammonia (R717) as a working fluid a flooded evaporator was modelled, assuming a vapour quality of x=1 at the inlet of the (low-stage) compressor. For other working fluids, a direct expansion evaporator with a compressor suction superheat of 5 K was modelled. The operating limits for the compressors were defined with maximum compressor discharge temperatures of 180 °C (Ommen et al., 2015).
In the design run of the evaporator and the condenser, pinch point temperature differences of 5 K were used. The RHE effectiveness was fixed to 0.6. For the calculation of the power consumption of

the hot water pump, a pressure drop in the condenser of 0.5 bar and an isentropic efficiency for the pump of 0.8 were assumed.
For the cycles working with R717, compressor data from Sabroe were used. For the other working fluids, a compressor from GEA Bock were used. The names of the compressors are shown in Table 1 together with the previous explained assumptions. The data for the fitting of the compressor polynomials were taken from Johnson Controls Denmark (1985-2019) and IPU (2008-2015) for the Sabroe- and Bock-compressors, respectively.

Table 1: Fixed input variables for heat pumps and water pump

Working fluid	R717	R134a, R290, R600a
Compressor suction superheat [K]	0	5
Max. discharge temperature [°C]	180	180
Pinch point temperature difference [K]	5	5
Regeneration heat exchanger effectiveness [-]	-	0.6
Water pressure drop in condenser [bar]	0.5	0.5
Pump isentropic efficiency [-]	0.8	0.8
Compressor model (one- and high-stage)	Sabroe HPX-708	Bock EX-HG 12P/60 4S
Compressor model (low-stage)	Sabroe SMC-112L	-

3. RESULTS

This section presents the screening of the HP system using storage tanks for gradual heating. The boundary conditions for the screening were presented in the previous section.

3.1. Working fluid and heat pump configuration

In the first screening, the influence of the working fluid and the HP configuration on the COP of the system was examined. Figure 3, right, shows the COP of the conventional HP as coloured columns for different working fluids and HP configurations. As seen, changing the HP configuration from one-stage to two-stage or including a RHE leads to an improvement in COP for each working fluid. The boxes on top of the columns show the range of COPs, when using the tank system for gradual heating with different number of circulations of water through the charge tank until it is completely charged.

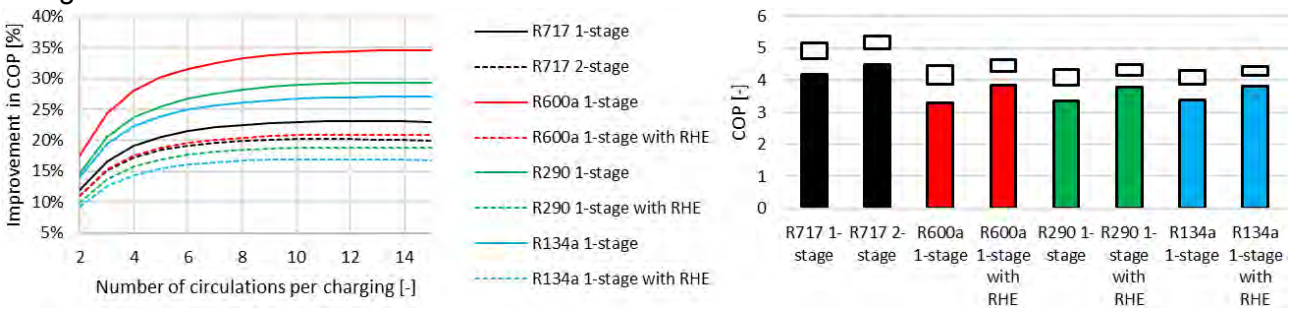

Figure 3: Left: Improvement in COP compared to conventional heat pump for different working fluids and heat pump cycles. Right: Coloured column depicts COP of conventional heat pump, box on top the range for different numbers of circulations during charging

Figure 3, left, shows the improvement of COP compared to a conventional HP for different working fluids and HP configurations and different numbers of circulations per charging cycle of the charge tank. The solid lines denote the improvement when using a simple one-stage HP and the dashed lines for two-stage HPs or with a RHE. It may be seen that the use of the tank system leads to bigger improvements for the simple one-stage HP configuration than for the other configurations. The difference in improvement between one-stage and two-stage HPs is smaller than between the one-stage HPs with and without RHE. It is also visible, that different working fluids show different behaviour. The biggest improvement in COP was achieved for a one-stage HP with R600a, with an improvement of up to 35 % and a minimum improvement for two circulations per charging cycle of 18 %.

3.2. Temperature Glide in Heat Sink

As a second parameter, the temperature glide in the heat sink was examined. Figure 4, left, depicts the maximum improvement in COP compared to a conventional HP for different temperature glides in the heat sink, working fluids and HP configurations. The values for a temperature glide of 40 K correspond to the maxima of the curves in Figure 3, left. It may be seen that the maximum improvement decreases with decreasing temperature, reaching an improvement of only 1.2 % for a one-stage HP with R600a and no improvement for a temperature glide of 5 K for a two-stage HP or RHE with R717 or R290 and R134a respectively.

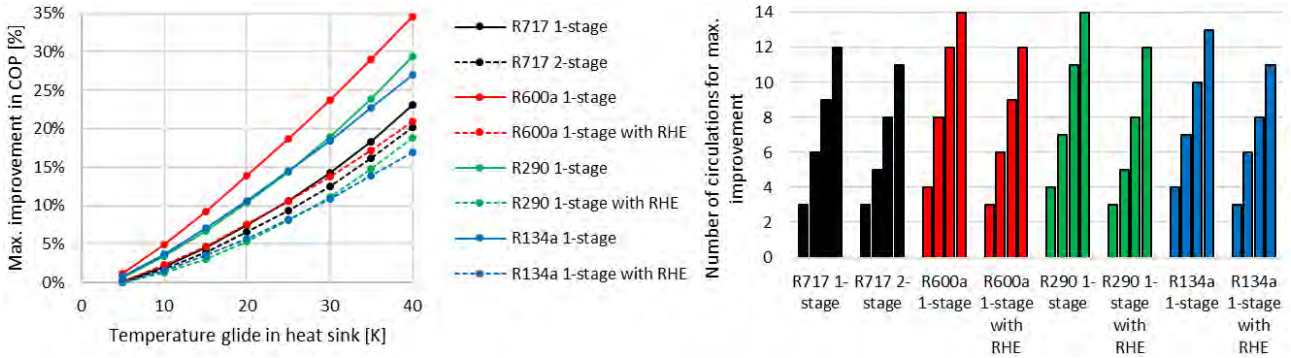

Figure 4: Left: Improvement in COP for varying temperature glide in heat sink. Right: Number of circulations with maximum COP for temperature glides of 10, 20, 30 and 40 K.

Figure 4, right, shows the optimum number of circulations per charging cycle for temperature glides of 10 K to 40 K in steps of 10 K. The fourth column of each working fluid and HP configuration shows the location of the maximum in Figure 3, left. It may be seen that the location of the maximum moves to lower numbers of circulations for decreasing temperature glides.

3.3. Temperature lift

The final screening investigates the influence of the temperature lift on the performance of the novel HP system. Figure 5, left, shows the maximum improvement in COP for different temperature lifts of 20 K to 60 K. The results with a temperature lift of 40 K coincide with the data for a temperature glide in the heat sink of 20 K in Figure 4, left. The data for the one-stage HP with R717 are shown only for temperature lifts of 20 K to 40 K. For higher temperature lifts, the discharge temperature exceeds the maximum allowed temperature of 180 °C. The highest improvement in COP was found for a one-stage cycle with R290 at a temperature lift of 20 K with 17 %. For temperature lifts above 20 K, the biggest improvement is achieved with a one-stage with R600a.

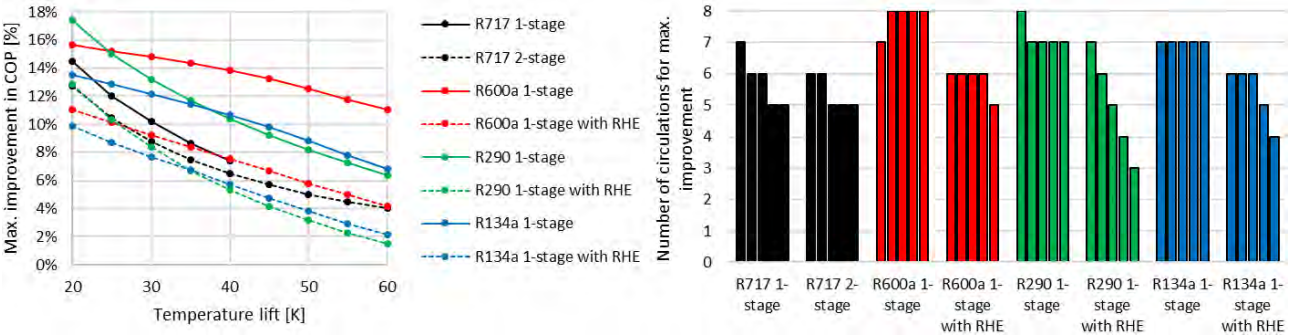

Figure 5: Left: Improvement in COP for varying temperature lifts. Right: Number of circulations with maximum COP for temperature lifts of 20, 30, 40, 50 and 60 K

For all investigated cases, the increase in temperature lift leads to lower maximum improvement. However, the slope of the curves shown in Figure 5, left, differs between the cases. While the curves of R717 and R290 are steeper at lower temperature lifts for all HP configurations, they are close to linear for R600a and R134a in a one-stage HP with RHE and for simple HP the get steeper with increasing temperature lifts.
Figure 5, right, shows the location of the maximum for temperature lifts between 20 K to 60 K in steps of 10 K. It shows some differences between the cases. For a one-stage cycle with R600a, the

number of circulations for the maximum improvement in COP increases with increasing temperature lifts. For a one-stage cycle with R134a, it remains constant at seven circulations and for all other cases it decreases with increasing temperature lifts.
Figure 6 shows the COP at different temperature lifts of a one-stage and two-stage cycle with R717 for a conventional HP and the novel system using storage tanks. As in Figure 5, left, the data for the one-stage cycle are shown only for temperature lifts of 40 K or lower, due to the limitations in the discharge temperature. As expected, all COPs decrease with increasing temperature lifts and the COP of a conventional one-stage HP is lower than the one of a conventional two-stage HP. As seen in the previous screenings and also in Figure 5, left, the introduction of the tank system leads to a bigger improvement for the one-stage cycle than for the two-stage cycle. In this case, this leads to higher COPs for a one-stage configuration with storage tanks than for a conventional two-stage HP for temperature lifts below 35 K. For a temperature lift of 20 K, the COP of the one-stage cycle with tanks of 6.48 reaches almost the COP of the two-stage HP with tanks of 6.66.

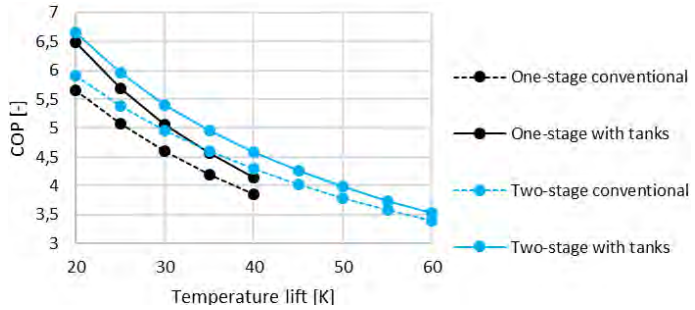

Figure 6: COP of one-stage and two-stage cycles with and without tank system with R717 for different temperature lifts

4. DISCUSSION

The conducted screenings showed the improvement potential of the novel storage system for different working fluids and HP configurations. However, the numerical results depend on the assumptions made for the calculations. A big influence derives from the choice of the compressors. Choosing another compressor would lead to different isentropic and volumetric efficiencies and thus for different COPs. Another influential factor are the assumptions for the electricity consumption of the water pump, i.e. the pressure drop in the condenser and the pump isentropic efficiency. Changing these values would change the maximum achievable improvement and the optimum number of circulation per charging cycle.
The assumption of constant UA-values of all heat exchangers after the design run was made for increasing the robustness and speed of the model. However, the varying mass flow rates of the working fluid and the water on the cold side could have an influence on the heat transfer coefficients and thereby on the performance. The use of the minimum temperature difference or the heat exchanger effectiveness as a design variable for the heat exchangers means that different heat exchanger sizes were considered for the screenings. Hence, the screening compared newly built HP systems to each other. For the upgrading of existing system, fixing the size of the heat exchangers would be more realistic and lead to different results than the ones presented in this work.
It should be mentioned, that the assumption of ideally stratified storage tanks and the neglect of dynamics of the HP means that in this work a best-case scenario in terms of COP was examined. In future work, the influence of thermal inertia and the control of the system should be investigated.
Within this work, only gradual heating with a tank system on the hot side was examined. Ommen et al. (2015) showed that the best performances for systems with serial heating are achieved, when serial heating and cooling is conducted at the same time. This corresponds to using the tank system at both hot and cold side. However, when using the tank system instead of serially connected heat pumps, the control and operation of the system becomes very complex. Further investigation on the potential of gradual heating and cooling and on the operation and control of such systems by dynamic models and experiments will be necessary.

5. CONCLUSION

The novel system, using a small charging tank and a bigger storage tank for gradual heating of process water showed significant potential for reduction in energy consumption. For the investigated

temperature sets, a one-stage heat pump with R600a as working fluid showed the biggest potential of improvement of all cases. When cooling water from 20 °C to 10 °C and heating water from 20 °C to 60 °C in 14 steps, the COP improvement was 35 % compared to a conventional heat pump, heating the water in one single step. The results showed that the improvement potential in COP decreases, when the heat pump configuration is changed from a simple one-stage cycle to a two-stage cycle or by adding a regeneration heat exchanger.
For all cases, a reduction of the temperature glide in the heat sinks leads to smaller improvement in COP. The trend of the maximum improvement showed to be independent from the working fluid and heat pump configuration. For some cases, the addition of the storage tanks does not lead to an improvement in COP at very low temperature glides.
Increasing the temperature lift between heat source and heat sink showed a decreasing improvement potential. The behaviour of the maximum improvement with increasing temperature lift differs between different working fluids. Further investigations on the reasons for these different behaviours will be necessary.
For R717, it was shown that for temperature lifts below 35 K, higher COPs can be achieved with a one-stage heat pump with storage tanks than with a two-stage cycle without storage tanks. For a temperature lift of 20 K, the tank system achieves similar COPs for one-stage and two-stage heat pumps.

ACKNOWLEDGEMENTS

This research project is financially funded by EUDP (Energy Technology Development and Demonstration). Project title: Highly Efficient and Simplified Thermodynamic Cycle with isolated heating and cooling – cost optimized (ISECOP), project number: 64017-05102.

REFERENCES

Bühler F., Nguyen T-V., Elmegaard B., 2016. Energy and exergy analyses of the Danish industry sector. Applied Energy, 184, 1447-1459.

F-Chart Software (LLC.), 1992-2018. Engineering Equation Solver,EES. V10.478 (21/8/2018). http://www.fchart.com/ees/. [accessed 10.01.2019]

IPU, 2008-2015. Pack Calculation Pro. V4.20.

Johnson Controls Denmark, 1985-2019. Sabroe MatchMaster Program COMP1. V26.70.

Löffler M. K., Griessbaum N., 2014. Storage devices for heat exchangers with phase change. Int. J. Refrigeration, 44, 189-196.

Olsen, L. et al., 2015. High efficient heat pump system using storage tanks to increase cop by means of the ISEC concept (part II, thermal storage system). Proceedings of the 24th IIR International Conference of Refrigeration, International Institute of Refrigeration.

Olsen, L. et al., 2016. Highly Efficient Thermodynamic Cycle with Isolated System Energy Charging (ISEC) – Final Report. Danish Technological Institute.

Ommen T. et al., 2015. Enhanced technical and economic working domains of industrial heat pumps operated in series. Proceedings of the 24th IIR International Conference of Refrigeration, International Institute of Refrigeration.

Rothuizen E. et al., 2014. High efficient ammonia heat pump system for industrial process water using the ISEC concept – part 1. Proceedings of the 11th Gustav Lorentzen Conference on Natural Refrigerants, Chinese Association of Refrigeration.

Rothuizen E. et al., 2015. High efficient heat pump system using storage tanks to increase COP by means of the ISEC concept – part 1. Proceedings of the 24th IIR International Conference of Refrigeration, International Institute of Refrigeration.

Wang K. et al., 2010. Investigation of the performance of a high-temperature heat pump using parallel cycles with serial heating on the water side. Int. J. Refrigeration, 33, 1142-1151

Manuscript ID: 1059
DOI: 10.18462/iir.icr.2019.1059

Semi-theoretical model of the wetting characteristics of aqueous ionic liquid on an aluminium finned-tube desiccant contactor

Niccolo GIANNETTI[(a)], Richard Jayson VARELA[(b)], Hifni ARIYADI[(c)], Seiichi YAMAGUCHI[(d)], Kiyoshi SAITO[(d)], Xin-Ming WANG[(e)], Hiroshi NAKAYAMA[(f)]

[(a)] Waseda Institute for Advanced Study, Waseda University, 1-6-1 Nishiwaseda, Shinjuku-ku, Tokyo 169-8050, Japan, niccolo@aoni.waseda.jp

[(b)] Research Organization for Open Innovation Strategy, Waseda University, 3-4-1 Okubo, Shinjuku-ku, Tokyo 169-8555, Japan, rjvarela@aoni.waseda.jp

[(c)] Department of Applied Mechanics and Aerospace Engineering, Waseda University, 3-4-1 Okubo, Shinjuku-ku, Tokyo 169-8555, Japan, hifni.ariyadi@aoni.waseda.jp

[(d)] Interdisciplinary Institute for Thermal Energy Conversion Engineering and Mathematics, Waseda University, 3-4-1 Okubo, Shinjuku-ku, Tokyo 169-8555, Japan, sei_yamaguchi@aoni.waseda.jp

[(e)] Evonik Japan Co., Ltd., 2-3-1 Nishi-Shinjuku, Shinjuku-ku, Tokyo 163-0938, Japan, xinming.wang@evonik.com

[(f)] Energy Applications R&D Center, Chubu Electric Power Co., Inc., 20-1Midori-ku, Nagoya-shi, Aichi, 459-8522, Japan, nakayama.hiroshi2@chuden.co.jp

ABSTRACT

A new design of an internally cooled desiccant contactor which uses a new ionic liquid (IL) solution as sorptive medium is targeted. To optimise its operative performance, a semi-theoretical model based on a variational thermodynamic principle is developed to predict the film rupture and wetting ability of the IL solution for different values of the IL mass fraction over a comprehensive range of liquid spray density. The minimum Reynolds number Reb allowing the film-like flow configuration and, below this value, the wetted fraction of the solid substrate are firstly formulated on an analytical basis. Successively, the theoretical formulation is used as a reference to minimise deviations between predicted results and measured data by calibrating dedicated characteristic coefficients. Predicted film rupture, wetting ability and wetting hysteresis behaviour are strongly affected by the IL mass fraction and found in good agreement with the measurements.
Keywords: Ionic Liquid, Liquid Desiccant, Modelling, Wettability

1. INTRODUCTION

Modern refrigeration technologies result in possibilities of considerable energy savings, provided that advanced modelling methods are available for optimizing the system design and controlling its performance in proximity of the maximum level. Heat exchangers constitute the fundamental transfer devices for realizing the desired output and minimizing the required input of these thermal systems. However, established modelling approaches for several of the main interfacial phenomena recurrent within heat exchangers are not presently available, and design as well as control methods of operative systems have so far relied on empirical rules of limited generality or trial-and-error procedures, leading to non-optimized operation. The empirical correlations commonly used in engineering design and control are analytical equations providing an estimation of the necessary parameters and requiring as an input few pieces of information related to the operative condition or the geometry of the element. The conventional process for obtaining this kind of formulations relies on preliminary experimental investigations followed by a numerical fitting to a product of power laws of dimensionless groups defined according to the Buckingham Theorem (Baker et al., 1991). However, due to the limited range and equipment-dependent characteristics of the experimental investigations, and the relatively “rigid” mathematical shape, the resulting correlations are limited in applicability and physical description.

In the modelling method suggested hereby, analytical formulations with equivalent ease of use are physically obtained from a thermodynamic extremum principle. Variational methods associated to extremum principles simplify the expression of complex, multivariable physical problems, and represent physical tools to obtain local and global mathematical formulations for problems that are less accessible from the vectorial standpoint of Newton's law. Extremum principles have led to critical results in theoretical as well as technical research areas (Bertola and Cafaro, 2008) despite their debated legitimacy and applicability (Reis, 2014) when applied to systems operating far from equilibrium (Grandy, 2008). Under this approach, the influential dimensionless groups are extracted and correlated to the required engineering output on the basis of the general physics of the problem. In this manner, the mathematical formulation of the correlation is not restricted to the product of power laws of dimensionless numbers, not limited to a specific geometry or working fluid and could characterise the phenomenon on a broader spectrum of conditions. Subsequently, the introduction of "corrective coefficients" (as in Giannetti et al, 2018a) while maintaining the mathematical formulation and the fitting to experimental results, gives an advanced kind of reliable semi-theoretical correlations, which still carry the fundamental physical interpretation of the phenomenon, where the corrective coefficients convey information about the quality of the simplifying assumptions introduced.

Owing to their high transfer capability, liquid films are frequently used in various transfer devices. Several corresponding technical circumstances require conditions that prevent the film from breaking into a series of rivulets, avoiding the formation of dry spots and the corresponding detrimental effect of having cramped transfer interfaces. By contrast, as the film thickness generally corresponds to the main transfer resistance, and to minimize the pumping power requirements, operability at low flow rates opens up to possibilities of enhanced transfer performance. Accordingly, the conditions under which the film breaks down and the extension of the resulting dry patches are of critical importance when predicting the effectiveness of these devices, as well as the efficiency of the system. Additionally, possible hysteresis behaviours can be critical for the proper dynamic characterization and control of the system. However, a general agreement on the mechanism of film rupture and partial wetting has not been reached.

This work targets film stability, wetting behaviour, and wetting hysteresis of a new ionic liquid (IL) solution as sorptive medium within a new design of an internally cooled desiccant contactor. The mathematical formulation of these phenomena is based on an extremum principle of classical Thermodynamics; a qualitative and quantitative validation of the results is presented with reference to the visual data captured on a dedicated experimental test section; finally, the theoretical formulation is used as a reference to minimise deviations between predicted results and measured data by calibrating dedicated characteristic coefficients for achieving a semi-theoretical formulation with high accuracy.

2. PHYSICAL MODEL

In desiccant systems, the air-solution contactor is a fundamental element for steady and efficient dehumidification and regeneration processes. In adiabatic contactors working as dehumidifiers, the desiccant solution temperature increases along the stream-wise direction owing to the absorption-heat release, and consequently decreases the local dehumidification capacity. Internally-cooled contactors (Fig. 1a) integrate a contemporary heat rejection process within the dehumidificator, and significant performance improvements, along with a major drop in size and cost, are expected.

In this work, as the working fluid employed (IL) differs from the standardly used lithium-cloride solution, aluminium is used without risk of corrosion in a finned-tube configuration with staggered tube arrays. Generally, ILs also exhibit high thermal and chemical stability, low volatility, excellent solubility with many organic compounds, and are non-flammable (Varela et al., 2018). Therefore, they are a promising alternative to be investigated for liquid desiccant systems and absorption processes in general. Aluminium is selected as the substrate because of its high thermal conductivity, low density, and low cost. The test section for the visualization of the IL solution wetting behaviour over the finned-tube contactor specifically considered and its dimensions are as shown in Fig. 1b (Giannetti et al., 2016).

As the performance of desiccant systems is strongly, but non-linearly, related to the transport performance of the contactor (directly associated to the), it is necessary to be able to estimate the extension of the transfer interfaces within the contactors in a comprehensive range of operative conditions for properly defining the operation strategy of these systems.

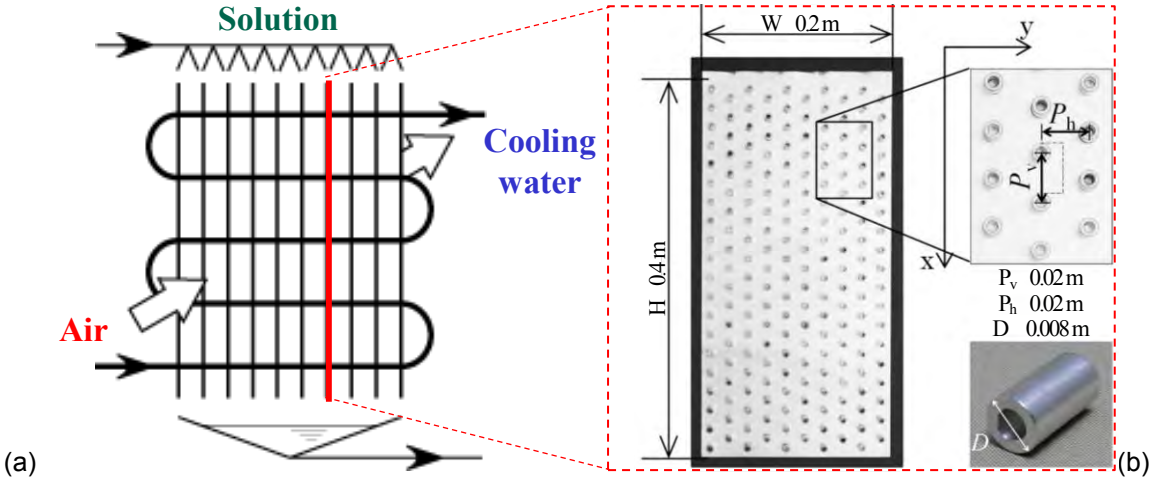

Figure 1: Dimensions of the test section of a vertical fin with cooling water tubes

2.1. Variational formulation

The following mathematical construct of the problem deviates from the intuitive Newtonian vectorial formulation by relying on the more abstract analytical formulation of extremum principles. This variational approach is based on the speculative assumption that physical phenomena can be described by relying on the principles of economy (Cline, 2017). Explicitly, the application of the principle of minimum energy (conceptually represented by Eq. 1) is based on the assumption that among the set of possible flow configurations, for a given flow rate, the one with minimal energy is the most likely to occur.

$$\frac{\partial E}{\partial \phi} = 0, \quad \frac{\partial^2 E}{\partial \phi^2} > 0 \qquad \text{Eq. (1)}$$

where E defines the total energy content (Eq. 2), and ϕ is a generalised geometric variable of the flow configuration. The principle is applied to the unit streamwise length δx of the flow configuration.

$$E = \left(\int_A \frac{1}{2}\rho u^2 dA + \int_S \sigma dS + \int_A \rho U dA + \int_A \rho g z dA + \ldots \right) \delta x \qquad \text{Eq. (2)}$$

In the following, as in previous related literature, the evaluation of E is limited to the kinetic energy E_K and surface tension energy E_σ contributions (Eq. 3). The first term is driven by gravity, which pushes toward flat isopotential interfaces, while the latter tends to generate round interfaces.

$$E = E_K + E_\sigma = \left(\int_A \frac{1}{2}\rho u^2 dA + \int_S \sigma dS = \int_A \frac{1}{2}\rho u^2 dA + \int_{Slv} \sigma_{lv} dS + \int_{Sls} \sigma_{ls} dS + \int_{Ssv} \sigma_{sv} dS \right) \delta x \qquad \text{Eq. (3)}$$

The integration over the phase-interfaces (liquid-solid S_{ls}, liquid-vapour S_{lv}, solid-vapour S_{sv}) or the cross-sectional area follows the solution of the streamwise momentum equation for defining the velocity distribution u, and the definition of two representative flow configurations with simplified flow geometries: a liquid film fully wetting the solid substrate and a rivulet with a circular cross-sectional shape representing the condition of partial wetting of the solid substrate (Fig. 2).
The principle of minimizing the energy of a given streamwise section of the film (as in Mikielewicz and Moszynski, 1976) enables the prediction of the rivulet wettability among the set of possible rivulet flow configurations with respect to the parameter X (Eq. 4) representing the ratio of the wet interface to the total surface of the solid substrate (Eq. 5), and the limit of stability of the uniform film (Eq. 6). The latter represents the transition between complete and partial wetting, and occurs at equivalent energy content provided the absence of related physical constraints.

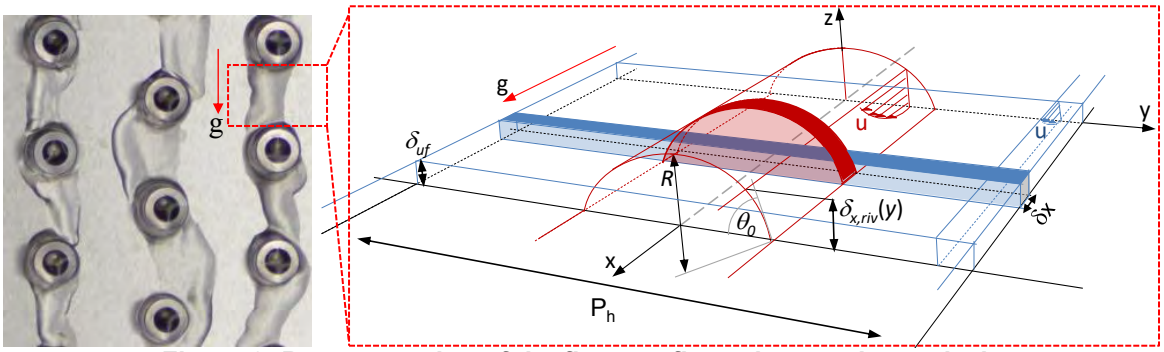

Figure 2: Representation of the flow configurations under analysis

$$\frac{\partial E_{riv}}{\partial X}=0, \quad \frac{\partial^2 E_{riv}}{\partial X^2}>0 \qquad \text{Eq. (4)}$$

$$X=\frac{S_{ls}}{S_{ls}+S_{sv}} \qquad \text{Eq. (5)}$$

$$E_{riv}=E_{uf} \qquad \text{Eq. (6)}$$

As the liquid flows laminarly, waveless over a flat solid wall of width λ, driven only by gravity g, under the same assumptions of the Nusselt integral solution for an isothermal plate, the parabolic velocity profile and the corresponding film thickness are commonly expressed in previous literature (see, for instance, Mikielewicz and Moszynski, 1976).

2.1.1. Film stability

Equation (7) represents the stability criterion of the uniform film (analytical details are given in Mikielewicz and Moszynski, 1976 and Giannetti et al., 2016) yielding to the estimation of the minimum Reynolds number (Eq. 9) that assures the complete wetting of the solid substrate.

$$\Delta_b^{\,5}+\left(1-\cos\theta_0\right)-G\left(\theta_0\right)\Delta_b^{\,3}=0 \qquad \text{Eq. (7)}$$

This equation expresses a univocal relationship $\Delta_b=\phi_b(\theta_0)$ between Δ_b and the contact angle θ_0 that is approximated by Eq. (8) with a deviation below 1% in the range $0<\theta_0<130°$.

$$\Delta_b \simeq 0.20\ln\theta_0+0.69 \qquad \text{Eq. (8)}$$

Since the film thickness can be estimated for the given velocity distribution of Nusselt solution, the parameter Δ_b (Eq. 9) is directly related to film Reynolds and modified Galileo numbers (Eq. 10).

$$\Delta_b=\left(\frac{\rho^3 g^2}{15\sigma\mu^2}\right)^{1/5}\delta_{uf,b} \qquad \text{Eq. (9)}$$

$$\mathrm{Re}_b=\left(\frac{3^5 g\mu^4}{4^5 15^3\rho\sigma^3}\right)^{-1/5}\Delta_b^{\,3}\simeq 6.77 Ga^{1/5}\Delta_b^{\,3} \qquad \text{Eq. (10)}$$

Yielding the following handling formulation of the minimum Reynolds number for the stability of the uniform film configuration (Eq. 11).

$$\mathrm{Re}_b \simeq 0.054\left(Ga_b\right)^{1/5}\left(\ln\theta_0+3.45\right)^3 \qquad \text{Eq. (11)}$$

2.1.2. Rivulet wetting ability

When the film flowrate is lower than that yielding the minimum Reynolds number in Eq. (11), the rivulet configuration shows lower energy content and, according to Eq. (4), the local wetting ratio X is given by Eq. (12) (Giannetti et al., 2016).

$$X = \left\{ \frac{2}{45} \frac{\psi(\theta_0)}{\sin\theta_0} \left[\frac{\theta_0}{\sin\theta_0} - \cos\theta_0 \right]^{-1} \right\}^{3/5} \frac{\sin\theta_0}{\gamma(\theta_0)} \left(\frac{9}{4} \frac{\mathrm{Re}}{We^3} \right)^{1/5} \qquad \text{Eq. (12)}$$

As shown in Giannetti et al. (2016), the geometrical functions of the contact angle ($\gamma(\theta_0)$, $\psi(\theta_0)$ and $G(\theta_0)$) are obtained by integrating kinetic energy and flow rate over the circular cross-sectional shape of the rivulet. Thus, given the thermo-physical properties of the desiccant solution and the contact angle of the solid-liquid pair, the stability of the film and the wetting ability of the rivulet are estimated. In order to simplify the expression of Eq. (12) without affecting its general physical connotation, the geometrical group (function of the only contact angle θ_0) is approximated as shown in Eq. (13).

$$\left\{ \frac{2}{45} \frac{\psi(\theta_0)}{\sin\theta_0} \left[\frac{\theta_0}{\sin\theta_0} - \cos\theta_0 \right]^{-1} \right\}^{3/5} \left(\frac{9}{4} \right)^{1/5} \frac{\sin\theta_0}{\gamma(\theta_0)} \simeq 0.27\theta_0^{-1.24} \qquad \text{Eq. (13)}$$

The direct theoretical outcomes of Eq.s (11), (12) and (13), calculated with reference to the thermo-physical properties of the IL and the contact angles in Table 1 tested by Varela et al. (2018), are compared to the experimental results from Giannetti et al. (2018)b in Fig.s 3(a).

Table 1 Contact angles of the IL solution on the aluminium substrate at 23°C

ω, %	12.8	21.3	32.0	39.9	50.8	62.4	69.7	75.5
θ_{0a}, °	105.9	99.8	86.3	83.4	78.0	74.7	79.3	74.2
θ_{0r}, °	84.9	66.3	58.8	59.2	49.4	54.7	47.5	47.3

The quantitative analysis of the results shows that to fully wet the fin surface from a dry state with a 34% IL solution, at constant temperature, it is necessary to increase the solution flow rate up to a Reynolds number of approximately 340. From this condition, the Reynolds number of the solution can be decreased to 100 while maintaining complete wetting. At higher IL mass fraction (for example 45%), complete wetting is achieved when the solution flow rate reaches a Reynolds number of circa 210, and, as the Reynolds number of the solution decreases, the liquid film breaking occurs at a film Reynolds of 60. The predicted values of the Reynolds number required for complete wetting and the minimum Reynolds number for the liquid film rupture in the remaining IL mass fraction are: 150 and 40 at 60% ω, 110 and 30 at 65% ω, 60 and 20 at 75% ω.

2.2. Semi-theoretical formulation

The theoretical shape of the film stability criterion expressed in Eq. (11) is maintained, and by introducing the characteristic coefficients C_0 and C_1 a semi-theoretical formulation of the minimum Reynolds number able to ensure complete wetting of the substrate is achieved (Eq. 14).

$$\mathrm{Re}_b \approx 0.054 C_0 \left(Ga_b \right)^{C_1/5} \left(\ln\theta_0 + 3.45 \right)^3 \qquad \text{Eq. (14)}$$

The characteristic coefficients C_2, C_3, and C_4, are introduced in Eq. (15) to match the actual wetting behaviour, the dependency on Weber and Reynolds number and the actual flow geometry.

$$X \approx 0.27 C_2 \theta_0^{-1.24 C_4} \left(\frac{\mathrm{Re}}{We^3} \right)^{C_3/5} \qquad \text{Eq. (15)}$$

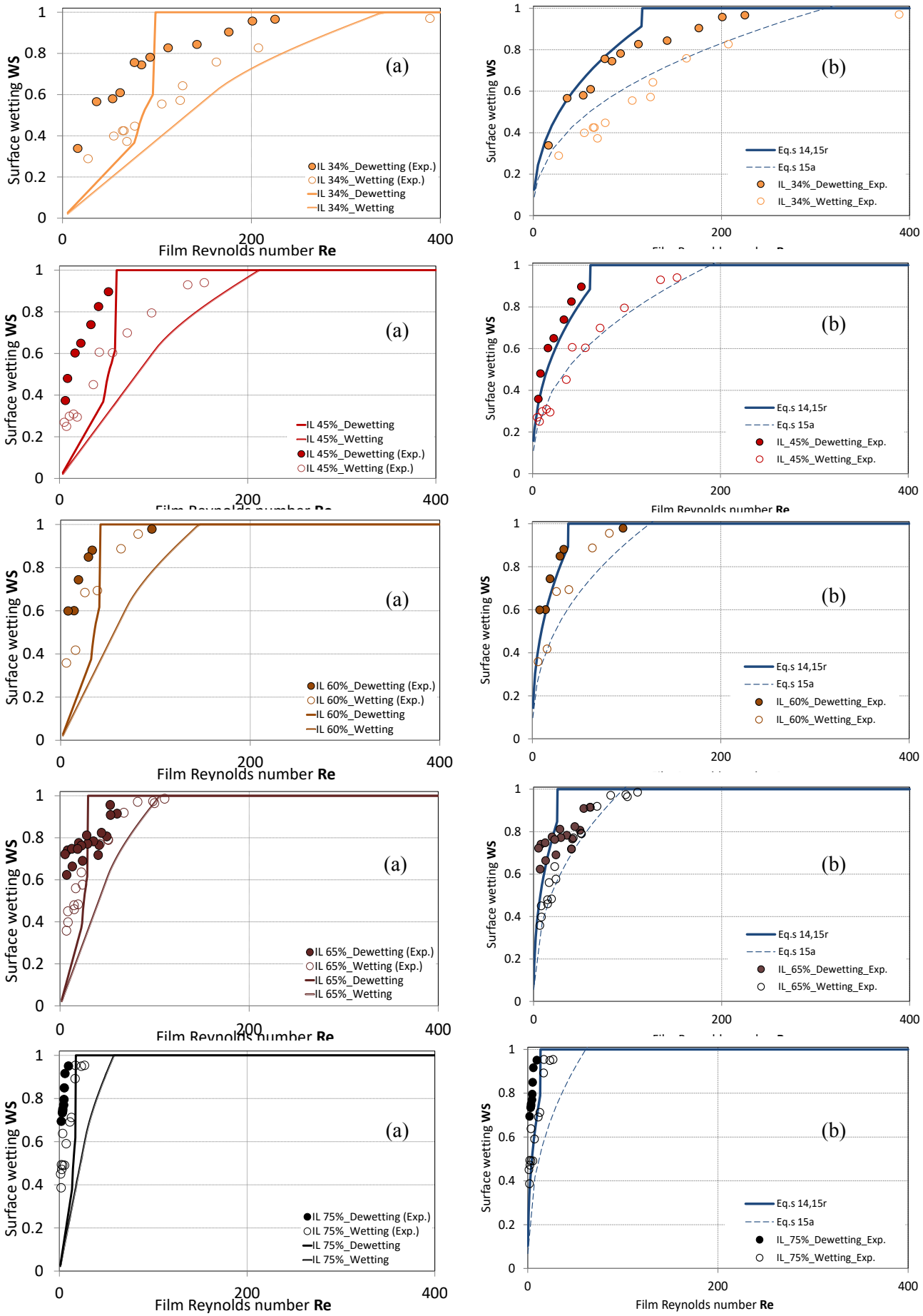

Figure 3: Comparison between experimental data and (a) theoretical or (b) semi-theoretical results

The deviation of the experimental data from the predicted results of Eq.s (14) and (15) is minimized, and the values summarized in Table 2 are obtained. The wetting behaviour of the desiccant solution is accurately predicted over the complete range of IL mass fraction (Fig.s 3 b) when using advancing contact angles for increasing flow rates (Eq. 15a) and receding contact angles for decreasing flow rates (Eq. 15r).

Table 2 Characteristic coefficients of the semi-theoretical formulation

C_0	C_1	C_2	C_3	C_4
0.47	1.28	3.07	0.35	0.73

The value of these coefficients represents the deviation of the semi-theoretical correlation from the formulation of the theoretical equations and the assumptions introduced when writing them. Specifically, C_0 and C_2 are related to the simplified geometry of the two flow configurations, which ignore waviness and more complex cross-sectional shapes. C_4 represents the limitation of the assumption of a single value of contact angle throughout the flow along the whole fin. Finally, C_3 and C_1 evaluate the importance of effects other than kinetics and surface tension (such as, heat and mass transfer or friction with the gaseous phase).

3. CONCLUSIONS

A semi-theoretical model was developed to predict film rupture and wetting ability of a new IL solution with respect to a new design of internally cooled desiccant contactor. The mathematical formulation was obtained from the implementation of the principle of minimum energy. From the analysis of these fundamental equations the hysteresis behaviour of the IL wetting ability and film stability was highlighted. It was recognized that this behaviour is intensified by the contact angle hysteresis phenomenon, and that lower values of the contact angle and surface tension, along with higher viscosity and density, improve the wettability of the desiccant solution with the increase in IL mass fraction; correspondingly, the film stability is expanded to lower Reynolds numbers, and the hysteresis behaviour becomes less substantial. On the other hand, as the mass fraction of IL increases, the viscosity of the sorptive solution increases and the thermal conductivity decreases, thus, adversely affecting heat and mass transfer. As a consequence, it cannot be concluded that it is always beneficial to operate with the highest IL mass fraction. A first experimental comparison over a comprehensive range of IL mass fraction and flow rates was presented, and the consistency of the results confirmed. The semi-theoretical formulation was obtained by introducing corrective coefficients calibrated with reference to the experimental data accurately predicts the minimum solution wetting rates for the whole range (34%-75%) of the IL mass fraction. As the wetting ability and the hysteresis behaviour over the complete wetting/dewetting cycles are precisely modelled, the model can be employed to optimize the component within real plants and consistently define an optimal control strategy to keep the system in proximity of its minimal energy consumption.

NOMENCLATURE

A	Cross-sectional Area (m^2)	S	Interface (m)
C	Characteristic coefficient	u	Stream-wise velocity ($m \cdot s^{-1}$)
D	Tube diameter (m)	W	Test section width (m)
E	Energy per unit stream-wise length ($J \cdot m^{-1}$)	We	Weber number
g	Gravity ($m \cdot s^{-2}$)	WS	Surface wetting
Ga	Galileo number	X	Wetting ratio
H	Test section length (m)	x	Local stream-wise direction (m)
P	Tube pitch (m)	y	Local transversal direction (m)
R	Rivulet radius (m)	z	Local normal direction (m)
Re	Reynolds number		

	Greek symbols		Subscripts
δ	Thickness (m)	a	Advancing
Δ	Dimensionless thickness	b	Film rupture
ϕ	Generic Geometrical variable	h	Horizontal
γ,ψ,G	Geometric functions of the contact angle	K	Kinetic
θ_0	Contact Angle (rad)	r	Receding
μ	Dynamic viscosity (Pa·s)	riv	Rivulet
ρ	Density ($kg \cdot m^{-3}$)	σ	Surface tension
σ	Surface tension ($J \cdot m^{-2}$)	uf	Uniform film
ω	Mass fraction ($kg_{IL} \cdot kg^{-1}$)	v	Vertical

REFERENCES

Baker, W.E., Westine, P.S., Dodge, F.T., 1991. Development of Model Laws from the Buckingham Pi Theorem, Fundamental Studies in Engineering 12, 19-31,

Bertola, V., Cafaro E., 2008. A critical analysis of the minimum entropy production theorem and its application to heat and fluid flow. International Journal of Heat and Mass Transfer 51, 1907-1912.

Cline, D., 2017. Variational Principles in Classical Mechanics. University of Rochester River Campus Libraries, Rochester, NY(U.S.A.).

Giannetti, N., Yamaguchi, S., Saito, K., 2016. Wetting behavior of a liquid film on an internally-cooled desiccant contactor. International Journal of Heat and Mass Transfer 101, 958–969.

Giannetti, N., Varela, R.J., Ariyadi, H., Yamaguchi, S., Saito, K., Wang, X.-M., Nakayama, H., 2018a. Semitheoretical Prediction of the Wetting Characteristics of Aqueous Ionic Liquid Solution on an Aluminum Finned-Tube Desiccant Contactor. Journal of Fluids Engineering, Transactions of the ASME 140(12), no. 121109.

Giannetti, N., Yamaguchi, S., Saito, K., Wang, X.M., Nakayama, H., 2018b. フィンチューブ型気液接触器におけるイオン液体水溶液の濡れ性の理論的検討 (Theoretical prediction of the wetting characteristics of aqueous ionic liquid on a finned-tube desiccant contactor). Annual Conference of the Japan Society of Refrigeration and Air Conditioning Engineering, September 4th –7th, 2018, Nihon University, Koriyama, Fukushima, Japan, C335.

Grandy, W.T., 2008. Entropy and the Time Evolution of Macroscopic Systems. Oxford University Press, New York.

Mikielewicz, J., Moszynski, J.R., 1976. Minimum thickness of a liquid film flowing vertically down a solid surface. International Journal of Heat and Mass Transfer 19, 771-776.

Reis, A.H., 2014. Use and Validity of Principles of Extremum of Entropy Production in the Study of Complex Systems. Ann. Phys. 346, 22–27.

Varela, R.J., Giannetti, N., Yamaguchi, S., Saito, K., Wang, X.M., Nakayama, H., 2018. Experimental investigation of the wetting characteristics of an aqueous ionic liquid solution on an aluminum fin-tube substrate. International Journal of Refrigeration 88, 472-482.

Manuscript ID: 1111
DOI 10.18462/iir.icr.201.1111

Field measurements of CO2 refrigeration systems with heat recovery in retrofitted ice rinks

Simon BOLTEAU [(a)], Cajus GRÖNQVIST[(a)], Jörgen ROGSTAM[(a)]

[(a)] Energi & Kylanalys AB, Prästgårdsgränd 4
Älvsjö 125 44, Sweden
simon.bolteau@ekanalys.se; cajus.gronqvist@ekanalys.se; jorgen.rogstam@ekanalys.se

ABSTRACT

Ice rinks have a high coinciding cooling and heating demand which turns them into ideal heat recovery applications. By using carbon dioxide (CO_2) as a refrigerant in a trans-critical operation, required high temperatures (e.g. for dehumidification, space heating and hot water) can be supplied which in combination with a suitable heating system design can result in very high heat recovery performance. This study compares the measured energy performance and life-cycle cost of five ice rinks in Sweden recently retrofitted from conventional refrigeration systems (HFC and ammonia) to trans-critical carbon dioxide refrigeration systems with heat recovery. The field measurements show that the operational energy use can be cut down by as much as 55% which makes the investment profitable in comparison with the previous conventional systems. Furthermore, in some cases the ice rink also became self-sufficient on its own recovered heat, eliminating the need for an external heating system.
Keywords: CO_2, Heat Recovery, Ice Rink, Measurement, Performance Indicators.

1. INTRODUCTION

Ice rinks consume a lot of energy. Statistics from Sweden show that a typical single ice sheet indoor rink with conventional technologies needs about 1 000 MWh purchased energy annually, with the refrigeration system, cooling capacity usually 250-350 kW, accounting for about 43% and space heating with hot water production for about 26%. Due to the regulations set by the EU for greenhouse gases as well as the age of several facilities, many ice rinks are today facing renovations which require sound decision-making to improve the overall performance. Meanwhile, energy monitoring and measurements carried out in ice rinks recently retrofitted with CO_2-based systems are providing actual data on the performance of this modern technology, which if further analyzed may help the decision-making process.

1.1. Technical Introduction to Ice Rinks

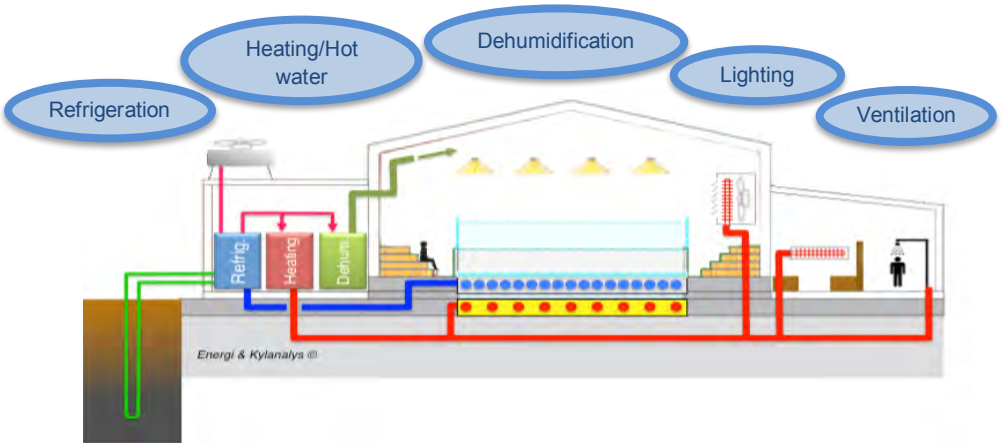

Figure 1: The general energy system layout of an ice rink with optimized heat recovery

Ice rink operation is mainly focused on the following energy systems: refrigeration, heating, dehumidification, lighting and ventilation. These “big five” systems, seen in Figure 1, normally account for more than 90% of the energy used in an ice rink (Rogstam et al., 2014). The systems interact which can be an advantage when utilized correctly. E.g. space heating, air movement and lighting inside the arena room will cause a heat load on the ice sheet. In order to maintain the desired ice temperature, the refrigeration system must extract this heat load from the ice. The extracted heat together with added heat from compressor work is eventually rejected on the warm side of the refrigeration system, often for the most part to the ambience. Optimizing the heat recovery process, where the rejected heat is instead used to cover the heating demands of the facility, is by far the biggest energy savings measure that can be done in today’s conventional ice rinks. It has been shown that when an ice rink has a well-designed heat recovery system it may even be self-sufficient on its own heat. (Rogstam and Bolteau, 2015)

1.2. Why CO_2 seems to be Well-suited for Ice Rink Refrigeration Systems

As mentioned before, the greatest source for lower energy consumption in an ice rink lies in the utilization of an optimized heat recovery system. CO_2 has very good properties in terms of heat recovery. Figure 2 shows the share of used available heat on the x-axis at corresponding temperatures on the y-axis. The temperatures of each refrigerant are at the compressor discharge level when starting from the left side, while getting cooled in the condenser/gas cooler as we move to the right. For example, when the refrigerant temperature reaches 35°C, only 19% of the available heat is extracted in the NH_3-case whereas more than 60% of the heat is available above 35°C for the CO_2. This advantage allows the CO_2 heat recovery system to cover all heating demands in a “typical” ice rink, reducing the cost of operation considerably which coupled with competitive investment and service costs, due to the rapid development of CO_2-based refrigeration systems in supermarkets, will yield long-term benefits for the owner.

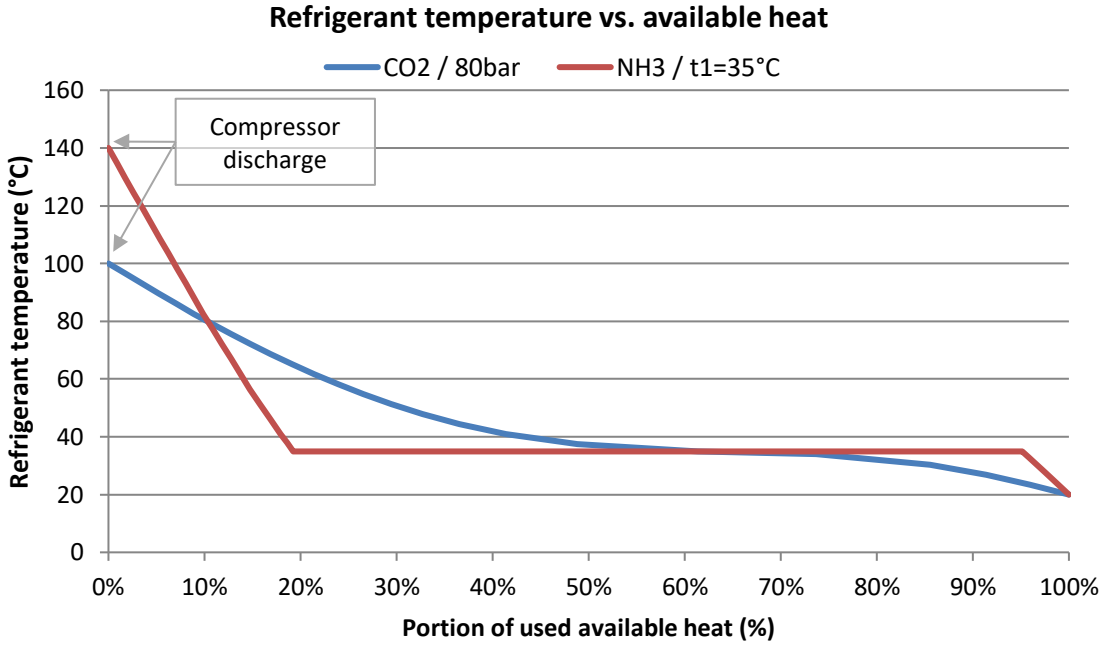

Figure 2: Comparison of the heat available between CO_2 and NH_3 (Rogstam et al., 2017)

Using CO_2 also as the secondary refrigerant in the distribution system brings several advantages over traditional solutions, e.g. calcium chloride and glycol. Perhaps the most prominent ones are that CO_2 utilizes phase change (evaporation) and has a low viscosity which leads to a considerably lower pumping power. Measurements done in traditional ice rinks indicate that about 20-25 % of the refrigeration system energy consumption stems from the auxiliary equipment, such as fans and pumps. By applying CO_2 as the secondary refrigerant, pumping power can be reduced to about 1 kW compared with traditional fluids which require 5-15 kW. Thus, the energy consumption of the auxiliary equipment in a CO_2 direct refrigeration system becomes less than 3 % of the grand total. However, in renovations where the rink

floor is left untouched, very good results can also be achieved by installing an indirect CO_2-system which uses for instance aqua ammonia as the secondary refrigerant in the existing plastic pipes.

2. CASE STUDIES – ICE RINKS IN SWEDEN

2.1. Facility A

Facility A is an average size heated ice rink (arena room temperature 8°C) with one ice sheet, which used to be cooled down by having a calcium chloride circuit connected to an ammonia refrigeration unit. The heating demand was mainly covered by district heating. In 2014, a new 250 kW CO_2 system with direct expansion into copper pipes in the rink floor was installed. The one stage heat recovery supplies a constant 60°C forward temperature. In addition, a geothermal storage is used for subcooling or as an alternative heat source, meaning that the refrigeration unit can guarantee heating even during off season.

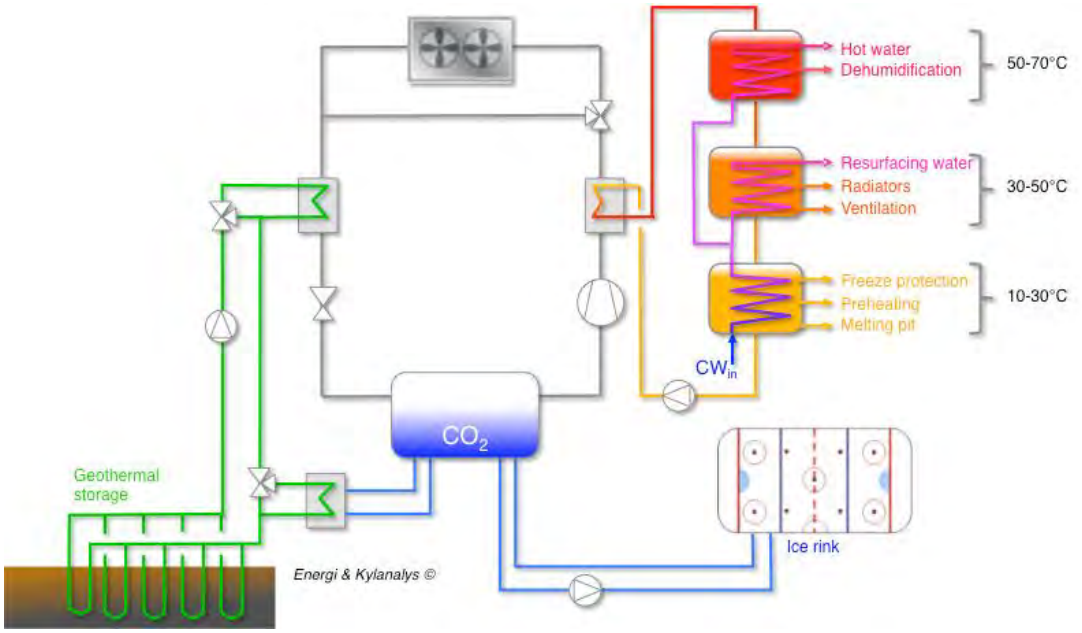

Figure 3: Overview of the system solution in Facility A

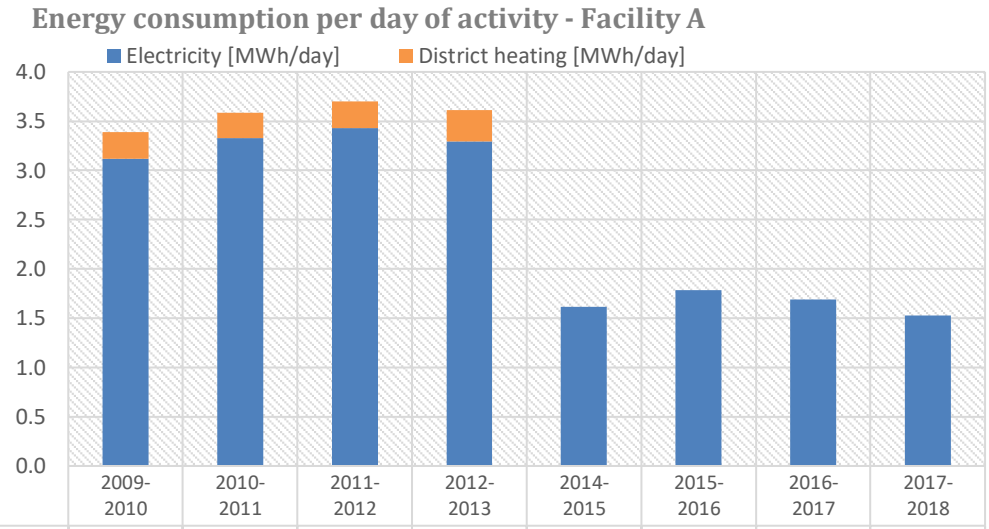

	2009-2010	2010-2011	2011-2012	2012-2013	2014-2015	2015-2016	2016-2017	2017-2018
District heating [MWh/day]	0.27	0.26	0.27	0.32	0.00	0.00	0.00	0.00
Electricity [MWh/day]	3.12	3.33	3.43	3.30	1.62	1.79	1.69	1.53

Figure 4: Facility A energy consumption

After the performed renovation the facility saved up to 55% on its energy consumption on the first year, from 3.62 to 1.62 MWh/day of activity. The ice rink reached its best performance during the 2017/2018 season, with a total use of 326 MWh electricity for a 7 month long period. Furthermore, the heat recovery system covers all the heating demands in the facility, making the ice rink selfsufficient on its own heat and eliminating the need for district heating. In fact there is excess heat still available, and the municipality has recently started to export 80-100 kW heat to the adjacent swimming hall.

2.2. Facility B

Facility B has two ice sheets (ice hockey and curling in separate buildings) and consists also of a sports hall. An R404a refrigeration system with calcium chloride running in the rink and curling floor pipes was used before to cover the cooling demand. The heating demand was mainly covered by district heating. In 2015 an indirect CO_2 refrigeration system replaced the old one. The existing secondary circuits were reused and retrofitted with aqua ammonia, reducing the pumping power demand. The new system provides a new complete one stage heat recovery function with a constant 60°C forward temperature. A new sorption dehumidifier benefits for instance from the recovered heat for reactivation.

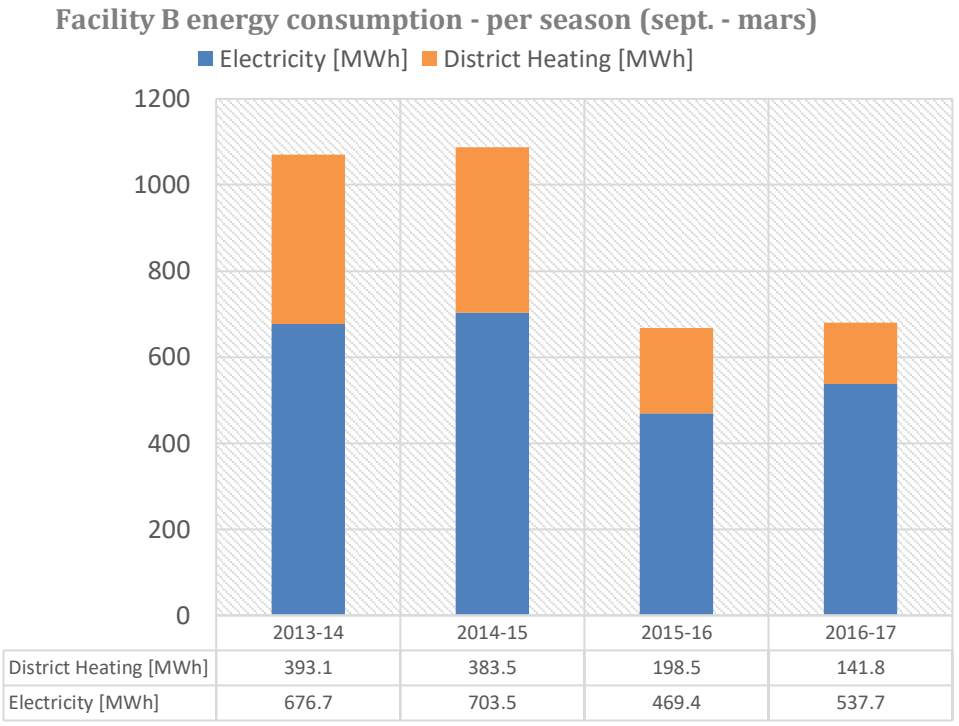

	2013-14	2014-15	2015-16	2016-17
District Heating [MWh]	393.1	383.5	198.5	141.8
Electricity [MWh]	676.7	703.5	469.4	537.7

Figure 5: Facility B energy consumption

Facility B has reduced its energy use by 39% after the refrigeration system renovation, from 5.1 to 3.1 MWh/day of activity, and Figure 5 shows the energy savings on a seasonal level. The control was improved even further for the season 2016-2017, leading to further reduction in district heating.

2.3. Facility C

Facility C is an average sized ice rink, which used to have an ammonia system covering the cooling demand in the heated arena (8°C). In 2014 the rink floor was replaced by a new one with new piping for the secondary refrigeration system, based on aqua ammonia. In 2017 the old ammonia compressors were replaced by a new CO_2 indirect system that was connected to the existing aqua ammonia circuit and equipped with a state of the art two stage heat recovery function that the new sorption dehumidifier can benefit for reactivation.

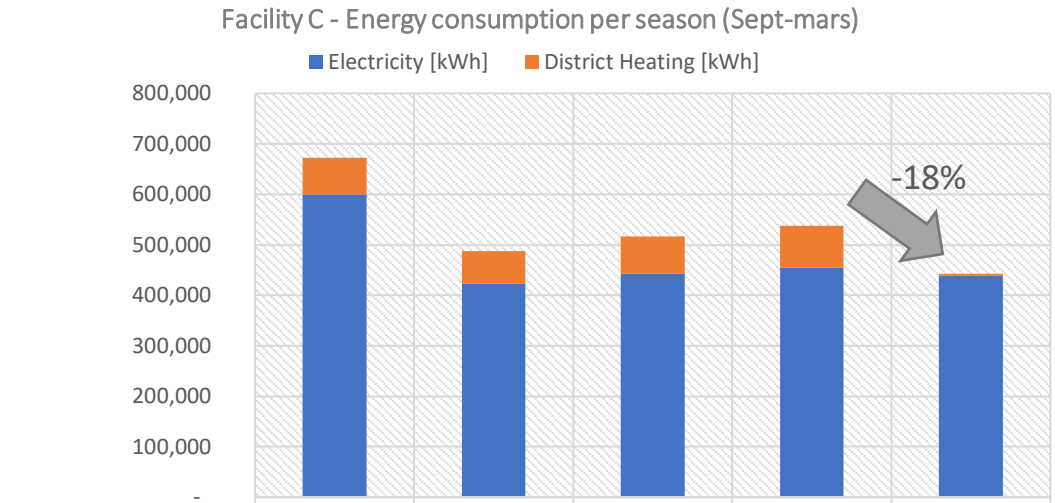

	2013-2014 Old ice rink	2014-2015 Old ice rink	2015-2016 Old ice rink	2016-2017 Old ice rink	2017-2018 New ice rink
District Heating [kWh]	72,672	64,516	72,922	84,014	4,444
Electricity [kWh]	600,470	423,031	443,205	453,925	438,380

Figure 6: Facility C energy consumption

Facility C reduced its energy consumption by 18% with the refrigeration system renovation from 2.52 to 2.07 MWh/day of activity, eliminating the need for district heating – only a residual 4 MWh consumption was left which can be fully eliminated by further optimizing the control of the heat recovery function. This means that the two stage heat recovery function meets the heating demand. Furthermore, like in the case of Facility A, Facility C is considering exporting excess heat to a swimming hall that potentially may be built next to it.

2.4. Facility D

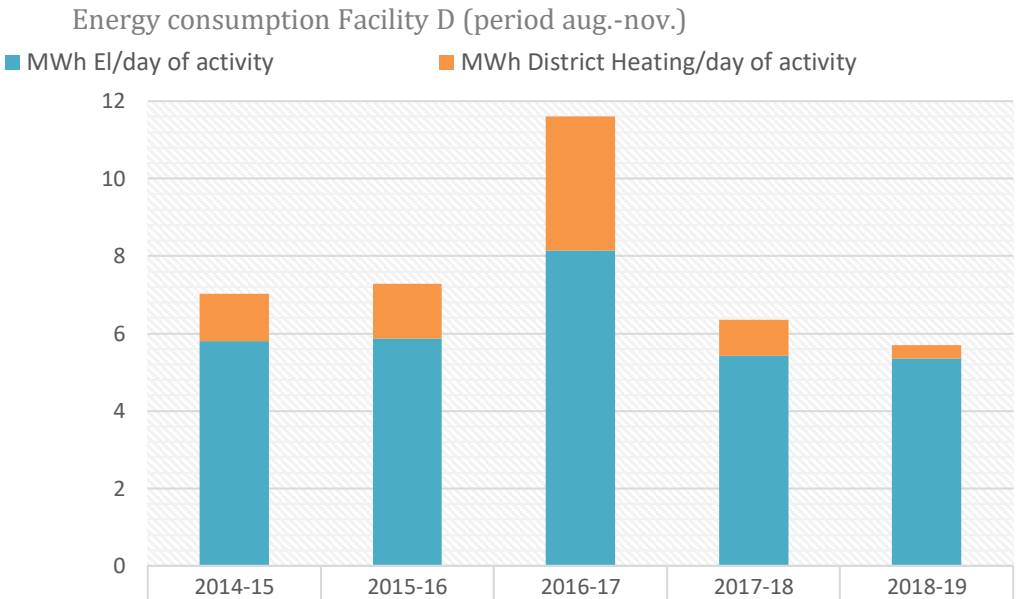

	2014-15	2015-16	2016-17	2017-18	2018-19
MWh District Heating/day of activity	1.2	1.4	3.5	0.9	0.4
MWh El/day of activity	5.8	5.9	8.1	5.4	5.3

Figure 7: Facility D energy consumption

Facility D has two ice sheets: one located in a 5800-spectator capacity arena (heated to 15°C) and the other one in a training hall. Before the renovation, the cooling demands were covered by an indirect ammonia refrigeration system providing its 600kW cooling capacity through a calcium chloride circuit. A heat recovery function also existed: a heat pump on the coolant circuit which covered a part of the heating demand. In 2017 a CO_2 indirect refrigeration unit replaced the ammonia one, and aqua ammonia replaced calcium chloride as the secondary refrigerant. The system is equipped with a two stage heat recovery function, from which e.g. a new sorption dehumidifier benefits by applying recovered heat.
During the season 2016-2017 the heat recovery function of the former refrigeration system was not in operation, which explains the energy consumption peak. The heating demand was during that season fully covered by the district heating. This allows for the calculation of the total heating demand that's covered by the new refrigeration unit's heat recovery function. Based on the most recent data, the two stage heat recovery function covers 88% of the heating demand in Facility D. If compared with a normal season of activity (2015-2016), the facility has reduced its energy consumption by 22% – from 7.3 to 5.7 MWh/day of activity.

2.5. Facility E

Facility E used to be a typical single sheet ice rink, with a heated arena room (around 8°C). An ammonia refrigeration unit was connected to a brine circuit in the rink floor. A heat recovery function provided up to 28°C for the preheating in the air handling unit. In 2016 a new CO_2 system was installed to replace ammonia, with direct expansion into new copper pipes that were laid in a layer of concrete above the existing rink floor. Furthermore, an additional ice sheet in a heated arena room (around 10°C) located in a brand-new building adjacent to the existing ice rink completes the facility in the 2017/2018 season. An optimized heat recovery system connected to the CO_2 system is designed to cover a large part of the heating demands in both ice rinks.

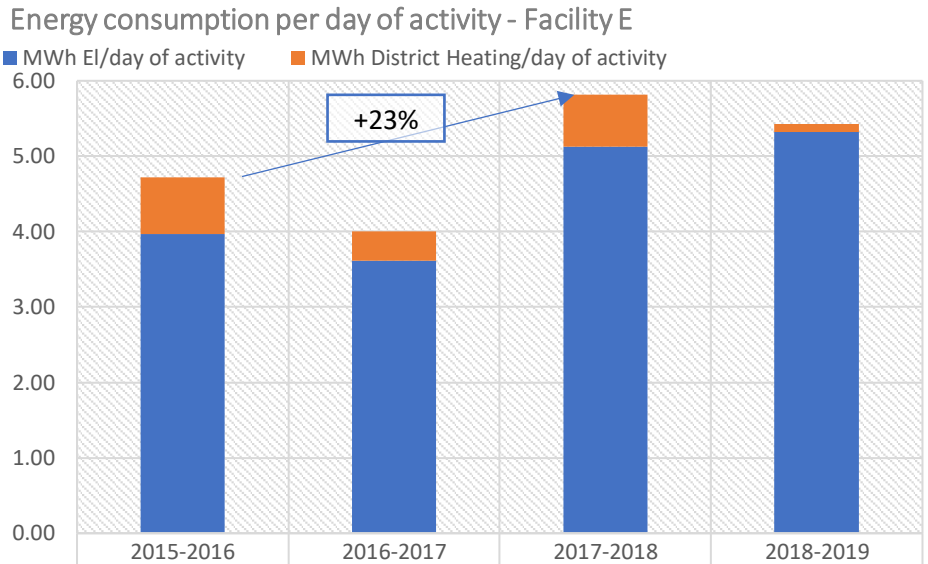

	2015-2016 Old ice rink [MWh]	2016-2017 One new ice rink [MWh]	2017-2018 Two new ice rinks [MWh]	2018-2019 Two new ice rinks [MWh]
MWh District Heating/day of activity	0.75	0.39	0.69	0.11
MWh El/day of activity	3.97	3.62	5.12	5.32

Figure 8: Facility E energy consumption

When Facility E still had only one ice sheet in operation the energy savings could easily be noticed from season 2015-2016 to 2016-2017, where the new refrigeration unit and its heat recovery function had reduced the energy consumption by 15% - from 4.72 to 4.00 MWh/day of activity. At this moment the heat recovery function was not used at its full capacity yet. When the new ice sheet was connected to

the unit for the season 2017-2018 the energy savings potential of the new system solution became more clearly visible. The CO_2 system is now able to run two ice sheets with an energy consumption that is only 23% higher than what the previous ammonia system needed when running one ice sheet. Moreover, season 2018-2019 looks even more promising since the controls have been improved, resulting in almost no district heating demand and only 15% higher consumption than the old system with only one ice sheet. Finally, plans are in the making to build a swimming hall in the vicinity of Facility E which opens up for the possibility of exporting excess heat from the heat recovery system.

2.6. Summary of all Cases – Life-cycle Cost Analysis

The financial performances of the new CO_2-based system solutions were evaluated in order to give a broad understanding of their benefits for the ice rink owner, which in all the studied cases were municipalities in Sweden. This was done through a life-cycle cost (LCC) analysis, where the old system was compared with the new one in each case study. Furthermore, the calculations have gone through a sensitivity and scenario analysis in order to test the robustness of the results and see how changes in e.g. economic outlook would affect the financial performance of each system. The economic lifespan of the LCC analysis has been set to 20 years, which is a reasonable timescale for these kinds of applications. The results presented in Figure 9 mainly reflect a normal economic outlook, where the nominal interest rate is set as 1,5% per year and the discount rate used by the municipalities in their investment decision-making is 2,5%. Investment (material & installation) and operating cost input are based on real data gathered from each case study, while the service related inputs for the different system solutions are based on a mix of data gathered from the case ice rinks, reports, and experts in the field in order to produce service cost estimations that can be used in the LCC analysis.

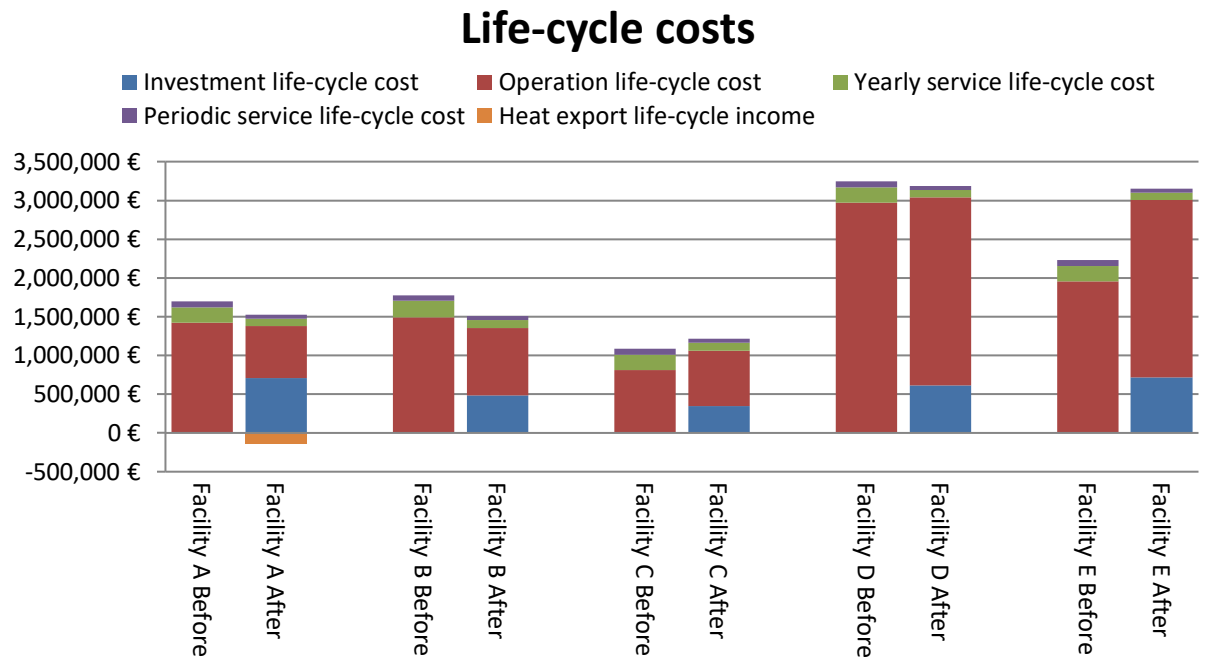

Figure 9: Life-cycle cost before/after analysis of all facilities

From Figure 9 it can generally be concluded that the savings achieved in performance already at this stage are having a profitable effect on the investments in the studied facilities (it should be repeated here that Facility E increased in size from one to two ice rinks). The only facility not showing clear financial benefit yet is Facility C. The reason for this is most likely related to the combination of lower heating demands in the facility as well as a shorter ice season (7 months) in comparison with the other studied facilities (8-9 months). However, as mentioned before, Facility C is considering exporting excess heat to a swimming hall that potentially may be built next to it. This would turn the tables and make the new system profitable compared to the old solution. The generated “income” from exporting excess heat

calculated in the case of Facility A is at this moment a highly conservative value, since it is based on data from the previous season when only halfway into it the export function was taken into use, with 90 MWh heat exported. It does, however, give an indication that the operational savings in ice rinks could be further maximized with a well utilized heat export strategy.

3. CONCLUSION

The aim of the study was to compare the measured energy performances and calculated life-cycle costs of five ice rinks in Sweden recently retrofitted from conventional refrigeration systems (HFC and ammonia) to trans-critical carbon dioxide refrigeration systems with optimized heat recovery. The field measurements of those five ice rinks in Sweden show that the operational energy use could be cut down by 18 to 55%. Furthermore, in some cases the ice rink also became self-sufficient on its own recovered heat, eliminating the need for an external heating system and opening up for the possibility to even export excess heat to a nearby facility.

As previously mentioned, the retrofits were also investigated in the form of a 20-year life-cycle cost analysis for each ice rink owner, where it was concluded that the savings gained in performance makes the investment in CO_2-based systems profitable in comparison with the previous conventional systems. The savings in performance could also be further maximized if coupled with a well utilized heat export strategy.

Finally, it should be commented that measured and gathered data from case studies like the ones presented in this paper play an important role in the development of estimation tools, where generated results regarding energy (Bolteau et al., 2018) and financial (Grönqvist and Rogstam, 2018) performance of modern refrigeration systems in ice rinks can be deemed reliable. This, as a result, should greatly aid the decision-making process in future ice rink renovation projects as well as in new construction projects.

NOMENCLATURE

CO_2	Carbon dioxide	NH_3	Ammonia
HFC	Hydrofluorocarbon	*LCC*	Life-cycle cost

REFERENCES

Bolteau, S., Kolasniewski, Y., Rogstam, J., 2018. Evaluation and modelling of ice rink energy usage. 13th IIR Gustav Lorentzen Conference, Valencia.

Grönqvist, C., Rogstam, J., 2018. Comparative life-cycle cost analysis of refrigeration systems in ice rinks. 13th IIR Gustav Lorentzen Conference, Valencia.

Rogstam, J., Beaini, C., and Hjert, J., 2014. Stoppsladd fas 4 - Energianvändning i svenska ishallar (in Swedish). Stockholm: EKA and the Swedish Ice Hockey Association. http://www.ekanalys.se/en/reports.

Rogstam, J., Bolteau, S. 2015. Ice rink of the future. Stockholm: EKA. http://www.ekanalys.se/en/reports.

Rogstam, J., Bolteau, S., Grönqvist, C. 2017. Cooling and heating ice rinks with CO_2. ASHRAE Journal, 59(8).

Manuscript ID: 1117
DOI: 10.18462/iir.icr.2019.1117

Performance of high temperature heat pump for simultaneous and efficient production of ice water and process heat

Christian SCHLEMMINGER[(a)], Eirik STARHEIM SVENDSEN[(a)], Sverre STEFFANUSSEN FOSLIE[(a)], Michael BANTLE[(a)], Opeyemi BAMIGBETAN[(b)], Petter NEKSÅ[(a)]

[(a)] SINTEF Energy Research, Kolbjørn Hejes Vei 1B, Trondheim, 7465, Norway, christian.schlemminger@sintef.nol

[(b)] NTNU. Dept. of Energy and process engineering, Trondheim, 7465, Norway

ABSTRACT

Industrial processes like milk production often require simultaneous cooling and heating at temperature of 1 °C to 10 °C and 90 °C to 120 °C, respectively. High temperature heat pumps (HTHP) with natural working fluids are a cost-, energy efficient and sustainable solution.

In this work a 20 kW_{th} lab scale cascade heat pump is analysed to predict the performance of a 300 kW_{th} pilot plant. The test campaign covers an evaporation temperature range of -1 °C to +1 °C and a condenser temperature range of 113 °C to 118 °C enabling ice-water chilling from 10 °C to 4 °C and a hot-water heating from 85 °C to 116 °C

A Combined heating and cooling $COP_{combined}$ of 2.6 to 2.8 was achieved for a temperature lift of 110 K to 80 K, respectively. This performance gives a primary energy saving potential of 57% and a potential CO_2-emission reduction of 94%.

It can be concluded that HTHP can produce simultaneously chilled/ice-water and hot-process water efficiently for processes like drying, sterilization, pasteurization.

Keywords: Refrigeration, High Temperature Heat Pump, Natural Working Fluids, Efficiency, Combined Heating and Cooling,

1. INTRODUCTION

Demands for process heat between up to 150 °C are estimated to 172 TWh/year on European basis (Nellissen and Wolf, 2015), an equivalent energy consumption of about 8500000 Norwegian households. The presented work focuses on technology development for combined heating and cooling which can be applied in processes as: sterilisation, pasteurisation, distillation and brewing. In such processes product heating, e.g. with pressurized hot-water, is followed by a product cooling (Elmegaard et al., 2017), (Wolf et al., 2014), (IEAHeatPumpCentre, 2014).

A combination of ice- and pressurized hot-water production using a heat pump enables the efficient use of renewable electricity as CO_2-lean primary energy source, which enables: a) increased process efficiency, b) reduction in operation costs and c) reduction in CO_2-emissions.

Standard heat pump technologies for industrial applications (>TRL8) are restricted by simultaneous heat source and heat sink temperatures in the range 30 °C to 70 °C and 70 °C to 100 °C (Elmegaard et al., 2017). Heat pumps working at heat sink temperatures >100 °C are scare and commonly defined as high temperature heat pumps HTHP (Arpagaus et al., 2018). Research challenges related to HTHP development are: i) extending the limits of heat supply temperature to higher values, ii) improving HTHP efficiency, iii) applying new environmentally friendly refrigerants and iv) increase the TRL level from 3 to 7, lab scale to industrial pilot scale, respectively.

The presented work addresses this research challenges by presenting a lab scale HTHP lifting heat form an ice-water production at 4 °C to a pressurized water based heat sink temperature up to 118 °C. Environmental friendly natural working fluids are applied having low values of ODP, GWP and TEWI. The elevated condensation temperatures restrict the available natural working fluids for the compression

heat pump cycle. Suitable working fluids available for condensation temperatures >100°C are water (R718), ammonia (R717), pentane (R601) and n-butane (R600) (Lemmon et al., 2013). Comparisons of available working fluids for the operation temperature and capacity range, also including synthetic, concluded that butane (R600) is most suitable (Bamigbetan et al., 2016), (Bamigbetan et al., 2018). For the targeted temperature lift >100 K a cascade-HTHP system was selected with propane (R290) in the low temperature cycle (LTC) and butane (R600) in the high temperature cycle (HTC), as depict in Fig. 1.

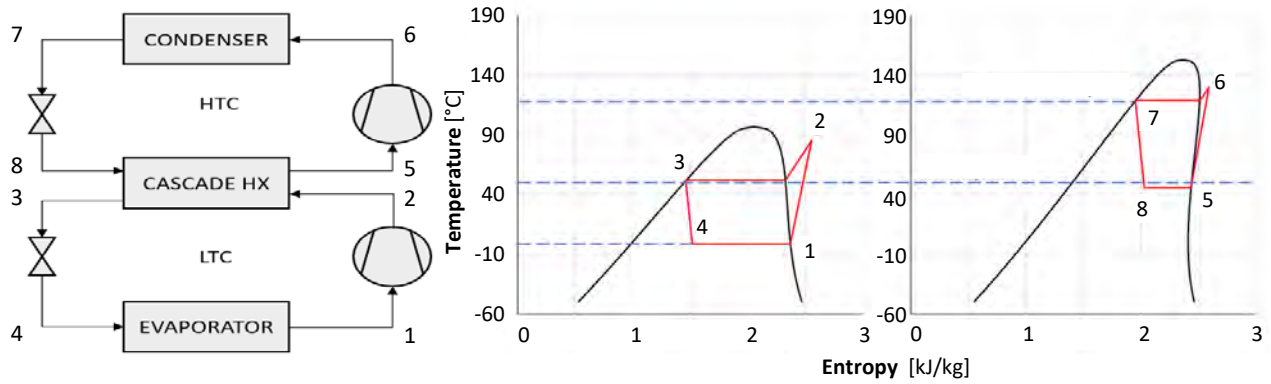

Figure 1: Simplified cycle and T-S diagram of R290/R600 cascade-HTHP

This work presents a detailed system analysis of a 20 kW_{th} R290/R600 cascade-HTHP lab scale system to show the technical feasibility, its energy efficiency an emission reduction potential.

2. MAIN SECTION

This section covered the design, measurement and analysis methods applied.

2.1. Test Setup Description

The R290/R600 cascade-HTHP (c-HTHP) is designed and build based on commercially available components as listed in Table 1.

Table 1 Main components of the c-HTHP

	Component	Manufacturer	Model
LTC - R290	LTC Compressor	DORIN	HEX551CC
	Evaporator	Kaori	K095 x 22
	Suction accumulator with internal HEX	CARLY	LCYE 69S
	High pressure receiver	KLIMAL	RCO139.40.4.80
	Frequency converter	Eaton	DA134046FB-B55C
	Electronic expansion valve	Carel	E2V14
HT – R600	HTC Compressor	DORIN	HEX1501CC
	Evaporator	Kaori	K070 x 60
	Suction accumulator with internal HEX	CARLY	LCYE 69S
	High pressure receiver	KLIMAL	RCO139.40.4.80
	Frequency converter	Eaton	DA134046FB-B55C
	Electronic expansion valve	Carel	E2V14

The working temperature range of the water-based heat sink and heat source was defined as 4 °C to 30 °C and 85 °C to 115 °C, respectively. The evaporator capacity is 10 kW at 10 °C water inlet and 4 °C water outlet. The condenser capacity is 20 kW at 100 °C water inlet and 120 °C water outlet temperature. The pinch point temperature of the heat exchangers is defined as 3 K.
A simplified P&ID schematic and the setup picture is depicted in Fig. 2. The temperature measurement range is -30 °C to 200 °C with an accuracy of ±1 K (absolute) and ±0,3 K (relative). Pressure measurement range is 1 bar to 30 bar with an accuracy of ±0.2 % FS BSL. The working fluids are measured separately by Coriolis mass flow meters with a measurement rang of 0,5 kg/min to 50 kg/min

and an accuracy of ±0.2 % FS. Heat source and heat sink water flow rates are measured using ultrasonic flow meters having an accuracy of ±2 % FS. Compressor speed and electric energy consumption can be manually adjusted using the frequency converters. The electric energy consumption reading has an uncertainty of ±1 %.
The c-HTHP setup was designed and manufactured in accordance to DIN EN 378. All working fluid containing components are placed within a separately ventilated cabinet, see Fig. 2. A gas detector and a ventilation control sensor are installed. The electricity supply into the cabinet is cut-off when the hydrocarbon concentration exceeds 800ppm and/or the ventilation is insufficient. The LTC and HTC are charged with 2.5 kg each.

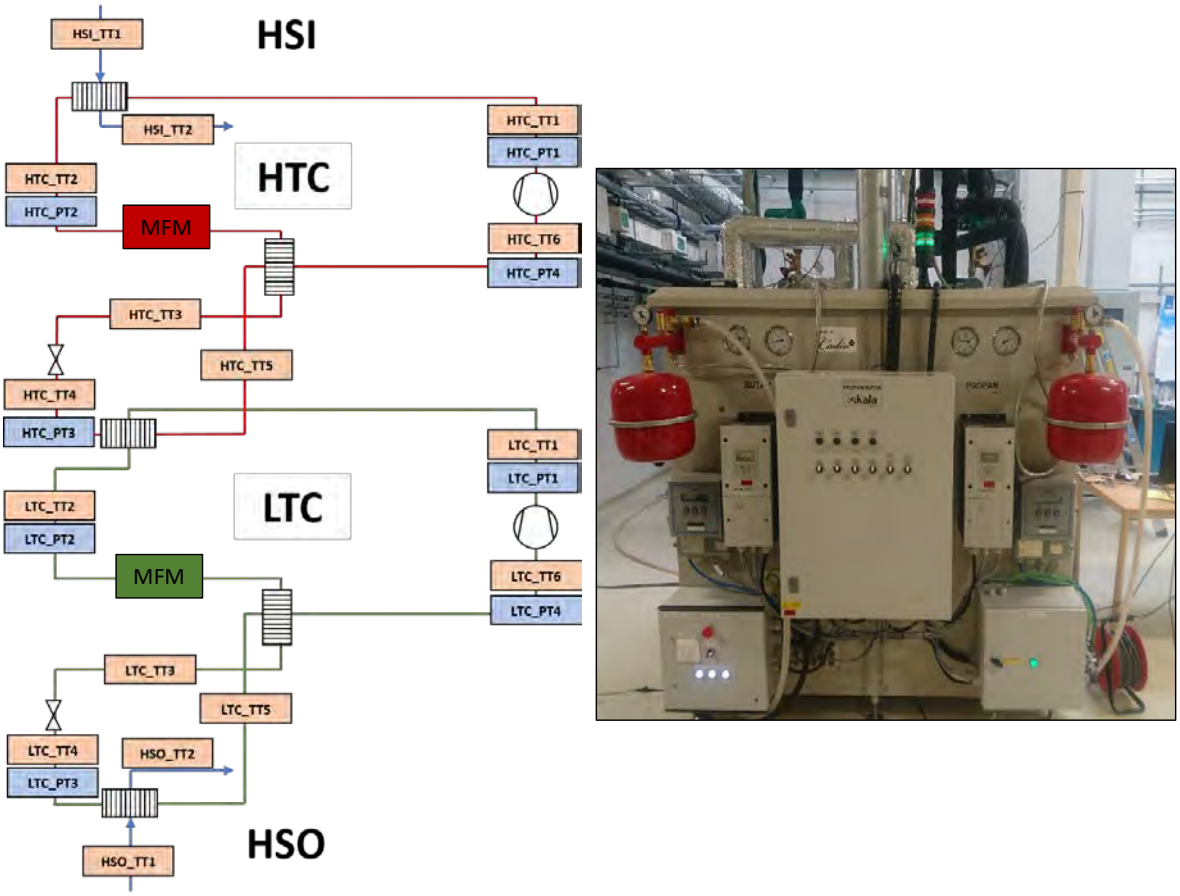

Figure 2: Simplified P&ID diagram (left) and picture of c-HTHP setup (right), (TT = Temperature Transmitter, PT = Pressure Transmitter, HIS = Heat Sink, HSO = Heat source)

2.2. Compressors

A standard R290-compressor was installed at the LTC. Evaporation temperatures exceed the standard working conditions of 10 °C of the compressor. The working temperature range was extended by Dorin for the specific test purpose. The standard condensation temperature working rang is limited to 65°C. The electric motor of the R290-compressor is suction gas cooled. The R600-compressor is a non-commercial prototype. It is modified to an operation range of 80 °C and 140 °C (160 °C) for suction and discharge temperature, respectively. This high temperature levels require a proper design and thermal management. The electric motor is suction gas cooled. It has an external gas manifold, the discharge temperature range is extended to 160 °C and the electric motor is about 25% overmentioned. Further, a suitable lubricant for high temperature applications and hydrocarbons was selected. Both compressors are semi hermetic, certified for use in ATEX 2014/34/EU zone 2. Operation frequency range is 35 Hz to 50Hz.

2.3. Experimental Campaign

The experimental campaign was designed to evaluate the coefficient of performance of the c-HTHP. As heat source water was cooled from 10 °C to 4 °C while pressurized hot-water was heated at the heat

sink side from 85 °C to 115 °C. The compressor frequency was increased in 5 Hz intervals from 35 Hz to 50 Hz. The seven measurements conducted are listed in Table 2.
The measurements were conducted at steady state condition, defined as stable heat source and heat sink in- and outlet temperature variations <±1 K. The measurement duration was minimum 10 minutes with a sampling rate of 1 second. Compressor electrical power consumptions and frequencies were recorded manually, whereas all other parameters were logged and post experimental averaged over the entire measuring period.

Table 2 Operating conditions of the experimental c-HTHP investigation

f [Hz]	Temperature [°C]						COP [-]		η [-]	Capacity [kW]		
	HSO			HSI								
HTC/ LTC	in	out	evap.	in	out	cond.	C_HSI +HSO	HSI+ HSO	C_HSI +HSO	cond.	evap.	el_ comp
35/35	9.8	4.8	0.8	83.9	112.5	113.4	6.2	2.84	0.46	19.0	8.45	9.7
40/35	9.1	3.7	-0.2	84.6	114.6	115.3	6.0	2.71	0.45	20.0	8.37	10.5
40/40	9.7	4.2	0.1	84.4	115.9	116.7	6.0	2.66	0.45	21.2	9.28	11.5
45/40	10.3	4.7	0.6	84.7	114.5	115.8	6.1	2.69	0.45	22.6	9.76	12.0
45/45	10.1	4.1	0.1	84.8	116.7	118.0	5.9	2.64	0.45	24.6	10.31	13.2
50/45	10.3	4.4	-0.1	84.8	116.1	117.6	6.0	2.63	0.45	25.7	10.62	13.8
50/50	9.9	3.9	-0.7	85.0	116.3	118.2	5.9	2.60	0.44	27.3	11.30	14.9

2.4. Data Analysis

Data analysis was carried out using Microsoft Excel 2016 in combination with the property database REFPORP 9.0 (Lemmon et al., 2013). All presented measurement values are minimum 10 minute averaged. The standard deviation was used as quality criteria and was below the measurement uncertainties.
Since heat source and heat sink is utilized in the application of simultaneous ice- and hot-water production a combined ideal COP based Carnot is defined as maximum thermal efficiency as given in Eq. (1).

$$COP_{C\_HSI+HSO} = \frac{T_{HSITT2} + T_{HSOTT2}}{T_{HSITT2} - T_{HSOTT2}} \quad \text{Eq. (1)}$$

The condenser capacity is determined by the measured working fluid mass flow and the enthalpy difference between condenser inlet and outlet, as described in Eq. 2.

$$\dot{Q}_c = \dot{m}_{R\_HTC} \cdot (h_{HTC1} - h_{HTC2}) \quad \text{Eq. (2)}$$

The evaporator capacity is determined in analogy, as given in Eq. 3.

$$\dot{Q}_E = \dot{m}_{R\_LTC} \cdot (h_{LTC5} - h_{LTC4}) \quad \text{Eq. (3)}$$

As the ideal COP, takes the combined coefficient of performance heat source and heat sink into account, see Eq.4.

$$COP_{HSI+HSO} = \frac{\dot{Q}_E + \dot{Q}_c}{P_{comp\_LTC} + P_{comp\_HTC}} \quad \text{Eq. (4)}$$

To benchmark the combined COP the Carnot-efficiency is defined as given in Eq. 5.

$$\eta_{c\_HSI+HSO} = \frac{COP_{HSI+HSO}}{COP_{C\_HSI+HSO}} \quad \text{Eq. (5)}$$

In addition to the system, the compressor characteristics were evaluated. The total compressor efficiency is calculated as given in Eq. 6 and the volumetric efficiency as defined in Eq. 7.

$$\eta_{Comp\_total} = \frac{\dot{m}_R \cdot (h_{is\_discharge} - h_{suction})}{\dot{P}_{el\_Comp}} \quad \text{Eq. (6)}$$

$$\eta_{Comp\_vol} = \frac{\dot{m}_R}{\rho_{suction} \dot{V}_{Comp}} \quad \text{Eq. (7)}$$

The compressor displacement is calculated, as given in Eq. 8, with a standard displacement at 50 Hz of 23.13 m^3/h and 48.8 m^3/h for LTC- and HTC-compressor, respectively.

$$\dot{V}_{Comp} = \frac{\dot{V}_{Comp}(50Hz) f_V}{3600 \cdot 50} \quad \text{Eq. (8)}$$

3. REULTS AND DISCUSSION

The results are presented with focus on compressor and system performance and close with the prediction of emission and cost reduction potential.

3.1. Compressor Characteristics

The total compressor and the volumetric efficiencies are plotted over the pressure ratios in Figure 3 and were determined das given in Eq. 6 and Eq. 7, respectively.

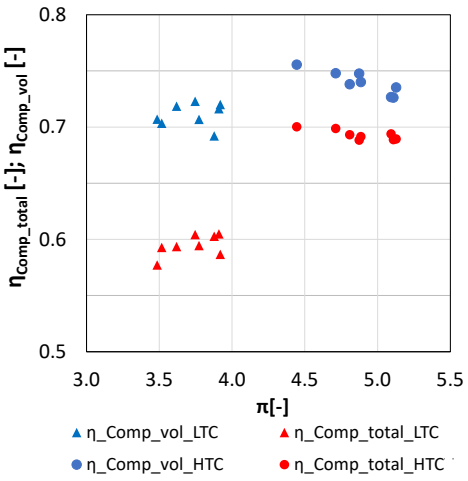

Figure 3: Compressor total compression efficiency and volumetric efficiency of experimental results

The total compressor and the volumetric efficiency are constant over the investigated pressure ration 3.5 to 4.0 and 4.4 to 5.2 for both the LTC- and the HTC-compressor, respectively. The total compressor efficiency is about 0.59 for the LTC-compressor and about 0.69 for the HTC-compressor. Even so the pips of the setup are insulated thermal losses occur between the compressor outlet and the temperature measurement position. The thermal losses are expected higher for the HTC-compressor, since the compressor head and the discharge manifold are external compared to the LTC-compressor. The volumetric efficiencies are in the range of 0.71 and 0.74 for the LTC- and the HTC-compressor respectively.

3.2. System Performance

The c-HTHP system performance is depict in Figure 4 as combined COP over the evaporation temperature. Further, the combined COP is plotted over the temperature lift which is defined as difference between evaporation and condensation temperature.

The measurement results show the expected increase of the combined COP by increasing evaporation temperature. Variations on HSI-inlet temperatures of ±5 K result in variations of ±5 % for the combined COP. For ice-water relevant evaporation temperatures range is 1 °C to +1 °C.
The variation of compressor frequency from 35 Hz to 50 Hz lead to an evaporator capacity increase from 8.37 kW to 11.3 kW. HSO-inlet-temperatures varied in the range of 9.1 °C to 10.3 °C resulting in a HSO-outlet temperature 3.7 °C – 4.8 °C.
The increase of compressor frequency resulted in increased temperature lift, as shown in Figure 4. HSI-inlet temperature was held constant with 84.5 °C ± 0.5 K. The condensation temperature increased from 113.4 °C to 118.2 °C effecting the HIS-outlet temperature 112.5 °C to 116.7 °C. The condenser capacity increased from 19.0 kW to 27.3 kW by increasing the compressor frequency. Consequently, decreased the combined COP. However, results the increased compressor frequency not significantly to a decreasing combined COP, indicated by the constant Carnot-efficiency as defined by Eq. 5 of 0.448 ±0.01, see Table 2.
The simultaneous production of ice- and pressurised hot-water with the developed c-HTHP system resulted in a combined COP range of 2.6 to 2.8.

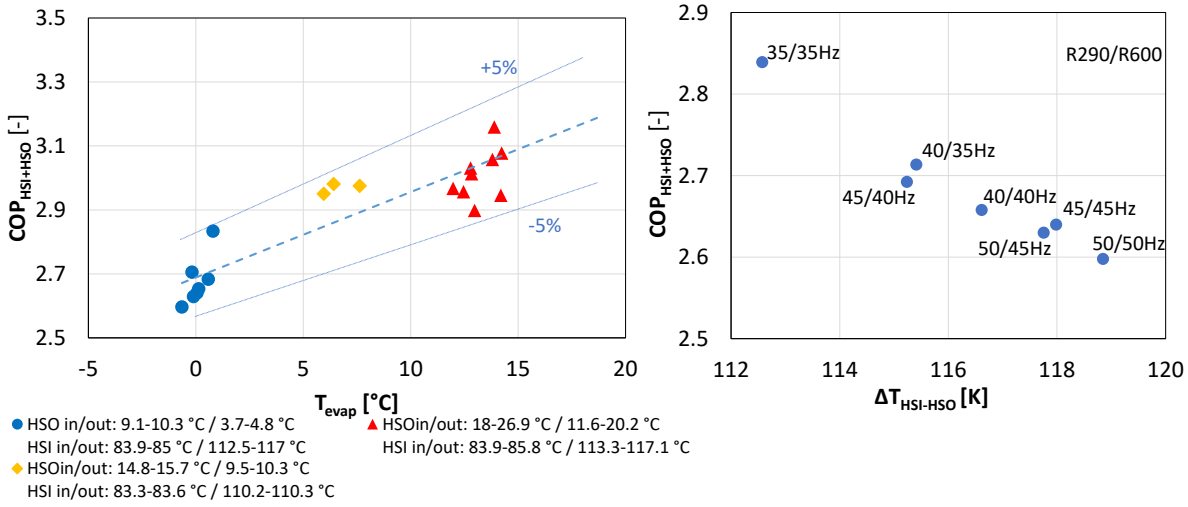

Figure 4: c-HTHP system performance: combined COP as function of evaporation temperature (left), combined COP as function of temperature lift (right)

A detailed investigation of the characteristic sate points of the cascade cycle at 50 Hz compressor frequency for both compressors, is given in Fig. 5.

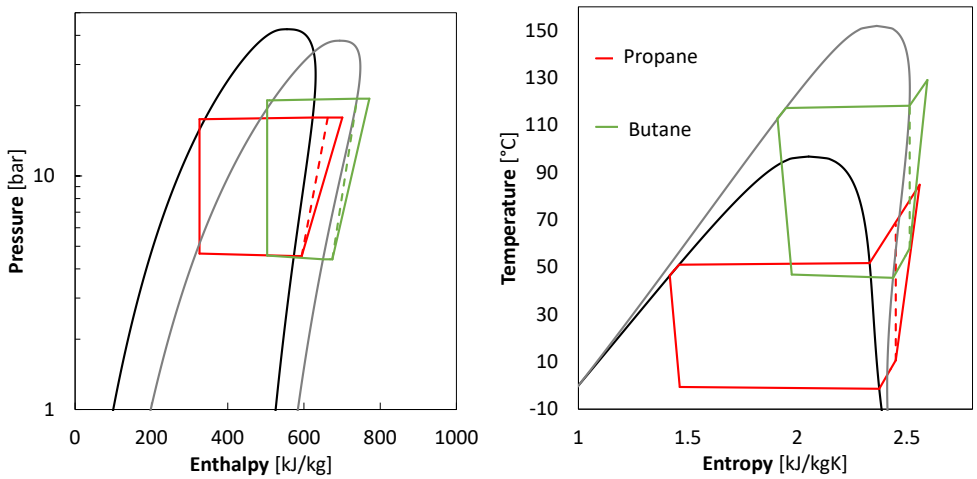

Figure 5: Characteristic sate points at 50 Hz operation for both compressors: log(p)-h diagram (left), T-S diagram (right)

It shows moderate working pressures of both cycles in a range of 4.5 bar to 21.5 bar. The super heat of the R290 cycle is about 15 K at the compressor suction, however the compressor discharge temperature reaches about 85 °C. The high efficiency of the R600-compressor indicates the necessity for sufficient superheat, otherwise compression into the two-phase region may occur. In the experiments a 13 K superheat was sufficient at the compressor suction side, resulting in discharge temperatures of about 130°C.
The T-S diagram reveals only 42 % R600 liquid are present after expansion. To enhance the cycle more R600-subcooling is suggested, further the implementation of ejectors for expansion work recovery would further improve the cycle.

3.3. Emission and Primary Energy Reduction Potential

The application of HTHP are the upgrade and utilisation of waste heat resulting in a replacement of fossil fuelled or direct electric heat supply. The investigated HTHP enables a high temperature lift enabling simultaneous production of ice- and pressurized hot-water. This additional cooling capacity available can either reduce the cooling load of existing chillers or increase the total cooling capacity of a production side.
A reference case is defined to evaluate the emission and cost reduction potential. The reference case assumes: gas fired hot-water production at the same temperature level as the HTHP with an efficiency of 0.85, ice-water production with a chiller having a COP of 4.5. CO_2-emissions for gas and electricity are 180 g_{CO2}/kWh_{th} and 22 g_{CO2}/kWh_{el}, respectively.
Standardised result for pressurised hot-water production are given in Table 3.

Table 3 Emissions and operating cost comparisons

	Reference case	HTHP
hot-water production [kW]	1	1
ice-water production [kW]	0.41	0.41
power required [kW]	0.09	0.54
gas boiler fuel [kW]	1.18	-
total energy required[kW]	1.27	0.54
total energy saving [kW]	0.72	
relative energy saving	57 %	
CO_2-reduction	94 %	

This simple comparison indicated significant primary energy saving by 57 %. For the production of 1,0 kWh pressurised hot-water and 0.41 kWh ice-water requires the reference case 151 g_{CO2}, whereas the HTHP only emits 8.5 g_{CO2}, a reduction by 94%.

4. CONCLUSIONS

A technology for efficient and CO_2-emission lean simultaneous production of ice- and pressurized hot-water was presented. This high temperature heat pump utilizes environmentally friendly natural working fluids with low ODP, GWP and TEWI values. Typical application of these type industrial size HTHP would be in processes like: sterilisation, pasteurisation, distillation and brewing etc..
The performance of the $30kW_{th}$ lab scale HTHP was analysed for an evaporation and condensation temperature operation range of 1 °C to +1 °C and 113.4 °C to 118.2 °C, respectively. A modified compressor was installed at the high temperature cycle of the cascade-HTHP system, enabling to increase standard equipment temperature limits. The total compressor efficiency was in the order of 0.74. The combined coefficient of performance was measured in a range of 2.6 to 2.8. This equals a Carnot-efficiency of 0.45 for a 119 K temperature lift.
The application of the developed cascade-HTHP system for simultaneous production of ice- and pressurised hot-water enables a significant reduction in primary energy consumption of 57 % and CO_2-emissions of 94% compared with a gas fired hot-water and chiller-based ice-water production.
The results show the great potential for industrial HTHP to increase industrial process efficiency and phase in of CO_2 lean electricity simultaneously.

ACKNOWLEDGEMENTS

This paper has been funded by HighEFF - Centre for an Energy Efficient and Competitive Industry for the Future, an 8-year Research Centre under the FME-scheme (Centre for Environment-friendly Energy Research, 257632/E20). The authors gratefully acknowledge the financial support from the Research Council of Norway and user partners of HighEFF.
The authors would also like to acknowledge the support of The Research Council of Norway and the industrial partners Equinor AS, Hydro Aluminium AS, Statkraft Varme AS, Vedde AS, member of TripleNine Group Vedde AS, Mars GmbH, TINE SA, Cadio AS, Hybrid Energy AS and EPCON Evaporation Technology AS through the grant NFR-243679 (HeatUp).

NOMENCLATURE

Symbol		*Index*	
COP	coefficient of performance (-)	*C*	Carnot
h	enthalpy (kJ×kg^{-1})	*c*	condenser
$\dot{m}$	mass flow rate (kg×s^{-1})	*Comp*	compressor
P	power (W)	*el*	electric
p	pressure (bar)	*HIS*	heat sink
$\dot{Q}$	heat flow (W)	*HSO*	heat source
T	temperature (K)	*HTC*	high temperature cycle (R600)
$\dot{V}$	volume flow (m^3×s^{-1})	*is*	isentropic
η	efficiency (-) or (W×W^{-1})	*LTC*	low temperature cycle (R290)
Π	Pressure ratio (-) or (bar/bar)	*E*	evaporator
ρ	density (m^3×kg^{-1})	*R*	refrigerant
		th	thermal

REFERENCES

Arpagaus, C., Bless, F., Uhlmann, M., Schiffmann, J., Bertsch, S.S., 2018. High temperature heat pumps: Market overview, state of the art, research status, refrigerants, and application potentials. Energy 152, 985-1010.

Bamigbetan, O., Eikevik, T.M., Nekså, P., Bantle, M., 2016. Evaluation of natural working fluids for the development of high temperature heat pumps, 12th IIR Gustav Lorentzen Conference on Natural Refrigerants (GL2016), Edinburgh, United Kingdom.

Bamigbetan, O., Eikevik, T.M., Nekså, P., Bantle, M., Schlemminger, C., 2018. Theoretical analysis of suitable fluids for high temperature heat pumps up to 125° C heat delivery. Int. J. Refrigeration 92, 185-195.

Elmegaard, B., Zühlsdorf, B., Reinholdt, L., Bantle, M., 2017. Book of presentations of the International Workshop on High Temperature Heat Pumps, International Workshop on High Temperature Heat Pumps. Technical University of Denmark (DTU).

IEAHeatPumpCentre, 2014. Annex 35: Application of Industrial Heat Pumps - Final Report (No. Report HPP-AN35-1&2), Borås, Sweden.

Lemmon, E.W., Huber, M.L., McLinden, M.O., 2013. NIST Standard Reference Database 23: Reference Fluid Thermodynamic and Transport Properties-REFPROP, Version 9.8 ed. National Institute of Science and Technology, Gaithersburg.

Nellissen, P., Wolf, S., 2015. Heat pumps in non-domestic applications in Europe: Potential for an energy revolution. Emerson Climate Technologies, Delta-ee 3rd Annual Heat Pumps & Utilities Roundtable.

Wolf, S., Fahl, U., Blesl, M., Voß, A., Jakobs, R., 2014. Analyse des Potenzials von Industriewärmepumpen in Deutschland. Institut für Energiewirtschaft und Rationelle Energieanwendung. Stuttgart. URL: http://www.ier.uni-stuttgart.de/publikationen/veroeffentlichungen/forschungsberichte/downloads/141216_Abschlussbericht_FKZ_0327514A.pdf (downloaded 01. 10. 2015).

Manuscript ID: 1125
DOI: 10.18462/iir.icr.2019.1125

Performance evaluation of CO_2-based mixture refrigerants in ground-source heat pump with ejector

Wei Wu[(a)]*, Michael Leung[(a)], Xianting Li[(b)]

[(a)]School of Energy and Environment, City University of Hong Kong, Hong Kong, China.
Email: weiwu53@cityu.edu.hk
[(b)]Department of Building Science, School of Architecture, Tsinghua University, Beijing, China.

ABSTRACT

Ground-source heat pumps (GSHPs) attract increasing interest but requires alternative refrigerants with low GWPs. This work investigates the performance of CO_2-based mixture refrigerants in GSHPs with ejector. R41, R32, R161 and R1270 are selected from different HFCs/HFOs/HCs to be blended with CO_2. These mixtures are compared for GSHPs with and without ejector under various compositions. Results indicate that the cooling capacity of each mixture increases with the CO_2 fraction; ejector increases the cooling capacities for CO_2/R41 but decreases those for CO_2/R32, CO_2/R161 and CO_2/R1270. Ejector increases the COP of pure refrigerants and mixtures with small temperature glides, but not with large temperature glides. Without ejector, mixtures always outperform CO_2 and outperform pure HFC/HFO/HC under lower CO_2 fractions. With ejector, mixtures outperform CO_2 under lower CO_2 fractions but never outperform pure HFC/HFO/HC. In addition, the discharge temperature with ejector is much higher for mixtures with large temperature glides.

Keywords: low GWP; CO_2; mixture refrigerant; ground-source heat pump; ejector; COP

1 INTRODUCTION

Ground-source heat pumps (GSHPs) are attracting increasing interest due to the high energy efficiency (Wu and Skye, 2018). The Kigali Amendment to Montreal Protocol requires to reduce hydrochlorofluorocarbons use (UNEP, 2016). It is necessary to seek low global-warming-potential (GWP) refrigerants for GSHPs. CO_2 is a promising candidate but suffers from low efficiency and high pressure (Kim et al., 2004). Various advanced vapor-compression cycles have been proposed to enhance the coefficient of performance (COP) of CO_2 heat pumps. These cycles include suction line heat exchanger (SLHX) cycle, ejector cycle, expander cycle, multiple-cooler cycle, and their combinations (Groll and Kim, 2007; Hu et al., 2016). The ejector is regarded to be an inexpensive and effective method for efficiency improvement (Elbel, 2011; Bai et al., 2015).

To lower the operating pressure of CO_2 heat pumps, CO_2-based mixture refrigerants have been investigated. The studied refrigerants blended with CO_2 include hydrofluorocarbons (HFCs), hydrofluoroolefins (HFOs) and hydrocarbons (HCs) (Dai et al., 2015). Apart from reducing the pressure of CO_2 heat pumps, CO_2-based mixture refrigerants can also increase the cycle COP. In addition, CO_2-based mixtures can also decrease the GWPs, lower the flammability, while increasing the volumetric capacity of HFCs, HFOs or HCs.

The objective of this work is to investigate the performance of CO_2-based mixture refrigerants in GSHPs with ejector. Different HFCs, HFOs and HCs are considered to select the suitable

candidates for CO_2 blends. The selected CO_2-based mixture refrigerants are compared for GSHPs with and without ejector under various mixture compositions.

2 METHODOLOGY

2.1 Refrigerant Property

Several widely investigated refrigerants from the categories of HFC, HFO and HC are chosen for analysis, with the basic information provided in Table 1.

Table 1. Basic information of the studied refrigerants (NIST, 2013; ASHRAE, 2016)

Category	Refrigerant	ODP	GWP	Boiling point (°C)	Critical point (°C)	Safety group
CO_2	CO_2	0	1	-78.5	31.0	A1
HFC	R134a	0	1370	-26.1	101.1	A1
	R152a	0	124	-24.0	113.3	-
	R161	0	12	-37.6	102.1	A2
	R32	0	675	-51.7	78.1	A2L
	R41	0	92	-78.3	44.1	-
HFO	R1234yf	0	4	-29.5	94.7	A2L
	R1234ze(E)	0	6	-19.0	109.4	A2L
HC	R290	0	3	-42.1	96.7	A3
	R600	0	4	-0.5	152.0	A3
	R600a	0	3	-11.7	134.7	A3
	R1270	0	2	-47.6	91.1	A3

The properties of the pure and mixture refrigerants are calculated using REFPROP (NIST, 2013). Fig. 1a shows the critical temperature versus the mixture composition. The critical temperature decreases as the CO_2 mass fraction increases, with CO_2/R41 showing the closest critical temperature to CO_2. Fig. 2b presents the condensing pressure versus the mixture composition under a condensing temperature of 28 °C (as defined in section 2.2). The condensing pressure increases as the CO_2 mass fraction increases, with CO_2/R41 showing the highest pressure and CO_2/R600 showing the lowest. Mixtures can effectively lower the operating pressures of CO_2 heat pumps.

Fig. 2 shows the temperature glides of the evaporating and condensing processes under an evaporating temperature of 5 °C and a condensing temperature of 28 °C (as defined in section 2.2). For both the evaporator and condenser, the temperature glide increases first and decrease later as the CO_2 mass fraction increases. CO_2/R41 has the lowest temperature glides, staying below 2 °C, while CO_2/R600 has the highest, reaching higher than 80 °C. To avoid a too large temperature glide, R41, R32, R161 and R1270 are chosen for further analysis.

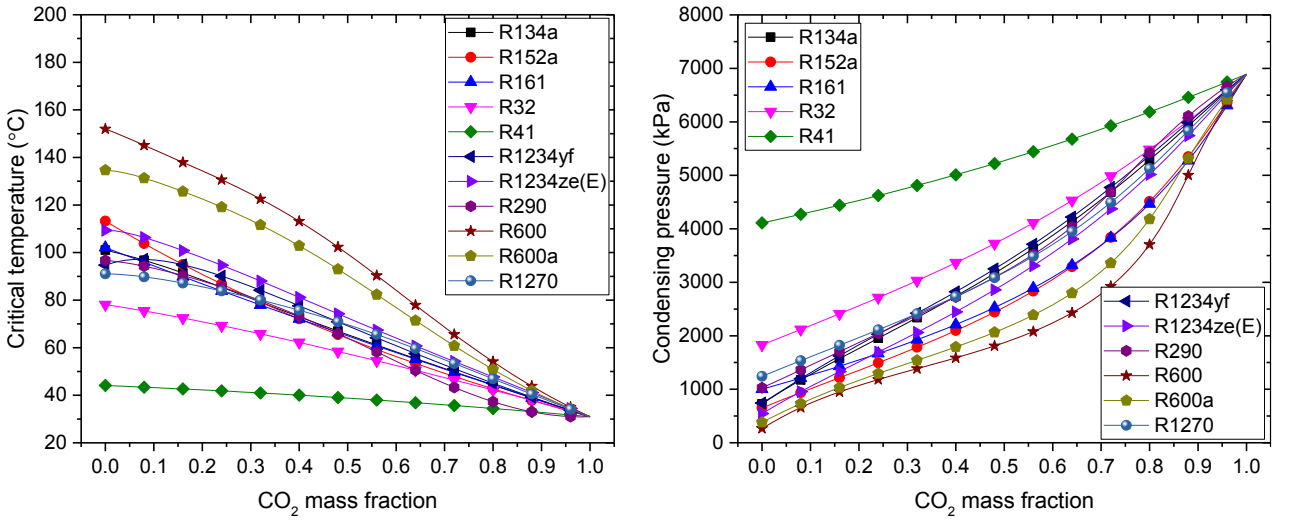

(a) Critical temperature (b) Condensing pressure

Figure 1: Critical temperature and condensing pressure of different mixture refrigerants

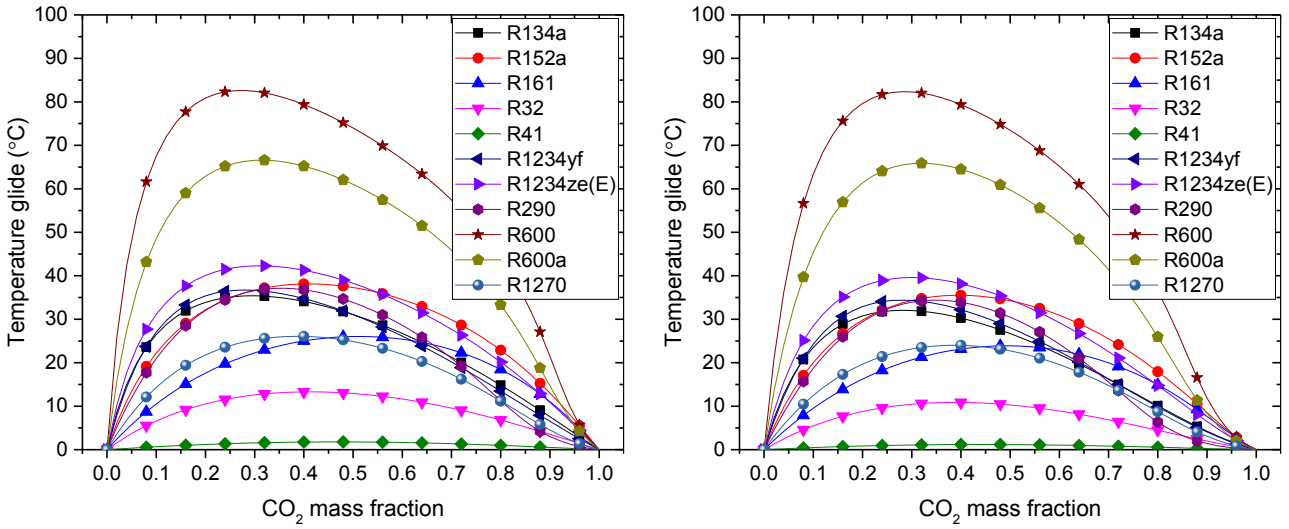

(a) Evaporator (b) Condenser

Figure 2: Temperature glides of different mixture refrigerants

The schematic diagram of the GSHP with ejector is illustrated in Fig. 3. The advantage of GSHP is that the relatively low temperature from the ground can increase the period of subcritical operation for CO_2 cycles (in cooling mode). While most studies on CO_2 cycles are for the transcritical mode, this work is focused on the subcritical mode.

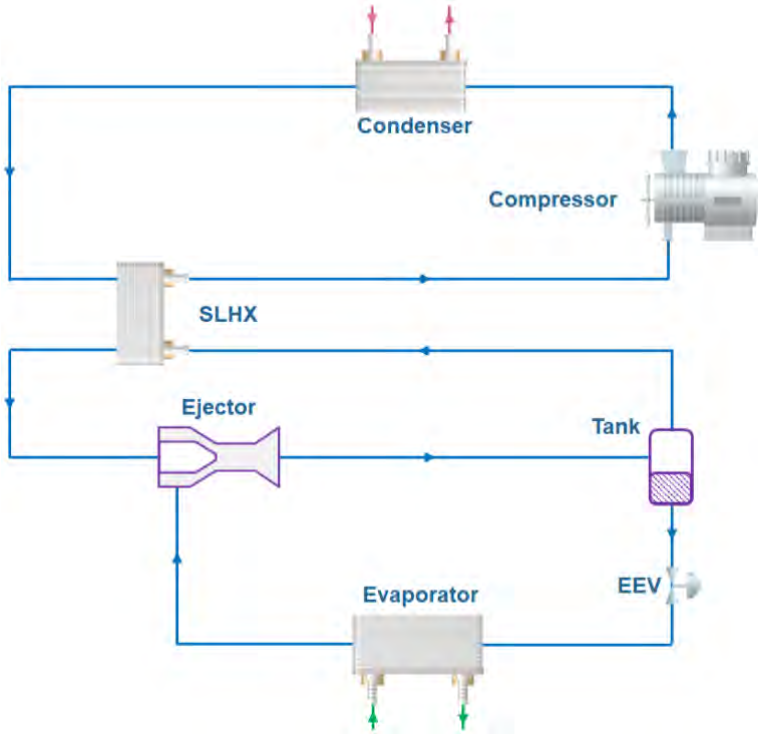

Figure 3: Schematic diagram of the GSHP with ejector

2.2 Heat Pump Model

To establish the thermodynamic model of the cycle, some commonly used assumptions are made: the system is in steady state; the flow resistance, pressure drops, and heat losses are ignored; the throttling process is isenthalpic. The expansion efficiencies of the motive and suction fluids and the efficiency of the diffusion process are set constants. The motive and suction fluids reach the same pressure at the inlet of the mixing section. The vapor refrigerant and the liquid refrigerant leaving the separator tank are both saturated. Kinetic energies of the refrigerant at the ejector inlet and outlet are both ignored.

The compositions of the mixtures entering and leaving the separator tank are different, it is assumed that the composition difference between the initial charged refrigerant and the refrigerant entering the separator tank is neglectable. This composition has a medium CO_2 fraction, while the vapor refrigerant leaving the separator tank has a higher CO_2 fraction, and the liquid refrigerant leaving the separator tank has a lower CO_2 fraction. The different levels of compositions are calculated by an iterative process.

Only the compressor model is introduced here due to the length limitation. A semi-hermetic reciprocating compressor is used for the GSHP. The compressor speed (N) is 1450 RPM @ 50 HZ, the bore diameter (D) is 22 mm, and the stroke (L) is 17 mm. The compressor displacement (m^3/s) rate is:

$$V_d = \frac{\pi}{4}\left(\frac{D}{1000}\right)^2 \frac{L}{1000}\frac{N}{60} \qquad \text{Eq. (1)}$$

Based on the measurements, the volumetric efficiency and total compressor efficiency are correlated to the pressure ratio (P_r) within the subcritical range:

$$\eta_v = 1.0212 - 0.0949P_r \qquad \text{Eq. (2)}$$

$$\eta_c = -0.6064 + 1.6912P_r - 0.8532{P_r}^2 + 0.1823{P_r}^3 - 0.0142{P_r}^4 \quad \text{Eq. (3)}$$

Thus, the refrigerant mass flow rate through the compressor is calculated by:

$$m_r = \eta_v V_d \rho_{suc} \quad \text{Eq. (4)}$$

Based on the definition of total compressor efficiency (the ratio of the power required for isentropic compression (W_i) to the actual power input (W_c)), the actual compressor power is calculated by:

$$W_c = \frac{W_i}{\eta_c} = \frac{m_r(i_{dis,i} - i_{suc})}{\eta_c} \quad \text{Eq. (5)}$$

The actual compressor discharge enthalpy is computed using the heat-balance equation of the compressor:

$$m_r(i_{dis} - i_{suc}) = W_c(1 - \gamma_{loss}) \quad \text{Eq. (6)}$$

where γ_{loss} is the ratio of the compressor heat lost to the ambient over the electrical power input to the motor, and is fit to functions of the pressure ratio:

$$\gamma_{loss} = \begin{cases} -0.3658 + 0.4484P_r - 0.0933{P_r}^2, & P_r < 2.2 \\ -0.0121 + 0.0842P_r, & P_r \geq 2.2 \end{cases} \quad \text{Eq. (7)}$$

Based on the standard test conditions specified by ISO 13256-2-1988 (ISO, 1998), the parameters for the analysis of the GSHP in cooling mode is listed in Table 2. The evaporating and condensing temperatures are different between pure and mixture refrigerants, and different value-setting methods yield different results (McLinden and Radermacher, 1987). In this work, the evaporating temperature is defined as the mean value of the bulb-point and dew-point temperature under the evaporating pressure, while the condensing temperature is defined as the mean value of the bubble-point and dew-point temperature under the condensing pressure.

Table 2. Parameters for the GSHP with ejector in cooling mode

Parameter	Value	Parameter	Value
Liquid entering evaporator (°C)	12	Liquid entering condenser (°C)	25
Liquid exiting evaporator (°C)	7	Liquid exiting condenser (°C)	30
Evaporating temperature (°C)	5	Condensing temperature (°C)	28
Superheating degree (°C)	5	Subcooling degree (°C)	2
SLHX effectiveness	0.8	Ejector efficiencies	Motive: 0.9; Suction: 0.9; Diffusion: 0.8

3 RESULTS AND DISCUSSIONS

3.1 Performance Comparison

The cooling capacity and COP are compared for the GSHPs with and without ejector using different mixtures, as shown in Fig. 4. For each mixture, the cooling capacity increases with the CO_2 mass fraction (Fig. 4a), due to the much higher volumetric capacity of CO_2 compared to other pure refrigerants. Comparing the GSHPs with and without ejector, ejector contributes to higher cooling

capacities for CO_2/R41 under all the compositions, while it leads to lower cooling capacities for CO_2/R32, CO_2/R161 and CO_2/R1270 under all the compositions except for the pure refrigerants. For all the pure refrigerants, ejector yields higher cooling capacities. The penalty of cooling capacity is larger for the mixtures with higher temperature glides (e.g., CO2/R161 and CO_2/R1270) or under compositions yielding higher temperature glides (e.g., CO_2 mass fraction of 0.3~0.8).

Fig. 4b indicates opposite COP trends for the GSHPs with and without ejector. With ejector, the COP generally decreases first and increases later as the CO_2 mass fraction increases. Without ejector, the COP slightly decreases for CO_2/R41 as the CO_2 mass fraction increases, while it increases first and decreases later for CO_2/R32, CO_2/R161 and CO_2/R1270. For all the pure refrigerants, ejector contributes to a higher COP.

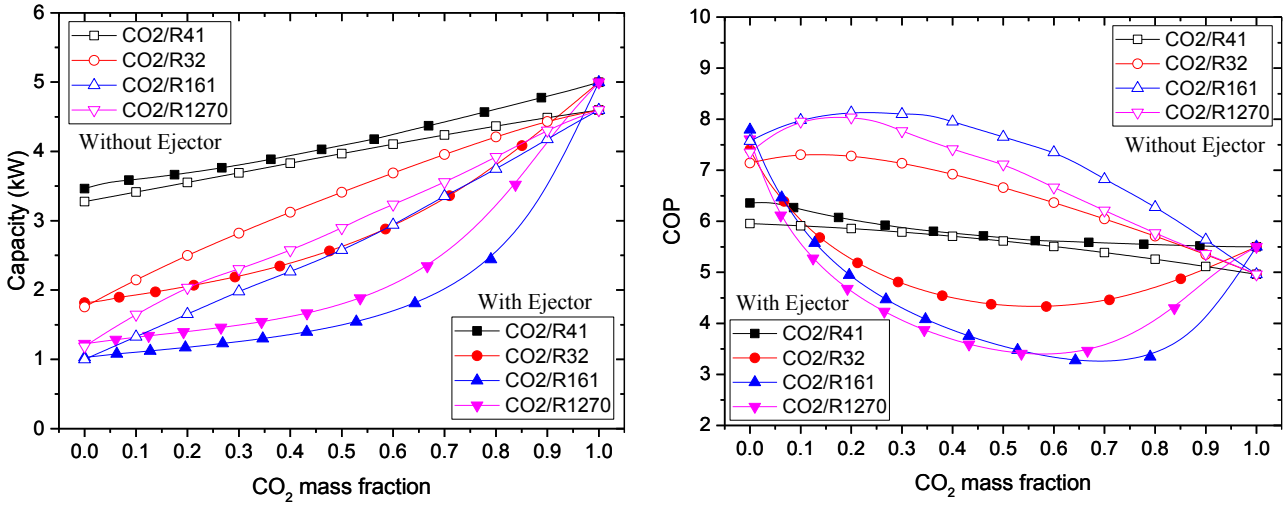

(a) Cooling capacity (b) Cooling COP

Figure 4: Performance comparison of the GSHPs with and without ejector

3.2 Discussions

The performance characteristics of the various refrigerants and cycles are explained in detail in this section.

3.2.1 Ejector improves the cycle performance of pure refrigerants

Fig. 5 presents the pressure-enthalpy (ph) diagrams of the GSHPs with and without ejector using pure CO_2. The two cycles have the same condensing pressure, while the ejector can lift the evaporating pressure by recovering the expansion loss. Thus, the pressure ratio of the compressor is lower and the inlet enthalpy of the evaporator is decreased, contributing to a higher COP and capacity. It is concluded that ejector is beneficial for all the pure refrigerants, with higher improvement for high-pressure refrigerants like CO_2 and R41.

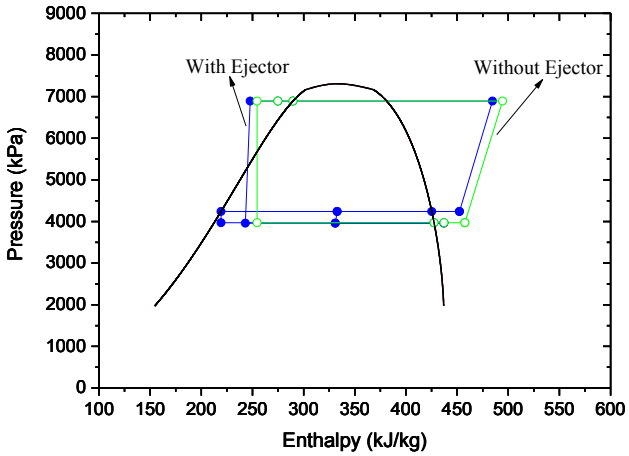

Figure 5: ph diagram of the GSHPs with and without ejector (pure CO_2)

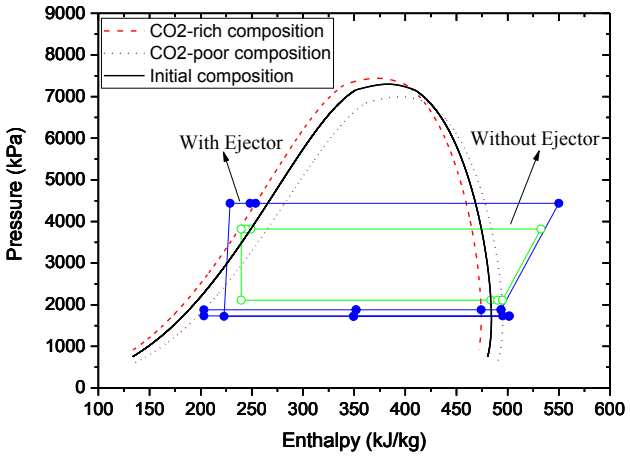

Figure 6: ph diagram of the GSHPs with and without ejector (50/50 CO_2/R32)

3.2.2 Ejector worsens the cycle performance of mixture refrigerants with large temperature glides

Fig. 6 compares the ph diagrams of the GSHPs with and without ejector using 50/50 CO_2/R32. The effect of the initial charged CO_2 fraction on the CO_2-rich composition (condenser side) and the CO_2-poor composition (evaporator side) is presented in Fig. 7. The mixture with lower temperature glides (CO_2/R41) shows small variations of compositions, while those with higher temperature glides (CO_2/R161 and CO_2/R1270) show large variations. The variations of composition lead to different ph profiles (Fig. 6) for the saturation lines. In addition, the CO_2-rich composition at the condenser side leads to higher condensing pressure while the CO_2-poor composition at the evaporator side leads to lower evaporating pressure. Consequently, the COP of the GSHP with ejector is lower than that without ejector (Figure 4b). This penalty is especially large given large temperature glides.

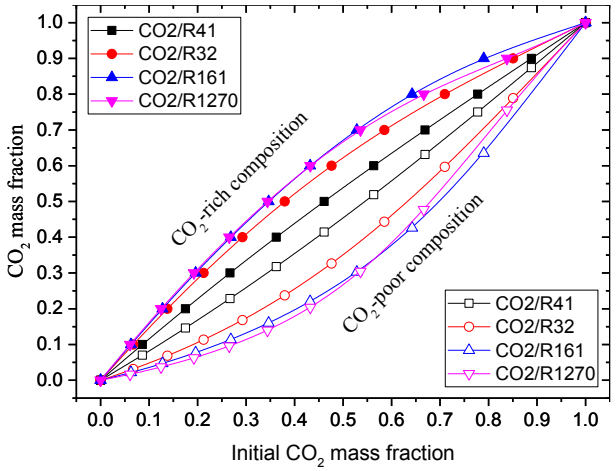

Figure 7: Compositions of GSHP with ejector

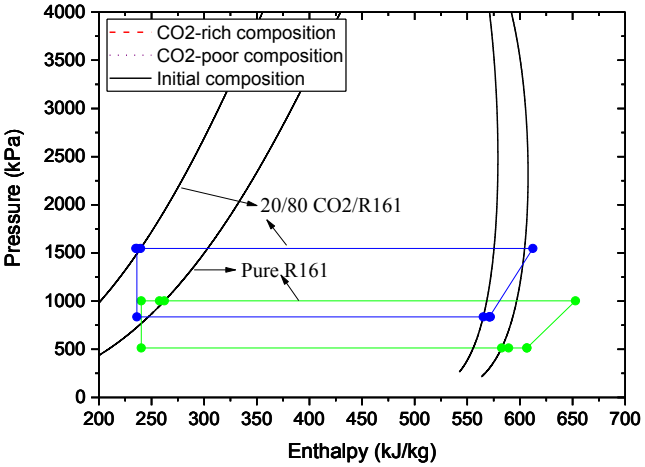

Figure 8: ph diagram of the GSHPs without ejector (pure R161 versus CO_2/R161)

3.2.3 Ejector improves the cycle performance of mixture refrigerants with small temperature glides

For CO_2/R41 with small temperature glides, the penalty caused by composition variation is overwhelmed by the benefit contributed by the pressure life of the ejector. Therefore, the ejector cycle always yields higher COPs for CO_2/R41 (Figure 4b), but the improvement is small under CO_2 mass fractions of 0.3~0.6 due to the increased temperature glides (Fig. 2).

3.2.4 Without ejector, mixtures always perform better than CO_2 and perform better than HFC/HFO/HC under lower CO_2 fractions

Fig. 8 compares the GSHPs without ejector using pure R161 and CO_2/R161 mixture. Compared to the pure R161, the CO_2/R161 mixture has a higher condensing pressure and a higher evaporating pressure. Whether the mixture brings about benefit or penalty depends on whether the pressure ratio increases or not. For the specific composition of 20/80 CO_2/R161, the pressure ratio decreases and thus the COP is higher than that of the pure R161 (Figure 4b). For other compositions (e.g., with CO_2 mass fraction above 0.6), the pressure ratio increases and thus the COP is lower.

3.2.5 With ejector, mixtures perform better than CO_2 under lower CO_2 fractions but never perform better than pure HFC/HFO/HC.

Fig. 9 compares the GSHPs with ejector using pure R161 and CO_2/R161 mixture. Compared to the pure R161, the CO_2/R161 mixture also has higher condensing and evaporating pressures, with the condensing pressure increases much more. Although the pressure lift contributed by ejector is higher for the mixture, the pressure ratio of the compressor is still much higher. Therefore, the COP is lower than that of the pure R161 (Figure 4b). Comparing the mixture with and without ejector (Figure 8 and Figure 9), it is seen that the evaporating pressure is much lower, and the condensing pressure is much higher for the GSHP with ejector (also indicated in Figure 6).

3.2.6 With ejector, the discharge temperature is much higher for mixtures with large temperature glides

Fig. 10 compares the TS diagrams of the GSHPs with ejector using pure CO_2 and 50/50 CO_2/R32. It indicates that the discharge temperature of the CO_2/R32 mixture is much higher than that of the pure CO_2. This is mainly caused by the large pressure ratio, so the large temperature glides should be avoided when determining the mixture composition.

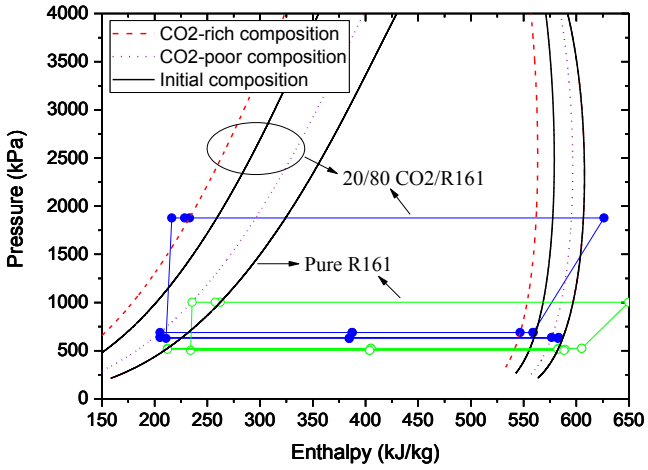

Figure 9: ph diagram of the GSHPs with ejector (pure R161 versus CO_2/R161)

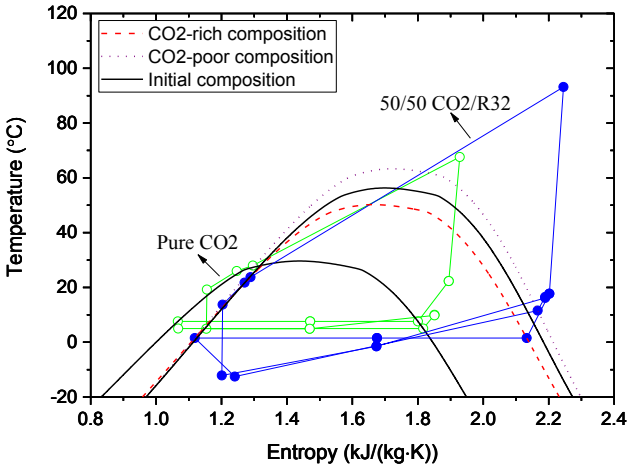

Figure 10: TS diagram of the GSHPs with ejector (pure CO_2 versus 50/50 CO_2/R32)

4 CONCLUSIONS

This work investigates the CO_2-based mixtures in GSHPs with ejector. R41, R32, R161 and R1270 are selected from different HFCs/HFOs/HCs for CO_2 blends, which are further compared for GSHPs with and without ejector under various compositions. The main conclusions are drawn as follows:
(1) For each mixture, the cooling capacity increases with the CO_2 mass fraction due to the higher volumetric capacity of CO_2. Ejector contributes to higher cooling capacities for CO_2/R41 but leads to lower cooling capacities for CO_2/R32, CO_2/R161 and CO_2/R1270. (2) Ejector increases the COP of

pure refrigerants and mixture refrigerants with small temperature glides but decreases the COP of mixture refrigerants with large temperature glides. (3) Without ejector, mixtures always perform better than CO_2 and perform better than pure HFC/HFO/HC under lower CO_2 fractions. (4) With ejector, mixtures perform better than CO_2 under lower CO_2 fractions but never perform better than pure HFC/HFO/HC. In addition, the discharge temperature with ejector is much higher for mixtures with large temperature glides.

ACKNOWLEDGMENTS

The work described in this paper was fully supported by a grant from City University of Hong Kong (Project No. 9610408).

NOMENCLATURE

D	diameter, mm	i	enthalpy, kJ/kg
L	stroke, mm	m	mass flow rate, kg/s
N	compressor speed, RPM	P_r	pressure ratio
V	compressor displacement, m^3/s	W	power, kW
η	compressor efficiency	ρ	density, kg/m^3
γ	ratio of compressor heat loss	COP	coefficient of performance

REFERENCES

ASHRAE, 2016. Standard 34-2016 Designation and Safety Classification of Refrigerants. ASHRAE, Atlanta.

Bai, T., Yan, G., Yu, J., 2015. Thermodynamic analyses on an ejector enhanced CO2 transcritical heat pump cycle with vapor-injection. Int J Refrig 58, 22-34.

Dai, B., Dang, C., Li, M., et al., 2015. Thermodynamic performance assessment of carbon dioxide blends with low-global warming potential (GWP) working fluids for a heat pump water heater. Int J Refrig 56, 1-14.

Elbel, S., 2011. Historical and present developments of ejector refrigeration systems with emphasis on transcritical carbon dioxide air-conditioning applications. Int J Refrig 34(7), 1545-1561.

Groll, E., Kim, J., 2007. Review of recent advances toward transcritical CO2 cycle technology. HAVC & R Res 13(3), 499-520.

Hu, H., Eikevik, T., Neksa, P., et al., 2016. Performance analysis of an R744 ground source heat pump system with air-cooled and water-cooled gas coolers. Int J Refrig 63, 72-86.

ISO, 1998. ISO 13256-2:1998. Water-source Heat Pumps-Testing and Rating for Performance-Part 2: Water-to-water and Brine-to-water Heat Pumps.

Kim, M., Pettersen, J., Bullard, C., 2004. Fundamental process and system design issues in CO2 vapor compression systems. Prog Energy Combust Sci 30(2), 119-174.

McLinden, M., Radermacher, R., 1987. Methods for comparing the performance of pure and mixed refrigerants in the vapour compression cycle. Int J Refrig 10(6), 318-325.

NIST, 2013. NIST reference fluid thermodynamic and transport properties–REFPROP, v9.1.

UNEP, 2016. Amendment to the Montreal Protocol on Substances that Deplete the Ozone Layer, Kigali.

Wu, W., Skye, H., 2018. Progress in Ground-source Heat Pumps Using Natural Refrigerants. Int J Refrig 92, 70-85.

Manuscript ID: 1131
DOI: 10.18462/iir.icr.2019.1131

Design of a system to produce domestic hot water based on a water to water heat pump booster

Estefania HERVAS-BLASCO[(a)], Emilio NAVARRO-PERIS[(a)], Jose M. CORBERÁN[(a)]

Instituto Universitario de Investigación en Ingeniería Energética, Universitat Politècnica de Valencia, Valencia, 46022, Spain, emilio.navarro@iie.upv.es

ABSTRACT

Domestic Hot Water (DHW) demand will remain similar in spite of the effort done to reduce energy consumption in houses. Heat pump (HP) is a potential technology to produce DHW due to its high efficiency. However, DHW application is characterized by high secondary temperature lifts for what HPs have been using transcritical cycles.
Under the European project "NEXTHPG", a water-to-water HP prototype (WtWHP) was developed. This HP stands out for: its high efficiency, the recuperation of the heat from wastewater mass flows and the use of natural refrigerants with subcritical cycles (propane).
The main objective of this work is to design a DHW production system integrating this WtWHP, a preheating heat exchanger, and a storage tank including the control strategy that leads to the maximum CO2 emissions reduction.
Keywords: Domestic Water, Heat Pump, Heat Recovery, Heat Source, R290.

1. INTRODUCTION

The building sector accounts for 21% of the total energy consumption, and almost 15% of that percentage is related to water heating for domestic hot water (DHW) (with a significant increase of that share being projected as room heating loads decrease) ("Energy consumption in households" EU). In addition, according to the European Environment Agency (EEA), the residential sector is responsible for 11.5% of total CO_2 emissions. Thus, improving water heating production within this sector is becoming unavoidable for a sustainable future, overall, taking into account that the employment of more efficient technologies and the introduction of passive houses mean that DHW becomes the most important thermal need of a building.
Most residential water heaters are equipped with conventional boilers that use electricity or fossil fuels. In spite of their simplicity and affordability, they are neither energetically nor environmentally desirable. Compared to these solutions, the demonstrated high efficiency of heat pumps (HPs) means they present one potential alternative for water heating, and they can operate in standalone form, avoiding the need for a back-up technology.
HPs have been widely used within many heating and cooling applications. However, most applications are characterized by low secondary fluid temperature lifts. In applications where high secondary fluid temperature lifts are required, either transcritical cycles capable to operate efficiently under high efficiencies with high temperature lifts or progressive heating processes with subcritical cycles to avoid the loss of performance due to temperature lifts around 50 K, are employed. Recently, researchers have been working on the optimization of HPs for that kind of applications and HPs with coefficients of performance (COPs) similar that those obtained with transcritical cycles have been developed. This is possible thanks to the applications of high (optimal) degrees of subcooling (Pitarch et al., 2018), (Pottker and Hrnjak, 2015) and the proper redesign of the HP. This kind of HP has been called a "Subcooled Heat Pump" (SHP).
One-step further deals with the integration of these SHPs within a real system in order to satisfy a real DHW demand.
Regarding heat recovery applications to produce DHW in the residential sector, not so much work can be found in the literature and usually the generalization of the presented results to other system configurations is not easy (Hua el al., 2010; Hepbasli et al., 2014).
This paper analyses a heat recovery system for DHW production in the residential sector based on such a SHP. Apart from the HP, a heat-recovery heat exchanger (HE) and a variable-volume storage

tank (ST) are integrated in the system. The sizing of the components and the definition of the operating control strategy in order to minimize the global energy consumption of the system are investigated. The results presented can yield valuable information for the next years, guiding the proper system design when the substitution of common DHW production technologies by HPs takes place in order to meet the requirements of new policies aimed towards a decarbonized energy sector.

2. MODEL DESCRIPTION

The system under analysis is presented in figure 1 (left) where heat recovery from water at 20ºC has been used to produce water at 60ºC. TRNSYS has been used in order to model the system. The main components of the system are a heat exchanger with an efficiency of 0.75, the SHP model described in (Pitarch et al., 2018) and a storage tank of variable volume (type 39). In order to define the load profile, the stochastic model described in VDI has been used.

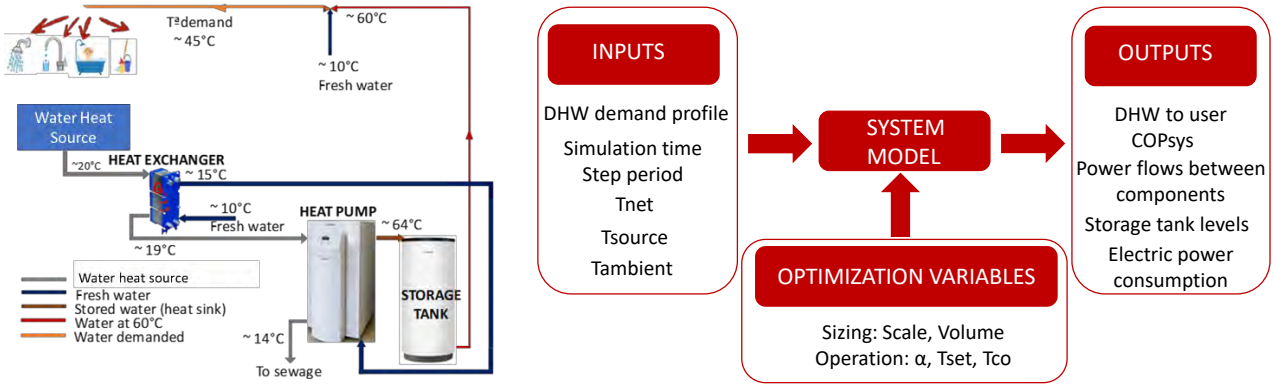

Figure 1: Scheme of the system under analysis (left). Structure of the model (right)

Fig. 1 (right) shows a scheme of the structure of the used model showing the input, the output and the optimization variables. In that scheme, scale is the size of the heat pump, volume is the size of the tank, alfa is the tank level when the heat pump switches on, Tset is the water tank temperature and Tco is the condenser outlet temperature.

Regarding the control algorithm, Fig. 2 summarizes the followed algorithm. The main source of irreversibility of the system arises from the addition of a ST. Thus, the control of the installation is based on the minimization of the temperature and the time that the water is stored in the ST. As the temperature of the stored water increases, so does the irreversibility. The minimum possible temperature of stored water considered in this work is 60 ºC. Hence, the control set temperature is T_{set} = 60 ºC.

In order to maintain a temperature of at least 60 ºC at the ST, the outlet temperature of the condenser in the HP needs to be some degrees higher. Specifically, based on the simulation results, the minimum outlet temperature to achieve this requirement stably is 64 ºC. Thus, from all the simulations, the water outlet temperature at the condenser is set to 64 ºC.

The minimum time for which the water is stored is dependent on both the volume (capacity of the ST) and the level of the water inside the tank. Dynamic control based on the water level inside the tank is required and both the volume and the level of the tank are parameters to be optimized. This control variable is called α and expresses the control level as a percentage of the volume according to Eq. (1).

$$Control\_level = \alpha \cdot Volume \tag{1}$$

where *Volume* is the capacity (size) of the tank. The determination of the optimal α is also an objective of this work.

A maximum ST level is also required to avoid overproduction; the maximum level set is based on the production capacity of the HP in one-time step as indicated in Eq. 2.

$$\max\_level = Volume - mw\_cond \cdot step \tag{2}$$

where *mw_cond* is the HP water mass flow rate production for a determined scale and *step* the simulation time step.
Finally, to preserve the durability of the HP, a maximum of nine starts within the same hour is recommended by manufacturers and has been considered in the control. This feature is programmed in the HP type.

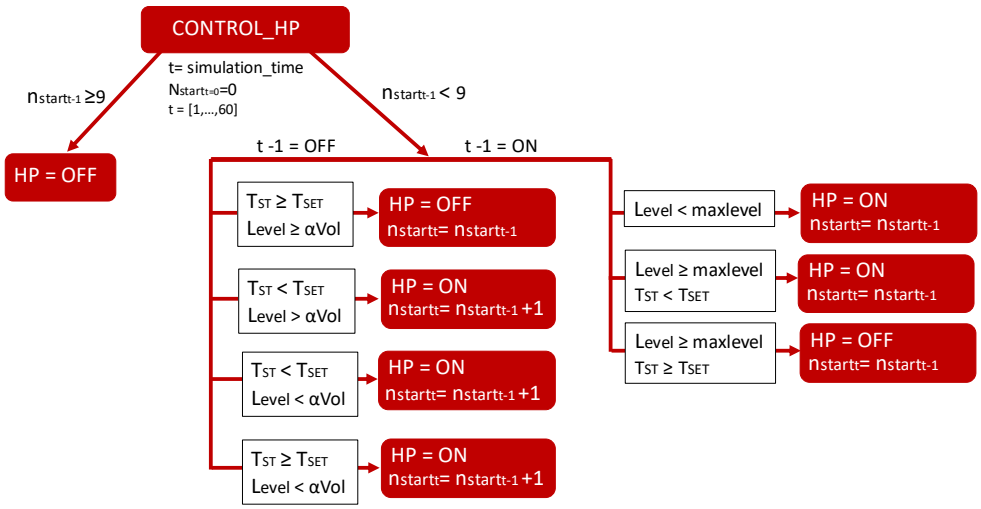

Figure 2: Control algorithm implemented for the system

The used control criteria are not based in two conditions, satisfy the demand 99% of the time and do not allow more than one-minute shortage at the same hour daily. The second condition is added in order to consider the particular user satisfaction characteristics of this type of hot water demand.
The optimization of CO2 emissions has been performed for a system considering all these constrains.

3. PERFORMED ANALYSIS

In order to minimize the CO2 emissions of this type of application an optimization of the HP heating capacity (*Scale*), the volume of the ST, and the control level (α) is carried out. The optimization has been made over one-year DHW demand profiles.
Three different sets of simulations, based on different demand sizes, have been performed, 20H, 10H, and 30H.
Figure 3 (left) describes the main inputs used in the parametric studies for each demand size.

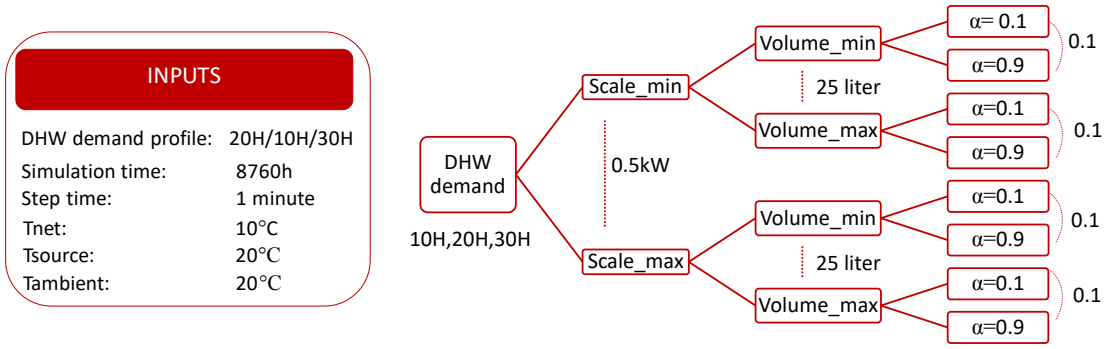

Figure 3: Inputs of the parametric studies (left). Parametric studies for each demand size. 0.5 kW scale increments, 25 litre ST size increments, and increments of 0.1 in α (right)

Fig. 3 (right) summarizes the parametric studies performed for each case:
- *Scale* variation range: it is expressed in terms of heating capacity (Qcond) and goes from the minimum size that meets the discomfort requirements to the size that satisfies an operating time of a minimum of 1.5 hours per day (in 0.5-kW steps).

- *Volume* variation range: for each heating capacity, the maximum and minimum ST sizes that meet discomfort levels are investigated (in 25-litre steps).
- *A* variation range: for each ST size, the variation of the control level in terms of the volume percentage, α, goes from 0.1 to 0.9 (in steps of 0.1).

The results presented have been obtained from more than 12000 simulations.

4. OBTAINED RESULTS

The initial sizing-configuration of the system has been developed based on the analysis of the demand for 20 multifamily houses. Table 1 shows the main results obtained. For the cases 1, 2 and 3 a constant demand profile has been considered, for the case 4 a variable profile demand calculated according VDI reference has been used.

Table 1. System analysis. Results for HP, HP+HE (20ºC), HP+HE (30ºC) and HP+HE+ST

System	HP	HP + HE	HP+HE	HP+HE+ST
Tsource (ºC)	20	20	30	20
Annual energy demand (kWh)	31283.2	31283.2	31283.2	31283.2
Average required heating power (kW)	3.57	3.57	3.57	3.57
Tco (ºC)	60	60	60	64
% capacity supplied by HE	0	10	30	10
COPhp	5.74	5.39	6.03	5.14
COPsys	5.71	5.95	8.5	5.2

From that analysis, it has been shown that the pre-heating heat exchanger allows an improvement of the system efficiency by up to 15% for the considered conditions, the importance of the HE increases as the water temperature of the source increases. The need for the ST is justified in order to satisfy the variable demand curve of this type of application, but it introduces a reduction in the annual system performance by 12% in the best case (variable volume tank with no stratification).
Figure 2 and Figure 3 give an example of the parametric studies performed with each demand size. In this case, a 20H load profile has been used. Figure 2 shows the annual CO_2 emissions associated with the system and Figure 3 the respective HP operating hours for the possible solutions (combinations HP-ST that meet comfort standards). The parametric studies are based on different sizes in 0.5-kW steps, but Figure 2 and Figure 3 outline only the three most representative ones: (a) the minimum HP size, (b) the optimal HP size, and (c) the maximum HP size.

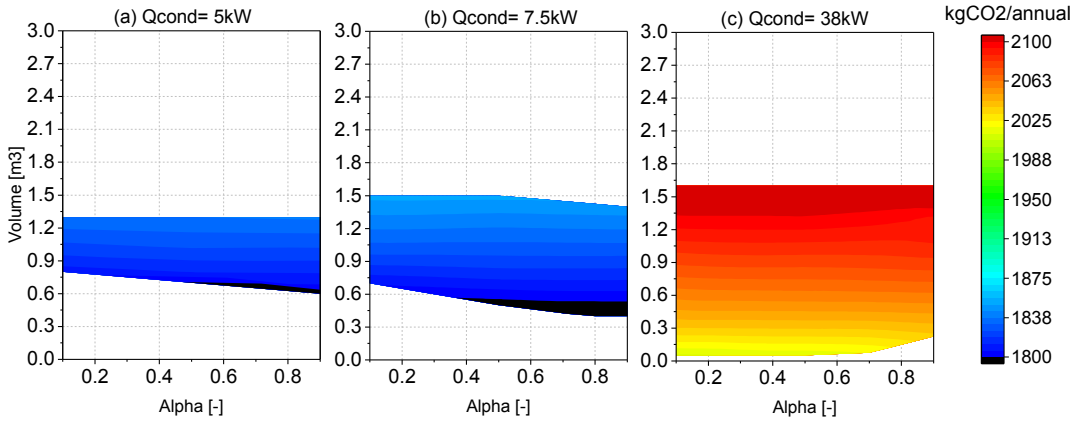

Figure 2: Annual CO2 emissions associated with the system as a function of the ST size (volume) and control level (α) for (a) the minimum HP size, (b) the optimal HP size, and (c) the maximum HP size. Only the solutions that meet the discomfort standards are represented

From Figure 2 and Figure 3, several comments can be done:

- Not all the combination sizes are possible solutions. In fact, there is a maximum ST size (depending on the HP size) capable of meeting the discomfort requirements. The region of possible solutions becomes larger as the HP size increases.

- The operating time depends mainly on the HP size. The ST size has a greater influence with small heating capacities. High volumes lead to higher operating times.
- Combinations of small HP-ST sizes lead to lower CO_2 emissions. Among the solutions, the best combinations from an energy point of view have the lowest ST size and high α but a longer operating production time.
- For a given HP size, CO_2 emissions increase linearly with the ST size.
- For a given HP size, an increase of approximately 5% from the minimum volume to the maximum volume takes place.
- Higher HP sizes lead to significantly higher CO_2 emissions (even though fewer operating hours are required). When the operating time increases from 1.5 $h \cdot day^{-1}$ to 12 $h \cdot day^{-1}$, the CO2 emissions increase by 15%.
- With high ST volumes, the control of the ST level (α) become less important. In these cases, the HP operating control is driven mainly by the ST temperature.
- With small ST volumes, the dominant control is α and it widens the solution region compared to when no control level is used, especially with small HP sizes (optimum). For instance, in (b), the minimum volume without the control level is 700 litres, while an ST tank 57% smaller (400 litres) is possible when high water level controls are applied.

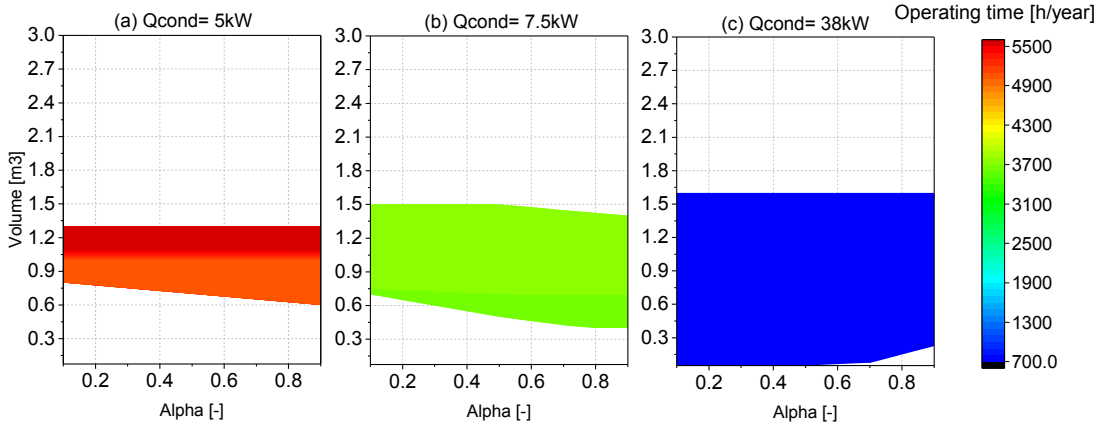

Figure 3: Annual HP operating hours function of the ST size (volume) and control level (α) for (a) the minimum HP size, (b) the optimal HP size, and (c) the maximum HP size. Only the solutions that meet the discomfort standards are represented

Similar results are obtained with other demand sizes and in all parametric simulations.
Following the approach shown in Figure 2 and Figure 3 but taking into account only the optimal control (α value), the binomial analysis of the ST-HP size is done for 10H, 20H, and 30H load demands.
Figure 4, shows the CO_2 emissions per house, for the solution maps (in terms of HP-ST size) and optimal α value for 10H, 20H, and 30H. To distinguish the influence of the demand size, the same scale has been used in each figure. Nevertheless, a magnified view of 10H has been considered in some cases.
The most remarkable conclusions from Figure 4 are:

- Higher aggregated demands lead to lower CO_2 emissions associated with each apartment.
- In all the cases, there is a small optimal region of HP-ST size combinations that lead to similar annual emissions for each demand type. The minimum emissions correspond to a line of solutions with the smallest ST and HP sizes in each case.
- For a given demand, CO_2 emissions vary by up to 20% from the optimal solution to the worst case.

Other relevant results obtained from these simulations is related to the influence of the selected demand profile. Recommending that end-users DHW demand at the most convenient moment from an energy point of view rather than on a random pattern, and “educating” them about this, could also be a solution compromised with the environment (as already happens with heating demand and other types of consumption).

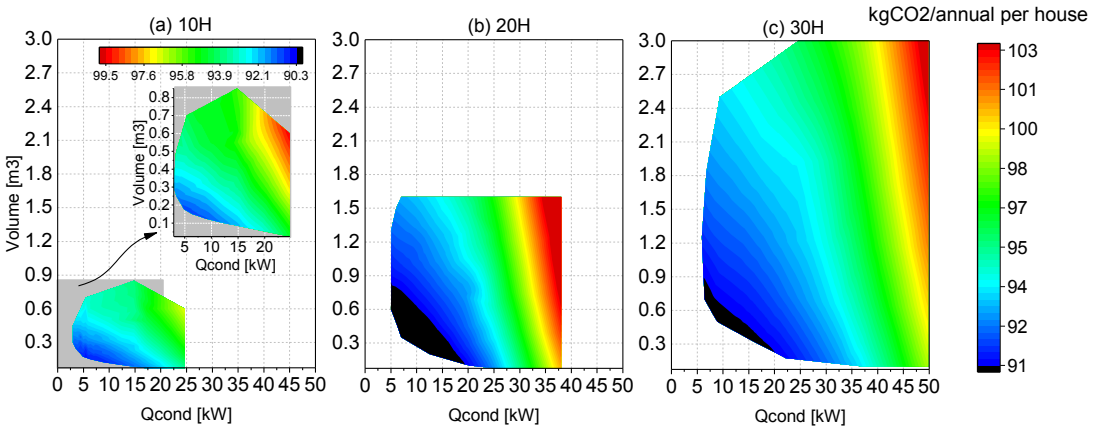

Figure 4: CO2 annual emissions per house for each HP-ST size and (a) 10H demand, (b) 20H demand, and (c) 30H demand

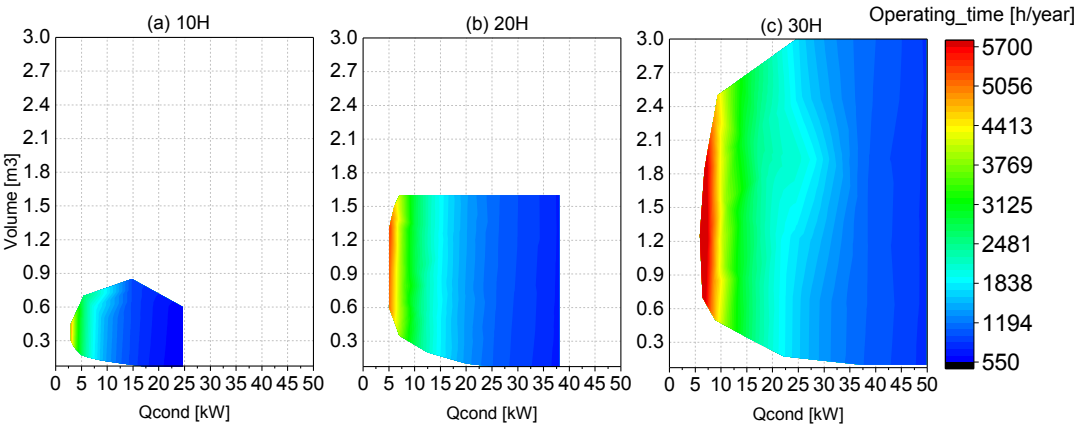

Figure 5: Annual HP operating hours for each HP-ST size and (a) 10H demand, (b) 20H demand, and (c) 30H demand

Fig. 5 shows the operating hours as a function of the hp size and tank volume for the three cases under study. According these results:

- A bigger solutions map leads to a wide range of operating times, from 1.5 h·day^{-1} to almost 16 h·day^{-1} in the 30H case, while with a smaller demand, where fewer combinations are possible, the range is from around 7 h·day^{-1} to 2 h·day^{-1}.
- Optimal solutions appear with high to medium operating time production.

Fig. 6 shows the values of the optimum α as a function of the heat pump size for several demand conditions. According that figure, the optimal solutions occur with small sizes and high values of α (0.9–0.8), which correspond to the solution in which the water is stored for the minimum time.

In fact, the smaller the ST size, the higher the value of α required to meet discomfort standards. Thereafter, medium α values lead to optimal solutions for medium ST sizes and low α values lead to the best solutions with high ST volumes.

Fig. 7 collects the optimal HP-ST sizes for each demand size and the best α values. In addition, the required annual operating hours are also represented as a function of the optimal binomial sizes. Green colour is used for 30H, blue for 20H, and orange for 10H. Dotted lines indicate the operating time and continuous lines represent ST sizes.

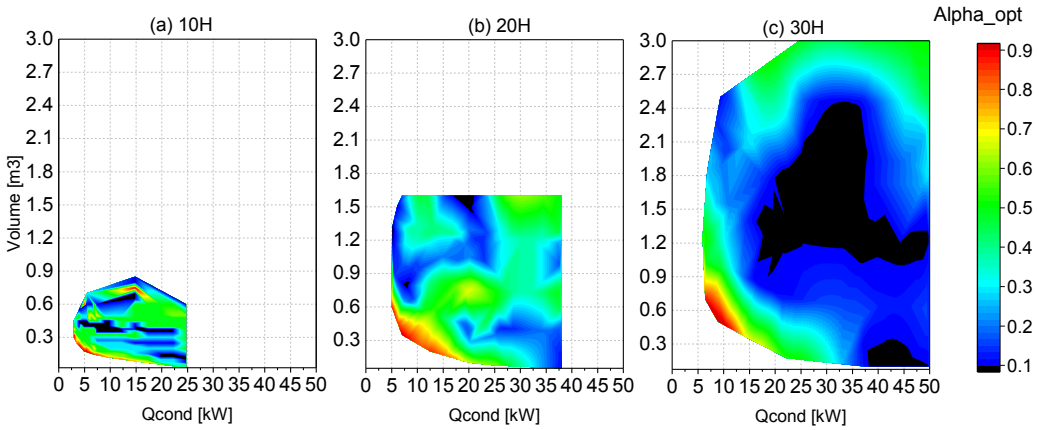

Figure 6: Optimal control level (α) values for each HP-ST size and (a) 10H demand, (b) 20H demand, and (c) 30H demand

Fig. 7 is useful for sizing an HP system for DHW production with the characteristics described in this work. According to the figure, with small HP sizes, there is a minimum ST size required, while as the HP size increases, lower ST volumes are possible. In addition, increasing the heating capacity of the HP does not always lead to lower ST volumes (due to discomfort requirements).

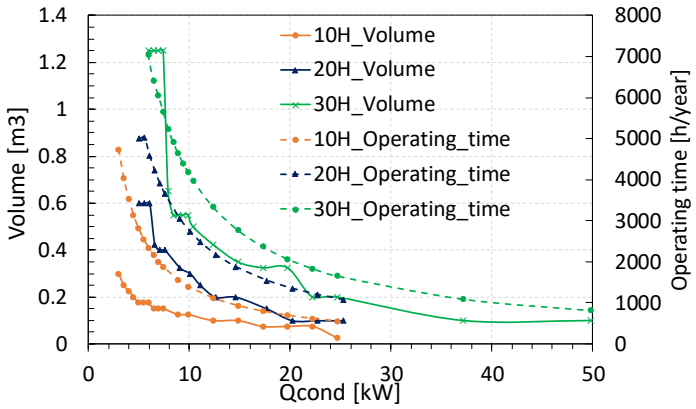

Figure7: Optimal HP-ST size combination and its associated annual operating time for demands of 10H, 20H, and 30H

Finally in order to get an order of magnitude of the performance of this system compared with other systems available in the market, table 2 shows CO2 emissions of several systems.

Table 2 Estimation of the CO2 emissions/year for several systems

HP	1803.9
HP+HE	1768.0
Gas Boiler	8568.9
Gas Boiler+ 50% Solar	4284.4

The results from the table shows the potential of using this kind of approach in order to reduce the total energy consumption in this type of system.

5. CONCLUSIONS

This work analyses a system to produce DHW from the recovery of low-grade temperature sources using HPs. The study is performed for an application based on the residential sector. The main components of the system are a pre-heating heat exchanger, an optimized HP, and a variable volume ST. DHW load profiles based on stochastic models for 10, 20, and 30 multifamily-houses

have been used in order to simulate the DHW demand profile. With these basic components, a model of the system has been developed in TRNSYS.
It should be mentioned that a unique optimal solution does not exist. A set of HP and ST size combinations with similar associated CO_2 emissions exists. In general, small sizes of both components (HP+ST) are preferred, allowing to minimize the time the water is stored.
In the literature rely on economic factors and are applicable only to specific situations. Energy-efficient solutions are not so commonly investigated even though they should be the focus in order to reduce CO_2 emissions. In addition, those types of solutions are independent of energy policies and are hence more general. From that point of view, the presented study aims to serve as a guide to the sizing of HP systems for DHW production based on the most efficient alternative. Economic factors could be used to match the energy aspects in a second step of the sizing process and can be adapted to the specific requirements.
The total savings of this kind of system has been estimated and with the proper system design and it could reach values of 4.8 times in terms of CO_2 reductions. These values have been obtained for a relatively low heat source temperature (20ºC) but the improvement could be significantly higher if the source temperature increases to 30-40ºC. It should be noted that the difference of using this kind of system with the proper design could reduce the CO_2 emissions in up to 20% compared with the same system with a non-optimized design.
Finally, the work presented aimed to find the optimal size and operation strategy of an HP-ST system in order to satisfy DHW production within the residential sector based on the minimization of the associated CO_2 emissions for a given demand profile. However, it should be pointed out that among the most influential variables in the final energy consumption of this type of system are those related to the user habits with regard to DHW use. Therefore, solutions to minimize the environmental impact associated with DHW production should take that point into account and should also imply the need for education and adoption of some habits in DHW use by the user that are environmentally friendly. From that point of view, this work has quantified the losses derived from the presence of peaks in the demand and these losses could represent up to 12% of the total energy consumption.

ACKNOWLEDGEMENTS

A short section may acknowledge special assistance, such as financial aid, help of guiding technical committees, individuals, or other groups. Part of the work presented was carried out by Estefanía Hervás Blasco with the financial support of a PhD scholarship from the Spanish government SFPI1500X074478XV0. The authors would also like to acknowledge the Spanish Ministerio de Economia y Competitividad through the project "Maximización de la Eficiencia y Minimización del Impacto Ambiental de Bombas de Calor para la Descarbonización de la Calefacción/ACS en los Edificios de Consumo Casi Nulo" with the reference ENE2017-83665-C2-1-P for the support given

REFERENCES

Energy consumption in households. http://ec.europa.eu/eurostat/statistics-explained/index.php/Energy_consumption_in_households (accessed 1 August 2018).

Pitarch, M., Navarro-Peris, E., Gonzalvez-Macia, J., Corberan, J.M., 2018. Experimental study of a heat pump with high subcooling in the condenser for sanitary hot water production. Sci. & Tech, for the Built, Env. 24(1) 105-114, 2018.

Pottker, G, Hrnjak, P., 2015. Effect of the condenser subcooling on the performance of vapor compression systems. Int, J, Refrig. 50,156–64.

VDI (Verein Deutscher Ingenieure). Referenzlastprofile von Ein-und Mehrfamilien-häusern für den Einsatz von KWK-Anlagen., 2008. Reference load profiles of single-family and multi-family houses for the use of CHP systems. VDI-Richtlinien.

Hua, K.J., Chou, S.K., Yang, W.M., 2010. Advances in heat pump systems: A review. Appl. Energy 87, 3611–24.

Hepbasli, A., Biyik, E., Ekren, O., Gunerhan, H., Araz, M., 2014. A key review of wastewater source heat pump (WWSHP) systems. Energy. Convers. Manag. 88, 700-722.

Manuscript ID: 1133
DOI: 10.18462/iir.icr.2019.1133

Performance Analysis on Developed EVI Air Source Heat Pump with Seasonal Heat Demand

Ming Jun HUANG[a], Yan Jun Dai[b], Nikhilkumar SHAH[a], Christopher WILSON[a], Neil J. HEWITT[a]

[a]Ulster University, Centre for Sustainable Technologies, Shore Road, Newtownabbey, Co. Antrim, Northern Ireland, BT370QB, UK, m.huang@ulster.ac.uk

[b]School of Mechanical Engineering, Shanghai Jiao Tong University, Shanghai, 200240, China

ABSTRACT

An optimised air source heat pumps (ASHP) using an economised vapour injection (EVI) compressor is integrated in a residential house for field trial and aimed to replace fossil-fuel boiler heating system. Due to the complex of operation strategy and ambient conditions, a good understanding of the EVI-ASHP performance under different operation conditions is essential. This study investigates and analyses the heating capacity and performance of the developed EVI ASHP in field trials for space heating and hot water supply for whole year with variable operation strategies and issues in details. The results of this study provide a solid basis for system operation improvement and scaling up applications of this kind of heat pump in the future.
Keywords: Domestic Air Source Heat Pump, COP, Field Trial, Heat Supply, Domestic Hot Water.

1. INTRODUCTION

In the UK energy use in domestic sector accounted for 29 % of the total energy consumption and 80 % of which is used for space heating and hot water (ECUK, 2017). In the European Union 14% of total energy consumption in the residential sector is for hot water production while in the UK 17% for the water heating. Retrofitting the existing domestic heating system using renewable energy sources, it could potentially reduce the energy consumption and carbon emission. Air source heat pumps (ASHP) utilise energy stored in the surrounding ambient at low temperatures and convert it to high temperature useful energy which is good practice for meeting buildings' heating demand in marine climate like UK because of high efficiency and lower cost (Hewitt et al., 2011; Chua et al., 2010). Studies have revealed that the efficiency of energy production equipment is influenced by the particular characteristics of heat consumption profile.

The ASHP using an economised vapour injection (EVI) compressor has the capability to overcome some of the difficulties of the high temperature lift operation (namely reduced heating capacity) that allows low liquid subcooling to be attained in the compression cycle while maintaining the high evaporator capacity to provide adequate heating during the cold ambient air period (Hewitt et al., 1991; Zhang et al., 2016). A research programme was developed to optimise the components and operating regime of an ASHP using the EVI compressor (Hewitt and Huang, 2008; Huang and Hewitt 2013). The results showed that the EVI-ASHP improved the heating capacity and COP by up to 23% and 5.4%, respectively under the standard test conditions in the lab.

An optimised Air source heat pumps (ASHP) using an economised vapour injection (EVI) compressor is integrated in a residential house for field trial and aimed to replace fossil-fuel boiler heating system. Due to the complex of operation strategy and ambient conditions, a good understanding of the EVI-ASHP performance under different operation conditions is essential. In is also, in order towards a more sustainable behaviour for energy and heat usage, studying the realistic energy consumption with the heat supply are necessary for optimizing the design and control operation of energy systems (Fuentes et al. 2018). Characterization of domestic heat demanding with supply performance would allow for designing innovative control strategies for heat supply systems based on consumption. This study investigates and analyses the heating capacity and performance of the developed EVI ASHP in field trials for space heating and hot water supply in a residential house in Belfast, Northern Ireland, UK for whole year with variable

operation strategies and issues in details. The results of this study provide a solid basis for system operation improvement and scaling up applications of this kind of heat pump in the future.

2. DESCRIPTION OF THE EVI ASHP HEATING SYSTEM FOR FIELD TRIAL

The operated EVI-ASHP system in the field trial has a nominal capacity of 12 kW heat (Copeland, 2016). The selected heating system retrofit house heated by the EVI ASHP is a typical UK semi-detached 3 bed-roomed family house with 105 m^2 in Carrickfergus, Northern Ireland. The household space heat distribution system and domestic hot water supply would be met by circulating pump transferring heat directly from the ASHP to the household, as shown schematically in Fig. 1. Circulating pump has a constant flow rate of 0.385 l/s. More detail description about the principle of EVI ASHP can be found in our previous work (Huang and Hewitt, 2013). The ASHP system has been operated through all year. Three particular periods have been chosen to study the performance of the ASHP aiming to have a close study on the heat supply to meet the space heating and hot water supply with variable demanding: 1) Feb/March for combined space heating and hot supply in the coldest ambient temperature period; 2) May for combined space heating and hot supply in the mild ambient period; and 3) Aug/ Sep for hot water supply only. The performance of the ASHP with energy consumption have been monitored and the data were recorded by a ΔT logger at 30 second intervals and stored for later analysis. Only the repeatable data for operating under similar ambient conditions were used for analysis.

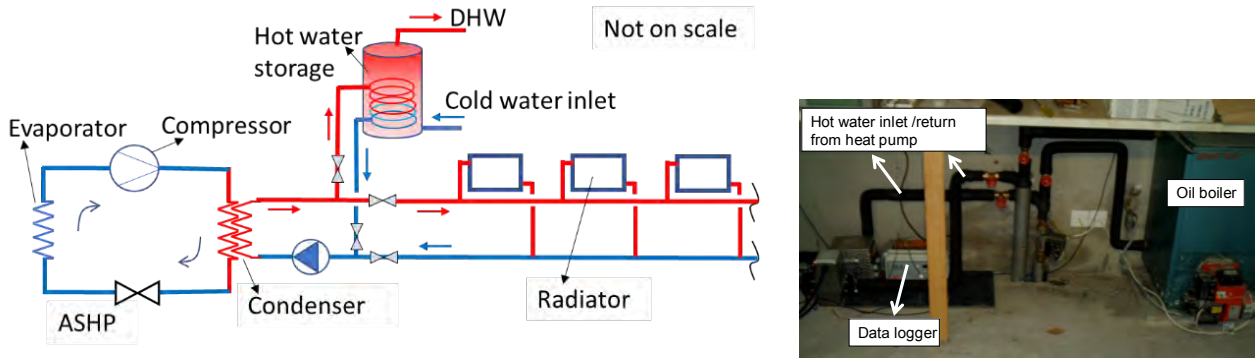

Figure 1: Schematic representation of ASHP integrated into a conventional domestic heating system

3. RESULTS AND DISCUSSIONs

3.1. EVI ASHP Performance in the Winter Operation

Fig. 2 presents the hot water inlet and return temperatures and heat supply to the household in continued 30 hours during March with an ambient temperature varies from around 0°C to 4°C. The ASHP is engaged during the early morning and late afternoon. It can be seen that the heat supply has been affected with the ambient temperature variation. The COPs are 3.42 and 3.93 respectively on the same period of the two days to reflect the influence of the ambient temperatures. More detailed temperature variations can be seen respectively in the two afternoon sessions (Fig. 3). When the ambient temperature is lower at the first day, the heating demand is higher but the supplied hot water temperature from ASHP takes longer time to reach the setting point 65/55 °C during the ramp up and on-off periods comparing to the higher ambient temperature in the second day. In order to keep the setting points with the system operation, the discharge temperature is higher and suction temperature is lower with the lower ambient temperature in the first day comparing the higher ambient temperature in the second day.

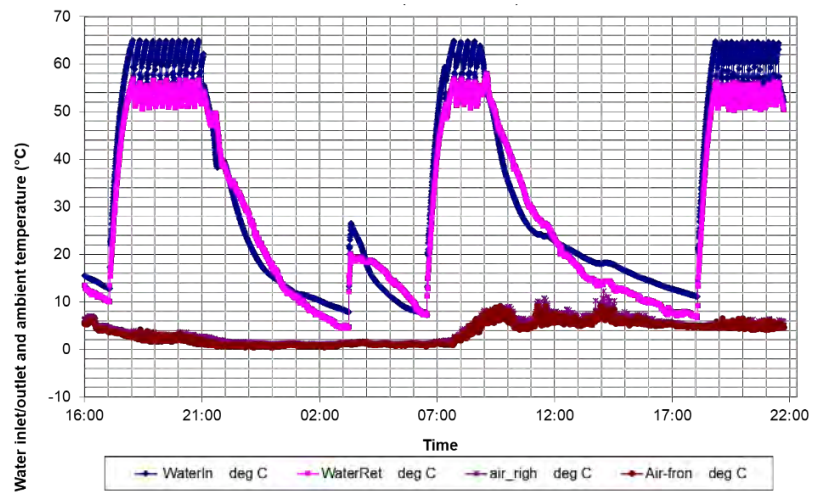

Hot water inlet / return with ambient temperature

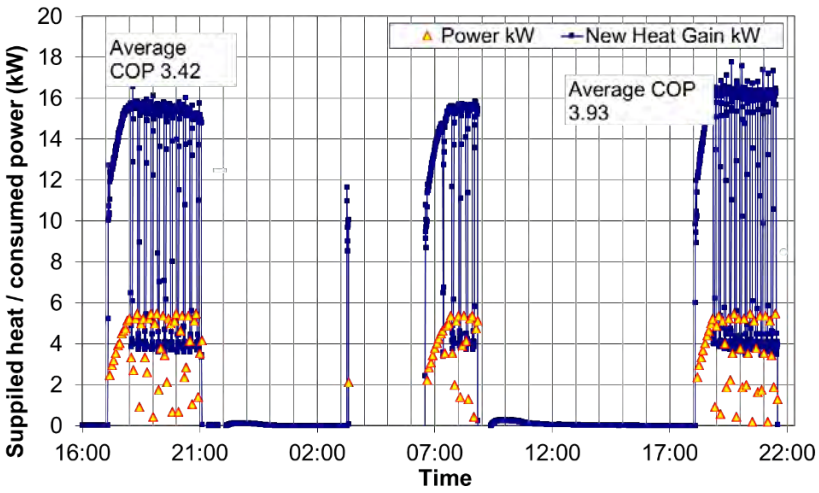

Heat supplied to the house by the ASHP

Figure 2: ASHP operated within 30 hours on March with hot water inlet/return temperatures and heat supply

3.2. Heat Supply by ASHP for Hot Water only Demand with and without Hot Water Withdraw

During summer there is no space heating demand but only for domestic hot water. The heat supplied by the ASHP is extracted by the water in the existing hot water tank with 1000 l capacity then used for hot water discharge in the household (see Fig. 1). The heat pump operated at the on-off setting points of 65/45 °C.

Comparisons of ASHP performance for the DHW supply only have been carried out with different hot water withdraw period by occupancies during charging the storage tank in Fig. 4. In order to limit the influence from other factors, the two situations are under the same ambient conditions. The blue lines with symbols represent hot water frequently withdrawn by the occupancies, by contrast, the yellow symbol lines represent a lack of water withdrawn. The ASHP performs similar on the discharge and condenser temperatures, but energies for longer time in the situation of the frequent hot water usage. The heat extracted by the hot water tank is increased when there is hot water withdraw from the hot water tank by the occupancies. It can be seen that the water withdrawn can cause an increase of heat extraction. The heat stored in the hot water tank is increased with higher COPs when there is hot water frequently withdrawn by the occupancies.

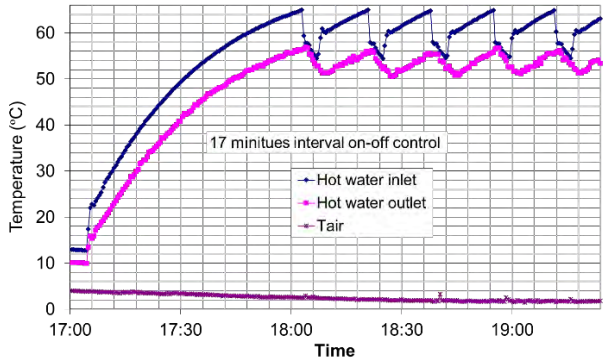

Hot water inlet/ return temp. on the First day

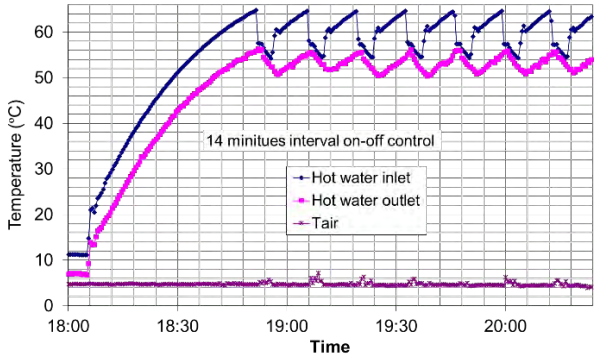

Hot water inlet/ return temp. on the Second day

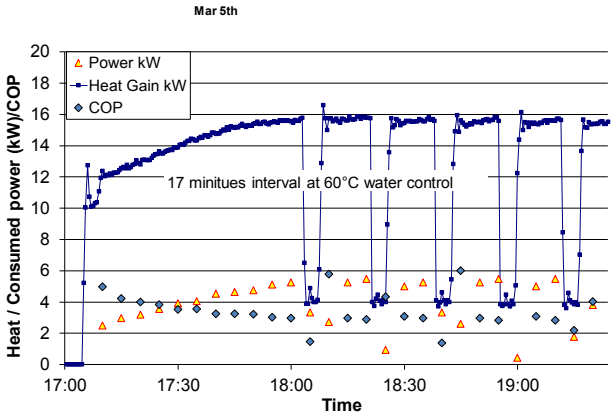

Heat /Power/COP on the First day

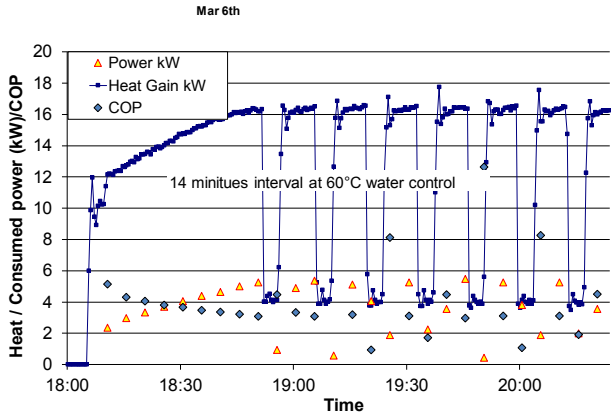

Heat /Power /COP supply on the Second day

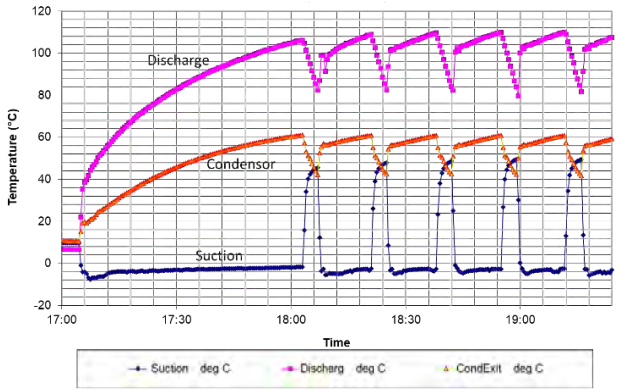

ASHP performance on the First day

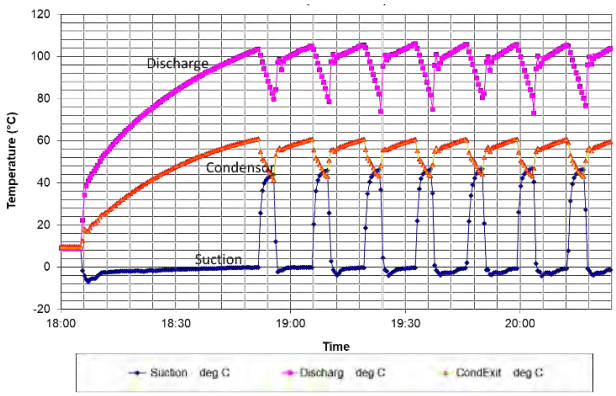

ASHP performance on the Second day

Figure 3: Detailed comparison of hot water inlet / return, heat supply to the household and ASHP performance along the cycle for the two days with respective time periods

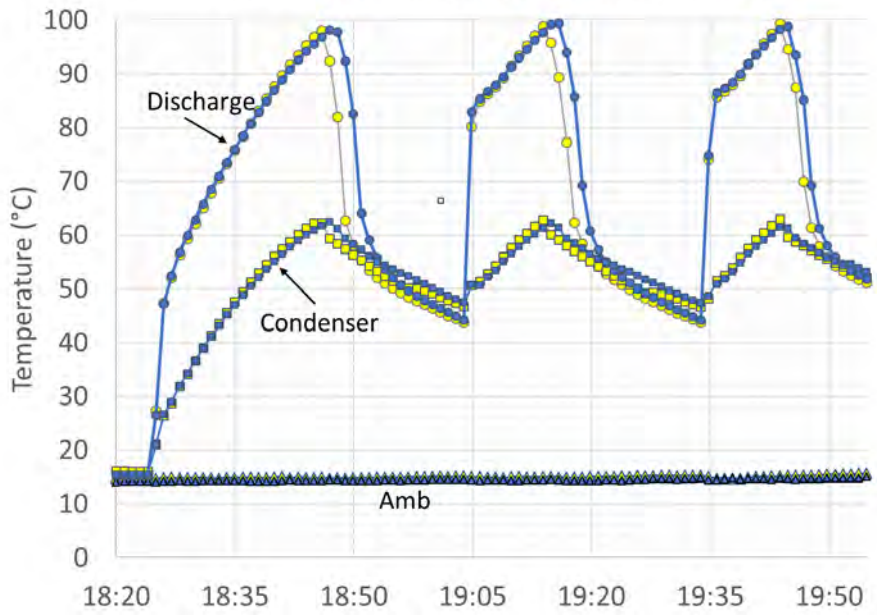

Discharge/Condenser temperature variations with same ambient temperatures

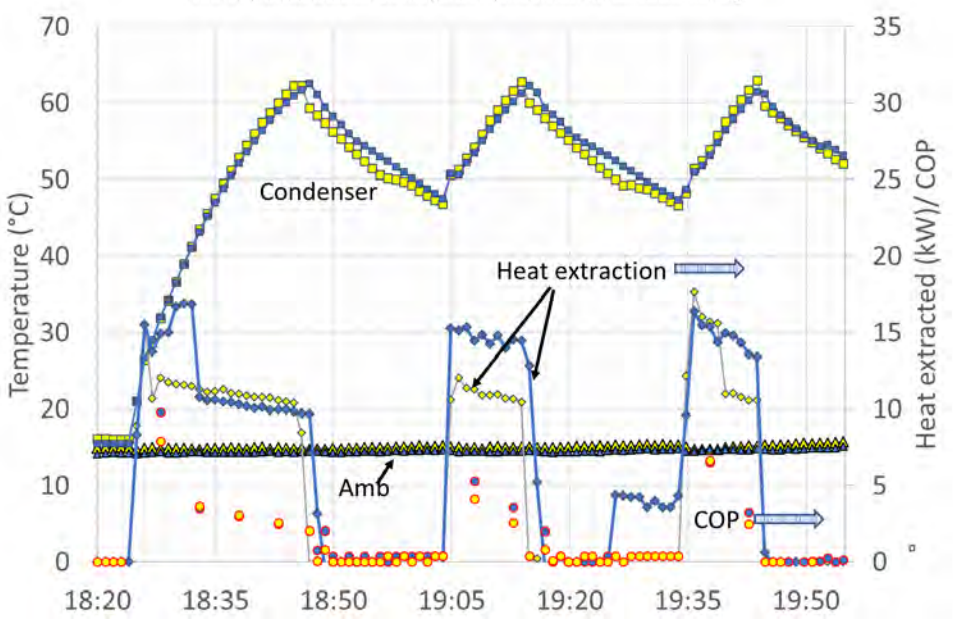

Condenser temperature variation along with heat extraction and COP during ASHP operation

Figure 4: Comparison of ASHP performance under different water discharge period for DHW supply only during summer with same ambient temperatures

3.3. Heat Supply by ASHP for Space Heating and Domestic Hot Water during Winter Period

During winter period the heat supplied by the ASHP is used for the house space heating and hot water withdraw (Fig. 1). The effect of ambient temperature to the performance of ASHP has been studied on the period in February. Fig. 5 represents the performance of the ASHP at the ambient temperatures at around 3 and 6 ℃. The AHSP is operated at the setting point of 60/40 ℃. The periods of the ramp up and on-off cycle are shorter while the discharge temperature is lower with higher heat extraction for the household when the ambient temperature is at 6 ℃ than at 3 ℃. Meanwhile the temperature rising rates are higher for the discharge and condenser temperatures at 6 ℃ than at 3 ℃.

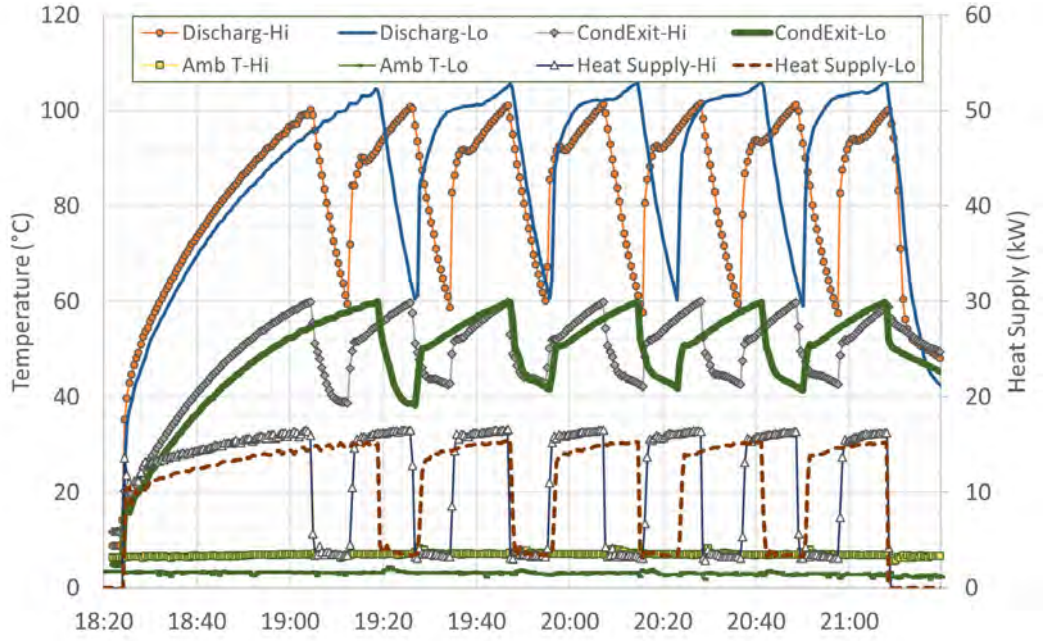

Figure 5: Ambient temperature influence onto the ASHP performance during winter operation between 3 and 6 ℃

3.4. Heat Supply by ASHP for Space Heating and Domestic Hot Water during Mild Period

Ramp up has some influence, but during on-off cycle, there is no significant difference.

The EVI ASHP performance during mild period of the year has been presented and compared with different ambient temperatures in Fig. 6. The hot water inlet temperature rising is quicker in the higher ambient temperature than in the lower ambient temperature. During off cycle period the heat is still extracted from the water. The heat extracted by the space heating system and hot water tank from the supplied hot water reaches to around 12 kW during the engaged period for both of the ambient temperatures at around 9C and 14 ℃. During the off cycle the circuit pump is still running and the heat extracted for space heating system can be seen at around 3kW. The heat extraction is a bit higher for the low ambient temperature situation than the high ambient temperature situation, but there is no significant difference with the ambient temperature at 9 ℃ and 14 ℃. However the discharge temperature in the vapor compression cycle is higher above 3 ℃ when the ambient temperature difference is 5 ℃.

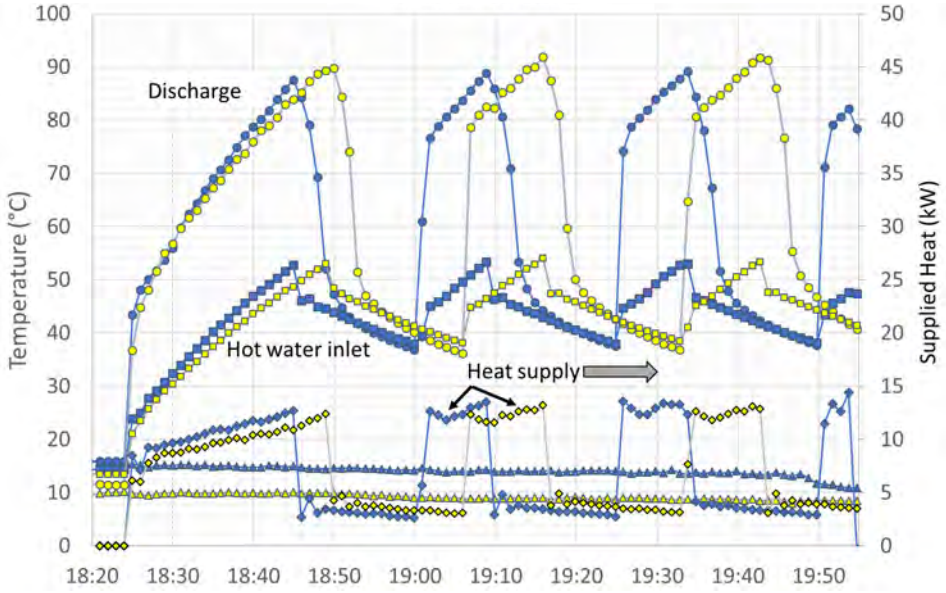

Figure 6: The performance of EVI ASHP for space heating and domestic hot water during mild period

3.5. Performance Comparison of the ASHP for Combined Space Heating and Domestic Hot Water and for Hot Water only

The hot water supplied by the heat pump is delivered to the house to meet the heat demand with constant water circuit pump. The performance of the ASHP with the supplied heat for hot water only and for the combined hot water and space heating with the heat pump operation setting points at 65/45 ℃ are analysed. The system under the ambient temperatures at 7°C and 3°C are selected to reflect the two cases respectively. The hot water inlet and outlet and heat supplied by the ASHP with ambient temperatures are presented in the Fig. 7. From the figure it can be seen that during the cold ambient temperature at around 3 ℃, the heat delivered by the ASHP to the house used for hot water and space heating is higher than the warm ambient temperature at around 7 ℃. The temperature ramp up rate of the water inlet is lower with the ambient temperature at 3 ℃ than at 7 ℃, i.e it takes longer time for the inlet water reaching the set point of 65 ℃ during the ramp up and on-off cycle. The inlet water temperature rising ratio keeps lower during the on-off cycle with the high heat demanding situation than for the low heat demanding which is only for hot water supply.

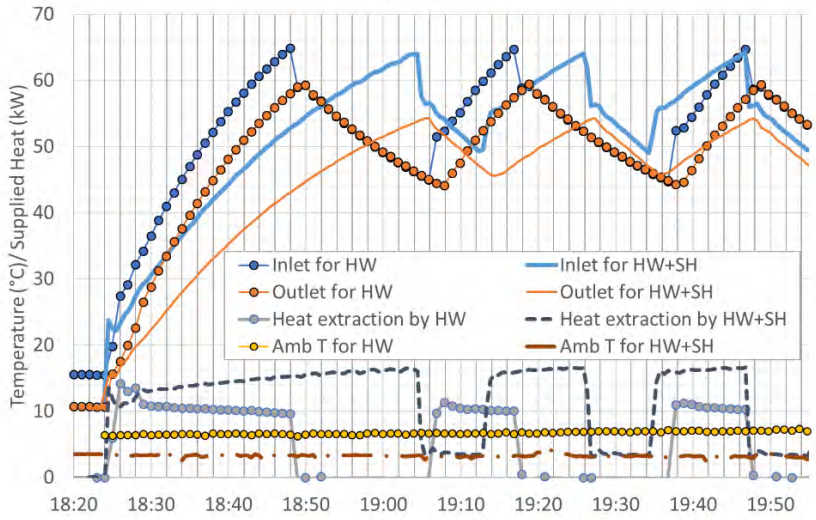

Figure 7: The comparisons of ASHP performance with the hot water supply only and combined hot water and space heating supply with 65/45 ℃ setting points

4. CONCLUSIONS

A laboratory evaluated EVI ASHP system has been integrated into a typical UK residential house for field trials. The issues and performance of the system on variable ambient conditions and operation conditions have been analysed and discussed in detail. The performance of the EVI ASHP with the heat demanding by the space heating and hot water have been analysed. It is expecting that these information can provide support information to optimise the system operation in the future. It has shown that such an EVI ASHP unit is capable of heating a typical N. Ireland family home and contributes the carbon emission reduction in the building sector, although more data from field trials needs to be collected to consolidate the optimised operation strategies.

ACKNOWLEDGEMENTS

The authors would like to acknowledge the support of EPSRC i-STUTE, EPSRC Lot-NET, H2020 CHESTER and INTERREG VA SPIRE 2.

REFERENCES

Chua KJ, Chou SK, Yang WM., 2010. Advances in heat pump systems: a review. Applied Energy, 87, pp. 3611-24.

Copeland, (2016), http://www.emersonclimate.eu/products.cfm, access in 2016.

ECUK, 2017, https://www.gov.uk/government/statistics/energy-chapter-1-digest-of-united-kingdom-energy-statistics-dukes.

Hewitt, N.J., McMullan J. T.,Murphy, N. E., 1991. Development of an alternative refrigeration cycle. Int J. Energy Research, Wileys, Chichester, Vol 15 (9), pp. 731-745.

Hewitt N.J. Huang M.J., 2008. Defrost cycle performance for a circular shape evaporator air source heat pump. Int. J. Refrigeration 31(3) 444-452.

Hewitt, N.J., Huang, M.J., Anderson, M., Quinn, M., 2011. Advanced air source heat pumps for UK and European domestic buildings, Applied Thermal Engineering 31,3713-3719, http://dx.doi.org/10.1016/j.applthermaleng.2011.02.005.

Huang, M.J. Hewitt, N.J., 2013. The experimental analysis of the effect of ambient factors on the defrosting of economised vapour injection compressor air source heat pump in marine climates. Int. J. Refrigeration 36, 820-827.

Fuentes, E., Arce, L., Salom J., 2018. A review of domestic hot water consumption profiles for application in systems and buildings energy performance analysis. Renewable and Sustainable Energy Reviews 81, 1530-1547.

Zhang, D., Li, J., Nan, J., Wang, L., 2016. Thermal performance prediction and analysis on the economized vapor injection air-source heat pump in cold climate region of China, Sustain. Energy Technol. Assess. 18, 127-133.

Manuscript ID: 1158
DOI: 10.18462/iir.icr.2019.1158

A field study on frosting suppression for air source heat pumps by adjusting operation strategies of multi-parallel compressors

Shi M. LIANG [a,b], Shi Q. Zhang [d], Wei WANG [a,c], Yu Y. SUN [a,c], Yi M. CUI [a,c], Zhao Y. LI [a,c], Shi M. DENG [e,a]

[a] Department of Building Environment and Facility Engineering, College of Architecture and Civil Engineering, Beijing University of Technology, Beijing,100124, China, mrwangwei@bjut.edu.cn

[b] Department of Management Engineering, Qingdao University of Technology, Linyi, 276000, China, liangshimin@emails.bjut.edu.cn

[c] Beijing Key Laboratory of Green Built Environment and Energy Efficient Technology, Beijing University of Technology, Beijing, 100124,China, mrwangwei@bjut.edu.cn

[d] The State Key Laboratory of Air-conditioning Equipment and System Energy Conservation, Zhuhai, 519707, China, newlife0427@163.com

[e] Department of Building Services Engineering, The Hong Kong Polytechnic University, Kowloon, Hong Kong SAR, China, besmd@polyu.edu.hk

ABSTRACT

Frosting is an unavoidable problem for air source heat pumps, especially in high humidity environment. It is necessary to develop efficient method for frosting suppression as well as defrosting. In this study, frosting suppression was achieved by adjusting the operation strategies of multi-parallel compressors. Field tests were conducted in Guiyang, China, where the average relative humidity in winter is over 80%. Two ASHP units with four fixed-speed compressors were chosen as comparing samples. Two operation strategies were compared for the frosting suppression performances of the units at part load. Test results shown that operation strategies can significantly affect the frosting suppression performance of the ASHPs. By optimizing the operation strategies, the frosting rate and the frosting-defrosting loss efficiency decreased by 38 % ~ 39 % and 31 % ~ 34 % thus leading to the heating efficiency and COP improving about 14 % ~ 22 % and 5 % ~ 14 %, respectively.
Keywords: Air Source Heat Pump, Frosting Suppression, Operation Strategy, Multi-Parallel Compressors.

1. INTRODUCTION

Air source heat pumps (ASHPs) have been widely used in buildings for space heating, due to their advantages of energy-saving and environmental protection in many parts of world. The European Union, Japan and China have successively identified ASHPs as a renewable energy technology. Recently, China has been promoting clean energy heating in an all-around way to reduce air pollution as a result of using coal for winter heating. With a series of related policies supported by Chinese government, such as “the Northern Area Winter Clean Energy Heating Plan 2017-21” issued in 2017, ASHPs has become the main utilization technology in clean energy heating projects and its application scale was further promoted. According to statistics, there were more than 1 million ASHP units have been applied to replace coal-fired home heating stoves from 2016 to 2018 in Beijing, and the total annual sales of ASHP units grow up to 2.9 million for Chinese manufactures in 2017, representing an increase of 43.7% from that in 2016 (Wang et al., 2019). It is expected that the Chinese ASHP market will continue to grow at a yearly increasing rate of more than 20 % over the next five years (Li, 2018).

When a space heating ASHP unit is operated in an ambient air with high humidity, frosting of its outdoor coil can be accumulated, as the temperature of the outdoor coil surface is both below a temperature of water freezing and ambient air dew point. Frosting blocks air flow passage of an outdoor coil of an ASHP unit, leading to the output heating capacity and coefficient of performance (*COP*) decreased by 30% ~ 60 % (Wang et al., 2013) and even its shutting down or damage (Li et al., 2014). Therefore, it is necessary to alleviate the negative effects of frosting and improve operating performances of frosting-defrosting cycles for an ASHP unit during its space heating operation.

Frosting suppression is a passive way to retard or suppress the frost growth on the ASHP, which is very helpful to improve frosting-defrosting performances of ASHP. Currently, a number of scholars have made extensive meaningful exploration on frosting suppression. These measures may be summarized as follows:

(1) Pretreating the inlet air. Some researchers tried to prevent frosting by using air pretreatment systems to dehumidify (Zhang et al., 2012) or heat the air before entering the outdoor coil of an ASHP unit (Wang et al., 2015). However, these measures of changing ambient air parameters were usually complex at high initial costs, and additional installation spaces were required. Furthermore, additional energy was also required to regenerate desiccant or to preheat inlet air. Consequently, this measure has not been widely used.

(2) Modifying surface properties. With respect to the former, studies on surface treatment using both hydrophilic and hydrophobic coatings have been extensively reported (Okoroafor et al., 2000; Wang et al., 2018). However, both hydrophilic and hydrophobic coatings have their own problems such as short service life, weak surface strength, poor durability, complex manufacturing process with high cost, etc. Therefore, while surface treatment is believed to be promising in suppressing frosting in the near future, and there are actually extensive related research activities going on, their current applications are limited.

(3) Employing additional external means**.** These external means would include ultrasonic vibration techniques (Wang et al., 2012), or to impose electrical and magnetic fields (Wang et al. 2004; Zhao et al. 2015). However, in practice, the use of ultrasonic vibration was of high initial and running costs, inconvenient with complex control, and the mechanism of applying electrical and magnetic fields to suppressing frosting was not adequately understood.

(4) Supplying heat for refrigerant in evaporator. The approaches were achieved by employing a heating accumulator to heat the refrigerant directly (Mei et al., 2002) or adding a hot gas bypass to inject a portion of the high temperature refrigerant into the evaporator (Byun et al., 2008). However, the improvement of frosting suppression is at the expense of additional energy or inherent output heating capacity, these approaches are also not used in practice as ideal options.

As a result, in practice, there have been few of the above studies that can be applied efficiently. Therefore, to further explore the efficient way of frosting suppression for ASHPS, a field study on frosting suppression for ASHPs by adjusting operation strategies of ASHP with multi-parallel compressors has been carried out and the study results are presented in this paper. The organization of the paper is as follows. Firstly, a detailed description of the field tests covering field meteorological condition, field ASHP unit, operation strategies and test cases, data reduction and instrumentations is presented. This is followed by reporting the field study results and their related discussion. Finally, a conclusion is given.

2. FIELD TEST

2.1 Environmental Condition

A field test was carried out in an office building in Guiyang. The city located in the typical mild and humid regions in China. The average ambient temperature (T_a) and relative humidity (*RH*) were 4.5 ^oC and 80 % during heating seasons, respectively. The ambient temperature was moderate, especially suitable for ASHP at heating mode. However, due to the high humidity in the region, frosting is a major problem for ASHPs operating in heating seasons. As shown in Fig.1, the meteorological parameters of typical annual during heating season in Guiyang were presented in the frosting map (Zhu et al., 2015). It indicated that most operating conditions for ASHPs distributed at the severe frosting zone, and the proportion of operating conditions at the severe frosting zone accounted for 76% of that at the total frosting zone. Therefore, severe frosting will occur on the

surfaces of outdoor coils for the ASHPs operating under these conditions, and the operating performances will be deteriorated seriously without an efficient way to reduce the negative effects of frosting.

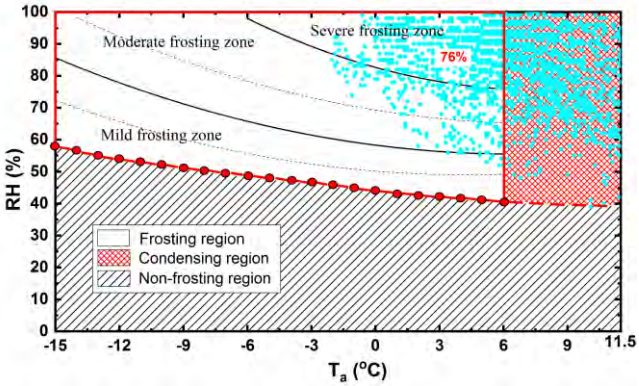

Figure 1: Meteorological parameters of Guiyang shown in the frosting map

2.2 Test Units and Instruments

To study the effect of the operation strategies on frosting suppression performances for the ASHPs with multiple compressors, two commercial ASHP units with same heating capacity were designed to supply heat for the building, which also had same configuration. The nominal input power and output heating capacity of each field ASHP unit were 15.7 kW and 54 kW, respectively. The nominal air flow rate of its outdoor axial fan was 21200 m^3 h^{-1}. The schematic of one field ASHP unit and photograph of the field ASHP units were presented in Fig. 2. Each field ASHP unit was configured with four fixed-speed compressors, two outdoor axial fan and two outdoor coils, which were equally distributed in two independent refrigerant loops. Each refrigerant loop owned two parallel compressors, one outdoor coil. The outdoor coils of each loop gained thermal energy from environment by convection of independent fans, and exchanged thermal energy by a coupled indoor coil with a water loop for the building simultaneously. Before the test, the operations of the two ASHP units were confirmed as normal and refrigerant charge volumes were same. During all tests, the field ASHP units started and stopped at the same time under same environment, and the return water temperature of the two ASHP units was setup at 40 ºC.

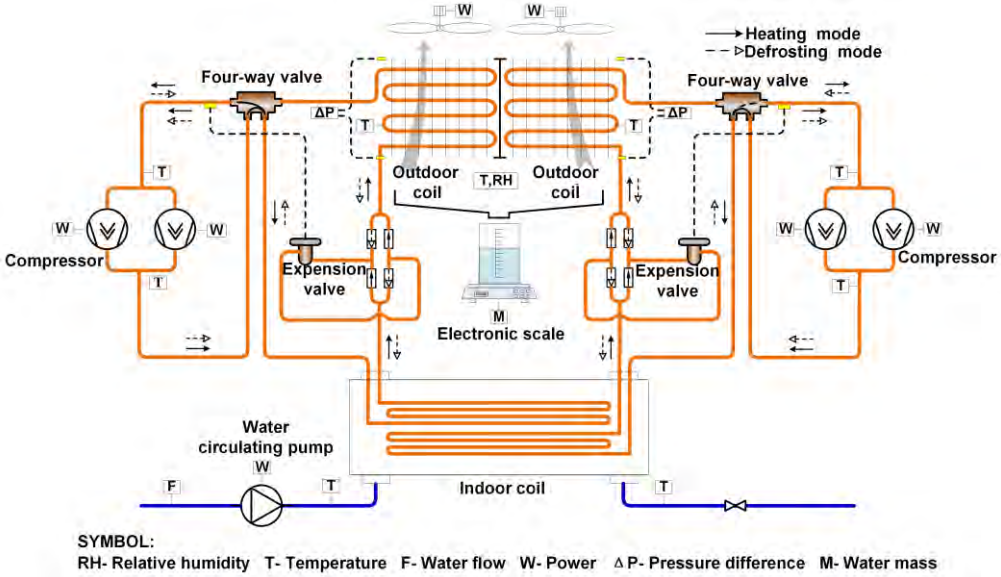

Figure 2: Schematics of the field ASHP unit

To compare the performances of the two ASHP units, a number of operating parameters of the two ASHP units were monitored during the field test, mainly including the T_a and RH, the T_{coil}, the compressor discharge and suction temperatures, the air side pressure drop across the outdoor coil, the supply and return water temperatures, the mass flow rate of water, the mass of melted frost collected in a frosting–defrosting cycle, the input power to the compressors, water pump and fans of

the field ASHP units. The installation positions of sensors were as shown in Figure 2. In addition, photographs of frosting on the outdoor coil surfaces of the two ASHP units were also taken to observe the frosting status of the outdoor coil surface. An automatic data acquisition system was used, with the monitoring devices/sensors detailed in Table 1.

Table 1. Information on the monitoring devices

Device	Number	Accuracy	Full scale
Temperature sensor	16	±0.15 ºC	−40 ~ 140 ºC
Temperature/humidity sensor	1	±0.15 ºC / ±5 %	−20 ~ 70 ºC / 0 ~ 100 %
Air Pressure difference	4	±1 Pa	0 ~ 100 Pa
Power meter	5	±1.0 %	--
Water flow meter	2	±0.5 %	0.5 ~ 10 $m^3 h^{-1}$
Video camera	2	--	15 megapixels
Electronic scale	2	±0.1 g	0 ~ 60 kg

2.3. Operation Strategies

For an ASHP unit equipped with multi-parallel compressors operating in different refrigerant loops, the number of operating compressors could be adjusted to adapt to the variation of the building requirements. Meanwhile, in case of the same number of operating compressors for the ASHP unit, by making the utmost use of the configured outdoor coils, the decrease of the heat transfer temperature difference (ΔT) could be achieved (Wang et al., 2006). According to the previous research results of Zhu et al., (2015), decreasing the heat transfer temperature difference (ΔT) was an efficiently way for suppression or retardation of frosting. Therefore, for the ASHP unit operating at part load, the optimization of operation strategies by changing the combinations of compressors, fans and outdoor coils could achieve the suppression or retardation of frosting under the frosting condition, thus resulting in the improvement of operating performances.

As shown in Fig. 3, there are two operation strategies for the test units operating in part load conditions. One is traditional strategy (S_1), in which only one refrigerant loop put into operating with two parallelly connected compressors. While, the other refrigerant loop shuts down. In the other strategy (S_2), two refrigerant loops were all put into operating, and for each loop only one compressor is operating. By contrast, the total air flow rate and the heat exchange area of the outdoor coils for the unit operating in S_2 were enlarged. This may cause the decrease of ΔT and the improvement of the output heating capacity. Therefore, it will be very helpful for frosting suppression and the improvement of the unit's performances operating in S_2.

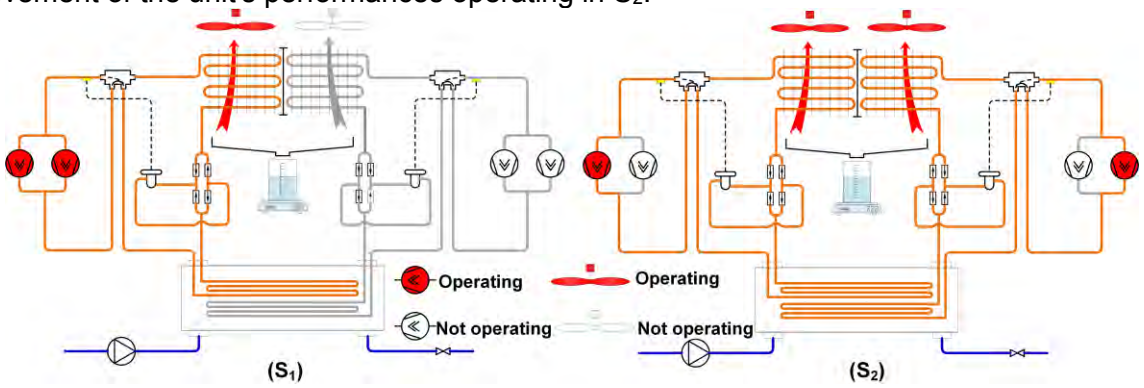

Figure 3: Operation strategies of the field ASHP units

2.4. Test Cases

To investigate the advantage of frosting suppression for the field ASHP unit operating in S_2, two test cases located in different frosting zones of frosting map (Zhu et al., 2015) were designed in this field study. The first case (Case 1) was located in severe frosting zone in frosting map, in which the average T_a and RH were about 1.92 °C and 87.66 %, and the second case (Case 2) was located in moderate frosting zone in frosting map, in which the average T_a and RH were about -1.46 °C and 69.87%. The details of the cases are shown in Table 2.

Table 2. Operating conditions of the field ASHP units

Case No.	T_a （°C）		RH （%）	
	Range	Average	Range	Average
1	1.79~2.22	1.92	86.11~88.7	87.66
2	-1.61~-1.06	-1.46	66.42~73.14	69.87

2.5. Data Reduction

According to Li et al., (2014) and Bai et al., (2018), the frosting-defrosting loss coefficient ε_L, heating efficiency η, and *COP* can be evaluated as follows:

$$\varepsilon_L = \frac{\Delta Q_{L1} + \Delta Q_{L2}}{Q_{NF}} \quad \text{Eq. (1)}$$

$$\eta = \frac{Q_{DF}}{Q_{NF}} \quad \text{Eq. (2)}$$

$$COP = \frac{Q_{DF}}{\int_0^t W dt} \quad \text{Eq. (3)}$$

Where ΔQ_{L1} is the heating energy loss during a frosting period, ΔQ_{L2} is heating energy loss during a defrosting period, Q_{NF} is the total heating energy gained in the same cycle with no frost, Q_{DF} is the effective heating energy during a frosting-defrosting cycle, t is the operating duration (min) of the ASHP units including the frosting-defrosting cycles, W is the instantaneous input power (kW) of the ASHP unit.

Moreover, the frosting rate v_f is used to describe the degree of frosting during the heating cycle. It is calculated as follows:

$$v_f = \frac{M_{dfw}}{t_{hc} \times A_{coil}} \quad \text{Eq. (4)}$$

Where M_{dfw} is the mass of melted frost collected in a frosting–defrosting cycle, A_{coil} is the heat transfer area of the outdoor coil.

3 TEST RESULTS AND DISCUSSION

Figure 5 shows the test results of Case 1. As seen from Fig. 5-1a, the T_a and *RH* is also relatively stable, which ranged from 1.79 °C to 2.22 °C, 86.11 % to 88.70 %, respectively. Moreover, the operating duration of the field ASHP units in this case is 195 min.

In Figure. 5-1, typical operating parameters, including air side pressure drop across the outdoor coil (ΔP), compressor discharge temperature (T_{dis}), compressor suction temperature (T_{suc}), ΔT, output heating capacity (q) and *COP*, are compared in S_1 and S_2. Figure. 5-1b shows the comparison of ΔP. The ΔP was increased by 28.95 Pa ~ 31.4 Pa and 10.57 Pa ~ 12.1 Pa, and the average increase rate of ΔP was achieved about 0.74 Pa/min and 0.21 Pa/min, respectively. It suggested that slower accumulation rate and lower frosting degree on outdoor coil surfaces were achieved in S_2 compared to that in S_1 thus achieving the improvement of operating conditions and performances. As seen from Figure. 5-1c, the increase of $T_{dis(S1)}$ was 38.6 ºC ~ 51.8 ºC, and that of $T_{dis(S2)}$ was 20.7 ºC ~ 25.1 ºC. Correspondingly, the decrease of $T_{suc(S1)}$ was 18.9 ºC ~ 20.7 ºC, and that of $T_{suc(S2)}$ was 7.1 ºC ~ 8.7 ºC. The field ASHP unit in S_2 led to a lower T_{dis} and a higher T_{suc} compared to that in S_1. The ΔT of the field ASHP units is shown in Figure. 5-1d. When the field ASHP units were operated in S_1 and S_2, the key parameter ΔT indicating the frosting degree was monitored. Results show $\Delta T_{(S1)}$ and $\Delta T_{(S2)}$ increased by 17.24 ºC ~ 17.79 ºC, 3.8 ºC ~ 4.1 ºC, respectively. The field ASHP unit in S_2 led to a lower ΔT compared to that in S_1. In addition, Figure. 5-1e and f presents the q and *COP*. The q and *COP* of the field ASHP unit in S_2 were higher than that in S_1. The q_{ave} was increased by 15 % from 23.5 kW to 27 kW, while the COP_{ave} was increased by 14 % from 3.15 to 3.6. Meanwhile the average input power in S_1 and S_2 can be calculated, which was the same reaching 7.5 kW.

Images of the outdoor coil surface, frosting rate (v_f), frosting-defrosting cycles (t), heating efficiency (η), and the frosting-defrosting loss frosting-defrosting loss coefficient (ε_L) are shown in Figure 5-2. It is clear that the degree of frosting on outdoor coil surfaces in S_2 is much less than that in S_1 shown in Figure. 5-2a. Fig. 5-2b and c show that the average frosting rate (v_{f_ave}) in S_2 was decreased by

39% from 0.95 g m^{-2} min^{-1} to 0.58 g m^{-2} min^{-1} compared to that in S_1, while the average frosting-defrosting cycle was prolonged from 49 min to 63.7 min. Furthermore, Figure. 5-2d and e present

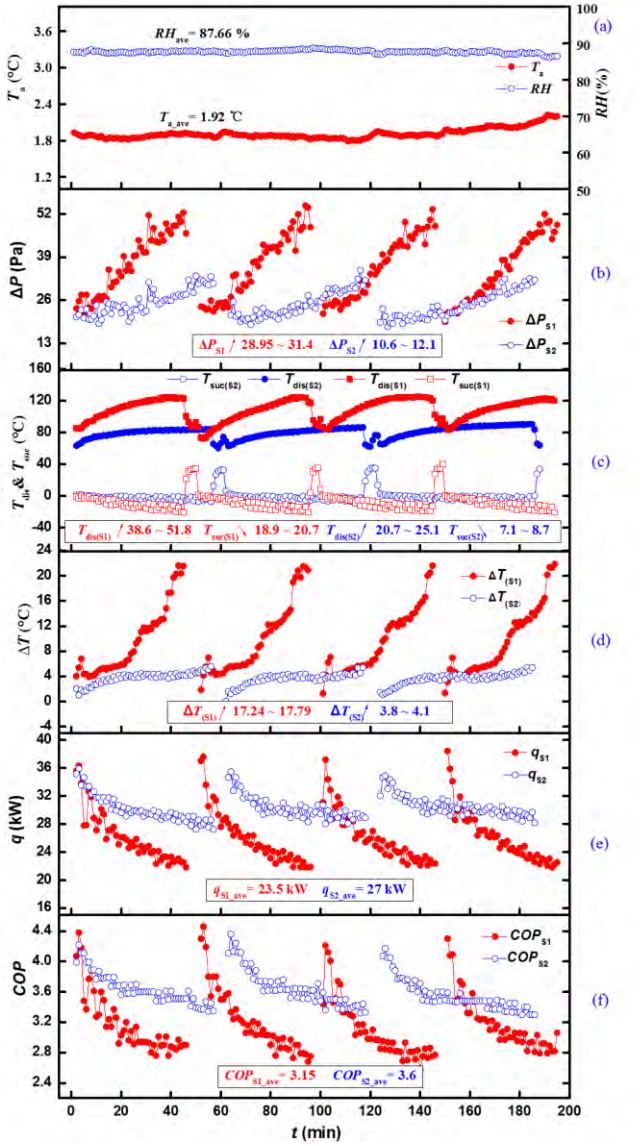

1) T_a, RH, ΔP, T_{dis}, T_{suc}, ΔT, q and COP

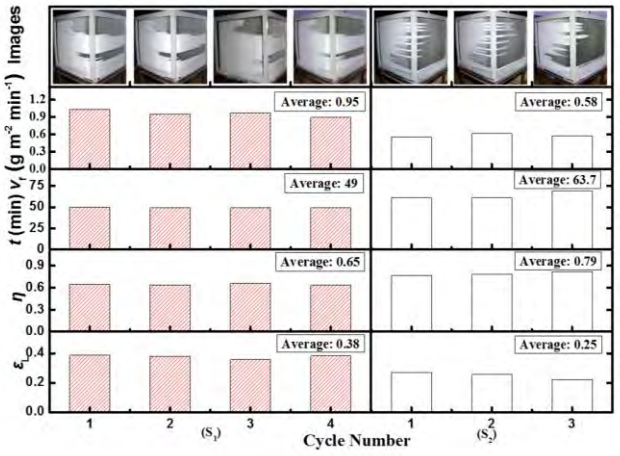

2) Images, v_f, t, η and ε_L

Figure 5: Test results of the field ASHP units in Case 1

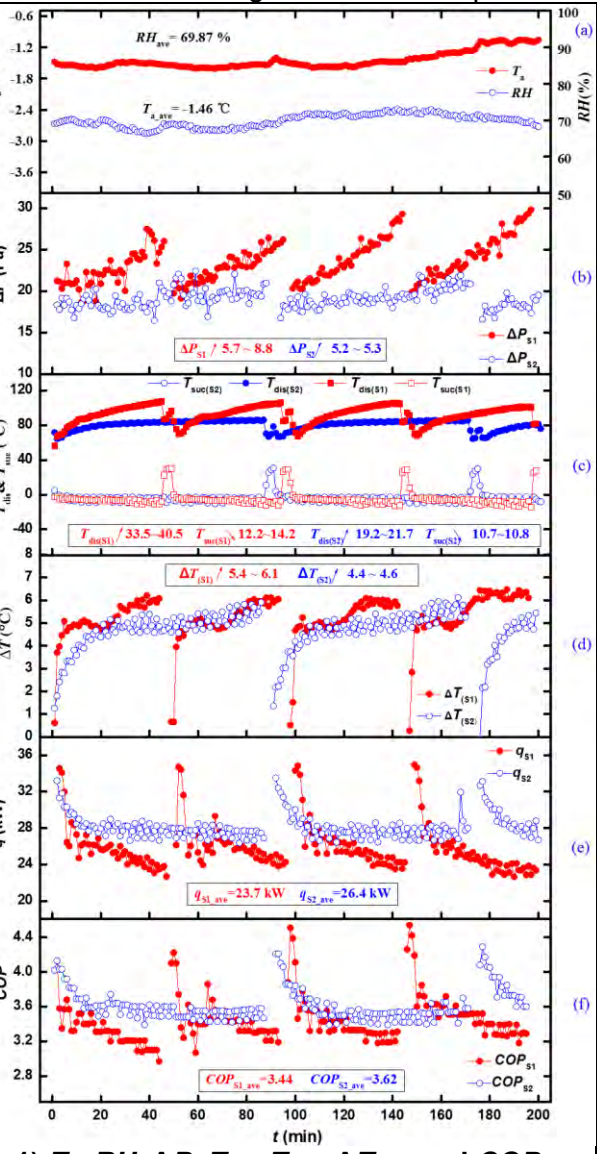

1) T_a, RH, ΔP, T_{dis}, T_{suc}, ΔT, q and COP

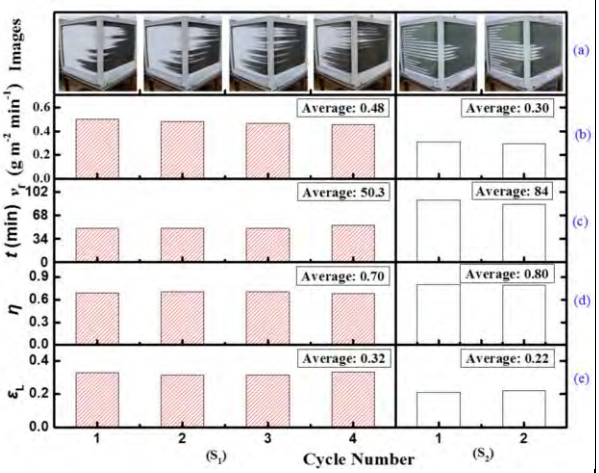

2) Images, v_f, t, η and ε_L

Figure 6: Test results of the field ASHP units in Case 2

that the field ASHP unit in S_2 leads to a higher η and a lower ε_L compared to that in S_1. The average heating efficiency (η_{ave}) was increased by 22 % from 0.65 to 0.79. The average frosting-defrosting loss efficiency (ε_{L_ave}) was decreased by 34 % from 0.38 to 0.25.

Figure. 6 shows the test results of Case 2. As seen from Figure. 6-1a, the T_a and RH is also relatively stable, which ranged from -1.61 °C to -1.06 °C, 66.42 % to 73.14 %, respectively. Moreover, the operating duration of the field ASHP units in this case is 200 min.

The detailed comparison of the operating parameters in S_1 and S_2, including ΔP, T_{dis}, T_{suc}, ΔT, q and COP, are shown in Figure 6-1. With the same analysis as the former, the $\Delta P_{(S1)}$ and $\Delta P_{(S2)}$ increased by 5.72 Pa ~ 8.79 Pa and 3.16 Pa ~ 4.12 Pa, and the average increase rate of ΔP was achieved about 0.14 Pa/min and 0.04 Pa/min, respectively. The results suggested that the frosting degree on the two coil surfaces was not severe in this case. However, better operating conditions and performances of the field ASHP units in S_2 were still achieved. As shown in Figure 6-1b to d, the field ASHP unit in S_2 led to a higher T_{suc} and a lower T_{dis}, ΔT compared to that in S_1. Meanwhile, the q_{ave} of the field ASHP unit in S_2 was increased by 11 % compared to that in S_1, while the COP_{ave} was increased by 5 %. The average input power in S_1 and S_2 was basically the same. Images of the outdoor coil surface, v_f, t, η and ε_L are shown in Figure 6-2. It is clear that the degree of frosting on outdoor coil surfaces in S_2 is lower than in S_1. Results shown that the v_{f_ave} in S_2 was decreased by 38% compared to that in S_1, while the average frosting-defrosting cycle was prolonged from 50.3 min to 84 min. Meanwhile, the η_{ave} was increased by 14 % and the ε_{L_ave} was decreased by 31 %.

As seen from the test results of Case 1 and 2, in the same environmental conditions, the degree of frost accumulated on outdoor coil surfaces for the field ASHP unit in S_2 was less than that in S_1 thus achieving better operating performances. The improvement of the frosting suppression performance for the field ASHP unit was attributed to the optimization of operation strategies by changing the combinations of compressor, fan and outdoor coil at part load to decrease ΔT. Although the input power of fans was increased for the field unit operating in S_2, due to the configured outdoor coils and fans fully utilized the total q and COP were still improved without any additional cost. Therefore, in severe frosting regions, the ASHP unit can be more adaptable to frosting conditions by optimizing the operation strategies.

4 CONCLUSIONS

In this paper, a field study on frosting suppression for ASHPs by adjusting operation strategies of ASHP with multi-parallel compressors is presented. The study was based on the two field ASHP units with same configuration, installed in Guiyang City in Southwest China, which is in a mild and humid region. The operating performances of the field units in two operation strategies were compared, when operated in two test cases respectively. By comparing the measured operating performances of the field ASHP units in same conditions, the frosting rate and the frosting-defrosting loss efficiency decreased by 38 % ~ 39 % and 31 % ~ 34 % thus leading to the heating efficiency and COP improving about 14 % ~ 22 % and 5% ~ 14%, respectively. It could be concluded that the way of adjusting operation strategies of multi-compressors had significant potential to achieve the frosting suppression for ASHP, further could improve the performances of the ASHP units operating under the severe frosting regions.

ACKNOWLEDGEMENTS

This work was supported partially by the National Key Research and Development Program of China (Grant No.2016YFC0700403), and the State Key Laboratory of Air-conditioning Equipment and System Energy Conservation (Grant No. SKLACKF201604).

NOMENCLATURE

A	area (m^2)	t	time (min)
M	mass (kg)	RH	relative humidity (%)
ΔP	Air pressure difference (Pa)	v	frosting rate (g m^{-2} min^{-1})
q	heating capacity (kW)	W	power (kW)

Q	heating energy (J)	η	heating efficiency (%)
ΔT	heat transfer temperature difference (°C)	T	temperature (°C)
ε	frosting-defrosting loss efficiency		

REFERENCES

Bai, X.X., Wang, W., Sun, Y.Y., Liu, J.D., Ge, Y.J., Deng, S.M., 2018. Operating performances of an ASHP unit operated in a mild and humid region using tube-encircled photoelectric sensor based defrosting initiation strategy. *Energy and Buildings, 177*, 140-153.

Byun, J.S., Lee, J., Jeon, C.D., 2008. Frost retardation of an air-source heat pump by the hot gas bypass method. Int. J. Refrig. 31, 328-334.

Li C.L., 2018. Hotspot Analysis of air source heat pump. Chinese Journal of Refrigeration Technology, 38(S1): 78-84. [In Chinese]

Li, L. T., Wang, W., Sun, Y. Y., Feng, Y. C., Lu, W. P., & Zhu, J. H., et al., 2014. Investigation of defrosting water retention on the surface of evaporator impacting the performance of air source heat pump during periodic frosting–defrosting cycles. Applied Energy, 135, 98-107.

Mei, V. C., Domitrovic, R. E., Chen, F. C., Kilpatrick, J. K., Finstad, C., Lubliner, M., et al., 2002. A frost-less heat pump. ASHRAE Transactions, 108, 452-459.

Okoroafor, E.U., Newborough, M., 2000. Minimising frost growth on cold surfaces exposed to humid air by means of crosslinked hydrophilic polymeric coatings. Appl. Therm. Eng. 20, 737-758.

Waddicor, D. A., Fuentes, E., Azar, M., Salom, J., 2016. Partial load efficiency degradation of a water-to-water heat pump under fixed set-point control. Appl. Therm. Eng, 106, 275-285.

Wang, C.C., Huang, R.T., Sheu, W.J., Chang, Y.J., 2004. Some observations of the frost formation in free convection: with and without the presence of electric field. International Journal of Heat & Mass Transfer. 47, 3491-3505.

Wang, D.Y., Tao, T.F., Xu, G.H., Luo, A., Kang, S.Y., 2012. Experimental study on frosting suppression for a finned-tube evaporator using ultrasonic vibration. Experimental Thermal & Fluid Science. 36, 1-11.

Wang, F., Liang, C.H., Zhang, X.S., 2018. Experimental study on frost suppression for ASHP combining superhydrophobic heat exchanger and air flow, Appl. Therm. Eng, 136, 666–673.

Wang, F., Wang, Z., Zheng, Y., Zhang, L., Hao, P., Chao, H., 2015. Performance investigation of a novel frost-free air-source heat pump water heater combined with energy storage and dehumidification. Applied Energy, 139(C), 212-219.

Wang, W., Feng, Y.C., Zhu, J.H., Li, L.T., Guo, Q.C., Lu, W.P., 2013. Performances of air source heat pump system for a kind of mal-defrost phenomenon appearing in moderate climate conditions. Appl. Energ. 112, 1138-1145.

Wang, W., Cui, Y.M., Sun, Y.Y., Deng, S.M., Wu, X., Liang, S.M., 2019. A new performance index for constant speed air-source heat pumps based on the nominal output heating capacity and a related modeling study. Energy & Buildings. 184, 205-215.

Wang, Y., Jiang, H.M., Ma, Z.L., 2006. Experiment and analysis of delaying frost of air-source heat pump water chiller-heater units by increasing the evaporator area. Heating Ventilating & Air Conditioning.

Zhao, H., Wang L., Lai, Y., Han J., Li, W., 2015. Effects of weak magnetic fields on frosting process on surface of copper tube. in: 24th IIR International Congress of Refrigeration, Yokohama, Japan.

Zhang, L., Fujinawa, T., Saikawa, M., 2012. A new method for preventing air-source heat pump water heaters from frosting. International Journal of Refrigeration, 35(5), 1327-1334.

Zhu, J.H., Sun, Y.Y., Wang, W., Deng, S.M., Ge, Y.J., Li, L.T., 2015. Developing a new frosting map to guide defrosting control for air-source heat pump units. Appl. Therm. Eng. 90, 782-791.

Manuscript ID: 1166
DOI: 10.18462/iir.icr.2019.1166

Comparison of zeotropic working fluid mixtures in different heat pump cycles

Benjamin ZÜHLSDORF[a,b], Jonas K. JENSEN[a], Lars O. REINHOLDT[b], Brian ELMEGAARD[a]

[a] Technical University of Denmark, Department of Mechanical Engineering, 2800 Kgs. Lyngby, Denmark, jkjje@mek.dtu.dk, be@mek.dtu.dk
[b] Danish Technological Institute, Energy and Climate, 8000 Århus, Denmark, bez@dti.dk, lre@dti.dk

ABSTRACT

Heat pumps are often integrated into boundary conditions with a temperature glide, resulting in inevitable inefficiencies due to heat transfer. Zeotropic mixtures have the potential to match the temperature profiles but require a screening procedure to select the best performing working fluid during the heat pump design. Hybrid compression-absorption heat pumps are an alternative technology, in which a recirculation pump can adjust the temperature profile of a pre-selected working fluid e.g., ammonia/water. This cycle is more complex but enables to avoid the working fluid screening. This paper compared the two approaches with each other and to pure working fluids to evaluate the potential under different boundary conditions. Both systems outperformed conventional systems using pure fluids. The optimal zeotropic mixtures were found to show the highest thermodynamic performances while the hybrid cycle with ammonia/water enabled more compact compression equipment.
Keywords: Heat Pump, Temperature Glide Matching, Working Fluid, Zeotropic Mixture.

1. INTRODUCTION

Heat pumps were found to be a future-proven technology enabling emission free and effective supply of heat. These characteristics facilitate their utilization in district heating and industry. The applications of heat pumps in district heating and industrial systems do however often imply that the heat source and the heat sink are experiencing temperature glides. Although the temperature glides imply a potential for considerably improving the thermodynamic performance of the heat pump, it is seldom exploited by conventional heat pump equipment originating from refrigeration applications.
Most vapour compression heat pumps are using pure working fluids or azeotropic working fluids mixtures, which are characterized by a constant temperature during evaporation and condensation. The resulting mismatch of the temperature profiles of the working fluid with the profiles of the sink and source stream corresponds to an increased amount of irreversibilities due to heat transfer and thereby to a limited thermodynamic system performance. Several studies, such as (Högberg et al., 1993; McLinden and Radermacher, 1987), have demonstrated the potential for improving the thermodynamic performance by selecting a zeotropic working fluid mixture with a good match of the temperature profiles with sink and source. Zühlsdorf et al. (2019) compared different approaches for the comparison of the working fluids and defined an approach to find the thermodynamically optimal working fluid on an economically fair basis. Zühlsdorf et al. (2018c) and Zühlsdorf et al. (2018d) presented working fluid screenings for different applications and outlined the potential to increase the thermodynamic performance by more than 30 % for simple cycle layouts. Zühlsdorf et al. (2018a) studied the impact of the temperature glide matching on the thermodynamic performance and found that the glide matching in the evaporator had a dominating impact.
The state of the art indicated that amount of irreversibilities due to heat transfer could be reduced to a minimum by a sophisticated working fluid choice for most of the applications. Considering a more sophisticated cycle layout might however yield additional performance improvements or enable obtaining a similar effect while requiring a smaller number of fluids considered during the screening.

Ammonia-water hybrid absorption-compression heat pumps are an example in which the cycle layout was adjusted to accommodate with the peculiarities of the ammonia-water mixture. Mixtures of ammonia and water have typically large and non-linear temperature glides, which may be controlled by a pump that operates in parallel to the compression process and determines the outlet quality of the evaporator. Hulten and Berntsson (1999) compared the performance of absorption heat pumps with vapour compression heat pumps using pure fluids and found the absorption heat pump to have an improved performance in applications with temperature glides larger than 10 K. Jensen et al. (2015a) determined the possible performances and supply temperatures using different commercially available equipment. Jensen et al. (2015b) analysed the working domains of ammonia-water hybrid heat pumps and indicated possible supply temperatures of up to 150 °C.
This paper aimed to create a basis for the comparison of ammonia-water hybrid compression-absorption heat pumps with a simpler cycle layout in combination with a sophisticated working fluid screening among working fluid mixtures by an analysis of the thermodynamic performances. Two cases were defined for which a simple cycle with a set of potential working fluid mixtures was compared to the hybrid heat pump using ammonia/water under consideration of thermodynamic and technical performance indicators.

2. METHODS

2.1. Case Study Description

The state of the art indicated that the choice of the optimal cycle and working fluid are dependent on the specific boundary conditions. As a basis for the comparisons, two cases studies were defined. The heat sink was assumed to be heated from 45 °C to 75 °C in both cases. The heat source was assumed to be cooled from 20 °C to 10 °C in Case I and from 35 °C to 10 °C in Case II. These cases correspond to applications as they could be found for supply to district heating networks from e.g., wastewater treatment plants in Case I (Bühler et al., 2018) and from e.g., data centres in Case II (Zühlsdorf et al., 2019).

2.2. Heat Pump Cycles and Modelling Assumptions

This chapter introduces the considered cycles including the assumptions for the thermodynamic modelling. As a reference, a basic cycle with an internal heat exchanger was chosen, as it was found to be promising in cases as described before (Zühlsdorf et al., 2019). Fig. 1 shows the layout of the internal heat exchanger (IHX) cycle. It is a single-stage vapour compression cycle with an internal heat exchanger, which recovers heat from the liquid line before the expansion for preheating the suction line in front of the compressor. The amount of heat transferred in the internal heat exchanger was defined by the minimum pinch point temperature difference and the definition to yield vapour in saturated conditions at the evaporator outlet.
Fig. 2 presents the layout of a hybrid vapour compression-absorption heat pump as it is commercially used with a working fluid mixture of ammonia and water. A pump is installed in parallel to the compressor, enabling to control the outlet state of the evaporator. The state can move into the two-phase zone, allowing variation of the temperature glide on the source side. The internal heat exchanger is installed to subcool the liquid before the throttling valve and preheat the liquid line after the pump. The liquid line is subsequently mixed with the discharge from the compressor and fed to the absorber. The working fluid mixture condenses during the heat rejection to the heat sink within the absorber. The liquid stream (state points 8-10) has a lower concentration of ammonia, while the concentration is higher in the gas stream (state points 1-2). The concentration in the remaining state points will be considered as the design concentration in the presentation of the results. The ratio of the liquid stream with the lean ammonia concentration $\dot{m}_9$ to the stream of the desorber $\dot{m}_8$ defines the recirculation ratio *f*. The recirculation factor was optimized with respect to a maximum COP.

$$f = \frac{\dot{m}_8}{\dot{m}_7} \qquad \text{Eq. (1)}$$

The models of both cycles consisted of energy and mass balances. The heat transfer processes were discretized in steps of equal heat transfer. The pressure levels were defined by minimum pinch point temperature differences within the heat exchangers. No heat losses from the components and

no pressure drops were considered. The numerical models of the IHX-cycle and a documentation were presented in (Zühlsdorf et al., 2018b). The models were implemented in Matlab 2018a (The MathWorks Inc., 2018) using medium properties from REFPROP 9.1 (Lemmon et al., 2013).

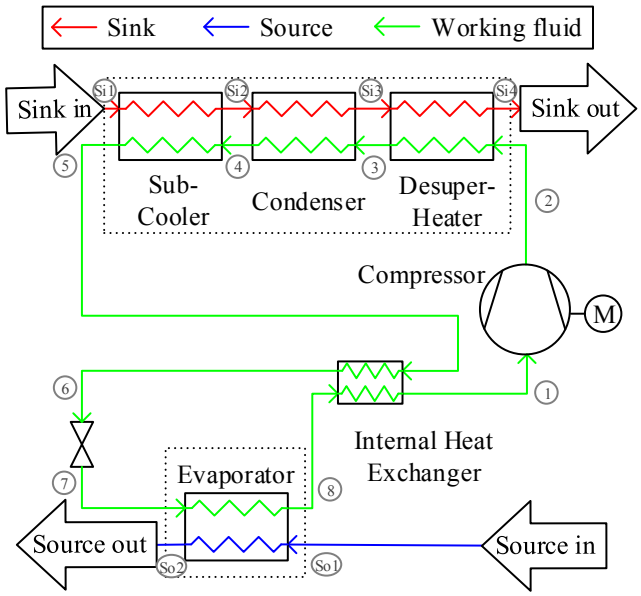

Figure 1: Vapour compression heat pump cycle with internal heat exchanger (IHX)

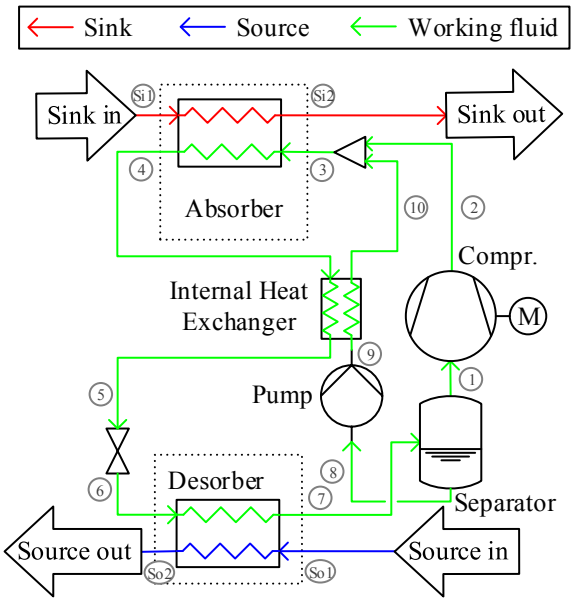

Figure 2: Hybrid absorption-compression heat pump cycle

Table 1 shows the component parameters that were assumed in the thermodynamic models. Both the pump and the compressor were modelled with an isentropic efficiency of 80 % and additionally considered a motor efficiency of 95 %. The heat exchangers were modelled with a minimum pinch point temperature difference of 3 K.

Table 1. Modelling assumptions

Isentropic efficiency of compressor and pump:	80 %
Motor efficiency:	95 %
Minimum pinch point temperature differences:	3 K

Different performance indicators were considered for the evaluation of the performance. The thermodynamic performance was evaluated by the coefficient of performance COP, which relates the amount supplied heat $\dot{Q}_{\mathrm{sink}}$ to the sum of the power consumed by the compressor $\dot{W}_{\mathrm{Comp}}$ and the pump $\dot{W}_{\mathrm{Pump}}$.

$$\mathrm{COP} = \frac{\dot{Q}_{\mathrm{sink}}}{\dot{W}_{\mathrm{Pump}} + \dot{W}_{\mathrm{Comp}}} \qquad \text{Eq. (2)}$$

The maximum achievable COP is defined by the Lorenz $\mathrm{COP}_{\mathrm{Lor}}$, which is defined by the theoretically ideal Lorenz cycle working with an isentropic compression and expansion between the thermodynamic average temperatures of sink $\bar{T}_{\mathrm{Sink}}$ and source $\bar{T}_{\mathrm{Source}}$ (Bejan et al., 1996; Lorenz, 1894). The Lorenz efficiency η_{Lor} relates the COP to the $\mathrm{COP}_{\mathrm{Lor}}$ and thereby enables comparing the performance of cycle working between different sink and source temperatures.

$$\eta_{\mathrm{Lor}} = \frac{\mathrm{COP}}{\mathrm{COP}_{\mathrm{Lor}}} = \frac{\mathrm{COP}}{\bar{T}_{\mathrm{Sink}} \Big/ (\bar{T}_{\mathrm{Sink}} - \bar{T}_{\mathrm{Source}})} \qquad \text{Eq. (3)}$$

Besides the thermodynamic performance, the volumetric heating capacity VHC was used as an indicator of the size of the compression equipment and thereby of the heat pump. It relates the supplied heat $\dot{Q}_{\mathrm{sink}}$ to the volume flow at the inlet of the compressor $\dot{V}_1$.

$$\mathrm{VHC} = \frac{\dot{Q}_{\mathrm{sink}}}{\dot{V}_1} \qquad \text{Eq. (4)}$$

The pressure levels in the evaporator p_{evap} and in the condenser p_{cond} were considered as further indicators of the technical feasibility of the cycle.

2.3. Working Fluid Screening

As a baseline, pure R-717 (ammonia) was evaluated for a standard cycle, which corresponds to the IHX cycle without the internal heat exchanger. The IHX-cycle was evaluated for a set of working fluids, which consisted of a number of pure fluids and all possible binary mixtures of these fluids. The following pure fluids were considered: R-744 (CO_2), R-1270 (propylene), R-290 (propane), R-E170 (DME), R-600a (iso-butane), R-600 (butane), R-601a (iso-pentane), R-601 (pentane).
These results were compared to the hybrid heat pump cycle using binary mixtures of R-717 (ammonia) and R-718 (water). Possible mixtures of R-717 and R-718 with one of the before mentioned working fluids were omitted, due to limited miscibility.

3. RESULTS

3.1. Case I: T_{Source} 20 °C → 10 °C, T_{Sink} 45 °C → 75 °C

Figure 3 shows the summary of the screening results for Case I. All binary mixtures that were evaluated for the IHX-cycle are included while selected mixtures are highlighted in colour. Additionally, the COP for the mixture of ammonia/water in the hybrid cycle is shown. The figure indicates that the best COPs for pure fluids are around 4.0 while the best zeotropic mixtures reach values of up to 4.5 in the IHX-cycle. It may furthermore be seen, that the hybrid heat pump cycle using 90 % ammonia / 10 % water is competitive to pure fluids in terms of COP.

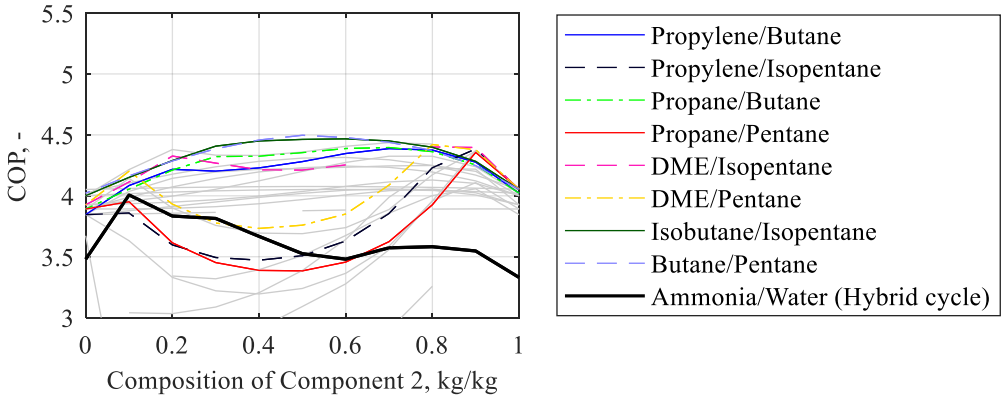

Figure 3: COP over mass composition of component 2 for the IHX-cycle and the hybrid cycle using ammonia/water

Table 2 presents additional performance indicators such as the volumetric heating capacity VHC, the evaporation pressure p_{evap} and the condensation pressure p_{cond} for selected working fluid mixtures, which showed promising results in all indicators. Additionally the Lorenz efficiency η_{Lor} was presented, considering the COP_{Lor} = 7.43 for Case I. The pure fluids reached Lorenz efficiencies of up to 55 % while the best mixtures exceed 60 %. Ammonia had a COP = 3.8, which is slightly lower than for the best pure fluids, but in turn had a high volumetric heating capacity indicating compact and cost-effective equipment.
The best COP of 4.5 was reached by 50 % butane / 50 % pentane, while the mixture had a VHC = 920 kJ·m^{-3}. The mixture 30 % propane / 70 % butane had a slightly lower COP of 4.3 but a higher VHC of 3700 kJ·m^{-3}.The hybrid heat pump with 90 % ammonia / 10 % water and f = 0.32 reached a COP of 4.0 while the VHC was 4800 kJ·m^{-3}. The pressures of all presented fluids were found to be within technical feasible constraints.

Table 2. Overview of key performance indicators for selected working fluid mixtures

Mixture	f	COP	η_{Lor}	VHC	p_{evap}	p_{cond}
	-	-	%	kJ·m^{-3}	bar	bar
Std-cycle						
Ammonia	-	3.76	51	6049	5.5	33.5
IHX-cycle:						
Iso-pentane	-	4.05	55	551	0.5	3.9
Iso-butane	-	4.00	54	1880	2.0	8.6
DME	-	3.93	53	3150	3.9	11.4
Propane	-	3.89	52	4513	3.9	18.2
50 % Butane / 50 % Pentane	-	4.50	61	924	0.8	5.0
30 % Propane / 70 % Butane	-	4.32	58	3656	4.5	18.3
80 % DME / 20 % Iso-pentane	-	4.33	58	2760	3.0	14.0
50 % Propylene / 50 % Butane	-	4.28	58	2971	3.5	15.1
Hybrid cycle:						
90 % Ammonia / 10 % Water	0.32	4.01	53	4797	4.8	23.2

Fig. 4 shows the temperature-heat-diagram of 50 % butane / 50 % pentane for the IHX cycle and Fig. 5 for 90 % ammonia / 10 % water for the hybrid compression-absorption cycle. The temperature profiles of the working fluid and the secondary streams were matching well, indicating minor losses.

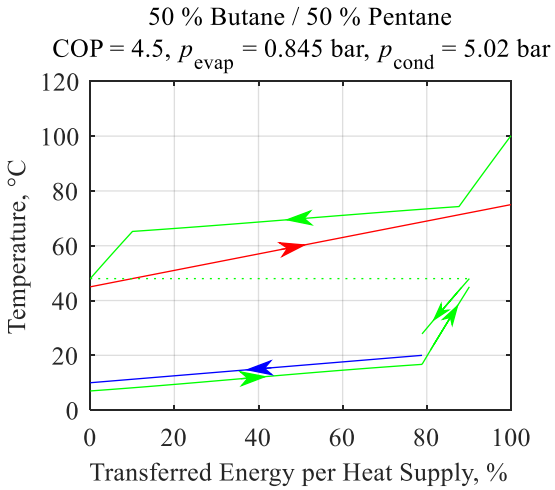

Figure 4: Temperature-heat-diagram of 50 % butane / 50 % pentane for the IHX cycle

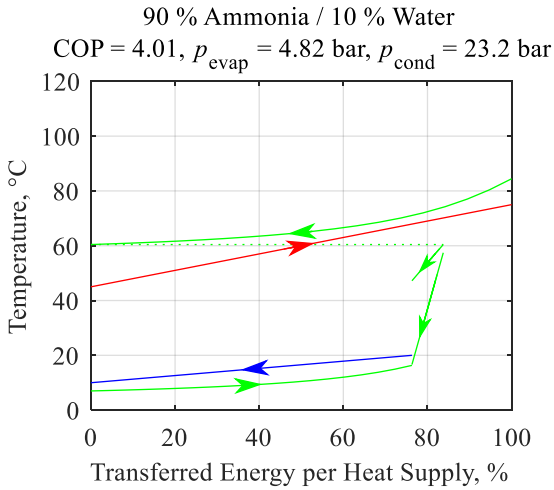

Figure 5: Temperature-heat-diagram of 90 % ammonia / 10 % water for the hybrid cycle

3.2. Case II: T_{Source} 35 °C → 10 °C, T_{Sink} 45 °C → 75 °C

Figure 6 and Table 3 show the corresponding results for Case II. The performance of the pure fluids was not impacted by the higher source inlet temperature and remained constant. The zeotropic mixtures in the IHX-cycle and the hybrid cycle using ammonia/water were however able to exploit the potential offered by the higher source inlet temperature. Promising results were the COP of 5.3 for 40 % DME / 60 % iso-pentane with a VHC = 1900 kJ·m^{-3} and the COP of 5.0 for 70 % propane / 30 % iso-pentane with a VHC = 3600 kJ·m^{-3}. The hybrid heat pump using 60 % ammonia / 40 % water reached a COP of 4.4 with a VHC = 2500 kJ·m^{-3} at f = 0.65, while 80 % ammonia / 20 % water had a slightly lower COP of 4.3 but a higher VHC = 4100 kJ·m^{-3} at f = 0.41.

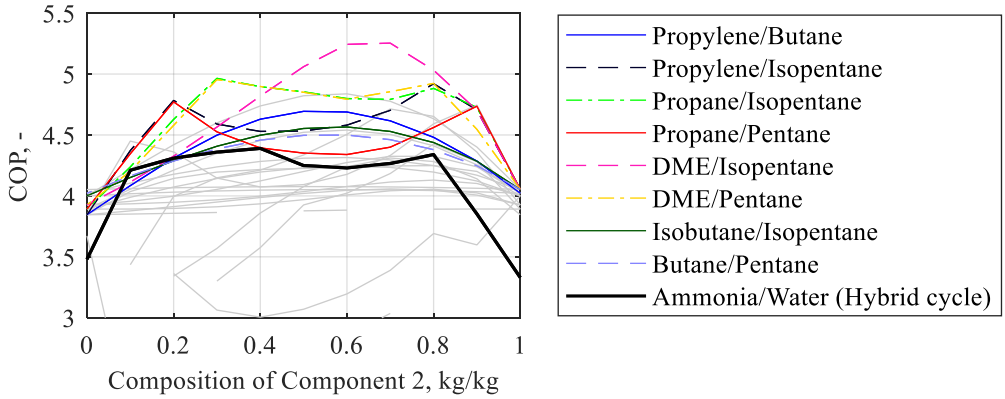

Figure 6: COP over mass composition of component 2 for the IHX-cycle and the hybrid cycle using ammonia/water

Table 3. Overview of key performance indicators for selected working fluid mixtures

Mixture	f	COP	η_{Lor}	VHC	p_{evap}	p_{cond}
	-	-	%	kJ·m^{-3}	bar	bar
Std-cycle						
Ammonia	-	3.76	42	6049	5.5	33.5
IHX-cycle:						
Iso-pentane	-	4.05	46	551	0.5	3.9
Iso-butane	-	4.00	45	1880	2.0	8.6
DME	-	3.93	44	3150	3.9	11.4
Propane	-	3.89	44	4513	3.9	18.2
40 % DME / 60 % Iso-pentane	-	5.25	59	1884	2.0	7.6
70 % Propane / 30 % Iso-pentane	-	4.96	56	3583	4.4	15.0
20 % Propylene / 80 % Iso-pentane	-	4.92	55	1288	1.3	5.8
50 % Iso-butane / 50 % Pentane	-	4.82	54	1208	1.2	5.7
Hybrid cycle:						
60 % Ammonia / 40 % Water	0.65	4.39	50	2482	2.2	11.0
80 % Ammonia / 20 % Water	0.41	4.31	48	4072	4.1	17.9

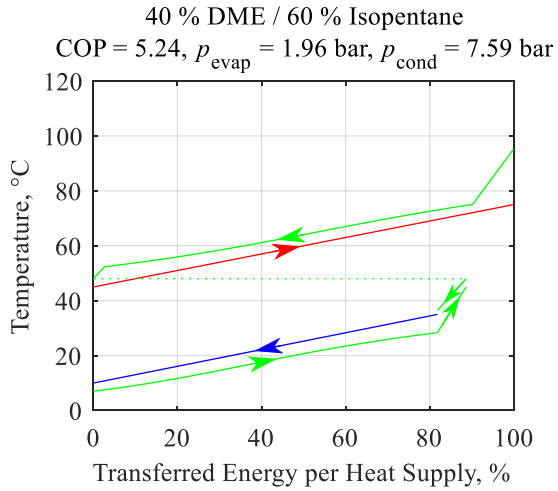

Figure 7: Temperature-heat-diagram of 40 % DME / 60 % Iso-pentane for the IHX cycle

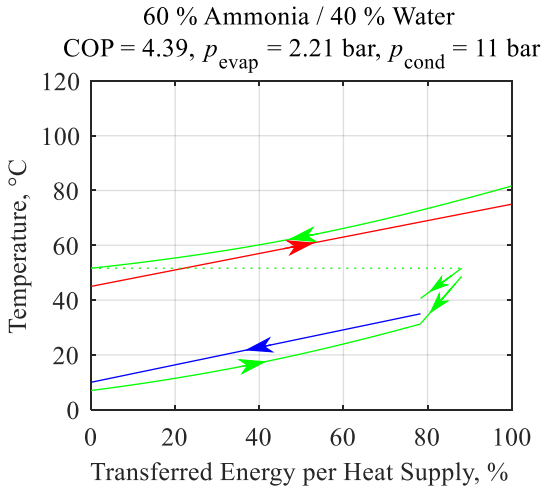

Figure 8: Temperature-heat-diagram of 60 % Ammonia / 40 % Water for the hybrid cycle

The maximum thermodynamic performance was COP_{Lor} = 8.9. The relative performances in terms of Lorenz efficiencies decreased for the pure fluids while the remained within the same magnitude

for the mixtures and the hybrid cycle. The pressure levels were found to be technically feasible, while ammonia in the standard cycle had the highest condensation pressure.
Figure 7 shows the temperature-heat-diagram for 40 % DME / 60 % iso-pentane in the IHX-cycle and Figure 8 for 60 % ammonia / 40 % water in the hybrid cycle. Both cycles are matching well with the temperature profiles of sink and source. While the presented mixtures had a slight mismatch on the sink side in Case I, the profiles are matching well on both sides for Case II.

4. DISCUSSION

The study considered the thermodynamic performance and different technical performance indicators for the evaluation and comparison of different working fluids and cycle layouts. Further aspects, such as the flexibility to accommodate with the peculiarities of the specific application during design and operation might be considered in further comparisons. While the standard cycles might be easier to design and operate, the hybrid cycle has a higher flexibility by controlling the circulation factor. While the mixture of ammonia and water was not competitive assuming simple cycles, competitive performances were found using the more complex hybrid cycle. In Case I with a temperature glide of 10 K on the source side, the hybrid heat pump cycle was competitive to the pure fluids, while the hybrid cycle outperformed the other pure fluids in terms of COP in Case II with a source glide of 25 K. These findings are consistent with the observations from (Hulten and Berntsson, 1999).
The screening of zeotropic working fluid mixtures enabled to find fluids, which outperformed the more complex hybrid cycle with ammonia/water. The benefit of introducing the circulation pump for was especially beneficial for the mixture of ammonia and water, as it typically implies large and non-linear temperature profiles during phase change. The zeotropic mixtures that yielded good performances in the IHX-cycle already had a well matching temperature profile, which suggests that only little additional benefits might be obtainable from increasing the cycle complexity to e.g., a hybrid cycle.

5. CONCLUSIONS

The study compared ammonia in a standard cycle without an internal heat exchanger, additional pure fluids in an IHX-cycle, a set of zeotropic mixtures in a standard cycle with an internal heat exchanger and a hybrid compression-absorption cycle using a mixture of ammonia/water. The comparison was conducted for two cases while Case I had a temperature glide in the source of 10 K and Case II of 25 K. For Case I, pure fluids, such as iso-pentane, reached a COP of 4.0, while ammonia had a lower COP of 3.8 but a higher volumetric heating capacity. The hybrid heat pump was competitive to the best pure fluids in terms of COP, while only pure ammonia reached a higher volumetric heating capacity. The zeotropic mixtures reached COPs of up to 4.5 while the volumetric heating capacities were lower than for ammonia and the hybrid cycle. For Case II, the performance increase of the zeotropic mixtures was higher, as they reached COPs of up to 5.2, while the performance of the pure fluids remained unchanged. The hybrid heat pump reached COPs of up to 4.4. The volumetric heating capacities of the hybrid cycle and the zeotropic mixtures in the IHX-cycle were comparable but lower than for pure ammonia.

It may be concluded that both the utilization of zeotropic mixtures with a simple cycle layout as well as the hybrid compression-absorption cycle with ammonia/water showed performances that outperformed pure fluids in COP while being competitive in terms of volumetric heating capacity. The performance increases were increasing for larger temperature glides in the heat source. The zeotropic mixtures showed higher thermodynamic performances than the hybrid cycle while the volumetric heating capacities were lower for high concentrations of ammonia.

ACKNOWLEDGEMENTS

This research project is financially funded by The Danish Council for Strategic Research in Sustainable Energy and Environment, under the project title: “THERMCYC –Advanced thermodynamic cycles utilizing low-temperature heat sources”.

REFERENCES

Bejan, A., Tsatsaronis, G., Moran, M., 1996. Thermal Design and Optimization, Thermal Design and Optimization. doi:10.1016/S0140-7007(97)87632-3

Bühler, F., Petrović, S., Ommen, T., Holm, F., Pieper, H., Elmegaard, B., 2018. Identification and Evaluation of Cases for Excess Heat Utilisation Using GIS. Energies 11, 762. doi:10.3390/en11040762

Högberg, M., Vamling, L., Berntsson, T., 1993. Calculation methods for comparing the performance of pure and mixed working fluids in heat pump applications. International Journal of Refrigeration 16, 403–413. doi:10.1016/0140-7007(93)90057-F

Hulten, M., Berntsson, T., 1999. The compression/absorption cycle – influence of some major parameters on COP and a comparison with the compression cycle. International Journal of Refrigeration 22, 91–106.

Jensen, J.K., Markussen, W.B., Reinholdt, L., Elmegaard, B., 2015a. On the development of high temperature ammonia-water hybrid absorption-compression heat pumps. International Journal of Refrigeration 58, 79–89. doi:10.1016/j.ijrefrig.2015.06.006

Jensen, J.K., Ommen, T., Markussen, W.B., Reinholdt, L., Elmegaard, B., 2015b. Technical and economic working domains of industrial heat pumps: Part 2 - Ammonia-water hybrid absorption-compression heat pumps. International Journal of Refrigeration 55, 183–200. doi:10.1016/j.ijrefrig.2015.02.011

Lemmon, E.W., Huber, M.L., McLinden, M.O., 2013. NIST Standard Reference Database 23: Reference Fluid Thermodynamic and Transport Properties-REFPROP, Version 9.1.

Lorenz, H., 1894. Beiträge zur Beurteilung von Kühlmaschinen. Zeitschrift des VDI 38, 62–68.

McLinden, M.O., Radermacher, R., 1987. Methods for comparing the performance of pure and mixed refrigerants in the vapour compression cycle. International Journal of Refrigeration 10, 318–325. doi:10.1016/0140-7007(87)90117-4

The MathWorks Inc., 2018. MATLAB R2018a.

Zühlsdorf, B., Jensen, J.K., Cignitti, S., Madsen, C., Elmegaard, B., 2018a. Analysis of temperature glide matching of heat pumps with zeotropic working fluid mixtures for different temperature glides. Energy 153, 650–660. doi:https://doi.org/10.1016/j.energy.2018.04.048

Zühlsdorf, B., Jensen, J.K., Elmegaard, B., 2019. Heat pump working fluid selection - Economic and thermodynamic comparison of criteria and boundary conditions. International Journal of Refrigeration 98, 500–513. doi:10.1016/j.ijrefrig.2018.11.034

Zühlsdorf, B., Jensen, J.K., Elmegaard, B., 2018b. Numerical models for the design and analysis of heat pumps with zeotropic mixtures, Rev01. doi:https://doi.org/10.11583/DTU.6825443

Zühlsdorf, B., Meesenburg, W., Ommen, T.S., Thorsen, J.E., Markussen, W.B., Elmegaard, B., 2018c. Improving the performance of booster heat pumps using zeotropic mixtures. Energy 154, 390–402. doi:https://doi.org/10.1016/j.energy.2018.04.137

Zühlsdorf, B., Riis Christiansen, A., Müller Holm, F., Funder-Kristensen, T., Elmegaard, B., 2018d. Analysis of possibilities to utilize excess heat of supermarkets as heat source for district heating. Energy Procedia - 16th International Symposium on District Heating and Cooling DHC2018 149, 276–285. doi:10.1016/J.EGYPRO.2018.08.192

Manuscript ID: 1169
DOI: 10.18462/iir.icr.2019.1169

Waste heat driven ammonia-water absorption chiller for high temperature residential-scale applications

Girish KINI[(a)], Michael TAMBASCO[(a)], Sriram CHANDRASEKARAN[(a)], Srinivas GARIMELLA[(a)]

(a) GWW School of Mechanical Engineering, Georgia Institute of Technology
Atlanta, 30318, USA, e-mail:sgarimella@gatech.edu

ABSTRACT

The development of a standalone waste-heat driven ammonia-water absorption chiller with a cooling capacity of 10.5 kW is presented. The system is designed to deliver cooling with a nominal COP of 0.6 for ambient temperatures as high as 40°C. To minimize the physical size of the system, heat and mass exchangers with novel microscale features and geometries are employed. Thermodynamic cycle modeling and heat and mass exchanger design and optimization methodologies are discussed. The chiller is fabricated as a packaged unit and its performance over a wide range of operating conditions demonstrated experimentally. This work validates the scalability of microchannel heat exchanger technology from a proof-of-concept laboratory scale device to a residential-scale absorption heat pump.
Keywords: Ammonia-water, Heat Exchanger, Microchannel, Waste Heat.

1. INTRODUCTION

Rising demand for space cooling is exerting enormous strain on electricity supply systems in many countries (IEA, 2018). Thermally activated refrigeration cycles such as the vapor absorption cycle can utilize low grade thermal energy, including waste heat, to provide cooling. In addition to reducing dependence on electricity grids, they are an attractive alternative to vapor compression systems as they utilize environmentally benign working fluids. Although the use of these cycles has typically been limited to large capacity industrial applications, advances in miniaturization of heat and mass exchangers allow for the development of small capacity absorption chillers for residential and small capacity applications (Garimella, 2003). Determan and Garimella (2012) presented a compact, monolithic heat pump (200 x 200 x 34 mm) that delivered 300 W of cooling at a COP of 0.375. Subsequently, Garimella et al. (2016) demonstrated a 3.3 kW cooling capacity microchannel absorption chiller as a packaged unit. The development and testing of a 10.5 kW cooling capacity ammonia-water absorption chiller is presented in this study.

2. CYCLE DESIGN AND MODELING

A schematic of the system under consideration is shown in Figure 1. The desorber uses the heat input and generates ammonia, which is purified in the rectifier and then proceeds to the condenser. After condensing, it flows through the expansion valve into the evaporator where it picks up heat from the conditioned space. The ammonia vapor from the evaporator and the dilute solution from the desorber recombine in the absorber, from which the concentrated solution is pumped back to the desorber to complete the cycle. Two recuperative heat exchangers, the solution heat exchanger, and the refrigerant precooler, are used to increase system efficiency. The waste heat is simulated using an electric circulation heater, which heats up a heat transfer oil coupled to the desorber. The condenser and absorber are hydronically coupled to the laboratory chiller in parallel. The evaporator is coupled to a water loop and provides the desired cooling to the conditioned space.

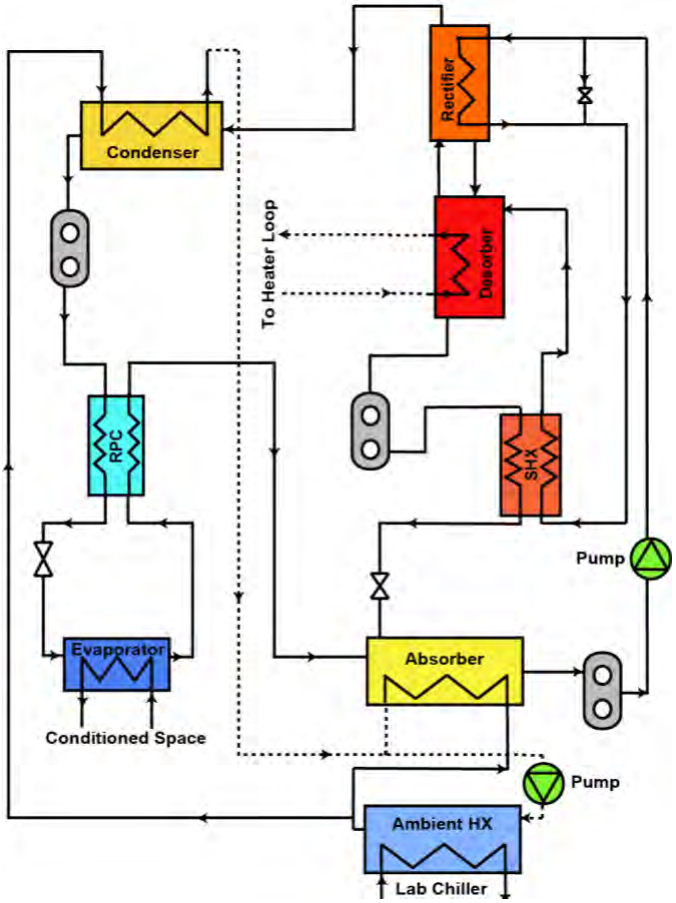

Figure 1: Schematic of absorption system

A thermodynamic cycle model is developed in Engineering Equation Solver (Klein, 2017). Mass, species and energy conservation equations are solved for each component iteratively. The system of equations is closed using assumptions on the quality for vapor inlet to the condenser and solution outlet of the desorber. The inputs to the model and key outputs are listed in Table 1. The cooling COP is calculated as shown in Eq. (1)

$$COP_{cooling} = \frac{\dot{Q}_{evap}}{\dot{Q}_{des}} \qquad \text{Eq. (1)}$$

Table 1: Cycle model inputs and outputs

Input	Value
Ambient temperature	40°C
Chilled water outlet temperature	12°C
Desorber coupling inlet temperature	162°C
Refrigerant Concentration	0.998

Output	Value
Evaporator duty	10.55 kW
Desorber duty	16.75 kW
$COP_{cooling}$	0.63

3. HEAT EXCHANGER DEVELOPMENT

3.1. Desorber and Rectifier

The desorber and rectifier are responsible for vapor generation and purification, respectively. A novel liquid-coupled desorber design incorporating the concept of diabatic distillation presented in Staedter and Garimella (2018) is utilized. The geometry is modified for the required vapor generation rates. Heat is applied to the ammonia-water working fluid through the heat transfer oil flowing in microchannel plates. The working fluid side is gravity driven and consists of an alternating pattern of trays. Each tray has regions that support simultaneous vapor generation and purification. The component consists of 12 working fluid sheets and 24 coupling fluid sheets. The working fluid sheets were machined while the coupling fluid sheets were photo-chemically etched. The design conformed to hydrodynamic limitations and operated between the weeping and flooding limits for the solution with vapor in counterflow. The rectifier design consists of a cavity filled with wire gauze packing where partial condensation occurs, thereby increasing the purity of the refrigerant. The generated reflux is gravity driven and flows back to the top of the desorber. The wire gauze enhances vapor-side heat transfer and provides surface area for liquid–vapor interaction to facilitate the diabatic distillation process.

3.2. Absorber

A vertically oriented baffled shell-and-tube heat exchanger serves as the absorber. Premixed solution/vapor mixture enters from the top into the shell side of the absorber and leaves as concentrated solution from the bottom. The coupling fluid is on the tube side, in counterflow with the shell-side fluid. The solution/vapor mixture flows in a serpentine path through the narrow tube bundle gaps created by the numerous small diameter tubes. The enhanced mixing created by this flow path aids in absorption mass transfer. Additionally, the small tubes provide high heat transfer coefficients for the coupling fluid, thereby reducing the overall heat transfer resistance. A small lip is provided on the baffles to enable solution pooling at each level, which further increases the solution/vapor interfacial area. A segmented heat and mass transfer model was developed for the absorber with the Colburn and Drew approach using the framework developed by Price and Bell (1974). The absorber is sized for a heat duty of 18.9 kW (the sum of all segment duties) that achieves complete absorption and provides the required subcooling in the concentrated solution. A schematic of the absorber and the internal details are shown in Figure 2.

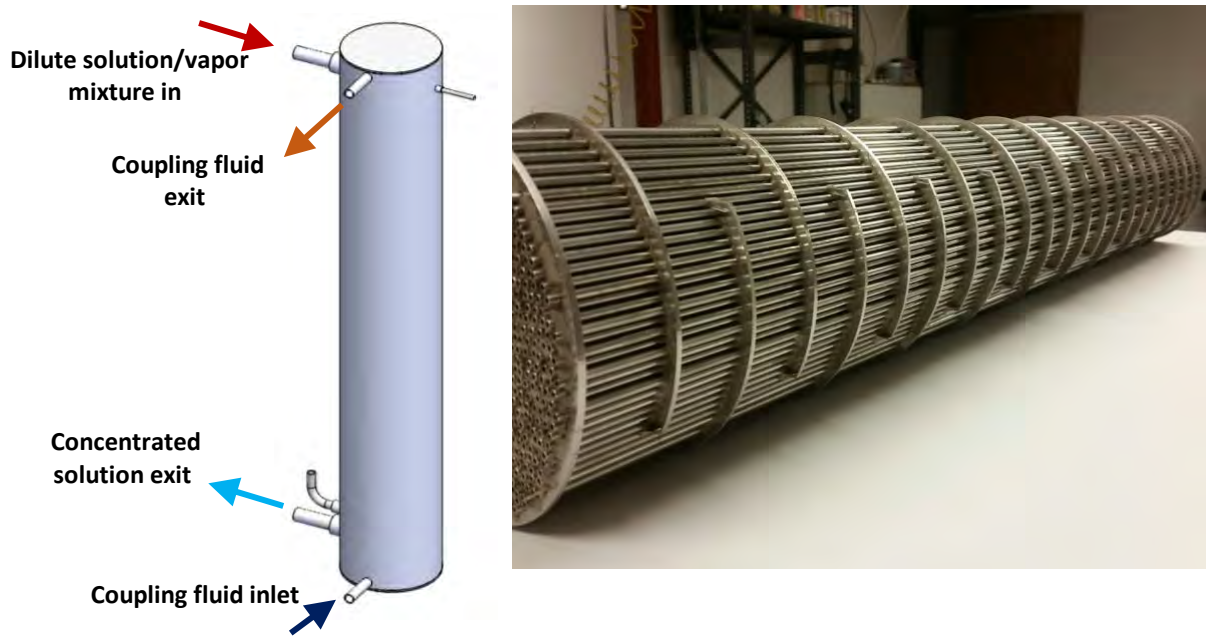

Figure 2: Absorber schematic (L); Tube bundle assembly (R)

3.3. Condenser, Evaporator, Refrigerant Precooler and Solution Heat Exchanger

These heat exchangers consist of an array of parallel, aligned alternating sheets with microscale features etched in them. These features facilitate the flow of various fluid streams and the associated heat and mass transfer. The design of these heat exchangers follows the methodology presented in Nagavarapu and Garimella (2011). The components are designed using models developed for the specific thermodynamic conditions, fluid composition and flow regime. The thermodynamic state points for each component are obtained from the cycle model. Component models utilize a segmented architecture that iteratively computes relevant fluid stream parameters at multiple locations by solving conservation equations in combination with a resistance network. The overall heat exchanger design provides the number of channels per sheet and number of sheets required to achieve the design duty under the constraints of overall component pressure drop, fluid maldistribution potential and fabrication considerations. The component CAD drawings are shown in Figure 3 and the corresponding details are summarized in Table 2.

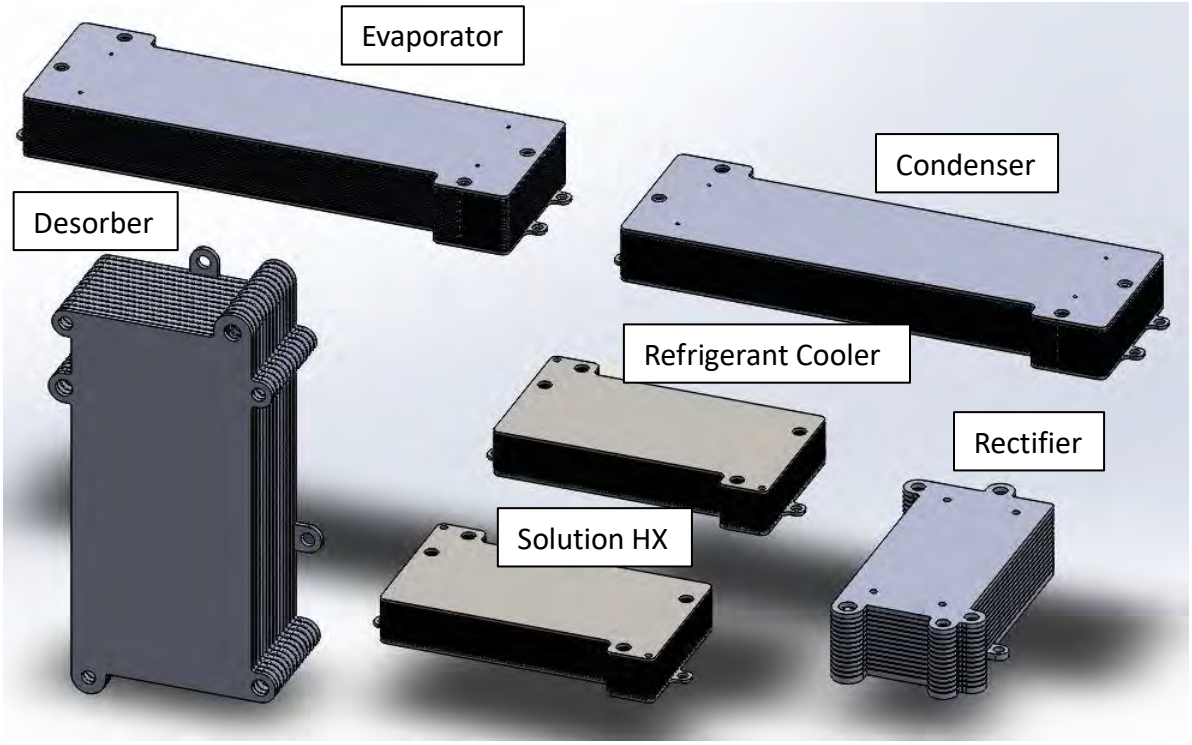

Figure 3: Heat exchanger geometries

The microchannel sheets are fabricated by photochemical etching. These sheets are then enclosed by cover plates and bonded together using vacuum brazing.

Table 2: Heat exchanger geometry details

Component	Type	Key dimensions
Desorber	Diabatic distillation column with microscale features, counterflow microchannel array	12 sets containing 1 working fluid sheet and 2 coupling fluid sheets per set
Rectifier	Microscale features with wire gauze packing, counterflow microchannel array	10 sets containing 1 wire gauze packed cavity and 1 coupling sheet

Absorber	Shell and tube, co-flow	955 tubes with OD 3.175 mm, ID 2.159 mm, 21 baffle plates
Condenser	Microchannel array, counterflow	Channel hydraulic diameter: 440 μm Number of sheets: 71 Number of channels per sheet: 89
Evaporator	Microchannel array, counterflow	Channel hydraulic diameter: 440 μm Number of sheets: 71 Number of channels per sheet: 89
Refrigerant Precooler	Microchannel array, counterflow	Channel hydraulic diameter: 440 μm Number of sheets: 67 Number of channels per sheet: 88
Solution heat exchanger	Microchannel array, counterflow	Channel hydraulic diameter: 440 μm Number of sheets: 51 Number of channels per sheet: 88

4. PROTOTYPE ASSEMBLY

Figure 4 shows a CAD model of the prototype unit with all components assembled. The overall size of the prototype is 0.6 m x 0.9 m x 1.0 m (L x W x H). The additional space shown in the figure would accommodate auxiliary components of the hydronic fluid-to-air heat exchangers. The connections to the heat source coupling heater and conditioned space simulation heater are shown.

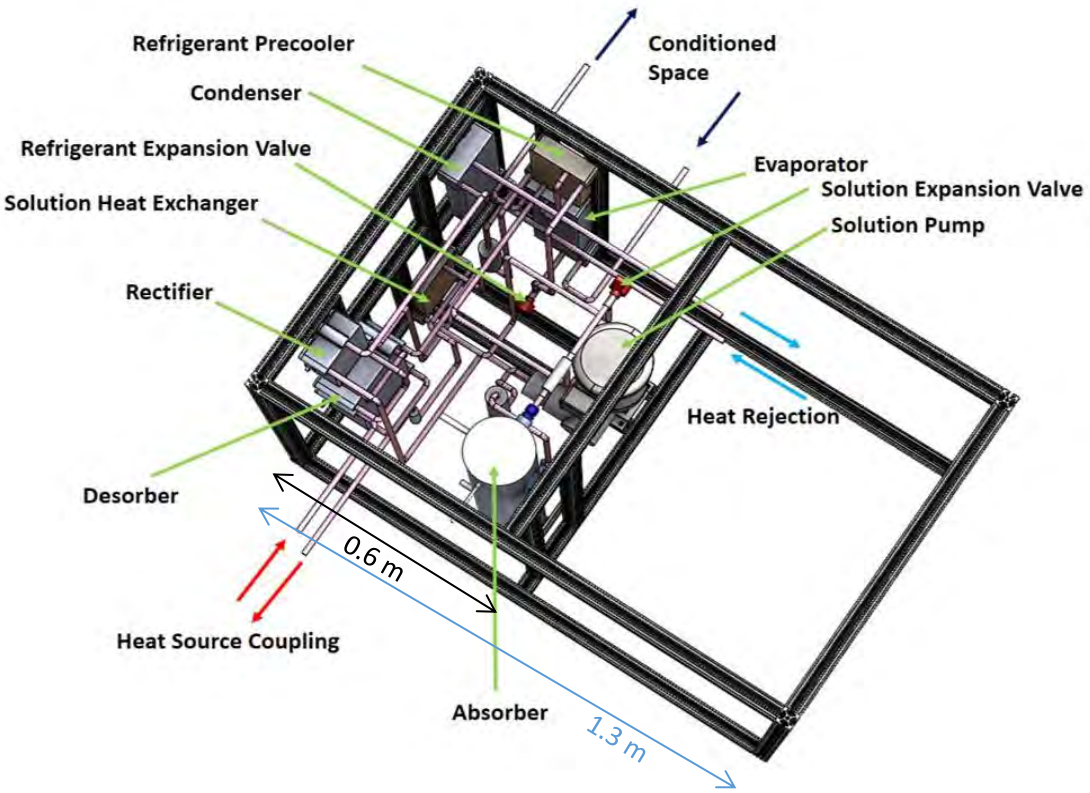

Figure 4: Prototype CAD

Figure 5 shows the assembled prototype system. The desorber is coupled to an electric heater on the right that circulates heat transfer oil. The evaporator coolant loop circulates water and contains a set of electrical heaters that maintain the temperature of the chilled water loop to the specified set-points. Both these loops are controlled by pulse-width modulated solid state controllers. Storage tanks are installed at the outlet of condenser, absorber and desorber. These tanks ensure appropriate fluid inventory in different parts of the system and allow for steady operation of the system. A positive displacement diaphragm pump is used to circulate the ammonia water mixture. The details of the instrumentation are provided in Table 3. Data acquisition and control is done using the National Instruments® LabVIEW™ platform. Steady-state data are recorded for a 20-minute duration at a rate of one scan per second. Control algorithms are implemented in the system for automated operation during steady-state and emergency shutdown in the event of equipment failure or high working fluid pressure.

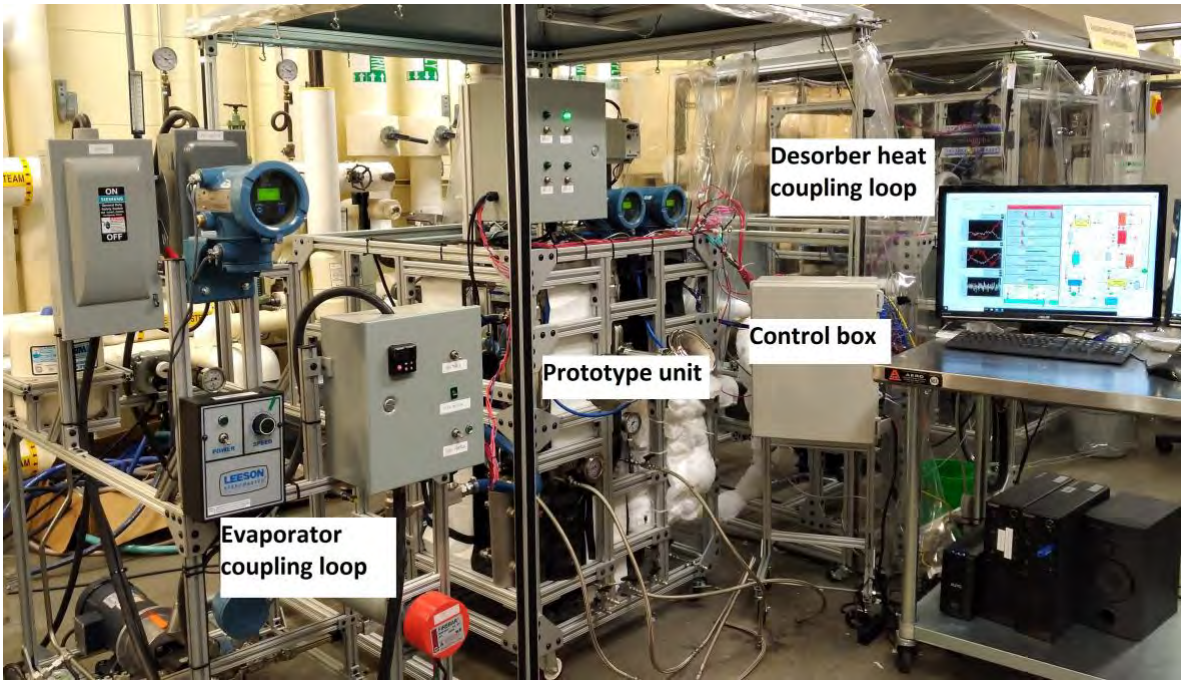

Figure 5: Assembled prototype system with all coupling loops and associated controls

Table 3: Equipment specification

Instrument	Manufacturer/Model	Range	Accuracy
Thermocouple	Omega® T-type	-250-300 °C	±0.5 °C
Pressure Transducer	Omega® 4-20mA Output absolute	0-1034.2 kPa 0-3447.3 kPa	±0.03%
Mass flow sensor (refrigerant and dilute solution)	Micromotion CMFS series	0-110 kg/hr	±0.1 %
Mass flow sensor (evaporator coupling)	Micromotion CMF series	0-108 kg/hr	±0.2 %
Solution pump	Hydracell P200		
Electronic valves	Carel E2V series	480 steps	
Heater controller	Watlow PM series		

5. EXPERIMENTAL RESULTS

Data are analyzed using time-averaged values of measured quantities that define inlet and outlet states for each heat exchanger as described in Lee et al. (2012). The evaporator duty is calculated using Eq.(2)

$$\dot{Q}_{evap} = \dot{m}_{cf,evap} Cp_{cf,evap} \left(T_{cf,evap,in} - T_{cf,evap,out} \right) \qquad \text{Eq. (2)}$$

Figure 6 shows the cooling duty, COP and coupling fluid temperatures of the evaporator and condenser for a sample set of test points. For test points 1-4, chilled water was supplied at 7.5°C and returned to the evaporator at 13.5°C. For test points 5-8, chilled water was supplied at 12.5°C and returned to the evaporator at 19.5°C. At design conditions specified in the cycle model, the system delivered 10.6 kW of cooling duty at a COP of 0.63. The grey bars represent the thermal lift against which the system is operating. It can be seen that this single-effect heat pump provides a cooling duty well over 10 kW for a wide range of conditions at COPs > 0.63 for almost all conditions. Even at a cooling water temperature of 40°C (Test Point 5) a cooling duty of 11 kW was achieved at a COP of 0.67.

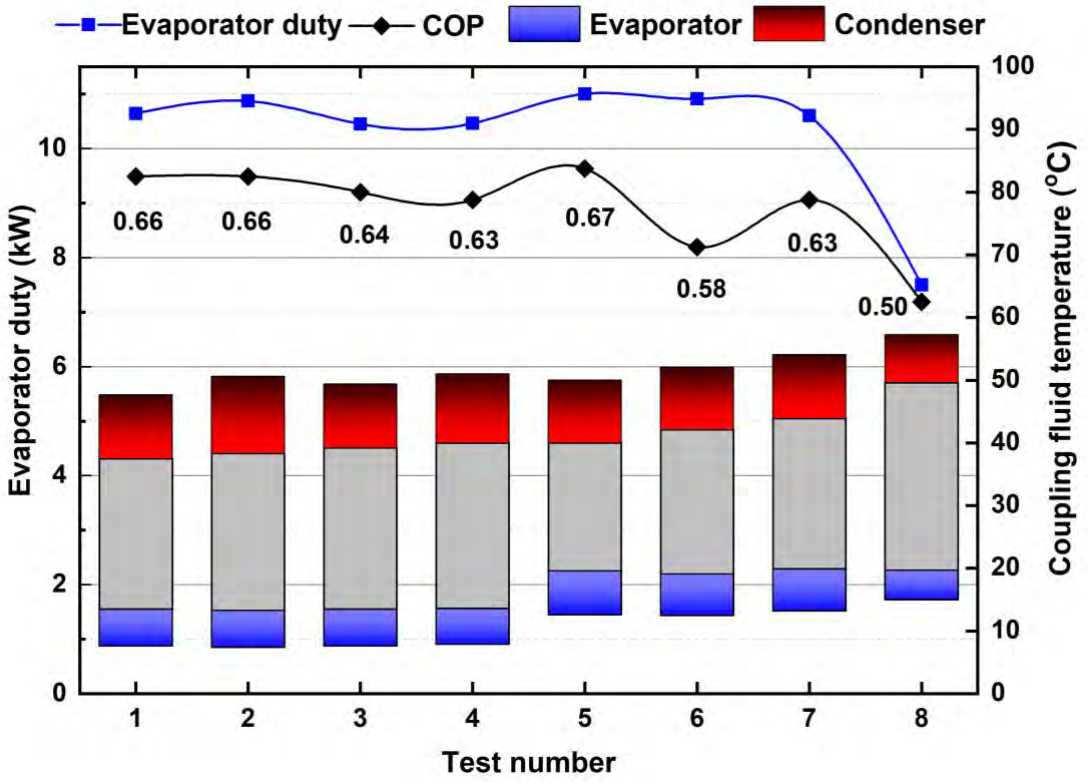

Figure 6: Experimental results for the prototype

6. CONCLUSIONS

The development of a compact waste-heat driven, residential-scale ammonia-water absorption chiller for high ambient temperatures is presented. Microscale heat and mass exchangers are utilized to provide 10.6 kW of cooling duty at a COP of 0.63 at design conditions. This demonstrates the scalability of microchannel technology from a proof-of-concept laboratory scale to residential-scale applications. With the feasibility of small-capacity absorption chillers demonstrated, high volume manufacturing methods shown here to fabricate microchannel components must be further refined to make them economically viable. This system can also be readily adapted to allow heating mode operation by simple switching of coupling fluid loops, thereby providing year-round service.

ACKNOWLEDGEMENTS

The authors acknowledge the financial support for this research through Advanced Research Projects Agency (ARPA-E), Department of Energy, USA Award # DE-0000842

NOMENCLATURE

Cp	Specific heat capacity (J kg^{-1}°C^{-1})	$\dot{Q}$	heat transfer rate (kW)
COP	coefficient of performance	T	temperature (°C)
$\dot{m}$	mass flow rate (kg s^{-1})		

Subscripts

cf	coupling fluid	$evap$	evaporator
des	desorber		

REFERENCES

Determan, M.D., Garimella, S., 2012. Design, fabrication, and experimental demonstration of a microscale monolithic modular absorption heat pump. Applied Thermal Engineering 47, 119-125.

Garimella, S., 2003. Innovations in energy efficient and environmentally friendly space-conditioning systems. Energy 28(15), 1593-1614.

Garimella, S., Keinath, C.M., Delahanty, J.C., Hoysall, D.C., Staedter, M.A., Goyal, A., Garrabrant, M.A., 2016. Development and demonstration of a compact ammonia–water absorption heat pump prototype with microscale features for space-conditioning applications. Applied Thermal Engineering 102, 557-564.

IEA, 2018. The Future of Cooling.

Klein, S.A., 2017. Engineering Equation Solver, F-Chart Software.

Lee, S., Bohra, L.K., Garimella, S., Nagavarapu, A.K., 2012. Measurement of absorption rates in horizontal-tube falling-film ammonia-water absorbers. International Journal of Refrigeration 35(3), 613-632.

Nagavarapu, A.K., Garimella, S., 2011. Design of Microscale Heat and Mass Exchangers for Absorption Space Conditioning Applications. Journal of Thermal Science and Engineering Applications 3(2), 021005-021005-021009.

Price, B.C., Bell, K.J., 1974. Design of binary vapor condensers using the colburn-drew equations. AIChE Symposium Series-Heat Transfer-Research and Design 70(138), 163-171.

Staedter, M.A., Garimella, S., 2018. Design and modeling of a microscale diabatic distillation column for small capacity ammonia–water absorption systems. International Journal of Refrigeration 94, 161-173.

Manuscript ID: 1184
DOI: 10.18462/iir.icr.2019.1184

Transcritical industrial heat pump using HFO's for up to 150°C hot air supply

Gisèle ABI CHAHLA[(1)], Yannick BEUCHER[(2)], Assaad ZOUGHAIB[(1)], Florence DE CARLAN[(2)], Jacques PIERUCCI[(3)]

[(1)] MINES ParisTech, PSL Research University, CES - Center for Energy efficiency of Systems, 5 rue Leon Blum, 91120 Palaiseau, France
assaad.zoughaib@mines-paristech.fr
[(2)] EDF Lab Les Renardières, Moret sur Loing et Orvanne, France
Florence.de-carlan@edf.fr
(3)R&D, Arjowiggins Graphic, Besse/Braye, France
jacques.pierucci@arjowiggins.com

ABSTRACT

Heat pumps may be used in drying processes to recover low-grade heat contained in moist exhaust air and supply the dryer. The heat pump design is limited technically by the level of process temperature and its performance optimization depends strongly on the difference between both temperature levels of process and effluents.
Using an exergy optimization methodology for heat pump integrations in industrial processes, a high temperature transcritical heat pump using the R-32 as working fluid was earlier proposed by the authors and experimentally demonstrated a 120°C hot air supply temperature.
In this paper, HFO's are considered to increase the air supply temperature to reach up to 150°C. Architecture technical options are also studied in order to improve the COP depending on the heat source and sink properties.
The prototype developed for the R-32 is adapted and used to validate the predicted performances. Its performance, when heating air from 90°C or 100°C to 150°C, is presented. The effluents are available at 82°C with different absolute humidities. The observed COP of the heat pump reached up to 3.72.
Keywords: Drying, Heat Recovery, HFO, Transcritical Cycle

1. INTRODUCTION

Due to the environmental concerns, improving energy efficiency of systems becomes a main challenge for all energy systems. This challenge implicates a better recovery of heat losses especially at high temperature in several industrial sectors. Indeed, a large amount of industrial sectors like paper drying needs heat at a high temperature range, typically 120°C-150°C, (Assaf 2010). In recent decades, studies dealt with the improvement of HPs energy efficiency especially those working at high temperature (Brown et al., 2009; Chamoun et al., 2012; Liu et al., 2012). Angelino (1994) demonstrated the advantages in an experimental point of view of the use of a transcritical HPs instead of subcritical HPs at high temperature for several stable fluids.
A thermodynamic model using Helmholtz multi-parametric equations to integrate the fluid properties was developed (Besbes et al., 2014) to predict the energy performances of transcritical HPs. And the results showed that 2 HFCs: R32, R134a and the HFO 1234yf have a great potential to maximize the energy efficiency of transcritical HPs at high temperature (120°C-130°C). This result led to a patent being registered (Peureux et al., 2014).
An experimental study dealing with the energy performance of a transcritical HP using the R32 as working fluid is presented by (Besbes et al., 2015). The operating conditions simulated a dryer

process. The heat source was humid air at 60°C (dew point at 45°C) and process air was heated from 60°C to 120°C. In this paper, the transcritical heat pump developed by Besbes et al. (2015) is adapted and used with the HFO 1234ze-E to increase the supply air temperature to 150°C.

2. EXPERIMENTAL METHODOLOGY

The experimental setup, designed in the previous work (Besbes et al., 2015), helped to demonstrate the high energy performance of a R32 transcritical HP. This experimental setup generates the conditions of an industrial dryer at the HP heat exchangers. Fig.1 provides the layout of a HP integrated with a preheater in a tunnel dryer. The effluents (moist air) preheat the ambient air moderately and get cooled to reach the saturation state. Then effluents pass through the evaporator to supply the HP with low grade heat. For this experimentation, only the HP energy performance was studied. The HP input operating conditions defined on the next paragraph were fixed with respect of the integration presented on Fig.1.

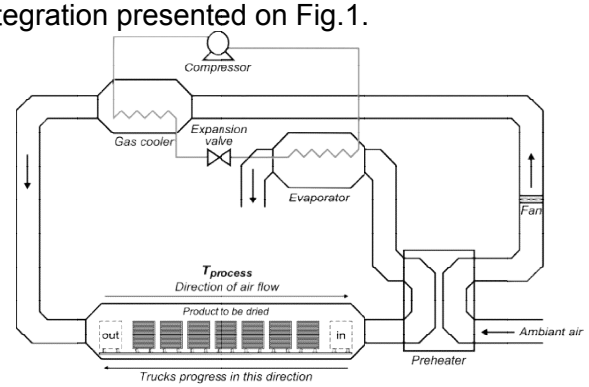

Figure 1:Schematic diagram of an integrated HP on a tunnel dryer process

2.1. Setup

To investigate the feasibility of delivering hot air at 150°C and the energy performance of the HFO1234ze-E transcritical HP system, the experimental setup is adapted and used. The main adaptation was the replacement of the lubricant. The fans were checked for their compatibility with higher temperature air. Moist air circulates on the cold loop. A schematic view of the experimental setup is shown in Fig. 2. The cold loop is composed of a steam humidifier, a fan, a heating resistor and valves to regulate the inlet evaporator air moisture content, temperature and mass flow rate. The hot loop is composed of a fan, a heating resistor, a valve system to control the temperature at the inlet of the gas cooler. Two sets of operating conditions are imposed on the test rig to try to get close to those of the typical drying processes (ADEME, 2006). For the first set (E1), the medium at the evaporator inlet is a humid air at 82°C with different level of absolute humidities ranging from 160 to 200 $gH_2O/kgDA$. The medium at the gas cooler inlet is an ambient air which was preheated from Tamb to 90°C to simulate the preheater of Fig.1, and the target temperature is fixed at 150°C.

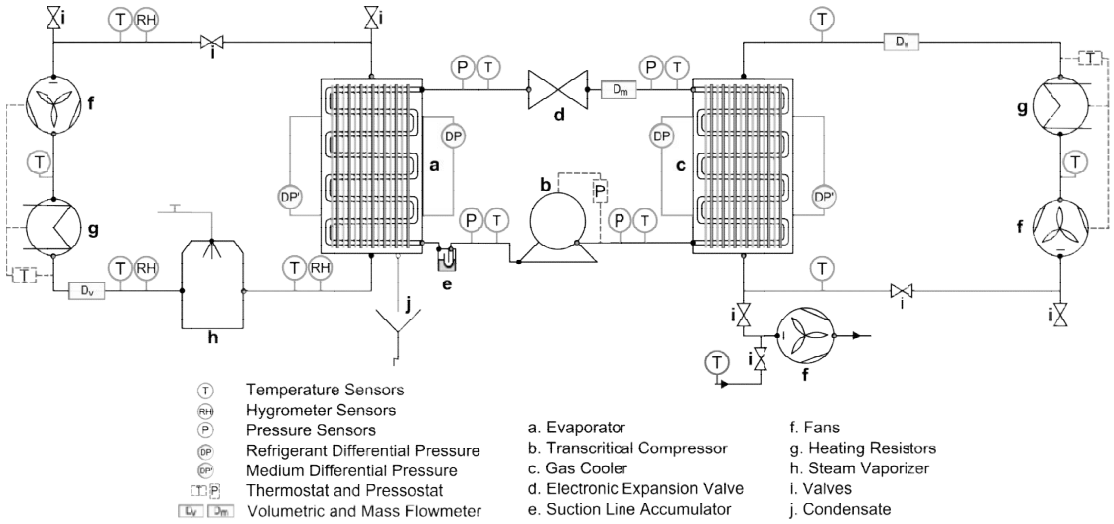

Figure 2: Test rig schematic view

For the second set (E2), the medium at the evaporator inlet is a humid air at 82°C with different level of absolute humidities ranging from 220 to 260 $gH_2O/kgDA$. The medium at the gas cooler inlet is an ambient air which was preheated from Tamb to 100°C, and the target temperature is fixed at 150°C.

The refrigerant loop is a single-stage vapour compression system. The following is a brief summary of the basic design and operating characteristics of the system:

- Refrigerant HFO1234ze-E was chosen as the working fluid of the heat pump (selected thanks to the methodology proposed in (Besbes et al, 2014). The critical temperature is equal to 109,4°C. And a polyolester synthetic oil (Reniso Triton se 170) was used as lubricant in the compressor.
- The gas cooler is an aluminium-finned stainless steel-tubes heat exchanger with dimensions of 0.30 m high x 0.60 m wide x 16 rows deep. The gas cooler has 1 circuit of 10 tubes per row of 12 mm external diameter and 2.5 mm pinch fins.
- The evaporator is an aluminium-finned stainless steel-tubes heat exchanger with dimensions of 0.72 m high x 0.75 m wide x 4 rows deep. The evaporator has 4 circuits of 6 tubes per row of 12 mm external diameter and 3 mm pinch fins.
- The compressor is a semi-hermetic reciprocating Bock HGX2/90 designed originally for R744 with a displacement of 7.70 m3/h at 50 Hz and a maximum discharge pressure of 13 000 kPa.
- A 3-phase induction motor is used to drive the compressor. The motor speed is controlled by a Danfoss, 3-phase, VLT HVAC frequency converter and the maximum input power of the motor is 11 kW.
- A CCM10 Danfoss electronic expansion valve designed for the R744 is used to control the refrigerant mass flow rate into the circuit and the gas superheat at the evaporator outlet.

Additional equipments of the heat pump included a suction line accumulator and compressor protection devices.

2.2. Instrumentation

The basic instrumentation required for evaluating the HP performance must include measurements of flow rate, temperatures, pressures and the electrical power input. Sensors were selected allowing defining the state conditions of the air and refrigerant at various localities shown in Fig.2. All the required readings were acquired at 10s intervals. Readings were considered for system performance analysis when they have been maintained steady for at least 20min.

Table 1 - List of measurement accuracies for the variables measured in the HP test rig

Measured property	Measuring sensors	Uncertainty on the value
Inlet and outlet refrigerant temperature	Class A RTD	±0.1 K
Inlet and outlet dry air temperature	Class A RTD	±0.1 K
Inlet and outlet air humidity	HC2-S ROTRONIC	±3% of measured value
Volume flow rate in the air loops	DEBIMO airfoil	±5%
Pressures in the air loops	CP300 KIMO	±0.5% + 1Pa
Pressures in the refrigerant circuit	PA21Y piezo resistive	±1%
Refrigerant mass flow rate	CORI FLOW	±0.2%
Compressor power input	3-Phase induction motor	±0.5%.

For the air loops, both dry and wet bulb temperature measurements were taken respectively at the gas cooler inlet and outlet and the evaporator inlet and outlet. The dry bulb temperatures were measured using stainless steel housing PT100 platinum resistance temperature devices (RTDs), and the wet bulb temperatures were measured by HC2-S ROTRONIC. At high relative humidity, the accuracy to measure the wet bulb temperature drops down. Thus, a lancing system was used to heat a moist air sample from the cold air loop. So the relative humidity decreases and the measure of the wet bulb temperature becomes more accurate. The volume flow rate was measured by the DEBIMO airfoil by KIMO for the two air loops. The differential pressures and pressures were measured by CP300 KIMO sensors. For the refrigerant circuit, temperatures and pressures were measured using respectively thermocouples and PA21Y piezo resistive pressure sensors, inserted through the walls of the refrigerant piping. As shown in Fig.2, locations of temperature and pressure sensors include the inlet and outlet of the compressor and gas cooler and the evaporator inlet. The refrigerant mass flow rate was measured by the CORI FLOW mass flow meter by BRONKHORST. The power input to the compressor was monitored using the Danfoss 3-phase induction motor and a wattmeter.

2.3. Experimental Tests

For all the tests performed in this work, the suction accumulator has been by passed to simplify the control. In our tests, the charge optimisation allows to reach the optimal high pressure. The expansion valve was controlled to maintain a reasonable super-heating value at the evaporator outlet, and simultaneously the motor speed compressor was controlled to reach the nominal point. The first tests served to determine the optimal refrigerant charge following the procedure proposed by Cho et al. (2005), Choi and Kim (2004) and Corberán et al. (2008). The optimal charge obtained for the first experimentations (7 kg) was kept for all the other operating conditions studied.
The tests series (E1) and (E2) were conducted at the full charge of the system under operating conditions introduced in previous paragraphs.

3. EXPERIMENTAL RESULTS AND DISCUSSION

Tests are performed using the experimental setup described earlier. The two experimentations set conditions are applied and for all the tests, the air exiting the gaz cooler attained 150°C. This temperature was controlled by adjusting the compressor rotating speed and the air flow rate. The control of the expansion valve insured a superheating of 5K for all the tests.
Table 2 gives the experimental results for both sets.
Results in table 2 show that the absolute humidity impacts directly the evaporator pressure.
Fig.3 shows the measured COP of the heat pump for each test. The COP is determined with an uncertainty of +/-3.3%.
The COP of the heat pump increases with the absolute humidity which is a direct consequence of the evaporating pressure increase. It is also noticed that the COP of the set E1 is higher than the COP of the set E2 even though the evaporator pressure is lower in set E1 than the one obtained in E2

Table 2 – Experimental results for the 2 experimentations sets (E1)and (E2)

		E1			E2		
Absolute humidity of input air temperature at the evaporator	g_{H2O}/kg_{DA}	160	180	200	220	240	260
Input air temperature at the evaporator	°C	82	82	82	82	82	82
Dew point of input air at the evaporator	*°C*	60.9	62.8	65.1	66.6	68.0	69.2
Input air temperature at the gas cooler	°C	90	90	90	100	100	100
Gaz cooler air outlet Temperature	°C	150	150	150	150	150	150
Gaz cooler pressure	*bar*	68.2	67.5	67.1	67.0	66.3	68.2
Evaporator pressure	*bar*	12.4	13	13.5	13.9	14.1	15.1
Evaporator capacity	*kW*	8.10	7.66	8.01	7.08	7.74	8.32
Gas cooler capacity	*kW*	11.34	10.54	11.15	10.13	11.01	11.79
Compressor power	*kW*	3.24	2.88	2.99	3.05	3.27	3.47

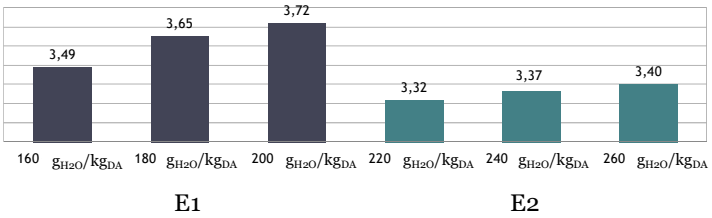

Figure 3: COP values for both sets (E1) and (E2)

Fig. 4 shows the evolution of vapor quality at the evaporator inlet for the realized tests.
The vapour quality at the inlet of the evaporator is significantly lower for the set E1 than the set E2. This is due mainly to the hot air inlet temperature (90°C for the set E1 and 100°C for the set E2) which impacts the refrigerant temperature at the outlet of the gaz cooler and hence the enthalpy at the inlet of the evaporator.

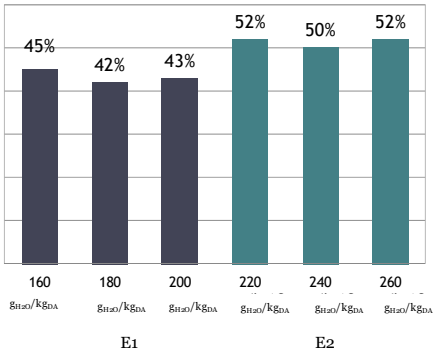

Figure 4 – Vapor quality at the inlet of the evaporator (in %)

Figure 5 shows on a T-H diagram how the change in the air inlet temperature impacts the cycle.

Indeed, as we can see in Fig. 5, the dashed part of the cycle is obtained for lower gaz cooler exit temperature. This temperature is directly impacted by the hot air inlet temperature. The resulting consequence is a lower vapour quality at the inlet of the evaporator and so a larger enthalpy change leading to an increased capacity at the evaporator for the same compression cost; which

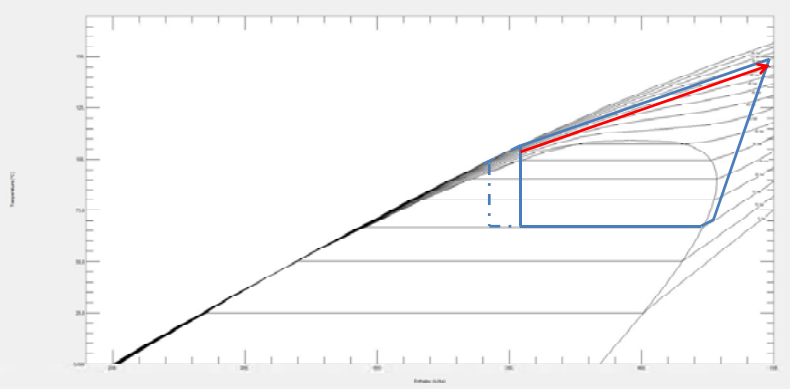

Figure 5: Effect of hot air inlet temperature on the cycle

explains the COP increase observed during the tests. This observation allows proposing technical options for improving the COP of such a heat pump using R-1234ze and supplying hot air at 150°C.

4. TECHNICAL OPTIONS FOR IMPROVING THE CYCLE

The experimental results presented in section 3 and their analysis have shown that the refrigerant temperature at the outlet of the gaz cooler will have a very important impact on the heat pump's COP. In the prototype, this temperature is directly linked to the hot air inlet temperature as it was highlighted between test sets E1 and E2.

One technical option, when the refrigerant properties are favourable, is to use an internal heat exchanger. Such a heat exchanger allows reducing the gaz cooler outlet temperature while increasing the superheat at the inlet of the compressor. Another technical option, which was studied for CO2 transcritical refrigeration cycles, is to use a parallel compression (Sarkar and Agrawal, 2010). Such a compression allows vapour compression on a smaller pressure difference reducing the main compressor input power.

Figures 6 and 7 show, in a T-H diagram, the simplified cycle including respectively the internal heat exchanger and the parallel compression.

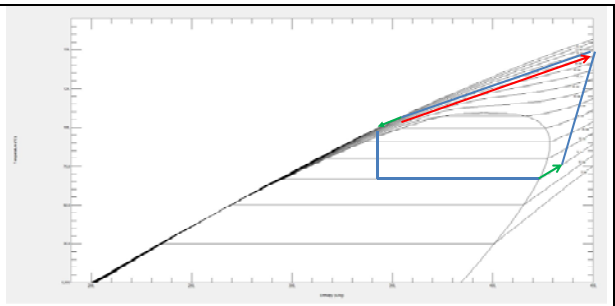

Figure 6 – T-H diagram of simplified transcritical cycle with IHX

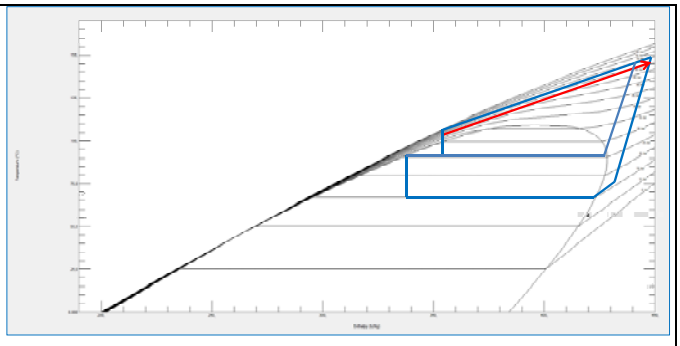

Figure 7 - T-H diagram of simplified transcritical cycle with parallel compression

These technical options where simulated for the first test of the E2 set (Evaporator air inlet temperature 82°C, absolute humidity 220 g/Kg_{da}, gaz cooler inlet air temperature 100°C). The simulation code is written in Python using Coolprop for the calculation of refrigerant properties. The main equations are first and second law and mass conservation. First the internal heat exchanger (IHX) was investigated, then the parallel compression and finally, combining both options.

The COP improvement is given in table 3.

Table 3 – COP improvement with IHX and parallel compression

Cycle	Transcritical	Transcritical+IHX	Transcritical+parallel compression	All options
COP	3.32	3.51	3.61	3.71

As we can see in table 3, parallel compression allows a 9% COP improvement. The use of IHX allows 6% COP improvement. The combination of the two options, by subcooling the liquid exiting the gaz cooler just before the first expansion, allows an improvement of 12% of the COP.
Indeed, both options allow the reduction of the evaporator inlet quality. This helps reducing the expansion valve losses. The parallel compression has an additional advantage of reducing the refrigerant mass flow to be compressed by the main compressor while compressing the rest of the mass flow at a lower pressure ratio.

5. CONCLUSIONS

The following conclusions can be drawn from the present analysis. The transcritical HP using the HFC 32 developped earlier has been able to supply 150°C hot air temperature by changing its working fluid to HFO-1234ze-E. The COP of the transcritical HP was measured for several operating conditions. In the worst operating conditions the HP presents a COP equal to 3.32 while it reached 3.72 for the most favourable ones. For the transcritical cycle, the vapor quality at the evaporator inlet is impacted by the conditions at the gaz cooler exit ones and affects the COP. Two technical options for improving the COP were simulated. They allow an improvement of 12% of the COP.

6. AKNOWLEDGEMENTS

The authors would like to aknowledge the financial support of ADEME through the TRANSPAC AMI project

7. REFERENCES

Angelino, G. Invernizzi, C., Supercritical heat pump cycles, International Journal of Refrigeration, Volume 17, Issue 8, 1994, Pages 543-554, ISSN 0140-7007.

Assaf, Khattar. 2010. Intégration D'une Pompe À Chaleur Dans Un Procédé Agroalimentaire - Simulation, Expérimentation et Intégration. Ph.D thesis, École Nationale Supérieure des Mines de Paris.

Besbes, Karim, Assaad Zoughaib, Florence De Carlan, and Jean-Louis Peureux. 2014. Exergy Based Methodology for Optimized Integration of Heat Pumps in Industrial Processes. International Refrigeration and Air Conditioning Conference at Purdue. http://docs.lib.purdue.edu/iracc/1435.

Besbes, Karim, Assaad Zoughaib, Florence De Carlan, and Jean-Louis Peureux. 2015. A R-32 TRANSCRITICAL HEAT PUMP FOR HIGH TEMPERATURE INDUSTRIAL APPLICATIONS. International Congress of Refrigeration, Yokohama.

Brown, J. Steven, Claudio Zilio, and Alberto Cavallini. 2009. The Fluorinated Olefin R-1234ze(Z) as a High-Temperature Heat Pumping Refrigerant. International Journal of Refrigeration 32(6): 1412–22. http://www.sciencedirect.com/science/article/pii/S0140700709000772 (February 14, 2014).

Chamoun, Marwan, Romuald Rulliere, Philippe Haberschill, and Jean Francois Berail. 2012. Dynamic Model of an Industrial Heat Pump Using Water as Refrigerant. International Journal of

Refrigeration 35(4): 1080–91.
http://www.sciencedirect.com/science/article/pii/S0140700711003082.

Cho, Honghyun, Changgi Ryu, Yongchan Kim, and Ho Young Kim. 2005. Effects of Refrigerant Charge Amount on the Performance of a Transcritical CO2 Heat Pump. International Journal of Refrigeration 28(8): 1266–73.

Choi, Jongmin, and Yongchan Kim. 2004. Influence of the Expansion Device on the Performance of a Heat Pump Using R407C under a Range of Charging Conditions. International Journal of Refrigeration 27: 378–84.

Corberán, Jose M., Israel O. Martínez, and José Gonzálvez. 2008. Charge Optimisation Study of a Reversible Water-to-Water Propane Heat Pump. International Journal of Refrigeration 31(4): 716–26. http://www.sciencedirect.com/science/article/pii/S0140700707002484 (December 12, 2014).

ADEME : Le sechage thermique. Rapport technique, ADEME, Département Industrie et Agriculture, 2006.

Liu, Zhaoyong, Li Zhao, Xuezheng Zhao, and Hailong Li. 2012. The Occurrence of Pinch Point and Its Effects on the Performance of High Temperature Heat Pump. Applied Energy 97: 869–75.

Meunier, Francis, Paul Rivet, and Marie-france Terrier. Froid Industriel 2ed.

Peureux, Bourig, Zoughaib, Besbes. Equipement including a heat pump for heating an external fluid with a large temperature differential. International Patent WO2014020255 (A1), 2014.

Sarkar J.,Agrawal N. Performance optimization of transcritical CO2 cycle with parallel compression economization. International Journal of Thermal Sciences. Volume 49, Issue 5, May 2010, Pages 838-843

Zhao, Chen Ru, and Pei Xue Jiang. 2011. Experimental Study of in-Tube Cooling Heat Transfer and Pressure Drop Characteristics of R134a at Supercritical Pressures. Experimental Thermal and Fluid Science 35(7): 1293–1303.

Manuscript ID: 1186
DOI: 10.18462/iir.icr.2019.1186

Trans-critical vapor compression cycle using butane (R600) as refrigerant for industrial waste heat recovery

Manuel VERDNIK, René RIEBERER, Heinz MOISI

Institute of Thermal Engineering, Graz University of Technology
Graz, 8010, Austria, manuel.verdnik@tugraz.at

ABSTRACT

By utilizing a trans-critical vapor compression cycle using hydrocarbons, the operating range of these natural refrigerants with low global warming potential and zero ozone depletion potential can be extended to higher temperature levels.
A single-stage cycle using a reciprocating (suction gas cooled) compressor and an internal heat exchanger for suction gas superheating has been modeled using Modelica and the TIL thermal component library. The simulation model has been validated by means of experimental data gathered with a R600 test rig operated at condensing temperatures up to 110°C.
The simulation model was modified to study the system behavior in trans-critical operation. Increasing the suction gas superheat lowers the values for the high-side pressure at which the maximum efficiency is reached, which could be utilized if the high-side pressure is limited by the used components. Through the application of an internal heat exchanger, the increase of superheat shows potential to increase the Coefficient of Performance (COP).
Keywords: Heat Recovery, High Temperature, Hydrocarbon, Trans-critical Cycle.

1. INTRODUCTION

With an energy consumption of 148 EJ, the industrial sector accounted for 37% of the world's total final energy consumption in 2016 (IEA, 2018). Recovering waste heat through the utilization of high temperature heat pumps can increase process efficiencies and decrease the use of fossil fuels, thus leading to a reduction in CO_2 emissions. In order to reduce the greenhouse gas emissions caused by the release of refrigerants to the atmosphere, the Kigali amendment to the Montreal protocol regulates a step-wise phase down of refrigerants with a high global warming potential (UNEP, 2016). Currently, heat supply temperatures up to 160°C are achievable with vapor compression heat pumps using the refrigerant R1336mzz-Z in the Viking Heat Booster (Viking, 2018). The Kobe Steel SGH 165 produces steam at 120 °C with a R245fa vapor compression heat pump and compresses it further to 165 °C (Arpagaus et al., 2018). Trans-critical vapor compression cycles allow an extension of the operating range of refrigerants beyond their critical temperature (Angelino and Invernizzi, 1994). Implemented with R744 (Lorentzen, 1990), this is a well-known technology (Austin and Sumathy, 2011), yet the application of other refrigerants is very limited. Besbes et al. (2015) developed a trans-critical R32 heat pump with a heat source temperature of 50°C and a heat sink temperature of 120°C.
The hydraulic layout and the t/h-diagram of a single-stage trans-critical vapor compression heat pump with an internal heat exchanger (IHX), using R600 as refrigerant is depicted in Fig. 1. After the compression to a high-side pressure exceeding the critical pressure of the refrigerant (37,96 bar), the heat rejection occurs at gliding temperature instead of condensation at constant temperature, as can be seen in the t/h-diagram in Fig. 1 (right). Without the relation between temperature and saturation pressure the necessary control of the high-side pressure can be obtained by adjusting the refrigerant mass in the according part of the cycle (Kim et al. 2004). In the observed cycle, this is realized with the pressure control valve (PCV) (Pos. 3). While the heat sink and source temperatures are boundary conditions set by the application, the suction gas superheat and the high-side pressure

can be adjusted to optimize the operation of the heat pump. To study the influence of these parameters, a simulation study based on a sub-critical test rig was carried out.
The sub-critical single-stage compression cycle equipped with a high-pressure receiver is modeled and validated with experimental data from a test rig, obtained by Moisi and Rieberer (2018). By adding a pressure control valve (PCV) at the receiver inlet (Pos. 3) as illustrated in Fig. 1, the high-side pressure can be raised above the critical pressure of the refrigerant, representing a trans-critical cycle with a medium pressure receiver. The test rig as well as the evaluation of the experimental data is described in Section 2, the simulation model is outlined in Section 3 and the results are presented in Section 4.

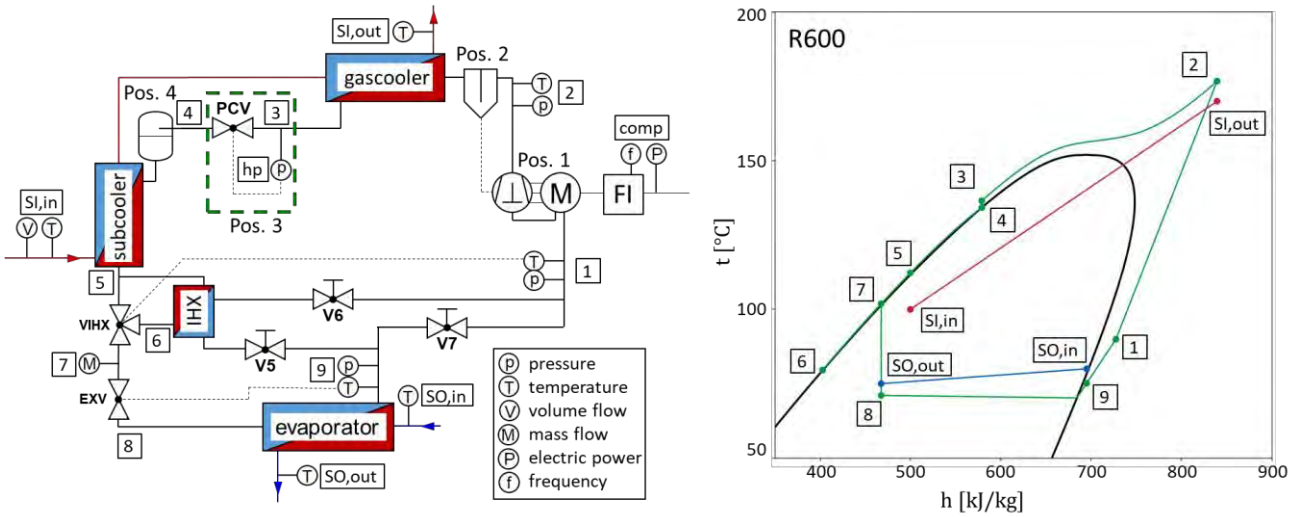

Figure 1: Hydraulic layout (left) and t/h-Diagram (right) of the studied trans-critical cycle

2. SUB-CRITICAL TEST RIG

The test rig of a sub-critical one-stage R600 high temperature heat pump has been developed during a preceding project (Moisi et al, 2018). The heat pump has a capacity of 45 kW at a heat source inlet/outlet temperature of 70/65 °C, a heat sink inlet/outlet temperature of 80/110 °C and an inverter frequency of 75 Hz (Moisi et al., 2017). The hydraulic layout depicted in Fig. 1 (left) corresponds to the refrigerant cycle of the sub-critical heat pump with the exception of the PCV. The suction gas superheating in the IHX can be adjusted with the 3-way-valve (VIHX). The IHX can be bypassed by closing the valves V5 and V6. A modified 30L-DLRX-13 separating hood reciprocating compressor (Pos. 1) from the project partner Frigopol equipped with a frequency inverter is used in the test rig. The modification of the compressor comprises a specially designed suction gas motor cooler to enable the necessary suction gas superheat needed to avoid wet compression due to an “overhanging” two-phase region of R600 (Moisi and Rieberer, 2016). To avoid accumulation of compressor lubricant in the refrigerant cycle, an oil separator (Pos. 2) is placed after the compressor. In sub-critical operation, the gascooler acts as condenser. The high-pressure receiver (Pos. 4) ensures saturated liquid state at the inlet of the subcooler. The electric expansion valve (EXV) regulates the refrigerant mass flow into the evaporator, thus controlling the suction gas superheat at the evaporator outlet. Brazed plate heat exchangers are used for the condenser, subcooler and evaporator. Water at a pressure of 2,5 bar is used in the heat sink and heat source cycles.

2.1. Measured Compressor and system efficiencies

Measurement data of the heat pump prototype at different operating points with an inverter frequency of 50 Hz, obtained by Moisi and Rieberer (2018), was used to evaluate the compressor and the system efficiencies. The positions of the sensors are depicted in Fig. 1. Relevant properties of R600 and water are obtained from the property database included in the software EES (2018). The overall isentropic efficiency, the internal isentropic efficiency and the volumetric efficiency of the compressor are calculated according to Eq. (1), Eq. (2) and Eq. (3) respectively.

$$\eta_{is,ov} = \frac{\dot{m}_{ref} \cdot (h_{ref,2s} - h_{ref,1})}{P_{el,comp}} \quad \text{Eq. (1)}$$

$$\eta_{is,i} = \frac{h_{ref,2s} - h_{ref,1}}{h_{ref,2} - h_{ref,1}} \quad \text{Eq. (2)}$$

$$\lambda_{vol} = \frac{\dot{m}_{ref}}{\rho_{ref,1} \cdot \dot{V}_{swept}} \quad \text{Eq. (3)}$$

The dependency of the compressor efficiencies on the pressure ratio is expressed by polynomials using the least squares approximation. Measured efficiencies as well as the approximations are depicted in Fig. 2.

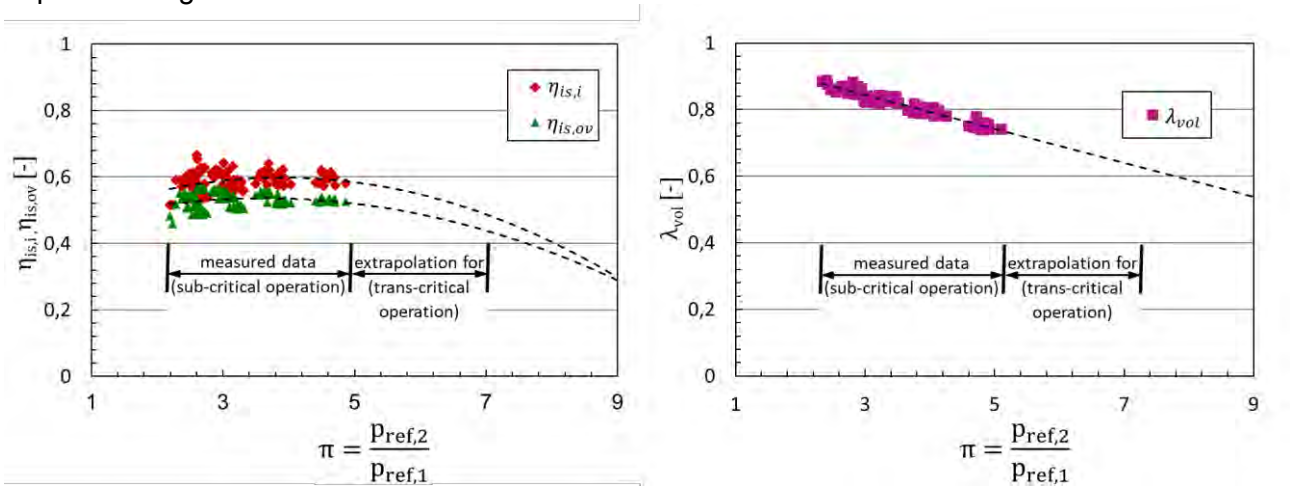

Figure 2: Overall isentropic and internal isentropic efficiency (left) and volumetric efficiency (right) of the Frigopol prototype compressor

The COP was evaluated with the measured heat release to the water cycle according to Eq. (4)

$$COP = \frac{\dot{Q}_{h,w}}{P_{el,comp}} = \frac{\dot{V}_{SI,in} \cdot \rho_{SI,in} \cdot cp_{SI,in} \cdot (t_{SI,out} - t_{SI,in})}{P_{el,comp}} \quad \text{Eq. (4)}$$

3. SIMULATION MODEL

The TIL Suite package (TLK-Thermo, 2018), containing model libraries for components and media properties in the object-based Modelica language, was used to develop the simulation model for this study. Predefined models of the package can be extended with user specific geometries or correlations for heat transfer and pressure drop.
First, the sub-critical test rig was modelled without the PCV according to the hydraulic layout in Fig. 1 with exception to the neglected oil separator. For the trans-critical operation, the PCV was added. The following sections describe the modelling of the compressor and the heat exchangers.

3.1. Compressor

The compressor was modelled using the “efficiency based compressor model” included in TIL with efficiencies according to Eqs. (1) to (3) deduced from measurement data as described in section 2.1 for the prototype compressor from Frigopol. In order to investigate a different compressor, data for a Bitzer 4VE-10P operated with R134a were retrieved from the manufacturer’s design software (Bitzer, 2018) to evaluate the efficiencies according to Eq. (1) and Eq. (3). Since there is no data for the compressor discharge temperature available in the software, the internal isentropic efficiency was assumed. The obtained polynomials as well as the nominal volumetric flow rate are listed in Table 1.

Table 1. Data used for modelling the compressor

	Frigopol 30L-DLRX-13 mod.	Bitzer 4VE-10P
$\eta_{is,ov}$	$0{,}4239 + 0{,}0619\pi - 0{,}0085\pi^2$	$0{,}6845 - 0{,}002\pi - 0{,}0004\pi^2$
$\eta_{is,l}$	$0{,}4211 + 0{,}0906\pi - 0{,}0116\pi^2$	$0{,}7600 - 0{,}002\pi - 0{,}0004\pi^2$
λ_{vol}	$0{,}9982 - 0{,}0512\pi$	$0{,}9747 - 0{,}0372\pi$
$\dot{V}_{swept}$ @ 50Hz	29,94 $m^3 \cdot h^{-1}$	34,7 $m^3 \cdot h^{-1}$

3.2. Heat Exchangers

The brazed plate heat exchangers are modeled with a finite volume approach and a discretization of 10 cells each. Geometrical data of the heat exchangers is listed in Table 2, a sinusoidal chevron pattern with a pattern angle of 60° is assumed for all heat exchangers.

Table 2. Geometrical data of the used heat exchangers

	Evaporator	Gascooler	Subcooler	IHX
Number of plates (-)	40	40	14	30
Length (mm)	466	476	250	250
Width (mm)	111	113	112,8	112,8
Pattern amplitude (mm)	1,91	1,68	1,91	1,91
Wall thickness (mm)	0,4	0,3	0,4	0,4

The heat transfer coefficients for evaporating and superheated R600 were calculated according to Longo et al. (2015), for condensing R600 the correlation by Akers et al. (1959) was used. Heat transfer coefficients for trans-critical operation were calculated using the correlation by Forooghi and Hooman (2014). The pressure drop in trans-critical operation, the heat transfer coefficient and pressure drop for liquid R600 in the subcooler and IHX as well as for the water side of the heat exchangers were calculated according to Martin (2013). The pressure drop during evaporation and condensation were calculated according to Longo et al. (2010) and Longo et al. (2012), respectively. The pressure drop for superheated R600 in the IHX was calculated according to Martin (2013).

4. RESULTS

4.1. Validation of the Model at Sub-critical Conditions

The COP measured at sub-critical operating points listed in Table 3 is compared with results from the simulation model, in both cases without the IHX. As can be seen from Fig. 3 (right), the relative deviation between simulation and experiment is less than 7% for all operating points.

Table 3. Experimentally investigated operation points (Moisi and Rieberer, 2018)

$t_{SO,in}$	50				60			70		80
$t_{SO,out}$	45				55			65		75
$t_{SI,in}$	50	60	70	80	60	70	80	70	80	80
$t_{SI,out}$	80	90	100	110	90	100	110	100	110	110
COP_{meas}	4.68	3.91	3.38	2.91	4.88	4.11	3.50	5.14	4.26	4.85

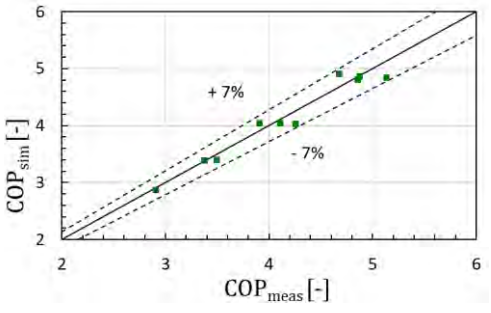

Figure 3. Comparison of simulated and measured COP at sub-critical conditions

4.2. Trans-critical Operation

Since the properties of a substance vary considerably in the vicinity of the critical point, the discretization of the gas cooler needs to be fine enough to consider these variations. In order to exclude the influence of the discretization of the gas cooler on the results of the simulation, the

variation of the COP with the high side pressure was investigated for different cell numbers in the gascooler. The value for the optimal high-side pressure at which the maximal COP occurs changed for simulations conducted with less than 80 cells. As more cells require more computational effort, especially during the initialization phase of the simulation, 80 cells were chosen as a tradeoff between computational effort and accuracy for the further simulations.

4.2.1. Optimal high-side pressure

At a fixed compressor inlet state, increasing the high-side pressure leads to an increase of the compressor outlet temperature (state point 2) and the required compressor power. Due to the heat rejection at gliding temperature in trans-critical operation and the curvature of a super-critical isobar, the location of the pinch point in the gascooler depends on the gas cooler inlet state and thus on the high-side pressure. At too low high-side pressures as depicted in Fig. 4 (left), the small temperature difference at the inlet of the gascooler affects the heat transfer, thus increasing the refrigerant temperature at the outlet of the gascooler (state point 3) and the subcooler (state point 5) and decreasing the heating capacity. Increasing the high-side pressure increases the temperature difference between refrigerant and heat sink medium at the inlet of the gascooler. This increases the heating capacity to the cost of increased compressor power. Fig. 4 (right) decipts a cycle with a too high high-side pressure. An optimum high-side pressure for achieving the highest COP at a certain operating point can be found as shown in Fig. 4 (middle).

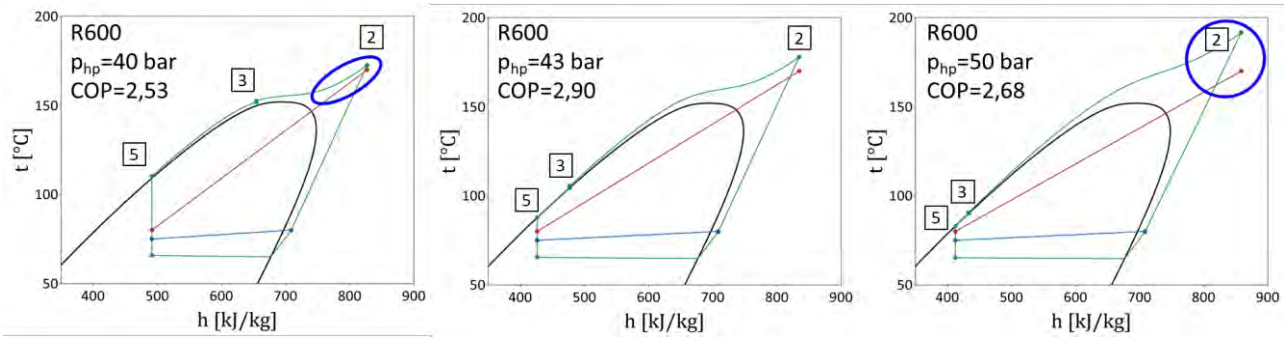

Figure 4: t/h-diagram for different high-side pressures at source inlet/outlet temperatures of 80/75 °C, sink inlet/outlet temperatures of 80/170 °C and a suction gas superheat of 15 K (without IHX)

4.2.2. Influence of the operating parameters

Simulation runs with different sink inlet temperatures but constant outlet temperature of 160 °C are shown in Fig. 5 (left). An increase in the sink inlet temperature leads to an increase of the refrigerant temperature at the subcooler outlet causing a decrease in the heating capacity (Moisi et al, 2018). Since the compressor power remains almost constant, a decline of the COP can be observed. The optimal value for the high-side pressure is not significantly influenced by the heat sink inlet temperature. Increasing the sink outlet temperature demands an increase of the high-side pressure. The increased compressor power leads to a drop of the maximal COP as can be seen in Fig. 5 (right).

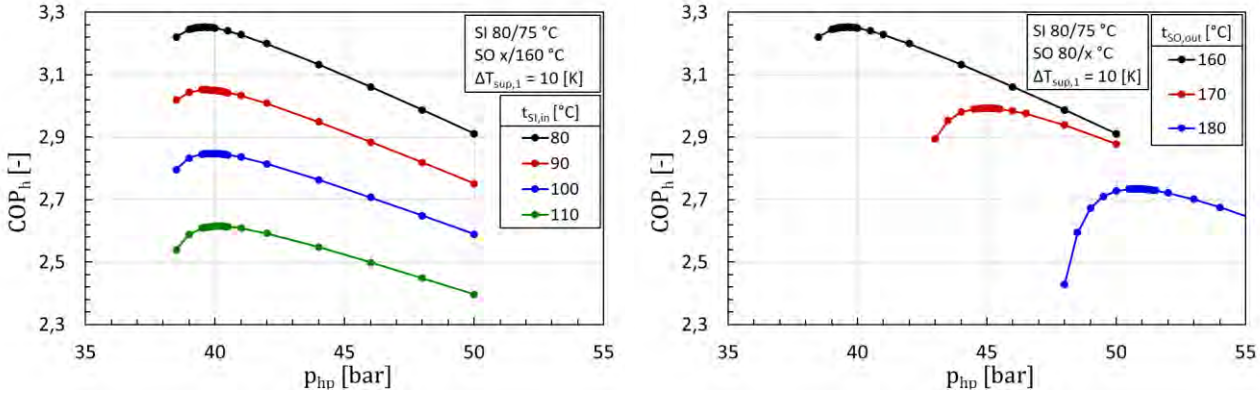

Figure 5: COP at varying sink inlet temperatures (left) and outlet temperatures (right) depending on the high-side pressure (without IHX)

The influence of a varying suction gas superheat realized in the evaporator (without using the IHX) can be observed in Fig. 6 (left). With increased superheat, the optimal high-side pressure drops. In cases where the maximum pressure is limited by components of the system, this can be used to reduce the necessary high-pressure level. However, as can be seen in Fig. 6 (right), the decreasing evaporation temperature at increasing superheat leads to a decrease in the heating capacity. The compressor power is almost constant because the decreased mass flow needs to be compressed at higher pressure differences. As a result, the COP decreases at increased superheat, which can clearly be seen in Fig. 6 (left).

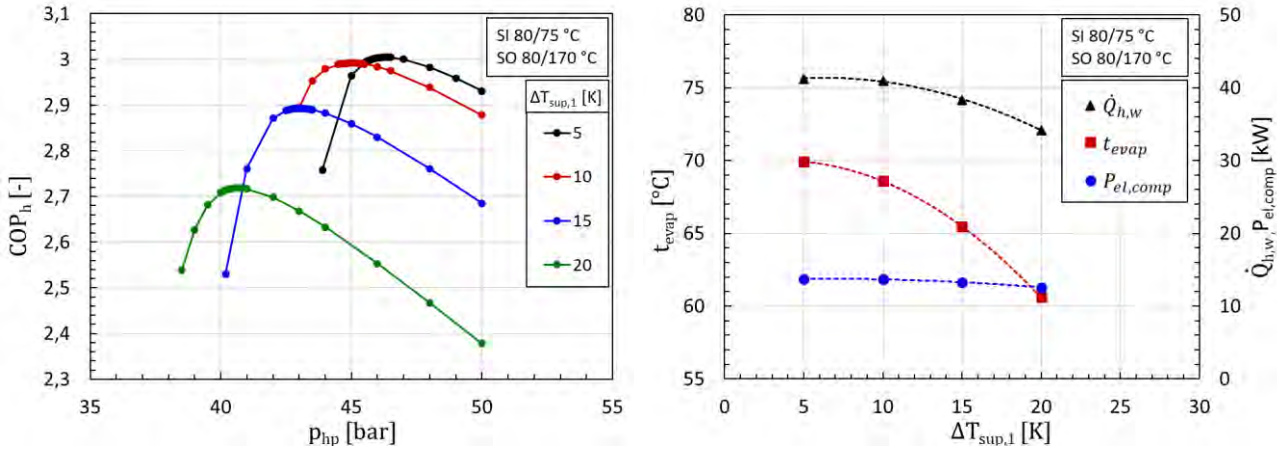

Figure 6: COP for different high-side pressures at varying suction gas superheat (left) and the influence of the superheat on evaporation temperature and capacities (right) (without IHX)

4.2.3. Possible improvements of the investigated cycle

The application of an internal heat exchanger as depicted in Fig. 1 enables an increase of the superheat without a decrease of the evaporation temperature. Fig. 7 (left) shows the COP at different values for suction gas superheat at the compressor inlet, where 5 K of superheat were obtained at the outlet of the evaporator and the rest was achieved using an IHX. As already observed without using the IHX, the optimal high-pressure drops but due to the IHX, the evaporation temperature does not decrease when increasing the suction gas superheat. As a result, the COP increases with increasing superheat because the compressor power remains almost constant while the heating capacity increases due to the increased superheat.

Another aspect for improvement is the used compressor. As can be seen from the efficiency data in Fig. 2, the prototype compressor is operated far outside the nominal operating range, thus leading to a deterioration of the efficiencies. Fig. 7 (right) shows the results with efficiency data for the Bitzer compressor as listed in Table 1. According to the simulation results, this compressor improves the COP and a further reduction of the optimal high-side pressure is possible.

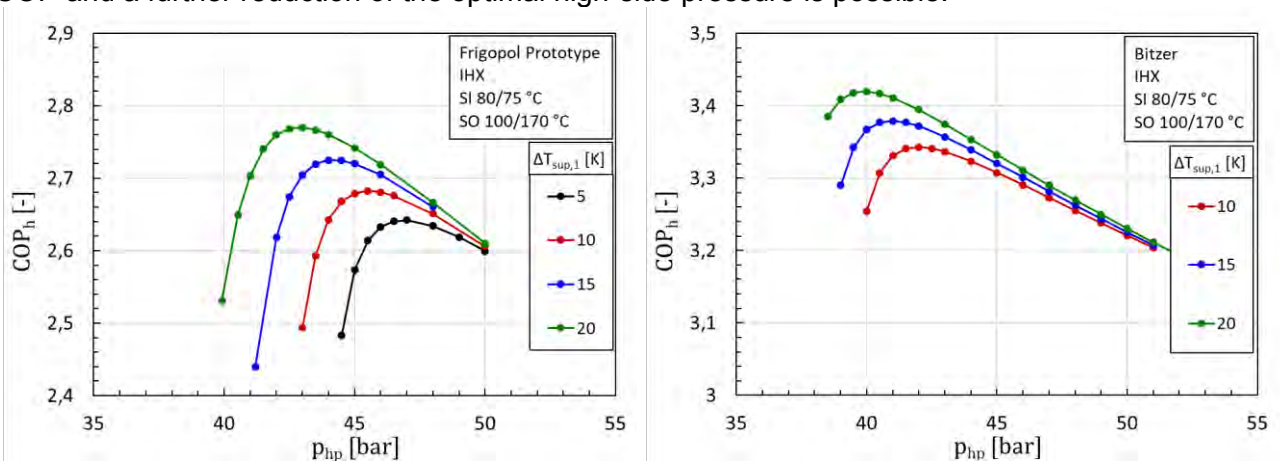

Figure 7: COP for different high-side pressures at varying suction gas superheat using an IHX with the Frigopol prototype compressor (left) and a Bitzer 4VE-10P (right)

5. CONCLUSIONS AND OUTLOOK

The introduced simulation model of a R600 high-temperature heat pump describes the COP of the sub-critical test rig with a deviation of less than 7% from the measured values.
By including a pressure control valve at the inlet of the receiver, trans-critical operation of the heat pump was investigated by means of simulation. The influence of the regulated high-side pressure on the COP showed an optimal value for each operating point that occurs at lower pressures if the suction gas superheat at the compressor inlet is increased. By using an internal heat exchanger, an increase of the COP by increasing the suction gas superheat is possible. At a heat source inlet/outlet temperature of 80/75 °C and a heat sink inlet/outlet temperature of 80/160 °C, the basic cycle without IHX using the Frigopol prototype compressor achieved a COP of 3.24 at a suction gas superheat of 5 K. At a sink inlet/outlet temperature of 100/170 °C, a COP of 2.64 was achieved. Using an IHX to raise the suction gas superheat to 20 K, the COP was improved to 2.77 while decrasing the high-side pressure from 47 to 43 bar. By using the Bitzer compressor, a further increase of the COP to 3.42 at a high-side pressure of 40 bar should be possible.
This study serves as the basis for the development of a prototype because application specific limitations of the components need to be taken into consideration. The model predicts compressor outlet temperatures 5-10 K higher than the sink outlet temperature at optimal high pressures, depending on the suction gas superheat. The expected high temperatures require special compressor lubricants such as Polyalphaolefin (PAO) oils. If suction gas cooled compressors are used, the maximum suction gas temperature represents a limit to the maximum evaporation temperature. The next steps will be to experimentally test the operating limits of the compressor such as the maximum high pressure and maximum suction gas temperature and then to develop a prototype for the trans-critical R600 vapor compression heat pump.

ACKNOWLEDGEMENTS

This work has been conducted in the course of the cooperative project “TransCrit” (FFG No.: 865083) under the cooperation of TU Graz and Frigopol Kälteanlagen GmbH. The project is funded by the Austrian Climate and Energy Fund and carried out within the Austrian Energy Research Program 2017.

NOMENCLATURE

1…9	state point
COP	Coefficient of Performance
cp	specific heat capacity (kJ·(kg·K)$^{-1}$)
$\eta_{is,ov}$	overall isentropic efficiency (-)
$\eta_{is,i}$	internal isentropic efficiency (-)
EXV	electric expansion valve
f	frequency (Hz)
h	specific enthalpy (kJ·kg^{-1})
IHX	internal heat exchanger
in	inlet
λ_{vol}	volumetric efficiency
meas	measured
$\dot{m}_{ref}$	refrigerant mass flow (kg·h^{-1})
out	outlet
p	pressure (bar)
p_{hp}	high-side pressure (bar)
PCV	pressure control valve
$P_{el,comp}$	electric power of the compressor (kW)
π	pressure ratio of the compressor (-)
$\dot{Q}_{h,w}$	heating capacity on water side (kW)
ref	refrigerant
ρ	density (kg·m^{-3})
s	isentropic change of state
SI	heat sink
sim	simulated
SO	heat source
ΔT_{sup}	suction gas superheat (K)
t	temperature (°C)
t_{evap}	evaporation temperature (°C)
V	valve
$\dot{V}$	volume flow
VIHX	3-way-valve internal heat exchanger
$\dot{V}_{swept}$	swept volume flow of the compressor (m^3·h^{-1})

REFERENCES

Akers, W.W., Deans, H.A., Crosser, O.K., 1959. Condensing heat transfer within horizontal tubes. Chemical Engineering Progress 54(10), 89-90

Angelino, G., Invernizzi, C., 1994. Supercritical heat pump cycles. International Journal of Refrigeration 17(8), 543-554

Arpagaus, C., Bless, F., Uhlmann, M., Schiffmann, J., Bertsch, S., 2018. High temperature heat pumps: Market overview, state of the art, research status, refrigerants, and application potentials. Energy 152, 985-1010

Austin, B., Sumathy, K., 2011. Transcritical carbon dioxide heat pump systems: A review. Renewable and Sustainable Energy Reviews 15(8), 4013-4029

Besbes, K., Youghaib, A., De Carlan, F., Peureux, J.-L., 2015. A R-23 transcritical heat pump for high temperature industrial applications. Proceedings of the IIR Conference of Refrigeration, Yokohama, Japan

Bitzer, 2018. Bitzer Software v. 6.9.2074, BITZER Kühlmaschinenbau GmbH, Sindelfingen, Germany

EES, 2018. Engineering Equation Solver v. 10.439, F-Chart Software, Madison, Wisconsin.

Forooghi, P., Hooman, K., 2014. Experimental analysis of heat transfer of supercritical fluids in plate heat exchangers. International Journal of Heat and Mass Transfer 74, 448-459

IEA, 2018. International Energy Agency. World Energy Balances: Overview (2018 Edition), https://webstore.iea.org/world-energy-balances-2018-overview (27.1.2019)

Kim, M., Pettersen, J., Bullard, C. W., 2004. Fundamental process and system design issues in CO2 vapor compression systems. Progress. in Energy and Combustion Science 30(2), 119-174

Longo, G.A., 2010. Heat transfer and pressure drop during hydrocarbon refrigerant condensation inside a brazed plate heat exchanger. International Journal of Refrigeration 33(5), 944-953

Longo, G.A., 2012. Hydrocarbon Refrigerant Vaporization Inside a Brazed Plate Heat Exchanger. Journal of Heat Transfer 134(10), 101801 1-10

Longo, G.A., Mancin, S., Righetti, G., Zilio, C., 2015. A new model for refrigerant boiling inside Brazed Plate Heat Exchangers (BPHEs). International Journal of Heat and Mass Transfer 91, 114-149

Lorentzen, G., 1990. Trans-critical vapour compression cycle device. Patent WO/07683

Martin, H., 2013. Druckverlust und Wärmeübergang in Plattenwärmeübertragern. In: Verein Deutscher Ingenieure, VDI-Wärmeatlas, Springer Vieweg, Berlin, 1687-1693

Moisi, H., Rieberer, R., 2016. Erforderliche Sauggasüberhitzung bei einer R600-Hochtemperaturwärmepumpe – Nutzung der Motorabwärme. Proc. Deutscher Kälte- und Klimatechnischer Verein (DKV)-Tagung. Kassel, Germany, November 2016, paper II.2.15.

Moisi, H., Rieberer, R., Verdnik, M., Baumhakel, A., 2017. Entwicklung einer R600-Hochtemperatur-Wärmepumpe - Simulation und erste Messungen. Proc. Deutscher Kälte- und Klimatechnischer Verein (DKV)-Tagung. Bremen, Germany, November 2017, paper AA IV 08

Moisi, H., Rieberer, R., 2018. Experimental Analysis of a R600 High Temperature Heat Pump. Proc. 13th IIR Gustav Lorentzen Conference. Valencia, Spain, June 2018, paper 1223

Moisi, H., Rieberer, R., Baumhakel, A., 2018. “HotCycle” – Final Project Report (FFG-Nr.: 848892). Insitute of Thermal Engineering, Graz University of Technology, Graz

TLK-Thermo, 2018. TIL Suite v.3.6.0, TLK-Thermo GmbH, Braunschweig, Germany

UNEP, 2016. The Kigali amendment to the Montreal Protocol: HFC phase-down, ozonaction fact sheet. 8th Meeting of the Parties to the Montreal Protocol, Kigali, Rwanda, UNEP, 1-7

Viking, 2018. Viking Heat Engines AS. Heat Booster. Product Information. http://www.vikingheatengines.com/upl/files/142690 (5.4.2018)

Manuscript ID: 1193
DOI: 10.18462/iir.icr.2019.1193

Thermodynamic analysis and selection of refrigerants for high-temperature heat pumps

José M. CORBERÁN[(a)], Abdelrahman H. HASSAN[(a),(b)], Jorge PAYÁ[(a)]

[(a)] Institute for Energy Engineering, Universitat Politècnica de València, Camino de Vera s/n, Valencia, 46022, Spain, corberan@ter.upv.es

[(b)] Mechanical Power Engineering Department, Faculty of Engineering, Zagazig University, Zagazig, 44519, Egypt, ahassan@iie.upv.es

ABSTRACT

This paper presents an analysis of the performance of high-temperature heat pumps using different refrigerants. A thermodynamic cycle model, considering minimum temperature difference at the heat exchangers pinch point, and reasonable pressure drop and efficiencies, has been developed. The source temperature was fixed at 80 °C, as a reference, while the temperature lift between sink and source was varied from 40 to 80 K to cover a wide range of applications. The selected refrigerants were categorized into three groups, wet, dry, and isentropic, based on the slope of saturated vapor curve on T-s diagram. The results showed that isentropic refrigerants, R-245fa, R-1233zd(E), and Butene, have the highest performance compared to dry and wet refrigerants. R-1233zd(E) is considered to be the most suitable one regarding performance and safety, however it only allows a maximum temperature lift of 73 K. Acetone seems to be a good candidate for higher temperature lifts.

Keywords: High-temperature Heat Pump, Modelling, Refrigerants, COP, Subcooler.

1. INTRODUCTION

To reduce the energy consumption and mitigate the negative impacts on environment, high-temperature heat pumps (HT-HPs) are considered to be an efficient solution. HT-HP is a promising technology that opens the door for several applications, one of the important applications is the industrial waste heat recovery. To imagine, in figures, the significant potential of industrial waste heat, Panayiotou et al. (2017) reported that this sector accounts for 370.41 TWh per year in the European industry. This heat represents a very valuable source, usually available between 40 and 80 °C, which could be reutilized by a HT-HP to produce hot water or steam at a temperature higher than 100 °C (Arpagaus et al., 2018). Another recent application is the compressed heat energy storage (CHEST), in which a HT-HP, driven by renewable energy sources (RES), is used to charge a high-temperature thermal energy storage (HT-TES) system in the periods of low demand; later, the thermal energy stored is discharged, using a heat engine (HE) cycle, to generate electricity during high demand peaks. CHEST system provides better integration of RES in the electricity grid and helps to overcome their intermittency (CHESTER, 2018).

Many authors in the literature have focused on assessing the performance of HT-HPs for different configurations, refrigerants, and values of temperature lift. To select the most suitable refrigerant for a HT-HP with temperature lift of 50 K and condensation temperature up to 150 °C, Reißner (2015) developed a simple idealized heat pump model equipped with an internal heat exchanger (IHX). For subcritical scenarios, the system was simulated for two subcooling (SC) values of 5 K and 35 K inside the condenser. The IHX is used only to improve slightly the coefficient of performance (COP) and generate the necessary superheat (SH) for dry refrigerants. The results showed that the refrigerants with higher critical temperature result to higher values of COP, and the effect of raising the subcooling degree on the system performance significantly depends on the refrigerant type. Finally, Reißner concluded that R-1336mzz(Z) and R-1233zd(E) are the best choices by thermodynamic suitability, with COP up to 6.6 and 6.84, respectively. A similar model was presented by Arpagaus et al. (2018) to compare the thermodynamic efficiency for different refrigerants. The main performance parameters were COP and volumetric heating capacity (VHC). The model's assumptions were: no pressure drop inside heat exchangers, constant isentropic efficiency of 0.7,

fixed SC value inside the condenser of 5 K, and fixed temperature lift of 70 K. They reported that the system performance for hydrofluoroolefins (HFO) refrigerants, R-1234ze(Z), R-1233zd(E), and R-1336mzz(Z), increases compared to R-245fa with condensing temperatures above 100 °C. Regarding the VHCs, R-1234ze(Z), R-600, R-1224yd(Z), R-245fa, and R-1233zd(E) give the most promising VHC values ranging from 2.5 to 3.4 $MJ \cdot m^{-3}$.

Fukuda et al. (2017) presented an exploratory assessment of a HT-HP used for heat recovery applications. The tested refrigerants were R-1234ze(Z), R-1233zd(E) and R-365mfc. They developed two configurations for the HT-HP cycle to raise the temperature of heat media to 160 °C with a waste heat at 80 °C. R-1234ze(Z) has a critical temperature of 150.1 °C, accordingly it was employed for transcritical cycles, such cycles are out of the frame of current paper. Regarding the single-stage with IHX subcritical cycle, the results showed that R-1233zd(E) has the better performance compared with R-365mfc. It has COP and pressure ratio values of 4.18 and 6.36, respectively. Furthermore, they stated that R-1233zd(E) cycle has irreversibility losses lower than R-365mfc by 21.7%.

In the literature, many thermodynamic models used to assess the HT-HPs performance are fundamental and do not consider many practical aspects such as different values of temperature lift, and pinch point and pressure drop inside heat exchangers. Furthermore, using IHX can enhance slightly the COP for some refrigerants, but it is not practical in some applications which require very high values of SC, more than 60 K (e.g. thermal energy storage systems). Also, using a subcritical system could result to a mismatch of temperature profiles inside the condenser, especially for applications that require a very high water-side temperature lift, more than 40 K (e.g. district heating (DH) and industrial applications). This mismatching increases the irreversibility associated with heat transfer through a finite temperature difference. All of these reasons motivated the authors to develop a more practical and flexible HT-HP model for different applications to be able to perform a more accurate comparison between the available refrigerants. The proposed model is equipped with a subcooler, after the condenser, to ensure a better match between refrigerant and secondary fluid temperature profiles. The proposed model considers the pinch point location, especially inside the subcooler, and pressure drop inside the heat exchangers. A range of temperature lift (ΔT_{lift}) values is considered, from 40 to 80 K. The ΔT_{lift} in the current study is defined as the difference between sink and source temperatures. Different refrigerants were analysed and compared to assess the thermodynamic performance of HT-HPs for various applications.

2. HT-HP MODEL DEVELOPMENT

2.1. Model Configurations and Assumptions

Fig. 1 shows the general configurations of the proposed HT-HP model. The proposed configurations are suitable for industrial applications, which require high temperature water (>100 °C) and saturated steam (Config. 1); or thermal energy storage applications, which require pumping the heat from low temperature level to store it in a HT-TES system (Config. 2). Regarding Config. 1, the pressurized water firstly enters the subcooler ($m_{wtr,in,subc}$) to heat it up to the temperature of the high-temperature water tank (HTWT). Then, part of it is directed to the condenser to generate saturated steam ($m_{stm,out,cond}$), and the rest exits the HTWT as saturated liquid water ($m_{wtr,out,HTWT}$).

In Config. 2 the pressurized water enters the subcooler from the low-temperature water tank (LTWT) and is heated up to the temperature of the HTWT in a closed loop. These two tanks represent the sensible heat storage system. As can be noticed that the condenser is replaced by a phase changing material heat storage (PCMHS) system to store the latent heat rejected from the refrigerant during condensation. In the current study, the outlet of refrigerant from the condenser/PCMHS is always assumed to be saturated liquid, and all the process of SC is done inside the subcooler. This leads to better matching and small temperature differences between the refrigerant and water.

These two configurations have been chosen because they allow taking advantage of both the two-phase (latent) and sensible heat exchange of subcritical cycles with a good approach to the corresponding secondary fluid, hence with high COP, see for instance the cycle depicted in Fig. 5.

The proposed model was developed using Engineering Equation Solver (EES) software (Klein, 2018).

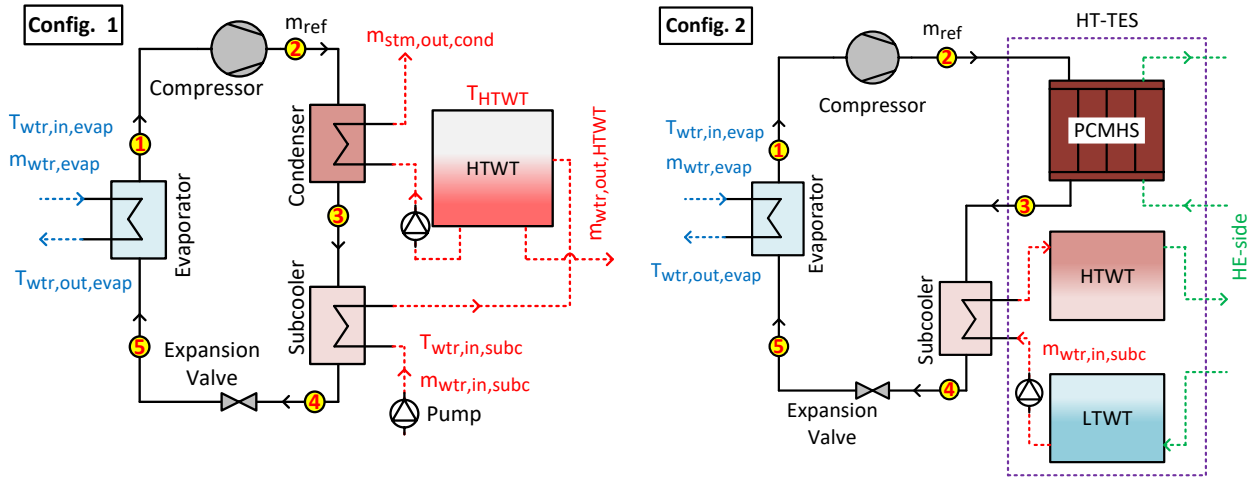

Figure 1: Different configurations for the proposed HT-HP model

The model assumptions are: the system runs under steady state conditions; the compressor has constant isentropic (η_s) efficiency of 0.7; the refrigerant mass flow rate (m_{ref}) is 1 kg·s^{-1}; the pressure drop in evaporator and condenser corresponds to 2 K and 0.5 K drop in the inlet saturation temperature, respectively; and all heat exchangers are counter flow with a fixed temperature difference at the corresponding pinch point (ΔT_{pp}) of 3 K. The main performance parameters to be evaluated are the COP, pressure ratio (Pr), discharge temperature (T_{dschrg}) and VHC. The VHC is the total heating effect per unit of swept volume, which gives an indication for the compressor size and its ability to pump the required thermal power. Table 1 summarizes the main performance parameters for the proposed HT-HP model.

Table 1. Performance parameters used in the present study

Parameter (unit)	Mathematical definition, based on Fig. 1
ΔT_{lift} (K)	$=T_{HTWT}-T_{wtr,in,evap}$
COP (-)	$=[(h_2-h_3)+(h_3-h_4)]/(h_2-h_1)$
Pr (-)	$=P_2/P_1$
T_{dschrg} (°C)	$=T_2$
VHC (MJ·m^{-3})	$=[(h_2-h_3)+(h_3-h_4)]/v_1$

2.2. Selection and Properties of Refrigerants for HT-HPs Applications

Selection of the proper refrigerant is a crucial decision for designing HT-HPs. One important aspect to choose a proper one is the required degree of SH after evaporation. Low SH values could result in wet compression, while high values could decrease the evaporation temperature and affect significantly the system performance. Based on this, the refrigerants could be classified into three groups based on the slope of saturated vapor curve on T-s diagram (dT/ds). The negative slope refrigerants are called “wet fluids”, the positive slope ones are called “dry fluids”, and near zero slop (semi-vertical slope) refrigerants are called “isentropic fluids” (Jockenhöfer et al., 2018). Fig. 2 compares between three different refrigerants correspond for each group.

As can be seen that the wet fluids do not require any SH, or very small value, in the outlet of evaporator, while the dry ones need a very high degree of SH to prevent the wet compression. On the other hand, the isentropic fluids need a moderate degree of SH that could be done inside the evaporator without side effects on the system performance.

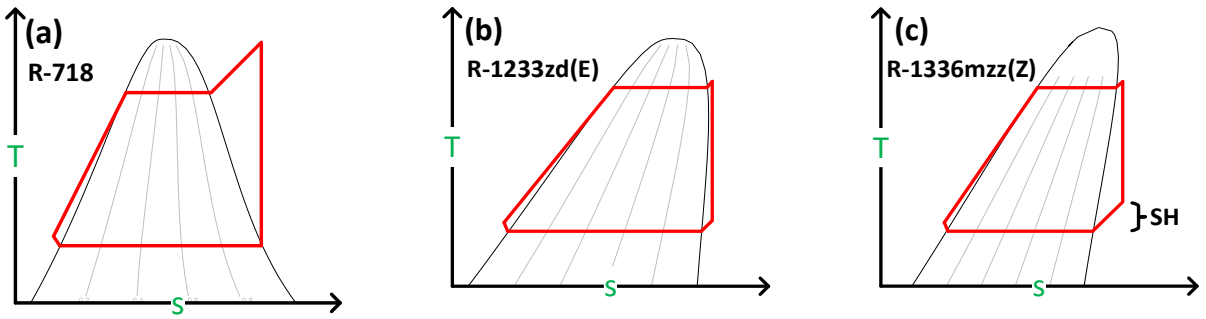

Figure 2: T-s diagram for: (a) R-718 (wet fluid), (b) R-1233zd(E) (isentropic fluid), and (c) R-1336mzz(Z) (dry fluid)

Other desirable criteria of the refrigerants used especially in HT-HPs applications are: zero ozone depletion potential (ODP=0); very low global warming potential (GWP<10); non-toxic; no or low flammability; high critical temperature (T_{crit}>145 °C) allowing for subcritical applications; low critical pressure (P_{crit}<3 MPa). Regarding the criteria discussed, Table 2 lists a sample of different refrigerants that could be employed in HT-HPs applications.

Table 2. Properties of selected refrigerants for HT-HPs (Arpagaus et al., 2018; Klein, 2018)

Group	Refrigerant	Type	T_{crit} (°C)	P_{crit} (MPa)	NBP[a] (°C)	ODP (-)	GWP (-)	SG[b]
Wet (W)	R-718 (water)	Natural	373.95	2.206	100.0	0	0	A1
	Acetone	HC[c]	235.0	4.7	56.0	0	<10	n.a.
Dry (D)	R-1336mzz(Z)	HFO[d]	171.3	2.9	33.4	0	2	A1
	R-365mfc	HFC[e]	186.85	3.266	40.2	0	804	A2
Isentropic (S)	R-1233zd(E)	HCFO[f]	166.5	3.62	18.7	0.0003	<1	A1
	R-245fa	HFC	154.01	3.65	15.1	0	858	B1
	Butene	HC	146.15	4.0	-6.3	0	<10	n.a.

[a]NBP: normal boiling point at 0.1013 MPa; [b]SG: safety group (ASHRAE, 2016); [c]HC: hydrocarbons; [d]HFO: hydrofluoroolefins; [e]HFC: hydrofluorocarbons; [f]HCFO: hydrochlorofluoroolefins.

3. RESULTS AND DISCUSSION

Fig. 3 shows the work ranges for refrigerants listed in Table 2. The work range is defined as the difference between critical temperature (T_{crit}) and normal boiling point (NBP). This gives an idea for the ability of refrigerant to reach a certain condensation temperature (T_{cond}) and its proximity to the critical point. In the present work, the values of T_{cond} range between 123 and 163 °C, as seen in Fig. 3.

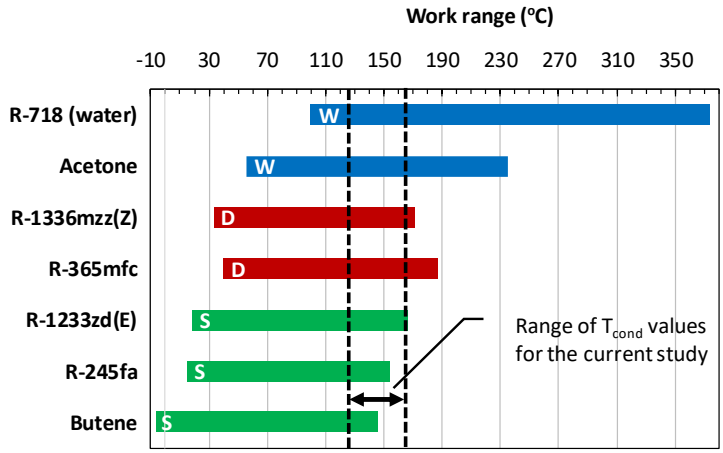

Figure 3: Work ranges for selected refrigerants and condensation temperature (T_{cond}) limits in the current work

Arpagaus et al. (2018) reported that for subcritical HT-HPs, the difference between T_{crit} and T_{cond} should be between 10 and 15 K to ensure a reasonable performance. Regarding this condition, it can be noticed that the R-718 (water), Acetone, and R-365mfc are the only refrigerants that could reach the maximum limit for the T_{cond} in the current work. The water has many desirable properties, such as very high latent heat and T_{crit}; however, because of its low vapor density it requires complicated multi-stage compression cycles with intercooling to cope the high values of pressure ratio and discharge temperature. Such cycles are out of the scope of the present work, so water has been excluded from the analysis.

In all simulations, the inlet water temperature to the evaporator ($T_{wtr,in,evap}$) was fixed at 80 °C, and the water-side temperature difference was set to 3 K. On the other hand, the inlet pressurized water to the subcooler ($T_{wtr,in,subc}$) was always assumed to be 5 K less than the $T_{wtr,in,evap}$. This is because we assume that if the value of $T_{wtr,in,subc}$ is very low and needs to be increased, it will be preheated firstly with the source hot water. A heat source at 80 °C has been chosen as a representative of potential sources of waste heat from solar production or industrial processes, with possible interconnection with district heating.

In the current study, all the SH is assumed to be done inside the evaporator. For wet fluids it was fixed at 1 K, while for isentropic fluids 5 K was set. On the other hand, the SH values for dry fluids were varied in each operating condition to ensure obtaining a minimum superheat value of 5 K at the inlet to the condenser.

Based on inlet conditions and model assumptions (Sub-section 2.1), the HT-HP's performance for the selected refrigerants is compared in Fig. 4. As can be noticed, Figs. 4a and b, that the isentropic fluids R-245fa, R-1233zd(E), and Butene have the highest COP and lowest Pr values compared with others. However, R-1233zd(E) is the only one that can reach a ΔT_{lift} up to 73 K (T_{cond}=156 °C) with reasonable COP, Pr, and T_{dschrg} values of 4.67, 5.68, and 164.3 °C, respectively. Also, it can be noticed that R-245fa has a very similar behaviour compared to R-1233zd(E), with slightly better COPs, till a ΔT_{lift}= 61 K (T_{cond}=144 °C); however, it is not recommended for its high GWP (≈ 858) and toxicity (Class B). Accordingly, R-1233zd(E) is considered to be a potential, environment-friendly, replacement for R-245fa.

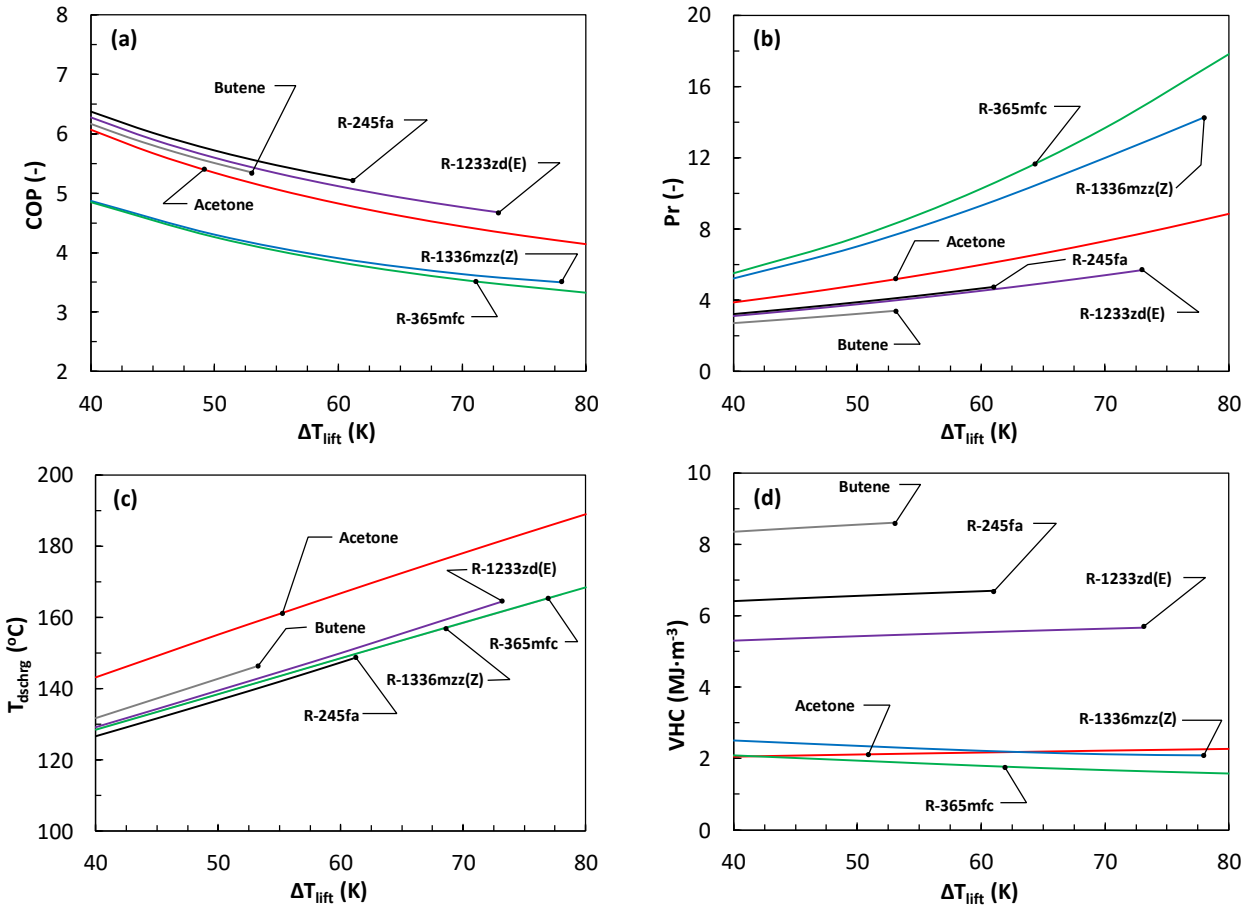

Figure 4: Performance parameters as a function of ΔT_{lift} for the selected refrigerants: (a) COP, (b) Pr, (c) T_{dschrg}, and (d) VHC

The wet fluid Acetone is the only refrigerant that can reach the maximum considered ΔT_{lift} of 80 K (T_{cond}=163 °C) with COP, Pr, and T_{dschrg} values of 4.14, 8.85, and 189 °C, respectively. Although, it clearly has very decent theoretical performance, the authors have not found experimental data in the literature regarding its real performance as refrigerant in this kind of application.
Contrarily, the dry fluids R-1336mzz(Z) and R-365mfc have the lowest COP and highest Pr values compared to other refrigerants. Although, R-365mfc can reach the maximum ΔT_{lift}= 80 K, it has the lowest COP of 3.33 and highest Pr of 17.82. As mentioned before the dry fluids need high SH values to prevent the wet compression. This, in turn, significantly decreases the evaporation temperature (T_{evap}) compared with wet and isentropic fluids. For example, R-365mfc requires SH of 31.6 K at ΔT_{lift} of 80 K. This results to Tevap= 45.4 °C, which is less than T_{evap} for wet and isentropic refrigerants by 26.6 K. Accordingly, for such refrigerants, it should be considered employing an external superheater to avoid such degradation in system performance.
Regarding the VHC, Fig. 4d shows that isentropic fluids have the highest values of VHC compared with others. Within the range of ΔT_{lift} studied, the average values of VHC for Butene, R-245fa, and R-1233zd(E) are 8.48, 6.58, and 5.49 MJ·m^{-3}, respectively. This implies smaller compressor size and lower cost for a given heating capacity. Generally, dry fluids express lower VHC compared to isentropic ones. R-365mfc shows the lowest average VHC (≈ 1.81 MJ·m^{-3}), which is about 67% lower than R-1233zd(E).
As previously indicated in Sub-section 2.1, the subcooler is considered to be a vital component of the system, especially for the applications that require high values of water-side temperature lift. To understand more this concept, Fig. 5 shows the T-s diagram for R-1233zd(E) at ΔT_{lift}= 40 K and water-side temperature profile inside subcooler and condenser (blue dashed line). As can be clearly noticed the small temperature differences and good matching between the refrigerant and water temperature profiles. The minimum temperature difference between the two profiles is 3 K, while the maximum is 9.2 K. The less the temperature differences between the two streams, the less the irreversibilities associated with the infinite heat transfer process. Optimization of subcooling in subcritical cycles leads to very high COPs and shows a great potential for water heating applications with high temperature lifts (Pitarch et al., 2017 and 2019).

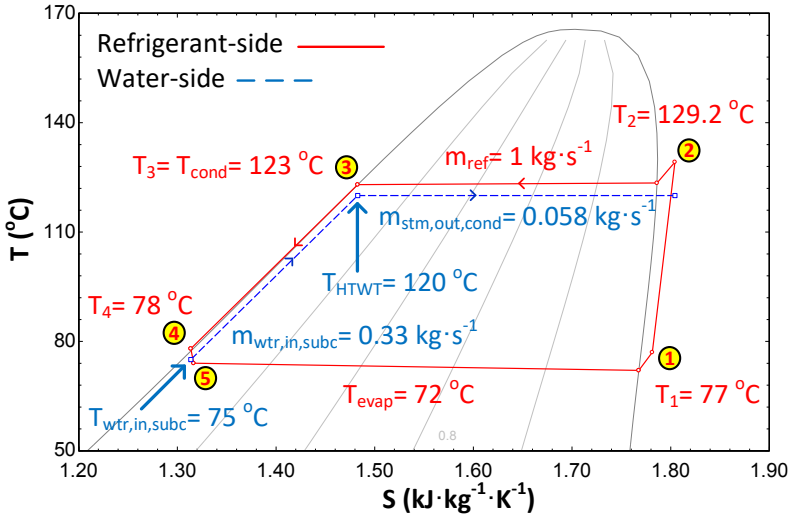

Figure 5: T-s diagram for R-1233zd(E) at ΔT_{lift}= 40 K, corresponds to T_{evap}=72 °C and T_{cond}= 123 °C, with η_s= 0.7, SH= 5K, and ΔT_{pp}=3 K

4. CONCLUSIONS

The thermodynamic performance of a HT-HP was evaluated using different refrigerants, for a ΔT_{lift} ranges between 40 and 80 K. The conclusions are summarized as follows:

- Isentropic refrigerants, R-1233zd(E), R-245fa, and Butene, show the best performance regarding COP, Pr, and VHC compared to dry and wet refrigerants.
- On the other hand, dry refrigerants, R-1336mzz(Z) and R-365mfc, have the lowest performance compared with others. The main reason for this is the high SH required to prevent the wet compression. This significantly decreases the evaporation temperature and,

consequently, the system performance. To prevent the performance degradation, it is very important to employ an external superheater.

- Only R-365mfc and Acetone can reach the maximum considered ΔT_{lift} of 80 K for the selected source temperature of 80 °C. However, the main disadvantages of R-365mfc are the high SH required (up to 31.6 K) to prevent wet compression, Class 2 flammability, and high GWP value of 804. The wet refrigerant Acetone shows a promising theoretical performance, however, there is no sufficient data, in the literature, about its real performance as refrigerant regarding the proposed HT-HP cycles.
- For a ΔT_{lift} up to 73 K, R-1233zd(E) is considered to be the best refrigerant in the current study, regarding thermal performance, environmental impact, and safety classification. R-1233zd(E) reaches ΔT_{lift}= 73 K (T_{cond}=156 °C) with COP, Pr, T_{dschrg}, and VHC values of 4.67, 5.68, 164.3 °C, and 5.66 MJ·m^{-3}.

ACKNOWLEDGEMENTS

Authors acknowledge the financial support provided by the project “ENE2017-83665-C2-1-P” funded by the “Ministerio de Ciencia, Innovación y Universidades” of Spain.

NOMENCLATURE

ΔT_{lift}	temperature lift (K)
ΔT_{pp}	pinch point (K)
COP	coefficient of performance (-)
h	enthalpy (kJ·kg^{-1})
m	mass flow rate (kg·s^{-1})
η_s	isentropic efficiency (-)
P	pressure (MPa)
Pr	pressure ratio (-)
s	entropy (kJ·kg^{-1}·K^{-1})
SC	subcooling (K)
SH	superheat (K)
T	temperature (°C)
v	specific volume (m^3)
VHC	volumetric heating capacity (MJ·m^{-3})

Subscripts:

HTWT	high-temperature water tank
cond	condenser/condensation
crit	critical
dschrg	discharge
evap	evaporator/evaporation
in	inlet
out	outlet
ref	refrigerant
stm	steam
subc	subcooler
wtr	water

REFERENCES

Arpagaus, C., Bless, F., Uhlmann, M., Schiffmann, J., Bertsch, S.S., 2018. High temperature heat pumps: Market overview, state of the art, research status, refrigerants, and application potentials. Energy 152, 985-1010.

ASHRAE, 2016. Standard 34-safety standard for refrigeration systems and designation and classification of refrigerants.

CHESTER, 2018. Compressed Heat Energy Storage for Energy from Renewable Sources (CHESTER) [WWW Document]. Europian Union’s Horizon 2020 Research and Innovation Programme. URL https://www.chester-project.eu

Fukuda, S., Kondou, C., Takata, N., Koyama, S., 2017. Thermodynamic Analysis on High Temperature Heat Pump Cycles Using Low-GWP Refrigerants for Heat Recovery. Proceedings of the 12th IEA Heat Pump Conference, Rotterdam, Netherlands.

Jockenhöfer, H., Steinmann, W.-D., Bauer, D., 2018. Detailed numerical investigation of a pumped thermal energy storage with low temperature heat integration. Energy 145, 665-676.

Klein, S.A., 2018. Engineering Equation Solver (Version V10.451), F-Chart Software.

Panayiotou, G.P., Bianchi, G., Georgiou, G., Aresti, L., Argyrou, M., Agathokleous, R., Tsamos, K.M., Tassou, S.A., Florides, G., Kalogirou, S., Christodoulides, P., 2017. Preliminary assessment of waste heat potential in major European industries. Energy Procedia 123, 335-345.

Pitarch, M., Hervas-Blasco, E., Navarro-Peris, E., Corberán, J.M., 2019. Exergy analysis on a heat pump working between a heat sink and a heat source of finite heat capacity rate. Int. J. Refrig. 99, 337-350.

Pitarch, M., Hervas-Blasco, E., Navarro-Peris, E., Gonzálvez-Maciá, J., Corberán, J.M., 2017. Evaluation of optimal subcooling in subcritical heat pump systems. Int. J. Refrig. 78, 18-31.

Reißner, F., 2015. Development of a Novel High Temperature Heat Pump System. PhD. thesis, Friedrich-Alexander-Universität Erlangen-Nürnberg, Nuremberg, Germany.

Manuscript ID: 1246
DOI: 10.18462/iir.icr.2019.1246

Large-scale mechanical vapor recompression drying process in superheated steam

Hans MADSBOLL [(a)], **Kasper G. LARSEN**[(b)]
[(a)] Danish Technological Institute, Kongsvang Allé 29, DK 8000 Aarhus C, hm@teknologisk.dk
[(b)] Enerdry A/S, Kongevejen 157, DK 2830 Virum, kgl@enerdry.dk

ABSTRACT

Large-scale fluid bed superheated steam drying units have been used for fibrous products such as sugarbeet pulp, and wood chips etc. as an energy efficient alternative to the standard method of heated air/flue gas in a drum dryer. The heat source is steam from nearby power plants due to the huge capacity requirements of steam at approx. 25 bar. An alternative to this method is the vapor recompression method, where steam is recompressed from approx. 3 bar to the inlet pressure of approx. 25 bar at design point operation. The benefits are significant energy savings and the use of electrical energy instead of fossil fuels. Such a unit has been modelled with a selection of centrifugal compressor designs. The model shows the energy balances, the pressure ratio, and the mass flow in the full drying unit, and it can be used to analyze part load operation, control strategy, energy consumption, preferred compressor characteristics etc.

1. INTRODUCTION

Industrial drying is a basic unit operation widely used in the process industry such as the food industry, the paper industry, the wood industry etc. In general, the drying process is centered on removing water from a product, and typically it consists of two phases. The first phase is where a part of the water can be removed simply by evaporation (free water), and the second, more complicated, phase is where the water is removed by diffusion. The drying process in question addresses the first part (evaporation), where various methods such as conveyer, drum dryers, and fluidized bed apply. The method of fluidized bed dryers is particularly useful for high capacity drying processes with lumps or chunks of the product, in this case fibrous products such as sugarbeet pulp, woodchips, etc.

2. DRYING IN SUPERHEATED STEAM

Typically, the product has an initial moisture content and a desired residual moisture content, and the operating conditions determine the residence time, the temperature level, the plant size etc. in combination with the specifics of the product. In the fluidized bed principle, the product is kept floating in the air. The air is flowing upwards with a relatively high speed, and the resulting drag force on the lump of product is larger than or equal to the gravity force.

The basic principle is that the product is kept floating in the air due to the air speed and the direction until it is dried to a sufficient residual moisture. Typically, the product is kept floating for 2-5 minutes, before it is dry. The drag force on the product is defined as

$$F_d = C_d \, ½ \, \rho_f \, u^2 \, \pi \, r^2$$

Where Fd is the drag force, Cd is the drag coefficient depending on the geometric shape of the product, typically in the range 0.5 – 1.0, ρ_f is the fluid density, u is the air flow speed, and r is the radius of the product in case of almost spherical lumps – otherwise the estimated area must replace $\pi \, r^2$.

In case of a spherical product lump, the gravity force Fg is

$$F_g = 4/3 \, \pi \, r^3 \, \rho_p \, g$$

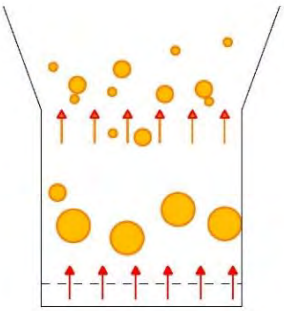

Figure 1: Fluidized bed dryer principle, the product is kept floating by means of the air flow

Figure 1 illustrates the basic principle and shows the real-life situation, where the size and density of the product lumps can vary quite a bit, and thus have somewhat different paths in the fluidized bed. The air flow is designed to handle this situation, and it can be adjusted to ensure the worst-case scenario size and moisture content to be sufficiently dry at product outlet. Hot air is led to the bottom of the dryer volume, and the product is heated as the air passes the product, and the heat transfer coefficient is important for the drying process. In general for a fluid bed dryer, the power consumption is typically in the order of 3500 – 6000 kJ/kg evaporated water as compared to the heat of evaporation 2250 kJ/kg in the typical temperature range, unless special measures show some kind of energy recovery.

Another method used for this type of products is rotary drum dryers. A large furnace is producing a hot flue gas, which is blown into the drum where a mixture of the product to be dried and the hot flue gas is mixed. The drying takes place in a mixture of flue gas, steam, and air. Due to the presence of air, some parts of the product to be dried is burned, and small particles are created. These particles are difficult to capture, and they are often released to the surroundings through the stack. By installing a steam dryer, the emissions of dust and VOC (volatile organic compounds) are eliminated. Furthermore, a large amount of energy is saved. On a standard large sugar factory, 50t/h of evaporation is required. Typically, a rotary drum dryer will use approx. 3000 kJ/kg corresponding to approx. 140 tons of coal per day for an application such as this one.

It is much more energy efficient to avoid the air as heat transfer media and use the steam instead. The basic principle is shown in figure 2. Steam is circulated in the dryer at a well-defined pressure – in this case 3 bar - by means of a fan, and it is superheated by the supply steam.

Steam is used as the media to transfer the energy to the product instead of air – thus evaporating the water from the product. The amount of evaporated steam is discharged at a separate outlet and is usually used for juice concentration in a sugar factory, or alternatively as boiler feed water preheating.

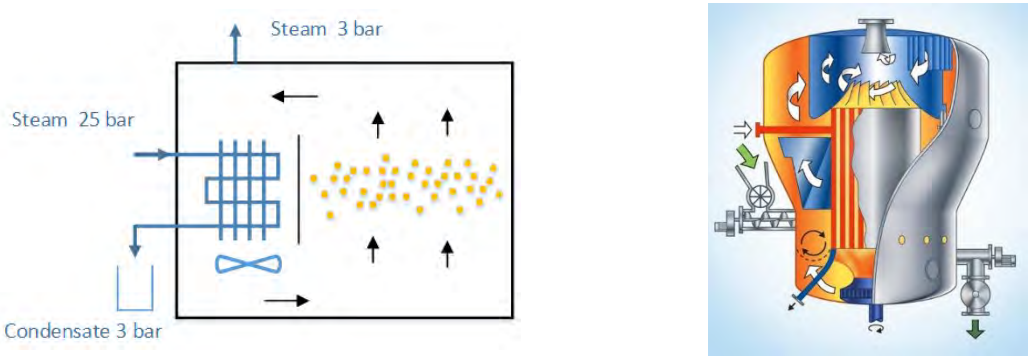

Figure 2: Drying by superheated steam – sketch of principle to the left, sketch of a unit to the right

If the low-pressure steam is completely lost, the energy consumption is the same as the heat of evaporation, i.e. approx. 2250 kJ/kg evaporated water plus the energy consumption for the fan in the order of 2-5 % of the added steam capacity. In case the entire amount of the 3-bar steam can be reused, the energy consumption is made of contributions from enthalpy loss due to steam pressure drop from 25 bar to 3 bar, fan power, and heat loss. The total is in the order of 20% of the heat of evaporation.

The capacity of the units in question is in the order of 10 – 70 MW heating – thus removing approx. 10 – 65 tons of water per hour, see figure 3. The only option to achieve such capacities is when the steam supplier is a power plant.

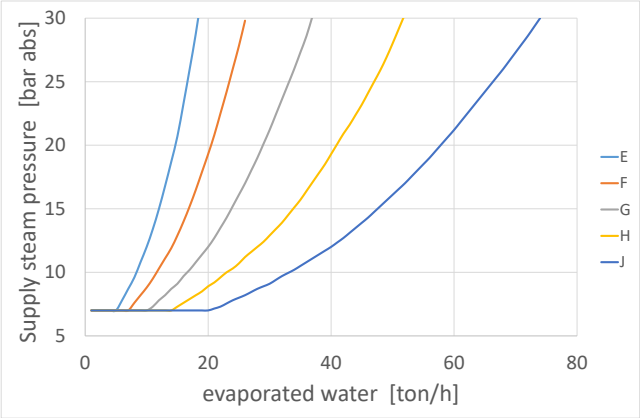

Figure 3: Capacity of the units as function of size and supply steam pressure

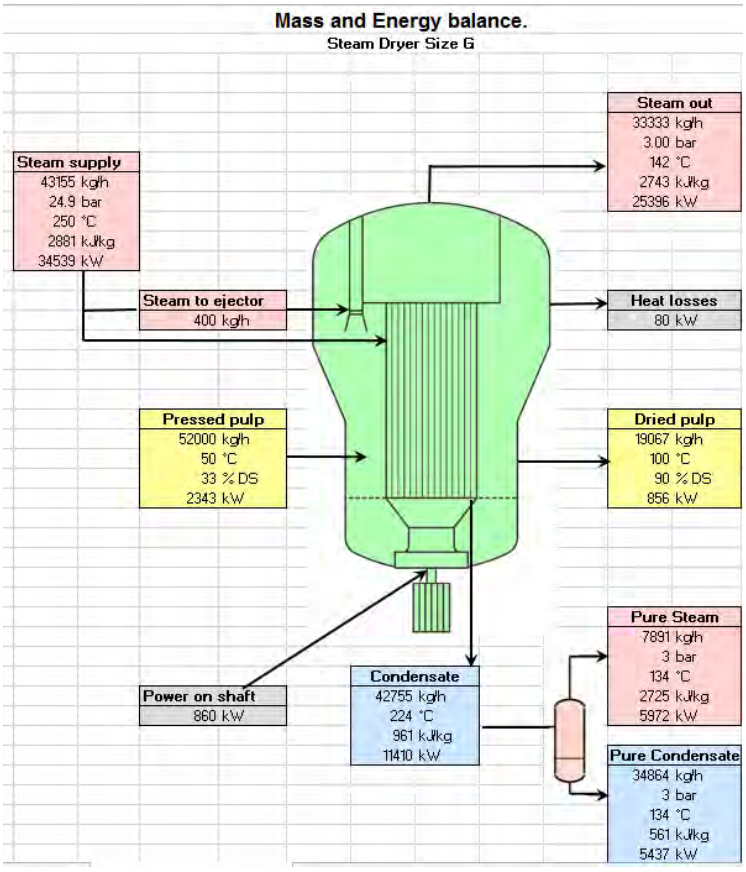

Figure 4: Mass and energy balance for the superheated steam dryer size G

Figure 4 shows the mass and energy balance for the large-scale dryer with superheated steam. In this example, 52 t/h product with 67% humidity is dried to 19 t/h product with 10% remaining humidity,

i.e. 33 t/h water is evaporated. The total energy consumption depends on the extent to which the energy bound in the condensate and the low-pressure steam can be used for other purposes. If there is absolutely no reuse of the steam and condensate, the energy consumption is approx. 3800 kJ/kg evaporated water – which is in the same category as drum dryers. However, if for example 80% of the steam, and if the condensate and the steam are used, the energy consumption can be as low as 650 kJ/kg.

A typical installation is illustrated in figure 5, where the power plant is operated in parallel with the superheated steam dryer and an evaporatrain for juice consentration, which is designed to make use of the relatively low-pressure steam.

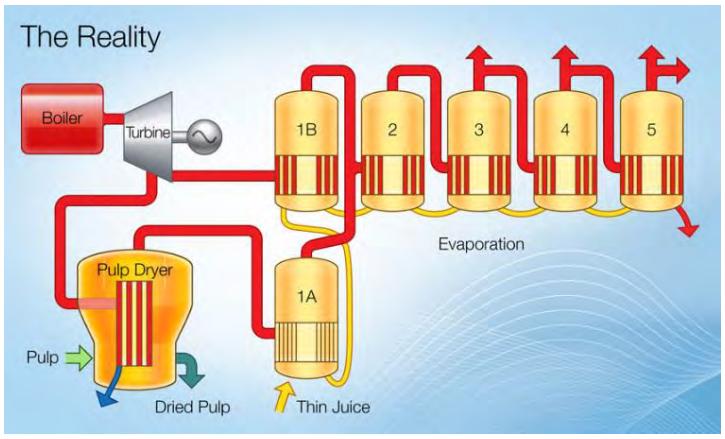

Figure 5: A typical installation where the steam supply is a power plant and the low-pressure steam is reused in a multi-flash dryer

The disadvantage of the system is that it is absolutely necessary to locate these units close to power plants and to reuse the low-pressure steam either for further processes or for heating in order to take advantage of the potential energy savings, which are available with the superheated water vapor drying method.

3. RECOMPRESSION WITH STEAM COMPRESSORS

There are some obvious advantages of introducing the steam compressors instead of the traditional steam supply system. The evaporated steam from the drying process is simply recompressed and condensated, which eliminate the need to find a suitable consumer or buyer of the large capacity of low-pressure steam in order to ensure the energy economy. This will allow the drying unit to operate autonomic without large steam suppliers or large steam end users. In addition, this type of dryers will contribute to the desired electrification of the process industry in order to eliminate fossil fuels from the future energy systems – a very important point.

The system is illustrated in figure 6, and the basic principle is that the amount of steam evaporated from the product in the drying process is lead to the water vapor (steam) compressor inlet. The compressor increases the pressure and thus the condensation temperature to some higher level, in the example to approx. 25 bar (235 °C). The energy of condensation is passed on to the circulating steam and thus superheats the steam to a value close to the condensation temperature in the heat exchanger. When the circulating steam has passed the wet product, the temperature of the steam is close to the saturation conditions. In this case, a rough estimate of the energy consumption is approx. 500 kJ/kg evaporated water for this standalone unit – independent of steam supply and reuse of low-pressure steam.

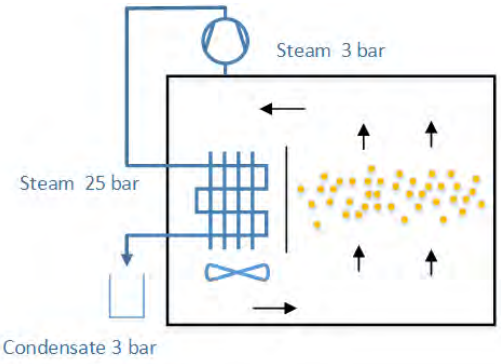

Figure 6: Basic principle of drying in superheated steam with vapor recompression

A mass and energy balance model has been established for the dryer with vapor recompression. The basic assumption is that centrifugal compressors with Ti impellers are used. This allows for a pressure ratio of approx. 2.3 per stage for water vapor. The maximum pressure ratio is rather low compared to for example air due to the relatively low atomic mass of water vapor. Thus, it is necessary to use three compressors in series to achieve the desired pressure ratio of 25/3 = 8.3. In the model, eight different compressor designs with corresponding compressor maps can be used to investigate the limitations and advantages of the various design options. Overall, a key dimensionless parameter for compressors is the specific speed defined by

$$Ns = \frac{n\sqrt{Q}}{\Delta ho^{3/4}}$$

where n is the rotational speed, Q is the volume flow, and Δho is the enthalpy increase in the compressor. The following figure shows the characteristics of the various values of the specific speed.

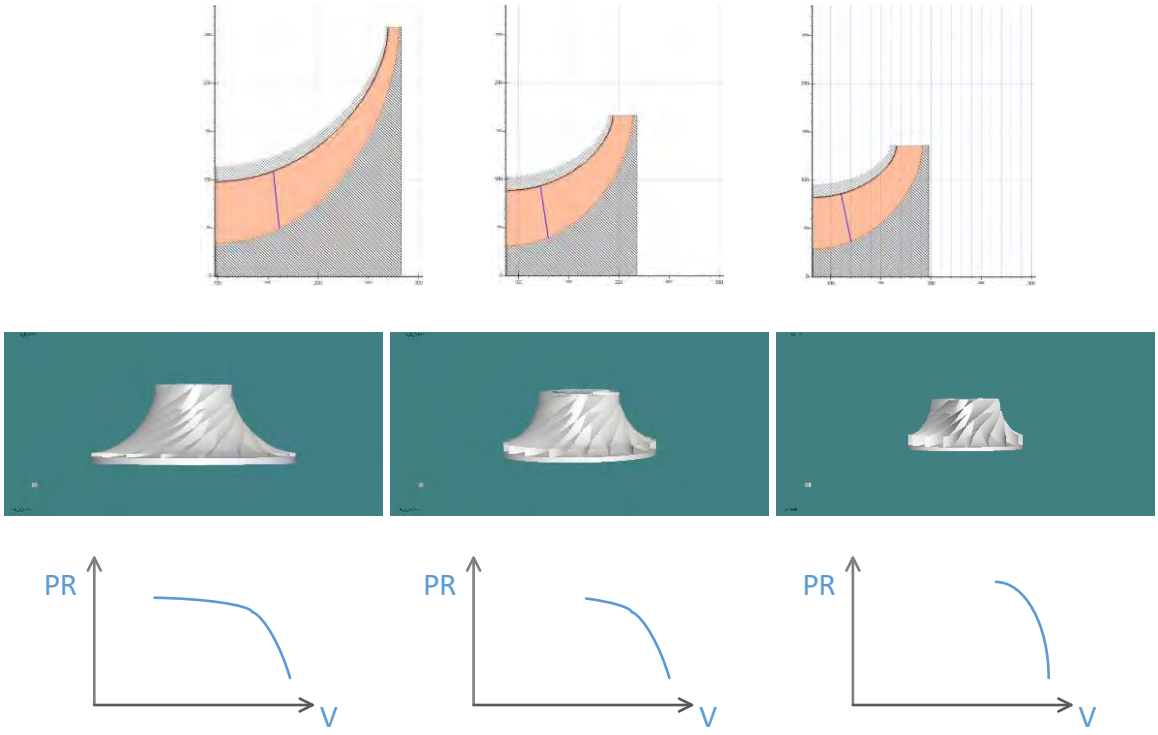

Figure 7: Illustration of the specific speed Ns for the values 0.5, 0.75, and 1.0, respectively, for the same design point operation specifications

In general, the lower Ns offers a larger operating range, which is a larger stall margin, while the maximum efficiency normally can be achieved at Ns close to 0.75 and the lowest cost for Ns is close to 1.0. As the capacity of the dryer is in the range of 15 to 65 MW, the corresponding variation in suction volume for the first low stage compressor is in the range of 4 m^3/s to 16 m^3/s. The following table shows the impeller diameter and the rotational speed for Ns = 0.75 impellers as a function of unit capacity. The total compressor diameter including diffuser and volute is in the order of 2 – 2.5 times the impeller diameter. The shown models are designed by means of the commercial compressor design software package COMPAL from ConceptsNREC, i.e. an industrial software package with calibrated loss models with map generation etc.

Evaporated water [t/h]	Heating capacity [MW]	1st stage suction volume [m^3/s]	1st stage impeller diameter [mm]	1st stage rotational speed [krpm]	Power consumption per stage [MW]
20	21.0	5.3	364	28.2	1.6
30	31.6	8.0	446	23.1	2.3
40	42.1	10.7	515	20.0	3.1
50	52.6	13.3	575	17.9	3.9
60	63.1	15.0	630	16.3	4.7

Figure 8 shows the mass and energy balance for the final model of the dryer with a selection of the three stage compressors.

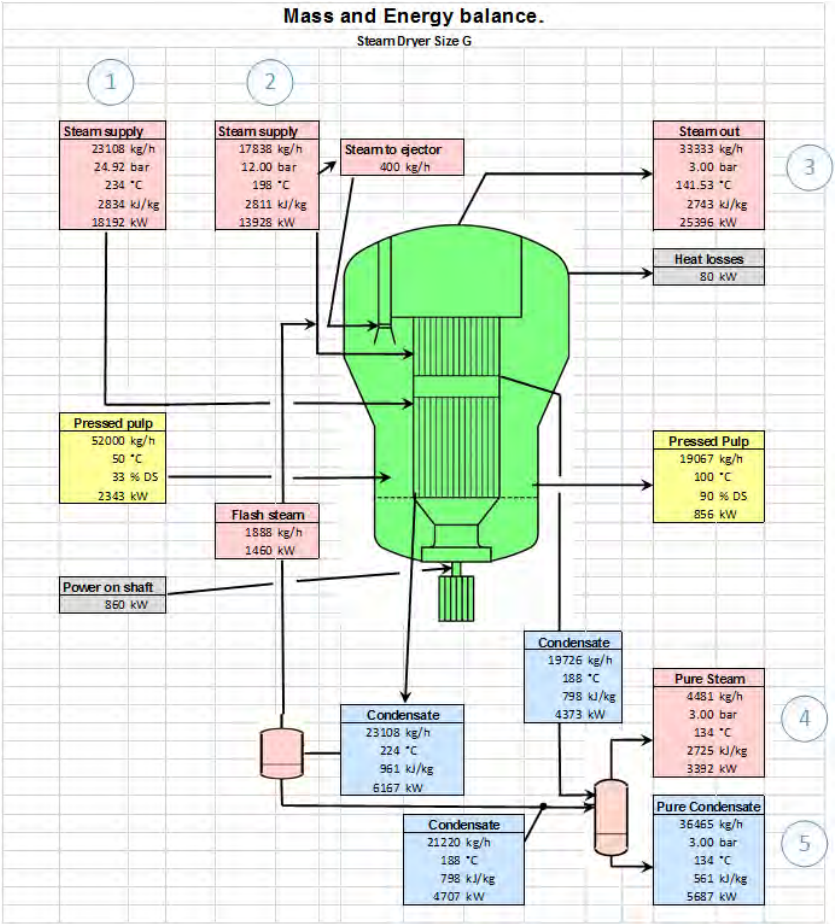

Figure 8: Mass and energy balance for the dryer in the compressor version

Figure 9 shows the specifications for the compressors at the design point for this particular compressor choice. The model operates with scalable compressors, and thus compressor maps, and it includes the option to design all three compressors as a function of the specifications for the

mass and energy balance for the dryer. The volume flow decreases – and thus the rotational speed increases – for the higher stages, but the power consumption is within the same range. The operating point for the three compressors is shown in figure 9, where the model has calculated the minimum energy consumption for the combination of the selected compressors. Intercooling is assumed between compressor stages.

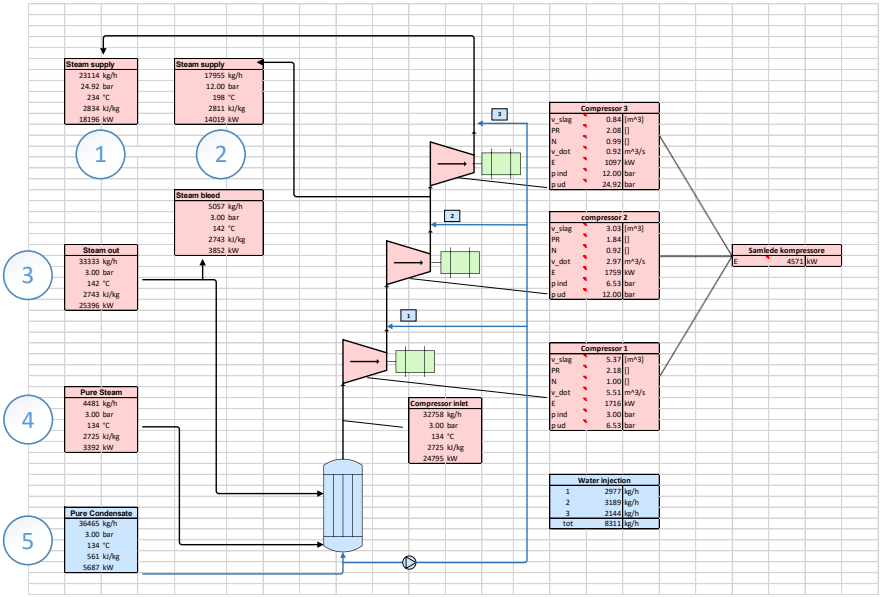

Figure 9: The corresponding compressor specifications at design point operation

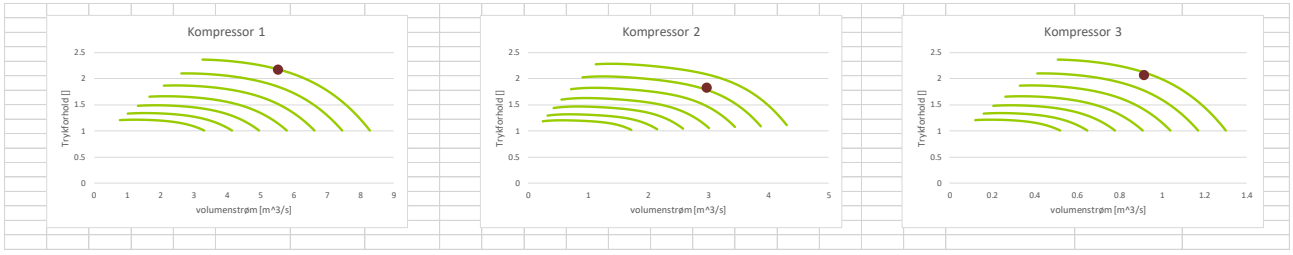

Figure 10: Operating points for the three compressors at design point

In this particular case, the power consumption is 590 kJ/kg evaporated water including the fan and the three compressors operating at the conditions of 3.0 bar inlet pressure and approx. 25 bar exit pressure (inlet pressure to the dryer heat exchanger). The type of compressors in question could be the integrally gear compressors produced by various large companies, e.g. Siemens, MAN, Kobelco, etc.

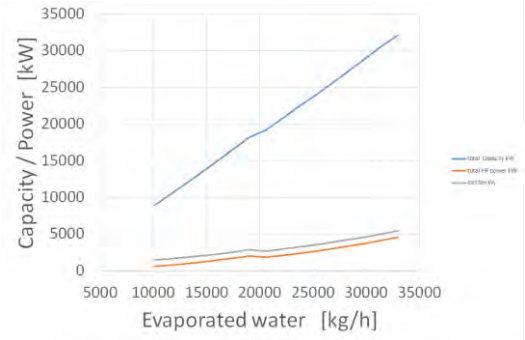

Figure 11: Heat exchanger capacity and total power consumption at part load conditions

In general, a better COP for the heat pump is obtained as the temperature lift decreases, and the model offers the opportunity to investigate part load operation. At some point, the capacity decrease causes a stall for the 1st stage compressor – and two stage operation applies (the two upper stages). As the capacity decreases, and thus the power consumption for the compressors as well, the relative importance of the fan power consumption increases and in general dominates at part loads below approx. 50 %. Thus, there is a potential to optimize dryer operation by regulating dryer pressure, fan speed, compressor design, etc. in order to minimize the total power consumption.

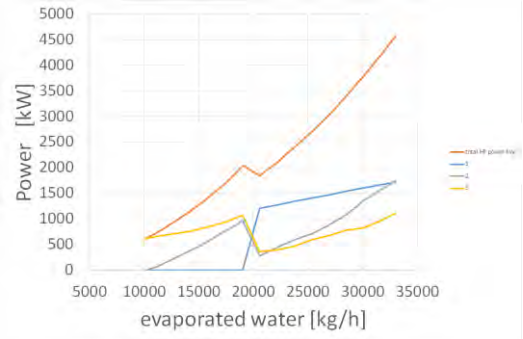

Figure 12: The corresponding compressor power consumption at part load

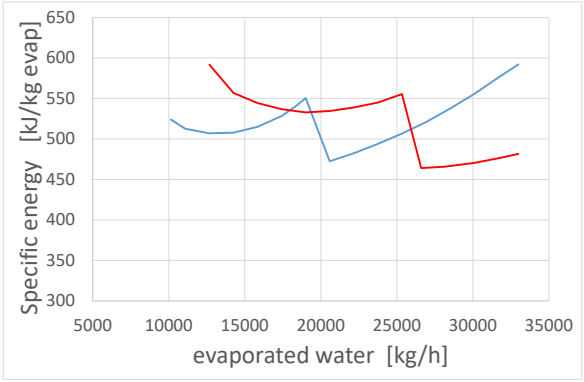

Figure 13: The corresponding power consumption at part load for the dryer size in question (blue) plus the next size (red)

Finally, another option for decreasing operating costs is to choose the next size dryer and thereby decrease the design point pressure. The example of 33 t/h evaporation is achieved by model G at 25 bar supply pressure. However, this can also be achieved by the larger H model at approx. 16 bar supply pressure (cf. figure 3). In that case, the specific energy consumption will be approx. 480 kJ/kg instead of 590 kJ/kg, and the specific application including expected operating period, full/part load etc. decides whether this is a better choice.

Currently, the main application for steam dryers is drying of sugar beet pulp, and the standard installation is steam supply from the power plant on the sugar factory. The amount of steam used is more or less the amount produced. The steam dryer with the standard setup works as a reduction station. No loss of energy, just loss of pressure (exergy). Alternatively a drum dryer which typically requires approx. 115 kg of coal per hour per ton water evaporation, all energy lost. For a large European unit based on sugar beets, the annual drum dryer consumption is approx. 20,000 tons coal. The steam dryer with compressor is a standalone unit, so it is comparable with a drum dryer. A drum dryer uses 3000 kJ/kg (gas), and the steam dryer with compressor uses app. 500 kJ/kg (electrical power). So in other words, the heat pump makes the steam dryer 6 times as efficient as the drum dryer. This is a good and cheap way of reducing CO2 emissions.

Manuscript ID: 1251
DOI: 10.18462/iir.icr.2019.1251

Control strategy of two stage CO2 heat recovery systems in ice rinks

Sotirios THANASOULAS[(a)], Jörgen ROGSTAM[(b)]

[(a)]Royal Institute of Technology (KTH), Energy Technology Department, Brinellvägen 68, Stockholm, 100 44, Sweden, soth@kth.se
[(b)] Energi & Kylanalys AB, Prästgårdsgränd 4
Älvsjö 125 44, Sweden, jorgen.rogstam@ekanalys.se

ABSTRACT

Heat recovery makes CO_2 trans-critical solutions more competitive. The heat recovery can be achieved in one stage or in two stages by using two de-superheaters in serial, because of the CO2 temperature profile. An Engineering Equation Solver (EES) model was developed in order to analyse what are the best operating conditions for an ice rink refrigeration system in 3 different heat recovery scenarios, respecting real de-superheater properties. The scenarios are an one stage which provides water heating from 20 ºC to 60 ºC, an one stage with 20 ºC to 70 ºC and a two stage with 20 ºC to 70 ºC. According to simulated results the refrigeration system can be more efficient if it operates under specific discharge pressure and subcooling. An optimum control strategy has been designed according to each scenario and the heat demand. Results show that the power consumption in the two-stage solution is 10% lower than the one stage scenario from 20 ºC to 60 ºC. The two-stage solution provides higher quality energy by consuming less electrical power.
Keywords: CO_2 Refrigerant, De-superheater, Heat recovery, Optimisation, Ice rinks, Control.

1. INTRODUCTION

Refrigeration systems with heat recovery solution in supermarkets and ice rinks have been evaluated. A comprehensive knowledge base is available together with several real installations. These installations give real data which can be compared with previous theoretical studies.
Ice rinks operate for a long term which means that they operate in wide range of different ambient temperatures. According to the ambient temperature, ice rinks have different energy demand per sector. The five big sectors in an ice rink are refrigeration, heating, ventilation, dehumidification and lighting systems (Rogstam et al., 2014)

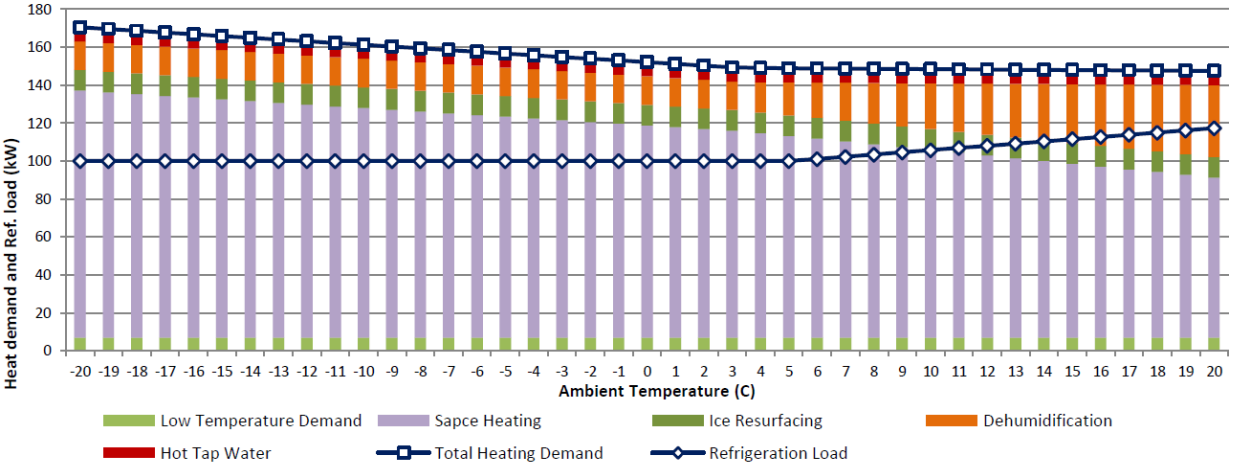

Figure 1: Regular ice rink demands (ROGSTAM, ABDI and SAWALHA, 2014)

According to Fig.1, the main energy user of an ice rink is the refrigeration system. A refrigeration system which uses CO_2 refrigerant can cover the heat demand by using heat reclaim. The heat reclaim is achieved using a heat exchanger, which is called de-superheater. This heat exchanger is placed between compressor and gas cooler (Fig.6a). It warms water which returns from the heating system.

The refrigeration cycle becomes more efficient after the use of subcooling because the enthalpy in the expansion device (h_s) becomes lower so the cycle can achieve the same cooling capacity (Q_c) having lower mass flow ($\dot{m}$) (Eq. 1), which means less energy consumption by the compressor. The enthalpy in the evaporator's outlet (h_2) is constant as it depends on the evaporator's temperature outlet which does not change.

$$Q_c = \dot{m}(h_2 - h_s) \quad \text{Eq. (1)}$$

The heat which is recovered ($Q_{recoved}$) is lower, for the same conditions (Eq. 2). The mass flow becomes lower, whilst the enthalpy inlet and outlet ($h_{des,out}$) of the de-superheater is constant. The enthalpy inlet of the desuperheater is equal to the enthalpy outlet of the compressor and is called discharge enthalpy ($h_{discharge}$).

$$Q_{recoverable} = \dot{m}(h_{discharge} - h_{des,out}) \quad \text{Eq. (2)}$$

The coefficient of performance for cooling purposes (COP_c) (Eq. 3) is not enough to represent how efficient is this refrigeration cycle, because of the heat which is reclaimed. The reason is that the heat recovery which is produced by a low COP_c cycle can be more profitable than using two different refrigeration cycles for heating and cooling respectively.

$$COP_c = \frac{Q_c}{E_{consumption}} \quad \text{Eq. (3)}$$

Sawalha introduced the definition of Heat Recovery Ratio (HRR) in order to define the limits of the effectiveness of the COP decrease (Sawalha, 2013):

$$HRR = \frac{Q_{recovered}}{Q_c} \quad \text{Eq. (4)}$$

2. DE-SUPERHEATER

CO_2 refrigeration in trans-critical operation is a very beneficial solution for an ice rink. It can reach to 120 bar discharge pressure, according to Sawalha (2008), which drives to high discharge temperature, enough to cover the ice rink's heat quality demand. Moreover, the temperature of CO_2 changes through the heat transfer, because CO_2 doesn't change phase (gas). As a result, the produced heat can be utilised more efficiently, since the temperature difference in the pinch point of a heat exchanger could be very close to 1K (Christesen, 2014). Pinch point refers to the closest point between the CO_2 temperature profile and the water temperature profile, through a heat exchanger.

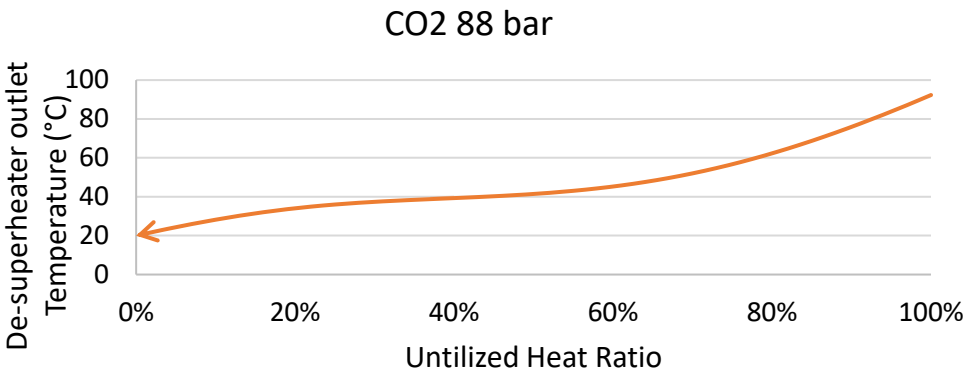

Figure 2: CO2 Temperature profile

Fig.2 illustrates the remaining unutilized heat per outlet temperature. Maximum utilisation of the produced heat is achieved when the CO_2 is condensed till 20 °C, which is equal to assumption for the water return temperature. Outlet temperature is the temperature of the refrigerant after the de-superheater. The line is not linear because CO_2 thermophysical properties change with the temperature.
The Unutilized Heat Ratio projects how much heat of the total recoverable heat has not been recovered for a specific de-superheater's refrigerant outlet temperature (Eq. 5). The unutilized heat is rejected via the gas cooler.

$$Unutilized\ Heat\ Ratio = \frac{Q_{recovered}}{Q_{recoverable}} \qquad \text{Eq. (5)}$$

When the discharge pressure becomes higher, the discharge temperature becomes higher as well. Discharge pressure and temperature are the pressure and temperature after the compressor. This affects the CO_2 temperature profile through the de-superheater. The curve of the temperature profile is moved upwards when the discharge pressure is higher. This drives to a smoother curve without parts which approach horizontal incline (Fig.3).

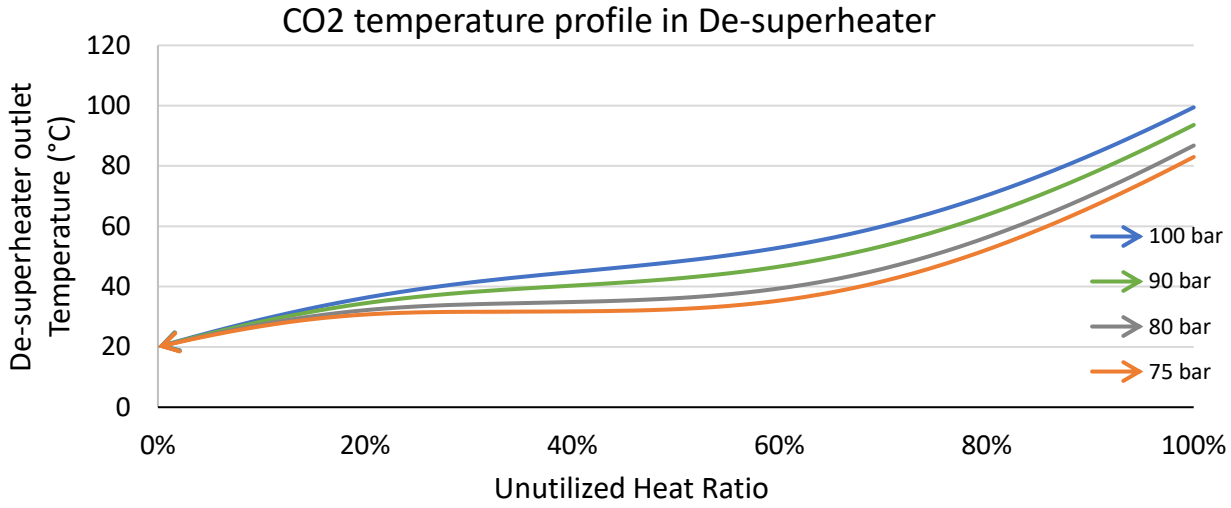

Figure 3: CO2 Temperature profile for different discharge pressure

The pinch point is very important for the heat transfer through the de-superheater; the water temperature profile should be adapted according to the pinch point and the CO_2 temperature profile (Fig.4). This means that the pinch point creates some constraints in the heat transfer giving disability of proper heat recovery (less recovered energy or lower supply water temperature). High approach

temperature (approach temperature is the temperature difference between water inlet and refrigerant outlet in de-superheater) is a consequence of the pinch point in a heat exchanger.

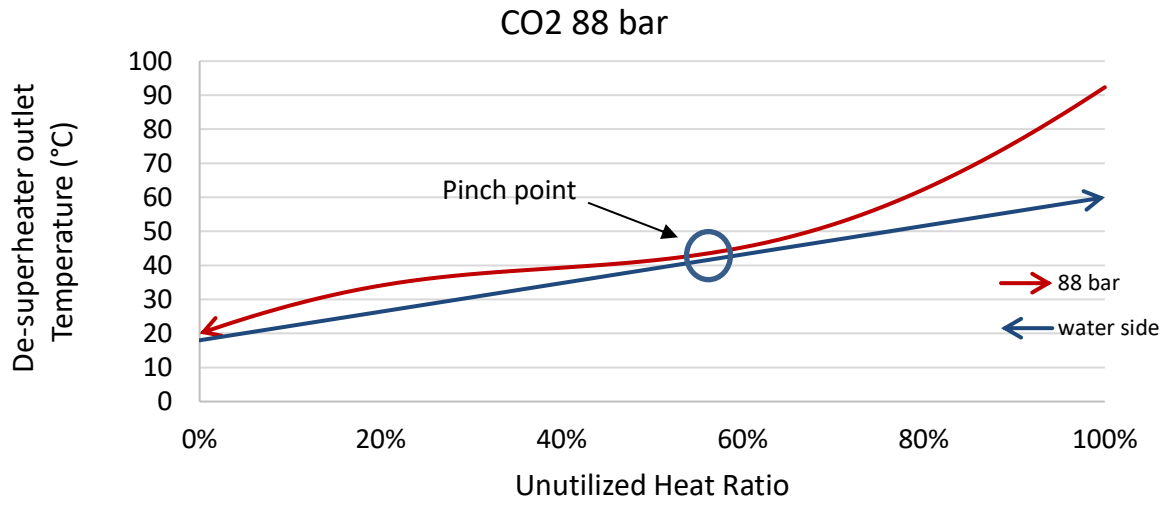

Figure 4: CO2 and water temperature profile through de-superheater

There are 2 solutions for more efficient heat transfer. Higher discharge pressure as it is explained above or use of 2 heat exchangers in series (two stage heat recovery) as it is illustrated in Fig.6b (heat transfer principle in Fig.5).

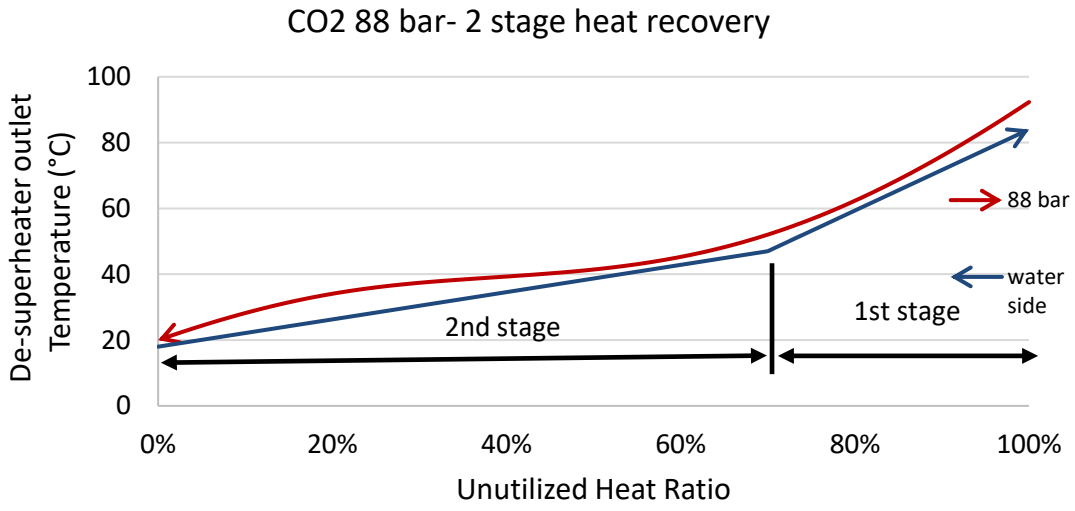

Figure 5: CO2 and water Temperature profile through De-superheaters, two stage heat recovery

3. MODELLING DETAILS

3.1. System Description

The reference system in this study is a regular ice rink CO_2 refrigeration cycle. The system consists of compressors' group, gas cooler and a receiver. The refrigerant is distributed under the ice rink with the help of pumps.

The energy could be recovered in either one or two stages. In the case of one stage the de-superheater is placed just before the gas cooler (Fig.6a). This used to be a common solution, but the same time is an inefficient solution.

The case of the two stages heat recovery gives a solution in that problem. Two de-superheaters are placed in series (Fig.6b) as the recovered energy to be divided in two parts. So, the high temperature

stage usually covers the 1/3 of the total requirement energy and the low temperature stage covers the rest 2/3 of the demand, according to Fig.1.

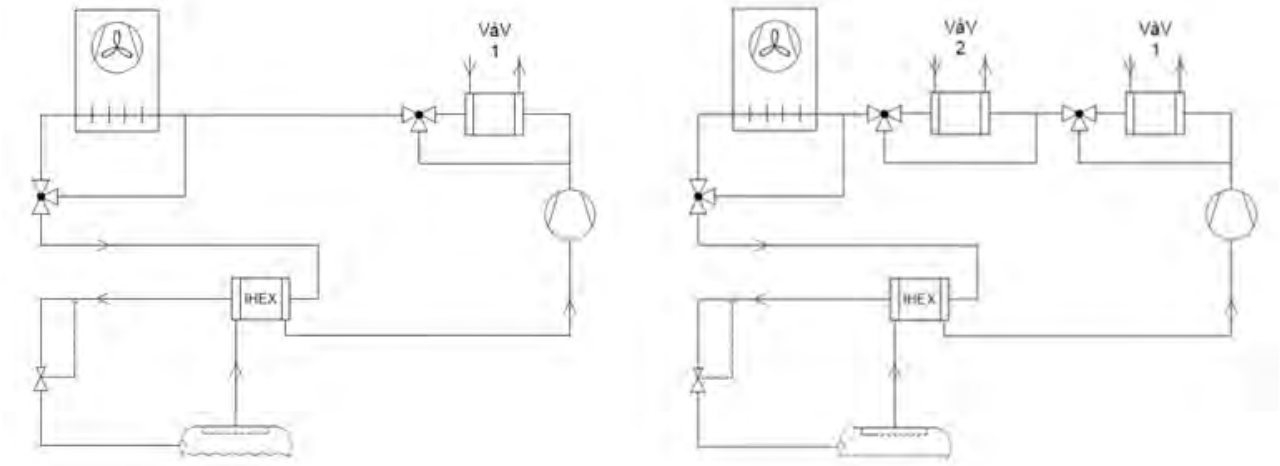

Figure 6: Refrigeration layout: a: 1stage heat recovery, b: 2stage heat recovery

3.2. Boundary conditions

It is assumed 130 kW of cooling demand and the evaporator temperature -8 ºC. It is also assumed 0 K internal superheating and 2 K external superheating, which creates losses in the system.
The efficiency of the compressor depends on the pressure ratio between the cold and warm side and it is based on manufacturer's data.
The CO_2 temperature after the gas cooler is estimated to be at least 10 ºC. Regardless of the ambient temperature, the gas cooler's fans operate to cool the refrigerant down to 10 ºC. The maximum temperature after the gas cooler is assumed 22 °C, because the temperature after the de-superheater can achieve a maximum low of 22 °C.
The water return in the de-superheater after the heating system is assumed to be at 20 °C. The high temperature stage heating system has 40 °C water return, in case of two stage heat recovery.

3.3. Control Strategy

The operation can be divided in 3 regions, which depend on the heat demand. In the first region the discharge pressure becomes higher to cover the heat demand, while the temperature after the gas cooler is constant. In the second region the discharge pressure is constant, while the temperature after the gas cooler becomes higher (less subcooling). In the third region, the gas cooler has been by-passed at all and the discharge pressure continues to be increased as to achieve the heat demand.

3.4. Scenarios

One stage heat recovery is usually used to provide hot water at 60 °C, in the first scenario thus water is heated from 20 °C to 60 °C through the de-superheater. In the second scenario, water is heated from 20 °C to 70°C, because sometimes the heat temperature demand is higher than 60 °C. In the third scenario, water is heated from 40 °C to 70 °C through the high temperature de-superheater and from 20 °C to 40 °C through the low temperature de-superheater. The share of the heat reclaim is 1/3 of the heat in the high temperature de-superheater and the rest 2/3 in the low temperature de-superheater.

4. RESULTS

An EES model was developed in order to analyse what are the best operating conditions for an ice rink refrigeration system in the 3 different heat recovery scenarios, respecting real de-superheater properties.

In every scenario, the system becomes less efficient in the second region, according to the control strategy. The COP_c becomes lower when the HRR is higher as it is visible in Figs. 7, 8 and 9. The heat recovery gain is significantly higher in comparison to the small loss of the system's performance.

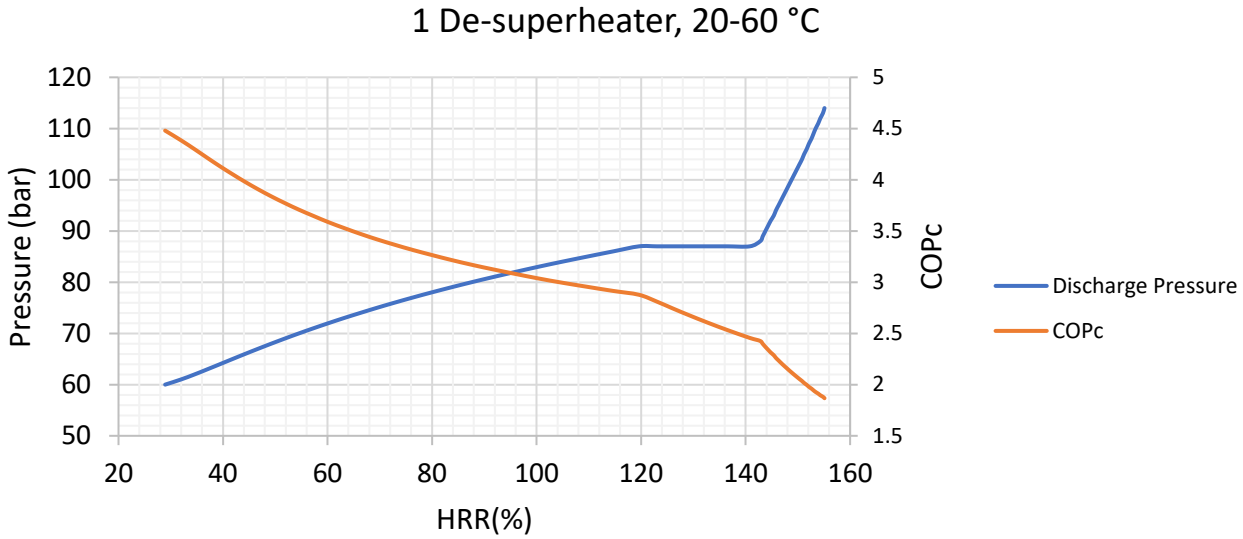

Figure 7: 1st Scenario: Optimun operation

The pressure in the second region is used as reference parameter to be compared to each scenario. This pressure could be called Optimum Constant Pressure (OCP). OCP is 87 bar in the first scenario, whilst 94-95 bar in the second scenario, for almost the same HRR range. The pressure should be 8 bar higher in order to be produced 10 °C warmer water.

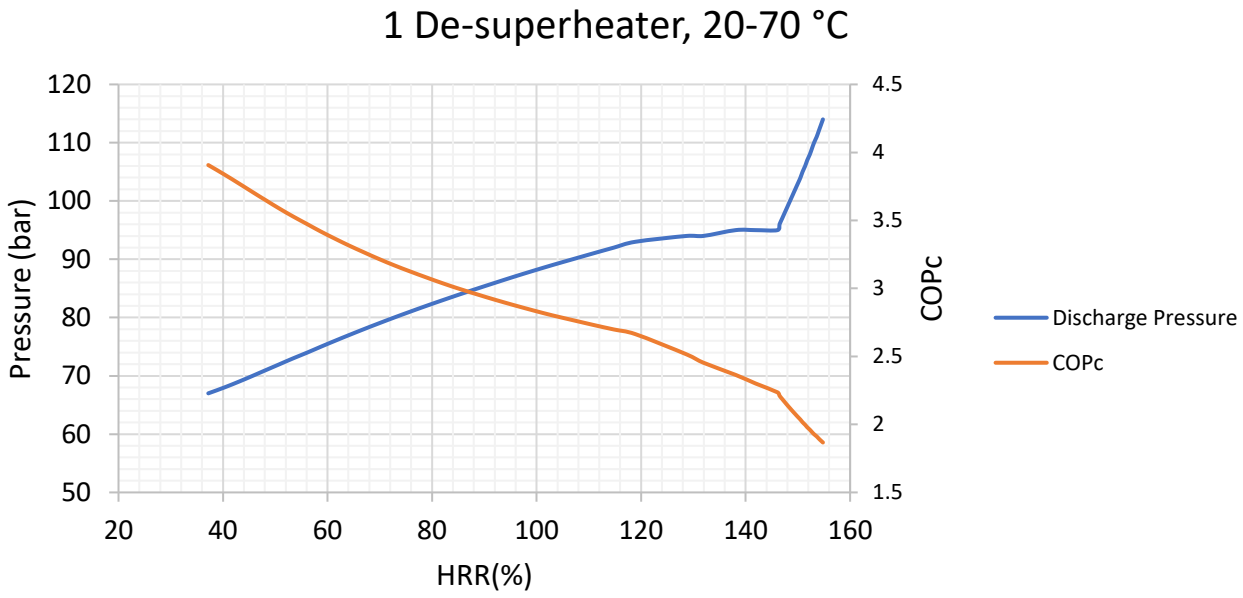

Figure 8: 2nd Scenario: Optimun operation

The third scenario has the same potential as the second, by having smaller OCP than in the first scenario. 81 bar of OCP shows that almost all the heat is utilized, and no heat is rejected via the gas cooler.

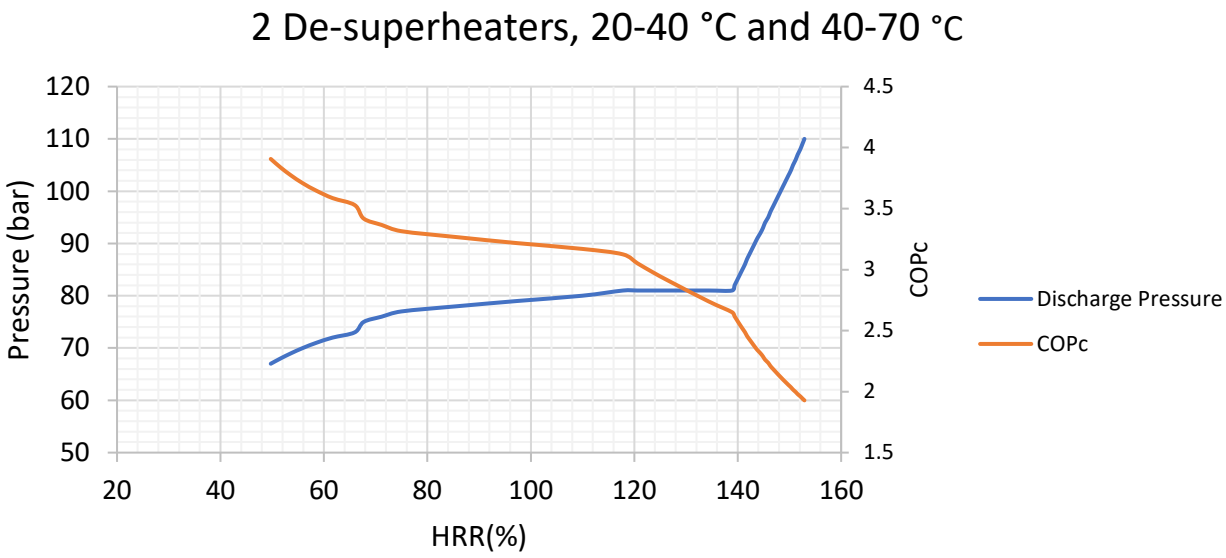

Figure 9: 3rd Scenario: Optimun operation

The COP_c is not enough to define the performance of one system. The best way for this comparison is the Global COP (COP_{Gl}) which defines the whole performance of these systems, as shown in Eq.6.

$$COP_{Gl} = \frac{Q_{recovered} + Q_c}{E_{consumption}} \qquad \text{Eq. (6)}$$

According to Fig.10 the first scenario has very good COP_{GL}, but this coefficient is 0.5 in the second scenario less when the supply water temperature demand is higher. For a system which operates more than 8 months this difference could have a big impact in the total energy consumption. But the COP_{GL} becomes 1.1 higher in case of two stage heat recovery (third scenario), which means that the performance is even better than the first scenario. So, higher quality energy is supplied for heating with better performance.

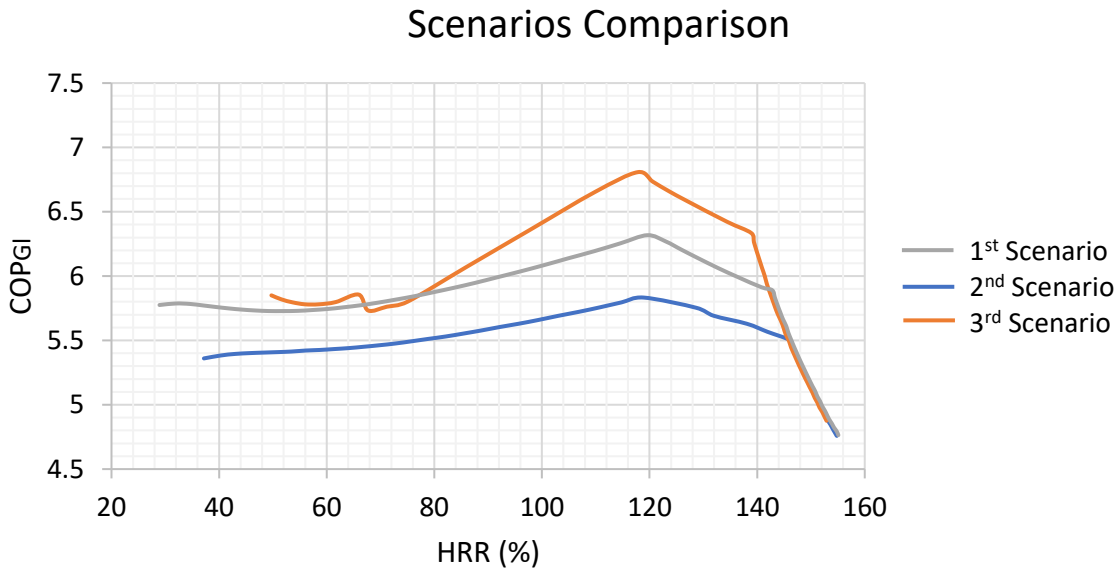

Figure 10: Global COP comparison

5. CONCLUSIONS

These systems could be more efficient if they operate in proper conditions. The proper control of these systems could provide better performance and even better quality of heat.
The water supply temperature could be higher than 60 ºC.
Moreover, the subcooling control is very important because it affects the energy that is recovered. The subcooling should be controlled according to the heating demand.
According to the heat demand and using proper hardware the system could recover higher quality of energy when the system's performance is better. Using two stage heat recovery instead of one stage heat recovery the water supply temperature is 10 ºC higher when the COP_{GL} is 10% higher for the same HRR range.
The system does not reject recoverable energy in case of two stage heat recovery because of smaller difference between the temperature profile of CO_2 and water through the de-superheater.

NOMENCLATURE

CO_2	Carbon dioxide	$\dot{m}$	CO_2 mass flow rate [kg×s^{-1}]
COP_c	Coefficient of Performance for cooling [-]	h_s	CO_2 enthalpy in expansion device [kJ×kg^{-1}]
COP_{GL}	Global Coefficient of Performance [-]	$h_{discharge}$	CO_2 enthalpy after compressor [kJ×kg^{-1}]
$E_{consumption}$	Compressors' power consumption [kW]	OCP	Optimum Constant Pressure [bar]
EES	Engineering Equation Solver	$h_{des,out}$	CO_2 enthalpy after desuperheater [kJ×kg^{-1}]
h_2	CO_2 enthalpy after evaporator [kJxkg^{-1}]	$Q_{recoverable}$	Recoverable Heat [kW]
HRR	Heat Recovery Ratio [-]	$Q_{recovered}$	Recovered Heat [kW]
Q_c	Cooling capacity [kW]		

REFERENCES

Christesen, R., 2014. Design of Heat Exchangers for Heat Recovery in Trans-critical CO2 Systems.

Sawalha, S., 2008. Carbon dioxide in supermarket refrigeration. Department of Energy Technology. Stockholm, Royal Institute of Technology. Doctoral thesis.

Sawalha, S., 2013. Investigation of heat recovery in CO2 trans-critical solution for supermarket refrigeration. International Journal of Refrigeration 36(1), 145-156.

Rogstam, J., 2010. Energy Usage Statistics and Saving Potential in Ice Rink. Proceedings of IIR Sustainable Refrigeration and Heat Pump Technology.

Rogstam, J., Abdi, A. and Sawalha, S., 2014. carbon dioxide in ice rink refrigeration. Proceedings of the 11th IIR Gustav Lorentzen Conference on Natural Refrigerants, Hangzhou, China.

Manuscript ID: 1253
DOI: 10.18462/iir.icr.2019.1253

High temperature industrial heat pumps utilising natural working fluids

Petter NEKSÅ [a,b], Michael BANTLE [a], Christian SCHLEMMINGER [a], Opeyemi BAMIGBETAN [b]

[a] SINTEF Energy Research
Trondheim, 7465, Norway petter.neksa@sintef.no
[b] NTNU. Dept. of Energy and process engineering
Trondheim, 7465, Norway

ABSTRACT

There is a large demand for heat typically in the temperature range 100-200ºC in different industries. This is today often covered by fossil fuel burning or direct use of electricity. Heat pumps has to a lesser extent been utilized due to higher investment cost and limited availability of systems for these temperatures.
With increasing focus on reduction of emissions and demand for improved energy efficiency the interest in development of high temperature heat pumps is increasing. Through the projects HeatUp and HighEFF the aim has been to develop heat pumps meeting the demands from industry utilizing natural working fluids.
The results show that the natural refrigerants hydrocarbons, steam and fluid mixture ammonia/water all can be applied successfully to supply the required temperatures and demands within different applications. This is supported by experimental results. Economic feasibility of implementation in the industry under different conditions are evaluated and discussed depending on country.
Keywords: Heat Pumps, Natural Refrigerants, Industrial, High Temperature, Energy Efficiency.

1. INTRODUCTION

The Paris agreement and later IPCC reports gives a clear recommendation that emissions of greenhouse gases (GHG) need to be reduced drastically in order to limit the global warming. Heat pumps may contribute to this by reducing electricity needs and by replacing fossil fuels for heating purposes.
For heat pumps the direct emissions related to HFC refrigerants is also important. Chlorine containing refrigerants are being phased out according to the Montreal protocol and phasing down the use of HFC refrigerants in order to reduce the GHG contribution from the sector will take place according to the Kigali amendment to the Montreal protocol.
Refrigerant selection for the future will therefore be principally between Natural refrigerants, e.g. hydrocarbons, ammonia, water, carbon dioxide or their mixtures, or to use new synthetic refrigerants. The society now have knowledge from three generations of synthetic fluorocarbons, all believed to have no negative environmental consequences when being introduced, but afterwards proved to have very negative consequences. It is therefore difficult to understand from a precautionary principle that one should rely on a new generation of synthetic fluids if sound alternatives can be found among the natural refrigerants. The natural refrigerants are naturally occurring in the biosphere and are therefore known to have no negative effects to the environment if they are leaked to the atmosphere.
For high temperature industrial heat pumps the refrigerant selection is very relevant since technology and concepts to a lesser degree exist in the market. Arpagaus (2019) gives an overview of definitions of a high temperature heat pump from the literature. In this publication we try to concentrate on heat pumps of medium to high capacity, from 100s of kW and higher, delivering heat partly or fully above

100ºC, thus covering the temperature range above the heat sink temperatures feasible by more off-the shelf technology.
Several sources have made mapping of the heat demands at different temperature levels in various industries (Apagaus et al., 2018 and Sevault et al., 2018). Some of them also map heat sources at different temperature levels (Huang et al., 2015). The general understanding is that there should be a considerable market potential for high temperature heat pumps. Still there is a need for further mapping. The potential varies from country to country depending on industry type and structure and because the coexistence of suitable heat sources to the demands need to be further mapped. In this respect industrial heating at temperature levels above 100ºC is somewhat special due to the high temperature lift required if the heat is to be absorbed from the ambient, unless the heat pump can benefit from serving cooling demands at this temperature level.
In this paper the latest results from the activity at SINTEF-NTNU within the area of high temperature heat pumps will be presented, with emphasis on activity in a competence building project named HeatUp and activity in the research center HighEFF. Focus has to a large extent been towards finding suitable technical solutions for use of natural refrigerants in this important application area for improved energy efficiency.

2. SUITABLE REFRIGERANTS

CFC-11 and CFC-114 were much considered working fluids for high temperature heat pumps in the 1980s. Due to their ODP and very high GWP, these fluids are obviously not alternatives anymore. Alternatives are now to be found in the group of natural refrigerants or new low-GWP synthetic refrigerants. Suitability for the given application, safety aspects, environmental compliance and in the end, very important, economic aspects, are important.
Screening of refrigerants is a common scientific exercise, often a first stage in approaching new applications. With todays thermodynamic libraries, many fluids may be compared relatively efficient according to defined criteria. Thereby comparing corresponding data for different fluids for predefined parameters, such as heat source and sink temperatures and component efficiencies. For fluids with relatively similar properties, the comparison becomes relatively easy, while fluids with somewhat different properties, e.g. carbon dioxide and water, can be more difficult to implement.
Bamigbetan et al. (2018a) made a screening of suitable fluids for heat delivery up to 125 ºC, focussing mainly on hydrocarbons and unsaturated HFCs, the so-called H(C)FOs. In general, for these fluids with relatively similar thermodynamic properties, the theoretical COP obtainable for given conditions was deferring with less than 10%. Such a difference may of course be important for the total energy efficiency, but on the other hand, other properties, like heat transfer capabilities and process and component adaptation could likely be influencing the differences in efficiency equally much. In this sense, it is very easy to put too much emphasis into relatively small differences in e.g. theoretical COP for given conditions. In the end a lot of practical and economic considerations will influence the choice.
Based on the history of negative experience with different generations of synthetic refrigerants from an environmental point of view, one approach may be to concentrate on finding suitable fluids among the natural refrigerants. This may require more efforts on solving engineering challenges related to e.g. flammability for hydrocarbons, pressure rating for carbon dioxide, high specific volume flows for water and toxicity for ammonia. All are however challenges that may be overcome in industrial applications, where standards and other non-technical aspects is less of a hinder for introducing e.g. flammable fluids, than in household and commercial applications.

3. TECHNOLOGIES AND RESULTS FOR DIFFERENT APPLICATIONS

Bamigbetan et al. (2017b) gives an overview of natural refrigerants in the perspective of high temperature heat pumps for vapor compression systems. It substantiates that it is possible to find suitable natural refrigerant alternatives for most applications, though technological advancements are required. Some such advancements are discussed here.

3.1. Hydrocarbons

Hydrocarbons are a family of fluids suitable to serve most temperature levels, from cryogenic temperatures to high temperature heat pumps, due to its overlapping vapor compression curves depending on the molecular weight of the different hydrocarbon molecules. They are also known to have very favourable transport properties, leading to good heat transfer properties, enabling efficient heat exchange.

A technological challenge is of course the flammability of the fluids, being categorised as A3 according to ISO 817. In industry, where these systems are to be installed, this can be handled safely by following the applicable standards and codes of good practice, but it is of course required to have proper training of personnel for installation, maintenance and operation.

Bamigbetan et al. (2018b) describes a laboratory prototype built up to investigate a butane-propane cascade heat pump able to deliver heating up to 115ºC at condensing temperatures up to 120ºC. The capacity of the prototype rig was 20 kW. Aim for a commercial size industrial plant is 300 kW.

Fig. 1a shows a process flow diagram of the laboratory plant. The system is built up with copper brazed plate heat exchangers and single stage compressors and expansion valves in each stage. The system is placed in a ventilated cabinet with leak detectors that stop the system in case of a system break down. The system is prepared for operation also with hydrocarbon mixtures as refrigerant but has so far only been tested with pure propane and butane.

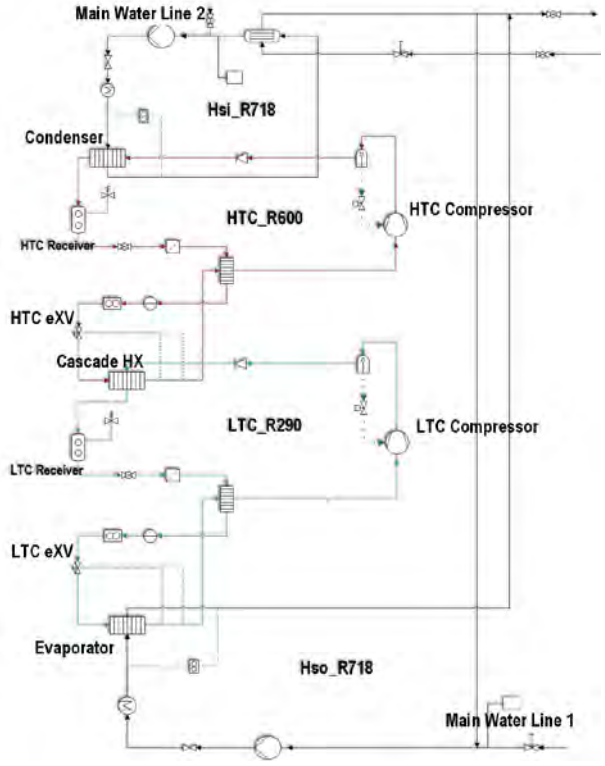



a) **b)**

Figure 1: a) Process flow diagram of the butane-propane cascade laboratory prototype b) Picture of ventilated cabinet with the hydrocarbon high temperature heat pump

Special attention was on the prototype butane compressor for the high temperature stage. The compressor installed is a four-cylinder semi-hermetic piston compressor made by Dorin. The butane stage will experience evaporation temperatures in the range of 40-60ºC. Temperature control to obtain sufficient motor cooling and to avoid excessive discharge temperatures is therefore a challenge. Further, installed in an ambient of room temperature it also requires special attention to avoid the suction gas to condense before entering the compressor. In order to enable proper monitoring, 11 temperature sensors and two pressure sensors was installed. The results of the testing so far look very promising. Operation with condensing temperatures up to 120ºC (about 21 bara) was performed over a longer period in the laboratory, without any visible degradation of the lubricant. The compressor is due to detailed investigation for possible wear when this is written.

Fig. 2 shows measured compressor efficiencies. As may be observed the efficiencies are very acceptable. The total compression efficiency measured as the isentropic work based on the suction pipe temperature for the given mass flow divided by the electric motor power consumption is between 70 and 75 % for all pressure ratios up to 5. More results may be found in Bamigbetan et al. (2018c, 2019).

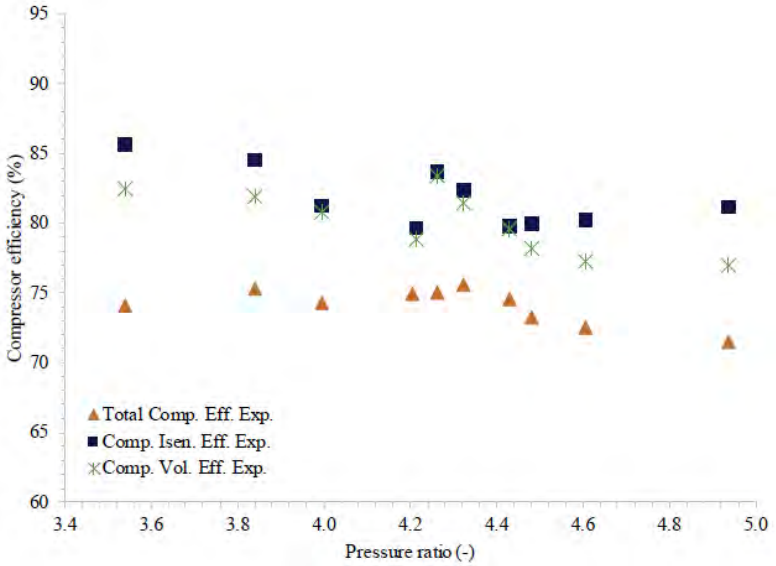

Figure 2: Compressor efficiencies of the prototype hydrocarbon compressor

Further testing in the laboratory pilot plant is planned to be performed with hydrocarbon mixtures as refrigerants. This may enable temperature adaptation for gliding temperature heat sink and source, thus potentially improving the efficiency for such applications. This was investigated from a theoretical point of view by Bamigbetan et al. (2016) for mixtures of propane, butane and pentane. The results showed the potential of improving the COP by up to 13.5% for temperature glides of respectively 10 and 30 K for the heat source and sink.

3.2. Water or Steam as Refrigerant

Water is a very good refrigerant, with good heat transfer characteristics and a very high heat of vaporisation. It is also abundant in the nature and dewatering by drying is a very important process in the industry.

For drying purposes, it is obviously a very interesting option to utilise the vapour from the drying process as refrigerant in an open type process. The concept is named mechanical vapour recompression (MVR). The vapour from drying is compressed, and the hot water vapour is used as heat source by condensation to heat and thus contribute to further drying of the product. It may also be used in steam driers, see Figure 3. Such systems can achieve very high coefficients of performance and are being used in e.g. the dairy industry.

Water may also be used in a closed cycle in a conventional vapor compression cycle. A challenge is however the very large swept volumes required for steam and the fact that evaporation below

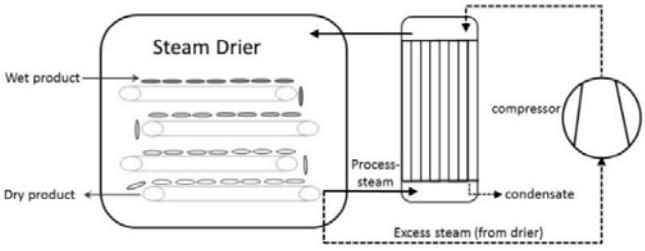

Figure 3: Simplified schematic layout of a superheated steam drier with energy recovery through mechanical vapour recompression

100ºC will happen at a sub-atmospheric pressure. The latter may be overcome by using steam in a high temperature stage with another refrigerant in the lower stage. The low stage, for instance using butane, will then be lifting the heat to temperatures above 100ºC, where the steam stage take over. Steam has the prospects of delivering heat at very high temperatures when compressed in oil-free compressors not affected by degradation of the lubricant, condensation temperatures up to 200ºC has been investigated in the HeaUP project. Potentially it could go higher.
Compressors of several types, e.g. screws and turbo compressors, or more fan like concepts, like roots blowers and centrifugal fans, exists in the market place. Thus, this type of systems can and are being built today. However, the existing compressors often become relatively costly for various reasons, for instance the fact that they for high temperatures need to do oil-free compression. Bantle et al. (2018a/b) describes development of a high speed turbo compressor based on a commercial turbo-charger for vehicles, able to run with speeds up to 80.000 rpm. Fig. 4a shows a picture of the prototype compressor and efficiency figures from the compressor tests are shown in Fig. 4b.

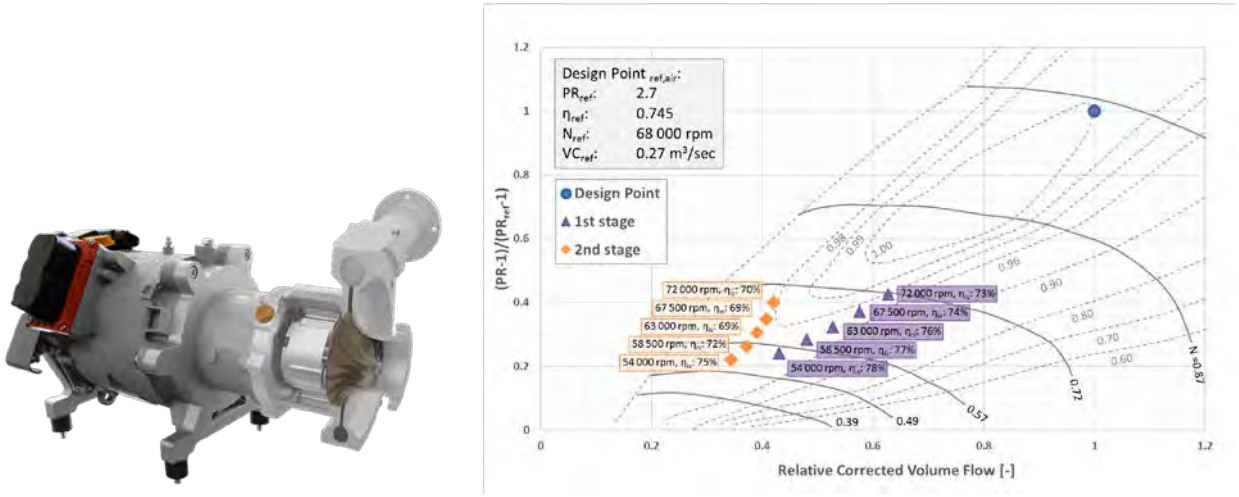

a) **b)**

Figure 4: a) Picture of the compressor, length 50 cm, width 40 cm and height 35 cm, 40 kg
b) Achieved measured efficiencies for the compressor

As seen from the picture and measures, the compressor is very compact and consequently it has the potential to reach a low cost. This, and the relatively high efficiency, may contribute to achieve cost efficient implementation of steam high temperature heat pumps.

3.3. Ammonia-Water

Ammonia is known to be a very good refrigerant and is the dominantly used refrigerant in industrial refrigeration systems. To reach condensing temperatures above 100ºC is however not feasible yet with standard equipment, even though 60 bar compressors has been introduced on the market, enabling temperatures close to 100ºC. One possibility might be to utilise it in a low temperature stage as investigated by Bamigbetan et al. (2017a).
Another possibility is to utilise ammonia in mixture with water in a compression-absorption cycle, see simplified process flow diagram in Fig. 5a. A great advantage of this cycle is that you may reach much higher temperatures with ammonia while operating at lower pressures. The cycle has gliding temperatures during heat absorption and rejection. These glides can be adjusted with different ratios of water-ammonia mixture in the system and solution circulation rates. In this way one may adjust the glides to match the temperature glides of the heat sink and source.
The cycle, also called the Osenbrück cycle, is shown schematically in a p – (1/T) diagram in Fig. 5b. As heat is absorbed by the zeotropic mixture of ammonia and water, a gas phase very rich in ammonia is formed. The gas and liquid are separated, and while the gas is compressed in an ordinary ammonia compressor, the weak solution is pumped in parallel to the high pressure. The two phases are then mixed and heat rejected in the absorber/condenser before throttled to the inlet of the desorber/evaporator.

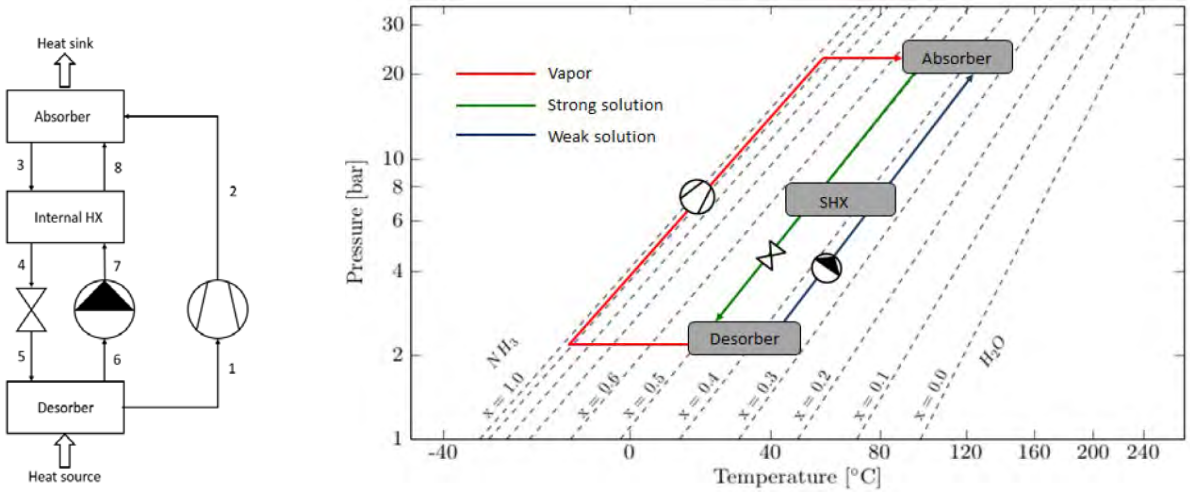

a) b)

Figure 5: a) Simplified process flow diagram of the vapour compression cycle b) Illustration of the process in a p - 1/T diagram

Several systems with this concept using 25 bar equipment have already been installed and are operating in the market (Nordtvedt et al., 2011). At this pressure rating heating up to 120ºC can be obtained. Ellingsen et al. (2018) presents a two-stage concept for heating at two different temperature level, which could be of interest in some industries, for example in dairies.

Wersland et al. (2017) investigated the cycle for heating of process water from 95-115ºC for a heat source temperature of 30ºC at varying loads from 10-130%. Absorber pressures required for this conditions varied from 26 to 27 bar, thus slightly above a standard pressure rating of 25 bar.

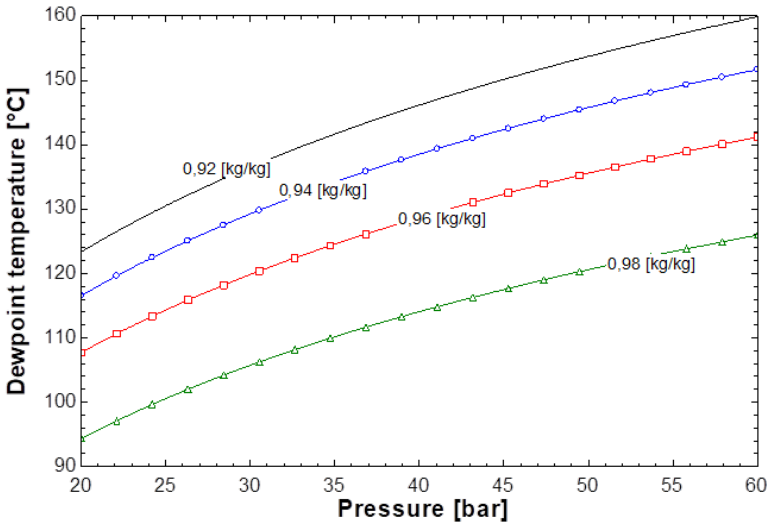

Figure 6: Dew point temperature at varying pressure for varying ammonia concentration in water

A very interesting possibility for reaching even higher temperatures opens with the new ammonia compressors, developed for higher pressures up to 60 bar. Figure 6 shows dewpoint temperatures as function of pressure for various mass fractions of ammonia in water. With 60 bar compressors, such a cycle should be able to deliver heating with temperature glides approaching 160ºC.

4. ECONOMIC CONSIDERATIONS

The economy of implementing high temperature heat pumps in the industry will vary very much depending of country, e.g. due to the ratio between gas and electricity price, and between industries, e.g. due to availability of heat sources to limit the required temperature lift or required installation cost, which may vary with a factor of 10 depending on if it is a brown or greenfield installation. An advantage is the high number of running hours in industry.

Figure 7 shows simple payback time as a function of the cost ratio of electricity to gas for an assumed COP and investment cost, gas versus a heat pump. In Norway, where the cost ratio is close to 1, it obviously becomes more favourable for implementation than in a country like Germany, where this ratio may be up to 4. An important factor here may be that the cost of emitting CO_2 must go up in the future if the countries should be able to comply with their obligation to reduce greenhouse gas emissions.

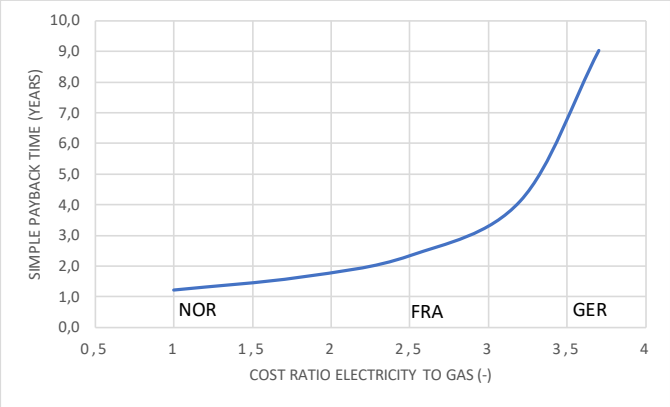

Figure: 7 Simple payback time vs cost ratio of electricity to gas
Additinal investment 550 EUR/kW, Gas price 0,06 EUR/kWh
COPhp 3,5 Running hours 8500 h/y

5. CONCLUSIONS

High temperature heat pumps can be an important possibility for enabling reduced energy use and limiting the greenhouse gas emissions from the industry.
Natural working fluids can offer heating at all relevant temperature levels for the industry, and thus avoiding the uncertainty of introducing new synthetic refrigerants that eventually may turn out to be harmful to the environment, as have been the case for the three first generations of halocarbons.
Characteristics of three categories of refrigerants utilising vapour compression principles, namely hydrocarbons, water and ammonia-water, has been discussed regarding their characteristics and specific development requirement based on recent research activities. All candidate natural working fluids have potential to fill market potential in different industries based on their characteristics.
Economic feasibility of implementation of high temperature heat pumps in the industry varies depending on the boundary conditions, which may vary very much between countries and individual industries. Increased cost on carbon emissions will benefit high temperature heat pump implementation.

ACKNOWLEDGEMENTS

This paper has been funded by HighEFF - Centre for an Energy Efficient and Competitive Industry for the Future, an 8-year Research Centre under the FME-scheme (Centre for Environment-friendly Energy Research, 257632/E20). The authors gratefully acknowledge the financial support from the Research Council of Norway and user partners of HighEFF.
The authors would also like to acknowledge the support of The Research Council of Norway and the industrial partners Equinor AS, Hydro Aluminium AS, Statkraft Varme AS, Vedde AS, member of TripleNine Group Vedde AS, Mars GmbH, TINE SA, Cadio AS, Hybrid Energy AS and EPCON Evaporation Technology AS through the grant NFR-243679 (HeatUp).

REFERENCES

Arpagaus, C., Bless, F., Uhlmann, M., Schiffmann, J. and Bertsch, S.S., 2018. High temperature heat pumps: Market overview, state of the art, research status, refrigerants and application potentials, Energy 152, pp 985-1010

Arpagaus, C., 2019. Hochtemperatur-Wärmepumpen. Marktübersicth, Stand der Technik und Anvendugngspotenziale, VDE Verlag, Berlin

Bamigbetan, O., Eikevik, T.M., Nekså, P. and Bantle, M., 2016. Evaluation of natural working fluids for the development of high temperature heat pumps, Proceedings of the 12th IIR Gustav Lorenzen Conference on Natural Refrigerants, Edinburgh

Bamigbetan, O., Eikevik, T.M., Nekså, P. and Bantle, M., 2017a. Extending ammonia high temperature heat pump using butane in a cascade system. Conf. proc. of the 7th IIR Conference on Ammonia and CO_2 refrigeration Technologies, Ohrid, Macedonia

Bamigbetan, O., Eikevik, T.M., Nekså, P. and Bantle, M., 2017b. Review of vapour compression heat pumps for high temperature heating using natural working fluids, Int. J. Refrigeration 80, pp. 197-211

Bamigbetan, O., Eikevik, T.M., Nekså, P., Bantle, M. and Schlemminger, C., 2018a. Theoretical analysis of suitable fluids for high temperature heat pumps up to 125 ºC heat delivery, Int. J. Refrigeration 92, pp. 185-195

Bamigbetan, O., Eikevik, T.M., Nekså, P., Bantle, M. and Schlemminger, C., 2018b. Experimental investigation of the performance of a hydrocarbon heat pump for high temperature industrial heating, Proceedings of 13th IIR Gustav Lorentzen conference on Natural Refrigerants, Valencia, 2018

Bamigbetan, O., Eikevik, T.M., Nekså, P., Bantle, M., Schlemminger, C. and Dallai, M., 2018c. Experimental investigation of a hydrocarbon pistion compressor for high temperature heat pumps, Proceedings of the 24th Int. compressor engineering conference, Purdue, July 9-12, 2018

Bamigbetan, O., Eikevik, T.M., Nekså, P., Bantle, M., Schlemminger, C., 2019, Experimental investigation of a prototype R-600 compressor for high temperature heat pump, Journal Energy 169, pp. 730-738

Bantle, M., Schlemminger, C., Tolstorebrov, I., Ahrens, M. and Evenmo, K. 2018a. Performance evaluation of two stage mechanical vapour recompression with turbo-compressors, Proceedings of 13th IIR Gustav Lorentzen conference on Natural Refrigerants, Valencia, 2018

Bantle, M., Schlemminger, C., Ahrens, M. and Evenmo, K. 2017. Kennfeld und Leistungsanalyse einer zweistufig Turbokompressor Brüden Verdictung, Proc. DKV-Tagung 2018, Aachen, AA II 2.04

Ellingsen, Ø.M., Kvalsvik, K.H. and Bantle, M., 2018. Two-stage high temperature hybrid heat pump with parallel heat sinks. Proceedings of 13th IIR Gustav Lorentzen conference on Natural Refrigerants, Valencia, 2018

Huang, B., Bühler, F., and Holm, F.M., 2015. Industrial Energy Mapping: THERMCYC WP6. Technical University of Denmark (DTU)

Nordtvedt, S.R., Horntvedt, B.R., Eikefjord, J. and Johansen, J. 2011. Hybrid heat pump for waste heat recovery in Norwegian food industry. Proc. of the 10th International heat pump conference

Sevault, A., Tranås, O.L. and Mazzetti, M. 2018. Industrial Excess Heat Recovery – Status of the Norwegian Industry, IEA IETS Annex XV report, ISBN 978-82-14-06921-1

Wersland, M.B., Kvalsvik, K.H., Bantle, M. 2017. Off-design of high temperature hybrid heat pump, Proc. of the 12th IEA Heat Pump Conference, Rotterdam, 2017

Manuscript ID: 1325
DOI: 10.18462/iir.icr.2019.1325

Radiation absorption and heat collection characteristics of graphene/paraffin composite phase change material

Lanxiong OUYANG [(a)], Guoying XU [(a)], Junhui YAN(a), Kai DU [(a)]

[(a)] Organization School of Energy and Environment, Southeast University, Nanjing, 8625210000, China, 220170590@seu.edu.cn

ABSTRACT

Based on the light-absorbing characteristic of graphene/paraffin composite phase change material (PCM), the solar radiation is directly absorbed by the nanoparticles added inside.
The purpose of this study is to investigate the performance of heat collecting of composite PCM and to explore the possibility of using it in integrated system of heat collection and storage.
The composite PCM with mass fractions of 0.01%, 0.025%, 0.05% and 0.1% were prepared. The extinction and absorption coefficient in solid and liquid phase was tested. The experiment was conducted to research the thermal performance of composite PCM.
It was concluded that the addition of graphene nanoparticles into paraffin significantly improves the absorption characteristics. Moreover, the composite PCM melted from the inside, which significantly enhanced the performance. This study verifies the feasibility of the composite PCM working in solar energy collecting and accumulating heat directly.
Keywords: Nanoparticles, Composite Phase Change Material, Heat Collecting, Heat Storage, Direct Light-Absorbing.

1. INTRODUCTION

Solar energy belongs to clean energy and is the richest source of energy on earth. The vacuum collector tube is adopted to make the working medium have the property of absorbing solar radiation by adding special nanoparticles into the working medium, which is not only a heat absorbing material, but also a heat carrying material(He, 2014).
The nanoparticles significantly improved the light absorption performance and increased the thermal conductivity and heat capacity (Wang et al., 2012). The absorption increased with the increase of mass fraction (Mu, 2011). It has been proved that nanofluid can be used as solar radiation absorption medium.
The solar radiation in the direct absorption and heat collection system is absorbed by the fluid working medium layer by layer, which is equivalent to put "internal heat source" into the fluid to improve the uniformity of the temperature distribution of the working substance in the pipe (Xu, 2015).
Solar thermal efficiency limits the use of solar energy due to its discontinuity and timeliness. To further solve this problem, researchers added the heat storage system to the solar heat collection. Phase change has a high heat storage density, but usually has a low thermal conductivity, which leads to a low heat storage and heat release rate.
The graphene nanoparticles not only have good thermal conductivity, but also show strong absorption performance in visible light, which is very suitable for recycling working medium of direct absorption solar collector (He, 2014). On the other hand, paraffin does not exist in the phenomenon of supercooling. The thermal cycle will not reduce the heat storage of paraffin, so paraffin is suitable for heat storage system (Hasnain and Gibbs, 1990).
In this paper, a new integrated method of solar energy collection and heat storage was proposed based on the good thermal conductivity and light absorption of the graphene-paraffin composite PCM. Graphene-paraffin composite PCM was used as both heat collector and heat storage medium. The main content of this article is arranged as follows: propose the integrated structure of heat collection and heat storage of composite PCM; study the thermal properties of composite PCM; study the radiation absorption mechanism and characteristics of composite PCM; experimental study on the heat-collecting properties of composite PCM; come to a conclusion.

2. RADIATION ABSORPTION AND HEAT COLLECTION CHARACTERISTICS

2.1. The Integrated Principle of Heat Accumulation and Heat Storage in Composite PCM

Based on direct absorb solar collector, an integrated system of heat collection and storage has been proposed. The composite PCM has great absorbing property of solar radiation and phase transition performance. It works as not only heat collecting but heat storage medium. The principle of the system is given in Fig.1. Working on transparent vacuum tube, the composite PCM absorbs solar radiation layer by layer, which is equivalent to put countless heat source into the composite PCM. On the other hand, the composite PCM can directly store energy. It reduces not only heat loss but also heat transfer resistance.

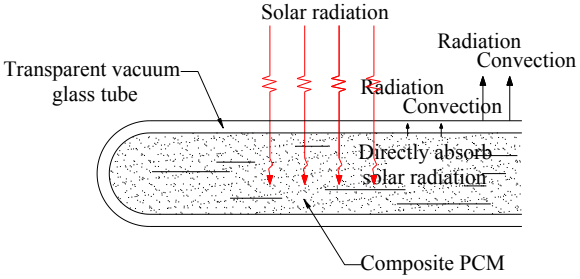

Figure 1: Integration of heat collecting and heat storage structure by using composite PCM

In terms of the composite PCM itself, the incorporation of graphene nanoparticles enhanced the heat transfer performance of the material. Besides that, the phase-change property of composite PCM makes the output heat of solar collector system more stable. This method has potential development in solar energy, especially in low temperature heat collection and storage.

2.2. Thermal Property of Composite PCM

Composite PCM with different mass fraction (0%, 0.01%, 0.025%, 0.05%, and 0.1%) has been prepared by two-step synthetic method. Graphene and graphite did not undergo chemical reactions, but only physically. All samples were uniform and stable. The thermal properties of composite PCM were tested by DSC, and the measured values are given in Table 1. The results show that the phase-transition temperature of the composite PCM is about 34℃. The addition of graphene had no significant effect on the latent heat of PCM.

Table 1. DSC test results of composite PCM

Mass Fraction (%)	Melting Temperature (℃)	Enthalpy Change of Melting ($J \cdot g^{-1}$)	Solidification Temperature (℃)	Enthalpy Change of Solidification ($J \cdot g^{-1}$)
0	33.76	215.91	34.45	215.47
0.025	34.07	214.15	34.79	215.14
0.05	34.08	214.45	34.74	214.78
0.1	33.98	210.94	34.74	212.95

2.3. Optical Property of Composite PCM

2.3.1. The mechanism of absorption of light by nanoparticles

In addition to absorption and transmission, nanoparticles also scatter light. Scattering refers to the deviation of some light from the original direction when light passes through an uneven material. Further, scattering includes refraction, reflection and other processes. Its propagation mechanism of light is shown in Fig. 2.

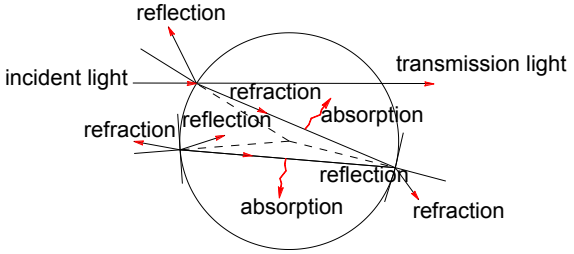

Figure 2: Light propagation mechanism of nanoparticles

The scattering process is actually the process of the collision of light and matter particles. The absorption refers to the absorption of light by particles as it passes through them. Transmission refers to the light except for scattering and absorption after passing particles.
If the distance between the nanoparticles is small and the particles are non-independent scattering, the coupling effect of the absorption characteristics of the particles must be considered. Therefore, the actual scattering of composite PCM is not simply the superposition of the dispersion degree of each group.

2.3.2. Test principle of extinction and absorption coefficient

According to the LAMBERT-BEER law, the absorbance can be expressed as:

$$A=log\frac{1}{\tau}=\varepsilon Cl \quad \text{Eq. (1)}$$

Where τ is the transmittance, ε is the molar extinction coefficient, l is the optical path length, and C is the concentration. The transmittance τ can be expressed as:

$$\tau=\frac{I_1}{I_0}=e^{-KeL_0} \quad \text{Eq. (2)}$$

Where I_0 is the intensity of incident light, I_1 is the intensity of transmission light, and the sample thickness is 0.01m. The extinction coefficient Ke can be expressed as:

$$Ke=100\times ln10^{A} \quad \text{Eq. (3)}$$

As shown in Fig. 3, the extinction coefficient is only measured transmitted, and the part beyond the transmission light is all taken as the absorption of the sample. So the scattering of the sample is classified as absorption. It can be concluded that the extinction coefficient doesn't distinguish between absorption and scattering. In order to explore the scattering characteristics of materials, the absorption coefficient is measured by a sphere to collect scattered and transmitted light. The scattered light is reflected several times in the detection instrument, with transmission light collected into the detector. The absorption coefficient Ka can be expressed as:

$$Ka=100\times ln10^{A'} \quad \text{Eq. (4)}$$

The absorbance A' is calculated by the intensity I_0 of incident light and the intensity I' of transmission light and scattering light. It can be concluded that the extinction coefficient is the sum of the absorption coefficient and scattering coefficient.

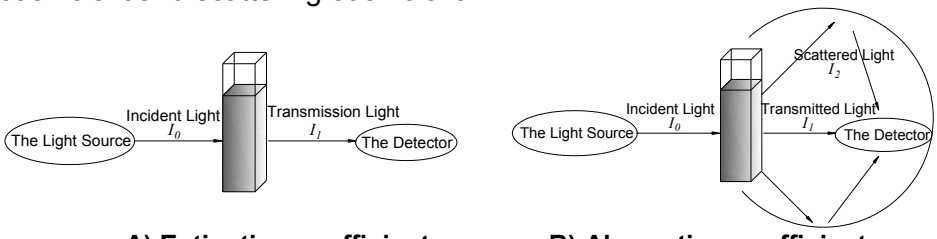

A) Extinction coefficient **B) Absorption coefficient**

Figure 3: Principles of optical coefficient

2.3.3. Extinction and Absorption Coefficient of Composite PCM with Different Concentrations

In this paper, the extinction coefficient and absorption coefficient of solid and liquid in visible light were tested. The test samples were shown in Fig 4, and the test results were shown in Figs 5 and 6.

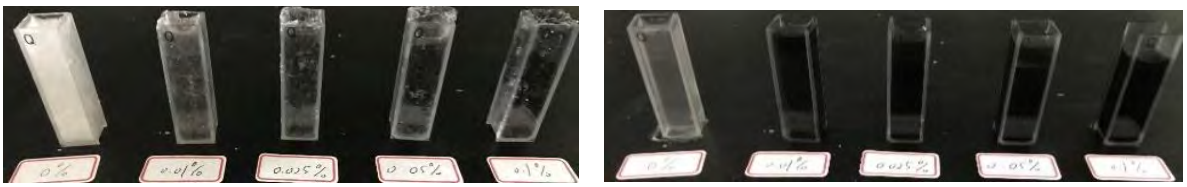

A) Composite PCM in solid state **B) Composite PCM in liquid state**

Figure 4: Testing sample

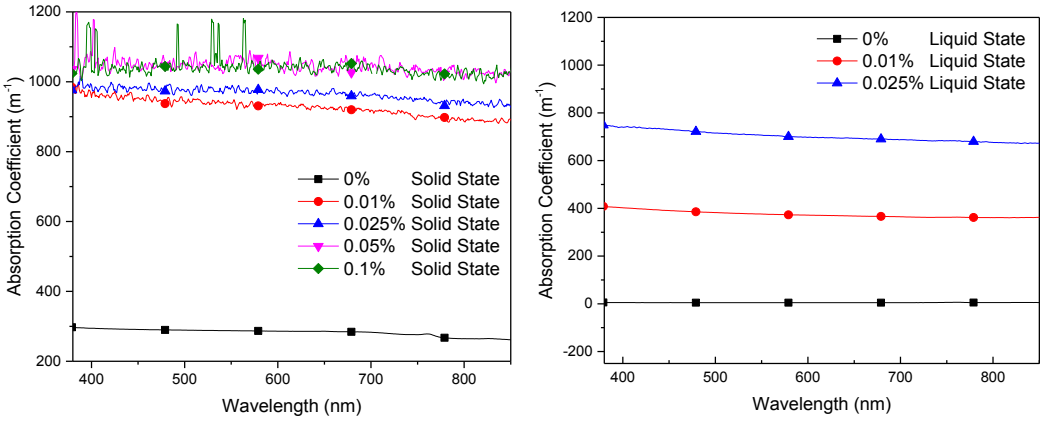

Figure 5: Absorption coefficient of composite PCM

It can be seen from Fig. 6 that the absorption coefficient of composite PCM with different concentrations in the visible light spectrum doesn't vary with wavelength. The addition of graphene significantly increases the absorption coefficient of composite PCM, and with the increase of graphene mass concentration, the absorption coefficient also increases, but the increase amplitude decreases. This is because the scattering degree of composite PCM is different. So there is an optimal mass concentration of composite PCM.

The absorption coefficient of solid is greater than that of liquid. For the composite PCM with a mass concentration of 0.01%, the absorption coefficient in liquid is 400 m^{-1} and absorption coefficient in solid is 950 m^{-1}. This is due to the change of the phase state of the base paraffin, but the increase of composite absorption is not the simple superposition of graphene nanoparticles and pure paraffin.

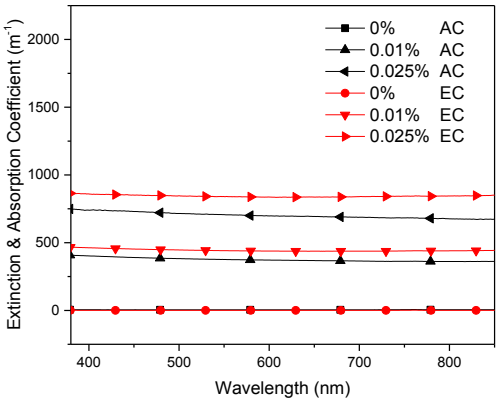

Figure 6: Comparison of extinction coefficient and absorption coefficient in liquid state

As can be seen from Fig. 7, in the visible light region, the absorption coefficient and extinction coefficient of pure paraffin in liquid are both 0, which means there is no absorption and scattering. For composite PCM in liquid state with mass concentration of 0.01% and 0.025%, the extinction coefficient is greater than the absorption coefficient, and the difference reflects the scattering of the material. The difference between the extinction coefficient and the absorption coefficient of the composite PCM in liquid state at the concentration of 0.025% is significantly greater than the

difference between the extinction coefficient and the absorption coefficient of the composite PCM in liquid state at the concentration of 0.01%.

2.4. Experimental Study on The Heat-Collecting Properties of Composite PCM

2.4.1. Analysis of temperature change in heat collecting process

In this paper, pure paraffin and composite PCM with mass concentration of 0.025% in a vacuum collector tube were selected as the experimental objects for outdoor heat collection experiment. Twelve temperature measurement points were arranged for each pipe, and four planes were selected in the vertical direction of the pipe, with three temperature measurement points in each plane, as shown in Fig. 7. The outdoor average temperature is 30.2 ℃. The average solar radiation is 214.5 W·m^{-2}. The intensity of solar radiation as shown in Fig. 8.

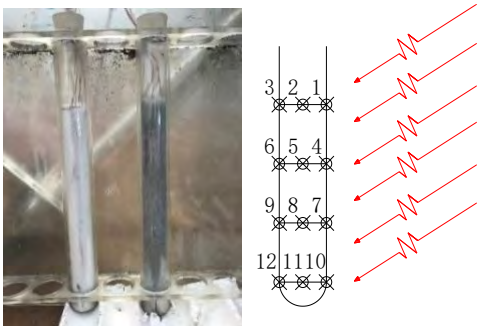

Figure 7: Experimental setup and measuring point arrangement

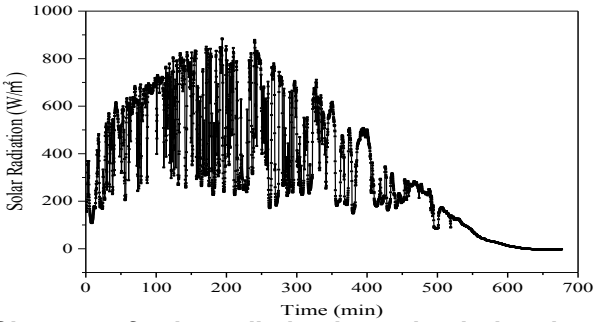

Figure 8: Changes of solar radiation intensity during the experiment

Fig. 9 shows that the temperature of the heat collection process changes with time. The temperature maintaining in the phase change temperature (34 ℃) instructs that material is melting. When the temperature is higher than the phase transition temperature, the point of PCM has been completely melt into liquid. The phase transition always begins at the top of the pipe, and then the liquid level gradually develops to the bottom. This is because the density of liquid paraffin is lower than that of solid paraffin. After the paraffin near the pipe wall melts, the liquid paraffin in the lower layer floats upward, resulting in the concentration of high temperature liquid paraffin in the upper part of the pipe.

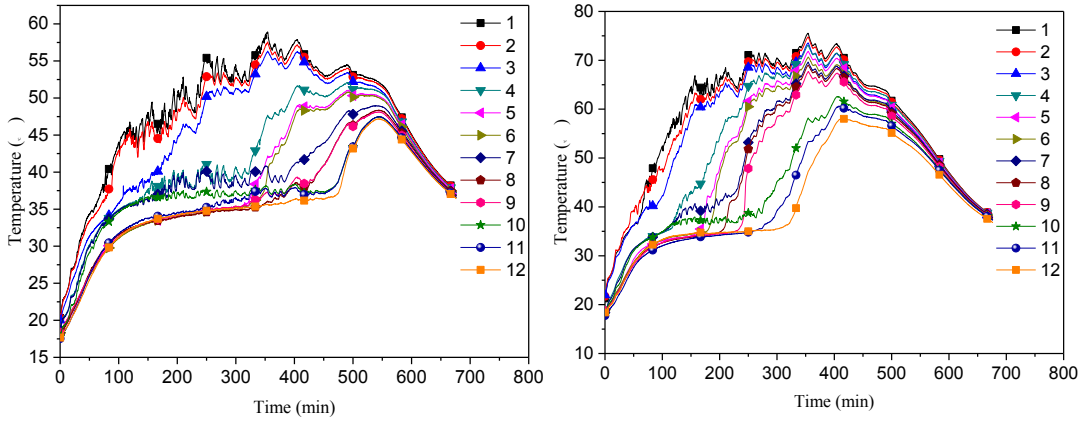

A) Pure paraffin **B) Composite PCM**

Figure 9: Changes of collector pipe temperature in different points during the experiment

The time it takes for the phase-change material to melt completely is defined as the total melting time. As can be seen from table 2, both pipes can completely melt under the same heat collection condition. Compared with pure paraffin wax, the addition of graphene nanoparticles significantly reduced the time required for the complete melting of the PCM and increased the maximum temperature that can be achieved during the experiment.

Table 2. Characteristic Parameters of Heat Collection

	Pure paraffin	Composite PCM
The highest local temperature of the process (℃)	54.3	73.4
Total melting time (min)	472	312
Average temperature at total melting time (℃)	46.6	58.8

As for the composite PCM, the addition of graphene improves the thermal conductivity of the material, which makes the internal heat exchange more intense, and the vertical temperature intersecting more obvious, thus shortening the time required for the complete melting of the composite PCM.

2.4.2. Analysis of heat collection efficiency of composite PCM

In the process of heat collection experiment, the instantaneous heat collection of composite PCM is calculated by Eq. (5):

$$Q_i=\int_i^{i+1}(m_{np}c_{np}+m_{bf}c_{bf})dt=\int_i^{i+1}(\emptyset_m c_{np}+(1-\emptyset_m)c_{bf})m_{nf}dt \qquad \text{Eq. (5)}$$

Where m_{np}, m_{bf} and m_{nf} are the mass of graphene, paraffin and composite PCM respectively. c_{np} and c_{bp} are the specific heat capacities of graphene and paraffin respectively. ∅ is the mass fraction of graphene.

The instantaneous heat collection efficiency of a single pipe can be expressed as:

$$\eta=\frac{Q_i}{AIT} \qquad \text{Eq. (6)}$$

The relationship between instantaneous efficiency and difference of normalized temperature can be expressed as:

$$\eta=\eta_0-U\times(\frac{t_i-t_a}{I}) \qquad \text{Eq. (7)}$$

Among them, η_0 is the intercept of the curve, i.e. the maximum instantaneous efficiency, which reflects the optical efficiency of the collector pipe. U is the heat dissipation coefficient, reflecting the heat dissipation of collector pipe; T_a is the ambient temperature, and I is the radiation intensity.

When the composite PCM completely melts, the net absorbed energy can be calculated from Eq. (8):

$$Q_{net}=Q_h+Q_s \qquad \text{Eq. (8)}$$

Where Q_h is the sensible heat of the PCM, Qs is the latent heat of the phase change, respectively calculated:

$$Q_h=(m_{np}c_{np}+m_{bf}c_{bf})\times(t'-t_0) \qquad \text{Eq. (9)}$$

$$Q_s=m_{nf}\times P \qquad \text{Eq. (10)}$$

Among them t' is the average temperature of the composite PCM melt completely, t_0 is initial average temperature of composite PCM; P is the heat storage capacity of composite PCM.

The cumulative amount of solar radiation from the initial moment to the moment of complete melting can be expressed as:

$$Q_{sum}=\int_0^{\tau}A_0S(T)d\tau \qquad \text{Eq. (11)}$$

The maximum instantaneous heat collection efficiency (η_0) of the composite PCM is 0.53456. But because of its radiation heat loss, heat dissipation coefficient (U) is 5.22048 J·m^{-2}·℃$^{-1}$. When completely melted, the net absorbed energy by the material accounts for 70.17% of the solar radiation energy, which is a high energy utilization.

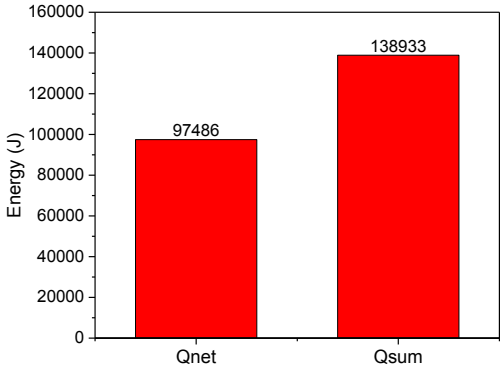

Figure 10: Net absorbed energy and solar radiation energy during melting

3. CONCLUSIONS

In this paper, the characteristics of spectral absorption and solar energy collection performance of graphene/paraffin composite PCM were tested and analyzed experimentally. The main conclusions are as follows: (1) The addition of graphene nanoparticles into paraffin can significantly improve the extinction coefficient and absorption coefficient, reaching the strong absorption level. It can be used for direct solar energy absorption and heat collection. The characteristics of absorption increase with the increase of graphene mass concentration, but the degree of increase decreased. Therefore, it is not necessary to use a high mass concentration. (2) Using composite PCM with a mass fraction of 0.025% in a vacuum collector pipe, the feasibility of direct heat collection and heat storage of graphene/paraffin composite PCM was verified by comparing it with pure paraffin. It has the potential to improve the performance of solar heat pump system. The heat storage and heat transfer properties of composite PCM will be further discussed in the future.

ACKNOWLEDGEMENTS

This research work was supported by the National Natural Science Foundation of China (No. 51676046).

NOMENCLATURE

A	absorbance	PCM	phase change material
A_0	area (m^2)	Q	quantity of heat (J)
C	concentration (mol·L^{-1})	S	solar radiation (W/m^2)
c	specific heat capacities (J /(kg℃))	T	time (min)
Ka	absorption coefficient	t	temperature (℃)
Ke	extinction coefficient	U	heat dissipation coefficient (J/m^2·℃)
L_0	optical path length (m)	τ	transmittance
I	intensity of light (Lux)	ε	molar extinction coefficient(L·mol^{-1}·m^{-1})
m	quality (kg)	η	instantaneous heat collection efficiency
P	heat storage capacity (J/kg)		

REFERENCES

Chen, L., 2017. Developing High-Performance Water Based Nanofluids for Direct Absorption Solar Collectors. Int D. South China University of Technology, Guangzhou, 46-52.

Deng, J., Furbo, S., Kong, W., Fan, J., 2018. Thermal performance assessment and improvement of a solar domestic hot water tank with PCM in the mantle. Int J. Energy & Buildings, 172.

Esen, M., 2004. Thermal performance of a solar cooker integrated vacuum-tube collector with heat pipes containing different refrigerants. Int J. Solar Energy 76(6), 751-757.

Hasnain, S. M., Gibbs, B. M., 1990. Prospects for harnessing renewable energy sources in Pakistan. Int J. Solar & Wind Technology 7(2), 321-325.

He, Q., 2014. Experimental investigation on radiation characteristic of nanofluids for direct absorption solar collectors. Int J. Applied Mechanics & Materials 881-883(3), 1095-1100.

Hosseinizadeh, S., Darzi, A., Tan, F., 2012. Numerical investigations of unconstrained melting of nano-enhanced phase change material (NEPCM) inside a spherical container. Int J. International Journal of Thermal Sciences 51(1), 77-83.

Kasaeian, A., 2017. Experimental investigation on the thermal behavior of nanofluid direct absorption in a trough collector. Int J. Journal of Cleaner Production 158, 276-284.

Ling-Bo, M., Ren-Yuan, Z., Xiu-Fang, K. E., 2010. Dispersion of Nano-copper in Cycle Fluids of Solar Collector. Int J. Nonferrous Metals 35, 134-136.

Mao L., Zhang R., Ke X., Chen X., 2007. Review of Direct Absorption-type Solar Energy Collection Systms. Int J. Materials Review 12, 12-15+23.

Motahar, S., Alemarajabi, A., Khodabandeh, R., 2017. Experimental investigation on heat transfer characteristics during melting of a phase change material with dispersed TiO2 nanop-articles in a rectangular enclosure. Int J. International Journal of Heat and Mass Transfer 109, 134-146.

Mu, L., 2011. Investigation of the Performance of Nanofluid-Based Direct Absorption Solar Collectors. Int D. Shanghai University of Electric Power, Shanghai, 35.

Pisut, T., Preeda C., 2017. Experimental study of a solar wall collector with PCM towards the natural ventilation of model house. Int J. Energy Procedia, 138.

Saidur, R., 2012. Evaluation of the effect of nanofluid-based absorbers on direct solar collector. Int J. International Journal of Heat and Mass Transfer 55(21), 5899-5907.

Wang, J., Xie, H., Xin, Z., 2009. Thermal properties of paraffin based composites containing multi-walled carbon nanotubes. Int J. Thermochimica Acta 488(1), 39-42.

Wang, W., Zhang, Q., Tang, L., Wu, M., 2012. Application of Nanofluids in Direct High flux solar collectors. Int J. New Chemical Materials 40(07), 118-120.

Wu, S., Tong, X., Gong, S., Peng, D., Xiao, S., 2014. Thermal Property of nano-GnPs/Paraffin heat storage phase change composite material. Int J. New Chemical Materials 42(07), 105-107.

Wu, Y., Zhou, L., Du X., Yang, Y., 2015. Extinction Effect and Near Field Thermal Radiation in Core-Shell Nanoparticle Arrays. Int J. Journal of Engineering Thermophysics 36(10), 2198-2202.

Xiang, Y., Gan, G., 2015. Optimization of building-integrated photovoltaic thermal air system combined with thermal storage. Int J. International Journal of Low-Carbon Technologies 10(2), 12-15.

Xu, G., Chen, W., Deng, S. 2015. Performance Evaluation of a Nanofluid-Based Direct Absorption Solar Collector with Parabolic Trough Concentrator: Int J. Nanomaterials 5(4), 2131-2147.

Zhang, K., Yu, L., 2000. Thermal Storage Technology in Solar Energy Utilization. Int J. Building Energy & Environment 02, 22-26.

Zhao, D., Li, Y., Dai, Y., 2011. Seasonal heat storage of solar in heating system. Int J. Solar Energy 03, 26-31.

Manuscript ID: 1341
DOI: 10.18462/iir.icr.2019.1341

Novel air conditioning system using desiccant coated heat exchanger

Tomohiro HIGASHI[(a)], Chaobin DANG[(a)], Eiji HIHARA[(a)], Li ZHANG[(b)]

[(a)]The University of Tokyo
5-1-5, Kashiwanoha, 277-8563, Japan, t.higashi@hee.k.u-tokyo.ac.jp
[(b)] Central Research Institute of Electric Power Industry
2-6-1, Nagasaka, Yokosuka, 240-0196, Japan, zhangli@criepi.denken.or.jp

ABSTRACT

The individual control of temperature and humidity is important for a comfortable ambient environment. Typically, conventional air-conditioning systems perform dehumidification while cooling. This may decrease efficiency; moreover, a drain tube is required. With regard to humidification, an additional humidifier and a supply of water are required, and no-feed water humidification is desired. The desiccant draws increasing attention to humidity control with high efficiency. In this study, a novel air-conditioning system using a desiccant coated heat exchanger (DCHE) is proposed. The system has a DCHE as the third heat exchanger in addition to the original evaporator and condenser, and the DCHE enables the system to control the ambient air temperature and humidity with high efficiency. A numerical simulation was carried out in order to estimate the system performance. The energy conservation of the proposed system was calculated by considering sensible and latent heat transfer.
Keywords: Air-conditioning, Desiccant, Humidification, Dehumidification.

1. INTRODUCTION

To reduce energy consumption and suppress greenhouse gas emissions, it is necessary to reduce the use of limited resources, such as fossil fuels, and to adopt renewable energy resources. The utilization of waste heat attracts increasing attention, and a desiccant system is a promising method to use waste heat for air-conditioning applications. A desiccant is a material that adsorbs moisture from the air. The adsorption of moisture from the air decreases the humidity of the air, and thus, dry air is circulated into the room. The waste heat is used in the desorption of the desiccant. In the study, we focused on an air-conditioning that uses a desiccant system. One of the most common devices that uses a desiccant for air-conditioning is the desiccant wheel (DW) (Guo et al., 2017). The desiccant is coated onto the surface of the DW, and it then rotates to continuously dehumidify the air. Waste heat is used for the desorption of the desiccant. However, adsorption and desorption on the DW are isenthalpic processes in which the temperature changes due to the latent heat of transport of the water. Therefore, the performance is potentially lowered.
In order to overcome this problem, a new waste heat driven air-conditioning system that uses a desiccant-coated heat exchanger (DCHE) is proposed in the study. The DCHE is a heat exchanger onto which a desiccant is coated. The coolant flowing in the DCHE maintains the temperature of the desiccant at a constant value during the adsorption/desorption processes, which can enhance the performance (Ge et al., 2010). We have investigated the heat and mass transfer characteristics of the DCHE using polymer sorbent, and built its calculation model (Higashi et al., 2017). Fig. 1 shows the DCHE used in the research. Polymer sorbent is coated on the surface of multi-port flat tubes and corrugated fins.

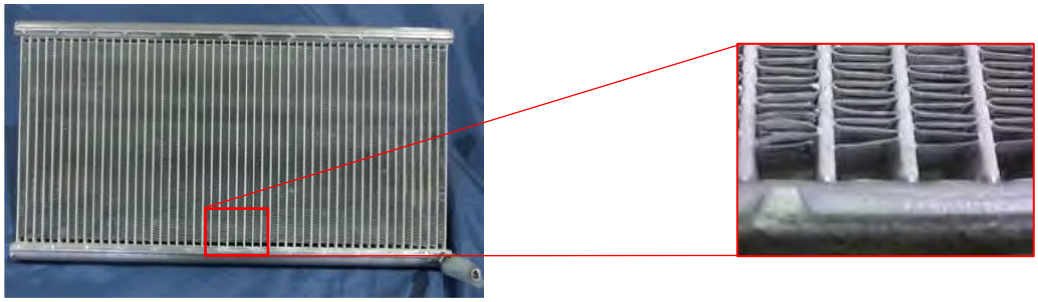

Figure 1: Desiccant coated heat exchanger

In this study, we proposed a hybrid air-conditioning system combining a DCHE and a compression refrigeration cycle. The DCHE performs humidification and dehumidification; further, the refrigeration cycle is responsible for cooling and heating, thus independently carrying out latent and sensible heat separation air-conditioning, while aiming at achieving energy saving and comfort. Furthermore, because cooling dehumidification is unnecessary during cooling operations in the summer, it is possible to perform a non-drain operation, i.e., dehumidification without water condensation on the surface of the heat exchanger. Finally, during heating operations in the winter, it is possible to perform no-feed water humidification that introduces moisture from the outside air. Though a room air-conditioner that takes in moisture from the outside air and performs humidification has been developed, the structure of its desiccant component is different, owing to which, we expected our hybrid air-conditioning system to exhibit higher energy saving performance. In this report, a calculation model of the hybrid air-conditioning system combining the DCHE calculation model and the refrigeration cycle calculation model was constructed, and its system performance was predicted. Cooling/heating demands and dehumidifying / humidifying demands were independently determined for comparison between the hybrid system and conventional air-conditioning methods.

2. HYBRID AIR-CONDITIONING SYSTEM

Fig. 2 shows a schematic diagram of a hybrid air-conditioning system where the DCHE and refrigeration cycle are combined. This system consists of a compressor (COMP), four-way valve, two heat exchangers (HEX1, HEX2), the DCHE, and two variable expansion valves (EXPV1, EXPV2). One variable expansion valve and the DCHE were added to the conventional room air-conditioner.

Fig. 3 shows each mode of operation. During cooling operations in the summer, the indoor heat exchanger works as an evaporator and the outdoor heat exchanger works as a condenser. In the case of the dehumidification operation, the EXPV 2 is fully opened, and DCHE works as an evaporator. Water vapor in indoor air is adsorbed by the DCHE, and dehumidification is carried out. When EXPV1 is fully opened, the DCHE works as a condenser, i.e., the adsorbed water is desorbed, and the moisture is exhausted to the outside air. The dehumidification is performed by alternating the dehumidification operation and the regeneration operation. This method results in a non-drain operation that does not cause condensation of water vapor in the evaporator. During heating operations in the winter, the indoor heat exchanger and the outdoor heat exchanger work as a condenser and an evaporator respectively. During the adsorption operation, the DCHE works as an evaporator and water vapor in outdoor air is adsorbed. The DCHE works as a condenser during the desorption operation. The adsorbed water is desorbed to the indoor air, and humidification is carried out as the next step.

Since only a single DCHE is installed in this hybrid system, dehumidification and humidification are carried out intermittently. Compared to the system consisting of two DCHEs, it is not possible to reduce the amount of desiccant under the same dehumidification / humidification rate. However, the advantages of a simplified refrigeration circuit and airflow switching mechanism have to be acknowledged and taken into consideration.

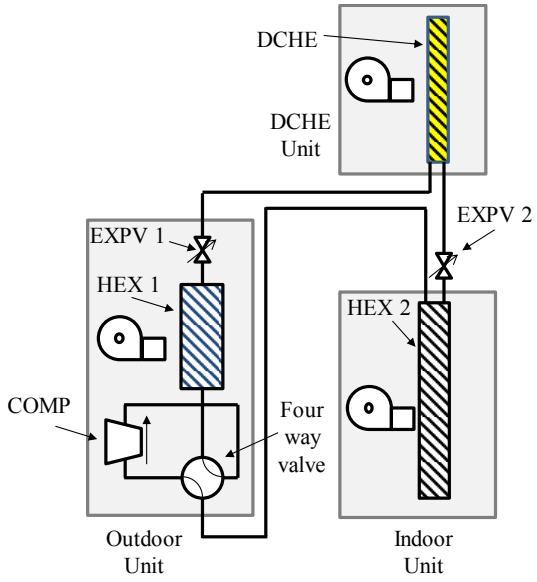

Figure 2: Schematic diagram of a hybrid system

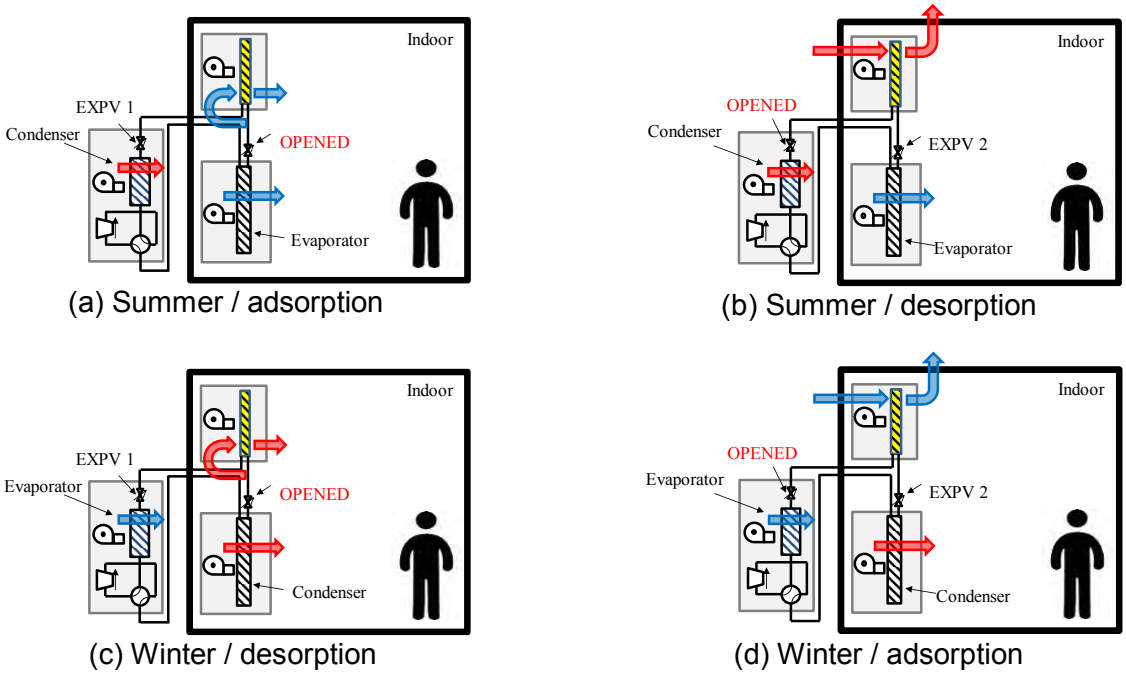

Figure 3: Modes of operation under each of the different conditions

3. CALCULATION METHODS

3.1. Calculation Model

The calculation model of the hybrid system was built, and used to predict system performance. The model was constructed by combining the DCHE calculation model and refrigeration cycle calculation model. Fig. 4 shows the DCHE calculation model. Multi-port flat tube heat exchangers with corrugated fins are assumed to have been used as shown in Fig. 4 (a). Fig. 4 (b) shows a cross-sectional view of this model. Heat transfer equations governing heat transfer from the air to the refrigerant, and mass transfer equations controlling the mass transfer process from the air to the desiccant layer were solved. The desiccant layer was assumed to be a homogeneous wall, and the heat conduction and mass diffusion of moisture in the layer were calculated. The thermal conductivity and diffusion coefficient were identified by comparison with the experimental results from a previous study. The polymer sorbent was assumed to be a desiccant material. Fig. 5 shows the adsorption

isotherm of the polymer sorbent.

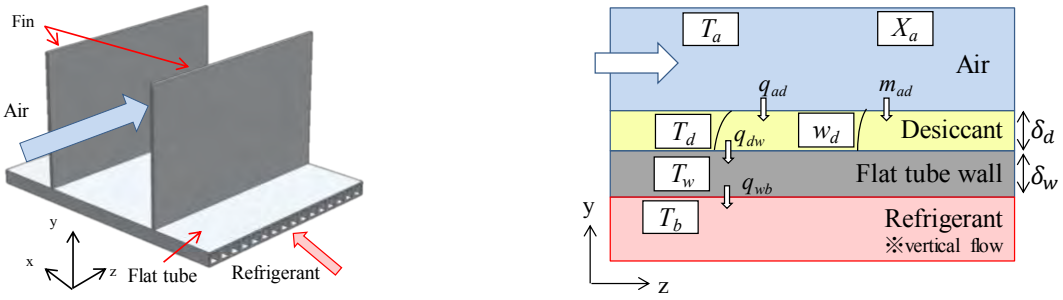

(a) Schematic view (b) Sectional view

Figure 4: DCHE calculation model

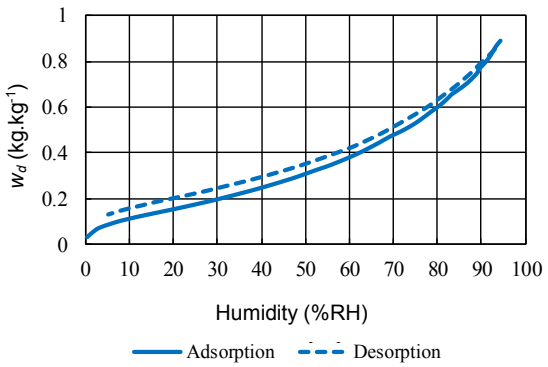

Figure 5: Adsorption isotherm

The temperature and the absolute humidity of the air are calculated by the following equations:

$$\rho_a c_{p,a} \frac{\partial T_a}{\partial t} + \rho_a c_{p,a} u_a \frac{\partial T_a}{\partial z} + \frac{l_a}{S_a} q_{ad} = 0 \qquad \text{Eq. (1)}$$

$$\rho_a \frac{\partial X_a}{\partial t} + \rho_a u_a \frac{\partial X_a}{\partial z} + \frac{l_a}{S_a} m_{ad} = 0 \qquad \text{Eq. (2)}$$

The thermal conduction and mass diffusion in the desiccant layer are expressed by the following equations:

$$\rho_d c_d \frac{\partial T_d}{\partial t} = \lambda_d \left(\frac{\partial^2}{\partial y^2} + \frac{\partial^2}{\partial z^2} \right) T_d \qquad \text{Eq. (3)}$$

$$\frac{\partial w_d}{\partial t} = D_d \left(\frac{\partial^2}{\partial y^2} + \frac{\partial^2}{\partial z^2} \right) w_d \qquad \text{Eq. (4)}$$

where λ_d in Eq. (3) is the equivalent thermal conduction and is equal to 0.11 Wm^{-1}K^{-1}, while D_d in Eq. (4) is the equivalent mass diffusion coefficient. Its temperature dependence is expressed by the following equation:

$$D_d(T) = D_0 \exp\left(-\frac{E_a}{RT}\right) \qquad \text{Eq. (5)}$$

where $D_0 = 9.0 \times 10^{-4}$ m^{2}s^{-1}, activation energy $E_a = 3.73 \times 10^4$ Jmol^{-1}, and gas constant $R = 8.314$ Jmol^{-1}K^{-1}.

The boundary conditions between the air and the desiccant layer are calculated by the following equations:

$$q_{ad} = h\left(T_a - Td|_{y=\delta_d}\right) = \lambda_d \frac{\partial T_d}{\partial y}\Big|_{y=\delta_d} - m_{ad}\gamma \quad \text{Eq. (6)}$$

$$m_{ad} = k_{ad}\left(X_a - X_{a,surface}\right) = \rho_d D_d \frac{\partial w_d}{\partial y}\Big|_{y=\delta_d} \quad \text{Eq. (7)}$$

In Eq. (6), q_{ad} is the heat flux, and γ is the latent heat of adsorption or desorption. In Eq. (7), m_{ad} is the mass flux of adsorption or desorption, and is proportional to difference between the absolute humidity of the air and the humidity at the surface of the desiccant layer. For further information, please consult the reference list.

The refrigeration cycle calculation model consists of a compressor, condenser, expansion valve, and evaporator. Thermal insulation efficiency of the compressor was assumed, and its outlet state of refrigerant was calculated from the difference in the corresponding values resulting from isentropic compression. Isenthalpic expansion was assumed at the expansion valve. Fig. 6 shows the calculation models of the condenser and the evaporator. Both were assumed to be fin tube heat exchangers. In each calculation cell, the outlet states of the air and the refrigerant were calculated from the inlet states.



(a) Schematic view (b) Calculation cell

Figure 6: Refrigeration cycle calculation model

Energy conservation of the air and the refrigerant are expressed by the following equations:

$$h_a \frac{T_{a,i} - T_{a,o}}{\ln\{(T_{a,i} - T_w)/(T_{a,o} - T_w)\}}\left(A_{tube} + \eta A_{fin}\right) = m_a\left(i_{a,i} - i_{a,o}\right) \quad \text{Eq. (8)}$$

$$h_r\left(T_w - T_{r,i}\right) = m_r\left(i_{r,o} - i_{r,i}\right) \quad \text{Eq. (9)}$$

where h_a and h_r are heat transfer coefficients at the air and the refrigerant side respectively, and η is fin efficiency.

The momentum conservation of the refrigerant is expressed by the following equation:

$$(P_i - P_o)\mathrm{S} = \tau l_{\mathrm{tube}} L_{cell} + m_r\{(1 - x_o)u_{l,o} + x_o u_{v,o} - (1 - x_i)u_{l,i} - x_i u_{v,i}\} \quad \text{Eq. (10)}$$

where τ is friction loss coefficient that was calculated by Colburn's equation. Eq. (10) shows the pressure loss of the refrigerant.

When condensation of water vapor occurs at the evaporator, the mass transfer coefficient was calculated by the Lewis equation as shown in Eq. (11).

$$k_a = \frac{h_a}{\rho_a c_{p,a}} \quad \text{Eq. (11)}$$

This model calculates the electricity consumption of the compressor and the evaporation temperature, etc. by using superheating, subcooling, and cooling (heating) capacity as input variables. The hybrid system calculation model was constructed by combining the DCHE calculation model and the refrigeration cycle calculation model. For comparison, we also predicted the performance of a conventional air-conditioner using the same model. In the conventional air-conditioner, cooling dehumidification in summer and humidification using a DW with an electric heater are assumed to be carried out. The electricity consumptions of the hybrid system and the conventional system were compared, and their energy saving performances were evaluated.

3.2. Calculation Conditions

In the performance evaluation of the systems, the demands of the cooling / heating capacity and the dehumidification / humidification rate were determined. In the conventional standard test to evaluate room air-conditioner performance, it is not possible to evaluate dehumidification / humidification performance properly because only the total heat load of the air is considered. Therefore in this study, latent heat load and sensible heat load demands were determined independently. Table 1 shows the demands in rating condition in summer, intermediate condition in summer, and rating condition in winter. In this calculation, it was assumed that two adults and two children live in a house whose floor area is 90 m^2. The magnitude of the dehumidification / humidification demands were calculated from the amount of ventilation and the extent of sweating. In intermediate condition in summer, the demand for dehumidification was equal to that in rating condition in summer, and the total heat demand was halved.

Table 1. Demanded cooling/heating capacities and dehumidification/humidification rate

Condition	Sensible heat (kW)	Latent heat (kW)	Dehumidification / humidification rate ($g.h^{-1}$)	Total heat (kW)
Rated in summer	4.89	0.71	1020	5.6
Intermediate in summer	2.09	0.71	1020	2.8
Rated in winter	6.7	0.52	750	7.22

Table 2 lists the geometrical properties of the indoor and outdoor heat exchangers and the DCHE. The amount of desiccant coated on the DCHE was 750g. Table 3 shows indoor and outdoor air characteristics. Air-conditioner performance test parameters prescribed by the JIS (Japanese industrial standard) were used. In the hybrid system when the conditions were that of summer, the evaporation temperature was set to be 1°C higher than the dew point temperature of the indoor air. This is to prevent water vapor condensation at the evaporator and to perform non-drain dehumidification.

Table 2. Geometrical properties of heat exchangers

	Width (mm)	Height (mm)	Depth (mm)
Indoor HEX	751	286	46
Outdoor HEX	1264	381	66
DCHE	450	300	80

Table 3. Indoor and outdoor air characteristics

	Dry bulb *T* (°C)	Wet bulb *T* (°C)
Summer indoor	27	19
Summer outdoor	35	24
Winter indoor	20	15
Winter outdoor	7	6

4. RESULTS

Fig. 7 shows the change in temperature and humidity of circulated air, the dehumidification rate, and cooling capacity in rated conditions in summer. The horizontal axis shows time while the vertical axis shows the values of each quantity. The initial 1080 seconds (18 minutes) was spent on a dehumidification operation, the next 240 seconds (4 minutes) was spent on regeneration operation, and a single cycle of complete operation lasts for 22 minutes. Each operation interval was adjusted to satisfy the demands shown in Table 1. In Fig. 7b, the dehumidification rate attained the maximum value at the beginning of the process, and decreased gradually. Because the evaporator does not perform dehumidification, it was not carried out at the same time as the regeneration operation.

Because the DCHE and the evaporator are responsible for dealing with latent heat and sensible heat respectively, separate air-conditioning to control each of these quantities could be carried out. In addition, it was clarified that the dehumidification rate could be controlled by adjusting the dehumidification and regeneration operation intervals. The characteristics of the supplied air were changed dynamically, following which, a time average of the system parameters was taken, and the performances of the system with the various dynamically adjusted parameters were compared.

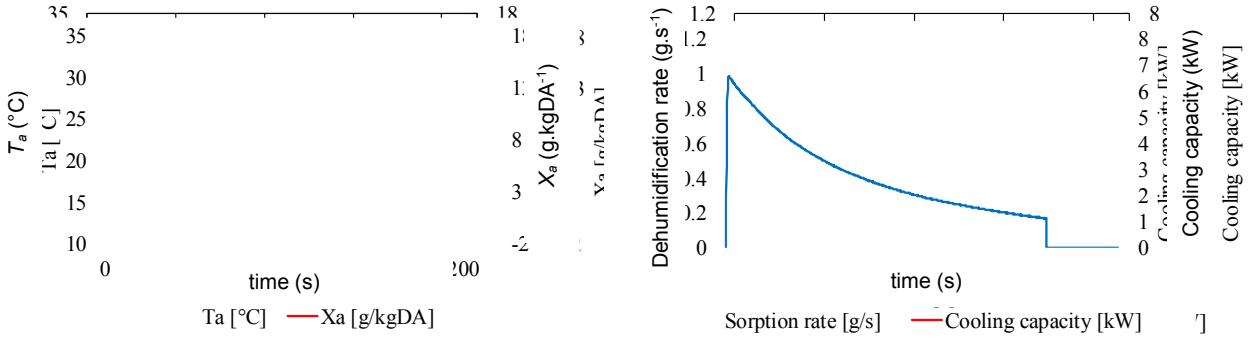

(a) Temperature and humidity of outlet air (b) Sorption rate and cooling capacity

Figure 7: Calculation results under rated conditions in summer

Table 4 shows the comparison in the performance between the hybrid system and the conventional system under rated condition in summer. Since the conventional system cannot control cooling load and dehumidification rate separately, a low evaporation temperature was required. The dehumidification rate became higher than demanded, which led to higher electricity consumption. Regarding the hybrid system, its dehumidification rate could be controlled to match the corresponding demand. The evaporation temperature could be higher than that in the conventional system. As a result, the electricity consumption could be reduced by about 24% as compared to the consumption in a conventional system.

Table 4. Comparison between the DCHE system and the conventional heat pump

	Conventional system	Hybrid system		
		Total	Evaporator	DCHE
Dehumidification rate ($g.h^{-1}$)	1532.7	1052.5	0	1052.5
Cooling capacity (kW)	5.60	5.63	3.70	1.93
Evaporation temperature (°C)	13.0		15.7	15.7
Electricity consumption (kW)	1.27	0.96		

Fig. 8 shows a comparison of electricity consumption under rated intermediate condition in summer, and rated condition in winter. The high energy saving performance of hybrid systems was revealed. In summer conditions, the requisite dehumidification rate could be achieved even with a high evaporating temperature that improved the efficiency of the refrigeration cycle itself. Non-drain operation was also achieved without cooling dehumidification. In winter condition, the hybrid system uses heat from the refrigeration cycle for the desorption of the desiccant while the conventional system uses the electric heater. Therefore, the electricity consumption could be reduced in the hybrid system. It was shown that the required humidification rate could be achieved through water-free humidification by adsorbing water from the outside air.

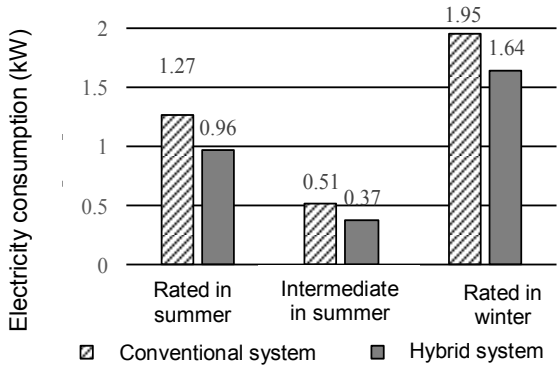

Figure 8: Comparison of electricity consumption

5. CONCLUSION

A Hybrid air-conditioning system combining a desiccant-coated heat exchanger and a refrigeration cycle was introduced. The demands for cooling / heating capacity and dehumidification / humidification rate were determined independently, and the system performance was compared to that of a conventional system. The high energy saving performance of the hybrid system was obviously apparent under all conditions. It was proven that non-drain dehumidification in summer, and water-free humidification in winter could be achieved.

ACKNOWLEDGEMENTS

This research was financially supported by the low carbon technology research and development program of the Ministry of the Environment.

NOMENCLATURE

A	surface area (m^2)	P	pressure (Pa)
c_p	specific heat at constant pressure ($J \times kg^{-1} \times K^{-1}$)	q_{ad}	heat flux ($W \times m^{-2}$)
D_d	equivalent mass diffusion coefficient ($m^2 \times s^{-1}$)	R	gas constant ($J \times mol^{-1} \times K^{-1}$)
E_a	activation energy ($J \times kg^{-1}$)	S	cross-sectional area (m^2)
h	heat transfer coefficient ($W \times m^{-2} \times K^{-1}$)	t	time (s)
i	Specific enthalpy ($J \times kg^{-1}$)	T	temperature (K)
k	mass transfer coefficient ($m \times s^{-1}$)	u	velocity ($m \times s^{-1}$)
l	cross-sectional perimeter (m)	w_d	moisture content in desiccant ($kg \times kg^{-1}$)
m	mass flow rate ($kg \times s^{-1}$)	X	absolute humidity ($kg \times kgDA^{-1}$)
m_{ad}	mass flux ($kg \times m^{-2} \times s^{-1}$)	x	quality of refrigerant (-)

Greek symbols

γ	adsorption/desorption heat ($J \times kg^{-1}$)	λ	thermal conductivity ($W \times m^{-1} \times K^{-1}$)
δ	thickness (m)	ρ	density ($kg \times m^{-3}$)
η	fin efficiency, -	τ	friction loss coefficient (-)

Subscripts

a	air	o	outlet
ad	air to desiccant	r	refrigerant
d	desiccant	v	vapor
i	inlet	w	flat tube wall, refrigerant tube wall
l	liquid		

REFERENCES

Guo, J., Lin, S., Bilbao, J. I., White, S. D., Sproul, A. B., 2017. A review of photovoltaic thermal (PV/T) heat utilization with low temperature desiccant cooling and dehumidification, Renewable and Sustainable Energy reviews, 67, 1-14.

Ge, T. S., Dai, Y. J., Wang, R. Z., Peng, Z. Z., 2010. Experimental comparison and analysis on silica gel and polymer coated fin-tube heat exchangers, Energy, 35, 2893-2900.

Higashi, T., Zhang, L., Saikawa, M., Dang, C., Hihara, E., 2017. Theoretical and experimental studies on isothermal adsorption and desorption characteristics of a desiccant-coated heat exchanger, Int. J. of Refrigeration, 84, 228-237.

Manuscript ID:1348
DOI: 10.18462/iir.icr.2019.1348

Hydrocarbons as natural refrigerants for heat pump water heating applications

Kashif Nawaz[(a)], Ahmed Elatar[(a)], Bo Shen[(a)], Van Baxter[(a)], Omar Abdelaziz[(a)]

[(a)]Oak Ridge National Laboratory[1]
Oak Ridge, TN 37831-6070, USA, nawazk@ornl.gov

ABSTRACT

Growing awareness of the potential environmental impacts of conventional refrigerants (CFCs and HFCs) has led to efforts to identify suitable refrigerants for various heat pump applications with minimum environmental impact. This study is focused on the performance evaluation of pure propane and isobutane as drop-in-replacement for R134a for heat pump water heating (HPWH). A component-based model is used to predict the performance. Key performance parameters such as unified energy factor, first hour rating and thermal stratification in the water tank are investigated. Appropriate experiments are conducted to validate the finding from model. Simulation and experimental findings suggest that both alternative refrigerants could provide comparable system performance to that of the baseline system containing R134a. System refrigerant charge and the condenser discharge temperature are established to investigate the potential of hydrocarbon refrigerants to substitute R134a without significant system modifications.
Keywords: Heat Pumps, Hydrocarbons, Natural Refrigerants, Hot Water Heating.

INTRODUCTION

Residential and commercial water heating accounts for approximately 10% of all residential and commercial site energy usage in the United States, making it the fourth largest energy end use in homes (DOE Building Technologies Office, 2016). On a global scale, in 2015 water heating consumed about 15–20% of residential energy for OEDC and non-OEDC countries as shown in Fig. 1.

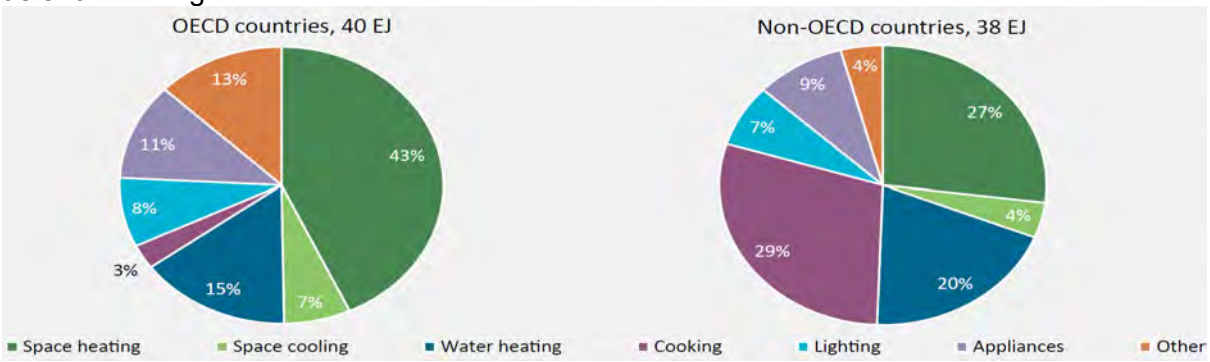

Fig. 1: End uses of residential energy consumed in OECD and non-OECD countries (International Energy Agency, 2016).

Despite recent advancements in energy efficiency, most residential water heaters are either conventional natural-gas-fired or electric storage heaters. While such systems are quite simple, they have very low system efficiency. Conversely, under appropriate conditions,

Notice: This manuscript has been authored by UT-Battelle, LLC, under contract DE-AC05-00OR22725 with the US Department of Energy (DOE). The US government retains and the publisher, by accepting the article for publication, acknowledges that the US government retains a nonexclusive, paid-up, irrevocable, worldwide license to publish or reproduce the published form of this manuscript, or allow others to do so, for US government purposes. DOE will provide public access to these results of federally sponsored research in accordance with the DOE Public Access Plan (http://energy.gov/downloads/doe-public-access-plan).

electrically driven, vapor compression heat pumps, or heat pump water heaters (HPWHs), represent a system opportunity with much higher thermal efficiency than conventional electric water heaters, resulting in significant energy savings.

Similar to conventional refrigeration or air-conditioning cycles, HPWHs use a vapor compression refrigeration cycle to transfer heat from a low temperature ambient to a high temperature reservoir, a hot water tank. A key parameter of interest is the working fluid used in the vapor compression cycle. Conventional HPWH systems deployed R-22, which is being phased down due to the high ozone depletion potential (ODP) associated with this fluid. R-134a emerged several years ago as the potential replacement, and most manufacturers have introduced systems with a reasonably higher unified energy factor (UEF) based on this refrigerant. However, concerns about possible global climate change have led to legislative action all around the world to phase down the use of hydrofluorocarbons (HFCs), including R-134a, in a range of heating, ventilation, air conditioning, and refrigeration (HVAC&R) applications, due to their relatively high global warming potential (GWP). Since HPWH systems are essentially heat pumps relying on the vapor compression refrigeration cycle, the technology has been equally affected (McLinden et al., 2017). Table 1 summarizes some familiar refrigerants with potential impact on the environment.

Table 1: Characteristics and environmental impact of different refrigerants

Refrigerant group	Refrigerant example	ODP	GWP_{100}	Atmospheric lifetime (years)	Flammability
CFCs	R11, R12, R115	0.6–1	4750–14400	45–1700	Nonflammable
HCFCs	R22, R141b, R124	0.02–0.11	400–1800	1–20	Nonflammable
HFCs	R407C, R32, R134a	0	140–11700	1–300	Nonflammable or mildly flammable
HFOs	R1234fy, R1234ze, R1234yz	0	0–12	-	Mildly flammable
Natural refrigerants	R744, R717, HC (R290, R600, R600a)	0	0	Few days	HCs: Highly flammable R717: Flammable R744:Nonflammable

A range of experimental, analytical, and numerical studies have evaluated the performance of HCs for various HVAC&R applications. Broadly, these refrigerant studies used either pure HCs, HC blends, or HC blends mixed with HFCs and hydrofluoroolefins (HFOs). Urchueguia et al. (2004) conducted an experimental study of a commercial refrigeration unit using R290 instead of R22. They concluded that the COP increased by 1–3% and the capacity decreased by 13–20% when R290 was used to replace R22. In another similar study. Lee and Su (2002) compared the performance of a domestic refrigeration system with R600a to replace R12 and R22. Khalid and Qusay (2014) investigated the performance of a residential air-conditioning system under high condensing temperatures using R22, R290, R407C, and R410A. They found that the cooling capacity and the power consumption for R410A were the highest among the four refrigerants and that R290 required less power and refrigerant charge for comparable performance to R22. Song et al. (2014) evaluated the performance of an air-conditioning system using R32 and R290 as substitute fluids for R22 and R410A. They found that at the rated conditions, the COP of R32 and R290 was significantly higher than that of R410A and R22. In another similar study, Zhou et al. (2010) considered R290 as a potential replacement for R22 in a split air-conditioning unit with different diameters of coiled capillary tubes and various operating conditions. They found that the cooling capacity of the system with R290 was lower than that with R22; however, the energy efficiency ratio was higher.

Multiple studies have focused on using HC mixtures as substitutes for conventional refrigerants. Chao and Teng (2014) studied the feasibility of using HC mixtures of R290 and R600a as alternative refrigerants in a small-sized refrigerator originally using R134a. They concluded from a no-load pull-down test that the optimal refrigerant charge for HCs was significantly lower than that for R134a. Rasti et al. (2012) used R436a (56% R290 and 44%

600a) as an alternative to R134a in a domestic refrigerator and concluded that the system's on-time ratio was reduced by 13% and that power consumption was reduced by 5.3% as compared to the original system with R134a. Mani and Selladurai (2008) conducted an experimental study using R290 and R600a (68% and 32% by mass, respectively) as a drop-in replacement for R12 and R134a and found that the HC mixture had a higher cooling capacity. It is important to note that trans-critical CO_2 HPWH technology also relies on a environmental friendly refrigerant, however, issues related to high pressure and variable flow rate pump system along with intermediate heat exchanger makes the technology less feasible compared to HC based HPWH system (Nawaz, 2017).

2. ANALYSIS STRATEGY

Modeling a HPWH system has been a challenge due to the varying complexities of the subsystems and the integration of the heat pump and water tank. The DOE/ORNL Heat Pump Design Model (HPDM) has been a reliable, public-domain platform for designing, optimizing, and analyzing heat pumps of varying complexity for both residential and commercial applications. The platform was used to develop a HPWH system model that included a wrapped tank condenser and accounted for features such as thermal stratification, piston effect, and mixing. The model was calibrated against measured test data and was used to evaluate HPWH performance.

The current study draws upon some component modeling aspects of a previous ORNL HPWH analysis for forced-flow designs (Baxter et al., 2011). Some of the key HPDM features important to the current study are described here. AHRI 10-coefficient compressor maps have been used to calculate mass flow rate and power consumption as shown by Eqs. (1) and (2), respectively, as function of evaporation and condensation temperatures (ANSI/AHRI 2010).

$$m = {}_1 + {}_2T_{evap} + {}_3T_{cond} + {}_4T_{evap}^2 + {}_5T_{evap}T_{cond} + {}_6T_{cond}^2 + {}_7T_{evap}^3 + {}_8T_{evap}^2T_{cond} + {}_9T_{cond}^2T_{evap} + {}_{10}T_{cond}^3 \quad \text{Eq. (1)}$$

$$W = {}_1 + {}_2T_{evap} + {}_3T_{cond} + {}_4T_{evap}^2 + {}_5T_{evap}T_{cond} + {}_6T_{cond}^2 + {}_7T_{evap}^3 + {}_8T_{evap}^2T_{cond} + {}_9T_{cond}^2T_{evap} + {}_{10}T_{cond}^3 \quad \text{Eq. (2)}$$

where T_{evap} and T_{cond} are the compressor suction and discharge saturation temperatures, and α and β are the compressor map coefficients for mass flow rate and power respectively. ${}_{1,2,...,10}$ and ${}_{1,2,...,10}$ are the mass flow rate and power coefficients respectively for compressor.

The HPDM uses a segment-to-segment modeling approach, which divides a single tube into numerous mini segments. Each tube segment has individual air-side and refrigerant-side entering states and considers possible phase transition; the ε-NTU approach has been used for heat transfer calculations within each segment. In addition to the functionalities of the segment-to-segment fin-tube condenser model, the evaporator model can simulate the dehumidification process. A wrapped tank condenser model was developed specifically for this investigation, using a segment-to-segment modeling approach. The flow-pattern-dependent heat transfer correlation published by Thome (2003) was used to calculate the condenser's two-phase heat transfer coefficient. The tank model includes the thermal conductivity of the thermal paste (used to ensure good contact between the wrapped tank condenser tubes and the tank wall) and the insulation covering the tank. Thus, heat loss from the tank was captured for the full time of the operation. The transient tank model accounts for one-dimensional water temperature stratification due to natural convention. Fig. 2 shows an example case (i.e., mixing caused by advection during water draw) for the CFD model used for the analysis. Additional details can be found in Elatar et al. (2017). A residential HPWH was considered as the baseline water-heating unit for performance evaluation and model calibration as shown in Fig 3. The performance of this unit has been evaluated previously at ORNL (Murphy et al., 2011).

3. RESULTS AND DISCUSSION

The US Department of Energy (DOE) initiated a rulemaking to consider amendments to its old test procedures for covered residential and commercial water heaters, as recommended in the American Energy Manufacturing and Technical Corrections Act. Based on the extensive testing, a new performance evaluation procedure was defined. In the new procedure, the tank water temperature set point is 125°F, and the test conditions for inlet water and ambient air temperature are prescribed as 58°F and 67.5°F (35–45% relative humidity), respectively. Key performance metrics used to evaluate and compare the performance of water heaters (WHs), including HPWHs, are listed below.

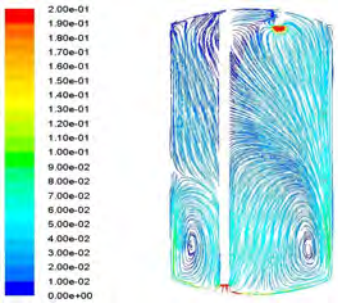

Fig. 2. Streamline for water flow in the tank during draw (m/s).

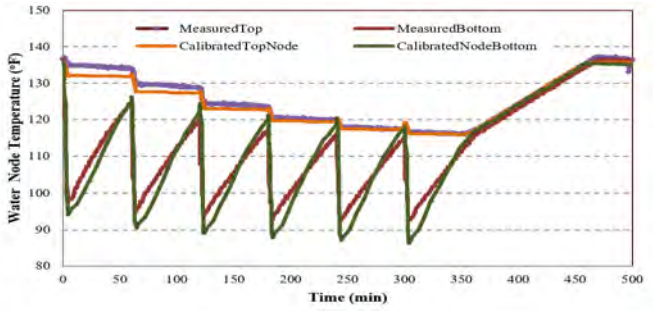

Fig. 3. Temperature stratification variation (measured vs. predicted).

3.1 First Hour Rating

FHR is a measure of the available hot water capacity of the WH (in gallons). Per the new DOE test method, hot water (125±15°F) is drawn from the tank as long as the temperature is more than 67±2°F higher than the entering water temperature. Once the temperature drops below the prescribed limit, the supply is stopped until the set point of 125±1.5°F is met again. Following the procedure, the total water drawn from the tank during 1 hour indicates the total capacity of the heat pump and electric resistance heaters.

3.2 Unified Energy Factor

UEF is a measure of system efficiency. It is defined as the ratio of the total heat delivered from the system (by heating the water) to the total power required to operate the system. Equation (3) describes the UEF.

$$UEF = \sum_{k=1}^{n} \frac{M_k c_p (T_s - T_i)}{W_i} \qquad \text{Eq. (3)}$$

In Eq. (3) k represents the individual hot water draw, considering that multiple draws are required by the test procedure and that n (total number of draws) can vary according to the method proposed by DOE (small, medium, and large usage pattern), and M is the total mass drawn for each respective draw. T_s, T_i, and W_i represent the supply water temperature, inlet water temperature, and total energy consumed by the unit (power times unit run time), respectively. The previous EF test procedure used a single water draw pattern—six equal water draws of ~10.7 gallons each spaced equally during the first 5 hours of the EF test—and applied it to all WHs (including HPWHs) with a storage tank. In contrast, the new method uses the measured FHR value to define the hot water draw pattern. The FHR analysis concluded that under all parametric conditions, the appropriate draw pattern for the HPWH unit being analyzed was for medium usage (FHR varied between 57 and 64 gallons).

4. PARAMETERS FOR PERFORMANCE EVALUATION

To optimize system performance, a parametric study was conducted to investigate the impacts of the condenser wrap pattern and the heat loss from the water storage tank. Two representative insulation effectiveness values were considered for the heat loss from the tank, 90% and 95%. The effectiveness is 90% when the tank loses 10% of the energy input to the water. The effectiveness is 95% when half that amount of energy is lost through the tank wall and insulation material to the environment. This essentially accounts for two values for the resistance to heat loss. Similarly, to explore the impact of condenser configuration, two different wrap patterns were considered for analysis as shown in Fig. 4. The counterflow pattern represents the flow of the refrigerant entering from the top section of the tank and moving downwards. In the parallel-counterflow configuration, the refrigerant enters close the middle of the tank, moves upwards, and then comes back to the middle section to continue downwards (identical to the pattern used by the prototype systems evaluated in the prior experimental study). In both cases, the refrigerant enters the system as superheated vapor, goes through a phase-change process, and exits as a subcooled liquid. Table 2 summarizes the cases considered in current study.

4. RESULTS AND DISCUSSION

FHR is a direct indication of system capacity. A larger FHR indicates a superior system capacity. It can be observed from Fig. 5 that R290 consistently shows a comparable FHR when compared with baseline R134a values, whereas R600a has an average FHR, close to 57 gallons (lower than R134a). Although the system's design parameters can have some secondary impact, the FHR is a direct indication of the volumetric capacity of the refrigerant. The low value for volumetric capacity for R600a can explain a relatively lower FHR.

Table 2. Simulation cases for parametric analysis

Case number	Wrap pattern	Tank insulation effectiveness (%)
1	Parallel-counterflow	90
2	Parallel-counterflow	95
3	Counterflow	90
4	Counterflow	95

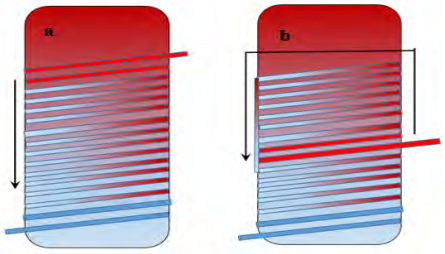

Fig. 4. Condenser wrap configurations: (a) counterflow, (b) parallel-counterflow.

Unified energy factor (UEF) is a direct measure of system efficiency. A larger UEF denotes a better performance. Fig. 6 presents the 24 hour UEF for different refrigerants as the design parameters vary. Heat loss from the tank is seen as a dominant factor, and UEF is higher for the cases with 95% tank insulation effectiveness. On the other hand, the condenser wrap pattern does not have any significant impact, as observed from the values presented in Fig. 6. Among the three refrigerants, R600a has the lowest UEF while for R134a and R290, the values are comparable.

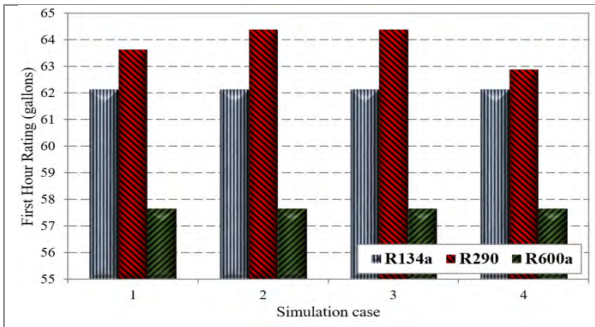

Fig. 5. First hour rating for different refrigerants

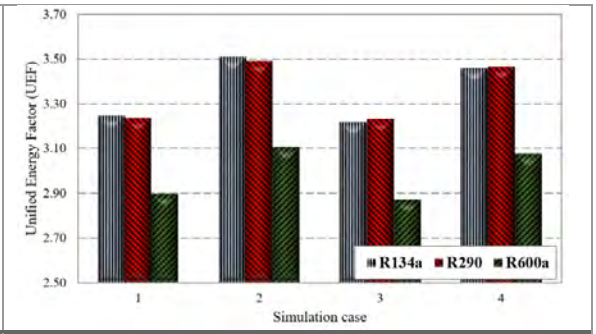

Fig. 6. Unified energy factor for different refrigerants

COP is the typical parameter used to describe the efficiency of a heat pump. It is important to recognize that COP, unlike UEF, represents the efficiency of the heat pump only and cannot be used to indicate the performance of the whole system. However, this is still an important parameter to consider as it shows the stand-alone performance of the heat pump. Fig. 7 presents COP for the different design options. Overall, COP is comparable for all design options, with slightly better performance for parallel-counterflow configuration and 95% tank insulation effectiveness. When the individual performance of different refrigerants is compared for a specific design option, COP is clearly lowest for R600a, as was the case for UEF.

An interesting relationship between insulation effectiveness and supply water temperature is presented in Fig. 8. A higher supply water temperature results in 90% thermal insulation (cases 1 and 3) because of the control mechanism to turn the heat pump on (T = 120°F) and off (T = 125°F), which ultimately lowers the system's UEF. The heat lost with the poorer thermal insulation causes the heat pump's run time to increase, leading to a higher average supply temperature.

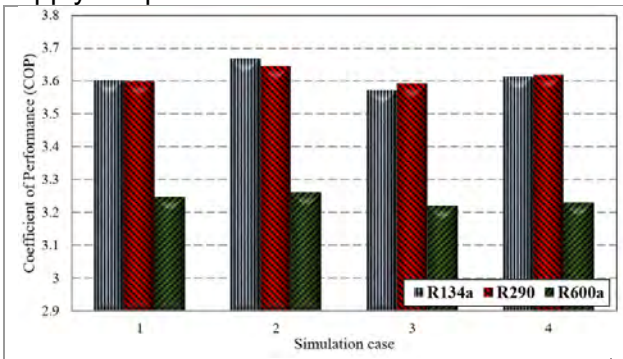

Fig. 7. Coefficient of performance

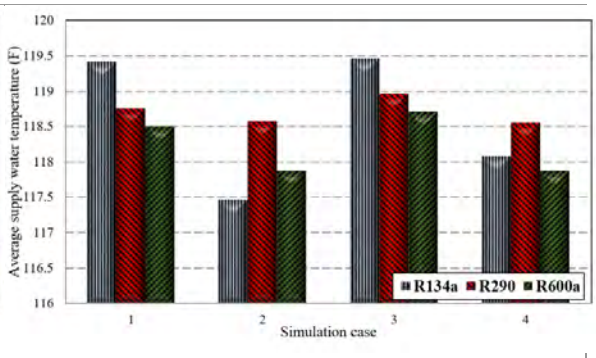

Fig. 8. Average supply water temperature

Total system charge is a critical parameter that has been the focus of continuous effort toward minimization, not only because refrigerants are expensive but also because class A3 refrigerants present serious safety concerns for any HVAC&R application. Fig. 9 compares total system charge in the evaporator and the condenser. Even though there is no significant difference in charge for various design options, it is interesting and encouraging that the charge required for both R290 and R600a is less than half that of the baseline R134a. This can be explained in terms of the lower molecular weights for the R290 and R600a refrigerants which are almost half that for R134a. This shows the potential of HC refrigerants to substitute for R134a and indicates that further development may allow an even smaller charge of flammable refrigerant to be successfully substituted to provide similar performance, thereby reducing safety concerns.

Fig. 10 presents the maximum condenser saturation temperature drop. For better heat transfer performance, a smaller temperature drop, which is directly related to the pressure drop through the condenser, is desired. As shown in Fig. 10, both design options with the parallel-

counterflow wrap pattern result in a lower condenser saturation temperature drop, while for the counterflow arrangement, it is higher. The higher condenser temperature drop can be related to the relative amount of condenser containing refrigerant vapor. Since for the counterflow arrangement there is a slower transfer of heat in the top part of the water tank, which contains relatively hot water (due to stratification), a longer heat exchanger length fraction in the vapor (higher pressure drop) region is required. In contrast, for a parallel-counterflow arrangement, vapor refrigerant entering close to the middle of the tank interacts with relatively cold water, ensuring a higher heat transfer rate and shorter vapor region. Analysis of the individual performance of the refrigerants shows that R290 has the lowest values. For counterflow arrangement, both R-134a and R600a show comparable performance; however, for parallel-counterflow configuration, R600a has a higher temperature drop. Since the saturation temperature drop directly depends on the saturation pressure drop, a condenser tube with relatively larger diameter can be helpful; however, this leads to a higher refrigerant charge, which is undesirable for the current application. For a drop-in-replacement study, it is desirable to have a comparable and preferably lower compressor discharge temperature for alternative refrigerants, as this ensures that a similar compressor with existing lubrication can be safely used. The issue is critical due to the flammable nature of refrigerants as well. Fig. 11 compares the compressor discharge temperature for various design options and indicates that maximum compressor discharge temperature is about 10°F lower for R600a and 1–2°F lower for R290 compared to the baseline refrigerant (R134a). This suggests that with respect to oil temperatures for both refrigerants, a safe substitution is possible without significant modification. However, since the volumetric capacity of R600a is lower, a relatively larger compressor is required for comparable performance (i.e., COP and UEF).

Thermal stratification in the storage tank has been studied extensively, and recent findings have shown that higher stratification can lead to improved UEF, a classical feature of CO_2-based HPWHs (Nawaz et al., 2017), since this can provide better heat transfer from the condenser tube to the water. Fig. 12 shows the relative water stratification for different refrigerants and design selections where the difference between the supply water temperature (exiting the water tank) and average tank water temperature is presented. There is no consistent trend when different design selections are compared, though cases 1 and 3 with 90% insulation effectiveness show slightly lower temperature differences. However, the relative water temperature difference is lowest for R600a on average, which is consistent with previous discussion regarding lower UEF and higher heat pump run time for this refrigerant.

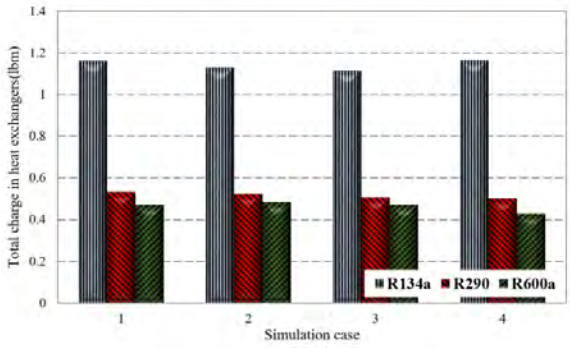

Fig. 9. Total charge in condenser and evaporator

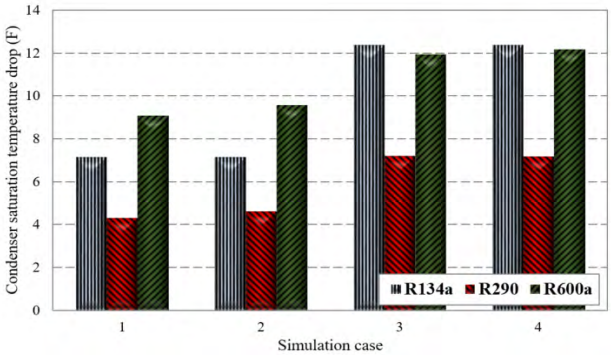

Fig. 10. Maximum condenser saturation temperature drop

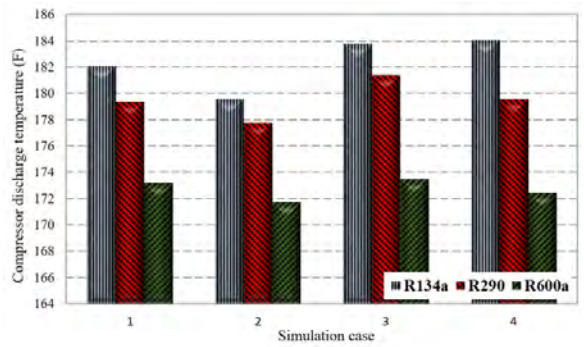

Fig. 11. Maximum compressor discharge temperature

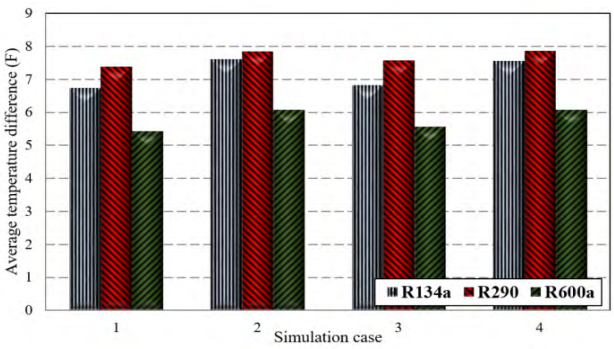

Fig. 12. Average difference between supply and tank bulk temperature

5. CONCLUSIONS

A simulation study of a wrapped-tank heat pump water heater has evaluated the feasibility of using R290 (propane) and R600a (isobutane) as natural refrigerants to substitute for R-134a. A model based on the DOE/ORNL Heat Pump Design Model was developed to account for both the heat pump and water tank designs, and it was used to study the impact of various design parameters. It has been found that both R134a and R290 showed comparable FHR and UEF. A relatively lower performance for R600a can be attributed to its relatively lower volumetric capacity, which can be resolved by increasing compressor size. The compressor discharge temperature was lower for R290 and R600a than it was for R134a. This suggests that compressors of similar design can be used with these refrigerants and that existing compressor lubricants are feasible. Total system charge for R290 and R600a was much smaller compared to the baseline system (at least 50% reduction). Considering the potential flammability of replacement refrigerants, which are safety class A3, the substitution of R290 or R600a would reduce safety concerns because a relatively smaller amount would be needed to operate the system. Considering the various performance parameters, R290 showed better prospects as a drop-in replacement for R134a, while R600a required a relatively larger compressor size to meet the baseline performance.

ACKNOWLEDGEMENTS

Funding for this work is provided by the US Department of Energy, Washington, DC. The authors thank Mr. Antonio Bouza, program manager for the DOE Office of Building Technologies.

NOMENCLATURE

AHRI	Air-Conditioning, Heating, and Refrigeration Institute	HC	hydrocarbon
		HFC	hydrofluorocarbon
CFC	chlorofluorocarbon	HFO	hydrofluoroolefin
CFD	computational fluid dynamics	HPDM	Heat Pump Design Model
COP	coefficient of performance	HPWH	heat pump water heater
EF	energy factor		
FHR	first hour rating		
GWP	global warming potential		
HVAC&R	heating, ventilation, air conditioning, and refrigeration		
ODP	ozone depletion potential		
OEDC	Organization for Economic Cooperation and Development		
UEF	unified energy factor		
WH	water heater		

REFERENCES

ANSI/AHRI Standard 540-99, 2010, “Positive Displacement Refrigerant Compressors and Compressor Units”, Air Conditioning and Refrigeration Institute, Arlington, VA.

ANSI/ASHRAE STANDARD 34, 2013. Designation and Safety Classification of Refrigerants.

Baxter, V. D., Murphy, R. W., Rice, C. K., Shen, B., Gao, Z., 2011. Analysis of Highly Efficient Electric Residential Heat Pump Water Heaters for Cold Climates, ORNL/TM-2011/278.

Chao, Y. C., Teng, T. P., 2014. Retrofit assessment of refrigerator using hydrocarbon refrigerants. Applied Thermal Energy, 66, 507–18.

Department of Energy rule making, 2013, “Energy conservation program for consumer products and certain commercial and industrial equipment: test procedures for residential and commercial water heaters” (10 CFR Parts 429, 430 and 431).

Emerging Technologies: HVAC, WH and Appliance-BTO Peer Review 2016.

Energy Technology Prospective 2016 (Report), International Energy Agency.

Khalid, A. J., Qusay, R. A., 2014. Experimental assessment of residential split type air-conditioning systems using alternative refrigerants to R-22 at high ambient temperatures. Energy Conversion Management, 86:496–506.

Nawaz, K., Shen, B., Elatar, A., Baxter, V. D., Abdelaziz, O., Performance Optimization of CO_2 HPWH System, International Journal of Refrigeration, 2017, 85, 213-218.

Lee, Y. S., Su, C. C., 2002. Experimental studies of isobutane (R600a) as the refrigerant in domestic refrigeration system, Applied Thermal Engineering, 22, 507–19.

Mani, K., Selladurai, V., 2008. Experimental analysis of a new refrigerant mixture as drop in replacement for CFC12 and HFC134a, International Journal of Thermal Science, 47,1490–5.

McLinden, M. O., Brown, J. S., Brignoli, R., Kazakov, A. F., Domanski, P. A., 2017, Limited Options for Low-Global-Warming-Potential Refrigerants, Nature Communications, 8-14476.

Murphy, R. W., V. D. Baxter, E. A. Vineyard, and R. L. Linkous, 2011, “Drop-in Evaluation of Refrigerant R1234yf in a Residential Integral Heat Pump Water Heater,” Proceedings of the 10th International Energy Agency Heat Pump Conference.

Nawaz, K., Shen, B., Elatar, A., Baxter, V. D., Abdelaziz, O., 2017. Performance analysis for CO_2 HPWH. International Journal of Refrigeration (in review)

Rasti, M., Hatamipour, M. S., Aghamiri, S. F., Tavakoli, M., 2012. Enhancement of domestic refrigerator's energy efficiency index using a hydrocarbon mixture refrigerant, Measurement, 45,1807–13.

Song, C., Shuangfeng, W., Zhongmin, L., 2014, Cycle performance of alternative refrigerants for domestic air-conditioning system based on a small finned tube heat exchanger, Applied Thermal Engineering, 64, 83–92.

Thome J. R., J. El Hajal and A. Cavallini, 2003, “Condensation in horizontal tubes, part 2: new heat transfer model based on flow regimes”, International Journal of Heat and Mass Transfer, 46(18), Pages 3365-3387.

Urchueguıa, J. F., Corberan, J. M., Gonzalvez, J., Dıaz, J. M., 2004. Experimental characterization of a commercial-size scroll and reciprocating compressor working with R22 and propane (R290) as refrigerant. Ecolibrium, 23–5.

Zhou, G., Zhang. Y., Yang, Y., Wang, X., 2010. Numerical model for matching of coiled adiabatic capillary tubes in a split air conditioner using HCFC22 and HC290, Applied Thermal Engineering, 30, 1477–87.

Manuscript ID: 1355
DOI: 10.18462/iir.icr.2019.1355

Ejector based climate control systems with heat and mass recuperation through the Maisotsenko cycle

Oleksii DRAKHNIA [a,d], Dmytro BUYADGIE[b,e], Olexiy BUYADGIE[b,e], Takahiko MIYAZAKI[d], Valeriy MAISOTSENKO[f] Andrei CHAMCHINE[g]

[a] Interdisciplinary Graduate School of Engineering Sciences, Kyushu University, Kasuga-koen 6-1, Kasuga-shi, Fukuoka 816-8580, Japan, drakhnia@kyudai.jp
[b] Wilson Engineering Technologies, Inc., 3330-I, Vincent Rd, Pleasant Hill, CA 94523, USA, buyadgie@wilsonet.org
[c] V.S. Martynovsky Institute of Refrigeration, Cryogenic Technologies and Eco Energetics of the Odessa National Academy of Food Technologies, 1/3, Dvoryans'ka str., 65026, Odessa, Ukraine, buyadgie@wilson-ukraine.com
[d] International Institute for Carbon-Neutral Energy Research (WPI-I2CNER), Kyushu University, 744 Motooka, Nishi-ku, Fukuoka 819-0395, Japan, miyazaki.takahiko.735@m.kyushu-u.ac.jp
[e] Wilson, Ejector Technology Lab, 15/13, Mikhailivs'ka str., 65005, Odessa, Ukraine, d.buyadgie@wilson-ukraine.com
[f] M-Cycle Corporation, 5628, South Idalia str., Centennial, CO 80015, USA, valeriymaisotsenko@gmail.com
[g] University of Central Lancashire, Preston PR1 2HE, UK, AChamchine@uclan.ac.uk

ABSTRACT

Electricity remains the main source of energy for conventional air-conditioning systems, while natural gas - is traditionally utilized for space heating. In both cases the thermodynamic processes are inefficient, as high-grade energy wastes its potential for the processes close to ambient temperatures. The paper describes the methods of multiplication of high, middle and low-grade heat to maximize the effect of space cooling and heating by combining thermally-driven ejector system with the heat recuperation process in the Maisotsenko cycle Heat and Mass Exchanger (HMX). Such a comprehensive and cost-efficient solution for space heating and cooling will help to lower the environmental loads at least twofold, save fossil fuels by 25-30%, displace 100% of the inhaled air at no extra cost and reduce by at least 10 times the energy consumption in the most intensive sector at the expense of the increased efficiency of the proposed technology over the existing systems.
Keywords: air-conditioning, binary mixture, ejector, heat pump, heating, recuperation, residential building

1. INTRODUCTION

During the centuries people used different types of fuel for space heating - from wood to hydrocarbons. Heat consumption increases significantly due to the increased population and industries that consume heat or generate power. There is a necessity appeared to reconsider a structure of fuel consumption.

The systems of comfortable climate conditions provide space heating and cooling represent right from the moment when they are required, so energy consumed for those processes is not stored. As a result of heat and mass exchange, heat and cold release into the atmosphere or intake into a cooled room that nullifies its exergy. Therefore, consumed energy or electricity is totally lost. Also, it should be mentioned that it is mostly high temperature heat and electricity consumed for those processes, but the useful effect does not take into account the exergy of the energy source.

Electric energy received by natural gas combustion is about 40-45% of utilized heat. At the same time, additional losses during its transfer to a long distance, reverse voltage conversion can reach up to 25%. The most reasonable way is to use combustion heat combined with solar heaters,

especially in areas with high solar insulation. Also, it is necessary to apply ejector-based heat pumps and hydrothermal air recuperation. This approach, calculated using the below set of equations, allows achieving theoretical COP of space heating up to 4 and air-conditioning up to 6-9.
Based on temperature difference of flows and warm- and cold ends approach only 15-20% of outlet air heat can be recovered, while heat and mass recovery allow utilizing of up to 75-80% of the outlet air enthalpy. Ejector Heat Pump (EHP) efficiency reaches up to 1.6-2.0. Provided heat losses though the walls reach from 70% to 20% of total losses, and heat sink from air exchange, respectively, from 30 up to 80%, the efficiency of the system, proposed in this paper can potentially reach 4 and even higher value at a proper room insulation (Table 1).

Table 1. Efficiency of the Maisotsenko Cycle HMX/EHP system at various heat losses parameters

№	Losses though insulation, %	Heat losses from air recuperation at various heat recovery rates, %		Total heat loss at various heat recovery rates, %		COP at conversion ratio of 1.8 and heat recuperation of 80%	COP at conversion ratio of 1.8 and heat recuperation of 75%
		80%	75%	80%	75%		
1	70	6	7.5	76	77.5	2.368	2.323
2	60	8	10	68	70	2.647	2.571
3	50	10	12.5	60	62.5	3.00	2.88
4	40	12	15	52	55	3.46	3.273
5	30	14	17.5	44	47.5	4.09	3.789
6	25	15	18.75	40	43.75	4.50	4.111
7	20	16	20	36	40	5.00	4.50

The conventional air-conditioning systems produce cold for both air-cooling and air dehumidification. In tropical climate zone, the ratio of the produced cooling capacity used for dehumidification can reach up to 80%. The calculated hydrothermal recuperation process allows removing up to 50% of moisture from the inlet air. EHP increases by 1.6-2.5 times the generation heat for cooling capacity production in Ejector Refrigeration System (ERS) comparing to heat from the gas heater or solar collectors. Overall effect of the proposed system is evaluated by the effect of heat and moisture recuperation and generation heat multiplication in the EHP (Table 2).

Table 2. Efficiency of combined HMX/ERS and HMX/ERS/EHP system at various cooling load on HMX

№	Cold production by Maisotsenko Cycle HMX, %	Cold production by ERS, %	Generation heat to cooling capacity ratio, %	COP of combined HMX/ERS	COP of combined HMX/ERS with heat pump*
1	50	50	60.83	1.644	3.633
2	55	45	54.76	1.826	4.036
3	60	40	48.68	2.054	4.54
4	65	35	42.59	2.352	5.197
5	70	30	35.51	2.816	6.223
6	75	25	30.41	3.288	7.267
7	80	20	24.34	4.108	9.08
8	85	15	18.25	5.479	12.109

* COP of the heat pump operating on steam at t_{gen}=170°C, t_{eva}=90°C, t_{cond}=100°C

The traditional space heating systems are distinguished from ancient fireplaces only by their 20-30%. higher efficiency. Artificial air-conditioning system appeared much later, but their energy consumption is on a level of space heating systems.
Also, space heating and air-conditioning systems usually represent separate units, except for vapour compression climate control systems. They are expensive and have a limited operating range in a space heating mode if the heat source is an ambient air. Heat utilizing air-conditioning system is a still a rare find due to its price and bulky design. Their efficiency is low at high temperatures or high ambient air humidity (Buker and Riffat, 2015; Buyadgie et al., 2015; Maisotsenko et al, 2003) and requires desiccant system to absorb the moisture before cooling the air.
First air-conditioning systems based on ejector technologies were developed and are constantly improving. Researchers conduct studies on new schematic solutions for climate control systems based on jet compressor (Besagni et al., 2016; Sarkar, 2012; Chen J. et al., 2011). Comparing to other studies of ejector systems, some reference papers studied thermopump and binary fluid

application. That significantly increases systems' efficiency and support for building a fully autonomous unit that depends on heat source only (Buyadgie, 2016; Dennis, 2016; Śmierciew et al., 2014; Buyadgie et al., 2010, 2012, 2012a; Guo et al., 2009).
The purpose of this study is to increase efficiency of the combined climate control and hot water supply system by full heat utilization and hydrothermal potential of combustion products, as well as outlet and inlet air potential.

2. HEAT SOURCES AND PRINCIPLES OF HEAT MULTIPLICATION

Fuel combustion is the main way of heat production, while natural gas is the most efficient for residential and commercial utilities application. It has high heating value up to 1150 Btu/ft^3, lower rate of harmful emissions into the atmosphere than coal or oil. Efficiency of combustion reaches up to 90-95%, which is significant achievement over the past century. If staged heat removal is applied up to 60-70°C, that is below a dew point, than the efficiency can even reach up to 103-107% (Kocheva and Kondratiev, 2015).
Solar thermal energy and various sources of exhaust heat can also be utilized for air-conditioning and space heating, though during the cold season solar radiation does not perfectly correlate with the heating needs. It also shall be taken into account that daily variations and limitations during daylight hours make the solar thermal source unstable. In any way, if those sources can increase temperatures of inlet air at an initial point, it will decrease load on furnace anyway. For air-conditioning, the maximum insolation level corresponds to maximum cold demand. Generally, solar thermal applications save in an average up to 40-60% of fuel.
Another reserve of heat is recuperation of outlet air. That is achieved by temperature difference and partial pressure of moisture in inlet and outlet air, which increases its enthalpy by several times.
Compatibility of heating/cooling systems components based on ejector technologies allows saving in cost of equipment as well as on a footprint and weight. At the same time, energy consumption in the most energy consuming sector (more than 50%) can be decreased by 5 times and more.
Primarily requirement to conditioning space in winter and summer seasons is availability of effective insulation. Heat in-and out- leak should be minimized along with radiative heat transfer and these factors should be considered during buildings design.

3. CONCEPTUAL DESIGNS OF COMPLEX CLIMATE CONTROL SYSTEM BASED ON EJECTOR TECHNOLOGIES FOR RESIDENTIAL SYSTEM

Combined climate control systems become more popular especially in regions where ambient temperature usually higher than 0°C.
Electrically driven combined systems are not that efficient, but convenient in service since they are universal and compact. Usually their price is lower than heater and air-conditioner separately.
Following that principle, based on single furnace utilizing combustion heat of natural gas, it is possible to develop same service units of several times higher efficiency. It will also serve to decrease the emissions and energy consumption in utility sector up to 5-10 times. Air recirculation strategy was modified to a continuous fresh air displacement.
Fig. 1 represents a simple diagram that contains gas water heater and heat and mass exchanger HMX (Maisotsenko et al., 2002, 2003; Maisotsenko and Galaka, 2018). During winter season, intake air is preheated by outlet air from the room and then heated up by furnace.
When HMX operates in air-conditioning mode, water evaporation in working channel provides cooling of product air (Maisotsenko et al., 2002, 2003; Maisotsenko and Galaka, 2018). Such system is effective in the areas where air relative humidity does not exceed 40%. As a result, energy consumption decreases by 2-3 times comparing to conventional heating or air-conditioning systems, and electricity consumption decreased by 3-4 times.
If the relative humidity is higher than 40% and ambient temperature is high, the parameters of supply air exceeds recommended comfortable parameters, relative humidity reaches 75-100%. In this case, climate control system is equipped with heat utilizing units that can operate at both cooling and heating modes. Than unit is ejector based, which differs by low price, energy efficiency and durability.
Fig. 2 and 3 represents the system with ejector unit operating in winter and summer modes.
Efficiency of the ejector unit operating in air-conditioning mode is defined by eq. 1:

$$\zeta = \frac{Q_{eva}}{Q_{gen}} = \omega \frac{q_{eva}}{q_{gen}} \qquad \text{Eq. (1)}$$

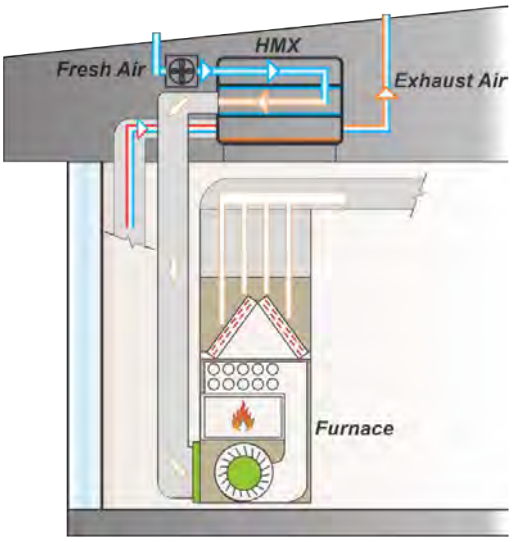

Figure 1: Schematic diagram of HMX and Furnace based system,

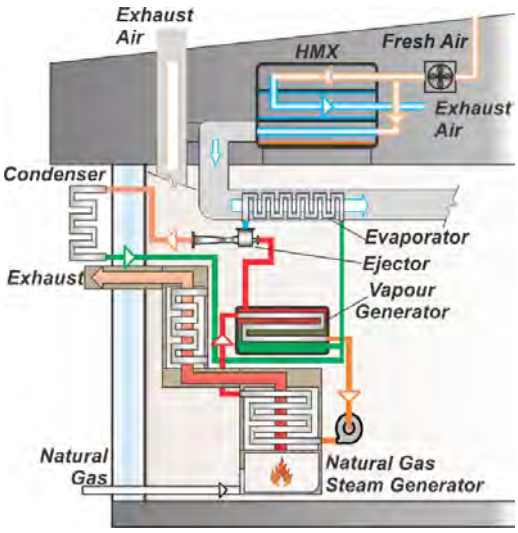

Figure 2: Schematic drawing of the system with HMX and ERS.

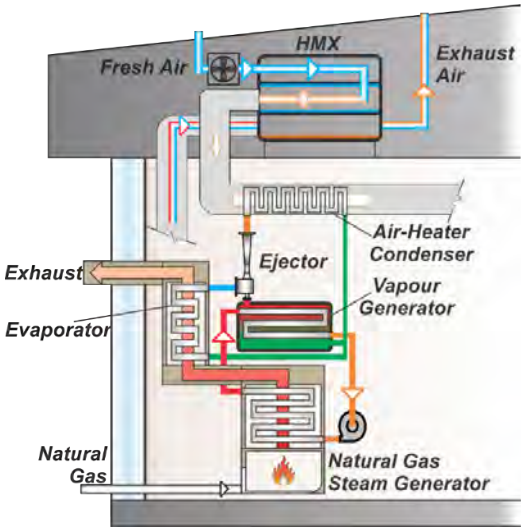

Figure 3: Schematic drawing of the system with HMX and EHP.

Efficiency of the ejector unit operating in air-conditioning mode with HMX is defined by eq. 2:

$$\zeta_{ERV} = \frac{Q_{HMX} + Q_{eva}}{Q_{gen}} \quad \text{Eq. (2)}$$

Efficiency of the ejector unit operating in air-conditioning mode with HMX/EHP is defined by eq. 3:

$$\zeta_{\varphi} = \frac{Q_{HMX} + Q_{eva}}{Q_{gen}} \varphi \quad \text{Eq. (3)}$$

Efficiency of the ejector unit operating in the heating mode is defined by eq. 4:

$$\varphi = \frac{Q_{gen} + Q_{eva}}{Q_{gen}} = 1 + \omega \frac{q_{eva}}{q_{gen}} = 1 + \zeta \quad \text{Eq. (4)}$$

Efficiency of the ejector unit operating in the heating mode with HMX is defined by eq. 5:

$$\varphi_{HMX} = \frac{Q_{gen} + Q_{eva} + Q_{HMX}}{Q_{gen}} \quad \text{Eq. (5)}$$

Entrainment ratio of an ejector is evaluated using method described by (Sokolov and Zinger, 1989), eq. 6.

$$\omega = \frac{K_1 \frac{a^{wf}_{gen,*}}{a^{mix}_{cond,*}} \lambda_{gen,A} - K_3 \lambda_{cond,C}}{K_4 \lambda_{cond,C} - K_2 \frac{a^{rf}_{eva,*}}{a^{mix}_{cond,*}} \lambda_{eva,B}}, \quad \text{Eq. (6)}$$

where

$$\Pi = \frac{P}{P_{eva}}$$

$$\lambda = \sqrt{\frac{k+1}{k-1}} \sqrt{1 - \Pi^{\frac{k-1}{k}}}$$

$$\gamma = \sqrt{\frac{k+1}{k-1}} \left(\frac{\Pi}{\Pi_*} \right)^{\frac{1}{k}} \sqrt{1 - \Pi^{\frac{k-1}{k}}}$$

$$K_1 = \varphi_1 \varphi_2 \varphi_3 = 0.834$$

$$K_2 = \varphi_2 \varphi_3 \varphi_4 = 0.812$$

$$\varphi_1 = 0.95, \varphi_2 = 0.975, \varphi_3 = 0.9, \varphi_4 = 0.925, \alpha = 0.5, \beta = 2$$

$$K_3 = 1 + \frac{\Pi_{cond,C} - \frac{P^{rf}_{eva}}{P^{mix}_{cond}} \left\{ \beta - \frac{(\beta - 1)}{2} \Pi_{eva,B} \left[1 + \left(\frac{P^{mix}_{cond}}{P^{rf}_{eva}} \right)^{1-\alpha} \left(\frac{\Pi_{cond,C}}{\Pi_{eva,B}} \right)^{1-\alpha} \right] \right\}}{\left(\frac{1}{\varphi_3} \frac{a^{mix}_{cond,*}}{a^{wf}_{gen,*}} \frac{P^{wf}_{gen}}{P^{mix}_{cond}} \right) k_{gen} \Pi_{gen,*} \lambda_{cond,C} \gamma_{gen,A} \beta}$$

$$K_4 = 1 + \frac{\Pi_{cond,C} - \Pi_{cond,B} \left\{ \beta - \frac{(\beta - 1)}{2} \left[1 + \left(\frac{P^{mix}_{cond}}{P^{rf}_{eva}} \right)^{1-\alpha} \left(\frac{\Pi_{cond,C}}{\Pi_{eva,B}} \right)^{1-\alpha} \right] \right\}}{\left(\frac{1}{\varphi_3} \frac{a^{mix}_{cond,*}}{a^{rf}_{eva,*}} \frac{P^{rf}_{eva}}{P^{mix}_{cond}} \right) k_{eva} \Pi_{eva,*} \lambda_{cond,C} \gamma_{eva,B} \beta}$$

where P the pressure (MPa);k adiabatic index; Π is the relative pressure; K_1 the integrated velocity coefficient of the working flow; K_2 the integrated velocity coefficient of the ejected flow; φ_1, φ_2, φ_3 and φ_4 are the experimental velocity coefficients; K_3 and K_4 are the integrated velocity coefficients; α and β are the empirical coefficients and γ the relative mass velocity; a the sound speed (m s^{-1}); *gen* the parameters of motive flow; *eva* the parameters of secondary flow; *cond* the parameters of mixed flow; *rf* the refrigerant flow parameters; *wf* the working flow parameters; *mix* the mixed flow parameters; *A* the nozzle outlet cross section area; *B* the mixing chamber inlet cross section area; *C* the mixing chamber outlet cross section area.

Considering, that ratio of specific evaporation heat of working and refrigerant fluid in Binary Fluid Ejector System is up to 1.5-2 times higher than Single Fluid Ejector System, efficiency of a Binary Fluid Ejector Heat Pump (BEHP) and Binary Fluid Ejector Refrigerating System (BERS) is higher by 1.5-1.25 times correspondently (Zhadan et al., 1981; Chen et al., 2011; Buyadgie et al., 2012).

As an example, the efficiency of the ERS operating on single R1233zd(E) at generation temperature 358K, condensation 308K, evaporation 285K, reaches 0.364, BERS operating on R1233zd(e)/Butane at the same parameters reaches 0.627. Also, efficiency of the single fluid EHP operating at generation temperature 413K, condensation 333K, evaporation 313K, reaches 1.577, BEHP operating at the same operating conditions equals to 1.85.

Efficiency of the systems proposed on Fig. 2 and 3 represented on Table 3 and Table 4 respectively.

Table 3. Efficiency of the combined HMX and EHP system at various ambient air parameters.

Ambient		HMX outlet		Q_{HMX}	Room Inlet		EHP		φ_{HMX}
t	RH	t	RH		t	RH	Q_{cond}	Q_{gen}	
°C	%	°C	%	kW	°C	%	kW	kW	
10	80%	10.5	100%	5.055	28	33.57%	17.862	9.655	2.374
5	80%	10.5	100%	14.598		33.57%	17.862	9.655	3.362
0	60%	10.5	100%	24.808		33.57%	17.862	9.655	4.419
-5	60%	7.45	100%	24.945		27.32%	20.918	11.307	4.056
-10	60%	4.3	100%	24.907		21.97%	24.069	13.010	3.764
-15	60%	1.1	100%	24.925		17.50%	27.266	14.738	3.541
10	60%	10.5	100%	8.919		33.57%	17.862	9.655	2.774
5	60%	10.5	100%	17.319		33.57%	17.862	9.655	3.644

Table 4. Efficiency of the combined HMX and ERS system at various ambient air parameters.

Ambient		HMX outlet		Q_{HMX}	Room Inlet		ERS		ζ_{HMX}	$\zeta\varphi$ φ=2.21
t	RH	t	RH		t	RH	Q_{eva}	Q_{gen}		
°C	%	°C	%	kW	°C	%	kW	kW		
35	55%	24	100%	6.224	22	100%	3.605	5.814	1.690	3.735
35	50%	24	94%	5.350		100%	2.277	3.673	2.076	4.588
35	45%	24	85%	5.332		96%	0.969	1.564	4.030	8.906
35	40%	24	75%	5.315		85%	0.966	1.559	4.030	8.906
35	35%	24	66%	5.298		74%	0.963	1.554	4.030	8.906
35	30%	24	57%	5.280		64%	0.960	1.548	4.030	8.906
35	25%	24	47%	5.263		53%	0.957	1.543	4.030	8.906

Ejector systems are close to commercialization, discussions about that are conducted for the past 10 years (Cizungu et al., 2001; Selvaraju et al., 2004; Huang et al., 2005; Śmierciew et al., 2014).

Systems' design proposed in the paper though slightly more costly than conventional ones but allows utilizing of combustion products enthalpy to dew point and increase efficiency by 1.5-2 times. At the same time, system can be applied in a wide range of climatic zones.

The cost of heating units based on prices for gas heater and compressor type air-conditioning systems is available, for example price for air-conditioning system with capacity of 5-6kW is $2,500 ("2019 Los Angeles Home AC Unit Cost | Los Angeles Central Air Cost," n.d.), boiler price is $7,384 ("2019 Los Angeles Home AC Unit Cost | Los Angeles Central Air Cost," n.d.). Proposed combined system consists of boiler, as a common part, 4 heat exchangers at a price $800, air duct, tubes, ejectors with total cost of $1,000. Thus, total cost of ejector-based system is $11,584, that is 11.5% higher than compressor-based system. Serial manufacturing of ejector-based system will decrease

the cost by 20-30%. For example, a price for 1 ejector varies from $300 to $500, while the price for serial production (from 1000 to 10,000 units) decreases from $50 to $12 per unit and depends on ejectors' fabrication method.

4. CONCLUSIONS

1. Climate control system proposed in the article is a low cost, simple and durable, allows to decrease fuel consumption by 3-5 times comparing to conventional systems.
2. Operation of any heat utilizing equipment depend on availability of effective heat, hydro- and steam insulation for operating in winter of summer modes. Otherwise, without proper control over residential operations, all advantages of new climatic systems would not be realized.
3. Solar heat application in winter mode and good insulation for both winter and summer allows to decrease fuel consumption up to 40-60%.
4. Ejector refrigerating systems and heat pumps operating on safe refrigerants and their mixtures allow in the best way utilize heat for space heating and air-conditioning, remaining a cheapest option.

NOMENCLATURE

P	pressure (MPa)	T	temperature (K)
Π	relative pressure (-)	t	Temperature (C)
a	sound speed, (m s^{-1})	γ	relative mass velocity (-)
λ	relative velocity (-)	k	adiabatic index
$K_1,K_2,$ K_3,K_4	integrated velocity coefficient (-)	ω	entrainment ratio
a	sound speed (m s^{-1})	$\varphi_1,\varphi_2,$ φ_3,φ_4	experimental velocity coefficient (-)

Abbreviations:

EHP	Ejector Heat Pump	*BEHP*	Binary Fluid Ejector Heat Pump
ERS	Ejector Refrigerating System	*BERS*	Binary Fluid Ejector Refrigerating System
HMX	Heat and Mass Exchanger	*RH*	Relative humidity

Subscripts:

gen	motive flow parameters	*eva*	secondary flow parameters
cond	mixed flow parameters	*out*	outlet parameter
A	nozzle outlet cross section	*B*	mixing chamber inlet cross section
C	mixing chamber outlet cross section		

Superscripts:

rf	refrigerant fluid	*wf*	working fluid
mix	binary fluid mixture	*out*	outlet parameter

REFERENCES

Besagni, G., Mereu, R., Inzoli, F., 2016. Ejector refrigeration: A comprehensive review. Renew. Sustain. Energy Rev. 53, 373–407.

Buker, M.S., Riffat, S.B., 2015. Recent developments in solar assisted liquid desiccant evaporative cooling technology—A review. Energy Build. 96, 95–108.

Buyadgie, D., Nichenko, S., Sechenyh, V., Buyadgie, O., Vasil'ev, I., 2010. Conceptual Design of Two-Stage Air-Conditioner. Proceedings of the 5th Asian Conference on Refrigeration and Air-Conditioning (ACRA2010), Tokyo, Japan. Paper 80.

Buyadgie, D., Buyadgie, O., Artemenko, S., Chamchine, A., Drakhnia, O., 2012. Conceptual design of binary/multicomponent fluid ejector refrigeration systems. Int. J. Low-Carbon Technol., vol. 7(2), 120–127.

Buyadgie, D., Buyadgie, O., Drakhnia, O., Artemenko, S., Chamchine, A., 2012a. Solar cooling technologies using ejector refrigeration systems. Energy Procedia 30(2012), 912-920.

Buyadgie, O., Buyadgie, D., Drakhnia, O., 2015. A Comparative Analysis of the Maisotsenko Cycle based Air-conditioning System: Ejector Cooling vs Desiccant. Proceedings of the 14th International Conference on Sustainable Energy Technologies (SET2015), Nottingham, UK. Paper 449.

Buyadgie, O., 2016. The Thermotransformation Processes Efficiency Enhancement in The Self-Contained Ejector Refrigerating Machines, PhD Thesis, The Odessa National Academy of Food Technologies, V.S. Martynovsky Institute of Refrigeration, Cryogenic Technologies and Eco-Energetics, Odessa, Ukraine.

Chen, J., Palm, B., Lundqvist, P., 2011. A new ejector refrigeration system with zeotropic mixtures. Proceedings of the 23rd International Congress of Refrigeration (ICR2011), Prague, Czech Republic, 2043-2050p.

Cizungu, K., Mani, A., Groll, M., 2001. Performance comparison of vapour jet refrigeration system with environment friendly working fluids. Appl. Therm. Eng. 21, 585–598.

Dennis, M., 2011. Characteristics of high-performance cooling systems using ejectors. International Conference on Solar Air Conditioning 2011, Ostbayerisches Technology Transfer Institute eV. Regensburg, Germany.

Guo, J., Shen, H.G.G., 2009. Modeling solar-driven ejector refrigeration system offering air conditioning for office buildings. Energy Build. 41, 175–181.

Huang, B.J., Hu, S.S., Lee, S.H., 2005. Development of an ejector cooling system with thermal pumping effect. Int. J. Refrig. 29(3), 476-484

Kocheva, M.A., Kondratiev, P.V., 2015. Stage utilization of combustion products heat. Stepwise the use of heat of products of combustion. Modern Problems of Science and Education Journal, 7(2015), 53-55.

Maisotsenko, V., Gillan, L.E., Heaton, T.L., Gillian A.D., 2002. Method and apparatus of indirect evaporation cooling. Patent US6,497,107.

Maisotsenko, V., Gillan, L.E., Heaton, T.L., Gillian A.D., 2003. Method and plate apparatus for dew point evaporative cooler. Patent US 6,581,402.

Maisotsenko, V., Galaka, O., 2018. Method and system for energy saving heating and humidifying of building using outside air. Patent US 9,982,907.

Sarkar, J., 2012. Ejector Enhanced vapour compression refrigeration and heat pump systems – A review. Renewable and Sustainable Energy Reviews 16, 6647-6659.

Selvaraju, A., Mani, A., 2004. Analysis of an ejector with environment friendly refrigerants. Appl. Therm. Eng. 24, 827–838.

Śmierciew, K., Gagan, J., Butrymowicz, D., Karwacki, J., 2014. Experimental investigations of solar driven ejector air-conditioning system. Energy Build. 80, 260–267.

Sokolov, E. Ya., Zinger, N.M., 1989. Jet Devices. Energoatomizdat, Moscow, 3rd Edn., 352 p.

Zhadan, S., Buyadgie, D., Peykov, A., Petrenko, V., Yurchenko, V., 1981. Application of fluids mixtures in ejector refrigeration machine (In Russian). Refrig. Eng. Technol. 32, 33–38.

2019 Los Angeles Home AC Unit Cost | Los Angeles Central Air Cost [WWW Document], n.d. URL https://www.improvenet.com/costs-near-me/los-angeles-new-ac-unit-cost (accessed 5.1.19).

Manuscript ID: 1370
DOI: 10.18462/iir.icr.2019.1370

Thermodynamic analysis of an absorption heat transformer based on experimental measurements

José L. CORRALES CIGANDA [(a)], Falk CUDOK [(a)], Manuel WAHL [(a)], Marvin SCHLOESSER [(a)], Dominik METZNER [(a)]

[(a)] Institut für Energietechnik, Technische Universität Berlin
Marchstr. 18, Berlin, 10587, Germany, jose.l.corralesciganda@tu-berlin.de

ABSTRACT

A prototype of an absorption heat transformer with a nominal capacity of 40 kW recovered heat has been investigated and compared with another prototype which measurements have been presented in a previous work (Cudok et al., 2017). The new prototype has been designed for upgrading industrial waste heat by recovering it at a temperature between 80 and 100°C and boosting it to a temperature level between 120 and 150°C. External heat balances obtained from measured external temperatures and flow rates combined with internal balances from enthalpy calculations of liquid and vapor flows have been used to get more insight into the internal process as occuring in real operation. The amount of adiabatic absorption in the absorber has been assessed (amounts up to 30% of the total referigerant absorbed), explaining the resulting heat flows in the main heat exchangers.
Moreover, an observed malfunction consisting of liquid refrigerant carry over from evaporator to absorber could be quantified with the results of the energy balances, explaining the deviation between measured coefficients of performance and expected ones.
Keywords: Heat Recovery, Enthalpy, Energy Balance, Absorption, Laboratory.

1. INTRODUCTION

This work aims to analyze the internal process of an absorption heat transformer (AHT) based on laboratory measurements, and to understand the differences between expected and obtained values for the coefficient of performance (COP). Two AHT prototypes are analysed by means of mass and energy balances: the first one presented in previous work, is able to work as an absorption chiller / heat pump or as a heat transformer (pr I). The second one (pr II) is based on the first one, but is adapted to be used only as a heat transformer and includes additional temperature sensors.

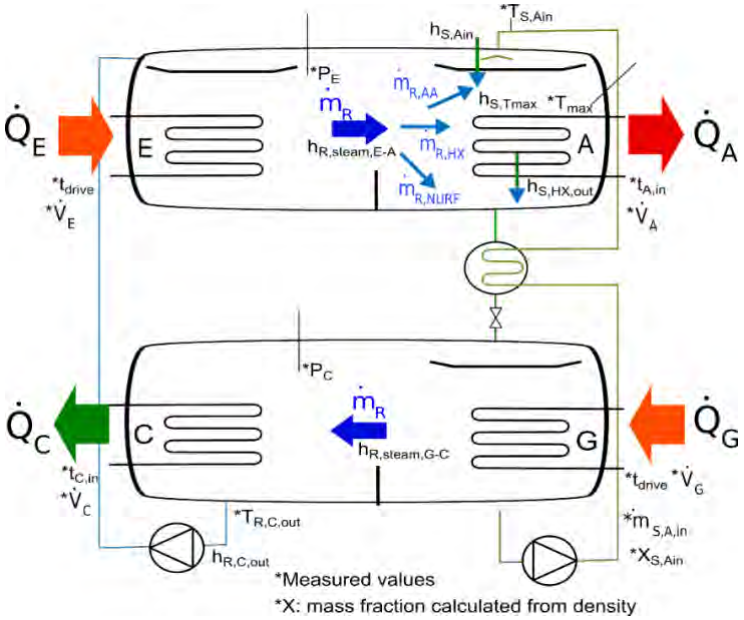

Figure 1: Absorption heat transformer scheme with measured values

, Measurement results of pr I have been presented in a previous work (Cudok et al., 2017) including the externally measured heat flows and a first estimation of the heat transfer coefficients. The same testrig used for pr I is used for the tests of pr II, that has been built with slighty different heat exchanger areas as table 1 shows. In a previous work, simulations of the AHT using different tools and thermodynamical property models but same physical model have been compared with one of the earliest measurements of the first prototype (Corrales Ciganda et al., 2016). This model has been used to define the new areas.

Prototype	A_A (m^2)	A_G/A_A (-)	A_E/A_A (-)	A_C/A_A (-)	$\dot{V}_{X=A,G,C,E}$ (m^3/h)	$\dot{m}_{sol}$ (kg/h)	$t_{C,in}$ (°C)	$t_{drive}=t_{GE,in}$ (°C)	$t_{A,in}$ (°C)
pr I	7.6	1	1	1	5	700	25-40	60-95	80-130
pr II	8.2	1.1	0.8	0.7	5	700	25/35	85/90/95	130

Table 1. HX Areas and measurement conditions for prototypes pr I and pr II

In this work, the results obtained with pr II are compared with the results obtained with pr I. Heat balances using external heat flows and internal mass and enthalpy flows have been calculated to understand the differences in the obtained results, and are used to derive the effectiveness of certain internal processes. These analyses revealed some inefficiencies that are usually not taken into account in most thermodynamical models of the cycle, and explain the differences between expected and measured COPs.

2. MEASUREMENTS: EXTERNAL HEAT FLOWS ANALYSIS

2.1. Experimental Results: Revaluated Heat Flows and COP

Fig. 2 presents the recovered heat flow rates measured for each AHT prototype ($\dot{Q}_A$) and its coefficient of performance, as a function of the double temperature difference $\Delta\Delta t$. The double temperature is an indicator for the driving temperature of the AHT, as presented in (Cudok & Ziegler, 2015) calculated using the definition from Eq. (1):

$$\Delta\Delta t = (t_G - t_A) - B \cdot (t_C - t_E) = B \cdot (t_E - t_C) - (t_A - t_{GE}) \qquad \textit{Eq. (1)}$$

The coefficient of performance for an AHT is defined as the useful high temperature heat flow rate transferred in the absorber divided by the total amount of waste heat flow rate transferred in generator and evaporator:

$$COP = \frac{\dot{Q}_A}{Q_G + \dot{Q}_E} \qquad \textit{Eq. (2)}$$

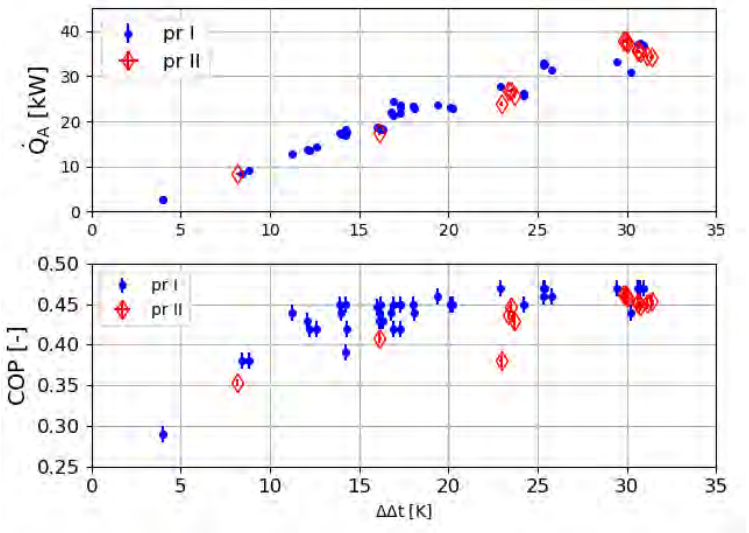

Figure 2: $\dot{Q}_A$ and COP vs. $\Delta\Delta t$ for pr I and pr II

Three sets of operating conditions have been consistently measured for pr II. The conditions correspond to the expected ones for a pilot plant prototype to be installed in the last phase of the Indus3Es project. The temperatures of the waste heat source have been variated between 85, 90 and 95°C with fixed inlet temperatures for the cooling water ($t_{C,in}$ =25°C) and for the higher temperature useful heat stream ($t_{A,in}$=130°C).These points had been previously measured for pr I and will be the basis for following analysis. For all measuremensts, flow rates at external circuits and solution pump has been set constant as presented in Table I.
The recovered higher temperatures heat flow rates measured with pr II are very similar to those measured with pr I. For example, for waste heat source temperatures of 95°C ($\Delta\Delta t$ around 30 K) the heat flow rates for pr I are between 36.9 and 37.4 kW. For the same waste heat source temperatures the results of pr II are between 34.3 and 37.8 kW, with a much bigger scatter. Regarding the COP, the values obtained for pr II are lower for the same operation conditions than those obtained for pr I.The differences seems to become bigger for points with lower $\Delta\Delta t$ values and lower heat flows. The differences could be caused by:

- Presence of non condensables gases during pr II measurements.
- Differences in effectiveness of the solution heat exchanger (SHX)
- Differences in heat losses to the surrounding environment
- Differences in adiabatic absorption efficiencies for same operation conditions
- Differences in non-usable refrigerant flows (NURF) between evaporator and absorber

The pressence of non-condensable gases has been investigated but could not be detected for any measurement. The effectiveness of the solution heat exchanger was calculated with measured temperatures and resulted in values between 77 and 81% for all tests of both prototypes (no significant differences). The following sections investigate if either differences in heat losses, differences in adiabatic absorption rates or differences in the amount of non-usable refrigerant flows can give a hint for the differences observed in the measurements.

2.2. AHT Energy Balances and Possible Heat Losses

If the heat balance of the AHT differs from zero at least one of the assumptions made for modelling is not valid. Either is the AHT not adiabatic or the measurements are not completely under steady state (thermal masses inside the AHT being still heated up or cooled down). Using all four heat flows entering/leaving the AHT we can write:

$$\dot{Q}_{bal,AHT} = \dot{Q}_A + \dot{Q}_G + \dot{Q}_E + \dot{Q}_C \qquad \textit{Eq. (3)}$$

Being $\dot{Q}_X$ the measured heat flow rates, that are positive when entering the AHT and negative when leaving it. Thus, a positive value for $\dot{Q}_{bal,AHT}$ indicates that heat is being stored within the AHT system or transferred to the surrounding environment (heat losses).

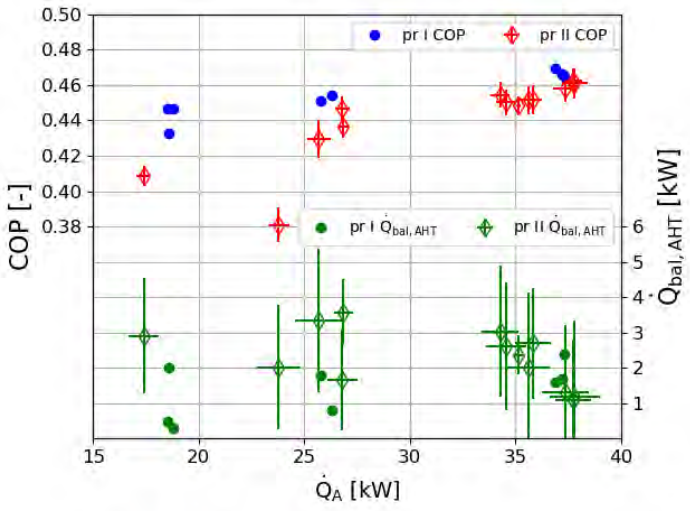

Figure 3: COP and $\dot{Q}_{bal,AHT}$ vs $\dot{Q}_A$ for pr I and pr II

Positive values for $\dot{Q}_{bal,AHT}$ are obtained for all measurements. Taking into consideration the measurement uncertainty, it can be affirmed for all measurements that the value for the unbalanced

heat flow lays between 0 and 5 kW. For measurements with $\dot{Q}_{,A}$ between 34 and 40 kW (t_{drive}=95°C) the obtained COP values for pr II (0.45-0.47) are similar to those of pr I (0.47) Same can be observed for measurements with revaluated heat flow around 25kW (t_{drive}=90°C) For even smaller $\dot{Q}_{,A}$ values (t_{drive}=85°C) the differences in obtained COP between pr I (0.41) and pr II (0.43-0.45) are beyond the measurement uncertainty. For this measurement with lower heat flow rates the influences of the non balanced heat flows on the COP is bigger. With an ideal zero value heat balance for the AHT, the difference between pr I and pr II COP values would be reduced : if the non balanced heat flows are substracted from the useful heat, the COP values would lay between 0.45 and 0.48 for pr I and between 0.43 and 0.47 for pr II. Other irreversibilites different than the heat losses must be responsible of the remaining difference.

3. MEASUREMENTS: INTERNAL ENTHALPY FLOWS ANALYSIS

3.1. Adiabatic Absorption

Another possible reason for the differences found between measured recovered heat flow rates for pr I and pr II is that the efficiency of the adiabatic absorption process is different.
In Fig. 1 the streams involved in the adiabatic absorption process are presented. The amount of refrigerant ideally adiabatically absorbed is calculated assuming adiabatic mixing and absorption up to saturated state. This can be expressed with the following equations, which are solved simultaneously using thermodynamic property functions and measured data: vessel pressure, and measured temperature, mass fraction and mass flow rate of the solution entering the absorber.

$$\dot{m}_{S,A,in} + \dot{m}_{R,AA,ideal} = \dot{m}_{S,Tmax,ideal} \qquad \textit{Eq. (4)}$$

$$\dot{m}_{S,A,in} \cdot h_{S,A,in} + \dot{m}_{R,AA,ideal} \cdot h_{R,steam,E-A} = \dot{m}_{S,Tmax,ideal} \cdot h_{S,Tmax,ideal} \qquad \textit{Eq. (5)}$$

$$\dot{m}_{S,A,in} \cdot X_{S,A,in} = \dot{m}_{S,Tmax,ideal} \cdot X_{S,Tmax,ideal} \qquad \textit{Eq. (6)}$$

with
$h_{\mathrm{S,A,in}} = h(p_{\mathrm{E}}, T_{\mathrm{S,A,in}}, X_{\mathrm{S,A,in}})$,$h_{\mathrm{S,Tmax,ideal}} = h_{\mathrm{sat}}(p_{\mathrm{E}}, X_{\mathrm{S,Tmax,ideal}})$, $T_{\mathrm{max,ideal}} = T_{sat}(p_{\mathrm{E}}, X_{\mathrm{S,Tmax,ideal}})$

once $T_{\mathrm{max,ideal}}$ is obtained, the adiabatic absorption effectiveness can be defined as:

$$\eta_{AA} = \frac{T_{max,meas} - T_{S,A,in}}{T_{max,ideal} - T_{S,A,in}} \qquad \textit{Eq. (7)}$$

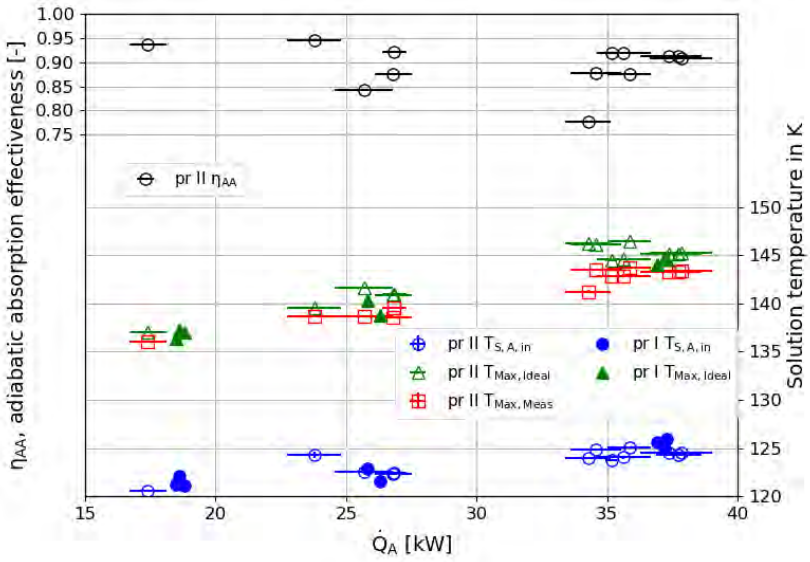

Figure 4: η_{AA} for pr II and measured temperatures for pr I and pr II

By comparing the maximal temperature measured after adiabatic absorption at the vessel with the ideal maximal temperature from the calculations above, we can obtain a value for the effectiveness of the adiabatic absorption.
The effectiveness calculations are presented only for measurements with pr II because measurements of the solution temperature inside the absorber after adiabatic absorption were not included when pr ! was investigated. Since the maximum temperature inside the vessel could be higher than the maximum temperature measured at the surface of the first tube rows of the absorber, the adiabatic absorption effectiveness could be higher than the presented values. Nevertheless, the values obtained are quite high (between 85 and 95%) and similar for all measured points. The differences between adiabatic absorption effectiveness calculated for prI and por II are not significant and do not seem to be the reason for neither the differences in COPs nor for the scatter in revaluated heat flow rates. Pr II was designed in order to obtain better adiabatic absorption than for pr I, so the adiabatic absorption effectiveness for pr I is expected to be lower.

3.2. Non-Usable Refrigerant Flows (NURF)

The non-usable refrigerant flows (NURF) can be defined as refrigerant flows between evaporator and absorber other than those being absorbed adiabatically or at the surface of the absorber heat exchanger tube bundles.
The total amount of refrigerant flow rate between generator and condenser is obtained from an energy balance at the condenser with the assumption of an condensation process without heat losses in steady state. The measured temperature of the liquid refrigerant leaving the condenser and the measured pressure inside the lower pressure vessel are used for the calculations.

$$\dot{m}_R = \frac{\dot{Q}_C}{(h_{R,steam,C-E} - h_{R,C,out})} \qquad \textit{Eq. (8)}$$

with

$$h_{R,steam,C-E} = h_{steam}(p_C, t_{drive}) \qquad \textit{and} \qquad h_{R,C,out} = h_{liquid}(p_C, T_{R,C,out})$$

In steady state conditions, the refrigerant mass flow rate from evaporator to absorber is the same as the flow rate from generator to condenser. At the same time, for an ideally insulated absorber this flow rate should be equal to the addition of the refrigerant flows adiabatically absorbed ($m_{R,AA}$) and absorbed at the tube bundle surface ($m_{R,HX}$). Writing an energy balance around the absorber we get

$$\dot{m}_{S,A,in} + (\dot{m}_{R,AA,ideal} + \dot{m}_{R,HX,ideal}) = \dot{m}_{S,HX,out} \qquad \textit{Eq. (9)}$$

$$\dot{m}_{S,A,in} \cdot h_{S,A,in} + (\dot{m}_{R,AA,ideal} + \dot{m}_{R,HX,ideal}) \cdot h_{R,steam,E-A} = m_{S,HX,out} \cdot h_{S,HX,out} \qquad \textit{Eq. (10)}$$

$$\dot{m}_{S,A,in} \cdot X_{S,A,in} = \dot{m}_{S,HX,out} \cdot X_{S,HX,out} \qquad \textit{Eq. (11)}$$

with $h_{R,steam,E-A} = h_{steam,sat}(p_E)$ *and* $h_{S,HX,out} = h_{sat}(p_E, X_{S,HX,out})$.

According to the definition for NURF given above, we can write:

$$\dot{m}_{NURF} = \dot{m}_R - (\dot{m}_{R,AA,ideal} + \dot{m}_{R,HX,ideal}) = \dot{m}_R - (\dot{m}_{R,AA} + \dot{m}_{R,HX}) \qquad \textit{Eq. (12)}$$

The obtained mass flow rates are plotted together with $\dot{m}_{R,AA}$ obtained with equations (4) to (6).
From the values obtained and shown in Fig. 5 it can be concluded that for the same revaluated heat output prototype pr I operates with less refrigerant flow rate than pr II.
The flow of adiabatically absorbed refrigerant is really similar for measurements with pr I and pr II, and accounts for around 18-20% of the total refrigerant flow in measurements with capacities between 35-40 kW and up to 29% for capacities around 18 kW. The calculated (minimal) amounts of NURF for measurements of pr II are between 2 and 5 times those (minimal) amounts calculated for measurements of pr I. These conclusions, however, must be taken very carefully, since the values obtained for NURF are within the uncertainty range for the calculated refrigerant mass flow rates.

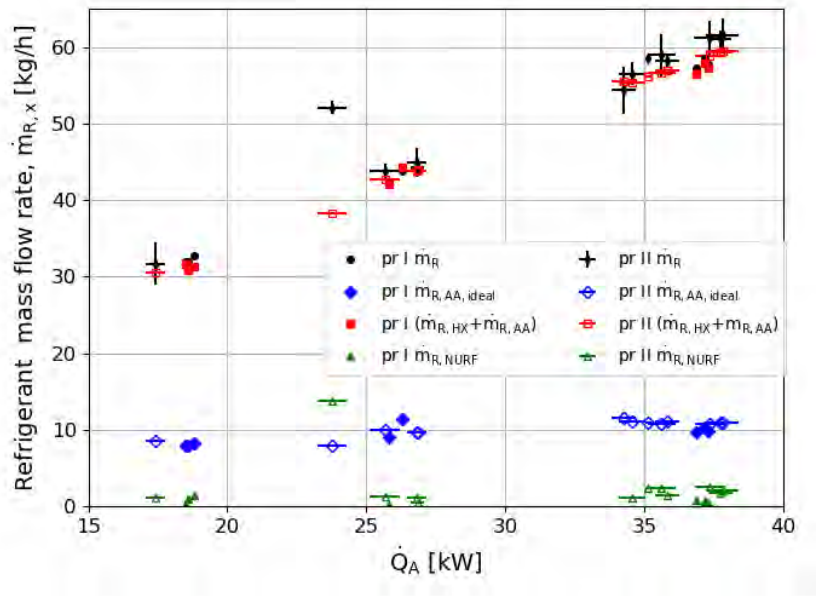

Figure 5: Refrigerant mass flow rates vs $\dot{Q}_A$

As explained in the text above, there is a mass flow of the non usable refrigerant flows from the evaporator into the absorber sump bypassing the heat exchanger tubes. It is possible that liquid refrigerant sprinkles directly into the absorber sump. It is also possible that refrigerant vapor flows from the evaporator to the absorber chamber, condenses at the shell tube and flows afterwards into the sump. A mixture of both procedures is also possible. In the case of liquid droplets the condenser and generator have to condense respectively generate that amount of non usable refrigerant on top of the refrigerant absorbed at the absorber. The evaporator evaporates the same amount of refrigerant the absorber absorbs. In the case of condensation at the shell tube at the absorber, the evaporator needs to evaporate the refrigerant absorbed by the absorber and additional the refrigerant condensed at the shell tube. In case liquid droplets the influence to the COP will be lower than in case refrigerant vapor condense at absorber shell tube.
To understand the influence of this non usable mass flow to the COP, its value excluding the heat input related to non-usable refrigerant flow for its calculation will be estimated. For the case “liquid refrigerant droplets” the following equations are used:

$$COP_{ld} = \frac{\dot{Q}_A}{(\dot{Q}_G - \dot{Q}_{G,NURF}) + \dot{Q}_E} \qquad Eq.\ (13)$$

The heat flow for the additional vapor generation in the generator is estimated by multiplication of the non-usable refrigerant mass flow rate and the specific heat of dilution $(r + l)$:

$$\dot{Q}_{G,NURF} = \dot{m}_{R,NURF} \cdot (r + l) \qquad Eq.\ (14)$$

In case of “vapor condensation” at the tube shell the corrected COP depends on the on $\dot{Q}_{G,NURF}$ and $\dot{Q}_{E,NURF}$ as following:

$$COP_{vd} = \frac{\dot{Q}_A}{(\dot{Q}_G - \dot{Q}_{G,NURF}) + (\dot{Q}_E - \dot{Q}_{E,NURF})} \qquad Eq.\ (15)$$

With

$$\dot{Q}_{E,NURF} = \dot{m}_{R,NURF} \cdot r \qquad Eq.\ (16)$$

The relation between the heat of vaporization r and the heat of dilution $(r + l)$ is described by the Dühring factor B (Ziegler, 1997):

$$r \cdot B = (r + l) \qquad Eq.\ (17)$$

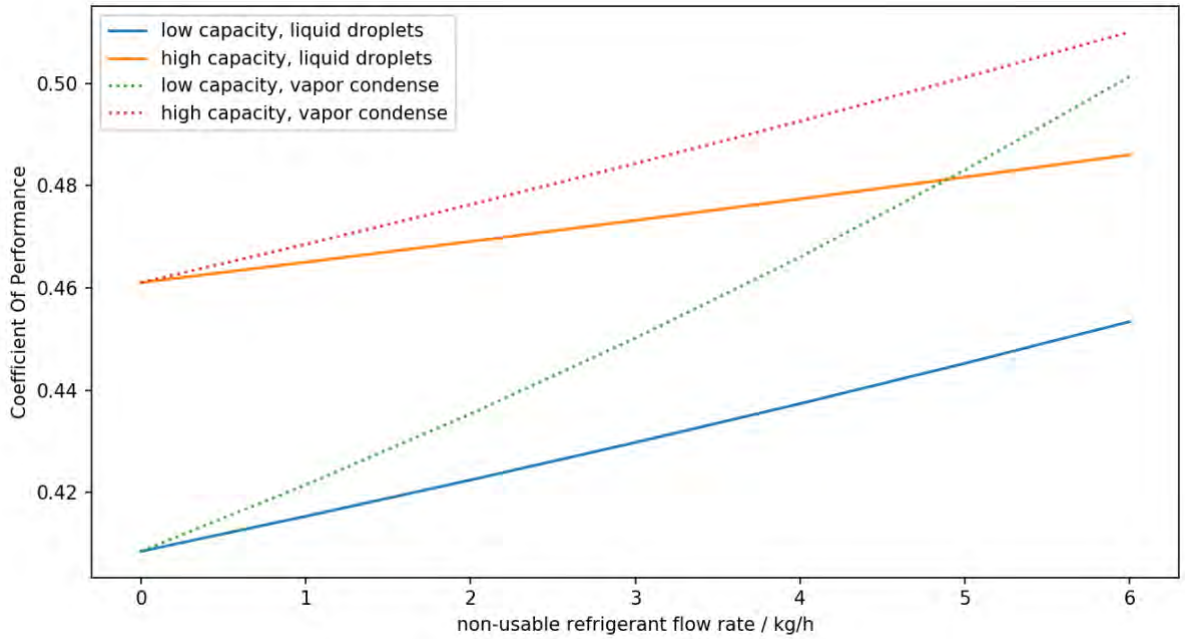

Figure 6: Effect of NURF on the COP

For two measurements, one with with low capacities ($\dot{Q}_{\mathrm{A}} = 17.39\ \mathrm{kW}, \dot{Q}_{\mathrm{E}} = 23.23\ \mathrm{kW}, \dot{Q}_{\mathrm{G}} = 19.34\ \mathrm{kW}$) and one with high capacities ($\dot{Q}_{\mathrm{A}} = 37.83\ \mathrm{kW}, \dot{Q}_{\mathrm{E}} = 43.10\ \mathrm{kW}, \dot{Q}_{\mathrm{G}} = 38.95\ \mathrm{kW}$) a variation of the non usable refrigerant mass flow rate ($0 \geq \dot{m}_{\mathrm{R,NURF}} \geq 6\ \mathrm{kg \cdot m^{-2}}$) by adaption the Eqs. (13) to (17) was done (see Fig. 6) In addition, it was assumed $r = 2200\ kJ/kg$ and $B = 1.15$.
This figure shows the corrected COP depending on the assumed non usable refrigerant flow. The mean value of the non usable refrigerant flow is around 4kg/h for the presented measurements (see Fig. 5). For the low capacity the corrected COP would be 44%, when the case “liquid droplets” will be compensated, and 46%, when the case “vapor condensate” will be compensate, instead of the measured COP of 41%. For the high capacity the measured COP of 46% will be corrected to 48% or 49% respectively. The diagram shows both case separately. The results of a non usable mass flow consist of sprinkling liquid droplets and condensing vapor will be between the particular curves.

4. CONCLUSIONS

The $\dot{Q}_{,\mathrm{A}}$ values measured with pr II are in the same range and only slightly smaller than those obtained for pr I and presented in (Cudok et al., 2017). The obtained COPs with pr II measurements were in in almost all cases lower than those obtained with measurements of pr I. One of the reasons for these differences in COP is the difference in heat losses to the surroundings, that was between 1 and 1.5 kW higher for pr II than for pr I, according to the energy balances.
The flow of refrigerant being adiabatically absorbed accounts for up to 30% of the total refrigerant flow. Calculated using the maximum temperature measurements inside the absorber of prototype pr II, at least 17% to 25% of the total flow of refrigerant is absorbed adiabatically (adiabatic absorption efficiencies in the range of 85-95%). It does not seem likely that differences in adiabatic absorption explain the differences in COP between pr I and pr II.
Higher Non Usable Refrigerant Flows (NURF) values have been obtained for pr II than for pr I. This NURF can be either liquid drops flow from the evaporator distribution system into the absorber sump, or steam flow condensing at any vessel surface. The amount of NURF is estimated to be between 2 and 7% of the refrigerant flow. This can reduce the COP between 1 and 3 percentual points.
Based on these analyses, differences in COP between the two prototypes can be explained by of the higher NURF values and increased heat losses for pr II compared to pr I. However, the scatter in recovered heat flows (up to 8%) for measurements of pr II under the same conditions cannot be explained by these reasons. The main hypothesis for this scatter in recovered heat flows is the different wetting of the absorber heat exchanger tube bundles during some tests, due to corrosion and particle accumulation in the solution circuit.

ACKNOWLEDGEMENTS

This work has been developed under the project “Indus3Es: Industrial Energy and Environmental Efficiency” funded by the Horizon 2020 framework of the European Union, Project No. 680738. http://www.indus3es.eu

NOMENCLATURE

Symbols			
A	Heat exchanger area (m²)	p	pressure (kPa)
AHT	Absorption heat transformer	pr I / II	Prototype 1 / 2
B	Dühring factor	$\dot{Q}$	Heat flow (kW)
COP	Coefficient of performance	r	Spec. heat of vaporization (kJ×kg^{-1})
DDT	Double temperature difference (K)	$r + l$	Spec. heat of dilution (kJ×kg^{-1})
η	Effectiveness	SHX	Solution heat exchanger
h	Spec. enthalpy (kJ×kg^{-1}×K^{-1})	t	External temperature (°C)
$\dot{m}$	Mass flow (kg×s^{-1})	T	internal temperature (°C)
NURF	Non-usable refrigerant flow	X	Mass fraction (kg×kg^{-1})

Indices			
A	Absorber	max	Maximal
AA	Adiabatic absorption	meas	Measurements
Bal	Energy balance	NURF	Non-usable refrigerant flow
C	Condenser	out	Outlet
drive	Driving	R	Refrigerant
E	Evaporator	rec	Recirculation at E
G	Generator	revaluated	Revaluated
HX	Heat exchanger bundle	S	Solution
in	Inlet	sat	Saturated
ld	Liquid droplets	*steam*	Steam
liquid	Liquid	*th*	Thermal
Ideal	Ideal		

REFERENCES

Corrales Ciganda, J. L. et al., 2016. Thermodynamic cycle models for the development of absorption heat transformers for the process industry. Nottingham, s.n., p. paper 320.

Cudok, F., Corrales Ciganda, J. L. & Kononenko, N., 2017. Experimental Results of an absorption heat transformer. Rotterdam, s.n., p. O 4.4.2.

Cudok, F. & Ziegler, F., 2015. Absorption heat converter and the characteristic equation method. Yokohama, s.n., p. paper 764.

Ziegler, F., 1997. Sorptionswärmepumpen. Erding: Forschungsberichte des Deutschen Klima- und Kältetechnischen Vereins e.V..

Manuscript ID: 1375
DOI: 10.18462/iir.icr.2019.1375

Compact Exhaust air/Supply air Heat Pump with Recirculation and Energy Recovery in Renovated Multi-storey-buildings

Fabian OCHS[(a)], Toni CALABRESE[(a)], Dietmar SIEGELE[(a)], Georgios DERMENTZIS[(a)]

[(a)] UIBK, Unit for Energy Efficient Buildings
Innsbruck, 6020, Austria, fabian.ochs@uibk.ac.at

ABSTRACT

A complete renovation package consisting of a decentralized (apartment size) exhaust-air heat pump for ventilation and heating installed in the kitchen and an air-to-water HP for domestic hot water preparation installed in the bathroom were developed. The very compact heat pumps are developed in order to enable the integration of these units into the window parapet or into the façade. The wall integration has a high potential in pre-fabrication and leads to an optimal solution for renovation of small apartments. The solutions aim to be cost effective, involving components and technologies with high efficiency and minimum noise emissions. With laboratory measurements and refrigerant cycle simulation, performance maps were generated for different compressor speeds and volume flows (supply, recirculation and additional ambient air) and depending on the source as well as on the extract air temperature and humidity. Control strategies were optimized by means of dynamic building simulations. A mock-up was installed and tested.
Keywords: Deep Renovation, Multi Family House, Compact Heat Pump, Performance, Indoor Air Quality, Energy Efficiency, Façade Integration.

1. INTRODUCTION

The building sector is responsible for a large percentage of the world energy requirements. Thus, a future sustainable energy system requires a deep renovation of existing buildings. While renovation to very low energy consumption by renovating with Passive House components to e.g. the so-called EnerPHit standard is well proven, the renovation of the HVAC system represents often a major hurdle in particular in multi-family homes. Non-disruptive renovation of flats is not trivial due to a number of complications (technical, economic, social). Innovative technologies and smart renovation strategies are required (see e.g. EU fp7 project iNSPiRe).
So-called Passive House compact hat pump units for ventilation, heating (optionally cooling) and domestic hot water (DHW) preparation consisting of a mechanical ventilation with heat recovery, an exhaust air heat pump and a small DHW store are a proven cost-effective and efficient technology that exist since more than 20 years. However, in spite of their name, market available systems are far too big to be installed in small flats or apartments of typical multi-family houses.
Within the EU fp7 project iNSPiRe and followed by the Austrian FFG project SalüH! cost-effective compact ventilation and heat pump units were developed as one of the possible solutions for energy renovation of small flats, especially in case of limited space Ochs et al. (2017a). Such a system can be completely integrated in the façade and thus minimizes the space required for renovation inside the flat. In addition, electricity required by the system can be potentially covered by a photovoltaic (PV) system installed on the roof or on the façade of the flat Calabrese et al. (2018a). An improved variant of such a system was developed and investigated. This new ventilation and heating concept is based on a supply air – exhaust air heat pump, with higher heating power and better control options of the system ensured by the use of a second condenser (i.e. desuperheater) with recirculation of secondary air.

2. CONCEPT

The supply air – exhaust air heat pump system with inverter technology is equipped in addition to the condenser which heats the supply air to max. 52 °C with a second condenser in which secondary air is heated. The secondary air is extracted from and supplied to the corridor (i.e. secondary air recirculation). The use of secondary air increases the heating power of the heat pump and gives the opportunity to split the power, allowing a better control of the heat pump system. The system uses the necessary ducts of the ventilation system to distribute space heating power plus one additional pair of ducts for the recirculation from the kitchen to the corridor. The air distribution system is placed in the corridor and supplies fresh air to the sleeping room, child room and living room. An electric radiator is placed in the bathroom for reasons of comfort.

The hydraulic scheme of the heating and ventilation system is shown in Fig. 1. The fresh air is heated by a pre-heater, an mechanical ventilation with heat recovery (MVHR), the condenser of the heat pump and, additionally, a post-heater if the power of heat pump is insufficient, before it is supplied and distributed to the flat. The air is extracted from bathroom and kitchen, cooled in the MVHR and its enthalpy is used as source for the heat pump. The evaporator of the heat pump is placed in the exhaust airflow after the energy recovery ventilation and uses the remaining enthalpy of the exhaust air. Additional ambient air can be used as source of the heat pump. The secondary air, extracted from the corridor of the flat, is heated in the desuperheater (i.e. “DESUP” in Fig. 1) and is supplied to the corridor.

One of the big advantages of such a system is the possibility to distribute heating power to the flat using the ventilation ducts. The mass balanced energy recovery ventilation (ERV) supplies fresh air to the sleeping room (SL), child room (CH) and living room (LI) and extracts air from the kitchen (KI) and bathroom (BA).

Fig. 1 shows a 3D view of the flat with a possible configuration of the proposed heating and ventilation system. In this case, the system is installed similar to a conventional HP split unit with an outdoor unit (but integrated in the façade of the flat) and an indoor unit (installed in the ceiling of the kitchen), see also [1]. The outdoor unit is integrated in the façade, while the indoor unit is installed on the ceiling of the kitchen. An air distribution system is installed in the corridor to supply air to the SL, LI and CH and collects air from the BA.

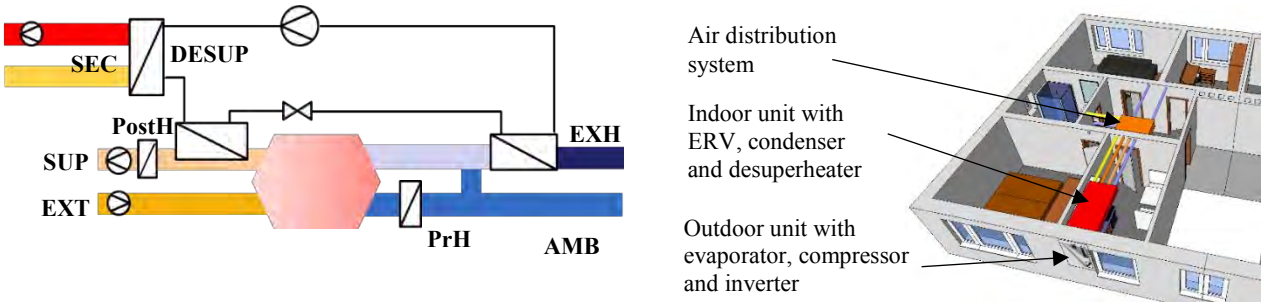

Figure 1: (left) Hydraulic scheme of the compact ERV and heat pump system with recirculation air. “PostH” and “PrH” represent the post-heater and the pre-heater, respectively. “DESUP” indicates the second condenser (i.e. desuperheater) of the heat pump that is used to heat the recirculation air in the corridor and (right) 3D view of the flat under investigation

3. FUNCTIONAL MODELS AND LAB TESTING

3.1. Indoor Unit

The compact unit was designed as a solution primarily for the case of limited space for energy renovation. The main components of the indoor unit are the ERV unit and the condenser and desuperheater of the heat pump. The functional model of the indoor unit that was tested in the lab of University of Innsbruck (UIBK) is shown in Fig. 2. The fresh air - optionally pre-heated in a pre-heater for frost-protection – is heated in the ERV unit and afterwards in the condenser of the heat pump before it is distributed in the corridor to the supply air rooms (i.e. SL, CH and LI). The extracted air (from bathroom and kitchen) is cooled in the ERV unit and is then driven to the evaporator

installed in the outdoor unit (Fig. 3, see below). The foam casing includes the duct of the secondary air that is extracted from the corridor, heated in the desuperheater and recirculated to the corridor.

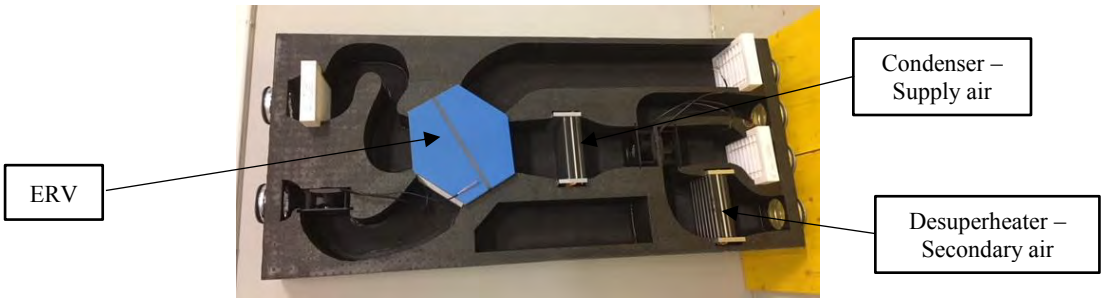

Figure 2: Functional model of the indoor unit of the supply air heat pump with recirculation of secondary air and integrated silencers (Photo: Siko Energiesysteme)

3.2. Outdoor Unit

Fig. 3 shows the outdoor unit of the proposed system installed into a prefabricated timber frame façade in the PASSYS test cell at the UIBK. As explained above, this configuration represents one of the possible solutions in which the outdoor unit is completely integrated into a façade and the indoor unit is installed in the flat. The inlets for the supply air, additional ambient air and exhaust air are visible on the façade.
On the photo of the mock-up in the so-called PASSYS test cell at UIBK (Fig. 3, right) the inlet of the supply air and the outlet of the exhaust air, as well as the inlet of the additional ambient air that is used as additional source of the heat pump can be seen. The main components contained in the outdoor unit are the compressor, the evaporator and the expansion valve of the heat pump, whereas the condenser and the desuperheater are installed in the indoor unit.

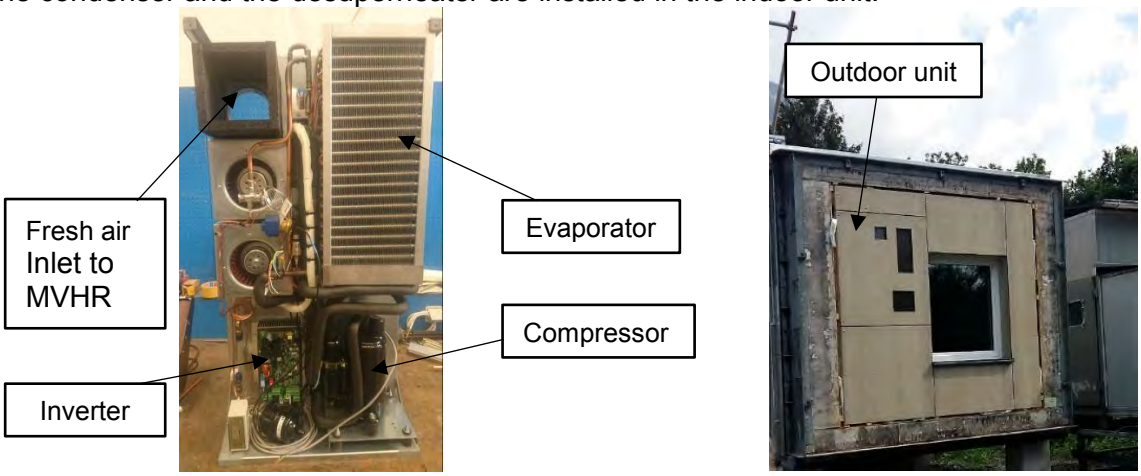

Figure 3: (left) Outdoor unit in the laboratory at the UIBK and (right) Outside view of the outdoor unit integrated into the prefabricated timber frame façade in the PASSYS test cell

4. SIMULATION STUDY

The proposed system was developed and tested in the laboratory and then modelled in the CARNOT/Simulink simulation environment. A simulation study for a flat of a typical multi-family house (MFH) was performed in order to investigate the performances of the heating system, as well as thermal comfort and indoor air quality (IAQ) in the flat.
Furthermore, the performance of this new system (i.e. with desuperheater with recirculation of secondary air) is compared with a reference system (i.e. supply air – exhaust air HP without desuperheater).

4.1. Reference Flat and Control of Ventilation and Heating System

The building under investigation is a typical central European multi-story building consisting of five stories and two symmetrical flats for each storey. The basement and the staircase are not heated.

The reference flat considered in this study is in the first floor oriented to the Northeast. The flat is occupied by 3 persons (ca. 23 m^2 per person). The daily schedule of the occupation profile is valid also during the weekend. An air change rate of 0.07 (h^{-1} due to infiltration through the façade is assumed.
The reference flat is shown in Fig. 4. The flat has a total heated area of 70.9 m² and it consists in six rooms: kitchen (KI), sleeping room (SL), corridor (CO), bathroom (BA), child room (CH) and living room (LI).
Figure 4 right hand side, shows a simplified block diagram of the heating system model created in CARNOT (Matlab/Simulink see previous section). The power of the heat pump is controlled with a temperature sensor installed in the corridor and, optionally, an additional temperature sensor is installed in the living room to avoid underheating in the suplly air rooms. This heating system with supply air and secondary air recirculation gives the possibility to heat the flat with two modes:

- If $T_{LI} < T_{SP}$, the supply air is used to heat the flat;
- If $T_{LI} > T_{SP}$, supply air and secondary air are used to deliver heating power

Where T_{LI} and T_{SP} represent the operative temperature of the living room and the set point temperature of the heating system, respectively.

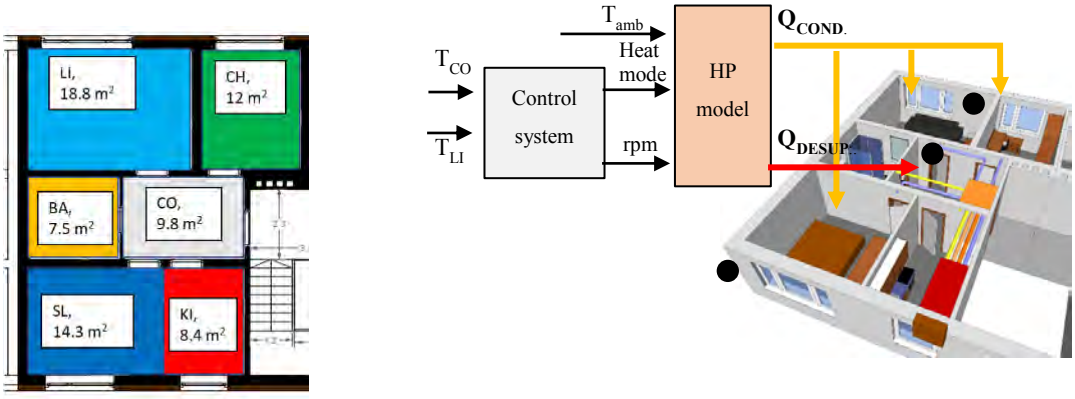

Figure 4: (left) Floor plan of the flat (70.9 m²) and (right) Block diagram of the system implemented in CARNOT, Matlab/Simulink. The black points indicate the position of the temperature sensors considered (i.e. ambient, CO and LI). "Heat mode" indicates the mode with which the power is delivered to the flat: with supply (i.e. condenser is activated) or with supply and secondary air (i.e. condenser and desuperheater are activated.

4.2. Simulation Platform, Modelling and Simulation Parameter

The simulation platform used is CARNOT, a toolbox extension for MATLAB/SIMULINK. UIBK developed a modified version of CARNOT toolbox (called carnotUIBK) with which an object of the building is created in MATLAB reading the information from an Excel file. This version of the CARNOT toolbox gives the possibility to change most relevant parameters (e.g. HVAC system, controls, model of door opening, etc.) easily in MATLAB/Excel.
The flat of the first floor oriented to Northeast was simulated, while the others flats (below, above and adjacent the flat simulated), basement, staircase and ambient are boundary conditions of the flat.
A balanced ERV unit (i.e. $V_{sup} = V_{ext}$) supplies 100 m³·h^{-1} of fresh air to the sleeping room (SL), child room (CH) and living room (LI) (40/20/40 m^3·h^{-1}, respectively) and extracts air from the kitchen (KI) and bathroom (BA) (60/40 m^3·h^{-1}, respectively). Sensible effectiveness (η_T) of 0.77 and latent effectiveness (η_ω) of 0.6 are taken based on measurement results. A secondary air flow rate of 100 m^3·h^{-1} were considered and an additional ambient air of 200 m^3·h^{-1} was used as source of the heat pump in addition to the exhaust air. All the doors of the flat were considered closed, except the doors of kitchen and living room.
Opening of the windows in summer period is considered for each room. Air exchange between two adjacent zones through the opening of the doors was modelled in MATLAB/SIMULINK, based on the equations used in the tool CONTAM Rojas et al. (2015). Additional information regarding the building model and the flat can be found in Calabrese et al. (2018b).

The moisture transport and buffering within the building envelope and the exchange of humidity between the walls and the ambient was taken into account. An annual building and system simulation of the reference flat of the MFH located in Innsbruck (Austria) was performed in CARNOT, Matlab/Simulink in order to investigate the energy performance of the proposed system (i.e. supply air – exhaust air heat pump with recirculation of secondary air) and the thermal comfort and the IAQ in the flat. A set point temperature of 21 °C for the heating system was assumed.

4.3. Performance Maps

The heat pump model is a dynamic model based on a look up table which is parameterized using measurement results. Two different sets of Performance Maps (PMs), derived from laboratory measurements, were implemented in CARNOT. Depending on the compressor speed (revolutions per minute, rpm), the ambient air temperature (T_{amb}) and "Heat mode" (i.e. with condenser or with condenser and desuperehater), total heating power and Coefficient of Performance (COP) of the heat pump are given. Fig. 5 (top) reports the PM in case of supply air heating and Fig. 5 (bottom) in case of supply and secondary air heating. In the letter case, the heating power was equally split between the condenser (50 %) and the desuperheater (50 %).
The ERV model was implemented, using the eta-NTU (eta_ω-NTU_ω) analytical approach, also parameterized using measurement results, see Ochs et al. (2017b).

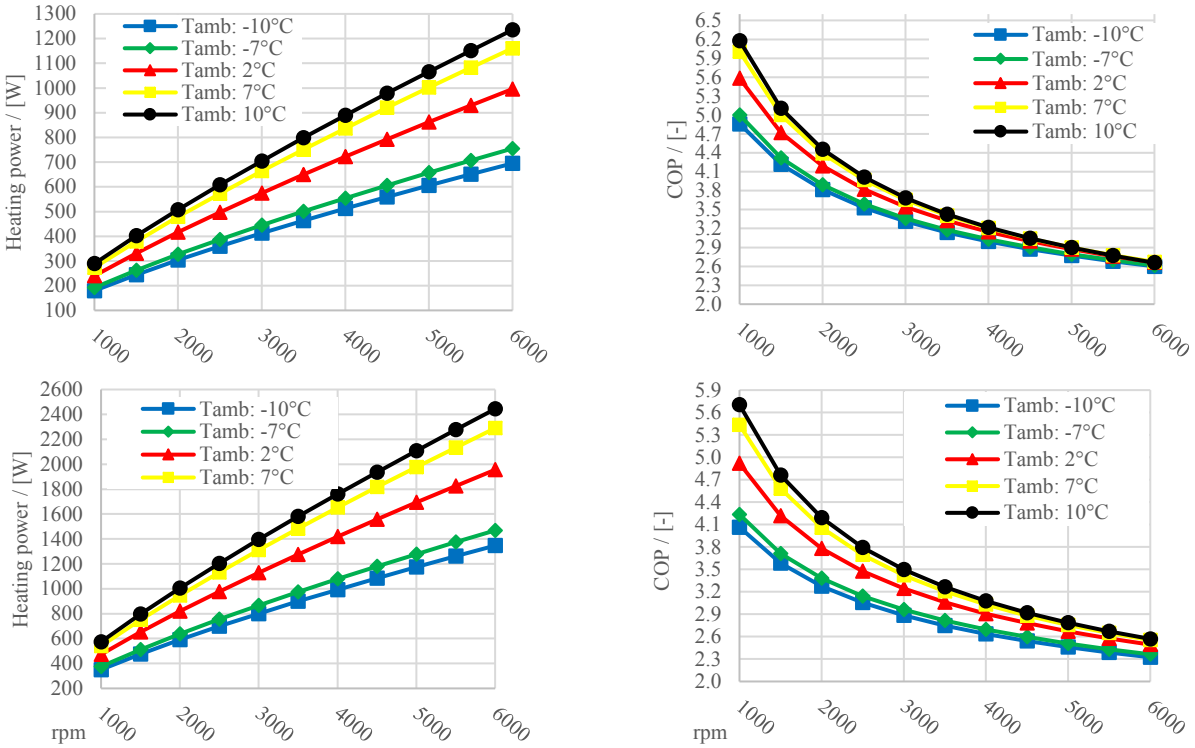

Figure 5: Performance map of the power of the heat pump (left) and the COP (right) depending on the rpm of the compressor and the ambient air temperature – (top) Heating with supply air and (bottom) Heating with supply and secondary air

4.4. KPI

Four Seasonal Performance Factors (SPFs) were defined according to the equations (1)-(4) in order to evaluate the energy performance of the components and of the system and to be able to compare it with a reference heating concept.
The seasonal performance factor of the heat pump, SPF_{HP}, incudes the electricity consumption of the two additional fans for the secondary air (Specific Fan Power (SFP) of 0.093 W·h·m^{-3}) and for the additional ambient air (SFP = 0.0565 W·h·m^{-3}). The electric power consumption of the fans $W_{el,Fans}$ is considered in the definition of SPF_{ERV} and indicates only the electricity consumption of the two fans for supply and extracted airflow rate (SFP = 0.4 W·h·m^{-3}). An additional consumption of 10 W was assumed for standby.

$$SPF_{HP} = \frac{(Q_{Condenser} + Q_{Desup})}{(W_{el,Compresssor} + W_{el,Vsec} + W_{el,Vamb})} \quad \text{Eq. (1)}$$

$$SPF_{sys} = \frac{(Q_{HP} + Q_{Post-heater} + Q_{Radiator})}{(W_{el,HP} + W_{el,Post-heater} + W_{el,Radiator})} \quad \text{Eq. (2)}$$

$$SPF_{ERV} = \frac{(Q_{Pre-heater} + Q_{HX})}{(W_{el,Pre-heater} + W_{el,Fans})} \quad \text{Eq. (3)}$$

$$SPF_{tot} = \frac{(Q_{ERV} + Q_{sys})}{(W_{el,ERV} + W_{el,sys})} \quad \text{Eq. (4)}$$

- $Q_{Condenser}$, Q_{Desup}: thermal energy delivered by the condenser and desuperheater, respectively
- $W_{el,Compresssor}$: electric consumption of the compressor
- $W_{el,Vsec}$: electric consumption of the secondary air fan
- $W_{el,Vamb}$: electric consumption of the fan for the additional ambient air
- $Q_{Post-heater}$, $W_{el,Post-heater}$: thermal and electric consumption of the post-heater, respectively
- $Q_{Radiator}$, $W_{el,Radiator}$ thermal and electricity energy of the electric radiator (bathroom)
- $Q_{Pre-heater}$, $W_{el,Pre-heater}$: thermal and the electric energy of the pre-heater
- Q_{HX}: thermal energy exchanged in the ERV unit during the heating season

4.5. Simulation Results

4.5.1. Thermal comfort and IAQ

The proposed system delivers a high level of IAQ and thermal comfort. The CO_2 concentration in the different rooms is shown in Fig. 6 (left). The IAQ is good in all the rooms. The child room is characterised by the maximum values of CO_2 detected (1025 ppm). Because of the assumption of closed doors in CH and SL and open door in LI and KI (see above), CO_2 concentration is slightly higher in CH and SL and levelled in LI.

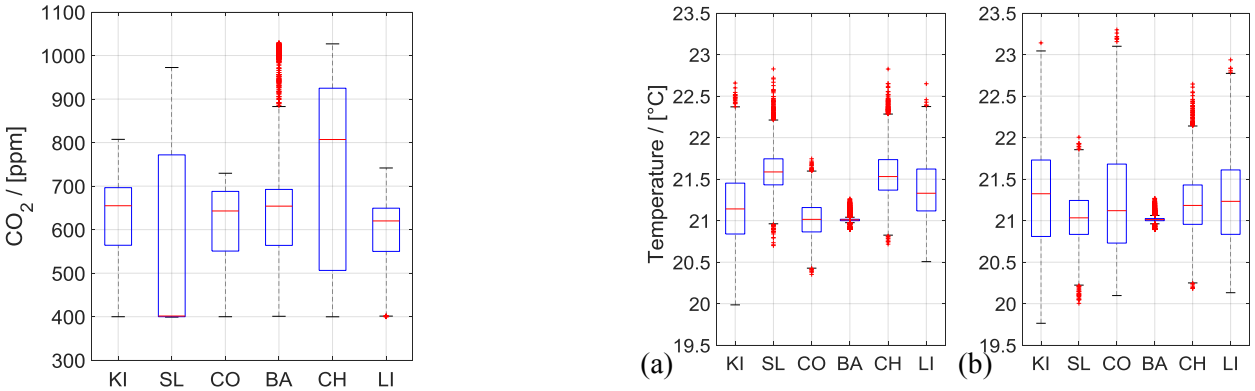

Figure 6: Box plot of (left) CO_2 concentration (hourly average values) for each room of the flat – ambient CO_2 concentration of 400 ppm (right) operative temperature (hourly average) for each room of the flat during the heating season in case of the supply air – exhaust air HP (a) or the supply air – exhaust air HP with secondary air (b)

Fig. 6 (right) shows the comparison between a conventional supply air heating system and the proposed systems with additional recirculation air with regard to the operative temperatures of the zones during the winter time. The well-known problem of overheating of supply air rooms (i.e. LI, CH and SL) in case of supply air heating can be avoided with the new system with recirculation, as an additional degree of freedom in the control is given by the possibility to split the heat flow to the condenser and the desuperheater. In both cases, an additional electric radiator installed in the bathroom is recommended for reasons of comfort. It keeps its temperature constant at 21 °C.

4.5.2. Energy performance

Fig. 7 and Table 1 show the comparison between the investigated system (i.e. supply air – exhaust air HP with secondary air) and the reference configuration without desuperheater in terms of energy performances (SPFs) and energy and electricity demand. Both systems have practically the same energy performances with a SPF_{HP} of 2.4 and a SPF_{tot} of 3.2. Because of the relative high share of the direct heating (i.e. electric radiator installed in the bathroom), SPF_{sys} is significantly lower compared to SPF_{HP}. The slightly higher temperature of the extracted air in case of secondary air system explains the higher SPF_{ERV} compared to the reference system. The energy performances of both systems is comparable, but the new system is able to ensure better thermal comfort in the flat (see Fig. 6). The slight overheating of the supply air rooms (i.e. SL, CH and LI) in case of the reference system explains the higher heating demand (30.5 $kWh \cdot m^{-2} \cdot a^{-1}$)) compared to the system in which secondary air is used (28.3 $kWh \cdot m^{-2} \cdot a^{-1}$) (see Table 1).

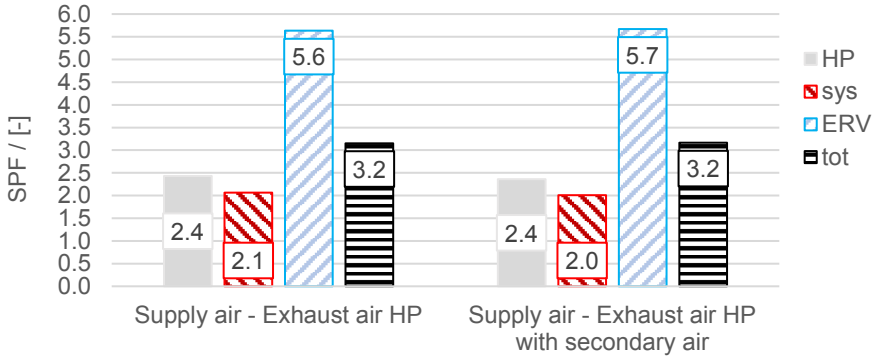

Figure 7: Annual SPFs (based on the equations (1) – (4), see section 4.3) for the proposed system (right) and comparison with the reference heating concept without desuperheater (left)

Table 1. Heating demand (HD), maximum hourly heating load (HL) and electricity demand (ED) for the proposed and the reference system. The additional electric power of the fans (for both systems) and for secondary air (only for system with secondary air) are taken into account

-	HD ($kWh \cdot m^{-2} \cdot a^{-1}$)	HL ($W \cdot m^{-2}$)	ED ($kWh \cdot m^{-2} \cdot a^{-1}$)
Supply air – exhaust air HP	30.5	17.3	14.8
Supply air – exhaust air HP with secondary air	28.3	22.7	14.1

Fig. 8 shows the heating power of the investigated heating system. The heating season lasts 8 months (1 October - 1 June) and 13% of the total heating energy is delivered through direct heating (i.e. heating of BA through electric radiator). Almost 50% of the total electricity consumption of the HVAC system is due to the compressor (see Fig. 8, right hand side), and also a relevant part is due to the ventilation system (32% of total electricity consumption during the heating season). The total electricity demand for the fans is higher as the MVHR works the entire year with a constant supply airflow rate of 100 $m^3 \cdot h^{-1}$).

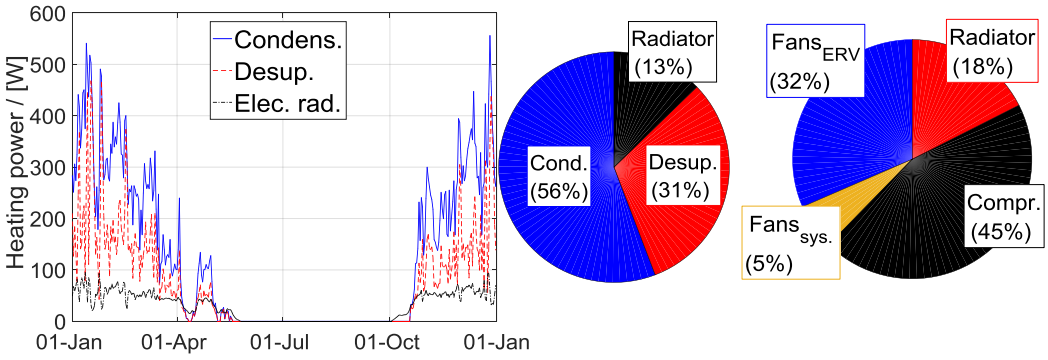

Figure 8: (left) Daily average values of the heating power, (centre) pie chart of the annual heating demand of the flat, and (right) pie chart of the electricity demand of the HVAC system

The heating demand is HD = 2005 kWh·a^{-1} or 28.3 kWh·m^{-2}·a) including energy recovery. The total electricity consumption (during the heating seasons) is 1456.4 kWh·a^{-1}. In Fig. 8, "$Fans_{ERV.}$" indicates the two fans (i.e. supply and extract air) of the ventilation system, while "$Fans_{sys.}$" represents the fans of the heating system (i.e. for secondary air, additional ambient air).

5. CONCLUSIONS

In the framework of the Austrian project SaLüH!, a new heating and ventilation concept based on a façade integrated supply air-exhaust air heat pump with secondary air recirculation was developed, tested in the laboratory and investigated by means of a simulation study in CARNOT, Matlab/Simulink. The proposed system is suggested as a solution for non-disruptive decentral renovation of flats in multi-family houses.

The system is, because of the additional degree of freedom for control by using secondary air recirculation heating able to ensure better thermal comfort compared to the reference supply air heating system in which heating is coupled to the hygienic air flow rate. Good IAQ with a maximum value of CO_2 of 1025 ppm is obtained in both systems.

Comparable energy performances were found for both systems (i.e. with or without desuperheater) with a SPF_{sys} of 2.0 and a SPF_{tot} (including ERV) of 3.2. The system performance could be further improved by reducing the share of direct electric heating (in the bathroom). However, as the system is supposed to be applied in flats with very low heating demand a SPF of 2 is acceptable. It has to be considered that such a system has to be compact and cost-effective and it competes direct electric heating or maybe mini-split heat pumps.

ACKNOWLEDGEMENTS

This work is part of the Austrian research project SaLüH! Renovation of multi-family houses with small apartments, low-cost technical solutions for ventilation, heating & hot water (2015-2018); Förderprogramm Stadt der Zukunft, FFG, Project number: 850085.

NOMENCLATURE

COP	Coefficient of performance (-)	rH	Relative humidity (-)
ED	Electricity demand (kWh)	SPF	Seasonal performance factor
HD	Heating demand (kWh)	T	Temperature (K)
HL	Heating load (W)	W	Work (kWh)
NTU	Number of transfer units (-)	η	effectiveness (-)
P	Power (W)	ω	Humidity ratio (-)
Q	Heat (kWh)		

REFERENCES

Calabrese T., Ochs F., Siegele D., Dermentzis G., 2018. Potential of covering electricity needs of a flat of a MFH with decentral compact heat pumps with PV – Simulation study for different DHW profiles and PV field sizes, in: EUROSUN 2018 10-13 September 2018, Rapperswil, Switzerland, 2018.

Ochs F., Dermentzis G., Siegele D., 2017a. Façade Integrated MVHR and Heat Pump. 12th Conference on Advanced Building Skins 2-3 October 2017, Bern, Switzerland.

Ochs F., Hauer M., Bianchi Janetti M., Siegele D. 2017b. Energy Performance of Membrane Energy Recovery Ventilation in Combination with an Exhaust Air Heat Pump, IBPSA 2017, USA

Rojas G., Spörk-Dür M., Venus D., Greml A., Krissmer L., Pfluger R., 2015. Lüften und Heizen in Passivhäusern in Österreich – Variantenvergleich auf Basis von Behaglichkeit und Nachhaltigkeit, Schriftenreihe 36/2015, Herausgeber bmvit

Manuscript ID: 1403
DOI: 10.18462/iir.icr.2019.1403

Simulation on the performance of gas-fired boiler with flue gas heat recovery utilizing gas engine driven heat pump

Wei CHEN[a,b], Sheng SHANG[a], Wenxing SHI[a], Baolong WANG[a], Yang CAO[b], Xianting LI[a]

[a] Department of Building Science, Tsinghua University, Beijing, 100084, P.R. China
[b] Institute of Building Environment and Energy, China Academy of Building Research, Beijing 100013, P.R. China

ABSTRACT

The gas-fired boiler for heating is an important way for space heating in China due to low pollutant emission. Meanwhile, because the flue gas temperature is much higher than the ambient, there is a great amount of waste heat in the flue gas. To effectively recover waste heat, a novel heat recovery system that integrated gas engine driven heat pump and condensation heat exchanger is proposed. A mathematical model is established to analyse the system performance. The results demonstrate that the ambient temperature has little impact on the heat recovery performance. The return water temperature is a key factor affecting the heat recovery performance. The efficiency will increase while the temperature of return hot water decreases. When the ambient temperature is 0°C, the system heat recovery efficiency can reach 14.3%, which is 5.3% higher than the condensing heat recovery of gas-fired boiler

Keywords: Gas-Fired Boiler, Deep Heat Recovery, Gas Engine Heat Pump, Flue Gas, Energy Saving.

1. INTRODUCTION

With the rapid development of urbanization, the heating consumption is larger and larger recent years in the north of China. It accounts for more than 24% of total building energy consumption (Building Energy Conservation Research Center. 2017). Though the coal fired boiler is the main way for space heating nowadays, its efficiency of energy utilization is low and pollutant emission is heavy (Jiang, 2000). Compared with the coal boiler, the efficiency of the gas fired boiler is much higher and the pollutant emission is less. Therefore, the gas fired boiler become an important way for space heating gradually. However, the exhausted gas temperature of the gas fired boiler is quite higher than ambient temperature. There is a great amount of waste heat in the flue gas, which contains more than 11% of latent heat (Xu et al., 2009). Recovering and reusing waste heat in the flue gas is an important way to improve the system efficiency, which draws the attention of a large number of researchers.

The simplest recovery system is sensible heat recovery. In the system, heat is recovered to preheat the supply air, and boiler efficiency can be promoted by 3-4% (Suntivarakorn and Treedet, 2016). But the latent heat cannot be recovered in sensible heat recovery system (Wei, 2017). The condensing heat recovery (CHR) was then developed to recover the latent heat from flue gas. Weber et al. (2002) analysed the feasibility of condensing heat recovery for recovering waste heat. Both Wang et al (2010) and Pan et al. (2010) investigated the performance of condensing heat recovery (CHR). Results indicated that a part of the latent heat can be recovered and the boiler efficiency can be improved by 8%. However, the exhausted gas temperature with condensing heat recovery is still high because of the limitation of the return water temperature. Therefore, total heat recovery was developed to recover heat from the flue gas in the low temperature range. Shang et al (2017) and Chen et al. (2017) proposed a deep total heat recovery system for gas fired boiler. The results show that the boiler efficiency can be enhanced by 13.4%, and exhausted gas temperature can be lower than 30 °C. But the area of heat exchanger is requested to be very large if exhausted flue gas temperature is expected to be further reduced. This means this kind of system will take up a lot of space.

In this paper, a novel heat recovery system (NHR) that integrated gas engine driven heat pump (GEHP) and condensation heat exchanger is proposed. A mathematical model is established to

analyse the system performance. The effect of main factors on the heat recovery efficiency of NH R system has been assessed. And the comparison between CHR and NHR is performed.

2. PRINCIPLE OF THE SYSTEM

Figure 1 presents the schematic of NHR system. The return water of heat supply network goes through the condenser of GEHP, the cylinder liner of the gas engine and the condensing heat exchanger successively, then returns to the boiler. The flue gas from the boiler and gas engine goes through the condensing heat exchanger and wall type heat exchanger to heat the return water and the circulation water, respectively, then exhausts to the ambient finally. The circulation water circulates among wall type heat exchanger, evaporator of GEHP and spray heat exchanger. The supply air is heated and humidified in the spray heat exchanger, then enters into the boiler.
A key factor of condensing heat exchanger is the dew point of flue gas. If the dew point of the flue gas is higher, the amount of heat transfer will be larger in the condensing heat exchanger due to larger latent heat recovered. Humidifying the supply air is beneficial to increase the dew point of the flue gas. On the other hand, GEHP can recover more heat from the flue gas by evaporator, to heat the return water, even the temperature of flue gas is low. Therefore, the temperature of flue gas will decrease further. That means more waste heat from the flue gas can be recovered and system efficiency will be promoted a lot.

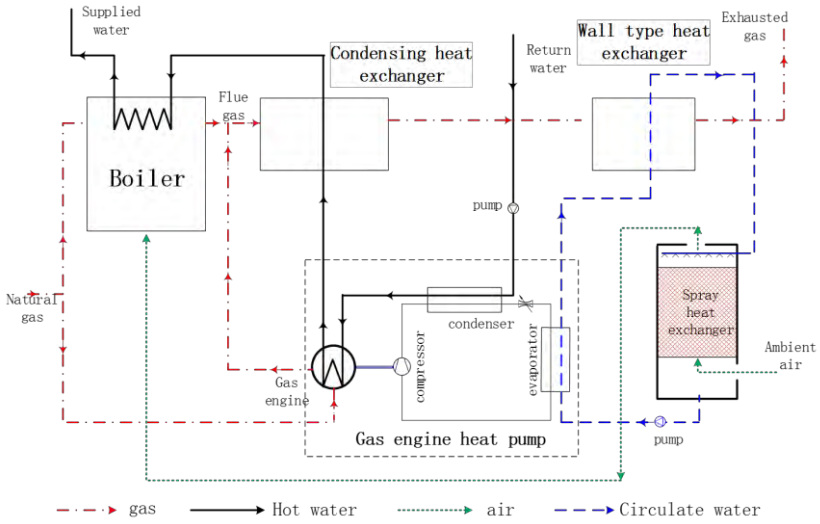

Figure 1: Schematic of NHR system

3. MATHEMATICAL MODEL OF THE SYSTEM

The mathematical model of NHR system contains three parts of the model: model of boiler, model of heat exchanger and model of GEHP.

3.1. Model of Boiler

The model of boiler is used to calculate the energy consumption of the natural gas. The return water of the heat supply network is 40 ºC. The flue gas temperature at the boiler outlet is 150 ºC (Bai, 2012). The heat capacity of the boiler is 650kW, and the primary energy efficiency for gas fired boiler is 0.9 (Yu, 2010). The primary energy consumption, i.e., natural gas consumption, is calculated by Eq. (1).

$$PE_{\text{boiler}} = \frac{Q_b}{\eta_b} \qquad \text{Eq. (1)}$$

Based on the chemical reaction of natural gas combustion, the mass flow rate of supply air and flue gas can be calculated. In order to grantee the security of the boiler, the excess air coefficient is taken as 1.2 (Khodabandeh et al., 2016). Moreover, the enthalpy of the flue gas can be calculated by Eq. (2).

$$i_g = \left(Cp_g + 1.84 d_g\right) \cdot T_g + r \cdot d_g \quad \text{Eq. (2)}$$

3.2. Model of Heat Exchangers

The model of heat and mass transfer model is used to calculate of performance of the condensing heat exchanger, wall type heat exchanger and spray heat exchanger. There are two types of heat exchanger: wall type heat exchanger (including condensing heat exchanger) and spray heat exchanger. A lumped parameter method is used in these two models (Kreith, 2012).
In the wall type heat exchanger, the heat transfer process is governed by conservation of energy and heat transfer equations which are shown in Eqs. (3) and (4).

$$m_g \cdot \left(i_{g,in} - i_{g,out}\right) = m_w \cdot Cp_w \cdot \left(T_{w,out} - T_{w,in}\right) \quad \text{Eq. (3)}$$

$$Q = h \cdot A \cdot \Delta T_m \quad \text{Eq. (4)}$$

In the spray heat exchanger, the heat transfer process is governed by conservation of energy and heat transfer equations. The equations are shown in Eq. (5-6).

$$m_a \cdot \left(i_{a,out} - i_{a,in}\right) = m_w \cdot Cp_w \cdot \left(T_{w,in} - T_{w,out}\right) \quad \text{Eq. (5)}$$

$$Q = h_m \cdot A \cdot \Delta i_m \quad \text{Eq. (6)}$$

The mass transfer process is governed by conservation of mass and mass transfer equation. The equations are shown in Eqs. (7) and (8).

$$w_a = m_a \cdot \left(d_{a,\text{out}} - d_{a,in}\right) \quad \text{Eq. (7)}$$

$$w_a = h_m \cdot A \cdot \Delta d_m \quad \text{Eq. (8)}$$

3.3. Model of GEHP

The model of GEHP is used to calculate the energy consumption of the gas engine and the outlet water temperature of the cylinder liner and evaporator. In the GEHP, the evaporator and condenser are a kind of wall type heat exchanger. The lumped parameter method is also used in this model. The calculation equations of evaporator and condenser are shown in Eqs. (9) and (10).

$$m_{ref} \cdot \left(i_{ref,in} - i_{ref,out}\right) = m_w \cdot Cp_w \cdot \left(T_{w,out} - T_{w,in}\right) \quad \text{Eq. (9)}$$

$$Q = h \cdot A \cdot \Delta T_m \quad \text{Eq. (10)}$$

The flue gas from gas engine is used to heat the water from condenser in the cylinder. The governed equations of heat exchanger process in cylinder are shown in Eqs. (11) and (12).

$$m_g \cdot Cp_g \cdot \left(T_{g,in} - T_{g,out}\right) = m_w \cdot Cp_w \cdot \left(T_{w,out} - T_{w,in}\right) \quad \text{Eq. (11)}$$

$$Q = h \cdot A \cdot \Delta T_m \quad \text{Eq. (12)}$$

The transmission efficiency axis which links the compressor with the gas engine is taken as 0.9. The efficiency of the gas engine and the primary energy consumption of the gas engine are calculated by Eq. (13) and Eq. (14) respectively. Eq. (13) is built on the product performance testing.

$$\eta_{eng} = 0.71 \cdot \left(0.2387 \cdot \alpha_{eng}^3 - 0.5307 \cdot \alpha_{eng}^2 + 0.3968 \cdot \alpha_{eng} + 0.2275\right) \quad \text{Eq. (13)}$$

$$E_{eng} = W_{com} / \eta_{eng} \cdot \eta_{tran} \quad \text{Eq. (14)}$$

3.4. System Performance Indexes

In order to evaluate the performance of the system, the heat recovery efficiency of NHR system is defined by Eq. (15).

$$\eta_{NHR} = Q_{rec} \Big/ \left(E_{boiler} + E_{eng} \right) \quad \text{Eq. (15)}$$

The total amount of heat recovered includes the amount of heat in evaporator, condensing heat exchanger and cylinder liner. Therefore, total amount of heat recovery is calculated by Eq. (16).

$$Q_{rec} = Q_{eva} + Q_{cyl} + Q_{chx} \quad \text{Eq. (16)}$$

The main and key component of CHR for the gas fired boiler is condensing heat exchanger. The calculation model of the condensing heat exchanger is the same as that described in section 3.2. The heat recovery efficiency of CHR is calculated by Eq. (17).

$$\eta_{CHR} = Q_{rec,CHR} \Big/ E_{boiler} \quad \text{Eq. (17)}$$

The simulation procedure is shown in Fig. 2. What we need input is ambient temperature, return water temperature and flue gas temperature from boiler. After that, the inlet water temperature of evaporator and humidity of spray heat exchanger outlet need to be assumed. Then solve the model of GEHP, condensing heat exchanger, wall type heat exchanger and spray heat exchanger. After all the processes above, the maximum error will be calculated. If the maximum error is accepted, then simulation is done. If not, the inlet water temperature of evaporator and humidity of spray heat exchanger outlet need to be adjusted to continue the calculation.

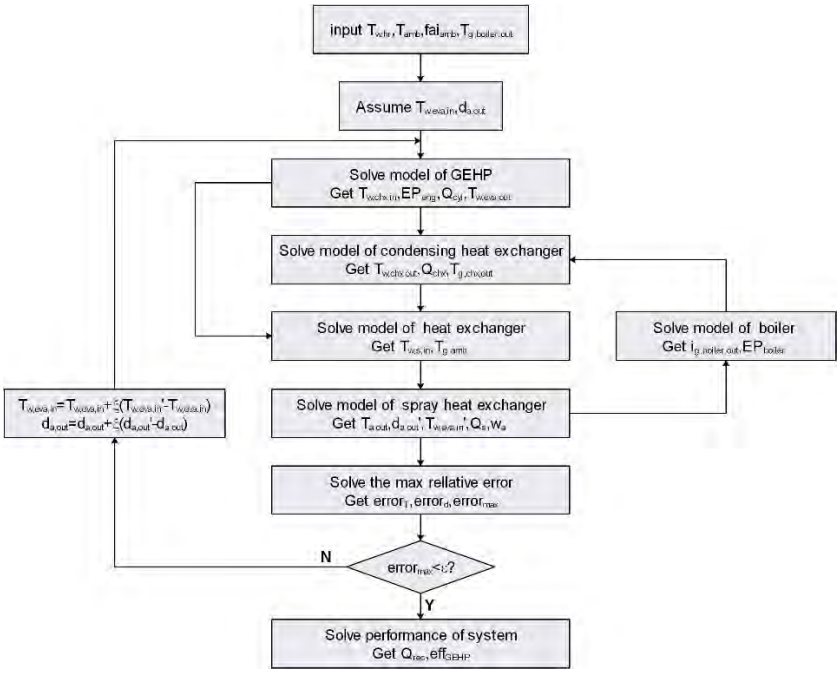

Figure 2: Simulation flowchart of NHR model

4. RESULTS AND DICUSSION

4.1. Effect of Ambient Temperature on the System Performance

Fig. 3(a) shows the relationships of ambient temperature with heat exchanged in heat exchangers. Fig. 3(b) shows the relationships of ambient temperature with heat recovery efficiency and exhausted gas temperature. The results reveal that when ambient temperature increase from -10 °C to10 °C, the amount of heat recovered increase from 102.6kW to 106.2kW. The increment is expected to be very slight. The main reason for this result is the number of moisture added into supply air is very small because of low temperature. In this case, the enthalpy of flue gas from the boiler increases a little. On the other hand, temperature of the return water is the same. The heat transfer effect of condensing heat exchanger is improved a little. The heat recovery efficiency is larger when the ambient temperature is higher, though the exhausted gas temperature is higher. Because higher ambient temperature means larger enhancement of flue gas enthalpy. When ambient temperature

increase from -10 ºC to10 ºC, the efficiency of heat recovered increase from 14.1% to 14.6%. Therefore, the ambient temperature has negligible impact on the performance of NHR.

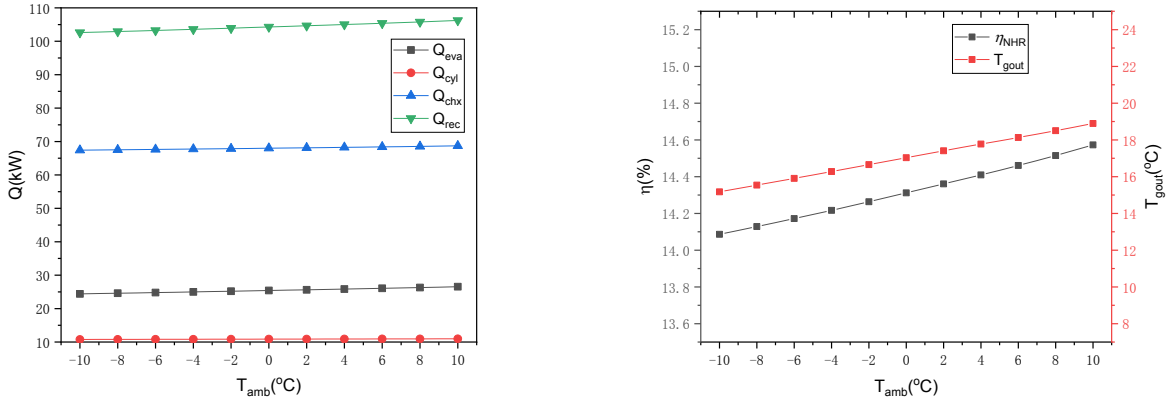

(a) (b)

Figure 3: Individual relationships of ambient temperature with heat exchanged in heat exchangers, heat recovery efficiency and exhausted gas temperature

When the ambient temperature is 0 ºC and the relative humidity is 40%, the total heat recovered is 104.22kW. In this case, and the heat recovery efficiency is 14.3%. Because considerable amount of heat from flue gas has been recovered, the exhausted gas temperature decreases to 17.03 ºC, which is much lower than any other heat recovery technologies.

4.2. Effect of Return Water Temperature on the System Performance

Fig. 4 shows the effects of return water temperature on heat exchanged in heat exchangers, heat recovery efficiency and exhausted gas temperature. The results indicate that when the return water temperature increase from 35 ºC to 45 ºC, the amount of heat recovered decrease from 108.1kW to 100.1kW. The change in the amount of heat recovered is obvious. The results show that the main change is the amount of heat in condensing heat exchanger. This is because the ambient temperature and relative humidity are the same, the enthalpy of flue gas from the boiler is almost the same, even lower when the return water temperature is lower. The return water temperature becomes the key factor of heat recovery efficiency. Lower return water means larger mean temperature difference in heat transfer of condensing heat exchanger. The heat recovery efficiency will be high to 14.9% when the return water temperature is 35 ºC. Therefore, the exhausted gas temperature can be lower than 14 ºC.

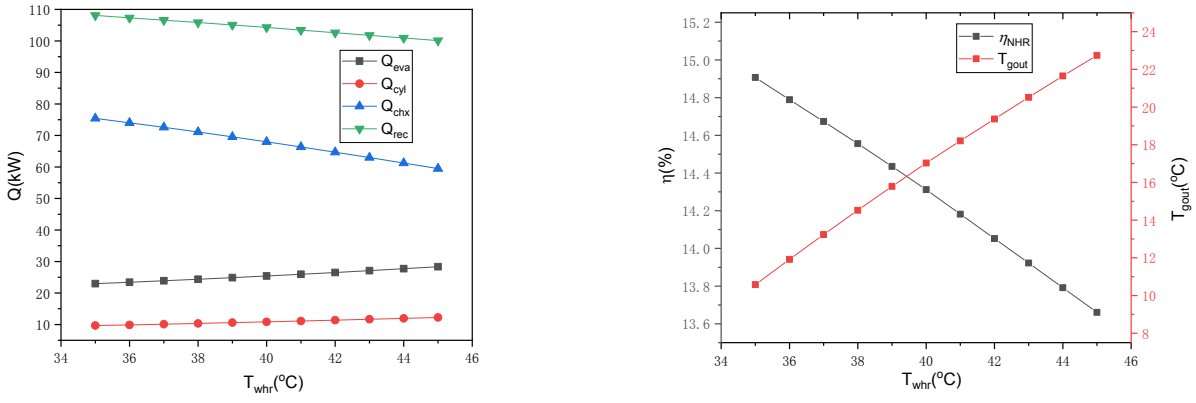

(a) (b)

Figure 4: Individual relationships of return water temperature with heat exchanged in heat exchangers, heat recovery efficiency and exhausted gas temperature

4.3. Comparison of NHR and CHR System

The difference of the CHR system from NHR system is that CHR system is without spray heat exchanger and GEHP. The return water goes through the condensing heat exchanger directly.
Fig. 5 shows the individual relationships of T_{amb} with heat recovery efficiency, T_{gout} and T_{dp} of CHR and NHR system. The dew point temperature is a function of humidity and dry bulb temperature.

According to the saturated vapor pressure, the dew point temperature can be estimated. The results reveal that the heat recovery efficiency of NHR is much high than that of CHR. When the ambient temperature is 0 ºC, the heat recovery efficiency can be promoted by 5.3%. What is more, the exhausted gas temperature of NHR is much lower than that of CHR. When the ambient temperature is 0 ºC, the exhausted gas temperature of CHR is 42.55 ºC, but 17.03 ºC in NHR. That means NHR recovers more waste heat from flue gas. On the other hand, the increased humidity of flue gas results in the increase of dew point temperature of flue gas because of the spray heat exchanger. Compared with CHR, largest increment of the dew point temperature of flue gas in NHR is 2.57 ºC. That means flue gas contains more latent heat, and its enthalpy is much high. Therefore, more heat can be recovered in the condensing heat exchanger in NHR.

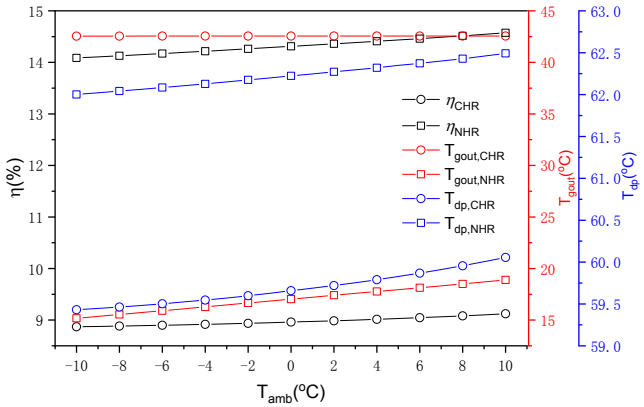

Figure 5: Individual relationships of ambient temperature with heat recovery efficiency, exhausted gas temperature and dew point temperature of CHR and NHR system

5. CONCLUSIONS

In this paper, a novel heat recovery system that integrated gas engine driven heat pump and condensation heat exchanger is proposed. A mathematical model is established to analyse the system performance. The main conclusions can be drawn as followed:

1. The ambient temperature has negligible impact on the performance of NHR. When ambient temperature increases from -10 ºC to10 ºC, the heat recovery efficiency increases from 14.1% to 14.6%.
2. The return water temperature is the key factor of the performance of NHR. The heat recovery efficiency will be high to 14.9% when the return water temperature is 35 ºC.
3. The heat recovery efficiency of NHR is much high than that of CHR. When the ambient temperature is 0 ºC, the heat recovery efficiency can be promoted by 5.3%.

ACKNOWLEDGEMENTS

This research is supported by the National Natural Science Foundation of China (Grant Nos. 51638010 and 51578306) and the Innovative Research Group of the National Natural Science Foundation of China (Grant No. 51521005).

NOMENCLATURE

A	area, m^2
Cp	specific heat at constant pressure, $kJ \times kg^{-1} \times K^{-1}$
d	humidity, $kg \times kg^{-1}$
h	heat transfer coefficient, $kW \times m^{-2} \times ºC^{-1}$
h_m	mass transfer coefficient, $kg \times m^{-2}$
i	enthalpy, $kJ \times kg^{-1}$
m	mass flow rate, $kg \times s^{-1}$
E	primary energy consumption, kW
Q	heat capacity/ heat exchanged, kW
T	temperature, ºC

Subscriptions

a	air
boiler	boiler
chx	condensing heat exchanger
com	compressor
cyl	cylinder liner
eng	gas engine
eva	evaporator
g	flue gas
in	inlet

w	mass transfer, kg×s^{-1}	*out*	outlet
W	power demand, kW	*rec*	heat recovery
α	part load rate of gas engine	*ref*	refrigerant
η	efficiency	*tran*	transmission shaft
Δd_m	logarithmic mean humidity difference, kg×kg^{-1}	*w*	water
Δi_m	logarithmic mean enthalpy difference, kJ×kg^{-1}		
ΔT_m	logarithmic mean temperature difference, °C		

REFERENCES

Bai C.L., Zhang D.L., 2012. Discussion on the gas-fired boiler energy saver -flue gas heat recovery technology. Appl Energy Technol (7):27-28.

Building Energy Conservation Research Center. 2017. 2017 annual report on China building energy efficiency. Beijing: China Architecture & Building Press.

Chen W, Shi W, Wang B, et al., 2017. A deep heat recovery device between flue gas and supply air of gas-fired boiler by using non-contact total heat exchanger. Energy Procedia 105: 4976-4982.

Jiang Y., 2000. Heating schemes analysis for medium and large cities in the North China. Hv & Ac 30(4):30-32.

Khodabandeh E, Pourramezan M, Pakravan MH, 2016. Effects of excess air and preheating on the flow pattern and efficiency of the radiative section of a fired heater. Appl Therm Eng 105:537–548.

Kreith F, Manglik RM, Bohn MS., 2012. Principles of heat transfer. Cengage learning.

Pan Z, Niu J, Lu CP, et al., 2010. Study on thermal efficiency of gas-fired vacuum hot water boiler with installing flue gas condensing waste-heat exchanger. In:Bioinformatics and biomedical engineering (iCBBE), 2010 4th international conference on. IEEE, 2010:1–4.

Suntivarakorn R, Treedet W., 2016. Improvement of boiler's efficiency using heat recovery and automatic combustion control system. Energy Procedia 100:193–7.

Shang S., Li X., Chen W., et al., 2017. A total heat recovery system between the flue gas and oxidizing air of a gas-fired boiler using a non-contact total heat exchanger. Appl. Energy, 207:613-623.

Wei M, Zhao X, Fu L, et al., 2017. Performance study and application of new coal-fired boiler flue gas heat recovery system. Appl Energy 188:121–129

Wang S. L., Wu Y. Y., Pan S. Y., et al., 2010. Impact of the Anticorrosion Films on the Condensing Heat Transfer of Flue Gas in Fin-Tube Heat Exchangers// International Heat Transfer Conference. 153-159.

Weber C, Gebhardt B, Fahl U., 2002. Market transformation for energy efficient technologies – success factors and empirical evidence for gas condensing boilers. Energy 27(3):287–315.

Xu J.F., Wang S.L., Pan S.Y., et al., 2009. Discussion on engineering application schemes of heat recovery technology of natural gas boilers. Hv & Ac 39(11):128-132

Yu CL., 2010. Discussions on different distract heating sources. Energy Conserv Technol 1:012.

Manuscript ID: 1436
DOI: 10.18462/iir.icr.2019.1436

Performance study of air source heat pump with multiple parallel outdoor units defrosting alternatively

NIU Jianhui [a,b], XU Shuxue [a], MA Guoyuan [a*], FAN Xiusong[a], LIU Shuailing[a]

[a] College of Environmental and Energy Engineering, Beijing University of Technology
Beijing,100124, China, zjknjh@163.com

[b] College of Energy and Environmental Engineering, Hebei University of Architecture
Zhangjiakou 075000, China

ABSTRACT

In order to solve the problem of reverse-cycle defrosting of large and medium air source heat pump, a new type of air source heat pump cycle with multiple parallel outdoor machines defrosting alternatively was proposed. Through switching valves to realize an outdoor machine defrosting, the rest of the outdoor machines are in the state of normal evaporative heat absorption at the same time. In the case of non-stopping heating, defrosting can be realized while recovering frost thawing cooling capacity. A test platform research system was built in artificial environment room. The law of the variation of the compressor suction, exhaust pressure and the system thermal performance in the condition of frost free, frosting and defrosting were discussed.

1. INTRODUCTION

A vapor compression air source heat pump absorbs heat from low temperature environment and transfers it to heat, so as to achieve the purpose of space heating in winter. It can both help to achieve energy saving and reduce air pollution emissions. For this reason, especially in recent decades, the application of air source heat pumps (ASHPs) is more and more extensive in the world (Hu, W.J. et al, 2011). In the past five years, in order to reduce or completely eliminate haze, with the vigorous promotion of the government, “coal to electricity” projects, especially in “Jing Jin Ji” area, have been implemented in rural areas. In winter, the original small coal-fired boilers has been replaced by air source heat pumps (ASHPs). But when ASHPs operate in winter, especially in high humidity and cold area, when the evaporator surface temperature is below 0°C, frost may be formed on the tube surface of its outdoor coil, which degrades performance significantly and even lead the ASHP unit to shut down. Consequently, defrosting is required to ensure the efficient operation of the system. Much research has been done on defrosting of air source heat pump at home and abroad (Melo et al, 2013; Li et al, 2014; Park et al, 2007; Ma et al, 2004; Huang et al, 2001). A number of studies experimentally investigated the defrosting methods and its effects (Kwak et al, 2010; Liu et al, 2018; Song et al, 2017; Ji et al, 2005;). The methods mainly include warm water spraying defrosting (Abdel-Wahed et al, 1983), electric heating defrosting (Kim et al, 2015), compressor shut down defrosting (Ameen et al, 1993), hot gas bypass defrosting (Choi et al, 2011) and reverse-cycle hot gas defrosting (Byun et al, 2006; Yao, 2004), etc. However, each of these existing defrosting methods has its own limitations and problems. For example, when air source heat pump defrosts in reverse cycle, sudden reversal of four-way reversing valve will not only cause sudden change of suction and exhaust pressure, but also cause mechanical loss of compressor (Li et al., 2014). For electric heating defrosting, it will consume too much electricity. Traditional defrosting methods either increase energy consumption or affect normal operation of heating. The cycle patterns that effectively avoided the two shortcomings were not proposed or studied thoroughly. The cold energy of the frost layer itself is not effectively recovered. In particular, it can be recycled into the heat pump itself to increase the energy efficiency of the heat pump.

In this study, a novel heat pump system with multiple parallel outdoor units defrosting alternatively

(HPMOD) was proposed. Through switching the valves, an outdoor unit defrosting can be realized, and at the same time the rest of the outdoor units are in normal evaporation and heat absorption. Without stopping heating, defrosting can be realized and the cold energy during defrosting process can be recovered to improve the operation efficiency and heating effect of the whole air source heat pump. An experimental apparatus of this novel air-source heat pump system was developed. A tested room with artificial load was constructed and the defrosting characteristics of the system under different working conditions had been experimentally investigated. Variations of system heating performance under the condition of different indoor air temperature and outdoor air temperature were obtained. The characteristics of defrosting under different working conditions were obtained.

2. HPMOD SYSTEM

In refrigeration and heat pump system, if the temperature of refrigerant liquid is lower than the saturation temperature under the same pressure, it is called sub-cooling. In the experiment, the high temperature liquid refrigerant from the condenser first enters a frosted evaporator. The frost layer on the evaporator fins is removed by sub-cooling and exothermic of the high temperature liquid refrigerant in the evaporator, which is called sub-cooling defrosting (SCD). After defrosting, the sub-cooled refrigerant is throttled and depressurized by expansion valve and then enters into other evaporators for normal evaporation and heat absorption. In this study, the new system named HPMOD system was shown in Fig.1. The system consists of compressor, indoor heat exchanger, throttle mechanism, outdoor heat exchanger, oil separator, liquid storage, gas-liquid separator and other accessories. Unlike ordinary units, outdoor units are composed of several evaporators in parallel. Through switching the solenoid valves, one of them can realize sub-cooling defrosting (SCD) and the rest ones evaporate and absorb heat normally at the same time. Thus, the functions of multiple outdoor units for defrosting without stopping heating can be realized. The main road liquid refrigerant is further sub-cooled which can increase the cooling capacity of the system. The superheat of the compressor is reduced.

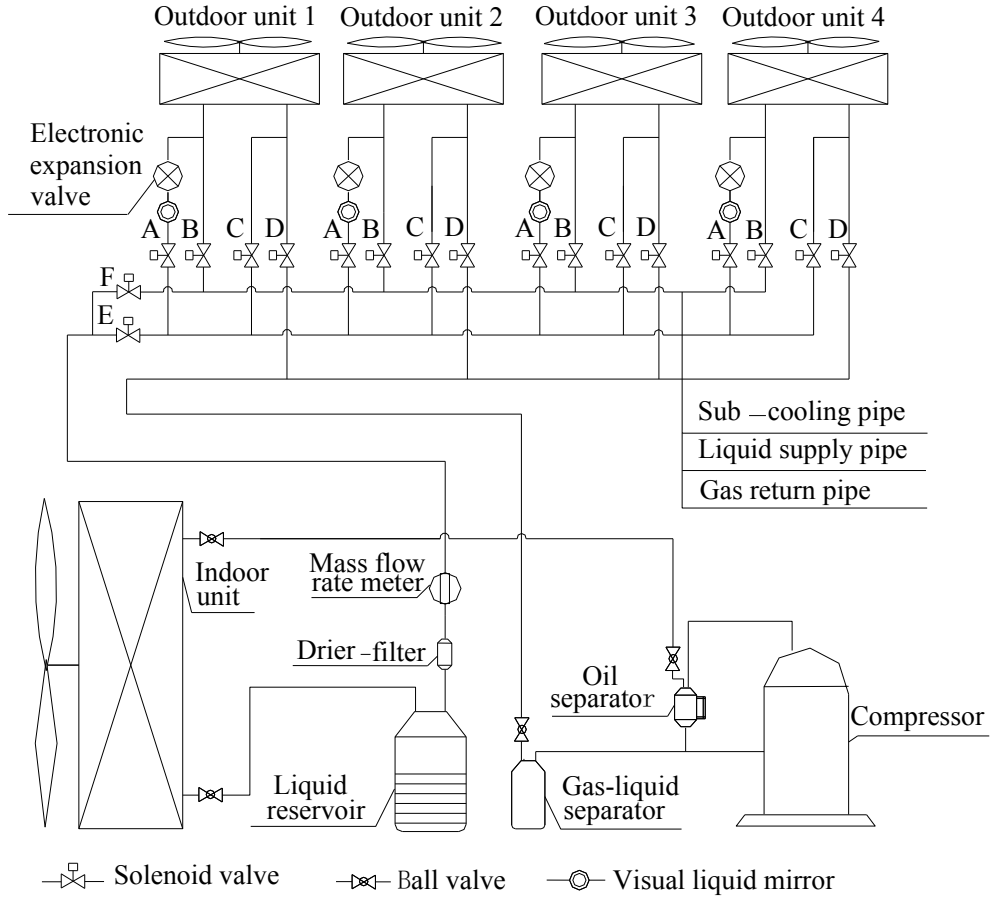

Figure 1: HPMOD system

The system has two heating operation modes; the specific working modes are as follows:
Mode 1: Common heating mode: all of the outdoor units are in normal evaporation and produce heating. The solenoid valve E on the liquid supply pipe and the solenoid valves A and D on the branch pipe of each outdoor unit are opened to realize the evaporation and heating of the liquid refrigerant in outdoor units after throttling.
Mode 2: Sub-cooling defrosting mode: one outdoor unit is in sub-cooling defrosting (SCD) and the others are in normal evaporation and heating. Close the solenoid valve E on the liquid supply pipe and open the solenoid valve F on the sub-cooling pipe. The solenoid valves B and C of the outdoor unit are opened; the refrigerant liquid is sub-cooled to remove the frost on the fins of the outdoor unit. At this time, the fan of the outdoor unit is stopped running. The two solenoid valves A and D of other outdoor units are opened for normal evaporation and produce heating. After throttled, the super-cooled liquid achieves heat absorption by normal evaporation, and the SCD units rotate alternately.

3. EXPERIMENTAL APPARATUS AND PROCEDURE

In order to further study the performance of the novel air source heat pump in frosting and defrosting process. An experimental device was built based on a Danfoss scroll compressor with rated input power of 4.13 kW. The outdoor unit was composed of 4 finned-tube evaporators in parallel. Each of them was made up of 4 rows and 4 loops of copper tubes and thin aluminum fins, and its outline dimension was 500X250X150mm in height, width and thickness, respectively. The indoor unit was a finned-tube air-cooled condenser. Which was made up of 4 rows and 12 loops of copper tubes and thin aluminum fins and its outline dimension was 800X1200X350mm in height, width and thickness, respectively. The model of CAREL E2V09BSF00 were adopted as electronic expansion valve. In addition, the device also consisted of an oil separator, a liquid storage, a gas-liquid separator and other accessories. R134a was used as refrigerant. The experimental ASHP unit was installed in an existing environmental chamber having a simulated indoor heated space and a simulated outdoor environment. The indoor and outdoor environment was controlled by the DX A/C system and two load generating units. The outdoor units were installed in the outdoor space, where the frosting/defrosting cycle operations were carried out. The schematic diagram for the plant was shown in Fig. 2.
The heating capacity is the enthalpy difference multiplied by the mass flow rate of the liquid refrigerant through them. The temperatures were measured by Pt100 and the pressures were measured by the model of Huba with accuracy of ±0.5% of full scale, the refrigerant mass flow rate was measured by a flow meter with the model of LZB-50 and its accuracy is ±0.2% of full scale. The compressor power was obtained by means of a high precision electrical measurement instrument with the model of DZFC-1 and its full scale is 10 kW. The date was obtained by HP34972A with the accuracy±0.2% of full scale. The enthalpy can be obtained from REFPROP 9.1.

Heating capacity Q:

$$Q = q\left(h_3 - h_4\right) \qquad \text{Eq. (1)}$$

Where, q is mass flow rate of liquid refrigerant throw condenser (kg s^{-1}), h_3 is the enthalpy in state point 3 (kJ kg^{-1}), h_4 is the enthalpy in state point 4 (kJ kg^{-1}).

Heating COP:

$$COP = \frac{Q}{P} \qquad \text{Eq. (2)}$$

Where, Q is the heat capacity (kW), and P is power input (kW).

The operating conditions were as follows: outdoor air temperature of −20~0℃ and air relative humidity of 0%~100%. For the fan speed of the condenser was controlled by frequency converter, the condensation temperature can be controlled of 40~48℃, vapor suction superheat can be controlled on 10 ℃ by electronic expansion valve.

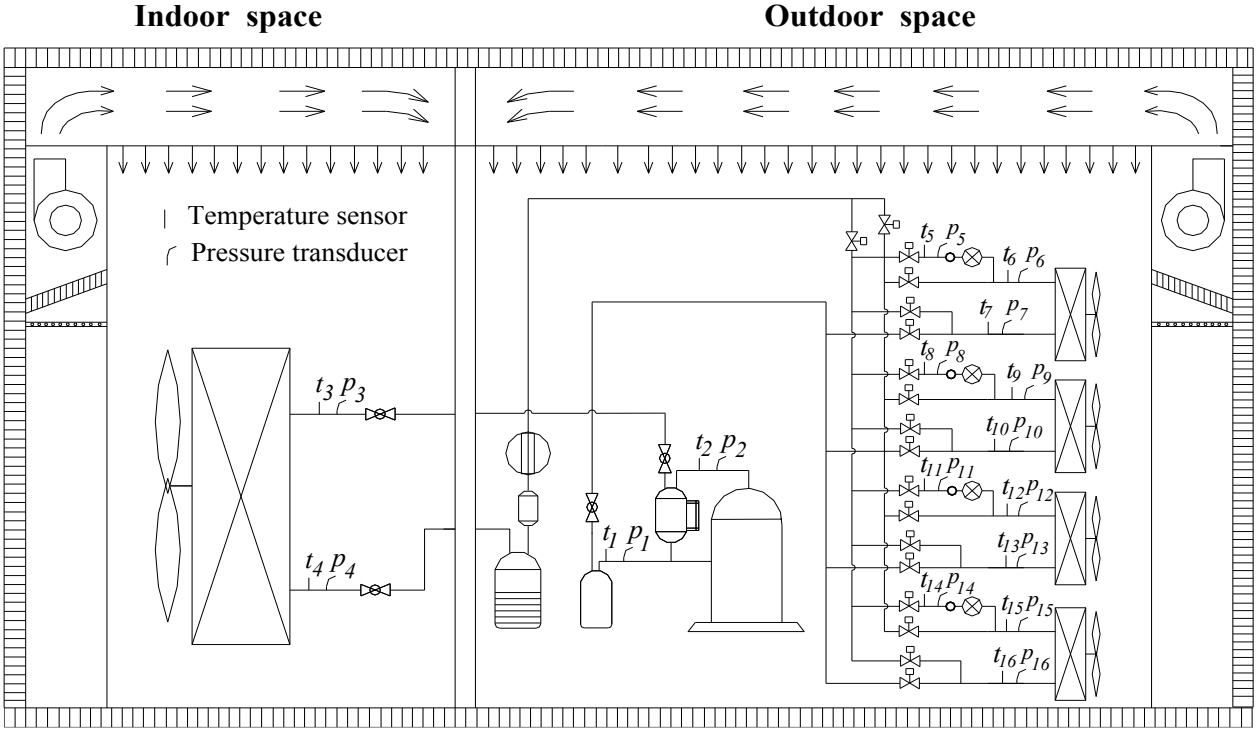

Figure 2: Schematic diagram of the experimental HPMOD system installed in an environmental chamber

When one outdoor evaporator was in sub-cooling defrosting process, its outlet sub-cooling liquid temperature would increase gradually with the defrosting process. When the evaporator outlet temperature reached to 15°C, the defrosting process was considered to be completed and another outdoor evaporator started to be defrosted in turn.

4. RESULTS AND DISCUSSION

4.1 Parameter Analysis under Specific Working Conditions

Figs. 3-5 showed the frosting and defrosting data of the HPMOD system when the evaporation temperature was -5℃, condensation temperature was 40℃ and the air relative humidity was 80%. From Fig. 3, it can be seen that when the solenoid valves were switched on or turned off to defrost, the suction pressure of the compressor dropped sharply at first then went up directly and then stabilized. There were two reasons about it. The first one was that the number of the evaporator changes from 4 to 3 immediately, the evaporation area decreased by about 1/4, which resulted in a significant decrease in the suction pressure of the compressor; the second reason was that the refrigerant liquid after condensation was not diverted to flow into evaporators to evaporate and absorb heat but was changed to flow into an outdoor evaporator wholly for sub-cooling defrosting, this resulted in a short-term insufficient suction of the compressor and a sharp drop in suction pressure. After a short time of buffering, the suction pressure went up sharply when the refrigerant liquid flowed out of the sub-cooling defrosting outdoor evaporator into the normal evaporating outdoor heat exchangers. The exhaust pressure had remained stable at about 1 MPa and fluctuated little.

From Fig. 4, it can be seen that when each outdoor unit rotated to defrost, the compressor's vapor

suction temperature and discharge temperature would decrease correspondingly. This was because that when an outdoor heat exchanger participated into sub-cooling defrosting, the main circuit liquid with a larger sub-cooling degree entered into other evaporators through electronic expansion valves, the superheat of the compressor vapor suction would drop instantaneously, finally this led to the decrease of the vapor suction temperature and vapor discharge temperature of the compressor. The exhaust temperature reached a maximum of about 85℃ when defrosting was required of each outdoor heat exchanger.

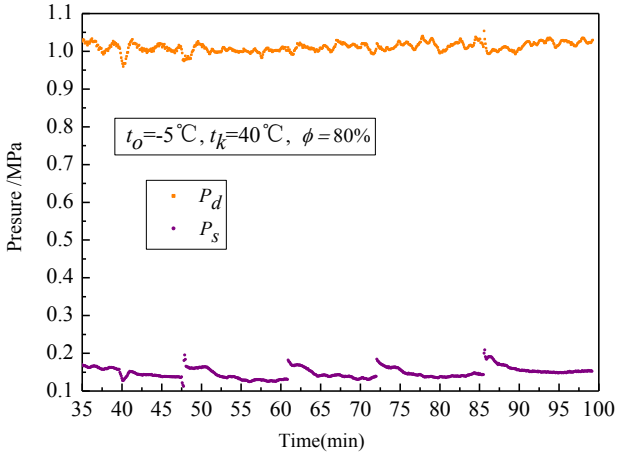

Figure 3: Variation of vapor suction and discharge pressure

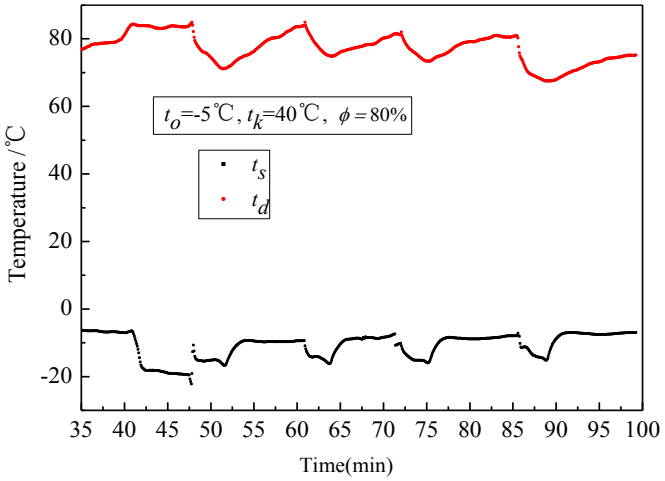

Figure 4: Variation of vapor suction and discharge temperature

From Fig. 5, it can be seen that the refrigerant flow rate fluctuated greatly in the process of sub-cooling defrosting alternatively. Related to the variation of the compressor vapor suction pressure, the lower the suction pressure was, the lower the refrigerant flow rate was and the refrigerant mass flow rate drops sharply and rises immediately. For example, at the start-up stage, the suction pressure of the compressor was about 0.17 MPa, the refrigerant mass flow rate was 93.8 kg h^{-1}; when the frosting process lasted to 2000s, the refrigerant mass flow rate was 83.4 kg h^{-1}; when defrosting began, the suction pressure of the compressor reduced to 0.15 MPa, and the refrigerant mass flow rate reduced to about 64 kg h^{-1}. The refrigerant flow rate tended to the pre-frosting level when the four outdoor units rotated to defrost and returned to normal mode.

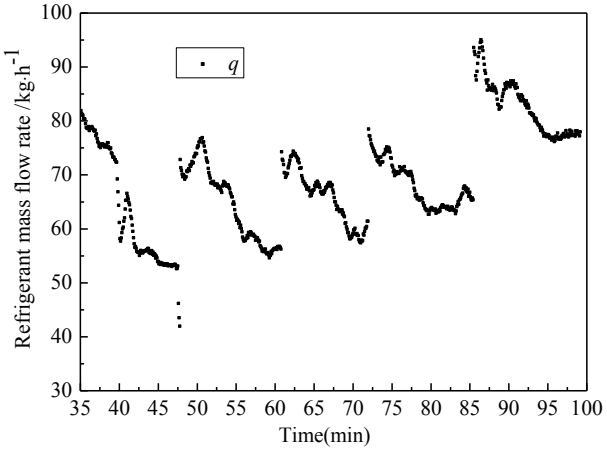

Figure 5: Variation of refrigerant mass flow rate

4.2 Data Analysis and Comparison under Different Working Conditions

From Fig. 6, it can be seen that at the same evaporation temperature and air relative humidity, the higher the condensation temperature, the longer the frosting process lasted, this was because that the higher the condensation temperature was, the greater the temperature difference and pressure difference of the compressor was. The lower the refrigerant circulating flow rate was, and the lower the refrigerant mass flow rate of evaporation and heat absorption in the outdoor heat exchanger was. Under the same conditions, the slower the frosting speed was, the longer the frosting time would be. When the condensation temperature was 40℃, the maximum heating capacity was about 4.5kW and the minimum heating capacity was about 3.0 kW in the process of defrosting. However, when the condensation temperature was 45℃, the maximum heating capacity was about 3.5kW and the minimum heating capacity was about 2.25kW.

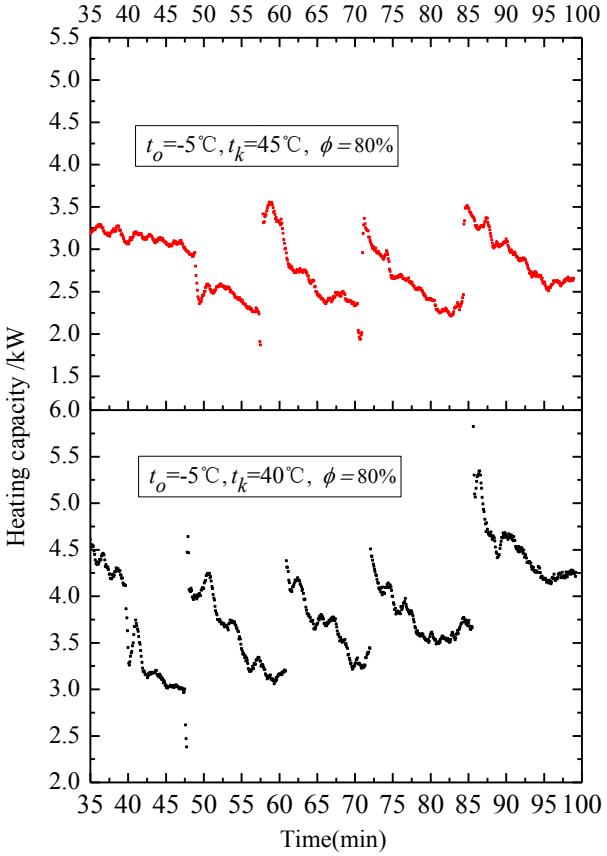

Figure 6: Heating capacity under different condensation temperature

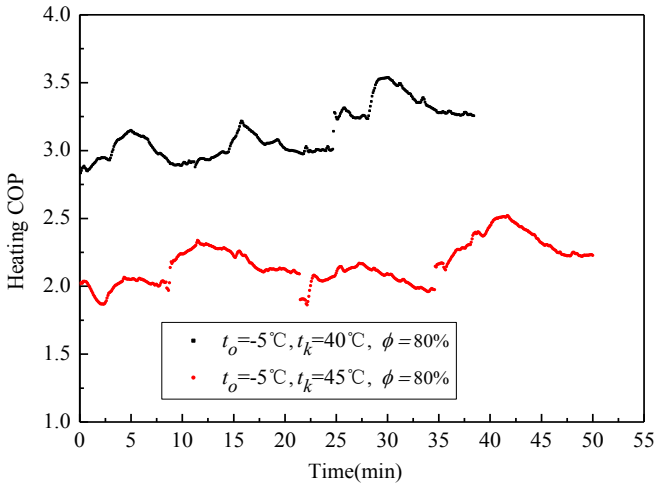

Figure 7: Heating COP under different condensation temperature

Fig. 7 was the heating COP under different condensation temperature, it was only in the process of subcooled defrosting. From it we can see although at different condensation temperature, the variation rule of heating COP was basically the same. The higher the condensation temperature, the lower the heating COP. When the condensation temperature was 40℃, the maximum heating COP was about 3.5 and the minimum heating COP was about 2.7 in the process of defrosting. However, when the condensation temperature was 45℃, the maximum heating COP was about 2.5 and the minimum heating COP was about 2.0.

5. CONCLUSIONS

In this paper, a novel air source heat pump system named as Heat Pump with Multiple Parallel Outdoor Units Defrosting alternatively (HPMOD) was designed, constructed and tested. The defrosting performances were experimentally investigated under different outdoor air temperature, air relative humidity and condensation temperature and etc. Based on the experimental results, the following conclusions were drawn:

1) The system can automatically defrost without stopping heating, the frost layer of a single outdoor evaporator can be removed in 6 minutes. In the process of sub-cooling defrosting, the compressor vapor suction pressure dropped sharply at first then went up directly and then deceased gradually. The compressor's vapor suction temperature and discharge temperature would decrease firstly and then increase gradually. The vapor suction temperature would come to a constant value at last.

2) Under different working conditions, the system heat capacity of the rotating defrosting process was about 2.25kWto 4.5kW and the heating COP was about 2.0 to 3.1.

ACKNOWLEDGEMENTS

This research was financed by Hebei provincial science and technology projects in 2017 (Grant No.17274515).

NOMENCLATURE

ASHP	*Air source heat pump*	*h*	*enthalpy (kJ kg-1)*
HPMOD	*Heat Pump with Multiple Parallel Outdoor Units Defrosting*	t_O	*Outdoor air temperature (℃)*
COP	*coefficient of performance*	t_k	*Condensation temperature (℃)*

P_s	*Vapor suction pressure (MPa)*	t_s	*Vapor suction temperature (℃)*
P_d	*Vapor discharge pressure (MPa)*	t_d	*Vapor discharge temperature (℃)*
Q	*Heating capacity (kW)*	ϕ	*relative humidity*
P	*Power input (kW)*	*1, 2, 3…*	*state points shown in the Figures*
q	*mass flow rate (kg s-1)*		

REFERENCES

Hu, W.J., Jiang, Y. Q., Qu, M.L., Ni, L., Yao, Y., Deng, S.M., 2011. An experimental study on the operating performance of a novel reverse-cycle hot gas defrosting method for air source heat pumps. Appl. Therm. Eng. 31,363-369.

Melo, C., Knabben, F.T., Pereira, P. V., 2013. An experimental study on defrost heaters applied to frost-free household refrigerators. Appl. Therm. Eng. 51(1), 239-245.

Li, L.T., Wang, W., Sun, Y. Y., 2014. Investigation of defrosting water retention on the surface of evaporator impacting the performance of air source heat pump during periodic frosting-defrosting cycles. Applied Energy 135,98-107.

Park, C. Y., Hrnjak, P. S., 2007. CO2 and R410A flow boiling heat transfer, pressure drop and flow pattern at low temperatures in a horizontal smooth tube. Int. J. Refrigeration 30 (1): 166-178.

Ma, G. Y., Ding, Y. J., Chai, Q. H., Jiang, Y., 2004. Experiment investigation of reverse cycle defrosting methods on air source heat pump with TXV as the throttle regulator. Int. J. Refrigeration 27(6), 671-678.

Huang, H., Li, Z. H., Yu, W. P., 2001. Simulation of defrosting process for air-cooled heat pump chiller. Journal of Southeast University (Natural Science Edition) 31(1),52-56.

Kwak, K., Bai, C., 2010. A study on the performance enhancement of heat pump using electric heater under the frosting condition: Heat pump under frosting condition. Appl. Therm. Eng. 30,539-543.

Liu, Z.B., Fan, P.Y., Wang, Q.H., Chi, Y., Zhao, Z.Q., Chi, Y.Y., 2018. Air source heat pump with water heater based on a bypass-cycle defrosting system using compressor casing thermal storage. Appl. Therm. Eng. 128,1420-1429.

Song, M.J., Gong, G.C., Mao, N., Deng, S.M., Wang, Z.H., 2017. Experimental investigation on an air source heat pump unit with a three-circuit outdoor coil for its reverse cycle defrosting termination temperature. Appl. Energy 204,1388-1398.

Ji, C. F., Huang, D., Yuan, X. L., 2005. Experimental study on frost and defrosting performance of air cooled heat pump chiller. Journal of Xi'an Jiao tong University.39(5),480-484.

Abdel-Wahed, R.M., Hifni, M.A., Sherif, S.A., 1983. Hot water defrosting of a horizontal flat plate cooling surface. Int. J. Refrigeration 6,152-154.

Kim, J.H., Choi, H.J., Kim, K.C., 2015. A combined dual hot-gas bypass defrosting method with accumulator heater for an air-to-air heat pump in cold region. Appl. Energy 147,344-352.

Ameen, F.R., Coney, J.E.R., Sheppard, C.G.W., 1993. Experimental study of warm-air defrosting of heat-pump evaporators, Int. J. Refrigeration 16,13-18.

Choi, H.J., Kim, B.S., Kang, D., Kim, K.C., 2011. Defrosting method adopting dual hot gas bypass for an air-to-air heat pump. Appl. Energy 88, 4544-4555.

Byun, J.S., Jeon, C.D., Jung, J.H., Lee, J.H., 2006. The application of photo-coupler for frost detecting in an air-source heat pump. Int. J. Refrigeration 29(2).191-198.

Yao, Y., Jiang, Y.Q., Deng, S.M., Ma, Z.L., 2004. A study on the performance of the airside heat exchanger under frosting in air source heat pump water heater/chiller unit. Int. J. Heat Mass Transfer 47 (17-18),3745-3756.

Li, L.T., Wang, W., Sun, Y. Y., Feng, Y.C., Lu, W.P., Zhu, J.H., Ge, Y.J., 2014. Investigation of defrosting water retention on the surface of evaporator impacting the performance of air source heat pump during periodic frosting-defrosting cycles. Appl. Energy 135, 98-107.

Manuscript ID: 1461
DOI: 10.18462/iir.icr.2019.1461

Assessment of the influence of the intermediate pressure on the optimal gas cooler pressure in a one-stage CO_2 heat pump with gas bypass for hot water generation

Fernando ILLÁN-GÓMEZ[(a)], José Ramón GARCÍA-CASCALES[(a)], Francisco Javier SÁNCHEZ-VELASCO[(a)], Víctor SENA-CUEVAS[(a)]

[(a)] Universidad Politécnica de Cartagena, DITF, ETSII
Cartagena, 30202, Spain, fernando.illan@upct.es

ABSTRACT

This work analyses the influence that the liquid receiver pressure has on the efficiency of a one-stage CO_2 heat pump water heater with gas bypass. The paper begins with the description of the experimental facility developed for the tests of these kind of heat pumps and continues with a theoretical discussion of the influence that the liquid receiver pressure has in the system's performance. Then the adjustment of the experimentally measured values of compressor power consumption and mass flow rate to typical AHRI correlations is presented. This adjustment is used in a simplified numerical model to assess the influence of the liquid receiver pressure in the system's performance. The model is finally compared to experimentally measured values of COP. The results show that the efficiency of this kind of system is always lower than that of a similar system without gas bypass, although at low gas cooler outlet temperatures the influence of the liquid receiver pressure is almost negligible and the system's efficiency is similar to that obtained without gas bypass.
Keywords: CO_2 Transcritical Cycle, Optimal Gas Cooler Pressure, Heat Pump Modelling.

1. INTRODUCTION

Buildings are responsible for around 30 % of the global final energy consumption (Ritchie, 2018), and more than 20 % of this energy is used for water heating (Dulac et al., 2013). According to Ritchie (2018), by 2040 water heating efficiency could improve by 43 % through the improvement of the efficiency of water heating equipment, for example increasing the deployment of heat pumps. On the other hand, the European Union (UE) and many others developed countries are developing regulations that aim to reduce the use of the fluorinated gases traditionally used as refrigerants in heat pumps, so important efforts must be made in developing heat pumps based in the use of low Global Warming Potential (GWP) refrigerants.

Many different authors are studying natural refrigerants as an alternative to fluorinated gases in domestic hot water heat pump systems and, particularly, carbon dioxide (R744) is getting a lot of attention from researchers, although most research studies are focused on air-source systems.

Tammaro et al. (2017) compared through numerical simulation the seasonal performance of two 40 kW air-water heat pump systems, one using CO_2 and the other using propane. They found that both fluids perform similarly in cold climates whereas in warm and average climates propane performs better. Ohkura et al. (2015) studied numerically the effect of tepid water extraction on the performance of a CO_2 heat pump water heating system. Minetto (2011) developed a theoretical and experimental study of an air-water CO_2 heat pump for domestic hot water production and presented a control method developed to maximize the COP of the system. Tammaro et al. (2016) studied the effect of the control strategy on the performance of an air-water CO_2 heat pump.

Most of the authors that are studding water-water CO_2 heat pumps have centered their attention in ground source heat pumps (Jin et al., 2016; Ghazizade-Ahsaee and Ameri, 2018). Others authors that have studied special applications of water-water CO_2 heat pumps are Stene (2005) or Liu et al. (2017).

Several authors, especially in Asia (Hepbasli et al., 2014; Shen et al., 2018), have studied the use of wastewater as heat source in heat pumps.

This paper focusses on the study of the influence that the liquid receiver pressure has on the efficiency of a one-stage CO_2 heat pump with gas bypass that recovers energy from wastewater for hot water generation.

2. EXPERIMENTAL FACILITY

Fig. 1 shows the experimental facility developed at the Technical University of Cartagena for the study of water-source heat pump water heaters. It consists of a primary refrigerant loop, represented by green lines in Fig. 1 and two auxiliary loops, represented by solid blue and solid red lines in the same figure. Although the facility allows studying four different configurations, only the one represented in Fig. 1 has been already tested.

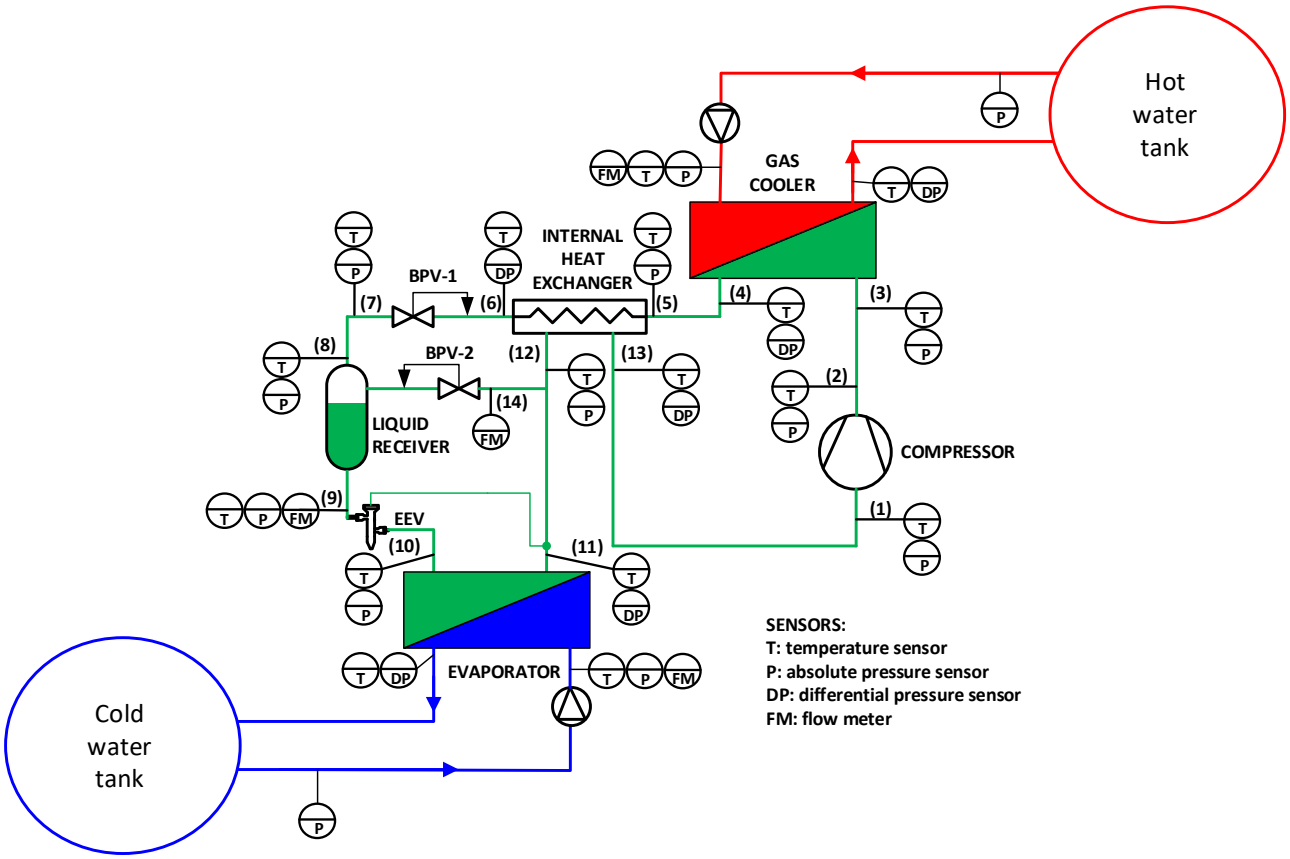

Figure 1: Sketch of the experimental facility

The refrigerant loop represented in Fig. 1 corresponds to a typical transcritical one stage CO_2 cycle with gas bypass. Two different electronic back pressure valves (BPV-1 and BPV-2) allow to control gas cooler and liquid receiver pressure, whereas an electronic expansion valve (EEV) controls the superheating at evaporator outlet. Temperature is measured using high precision resistance temperature detectors (RTDs), whereas pressure is measured using absolute pressure transmitters. Pressure drop in every heat exchanger is measured using differential pressure transmitters. Two Coriolis effect mass flow meters are used to measure the refrigerant mass flow rate flowing through the evaporator and the gas bypass. Finally, an energy counter, not represented in Fig. 1, measures the energy consumption in the compressor.

Two water loops are used to act as cold and hot reservoirs. The cold water loop provides water to the evaporator, acting as a greywater source. The hot water loop provides water to the gas cooler, acting as domestic hot water storage tank. The temperature at the inlet as well as the water flow rate through the heat exchangers in both loops can be accurately controlled using PID controllers. Alternatively, the system also allows controlling the temperature at the inlet and the outlet of the heat exchangers. Temperature and pressure of water at heat exchangers inlet and outlet, as well as water

flow rate are accurately measured, allowing a double check of the evaporator and gas cooler performance measurement.
All the variables measured are monitored and controlled with an interface developed in LabView®, National Instrument data acquisition software. This interface also allows controlling the system by acting over water flow and temperature in both hot and cold water loops, in order to guarantee stationary test conditions. Each experimental point is obtained as the averaged value for the 90 experimental data measured for each variable during 1800 seconds of steady-state conditions. Steady-state conditions are assumed when the standard deviation is lower than 1% for each parameter experimentally measured.

3. INFLUENCE OF INTERMEDIATE PRESSURE ON SYSTEM'S PERFORMANCE

The gas bypass in transcritical one-stage CO_2 systems is typically introduced to reduce the pressure in distribution systems, making possible to use standard pressure components in the lines that distribute liquid to the evaporators.
Additionally, thanks to the gas bypass the quality at the evaporator inlet is reduced, allowing for smaller evaporators, while the heat transfer in the evaporator is increased (Fritschi et al., 2017). This can also reduce the flow maldistribution when mini or micro channel multiport tubes are used for the evaporator (Kim et al., 2004).
On the other hand, the gas bypass affects the fluid properties at compressor suction and thus could affect the system's performance.
Fig. 2 shows a typical pressure-enthalpy diagram for the facility represented in Fig. 1. It has been obtained for an evaporation temperature of 5 ºC (evaporation pressure 39.7 bar), a superheating of 5 K, a gas cooler pressure of 80 bar, a refrigerant temperature of 25 ºC at the gas cooler outlet and a liquid receiver pressure of 50 bar, assuming that the internal heat exchanger has been bypassed.

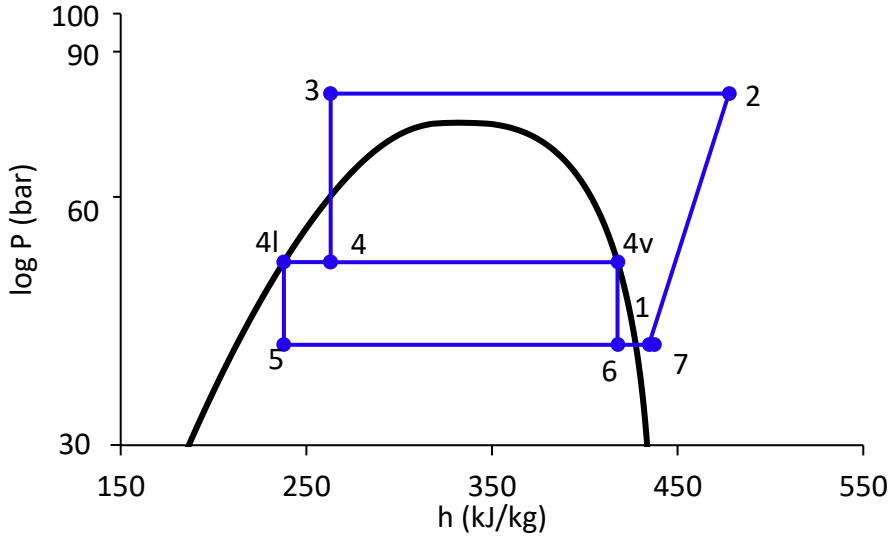

Figure 2: Pressure-enthalpy diagram

Fig. 3 shows the same cycle when the liquid receiver pressure varies between the two theoretical extreme values. The maximum liquid receiver pressure is around 60 bar (Fig. 3a), corresponding to the situation when the fluid enters at the liquid receiver as saturated liquid, whereas the minimum pressure (Fig. 3b) corresponds to the evaporation pressure (around 40 bar).
When the liquid receiver pressure equals the evaporation pressure (Fig. 3b), all the vapor goes through the gas bypass and the evaporator only receives liquid. At the evaporator outlet, the superheated vapor (SH=5 K) is mixed with the saturated vapor that comes from the gas bypass and the mix have a superheating of 3.75 K. As the liquid receiver pressure increases (Fig. 2), the mass flow rate through the gas bypass decreases, but the quality in point 6 also decreases. Initially the superheating in point 1 decreases until it reaches a minimum value (for the conditions represented in Fig. 2 and Fig. 3, that minimum is around 3.48 K, obtained for a liquid receiver pressure of 48 bar). If the liquid receiver pressure increases over that value, the superheating begins to increase. At

maximum liquid receiver pressure, there is no vapor in the receiver and all the refrigerant passes through the evaporator and the superheating reaches its maximum value (5 K).

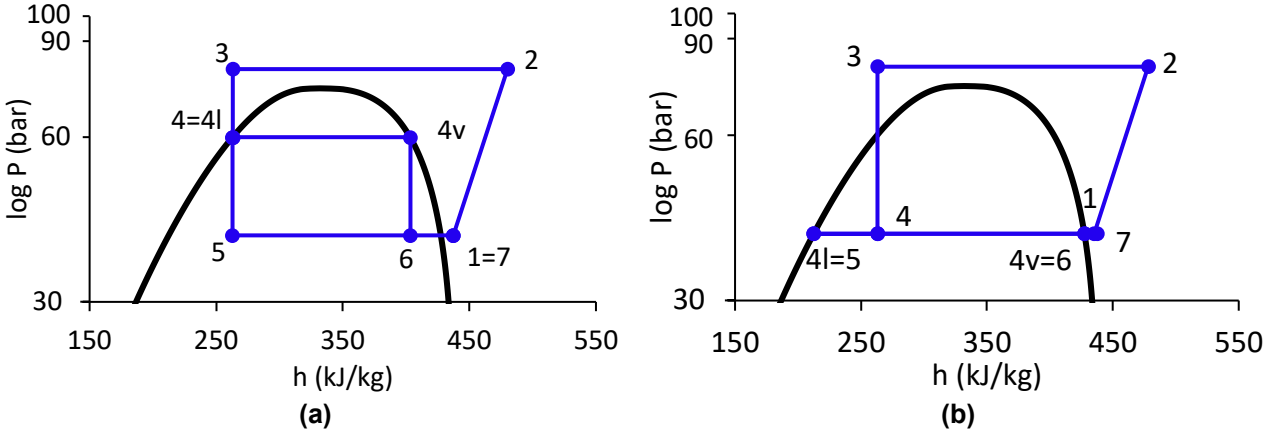

Figure 3: Influence of liquid receiver pressure on thermodynamic cycle

The efficiency of the system can be obtained using Eq. (1):

$$COP = \frac{h_2 - h_3}{h_2 - h_1} \qquad \text{Eq. (1)}$$

Since, as discussed previously, the liquid receiver pressure affects the conditions at compressor suction (affects h_1), it could affect also the system efficiency.
The rating of the compressor power input, refrigerant mass flow rate and refrigerating capacity are provided by most CO_2 compressor manufacturer according to AHRI Standard 571-2012, which established that those values shall be presented using a third degree polynomial equation, that only depends on the discharge and suction temperature. Additionally, superheating strongly affects the isentropic and volumetric efficiency in a reciprocating compressor (Morriesen and Deschamps, 2012) and therefore the liquid receiver pressure could affect the compressor behavior.
In order to obtain the influence that suction conditions have on compressor performance, several experimental tests have been developed in the facility described in section 2.1.
According to the manufacturer, the compressor mas flow rate can be obtained using Eq. (2) and the power consumption is given by Eq. (3):

$$\dot{m}_m = C_1 + C_2 \cdot T_0 + C_3 \cdot p_c + C_4 \cdot T_0^2 + C_5 \cdot T_0 \cdot p_c + C_6 \cdot p_c^2 \qquad \text{Eq. (2)}$$

$$\dot{W}_m = C_1 + C_2 \cdot T_0 + C_3 \cdot p_c + C_4 \cdot T_0^2 + C_5 \cdot T_0 \cdot p_c + C_6 \cdot p_c^2 + C_7 \cdot T_0^3 + C_8 \cdot p_c \cdot T_0^2 + C_9 \cdot T_0 \cdot p_c^2 + C_{10} \cdot p_c^3 \qquad \text{Eq. (3)}$$

where T_0 is the evaporating temperature in degrees Celsius, p_c is the discharge pressure in bar and coefficients C_1 to C_{10} are given in Table 1.

Table 1. Coefficients for compressor mass flow rate and power consumption

-	C_1	C_2	C_3	C_4	C_5	C_6	C_7	C_8	C_9	C_{10}
$\dot{m}_m$	0.040044	0.001141	-0.000197	$1.08 \cdot 10^{-5}$	$-1.7 \cdot 10^{-6}$	$5.5 \cdot 10^{-7}$	-	-	-	-
$\dot{W}_m$	-1904.9	-77.21	78.17	-1.033	1.195	-0.5297	-0.0048	0.0052	-0.0032	0.0014

Blue dots in Fig. 4 represent the results obtained when the experimentally measured values of mass flow rate and power consumption are compared to the values obtained using Eq. (2) and Eq. (3). Since there is a clear deviation between measured and calculated values, new superheat correction formulas based on suction densities, similar to the expression proposed in the appendix D of AHRI Standard 540-2015, are proposed (Eq. (4) and Eq. (5)). The results obtained using those equations are plotted in red dots in Fig. 4. Although according to that appendix D of AHRI Standard 540-2015, a change of superheat has negligible impact on power consumption, the results presented in Fig. 4.a show a better adjustment to experimental data when the manufacturer correlation is corrected using suction density.

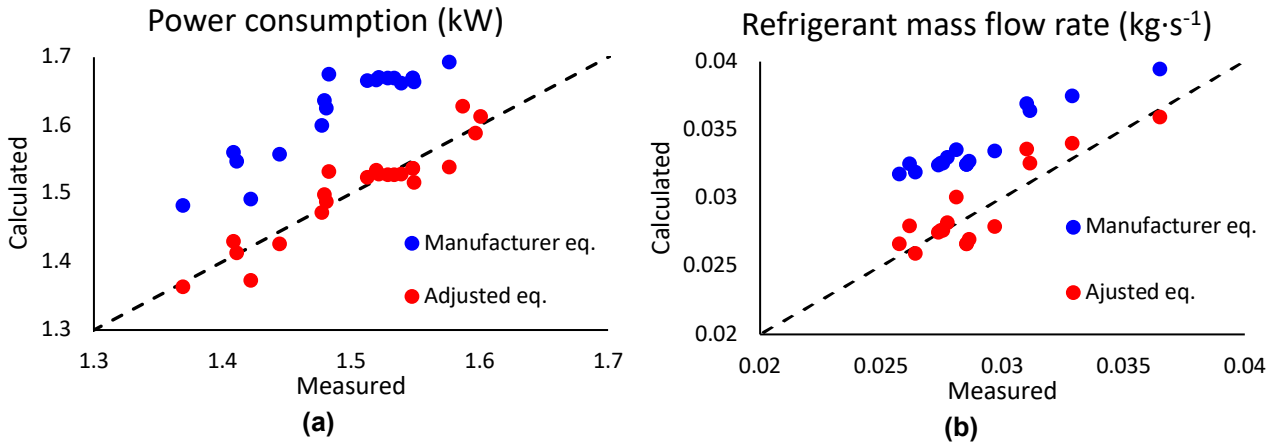

Figure 4: Experimentally measured Vs calculated values of compressor power consumption and mass flow rate

The expressions for the adjusted mass flow rate and power consumption are given by Eq. (4) and Eq. (5):

$$\dot{m}_{ad} = -0.00946 \cdot \dot{m}_m + 1.24215 \cdot \frac{\rho_1}{\rho_0} \qquad \text{Eq. (4)}$$

$$\dot{W}_{ad} = 0.84187 \cdot \dot{W}_m + 0.09047 \cdot \frac{\rho_1}{\rho_0} \qquad \text{Eq. (5)}$$

where ρ is the refrigerant density, the subscript 0 refers to saturated vapor at evaporation pressure and the subscript 1 refers to actual suction conditions.
According to Eq. (1), the system COP depends on any parameter that can affect the refrigerant enthalpy at compressor inlet (h_1) and outlet (h_2) or gas cooler outlet (h_3).
Enthalpy at compressor inlet (h_1) depends on the evaporation pressure, the superheating degree and, as discussed previously, the liquid receiver pressure.
Enthalpy at compressor outlet (h_2) can be obtained using Eq. (6):

$$h_2 = h_1 + \frac{\dot{W}_{ad}}{\dot{m}_{ad}} \qquad \text{Eq. (6)}$$

Consequently, it depends on the compressor discharge pressure, besides all parameter that affect enthalpy at compressor inlet (h_1).
Finally, the enthalpy at the gas cooler outlet (h_3) is a function of the pressure and temperature at gas cooler outlet.
Therefore, neglecting pressure drops and heat losses in the whole system, its COP depends on evaporation pressure, superheating degree, liquid receiver pressure, gas cooler pressure and gas cooler outlet temperature. Since in typical applications evaporation pressure and gas cooler outlet temperature are fixed and the superheating degree is kept constant, for a given application the system COP will depend on the gas cooler pressure and the liquid receiver pressure.

4. RESULTS AND DISCUSSION

A simplified numerical model has been developed in order the asses the influence that the liquid receiver pressure has on the system's efficiency, considering a domestic water heater that recovers energy from greywater at temperatures between 15 and 35 °C. The evaporation temperature has been varied between 5 and 25 °C and the superheating degree has been considered constant and equal to 5 K. The gas cooler outlet temperature has been varied between 10 °C and 50 °C and no intermediate heat exchanger has been considered.
Fig. 5 shows the influence that the liquid receiver pressure has on system COP for the optimal gas cooler pressure calculated in each condition. For gas cooler temperatures below the critical temperature of CO_2 (30.978 °C), the optimal gas cooler pressure is the critical pressure, although in this work the minimal gas cooler pressure has been fixed at 75 bar. Therefore, for a gas cooler outlet temperature of 20 °C, the maximum liquid receiver pressure (the pressure at which the fluid leaves the back pressure valve as saturated liquid) is 54.27 bar, lower that the saturation temperature

corresponding to 20 °C, so only evaporation temperatures of 5, 10 and 15 °C has been considered for this condition. On the other extreme, for a gas cooler outlet temperature of 50 °C and a evaporation temperature of 5 °C, the optimal gas cooler pressure is 125 bar and liquid receiver pressures below 49.3 bar will lead to wet vapor conditions at compressor suction, so these conditions have not been taken into account if Fig. 5d.

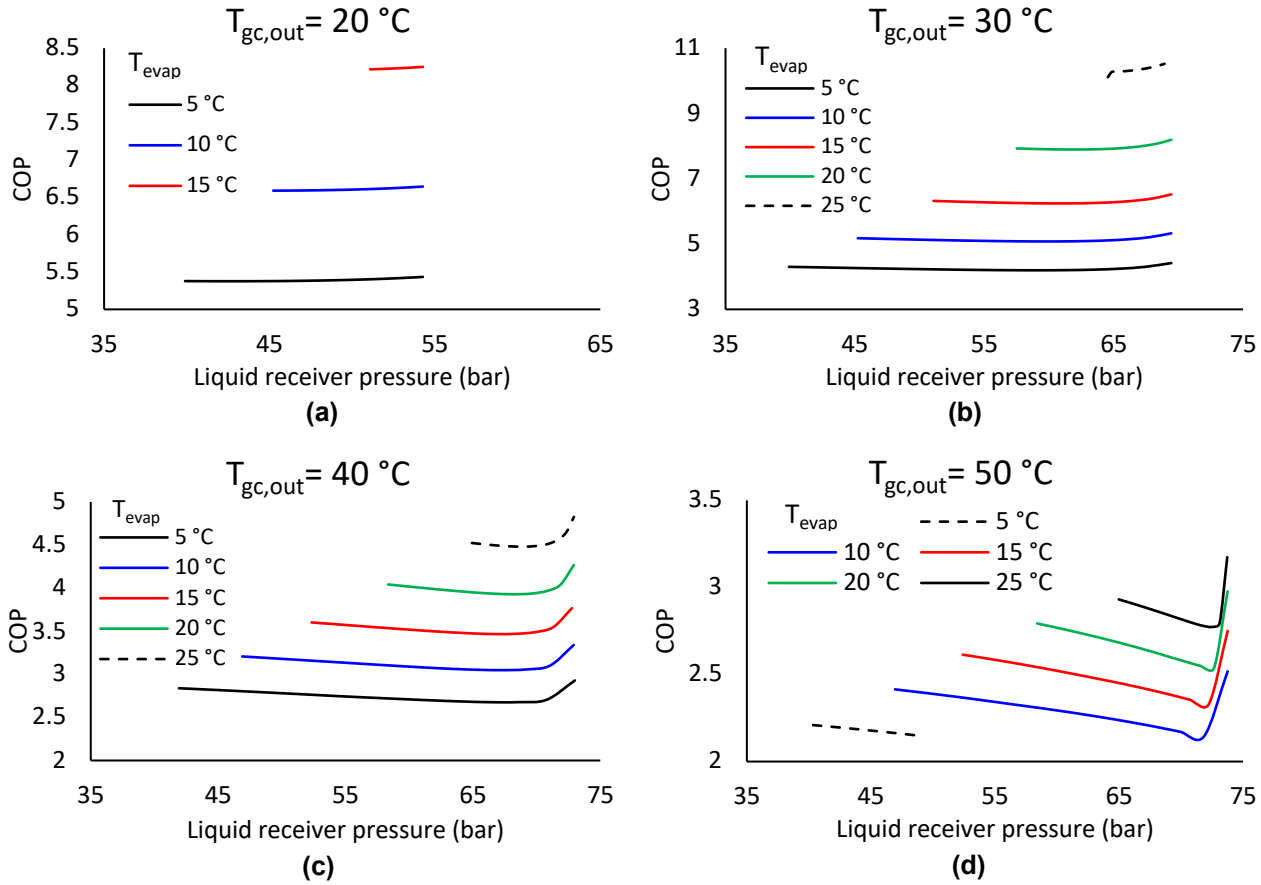

Figure 5: Influence of liquid receiver pressure on system's COP at different evaporation and gas cooler outlet temperatures

According to Fig. 5, the behavior is quite similar in all cases. In most cases the COP decreases initially as liquid receiver pressure increases from evaporation pressure, reaching a minimum value and then increases until it reaches its maximum value for the higher liquid receiver pressure.
That means that, from the energy efficiency point of view, a system with liquid receiver but without gas bypass will have always a better performance than a similar system with gas bypass, although as discussed previously, the gas bypass may have others advantages.
Nevertheless, as Fig. 5 shows, the influence of liquid receiver pressure is almost negligible at low gas cooler outlet temperature. As that temperature increases, the influence of liquid receiver pressure becomes stronger and therefore it must be carefully selected in order to not compromise the system's efficiency.
This theoretical behavior has been experimentally confirmed as shown in Fig. 6. The blue dots represent the experimentally measured COP. The red dots represent the COP calculated using the experimentally measured values of superheating, evaporation temperature and gas cooler outlet temperature and pressure. The black dashed line represents the COP calculated for the setpoint conditions (T_{evap}=10 °C, $T_{gc,out}$=25 °C, P_{gc}=74.8 bar, SH=5 K). As it can be seen, calculated and measured point are in good agreement and confirm the validity of the numerical model.

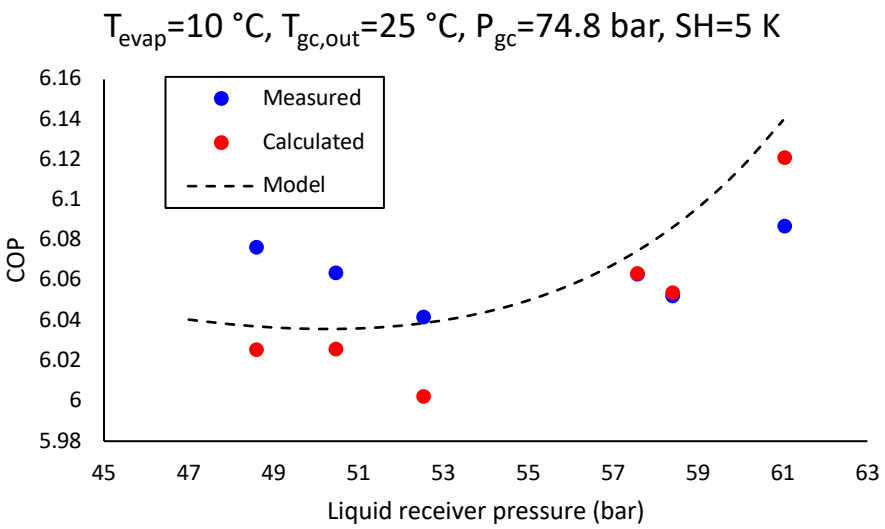

Figure 6: Experimentally measured Vs calculated COP

5. CONCLUSIONS

The influence of the liquid receiver pressure in the efficiency of a transcritical single stage CO_2 heat pump with gas bypass for hot water generation has been theoretically discussed. Compressor power consumption and mass flow rate have been experimentally modelled in order to be included in a simplified numerical model. According to the model, the efficiency of this kind of system reaches its maximum value for the highest liquid receiver pressure and is always lower than for a similar system without gas bypass. At low gas cooler outlet temperatures the influence of the liquid receiver pressure is almost negligible and the system's efficiency is similar to that obtained without gas bypass. These conclusions are supported by experimental results.

ACKNOWLEDGEMENTS

This work has been financed by projects ENE2014-53311-C2-1-P and ENE2017-83665-C2-2-P financed by the Ministry of Economy, Industry and Competitiveness and the European Regional Development Fund.

NOMENCLATURE

h	specific enthalpy (kJ/hg)	$\dot{m}$	mass flow rate ($kg \cdot s^{-1}$)
p	pressure (bar)	T	temperature (K)
$\dot{W}$	compressor power consumption (kW)		

REFERENCES

AHRI Standard 571-2012, 2012, Performance Rating of Positive Displacement Carbon Dioxide Refrigerant Compressors and Compressor Units. Air-Conditioning, Heating, and Refrigeration Institute, Arlington, VA, U.S.A., 26 p.

AHRI Standard 540-2015, 2015, Performance Rating of Positive Displacement Compressors and Compressor Units. Air-Conditioning, Heating, and Refrigeration Institute, Arlington, VA, U.S.A., 19 p.

Dulac J., LaFrance M., Trudeau N. Yamada H., 2013. Transition to sustainable buildings. Strategies and opportunities to 2050. IEA Publications, France, 284 p.

Fritschi H., Tillenkamp F., Löhrer R., M. Brügger M., 2017, Efficiency increase in carbon dioxide refrigeration technology with parallel compression. Int. J. Low Carbon Tech. 12, 171-180.

Ghazizade-Ahsaee H., Ameri M., 2018. Energy and exergy investigation of a carbon dioxide direct-expansion geothermal heat pump. Appl. Therm. Eng. 129, 165-178.

Hepbasli A., Biyik E., Ekren O., Gunerhan H., Araz M., 2014. A key review of wastewater source heat pump (WWSHP) systems. Energy Convers. Manage. 88, 700-722.

Jin Z., Eikevik T.M., Nekså P, Hafner A., 2016, Investigation on CO_2 hybrid ground-coupled heat pumping system under warm climate. Int. J. Refrigeration 62, 145-152.

Kim M.H., Pettersen J., Bullard C.W., 2004, Fundamental process and system design issues in CO_2 vapor compression systems. Prog. Energ. Combust. 30, 119-174.

Liu F., Zhu W., Cai Y., Groll E.A., Ren J., Lei Y., 2017. Experimental performance study on a dual-mode CO2 heat pump system with thermal storage. Appl. Therm. Eng. 115, 393-405.

Minetto S., 2011. Theoretical and experimental analysis of a CO_2 heat pump for domestic hot water. Int. J. Refrigeration 34, 742-751.

Morriesen A., Deschamps C.J., 2012. Experimental investigation of transient fluid flow and superheating in the suction chamber of a refrigeration reciprocating compressor. Appl. Therm. Eng. 41, 61-70.

Ohkura M., Yokoyama R., Nakatama T., Wakui T., 2015. Numerical analysis on performance enhancement of a CO_2 heat pump water heating system by extracting tepid water. Energy 87, 435-447.

Ritchie, J. (co-ordinator), 2018. Energy efficiency 2018. Analysis and outlooks to 2040. IEA Publications, France, 170 p.

Shen C., Lei Z., Wang Y., Zhang C., Yao Y., 2018. A review on the current research and application of wastewater source heat pumps in China. Therm. Sci. Eng. Prog. 6, 140-156.

Stene J., 2005. Residential CO_2 heat pump system for combined space heating and hot water heating. Int. J. Refrigeration 28, 1259-1265.

Tammaro M., Mauro A.W., Montagud C., Corberán J.M., Mastrullo R., 2016. Hot sanitary water production with CO_2 heat pumps: Effect of control strategy on system performance and stratification inside the storage tank. Appl. Therm. Eng. 101, 730-740.

Tammaro M., Montagud C., Corberán J.M., Mauro A.W., Mastrullo R., 2017. Seasonal performance assessment of sanitary hot water production systems using propane and CO_2 heat pumps. Int. J. Refrigeration 74, 224-239.

Manuscript ID: 1471
DOI: 10.18462/iir.icr.2019.1471

Development of hybrid VRF using R32 refrigerant

Soshi IKEDA[(a)], Jun NISHIO[(a)], Katsuhiro ISHIMURA[(b)], Hiroyuki OKANO[(b)]

[(a)] Advanced Technology R&D Center, Mitsubishi Electric Corporation
Hyogo, 661-8661, Japan, Ikeda.Soshi@ay.MitsubishiElectric.co.jp
[(b)] Air-Conditioning & Refrigeration System Works, Mitsubishi Electric Corporation
Wakayama, 640-8686, Japan

ABSTRACT

In order to prevent any further increase on the global warming threshold, the HVAC market is still focused on improving energy efficiency and reducing greenhouse gases. Therefore the market is still keen on adopting low-GWP air conditioning products. R32 refrigerant is considered as a mild-flammable refrigerant and when applied to a VRF system, it often requires additional safety measures such as shut-off valves, alarm and ventilation thereby causing more strain on the design and installation aspect of a R32 VRF system. Water based air conditioning system 'Hybrid VRF' was developed to mitigate this issue as it can still be designed, installed & commissioned as a VRF system, however reduces the requirement for any additional safety measures when R32 refrigerant is used.
Keywords: GWP, R32 Refrigerants, Hybrid VRF, Water-Based Multi Air Conditioning System, Lower Flammability.

1. INTRODUCTION

From a desire to prevent global warming, demands to reduce greenhouse gas emissions and save energy are increasing, and it is necessary to convert to low-GWP refrigerant in air conditioning equipment. Compact air conditioners such as room air conditioners are being switched from the current R410A refrigerant to R32 refrigerant which has GWP as low as 675 and is superior in terms of performance. However, when a lower flammability refrigerant such as R32 refrigerant is applied to an air conditioner that individually controls each indoor unit such as a building multi air conditioner, since there are many cases where additional safety measures such as mechanical ventilation and shutoff valves are required when installing in small rooms, there are problems in equipment design and construction. Therefore, the world's first water-based multi air conditioning system with 2-pipe heat recovery functions "Hybrid VRF" was developed. This system converts the medium from refrigerant to water in the middle of the route to the indoor unit from the outdoor unit and conveys it into the room, and R32 refrigerant was applied to it, and it realized the same workability as VRF without additional safety measures.
In this report, we describe the outline of a water-based multi air conditioning system for a building (hereinafter referred to as R32-Hybrid VRF) to which R32 refrigerant is applied, product characteristics and applied technology, the efficiency of air conditioning system, the reduction effect of refrigerant mass and the greenhouse gas emissions converted to CO_2.

2. OUTLINE OF R32-HYBRID VRF

2.1. Characteristics of R32 Refrigerant

Table 1 shows basic characteristics of R32 refrigerant. It shows GWP, flammability, normal boiling point, theoretical COP and pressure drop of R410A refrigerant and R32 refrigerant, and theoretical COP and pressure drop are indicated by R410A refrigerant ratio. R32 refrigerant, whose GWP is about 1/3 of the R410A refrigerant, has a theoretical COP of 102 percent and a pressure drop of 64 percent. Performance of air conditioners using R32 refrigerant improves by improving theoretical COP and reducing pressure drop. However, in order to apply R32 refrigerant, which can be flammable, to an air conditioner in which indoor units are individually controlled, it is necessary to

reduce the risk through additional safety measures such as mechanical ventilation and shutoff valves when installing in a small room.

Table 1. R32 refrigerant characteristics

-	R410A	R32
GWP※1 ($kg_{(CO2)}$/kg)	2088	675
Flammability※2 (-)	A1	A2L
Boiling point (℃)	-51.4	-51.7
Theoretical COP ratio※3 (percent)	100	102
Pressure drop ratio※3,4 (percent)	100	64

※1 IPCC 4th Assessment Report, ※2 ASHRAE34
※3 Condensing temperature 50℃, Evaporating temperature 5℃, Subcooling 10K, Superheating 3K, ※4 Suction side

2.2. Outline of Hybrid VRF

The systems of VRF and Hybrid VRF are shown in Figs. 1 and 2. Hybrid VRF is composed of an outdoor unit, a Branch Controller and a plurality of indoor units as well as a VRF having heat recovery functions. A pair of pipes connect the outdoor unit and the Branch Controller, and the Branch Controller and the indoor unit. While VRF carries heat between the outdoor unit and the indoor unit with refrigerant, Hybrid VRF carries heat between the outdoor unit and the Hydro Branch Controller with refrigerant, and carries heat between the Hydro Branch Controller and the indoor units with water. Therefore, Hybrid VRF can eliminate the use of refrigerant from the Hydro Branch Controller to the indoor unit. In addition, by installing the Hydro Branch Controller above the ceiling in the upper part of the room, it is possible to prevent direct refrigerant leakage indoors, especially in small rooms, and even if applying R32 refrigerant with lower flammability, no additional safety measures are required.
Fig. 3 shows the Hydro Branch Controller, which is a key part of the Hybrid VRF. The Hydro Branch Controller consists of two plate heat exchangers, valve blocks and two pumps. The plate heat exchanger exchanges heat between refrigerant supplied from the outdoor unit and water flowing from the indoor unit. The valve block switches the flow path of water circulating between the Hydro Branch Controller and the indoor unit. The pump circulates water between the Hydro Branch Controller and the indoor unit.
Water flowing out of the pump exchanges heat in the plate heat exchanger and is cooled or heated. The cold/hot water flowing out of the plate heat exchanger is distributed to each indoor unit by the valve blocks, and exchanges heat with air in the indoor unit. Water flowing from the indoor unit circulates by being distributed to the two pumps by the valve blocks.

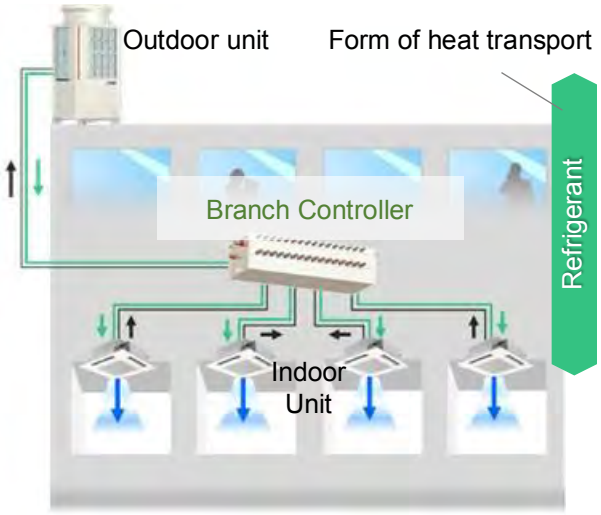

Figure 1: VRF

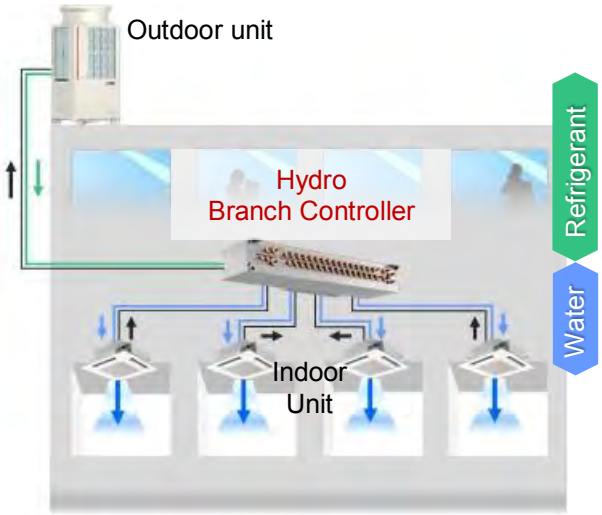

Figure 2: Hybrid VRF

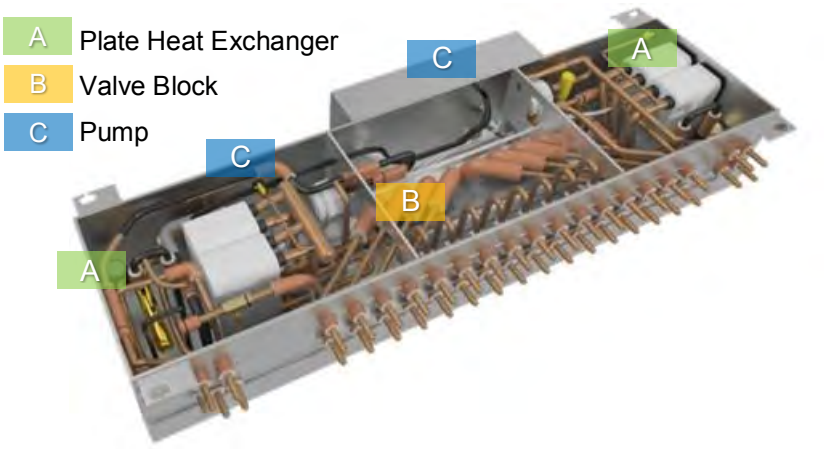

Figure 3: Hydro Branch Controller

3. PRODUCT FEATURES AND APPLIED TECHNOLOGY

3.1. Environmentally-Conscious System

The R32-Hybrid VRF is an environment combining the advantages of R32 refrigerant where GWP is about 1/3 of R410A refrigerant and those of the Hybrid VRF that can reduce the refrigerant mass by transferring heat from the Hydro Branch Controller to the indoor unit with water, and it is the world's first system to apply R32 refrigerant for water-based multi air conditioning system with 2-pipe heat recovery functions, with individually controlled indoor units.
Fig. 4 shows the greenhouse gas emissions converted to CO_2. Details of calculation conditions, refrigerant mass and greenhouse gas emissions will be explained in the section 4 "REDUCTION IN REFRIGERANT MASS AND GREENHOUSE GAS EMISSIONS". In the case shown in Fig. 4, the R32-Hybrid VRF can reduce greenhouse gas emissions by 84 percent : % from the R410A-VRF.

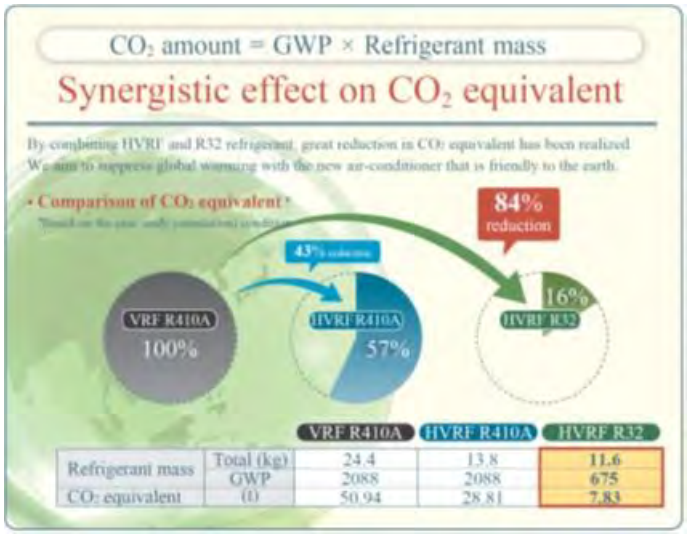

Figure 4: Greenhouse gas emissions converted to CO_2

3.2. 2-pipe Heat Recovery System

In the R32-Hybrid VRF, simultaneous operation of cooling and heating can be performed by connecting two refrigerant pipes from the outdoor unit to the Hydro Branch Controller, generating cold water and hot water at the same time by a Hydro Branch Controller, and supplying it to the indoor unit.
The refrigerant and water circuit in each operation mode is shown in Fig. 5. There are three operation modes of the R32-Hybrid VRF: heating operation, cooling operation and simultaneous cooling and heating operation.

3.2.1. Heating operation

In order to generate the hot water necessary for heating the interior, the two plate heat exchangers act as condensers. The water circulating in the heating indoor unit exchanges heat with high temperature and high pressure gas refrigerant in a plate heat exchanger, is heated to become hot water, and is supplied to the indoor unit. In this operation, the outdoor heat exchanger acts as an evaporator to absorb heat from the outdoor air.

3.2.2. Cooling operation

In order to produce the cold water necessary for cooling the interior, the two plate heat exchangers act as evaporators. The water circulating in the indoor unit to be cooled exchanges heat with a low temperature and low pressure two phase refrigerant in a plate heat exchanger, is cooled to become cold water, and is supplied to the indoor unit. In this operation, the outdoor heat exchanger acts as a condenser to radiate heat to the outdoor air.

3.2.3. Simultaneous cooling and heating

In order to generate hot and cold water necessary for cooling and heating the interior, the two plate heat exchangers act as condensers and evaporators, respectively. The water circulating in the heating indoor unit exchanges heat with high temperature and high pressure gas refrigerant in a plate heat exchanger acting as a condenser, is heated to become hot water and is supplied to the indoor unit. The refrigerant condensed and liquefied in the condenser passes through the expansion valve, becomes a low temperature and low pressure two-phase refrigerant, and then flows into the plate heat exchanger functioning as an evaporator. The water circulating in the indoor unit to be cooled exchanges heat with a low-temperature and low pressure two phase refrigerant in a plate heat exchanger and is cooled to cold water and supplied to the indoor unit. In this operation, the outdoor heat exchanger acts as a condenser or an evaporator according to the indoor heating and cooling load conditions. When the indoor cooling load is larger than the heating load, the outdoor heat exchanger acts as a condenser to radiate a part of the heat absorbed by cooling to the outdoor air. When the indoor heating load is larger than the cooling load, the outdoor heat exchanger acts as an evaporator to absorb a part of the heat radiated by heating from the outdoor air.

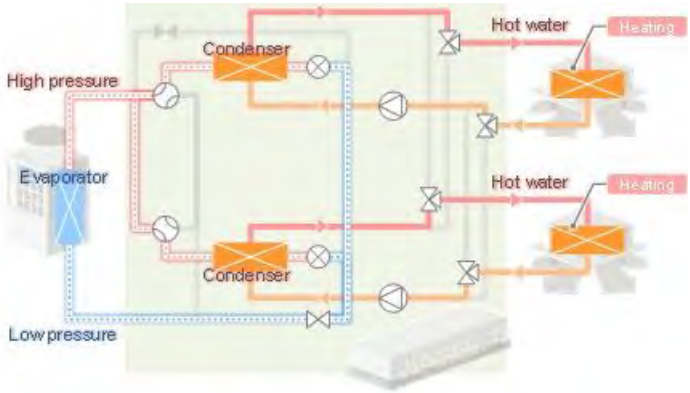

(a) Heating operation

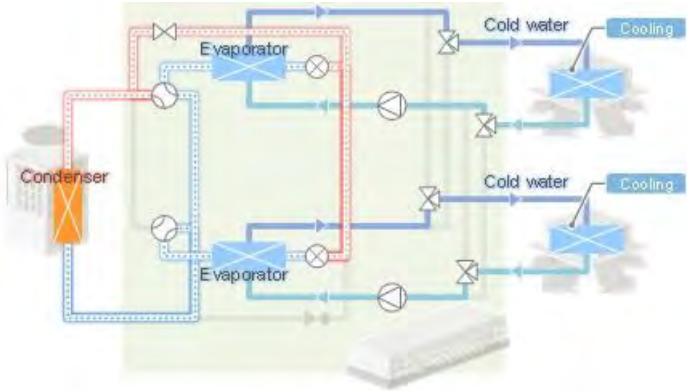

(b) Cooling operation

Figure 5: Refrigerant and water circuit diagram in different operation modes

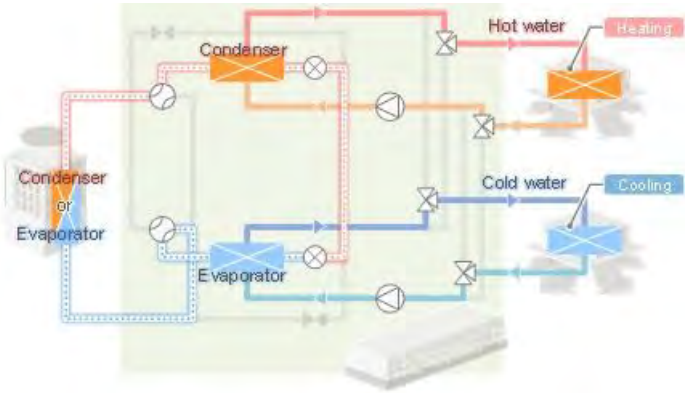

(c) Heating and Cooling operation

Figure 5: Refrigerant and water circuit diagram in different operation modes

3.3. Provincial Design and Construction

A comparison with a 4-pipe system is shown in Fig. 6. Since the R32-Hybrid VRF is a package system including valves, pumps, and heat exchangers in a Hydro Branch Controller, its components are fewer in number than those of the 4-pipe chiller system, so it can simplify system design.
A comparison with a 3-pipe system is shown in Fig. 7. Since the R32-Hybrid VRF is a 2-pipe system, the number of piping connections is fewer than for a 3-pipe VRF system, and piping construction can be reduced.

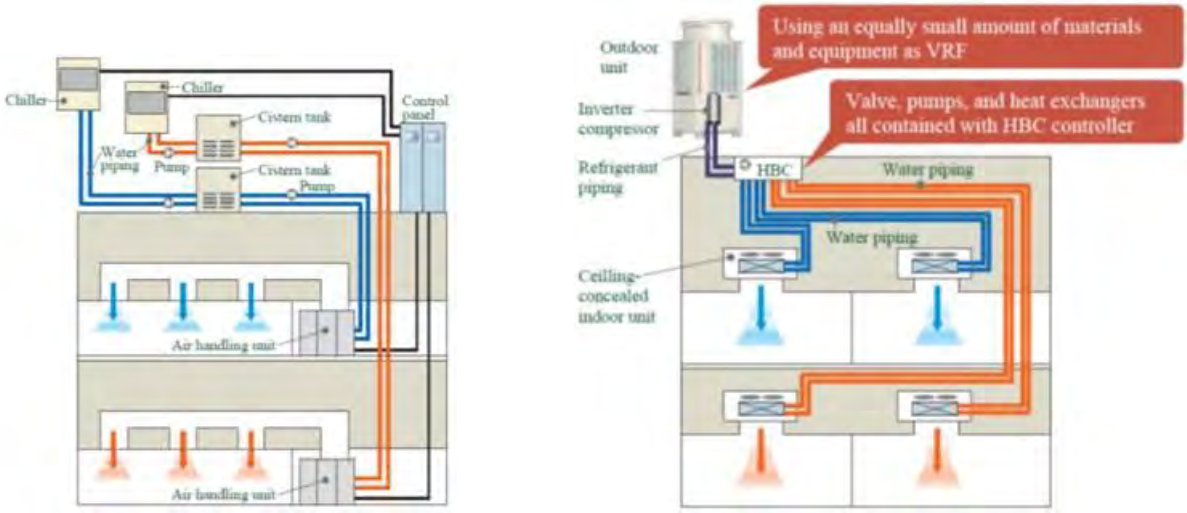

(a) 4-pipe chiller system (b) R32-Hybrid VRF (2-pipe heat recovery system)

Figure 6: Comparison against the 4-pipe system



(a) 3-pipe system (b) R32-Hybrid VRF

Figure 7: Comparison against the 3-pipe system

3.4. Prevent Leakage of Refrigerant into the Room

The installation image of the R32-Hybrid VRF is shown in Fig. 8. The R32-Hybrid VRF transfers heat from the Hydro Branch Controller to the indoor unit with water to restrict the area through which the refrigerant flows, so that it is possible to prevent direct refrigerant leakage to the room, especially to the small room.

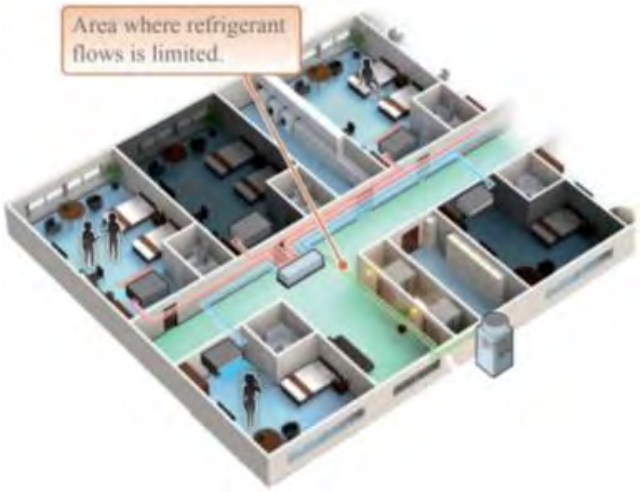

Figure 8: Installation image of R32-Hybrid VRF

4. EFFICIENCY OF AIR CONDITIONING SYSTEM

Table 2 shows the system conditions for the efficiency of air conditioning system. It is assumed to be applied to a hotel with 20 rooms of the same size. For the outdoor unit, the indoor unit, and the Branch Controller, the air conditioning capacity of 33.5 kW × 1 unit, 2.2 kW × 20 units and 16 branch + 4 branch devices were selected. The refrigerant pipe lengths of VRF and Hybrid VRF were 264 m and 40 m respectively. The refrigerant piping length from the outdoor unit of the VRF and the Hybrid VRF to the Branch Controller was 40 m in each. Table 3 shows the calculation conditions for the efficiency of air conditioning system.

Comparison of COP of air conditioning system is shown in Fig. 9, Table 4. The COP is indicated by R410A-VRF ratio. The COP is calculated by dividing the heating and cooling capacity by the air conditioning system input. The COP of heating of the R410A-VRF, the R410A-Hybrid VRF and the R32-Hybrid VRF are 100 percent, 91 percent and 94 percent, respectively. The COP of cooling of the R410A-VRF, the R410A-Hybrid VRF and the R32-Hybrid VRF are 100 percent, 88 percent and 101 percent, respectively. The COP of average of heating and cooling of the R410A-VRF, the R410A-Hybrid VRF and the R32-Hybrid VRF are 100 percent, 90 percent and 98 percent, respectively. The COP of R410A-Hybrid VRF is dropped by 10 percent relative to R410A-VRF due to the heat exchange loss between the refrigerant and water. The COP of R32-Hybrid VRF is equivalent to the R410A-VRF by improving theoretical COP and reducing pressure loss.

Table 2. system condition

Application image		Hotel(20 rooms/same size)
Outdoor unit		33.5 kW(Cooling Capacity)×1
Indoor unit		2.2 kW(Cooling Capacity)×20
Branch controller		16 ports + 4 ports sub(VRF/Hybrid VRF)
Total refrigerant piping length		264 meters (VRF),40 meters (Hybrid VRF)
Piping length Outdoor unit – Branch controller		40 meters(VRF/Hybrid VRF)
Main pipe size	High	19.05 millimeters (R410A),15.88 millimeters (R32)
	Low	22.2 millimeters

Table 3. Calculation condition

-	Heating	Cooling
Air temperature of outdoor (dry bulb/wet bulb) (℃)	7.0/6.0	35.0/27.0
Air temperature of indoor (dry bulb/wet bulb) (℃)	20.0/15.0	27.0/19.0
Capacity (kW)	37.5	33.5
Input (kW)	(Outdoor + Branch controller + Indoor)	
Air flow of outdoor (m^3/min)	185	185
Air flow of indoor (m^3/min)	8.5 (VRF) 10.5 (Hybrid VRF)	8.5 (VRF) 10.5 (Hybrid VRF)

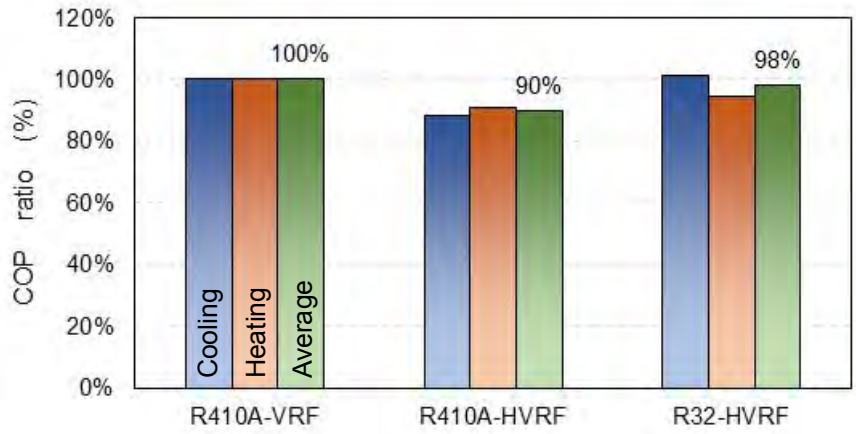

Figure 9: Comparison of efficiency of air conditioning system

Table 4. Comparison of efficiency of air conditioning system

-		VRF R410A	Hybrid VRF R410A	Hybrid VRF R32
Efficiency ratio (%)	Heating	100	91	94
	Cooling	100	88	101
	Average	100	90	98

5. REDUCTION IN REFRIGERANT MASS AND GREENHOUSE GAS EMISSIONS

The system conditions are the same as Table 2. Comparison of refrigerant mass is shown in Fig. 10, Table 5. The refrigerant mass of the R410A-VRF, the R410A-Hybrid VRF and the R32-Hybrid VRF are 24.4 kg, 13.8 kg and 11.6 kg, respectively. The R32-Hybrid VRF can reduce refrigerant mass by 52 percent compared to the R410A-VRF. A breakdown of the refrigerant mass reduction effect of the R32-Hybrid VRF is 43 percent by the Hybrid VRF conversion, 9 percent by R32 refrigerant conversion and downsize of refrigerant piping from the outdoor unit to the Branch Controller.

Table 6 compares the greenhouse gas emissions converted to CO_2. The greenhouse gas emissions of the R410A-VRF, the R410A-Hybrid VRF and the R32-Hybrid VRF are 50.94 t, 28.81 t, and 7.83 t, which are multiplied by the refrigerant mass of R410A refrigerant and R32 refrigerant by GWP. The R32-Hybrid VRF can reduce greenhouse gas emissions by 84 percent for the R410A-VRF.

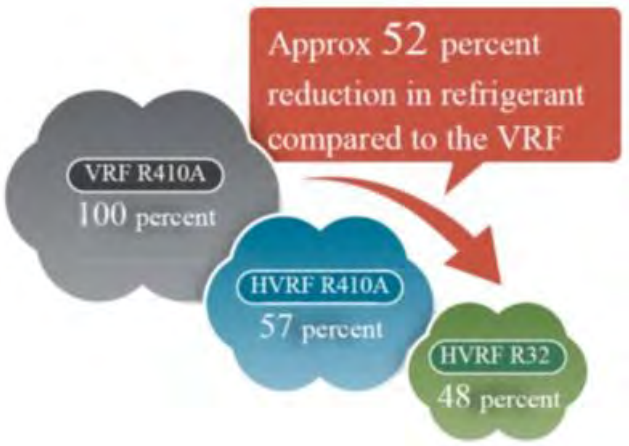

Figure 10: Comparison of refrigerant mass

Table 5. Comparison of refrigerant mass

-		VRF R410A	Hybrid VRF R410A	Hybrid VRF R32
Total refrigerant piping length (meters)		264	40	40
Main pipe size (millimeters)	High	19.05	19.05	15.88
	Low	22.2	22.2	22.2
Refrigerant mass (kg)		24.4	13.8	11.6

Table 6. Comparison of greenhouse gas emissions converted to CO_2

-	VRF R410A	Hybrid VRF R410A	Hybrid VRF R32
Refrigerant mass (kg)	24.4	13.8	11.6
GWP ($kg_{(CO2)}$/kg)	2088	2088	675
CO_2 equivalent (t)	50.94	28.81	7.83

6. CONCLUSIONS

The world's first water-based multi air conditioning system with 2-pipe heat recovery function "Hybrid VRF" was developed. This system converts the medium from refrigerant to water in the middle of the route from the outdoor unit to the indoor unit and conveys it into the room, and it applies R32 refrigerant and realizes the same workability as VRF without additional safety measures. Product features and application technologies of the R32-Hybrid VRF, the reduction effect of the refrigerant mass and the greenhouse gas emissions were described.

(1) The R32-Hybrid VRF is an environmentally conscious system that realizes GWP reduction by applying R32 refrigerant and reducing the refrigerant mass by using water. It is the world's first water-based multi air conditioning system with 2-pipe heat recovery function which applied R32 refrigerant.

(2) The R32-Hybrid VRF can produce simultaneous cooling and heating operation by simultaneously producing cold/hot water and supplying it to indoor units.

(3) Since the Hybrid VRF has a 2-pipe packaging system, it can simplify design and reduce materials and equipment, compared with a 4-pipe chiller system or a 3-pipe VRF system.

(4) The R32-Hybrid VRF can prevent direct refrigerant leakage into the room by limiting the area where the refrigerant flows.

(5) In the case assumed this time, the COP of R32-Hybrid VRF is equivalent to the R410A-VRF by improving theoretical COP and reducing pressure loss.

(6) In the case assumed this time, the R32-Hybrid VRF was able to reduce greenhouse gas emissions converted to CO_2 to 84 percent that of the R410A-VRF.

Manuscript ID: 1521
DOI: 10.18462/iir.icr.2019.1521

A dual-function absorption heat pump cycle for space conditioning and water purification

Daniel B. BOMAN[(a)], Srinivas GARIMELLA[(a)]

[(a)]Sustainable Thermal Systems Laboratory,
GWW School of Mechanical Engineering,
Georgia Institute of Technology,
Atlanta, GA, 30332, sgarimella@gatech.edu

ABSTRACT

A dual-function absorption heat pump cycle is developed for graywater purification and space conditioning. This cycle extracts vapor directly from an impure feed in the evaporator and collects condensate in the condenser while running membrane distillation in parallel with the desorber to allow additional water production. Thermodynamic modeling of this cycle is conducted by solving mass, species, and energy balances for each of the cycle components. Lithium bromide is used as the absorbent. Baseline performance of the cycle is determined at a set of operating conditions associated with a single-family home in the U.S. Parametric studies are conducted to determine water flows and performance over a range of water loads. The energy ratio of the cycle, which measures the total useful output as a function of power input, peaks above 1.5 for cooling mode and 1.6 for heating mode.
Keywords: Absorption, Heat Pump, Waste Recovery, Water Purification.

1. INTRODUCTION

With increasing concerns about sustainability, efforts are being made to extract more utility from available resources. Although initial development of space heating, space cooling, power generation, fuel production, and water purification techniques proceeded along separate paths and resulted in separate facilities, in recent years, engineers have sought to combine these disparate functions into cogeneration or polygeneration facilities that demonstrate enhancements in performance (Murugan and Horák, 2016; Wu and Wang, 2006). Similar strategies have been considered in the water purification space, where adsorption desalination (Ng et al., 2012; Youssef et al., 2015), humidification-dehumidification desalination (Nada et al., 2015), and absorption desalination (Wang and Lior, 2011) have been combined with cooling.

Indoor residential water use in the United States is on average 522 liters per household per day (DeOreo et al., 2016), of which 60% is discharged as graywater. A graywater purification method with a 90% recovery rate, therefore, could reduce indoor water use by approximately 54%, resulting in a water savings of over 60 million cubic meters per day nationwide. To achieve this, modifications are made to a single-effect absorption heat pump, allowing the system to perform water purification in addition to heating and cooling. Two methods of water purification are considered – one that takes advantage of the inherent operating strategy of the absorption heat pump, and one that provides additional capacity when needed. The heat pump is modeled thermodynamically, and performance is calculated using appropriate figures of merit.

2. CYCLE DEVELOPMENT

A single-effect absorption heat pump with a non-volatile absorbent consists of four primary heat exchangers (desorber, condenser, evaporator, and absorber), a pump, two expansion valves, and a recuperative solution heat exchanger (SHX), and operates in the following manner. The cycle begins with dilute solution flowing into the desorber, where heat is added from a low-grade heat source to evolve refrigerant from the solution. The refrigerant then condenses in the condenser, where it

rejects heat, and flows through an expansion valve to the evaporator, where it receives heat at low temperature to provide cooling. The resulting vapor flows into the absorber, where it is absorbed into the concentrated solution returning from the desorber. The dilute solution is then pumped from the absorber through the SHX back to the desorber to begin the cycle anew.
Cooling can be achieved in an absorption heat pump by coupling the evaporator to the conditioned space. In this case, heat from the absorber and condenser must be rejected. Heating can be achieved by coupling the absorber and/or condenser to the conditioned space. In heating mode, additional heat must be provided to the evaporator.

2.1. Modifications to Allow Water Purification

An absorption heat pump using water as the refrigerant, such as one using the water-LiBr working pair, is an excellent candidate as a water purifier, as between the inlet of the evaporator and the outlet of the condenser, the water undergoes two distillation processes – one in the evaporator and one in the desorber. The challenge, then, is to ensure that if pure water is extracted in the condenser, it is replenished prior to entering the evaporator so that the required cooling capacity can be satisfied. This can be achieved by introducing graywater into the evaporator to satisfy the required refrigerant flow rate in either cooling or heating mode.
For cases when the water load exceeds that at which all of the refrigerant would be extracted in the condenser, a secondary method of water purification must be incorporated in the cycle. As the cycle must operate at subatmospheric pressure, using a membrane to allow the graywater to be purified to remain at positive pressure is beneficial. There are two membrane-based methods of water purification that could be incorporated: forward osmosis and membrane distillation. For this work, membrane distillation is selected because there is no direct contact between the fluids on the two sides of the membrane; this eliminates concerns about the potential for the absorbent to diffuse through the membrane if the absorbent solution is used as the draw solution for forward osmosis. Figure 1 shows the open-loop heat pump cycle in cooling mode (Figure 1a) and heating mode (Figure 1b) with MD incorporated. Note that the graywater used to cool the absorber and condenser is used to drive the evaporator during heating mode. Membrane distillation (MD) is incorporated into the desorber as vapor-gap MD, with the vapor generated proceeding directly to the condenser.
One of the advantages of adding graywater purification to an absorption heat pump is the inherent presence of a liquid heat transfer medium for heat rejection from the absorber and condenser. This allows the construction of more compact heat and mass exchangers, which results in a smaller system footprint. The heat received by the graywater as it travels through the cycle is rejected to the ground through a ground-coupled heat exchanger.

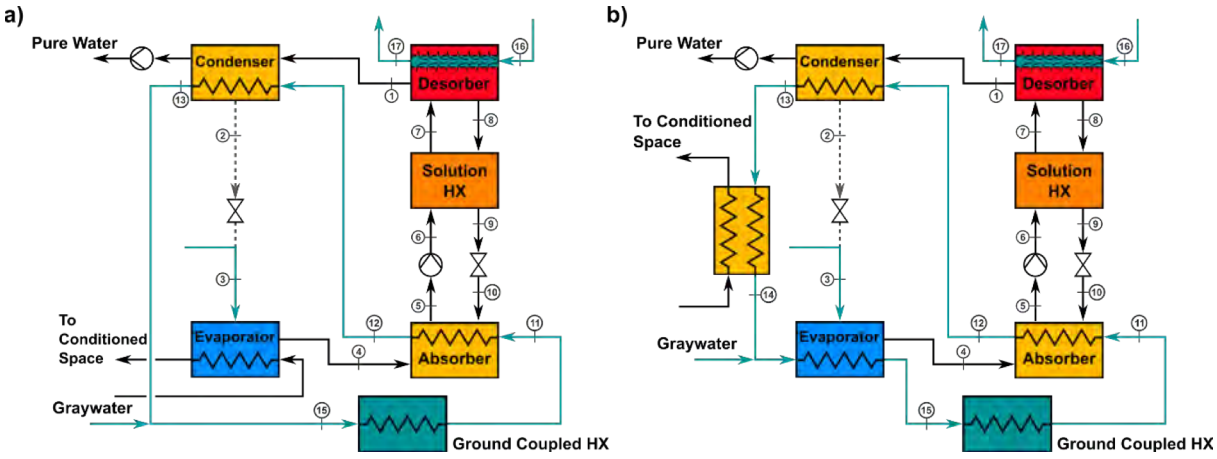

Figure 1: Schematic of an absorption heat pump and water purification cycle with MD for additional purification in a) cooling mode and b) heating mode

2.2. Thermodynamic Modeling

The figure of merit used to describe cycle performance is the energy ratio, which gives the ratio of useful cycle output to cycle power input and is the combination of two other figures of merit: the coefficient of performance (COP) and the standard gained output ratio (SGOR):

$$\mathrm{ER} = \mathrm{COP} + \mathrm{SGOR} \qquad \text{Eq. (1)}$$

The COP is the ratio of the thermal load to the cycle power input. Because the thermal load differs in cooling mode and heating mode, a different COP must be defined for each mode:

$$\mathrm{COP}_c = \frac{\dot{Q}_e}{\dot{Q}_{in} + \dot{W}_{pump}} \qquad \text{Eq. (2)}$$

$$\mathrm{COP}_h = \frac{-\dot{Q}_{cs}}{\dot{Q}_{in} + \dot{W}_{pump}} \qquad \text{Eq. (3)}$$

The negative sign on the heat transfer to the conditioned space is because heat transfer is defined as positive when entering the cycle. In cycles that use water as the refrigerant, pump work may be neglected as it is typically four orders of magnitude smaller than the heat transfer.

The gained output ratio is used in the desalination literature and is the ratio of the mass of water produced to the mass of steam used to provide heat for the purification process (Ghalavand et al., 2015). Because the heat of vaporization of water is a function of temperature, a temperature of 100°C is assumed for the steam. This can be used to convert the cycle energy input into an equivalent mass of steam and yield a dimensionless SGOR:

$$\mathrm{SGOR} = \frac{\dot{m}_w \times 2257\ \mathrm{kJ\ kg^{-1}}}{\dot{Q}_{in} + \dot{W}_{pump}} \qquad \text{Eq. (4)}$$

The quantities necessary to compute the figures of merit for the cycle are determined by performing mass, species, and energy balances on the cycle components. The operating conditions for the cycle are fixed by specifying the outlet temperatures of the desorber, absorber, condenser, and evaporator, the ground temperature, the SHX effectiveness, the pump efficiency, the thermal load and daily water production, and the closest approach temperature differences in the absorber, condenser, and ground heat exchanger. These values are shown in Table 1. The graywater is modeled as a NaCl solution with an initial concentration of 1 wt%. The steady-state concentration depends on the recovery. It should be noted that this is an extremely conservative estimate. (The approximate concentration of NaCl that gives the same osmotic pressure as the synthetic graywater formulation proposed by Hourlier et al. (2010) is 0.045 wt%.)

The following assumptions are used to conduct the cycle analysis:

1. Dilute solution leaving the absorber, concentrated solution leaving the desorber, liquid refrigerant leaving the condenser, and refrigerant vapor leaving the evaporator are in saturated states at their component outlet temperatures. In addition, the vapor leaving the desorber is at the desorber solution outlet (instead of inlet) temperature, which is a conservative estimate.
2. There is no pressure drop between components.
3. The fluid flowing through the condenser and evaporator is pure water.
4. The throttling valves operate isenthalpically.
5. Fluid flowing through the pumps is incompressible.

Table 1. Cycle baseline operating parameters

Parameter	Value
Absorber Temperature (T_a)	35°C
Desorber Temperature (T_d)	100°C
Condenser Temperature (T_c)	50°C
Evaporator Temperature (T_e)	5°C
Ground Temperature (T_{ground})	11°C
HTF Return Temperature ($T_{HTF,in}$)	28°C
Closest Approach Temperature (CAT)	2°C
Pump Efficiency (η_p)	0.85
SHX Effectiveness (ε_{SHX})	0.85
Cooling Load	10.5 kW
Heating Load	15 kW
Water Loads (DWP)	340 kg day^{-1}, 600 kg day^{-1}
Recovery (R)	0.9

The mass balance on the evaporator is:

$$\dot{m}_r = \dot{m}_{e,in} + \dot{m}_{r,loop} \quad \text{Eq. (5)}$$

where $\dot{m}_{e,in}$ is the net mass flow rate of graywater into the evaporator and $\dot{m}_{r,loop}$ is the mass flow rate of water from the condenser to the evaporator.
The absorber mass balance is:

$$\dot{m}_{dil} = \dot{m}_{conc} + \dot{m}_r \quad \text{Eq. (6)}$$

where $\dot{m}_{dil}$ is the mass flow rate of dilute solution and $\dot{m}_{conc}$ is the mass flow rate of concentrated solution.
The desorber mass balance is:

$$\dot{m}_{conc} + \left(\dot{m}_r + \dot{m}_{MD,d}\right) = \dot{m}_{dil} + \dot{m}_{MD,d} \quad \text{Eq. (7)}$$

where $\dot{m}_{MD,d}$ is the mass flow rate of water into the desorber via membrane distillation. It should be noted that the MD flow rate terms on both sides of the equation will cancel, but both are included here to show that water enters the desorber via MD and then exits with the refrigerant stream to flow into the condenser.
The evaporator mass balance is:

$$\dot{m}_{r,c} + \dot{m}_{gray,e,in} = \dot{m}_v + \dot{m}_{gray,e,out} \quad \text{Eq. (8)}$$

where the first term is the water flowing from the condenser to the evaporator and $\dot{m}_v$ is the mass flow rate of vapor flowing from the evaporator to the absorber.
The species balance on the absorber or the desorber is:

$$\dot{m}_{conc} w_{conc} = \dot{m}_{dil} w_{dil} \quad \text{Eq. (9)}$$

where w is the mass fraction of absorbent in the stream in question.
The species balance on the evaporator is:

$$\dot{m}_{gray,e,in} w_{gray,e,in} = \dot{m}_{gray,e,out} w_{gray,e,out} \quad \text{Eq. (10)}$$

Energy balances are calculated on two loops to determine the figures of merit. The first is the solution and refrigerant in the heat pump portion of the cycle. For this loop, the energy balance on the condenser is:

$$\dot{Q}_c = \left(\dot{m}_r + \dot{m}_{MD,d}\right)\left(h_2 - h_1\right) \quad \text{Eq. (11)}$$

where h_i is the specific enthalpy of the solution or refrigerant at state i, as shown in Figure 1.
The energy balance on the evaporator is:

$$\dot{Q}_e = \dot{m}_r h_4 - \dot{m}_{r,loop} h_3 - \dot{m}_{e,in} h_{11} \quad \text{Eq. (12)}$$

The energy balance on the absorber is"

$$\dot{Q}_a = \dot{m}_{dil} h_5 - \dot{m}_{conc} h_{10} - \dot{m}_r h_4 \quad \text{Eq. (13)}$$

The energy balance on the desorber is

$$\dot{Q}_d = \dot{m}_{conc} h_8 + \left(\dot{m}_r + \dot{m}_{MD,d}\right) h_1 - \dot{m}_{dil} h_7 \quad \text{Eq. (14)}$$

The heat transferred in the SHX is determined using the definition of the effectiveness:

$$\dot{Q}_{SHX} = \varepsilon \dot{Q}_{SHX,max} \quad \text{Eq. (15)}$$

where:

$$\dot{Q}_{SHX,max} = \min\left\{\dot{m}_{dil}\left(h_{7,max} - h_6\right), \dot{m}_{conc}\left(h_8 - h_{9,min}\right)\right\} \quad \text{Eq. (16)}$$

and

$$\begin{aligned} h_{7,max} &= h\left(T_8, w_{dil}\right) \\ h_{9,min} &= h\left(T_6, w_{conc}\right) \end{aligned} \quad \text{Eq. (17)}$$

The remaining state points are then determined by applying two energy balances on the SHX:

$$\dot{Q}_{SHX} = \dot{m}_{dil}\left(h_7 - h_6\right) \quad \text{Eq. (18)}$$

$$\dot{Q}_{SHX} = \dot{m}_{conc}\left(h_8 - h_9\right) \quad \text{Eq. (19)}$$

The second loop that is used to calculate the thermodynamic performance of the cycle is the graywater loop, which consists of graywater entering as the coupling fluid at state 11 and receiving heat from the absorption heat pump in the absorber and condenser. In the heating mode, the graywater additionally passes through the conditioned space heat exchanger to deliver energy to the conditioned space and through the evaporator to prevent freezing. The energy balance on the absorber for the graywater is:

$$-\dot{Q}_a = \dot{m}_g\left(h_{12} - h_{11}\right) \quad \text{Eq. (20)}$$

The energy balance on the condenser for the graywater is:

$$-\dot{Q}_c = \dot{m}_g\left(h_{13} - h_{12}\right) \quad \text{Eq. (21)}$$

In cooling mode, following the condenser, the graywater flows through the ground heat exchanger before returning to state 11. In heating mode, the graywater also flows through the conditioned space

heat exchanger and the evaporator. The energy balance on the conditioned space heat exchanger is:

$$\dot{Q}_{cs} = \dot{m}_g \left(h_{14} - h_{13} \right) \quad \text{Eq. (22)}$$

The energy balance on the graywater side of the evaporator is:

$$-\dot{Q}_e = \left(\dot{m}_g - \dot{m}_{MD,d} \right) \left(h_{15} - h_{14} \right) \quad \text{Eq. (23)}$$

The reduction in flow rate from the nominal graywater flow rate is because graywater extracted from the condenser at state 14 is heated to state 16 to replenish the water entering the system via MD.
The amount of water recovered from the graywater can be expressed using the recovery, which is the amount of pure water produced per unit mass of feed. The initial concentration of dissolved solids in the graywater and the recovery are used to determine the concentration of dissolved solids in the graywater in the cycle.
Properties of the NaCl solution are calculated using the work of Clarke and Glew (1985). The properties of the remaining substances are calculated using the Engineering Equation Solver (EES) platform (Klein, 2017). The system of equations comprising the model and the thermodynamic properties of the working fluids are solved simultaneously using EES.

3. RESULTS AND DISCUSSION

Variation in water flows through the cycle is studied as a function of the daily water production rate. The mass flow rates of looped refrigerant, graywater input to the evaporator, and MD input are shown in Fig. 2 for cooling mode and Fig. 3 for heating mode. From these figures, two modes of operation can be defined – a low water mode, in which some of the refrigerant is looped from the condenser to the evaporator, and a high water mode, in which additional pure water is generated via MD. The balanced water point is the point at which all of the graywater supplied to the cycle to satisfy the thermal load is extracted to satisfy the water load.
The flow rate trends in heating mode differ from those in cooling mode. In heating mode, once the cycle begins operating in the high water mode, the graywater input to the evaporator begins to decrease rather than remaining constant. This is because the water added via MD rejects heat as it condenses, which provides additional heat to the conditioned space.
The performance of the cycle in cooling and heating modes is shown in Fig. 4 as a function of the water production. For both modes of operation, the ER peaks at the balanced water operating point and decreases as the load ratio is increased or decreased from this point. In the low water mode, the energy input is constant, while the useful output increases as the load ratio increases. In the high water mode, both the energy input and useful output increase, but the energy required to heat the

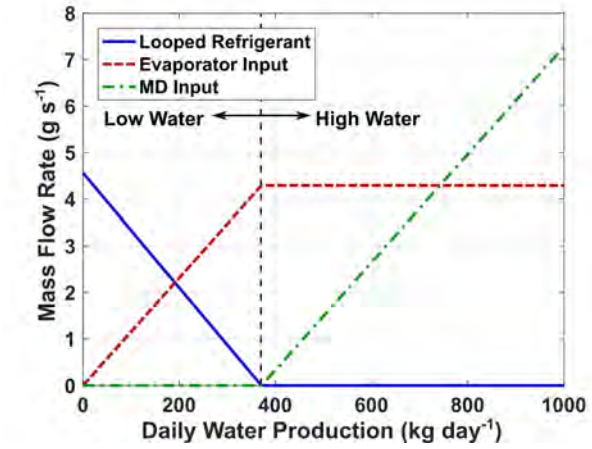

Figure 2: Water flow rates as a function of cycle water load for cooling mode

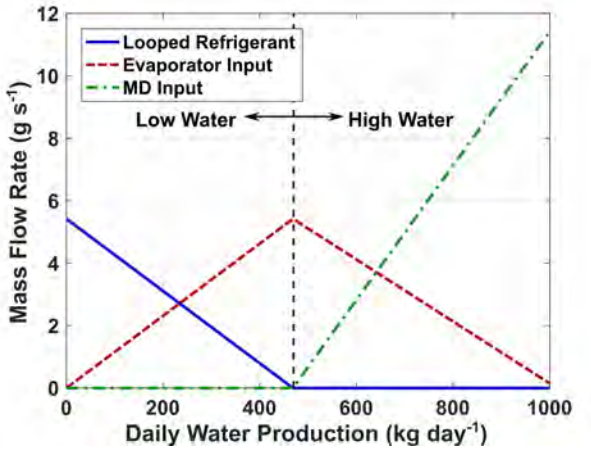

Figure 3: Water flow rates as a function of cycle water load for heating mode

graywater to the MD temperature increases more quickly than the increase in water production, which results in a decrease in ER.

In an ideal heat pump, the heating COP at corresponding conditions could be as high as (cooling COP + 1.) This does not occur for the proposed cycle for two reasons. The first is the limit imposed on the temperature of the conditioned-space heat exchanger, which prevents all of the heat added to the graywater in the absorber and condenser from being transferred to the conditioned space. The second is heat transfer to the ground. In the basic configuration, the temperature of the graywater leaving the evaporator is higher than the temperature of the graywater leaving the ground-coupled heat exchanger. Rejecting this heat to the ground requires that it be added again in the absorber. Therefore, a reconfiguration of the cycle with a bypass is proposed. The performance of this cycle is shown as a green line in 4. Some fraction of the graywater bypasses the ground heat exchanger, allowing retention of some of the energy in the stream and increasing performance of the cycle. This also pushes the peak to a higher daily water production, as performance does not begin to decrease until the full graywater flow cannot bypass the ground heat exchanger.

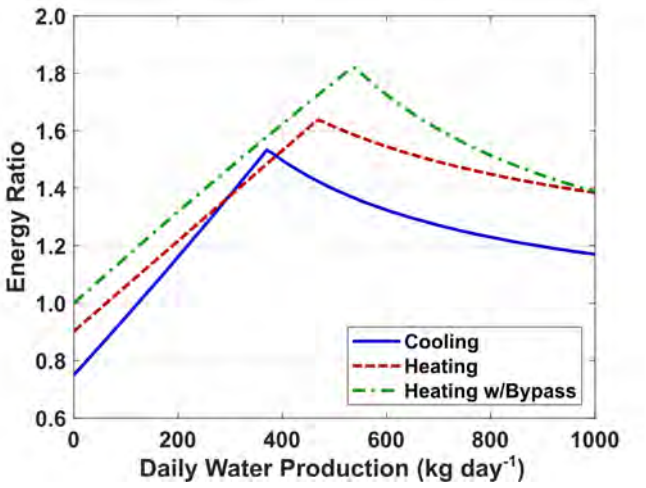

Figure 4: Energy ratio as a function of water load in cooling and heating mode

4. CONCLUSIONS

A reconfiguration of an absorption heat pump to enable graywater purification for direct potable reuse as a secondary function is developed. The reconfiguration changes a water-based absorption heat pump from a closed-loop cycle to an open-loop cycle and adds a membrane distillation module. A thermodynamic model of the modified absorption heat pump is developed and used to simulate its performance over a range of load ratios, which reveals the presence of low water and high water operating modes. The ER of the cycle peaks at the balanced water operating mode, exceeding 1.5 for cooling mode and 1.6 for heating mode in the base configuration. Reconfiguring the cycle in heating mode so that the graywater bypasses the ground heat exchanger results in an increase in performance for all load ratios at the baseline ground temperature.

NOMENCLATURE

COP	coefficient of performance	SGOR	standard gained output ratio
DWP	daily water production (kg day^{-1})	T	temperature (°C)
h	specific enthalpy (kJ kg^{-1})	w	weight fraction
$\dot{m}$	mass flow rate (kg s^{-1})	ε	effectiveness
$\dot{Q}$	heat transfer rate (kW)	η_p	pump efficiency

Subscripts

a	absorber	e, in	graywater flow into evaporator
c	condenser	g	graywater
$conc$	concentrated solution	max	maximum
cs	conditioned space	MD,d	from membrane distillation
d	desorber	min	minimum
dil	dilute solution	SHX	solution heat exchanger
HTF, in	conditioned space HX return	r	refrigerant
e	evaporator	$r, loop$	looped refrigerant

REFERENCES

Clarke, E.C.W., Glew, D.N., 1985. Evaluation of the Thermodynamic Functions for Aqueous Sodium Chloride from Equilibrium and Calorimetric Measurements below 154 °C. Journal of Physical and Chemical Reference Data 14(2), 489-610.

DeOreo, W.B., Mayer, P., Dziegielewski, B., Kiefer, J., 2016. Residential End Uses of Water, Version 2: Executive Report. Denver, CO, Water Research Foundation.

Ghalavand, Y., Hatamipour, M.S., Rahimi, A., 2015. A review on energy consumption of desalination processes. Desalination and Water Treatment, 1-16.

Hourlier, F., Masse, A., Jaouen, P., Lakel, A., Gerente, C., Faur, C., Le Cloirec, P., 2010. Formulation of synthetic greywater as an evaluation tool for wastewater recycling technologies. Environmental Technology 31(2), 215-223.

Klein, S.A., 2017. EES - Engineering Equation Solver. Middleton, WI, F-Chart Software.

Murugan, S., Horák, B., 2016. Tri and polygeneration systems - A review. Renewable and Sustainable Energy Reviews 60, 1032-1051.

Nada, S.A., Elattar, H.F., Fouda, A., 2015. Performance analysis of proposed hybrid air conditioning and humidification–dehumidification systems for energy saving and water production in hot and dry climatic regions. Energy Conversion and Management 96, 208-227.

Ng, K.C., Thu, K., Saha, B.B., Chakraborty, A., 2012. Study on a waste heat-driven adsorption cooling cum desalination cycle. International Journal of Refrigeration 35(3), 685-693.

Wang, Y., Lior, N., 2011. Proposal and analysis of a high-efficiency combined desalination and refrigeration system based on the LiBr–H_2O absorption cycle—Part 1: System configuration and mathematical model. Energy Conversion and Management 52(1), 220-227.

Wu, D.W., Wang, R.Z., 2006. Combined cooling, heating and power: A review. Progress in Energy and Combustion Science 32(5-6), 459-495.

Youssef, P.G., Mahmoud, S.M., Al-Dadah, R.K., 2015. Performance analysis of four bed adsorption water desalination/refrigeration system, comparison of AQSOA-Z02 to silica-gel. Desalination 375, 100-107.

Manuscript ID: 1537
DOI: 10.18462/iir.icr.2019.1537

Alternative energy storage using a domestic hot water solar-assisted heat pump with PV collector/evaporator and HC refrigerant

C.A. ISAZA-ROLDAN[(a)], William QUITIAQUEZ [(b)], César NIETO-LONDOÑO [(a)], Luis TOAPANTA [(b)], Isaac SIMBAÑA [(b)]

[(a)] Universidad Pontificia Bolivariana de Medellín
Medellín, 050031, Colombia, cesar.isaza@upb.edu.co, cesar.nieto@upb.edu.co
[(b)] Universidad Politécnica Salesiana
Quito, EC170607, Ecuador, wquitiaquez@ups.edu.ec, ltoapanta@ups.edu.ec
asimbana@ups.edu.ec

ABSTRACT

This work presents the thermodynamic analysis of a direct-expansion solar-assisted heat pump to provide domestic hot water. An aluminum bare collector/evaporator and a compressor that uses refrigerant R600a as working fluid compose the system. Boiling and condensation temperatures are -8 and 54.4 °C, respectively. The system test is conducted under different weather conditions (i.e. rainy, cloudy and clear day), obtaining a variation of the coefficient of performance between 4.07 and 6.72 for an average solar radiation in the range of 451.6 and 721.5 $W \cdot m^{-2}$. The water final temperature attains a value between 47.7 and 58.6 °C. The system works with solar energy, both thermal and photovoltaic, to replace conventional energy sources conducing to decrease the carbon reduction factor (CFC) in 89.5 % being lower than the 1977.2 kg of annual CO_2 emissions produced by an electric shower.
Keywords: Heat Pump, Solar Energy, Direct Expansion.

1. INTRODUCTION

The economic and social development have conducted to an increase in energy demand, mainly supported by burning of fossil fuels. According to Weldekidan, Strezov and Town (2018), fossil fuels reserves will deplete in seventy years. A 45 % of domestic hot water is obtained burning fossil fuels and a 24 % using electric energy having only a 13 % heated by thermal solar energy (Moore, Urmee, Rezvani and Baverstock, 2017). Domestic energy consumes about 26.8 % of the total energy demand where water-heating systems are the main energy consumption application. This consumption represents a 19 % of worldwide greenhouse gas emissions caused by using fossil fuels (Casanovas-Rubio and Armengou, 2018). By implementing a solar-assisted system, it will help to reduce emissions associated with burning fuels, preserving the environment and improving the operational and installation costs. An alternative manner to get hot domestic water is by implementing a direct-expansion solar-assisted heat pump (DX-SAHP). This type of system works within a vapor-compression refrigeration cycle, where the evaporator also works as a solar collector. A review carried out by Poppi, Sommerfeldt, Bales, Madani and Lundqvist (2018) shows several theoretical and experimental studies of DX-SAHP systems, the most of them emphasize about of a performance analysis. A DX-SAHP is a viable option to replace conventional water heaters, due to its higher performance against conventional gas or electric water heaters and by the reducing in 30 % the electric consumption and decreasing of operating costs from 13 to 25 %.
DX-SAHP improves can be attained by implementation of renewable source. Kong, Sun, Dong, Jiang and Li (2018), studied the performance of a DX-SAHP system using R-134a as working fluid. That system presented important advantages, like a superior thermodynamic performance related with a

higher coefficient of performance (COP), a lower system cost and a long-life time. The heating water reached a final temperature between 50 to 60.3 °C depending of the weather conditions, while the COP reduces its value in a 20.8 %.
Mohanraj, Belyayev, Jayaraj and Kaltayev (2018), show a refrigeration compression process using only by using absorbed heat from the solar radiation. Despite this type of heat pumps has high efficiencies, local weather conditions affect its performance, including ambient temperature and wind speed. A thermodynamic analysis of this system allows establishing that the generated energy is 2.09 kW with an average COP of 2.57.
Omojaro and Breitkopf (2013), shown that DX-SAHP systems are 75 % used for water heating, 19 % for space heating and the remaining on cooling. They found similar studies about designing and optimization of applications, aiming to reduce the overall cost system and improving collector's efficiency. The authors concluded that the solar collector is the main component, pre-heating the refrigerant before it passes through the compression process. Finally, they prove that the coefficient of performance decreases while water's temperature increase.
Cerit and Erbay (2013), studied experimentally the effect of roll-bond evaporator´s design on the performance of a heat pump. They concluded that as the number of passes increase the system's performance improves: e.g., 8 passes implies a COP value of 3.30, compared with 3.14 and 2.42 for 4 and 2 passes, respectively.
Sun, Wu, Dai and Wang (2014), showed that other factors beyond the climatological ones influence the collector/evaporator performance. Their experimental study demonstrated an improvement on the roll-bond collector performance by optimizing the geometry of the flow channel pattern. The whole system performance was increased by improving the heat conduction imposing a uniform temperature through the roll-bond collector surface and a reducing the approaching temperature to the saturation point.
Tagliafico, Scarpa and Valsuani (2014), conducted an experimental performance analysis of a DX-SAHP to confirm the efficiency of these systems in cloudy and rainy weather conditions. They showed that solar-assisted heat pumps could save around of 50 % in primary energy.
Based on the foregoing, the main objective of this study is to perform an experimental analysis of a DX-SAHP prototype by using R600a as a working fluid under very diverse weather conditions such as clear, cloudy and rainy to determine the best weather conditions to reach the highest performance. Fig. 1 shows the order of the process, where each step describes the activities to do. Experimental tests were done at an altitude of 2850 meters above sea level (0°15'32.1552"S, 78°33'12.87"W) in Quito, a city closest to the equator. A DX-SAHP is a high performance system to get hot domestic water using electric energy provided from photovoltaic system, additionally and an environmentally friendly refrigerant was used. This is an ideal application due to water does not surpass a temperature of 70 °C, a reachable goal using only solar energy.
This paper has the following structure. Section 2 presents the description of the DX-SAHP system developed. Section 3 details the theoretical model applied to perform the energy balances of each component. Section 4 discusses the obtained experimental results considering the different weather and system performance. Section 5 details conclusions and recommendations regarding the results obtained.

2. SYSTEM DESCRIPTION

A DX-SAHP works within a vapor-compression refrigeration cycle, gaining heat from hot surroundings to warm water, contained in a storage tank. A bare flat-plate solar collector/evaporator composes the system and boils the refrigerant with the solar radiation. The installed compressor has a power of 86 W and use R600a as working fluid and PV panels power it. Other used component is the condenser, built with a copper pipe submerged in an acrylic storage tank where the heat transfer takes places to condense the refrigerant to start the cycle again. Finally, a thermostatic expansion valve reduces the refrigerant temperature and pressure before it enters into the evaporator. Table 1 summarizes the information of the components of the system. The thermodynamic analysis was done in an ideal refrigeration cycle, considering saturated and overheated vapor at the inlet and outlet of the compressor, respectively, saturated liquid at the condenser outlet and a mixture entering

to the evaporator. Fig. 2 shows the layout of each used component including the manometers and thermocouples.

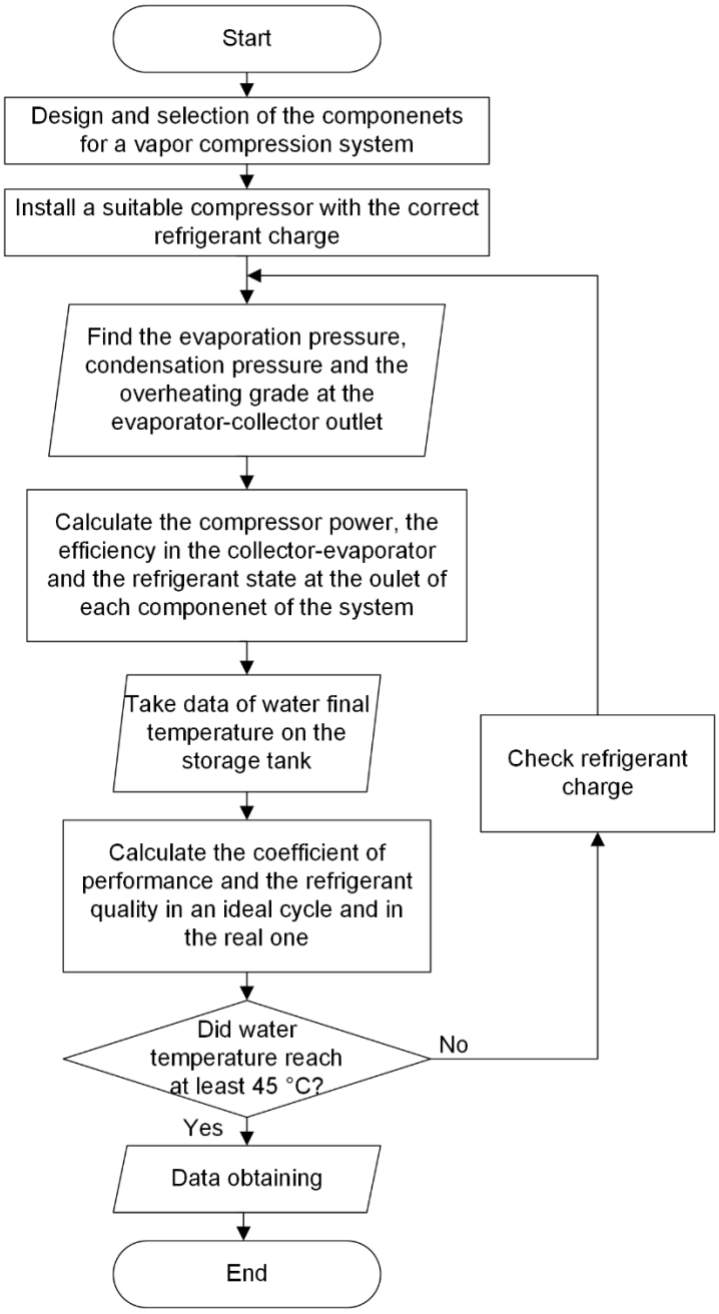

Figure 1: Flow diagram of the investigation process

Table 1. Description of each component of the system

Component	Description
Collector/evaporator	Bare aluminum flat-plate of 1.5 m^2
Compressor	Danfoss BD35K
Condenser	Copper pipe of 1/4 in for 10 liters of water
Expansion valve	Thermostatic type

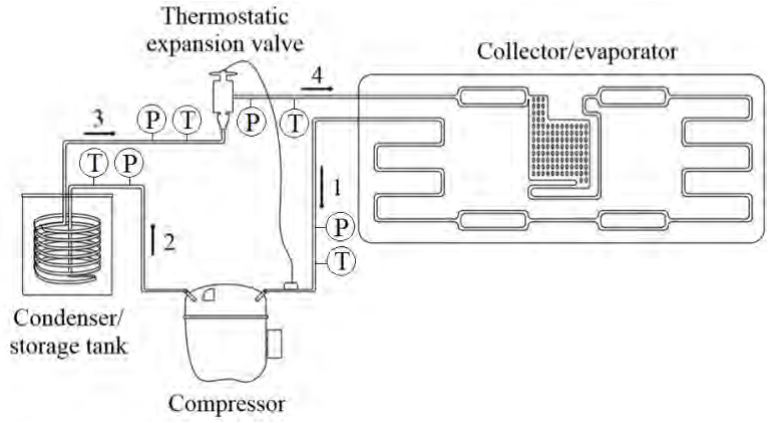

Figure 2: DX-SAHP components (P is a manometer and T is a thermocouple)

3. THEORETICAL MODEL

This investigation concerns a thermodynamic experimental analysis of DX-SAHP system. The data collection process started with several tests to calibrate the system until it gives an appropriate performance and then complete experimental tests to get the data, including pressure, temperature and climatic conditions, like radiation and ambient temperature. Mathematical models for solar radiation and thermodynamic balances in the refrigeration cycle allows processing and evaluating the performance of the system. The analysis includes evaluate enthalpies evaluation as function of the measured pressure and temperature values at inlet and outlet of each component.

3.1. Solar Angles

According to Stanciu C. and Stanciu D. (2014), the slope solar angle (δ) is function of the day of the year (N):

$$\delta = 23.45 \cdot \sin\left[\frac{360}{365}\cdot(284+N)\right]. \quad \text{Eq. (1)}$$

It is important to consider the latitude ($\emptyset$) of the closest location to the system position. For a bare collector/evaporator, the equation reported by Hafez, Soliman and Ismail (2017) permits to obtain the tilt angle (β):

$$\beta = \phi - \delta\,. \quad \text{Eq. (2)}$$

The incidence angle (Θ) of the solar beam for an oriented surface in any direction is follows (Kalogirou, 2014):

$$\cos\theta = (\sin\delta\cdot\sin\phi\cdot\cos\beta) - (\sin\delta\cdot\cos\phi\cdot\sin\beta\cdot\cos\gamma) + (\cos\delta\cdot\cos\phi\cdot\cos\beta\cdot\cos\omega)\ldots$$
$$\ldots + (\cos\delta\cdot\sin\phi\cdot\sin\beta\cdot\cos\gamma\cdot\cos\omega) + (\cos\delta\cdot\sin\beta\cdot\sin\gamma\cdot\sin\omega) \quad \text{Eq. (3)}$$

For this investigation, the inclination of the surface must be verified, due to it may be with a slope to the north or south, so Y = 180 and 0 °, respectively (Seme, Štumberger and Hadz, 2016). Therefore, equation 3 can reduce:

$$\cos\theta = \sin\delta\cdot\sin(\varphi+\beta) + \cos\delta\cdot\cos\omega\cdot\cos(\varphi+\beta). \quad \text{Eq. (4)}$$

$$\cos\theta = \sin\delta\cdot\sin(\varphi-\beta) + \cos\delta\cos\omega\cdot\cos(\varphi-\beta). \quad \text{Eq. (5)}$$

The solar angle (ω) can be calculated from the number of minutes that exist between the local solar noon and a specific hour as follows (Kalogirou, 2014):

$$\omega = \pm\ 0.25(\text{Number of minutes from local solar noon}). \quad \text{Eq. (6)}$$

There is an angle between the solar beams and a horizontal surface called solar altitude angle (α). This angle has a relation with the zenith angle (ψ) given by the equation reported by Jamil, Siddiqui and Akhtar (2016):

$$\sin\alpha = \cos\psi = \sin\varphi \cdot \sin\delta + \cos\varphi \cdot \cos\delta \cdot \cos\omega . \quad \text{Eq. (7)}$$

The solar azimuth angle depends of the solar angle, solar slope angle and solar altitude angle. Therefore, it can be calculated as follows (Kalogirou, 2014):

$$\sin z = \frac{\cos\delta \cdot \sin\omega}{\cos\alpha} . \quad \text{Eq. (8)}$$

The sunset angle (ω_{ss}) is given by the equation reported by Duffie and Beckman (2013):

$$\cos\omega_{ss} = -\tan\phi \cdot \tan\delta \ . \quad \text{Eq. (9)}$$

The following subsections present the thermodynamic analysis for each component of the system.

3.2. Collector/Evaporator

The useful gained heat in the collector/evaporator in terms of change of the refrigerant enthalpy is expressed by (Abdul Aziz, Mat and Sopian, 2013; Hawlader, Chou and Ullah, 2001; Kjellsen, 2016):

$$\dot{Q}_{evap} = \dot{m} \cdot \Delta h_{evap} , \quad \text{Eq. (10)}$$

where $\dot{Q}_{evap}$ is the heat rate of the refrigerant, h is the specific enthalpy at the evaporator inlet and outlet respectively. The refrigerant mass flow rate ($\dot{m}$) is calculated by (Chen and Yu, 2017):

$$\dot{m} = \frac{N \cdot \eta_V \cdot V_d}{v_{in}} . \quad \text{Eq. (11)}$$

The volumetric efficiency (η_V) is 95 %, meanwhile the rotary speed for the compressor (N) is 3500 rpm, and its volumetric displacement (V_d) is 300 cm^3 and the specific volume at the compressor inlet (v_{in}) is calculated at a given pressure and temperature.

3.3. Compressor

The power for the compression ($\dot{W}_i$) using the refrigerant enthalpy change can be calculated with the equation reported by Kara, Ulgen and Hepbasli (2008) and Wang et al. (2017):

$$\dot{W}_i = \dot{W}_{comp} \cdot \eta_{comp} . \quad \text{Eq. (12)}$$

The required power for the compressor ($\dot{W}_{comp}$) can be evaluated as mention Deng and Jianlin (2016) and Xu, Deng, Zhang, Yang and Zhang (2009):

$$\dot{W}_{comp} = \dot{m} \ \frac{\Delta h_{comp}}{\eta_{comp}} , \quad \text{Eq. (13)}$$

where, η_{comp}, is the compressor performance indicated by the manufacturer.

3.4. Condenser

In any heat pump, the condenser capacity or the condensation heat rate ($\dot{Q}_{cond}$) is function of the enthalpy change and it can be evaluated by (Chow, Bai, Fong and Lin 2012; Huang, Ji, Xu and Li, 2016):

$$\dot{Q}_{cond} = \dot{Q}_{evap} + \dot{W}_{comp} = \dot{m} \ \cdot \Delta h_{cond} . \quad \text{Eq. (14)}$$

3.5. Thermostatic expansion valve

The throttling process in the expansion valve is isenthalpic, meaning that the specific enthalpy at the inlet and outlet are same as (Li, Wang, Wu and Xu, 2007; Youssef, El-Telbany and Zekry, 2017):

$$h_{val,in} = h_{val,out} . \quad \text{Eq. (15)}$$

3.6. Coefficient of performance

Malali, Chaturvedi and Abdel-Salam (2016) have demonstrated that a solar assisted heat pump can achieve very high coefficient of performance (COP), from 2 to 6 and higher depending the location. The COP is calculated by (Kong, Li, Lin and Yang, 2017):

$$COP = \frac{\dot{Q}_{cond}}{\dot{W}_{comp}} . \quad \text{Eq. (16)}$$

4. RESULTS AND DISCUSSION

This section shows the results for the tests performed to establish the system behavior under different weather conditions. Each test lasted for 75 minutes, testing the DX-SAHP performance under solar radiation and ambient temperature variations. It is important to mention that each test was done at the same time of the day, starting at 11:00, since July until November 2018. A Fluke Ti400 infrared camera was used to corroborate measured temperature by the installed thermocouples where the estimated uncertainty has been provided for measurements about ± 2 %. Fig. 3 shows the taken images from collector/evaporator and the condenser-storage tank.



(a) (b)

Figure 3: Infrared images (a) collector/evaporator (b) condenser-storage tank

For each test, minimum, maximum and average data for the ambient temperature, radiation and water final temperature were taken as it is shown in Table 2.

Table 2. Test daily information

Parameter	Test 1	Test 2	Test 3	Test 4
Climatic condition	Rainy	Cloudy	Clear	Clear
Ambient temperature (°C)	18.7	20	21	20.7
Min. radiation ($W \cdot m^{-2}$)	380.5	412.2	390.2	400.4
Max. radiation ($W \cdot m^{-2}$)	850.6	842.3	1100.2	950.9
Average radiation ($W \cdot m^{-2}$)	451.6	640.4	745.2	675.65
Water final temperature (°C)	47.7	56.5	58.6	57.4
Average wind speed ($m \cdot s^{-1}$)	0.9	1.0	1.4	1.6

As is observed from the results above, the system, performance increases when it operates under favorable conditions (clear days), however the tests during unfavorable days (cloudy and rainy days) show that the system can increase the water temperature up to 40 °C.
Solar irradiation is in function of the local weather conditions, time of the year and site latitude. Test 4 was done under clear sky presenting a minimum and maximum ambient temperature of 20.3 and 21.3 °C, respectively and the average water temperature during this test was 43 °C. The weather conditions increase the system performance. In Test 4, the maximum value of wind velocity was 2.8 $m \cdot s^{-1}$, with an average ambient temperature on 20.7 °C and solar irradiation of 675.65 $W \cdot m^{-2}$, approximately. The wind speed fluctuation does not have a constant behavior; therefore, it is going to influence on the gained heat in the collector/evaporator. Minimum and maximum values of wind speed in a clear day are 0.4 and 2.8 $m \cdot s^{-1}$, respectively.
Fig. 4 presents the solar irradiation during the hours the tests were performed. The maximum solar radiation value during clear conditions was of 1100.2 $W \cdot m^{-2}$. The heating time to increase the water temperature around 50 °C was near 35 minutes for the clear conditions (Test 3) with an average solar irradiation value of 745.2 $W \cdot m^{-2}$ and ambient temperature of 21 °C. However, during cloudy conditions, the water barely increases its temperature to 40 °C for the same period time (35 minutes) with an average solar irradiation of 745 $W \cdot m^{-2}$.

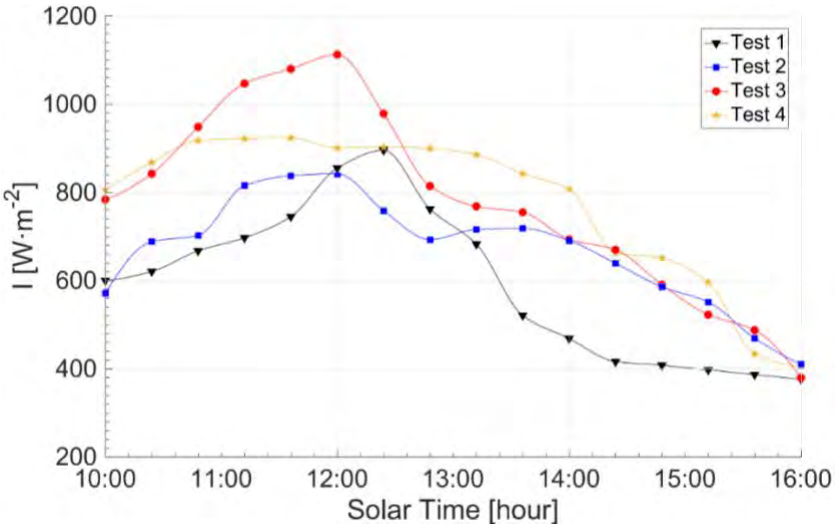

Figure 4: Total solar irradiation on characteristic days

The water gains the released heat at the condenser and increases its temperature during the test as shown in Fig. 5a. The highest temperature is near 60 °C, and is obtained throughout Test 3 (clear conditions). During cloudy conditions (Test 2), the maximum water temperature was 48 °C along the test, despite the reduction in the solar irradiation the water raise its temperature in more than 20 °C respect the initial condition.
Fig. 5b shows values for calculated COP with Eq. (16) through the all tests. On the Test 3, for an average solar irradiation of 745.2 $W \cdot m^{-2}$, the average COP was 4.8; and for a value of 640.4 $W \cdot m^{-2}$, COP was 6.1. In both cases, the water temperatures were 52 and 56 °C, respectively. These values have relation with the ambient temperature during the tests that was 18 and 18.6 °C, respectively. When the solar radiation or ambient temperature increased, the COP of the system increased and the heating time reduced.
Due to this system works with solar energy, it depends on the available solar irradiation, reaching the highest performance at noon (as can be seen in Fig. 4). Fig. 6a shows that the system performance is higher when the solar irradiation has the high values. When received radiation on the surface of the collector/evaporator was 380 $W \cdot m^{-2}$, the value of COP was 4.2. Meanwhile, a radiation that reaches to 1100 $W \cdot m^{-2}$ improved the COP of the system by 62 %, allowing to the water to reach 58.6 °C in 75 minutes, approximately. A similar situation occurs in Fig. 6b. The water may reach a higher final temperature when solar radiation is high and this value depends of ambient temperature. An obtained water temperature during Test 1 was 58 °C with 700 $W \cdot m^{-2}$ and 20.5 °C, as average values of solar radiation and ambient temperature, respectively, finally the obtained COP

under these conditions was 6.4. Results of Figs. 4, 6a and 6b indicate that when the ambient temperature and solar radiation increase, the COP of the system and water temperature increase, besides the heating time decreased. The weather conditions modify the system performance.

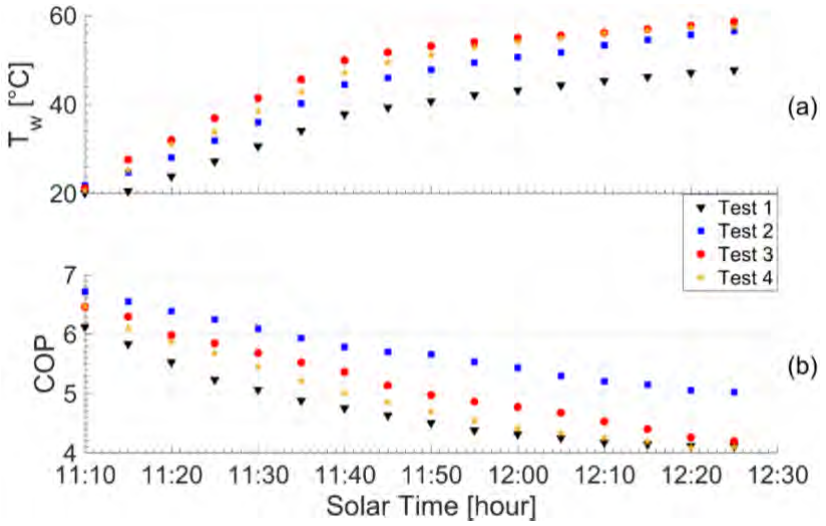

Figure 5: Variation of (a) water temperature (b) COP

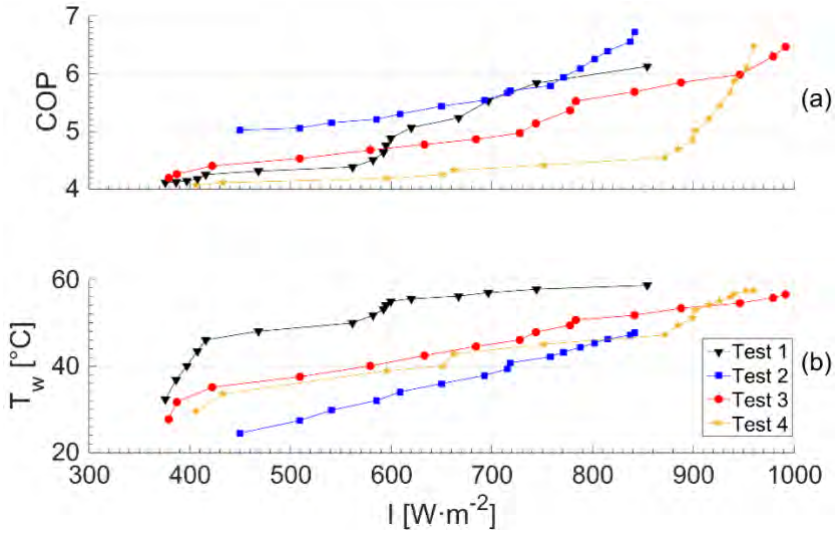

Figure 6: Solar radiation against (a) COP (b) water temperature

The highest gained heat by the collector/evaporator was 305.88 W (Test 2) with a velocity of 2.8 m·s^{-1}, solar radiation of 900 W·m^{-2} and ambient temperature at this time was 20.5 °C. Comparing the previous gained heat with the other conditions (Test 1), for an ambient temperature, solar radiation and wind velocity of 19.4 °C, 750 W·m^{-2} and 0.8 m·s^{-1}, respectively, the gained heat decreased a 11 %, approximately. Fig. 7 shows the variation of gained heat in the evaporator calculated with Eq. (10). It demonstrates the influence of parameters such as solar radiation and ambient temperature in the gained heat by the collector/evaporator. Superheated refrigerant goes out from the evaporator to enter in the compressor, increasing its temperature and pressure, and then it enters in the condenser, which acts a heat exchanger where the refrigerant released the gained heat into the storage tank to heat water. In the condenser, the minimum released values were 266 and 297 W at the end of Test 1 and 2, respectively. This value was obtained by applying Eq. (14) and was affected by low radiation and ambient temperature, 380.5 W·m^{-2} and 18.7 °C, respectively, for Test 1, meanwhile for Test 2, the lowest radiation was 412.2 W·m^{-2}. The maximum value of released heat in the condenser was 359.58 and 326.32 W at the beginning of Test 2 and 1,

respectively. During these tests, there was an ambient temperature of 19 °C, however, in the course of the test, it presents a solar irradiation of 1100 $W \cdot m^{-2}$. In addition, it is possible to affirm that solar radiation influences on the system performance.

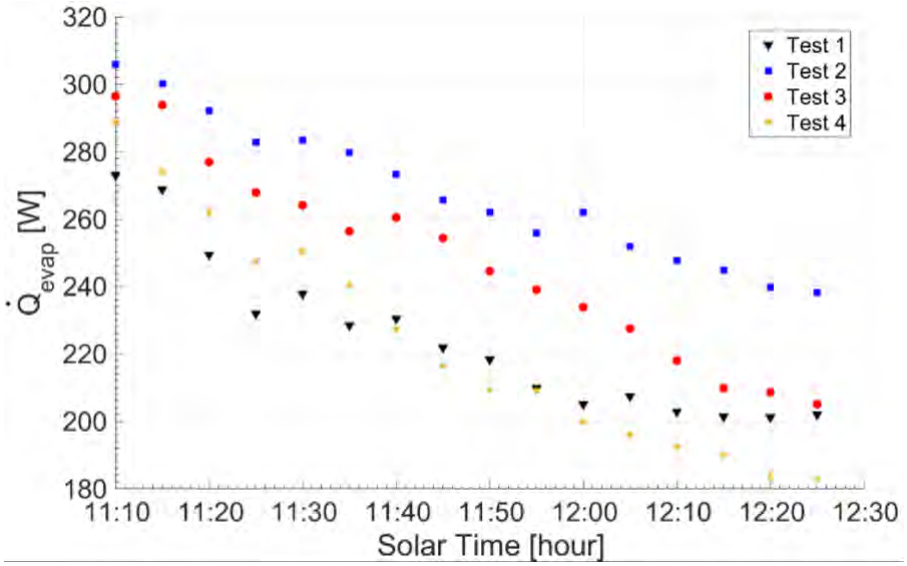

Figure 7: Gained heat by the collector/evaporator

The correct operation of the system depends on the compressor, which uses refrigerant as working fluid. The compressor outlet pressure is in relation with the water heating time as Fig. 8 shows. In the vapor-compression refrigeration cycle, low-pressure refrigerant enters to a solar collector/evaporator and it boils completely by absorbing heat from incident solar energy and surroundings. Exiting vapor from the solar collector/evaporator, in a moderately superheated condition, enters in the compressor, where refrigerant pressure and temperature increase during the compression process. The maximum pressure at the compressor outlet was 779.78 kPa on rainy conditions (Test 1). When the compressor reaches 60 °C, it will stop for safety.

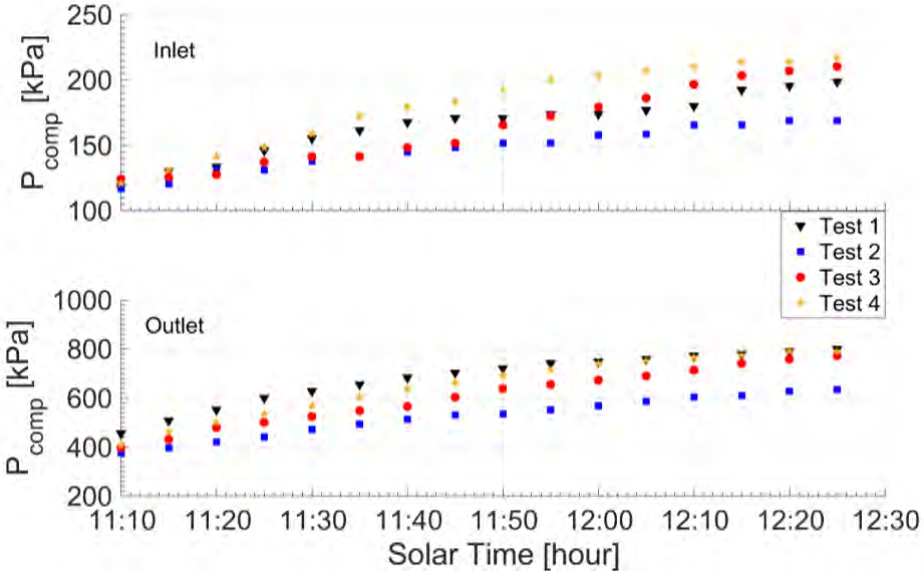

Figure 8: Pressure variation in the compressor

The power demand depends on the mass flow rate, whose variation in time is presented in Fig. 9. This parameter was calculated by applying Eq. (11). The compressor consumption power per mass unit increases greatly while the specific heating capacity increases slightly, resulting in the considerable decline of COP from 6.2 to 4.2 during rainy conditions.

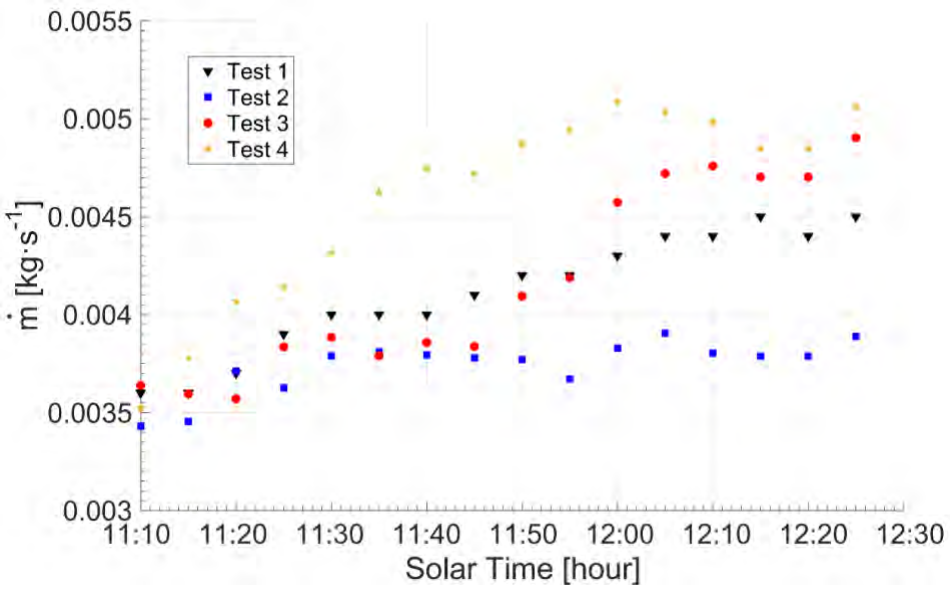

Figure 9: Mass flow rate variation

Besides, COP value decreased from 6.5 to 4.4 for the clear conditions tests. While the system requires more refrigerant mass flow rate due to the operation and climatic conditions, the compressor will increase its energy consumption. The relationship between the compressor power consumption against the mass flow rate required by the system is shown in Fig. 10. Results indicate that a reducing heating time produces a decrease in the total energy consumption of the compressor.

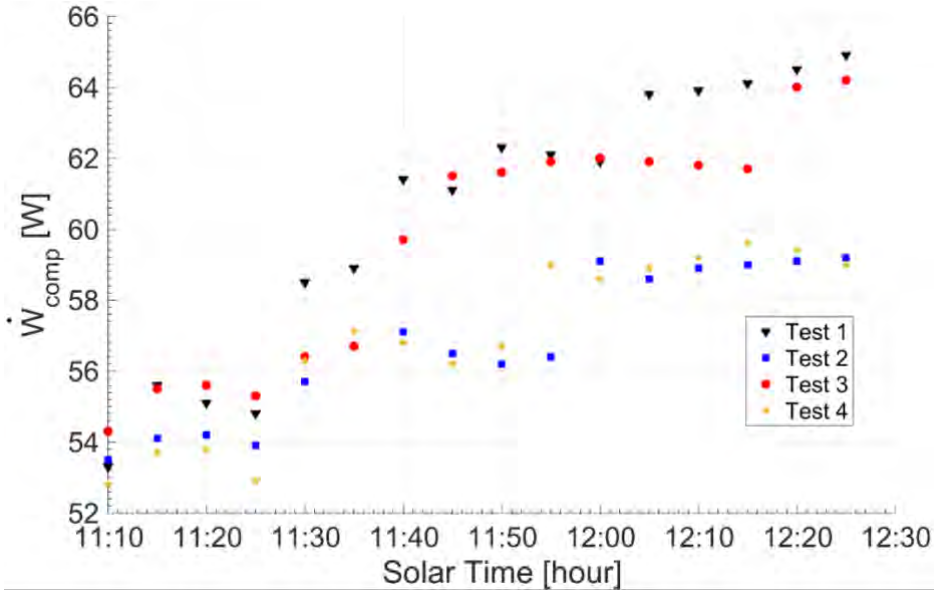

Figure 10: Compressor power variation

5. CONCLUSIONS

A bare collector/evaporator used in a DX-SAHP was studied with a thermodynamic analysis to determinate its performance under several weather conditions. The following conclusions were obtained from this investigation:

Even though the performance is influenced by the weather condition and available solar radiation, the system attains an optimum operating condition in any type of weather conditions; with clear sky,

COP reached a maximum value of 6.72 with an average solar radiation of 721.58 $W \cdot m^{-2}$. However, it also had a COP of 4.07 with a low level of radiation, about of 451.6 $W \cdot m^{-2}$, in average.
Heated water has an almost constant heating process. It depends of the incident solar radiation on the collector/evaporator and the ambient temperature. In clear conditions, water reached a final temperature of 58.6 °C and with a cloudy and rainy weather, water final temperature was 47.7 °C. When the solar radiation or ambient temperature increase, heating time decreases and COP of the system increases.
The carbon reduction factor (CFC) with a maximum COP of 6.72 is 89.5; therefore, by the implementation of this system to replace a conventional electric heating system, there will be a significant reduction in the CO_2 emissions, about a 91 % comparing it with the conventional systems.

ACKNOWLEDGEMENTS

The authors want to express a deep gratitude to the Renewable Energies and Mechanical Implementation of SMEs Research Group of the Universidad Politécnica Salesiana in Ecuador and the Energy and Thermodynamic Research Group of the Universidad Pontificia Bolivariana in Colombia, for supporting the accomplishment of this research.

NOMENCLATURE

N	*Number of the day of the year [dimensionless]*
Q	*Heat [W]*
m	*Mass flow rate [$kg \cdot s^{-1}$]*
h	*Enthalpy [$kJ \cdot kg^{-1}$]*
W_i	*Requiered power [W]*
W	*Power [W]*
A	*Area [m^2]*
I	*Solar radiation instensity [$W \cdot m^{-2}$]*
t	*Time [s]*

Greek symbols

η	*Efficiency*
δ	*Slope solar angle*
φ	*Latitude*
β	*Tilt angle*
θ	*Incidence angle*
γ	*Azimuth angle*
ω	*Solar angle*
α	*Altitude angle*
ψ	*Zenith angle*
z	*Solar azimuth angle*

Subscripts

evap	*Evaporator*
cond	*Condenser*
comp	*Compressor*
val	*Expansion valve*
in	*Inlet*
out	*Outlet*

REFERENCES

Abdul Aziz, M., Mat, S., & Sopian, K. (2013). Technology Review of Solar Assisted Heat Pump System for Hot Water Production. *Latest Trends in Renewable Energy and Environmental Informatics, 8*, 65-75.

Casanovas-Rubio, M., & Armengou, J. (2018). Decision-making tool for the optimal selection of a domestic water-heating system considering economic, environmental and social criteria:

Application to Barcelona (Spain). *Elsevier - Renewable and Sustainable Energy Reviews, 91*, 741-753.
Cerit, E., & Erbay, L. (2013). Investigation of the effect of rollbond evaporator design on the performance of direct expansion heat pump experimentally. *Energy Conversion and Management, 72*, 163-170. doi:10.1016/j.enconman.2012.09.034
Chen, J., & Yu, L. (2017). Theoretical analysis on a new direct expansion solar assisted ejector-compression heat pump cycle for water heater. *Elsevier - Solar Energy*(142), 299-307.
Chow, T. T., Bai, Y., Fong, K., & Lin, Z. (2012). Analysis of a solar assisted heat pump system for indoor swimming pool water and space heating. *Elsevier - Applied Energy, 100*, 309-317.
Deng, W., & Jianlin, Y. (2016). Simulation analysis on dynamic performance of a combined solar/air dual source heat pump water heater. *Elsevier - Energy Conversion and Management, 120*, 678-387.
Duffie, J., & Beckman, W. (2013). *Solar Engineering of Thermal Processes.* New Jersey: Wiley & Sons, Inc.
Hafez, A., Soliman, A., & Ismail, I. (2017). Tilt and azimuth angles in solar energy applications – A review. *Renewable and Sustainable Energy Reviews, 77*, 147-168.
Hawlader, M., Chou, S., & Ullah, M. (2001). The performance of a solar assited heat pump water heating system. *Elsevier - Applied Thermal Engineering, 21*, 1049-1065.
Huang, W., Ji, J., Xu, N., & Li, G. (2016). Frosting characteristics and heating performance of a direct-expansion solar-assisted heat pump for space heating under frosting conditions. *Elsevier - Applied Energy*(171), 656-666.
Jamil, B., Siddiqui, A., & Akhtar, N. (2016). Estimation of solar radiation and optimum tilt angles for south-facing surfaces in Humid Subtropical Climatic Region of India. *Engineering Science and Technology, an International Journal, 19*(4), 1826-1835.
Kalogirou, S. (2014). *Solar Energy Engineering - Processes and Systems.* Oxford: Elsevier, Inc. Academic Print.
Kara, O., Ulgen, K., & Hepbasli, A. (2008). Exergetic assessment of direct-expansion solar-assisted heat pump systems: Review and modeling. *Elsevier - Renewable and Sustainable Energy Reviews, 12*, 1383-1401.
Kjellsen, P. (2016). *Simulations and experiments on a Solar-Assisted Heat Pump Water Heater.* Trondheim: NTNU.
Kong, X. Q., Li, Y., Lin, L., & Yang, Y. G. (2017). Modeling evaluation of a direct-expansion solar assisted. *International Journey of Refrigeration*(76), 136-146.
Kong, X., Sun, P., Dong, S., Jiang, K., & Li, Y. (2018). Experimental performance analysis of a direct-expansion solar-assisted heat pump water heater with R134a in summer. *Elsevier - International Journal of Refrigeration*.
Li, Y., Wang, R., Wu, J., & Xu, Y. (2007). Experimental performance analysis on a direct-expansion solar-assisted heat pump water heater. *Elsevier - Applied Thermal Engineering, 27*, 2858-2868.
Malali, P., Chaturvedi, S., & Abdel-salam, T. (2016). An approximate method for prediction of thermal performance of direct expansion-solar assisted heat pump (DX-SAHP) systems for water heating applications. *Elsevier - Energy Conversion and Management, 127*, 416-423.
Mohanraj, M., Belyayev, Y., Jayaraj, S., & Kaltayev, A. (2018). Research and developments on solar assisted compression heat pump systems – A comprehensive review (Part A: Modeling and modifications). *Elsevier - Renewable and Sustainable Energy Reviews, 83*, 90-123.
Moore, A., Urmee, T., Rezvani, S., & Baverstock, G. (2017). Life cycle assessment of domestic hot water systems in Australia. *Elsevier - Renewable Energy, 103*, 187-196.
Omojaro, P., & Breitkopf, C. (2013). Direct expansion solar assisted heat pumps: A review of applications and recent research. *Elsevier - Renewable and Sustainable Energy Reviews, 22*, 33-45.
Poppi, S., Sommerfeldt, N., Bales, C., Madani, H., & Lundqvist, P. (2018). Techno-economic review of solar heat pump systems for residential heating applications. *Elsevier - Renewable and Sustainable Energy Reviews, 81*, 22-32.
Seme, S., Štumberger, B., & Hadz, M. (2016). A novel prediction algorithm for solar angles using second derivative of the energy for photovoltaic sun tracking purposes. *Solar Energy, 137*, 201-211.

Stanciu, C., & Stanciu, D. (2014). Optimum tilt angle for flat plate collectors all over the World – A declination dependence formula and comparisons of three solar radiation models. *Energy Conversion and Management, 81*, 133-143.

Sun, X., Wu, J., Dai, Y., & Wang, R. (2014). Experimental study on roll bond collector/evaporator with optimized channel used in direct expansion solar assisted heat pump water heating system. *Applied Thermal Engineering, 66*(1-2), 571-579.

Tagliafico, L., Scarpa, F., & Valsuani, F. (2014). Direct expansion solar assisted heat pumps. A clean steady state approach for overall performance analysis. *Applied Thermal Engineering, 66*, 216-226.

Wang, Z., Guo, P., Zhang, H., Yang, W., & Mei, S. (2017). Comprehensive review on the development of SAHP for domestic hot water. *Elsevier - Renewable and Sustainable Energy Reviews, 72*, 871-881.

Weldekidan, H., Strezov, V., & Town, G. (2018). Review of solar energy for biofuel extraction. *Elsevier - Renewable and Sustainable Energy Reviews, 88*, 184-192.

Xu, G., Deng, S., Zhang, X., Yang, L., & Zhang, Y. (2009). Simulation of a photovoltaic/thermal heat pump system having a modified collector/evaporator. *Solar Energy, 83*, 1967-1976.

Youssef, A., El-Telbany, M., & Zekry, A. (2017). The role of artificial intelligence in photo-voltaic systems design and control: A review. *Elsevier - Renewable and Sustainable Energy Reviews, 78*, 72-79.

Manuscript ID: 1550
DOI: 10.18462/iir.icr.2019.1550

Experimental study on the wetting characteristics of a liquid-level-lifting type asymmetrical overflow distributor

Yuhao YI[(a)], Tianle HU[(a)], Xiaoyun XIE[(a)*], Yi JIANG[(a)]
[(a)] Building Energy Research Center, Tsinghua University
Beijing, 100084, People's Republic of China, 13241203123@163.com

ABSTRACT

Shell-tube falling film structure is commonly adopted for the main components in absorption heat pump (AHP). However, this structure leads to a large size. This work aimed to develop a detachable plate-type falling film heat transfer structure, to present a liquid-level-lifting type asymmetrical overflow distributor system to miniaturize the AHP system.
In this work, a specific experimental system was developed. The experimental study under different solution temperatures and distributor dimensions were carried out to find the key factors which influence the wetting characteristics.
A structure with optimal wetting performance was determined under the rated flow after the study. The overall wetting rate reached 95%, and the average thickness of liquid film was as low as 0.44mm. An optimized distributor with ideal wetting performance was presented, which promote the development of the detachable plate-type falling film AHP and the application of absorption technology.
Keywords: Absorption Heat Pump; Plate-type Falling Film; Overflow Liquid Distribution; Wettability

1. INTRODUCTION

An absorption heat pump (AHP) is a thermally driven device that can complete the heat conversion of different grades of thermal energy (T.Hu et al., 2017). Nowadays, a new method of heating by using this system has been proposed to achieve long-distance heat transportation (Y.Li et al., 2011). However, the large size and high cost of traditional AHP limits greater application of absorption technology. For an absorption refrigeration unit with a cooling capacity between 10 and 30 kW, the required volume per unit of cooling capacity is approximately 0.04 $m^3 \cdot kW^{-1}$, while the required unit cooling capacity is only 0.02 $m^3 \cdot kW^{-1}$ of the compression refrigeration unit in the same cooling capacity range (Ruiz G et al., 2011). Conventional AHP uses a shell-and-tube heat exchange structure, which causes the large size (Yau.Y.H et al., 2010). Therefore, a new appropriate heat exchanger form should be researched.
In recent years, different scholars have done a lot of research in different directions such as plate-fin, plate and micro-channel structure (Z.C et al., 2003; Cerezo J et al., 2009; Delahanty J.C. et al., 2015). From the report, the plate-fin structure has the problem that the effect of the fins is not obvious, and the structure is not compact enough (Z.C et al., 2003). What's more, there is no subsequent reports have been reported. The micro-channel structure only made an attempt to ammonia absorption chillers in small capacity (Delahanty J.C. et al., 2015). It has the problem of great process difficulty which can't be used in large-scale engineering applications. Therefore, this paper studies the plate-type falling film absorption heat pump system.
At present, there have been many articles on the research and performance test of the plate type falling film heat exchanger. Mehdi et al. (2015) designed an embossed sheet structure and tested the heat transfer performance. The heat pump could reach the absorption rate of 0.004 $kg \cdot m^{-2} \cdot s^{-1}$ at the design temperature. Benoit et. al. (2017) designed a vertical trough-type falling film structure, which achieved an absorption rate of 0.007 $kg \cdot m^{-2} \cdot s^{-1}$ at low solution flow rates. Yan et al. (2017) conducted a plate-type falling film experiment on liquids with different viscosities, and tested the wetting rate and film thickness. The conclusion was that the film thickness is inversely related to the viscosity. Armel et al. (2014) tested the falling film wetting performance of a single vertical corrugated plate at different solution flows, which found that the wetting rate is higher than the reverse when the flow rate changes from large to small. Al-Sibai et. al. (2005) researched the fluctuation of plate-type

falling film, which found the factors affecting the flow of liquid film are not only the Reynolds number (Re), but also the length of the plate.
Currently, scholars mainly focus on the heat exchange performance of the plate-type absorption heat pump, without considering the problems which may arise in actual engineering. The unit usually has problems that the gas brings solution from generator to evaporator, and the equipment can't be disassembled without destroying the vacuum. Research on the design of plate-type falling film liquid separator has appeared vacancy. There is no special structure of plate-type falling film liquid distributor has been designed. Accordingly, our previous study designed a new structure of plate-type falling film liquid distributor, which can effectively solve the problem of gas bringing solution, and achieve the disassembly of the equipment without breaking the vacuum (T.Hu et al., 2017), this paper also designed different plate textures. In this paper, an experiment was done to tested the wetting rate of the new structure, and the structure of the liquid distributor and the texture of the plate were optimized to achieve a high wetting rate at low density of liquid distribution.

2. FIRST GENERATION OF LIQUID DISTRIBUTOR

In order to solve the problems mentioned earlier, a liquid-level-lifting type asymmetrical overflow distributor system was proposed, first we used the first generation for wetting characteristics experiment. The obtained wetting rate is not great in low solution flow.

2.1. The structure of first generation equipment

Fig. 1 shows the structure of first generation liquid distributor (T.Hu et al., 2017). This liquid distributor can be used in all the heat exchangers of absorption heat pump. When it works in the generator, the solution enters vertically from two sides of the structure shown in Fig. 1(c), and overflows to the inside respectively. Then, the falling film flow state is formed. A 30 mm long baffle is designed on both sides of the solution falling film passage, and the generated steam is discharged from the steam passage inside the baffle plate, as a result, the steam does not bring solution.

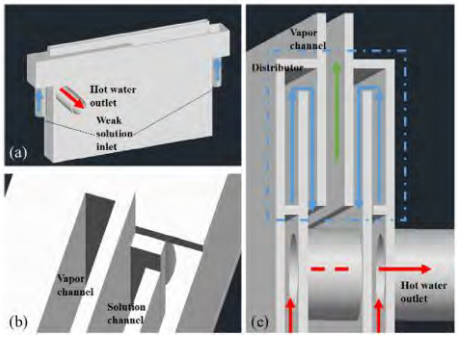

Figure 1: Drawings of the first generation liquid distributor: (a) front view; (b) top vie; and (c) cross-sectional view

On this basis, our previous study designed a multi-channel heat and mass exchanger (HMX) (T.Hu et al., 2019), which can achieve to disassemble the equipment without breaking vacuum. Fig. 2 shows the design concept of HMX. The green and gray parts are steam channels, which are in a vacuum state. The orange portion is an atmospheric water channel formed by splicing two independent units. After the two modules are spliced together, the equipment can be used as a generating-condensing module or an absorbing-evaporating module. When the HMX needs to be disassembled, it can be disassembled into two separate modules for periodic cleaning, while the vacuum channel will not be destroyed.

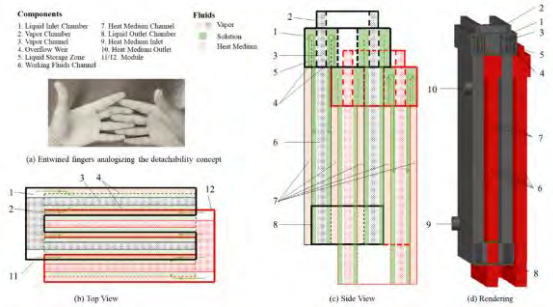

Figure 2: Conceptual sketch of a detachable heat and mass exchanger

2.2. Test system

Fig. 3(a) shows the layout of the experimental setup, while Fig. 3(b) shows the actual photo of the whole test system. A sufficient amount of lithium bromide solution is installed in the effusion tank. When the solution pump is turned on, the solution flows along the tube to the solution box. Then the solution enters the liquid distributor and starts falling film flow. Finally, the solution flows down from the plate and returns to the effusion tank. The flow and wetting characteristics of the solution on the liquid distributor and plate can be studied.

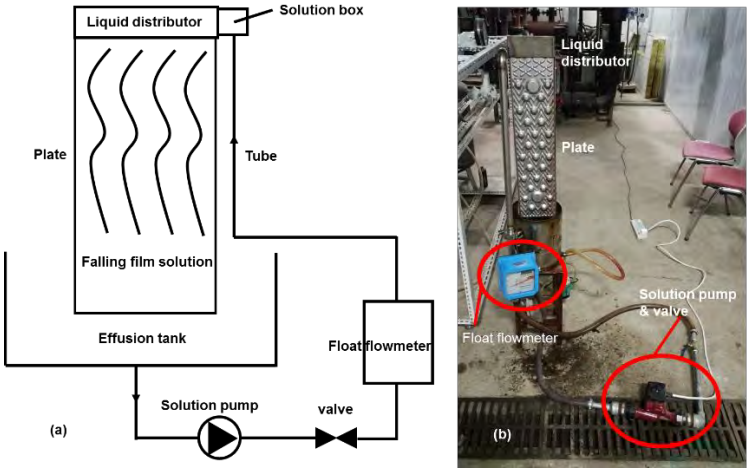

Figure 3: Test system of wetting characteristics of liquid distribution: (a) layout; (b) actual system

A valve is installed on the tube to adjust the flow rate of the solution. We can use it to change liquid density. Specific experimental parameters are shown in Table 1. In order to study the relevant factors affecting the flow characteristics more effectively, the experiment is carried out under atmospheric pressure. Both water and lithium bromide solutions are tested under different densities of liquid distribution. The concentration of lithium bromide solution is the same as that inside the actual unit, but the specific experimental temperature is lower than actual working temperature. Referring to the research method of Al-Sibai et al. (2005), the solution was dyed with a small amount of carmine, and the wetting rate was calculated by taking a photo of the plate-type falling film unit. Fig. 4 shows the calculation method. Photoshop is used to obtain the pixel of the colored part and the overall pixel value, then we can get the wetting rate η_{wet}. The calculation formula is shown in Eq. (1).

$$\eta_{wet} = Pix_{wetting} / Pix_{total} \times 100\% \quad \text{Eq. (1)}$$

where $pix_{wetting}$ and pix_{total} is the pixel value of the colored part and overall pixel value.

Table 1. Related parameters of the wetting characteristics experiment

Experimental environment	Experimental fluent	
Atmospheric pressure	Lithium bromide aqueous solution	Water
	3.7-15.6 ℃ ; 1.42 g·cm^{-3}; 42 wt.%	10.3 °C; 1.0 g·cm^{-3}
Fluid dye	Experimental instrument	
Carmine (less than 1 wt.%)	SONY HDR-PJ760	Float flowmeter (>40 L·h^{-1})

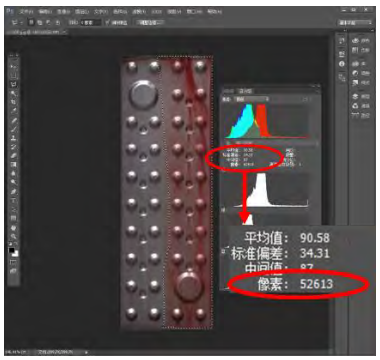

Figure 4: The method for calculating the wetting rate

2.3. Test result of wetting characteristics

Fig. 5 shows the wetting characteristics of the solution at different flow rates. All of the experimental phenomena in the figure can be repeated. The upper and lower rows are the experimental results of the flow rate from small to large and from large to small. According to the method of the previous section, the wetting rate is calculated, and the curve of the wetting rate as a function of the density of liquid distribution can be plotted.

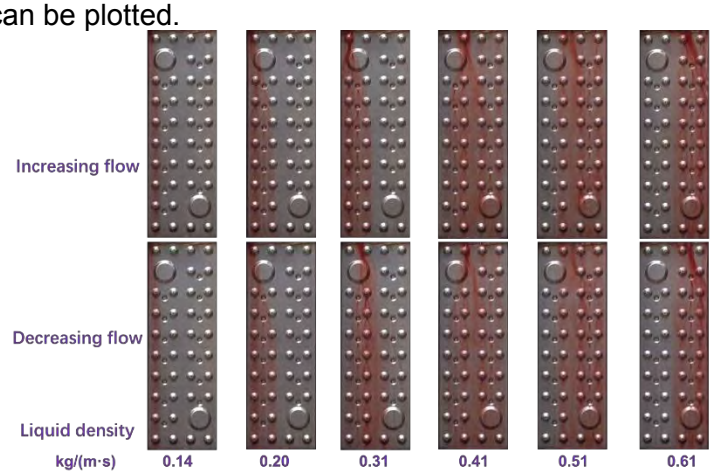

Figure 5: Wetting characteristics of solutions at different flow rates

Fig. 6 shows the results of the testing wetting rate of water and lithium bromide solution at different liquid density. The red and blue curves in the figure are the wetting rate of decreasing flow rate and increasing flow rate when the fluid is water. When the fluid is a solution, the change in flow rate has little effect on the actual wetting characteristics. From the curve in Fig. 6, the following two results can be obtained: 1). If the flow rate is too large or too small, the fluid will bias flow. Therefore, the asymmetric liquid distribution system has the best flow rate. In our test, the best flow rate occurs at the density of liquid distribution of 0.26-0.4 $kg \cdot m^{-1}s^{-1}$; 2). At the same flow rate, the wetting rate of decreasing flow rate is greater than the test result of the increasing flow rate, and the deviation is most significant near the optimum flow rate. For water, at the density of liquid distribution of 0.27 $kg \cdot m^{-1}s^{-1}$, the wetting rate of decreasing flow is 78%, while the wetting rate of increasing is just 40%. The latter wetting rate is 38% less than the former. According to the results of Lee et al. (2002), there is inertia in the vertical plate falling film flow. Our test has found the wetting characteristics obtained by gradually decreasing the flow rate after wetting the plate surface in advance are better, which is consistent with the results of Al-Sibai (2005). In addition, our study has found that the effect of flow inertia on water is greater than the effect on the lithium bromide solution.

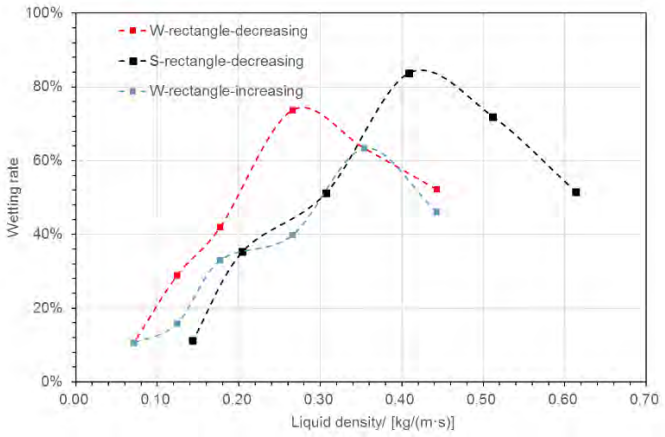

Figure 6: Wetting rate of different fluids at different density of liquid distribution

The tests in Fig. 6 adopt the plate with bubble-like groove of rectangular arrangement, while Fig. 7 shows the results of the plates with bubble-like groove of different arrangement. The rectangular curve in Fig. 7 is the result of the rectangular arrangement plate, and the rhombic curve is the result of the rhombic arrangement plate. When the density of liquid distribution is small, the wetting rates of the two arrangements are similar, but when the density of liquid distribution is large, the corrugated plate of the rhombic arrangement can avoid the bias flow, and the wetting rate is significantly better than the corrugated plate of the rectangular arrangement. At the high density of liquid distribution of 0.6 $kg \cdot m^{-1}s^{-1}$, the wetting rate of rhombic arrangement is 91%, while that of rectangular arrangement is only 49%. The latter wetting rate is 42% less than the former.

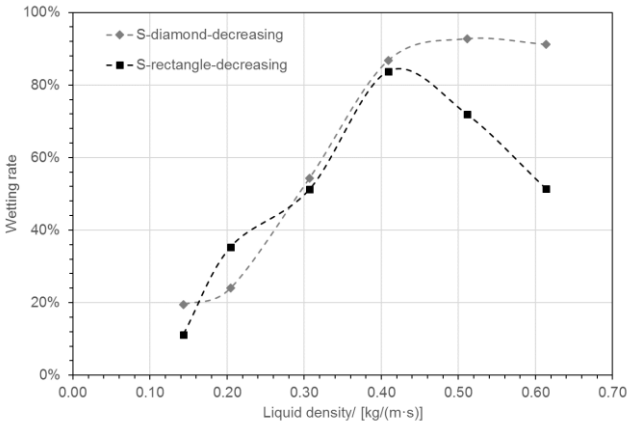

Figure 7: Wetting rate of different bubble-like groove arrangement at different densities of liquid distribution

All the above test results shows low wetting rate under the small density of liquid distribution. Therefore, the wetting characteristics of the first generation liquid distributor under the small liquid density are not good, and the structure of the liquid distributor needs to be improved and optimized.

3. STRUCTURAL OPTIMIZATION OF LIQUID DISTRIBUTOR

We found in the test that there are two factors affecting the wetting characteristics of the plate-type falling film. The first factor is the liquid distributor and the second is the corrugated structure of the plate. Since the plate type falling film flow can only be distributed once, it is required to make the liquid flow uniformly and completely from the full plate. The first generation did not achieve it at a small density of liquid distribution, so the structure of liquid distributor needs to be optimized. In addition, the first generation of plate adopts the bubble-like groove arrangement. It is tested that the water side had a low heat transfer coefficient (T.Hu et al., 2019). Therefore, it is necessary to design a suitable corrugated structure on the plate, which can not only enhance the heat transfer coefficient of water side, but also show the high wetting characteristics of solution side.

3.1. Structural optimization of liquid distributor

Fig. 8 shows the structural parameters of the liquid distributor. The key dimensions affecting the wetting characteristics of plate-type falling film are H_{in}, H_1 and H_2. Among them, H_{in} is the height of the solution inlet, H_1 is the highest height that liquid level can be lifted, and H_2 is the height of the groove from the upper wall. In the actual optimization plan, we design the height of H_1 is 60mm, then we change the height of H_{in} and H_2 to carry out multiple experiments. Finally, we can find the optimum size, and explore the law at the same time.

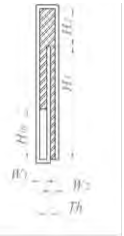

Figure 8: Structure of liquid distributor

The experimental parameters of the optimizing liquid distributor is shown in Table 2. The specific experimental setup is the same as it in Chapter 2, and the experiment is still tested under atmosphere pressure. In order to study the properties of liquid distribution, we use a vertical plate as the plate structure. We use the same method of Chapter 2 to calculate the wettiing rate of the plate to represent the actual properties of liquid distribution. The higher the wetting rate, the better the properties of it.

Table 2. Related parameters of the wetting characteristics experiment

Experimental environment	Experimental fluent	
Atmospheric pressure	Lithium bromide aqueous solution	
	8.1-20.2 ℃ ; 1.433 g·cm^{-3}; 42 wt.%	
Fluid dye	Experimental instrument	
Carmine (less than 1 wt.%)	SONY HDR-PJ760	Float flowmeter (>40 L·h^{-1})

3.2. Test result of wetting characteristics

Fig. 9(a) shows the actual wetting characteristics of test results for different solution inlet heights, where the H_2 height is a constant 5 mm. From the curve in Fig. 9(a), it is a significant influence on the effect of liquid distribution by changing the solution inlet height. The flow rate of the optimum wetting rate is also different at different heights of H_{in}. The optimum flow rate at 20mm height is between 80-90 L·h^{-1}, the optimal flow rate at 30mm height is between 100-125 L·h^{-1}, and the optimal flow rate at 40mm height is over 125 L·h^{-1}. With the increase of inlet height H_{in}, the optimum flow rate of liquid distribution will also increase. At the low density of liquid distribution of 0.15 kg·m^{-1}s $^{-1}$, the wetting rate in 40 mm inlet height is 38%, while 30% in 30mm H_{in}, and 18% in 20mm H_{in}. Under the experimental conditions, the plate has a highest wettability with a height of 30 mm. However, the high wetting rate of the plate occurs at a large flow rate (over 100 L·h^{-1}). At the small density of liquid distribution, the wetting rate of plate at different H_{in} is less than 40%. The wetting charcteristics is not ideal by just changing the inlet height H_{in}.

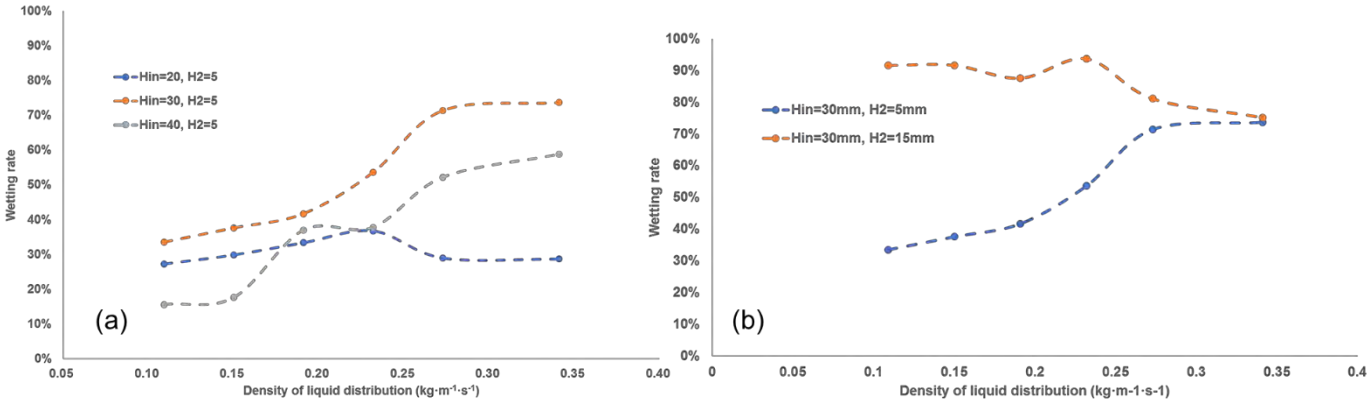

Figure 9: Wetting rate of different liquid distributor of H_{in} or H_2 at different density of liquid distribution: (a) different H_{in}, and (b) different H_2

Fig. 9(b) shows the actual wetting characteristics results for different H_2, where H_{in} takes an optimum value of 30 mm. From the curve of Fig. 9(b), increasing H_2 has a significant effect on the wetting characteristics. When the height of H_2 is 15mm, the wetting rate tested under small density of liquid distribution is significantly improved, and the average wetting rate reaches 95%. At the low density of liquid distribution of 0.15 kg·m^{-1}s $^{-1}$, the wetting rate of 15 mm H_2 reaches 92%, while the wetting rate of 5 mm H_2 at the same density of distribution is only 38%. The wetting rate of former is 2.42 times of the latter. The optimized liquid distributor can meet the working requirements of actual heat exchanger. The reason for this result is that when the height of H_2 is small, the fluid comes into contact with the upper wall. It would create a force that prevents the solution falling film uniformly. Therefore, when the hieght of H_2 raising until the solution does not contact with the upper wall, the force disappears. The solution is unformly distributed on the cross section of the liquid distributor, and only freely dropped by gravity. As a result, the solution can cover the whole plate and form falling

film flow. Thereby, the plate can obtain a high wetting rate. When the density of liquid distribution is large, bias flow becomes the main factor, resulting in similar results of wetting characteristics with different height of H_2. The wetting rate drops to 75%, which is 0.82 times of the wetting rate in the low desnity of liquid distribution.

3.3. Simplified calculation of liquid film thickness

Finally, we theoretically calculate the film thickness obtained in Sec.3.2. The following assumptions were made to simplify the calculation：
1. The solution overflows from the full width of the liquid distributor, and the solution film has the same thickness at the same height;
2. Ignore surface tension, viscous force and inertial force of the interface between air and solution.
The calculation parameters are as follows:
H_{in}: 30 mm; H_2: 15 mm; b (the width of the liquid distributor): 150 mm;
G_v (the inlet flow rate of the solution): 55 $L \cdot h^{-1}$.
In the free falling film flow of the plate, the Reynolds number can be calculated in Eq. (2).

$$\mathrm{Re} = \frac{4\Gamma}{\mu} \qquad \text{Eq. (2)}$$

Where Γ is mass flow rate per unit length in $kg \cdot m^{-1}s^{-1}$, μ is dynamic viscosity in $kg \cdot m^{-1}s^{-1}$.
For vertical plate, Γ can be calculated in Eq. (3), and Re can be calculated in Eq. (4).

$$\Gamma = \frac{\rho G_v}{b} \qquad \text{Eq. (3)}$$

$$\mathrm{Re} = \frac{4\rho G_v}{\mu b} \qquad \text{Eq. (4)}$$

Where ρ is solution density in $kg \cdot m^{-3}$. Accroding to Eq. (4), the Re can be calculated, The value of Re is 146. According to the existing research (Al-Sibai F. et al., 2005), the Reynolds number is between 20 to 1000 ~ 2000. The flow pattern of liquid film is fluctuating laminar flow. According to Nusselt falling film theory, in the initial stage of falling film, the thickness of liquid film is constant, which satisfies the film thickness formula in Eq. (5):

$$\delta = \left(\frac{3\Gamma\mu}{\rho^2 g}\right)^{\frac{1}{3}} \qquad \text{Eq. (5)}$$

Where g is gravitational constant (9.81 $m \cdot s^{-2}$), as a result, the result of film thickness is 0.44 mm, which is suitable for falling film heat transfer process.

4. CONCLUSIONS

A liquid-level-lifting type asymmetrical overflow distributor system is proposed in this paper to miniaturize the AHP system. The corrugations of the plate has an effect on the wetting characteristics. A suitable structure of plate should be found to improve both the heat transfer performance on the water side and the wetting characteristics on the solution side. Some structural optimization schemes have been proposed to improve the wetting characteristics of the system. Some conclusions can be made as follows:
1) The asymmetric liquid distribution system has the best flow rate. The best flow rate occurs at the density of liquid distribution of 0.26-0.4 $kg \cdot m^{-1}s^{-1}$, If the flow rate is too large or too small, the fluid will bias flow;
2) Different flow characteristics can influence the wetting rate. For water, at the density of liquid distribution of 0.27 $kg \cdot m^{-1}s^{-1}$, the wetting rate of decreasing flow is 78%, while the wetting rate of incresasing is just 40%. The latter wetting rate is 38% less than the former;
3) It is a significant influence on the effect of liquid distribution by changing the solution inlet height. Under the experimental conditions, the plate has a highest wetting rate with a height of 30 mm. The average wetting rate is 35% in low desnity of liquid distribution, which is 1.25 times than that of 40 mm H_{in}, and 2.33 times than that of 20 mm H_{in};
4) When the height of the groove from the upper wall is 15mm, the average overall wetting rate reaches 95%, and the average thickness of liquid film was as low as 0.44mm. At the low density of liquid distribution of 0.15 $kg \cdot m^{-1}s^{-1}$, the wetting rate reaches 92%, which is 2.42 times of the wetting

rate in 5 mm H_2, the optimized liquid distributor can meet the working requirements of actual heat exchanger.

ACKNOWLEDGEMENTS

The authors gratefully acknowledge the support from the National Natural Science Foundation of China (grant numbers 51306098, 51138005), the innovative Research Groups of National Natural Science Foundation of China (grant number 51521005), and Tsinghua University Initiative Scientific Research Program (No. 20151080470).

NOMENCLATURE

H	height (m)	η_{wet}	wetting rate (%)
b	width (m)	G	volume flow rate (m^3s^{-1})
Γ	density of liquid distribution ($kg \cdot m^{-1}s^{-1}$)	ρ	density ($kg \cdot m^{-3}$)
μ	dynamic viscosity ($kg \cdot m^{-1} \cdot s^{-1}$)	δ	film thickness (m)
g	gravitational constant (9.81 $m \cdot s^{-2}$)	Re	Reynolds number

REFERENCES

Al-Sibai, F, 2005. Experimentelle untersuchung der strömungscharakteristik und des wärmeübergangs bei welligen rieselfilmen. [Dissertation]. Aachen: RWTH-Aachen.

Benoît, Michel, Nolwenn, Le, Pierrès, Stutz, B., 2017. Performances of grooved plates falling film absorber[J]. Energy, 138.

Cerezo, J., et al., 2009. Experimental study of an ammonia–water bubble absorber using a plate heat exchanger for absorption refrigeration machines. Applied Thermal Engineering, 29(5-6): 1005-1011.

Delahanty, J., C., S., Garimella, and M., A., Garrabrant, 2015. Design of compact microscale geometries for ammonia–water desorption. Science and Technology for the Built Environment, 21(3): 365-374.

García-Hernando, N., Almendros-Ibáñez, J., A., Ruiz, G., et al., 2011. On the pressure drop in Plate Heat Exchangers used as desorbers in absorption chillers[J]. Energy Conversion and Management, 52(2): 1520-1525.

Gonda, A., Lancereau, P., Bandelier, P., et al., 2014. Water falling film evaporation on a corrugated plate[J]. International Journal of Thermal Sciences, 81: 29-37.

Lee, K., B., et al., 2002. Comparison of Heat and Mass Transfer in Falling Film and Bubble Absorbers of Ammonia-Water. Experimental Heat Transfer, 15(3): 191-205.

Lu,Y., Stehmann, F., Yuan, S., et al., 2017. Falling film on a vertical flat plate–Influence of liquid distribution and fluid properties on wetting behavior[J]. Applied Thermal Engineering.

Mortazavi, M., Nasr, Isfahani, R., Bigham, S., et al., 2015. Absorption characteristics of falling film LiBr (lithium bromide) solution over a finned structure[J]. Energy, 87: 270-278.

T. Hu, X. Xie, Y. Jiang, 2017. Design and experimental study of a plate-type falling-film generator for a LiBr/H2O absorption heat pump. International Journal of Refrigeration, 74: 302-310.

T. Hu, X. Xie, Y. Jiang., 2019. A detachable plate falling film generator and condenser coupling using lithium bromide and water as working fluids. International Journal of Refrigeration, 98: 120-128.

Yau. Y. H, Ahmadzadehtalatapeh, M., 2010. A review on the application of horizontal heat pipe heat exchangers in air conditioning systems in the tropics[J]. Applied Thermal Engineering, 30(2): 77-84.

Y. Li, F. Lin, S. Zhang, X. Zhao, 2011. A new type of district heating system based on distributed absorption heat pumps. Energy, 36(7): 4570-4576.

Zhuoming C., et al., 2003. Structure and performance study of LiBr absorption chiller based on whole-plate-fin heat-exchanger. Journal of refrigeration, 24(1): 28-32.

Manuscript ID: 1570
DOI: 10.18462/iir.icr.2019.1570

Dynamic behavior study of multi-section vertical absorption heat exchanger

Chaoyi ZHU[(a)], Xiaoyun XIE[(a)]*, Yi JIANG[(a)]

[(a)] Building Energy Research Center, Tsinghua University
Beijing, 100084, China, xiexiaoyun@tsinghua.edu.cn

ABSTRACT

Multi-section vertical absorption heat exchanger (MVAHE) is a novel heat exchanger applied in district heating system. In field application, the MVAHE faces many challenges like sudden black out and heat source break down. Therefore, dynamic behavior study is critical to reach higher stability and better heat exchange performance. The working fluid flows through several sections inside MVAHE under gravity and section vapor pressure difference. An intensive distributed parameter dynamic model is built to study the pressure and liquid level response under transient conditions. The model is validated by test result. Start-up process is studied in detail. A better control strategy is recommended.
Keywords: Absorption Heat Pump, Absorption Heat Exchanger, Dynamic Modelling, District Heating.

1. INTRODUCTION

A novel district heating system using low-grade waste heat from power plants and industries as heat source was proposed in recent years by Fu et al. (2008) to reduce primary energy consumption for heating. Absorption heat exchanger (AHE) is a novel heat exchanger to finish heat exchange from primary water to secondary water and to reduce outlet primary water temperature for waste heat collection (Xie and Jiang, 2017). The AHE consists of an absorption heat pump (AHP) and a plate heat exchanger (HEX) as shown in Fig. 1a. Unlike conventional absorption chiller or AHP, the AHP applied in AHE has larger external fluid inlet/outlet temperature difference in condenser and evaporator and larger pressure difference range, as shown in Table 1. Therefore, advanced design should be introduced to enable better performance.

Multi-section vertical absorption heat exchanger (MVAHE) was proposed and developed (Jiang et al., 2013; Zhu et al., 2016). The absorber and evaporator are divided into three sections from top to bottom to provide three evaporating processes for the 15K~20K inlet/outlet water temperature difference in evaporator. U-pipe is applied to let the solution or refrigerant water flow from the upper section to the lower section and to separate the vapor space of the two sections. Orifice plate is applied in each section of generator, absorber, and evaporator to distribute liquid equally to heat transfer pipes and to realize falling film heat and mass transfer process. The hot primary water flows through the generator, the HEX, and the evaporator in succession, then returns to the heat source. The cold secondary water is divided into two flows, the first one flows through absorber and condenser in succession, and the second one flows through HEX. The two flows meet together after being heated, and then flow to rooms for space heating. The structure is shown in Fig. 1b.

Table 1. Difference between Conventional Absorption Chiller or AHP and AHE

Parameters	Conventional	AHE
Condenser inlet/outlet temp [℃]	30/35	40/55
Evaporator inlet/outlet temp [℃]	12/7	45/25
(Inlet T)-(Outlet T) [K]	**ΔT=5** →	**ΔT=15~20**
(Condensing P)-(Evaporating P) [kPa]	**ΔP=4.6~6** →	**ΔP=4.4~21**

In MVAHE, the internal working solution or refrigerant flows from upper section to lower section naturally. The driven force of the flow includes liquid level difference and pressure difference between two sections. Therefore, the stability of the MVAHE highly relies on stable liquid level and

pressure difference. The dynamic response of liquid level and pressure should be studied to further improve the stability of MVAHE.

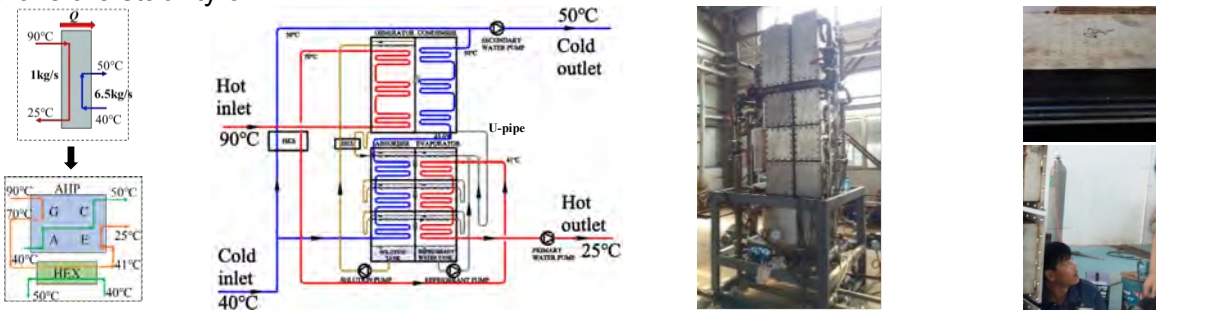

(a) Basic process (b) Internal structure and process (c) Developed MVAHE (d) Orifice plate and U-pipe

Figure 1: Absorption Heat Exchanger

Previous dynamic modeling works about AHP or absorption chiller mainly focused on the change of heating or cooling rate, flow rate, and COP (Jeong et al., 1998; Zinet et al., 2012; Viswanathan et al., 2013; Kohlenbach and Ziegler, 2008a,b). Some studies also focused on advanced strategy to shorten start-up time (Kim and Park, 2007; Xu et al., 2016) and to avoid crystallization (Shin et al., 2009). However, the author can barely find study paying attention to internal working fluid flow process especially natural flow process in such a complicated system. The flow model is over simplified to reveal the real condition. Therefore, a new dynamic model that is able to accurately calculate the nine liquid tank levels (including orifice plate distribution tanks, solution tank, and refrigerant tank), six U-pipe liquid levels, and four vessel pressures at any instant should be developed to study the dynamic behavior of MVAHE under challenging transient conditions.

2. MODELING

This study focuses on the complicated various chamber pressures and liquid levels change in a MVAHE under dynamic conditions. A dynamic model is developed to address the limitations of other models applied in previous works and to realize effective pressure and liquid level calculation. To reduce the complexity of the model, following assumptions are employed:

a) The MVAHE is insulated from its surroundings and thus, the heat exchange between the AHE and the ambient is neglected;
b) The heat transfer pipes in the condenser and evaporator are covered completely with saturated water film;
c) The pressure drop of vapor flowing from generator to condenser or from evaporator to absorber is neglected;
d) The vapor in each chamber is mixed uniformly. Therefore, each chamber has unique vapor property (e.g., pressure, density, specific enthalpy).

2.1. Heat and Mass Transfer Model

Distributed parameter method is applied to build the heat and mass transfer model. For generating or absorbing process, the heat transfer process and mass transfer process are considered separately. This method is chosen because it is not suitable to define mean temperature difference for solution generating and absorbing processes (Li, 2016).

In generator, the heat source fluid inside pipes transfers heat through pipes to solution. The solution is heated and the mass transfer between solution mainstream and surface saturated solution film begins. Therefore, vapor is generated to the chamber and the solution is concentrated. The surface saturated solution film has concentration controlled by mainstream temperature and chamber vaopr pressure:

$$x_{sat,g} = x_{sat}(P_{gc}, t_{s,g}) \quad \text{Eq. (1)}$$

the mass transfer rate is controlled by mass transfer coefficient h_m and local concentration difference between mainstream and surface:

$$d\dot{m}_{v,g} = (x_{sat,g} - x_{s,g})\rho_s h_m dA_g \quad \text{Eq. (2)}$$

the heat transfer process is modeled as follows:

$$d\dot{q}_{ts,g} = (t_{tu,g} - t_{s,g})k_{ts}dA_g \quad \text{Eq. (3)}$$

$$d\dot{q}_{ft,g} = (t_{w,g} - t_{tu,g})k_{ft}dA_g \quad \text{Eq. (4)}$$

In condenser, the saturated water covering pipes has temperature calculated by chamber pressure:

$$t_{sat,c} = t_{sat}(P_{gc}) \quad \text{Eq. (5)}$$

and the heat transfer rate is modeled as shown in Eq. (6) to (7):

$$d\dot{q}_{rt,c} = (t_{sat,c} - t_{tu,c})k_{rt}dA_c \quad \text{Eq. (6)}$$

$$d\dot{q}_{tf,c} = (t_{tu,c} - t_{w,c})k_{tf}dA_c \quad \text{Eq. (7)}$$

In generator-condenser vessel, the heat and mass transfer process can be illustrated by Fig. 2.

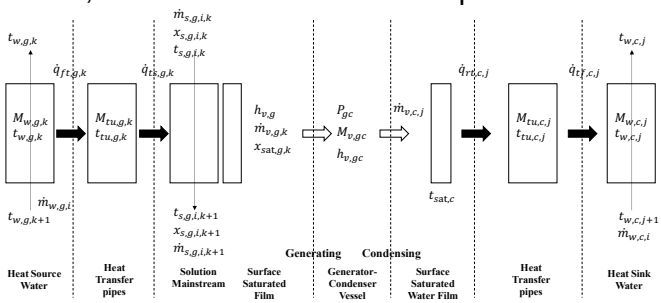

Figure 2: Generating and condensing process

The heat and mass transfer model in absorber and evaporator can be developed using similar method, as shown in Eq. (8) to Eq. (14)

$$x_{sat,a} = x_{sat}(P_{ae}, t_{s,a}) \quad \text{Eq. (8)}$$

$$d\dot{m}_{v,a} = (x_{s,a} - x_{sat,a})\rho_s h_m dA_a \quad \text{Eq. (9)}$$

$$d\dot{q}_{st,a} = (t_{s,a} - t_{tu,a})k_{st}dA_a \quad \text{Eq. (10)}$$

$$d\dot{q}_{tf,a} = (t_{tu,a} - t_{w,a})k_{tf}dA_a \quad \text{Eq. (11)}$$

$$t_{sat,e} = t_{sat}(P_{ae}) \quad \text{Eq. (12)}$$

$$d\dot{q}_{tr,e} = (t_{tu,e} - t_{sat,e})k_{tr}dA_e \quad \text{Eq. (13)}$$

$$d\dot{q}_{ft,e} = (t_{w,e} - t_{tu,e})k_{ft}dA_e \quad \text{Eq. (14)}$$

2.2. Natural Flow Model

The solution and refrigerant water flow from top section to bottom section under pressure difference and gravity effect. The input of natural flow model is essential to determine the flow rate in each section and to reveal solution or refrigerant transport delay. Natural flow model mainly includes orifice plate liquid flow model and U-pipe flow model.

2.2.1. Orifice plate flow model

The liquid level above orifice plate is the driven force to overcome the pressure drop of fluid flowing through orifice. Therefore, the fluid flow velocity through orifice is a function of fluid property and liquid level. This function was tested before building the model. The connection between orifice plate pressure drop and solution flow velocity through orifice is shown in Fig. 3. For each fluid, there is a similar function as shown in Eq. (15).

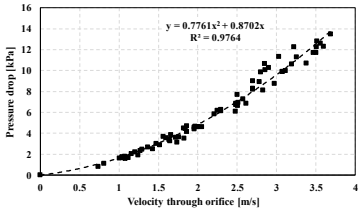

Figure 3: Pressure drop of solution flowing through orifice

$$u = f(\rho, H) \quad \text{Eq. (15)}$$

In dynamic modelling, the liquid level above orifice plate is changing along with time. Therefore, the distribution flow rate of liquid in each section can be calculated.

2.2.2. U-pipe flow model

U-pipe is applied to separate the vapor space of two vessels and to provide liquid flow channel. The U-pipe flow model will determine the flow rate from upper section to lower section as well as the liquid level in the U-pipe.

The U-pipe model is shown in Fig. 4. Three flow rates are considered: the U-pipe inlet flow rate $\dot{m}_{upipe,inlet}$, the U-pipe inside flow rate $\dot{m}_{upipe,inner}$, and the U-pipe outlet flow rate $\dot{m}_{upipe,outlet}$. The inlet flow rate is an independent parameter for U-pipe flow model. The inside flow rate is a function of U-pipe inlet pressure $P_{upipe,inlet}$, outlet pressure $P_{upipe,outlet}$, downstream liquid column height $H_{upipe,downward}$, upstream liquid column height $H_{upipe,upward}$, and liquid properties. The outlet flow rate is the actual inlet flow rate to the lower section. At the beginning of a U-pipe flow, the pipe is empty or at least half-empty, the upstream liquid column height $H_{upipe,upward}$ is smaller than U-pipe upward height $L_{upipe,upward}$, and the outlet flow rate is zero. Otherwise, the upstream liquid level reaches U-pipe exit, and the outlet flow rate equals to inside flow rate.

The downward stream liquid column height is controlled by inlet flow rate and inside flow rate. When $H_{upipe,downward}$ is larger than U-pipe height, the liquid will accumulate above the inlet of U-pipe, and the smoothly U-pipe natural flow is blocked. This may happen when U-pipe flow pressure drop is higher than design condition or the outlet pressure is higher than inlet pressure. The upstream liquid column height is influenced by inside flow. The maximum height is U-pipe height. With the input of U-pipe flow model, the dynamic model can calculate start-up process where the time delay to refill each U-pipe cannot be ignored. The dynamic model can also simulate the condition when natural flow is blocked and the liquid level is higher than U-pipe inlet point.

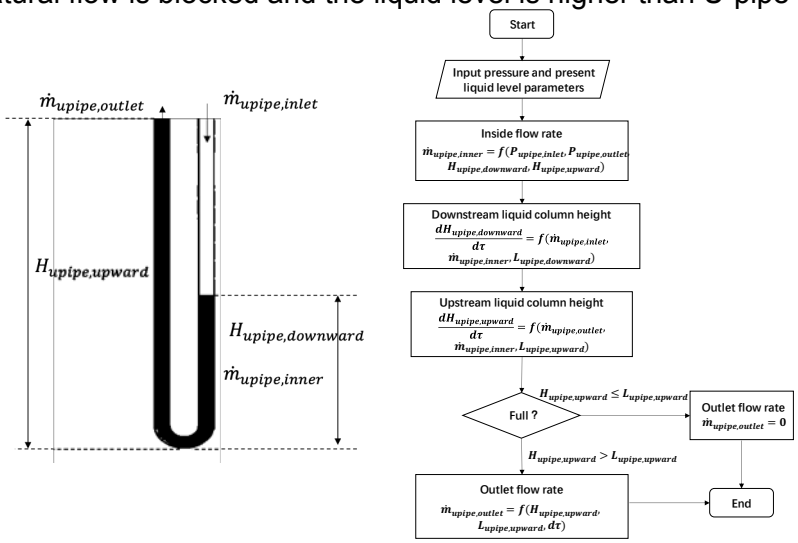

(a) U-pipe flow (b) Calculation process

Figure 4: U-pipe flow model

2.3. Dynamic Modeling

2.3.1. Liquid tank model

Inside a MVAHE, there are a lot of liquid tanks including the tank above each orifice plate, the solution tank, and the refrigerant water tank. Conservation equations are used to determine the properties of liquid inside the tanks (mass, enthalpy, and concentration) at any instant.

$$\frac{dM}{d\tau} = \dot{m}_{in} - \dot{m}_{out} \quad \text{Eq. (16)}$$

$$\frac{d(Mh)}{d\tau} = (\dot{m}h)_{in} - (\dot{m}h)_{out} \quad \text{Eq. (17)}$$

$$\frac{d(Mx)}{d\tau} = (\dot{m}x)_{in} - (\dot{m}x)_{out} \quad \text{Eq. (18)}$$

2.3.2. Pressure calculation

Pressure calculation is crucial in this study because it matters the calculation of natural flow rate and liquid level change. In this model, the vapor pressure is determined by calculating the vapor properties (specific enthalpy, specific volume) in the chamber, as shown in Eq. (19) to Eq. (22).

$$\frac{dM_v}{d\tau} = \dot{m}_{v,in} - \dot{m}_{v,out} \quad \text{Eq. (19)}$$

$$\frac{d(M_v h_v)}{d\tau} = (\dot{m}_v h_v)_{in} - (\dot{m}_v h_v)_{out} \quad \text{Eq. (20)}$$

$$v = \frac{V_{vessel}}{M_v} \quad \text{Eq. (21)}$$

$$P = f(h_v, v) \quad \text{Eq. (22)}$$

3. START-UP PROCESS STUDY AND MODEL VALIDATION

In this section, the developed model is validated by field test result. The start-up process is chosen for the validation because this process has transient pressure, flow rate, and temperature change at the same time, making it the most difficult process to simulate.

3.1. Start-up Process Field Test

A MVAHE with one-section generator-condenser unit and three-section absorber-evaporator unit is chosen for the test. Present start-up procedure is turning on solution pump and refrigerant pump first, the equipment is running at cold mode where no heat source or heat sink is introduced. After solution and refrigerant flow into each vessel and that liquid level above each orifice plate is stable, the hot water pump and the cooling water pump begin to work. The machine switches to heating mode. The pressure change in each section under two different modes are shown in Fig. 5.

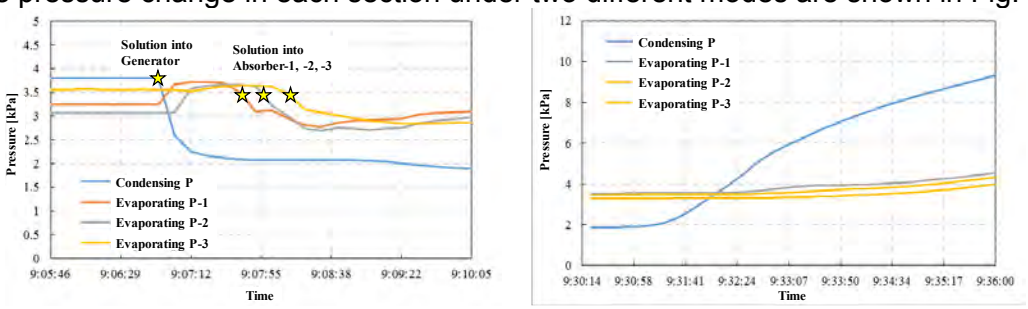

(a) Cold mode (b) Heating mode

Figure 5: Start-up process pressure change

In cold mode, the pressure of each section decreased when solution enters. The solution entered each section with clear time delay. Therefore, the pressure of each section from top to bottom dropped one after another. The pressure in generator-condenser unit (Condensing P) was lower than the others. This interfered the U-pipe flow from generator to absorber. Solution was observed to accumulate at the bottom of generator (inlet of U-pipe connecting generator and absorber).
In heating mode, the condensing pressure was rising, a decreasing pressure gradient from top section (Condensing P) to bottom section (Evaporating P-3) was gradually developed. This pressure gradient ensured that the inlet pressure was higher than outlet pressure for each U-pipe and guaranteed stable natural flow. The solution level at bottom of generator disappeared.

3.2. Model Validation with Test Result

The same start-up condition is calculated by the dynamic model developed in this study. The agreement with test result is shown in Fig. 6 and Fig. 7. The calculated pressure value and changing trend fit well with test result.
The liquid level change is also calculated. Fig. 8 shows the solution level change at inlet of U-pipe from generator to absorber. In cold mode, the liquid level is rising beyond inlet point of U-pipe and solution begins to accumulate at bottom of generator. While in heating mode, this liquid level is lower and lower, the solution accumulation disappears. The calculated result meets test observation.

3.3. Control Strategy to Avoid Solution Accumulation

Solution accumulation may lead to many problems including unstable natural flow and solution overflow into refrigerant. The reason is that condensing pressure is lower than evaporating pressure-1 when solution and refrigerant enter each section in cold mode. After trying several methods using the dynamic model, the authors suggest that inputting heat source and heat sink fluid before turning on solution pump and refrigerant pump can keep condensing pressure higher than evaporating pressure and avoid solution accumulation. The pressure change and liquid level change are calculated and shown in Fig. 9. The liquid column height on downward side is always smaller than U-pipe height and solution accumulation will not happen.

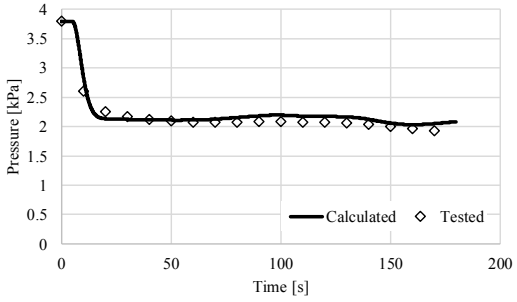

(a) Condensing pressure

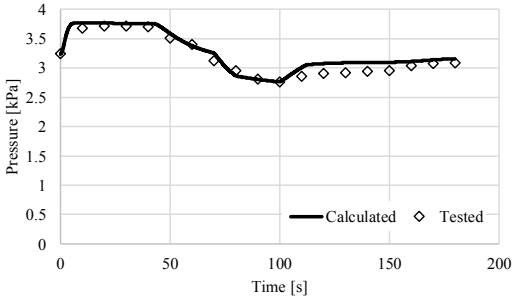

(b) Evaporating pressure-1

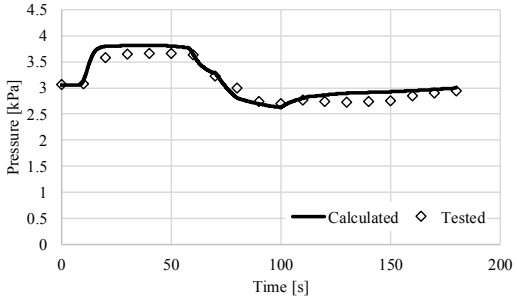

(c) Evaporating pressure-2

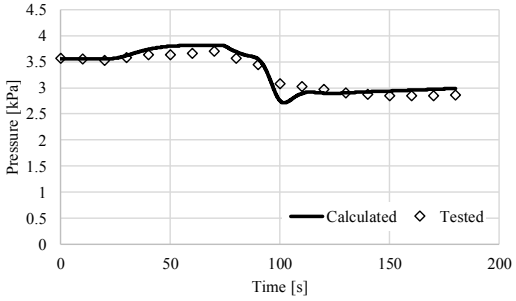

(d) Evaporating pressure-3

Figure 6: Cold mode pressure

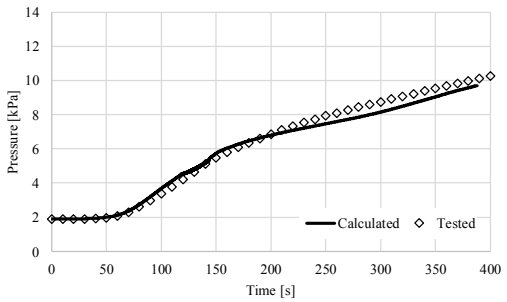

(a) Condensing pressure

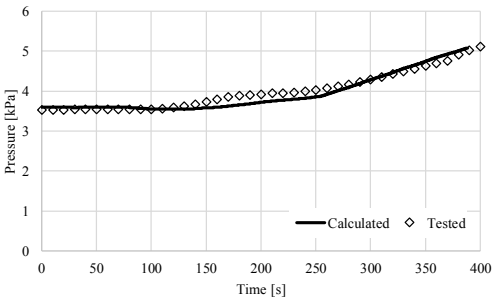

(b) Evaporating pressure-1

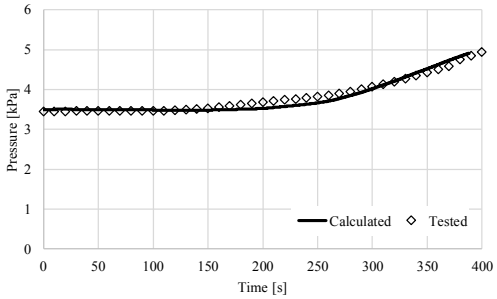

(c) Evaporating pressure-2

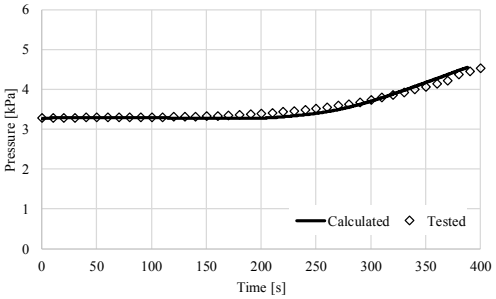

(d) Evaporating pressure-3

Figure 7: Heating mode pressure

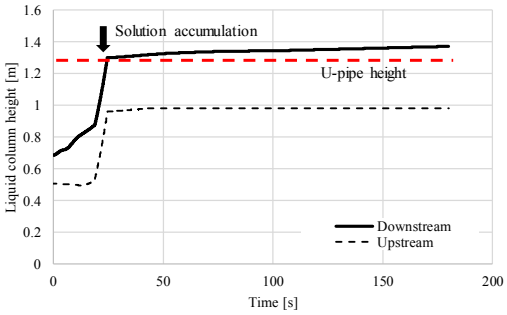

(a) Cold mode accumulation happens

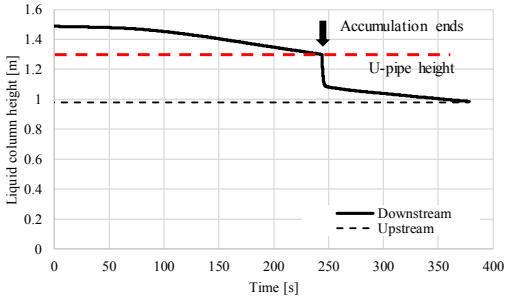

(b) Heating mode accumulation disappears

Figure 8: Liquid level change and solution accumulation

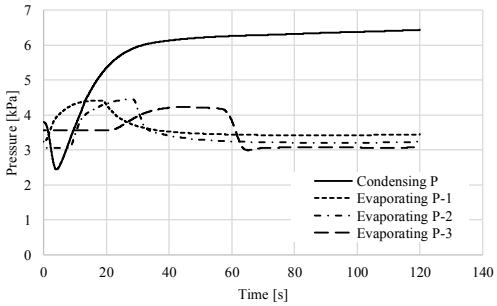

(a) Pressure change

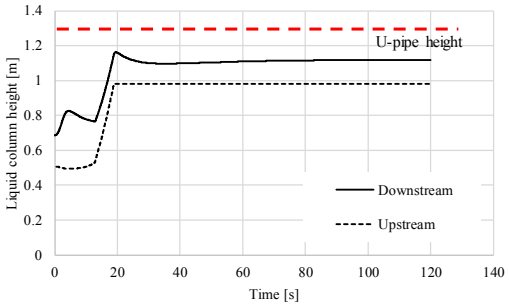

(b) Liquid level change

Figure 9: Improved start-up procedure

4. CONCLUSION

In this study, a dynamic model is developed to study the pressure change and liquid level change in MVAHE under transient conditions. A distributed-parameter heat and mass transfer model is applied. The natural flow model for orifice plate and U-pipe are introduced to calculate flow rate and liquid level change. The model is validated by test result. Start-up process is meticulously studied and an improved start-up control strategy is suggested. This model will be helpful to study more conditions and to further improve the stability of MVAHE.

ACKNOWLEDGEMENTS

The authors gratefully acknowledge the support from the National Natural Science Foundation of China (Grant number 51306098, 51138005), the Innovative Research Group of National Natural Science Foundation of China (Grant number 51521005), and the Tsinghua University Initiative Scientific Research Program (No. 20151080470).

NOMENCLATURE

A	heat and mass transfer area [m^2]	P	pressure [kPa]
H	height [m]	$\dot{q}$	heat rate [kW]
h	specific enthalpy [$kJ \times kg^{-1}$]	t	temperature [℃]
h_m	mass transfer coefficient [$m \times s^{-1}$]	V	volume [m^3]
k	heat transfer coefficient [$kW \times m^{-2} \times K^{-1}$]	v	specific volume [$m^3 \times kg^{-1}$]
M	mass [kg]	x	solution concentration
$\dot{m}$	mass flow rate [$kg \times s^{-1}$]	ρ	density [$kg \times m^{-3}$]

Subscripts:

sat	saturated	*gc*	generator-condenser vessel
s	solution	*ae*	absorber-evaporator vessel
v	vapor	*g*	generator/generating
w	water	*a*	absorber/absorbing
tu	heat transfer tube	*c*	condenser/condensing
ts, st	transfer between solution and tube	*e*	evaporator/evaporating
tr, rt	transfer between refrigerant and tube	*tf, ft*	transfer between fluid and tube

REFERENCES

Fu, L., Jiang, Y., Zhang, S., (2008). District heating system based on Co-ah cycles in combined heating and power systems. *J. Tsinghua Univ*. 48 (9), 1377–1380.

Jiang, Y., Xie, X., Fu, L., Zhang, S., (2013). A new type of fundamental unit of the absorption refrigerator realizing large temperature lift/drop. *Chinese Patent* No. CN101852510B.

Jeong, S., Kang, B. H., & Karng, S. W. (1998). Dynamic simulation of an absorption heat pump for recovering low grade waste heat. *Applied thermal engineering*, 18(1-2), 1-12.

Kim, B., & Park, J. (2007). Dynamic simulation of a single-effect ammonia–water absorption chiller. *International Journal of Refrigeration*, 30(3), 535-545.

Kohlenbach, P., & Ziegler, F. (2008a). A dynamic simulation model for transient absorption chiller performance. Part I: the model. *International journal of refrigeration*, 31(2), 217-225.

Kohlenbach, P., & Ziegler, F. (2008b). A dynamic simulation model for transient absorption chiller performance. Part II: Numerical results and experimental verification. *International journal of refrigeration*, 31(2), 226-233.

Li, J.(2016). Research on Heat and Mass Transfer and Match Properties of Absorber in Absorption Heat Pump. Doctoral dissertation, Tsinghua University, Beijing, China.

Shin, Y., Seo, J. A., Cho, H. W., Nam, S. C., & Jeong, J. H. (2009). Simulation of dynamics and control of a double-effect LiBr–H2O absorption chiller. *Applied Thermal Engineering*, 29(13), 2718-2725.

Viswanathan, V. K., Rattner, A. S., Determan, M. D., & Garimella, S. (2013). Dynamic model for a small-capacity ammonia–water absorption chiller. *HVAC&R Research*, 19(7), 865-881.

Xie, X., & Jiang, Y. (2017). Absorption heat exchangers for long-distance heat transportation. *Energy*, 141, 2242-2250.

Xu, Y. J., Zhang, S. J., & Xiao, Y. H. (2016). Modeling the dynamic simulation and control of a single effect LiBr–H2O absorption chiller. *Applied Thermal Engineering*, 107, 1183-1191.

Zhu, C., Xie, X., & Jiang, Y. (2016). A multi-section vertical absorption heat exchanger for district heating systems. *International Journal of Refrigeration*, 71, 69-84.

Zinet, M., Rulliere, R., & Haberschill, P. (2012). A numerical model for the dynamic simulation of a recirculation single-effect absorption chiller. *Energy Conversion and Management*, 62, 51-63.

Manuscript ID: 1579
DOI: 10.18462/iir.icr.2019.1579

A novel heat-driven thermoacoustic refrigeration system for food refrigeration applications

Huizhi Wang[(a), (b)], Limin Zhang[(a)], Jianying Hu[(a)], Guoyao Yu[(a)], Zhanghua Wu[(a)], Ercang Luo[(a), (b)]

[(a)] Key Laboratory of Cryogenics, Technical Institute of Physics and Chemistry, Chinese Academy of Sciences, Beijing 100190, China, liminzhang@mail.ipc.ac.cn & ecluo@mail.ipc.ac.cn

[(b)] University of Chinese Academy of Sciences, Beijing 100190, China, liminzhang@mail.ipc.ac.cn & ecluo@mail.ipc.ac.cn

ABSTRACT

Heat-driven thermoacoustic refrigerator is promising in harvesting medium-temperature heat energy due to its remarkable advantages of totally no moving components and environmental friendliness. In this work, a novel looped heat-driven thermoacoustic refrigeration system for refrigerated trucks is tested and analyzed. In the experiments, under a heating temperature of 300 °C and an ambient temperature of 30 °C, a total cooling capacity of 3.58 kW and a coefficient of performance of 0.18 were achieved with a refrigeration temperature of -10 °C. This novel looped heat-driven thermoacoustic refrigeration system exhibits a potential advantage in the cooling efficiency and specific power for refrigerated trucks and fishing vehicles.

Key words: thermoacoustic refrigerator; no moving component; environmental friendliness; refrigerated truck; fishing vehicle

1. INTRODUCTION

Refrigeration is used in all stages of the food chain to slow the physical, microbiological and chemical activities that cause deterioration in foods (Tassou et al., 2010). Although the vapor compression cycle is well established in food refrigeration, the rising cost of electricity and pressure to reduce the environmental impacts and carbon footprint of food production have renewed interest in heat driven technologies that could bring economic and environmental advantages over the conventional vapor compression cycle in future. In recent years, directly harnessing the waste heat of exhaust gas in refrigeration is booming (Xu and Wang, 2018., Zhu et al, 2016), especially for refrigerated trucks and fishing vehicles. Of which, heat-driven thermoacoustic refrigeration (HD-TAR) might be an effective approach to exploit the exhaust waste heat of refrigerated trucks and fishing vehicles due to its advantages of high reliability and compactness. In such a system, a thermoacoustic engine (TAE) is capable of converting exhaust waste heat to acoustic work and drives a thermoacoustic refrigerator (TAR) to generate cooling effect without any moving mechanical components. According to the internal acoustic field characteristics, HD-TARs are typically classified into ‘standing-wave’ (Adeff and Hofler, 2000) and ‘traveling-wave’ (Ceperley, 1979). The latter has been proved to outperform the former in the thermal efficiency due to the intrinsic reversibility.

To achieve high-efficiency traveling-wave acoustic field in HD-TARs, some typical structures were proposed: Luo’s two-looped configuration achieved a total cooling capacity of 435 W and an overall COP of 0.18 with a temperature drop of 27 °C (Luo et al, 2006), and de Blok’s single-looped configuration reached a total cooling capacity of 95 W pumping from -45 °C to 25 °C (De Block, 2012). However, they both suffer from acoustic power mismatch between the TAE and the TAR which brings about essential issues of low specific power and poor thermal efficiency. For the single-looped HD-TAR with a heating temperature of 200-300 °C and a refrigeration temperature drop of 30-50 °C, a stage ratio of 1:1 between the TAE and TAR has been proven to be of higher efficiency and power density theoretically and experimentally (Wang et al, 2018., De Block, 2018). In 2018, de Blok’s single-looped configuration of two stage TAE driven two stage TAR achieved a total cooling capacity of 18 kW with a cooing temperature of -10 °C and an ambient temperature of 30 °C (De Block, 2018), which verifies the huge potential for the single-looped HD-TAR applied in practice. The main obstacle to use HD-TARs in practice is the relatively low thermal efficiency.

Based on the analysis of optimal acoustic field affected by cooling temperature (Luo et al, 2019), a traditional cumbersome resonance tube between the TAE and TAR is no longer required for a room temperature HD-TAR. A novel looped HD-TAR with a TAE and a TAR direct coupling in each thermal-to-cold conversion unit is proposed, designed and investigated. Our preliminary experimental results have been reported as a short communication article (Wang et al, 2019). In this paper, the novel looped HD-TAR for food refrigeration applications is calculated and tested. Overall performance parameters of cooling capacity and COP are investigated under different heating temperature and refrigeration temperature.

2. ESTABLISHMENT OF THE NOVEL LOOPED HD-TAR SYSTEM

As shown in Figure. 1, the novel looped HD-TAR includes three identical subunits, which consists of a TAE, a TAR and a resonance tube in sequence. Each TAE comprises an ambient heat exchanger 1, a regenerator 1, a hot heat exchanger and a thermal buffer tube 1. Each TAR comprises an ambient heat exchanger 2, a regenerator 2, a cold heat exchanger, a thermal buffer tube 2 and a flow straightener. Main component dimensions of the novel looped HD-TAR are listed in Table 1. All heat exchangers are of shell-tube type with the tube diameter of 1 mm. The hot heat exchanger is a key thermoacoustic component capable of absorbing external heating power and the ambient heat exchanger is used to reject heat to the circulating water, thus a temperature gradient across the regenerator 1 of the TAE could be established. When this axial temperature gradient exceeds a critical value, a self-excited thermoacoustic oscillation will occur at the beginning and acoustic power will be enlarged. Amplified acoustic power is consumed partially in the regenerator 2 of the TAR to attain cooling capacity and the remaining acoustic power from the resonance tube is recycled into the next subunit. The length of the tapered compliance tube is extended to 150 mm to suppress the jet between the ambient heat exchanger 1/thermal buffer tube 2 and resonance tube (Backhaus and Swift, 2000). In order to place an elastic membrane to suppress the global DC flow, there is a cavity with a length of 30 mm and a diameter of 110 mm at the entrance of the TAE (Gedeon, 1997). According to the previous work, a stage number of three is found to be a good tradeoff between power and efficiency. The following calculations are conducted by the commercial software SAGE based on the thermodynamic and dynamic equations (Gedeon, 1995). Some parameters are given to evaluate the performance of the novel looped HD-TAR system. The overall coefficient of performance (COP) for the looped HD-TAR is defined as

$$COP = Q_c / Q_h \qquad \text{Eq. (1)}$$

where Q_c and Q_h refer to the cooling capacity and heating power, respectively.

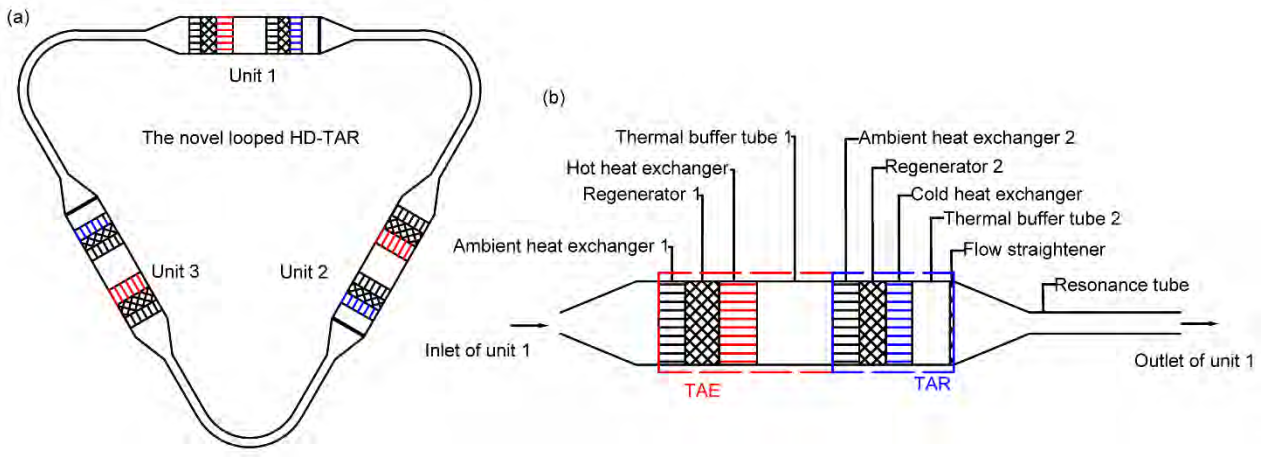

Figure 1: The model of the novel looped HD-TAR

Table 1. Main dimensions of the novel looped HD-TAR (mm)

Component		Inner diameter	Length	Other
TAE	Ambient heat exchanger 1	102	35	0.18 porosity
	Regenerator 1	107	45	120-mesh stainless steel screens
	Hot heat exchanger	102	50	0.18 porosity

	Thermal buffer tube 1	110	100	
TAR	Ambient heat exchanger 2	102	35	0.18 porosity
	Regenerator 2	107	35	120-mesh stainless steel screens
	Cold heat exchanger	102	35	0.18 porosity
	Thermal buffer tube 2	110	50	
	Flow straightener	110	5	20-mesh copper screens
Resonance tube		28	3000	

As shown in Figure. 2, the experimental apparatus comprises a looped HD-TAR subsystem, a thermal oil circulating subsystem, three propylene glycol circulating subsystems, a water circulating subsystem. Hot heat exchangers were heated by the thermal oil and the total heating power was acquired indirectly through the multiplication of voltage and current. In addition, the Hot heat exchangers were insulated by the Silicate-aluminum insulation with the thickness of 60 mm to reduce the heat loss. A calibrated PT100 platinum resistance thermometer was located at the outlet of hot heat exchangers to measure the heating temperature of the thermal oil. Cold heat exchangers were heated by the propylene glycol and the cooling capacity was measured by a power meter. Similarly, cold heat exchangers were insulated by the multi-layer Foam insulation to reduce the cooling capacity loss. Three calibrated PT100 platinum resistance thermometers were deployed in the reservoir to measure the local temperature of the propylene glycol. All ambient heat exchangers are cooled by the water with the temperature of 30 °C. The working gas is helium with a mean pressure of 10 MPa. Additionally, an elastic membrane was placed in the entrance of Unit 3 to suppress the global DC flow.

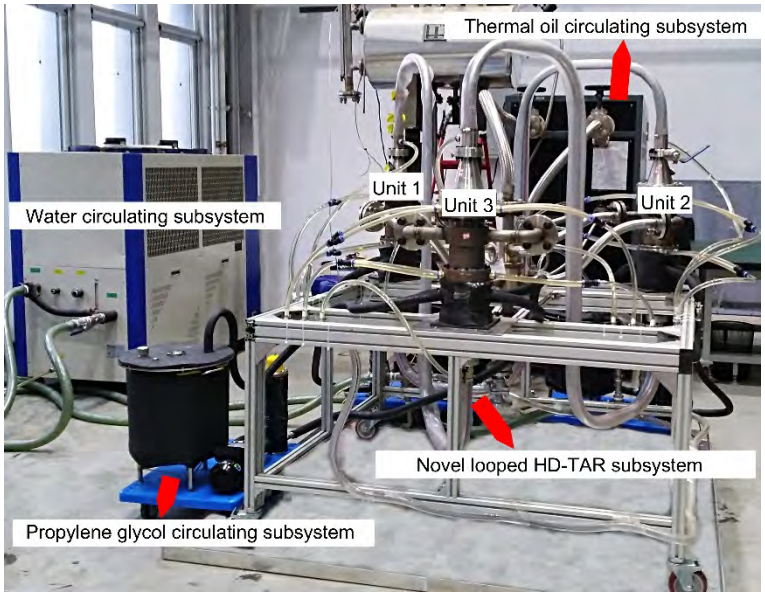

Figure 2: Experimental apparatus of the novel looped HD-TAR system

3. RESULTS AND DISCUSSIONS

To test and analyze performances of the whole system, a series of experiments and calculations have been carried out. When the heating temperature reached 80 °C, the looped HD-TAR began to self-excite with a resonance frequency of about 56 Hz. With the rise of heating temperature, the refrigeration temperature began to drop. When the thermal oil temperature at the outlet of hot heat exchanges reached 260 °C and 300 °C, the propylene glycol temperature at the entrance of cold heat exchanges was fixed at 0 °C, -5 °C, -10 °C and -15 °C, respectively. Figure. 3 illustrates experimental and calculated results of overall cooling capacity under different refrigeration temperature. When the refrigeration temperature changes from -15 °C to 0 °C, overall cooling capacity ranges from 2.02 kW to 3.75 kW with a heating temperature of 260 °C and it ranges from 2.95 kW to 4.93 kW with a heating temperature of 300 °C. The COP of the looped HD-TAR under different refrigeration temperature is presented in Figure. 4. As shown in figure, COP rises with the increase of the refrigeration temperature and covers a range of 0.15-0.24. Compared with the

previously reported heat-driven refrigeration technology for refrigerated trucks and fishing vehicles, the experimental results exhibit certain advantages in COP and cooling capacity. However, a large deviation of approximately 55% could be readily observed between experimental and calculated results. One reason might consist in the unaccounted heat loss between the heat transfer fluid and solid wall in all the heat exchangers. Another reason might lie in the numerical model which underestimates the cooling capacity loss induced by the complicated flow and heat transfer in the thermal buffer tube 2. In the near future, multidimensional simulations by using computational fluid dynamics will be carried out to identify the quantity of the losses and improvement will be made accordingly.

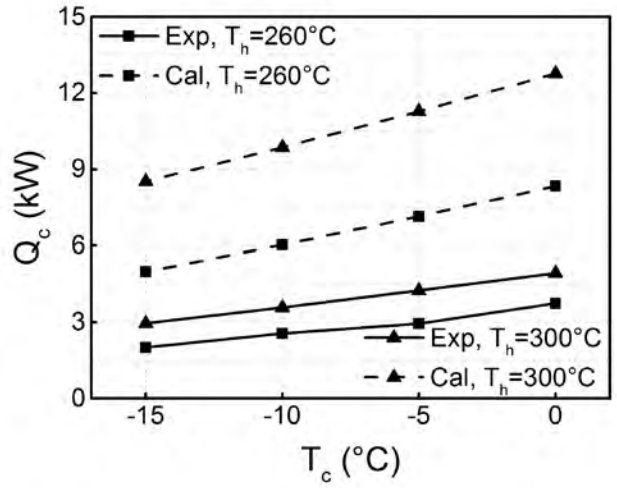

Figure 3: Experimental and calculated results of overall cooling capacity under the heating temperature of 260 °C and 300 °C

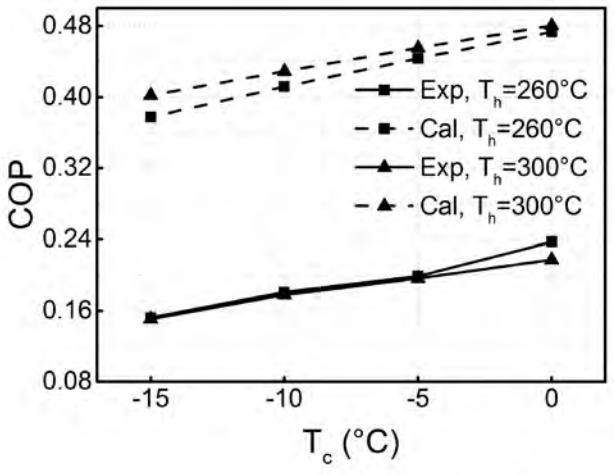

Figure 4: Experimental and calculated results of COP under the heating temperature of 260 °C and 300 °C.

4. CONCLUSIONS

A novel looped HD-TAR system for food refrigeration applications is investigated and analyzed under different refrigeration temperature. With regard to a typical condition of a heating temperature of 300 °C and an ambient temperature of 30 °C, a total cooling capacity rises from 2.95 kW to 4.93 kW and a COP ranges from 0.15 to 0.22 when refrigeration temperature change from -15 °C to 0 °C. Experimental results show a good prospect for food refrigeration applications for recovering waste heat of refrigerated trucks and fishing vehicles. The reasonable design of the heat exchangers and thermal buffer tube will be desirable for the improvement of the refrigeration performance in future.

ACKNOWLEDGEMENTS

This work was financially supported by the National Key Research and Development Project of China (No. 2016YFB0901403) and the National Natural Science Foundation of China (No. 51506211).

NOMENCLATURE

COP	coefficient of performance	Q_c	cooling capacity (W)
Q_h	heating power (W)	T_c	cooling temperature (°C)

REFERENCES

Tassou, S. A., Lewis, J. S., Ge, Y. T., Hadawey, A., Chaer, I., 2010. A review of emerging technologies for food refrigeration applications. Appl. Therm. Eng 30(4), 263-276.

Xu, Z. Y., Wang, R. Z., 2018. Comparison of absorption refrigeration cycles for efficient air-cooled solar cooling. Sol. Energy 172, 14-23.

Zhu, F. Q., Jiang, L., Wang, L. W., Wang, R. Z., 2016. Experimental investigation on a MnCl2, CaCl2, NH3, resorption system for heat and refrigeration cogeneration. Appl. Energy 181, 29-37.

Adeff, J. A., Hofler, T. J., 2000. Design and construction of a solar-powered, thermoacoustically driven, thermoacoustic refrigerator. J. Acoust. Soc. Am 107(6), 37-42.

Ceperley, P. H., 1979. A pistonless Stirling engine--The traveling wave heat engine. J. Acoust. Soc. Am 66(5), 1508-1513.

Luo, E. C., Dai, W., Zhang, Y., Ling, H., 2006. Thermoacoustically driven refrigerator with double thermoacoustic-stirling cycles. Appl. Phys. Lett 88(7), 074102(1-3).

De Block, K., 2012. Multi-stage traveling wave thermoacoustics in practices. Proceeding of the 19th International Congress on Sound and Vibration, Vilnius, Lithuania, 1-8.

Wang, H. Z., Yu, G. Y., Hu, J. Y., Wu, Z. H., Zhang, L. M., Luo, E. C., 2018. A novel looped low-temperature heat-driven thermoacoustic refrigerator operating in room temperature range. Proceeding of the 10th International Conference on Applied Energy, Hong Kong, China.

De Block, K., 2018. Technology and application of thermoacoustic heat transformers[R]. MVO/NAP-Workshop. https://www.napnetwerk.nl/download/?id=12183.

Luo, K. Q., Hu, J. Y., Luo, E. C., Zhang, L. M., Sun, Y. L., Zhou, Y., 2019. Theoretical investigation on the optimal PU phase relationships of regenerative cooling systems with highest efficiency. Cryogenics, 98, 5-11.

Wang, H. Z., Zhang, L. M., Yu, G. Y., Hu, J. Y., Luo, E. C., Ma, Y., Jiang, C., Liu, X. X., 2019. A looped heat-driven thermoacoustic refrigeration system with direct-coupling configuration for room temperature cooling. Sci. Bull 64, 8-10.

Backhaus, S., Swift, G. W., 2000. A thermoacoustic-Stirling heat engine: Detailed study. J. Acoust. Soc. Am 107(6), 3148-3166.

Gedeon, D., 1997. DC Gas Flows in Stirling and Pulse Tube Cryocoolers. In: Ross, R. G., Cryocoolers 9, Springer, Boston, MA, 385-392.

Gedeon, D., 1995. Sage: Object-Oriented Software for Cryocooler Design. In: Ross, R. G., Cryocoolers 8, Springer, Boston, MA, 281-292.

Manuscript ID: 1594
DOI: 10.18462/iir.icr.2019.1594

A novel flue gas total heat recovery system combining direct-contact condensation with liquid desiccant absorption

Xiaoyue ZHANG[(a)], Junda WU[(a)], Zhen LI[(b)]

[(a)] Key Laboratory of Thermal Science and Power Engineering of Ministry of Education, Tsinghua University
Beijing, 100084, China, xy-zhang15@mails.tsinghua.edu.cn
[(b)] Beijing Key Laboratory of Heat Transfer and Energy Conversion, Tsinghua University
Beijing, 100084, China, lizh@tsinghua.edu.cn

ABSTRACT

A condensing boiler is unable to effectively recover a large amount of latent heat carried with the water vapor in the flue gas of natural gas boilers. A heat recovery system combining direct-contact condensation with liquid desiccant absorption is then proposed in this paper. The water vapor in the flue gas is partially condensed in the direct-condenser and further absorbed by the liquid desiccant. A case study of a gas-fired boiler with this heat recovery system shows that the boiler equivalent thermal efficiency based on the natural gas lower heating value can reach 104.7% when the return water temperature is 40°C. The relative humidity of the discharged flue gas is only 30%, which avoids the formation of white smoke. This system also contributes to the mitigation of NOx and CO_2 emissions. A parametric analysis indicates that the lower the return water temperature, the better the performance of this system.
Keywords: Absorption System, Combined Heat Pump Boiler, Heat Recovery, Liquid Desiccant.

1. INTRODUCTION

Due to increasingly serious environmental problems and haze weather facing China, coal-fired boilers in district heating are being replaced with gas-fired boilers whose flue gases are relatively clean. The water vapor content in the flue gas of natural gas boilers is very high and the humidity ratio of the flue gas can be as high as 120 $g \cdot kg^{-1}$. A large amount of latent heat is carried with the water vapor in the flue gas. Thus, there is a great potential for the improvement of the boiler efficiency and a total heat recovery including latent heat recovery from the flue gas is significant. Besides, flue gases with high humidity will form white smoke which may facilitate pollutant attachment and aggravate haze together with NOx emissions. So it would be better if the flue gas can be dehumidified and the NOx emissions can be mitigated along with heat recovery.

In heating networks, condensing boilers are common boilers with heat recovery using the return water as the cooling medium to cool the flue gas below its dew point. The heat recovery unit is usually an indirect-contact heat exchanger where the water vapor in the flue gas is condensed with the corresponding latent heat released to the return water. When the return water temperature is 41°C, the boiler efficiency could increase from 90.1 to 95.8% after a conventional natural gas boiler is retrofitted into a condensing boiler (Che et al., 2004). However, the heat recovery of a condensing boiler is restricted by the return water temperature. When the return water temperature is high and close to the dew point temperature of the flue gas, which is about 55°C, the water vapor can hardly be condensed and the heat recovery is then substantially reduced. Thus, heat pumps are usually applied to this system, producing low-temperature chilled water to recover the latent heat which is then transported to the return water. Heat pumps are classified as vapor compression heat pumps and absorption heat pumps. The combined vapor compression heat pump boiler is simple but its main drawback is the high electric power consumption (Chen et al., 2012). Qu et al. (2014) experimentally investigated the performance of a natural gas boiler using an absorption heat pump for heat recovery, showing that the boiler efficiency was improved by 10%. However, the heat exchangers in these systems are indirect-contact heat exchangers, with low heat transfer capability and potential corrosion problems. Zhu et al. (2014) combined an absorption heat pump with a direct-contact heat exchanger which is a spray tower, where the chilled water produced by the heat pump

contacts directly with the flue gas. This scheme improved the heat capacity of a gas boiler by nearly 12%. The flue gases of both the condensing boiler and the combined heat pump boiler are discharged to the atmosphere at saturation, which still forms white smoke. Lazzarin et al. (1992) proposed a total heat recovery method based on liquid desiccant dehumidification cycle, which was called open cycle absorption heat pump (OAHP). Unlike the condensing method, the water vapor in the flue gas is absorbed by the liquid desiccant driven by vapor pressure difference and thus the flue gas does not need to be cooled below its dew point. Wang et al. (2016) conducted an experiment on the performance of an open cycle absorption heat pump using lithium bromide aqueous solution as the liquid desiccant. The results showed that this system outperformed the condensing gas-fired boilers by 21.2% in heat recovery when the return water temperature is 45°C. However, in this system, a large amount of water vapor is absorbed solely by the desiccant, increasing the load and size of the absorber and regenerator. Another drawback of this system might be the contamination from the flue gas to the liquid desiccant.

Thus, a novel total heat recovery system combining a direct-contact condenser with an open absorption heat pump based on liquid desiccant will be introduced in this paper. This newly proposed system uses the direct-contact condenser to share the moisture load with the absorber and can avoid the contamination to the desiccant as well. The heat recovery of this system will be calculated based on a typical heating condition. Then, a parametric analysis will be conducted by changing the temperature of the return water. Economic feasibility and environmental compatibility will also be analyzed to evaluate the system.

2. SYSTEM DESCRIPTION

Fig. 1 shows the diagram of the proposed flue gas heat recovery system combining direct-contact condensation with liquid desiccant dehumidification. This heat recovery system mainly consists of a flue gas direct-contact condenser, an absorber, a regenerator, a steam condenser and two heat exchangers (HX). The regenerator is a vapor/steam generator, where natural gas is consumed to heat the desiccant solution so that the water absorbed by the desiccant is evaporated and the desiccant solution is regenerated/concentrated. The flue gas from the regenerator, together with the flue gas from the boiler, then flows into the direct-contact condenser. The flue gas condenser is actually a packed bed tower. The circulating water is sprayed from the top to directly contact with the flue gas and, due to the high humidity ratio, the water vapor in the flue gas is partially condensed into the circulating water. After being preliminarily cooled and dehumidified in the condenser, the flue gas enters the absorber to be further dehumidified. The absorber is also a packed bed tower, where the relatively cold and concentrated desiccant solution contacts with the flue gas and the water vapor in the flue gas is further absorbed by the desiccant. Finally, the flue gas is discharged to the atmosphere at a lower temperature and humidity. After absorbing water vapor, the desiccant solution is diluted and part of the solution then flows through a three-way valve and enters the regenerator. The evaporated water vapor in the regenerator flows into the steam condenser, releasing condensation heat to a branch of the return water. The concentrated solution from the regenerator, after being mixed with the other part of the diluted solution, flows into a heat exchanger to be cooled by a branch of the return water before being sprayed into the absorber.

As can be seen, the flue gas condenser shares the vapor absorption load with the absorber, which significantly reduces the size of the absorber and the regenerator. A little amount of alkali liquor is added to the circulating water to help absorb CO_2 and soluble NOx, which can not only mitigate the CO_2 and NOx emissions but also avoid their contamination to the liquid desiccant in the absorber. After recovering the sensible heat and part of latent heat from the flue gas, the circulating water transfers the heat to a branch of the return water through a HX. The three branches of preheated return water then converge and enter the boiler to be further heated. Non-condensable gases like O_2 will be carried into the regenerator, causing corrosion problems. As the steam condenser is connected with the regenerator, the gathering of non-condensable gases may also deteriorate the condensation performance. Thus, a vacuum pump is used to bleed the gases and the desiccant solution is concentrated under low pressure, which not only alleviates the corrosion but also lowers the boiling point of the solution. As the flowrate of the desiccant is large, only part of the desiccant solution flows through the three-way valve into the regenerator to reduce the heat needed to boil the desiccant. This will also reduce the gases carried into the regenerator.

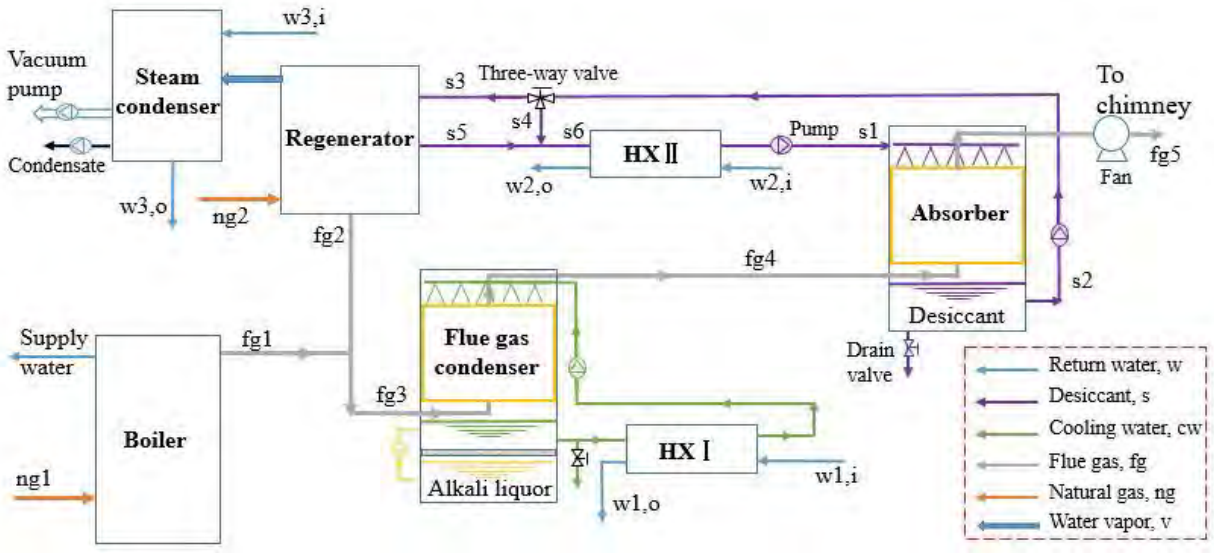

Figure 1: Diagram of the heat recovery system combining direct-contact condensation and desiccant absorption

3. CASE STUDY

3.1. Assumptions, Modelling and Input Parameters

All the components of the proposed system are essentially heat exchangers except the flue gas condenser and the absorber which are packed bed tower. The parameters of the heat exchangers are calculated based on heat and mass balances and pinch point temperature differences. The pinch point temperature differences in HXI, HXII and the steam condenser are 5 K, 5 K and 10 K, respectively. The thermal efficiency of the regenerator is assumed the same as that of the original boiler which is 92% based on the natural gas lower heating value, with a flue gas temperature of 120°C. The humidity of the flue gas from the regenerator and from the boiler is also equal, which is calculated according to the model provided in the literature (Zhang and Li, 2019). The outdoor air temperature and relatively humidity of air are 0°C and 40% in heating seasons. The flue gas condenser and the absorber are calculated using the finite difference model of adiabatic counter-flow packed towers (Factor and Grossman, 1980) with the lithium bromide water solution as the liquid desiccant. A natural gas boiler with a heating capacity of 7 MW is simulated for floor heating occasions where the temperatures of the supply and return water are 50°C and 40°C. Other input parameters are listed in Table 1. A regeneration flowrate ratio of 0.5 means half of the solution from the absorber enters the regenerator through the three-way valve.

Table 1. Input parameters of the proposed system for simulation

Circulating water flowrate	Flowrate of each return water branch	Absorber inlet solution flowrate	Absorber inlet solution concentration	Regeneration flowrate ratio
13.3 kg·s^{-1}	25.0 kg·s^{-1}	8.0 kg·s^{-1}	50.0%	0.5

3.2. Simulation Results

Fig. 2 shows the simulation results of this proposed system. As can be seen, the humidity ratio of the flue gas is reduced by 56 g·kg^{-1} in the direct-contact condenser, approximately equal to the humidity ratio reduction in the absorber which is 50 g·kg^{-1}. This means that the flue gas condenser shares equally considerable latent heat load compared to the absorber. The temperature of the flue gas is reduced to 47.8°C after the direct-contact condenser, which benefits the following dehumidification process in the absorber. The flue gas is ultimately discharged to the atmosphere with a humidity ratio of only 22 g·kg^{-1}, which means that most of the latent heat carried with the water vapor is recovered. Besides, the water vapor absorbed by the desiccant is finally transported to the steam condenser and the distilled water with a flowrate of 0.43 t·h^{-1} can thus be recovered for boiler

replenishment. The concentration changes in the desiccant solution are small due to a large flowrate. The concentration of the solution at the regenerator outlet is 52.4%, far from the crystallization point. The total natural gas consumption of the whole system is 676 $Nm^3 \cdot h^{-1}$, reduced by about 13.7% compared with the original boiler which consumes 783 $Nm^3 \cdot h^{-1}$ of natural gas.

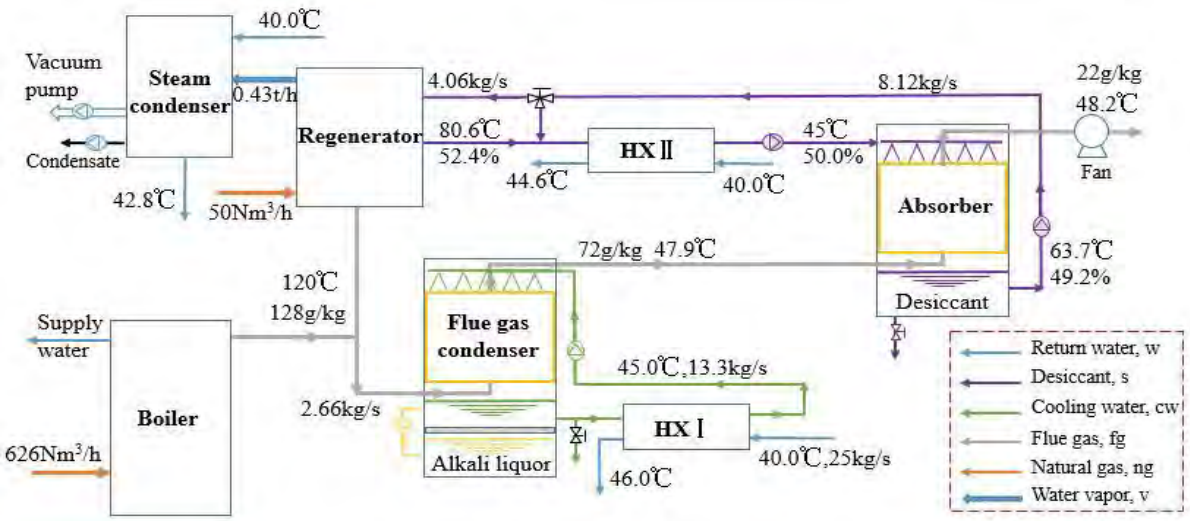

Figure 2: Simulation results of the proposed system

3.3. Environmental Compatibility

Fig. 3 shows the parameters of the flue gas discharged to the atmosphere on a psychrometric chart. In the chart, *O*, *Y*, *Z* represents the states of the outdoor air, the flue gas after the direct-condenser and the flue gas after the absorber. As can be seen, if the flue gas is discharged to the atmosphere after the direct-contact condenser and mixed with the outdoor air around the chimney, the state of the mixed gas will be on the dashed line which is in the fog zone and white smoke will thus be formed. In contrast, if the flue gas is discharged after the absorber, the relative humidity of the flue gas is only 30% and the state of the mixed gas will be on the solid line. In this case, the formation of white smoke will be avoided with this heat recovery system. Moreover, the NOx and CO_2 emissions are also mitigated due to the alkali liquor additive in the condenser. NOx emissions can be further mitigated by installing an ozone generator to oxidize the insoluble NO to soluble NOx. With the condensation of water vapor, the flowrate of the circulating water will increase and the redundant water needs to be drained periodically. The drainage is neutral or weakly alkaline, which meets the environmental requirements. Thus, this proposed heat recovery system is environmentally friendly.

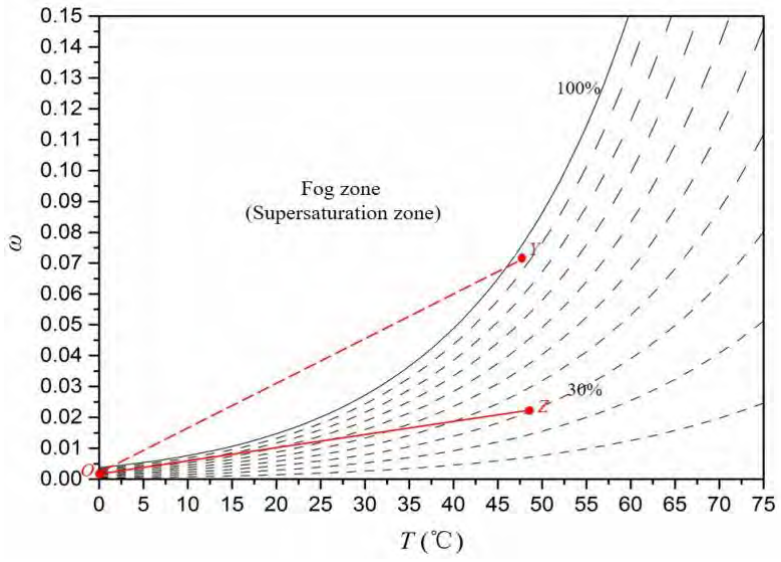

Figure 3: Parameters of the flue gas on a psychrometric chart

4. ECONOMIC FEASIBILITY AND PARAMETRIC ANALYSIS

4.1. Economic Feasibility

Although the heat recovery of the proposed system is considerable, this system also consumes extra electric power for pumps and the fan. An equivalent thermal efficiency of the boiler, η_e as shown in Eq. (1), is then introduced to evaluate this system by taking the electric power into consideration.

$$\eta_e = m_w c_w \Delta T \left((V_1 + V_2) Q_{lcv} + W_p \eta_{gp}^{-1} \right)^{-1} \quad \text{Eq. (1)}$$

where m_w and c_w are the total mass flowrate and the specific heat capacity of the return heating water, ΔT is the temperature rise of the supply water over the return water, V_1 and V_2 are the consumed standard volume of natural gas in the boiler and the regenerator, Q_{lcv} is the lower heating value of natural gas (35 MJ per standard cubic meter), W_p is the total extra electric power consumed by the pumps and the fan, η_{gp} is the power efficiency of gas-fired generators which is 38% (Wen et al., 2018). Since the thermal efficiency is based on the lower heating value of natural gas instead of the higher heating value, the thermal efficiency can theoretically exceed 100%. The extra electric power consumption of the pumps and the fan in this system are estimated in Table 2. The equivalent thermal efficiency of the boiler is 104.7% when the return water temperature is 40°C, which is much higher than that of the original boiler (92%).

Table 2. Extra electric power consumption of the pumps and the fan (kW)

Circulating water pump	Solution pump before absorber	Solution pump after absorber	Return water pump	Vacuum pump	Fan
1.1	2.2	1.1	30	1.5	7.5

All components are made of stainless steel to avoid corrosion. The heat exchanger area and the area of the packing in the flue gas condenser and absorber are listed in Table 3, according to which the costs of the main components are estimated. The specific surface area of the packing is 250 $m^2 \cdot m^{-3}$. The regenerator is a steam boiler with a heating capacity of about 0.5 MW and costs CNY300000 which is relatively expensive due to the stainless steel materials. Thus, the equipment investment totals about CNY477000. For a natural gas price of CNY2.28 per standard volume and an electricity price of CNY0.8 per kilowatt hour, the heat recovery system can save CNY208.5 per hour. If the boiler continuously operates at full load, the payback period is 2288 hours which is just over one year (one heating season). Therefore, the proposed system is energy-efficient and its economic feasibility can be ensured.

Table 3. Heat exchange area (m^2) and costs (CNY) of the main components

	HXI	HXII	Steam condenser	Flue gas condenser	Absorber
Area	23	23	13	820	820
Cost	19000	19000	11000	64000	64000

4.2. Parametric Analysis

The return water temperature is a key parameter that influences the performance of heat recovery systems. For floor heating networks, the return water temperature typically ranges from 35 to 45°C. Fig. 4a shows that with increasing return water temperature, the humidity ratio of the discharged flue gas increases and the boiler equivalent thermal efficiency decreases. The thermal efficiency based on natural gas lower heating value increases from 103.0 to 105.8% when the return water temperature decreases from 45 to 35°C. Fig. 4b shows that the humidity ratio reduction in the direct-contact condenser increases with decreasing return water temperature since more water vapor is condensed in the condenser for lower return water temperatures. Therefore, a lower return water temperature is better for the system energy efficiency, and the direct-contact condenser will play a more important role in the case of low return water temperature.

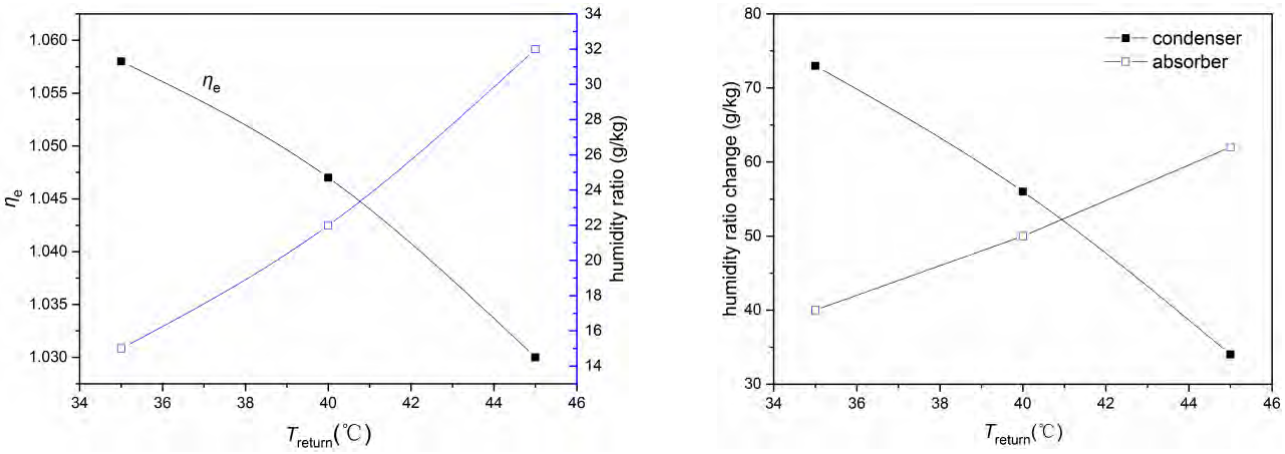

Figure 4: Parametric analyses of the heat recovery system with the variation of return water temperature

5. CONCLUSIONS

A flue gas heat recovery system combining a direct-contact condenser with a liquid desiccant absorption cycle is proposed in this paper. The thermal efficiency of the boiler with this heat recovery system ranges between 103.0 to 105.8% in typical floor heating conditions. The relative humidity of the discharged flue gas is so low that the formation of white smoke is avoided. Besides, NOx and CO_2 emissions can also be mitigated. This system is energy-efficient and environmentally friendly and thus its application is promising.

ACKNOWLEDGEMENTS

This research was sponsored by the National Natural Science Foundation of China (Grant No. 51776103) and the Science Fund for Creative Research Groups (Grant No. 51621062).

REFERENCES

Che, D., Liu, Y., Gao, C., 2004. Evaluation of retrofitting a conventional natural gas fired boiler into a condensing boiler. Energy Conv. Manag. 45(20), 3251-3266.

Chen, Q., Finney, K., Li, H., Zhang, X., Zhou, J., Sharifi, V., Swithenbank, J., 2012. Condensing boiler applications in the process industry. Appl. Energy 89(1), 30-36.

Factor, H.M., Grossman, G., 1980. A packed bed dehumidifier/regenerator for solar air conditioning with liquid desiccants. Sol. Energy 24(6), 541-550.

Lazzarin, R. M., Longo, G. A., Piccininni, F., 1992. An open cycle absorption heat pump. Heat Recovery Syst. CHP 12(5):391-396.

Qu, M., Abdelaziz, Q., Yin, H., 2014. New configurations of a heat recovery absorption heat pump integrated with a natural gas boiler for boiler efficiency improvement. Energy Conv. Manag. 87, 175-184.

Wang, Z., Zhang, X., Li, Z., 2016. Evaluation of a flue gas driven open absorption system for heat and water recovery from fossil fuel boilers. Energy Conv. Manag. 128, 57-65.

Wen, H., Song, J., Zhang, Y., 2018. Effect of power generation efficiency on economy of distributed energy system. Gas & Heat 1, 12-15.

Zhang, X., Li, Z., 2019. A liquid-desiccant-based heat recovery system for gas-fired boilers in district heating networks. ASHRAE transactions. (Volume and pages not available yet)

Zhu, K., Xia, J., Xie, X., Jiang, Y., 2014. Total heat recovery of gas boiler by absorption heat pump and direct-contact heat exchanger. Appl. Therm. Eng. 71(1), 213-218.

Manuscript ID: 1638
DOI: 10.18462/iir.icr.2019.1638

Development of a two-stage absorption-resorption heat pump cycle with multiple internal heat recovery for space heating

Teng JIA[(a)(b)], Yanjun DAI[(a)(b)]

[(a)] Institute of Refrigeration and Cryogenics, Shanghai Jiao Tong University
Shanghai, 200240, China, yjdai@sjtu.edu.cn
[(b)] Engineering Research Center of Solar Power and Refrigeration, MOE
Shanghai, 200240, China, yjdai@sjtu.edu.cn

ABSTRACT

Ammonia-water absorption-resorption heat pump (ARHP) is a promising technology for efficient use of low-temperature heat for space heating. In this paper, a two-stage balanced ARHP cycle with multiple internal heat recovery is proposed. The objective of this work is to study performance of the novel cycle and stress utilization of low-temperature solar heat for space heating. A mathematical model is built to obtain COP values, heat supply temperature, heat inputs/outputs and solution circulation ratios at different feasible high pressure/medium pressure/low pressure ($P_H/P_M/P_L$) values. The results showed that the maximum COP of 1.37 and heat supply temperature of 46.1 °C can be obtained when $P_H/P_M/P_L$ is 1.75/1.10/0.375 MPa under given working conditions. Minimum ambient temperature and heat source temperature to drive the cycle are -17.4 °C and 77 °C, respectively, highlighting the potential of integrating the cycle with commonly used non-tracking solar collectors for space heating.
Keywords: Ammonia-Water, Two-Stage Absorption-Resorption, Heat Recovery, Space Heating.

1. INTRODUCTION

Winter space heating and domestic hot water supply of buildings consumes an essential part of the primary energy in northern China. Heat pumps show great advantages over conventional heating and domestic hot water supply systems which directly or indirectly depend on fossil fuel combustion at low energy conversion efficiency and can help alleviate the severe hazy weathers in northern China caused by coal-dominated energy structure.

Compared to vapor compression heat pumps (VCHPs), thermally activated absorption heat pumps (AHPs) gain popularity in space heating and hot water supply by the ability to be integrated with diverse heat sources, such as gas combustion (Dai et al., 2018), solar energy (Shirazi et al., 2018), biomass energy (Gironès et al., 2018) and waste heat (Kalinowski et al., 2009). However, the heat source temperature demand for conventional AHPs and GAX-based ones are much high (above 120 °C), which limits its integration with commonly used non-tracking solar collectors (Dai et al., 2018; Gomez et al., 2008). In order to extend solar contribution, many researches have attempted to lower the heat source temperature demand of AHPs. The cut-in point is to improve the internal cycle based on conventional AHP cycles.

An absorption-resorption heat pump (ARHP) cycle can be built by substituting the condenser and evaporator in an AHP cycle with a high-pressure absorber and a low-pressure generator, respectively. Baehr (1981) investigated the utilization of the ARHP for building heating aiming to reduce the relatively high condenser pressure and pressure-ratio. It was pointed out that the advantage of having lower condenser-pressures than the conventional AHP cycle must be inevitably paid for with lower COP values. Du et al. (1991 and 1993) theoretically and experimentally investigated an ammonia-water ARHP system for hot water supply which was equipped with two solution pumps and the heat source temperature is up to 150 °C. Jia et al. (2018) theoretically developed a single-stage ARHP cycle with internal heat recovery for building floor heating purpose, which could be driven by solar heat of above 85 °C provided by mass-produced compound parabolic collectors (CPCs) or evacuated tube collectors (ETCs). The cycle could work when the ambient temperature is over -7.5 °C. Jia et al. (2019) further proposed an improved solar-assisted dephlegmator-free single-stage ARHP cycle which implements the internal solution

circulation depending on only one solution pump. The cycle could be operated when solar heat temperature is over 82 ºC and ambient air temperature is above -5.8 ºC.
Although the aforementioned ARHP cycles can be driven by low-temperature solar heat to some extent, the heat supply temperature is not high enough to meet the requirement of various types of heating terminals. Moreover, the low ambient temperature adaptability is not enough to meet the heating needs in cold regions below -10 ºC.

2. CYCLE DEVELOPMENT AND ANALYSIS

2.1. Two-Stage ARHP Cycle

This paper seeks to develop a novel two-stage ARHP cycle to further reduce the heat source demand, to enhance the low ambient temperature adaptability and simultaneously raise the heat supply temperature based on the single-stage ARHP cycle (Jia et al.,2019).

2.1.1. Cycle development

As shown in Figure 1, the two-stage ARHP cycle can be developed based on the single-stage cycle by lifting P_H or reducing P_L or both simultaneously. A medium-pressure part composed of a generator and an absorber is added. The medium-pressure generator (MPG) is expected to be driven by solar heat of the same temperature level as that for the high-pressure generator (HPG). The medium-pressure absorber (MPA) can release more absorption heat which contributes to lifting the heating capacity. Larger pressure drop from P_H to P_L during the throttling process helps reduce temperature of the stream entering the low-pressure generator (LPG), thus enhancing the low ambient temperature adaptability. Larger temperature of solution flowing out of the high-pressure absorber (HPA) in the two-stage ARHP cycle contributes to higher heat supply temperature. Moreover, temperature overlap between the MPG and low-pressure absorber (LPA) provides the possibility to extract some of the absorption heat to the generator within the cycle by heat exchangers which therefore leads to a higher COP (Jawahar et al., 2010).

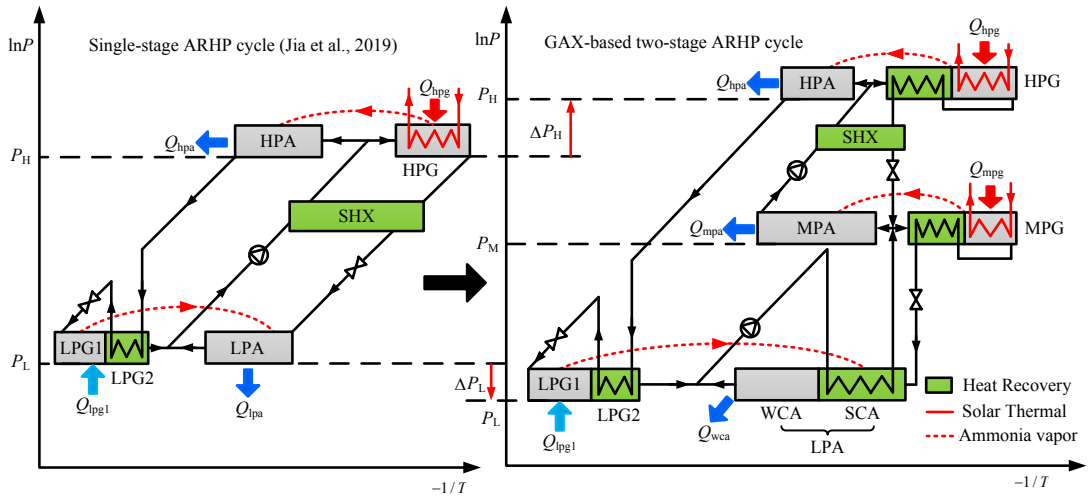

Figure 1: Development of two-stage ARHP cycle based on the single-stage cycle (Jia et al., 2019)

2.1.2. Detailed cycle description

The detailed schematic diagram of the novel two-stage ARHP cycle is depicted in Figure 2. The cycle consists of HPG, HPA, MPG, MPA, LPG, LPA, solution heat exchanger (SHX), vapor-solution heat exchanger (VSHX), solution mixing tank (SMT), solution mixing/separation tank (SMST), solution separation tank (SST), three throttle valves (TV1, TV2 and TV3) and two solution circulation pumps (SP1 and SP2). Multiple internal heat recovery can be achieved in LPG2, HPG, MPG, SCA and SHX. To functionally distinguish different heat sources for the low-pressure generation process, LPG is divided into two parts: LPG1 extracting heat (Q_{lpg1}) from ambient air and LPG2 recovering heat (Q_{lpg2}) from HPA outlet warm solution. In HPG and MPG, heat of the outlet solutions can be recovered to preheat the inlet solutions by heat recovery coils arranged inside. LPA can also be divided into two parts: solution-cooled absorber (SCA) which recovers part of low-pressure absorption heat to preheat the pump outlet solution, and water-cooled absorber

(WCA) which delivers the remaining absorption heat to the return/supply water stream. The cycle contains three inner sub-cycles and ammonia-water is employed as the working pair.

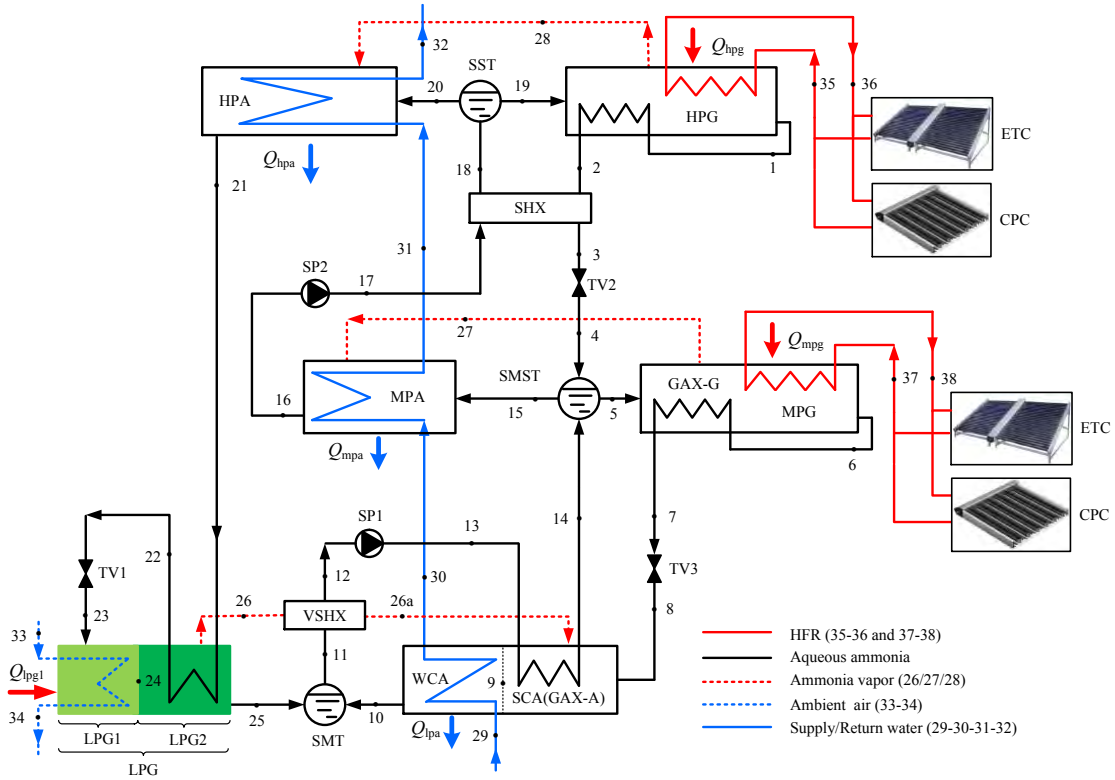

Figure 2: Schematic diagram of the proposed two-stage ARHP cycle

2.2. Mathematical Model

2.2.1. Assumptions

The thermodynamic properties of ammonia-water solutions and vapour streams are obtained by REFPROP 9.1 (2013). The following assumptions were made to simplify the calculation process.
(1) The system runs in a steady state and pressure drops along the pipes are neglected;
(2) Power inputs of solution pumps are negligible compared to heat inputs of generators and heat outputs of absorbers.
(3) The depressurizing processes in throttle valves are isenthalpic.
(4) The solutions out from SCA, WCA, LPG1, LPG2, MPA, MPG, HPA and HPG are all saturated.
(5) Vapor out at outlet of LPG, MPG and HPG are all saturated.

2.2.2. Thermodynamic model of cycle components

All the components can be analysed based on mass, energy and species (NH_3) mass conservation equations, which are separately given as follows (Han et al., 2017):

$$\sum_i m_{in} - \sum_i m_{out} = 0 \qquad \text{Eq. (1)}$$

$$\sum_i (m_{in} \cdot x_{in}) - \sum_i (m_{out} \cdot x_{out}) = 0 \qquad \text{Eq. (2)}$$

$$\left(\sum_i (m_{in} \cdot h_{in}) - \sum_i (m_{out} \cdot h_{out})\right) + \left(\sum_i Q_{in} - \sum_i Q_{out}\right) + \left(\sum_i W_{in} - \sum_i W_{out}\right) = 0 \qquad \text{Eq. (3)}$$

Coefficient of performance (COP) is adopted to evaluate the cycle performance, given by

$$COP = \frac{Q_{hpa} + Q_{mpa} + Q_{wca}}{Q_{hpg} + Q_{mpg}} \qquad \text{Eq. (4)}$$

2.2.3. Model validation

When P_H equals to P_L in the proposed two-stage ARHP cycle, it turns into a single-stage ARHP cycle. To validate the simulation model, the results in this paper have been compared to the

simulation results presented in the literatures in Table 1. It can be found that the results in this paper were perfectly consistent with those in the literatures.

Table 1. Validation of the mathematical model

$P_H/P_M/P_L$ (MPa)	$T_1/T_{10}/T_{16}/T_{21}/T_{24}$ (ºC)	COP in this work	COP in Refs.	Relative deviation
1.50/1.50/0.35	145/45/55/55/15	1.295	1.270 (Du et al., 1991)	2.95%
1.40/1.40/0.32	90/35/40/40/0	1.200	1.228 (Jia et al., 2018)	2.28%
1.50/1.50/0.35	90/35/40/40/0	1.282	1.305 (Jia et al., 2019)	1.76%

2.3. Performance Analysis

In this paper, a case was investigated to seek the proper path to develop two-stage ARHP cycle based on the single-stage ARHP cycle. The case can be described as: If P_H values of the single- and two-stage ARHP cycle are equal, P_L and temperature of stream at LPG1 inlet of the two-stage cycle can be lower than those of the single-stage cycle (by ΔP_L and ΔT_a, respectively), making it possible for the proposed cycle to work at lower ambient air temperatures, as shown in Figure 3.

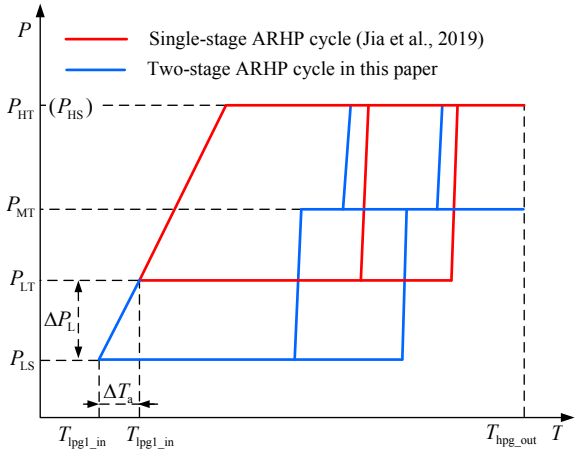

Figure 3: Comparison between the single-stage and the two-stage ARHP cycle in P-T diagram

The initial working conditions are given in Table 2.

Table 2. Initial working conditions

Working Conditions	Value (ºC)
Ambient air temperature	5
Temperature of return water (29)	30
Temperature of solution (10) out from LPA	35
Temperature of solution (16) out from MPA	40
Temperature of solution (21) out from LPA	45
Temperature of solution (1) out from HPG	90
Temperature of solution (6) out from MPG	90
Cold end temperature difference of SHX	5

2.3.1. Feasible design combination of P_H/P_L

Based on the working conditions given in Table 2, feasible P_H/P_L combination set to enable the cycle is obtained, as the shaded area shows in Figure 4. It can be seen that the feasible P_H values are restricted in the range from 1.50 MPa to 1.75 MPa. For each P_H value within this range, there exist corresponding and certain P_L ranges to effect the cycle. The feasible P_L range becomes narrower with the increasing of P_H value. It is because that higher P_H values result in larger concentration of outlet solutions from HPG and HPA (solution (1) and (21)), which flows into low-pressure side and ultimately allows the LPG and LPA to work in a wider P_L range. It should be pointed out that the feasible P_H/P_L pair area varies when working conditions change.

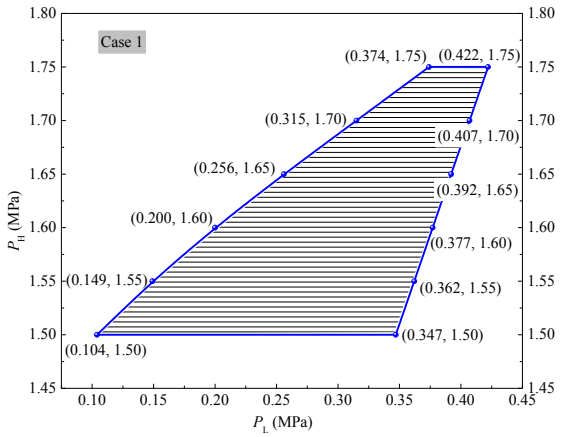

Figure 4: Feasible P_H/P_L range to effect the proposed cycle in the studied case

2.3.2. Effect of P_H/P_L on P_M range and COP

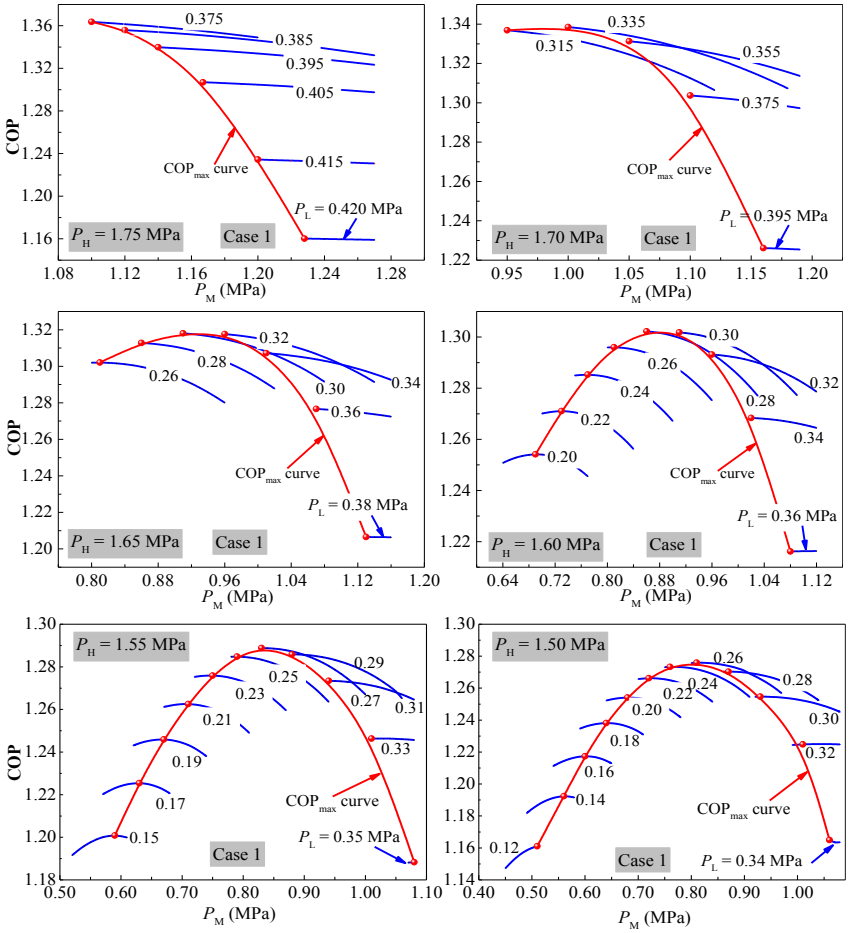

Figure 5: Feasible PM ranges and the corresponding COP values

Based on the feasible P_H/P_L pair area illustrated in Figure 4, effect of P_H/P_L pair values on feasible P_M range and that of $P_H/P_M/P_L$ combination on the cycle COP are studied, as shown in Figure 5. It can be seen that for given P_H/P_L value, there exists a certain P_M range and COP varies with the changing of $P_H/P_M/P_L$ combination value. For most cases, COP firstly increases with the increasing of P_M value and then decreases, so maximum COP values and optimum P_M values can be found. It is also obvious from Figure 5 that for given P_H value, optimum P_M value ascends with the increasing of P_L value while the maximum COP value firstly increases and then decreases with the increasing of P_L value. Therefore, there exist global optimum COP and $P_H/P_M/P_L$ values for the studied case, which are 1.37 and 1.75/1.10/0.375 MPa, respectively.

2.3.3. Heat supply temperature

Figure 6 describes the variation of the heat supply temperature (T_{hs}) with $P_H/P_M/P_L$ combination values. Restricted by the minimum heat transfer temperature difference of cycle internal heat exchange components, return/supply temperature lift in WCA are set as 5 ºC. T_{hs} depends on both the ratio of Q_{mpa} and Q_{wca} and the ratio of Q_{hpa} and Q_{wca}. It can be seen that for given P_H/P_L value, T_{hs} decreases with the increasing of P_M within its range. It is because that higher P_M value enhances the absorption process in MPA while simultaneously weakens that in HPA. In other words, with the increasing of P_M value, the ratio of Q_{mpa} and Q_{wca} increases while the ratio of Q_{hpa} and Q_{wca} decreases. The above two effects are contradictory when it comes to T_{hs}, and the integrated results is that T_{hs} decreases with the increasing of P_M value. It is obvious that for given P_H/P_M, T_{hs} ascends with the increasing of P_H value. The reason is that when P_H value increases, solution flowing out of HPA becomes stronger and more refrigerant vapor can be absorbed in HPA, resulting in more absorption heat output and larger ratio of Q_{hpa} and Q_{wca}. Therefore, T_{hs} increases accordingly.

For the studied case, the maximum T_{hs} ($T_{hs,max}$) under given working conditions reaches 49.8 ºC when $P_H/P_M/P_L$ is 1.75/1.20/0.415 MPa, where the COP is 1.23, which can basically meet the temperature demand of fan coil heating. When the cycle is operated at its maximum COP of 1.37, T_{hs} can still reach 46.1 ºC, which can meet the temperature demand of building floor heating. Besides, it is obvious from Figure 6 that, most of T_{hs} values corresponding to feasible $P_H/P_M/P_L$ values are above 40 ºC. In other words, the case is especially suitable for building floor heating.

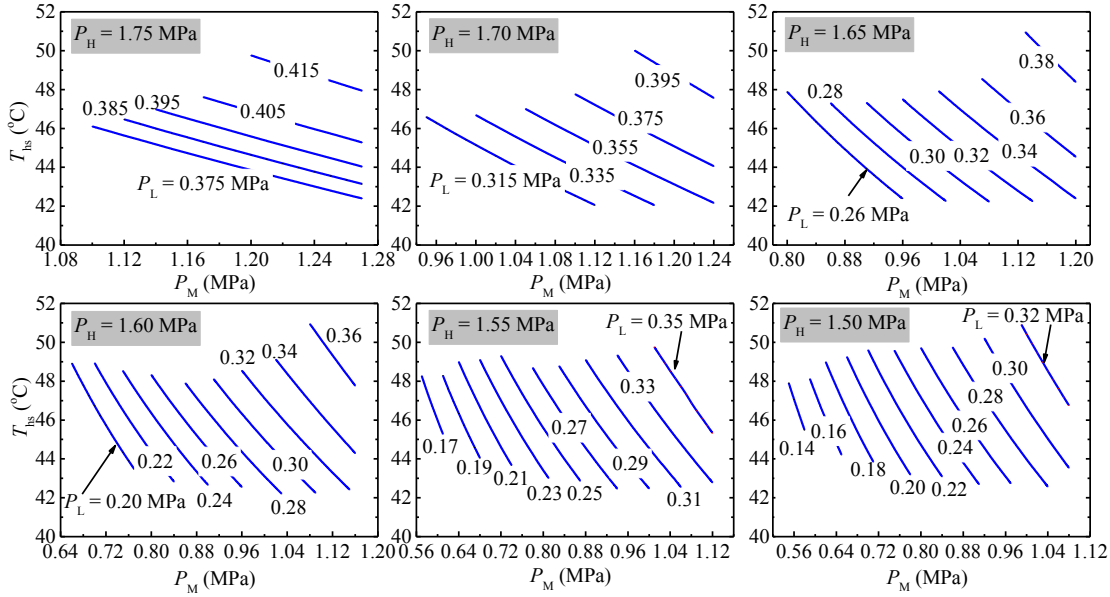

Figure 6: Heat supply temperature versus $P_H/P_M/P_L$ combination

2.3.4. Minimum ambient air temperature

Minimum ambient air temperature ($T_{a,min}$) to enable the cycle was investigated to validate the greater low ambient air temperature adaptability of the novel cycle than the single-stage cycle, as shown in Figure 7. For different $P_H/P_M/P_L$ values, there exists an exact $T_{a,\,min}$ value to enable the cycle, and for given P_H value, $T_{a,min}$ ascends with the increasing of P_L value. For the studied case, $T_{a,\,min}$ can be low to -17.4 ºC, indicating that the two-stage cycle has greater low-temperature adaptability than the single-stage cycle for which $T_{a,\,min}$ is -5.8 ºC (Jia et al., 2019).

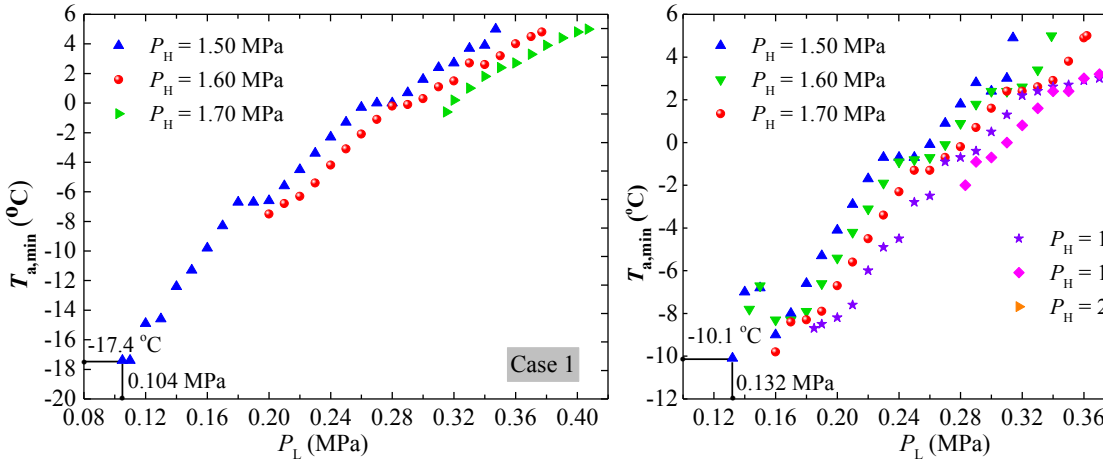

Figure 7: Minimum ambient air temperature versus $P_H/P_M/P_L$ combination

2.3.5. Heat source temperature demand

Heat source temperature (T_h) level was calculated to validate the possibility of integrating more economical stationary solar collectors with the proposed cycle for space heating, as illustrated in Figure 8. It can be seen that for given P_H/P_L value, when T_h is low, COP directly increases with the increasing of P_M. When T_h gets larger than 81 ºC here, COP turns to firstly increase and then descend with the increasing of P_M. When T_h gets larger than 85 ºC, COP becomes to directly decline with the increasing of P_M. For the studied case, the minimum heat source temperature to drive the cycle is 77 ºC, indicating that the two-stage cycle further lowers the heat source temperature demand based on the single-stage cycle for which $T_{h,min}$ is 82 ºC under the same working conditions. The two-stage cycle can contribute to enhancing solar fraction and working time when ARHPs are integrated with economical stationary solar collectors for space heating. Moreover, the cycle COP can be up to 1.40 when the heat source temperature gets above 100 ºC.

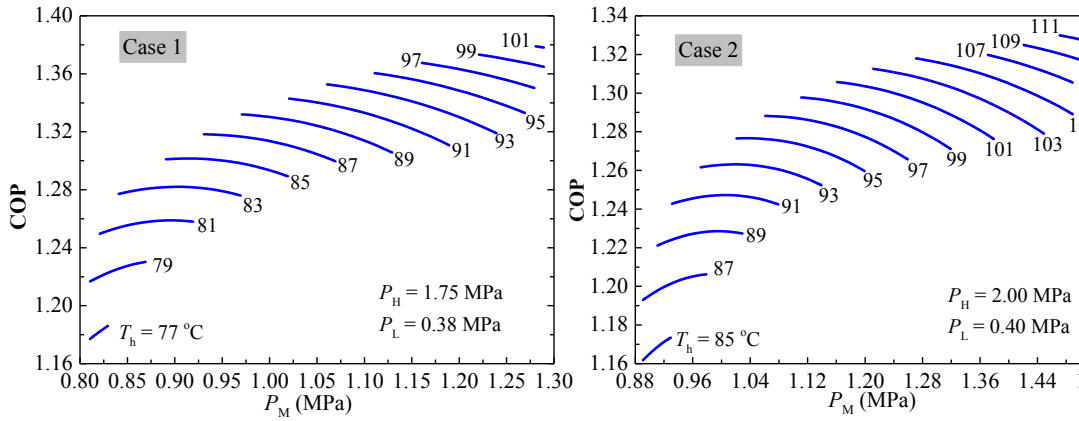

Figure 8: Effect of heat source temperature (T_h) on COP

3. CONCLUSIONS

This paper proposes and theoretically investigates a novel two-stage ARHP cycle with multiple internal heat recovery for space heating at lower ambient temperatures. The main results are:

(1) The feasible high pressure range for the studied case is 1.50~1.75 MPa. For each P_H value within the range, there exists a certain corresponding P_L range, and each P_H/P_L value corresponds to a certain P_M range to enable the novel cycle.

(2) For the studied case, the cycle has the highest COP of 1.37 where the heat supply temperature can reach 46.1 ºC and can meet the temperature demand of building floor heating.

(3) Minimum ambient temperature for the cycle is -17.4 ºC, indicating that the two-stage cycle has greater low temperature adaptability than the single-stage cycle under the same working conditions.

(4) Heat source temperature demand of the novel cycle is above 77 ºC, meaning that the two-stage cycle could work within a wider heat source temperature range than the conventional AHP cycle and the single-stage ARHP cycle.

ACKNOWLEDGEMENTS

This paper is supported by the key project of the National Natural Science Foundation of China under the contract No. 51736006.

NOMENCLATURE

AHP	absorption heat pump	ARHP	absorption-resorption heat pump
CPC	compound parabolic collector	ETC	evacuated tube collector
HPA	high pressure absorber	HPG	high pressure generator
LPA	low pressure absorber	LPG	Low pressure generator
MPA	medium pressure absorber	MPG	medium pressure generator
SCA	solution-cooled absorber	SHX	solution heat exchanger
SMT	solution mixing tank	WCA	water-cooled absorber
VCHP	vapor compression heat pump	VSHX	vapor-solution heat exchanger
h	specific enthalpy (kJ/kg)	*m*	mass flow rate (kg/s)
P	pressure (MPa)	*Q*	heat transfer rate (kW)
T	temperature (^{o}C/K)	*W*	work (kW)
x	solution concentration (kg/kg)		

REFERENCES

Dai E.Q., Lin M., Xia J.H., Dai Y.J. 2018. Experimental investigation on a GAX based absorption heat pump driven by hybrid liquefied petroleum gas and solar energy. Sol. Energy 169, 167-178.

Shirazi A., Taylor R.A., Morrison G.L., White S.D., 2018. Solar-powered absorption chillers: A comprehensive and critical review. Energy Convers. Manag. 171, 59-81.

Gironès V.C., Moret S., Peduzzi E., Nasato M., Maréchal F., 2018. Optimal use of biomass in large-scale energy systems: Insights for energy policy. Energy 137, 789-797.

Kalinowski P., Hwang Y.H., Radermacher R., Hashimi S.A., Rodgers P., 2009. Application of waste heat powered absorption refrigeration system to the LNG recovery process. Int. J. Refrigeration 32, 687-94.

Gomez V.H., Vidal A., Best R., Garcia-Valladares O., Velázquez N., 2008. Theoretical and experimental evaluation of an indirect-fired GAX cycle cooling system. Appl. Therm. Eng. 28(8-9), 975-987.

Baehr H.D., 1981. The COP of absorption and resorption heat pumps with ammonia-water as working fluid. Int. J. Refrigeration 4(2), 83-86.

Du K., Yang S.W., Zhang S.Q., 1991. Experimental analysis and research of an aqua ammonia absorption-resorption heat pump. J. Eng. Thermophy. 3(12), 229-233. (in Chinese)

Du K., Yang S.W., Zhang S.Q., 1993. Performance simulation and analysis of aqua ammonia absorption-resorption heat pump, J. Southeast Univ. 2(23), 26-32. (in Chinese)

Jia T., Dai Y.J., 2018. Development of a novel unbalanced ammonia-water absorption-resorption heat pump cycle for space heating. Energy 161, 251-265.

Jia T., Dai E.Q., Dai Y.J., 2019. Thermodynamic analysis and optimization of a balanced-type single-stage NH_3-H_2O absorption-resorption heat pump cycle for residential heating application. Energy 171, 120-134.

Jawahar C.P., Saravanan R., 2010. Generator absorber heat exchange based absorption cycle-A review. Renew. Sustain. Energy Rev. 14(8), 2372-2382.

Han B.C., Cheng W.L., Li Y.Y., Nian Y.L., 2017. Thermodynamic analysis of heat driven Combined Cooling Heating and Power system (CCHP) with energy storage for long distance transmission. Energy Convers. Manag. 154, 102-117.

Manuscript ID: 1641
DOI: 10.18462/iir.icr.2019.1641

Exergy analysis of vapour injection system with intermediate heat exchanger using R32/R1234ze(E) mixture

Zuo CHENG [(a)], Baolong WANG [(a)], Wenxing SHI [(a)] , Xianting LI [(a)]

[(a)] Department of Building Science, School of Architecture, Tsinghua University
Beijing, 100084, China, wangbl@tsinghua.edu.cn

ABSTRACT

Refrigerant mixtures are regarded as potential alternatives in the field of air conditioning and heat pumps because rare pure refrigerants can totally meet all the requirements of environmental, thermodynamic and safety properties. Meanwhile, as an effective means, vapour injected system is widely applied to improve the system performance of heat pump under large compression ratio, especially the intermediate heat exchanger system for refrigerant mixtures.
However, with regard to this potential system, it is still lack of further analysis, especially the exergy analysis. In this study, the exergy destruction method is applied to analyse quantitatively temperature matching degree of heat exchangers and system performance. Meanwhile, multiple working conditions are covered in analysis.

Keywords: Refrigerant Mixtures, Vapour Injection, Exergy Destruction, Intermediate Heat Exchanger.

1. INTRODUCTION

Influenced by ozone depletion and global warming crisis, most of refrigerants are being phased down owing to their high GWP. While according to the latest authoritative research (Mclinden et al., 2017), none refrigerant that can accomplish all requirements at the same time, and the mixed refrigerants provide more flexibility in searching for new alternatives. So refrigerant mixtures are required.
At the same time, the key issue in the heat pump system that has been focused but still needs to be addressed is the poor performance under large pressure ratio. Gas injected system is widely considered as a good solution to this problem (Xu et al., 2011) because it can increase the heating capacity and improve the system energy efficiency at low ambient temperature. Ma et al. (2003) analysed the performance of improved gas injected system under different condensing and evaporating temperature, it was founded that this technology can help system run smoothly for a long time when the ambient temperature was near -15°C and exhibited larger COP than conventional heat pump system. There are also some researchers concentrated in the gas injected system with refrigerant mixtures. Jung *et al.* (1999) simulated the multi-stage heat pumps with a heat exchanger economizer. R22/R142b/R134a, R32/R134a, R125/R134a mixtures were studied. The results indicated that the three-stage heat pump is up to 27.3% more energy efficient than the conventional single-stage with pure refrigerant. D'Angelo *et al.* (2016) presented a performance evaluation of a gas injected refrigeration system using R290/R600a. The results showed that the maximum COP was obtained for a mixture containing 40 wt% R290 and the COP was enhanced 16–32% by gas injection. Our previous study (Wang et al., 2018) analysed the vapour injected system with R32/R1234ze(E) mixtures and found that the system with intermediate heat exchanger (IHX) is better than flash tank system.
However, with regard to this potential system, it is still lack of further analysis, especially the exergy analysis. In this research, R32/R1234ze(E) mixtures are chosen as typical refrigerant pairs for its great potential in the future, the exergy destruction method is applied to evaluate the temperature matching degree and analyse the exergy destruction of each component and their relation between it and the energy efficiency of IHX vapour injection system. Meanwhile, four different evaluation working conditions are taken into account to illustrate the effect of working conditions.

2. METHODOLOGY

A vapour injected heat pump with IHX are modelled in this section. To make the results comparable, the parameters of the condenser, evaporator and compressor are kept same. In order to simplify the simulation properly, the following assumptions are made:

- The superheated degree of at the evaporator outlet is fixed as 5K and the subcooling degree at the condenser outlet is fixed as 3K;
- The vapour at the injection outlet is saturated.
- The difference between the charged composition and circulation composition in condenser is neglected.

2.1. Working Conditions

Working conditions are essential factors affecting the performance of the zeotropic two-stage compression system. In this research, the constant refrigerant parameters working conditions and constant outer fluid parameters working conditions both are considered. The detailed descriptions are listed in Table 1. In the constant refrigerant parameters working conditions, three different definitions of evaporating and condensing temperatures are discussed separately. Among constant outer fluid parameters working conditions, the inlet temperature and the mass flowrate at the evaporator and the condenser are both fixed in condition 1; the inlet and the outlet temperature at the evaporator and the condenser as well as heating capacity are both fixed in condition 2; on the basis of condition 2, the compression process is assumed to be isentropic compression to avoid possible effects of unreasonable compressor designs for different refrigerants.

Table 1. Working conditions

Working conditions	Descriptions		
1	Mode1	Mode2	Mode3
	$T_{e,dew}$ = -10˚C; $T_{c,bub}$ = 45˚C	$T_{e,bub}$ = -10˚C; $T_{c,dew}$ = 45˚C	$T_{e,ave}$ = -10˚C; $T_{c,ave}$ = 45˚C
2	$T_{w,c,in}$ = 40˚C; $T_{HTF,e,in}$ = 0˚C; $m_{w,c,in}$ = 0.55kg/s; $m_{HTF,e,in}$ = 0.7kg/s		
3	$T_{w,c,in}$ = 40˚C; $T_{w,c,out}$ = 45˚C; $T_{HTF,e,in}$ = 0˚C; $T_{HTF,e,out}$ = -5˚C; Q = 10kW		
4	$T_{w,c,in}$=40˚C; $T_{w,c,out}$=45˚C; $T_{HTF,e,in}$=0˚C; $T_{HTF,e,out}$=-5˚C; Q=10kW (Isentropic compression)		

2.2. Model

The REFPROP 9.1 (Lemmon et al., 2013) are linked to calculate the thermodynamic properties of the refrigerants. The mixing model (Kunz and Wagner, 2012) applicable for R32 and R1234ze(E) mixtures is adopted.

Scroll compressor is adopted in this research. In our previous study, a detailed compressor model suitable for vapour injection system using refrigerant mixtures has been developed (Wang et al., 2018), the configuration parameters of the system used in simulations are shown in Table 2.

Table 2. Scroll compressor configuration parameters

Base circle radius (mm)	Thickness of scroll (mm)	Height of scroll (mm)	Cycles of scroll	Injection port position (°)	Injection port area (mm2)
2.70	3.68	35.7	2.79	0	50.27

.

Table 3. Heat exchangers configuration parameters

	Length (mm)	Inside diameter of outer tube (mm)	Inside diameter of outer tube (mm)	Inside diameter of inner tube (mm)	Number of inner tube
Evaporator	6200	37	9.52	8.72	6
Condenser	6200	42.6	9.52	8.72	10

A distributed parameter model of double pipe heat exchanger is adopted to simulate the heat exchange process accurately. In the calculation for each section, local properties such as the compositions, specific heat, coefficient of viscosity, and heat conductivity coefficient are adopted, and on basis of these properties the overall heat transfer coefficient in every section is calculated. Moreover, the heating transfer fluids in evaporator side is a mixture of 40: 60% (by volume) of ethylene glycol and water.

2.3. Estimation Parameter

The relevant parameters of the first law of thermodynamics are listed as follows:

$$Q_c = m_r \cdot \left(h_{con,in} - h_{con,out} \right) \quad \text{Eq. (1)}$$

$$COP = \frac{Q_c}{W} \quad \text{Eq. (2)}$$

The traditional component exergy destruction parameters, such as compressor exergy destruction $Ex_{d,com}$, first and second throttling exergy destruction $Ex_{d,thro,fir}$ and $Ex_{d,thro,sec}$ are calculated according to Ahamed et al. (2011).

In this research, temperature matching degree is taken into account. Actually as the most remarkable feature and significant potential of refrigerant mixtures, temperature matching degree was mentioned in the previous study but lack of further and quantitative analysis. With respect to the quantitative description of temperature matching degree, Jin et al. (2011) evaluated the temperature matching degree with temperature difference variance during heat exchange and screened optimal refrigerant mixtures. This method can clearly descript quantitatively the temperature matching degree but was difficult to link it with energy efficiency directly. Recently, Zühlsdorf et al. (2018) descript the temperature matching degree with exergy destruction. In their study, exergy destruction was divided into two parts, the exergy destruction caused by finite heat transfer area and un-matching process during heat exchanger. Owing to the tight link between exergy and energy efficiency, this method is expected to be further applied in the system analysis using refrigerant mixtures. So this method is applied in this research. As mentioned above, exergy destruction Ex_d at evaporator, condenser and IHX are both divided to two parts, the exergy destruction caused by finite heat transfer area $Ex_{d,pinch}$ and un-matching process during heat exchanger $Ex_{d,unmatch}$. The un-matching degree $\alpha_{unmatch}$ is defined as the ratio of $Ex_{d,unmatch}$ and Ex_d. Taking the evaporator as an example to represent all heat exchangers, the above definition are listed as follows:

$$Ex_{d,e} = \int T_0 \left(\frac{1}{T_{r,e}} - \frac{1}{T_{HTF,e}} \right) dQ \quad \text{Eq. (3)}$$

$$Ex_{d,e,pinch} = \int T_0 \left(\frac{1}{T_{HTF,e} - \Delta T_{pinch,e}} - \frac{1}{T_{HTF,e}} \right) dQ \quad \text{Eq. (4)}$$

$$Ex_{d,e,unmatch} = \int T_0 \left(\frac{1}{T_{r,e}} - \frac{1}{T_{HTF,e} - \Delta T_{pinch,e}} \right) dQ \quad \text{Eq. (5)}$$

$$\alpha_{unmatch,e} = \frac{Ex_{d,e,unmatch}}{Ex_{d,e}} \quad \text{Eq. (6)}$$

where, T_0 is the reference temperature, which is defined as the ambient temperature 313.15K, $\Delta T_{pinch,e}$ is the pinch temperature difference during heat transfer process.

In addition, the exergy efficiency is defined as follows:

$$\eta_{ex} = 1 - \frac{Ex_{d,e} + Ex_{d,c} + Ex_{d,IHX} + Ex_{d,com} + Ex_{d,thro,fir} + Ex_{d,thro,sec}}{W} \quad \text{Eq. (7)}$$

3. RESULTS

In this section, one constant refrigerant parameters and three constant outer fluid parameters working conditions are both covered in the exergy analysis. In order better illustrate the system performance and the temperature matching relationship, the whole composition range of R32/R1234ze(E) mixtures is considered, the molar fraction of R32 changes from 0 to 100% in increments of 10%.

3.1. Thermodynamic Performance

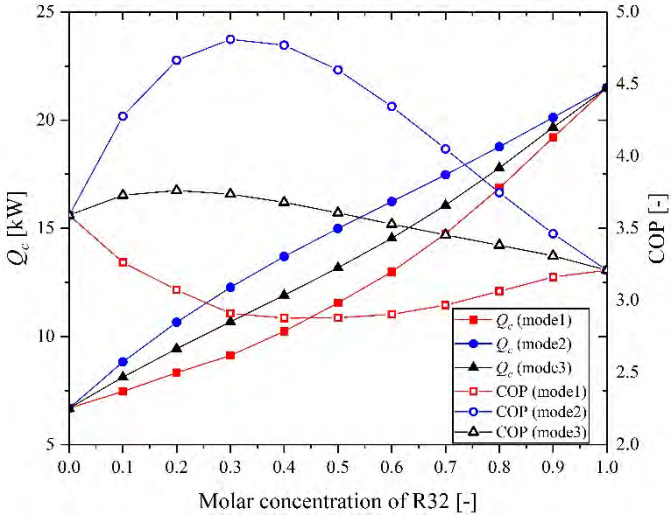

Figure 1: Heating capacity and COP

In this performance analysis, though the same evaporating and condensing temperature is fixed, according to Table 1, three definition modes are involved. From Fig. 1, it can be seen that the heating capacity of each modes increase with the increase of R32 concentration, which is caused by its larger latent heat of R32. Then it is illustrated that the COP changing trend varies from different operating modes. In mode 1, evaporating dew temperature and condensing bubble temperature are fixed, with the addition of R32, the temperature glide at evaporator and condenser increase firstly and then decrease, which causes the average evaporating temperature decreasing firstly and then increasing, there is a completely opposite trend at the condenser simultaneously. So in this mode, the system COP decreases firstly and then increases. On the contrary, the definition of evaporating bubble temperature and condensing dew temperature in mode 2 results in different changing trend of average evaporating and condensing temperature and opposite COP changing trend. In mode 3, the definition of average evaporating and condensing temperature brings the possibility of multiple COP changes, which is just one of them.

3.2. Fixed Inlet Temperature and Mass Flowrate of HTF and Water

This working condition is a common operating condition. The heating capacity, COP and exergy efficiency are listed in Fig. 2(a), it can be seen that heating capacity also increase with R32 concentration increases, while COP decreases, which is mainly caused by larger adiabatic index of R32 and illustrated in our previous study (Wang et al., 2018). It is also notable that the exergy efficiency is consistent with the COP trend, which illustrate that the following exergy estimating method of heat transfer matching degree can be closely linked with system energy efficiency. The whole exergy destruction in condenser, evaporator and IHX and un-matching degree in each heat exchanger are obtained in Fig. 2(b), firstly it can be seen that the exergy destruction in IHX is small compared with evaporator and condenser, then the un-matching degree in the three heat exchanger is analysed respectively. For evaporator, using pure refrigerant brings smaller un-matching degree, which is caused by small setting HTF temperature difference. The matching degree trend in condenser is a little complex because another superheating region affects the matching relationship in condenser. For IHX, using refrigerant mixtures brings better temperature matching degree, when the R32 molar concentration is 0.3, the un-matching degree is smallest. At the same time, it is notable that the temperature matching is difficult to reach simultaneously for all the heat exchanger in the system, then due to the higher capacity with R32 in three heat exchangers, the whole exergy destruction in three heat exchangers increases with more R32.

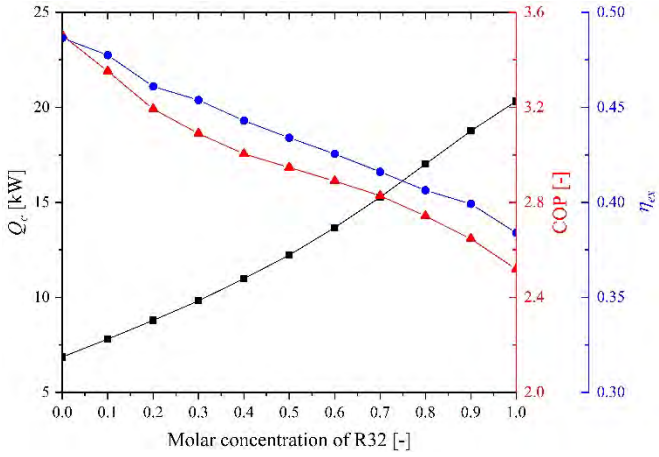

(a) Heating capacity, COP and exergy efficiency

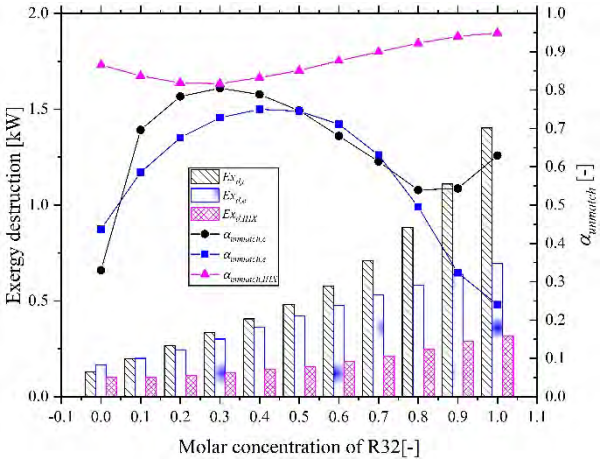

(b) Exergy destruction and un-matching degree in heat exchanger

Figure 2: Heating capacity, COP and exergy parameters in working condition 2

3.3. Fixed Inlet and Outlet Temperature and Heating Capacity

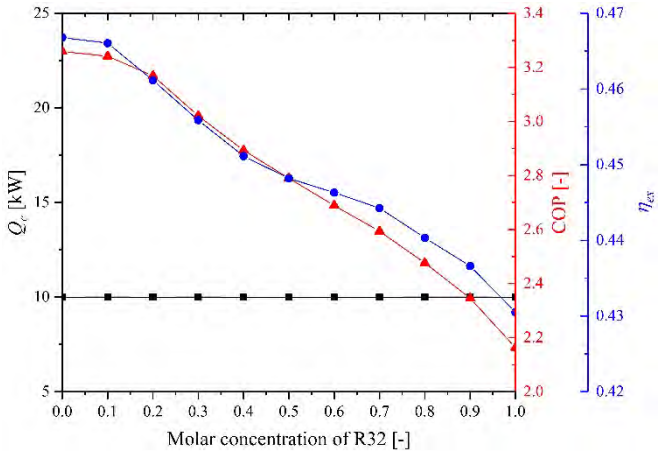

(a) Heating capacity, COP and exergy efficiency

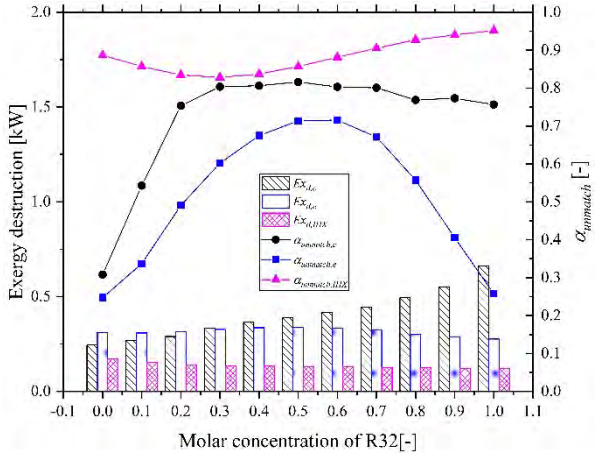

(b) Exergy destruction and un-matching degree in heat exchanger

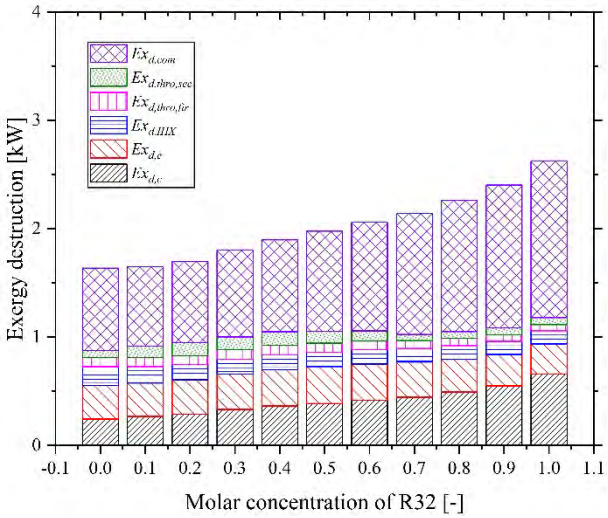

(c) Exergy destruction of each component

Figure 3: Heating capacity, COP and exergy parameters in working condition 3

Actually this is another common working condition. The heating capacity, COP and exergy parameters are listed in Fig. 3. Compared with working condition 2, the whole trend of COP, the un-matching degree in evaporator and IHX do not varies much. While the un-matching degree in condenser does not change apparently from 40%~100%, because lower compressor frequency for higher R32 concentration brings relatively lower compression efficiency and larger superheated

region, this region enhance the un-matching degree on the basis of working condition 2. On the other hand, it can be obtained that, different from working condition 2, the exergy destruction in evaporator increases firstly and then decrease, that in IHX decreases firstly and then increases, which is closely linked with the un-matching degree under the same capacity. While for the condenser, the exergy destruction still increases with more R32, which is probably caused by larger pinch exergy destruction. In Figure 3(c), the exergy destruction of each component are analysed, it can be obtained that for each refrigerant composition, the exergy destruction of compressor is dominant. Moreover, the ratio of compressor destruction increases with more R32, which causes the lower exergy efficiency and COP.

3.4. Fixed Inlet and Outlet Temperature and Heating Capacity (Isentropic Compression)

On the basis of analysis to working condition 3, it can be seen that compressor is a decisive influence factor. However the compressor and the corresponding operating frequency may not be the most suitable for that composition. So in this working condition, the compression process is assumed to be isentropic compared with working condition 3.

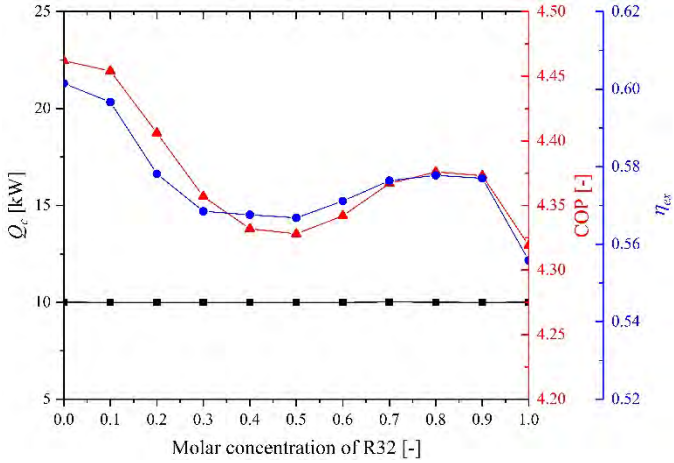

(a) Heating capacity, COP and exergy efficiency

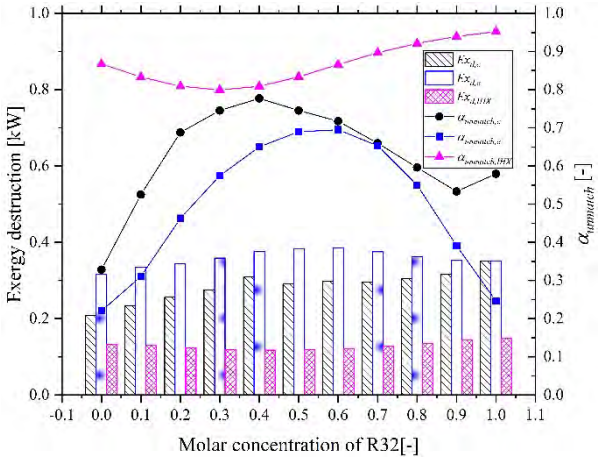

(b) Exergy destruction and un-matching degree in heat exchanger

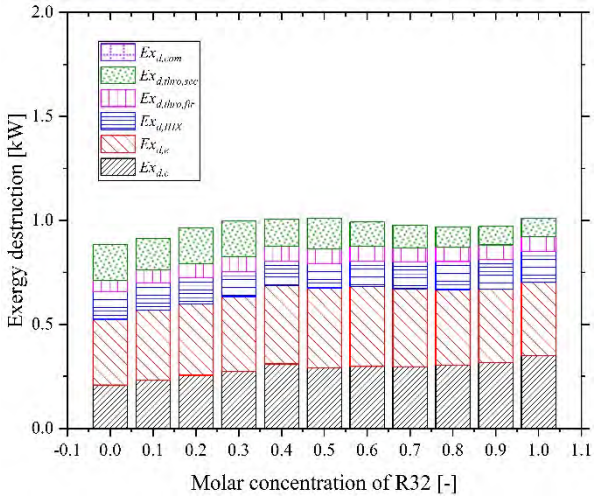

(c) Exergy destruction of each component

Figure 4: Heating capacity, COP and exergy parameters in working condition 3

Firstly it can be found that the COP and exergy efficiency do not changes regularly as the above two working conditions. With the R32 increasing, COP decreases firstly and then increases, lastly decreases. As for the exergy destruction and un-matching degree in heat exchanger, the un-matching degree is similar with working condition 2 as illustrated before, while the exergy destruction is strongly connected with the un-matching degree with the same capacity. Moreover, it can be drawn from Fig. 4(c) that the whole exergy destruction has not been increased with R32 increasing, rather influenced by the exergy destruction in heat exchanger and corresponding temperature matching degree. In that case, the exergy destruction in evaporator is dominant.

4. CONCLUSIONS

Based on a comprehensive model of vapour injection heat pump with IHX using R32/R1234ze(E), the exergy destruction method is applied to analyse the quantitative temperature matching degree of evaporator, condenser and IHX and corresponding effect on total exergy destruction and system performance. Meanwhile, one thermodynamic working condition and three actual operating working conditions are compared and covered to better realize the temperature matching degree. The main research conclusions are as follows:

- Compared with evaporator and condenser, the exergy destruction in IHX is relatively smaller and its matching degree is hard to affect the performance;
- It is hard to reach temperature matching simultaneously in three heat exchanger in IHX vapour injection system. 30% R32 is the best temperature matching for IHX, 100% for evaporator and 0% for condenser under fixed inlet temperature and mass flowrate of HTF and water;
- Compressor is a dominant exergy destruction component, which will directly influence the assessment of exergy efficiency

ACKNOWLEDGEMENTS

This research is funded by the China National Key R&D Program “Solutions to Heating and Cooling of Buildings in the Yangtze River Region” (Grant No. 2016YFC0700304) and the National Natural Science Foundation of China (Grant No. 51676104).

NOMENCLATURE

Q_c	heating capacity (kW)	Ex_d	exergy destruction (kW)
T	temperature (K)	T_0	reference temperature (K)
W	power consumption (kW)		
e	evaporator	*c*	condenser
com	compressor	*thro*	throttle
fir	first	*sec*	second
η_{ex}	exergy efficiency		
COP	coefficient of performance	HTF	heat transfer fluid
IHX	intermediate heat exchanger		

REFERENCES

Ahamed, J.U., Saidur, R., Masjuki, H.H., 2011. A review on exergy analysis of vapor ompression refrigeration system. Renew. Sustain. Energy Rev. 15 (3), 1593–1600.

D’Angelo, J.V.H., Aute, V., Radermacher, R., 2016. Performance evaluation of a vapor injection refrigeration system using mixture refrigerant R290/R600a. Int. J. Refrig. 65, 194–208.

Gao, P., Zhao, L., 2008. Theoretical and experimental investigation on components’ proportion of zeotropic mixtures based on relation between temperature and enthalpy during phase change. Energy Convers. Manage. 49(6), 1567–73.

Jung, D., Kim, H.J., Kim, O., 1999. Study on the performance of multi-stage heat pumps using mixtures. Int. J. Refrig. 22, 402–413.

Jin, X., Zhang, X., 2011. A new evaluation method for zeotropic refrigerant mixtures based on the variance of the temperature difference between the refrigerant and heat transfer fluid. Energy Convers. Manage. 52, 243–249.

McLinden, M.O., Steven Brown, J., Brignoli, R., Kazakov, A.F., Domanski, P.A., 2017. Limited options for low-global-warming-potential refrigerants. Nat. Commun. 8, 14476.

Ma, G., Chai, Q., Jiang, Y., 2003. Experimental investigation of air-source heat pump for cold regions. Int. J. Refrig. 26, 12-18.

Venkatarathnam, G., Murthy, SS., 1999. Effect of mixture composition on the formation of pinch points in condensers and evaporators for zeotropic refrigerant mixtures international. Int. J. Refrig. 22, 205–15.

Wang, B., Cheng, Z., Shi, W., Li, X., 2017. Numerical study of gas injected heat pump using zeotropic R32/R1234ze(E) mixture: Comparison of two type economizers. Appl. Therm. Eng. 142, 410-420.

Xu, X., Hwang, Y., Radermacher, R., 2011. Refrigerant injection for heat pumping/air conditioning systems: Literature review and challenges discussions. Int. J. Refrig. 34, 402–415.

Zühlsdorf, B., Jensen, J., Cignitti, S., Madsen, C., Elmegaard, B., 2018. Analysis of temperature glide matching of heat pumps with zeotropic working fluid mixtures for different temperature glides. Energy. 153, 650-660.

Manuscript ID: 1644
DOI: 10.18462/iir.icr.2019.1644

Comparing integrating configurations of latent heat storage in heat pump heating systems

Tianhao XU[(a)], Yingrui HAO[(a)], Samer SAWALHA[(a)]

[(a)] Royal Institute of Technology (KTH), Energy Technology Department, Brinellvägen 68, Stockholm, SE-100 44, Sweden, txu@kth.se

ABSTRACT

Short-term latent heat thermal energy storage (LHTES) can be integrated in building heating systems for performing load shifting from on- to off-peak hours. In this study, the coupling effects of LHTES integration in heat pump heating systems are investigated for a multi-family building in Stockholm. As the reference heat pump provides heat in two separate heat exchangers, a de-superheater for domestic hot water and a condenser for space heating, two configurations for LHTES integration with the two respective heat exchangers are compared using a quasi-stationary mathematic system model. The performances of the two integrating configurations are also compared with the basic heat pump heating scenario (no heat storage) regarding the total electricity consumption, the seasonal performance factor (SPF), and the electric bills for end-users over a selected heating-season week. The simulation results reveal that, while using the condenser for charging an LHTES unit containing phase change materials melted at 58 ºC inevitably increases the total electricity consumption in the heating system relative to the basic scenario, using the desuperheater instead for LHTES charging can reduce the total electricity consumptions and bills of 24 kWh and 173 SEK (17€), respectively, during that specific week.
Keywords: Thermal Energy Storage, Phase Change Materials, Heat Pump, Space Heating, Load Shifting

1. INTRODUCTION

Integrating thermal energy storage (TES) units with HVAC (heating, ventilation and air-conditioning) systems has been recognized as an effective measure to decarbonize the heating and cooling sectors in buildings by enabling the incorporation of renewable energy sources and facilitating peak-load shifting. Space heating demand, taking over the largest portion of final energy consumption in buildings within the European context, has been increasingly handled by heat pump (HP) technologies. To investigate the coupling effects of TES and HP in hydronic heating systems, a number of experimental and simulation studies have been conducted. In these studies, latent heat thermal energy storage (LHTES) has attracted most research interests as it is featured with high storage density and small temperature swing compared with the sensible heat storage. In principle, LHTES can enable the coupled HP to be deactivated during periods with economically or environmentally unfavourable conditions (Pardiñas et al., 2017), such as on-peak hours, acting as a heat source for keeping indoor climates through releasing the previously stored heat to heating terminals.

However, few researchers delved into optimizing the integrating configuration and control strategies of HP-LHTES integrated systems (Zhu et al., 2014). Within the scope of HP-LHTES integrated systems without solar thermal incorporation, the existing system performance analyses focused on a single scenario as found in literatures: the heat carried by heat transfer fluids (HTFs, water in most cases) for charging LHTES, is produced by the condenser of an HP through parallel hydraulic connections (Moreno et al., 2014). In such configurations, as LHTES commonly requires high-temperature HTFs to melt phase change materials (PCMs) in a time-efficient way, one normally has to impose a large condensation temperature lift in the HP vapor compression cycle, often deteriorating heating COPs. This operating condition is not

necessary in basic HP heating systems where LHTES is not installed. This problem has been addressed in some previous studies. For instance, Agyenim and Hewitt (2010) restrict the HTF supply temperature down to 62.9 °C to melt RT58, a commercial paraffin with a peak melting point of 58 °C, in a performance analysis of an HP-LHTES integrated system, whereas an HTF supply temperature of 76.7 °C can increased the overall heat transfer coefficient by 45%. There remains a need for an optimal design that can ensure the satisfactory charging/discharging thermal performance of LHTES without decreasing HP efficiency in an integrated system.
In the present study, an alternative integrating method is proposed regarding utilizing a desuperheater in an HP cycle for LHTES charging. In this configuration, the desuperheater water outlet, of which the temperature can be controllably high thanks to direct hot gas desuperheating at the compressor discharging port, can be directly exploited to melt PCMs in LHTES without compromising the heating COP as in the condenser heating configuration. To predict the potential savings in electricity consumptions and bills, a basic HP heating system (Case 0) and two different HP-LTHES integrated systems, one utilizes the condenser for LHTES charging (Case 1) and the other utilizes the desuperheater (Case 2), are modelled and compared for a typical Swedish multi-family residence which employs hydronic radiators as the heating terminal. The paper is organized as follows: first, the layouts of Case 0–2 are displayed and explained; then, the two main components (HP and LHTES), which have been tested as prototypes in KTH Energy Technology Department, are briefly introduced; the validated sub-model of each component is built and incorporated in a mathematic system model. Last, the system performances of Case 0–2 are presented by two means:(1) the evolution of HP and LHTES operating statuses over a heating-season week in Stockholm, and (2) the total electricity consumptions and tariffs, as well as the seasonal performance factor (SPF) of the integrated system during the week.

2. METHODOLOGY

2.1. Backgrounds of LHTES Applications

In Sweden, district heating and electricity networks normally show two peak periods, morning and evening, in terms of heat and electricity generation capacity; the peak heat and/or power plants, mostly based on fossil fuels, are forcedly activated to meet the peak demands. The on-peak electricity trading prices are accordingly raised by the producers, indicated by Nord Pool, the electricity trading platform in Nordic regions. For end-users who adopt variable price contracts of purchasing electricity from the grid, reducing on-peak electricity usage can hence save their electric bills, as the real-time electricity tariffs end-users are charged with are mostly affected by the trading prices. Therefore, dwellings with independent heating devices see potentials of shifting heating demands from on- to off-peak hours by means of applying heat storage in heating systems. LHTES, as an emerging energy-dense heat storage technology, is investigated in the present case study of assuming its integration in a heat pump heating system of a multi-family building in Stockholm. Here, the load shifting strategy from on- to off-peak hours is evaluated; the heat is stored in the coupled LHTES unit during a typical daily off-peak period, starting from late-night and ending in early-morning hours, and then recovered during on-peak hours with highest electricity tariffs in a day.

2.2. Layouts of HP-LHTES Integrated Systems

In a common Swedish residential HP heating system, radiators are typically arranged in a 2-pipe distribution system with a parallel connection to an HP (denoted as Case 0 as the base heating scenario; see Fig. 1a). With this configuration, two circulation pumps are required for the HP and the heat distribution circuits, respectively. In this case, an air-source heat pump (ASHP) is selected for investigation, and an external electric heater is deployed at the heat distribution circuit for supplementary heating when the outdoor temperature drops below the balance temperature.
Fig. 1b and 1c illustrate two different layouts of LHTES integrated heating systems for charging; the common layout for discharging is shown in Fig. 1d. To the best of authors' knowledge, the existing studies mostly investigated the integrated configuration of Case 1 (Fig. 1b), where a parallel LHTES branch is configured between the ASHP's condenser and the by-pass line. For

instance, Hamada and Fukai (Hamada and Fukai 2005) presented such designs of an on-field experimental setup for testing LHTES integrated solutions in a commercial building. In this configuration, heat transfer fluid (water) supply temperature, expressed as $T_{LHTES,in}$ in Fig.1b, is mandatorily kept to be at least 65 °C for melting PCMs and thereby enabling latent heat storage. If $T_{LHTES,in}$ is higher than the radiator supply temperature, $T_{rad,s}$, determined by the so-called heating curve, the condensation temperature has to be raised in a way that the water outlet temperature at the condenser, $T_{cond,out}$, should be at lowest equal to $T_{LHTES,in}$ to fulfil the supply temperature requirements for LHTES charging. Such condensation temperature lifts are not necessary in Case 0, the basic heating scenario.

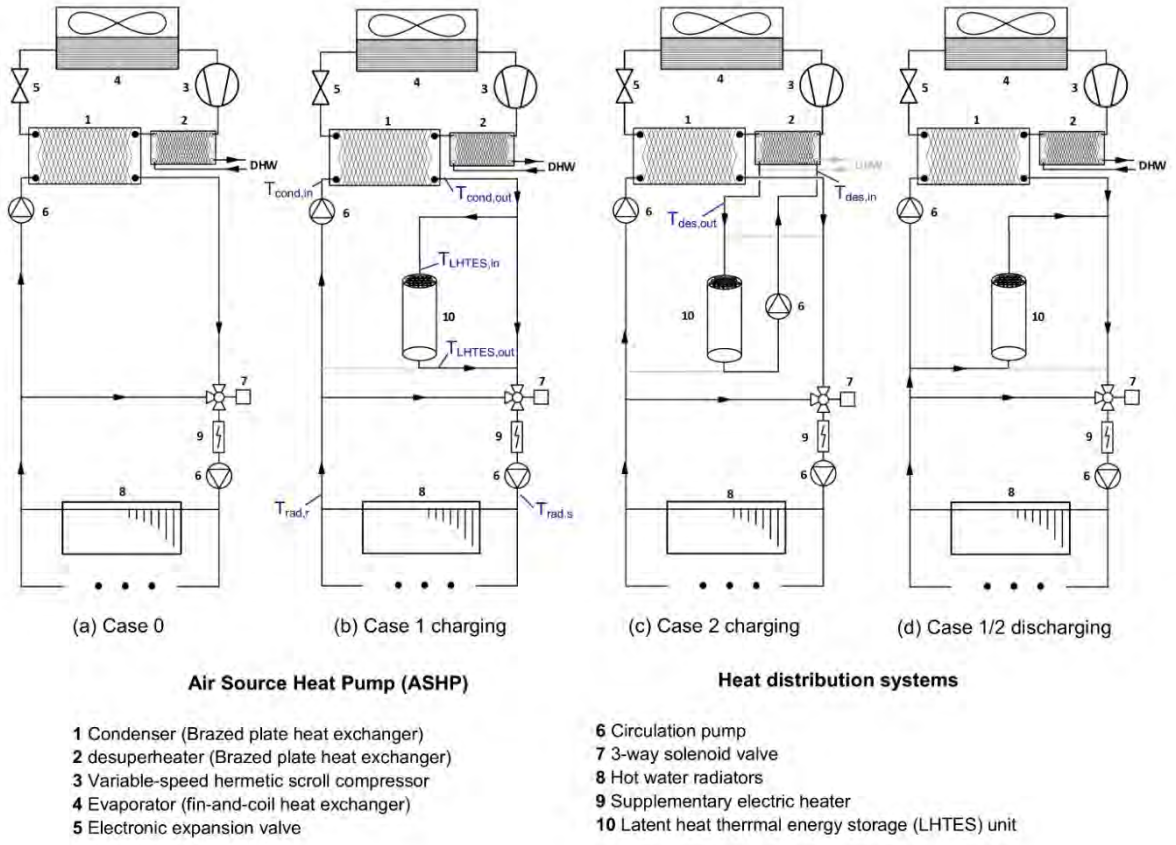

Figure 1: layouts of LHTES integrated heating systems

As the novelty of the present study, the configuration of Case 2, displayed in Fig.1c, is proposed as a design that utilizes the desuperheater, which is originally dedicated for producing DHW in commercial HPs, to charge LHTES by taking advantages of its higher water outlet temperature compared with that of the condenser. According to previous studies, $T_{des,out}$ can be increased up to 80 °C in the reference HP prototype with a working condensation temperature of around 46 °C (Xu et al., 2018); by properly controlling the desuperheater water flowrate and identifying the matched temperature profile ($T_{des,out}$=65 °C), LHTES can be successfully charged with desuperheater outlet water without deliberately increasing condensation temperatures as Case 1. In this scenario, an HP can be driven with off-peak electricity to charge the LHTES with the desuperheater during the late night-time hours when there is barely DHW demand.

On the other hand, the discharging flow configuration for both Case 1 and 2 is displayed in Fig. 1d as both cases share the same configuration. In principle, the stored heat is released to a diverted branch of flow for LHTES discharging in the heat distribution system.

2.3. Modelling and Analysis

To compare the overall energy efficiency of the three different configurations, a quasi-steady state system model developed through EES (Engineering Equation Solver) was created, comprising of three individual sub-models for predicting the thermal performances of three key

elements, ASHP, LHTES, and radiators. The ASHP and LHTES sub-models are based on the experimental investigations reported in the author's previous works. The condenser and desuperheater configurations in the reference HP are illustrated in Fig. 2a, and the structure of LHTES tank is shown in Fig. 2b.

First, the ASHP sub-model is constructed based on a performance map, generated by a validated R290 HP model using a vapour compression software package, IMST-ART. The detailed experimental results of the R290 HP prototype and the validation information of the IMST-ART model have been reported by the authors in a previous work (Xu et al., 2016). The condenser and desuperheater are both brazed plate heat exchangers but with different nominal capacities of 40 kW and 6.5 kW, respectively, and the variable-speed compressor in the HP prototype can work with a maximum speed of 65 Hz according to the manufacturer.

Second, LHTES is modelled by generating a performance map involving the transient behaviours of charging/discharging rates and $T_{LHTES,out}$, which were obtained through a comprehensive experimental campaign. The tested LHTES unit is a 0.38 m^3 stainless steel storage tank containing 50 cylindrically encapsulated PCMs. the used PCM is a commercial salt hydrate with a melting temperature range of 57 to 63 °C. The details of the testing facility can be found in the author's previous work (Xu et al., 2019). In the model, the size of the simulated LHTES unit is scaled up on different levels in Case 1 and Case 2 due to the variability in the heat capacitance of charging provided by the HP; the evaluation is further presented in Section 3.2.

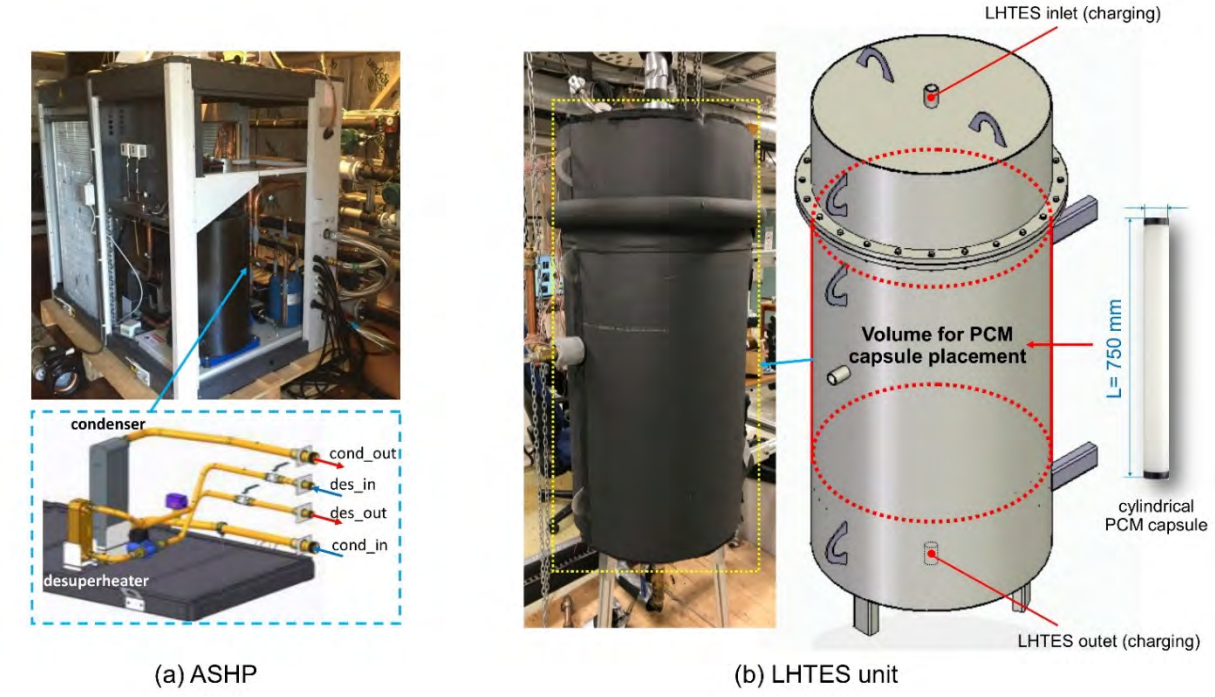

Figure 2: Illustrations of the experimental set-up: (a) ASHP; (b) LHTES

Third, the heat distribution system is modelled in terms of the heating capacity, supply/return temperature ($T_{rad,s}$/$T_{rad,r}$), and water flowrate of a typical design of radiator heating systems in a Swedish multi-family building. $T_{rad,s}$/$T_{rad,r}$ is set to 55/45 °C at the design outdoor temperature (DOT=-16 °C) and their variations at different outdoor temperatures are determined by a heating curve. The present model simplifies the thermal comfort consideration by assuming that the set-point control of indoor air temperature (20 °C) is at all time nodes perfectly achieved through the smart control of the ASHP at variable speeds, producing heat for radiators and LHTES at desirable capacities, and the 3-way solenoid valve, which instantly modulates the mixing/separation of the water flow of AHHP circuit and LHTES branch to fulfil the requirements of $T_{rad,s}$.

With load shifting strategies implemented, the COP and heating capacity of ASHP are accordingly affected and thereby influence the overall system performance. As one of the metrics for comparing the energy efficiency of different scenarios, the seasonal performance

factor of the system is calculated according to Eq. (1) over a heating-season week in Stockholm. The total electricity consumptions constitute of three parts, ASHP, circulation pumps in heat distribution systems, and the supplementary electrical heaters if necessary. Also, the total electric bills for space heating are compared amongst three cases as the economic evaluation of heat storage integration.

$$SPF_{sys} = \frac{\int \dot{Q}_{HP}\, dt}{\int P_{HP}\, dt + \int P_{pump}\, dt + \int P_{el.heater}\, dt} \qquad \text{Eq. (1)}$$

3. LOAD SHIFTING ANALYSIS

3.1. Sizing LHTES Units in Integrated Systems

In principle, completely shifting the on-peak heating loads to off-peak hours is the most desirable operating strategy. Yet, two factors restrict the implementation of such a strategy in the investigated system: (1) the intrinsic declining tendency of charging/discharging rates in general LHTES applications, and (2) the availability of heating capacity provided by the heat exchanger for LHTES charging. For the former aspect, the experimental results indicate that a complete discharging process of the LHTES unit lasts for approximately 5 hours, showing quasi-exponentially decreasing discharging rates. Consequently, the LHTES unit can be sized in a way that its initial maximum heat releasing power fully covers the heating demands as long as possible during on-peak hours, so meanwhile the HP can be utterly averted from operation. On the other hand, the amount of heat that can be feasibly released during on-peak hours is substantially dependent on the preceding charging process, which is concerned with the second factor. Case 1 and 2 employs different heat exchangers at the sink to provide heating for LHTES, which is necessarily taken into account when evaluating the appropriate LHTES unit sizing.

For Case 1, HP is mandatorily operated with a condensation temperature of at least 60 °C to ensure $T_{cond,out}$ at 65 °C. With a maximum compressor speed (65Hz), the extra heating capacity deliberately produced by the condenser for the purpose of LHTES charging can be sustained above 20 kW in most off-peak hours. The abundance in available heating capacity for LHTES charging enables the LHTES unit to be sized primarily based on the criteria of covering the on-peak heating demands. Therefore, the LHTES volume is scaled up to 1.3 m^3 with a capacity of incorporating 290 PCM capsules for Case 1. The estimated thermal storage capacity is approximately 100 kWh.

For Case 2, the LHTES unit is connected with the desuperheater in serial; the desuperheater has a much smaller heat transfer area (0.64 m^2) compared with the condenser (3.98 m^2) in the original design of the ASHP prototype. Compared with Case 1, the available heat in the desuperheater for charging LHTES is much more limited, regardless of the compressor speed, because of its small heat transfer area and limited heat content from superheated gas that is available for exploitation. Along a charging process, the charging rate in LHTES considerably decreases and $T_{LHTES,out}$ ($T_{des,in}$ equals to $T_{LHTES,out}$ with the present serial connection, see Fig. 3c) accordingly increases, to be specific, above 60 °C after 1.5 hour of charging according to the experimental observations. As the HP condensation temperature of Case 2 is kept as low as that of Case 0, the basic HP heating scenario, the compressor discharge temperature is at most around 83 °C, which leaves a limited margin for heat transfer from superheated gas to water flow in the desuperheater, and thus leading to a considerably lower heating capacity for LHTES charging (below 4 kW after 1.5 hours of charging). As a result, the LHTES unit in Case 2 can only be designed with a heat storage capacity of approximately 48 kWh (120 PCM cylinders); unlike Case 1, the primary restriction on the size stems from the availability of heating capacity in the desuperheater.

3.2. Performance Analysis

The main operating parameters of the HP-LHTES integrated system are presented during the investigated heating-season week. Fig. 3 illustrates the modelling results presented on a half-

hour basis: the hatched area represents the required HP heating capacity without LHTES integration (Case 0) while the yellow solidly filled area represents the HP heating capacity with load shifting implemented of Case 1 (Fig. 3a) and Case 2 (Fig. 3b). The electricity tariffs that the end-users are charged with during this specific week are shown as the red curves. It is observed that Case 1 shows a larger amount of heating load shifted, which allows the HP to be deactivated for a longer on-peak period (2.5 hours) than Case 2 (1.0 hour), due to the larger volume of the LHTES unit.

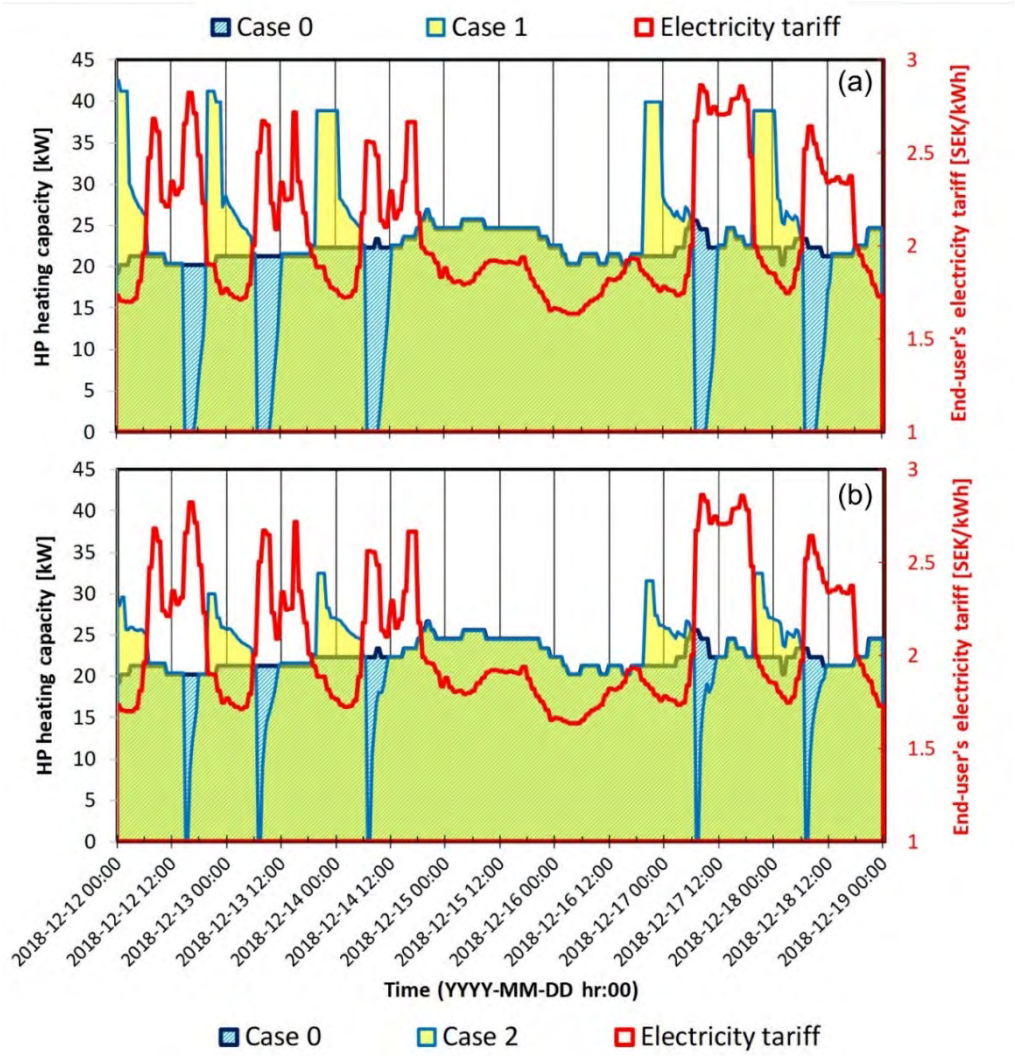

Figure 3: Comparisons of HP heating capacity: (a) Case 0 and 1; (b) Case 0 and 2

Fig. 4 displays the working statuses of the HP and LHTES, respectively. As illustrated by Fig. 4a, the compressor can be operated at a maximum speed of 65 Hz for LHTES charging in Case 1 but not necessarily in Case 2 due to the smaller volume of the LHTES unit. Generally, higher HP power consumptions of Case 1 are found because of its higher heating capacity and lower COP. Fig. 4b shows the evolution of heat storage capacity in LHTES with consecutive charging and discharging processes.

To summarize, Table 1 lists the key performance indicators of the basic HP heating systems and LHTES-integrated systems regarding the electricity use and SPF. Compared with Case 0, a higher total electricity consumption as well as a lower SPF is discovered for running the HP-LHTES integrated with Case 1 configuration, largely because of the HP operation with lower COPs as charging LHTES requires. The load shifting from on- to off-peak hours defeats the purpose of reducing electricity bills for end-users, as higher electricity tariffs are found for Case 1. However, Case 2 configurations exhibit potential savings in both the electricity consumptions and bills relative to Case 0 and 1. The total electricity consumption is reduced by around 8% by using desuperheater to charge the LHTES unit rather than the condenser. The economic aspect is analysed for investing such a plug-in LHTES unit in the Case 2 scenario. With

estimation of a total capital cost at 39440 SEK (3944€) combining the costs of PCMs, a storage tank, and a circulation pump, the discounted payback period would be 11.2 years assuming that a weekly electric bill saving of 17€ is achieved throughout entire heating seasons.

Table 1. Comparisons of performance indicators amongst three cases over the week

	Case 0	Case 1	Case 2
SPF_{sys} (-)	2.41	2.25	2.42
End-user's electricity consumption (kWh)	3132	3356	3108
End-user's electric bills (SEK) [a]	6444	6564	6271
Discounted payback periods (yr) [b]	-	-	11.2
[a] 1 SEK ≈ 0.1 €; [b] Calculation is based on a discount rate of 4%.			

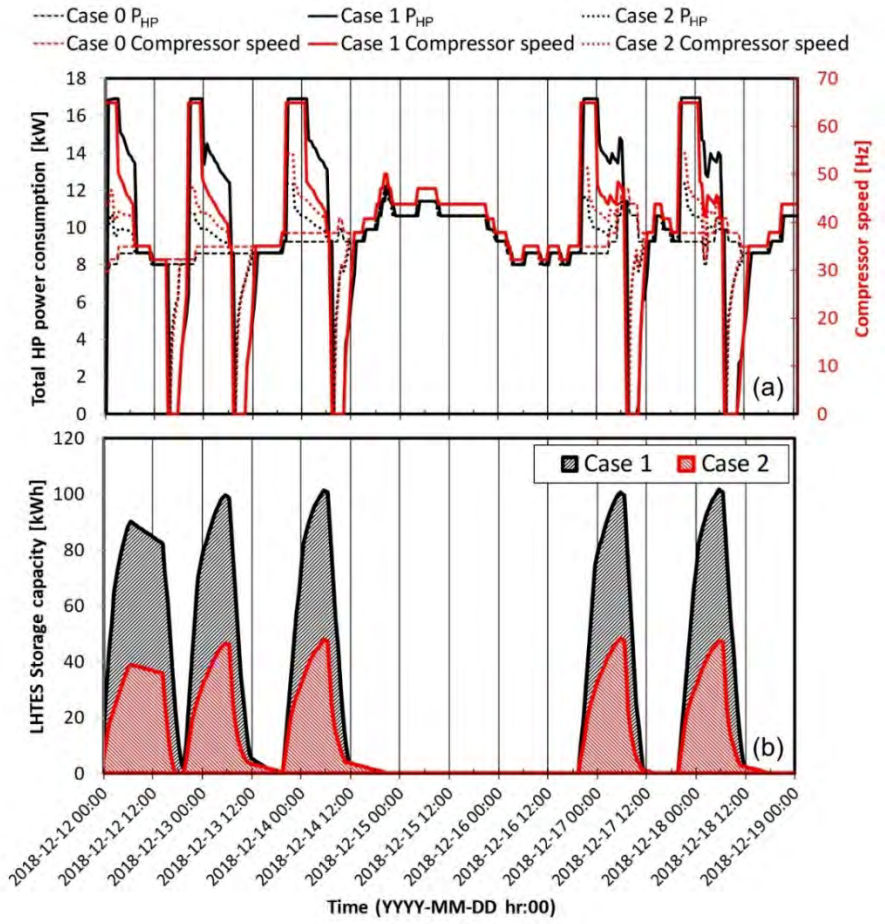

Figure 4: Working statues of the main components: (a) HP; (b) LHTES unit

4. CONCLUSIONS

This study theoretically investigates two LHTES-integrated HP heating systems, one of which uses the condenser for charging LHTES (Case 1) and the other uses the desuperheater (Case 2), aimed for typical multi-family dwellings in Stockholm. Quasi-stationary system models on a half-hour basis are built for evaluating the performances of these two integrating configurations where the storage unit is utilized for peak heating load shifting. The performance indicators, including the system's SPF, the total electricity consumption, and bills of heating for the end-users, are calculated for both integrating configurations and the basic heating system without storage device (Case 0) over a chosen heating-season weak. The transient working statues of HP and LHTES in the integrated systems are revealed for both Case 1 and Case 2. The simulation results indicate that using the condenser (Case 1) to charge the LHTES unit leads to increased total electricity consumptions (7.2%) and bills (1.9%) compared with the basic

heating systems owing to the necessity of increasing HP's condensation temperature. But utilizing the desuperheater (Case 2) for charging LHTES instead can decrease the bill by 17€/week (around 3%) because it brings negligible influences on the HP's condensation temperature and thereby the total electricity consumptions.
There are a few limitations of the present study which can be improved in the future work:

- The quasi-stationary system model can be improved with a finer time discretization, so that the transient HP and LHTES operating statues can be interpreted more in details;
- The LHTES charging/discharging thermal performances can be improved by better PCM encapsulation designs. Future work can include optimizing the heat transfer aspect of the LHTES unit and simulating its improved thermal performances in an HP-LHTES integrated system.

ACKNOWLEDGEMENTS

The first author would like to express his gratitude to the Chinese Scholarship Council (CSC) for the stipend. The Swedish Energy Agency is thanked for its financial supports.

NOMENCLATURE

(AS)HP	(air-source) heat pump	*LHTES*	latent heat thermal energy storage
Q	heating capacity (kW)	*P*	power consumption (kW)
HTF	heat transfer fluid	*PCM*	phase change material
T	temperature (°C)	*SPF*	seasonal performance factor (-)

REFERENCES

Agyenim, F., Hewitt N., 2010. The development of a finned phase change material (PCM) storage system to take advantage of off-peak electricity tariff for improvement in cost of heat pump operation. Energy and Buildings 42(9), 1552-1560.

Hamada, Y., Fukai J., 2005. Latent heat thermal energy storage tanks for space heating of buildings: Comparison between calculations and experiments. Energy Conversion and Management 46(20): 3221-3235.

Moreno, P., Solé C., Castell A., Cabeza L. F., 2014. The use of phase change materials in domestic heat pump and air-conditioning systems for short term storage: A review. Renewable and Sustainable Energy Reviews 39(Supplement C): 1-13.

Pardiñas, Á. Á., Alonso, M. J., Diz, R., Kvalsvik, K. H. Fernández-Seara, J., 2017. "State-of-the-art for the use of phase-change materials in tanks coupled with heat pumps." Energy and Buildings 140: 28-41.

Xu, T., Chiu, J. N., B. Palm and S. Sawalha, 2019. "Experimental investigation on cylindrically macro-encapsulated latent heat storage for space heating applications." Energy Conversion and Management 182: 166-177.

Xu, T., Navarro-Peris E., Piscopiello S., Sawalha S., Corberán J. M., Palm B., 2018. Large-capacity propane heat pumps for dhw production in residential buildings. Refrigeration Science and Technology.

Xu, T., Sawalha, S., Mazzotti W., Björn P., 2016. Performance Evaluation of a Large Capacity Air-Water Heat Pump Using Propane as Refrigerant. Proceedings of 12th IIR-Gustav Lorentzen Conference on Natural Refrigerants-GL2016, Edingburgh, UK, IIR.

Zhu, N., Hu, P., Xu, L., Jiang, Z., Lei, F., 2014. Recent research and applications of ground source heat pump integrated with thermal energy storage systems: A review. Applied Thermal Engineering 71(1): 142-151.

Manuscript ID: 1668
DOI: 10.18462/iir.icr.2019.1668

A Gas-Fired Heat-Driven Thermoacoustic Heat Pump for Winter Heating

Yanlei SUN [a, b], Jianying Hu [a, b*], Ercang LUO [a, b*], Limin ZHANG [a], Kaiqi LUO [a, b], Zhanghua WU [a, b]

[a] CAS Key Laboratory of Cryogenics, Technical Institute of Physics and Chemistry
Beijing, 100190, China, jyhu@mail.ipc.ac.cn & ecluo@mail.ipc.ac.cn
[b] University of Chinese Academy of Sciences
Beijing, 100049, China, jyhu@mail.ipc.ac.cn & ecluo@mail.ipc.ac.cn

ABSTRACT

Gas-fired heating is more environmentally friendly than coal-fired heating, but it results in extensive exergy loss because the heating supply temperature is much lower than the combustion temperature. We proposed a new gas-fired heat-driven thermoacoustic heat pump system. The SAGE program was used to simulate and optimize the system. With heating supply temperature of 333K and surrounding temperature of 273K, the system achieved a COPh of 1.72, corresponding to a relative Carnot efficiency of 44.43%. In addition, the simulation results also showed that the heat pump performance is sensitive to the system parameters.
Keywords: Gas-fired, Thermoacoustic, Heat-Driven Heat Pump, COPh, Sensitivity.

1. INTRODUCTION

Rapid developments in Chinese economy have led to rapid growth in total societal energy consumption, especially with regards energy consumption in buildings. Heating, ventilation, and air-conditioning devices and domestic hot water accounts for in excess of two-thirds of the energy consumption in buildings in China. The proportion of energy consumption from heating is large (Li, 2016). The energy consumption for winter heating in northern China must be reduced to maintain residents' living quality (Zhao, 2014). Conventional heating methods in northern China include centralized heating based mainly on the burning of fossil energy to produce hot water. Besides cogeneration, most heating methods have low energy efficiency and high pollution (Wu, 2013) and (Wu, 2013). As an environmentally friendly, energy-saving and efficient air-conditioning system, heat pumps can pump heat from low-temperature heat sources (such as air, water and solar energy) and improve the heat temperature by consuming a small fraction of mechanical power, which provides an effective measure to protect the environment and minimise power shortages (Zhao, 2013) and (Tong, 2012). With the implementation of the Coal-to-Gas Program in China, a heat-driven heat-pump technology can play an important role in decreasing pollutant emissions and improving the quality of life of residents because of its advantages of high efficiency, high reliability and low pollution.

The Stirling machine is a heat engine that is based on the Stirling cycle. The Stirling cycle was first proposed by Robert Stirling in 1816 and was used in engines (Graham, 1985). In 1862, Kirk used the reverse Stirling cycle in refrigeration experiments, and promoted the development of Stirling heat pumps. In 1964, Beale of the United States proposed the concept of a free-piston Stirling engine in which the crank-link mechanism was eliminated compared with the traditional Stirling machine. The dynamic piston and ejector were not subjected to lateral forces during the axial movement. The contact seal was replaced by a gas seal, depending on the leaf spring and the gas bearing, which improved the reliability and stability of the system (Beale, 1976). However, researches on duplex free-piston Stirling heat pumps were rarely reported. Only Sunpower of the United States and Kawasaki of Japan have reported the use of duplex free-piston Stirling heat pumps (Rix, 1989). Fig. 1.a provides a schematic diagram of the mechanism of the duplex free-piston Stirling heat pump developed by Sunpower in 1983. The structure uses a free-piston Stirling heat pump that is driven by a free-piston Stirling engine, which shares the same power piston. The mechanical output of the Stirling engine drives the Stirling heat pump. The cold-end of the engine operates at the same

temperature as the hot-end of the heat pump, which increases the coefficient of performance (COP). In 2006, Boucher et al. of France proposed a structure in the form of an opposed free-piston Stirling engine (Boucher,2007), in which an asynchronous linear motor was used for coupling. The heat released from the cold-end of the engine was used to supply heat to the outside. To resolve the problem of impedance matching between the engine and the heat pump (or refrigerator), in 2016, Li et al. of China devised a new type of resonant tube-coupled duplex Stirling refrigerator structure (Li, 2016). The free-piston Stirling engine was matched with the free-piston Stirling refrigerator with a resonant tube, as shown in Fig. 1.b. The resonance tube was too long, which resulted in large system occupation and huge loss of acoustic power. In response to this problem, in 2017, Hu et al. of China proposed using a light-load liner alternator to couple a Stirling refrigerator and a Stirling engine, and analysed the parameter sensitivity on this structure (Hu, 2017). In this configuration, the resonant piston transferred acoustic power and coupled the engine and the refrigerator. This system was more compact with a lower loss of acoustic power.

Based on the above research, we proposed a gas-fired heat-driven thermoacoustic heat pump, which uses a light-load liner alternator to couple a thermoacoustic Stirling prime mover and a thermoacoustic Stirling heat pump. We introduced the system and simulated the structure with SAGE software and then we discussed the influence of the key parameters on the system before providing the conclusions.

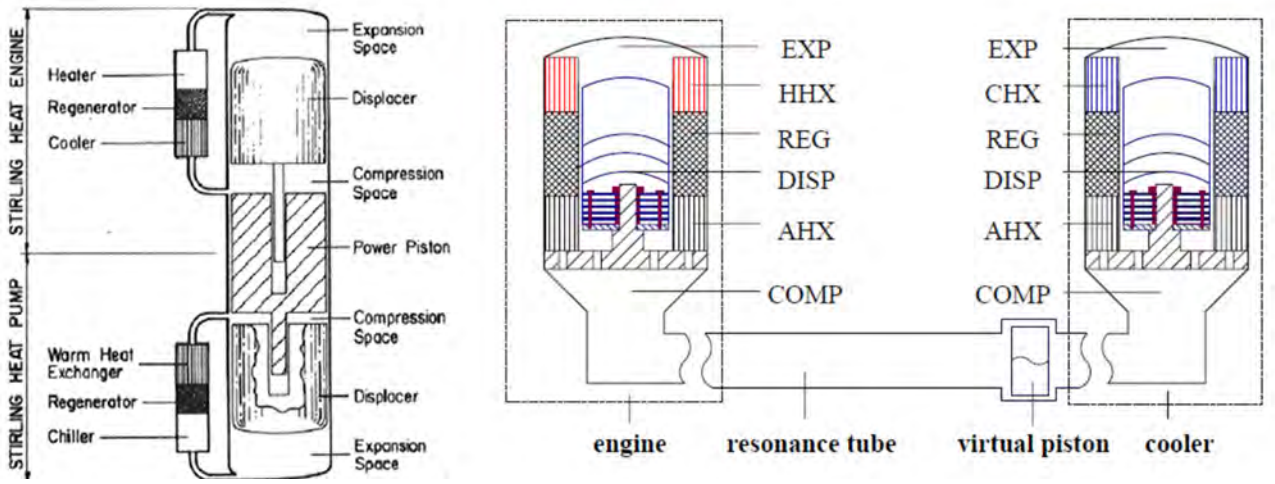

Figure 1: Schematic of a duplex Stirling heat pump (a) and a heat-driven duplex Stirling cooler with a resonance tube (b)

2. SYSTEM AND NUMERICAL MODEL

The gas-fired heat-driven thermoacoustic heat pump consists of a thermoacoustic Stirling prime mover, a light-load liner alternator and a thermoacoustic Stirling heat pump, as shown in Fig. 2. Among them, the thermoacoustic Stirling prime mover is mainly composed of an expansion chamber, a hot-end heat exchanger (HHX), a regenerator, a displacer, an ambient heat exchanger (AHX) and a compression chamber. The thermoacoustic Stirling heat pump is composed mainly of an expansion chamber, an ambient heat exchanger (AHX), a regenerator, a displacer, a cold-end heat exchanger (CHX) and a compression chamber. The light-load linear alternator is located between the thermoacoustic Stirling engine and the thermoacoustic Stirling heat pump, as a resonating piston, to match the acoustic field on the left and right sides of the linear alternator.

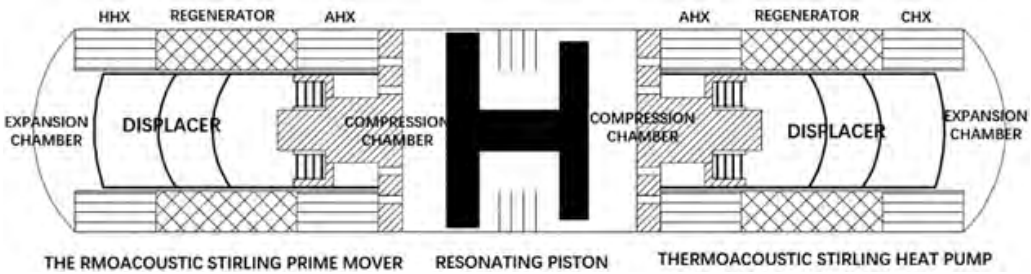

Figure 2: Schematic of gas-fired heat-driven thermoacoustic heat pump

2.1. Working Mechanism

The main working mechanism of the system is as follows. After absorbing high-grade heat from natural-gas combustion, the thermoacoustic Stirling prime mover establishes a positive temperature gradient at both ends of the regenerator. In the regenerator, heat is converted gradually into acoustic power along the increasing direction of the temperature gradient. In the expansion chamber, acoustic power is collected and transferred to the compression chamber by the displacer. In the compression chamber, part of the acoustic power flows to the light-load liner alternator, and the other part of the acoustic power is amplified again through the ambient heat exchanger, the regenerator and the hot-end heat exchanger. The acoustic power is enlarged and looped back and forth. Because of the mechanical damping of the light-load liner alternator, the acoustic power that flows through the light-load liner alternator is dissipated. The remainder flows into the compression chamber of the thermoacoustic Stirling heat pump. In the thermoacoustic Stirling heat pump, the acoustic power that flows in and the acoustic power that is recovered by the displacer are combined and flow into the ambient heat exchanger, the regenerator and the cold-end heat exchanger. The mixed acoustic power is consumed gradually against the direction of the temperature gradient. The Stirling thermoacoustic prime mover absorbs heat from the natural gas combustor, generates acoustic power and supplies heat for an indoor heating supply. The thermoacoustic Stirling heat pump consumes acoustic power to extract heat from the environment and increases the temperature to warm the circulating water. The total output heating power could be several times larger than the acoustic power, so the primary energy-utilization efficiency of the heat-driven pump is obviously higher than the simple combustion heat. The light-load liner alternator makes the thermoacoustic Stirling prime mover and the thermoacoustic Stirling heat pump achieve a traveling-wave acoustic field. The displacement of the alternator's piston indicates whether the system is operating normally.

2.2. Evaluation Mechanism

The commercially available software SAGE version-10 was used to simulate the system. The software performs one-dimensional modelling calculations based on the concept of a node-analysis method, and obtains numerical calculation results by solving the coupled N–S equations (Gedon, 2011). To evaluate the system performance, the overall coefficient of performance (COPh), the output heating power and the relative Carnot efficiency of the entire system were introduced.
The COPh of the entire system is defined as:

$$Q_{pump} = Q_{pump,hp} + Q_{pump,pr} \quad \text{Eq. (1)}$$

$$COP_h = Q_{pump} \cdot Q_{heating}^{-1} \quad \text{Eq. (2)}$$

where Q_{pump}, $Q_{pump,hp}$, $Q_{pump,pr}$ and $Q_{heating}$ are the output heating power of the entire system, the output heating power of the thermoacoustic Stirling heat pump, the output heating power of the thermoacoustic Stirling prime mover and the input heating power of the hot-end of the thermoacoustic Stirling prime mover in W, respectively.
The relative Carnot efficiency of the system is given by:

$$\eta = Q_{pump}\left(1 - T_0 \cdot T_r^{-1}\right)\left[Q_{heating}\left(1 - T_0 \cdot T_h^{-1}\right)\right]^{-1} \quad \text{Eq. (3)}$$

where T_h, T_r, T_0 are the hot-end temperature of the prime mover, the heating supply temperature and the surrounding temperature in K, respectively.
By obtaining the displacement of the light-load linear alternator and the operating frequency of the system, it can be determined whether the system operates normally.

2.3. Geometry Details and Operating Conditions

The system is mainly composed of a thermoacoustic Stirling prime mover, a light-load linear alternator and a thermoacoustic Stirling heat pump. The geometric details of the design are shown in Tables 1–3.

Table 1. Geometric parameters of the thermoacoustic Stirling prime mover

Components	Parameters
Expansion Chamber	90 cm^3
HHX	80mm long, 56 channels: width 1mm, high 10mm, thickness 1mm
Regenerator	70mm long, equivalent diameter 60mm, porosity 0.8
AHX	60mm long,1125tubes: inner diameter 0.8mm, thickness 0.4mm
Displacer	100mm long, diameter 88mm, weight 0.56kg
Compression Chamber	400 cm^3

Table 2. Geometric parameters of the light-load linear alternator

Components	Parameters
Alternator	100mm long, diameter 76.45mm, weight 7 kg, mechanical damping (Rm) 40kg/s, spring stiffness(K) 8.119x10^3N/m, piston area ratio 0.989

Table 3. Geometric parameters of the thermoacoustic Stirling heat pump

Components	Parameters
Expansion Chamber	118 cm^3
AHX	60mm long, 1531tubes: inner diameter 0.8mm, thickness 0.4mm
Regenerator	40mm long, equivalent diameter 70mm, porosity 0.8
CHX	50mm long, 1531tubes: inner diameter 0.8mm, thickness 0.4mm
Displacer	100mm long, diameter 100mm, weight 0.7735kg
Compression Chamber	300 cm^3

The operating conditions of the system design are shown in Table 4.

Table 4. System-design conditions

Operating Frequency	Working Medium	Average Pressure	Hot-End Temperature	Heating Supply Temperature	Surrounding Temperature
45Hz	He	6MPa	923K	333K	273K

2.4. Results

With the displacement of the light-load liner alternator and working frequency of the system fixed at 9 mm and 45 Hz, it was found that the input and the output heating power were 3202 W and 5500 W, respectively. The COPh and relative Carnot efficiency of the system reached 1.72 and 44.43%, respectively. The calculation results are shown in Table 5.

Table 5. System calculation results

Displacement of the Light-Load Liner Alternator (mm)	Input Heating Power (W)	Output Heating Power (W)	COP_h	η
9.000	3202	5500	1.72	44.43%

3. INFLUENCE OF KEY PARAMETERS

Because of uncertainties in working conditions, it is difficult for the system to achieve the desired design state, and parameters will deviate from the design value. Therefore, understanding the sensitivity of the system performance to parameter changes will play a vital role in system control and efficiency improvement. We focus on the influence of temperature and average pressure on the thermodynamic performance.

3.1. Influence of Temperature on Thermodynamic Performance

By changing the hot-end temperature of the prime mover and surrounding temperature, the system-performance curve as a function of temperature can be obtained, as shown in Fig. 3. When the surrounding temperature increases, the onset temperature of the system decreases gradually, and the output heating power of the entire system, COPh, and the displacement of the light-load liner alternator increase accordingly. An increase in the surrounding temperature is conducive to system work. When the surrounding temperature is constant, the displacement of the light-load liner alternator, the output heating power of the entire system, and the COPh improve significantly as the hot-end temperature of the prime mover increases. The COPh and relative Carnot efficiency of the system will have a maximum value with an increase in the hot-end temperature of the prime mover, as shown in Fig. 3.c. With the surrounding temperature of 273K and hot-end temperature of 925K, the system obtains the COPh extreme value of 1.719. When the surrounding temperature is 293K, the system obtains the COPh maximum value of 1.84 at the hot-end temperature of 800K. When the surrounding temperature is 313K, the system obtains the COPh extreme value of 1.966 at the hot-end temperature is 700K. It can be concluded that with the surrounding temperature increase, the maximum COPh gradually increases and the corresponding hot-end temperature gradually decreases.

The above calculation results show that the parameters of the displacement of the light-load liner alternator, the output heating power of the entire system and the COPh are sensitive to temperature changes of the system heat source. Because the frequency of the system operation increases only slightly with an increase in temperature, as shown in Fig. 3.b, the frequency is insensitive to changes in system heat-source temperature.

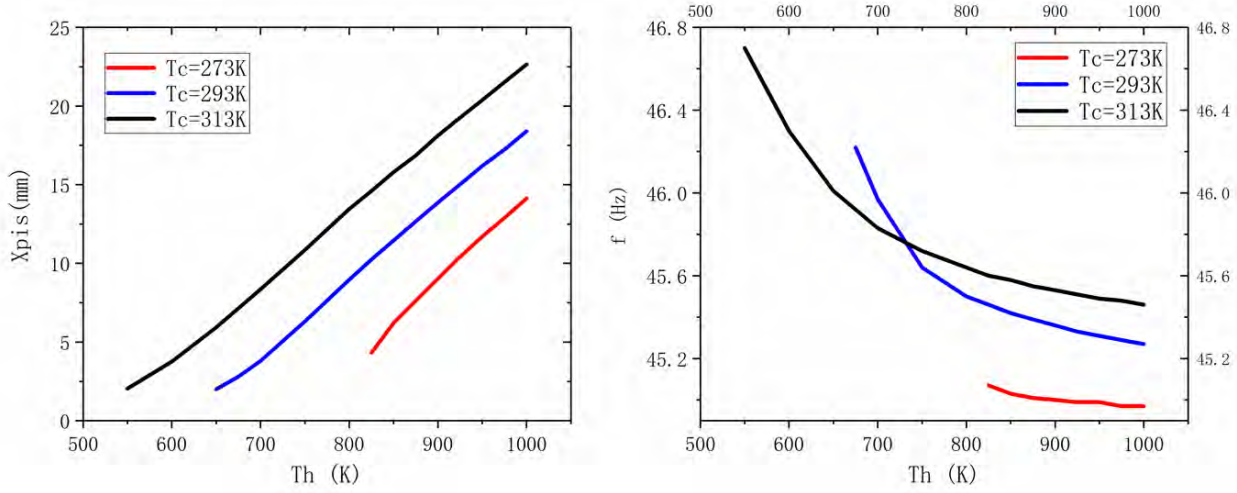

(a) **(b)**

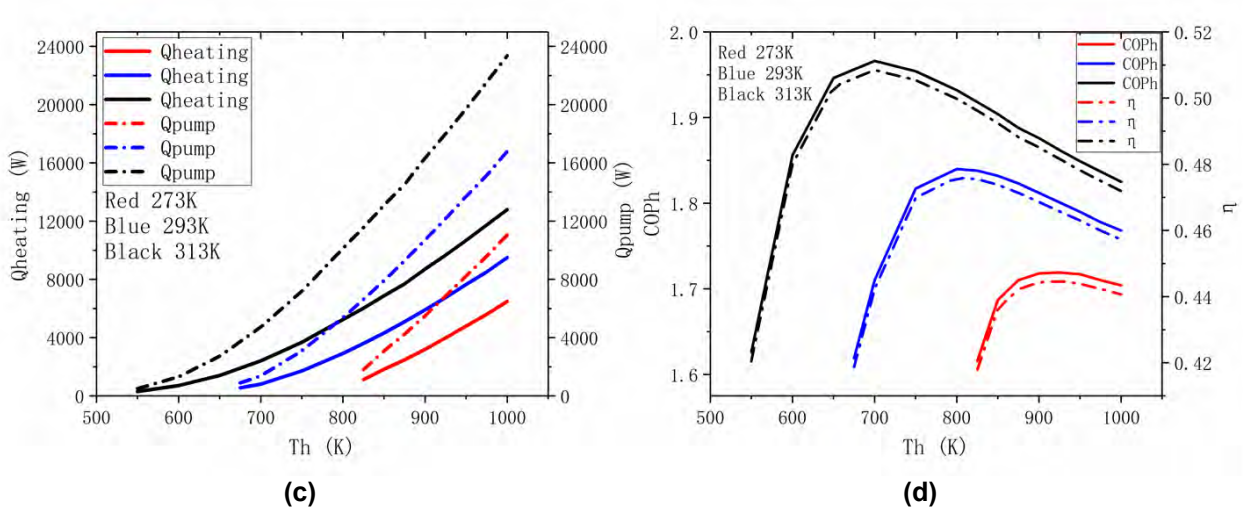

(c) (d)

Figure 3: Influence of temperature on thermodynamic performance: X_{pis} vs. T_h (a), f vs. T_c (b), $Q_{heating}$ and Q_{pump} vs. T_h (c), COPh and η vs. T_h (d)

3.2. Influence of Average Pressure on Thermodynamic Performance

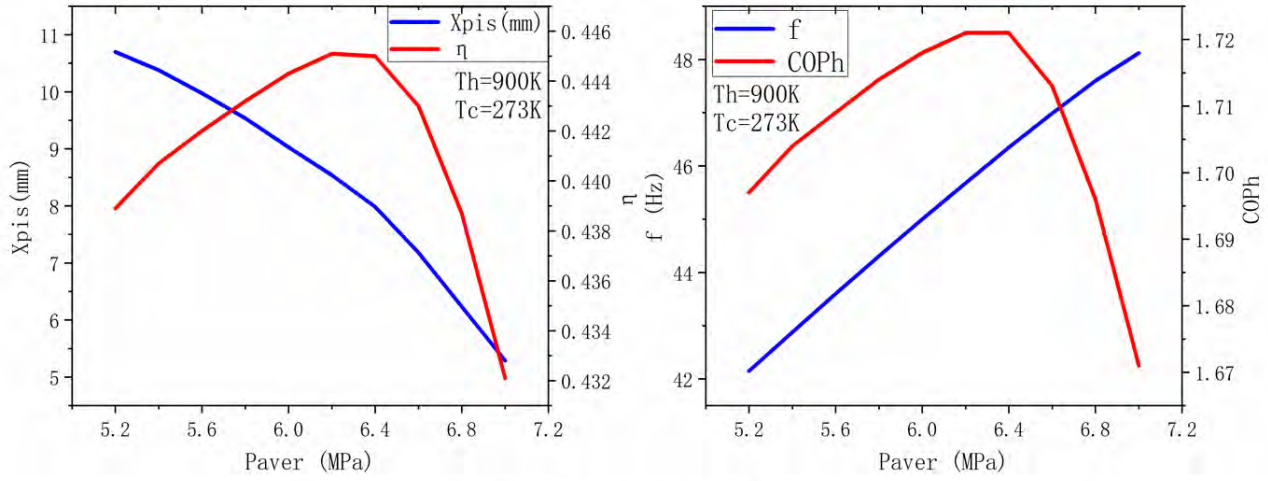

(a) (b)

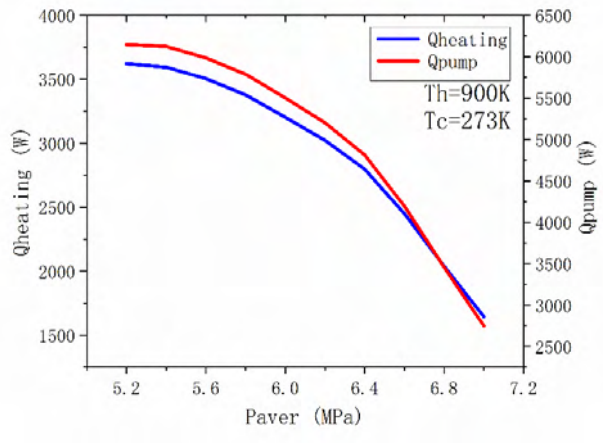

(c)

Figure 4: Influence of average pressure on thermodynamic performance: X_{pis} and η vs. P_{aver} (a), f and COPh vs. P_{aver} (b), $Q_{heating}$ and Q_{pump} vs. P_{aver} (c)

Fig. 4 shows the influence of average pressure changes on the thermodynamic performance. Fig. 4.a and b show that the thermoacoustic Stirling prime mover and the thermoacoustic Stirling heat pump are matched because of the action of the light-load liner alternator. Where the other design parameters of the system are determined, the COPh and relative Carnot efficiency of the entire system increase with an increase in average pressure and an extreme efficiency result. As the pressure increases, the COPh and relative Carnot efficiency increase gradually, and they decrease after reaching an extreme value. The system has the highest COPh and relative Carnot efficiency at 6.2 MPa, which is fixed at 1.721 and 0.4451, respectively.
Fig. 4.a and c show that as the pressure increases, the displacement of the light-load liner alternator, the output heating power and the input heating power decrease gradually. The decreasing trend increases gradually with an increase in pressure. To obtain a larger output heating power in the system, a reduction in average system pressure is required.
Fig. 4.b shows that on condition that the other design parameters of the system are determined, the operating frequency of the system increases gradually in an approximately positive linear manner as the pressure increases. If the system frequency is too high, the heat-exchange effect between the system and the external environment and the heat-transfer performance of the regenerator will decrease. It can be an explanation for the sharp decrease in the COPh when the pressure is higher than the optimum value,
The above calculation results indicate that the parameters of the displacement of the light-load liner alternator, the output heating power, the COPh and the frequency are all sensitive to the variation of average pressure. Therefore, the variation of average pressure needs to be considered during operation.

4. CONCLUSIONS

In this paper, a gas-fired heat-driven thermoacoustic Stirling heat pump was proposed. The full heat-driven pump was numerically simulated and analysed based on the SAGE program. It is shown that the novel heat-driven pump has excellent performance. The result shows that with the hot-end temperature of the prime mover, the heating and the surrounding temperatures of the heat pump fixed at 923K, 333K, 273K, and frequency of 45Hz, the system can achieve a COPh of 1.72 and a relative Carnot efficiency of 44.43%. With the light-load liner alternator displacement fixed at 9mm, the input heating power and the output heating power were 3202W and 5500W. In addition, the simulation results also showed that the heat pump performance is sensitive to the system parameters. The parameters of the displacement of the light-load liner alternator, the output heating power of the entire system, the COPh are sensitive to the system temperature and average pressure and the frequency is only sensitive to the change of average pressure.

ACKNOWLEDGEMENTS

This work was supported financially by the Key Research and Development Program of China (Contract No. 2017YFB0903603) and the National Sciences Foundation of China (Grant No. 51627809, 51576204 and 51876213).

NOMENCLATURE

Q_{pump}	output heating power of the entire system (W)	$Q_{pump,hp}$	output heating power of the thermoacoustic Stirling heat pump (W)
$Q_{pump,pr}$	output heating power of the thermoacoustic Stirling prime mover (W)	$Q_{heating}$	input heating power of the hot-end of the thermoacoustic Stirling prime mover (W)
COPh	overall coefficient of performance	η	relative Carnot efficiency

T_0	surrounding temperature (K)	T_r	heating supply temperature (K)
T_h	hot-end temperature of the prime mover (K)	X_{pis}	displacement of the light-load liner alternator (mm)
f	operating frequency (Hz)	P_{aver}	average pressure (MPa)

REFERENCES

Li, X.T., Song, P.Y., Shi, W.X., Wang, B.L., 2016. Novel heat pump with high efficiency for the whole year: Flexible heat pump. HV&AC 46(12),1-7.

Zhao, Y., Chen, Y.Y., Luo, E.C., Zhou, Y., 2014. Numerical Simulation and Experimental Study on a Liner-compressor Driven Traveling-wave Thermoacoustic Heat Pump. Journal of Refrigeration (5),7-13.

Wu, W., Shi, W.X., Wang, B.L., Li, X.T.,2013. Approaches and Comparative Analysis for Performance Improvement of Air Source Absorption Heat Pump in Cold Regions. Journal of Refrigeration 34(5),1-7.

Wu, W., Li, X.T., Shi, W.X., Wang, B.L., 2013. Low evaporating temperature absorption heat pump used for heating and domestic hot water in Northern China. HV&AC 43(8),86-93.

Yang, Z., Wang, W.B., Wu, X.,2013. Thermal modeling and operating tests for a gas-engine driven heat pump working as a water heater in winter. Energy & Buildings 58,219–226.

Tong, H., Luo, E.C., 2012. Double-acting traveling-wave thermoacoustic heat pump for high-temperature range driven by linear compressor. CRYOGENICS (4), 18-23.

Graham, W.P.D., J., R.S.P.D.,1985. Free piston stirling engines. Springer Berlin, Heidelberg ,268p.

Beale, W.T., 1976.Power piston actuated displacer piston driving means for free-piston Stirling cycle type engine. U.S. Patent No. 3, 937, 018. 10.

Rix, D.H, 1989.The potential of the Stirling cycle heat pump. Proceedings of the Institution of Mechanical Engineers, Part A: Journal of Power and Energy 203.4, 245-254.

Boucher, J., Lanzetta, F., Nika P.,2007. Optimization of a dual free piston Stirling engine. Applied Thermal Engineering 27(4), 802-811.

Li, X.W., Yu, G.Y., Wang, X.T., Dai, W., Luo, E.C., 2016. Numerical study on a new type resonance tube coupled duplex Stirling cooler. CRYOGENICS (5),15-21.

Hu, J.Y., Luo, E.C., Dai, W., Zhang, L.M.,2017. Parameter sensitivity analysis of duplex Stirling coolers. Applied Energy 190, 1039-1046.

Gedeon D., 2011. Sage version 10: user's manual. Gedeon Associates, Athens, 432p.

Manuscript ID: 1694
DOI: 10.18462/iir.icr.2019.1694

Applications of absorption heat exchangers for kinds of waste heat recovery systems

Yi JIANG[(a)*], Xiaoyun XIE[(a)]

[(a)] Building Energy Research Center, Tsinghua University
Beijing, 100084, China, jiangyi@tsinghua.edu.cn

ABSTRACT

Absorption Heat Exchanger (AHE) is a kind of new heat exchange concept put forward in recent years, by which un-matching heat transfer processes could be realized. Kinds of applications of the AHEs for industries waste heat recovery are introduced in this paper, including condensing heat recovery in CHP plant, long distance heat transportation system, low grade waste heat recovery system in steel plants and fast cooling systems in beverage production process. Real projects for the above typical applications are introduced, including waste heat recovery in Datong First CHP plant, Taiyuan Gujiao CHP plant, Qianxi steel plants and so on. The energy consumption results are shown for each project. The suitable application system structures of AHEs are discussed finally, and then the design principle of using AHEs in different systems is given.
Keywords: Absorption System, Industrial Application, Heat Exchanger, Heat Pump, Optimization, System Absorption.

1. INTRODUCTION

The energy consumption for buildings takes more than 20% of the total national energy consumption in China (Building Energy Research Centre, Tsinghua University, 2015), in which the district heating systems in north of China takes about 24% of the total building energy consumption. For ordinary heating systems, the main heat sources are the steam extracted from CHP plants with temperature higher than 100 ℃ and the boilers. The designed indoor temperature in heating seasons is only 18~22℃, while the temperature of the heat source, take the coal boilers for example, is higher than 500℃, which leads to big waste of energy quality.

In another hand, there exists enormous waste heat exhausted in kinds of industries, which can take 50% of the total input energy for the industry, and the energy consumption of industries takes more than 60% of the total national energy consumption. Furthermore, the waste heat with low temperature, lower than 80℃ takes the main part of the total waste heat. There are kinds of methods to recover the wasted heat for use, most of which are for the craft processes themselves. While the low temperature waste heat is really the most suitable heat source for building heating system, how to recover the wasted heat for building heat system is the hot topic in recent years.

Absorption heat pumps(AHPs) have been used for this purpose in several big scale projects for district heating systems in China, by which the condensed wasted heat of CHP plants (Li, 2011), the waste heat from steel plants (Fang, 2013) are recovered. For AHP systems, the heat source with high temperature is the driven force. If the temperature of the waste heat is lower than 40℃, it is not easy to recover all of the waste heat as the heat source is not enough. Second, as the plants are always far from the cities, the waste heat must be transported for a long distance. How to increase the transportation temperature difference is the key problem. Thus, a new concept, absorption heat exchangers (AHEs) are prompted (Fu, 2008), by which the return water temperature can be low to 20℃. By using the AHEs, first, part of the waste heat can be recovered by the return water directly, second, the transportation temperature difference can be enlarged significantly.

Thus, in this paper, applications of AHEs are introduced, including waste heat recovery of CHP plants, waste heat recovery of kinds of industries, fast cooling systems and so on. Different scales of real AHEs were developed and the field testing results are introduced to show the level of the performance of the developed AHEs.

2. PRINCIPLE OF ABSORPTION HEAT EXCHAGNERS

2.1. Principle of two Types of AHE

The principle of absorption heat exchangers (Fu, 2008, Xie and Jiang, 2017) are shown in Fig. 1.

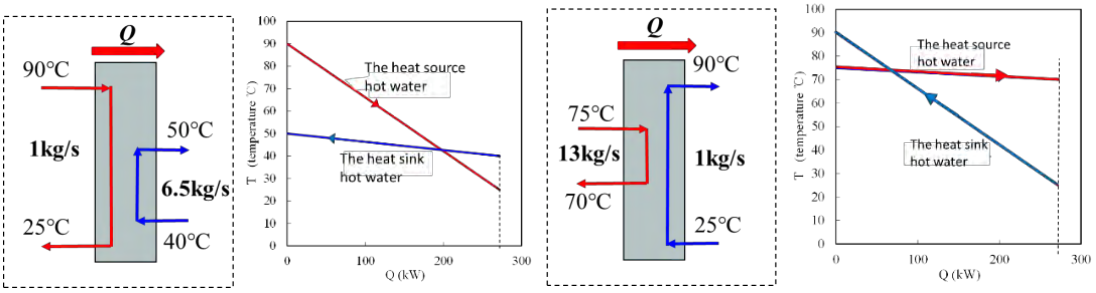

(a) The first type of AHE (b) the second type of AHE

Figure 1: Principle of AHEs

There are two types of AHE. For the first type of AHE (type I), the flow rate of the heat source is much lower than that of the heat sink, and the outlet temperature of the heat source hot water can be lower than the inlet temperature of heat sink hot water, as the T-Q chart shows. For the second type of AHE (type II), the flow rate of the heat sink is much lower than that of the heat source, and the outlet temperature of the heat sink hot water can be higher than the inlet temperature of the heat source, as the T-Q chart shows. To achieve un-matching heat transfer processes is the most important feature of the two types of AHEs. How to realize the above trans-normal functions of AHEs? In fact in the AHE, the main components are an absorption heat pump and a common heat exchanger (Fu, 2008; Xie and Jiang, 2017), as Fig. 2 shows. The principle of the AHEs in detail are not discussed here.

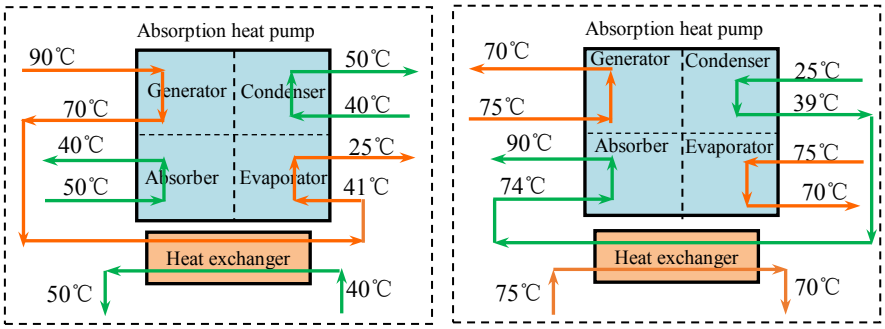

(a) The first type of AHE (b) The secondary type of AHE

Figure 2: Principle of the two types of AHE

2.2. The Main Performance Description Method of AHEs

The temperature efficiency Xie and Jiang, 2017) is used to describe the basic heat transformation performance of AHEs, which is shown in Eq. (1)~(2).

$$\varepsilon_I = \frac{t_{1,in} - t_{1,o}}{t_{1,in} - t_{2,in}} \quad \text{Eq. (1)}$$

$$\varepsilon_{II} = \frac{t_{2,o} - t_{2,in}}{t_{1,in} - t_{2,in}} \quad \text{Eq. (2)}$$

Eq. (3) shows the fitting equation of the temperature efficiency. The main factors to influence the temperature efficiency are the flow rate ratio and the running flow rate. The two sides temperature also influence the temperature efficiency, but with much slight effect.

$$\varepsilon = \varepsilon^0 + a \cdot (1/m - 1/m_0) + b \cdot (G - G_0) + ks \cdot (t_{1,in} - t^0_{1,in}) + kr \cdot (t_{2,in} - t^0_{2,in}) \quad \text{Eq. (3)}$$

Where m represents the flow rate ratio($m \geq 1$), G represents the lower flow rate of the two sides, ε^0 , m_0 , G_0, $t^0_{1,in}$, $t^0_{2,in}$, G_0 represents the parameters under the rated working condition. a,b, ks, kr are constants, which depend on the different process structures.
Take one developed three stage AHE as an example, the value of the above parameters are: ε^0=1.307, G_0=0.7 kg/s, m_0 =10.57, $t^0_{1,in}$ =90℃, $t^0_{2,in}$ =40℃, a=0.484, b=0.169, ks=-1.599E-03 ℃$^{-1}$, kr=-3.760E-03 ℃$^{-1}$

3. APPLICATION SYSTEMS OF ABSORPTION HEAT EXCHANGERS

The absorption heat exchangers have been applied in kinds of real systems to realize the demanded extremely un-matching heat transfer processes, including the CHP systems to recover condensed waste heat, the long-distance transportation system of low grade heat, the fast cooling systems and so on, which are introduced in the following.

3.1. CHP systems to recover condensed waste heat

CHP system is one of the common heat sources of district heating systems, which take 42% of the total heat sources of heating systems in China (Building Energy Research Centre, Tsinghua University, 2015). For common CHP systems, as shown in Fig. 3a, the heat source is only the extracted steam from the steam engine, and the primary hot water is heated by the extracted steam through steam-water heat exchangers (HEs), and at the terminal heat stations, the secondary hot water is heated by the primary hot water through water-water HEs. A case of the heat transfer processes of the common CHP systems is shown in Fig. 3b. At the CHP plants, as the steam changing phase when it releasing heat, and there is a big in-out temperature difference of the primary hot water for long distance transportation purpose, the heat transfer process carried out in the steam-water heat exchanger is an extremely un-matching heat transfer process, also called “triangle heat transfer process”. For this kind of heat transfer process, there exists large heat transfer loss caused by extremely un-matching flow rate of two sides, also called entransy dissipation (Guo, 2010) even if the heat transfer area tents to be infinite. To decrease the entransy dissipation is the key to decrease the energy consumption of CHP systems.

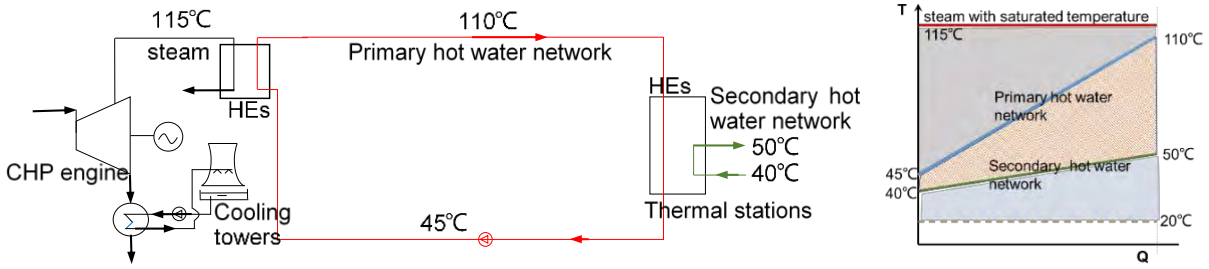

(a) System principle (b) T-Q chart

Figure 3: Common CHP systems

By using AHPs and AHEs, a new kind of CHP system is prompted (Fu, 2008), as shown in Fig. 4. The corresponding T-Q chart to express the heat transfer processes of the novel system is shown in Fig. 5. At the terminal thermal stations, the AHEs are used instead of common HEs to return the primary hot water with much lower temperature, for this case, 20℃, which is 25K lower than that of common HEs and is 20K lower than the inlet temperature of secondary hot water. At the CHP plants, the return hot water with low temperature is first pumped into at the HEs to be heated by the circulation water first, and then is pumped into the absorbers and condensers of AHPs to be heated further, and finally is pumped into the steam-water heat exchanger to be heated by the steam to the supply temperature, for this case,110℃. By using the circulation water HEs and the AHPs, the heat of the waste steam can be recovered, which can make the total supply heat increased 30% or to save the extracted steam to generate more electricity to supply the same quantity of heat. Furthermore, the transportation temperature difference of the primary hot water is also enlarged to be 1.6 times of that for common CHP systems, the heat transportation ability of the primary hot water network is increased 60%. Compared the T-Q charts with the common system, the entransy

dissipation of the heat transfer processes in the AHP and the AHE process are both decreased significantly. This kind of novel CHP system using AHEs have been applied in several real large-scale projects in China (Sun, 2014).

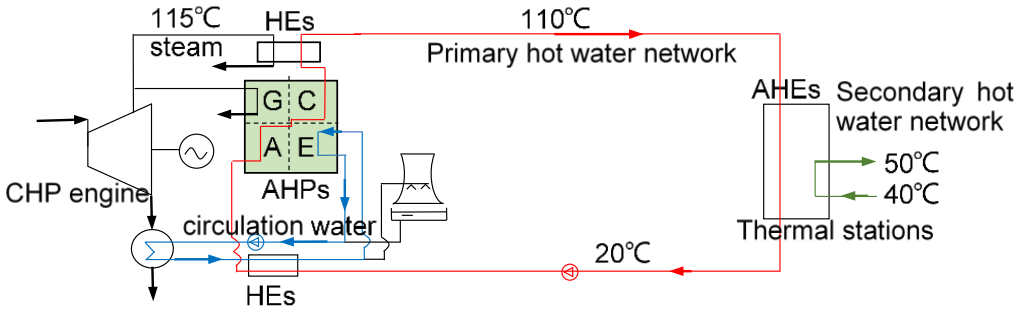

Figure 4: Condensed waste heat recovery system using AHEs

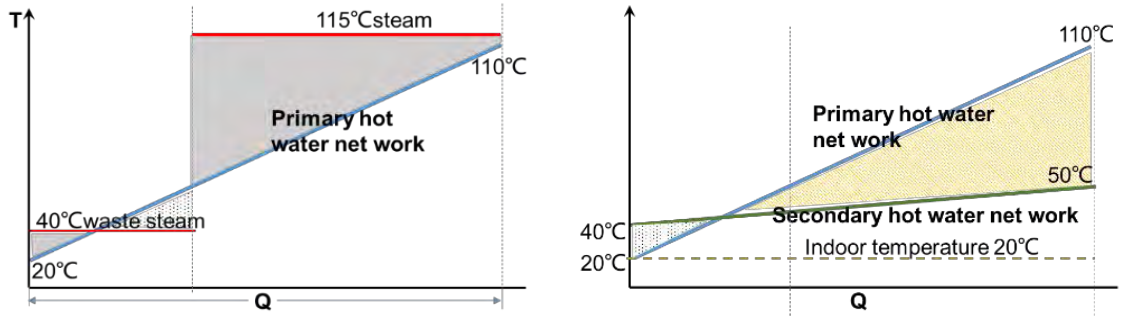

(a)AHP process in CHP plant (b) AHE process in terminal thermal stations

Figure 5: Heat transfer processes in T-Q chart for the new CHP systems

3.2. AHEs for Long Distance Heat Transportation

Another important application of AHEs is to recover industrial waste heat as the heat source of district heating systems. The industrial waste heat at 30~80℃ takes a big part of the total industrial waste heat, while very hard to recover according to its low grade. However, this part of waste heat can be the heat source for district heating system. As the waste heat is always far from the buildings, it is needed to be transported for a long distance. Thus, a novel system using the two types of AHEs is prompted (Xie and Jiang, 2017), as shown in Fig. 6.

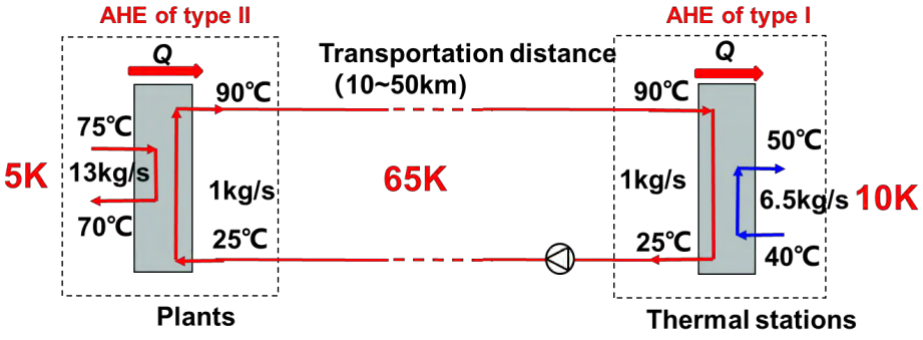

Figure 6: AHEs for long distance heat transportation

For this system, the AHEs of type II are applied at the industry plants to recover the waste heat and to transform the heat from low in-out temperature difference to high in-out temperature difference, as Fig. 6 shows, from 5K to 65K. Then, the hot water with high in-out temperature difference is transported through the primary hot water network with long distance to the terminal thermal stations. At the thermal stations, the AHEs of type I are applied to transfer heat from the primary hot water network to the secondary hot water side for building use, and meanwhile to transform the heat from high in-out temperature difference to low in-out temperature difference, as Fig. 6 shows, form 65K to 10K, as the hot water with high flow rate and low in-out temperature difference is needed for heating of buildings. The higher the transportation temperature difference(TTD) of the primary hot

water network, the longer the transportation distance can be realized. The TTD of the primary hot water network depends on the temperature efficiency of the two types of AHEs and the temperature difference between the inlet temperature of the waste heat and the inlet temperature of the secondary hot water (Xie and Jiang, 2017), as shown by Eqs. (4)~Eq. (5).

$$TTD=K(t_{s,in}-t_{r,in}) \quad \text{Eq. (4)}$$

$$K=\frac{1}{\frac{1}{\varepsilon_I}+\frac{1}{\varepsilon_{II}}-1} \quad \text{Eq. (5)}$$

Where $t_{s,in}$ represents the inlet temperature of the industrial waste heat, $t_{r,in}$ represents the inlet temperature of the secondary hot water, ε_I *and* ε_{II} respectively represents the temperature efficiency of the two types of AHEs. K is called the amplifying factor, which represents the amplification of the TTD of this system compared with the limit TTD of common system using only common heat exchangers.

The higher the temperature efficiency of the AHEs, the higher the TTD, and the amplifying factor K can reach 1.5~2.

This new system can be used for CHP system using backpressure turbine, as Fig. 7a shows. The AHEs of type II are installed at the CHP plants and the AHE of type I are applied at the thermal stations. Using the novel system, the condensing temperature of the waste steam can be decreased to 75 ℃ to realize a 65K TTD of the primary hot water network.

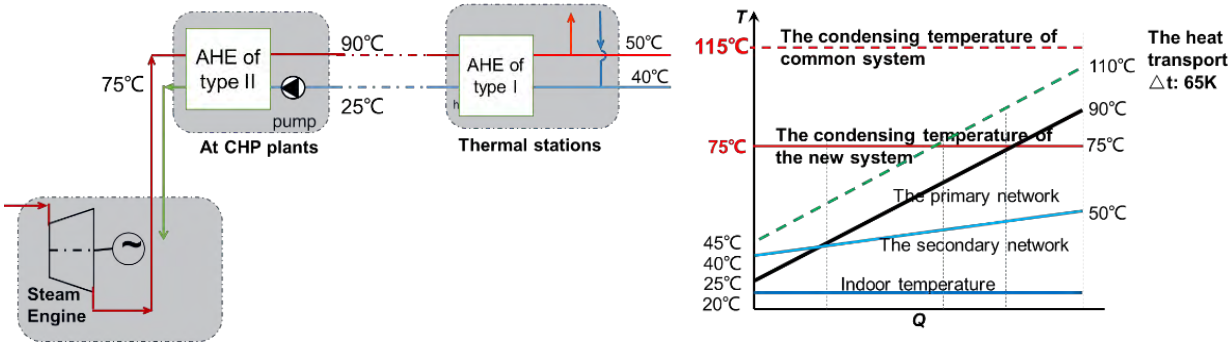

(a) System principle (b)T-Q chart

Figure 7: AHEs system applied in CHP systems using backpressure turbine

Fig. 7b shows the T-Q chart of this system. The comparison results with the common system is also given by Fig. 7(b). The common system is composed of just common heat exchangers between the waste steam and the primary hot water and between the primary hot water and the secondary hot water. To get the same TTD of the primary hot water network, the condensing temperature of the waste steam for the common system is at 115℃. Thus, using the novel AHEs system, the condensing temperature of the waste steam can be 40 K lower, by which to generate more electricity.

This kind of system can also be used for heating system of swimming pool nuclear reactor to realize long distance transportation of the nuclear reactor heat for buildings heating, as shown in Fig. 8, which well meets the demand of long distance of the nuclear reactor from the cities.

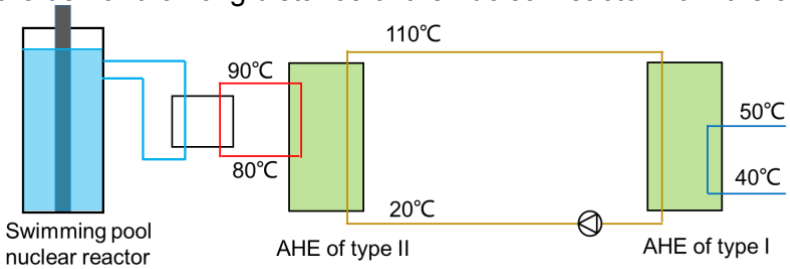

Figure 8: T-Q chart of AHEs system for district heating of backpressure turbine

3.3. Absorption Heat Exchangers for Fast Cooling Processes

The AHEs can also be used for fast cooling processes in chemical industry processes, food cooling processes and so on. The principle of the common fast cooling processes is shown in Fig. 9, to cool the material with high temperature (95℃) to low temperature (18℃), the mechanical chiller is used to produce cold water with temperature (15℃) lower than the demanded outlet temperature of the material. The cooling process is also shown in the T-Q chart, from which we can see that it is an extremely unmatching heat transfer process. Thus, using the first type of AHE, as Fig. 10 shows, the mechanical chiller can be cancelled, the cold water with temperature lower than the demanded outlet temperature of the material can be produced by the AHE with the other side to be only cooling water (30~35℃). By decreasing the entransy loss of the extremely unmatching heat transfer processes, the cooling source temperature can be lifted to realize the same cooling demand of the material.

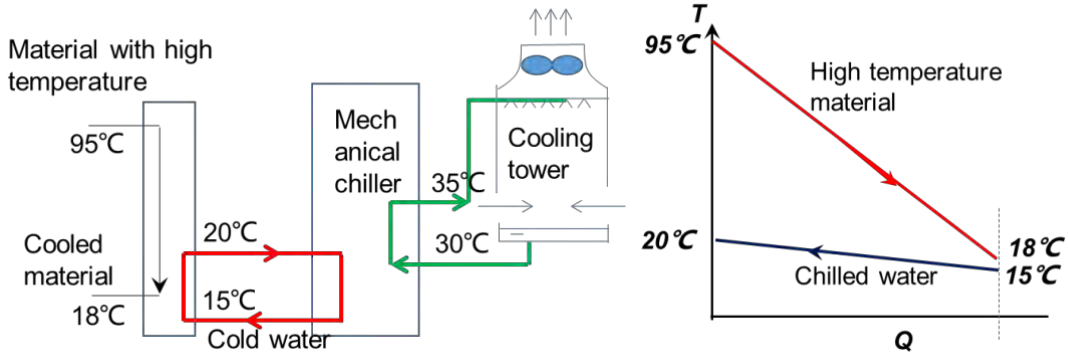

Figure 9: Common fast cooling system using mechanical chillers

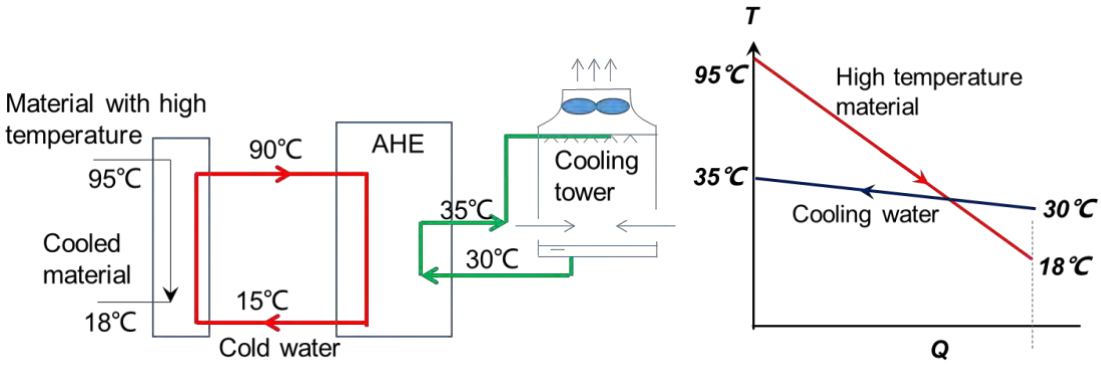

Figure 10: Novel fast cooling system using AHEs

4. DEVELOPMENT OF ABSORTPION HEAT EXCHANGERS

Different scales of real devices of AHEs have been developed, as Fig. 11 shows, the heat transfer quantity is from 200kW~10MW. These developed AHEs have been applied in real projects in China, such as the long distance heat supply system of Taiyuan Gujiao CHP plant, the building type heating system using in Chifeng city, Huhehaote city, Qianxi city and so on.





6MW 8MW 10MW

Figure 11: Different scales of developed AHEs

The testing performance of the different scales of AHEs are shown in Table 1, which indicates that the developed AHEs are running well in real projects.

Table 1: Testing performance of AHEs using in Taiyuan Gujiao project

Scales of AHE	Load rate	ε_I	$t_{1,in}$	$t_{1,o}$	$t_{2,in}$	$t_{2,o}$
1MW	29%	1.263	103.6	29.2	44.7	50
2MW	31.1%	1.339	107.6	19.8	42.3	49.3
6MW	43.3%	1.32	106.8	19.8	40.9	50.9
8MW	48.92%	1.363	112.9	20.1	44.8	53.7

Where $t_{1,in}$ represents the inlet temperature of the primary hot water, $t_{1,o}$ represents the outlet temperature of the primary hot water, $t_{2,in}$ represents the inlet temperature of the secondary hot water, $t_{2,o}$ represents the outlet temperature of the secondary hot water.

5. CONCLUSIONS

As important waste heat recovery and heat transformation devices, AHEs have been used in more and more real applications, especially to realize un-matching heat transfer problem. Several real applications of AHEs are concluded in this paper, these are:

1. Using the first type of AHE combined AHP system to recover the waste steam heat of CHP plants to significantly decrease the entransy dissipation of common systems, which can make the supply heat increased 30% and the heat transportation ability of the primary hot water network increased 60%.
2. Using the two types of AHEs to realize low grade heat long distance transportation, which can applied in backpressure CHP plants to decrease the backpressure to generate more electricity, the swimming pool nuclear reactor heating systems and so on, the TTD of the primary hot water can be amplified to 1.5~2 times of that for common systems
3. Using the first type of AHE to realize industry fast cooling system, which can make the mechanical chiller be cancelled and just using cooling tower to save the electricity.
4. Different scales of AHEs have been developed and applied in real projects, from the testing results, the temperature efficiency of the developed AHEs was reaching 1.26~1.36, which indicates good performance of the developed devices.

ACKNOWLEDGEMENTS

The authors gratefully acknowledge the support from the National Natural Science Foundation of China (grant numbers 51306098, 51138005), the innovative Research Groups of National Natural Science Foundation of China (grant number 51521005), and Tsinghua University Initiative Scientific Research Program (No. 20151080470).

NOMENCLATURE

AHE Absorption heat exchanger
AHP Absorption heat pump

subscripts
I The first type of AHE

CHP	Combined heating and power	*II*	The second type of AHE
K	Amplifying factor	*1*	Primary hot water
m	flow rate ratio	*2*	Secondary hot water
TTD	Transportation temperature difference (K)	*in*	inlet
t	temperature (℃)	*o*	outlet
ε	Temperature efficiency		

REFERENCES

Building Energy Research Centre, Tsinghua University, 2015. Annual Report of China Building Energy Efficiency. Beijing, China Architecture & Building Press 2-10,44-46.

Fang, H., Xia, J.J., Zhu, K., et al, 2013. Industrial waste heat utilization for low temperature district heating. Energy Policy 62, 236-246.

Fu, L., Jiang, Y., Zhang, S.G., 2008. District heating system of CHP plants based on co-ah cycle. J Tsinghua Univ (Sci & Tech) 48(9): 1377-1380,1412.

Guo, Z.Y., Liu, X.B., Tao, W.Q., et al, 2010. Effectiveness–thermal resistance method for heat exchanger design and analysis. International Journal of Heat and Mass Transfer 53(13-14): 2877-2884.

Li, Y., Fu, L., Zhang, S.G., et al, 2011. A new type of district heating method with co-generation based on absorption heat exchange (co-ah cycle). Energy Conversion and Management 52(2), 1200-1207.

Sun, J., Fu, L., Sun, F.T., et al, 2014. Experimental study on a project with CHP system basing on absorption cycles. Applied Thermal Engineering 73(1): 732-738.

Xie, X.Y., Jiang,Y.,2017. Absorption heat exchangers for long-distance heat transportation. Energy, 141, 2242-2250.

Manuscript ID: 1715
DOI:10.18462/iir.icr.2019.1715

Effect of surface roughness on heat transfer in a thermal energy storage system employing microencapsulated phase change material slurry

Othman F. ALASFOOR[(a)], S.A. SHERIF[(b)]

[(a)] University of Florida
Gainesville, FL 32611-6300, USA, ofalasfoor@ufl.edu
[(b)] University of Florida
Gainesville, FL 32611-6300, USA, sasherif@ufl.edu

ABSTRACT

This study examines the effect of surface roughness on the heat transfer efficiency factor in a thermal energy storage system employing microencapsulated phase change material (MEPCM) slurry. The heat transfer efficiency factor is defined as the mean Nusselt number ratio for a MEPCM slurry with and without surface roughness. The model employed is applicable to a laminar and hydrodynamically fully developed MEPCM slurry flowing inside a tube using a two-dimensional convective heat transfer model. The surface roughness effect was incorporated into the model using a surface enlargement function defined as the surface area ratio of a MEPCM with and without surface roughness. A range of surface enlargement values were used to calculate the heat transfer efficiency factor under a host of conditions. Results show that as the surface roughness of the MEPCM's increases, the heat transfer efficiency factor decreases. This result emphasizes the need to incorporate surface roughness into MEPCM slurry models in order to avoid over-predicting the heat transfer rate in such systems.
Keywords: Energy Efficiency, Energy Storage, Heat Transfer, Nusselt Number, Phase-Change Material, Roughness, Suspension, Thermal Storage.

1. INTRODUCTION

It is estimated that in 2030, solar energy will be able to cover 50% of low and medium temperature heating demand within Europe (Heating, 2009). Solar thermal collectors are among the many components employed for heat collection in a solar energy system (Serale et al., 2015; Serale et al., 2016). Solar collectors have been a topic of research and development for a very long time (Hottel and Woertz, 1942). Unfortunately, one of the main difficulties facing the widespread utilization of solar thermal collectors is finding more effective means to store thermal energy.

Energy storage in general can be utilized to reduce or eliminate peaks of electricity demand during peak operating hours (Delgado et al., 2012). Electric energy storage and hydro storage are among the most common forms of energy storage that are currently available with many studies to back them up. Thermal energy storage is also among those main forms of energy storage and it has many promising benefits and various potential thermal energy applications. Thermal energy storage is either available as sensible heat storage or latent heat storage. Currently, latent heat storage is receiving so much attention due to its advantages that include having higher thermal storage capacity along with its ability to store heat within a relatively small temperature range because of phase change (Goel et al., 1994).

These latent energy storage systems use phase changing materials (PCMs) for thermal storage. Many studies have been conducted to improve PCMs and one of the means of improvement is to encase them in protective capsules. These capsules serve the purpose of improving heat transfer by increasing the surface area and preventing the PCM from leaking when existing in the liquid phase, thus making it a lot easier to handle (Nomura et al., 2015; Telkes, 1980). Additional improvement to the heat transfer can be achieved by microencapsulating the PCM which would make it possible to mix the latter with a carrier fluid. This will make them usable as a heat transfer

fluid in a large number of applications (Nomura et al., 2015). These fluids are called suspensions or slurries and they combine the advantages of both heat transfer and energy storage media (Charunyakorn et al., 1991) because of the phase changing materials contained within them and because of the fact that during phase change, these slurries have a much higher specific heat than single phase fluids (Hu and Zhang, 2002). Slurries can also help reduce pumping power due to their higher heat capacity (Kasza and Chen, 1982). Higher heat capacities will help transport larger amounts of heat with smaller flow rates, and hence smaller pumping power. Many studies have been done to understand the heat transfer behavior of such slurries for different materials and conditions (Roy and Sengupta, 1991) both experimentally (Goel et al., 1994) and numerically (Charunyakorn et al., 1991; Hu and Zhang, 2002; Zhang and Faghri, 1995; Zhang et al., 2003). They resulted in promising improvements and deeper understanding of this field along with many potential applications that are in need of such technologies including solar energy (Serale et al., 2015; Serale et al., 2016), HVAC (Wang and Niu, 2009) and heat exchangers (Gschwander et al., 2005; Hu and Zhang, 2002).

The main purpose of the study upon which this paper partly reports is to look at the problem of modelling the heat transfer behavior of microencapsulated phase change material slurries by examining the effect of surface roughness of the micro particles in the slurry. The effect of surface roughness on heat transfer has become an interesting field of research and is gaining popularity among researchers. Many studies have already been done to investigate surface roughness effect with insightful results (Achenbach, 1977; Dierich and Nikrityuk, 2013). Existing theoretical models are expected to explain physical behavior, but one of the factors that seems to have been neglected in many of these models is the surface roughness of the object being studied and how it could increase the overall surface area of that object, thus affecting its heat transfer characteristics (Dierich and Nikrityuk, 2013, 2010) In this work, an attempt will be made to quantify the effect of surface roughness on the heat transfer characteristics

2. ANALYSIS

The model used in this study to numerically simulate the forced convective heat transfer of a microencapsulated phase change material (MEPCM) slurry, as demonstrated in Figure 1 and Figure 2, is based on the combined work of (Charunyakorn et al., 1991) along with that of (Alisetti and Roy, 2000) and (Zhang et al., 2003) regarding the effective specific heat model and the modified Nusselt number. The model was then coupled with the approach of (Dierich and Nikrityuk, 2013) to incorporate the effect of the thickness of the roughness layer.

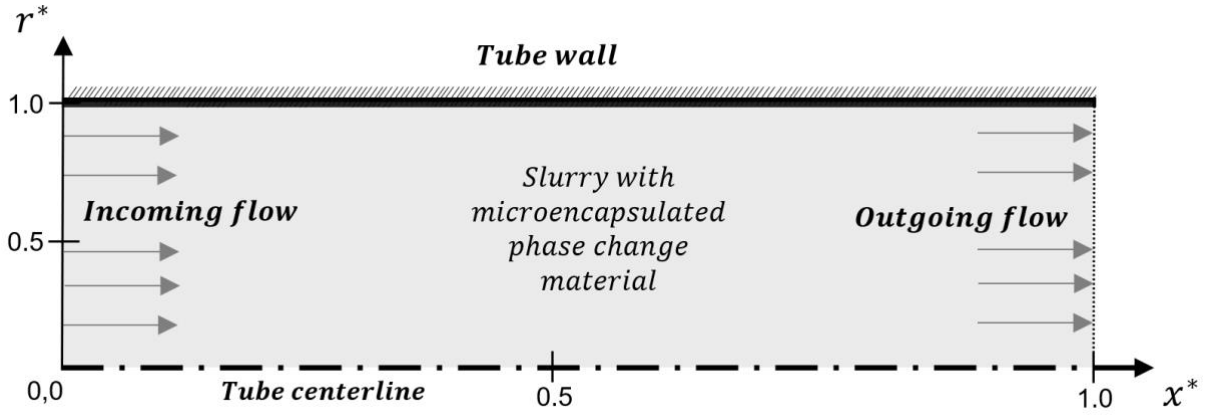

Figure 1: Slurry with microencapsulated phase change material flowing inside a tube.

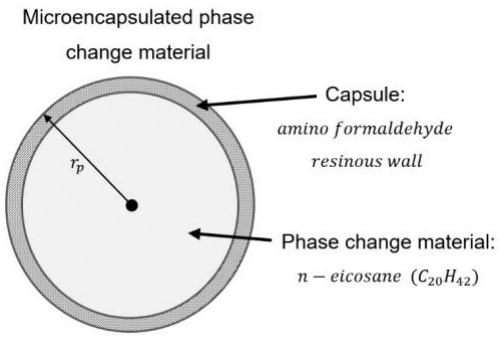

Figure 2: Microencapsulated phase change material particle.

The model employs the following assumptions (Zhang et al., 2003): (a) incompressible fluid; (b) continuum; (c) nuclear, electromagnetic and radiation energy transfers are neglected; (d) the slurry is flowing in a circular tube in fully developed flow; (e) phase change occurs between the temperatures T_1 and T_2; (f) the volumetric concentration is kept below 25% to ensure the validity of the Newtonian fluid assumption (Rutgers, 1962) and (Charunyakorn et al., 1991); (g) $T_i \leq T_1$; (h) uniform distribution of the micro particles in the slurry; (i) both axial conduction and viscous dissipation are neglected; (j) no heat generation in the flow; (k) all thermophysical properties are constant except the specific heat which is temperature-dependent during phase change; (l) the MEPCM slurry is homogeneous but the thermal conductivity is a function of the local shear and varies across the flow; and (m) the drag effect due to the micro particle surface roughness is neglected (Dierich and Nikrityuk, 2013). The two-dimensional steady state energy equation is used in cylindrical coordinates (x, r) as given by (Zhang et al., 2003)

$$\rho_b C_{p,b}\left(u\frac{\partial T}{\partial x}\right)=\frac{1}{r}\frac{\partial}{\partial r}\left(rk_e\frac{\partial T}{\partial r}\right) \qquad \text{Eq.(1)}$$

With the following boundary conditions, $T|_{x=0}=T_i$, $\left.\frac{\partial T}{\partial r}\right|_{r=0}=0$ and $T|_{r=r_0}=T_w$. The effective thermal conductivity of the slurry k_e (Charunyakorn et al., 1991) is calculated using k_b from Maxwell's relation (Maxwell, 1954) as given by

$$k_b=k_f\cdot\frac{2+\frac{k_p}{k_f}+2c\left(\frac{k_p}{k_f}-1\right)}{2+\frac{k_p}{k_f}-c\left(\frac{k_p}{k_f}-1\right)} \qquad \text{Eq.(2)}$$

The conductivity enhancement factor f (Charunyakorn et al., 1991) is given by

$$\begin{cases} f=1+BcPe_p^m=1+\left\{Bc\ 8^m\left[Pe_f\cdot\left(\frac{r_{p0}}{r_0}\right)^2\right]^m\cdot(r^*)^m\right\} \\ Pe_p=\left[8\cdot Pe_f\cdot\left(\frac{r_{p0}}{r_0}\right)^2\cdot r^*\right], \quad Pe_f=\left(\frac{2r_0u_m}{\alpha_f}\right) \\ B=3.0, \quad m=1.5, \quad Pe_p<0.67 \\ B=1.8, \quad m=0.18, \quad 0.67\leq Pe_p\leq 250 \\ B=3.0, \quad m=\frac{1}{11}, \quad Pe_p>250 \end{cases} \qquad \text{Eq.(3)}$$

The modified Nusselt number is given by

$$Nu_x=\frac{h_m\cdot 2r_0}{k_b}=\frac{2r_0q_w^{"}}{k_b(T_w-T_i)} \qquad \text{Eq. (4)}$$

The dimensionless boundary conditions are

$$\theta|_{x^*=0} = 0\,, \qquad \left.\frac{\partial\theta}{\partial r_1}\right|_{r^*=0} = 0\,, \quad \theta|_{r^*=1} = 1 = \theta_w \qquad \text{Eq. (5)}$$

Thus, the dimensionless energy equation becomes

$$C_p^* \cdot \left(1 - r^{*2}\right) \cdot \frac{\partial\theta}{\partial x^*} = 2f\frac{\partial^2\theta}{\partial r^{*2}} + \frac{\partial f}{\partial r^*}\frac{\partial\theta}{\partial r^*} \qquad \text{Eq. (6)}$$

The correlation for variable specific heat during phase change (Alisetti and Roy, 2000) is given by

- $For\ \theta < M_L \quad or \quad \theta > M_L + M_r$

$$C_p^* = 1 \qquad \text{Eq. (7)}$$

- $For\ M_L \le \theta \le M_L + M_r$

$$C_p^* = 1 + \frac{\pi}{2}\left(\frac{1}{Ste \cdot M_r} - c_{mass} \cdot \frac{C_{p,s}}{C_{p,b0}}\right) \cdot sin\left(\pi \cdot \frac{\theta - M_L}{M_r}\right) \qquad \text{Eq. (8)}$$

The properties of water, microencapsulated phase change materials and slurry for different MEPCM concentrations are as reported by Goel et al. (Goel et al., 1994). Whereas the values of the relevant parameters are as reported by Zhang et al. (Zhang et al., 2003). The energy equation is solved using the finite difference method in MATLAB. The discretization of that equation is done according to the finite difference method using forward differencing in the axial direction and central differencing in the radial direction (Zhang et al., 2003) with a grid step of $\Delta x^* = 0.0005$ and $\Delta r^* = 0.025$. The modified Nusselt number is then used along with the dynamic viscosity ratio (Goel et al., 1994) and (Charunyakorn et al., 1991) to calculate the mean Nusselt number. The dynamic viscosity ratio is a correction factor used to account for the higher bulk viscosity of the slurry with the micro particles when compared to a slurry without the micro particles under the same conditions. The mean Nusselt number with the correction factor can be expressed as follows (Charunyakorn et al., 1991):

$$Nu_{av} = \left(\frac{\mu_b}{\mu_f}\right)^{0.14} \cdot \frac{1}{x^*}\int_0^{x^*} Nu_{x,m}\, dx^* \qquad \text{Eq. (9)}$$

The surface roughness effect can then be incorporated into the model by using the modified heat transfer efficiency factor E_f (Dierich and Nikrityuk, 2013). The latter quantity represents the ratio of the mean Nusselt number of the slurry with surface roughness Nu_{av} to that without the surface roughness Nu_{av}^0. The surface enlargement S_{ef} (Dierich and Nikrityuk, 2013) is the ratio of the surface area of the micro particle with surface roughness S_{rough} to that without surface roughness S_0. The surface roughness effect is then incorporated into the model using the following equation:

$$f = 1 + \left[Bc\ 8^m \left(S_{ef}\right)^m (r^*)^m\right] \qquad \text{Eq. (10)}$$

The behavior of the heat transfer efficiency factor E_f with the surface enlargement S_{ef} is then plotted for a range of values as will be discussed in the following section. This is done by repeatedly solving the model in MATLAB for each single value of the surface enlargement S_{ef} to get the corresponding value of the heat transfer efficiency factor E_f. The resultant plots will be shown to demonstrate how the change in the thickness of the roughness layer affects the mean Nusselt number and the convection heat transfer.

3. RESULTS

Fig. 3 shows contours of the dimensionless temperature of the slurry without the surface roughness effect as the slurry enters the tube with an inlet temperature and as it is subjected to heating under a constant tube wall temperature.

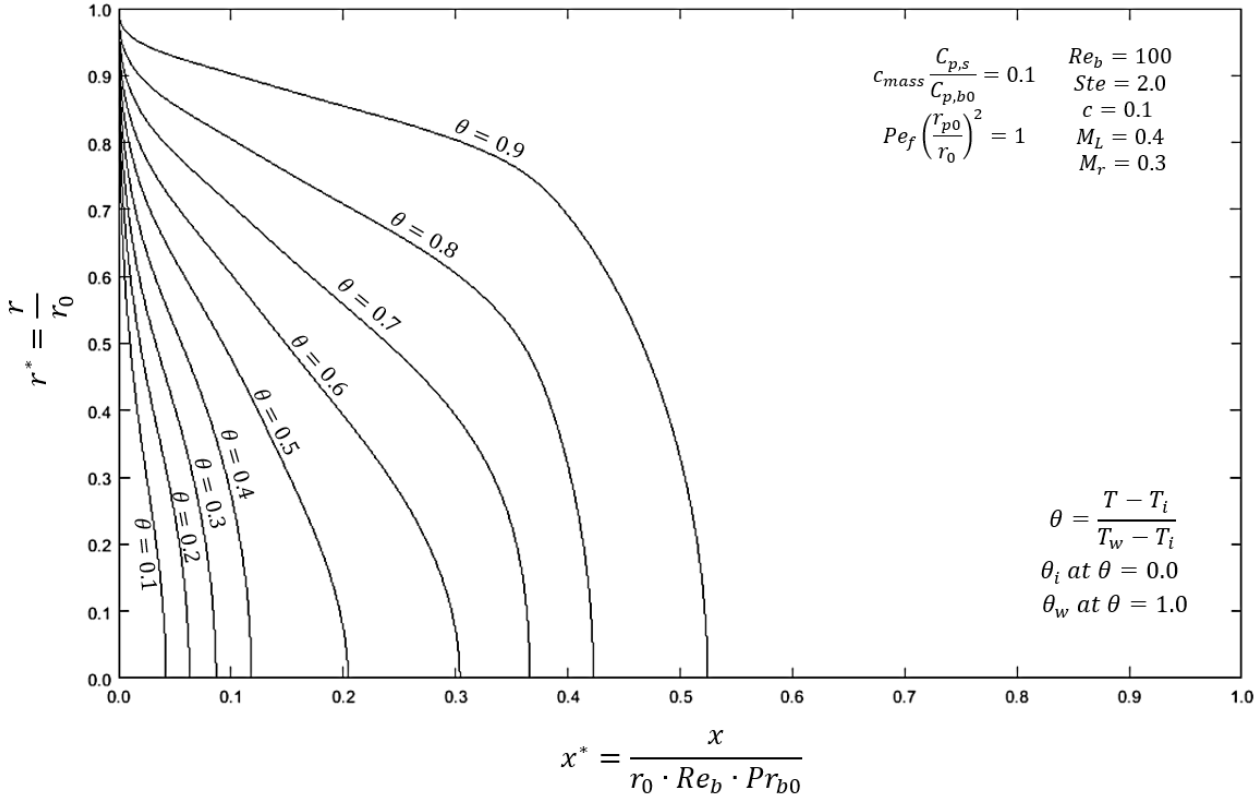

Figure 3: Contours of the dimensionless temperature θ as a function of x^* and r^*.

Fig. 4 displays a similar behavior to that reported by both Zhang et al. (Zhang et al., 2003) and Alisetti and Roy (Alisetti and Roy, 2000), with some differences in their respective results. Many qualification runs were conducted for the model presented in this work for different mesh sizes and boundary conditions, and higher-order finite differencing methods to investigate whether or not the differences observed among the three models are physical or are caused by non-physical effects. Quantitatively speaking, a calculated average difference of 27.8% was observed between the present model and that of Alisetti and Roy (Alisetti and Roy, 2000), while an average difference of 36.7% was observed relative to that of Zhang et al. (Zhang et al., 2003).

An explanation of the above differences can be given by further looking into the model used in this study by itself. This model can basically be viewed as a compilation of three modules. The first module pertains to how the model used by (Charunyakorn et al., 1991) treated the dimensionless energy equation [given by Eq. (6)], the definition of the dimensionless axial coordinate, the dynamic viscosity ratio which was used as a correction factor [see Eq. (9)], and the correlation used for the effective thermal conductivity k_e. The second module pertains to the effective specific heat model developed by Alisetti and Roy (Alisetti and Roy, 2000) as given by Eq. (8). Specifically, it pertains to incorporating the effect of phase change into the model. The third module pertains to using the approach developed by Zhang et al. (Zhang et al., 2003) for the modified Nusselt number as given by Eq. (4). Specifically, they used the modified Nusselt number along with the effective specific heat model developed by Alisetti and Roy (Alisetti and Roy, 2000) to numerically solve their problem. It is important to note that the modified Nusselt number reported by Zhang et al. (Zhang et al., 2003) was introduced to account for the fact that they used the inlet fluid temperature instead of the bulk mean temperature. Typically, the bulk mean temperature of the fluid incorporates the specific heat in its definition, which in this case is a variable quantity during the phase change process. Thus, their

attempt to avoid dealing with the bulk mean temperature to avoid the variability of the specific heat during the phase change process had to be somehow corrected for. Unfortunately, verification of the model was not possible because there are no available analytical solutions for the problem due to the complexity of the model (Alisetti and Roy, 2000). Also, the available experimental data for laminar flows are limited to the constant heat flux boundary condition case. Furthermore, whatever data that may be available should only be used for qualitative comparisons because the degree of subcooling for all the known experiments is not known in an exact way (Alisetti and Roy, 2000).

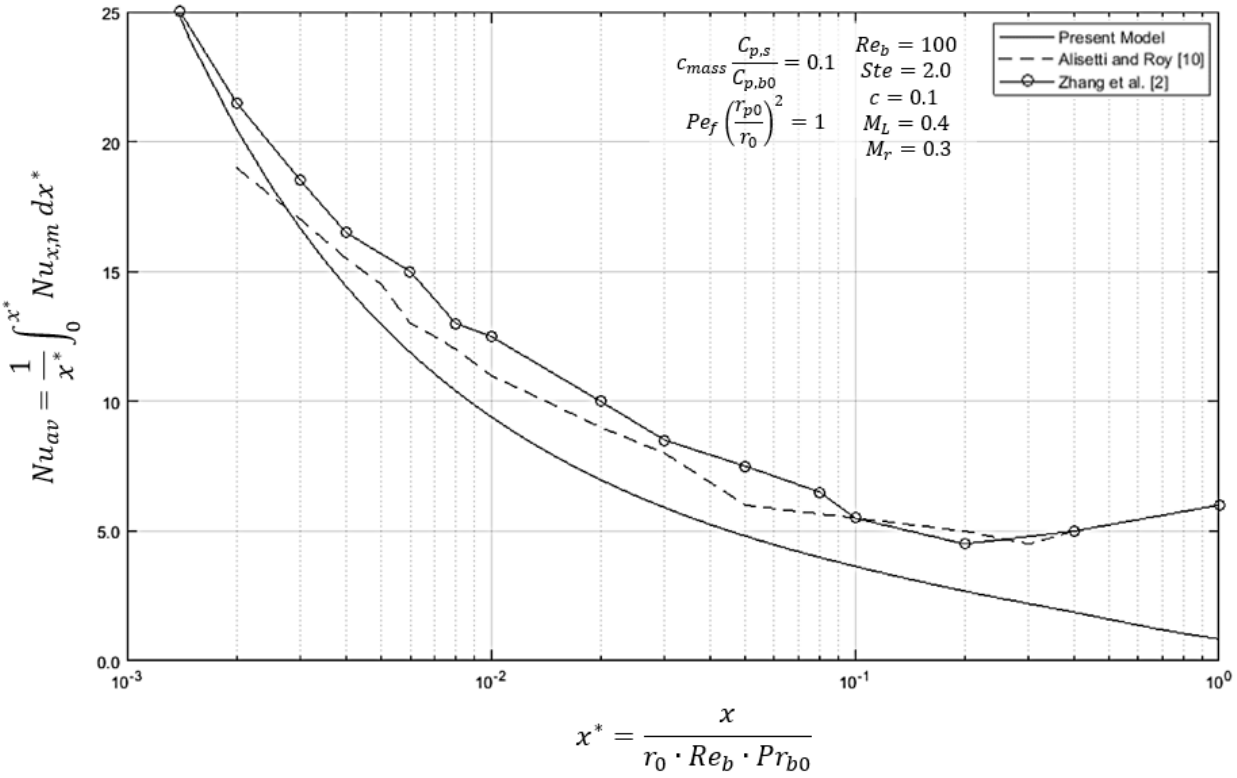

Figure 4: Comparison of model results with those of Alisetti and Roy (Alisetti and Roy, 2000) and Zhang et al. (Zhang et al., 2003)

The heat transfer efficiency factor which ranges from $0 \leq E_f \leq 1$ has been calculated for a range of values of the surface enlargement which ranges from $1 \leq S_{ef} \leq 1.5$ to quantify the behavior of the slurry. The results are shown in Fig. 5 and Fig. 6. As expected, the heat transfer efficiency factor E_f decreases as the surface enlargement S_{ef} increases. This means that the Nusselt number of the slurry with surface roughness is less than that of a slurry without surface roughness. The reason is related to the fact that for the case of the MEPCM slurry, the thermal conductivity is not constant and is represented by the effective conductivity, k_e. Also, the effective conductivity is related to the conductivity enhancement function f which was modified to include the surface roughness effect as in Eq. (10).

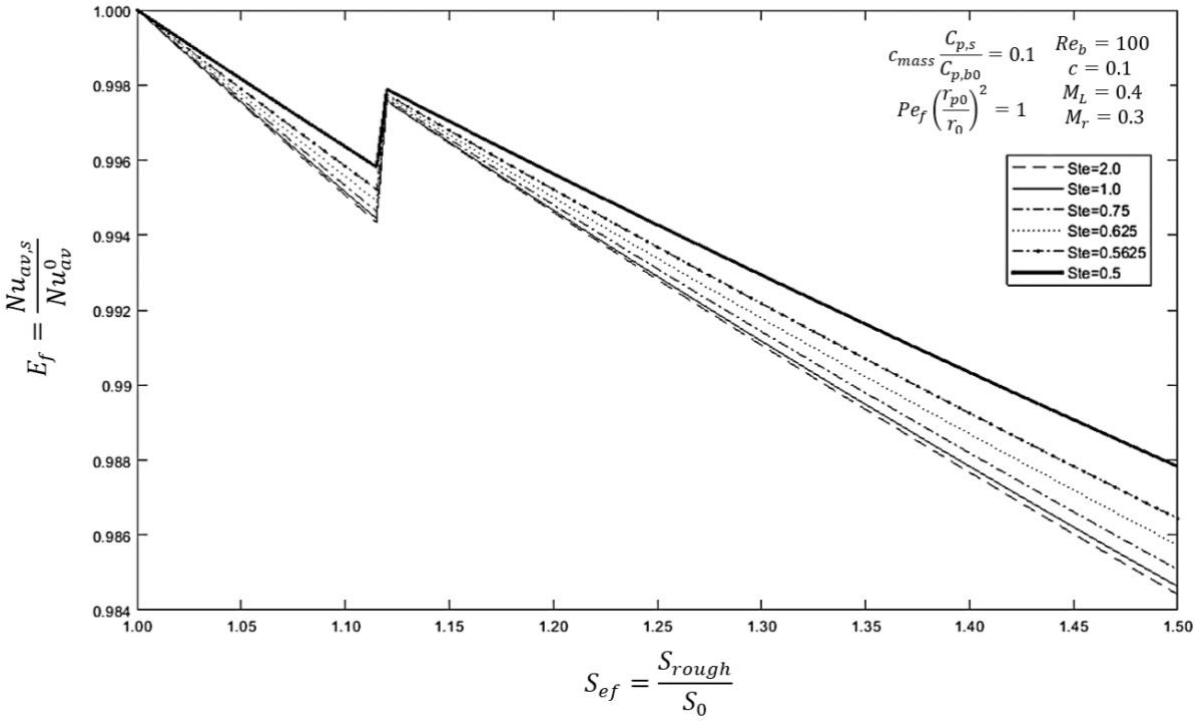

Figure 5: Effect of the Stefan number Ste on the heat transfer efficiency factor E_f as a function of the surface enlargement S_{ef}.

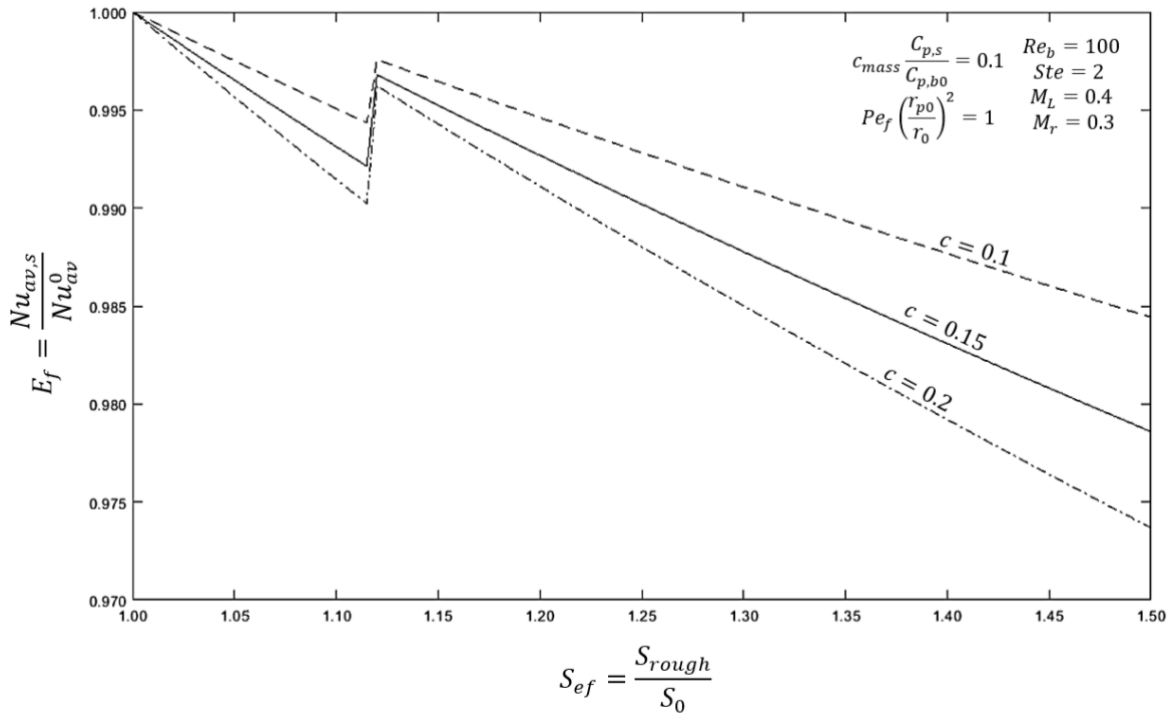

Figure 6: Effect of the volumetric concentration c on the heat transfer efficiency factor E_f as a function of the surface enlargement S_{ef}.

Fig. 7 shows how the values of the conductivity enhancement function f increase as the surface enlargement S_{ef} increases. An increase in the conductivity enhancement function results in an increase in the effective thermal conductivity k_e of the slurry, which in turn causes an increase in the heat transfer by conduction in the slurry. This results in a decrease in the value of the mean Nusselt number for the slurry with the surface roughness effect.

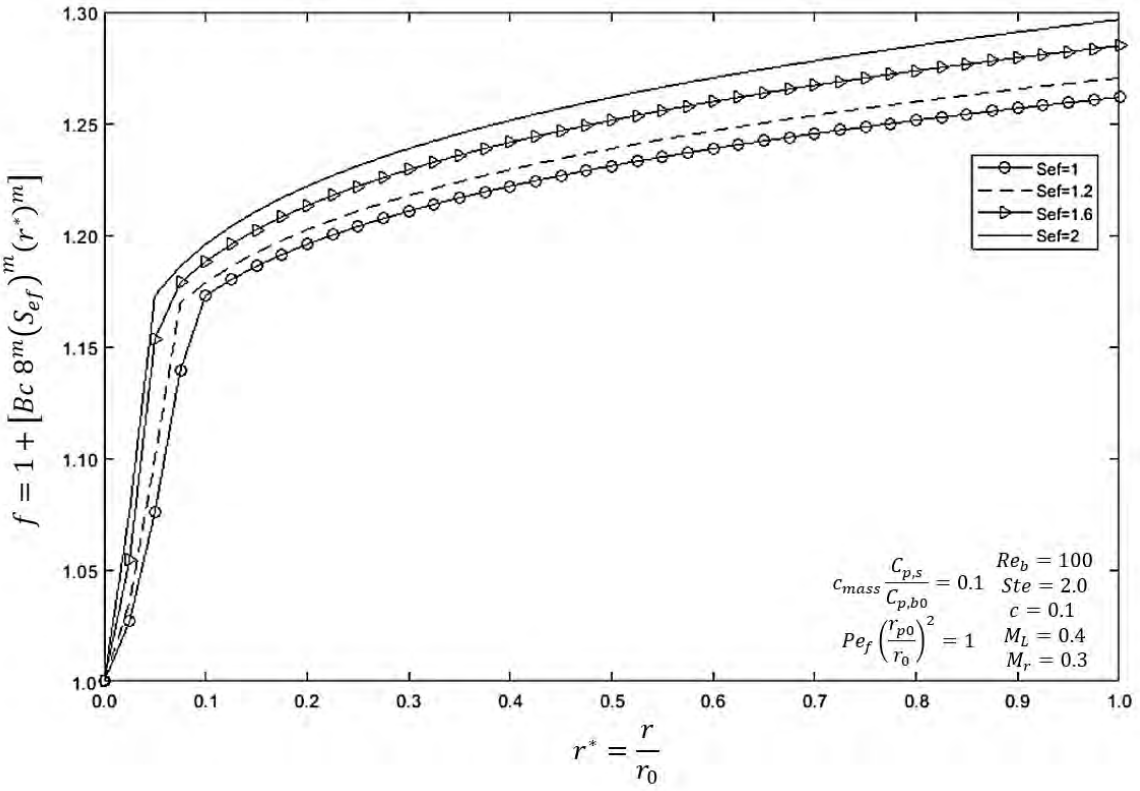

Figure 7: Effect of the surface enlargement S_{ef} on the conductivity enhancement function f.

The aforementioned behavior conforms with the behavior observed in the study conducted by (Dierich and Nikrityuk, 2013), despite the major differences in their analysis relative to that reported here. It is important to point out that the analysis of (Dierich and Nikrityuk, 2013) employed a different model and solution technique for the problem, and that their control surface was the cylindrical particle itself. This is fundamentally different than the control surface used here; namely the slurry with the suspended micro particles. Also, the heat transfer efficiency factor E_f used in their study was based on the surface averaged Nusselt number of the cylindrical particle which is different than the mean Nusselt number of the slurry employed here. The effect of changing different parameters on the heat transfer efficiency factor E_f has been investigated and plotted. The Stefan number Ste effect on the heat transfer efficiency factor E_f is shown in Fig. 5. Several Stefan number values were used and the results show that E_f reaches its lowest values for the case when $Ste = 2$. This signifies a much higher difference between the values of the mean Nusselt number of the slurry with surface roughness and the slurry without surface roughness.

The aforementioned behavior is caused by the fact the MEPCM particle consists of two parts, a capsule and a PCM core, as shown in Fig. 2. The PCM core is made of a phase changing hydrocarbon called $n - eicosane$ $(C_{20}H_{42})$ (Goel et al., 1994) that is more susceptible to be affected by latent heat than by the sensible heat. This is not the case for the capsule since it is made from an $amino\ formaldahide\ resinous\ wall$ that doesn't undergo phase change and therefore it is more susceptible to be affected by sensible heat than latent heat. Furthermore, the capsule wall is the part that is affected by the surface roughness which further increases its susceptibility to be affected by sensible heat (as opposed to latent heat). So, by combining both effects of a high Stefan number (Ste=2) relative to the other values, and increasing the surface roughness of the capsule wall, this will eventually cause a more profound reduction in the mean Nusselt number of the slurry with surface roughness which will eventually result in a much lower value of the heat transfer efficiency factor E_f as demonstrated in Fig. 5.

Figure 6 displays the effect of the volumetric concentration c on the heat transfer efficiency factor E_f. Three values of the volumetric concentration were used, $c = 0.1, c = 0.15\ and\ c = 0.2$. It appears that

E_f reaches its lowest values for the case with $c = 0.2$ which is a slurry with 20% concentration of MEPCM particles. This is caused by the fact the volumetric concentration c has a direct effect on the value of the conductivity enhancement function as given by Eq. (10). Also, as the concentration increases, f will also increase. This causes an increase in the thermal conductivity which further lowers the mean Nusselt number of the slurry. There is however what seems to be an abnormal behavior in both Fig. 5 and Fig. 6 where there is a sharp increase in the value of the heat transfer efficiency factor at approximately $S_{ef} = 1.12$. This behavior requires further investigation as it could be caused by the possible inability of the available models to fully simulate the behavior of the MEPCM slurry with the added surface roughness effect.

4. CONCLUSIONS

An investigation has been conducted to study the effect of the surface roughness of microencapsulated phase change materials (MEPCM) that are suspended in a slurry that is both laminar and hydrodynamically fully developed flowing inside a tube with a constant wall temperature. The main performance parameters in the study are the heat transfer efficiency factor E_f and the surface enlargement S_{ef}. The model described in this paper was developed incorporating the analyses of (Charunyakorn et al., 1991), (Zhang et al., 2003) and (Alisetti and Roy, 2000) for the MEPCM slurry along with the analysis of (Dierich and Nikrityuk, 2013) in incorporating the surface roughness effect. Verification of the model used in this study agrees qualitatively with (Zhang et al., 2003) and (Alisetti and Roy, 2000) but not quantitatively due to the differences between the models. However, the overall behavior of the main parameters were as expected and in line with those of (Dierich and Nikrityuk, 2013), despite the major differences in the analysis. The results showed that the heat transfer efficiency factor decreases as the surface enlargement increases. This means that as the surface roughness increases, the mean Nusselt number of the slurry decreases. The effect of the Stefan number and the volumetric concentration c on the heat transfer efficiency factor were also investigated and the results showed that the heat transfer efficiency factor reaches its lowest values when either or both Ste or c increase. This typically results in a further decrease in the mean Nusselt number of the slurry with the surface roughness.

The results reported here emphasize the importance of accounting for surface roughness effects. Not doing so risks over-predicting the heat transfer rate. This seems to have been a pervasive problem in a good number of past studies. Future studies should take surface roughness into their consideration in order to develop better models and get more realistic results. Also, more research should be done to develop specific geometric surface roughness models that could map the topography of the particle in order to find more accurate methods to incorporate the surface roughness effect in the heat transfer equations. Last but not least, more experimental studies should be done to present the actual values of the surface roughness layer and its thickness for various materials.

ACKNOWLEDGEMENTS

The authors would like to thank Dr. Siddharth Thakur, Dr. Ryan Houim and Dr. S. Moussa Mirehei. The authors are grateful to the support of the Department of Mechanical and Aerospace Engineering at the University of Florida. The first author acknowledges the financial support of the Government of Kuwait and Kuwait University in funding his graduate studies at the University of Florida.

NOMENCLATURE

Latin Symbols

c	volumetric concentration of micro particles	T	temperature (K)
c_{mass}	mass concentration of micro particles	T_1	lower phase change temperature limit (K)

C_p	specific heat (kJ×kg^{-1}×K^{-1})
C_p^*	dimensionless specific heat $C_p^* = \frac{C_{p,b}}{C_{p,b0}}$
E_f	heat transfer efficiency factor $E_f = \frac{Nu_{av}}{Nu_{av}^0}$
f	conductivity enhancement function
h_{fs}	phase change material latent heat of fusion (kJ×kg^{-1})
h_m	modified convective heat transfer coefficient
k	thermal conductivity (W×m^{-1}×K^{-1})
k_e	effective thermal conductivity of slurry (W×m^{-1}×K^{-1}) $k_e = f k_b$.
$\mathrm{M_L}$	dimensionless initial subcooling $M_L = \frac{T_1 - T_i}{T_w - T_i}$
$\mathrm{M_r}$	dimensionless phase change temperature range $M_r = \frac{T_2 - T_1}{T_w - T_i}$
$\mathrm{Nu_{x,m}}$	modified local Nusselt number
$\mathrm{Nu_{av}}$	mean Nusselt number
$\mathrm{Nu_{av,s}}$	mean Nusselt number with surface roughness effect
$\mathrm{Nu_{av}^0}$	mean Nusselt number without surface roughness effect
Pe	Peclet number
Pr	Prandtl number $Pr_{b0} = \frac{\nu_b}{\alpha_{b0}} = \frac{\rho_b C_{p_{b0}} \nu_b}{k_b}$
r	radial coordinate (m)
r_0	tube radius (m)
r_p	micro particle radius (m)
r_{p0}	micro particle radius without surface roughness (m)
r_{ps}	micro particle radius with surface roughness (m)
r^*	dimensionless radial coordinate $r^* = \frac{r}{r_0}$
Re	Reynolds number $Re_b = \frac{2 r_0 u_m}{\nu_b}$
S_{ef}	surface enlargement $S_{ef} = \frac{S_{rough}}{S_0} = \left(\frac{r_{ps}}{r_{p0}}\right)^2$
S	surface area (m^2) $S = 4\pi r^2$
Ste	Stefan number
S_0	micro particle surface area without surface roughness (m^2)
S_{rough}	micro particle surface area with surface roughness (m^2)
T_2	upper phase change temperature limit (K)
T_i	Inlet temperature of slurry (K)
u	axial velocity (m×s^{-1}) $u = 2u_m\left[1 - \left(\frac{r}{r_0}\right)^2\right]$
u^*	dimensionless axial velocity $u^* = \frac{u}{u_m}$
x	axial coordinate, m
x^*	dimensionless axial coordinate $x^* = \frac{x}{r_0 \cdot Re \cdot Pr_{b0}}$

Greek Symbols

α	thermal diffusivity (m^2×s^{-1})
θ	dimensionless temperature $\theta = \frac{T - T_i}{T_w - T_i}$
μ	dynamic viscosity (N×s×m^{-2})
ν	kinematic viscosity (m^2×s^{-1})
ρ	Density (kg×m^3)

Subscripts

b	bulk fluid (slurry)
$b0$	slurry without phase change
l	liquid
s	solid
f	suspending fluid
p	microcapsule particle
w	tube wall
x	local
m	modified
ps	particle with surface roughness
$p0$	particle without surface roughness
e	effective

Superscripts

*	Dimensionless
0	Without surface roughness effect

REFERENCES

Alisetti, E. L., Roy, S. K., 2000, Forced convection heat transfer to phase change material slurries in circular ducts. Journal of Thermophysics and Heat Transfer, 14(1), 115-118.

Charunyakorn, P., Sengupta, S., Roy, S., 1991, Forced convection heat transfer in microencapsulated phase change material slurries: flow in circular ducts. International journal of heat and mass transfer, 34(3), 819-833.

Delgado, M., Lázaro, A., Mazo, J., Zalba, B., 2012, Review on phase change material emulsions and microencapsulated phase change material slurries: materials, heat transfer studies and applications. Renewable and Sustainable Energy Reviews, 16(1), 253-273.

Dierich, F., Nikrityuk, P., 2013, A numerical study of the impact of surface roughness on heat and fluid flow past a cylindrical particle. International Journal of Thermal Sciences, 65, 92-103.

Dierich, F., Nikrityuk, P., 2010, A numerical study of the influence of surface roughness on the convective heat transfer in a gas flow. Computer Modeling in Engineering & Sciences(CMES), 64(3), 251-266.

Goel, M., Roy, S. K., Sengupta, S., 1994, Laminar forced convection heat transfer in microcapsulated phase change material suspensions. International journal of heat and mass transfer, 37(4), 593-604.

Gschwander, S., Schossig, P., Henning, H.-M., 2005, Micro-encapsulated paraffin in phase-change slurries. Solar Energy Materials and Solar Cells, 89(2-3), 307-315.

Heating, S., 2009, Cooling for a Sustainable Energy Future in Europe (Revised). European Solar Thermal Technology Platform (ESTTP).

Hottel, H., Woertz, B., 1942, Performance of flat-plate solar-heat collectors. Trans. ASME, 64.

Hu, X., Zhang, Y., 2002, Novel insight and numerical analysis of convective heat transfer enhancement with microencapsulated phase change material slurries: laminar flow in a circular tube with constant heat flux. International journal of heat and mass transfer, 45(15), 3163-3172.

Kasza, K. E., Chen, M. (1982). *Development of enhanced heat transfer/transport/storage slurries for thermal-system improvement*. Retrieved from

Maxwell, J. C., 1954, A Treatise on Electricity and Magnetism. (3rd Edn), I, 440-441,.

Nomura, T., Zhu, C., Sheng, N., Saito, G., Akiyama, T., 2015, Microencapsulation of metal-based phase change material for high-temperature thermal energy storage. Scientific reports, 5, 9117.

Roy, S. K., Sengupta, S., 1991, An evaluation of phase change microcapsules for use in enhanced heat transfer fluids. International communications in heat and mass transfer, 18(4), 495-507.

Rutgers, I. R., 1962, Relative viscosity of suspensions of rigid spheres in Newtonian liquids. Rheologica Acta, 2(3), 202-210.

Serale, G., Fabrizio, E., Perino, M., 2015, Design of a low-temperature solar heating system based on a slurry Phase Change Material (PCS). Energy and Buildings, 106, 44-58.

Serale, G., Goia, F., Perino, M., 2016, Numerical model and simulation of a solar thermal collector with slurry Phase Change Material (PCM) as the heat transfer fluid. Solar Energy, 134, 429-444.

Telkes, M. (1980). Phase change thermal storage materials with crust forming stabilizers. In: Google Patents.

Wang, X., Niu, J., 2009, Performance of cooled-ceiling operating with MPCM slurry. Energy Conversion and Management, 50(3), 583-591.

Zhang, Y., Faghri, A., 1995, Analysis of forced convection heat transfer in microencapsulated phase change material suspensions. Journal of Thermophysics and Heat Transfer, 9(4), 727-732.

Zhang, Y., Hu, X., Wang, X., 2003, Theoretical analysis of convective heat transfer enhancement of microencapsulated phase change material slurries. Heat and Mass Transfer, 40(1-2), 59-66.

Manuscript ID: 1750
DOI: 10.18462/iir.icr.2019.1750

Performance improvement of a residential heat pump water heater by modifying stratification of water temperature

Ce SHI[(a)], Pega HRNJAK[(a)(b)]

[(a)] Department of Mechanical Science and Engineering,
University of Illinois at Urbana-Champaign
1206 West Green Street, Urbana, IL 61801, United States
Phone: (217) 721-1755, Email: ces3@illinois.edu
[(b)] Creative Thermal Solutions, Inc., 2209 N Willow Rd, Urbana, IL, 61802, United States
Phone: (217) 721-1755, Email: pega@illinois.edu

ABSTRACT

This paper presents experimental operation of a heat pump water heater (HPWH) at various draw rates to investigate the effect of tank stratification on system performance.
Measurements are made both on refrigerant and water sides. Exergy analysis and mixing coefficient were introduced to characterize tank stratification. Performance is evaluated based on COPsys and recovery efficiency as measures. Results show that with increase of draw rate, stratification worsens causing higher condensing temperature, which results to lower system performance.
Three-Dimensional Computational Fluid Dynamics (CFD) method was introduced to describe and explore the thermal tank numerically. The results from experiments for effect of draw rate on stratification agrees with CFD results.
Performance of HPWHs is strongly influenced by the thermal stratification in the water tank. Destratification and mixing is more pronounced as draw rate increases. Improvement options are discussed that can improve performance with asymptotic approach to a perfectly stratified tank.
Keywords: CFD, COP, Entropy, Exergy, Heat Pump Water Heater, Mix, Stratification.

1. INTRODUCTION

Heat pump water heaters (HPWHs) are increasingly used for residential heating applications. They offer higher efficiency than conventional electric resistance water heaters and reduce the energy consumption. Therefore, HPWH is a more environmentally friendly surrogate for residential heating. Numerous research has been conducted on the performance of HPWHs with various complex parameters, such as the working fluid, tank size, water draw flow rate, heat exchangers, etc. Various analysis approach has been developed, such as the entropy generation, exergy loss and energy analysis, for individual components as well as the whole HPWH system.
One of the questions is to find a good design on the tank side that would provide good efficiency at various user patterns. After certain amount of hot water has been used and replaced with cold water at a certain flow rate, it is of interest to investigate how much electricity is needed to bring the water temperature in the tank back to the temperature before consumption and how the water usage amount and the draw rate affect the energy efficiency.

2. EXPERIMENTATION

2.1 Experimental Facility

Fig. 1 and Fig. 2 illustrate a schematic drawing of the HPWH system and the experimental setup. It is a modified facility from Li and Hrnjak (2018). The experimental facility is instrumented on the base of a residential heat pump water heater unit, which contains an evaporator, a low-pressure side accumulator, a back pressure reciprocating compressor, an electronic expansion valve, a wrap-around coil condenser, and a water tank. R134a was chosen as the refrigerant and POE 22 is used for the compressor. The condenser has two parallel aluminium coil tubes which are wrapped around

the stainless-steel tank wall. The capacity of the water tank is 250 liters.

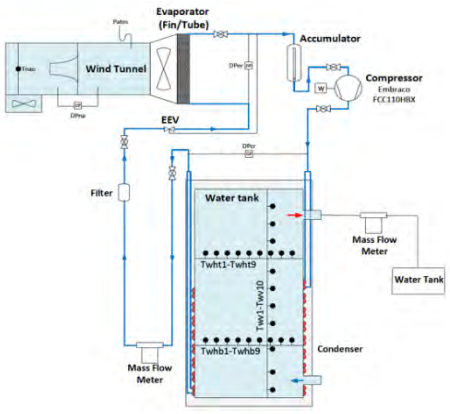

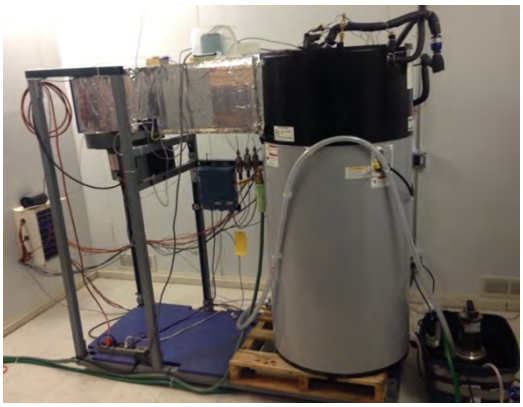

Figure 1: Schematic drawing of the HPWH system

Figure 2: Experimental Setup



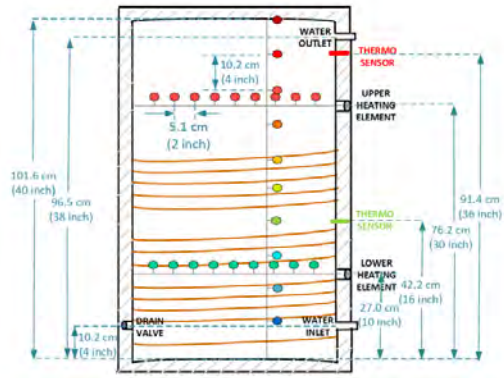

Figure 3: Thermo sensors and heating elements in the HPWH

Figure 4: Locations of various elements

Fig. 3 shows the original design for this HPWH unit contains two immersed electric resistance heating elements to operate instead of heat pump system when demand or temperature difference exceeds ability of the heat pump to supply hot water. For research purpose, the heating elements have been removed, so that the water heating process only depends on the vapor-compression cycle.

Fig. 4 shows that 28 Thermocouples are put in the water tank to monitor the temperature change during the operation, 10 of them are placed vertically with 10cm interval, rest are placed horizontally at two levels: 27 and 76cm above the bottom.

2.2 Experimental Procedures

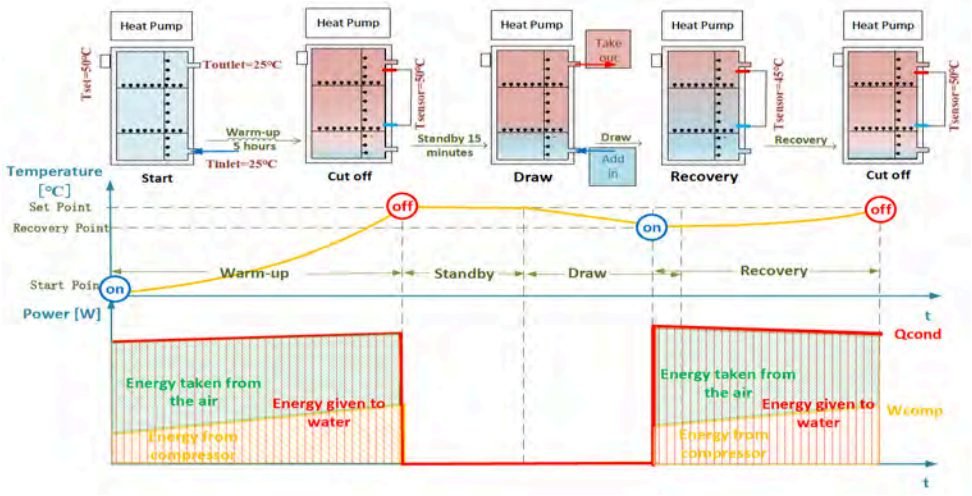

Figure 5: Experimental procedures

Fig. 5 shows the experimental procedures. First, fill the tank with cold water at 25℃, set the set-point at 50℃. Then run the heat pump until it cut off automatically. A 15-minute standby period is followed by a given gallon water draw with constant draw rate, at the same time refill the tank with cold water to keep tank full at all time. During the draw period, when the sensor temperature decreases to the recovery point, the heat pump automatically restarts by its controller, the system heats up until it reaches to the set point and shuts off again.

2.3 Methods for Characterizing Tank Mixing

The stream of cold water entering the hot storage tank through the inlet port causes turbulent mixing and entrainment of surrounding region close to the tank entrance, even when the water is being charged at a relatively low velocity.

Mixing with different temperatures always results in entropy generation and exergy loss (Haller et al., 2010). When storage tank is maintaining better stratification, less entropy and exergy loss is generated (Haller et al., 2010). Therefore, entropy generation and exergy loss have been conducted here to characterize the "usefulness" of the energy stored in the tank. The specific exergy can be quantified according to the Eq. (1) and (2). And the values for each of the ten thermocouples were summed up to represent the exergy stored in the tank.

$$s_{tank} = \sum_{i=1}^{n} s_i = \sum_{i=1}^{n} \frac{Q}{T_i} \quad \text{Eq. (1)}$$

$$E_{x\,tank} = \sum_{i=1}^{n} E_{xi} = \sum_{i=1}^{n} (h_i - h_0) - T_0\,(s_i - s_0) \quad \text{Eq. (2)}$$

Mixing causes the loss of capacities during the draw period. Mixing coefficient is defined to express two dimensionless numbers, Richardson and Reynolds number, as it shown in Eq. (3) and (4). A higher mixing coefficient indicates greater mixing in the thermal storage tank (Nelson, et al., 1999).

$$Z = 1.688\times10^{4}\left(\frac{Re}{Ri}\right)^{0.67} \quad \text{Eq. (3)}$$

$$Ri = \frac{g\beta(T_{initial} - T_{inlet})L}{v^2} \quad \text{Eq. (4)}$$

Where, Ri is the convection Richardson number that is calculated from the temperatures, *v* is the bulk flow velocity and Re is the Reynolds number which is based on the average velocity of the flow.

2.4 Methods for Evaluating System Recovery Performance

Industry defined "Recovery Efficiency" to evaluate the recovery performance from the water side:

$$\eta_{recovery} = \frac{Energy\ in\ the\ water\ delivered\ at\ outlet}{Electricity\ input\ to\ HPWH\ system} = \frac{M_{draw}C_{p,r}(\overline{T}_{out} - \overline{T}_{in})}{W_{comp} + W_{auxiliary}} \quad \text{Eq. (5)}$$

At the same time, COP_{system} is defined as the ratio of condensing capacity and electricity input to HPWH system.

$$COP_{system} = \frac{Condensing\ capacity}{Electricity\ input\ to\ HPWH\ system} = \frac{Q_{cond}}{W_{comp} + W_{auxiliary}} \quad \text{Eq. (6)}$$

2.5 Effect of Draw Rate on System Performance

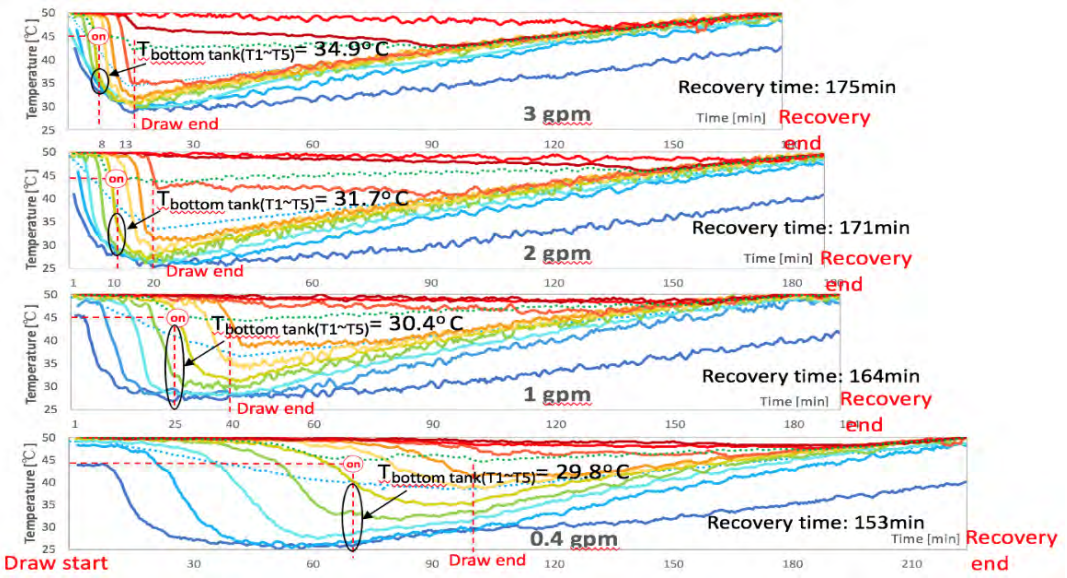

Figure 6: Vertical temperature measured by constant 152 l draw amount indicates a warmer bottom tank with higher draw rate when compressor restarts

Fig. 6 shows the temperature change by constant draw amount with different draw rate changing from 25 to 189 g/s. It indicates that longer time is required to recover the temperature at increasing draw rate. When the compressor starts, a warmer bottom tank is achieved at higher draw rate.
Fig. 7 indicates that the condensing temperature could be affected by the bottom tank condition. The higher draw rate that remains a warmer bottom tank temperature results to a higher condensing temperature.

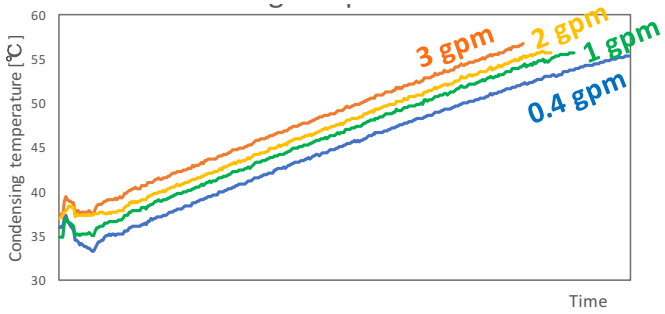

Figure 7: The warmer bottom tank results to a higher condensing temperature

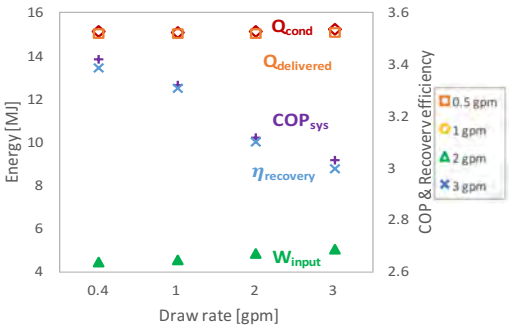

Figure 8: HPWH performance decrease (14%) with the increase of draw rate from 25 to 189 g/s (0.4 to 3 gpm)

Fig. 8 again indicates the two evaluations COPsys and recovery efficiency coincide well with each other. It shows that with the same water draw amount, the energy delivered at the outlet remains unchanged, so the system performance depends on how much electricity it used during the recovery period. With higher condensing temperature, the compressor draws more power, we could see there is a 14% recovery efficiency decrease from 25 to 189 g/s which means that in order to bring the tank water back to the same condition as at the beginning, more electricity need to be used at higher draw rate.

2.6 Effect of Draw Rate on Mixing in Thermal Storage Tank

When adding same amount of cold water into the storage tank at different draw rate, each tank obtains the same internal energy. However, on a charge perspective, the tank with higher draw rate would achieve greater entropy generation and exergy due to the mixing. F. 9 illustrates the entropy generation and exergy loss at different draw rate from 20 liters to 140 liters of the draw.
It shows that the entropy increases and entropy decreases with the increment of draw rate, which indicates when drawing the same amount of water faster, more stratification would be destroyed and greater mixing happens in the storage tank. Furthermore, this trend becomes more obvious with higher draw amount, entropy generates from 0.8% at 20 liters to 6% at 140 liters, while exergy losses from 1.1% at 20 liters to 12.2% at 140 liters.

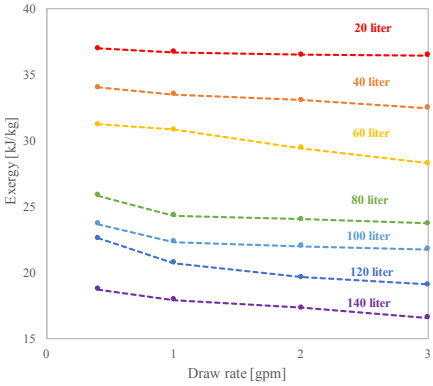

Figure 9: Higher draw rate causes more exergy loss

Richardson number indicates the importance of natural convection relative to the forced convection. Lower Richardson number represents that the natural convection is negligible while larger Richardson number indicates forced convection can be neglected. In the HPWH storage tank, stratification is driven by the natural convection, and the inlet jet flow results in forced convection in the thermal tank. Figs. 10 and 11 illustrates the Richardson number and mixing coefficient among the tank height at different draw rate from 25 to 189 g/s (0.4 gpm to 3 gpm). It could be found that higher draw rate obtains lower Richardson number and higher mixing coefficient, which indicates worse stratification and greater mixing. Furthermore, compared with bottom tank level, the upper tank obtains higher Richardson number as well as lower mixing coefficient, hence the upper tank remains lower mixing and better stratification since the inlet jet is located at the tank bottom.
When focusing on one certain draw rate, it could be noted that during the draw period at constant draw rate, the mixing in the lower tank level increases with the draw amount while the upper tank remains almost the same.

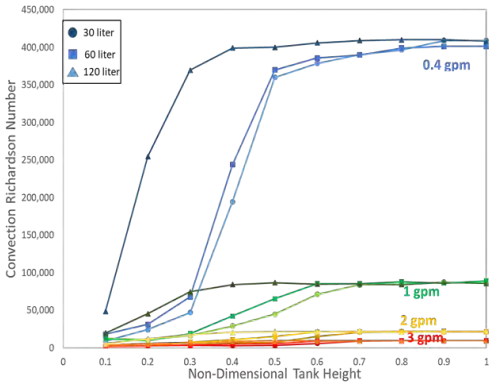

Figure 10: Lower Richardson number with draw rate indicates greater mixing in the storage tank

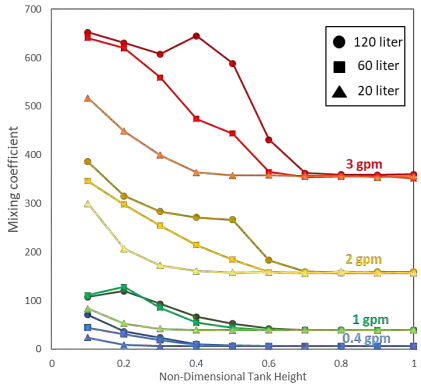

Figure 11: Higher mixing coefficient with draw rate indicates greater mixing in the storage tank

3. NUMERICAL MODELLING OF MIXING

Three-dimensional CFD model is carried out to explore the thermal tank mixing numerically. The geometry is created in DESIGN MODELER and the mesh is generated in MESH, an approximately 500,000-element grid has been performed. Fluent 17.2 has been used as the CFD solver to obtain the temperature and velocity contour inside the tank.

3.1 Effect of Draw Rate on Mixing

Various draw rates from 1 to 3 gpm at same draw amount have been simulated. Fig. 12 shows that as the cold water is discharging at higher rate than the water convection rate inside the tank, a free shear layer is developed results in mixing and entrainment of the surroundings.
With a smaller draw rate at the constant draw amount, the bottom tank obtains more blue area and the height of mixed water is lower. This indicates when slowly drawing the water, the cold water concentrates more at the bottom and hot water is kept in the tank as much as possible. It coincides well with the experiment part that a warmer bottom tank would be achieved when drawing faster, which illustrate a worse stratification in the water tank.

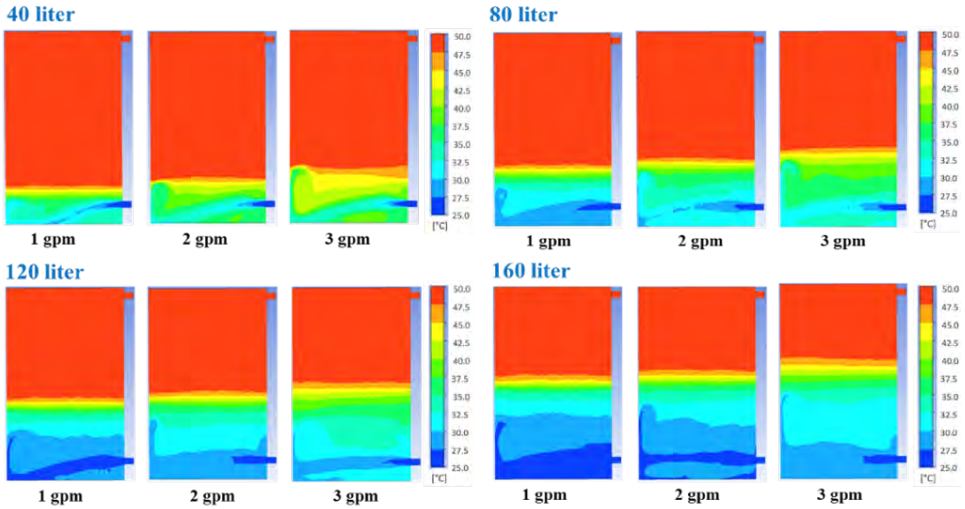

Figure 12: Temperature contours at different draw rates, in time during 152 l draw amount

3.2 Effect of Entrance Structure on Mixing

Another way to control stratification is by adding additional structures. Therefore, Fig. 13 lists two configurations, one with an expanding nozzle connected to the tank inlet which the diameter is two times of the original inlet diameter. Another is considered with a baffle a little bit above the inlet, which the porosity is about 50%.

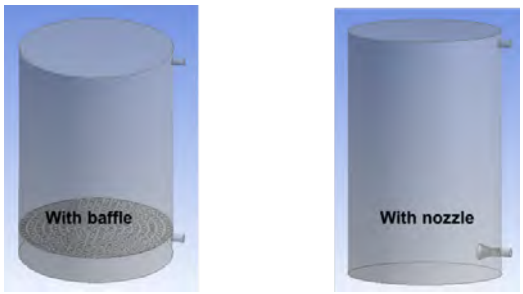

Figure 13: Geometry of two tank configurations

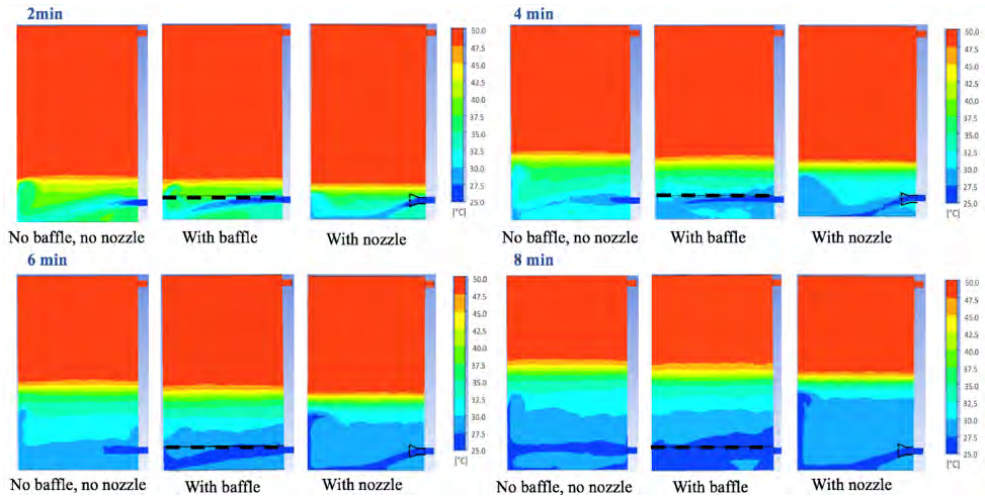

Figure 14: Temperature contours in three configurations, for 0.25m/s velocity at the inlet tube, in time during 152 liter total water draw amount (indicate less mixing with baffle or nozzle)

Fig. 14 shows the temperature contours without baffle and nozzle, with only baffle and with only nozzle. It is obvious to find that with baffle and with nozzle, the height of mixed water is lower, which means more hot water is maintained in the tank. Without the baffle and nozzle, the cold water in the tank spreads more and destroys the tank stratification more. Besides, there is a larger low-temperature area below the baffle, which indicates the baffle controls mixing so that cold water could be limited to a smaller area. Compared with baffle and nozzle, the tank with nozzle remains a lower mixed water height during the draw period.

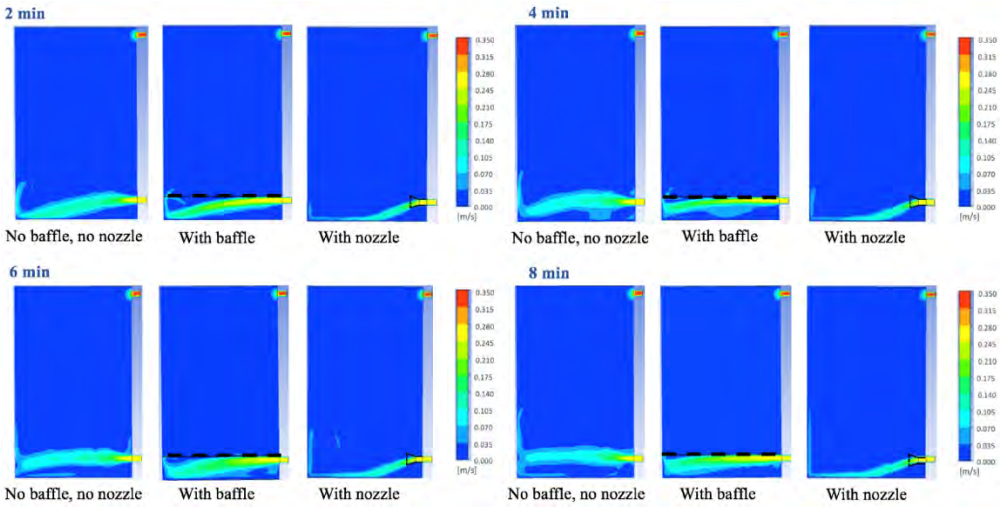

Figure 15: Velocity contours in three configurations, for 0.25m/s velocity at the inlet tube, in time during 152 l total water draw amount (indicate less mixing with baffle or nozzle)

Fig. 15 shows the velocity contours without baffle and nozzle, with only baffle and with only nozzle. The one with nozzle has the lowest velocity gradient that it holds the smallest area where velocity is greater than 0. And the tank with nothing inside holds the largest velocity gradient area. Therefore, the conclusion can be drawn that by limiting the mixing near the inlet area and reducing the inlet velocity, the tank stratification could be maintained better.

3.3 Effect of Inlet Location on Mixing

Another way of promoting stratification by tank design is the inlet location.

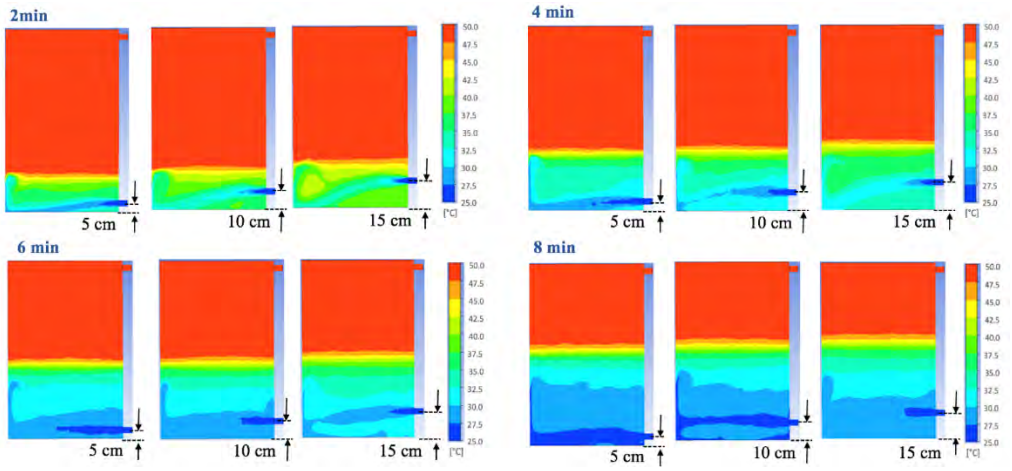

Figure 16: Temperature contours in three inlet positions, for 0.25m/s velocity at the inlet tube, in time during 152 l total water draw amount

As it shown in Fig. 16, three different inlet locations are considered in this paper, 5 cm, 10 cm and 15 cm away from the tank bottom respectively. Lower inlet position obtains larger cold area at the bottom and larger hot water at upper tank, indicates that the stratification is directly impacted by the inlet design, in order to have less mixing and better stratified tank, the inlet should be placed as close as possible to the tank bottom.

4. CONCLUSIONS

In this paper, the HPWH performance in different draw conditions has been investigated. For constant draw rate, draw amount does not affect system efficiency (COP) significantly. Only 3% of performance difference exists with the increase of draw amount from 50% of the tank capacity to 100%.

Higher draw rate results in more mixing. Entropy, Richardson Number and Mixing Coefficient are introduced to characterize the stratification level of the thermal storage tank. Less entropy generation, higher Richardson Number and lower Mixing Coefficient indicate a better stratified thermal tank.

To better understand the mixing and stratification in the water tank, the 3D CFD simulation has been used as an effective tool to investigate the impact of the water tank parameters. The results from experiments for effect of draw rate on stratification agrees with the CFD results. Entrance effect has also been explored on stratification. A tank with higher inlet position obtains greater mixing. Baffles and nozzles can be used as effective tools to reduce mixing in the thermal tank.

NOMENCLATURE

Symbol:			Subscript:	
Q	capacity	(kW)	r	refrigerant
W	power	(kW)	i	tank layer
ρ	density	(kg/m^3)	str	stratified
T	temperature	(K)	mix	mixed
E_i	energy	(J)	comp	compressor
V	volume	(m^3)	cond	condenser
y	vertical distance	(m)	in	inlet
c_p	specific heat capacity	(kJ/kg °C)	out	outlet
M	momentum of energy	(J m)	sys	system
N	number of tank layers			
η	efficiency			

REFERENCES

Li, W., Hrnjak, P., 2018. Experimentally validated model of heat pump water heater in heating-up transients. International Journal of Refrigeration 88, 420-431.

Haller, M.Y., Yazdanshenas, E., Andersen, E., Bales, C., Streicher W., Furbo, S., 2010. A method to determine stratification efficiency of thermal energy storage processes independently from storage heat loss. Solar Energy Vol. 84, No. 6, 997-1007.

Nelson, J.E.B., Balakrishnan, A.R., Srinivasa Murthy, S., 1999. Experiments on stratified chilled-water tanks. International Journal of Refrigeration 22, 216-234.

Manuscript ID: 1791
DOI: 10.18462/iir.icr.2019.1791

COP tests of a Rotation Heat Pump

Andreas LÄNGAUER[(a)], Bernhard ADLER[(a)], Christian RAKUSCH[(a)], Karl PONWEISER[(b)]

[(a)] ecop Technologies GmbH
Vienna, 1230, Austria, office@ecop.at
[(b)] TU Wien
Vienna, 1040, Austria, karl.ponweiser@tuwien.ac.at

ABSTRACT

A completely new way of using an ecologically friendly, not flammable and nontoxic working gas for heat pump applications is realized in the Rotation Heat Pump (RHP) by using a Joule process instead of a Rankine Process. Substantiated by a working fluid which is always gaseous, it is possible to obtain a sensible heat transfer at sink and source.
The main problem to accomplish an efficient Joule process in heat pumps, the compressing of the gas, is based on a centrifugal potential which allows a compression efficiency of more than 99%.
Another major advantage of the Joule process within the RHP is the possibility to change the temperature range from -20 up to 150 °C without affecting the coefficient of performance (COP) considerable. The COP is mainly determined by the temperature spread between sink and source.
Latest tests on the first industrial RHP validate the function and possibilities of this new technology.
Keywords: Rotation Heat Pump, High Temperature, COP, Energy Efficiency, Centrifugal Potential.

1. INTRODUCTION

The main problems of high temperature heat pumps are related to the lubrication of the compressor combined with the aim to use nontoxic, not flammable and low global warming potential (GWP) working fluids. Considering these facts, the Rotation Heat Pump, which is based on a Joule process has been developed and is built now. A compression based on a centrifugal potential and a noble gas as working fluid, eliminate the named problems. Some general calculations and technical details should help to understand the function before the results of tests are shown. The setup of the test rig, including several points for measuring essential values will be described as well. A lookout for further concepts and possibilities of applications including different processes will finally be given.

2. MAIN PRINCIPLE, DESIGN AND CALCULATION

The basic design of a Rotation Heat Pump consists of a rotor on which the heat exchangers and pipes are mounted and a housing which encloses the rotor. The rotating domain is filled with an ecologically friendly working fluid, consisting of different noble gases in the gaseous system and water in the sink and source system. Further necessary components like electrical devices and pumps are mounted on the main rig. In Fig. 1 the complete design is shown while the upper case is removed (left) and the principle of the rotor including heat exchangers and pipes is represented (right).

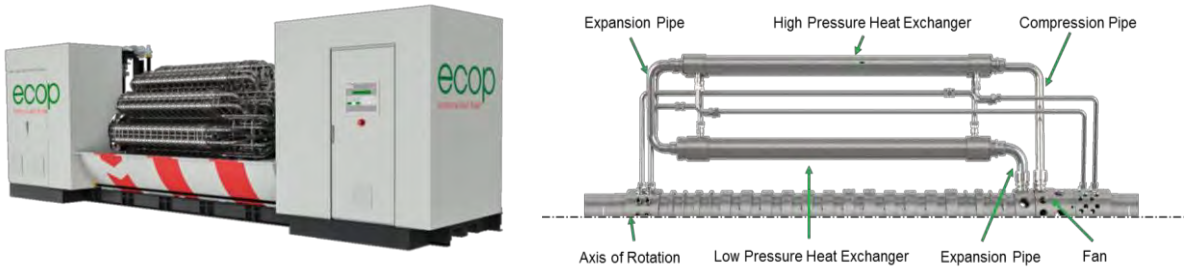

Figure 1: Design of a Rotation Heat Pump

In the following sections a short overview of the principle and function is given. In addition, the calculation of the COP of the Joule Cycle is given.

2.1. The Counter Clockwise Joule cycle in a Rotation Heat Pump

The main difference between conventional heat pumps and a Rotation Heat Pump is based on the thermodynamic cycle. The mainly used Vapor Compression Heat Pump Cycle, is replaced by the Joule Cycle. This has been described in various papers before e.g. Adler et. al (2011), Adler and Riepl (2014), Adler and Mauthner (2017). Since the process is not common used, a short description corresponding to the design is given.
In Fig. 2 the thermodynamic process is shown in a Temperature-Entropy diagram, including some characteristic points.
Starting at 1, the compression caused by the rotation of the working fluid containing system leads to increased pressure and temperature at point 2. During the process 2 to 3, thermal energy is transferred from the hot gas to the water of the sink via the high-pressure heat exchanger. The expansion from 3 to 4 is followed by the low-pressure heat exchanger, where the temperature of the gas is lower than the source temperature. Based on this temperature difference, sensible heat is transferred from the source to the gas and increasing its temperature (4-5). Going to the inner diameter from 5 to 5.1 the gas expands further going along with a temperature decrease. The final step to close the cycle is a pressure increase (5.1 to 5.2) provided by a fan. This is necessary to overcome the pressure losses due to the fluid movement and the divergence of the isobars with increasing entropy.

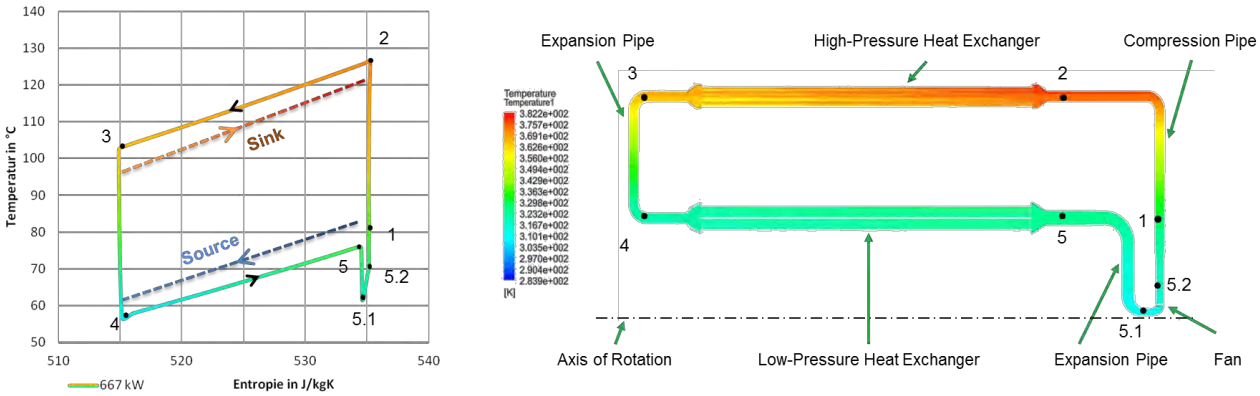

Figure 2: Joule cycle (left) and corresponding design (right) of a Rotation Heat Pump

While most applications use a compressor to increase pressure and temperature, which efficiency is essential for the COP of the system, the main compression in an RHP is based on a centrifugal potential. This is the key factor which leads to a very high efficiency of the cycle. For the main compression of the gas only frictional losses have to be compensated.
Fig. 3 shows the system including sink and source connections and flow paths.

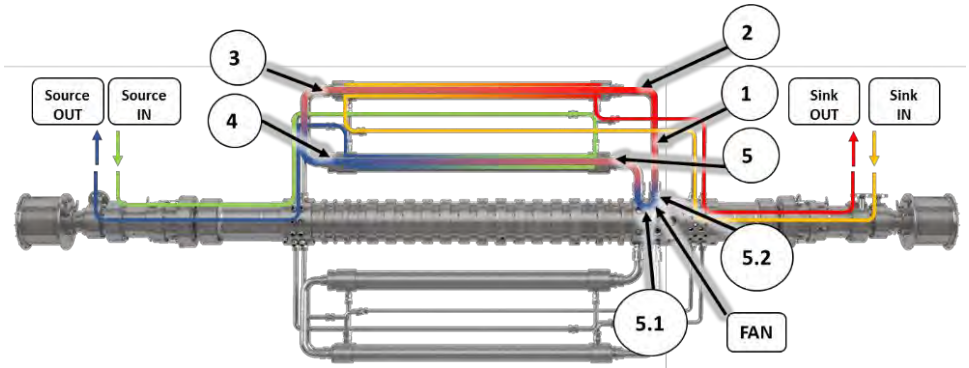

Figure 3: Rotation Heat Pump including connections and process-points

The described system correlates with the tested system. The results are shown in the chapter Testing.

2.2. Calculation of the Coefficient of Performance (COP) for a RHP

One of the most common dimensionless parameters for heat pumps is the coefficient of performance, since it represents the ratio of electrical power consumption and thermal power output. This in fact shows how efficient a heat pump is. In conventional systems the electrical power consumption is often measured at the electrical contacts of the compressor which means that the control system is not regarded. The thermal power output is based on the mass flow and increase of temperature at the heat sink in combination with the specific heat capacity.
To get a comparable value for a Rotation Heat Pump the electrical power consumption is based on the power of the fan engine plus the power of the rotor engine. The thermal power is calculated as mentioned above for conventional systems. Finally, the COP can be described as:

$$COP = \frac{\dot{Q}_{sink}}{P_{electric}} \qquad \text{Eq. (1)}$$

where $\dot{Q}_{sink}$ is the thermal power at sink and $P_{electric}$ is the electrical power consumption, all given in W. Because of the fact, of having two devices for the electrical power consumption, the COP can be calculated using both as explained or just the electrical power for the fan. Using only the electrical power consumption for the fan for evaluating the COP, it can be seen as efficiency of the process itself. Therefore, it is named $COP_{Process}$ in the next sections and diagrams.

3. TESTING

In the following chapter the setup of the test system, the installed sensors, and the measurement system is described. This setup has been used for evaluating the afterwards shown results of the Rotation Heat Pump K7. The test rig is installed at the production site of the company where the RHP has been manufactured as well. It includes the RHP, heat exchangers, control valves, pumps, expansion tanks, coolers, sensors, and the whole pipe system.
Since there have been many different test scenarios, some specific and representative design points have been picked. They are shown in the following diagrams.

3.1. Setup of Test Rig, Sensors, and Measurement Procedure

For testing a Rotation Heat Pump no specific equipment compared to similar applications is necessary. Essential are for example temperature and mass flow sensors at sink and source as well as devices for measuring the electrical power consumption. The calibration of these sensors has been done before starting the tests. A specific list of relevant sensors and where they are located is given in Table 1. Additionally, Fig. 3 and Fig. 4 show the test rig and RHP K7 including sensor positions.



Figure 4: Overview test rig and RHP K7

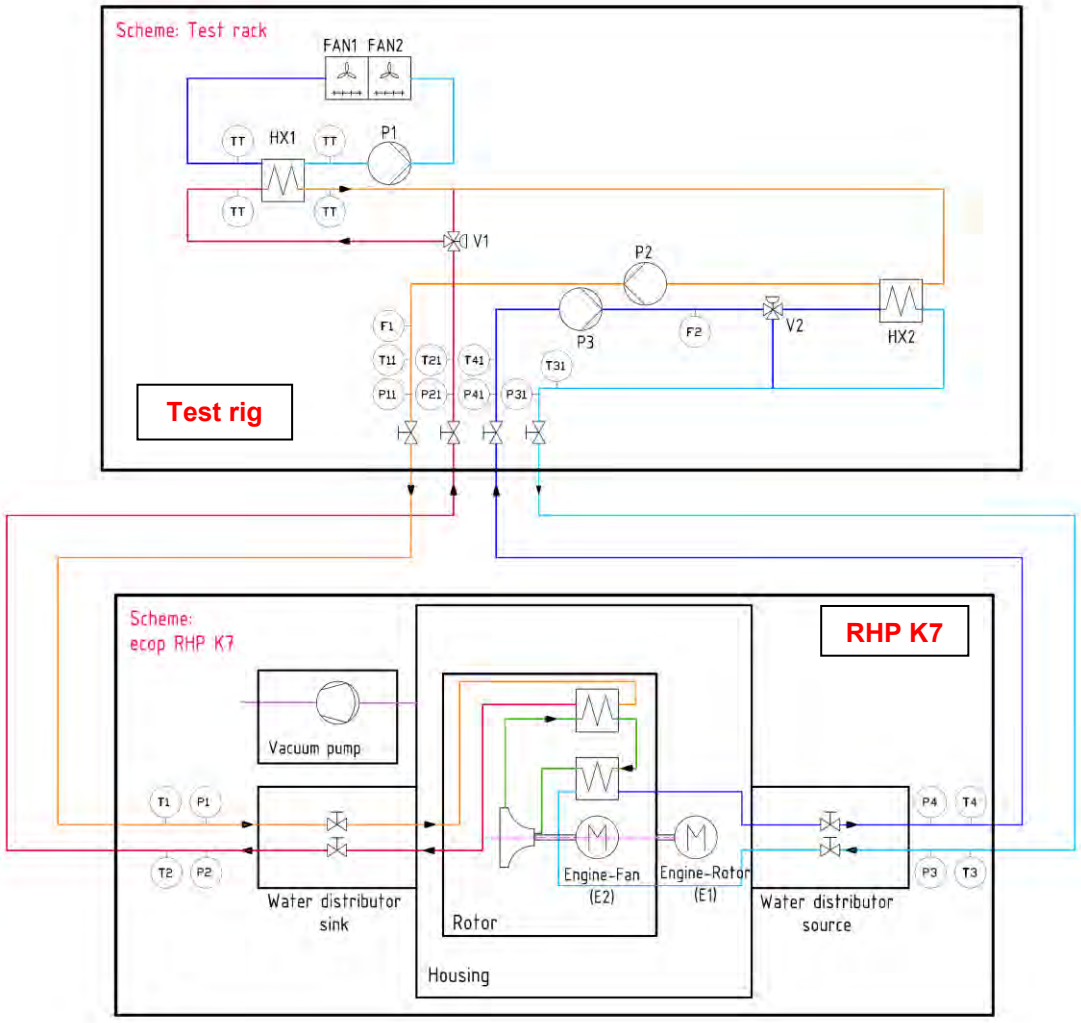

Figure 5: Simplified scheme of the test rig and RHP K7

These sensors are connected via a bus-system to the programmable logic controller where the measured values are logged in a text file to be used for further analyses and calculations afterwards. The electrical power consumption is evaluated via the frequency converters (FC) and the controller.

Table 1. Used sensors and their positions in the test system

Type of Sensor	Measurand	Position	Accuracy class
Pt 100	Temperature	Source in (T3)	A
Pt 100	Temperature	Source out (T4)	A
Pt 100	Temperature	Sink in (T1)	A
Pt 100	Temperature	Sink out (T2)	A
Magnetic-inductive	Mass flow	Source in (F2)	+/- 0,2 %
Magnetic-inductive	Mass flow	Sink in (F1)	+/- 0,2 %
Output of FC	Electrical power	Frequency converter (main rotor) (E1)	-
Output of FC	Electrical power	Frequency converter (fan) (E2)	-

The test procedure is divided in long-term-tests and short-term-tests where the first ones are considered for constant machine parameters for more than 8 hours. The short-term-tests are regarded to reach a specific design point and keep the state constant as long as it takes the system to be stable. This usually doesn't exceed more than one hour, mostly it only takes a few minutes. The presented results are mainly from short term tests, where the duration of the test is given on the abscise in the diagrams. Due to some sensor noise, specific values like COP, thermal power and

electrical power have been arithmetically averaged over 40 values (+/-20 values). The sampling rate of the logging is 5 seconds, so the averaged values display a mean over 200 s. If a value is averaged, it is mentioned in the diagram at the curve title with "_ave". Calculated values are related to the sensor signals and since there are given tolerances there is a possible deviation which is not considered and presented in this paper.

3.2. Results of Testing

The testing of the Rotation Heat Pump showed that in terms of COP it is working in at least the same range or providing a higher COP as conventional heat pumps which are using standard refrigerants. Essential intensive thermodynamic properties like temperature of sink and source are shown as well as other process parameters like mass flow, electrical power consumption and rotational speed of the rotor.
Fig. 6 shows a simulation of the Joule Cycle for the first shown test case and set of parameters, based on real gas properties provided by the National Institute of Standards and Technology (NIST) database. The temperature curves of sink and source in relation to the heat transfer are simplified but in terms of heat transfer coefficient, logarithmic temperature difference and total heat transferred based on standard functions for heat exchangers.

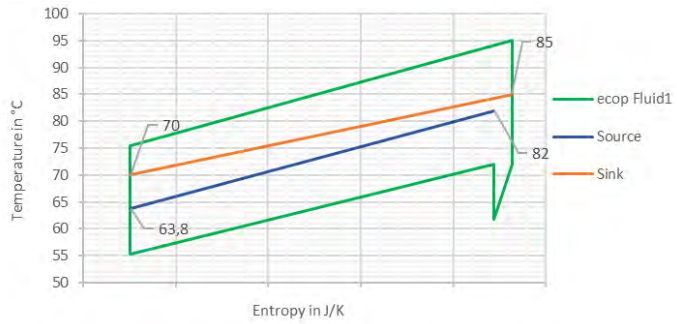

Figure 6: State diagram of the cycle, put up by calculated significant values of the process including the temperature of source and sink

The following diagrams, Fig. 7 and Fig. 8 show the results of short term tests using described formulas and measured values. This first example case illustrates the process at almost constant temperature of sink and source. The slow drift of the temperatures of around 5 K/h is caused by the heat exchanger HX1 in combination with the valve V1. Since it is a closed system and there is electrical power input, energy is finally transformed into heat which has to be transferred out of the system. The mass flow through HX1 is controlled using the valve V1 which is connected to the main control system. Because there is no feedback control and the value is set by hand, the exact value for constant temperatures couldn't be found for this test. All other values remain relatively constant. The rotational speed of the main rotor in this case was around 1200 rpm where it was possible to increase the temperature of the sink of approximately 15 K and decrease the source of around 15 K. The temperature spread between "T sink out" and "T source in" is around 3 K. This value depends basically on the rotational speed and the mass flow of sink and source as well as the mass flow of the working fluid. For this process and the given boundary conditions the calculated COP results in a value of around 6.

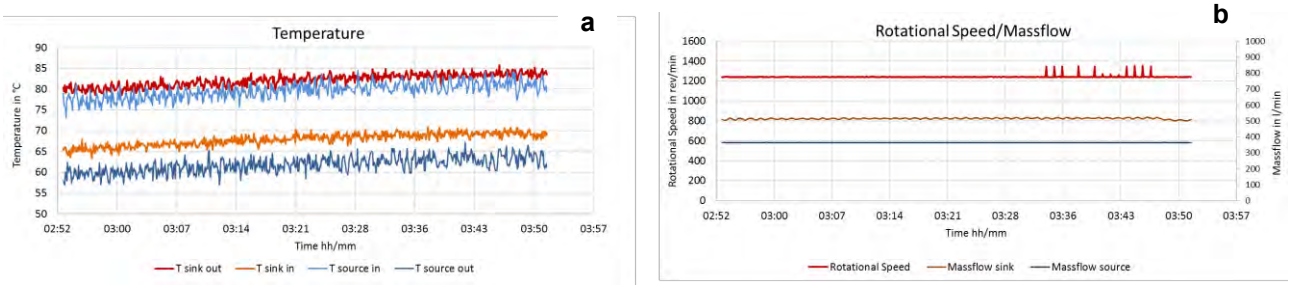

Figure 7: Temperature of sink and source (a), mass flow and rotational speed (b)

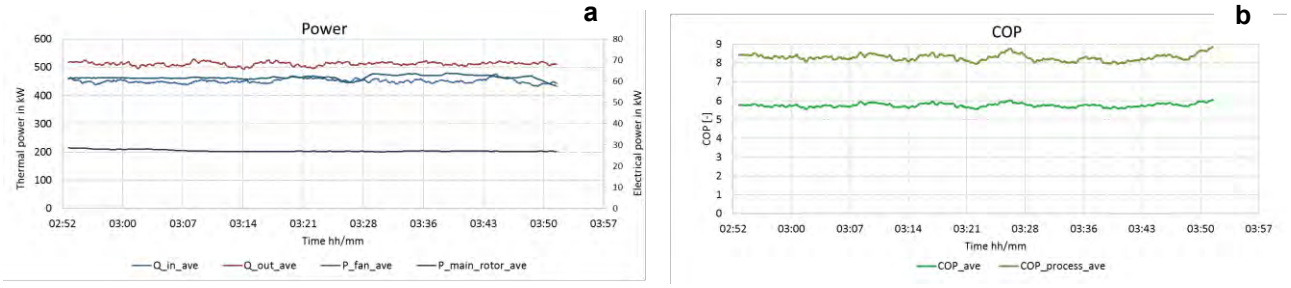

Figure 8: Thermal and electrical power (a), COP (b)

The second set of test results show the flexibility of the process over a given temperature range. This should only be an example, for the process itself it is possible to use a wider range. Fig. 9 and Fig. 10 show measured and calculated values over time. This curve shape can be realized by adapting the position of valve V1. So, for the descend of the temperatures till 05:50, the valve was more opened compared to the second half of the curve where the temperatures ascend. The rotational speed of the main rotor and the mass flow of sink and source are corresponding to the first example above. A different position of valve V2, which is controlling the mass flow of the source through the heat exchanger HX2, results in another temperature spread. In this case the spread between “T sink out” and T source in” is approximately 10 K. Because of less thermal power transferred, compared to the first case, the COP results in a value of around 5 as shown in Fig. 10. The small peak of the COP at 05:31 is caused by a short time when the electrical power consumption of the fan was less than before and afterwards. This may be caused by changed flow conditions in the gaseous system, especially at the fan. Anyway, it is clearly noticeable that the temperature level of the system can be adapted and changed during the process while the COP is not nameable affected.

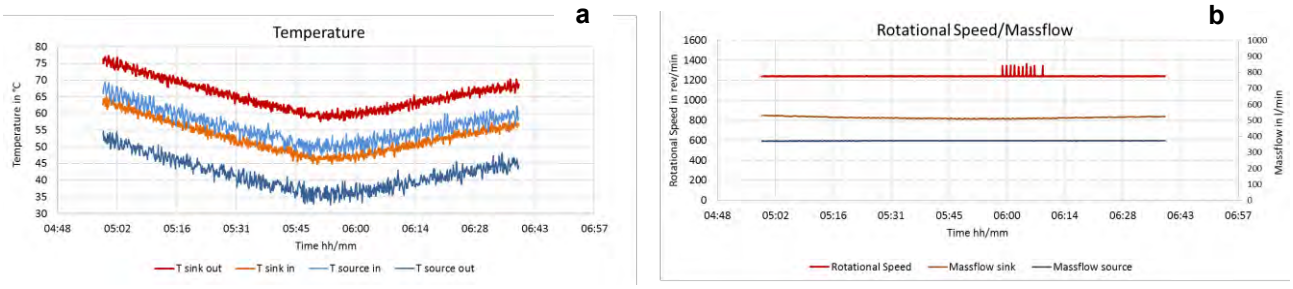

Figure 9: Temperature of sink and source (a), mass flow and rotational speed (b)

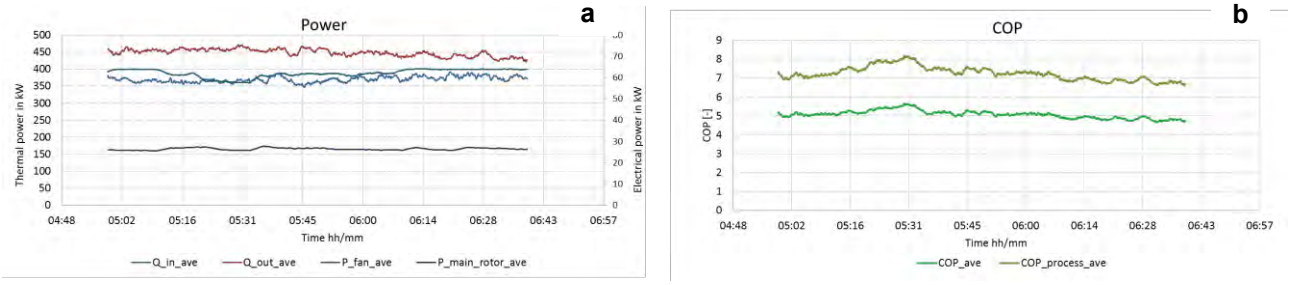

Figure 10: Thermal and electrical power (a), COP (b)

The last example shows the step response of the system, therefore the transferred heat between sink and source was adjusted in a relatively short time (<1min). The variation takes place at 04:26, when the temperature of “T sink in” and “T source in” approach each other. This test scenario could be a Dirac jump because more or less power is requested at the sink in a short time period. The jump shown in Fig. 11 (a) results in a decrease of thermal power, Fig. 12. Because of the averaging the step is displayed as a ramp and not instantaneously as the temperatures show. Additionally, the COP drops from around 6 to 5 which is the result of less thermal power transferred while the electrical power consumption remains almost constant.

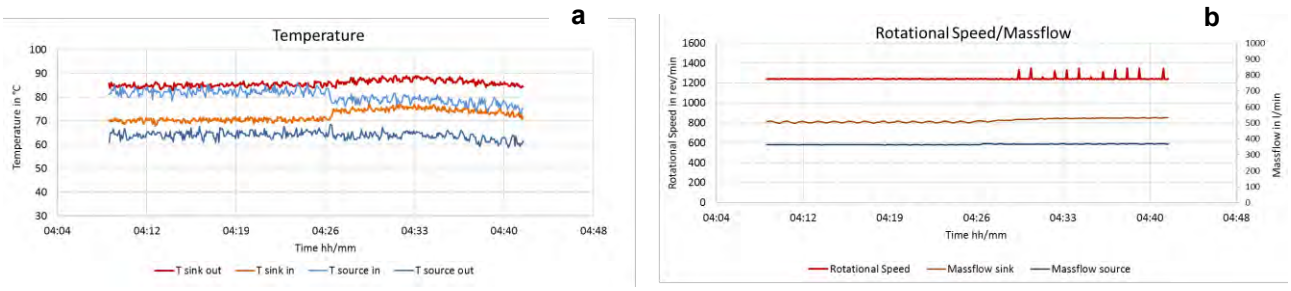

Figure 11: Temperature of sink and source (a), mass flow and rotational speed (b)

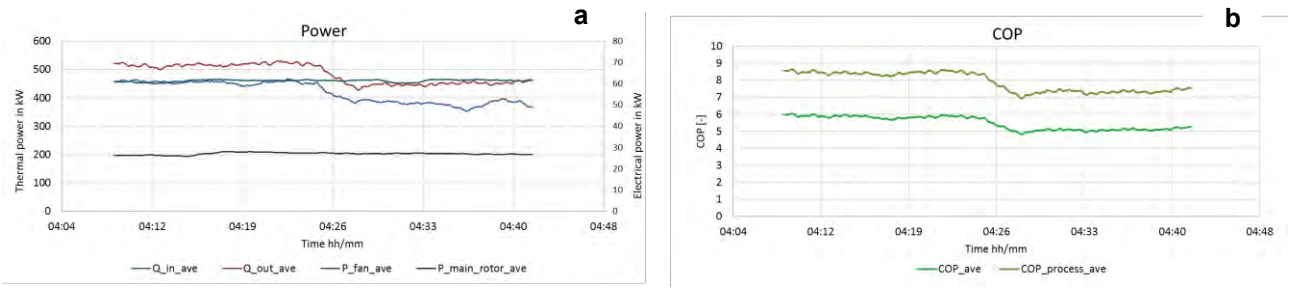

Figure 12: Thermal and electrical power (a), COP (b)

One more test was done at a higher rotational speed of the main rotor in combination with changing temperatures at sink and source. The case, shown in Fig. 13 and Fig. 14, describes a drift from around 68°C up to around 91°C of the sink outlet temperature at a speed of 1400 rpm. The mass flow of sink and source is controlled to be at a constant value of 450 l/min. Compared to the previous cases the power for the main rotor is slightly higher at this speed. This is caused by the increased losses of for example bearings and sealings. The temperature drift for this case has been done by changing the value of valve V1 in a way that less heat is transferred out of the system. In terms of the COP there is no significant change during the whole time of the test case, including the drift to a higher temperature level, starting at 05:02, as well. Because of the heat transferred and a higher temperature spread between sink and source, more electrical power is needed as shown in Fig. 14. This affects primary the power of the fan because of changed conditions of the process. For a closed cycle it is necessary to compensate the divergence of the isobars which in fact results in a higher pressure increase to be provided by the fan.

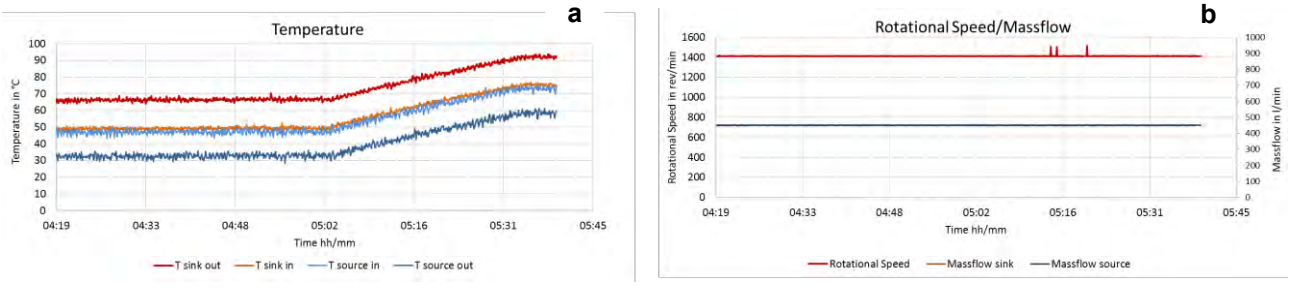

Figure 13: Temperature of sink and source (a), mass flow and rotational speed (b)

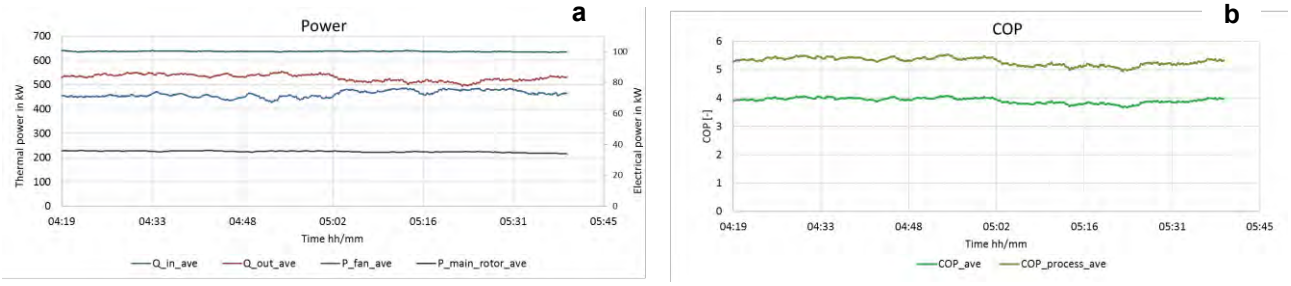

Figure 14: Thermal and electrical power (a), COP (b)

4. CONCLUSIONS

The operation and testing of the RHP showed that the principle and theory of the Joule Cycle is working for this application as predicted, as well as that it is very effective and opens a wide range of further heat pump applications not used right now. Not only the possible higher temperatures but also the sensible heat transfer are unique as well as the usage of a Joule Cycle for a heat pump. This means in combination with an environmentally friendly working fluid where the GWP=0, which is nontoxic and not flammable that by use of the presented machine the CO_2 emissions of many applications can be considerably reduced in a save way.
The described system of the test rig and the Rotation Heat Pump were used for evaluating different COP values and show the dependence on different parameters. Actual test cases include results for constant boundary conditions and stationary operation, variation of the temperature range and system responses for a step at the sink and source inlet temperature. A simulation based on analytical calculations shows good accordance with the test results. Based on the tests shown in this paper, some more test cases will be scheduled where even more knowledge about the Rotation Heat Pump and its function will be generated. This includes cases for high temperature applications as well as different scenarios for industrial applications.

ACKNOWLEDGEMENTS

This project has received funding from the European Union's Horizon 2020 research and innovation programme under grant agreement No 823463.

REFERENCES

Adler B. et al., 2011. Centrifugal compression turbo heat pump made by ECOP. 10th IEA Heat Pump Conference, Tokyo, Japan

Adler B., Riepl, S., 2014. Heat pump for process industry. 11th IEA Heat Pump Conference, Montreal, Canada

Adler B., Mauthner R., 2017. Rotation Heat Pump (RHP). 12th IEA Heat Pump Conference, Rotterdam, Netherlands

Manuscript ID: 1815
DOI: 10.18462/iir.icr.2019.1815

Experimental Study on a Water and Air Source High-Temperature Heat Pump Using a Low GWP Refrigerant

Choyu Watanabe[(a), (b)], Toshiyuki Nakamura[(a)], Motoki Yamada[(a)], Tomoyuki Yamada[(a)], Atsuki Hattori[(a)], Tadayoshi Aono[(a)], Shuto Tomita[(a)]

(a) Graduate School of Engineering of Nagoya University
Nagoya, 463-8603, Japan, watanabe.choyu@ng.mbox.nagoya-u.ac.jp
(b) Chubu Electric Power Co., Inc.
Nagoya, 459-8522, Japan, Watanabe.Chouyuu@chuden.co.jp

ABSTRACT

A high-temperature heat pump using a low GWP refrigerant, such as R1234yf or R454C, were experimentally investigated to supply hot water. The temperature of hot water ranged from 45 °C to 90 °C for R1234yf and ranged from 45 °C to 75 °C for R454C, while the temperature of supplied water ranged from 6 °C to 24 °C. The temperature of heat sources ranged from 7 °C to 25 °C. Degrees of sub-cooling of sub-critical heat pump cycles ranged from 10 °C to 70 °C because large temperature-rise was needed to heat supplied water. A test apparatus and measurement system were presented. The test results using R1234yf and a water-source evaporator were discussed in comparison with the test results of the former work using R1234yf and an air-source evaporator. The test results using R1234yf and a water-source evaporator were discussed in comparison with the test results using R454C.
Keywords: Low GWP Refrigerant, R1234yf, R454C, COP, Energy Efficiency

1. INTRODUCTION

Heat pump technology is important to boost the reduction of CO_2 emissions, reduce primary energy consumption and increase the amount of renewable energy usage due to high energy efficiency of heat pumps. To further enhance these effects, the development and spread of high temperature heat pumps for hot water supply and re-heating of hot water circulation must be supported. For example, air source heat pumps using R134a as a refrigerant for re-heating hot water circulation have been applied to cutting and washing processes in automobile parts factories (Watanabe, 2017).
The low GWP refrigerants, such as R1234yf and R454C, are expected as the next generation refrigerants for heat pumps. A water source high-temperature heat pump using R1234yf (Watanabe et al., 2017) and an air source high-temperature heat pump using R1234yf (Watanabe et al., 2018) has been investigated. However, heating capacity and heating COP did not reach expected values. Because evaporation temperature could not be controlled properly with a thermostatic expansion valve with internal pressure equalization due to the pressure drop in distributors to a plurality of refrigerant passages of an air source evaporator.
In this paper, a water source high-temperature heat pump using R1234yf or R454C with thermostatic expansion valves with external pressure equalization are experimentally investigated to supply hot water. A test apparatus and measurement system are presented. Test results using R1234yf and a water source evaporator are discussed in comparison with the test results of the former work using R1234yf and an air source evaporator (Watanabe et al., 2018). The test results using R454C and a water source evaporator are discussed in comparison with the test results using R1234yf.

2. REFRIGERANTS FOR HIGH-TEMPERATURE HEAT PUMPS

Properties of refrigerants for high-temperature heat pumps are shown in Table 1. GWP (100 years), safety, critical pressure, critical temperature and boiling point temperature of each refrigerant are described for R1234yf, R1234ze(E), R454C, R32, R410A, R134a and R290 in this table. R454C is composed of R1234yf (78.5 mass%) and R32 (21.5 mass%). When we selected refrigerants in this

paper, we though the refrigerants to be removed, whose GWP (100 years) is higher than 150, or whose flammability is high. Further, we thought the refrigerants to be removed, whose boiling point temperature is higher than -25 °C because the lowest evaporation temperature of a sub-critical cycle is -25 °C, assumed that the lowest temperature of heat source air is -15 °C and the lowest evaporation temperature is lower by 10 K than the temperature of heat source air. R1234yf and R454C were selected because they were not removed.

Table 1. Properties of refrigerants for high-temperature heat pumps

Classification	Refrigerant	Chemical formula	GWP_{100}	Safety [3]	Critical point		Boiling point [4] (°C)
					Pressure (M Pa)	Temperature (°C)	
HFO	R1234yf	$CF_3CF=CH_2$	<1 [1]	A2L	3.38	94.7	-29.5
	R1234ze(E)	Trans-$CHF=CHCF^3$	<1 [1]	A2L	3.64	109.4	-19.0
HFO & HFC	R454C	-	146 [1]	A2L	4.69	88.5	-45.9
HFC	R32	CH_2F_2	677 [1]	A2L	5.78	78.1	-51.7
	R134a	CF_3CH_2F	1,300 [1]	A1	4.06	101.1	-26.1
Natural refrigerant	R290	C_3H_8	3 [2]	A3	4.24	106	-42.1

1) Values of Global Warming Potential 100 year according to Appendix 8.A, the 5th final report of IPCC WG1.
2) Values of Global Warming Potential 100 year for R290 according to Table 2.15, IPCC Fourth Assessment Report.
3) A: lower toxicity, B: higher toxicity, 1: no flame propagation, 2L: lower flammability with a maximum burning velocity of ≤10 cm/s, 2: lower flammability with a maximum burning velocity of >10 cm/s, 3: higher flammability classified according to ISO 817:2014.
4) Temperature at which the liquid boils under standard atmosphere, 0.1013 MPa.

3. EXPERIMENTAL APPARATUS FOR HIGH-TEMPERATURE HEAT PUMPS

Figure 1 shows the schematic drawing of an experimental apparatus for high-temperature heat pump and measure points. Figure 2 shows the outside view of the apparatus. The apparatus consists of a refrigerant circuit of a heat pump cycle, heat sink water circuit to measure heating capacity and heat source water circuit to use a water source evaporator. The refrigerant circuit consists of a compressor, a water-cooled condenser, a receiver, a water-cooled sub-cooler, two expansion valves for R1234yf and R454C, an air-source evaporator with a fan, a water-source evaporator, an accumulator and sight glasses. The condenser, sub-cooler and water-source evaporator are all copper-brazed stainless-steel plate type heat exchangers. The receiver is arranged between the condenser and the sub-cooler. The semi-hermetic reciprocating compressor 2KES-05Y made by Bitzer was adopted. The compressor has two cylinders, a bore diameter of 30 mm, a stroke of 33 mm and a displacement volume of 490 m^3/h when the frequency of power source is 60 Hz. The maximum discharge pressure is 3.2 MPa, and the maximum suction pressure is 1.9 MPa. The compressor has a 3-phase 200V induction motor, which has a maximum output of 1.8 kW. The heat sink water circuit consists of a heat sink water tank, an auxiliary chiller, a heat sink water pump driven by an inverter and a fan coil unit. The inner volume of the heat sink water tank is 0.035 m^3. Supplied water is heated in the sub-cooler and condenser. The heat of hot water is dissipated to ambient air in the fan coil unit. The heat source water circuit consists of a heat source water tank, a heat source water pump driven by an inverter, and a heat exchanger between heat source water and heat sink water. The inner volume of the heat source water tank is 0.035 m^3.

Refrigerant pressure was measured with piezo-resistance pressure transducers. Refrigerant temperature was measured with copper-constantan thermo-couples attached on outside surfaces of copper tubes in which refrigerant flows. Mass flow rate of refrigerant was measured with a Coriolis flowmeter. Water temperature was measured with platinum resistor temperature sensors inserted in the water pipes. Flow rate of water was measured with two electromagnetic flowmeters.

4. EXPERIMENTAL CONDITIONS

Experimental conditions of the former work (Watanabe et al., 2018) are shown in Table 2 according to JIS C 9220-2011. Dry bulb air temperature, wet bulb air temperature, water supply temperature and hot water temperature are shown for each season condition in Table 2. Figure 3 shows the air-source evaporator and thermostat expansion valve with internal pressure equalization of the former work (Watanabe et al., 2018). Heating capacity and heating COP did not reach expected values. Because evaporation temperature could not be controlled properly with a thermostatic expansion valve with internal pressure equalization due to the pressure drop in distributors to a plurality of refrigerant passages of an air source evaporator. Experimental conditions of this work are shown in Table 3. Source water temperature, water supply temperature and hot water temperature are shown for each season condition in Table 3. Maximum hot water temperature is 75 °C for R454C while that is 90 °C for R1234yf. Because the critical temperature of R454C is lower than that of R1234yf. Figure 4 shows the water-source evaporator and thermostat expansion valve with external pressure equalization newly adopted in this work to enable proper control of expansion.

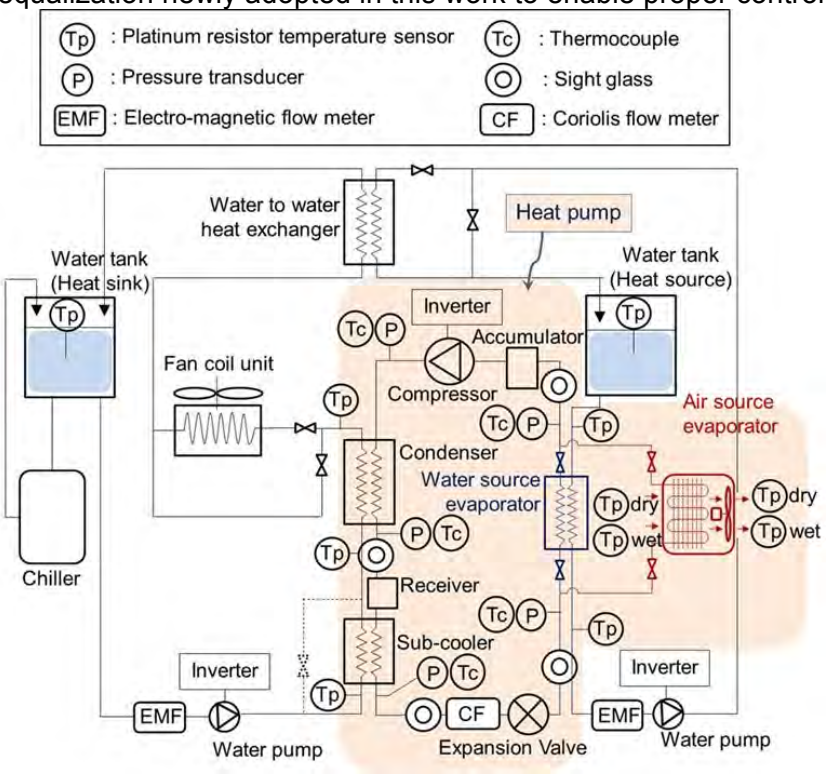

Figure 1: Schematic drawing of an experimental apparatus and measure points

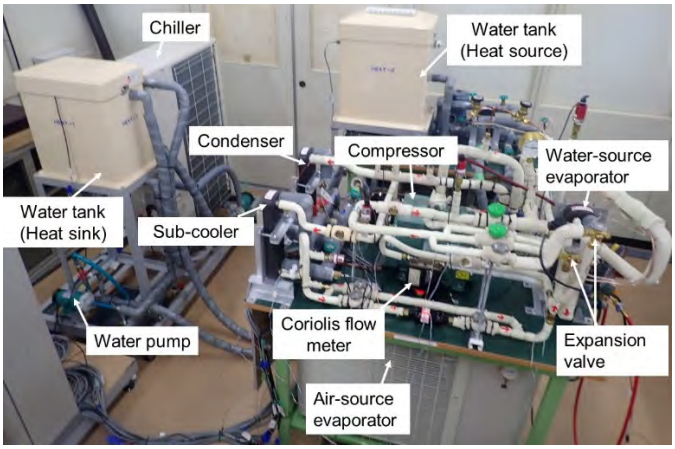

Figure 2: Outside view of an experimental apparatus for high-temperature heat pumps

Table 2. Experimental conditions (R1234yf air-source heat pump) (Watanabe et al., 2018)

Season	Heat source air temperature (°C, dry bulb)	Heat source air temperature (°C, wet bulb)	Water supply temperature (°C)	Hot water temperature (°C)
Summer	25	21	24	45, 65, 80, 90
Midterm	16	12	17	45, 65, 80, 90
Winter	7	6	9	45, 65, 80, 90
Frost	2	1	5	45, 65, 80, 90

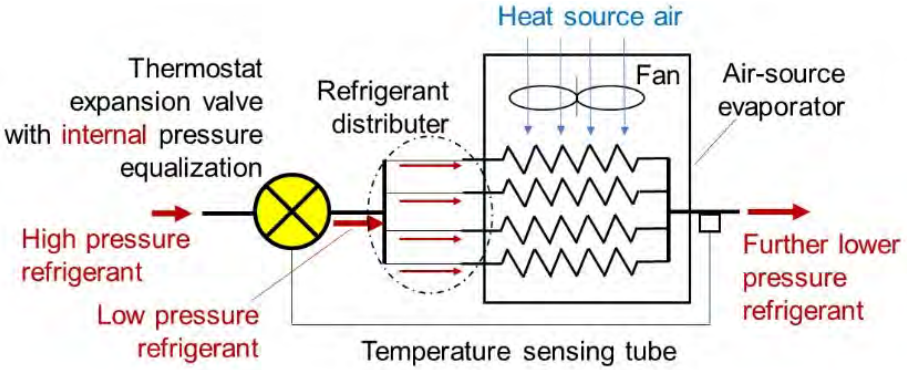

Figure 3: Air-source evaporator and thermostat expansion valve with internal pressure equalization (Watanabe et al., 2018)

Table 3. Experimental conditions (water-source heat pump)

Season	Heat source water temperature (°C)	Water supply temperature (°C)	Hot water temperature (°C)	
			R1234yf	R454C
Summer	25	24	45, 65, 80, 90	45, 65, 75
Midterm	16	17	45, 65, 80, 90	45, 65, 75
Winter	7	9	45, 65, 80, 90	45, 65, 75

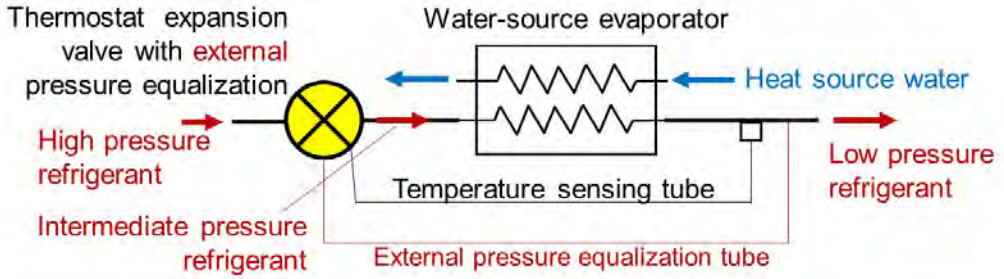

Figure 4: Water-source evaporator and thermostat expansion valve with external pressure equalization

5. EXPERIMENTAL RESULTS AND DICCUSSION

Fig. 5 shows heating COP versus hot water temperature (45 °C, 65 °C, 80 °C and 90 °C) and heating capacity versus hot water temperature for each season condition. Square marks show the test results using R1234yf, the water-source evaporator and thermostat expansion valve with external pressure equalization obtained in this work. And solid lines show approximate curves obtained from experiment points. Circle marks show the test results using R1234yf, the air-source evaporator and thermostat expansion valve with internal pressure equalization obtained in the former work (Watanabe et al., 2018). And dashed lines show approximate curves obtained from the experiment points. Blue marks and lines show the test results and approximate curves under the summer condition. Orange marks and lines show the test results and approximate curves under the midterm condition. Grey marks and lines show the test results and approximate curves under the winter condition. Heating capacities and heating COPs obtained in this work are larger than those obtained in the former work. The increase of heating capacities and heating COPs are the largest under the

summer condition, the median under the midterm condition and the smallest under the winter condition.

Fig. 6, Fig. 7 and Fig. 8 shows pressure–enthalpy diagrams and temperature–entropy diagrams of the heat pump cycles drawn using CYCLE_D (Brown, J.S. et al., 2009). Red marks and lines show the heat pump cycles using R1234yf, the water-source evaporator and thermostat expansion valve with external pressure equalization obtained in this work. Blue marks and lines show the test results using R1234yf, the air-source evaporator and thermostat expansion valve with internal pressure equalization obtained in the former work (Watanabe et al., 2018). Fig. 6 shows the test results under the summer condition and hot water temperature 45 °C. Fig. 7 shows the test results under the midterm condition and hot water temperature 65 °C. Fig. 8 shows the test results under the midterm condition and hot water temperature 90 °C. In all cases of Fig. 6, Fig. 7 and Fig. 8, evaporation pressures and evaporation temperatures rise in the heat pump cycles obtained in this work in comparison with the heat pump cycles obtained in the former work. The rise of evaporation pressure and temperature shows the largest value in Fig. 6, the median value in Fig. 7 and the smallest value in Fig. 8. Because the mass flow rate of the refrigerant is the largest value and the evaporation pressure of the refrigerant is the lowest in Fig. 6; the mass flow rate of the refrigerant is the median value and the evaporation pressure of the refrigerant is the median value in Fig. 7; the mass flow rate of the refrigerant is the smallest value and the evaporation pressure of the refrigerant is the largest in Fig. 8.

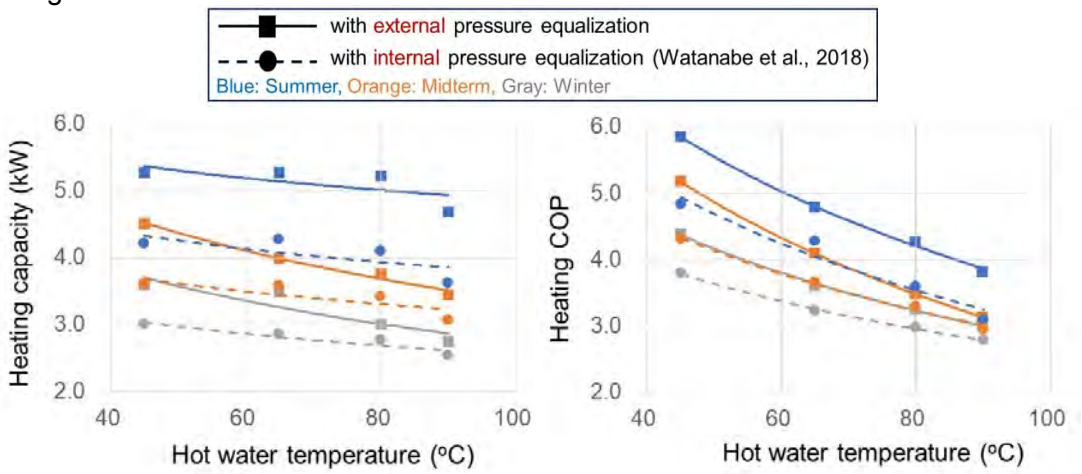

Figure 5: Experimental data regarding heating capacity and heating COP for hot water temperature

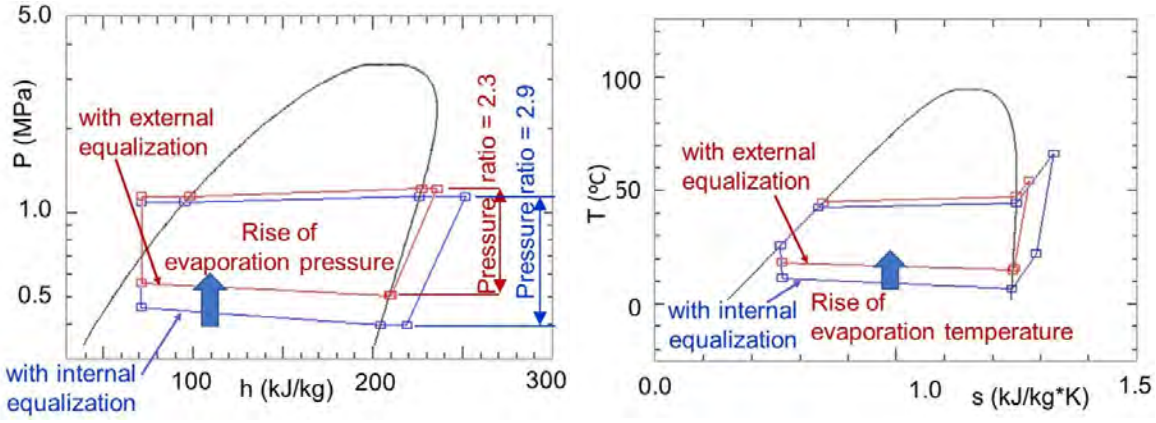

Figure 6: P-h and T-s diagrams (R1234yf, summer, hot water temperature: 45 °C)

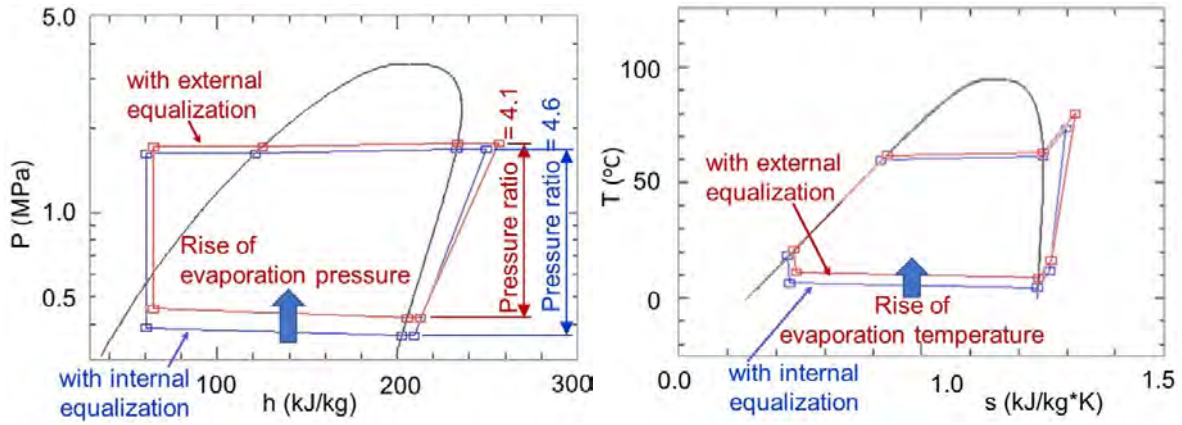

Figure 7: P-h and T-s diagrams (R1234yf, midterm, hot water temperature: 65 °C)

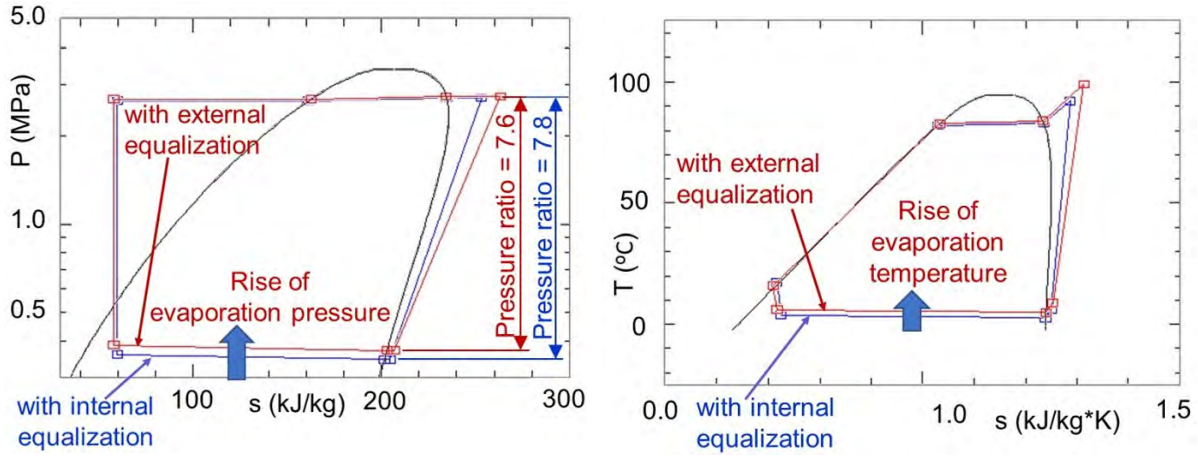

Figure 8: P-h and T-s diagrams (R1234yf, winter, hot water temperature: 90 °C)

Fig. 9 shows heating COP versus hot water temperature (45 °C, 65 °C and 75 °C for R454C; 45 °C, 65 °C, 80 °C and 90 °C for R1234yf) and heating capacity versus hot water temperature for each season condition. Square marks show the test results using R454C, the water-source evaporator and thermostat expansion valve with external pressure equalization obtained in this work. And solid lines show approximate curves obtained from experiment points. Circle marks show the test results using R1234yf, the water-source evaporator and thermostat expansion valve with external pressure equalization obtained in this work. And dashed lines show approximate curves obtained from the experiment points. Blue marks and lines show the test results and approximate curves under the summer condition. Orange marks and lines show the test results and approximate curves under the midterm condition. Grey marks and lines show the test results and approximate curves under the winter condition. Heating capacities of R454C are larger than those of R1234yf. However, heating COPs of heat pump cycles using R454C are smaller than those of R1234yf because the heating capacities and cooling capacities of R454C are larger than those of heat pump cycles using R454C R1234yf using the same condenser and evaporator.

Fig. 10-12 shows pressure–enthalpy diagrams and temperature–entropy diagrams of the heat pump cycles drawn using CYCLE_D (Brown, J.S. et al., 2009). Red marks and lines show the heat pump cycles using R454C, the water-source evaporator and thermostat expansion valve with external pressure equalization obtained in this work. Blue marks and lines show the test results using R1234yf, the water-source evaporator and thermostat expansion valve with external pressure equalization obtained in this work. Fig. 10 shows the test results under the summer condition and hot water temperature 45 °C. Fig. 11 shows the test results under the midterm condition and hot water temperature 65 °C. Fig. 12 shows the test results under the midterm condition and hot water temperature 75 °C for R454C, and 90 °C for R1234yf. In both cases of Fig. 10 and Fig. 11, condensation and evaporation pressures of R454C are higher than those of R1234yf in the heat

pump cycles while condensation and evaporation temperatures of R454C are approximately equal to those of R1234yf. In Fig. 12, condensation pressures and evaporation temperatures of R454C are approximately equal R1234yf while evaporation pressures and condensation temperatures of R454C are higher than those of R1234yf.

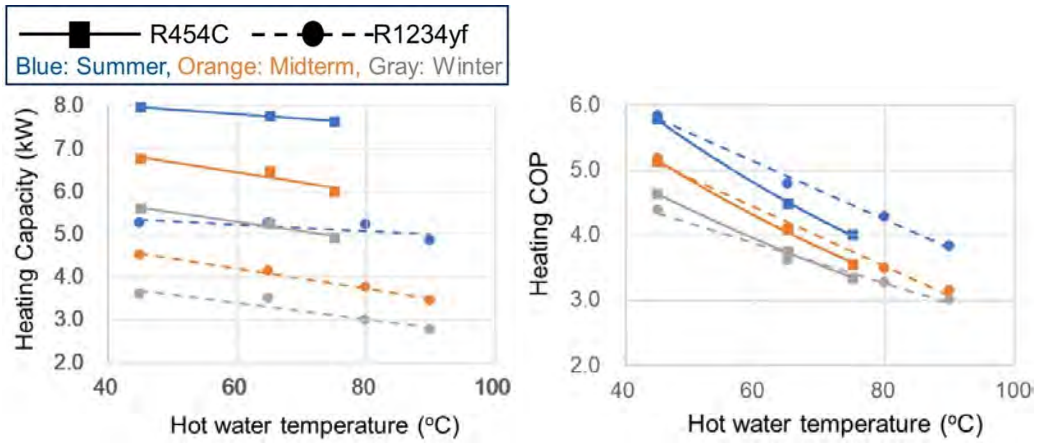

Figure 9: Experimental data regarding heating capacity and heating COP for hot water temperature

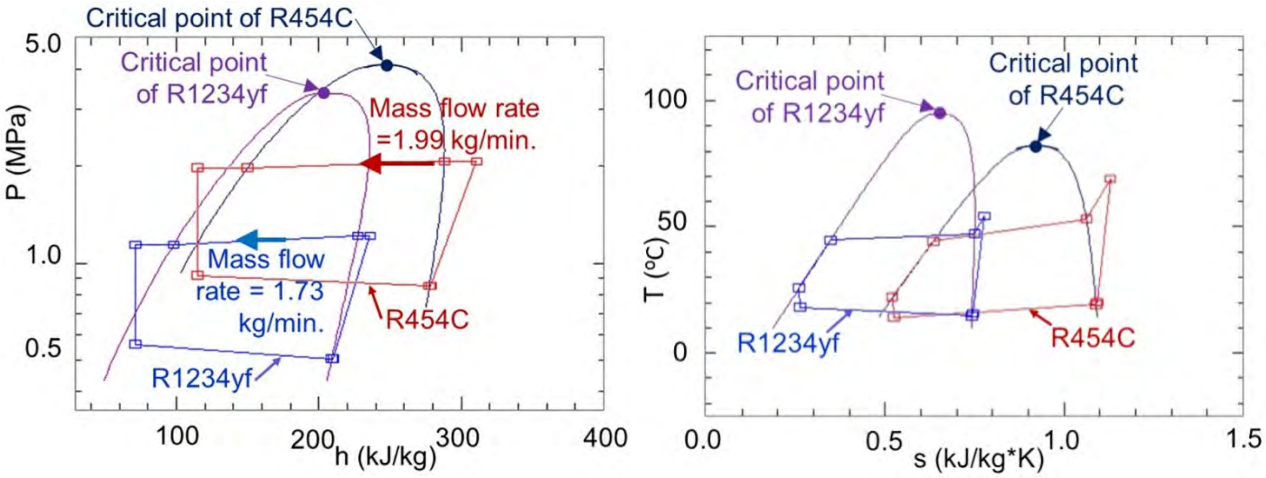

Figure 10: P-h and T-s diagrams (summer, hot water temperature: 45 °C)

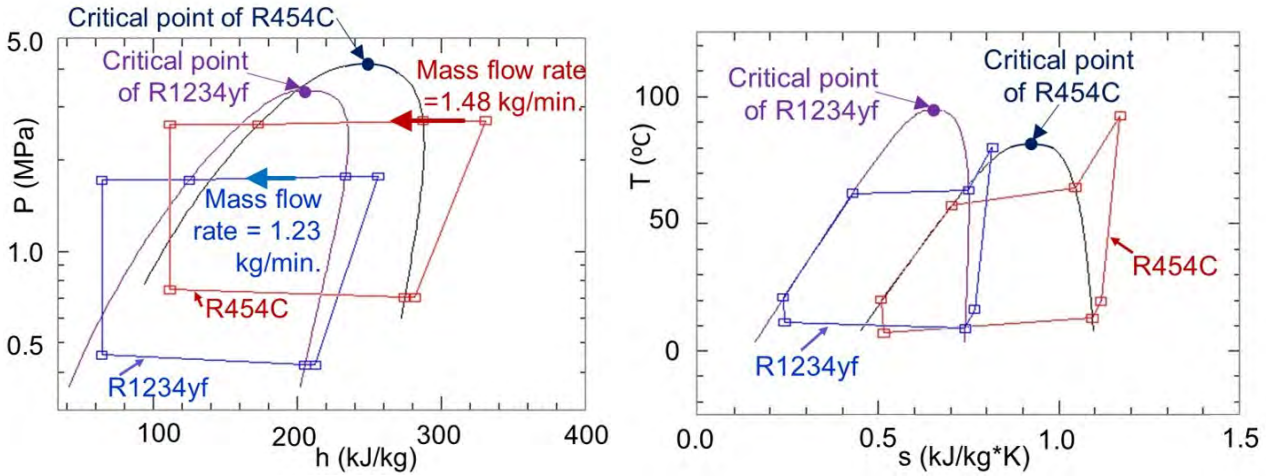

Figure 11: P-h and T-s diagrams (midterm, hot water temperature: 65 °C)

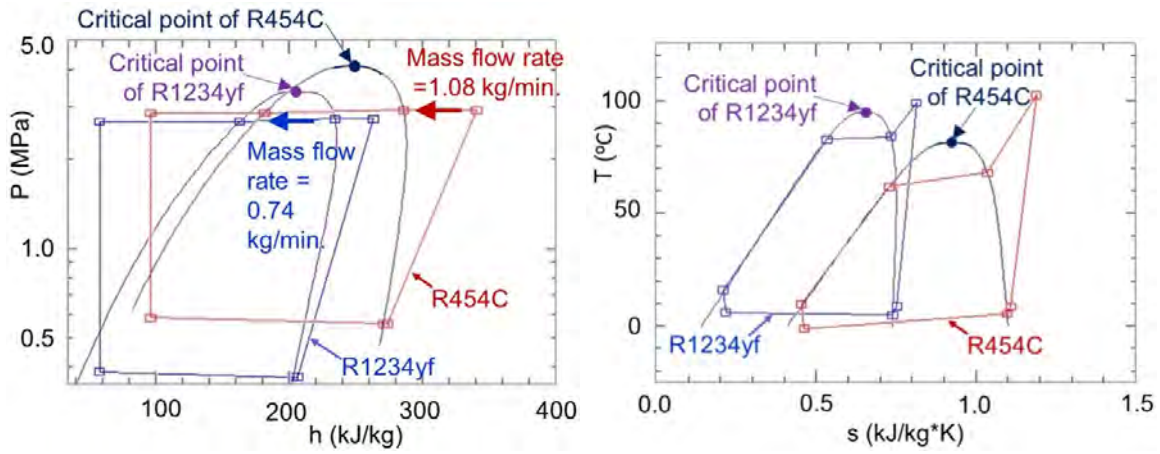

Figure 12: P-h and T-s diagrams (winter, hot water temperature: 75 °C for R454C, 90 °C for R1234yf)

6. CONCLUSIONS

The high-temperature heat pump using a low GWP refrigerant, such as R1234yf or R454C, were experimentally investigated to supply hot water. The temperature of hot water ranged from 45 °C to 90 °C for R1234yf and ranged from 45 °C to 75 °C for R454C, while the temperature of supplied water ranged from 6 °C to 24 °C.

Heating capacities and heating COPs obtained using R1234yf and a thermostat expansion valve with external pressure equalization are larger than those obtained using R1234yf and a thermostat expansion valve with internal pressure equalization.

Heating capacities of heat pump cycles using R454C are larger than those of heat pump cycles using R1234yf. However, heating COPs of heat pump cycles using R454C are smaller than those of heat pump cycles using R1234yf because the heating capacities and cooling capacities of R454C are larger than those of R1234yf using the same condenser and evaporator.

ACKNOWLEDGEMENTS

This study has been conducted as Creative Experiments for Comprehensive Engineering of Graduate School of Engineering of Nagoya University.

NOMENCLATURE

P	pressure (MPa)	h	specific enthalpy (kJ×kg^{-1})
T	temperature (°C)	s	specific entropy (kJ×kg^{-1}×K^{-1})

REFERENCES

Watanabe, C., 2017, Application of Heat Pumps to Cutting and Washing Processes, European Heat Pump Summit 2017, No. 3.

Watanabe, C. et al., 2017. Theoretical and Experimental Study on Air-source High-Temperature Heat Pumps Using a Low GWP Refrigerant. Proceedings of the 9th Asian Conference on Refrigeration and Air-conditioning, Japan Society of Refrigerating Air conditioning Engineers, o.3.3.2.

Watanabe, C. et al., 2018. Theoretical and Experimental Study on High-Temperature Heat Pumps Using a Low GWP Refrigerant. Proceedings of the 12th Heat Pump Conference 2017, International Energy Agency, A325.

Brown, JS et al., 2009. CYCLE_D: NIST Vapor Compression Cycle Design Program -Version 5.0 (NIST Standard Reference Database 49).

Manuscript ID: 1869
DOI: 10.18462/iir.icr.2019.1869

Development of Ammonia-Water Hybrid Absorption-Compression Heat Pumps

Marcel Ulrich AHRENS, Armin HAFNER and Trygve Magne EIKEVIK

Norwegian University of Science and Technology - NTNU,
Kolbjørn Hejes vei 1B, 7491 Trondheim, Norway,
marcel.u.ahrens@ntnu.no

ABSTRACT

In this paper, investigations on the development of industrial high temperature heat pumps are carried out based on the analysis of the current available components. Ammonia-water hybrid heat pumps combine technologies of an absorption and compression heat pump with a mixture of ammonia and water as refrigerant. The functionality of this process was already been proven in the industrial sector using standard components. In this study, currently available components are investigated for utilization in a hybrid heat pump test facility able to operate at elevated high side pressures to achieve exit temperatures on the secondary fluid side of 140 °C to 180 °C. Critical components are identified and discussed based on defined process requirements. Subsequently, an overview of available components enabling process parameters with a high side pressure of up to 60 bar are presented and necessary adjustments for the use in the planned test facility are discussed.
Keywords: Industrial High Temperature Heat Pump, Hybrid Absorption-Compression Heat Pump, Ammonia-Water Mixture.

1. INTRODUCTION

Conti et al. (2016) have stated an increasing energy demand in the industrial sector in recent years with a clear trend for the future. In addition, in various industrial processes large amounts of low grade waste heat are not exploited due to the lack of waste heat utilization. Arpagaus et al. (2018) have found that industrial processes with a large heat demand in the temperature range up to 150 °C and useable waste heat streams in particular have a great potential for high temperature heat pump applications. Simultaneously, the demand for environmentally benign working fluids such as the natural fluids, ammonia and water, become more dominant.

Due to the given properties, hybrid absorption-compression heat pumps (HACHP) with a zeotropic ammonia-water mixture as working fluid provide a good solution for industrial high temperature heat pump applications. The working principle of this system is based on the Osenbrück cycle, which extends a vapour compression heat pump with an additional solution circuit (Osenbrück, 1895). This extension provides the typical properties of HACHP systems such as the attainable high sink temperature combined with high temperature lift and non-constant temperature glide. For this reason, the ammonia-water HACHP concept is interesting for industrial high temperature applications as for instance the utilization of waste heat streams. Furthermore, the functionality of this process in the industrial sector have already been proven by Nordtvedt et al. (2013) using standard available refrigeration components and achieving sink outlet temperatures up to 120 °C.

In recent years, various authors, such as Jensen (2015) and Nordtvedt (2005), have investigated the HACHP system to identify challenges and potentials for the optimization of process parameters. The development was constantly pushed forward due to the increasing interest in the use of ammonia in refrigeration systems and the associated efforts to optimize the components. They determined that the compressor is a dominant constraint on achievable process conditions due to the limitation of high pressure and discharge temperature. In addition, there is a lack of knowledge and experience in operating the system with higher operating parameters. In particular, this relates to the design of the absorber and the expiration of the absorption process at high pressures and temperatures. The focus of this study is therefore to identify available compressor and absorber solutions for the development of a planned HACHP test facility that can operate at high pressure levels and reach sink outlet temperatures of 140 °C to 180 °C.

In the further course, the general functionality and advantages of the HACHP system are presented. In addition, the characteristics and requirements of the planned test facility are discussed. Subsequently, the focus is placed on the identification of critical components to achieve the defined operating parameters. For this purpose, functions and requirements are defined and possible concepts and solutions for use in high temperature operation are demonstrated. Finally, the results of the study are presented and discussed with regard to usability in the development of the planned test facility considering the given requirements.

2. THE AMMONIA-WATER HYBRID ABSORPTION-COMPRESSION HEAT PUMP

This section deals with the description of the general HACHP cycle as well as the discussion of the characteristics and requirements of the planned test facility.

2.1. Hybrid Heat Pump Cycle with an Ammonia-Water Mixture as Working Fluid

Fig. 1a shows a simplified representation of the Osenbrück cycle, the most basic HACHP cycle. This basic cycle consists of seven main components: three heat exchangers, a liquid-vapour separator, an expansion valve, a solution pump and a compressor. Throughout the entire heat transfer process with the heat source in the desorber, the ammonia-water mixture is in the two-phase region and the ammonia concentration in the liquid phase decreases. Due to incomplete evaporation, a two-phase mixture leaves the desorber (1). A liquid-vapour separator is applied to separate the phases and ensure that only vapour enters the compressor (2) to be compressed to the high pressure side of the cycle (3). The liquid phase, characterized as weak solution, is sent to the solution pump (4) where the pressure level is increased (5). Then, the weak solution passes through an internal heat exchanger (IHX) to increase liquid temperature and improve overall cycle performance (5-6). After the IHX and compressor, the liquid and vapour streams are mixed which typically results in a liquid-vapour mixture (7). In the absorber, vapour is absorbed into the liquid phase rejecting heat to the heat sink. The ammonia concentration in the liquid phase gradually increases, so that the saturated liquid out of the absorber is called strong solution (7-8). Heat is transferred from the strong to the weak solution stream in the IHX (8-9) before the solution is expanded to the low pressure level (9-10) to return to the desorber.

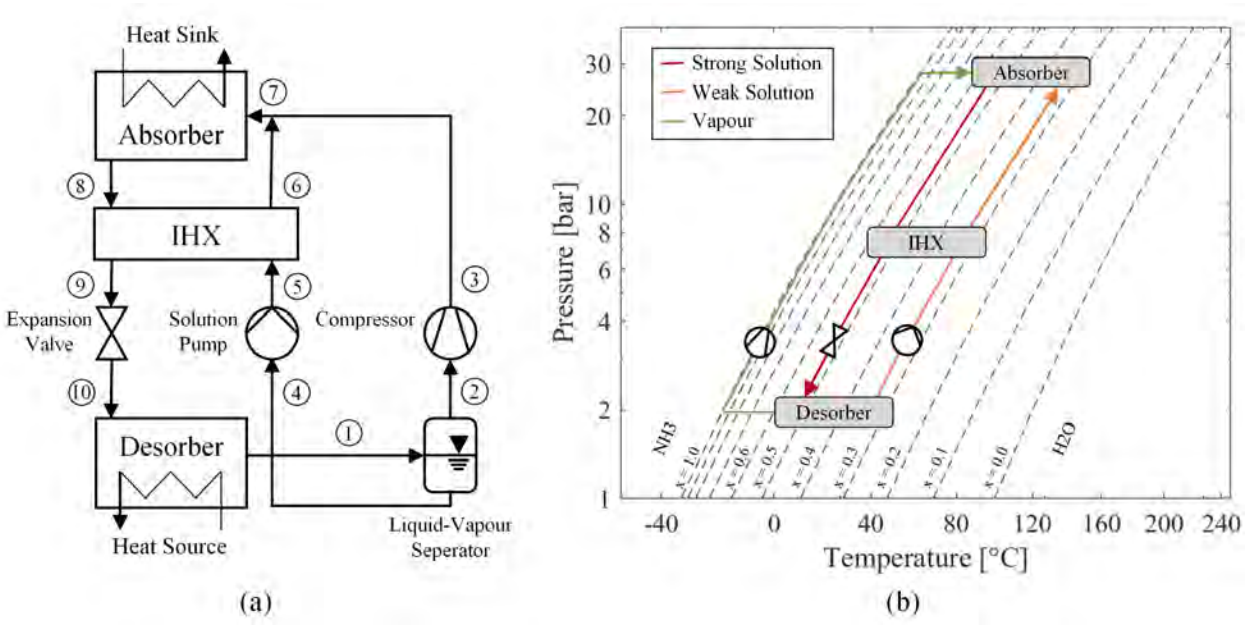

Figure 1: (a) Simplified representation of an absorption-compression hybrid heat pump cycle (b) PTX diagram of saturated liquid for an ammonia-water mixture with hybrid heat pump components

Fig. 1b shows a pressure-temperature-concentration (PTX) diagram of saturated liquid for an ammonia-water mixture including main components and flows of a hybrid heat pump cycle. This representation illustrates the overall functionality and properties of the system, not the actual compression paths. As mentioned by Jensen et al. (2014), the HACHP system has two additional

degrees of freedom compared to conventional vapour compression systems. This ensures the high flexibility and adaptability of the operating parameters to given boundary conditions.
Based on the simplified cycle (see Fig. 1), authors such as Nordtvedt (2005), Kim et al. (2012) and Jensen (2015) examined various process modifications. These include additional components, such as further heat exchangers or circulation and cooling circuits. This allows the system to be further adapted and improved, but complexity has also increased. The following properties and advantages of the system were claimed:

- The ability to vary the composition of the working fluid and circulation ratio increases the flexibility of the system and makes it easier to adapt to temperature fluctuations and heat capacities. By controlling the ammonia concentration of the weak solution, various operating conditions can be achieved and the operation improved.
- Compared to conventional vapour compression heat pumps, which use pure ammonia as the working fluid, higher sink temperatures can be achieved at relatively low discharge pressure.
- Occurring temperature glides due to the use of a zeotropic working fluid during the absorption and desorption process can be adapted to the gliding temperatures of heat sinks and heat sources. This reduces the irreversibility of the system and allows a high temperature rise with comparatively high COP for many operating conditions, and in particular for waste heat applications.

2.2. Characteristics and Requirements of the Planned Hybrid Heat Pump Test Facility

As previously discussed, there is an increasing interest in utilizing waste heat streams of industrial processes using high temperature heat pump applications. The focus of recent years has been on developing and improving existing cycles and components. In addition, the numerical analysis of Jensen (2015) has extensively investigated the potential and requirements of the HACHP system for achieving sink outlet temperatures above the current limit of around 120 °C.
The aim of developing the planned HACHP test facility is to increase the achievable outlet temperatures on the secondary side up to 140 °C to 180 °C and to optimize the system by taking advantage of the developments and improvements of recent years. In addition, the optimization of process parameters and components should be possible. To achieve these goals, the following characteristics are defined for the planned test facility:

- The components of the system must be designed and selected to operate at high temperatures and high pressures to achieve the desired sink outlet temperature.
- In order to test and optimize various operating conditions, it must be possible to vary the weak solution composition as well as the heat source and heat sink temperatures.
- To test and optimize different components of the HACHP cycle, the respective connections of the components must be designed interchangeably.
- In order to ensure the necessary flexibility of the system, auxiliary equipment and measuring instruments must have a sufficiently wide range to cover all possible operating conditions.
- The mass and energy flows must be regarded as relatively small, since it is a laboratory test facility.

Due to the ammonia-water mixture as the working fluid and the desired operating conditions, additional requirements such as material compatibility and oil-free operation are placed on the system:

- When designing the system and selecting the components, attention must be paid to material compatibility. All wetted parts must be made of ammonia-compatible material. Ammonia and hydrous ammonia are fully compatible with materials such as iron, steel, stainless steel and aluminium, but cause corrosion problems in contact with copper, zinc and copper-based alloys (Stene, 2008).
- The oil-free operation of components such as the compressor is desirable to keep the system and in particular the heat exchanger free of lubricant oil. Especially high temperatures and the possible water content in the vapour stream make the oil separation more complex and expensive. The incomplete separation results in lubricating oil in other components of the system, such as the heat exchanger, which affects the heat transfer properties (Zaytsev and Infante Ferreira, 2002).

3. INVESTIGATION OF COMPONENTS FOR USE IN HYBRID HEAT PUMPS

This section is focused on critical components in the design of the planned test facility to achieve the defined characteristics and requirements. Based on Jensen (2015) and Nordtvedt et al. (2013), the compressor for the compression of the ammonia vapour is a critical component of the HACHP system and leads to limitations for the achievable operation parameters. Another critical component is the absorber for the absorption process at the planned high pressure and temperature level, as there is a lack of knowledge and experience for these operating areas. In the further course, the functions and requirements for these components are defined and possible concepts and solutions for use in the planned HACHP test facility are presented and discussed.

3.1. Compressor Solutions for use in Hybrid Heat Pumps at High Temperature Operation

In the HACHP system, the compressor takes over the compression of the ammonia vapour after the liquid-vapour separator from the low pressure to the high pressure level (see Figure 1). As inlet condition for the ammonia vapour at the compressor inlet, a pressure of approximately 2 bar and a temperature of 60 °C are assumed. In addition to the general requirements for components for use in the planned test facility with ammonia-water mixture as working fluid, further requirements are defined based on the desired operating conditions for the compressor used. In order to achieve a high temperature lift and outlet temperatures on the secondary side of 140 °C to 180 °C, a high discharge pressure and pressure ratio are required. For this purpose, the compressor must withstand a discharge temperature of at least 180 °C. According to Neskå et al. (1998), operation with normal lubricants should be possible for discharge temperatures up to 180 °C. Due to the design and properties of the system, it is possible that the ammonia vapour contains a low water content. Therefore, the compressor must be resistant to small amounts of liquid in the vapour stream during the compression.

The investigations of Arpagaus et al. (2018) and other authors have shown that various compressor concepts and solutions are possible for ammonia vapour compression in high temperature heat pump applications. Based on the higher pressure ratios that can be achieved and the smaller swept volume compared to dynamic compression systems, positive displacement compressors, such as the piston and screw compressor, have been identified as promising approaches. Possible concepts and solutions for the compression are presented below.

A basic solution for the compressor system is the compression in one compressor stage. This is possible for pressure ratios and inlet conditions in the appropriate range, depending on the compressor selected. To achieve higher pressure levels with increasing inlet conditions and discharge temperature, the modification of the process cycle as well as the further improvement of the compressors are suitable solutions.

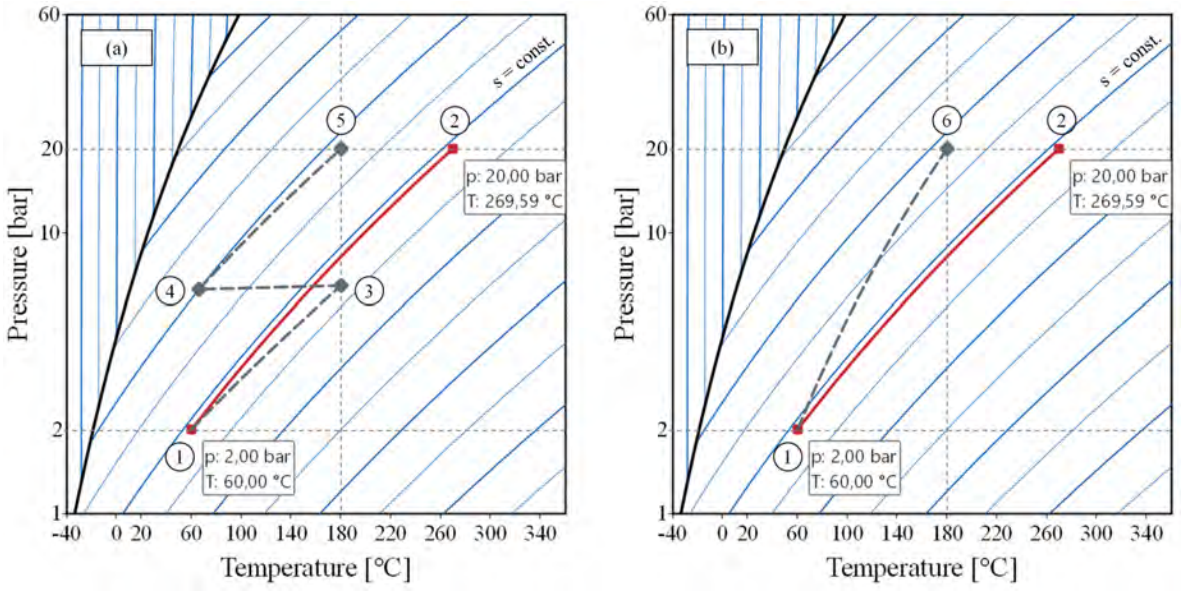

Figure 2: Log p-T diagram of pure ammonia including an isentropic compression compared to (a) two-stage compression with intercooling and (b) one-stage compression with cooling and liquid injection

Fig. 2 shows the isentropic compression (1-2) of pure ammonia in a log p-T diagram from the previously defined input conditions (1) to a freely defined pressure of 20 bar (2). A discharge temperature of almost 270 °C is achieved. Due to the relatively low density and specific heat capacity of ammonia in the superheated vapour phase, the discharge temperature occurring during compression is comparatively high (Stene, 2008). In the ideal case, this is far above the indicated maximum temperature and is even higher for the real compression due to irreversibility. This leads to many problems, such as chemical decomposition of the working fluid, carbonization of the lubricant and collapse of seals (Jensen, 2015). In addition, high discharge temperatures reduce the COP of the HACHP system.

Jensen (2015) discussed different process modifications to achieve the desired pressure rise by holding the discharge temperature in an acceptable range for the compressor. The first possible modification, as shown in Fig. 2a shows a two-stage compression (1-5), whereby the gas is cooled down again after reaching a temperature of 180 °C by an additional IHX (3-4). This two-stage compression can provide a higher pressure level and sink temperature, as the discharge gas temperature is reduced during the compression process. The investigation results have shown, that the option of an additional IHX installed behind the contained IHX caused the lowest cost increase and the highest discharge gas temperature decrease (see Fig. 1).

Another promising concept is the use of a liquid-resistant compressor with the implementation of an injection of the strong solution before or after the IHX. Fig. 2b shows a possible one-stage compression with cooling and liquid injection during the compression process (1-6). The injection can take place on various tasks and can be used for seal cooling and for lowering the discharge temperature through the compression. Zaytsev and Infante Ferreira (2002) investigated the various effects of the additional injection of ammonia-water mixture into the compressor. In general, the liquid injection has positive influence of the compressor volumetric and isentropic efficiency. On the other hand, the liquid injection leads to various challenges due to the complexity of the evaporation processes during the compression. However, oil-free compressors with liquid injection capable of achieving the desired parameters are not readily available.

All approaches have individual advantages and challenges for use in HACHP systems at high temperature operation. Table 1 gives an overview of the previously mentioned and discussed advantages and challenges of the different solutions for the ammonia vapour compression.

Table 1. Overview of solutions for the ammonia vapour compression

	Single-Stage	Multi-Stage	Liquid Injection
Advantages	Lower installation costs	Possible intercooling	Oil-free operation
Challenges	High discharge temperature	Higher complexity	Evaporation process

3.2. Absorber Solutions for use in Hybrid Heat Pumps at High Temperature Operation

Jung et al. (2014) identified the absorber as one of the most significant components in the HACHP system. As mentioned by Nordtvedt et al. (2013), the operation of the hybrid heat pump cycle with ammonia-water as zeotropic mixture leads to large non-constant temperature glides during the desorption and absorption processes. In the absorber, the ammonia concentration in the liquid phase increases due to the absorption of the vapour. The saturation temperature of the mixture decreases from the inlet to the outlet of the heat exchanger due to the considerably lower boiling point of ammonia compared to water. During this absorption process, heat is transferred to the coolant on the secondary fluid side.

For the use of an absorber for the absorption process in a HACHP system, various requirements for the properties of the heat exchanger are defined. In addition to the general requirements, such as the minimization of size and pressure losses, the suitability for the given operating parameters must be considered for use in the planned test facility. Based on Kang et al. (2000), a high area density [m^2/m^3] of the heat transfer surface combined with a high overall heat transfer coefficient is required to achieve a compact size of the heat exchanger. Furthermore, the generation of a good mixture of the vapour and liquid phases and the complete and continuous wetting of the heat transfer surfaces are important.

For the construction of the absorber, different heat exchanger types and absorption modes are available. Previous work has used tube and shell as well as plate heat exchanger types with different orientations and flow directions. Based on Kang et al. (2000), the falling film and bubble absorption

modes were recommended for use in HACHP systems. In the further course, possible solutions and concepts will be presented and discussed.
Minea and Chiriac (2006), for example, used a horizontally arranged shell and tube heat exchanger with a falling film for their investigation of the HACHP system. In this case, the weak solution slides as a thin film on the outside of the horizontal tubes from top to bottom. The ammonia vapour fills the free space and is absorbed into the liquid film with the release of heat to the coolant in the tubes. They mentioned that the driving force for the absorption and amount of mass transfer are related to the ammonia vapour pressure and concentration as well as the composition of the liquid and mass transfer resistance.
An et al. (2013) investigated a vertical plate heat exchanger with bubble absorption mode. Here, the weak solution and ammonia vapour entered the absorber at the bottom and flow to the top with the coolant in counter-flow direction from the top to the bottom. They found that the absorber internal pressure has more effect on the coolant temperature difference than the geometric conditions. In addition, the absorber aspect ratio of the length to the gap between the plates has more effect on the overall heat transfer coefficient than the ratio of the width to the gap.
Due to the investigations carried out and the results obtained, the plate heat exchanger type is increasingly being used for HACHP applications. The ammonia-water mixture can flow downwards as in a falling film type of absorber or upwards as in a bubble type absorber. Jung et al. (2014) stated, that the plate heat exchanger is able to transfer heat very efficiently during the absorption process due to the large surface area and corrugated plates. The plates can be pressed with different shapes to increase the turbulence, fluid distribution and surface area. Because of these capabilities, the design can be much more compact compared to shell and tube heat exchangers. In addition, the plate heat exchanger type can provide a high heat transfer coefficient, good wettability and mixing of the liquid and vapour phases. Figure 3 shows a schematic representation of a plate heat exchanger with falling film and bubble absorption mode. The specified flow directions can be varied depending on the application.

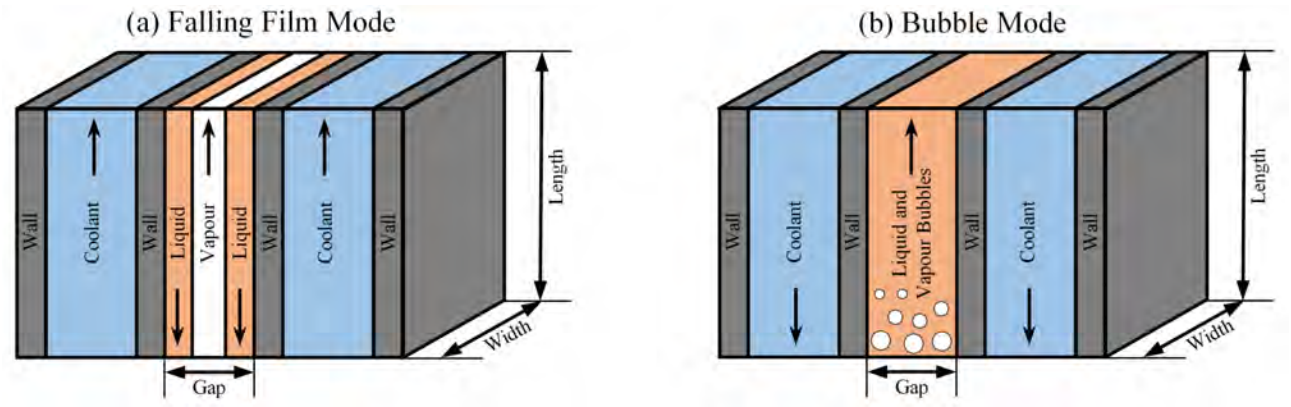

Figure 3: Representation of a plate heat exchanger with falling film and bubble absorption mode

One of the major challenges in using plate heat exchangers for two-phase applications is to ensure good distribution at the inlet and mixture of liquid and vapour over the entire length of the absorber. Because of the easier distribution of the vapour phase, the bubble absorption mode has an advantage over the falling film. In addition, the falling film is susceptible to solvent flow instabilities, which can significantly affect absorption and heat transfer rates (Kang et al., 2000). Table 2 gives an overview of the previously mentioned and discussed advantages and challenges of the different solutions for the absorber design and ammonia absorption mode.

Table 2. Overview of solutions for absorber design and ammonia absorption mode

	Plate Heat Exchanger	Falling Film Mode	Bubble Mode
Advantages	Compact design and good mixing conditions	Low pressure drop and high heat transfer coefficient	High absorption and heat transfer rate
Challenges	Distribution of the mixture	Solvent flow instabilities	Distribution over total length

4. RESULTS AND DISCUSSION

Based on the defined characteristics and requirements of the planned HACHP test facility and the corresponding requirements for the identified critical components, available solutions on the market were investigated. The investigation has shown that the compressor for the ammonia compression is the main constraint to achieve higher process parameter such as the high pressure and temperature level.
Ahrens et al. (2019) conducted a study focusing on available ammonia compressors for HACHP systems in high temperature operation. The results have shown, that various solutions from different manufacturers are currently available on the market. However, to the best knowledge of the author, the available compressors do not achieve the defined requirements for the use in the planned hybrid heat pump facility. It is not possible to operate at high pressure and to achieve exit temperatures on the secondary side of 140 °C to 180 °C. For the development of the planned hybrid heat pump test facility, modifications of the system must be considered. Possible adjustments have already been discussed and may include the division of the compression process or the integration of additional cooling options.
The investigation on the absorber has shown that various solutions are currently available on the market. Plate heat exchangers can be used with the presented absorption modes. The use of both methods by subdividing the absorption process is also possible, as described and used by Nordtvedt (2005). Overall, the available solutions can be operated at the required pressure and temperature levels. Based on these results, the planning and operation of the planned test facility is possible, although the achievable efficiency of the absorption process and heat transfer may not be optimal. In addition, the lack of knowledge and experience for the absorption process and the design of the absorber for the planned operating areas can be improved.
For the further development of the HACHP test facility, the examination of a solution for the ammonia compression is the major challenge. Despite this fact, the design and operation of the absorber should be possible in an acceptable range. Overall, the development of the planned test facility can help to expand knowledge and experience in design and operation and to support the further development of the components.

5. CONCLUSIONS

The aim of this study was the identification and evaluation of suitable components for the development of a planned ammonia-water hybrid absorption-compression heat pump test facility. At the beginning, the general functionality and advantages of the HACHP system were presented. In addition, the characteristics and requirements of the planned test facility were discussed. Subsequently, the focus was placed on the critical components identified to achieve the defined operating parameters. Here, the compressor for the ammonia compression and the absorber for the absorption process at high temperatures and pressures were identified as possible limitations. For this reason, functions and requirements were defined and possible concepts and solutions for use in high-temperature operation were presented and discussed. Finally, the results of the study were presented and discussed with regard to usability in the development of the planned test facility considering the given requirements.
The investigation has shown, that due to the increasing interest and use of ammonia for industrial heat pump applications, a growing range of compressors with high pressures up to 60 bar is available on the market. The use of currently available compressors is not possible without adjustments due to the special requirements for use in the planned test facility. For the absorber, a general use of the available solutions under the given conditions should be possible. However, design and efficiency may not be optimal due to lack of experience in the planned operating area. In general, experience in the operation and improvement of main components as well as the entire cycle can be gained by developing a HACHP test facility.

ACKNOWLEDGEMENTS

The work is part of HighEFF - Centre for an Energy Efficient and Competitive Industry for the Future, an 8-year Research Centre under the FME-scheme (Centre for Environment-friendly Energy Research, 257632). The authors gratefully acknowledge the financial support from the Research Council of Norway and user partners of HighEFF.

REFERENCES

Ahrens, M.U., Hafner, A., Eikevik, T.M. 2019. Compressors for ammonia-water hybrid absorption-compression heat pumps. In 8th IIR Conference: Ammonia and CO2 Refrigeration Technologies, Ohrid.

An, S.S., Jung, C.W., Kim, M., Park, S.R., Kang, C., Kang, Y.T. 2013. Experimental and simulation study on the plate absorber for hybrid heat pump system. Journal of Mechanical Science and Technology 27 (12), 3903-3909.

Arpagaus, C., Bless, F., Uhlmann, M., Schiffmann, J., Bertsch, S.S. 2018. High temperature heat pumps: Market overview, state of the art, research status, refrigerants, and application potentials. Energy 152, 985-1010.

Conti, J., Holtberg, P., Diefenderfer, J., LaRose, A., Turnure, J.T., Westfall, L. 2016. International energy outlook 2016 with projections to 2040 (No. DOE/EIA-0484 (2016)). USDOE Energy Information Administration (EIA), Washington, DC (United States). Office of Energy Analysis.

Jensen, J.K., Reinholdt, L., Markussen, W.B., Elmegaard, B. 2014. Investigation of ammonia/water hybrid absorption/compression heat pumps for heat supply temperatures above 100 °C. In Proceedings of the International Sorption Heat Pump Conference (ISHPC 2014) Vol.1, Center for Environmental Energy Engineering, 311-320.

Jensen, J.K. 2015. Industrial heat pumps for high temperature process applications – A numerical study of the ammonia-water hybrid absorption-compression heat pump. Technical University of Denmark, Kongens Lyngby.

Jung, C.W., An, S.S., Kang, Y.T. 2014. Thermal performance estimation of ammonia-water plate bubble absorbers for compression/absorption hybrid heat pump application. Energy 75, 371-378.

Kang, Y.T., Akisawa, A., Kashiwagi, T. 2000. Analytical investigation of two different absorption modes: falling film and bubble types. International Journal of Refrigeration 23, 430-443.

Kim, J., Park, S-R., Baik, Y-I., Chang, K-C., Ra, H-S, Kim, M., Kim, Y. 2012. Experimental study of operating characteristics of compression/absorption high-temperature hybrid heat pump using waste heat. Renewable Energy 54 (2013), 13-19.

Minea, V., Chiriac, F. 2006. Hybrid absorption heat pump with ammonia/water mixture – Some design guidelines and district heating application. International Journal of Refrigeration 29, 1080-1091.

Neskå, P., Rekstad, H., Reza Zakeri, G., Schiefloe, P.A. 1998. CO2-heat pump water heater: characteristics, system design and experimental results. International Journal of Refrigeration, Vol. 2, No. 3, 172-179.

Nordtvedt, S.R. 2005. Experimental and theoretical study of a compression/absorption heat pump with ammonia/water as working fluid. Norwegian University of Science and Technology, Trondheim.

Nordtvedt, S.R., Horntvedt, B.R., Eikefjord, J., Johansen, J. 2013. Hybrid heat pump for waste heat recovery in Norwegian food industry. Thermally driven heat pumps for heating and cooling, 57-61.

Osenbrück, A. 1895. Verfahren zur Kälteerzeugung bei Absorptionsmaschinen. Deutsches Reichspatent DPR 84084.

Stene, J. 2008. Design and application of ammonia heat pump systems for heating and cooling of non-residental buildings. In 8th IIR Gustav Lorentzen Conference, Copenhagen.

Zaytsev, D., Infante Ferreira, C.A. 2002. Screw Compressor for Ammonia-Water Heat Pump Lubricated by The Process Mixture. International Compressor Engineering Conference. Paper 1581.

Manuscript ID: 1876
DOI: 10.18462/iir.icr.2019.1876

Experimental measurements and techno-economic analysis of a compact DHW heat pump powered by photovoltaic energy

F. AGUILAR[(a)], D. CRESPÍ [(a)], P.V. QUILES [(a)]

[(a)] University Miguel Hernández of Elche

Elche, 03201, Spain, pedro.vicente@umh.es

ABSTRACT

Heat pumps are expected to become the most widely used system for the production of domestic hot water (DHW) in dwellings in the coming years in Europe. The total decarbonisation of Europe's energy system by 2050 is currently producing changes in the sector, where traditional boiler companies have started to market heat pumps.
This study analyses the performance of a compact heat pump for DHW production, which is simultaneously powered by PV panels (470 Wp) and the grid. The system (PV-HP) is designed to consume the energy produced by the PV panels in two ways: to drive the compressor or to power an electrical resistance within the water accumulator. The seasonal performance factor (SPF) of the analyzed system is around 9, which means that 1 kWh of grid electricity produces 9 kWh of thermal energy for DHW.
The techno-economic analysis shows the benefits of this system when it is compared to a DHW heat pump without PV and a standard boiler.
Keywords: Domestic Hot Water, Water Heater, Heat Pump, Photovoltaic Energy, Solar Energy.

1. INTRODUCTION

The European Union has established a roadmap in order to accomplish the goals which have been set in the “Paris Agreement”. For example, the EU has set a binding target to reduce emissions by at least 40% below 1990 levels by 2030.
In this framework, efficient heat pumps with the support of solar energy (thermal or photovoltaic), will probably be the future facilities for many decarbonized buildings in 2050, and they are now an interesting solution to be considered to meet the nZEB requirements.
In recent years, photovoltaic solar energy has been considered in the performance of the heat pump as a whole system. Recently published review of Mohanraj et al. (2018) includes a section about “solar photovoltaic assisted heat pump water heaters”. Poulet and Outbib (2016) analyzed hybrid systems using renewable energy sources without any connection to an electrical network. After their experience, they came to the conclusion that the optimal design consists of photovoltaic panels + air/water heat pumps with improved control which includes strategies based on the weather forecast. Thygesen and Karlsson (2014) concluded that thermal storage (instead of electrical storage) and eventually a “PV controlled heat pump” is the most cost effective system, since the objective should be to reduce the purchase of electricity. Kato and Suzuoki (2014) carried out simulations to demonstrate that it is possible to use heat pump water heaters in homes to improve the operation of the electricity network in residential areas with many photovoltaic installations.
The approach of the authors (Aguilar et al. (2016)) focused on improving the performance of a photovoltaic assisted heat pump for domestic water heating applications. The photovoltaic panels were connected directly to the unit and the photovoltaic electricity was only consumed in the system: either in the compressor or in the electric heater. The heat pump analyzed was an ON/OFF unit with a nominal heating capacity of 1.5 kW and a nominal electrical consumption of 470W (nominal COP=3.19). The system had a thermal storage of 190 liters and no batteries.

2. EXPERIMENTAL WORK

2.1. System Description

The designed system was mainly composed of: a domestic hot water heat pump with a nominal heating capacity of 1.5 kW and a nominal electrical consumption of 470 W (nominal COP=3.19), a

PV facility with a total peak power of 470 W_p and a grid connection. Also, the PV panels were connected a MPPT micro-converter in order to change the direct current (24-30 VDC) to alternating current (230 VAC).
Tables 1 and 2 show the technical characteristics of the heat pump for DHW and the ones of the photovoltaic panels, respectively.

Table 1. Technical characteristics of the heat pump

MIDEA Compak KHP 15 190	Symbol	Unit	Eco
Thermal Capacity	Q_{HP}	W	1500
Compressor Power	$P_{E\text{-}COMP}$	W	470
COP	COP	-	3.19
Refrigerant	---	---	R134a
Evaporator Fan Power	$P_{E\text{-}FAN}$	W	30
Tank Volume	Vol.	L	190

Table 2. Technical characteristics of the PV panels

Eurener 235	Symbol	Unit	Nom.
Nominal power	$P_{N,PV}$	W	235
Panel surface area	A_{PV}	m^2	1.67
Efficiency	Eff_{PV}	%	13.74
Inclination angle	α	º	45
Orientation angle	β	º	0º South

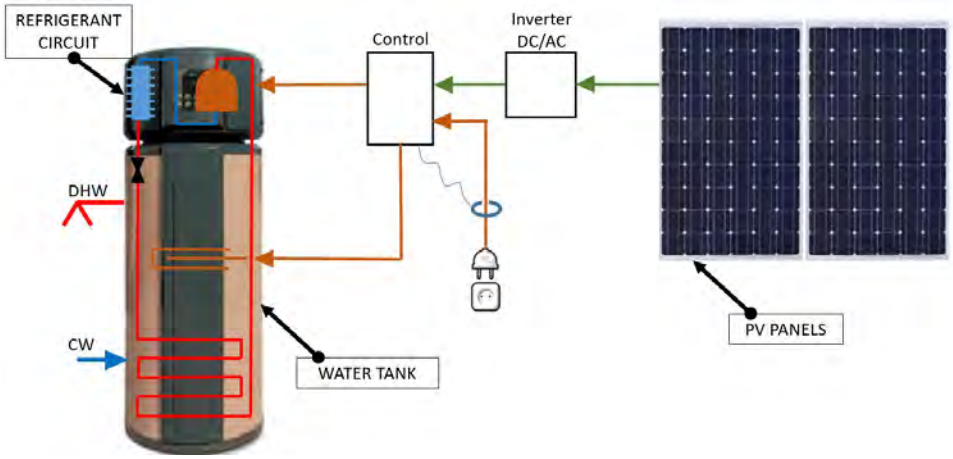

Figure 1: Photovoltaic assisted heat pump (PV-HP) for domestic hot water production

The heat pump is simultaneously powered by the grid and by the PV panels, although the system was designed to prioritize the PV energy supply over the one from the grid. As a result, primary energy and CO_2 emissions are maximized. The coupling between the heat pump, the photovoltaic panels and the electrical network is carried out by means of a network current inhibitor.
Besides, an electrical resistance inside the water tank of the heat pump consumes the electrical energy produced by the PV facility when the heat pump is not working. Thus, the total energy produced by the PV panels is profited in system (by the heat pump if it is working or by the electrical resistance if it is not). The energy from the grid is only necessary if the PV energy is not enough to power the heat pump.
Fig. 1 shows a schematic representation of the described system of the photovoltaic domestic hot water heat pump.

2.2. Experimental Facility

The previously described system was installed on the roof of the University's research laboratory located in Elche (Southeast of Spain).
An experimental facility was specifically built in order to test and to analyze the performance of the system (PV-HP) under real conditions. This facility is represented in Fig. 2 where the subsystem "A" consists on a compact heat pump water heater for domestic water production, which includes: the refrigerant cycle, the water tank and the electrical heater or resistance.
The subsystem B is composed of two PV panels, a grid connection and the necessary devices in charge of managing and integrating these two energy sources (a network current inhibitor, electrical protections, etc.).
Finally, the subsystem "C" is the system used to simulate domestic hot water consumptions without wasting water. An auxiliary tank of this subsystem receives hot water at 55-60ºC from the heat pump, while the water chiller cools it down to 12–15°C.

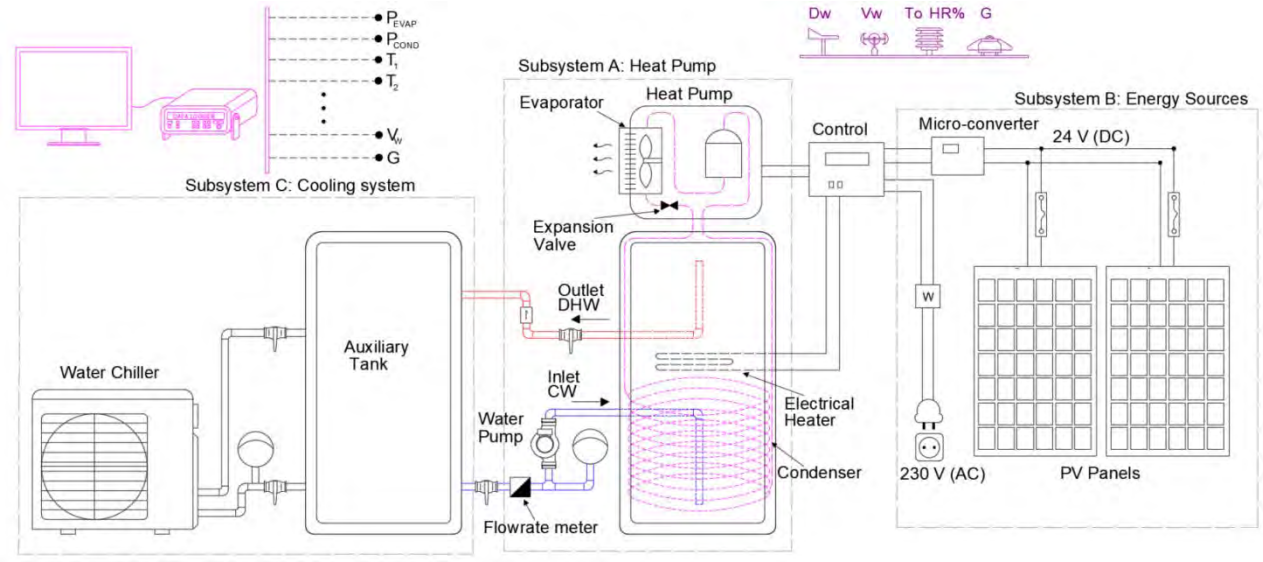

Figure 2: Experimental facility

Besides, several probes and measuring instruments have been installed along the facility in order to measure: meteorological data, refrigerant cycle temperatures and pressures, water flowrate and power consumptions (from the grid and from the PV panels). All the instruments and probes are connected to a HP 34970A Data Acquisition Unit, which makes recordings every 2 minutes.

2.3. Experimental Method

In order to analyze the performance of the described system under real conditions, a water consumption profile was designed to imitate the hot water consumption of a typical four member's family with a total demand of 132 liters per day at 55ºC. Each draw was programmed to last 5:30 minutes, following the draw profile shown in Table 3.

Table 3. Tapping Cycle

Flowrate	Tappings						TOTAL (Liters)
	7:30	8:15	10:00	13:45	21:00	22:00	
4 L·min^{-1}	22 L	22 L	22 L	22 L	22 L	22 L	132

In every experiment the heat pump was engaged at 12:00 and remained so until the water reached a temperature of 55ºC, at which point it was disconnected. Therefore, the photovoltaic contribution could be maximized. The water inlet temperature was kept between 12 and 15ºC by using the water chiller.

This experimental work was carried out during an entire year, so winter and summer results could be obtained. The facility was working with few interruptions (small adjustments and repairs), so that more than 240 days could be analyzed (20 days/month). In order to clarify the behaviour of the system, the experimental test results for one day are analyzed next.
Fig. 3a shows the meteorological data (solar irradiance at 45º and outdoor temperature) on June, 23th. As it can be see, it was a cloudy day, where the total solar irradiation over the PV panels plane was 6.44 kWh/m^2, the average outdoor temperature was 25.1ºC and the average temperature during the working hours of the heat pump was 28.7ºC.
The temperature on the 4 main points of the refrigerant cycle are shown in Fig. 4b. As it can be seen in this figure the heat pump was working between 12 pm and few minutes after 3 pm. At 13:45 there is a domestic hot water consumption and this affects to the refrigerant temperatures.

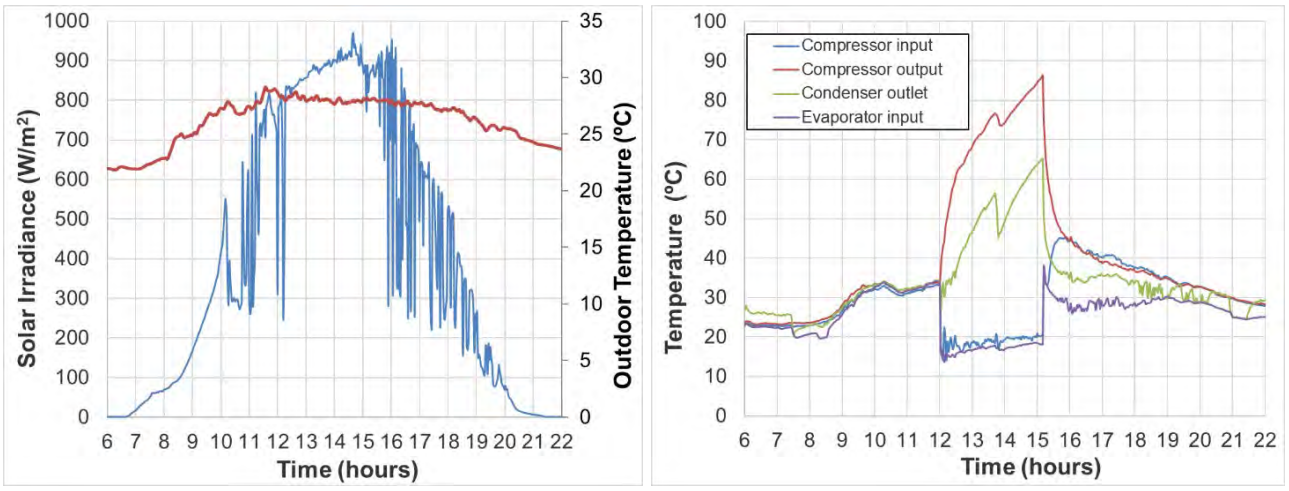

a) b)

Figure 3: a) Meteorological data; b) Temperatures on the refrigerant cycle (June, 23th)

Fig. 4a shows the curves of the solar photovoltaic energy produced by the PV panels (P_{PV}) and the energy consumed by the heat pump (P_{HP}). Different shades of gray have been used in order to explain the origin and destination of each energy flux.
Thus, the area in middle grey corresponds to PV production which is consumed by the heat pump ($E_{PV,HP}$). Dark grey area corresponds to the energy consumed by the heat pump which is provided by the grid ($E_{GRID,HP}$). The electricity consumption from the grid is due to difference between the PV panels production and the heat pump consumption. Finally, light grey is used for the energy produced by the PV panels which is consumed by the electrical ($E_{PV,ELEC}$), which happens when there is PV production but the heat pump is not working.
Consequently, the sum of the middle grey area and dark grey area results in the total electric consumption of the heat pump ($E_{TOT,HP}$).. The sum of the three areas (dark, middle and light grey) is the total electricity consumption, including the heat pump and the electrical resistance ($E_{TOT,SYST}$).
The value of these energy fluxes have been included in the figure for clarification.
By using the methodology described by Aguilar et al. (2016), the useful heat flux provided to the water by the heat pump may be obtained from the experimental measurements.
Fig. 4.b shows the thermal useful power provided to the water (Q_{TOT}), which is the sum of the heat fluxes provided by the heat pump (dark grey area, Q_{HP}) and by the electrical resistance (light grey area, Q_{ELEC}). It is noteworthy, that the thermal power provided by the electrical resistance is calculated as the power provided by the PV panels to the resistance.

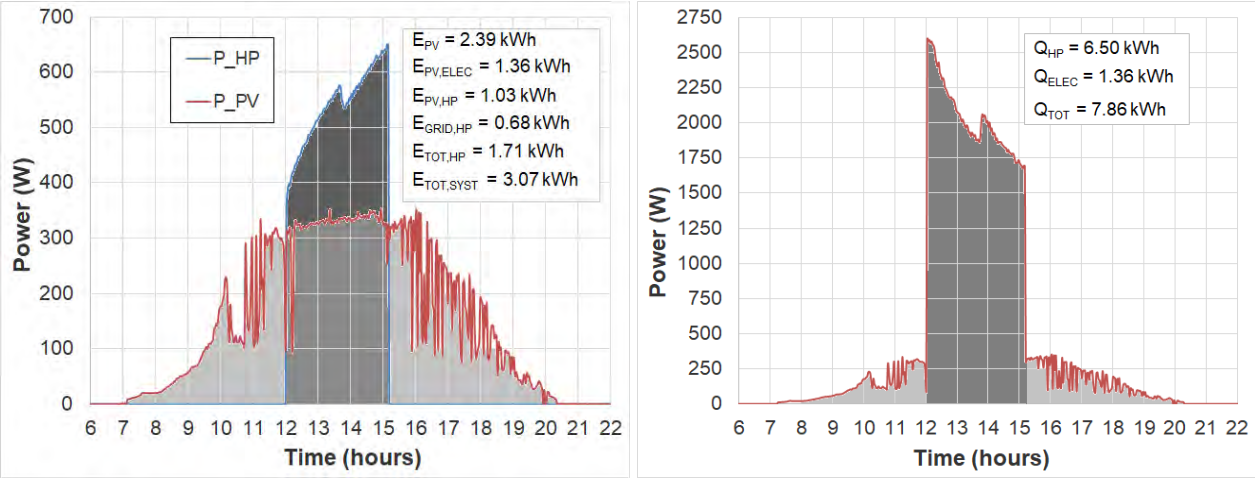

a) b)

Figure 4: a) PV energy and grid energy; b) Thermal power, (June, 23th)

As it is exposed by Aguilar et al. (2016) two Seasonal Performance Factor can be defined. On the one hand, the Seasonal Performance Factor of the heat pump (SPF_{HP}) is known as the ratio between the thermal energy supplied by the heat pump (Q_{HP}) and its total electrical consumption ($E_{TOT,HP}$), as shown in Eq. (1):

$$SPF_{HP} = \frac{Q_{HP}}{E_{TOT,HP}} = \frac{6.50}{1.71} = 3.80 \qquad \text{Eq. (1)}$$

On the other hand, the Seasonal Performance Factor of the system (SPF_{SYST}) is defined as the relation between the total heat given to the water (Q_{TOT}) and the energy taken from the grid ($E_{GRID,HP}$). (see Eq. (2)). This parameter does not take into account the photovoltaic energy because it is a renewable source.

$$SPF_{SYS} = \frac{Q_{SYST}}{E_{GRID,HP}} = \frac{6.50+1.36}{0.68} = 11.56 \qquad \text{Eq. (2)}$$

Also, two key performance factors were defined in order to take into account the solar energy used by the system.
The solar contribution of the heat pump is calculated by following Eq. (3):

$$SC_{HP} = \frac{E_{PV,HP}}{E_{PV}} = \frac{1.03}{2.39} = 0.4309 \approx 43.1\% \qquad \text{Eq. (3)}$$

The solar contribution of the system is known as:

$$SC_{SYS} = \frac{Q_{ELEC}+Q_{HP}\cdot SC_{HP}}{Q_{ELEC}+Q_{HP}} = \frac{1.36+6.50\cdot 0.43}{1.36+6.50} = 0.5294 \approx 52.9\% \qquad \text{Eq. (4)}$$

3. ANNUAL RESULTS

The experimental method described in point 2.3 was used to analyse the behaviour of the system during the whole year. Table 4 summarizes the monthly average values by taken into account all the energy fluxes previously described. This average results have been used to calculate the Seasonal Performance Factor and the Solar Contribution of the system.
The total DHW demand of this typical 4 member's family was of 2247.6 kWh, while the energy losses of the tanks resulted of 596.6 kWh. Then the total thermal energy demand supplied by the system (HP + Electrical Heater) was of 2844.3 kWh.
The electrical energy demanded by the heat pump was of 715.1 kWh (317.6 from the grid and 403.7 from the PV panels), so the SPF of the heat pump was of 3.42. However, if the energy supplied by the PV panels were not taken into account, the system reached a SPF of 8.91, with a Solar Contribution close to 60%.

Table 4. Results of energy fluxes, Average daily results in kWh·day^{-1} - Total results in kWh·year^{-1}

-	$E_{TOT,HP}$	$E_{GRID,HP}$	$E_{PV,HP}$	$E_{PV,ELEC}$	E_{PV}	Q_{HP}	Q_{ELEC}	Q_{TOT}	Q_{DHW}	Q_{LOSS}
January	2.30	0.90	1.40	0.61	2.02	6.94	0.61	7.55	5.56	2.15
February	2.28	0.98	1.43	0.75	2.18	6.90	0.75	7.65	5.67	2.02
March	2.12	1.01	1.17	0.91	2.08	6.65	0.91	7.56	5.55	1.89
April	2.05	0.68	1.37	1.22	2.59	7.51	1.22	8.74	6.69	1.74
May	1.96	0.87	1.09	1.10	2.19	7.17	1.10	8.27	6.38	1.71
June	1.77	0.81	0.97	1.24	2.21	6.48	1.24	7.72	6.53	1.36
July	1.68	0.71	0.98	1.41	2.39	6.39	1.41	7.80	6.69	1.19
August	1.64	0.76	0.88	1.35	2.23	6.43	1.35	7.78	6.66	1.14
Sept.	1.67	0.80	0.87	1.27	2.14	6.34	1.27	7.61	6.42	1.20
Oct.	1.80	0.76	1.04	1.15	2.19	6.41	1.15	7.56	6.31	1.44
Nov.	2.03	1.13	0.89	0.72	1.62	6.54	0.72	7.26	5.74	1.77
Dec.	2.23	1.04	1.20	0.72	1.92	6.78	0.72	7.50	5.67	2.03
Total	715.1	317.6	403.7	379.2	782.9	2449.2	379.2	2844.2	2247.6	596.6
Average	1.96	0.87	1.11	1.04	2.15	6.71	1.04	7.75	6.16	1.63

4. TECHNO-ECONOMIC ANALYSIS

This part of the study is focused on analysing the techno-economic viability of the PV heat pump in comparison with conventional DHW systems. The compared solutions are:

- PV-HP: It consists of the PV supported heat pump previously analysed.
- HP: The same heat pump, but without PV panels.
- Boiler. A natural gas boiler with a seasonal efficiency of 92%.

Table 5 shows the energy conversion factors and the emissions factors used in Spain for electricity and Natural Gas. The results showed in Table 6 have been obtained by applying these conversion factors to the energy demand from Table 4.

Table 5. Conversion factors for Spain (IDAE, 2016)

-	Units	Value
Non-Renewable Primary Energy for Electricity	$kWh_{nRPE} \cdot kWh_E^{-1}$	2.0
Non-Renewable Primary Energy for Natural Gas	$kWh_{nRPE} \cdot kWh_{NG}^{-1}$	1.2
CO_2 emissions for Electricity	$kgCO_2 \cdot kWh_E^{-1}$	0.357
CO_2 emissions for Natural Gas	$kgCO_2 \cdot kWh_{NG}^{-1}$	0.252

Table 6. Thermal analysis

	Units	PV-HP	HP	Boiler
DHW Demand	kWh	2247.6	2247.6	2247.6
Tank Losses	kWh	596.6	596.6	0.0
Total Demand	kWh	2844.2	2844.2	2247.6
SPF	---	8.91	3.42	0.92
Grid Consumption	kWh_E	317.6	830.4	44.9
Gas Consumption	kWh_{NG}	0.0	0.0	2.442.0
Non-RPE	kWh_{nRPE}	635.2	1663.3	3021.7
CO_2 Emissions	$kgCO_2$	113.4	269.9	631.7

According to the results from Table 6, the PV-HP water heater has the lowest Non-renewable primary energy consumption and the lowest CO_2 emissions.

Table 7 includes the total estimated investment costs, all the necessary investments for the construction and the commissioning of the facilities have been considered.

Table 7. Total investment costs, in €

	PV-HP	HP	Boiler
• INVESTMENT IN EQUIPMENTS			
PV Panels	700	0	0
Heat Pump	1200	1200	0
Boiler	0	0	1200
TOTAL INVESTMENT IN EQUIPMENTS	1900	1200	1200
• OTHER INVESTMENTS			
Design, planning and commissioning	200	200	60,0
General costs associated to works	380	240	240
Indirect costs and industrial benefits	95	60	60
TOTAL OTHER INVESTMENTS	675	500	360
TOTAL INVESTMENT COSTS	2575	1700	1560

The photovoltaic panels price drop along the last years (from 6 €/W_P in 2010 to less than 2 €/W_P in 2018), reduces significantly the price of the PV-HP system.
Table 8 summarizes the annualized costs for the analysed solutions. The period under consideration for the study is 25 years, which is also the lifetime of the PV panels. An inflation rate of 3%and a market discount rate of 3% have been also considered. On the one hand, the energy cost of electricity is 0.15 €/kWh and its power cost 40 €/kW/year. On the other hand, the energy and power cost of natural gas are 0.05 €/kWh and 60 €/kW/year, respectively.

Table 8. Annualized costs, in €·years^{-1}

	PV-HP	HP	Boiler
• REPLACEMENT COST			
PV panels (25 years)			
Heat Pump (18 years)	18.1	18.1	
Boiler (18 years)			18.1
TOTAL REPLACEMENT COST	18.1	18.1	18.1
• MAINTENANCE COSTS			
PV panels	30		
Heat Pump	60	60	
Boiler			60
TOTAL MAINTENANCE COSTS	90	60	60
• OPERATION ENERGY COSTS			
Energy Cost (Electricity or Gas)	47.6	125.0	128.9
Power Cost (Electricity or Gas)	40.0	40.0	60.0
TOTAL OPERATION ENERGY COSTS	87.6	165.0	188.9
ANNUALIZED COSTS			
Investment	119.0	78.5	72.1
Replacement	18.1	18.1	18.1
Maintenance	87.4	58.3	58.3
Electricity	85.1	160.2	183.3
TOTAL ANNUALIZED COSTS	309.6	315.1	331.8

5. CONCLUSIONS

A techno-economic analysis of a domestic hot water heat pump supported by photovoltaic panels has been carried out by using the results from a previous experimental work of one year. The heat pump assisted by photovoltaic panels (PV-HP) has been compared to other typical solutions for domestic hot water production. The main conclusions of the experimental analysis are:

- For a DWH demand of 2247.6 kWh·year^{-1}, the proposed system has a consumption of non-renewable primary energy of 635.2 kWh_{nRPE}·year^{-1}, while the heat pump without PV support has 1663.3 kWh_{nRPE}·year^{-1} (2.6 times higher) and the boiler has 3021.7 kWh_{nRPE}·year^{-1} (4.8 times higher).
- The investment cost of the proposed system is 50% higher than the heat pump without photovoltaic panels and 65% higher than the boiler.
- The annualized cost of the three solutions is similar, which is a positive result for the proposed solution (PV-HP), since it is much more efficient.

NOMENCLATURE

E	Electrical energy (kWh)
P	Electrical power (kW or W)
Q	Thermal energy (kWh)
$\dot{Q}$	Thermal power (kW or W)
T	Temperature (ºC)

DHW	Domestic Hot Water
ELEC	Electrical Heater
HP	Heat Pump
PV	Photovoltaic
SYS	System
SPF	Seasonal Performance Factor
SC	Solar Contribution
ST	Solar Thermal Installation
TOT	Total
LOSS	Thermal Losses

REFERENCES

Aguilar FJ, Aledo S, Quiles PV.,2016, Experimental study of the solar photovoltaic contribution for the domestic hot water production with heat pumps in dwellings. Applied Thermal Engineering 101, 379-389.

Kato T, Suzuoki Y., 2014, Autonomous scheduling of heat-pump water heaters for mitigating voltage rise caused by photovoltaic power generation systems. Applied Thermal Engineering 71, 652-657.

Mohanraj M, Belyayev Ye, Jayaraj S, Kaltayev A, 2018. Research and developments on solar assisted compression heat pump systems – A comprehensive review (Part-B: Applications). Renewable and Sustainable Energy Reviews 83, 124-155.

Poulet P, Outbib R., 2015, Energy production for dwellings by using hybrid systems based on heat pump variable input power. Applied Energy. 147, 413-429.

Thygesen R, Karlsson B., 2014, Simulation and analysis of a solar assisted heat pump system with two different storage types for high levels of PV electricity self-consumption. Solar Energy. 103,19-27.

Manuscript ID: 1878
DOI: 10.18462/iir.icr.2019.1878

Performance testing of a geothermal heat pump system in a Canadian residential building

Mohamed R.H. ABDEL-SALAM*, Aqeel ZAIDI

Technology Development, Enbridge Gas Inc.
500 Consumers Rd, M2J 1P8, Toronto, Canada

moa030@usask.ca

ABSTRACT

Geothermal heat pump systems (GHPSs) are more energy efficient than traditional HVAC systems for space heating and cooling applications in buildings. In this paper, the thermal performance of a vertical closed-loop GHPS installed in a single-family residential building located in Innisfil, Canada, is tested, analyzed and evaluated when operated in the cooling mode throughout the hottest week of the year. Results show that the maximum and minimum coefficient of performances (COPs) of the GHPS are 11.1 and 10.7, respectively, and variation of outdoor air temperature has no influence on the COP of the GHPS. The average temperatures of water leaving and entering the ground loop are 13.0ºC and 15.4ºC, respectively. Further, the average evaporator and condenser temperatures are 4.6ºC and 17.9ºC, respectively. It is concluded that compared to conventional air-source heat pumps (ASHPs), the tested GHPS can significantly reduce space cooling energy consumption in Canadian residential buildings.

Keywords: Air-Conditioning, Coefficient of Performance (COP), Energy Saving, Geothermal Heat Pump System.

1. INTRODUCTION

Compared to conventional air-source heat pumps (ASHPs), geothermal heat pump systems (GHPSs) are more energy efficient for space heating and space cooling applications in buildings (Urchueguía et al. 2008; Hwang et al. 2009; Zhai and Yang 2011; Michopoulos et al. 2013; Kharseh et al. 2015; Zhai et al. 2017). Fig. 1 shows a schematic of a vertical closed-loop GHPS. Like ASHPs, GHPSs are composed of a vapor compression cycle, where supply air is cooled in the evaporator during the cooling season and heated in the condenser during the heating season. The main difference between GHPSs and AHPSs is GHPSs include a ground heat exchanger which is used to extract the thermal energy of the ground to provide space heating during the heating season and reject thermal energy of the building to the ground during the cooling season. The main objective of this work is to monitor, analyze, and evaluate the cooling performance of a 14.3-kW vertical closed-loop GHPS installed in a single-family residential building in Innisfil, Canada. The GHPS performance was monitored, analyzed and evaluated throughout the hottest week of the year (June 29th to July 5th, 2018).

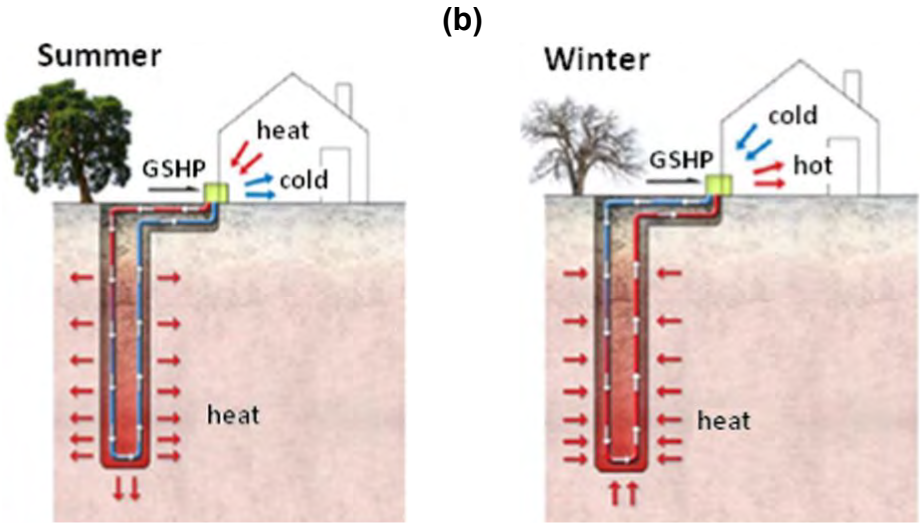

Figure 1: Schematic of a vertical closed-loop geothermal heat pump system (a) cooling mode (b) heating mode (Johnston et al. 2011)

2. THE GEOTHERMAL HEAT PUMP SYSTEM

The GHPS was installed in a bungalow located in Innisfil (latitude 44°29'N and longitude 79°33'E), Canada. The bungalow was built in 2017 and has a total conditioned space of 328 m^2. The average thermal resistance (R-value) of the building's walls and ceiling are 3.3 $m^2K \cdot W^{-1}$ and 10.45 $m^2K \cdot W^{-1}$, respectively. The windows are energy efficient with a total surface area of 24 m^2. The NFRC rating of the windows is R-value of 0.63 $m^2K \cdot W^{-1}$ and SHGC of 0.24. The peak cooling load of this bungalow is 6 kW.

Table 1 gives the specifications of the GHPS tested in this work. The cooling capacity of the GHPS is 14.3 kW with a 17.5 kW ground loop. The GHPS has a vertical closed-loop with 5 boreholes where there is one polyethylene U-tube in each borehole. The depth of the boreholes is 60 m and the inner diameter of the polyethylene U-tube is 19 mm. The GHPS is equipped with a variable capacity compressor and a desuperheater. The desuperheater uses the waste heat to preheat the domestic water which helps reduce domestic hot water power consumption and cost.

Table 1. GHPS specifications.

Cooling capacity (kW)	14.3
Loop size (kW)	17.5
EER	36 - 41
Compressor	Variable capacity scroll
Blower	ECM variable speed
Stages	Variable capacity
Refrigerant	R-410A

The power consumption of the compressor, fan, and ground pump, compressor suction and discharge pressures, evaporator temperature, condenser temperature, superheating, subcooling, water inlet and outlet temperatures and flow rate through the ground loop, set room temperature, and actual room temperature were monitored and data was recorded every 10 seconds. The performance of the GHPS is evaluated based on the overall coefficient of performance (COP_{sys}). COP_{sys} is the ratio between the energy removed from the conditioned space and the total power consumption of the compressor, fan, and ground pump. Equation (1) was used to calculate the COP_{sys} of the GHPS tested in this study.

$$COP_{sys} = \frac{\dot{m}_{air}\left(h_{air,inlet} - h_{air,outlet}\right)}{\dot{W}_{compressor} + \dot{W}_{fan} + \dot{W}_{pump}} \quad \text{Eq. (1)}$$

Where $\dot{m}_{air}$ is the air mass flow rate (kg·s^{-1}), $h_{air,inlet}$ is the return air enthalpy (kJ·kg^{-1}), $h_{air,outlet}$ is the supply air enthalpy (kJ·kg^{-1}), $\dot{W}_{compressor}$ is the compressor power consumption (W), $\dot{W}_{fan}$ is the fan power consumption (W), and $\dot{W}_{pump}$ is the power consumption of the ground loop pump (W).

3. RESULTS AND DISCUSSION

The cooling performance of the GHPS was monitored throughout the hottest week of the year (June 29th to July 5th, 2018). The outdoor air temperature was obtained from Environment and Natural Resources Canada. The average daily outdoor air temperature, set room temperature and actual room temperature are shown in Fig. 2. The average daily outdoor air temperature ranged between 22.3ºC and 27.7ºC. Fig. 2 shows that the GHPS was able to maintain the desired indoor air temperature where the set and actual room temperatures were maintained nearly constant at 25ºC throughout the entire week.

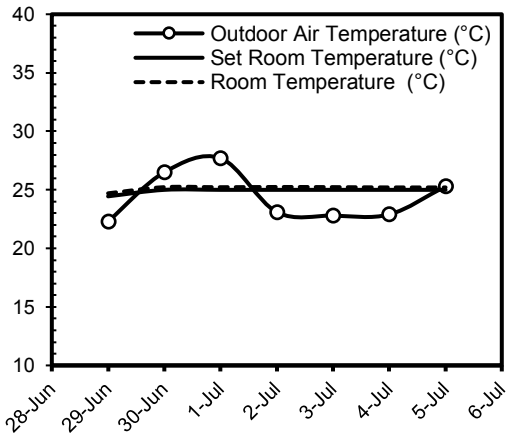

Figure 2: Average daily outdoor air temperature, set room temperature and actual room temperature throughout the hottest week of the year.

The average daily outdoor air temperature and COP_{sys} of the GHPS are shown in Fig. 3. Unlike ASHPs where the COP strongly depends on the outdoor air temperature (i.e, COP decreases as outdoor air temperature increases), Fig. 3 shows that although the average daily outdoor air temperature changed by up to 5.5ºC throughout the week, the COP_{sys} of the GHPS was maintained nearly constant. Thus, variation of outdoor air temperature had negligible influence on the COP_{sys} of the GHPS. This is because the ground temperature remains relatively constant throughout the entire summer. Fig. 3 shows that the COP_{sys} of the GHPS was maintained nearly constant at 11 throughout

the entire week. The average cooling COP of ASHPs ranges between 2 and 5, where ASHPs run at low COPs during the hottest week of the year. Therefore, compared to ASHPs, the GHPS is much more energy efficient and can significantly reduce space cooling energy consumption and greenhouse gas (GHG) emissions.

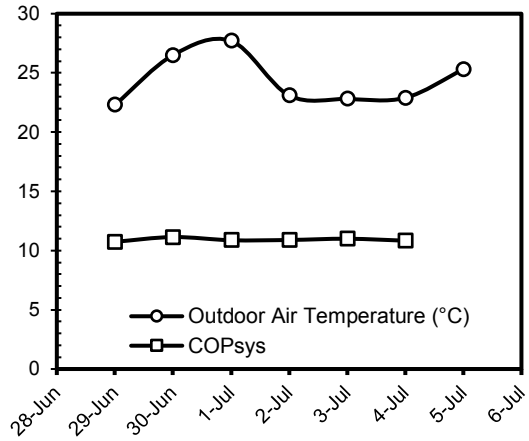

Figure 3: Average daily outdoor air temperature and COP_{sys} of the GHPS throughout the hottest week of the year.

Fig. 4a shows the daily total cooling loads and total power consumption of the GHPS. The total cooling load throughout the week was 525.3 kWh and the total power consumption was 50.3 kWh. The peak daily cooling energy demand of the building was 92.6 kWh and occurred on June 30th and the peak power consumption of the GHPS was 8.7 kWh and occurred on July 1st. Further, the cooling load and total power consumption varied by up to 51% and 47%, respectively, throughout the week. Fig. 4b shows the daily compressor, ground pump, and fan power consumption of the GHPS. It is clear that the compressor was responsible for the largest portion of the total power consumption, where the compressor, ground pump and fan were responsible for 85.7%, 9.6% and 4.7%, respectively, of the total power consumption of the GHPS. Moreover, the compressor power consumption was sensitive to the cooling load variation, whereas variation of cooling load had a negligible influence on the power consumption of fan and ground pump.

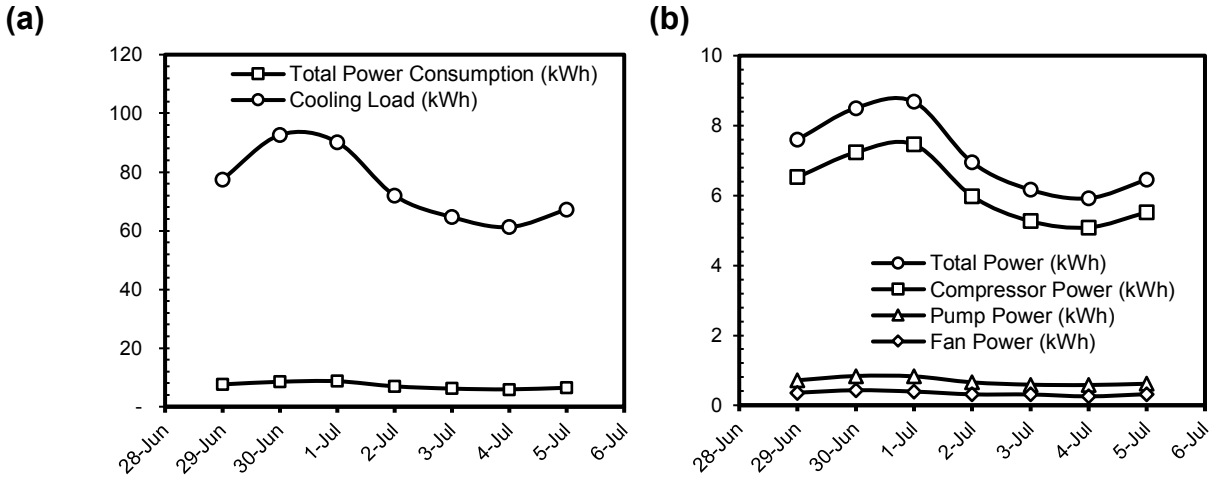

Figure 4: (a) daily total power consumption and cooling load, (b) daily compressor, fan, ground loop pump and total power consumption of the GHPS.

Fig. 5 shows the average daily ground loop entering water temperature (EWT), leaving water temperature (LWT), and water flow rate of the GHPS. The difference between the LWT and EWT was

maintained constant at 2.4ºC throughout the entire week. The average LWT, EWT and water flow rate were maintained nearly constant throughout the entire week. The average LWT, EWT, and water flow rate were 13.0ºC, 15.4ºC, and 35.4 $L \cdot min^{-1}$, respectively.

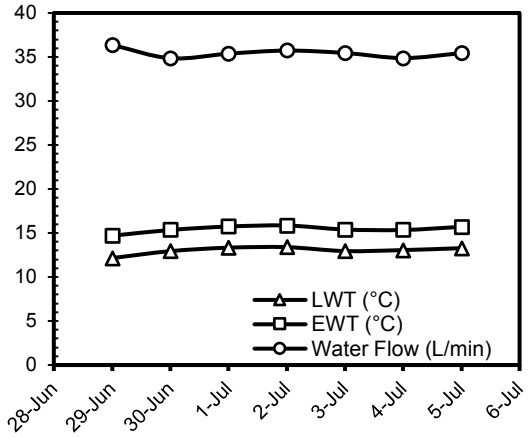

Figure 5: Average daily leaving water temperature, entering water temperature, and water flow rate through the ground loop.

Fig. 6a shows the average daily condenser temperature, evaporator temperature, superheating and subcooling of the GHPS. The average condenser and evaporator temperatures throughout the entire week were 17.9ºC and 4.6ºC, respectively, and the average superheating and subcooling were 7.2ºC and 1.8ºC, respectively. The GHPS tested in this work is equipped with a variable capacity compressor. The average daily compressor suction and discharge pressures are shown in Fig. 6b. The suction and discharge pressures were maintained nearly constant throughout the entire week at 829 kPa and 1,255 kPa, respectively.

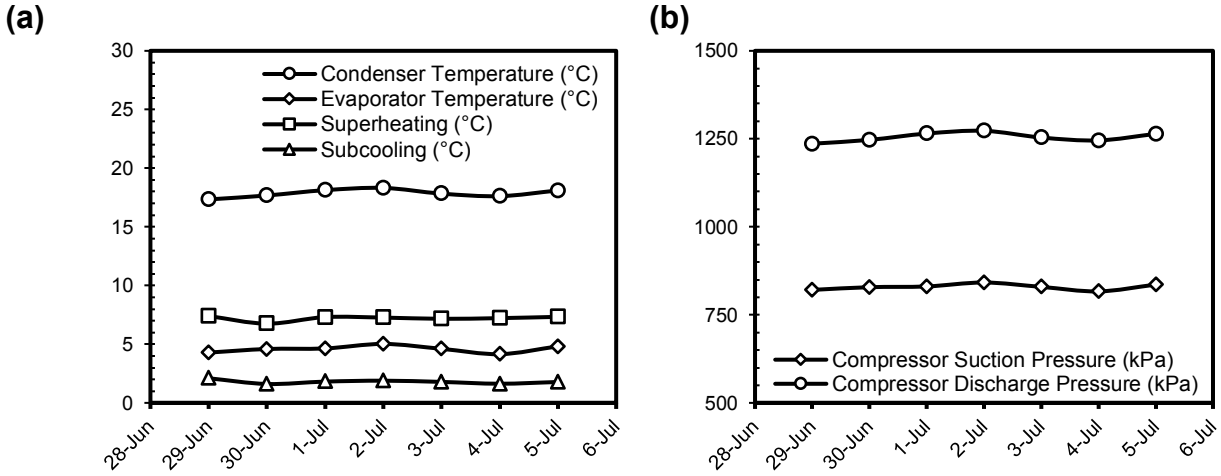

Figure 6: (a) average daily condenser temperature, evaporator temperature, superheating and subcooling, (b) average daily compressor suction pressure and discharge pressure.

4. CONCLUSIONS

The cooling performance of a 14.3-kW vertical closed-loop GHPS was monitored, analyzed and evaluated throughout the hottest week of the year. The GHPS was installed in a single-family detached house (328 m^2 new construction bungalow) in Innisfil, Canada. Results show that the GHPS was able to meet the building's peak cooling load. The minimum and maximum overall COPs of the GHPS are 10.7 and 11.1, respectively. The average temperatures of water leaving and entering the

ground loop were 13.0ºC and 15.4ºC, respectively. Unlike ASHPs, the outdoor air temperature had a negligible influence on the COP_{sys} of the GHPS. It is concluded that compared to conventional ASHPs, GHPS can achieve significant energy savings (up to 450%) when used for residential space cooling applications in Ontario, Canada.

NOMENCLATURE

Parameter	Description	Unit
$h_{air,inlet}$	return air enthalpy	kJ·kg^{-1}
$h_{air,outlet}$	supply air enthalpy	kJ·kg^{-1}
$\dot{m}_{air}$	air mass flow rate	kg·s^{-1}
$\dot{W}_{compressor}$	compressor power consumption	W
$\dot{W}_{fan}$	fan power consumption	W
$\dot{W}_{pump}$	ground loop pump power consumption	W
Acronyms		
ASHP	Air-Source Heat Pump	
COP	Coefficient of Performance	
ECM	Electronically Commutated Motor	
EWT	Entering Water Temperature	
GHG	Greenhouse Gas	
GHPS	Geothermal Heat Pump System	
HVAC	Heating, Ventilation, and Air-Conditioning	
LWT	Leaving Water Temperature	
NFRC	National Fenestration Rating Council	
SHGC	Solar Heat Gain Coefficient	

REFERENCES

Environment and Natural Resources Canada (http://climate.weather.gc.ca/).

Hwang Y., Lee J.K., Jeong Y.M., Koo K.M., Lee D.H., Kim I.K., Jin S.W., Kim S.H., 2009. Cooling performance of a vertical ground-coupled heat pump system installed in a school building. Renewable Energy 34, 578-582.

Johnston I.W., Narsilio G.A., Colls S., 2011. Emerging geothermal energy technologies. KSCE Journal of Civil Engineering 5(4), 643-653.

Kharseh M., Al-Khawaja M., Suleiman M.T., 2015. Potential of ground source heat pump systems in cooling-dominated environments: Residential buildings. Geothermics 57, 104-110.

Michopoulos A., Zachariadis T., Kyriakis N., 2013. Operation characteristics and experience of a ground source heat pump system with a vertical ground heat exchanger. Energy 51, 349-357.

Urchueguía J.F., Zacarés M., Corberán J.M., Montero Á., Martos J., Witte H., 2008. Comparison between the energy performance of a ground coupled water to water heat pump system and an air to water heat pump system for heating and cooling in typical conditions of the European Mediterranean coast. Energy Conversion and Management 49, 2917-2923.

Zhai X.Q., Yang Y., 2011. Experience on the application of a ground source heat pump system in an archives building. Energy and Buildings 43, 3263-3270.
Zhai X.Q., Cheng X.W., Wang R.Z., 2017. Heating and cooling performance of a minitype ground source heat pump system. Applied Thermal Engineering 111, 1366-1370.

Manuscript ID: 217
DOI: 10.18462/iir.icr.2019.0217

Performance analysis of the metamaterial based cool roof for single-family houses

Saihong TANG, Kai ZHANG*, Lufang CHEN, Mingquan MA, Fei LI, Xiaofeng NIU

College of Urban Construction, Nanjing Tech University
Nanjing, 210009, China, kai.zhang.ch@njtech.edu.cn

ABSTRACT

Cool roof with high solar reflectance and high emittance has been demonstrated as an effective way to mitigate heat gain from buildings. The newly proposed metamaterial based radiative cooling surface (MRCS), has an average daily cooling power of 110 $W.m^{-2}$, shows high technical potential for the application in buildings as cool roof. The single-family houses are excellent end users of MRCS roof account for the relatively low cooling load but high ratio of roof area to floor area. To investigate the cooling performance of MRCS roof, three kinds of roof (i.e., MRCS roof, shingle roof, and light-colored roof) are employed in a two-floor single-family house. The cooling benefit of MRCS roof is analyzed with EnergyPlus. The results show that the annual cooling electricity consumption of the house with MRCS roof can be reduced by 15.8% and 8.6% compared to the house with shingle roof and light-colored roof, respectively.
Keywords: Cool roof, Radiative cooling, Passive cooling, Energy saving.

1. INTRODUCTION

The climate zones of marine west coast, mediterranean, wet tropical, and arid receive about 1300 to 1900 $kWh.m^{-2}$ annual-averaged solar radiation (Testa and Krarti, 2017, Zingre et al., 2015a, Suehrcke et al., 2008, Akbari and Konopacki, 2004). And nearly 30% of the solar radiation will be converted into the indoor heat gains of buildings, including 19% through walls and 11% through roof (Zingre et al., 2015b). The building surface with high solar reflectance and high emittance (e.g., cool roof) has been demonstrated as an effective way to mitigate the heat gain from roof accounts for the radiative cooling between cool roof and outer space (Zingre, 2014).

Many attentions had been paid on the cooling energy saving potential of cool roof (Synnefa and Santamouris, 2012). Pisello et al. (2013) studied the cooling efficiency of coupled passive-active cooling system in an industrial building by integrating with cool roof. The results showed that the cool roof was able to eliminate the suction air overheating of the heat pump external units, and the indoor air temperature of the room space was decreased by 2-4 °C. Romeo and Zinzi (2013) indicated that the combination of the moderate thermal insulation and cool roof could significantly improve the cooling efficiency of non-residential buildings in southern European countries. Pisello and Cotana (2014) investigated the effect of cool roof on a traditional residential building in central Italy based on the year-round monitoring data. Their results showed that the cool roof could reduce the attic temperature by up to 4.7 °C during the hottest period of summer. Zingre et al. (2015) proposed a new RTTV (i.e., room thermal transfer value) index to calculate the annual average heat gain from the roof, which could be used to indicate the cooling benefit of cool roofs. Although radiative cooling technologies had been proposed for many years, the applications were limited to nighttime conditions since the mismatch of radiative cooling and solar radiation in the daytime (Spanaki et al., 2014, Cotana et al., 2014, Hu et al., 2016). The newly proposed metamaterial based radiative cooling surface (MRCS), which can be used for both nocturnal and diurnal radiative cooling, shows high technical potential for the application in buildings as the cool roof (Zhai et al., 2017). However, the MRCS has an average daily cooling power of 110 $W.m^{-2}$ accounts for direct thermal measurement (Zhang et al., 2018) which is relative lower to the cooling load of industry buildings. And the cool roof has always only benefit to the top floor of the building. Thus, the single-family houses are excellent end users of the MRCS roof account for the relatively low cooling load but high ratio of roof area to floor area.

To investigate the cooling performance of MRCS roof, three kinds of roof (i.e., MRCS roof, shingle roof, and light-colored roof) were employed in a two-floor single-family house. The cooling benefit of MRCS roof was analyzed by using EnergyPlus. Ant then the cooling electricity saving potential of the house with MRCS roof was discussed in detail by comparing with the house with shingle roof and light-colored roof.

2. METHODS

2.1. Description of Model

A two-floor single-family house located at San Francisco, CA of the U.S. was selected to investigate the cooling performance of MRCS roof. The model originated from the U.S. Department of Energy (DOE) had eight windows and two doors on the building envelopes, and the orientation of the house had been defined in this model (Online resource, 2019a). The dimension and the detailed parameters were given in Fig. 1 and Table 1. The weather data employed in this study was also from online resource of U.S. DOE (Online resource, 2019b).

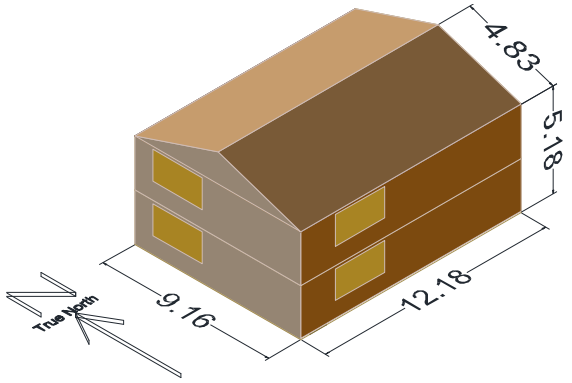

Figure 1: Sketch of the two-floor single-family house

Table 1. Detailed parameters of the two-floor single-family house

Items	Description
Floor area	204 m^2
Roof area	118 m^2
Window-wall ratio	10%
Occupants	3
Air conditioning system	Split air conditioner
Indoor air temperature setpoint	Cooling: 24 °C Heating: 22 °C
Thermal resistance	Wall: R13 Roof: R7
Thermal emittance	MRCS roof: 0.93 Light-colored roof: 0.87 Shingle roof: 0
Solar absorptance	MRCS roof: 0.04 Light-colored roof: 0.31 Shingle roof: 0.75

To clearly indicate the cooling performance of MRCS roof, three type roofs were employed in this study, including MRCS roof, shingle roof (i.e., typical roof of the residential building in the U.S.), and light-colored roof (i.e., typical cool roof). The model was simulated by using EnergyPlus, in which the two-floor single-family house was divided into two zones (i.e., living zone and attic zone). The living zone was conditioned by a split air conditioner, and the attic zone was unconditioned. The detailed parameters were also introduced in Table 1.

2.2. Heat Transfer from Cool Roof

As shown in Fig. 2, the heat transfer from the cool roof was relative complex. In Fig. 2, the q_{cond} was the heat conduction from the cool roof to the attic zone, the q_{sol} was the solar absorption by the cool roof, the q_{conv} was the convective heat transfer between the cool roof and ambient air, and the q_{rad} was the heat transfer between the cool roof and outer space through radiative cooling.

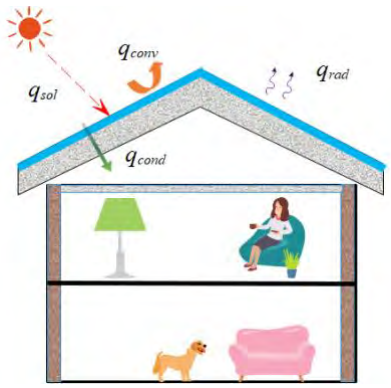

Figure 2: Schematic of heat transfer for cool roof

The models of above heat transfer progress were as follows (Zhang et al., 2014, Zhang et al., 2018):

$$q_{cond} = \frac{\alpha}{\delta}\Delta T \quad \text{Eq. (1)}$$

$$q_{sol} = \lambda I_{sol} \quad \text{Eq. (2)}$$

$$q_{conv} = h\left(T_{surf} - T_{amb}\right) \quad \text{Eq. (3)}$$

$$q_{rad} = \sigma\varepsilon_{surf}\left(T^4_{surf} - T^4_{sky}\right) \quad \text{Eq. (4)}$$

where α is the heat conductivity coefficient in W.mK, δ is the thickness of the roof in m, $\triangle T$ is the temperature difference between roof and attic zone in K, λ is solar absorption coefficient, I_{sol} is the incident solar radiation in W.m^{-2}, h is the convective heat transfer coefficient in W.m^{-2}K, T_{surf} is the surface temperature of cool roof in K, T_{amb} is the ambient air temperature in K, σ is the Stefan-Boltzmann constant in W.m^{-2}K^{-4}, which is 5.67×10^{8}, ε_{surf} is the emittance of cool roof, T_{sky} is the effective sky temperature in K.

In Eq. (3), h was derived from (Bliss, 1961, Clark and Allen, 1978):

$$h = h_n + h_f \quad \text{Eq. (5)}$$

$$h_n = \begin{cases} \dfrac{9.482\left|T_{surf} - T_{amb}\right|^{\frac{1}{3}}}{7.238 - \left|\cos\alpha\right|} \left(T_{surf} < T_{amb}\right) \\ \dfrac{1.810\left|T_{surf} - T_{amb}\right|^{\frac{1}{3}}}{1.382 + \left|\cos\alpha\right|} \left(T_{surf} > T_{amb}\right) \end{cases} \quad \text{Eq. (6)}$$

$$h_f = 2.537 W_f R_f \left(\frac{PV_z}{A_s}\right)^{\frac{1}{2}} \quad \text{Eq. (7)}$$

where h_n is the natural convection component in W.m^{-2}K, h_f is the forced convection component in W.m^{-2}K, W_f is the wind direction modifier, R_f is the roughness multiplier of roof, P is the perimeter length of roof in m, V_z is the local wind speed in m.s^{-1}, A_S is the area of roof in m^2.
In Eq. (4), T_{sky} could be calculated by (Collins and Parker, 1998):

$$T_{sky} = \varepsilon_{sky}^{\frac{1}{4}} T_{amb} \quad \text{Eq. (8)}$$

$$\varepsilon_{sky} = 0.711 + 0.56(\frac{T_d}{100}) + 0.711(\frac{T_d}{100})^2 \quad \text{Eq. (9)}$$

where ε_{sky} is the average spectral and directional longwave emissivity/absorptivity of the atmospheric of cool roof, T_d is the ambient dewpoint temperature in K.

3. RESULTS AND DISCUSSION

3.1. Cooling Benefit of MRCS Roof

The cold energy from cool roof (i.e., light-colored roof or MRCS roof) was generated by the radiative cooling, which could be considered as a kind of “free” cooling. The benefit of this cold energy could result in a reduction of the cooling load addressed by the split air conditioner. It also meant that the decreased cooling load would be covered by the cold energy produced by the cool roof. The cooling load afforded by the split air conditioner was calculated by using EnergyPlus for the house with these three kinds of roof separately. As shown in Fig. 3, the cooling load was significantly reduced while the light-colored roof or MRCS roof was employed. Especially for the application of MRCS roof, the annual cooling loads were reduced by 16.3% and 8.5% compared to shingle roof and light-colored roof, respectively. Although the cooling load could be reduced by applying the light-colored roof compared with the shingle roof, the cooling benefit was still lower than the MRCS roof accounts for the relative higher solar absorptance.

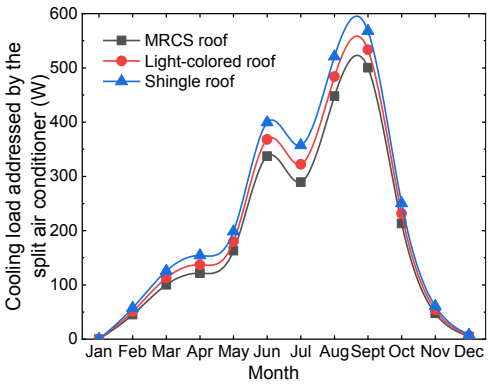

Figure 3: Cooling load addressed by the split air conditioner

3.2. Annual Cooling Electricity Saving Potential

As mentioned in section 3.1, the cooling load afforded by the split air conditioner of the building with MRCS roof was significantly reduced compared to that in the buildings with shingle roof and light-colored roof. This will shorten the running period of the split air conditioner, and thus resulting in a reduction of cooling electricity consumption. The annual cooling electricity consumption of the house with three kinds of roof were shown in Fig. 4. Both of MRCS roof and light-colored roof could reduce the energy consumption of the building, and the annual cooling electricity consumption of MRCS roof and light-colored roof were decreased by 87.66 kWh and 44.67 kWh compared to that of shingle roof, respectively. Thus, more cooling benefit could be achieved by applying the MRCS roof. For the house with MRCS roof, the annual cooling electricity consumption was about 465.6 kWh, which was 15.8% and 8.6% lower to that of the house with shingle roof and light-colored roof, respectively.

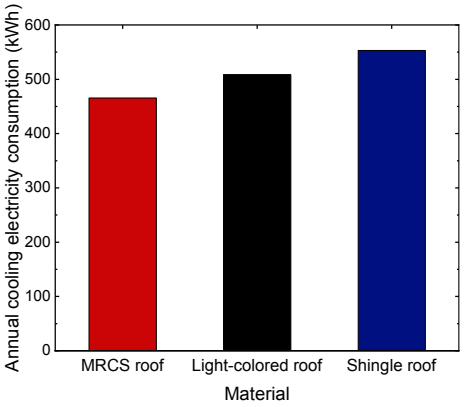

Figure 4: Annual cooling electricity consumption

3.3. Comparison of Monthly Cooling Electricity Consumption

To clearly indicate the cooling performance of MRCS roof, the monthly cooling electricity consumption of the selected two-floor single-family house for the three kinds of roof were presented in Fig. 5. Most of the cooling electricity was consumed in cooling season (i.e., June to September) accounts for the higher cooling demand. In the cooling season, the average monthly cooling electricity consumption of the house with MRCS roof was 80.5 kWh, resulting a reduction of 14.7% and 7.8% by comparing with the house using shingle roof and light-colored roof, respectively. Although small cooling demand was required in the cold month (i.e., November to March), the percentage of cooling electricity saving achieved by applying the MRCS roof was higher than that in cooling season. And the cooling electricity consumption of the house with MRCS roof was reduced by 21.1% and 11.5% compared to the house with shingle roof and light-colored roof respectively in the cold month.

The detailed results were all presented in Table 2. In addition, the orientation and slope angle of the roof also have significant effects on the cooling performance of the cool roof, and the detailed effects will be conducted in our future study.

Table 2. Detailed cooling load and cooling electricity consumption

Months	MRCS roof		Light-colored roof		Shingle roof	
	Cooling load (W)	Cooling electricity (KWh)	Cooling load (W)	Cooling electricity (KWh)	Cooling load (W)	Cooling electricty (KWh)
Jan	0	0	0	0	0	0
Feb	45.14	8.26	50.87	9.29	57.32	10.42
Mar	100.33	20.75	112.84	23.26	125.71	25.91
Apr	121.57	24.72	137.29	27.83	154.31	31.21
May	162.85	34.77	179.76	38.25	198.23	42.07
Jun	337.19	69.95	368.17	76.29	399.45	82.71
Jul	289.16	58.15	322.39	65.03	357.1	72.2
Aug	447.73	93.95	483.77	101.53	520.96	109.3
Sept	500.29	100.27	533.42	106.96	567.9	113.87
Oct	213.31	44.85	231.61	48.73	250.23	52.6
Nov	47.42	9.1	54.12	10.31	60.79	11.59
Dec	4.81	0.79	6.23	1.07	7.69	1.34

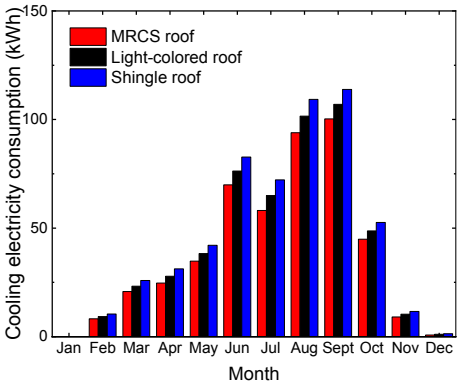

Figure 5: Monthly cooling electricity consumption

4. CONCLUSION

In order to study the energy saving potential of MRCS roof, the cooling performance of the building with three kinds of roof (i.e., MRCS roof, shingle roof, and light-colored roof) were compared in a two-floor single-family house located at San Francisco, CA of the U.S. The cooling load addressed by the MRCS roof was analyzed, and both annual and monthly cooling electricity consumption of the split air conditioner were discussed in detail for the house with MRCS roof. The main conclusions were as followings:

- By employing the MRCS roof, the cooling load afforded by the split air conditioner of the two-floor single-family house was decreased by 16.3% and 8.5% compared to the house with shingle roof and light-colored roof, respectively.
- The annual cooling electricity consumption of the house with MRCS roof was 15.8% and 8.6% lower to that with shingle roof and light-colored roof.

ACKNOWLEDGEMENTS

This work is supported by grants from the National Natural Science Foundation of China (No. 51878342) and Jiangsu Provincial Department of Housing and Urban Rural Construction (No. 2018ZD067).

NOMENCLATURE

A_S	roof area (m^2)	h	convective heat transfer coefficient ($W.m^{-2}K$)
h_f	forced convection component of roof ($W.m^{-2}K$)	h_n	Nature convection component of roof ($W.m^{-2}K$)
I_{sol}	incident solar radiation ($W.m^{-2}$)	α	heat conductivity coefficient ($W.m^{-2}K$)
P	perimeter length of roof (m)	R_f	roughness multiplier of roof
T_{amb}	ambient air temperature (K)	T_d	ambient dewpoint temperature (K)
T_{sky}	effective sky temperature (K)	T_{surf}	surface temperature of cool roof (K)
ΔT	the temperature difference between the two sides of the roof (K)	V_z	local wind speed ($m.s^{-1}$)
W_f	wind direction modifier	ε_{sky}	average spectral and directional longwave emissivity/absorptivity of the atmospheric
ε_{surf}	emittance of cool roof	σ	Stefan-Boltzmann constant ($W.m^{-2}K^{-4}$)
λ	solar absorption coefficient	δ	Thickness of the roof (m)

REFERENCES

Akbari, H., Konopacki, S., 2004. Energy effects of heat-island reduction strategies in Toronto, Canada. Energy 29, 191-210.

Bliss, Jr RW., 1961. Atmospheric radiation near the surface of the ground: a summary for engineers. Sol Energy 5, 103–120.

Clark G., Allen C., 1978. The estimation of atmospheric radiation for clear and cloudy skies. In: Proc 2nd National Passive Solar Conference, p, 675–678.

Collins, T., Parker, S., 2015. Technology Installation Review: WhiteCap Roof Spray Cooling System. Pacific Northwest National Laboratory, Richland, WA Accessed October, 1998.

Cotana, F., Rossi, F., Filipponi, M., Coccia, V., Pisello, AL., Bonamente, E., et al. 2014. Albedo control as an effective strategy to tackle Global Warming: a case study. Appl Energy 130, 641–647.

Hu, M., Pei, G., Wang, Q., Li, J., Wang, Y., Ji, J., 2016. Field test and preliminary analysis of a combined diurnal solar heating and nocturnal radiative cooling system. Appl Energy 179, 899–908.

Pisello, A.L., Cotana, F., 2014. The thermal effect of an innovative cool roof on residential buildings in Italy: Results from two years of continuous monitoring. Energ Buildings 69, 154-164.

Pisello, A.L., Santamouris, M., Cotana, F., 2013. Active cool roof effect: impact of cool roofs on cooling system efficiency. Adv Build Energ Res 7, 209-221.

Raman, A., Anoma, M., Zhu, L., Rephaeli, E., Fan, S., 2014. Passive radiative cooling below ambient air temperature under direct sunlight. Nature 515, 540-544.

Romeo, C., Zinzi, M., 2013. Impact of a cool roof application on the energy and comfort performance in an existing non-residential building. A Sicilian case study. Energ Buildings 67, 647-657.

Sabbagh, J., Khalifa, A., Olwi, I., 1993. Development of passive dry cooling system for power plants in arid land. Sol Energy 51, 431-447.

Spanaki, A., Kolokotsa, D., Tsoutsos, T., Zacharopoulos, I., 2014. Assessing the passive cooling effect of the ventilated pond protected with a reflecting layer. Appl Energy 123, 273–280.

Suehrcke, H., Peterson, E., Selby, N., 2008. Effect of roof solar reflectance on the building heat gain in a hot climate. Energ Buildings 40, 2224-2235.

Synnefa, A., Santamouris, M., 2012. Advances on technical, policy and market aspects of cool roof technology in Europe: The Cool Roofs project. Energ Buildings 55, 35-41.

Testa, J., Krarti, M., 2017. A review of benefits and limitations of static and switchable cool roof systems. Renew Sust Energ Rev 77, 451-460.

Zhai, Y., Ma, Y., David, S., Zhao, D., Lou, R., Tan, G., Yang, R., Yin, X., 2017. Scalable-manufactured randomized glass-polymer hybrid metamaterial for daytime radiative cooling. Science 355, aai7899.

Zhang, K., Zhao, D., Zhai, Y., Yin, X., Yang, R., Tan, G., 2017. Modelling study of the low-pump-power demand constructal T-shaped pipe network for a large scale radiative cooled-cold storage system. Appl Therm Eng 127, 1564-1573.

Zhang, K., Zhao, D., Yin, X., Yang, R., Tan, G., 2018. Energy saving and economic analysis of a new hybrid radiative cooling system for single-family houses in the USA. Appl Energ 224, 371-381.

Zhang, X., Zhu, T., An, Q., Ren, Z., Mei, F., 2014. Heat Transfer, sixth ed., China Architecture & Building Press, Beijing.

Zingre, K., 2014. Building energy savings using high-albedo-high-emittance (cool) roof materials. Doctoral Dissertation, Nanyang Technological University 2014.

Zingre, K., Wan, M., Wong, S., Toh, W., Lee, I., 2015a. Modelling of cool roof performance for double-skin roofs in tropical climate. Energy 82, 813-826.

Zingre, K., Wan, M., Tong, S., Li, H., Chang, V., Wong, S., Toh, W., Lee, I., 2015b. Modeling of cool roof heat transfer in tropical climate. Renew Energy 75, 210-223.

Zingre, K., Wan, M., Yang, X., 2015c. A new RTTV (roof thermal transfer value) calculation method for cool roofs. Energy 81, 222-232.

Online source, retrieved on January 24, 2019a, https://www.energycodes.gov/development/residential

Online source, retrieved on May 11 2019b, https://energyplus.net/weather-location/north_and_central_america_wmo_region_4/USA/CA/USA_CA_San.Francisco.Intl.AP.724940_TMY3

Manuscript ID: 283
DOI: 10.18462/iir.icr.2019.0283

Relationship between specific energy consumption and size of supermarket stores

Alan FOSTER, Tim BROWN, Judith EVANS and Graeme MAIDMENT

London South Bank University, Churchill Building, North Somerset, Langford, UK,

alan.foster@lsbu.ac.uk.

ABSTRACT

Energy consumption data for 2017 were analysed for 190 retail (supermarket) stores from one retailer in the UK. The relationship between energy consumption and store size was investigated. The mean energy intensity defined by the ratio of electrical energy consumption across the sales floor area was 866 kWh.m^{-2}.yr^{-1} for an average sales floor area of 469 m^2. Plotting energy intensity against store size showed that smaller stores had a higher energy intensity. Measuring energy intensity using electrical energy consumption, total energy consumption, sales or gross floor area, perimeter area of the store and store volume all showed a similar trend. Electrical energy consumption is well correlated with refrigeration capacity (r^2 = 0.779), however, it is has a slightly better correlation with sales floor area (r^2 = 0.883). . When including these data with other data from previous studies, it can be seen that large stores (supermarkets) had an approximately constant energy intensity (decreasing slightly with increased floor area) and smaller stores (convenience) had a much higher energy intensity which increases strongly with decreasing floor area. Therefore to represent stores ranging from small to large a power law relationship is required.

Key words: Benchmarking, supermarket, energy consumption, retail

1 INTRODUCTION

In the UK, the retail sector accounts for 4.3 million tonnes of oil equivalent (MTOE) per year or 9.9 $MtCO_{2e}$ emissions (Lee *et al*., 2009). Seventy per cent of this energy use is from electricity. Foster *at al.* (2018) showed that refrigeration accounts for an average of 33% of total electrical energy for a UK retailer (based on 565 stores).

Comparing energy consumptions between different stores is not sensible unless the size of the store is taken into account, e.g. a large store should use more energy than a smaller store. Therefore, energy intensity, sometimes called specific energy consumption, is considered a useful metric to compare the energy efficiency of different size retail stores. Energy intensity is calculated by taking a metric of the energy consumption (the dividend) and dividing by another metric of the size of the store (the divisor) which normalises the data to allow comparisons between different size stores. The two dividends used are either the electrical energy consumption (EEC) or the total energy consumption (TEC), which includes natural gas. The two divisors used are either the gross floor area (GFA) or the sales floor area (SFA). There is no standard measurement and therefore data is often presented using either a dividend or divisor, making it difficult for comparisons.

Tassou *et al.* (2011) showed that energy consumption and emissions from supermarkets varies widely and can depend on many factors such as the type and size of the store, business and merchandising practices and refrigeration and environmental control systems used. Their data showed that electrical energy intensity plotted against SFA followed a power law with almost constant electrical intensity at high sales area and electrical intensity rising rapidly for small sales area. For small (convenience) stores with self-contained ‘integral’ refrigeration equipment, energy intensities were approximately 300 kWh.m^{-2}.yr^{-1} higher than stores using predominantly centrally located ‘remote’ refrigeration equipment. They also showed the standard deviation of the stores

with integral refrigeration was also slightly higher than the stores with remote refrigeration. Other factors that were considered to have an important influence on the electrical energy intensity of convenience stores, were the balance between temperature controlled (refrigerated) and ambient products and the balance between frozen and chilled food cabinets.

Chung *et al* (2006) showed energy intensity was affected by building age, floor area, operation schedule, number of customers and occupants' behaviour. Foster *et al.* (2018) showed energy intensity was related to store age and opening hours. In data from one UK retailer's stores Foster *et al.* (2018) showed energy intensity decreasing linearly with floor area and energy intensities which were significantly lower than those presented by Tassou *et al.* (2011).

This paper analyses recent, so far unpublished, UK supermarket energy intensities from a retailer with predominantly smaller stores than those previously analysed by Foster *et al.* (2018).

Different ways of calculating energy intensity and the relationship between the size of stores' refrigeration systems and energy intensities are investigated. The paper also compares the new data on smaller stores with previously published data on mainly larger stores to better ascertain the relationship of energy intensity over a large range of store sizes.

2 METHOD

Energy consumption data for 2017 was analysed for 190 retail stores from one retailer in the UK.

Energy intensity was calculated using both EEC and TEC as the dividend and SFA and GFA as the divisor. Energy intensities were also calculated using two other divisors, perimeter area (PA) and store volume (SV)

As the heat flow due to conduction into and out of a building through the walls is generally proportional to the total surface area of all sides of the building (including floor and roof), it was considered that energy consumption may better correlate with the perimeter surface area, which in this analysis was termed PA. The height of each of the stores was unknown, however the retailer approximated that convenience stores (SFA < 280 m^2) had a celling height of 3.2 m and that supermarkets (SFA > 280 m^2) had a celling height of 5 m.

It was also considered that energy consumption may also correlate well with store volume, so both sales volume (SV) (SFA x height of store) and gross volume (GV) (GFA x height of store) were used in the analysis.

In smaller stores, refrigerated food typically takes up a greater proportion of floor area than it does in larger stores as larger stores will merchandise more non-grocery products. As refrigeration is responsible for a large part of the energy used by stores (33% of electrical consumption according to Foster *et al.*, 2018), refrigeration capacity (RC) was considered to assess whether it correlated well with energy intensity.

3 RESULTS

3.1 Relationship between energy consumption and size of store

Table 2 shows the mean and standard deviation (SD) of the different energy consumptions and floor areas for the supermarket stores.

Table 1. Mean and standard deviation of energy consumption and store areas.

	Mean	SD
Gross floor area (m^2)	738	741
Sales floor area (m^2)	469	493
Electrical energy consumption ($MWh.year^{-1}$)	327	283
Total energy consumption ($MWh.year^{-1}$) (gas+electrical)	371	352

EEC was plotted against SFA in Figure 1. A good linear relationship is shown (r^2 = 0.870). However, the linear regression does not go through zero, with an offset of 75.8 ± 20.2 $MWh.yr^{-1}$ within a 95% confidence band.

This offset did not seem significant when looking at all the total data set, however, when examining only the smaller stores (Figure 2), it is obvious that the offset was a significant part of the energy consumption for smaller stores.

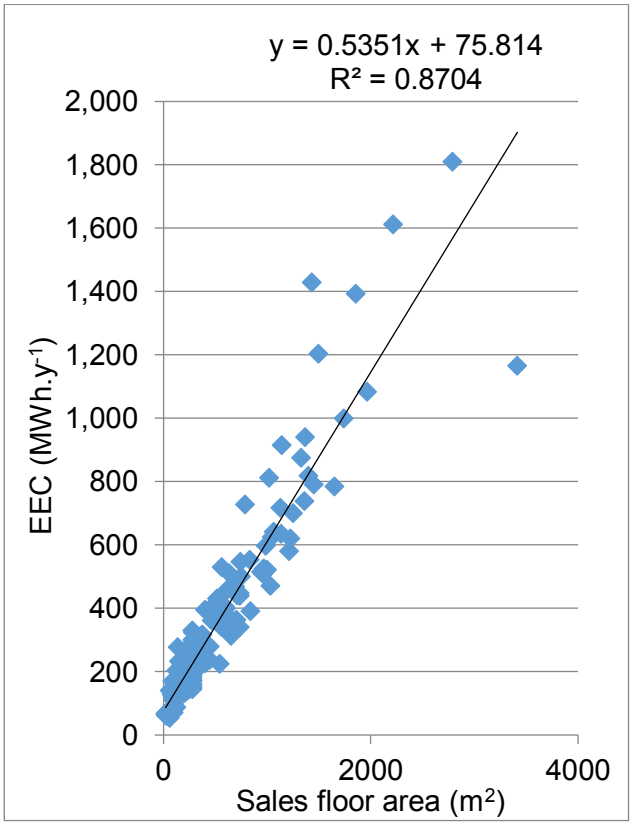

Figure 1. EEC against SFA for all stores.

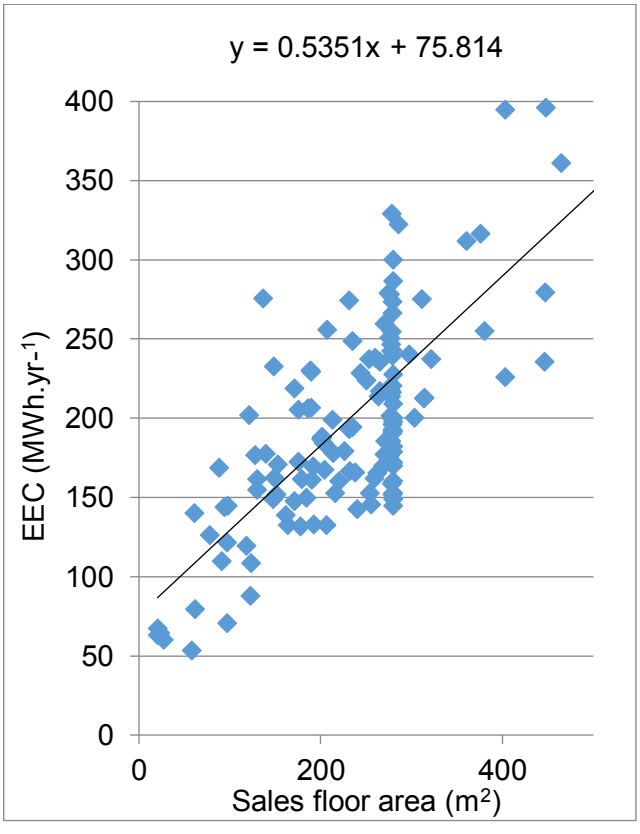

Figure 2. EEC against SFA for the smaller stores.

3.2 Relationship between energy intensity and size of store

Table 2 shows the mean and standard deviation (SD) values for the different energy intensities examined. As can be seen there is a large standard deviation of all of the energy intensities. The two energy intensities based on store volume had standard deviations larger than 50% of the mean. The lowest standard deviation as a proportion of the mean (33%) was based on perimeter area.

Table 2. Mean and standard deviation of supermarket store parameters.

	Mean	SD	% SD/mean
EEC/SFA (kWh.year^{-1}.m^{-2})	866	408	47
EEC/GFA (kWh.year^{-1}.m^{-2})	533	239	45
TEC/GFA (kWh.year^{-1}.m^{-2})	568	244	43
EEC/PA (kWh.year^{-1}.m^{-2})	193	64	33
EEC/SV (kWh.year^{-1}.m^{-3})	243	143	59
EEC/GV (kWh.year^{-1}.m^{-3})	157	84	54

In cases where there is so much variance around the mean, it is common in the literature to plot the energy intensity against the divisor. If the results give a flat line then the energy intensity is an ideal way of comparing stores of different sizes, as the value is constant for different store sizes. If the energy intensity is not constant then a relationship between the energy intensity and the size of store can be shown by line fitting (regression analysis).

Figure 3 shows energy intensities plotted as EEC/SFA, EEC/GFA, TEC/GFA, EEC/PA, EEC/SV and TEC/GV. All energy intensities show a similar power law relationship to that given by Tassou *et al.* (2011).

A better correlation coefficient (r^2) is shown when the energy intensity is based on volume rather than area. EEC/SV and TEC/GV give r^2 values of 0.77 and 0.63 respectively, which are higher than the r^2 of 0.54 from the usually reported EEC/SFA.

If we wish to compare energy intensities between stores there is clearly less variance between the predicted and actual values if we use a power law relationship, and this relationship shows less variance when volume is used as the divisor. If we wish to use mean data and not consider energy intensity varying with size, then it is better to use perimeter area as the divisor, as this gives the lowest %SD/mean.

3.3 Effect of refrigeration

RC values were not available for all stores and therefore the number of samples in the analysis was reduced to 139. When RC was plotted against SFA (Figure 4), a slope with a statically significant (P>0.95) positive offset is shown, much like when EEC is plotted against SFA. This shows that smaller stores have proportionally more refrigeration capacity as can be seen when RC/SFA is plotted against SFA (Figure 5). As a significant part of the energy consumption of the store is through refrigeration, this indicates that this is a reason for increased energy intensity in smaller stores.

Figure 6 shows EEC vs RC and EEC vs SFA for the reduced (139 samples) data set. There was a good correlation between EEC and RC (r^2 = 0.779), however, this was not as high as that for EEC vs SFA (r^2 = 0.883). This was due to the quality of the data, where SFA is more accurately known than RC and also because RC is not the actual refrigeration capacity of the store but a nominal value specified when the refrigeration system was contracted.

A multiple regression of EEC using both SFA and RC was carried out. This only reduced the standard error from 80.3 to 79.6 (MWh.m^{-2}.yr^{-1}) compared to a single regression using SFA as the factor and therefore was not considered useful.

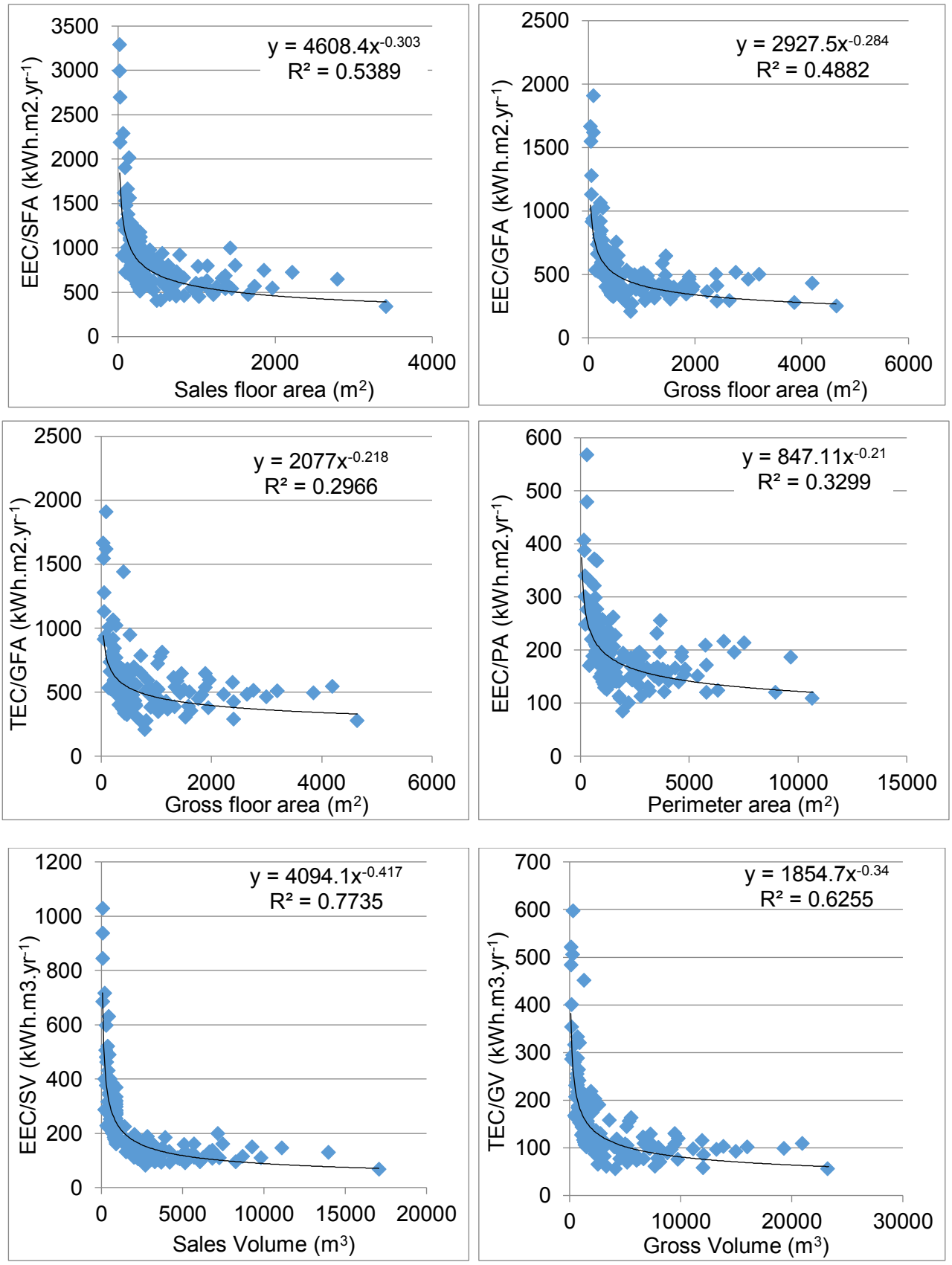

Figure 3. Power law regression for energy intensity intensities plotted as EEC/SFA, EEC/GFA, TEC/GFA, EEC/PA, EEC/SV and TEC/GV.

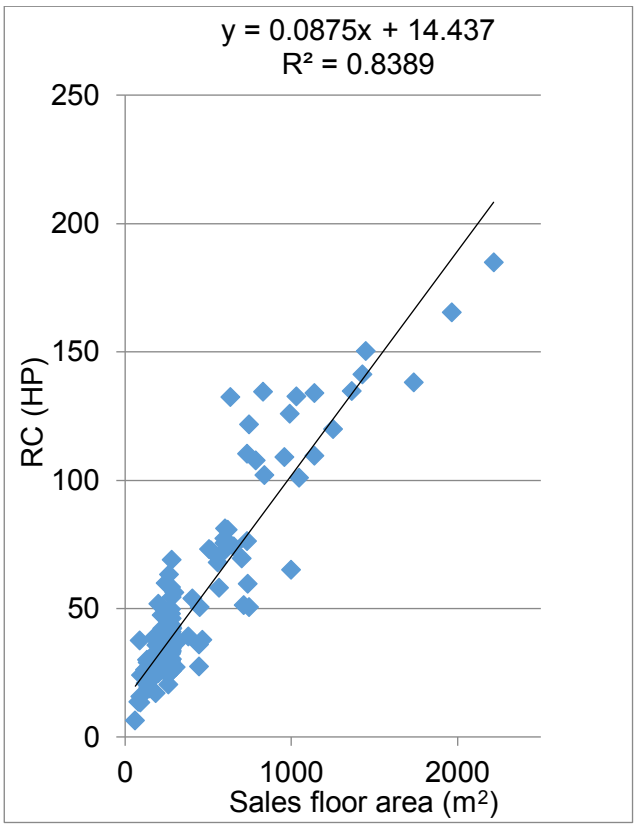

Figure 4. RC plotted against SFA.

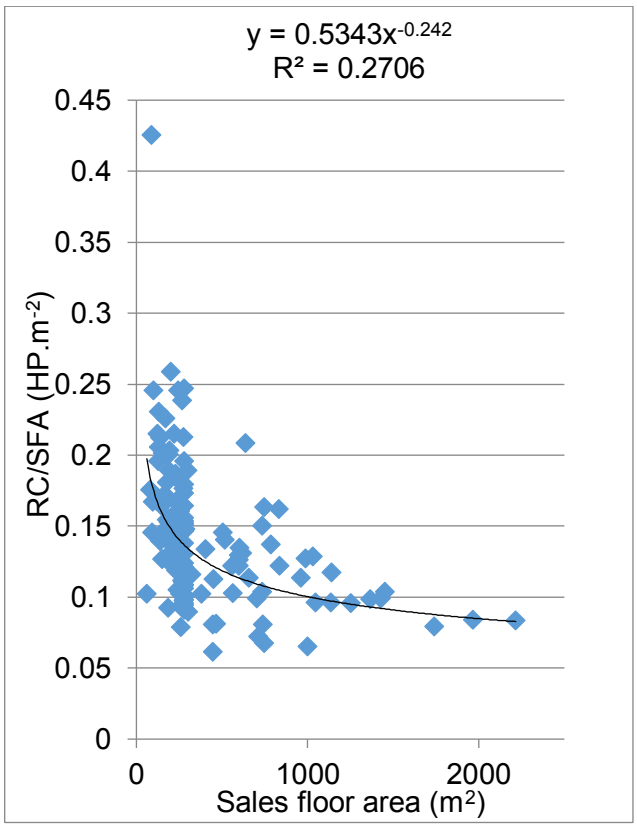

Figure 5. RC/SFA plotted against SFA.

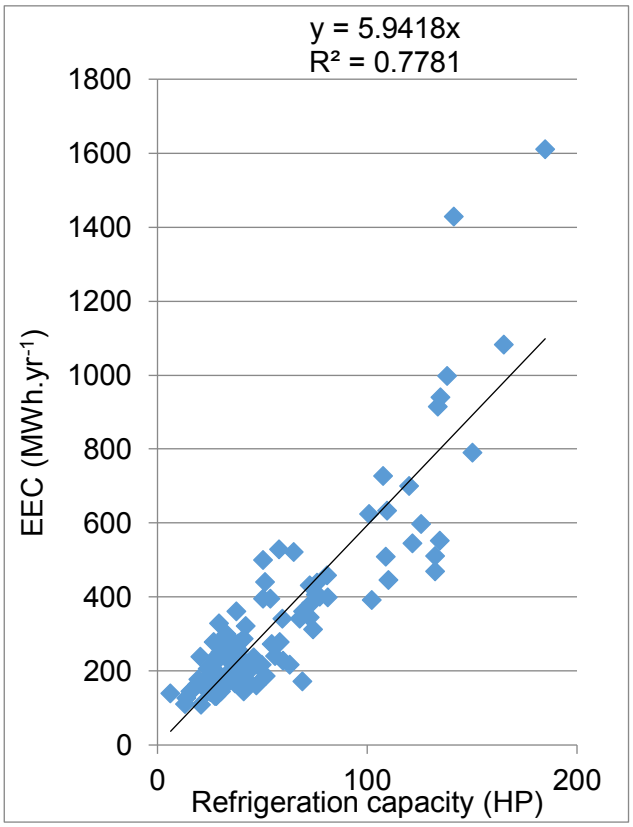

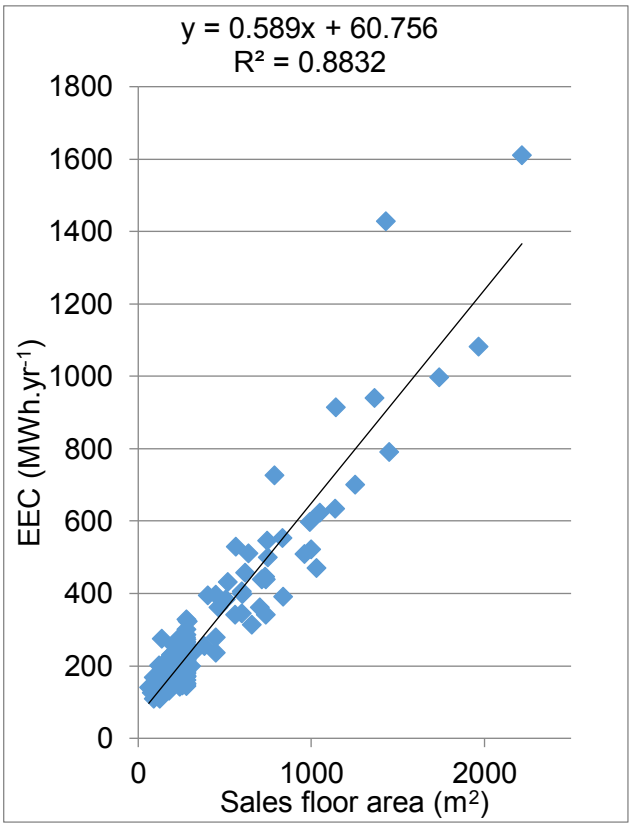

Figure 6. EEC vs RC (left) and EEC vs SFA (right).

3.4 Comparison with other studies

Data from a different UK retailer's stores (Foster *et al.*, 2018) showed a linear relationship between EEC/SFA and SFA, with EEC/SFA reducing slightly with increasing SFA. Average EEC/SFA was 566 kWh.m^{-2}.yr^{-1} and average SFA was 3,306 m^2. This was very different to the data presented in this paper with an average EEC/SFA of 866 kWh.m^{-2}.yr^{-1} and a non-linear relationship with SFA. However, the average SFA for this study was 469 m^2 and as we have shown the EEC/SFA is very dependent on SFA. Figure 7 shows EEC/SFA plotted for both data sets, the figure on the right includes all data and the figure on the left only stores below 4,000 m^2 SFA.

It can be seen that when EEC/SFA values from this study are plotted with those from Foster *et al.* (2018) there is a good match between stores with similar SFAs. This study covers the small SFAs where there is a power law relationship and Foster *et al.* (2018) covers large SFAs where there is a linear relationship.

The inverse power relationship observed by Tassou *et al.* (2011) was seen in this study. For SFA below 280 m^2 Tassou *et al*. (2011) showed an average EEC/SFA of 1480 kWh.m^{-2}.yr^{-1}. Data from this study showed a similar EEC/SFA at the very low SFAs but once SFA reached approximately 280 m^2 the EEC/SFA dropped to approximately 750 kWh.m^{-2}.yr^{-1} which is about half that in the Tassou *et al.* (2011) study. As stated in Foster *et al.* (2018) the reason for this difference is not obvious.

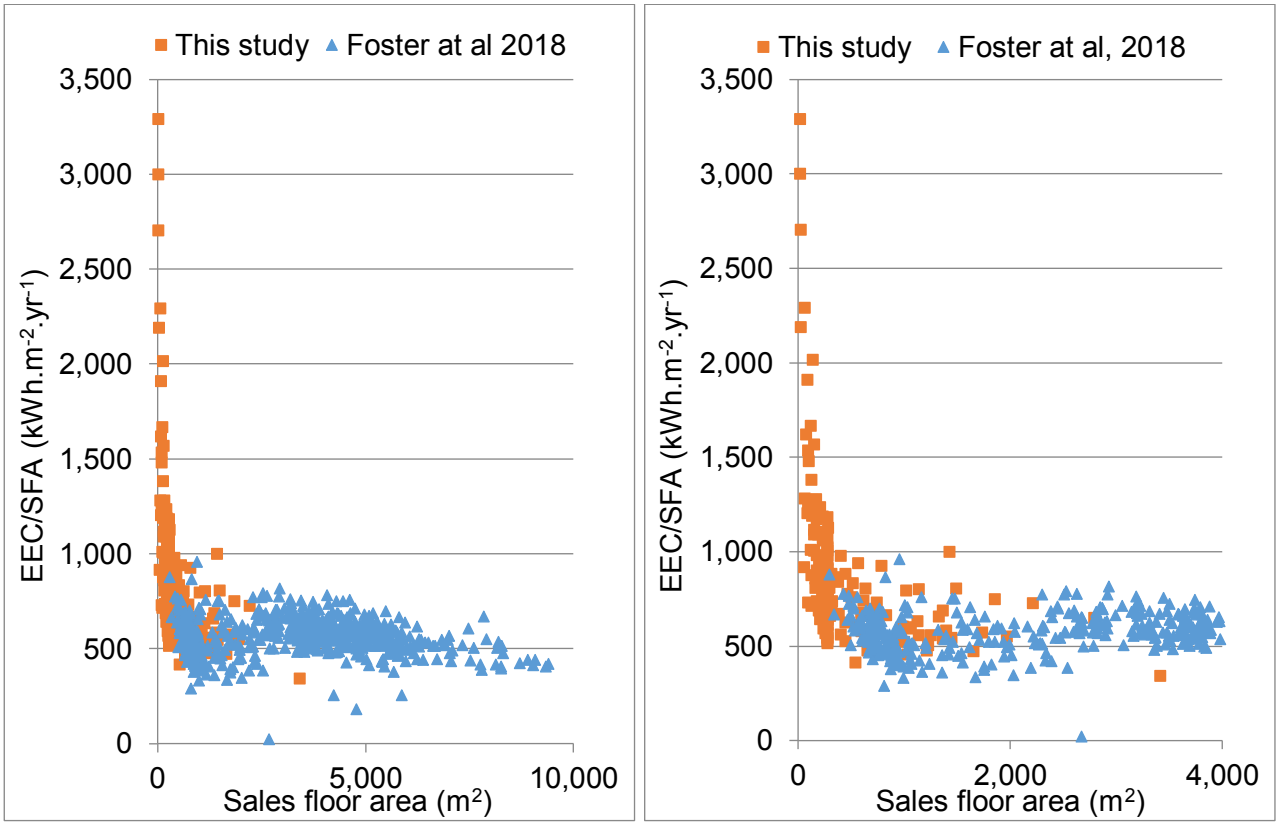

Figure 7. SEEC v SFA for this study and a previous study. Left figure includes all SFAs and right figure SFAs below 4000 m^2.

4 DISCUSSION AND CONCLUSIONS

This study of small supermarket stores complements a previous study on larger stores (Foster *et al.* 2018) and thus provides recent energy consumption data to allow benchmarking comparisons.

Large 'supermarket' stores have been shown to have an approximately constant energy intensity (decreasing slightly with increased floor area). Smaller 'convenience' stores have a much larger energy intensity which increases strongly with decreasing floor area. This can be represented by a power law relationship between energy intensity and store size or a linear relationship with a positive offset between energy consumption and store size.

Calculating energy intensity using electrical or gross energy and sales, floor, perimeter or volume shows a similar pattern. When looking at the energy intensity irrespective of store, using the PA as the divisor gives the smallest variance in the data. When using a power law relationship between energy intensity and store size, using store volume as the divisor gives the smallest variance.

EEC is well correlated with RC, however, it has a slightly better correlation with SFA.

5 ACKNOWLEDGEMENTS

This work was carried out as part of the EPSRC i-STUTE EUED energy centre and End Use Energy Demand Centres Collaborative Projects (EP/P006779/1).

NOMENCLATURE

EEC Electrical energy consumption ($MWh.yr^{-1}$)

PA Perimeter area (m^2)

RC Refrigeration capacity (Horse power)

SFA Sales floor area (m^2)

TEC Total energy consumption ($kWh.m^{-2}.yr^{-1}$)

TFA Total floor area (m^2)

6 REFERENCES

Chung, W., Hui, Y., Lam, Y., 2006. Benchmarking the energy efficiency of commercial buildings. Applied Energy 83, 1–14.

Foster, A., Evans, J., Maidment G., 2018. Benchmarking of supermarket energy consumption. Proceedings of the 5th IIR Conference on Sustainability and the Cold Chain, Beijing, China.

Lee, P., Bartlett, C., Eatherley, D., 2009. Quantification of the potential CO_2 savings from resource efficiency in the UK - An evaluation of the benefits of low-cost / no-cost improvements in UK industry and commerce for Defra. Oakdene Hollins Ltd.

Tassou, SA., Ge, YT., Hadawey, A., Marriott, D., 2011. Energy consumption and conservation in food retailing. Applied Thermal Engineering. 31, 147–156.

Manuscript ID: 885
DOI: 10.18462/iir.icr.2019.0885

Evaluation of the heat and energy performance of a datacenter by a new efficiency index: energy usage effectiveness design - EUED

Alexandre F. SANTOS[a, b], Heraldo J.L. DE SOUZA[a], Pedro D. GASPAR[b, c]

[a] FAPRO - Faculdade Profissional, www.fapro.com.br
[b] University of Beira Interior, Rua Marquês d'Ávila e Bolama, 6201-001, Covilhã, Portugal, dinis@ubi.pt
[c] C-MAST - Centre for Mechanical and Aerospace Science and Technologies, University of Beira Interior, Covilhã, Portugal.

ABSTRACT

Data Centers are growing steadily worldwide and they are expected to continue on growing up to 53% in 2020. Due to this growth the energy efficiency in this type of building is essential. There are methodologies to measure this efficiency; one example is PUE (Power Usage Effectiveness). The unit suggested for measuring efficiency at the design stage would be the EUED (Energy Usage Efficiency Design) with this will be used data to use "free cooling" and adiabatic system in some cases, a comparison will be made only considering the equipment in the worst situation. It also uses the study of enthalpy utilization as a new methodology to obtain the results. By doing so, differences were found, between cities than 1.21% of São Paulo in relation to Curitiba and 10.61% of Rio de Janeiro in relation to Curitiba. The indices obtained by applying the EUED index were 1.245 $kW \cdot kW^{-1}$ for Curitiba, 1.260 $kW \cdot kW^{-1}$ for São Paulo and 1.377 $kW \cdot kW^{-1}$ for Rio de Janeiro, respectively, giving a difference of 16.86% for Curitiba of 16.19% for São Paulo and 10.31% for Rio de Janeiro in relation to PUE COA (Power Usage Effectiveness Constant Outdoor Air).

Keywords: Data Centers, PUE, EUED, Data Center Cooling.

1. INTRODUCTION

Mobile traffic is expected to grow almost fourfold in less than a decade – from 3.9 ZB (ZetaBytes) in 2015 to 14.1 ZB per year by 2020, according to Converge Comunicações, the main Brazilian communication group dedicated to the Information and Communication Technology (ICT) market. The data comes from Cisco Systems' Sixth Annual Global Cloud Index (2015-2020) which attributes this expansion to the increasing enterprise migration of IT systems to cloud and its ability to expand quickly and efficiently to support more workloads than that of traditional data centers (DCs).
With higher DC virtualization rates, cloud operators will be able to offer a greater variety of services to businesses and consumers with optimal performance. According to the analysis, the cloud will dominate and exceed traditional DC growth by 2020 when 92% of the workload will be processed by cloud DC and 8% by traditional DCs.
Moreover by 2020, $298 million dollars or 68% of the cloud workload will be placed in public cloud data centers, compared to $66.3 million dollars or 49% recorded in 2015 – a 35% compound annual growth rate between 2015 and 2020. Resources like Internet of Things (IoT) and Big Data will boost the market. IoT will be a great data generator, reaching 600 ZB per year by 2020 which is 275 times greater than the projected traffic between DCs and devices / end users (2.2 ZB) – 39 times greater than the total traffic of DCs (15.3 ZB). Big Data is already driving the overall growth of storing data. Data stored in data centers will increase fivefold by 2020, reaching 915 Exabyte (EB) – an increase of 5.3 times (a compound annual growth rate of 40%) from the 171 level EB in 2015.
For the first time, Cisco also quantified and analysed the impact of hyper scale DCs which are expected to grow from 259 in 2015 to 485 by 2020. DC hyper scale traffic is expected to increase fivefold over the next five years. These infrastructures will account for 47% of installed servers.

With the growth of DCs, one of the major challenges is to improve the performance and efficiency of DCs, largely due to the heat dissipated by the servers, while the enormous number of equipment installed to increase the storage capacity also greatly in-creases the electrical power and consequently the heat dissipation. To improve heat dissipation, some DCs even moved to places where average air temperature is lower – places like the Arctic Circle or Sweden – to achieve better energy efficiency in the cooling process.
Efficiency metrics are defined and standardized to compare the efficiency of DC systems and their operating costs. A global consortium of IT equipment manufacturers, technology companies, government, education and R&D institutions, class associations and other sectors of society have also been set up to discuss, develop and recommend best practices for energy efficiency along with emission of CO^2. One such metric is Power Us-age Effectiveness (PUE) defined by The Green Grid (2012) as an instrument to measure the energy efficiency of a DC. The parameter is the ratio of the total energy consumed by a DC and the power supplied to the IT equipment. The ideal PUE value would be 1.0. There are already reported cases of DCs with PUE = 1.02 (Saylor *et al.*, 1998).
There are other factors that do not touch this research work, for example: energy availability, and seismic risk, focusing exclusively on areas of greater impact beyond the IT equipment itself such as thermal areas. A typical DC (with PUE = 2.1) has the following distribution of electricity consumption (Rasmussen, 2012).

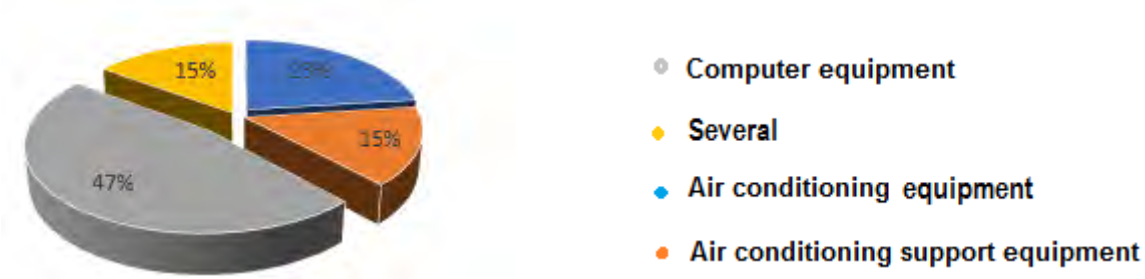

Figure 1: Distribution of electricity consumption in a typical DC (Rasmussen, 2012).

The point is that in a typical DC, except for the 47% out of the remaining 53% of electrical consumption used in computer equipment, the air conditioning system is responsible for 38% of total electricity consumption. IT and air conditioning correspond to about 72% of all electrical consumption in the infrastructure. Since the emphasis of this work is not directed at the efficiency of computer equipment, the idea is to use an index that can help investors to have the needed support when deciding the most suitable place for the installation of a DC, using an abacus with simple and basic elements. According to EY (2015), executives need to "Increase the speed of decision making and the efficiency of project execution to take advantage of windows of opportunity".
One such metric is called Power Usage Effectiveness (PUE), defined by The Green Grid (2012) as an instrument to measure the energy efficiency of a DC. This parameter is the ratio of the total power consumed by a DC and the power supplied to the IT equipment. The ideal PUE value would be 1.0. Already reported cases of CD with PUE = 1.02.
According to EY (2015), executives need to "Increase the speed of decision making and the efficiency of project execution to take advantage of windows of opportunity."
A truly accurate metric will be to create a new index called Energy Usage Effective-ness Design (EUED). This metric will emphasize the outside characteristics of the DC, studying the weather and geothermal characteristics.
To do so, a pre-project study using natural indexes can accelerate decision making at the most appropriate location for the location of a thermal DC, i.e., making use of an index involving four elements. In the correlation, the index for decision making will consist of the following parameters:

- Dry air bulb temperature;
- Wet bulb temperature of air;
- Soil temperature (geothermal);
- Dew point temperature of air.

And the air behaviour in relation to the cited parameters. These parameters will fuel a new efficiency index in DCs that will be Energy Usage Effectiveness Design (EUED), which works with an emphasis on energy rather than power such as PUE. In addition to the PUE (Power Usage Effectiveness), defined by The Green Grid (2012), the Thermal Guidelines for Data Processing Environments already have some simulations for the use of "Free cooling" for some cities of the United States of

America, like Chicago. However, in this work the evaporative and geothermal adiabatic systems are included in the simulations to create the new index Energy Usage Effectiveness Design (EUED) to evaluate DCs instead of PUE. This work shows the analysis of ASHRAE Thermal Guidelines for Processing (2015) for 3 target cities.
Intended for the calculation of the EUED and subsequent comparison with the PUE values, the analysis, and discussion of results, aimed to obtain a higher level of information to be used in decision making for a place to install a DC

2. SELECTED CITIES AND THEIR CHARACTERISTICS

Looking at the comparison metrics, the article will be based on a high-density Datacenter. The chosen cities of similar characteristics are:

- Curitiba, Paraná, Brazil;
- São Paulo, São Paulo, Brazil;
- Rio de Janeiro, Rio de Janeiro, Brazil.

The cities are close to large basins, (based by the Brazilian Association of Technical Standards – ABNT) (NBR 16401, 2008), and have similar characteristics:

Table 1. Data from the cities of Curitiba, São Paulo, and Rio de Janeiro (NBR 16401, 2008)

City	Year frequency	DB (°C)	WB (°C)	Altitude (m)
Curitiba	0.4 %	30.9	23.2	908
Curitiba	1.0%	29.8	22.6	908
Curitiba	2.0%	28.7	22.0	908
São Paulo	0.4%	32.0	23.2	803
São Paulo	1.0%	31.0	22.6	803
São Paulo	2.0%	30.0	22.1	803
Rio Janeiro	0.4%	34.0	26.6	3
Rio Janeiro	1.0%	32.7	26.2	3
Rio Janeiro	2.0%	31.8	25.8	3

The difference between the dry bulbs of cities Curitiba and São Paulo is 3.56% and Curitiba and Rio de Janeiro is 10.03%, and for psychrometric effects, the altitude of Curitiba is 908 m, São Paulo is 803 m and Rio de Janeiro is 3 m.
For comparison purposes, a high density DC of 414 m² is used, measuring 28.8x14.4 m, and with a heat dissipation of equipment (347.3 kW of sensible heat, that is 0.84 $kW \cdot m^{-2}$), and an internal thermal load of 48 kW (conduction, lighting = 8 kW in total), people and others (40 kW of losses in Nobreak and others) – 8 equipment were selected (4 active equipment and 4 reserved) of 30 TR "dual Fluid", with 85% Sensitive Heat Factor, as shown in Fig. 2 and Table 2.

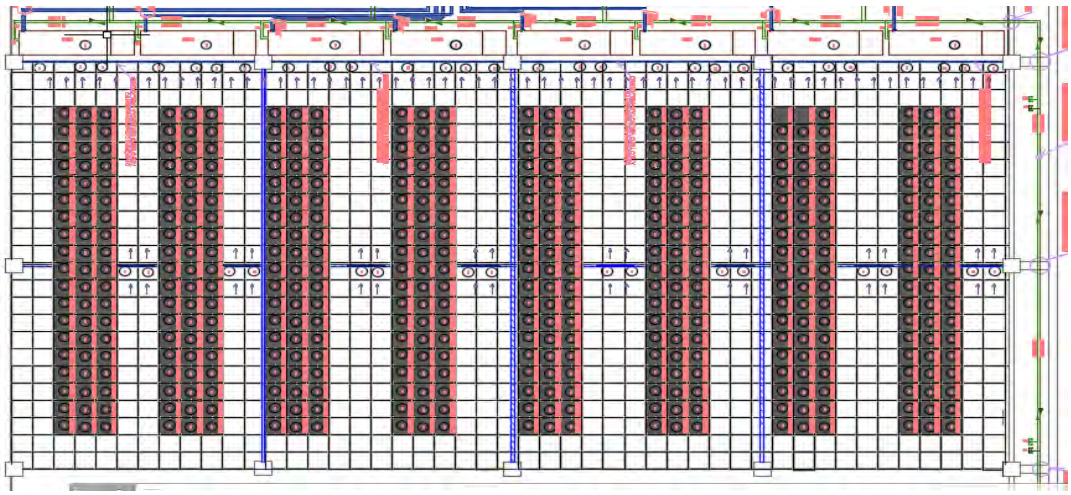

Figure 2: Data Center scheme

The standard air conditioning equipment used in DCs of dual fluid has the features detailed in Table 2.

Table 2. Feature standard air conditioning equipment used in DCs of Dual fluid (EMERSON NETWORK POWER, 2016)

Model	Units	L99
Total cooling capacity	kW	194.6
Sensible cooling capacity	kW	89.3
SHR		0.85
EER		3.40
Number of compressors	N	2
Number of compressors	N	2
Air delivery	$m^3 \cdot h^{-1}$	21100
Max. ESP	Pa	90
Sound pressure level	dB(A)	66.9
Width	Mm	2550
Depth	Mm	890

The approximate capacity of 30 TR (Cooling Tonnage or 104.6 kW, for each of the eight equipment, being 1 active and another reserved), has an Energy Efficiency Rate (EER) of 3.4 $kW \cdot kW^{-1}$ (in the condition of direct expansion), i.e. the power feeding point of the air conditioning to meet the thermal load will be 123.5 kW, therefore, the PUE COA will be as follows:
PUE COA= Total energy (data equipment + air conditioning + lighting + losses of nobreak and inverters, and others) / data equipment energy:

(347.3+123.05+8+40) / (347.3) = 1.50 $kW \cdot kW^{-1}$

This value of 1.50 $kW \cdot kW^{-1}$ is an excellent value since a typical DC already quoted above is 2.1 $kW \cdot kW^{-1}$.
These yields of air conditioning equipment were based on an air inlet temperature in the condenser from 33 to 35°C, a condition close to the two cities already mentioned, i.e. the PUE of the two cities would be the same.

3. COMPARING PUE COA AND EUED

The PUE COA (Power Usage Effectiveness Constant Outdoor Air) is the same PUE index, but with an emphasis on the external temperature at the mean of 0.4% of the current higher temperatures of NBR 16401. Unlike the PUE already mentioned that works only with power indexes, the index created in this EUED article works with the 8760 hours (the metrics being the usage of energy instead of power, which is already a suggestion for the ISO 50006 where they have been using, for commercial buildings, the metric of $kWh \cdot m^{-2}$).
Using annual dry bulb temperature indexes associated with the coincident dew point temperature (data from the ASHRAE Weather Data Viewer), they obtain EUED indexes, classified as:

- Free Cooling - System that allows the use of the enthalpic characteristics of the external air to acclimatize an enclosure;
- Evaporative - Adiabatic cooling, which consists of cooling the environment using the wet bulb temperature;
- COP - Performance coefficient, which is used to evaluate the relationship between the refrigeration capacity and the work spent to do it.

Based on an inflation temperature of 20°C on average, we worked with the EUED methodology, with the following factors:

- When the temperature is below 20°C, and the enthalpy is below 18.4 $BTU \cdot LB^{-1}$, Free Cooling will only be used;
- When the temperature is between 15 to 24°C, and the enthalpy of 18.4 to 24 $BTU \cdot LB^{-1}$, the Evaporative system will be used;
- When the temperature is at any point above 20°C, and above 24 $BTU \cdot LB^{-1}$, the normal system will be used under the following conditions:

- Air inlet temperature between 24 and 27°C = COP 1;
- Air inlet temperature between 27 and 30°C = COP 2;
- Air inlet temperature between 30 and 33°C = COP 3;
- Air inlet temperature above 33°C in any condition = COP 4.

In order to simulate the conditions of COP 1, COP 2, COP 3, and COP 4, the Cool pack software (where it was initiated by condition 4) was used to simulate a standard isentropic coefficient to be able to identify the COP with the variation in the condensation temperatures, for the temperature effect of condensation was used by default; that is the average air in-take temperature for each situation added to 11°C, with the following conditions:

Table 3. Distribution of electricity consumption in a typical DC

Cases	Power of base equipment (kW)	Condensing temperature (ºC)	Evaporation temperature (ºC)	Cooling Fluid	COP ($kW \cdot kW^{-1}$)
COP 1	104.5	36.5	5	R 410 A	4.381
COP 2	104.5	39.0	5	R 410 A	4.101
COP 3	104.5	42.5	5	R 410 A	3.745
COP 4	104.5	44.0	5	R 410 A	3.633

- The calculation for COP 4 should consider fans powered at 7.36 kW; that is, in the case of study COP 4, the value of the COP without the fans reaches 4.829. To achieve the COP with the fans, the following equation will be used: (104.5 / 21.64 kW from compressors + 7.36 kW from fans) = 3.633 $kW \cdot kW^{-1}$.
- COP 3 considered fans powered at 7.36 kW, that is: a COP of 5.087, with the fans, goes to (104.5 / (20.54 kW from compressors + 7.36 from fans) = 3.745 $kW \cdot kW^{-1}$.
- COP 2 having fans powered at 7.36kW, the COP will be (104.5 kW / (18.12 from compressors + 7.36 from fans) = 4.101 $kW \cdot kW^{-1}$; and without fans it will go up to 5.768 $kW \cdot kW^{-1}$.
- And finally, COP 1 with fans powered at 7.36 kW, the COP will be (104.5 kW / (16.49 + 7.36) = 4.381 $kW \cdot kW^{-1}$; while the COP without fans will go to 6.338 $kW \cdot kW^{-1}$.

From the COPs obtained by the CoolPack software and the basic data of the enthalpy system methodology for DCs, a system of wide psychrometric coverage was elaborated for all possible external temperature points, either for "Free Cooling", Evaporative or just Cooling (see Fig. 3).

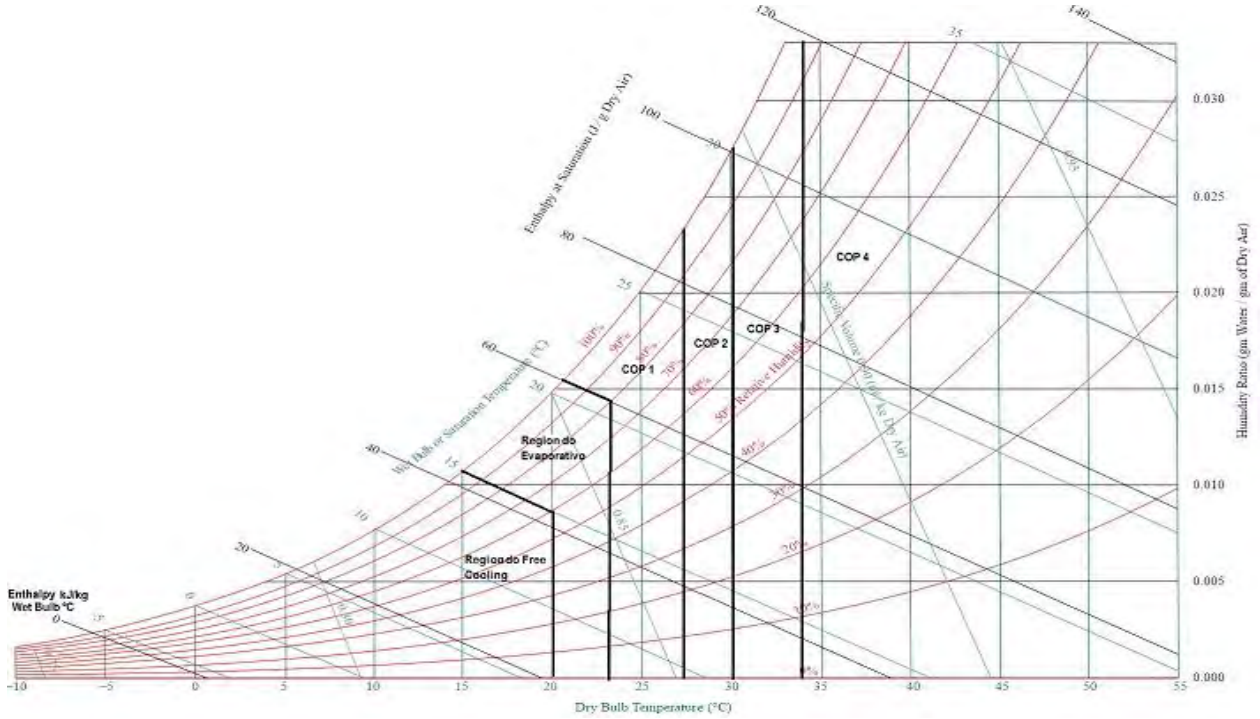

Figure 3: Psychrometric chart (COOLPACK, 2016)

Using the ASHRAE weather data viewer (ASHRAE, 2013), the association of the dry-bulb temperature frequencies with the coincident dew point temperatures was defined as the method; and at each point, the enthalpy associated with this relation was found in the following cumulative frequencies for each system and city (Table 5):

Table 4. Data for psychrometric chart

Operating system	Total Thermal Charge	COP ($kW \cdot kW^{-1}$)	Power (kW)
Free Cooling	395.3	19.180	20.610
Evaporative	395.3	16.780	23.558
COP 1	395.3	4.381	90.231
COP 2	395.3	4.101	96.391
COP 3	395.3	3.795	105.554
COP 4	395.3	3.633	108.808

Table 5. Frequency in hours of usage

Operating system	Curitiba hours	São Paulo hours	Rio Janeiro Hours
Free Cooling	4410.000	2574.191	159.515
Evaporative Cooling	3453.887	4713.820	2131.860
COP 1	579.743	906.945	4536.432
COP 2	269.874	434.482	1108.059
COP 3	45.987	122.639	554.971
COP 4	0.509	7.922	269.163

Using the same ASHRAE software, selecting the EUED index as proposed, it classified the frequencies in working hours for the three cities. It is noteworthy that between cities there are differences. In Curitiba the evaporative system, when the temperature is between 15 to 24°C and the enthalpy of 18.4 to 24 BTU/LB, had a higher frequency, which is 3453.887 hours; São Paulo 4713.20 hours, and Rio de Janeiro 2131.860 hours of frequencies. With a Free Cooling, with a temperature below 20°C and the enthalpy lower than 18.4 $BTU \cdot LB^{-1}$, Curitiba has 4410 hours of frequency, the São Paulo have 2574.191 hours, and Rio de JANEIRO 159.515 hours.
According to Table 5, it is verified that with the rules proposed in the EUED, 6 levels were classified: Free Cooling; Evaporative; COP 1; COP 2; COP 3; COP 4. The cities of Curitiba, São Paulo and Rio de Janeiro, have different air consumption energy according to their temperature and enthalpy. In a period of 8760 hours, São Paulo used 18.06% more energy than Curitiba, and Rio de Janeiro 57.35% more energy than Curitiba. Another view in this table shows the relation between COP and energy. The higher the COP the lower is the energy consumption (see Table 6).
Energy consumption with infrastructure, which is the sum of energy consumption plus air conditioning, equipment, lighting and other equipment, between cities show a difference of more than 1.21% for São Paulo in relation to Curitiba; and 10.61 % for Rio de Janeiro in relation to Curitiba. The indexes obtained with application of the EUED index were, respectively, 1.245 $kW \cdot kW^{-1}$ for Curitiba, 1.260 $kW \cdot kW^{-1}$ for São Paulo, and 1.377 $kW \cdot kW^{-1}$ for Rio de Janeiro, showing a difference of 16.86% for Curitiba, São Paulo 16.19%, and 10.31% for Rio de Janeiro in relation to the PUE, as shown in Table 8.

Table 6 - Calculations using index EUED rules.

Operating system	Thermal Load Total (kW)	COP ($kW \cdot kW^{-1}$)	Power (kW)	Curitiba (h)	São Paulo (h)	Rio de Janeiro (h)
Free Cooling	395.3	19.180	20.610	4410.000	2574.191	159.515
Evaporative cool.	395.3	16.780	23.558	3453.887	4713.820	2131.860
COP 1	395.3	4.381	90.231	579.743	906.945	4536.432
COP 2	395.3	4.101	96.391	269.874	434.482	1108.059
COP 3	395.3	3.745	105.554	45.987	122.639	554.971
COP 4	395.3	3.633	108.808	0.509	7.922	269.163

Table 7. Final results in the calculations using the EUED index rules

Infra Rio Janeiro kW/h year	4190415.928
Infra Curitiba kWh year	3788397.606
Infra São Paulo kWh year	3834530.819
EUED Curitiba	1.245
EUED São Paulo	1.260
EUED Rio de Janeiro	1.377
DIFFERENCE EUED/PUE COA Curitiba year	16.86%
DIFFERENCE EUED/PUE COA São Paulo year	16.19%
DIFFERENCE EUED/PUE COA Rio de Janeiro year	10.31%

Table 8. Comparison of PUE COA, EUED, COP PUE COA and COP EUED

CITIES	PUE COA	EUED	COP PUE COA	COP EUED
Curitiba	1.455	1.245	3.745	13.553
São Paulo	1.467	1.260	3.642	11.481
Rio de Janeiro	1.481	1.377	3.463	5.629

Figure 4 shows the comparative information of the COP PUE COA and COP EUED. The COP EUED, COP is much larger than the other cities compared, so this is the best way to map the possibilities in the project and to have satisfactory results in the installations of new DCs.

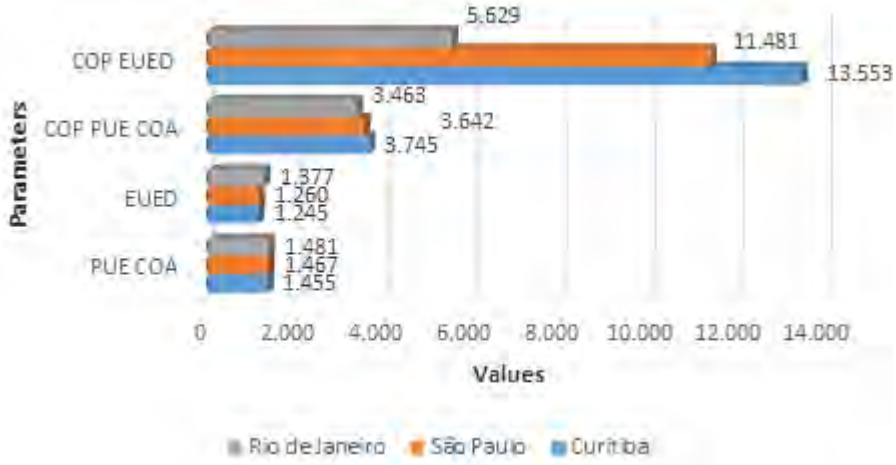

Figure 4: Comparison of COP PUE COA and COP EUED

4. CONCLUSIONS

The proposed EUED index is a more reliable index compared to the PUE to analyse energy efficiency in new DCs by the fact that it uses energy rather than power for comparison between systems as a metric. Enthalpy is an essential tool for choosing the best place to insulate a DC, for the holistic view it understands. Energy consumption with infrastructure, which is the sum of energy consumption with air conditioning, equipment, lighting and other equipment, between the cities gives a difference to more than 1.21% of São Paulo in relation to Curitiba and 10.61% of Rio de Janeiro in relation to Curitiba. The indices obtained with application of the EUED were, respectively, 1.245 $kW \cdot kW^{-1}$ for Curitiba, 1.260 $kW \cdot kW^{-1}$ for São Paulo and 1.377 $kW \cdot kW^{-1}$ for Rio de Janeiro, giving a difference of 16.86% for Curitiba, 16.19% for São Paulo and 10.31% for Rio de Janeiro in relation to PUE COA.

REFERENCES

ASHRAE, 2011. Thermal Guidelines for Data Processing Environments. 3rd Edition. ASHRAE Datacom series. 2011. ASHRAE. Technical Committee (TC) 9.9 - Mission Critical Facilities, Technology Spaces, and Electronic Equipment. ASHRAE.

ASHRAE, 2014. Thermal Guidelines for Data Processing Environments. 4rd Edition. ASHRAE.

ASHRAE, 2014. Technical Committee (TC) 9.9 - Mission Critical Facilities, Technology Spaces, and Electronic Equipment. ASHRAE.

ASHRAE, 2009. Guide Pocket ASHRAE. 7th edition.

ASHRAE. ASHRAE Weather Data Viewer Software. Available www.ashrae.org.

ABNT, 2008. ABNT 16401: Instalações de ar-condicionado - Sistemas centrais e unitários, qualidade do ar interior. Rio de Janeiro.

Cisco, 2015. Cisco Global Cloud Index: Forecast and Methodology. 2014–2019. White Paper FLGD 12624, Cisco.

Cisco, 2015. Cisco Visual Networking Index: Forecast and Methodology. 2014–2019. White Paper FLGD 12352, Cisco.

EMERSONNETWORKPOWER. Característica do equipamento Dual fluid (LIEBERT). available http://www.emersonnetworkpower.com/en-US/Brands/Liebert/Pages/default.aspx.

EPA, 2007. Report to Congress on Server and Data Center Energy Efficiency, Public Law 109-431, U.S. Environmental Protection Agency (EPA), ENERGY STAR Program.

EXAME, 2007. Datacenters. Revista Exame. São Paulo.

EY, 2015. Lessons from change: building a better working world. Ernst & Young.

Filho, D.P. & Santos, J.A., 2001. Metodologia científica. Editora Futura. São Paulo.

Harriman III & Lstiburek, 2009. The ASHRAE Guide for Buildings in Hot & Humid Climates. Second Edition, new content. ASHRAE.

IDC, 2014. Worldwide Datacenter Census and Construction 2014–2018 Forecast: Aging Enterprise Datacenters and the Accelerating Service Provider Buildout. Doc # 251830 - Market Analysis, International Data Corporation (IDC).

ISO 50006, 2014. Energy management systems -- Measuring energy performance using energy baselines (EnB) and energy.

Kavanaugh & Raffery, 2014. Geothermal Heating and Cooling. First Edition, Design of Ground Source. ASHRAE.

Koomey, J., 2011. Growth in Datacenter electricity use 2005 to 2010. Oakland, CA: Analytics Press.

NRDC, 2014. America's Data Centers Are Wasting Huge Amounts of Energy. Issue Brief, iB: 14-08-a, Natural Resources Defense Council (NRDC).

Rasmussen, N., 2012. Implementing Energy Efficient Data Centers. White Paper 114. Schneider Electric's Data Center Science Center. Schneider-Electric.

Santos, A.F.R.S., 2014. Análise de temperaturas geotérmicas para aplicação de bombas de calor no Paraná (Brasil). Curitiba.

Steinbrecher, R.A. & Schmidt, R., 2014. Performance indicators (EnPI) -- General principles and guidance.

Steinbrecher, R.A. & Schmidt, R., 2011. Data Center Environments: ASHRAE's Evolving Thermal Guidelines. ASHRAE Journal, pp. 42.

The Green Grid, 2012. PUE™: A comprehensive examination of the metric. White paper #49 (Eds: V. Avelar, D. Azevedo, A. French), The Green Grid.

Thibodeau, P., 2014. Data centers are the new polluters. ComputerWorld.

3M, 2015. Two-Phase Immersion Cooling: A revolution in data center efficiency. 3M.

Manuscript ID: 908
DOI: 10.18462/iir.icr.2019.0908

Building energy management in energy-hub manner based on economic model predictive control

Jiangyu WANG[(a)], Jiangyan LIU[(b)], Guannan LI[(c)], Yabin GUO[(a)], Huanxin CHEN[(a)], Yue YUAN[(d)], Yao HUANG[(a)]

[(a)] Department of Refrigeration & Cryogenics, Huazhong University of Science and Technology
Wuhan, 430074, China, jywang_2016@hust.edu.cn(J.W), guoyb_h@hust.edu.cn(Y.G),chenhuanxin@tsinghua.org.cn(H.C),yaohuang@hust.edu.cn(Y.H)
[(b)] College of power engineering, Chongqing University
Chongqing, 400045, China, liujiangyan@hust.edu.cn
[(c)] School of Urban Construction, ,Wuhan University of Science and Technology
Wuhan, 430065, China, leegna@163.com
[(d)] China-Eu Institute for clean and Renewable Energy, Huazhong University of Science and Technology
Wuhan, 430074, China, m201671238@hust.edu.cn

ABSTRACT

Building sector accounts for nearly 40% of the global energy consumption. Energy-hub is attached attentions for the energy/cost saving and load shifting of building. In this paper, we proposed a model predicted control (MPC) based demand-side building energy management framework in the energy-hub structure. Simulations in four scenarios with dynamic electricity price were conducted on a building to investigate the energy saving potential under the proposed framework. In scenario 1 and 2, building climate control and economic control were employed to track the indoor temperature setpoint and minimize the cost respectively. In the scenario 3, a typical demand response problem with electric storage device was studied while an additional on-site generation component was considered in scenario 4. The results demonstrate that scenario 2 can achieve 21% cost saving compared to scenario 1. Furthermore, scenario 3 and 4 can achieve nearly 20% and 31% cost saving compared to scenario 2.
Keywords: Model Predictive Control, Energy Hub, Building Climate Control, Demand Response, Demand-Side Energy Management.

1. INTRODUCTION

Building energy consumption accounts for approximately 40% of the global energy demand (Kolokotsa et al., 2011), and heating, ventilation and air-conditioning(HVAC) system account for a large part. Meanwhile, heating and cooling power always increase the peak load demand which means the plant capacity need be increased to meet the system peaks. That causes disproportionately high social costs since the plant is not dispatched at the off peak hours (Kircher and Zhang, 2015). In this context, demand-side energy management (DSEM) program which aims at reducing the building peak load, has elicited extensive attention.

More specifically, building have considerable demand response potential due to the thermal storage capacity (Wang et al., 2014). Furthermore, HVAC system can utilize the storage characteristics to shift the heating or cooling load demand away from peak hours without sacrificing the indoor comfort level. From this point, DSEM can employ HVAC equipment to shape the end-users' energy consumption profiles to achieve the load shifting and cost saving under the dynamic electricity prices. However, it is challenging to reduce considerable peak load demand solely by the thermal storage capacity of building. On the one hand, curtailing heating power blindly in the peak hours of winter may cause negative influence on the comfort level of occupants due to the limited thermal storage capacity. On the other hand, the optimization-based HVAC control method is necessary for maximizing economic benefits while minimizing the impact on the thermal comfort level.

Energy hub, which allows the building to connect with the grid, thermal/electricity storage component and on-site generation, is a promising option for extending the pool of demand response resources. Under the framework of energy hub, building operators can employ the battery to store electricity energy at the low prices time and discharge the energy to HVAC system at the peak hours. Furthermore, generation element (i.e. wind turbines, solar photovoltaic panels) can even provide "free" renewable energy to reduce stress towards main grid.

However, it will bring difficulties to the controller design with those components involved in the demand response program. For example, the charge and discharge power of a battery is limited. A proportion-integrals-differential(PID) controller can hardly deal with those constraints while maintaining the comfort level. Although some heuristic strategies have been employed on the building with thermal storage systems, they cannot deal with time-varying economic demand response policy (Kircher and Zhang, 2015).

As a typical optimization-based control method, model predictive control(MPC) has been widely applied to control buildings HVAC to meet comfort or economics goals. (Ma et al., 2012) employed economic MPC(EMPC) to reduce a multi-zone commercial building demand in the co-simulation environment with EnergyPlus (Crawley et al., 2001). Results demonstrate that EMPC can achieve the highest energy and cost saving compared to the baseline and other control strategies. (Široký et al., 2011) investigated the energy saving potential of a building heating system. 15%~28% of energy savings are achieved by MPC. (Ma et al., 2012) employed MPC to operate the building cooling systems equipped with a water tank. Results show that MPC can reduce the electricity cost and improve the energy efficiency of the central plant. An economic MPC was adopted to control the heat pumps of the house in smart grid (Halvgaard et al., 2012). Nearly 25 ~35% of the electricity cost saving are achieved by MPC controller compared to the traditional operation of heat pumps. (Oldewurtel et al., 2010) and (Avci et al., 2013) investigate the potential of peak electricity demand reduction by using MPC and real-time pricing. However, there are currently few studies which investigate and compare the potential of energy saving and cost benefits in the structure of energy hub with different components.

In this paper, we propose a MPC-based simulation framework for building DSEM under the energy-hub structure. The framework can be flexibly used for building comfort control or assess the energy saving potential under the user-specified demand response schemes in the presence of storage and generation components. The framework is applied to a simple one-room building with a Time-of-Use(TOU) prices under the structure of energy-hub. Besides, we develop an open-source toolbox EMPC (https://github.com/jywang2016/EMPC) for researchers interested in this filed.

This paper is organized as follows. In section 2, the framework and components dynamics are described. Section 3 provides information on the case study while the simulation results are presented in section4. Section 5 is the conclusion and further work.

2. FRAMEWORK AND MODELS

2.1. Proposed Framework

The schematic of proposed framework is shown in Fig. 1. The left-side of the framework schematic is the flowchart of MPC solving and the right-side is the diagram of the energy-hub structure. The data from elements about electricity usage or generation will be recorded in the building data management system(BDMS). Meanwhile, the building operators can also collect the constraints information, for example, time-varying temperature range as shown in the grey blocks in Fig. 1.

According to the components involved in energy management, the framework will generate three types of MPC controllers with different constraints and optimization objectives. Furthermore, these optimization problems will be solved iteratively by the computing platform which consists of R and an open-source solver ECOS (Domahidi et al., 2013). More specifically, the first type of MPC controller aims to conduct the building climate control to track the reference temperature curve. A typical demand response problem with storage component can be solved by the second type of MPC controller. Finally, in order to achieve cost or energy saving, the third type of MPC controller takes the on-site generation element into consideration. Note that the narrow division of MPC controller is just for the convenience of distinction.

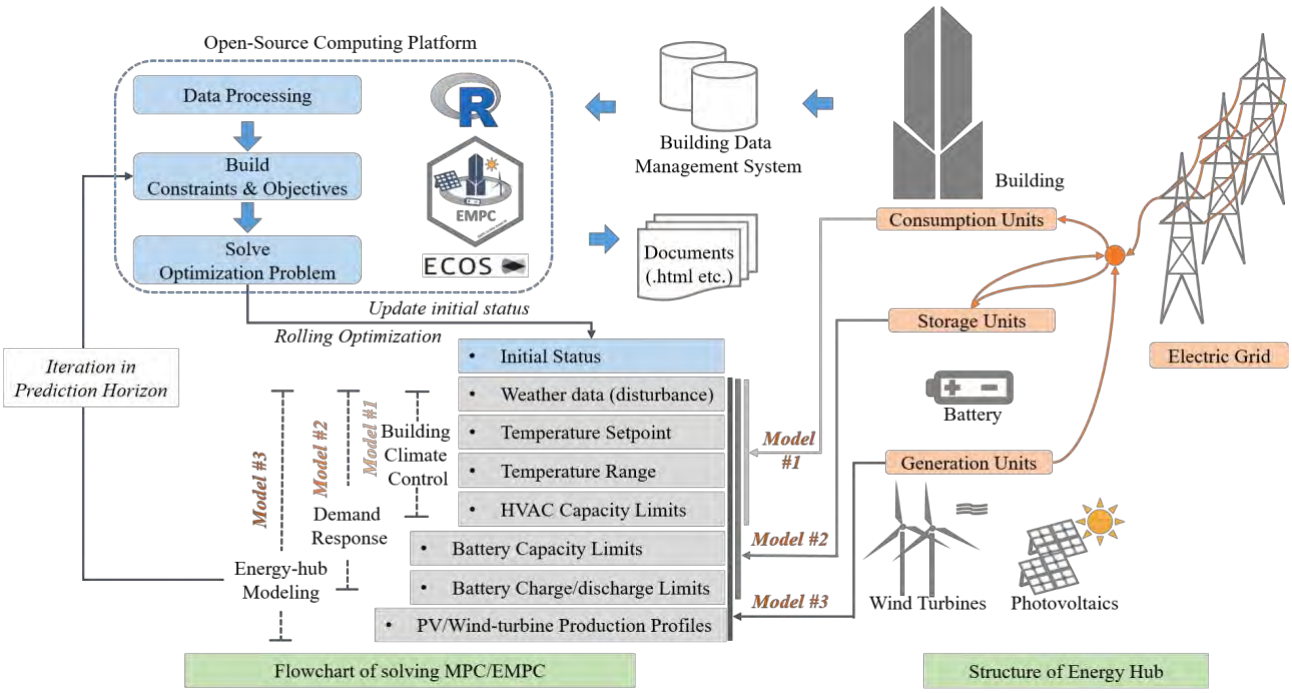

Figure 1: Framework of MPC-based demand-side management system

2.2. Mathematic Models

2.2.1. Building Dynamics

The discrete-time state space model is used to capture the thermal dynamics is shown in Eq. (1).

$$X_{k+1} = AX_k + B_u u_k + B_d d_k$$
$$Y_k = CX_k \qquad \text{Eq. (1)}$$

where *k* is the index of time step, *x* is the state, *u* is the HVAC input (i.e. the power of electric heater in this paper) in kW, *d* is the weather disturbances, *Y* is the indoor temperature in degree centigrade.

2.2.2. Storage Element Model

The charge and discharge characteristics of the storage element is shown in Eq. (2).

$$X_{s,k+1} = A_s X_{s,k} + B_s u_{s,k} \qquad \text{Eq. (2)}$$

where x_s indicates the storage capacity in kWh, us indicates the charge or discharge power in kW.

2.2.3. On-site Generation Element Model

We employ the photovoltaic(PV) as the on-site generation component. The formulation details about usable electrical power produced by a PV can be found in (DoE, U.S., 2010).

2.3. MPC Algorithm

The MPC policy is calculated by solving an optimization problem at each stage. The first element of the solution at each stage will be implemented. In this paper, MPC is conducted for building climate control and economic control.

2.3.1. Climate MPC

The objective and constraints of climate MPC controller are as shown in Eq. (3).

$$
\begin{aligned}
&min\, J(u) = \sum_{k=1}^{N} (T_{set,k} - Y_k)^2 \\
&s.t.\ T_{k,\min} - s \le Y_k \le T_{k,\max} + s \\
&\quad u_{\min} \le u_k \le u_{\max}
\end{aligned}
\qquad \text{Eq. (3)}
$$

where *J* is the objective function need to be minimized, T_{set} is the temperature set point, N is the control horizon, subscripts min and max indicate the lower and upper value of the variable respectively. The calculated indoor temperature Y is constrained by Eq. (1). Since the initial value of Y may be too low to violate the constraints, we include slack variable *s(s>0)* and a large penalty factor p to make the MPC problem feasible. Besides, we formulate the objective function J in a squared form instead of multiply of two matrices because the Y is a scalar in this paper.

2.3.2. Economic MPC

The economic MPC controller aims at satisfying the user's comfort with the lowest cost. The optimization problem of economic MPC with just building element involved is shown in Eq. (4).

$$
\begin{aligned}
&min\, J(u) = \sum_{k=1}^{N} c_k u_k + ps \\
&s.t.\ T_{k,\min} - s \le Y_k \le T_{k,\max} + s \\
&\quad u_{\min} \le u_k \le u_{\max}
\end{aligned}
\qquad \text{Eq. (4)}
$$

where *c* is electricity price. With storage element involved in the constraints development, the optimization problem is shown in Eq. (5).

$$
\begin{aligned}
&min\, J(u) = \sum_{k=1}^{N} c_k e_k + ps \\
&s.t.\ T_{k,\min} - s \le Y_k \le T_{k,\max} + s \\
&\quad u_{\min} \le u_k \le u_{\max} \\
&\quad X_{s,\min} \le X_{s,k} \le X_{s,\max} \\
&\quad u_{s,\min} \le u_{s,k} \le u_{s,\max} \\
&\quad e_k = max(u_k + u_{s,k}, 0)
\end{aligned}
\qquad \text{Eq. (5)}
$$

Compared to Eq. (4), the constraints of battery capacity and charge/discharge power are considered. In addition, the net power consumption *e* is the sum of battery charge/discharge power and heater power. Besides, *e* should be added generation power when the on-site generation element is considered. To prevent battery from reinjecting power into the main grid, we assume e≥0.

3. CASE STUDY

3.1. Data Generation

In this paper, a one-zone building located in the Wuhan City(China) was simulated in EnergyPlus for data generation. We conducted a simulation in the middle of January over one week. The state-space model as shown in Eq. (1) was obtained by solving a resistance capacity model.

An electric heater with a maximum power of 3kW is used to control the temperature of the building. We assumed that the electricity price is 0.2$/kWh between 10 am and 16 pm, while the price is 0.04$/kWh at rest of the day. The indoor temperature set point is shown in Table 1. In addition, we also assumed there is a battery with capacity of 6kWh. The generation power profile was collected from EnergyPlus simulation.

3.2. Control Scenarios

Four scenarios of MPC-based DSEM was set up and the corresponding configuration was as shown in Table 1. In the first scenario, the MPC was employed to track the constant temperature set point while the time-varying constraints were adopted in the remaining scenarios. In the third and fourth scenarios, we assumed that the target building was equipped with a battery and an additional PV panel. In all scenarios, the control horizon of MPC controllers is 24, namely 6 hours since the time step is 15 minutes.

Table 1. Configuration of different scenarios

Scenarios ID	Control Type	T_{set} (°C)	Storage	Generation
s1	Climate control	24	-	-
s2	Economic control	$[22,26]\ t \in [8:00,18:00]$	-	-
s3	Economic control	$[20,28]\ t \notin [8:00,18:00]$	Battery	-
s4	Economic control		Battery	PV

4. RESULTS

4.1. Indoor Air Temperature

The indoor temperature in the simulation of four scenarios are shown in Fig. 2. The areas covered by the light blue blocks indicate periods of high electricity price. The grey dotted lines represent the upper and lower limits of the indoor temperature respectively. It should be noted that since the initial temperature of the building is 12 degrees Celsius, temperature values of the first three moments in four scenarios are lower than 20. First three points in each profile in all scenarios are neglected.

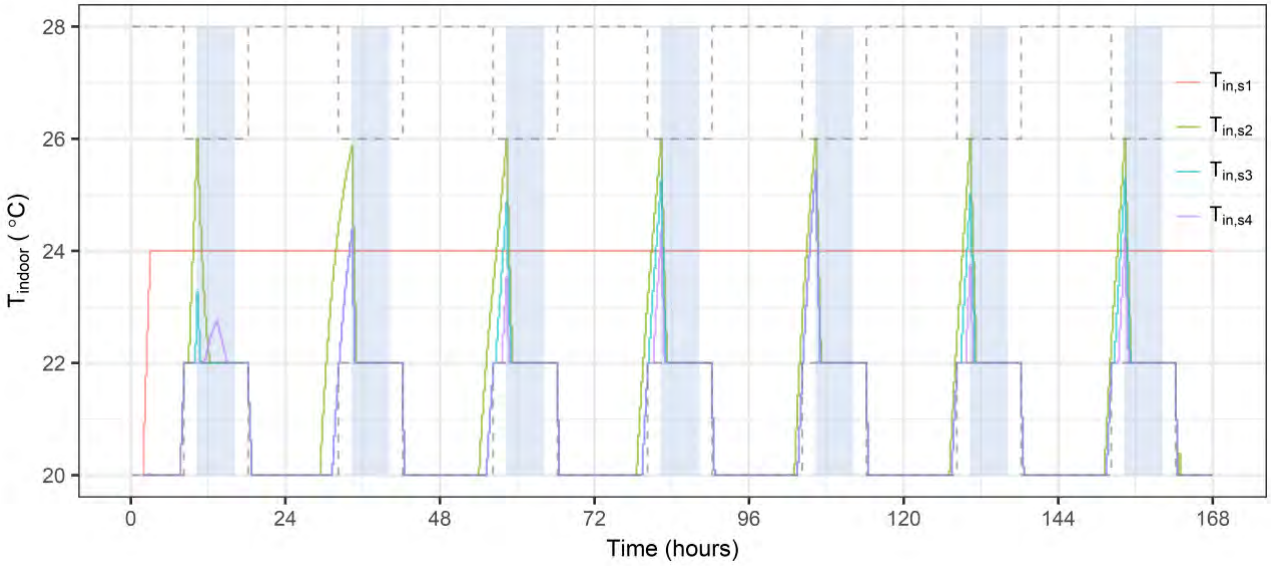

Figure 2: Indoor air temperature profiles of simulated building under different scenarios

It can be observed that the MPC controller in scenario 1 can increase and maintain the indoor temperature to 24 °C. In scenario 2, the MPC controller try to increase the indoor temperature to the upper limit before the high electricity price period. In the way, the heat storage characteristics of the building envelope are utilized to reduce the electricity consumption during the high price period, thus reducing the total cost. Interestingly, the controllers under scenarios 3 and 4 were not keen to over-heat the indoor air too much. This is because the battery or PV can supply enough power to the electric heater during periods of high electricity prices. The battery tends to store energy when the price is low and discharge it to heater when the electricity price is high. The PV generate electricity with “free-cost”. Therefore, compared to scenario 2, the controllers will avoid maximize the room temperature in scenario 3 and 4 prematurely because there is a cheaper or nearly free energy resource supply in the high price periods.

4.2. Power Consumption

All the profiles of the input power of the heater and the charge/discharge power of the battery under four scenarios are shown in Fig. 3. The orange curve in the second subgraph is the power generation of the PV. Both the power of battery discharge and PV generation are negative.

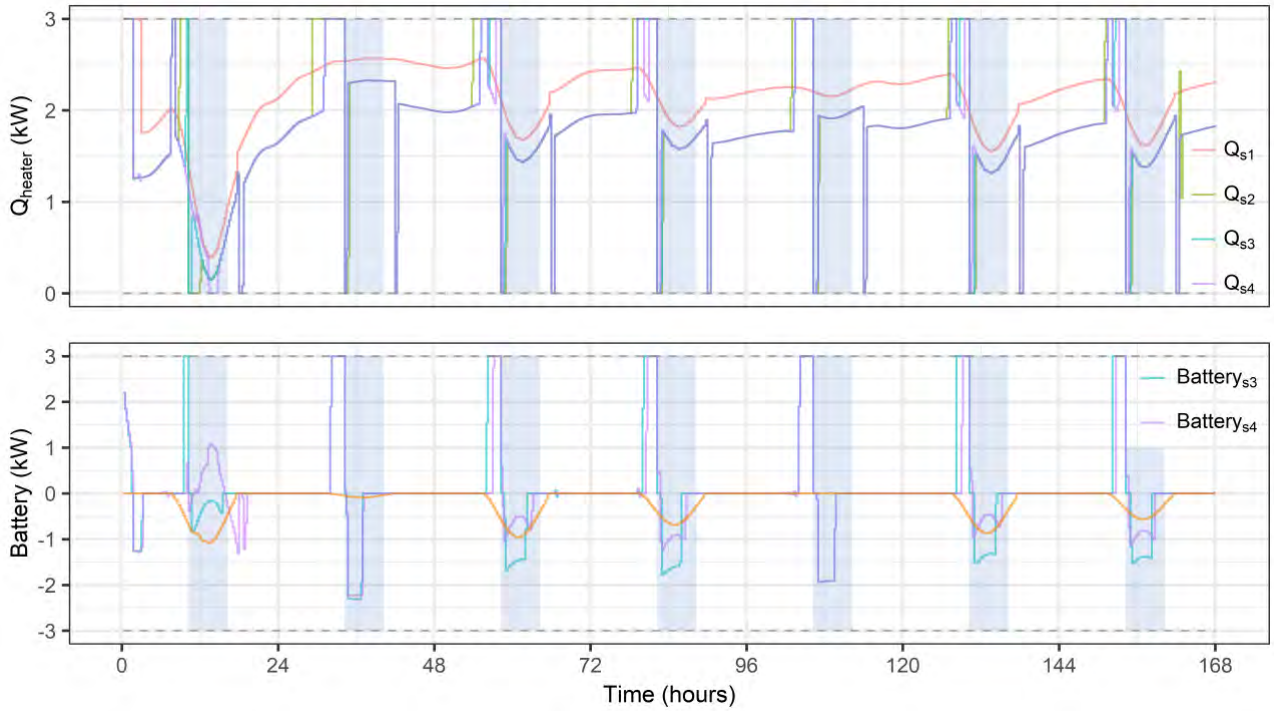

Figure 3: Heater, battery and PV energy usage/ generation profiles

It can be observed from the first subgraph that MPC controller in scenario 1 tends to maintain the indoor temperature around 24 °C. In other word, it aims at temperature tracking instead of cost-saving. Therefore, the input power to heater in scenario 1 is the highest than others at most of the time.

Compared to scenario 3 and 4, the MPC controller of scenario2 tends to increase the input power of the heater in advance. This is because there is neither a battery nor a PV for the controller to supply cheap or free power in the high price periods. Controller in scenario2 use as much as possible electricity at the cheap price duration. This phenomenon is consistent with the conclusion obtained from Fig. 2.

Subgraph 2 indicated that the electricity of scenario 3 mainly comes from the discharge during the high price period. Compared to scenario 3, the battery of scenario 4 have less charge or discharge because the PV can afford a considerable portion of the power supply.

4.3. Electricity Cost

In the one-week control simulation, the total cost in the four scenarios is shown in Table 2. The total cost is calculated from the electricity purchased from the main grid.

Table 2. Total electricity cost over one-week simulation

Scenarios No.	s1	s2	s3	s4
Cost/($/week)	26.46	20.79	16.51	14.17

The MPC controller in scenario 2 saved nearly 21.43% of the electricity cost by utilizing the heat capacity of the building, compared to which in scenario 1. Furthermore, compared to scenario 2, 20.59% of the electricity cost is saved through the battery element to expand the demand response capability of the building in scenario 3. Finally, we saved 31.8% of the electricity cost by using both of the battery and PV element compared to the scenario 2.

5. CONCLUSIONS

In this work, a MPC-based DSEM framework was proposed to investigate the demand response potential by controlling the HVAC system. Besides the fundamental elements (i.e. main grid and building), the energy storage and on-site generation component were also considered under the structure of energy-hub. Four scenarios with different control purposes and participating components were studied. Three conclusions were concluded as follows.

1) We demonstrated that this framework can navigate the trade-off between occupancy comfort and economic environment by utilizing the heat storage capacity of building envelope. The framework can achieve nearly 21% of electricity bills savings while maintaining building climate, compared to MPC with constant temperature set point.
2) This framework can achieve furthermore cost saving by taking storage and generation components into account. Compared to scenario 2, scenario 3 and 4 saved about 20% and 31% of the electricity bills, respectively.
3) For the end-users, the framework can be used to assist in the selection of storage and generation elements for the building to achieve energy or economic saving. For the producers, the framework can be used to design dynamic energy prices to encourage building operators to shift load.

We have developed an open source package called EMPC as an example of this framework implementation. We hope to develop an interface between EMPC and EnergyPlus for the co-simulation purpose.

ACKNOWLEDGEMENTS

This research was financially supported by the National Natural Science Foundation of China (Grants 51876070 and 51576074).

NOMENCLATURE

X	building state(°C)	p	penalize factor(-)
X_s	battery state(kWh)	s	slack variable(-)
u	heater input power(kW)	c	electricity price($/kWh)
u_s	charge/discharge power(kW)	e	net power consumption(kW)
J	objective function(-)	T_{set}	indoor temperature set point(°C)

REFERENCES

Kolokotsa, D. E. K. D., Rovas, D., Kosmatopoulos, E., & Kalaitzakis, K. (2011). A roadmap towards intelligent net zero-and positive-energy buildings. Solar Energy, 85(12), 3067-3084.

Kircher, K. J., & Zhang, K. M. (2015, July). Model predictive control of thermal storage for demand response. In American Control Conference (ACC), 2015 (pp. 956-961). IEEE.

Wang, S., Xue, X., & Yan, C. (2014). Building power demand response methods toward smart grid. HVAC&R Research, 20(6), 665-687.

Ma, J., Qin, J., Salsbury, T., & Xu, P. (2012). Demand reduction in building energy systems based on economic model predictive control. Chemical Engineering Science, 67(1), 92-100.

Crawley, D. B., Lawrie, L. K., Winkelmann, F. C., Buhl, W. F., Huang, Y. J., Pedersen, C. O., ... & Glazer, J. (2001). EnergyPlus: creating a new-generation building energy simulation program. Energy and buildings, 33(4), 319-331.

Široký, J., Oldewurtel, F., Cigler, J., & Prívara, S. (2011). Experimental analysis of model predictive control for an energy efficient building heating system. Applied energy, 88(9), 3079-3087.

Ma, Y., Borrelli, F., Hencey, B., Coffey, B., Bengea, S., & Haves, P. (2012). Model predictive control for the operation of building cooling systems. IEEE Transactions on control systems technology, 20(3), 796-803.

Halvgaard, R., Poulsen, N. K., Madsen, H., & Jørgensen, J. B. (2012, January). Economic model predictive control for building climate control in a smart grid. In Innovative Smart Grid Technologies (ISGT), 2012 IEEE PES (pp. 1-6). IEEE.

Oldewurtel, F., Ulbig, A., Parisio, A., Andersson, G., & Morari, M. (2010, December). Reducing peak electricity demand in building climate control using real-time pricing and model predictive control. In CDC (pp. 1927-1932).

Avci, M., Erkoc, M., Rahmani, A., & Asfour, S. (2013). Model predictive HVAC load control in buildings using real-time electricity pricing. Energy and Buildings, 60, 199-209.

Domahidi, A., Chu, E. and Boyd, S., 2013, July. ECOS: An SOCP solver for embedded systems. In Control Conference (ECC), 2013 European (pp. 3071-3076). IEEE.

DoE, U. S. (2010). Energyplus engineering reference. The reference to energyplus calculations.

Manuscript ID: 966
DOI: 10.18462/iir.icr.2019.0966

Quantification of energy flexibility from air conditioning of residential buildings

Alice MUGNINI[(a)], Fabio POLONARA[(a)(b)], Alessia ARTECONI[(a)]

[(a)] Dipartimento di Ingegneria Industriale e Scienze Matematiche, Università Politecnica delle Marche, via Brecce Bianche 1, 60131 Ancona, Italy, a.mugnini@pm.univpm.it, f.polonara@univpm.it, a.arteconi@univpm.it

[(b)] Consiglio Nazionale delle Ricerche (CNR): Construction Technologies Institute, Viale Lombardia 49, 20098, San Giuliano Milanese, (MI), Italy

ABSTRACT

Air conditioning (AC) for buildings is an energy demanding sector, showing an increasing trend in energy use worldwide. For this reason, demand side management (DSM) strategies addressing building thermal cooling loads have a paramount importance. In this paper several air conditioning systems are considered, composed of chillers and different distribution systems, such as radiant ceiling (panels and concrete ceiling), fan coils and splitters. The energy flexibility they can provide is quantified at design condition by means of a dedicated methodology, thus their performance is compared. Furthermore, the effect of their combination on the overall operating energy flexibility achievable is evaluated in order to draw some guidelines for optimal strategies of energy flexibility exploitation.
Keywords: DSM, Air Conditioning, Chiller, Heat Pump.

1. INTRODUCTION

The International Institute of Refrigeration (IIR) estimates that the total number of refrigeration, air-conditioning and heat-pump systems in operation worldwide is roughly 3 billion, accounting for about 17% of the overall electricity used (IIR, 2015). In particular, space cooling is the fastest growing end energy use in buildings, having increased by 3.3% a year since 2010 (IEA, 2018). Therefore, especially in summer season, the electricity demand will tend to increase, both in terms of average demand and peak, being the building sector one of the most energy-consuming worldwide (in Europe it accounts for about 40% of global energy consumption). Moreover, as promoted by the European Directive 2009/28/EC (2009), renewable energy sources (RES), whose nature is hardly foreseeable, will be more and more widespread as large-scale generation system. To limit grid instability and reduce overall demand, the building sector can provide a big contribution through the application of Demand Side Management (DSM) programs. DSM is meant as those actions addressed to modify the final user's electricity consumption in relation to the needs of the grid.

Many literature studies assessed the potential electric flexibility of buildings provided by managing their thermal demand for heating space (Foteinaki et al., 2018). However, for cooling applications, a smaller number of works are available, although its potential is undoubtable. Arteconi and Polonara (2018) highlighted how, adding a thermal energy storage (TES) to an air conditioning (AC) system, allows to obtain different benefits (e.g. reduction of the installed capacity, increase of the operational flexibility, potential energy costs reduction). Different systems can be used as TES in building cooling applications (Gang, 2015). Hasnain (1998) evaluated the coupling of a thermally stratified chilled water storage (sensible TES) or an ice storage (latent TES) to a chiller for air conditioning. It was demonstrated that a full storage strategy (realized by shifting the entire peak cooling load to off-peak hours) allows to obtain peak electricity demand reduction up to 80–90% for short peak demand electricity periods. Li el al. (2019) studied the potential of the thermal inertia introduced by the building envelope as passive storage in cooling applications. Through an on-off control, they estimated a 18.73% reduction of the peak electricity consumption due to the energy stored in the envelope of a commercial building coupled with an air-conditioning system. The building envelope inertia can also be exploited in an active way, if a radiant surface (ceiling or floor) is used for cooling (Arteconi et al.,

2014). In this case, the ceiling/floor is a radiating surface, while the concrete acts like a thermal storage cooled by water.
The objective of this work is to evaluate the potential energy flexibility that different AC residential systems can provide. Low, medium and high inertia distribution systems, such as split system, fan coil, ceiling panels and concrete ceiling radiant cooling, coupled with a heat pump are considered. Firstly, through dynamic simulations, a single indicator (the Flexibility Performance Indicator, FPI) (Mugnini et al., 2018) is calculated to quantify and compare their energy flexibility performance at design conditions. Secondly, the effect of their aggregation on the achievable overall flexibility is evaluated in operating mode, by assuming different DSM strategies. The goal of the analysis is to provide guidelines for an effective exploitation of aggregated flexibility provided by space cooling.

2. METHODS

In this section the energy flexibility quantification methodology is explained. Section 2.1 describes the energy flexibility labelling procedure (Mugnini et al., 2018), while Section 2.2 reports how the operating flexibility of the AC systems is conducted.

2.1 Flexibility Performance Indicator Calculation

The FPI calculation requires a transient building simulation tool, even if it refers to design conditions, since the building energy demand strongly depends on external environment conditions variability and on the dynamic of its thermal response in DMS applications. For this purpose, Trnsys 17 (Solar Energy Laboratory, 2012a) is used in this work. Furthermore standard boundary conditions (SBC) have to be uniquely defined. The first one is represented by the indoor comfort conditions: the acceptable temperature comfort band is 24-26°C and relative humidity (RH) can vary between 50-70%. For the external environment, a typical meteorological year (TMY) must be used as climatic file for the simulations. Moreover, the demand response (DR) event must be fixed. A DR is a particular DSM application, defined as 'changes in electric usage implemented directly or indirectly by end-use customers/prosumers from their current/normal consumption/injection patterns in response to certain signals', typically price signals (Gellings, 2009). For its importance on reducing the peak energy demand and installed power capacity a peak shaving strategy (PSS) is selected. It consists of interrupting power supply to the cooling systems at the electrical system peak power demand time until the internal comfort conditions reach the upper boundary (response period). Then the cooling system is switched on and the event can be considered ended when the initial comfort conditions are restored (recovery period).
The FPI calculation method is based on the comparison between the building behaviour during the DR event and the reference one (e.g. without the DR event). Eq. 1 shows the FPI formulation.

$$FPI = \frac{1}{4}\left(p_1 \cdot t^*_{res} + p_2 \cdot \dot{P}^*_{res} - p_3 \cdot t^*_{rec} + p_4 \cdot \eta_{DR}\right) \quad \text{Eq. (1)}$$

It is defined in a dimensionless form as weighted average of four contributions, where the asterisk indicates the dimensionless terms and the p_i the contributions weight. These contributions account for all the different energy flexibility typical aspects: time, capacity and power (Reynders et al., 2017). The first one is the response time t_{res} [hours] referred to 24 hours (p_1=60). The second one is the committed power $\dot{P}_{res}$ [kW_e], normalized to the installed rated power with a weight of 20% (p_2=20). It is defined as the integral of the difference between the building reference power demand and its power demand during the DR event divided by the duration of the response phase, t_{res}. The latter is the third contribution, the recovery time t_{rec} [hours] and in Eq.1 is referred to 24 hours (p_3=10). Finally, there is the DR energy efficiency η_{DR} (p_4=10). It is calculated as the ratio between the actual energy variation E_{DR} [kWh_e] achieved during the DR event and the building electricity use in reference operation during the whole DR event. In the FPI formulation, a greater weight is assigned to those parameters that represent the interaction of the building with the grid side t_{res} and $\dot{P}_{res}$, since they refer to the period when the cooling system is switched of.
Based on FPI values, a flexibility class distinction can be made: building is located in class D if FPI is less than 4, while the class became C if it is between 4 and 5.5. Class B goes from 5.5 to 8, A1 from 8 to 10, A2 from 10 to 20 and, if FPI is more than 20 the flexibility class become the higher A3.

2.2 Evaluation of Operational Flexibility

In order to evaluate the operating energy flexibility achievable through residential cooling demand management, the effect of different AC systems combinations in a DMS scenario is presented. The DR event is a peak shaving strategy starting at 12:00 (the same defined in Section 2.1) when the cooling system is switched off until the internal comfort bound is reached. Two different requests for energy flexibility are modelled for each single user: high flexibility demand (HFD) and low flexibility demand (LFD). As the evaluation is focused on thermostatically controlled loads (TCL), HFD exploits the overall comfort range available (internal set-point starting from 24°C and 60% RH can reach 26°C and/or 70%RH). LFD, instead, consists in requesting a smallest comfort variation (maximum temperature and humidity achievable: 25°C end/or 65%HR). The HFD and LFD strategies are applied in several configurations to the AC systems in order to achieve different goals (e.g. instantaneous peak reduction, minimum user involvement or peak reduction for long periods): all of the them are involved at the same time or only some of them are involved or they are called to participate to the DR event one after another.

3. CASE STUDY

In this section the building and the AC systems are described. In order to evaluate the energy flexibility potential obtainable from the aggregation of the different cooling systems, a single building, composed of four apartments, is modelled. It is located in Rome (41°47' N, 12°14' E), where summer is quite hot with an average daily temperature of 26.5°C for August (the warmer month) (UNI, 2016a). In the first part a description of the building construction characteristics is reported, then the considered AC systems are described.

3.1 Building Features

A single building composed of four climatic zones (apartments) is modelled in TRNBUILT (Solar Energy Laboratory, 2012b). For the climatic class D, the envelope thermal transmittances (U-values) are extrapolated from the Italian regulation D.M. 26 June 2015 (Italian Ministry of Economic Development, 2015), since it is representative of a consistent share of the building stock where modern cooling system can be integrated. The wall composition and thermal properties of the construction materials were extrapolated from the Italian building norms: UNI/TR 11552 (2014). A hollow bricks masonry with cavity thermal insulation is used for external walls (U=0.36 $Wm^{-2}K^{-1}$), while internal walls are realized as insulated structure in perforated bricks (U=0.58 $Wm^{-2}K^{-1}$). The ceiling is modelled with reinforced brick-concrete slab and has a high insulation level (U=0.28 $Wm^{-2}K^{-1}$); a concrete high insulated floor (U=0.36 $Wm^{-2}K^{-1}$) is adopted. Windows with double glass (argon filled) and aluminum frame (U=2.12 $Wm^{-2}K^{-1}$) are used.

All the dwellings have a 100 m^2 living area and a 21% of window surface area rate was assumed (Italian Ministry of Economic Development, 1975). The air changes per hour (ACH) are equal to 0.5 h^{-1} and an occupancy density of 30 m^2 per person with a corresponding internal gain of 120 Watt/person is considered. Artificial light density of 10 Wm^{-2} is introduced too.

3.2 AC Systems

Four different AC systems, whose distribution systems have different thermal inertia, are taken into account. They are sized on the basis of the peak cooling demand (Pizzetti, 1986). In Rome, the cooling peak load, with the outside design condition suggested by Italian standard UNI 10349-2 (2016b) and an internal temperature of 25°C with 60% RH is about 5.7 kW_t, of which 4.5 kW_t sensible and 1.2 kW_t latent.

The modelled cooling systems are:

i. Air source heat pump (AHP) with direct expansion split system (SS). In this system the indoor air cooling is realized by direct contact with the evaporator in which the refrigerant flows. The AHP is modelled with Type 954 and it is sized to cover the overall thermal load, since the same unit treats both the sensitive and the latent contribution. With this system only the temperature can be used as comfort limit condition for the DR event, since a RH punctual control is not possible. It is the system with lower thermal inertia. However, it is introduced for its large diffusion due to its inexpensiveness and installation easiness.

ii. Air to water heat pump (WHP) with fan coil units (FCU). The WHP, whose performance is derived from a manufacturer catalogue (Viessman, 2016), is modelled with Type 941 and it is sized to provide only the sensible load. FCU lower the air temperature below its dew point, managing in this way also the latent heat contribution, however, also in this case, a RH punctual control is not possible. Although characterized by a low thermal inertia as split systems, the presence of a water loop allows the addition of a TES, with consequent increase in thermal inertia. In this case a 200 liters cold water tank (autonomy 30 minutes) is added in order to model a medium thermal inertia AC system.
iii. Air source heat pump (WHP) and air dehumidifier (AD) with ceiling panels (CP). The WHP (Viessman, 2016) is sized to cover only the amount of sensible heat. The treatment of latent heat is entrusted to an internal AD, modelled with Type 688. In this case, both the internal temperature and relative humidity can be controlled. The chilled ceiling is composed of pipes set on panels in the first internal layer of the roof, for this reason it is considered a medium thermal inertia system if compared with radiant cooling concrete ceiling.
iv. Air source heat pump (WHP) and air dehumidifier (AD) with radiant cooling concrete ceiling (CC). It is modelled as a massive active layer in the ceiling stratigraphy. Even in this case the treatment of latent heat is entrusted to an internal AD (Type 688). This distribution system has the highest thermal inertia, since the pipes are embedded in a concrete layer of 0.1 m.

Fig. 1 shows a scheme of the 4 apartments building with their different cooling systems.

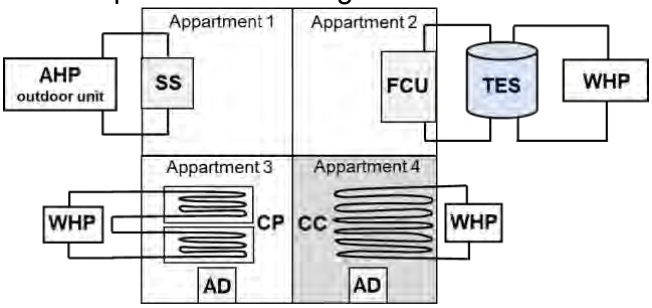

Figure 1: Schematics of the cooling systems in the considered building.

4. RESULT AND DISCUSSION

In this section the simulation results are presented. In the first section the energy flexibility performance of the four cooling systems is compared thought the FPI calculation. Then, the effect of the combination of different energy flexibility sources is evaluated in operating conditions.

4.1 AC Systems Flexibility Performance Comparison

According to the methodology illustrated in Section 2.1, the DR representative summer day is August 18, when the TMY average daily temperature is 26.54°C (UNI, 2016a) and the DR starting time is 12.00 pm, when frequently the Italian electric demand has a peak in summer weekdays (Terna Spa, 2019).

Table 1 summarizes the flexibility parameters and the FPI calculation for all the cooling systems. All of them have low design energy flexibility since the FPI remains always between 4.1 and 5.5 (Class C or B). Focusing on the SS and FCU systems, a very similar behaviour can be observed between them. The TES coupled with FCU allows to obtain a response time 22 minutes longer than the SS. As Fig. 2(a) shows, due to the cold-water tank discharge, from time 12 hours to 12.7 hours, when the WHP is off, the indoor temperature continues to comply with the initial set-point. However, from the electricity consumption point of view, the adoption of FCU with a TES produces less savings in committed power and actual energy use, which negatively affect the FPI calculation.

Table 1. Flexibility parameters for the modelled AC systems, FPI calculation and labelling

AC system	t_{res} (hours)	$\dot{P}_{res}$ (kW_e)	t_{rec} (hours)	E_{DR} (kWh_e)	FPI	Flexibility class
SS	1.65	0.42	0.20	3.26	5.0	C
FCU	2.02	0.18	0.22	1.54	4.1	C
CP	1.65	0.91	5.40	3.78	5.5	B
CC	1.15	0.89	3.17	2.02	5.3	C

As said before, these AC systems do not allow a punctual RH control, so the DR phases are determined by the indoor temperature only. Instead, in CP and CC systems, where an air dehumidifier is installed, the response and the recovery period are ruled by both of them.
It can be immediately noted that, even if a distribution system with a higher thermal inertial (CP or CC) is adopted, the response time, t_{res}, remains rather low (Table 1), since the RH conditions affect a lot the building behaviour. Moreover, the thermal inertia has an impact on the speed with which the RH increases, and so on the comfort limit condition that is reached first. When there is more thermal inertia, indeed, the internal temperature tends to rise more slowly, and the relative humidity increases faster, as it can be seen in Fig. 2(b). The CC system provides a higher inertia than CP and the RH reaches firstly the limit conditions, t_{res} is 30% lower for CC than CP (determining a lower E_{DR} value). However, when the response period ends, the indoor temperature in CP system reaches 25.7°C, while for CC about 25°C. This fact affects the recovery period, which for CP is 2 hours and 12 minutes higher than for CC. $\dot{P}_{res}$ is almost the same for CC and CP as well as the WHP size.
This analysis makes possible to conclude that, for the modelled dwellings in summer period there is a low overall design energy flexibility performance. The thermal inertia seems to affect positively the response duration only if the control system is just temperature-based. If a more accurate control of the comfort condition is possible (both temperature and relative humidity), its influence on the response period is mitigated. However, this last case allows to obtain a little improvement in flexibility performance.

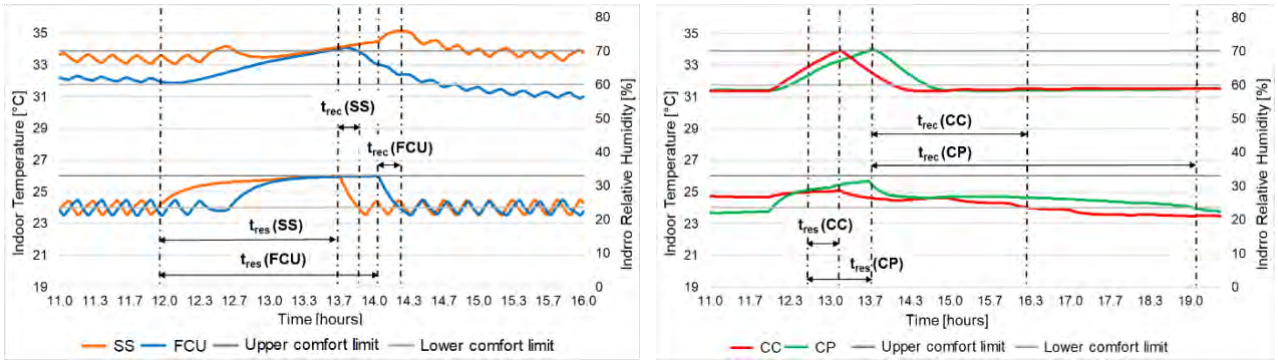

(a) **(b)**

Figure 2: Indoor temperature and comfort bounds during the DR event. (a) Comparison between SS and FCU. (b) Comparison between CP and CC

4.2 AC Systems Flexibility Combination Evaluation

In this section the aggregated energy flexibility obtained from the different AC systems during a DR event is evaluated. The DR strategy consists in an electricity demand reduction at Italian summer peak electric demand time (12.00 pm) and the same day used for the flexibility labelling method is considered. Fig. 3 shows the overall electricity demand for the 4 apartments building without DR event and its breakdown in the different AC contributions in a time period of 1 hour (from 12.00 to 1.00 pm). Four electric power levels can be distinguished: a base load of 5 kW_e, an intermediate load of 7 kW_e, and two power peaks: 10 kW_e and 12 kW_e (the latter is obtained when all the systems are working together).
Since the indoor comfort is still guaranteed for more than 1 hours (t_{res} in Table 1), if a high flexibility demand (HFD) strategy is applied independently at each cooling system, the aggregated demand becomes zero for the whole hour as showed in Fig. 4 (the aggregated response period ends at 13.15 hours). A different situation can be noted if, instead, a low flexibility demand (LFD) strategy is applied. Looking at the dotted line in Fig. 4, a power demand of about 5 kW_e is requested after 0.1 hours from the DR programme activation. This is due to the shorter response time that the systems present in case of restricted comforts limits. Especially, the apartment with splitters (SS) reaches the indoor temperature of 25°C in 0.13 hours. In the same way, the fan-coil (FCU) system response period is 0.78 hours, while 0.47 and 0.60 hours are respectively the values of t_{res} for ceiling panels (CP) and concrete ceiling (CC) radiant cooling. However, if a LFD strategy is applied to all the considered AC systems together, the electricity consumption is also zero, even if for a limited time (about 8 minutes). This effect cannot be obtained if only a few AC systems are involved with a LFD strategy.

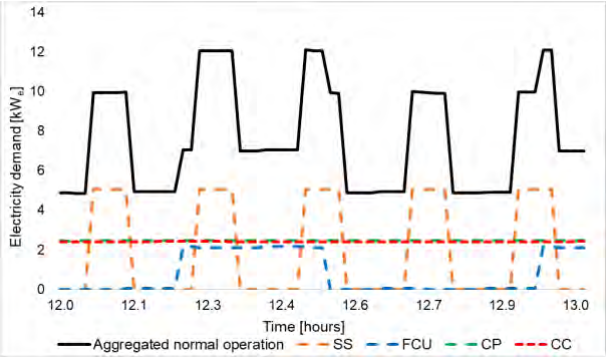

Figure 3: Electricity aggregated demand. Total and single contributions

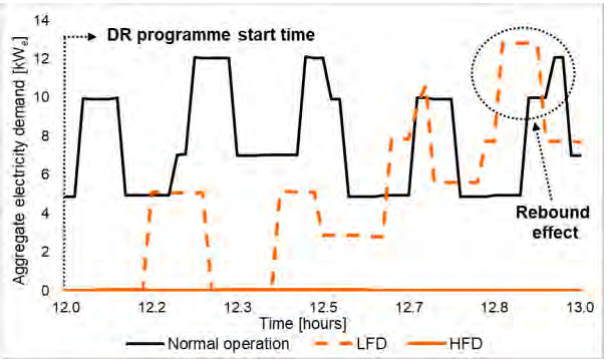

Figure 4: Electricity aggregated demand. HFD or LFD activated together for all user

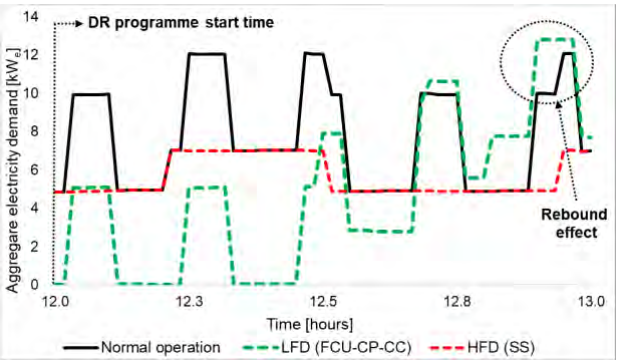

Figure 5: Electricity aggregated demand. HFD to SS AC system compared with LFD to all the others (FCU, CC and CP)

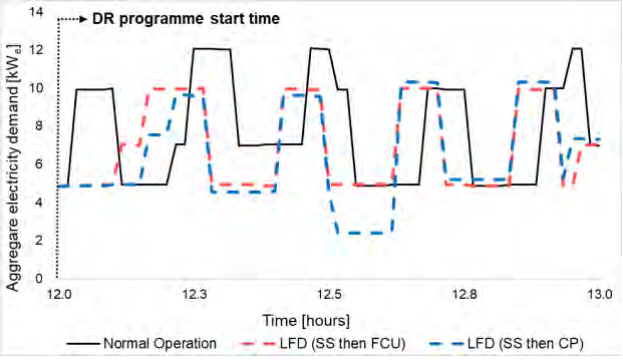

Figure 6: Electricity aggregated demand. LFD in sequence. Comparison between FCU after SS and CP after SS

Table 2 reports the percentage of time (in the considered hour between 12:00 and 13:00 h when the network requires flexibility) in which the aggregated demand remains below the power threshold levels described above (7, 10 and 12 kW_e). Since the SS electric load is the highest contribution in the aggregated demand (it accounts for about 42% of the demanded power when all the cooling systems are on), a possible DR strategy could be the HFD configuration applied only to it (green dotted curve in Fig. 5). In this way for the whole considered hour, the aggregated electricity demand stays always below 10 kW_e. Furthermore, the total power is reduced to the base load for about 13.2 minutes (22% of the considered hour), as showed in Table 2. Since the SS power demand is of the same order of magnitude of the aggregated demand of the other 3 cooling systems (FCU, CC and CP), in Fig. 5 the latter strategy is compared to a possible LFD configuration applied to them. In this last case a flattening of the highest peaks is not obtained for the whole considered hour (Table 2) but, the base load is maintained for about 50% of the time.

In order to request a smaller variation of the temperature comfort bound to the final users, the effect of a LFD configuration with subsequent calls of the 4 AC systems is investigated. The DR operator, in order to minimize the involvement of the individual user, which must be economically incentivized, could evaluate to call them one by one in this manner: once the first user has reached its restricted comfort limit, another one is called and so on.

Fig. 6 reports the aggregated power in case FCU or CP systems are called after SS. Split system is chosen as first call since its power is high, but its response period is very low (Table 2).

In both cases, as shown in Table 2, the base load is maintained for a short time (12% and 17% of the flexibility hour respectively for SS-FCU and SS-CP). While, for both cases, the aggregated electricity demand always remains lower than the maximum power peak threshold (12 kW_e).

Concluding, the results show that if the aggregated electricity power wants to be maintained below the base power threshold for a longer time, the DR strategy should involve all the users with a LFD configuration in order to get a compromise among load redaction, comfort variation and duration of the aggregated response period. As alternative a LFD configuration with subsequent calls guarantees that the power demand on average is higher, but always lower than the maximum

threshold. Instead a HFD strategy only applied to the most energy demanding AC system (SS) allows a peak power reduction more important (always below 10 kW).

Table 2. Percentage of time (in the 12.00-1.00 pm hour) in which the aggregated demand remains below the considered thresholds

DR Strategy	Below 7 kW_e	Below 10 kW_e	Below 12 kW_e
LFD to all systems	63%	70%	85%
HFD to SS	22%	100%	100%
LFD to SS	17%	17%	22%
LFD to FCU, CC and CP	50%	70%	90%
Sequence LFD (SS then FCU)	12%	17%	100%
Sequence LFD (SS then CP)	17%	22%	100%

Eventually, it is important to note that, a PSS DR programme affects the aggregated electric demand trend also during the time after the event (recovery period). In Fig. 4 and 5, where the DR events end before 1.00 pm, a late peak (about 12.5 kW_e) larger than the highest in normal operation (in Fig.1) can be observed (for Fig. 6 the rebound effect happens after 13:00 h and it is not visible in the graph). This aspect should also be taken into consideration by a grid operator to minimize the rebound effect of the events on the network.

5. CONCLUSIONS

Purpose of this work was the energy flexibility characterization of residential AC sector. In order to do it, a design and an operating evaluation were conducted. In the first case a flexibility labelling methodology was applied to space cooling systems with different characteristics in terms of thermal inertia and indoor comfort control: SS, FCU, CP and CC coupled with a heat pump. These systems were modelled in four apartments belonging to the same building, thus to consider in operating mode the aggregated electricity demand for the whole building. Even if the obtained design flexibility performances were low (all the systems have flexibility class C or B), all the AC systems had response times of more than one hour.

Operatively, this fact allows the reduction to zero of the aggregated power for 1.18 hours, if a DR strategy with a high flexibility demand (HFD) configuration is applied (i.e. variation of 2°C for the temperature and 10% for RH) to all the AC systems at the same time. The aggregated demand is, instead, zero for about 38 minutes with a low flexibility demand (LFD, i.e. variation of 1°C for the temperature and 5% for RH). Alternative combinations of the energy flexibility provided by the different AC systems were tested. The results showed that good performance, in terms of time with reduced power and maximum peak power demand, can be reached with a HFD strategy applied only to the highest energy demand user (AC with splits). On the other hand, the involvement of AC systems with higher thermal inertia allows to maintain the aggregated base load threshold for about 30 minutes, even with a LFD. A DR strategy with subsequent calls of the different users was also analysed. An LFD strategy applied firstly to the AC split system and secondly to an higher thermal inertia AC systems (FCU or CP) allows to maintain the peak demand always lower than the maximum power threshold (12 kW_e).

Concluding, the analysis showed that good energy flexibility performance in operation mode can be achieved by means of cooling demand management in buildings even with limited comfort bound variation requested to the users.

ACKNOWLEDGEMENTS

This work has been supported by MIUR of Italy in the framework of PRIN2015 project: “Clean heating and cooling technologies for an energy efficient smart grid”, Prot. 2015M8S2PA.

REFERENCES

Arteconi, A., Costola, D., Hoes, P., Hensen, J.L.M., 2014. Analysis of control strategies for thermally activated building systems under demand side management mechanisms. Energy Build, 80, 384–393.

Arteconi, A., Polonara, F., 2018. Assessing the demand side management potential and the energy flexibility of heat pumps in buildings. Energies 11, 1846.

European Parliament, 2009. Directive 2009/28/EC of 23 April 2009 on the promotion of the use of energy from renewable sources and amending and subsequently repealing Directives 2001/77/EC and 2003/30/EC. Official Journal of the European Union.

Foteinaki, K., Li, R., Heller, A., Rode, C., 2018. Heating system energy flexibility of low-energy residential buildings. Energy Build. 180, 95–108.

Gang, L., Hwang, Y., Radermacher, R., 2015. Review of cold storage materials for air conditioning application. Int. j. Refrig. 35, 2053-2077.

Gellings, C.W., 2009. Enabling Energy Efficiency and Demand Response, The Smart Grid, The Fairmont Press, Lilburn, 134-141.

Hasnain, S.M., 1998. Review on sustainable thermal energy storage technologies, Part 2: Cool thermal storage. Energy Convers. Manag, 39, 1139–1153

International Energy Agency (IEA), 2018. Cooling in buildings. Tracking Clean Energy Progress.

International Institute of Refrigeration (IIR), 2015. The Role of Refrigeration Industry in the Global Economy, 29th Inform. Note on Refrigeration Technology, Paris.

Italian Ministry of Economic Development, 1975. Italian Ministerial Decree of 5th July 1975: Modification to the ministerial instructions dated 20th June 1896 concerning the minimal height and the main hygienic-sanitary requirements in housing units. Gazzetta ufficiale.

Italian Ministry of Economic Development, 2015. Decree of 26 June 2015 - Application of Calculation Methods for Energy Performance and Definition of Minimum Building Requirements. Gazzetta Ufficiale.

Li, W., Yang, L., Ji, Y., Xu, P., 2019. Estimating demand response potential under coupled thermal inertia of building and air-conditioning system. Energy Build. 182, 19–29.

Mugnini, A., Polonara, F., Arteconi, A., 2018. Design Energy Flexibility for Italian Residential Buildings. In Proceedings of the 5th International High-Performance Buildings Conference at Purdue, 330-340.

Reynders, G., Diriken, J., Saelens, D., 2017. Generic Characterization Method for Energy Flexibility: Applied to Structural Thermal Storage in Residential Buildings. App. Energy 198, 192–202.

Solar Energy Laboratory, 2012a. Trnsys 17. Using the Simulation Studio.” University Wisconsin-Madison 2, Volume 2, 1–29.

Solar Energy Laboratory, 2012b. Trnsys 17. Multizone Building modelling with Type56 and TRNBuild. Volume 5, University Wisconsin-Madison 2, 1–230.

Pizzetti, C.,1986. Condizionamento dell’aria e refrigerazione. Teoria e calcolo degli impianti.

Terna Spa, 2018. Daily Italian electricity demand. [Online]. Available: http://www.terna.it/.

UNI, Italian Standards organization, 2014. UNI/TR 11552. Abacus of the structures constituting the opaque envelope of the thermophysical buildings.

UNI, Italian Standards organization, 2016a. UNI 10349-1: Heating and Cooling of Buildings - Climatic Data - Part 1: Monthly Means for Evaluation of Energy Need for Space Heating and Cooling and Methods for Splitting Global Solar Irradiance into the Direct and Diffuse Parts and for Calculate the Sol.

UNI, Italian Standards organization, 2016b. UNI 10349-2: Heating and Cooling of Buildings - Climatic Data - Part 2: Data for Design Load.

Viessmann, 2016. VITOCAL 200-S, Air to water heat pump with DC inverter technology for heating and cooling.

Manuscript ID: 1046
DOI: 10.18462/iir.icr.2019.1046

Proof of concept for a building integrated solid state heat pump

Sietze VAN DER SLUIS[(a)]
[(a)] SAINT TROFEE
Zutphen, 7205AR62, The Netherlands, sietze@sainttrofee.nl

ABSTRACT

A proof of concept has been produced for a solid state building integrated heat pump. This "ActiveWall" heat pump is designed as part of the outer wall of a building, and therefore does not occupy any useful building space. The outdoor side of the ActiveWall has a photovoltaic (PV) surface.
The heat pump is based on thermoelectric cooling, which is generally known to have a poor efficiency, but is actually quite efficient at low temperature differences such as those occurring in heating and cooling of buildings in moderate climates. Due to its PV surface, the yearly net electricity use for heating and cooling with ActiveWall is very low.
The ActiveWall uses very large heat exchange surfaces and natural convection heat transfer to avoid the necessity of additional fans. Thus, the overall concept does not contain any moving parts, which provides ActiveWall with a long life and low maintenance.
Keywords: Building, Heat Pump, Photovoltaic Panel, Thermoelectric Cooling.

1. INTRODUCTION

Under the Energy Performance of Buildings Directive (EPBD) each EU Member State must present a roadmap towards a low and zero-emission building stock in the EU by 2050. Consequently, houses that will be built in the coming years already need to have a near zero emission, as they will be part of the 2050 building stock. That's why already now new regulations see the light, such as in The Netherlands, where new houses must have a primary fossil energy use of less than 25 $kWh \cdot m^{-2}$ per year as of the beginning of 2020. Calculations show that the use of heat pumps is just about inevitable in order to achieve that goal (van der Heide et al., 2016). So roughly speaking, as of 2020 all new houses in the Netherlands will have a heat pump. And it is very likely that similar legislation, stimulating the use of heat pumps, will apply in most other EU member states.
Heat pumps today are expensive compared to gas boilers, they are heavy, and take up more space. Air source heat pumps are popular, but there are concerns about the noise of the evaporator fans. And many heat pumps today still contain refrigerants with a high global warming potential (GWP).
In the early days, a few decades ago, the predominant type of heat pump used in The Netherlands for single family housing was a water/water heat pump with ground source heat exchangers (GSHX). The design of such a heat pump is straightforward, because the temperature level of the (earth) source is quite constant and no defrosting is needed. Plate heat exchangers could be used as evaporator and condenser. Plot sizes in The Netherlands are small, so vertical GSHX were used in the form of polyethylene U-tubes with lengths in the order of 50 – 150 m. The costs for drilling holes and installing the GSHX were considerable.
Nowadays, air source heat pumps are popular. New inverter driven compressors can adjust easily to varying outdoor air conditions, and defrosting is performed by reversing the heat pump cycle. The defrosting sometimes causes concern, because there is no heat source available except taking heat "back" from the load where it was supplied to in the first place (in heating mode). But in a climate like in The Netherlands, heating days with sub-zero outdoor temperatures are limited

(and becoming less). Thus, with a good evaporator / fan design, defrosting needs are limited. The evaporator fans however do cause a new concern in densely populated areas: noise problems.
The most common heat rejection system, for both water source and air source heat pumps, is floor heating. Floor heating is appreciated for its comfort, but the drawback of floor heating is that it is slow to respond. It is not really a technical problem, with intelligent thermostats that can be set to start heating hours in advance of the actual comfort demand, and to maintain a relatively high night setting. But in terms of energy consumption, both the long preheating time and the high night setting are wasteful. Figure 1 shows average load profiles for a set of some 700 monitored heat pumps in the UK, at two outdoor temperatures (Love et al., 2017).

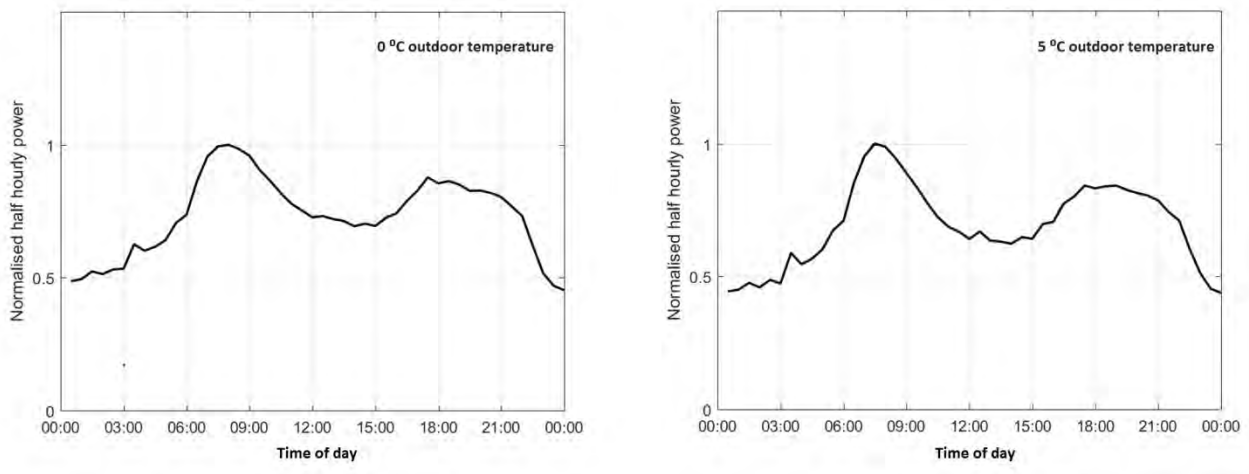

Figure 1: Measured heat pump load profiles at 0 ^{0}C and at 5 ^{0}C outdoor temperature

At night, when heating is not really required, heat pumps still run continuously at over 50% of capacity. A fact that is not taken into account when judging the performance of a heat pump in relation to other heating systems, based on heat pump COP only (however good that may be).
Furthermore, (water) distribution system losses are in the order of 3 - 7 % (Dieleman, 2001).
Due to the nightly energy use and the distribution losses, the real energy consumption of conventional heat pumps with floor heating is higher than we would expect on the basis of heat load and COP only. Together with the concerns noted before, relating to costs, size, noise and to a lesser extent, refrigerant GWP, we have been looking for an alternative without these drawbacks. And we have a surprising alternative, “ActiveWall”, based on thermoelectric heating and cooling.

2. THERMOELECTRIC HEATING AND COOLING

Thermoelectric elements make use of the Peltier effect to create a heat flow through the junction of two materials when a voltage is applied. They are often called Peltier elements. Commercially available Peltier elements or modules are made of p-type and n-type semiconductors, and include a large number of junctions on a small area. They are usually equipped with large heat sinks and fans for forced air circulation (Figure 2). They are usually presented as “coolers” but in fact they are heat pumps that can easily be reversed by reversing the polarity of the applied voltage.

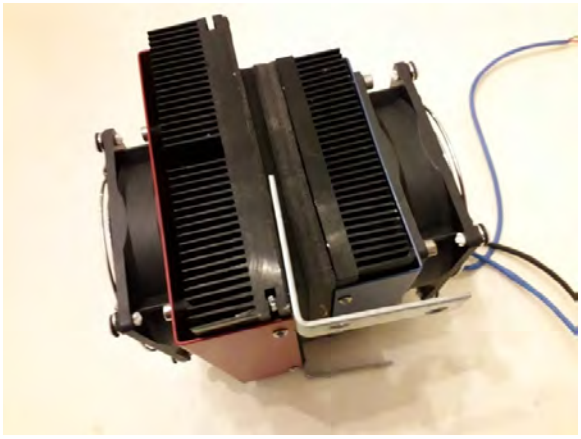

Figure 2: Thermoelectric heat pump assembly with heat sinks and fans.

From a historical point of view, reports on using thermoelectric modules for air-conditioning can be found as early as the 1960's. Several manufacturers produce thermoelectric air conditioners, which are mostly intended for cooling of small enclosures containing high power electronics. There are some more recent reports and patent applications describing thermoelectric air conditioners for space cooling (Kim, 2001 and Rawat, 2013). Achille Messac introduced an Active Building Envelope which is a combination of a thermoelectric cooler (TEC) and a solar panel (PV) to cool buildings (Messac, 2005). In this design the TEC makes use of the well-known conventional bulky heat exchanger fins (Figure 3).

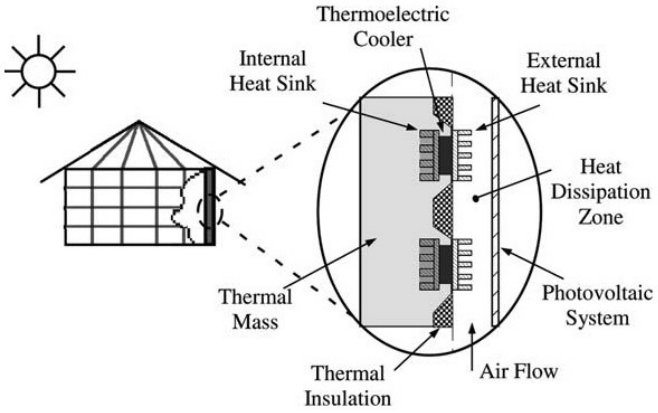

Figure 3: Schematic drawing of an Active Building Envelope as proposed by Messac (2005)

The reputation of thermoelectric elements is that they have a very "bad" COP. Let's have a look at the basic formulas that govern a thermoelectric module operation. There are three important module characteristics to start with: Sm, Rm and Km. The module Seebeck coefficient Sm ($V \cdot K^{-1}$) gives the relation between the voltage over the module and the temperature difference ΔT (in K) over the module. The module electrical resistance Rm (in ohm) gives the relation between the Voltage V applied over the module (in volt), and the current I through the module (in ampere). Finally, the module thermal conductance Km (in $W \cdot K^{-1}$) gives the "loss" due to internal heat leakage from hot side to cold side. The 2 basic formulas for the module cooling load Qc (in watt) in relation to the cold side temperature Tc (in K) and for the module power consumption P (in watt) are:

$$Qc = Sm \cdot I \cdot Tc - ½\, Rm \cdot I^2 - Km \cdot \Delta T \qquad \text{Eq. (1)}$$

$$P = Sm \cdot I \cdot \Delta T + Rm \cdot I^2 \qquad \text{Eq. (2)}$$

The term with Sm in the cooling load is the desirable effect we're after. The term with Rm describes Ohmic heating, which is a "loss" term, as is the term with the thermal conductance Km. In the limit where the loss terms become negligible, we would have:

$$\lim_{(Rm\to 0, Km\to 0)} COP = {Qc}/{P} = {(Sm \cdot I \cdot Tc)}/{(Sm \cdot I \cdot \Delta T)} = {Tc}/{\Delta T} \qquad \text{Eq. (3)}$$

This is the exact same (ideal) COP that we see in a classical compression refrigeration cycle. The term in eq. (1) with the thermal conductance Km is the thermal shortcut from the hot side to the cold side. At low values of current (I) and a high value of externally applied temperature difference, it can cause some unconventional effects, such as negative cooling loads, negative cooling COP values, and corresponding heating COP values below 1 (figure 4). At lower values of current and temperature difference than shown in figure 4, the COP is higher, e.g. COP = 12 at 0,5 A and 2 K.

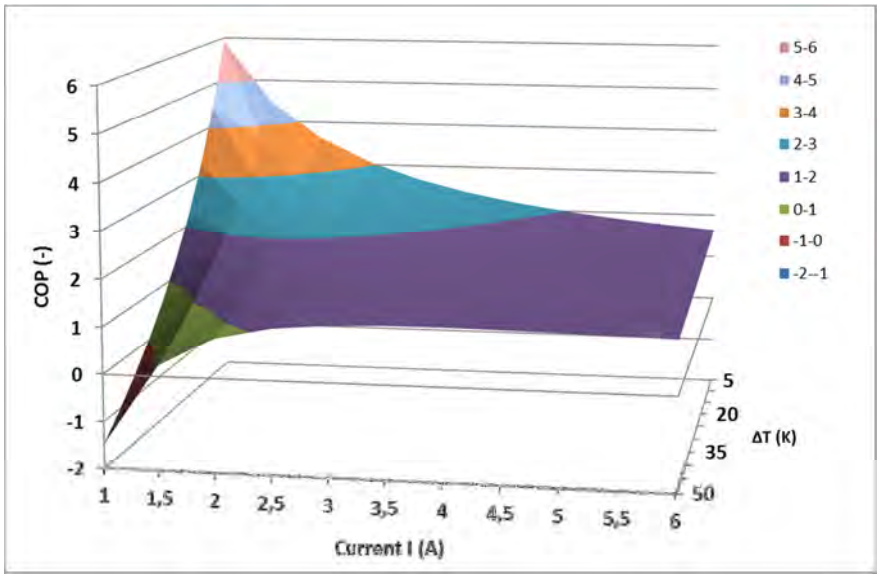

Figure 4: COP for a thermoelectric element as function of current and temperature difference ΔT.

In the past, thermoelectric elements were relatively expensive. But as with all semiconductor products, the costs of thermoelectric elements have been decreasing over the years. Nowadays a TEC1-12706 element with Qc(optimum) = 7,5 Watt can come at a price of around 0,79 € which is equivalent to some 105,- €/kW. (The designation TEC1-12706 relates to a thermoelectric 1-layer module with 127 junctions and a maximum current of 6 Amperes).

3. HEAT EXCHANGER DESIGN

In order to achieve an acceptable COP, the heat exchangers on the hot side and the cold side of the thermoelectric element need to have a good heat transfer. Nevertheless, we want to avoid the use of the conventional aluminium finned heat sinks with forced air circulation, mainly because we do not want any moving parts (fans) in our design.
The overall concept for ActiveWall is that it will be a heat pump integrated in the walls of a building, similar to the idea of the Active Building Envelope (ABE) shown in Figure 3. In our case however, in contrast to the original ABE, we will not use a thermal mass on the indoor side, but a large surface flat heat exchanger that directly heats or cools the indoor air. In this way we will have a heated or cooled indoor wall which offers the benefits of radiant heating and cooling. Likewise, we want to extend the heat exchanger surface on the outside over the entire wall, instead of the localized external heat sinks in the ABE of Figure 3.

Without forced air circulation, we will have a surface heat transfer coefficient α for free convection with a value in the order of only 5 W/(m².K). For practical (end-user) reasons of appearance and cleaning, we want to have a smooth surface on the indoor side. Then, in order to increase the heat exchange surface per m² of visible indoor wall, we can only increase the surface of the heat exchanger by means of interior air channels. These air channels will be placed vertically to allow for a natural convection air flow. The dimensions of these channels can range from mini-channels to large size channels with a diameter in the cm range. In our first proof of concept we have used rectangular air channels with 13 mm sides.
Thermoelectric elements themselves have a small heat transfer area, the most common sizes are 30 x 30 mm² or 40 x 40 mm². The thermoelectric heat flow through this small surface must be conducted over the much larger surface of the heat exchanger, without introducing large temperature differences. We have used finite element modelling (FEM) to calculate the temperature differences over the heat exchanger surface.

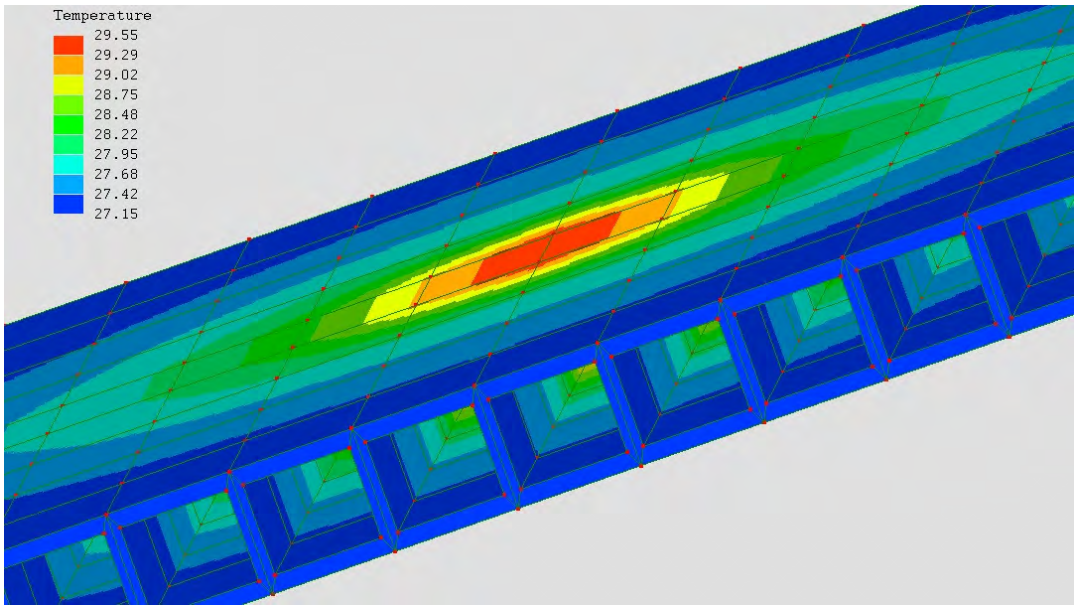

Figure 5: Result of FEM modelling, calculated temperature distribution (ºC) over an ActiveWall (air) heat exchanger (proof of concept) with a thermoelectric heat source attached. Air temperature 20 ºC

4. SCOP AND ENERGY USE

To make an appraisal of the seasonal coefficient of performance (SCOP) and the yearly energy use, we have made a year-round building simulation with EnergyPlus™, a whole building energy simulation program (https://energyplus.net). With this simulation we obtained hourly values for the outdoor temperature, indoor temperature and heat load for a reference building module in a Dutch climate. As discussed in the introduction, we did not include night heating in the model. ActiveWall is a fast responding system. It is able to deliver the heating peaks that occur in the morning when the heating is switched on, as calculated by the building energy simulation program.
We used the characteristics of the ActiveWall heat exchangers and those of the selected thermoelectric elements to calculate, for each hour, the power input to the thermoelectric elements needed to deliver the required heat load at the momentary outdoor- and indoor temperatures. This was done based on its specific performances for a number of commercially available thermoelectric elements. We found the best performance at an average heating power of 5 Watt per element. These elements can deliver a maximum cooling power Qc(max) of 26 Watt.

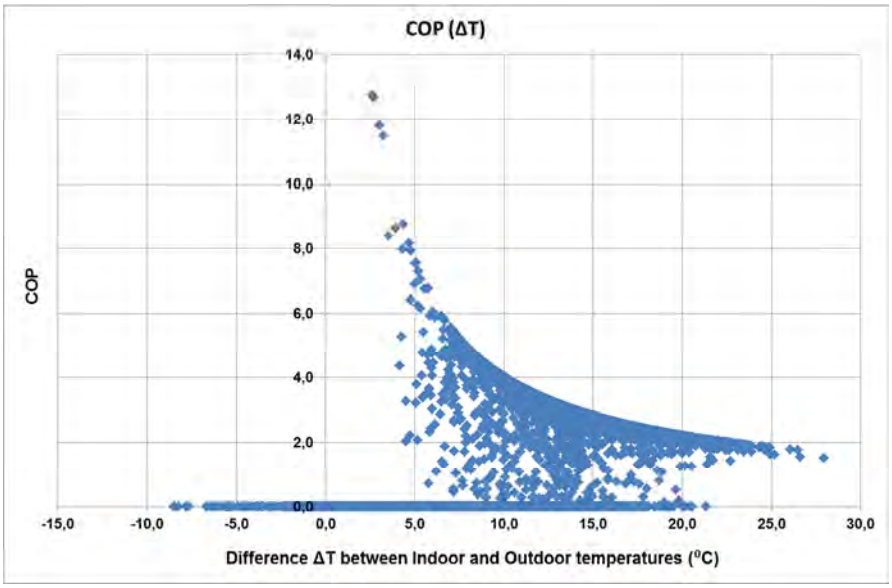

Figure 6: Calculation results for heating COP for all individual hours over an entire year

Based on the these calculation results, we can calculate a SCOP of 2,6. Of course, this is not high compared to modern heat pumps with a COP value of 4 at A2/W35.
But like we argued in the introduction, it is better to compare the yearly energy consumption rather than just COP values, because these do not include night losses and distribution losses. Also, the use of large surface radiant heating as in ActiveWall allows for a slightly lower temperature setting than conventional heating, to obtain the same comfort level. For the building module as a whole, we calculated a yearly heat requirement of 2003 $kWh_{(th)}$ and a corresponding energy use for ActiveWall of 779 $kWh_{(e)}$. For the same building unit we calculated a yearly heat requirement of 2802 $kWh_{(th)}$ and a corresponding energy use of 722 $kWh_{(e)}$ for a heat pump with COP = 3,88. In this way the ActiveWall energy consumption is only 8 % higher.
The ActiveWall concept includes, besides the thermoelectric layer, a second layer of photovoltaic elements. Our calculations show that the PV surface power generation equals the (net) Activewall energy consumption for heating and cooling in western-, central- and southern Europe.

5. PROOF OF CONCEPT MODEL

Based on the design considerations, we constructed a proof of concept model, mainly for purposes of demonstration and dissemination. The heat exchangers in this case are not extruded in one part, but are built from smaller square tubes mainly out of cost considerations. This impedes the heat conduction over the exchanger area to a great extent. Consequently the performance of the model could not obtain design values, nevertheless the functioning can be clearly demonstrated.



Figure 7: ActiveWall Proof of Concept model

6. ACTIVEWALL AND MODULAR BUILDING

ActiveWall is a concept under development, and not yet ready for market introduction. However, it is not difficult to imagine where ActiveWall would fit in perfectly, based on its USP's. Market segments like modular office buildings and semi-permanent housing facilities are perfectly suited for ActiveWall. To begin with, because the modules are not manufactured on site but are prefabricated in a controlled environment. But more importantly, because ActiveWall does not occupy any useful space, which is important for small semi-permanent housing modules. The fact that ActiveWall does not need to be connected to technical installations can further reduce the building time in the already fast modular building process. And for the end user, the fact that ActiveWall is totally silent and does not need maintenance are real advantages.



Figure 8: ActiveWall is ideally suited for use in modular building

The ActiveWall concept consists not only of an inner wall that comprises the thermoelectric elements and heat exchangers, but also of an outer wall with vertical solar panels. The inner- and outer wall can be constructed separately, as for example in Figure 8, with a spacing in between them to allow for free air circulation.
The ActiveWall concept with both thermoelectric and photovoltaic layers present, will act as an indoor cooling solution in summertime. It is then actually a "solar cooling" system, but far more simple than the common solar cooling systems using thermal collectors and absorption cooling.

7. CONCLUDING REMARKS

ActiveWall is a new wall-integrated heat pump concept based on thermoelectric elements. It has no moving parts, which makes it reliable, low maintenance and above all, silent. There is no additional space needed for technical systems, so ActiveWall is space-saving. The "bare" COP is not high, but still acceptable because of the relative small temperature differences in space heating and cooling. The yearly energy use is competitive with conventional heat pumps because there are no distribution losses, night heating can be avoided and heating is both convective and radiant. When the outdoor side of ActiveWall is covered with PV, the power generated can cover the net energy use for heating and cooling.
We have made costs calculations for ActiveWall including material costs, the costs for electronic control and manufacturing costs. These initial calculations show that ActiveWall can be cost competitive to air source heat pumps in terms of investment. These calculations do not yet include the avoided costs for (wall) construction materials.

REFERENCES

van der Heide, J., Vreemann, H.L., Haytink, T.G., 2016. Onderzoek innovatieve opties BENG (Bijna Energie Neutrale Gebouwen). Rijksdienst voor Ondernemend Nederland (RVO), Utrecht, 83 pages (in Dutch).

Dieleman, M., Breembroek, G., 2001. Domestic heating and cooling distribution and ventilation systems and their use with residential heat pumps. Heat Pump Centre (IEA-HPT), Boras.

Love, J., Smith, A.Z.P., Watson, S., Oikonomou, E., Summerfield, A., Gleeson, C., Biddulph, P., Chiu, L.F., Wingfield, J., Martin, C., Stone, A., Lowe, R.,2017. The addition of heat pump electricity load profiles to GB electricity demand: Evidence from a heat pump field trial. Applied Energy 204,, 332-342.

Kim C.M., 2001. Air conditioner for individual cooling/heating. US Patent application no. US2001/0005990 A1 of Jul. 5.

Rawat, M.K., 2013. A review on developments of thermoelectric refrigeration and air conditioning systems: a novel potential green refrigeration and air conditioning technology. International Journal of emerging technology and advanced engineering Vol. 3, special issue 3 (2013)

Messac, A., Khire, R.A., Van Dessel, S., 2005. Design of thermo electric heat pump unit for active building envelope systems. International Journal of heat and Mass Transfer 48 (2005), 4028-4040.

Manuscript ID: 1330
DOI: 10.18462/iir.icr.2019.1330

Rigorous assessment of low GWP refrigerants in heat pumps from an ecologic perspective using life cycle assessment

Christian VERING, Moritz LAUSTER, Dirk MUELLER

Institute for Energy Efficient Buildings and Indoor Climate
Aachen, 52074, Germany, cvering@eonerc.rwth-aachen.de

ABSTRACT

Enhancing the significance of global warming and systematically reducing greenhouse gas emissions can be established by utilizing transparent assessment methodologies. Within this work, we contribute to the estimation of carbon dioxide equivalent emission impact of different refrigerants for direct and indirect emissions. Regarding heat pump heating systems in dynamic heat supply systems for a whole lifecycle, comparable boundary conditions are chosen. Direct emissions correlate to the static GWP value of a refrigerant and the refrigerant charge of the heat pump. Indirect emissions occur in the production, distribution, operation and disposal of the heat pump with special respect to the refrigerant.
This approach allows a direct comparison of the impact of low GWP refrigerants on lifecycle carbon dioxide equivalent emissions. We state that, if we do not reduce indirect emissions by increasing efficiency or obtaining PV electricity, the GWP of the chosen refrigerant is rather irrelevant.
Keywords: Ecologic Assessment, Refrigerant Impact, Carbon Dioxide Emissions.

1. INTRODUCTION

The advancing climate change is mainly due to the emission of greenhouse gases (GHG) into the Earth's atmosphere. This occurs exemplarily through the combustion of fossil fuels (BMWi, 2018). Therefore, it is necessary to identify saving potentials. In Germany, about one third of overall GHG emissions relate to the buildings sector and 81 % of these are used to provide space heating and domestic hot water (Statista, 2018).
Regarding heat supply of residential buildings in Germany, heat generation technologies mainly base on combustion of fossil fuels. Gas condensing boilers are state of the art technology, but also gas and oil low-temperature boilers are widely used (Statista, 2018). Thus, carbon dioxide (CO_2) is a combustion product of heat supply. Regarding high technology efficiencies, a direct CO_2 reduction can only be achieved by decreasing the heat demand. User related demand reduction as well as better insulation standards aim for this goal. However, user related demand reduction is a renunciation and better insulation is very expensive in most cases. Therefore, alternative technologies with high efficiencies are promising to systematically reduce CO_2 emissions of residential buildings.
Heat pump heating systems are awarded to be a key technology decreasing CO_2 emissions in the building energy sector by electrifying heat supply. Heat pumps use electric energy to utilize ambient heat on pretended temperature levels using a refrigerant. The structure of heat pump's emissions differ from conventional technologies. Opposed to nearly 100 % direct emissions of boilers during operation, heat pump emissions are both direct and indirect. On the one hand, direct emissions relate to refrigerant leakage and its Global Warming Potential (GWP). On the other hand, indirect emissions refer to emissions covered in the conversion of electric energy.
National and international regulations like Montreal Protocol or F-Gas-Regulation aim for a systematical reduction of GHG emissions by phase downs. Implied refrigerant phase downs are shown in Fig. 1 for both regulations. It is obvious that a reduction of refrigerant selling amount by 79 % in the EU until 2030 and by 85 % internationally until 2040 is very challenging. In addition, refrigerant prices increased dramatically within the first two years up to 750 % (Vering, 2018). Summing up these points, both phase downs require alternative refrigerants for heat pump heating systems in order to be affordable, efficient and sustainable.

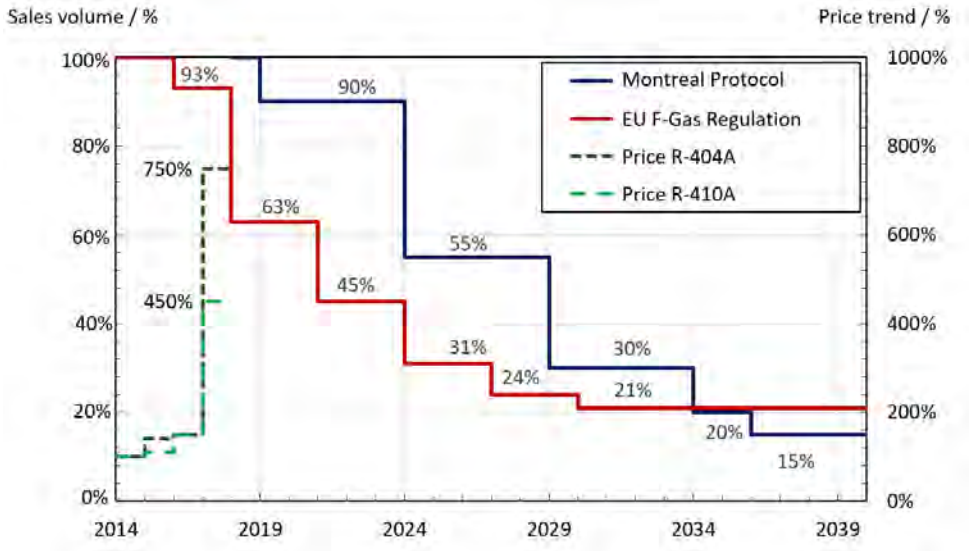

Figure 1: Refrigerant phase down regarding Montreal Protocol and F-Gas-Regulation as well as price development of two typical high GWP synthetical refrigerants.

Different key values assess the sustainability of refrigerants. The most common one is the static parameter GWP. Besides, Total Equivalent Warming Impact (TEWI) and Life Cycle Climate Performance (LCCP) extend this approach by different auxiliary equations regarding the lifecycle of the product. A holistic approach to assess ecologic consequences of a product, service or application, is Life Cycle Assessment (LCA) regarding normative standards (DIN EN ISO 14040). Within this paper, a short comparison of the methodologies is performed by introducing main differences regarding considered periods. In addition, we use these methodologies to evaluate the impact of different refrigerants on heat pump's emissions compared to condensing gas boiler technology in the German building stock.

Theoretically, the number of suitable refrigerants is around 1.000 (McLinden, 2017). McLinden et al. do an assessment of refrigerants compared to R-410A in (McLinden, 2017) and recommend different ones regarding the static parameters Coefficient of Performance (*COP*) and volumetric cooling capacity. However, they do not concern dynamic behaviour of the refrigerant circuit. Therefore, we introduce dynamic building performance simulations in Modelica to consider dynamic system behaviour.

Thereby, this work contributes to the ecologic assessment of heat pump heating systems in the building stock with respect to the refrigerant impact. We show

- in Chapter 2 different assessment methodologies for various lifetime periods. We introduce GWP, TEWI, LCCP and LCA for the evaluation of carbon dioxide equivalent emissions and compare them to each other.
- The simulation setup is presented in Chapter 3. Thereby, we focus on a dynamic simulation model of a building energy system linked to an efficiency based model of a heat pump considering the effect of different thermodynamic refrigerant properties. Transport properties are not considered yet.
- Utilizing the setup in Chapter 4, it is possible to calculate different carbon dioxide emissions for each refrigerant and compare it to both, other refrigerants as well as other technologies.
- Finally, we summarize and conclude our findings in Chapter 5.

2. METHODOLOGY

Within this contribution, we suggest a system decomposition to simplify it into solvable partial problems. In Fig. 2 a horizontal and a vertical decomposition is shown. In the horizontal layer, there is the background system with its energy sources, electricity and refined products linked to the heat supply system. On the right hand side, the building with its heat load, various water demands, insulation and thermal mass is connected to the heat supply system via a transfer system. A vertical separation indicates different LCA-periods of the supply system. We distinguish between production, operation and disposal.

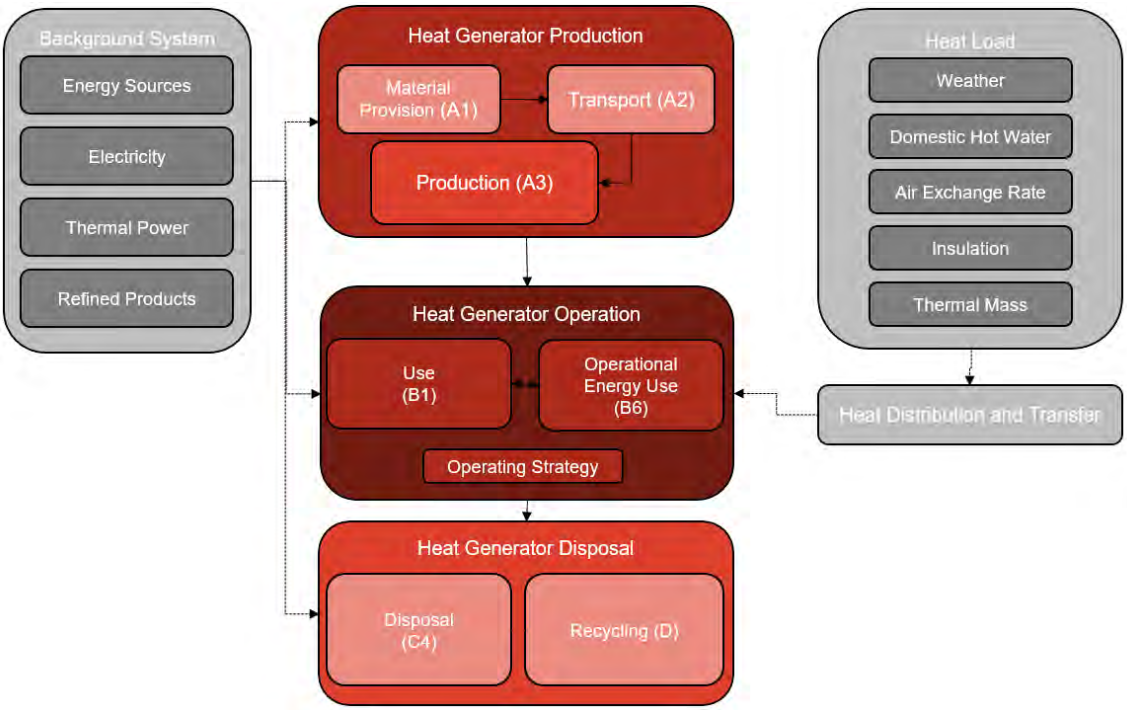

Figure 2: Periods of a heat pump lifecycle considering the background system and interaction with the building physics.

In the production period, there is raw material supply (A1), transport to production (A2) and the production process itself. During operation, we assume the use of the heat supply system (B1) as well as energy demands for the plant periphery (B6) to be relevant. Within the disposal period, there is the removal of the supply system and parts for recycling.
In each period, various amounts of emissions accrue that need to be considered for the whole lifecycle of the technology. As introduced in Chapter 1, four methods for ecological assessment are presented within this paper. These are GWP, TEWI, LCCP and LCA. In Fig. 3, these methodologies are related to their assessment of a heat supply technology lifetime. Especially, LCA distinguishes between two periods called cradle-to-grave (ctg) and gate-to-gate (gtg). The first method (ctg) assesses the whole lifecycle whereas gtg considers the lifecycle from the transport to location of operation until the disposal without recycling.

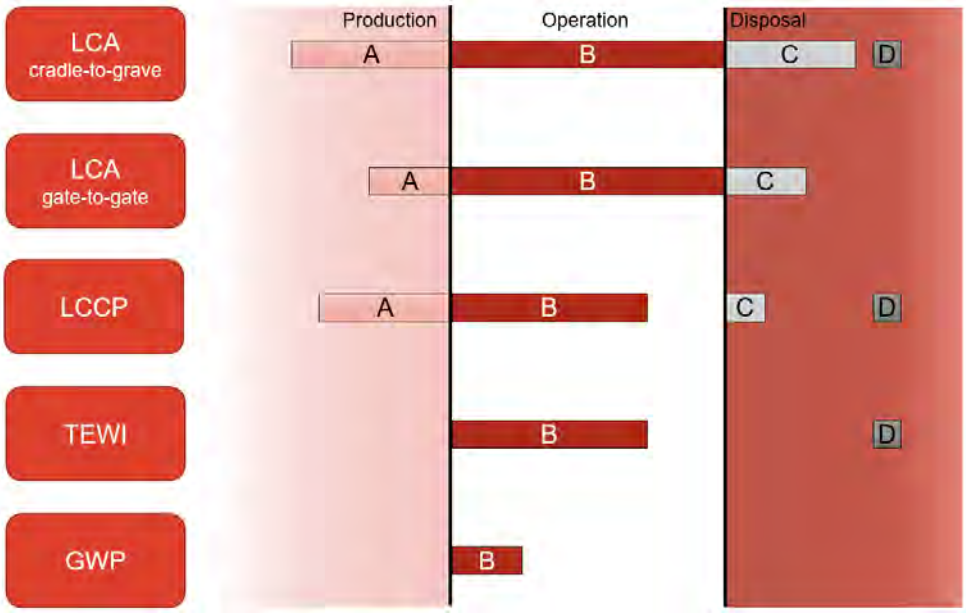

Figure 3: Ecological assessment regarding different periods of a lifecycle using the methodologies GWP, TEWI, LCCP and LCA.

In addition, LCCP takes these phase into account and adds up parts of the recycling phase. Herein, static boundary conditions are used. TEWI reduces complexity of the assessment period by considering the operation and parts of the recycling phase. That means assessments can be calculated with less information about the system. Lastly, the GWP is a static parameter, which compares the impact of different refrigerants considering their equivalent CO_2 emissions.
Within this paper, we use GWP to classify different refrigerants in low GWP and high GWP refrigerants a priori. This methodology only allows to derive direct emissions of the system, whereas TEWI, LCCP and LCA consider indirect emissions of the background system as well. We calculated with LCCP that the impact of production, disposal and recycling is negligible compared to the operation period, if we consider the lifecycle of a technology. This allows doing LCA for the gtg period, which is the presented methodology within this paper.
Assessing the lifecycle with LCA, energy and mass balances need to be derived for the considered system. We use the system presented in Fig. 2 separated in background system, heat supply system and building energy system. The functional unit is the heat demand of the building, as it needs to be the same for the heat pump and the reference gas boiler system. Focusing on the operation of the system, a dynamic simulation model is implemented in Modelica that calculates the demands for a lifecycle. The heat pump considers different refrigerants to assess their impact on both direct and indirect emissions over the lifecycle. The modelling setup is presented in Chapter 3.

3. MODELLING AND ASSESSMENT SETUP

The modelled system consists of a reference house, a condensing gas boiler or an air-to-water heat pump with an electrical backup heater. Both are linked to two storages to provide space heating by a buffer storage as well as domestic hot water. The house is represented by its heating demand throughout the lifecycle of 18 years. Heat is provided by the heat pump system, which is modelled using a refrigerant dependent *COP* multiplied with a constant efficiency factor for air-water heat pumps of 0.5, which is typical for On/Off-controlled heat pumps. The electrical backup heater has an efficiency of 1. For the calculation of the *COP* the same ambient temperature data is used, which was used to perform the heating demand analysis for the reference building (Constantin, 2014). It is a typical building for the German building stock with a year of construction about 1960. It has an insulation standard following WSchV84 and a net area of 150 m², which represents a wide range of buildings in Germany.
The location of the building exemplarily is Aachen with a standard outside temperature of -12 °C. We assume domestic hot water profiles (here: profile M) and an air exchange rate of $n = 0{,}5\ h^{-1}$. A detailed model description is presented in Constantin et al. 2014). Two typical control strategies are implemented for demand-oriented operation. A hysteresis control with a target temperature of $t_{DHW} = 50\ °C\ \pm 5\ °C$ is provided for the domestic hot water. A heating curve is set with a base point of 20 °C at heating limit temperature and a gradient of -1 for the buffer storage tank. The heating limit temperature is set to $t_{HG} = 15\ °C$ and the bivalence temperature is set to $t_{Biv} = -2\ °C$. Considering dynamic boundary conditions allows assessing the dynamics of the system.
Typical refrigerants for the application in heat pumps are shown in Fig. 4 (McLinden, 2017). All refer to the reference of R-410A. That makes it possible to compare them in a simulation study. We setup a heat pump model with performance data of R-410A in the reference case. The other cases are calculated with a corrected *COP* compared to R-410A. Regarding cooling capacity, we adapt the heat pump size ensuring comparable results for the discussion.
Within this study, we investigate five typical refrigerants in heat pumps. The refrigerants are R-410A, R-32, R-1234yf, R-290 (propane) and R-1270 (propene). R-410A is a typical high GWP refrigerant (GWP = 1920) that is commonly applied in heat pumps. A high pressure, lower GWP refrigerant is R-32 with a GWP = 677. A typical low GWP refrigerant is the halogenated R-1234yf with a GWP about 1. Non-halogenated refrigerants can be hydrocarbons like propane with GWP = 3 and propene with GWP = 1 (IPCC, 2013).
Direct CO_2 emissions of these refrigerants correlate to the amount within the heat pump, which is required to provide the heat demand. Considering synthetic refrigerants, an amount of 0.3 kg/kW is necessary to run a heat pump. The value for hydrocarbons is 0.15 kg/kW. Using these values at a nominal heating power of the reference heat pump, we calculate 3 kg of synthetic and 1.5 kg of natural refrigerants to be necessary (United Nations Environment Programme, 2015).

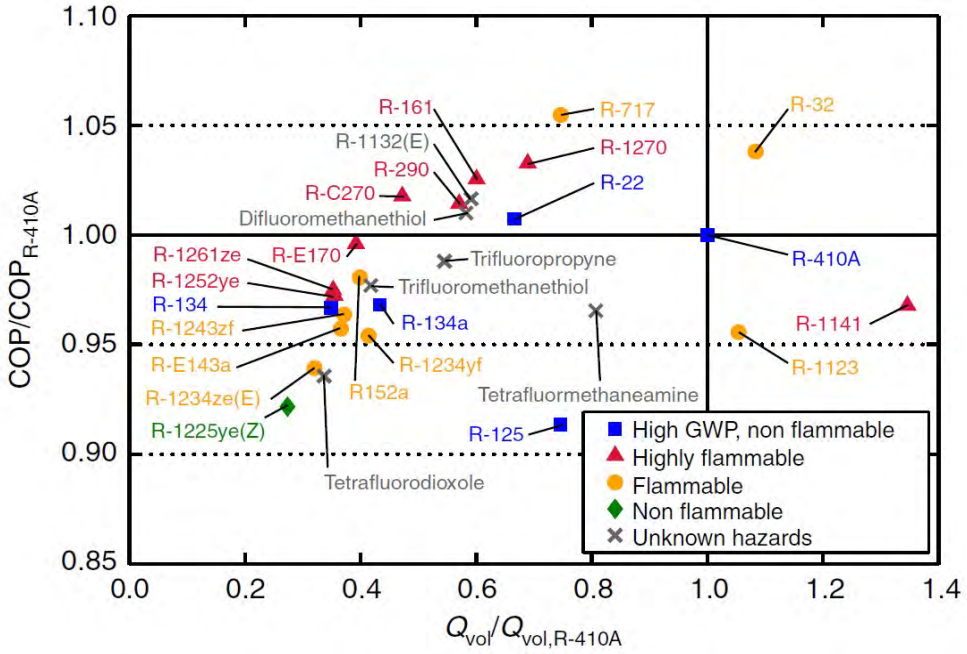

Figure 4: Coefficient of Performance and cooling capacity of different refrigerants related to R-410A.

Calculating the whole potential of CO_2 emissions of each refrigerant, Fig. 5 shows that R-410A has the highest direct CO_2 emission with 5772 kg compared to the lowest of R-1234yf and R-1270 with 3 kg CO_2. These amounts emit, if the completely refrigerant mass leaves the heat pump exemplarily because of leakage. However, typical leak rates are about 5 % per year (Ashford, 2006). Additionally, we do not assume the *SCOP* to be a function of filling capacity, which overestimates the performance minimally.

Focusing on heat pumps' indirect emissions, which occur because of electricity that is required for running the heat pump and the backup heater, the primary energy factor of electricity needs to be determined. In Germany, this factor is 489 g CO_2 /kWh in 2018. Because of a changing energy supply system, a regression by about 1.6 % per year is assumed (Greiner, 2016).

Regarding the condensing gas boiler, an efficiency of 1,09 and a primary energy factor of natural gas of 205 g CO_2/kWh is used in the calculation procedure (Greiner, 2016). For the different refrigerants and gas condensing boilers, dynamic system simulations are performed with Dymola. The results are shown and discussed in Chapter 4.

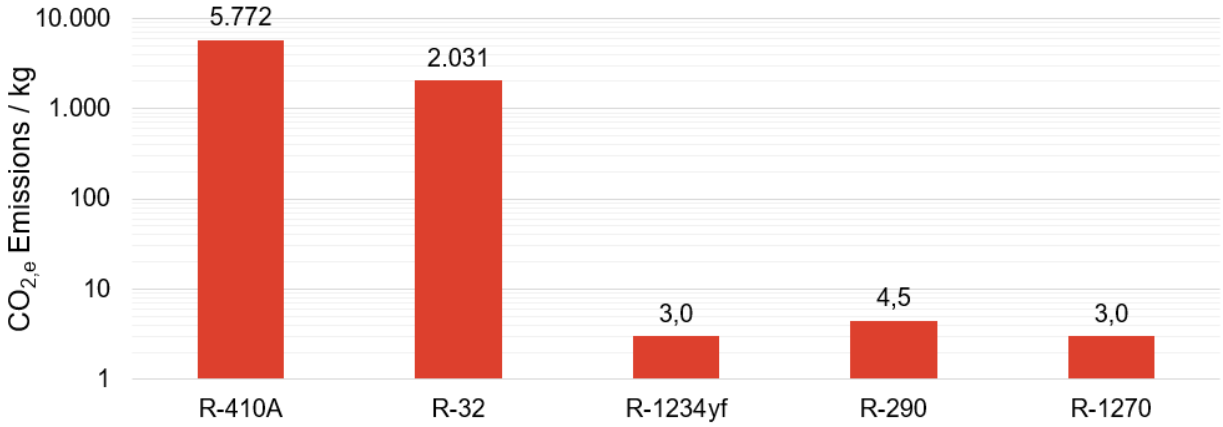

Figure 5: Potential of direct CO_2 emissions of different refrigerants.

4. DISCUSSION

In Fig. 6, final scenario results are depicted. The condensing gas boiler emits about 73.000 kg CO_2 over its lifecycle. All heat pump heating systems do emit less CO_2 compared to the condensing gas boiler, which indicates that a change of technology is appropriate ecologically. CO_2 emissions of the electrical backup heater is below 5 % in each heat pump scenario.
The lowest emission over the whole lifecycle was determined about 68.000 kg CO_2 with the heat pump that uses R-32 as refrigerant. This is a reduction compared to conventional technology by about 7 %.
R-32 has a GWP of 677. Assuming a leak rate of 5 % per year, direct CO_2 emissions of R-32 are about 1224 kg CO_2. These are 2 % of overall emissions for the whole R-32 heat pump lifecycle. R-410A has the highest direct emissions with a maximum about 10 %. Referring low GWP refrigerants R-1234yf, R-290 and R-1270, direct emissions are below 1 % compared to the lifecycle emissions.

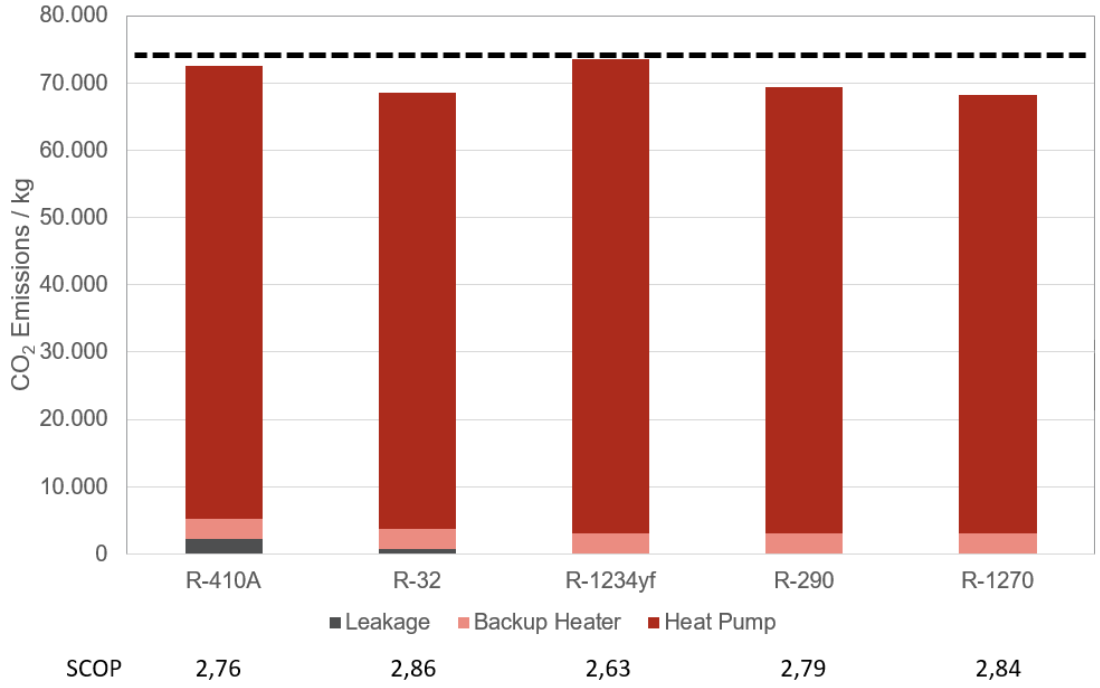

Figure 6: CO_2 equivalent emissions of different heat supply systems over the whole lifecycle.

Regarding the conventional technology, all heat pump heating systems emit less CO_2 than the reference technology. Considering the different refrigerants within the heat pumps, different systems' seasonal coefficients of performance are calculated. The highest *SCOP* has the R-32 system with 2.86 compared to the lowest of R-1234yf of 2.63. Hence, R-32 has the lowest and R-1234yf has the highest indirect CO_2 emissions due to the primary energy factor of electricity. These emissions can be reduced by both reducing the primary energy factor as well as increasing the systems' *SCOP*. Moreover, this context is consolidated in Fig. 7. The diagram shown has three dimensions. On the ordinate, there are calculated CO_2 emissions for the lifecycle. The GWP is shown on the abscissa. The third dimension is the systems' *SCOP* represented by different levels. The gas boiler technology is depicted with the dashed line. It is obvious, that heat pump heating systems can ecologically be an alternative heating technology for *SCOP*s higher than 2,6 in Germany.

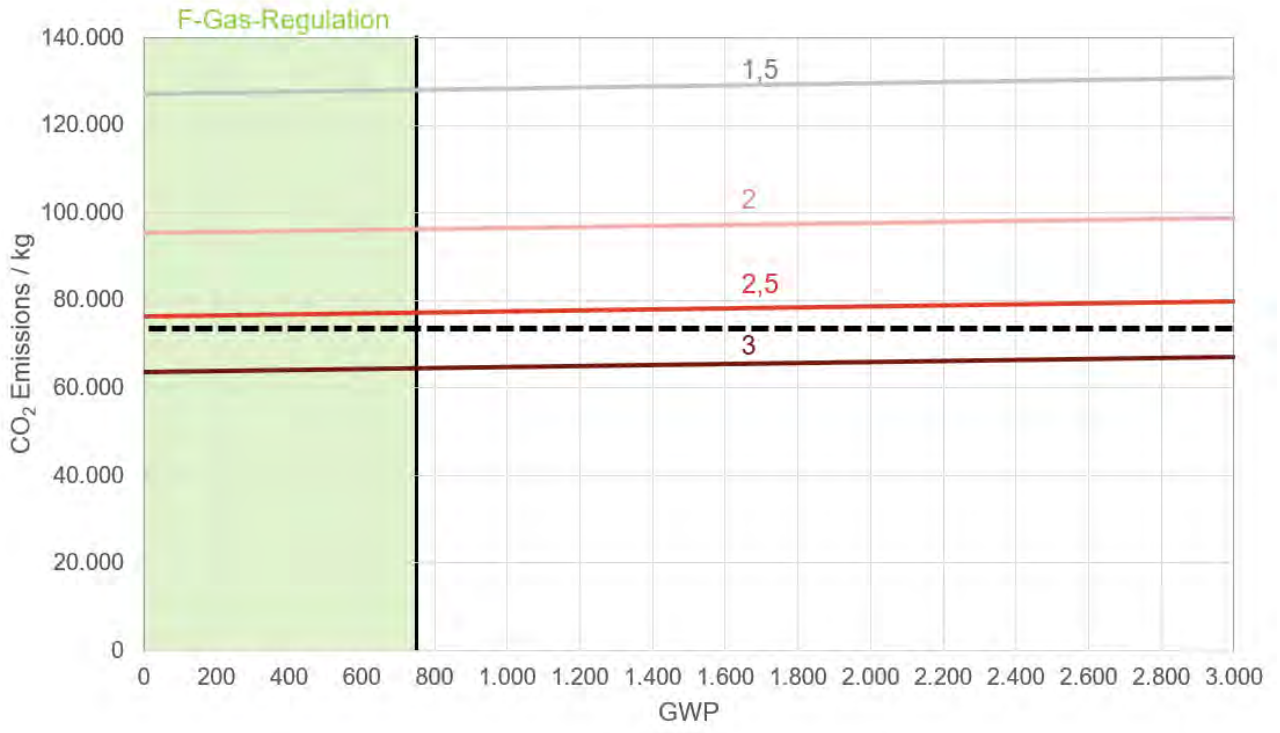

Figure 7: Comparison of different GWP and SCOPs regarding overall CO_2 emissions.

Different progresses show, that for a constant primary energy factor, it is ecologically more beneficial to increase the *SCOP* than to decrease the refrigerant's GWP. The difference in overall CO_2 emissions regarding different GWPs is rather irrelevant compared to an increase in *SCOP*. In addition attributing these calculations to e.g. F-Gas-Regulation, we see the green-deposited area that shows the maximum allowed GWP. This area compared to the effect of the GWP on overall emissions is quite small, so that many thermodynamic propitious refrigerants cannot be chosen for future heat pump developments. Involving the *SCOP*, this might not lead to integral best solutions.

5. CONCLUSION

Within this work, we apply life cycle assessment to estimate the impact of different refrigerants on CO_2 emissions of heat pump heating systems regarding its lifecycle. For this, we use dynamic building simulations to determine the dynamics of the system and the impact of operation in a typical residential building as use case. Thus, it is possible to distinguish between direct and indirect CO_2 emissions. Classifying different refrigerants in heat pumps, we compare these systems against a condensing gas boiler for boundary conditions in Germany.

The results show that all heat pump heating systems with a *SCOP* above 2.6 are ecologically beneficial compared to condensing gas boilers. Applying high GWP refrigerants, direct emissions are in maximum about 10 % of overall emissions. A change to low GWP solutions prove that direct emissions are lower than 1 % e.g. for R-290 or R-1234yf compared to the lifecycle emissions with primary energy factors from Germany. However, the overall CO_2 emissions are not related to the refrigerant with the lowest GWP, but to R-32, which has a GWP of 677 and reduces indirect emissions significantly. That shows that the impact of *SCOP* and indirect emissions is higher than the GWP's impact, respectively.

A reduction of indirect emissions in Germany can be done by a reduction of primary energy factor e.g. by obtaining PV electricity or by an increase of *SCOP*. In both cases, these consequences have a higher impact than the application of low GWP refrigerants with a not optimal thermodynamic performance. Therefore, we state that the refrigerants' GWP impact is rather irrelevant, respectively. From an ecologic point of view, it is necessary to firstly choose the refrigerant regarding thermodynamic performance and secondly go for low GWP solutions.

NOMENCLATURE

COP	Coefficient of Performance	GWP	Global Warming Potential
η_e	Backup heater efficiency	η_b	Condensing gas boiler efficiency
LCA	Life Cycle Assessment	LCCP	Life Cycle Climate Performance
n	Air-exchange rate	$\dot{Q}$	Cooling capacity (kW)
SCOP	Seasonal coefficient of performance	t_{biv}	Bivalence temperature
t_{HG}	Heating limit temperature	t_{DHW}	Domestic hot water set temperature
TEWI	Total Equivalent Warming Impact		

REFERENCES

BMWi, 2018. Energieeffizienz in Zahlen, URL: https://www.bmwi.de/Redaktion/DE/Publikationen/Energie/energieeffizienz-in-zahlen-2018.pdf?__blob=publicationFile&v=6.

Statista, 2018. Bestand zentraler Wärmeerzeuger für Heizungen in Deutschland nach Kategorie im Jahr 2017 (in Millionen Stück), URL: https://de.statista.com/statistik/daten/studie/165282/umfrage/gesamtbestand-der-zentralen-waermeerzeuger-in-deutschland/.

Vering, C. et al., 2018. Potentielle Kältemittel für Wärmepumpen in der Heizungstechnik, in Kälte Klima Aktuell, 05/2018.

DIN EN ISO 14040, Environmental management - Life cycle assessment - Principles and framework (ISO 14040:2006), 2006. German and English version EN ISO 14040.

McLinden M. O. et al., 2017. Limited options for low-global-warming-potential refrigerants. Nature Communications 8, 1-9.

Constantin, A. et al., The Modelica HouseModels Library: Presentation and Evaluation of a Room Model with the ASHRAE Standard 140, Modelica Conference, 2014.

IPCC, 2013: Anthropogenic and Natural Radiative Forcing. In: Climate Change 2013: The Physical Science Basis. Contribution of Working Group I to the Fifth Assessment Report of the Intergovernmental Panel on Climate Change [Stocker, T.F., D. Qin, G.-K. Plattner, M. Tignor, S.K. Allen, J. Boschung, A. Nauels, Y. Xia, V. Bex and P.M. Midgley (eds.)], Cambridge University Press, Cambridge, United Kingdom and New York, NY, USA.

United Nations Environment Programme, Montreal Protocol on Substances that Deplete the Ozone Layer: Refrigeration, Air-Conditioning and Heat Pumps Technical Options Committee (RTOC): Assessment 2014 and 2015.

Ashford, P. et al., 2006. Emissions of fluorinated substances for ozone depleting substances. In IPCC Guidelines for International Greenhouse Gas Inventories.

Greiner, B., Hermann, H. Sektorale, 2016. Emissionspfade in Deutschland bis 2050. In Arbeitspaket 1.2 im Forschungs- und Entwicklungsvorhaben des Bundesministeriums für Umwelt, Naturschutz, Bau- und Reaktorsicherheit: Wissenschaftliche Unterstützung zur Erstellung und Begleitung des Klimaschutzplans 2050.

Manuscript ID: 1499
DOI: 10.18462/iir.icr.2019.1499

Analysis on the characteristic of heat absorbed by the pipes in pipe-embedded double-skin façade (PDSF)

Shuai YAN, Xianting LI

Department of Building Science, Beijing Key Laboratory of Indoor Air Quality Evaluation and Control, Tsinghua University, Beijing, 100084, China,
xtingli@tsinghua.edu.cn

ABSTRACT

Pipe-embedded double-skin façades (PDSFs) could release the overheating problem in conventional double-skin façades (DSFs). The characteristic of heat absorbed by pipes, which is related with the additional energy consumption of PDSF, is not clearly investigated. In this study, three indexes, convective heat transfer coefficient, equivalent temperature and fraction of solar heat absorbed by pipes, are proposed to reflect heat absorbed by pipes. The characteristic of PDSF with different external and internal glazing are compared. The results show that: 1) the heat absorbed by pipes is classified into convective and solar heat; 2) the convective heat transfer coefficient is dependent on the thickness of both external and internal glazing. The fraction of solar heat absorbed by pipes is mainly dependent on the external glazing and 3) when the total thickness of external and internal glazing is fixed, it is better to apply better insulated glazing to the external.
Keywords: Pipe-Embedded Envelope, Double-Skin Façade, Building Envelope, Building Energy Efficiency, Thermal Network Model.

1. INTRODUCTION

Glass curtains are widely used in high-rise buildings. However, heat transfer through a transparent building envelope in summer is significant, leading to the greenhouse effect as well as increased building cooling load (Annunziata et al., 2016). To reduce the heat gain of a transparent building envelope, many works have been conducted, and they can be classified into two categories: enhanced shading and the substitution of advanced glass (Kirimtat and Krejcar, 2018). External shading is a widely used shading technology that blocks solar radiation efficiently. However, it requires expensive maintenance because the shading is exposed to an ambient environment and affects the original appearance of the building (Nikoofard et al., 2011).Regarding the substitution of advanced glass, high-reflectance glass and photochromic glass are two types of representative superior glass in the state-of-art research (Rezaei et al., 2017). Nevertheless, high-reflectance glass results in light pollution, and photochromic glass is expensive (Aste et al., 2018). To ensure better performance in summer with reasonable cost, the double-skin façade (DSF), which is considered as middle shading, has been globally used owing to its aesthetic appearance and modern concept (Ghaffarianhoseini et al., 2016).

Conventionally, DSF consists of two glass panels, which are integrated with Venetian blinds in the cavity. In addition, there are openings in DSF for ventilation (Manz, 2004). The performance and applicability of DSF have been conducted through many researches, which have shown remarkable energy-saving potential, especially in hot and sunny climates (Barbosa and Ip, 2014; Alberto et al., 2017). However, there is an important challenge confronted by conventional DSF: the high risk of unacceptable performance due to the overheating problem (Ghaffarianhoseini et al., 2016). Previous research has indicated that the shading device can be heated to 50–60 °C when solar radiation is extremely strong (Flores et al., 2015).

To avoid the overheating problem, Shen and Li (2016) proposed a system that embedded pipes in the Venetian blinds of DSF, which was named the pipe-embedded double-skin façade (PDSF). In their design, water is produced by natural energy, thus, the efficiency of the system is high. In addition, the initial investment is acceptable compared with DSF because the only difference between PDSF and DSF is the embedded pipes. The heat transfer characteristics of a typical PDSF was investigated by computational fluid dynamics (CFD) software and results show that the inner

surface temperature can be reduced drastically compared with conventional DSF, benefitting not only energy consumption but also thermal comfort.
Previous research mainly concentrated on the indoor heat gain reduction of the PDSF over other glazing technologies. However, the characteristic of heat absorbed by pipes in PDSF is not clearly investigated. It is clear that PDSF would consumes more additional energy because of the production and delivery of the water for embedded pipes compared with ventilated DSF. In fact, the additional energy consumption mainly depends on the heat absorbed by the pipes. In this way, it's important to study the heat absorbed by the pipes in the case of PDSF, which would help to better demonstrate the superiority of PDSF over other glazing technologies.
In this paper, the description of PDSF and its thermal network is presented in section 2. In the meanwhile, three indexes for the description of heat absorbed by pipes are proposed. The characteristic of PDSF with different external and internal glazing thickness are compared and discussed with the proposed indexes in section 3.

2. METHODOLOGY

The configuration of PDSF is shown at first in this section. Then, the thermal network is presented based on its heat transfer characteristic. Three indexes to describe heat absorbed by pipes were proposed at last.

2.1 Description of PDSF

The schematics of DSF and PDSF are shown as Fig. 1. The same as conventional DSF, PDSF is made up of external, internal glazing and middle shading blinds. Different to DSF, solar radiation is designed to be removed with the pipes embedded in the case of PDSF rather than ventilation, thus air openings are removed. The water in the pipes of PDSF can be produced by the cooling tower, ground source heat exchanger etc.(Shen and Li, 2016).
Although transmitted visible solar radiation can be reduced by shading in DSF, a great amount of radiation heat would be absorbed by the blind and then lead to convective heat transfer to indoor in the case of DSF, which is the so-called absorption-conduction heat transfer (Baenas and Machado, 2017). Based on the configuration of PDSF, the embedded pipes in PDSF are designed to remove such absorption-conduction heat transfer, so it can avoid the overheating problem.

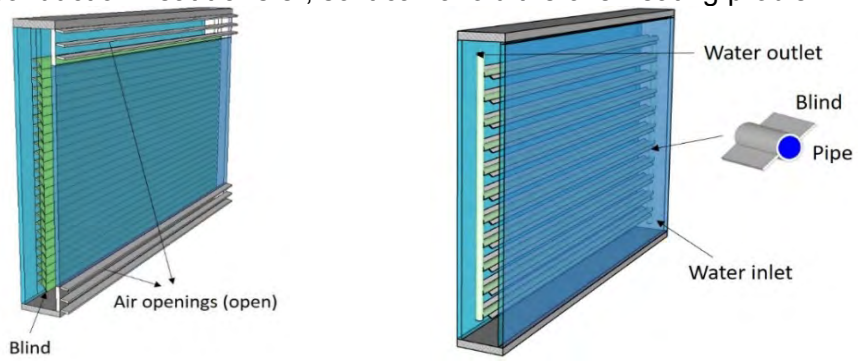

a) Conventional DSF **b) PDSF**

Figure 1: Configurations of the traditional DSF and PDSF

2.2 Thermal Network of PDSF

Similar to DSF, short wave solar heat, conductive, convective and longwave radiative heat transfer exists in the heat transfer process of the PDSF. To be specific, conductive heat refers to the heat transferred between two sides of internal and external glazing. The convective heat transfer exists inside the cavity of PDSF. In the meantime, longwave radiative heat is transferred between shading and glazing. The schematic diagram of heat transfer in PDSF is shown as Fig. 2. The thermal resistance of each kind is calculated with Eqs. (1) - (3).

$$R_{cond} = \delta/\lambda \quad \text{Eq. (1)}$$

$$R_{conv} = 1/h_c \quad \text{Eq. (2)}$$

$$R_{rad} = \sigma({T_1}^2 + {T_2}^2)\times(T_1 + T_2)\Big/\left[\left(\frac{1}{\varepsilon_1} - 1\right) + \left(\frac{1}{\varepsilon_2} - 1\right) + \frac{1}{F_{1,2}}\right] \quad \text{Eq. (3)}$$

where R_{cond}, R_{conv} and R_{rad} are conductive, convective and long wave radiative resistance, respectively, $m^2\times K\times W^{-1}$; δ is the thickness of glass, m ; λ is thermal conductivity, $W\times m^{-1}\times K^{-1}$; h_c is convective heat transfer coefficient, $W\times m^{-2}\times K^{-1}$; σ is Stefan-Boltzmann constant, $W\times m^{-2}\times K^{-4}$; T_1 and T_2 are the temperature of two surface participating in long wave radiative heat transfer, K; ε is the hemispherical emissivity; $F_{1,2}$ is the view factor between two surfaces.

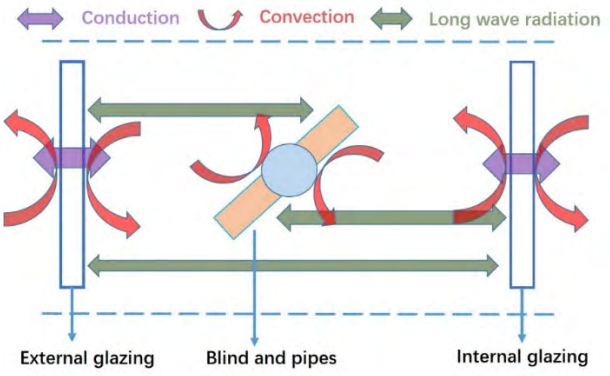

Figure 2: Schematic diagram of PDSF heat transfer

As shown in Fig. 2, the heat transfer of PDSF is similar to that of DSF. In DSF researches, the thermal network method is a popular approach to provide a distinct understanding of comprehensive heat transfer (Oliveira et al., 2016). With the assistance of the thermal network model in DSF, the thermal network of PDSF is obtained based on the following assumptions:

1) Thermal stratification and the heat transfer in the vertical direction are neglected since the temperature difference in the cavity is quite small in previous researches (Shen and Li, 2016; Shen and Li, 2017);
2) The thermal mass of PDSF is neglected thus heat transfer is considered as steady state, since the PDSF and DSF have similar structures and the DSF thermal mass is neglected in many studies (Xue and Li, 2015);
3) The thermal conduction resistance of the blinds and the resistance between water and blind are neglected because the heat transfer coefficient inside the pipe is larger than that of air. In addition, the size of the blind is usually small (Shen and Li, 2016; Shen and Li, 2017);
4) The long-wave radiative heat transfer coefficient is considered as a constant (Baenas and Machado, 2017). The temperature magnitude in this study is approximately 300 K;

Based on these assumptions, the thermal network is used to reveal the heat transfer of the PDSF, as shown in Fig. 3, where $T_{rad,out}$, $T_{conv,out}$, T_{indoor} and T_{water} are the outdoor radiative, convective temperature, indoor set-point and water temperature, respectively, °C; $R_{rad,out}$ and $R_{conv,out}$ are the long-wave radiative and convective thermal resistance between the outdoor environment and the external glass, $m^2\times K\times W^{-1}$; R_{in} is the combined resistance considering both long-wave radiative and convective heat transfer between the glass surface and the indoor space (Baenas and Machado, 2017), $m^2\times K\times W^{-1}$; $R_{cond,eg}$ and $R_{cond,ig}$ are the conductive resistance of the external and internal glass, $m^2\times K\times W^{-1}$; $R_{conv,gap}$ and $R_{conv,bl}$ are the thermal resistance for convective heat transfer of the gap and shading blind, $m^2\times K\times W^{-1}$; $R_{rad,eg-bl}$, $R_{rad,ig-bl}$ and $R_{rad,eg-ig}$ are the radiative thermal resistance between the external glass and blind, internal glass and blind, and external glass and internal glass, respectively, $m^2\times K\times W^{-1}$; HA_{eg}, HA_{bl} and HA_{ig} are the solar heat absorbed by the external glass, shading blind and internal glass, $W\times m^{-2}$.

The overall optical property of PDSF is obtained with the optical property of glazing and blinds (Oliveira et al., 2016; Wang and Chen, 2016; Zhang et al. 2016; Su et al., 2017). Thus, solar heat absorbed by external, internal glass and shading are calculated with the absorption coefficient and solar intensity, shown as Eqs. (4) - (6):

$$HA_{eg} = \alpha_{eg} \times I \quad \text{Eq. (4)}$$

$$HA_{bl} = \alpha_{bl} \times I \quad \text{Eq. (5)}$$

$$HA_{ig} = \alpha_{ig} \times I \quad \text{Eq. (6)}$$

where α_{eg}, α_{bl} and α_{ig} are absorptivity of external glass, shading blind and internal glass, respectively, which reflect the optical property; I is solar radiation intensity, W×m^{-2}.

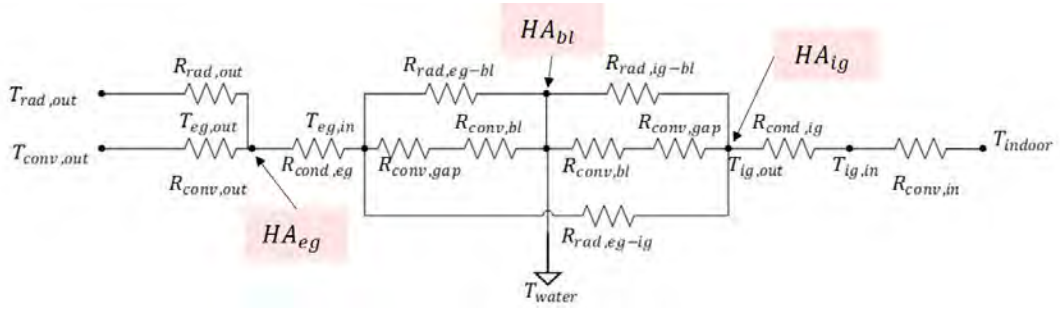

Figure 3: The thermal network of PDSF

2.3 Indexes to Describe Heat Absorbed by the Pipes

The thermal network in Fig. 3 is a linear system thus the heat absorbed by the pipes can be calculated by the superposition of the contribution from outdoor air temperature, outdoor radiative temperature, indoor temperature and the solar heat absorbed by each component. To be specific, heat absorbed by pipes can be calculated with Eq. (7):

$$Q_{pipe} = (K_{pipe} \times (T_{pipe,out} - T_{water}) + SHAP \times I) \times A \quad \text{Eq. (7)}$$

where K_{pipe} is the convective heat transfer coefficient for heat absorbed by pipes, which is defined as the heat absorbed by pipes per area of window when the difference of $T_{pipe,out}$ and water temperature is 1°C and the solar radiation is zero, W×m^{-2}×K^{-1}; $T_{pipe,out}$ is the equivalent temperature , which is an integrated value of outdoor air temperature, radiative temperature and indoor set point, °C; $SHAP$ is the fraction of solar heat absorbed, which is defined as the ratio of solar heat absorbed by pipes and solar radiation for per area of window.

With K_{pipe} and $T_{pipe,out}$, one can get the convective heat transfer through the pipes. In addition, $SHAP$ is the fraction of solar heat absorbed by pipes, which is used to reflect the contribution of solar radiation in total heat absorbed by pipes.

The expressions of K_{pipe}, $T_{pipe,out}$ and $SHAP$ are shown as Eq.(8) through Eq.(10). Since the weighting of each temperature in equivalent temperature $T_{pipe,out}$ is only dependent on the façade structure, the weighting of ambient is selected to reflect the weighting of outdoor convective and radiative temperature in $T_{pipe,out}$, shown as Eq.(11). When calculating the equivalent resistance between outdoor air and pipes, the other temperature is kept the same as water temperature and solar radiation is set as zero:

$$K_{pipe} = \frac{1}{R_{equ,pipe}} = \frac{1}{R_{equ,pipe}^{conv,out}} + \frac{1}{R_{equ,pipe}^{rad,out}} + \frac{1}{R_{equ,pipe}^{indoor}} \quad \text{Eq. (8)}$$

$$T_{pipe,out} = \frac{R_{equ,pipe}}{R_{equ}^{conv,out}} \times T_{conv,out} + \frac{R_{equ,pipe}}{R_{equ}^{rad,out}} \times T_{rad,out} + \frac{R_{equ,pipe}}{R_{equ}^{indoor}} \times T_{indoor} \quad \text{Eq. (9)}$$

$$SHAP = \alpha_{ig} \times \beta_{ig} + \alpha_{eg} \times \beta_{eg} + \alpha_{bl} \quad \text{Eq. (10)}$$

$$W_{pipe}^{ambient} = 1 - \frac{R_{equ,pipe}}{R_{equ,pipe}^{indoor}} \quad \text{Eq. (11)}$$

where R_{equ} is the equivalent resistance for PDSF, $m^2 \times K \times W^{-1}$, where $R_{equ,pipe}^{conv,out}$, $R_{equ,pipe}^{rad,out}$ and $R_{equ,pipe}^{indoor}$ are the equivalent resistance to convective heat absorbed by pipes from outdoor air, radiant ambient and indoor, respectively, $m^2 \times K \times W^{-1}$; β_{ig} is the ratio of the absorption-conduction heat from the internal glass to the heat absorbed by the internal glass; β_{eg} is the ratio of the absorption-conduction heat from the external glass to the heat absorbed by the external glass.
So far, K_{pipe}, $T_{pipe,out}$ and $SHAP$ are put forward for the description of heat absorbed by the pipes. The equivalent resistance $R_{equ,pipe}$ equals to the three resistances connected in parallel. $R_{equ,pipe}$ is the inverse of K_{pipe}, as Eq. (8). $SHAP$ is used to estimate the solar heat absorbed by the pipes, which is expressed as Eq. (10). It consists of absorption-conduction heat from external and internal glazing as well as the heat absorbed by the shading blinds. In the meantime, $T_{pipe,out}$ is an integrated temperature of outdoor convective, radiative and indoor temperature, °C; the weighting is only dependent on the equivalent resistances, shown as Eq. (11).

3. HEAT TRANSFER CHARACTERISTIC OF THE PIPES

Conventionally, the thickness of external and internal glass would have an impact on the overall optical and thermal property of PDSF. The thicker the glass is, the more expensive the investment is. However, the width of the cavity is usually fixed since the space for glazing is very limited in buildings thus the characteristic of PDSF under different cavity width is not discussed. The $\boldsymbol{K_{pipe}}$, $\boldsymbol{SHAP}$ and $\boldsymbol{W_{pipe}^{ambient}}$ under different external and internal glass combinations are compared and analysed.

The property of the glass and blinds in the adopted PDSF is shown as Table 1, which is widely used in the studies of PDSF (Shen and Li, 2016; Shen and Li, 2017).

Table 1. Thermal and optical property of the glass and blinds in PDSF

-	Glazing	Venetian blinds
Material	stalinite	aluminum
Thickness(mm)	9	2
Heat conductivity coefficient($W \times m^{-1} \times K^{-1}$)	0.28	180
Refractive index	1.4	/
Absorptivity (m^{-1})	5	/
Transmissivity	/	0.1

3.1 K_{pipe} under Different Glass Combinations

Fig. 4 shows convective heat transfer coefficient, K_{pipe}, under investigated glass combination. From the tendency of curves, it is observed that this coefficient is influenced by insulation of both external

and internal glass. Among the studied cases, heat transfer coefficient of the best insulation is 4.7 W×m^{-2}×K^{-1}, which is only 74% of the worst insulation 6.4 W×m^{-2}×K^{-1}. Reduction of convective heat transfer coefficient of pipes is outstanding when insulation of glass is not sufficient. Once the insulation of external and internal glass is good enough, there is no further benefits for adding insulation. It could be explained that though total heat transfer coefficient is dependent on glass insulation, convective heat transfer inside cavity is still limited.

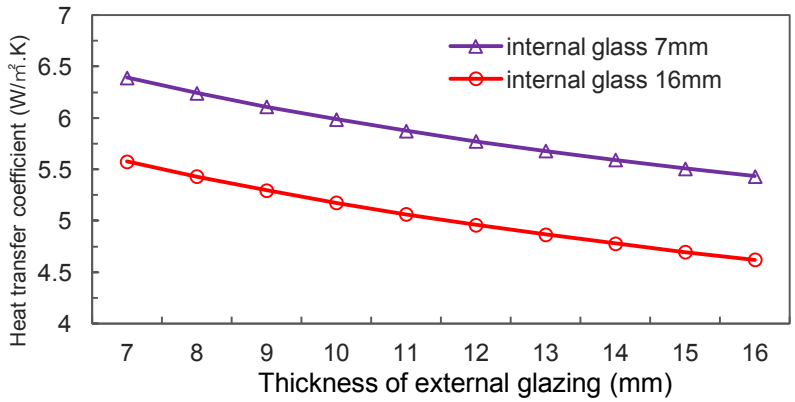

Figure 4: K_{pipe} of different combination of external and internal glass

3.2 $SHAP$ under Different Glass Combinations

Fraction of solar heat absorbed by pipes, $SHAP$, under different glass combination, is shown as Fig. 5. Results shows that among the studied cases, fraction of the removed solar heat through pipes is around 60 percent, which indicates most of the solar radiation is removed by water pipes. The tendency in these curves shows the percentage of solar heat removed by water increases with the decrease of external glass thickness and the increase of internal glass thickness. This can be accounted that the thicker external glass would permit less solar radiation penetrated, thus the solar radiation percentage decrease with the increases of external glass thickness. In addition, solar radiation absorbed by internal glass would transfer into the convective heat and cooled by the blind thus the fraction would increase with the increase of internal glass thickness. However, the increase is not remarkable because radiation absorbed by internal glass is very limited.

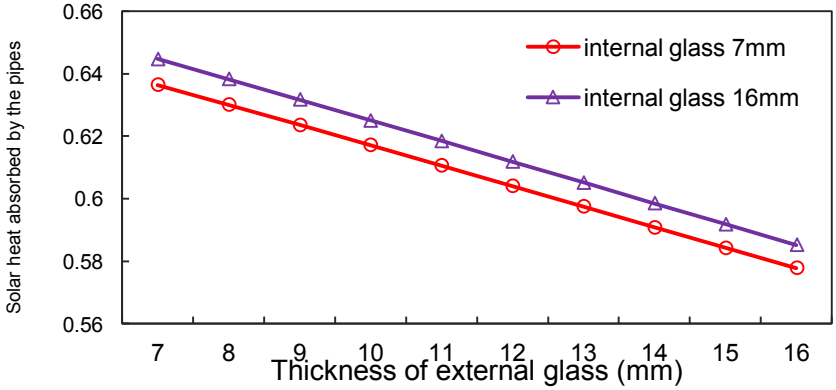

Figure 5: $SHAP$ of different combination of external and internal glass

3.3 $W_{pipe}^{ambient}$ under different glass combinations

Fig. 6 illustrates the weighting factor of ambient, $W_{pipe}^{ambient}$, under different glass combination. If the thickness of external glass is equal to that of internal glass, the weighting factor is around 0.5. In fact, $W_{pipe}^{ambient}$ indicates the relative degree of thermal resistance value of ambient and indoor. In other words, the $W_{pipe}^{ambient}$ would exceeds 0.5 when equivalent resistance between ambient and water is smaller than that between indoor and water. The larger difference, the larger $W_{pipe}^{ambient}$.

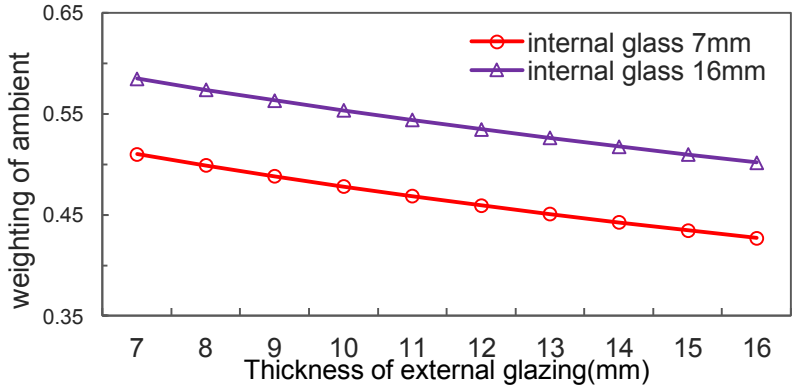

Figure 6: $W_{pipe}^{ambient}$ of different combination of external and internal glass

3.4 Discussion

If the total thickness of external and internal glass is fixed, the variation in K_{pipe} among different glass combinations is limited. However, $SHAP$ would reduce with the increase of external glass thickness. Moreover, the outdoor air temperature is usually higher than the indoor set point thus the reduction in $W_{pipe}^{ambient}$ will decrease the total convective heat transfer through pipes. In general, it is suggested that better insulated glass be installed at the external to reduce the heat absorbed by the pipes.

4. CONCLUSIONS

To evaluate the heat absorbed by the pipes in PDSF, three indexes were proposed based on its thermal network in this paper. The characteristic of the PDSF under different combinations of external and internal glazing were compared and analysed through the proposed indexes. The specific conclusions are as follows:

1) The heat absorbed by pipes in PDSF can be classified into convective heat and solar heat. The convective heat is calculated by the convective heat transfer coefficient, K_{pipe}, and difference between water temperature and equivalent temperature $T_{pipe,out}$. The solar heat absorbed can be estimated by the solar heat absorbed by pipes, $SHAP$, multiply solar intensity;
2) K_{pipe} is dependent on the thickness of both external and internal glazing, the thicker glazing, the lower K_{pipe}. $SHAP$ is about 0.6 in the investigated cases and it's mainly dependent on the external glazing;
3) When the total thickness of external and internal glazing is fixed, it is recommended to apply better insulated glazing to the external to reduce heat absorbed by pipes.

ACKNOWLEDGEMENTS

This study was supported by the national natural science foundation of china (grant no. 51578306 and grant no. 51638010).

NOMENCLATURE

A	area of the window (m^2)	*F*	view factor of two surfaces
HA	Solar heat absorbed ($W \times m^{-2}$)	*I*	solar intensity ($W \times m^{-2}$)
K	convective heat transfer coefficient ($W \times m^{-2} \times K^{-1}$)	*Q*	heat absorbed by pipes ($W \times m^{-2}$)
SHAP	fraction of solar heat absorbed by pipes	*T*	Temperature (°C)
W	Weighting of the temperature	α	short-wave solar absorptivity
β	ratio of absorption-conduction heat	λ	thermal conductivity ($W \times m^{-1} \times K^{-1}$)
δ	thickness of the glass (m)		

ABBREVIATIONS

CFD	computational fluid dynamics
DSF	double-skin facade
PDSF	pipe-embedded double-skin facade

REFERENCES

Alberto, A., Ramos, N. M. M., Almeida, R. M. S. F., 2017. Parametric study of double-skin facades performance in mild climate countries. Journal of Building Engineering 12, 87-98.

Annunziata, E., Testa, F., Iraldo, F., Frey, M., 2016. Environmental responsibility in building design: an Italian regional study. Journal of Cleaner Production 112, 639-648.

Aste, N., Leonforte, F., Piccolo, A., 2018. Color rendering performance of smart glazings for building applications. Solar Energy 176, 51-61.

Baenas, T., Machado, M., 2017. On the analytical calculation of the solar heat gain coefficient of a BIPV module. Energy and Buildings 151, 146-156.

Barbosa, S., Ip, K., 2014. Perspectives of double skin façades for naturally ventilated buildings: A review. Renewable and Sustainable Energy Reviews 40, 1019-1029.

Flores, Larsen, S., Rengifo, L., Filippín, C., 2015. Double skin glazed façades in sunny Mediterranean climates. Energy and Buildings 102, 18-31.

Ghaffarianhoseini, A., Ghaffarianhoseini, A., Berardi, U., Tookey, J., Li, D. H. W., Kariminia, S. 2016. Exploring the advantages and challenges of double-skin façades (DSFs). Renewable and Sustainable Energy Reviews 60, 1052-1065.

Kirimtat, A., Krejcar, O., 2018. A review of infrared thermography for the investigation of building envelopes: Advances and prospects. Energy and Buildings 176, 390-406.

Manz, H., 2004. Total solar energy transmittance of glass double façades with free convection. Energy and Buildings 36(2), 127-136.

Nikoofard, S., Ugursal, V. I., Beausoleil-Morrison, I., 2011. Effect of external shading on household energy requirement for heating and cooling in Canada. Energy and Buildings 43(7), 1627-1635.

Oliveira Panão, M. J. N., Santos, C. A. P., Mateus, N. M., Carrilho da Graça, G., 2016. Validation of a lumped RC model for thermal simulation of a double skin natural and mechanical ventilated test cell. Energy and Buildings 121, 92-103.

Shen, C., Li, X., 2016. Solar heat gain reduction of double glazing window with cooling pipes embedded in venetian blinds by utilizing natural cooling. Energy and Buildings 112, 173-183.

Shen, C., Li, X ., 2017. Potential of Utilizing Different Natural Cooling Sources to Reduce the Building Cooling Load and Cooling Energy Consumption: A Case Study in Urumqi. 10(3):366-.

Su, Z., Li, X., Xue, F., 2017. Double-skin façade optimization design for different climate zones in China. Solar Energy 155, 281-290.

Wang, Y., Chen, Y., 2016. Modeling and calculation of solar gains through multi-glazing facades with specular reflection of venetian blind. Solar Energy 130, 33-45.

Xue, F., Li, X., 2015. A fast assessment method for thermal performance of naturally ventilated double-skin façades during cooling season. Solar Energy 114, 303-313.

Manuscript ID: 1518
DOI: 10.18462/iir.icr.2019.1518

Autonomy of low energy residential houses in Belgium using photovoltaic panels and energy storage

Hugo MONTEYNE[(a)], Katarina SIMIC[(a)], Marija LAZOVA[(a)]
Jelle LAVERGE[(b)], Michel DE PAEPE[(a),(c)]

[(a)] Department of Flow, Heat and Combustion Mechanics, Ghent University – UGent
Ghent, 9000, Belgium, Michel.DePaepe@UGent.be
[(b)] Department of Architecture and Urban Planning, Ghent University – UGent
Ghent, 9000, Belgium, Jelle.Laverge@UGent.be
[(c)] Flanders Make, core lab UGent-EEDT
Ghent, 9052, Belgium, Jeroen.DeMaeyer@UGent.be

ABSTRACT

A building can be considered to be a zero energy building if the energy use of the building is compensated with on-site produced renewable energy on a yearly basis. This paper investigates the possibility of low energy buildings using photovoltaic PV solar panels in combination with energy storage systems to become zero energy or a (partly) autonomous building. A detached residential building with underfloor heating, air to water heat pump and photovoltaic panels PV is considered for this case study. The building is modelled in three energy performance levels, 15, 30 and 60 $kWh.m^{-2}.a^{-1}$. All three energy performance levels ensure comfort heating. A user profile for domestic hot water is implemented according to Ecodesign. The energy use profile for appliances is taken from field measurements. Maximum autonomy of the three different buildings, using energy storage, results in 73%, 67% and 60% respectively for 100m² PV panel use and the selected boundary conditions of this research.
Keywords: Energy Efficiency, Energy Storage, Heat Pump, Residential Building, Solar Energy.

1. INTRODUCTION

In the European Union (EU), the total final energy use was measured to be equal to approximately 1.084 Mtoe (Bertoldi et al., 2018). The term final energy represents the amount of energy that is actually used by the end consumer. According to statistics, final energy is principally used by four sectors: transport, residential, industry and services. The residential sector accounts for 25.38% of the final total energy use in EU (Bertoldi et al., 2018). On the other hand, residential buildings account for a share of 75% of the total building stock in EU (De Boeck et al., 2015).
Households use energy for different purposes: space and water heating, space cooling, cooking, lighting, electrical appliances. Statistical surveys carried out by the official organization of the EU have shown that the used energy in dwellings is mostly taken by space heating (64.7%) and domestic hot water production (14.5%), while consequential production of energy for covering both of the thermal needs accounts for 79.2% of total final energy use (Eurostat, 2018). The same study has shown that natural gas, fossil fuel, plays an important role in providing energy to satisfy the energy needs for an average dwelling in Europe. In fact, gas is still responsible for providing 43.4% of the heat for space heating, 47.9% for water heating and 33.1% for cooking needs. Present world society has a clear awareness of the transient of the fossil fuel energy sources. As a matter of fact, renewable energy sources are finding an outstanding breakthrough in the market. According to the official statistical data (Eurostat, 2018), renewables cover 22.2% of the energy needs for space heating, 9.6% for hot water production following 4.2% for cooking in EU. The future expectations over energy use in novel as well as in refurbished buildings testify about optimal use of energy and definite implementation of renewable energy sources and accompanying technology.

With each novel directive, European legislation intends to push building stock to near zero or zero energy buildings. A building can be considered to be a zero energy building (ZEB) if the energy use of the building is compensated with on-site produced renewable energy on a yearly basis. As stated by Agostino and Delia (2015) a zero energy building compensates its total energy use for heating, ventilation, domestic hot water and appliances by renewable energy produced on site. In the case of zero energy building, energy demand and energy production are shifted over the seasons. Fig. 1 shows change in energy demand for comfort heating versus electrical energy production using 50 m^2 photovoltaic (PV) solar panel for a full year time. It can clearly be seen that energy demand has completely contradictory behaviour when compared to the energy production at the given moment for all different building energy performances. A 15 $kWh.m^{-2}.a^{-1}$ building has a reduced heating demand during the offseason due to the high passive solar gains but still has a significant energy use during the coldest winter period with low solar radiation, not enough to compensate the heat losses of the building. When no sufficient energy storage is used the electricity grid is utilized as virtual energy storage. To get an autonomous building, energy storage is needed on site to bridge the time shift.

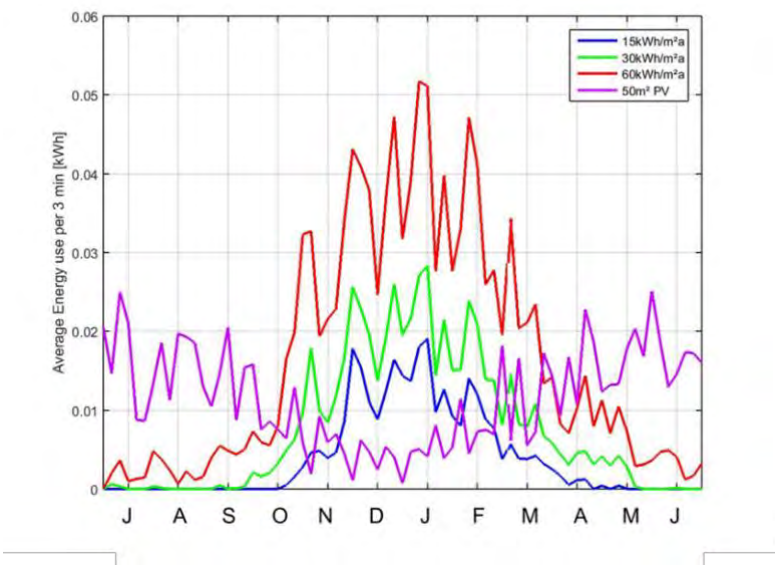

Figure 1: The energy demand of a 15, 30 and 60 $kWh.m^{-2}.a^{-1}$ building and energy production 50m² PV

Weitemeyer et al. (2015) highlighted that energy storage and/or curtailment will be required once the renewable energy ratio surpasses 50% in covering overall energy demand with joint use of flexible power plants. Later research performed by Child et al. (2017) and Child et al. (2018) have confirmed the same share of renewable energy production ratio value.

This paper investigates the possibility of low energy buildings using photovoltaic (PV) solar panels with efficiency of 16% in combination with energy storage systems to become a partly autonomous building. This part of the research focuses on different building envelopes, the needed amount of renewable energy and the needed energy storage to reduce the dependency from the grid. The importance of having a vigorous building envelop resulting in the lower necessity of taking the energy from the grid or to have a higher autonomy intends to be the goal of the research. Non-technical people pretend that a lower energy performance of the building can be compensated by extra renewable energy production on site. This is mathematically correct on a yearly basis if only the total energy use is considered. This paper highlights the incontrovertible advantage of higher building performance.

In the following text, 15 $kWh.m^{-2}.a^{-1}$, 30 $kWh.m^{-2}.a^{-1}$ and 60 $kWh.m^{-2}.a^{-1}$ building levels will be represented as B15, B30, B60 buildings respectively in order to facilitate the understanding of the results.

2. METHODOLOGY

2.1. Observed Case

A detached residential building with underfloor heating, air to water heat pump and photovoltaic panels (PV) is considered for this case study. The building is modelled in three energy performance levels of 15, 30 and 60 kWh.m^{-2}.a^{-1}. All three buildings are assumed to be located in the area of Brussels, Belgium. Therefore, the chosen outdoor boundary conditions are corresponding to the available weather data conditions of Brussels. This study is focussing on one building design with one set of building parameters for each investigated energy performance of the building. However, it is important to mention that a building with the same energy performance but with a different orientation and different window construction will change the energy load profile for heating on a daily basis. Previously, it has been ensured that all three energy performance levels are fulfilling the comfort heating demand with respect to the heat losses. The buildings are assumed to be constantly heated with the indoor set point temperature at 20ºC.
The only difference in the energy use of the investigated buildings is the energy performance of the building envelope. Due to different heating demand, the electrical energy use is 689, 1378 and 2756 kWh.a^{-1} for the 15, 30 and 60 kWh.m^{-2}.a^{-1} building for comfort heating while all three houses have the same demand of 848 kWh.a^{-1} for domestic hot water and 5011 kWh.a^{-1} for the appliances. This brings the total electricity use on 6548, 7237 and 8615 kWh.a^{-1} for each energy performance building level respectively.

2.2. Simulation Tools and Strategy

The buildings and the systems are modelled in software package TRNSYS17 (Solar Energy Laboratory, 2009), using TRNFlow to calculate the ventilation, in- and exfiltration of the buildings. In addition, several MATLAB (2015) scripts were used in order to calculate relations between produced heat by the air to water heat pump and energy stored by the energy storages. Data analysis was also performed using the MATLAB software package. Fig. 2 illustrates the simulation methodology.

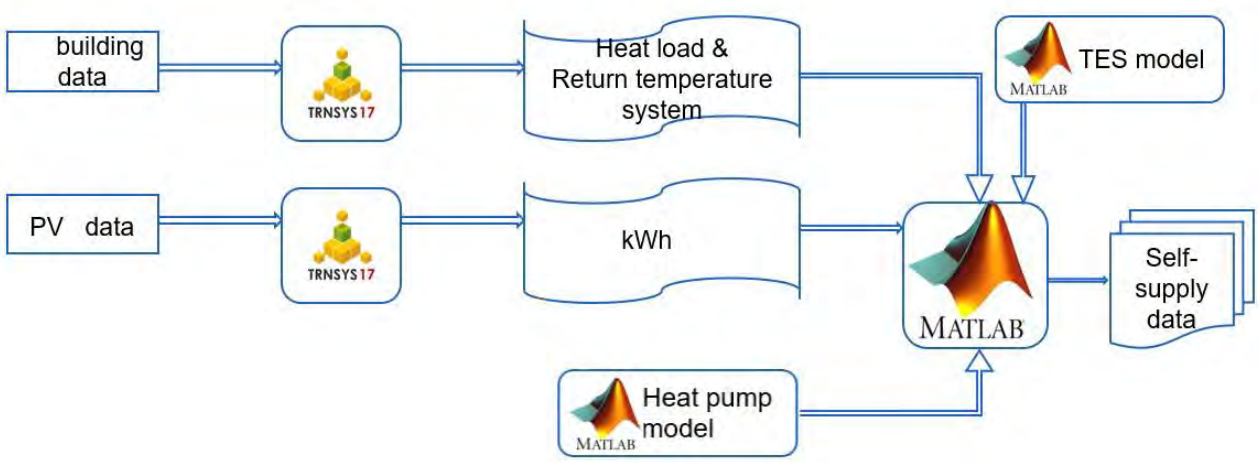

Figure 2: Simulation methodology

Therefore, TRNSYS simulation results are used as input to the storage and the heat pump model, while installation models are developed in a MATLAB script. The calculation of the heating demand and energy supply is thus decoupled from the installation simulation. As a result, the simulation is speeded up sufficiently to evaluate a multitude of energy production and energy storage combinations.
The simulations of the energy performance were done with a time step of 3 minutes. At each time step, the following data were calculated:

- the heating demand of the building
- the return water temperature of the underfloor heating
- the mass flow rate in the underfloor heating
- the thermal power production by the heat pump and energy use of the heat pump
- the solar power production of the photovoltaic solar panels

- the status of the thermal and electrical storage

The energy exchange between the building, the energy buffers and the electrical grid is integrated in the post-processing method using a control strategy which is the same for all analysed cases. The strategy covers the energy balance of the whole building system and it is met at each time step.
The domestic hot water (DHW) production has priority on the heating load of the building. The comfort demand of 40°C DHW at each time step must be guaranteed.

2.3. Used Input Data

A user profile for domestic hot water is implemented according to Ecodesign requirements. The used profile in this study is a medium user profile (3XS) coming from the regulation of the European Commission, (813/2013).
Outdoor conditions are simulated by using the Meteonorm climate data. The data are coming from the official Royal weather station located in Uccle (Belgium). Besides the outdoor temperature, data files are containing as well the information over the solar radiation, the position of the sun, outdoor relative humidity, sky cover etc.
On the other hand, the energy use profile for appliances is taken from field measurements during the Linear project (D'hulst et al., 2015) where the energy use is measured over more than a full year on a time step basis of 15 minutes. The profile of the appliance use is appropriate for a young family with two young children living in a detached house. Both parents are having full-time employment. In the original project, the heating and the DHW production of this case study house were supplied by a gas boiler. For cooking, an electric stove was used. The total electricity use for this case was determined to be 5010 $kWh.a^{-1}$.

2.4. Investigated Energy Storage Systems

As it was shown before, optimum renewable energy production and energy requirement are shifted in time. By introducing energy storages to the system the impact of this phenomenon may be significantly mitigated. Electricity production out of photovoltaic panels has the peak production around noon. On the other hand, air to water heat pumps have their maximum COP at the same time due to maximal daily outdoor temperature. Since the energy demand shows to be disproportionate to the optimum energy production, there is a clear necessity of having energy storage in order to increase the energy autonomy of a dwelling.
In this study, both electrical energy storage (EES) and thermal energy storage (TES) are considered for the purpose of the autonomy analysis. Several different capacities of both EES and TES, as well as their combination with different PV sizes, are considered by the analysis. The charging and discharging losses of the EES are assumed and kept fixed at 10%.The results of the research are given in the next section of the paper.

3. RESULTS

Autonomy for three different energy performing buildings was analysed for several different energy storages and PV surface sizes. Electrical energy storage is evaluated for 0, 2000, 4000 and 8000 Wh. On the other hand, thermal storage is evaluated for 0, 500, 1000 and 2000 litre of volume. All sizes used for evaluation of impact to building autonomy are realistic and taken as standardized capacities provided by relevant manufacturers of the equipment.
In real use, a different combination of EES and TES sizes are possible. Depending on the energy need and principally on investment costs, different solutions are to be found in modern households. Different energy storage systems will be compared to the basic system without energy storage and without renewable energy production. The last baseline has per definition an autonomy of 0% which means that all needed energy has to be supplied by the grid. Autonomy stands for the independence from the grid or fraction of the load covered by on-site generation. In this study, the autonomy of different dwellings is evaluated based on the solar fraction. As shown on the Eq. (1) and based on the research performed by Widen et al. (2009), the solar fraction is defined as the ratio between energy supplied from the grid and total electricity demand:

$$solar\ fraction = 100 - \frac{energy\ supply\ grid}{total\ electricity\ demand} \qquad \text{Eq. (1)}$$

3.1. Autonomy of the 15, 30, 60 kWh.m^{-2}.a^{-1} Energy Performance Level Building in Belgium

Fig. 3, Fig. 4 and Fig. 5 illustrate which solar fractions can be realized with PV areas up to 100m² combined with different sizes of electrical and thermal energy storage for all three energy performance levels. Small thermal storage has always a significant improvement on the solar fraction. However, the increment of the size of the TES without an introduction of the EES does not give further notable improvement except for the least energy efficient building. Nevertheless, EES brings higher grid independency even for the smallest battery capacity. In fact, the impact of using the small scale electrical battery brings higher solar fraction than the use of the biggest TES for B15 and B30 building cases. The higher impact of EES is due to the fact that the thermal energy storage is only used during the heating season and the EES is used during the entire year.
Fig. 3 shows autonomy results of the B15 building. The B15 building has an autonomy of 30% (solar fraction) in the absence of any energy storage and use of 100m^2 PV solar panels. Without energy storage and 50m² PV, a solar fraction of 25% is achieved (remaining energy requirement is 4911 kWh.a^{-1}). Using the same PV area and introducing a thermal energy storage of 2000l increases the solar fraction up to 31%, leaving the remaining energy requirement to be 4812 kWh.a^{-1}.

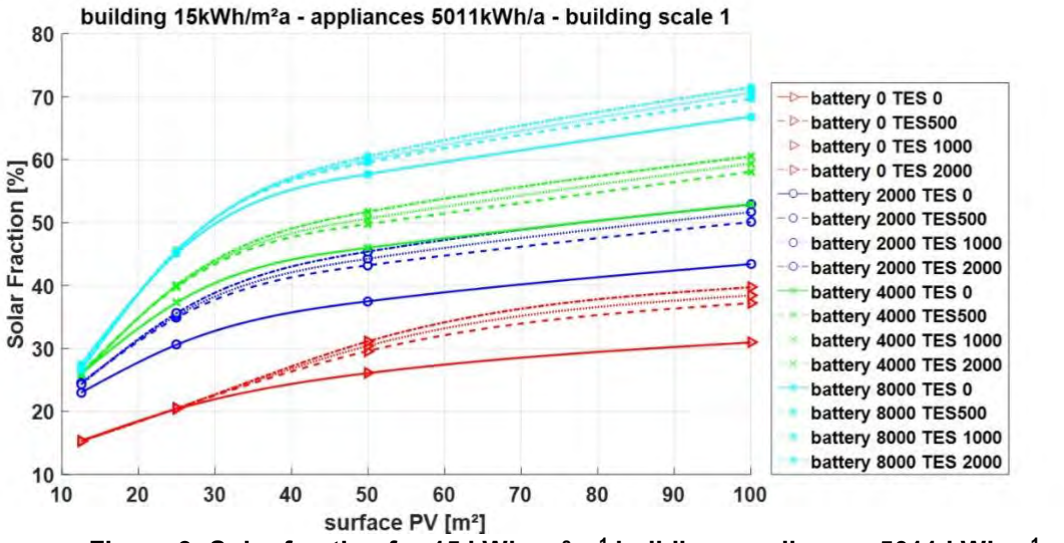

Figure 3: Solar fraction for 15 kWh.m^{-2}.a^{-1} building, appliances 5011 kWh.a^{-1}

Representation of the autonomy for all three building performances allows determination of the needed renewable energy and energy storage to get to the same energy supply from the grid.
The B15 building has a total energy demand of 6548 kWh.a^{-1}. A PV surface of 5m² is needed for the B30 and 30m² PV for the B60 to get the same electricity demand as the B15 on yearly basis using the grid as storage. In case the same supply from the grid is targeted as the B15, without using the grid as a storage system, the B30 needs 9,52% solar fraction. This can be reached by means of 5m² PV panel. However, the B60 building would require a 24% solar fraction which needs 83m² PV or 30m²PV and 2000l TES or 25m² PV and 2000 Wh battery.

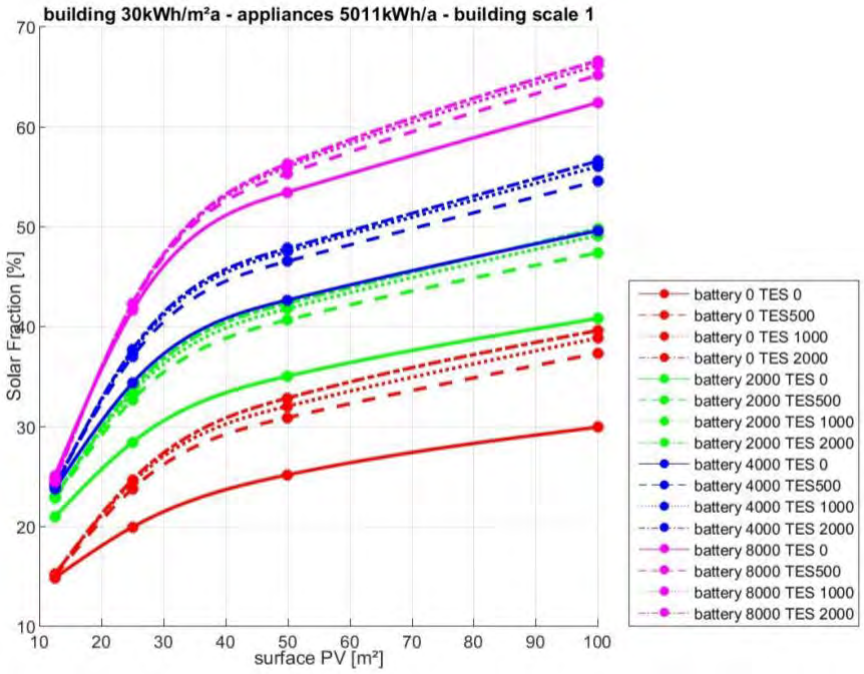

Figure 4: Solar fraction for 30 kWh.m^{-2}.a^{-1} building, appliances 5011 kWh.a^{-1}

According to the first definition of zero energy building (ZEB), in order to make all three buildings ZEB, a PV area of 44, 49 and 58m² is needed. This results in the autonomy of 26%, 25% and 22% for the B15, B30 and B60 and leading the supply from the grid as energy storage to become 4845, 5428 and 6720 Wh. To bring all buildings on the same energy supply from the grid of 4845 Wh, the B30 building needs a solar fraction of 33% which includes 50m² PV with 2000l TES or 24m² PV with a 4000 Wh battery or 100m² PV with 700l TES.
The B60 building, however, needs, in this case, a solar fraction of 44% which opens four possibilities. The first is to have a 60m² PV solar panel with a 4000 Wh battery. Then, the second could be to have a 2000l TES and 2000 Wh battery or 28m² PV with an 8000 Wh battery. The last option requires a 100m² PV solar panel with 1000l TES with an 2000 Wh battery. The lower the energy performance of the building, the bigger PV solar panel surface and energy storage is needed to get the same energy supply from the grid.

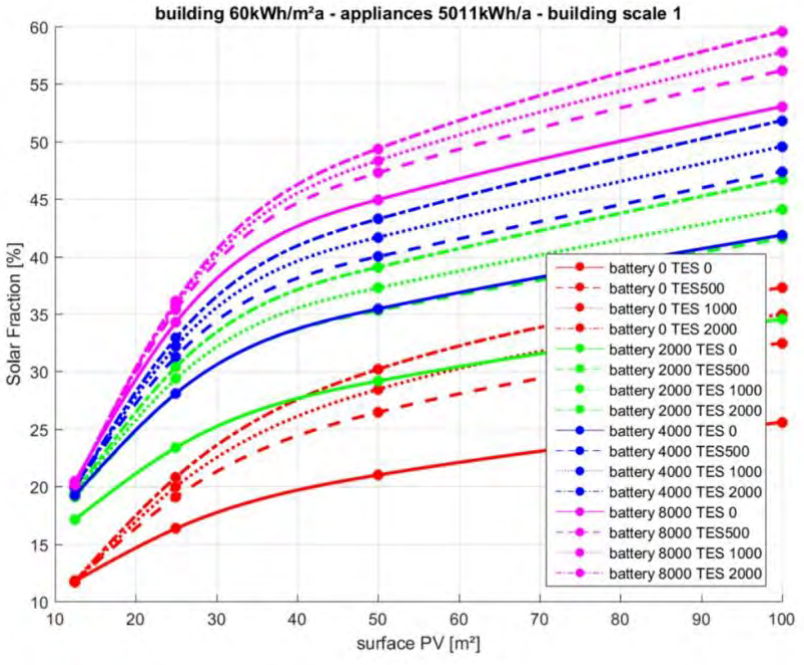

Figure 5: Solar fraction for 60 kWh.m^{-2}.a^{-1} building, appliances 5011 kWh.a^{-1}

The highest autonomy for maximal battery and thermal storage capacity and PV surface area of 100m^2 proves to be 72%, 67% and 60% for B15, B30 and B60. Therefore, for the boundary conditions used in this study, it is determined to be impossible to achieve 100% grid independence for neither of the analysed building envelops using the roof as available PV area.

3.2. The Remaining Energy Requirement for the three Buildings with Different Battery Use

Since every different building has different energy requirements due to heat demand, it becomes clear that one size of battery will have a different impact to the remaining energy needs that have to be taken from the grid. Fig. 6 illustrates the remaining energy supply from the grid for different battery sizes for the three levels of building energy performance. Following the result on Fig. 6 it becomes evident that for using e.g. 2000 kWh.a^{-1} from the grid, a 15 kWh.m^{-2}.a^{-1} building will require a battery size of 7500 Wh, while the 30 kWh.m^{-2}.a^{-1} needs to have a double-sized battery of 15000 Wh. The 60 kWh.m^{-2}.a^{-1} building cannot reach the example chosen level of limited energy supply.

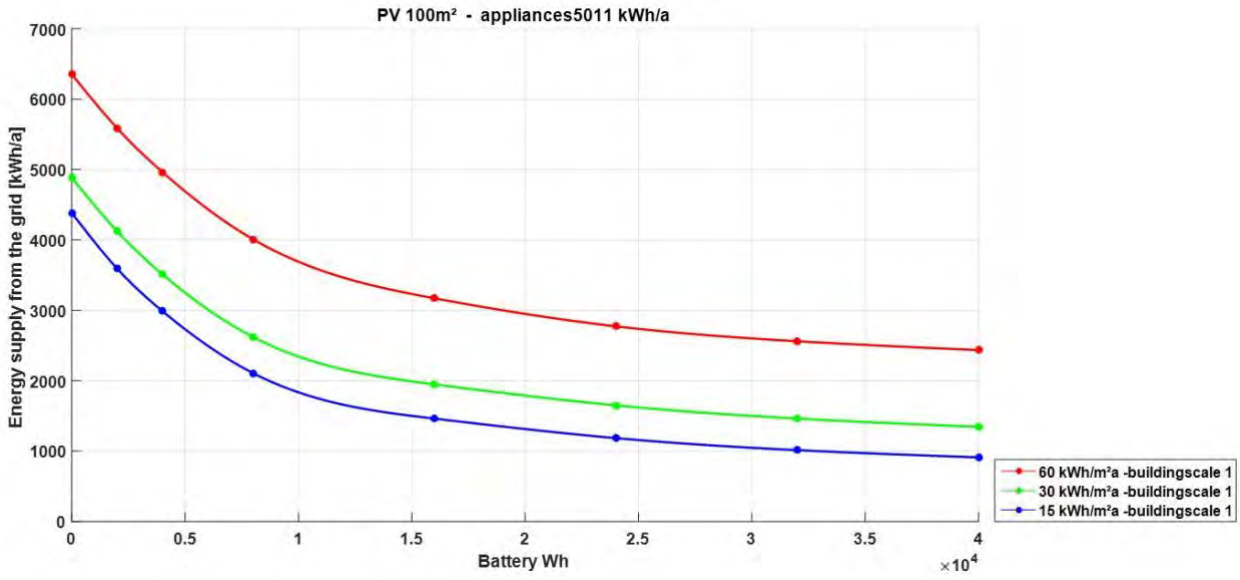

Figure 6: The capacity of EES in order to have the same remaining energy requirement for all three buildings for 100m^2 PV panel area and 5011 kWh.a^{-1} electricity use

The lower the energy performance of the building the more difficult it is to compensate the lower building performance with extra energy storage.

3.3. Financial Aspect

In this chapter, an order of magnitude of the financial impact will be given through a partial financial evaluation on the electrical energy storages (batteries). As part of the study, different battery capacitates are adopted to evaluate the level of the buildings autonomy to the grid that can be achieved.

In 2017, the cost of a battery was approximately 1000€ per kWh capacity. The price corresponds to the average price of the Li-Ion batteries that can be applied to the entire capacity range used in this research. Assuming a lifecycle of the building of 30 years means that the battery has to be replaced two times during the mentioned period. This also means that the magnitude of the extra investment is 15000€ for the case of 15 kWh.m^{-2}.a^{-1} building and 30000€ for the 30 kWh.m^{-2}.a^{-1} building.

Another interesting aspect is the ageing of the equipment. The storage capacity of a battery decreases due to cycling ageing and calendar ageing. In the scientific literature, many studies have been addressing the life cycles of the batteries for the application in the electric vehicles. Compared to the batteries of the electric vehicles, the batteries in buildings application have significantly more stable working conditions. The changing of the battery is spread over a range of 12 hours while only the overshoot of the produced energy is actually stored in the batteries. The ageing of the EES is not considered in this research. Several experimental studies have shown that batteries in buildings

application will have a much longer life cycle when compared to others. However, further research over the matter is certainly needed in the close future. Improving the energy performance of the building envelop and building system should be the first step before considering using energy storage.

4. CONCLUSIONS

Long-term targets set out in European Union Roadmap-2050 request emissions from the building stock, with the largest share of housing stock, to be cut by around 90% till the year 2050. Both energy efficiency measures and the transit from fossil fuels to decarbonized electricity, e.g. by using heat pumps merged with renewable energy are indispensable for reaching those ambitious targets. Balancing intermittent renewable energy supply through pro-active demand-side management and energy storage will serve as leading instruments in order to reduce the energy use of residential buildings.

In this research, using simulation tools, several aspects of different energy efficiency level buildings have been analysed. Using realistic sizing of building integrated systems including electrical and thermal energy storage as well as photovoltaic panels results in significant reductions of energy supply from the grid. For the boundary conditions used in this research, results show the impossible reach of energy independence from the grid in Belgium. The maximum obtained autonomy was shown to be 72% for the 15 $kWh.m^{-2}.a^{-1}$ with EES of 8000 Wh, TES of 2000l and PV panel surface of $100m^2$, while the maximum autonomy for the 30 and 60 $kWh.m^{-2}.a^{-1}$ buildings results in 67% and 60% respectively. On the other hand, if the area for using the PV solar panels is limited to $52m^2$, maximum autonomy of the three different building energy levels results in 61%, 57% and 50% respectively.

Local energy storage can significantly increase the autonomy of buildings using on-site produced renewable energy. However, the high investment of energy storage and the limited life cycle of the equipment is still a threshold.

Without a proper design of the building envelop in order to significantly reduce the energy demand, large investments in renewable energy production and storage equipment cannot make a typical residential building in Belgium autonomous. To contribute to the aspirations of the EU, refurbishment of existing buildings and construction of new ones in order to meet high energy performance of the building envelop and the building systems will be inevitable.

ACKNOWLEDGEMENTS

This research was supported by the Burnay Price donated by ATIC (Royal Society for Heating, Ventilation and Climatisation). The financial support is gratefully acknowledged.

REFERENCES

Bertoldi, P., Diluiso, F., Castellazzi, L., Labanca, N., Serrenho, T., 2018. Energy Consumption and Energy Efficiency Trends in the EU-28 2000-2005. European Commission report, 1-175.

Child, M., Breyer, C., Bogdanov, D., Fell, H.-J., 2017. The of storage technologies for the transition to a 100 % renewable energy system in Ukraine. 11th International Renewable Energy Storage Conference IRES 2017, Energy procedia 135, 410–423.

Child, M., Ilonen, R., Vavilov, M., Kolehmainen, M., Breyer, C., 2018. Scenarios for sustainable energy in Scotland. Wiley, 1–19.

D'hulst, R., Labeeuw, W., Beusen, B., Claessens, S., Deconinck, G., Vanthournout, K., 2015. Demand response flexibility and flexibility potential of residential smart appliances: Experiences from large pilot test in Belgium. Appl. Energ., 155, 79–90.

D'Agostino, D., 2015. Assessment of the progress towards the establishment of definitions of Nearly Zero Energy Buildings (nZEBs) in European Member States. Journal of Building Engineering, 1, 20–32.

De Boeck, L., Verbeke, S., Audenaert, A., De Mesmaeker, L., 2015. Improving the energy performance of residential buildings: A literature review. Renew. Sust. Energ. Rev., 52, 960–975.

European Commission., 2013. COMMISSION REGULATION (EU) No 813/2013 of 2 August 2013 implementing Directive 2009/125/EC of the European Parliament and of the Council with regard to ecodesign requirements for space heaters and combination heaters. Official Journal of the European Union, (813), 136–161.

Eurostat., 2018. Energy consumption in households, (March 2018), 1–9. Retrieved from https://ec.europa.eu/eurostat/statistics-explained/index.php/Main_Page

MATLAB and Statistics Toolbox Release R2015b, The MathWorks, Inc., Natick, Massachusetts, United States., 2015. Massachusetts, United States of America.

Solar Energy Laboratory, University of Wisconsin- Madison., 2009. Trnsys 17 (Vol. 4).

Weitemeyer, S., Kleinhans, D., Vogt, T., Agert, C., 2015. Integration of Renewable Energy Sources in future power systems : The role of storage. Renew. Energ., 75, 14–20.

Widen, J., Wackelgard, E., Lund, P. D., 2009. Options for improving the load matching capability of distributed photovoltaics : Methodology and application to high-latitude data. Sol. Energy, 83, 1953–1966.

Manuscript ID: 1770
DOI: 10.18462/iir.icr.2019.1770

Parametric study by means of 3D CFD to improve the airflow pattern and temperature distribution in data center rooms

Diogo G.C.S. MACEDO [(a)], Radu GODINA [(a,b)], Pedro D. GASPAR [(a,b)], Pedro D. SILVA [(a,b)] ,Miguel T. COVAS [(c)]

[(a)] Department of Electromechanical Engineering, University of Beira Interior
Covilhã, 6201-001 Portugal
[(b)] C-MAST - Centre for Mechanical and Aerospace Science and Technologies, Covilhã, Portugal
Covilhã, 6201-001 Portugal, dinis@ubi.pt
[(c)] ALTICE/MEO - Serviços de Comunicações e Multimédia, SA, Quinta Grila DATACENTER
Covilhã, 6200-292, Portugal

ABSTRACT

The processing efficacy and energy efficiency of data centers (DC) is directly related with the cooling performance of the air-conditioning systems. The cooling effectiveness depends on airflow pattern and temperature distribution. This paper presents the parametric study of three-dimensional (3D) computational fluid dynamics (CFD) models to improve these technical characteristics. In this case study the most suitable thermal load, as deemed by the organization, of the heat flow boundary condition is simulated and studied for maximum and minimum airflow. The analysis of the numerical results provides a prediction of the thermal performance, i.e., the lower values and spatial gradients (hot spots) of air temperature and velocity while maintaining the computational processing requirements. These results allow the development of an optimized CFD model for setting up the operational parameters of CRAC systems for DC rooms.
Keywords: Computational Fluid Dynamics, Computer Room Air Conditionings, Data Centers, Air-conditioning Systems, Hot Spots, Energy Efficiency.

1. INTRODUCTION

In the last decades the Data Centers (DCs) have undergone a significant evolution, adopting more efficient techniques and practices, but their energy consumption continues very high. By 2015 this consumption accounted for around 1.3% of world energy consumption (Díaz et al., 2017). Due to the increased need for data storage, there is a trend to build larger DCs, thereby increasing energy consumption, which leads to increased concern about minimizing the environmental impact, reducing energy consumption costs, and optimizing the energy performance (Dayarathna et al., 2016). As expected, power consumption for DC cooling has been increasing over the years, due to the large increasing amount of information technology (IT) systems that DC rooms hold. This is due to the advance of the technology that causes the continuous components miniaturization, which allows the installation of more components in the same space. This requires adequate cooling so that there is no high temperature or humidity gradients or spots, as these factors lead to deficiencies in the operation of electronic equipment (Song et al., 2015). The constant escalation in the recent years of the heat density of IT servers caused a rise of 40% in the energy consumption of data centers' cooling systems (Nada et al., 2016a). The energy efficiency of DCs is very dependent on their thermal performance. Since the refrigeration system is a relevant energy consumer in these infrastructures, the development of parametric studies that predict the variation of relevant quantities in the airflow and heat transfer processes, depending on the layout, dimensions and operational characteristics of devices and systems, can translate into improvements in the thermal performance of the infrastructure, and simultaneously of energy efficiency. The results can be tested in the next phases of the DC infrastructure, with the prospect of achieving additional gains in reducing energy consumption (Zhang et al., 2018). Computational Fluid Dynamics (CFD) is a set of numerical methods for obtaining an approximate solution to a problem of fluid dynamics and/or heat transfer. The equations that come into play are those of fluid mechanics and heat transfer, solved by numerical methods. The solution is approximate and not exact for several reasons. However, thanks to the development of digital methods and increasingly powerful computers with a large memory capacity, the CFD allows having very

satisfactory solutions. This is more than enough in certain areas of industry where very often a prediction of the order of magnitude of average values is amply sufficient (Wendt, 2009). This topic has been gaining interest and several researchers have been drawing attention to such types of studies (Li and Kandlikar, 2015). Nadjahi et al. (2018) review the thermal management and novel cooling strategies for data center and addresses energy saving procedures/techniques/ technologies. Nada et al. (2016b) simulate the thermal performance of DCs considering different configurations of CRAC units and physical separations of cold and hot aisles. The authors concluded that the performance strongly depends on the racks location. A thermal management system for a small data center incorporating noise reduction is proposed by Zhou et al. (2018) and is verified by experimental testing. The authors argue that his solution avoids the formation of hot spots. Ni et al. (2017) used CFD to model the airflow in a data center with floor air supply to identify the optimal conditions of air distribution that provide the best energy savings. Distinct airflow strategies for data centers are analyzed in Behere (2015) and different approaches for the optimization of the airflow are proposed. A fast-executing hybrid lumped capacitance-CFD model for the simulation of data center transient thermal events is proposed by Erden et al. (2014). The model effectively predicts such events since the results of study were compared with experimental data acquired from a three-rack data-center test cell. However, the abovementioned studies lack complexity since the proposed models are fairly simple and focus on small data centers with a low number of racks. For this reason, such types of studies are simulated in a short period of time and are validated without difficulty.
This paper presents the parametric study of three-dimensional computational fluid dynamics model to improve airflow pattern and temperature distribution of a real data center room with substantial dimensions and considering 208 racks. This data center is located in an average European city. In this case study the proper thermal load, as deemed by the organization, of the heat flow boundary condition is simulated and studied for maximum and minimum air flow velocity. ANSYS™ Fluent package is used to simulate the airflow and heat transfer processes in the room. This paper is organized as follows. In section 2 the proposed model and the computational processing requirements are described. The results are shown and analyzed in section 3. Finally, in chapter 4 the concluding remarks are given.

2. MODEL DESCRIPTION

The geometric model was developed taking into account the characteristics of computational processing in order to avoid divergence patterns during the simulations run. Thus, the three-dimensional geometry was simplified in order to avoid a highly complex mesh. A complex mesh requires high computational processing, which leads to an increase of time running each simulation, being necessary every so often to adjust the mesh to the availability of time and processing capacity of the simulating tools. In order to achieve such scenario, the racks are represented as parallelepipeds, and the cables, rails, access doors and fixtures have been concealed to facilitate the construction of the mesh. In the case of illumination, these were concealed not only by the complexity they would generate in the developed mesh, but also because they were disconnected during the operation of the IT room, thus generating no heat.
The continuity, momentum, energy equations and the standard k-ε model equations are based on the equations exposed in Ni et al. (2017) and Hoang et al. (2000). The constants of the standard k-ε model: σ_k, σ_ε, $C_{1\varepsilon}$, $C_{2\varepsilon}$ e C_μ are set to the following values 1, 1.3, 1.44, 1.92 and 0.09, respectively, as provided by Hoang et al. (2000).
The CFD software used for this simulation was ANSYS™ Fluent. To perform the numerical simulation it was necessary to elaborate a three-dimensional geometry of the IT room with its 208 racks. The number of nodes is 1 183 613, the number of control volumes is 2 341 172, the Aspect Ratio is 1.645 and the skewness is 0.177. These numbers required a high computational power. This geometry was developed in AutoCAD 2017 software and later exported to a compatible format (.sat) with Ansys Software. The 3D geometry developed for the present study can be observed in Fig. 1.

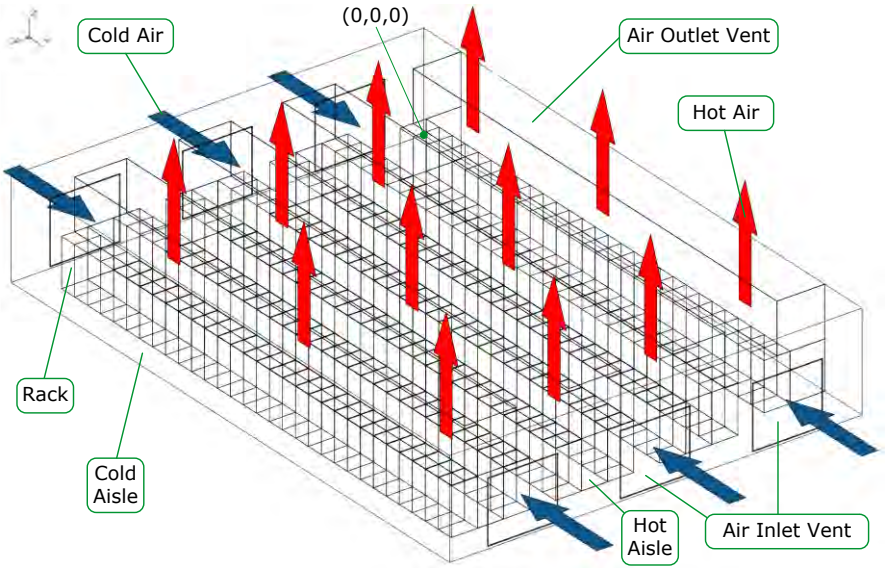

Figure 1: Three-dimensional geometry of the studied data center room

The resulting mesh consists of tetrahedral elements (cold aisles) and hexahedral (hot aisles and racks). This solution was adopted because the mesh would have a high number of control volumes if only the mesh were used with tetrahedral elements. This solution was employed due to the fact that having only tetrahedral elements, albeit the ideal model, it was not possible due to extremely high computational power required for this purpose.

2.1. Boundary Conditions

The boundary conditions defined in the numerical models were based on the data collected in the DC room. To the values collected was also added the value of pressure loss in the racks provided by North (2011) in which 80% perforation causes a pressure loss of 7.5 Pa. It is important to point out that from now on all coordinate values and parameters are presented in a non-dimensional way to simplify the comparison between case studies. The dimensionless quantities of the values to be considered are the value 0 for the minimum value and the value 1 for the maximum value. The maximum height value of the rack is 0.489. It should be noted that in the case of temperature, the maximum value corresponds to a temperature value that exceeds the operating specifications of the racks. That is, it is an air temperature value with the possibility of malfunctioning or damage to the equipment included in the IT rooms, which are intended with uninterrupted operation.

The equations previously mentioned are solved at the fluid zone, that is, it contains the control volumes where these equations are solved. The fluid used in the present study is air, considered to be incompressible, which means that the values of the values presented in Table 1 are constant and the gravitational acceleration was considered as g = 9.81 $m \cdot s^{-2}$. The fluid zone was considered with the dimensionless temperature of 7.09×10^{-4}. A solution converges when all the residuals reach the stopping criterion, $\lambda = 1 \times 10^{-3}$ for all variables, except for the energy variable that assumes a stop criterion of $\lambda = 1 \times 10^{-6}$. The factors concerning relaxation were the ones given by the default settings of the software.

The iterative process of the various numerical models was defined to be 1500 iterations, since it was concluded that the solution would not reach the stopping criterion. However, the possible convergence was easily achieved by using 1500 iterations since the variables stabilized before this number of iterations.

Table 1. Atmospheric properties if the air

Constants	Values
Specific mass	ρ = 1.21 $kg \cdot m^{-3}$
Dynamic viscosity	$\mu = 1.82528 \times 10^{-5}$ $kg \cdot m^{-1} \cdot s^{-1}$
Thermal conductivity	k = 0.0256706 $W \cdot m^{-1} \cdot K^{-1}$
Specific heat	C_p = 1006.14 $J \cdot kg^{-1} \cdot K^{-1}$

3. SIMULATION RESULTS AND ANALYSIS

In this case study, case study 1, the most suitable thermal load, as considered by the organization, of the heat flow boundary condition is simulated and studied for maximum and minimum air flow velocity. In this case study the changes in boundary conditions are as follows: the typical dimensionless thermal load dissipated by the racks: q_{adm} = 0.340 and the minimum dimensionless air flow velocity: v_{adm} = 0.

In the Figs. 2, 3 and 4 it is possible to observe the predictions of dimensionless temperature field for this case study.

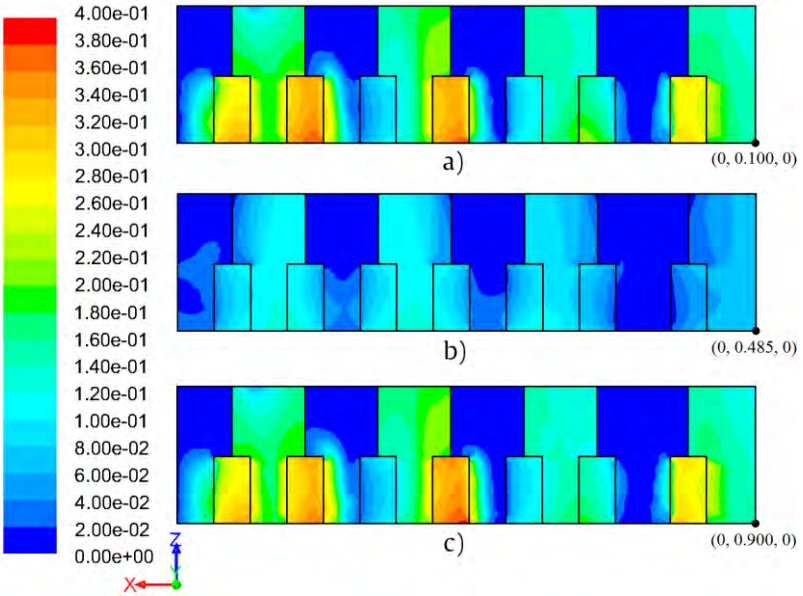

Figure 2: Dimensionless temperature fields in the *x-z* plane for a) y_{adm} = 0.100, b) y_{adm} = 0.485 and c) y_{adm} = 0.900.

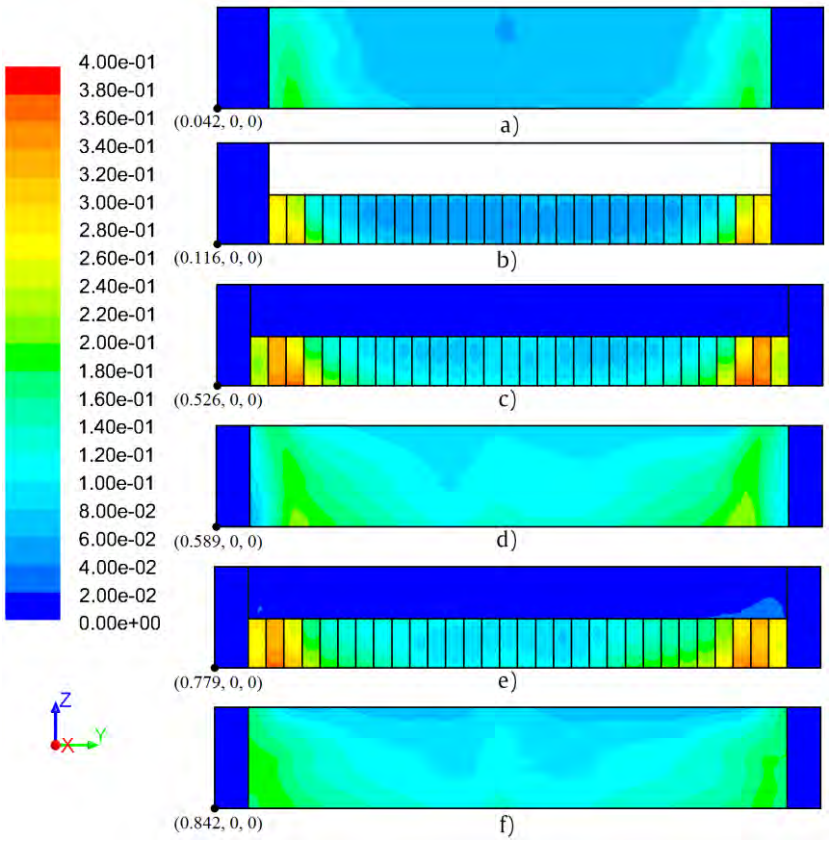

Figure 3: Dimensionless temperature fields in the *y-z* plane for a) x_{adm} = 0.042, b) x_{adm} = 0.116, c) x_{adm} = 0.526, d) x_{adm} = 0.589, e) x_{adm} = 0.779 and f) x_{adm} = 0.842

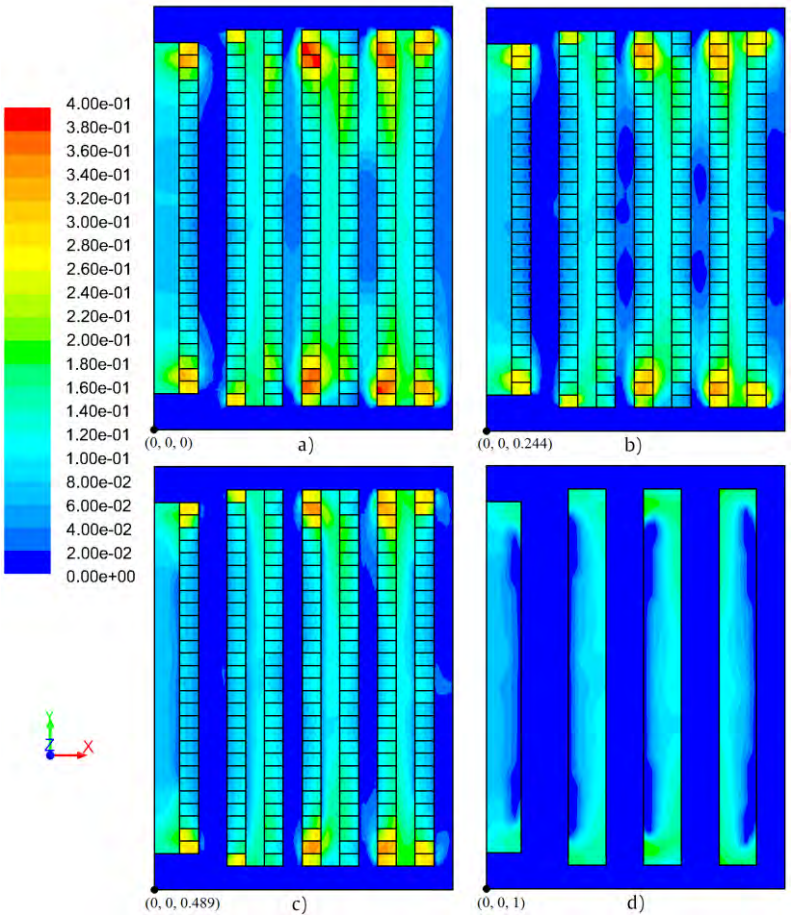

Figure 4: Dimensionless temperature fields in the *x-y* plane for a) z_{adm} = 0, b) z_{adm} = 0.244, c) z_{adm} = 0.489, d) z_{adm} = 1

By observing Fig. 3 it can be predicted several hots spots at the extremity of the rack lines. This is confirmed also by observing the *y* and *z* planes, as depicted by Figs. 2 and 4, respectively. These hot spots are considered to be of values of dimensionless temperature higher than T_{adm} > 0.350. It can also be observed in Fig. 4a) that the heat is more intense at the base of the racks due to lower airflow in this zone. This happens because the airflow is more intense in the middle of the air vents and not at the bottom.

In case 2, the changes in boundary conditions are as follows: the typical dimensionless thermal load dissipated by the racks: q_{adm} = 0.340 and the maximum dimensionless airflow velocity: v_{adm} = 1. Figs. 5, 6 and 7 show the predictions of the dimensionless temperature field for this case study.

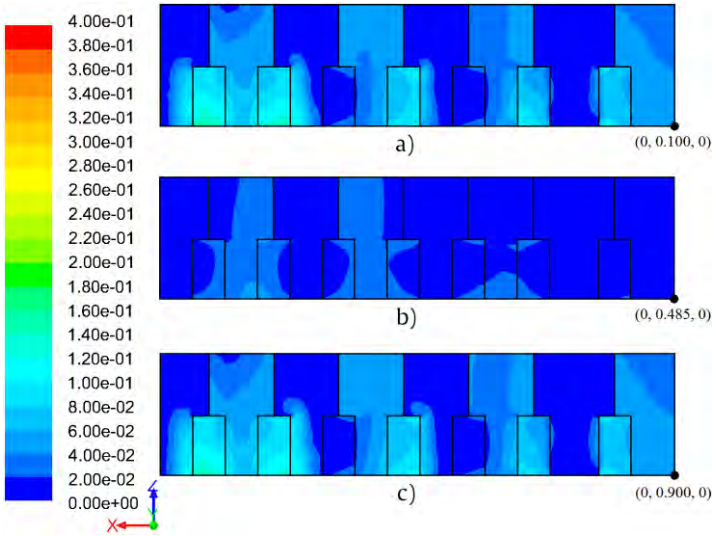

Figure 5: Dimensionless temperature fields in the *x-z* plane for a) y_{adm} = 0.100, b) y_{adm} = 0.485 and c) y_{adm} = 0.900

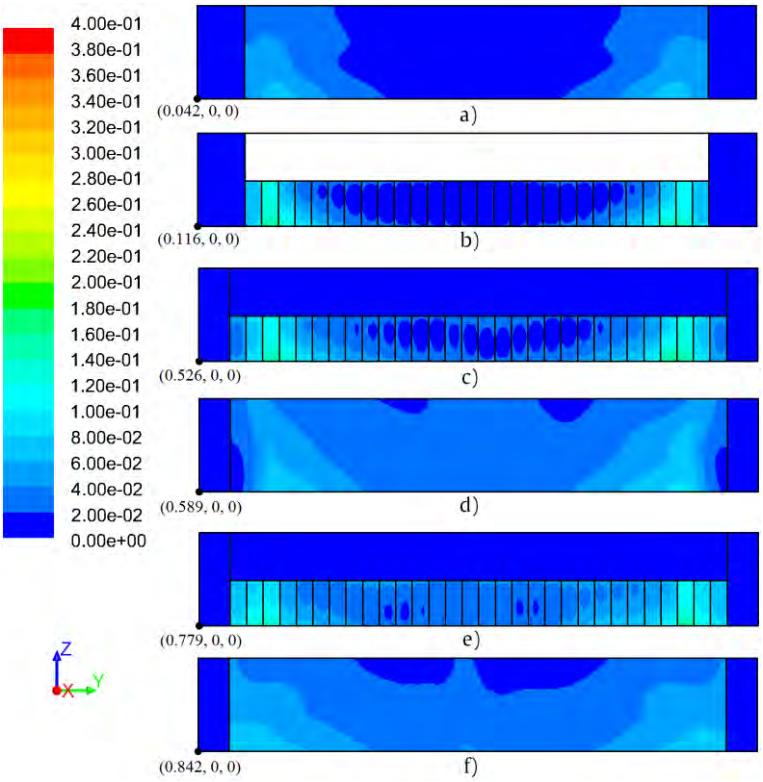

Figure 6: Dimensionless temperature fields in the *y-z* plane for a) x_{adm} = 0.042, b) x_{adm} = 0.116, c) x_{adm} = 0.526, d) x_{adm} = 0.589, e) x_{adm} = 0.779 and f) x_{adm} = 0.842

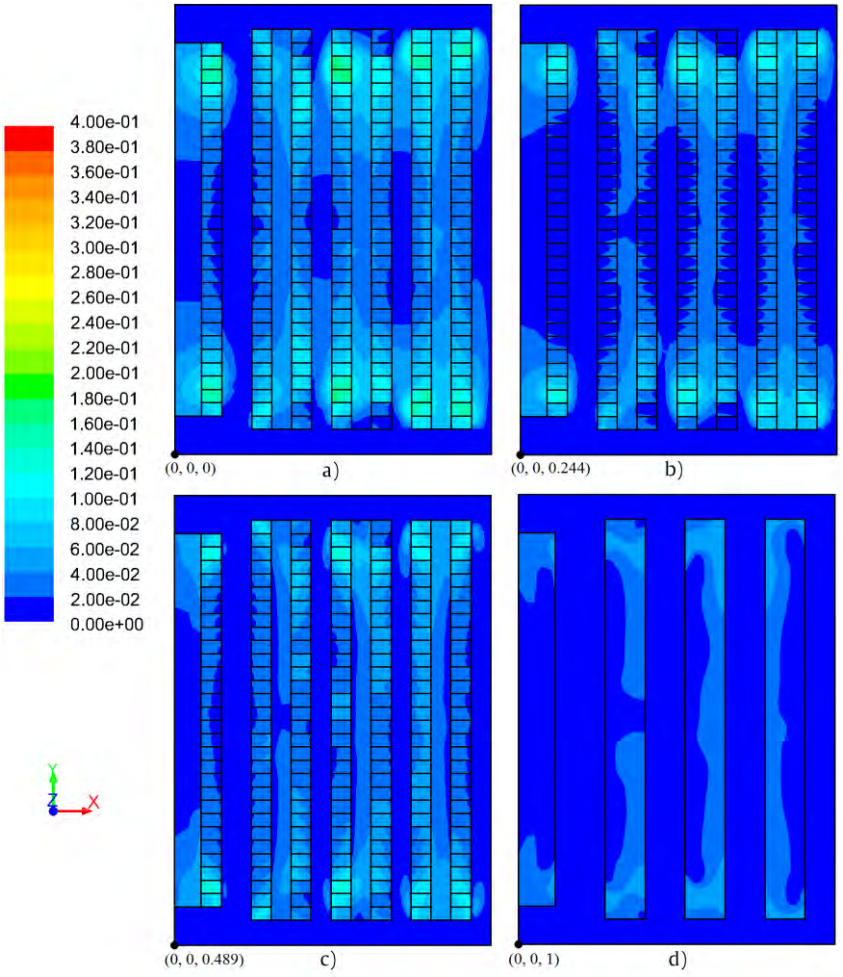

Figure 7: Dimensionless temperature fields in the *x-y* plane for a) z_{adm} = 0, b) z_{adm} = 0.244, c) z_{adm} = 0.489, d) z_{adm} = 1

It should be noticed that in both case studies the scale was changed in order to perceive the differences of temperature in the DC room. Thus, the scale ranges from 0 to 0.4 dimensionless. By observing Figs. 5, 6 and 7 it can be noticed that there is no formation of hot spots. This condition occurs due to the maximum air airflow, and consequently, maximum air velocity possible. Therefore, all the heated air is exhausted successfully. Even with this air velocity it is possible to predict that the warmer air is located at the extremity of the rack lines. By comparing Fig. 7a) with Fig. 7c) it is possible to confirm that the heat is more intense at the base of the racks. The numerical model is validated by 3 measurements made and supplied by the data center.

The hot spots observed at the extremities of the lines of the racks occur due to the improper airflow in these locations, as shown in Figs. 8a) and 8b). However, in the middle of the room, represented by Fig. 8b), the air flows as intended. The poor airflow that occurs at the extremities of the racks' lines exists due to a deficient layout of the DC room. This can be noticed by observing the zoomed section of Fig. 8a) in which the air flows incorrectly from the hot aisle to the cold aisle, in the zoomed section from left to right. The correct direction of the air should be from the cold aisle to the hot aisle, as shown in the zoomed section of Fig. 8b).

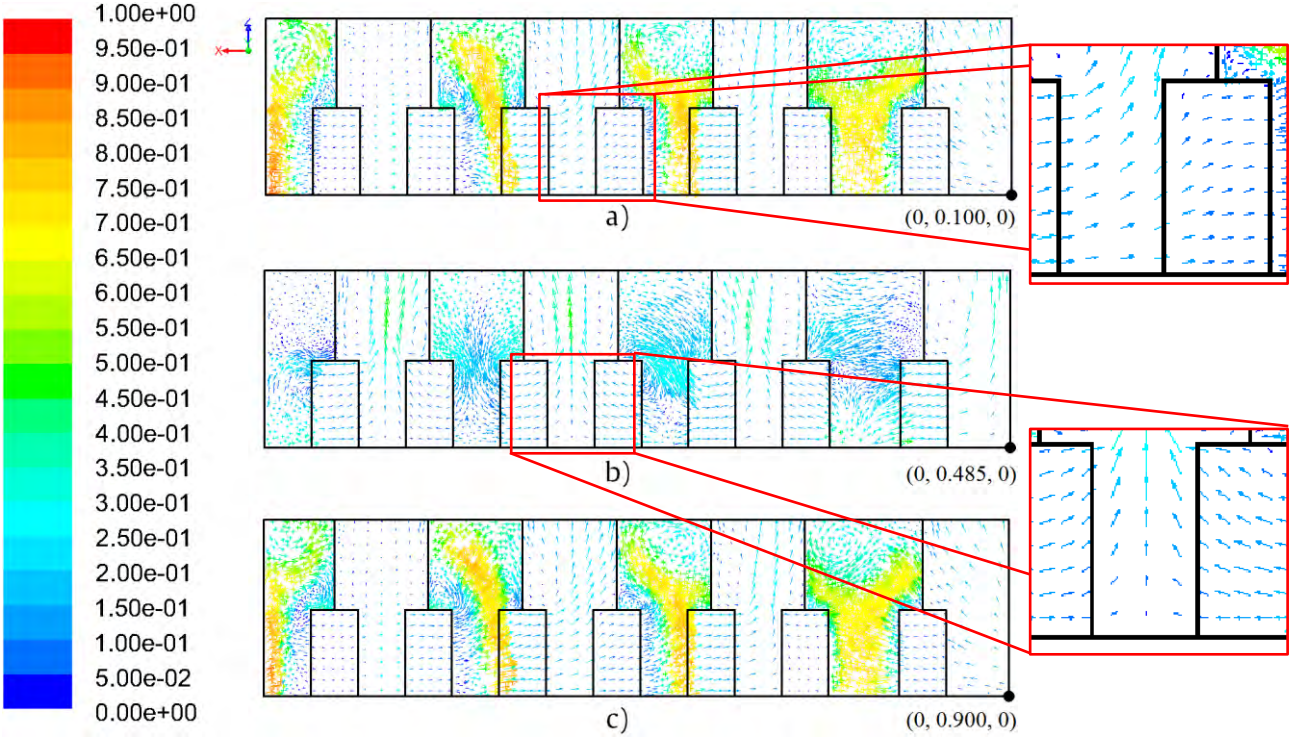

Figure 8: Dimensionless velocity vectors profiles for the *x-y* plane a) y_{adm} = 0.100, b) $y_{adm.}$ = 0.485, and c) $y_{adm.}$ = 0.900

4. CONCLUSIONS

In this paper a parametric study of CFD models to study the airflow of a data center room with 208 racks was presented. Two case studies were simulated with the most suitable thermal load, as deemed by the organization that provided the data in which the heat flow boundary condition is simulated and studied for maximum and minimum air velocity. The analysis of the numerical results showed that no hot spots occur in the case study with the maximum air flow and several hot spots occur in the case study with the minimum air flow. These hot spots are observed at the extremities of the lines of the racks and occur due to the improper airflow in these locations. Both case studies confirm this scenario. The poor air flow at the extremities of the lines of the racks occurs due to a deficient layout of the room. This study confirmed that the layout of the room is not ideal. A solution could be the removing at least a few racks from both lines' extremities in order to enable a more adequate air flow in that location.

ACKNOWLEDGEMENTS

The current study was funded in part by Fundação para a Ciência e Tecnologia (FCT), under project UID/EMS/00151/2013 C-MAST, with reference POCI-01-0145-FEDER-007718.

REFERENCES

Behere, S., 2015. Airflow Optimization In Data Centers. Energy Eng. 112, 33–54. https://doi.org/10.1080/01998595.2015.11414491

Dayarathna, M., Wen, Y., Fan, R., 2016. Data Center Energy Consumption Modeling: A Survey. IEEE Commun. Surv. Tutor. 18, 732–794. https://doi.org/10.1109/COMST.2015.2481183

Díaz, A.J., Cáceres, R., Cardemil, J.M., Silva-Llanca, L., 2017. Energy and exergy assessment in a perimeter cooled data center: The value of second law efficiency. Appl. Therm. Eng. 124, 820–830. https://doi.org/10.1016/j.applthermaleng.2017.06.066

Erden, H.S., Khalifa, H.E., Schmidt, R.R., 2014. A hybrid lumped capacitance-CFD model for the simulation of data center transients. HVACR Res. 20, 688–702. https://doi.org/10.1080/10789669.2014.930280

Hoang, M.L., Verboven, P., De Baerdemaeker, J., Nicolaï, B.M., 2000. Analysis of the air flow in a cold store by means of computational fluid dynamics. Int. J. Refrig. 23, 127–140. https://doi.org/10.1016/S0140-7007(99)00043-2

Li, Z., Kandlikar, S.G., 2015. Current Status and Future Trends in Data-Center Cooling Technologies. Heat Transf. Eng. 36, 523–538. https://doi.org/10.1080/01457632.2014.939032

Nada, S.A., Said, M.A., Rady, M.A., 2016a. Numerical investigation and parametric study for thermal and energy management enhancements in data centers' buildings. Appl. Therm. Eng. 98, 110–128. https://doi.org/10.1016/j.applthermaleng.2015.12.020

Nada, S.A., Said, M.A., Rady, M.A., 2016b. CFD investigations of data centers' thermal performance for different configurations of CRACs units and aisles separation. Alex. Eng. J. 55, 959–971. https://doi.org/10.1016/j.aej.2016.02.025

Nadjahi, C., Louahlia, H., Lemasson, S., 2018. A review of thermal management and innovative cooling strategies for data center. Sustain. Comput. Inform. Syst. 19, 14–28. https://doi.org/10.1016/j.suscom.2018.05.002

Ni, J., Jin, B., Zhang, B., Wang, X., 2017. Simulation of Thermal Distribution and Airflow for Efficient Energy Consumption in a Small Data Centers. Sustainability 9, 664. https://doi.org/10.3390/su9040664

North, T., 2011. Understanding How Cabinet Door Perforation Impacts Airflow. BICSI News Mag. 36–42.

Song, Z., Zhang, X., Eriksson, C., 2015. Data Center Energy and Cost Saving Evaluation. Energy Procedia, Clean, Efficient and Affordable Energy for a Sustainable Future: The 7th International Conference on Applied Energy (ICAE2015) 75, 1255–1260. https://doi.org/10.1016/j.egypro.2015.07.178

Wendt, J. (Ed.), 2009. Computational Fluid Dynamics: An Introduction, 3rd ed. Springer-Verlag, Berlin Heidelberg.

Zhang, K., Zhang, Y., Liu, J., Niu, X., 2018. Recent advancements on thermal management and evaluation for data centers. Appl. Therm. Eng. 142, 215–231. https://doi.org/10.1016/j.applthermaleng.2018.07.004

Zhou, C., Yang, C., Wang, C., Zhang, X., 2018. Numerical simulation on a thermal management system for a small data center. Int. J. Heat Mass Transf. 124, 677–692. https://doi.org/10.1016/j.ijheatmasstransfer.2018.04.005

Manuscript ID: 1891
DOI: 10.18462/iir.icr.2019.1891

Development of thermal energy storage system for peak thermal demand of apartment using phase change material

Hyo Jae JEONG[(a)], Dongho PARK[(a)], Sung Yong PARK[(b)], Dong An CHA[(a)], Jong Hyeon PECK[(a)], Kyung Min KIM[(b)], Won Seok CHANG[(b)], Mun Sei OH[(b)]

[(a)]Thermal & Fluid System R&D Group, Korea Institute of Industrial Technology (KITECH), Cheonan, 31056, South Korea, hyojae.jeong@kitech.re.kr, senna@kitech.re.kr, cdongan@kitech.re.kr, pjh6240@kitech.re.kr

[(b)]New Technology Research Department, Korea District Heating Corporation (KDHC), Yongin, 17099, South Korea, sy215@kdhc.co.kr

ABSTRACT

Thermal energy storage technology can solve a problem of time discrepancy between heat supply and demand by using sensible or latent heat storage. Generally, the storage media of sensible heat storage is water. There is advantage of latent heat storage using phase change material (PCM), since both of sensible and latent heats can be used for heat storage. Therefore, the latent heat storage has high energy density than that of sensible heat storage. Recently, the latent heat storage has been widely considered in order to apply to control temperature in building, cold food chain, air conditioning, and so on. In this study, thermal energy storage system using solid-liquid PCM was developed to respond peak thermal demand of apartment. The thermal demand in apartment is generally peaked in the morning and at night. Since the imbalance of thermal demand during a day, the heat supply system of the apartment should be installed as large scale system to cover the peak thermal demand. Note that the capital and operational costs of heat supply system become high to cover the peak thermal demand. Therefore, it was necessary to develop thermal energy storage for charging heat at normal thermal demand and discharging heat at peak thermal demand. PCM in the latent heat storage was developed to discharge heat at the peak of thermal demand. The melting temperature of PCM applied to this study was 78 °C. The hot water supplied from Korea District Heating Corporation (KDHC) had high pressure as high as 15 bar. Therefore, the latent heat storage was designed with shell-tube structure. In this presentation, the progress of project to develop latent heat storage system and preliminary test results are provided.

Keywords: Latent Heat Storage, Thermal Demand, Apartment, Phase Change Material, Shell-Tube Heat Exchanger.

1. INTRODUCTION

Thermal energy storage technology can solve a problem of time discrepancy between heat supply and demand by using sensible or latent heat storage. Sensible heat storage depends on the material's specific heat capacity (Cunda and Eames, 2016). Generally, the storage media of sensible heat storage is water. There is advantage of latent heat storage using phase change material (PCM), since both of sensible and latent heats can be used for heat storage. Therefore, the latent heat storage has high energy density than that of sensible heat storage. On the other hand, volumetric expansions of latent heat storage during the melting process can reach 10–15% for some materials (Cunda and Eames, 2016).

Recently, the latent heat storage has been widely studied for application to control temperature in building, cold food chain, air conditioning, and so on. Medium and large scale latent heat storage systems with solar thermal collectors could be applied to centralized air conditioning and district heating networks for hospitals, commercial centres, and office buildings (Agyenim et al., 2010, Gil et al., 2013, Gil et al., 2013, Colella et al., 2012, Kensby et al., 2015)). The latent heat storage could be also applied to Organic Rankine cycle (ORC) driven by solar thermal energy to avoid destabilization of ORC system by short term weather irregularities (clouds, fog, etc.) (Vivian et al.,

2015, Higgo and Zhang, 2015). The latent heat storage may also have applied to food and beverages industry (beer, milk, chocolate, cheese, coffee, canned food, etc.) to achieve optimum temperatures during shipping (Agyenim et al., 2010).
In this study, thermal energy storage system using solid-liquid PCM was developed to respond peak thermal demand of apartment. The thermal demand in apartment is generally peaked in the morning and at night. Since the imbalance of thermal demand during a day, the heat supply system of the apartment should be installed as large scale system to cover the peak thermal demand. Note that the capital and operational costs of heat supply system become high to cover the peak thermal demand. Therefore, it is necessary to develop thermal energy storage for charging heat at normal thermal demand and discharging heat at peak thermal demand.
PCM in the latent heat storage was decided to discharge heat at the peak thermal demand in this study. It was important that the PCM should have a relative high latent heat and stability in its molten state (Cunda and Eames, 2016). The melting temperature of PCM applied to this study was 78 °C. Note that thermal conductivity of commonly used PCMs is generally from 0.2 to 0.7 W/m-K (Cunda and Eames, 2016). Therefore, heat exchanger should be designed as complexed geometry in order to obtain sufficient heat transfer rate during heat charging or discharging. Hot water supplied from Korea District Heating Corporation (KDHC) had high pressure as high as 15 bar. In this study, the latent heat storage was designed with shell-tube structure with narrow tube interval to enhance heat transfer rate and be durable the pressure. In this presentation, the progress of project to develop latent heat storage system and preliminary test results are provided.

2. DESIGN OF EXPERIMENTAL SETUP

2.1. Development of Phase Change Material

In order to decide PCM for the latent heat storage, 5 PCMs previously developed by our research group were considered. Each PCM were tested using Differential scanning calorimeter (DSC) to examine the required amounts and melting temperature of PCM. Note that it is possible to obtain results such as melting temperature and latent heat using DSC. The DCS results of PCMs are listed in Table 1. Since hot water supply system (not heating system) in the apartment was considered in this study, the temperature of heat charging should be around 80 °C. Therefore, A12 was selected in this study because its melting temperature was close to the required temperature.

Table 1. DSC results of PCMs.

Code[1)]	Melting temperature (°C)	Latent heat (J/g)	Heat capacity (J/g-K)	Density(kg/m^3)
A12	78	285.1	1.2(solid)/1.3(liquid)	2,180 (solid)
HT7	44	176.6	1.7(solid)/2.3(liquid)	1,004 (solid)
HT54	54	190.8	1.7(solid)/2.4(liquid)	990 (solid)
W02	62	200.0	1.9(solid)/2.8(liquid)	989 (solid)
HT68	68	195.7	1.6(solid)/2.2(liquid)	965 (solid)

[1)]Code name of PCMs developed by Korea Institute of Industrial Technology

2.2. Design of Latent Heat Storage

The pressure and temperature of hot water supplied from KDHC to the apartment were around 15 bar and 115 °C, respectively. Therefore, the latent heat storage should be durable for high pressure and temperature. In this study, shell-tube structure was applied to the latent heat storage. The outside dimeter and length were 800 and 1600 mm, respectively. The thickness of shell was 8 mm. The outside diameters and number of tubes were 3/4 inch and 450, respectively. The tube interval was optimised by CFD (computational fluid dynamics) modelling regarding the time of heat charging and discharging. All the components of storage was made by using stainless steel 304. The amount of PCM in the latent heat storage was about 1,200 kg. Therefore, the total latent heat of storage could be calculated as 81,600 kcal. The designed latent heat storage is detailed in Figure 1 and 2. The storage was insulated by ethylene propylene diene monomer insulation of 30 mm.

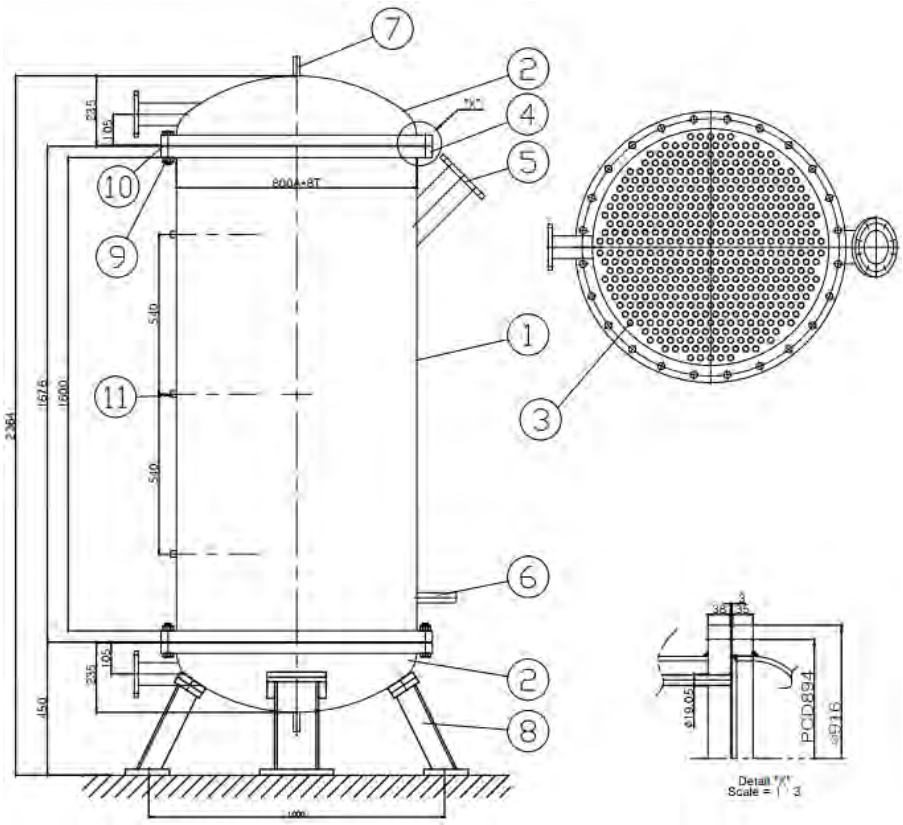

Figure 1. Design of latent heat storage.

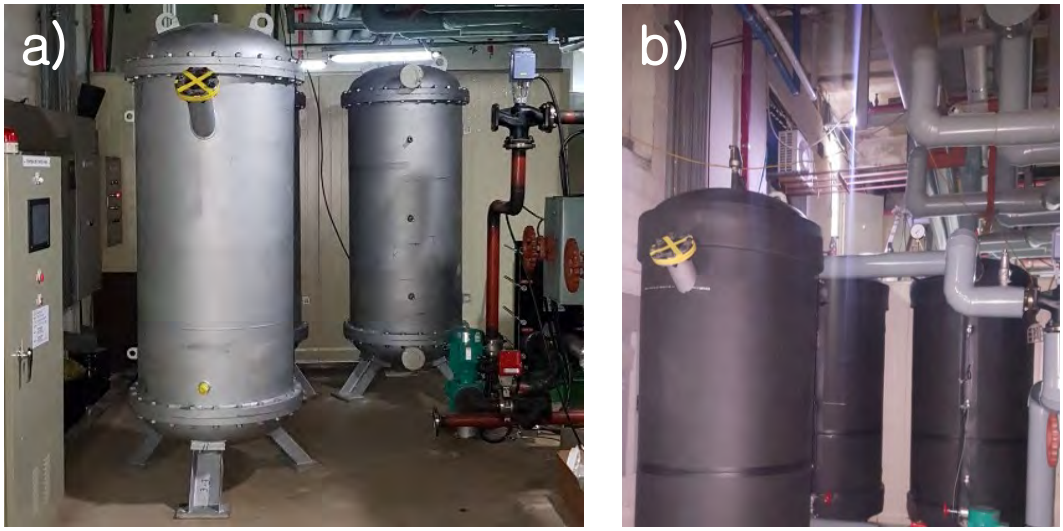

Figure 2. Pictures of installed latent heat storage: a) without insulation, b) with insulation.

2.3. Latent Heat Storage System Configuration

The maximum hot water load of apartment was 229 Mcal/h. In this study, three of latent heat storage were installed in the system. All the storage were connected as parallel between main supply pipe of KDHC and thermal demand side in the apartment. The heat of latent heat storage was charged by hot water supplied from KDHC in the day time. The heat was discharged from the latent heat storage when the thermal demand was increased in the morning or at night. There was a plate heat exchanger was installed at the outlet of storage in order to heat exchange between water supplied from storage and supply water heated to hot water. The detail system configuration is shown in Figure 3. The latent heat storage system could be monitored and controlled by Programmable Logic Controller (PLC) as shown in Figure 4. In order to temperature distributions of the latent heat storage, the temperatures were measured using 42 channels data acquisition system as shown in Figure 4.

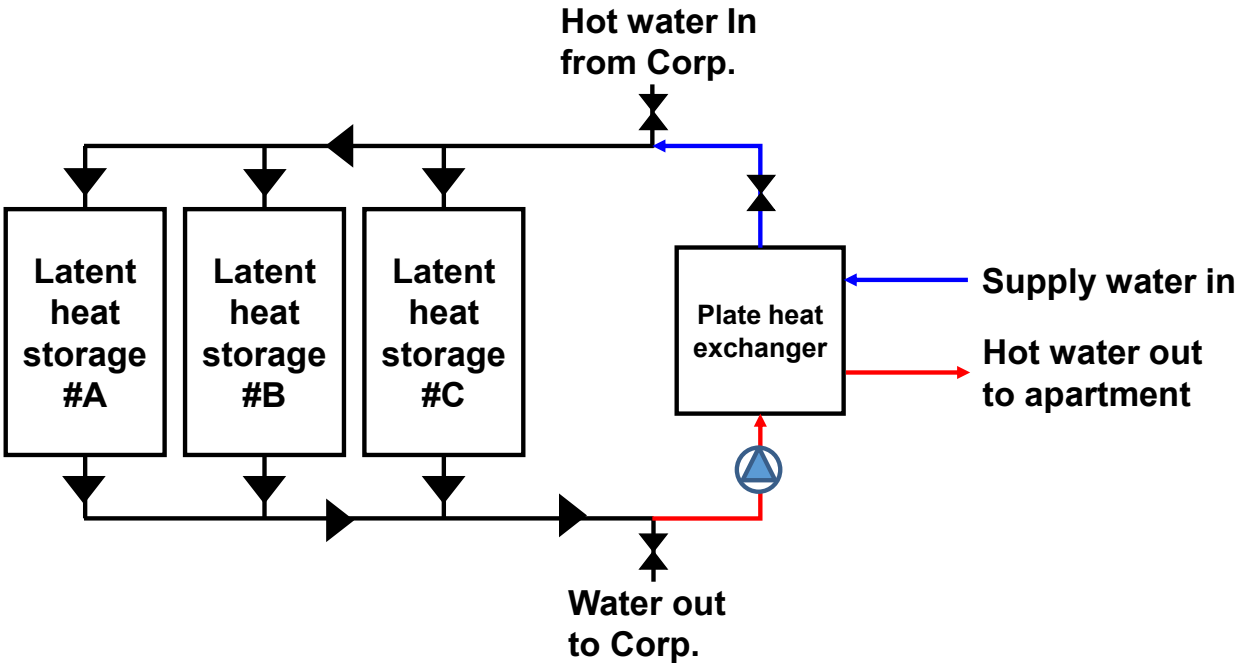

Figure 3. Configuration of latent heat storage system.



Figure 4. PLC and 42 channels temperature measurement point.

3. RESULTS

Figure 5 shows the preliminary test results of latent heat storage. In Figure 5, 'Hot water in' and 'Hot water out' indicate the hot water supplied from KDHC. And, 'Return water to storage' and 'Hot water out to apartment' indicate return water from plate heat exchanger to the latent heat storage and hot water heated in the plate heat exchanger, respectively. As shown in Figure 5, the storage temperature was maintained constant as PCM's melting temperature from 100 to 400 min after heat charging started. Therefore, it could be concluded that the PCM was on phase change state. The temperature discrepancy between 'hot water in' and 'hot water out' was about 35 °C after heat charging was stable. In the preliminary test, the heat was charged in the storage during 350 mins. Since the temperature of storage was not higher than melting temperature, it could be concluded that the heat charging process was not finished for 350 mins. After heat charging, heat discharging test was conducted for 400 mins. Temperatures of 'return water to storage' and 'hot water out to apartment' were fluctuated because of thermal demand variation of apartment during heat discharging. The preliminary results in Figure 5 were obtained by latent heat storage #B only. In further tests, heat charging and discharging process will be conducted using all the latent heat storage according to thermal demand of the apartment.

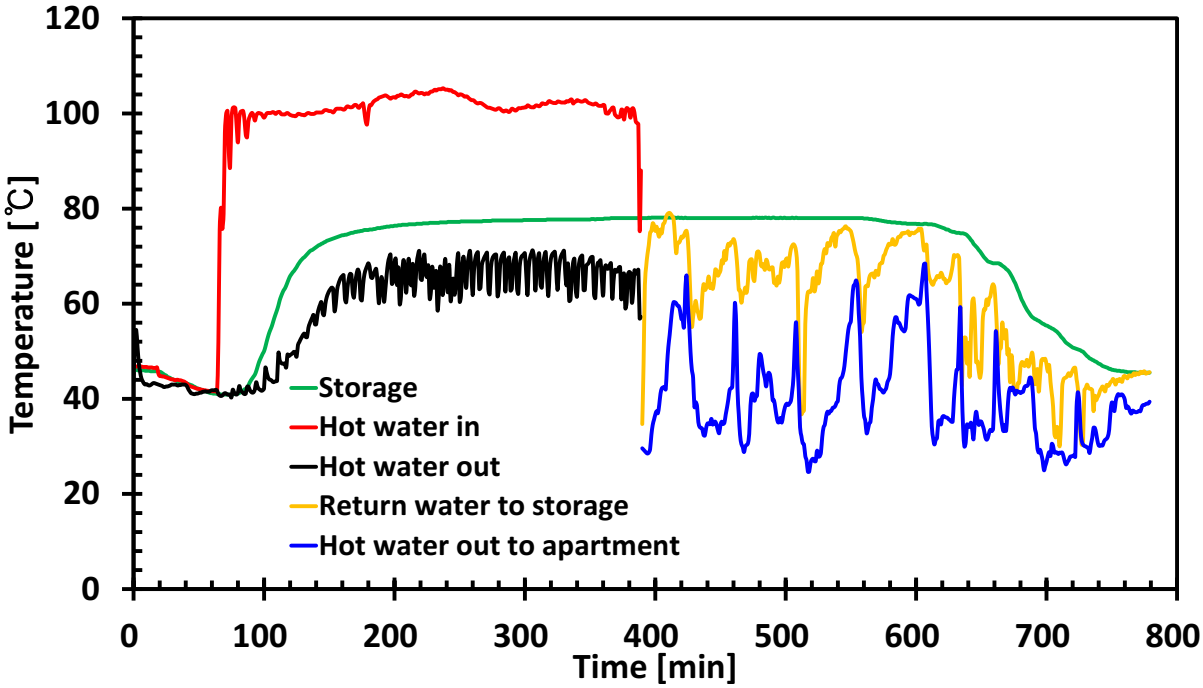

Figure 5. Preliminary test results of latent heat storage.

4. CONCLUSIONS

The latent heat storage system was developed to respond the imbalance of thermal demand of apartment during a day A12 PCM was selected in this study because its melting temperature of 78 °C was close to the required temperature of 80 °C for heat charging. The shell-tube structure was applied to the latent heat storage to be durable for pressure and temperature of hot water of 15 bar and 115 °C supplied from KDHC. Three of latent heat storage were installed in the system to respond the maximum hot water load of apartment was 229 Mcal/h. In this presentation, the preliminary results of the latent heat storage system were obtained by latent heat storage #B only. In further tests, heat charging and discharging process will be conducted using all the latent heat storage according to thermal demand of the apartment.

ACKNOWLEDGEMENTS

This work was supported by the Korea District Heating Corporation (KDHC) (A Study on the Application of Thermal Energy Storage System on the User's Side, 20/2/2018~19/8/2019).

REFERENCES

Agyenim F., Hewitt N., Eames P., Smyth M., 2010. A review of materials, heat transfer and phase change problem formulation for latent heat thermal energy storage systems (LHTESS). Renewable & Sustainable Energy Reviews 14, 615-28.

Colella F., Sciacovelli A., Verda V., 2012. Numerical analysis of a medium scale latent energy storage unit for district heating systems. Energy 45, 397–406.

Cunda J.P., Eames P., 2016. Thermal energy storage for low and medium temperature applications using phase change materials – A review. Applied Energy 177, 227-38.

Gil A., Oró E., Peiró G., Álvarez S., Cabeza L.F., 2013. Material selection and testing for thermal energy storage in solar cooling. Renewable Energy 57, 366–71.

Gil A., Barreneche C., Moreno P., Solé C., Inés Fernández A., Cabeza L.F., 2013. Thermal behaviour of d-mannitol when used as PCM: comparison of results obtained by DSC and in a thermal energy storage unit at pilot plant scale. Applied Energy111, 1107–13.

Higgo A.R., Zhang T.J., 2015. Characterization of a compact organic rankine cycle prototype for low-grade transient solar energy conversion. Energy Procedia 69, 1113–22

Kensby J., Trüschel A., Dalenbäck J-O. 2015. Potential of residential buildings as thermal energy storage in district heating systems – results from a pilot test. Applied Energy 137, 773–81.

Vivian J., Manente G., Lazzaretto A., 2015. A general framework to select working fluid and configuration of ORCs for low-to-medium temperature heat sources. Applied Energy 156, 727–46.